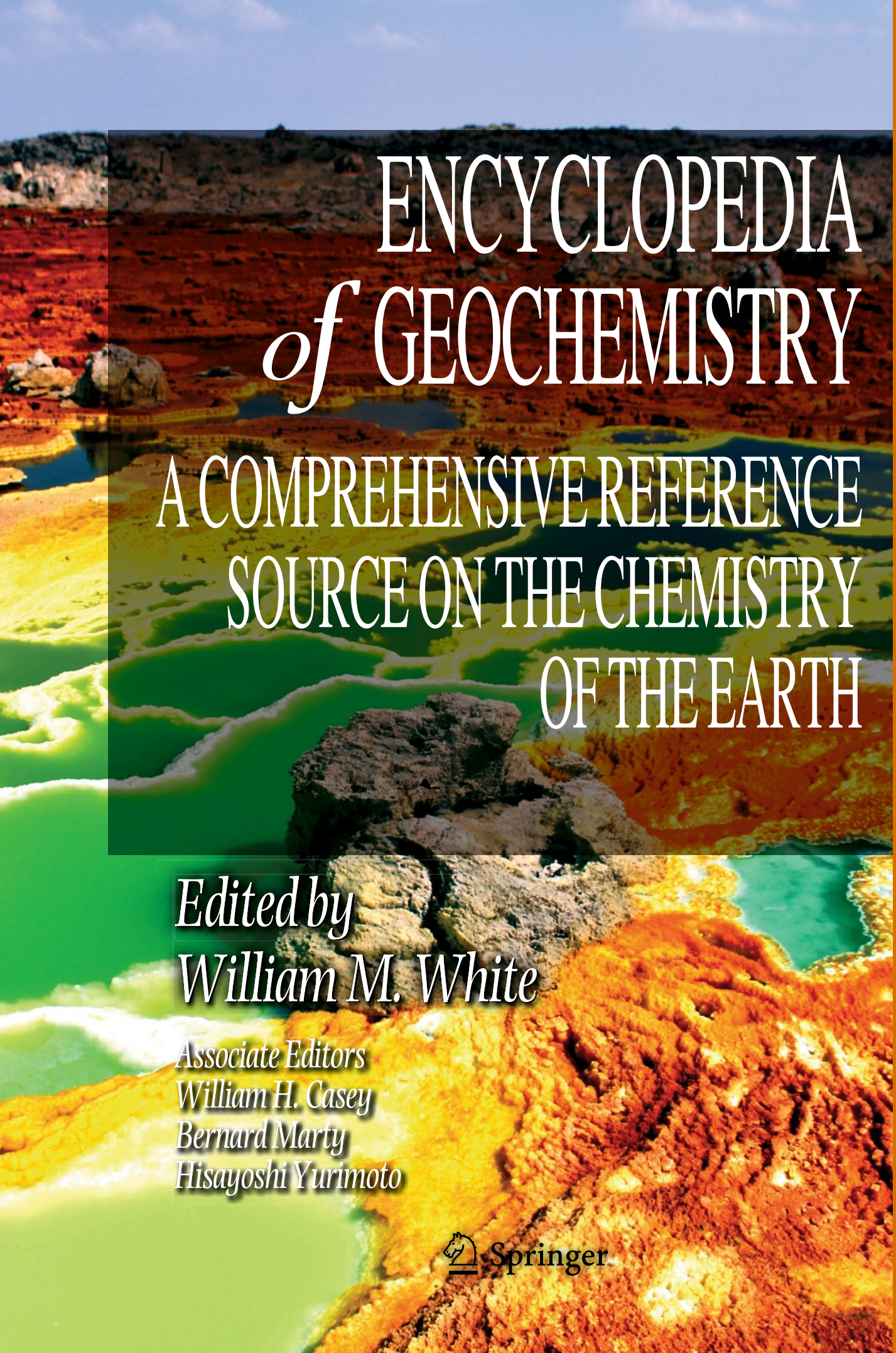

ENCYCLOPEDIA of GEOCHEMISTRY

A COMPREHENSIVE REFERENCE SOURCE ON THE CHEMISTRY OF THE EARTH

Edited by
William M. White

Associate Editors
William H. Casey
Bernard Marty
Hisayoshi Yurimoto

Springer

ENCYCLOPEDIA of EARTH SCIENCES SERIES

ENCYCLOPEDIA *of* GEOCHEMISTRY

Encyclopedia of Earth Sciences Series

ENCYCLOPEDIA OF GEOCHEMISTRY

Volume Editor

After receiving his B.A. in geology from the University of California, Berkeley, William White earned a Ph.D. in oceanography from the University of Rhode Island in 1977. White did postdoctoral work at the Carnegie Institution of Washington and at the US Geological Survey in Denver between 1977 and 1980. From 1980 to 1985 he was a staff scientist at the Max Planck Institut für Chemie in Mainz, Germany, and then spent a year as associate professor in the College of Oceanography at Oregon State University. White joined the Cornell faculty in 1986 where he currently serves as professor of earth and atmospheric sciences. He spent 7 months of 1995 as a visiting professor at the École Normale Supérieure de Lyon and the Université de Rennes, served as a visiting professor at the Université de Brest in 2001–2002, and was a Merle Tuve Senior Fellow at Carnegie Institution of Washington in 2002. White is a fellow of the Geochemical Society and the American Geophysical Union. He served as founding editor of the electronic journal *Geochemistry, Geophysics, Geosystems* (G-cubed) from 1999 to 2005.

Associate Editors

William H. Casey
University of California
Department of Chemistry and Department of Earth and Planetary Sciences
Davis, CA, USA

Bernard Marty
Centre de Recherches Pétrographiques et Géochimiques (CRPG), CNRS
Institut Universitaire de France, Ecole Nationale Supérieure de Géologie
Vandoeuvre-les-Nancy, France

Hisayoshi Yurimoto
Hokkaido University
Natural History Sciences
Sapporo, Japan

Aims of the Series

The *Encyclopedia of Earth Sciences Series* provides comprehensive and authoritative coverage of all the main areas in the Earth Sciences. Each volume comprises a focused and carefully chosen collection of contributions from leading names in the subject, with copious illustrations and reference lists.
These books represent one of the world's leading resources for the Earth Sciences community. Previous volumes are being updated and new works published so that the volumes will continue to be essential reading for all professional earth scientists, geologists, geophysicists, climatologists, and oceanographers as well as for teachers and students. See the back of this volume for a current list of titles in the *Encyclopedia of Earth Sciences Series*. Go to http://www.springerlink.com/reference-works/ to visit the "Earth Sciences Series" online.

About the Series Editor

Professor Charles W. Finkl has edited and/or contributed to more than eight volumes in the *Encyclopedia of Earth Sciences Series*. He has been the Executive Director of the Coastal Education and Research Foundation and Editor-in-Chief of the international *Journal of Coastal Research* for the past 35 years. He is also the Series Editor of the Coastal Research Library (Springer). In addition to these duties, he is Distinguished University Professor Emeritus at Florida Atlantic University (FAU) (Boca Raton, Florida). He is a graduate of Oregon State University (Corvallis) and the University of Western Australia (Perth). Work experience includes the International Nickel Company of Australia (Perth), Coastal Planning & Engineering (Boca Raton, Florida), and Technos Geophysical Consulting (Miami, Florida). He has published numerous peer-reviewed technical research papers and edited or co-edited and contributed to many books. Dr. Finkl is a Certified Professional Geological Scientist (Arvada, Colorado), a Certified Professional Soil Scientist (Madison, Wisconsin), a Certified Wetland Scientist (Lawrence, Kansas), and a Chartered Marine Scientist (London). Academically, he served as a Demonstrator at the University of Western Australia, Courtesy Professor at Florida International University (Miami), Program Professor and Director of the Institute of Coastal and Marine Studies at Nova Southeastern University (Port Everglades, Florida), and Full Professor at FAU. During his career, he acquired field experience in Australia; the Bahamas; Puerto Rico, Jamaica; Brazil; Papua New Guinea and other SW Pacific islands; southern Africa; Western Europe; and the Pacific Northwest, Midwest, and Southeast USA. Dr. Finkl is a member of several professional societies including the Geological Society of America; Soil Science Society of America; Institute of Marine Engineering, Science and Technology; and the Society of Wetland Specialists. He is a recipient of the International Beach Advocacy Award (Florida Shore & Beach Preservation Association), Certificate of George V. Chilingar Medal of Honor (Russian Academy of Natural Sciences), and Lifetime Commitment to Coastal Science Award (International Coastal Symposium).

Founding Series Editor

Professor Rhodes W. Fairbridge (deceased) has edited more than 24 Encyclopedias in the Earth Sciences Series. During his career he has worked as a petroleum geologist in the Middle East, been a WWII intelligence officer in the SW Pacific, and led expeditions to the Sahara, Arctic Canada, Arctic Scandinavia, Brazil, and New Guinea. He was Emeritus Professor of Geology at Columbia University and was affiliated with the Goddard Institute for Space Studies.

ENCYCLOPEDIA OF EARTH SCIENCES SERIES

ENCYCLOPEDIA *of* GEOCHEMISTRY

A Comprehensive Reference Source on the Chemistry of the Earth

edited by

WILLIAM M. WHITE
Cornell University, Ithaca, NY, USA

With Associate Editors

WILLIAM H. CASEY
University of California, Davis, CA, USA

BERNARD MARTY
CNRS Institut Universitaire de France, Vandoeuvre-les-Nancy, France

HISAYOSHI YURIMOTO
Hokkaido University, Sapporo, Japan

Springer

Library of Congress Control Number: 2018930990

ISBN: 978-3-319-39311-7
This publication is available also as:
Electronic publication under ISBN 978-3-319-39312-4 and
Print and electronic bundle under ISBN 978-3-319-39313-1

Cover illustration: The poly-extreme hydrothermal terraces of Dallol, Afar Triangle, Ethiopia. Hydrothermal chimneys and miniature geysers discharge high temperature (105–108 °C), oxygen-free, hyper-acidic (pH ~ 0), and Fe-rich (26 g/L of Fe) brines, creating a series of colorful terraces and pools. Unlike other hydrothermal sites where the colors are related to the presence of microorganisms, the color palette of Dallol results from the slow oxidation of aqueous ferrous species and precipitation of Fe(III)-chlorides/-oxyhydroxides/-sulfates. Photograph was taken during the fieldtrip of 2017 in the framework of the ERC grant Prometheus. Electra Kotopoulou, Spanish National Research Council (IACT-CSIC-UGR), Spain.

Printed on acid-free paper

This Springer imprint is published by Springer International Publishing AG, part of Springer Nature.
The registered company address is: Gewerbestrasse 11, 6330 Cham, Switzerland

Contents

Contributors xv

Preface xxxi

Acknowledgments xxxiii

Ab Initio Calculations 1
David A. Dixon

Achondrites 7
Akira Yamaguchi, Jean-Alix Barrat and Richard Greenwood

Acid Deposition 12
Gregory B. Lawrence

Acid–Base Reactions 15
Carl O. Moses

Activation Parameters: Energy, Enthalpy, Entropy, and Volume 19
William H. Casey and C. André Ohlin

Activity and Activity Coefficients 21
Barry R. Bickmore and Matthew C. F. Wander

Alkali and Alkaline Earth Metals 23
Ricardo Arevalo Jr.

Aluminum 27
Mainak Mookherjee

Analytical Techniques 29
William M. White

Anthropogenic CO_2 34
Klaus S. Lackner

Antimony 37
Jacqueline R. Houston

Aqueous Solutions 39
Barry R. Bickmore and Matthew C. F. Wander

Archeological Geochemistry 42
Patrick Degryse and R. Alexander Bentley

Argon 53
Mark A. Kendrick

Argon Isotopes 56
Philippe Sarda

Arsenic 58
Monica Vasiliu and David A. Dixon

Astatine 59
Monica Vasiliu and David A. Dixon

Atmophile Elements 60
Daniele L. Pinti

Atmospheric Evolution 62
Colin Goldblatt

Atomic Absorption, Inductively Coupled Plasma Optical Emission Spectroscopy, and Infrared Spectroscopy 76
Michael A. Rutzke

Atomic Number, Mass Number, and Isotopes 83
Russell S. Harmon

Authigenesis 85
Norbert Clauer

Barium 91
William M. White

Beryllium 93
Jeffrey G. Ryan

Beryllium Isotopes 95
Paul R. Bierman and Eric W. Portenga

Biogenic Methane 100
Dariusz Strąpoć

Biogeochemistry 107
Hilairy Ellen Hartnett

Biological Pump 111
Sarah L. C. Giering and Matthew P. Humphreys

Biomarker: Assessment of Thermal Maturity 116
Kenneth E. Peters and J. Michael Moldowan

Biomarkers: Coal 123
Achim Bechtel and Wilhelm Püttmann

Biomarkers: Petroleum 136
Meng He, J. Michael Moldowan and Kenneth E. Peters

Biopolymers and Macromolecules 148
Markus Kleber and Patrick Reardon

Bismuth 153
Cristiana L. Ciobanu and Nigel J. Cook

Black Shales and Sapropels 155
Kay-Christian Emeis

Boron 156
Christophe Lécuyer

Boron Stable Isotopes 162
Gavin L. Foster, Christophe Lécuyer and Horst R. Marschall

Bromine 167
Hélène Bureau

Cadmium 171
Monica Vasiliu and David A. Dixon

Caesium 172
Gray E. Bebout

Calcium 177
Christophe Lécuyer

Calcium Isotopes 181
Juraj Farkaš

Calorimetry 186
Masaki Akaogi

Carbon 187
Adrian Jones

Carbon Cycle 191
Elizabeth A. Canuel and Amber K. Hardison

Carbon Isotopes 194
Thomas Wagner, Clayton R. Magill and Jens O. Herrle

Carbonate Compensation Depth 204
Ryan J. Woosley

Carbonate Minerals and the CO_2-Carbonic Acid System 206
Abraham Lerman and Fred T. Mackenzie

Cerium 226
Catherine Chauvel

Chalcophile Elements 229
Sarah-Jane Barnes

Chelation 233
Corey D. Pilgrim

Chemical Bonds 234
Barry R. Bickmore and Matthew C. F. Wander

Chemical Weathering 237
Jérôme Viers and Priscia Oliva

Chlorine 241
Mark A. Kendrick

Chlorine Isotopes 244
Magali Bonifacie

Chondrites 248
Sara Russell

Chondrules 251
Rhian Jones

Chromium 255
Monica Vasiliu and David A. Dixon

Chromium Isotopes 256
Devon B. Cole, Xiangli Wang, Liping Qin, Noah J. Planavsky and Christopher T. Reinhard

Clapeyron's Equation 262
Masaki Akaogi

Clay Membranes 263
Ian C. Bourg

Clay Minerals 265
Josh Wimpenny

Coal 275
Stephen F. Greb, Cortland F. Eble and James C. Hower

Cobalt 291
Olivier Pourret and Michel-Pierre Faucon

Colloids 294
Jean-François Boily

Complexes 297
Jay R. Black

Compound-Specific Isotope Analysis 300
Yi Ge Zhang

Copper 303
Xingcheng Liu and Xiaolin Xiong

Copper Isotopes 305
Paul Savage

Cosmic Elemental Abundances 310
Herbert Palme

Cosmogenic Nuclides 317
Rainer Wieler

Critical Points 325
William H. Casey and Peter A. Rock

Critical Zone 326
Justin B. Richardson

Crystal Chemistry 331
Dana T. Griffen

Crystal Field Theory 340
Hans Keppler

Debye-Hückel Equation 345
Jay R. Black

Density Functional Theory 347
David A. Dixon

Diagenesis 353
Isabel P. Montañez and Laura J. Crossey

Diffusion 363
Yan Liang

Dissolved Organic Matter (DOM) 375
Hilairy Ellen Hartnett

Dolomite and Dolomitization 378
Jennifer A. Roberts

Dysprosium 381
Scott M. McLennan

Earth's Atmosphere 383
Daniele L. Pinti

Earth's Continental Crust 392
Roberta L. Rudnick

Earth's Core 418
William F. McDonough

Earth's Oceanic Crust 430
Michael Perfit

Electron Probe Microanalysis (EPMA) 439
Stuart Kearns

Electronegativity 442
Barry R. Bickmore and Matthew C. F. Wander

Elements: Metalloids 445
David A. Dixon and Monica Vasiliu

Enthalpy 446
Carl O. Moses

Entropy 447
Carl O. Moses

Epigenesis 453
Jamie J. Wilkinson

Equilibrium 455
Heinz Gamsjäger

Equilibrium Constant 456
Erich Königsberger

Erbium 460
Scott M. McLennan

Europium 462
Matthias Willbold

Evaporites 464
John Warren

Experimental Mineralogy and Petrology 471
Charles A. Geiger and Tatsuhiko Kawamoto

Ferromanganese Crusts and Nodules: Rocks That Grow 477
Kira Mizell and James R. Hein

Fick's Law 483
Isao Sakaguchi

Fission Track Analysis 484
Stuart N. Thomson

Fluid Inclusions 488
Robert J. Bodnar

Fluid–Rock Interaction 492
William E. Glassley, Laura J. Crossey and Isabel P. Montanez

Fluorine 495
Kenneth T. Koga and Estelle F. Rose-Koga

Formation and Evolution of the Earth 498
Francis Albarède

Fractional Crystallization and Assimilation 513
Frank Spera and Melissa Scruggs

Free Energy 518
Carl O. Moses

Fugacity 521
Christopher A. Colla and William H. Casey

Gadolinium 525
Scott M. McLennan

Gallium 526
Munir Humayun

Gas Chromatography–Mass Spectrometry (GC–MS) 530
Patricia M. Medeiros

Gas Hydrates 535
Rajnish Kumar and Praveen Linga

Gas Source Mass Spectrometry (GS-MS) 541
Masahiko Honda and Allan R. Chivas

Geochemical Classification of Elements 545
Cin-Ty Lee

Geochemical Exploration 549
John F. H. Thompson

Geochemical Reference Materials 553
Thomas C. Meisel

Geochemical Thermodynamics 554
William H. Casey and Peter A. Rock

Geochemistry 561
William M. White

Geochronology and Radiogenic Isotopes 571
Jeff Vervoort

Geologic Time Scale 586
Mark D. Schmitz

Geoneutrinos 589
William F. McDonough

Geothermal Systems 592
Adam J. Hawkins and Jefferson W. Tester

Geothermometry and Geobarometry 597
Keith Putirka

Germanium 615
Louis A. Derry

Giant Impact Hypothesis 617
Hidenori Genda

Gibbs-Duhem Equation 620
William H. Casey and Peter A. Rock

Gold 622
Monica Vasiliu and David A. Dixon

Gouy-Chapman Theory 623
Garrison Sposito

Hafnium 629
Janne Blichert-Toft

Hafnium Isotopes 631
Janne Blichert-Toft

Halide Minerals 636
John Warren

Halogens 645
Mark A. Kendrick

Heat Capacity 649
Brian F. Woodfield

Heat-Producing Elements (HPEs) 652
Hugh StC O'Neill

Helium 657
Yuji Sano

Helium Isotopes 659
Yuji Sano

Henry's Law 663
William M. White

High Field Strength Elements 664
Vincent J. M. Salters

High-Resolution Mass Spectrometry 666
Elizabeth B. Kujawinski

History of Geochemistry 670
William M. White

Holmium 683
Scott M. McLennan

Hydrocarbons 685
John K. Volkman

Hydrogen 693
James G. Brophy and Arndt Schimmelmann

Hydrogen Isotopes 696
Arndt Schimmelmann and Peter E. Sauer

Hydrologic Cycle 701
Giuseppe Mascaro

Hydrothermal Alteration 704
Andri Stefánsson and Barbara I. Kleine

Hydrothermal Solutions 706
Jean-François Boily

Hydrothermal Vents 711
Wolfgang Bach and Eoghan P. Reeves

Hypogene 715
Barbara I. Kleine and Andri Stefánsson

Incompatible Elements 719
Catherine Chauvel

Indium 721
Monica Vasiliu and David A. Dixon

Inductively Coupled Plasma Mass Spectrometry (ICP-MS) 723
Maria Schönbächler

Iodine 728
Hélène Bureau

Ion Exchange Chromatography 731
Maria Schönbächler

Ion Microprobe 736
Kazuhide Nagashima

Ionic Radii 738
Hugh Rollinson and Jacob Adetunji

Iridium 743
Thomas C. Meisel

Iron 745
Munir Humayun

Iron Formations 751
Clark M. Johnson

Iron Isotopes 756
Noah J. Planavsky and Vincent Busigny

Iron Meteorites 762
Henning Haack

Isotope Dilution 767
Jon Woodhead

Kerogen 771
Steven Petsch

Kinetics of Geochemical Processes 775
Don Sparks

Krypton 784
Greg Holland

Laboratory Simulations of Organic Geochemical Processes at Elevated Temperatures 789
Jeffrey S. Seewald

Lanthanide Rare Earths 792
Scott M. McLennan

Lanthanum 799
Catherine Chauvel

Large-Ion Lithophile Elements 800
Catherine Chauvel and Roberta L. Rudnick

Laser Ablation – Inductively Coupled Plasma Mass Spectrometry 801
Takafumi Hirata

Lead 811
Dominique Weis

Lead Isotopes 813
Dominique Weis

Lipids (Bacteria and Archaea) 818
Ann Pearson

Lithium 822
Jeffrey G. Ryan

Lithium Isotopes 824
Jeffrey G. Ryan

Lithophile Elements 827
Frances E. Jenner and Hugh StC O'Neill

Low-Temperature Geochemistry 828
Tori Z. Forbes

Luminescence 835
Tori Z. Forbes

Lutetium 839
Scott M. McLennan

Magmatic Process Modeling 841
Mark Ghiorso

Magnesium 853
Fang-Zhen Teng

Magnesium Isotopes 856
Fang-Zhen Teng

Magnetism 860
H. Tsunakawa and Y. Yamamoto

Manganese 864
Tammie L. Gerke and Brenda J. Little

Mantle Geochemistry 867
Andreas Stracke

Marine Sediment 878
Ann G. Dunlea, Rachel P. Scudder and Richard W. Murray

Mass Transfer 892
Peter C. Lichtner

Mercury 895
Charles N. Alpers

Mercury Isotopes 900
Bridget A. Bergquist

Metamorphic Reactions and Processes 906
Eleanor C. R. Green

Meteorites 917
Michael K. Weisberg

Mid-Ocean Ridge Basalts (MORB) 924
Charles H. Langmuir

Mineral Defects 932
Kurt Schwartz and Maik Lang

Mineral Genesis 936
Alain J. Baronnet

Mineralogy 943
Michael F. Hochella Jr.

Molybdenum 947
Anthony Chappaz, Jennifer B. Glass and Timothy W. Lyons

Molybdenum Isotopes 950
Jane Barling, Jie Yang and Yu-Hsuan Crystal Liang

Native Minerals 957
Satoshi Matsubara

Natural Gas 961
Giuseppe Etiope

Neodymium 965
Michael Bizimis and Howie D. Scher

Neodymium Isotopes 967
Michael Bizimis and Howie D. Scher

Neon 973
Manuel Moreira

Neon Isotopes 975
Moreira Manuel

Neutron Activation Analysis 978
James R. Budahn

Nickel 980
William L. Griffin and Mathieu Chassé

Niobium 983
Carsten Münker

Nitrogen 985
Pierre Cartigny

Nitrogen Cycle 987
Monica M. Palta and Hilairy Ellen Hartnett

Nitrogen Isotopes 991
Pierre Cartigny and Vincent Busigny

Noble Gases 1003
Chris J. Ballentine and Peter H. Barry

Nuclear Magnetic Resonance 1009
Corey D. Pilgrim

Nucleosynthesis 1014
Jitendra Nath Goswami

Nutrients 1019
J. A. Brandes

Ocean Biochemical Cycling and Trace Elements 1023
Hein J. W. de Baar, Steven M. A. C. van Heuven and Rob Middag

Ocean Salinity, Major Elements, and Thermohaline Circulation 1042
Hein J. W. de Baar, Steven M. A. C. van Heuven and Rob Middag

Oceanic Island Basalts 1048
Matthew Gerard Jackson

Oil Seeps and Coastal Bitumen 1052
David McKirdy, Andrew Ross and Asrarur Talukder

Oil Shale 1055
Justin E. Birdwell

Oil-Oil and Oil-Source Rock Correlations 1057
Norelis D. Rodriguez

Oklo Natural Nuclear Reactors 1059
Mark J. Rigali

Onuma Diagrams 1062
Chenguang Sun

Ore Deposits 1063
Michel Cuney

Organic Facies 1075
R. Paul Philp

Organic Geochemistry 1081
John K. Volkman

Organic Matter Degradation and Preservation 1094
Sandra Arndt and Douglas Edward LaRowe

Organic Matter in Fossils 1099
A. D. Muscente, Andrew D. Czaja, Leigh Anne Riedman and Caitlin Colleary

Organics: Sources and Depositional Environments 1103
Elisabeth Sikes

Osmium 1109
Richard J. Walker

Osmium Isotopes 1111
Richard J. Walker

Oxidation-Reduction Reactions and E_h-pH (Pourbaix) Diagrams 1115
William H. Casey

Oxide Minerals 1120
Patrick Nadoll

Oxygen 1124
Edward D. Young

Oxygen Isotopes 1129
Hisayoshi Yurimoto

Ozone and Stratospheric Chemistry 1135
Slimane Bekki and Joël Savarino

Paleoclimatology 1147
Larry C. Peterson

Paleoenvironments 1160
B. D. A Naafs and R. D. Pancost

Paleoproductivity 1163
Gerold Wefer

Paleotemperatures 1166
Jennifer E. Hertzberg and Matthew W. Schmidt

Palladium 1172
James M. Brenan

Paragenesis 1175
Denton S. Ebel and Robert J. Kamilli

Partial Melting 1180
Paul D. Asimow

Particle-Induced X-Ray Emission (PIXE) 1185
Masanori Kurosawa

Partitioning and Partition Coefficients 1186
Chenguang Sun

Peat 1197
Thomas J. Kelly, Ian T. Lawson and Lydia E. S. Cole

Periodic Table 1201
Karen Harpp

Petroleum 1207
Philippe Ungerer

Phase Equilibria 1220
Robert W. Luth

Phosphorus 1231
Karl B. Föllmi

Platinum 1233
James M. Brenan

Platinum Group Elements 1236
Igor S. Puchtel

Poisson-Boltzmann Equation 1240
Joan E. Curry

Polonium 1241
Monica Vasiliu and David A. Dixon

Polyoxometalates and Other Metal-Oxo Clusters in Nature 1242
May Nyman

Porphyrins 1247
J. William Louda

Potassium 1253
Ricardo Arevalo Jr.

Praseodymium 1257
Scott M. McLennan

Precambrian Geochemistry 1258
Tsuyoshi Komiya

Precambrian Organic Matter 1266
Roger Summons

Presolar Grains 1273
Peter Hoppe

Programmed Temperature Pyrolysis 1276
Kenneth E. Peters and Leonardo Briceño Rodriguez

Promethium 1286
Scott M. McLennan

Protactinium 1287
Julie Prytulak

Quantum Numbers 1291
David A. Dixon

Radioactivity 1295
Don Porcelli

Radium 1298
William M. White

Radon 1301
Don Porcelli

Raman Microspectroscopy 1303
András Gorzsás

Refractory Inclusions in Chondritic Meteorites 1307
Alexander N. Krot and Glenn J. MacPherson

Rhenium 1312
James M. Brenan

Rhodium 1314
Thomas C. Meisel

Rubidium 1316
Oliver Nebel

Ruthenium 1318
Thomas C. Meisel

Samarium 1321
Michael Bizimis and Howie D. Scher

Scandium 1323
Iain M. Samson and Mathieu Chassé

Selenium 1326
Monica Vasiliu and David A. Dixon

Siderophile Elements 1328
James M. D. Day

Silicate Melts 1330
Pascal Richet

Silicate Minerals 1334
Ritsuro Miyawaki

Silicon 1335
Monica Vasiliu and David A. Dixon

Silicon Isotopes 1337
Anat Shahar

Silver 1340
Helen Mango

Sodium 1344
Jérôme Gaillardet

Soils 1347
Johannes Lehmann

Solid Solution/Exsolution 1352
C. Noguera and B. Fritz

Solubility 1359
Jean-François Boily

Stable Isotope Geochemistry 1367
William M. White

Standard States 1374
William H. Casey and Peter A. Rock

Stoichiometry 1376
Anna F. Oliveri

Strontium 1377
Oliver Nebel

Strontium Isotopes 1379
Oliver Nebel and Jessica A. Stammeier

Subduction Zone Geochemistry 1384
Terry Plank

Sulfate Minerals 1392
Andrew G. Christy

Sulfide Minerals 1394
Andrew G. Tomkins and Bree Morgan

Sulfur 1397
James Farquhar

Sulfur Cycle 1399
Martin A. Schoonen

Sulfur Isotopes 1402
James Farquhar

Supergene 1409
Martin Reich

Surface Geochemistry 1410
Christian Ludwig and William H. Casey

Synchrotron X-Ray Fluorescence Analysis 1415
Juan S. Lezama Pacheco and Scott E. Fendorf

Tantalum 1419
Carsten Münker

Technetium 1421
Yoshio Takahashi

Tellurium 1423
Yoshio Takahashi

Terbium 1425
Scott M. McLennan

Thallium 1426
Josh Wimpenny

Thallium Isotopes 1429
Sune G. Nielsen

Thermal Ionization Mass Spectrometry 1433
John C. Lassiter

Thermogravimetry 1435
Jiri Kucerik

Thorium 1439
Vincent J. M. Salters

Thulium 1441
Scott M. McLennan

Tin 1443
William M. White

Titanium 1445
Jay B. Thomas

Trace Elements 1451
William M. White

Transition Elements 1452
Dante Canil

Tungsten 1455
George R. Helz

Tungsten Isotopes 1458
Thorsten Kleine

Unified Atomic Mass Unit, Avogadro Constant, and Mole 1463
Norman E. Holden

Uranium 1464
Vincent J. M. Salters

Uranium Decay Series 1468
Bernard Bourdon

Van der Waals Force 1473
Taku Tsuchiya

Vanadium 1474
Olivier Pourret and Aline Dia

Volcanic Gases 1476
Alessandro Aiuppa and Fabrice Gaillard

Volcanism 1480
Nick Rogers

Water 1487
Carl O. Moses

Xenon 1497
Sujoy Mukhopadhyay

Xenon Isotopes 1500
Sujoy Mukhopadhyay

X-Ray Diffraction 1508
Tori Z. Forbes

X-Ray Fluorescence Analysis 1511
Izumi Nakai

Ytterbium 1517
J. H. L. Voncken

Yttrium 1518
J. H. L. Voncken

Zinc 1521
Joël Brugger

Zinc Isotopes 1524
Frédéric Moynier

Zirconium 1528
Carsten Münker

Author Index 1531

Subject Index 1533

Contributors

Jacob Adetunji
Geoscience
University of Derby
Derby, UK

Alessandro Aiuppa
Dipartimento DiSTeM
Università di Palermo
Palermo, Italy
and
Sezione di Palermo
Istituto Nazionale di Geofisica e Vulcanologia
Palermo, Italy

Masaki Akaogi
Department of Chemistry
Gakushuin University
Tokyo, Japan

Francis Albarède
Laboratoire de Géologie de Lyon
Ecole Normale Supérieure de Lyon
Lyon Cedex 7, France

Charles N. Alpers
U.S. Geological Survey
California Water Science Center
Sacramento, CA, USA

Ricardo Arevalo Jr.
Planetary Environments Lab
NASA Goddard Space Flight Center
Greenbelt, MD, USA

Sandra Arndt
BGeosys, Department Geoscience, Environment and Society (DGES)
Université Libre de Bruxelles
Bruxelles, Belgium

Paul D. Asimow
Division of Geological and Planetary Sciences
California Institute of Technology
Pasadena, CA, USA

Wolfgang Bach
Department of Geosciences and MARUM Center for Marine Environmental Research
University of Bremen
Bremen, Germany

Chris J. Ballentine
Department of Earth Sciences
University of Oxford
Oxford, UK

Jane Barling
Department of Earth Sciences
University of Oxford
Oxford, UK

Sarah-Jane Barnes
Sciences de la Terre
Université du Québec à Chicoutimi
Chicoutimi, QC, Canada

Alain J. Baronnet
Aix-Marseille Université, CNRS, CINAM
Campus Luminy
Marseille, France

Jean-Alix Barrat
U.B.O.-I.U.E.M
CNRS UMR 6538 (Domaines Océaniques)
Plouzané, France

Peter H. Barry
Department of Earth Sciences
University of Oxford
Oxford, UK

Gray E. Bebout
Department of Earth and Environmental Sciences
Lehigh University
Bethlehem, PA, USA

Achim Bechtel
Department of Applied Geoscience and Geophysics
Petroleum Geology
Montanuniversitaet Leoben
Leoben, Austria

Slimane Bekki
LATMOS-IPSL (Laboratoire Atmosphères, Milieux, Observations Spatiales)
Sorbonne Universités-UPMC, Paris Saclay-UVSQ, CNRS
Paris, France

R. Alexander Bentley
Comparative Cultural Studies and Hobby School of Public Affairs
University of Houston, McElhinney Hall
Houston, TX, USA

Bridget A. Bergquist
Department of Earth Sciences
University of Toronto
Toronto, ON, Canada

Barry R. Bickmore
Department of Geological Sciences
Brigham Young University
Provo, UT, USA

Paul R. Bierman
Department of Geology
University of Vermont
Burlington, VT, USA

Justin E. Birdwell
Central Energy Resources Science Center
U.S. Geological Survey
Denver, CO, USA

Michael Bizimis
Earth and Ocean Sciences
University of South Carolina
Columbia, SC, USA

Jay R. Black
School of Earth Sciences
The University of Melbourne
Melbourne, VIC, Australia

Janne Blichert-Toft
Laboratoire de Géologie de Lyon
Ecole Normale Supérieure de Lyon, Université Claude Bernard Lyon 1, CNRS
Lyon, France

Robert J. Bodnar
Department of Geosciences
Virginia Tech
Blacksburg, VA, USA

Jean-François Boily
Department of Chemistry
Umeå University
Umeå, SE, Sweden

Magali Bonifacie
Institut de Physique du Globe de Paris
Sorbonne Paris Cité, Université Paris Diderot
Paris, France

Bernard Bourdon
Laboratoire de Géologie de Lyon
Université de Lyon
Lyon, France
and
ENS-Lyon
Université Lyon 1, CNRS, UMR 5276 LGLTPE
Lyon, France

Ian C. Bourg
Department of Civil and Environmental Engineering and Princeton Environmental Institute
Princeton University
Princeton, NJ, USA

J. A. Brandes
Skidaway Institute of Oceanography and Department of Marine Science
University of Georgia
Savannah, GA, USA

James M. Brenan
Department of Earth Sciences
Dalhousie University
Halifax, NS, Canada

James G. Brophy
Department of Earth and Atmospheric Sciences
Indiana University
Bloomington, IN, USA

Joël Brugger
School of Earth, Atmosphere and the Environment
Monash University
Clayton, Australia

James R. Budahn
U.S.Geological Survey
Denver, CO, USA

Hélène Bureau
Institut de Minéralogie, de Physique desMatériaux et de Cosmochimie (IMPMC)
Sorbonne Universités – UPMCUniv. Paris 06, CNRSUMR 7590, MuséumNational d'Histoire Naturelle
Paris, France

Vincent Busigny
Institut de Physique du Globe de Paris
Sorbonne Paris Cité, Université Paris Diderot
Paris, France

Dante Canil
School of Earth and Ocean Sciences
University of Victoria
Victoria, BC, Canada

Elizabeth A. Canuel
Department of Physical Science, Virginia Institute of Marine Science
College of William & Mary
Gloucester Point, VA, USA

Pierre Cartigny
Institut de Physique du Globe de Paris
Sorbonne Paris Cité, Université Paris Diderot
Paris, France

William H. Casey
Department of Chemistry and Department of Earth and Planetary Sciences
University of California
Davis, CA, USA

Anthony Chappaz
Department of Earth and Atmospheric Sciences
Central Michigan University
Mount Pleasant, MI, USA

Mathieu Chassé
Institut de minéralogie, de physique des matériaux, et de cosmochimie (IMPMC)
Sorbonne universités – UPMC
Paris, France

Catherine Chauvel
ISTerre
University Grenoble Alpes, CNRS
Grenoble, France

Allan R. Chivas
GeoQuEST Research Centre, School of Earth and Environmental Sciences
University of Wollongong
Wollongong, NSW, Australia
and
Department of Earth Sciences
University of Adelaide
Adelaide, SA, Australia

Andrew G. Christy
School of Earth and Environmental Sciences
University of Queensland
St Lucia, QLD, Australia
and
Geosciences
Queensland Museum
Hendra, QLD, Australia

Cristiana L. Ciobanu
School of Chemical Engineering
The University of Adelaide
Adelaide, SA, Australia

Norbert Clauer
Laboratoire d'Hydrologie et de Géochimie de Strasbourg
CNRS - Université de Strasbourg
Strasbourg, France

Devon B. Cole
Department of Geology and Geophysics
Yale University
New Haven, CT, USA

Lydia E. S. Cole
Department of Zoology, Biodiversity Institute
University of Oxford
Oxford, UK

Christopher A. Colla
Department of Chemistry and Department of Earth and Planetary Sciences
University of California
Davis, CA, USA

Caitlin Colleary
Department of Geosciences
Virginia Tech
Blacksburg, VA, USA

Nigel J. Cook
School of Chemical Engineering
The University of Adelaide
Adelaide, SA, Australia

Laura J. Crossey
Department of Earth and Planetary Sciences
University of New Mexico
Albuquerque, NM, USA

Michel Cuney
GeoRessources
University of Lorraine, CNRS, CREGU
Vandoeuvre les Nancy, France

Joan E. Curry
Department of Soil, Water and Environmental Science
University of Arizona
Tucson, AZ, USA

Andrew D. Czaja
Department of Geology
University of Cincinnati
Cincinnati, OH, USA

James M. D. Day
Scripps Institution of Oceanography
University of California San Diego
La Jolla, CA, USA

Hein J. W. de Baar
NIOZ Royal Netherlands Institute for Sea Research
Department of Ocean Systems (OCS), and Utrecht University
Den Burg, The Netherlands

Patrick Degryse
Earth and Environmental Sciences, Division Geology
Centre for Archaeological Sciences, KU Leuven
Leuven, Belgium

Louis A. Derry
Department of Earth and Atmospheric Sciences
Cornell University
Ithaca, NY, USA

Aline Dia
Géosciences Rennes
Rennes, France

David A. Dixon
Department of Chemistry
University of Alabama
Tuscaloosa, AL, USA

Ann G. Dunlea
Woods Hole Oceanographic Institution
Woods Hole, MA, USA

Denton S. Ebel
Department of Earth and Environmental Sciences
Columbia University
New York, NY, USA

Cortland F. Eble
Kentucky Geological Survey
University of Kentucky
Lexington, KY, USA

Kay-Christian Emeis
Department of Earth Sciences
Hamburg University
Hamburg, Germany

Giuseppe Etiope
Sezione Roma 2
Istituto Nazionale di Geofisica e Vulcanologia
Rome, Italy

Juraj Farkaš
Department of Earth Sciences, School of Physical Sciences
University of Adelaide
Adelaide, South Australia, Australia
and
Department of Geochemistry
Czech Geological Survey
Prague, Czech Republic

James Farquhar
Department of Geology and Earth System Science Interdisciplinary Center
University of Maryland
College Park, MD, USA

Michel-Pierre Faucon
UniLaSalle
Beauvais Cedex, France

Scott E. Fendorf
Department of Geology
Stanford University
Menlo Park, CA, USA

Karl B. Föllmi
Institute of Earth Sciences
University of Lausanne
Lausanne, Switzerland

Tori Z. Forbes
Department of Chemistry
University of Iowa
Iowa City, IA, USA

Gavin L. Foster
Ocean and Earth Science, National Oceanography Centre Southampton
University of Southampton
Southampton, UK

B. Fritz
Laboratoire d'Hydrologie et Géochimie de Strasbourg
Université de Strasbourg/EOST, CNRS
Strasbourg Cedex, France

Fabrice Gaillard
Institut des Sciences de la Terre
Université d'Orléans-BRGM
Orléans, France

Jérôme Gaillardet
Institut de Physique du Globe de Paris
Paris, France

Heinz Gamsjäger
Leoben, Austria

Charles A. Geiger
Department of Chemistry and Physics of Materials
Section Mineralogy
University of Salzburg
Salzburg, Austria

Hidenori Genda
Earth-Life Science Institute (ELSI)
Tokyo Institute of Technology
Tokyo, Japan

Tammie L. Gerke
Department of Geology and Environmental Earth Science
Miami University Middletown
Middletown, OH, USA

Mark Ghiorso
OFM Research
Seattle, WA, USA

Sarah L. C. Giering
Ocean Biogeochemistry and Ecosystems
National Oceanography Centre
Southampton, UK

Jennifer B. Glass
School of Earth and Atmospheric Sciences
Georgia Institute of Technology
Atlanta, GA, USA

William E. Glassley
Department of Earth and Planetary Sciences
University of California
Davis, USA

Colin Goldblatt
School of Earth and Ocean Sciences
University of Victoria
Victoria, BC, Canada

András Gorzsás
Department of Chemistry
Umeå University
Umeå, Sweden

Jitendra Nath Goswami
Physical Research Laboratory
Ahmedabad, India

Stephen F. Greb
Kentucky Geological Survey
University of Kentucky
Lexington, KY, USA

Eleanor C. R. Green
Institute of Geochemistry and Petrology
ETH Zürich
Zürich, Switzerland

Richard Greenwood
Planetary and Space Sciences, Department of Physical Sciences
The Open University
Milton Keynes, UK

Dana T. Griffen
Geology Department
Brigham Young University
Provo, UT, USA

William L. Griffin
Earth and Planetary Sciences
Macquarie University
North Ryde, NSW, Australia

Henning Haack
Maine Mineral and Gem Museum
Bethel, ME, USA

Amber K. Hardison
Marine Science Institute
The University of Texas at Austin
Port Aransas, TX, USA

Russell S. Harmon
North Carolina State University
Raleigh, NC, USA

Karen Harpp
Department of Geology
Colgate University
Hamilton, NY, USA

Hilairy Ellen Hartnett
School of Earth and Space Exploration and School of Molecular Sciences
Arizona State University
Tempe, AZ, USA

Adam J. Hawkins
Earth and Atmospheric Sciences
Cornell University
Ithaca, NY, USA

Meng He
Department of Geological and Environmental Sciences
Stanford University
Stanford, CA, USA

James R. Hein
Pacific Coastal and Marine Science Center
U.S. Geological Survey
Santa Cruz, CA, USA

George R. Helz
Departments of Geology and Chemistry
University of Maryland
College Park, MD, USA

Jens O. Herrle
Institute of Geosciences
Goethe University Frankfurt
Frankfurt, Germany

Jennifer E. Hertzberg
Department of Marine Sciences
University of Connecticut
Groton, CT, USA

Takafumi Hirata
Geochemical Research Center
The University of Tokyo
Tokyo, Japan

Michael F. Hochella Jr.
Department of Geosciences
Virginia Tech
Blacksburg, VA, USA
and
Geosciences Group
Pacific Northwest National Laboratory
Richland, WA, USA

Norman E. Holden
National Nuclear Data Center
Brookhaven National Laboratory
Upton, New York, USA

Greg Holland
School of Earth and Environmental Sciences
University of Manchester
Manchester, UK

Masahiko Honda
Research School of Earth Sciences
The Australian National University
Canberra, ACT, Australia

Peter Hoppe
Particle Chemistry Department
Max Planck Institute for Chemistry
Mainz, Germany

Jacqueline R. Houston
CSUS – California State University
Sacramento, CA, USA

James C. Hower
Center for Applied Energy Research
University of Kentucky
Lexington, KY, USA

Munir Humayun
Department of Earth, Ocean and Atmospheric Science
Florida State University
Tallahassee, FL, USA

Matthew P. Humphreys
Ocean and Earth Science
University of Southampton
Southampton, UK

Matthew Gerard Jackson
Department of Earth Science
University of California Santa Barbara
Santa Barbara, CA, USA

Frances E. Jenner
Department of Environment, Earth and Ecosystems
The Open University
Milton Keynes, Buckinghamshire, UK

Clark M. Johnson
Department of Geoscience
University of Wisconsin
Madison, WI, USA

Adrian Jones
Department of Earth Sciences
University College London
London, UK

Rhian Jones
School of Earth and Environmental Sciences
The University of Manchester
Manchester, UK

Robert J. Kamilli
Tucson Office – Geology, Minerals, Energy and Geophysics Science Center
U.S. Geological Survey
Tucson, Arizona, USA

Tatsuhiko Kawamoto
Institute for Geothermal Sciences, Graduate School of Science
Kyoto University
Kyoto, Japan

Stuart Kearns
School of Earth Sciences
University of Bristol
Bristol, UK

Thomas J. Kelly
School of Geography
University of Leeds
Leeds, UK

Mark A. Kendrick
Research School of Earth Sciences
Australian National University
Canberra, ACT, Australia

Hans Keppler
Bayerisches Geoinstitut
University of Bayreuth
Bayreuth, Germany

Markus Kleber
Department of Crop and Soil Science
Oregon State University
Corvallis, OR, USA

Barbara I. Kleine
Institute of Earth Sciences
University of Iceland
Reykjavík, Iceland

Thorsten Kleine
Institut für Planetologie
University of Münster
Münster, Germany

Kenneth T. Koga
Laboratoire Magmas et Volcans
Université Blaise Pascal – CNRS
Clermont-Ferrand, France

Tsuyoshi Komiya
Department of Earth Science and Astronomy
The University of Tokyo
Tokyo, Japan

Erich Königsberger
Chemical and Metallurgical Engineering and Chemistry
School of Engineering and Information Technology
Murdoch University
Murdoch, WA, Australia

Alexander N. Krot
Hawai‘i Institute of Geophysics and Planetology
University of Hawai‘i at Mānoa
Honolulu, HI, USA

Jiri Kucerik
Institute of Chemistry and Technology of Environmental Protection, Faculty of Chemistry
Brno University of Technology
Brno, Czech Republic

Elizabeth B. Kujawinski
Marine Chemistry and Geochemistry
Woods Hole Oceanographic Institution
Woods Hole, MA, USA

Rajnish Kumar
Department of Chemical Engineering
Indian Institute of Technology
Chennai, India

Masanori Kurosawa
Faculty of Life and Environmental Sciences
University of Tsukuba
Tsukuba, Ibaraki, Japan

Klaus S. Lackner
School of Sustainable Engineering and the Built Environment
Arizona State University
Tempe, AZ, USA

Maik Lang
Department of Nuclear Engineering
University of Tennessee
Knoxville, TN, USA

Charles H. Langmuir
Department of Earth and Planetary Sciences
Harvard University
Cambridge, MA, USA

Douglas Edward LaRowe
Department of Earth Sciences
University of Southern California
Los Angeles, CA, USA

John C. Lassiter
Department of Geological Sciences, Jackson School of Geosciences
University of Texas at Austin
Austin, TX, USA

Gregory B. Lawrence
New York Water Science Center
U.S. Geological Survey
Troy, NY, USA

Ian T. Lawson
Department of Geography and Sustainable Development
University of St Andrews
Edinburg, Scotland, UK

Christophe Lécuyer
Laboratoire de Géologie de Lyon, LGL-TPE
CNRS UMR 5276, Université Claude Bernard Lyon 1 and Institut Universitaire de France
Lyon, France

Cin-Ty Lee
Department of Earth Science MS-126
Rice University
Houston, TX, USA

Johannes Lehmann
Soil and Crop Science, School of Integrative Plant Science
Cornell University
Ithaca, NY, USA

Abraham Lerman
Department of Earth and Planetary Sciences
Northwestern University
Evanston, IL, USA

Juan S. Lezama Pacheco
School of Earth, Energy, and Environmental Sciences
Stanford University
Menlo Park, CA, USA

Yan Liang
Department of Earth, Environmental and Planetary Sciences
Brown University
Providence, RI, USA

Yu-Hsuan Crystal Liang
Institute of Earth Sciences
Academia Sinica
Nangang, Taipei, TAIWAN

Peter C. Lichtner
OFM Research—Southwest
Santa Fe, NM, USA

Praveen Linga
Department of Chemical and Biomolecular Engineering
National University of Singapore
Singapore, Singapore

Brenda J. Little
Naval Research Laboratory
Stennis Space Center
Hancock County, MS, USA

Xingcheng Liu
Guangzhou Institute of Geochemistry
Chinese Academy of Sciences
Guangzhou, China

J. William Louda
Department of Chemistry and Biochemistry and the Environmental Sciences Program
Florida Atlantic University
Boca Raton, FL, USA

Christian Ludwig
Paul Scherrer Institute (PSI)
Villigen, Switzerland
and
École Polytechnique Fédérale de Lausanne (EPFL)
Lausanne, Switzerland

Robert W. Luth
Department of Earth and Atmospheric Sciences
University of Alberta
Edmonton, AB, Canada

Timothy W. Lyons
Department of Earth Sciences
University of California – Riverside
Riverside, CA, USA

Fred T. Mackenzie
Department of Oceanography, School of Ocean and Earth Science and Technology
University of Hawai'i at Manoa
Honolulu, HI, USA

Glenn J. MacPherson
Smithsonian Institution
Washington, DC, USA

Clayton R. Magill
Lyell Centre for Marine and Earth Science and Technology
Heriot-Watt University
Edinburgh, UK

Helen Mango
Department of Natural Sciences
Castleton University
Castleton, VT, USA

Horst R. Marschall
Department of Geology and Geophysics
Woods Hole Oceanographic Institution
Wood Hole, MA, USA
and
Institut für Geowissenschaften
Goethe-Universität Frankfurt
Frankfurt am Main, Germany

Giuseppe Mascaro
School of Sustainable Engineering and the Built Environment
Arizona State University
Tempe, AZ, USA

Satoshi Matsubara
Department of Geology and Paleontology
National Museum of Nature and Science
Tokyo, Japan

William F. McDonough
Department of Geology
University of Maryland
College Park, MD, USA

David McKirdy
Department of Earth Sciences, School of Physical Sciences
The University of Adelaide
Adelaide, SA, Australia

Scott M. McLennan
Department of Geosciences
Stony Brook University
Stony Brook, NY, USA

Patricia M. Medeiros
Department of Marine Sciences
University of Georgia
Athens, GA, USA

Thomas C. Meisel
General and Analytical Chemistry
Montanuniversität Leoben
Leoben, Austria

Rob Middag
NIOZ Royal Netherlands Institute for Sea Research
Department of Ocean Systems (OCS), and Utrecht University
Den Burg, The Netherlands

Ritsuro Miyawaki
Department of Geology
National Museum of Nature and Science
Tokyo, Japan

Kira Mizell
Pacific Coastal and Marine Science Center
U.S. Geological Survey
Santa Cruz, CA, USA
and
Department of Ocean Sciences
University of California, Santa Cruz
Santa Cruz, CA, USA

J. Michael Moldowan
Biomarker Technologies, Inc.
Rohnert Park, CA, USA

Isabel P. Montañez
Department of Earth and Planetary Sciences
University of California
Davis, CA, USA

Mainak Mookherjee
Earth, Ocean and Atmospheric Sciences
Florida State University
Tallahassee, FL, USA

Manuel Moreira
Institut de Physique du Globe de Paris
Sorbonne Paris Cité, UMR CNRS 7154, Université Paris Diderot
Paris, France

Bree Morgan
School of Geosciences
The University of Sydney
Camperdown, NSW, Australia

Carl O. Moses
Provost and Vice President for Academic Affairs
Grand View University
Des Moines, IA, USA

Frédéric Moynier
Institut de Physique du Globe de Paris
Université Paris Diderot, Sorbonne Paris Cité
Paris, France
and
Institut Universitaire de France
Paris, France

Sujoy Mukhopadhyay
Department of Earth and Planetary Sciences
University of California Davis
Davis, CA, USA

Carsten Münker
Institut für Geologie und Mineralogie
Universität zu Köln
Köln, Germany

Richard W. Murray
Department of Earth and Environment
Boston University
Boston, MA, USA

A. D. Muscente
Department of Earth and Planetary Sciences
Harvard University
Cambridge, MA, USA

B. D. A. Naafs
Organic Geochemistry Unit, School of Chemistry
University of Bristol and Cabot Institute
Bristol, UK

Patrick Nadoll
GeoZentrum Nordbayern, Geochemistry – Economic Geology
Friedrich-Alexander-University Erlangen-Nuremberg
Erlangen, Germany

Kazuhide Nagashima
Hawai‘i Institute of Geophysics and Planetology
University of Hawai‘i at Mānoa
Honolulu, HI, USA

Izumi Nakai
Department of Applied Chemistry
Tokyo University of Science
Tokyo, Japan

Oliver Nebel
School of Earth, Atmosphere and Environment
Monash University
Clayton/Melbourne, VIC, Australia

Sune G. Nielsen
Department of Geology and Geophysics
Woods Hole Oceanographic Institution
Woods Hole, MA, USA

C. Noguera
Institut des Nanosciences de Paris
CNRS-Sorbonne Universités, UPMC University Paris 06
Paris, France

May Nyman
Department of Chemistry
Oregon State University
Corvallis, OR, USA

C. André Ohlin
Department of Chemistry
Umeå University
Umeå, Sweden

Priscia Oliva
CNRS/IRD
Paul Sabatier University
Toulouse, France

Anna F. Oliveri
Department of Chemistry, Department of Earth and Planetary Sciences
University of California
Davis, CA, USA

Hugh StC O'Neill
Research School of Earth Sciences
Australian National University
Acton, Australia

Herbert Palme
Forschungsinstitut und Naturmuseum Senckenberg
Frankfurt am Main, Germany

Monica M. Palta
Department of Environmental Studies and Science
Pace University
New York, NY, USA

R.D. Pancost
Organic Geochemistry Unit, School of Chemistry
University of Bristol and Cabot Institute
Bristol, UK

Ann Pearson
Department of Earth and Planetary Sciences
Harvard University
Cambridge, MA, USA

Michael Perfit
Department of Geological Sciences
University of Florida
Gainesville, FL, USA

Kenneth E. Peters
Schlumberger
Mill Valley, CA, USA
and
Department of Geological Sciences
Stanford University
Stanford, CA, USA

Larry C. Peterson
Rosenstiel School of Marine and Atmospheric Science
University of Miami
Miami, FL, USA

Steven Petsch
Department of Geosciences
University of Massachusetts Amherst
Amherst, MA, USA

R. Paul Philp
ConocoPhillips School of Geology and Geophysics
University of Oklahoma
Norman, OK, USA

Corey D. Pilgrim
Department of Chemistry
University of California, Davis
Davis, CA, USA

Daniele L. Pinti
GEOTOP, Research Center on the Dynamics of Earth System
Université du Québec à Montréal
Montréal, QC, Canada

Noah J. Planavsky
Department of Geology and Geophysics
Yale University
New Haven, CT, USA

Terry Plank
Lamont-Doherty Earth Observatory
Columbia University
Palisades, NY, USA

Don Porcelli
Department of Earth Sciences
Oxford University
Oxford, UK

Eric W. Portenga
Department of Geography and Geology
Eastern Michigan University
Ypsilanti, MI, USA

Olivier Pourret
UniLaSalle
Beauvais Cedex, France

Julie Prytulak
Department of Earth Science and Engineering
Imperial College London
London, UK

Igor S. Puchtel
Department of Geology
University of Maryland
College Park, MD, USA

Keith Putirka
Department of Earth and Environmental Sciences
California State University – Fresno
Fresno, CA, USA

Wilhelm Püttmann
Institute for Atmospheric and Environmental Sciences
Department of Environmental Analytical Chemistry
Goethe University
Frankfurt am Main, Germany

Liping Qin
Department of Earth and Space Science
China University of Science and Technology
Hefei, Hubei, China

Patrick Reardon
Nuclear Magnetic Resonance Facility
Oregon State University
Corvallis, OR, USA

Eoghan P. Reeves
Department of Earth Science and Centre for Geobiology
University of Bergen
Bergen, Norway

Martin Reich
Department of Geology and Andean Geothermal Center of Excellence (CEGA), FCFM
Universidad de Chile
Santiago, Chile

Christopher T. Reinhard
School of Earth and Atmospheric Science
Georgia Institute of Technology
Atlanta, GA, USA

Justin B. Richardson
Dept. of Earth and Atmospheric Sciences
Cornell University
Ithaca, NY, USA

Pascal Richet
Institut de Physique du Globe de Paris
Paris, France

Leigh Anne Riedman
Department of Earth and Planetary Sciences
Harvard University
Cambridge, MA, USA

Mark J. Rigali
Sandia National Laboratories
Albuquerque, NM, USA

Jennifer A. Roberts
Department of Geology
University of Kansas
Lawrence, KS, USA

Peter A. Rock
College of Math and Physical Sciences, Department of Chemistry
University of California
Davis, CA, USA

Leonardo Briceño Rodriguez
Schlumberger
Mexico City, Mexico

Norelis D. Rodriguez
Chevron Energy Technology Company
Houston, TX, USA

Nick Rogers
School of Environment, Earth and Ecosystem Sciences
The Open University
Milton Keynes, UK

Hugh Rollinson
Geoscience
University of Derby
Derby, UK

Estelle F. Rose-Koga
Laboratoire Magmas et Volcans
Université Blaise Pascal – CNRS
Clermont-Ferrand, France

Andrew Ross
CSIRO Earth Science and Resource Engineering (CESRE)
Kensington, NSW, Australia

Roberta L. Rudnick
Department of Earth Science
University of California
Santa Barbara, CA, USA
and
Department of Geology
University of Maryland
College Park, MD, USA

Sara Russell
Department of Earth Sciences
The Natural History Museum
London, UK

Michael A. Rutzke
College of Agriculture and Life Sciences Nutrient Analysis Lab
Cornell University
Ithaca, NY, USA

Jeffrey G. Ryan
School of Geosciences
University of South Florida
Tampa, FL, USA

Isao Sakaguchi
National Institute for Materials Science
Tsukuba, Ibaraki, Japan

Vincent J. M. Salters
National High Magnetic Field Laboratory and Department of Earth, Ocean and Atmospheric Sciences
Florida State University
Tallahassee, FL, USA

Iain M. Samson
Department of Earth and Environmental Sciences
University of Windsor
Windsor, ON, Canada

Yuji Sano
Atmosphere and Ocean Research Institute
Univertsity of Tokyo
Kashiwa, Japan

Philippe Sarda
GEOPS, Univ. Paris-Sud, CNRS
Université Paris-Saclay, Rue du Belvédère
Orsay, France

Peter E. Sauer
Department of Earth and Atmospheric Sciences
Indiana University
Bloomington, IN, USA

Paul Savage
Department of Earth and Environmental Sciences
University of St Andrews
St Andrews, UK

Joël Savarino
Laboratoire de Glaciologie et Géophysique de l'Environnement
Université Grenoble-Alpes, UMRCNTS/UGA
Grenoble, France

Howie D. Scher
Earth and Ocean Sciences
University of South Carolina
Columbia, SC, USA

Arndt Schimmelmann
Department of Earth and Atmospheric Sciences
Indiana University
Bloomington, IN, USA

Matthew W. Schmidt
Department of Ocean, Earth and Atmospheric Sciences
Old Dominion University
Norfolk, VA, USA

Mark D. Schmitz
Department of Geosciences
Boise State University
Boise, ID, USA

Maria Schönbächler
Institute of Geochemistry and Petrology
ETH
Zurich, Switzerland

Martin A. Schoonen
Brookhaven National Laboratory
Upton, NY, USA
and
Department of Geosciences
Stony Brook University
Stony Brook, NY, USA

Kurt Schwartz
GSI Helmholtz Center for Heavy Ion Research
Darmstadt, Germany

Melissa Scruggs
Department of Earth Science
University of California Santa Barbara
Santa Barbara, CA, USA

Rachel P. Scudder
Texas A&M University
College Station, TX, USA

Jeffrey S. Seewald
Marine Chemistry and Geochemistry Department
Woods Hole Oceanographic Institution
Woods Hole, MA, USA

Anat Shahar
Geophysical Laboratory
Carnegie Institution for Science
Washington, DC, USA

Elisabeth Sikes
Department of Marine and Coastal Sciences
Rutgers the State University of New Jersey
New Brunswick, NJ, USA

Don Sparks
Department of Plant and Soil Sciences
University of Delaware
Newark, DE, USA

Frank Spera
Department of Earth Science
University of California Santa Barbara
Santa Barbara, CA, USA

Garrison Sposito
Environmental Science, Policy and Management
University of California
Berkeley, CA, USA

Jessica A. Stammeier
Institute of Applied Geosciences
Graz University of Technology
Graz, Austria

Andri Stefánsson
Institute of Earth Sciences
University of Iceland
Reykjavík, Iceland

Andreas Stracke
Institut für Mineralogie
Westfälische Wilhelms-Universität
Münster, Germany

Dariusz Strąpoć
Geoservices
Schlumberger
Roissy, France

Roger Summons
Earth, Atmospheric, and Planetary Sciences Department
Massachusetts Institute of Technology
Cambridge, MA, USA

Chenguang Sun
Department of Earth, Environmental and Planetary Sciences
Rice University
Houston, TX, USA

Yoshio Takahashi
Graduate School of Science
The University of Tokyo
Tokyo, Japan

Asrarur Talukder
CSIRO Earth Science and Resource Engineering (CESRE)
Kensington, NSW, Australia

Fang-Zhen Teng
Isotope Laboratory, Department of Earth and Space Sciences
University of Washington
Seattle, WA, USA

Jefferson W. Tester
Earth and Atmospheric Sciences
Cornell University
Ithaca, NY, USA
and
School of Chemical and Biomolecular Engineering
Cornell University
Ithaca, NY, USA

Jay B. Thomas
Department of Earth Sciences, 204 Heroy Geology Laboratory
Syracuse University
Syracuse, NY, USA

John F. H. Thompson
Department of Earth and Atmospheric Sciences
Cornell University
Ithaca, NY, USA

Stuart N. Thomson
Department of Geosciences
University of Arizona
Tucson, AZ, USA

Andrew G. Tomkins
School of Earth, Atmosphere and Environment
Monash University
Melbourne, VIC, Australia

Taku Tsuchiya
Geodynamics Research Center
Ehime University
Matsuyama, Ehime, Japan

H. Tsunakawa
Department of Earth and Planetary Sciences
Tokyo Institute of Technology
Tokyo, Japan

Philippe Ungerer
Materials Design S.A.R.L.
Montrouge, France

Steven M. A. C. van Heuven
NIOZ Royal Netherlands Institute for Sea Research
Department of Ocean Systems (OCS), and Utrecht University
Den Burg, Texel, The Netherlands

Monica Vasiliu
Department of Chemistry
University of Alabama
Tuscaloosa, AL, USA

Jeff Vervoort
Geological Sciences
School of the Environment, Washington State University
Pullman, WA, USA

Jérôme Viers
CNRS/IRD
Paul Sabatier University
Toulouse, France

John K. Volkman
Oceans and Atmosphere Flagship
CSIRO
Hobart, TAS, Australia

J. H. L. Voncken
Faculty of Civil Engineering and Geosciences, Department of Geosciences and Engineering, Section Resource Engineering
Delft University of Technology
Delft, The Netherlands

Thomas Wagner
Lyell Centre for Marine and Earth Science and Technology
Heriot-Watt University
Edinburgh, UK

Richard J. Walker
Department of Geology
University of Maryland
College Park, MD, USA

Matthew C. F. Wander
Department of Geological Sciences
Brigham Young University
Provo, UT, USA

Xiangli Wang
Department of Geology and Geophysics
Yale University
New Haven, CT, USA

John Warren
Petroleum Geoscience Prog.
Chulalongkorn University
Bangkok, Thailand

Gerold Wefer
MARUM – Center for Marine Environmental Sciences
University of Bremen
Bremen, Germany

Dominique Weis
Pacific Centre for Isotopic and Geochemical Research
Earth, Ocean and Atmospheric Sciences
University of British Columbia
Vancouver, BC, Canada

Michael K. Weisberg
Department of Physical Sciences, Earth and Planetary Sciences, Kingsborough Community College and Graduate Center
City University of New York
New York, USA

William M. White
Department of Earth and Atmospheric Sciences
Cornell University
Ithaca, NY, USA

Rainer Wieler
Department of Earth Sciences, Institute of Geochemistry and Petrology
ETH Zürich
Zürich, Switzerland

Jamie J. Wilkinson
Department of Earth Sciences
Natural History Museum
London, UK
and
Department of Earth Science and Engineering
Imperial College
London, UK

Matthias Willbold
School of Earth, Atmospheric and Environmental Sciences
University of Manchester
Manchester, UK

Josh Wimpenny
Nuclear and Chemical Sciences Division
Lawrence Livermore National Laboratory
Livermore, CA, USA

Brian F. Woodfield
Department of Chemistry and Biochemistry
Brigham Young University
Provo, UT, USA

Jon Woodhead
School of Earth Sciences
The University of Melbourne
Melbourne, VIC, Australia

Ryan J. Woosley
Department of Ocean Science
University of Miami, Rosenstiel School of Marine and Atmospheric Sciences
Miami, FL, USA

Xiaolin Xiong
Guangzhou Institute of Geochemistry
Chinese Academy of Sciences
Guangzhou, China

Akira Yamaguchi
Antarctic Meteorite Research Center
National Institute of Polar Research
Tokyo, Japan
and
Department of Polar Science
School of Multidisciplinary Science, SOKENDAI (The Graduate University for Advanced Studies)
Tokyo, Japan

Y. Yamamoto
Center for Advanced Marine Core Research
Kochi University
Kochi, Japan

Jie Yang
School of Earth and Environmental Sciences
University of St Andrews
Fife, UK

Edward D. Young
Department of Earth, Planetary, and Space Sciences
UCLA
Los Angeles, CA, USA

Hisayoshi Yurimoto
Natural History Sciences
Hokkaido University
Sapporo, Japan

Yi Ge Zhang
Department of Oceanography
Texas A&M University
College Station, TX, USA

Preface

Few fields within the earth sciences have grown as rapidly or had as great an impact as geochemistry. The impact of geochemistry has been vast and greatly influenced our understanding of virtually every aspect of this planet, its neighbors, and the life that makes it so unique.

As an example, consider what Darwin wrote in 1859 in *Origin of Species*: "*If the theory* [evolution] *be true*, *it is indisputable that before the lowest Cambrian stratum was deposited, long periods elapsed. . .and that during these vast periods, the world swarmed with living creatures. But to the question why we do not find rich fossiliferous deposits belonging to these assumed earliest periods before the Cambrian system, I can give no satisfactory answer*." Darwin understood that the Precambrian comprised "long periods" but had no idea how long. Geochemistry, in particular analysis of radioactive elements and their daughter products, provided the answer: four billion years. While the answer to " how long" could have been given more than half a century ago, the answer to his question "why" has only become apparent within the last decade, and that answer also comes from geochemistry. Recent studies of redox-sensitive metals such as uranium and molybdenum in ancient marine sediments have revealed that although the Earth's atmosphere first became oxidizing about 2.3 billion years ago, oxygen levels remained too low to support animal life for nearly another 2 billion years. Animals appear in the fossil record shortly, geologically speaking, after that rise.

Why oxygen levels began to rise in the Neoproterozoic remains unclear, but biomarkers in sediments of the time hint at possible answers. Biomarkers are fragments of original biomolecules that survive in sediment and contain clues to ancient environments and operation of the carbon cycle. The carbon cycle is intimately connected to both the oxygen cycle through photosynthesis, respiration, and burial of organic carbon and climate through the greenhouse gases CO_2 and CH_4.

In another example, Louis Agassiz first recognized that the Earth had experienced extensive recent glaciation in the first half of the nineteenth century. Only in the last half of the twentieth century has geochemistry, particularly the analysis of oxygen and hydrogen isotope ratios, provided answers to the when and why of the Agassiz's "Ice Ages." Geochemistry continues to provide all the main tools for paleoclimate analysis. Understanding what controlled climate in the past is key to predicting how it will change in the future. This is, of course, critical, because humans have shifted the balance in the carbon cycle by burning anciently buried organic carbon, and climate is changing as a consequence.

Geochemistry is also revealing the workings of the Earth's interior. Thermobarometers based on the distribution of elements between different minerals reveal the temperatures of metamorphism and crystallization in magma chambers. Combined with geochronometers, they can reveal the rates of these processes and the rates at which mountains rise and erode. The 1960s James Bond film proclaimed that "Diamonds are Forever," but it is zircon that holds the record for longevity. Because zircons concentrate uranium, they are natural clocks. Chemical and isotopic analysis of zircons reveals that creation of the continents began 4.4 billion years ago and proceeded subsequently in pulses that appear to correspond to times of supercontinent formation.

We have learned that geochemical cycles extend to the base of the mantle. Water, carbon, nitrogen, and sulfur are carried into the mantle at subduction zones. Isotopic analyses, among other approaches, reveal that these are then carried upward in mantle plumes, which seismic imaging show rise from the base of the mantle, and are released back to the surface by "hot spot" volcanoes such as Hawaii, Réunion, etc. These deep cycles operate much more slowly than surficial ones, as the discovery of the mass independently fractionated isotopic signature of Archean atmospheric sulfur in lavas from volcanoes of French Polynesia demonstrates.

Geochemistry has its roots in the ancient arts of metallurgy, refining elements from the Earth, and alchemy, transforming those elements into new ones. The latter proved fruitless, of course, but transforming elements

into new ones happens continually in stellar interiors, supernovae, and neutron star mergers. The disparate isotopic signatures of these various nucleosynthetic processes are found in meteorites – the "left-overs" from solar system formation 4.5 billion years ago. The impact of geochemistry thus extends to understanding how planetary systems form and how the cosmos has evolved.

The beginnings of metallurgy mark the transition of humanity out of the Stone Age and the founding of modern civilization. Many of the metals that the ancients mined and refined, such as copper, tin, lead, and iron, are still essential to us, but modern society depends increasingly on a vast array of less common elements: as many as 70 different elements are components of smart phones, including lithium, yttrium, rare earths, indium, tantalum, gallium, and antimony. Many of these and others such as cadmium, tellurium, and thallium are increasingly needed as we transition to carbon-free, energy efficient societies. Finding sufficient sources of them requires understanding their behavior in nature and the processes that concentrate them. At the same time, many of these elements are toxic or form environmentally destructive compounds. Geochemistry is essential both in supplying society's resources and dealing with its wastes.

Many ore deposits are formed as a result of hydrothermal activity. The cover photo of the colorful salt deposits of the Dallol dome in the Danakil depression of Ethiopia is an example of such activity, and it also illustrates how all aspects of geochemistry are ultimately interconnected. There, a mantle plume causes rifting and volcanism. The magmatic heat drives a mixture of magmatic volatiles, formation brines, and groundwater upward through layers of basalt and evaporites, dissolving a variety of elements from both. Once this hot, acidic solution reaches the surface, cooling and reaction with atmospheric oxygen result in precipitation. Thus, the resulting salts are ultimate products of all of the Earth: its interior, the oceans, and the atmosphere.

The point is that the scope of geochemistry is so vast that it is impossible for any one person to know the entire field. This is *raison d'etre* for this encyclopedia. The 331 entries include brief summaries of the behavior of the naturally occurring chemical elements, and their isotopes in many cases, brief definitions of important terms such as quantum numbers, overviews of important topics such as evaporites, and extensive reviews of broad topics such as the formation and evolution of the Earth. All of these entries are written by experts on the subject. None of them are exhaustive, rather they are meant to acquaint the reader with the topic and, with the references at the end of each entry, provide a point of departure for further understanding. The encyclopedia is aimed at students, teachers, professionals working in other aspects of earth science, and anyone wanting to understand more about the chemistry of nature. Given, again, the vast scope of geochemistry, we expect it should also be useful to geochemists needing to understand topics outside their own area of specialty.

William M. White
Ithaca, NY
December 2017

Aknowledgments

The editors wish above all to thank the hundreds of scientists from academia, industry, and government organizations who have graciously contributed their time and effort in writing the entries that comprise this encyclopedia. It is primarily their efforts which have produced this volume. We would also like to thank the many other hundreds of scientists who have provided peer reviews for these entries and improved them with their constructive comments. Finally, we would like to thank the Springer team, Petra van Steenbergen, Sylvia Blago, and Johanna Klute for their work and assistance in assembling this volume.

William H. Casey
Bernard Marty
William M. White
Hisayoshi Yurimoto

A

Ab Initio Calculations

David A. Dixon
Department of Chemistry, University of Alabama, Tuscaloosa, AL, USA

Definition

Molecular orbital theory is an approach to solving the Schrödinger equation for the motion of electrons in molecules (as well as atoms). Such calculations are known as *ab initio* (from first principles) electronic structure calculations. The molecular orbitals are usually expressed as sums of atomic orbitals, and the rules of quantum mechanics including the Pauli exclusion principle are followed. The use of molecular orbital theory ranges from qualitative where it is used to provide a description of the electron occupancy in a molecule to explain experimental results from photoelectron spectroscopy and electronic spectroscopy to extremely quantitative with a focus on precise predictions of molecular energetics and spectroscopic parameters.

Overview

Molecules contain electrons which have a low enough mass that the laws of quantum mechanics must be used to describe them if the electronic structure of an atom or molecule needs to be studied. In order to predict the energy of the electrons in a molecule by solving the Schrödinger equation for the electronic motion, we make the Born-Oppenheimer approximation based on the fact that the electrons are 1836 times lighter than the smallest nuclear mass (the proton or the H atom nucleus) so that we can separate the electronic and nuclear motion. The Born-Oppenheimer approximation underlies all of how we interpret molecular structure and spectroscopy as it effectively states that the electrons readjust immediately as the nuclei move in a molecule (Hehre et al. 1986; Hirst 1990; Grant and Richards 1995; Lowe and Peterson 2006; Levine 2014; Foresman and Frisch 2015).

Current electronic structure methods are based on the solution of the time-independent Schrödinger wave equation

$$H\Psi = E\Psi \tag{1}$$

for the motion of electrons in atoms and molecules including complexes and charged systems, where H is the Hamiltonian operator which is Hermitian, Ψ is the wave function, and E is the energy. Equation 1 is an eigenvalue equation and can only be solved analytically for very simple systems usually involving a single electron. Initially, the Hamiltonian did not include relativistic effects, but recently, it has become possible to solve the relativistic Schrödinger equation for electronic motion as such solutions are needed to describe molecules containing heavy elements which play an important role in many environmental geochemical issues (Pykkö and Descleaux 1979; Wilson 1988; Reiher 2012).

For a molecular system, the exact nonrelativistic Hamiltonian in atomic units (the electron mass and charge, Planck's constant divided by 2π, and the Coulomb constant are all set to unity) is given by

$$-\sum_{i=1}^{n}\frac{1}{2}\nabla_i^2-\sum_{i=1}^{n}\sum_{A=1}^{M}\frac{Z_A}{r_{iA}}+\sum_{i=1}^{n}\sum_{j>i}^{n}\frac{1}{r_{ij}}-\sum_{A=1}^{M}\frac{1}{2M_A}\nabla_A^2+\sum_{A=1}^{M}\sum_{B>A}^{M}\frac{Z_AZ_B}{R_{AB}} \tag{2}$$

In Eq. 2, the capital letters correspond to the M nuclei, and the lower case letters correspond to the n electrons. In atomic units, the mass of a nucleus is in terms of the mass of an electron. The first term represents the kinetic energy of the electrons and includes the quantum operator for the

W. M. White (ed.), *Encyclopedia of Geochemistry*,
https://doi.org/10.1007/978-3-319-39312-4

momentum squared (K.E. = $p^2/2$ m). The second term is the kinetic energy of the nuclei, and in the Born-Oppenheimer approximation, does not depend on the electronic wave function so it can be calculated classically. The third term is the potential energy due to the Coulombic attraction of the i^{th} electron to the A^{th} nucleus, is the term in the Hamiltonian representing the force that holds electrons to the nucleus, and is responsible for the stability of the system. This term is relatively cheap to compute. The fourth term is the inter-electron repulsion energy and this is the difficult term to calculate. The reason for this is that the electrons are not points but are probability distributions based on their wave-like properties, their deBroglie wavelengths. In addition, due to the Pauli exclusion principle, a nonclassical component, the exchange integral is introduced. The final term is the internuclear repulsion energy, and again the Born-Oppenheimer approximation makes this term classical and independent of the electronic wave function. The atomic unity of energy is the hartree which is twice the ionization potential of the H atom and equals 4.359744×10^{-18} J. The atomic unit of distance is the bohr, the most probable distance of the electron from the proton in the 1 s orbital of the H atom, and equals $5.2917721 \times 10^{-11}$ m.

Quantum chemical molecular orbital (MO) theory methods can usually be classified either as *ab initio* or semi-empirical. The first label, *ab initio*, means "from the beginning" = first principles and uses no empirical parameters. This category includes the starting level Hartree-Fock (HF) approach and methods that include a treatment of the electron correlation including configuration interaction (CI), many-body perturbation theory (MBPT), coupled-cluster (CC) theory, and other approaches. The second category, semiempirical (SEMO), includes methods which make significant approximations to substantially reduce the number of integrals and then use empirical parameters to evaluate the integrals that are kept in a minimal basis set. These methods include the modified neglect of differential overlap (MNDO) (Dewar and Thiel 1977), Austin Model 1 (AM1) (Dewar et al. 1985), and Stewart's PMn ($n = 3, 6, 7$) (Stewart 2013). The goal of SEMO methods is to reproduce experiment or equivalently very accurate correlated molecular orbital theory calculations.

An advantage of computational molecular orbital theory methods is that many properties can be calculated to varying degrees of accuracy depending on the amount of computation. Examples of these properties are given in Table 1.

There is always a compromise between computational speed and accuracy. We define "chemical accuracy" for thermochemistry as 1 kcal/mol or about 4 kJ/mol (1 kcal/mol = 4.184 kJ/mol), for structures as ±0.005 Å, and for spectroscopy as ±5 cm^{-1} for vibrational frequencies. As an example of the need for accurate calculations, if one has a 50:50 starting mixture of two components, a change in the free energy ΔG of 5.86 kJ/mol leads to a change in the equilibrium constant of a factor of 10 leading to a 10:1 mixture at 25 °C. A factor of 2–4 in a rate constant can have an impact on whether a compound will degrade quickly in the environment so that there will be little if any impact, for example, on atmospheric infrared absorption. A factor of 10 in a rate constant at room temperature (25 °C) corresponds to a change in the activation energy of 5.86 kJ/mol.

Ab Initio Calculations, Table 1 Properties obtainable from quantum mechanical methods

Molecular structures (rotational spectra)
Vibrational energy levels (infrared and Raman spectra)
Nuclear magnetic resonance (NMR) chemical shifts
Electronic energy levels (UV and visible spectra)
Accurate thermochemistry (gas phase)
Potential energy surfaces (barrier heights, transition states)
Ionization potentials (photoelectron and X-ray spectra)
Electron affinities
Dipole moments
Polarizabilities
Electron density maps and population analysis

Hartree-Fock (HF) Theory

The simplest first principles solution in the molecular orbital theory approach is Hartree-Fock theory, a self-consistent method, which describes the energy of an electron in the average field of the other n–1 electrons. This approximation makes Hartree-Fock theory much simpler than the full N-body problem. The HF method is based on using a Slater determinant for the molecular orbitals, and each molecular orbital is expanded as a linear combination of atomic orbitals (LCAO). The Hartree-Fock method iteratively solves for the linear expansion coefficients (the quantities which determine which atomic orbitals make up the molecular orbitals) until they do not change within a prescribed limit within successive iterations. The Hartree-Fock molecular orbitals represent an approximation to the solution of the electronic Schrödinger equation. In many cases where the properties are not good to first order, this approximation can give poor results, for example, covalent bond energies. The HF method can provide a set of starting orbitals that can be used to substantially improve the results with more accurate methods. A key correction to deal with is the Coulomb hole, which arises because the motions of electrons in an orbit are correlated. The HF approach does not properly treat the interaction of an electron with the other electron in a doubly occupied orbital as it allows the electrons to overlap which is not possible due to Coulomb's law so the motion of the electrons

is correlated (they repel each other). This is known as dynamic correlation.

One of the great triumphs of modern quantum chemistry has been the development of analytical derivative methods which allow one to find minimum energy structures and then to characterize these structures as minima, transition states, saddle points, etc. The first derivatives of the energy E with respect to the nuclear coordinates x can be used in efficient search algorithms to find minimum energy structures. Remember that $dE/dx = 0$ defines a minimum or a maximum. Given the second derivatives of the energy with respect to the nuclear coordinates, one can characterize the minima and obtain the force constants and thus the vibrational spectra. Remember that d^2E/dx^2 defines the curvature at the place where $dE/dx = 0$. If $d^2E/dx^2 > 0$, then the structure is a minimum, and if $d^2E/dx^2 < 0$, it is a maximum. If there is only one negative d^2E/dx^2, the structure is a transition state.

Basis Sets

Ab initio electronic structure computations are almost always carried out numerically using a basis set of atomic orbitals as matrix/vector operations can be fast on computers, and such an approach connects to simple chemical descriptions of how the electrons in atoms form bonds in molecules. It is important to choose a basis set that is large enough to give a good description of the molecular wave function. The basis set is often described as the one-particle problem. Typically, the basis functions are centered on the atoms and so are called atomic orbitals. These atom-centered basis functions are usually chosen to be Gaussian-type orbitals (GTOs), which have the form

$$\mathrm{GTO}(x, y, z) = x^a y^b z^c \exp\left(-\xi r^2\right) \tag{3}$$

where x, y, z are the local (atom-centered) Cartesian coordinates, *a, b, c* are positive integers which describe the angular momentum of the orbital, r is the radial distance to the atomic center, and ξ is an exponent optimized in some way to provide the best values for a set of properties. Unlike hydrogen atom orbitals, GTOs do not have radial nodes, but radial nodes can be obtained by combining different GTOs. An atomic basis function is usually given as a fixed linear combination of GTOs, a contracted Gaussian basis function, where the coefficients are obtained from an electronic structure calculation usually on an atom. The smallest basis set to give practically useful results is a polarized double-ζ set which has two sets of orbitals for each orbital in the minimal set needed to describe an atom plus a set of functions with a value of the angular momentum quantum number one higher than needed for a minimal basis set. As an example, for C, there are two 1 s orbitals, two 2 s orbitals, 2 sets of 3 2p orbitals and one set of 5 d orbitals. As the core electrons do not usually participate in the chemistry of the valence electrons, the core is often treated by a single set of orbitals to reduce the computational expense giving a split valence basis set. The most commonly used split valence double-zeta plus polarization basis set is Pople's 6–31G* or 6–31G(d) basis.

Much larger basis sets are needed for treating the correlation energy, and a number of such sets have been developed including atomic natural orbitals (Almlöf and Taylor 1991; Neese and Valeev 2011) and correlation consistent basis sets (Dunning 1989). By exploiting the systematic convergence properties of the correlation consistent basis sets including additional diffuse functions (Kendall et al. 1992), it is possible to obtain accurate estimates of the complete basis set (CBS) limit (Feller et al. 2011) without having to resort to such extremely large basis sets that would unavoidably limit calculations to small diatomic molecules (Peterson 2007). Such basis sets are being developed for the entire periodic table and are currently available for elements up to Z = 86, excluding the lanthanides which are under development and for some of the actinides with the remainder under development. An advantage of a consistent set of basis sets that converges to the CBS limit is the elimination of the 1-particle truncation problem arising from basis set incompleteness. This provides a measure of the intrinsic error associated with a given n-particle method. In addition, issues with basis set superposition error (BSSE) are minimized.

The high atomic numbers (Z) of the heavier elements beyond the second row imply that relativistic effects must be properly included to attain even semiquantitative accuracy (Wilson 1988; Hess and Dolg 2002; Reiher 2012; Dolg 2015). For many of the properties of interest, the core electrons are chemically inert. It is possible to eliminate the core contributions from direct consideration by using small-core pseudopotentials or relativistic effective core potentials (RECPs) (Küchle et al. 1998; Reiher 2012). This is equivalent conceptually to ignoring the correlation effects of the 1 s electrons for second row atoms like S and Cl. Recently, Peterson and coworkers have developed correlation consistent basis sets in combination with effective core potentials from the Stuttgart/Köln group for all of the main group atoms and transition metals enabling reliable predictions for compounds containing most of the elements in the periodic table (Peterson 2015). Good sources for the basis sets are the EMSL Basis Set Exchange website (Feller 1996; Schuchardt et al. 2007; EMSL) and the K. Peterson website at Washington State University (Peterson). Many computer programs have basis sets embedded in them, but

one should take care to make sure that the basis sets are implemented the same in different programs and even in different versions of the same program when calculating various quantities.

Electron Correlation Methods

Many methods have been developed to treat the n-particle or correlation energy problem. The simplest method is second-order Møller-Plesset (MP2) (Møller and Plesset 1934; Pople et al. 1976) which is based on a perturbation theory expansion and can be extended to higher orders. The most common reliable methods that one can use to treat the correlation problem adequately are coupled-cluster-based approaches (Bartlett and Musial 2007). Until the last 20 years, it was believed that most of the problems in the accurate treatment of molecular systems were due to the difficulties in treating the n-particle problem. In fact, based on full configuration interaction benchmark studies, it has been found that many of the problems previously attributed to the solution of the n-particle problem were actually due to deficiencies in the solution of the 1-particle problem, the choice of the atomic orbital basis sets (Dunning 1989). There is a good understanding today of the means to solve many problems to chemical accuracy, and there is a growing consensus that for systems based predominantly on a single configuration, the coupled cluster with all single and double excitations plus a correction for the connected triples (CCSD(T)) method can provide such results. However, the computational cost can be very high as one must use very large extended basis sets and the CCSD (T) scales as N^7 where N is the number of basis set functions. Recently developed F12 methods utilize a Slater-type correlation factor, $F_{12} = e^{-\gamma r_{12}}$, and exhibit significantly faster convergence toward the CBS limit, especially for geometries and frequencies (Kutzelnigg 1985; Adler et al. 2007; Helgaker et al. 2008; Knizia et al. 2009; Peterson et al. 2012b; Feller 2015).

For cases with multireference (MR) character or when more accurate results (<1 kcal/mol) are needed, extension of the correlation treatment beyond CCSD(T) is required. This can be done by performing calculations with higher order coupled-cluster methods (CCSDT, CCSDT(Q), CCSDTQ, etc.) to estimate the remaining contributions between full CI (FCI) and CCSD(T). Another approach is to use multireference methods with some additional treatment for electron correlation such as configuration interaction (MRCI) or perturbation theory methods (CASPT2). The idea of configuration interaction is to take a set of Slater determinants generated by promoting electrons from the HF occupied orbitals to the unoccupied orbitals. We represent the wave function as a sum of these Slater determinants with a set of optimized coefficients which describe how much a Slater determinant contributes to the overall wave function. As the coefficients of each determinant are optimized, CI is a variational approach. An issue with any truncated configuration interaction calculation is that they are not size consistent (proportional to the number of electrons as the distance between them gets large). An MR wave function is one where a single configuration wave function is not a good representation of the molecule, e.g., N_2 dissociating to large R or NO_3 an open shell molecule with 3 equivalent Lewis dot structures or O_3 with 2 equivalent Lewis dot structures. This type of correlation is known as static correlation. In the MR approach, one writes the molecular wave function as a sum of configuration state functions (CSF) and varies both the expansion coefficients of the CSFs and those of the molecular orbitals in each CSF. MRCI uses the MR wave function as the starting point for additional CI calculations to get an estimate of the dynamic correlation. This is a computationally very expensive process. One issue with MRCI methods is the choice of the active electrons and orbitals which are to be optimized. This is relatively straightforward for smaller systems such as N_2 where the active space consists of the $\sigma(2\,s)^2$ and $\sigma^*(2\,s)^2$ and $\sigma(2p)^2$ and $\pi(2p)^4$ electrons and orbitals and the unoccupied (virtual) $\sigma^*(2p)$ and $\pi^*(2p)$ orbitals to give what is known as a complete active space or CASSCF. The choice of the CASSCF can get quite complicated for larger molecules with more electrons, and there is currently a rough limit of about 16 electrons in 16 active orbitals due to computational cost.

An example of how to use high accuracy calculations to get the heat of formation from the calculated total atomization energy in combination with accurate experimental heats of formation of the atoms at 0 K is now given, the Feller-Peterson-Dixon (FPD) method (Dixon et al. 2012; Feller et al. 2012; Peterson et al. 2012a). The expression for the zero point inclusive, total atomization energy (TAE = ΣD_0), is given by the following expression:

$$\begin{aligned} TAE &= \Sigma D_0 \\ &= \Delta E_{elec}(CBS) + \Delta E_{CV} + \Delta E_{SR} + \Delta E_{SO} \\ &\quad + \Delta E_{HO} + \Delta E_{ZPE} \end{aligned} \tag{4}$$

The various energy terms in the calculation are treated as accurately as possible, exploiting the fact that each piece can be handled with different levels of approximation. The best available appropriate geometry for each computational level should be used. The first term in the energy expression is the electronic energy contribution of the "valence electrons," which we will take to be the complete basis set (CBS) limit of the CCSD(T) energy. For molecular systems with wave

functions dominated by a single Slater determinant, this is an appropriate approach. The second term is the correlation of the outer-core electrons with themselves and with the valence electrons, the core-valence term. If possible, this contribution is also estimated at the CBS limit. The third and fourth terms deal with the effects of relativity with the third term accounting for scalar relativistic effects and the fourth term dealing with the spin orbit interaction for atoms and molecules. The fifth term deals with corrections to the TAE beyond the CCSD (T) level. The final value is the zero point energy, which will be negative and decrease the TAE. The TAE, i.e., the enthalpy for reaction (2), can then be used to calculate the heat of formation of the molecule $A_aB_bC_c$ at 0 K from reaction (5) with expression (6).

$$A_aB_bC_c \rightarrow aA + bB + cC \tag{5}$$

$$\Delta H_f{}^{0K}(A_aB_bC_c) = a\Delta H_f{}^{0K}(A) + b\Delta H_f{}^{0K}(B) + c\Delta H_f{}^{0K}(C) - \Sigma D_0 \tag{6}$$

Solvation Effects

Geochemical applications often require the treatment of aqueous systems. In order to include the effects of solvation, one has to use either explicit solvent molecules in the calculation which is computationally very expensive due to the large number of atoms and electrons involved and the many solvent molecule conformations or self-consistent reaction field (SCRF) approaches (Tomasi et al. 2005) or some combination (Gutowski and Dixon 2006). One SCRF approach is the Conductor-like Screening Model (COSMO) originally developed by Klamt (Klamt and Schümann 1993; Klamt 2005). This approach starts by determining the interaction of a dipole in the center of a conducting sphere field given by Eq. (7)

$$\Delta E = -\frac{1}{2}\sum_{ij}\frac{q_i q_j R}{\sqrt{R^4 - 2R^2 \boldsymbol{r_i r_j} + r_i^2 r_j^2}} \tag{7}$$

where R is the radius of the surrounding conducting sphere, q is the charge, $\boldsymbol{r}$ is the position vector of the charge with respect to the spherical center, and r is the distances of the charge from the center. When combined with the dielectric scaling function for dipoles derived by Kirkwood, this basic model gave good results. Although this exact solution works well for many systems, a more realistic cavity shape is needed. The resulting Green's function takes the form of:

$$G_S^X = -\frac{1}{2}f(\varepsilon)Q^X B^t A^{-1} \equiv \frac{1}{2}Q^X D Q^X \tag{8}$$

where G_S^X is the total free-energy gain, $f(\varepsilon)$ is the dielectric scaling factor, Q^X is charge density, A is the Coulomb interaction matrix of the surface segments, B is an operator that generates a potential from the charge density, t is the matrix transposition, and matrix D is the Green's function of the continuum. This is essentially an additional charge-charge interaction to the charge density, Q^X, of the Coulomb interaction energy. Note that SCRF approaches give a free energy of solvation. The reaction free energies in solution at 298 K can be predicted by combining $\Delta G_{solvation}$ with ΔG_{gas} to get $\Delta G_{solution}$. ΔG_{gas} is obtained by taking ΔH_{gas}(298 K) value and combining it with ΔS_{gas}(298 K) using calculated frequencies and geometries with the usual statistical mechanical approaches and the equation $\Delta G = \Delta H - T\Delta S$. There are many additional solvation approaches, and another common one is the SMD approach developed by Cramer and Truhlar (Marenich et al. 2009).

Conclusions

Ab initio molecular orbital theory is currently the best current way to get "the right answer for the right reason" (Borden et al. 2002) for a broad range of molecular properties and energetics. Reliable heats of formation for gas phase molecules containing most atoms in the periodic table can be obtained to chemical accuracy of ± 1 kcal/mol by using composite methods such as FPD, although these methods are computationally expensive. Such methods also provide reliable predictions of nonbonded interactions, which are important in geochemical applications but difficult to predict with most density functional theory exchange-correlation functionals. Similar high-level predictions can be made for structures and spectroscopic properties. For example, reliable calculated vibrational frequencies can be used to determine the correct isotope fractionation factors (Rustad et al. 2010) as was done for the fractionation of ^{11}B and ^{10}B between $B(OH)_3$(aq) and $B(OH)_4^-$(aq), which has been used in paleoclimate studies to estimate the pH of the oceans on timescales of 20 my (Hemming and Hanson 1992). Improvements in methods are still being made especially for molecules with multireference character, solvent effects, and the solid state (Yang et al. 2014).

Cross-References

- ▶ Aqueous Solutions
- ▶ Free Energy
- ▶ Geochemical Thermodynamics

References

Adler TB, Knizia G, Werner H-J (2007) A simple and efficient CCSD(T)-F12 approximation. J Chem Phys 127:221106. (4 pages)

Almlöf J, Taylor PR (1991) Atomic natural orbital (ANO) basis sets for quantum chemical calculations. Adv Quantum Chem 22:301–373

Bartlett RJ, Musial M (2007) Coupled-cluster theory in quantum chemistry. Rev Mod Phys 79:291–352

Borden WT, Handy NC, Schaefer HF, Davidson ER (2002) Molecular quantum mechanics: the right answer for the right reason: the proceedings of an international conference in Honor of Professor Ernest R. Davidson, held at the University of Washington, Seattle, 21–25 July 2001. Taylor & Francis, London

Dewar MJS, Thiel W (1977) Ground states of molecules. 38. The MNDO method. Approximations and parameters. J Am Chem Soc 99:4899–4907

Dewar MJS, Zoebisch EG, Healy EF, Stewart JJP (1985) Development and use of quantum mechanical molecular models. 76. AM1: a new general purpose quantum mechanical molecular model. J Am Chem Soc 107:3902–3909

Dixon DA, Feller D, Peterson KA (2012) A practical guide to reliable first principles computational thermochemistry predictions across the periodic table. In: Ralph AW (ed) Annual reports in computational chemistry, vol 8. Elsevier, Amsterdam, pp 1–28

Dolg M (ed) (2015) Computational methods in lanthanide and actinide chemistry. Wiley, New York

Dunning TH Jr (1989) Gaussian basis sets for use in correlated molecular calculations. I. The atoms boron through neon and hydrogen. J Chem Phys 90:1007–1023

EMSL basis set library: https://bse.pnl.gov/bse/portal

Feller D (1996) The role of databases in support of computational chemistry calculations. J Comput Chem 17:1571–1586

Feller D (2015) A statistical electronic structure calibration study of the CCSD(T*)- F12b method for atomization energies. J Phys Chem A 119:7375–7387

Feller D, Peterson KA, Hill JG (2011) On the effectiveness of CCSD(T) complete basis set extrapolations for atomization energies. J Chem Phys 135:044102. (18 pages)

Feller D, Peterson KA, Dixon DA (2012) Further benchmarks of a composite, convergent, statistically calibrated coupled cluster based approach for thermochemical and spectroscopic studies. Mol Phys 110:2381–2399

Foresman JB, Frisch Æ (2015) Exploring chemistry with electronic structure methods, 3rd edn. Gaussian, Inc., Wallingford

Grant GH, Richards WG (1995) Computational chemistry. Oxford University Press, Oxford

Gutowski KE, Dixon DA (2006) Predicting the energy of the water exchange reaction and free energy of solvation for the uranyl ion in aqueous solution. J Phys Chem A 110:8840–8856

Hehre WJ, Radom L, Schleyer PVR, Pople JA (1986) Ab initio molecular orbital theory. Wiley-Interscience, New York

Helgaker T, Klopper W, Tew DP (2008) Quantitative quantum chemistry. Mol Phys 106:2107–2143

Hemming NG, Hanson GN (1992) Boron isotopic composition and concentration in modern marine carbonates. Geochim Cosmochim Acta 56:537–554

Hess BA, Dolg M (2002) Relativistic quantum chemistry with pseudopotentials and transformed Hamiltonian, Wiley series in theoretical chemistry, vol 57. Wiley, Chichester

Hirst DM (1990) A computational approach to chemistry. Blackwell Scientific, Oxford

Kendall RA, Dunning TH Jr, Harrison RJ (1992) Electron affinities of the first-row atoms revisited. Systematic basis sets and wave functions. J Chem Phys 96:6796–6806

Klamt A (2005) Quantum chemistry to fluid phase thermodynamics and drug design. Elsevier, Amsterdam

Klamt A, Schümann G (1993) A new approach to dielectric screening in solvents with explicit expressions for the screening energy and its gradient. J Chem Soc Perkin Trans 2:799–805

Knizia G, Adler TB, Werner H-J (2009) Simplified CCSD(T)-F12 methods: theory and benchmarks. J Chem Phys 130:054104. (20 pages)

Küchle W, Dolg M, Stoll H, Preuss H. Pseudopotentials of the Stuttgart/Dresden Group 1998 (Revision: Tue Aug 11, 1998). http://www.theochem.uni-stuttgart.de/pseudopotentiale

Kutzelnigg W (1985) The r_{12}-dependent terms in the wave function as closed sums of partial wave amplitudes for large *l*. Theor Chim Acta 68:445–469

Levine I (2014) Quantum chemistry, 7th edn. Pearson, New York

Lowe JP, Peterson KA (2006) Quantum chemistry, 3rd edn. Elsevier, Amsterdam

Marenich AV, Cramer CJ, Truhlar DG (2009) Universal solvation model based on solute electron density and a continuum model of the solvent defined by the bulk dielectric constant and atomic surface tensions. J Phys Chem B 113:6378–6396

Møller C, Plesset MS (1934) Note on the approximation treatment for many-electron systems. Phys Rev 46:618–622

Neese F, Valeev EF (2011) Revisiting the atomic natural orbital approach for basis sets: robust systematic basis sets for explicitly correlated and conventional correlated ab initio methods? J Chem Theory Comput 7:33–43

Peterson K (2007) A. Gaussian basis sets exhibiting systematic convergence to the complete basis set limit, Chapter 11. In: Spellmeyer DC, Wheeler RA (eds) Annual reports in computational chemistry, vol 3. Elsevier, Amsterdam, pp 195–206

Peterson KA (2015) Correlation consistent basis sets for actinides; I. The Th and U atoms. J Chem Phys 142:074105. (14 pages)

Peterson KA. http://tyr0.chem.wsu.edu/~kipeters/basis.html

Peterson KA, Feller D, Dixon DA (2012a) Chemical accuracy in ab initio thermochemistry and spectroscopy: current strategies and future challenges. Theor Chem Accounts 131:1–20

Peterson KA, Dixon DA, Stoll H (2012b) The use of explicitly correlated methods on XeF_6 predicts a C_{3v} minimum with a sterically active, free valence electron pair on Xe. J Phys Chem A 116:9777–9782

Pople JA, Binkley JS, Seeger R (1976) Theoretical models incorporating electron correlation. Int J Quantum Chem Symp 10:1–19

Pykkö P, Descleaux JP (1979) Relativity and the periodic system of elements. Acc Chem Res 12(8):276–281

Reiher M (2012) Relativistic Douglas–Kroll–Hess theory. Wiley Interdiscip Rev Comput Mol Sci 2:139–149

Rustad JR, Bylaska EJ, Jackson VE, Dixon DA (2010) Calculation of boron-isotope fractionation between $B(OH)_3$(aq) and $B(OH)_4^-$(aq). Geochim Cosmochim Acta 74:2843–2850

Schuchardt KL, Didier BT, Elsethagen T, Sun L, Gurumoorthi V, Chase J, Li J, Windus TL (2007) Basis set exchange: a community database for computational sciences. J Chem Inf Model 47:1045–1052

Stewart JJP (2013) Optimization of parameters for semiempirical methods VI: more modifications to the NDDO approximations and re-optimization of parameters. J Mol Model 19:1–32

Tomasi J, Mennucci B, Cammi R (2005) Quantum mechanical continuum solvation models. Chem Rev 105:2999–3094

Wilson S (1988) Methods in computational chemistry, Relativistic effects in atoms and molecules, vol 2. Plenum Press, New York

Yang J, Hu W, Usvyat D, Matthews D, Schuetz M, Chan GK-L (2014) Ab initio determination of the crystalline benzene lattice energy to sub-kilojoule/mole accuracy. Science 345:640–643

Achondrites

Akira Yamaguchi[1,2], Jean-Alix Barrat[3] and Richard Greenwood[4]
[1]Antarctic Meteorite Research Center, National Institute of Polar Research, Tokyo, Japan
[2]Department of Polar Science, School of Multidisciplinary Science, SOKENDAI (The Graduate University for Advanced Studies), Tokyo, Japan
[3]U.B.O.-I.U.E.M, CNRS UMR 6538 (Domaines Océaniques), Plouzané, France
[4]Planetary and Space Sciences, Department of Physical Sciences, The Open University, Milton Keynes, UK

Definition

Achondrites are meteorites that formed by varying degrees of melting and differentiation on their parent bodies. They are divided into asteroidal and planetary achondrites. Asteroidal achondrites are remnants of differentiated planetesimals and protoplanets that existed shortly after the formation of the Solar System. They are partially to totally melted rocks. Planetary achondrites represent material derived from large planetary bodies (the Moon and Mars) and formed by complex igneous processing.

Introduction

This section covers achondrites and achondritic clasts in stony-iron meteorites (Table 1). Achondrites comprise ~6% of the global collection. Achondrites were derived either from asteroids (asteroidal achondrites) or larger planetary bodies (planetary achondrites). Asteroidal achondrites are broadly classified into primitive and differentiated types. Primitive achondrites experienced partial melting and preserve isotopic and some chemical signatures of their precursor chondritic materials (Fig. 1). They include the acapulcoite-lodranite clan, the winonaites and silicate inclusions in IAB-IIICD irons, achondritic inclusions in IIE irons, brachinites, and ureilites. Differentiated achondrites are igneous rocks with highly fractionated compositions. They include the HED meteorites (acronym of Howardites, Eucrites, and Diogenites), angrites, aubrites, and mesosiderite silicate clasts. The petrologic characteristics and oxygen isotopic homogeneity of these groups (Fig. 1) indicates that their parent bodies experienced global-scale melting. Asteroidal achondrites originated from planetesimals and protoplanets that accreted shortly after the formation of the Solar System. Planetary achondrites, include lunar and Martian meteorites and formed in large part from a wide variety of magmas produced as a result of complex igneous processing. They generally have much younger ages than those of asteroidal achondrites. Modern classification schemes for achondrites are presented by Hutchison (2004), Weisberg et al. (2006), Krot et al. (2014), and Mittlefehldt (2014). Detailed information for individual achondrite groups is provided in the review papers of Benedix et al. (2014), Goodrich et al. (2004), Greenwood et al. (2012), Keil (2010, 2012, 2014), Korotev (2005, 2016), McSween and McLennan (2014), Mittlefehldt et al. (1998), Mittlefehldt (2014, 2015), Warren and Taylor (2014), and the Meteoritical Bulletin Database (2016). The descriptions of individual achondrite groups below are given in approximate order of differentiation, from least melted to most extensively melted.

Acapulcoites and Lodranites

Isotopic and petrological evidence indicates that the acapulcoites and lodranites were derived from a single parent body (e.g., McCoy et al. 1997). Acapulcoites and lodranites are equigranular, recrystallized rocks composed of orthopyroxene, olivine, diopside, plagioclase, Fe,Ni metal, schreibersite, troilite, whitlockite, Cl-apatite, chromite, and graphite. The constituent minerals are similar to those in ordinary chondrites. Acapulcoites are finer-grained (150–230 μm) with chondritic abundance of major minerals and lodranites are coarser-grained (340–700 μm) and depleted in troilite and plagioclase. Mg# (= 100× molar Mg/(Mg + Fe)) of mafic minerals (olivine $Fa_{3–13}$) are higher than those of ordinary chondrites. Acapulcoites and lodranites are considered to be residues after ~10–20% partial melting. The degree of partial melting is significantly higher in the lodranites than in the acapulcoites.

Winonaites and Silicate Clasts in IAB and IIICD Irons

Winonaites and silicate clasts in IAB and IIICD irons may have originated from the same source based on their similar oxygen isotopic and mineralogical compositions (e.g., Benedix et al. 1998). Winonaites are fine- to medium-grained (55–230 μm) equigranular rocks mainly composed of olivine and pyroxene and are petrologically similar to acapulcoites and lodranites. Minor minerals include schreibersite, daubréelite, and alabandite. The Mg# values of mafic minerals (olivine $Fa_{1–8}$) are between H and E chondrites and are higher than those of the acapulcoite-lodranite clan. Most are unbrecciated rocks. Some contain relict chondrules. Winonaites and IAB inclusions experienced partial melting of both Fe, Ni-FeS, and silicate materials.

Achondrites, Table 1 Characteristics of major groups of achondrites and achondritic clasts in stony-iron meteorites

Group	Textures	Major minerals	Fa in olivine	$\Delta^{17}O$	Statistics[a]	Petrogenesis
Asteroidal achondrites						
Primitive achondrites						
Acapulcoites-lodranites	Equigranular	ol, px, feld, FeNi-FeS	3–13	−1.39 to −0.81	0.26%	Partial melting
Winonaites	Equigranular	ol, px, feld, FeNi-FeS	1–8	−0.60 to −0.24	0.05%	
Brachinites	Granular	ol, px	30–35	−0.39 to −0.11	0.07%	
Ureilites	Granular	px, ol	3–26 (cores)	−2.45 to −0.35	0.79%	
IIE silicates (achondritic)	Equigranular	px, ol, FeNi-FeS	15–20	0.63–0.78		
Differentiated achondrites						
Angrites	Igneous	Ca-Al-Ti px, ol	Vary widely	−0.003 to −0.042	0.04%	Global-scale melting (magma ocean?)
Aubrites	Coarse-grained	px, ol	0	−0.02 to 0.08	0.14%	
HED meteorites					3.17%	
Howardites	Brecciated		Vary widely			
Eucrites	Brecciated, basaltic/gabbroic	px, feld, sil		−0.246 to −0.230		
Diogenites	Brecciated, coarse-grained	px, ol	27–35	−0.247 to −0.231		
Mesosiderites	Brecciated	px, pl, ol, FeNi-FeS	8–42	−0.265 to −0.231	0.42%	
Main-group pallasites	Coarse-grained	ol, px, FeNi-FeS	11–18	−0.194 to −0.165	0.10%	
Planetary achondrites						
Lunar meteorites				−0.012 to 0.018	0.45%	Complex igneous processing (wide variety of magmas)
Feldspathic	Brecciated	pl, px, ol	Vary widely			
Mingled	Brecciated		Vary widely			
Mare	Brecciated, basaltic	px, pl	Vary widely			
Martian meteorites				0.300–0.327	0.31%	
Basaltic shergottites	Basaltic	px, pl				
Iherzolitic shergottite	Coarse, poikilitic		34–40			
Nakhlites	Coarse-grained	px	70–83			
Chassignites	Coarse-grained	ol	21–47			
ALH 84001	Coarse-grained	px				
NWA 7533, 7034 etc.	Brecciated					

[a]Statistics of approved meteorite fall and finds. Total number of meteorites is 52,782 (as of Jan 4, 2016)

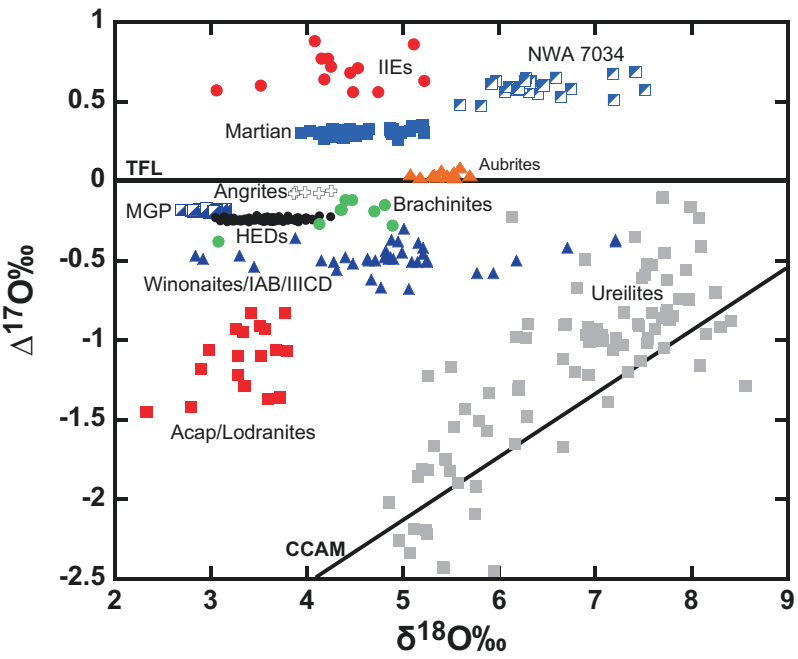

Achondrites, Fig. 1 Oxygen isotopic compositions of achondrites. *TFL* terrestrial fractionation line, *CCAM* carbonaceous chondrite anhydrous minerals

Brachinites

Brachinites are olivine-rich rocks (dunitic or wehrlites) (olivine: 73–93 vol%, $Fa_{27–36}$), with minor to trace amounts of augite, plagioclase, orthopyroxene, chromite, Fe-sulfide, phosphates, and Fe,Ni metal. The brachinite group is poorly defined, such that there are many petrologically similar, "brachinite-like" achondrites, such as *Divnoe*, whose relationship with the brachinite group is presently unknown. Brachinites have lithophile and siderophile element abundances that display variable depletions compared to chondrites. The presence of a lineation and foliation defined by alignment of olivine in some brachinites and *Divnoe* suggests that they may have formed as igneous cumulates. Feldspar-rich meteorites, GRA 06128 and 06129 could be genetically related to brachinites (Day et al. 2012).

Ureilites

Ureilites are the second largest group of achondrites after the HED meteorites. Ureilites are ultramafic rocks mainly composed of olivine and pyroxene with interstitial carbon-bearing phases (<5 vol%). The proportion of olivine and pyroxene varies widely. Minor minerals include carbon polymorphs (graphite, diamond, lonsdaleite, and chaoite), Fe,Ni metal (kamacite), and exceptionally chromite and plagioclase. Most ureilites are unbrecciated. Except for rims and veins in olivine, silicates (i.e., olivine cores and pyroxenes) are quite uniform in Fe/Mg ratios within any given ureilite. However, compositions from one sample to another exhibit considerable variation, as shown by the olivine-cores, which range from Fa_3 to Fa_{26}. Mineralogical evidence indicates that ureilites equilibrated at high temperatures (1200–1300 °C) and subsequently experienced rapid cooling, consistent with impact-excavation or disruption of their parent body (Takeda 1987). A few ureilites are fragmental breccias composed of typical monomict ureilite clasts, plus a variety of other lithic clasts and mineral fragments.

Compared to chondrites, bulk ureilites are depleted in Al and have fractionated rare earth element (REE) patterns. Refractory siderophile elements are roughly chondritic (~0.1–2× CI). Ureilites retain high concentrations of fractionated planetary type noble gases. Oxygen isotopic compositions plot close to the carbonaceous chondrite anhydrous mineral (CCAM) line.

Ureilites are residues after >15% partial melting. Feldspathic clasts found in some polymict ureilites, including the Almahata Sitta fall, are remnants of lavas extracted from ureilites.

IIE Silicate Clasts

IIE iron meteorites contain a wide variety of silicate inclusions from primitive, chondritic to highly differentiated (basaltic partial melts) types (Mittlefehldt et al. 1998). Oxygen isotopic compositions indicate a genetic relationship between IIE silicate clasts and the H chondrites. The silicate clasts give a range of radiometric dates, from ~3.7–4.5 Ga, which may represent impact ages. There are two principal end member models for the origin of the IIE silicate clasts, endogenous igneous processes, or impact melting of an H chondritic parent body (McDermott et al. 2016).

Angrites

Angrites are a small group of achondrites with an unusual mineralogy and bulk composition. Their oxygen isotopic compositions fall on a well-constrained mass fractionation line consistent with a high degree of partial melting (Greenwood et al. 2005). They are medium to coarse-grained igneous, unbrecciated rocks mainly composed of Ca-Al-Ti rich pyroxene, Ca-rich olivine, anorthositic plagioclase and a range of minor minerals including: spinel, troilite, kirschteinite, whitlockite, titanomagnetite, and Fe, Ni metal. They are subdivided into plutonic and volcanic varieties. Angrites are highly depleted in alkali elements but are not very depleted in the highly volatile elements (e.g., Br, Se, Zn, In, and Cd). Although they are unbrecciated, angrites contain moderate abundances of siderophile elements. Angrites are believed to have formed by partial melting of primitive sources under oxidizing conditions. However, an impact melt origin has been proposed to account for their relatively high abundance of siderophile elements (Riches et al. 2012). Angrites are known to be amongst the most ancient basalts in the Solar System (Schiller et al. 2015).

Aubrites

Aubrites (or enstatite achondrites) are the most reduced achondrites. They comprise unbrecciated rocks, as well as regolith and fragmental breccias. They mainly consist of nearly FeO-free enstatite (75–98 vol%) with variable amounts of plagioclase, high-Ca pyroxene, and forsterite. Other constituent phases include Si-bearing Fe,Ni metal, oldhamite, daubréelite, ferroan alabandite, caswellsilverite, djerfisherite, niningerite, and schreibersite. Aubrites are igneous rocks formed by melting and differentiation of enstatite chondrite-like precursors. However, their relationship with known enstatite chondrites has not yet been established.

HED Meteorites

HED meteorites represent the largest group of achondrites. Monomict or unbrecciated eucrites and diogenites have essentially the same oxygen isotopic compositions ($\Delta^{17}O$), indicating that they are derived from a single source (Greenwood et al. 2015), probably asteroid 4 Vesta. Eucrites are divided into basaltic (noncumulate) and cumulate eucrites. They are mainly composed of pyroxene and plagioclase; minor phases include silica minerals, ilmenite, chromite, troilite, Fe,Ni metal, and Ca-phosphates (apatite and merrillite). Trace minerals include baddeleyite and zircon. Basaltic eucrites, which experienced varying degrees of shock and thermal metamorphism, are subdivided into four chemical groups (trends): main group, Nuevo Laredo trend, Stannern-trend, and residual eucrites (e.g., Yamaguchi et al. 2009). Diogenites are orthopyroxenites or harzburgites (olivine abundances up to 80 vol%). Most of them are brecciated, coarse-grained rocks and recrystallized breccias. They are composed of orthopyroxene and olivine, with minor chromite, silica minerals, and Fe,Ni metals.

HED polymict breccias are divided into polymict eucrites, howardites, and polymict diogenites (Delaney et al. 1983). The boundaries between these various types are not clear and form a continuum with respect to different types of lithic clasts and mineral fragments. Polymict eucrites contain >90 vol% eucritic clasts and polymict diogenites contain >90 vol% diogenitic clasts. The polymict breccias may contain minor exotic materials, such as chondritic clasts and Fe, Ni metals.

Geochemical evidence suggests that basaltic eucrites are residual melts after extensive fractional crystallization in a magma ocean (e.g., Righter and Drake 1997). The origin of diogenites seems to be more complex. They may have formed as cumulates after magma ocean crystallization, or alternatively crystallized in intrusions within the early-formed eucritic crust (Barrat et al. 2008). It is likely that eucrites and diogenites crystallized shortly after the formation of the Solar System. In a similar manner to lunar crustal rocks, their parent body experienced a heavy meteorite bombardment from ~4.4–3.0 Ga that resulted in the formation of most HED polymict breccias (Bogard 2011).

Mesosiderites

Mesosiderites are polymict breccias (stony-irons) consisting of silicates and Fe,Ni metal (>20 vol%). The silicate clasts are very similar to HED meteorites. Mesosiderites are classified into three petrologic classes on the basis of increasing orthopyroxene abundances, from A (basaltic) to B (more ultramafic) to C (orthopyroxenites). They are also subdivided into four metamorphic grades based on silicate textures, from grade 1 (lowest) to 4 (highest). The silicate fraction consists of mineral and lithic clasts in a fine-grained (recrystallized) or igneous matrix. The most common types are basalts, gabbros, and orthopyroxenites. Basaltic and gabbroic clasts are petrologically similar to eucrites. However, some basaltic clasts have low FeO/MnO in mafic silicates and show extreme REE depletions with very large positive Eu anomalies. The composition of Fe,Ni metal is roughly similar to that of the IIIAB irons. HED meteorites and mesosiderite silicates have identical oxygen isotopic compositions, consistent with a common source (e.g., Greenwood et al. 2015). Petrologic and geochemical features of mesosiderite silicate clasts can be explained by complex igneous processes or by metamorphism and partial melting resulting from metal-silicate mixing on a parent body similar to Vesta (Table 1).

Pallasites

Pallasites consist of subequal amounts of silicate (mostly, olivine) and Fe,Ni metal. Minor minerals include troilite, chromite, schreibersite, pyroxene, phosphates, and phosphoran olivine (Bosenberg et al. 2012). Sizes of individual olivine grains are up to a few centimeter. They are divided into main group pallasites, the Eagle Station group, the pyroxene pallasite grouplet, and ungrouped pallasites (e.g., *Milton*). They have distinct oxygen isotopic, mineral, and metal compositions. Pyroxene pallasites contain pyroxene (<3 vol%). It is widely thought that pallasites formed by mixing of molten Fe,Ni metal from the core of one asteroid with mantle from another differentiated asteroids. Based on oxygen isotopic compositions, the pallasites are derived from at least five parent bodies.

Lunar Meteorites

Lunar meteorites are crustal rocks from the Moon. They are divided into feldspathic breccias, mixed breccias of basalts and anorthosites, KREEP-rich (K, Rare Earth Elements, and P) breccias, and mare basalts. Feldspathic breccias are mostly composed of plagioclase with minor olivine and pyroxene and have high Al_2O_3 (26–31%), low FeO (3–6%), and low incompatible elements. Mare basalts have high FeO (18–22%) and moderately low Al_2O_3 (8–10%) (Korotev 2005). KREEP-rich breccias have very high concentrations of incompatible elements.

Lunar meteorites provide a more representative sampling of the lunar crust than the samples obtained by Apollo and Russian Luna missions that collected rocks and regoliths almost exclusively from the equatorial regions of the Procellarum KREEP Terrane. Feldspathic breccias represent ancient lunar crust that formed ~4.4–4.5 Ga. The precursors to the feldspathic breccias may originally have been cumulate

rocks that floated on the top of a global magma ocean. KREEP-rich rocks are contaminated with the final dregs of the magma ocean. Alternative models for crust formation, such as serial volcanisms, have also been suggested. Almost all highland rocks were brecciated during the cataclysmic bombardment ~3.9 Ga. Mare basalts formed during later volcanism and continued to ~1.2 Ga on the basis of remote-sensing data (Hiesinger et al. 2003).

Martian Meteorites

Martian meteorites are crustal rocks from Mars. They are shergottites, nakhlites, chassignites, orthopyroxenite (*ALH 84001*), and polymict breccias (e.g., *NWA 7034* and paired rocks) (Agee et al. 2013; Humayun et al. 2013). The former three were collectively called "SNC meteorites." Shergottites are divided into basaltic, lherzolitic, and olivine-phyric types and mainly consist of pyroxene, maskelynite (transformed from plagioclase), and minor minerals. Nakhlites are clinopyroxenites. Chassignites are dunites. Basaltic and olivine-phyric shergottites, and nakhlites are volcanic rocks formed in lava flows. Other SNC meteorites are plutonic rocks. The polymict breccias are compositionally similar to Martian regolith and have an oxygen isotopic composition distinct from other Martian meteorites. Some Martian meteorites experienced aqueous alteration after crystallization. The ages are generally younger than those of asteroidal achondrites varying from 4.4–0.2 Ga (Nyquist et al. 2001; Humayun et al. 2013).

Ungrouped Achondrites

There are ~70 ungrouped achondrites consisting of ~30 "groups." The largest group is similar to brachinites ("brachinite-like"). There are 17 basaltic achondrites that are petrologically similar to basaltic eucrites but have distinct O-isotopic compositions (e.g., *NWA 011*). These meteorites could have been derived from the crust of differentiated bodies similar to Vesta. *NWA 6704* and paired rocks are orthopyroxenites. *NWA 7325* and paired rocks are olivine gabbros and have a reduced mineralogy. These rocks formed from an unusual melt characterized by very low REE abundances and a very large positive Eu anomaly, generated by the remelting of an ancient gabbroic lithology (Barrat et al. 2015).

Summary

Achondrites represent samples from several tens of differentiated asteroids. Asteroidal achondrites record early differentiation of planetesimals that took place a few million years after the formation of the solar system. Planetary achondrites provide important information about the differentiation processes that took place on larger bodies. The number of achondrite samples is currently expanding rapidly, due in large part to ongoing collection activities in hot and cold desert regions. These new samples provide a wealth of evidence concerning the magmatic and metamorphic processes that took place on their parent bodies.

Cross-References

- ▶ Iron Meteorites
- ▶ Meteorites

References

Agee CB, Wilson NV, McCubbin FM, Ziegler K, Polyak VJ, Sharp ZD, Asmerom Y, Nunn MH, Shaheen R, Thiemens MH, Steele A, Foel ML, Bowden R, Glamoclija M, Zang Z, Elardo SM (2013) Unique meteorite from early Amazonian Mars: water-rich basaltic breccia Northwest Africa 7034. Science 339:780–785

Barrat JA, Yamaguchi A, Zanda B, Bollinger C, Bohn M (2008) Relative chronology of crust formation on asteroid Vesta: insights from the geochemistry of diogenites. Geochim Cosmochim Acta 74:6218–6231

Barrat JA, Greenwood RC, Verchovsky AB, Gillet P, Bollinger C, Langlade JA, Liorzou C, Franchi IA (2015) Crustal differentiation in the early solar system: clues from the unique achondrite Northwest Africa 7325 (NWA 7325). Geochim Cosmochim Acta 168:280–292

Benedix GK, McCoy TJ, Keil K, Bogard DD, Garrison DH (1998) A petrologic and isotopic study of winonaites: evidence for early partial melting, brecciation, and metamorphism. Geochim Cosmochim Acta 62:2535–2553

Benedix GK, Haack H, McCoy TJ (2014) Iron and stony-iron meteorites. In: Davis AM (ed) Treatise on geochemistry, vol 1, 2nd edn. Elsevier, Amsterdam, pp 267–285

Bogard DD (2011) K-Ar ages of meteorites: clues to parent-body thermal histories. Chem Erde 71:207–226

Bosenberg JS, Delaney JS, Hewins RH (2012) A petrological and chemical reexamination of Main Group pallasite formation. Geochim Cosmochim Acta 89:134–158

Day JMD, Walker RJ, Ash RD, Liu Y, Rumble D III, Irving AJ, Goodrich CA, Tait K, McDonough WF, Taylor LA (2012) Orgin of felsic achondrites graves Nunataks 06128 and 06129 and ultramafic brachinites and brachinite-like achondrites by partial melting of volatile-rich primitive parent bodies. Geochim Cosmochim Acta 81:94–128

Delaney JS, Takeda H, Prinz M, Nehru CE, Harlow GE (1983) The nomenclature of polymict basaltic achondrite. Meteoritics 18:103–111

Goodrich CA, Scott ERD, Fioretti AM (2004) Ureilitic breccias: clues to the petrologic structure and impact disruption of the ureilite parent asteroid. Chem Erde 64:283–327

Greenwood RC, Franchi IA, Jambon A, Buchanan PC (2005) Widespread magma oceans on asteroidal bodies in the early Solar System. Nature 435:916–918

Greenwood RC, Franchi IA, Gibson JM, Benedix GK (2012) Oxygen isotope variation in primitive achondrites: the influence of primordial, asteroidal and terrestrial processes. Geochim Cosmochim Acta 94:146–163

Greenwood RC, Barrat JA, Scott ERD, Haack H, Buchanan PC, Franchi IA, Yamaguchi A, Johnson D, Bevan AWR, Burbine TH (2015) Geochemistry and oxygen isotope composition of main-group pallasites and olivine-rich clasts in mesosiderites: implications for the "Great Dunite Shortage" and HED-mesosiderite connection. Geochim Cosmochim Acta 169:115–136
Hiesinger H, Head JW III, Wolf U, Jaumann R, Neukum G (2003) Ages and stratigraphy of mare basalts in Oceanus Procellarum, Mare Nubium, Mare Cognitum, and Mare Insularum. J Geophys Res 108. doi:10.1029/2002JE001985
Humayun M, Nemchin A, Zanda B, Hewins RH, Grange M, Kennedy A, Lorand J-P, Gopel C, Fieni C, Pont S, Deldicque D (2013) Origin and age of the earliest Martian crust from meteorite NWA 7533. Nature 503:513–517
Hutchison R (2004) Meteorites: a petrologic and isotopic synthesis. Cambridge University Press, Cambridge
Keil K (2010) Enstatite achondrite meteorites (aubrites) and the histories of their asteroidal parent bodies. Chem Erde 70:295–317
Keil K (2012) Angrites, a small but diverse suite of ancient, silica-undersaturated volcanic-plutonic mafic meteorites, and the history of their parent asteroid. Chem Erde 72:191–218
Keil K (2014) Brachinite meteorites: partial melt residues from an FeO-rich asteroid. Chem Erde 74:311–329
Korotev RL (2005) Lunar geochemistry as told by lunar meteorites. Chem Erde 65:297–346
Korotev RL (2016) Lunar meteorites. http://meteorites.wustl.edu/lunar/. Accessed 1 Jan 2016
Krot AN, Scott ERD, Goodrich CA, Weisberg MK (2014) Classification of meteorites and their genetic relationships. In: Davis M (ed) Treatise on geochemistry, vol 1, 2nd edn. Elsevier, Amsterdam, pp 1–63
McCoy TJ, Keil K, Clayton RN, Mayeda TK, Bogard DD, Garrison DH, Wieler R (1997) A petrologic and isotopic study of lodranites: evidence for early formation as partial melt residues from heterogeneous precursors. Geochim Cosmochim Acta 61:623–637
McDermott KH, Greenwood RC, Scott ERD, Franchi IA, Anand M (2016) Oxygen isotope and petrological study of silicate inclusions in IIE iron meteorites and their relationship with H chondrites. Geochim Cosmochim Acta 173:97–113
McSween HY, McLennan SM (2014) Mars. In: Davis AM (ed) Treatise on geochemistry, vol 1, 2nd edn. Elsevier, Amsterdam, pp 251–300
Meteoritical Bulletin Database (2016) https://www.lpi.usra.edu/meteor/metbull.php. Accessed 4 Jan 2016
Mittlefehldt DW (2014) Achondrites. In: Davis AM (ed) Treatise on geochemistry, vol 1, 2nd edn. Elsevier, Amsterdam, pp 235–265
Mittlefehldt DW (2015) Asteroid (4) Vesta: I. The howardite-eucrite-diogenite (HED) clan of meteorites. Chem Erde 75:155–183
Mittlefehldt DW, McCoy TJ, Goodrich CA, Kracher A (1998) Non-chondritic meteorites from asteroidal bodies. In: Papike JJ (ed) Planetary materials, Reviews in mineralogy, vol 36. Mineralogical Society of America, Washington, DC, pp 4.1–4.195
Nyquist LE, Bogard DD, Shih C-Y, Greshake A, Stöffler D, Eugster O (2001) Ages and geologic histories of martian meteorites. Chronol Evol Mars 96:105–164
Riches AJV, Day JMD, Walker RJ, Simonetti A, Liu Y, Neal CR, Taylor LA (2012) Rhenium-osmium isotope and highly-siderophile-element abundance systematics of angrite meteorites. Earth Planet Sci Lett 353–354:208–218
Righter K, Drake MJ (1997) A magma ocean on Vesta: core formation and petrogenesis of eucrites and diogenites. Meteorit Planet Sci 32:929–944
Schiller M, Connelly JN, Glad AC, Mikouchi T, Bizzaro M (2015) Early accretion of protoplanets inferred from a reduced inner solar system ^{26}Al inventory. Earth Planet Sci Lett 420:45–54
Takeda H (1987) Mineralogy of Antarctic ureilites and a working hypothesis for their origin and evolution. Earth Planet Sci Lett 81:358–370
Warren PH, Taylor GJ (2014) The moon. In: Davis AM (ed) Treatise on geochemistry, vol 1, 2nd edn. Elsevier, Amsterdam, pp 559–599
Weisberg MK, McCoy TJ, Krot AN (2006) Systematics and evaluation of meteorite classification. In: Lauretta DS, McSween HY Jr (eds) Meteorite and early solar system II. The University of Arizona Press, Tucson, pp 19–52
Yamaguchi A, Barrat JA, Greenwood RC, Shirai N, Okamoto C, Setoyanagi T, Ebihara M, Franchi IM, Bohn M (2009) Crustal partial melting on Vesta: evidence from highly metamorphosed eucrites. Geochim Cosmochim Acta 73:7162–7182

Acid Deposition

Gregory B. Lawrence
New York Water Science Center, U.S. Geological Survey, Troy, NY, USA

Definition

Acid deposition, often referred to as acid rain, is a term used to describe the deposition of pollutant-derived chemical compounds from the atmosphere to the Earth's surface. These compounds result from emissions produced by fossil fuel combustion for energy production and vehicular use and from agricultural practices that create air pollution. Some of the pollutants can be deposited relatively close to the emission source, but others can be transported hundreds of miles from the source before being deposited. Much of the acid deposition occurs in a strongly acidic form as sulfuric or nitric acid (H_2SO_4 or HNO_3), but some compounds are deposited in nonacidic forms that can be transformed into acids through complex ecosystem processes. In particular, nitrogen deposited as NH_3 or nitrogen oxides (NO_x) can be converted to HNO_3 through a series of biochemical transformations involving both plants and microbes.

Landscape Sensitivity to Acid Deposition

Deposition occurs in the form of rain, snow, and sleet (termed wet deposition) when precipitation is occurring, as well as particles and gases (termed dry deposition) and fog (termed cloud deposition). Some acid deposition falls directly onto water surfaces, but because the surface area of freshwater lakes and streams is small relative to the surface area of land (less than 7% in the United States), the vast majority of acid deposition interacts with terrestrial ecosystems before reaching surface waters. This is a key factor, because the geochemical makeup of soil and underlying till and bedrock determines the impact that acid deposition will have on both terrestrial and aquatic ecosystems.

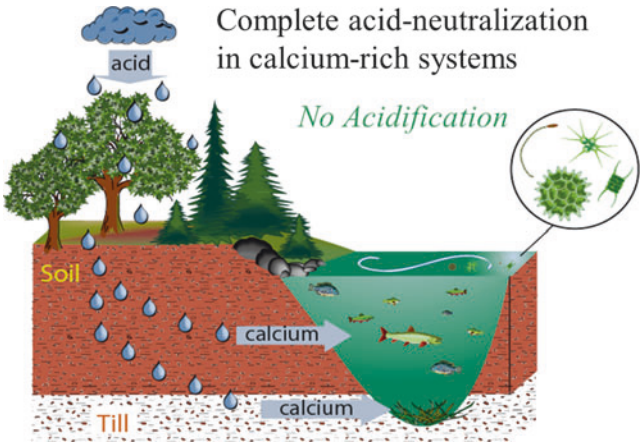

Acid Deposition, Fig. 1 Landscapes with abundant Ca in the soil and subsoil (till in glaciated regions, weathered bedrock or saprolite in unglaciated regions) effectively neutralize acid deposition, preventing harmful effects to terrestrial and aquatic ecosystems

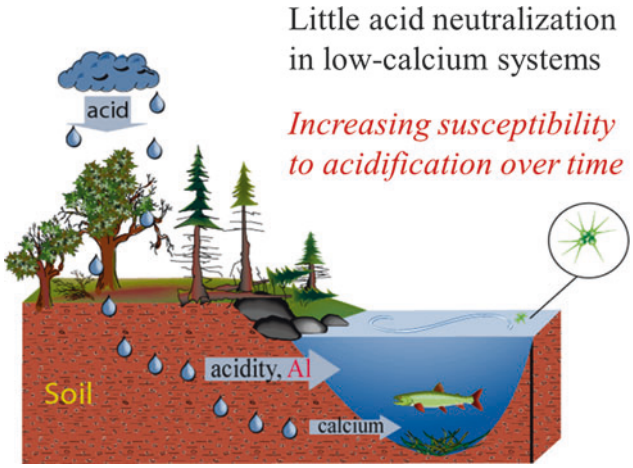

Acid Deposition, Fig. 2 Landscapes developed from slowly weathering rocks with low Ca content have limited acid-neutralizing ability. Acid deposition depletes the naturally low levels of Ca causing acidification of soils and surface waters

As deposited acids move in solution through soil and deeper pathways en route to surface waters, they can be neutralized through (1) the consumption of H^+ by dissolution of minerals; (2) electrostatic exchange between H^+ and base cations that are adsorbed to particle surfaces such as calcium (Ca), magnesium (Mg), sodium (Na), and potassium (K); (3) adsorption of SO_4^{2-} to soil particles (particularly in non-glaciated soils); (4) uptake of nitrate by vegetation; and (5) conversion of deposited nitrogen into gaseous N_2 (termed denitrification). If the soil and subsoil are rich in base cations, such as those derived from carbonates, acid deposition will be fully neutralized with little or no effects on aquatic and terrestrial ecosystems (Fig. 1). However, some landscapes are derived from bedrock types such granite or gneiss, which weather slowly and are comprised of minerals poor in base cations. In these landscapes, the limited buffering of acid inputs is not sufficient to prevent surface water acidification (Fig. 2). For this reason, the impact of acid deposition can vary from little or no effect on soils and surface waters to severe acidification depending upon the mineralogical composition of the predominant rock types of the landscape. Upland areas that are typically forested most often have bedrock types with limited ability to neutralize acids. This characteristic plus high levels of precipitation make these areas the most susceptible to acid deposition. The rate of acid deposition plays an important role in determining the severity of effects. Proximity to emission sources and location relative to prevailing winds are important factors in determining the levels of acidic deposition to which an area is exposed.

History of Acid Deposition Effects

Negative environmental effects of air pollution from fossil fuel combustion were documented for areas of central and northern Europe, and for eastern North America by the mid-1900s, and for eastern Europe and Southeast Asia by the late 1900s. However, acidification of surface waters first became apparent in Scandinavia in the 1960s and in North America in the 1970s from observations of fish kills. It's estimated that acid deposition levels peaked throughout eastern North America (Driscoll et al. 2001) and much of Northern Europe during the 1970s (Wright et al. 2005). The data collected by the National Atmospheric Deposition Program, established in the late 1970s to monitor acid deposition throughout the United States, showed that sulfur deposition decreased by as much as 70% from 1980 to 2010 (http://nadp.sws.uiuc.edu/; accessed March 5, 2017) with similar or larger decreases achieved in Europe, largely as a result of various forms of government legislation that reduced air pollution, such as the 1970 Clean Air Act Amendments in the United States.

Effects of acid deposition on aquatic ecosystems caused widespread concern that led to a rapid development of monitoring and research programs. Fish as well as many other forms of aquatic life were found to be sensitive to the decreased pH, but the primary toxicant was identified as inorganic monomeric aluminum (Al), a group of aluminum compounds released from the soil by the acid deposition. Although Al occurs naturally in the soil, it is not converted into harmful forms without the addition of acidic deposition. In the early stages of acid deposition research, the importance of acidity derived from atmospheric pollution was questioned relative to natural acidity produced by decomposition of plant material (Krug and Frink 1983). This natural organic acidity was found to be a significant factor in lowering the pH of some surface waters, and organic acids moving through soil were known to mobilize Al (Fakhraei and Driscoll 2015). However, through the process of organic acid mobilization,

Al becomes complexed with organic anions, rendering it innocuous to aquatic ecosystems. In sharp contrast, the strong mineral acids (H_2SO_4 and HNO_3) that comprise acid deposition release Al in several inorganic forms that negatively impact all levels of the aquatic food chain. As a result, surface waters in many poorly buffered regions became episodically or chronically toxic to aquatic biota, thereby degrading aquatic ecosystems and rendering some lakes and streams incapable of supporting fish populations.

Terrestrial effects of acid deposition were first suggested by mass die-offs of red spruce (*Picea rubens* Sarg.) trees in the mountains of the Northeastern US and Norway spruce (*Picea abies* H. Karst.) in countries such as Germany and the Czech Republic the early 1980s. Some forests lost up to 50% of the trees without any apparent natural cause. By the 1990s elevated mortality of red spruce was also being seen at relatively low elevations in the United States, such as the Western Adirondack Region of New York (Lawrence et al. 1997). Research through the 1980s and 1990s focused on direct effects of acid deposition on foliage. Extensive periods of acidic fog at high-elevation sites were found to damage spruce needles, which eventually led to mortality. However, a widely cited paper published in 1988 (Shortle and Smith 1988) drew the first link between red spruce decline and acid deposition effects on soils. At that time, effects of acid deposition on soils were unclear, but this study spurred increased research on possible soil effects of acid deposition. Eventually, the primary cause of widespread red spruce decline was determined to be depletion of soil calcium from enhanced leaching by acid deposition (Schaberg et al. 2001).

The Key Role of Soils

Possible effects on soils had been suspected soon after the discovery of acid deposition, but without soil data that predated the onset of the problem, knowledge of soil effects was limited largely to theory. In the early 1980s, a renowned German soil scientist developed the conceptual model of how acid deposition affected soils through a three-stage process (Ulrich 1983). In the first stage, release of base cations through weathering of primary and secondary minerals is sufficient to fully buffer the elevated inputs of acids. However, in soils with small amounts of rapidly weatherable minerals, due to long-term natural weathering, or in soils developed from slowly weathering silicate minerals, the rate of acid buffering from weathering could be exceeded by the rate of acid inputs from acid deposition. This condition leads to phase 2 in which buffering of acid deposition would be dependent on exchange between base cations adsorbed to soil particle surfaces and protons (H^+) in soil solution. Replenishment of adsorbed base cations is ultimately dependent on weathering, so if acid deposition levels exceed weathering rates, the buffering of acidity through cation exchange will lead to depletion of exchangeable base cations. This condition leads to phase 3 in which buffering of acidity shifts to release of inorganic Al to soil solution. Once in solution, various chemical species of inorganic Al become mobile in association with SO_4^{2-} and NO_3^-, enabling movement from soils to surface waters.

Ulrich's theory explained the acidification of surface waters, and by the early 2000s, data from soil resampling studies showed that depletion of exchangeable Ca concentrations was common in regions where surface water acidification occurred (Warby et al. 2009). The link between soil Ca depletion and Al mobilization was fully confirmed with archived soils from northwestern Russia that showed depletion of exchangeable Ca between 1926 and 1964, followed by little further Ca depletion, but a pronounced mobilization of Al from 1964 to 2001 (Lawrence et al. 2005). Quantification of these soil changes resulting from acidification was an important step to aid in the assessment of ecosystem recovery responses from declining acid deposition levels.

Once it had been established that acid deposition had depleted soils of Ca, research on ecosystem effects of acid deposition expanded beyond acidification to evaluate the direct effects of decreased Ca availability. Because Ca is an essential nutrient for plants and animals, depletion of soil Ca can have negative effects on both terrestrial and aquatic species. In addition to red spruce mortality, loss of soil Ca has also been linked to decreased growth and increased mortality of sugar maple trees, decreases in abundance of some songbird species, decreased abundance and diversity of terrestrial snails, and negative effects on zooplankton in lakes and benthic algae in streams (Lawrence et al. 2016).

The Status of Recovery from Acid Deposition in 2017

The large decrease in acid deposition levels in North America dating back to the early 1980s led to partial recovery of surface waters in the late 1990s. The most pronounced change has been the decrease in inorganic Al concentrations, although recovery has also been seen with increases in pH and acid-neutralizing capacity (Driscoll et al. 2001). Nevertheless, in 2017, surface waters that experience toxic levels of inorganic Al during periods of high stream flow remained common in the most acid-sensitive landscapes. Furthermore, increases in the organic acidity of surface waters that have occurred during the period of recovery have slowed the increase of pH and ANC, although this response is likely to represent a return to pre-acid deposition conditions and therefore is likely to be tied to recovery (Monteith et al. 2007).

Evidence of soil recovery from acidification effects was first shown in a study covering a large region of the Northeastern United States and eastern Canada (Lawrence et al. 2015). Sites

showing the greatest decrease in acid deposition also showed the strongest recovery response. Decreases in Al in surface or near-surface organic soils indicated that Al mobilization had decreased markedly and decreases in Ca were no longer seen. However, the soil recovery identified in 2015 must be considered to be in its early phase. In the upper mineral soil, Al continues to show increases. Although this increase could indicate further acidification, it may also indicate a recovery phase as Al moves downward from the organic horizons to be immobilized in the upper mineral soil (Lawrence et al. 2015). The widespread decreases in surface water Al concentrations support the interpretation that Al has become less mobile within the soil profile. Overall, monitoring of soils and waters indicates continued progress toward full recovery, but uncertainties remain regarding the rate at which soils will recover, and these uncertainties carry over into the chemical recovery surface waters. Biological recovery of terrestrial and aquatic ecosystems remains dependent on chemical recovery and therefore has also shown limited recovery. The legacy of acid deposition effects on terrestrial and aquatic ecosystems seen in 2017 is likely to persist over future decades.

Cross-References

- ▶ Acid–Base Reactions
- ▶ Aluminum
- ▶ Calcium
- ▶ Chemical Weathering
- ▶ Nitrogen Cycle
- ▶ Soils
- ▶ Sulfur
- ▶ Water

References

Driscoll CT, Lawrence GB, Bulger AJ, Butler TJ, Cronan CS, Eagar C, Lambert KF, Likens GE, Stoddard JL, Weathers KC (2001) Acidic deposition in the northeastern United States: sources and inputs, ecosystem effects, and management strategies. Bioscience 51(3):180–198

Fakhraei H, Driscoll CT (2015) Proton and aluminum binding properties of organic acids in surface waters of the northeastern, USA. Environ Sci Technol 49:2939–2947

Krug JC, Frink (1983) Acid rain on acid soil: a new perspective. Science 221:520–525

Lawrence GB, Burns DA, Riva-Murray K (2016) A new look at liming as an approach to accelerate recovery from acidic deposition effects. Sci Total Environ 562:35–46

Lawrence GB, David MB, Bailey SW, Shortle WC (1997) Assessment of calcium status in soils of red spruce forests in the northeastern United States. Biogeochemistry 38:19–39

Lawrence GB, Hazlett PW, Fernandez IJ, Ouimet R, Bailey SW, Shortle WC, Smith KT, Antidormi MR (2015) Declining acidic deposition begins reversal of forest-soil acidification in the northeastern U.S. and eastern Canada. Environ Sci Technol 49:13103–13111

Lawrence GB, Lapenis AG, Berggren D, Aparin BF, Smith KT, Shortle WC, Bailey SW, Varlyguin DL, Babikov B (2005) Climate dependency of tree growth suppressed by acid deposition effects on soils in Northwest Russia. Environ Sci Technol 39:2004–2010

Monteith DT, Stoddard JL, Evans CD, de Wit HA, Forsius M, Hogasen T, Wilander A, Skjelkvale BL, Jeffries DS, Vuorenmaa J, Keller B, Kopacek J, Vesely J (2007) Dissolved organic carbon trends resulting from changes in atmospheric deposition chemistry. Nature 450:537–541

Schaberg PG, DeHayes DH, Hawley GJ (2001) Anthropogenic calcium depletion: a unique threat to forest ecosystem health? Ecosyst Health 7:214–228

Shortle WC, Smith KT (1988) Aluminum-induced calcium deficiency syndrome in declining red spruce. Science 240(4855):1017–1018

Ulrich B (1983) Soil acidity and its relations to acid deposition. In: Ulrich B, Pankrath J (eds) Effects of accumulation of air pollutants in forest ecosystems. D. Reidel, Dordrecht, pp 127–146

Warby RAF, Johnson CE, Driscoll CT (2009) Continuing acidification of organic soils across the northeastern USA: 1984–2001. Soil Sci Soc Am J 73:274–284

Wright RF, Larssen T, Camarero IL, Cosby BJ, Ferrier RC, Helliwell R, Forsius M, Jenkins A, Kopacek J, Maier V, Moldan F, Posch M, Rogora M, Schopp W (2005) Recovery of acidified European surface waters. Environ Sci Technol 39:64a–72a

Acid–Base Reactions

Carl O. Moses
Provost and Vice President for Academic Affairs, Grand View University, Des Moines, IA, USA

Acid–base concepts provide one of the most important and enduring foundations for correlating chemical reactivity. A *general theory* of acid–base reactivity has yet to be developed but, in fact, there may be little need in view of the utility of the various concepts that provide a framework for understanding and, in many cases, quantitatively accounting for or predicting chemical reactivity. Several such frameworks are available, but this entry focuses on two concepts that have contributed significantly to geochemistry: Brønsted-Lowry acidity and Lewis acidity. In addition to reactions in aqueous solution (the focus of this entry), both Brønsted-Lowry and Lewis acid–base reactions occur at the interface between mineral surfaces and aqueous solutions. Surface acidity and the consequent formation of surface complexes constitute a very active area of current research (see ▶ "Surface Geochemistry"), owing to the fundamental importance of acid–base reactivity in explaining and correlating processes (e.g., dissolution and precipitation, ion exchange, catalysis) in heterogeneous systems (Huang 1981; Schindler 1981; Davis and Kent 1990; Stumm 1992).

Originally published in : Marshall CP, Fairbridge RW (eds) Encyclopedia of Geochemistry, Springer Netherlands, 1999

The Braønsted-Lowry Concept

The most familiar acid–base concept is the Brønsted-Lowry definition: an acid donates a proton (i.e., hydrogen ion, H^+), and a base accepts a proton (Eq. 1).

$$\text{acid} = \text{base} + H^+ \tag{1}$$

The Brønsted-Lowry concept broadened the antecedent Arrhenius concept, with which it is often confused. According to Arrhenius, acids donate H^+ and bases donate OH^- (hydroxide ion); furthermore, water was the requisite solvent system. As it was recognized that electrolyte dissociation takes place in other solvents, it was also recognized that basicity can be treated as the inverse of acidity and not restricted to OH^-. The Brønsted-Lowry concept thus broadens the notion of base as any species capable of combining with H^+. The hydrogen ion acquired a special status in early studies of electrolyte dissociation owing to its small size, very high charge density, high mobility, and complete lack of electrons. It is natural that while the Brønsted-Lowry concept broadened the concept of a base, the definition of an acid remains restrictive.

A general acid dissociation reaction and its equilibrium constant $K_{\text{acid, HA}}$ are written, respectively, as

$$HA = H^+ + A^- \text{ and } K_{\text{acid,HA}} = \frac{a_A - a_{H^+}}{a_{HA}}, \tag{2}$$

where a_i represents the activity of species i (activity is a thermodynamic concept related to concentration: $a_i = \gamma_i m_i$, where m is molality (mol kg^{-1}) and γ is the solution composition-dependent activity coefficient; see ▶ "Equilibrium Constant" and Activity and activity coefficients). For a general base, B, we write:

$$B + H^+ = BH^+ \text{ and } K_{\text{base,B}} = \frac{a_{BH^+}}{a_B a_{H^+}}. \tag{3}$$

Base association is thus the reciprocal of acid dissociation, in accord with the definition in Eq. 1. We could write:

$$K_{\text{base},A^-} = \frac{a_{HA}}{a_A - a_{H^+}} = K^{-1}_{\text{acid,HA}}$$

or:

$$K_{\text{acid},BH^+} = \frac{a_B a_{H^+}}{a_{BH^+}} = K^{-1}_{\text{base, B}},$$

and we observe that:

$$\left(K_{\text{base},A^-}\right)\left(K_{\text{acid,HA}}\right) = 1 \quad \text{and}$$
$$\left(K_{\text{acid},BH^+}\right)\left(K_{\text{base, B}}\right) = 1.$$

The magnitudes of K_{acid} and K_{base} indicate the relative strengths of acids or bases. Smaller values of K_{acid} reflect a smaller tendency for an acid to dissociate (a weaker acid), while smaller values of K_{base} reflect a smaller tendency for a base to acquire a proton (a weaker base). Equations 2 and 3 are hypothetical representations, however, because protons are too reactive to exist independently. A Bronsted-Lowry acid–base reaction is a proton *transfer,* so a proton-donation reaction such as Eq. 2 must be coupled with a proton-acceptance reaction such as Eq. 3. In general,

$$\begin{aligned} HA = A^- + H^+ \quad & K_{\text{acid}} = \frac{a_A - a_{H^+}}{a_{HA}} \\ B + H^+ = BH^+ \quad & K_{\text{base}} = \frac{a_{BH^+}}{a_H + a_B} \\ \hline HA + B = BH^+ + A^- \quad & K_{AB} = \frac{a_A - a_{BH^+}}{a_{HA} a_B} = K_{\text{acid}} K_{\text{base}} \end{aligned} \tag{4}$$

Neither K_{acid} nor K_{base} can be measured independently of one another, owing to the need to couple proton donations and acceptances.

H_2O is an *amphoteric* solvent (i.e., it can behave both as an acid and as a base). The autoprotolysis reaction (Eq. 5) involves one H_2O that behaves as an acid and donates H^+ and another H_2O that acts as a base and accepts H^+.

$$H_2O + H_2O = H_3O^+ + OH^- \tag{5}$$

Equation 5 represents the coupling of $H_3O^+ = H_2O + H^+$ (K_{acid}, H_3O^+) and $OH^- + H^+ = H_2O$ ($K_{\text{base, OH}^-}$). The autoprotolysis equilibrium constant is $K_w = a_{H3}{}^{o+} a_H{}^-$ in which the mass-action expression for K_w is written without a denominator because we assume that the solution is sufficiently dilute that $a_{H2}{}^o \rightarrow 1$. Following the coupling scheme in Eq. 4, K_{AB}, $H_2O = K_{\text{acid,H}_3\text{O}^+} K_{\text{base,OH}^-}$, so $K_W = K^{-1}_{AB,\text{H}_2\text{O}}$ (at 25°C, $K_W = 10^{-14}$). The formalism of using H_3O^+ for the acid species of water is often relaxed, and K_w is called the hydrolysis constant for $H_2O = H^+ + OH^-$. Similarly, Eq. 2 is used as a prototypical acid dissociation. Using H^+ as a shorthand notation for H_3O^+ is harmless as long as we remember that protons have no independent existence and are transferred in coupled reactions.

In aqueous solutions, Braønsted-Lowry acid dissociation reactions are coupled to the inverse of H_3O^+ dissociation by the scheme in Eq. 4, i.e., H_2O is the proton-accepting base, so $HA + H_2O = H_3O^+ + A^-$, and $K_{AB} = K_{\text{acid,HA}} K^{-1}_{\text{acid}}$, H_3O^-. The K_a values reported in the literature for aqueous Bronsted-Lowry acids (e.g., $H_2CO_3 = HCO^-{}_3 + H^+$, $K_a = 10^{-6.35}$) are understood to be the same as K_{AB} and implicitly include the inverse dissociation of H_3O^+ (e.g., $H_2CO_3 + H_2O = HCO^-{}_3 + H_3O^+$, $K_{AB} = 10^{-6.35}$). Similarly, aqueous Bronsted-Lowry base-association reactions are

coupled to the inverse of OH^- association, giving $B + H_2O - BH^+ + OH^-$, for which the reported K_b values are $K_{AB} - K_{BK} = K_{base,B}$, K^{-1}_{base,OH^-} (e.g., $NH_3 + H_2O = NH^+_4 + OH^-$, $K_b = 10^{-4.75}$). Generally, for an aqueous acid and its conjugate base, $K_a K_b = K_W$ (e.g., $NH^+_4 = NH_3 + H^+$, $K_a = 10^{-9.25}$).

Braønsted-Lowry acid–base reactivity plays a fundamental role in geochemistry because so many geochemical processes involve proton transfers. The hydration of oxide gases generally yields acids that may dissociate to yield protons in aqueous solution (e.g., $CO_2 \rightarrow H_2CO_3$, $SO_3 \rightarrow H_2SO_4$; see Acid deposition). Furthermore, many mineral dissolution reactions involve the consumption or production of protons in solution and are, in fact, promoted by the amphoteric character of H_2O.

pH

The Braønsted-Lowry proton-transfer concept of acidity also leads to the familiar concept of pH, which provides a reference scale for the relative H^+ concentration of different solutions in a given protonic solvent. The definition of pH is based on using the prefix "p" to mean the "negative base-10 log of" the indicated quantity, and the "H" indicates the quantity a_{H^+} Eq. 6 for aqueous solutions).

$$\mathrm{pH} \equiv -\log a_{H_3O^+} \tag{6}$$

With the p-notation, we can also write $pK_w = \mathrm{pH} + \mathrm{pOH} =$ 14 (at 25 °C). A neutral pH is the pH where $a_{H_3O^+} = a_{OH^-}$ ($\mathrm{pH_{neutral}} = \mathrm{pOH_{neutral}}$), so $PK_W = 2\mathrm{pH_{neutral}}$; at 25 °C therefore, $\mathrm{pH_{neutral}} = 7$. The conventional limits of the aqueous pH scale are 0 ($a_{H_3O^+} = 1$, $a_{OH^-} = 10^{-14}$) and 14 $a_{OH^-} = 1$), but concentrated solutions of strong acids can have pH < 0 and concentrated solutions of strong bases can have pH > 14. Measurements of pH in such concentrated solutions are quite difficult, owing to the need for significant activity coefficient corrections and the often nonlinear character of device or indicator calibrations. In natural waters, pH values outside the range 3–11 are uncommon, and most living organisms are best suited to a significantly narrower range of near-neutral values. Butler (1964) elaborates on the calculation of pH and other parameters of Brønsted-Lowry acid–base reactivity in solution.

The Lewis Acid Concept

The Lewis concept is based on the donation and acceptance of bonding electrons. Lewis acids and bases are not to be confused with reducing and oxidizing agents whose oxidation states change by virtue of electron transfers without bonding. A Lewis acid has a vacant orbital that can accept a pair of electrons, and a Lewis base has at least one pair of valence electrons that are not being used for a bond (Jensen 1980). Lewis acidity is a broader concept than Braønsted-Lowry acidity, but all Brønsted-Lowry bases are also Lewis bases because the portion is a Lewis acid. Lewis acid–base reactivity involves the formation of *coordination complexes* (also called *adducts*; Eq. 7).

$$\mathrm{A} + : \mathrm{B} = \mathrm{A} : \mathrm{B} \tag{7}$$

The use of the: emphasizes the electron donation and acceptance. In the specific case where A is a metal ion, :B is often termed a *ligand.* A Lewis acid may also be called an *electrophile*, and its acidity is *electrophilic* in nature, owing to its tendency to react with an electron-rich species. The corresponding terms for a Lewis base are *nucleophile* and *nucleophilic.*

Depending on the reactants, Lewis acid reactions like Eq. 7 are usually coupled with Lewis base reactions (the inverse of Eq. 7). A coupled complexation reaction thus involves the exchange of acids and bases: $A_1B_1 + A_2B_2 = A_1B_2 + A_2B_1$.

Lewis acidity is an especially useful concept for understanding the formation of complexes in aqueous solution and for rationalizing or correlating the relative stability of complexes. Under the Lewis concept, cations are acids, anions are bases, and salts are complexes. For example, solid Na·$\ddot{\mathrm{C}}$l is a complex of acidic Na^+ and basic $\cdot\ddot{\mathrm{C}}\mathrm{l}^-$. In solution, cations (generally metal ions, Me^{x+}) are coordinated with basic ligands (L^{y-}), $MeL_n^{(x+)-(n(y-))}$, where n is the ligand number. Neutral species can also behave as acids or bases, depending on their ability to accept or donate electron pairs. H_2O can bond as a base via the oxide anion (e.g., with Fe^{3+}, $Fe(H_2O)^{3+}_6$); in these hydration complexes, the ligand number is the hydration number. Owing to its polar nature, H_2O can also be a Lewis acid via hydrogen bonding and, thereby, hydrate base anions (e.g., with Cl^-, $(OH_2)_n Cl^-$). For example, in aqueous solution,

$$Fe(H_2O)^{3+}_6 + (OH_2)_n Cl^- = FeCl(H_2O)^{2+}_5 + (n+1)H_2O.$$

Although such reactions are coupled, we usually write $Fe^{3+} + Cl^- = FeCl^{2+}$, and the formation (association) constant, $K_{FeCl^{2+}}$, implicitly includes the acid–base exchange of H_2O molecules.

In the absence of other ligands, an aqueous cation is surrounded by a hydration "sphere" in which the H_2O molecules are positioned according to the coordination geometry of the cation and oriented with their protons away from the cation; for example, Fe^{3+} tends toward octahedral coordination, so its primary hydration sphere contains 6 H_2O molecules. Outside the primary hydration sphere, there is a more diffuse zone of H_2O molecules whose movement and position

are influenced somewhat by the charge on the cation; this secondary hydration sphere is not constrained to the cation's coordination geometry, and the number of H_2O molecules in the secondary sphere is less determinate. In a hydrated Lewis acid, the repulsive force between the cation and a proton on a coordinated H_2O is approximately proportional to z, the charge of the cation, and r^{-1}, the distance between the cation and the proton. In the literature, various ionic potential functions $I_P = z^p/r^q$ are used; usually, $p = 1$ or 2, and $q = 1$. In any case, increased I_P gives increased hydration (i.e., larger n) and increased tendency to eject H^+ from the complex and form a metal-hydroxide complex (e.g., $FeOH(H_2O)^{2+}_5$). Owing to their large size, anions have small I_P and are generally only weakly hydrated; n is often indeterminate for an anion.

There are two types of Lewis complexes of metals and non-H_2O ligands in aqueous solution. In an *inner-sphere complex,* the ligand displaces an H_2O molecule from the primary hydration sphere and resides in one of the cation's coordination sites. In an *outer-sphere complex* (sometimes called an ion pair), the ligand resides outside the primary hydration sphere; the ligand is shielded from direct interactions with the cation by the H_2O molecules of the primary hydration sphere. A given complex is generally not purely inner-sphere or outer-sphere, but the character of the complex can be dominated by one type or the other in the same sense that bonds are dominated by covalent bonding (inner-sphere; short-range forces with lots of electron sharing between cation and ligand) or electrostatic bonding (outer-sphere; long-range forces with little electron sharing). Inner-sphere complexes are characterized by greater stability and larger association constants than outer-sphere complexes.

There is no widely used method of or scale for quantitatively comparing Lewis acid–base strengths that compares with the pK_a–pH relationships of Brønsted-Lowry acids. Any Lewis acid–base reaction does, of course, have an equilibrium constant, but the problem lies in establishing a reference acid against which the strength of other acids can be compared in the necessary coupling reaction and, similarly, establishing a reference base for measuring basicity. In aqueous solutions, the Brønsted-Lowry definition points clearly toward H_3O^+ as the reference acid and OH^- as the reference base, but the benefits of the broader Lewis definition come at the expense of less clarity with respect to references. The magnitude of ΔH (enthalpy change) for a reaction represents the strength of the bonds made or broken, and efforts have been made to use multiple parameters relating to electrophilicity and nucleophilicity of reactants to predict ΔH for complexation reactions (e.g., Drago and Wayland 1965) or to predict K (Edwards 1954). In either case, the computed values provide a basis for predicting the relative stability of complexes.

On the other hand, the proton is a rational choice for a reference Lewis acid in aqueous solution. The proton is small and unpolarizable, and it has a very high I_P. If the proton thus defines one end of a scale of Lewis acidity, the opposite end would be represented by a large, polarizable cation with low I_P (e.g., Ag^+ and Hg^{2+}). Bases could then be classified according to their reactivity with acids. It is observed that bases in which the donor atoms are relatively small and unpolarizable tend to bond with acids at the proton end of the Lewis acidity scale in preference to acids at the opposite end and vice versa.

Although it is not quantitative, the principle of hard and soft acids and bases (HSAB, also known as Pearson's Rule) has proved to be very useful in correlating the relative stability of complexes along the lines of such a qualitative scale (Pearson 1973). HSAB holds that hard acids tend to combine with hard bases, while soft acids tend to combine with soft bases. If B_2 is softer than B_1 and A_2 is softer than A_1, the exchange reaction $A_1B_2 + A_2B_1 = A_1B_1 + A_2B_2$ tends to proceed to the right ($K > 1$). Acids and bases are thus each classified into three categories: (a) hard species that are smaller, more charge-dense, and less polarizable, (b) soft species that are larger, less charge-dense, and more polarizable, and (c) borderline species. The borderline category allows for the qualitative and relative nature of the correlation and for the fact that molecular environment (e.g., the presence of different ligands) can influence the relative hardness of a species.

The geochemical significance of Lewis acid–base reactivity lies in two areas. In the first, the specificity or sequence of reactivity of one species (a cation, an anion, a mineral surface site) with others can often be explained according to Pearson's rule. The second area of significance is the formation or relative stability of aqueous complexes, which generally promotes the mobility of elements in the hydrosphere by enhancing their solubility.

Acidic and Basic Rocks

Although it is not common to see these designations in current literature, the older literature often refers to "acidic rocks" and "basic rocks." Those designations have much more to do with a classification of rocks on the basis of their composition than on the basis of their reactivity, which is the principal use of acid–base concepts in other contexts. The origin of the term "acid rock" is the tendency of non-metal oxides to form acids when they dissolve in water (e.g., $SiO_2 + 2H_2O = H_4SiO_{4(aq)}$; silicic acid is a weak acid). Hence rocks rich in silica (those containing large proportions of quartz or feldspar) have been called acidic. "Basic rock" originates in the tendency of metal oxides to form bases upon

dissolution (e.g., $MgO + H_2O = Mg^{2+} + 2OH^-$), and rocks rich in iron oxide or alkali earth oxides have been called basic. The more common recent trend is to reserve acidic and basic for descriptions of reactivity and to use terms like silicic, felsic, or mafic to describe the composition of rocks. "Alkaline" is a synonym for "basic,," but it has also been used to describe rocks rich in the alkali metals sodium or potassium. It is still common for such rocks to be referred to as alkaline, although "sodic" and "potassic" are clearer alternatives. It is also true that terms like "base metal" and "acid alteration" occur frequently in the literature, where they often lead to some confusion if they are used without a clear explanation of their meaning in context.

Cross-References

- Acid Deposition
- Aqueous Solutions
- Carbonate Minerals and the CO_2-Carbonic Acid System
- Fluid–Rock Interaction
- Hydrothermal Solutions
- Oxidation-Reduction Reactions and Eh-pH (Pourbaix) Diagrams
- Stoichiometry
- Water

References

Butler JN (1964) Ionic equilibrium: a mathematical approach. Addison-Wesley, Reading. 547 pp
Davis JA, Kent DB (1990) Surface complexation modeling in aqueous geochemistry. In: Hochella MF Jr, White AF (eds) Mineral-water interface geochemistry, Reviews in mineralogy, vol 23. Mineralogical Society of America, Washington, DC, pp 177–260
Drago RS, Wayland BB (1965) A double-scale equation for correlating enthalpies of Lewis acid-bases interactions. J Am Chem Soc 87:3571–3577
Dzombak DA, Morel FMM (1990) Surface complexation modeling: hydrous ferric oxide. Wiley, New York. 393 pp
Edwards JO (1954) Correlation of relative rates and equilibria with a double basicity scale. J Am Chem Soc 76:1540–1547
Huang CP (1981) The surface acidity of hydrous solids. In: Anderson MA, Rubin AJ (eds) Adsorption of inorganics at solid–liquid interfaces. Ann Arbor Science, Ann Arbor, pp 183–217
Jensen WB (1980) The Lewis acid–base concept. Wiley, New York. 364 pp
Pearson RG (ed) (1973) Hard and soft acids and bases, Benchmark papers in inorganic chemistry. Dowden/Hutchinson and Ross, Stroudsburg. 480 pp
Schindler PW (1981) Surface complexes at oxide-water interfaces. In: Anderson MA, Rubin AJ (eds) Adsorption of inorganics at solid–liquid interfaces. Ann Arbor Science, Ann Arbor, pp 1–49
Stumm W (1992) Chemistry of the solid-water Interface. Wiley, New York. 428 pp

Activation Parameters: Energy, Enthalpy, Entropy, and Volume

William H. Casey[1] and C. André Ohlin[2]
[1]Department of Chemistry and Department of Earth and Planetary Sciences, University of California, Davis, CA, USA
[2]Department of Chemistry, Umeå University, Umeå, Sweden

Definition

Activation parameters are used in chemical kinetics to describe the equilibrium between reactants of a chemical reaction and a single, unstable molecule called a transition state.

Transition State Theory and Elementary Versus Overall Reactions

Transition-state theory is the central underpinning of all chemical kinetics. It postulates that for elementary reactions, there is equilibrium between reactants and an unstable form called the transition state, which is a single molecule. The equilibrium is conventional in all ways except that the transition state has a loose vibrational mode that dissociates and leads to products (Glasstone et al. 1941). The thermodynamic terms that describe this activated equilibrium between the reactants and the transition state are called activation parameters and have exact analogues with the standard thermodynamic parameters that describe a conventional equilibrium between the reactants and the products in a reaction. However, the transition state determines the rate of reaction is unstable.

For geochemists, it is essential to understand the definition and scope of an elementary reaction – these are reactions that have a single energy barrier between reactants and products. Thus, the rotation of a methyl group from staggered to eclipsed orientation could be an elementary reaction. Transfer of a proton from a metal-bound water molecule to a bulk water one could be an elementary reaction. Transfer of a solvation water molecule to the bulk could be an elementary reaction. The key is that one can follow the movement of each atom over the single-step barrier.

Reactions that do not consist of a single molecular step and concerted motions are overall reactions. Inversion of the structure of cyclohexane from *chair* to *boat* conformation is *not* an elementary reaction because intermediate states can be identified, even though the molecule doesn't dissociate. Thus, geochemical reactions such as:

$$SiO_2(s) + 2H_2O(l) = H_4SiO_4(aq) \quad (1)$$

are *not* elementary reactions because one cannot enumerate the actual concerted motions of each atom in the reacting structure as the reaction proceeds at the molecular scale. There must be hundreds or thousands of elementary reactions, each of which has an energy barrier. The energy landscapes for geochemical reactions are complicated, not simple.

Transition state theory can be adapted to treat overall reactions but with enormous loss of information (Boudart 1976; Boudart and Djega-Mariadasson 1984; Lichtner 2016) so that these become effectively empirical relations. Even simple isotope-exchange reactions, involving molecules where the structures can be known with complete confidence and which can be studied in excruciating experimental detail, usually proceed via metastable states and many steps (Casey and Rustad 2016; Rustad 2010; Rustad and Casey 2012).

Activation Parameters

For true single-step reactions, the activation energy is defined as the energy that must be surmounted for reactants to reach the transition state (Fig. 1). Note that there is a single barrier and no intermediates. Practically the activation energy, E_a, is estimated from the temperature dependence of a reaction rate coefficient or, in rare but increasingly frequent cases, from electronic-structure calculations.

Because transition state theory postulates an equilibrium between reactants and the transition state, the conventional derivative properties of an equilibrium constant have exact analogues in chemical kinetics. The temperature variation of the rate coefficient yields the familiar Arrhenius rate law:

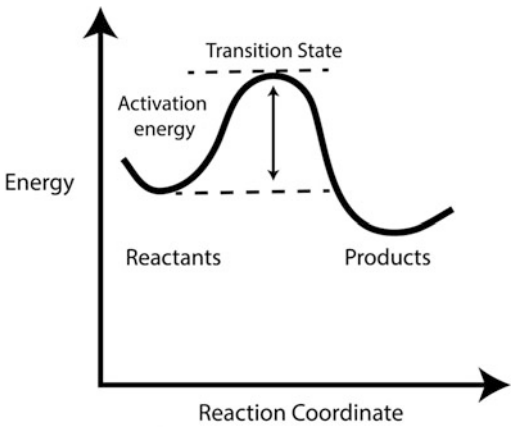

Activation Parameters: Energy, Enthalpy, Entropy, and Volume, Fig. 1 The activated equilibrium for an elementary reaction has a single energy barrier

$$k = A_o e^{\frac{-E_a}{RT}} \tag{2}$$

where A_o is an empirical pre-exponential term that can be interpreted to include activation entropies and activity coefficients. The similarity of this expression to the conventional Van't Hoff expression for the temperature variation of an equilibrium constant is not accidental:

$$\left(\frac{\delta \ln k^{\neq}}{\delta\left(\frac{1}{T}\right)}\right)_P = \frac{-\Delta H^{\neq}}{R} \tag{3}$$

Similarly the pressure variation of the activated equilibrium yields activation volumes:

$$\left(\frac{\delta \ln k^{\neq}}{\delta P}\right)_T = \frac{-\Delta V^{\neq}}{RT} \tag{4}$$

and the activation enthalpy relates to the activation energy via:

$$E_a = H^{\neq} + RT \tag{5}$$

where E_a is the activation energy derived from the Arrhenius equation (analogous to the Van't Hoff equation of equilibrium thermodynamics), The parameter $H^{\neq}$ is the enthalpy of activation, R is the gas constant, and T is the temperature in Kelvins.

The activation barriers for common reactions in aqueous solutions vary from about 20 kJ/mol for the cost of solute diffusion to the exchange of a water bound in $[Ir(OH_2)_6]^{3+}$ with a bulk water, which has an activation enthalpy of over 130 kJ/mol (Helm and Merbach 2005). For aqueous reactions, there is usually a strong correlation between the logarithm of the rate coefficient and the activation energy or enthalpy. For homoleptic ligand-exchange reactions, such as exchange of a bulk water for a water bound in an inner solvation sphere of a metal, the activation volume, $\Delta V^{\neq}$, is used to infer the form of the transition state. Because a bulk water is much more loosely packed than a solvation-shell water, a positive $\Delta V^{\neq}$ value is used to infer a reaction pathway that has considerable dissociative character, meaning that the reaction involves a decrease in coordination number in the transition state. Conversely a negative $\Delta V^{\neq}$ value is used to infer gain in coordination number of the metal during the ligand-exchange reaction. In reality most reactions fall intermediate between these extremes.

Conclusion

Activation parameters are experimental parameters that shed light into the relationship between the rate of an elementary reaction, the motions of the atoms, and the changes in bonding

as the reaction proceeds. In most geochemical systems, activation parameters correspond to overall reactions and are composites from many steps. Thus they can vary with solution composition and experimental conditions as the relative importance of different steps varies (e.g., Casey and Sposito 1992).

Cross-References

- ▶ Enthalpy
- ▶ Entropy
- ▶ Equilibrium
- ▶ Geochemical Thermodynamics
- ▶ Kinetics of Geochemical Processes
- ▶ Water

References

Boudart M (1976) Consistency between kinetics and thermodynamics. J Phys Chem 80:2869–2870

Boudart M, Djega-Mariadasson G (1984) Kinetics of heterogeneous catalytic reactions. Princeton University Press, Princeton. 242 pp

Casey WH, Rustad JR (2016) Pathways for oxygen-isotope exchange in two model oxide clusters. New J Chem 40:898–905

Casey WH, Sposito G (1992) On the temperature dependence of mineral dissolution rates. Geochim Cosmochim Acta 56:3825–3830

Glasstone S, Laidler KJ, Eyring H (1941) The theory of rate processes. Princeton University, New York

Helm L, Merbach AE (2005) Inorganic and bioinorganic solvent exchange mechanisms. Chem Rev 105:1923–1959

Lichtner PC (2016) Kinetic rate laws invariant to scaling the mineral formula unit. Am J Sci 316:437–469

Rustad JR (2010) Elementary reactions in polynuclear ions and aqueous-mineral interfaces: a new geology. Adv Inorg Chem 62:391–436

Rustad JR, Casey WH (2012) Metastable structures and isotope exchange reactions in polyoxometalate ions provide a molecular view of oxide dissolution. Nat Mater 11:223–226

Activity and Activity Coefficients

Barry R. Bickmore and Matthew C. F. Wander
Department of Geological Sciences, Brigham Young University, Provo, UT, USA

Definition

The *activity* of a chemical entity is a dimensionless quantity derived by multiplying a correction factor (called an *activity coefficient*) by some measure of its molar abundance, such as molar concentration (molarity), molality, partial pressure, or mole fraction. See Eq. 1, where (a_i) is the activity of a species or component i, γ_i is the activity coefficient, and x_i is a measure of molar abundance.

$$a_i = \gamma_i x_i \tag{1}$$

Activities are thus used as "effective concentrations" and are necessary to the extent that chemical behavior is not *ideal* – i.e., strictly proportional to molar abundance – and so $\gamma_i \neq 1$. Formally, a_i is defined by Eq. 2, where it described as a function of the difference between the chemical potential of i (μ_i) and its chemical potential in some standard state $\left(\mu_i^{\ominus}\right)$, temperature ($T$), and the gas constant (R).

$$a_i = e^{\left(\mu_i - \mu_i^{\ominus}\right)/RT} \tag{2}$$

Molar Abundance and Ideal Behavior

Many foundational advances in chemistry were based on the recognition that various behaviors of atoms and molecules are roughly proportional to their local abundance (Levere 2001). The pressure of a gas at constant volume and temperature is proportional to the number of molecules present (Avogadro's law and the Ideal Gas law). The concentration of a dissolved gas is proportional to its partial pressure in the gas phase (Henry's law). The vapor pressure of each liquid in a mixture is proportional to both the vapor pressure of each pure component and its mole fraction in the mixture (Raoult's law).

That such behaviors *should* be proportional to molar abundance is intuitively obvious and can be illustrated by a simple example. Consider a chemical reaction, A + B → AB. The rate at which molecules A and B react necessarily depends on how often they encounter one another. If the number of A molecules in the available space is doubled, then the B molecules will be twice as likely to encounter them.

Therefore, many standard equations describing chemical behavior, especially rate laws and mass action (equilibrium constant) expressions, are intentionally formulated to reflect the expected proportional behavior. Chemists consider systems that act strictly in this manner to be behaving *ideally*.

The activity and the corresponding standard state chemical potential is always tied to a particular scale of molar abundance, generally mole fraction for all condensed phase solutions, except that activities for solutes in aqueous solutions are linked to the molal concentration scale (Robinson and Stokes 1965). The *fugacity* of gases, which is closely related to activity, is based on partial pressures (Atkins and Jones 2008). Therefore, although activity is dimensionless, one must take care to use the appropriate scale with a particular tabulation or model of activity coefficients.

At the standard state, the activity coefficient is equal to 1, denoting ideal behavior, but the choice of what that standard state should be is arbitrary. For chemical entities measured on the mole fraction scale in condensed phases, this corresponds to a pure substance, where the mole fraction is equal to 1. For dissolved species in aqueous solutions, the standard state is a hypothetical state of infinite dilution, extrapolated from experimental data.

Nonideal Chemical Behavior and Activity

Real chemical systems always diverge from ideal behavior to some degree because of interactions (attraction or repulsion) between the chemical entities involved and their surroundings. One classic example is Johannes van der Waals's analysis of deviations of real gas behavior from the Ideal Gas Law (Levere 2001). He noted that real gases tend to deviate most from ideal behavior at low temperatures and high pressures – i.e., when one would expect the gas molecules to be closer to one another – and showed that the observed behavior could be explained by assuming short-range attraction between them. This also explained how condensation of gases into liquid form is possible.

Any interaction other than simple chemical reaction or elastic collision (a collision in which kinetic energy is conserved) will contribute to nonideal behavior, and the closer the chemical entities involved approach one another, the more pronounced such effects will be. Therefore, the simplest models to predict activity coefficients tend to focus on longer-range forces and are only accurate under a limited range of conditions. More accurate models extend that range by, at least implicitly, taking into account increasingly complex interactions between the chemical entities involved.

In dilute aqueous solutions (Wolery 1990), for instance, activity coefficients depend mostly on long-range electrical forces, so the simplest models for estimating activity coefficients are solely based on the formal charge (Z_i) of individual ions and the total ionic strength (I) of the solution. For example, Eq. 3 shows one form of the Debye-Hückel equation, where A_γ is a constant for a given temperature. Equation 4 shows the Davies equation, in which 0.2 is sometimes replaced by 0.3.

$$\ln \gamma_i = \frac{-A_\gamma Z_i^2 \sqrt{I}}{1 + 1.5\sqrt{I}} \tag{3}$$

$$\ln \gamma_i = -A_\gamma Z_i^2 \left(\frac{\sqrt{I}}{1 + \sqrt{I}} - 0.2I \right) \tag{4}$$

The Debye-Hückel equation is reasonably accurate in solutions up to 0.1–0.3 molal ionic strength, while the Davies equation is useful up to ~0.5 molal ionic strength. In more concentrated solutions, however, both models fail badly because other factors become more important when dissolved species are forced closer together. Both equations predict $\gamma_i = 1$ for uncharged species, for instance, but this could only be accurate over short distances if the distribution of charge around neutral species like silicic acid (H_4SiO_4) could be approximated by a point or spherical charge. Therefore, molecular shapes, electronegativity differences among atoms, the tendency to pair with neighboring ions, and the disruption of surrounding water structure, all of which could be very different among individual species with the same formal charge, begin to dominate the behavior of aqueous species (Pitzer 1991).

Both the Debye-Hückel and Davies equations imply a monotonic decrease in γ_i with increasing ionic strength, but in high ionic strength solutions, γ_i values often actually start to climb, and may even rise to values greater than 1. Improved activity coefficient models must, therefore, incorporate increasing levels of detail regarding how the solute species interact with one another. This is often done by introducing interaction terms for every pair of dissolved species. For example, to estimate the activity coefficient for Na^+ in a high ionic strength solution containing dissolved Na^+, Cl^-, H^+, and OH^-, one would have to account for interactions between Na^+ and every other species present. One common method for implementing this is the Specific Ion Interaction Theory (SIT) of Brønsted (1922), Guggenheim (Guggenheim and Turgeon 1955), and Scratchard (1936), shown in Eq. 5. Here, a Debye-Hückel term dominates at low ionic strengths, but a summation of pair-wise interaction terms, which depend on interaction coefficients specific to the species i and all other species $j(\varepsilon_{i,j})$ and the molal concentrations of all other species (m_j).

$$\log_{10} \gamma_i = \frac{-A_\gamma Z_i^2 \sqrt{I}}{1 + 1.5\sqrt{I}} + \sum\nolimits_j \varepsilon_{i,j} m_j \tag{5}$$

To estimate activity coefficients in the most concentrated brines, however, one needs to take into account interactions between triplets, in addition to pairs, of species. Pitzer's equations (Pitzer 1991) include such interaction terms, but also make pair-wise interaction terms functions of ionic strength. The most famous Pitzer-based model among geochemists is the Harvie-Møller-Weare (Harvie et al. 1984) model for the sea-salt system at 25 °C, which can accurately reproduce the solubilities of salts in highly concentrated brines up to 14 molal ionic strength.

As interaction terms for pairs and triplets of species are added, activity coefficient models can be made more and more accurate over a wider range of conditions, but the information required to calibrate the models increases exponentially as more species are added to the solution, to the

point that it can be prohibitive to use Pitzer, or even SIT, models for very complex solutions.

There is an extensive literature dealing with activity coefficients in nonaqueous phases such as solid solutions, gases, and silicate melts. For an introduction to this, see Nordstrom and Munoz (1985) and references cited therein.

Summary and Conclusions

Attractive or repulsive interactions between chemical components or species cause them to behave in a "nonideal" manner. That is, their reactivity is not strictly proportional to their molar abundance (molar concentration, molality, partial pressure, mole fraction). When using equations to describe chemical kinetics and equilibrium, therefore, chemists account for nonideality by replacing measures of molar abundance with activity, which is a dimensionless "corrected" concentration obtained by multiplying a correction factor (activity coefficient) by the molar abundance. Standard models to estimate activity coefficients vary widely in their complexity and accuracy.

Cross-References

- ▶ Aqueous Solutions
- ▶ Chemical Bonds
- ▶ Electronegativity

References

Atkins P, Jones L (2008) Chemical principles: the quest for insight. W. H. Freeman and Company, New York. 787 p

Brønsted JN (1922) Studies on solubility IV. The principle of the specific interaction of ions. J Am Chem Soc 44:877–898

Guggenheim EA, Turgeon JC (1955) Specific interaction of ions. Trans Faraday Soc 51:747–761

Harvie CE, Møller N, Weare JH (1984) The prediction of mineral solubilities in natural waters: the Na-K-Mg-Ca-H-Cl-SO_4-OH-HCO_3-CO_3-CO_2-H_2O system to high ionic strengths at 25 °C. Geochim Cosmochim Acta 48:723–751

Levere TH (2001) Transforming matter: a history of chemistry from Alchemy to the Buckyball. Johns Hopkins University Press, Baltimore. 232 p

Nordstrom DK, Munoz JL (1985) Geochemical thermodynamics. The Benjamin/Cummings Publishing Company, Menlo Park. 477 p

Pitzer KS (1991) Ion interaction approach: theory and data correlation. In: Pitzer KS (ed) Activity coefficients in electrolyte solutions. CRC Press, Boca Raton

Robinson RA, Stokes RH (1965) Electrolyte solutions. Butterworths, London. 571 p

Scratchard G (1936) Concentrated solutions of strong electrolytes. Chem Rev 19:309–327

Wolery TJ (1990) On the thermodynamic framework of solutions (with special reference to aqueous electrolyte solutions). Am J Sci 290: 296–320

Alkali and Alkaline Earth Metals

Ricardo Arevalo Jr.
Planetary Environments Lab, NASA Goddard Space Flight Center, Greenbelt, MD, USA

A

Introduction

The alkali and alkaline earth metals comprise the first two columns of the periodic table, traditionally referred to as Groups IA and IIA, respectively (Fig. 1). Although H is technically considered a member of Group IA, it is not an alkali metal like the rest of the elements in this column; rather, H is a highly volatile non-metal and the smallest and lightest atom of them all. From lithium (Li) through francium (Fr) in Group IA, and beryllium (Be) through radium (Ra) in Group IIA, the rest of the alkali and alkaline earth metals share a number of physical characteristics, such as: malleability, ductility, electrical/thermal conductivity, and reactivity at standard temperature and pressure. Although often associated with biological systems and dietary supplements, alkali and alkaline earth metals represent an extraordinarily important and versatile suite of elements that can be applied as geochemical tracers for a multitude of planetary processes. Moreover, many of these elements are extraordinarily common in geological materials; for example, calcium (Ca), magnesium (Mg) and sodium (Na) represent the 5th, 6th and 7th (respectively) most abundant elements in the Earth's continental crust (Rudnick and Gao 2003).

Chemistry and Geochemical Behavior

The exploitation of alkali and alkaline earth metals as serviceable geo- and/or cosmochemical proxies is enabled by the systematic and predictable behavior of these elements in planetary environments, which is controlled ultimately by their distinctive electronic configurations. All of the Group IA and IIA elements, including H, belong to the s-block of the periodic table. Although He is also technically an s-block element, it is not described here as it falls into Group VIIIA. The alkali metals representing Group IA are characterized by a single outer shell electron held in an *s* (spherical) orbital; *s* orbitals may only be occupied by a maximum of two electrons with opposite spin directions, following the Pauli Exclusion Principle. The alkaline earth metals, on the other hand, are characterized by "full" outer *s* orbitals.

Because *s* orbital electrons are only loosely bound (relative to electrons occupying *p*, *d* and/or *f* orbitals), Group IA and

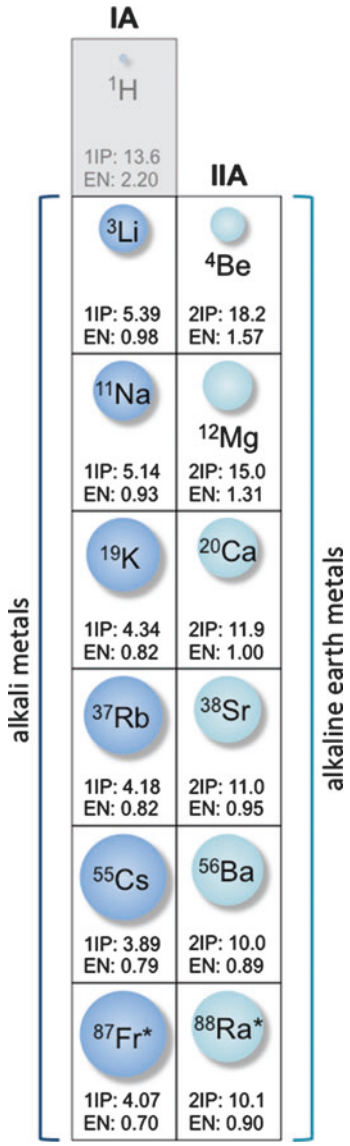

Alkali and Alkaline Earth Metals, Fig. 1 Isolation of the alkali and alkaline earth metals (Groups IA and IIA, respectively) from the rest of the periodic table. Relative atomic radii (depicted as spheres), and absolute values for first and second ionization potentials (labeled as 1IP and 2IP, respectively, in eV) and electronegativities (EN, following the Pauling scale) are taken from (CRC 2001). Francium (Fr) and radium (Ra) are highly unstable, and thus labeled with an asterisk

IIA elements are characterized by large atomic radii, low electronegativities and high reactivities. The alkali metals are defined by the lowest first ionization potentials (1st IP, the energy required to remove a single electron from the neutral atom) of all the elements, with cesium (Cs) defining the lowest 1st IP (3.89 eV; (CRC 2001)) of the group. In comparison, the alkaline earth metals are defined by some of the lowest second ionization potentials (2nd IP), with barium (Ba) defining the lowest 2nd IP (10.00 eV; (CRC 2001)) of all the stable elements.

The homologous behavior of the elements in each Group enables substitution for one another in mineral lattices. For example, because ions of potassium (K^+) and rubidium (Rb^+) share identical valence states and similar ionic radii as members of Group IA, Rb^+ is easily substituted into the cation site designated for K^+ in micas and potassic feldspars. Minimal work is required to substitute Rb^+ for K^+, as no charge balancing is required, nor significant strain imposed on the mineral lattice (Wood and Blundy 2003); in contrast, fitting ions of scandium (Sc^{3+}) or uranium (U^{6+}) into the same site would require a coupled substitution to achieve electroneutrality, plus significantly more strain energy.

Despite their common electronic structures, the alkali and alkaline earth metals vary widely in their relative volatilities, as measured by their respective 50% condensation temperatures at a total pressure of 10^{-4} bar (Fig. 2). The condensation temperature of an element is controlled primarily by its geochemical affinity as well as the presence of a suitable host phase during condensation of the solar nebula. All of the elements within Group IA are considered moderately to highly volatile, with condensation temperatures ranging from 1140 K down to 800 K (Lodders 2003). In general, the elements in this group become progressively more volatile with size/mass; Li is the least volatile in the group, whereas Cs is the most (note Fr is unstable). In contrast, the elements of Group IIA are substantially more refractory with condensation temperatures extending from 1300 to 1500 K; no obvious trend in volatility is exhibited as a function of size/mass in this group. All of the alkali and alkaline earth metals are characterized as lithophile (or oxygen-loving) elements as they are hosted primarily in the silicate portion of the earth, with only negligible to trace amounts estimated in the planet's core (McDonough 2003; Murthy et al. 2003; Corgne et al. 2007).

Due to their large atomic (and ionic) radii and their abundances in silicate rocks and minerals, alkali and alkaline earth metals are often referred to as Large Ion Lithophile Elements (LILE) in the geological community. In general, all of these elements are fluid mobile (Taylor and McLennan 1985) and thus commonly associated with metasomatism, hydrothermal alteration and slab dehydration processes, to name a few examples. Other than Ca, Mg and Na, the rest of the alkali and alkaline earth metals behave largely as incompatible trace elements during differentiation of the Earth's silicate shell; that is to say, they prefer to migrate into the melt rather than remain behind (during melting) or be forced into a crystal lattice (during crystallization). Consequently, most of the alkali and alkaline earth metals are concentrated in the continental crust relative to the modern mantle (Hofmann 1988).

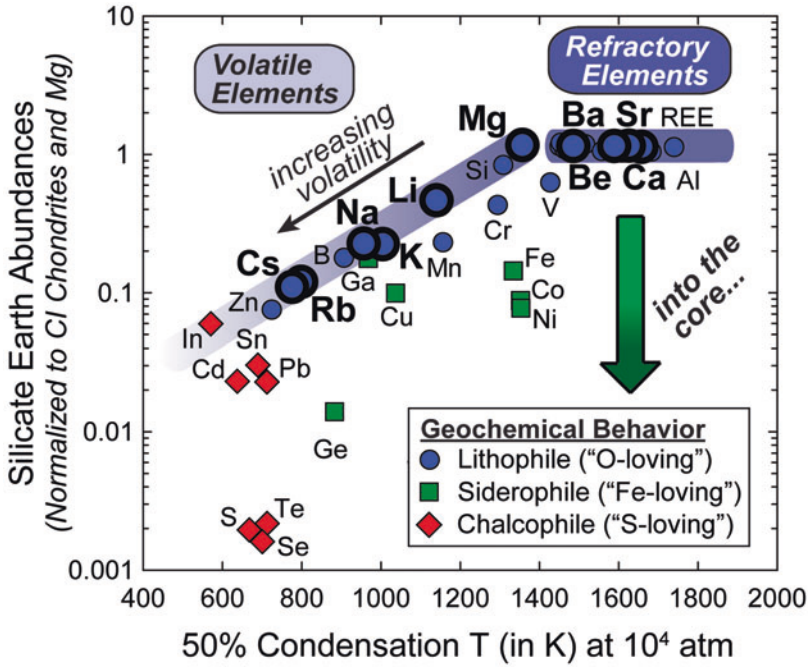

Alkali and Alkaline Earth Metals, Fig. 2 Elemental abundances in the silicate portion of the Earth plotted relative to 50% condensation temperatures at 10^{-4} bar total pressure, a measure of elemental volatility. Siderophile (iron-loving) and chalcophile (sulfur-loving) elements that plot below the volatility trend line, as defined by lithophile (oxygen-loving) elements, are likely depleted due to sequestration into the core. In general, alkali metals become increasingly more volatile with size/mass, whereas all of the alkaline earth metals are considered refractory in nature. All members of Groups IA and IIA behave as lithophile elements. Figure modified from (McDonough and Sun 1995). Condensation temperatures from (Lodders 2003)

Geological Applications

The characteristic attributes of the alkali and alkaline earth metals (some of which are described above), and the homologous behavior of the respective constituents of each Group in geological materials, make these elements particularly useful as geochemical proxies for a number of terrestrial processes. For example, Li abundances and isotopic exchange between aqueous and silicate systems provides important information on chemical weathering processes, including erosion rates, provenances, local temperatures, and pH conditions (Chan et al. 1992; Pistiner and Henderson 2003; Teng et al. 2004; Kısakűrek et al. 2005; Misra and Froelich 2012). Anthropogenic ^{137}Cs, with a half-life on the order of 30 years, has found employment as a tracer of: (i) soil erosion (Walling et al. 1999); (ii) sedimentation rates (Pennington et al. 1973); and, (iii) runoff (Rogowski and Tamura 1965) in environments that have been exposed to nuclear fission byproducts. Ratios of strontium (Sr), Mg and Ba to Ca captured by reef-building corals (Gagan et al. 1998), the carbonate shells of benthic foraminifera (Lea et al. 1999) and aragonitic ear stones of marine fish (Bath et al. 2000) have been used to map fluctuations in sea surface paleotemperatures and reconstruct global ocean nutrient content, circulation dynamics and fluxes.

Alkali and alkaline earth metals also serve as witnesses of the accretion and internal differentiation of other planetary bodies. Due to the lower condensation temperature of K relative to Th and U (Lodders 2003), K/Th and K/U ratios measured via orbiting spacecraft have been invoked as gauges of the volatile element depletion of Mercury, Venus, Mars, the moon, and the asteroid Vesta (Vinogradov et al. 1973; Prettyman et al. 2006; Taylor et al. 2006; Peplowski et al. 2011; Prettyman et al. 2015). Uniform Be and Mg initial isotopic compositions measured in terrestrial materials, calcium-aluminum inclusions (CAIs) and hibonite grains derived from chondritic meteorites indicate that the solar nebula was relatively well mixed during accretion of the inner solar system (McKeegan et al. 2000; Marhas et al. 2002; Teng et al. 2010). Short-lived ^{41}Ca ($t_{1/2}$ = 0.10 Myr) and ^{26}Al ($t_{1/2}$ = 0.72 Myr), which together track with stable ^{40}Ca, implicate a nucleosynthetic origin (likely an asymptotic giant branch or more massive star) for of these valuable geochronometers and early sources of radiogenic heat (Srinivasan et al. 1996; Sahijpal et al. 1998; Huss et al. 2009).

More applications of the alkali and alkaline metals as geo- and/or comoschemical proxies of planetary processes can be found in the chapters dedicated to each element. Unfortunately, the highly unstable natures of Fr and Ra complicate the use of their abundances and/or isotopes as mainstream geological tools.

Summary

Alkali (Group IA) and alkaline earth metals (Group IIA) share a host of common physicochemical attributes. The homologous behavior of each Group allows for substitution of major elements (e.g., Na) with less abundant elements (e.g., K, Rb

and Cs) in designated structural sites within mineral lattices. Together, the alkali and alkaline earth metals define the LILE, are highly soluble in aqueous solutions (and thus fluid-mobile), and generally incompatible during mantle melting and subsequent crystallization of magmas (with the notable exceptions of Ca, Mg and Na). However, the alkali metals are significantly more volatile than the alkaline earth metals. Because both Groups of elements are often found in appreciable quantities in many geological materials, including those derived from the Earth as well as other planetary bodies, they have been exploited as tracers for a litany of geological processes, fractionation mechanisms and source contributions/provenances.

Cross-References

- ▶ Large-Ion Lithophile Elements
- ▶ Periodic Table

References

Bath GE, Thorrold SR, Jones CM, Campana SE, McLaren JW, Lam JWH (2000) Strontium and barium uptake in aragonitic otoliths of marine fish. Geochim Cosmochim Acta 64:1705–1714

Chan LH, Edmond JM, Thompson G, Gillis K (1992) Lithium isotopic composition of submarine basalts: implications for the lithium cycle in the oceans. Earth Planet Sci Lett 108:151–160

Corgne A, Keshav S, Fei YW, McDonough WF (2007) How much potassium is in the Earth's core? New insights from partitioning experiments. Earth Planet Sci Lett 256:567–576

CRC (2001) Handbook of chemistry and physics, 82nd edn. CRC Press, Boca Raton

Gagan MK, Ayliffe LK, Hopley D, Cali JA, Mortimer GE, Chappell J, McCulloch MT, Head MJ (1998) Temperature and surface-ocean water balance of the Mid-Holocene Tropical Western Pacific. Science 279:1014–1018

Hofmann AW (1988) Chemical differentiation of the Earth: the relationship between mantle, continental crust, and oceanic crust. Earth Planet Sci Lett 90:297–314

Huss GR, Meyer BS, Srinivasan G, Goswami JN, Sahijpal S (2009) Stellar sources of the short-lived radionuclides in the early solar system. Geochim Cosmochim Acta 73:4922–4945

Kısakűrek B, James RH, Harris NBW (2005) Li and δ^7Li in Himalayan rivers: proxies for silicate weathering? Earth Planet Sci Lett 237:387–401

Lea DW, Mashiotta TA, Spero HJ (1999) Controls on magnesium and strontium uptake in planktonic foraminifera determined by live culturing. Geochim Cosmochim Acta 63:2369–2379

Lodders K (2003) Solar system abundances and condensation temperatures of the elements. Astrophys J 591:1220–1247

Marhas KK, Goswami JN, Davis AM (2002) Short-lived nuclides in Hibonite grains from Murchison: evidence for solar system evolution. Science 298:2182–2185

McDonough WF (2003) Compositional model for the Earth's core. In: Carlson RW (ed) Treatise on geochemistry. Elsevier-Pergamon, Oxford, pp 547–568

McDonough WF, Sun S (1995) The composition of the Earth. Chem Geol 120:223–253

McKeegan KD, Chaussidon M, Robert F (2000) Incorporation of short-lived ^{10}Be in a calcium-aluminum-rich inclusion from the Allende meteorite. Science 289:1334–1337

Misra S, Froelich PN (2012) Lithium isotope history of Cenozoic seawater: changes in silicate weathering and reverse weathering. Science 335:818–823

Murthy VR, van Westrenen W, Fei Y (2003) Experimental evidence that potassium is a substantial radioactive heat source in planetary cores. Nature 423:163–165

Pennington W, Tutin TG, Cambray RS, Fisher EM (1973) Observations on lake sediments using fallout ^{137}Cs as a tracer. Nature 242:324–326

Peplowski PN, Evans LG, Hauck SA, McCoy TJ, Boynton WV, Gillis-Davis JJ, Ebel DS, Goldsten JO, Hamara DK, Lawrence DJ, McNutt RL, Nittler LR, Solomon SC, Rhodes EA, Sprague AL, Starr RD, Stockstill-Cahill KR (2011) Radioactive elements on mercury's surface from MESSENGER: implications for the planet's formation and evolution. Science 333:1850–1852

Pistiner JS, Henderson GM (2003) Lithium-isotope fractionation during continental weathering processes. Earth Planet Sci Lett 214:327–339

Prettyman TH, Hagerty JJ, Elphic RC, Feldman WC, Lawrence DJ, McKinney GW, Vaniman DT (2006) Elemental composition of the lunar surface: analysis of gamma ray spectroscopy data from lunar prospector. J Geophys Res Planets 111

Prettyman TH, Yamashita N, Reedy RC, McSween HY Jr, Mittlefehldt DW, Hendricks JS, Toplis MJ (2015) Concentrations of potassium and thorium within Vesta's regolith. Icarus 259:39–52

Rogowski AS, Tamura T (1965) Movement of ^{137}Cs by runoff, erosion and infiltration on the alluvial Captina silt loam. Health Phys 11:1333–1340

Rudnick RL, Gao S (2003) Composition of the continental crust. In: Rudnick RL (ed) The crust. Elsevier-Pergamon, Oxford, pp 1–64

Sahijpal S, Goswami JN, Davis AM, Grossman L, Lewis RS (1998) A stellar origin for the short-lived nuclides in the early solar system. Nature 391:559–561

Srinivasan G, Sahijpal S, Ulyanov AA, Goswami JN (1996) Ion microprobe studies of Efremovka CAIs: II. Potassium isotope composition and 41Ca in the early solar system. Geochim Cosmochim Acta 60:1823–1835

Taylor SR, McLennan SM (1985) The continental crust: its composition and evolution. Blackwell, Oxford

Taylor GJ, Boynton W, Brückner J, Wänke H, Dreibus G, Kerry K, Keller J, Reedy R, Evans L, Starr R, Squyres S, Karunatillake S, Gasnault O, Maurice S, d'Uston C, Englert P, Dohm J, Baker V, Hamara D, Janes D, Sprague A, Kim K, Drake D (2006) Bulk composition and early differentiation of Mars. J Geophys Res Planets 111

Teng FZ, McDonough WF, Rudnick RL, Dalpé C, Tomascak PB, Chappell BW, Gao S (2004) Lithium isotopic composition and concentration of the upper continental crust. Geochim Cosmochim Acta 68:4167–4178

Teng F-Z, Li W-Y, Ke S, Marty B, Dauphas N, Huang S, Wu F-Y, Pourmand A (2010) Magnesium isotopic composition of the Earth and chondrites. Geochim Cosmochim Acta 74:4150–4166

Vinogradov AP, Surkov YA, Kirnozov FF (1973) The content of uranium, thorium, and potassium in the rocks of Venus as measured by Venera 8. Icarus 20:253–259

Walling DE, He Q, Blake W (1999) Use of ^{7}Be and ^{137}Cs measurements to document short- and medium-term rates of water-induced soil erosion on agricultural land. Water Resour Res 35:3865–3874

Wood BJ, Blundy JD (2003) Trace element partitioning under crustal and uppermost mantle conditions: the influences of ionic radius, cation charge, pressure, and temperature. In: Carlson RW (ed) The mantle and core. Elsevier-Pergamon, Oxford, pp 395–424

Aluminum

Mainak Mookherjee
Earth, Ocean and Atmospheric Sciences, Florida State University, Tallahassee, FL, USA

Element Data
Atomic Symbol: **Al**
Atomic Number: **13**
Atomic Weight: 26.98 g/mol
Isotopes and Abundances: ^{27}Al 100%, ^{26}Al (short-lived)
1 Atm Melting Point: 660.3 °C
1 Atm Boiling Point: 2519 °C
Common Valences: 3+
Ionic Radii: 53 pm (4-fold); 67.5 pm (6-fold)
Pauling Electronegativity: 1.61
First Ionization Energy: 577.5 kJ/mol
Chondritic (CI) Abundance: 0.84%[1]
Silicate Earth Abundance: ~2.3%
Crustal Abundance: 8.45%[2]
Seawater Abundance: 1–2 × 10^{-9} kg/L
Core Abundance: ~0
[1]McDonough and Sun (1995)
[2]Rudnick and Gao (2014)

Properties

A metallic element that is silver-white in color, weighs less, does not readily oxidize, i.e., resistant to corrosion, ductile, malleable, and is a good electrical conductor. The metal occurs as oxides, hydroxides, and aluminosilicate minerals in the Earth's crust.

History and Use

In 1825, Danish physicist Hans Christian Oersted obtained aluminum by heating aluminum chloride with potassium. However the aluminum was impure. In 1827, German chemist Friedrich Wöhler used similar method to obtain pure aluminum by heating aluminum chloride with sodium instead of potassium. The name for aluminum is derived from the Latin name for alum – "alumen" meaning bitter salt.

In the present day, aluminum is mined from bauxite deposits and reduced to metallic state. Metallic aluminum is widely used in our daily life. Use of metallic aluminum ranges from kitchen appliances, packaging, construction materials, transport industry, to electricity cables. Owing to its lighter weight and high strength-to-weight ratio, aluminum alloys are extensively used in manufacturing aircraft, spacecraft, and freight cars, and also in high-speed trains. Aluminum alloys are also extensively used in modern ships owing to their resistance to corrosion in both fresh-water and sea-water. Modern energy efficient skycrapers, pavilions, and sports facility, all use aluminum alloys. Around 25% of all aluminum produced world-wide is used for modern construction.

Isotopes and Cosmochemistry

The only stable isotope of aluminum is ^{27}Al. Aluminum also has several other isotopes, among them ^{26}Al is a short-lived cosmogenic radionuclide with half-life ($\tau_{1/2}$) of 7×10^5 year. ^{26}Al is likely to have played an important role in producing heat during the initial accretion stages of terrestrial planets (Hostetler and Drake 1979). Together with ^{10}Be, ^{26}Al in quartz provides valuable constraints on rates of surface processes including uplift, erosion (Balco et al. 2008), denudation, sedimentation (Hippe et al. 2012, von Blanckenburg and Willenbring 2014) and de-/glaciation (Ivy-Ochs and Briner 2014). Evidence of the existence of ^{27}Al is found mainly in calcium-aluminum rich inclusions (CAI), which are light colored inclusions in carbonaceous chondrite meteorites. CAIs are submillimeter to centimeter sized inclusions and are likely have formed by condensation at high temperature in the protoplanetary disks. Recent studies indicate that CAIs are one of the oldest (4568.2 million years) known materials in the solar system (Bouvier and Wadhwa 2010).

Mineralogy and Geochemistry

Based on Goldschmidt's classification, aluminum is primarily a lithophile element. In the Earth, together with silicon and oxygen, it forms a wide variety of aluminosilicate minerals that dominate all rock types including igneous, metamorphic, and sedimentary rocks. Igneous rocks such as basalts are composed of aluminosilicate framework minerals such as feldspar [$(K,Na)AlSi_3O_8$-$Ca_2Al_2Si_2O_8$]. Aluminosilicate polymorphs such as kyanite, andalusite, and silimanite [Al_2SiO_5] are often found in metamorphic rocks and provide valuable clues to the pressure-temperature conditions prevailing during the formation of the rock. Aluminum is also an important constituent of clay minerals such as kaolinite [$Al_2Si_2O_5(OH)_4$], which forms due to weathering and often associated with sedimentary rocks. In most aluminosilicate minerals, the [Al-O-Al] bonds are energetically unstable

with respect to [Al-O-Si] arrangement. The [Al-O-Si] arrangement better conforms to Pauling's electrostatic valence principle and is often referred to as "aluminum avoidance principle" (Loewenstein 1954). Calorimetric results on aluminosilicate minerals and glasses also indicate that reactions such as [Si-O-Si] + [Al-O-Al] = 2 [Si-O-Al] are energetically favorable by 40–100 kJ/mol (Navrotsky et al. 1982). Aluminum is a minor element in many of the major minerals in mantle rocks such as peridotites. Through coupled substitution [$Si^{4+} = Al^{3+}+H^{+}$], aluminum plays important role in sequestering water in mantle mineral phases including enstatite pyroxene [$MgSiO_3$] (Mierdel et al. 2007) and stishovite [SiO_2] (Pawley et al. 1993). In addition, incorporation of aluminum in hydrous phases enhances the thermodynamic stability (Ohtani et al. 2001; Bromiley and Pawley 2003) thus providing viable mechanism for transporting water into the deep Earth. Based on high-pressure studies it is also known that aluminum also stabilizes a suit of minor mineral phases in the deeply subducted oceanic and continental crust, such as hollandite [$(K,Na)AlSi_3O_8$], new aluminous phase (NAL) [$CaMg_2Al_6O_{12}$], and calcium ferrite [$(Ca,Mg)Al_2O_4$] (Irifune and Ringwood 1993, 1994; Mookherjee and Steinle-Neumann 2009; Mookherjee 2011). These aluminous phases have a wide range of chemistry and could host large alkali cations such as sodium and potassium in their crystal structure [$(Na,K)AlSiO_4$] (Miyajima et al. 2001; Mookherjee et al. 2012).

At deep crustal conditions where fluids and aluminosilicate minerals interact, the solubility silicon and aluminum in aqueous fluids are quite distinct. Silicon solubility is significantly greater than aluminum. Silica [SiO_2] initially dissolves in aqueous fluid as [$Si(OH)_4$] monomer and eventually forms dimer [$(OH)_3$-Si-O-Si-$(OH)_3$] and higher order polymers (Zotov and Keppler 2002). Unlike silicon, solubility of aluminum in neutral aqueous fluid is low (Walther 1997; Tropper and Manning 2007). At elevated pH the dominant aluminum species in aqueous fluid is [$Al(OH)_4^{1-}$] (White 2013). Unlike silicon, aluminum does not readily polymerize in aqueous fluids (Mookherjee et al. 2014) at neutral chemistry. Elevated pH or complexation with silica might enhance aluminum solubility by affecting speciation.

Biological Utilization and Toxicity

Some studies have hinted that adults who are exposed to high levels of aluminum may develop Alzheimer's disease. However, other results do not agree with these findings. So at present, the exposure to high levels of aluminum and Alzheimer's disease is highly contentious.

Children exposed to high levels of aluminum may develop bone disease since aluminum in the stomach may prevent adsorption of phosphate, which is required for growth of healthy bones.

Plants, however, are affected by aluminum toxicity. Most of the aluminum in the soil is often bound by ligands or aluminosilicates. However, lowering of the pH caused by irrigation practices or acid rain often releases Al^{3+} in the soil, which affects the growth and productivity of plants (Delhaize and Ryan 1995). Active research is being pursued to enhance understanding and also to engineer plants with higher tolerance towards aluminum toxicity.

Summary

Aluminum is the third most abundant element in the Earth's crust. Together with silicon and oxygen, it forms the framework of wide variety of oxides, hydroxides, and aluminosilicate minerals that are stable in the Earth's crust and mantle. Aluminum plays an important role in the water transport in the deep Earth. Aluminum metal is used in materials of daily use and almost 100% of aluminum is recyclable. Aluminum is typically not toxic but children should be protected from high levels of exposure.

Cross-References

- Acid Deposition
- Beryllium Isotopes
- Clay Minerals
- Complexes
- Cosmogenic Nuclides
- Earth's Continental Crust
- Lithophile Elements
- Mantle Geochemistry
- Magnesium Isotopes
- Ore Deposits
- Periodic Table
- Refractory Inclusions in Chondritic Meteorites

References

Balco G, Stone JO, Lifton NA, Dunai TJ (2008) A complete and easily accessible means of calculating surface exposure ages or erosion rates from ^{10}Be and ^{26}Al measurements. Quart Geochronol 3:174–195

Bouvier A, Wadhwa M (2010) The age of the solar system redefined by the oldest Pb-Pb age of a meteorite inclusion. Nat Geosci 3:637–641

Bromiley GD, Pawley AR (2003) The stability of antigorite in the systems $MgO-SiO_2-H_2O$ (MSH) and $MgO-Al_2O_3-SiO_2-H_2O$

(MASH): the effects of Al^{3+} substitution on high-pressure stability. Am Mineral 88:99–108
Delhaize E, Ryan PR (1995) Aluminum toxicity and tolerance in plants. Plant Physiol 107:315–321
Hippe K, Kober F, Zeilinger G, Ivy-Ochs S, Maden C, Wacker L, Kubik PW, Wieler R (2012) Quantifying denudation rates and sediment storage on the eastern Altiplano, Bolivia using cosmogenic ^{10}Be, ^{26}Al, and in situ 14C. Geomorphology 179:58–70
Hostetler CJ, Drake MJ (1979) On the early global melting of the terrestrial planets. In: Abstracts of papers presented to the conference on the lunar highlands crust. Sponsored by the Lunar Science Institute, LPI Contribution 394, edited by P. C. Robertson
Irifune T, Ringwood AE (1993) Phase transformations in subducted oceanic crust and buoyancy relationships at depths of 600–800 km in the mantle. Earth Planet Sci Lett 117:101–110
Irifune T, Ringwood AE (1994) Subduction of continental crust and terrigenous and pelagic sediments: an experimental study. Earth Planet Sci Lett 126:351–368
Ivy-Ochs S, Briner JP (2014) Dating disappearing ice with cosmogenic nuclides. Elements 10:351–356
Loewenstein W (1954) The distribution of aluminum in the tetrahedral of silicates and aluminates. Am Mineral 39:92–96
McDonough WF, Sun SS (1995) The composition of the Earth. Chem Geol 120:223–253
Mierdel K, Keppler H, Smyth JR, Langenhorst F (2007) Water solubility in aluminous orthopyroxene and the origin of Earth's atmosphere. Science 315:364–368
Miyajima N, Yagi T, Hirose K, Kondo T, Fujino K, Miura H (2001) Potential host phase of aluminum and potassium in the Earth's lower mantle. Am Mineral 86:740–746
Mookherjee M (2011) Mid-mantle anisotropy: elasticity of aluminous phases in subducted MORB. Geophys Res Lett 38:L14302. https://doi.org/10.1029/2011GL047923
Mookherjee M, Steinle-Neumann G (2009) Detecting deeply subducted crust from the elasticity of hollandite. Earth Planet Sci Lett 288:349–358
Mookherjee M, Karki BB, Stixrude L, Lithgow-Bertelloni C (2012) Energetics, equation of state, and elasticity of NAL phase: potential host for alkali and aluminum in the lower mantle. Geophys Res Lett 39:L19306
Mookherjee M, Keppler H, Manning CE (2014) Aluminum speciation in aqueous fluids at deep crustal pressure and temperature. Geochim Cosmochim Acta 133:128–141
Navrotsky A, Peraudeau G, McMilan P, Coutures JP (1982) A thermochemical study of glasses and crystals along the joins silica-calcium aluminate and silica-sodium aluminates. Geochim Cosmochim Acta 46:2039–2047
Ohtani E, Litasov K, Suzuki A, Kondo T (2001) Stability field of new hydrous phase δ-AlOOH, with implications for water transport into deep mantle. Geophys Res Lett 28:3991–3993
Pawley AR, McMillan PF, Holloway JR (1993) Hydrogen in stishovite, with implications for mantle water content. Science 261:1024–1026
Rudnick RL, Gao S (2014) 4.1 – Composition of the continental crust. In: Holland HD, Turekian KK (eds) Treatise on geochemistry, 2nd edn. Elsevier, Oxford, pp 1–51
Tropper P, Manning CE (2007) The solubility of corundum in H_2O at high pressure and temperature and its implications for Al mobility in the deep crust and upper mantle. Chem Geol 240:54–60
Von Blanckenburg F, Willenbring JK (2014) Cosmogenic nuclides: dates and rates of Earth-surface changes. Elements 10:341–346
Walther JV (1997) Experimental determination and interpretation of the solubility of corundum in H_2O between 350 and 600 °C from 0.5 to 2.2 kbar. Geochim Cosmochim Acta 61:4955–4964
White WM (2013) Geochemistry. Wiley-Blackwell, Hoboken, p 660
Zotov N, Keppler H (2002) Silica speciation in aqueous fluids at high pressure and high temperature. Chem Geol 184:71–82

Analytical Techniques

William M. White
Department of Earth and Atmospheric Sciences, Cornell University, Ithaca, NY, USA

Definition

Geochemical analytical techniques are used to determine the elemental, molecular, and isotopic compositions of natural materials including rocks, fluids, gases, and their components. They are also used to characterize molecular or crystal structure of these materials and the valance states of their constituent atoms, the nature of chemical bonds between them, and the nature and rates of reactions. This entry only summarizes the broad principles and applications of various analytical techniques; details of these techniques are reviewed in individual entries.

Compositional and Isotopic Analysis

The objective of elemental analysis is to quantify the relative proportions of the chemical elements in a sample. In principle, all chemical elements are present in most natural materials, although not necessarily at detectable levels. Generally, just a few elements make up more than 95% of these materials; these are generally referred to as the *major* elements, components, salts, etc. Some techniques have the sensitivity to analyze only major elements; other techniques have been developed to determine trace element abundances. The technique employed will depend on the abundance of the elements of interest. In some cases, the most abundant components are not determined by analysis. For example, oxygen is the most abundant element in most rocks, but its abundance is often inferred rather than determined. Similarly, the amount of water, and by extension the amount of O and H in aqueous solutions, is rarely directly determined.

Modern elemental analysis is almost always instrumental, having replaced earlier gravimetric and colorimetric methods over the course of the twentieth century. There are several broad classes of these techniques. The first are "spectroscopic" techniques in which abundance of elements or compounds is determined by measuring the amount of characteristic electromagnetic radiation either adsorbed or emitted by them. The second is mass spectrometric techniques in which a sample or a part of it is ionized, the ions separated by mass, and counted. A third class of techniques measures other particles, such as emitted beta or alpha particles, neutrons, geoneutrinos, or back-scattered electrons, but

these techniques have limited application. In most techniques, calibration against a geochemical reference material is necessary.

Spectroscopic Techniques

These techniques vary by the nature of the radiation employed, whether it is natural or induced, the materials analyzed, and whether emission or absorption is measured. The radiation varies from infrared to gamma. Infrared radiation is associated with molecular vibrations and rotations. For example, infrared absorption is used to routinely determine the abundances of CO_2, CH_4, and other trace gases in the atmosphere, either in flasks using artificial illumination or directly in the atmosphere using solar illumination (e.g., Vanderkluysen et al. 2014; Wunch et al. 2011) and to determine the abundance of CO_2 and H_2O in volcanic glasses (Dixon et al. 1988).

Techniques of atomic adsorption and atomic emission spectroscopy are based on the adsorption or emission of photons in or near the optical spectrum as electrons surrounding atoms transition between quantized energy levels. In atomic adsorption spectrometry (AAS), a sample solution is atomized in a flame or a graphite furnace and illuminated with the emission spectrum of the element of interest. The intensity of this light absorbed by the sample is proportional to the concentration of the element in it. In atomic emission spectroscopy, electrons in a sample are excited into higher energy states, either thermally (flame emission spectroscopy or flame photometry), through electrical discharge (spark and arc atomic emission spectroscopy), or in a radio-frequency-induced inductively coupled argon plasma (variously known as inductively coupled plasma optical emission spectroscopy (ICP-OES) or inductively coupled plasma atomic emission spectroscopy (ICP-AES)). Regardless of the excitation method, the principle is same: electrons decay to lower states by emitting photons with energy/wavelength characteristic of the element. Consequently, the intensity of light at that wavelength is proportional to the element's abundance in the sample. Of these techniques, ICP-OES is rapidly replacing older techniques such as AAS and flame photometry as it allows for simultaneous measurement of most naturally occurring elements because the higher temperatures in the plasma result in greater intensities and more complete breakdown of compounds, leading to greater sensitivity and accuracy (Hou et al. 2006).

For the most part, these optical techniques are most readily used to analyze aqueous solutions (although electrothermal vaporization is possible). This is ideal for water samples, but a disadvantage for rock and soil samples. In contrast, x-ray fluorescence (XRF) is ideally suited for analysis of solids. This technique has a long history, having been first used by Victor Goldschmidt in the early twentieth century. The principle involved is similar to optical techniques in that it is based on detecting photons emitted by electrons as they decay from excited states. The difference is that in XRF electrons in inner shells are excited by illuminating the sample with x-rays; the energy difference between states of inner electrons is greater than those of outer electrons excited in optical techniques, and consequently they emit photons in the x-ray rather than optical part of the spectrum. This technique has the advances of relatively little sample preparation and an ability to quantify many trace elements as well as the major constituents of materials. Most XRF analysis is done with x-rays generated with a cathode-ray tube; synchrotrons are capable of producing a much more intense photon beam. Thus, synchrotron-XRF allows greater sensitivity and analysis at micron-scale resolution (e.g., Dyl et al. 2014).

X-ray emission can also be induced by bombardment with energetic particles. This allows for some variations on the XRF technique such as electron probe microanalysis (EPMA), in which x-ray emission is induced by bombardment with an energetic electron beam, and particle-induced x-ray emission (PIXE), in which it is induced by bombardment with a proton or alpha particle beam. These techniques are particularly appropriate for in situ microanalysis. With a beam diameter of 10 μm and less, the electron microprobe has become the standard method for quantitative analysis of major and minor elements in solid phases or parts of phases (such as inclusions or crystal zones) as well as qualitative mapping of those phases. Synchrotron-based micro-PIXE has sufficient sensitivity that trace element concentrations can also be measured and mapped. A PIXE instruments utilizing ^{210}Po-sourced alpha particles aboard the NASA's *Curiosity* rover has provided in situ analysis of Martian materials.

Gamma rays are produced by quantized nuclear energy state transitions associated with radioactive decay and hence can be also used to quantify the amount of an element. There are two approaches to gamma-ray spectroscopy: the first measures gamma-ray emissions of naturally occurring radionuclides, and the second measures gamma rays emitted by radionuclides produced by neutron bombardment. In gamma-ray logging, a gamma spectrometer is lowered down a borehole to determine the concentrations of K, Th, and U in the adjacent rock as a function of depth (e.g., Hampson et al. 2005). Gamma-ray spectrometers can also be flown in aircraft to survey the distribution of natural and man-made (e.g., Fukushima accident) radioactive elements. Finally, gamma-ray spectrometers have frequently been flown on spacecraft for elemental analysis of surfaces of other solar system bodies. In addition to gamma rays emitted by K, U, and Th, cosmic rays impacting on the surfaces of bodies with little or no atmosphere initiate nuclear reactions producing

unstable nuclides, which then decay emitting characteristic gamma rays. Used in conjunction with neutron detectors, the abundances of a number of elements, including O, Mg, Al, Si, Cl, Ca, Ti, and Fe (Prettyman 2007) can be determined. In the second approach, known as *neutron activation analysis*, a sample is irradiated with neutrons in a reactor. Some of those neutrons are captured by sample nuclei to produce radioactive isotopes, which then decay with the emission of a characteristic gamma-ray spectrum. The technique can be applied directly to solids and has the advantage of requiring relatively little preparation and being extremely sensitive for elements with high neutron capture cross sections, such as many of the rare earths and noble metals. The disadvantage is that abundances of elements with low neutron capture cross sections, such as Nb, cannot be determined.

Mass Spectrometric Techniques

Two broad classes of mass spectrometers are employed by geochemists. The first is so-called isotope ratio mass spectrometry (IRMS), which are primarily designed to determine isotopic compositions but can also be used to determine elemental abundances. The second is designed to analyze organic molecules. In both classes, ions are formed in the mass spectrometer's source, accelerated by an electric field, separated by mass-to-charge ratio in the analyzer section, and the ion current measured or individual ions counted by a detector. Isotope ratio mass spectrometers are, of course, the primary tool of stable and radiogenic isotope geochemists and geochronologists. High-precision isotope ratio determination generally requires a Nier-type magnetic sector instrument (Nier 1940) and pre-purification of the element of interest, for example, by ion exchange chromatography, cryogenic separation of gases, or in-line gas chromatography. From a perspective of elemental analysis, they have the ability to accurately and precisely analyze elements in geologic materials at concentration levels well below the effective detection limit of spectroscopic techniques. One approach to elemental analysis is isotope dilution, in which a known amount of "spike," a purified isotope of the element of interest, is added to the sample. The isotope ratio of the sample-spike mixture is then measured and the abundance of that element calculated from it. Isotope dilution can be used with a variety of ion source designs, including gas source (GCMS), spark source, inductively coupled plasma (ICP-MS), and thermal ionization (TIMS). Although highly accurate, it is time-consuming. The other approach is to measure the ion beam intensity of specific isotopes and comparing that to the ion beam intensity in a standard. This is the basis of spark source mass spectrometry as well as inductively coupled plasma mass spectrometry (ICP-MS), which has now almost entirely supplanted the former. As in optical techniques, samples are usually introduced into an ICP-MS in solution, although other introduction methods such as hydride generation can be used. In laser ablation-ICP-MS (LA-ICP-MS), material is ablated from a small pit of a solid sample with a laser and the ablated material carried into the plasma by a gas stream. This allows for direct analysis of elemental abundances or isotope ratios in minerals and other geologic solids on spots with a radius as small as 5 μm.

Ion microprobes, or secondary ionization mass spectrometry (SIMS), are instruments designed for isotopic and chemical microanalysis. A primary ion beam, often O or Cs, sputters secondary ions from a small (nm to μm scale) region of the polished surface of a sample, and the secondary ions are extracted by an electric field into a mass spectrometer. Such instruments require higher mass resolution than conventional isotope ratio mass spectrometers to avoid interferences. Among other things, these instruments have been particularly useful in dating complex zircons, including Earth's oldest surviving mineral grains (Wilde et al. 2001) and evaluating intracellular and metabolic processes (e.g., Orphan et al. 2009).

Because of their extreme rarity, cosmogenic nuclides such as ^{14}C, ^{10}Be, and ^{26}Al are measured by accelerator mass spectrometers. In accelerator mass spectrometers, ions are initially separated in a sector mass spectrometer, then stripped of electrons, and accelerated to very high energies (200 kV–2 MV compared to $\leq$10 kV in conventional mass spectrometers) before entering a second-stage mass spectrometer and a detector. This is highly effective in eliminating isobaric interferences allowing quantification of isotope ratios as low as 10^{-12}–10^{-18}.

Mass spectrometers used for analysis of organic compound analysis are generally combined with liquid (LC) or gas chromatographs (GC) and a variety of hard (electron impact) or soft (electrospray or chemical) ionization techniques. Different compounds move through the chromatographic column at different speeds depending on their properties and the nature of the stationary phase. Thus, in liquid and gas chromatography-mass spectrometry (GC-MS), compounds will enter the mass spectrometer sequentially. In the case of hard impact ionization, compounds typically partially breakdown into fragments, producing a characteristic distribution of mass/charge ratios. From that, the elemental formula can be reconstructed. In contrast, the softer ionization techniques fragment less and thus can retain a suite of molecular ion peaks from a complex mixture. GC-MS and LC-MS instruments typically utilize a quadrupole or time-of-flight mass spectrometer rather than the sector design of IRMS due to their ability to very quickly scan the mass spectrum. Compound-specific isotope analysis (CSIA) operates in a similar manner employing a liquid

or gas chromatograph to separate organic compounds, but employs a sector-design IRMS rather than a quadrupole. High-resolution mass spectrometry (time-of-flight or ion-cyclotron resonance) is necessary in studying large macromolecules common in nature that contain a distribution of isotopes resulting in different components having nearly identical m/z ratios. For example, ^{14}N differs from $^{12}C^{1}H_2$ by 0.0126 u. Resolving these as individual ions requires a mass resolution of only 0.1%, but resolving them as constituents of a molecule of mass 500 u would require a resolution of 2 ppm.

Crystalline, Molecular, Oxidation State, and Chemical Bonding Characterization

Determination of mineral structure is generally done by x-ray diffraction (XRD). Samples are irradiated by monochromatic x-rays, which are diffracted by the crystal lattice. The angle of diffraction is a function of the interatomic spacing, which is in turn characteristic of the crystal structure. Because the crystal structure and x-ray diffraction patterns of nearly all minerals are known, XRD can be used to determine the minerals present and their relative abundances in a rock or soil sample. This kind of analysis is generally done with a powdered sample. XRD can, of course, be used to determine crystalline structure when it is not already known. This type of research is often conducted on single crystals.

The absorption techniques described above measure the absorption photons with energies corresponding to quantized molecular or atomic transitions. However, when a sample is irradiated, some photons are inelastically scattered, i.e., they lose or gain some fraction of their original energy. This results in a shift in wavelength. Raman spectroscopy exploits this inelastic photon scattering. Samples are irradiated with intense monochromatic radiation, which can range from x-ray to infrared, and the intensity of the inelastically scattered photons measured as a function of wavelength shift. This shift depends on the nature of atoms and molecules, their chemical bonds, and their rotational and vibrational motions. From analysis of the distribution of these energies, inferences about the presence of certain functional groups, conformations and symmetry of the molecules, anisotropy, chirality, and polymer and crystal orientations can be drawn. Since the scattering depends in part on the atoms present, Raman spectroscopy also provides semiquantitative analysis and information on crystal structure that compliments other techniques ranging from infrared spectroscopy to XRD. It can also be used to measure temperature and pressure in experiments. Raman spectroscopy is nondestructive, requires minimal sample preparation, and can be used at high spatial resolution, 10 μ and less for Raman microspectroscopy.

X-ray near-edge absorption spectroscopy (XANES) is used to interrogate the chemical state, such as valence, coordination number, bonding distances, etc., of atoms in soil minerals, volcanic glasses, etc. XANES exploits the absorption of x-rays by atoms as a function of the energy (or equivalently, wavelength) of an x-ray beam generated by a synchrotron. Whereas XRF utilized a photon source of fixed energy, XANES uses an x-ray beam of tunable energy. Absorption increases sharply when the energy of the incident photon matches the energy of an electron in a specific inner atomic orbital – this is the absorption edge. The energy of the edge is a function of the oxidation state of the atom (a higher oxidation state requires more energetic x-ray to excite inner electrons because the nucleus is less shielded). The edge also has structure (i.e., variation in absorption efficiency as a function of energy) that results from scattering resonances of the electrons ejected at low kinetic energy. This in turn depends on the position of neighboring atoms including interatomic distances and bond angles. XANES has been used, among other things, to determine Fe^{3+}/Fe^{2+} ratios in volcanic glasses (e.g., Kelley and Cottrell 2009).

Mössbauer spectroscopy exploits small changes in the energy of gamma-ray absorption by a nucleus due to factors such as transition of electrons within its orbital, the surrounding electric field gradient, and interaction between the nucleus and a surrounding magnetic field. In this technique, the sample is illuminated by gamma rays emitted by a nucleus identical to the one in the sample being studied, most commonly ^{57}Fe (the daughter of radioactive ^{57}Co). The gamma-ray source is moved toward and away from the sample during analysis, resulting in Doppler shifts in gamma-ray energy and absorbance measured as a function of energy. Oxidation state and information on the local crystallographic and chemical environment of Fe nuclei can then be determined from the absorption spectrum. The application of this technique is broad including study of redox reactions in sediments and soils, oxidation state of mantle rocks and melts, and iron isotope fractionation (e.g., Polyakov and Mineev 2000). Mössbauer spectrometers have been included in the instrumentation package of NASA's Martian rovers.

Nuclear magnetic resonance (NMR) spectroscopy exploits the intrinsic "spin" of protons and neutrons. Because the spins of paired nucleons cancel, only nuclei with an odd number of protons or neutrons have a net spin. The spin of such nuclei will align with that of an applied magnetic field. Application of radio-frequency (RF) radiation of the appropriate frequency (the resonant frequency) can then excite

these nuclei into higher spin states. The precise energy difference between spin states and hence the precise RF frequency that must be absorbed for the transition to occur will depend on the atomic environment of the nucleus as a consequence of electrons in the vicinity of the nucleus. As a result of this so-called chemical shift, NMR spectroscopy can be used to explore the structure, dynamics, and chemical environment of atoms. It has been used, among other things, to explore the structure of aluminosilicate glasses (analogies of silicate liquids) (e.g., Gambuzzi et al. 2014), the structure of kerogen and humic substances (e.g., Mann et al. 1991), and reaction rates in aqueous solutions (e.g., Harley et al. 2011).

Summary

Geochemists have a wide variety of analytical instruments at their disposal to characterize the nature and composition of the atmosphere, aqueous solutions, rocks, minerals, and soil. Much of the progress in geochemistry has come from the enormous innovation in analytical techniques over the last century.

Cross-References

- Atomic Absorption, Inductively Coupled Plasma Optical Emission Spectroscopy, and Infrared Spectroscopy
- Compound-Specific Isotope Analysis
- Cosmogenic Nuclides
- Electron Probe Microanalysis (EPMA)
- Gas Chromatography–Mass Spectrometry (GC–MS)
- Gas Source Mass Spectrometry (GS-MS)
- Geochemical Reference Materials
- Geochronology and Radiogenic Isotopes
- Geoneutrinos
- Inductively Coupled Plasma Mass Spectrometry (ICP-MS)
- Ion Exchange Chromatography
- Ion Microprobe
- Isotope Dilution
- Laser Ablation – Inductively Coupled Plasma Mass Spectrometry
- Neutron Activation Analysis
- Nuclear Magnetic Resonance
- Organic Geochemistry
- Particle-Induced X-Ray Emission (PIXE)
- Raman Microspectroscopy
- Refractory Inclusions in Chondritic Meteorites
- Stable Isotope Geochemistry
- Synchrotron X-ray Fluorescence Analysis
- Thermal Ionization Mass Spectrometry
- Trace Elements
- X-ray Diffraction
- X-Ray Fluorescence Analysis

References

Dixon JE, Stolper E, Delaney JR (1988) Infrared spectroscopic measurements of CO_2 and H_2O in Juan de Fuca ridge basaltic glasses. Earth Planet Sci Lett 90(1):87–104. https://doi.org/10.1016/0012-821X(88)90114-8

Dyl KA, Cleverley JS, Bland PA, Ryan CG, Fisher LA, Hough RM (2014) Quantified, whole section trace element mapping of carbonaceous chondrites by synchrotron X-ray fluorescence microscopy: 1. CV meteorites. Geochimica et Cosmochimica Acta 134:100–119. https://doi.org/10.1016/j.gca.2014.02.020

Gambuzzi E, Pedone A, Menziani MC, Angeli F, Caurant D, Charpentier T (2014) Probing silicon and aluminium chemical environments in silicate and aluminosilicate glasses by solid state NMR spectroscopy and accurate first-principles calculations. Geochim Cosmochim Acta 125:170–185. https://doi.org/10.1016/j.gca.2013.10.025

Hampson GJ, Davies W, Davies SJ, Howell JA, Adamson KR (2005) Use of spectral gamma-ray data to refine subsurface fluvial stratigraphy: late Cretaceous strata in the Book Cliffs, Utah, USA. J Geol Soc 162(4):603–621

Harley SJ, Ohlin CA, Casey WH (2011) Geochemical kinetics via the Swift–Connick equations and solution NMR. Geochim Cosmochim Acta 75(13):3711–3725. https://doi.org/10.1016/j.gca.2011.04.009

Hou X, Amais RS, Jones BT, Donati GL (2006) Inductively coupled plasma optical emission spectrometry. In: Encyclopedia of Analytical Chemistry, vol. Wiley, Chichester, UK. https://doi.org/10.1002/9780470027318.a5110.pub3

Kelley KA, Cottrell E (2009) Water and the oxidation state of subduction zone magmas. Science 325(5940):605–607. https://doi.org/10.1126/science.1174156

Mann AL, Patience RL, Poplett IJF (1991) Determination of molecular structure of kerogens using 13C NMR spectroscopy: I. The effects of variation in kerogen type. Geochim Cosmochim Acta 55(8):2259–2268. https://doi.org/10.1016/0016-7037(91)90102-B

Nier AO (1940) A mass spectrometer for routine isotope abundance measurements. Rev Sci Instrum 11(7):212–216

Orphan VJ, Turk KA, Green AM, House CH (2009) Patterns of 15 N assimilation and growth of methanotrophic ANME-2 archaea and sulfate-reducing bacteria within structured syntrophic consortia revealed by FISH-SIMS. Environ Microbiol 11(7):1777–1791. https://doi.org/10.1111/j.1462-2920.2009.01903.x

Polyakov VB, Mineev SD (2000) The use of Mössbauer spectroscopy in stable isotope geochemistry. Geochim Cosmochim Acta 64(5):849–865. https://doi.org/10.1016/S0016-7037(99)00329-4

Prettyman TH (2007) Remote chemical sensing using nuclear spectroscopy. Enc Sol Syst 2:765–786

Vanderkluysen L, Burton MR, Clarke AB, Hartnett HE, Smekens J-F (2014) Composition and flux of explosive gas release at LUSI mud volcano (East Java, Indonesia). Geochem Geophys Geosyst 15(7):2932–2946. https://doi.org/10.1002/2014GC005275

Wilde SA, Valley JW, Peck WH, Graham CM (2001) Evidence from detrital zircons for the existence of continental crust and oceans on the earth 4.4 Gyr ago. Nature 409:175–178

Wunch D, Toon GC, Blavier J-FL, Washenfelder RA, Notholt J, Connor BJ, Griffith DWT, Sherlock V, Wennberg PO (2011) The total carbon column observing network. Philosophical Transactions of the Royal Society A: mathematical. Phys Eng Sci 369(1943):2087–2112. https://doi.org/10.1098/rsta.2010.0240

Anthropogenic CO_2

Klaus S. Lackner
School of Sustainable Engineering and the Built Environment, Arizona State University, Tempe, AZ, USA

Synonyms

Anthropogenic carbon dioxide; Human-generated carbon dioxide

Definition

Carbon dioxide, generated by human activities, that enters the natural carbon cycle (usually through the atmosphere).

Anthropogenic carbon dioxide, chemical formula CO_2, is produced in the chemical conversion of various carbon bearing compounds or by releasing CO_2 from geological reservoirs that without human interference would have remained isolated from the more mobile carbon pools in the atmosphere, the ocean, and the biosphere.

Sources of Anthropogenic CO_2

Generation of anthropogenic CO_2 began with the introduction of fire and the combustion of biomass, which mainly produces CO_2 and H_2O. Until the industrial revolution, anthropogenic CO_2 production remained small compared to the natural carbon cycle and was essentially balanced by the uptake of CO_2 by plants. For biomass to be burned, it first has to grow. The carbon balance was more seriously upset with the introduction of coal as an important heating fuel in Britain in the late eighteenth century at the dawn of the industrial revolution (Christianson 2000). Coal consumption grew rapidly during the nineteenth century. Prior to the industrial revolution, the occasional use of coal and oil that spontaneously comes to the surface was insignificant. By contrast, the industrialization of Britain was based on large-scale consumption of coal, and coal energy became a major foundation of modern societies. Initially, coal simply replaced wood for heating, but then took a role in powering the steam engines (Newcomb's first steam engine) (Christianson 2000) driving the pumps that kept coalmines dry. As steam engines improved, their uses spread to many different applications revolutionizing modern societies. Add to this the invention of modern steel making with coke produced from coal, and the combustion of coal released so much CO_2 to the atmosphere that it became an important and additive player in the overall carbon cycle. The rate of anthropogenic CO_2 generation accelerated even more at the end of the nineteenth century with the introduction of petroleum, which is easily refined into convenient liquid fuels like gasoline, kerosene, diesel, and jet fuel. Finally, natural gas was added to the mix, and today's CO_2 emissions from fossil fuel combustion exceed 30 billion metric tons per year. Coal, oil, and gas each contributes comparable amounts (Fig. 1).

Other anthropogenic releases of CO_2 result from the calcination of carbonates, usually lime stone, mainly in the production of cement. About half of the CO_2 in cement making results from fuel combustion, the remainder is the CO_2 freed as limestone (calcium carbonate) is converted to

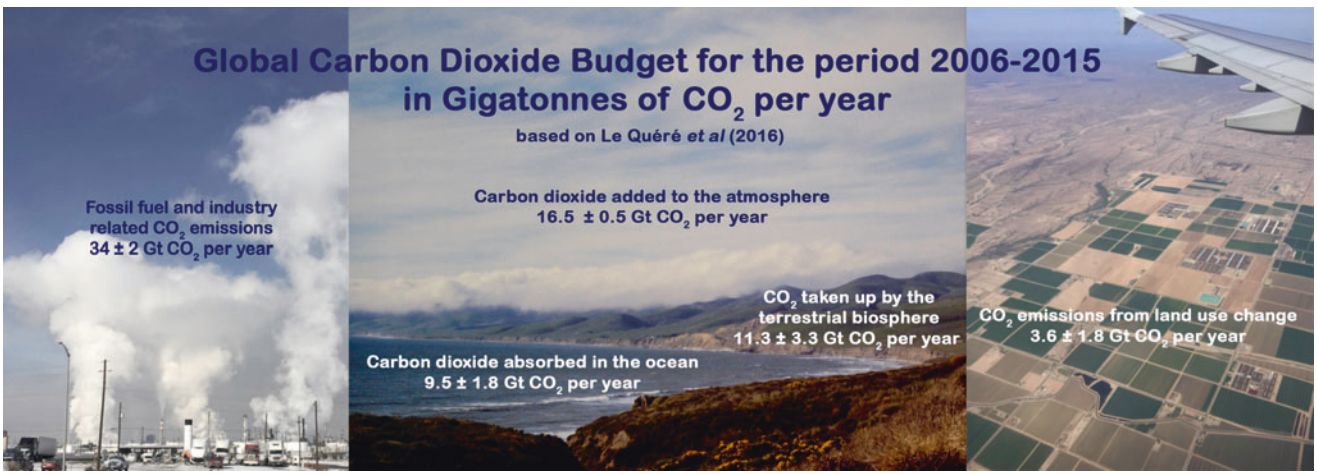

Anthropogenic CO_2, Fig. 1 The global carbon dioxide budget for the decade from 2006 to 2015. The budget numbers are given in Gigatonnes of carbon dioxide per year and reflect a 10 year average. The anthropogenic fuel cycle liberates carbon from fossil fuel resources and land use. The carbon, mainly in the form of carbon dioxide enters the atmosphere, and redistributes itself between the atmosphere, the ocean and the terrestrial biosphere. Most of the CO_2 in the ocean is dissolved inorganic carbon. Most of the carbon stored in biomass is organic matter. Here the numbers are given in terms of CO_2 masses, but often they are given in terms of carbon. One ton of carbon equals 3.67 tons of CO_2. The carbon dioxide flows have been adapted from Le Quéré C et al. (2016), Global carbon budget 2016. Earth Syst Sci Data 8(2):605.)

lime (calcium oxide). The cement industry produces about 7% of all anthropogenic CO_2 emissions (calculated from data provided by van Oost 2016 and Fischedick et al. 2014).

Not all of the carbon present in oil, coal, or gas that is extracted from the ground is directly oxidized to CO_2, some is incorporated into other chemical compounds, for example, plastics, asphalt, or carbon for carbon black in tires or in carbon electrodes. Some of these carbon-based materials will persist in the environment for long times, but many will degrade over time producing CO_2 in the process; others will be combusted in waste incineration plants that again release anthropogenic CO_2.

Finally, anthropogenic sources include CO_2 from underground gas reservoirs that are either tapped for their CO_2 content or produce CO_2 as an unintended byproduct. For example, many natural gas wells contain significant amounts of CO_2 that is co-produced with methane. In most cases, the CO_2 will have to be removed from the gas before it can be distributed to customers. For example, the Sleipner Field in the North Sea operated by Statoil produces a gas that contains about 10% carbon dioxide, too much to leave it in the gas (IPCC 2005).

Adding up the total carbon mobilized by human activities (Ciais et al. 2013), including the sources mentioned above and carbon released from deforestation and land use changes, minus the uptake induced by human activities for example in reforestation, still leaves a net release of CO_2 of 33 billion tons per year, or nine billion tons of mobilized carbon. Even though this is much smaller than the natural annual flow of carbon from the atmosphere into biological reservoirs (on the order 170 billion metric tons of carbon per year), it matters because it is not matched by an opposing flow. Photosynthesis with its large uptake and release rates causes an annual fluctuation of about 6 parts per million by volume (ppm) in the atmosphere, but does not lead to a significant change in the annual average concentration. By contrast, human emissions currently raise CO_2 concentration by about 2.2 ppm per year. Since the beginning of the industrial revolution, the CO_2 concentration in the atmosphere rose from 280 to 410 ppm in May of 2017.

Environmental Concerns Over Anthropogenic CO_2 Emissions

Anthropogenic CO_2 emissions have become a large environmental concern as they represent by far the largest contribution to human-induced climate change. Excess CO_2 redistributes itself between the atmosphere, the ocean, and the biosphere. The surface ocean is in equilibrium with the atmosphere, but the deep ocean will take many centuries to adjust to changes in the atmosphere. In equilibrium, about 80% of the excess CO_2 will end up in the ocean. Roughly half the CO_2 emitted to the atmosphere will stay there for centuries. Over tens of thousands of years, natural removal of CO_2 from the combined atmosphere/ocean/biosphere system proceeds by geochemical processes that produce mineral carbonates (Archer et al. 2009).

As a greenhouse gas in the atmosphere, CO_2 causes global warming. Dissolved as carbonic acid in the ocean, it changes the ocean pH, and with it the carbonate chemistry of the ocean, which is important to many calcifying organisms like corals. Lastly, CO_2 leads to worldwide eutrophication of bioecosystems with concomitant imbalances.

Computational models corroborate and even strengthen the simple and physical story that CO_2 emissions are cumulative and tend to pile up in the atmosphere. Models all agree (MacDougall 2015) that the warming caused by CO_2 emissions is driven by total cumulative emission and does not depend on the shape of the emission profile. Models suggest that the reduction of the greenhouse effect due to uptake of CO_2 into the ocean is compensated for by the gradual warming of the ocean. The temperature increase will stop when emissions stop, but excess temperatures will persist for about a millennium (Solomon et al. 2009). Moreover, models agree that the expected warming is simply linear in the cumulative emissions, which hints at complex feedback mechanisms because the underlying greenhouse effect is logarithmic in the CO_2 concentration.

Policy makers and climate change scientist agree that climate change needs to be kept to a manageable level. Most countries of the world including the United States, China, and European Union signed and ratified the 1992 United Nations Framework Convention on Climate Change in Rio de Janeiro that obligates all parties to prevent dangerous levels of climate change. Today, the Intergovernmental Panel on Climate Change (IPCC) discusses a 2°C rise over preindustrial global temperatures as a threshold beyond which warming poses severe risks to humans and the environment (IPCC 2014). This corresponds to about 450 ppm of CO_2 in the atmosphere, or 45 ppm above the current level. The 21st United Nations Conference of the Parties on Climate Change in Paris in 2015 resulted in an agreement that reaffirms the 2°C limit and adds that the world should be aiming for a temperature increase of no more than 1.5°C leaving very little room for additional CO_2 emissions.

Balancing the Carbon Budget

Stabilizing the CO_2 concentration in the atmosphere at any reasonable level requires balancing the anthropogenic carbon budget. This in turn means that fossil fuel combustion must either be eliminated completely by moving to nonfossil energy sources or the remaining fossil fuel consumption has to be balanced by the safe and permanent disposal of an

equivalent amount of CO_2. Renewable energy including solar and biomass or nuclear energy could replace oil, coal, and gas, which today comprise more than 80% of the world's primary energy consumption. To the extent that fossil fuels will still be used, e.g., as jet fuels in the aviation industry, disposal of an equivalent amount of CO_2 will become necessary. Disposal processes are referred to as carbon sequestration or carbon capture and storage (IPCC 2005). Carbon dioxide storage could involve the injection of CO_2 into deep underground reservoirs, where it would occupy the pore space in a manner similar to how oil and gas are naturally stable in geological reservoirs. A second option is to bind CO_2 to natural minerals that react with carbon dioxide and water to form carbonate salts or bicarbonate salts. This process is referred to as mineral sequestration (Lackner et al. 1995). Bicarbonates tend to be water-soluble and would end up in the ocean, and carbonates are often insoluble and form minerals like limestone or calcium carbonate. Such mineralization processes occur naturally and are known as geological weathering. In their natural form, they are far too slow to keep up with anthropogenic CO_2 production, but over tens or hundreds of thousands of years, they will reinstate the natural carbon balance of the system. For practical carbon dioxide storage, mineralization would need to be accelerated by many orders of magnitude. A third option, which actually was the first to be proposed (Marchetti 1977), is to put the CO_2 into the ocean, either by dissolving it in the water column or forming lakes of CO_2 at the ocean floor. However, ocean storage of CO_2, which in water turns to carbonic acid, has been criticized on environmental grounds. The capacity of the ocean to hold sufficient CO_2 for a sufficient time may not be available. At the present rate of three trillion tons per century, CO_2 production in the coming century could easily be several trillion tons. For comparison, Lake Michigan contains 5 trillion tons of water. Ocean circulation turns over the ocean in roughly 1000 years. Considering that it will take natural processes many thousands of years to eliminate the excess CO_2, a residence time in the ocean of less than a thousand years would be too short. Similar concerns over capacity and storage time have been raised about storing anthropogenic CO_2 in the standing biomass.

Before CO_2 can be stored, it must be collected or captured. In the case of biomass growth, capture is part of the natural process of photosynthesis. For other approaches to carbon sequestration, there need to be active processes to collect CO_2. The most suitable locations for capture are the big point sources of CO_2, like power plants, refineries, steel plants, and cement plants (IPCC 2005). Among these point sources, power plants tend to be bigger and in aggregate produce much more CO_2 than other point sources. Natural gas wells frequently co-produce CO_2 that needs to be sequestered. One of the largest CO_2 disposal effort is at the above-mentioned Sleipner Gas Field in the North Sea, where the Norwegian oil company Statoil separates the CO_2 from the natural gas at the well site and injects about one million tons of CO_2 per year into a deep saline aquifer 800 m below the seafloor (Arts et al. 2008).

Point source capture could involve retrofitting existing power plants, building new power plants with more efficient and more integrated CO_2 capture. In order to truly close the anthropogenic carbon cycle, it is not sufficient to reduce emissions or capture a large fraction of the CO_2 that is produced in the combustion process, but it will be necessary to collect all of the CO_2, even that which escapes into the atmosphere. Moreover, it may become necessary to create negative emissions where CO_2 that has already been emitted is removed from the environment. Unless emissions are reduced much more rapidly than today an overshoot scenario becomes unavoidable, and some climate scientists consider it already necessary (Hansen et al. 2013).

Collection from the environment, for example directly from the atmosphere, also makes it possible to balance out emissions from sectors of the economy that do not lend themselves to point source capture, because emissions are distributed and mobile and individually small (Lackner 2014). Vehicles, ships, and airplanes may carry fuel that is converted at the point of consumption into CO_2 and H_2O. While point source capture, for example, from flue gas can go back to well-established scrubbing technologies using, for example, amine solutions to bind CO_2 that is regenerated during a heating step, capture from ambient air requires innovative approaches, which are being developed, or combust biomass, which during its growth collected CO_2 from the atmosphere, in power plants that capture their own CO_2 and permanently dispose of it.

Conclusion

In summary, human activities have profoundly altered the natural carbon cycle on Earth by converting stable carbon from deep underground into CO_2 that flows through the mobile carbon pool. This pool includes the atmosphere, the ocean, and biomass. Since natural processes for balancing the carbon cycle are too slow to prevent the accumulation of excess CO_2 in the atmosphere, options for managing anthropogenic CO_2 and balancing the world's carbon budget are being developed.

Cross-References

- ▶ Atmospheric Evolution
- ▶ Carbon
- ▶ Carbon Cycle

▶ Carbonate Minerals and the CO_2-Carbonic Acid System
▶ Earth's Atmosphere
▶ Natural Gas
▶ Ocean Biochemical Cycling and Trace Elements
▶ Ocean Salinity, Major Elements, and Thermohaline Circulation
▶ Petroleum

References

Archer D et al (2009) Atmospheric lifetime of fossil fuel carbon dioxide. Annu Rev Earth Planet Sci 37:117–134
Arts RJ et al (2008) Ten years' experience of monitoring CO_2 injection in the Utsira Sand at Sleipner, offshore Norway. First Break 26(1):65
Christianson GE (2000) Greenhouse: the 200 year story of global warming. Penguin Books, New York
Ciais P, Sabine C, Bala G, Bopp L, Brovkin V, Canadell J, Chhabra A, DeFries R, Galloway J, Heimann M, Jones C, Le Quéré C, Myneni RB, Piao S, Thornton P (2013) Carbon and other biogeochemical cycles. In: Stocker TF, Qin D, Plattner G-K, Tignor M, Allen SK, Boschung J, Nauels A, Xia Y, Bex V, Midgley PM (eds) Climate change 2013: the physical science basis. contribution of working group I to the fifth assessment report of the intergovernmental panel on climate change. Cambridge University Press, Cambridge, UK/New York
Fischedick M, Roy J, Abdel-Aziz A, Acquaye A, Allwood JM, Ceron J-P, Geng Y, Kheshgi H, Lanza A, Perczyk D, Price L, Santalla E, Sheinbaum C, Tanaka K (2014) Chapter 10 industry. In: Edenhofer O, Pichs-Madruga R, Sokona Y, Farahani E, Kadner S, Seyboth K, Adler A, Baum I, Brunner S, Eickemeier P, Kriemann B, Savolainen J, Schlömer S, von Stechow C, Zwickel T, Minx JC (eds) Climate change 2014: mitigation of climate change. Contribution of working group III to the fifth assessment report of the intergovernmental panel on climate change. Cambridge University Press, Cambridge, UK/New York
Hansen J, Kharecha P, Sato M, Masson-Delmotte V, Ackerman F, Beerling DJ, Hearty PJ, Hoegh-Guldberg O, Hsu SL, Parmesan C, Rockstrom J (2013) Assessing "dangerous climate change": required reduction of carbon emissions to protect young people, future generations and nature. PLoS One *8*(12):e81648
IPCC (2005) In: Metz B, Davidson O, de Coninck H, Loos M, Meyer L (eds). IPCC special report: Carbon dioxide capture and storage. Cambridge University Press, Cambridge, UK, pp 431
IPCC (2014) Climate change 2014: synthesis report. Contribution of working groups I, II and III to the fifth assessment report of the intergovernmental panel on climate change [Core Writing Team, RK Pachauri, LA Meyer (eds)]. IPCC, Geneva, 151 pp
Lackner KS (2014) The use of artificial trees. Issues Environ Sci Technol 38(2014):80–104
Lackner KS et al (1995) Carbon dioxide disposal in carbonate minerals. Energy 20(11):1153–1170
MacDougall AH (2015) The transient response to cumulative CO_2 emissions: a review. Curr Clim Change Rep 2:39–47. https://doi.org/10.1007/s40641-015-0030-6
Marchetti C (1977) On geoengineering and the CO_2 problem. Clim Chang 1(1):59–68
Solomon S, Plattner GK, Knutti R, Friedlingstein P (2009) Irreversible climate change due to carbon dioxide emissions. Proc Natl Acad Sci 106(6):1704–1709
van Oost HG (2016) Cement, USGS minerals information. In: Mineral commodity summaries. http://minerals.usgs.gov

Antimony

Jacqueline R. Houston
CSUS – California State University, Sacramento, CA, USA

Element Data
Antimony (Sb: atomic weight 121.76) is a silvery metalloid with common oxidation states of (−3), (+3) and (+5). Antimony has two stable isotopes: ^{121}Sb (natural abundance of 57.36%) and ^{123}Sb (natural abundance of 42.64%).

Properties

Antimony has four allotropes, which include the blue-white metalloid, the most common allotrope of antimony, and three meta-stable allotropes, yellow, black and explosive. Antimony forms a variety of chemical compounds such as chlorides ($SbCl_3$), fluorides (SbF_3), oxides (Sb_2O_3 and Sb_4O_{10}) and sulfides (Sb_2S_3) (Greenwood and Earnshaw 1997; Wiberg et al. 2001).

History and Use

Antimony has found many commercial applications. Antimony trioxides (Sb_2O_3) are most often used as fire retardants in foam filled furniture, accounting for roughly 60% of its commercial production. Antimony is also used as an alloying material for lead-acid batteries, bullets, and solder (roughly 20% of commercial use). Other applications include the use of antimony sulfides and oxides in pigments, as catalysts for the production of polyethyleneterphthalate and in the production of glasses and pyrotechnics (Butterman and Carlin Jr 2003).

Antimony Minerals

Although the abundance of antimony in the Earth's crust is less than 0.5 parts per million, it forms over a hundred mineral species, many of which are sulfide minerals. In reducing environments with high sulfide concentrations, such as those found in hydrothermal ore deposits, sulfide containing minerals such as stibnite form readily (Sb_2S_3, Fig. 1). The metal ore stibnite often occurs as iridescent needles and is mined in only a few countries, with China

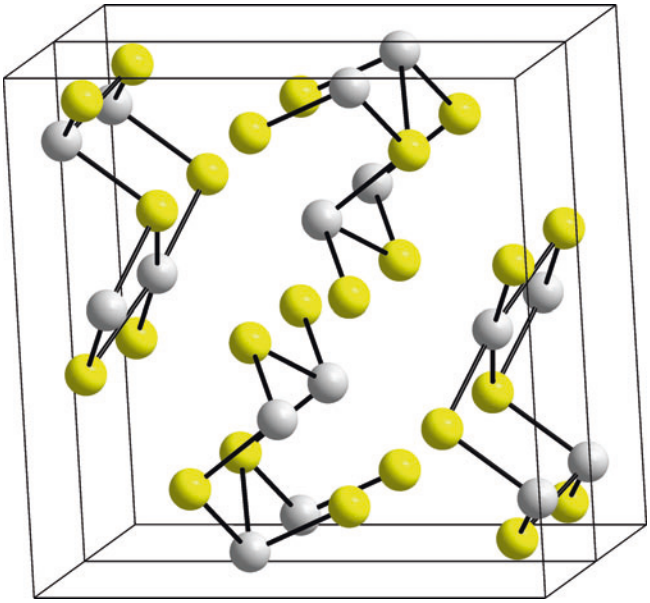

Antimony, Fig. 1 Structure of stibnite (Source: American-Mineralogist-Crystal-Structure-Database: Stibnite. Permission granted to copy under GNU Free Documentation License)

being the largest producer (Carlin Jr 2011). The metal ore has a specific gravity of 4.63 and belongs to the orthorhombic crystal class system. Other antimony minerals include kermesite (Sb_2S_2O), ullmannite (NiSbS), valentinite (Sb_2O_3), and tetrahedrite (Cu_3SbS_3). Additionally, minerals such as cervantite[Sb(III)Sb(V)O_4] demonstrate that antimony can exist in more than one oxidation state within one mineral phase.

Aqueous Geochemistry

Weathering of rocks, soil runoff, and anthropogenic activities contribute to the occurrence of antimony in natural waters. Because aqueous antimony has two common oxidation states in natural systems (+3 and +5), its speciation primarily depends on the oxidative conditions. Under oxic conditions, dissolved antimony is primarily present as $[Sb(OH)_6]^-$ (pH values > 2.5) in which Sb is present in the (+5) oxidation state (Krupka and Serne 2002). Contrary to thermodynamic data (Baes and Mesmer 1976; Krupka and Serne 2002), several studies have suggested that metastable Sb(+3) has also been found under oxic conditions, which may have resulted from biotic processes and when antimony oxidation rates are slow (Krupka and Serne 2002). Under moderately reducing conditions, the speciation is dominated by the $Sb(OH)_3$ species (pH 2–12) in which the antimony is in the (+3) oxidation state. As one would expect, the adsorption of antimony to mineral surfaces in aqueous environments is determined by the speciation of antimony. The hydrolytic anion, $[Sb(OH)_6]^-$ is the dominant species under oxic conditions and over a relatively wide pH range. Under acidic conditions, where the mineral surface is positively charged, adsorption of $[Sb(OH)_6]^-$ is greatest. At near neutral pH to basic pH conditions, electrostatic repulsion between the negatively charged mineral surface and the anionic $[Sb(OH)_6]^-$ complex reduces the likelihood of adsorbed antimony. As a result, under oxic and somewhat basic conditions, antimony is thought to be highly mobile in the natural environment (Krupka and Serne 2002).

Summary

Compared to other elements, little is known regarding the geochemical behavior of antimony. In natural waters, the common oxidation states of antimony are (+3 and +5) in which the hydrolytic anion $[Sb(OH)_6]^-$ is thought to be the dominant species under oxic conditions and pH range of 2–12. Even though the abundance of antimony is low in the Earth's crust, antimony is known to form over a hundred mineral species including the metal ore stibnite.

Cross-References

- Aqueous Solutions
- Geochemistry
- Mineralogy
- Ore Deposits
- Oxidation-Reduction Reactions and Eh-pH (Pourbaix) Diagrams
- Sulfide Minerals

References

Baes CF Jr, Mesmer RF (1976) The hydrolysis of cations. Wiley, New York

Butterman C, Carlin JF Jr (2003) Mineral commodity profiles: antimony. U.S. Geological Survey, Mineral Commodity Summaries, Internal Government Report. http://minerals.usgs.gov/minerals/pubs/#mcs

Carlin JF Jr (2011) Mineral commodity summaries: antimony. U.S. Geological Survey, Mineral Commodity Summaries, Internal Government Report. http://minerals.usgs.gov/minerals/pubs/#mcs

Greenwood NN, Earnshaw A (1997) Chemistry of the elements, 2nd edn. Butterworth-Heinemann, Oxford

Krupka KM, Serne RJ (2002) Geochemical factors affecting the behavior of antimony, cobalt, europium, technetium, and uranium in vadose sediments. PNNL-14126 Pacific Northwest National Laboratory, Richland

Wiberg E, Wiberg N, Holleman AF (2001) Inorganic chemistry. Academic, San Diego

Aqueous Solutions

Barry R. Bickmore and Matthew C. F. Wander
Department of Geological Sciences, Brigham Young University, Provo, UT, USA

Definition

An *aqueous* solution is one in which the *solvent* is liquid water. That is, *solute* (dissolved) ions and molecules are surrounded by water molecules and incorporated into the network of bonds within the water. The dissolved species then spread throughout the water.

Aqueous Solutions in Geochemistry

In geochemistry, by far the most important solvent is water. In general, geochemists divide natural waters into three types: freshwaters (including rain, rivers, lakes, and shallow groundwaters), seawater, and brines (including evaporative basins, many hydrothermal waters, and deep groundwaters). Natural waters also may be intermediates between these types, formed by mixing (e.g., estuarine waters from seawater and river water) or by evaporation (e.g., a brine from partial evaporation of seawater). The typical chemical characteristics of natural waters are shown in Table 1.

Aqueous solutions are the reservoirs or the means of transport for elements in biochemical and geochemical cycles and, thus, are the primary media through which matter and energy are exchanged at the Earth's surface. The chemical reactions effecting this exchange may be of five types: acid/base, complexation, oxidation/reduction, dissolution/precipitation, and adsorption/partitioning reactions. Many of these reactions also may be biologically mediated. The compositions of aqueous solutions reflect the extent of reaction with sediments, rocks, or gases. All the properties of aqueous solutions are strongly linked to their molecular-scale structure.

Structure

Water structure is dominated by two factors: (1) lone-pair effects causing the bent structure of the water molecule, resulting in an electrical dipole, and (2) the preference of H atoms for asymmetrical bonding between O atoms, resulting in weaker attractions between H_2O molecules than within them.

The H-O bonds within and between water molecules generally exhibit bond orders greater than ~0.65 and less than ~0.35, respectively, with the most common values about 0.83 and 0.17 (Brown 2002; Bickmore et al. 2009) (see ▶ "Chemical Bonds"). In pure water, nearly all H atoms are bound strongly to one O atom within the molecule, and to one or (less commonly) more O atoms on other molecules. This results, on average, in a distorted tetrahedral distribution of H atoms around each O atom, with molecules associated in various cluster and ring formations on a larger scale (Bunker and Casey 2016).

When other species are dissolved, the water molecules reorient themselves around the ions and molecules, to some extent altering the original structure of the solution and the ability of the water molecules to reorient themselves in response to changes in local conditions. The H atoms in water are oriented to bond with any negatively charged atoms, and the O atoms orient themselves to bond with positively charged atoms.

The local bonding environments generated by this reorganization are remarkably similar to those found in oxide solids. Al^{3+} ions, for instance, would typically be found surrounded by four to six O^{2-} ions, just as in the structures of common minerals. Larger, low-charge ions like K^+ would typically be connected to the surrounding O^{2-} via a larger number (8–12) of weaker bonds. The bonding environments of the O^{2-} atoms would be determined by bond order considerations and lone-pair effects. In other words, these local bonding environments can largely be rationalized in terms of Pauling's Rules for crystal structures (Bunker and Casey 2016).

Thermodynamic Description

Thermodynamic description of an aqueous solution requires that two properties be defined for the solvent water and each dissolved species: concentration and activity. Concentration is usually expressed in units of molarity (mol/L) or molality (mol/kg of solvent). The latter is the most broadly useful because the mass of water, as opposed to its volume, is invariant with temperature, pressure, and solute content. Activity (see ▶ "Activity and Activity Coefficients") is a unitless quantity that is the concentration of a species multiplied by a correction factor (activity coefficient) necessary to account for changes in chemical behavior related to interactions between species and changes in local water structure. By convention, activity coefficients of dissolved species in aqueous solutions are 1 at infinite dilution and vary from that value at higher solute concentrations. Typically, values are <1 at low to moderate concentrations, but then can rise to >1 in very concentrated brines. The activity of pure water is 1, and

Revised and expanded from Burton EA (1999) Aqueous Solutions. In: Marshall CP and Fairbridge RW (Eds) Encyclopedia of Geochemistry, Kluwer Academic Publishers

Aqueous Solutions, Table 1 Chemical characteristics of natural waters. Data from several sources (Baas Becking et al. 1960; Collins 1975; Millero and Schreiber 1982; Berner and Berner 1987; Boggs 1992)

Environment	pH	Eh range (V)	Major ions in order of abundance	Dissolved organic carbon (mg/L)
Rainwater				
Continental	4–6	Oxic	SO_4^{2-}, Ca^{2+}, Cl^-, NO_3^-, Na^+, K^+, NH_4^+, Mg^{2+}	?
Marine and coastal	5–6	Oxic	Cl^-, Na^+, SO_4^{2-}, Mg^{2+}, Ca^{2+}, K^+, NO_3^-, NH_4^+	?
Rivers	5–9	0.3–0.5	HCO_3^-, Ca^{2+}, $H_4SiO_4°$, SO_4^{2-}, Cl^-, Na^+, Mg^{2+}, K^+	<1 to >30
Lakes				
Fresh	5.9	−0.1–0.5	HCO_3^-, Ca^{2+}, $H_4SiO_4°$, SO_4^{2-}, Cl^-, Na^+, Mg^{2+}, K^+	<1 to >100
Saline	5–10	−0.1–0.5	Cl^-, Na^+, SO_4^{2-}, HCO_3^-, Mg^{2+}, K^+, Ca^{2+}, $H_4SiO_4°$	<1 to >100
Shallow groundwater	6–8.5	−0.1–0.45	HCO_3^-, SO_4^{2-}, Ca^{2+}, Na^+, Cl^-, Mg^{2+}, $H_4SiO_4°$, K^+	<1 to 20
Marine	7.5–8.4	0.2–0.4	Cl^-, Na^+, SO_4^{2-}, Mg^{2+}, Ca^{2+}, K^+	<0.1 to 3
Evaporative marine	7.5–9.0	Oxic or anoxic	As for marine then inc. Mg^{2+} with mineral precipitation	?
Brackish marine	7.5–8.4	Oxic or anoxic	As for marine	?
Deep connate groundwater	6.0–8.0	−0.25–0.4	Cl^-, Na^+, K^+, SO_4^2, Ca^{2+}, Mg^{2+}	<10 to 4500

decreases with increasing solute concentrations. For most natural solutions, however, the activity of water remains close to one. Even for seawater, the activity of water is >0.98, and so it is usually treated as a constant except in association with the most concentrated brines (Stumm and Morgan 1995). Activity coefficients are estimated via a wide variety of models, the simplest of which take into account only the formal charges of the ions in solution and the overall ionic strength. For solutions with ionic strengths greater than ~0.5 molal, however, it is necessary to use more complex formulations, such as Pitzer or Specific Ion Interaction Theory models (Langmuir 1997). For hydrothermal solutions, geochemists often use the model of Helgeson and coworkers (Helgeson et al. 1981).

Acid-Base Reactions

An acid, in the Brønsted-Lowry definition, is a species that can dissociate and donate H^+ to an adjacent water molecule to create H_3O^+. The adjacent water molecule is usually ignored and H_3O^+ abbreviated as H^+, so that an acid dissociation reaction is written as $HB \leftrightarrow H^+ + B^-$, where HB is the acid and B^- is the conjugate base. A base is a species that can accept H^+ in the reverse reaction. A given aqueous solution is designated as "acidic" or "basic" based on the relative concentrations of H^+ and OH^- ions, acidic solutions being those with more H^+.

The acidity/basicity of a solution is commonly characterized according to the pH scale, where pH is the negative of the base-10 logarithm of the H^+ activity (equal to the H^+ concentration in dilute solutions). Most natural waters have pH values between 5 and 9.

The most fundamental acid-base reaction is water dissociation, written $H_2O \leftrightarrow H^+ + OH^-$. The equilibrium constant for this reaction (K_w) is 10^{-14} at 25 °C, which implies that a "neutral" solution (i.e., one in which there are equal activities of H^+ and OH^-) has ~10^{-7} molal of both ions, assuming activity coefficients of ~1. In a neutral solution at 25 °C, therefore, pH = 7. The value of K_w changes with temperature, however, so that at 100 °C, for instance, $K_w = 10^{-12.25}$, and under neutral conditions the H^+ and OH^- concentrations would be ~$10^{-6.125}$ molal. In other words, the neutral solution pH is 6.125 at 100 °C.

In addition to H^+ (or H_3O^+) and OH^-, the most common ions in natural waters participating in acid-base reactions are HCO_3^- and CO_3^{2-}-, which act as bases, and dissolved CO_2 ($H_2CO_3°$) and silica ($H_4SiO_4°$), which act as acids. (Some species, like HCO_3^- or water itself, can act as either an acid or a base.) Any metals in solution, via hydrolysis, also can act as acids. (In hydrolysis, water molecules surrounding a metal cation dissociate.) In acid rain, nitrogen and sulfur species may be important acids.

The equilibrium constants for acid dissociation reactions are usually abbreviated as K_a or pK_a (the negative of the base-10 logarithm of K_a). Mathematically, it works out that the pK_a value for a given acid dissociation reaction equals the pH at which the acid and its conjugate base have equal concentrations. For example, pK_a = 9.84 for the dissociation of silicic acid ($H_4Si0_4°$), so at pH = 9.84, there would be equal concentrations of $H_4Si0_4°$ and $H_3Si0_4^-$.

Acid-base reactions play critical roles in rock weathering. Rainwater is a low ionic strength, dilute aqueous solution with a pH value of about 5.7 resulting from the equilibration of water with atmospheric CO_2 (Langmuir 1997). In percolating through soil, the solution becomes much more acidic

from re-equilibration with soil gas $C0_2$, which is typically about 10 times higher than the atmospheric value. In the underlying rock, this solution is highly corrosive with respect to basic minerals, such as carbonates and feldspars. As these minerals dissolve, the solution pH rises and the solution becomes more concentrated in ions such as Ca^{2+}, Na^{+}, Mg^{2+}, K^{+}. These ions may subsequently participate in precipitation reactions to form authigenic carbonates, clays, or metal hydroxides. At the other end of the natural solution spectrum from unreacted rainwater is seawater. Reflective of the aggregate effects of innumerable water-rock interactions, seawater is a high ionic strength solution, with a basic pH of about 8.2.

Complexation

In aqueous solutions, complexation can occur between solute species and water molecules, hydrogen ions, hydroxide ions, or other solute species, resulting in charged or uncharged complexes. The tendency to form complexes is related to the relative attraction between the solute species versus that between those species and water molecules.

Metals form some of the most important complexes in natural waters. These consist of a central metal ion and electron-donating ligand, forming a complex with negative, positive, or neutral charge. The complexed metal may have a different oxidation state to the free metal ion and, thus, have a different reactivity. In particular, complexation often results in increased metal solubility and leaching. In many waters, natural organic molecules, such as amino acids and humic substances, and anthropogenic pollutants, such as EDTA, are important complexing agents. Many biological processes rely on metal complexes to maintain metals in solution during cell transport processes.

Oxidation-Reduction Reactions

In oxidation-reduction (redox) reactions, water plays a critical role acting as an electron donor or acceptor. The stability limits for Eh-pH diagrams are defined by the stability limits for water according to the reactions:

$$O_{2(g)} + 4\,H^{+} + 4e^{-} = 2\,H_2O$$
$$2\,H^{+} + 2e^{-} = H_2(g)$$

The upper and lower limits usually are set by convention using partial pressures of O_2 at 1 and $10^{-83.1}$ atm (Drever 1982).

The predominant elements involved in redox reactions are carbon, nitrogen, oxygen, sulfur, iron, and manganese. With water in equilibrium with atmospheric oxygen (PO_2 = 0.21 atm), carbon should be present only as dissolved CO_2, HCO_3^{-}, CO_3^{2-}, nitrogen as NO_3^{-}), sulfur as SO_4^{2-}, iron as FeOOH or Fe_2O_3, and manganese as MnO_2. More reduced species, such as H_2S, CH_4, and free Fe^{2+} and Mn^{2+} (as hydrated forms), are common in surface environments, however, and their presence reflects the importance of biological processes in creating reducing microenvironments and regulating natural aqueous solution chemistry.

Dissolution/Precipitation Reactions

Whether a mineral will dissolve or precipitate from a solution of a given composition can be estimated using thermodynamic criteria. Computer models, such as WATEQ (Truesdell and Jones 1974), SOLMINEQ (Kharaka and Barnes 1973), REDEQL (Morel and Morgan 1972), PATI-II (Helgeson et al. 1970), and the various more recent computer codes derived from these models, use input solution ion concentrations to calculate ion speciation and the saturation states of the water with respect to the possible minerals which could form from or might have dissolved to produce a water of such composition. Once again, the tendency for compounds to precipitate or dissolve depends on the relative attraction between the species combined in the solid versus that between those species and water molecules (Brown 2002).

The kinetics of reactions in aqueous solutions also must be considered, however. Although the thermodynamic driving force for a given reaction may be significant, there may be species in solution which inhibit reaction progress. A well-known example is the oversaturation of surface seawater with respect to calcite, which is maintained because dissolved sulfate and magnesium inhibit the progress of the precipitation reaction.

Adsorption/Partitioning Reactions

Solute and colloidal transport in aqueous solutions are strongly dependent on the properties of solid-solution interfacial regions. The surfaces of natural minerals in contact with aqueous solution are often electrically charged due to local charge imbalances. This induces concentration gradients between the ions around these surfaces, and when in contact with water there is an offsetting imbalance of electrical charge in solution at and near the solid surface, because solute ions of opposite charge are attracted to the charged surface, and ions of the same charge are repelled. Therefore, chemical models involving functional groups on solid surfaces must employ electrostatic corrections to bulk ionic concentrations/activities. This "electric double layer" (i.e., the layer of altered ionic concentrations at the interface) decreases in thickness with increasing ionic strength. This allows suspended solid particles to approach each other more closely, promoting aggregation (Stumm 1992).

The polar nature of water molecules also influences the transport and partitioning of molecules that are not necessarily

ionic. That is, molecules with more polar bonds tend to strongly attract polar water molecules, and so are "hydrophilic," whereas those with less polar or fully covalent bonds tend to be "hydrophobic." Therefore, hydrophobic compounds like waxes tend to partition at solid-solution interfaces.

Summary and Conclusion

Aqueous solutions provide one of the major means of chemical transformation and transport near the surface of the Earth. They provide a liquid-phase oxide network similar to the solid-phase oxide networks of most minerals, so that ions may be dissolved, transported, and recombined in various ways. The characteristics of the chemical bonds involving water molecules, including their spatial distribution as influenced by lone-pair effects, are at the heart of water's unique properties.

Cross-References

- Acid Deposition
- Acid–Base Reactions
- Activity and Activity Coefficients
- Calorimetry
- Chelation
- Chemical Bonds
- Clay Membranes
- Earth's Oceanic Crust
- Fluid–Rock Interaction
- Gibbs-Duhem Equation
- Hydrothermal Solutions
- Low-Temperature Geochemistry
- Standard States
- Stoichiometry
- Water

References

Baas Becking LGM, Kaplan IR, Moore D (1960) Limits of the natural environments in terms of pH and oxidation-reduction potentials. J Geol 68:243–284
Berner EK, Berner RA (1987) The global water cycle: geochemistry and environment. Prentice-Hall, Englewood Cliffs. 397 p
Bickmore BR, Rosso KM, Brown ID, Kerisit S (2009) Bond-valence constraints on liquid water structure. J Phys Chem A 113:1847–1857
Boggs SJ (1992) Petrology of sedimentary rocks. Macmillan, New York. 707 p
Brown ID (2002) The chemical bond in inorganic chemistry: the bond valence model. Oxford University Press, New York. 278 p
Bunker BC, Casey WH (2016) The aqueous chemistry of oxides. Oxford University Press, New York. 604 p
Burton EA (1999) Aqueous solutions. In: Marshall CP, Fairbridge RW (eds) Encyclopedia of geochemistry. Kluwer, Dordrecht/Boston
Collins AG (1975) Geochemistry of oilfield brines. Elsevier, Amsterdam. 496 p
Drever JI (1982) The geochemistry of natural waters. Prentice-Hall, Englewood Cliffs. 388 p
Helgeson HC, Brown TH, Nigrini A, Jones TA (1970) Calculations of mass transfer in geochemical processes involving aqueous solutions. Geochim Cosmochim Acta 32:569–592
Helgeson HC, Kirkham DH, Flowers G (1981) Theoretical prediction of the thermodynamic behavior of aqueous electrolytes at high pressures and temperatures: IV. Calculation of activity coefficients and standard and relative partial molal properties to 600C and 5 kb. Am J Sci 281:1249–1516
Kharaka YK, Barnes I (1973) SOLMINEQ: solution-mineral equilibrium computations. In: N.T.I.S.T.R. PB214-899 Ed
Langmuir D (1997) Aqueous environmental geochemistry. Prentice Hall, Upper Saddle River. 600 p
Millero FT, Schreiber DR (1982) Use of the ion pairing model to estimate activity coefficients of the ionic components of natural waters. Am J Sci 282:1508–1540
Morel FMM, Morgan JJ (1972) A numerical method for computing equilibria in aqueous systems. Environ Sci Technol 6:58–67
Stumm W (1992) The chemistry of the solid-water interface. Wiley, New York. 428 p
Stumm W, Morgan JJ (1995) Aquatic chemistry: chemical equilibria and rates in natural waters. Wiley, New York. 1040 p
Truesdell AH, Jones BF (1974) WATEQ: a computer program for calculating chemical equilibria of natural water. J Res US Geol Surv 2:233–248

Archeological Geochemistry

Patrick Degryse[1] and R. Alexander Bentley[2]
[1]Earth and Environmental Sciences, Division Geology, Centre for Archaeological Sciences, KU Leuven, Leuven, Belgium
[2]Comparative Cultural Studies and Hobby School of Public Affairs, University of Houston, McElhinney Hall, Houston, TX, USA

Definition

Archaeological geochemistry is the discipline which integrates geochemical analysis techniques and methods into the study of the human past, to answer questions on subsistence, migration, environment, and the transport and use of natural raw materials.

Introduction

Archaeology is an interdisciplinary science par excellence. In its quest to reconstruct human behavior in the natural and cultural environment in the past, it uses knowledge and techniques from many different academic disciplines. As the exact sciences are increasingly integrated into archaeological

research throughout the world, a range of geochemical tools are applied to archaeological questions dating from early hominins of the Plio-Pleistocene to Paleolithic hunter-gatherers, early Neolithic farmers, and great early state civilizations. Archaeological geochemistry began with the investigation of ancient materials, particularly stone and pottery. More recently, archaeological chemistry has seen a growth of biogeochemical tools applied to human and plant remains as part of an integrated science of the Anthropocene, as human societies first began to substantially transform their environment (Smith and Zeder 2013).

With the spectacular growth of this field in the last decades, certain topics are not covered in this entry. One of those subjects is geochronology, even though isotopic systems such as K-Ar, Rb-Sr, U-Th-Pb, and U-decay series are used both to refine and extend archaeological dating beyond the limits of radiocarbon dating (e.g., Deino et al. 1998). U-series dates on calcite flowstone growths on the surfaces of paintings, for example, have shown the world's earliest cave art is both surprisingly old (~40 kyr ago) and geographically extensive (Aubert et al. 2014; Pike et al. 2012).

As much as we would like to cover these and related topics, we focus mainly on two primary lineages of archaeological geochemistry. The first is the elemental and isotopic characterization of inorganic materials to infer provenance and production. The second is the biogeochemical characterization of organic materials to infer diet, migration, and subsistence practices.

Geochemical Study of Inorganic Materials

In archaeology, ancient artifacts are not simply materials intended for classification, but they are direct proof of how ancient production and technology evolved. The better we understand the different contexts in which people used and produced artifacts, the more likely we are to understand their everyday life, crafts, or trade. By characterizing material exchange, aspects of social stratigraphy and standard of living can be documented as well.

While archaeological chemistry dates to eighteenth- and nineteenth-century studies of Greco-Roman coins and Roman pigments and pottery (Pollard and Heron 2008), the use of exact scientific tools mainly developed after World War II (Peacock 1970). Since the 1970s, exact scientific techniques for provenancing, especially optical microscopy and an array of chemical analysis, have been used more and more frequently and on more and more material categories.

Provenance Studies

An essential assumption in provenance studies – measuring some property to trace an artifact to its particular source or production site – is that the between-source differences must exceed within-source variation (Weigand et al. 1977). In general, many techniques from the geosciences are applied to study the source of raw materials for ancient craft production in different chronological-geographical contexts and on different artifact types (pottery, vitreous materials, metals), in which trace element profiles and isotopic analysis have proven essential (Henderson 2000; Pollard and Heron 2008).

Just about every element of the periodic table has been used at some time to compare the typical composition of resource materials to that of archaeological artifacts. Depending on the nature of the materials analyzed (e.g., clay compared to ceramic, sand to glass, ore to metal), elements are chosen for their occurrence as major or trace element and the nature of the geological-mineralogical information they provide. Multimethod provenance studies will often combine petrography and chemical techniques such as (but not exclusive to) element and isotope ratio analysis.

Provenance of Pottery and Glass

The provenance determination of stone and ceramics is often accomplished through chemical and mineralogical-petrographic analysis (e.g., Degryse and Braekmans 2014; Kempe and Harvey 1983). In such studies, the analytical data from stone objects or ceramics are compared to the geological characteristics of the potential raw material sources, such as stone quarries, mines, soil surveys, and clay pits. For example, aluminum, magnesium, and potassium are typical major elements, which provide information on the type of clay minerals used for ceramic manufacturing. However, since most clays have similar, if not overlapping, major element compositions, there is little resolution in such analysis to distinguish different ceramic origins. The variation in trace elements, such as the transition metals or the rare earth elements (REEs), may then be much more useful to distinguish different raw materials used. Overall, trace element analysis has been successful in answering archaeological questions on ceramic raw material provenance, recipes, and manufacturing processes and technological (r)evolutions (Fig. 1). In provenance studies of ceramics, since the introduction of petrography and geochemistry in the 1950s and 1960s (e.g., Peacock 1970), these techniques have been used routinely over the years.

As for glass, some diagnostic chemical compositions of ancient glass provide a characterization which suggest a specific source. The first regular production of glass uses four basic components (Degryse and Braekmans 2014): silica as a network former, a network modifier or flux (alkali and/or lead), stabilizers (usually lime), and colorants (in the form of many different possible metals). Specific compositions of glass production may indicate certain sources, technical processes, and ages (Brill 1999; Sayre and Smith 1961). The elements magnesium, potassium, and phosphorous separate the earliest plant ash-based glasses, in which quartz pebbles

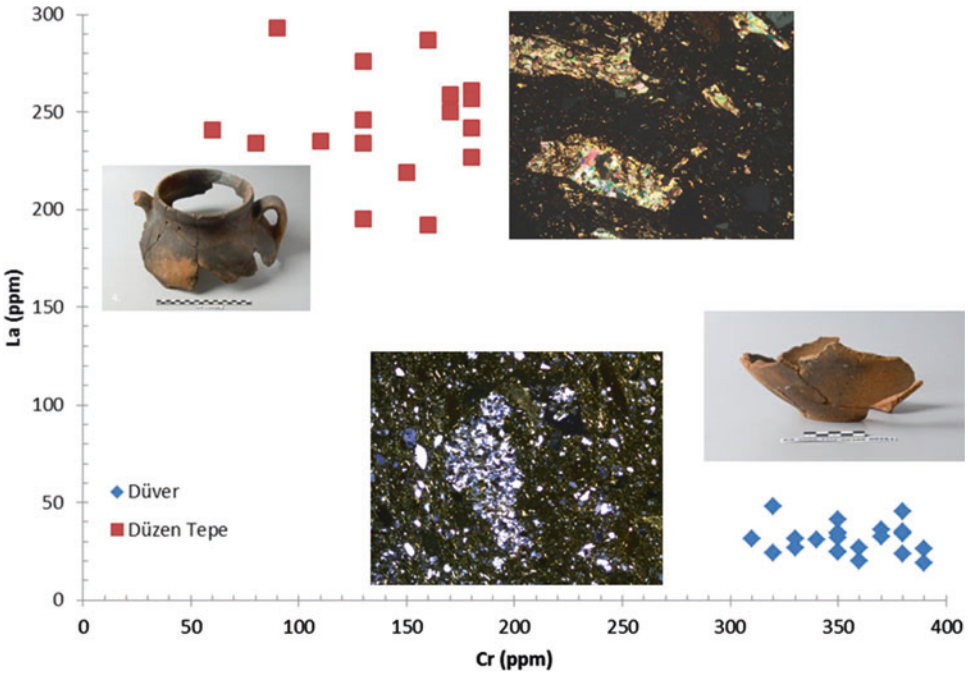

Archeological Geochemistry, Fig. 1 Comparison of the La-Cr trace element content and a micrograph of Iron Age ceramics from the sites of Tepe Düzen (*squares*) and Düver (*diamonds*) (SW Turkey – 20 km apart), indicating the use of two different clay raw material sources (Data from Braekmans et al. 2011)

and plant ashes were used as flux, from natron-based glasses of the Mediterranean and Europe, which contained soda-rich minerals, crushed lime, and quartz sand. Usually, contents higher than 1.5% in both magnesia and potash are thought to prove the use of plants as a flux. Elements like iron, titanium, and aluminum are usually related to the concentrations of specific minerals (feldspars, clays, etc.) in the silica source of the glass (Freestone 2006).

Some minor elements in ancient glass were added to color or decolor the material, such as cobalt in dark-blue glass or copper in lighter blue or greenish glass, or opacity imparted through addition of antimony, tin, or lead. Since these coloring elements were often added in the form of ores (e.g., stibnite), minerals (e.g., alum), or metals (e.g., bronze), these elements do not source the raw material of the glass itself but indicate the source of the colorant/opacifier. Trace elements in glass can also help to separate compositional groups and assign individual objects to them (Brill 1999; Shortland et al. 2007). Egyptian and Mesopotamian glasses, for example, are distinguishable particularly by their concentrations of titanium, zirconium, chromium, and lanthanum, which may reflect different geological sources, plant ash compositions, silica sources, and/or contamination of the melt by clay or grinding debris (Rehren and Pusch 2005; Shortland et al. 2007). In Roman natron glass, for another example, the REE content has been shown to be dependent on the clay fraction of the sand and is identical for most possible provenance areas in the Mediterranean. Elements such as zirconium, hafnium, titanium, etc. are controlled by heavy mineral concentrations in sand and offer potential as indicators of glass provenance (Degryse and Shortland 2009). For instance, Schibille et al. (2016) proposed a new classification scheme for the composition of first millennium natron glass, in which the ratios TiO_2/Al_2O_3 versus Al_2O_3/SiO_2 distinguish an Egyptian versus a Syro-Palestinian primary origin (Fig. 2a). Glazes applied to clay bodies have similar compositional features to contemporary glass (Tite and Shortland 2008).

Strontium and neodymium isotopes, discussed more below, have been used to trace the provenance of vitreous materials including ceramics and glass (Degryse 2012). As shown in Fig. 2b, neodymium isotopic analysis of ancient glass identifies the sources of non-quartz minerals in the silica raw material used to make this glass (Degryse 2014). The element boron is inherited in glass through the flux, and the boron isotopic composition of evaporites has been used to distinguish different sources of natron raw material (Devulder et al. 2014, 2015).

Metals and their Geologic Sources

The analysis of metal alloys involves the identification of the presence/absence of a sufficient concentration of a particular element to conclude that it has a significant effect on the properties of the alloy and is not just an impurity. Nevertheless, care has to be taken as to the intent of the early metallurgists in mixing metals to obtain certain properties. Copper alloys are often assigned to categories such as bronze (Cu + Sn), leaded bronze (Cu + Sn + Pb), antimonal copper (Cu + Sb), arsenical copper (Cu + As), brass (Cu + Zn with or without Pb), or gunmetal (Cu + Zn + Sn with or without Pb).

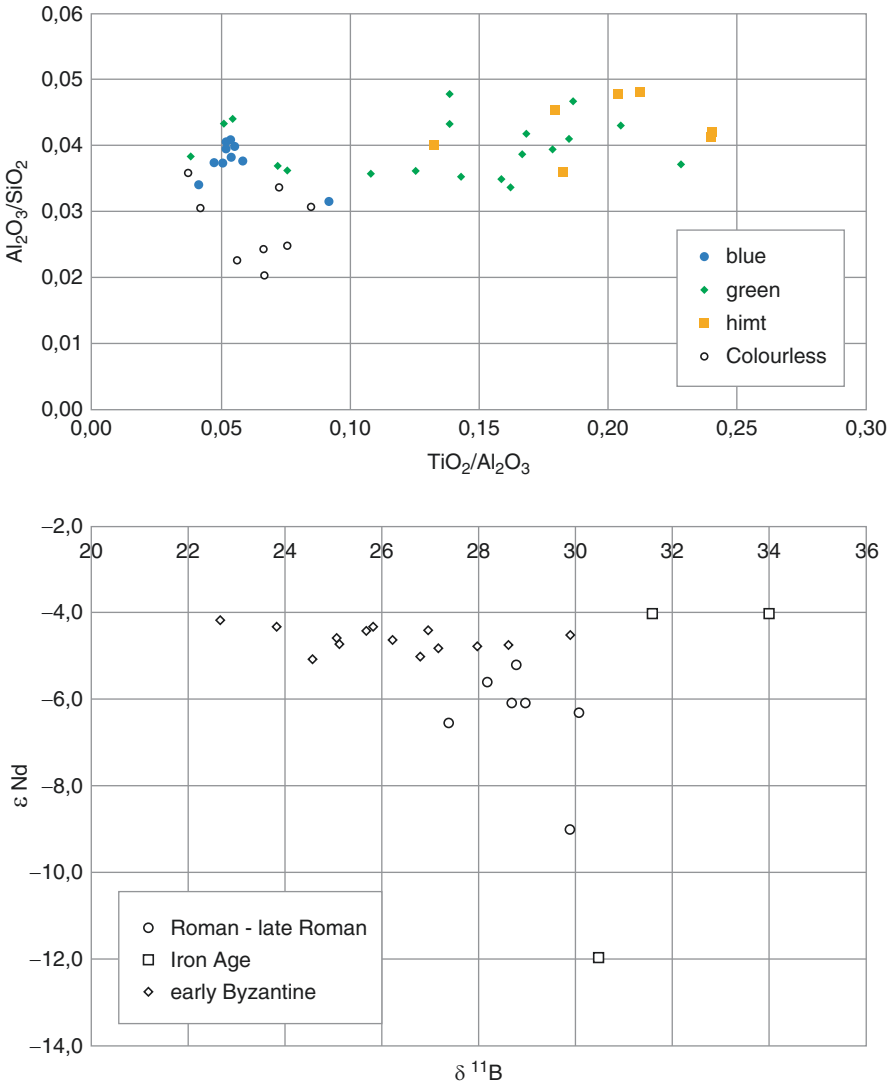

Archeological Geochemistry, Fig. 2 (**a**) Plot of the TiO_2/Al_2O_3 versus Al_2O_3/SiO_2 ratio in sixteenth- to seventeenth-century AD glass from Sagalassos (Turkey), distinguishing the Egyptian primary origin of the local "*yellow-brown*" HIMT glass from the Syro-Palestinian primary origin of the local *blue* and *colorless glass* and the locally recycled nature of the *green glass* (Degryse et al. 2006). (**b**) Plot of the ε_{Nd} versus $\delta^{11}B$ isotopic composition of Iron Age to early Byzantine natron glass from around the Mediterranean. The range in ε_{Nd} indicates the use of silica raw materials from the Eastern Mediterranean ($-6 < \varepsilon_{Nd} < -4$) as well as (rarely) from the Western Mediterranean ($\varepsilon_{Nd} < -6$), while the $\delta^{11}B$ is typical for North African natron sources from evaporitic lakes in Tunisia, Libya, and Egypt (Data from Devulder et al. (2014) and Degryse (2014))

An element is then considered significant if it is present at a concentration of more than about 1% for tin, antimony, and arsenic and 2% for lead (Pike 2002). Trace elements are commonly used to assign metal (alloys) to ore sources. Typically, for example, the contents of bismuth, cobalt, silver, gold, zinc, nickel, and iron are used fin tracing copper alloys. However, this needs to be treated with care as recycling and reuse of metal may significantly influence their composition. Also, (s)melting may have had a dramatic effect on the concentrations of many minor and trace elements (Wilson and Pollard 2001; Rehren 2008). As the chemical relationship between raw materials and metal artifacts made from them may have been altered, provenance of and trade in metal artifacts have been addressed using heavy radiogenic isotopes of strontium, neodymium, and lead (Degryse 2012). The isotopic composition of a raw material is dependent on the geological age and origin of that material. Heavy isotopes are not fractionated during technical processing due to their relatively high masses and low internal relative mass differences. As melting will hence have had little effect on isotope ratios, these may be used in tracing raw materials in craft production. The isotopic composition of the artifact will be identical, within analytical errors, to the raw material (mixture) from which it was derived, while the signatures of different raw materials used, and hence the resulting artifacts, may differ (Brill and Wampler 1965).

Lead isotopes were one of the first used to investigate ancient materials, in particular to trace the provenance of lead, silver, and bronze metal (mainly from the Mediterranean Bronze Age period) since the 1960s. These efforts, but also the disadvantages and controversy around the use of Pb isotopes, have been extensively reviewed (Pollard 2009). Lead isotopic analysis has also been used to study a range of archaeological vitreous materials and to provenance ancient iron (Degryse 2012) and copper alloys using lead isotope mixing models (Pollard and Bray 2015). Elsewhere in the world, lead isotope analyses have been used to source

copper, tin, and bronze objects from late prehistoric Myanmar to known prehistoric copper mines elsewhere in Southeast Asia (Pryce et al. 2016).

Tin was another vital commodity in ancient times, but the provenance of prehistoric tin, used for the production of bronze from the third millennium BC onward, is still unsolved. Since lead in ancient bronze comes mostly from the copper ore, lead isotopic analysis cannot be applied for determining the provenance of tin (Begemann et al. 1999). Analysis of tin isotope ratios (Gale 1997) with large sample sizes has shown homogeneous isotopic compositions within ore deposits and significantly different between deposits (Haustein et al. 2010). Isotopic analysis also provides a means to investigate the provenance of antimony in glass and ores (e.g., Lobo et al. 2014), which may reveal that the origin of antimony in early glass coincides with its use in metallurgy in the Caucasus in the Bronze Age (Degryse et al. 2015).

For inorganic materials, new analysis technologies include laser ablation multi-collector ICP-MS (Devulder et al. 2015) and portable X-ray fluorescence spectrometers (Tykot 2016). Because these methods are fast and fairly nondestructive to the artifacts, they will likely become more widespread in the near future.

Geochemical Study of Organic Materials

Organic Residues

Answering questions on diet is approached through the analysis of preserved biomolecular components of residues in and on archaeological materials, usually ceramics. This biomarker approach looks at compound-specific isotope compositions of a range of major biochemical components of animals and plants (Cramp and Evershed 2014). A wide range of biochemicals including lipids and proteins can be derived from human and animal remains and particularly in pottery, which preserves the biochemical remains of animal fats, waxes, or dairy products (Cramp and Evershed 2014). Molecular and stable isotopic techniques now exist for identifying the fats of the major classes of domesticated animals, i.e., ruminants versus nonruminants, and of some hunted terrestrial species (e.g., Copley et al. 2003; Outram et al. 2009). This led to a series of discoveries in identifying the world's oldest dairy residues on pottery remains (Copley et al. 2003; Dunne et al. 2012; Salque et al. 2013; Smyth and Evershed 2015) – in each case centuries or millennia earlier than had hitherto been assumed. The organic residue work can involve painstaking preparation and analysis of hundreds of potsherds over a wide geographical range (Salque et al. 2013). Compound-specific stable isotope measurements in fatty acids are made using a gas chromatograph (GC) linked to an isotope ratio mass spectrometer (IRMS). The typical means of identifying dairy fats is by a plot of the $\delta^{13}C$ values in the $C_{16:0}$ fatty acid versus $\delta^{13}C$ in the heavier $C_{18:0}$ fatty acid (Fig. 3). Ruminant dairy fats typically plot with $\delta^{13}C$ in the $C_{18:0}$ about 3–5 per mil lower than in adipose fats from meat.

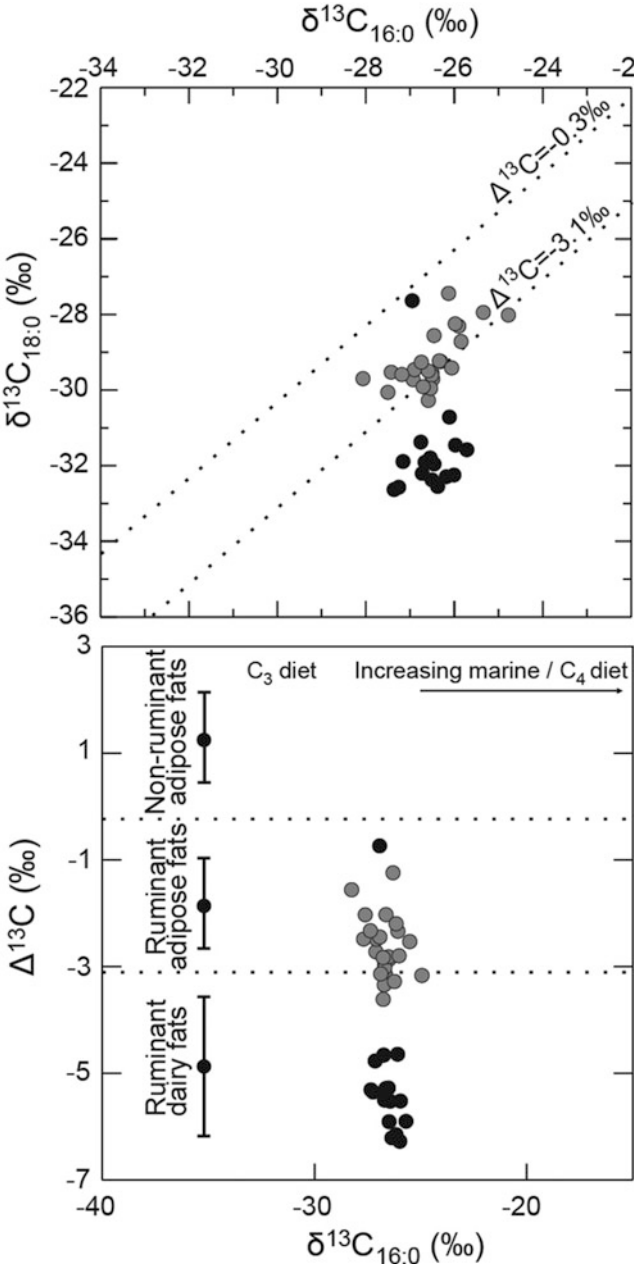

Archeological Geochemistry, Fig. 3 Isotopic distributions in animal fat residues extracted from Neolithic sieves and cooking pots from the sixth millennium BC in Northern Europe (Salque et al. 2013). The *top* shows $\delta^{13}C$ in the $C_{16:0}$ and $C_{18:0}$ fatty acids, with one data point for each vessel, the sieves shown in *black* and the cooking pots in *gray*. The *bottom* shows $\Delta^{13}C$ values = ($\delta^{13}C_{18:0} - \delta^{13}C_{16:0}$) of the extracts plotted against their $\delta^{13}C_{16:0}$. Ranges on the *left* show expected $\Delta^{13}C$ values for a global database. Note how the cheese sieves contained residues of dairy fats (Modified after Salque et al. (2013), with kind permission from Mélanie Roffet-Salque)

Diet and Environment

Inferences concerning migration, diet, climate, and subsistence can be made through the identification and quantification of animal and plant remains found at archaeological sites. Hydrogen isotope values in animal fats, for example, bioaverage local water sources and thus can act as proxies for the climate (temperature/precipitation) of the region in which the animals were raised (Outram et al. 2009).

Contamination due to the uptake and diffusion of chemical elements or other alteration processes, like dissolution or erosion, can change the composition and distort the results of environmental and dietary studies. Compositional studies on fossilized bone have provided information on various aspects of the paleoenvironment because of diagenetic changes during the fossilization process of buried bone (Denys et al. 1996). The nature and degree of diagenesis have been evaluated through the study of changes in the fossil bones' chemical composition (Hedges 2002).

Stable isotope analysis of animal and human remains is mainly used for diet reconstruction. Traditional carbon and nitrogen isotope analysis of bulk collagen in bone, and recently in individual amino acids, is used to estimate dietary patterns. The isotopic signal in bone collagen reflects dietary inputs averaged over at least the last decade of life but often with a particular emphasis on the period of adolescence (Hedges et al. 2007; Stenhouse and Baxter 1979). As the stable isotope signals in aquatic food products (freshwater and marine species) are different from those in terrestrial organisms, and as they are variable according to the organism's place in the food chain (which are shorter in terrestrial environments), the contribution of various food stuff to the former human diet can be evaluated through the analysis of stable isotopes (Fig. 4).

Carbon isotopes ^{12}C and ^{13}C fractionate during primary production of organic matter during photosynthesis, such that C_3 plants (e.g., most plants including rice, wheat, etc.) have $\delta^{13}C_{PDB}$ values between −23 and −34‰ (Heaton 1999). The C_4 plants, adapted to hot and dry climates, fix CO_2 more efficiently than C_3 plants, via a 4-carbon acid (hence C4), and exhibit less isotopic fractionation of carbon than C_3 plants. C_4 plants include tropical grasses and importantly teosinte and maize in the new world and sorghum and millet in the old world. The $\delta^{13}C_{PDB}$ value in C_4 plants ranges from about −10 to −18‰ (O'Leary 1988). There are a number secondary effects on $\delta^{13}C$ in plants, including temperature, humidity, forest density, altitude, and insolation (Heaton 1999). In animals and humans, the major causes of $\delta^{13}C$ variations include consumption of marine resources, generally enriched in ^{13}C by several per mil compared to terrestrial C_3 plant foods and meat consumption, whereby $\delta^{13}C$ increases by about one per mil per trophic level (Schoeninger and DeNiro 1984).

Applications of bulk $\delta^{13}C$ and $\delta^{15}N$ in archaeological bone collagen over the past 40 years (Lee-Thorp 2008) have mainly focused on differentiating between diets based on marine and terrestrial protein sources and diets that emphasizing C_3 versus C_4 plants and estimating dietary trophic level. By analyzing different tissues (dentine, rib, and femur) from the same individual, a dietary history can be established from childhood to the last few years of their life. Carbon isotopes have most frequently been measured in bone collagen, in which ^{13}C is enriched by about +5‰ relative to diet, but measurement of $\delta^{13}C$ can also be done in the carbonate fraction of tooth enamel, enriched by about 9.4‰ relative to the whole diet (Ambrose et al. 1997; Koch et al. 1995). Since these materials represent different

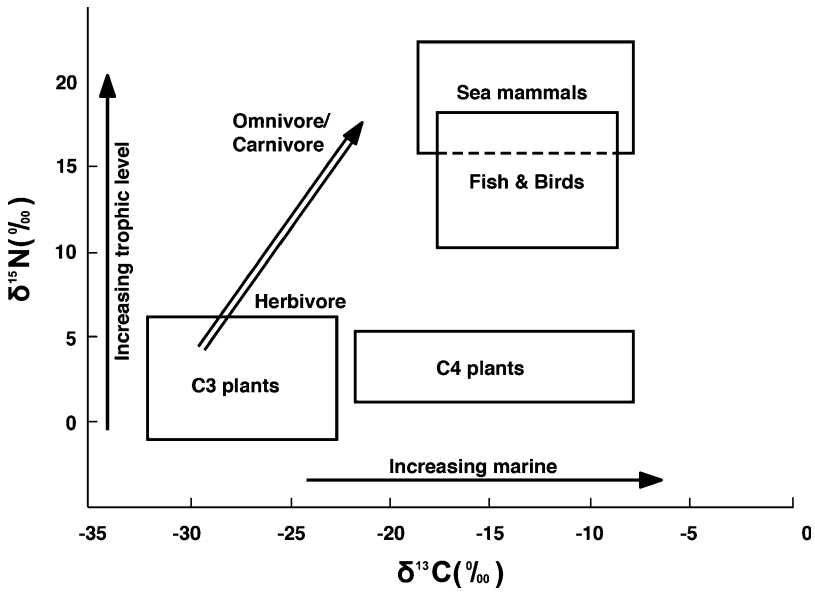

Archeological Geochemistry, Fig. 4 Conceptual plot of the use of carbon and nitrogen isotope ratios, measured on bone collagen, in diet reconstructions

biomolecular pathways – collagen representing protein in the diet, tooth enamel apatite reflecting the whole diet – additional value is gained by observing the differences in $\delta^{13}C$ measured in more than one of these tissues (Schoeninger 2009).

Using these end-members for a linear mixing model, $\delta^{13}C$ has been used to estimate percentages of marine foods in the diet, despite the uncertainties regarding $\delta^{13}C$ in coastal food webs and in apatite itself (e.g., Prowse et al. 2004; Schoeninger and DeNiro 1984). A pure C_3 plant diet might yield $\delta^{13}C$ of −16‰ in enamel carbonate, for example, versus a pure marine diet at − 4.6‰, such that each 1‰ of $\delta^{13}C$ change is modeled as reflecting 9% dietary change along the continuum (Ambrose et al. 1997). This can be complemented by sulfur isotope analysis where there is a question of freshwater versus marine food uptake (Bocherens et al. 2015; Richards et al. 2003).

Nitrogen is derived from dietary protein and used by the body to synthesize amino acids. Averaged in bone collagen as signature of the whole diet, the bulk $\delta^{15}N$ in collagen has long been assumed to reflect trophic level, with about 3–4‰ increase in $\delta^{15}N$ per trophic level, from plants to herbivores to carnivores, as this trophic effect continues up the food chain (Schoeninger and DeNiro 1984). Diets based on legumes tend to exhibit lower $\delta^{15}N$ values, because legumes have nitrogen fixed for them by bacteria and have $\delta^{15}N$ close to 0‰. $\delta^{15}N$ is usually measured in concert with bulk $\delta^{13}C$ in collagen, and innovative new case studies include a comparison of palaeogenetic data versus $\delta^{13}C$, $\delta^{15}N$, and $\delta^{34}S$ in Neolithic human skeletons, which identified two distinct human groups coexisting across a frontier for millennia (Bollongino et al. 2013).

Because bulk $\delta^{13}C$ and $\delta^{15}N$ analyses of collagen, however, only reflect an average across the constituent amino acids, a notable advance lies in measuring $\delta^{13}C$ and $\delta^{15}N$ in specific compounds separated by gas chromatography, including amino acids and cholesterol extracted from skeletal materials (e.g., Naito et al. 2013; Styring et al. 2015). Compared to bulk C and N isotopes from bone collagen, $\delta^{13}C$ in different amino acids, such as glycine versus phenylalanine, carries additional information due to different biochemical pathways from the diet (e.g., Choy et al. 2010; Styring et al. 2015). Measuring $\delta^{15}N$ in amino acids helps resolve the ambiguities of bulk $\delta^{15}N$ signal (e.g., from nutrient recycling) and has been used, for example, to identify early agricultural manuring (Bogaard et al. 2013). Also, since amino acids can be prepared by acid hydrolysis of a subsample of collagen used for the bulk analyses, bulk $\delta^{13}C$ and $\delta^{15}N$ analyses are increasingly used as a screening method to select well-preserved and "interesting" (e.g., exceptional bulk values) samples for compound-specific isotopic analysis.

Mobility

By substituting as a + 2 cation for calcium, elements similar to Ca, including Sr, Ba, and Pb, are permanently preserved in the mineral phase (hydroxyapatite) of archaeological tooth enamel, which is more resistant to post-burial contamination with respect to these elements than bone (Kamenov and Gulson 2014; Trickett et al. 2003; Willmes et al. 2016). As they have large atomic mass and therefore relatively small mass differences between their respective isotopes, isotopes of Sr, Ba, or Pb enter the food chain without fractionation relative to their weathered geologic sources (Bentley 2006; Ericson 1985; Evans et al. 2015; Kamenov and Gulson 2014). In tooth enamel, the isotope signature therefore reflects the concentration-weighted average of those sources while the enamel was forming (Beard and Johnson 2000). For settled communities, a parsimonious interpretation of a "nonlocal" isotope signature in tooth enamel is that the person was an immigrant, but often another possibility is that the person spent substantial childhood time elsewhere (e.g., a childhood hunter-gatherer who later joined a settled community).

The most widely used of these systems is the strontium isotope signature ($^{87}Sr/^{86}Sr$) in tooth enamel (Ericson 1985). High-profile applications include an exceptionally well-preserved bog body from the Bronze Age of Denmark, ca. 3400 BP, whose bones, teeth, and even woolen clothing were traced using strontium isotopes (Frei et al. 2015). Geology provides a general basis for what we expect the biologically available $^{87}Sr/^{86}Sr$ to be in different areas, and maps of bioavailable strontium or Sr maps are becoming more common (Evans et al. 2010; Frei and Price 2012; Hodell et al. 2004; Montgomery et al. 2006). One challenge to mapping $^{87}Sr/^{86}Sr$ is its environmental variability in soils and plants (Sillen et al. 1998). The $^{87}Sr/^{86}Sr$ in tooth enamel reflects a concentrated-weighted average of all inputs during enamel formation, with much lower coefficient of variation than within their environmental sources (Burton and Price 2003; Bentley 2006; Montgomery et al. 2010). Due to this bioaveraging effect, while stream or groundwater can be good proxies for bioavailable $^{87}Sr/^{86}Sr$ (Montgomery et al. 2006), archaeological tooth enamel in animals is often good for mapping $^{87}Sr/^{86}Sr$ (Bentley and Knipper 2005). For coastal settings, however, seaspray or precipitation can supply significant Sr of marine derivation ($^{87}Sr/^{86}Sr = 0.7092$), presenting a challenge to untangling the various contributions of coral reefs, seaspray, and seafood in the diet. Measuring Ba/Sr in tooth enamel can help triangulate the food sources from enamel samples because seawater has orders of magnitude lower Ba/Sr ratios than typical terrestrial environments (Bentley et al. 2007; Burton and Price 2003).

Micro-sampling across a human or animal tooth, either by laser ablation or by micro-milling, provides $^{87}Sr/^{86}Sr$

measurements within a single tooth. Measurements along the growth of a cow's tooth, for example, track its mobility over about 2 years of its life (Gron et al. 2016; Montgomery et al. 2010). A challenge in measuring $^{87}Sr/^{86}Sr$ by the laser ablation method, LA-ICP-MS, however is the isobaric interferences at atomic masses from 84 to 88, including inert gasses used by the mass spectrometer and from the source material itself (Nowell and Horstwood 2009). Instrumental correction methods are improving, however (Müller and Anczkiewicz 2016; Willmes et al. 2016), and the noise in the LA-ICP-MS data can also be smoothed through a moving average of the raw signal (Lewis et al. 2014). Nevertheless, the best accuracy is still achieved through TIMS analysis on micro-drilled samples in which the strontium is purified through traditional column chemistry (Müller and Anczkiewicz 2016; Nowell and Horstwood 2009).

For over 40 years, studies of Pb isotopes – radiogenic isotopes ^{206}Pb, ^{207}Pb, and ^{208}Pb versus the non-radiogenic isotope ^{204}Pb – have been used to identify anthropogenic sources of lead in humans, whose blood, teeth, and bones incorporate trace amounts of Pb from the local environment through dust and soil particulates (Evans et al. 2015; Kamenov and Gulson 2014). Homogeneous anthropogenic sources have dominated atmospheric Pb for centuries – from silver and lead mining 3000 by the ancient Greeks and Romans to the leaded gasoline in the twentieth century – as visible in the $^{207}Pb/^{206}Pb$ signatures in peat core records and in modern human teeth (Kamenov and Gulson 2014; Shotyk et al. 1998). In pre-metal prehistoric times, however, Pb concentrations in the environment and the human body were several orders of magnitude lower, i.e., less than 1 ppm in human teeth (Chiaradia et al. 2003; Kamenov and Gulson 2014). Lead isotopes in the biosphere have been mapped in the United States at coarse resolution (Keller et al. 2015). In the Mayan region of the Yucatan Peninsula, regional differences Pb isotopes between limestone-rich lowlands and metamorphic or volcanic highlands make this a promising region for lead isotope studies of Mayan human and animal remains (Sharpe et al. 2016).

Geographic origins are reflected in enamel $\delta^{18}O$ values measured in animals that take in much of their oxygen through ingested water (Kohn 1996). Oxygen isotopes can be measured in either the phosphate or structural carbonate fraction of tooth enamel, with a fixed offset in $\delta^{18}O$ between the two materials (Bryant et al. 1996). In precipitation, $\delta^{18}O$ depends on the source water, temperature, distance from the coast, altitude, rain shadow effects, and other aspects of the hydrologic cycle (Bowen and Wilkinson 2002). The altitude effect is about 1–2‰ reduction in $\delta^{18}O$ per 1000 m (Poage and Chamberlain 2001). In mammals, the oxygen isotopic composition of skeletal matter is controlled by drinking water, food, and atmospheric oxygen, but as moderated by complex physiological fractionations (Kohn 1996; Kohn and Cerling 2002). Due to the time-averaging effect of enamel formation, however, measurements of $\delta^{18}O$ in sequential samples of livestock teeth can reveal seasonal herd movements (Balasse et al. 2012) or serve as a proxy for paleoclimate (Sarkar et al. 2016). In humans, drinking water can include different geographic sources such as precipitation, stream, and groundwater. Humans with a consistent water supply, such as groundwater from wells in prehistoric Britain, may yield tooth enamel with $\delta^{18}O$ variation of 1‰ or less within a sedentary community (Budd et al. 2004). This is not always the case, however. In tropical regions, $\delta^{18}O$ in enamel may vary more within populations than between them, whereas in alpine regions, like the Andes or Alps, both seasonal differences and altitudinal effects in meteoric water $\delta^{18}O$ may be larger than differences between groups.

Overall, by combining isotope signatures with all the archaeological details and genetic (DNA) analyses, such elusive phenomena such as prehistoric kinship and the origin of social inequality can be identified. For example, Sr, O, and C isotope measurements in tooth enamel, compared with heritable dental traits, revealed group structure among the victims of a Neolithic massacre buried in a mass grave at Talheim, Germany (Bentley et al. 2008). Given evidence for differential land access in the Neolithic, from carbon and nitrogen isotopes in plant and animal remains (Bogaard et al. 2011; Fraser et al. 2013) as well as strontium isotopic signatures in humans such as the example shown in Fig. 5, others have looked for and found different animal husbandry patterns in prehistoric domestic animal teeth (Balasse et al. 2012, 2016; Gron et al. 2016; Madgwick et al. 2012; Montgomery et al. 2010). These inferences about land use are combined with evidence from plant remains to reconstruct the food webs (Fraser et al. 2013), climate change (Riehl et al. 2008), or land management practices (Wallace et al. 2015; Bogaard et al. 2013).

Conclusion

Chemical and isotopic analyses are a means to characterize the origin and/or nature of raw materials used in artifact production and therefore contribute to models of trade, manufacture, and ancient economy. The combination of isotopic results with the macroscopic analysis of the human, animal, and plant remains from archaeological sites can create a clearer picture of the dietary patterns and natural environment of a society. New instrumentation continually makes new analysis possible first for specialists and then later for archaeologists more widely. Ideally, a full archaeological interpretation should combine chemical results with evidence from archaeological excavations,

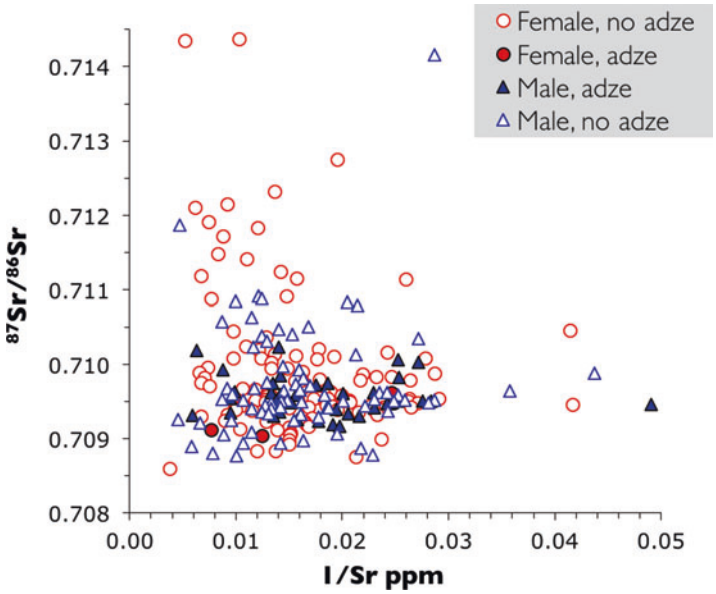

Archeological Geochemistry, Fig. 5 $^{87}Sr/^{86}Sr$ in archaeological human enamel samples from early Neolithic sites across Central Europe, where early Neolithic farmers preferred the rich loess soil ($^{87}Sr/^{86}Sr$ between 0.709 and 0.710). Most males buried with distinctive Neolithic stone adzes (*filled triangles*) yielded $^{87}Sr/^{86}Sr$ within the *loess* range, with lower variance than the rest of the sample ($p < 0.01$). Most individuals outside this range were females or males without adzes ($p < 0.01$). As males with adzes yielded strontium isotope signatures consistent with their preferred loess soils, the implication is that males without adzes were not cultivating their food in local soils; perhaps they were pastoralists or they had to farm less optimal uplands (Modified after Bentley et al. (2012))

historical sources, and typo-chronological study. The use of techniques adapted from the geosciences and developments in microanalysis and in (semi-) nondestructive analysis of archaeological materials (Neff 2012; Resano et al. 2010) have allowed to look at archaeological research questions in an entirely new way.

Cross-References

- Antimony
- Boron Stable Isotopes
- Copper
- Geochronology and Radiogenic Isotopes
- Inductively Coupled Plasma Mass Spectrometry (ICP-MS)
- Ion Exchange Chromatography
- Inductively Coupled Plasma Mass Spectrometry (ICP-MS)
- Lanthanide Rare Earths
- Lead
- Neodymium Isotopes
- Oxygen Isotopes
- Silicon
- Stable Isotope Geochemistry
- Strontium Isotopes
- Thermal Ionization Mass Spectrometry
- Trace Elements

References

Ambrose SH, Butler BM, Hanson DB, Hunter-Anderson RL, Krueger HW (1997) Stable isotopic analysis of human diet in the Marianas archipelago, western Pacific. Am J Phys Anthropol 104:343–361

Aubert M, Brumm A, Ramli M, Sutikna T, Saptomo EW, Hakim B, Morwood MJ, van den Bergh GD, Kinsley L, Dosseto A (2014) Pleistocene cave art from Sulawesi, Indonesia. Nature 514:223–227

Beard BL, Johnson CM (2000) Strontium isotope composition of skeletal material can determine the birth place and geographic mobility of humans and animals. J Forensic Sci 45:1049–1061

Balasse M, Boury L, Ughetto-Monfrin J, Tresset A (2012) Stable isotope insights ($\delta^{18}O$, $\delta^{13}C$) into cattle and sheep husbandry at Bercy (Paris, France, 4th millennium BC): birth seasonality and winter leaf foddering. Environ Archaeol 17:29–44

Balasse M, Evin A, Tornero C, Radu V, Fiorillo D, Popovici D, Andreescu R, Dobney K, Cucchi T, Bălăşescu A (2016) Wild, domestic and feral? Investigating the status of suids in the Romanian Gumelniţa (5th mil. cal BC) with biogeochemistry and geometric morphometrics. J Anthropol Archaeol 42:27–36

Begemann F, Kallas K, Schmitt-Strecker S, Pernicka E (1999) Tracing ancient tin via isotope analysis. In: Hauptmann A, Pernicka E, Rehren T, Yalcin U (eds) The beginnings of metallurgy, Der Anschnitt Beiheft 9. Deutsches Bergbau-Museum, Bochum, pp 277–284

Bentley RA (2006) Strontium isotopes from the earth to the archaeological skeleton: a review. J Archaeol Method Theory 13:135–187

Bentley RA, Knipper C (2005) Geographic patterns in biologically-available strontium, carbon and oxygen isotopes signatures in prehistoric SW Germany. Archaeometry 47:629–644

Bentley RA, Buckley HR, Spriggs M, Bedford S, Ottley CJ, Nowell GM, Macpherson CG, Pearson DG (2007) Lapita migrants in the Pacific's oldest cemetery. Am Antiq 72:645–656

Bentley RA, Price TD, Wahl J, Atkinson TC (2008) Community structure in the Neolithic community of Talheim. Antiquity 82:290–304
Bentley RA, Bickle P, Fibiger L, Nowell GM, Dale CW, Hedges REM, Hamilton J, Wahl J, Francken M, Grupe G, Lenneis E, Teschler-Nicola M, Arbogast R-M, Hofmann D, Whittle A (2012) Community differentiation and kinship among Europe's first farmers. Proc Natl Acad Sci U S A 109:9326–9330
Bocherens H, Drucker DG, Germonpré M, Oliva M (2015) Reconstruction of the Gravettian food-web at Predmostí I using multi-isotopic tracking (^{13}C, ^{15}N, ^{34}S) of bone collagen. Quat Int 359–360:211–228
Bogaard A, Fraser R, Heaton THE, Wallace M, Vaiglova P, Charles M, Jones G, Evershed RP, Styring AK, Andersen NH, Arbogast R-M, Bartosiewicz L, Gardeisen A, Kanstrup M, Maier U, Marinova E, Ninov L, Schäfer M, Stephan E (2013) Crop manuring and intensive land management by Europe's first farmers. Proc Natl Acad Sci U S A 110:12589–12594
Bogaard A, Strien H-C, Krause R (2011) Towards a social geography of cultivation and plant use in an early farming community: Vaihingen an der Enz, south-west Germany. Antiquity 85:395–416
Bollongino R, Nehlich O, Richards MP, Orschiedt J, Thomas MG, Sell C, Fajkošová Z, Powell A, Burger J (2013) 2000 years of parallel societies in stone age Central Europe. Science 342:479–481
Bowen GJ, Wilkinson B (2002) Spatial distribution of δ18O in meteoric precipitation. Geology 30:315–318
Braekmans D, Degryse P, Poblome J, Neyt B, Vyncke K, Waelkens M (2011) Understanding ceramic variability: an archaeometrical interpretation of the classical and Hellenistic ceramics at Düzen Tepe and Sagalassos (Southwest Turkey). J Archaeol Sci 38(9):2101–2115
Brill RH (1999) Chemical analyses of early glasses. Corning Museum of Glass, Corning
Brill RH, Wampler JM (1965) Isotope studies of ancient lead. Am J Archaeol 71:63–77
Bryant JD, Koch P, Froelich PN, Showers WJ, Genna BJ (1996) Oxygen isotope partitioning between phosphate and carbonate in mammalian apatite. Geochim Cosmochim Acta 60:5145–5148
Budd P, Millard A, Chenery C, Lucy S, Roberts C (2004) Investigating population movement by stable isotope analysis. Antiquity 78:127–140
Burton JH, Price TD (2003) The use of barium and strontium abundances in human skeletal tissues to determine their geographic origins. Int J Osteoarchaeol 13:88–95
Chiaradia M, Gallay A, Todt W (2003) Different contamination styles of prehistoric human teeth at a Swiss necropolis (Sion, Valais) inferred from lead and strontium isotopes. Appl Geochem 18:353–370
Choy K, Smith CI, Fuller BT, Richards MP (2010) Investigation of amino acid $\delta^{13}C$ signatures in bone collagen to reconstruct human palaeodiets using LC-IR-MS. Geochim Cosmochim Acta 74:6093–6111
Copley MC, Berstan R, Dudd SN, Docherty G, Mukherjee AJ, Straker V, Payne S, Evershed RP (2003) Direct chemical evidence for widespread dairying in prehistoric Britain. Proc Natl Acad Sci U S A 100:1524–1529
Cramp LJE, Evershed RP (2014) Reconstructing aquatic resource exploitation in human prehistory using lipid biomarkers and stable isotopes. In: Holland HD, Turekian KK (eds) Treatise on geochemistry: archaeology and anthropology. Elsevier, Amsterdam, pp 319–339
Degryse P (2012) Archeometric applications. In: Vanhaecke F, Degryse P (eds) Isotopic analysis, fundamentals and applications using ICP-MS. Wiley-VCH Verlag GmbH & Co. KG, Weinheim, pp 373–390
Degryse P (ed) (2014) Glass making in the Greco-Roman World, studies in archaeological sciences 4. Leuven University Press, Leuven
Degryse P, Braekmans D (2014) Elemental and isotopic analysis of ancient ceramics and glass. In: Cerling T (ed) Treatise on geochemistry: archaeology and anthropology, Chapter 14. Elsevier, Oxford, pp 191–207
Degryse P, Shortland AJ (2009) Trace elements in provenancing raw materials for Roman glass production. Geol Belg 12(3–4):135–143
Degryse P, Shortland AJ (2013) Nourishing archaeology and science. Proc Natl Acad Sci U S A 110(51):20352–20353
Degryse P, Schneider J, Haack U, Lauwers V, Poblome J, Waelkens M, Muchez P (2006) Evidence for glass 'recycling' using Pb and Sr isotopic ratios and Sr-mixing lines: the case of early Byzantine Sagalassos. J Archaeol Sci 33(4):494–501
Degryse P, Lobo L, Shortland AJ, Vanhaecke F, Blomme A, Painter J, Gimeno D, Eremin K, Greene J, Kirk S, Walton M (2015) Isotopic investigation into the raw materials of late bronze age glass making. J Archaeol Sci 62:153–160
Deino AL, Renne PR, Swisher CC (1998) $^{40}Ar/^{39}Ar$ dating in paleoanthropology and archeology. Evol Anthropol 6(2):63–75
Denys C, Williams CT, Dauphin Y, Andrews P, Fernandez-Jalvo Y (1996) Diagenetical changes in Pleistocene small mammal bones from Olduvai bed I. Palaeogeogr Palaeoclimatol Palaeoecol 126:121–134
Devulder V, Vanhaecke F, Shortland A, Mattingly D, Jackson C, Degryse P (2014) Boron isotopic composition as a provenance indicator for the flux raw material in Roman natron glass. J Archaeol Sci 46:107–113
Devulder V, Gerdes A, Vanhaecke F, Degryse P (2015) Validation of the determination of the B isotopic composition in Roman glasses with laser ablation multi-collector inductively coupled plasma-mass spectrometry. Spectrochim Acta B At Spectrosc 105:116–120
Dunne J, Evershed RP, Salque M, Cramp L, Bruni S, Ryan K, Biagetti S, di Lernia S (2012) First dairying in green Saharan Africa in the fifth millennium BC. Nature 486:390–394
Ericson JE (1985) Strontium isotope characterization in the study of prehistoric human ecology. J Hum Evol 14:503–514
Evans JE, Montgomery J, Wildman G, Boulton N (2010) Spatial variations in biosphere $^{87}Sr/^{86}Sr$ in Britain. J Geol Soc London 167:1–4
Evans JA, Pashley V, Richards GJ, Brereton N, Knowles TG (2015) Geogenic lead isotope signatures from meat products in Great Britain. Sci Total Environ 537:447–452
Fraser RA, Bogaard A, Schäfer M, Arbogast RM, Heaton THE (2013) Integrating botanical, faunal and human stable carbon and nitrogen isotope values to reconstruct land use and palaeodiet at LBK Vaihingen an der Enz, Baden-Württemberg. World Archaeol 45(3):492–517
Freestone IC (2006) Glass production in late antiquity and the early Islamic period: a geochemical perspective. In: Maggetti M, Massiga B (eds) Geomaterials in cultural heritage, Special publications, vol 257. Geological Society of London, London, pp 201–216
Frei KM, Price TD (2012) Strontium isotopes and human mobility in prehistoric Denmark. Archaeol Anthropol Sci 4:103–114
Frei KM, Mannering U, Kristiansen K, Allentoft ME, Wilson AS, Skals I, Tridico S, Nosch ML, Willerslev E, Clarke L, Frei R (2015) Tracing the dynamic life story of a Bronze Age Female. Sci Rep 5:10431
Gale NH (1997) The isotopic composition of tin in some ancient metals and the recycling problem in metal provenancing. Archaeometry 39:71–82
Gron KJ, Montgomery J, Nielsen PO, Nowell GM, Peterkin JP, Sørensen L, Rowley-Conwy P (2016) Strontium isotope evidence of early Funnel Beaker Culture movement of cattle. J Archaeol Sci Rep 6:248–251
Haustein M, Gillis C, Pernicka E (2010) Tin isotopy – a new method for solving old questions. Archaeometry 52:816–832
Heaton THE (1999) Spatial, species, and temporal variations in the $^{13}C/^{12}C$ ratios of C_3 plants. J Archaeol Sci 26:637–649
Hedges REM (2002) Bone diagenesis: an overview of processes. Archaeometry 44:319–328
Hedges REM, Clement JG, Thomas CDL, O'Connell TC (2007) Collagen turnover in the adult femoral mid-shaft. Am J Phys Anthropol 133:808–816

Henderson J (2000) The science and archaeology of materials. Routledge, London
Hodell DA, Quinn RL, Brenner M, Kamenov G (2004) Spatial variation of strontium isotopes ($^{87}Sr/^{86}Sr$) in the Maya region. J Archaeol Sci 31:585–601
Kamenov GD, Gulson BL (2014) The Pb isotopic record of historical to modern human lead exposure. Sci Total Environ 490:861–870
Keller AT, Regan LA, Lundstrom CC, Bower NW (2015) Evaluation of the efficacy of spatiotemporal Pb isoscapes for provenancing of human remains. Forensic Sci Int 261:83–92
Kempe DRC, Harvey AP (1983) The petrology of archaeological artefacts. Clarendon Press
Koch PL, Heisinger J, Moss C, Carlson RW, Fogel ML, Behrensmeyer AK (1995) Isotopic tracking of change in diet and habitat use in African elephants. Science 267:1340–1343
Kohn MJ (1996) A predictive model for animal $\delta^{18}O$: accounting for diet and physiological adaptation. Geochim Cosmochim Acta 60:4811–4829
Kohn MJ, Cerling TE (2002) Stable isotope compositions of biological apatite. Rev Mineral Geochem 48:455–488
Lee-Thorp JA (2008) On isotopes and old bones. Archaeometry 50:925–950
Lewis J, Coath CD, Pike AWG (2014) An improved protocol for $^{87}Sr/^{86}Sr$ by LA-ICP-MS using oxide reduction and a customised plasma interface. Chem Geol 390:173–181
Lobo L, Degryse P, Shortland A, Eremin K, Vanhaecke F (2014) Copper and antimony isotopic analysis via multi-collector ICP-mass spectrometry for provenancing ancient glass. J Anal At Spectrom 29:58–64
Madgwick R, Mulville J, Stevens RE (2012) Isotopic analysis of fauna from British middens of the late Bronze Age. Environ Archaeol 17:126–140
Montgomery J, Evans JA, Wildman G (2006) $^{87}Sr/^{86}Sr$ isotope composition of bottled British mineral waters for environmental and forensic purposes. Appl Geochem 21:1526–1534
Montgomery J, Evans JA, Horstwood MSA (2010) Evidence for long-term averaging of strontium in bovine enamel using TIMS and LA-MC-ICP-MS strontium isotope intra-molar profiles. Environ Archaeol 15:32–42
Müller W, Anczkiewicz R (2016) Accuracy of laser-ablation (LA)-MC-ICPMS Sr isotope analysis of (bio)apatite – a problem reassessed. J Anal At Spectrom 31:259–269
Naito YI, Chikaraishi Y, Ohkouchi N, Drucker DG, Bocherens H (2013) Nitrogen isotopic composition of collagen amino acids as an indicator of aquatic resource consumption. World Archaeol 45:338–359
Neff H (2012) Laser ablation ICP-MS in archaeology. In: Lee MS (ed) Handbook of mass spectrometry. Wiley, New York, pp 829–843
Nowell GM, Horstwood MSA (2009) Comments on Richards et al. J Archaeol Sci 36:1334–1341
O'Leary MH (1988) Carbon isotopes in photosynthesis. BioScience 38:328–336
Outram AK, Stear N, Bendrey R, Olsen S, Kasparov A, Zaibert V, Thorpe N, Evershed RP (2009) Earliest horse harnessing and milking. Science 323:1332–1335
Peacock DPS (1970) The scientific analysis of ancient ceramics: a review. World Archaeol 1:375–389
Pike AWG (2002) Analysis of Caucasian metalwork – the use of antimonal, arsenical and tin bronze in the Late Bronze Age. In: Curtis J, Kruszynski M (eds) Ancient Caucasian and related material in the British museum, the British museum occasional paper 121. British Museum, London, pp 87–98
Pike AWG, Hoffmann DL, García-Diez M, Pettitt PB, Alcolea J, De Balbín R, González-Sainz C, de las Heras C, Lasheras JA, Montes R, Zilhão J (2012) U-series dating of Paleolithic art in 11 caves in Spain. Science 336:1409–1413
Poage MA, Chamberlain CP (2001) Empirical relationships between elevation and the stable isotope composition of precipitation and surface waters. Am J Sci 301:1–15
Pollard AM (2009) What a long strange trip it's been: lead isotopes in archaeology. In: Shortland AJ, Freestone IC, Rehren T (eds) From mine to microscope: advances in the study of ancient technology. Oxbow Books, Oxford, pp 181–189
Pollard AM, Bray PJ (2015) A new method for combining lead isotope and lead abundance data to characterize archaeological copper alloys. Archaeometry 57:996–1008
Pollard AM, Heron C (2008) Lead isotope geochemistry and the trade in metals. Chapter 9. In: Archaeological chemistry, 2nd edn. The Royal Society of Chemistry, Cambridge, UK, pp 302–345
Prowse T, Schwarcz HP, Saunders S, Macchiarelli R, Bondioli L (2004) Isotopic paleodiet studies of skeletons from the Imperial Roman-age cemetery of Isola Sacra, Rome, Italy. J Archaeol Sci 31:259–272
Pryce TO, Htwe KMM, Georgakopoulou M, Martin T, Vega E, Rehren T, Win TT, Petchey P, Innanchai J, Pradier B (2016) Metallurgical traditions and metal exchange networks in late prehistoric central Myanmar, c. 1000 BC to c. AD 500. Archaeol Anthropol Sci. https://doi.org/10.1007/s12520-016-0436-7. (in press)
Rehren T (2008) A review of factors affecting the composition of early Egyptian glasses and faience: alkali and alkali earth oxides. J Archaeol Sci 35:1345–1354
Rehren T, Pusch EB (2005) Late Bronze Age glass production at Qantir-Piramesses, Egypt. Science 308:1756–1758
Resano M, García-Ruiz E, Vanhaecke F (2010) Laser ablation – inductively coupled plasma mass spectrometry in archaeometric research. Mass Spectrom Rev 29:55–78
Richards MP, Fuller BT, Sponheimer M, Robinson T, Ayliffe L (2003) Sulphur isotope measurements in archaeological samples. Int J Osteoarchaeol 13:37–45
Riehl S, Bryson R, Pustovoytov K (2008) Changing growing conditions for crops during the Near Eastern Bronze Age (3000–1200 BC): the stable carbon evidence. J Archaeol Sci 35:1011–1022
Salque M, Bogucki PI, Pyzel J, Sobkowiak-Tabaka I, Grygiel R, Szmyt M, Evershed RP (2013) Earliest evidence for cheese making in the sixth millennium BC in northern Europe. Nature 493:522–525
Sarkar A, Mukherjee AD, Bera MK, Das B, Juyal N, Morthekai P, Deshpande RD, Shinde VS, Rao LS (2016) Oxygen isotope in archaeological bioapatites from India. Sci Rep 6:26555
Sayre EV, Smith RW (1961) Compositional categories of ancient glass. Science 133:1824–1826
Schibille N, Sterrett-Krause A, Freestone IC (2016) Glass groups, glass supply and recycling in late Roman Carthage. Archaeol Anthropol Sci. https://doi.org/10.1007/s12520-016-0316-1
Schoeninger MJ (2009) Stable isotope evidence for the adoption of maize agriculture. Curr Anthropol 50:633–640
Schoeninger MJ, DeNiro MJ (1984) Nitrogen and carbon isotopic composition of bone collagen from marine and terrestrial animals. Geochim Cosmochim Acta 48:625–639
Sharpe AE, Kamenov GD, Gill A, Hodell DA, Emery KF, Brenner M, Krigbaum J (2016) Lead (Pb) isotope baselines for studies of ancient human migration and trade in the Maya region. PLoS One 11(11): e0164871
Shortland AJ, Rogers NW, Eremin K (2007) Trace element discriminants between Egyptian and Mesopotamian Late Bronze Age glasses. J Archaeol Sci 34:781–789
Shotyk W, Weiss D, Appleby PG, Cheburkin AK, Frei R, Gloor M, Kramers JD, Reese S, Van der Knaap WO (1998) History of atmospheric lead deposition since 12,370 14C yr BP from a peat bog, Jura Mountains, Switzerland. Science 281:1635–1640
Sillen A, Hall G, Armstrong R (1998) $^{87}Sr/^{86}Sr$ ratios in modern and fossil food-webs of the Sterkfontein valley. Geochim Cosmochim Acta 62:2463–2478

Smith BD, Zeder MA (2013) The onset of the Anthropocene. Anthropocene 4:8–13
Smyth J, Evershed RP (2015) Milking the megafauna: using organic residue analysis to understand early farming practice. Environ Archaeol 21(3):214–229
Stenhouse MJ, Baxter MS (1979) The uptake of bomb ^{14}C in humans, in radiocarbon dating. In: Berger R, Suess HE (eds) Radiocarbon dating. University of California Press, Berkeley, pp 324–341
Styring AK, Fraser RA, Arbogast RM, Halstead P, Isaakidou V, Pearson JA, Schäfer M, Triantaphyllou S, Valamoti SM, Wallace M, Bogaard A, Evershed RP (2015) Refining human palaeodietary reconstruction using amino acid $\delta^{15}N$ values of plants, animals and humans. J Archaeol Sci 53:504–515
Tite M, Shortland AJ (2008) Production technology of faience and related early vitreous materials, Oxford University School of Archaeology Monograph, vol 72. Oxford University School of Archaeology, Oxford, pp 187–198
Trickett MA, Budd P, Montgomery J, Evans J (2003) An assessment of solubility profiling as a decontamination procedure for the Sr-87/Sr-86 analysis of archaeological human skeletal tissue. Appl Geochem 18:653–658
Tykot RH (2016) Using non-destructive portable x-ray fluorescence spectrometers on stone, ceramics, metals, and other materials in museums. Appl Spectrosc 70:42–56
Wallace M, Jones G, Charles M, Fraser R, Heaton THE, Bogaard A (2015) Crop water availability in Neolithic and Bronze Age Western Asia and Aegean inferred directly by stable carbon isotope analysis. PLoS One 10(6):e0127085
Weigand PC, Harbottle G, Sayre EV (1977) Turquoise sources and source analysis: Mesoamerican and the Southwestern U.S.A. In: Earle TK, Ericson JE (eds) Exchange systems in prehistory. Academic Press, New York, pp 15–34
Willmes M, Kinsley L, Moncel MH, Armstrong RA, Aubert M, Eggins S, Grün R (2016) Improvement of laser ablation in situ micro-analysis to identify diagenetic alteration and measure strontium isotope ratios in fossil human teeth. J Archaeol Sci 70:102–116
Wilson L, Pollard AM (2001) The provenance hypothesis. In: Brothwell DR, Pollard AM (eds) Handbook of archaeological sciences. Wiley, New York

Argon

Mark A. Kendrick
Research School of Earth Sciences, Australian National University, Canberra, ACT, Australia

Element Data
Atomic Symbol: Ar
Atomic Number: 18
Atomic Weight: 39.984
Isotopes and Abundances: ^{40}Ar (99.6%), ^{38}Ar (0.06%), and ^{36}Ar (0.34%)
1 Atm Melting Point: 83.95 K
1 Atm Boiling Point: 87.29 K
(*continued*)

Common Valences: 0
First Ionization Potential: 1520.6 kJ mol^{-1}
Chondritic (CI) Abundance: ~10^{-6} mol g^{-1} (~93 ppm by mass)
Silicate Earth Abundance: ~10^{-12} mol ^{36}Ar g^{-1} (parts per trillion range)
Crustal Abundance: $<10^{-11}$ mol ^{36}Ar g^{-1}
Seawater Abundance: ~1–2 × 10^{-8} mol ^{36}Ar g^{-1}

Properties

Argon is the most abundant noble gas and accounts for 0.934 volume % of dry air. Argon has a calculated atomic radius of 0.71 Å and a van der Waals radius of 1.88 Å. Argon is a colorless, odorless, tasteless, nontoxic gas at room temperature, and like the other noble gases in group 18 of the periodic table, Ar usually has a full valence shell of electrons and does not form chemical bonds. Chemical inertness and volatility are defining features of group 18 gases which exist in monatomic states and are commonly known as the noble, inert, or rare gases. This behavior is further emphasized by the name argon which is derived from the Greek *argos* meaning lazy, idle, or inactive.

Argon has three stable isotopes: ^{40}Ar now dominates on all rocky planets and meteorites because it is produced by radioactive decay of ^{40}K, which has a half-life of 1.25 Ga. The scarce ^{38}Ar and ^{36}Ar isotopes are not significantly produced by any radiogenic or nucleogenic pathway and are therefore regarded as primordial isotopes on Earth. The ^{37}Ar and ^{39}Ar isotopes are short-lived radionuclides with half-lives of 35 days and 269 years, respectively, that are exploited by ^{40}Ar-^{39}Ar dating (below) but are only produced at very low levels in the Earth's crust (Chang 2015; McDougall and Harrison 1999).

Discovery and Utility

Argon was the first noble gas to be isolated (Rayleigh and Ramsay 1894). The first hint of its existence came in 1766 when Henry Cavendish noted that 1% of the gas in air could not be chemically combined. However, argon was only isolated from air and identified as a new element in 1894 (Rayleigh and Ramsay 1894). Its isolation followed some months after Lord Rayleigh and Sir Ramsey first noted that nitrogen purified from decomposing ammonium nitrite appeared to be 0.5% lighter than nitrogen purified from air. The discrepancy that indicated the presence of an unknown heavier gas contaminating atmospheric nitrogen and argon was later isolated from this mixture by reaction with heated

magnesium. The residual gas had a volume of ~1% the original volume of air and was shown to have distinct spectral lines.

Argon has a number of industrial and scientific applications, and it is produced for these purposes by fractional distillation of liquefied air, together with liquid nitrogen and liquid oxygen. Due to its abundance, argon is the cheapest noble gas used for industrial processes. Argon is used to sparge dissolved gas impurities from molten metals including steel; it is used in some types of arc welding/cutting of reactive metals and in the production of reactive elements and growing crystals. Argon is used as a preservative to displace moisture and air from some food and medicine packages. The low thermal conductivity of argon means it can be used to fill the gap in sealed double glazing units. The inert chemical and characteristic electrical properties of Ar are used in lighting: argon prevents oxidation of the filament in incandescent light bulbs and produces a characteristic violet/lilac light in gas-discharge lamps. Argon is used in science to provide inert atmospheres within glove boxes and can be used as a carrier gas for gas chromatography or laser ablation inductively coupled plasma mass spectrometry. The breakdown of ArF is used to produce 193 nm light in Excimer lasers.

Distribution in the Cosmos and on Earth

Argon is the tenth most abundant element in the solar system accounting for ~3 atoms per million (~93 ppm by mass or ~10^{-6} mol g^{-1}) of the solar photosphere, where it is dominated by the non-radiogenic ^{36}Ar and ^{38}Ar isotopes and is similarly abundant as calcium (Ca) and aluminum (Al) (Lodders 2003). The high volatility of Ar, which has a 50% condensation temperature of 48 K at 10^{-4} bar (Lodders 2003), means that it is strongly depleted in chondritic meteorites that condensed from the solar nebula. Argon and other noble gases are further depleted in differentiated terrestrial planets like Earth, where they are strongly partitioned into the atmosphere and regarded as atmophile elements. The Earth's atmosphere is estimated to have a total Ar inventory of 1.7×10^{18} mols equivalent to ~70 trillion tons (Ozima and Podosek 2002). The absolute abundance of argon within the Earth is subject to substantial uncertainty; however, the atmosphere probably contains 95–99% of all $^{36\text{-}38}$Ar on Earth and 50–95% of all ^{40}Ar. Given the crust and mantle contain K, they have uniformly higher ^{40}Ar/^{36}Ar than the atmosphere. However, the proportion of ^{40}Ar outgassed from the Earth hinges on how the K content of the Earth is estimated. Argon has a total abundance on Earth on the order of 10–20 ppb with primordial $^{36\text{-}38}$Ar in the parts per trillion range (e.g., ~10^{-12} mol g^{-1}). Primordial Ar is therefore approximately a million times less abundant on Earth than in the Sun, which explains why noble gases like Ar are also known as rare gases.

Seawater represents Earth's second largest Ar reservoir, after the atmosphere, and has a typical Ar concentration of ~$1–2 \times 10^{-8}$ mol g^{-1}, with the absolute concentration varying as a result of solubility fluctuations related to temperature and salinity (Ozima and Podosek 2002). Argon does not usually form chemical bonds, but it can be adsorbed onto mineral surfaces via van der Waals forces. If present, argon is trapped in fluid inclusions in minerals, and it is also incorporated in lattice defect structures and vacant ring sites in hydrous minerals (Jackson et al. 2015). Maximum ^{36}Ar concentrations of 10^{-11} mol g^{-1} have been reported for hydrous minerals and sediments (Kendrick et al. 2013), whereas the mantle has an estimated ^{36}Ar concentration of only ~$2–3 \times 10^{-15}$ mol g^{-1}. Some ionic molecules containing Ar have been formed under laboratory conditions including the hydrate ion ArH^+ which forms readily under vacuum conditions and short-lived molecules such as ArF and HArF. Argon is also trapped in the lattice structure of gas hydrate.

Significance in Geochemistry, Geochronology, and the Composition of Air

The radioactive decay of ^{40}K to ^{40}Ar forms the basis of one of the most widely used geochronometers in Earth science today (McDougall and Harrison 1999). The radioactive decay of ^{40}K is branched: it decays to produce 11.2% ^{40}Ar via electron capture and 88.8% ^{40}Ca via beta decay. However, the strong depletion of argon on Earth means that radiogenic ^{40}Ar is much easier to measure than radiogenic ^{40}Ca and ^{40}Ar is therefore the most important decay product for geochronology. The 1.25 Ga half-life of ^{40}K decay has enabled the K-Ar dating technique to be applied to primitive meteorites that represent some of the oldest objects in the solar system, down to events occurring at sub-million year timescales. Most modern "K-Ar" ages are obtained via the ^{40}Ar-^{39}Ar technique. In this technique the geological sample is irradiated in a nuclear reactor to convert a small portion of the samples ^{39}K into ^{39}Ar via a neutron reaction. K is then measured via the irradiation-produced ^{39}Ar proxy isotope by mass spectrometry together with ^{40}Ar. This technique has the advantages that K and Ar are measured simultaneously and possible ^{40}Ar-loss can be assessed via age spectra diagrams. It also provides very high precision and its high sensitivity enables application to materials with young ages in the tens of thousands of years age range (McDougall and Harrison 1999).

The importance of Ar in geochronology means that there has been great interest in precisely determining its isotopic composition in air (Table 1). The IUGS subcommission on geochronology recommended an atmospheric ^{40}Ar/^{36}Ar ratio of 295.5 ± 0.5 (Steiger and Jager 1977), which has been widely used, but includes a rounding error compared to the value of 296 originally recommended by Nier (1950)

Argon, Table 1 Isotopic composition of Ar in air

	$^{40}Ar/^{36}Ar$	$^{38}Ar/^{36}Ar$
Nier (1950)	296.0 ± 0.5	0.1880 ± 0.0004
IUGS	295.5 ± 0.5	
Lee et al. (2006)	298.6 ± 0.3	0.1885 ± 0.0003
Valkiers et al. (2010)	298.7 ± 0.1	0.1898 ± 0.0002

(Table 1). More recent determinations suggest a $^{40}Ar/^{36}Ar$ ratio about 1% higher than Nier's value (Lee et al. 2006; Valkiers et al. 2010). It has not yet been possible to reproduce the abundance of all three argon isotopes at the quoted levels of uncertainty (Table 1); however, Mark et al. (2011) suggests that the combined $^{40}Ar/^{36}Ar$ and $^{38}Ar/^{36}Ar$ values of Lee et al. (2006) show the greatest internal consistency. Until consensus is reached regarding the best $^{40}Ar/^{36}Ar$ ratio for air, the value adopted for measurement calibration should ideally be stated.

The second major use of Ar is as a geochemical tracer. The $^{40}Ar/^{36}Ar$ composition of fluid inclusions in crustal minerals is sensitive to the introduction of atmospheric components with low $^{40}Ar/^{36}Ar$, whereas mantle (or ancient crustal) fluids have elevated $^{40}Ar/^{36}Ar$. As a result of degassing ^{40}Ar from the mantle and crust, the atmospheric $^{40}Ar/^{36}Ar$ ratio has increased over Earth history (Cadogan 1977; Pujol et al. 2013). The argon isotope signature of the mantle provides information about mantle degassing and re-gassing through subduction recycling. The maximum $^{40}Ar/^{36}Ar$ of the mantle sampled by mid-ocean ridge basalt is ~40,000 (Moreira et al. 1998), whereas the mantle sampled by ocean island basalts (e.g., Hawaii, Iceland) has a substantially lower $^{40}Ar/^{36}Ar$ of $<$15,000 because it is less degassed and contains more primordial ^{36}Ar (Mukhopadhyay 2012). The $^{38}Ar/^{36}Ar$ of the mantle is of considerable interest for identifying the primordial origin of noble gas in the mantle. Most recent analyses suggest the mantle and atmosphere have indistinguishable $^{38}Ar/^{36}Ar$ that is slightly higher than the solar value (Holland and Ballentine 2006; Raquin and Moreira 2009). This is consistent with the possibility that atmospheric noble gases have been extensively cycled into the mantle by subduction (Holland and Ballentine 2006); however, the ultimate origin of noble gases in the mantle and atmosphere remain an area of active debate.

Summary

Argon is the most abundant noble gas accounting for 0.934% of dry air. As a result of its abundance, argon was the first noble gas to be chemically isolated and is the cheapest noble gas used in industrial processes. Argon has three stable isotopes; ^{40}Ar is produced by radioactive decay of ^{40}K, whereas ^{38}Ar and ^{36}Ar are primordial isotopes on Earth. Argon is strongly depleted on Earth and concentrated in the atmosphere. The ^{40}Ar-^{39}Ar method is a powerful and widely used geochronometer. The variable distribution of Ar isotopes between Earth's mantle, crust, and atmosphere provides important constraints on mantle outgassing, fluid flow in the crust and subduction-recycling.

Cross-References

- ▶ Argon Isotopes
- ▶ Geochronology and Radiogenic Isotopes
- ▶ Noble Gases

References

Cadogan PH (1977) Palaeoatmospheric argon in Rhynie chert. Nature 268:38

Chang J (2015) Table of nuclides, KAERI (Korea Atomic Energy Research Institute). Available at: http://atom.kaeri.re.kr/ton/. Retrieved Oct 2015

Holland G, Ballentine CJ (2006) Seawater subduction controls the heavy noble gas composition of the mantle. Nature 441:186–191

Jackson CRM, Parman SW, Kelley SP, Cooper RF (2015) Light noble gas dissolution into ring structure-bearing materials and lattice influences on noble gas recycling. Geochim Cosmochim Acta 159:1–15

Kendrick MA, Honda M, Pettke T, Scambelluri M, Phillips D, Giuliani A (2013) Subduction zone fluxes of halogens and noble gases in seafloor and forearc serpentinites. Earth Planet Sci Lett 365:86–96

Lee JY, Marti K, Severinghaus JP, Kawamura K, Yoo HS, Lee JB, Kim JS (2006) A redetermination of the isotopic abundances of atmospheric Ar. Geochim Cosmochim Acta 70:4507–4512

Lodders K (2003) Solar system abundances and condensation temperatures of the elements. Astrophys J 591:1220–1247

Mark DF, Stuart FM, de Podesta M (2011) New high-precision measurements of the isotopic composition of atmospheric argon. Geochim Cosmochim Acta 75:7494–7501

McDougall I, Harrison TM (1999) Geochronology and thermochronology by the $^{40}Ar/^{39}Ar$ method, 2nd edn. Oxford University Press, New York

Moreira M, Kunz J, Allegre C (1998) Rare gas systematics in popping rock: isotopic and elemental compositions in the upper mantle. Science 279:1178–1181

Mukhopadhyay S (2012) Early differentiation and volatile accretion recorded in deep-mantle neon and xenon. Nature 486:101–104

Nier AO (1950) A redetermination of the relative abundances of the isotopes of carbon, nitrogen, oxygen, argon and potassium. Phys Rev 77:789–793

Ozima M, Podosek FA (2002) Noble gas geochemistry, 2nd edn. Cambridge University Press, Cambridge

Pujol M, Marty B, Burgess R, Turner G, Philippot P (2013) Argon isotopic composition of Archaean atmosphere probes early earth geodynamics. Nature 498:87–90

Raquin A, Moreira M (2009) Atmospheric $^{38}Ar/^{36}Ar$ in the mantle: implications for the nature of the terrestrial parent bodies. Earth Planet Sci Lett 287:551–558

Rayleigh L, Ramsay W (1894) Argon, a new constituent of the atmosphere. Proc R Soc Lond 57:265–287

Steiger RH, Jäger E (1977) Subcommission on geochronology – convention on use of decay constants in geochronology and cosmochronology. Earth Planet Sci Lett 36:359–362

Valkiers S, Vendelbo D, Berglund M, de Podesta M (2010) Preparation of argon primary measurement standards for the calibration of ion current ratios measured in argon. Int J Mass Spectrom 291:41–47

Argon Isotopes

Philippe Sarda
GEOPS, Univ. Paris-Sud, CNRS, Université Paris-Saclay, Rue du Belvédère, Orsay, France

Introduction

Argon (Ar) has three natural isotopes with masses 36, 38, and 40. ^{36}Ar and ^{38}Ar are stable, that is, they are not radioactive, and they are also not produced by radioactivity processes. In detail, these isotopes can be produced in tiny amounts by rare reactions such as the β^-radioactive decay of ^{36}Cl *yielding* ^{36}Ar. Besides such minor productions, the isotopes ^{36}Ar and ^{38}Ar have been essentially produced in stars before solar system formation. They are therefore mostly primordial in origin and they bear a message about the processes that occurred at and before planetary formation.

Argon-40 is not radioactive but is produced by the decay of ^{40}K, a rare isotope of potassium. Models of nucleosynthesis indicate that ^{40}Ar is produced in stars in tiny amount compared to ^{36}Ar and ^{38}Ar (e.g., $^{40}Ar/^{36}Ar \sim 10^{-4}$). Thus, practically all ^{40}Ar present in Earth is radiogenic. The terrestrial atmosphere presents a concentration of argon of 0.934 mol.% (dry air), mainly made of ^{40}Ar ($^{40}Ar/^{36}Ar = 298.6$ in air), as a result of the production of ^{40}Ar in the crust and mantle through time and its accumulation in the atmosphere. Potassium-40 decays to ^{40}Ar with a half-life of 1.25 Ga. Potassium has three isotopes with masses 39, 40, and 41, and only ^{40}K is radioactive, with the particularity that it can decay following two schemes, one being a β^-radioactivity producing ^{40}Ca, and the other one being an electronic capture producing ^{40}Ar. The fact that ^{40}Ar is essentially radiogenic is fully confirmed by isotopic measurements of meteorites, which show extremely low $^{40}Ar/^{36}Ar$ isotopic ratios. Indeed, in outer space and extraterrestrial objects, i.e., in environments other than telluric planets, ^{36}Ar and ^{38}Ar are much more abundant that ^{40}Ar.

Atmospheric Argon Isotopes

From a historical point of view, the high abundance of ^{40}Ar in air, an anomaly compared to ^{36}Ar and ^{38}Ar (and other noble gases), led German physicist Carl Friedrich von Weizsäcker, in the middle of the twentieth century, to suspect that (i) ^{40}Ar was radiogenic, (ii) a new, radioactive, isotope of potassium existed that had to be ^{40}K (only ^{39}K and ^{41}K were known at that time), and (iii) ^{40}K could decay by a new scheme, unknown at that time, that had to be electronic capture (von Weizsäcker 1937). A beautiful reasoning based on a geochemical observation.

The terrestrial atmosphere is the main noble gas reservoir with a fast mixing timescale of the order of a few years. It therefore constitutes a convenient international isotope standard for noble gases. The isotopic composition of atmospheric argon, given as $^{38}Ar/^{36}Ar$ and $^{40}Ar/^{36}Ar$, is thus the interlaboratory reference. The normalization to ^{36}Ar is based on the fact that ^{36}Ar is the most abundant of the nonradiogenic isotopes, hence the easiest to measure with the smallest uncertainty. Measurements of argon isotopes in air have long shown that ^{36}Ar is about five times more abundant than ^{38}Ar, and that ^{40}Ar is roughly 300 times more abundant than ^{36}Ar (and thus, 1500 more abundant than ^{38}Ar).

Until recently, the recommended values were those obtained by Alfred O. Nier (1950, who proposed. $(^{38}Ar/^{36}Ar)_{\mathrm{AIR}} = 0.1880 \pm 0.0003$ (1σ) and $(^{40}Ar/^{36}Ar)_{\mathrm{AIR}} = 295.5 \pm 0.5$ (1σ). These values were adopted and recommended by the International Union of Geological Sciences in 1977 (Steiger and Jäger 1977). Since then, the $(^{40}Ar/^{36}Ar)_{\mathrm{AIR}}$ ratio was found slightly different by Lee et al. (2006), with a value of 298.6 ± 0.1 (1σ). Lee et al. (2006) also confirmed the value of Nier for the $(^{38}Ar/^{36}Ar)_{\mathrm{AIR}}$ ratio, with a measured value of 0.1885 ± 0.0001 (1σ).

In addition to ^{36}Ar, ^{38}Ar and ^{40}Ar, two radioactive Ar isotopes are used in geochronology in the so-called ^{39}Ar-^{40}Ar dating method. Neutron activation of potassium-40 produces ^{39}Ar, which β^- decays to ^{39}K with a half-life of 268 years. ^{37}Ar is also produced by neutron activation of ^{40}Ca and decays by electronic capture to ^{37}Cl, with a half-life of 35 days. The rocks or minerals to be dated are therefore radioactive and demand caution when manipulated. Some advanced mass-spectrometers can measure the five argon isotopes simultaneously, i.e., masses 36, 37, 38, 39, and 40, by using the so-called multicollection technique, where the five isotopes are received in five collectors (Faraday cups or electron multipliers).

Geochemists use the argon isotopes for two main applications, geochronology and isotope tracing of geological phenomena.

Radiochronometric Dating with Argon Isotopes

The method consists in measuring the concentrations of ^{40}Ar, and of ^{40}K, which permit to calculate, from the equation of radioactivity, an age based on the assumption that the object to be dated did not lose or gain any argon or potassium isotopes ("closed-system hypothesis"). In practice, the $^{40}Ar/^{36}Ar$ ratio is also measured, which permits to correct the amount of ^{40}Ar from the contribution of atmospheric argon. Under the assumption that ^{36}Ar is from air, the contribution of atmospheric ^{40}Ar is estimated by multiplying

^{36}Ar by the $(^{40}Ar/^{36}Ar)_{AIR}$ ratio of 298.6. Removing this contribution from total ^{40}Ar permits to estimate the amount of radiogenic ^{40}Ar produced in the sample by the decay of ^{40}K.

The basic method, called *K-Ar* dating, or ^{40}K-^{40}Ar, requires splitting the sample to be dated into two aliquots. *Ar* isotopes are extracted from one aliquot by heating under high vacuum and analyzed by static mass spectrometry. The *K* concentration is measured on the other aliquot after acid dissolution and usually with an optical method such as atomic absorption. The *K-Ar* dating method is suitable for samples that have been emplaced at the surface of the Earth and thus may have incorporated present atmospheric argon. This is often the case of volcanic samples, which cool rapidly at the surface of the Earth. However, if argon incorporated during rock/mineral cooling (often called "initial argon") is not atmospheric, then the *K-Ar* method is problematic because it is then difficult to correct for initial argon. Such a problem arose when attempting to date volcanic samples from Mid-Ocean Ridges in the 1960s. It was found that the initial Ar isotope composition was non-atmospheric, with a $^{40}Ar/^{36}Ar$ ratio much higher than the atmospheric value. This eventually led to the identification of strongly radiogenic argon in the mantle of the Earth, a trace of the massive and very ancient degassing of our planet (see below).

The difficulty of evaluating the isotopic composition of initial argon led to the development of a more sophisticated K-Ar dating method, the so-called *Ar-Ar* method, or ^{39}Ar-^{40}Ar method, where ^{40}K is transformed into ^{39}Ar by neutron activation. Combined with stepwise heating extraction of both natural and neutron-produced Ar isotopes, this method permits to identify radiogenic ^{40}Ar produced in-situ by the decay of ^{40}K from inherited ^{40}Ar. Another advantage of this method is that only one aliquot of the sample is used to determine both the parent (^{40}K) and the daughter (^{40}Ar) isotope amounts by static mass spectrometry. The sample is usually heated in several temperature steps, and the five Ar isotopes are measured for each step (see above). An age is calculated for each step and the results are represented in a diagram showing age versus fraction of Ar released. When several successive steps give the same age within analytical uncertainty, this is called a "plateau" and this age is considered reliable (previous steps being perturbed by Ar loss or mixing with air). This elegant method was developed in the 1960s by Merrihue and Turner (1966).

Tracing Geological Processes with Argon Isotopes

Argon isotopes can also be used to trace geological phenomena. We take the example of the generation of the atmosphere by degassing of the Earth's interior. When, in the 1960s, several scientists attempted to date fresh basaltic samples from Mid-Oceanic Ridge axes using the *K-Ar* method, they found ages of tens to hundreds of million years, at odds with the very young character of ridge axes (Ozima and Kudo 1972). The problem was that the initial $^{40}Ar/^{36}Ar$ ratio was much higher than the atmospheric value. As these basalts came directly from the mantle beneath the ridge, and because isotopes with such high masses as argon are certainly very little isotopically fractionated, the meaning of these measurements was that mantle argon was different from atmospheric argon. This discovery prompted efforts from the noble gas community to identify the isotopic composition of Ar trapped in such samples of Mid-Ocean Ridge basalts (MORBs), by extracting gases either by progressive heating of the samples or by vacuum crushing. These samples contained very little Ar, but, upon progressive heating, they degassed Ar with $^{40}Ar/^{36}Ar$ ratios that were increasingly higher with increasing temperature. Such "exotic" $^{40}Ar/^{36}Ar$ ratios could reach extremely high values, up to 20,000 (Sarda et al. 1985). Values close to 30,000 are not rare (Moreira et al. 1998), and the highest values reach ~40,000. Because Mid-Ocean Ridge basalts are sampling magmas from the underlying mantle, such extreme ratios were likely to represent the mantle Ar isotope composition. Why was mantle argon so radiogenic compared to atmospheric argon? The answer to this question is that this radiogenic character is the geochemical record of both very strong and very early degassing of the Earth. A $^{40}Ar/^{36}Ar$ isotopic ratio of 30,000 is about 100 times the value of air argon, and this means that ^{36}Ar in the present mantle is just 100 times lower than it was initially. Simple calculations using the ^{40}K decay constant show that, for the present $^{40}Ar/^{36}Ar$ ratio in the mantle to be so high, degassing of ^{36}Ar from the mantle into the atmosphere must have occurred within the first 100 million years of the Earth's existence (Sarda et al. 1985).

Among the rare gases, xenon also bears the same message, when using the extinct β^- radioactivity of iodine-129 (^{129}I) that yields ^{129}Xe with a half-life of 16 Ma. Using both xenon and argon systematics, degassing can be modeled using simple first-order kinetics, combined with the decay constants appropriate for *K-Ar* and *I-Xe*. This gives a picture of the degassing kinetics during the 4.5 billion years: clearly two stages are present (Allègre et al. 1983). A very strong degassing stage, with degassing rate decreasing very fast, occurred during the first 100 million years or so, and this stage was followed by about four billion years of more gentle degassing, with a degassing rate analogous to the present one. The first stage could represent degassing that occurred during planet growth or during the magma ocean stage of the young Earth, while the second stage could represent the times when the mantle became solid and animated by solid-state convection.

Concurrently, ^{40}Ar produced by the decay of ^{40}K accumulated in the atmosphere, with the $(^{40}Ar/^{36}Ar)_{AIR}$ increasing with time. The accumulation rate depends of the degassing rate of the mantle and of the continental crust, the latter being a major reservoir of potassium. Thus, the $(^{40}Ar/^{36}Ar)_{AIR}$ ratio of ancient air might have the potential to trace the geodynamics of the mantle and crust. In agreement with this possibility, a $(^{40}Ar/^{36}Ar)_{AIR}$ ratio of 143 ± 24 (1σ) was measured in 3.5 Ga-old fluid inclusions, presumably representing the Ar isotope composition of air at this time (Pujol et al. 2013). This result allowed these authors to propose a major crustal growth event ~3 Ga ago.

Conclusion

The isotopic composition of argon is widely used in Earth sciences, mainly for two purposes. The decay of potassium-40 to argon-40 led to the development of the so-called "K-Ar" geochronology, probably the most widely used method for dating rocks and minerals. For example, this method permitted to date oceanic rocks which, combined with paleomagnetism, provided the definite proof of plate tectonics. Combined with the volatile character of argon, this decay scheme has the potential to trace geological processes involving transfer of volatile species between geochemical reservoirs. This approach showed that the terrestrial atmosphere is an ancient reservoir which formed within the first tens to hundreds of Ma of the Earth's history.

Cross-References

- ► Atmospheric Evolution
- ► Geochronology and Radiogenic Isotopes
- ► Mid-Ocean Ridge Basalts (MORB)
- ► Noble gases

References

Allègre CJ, Staudacher T, Sarda P, Kurz M (1983) Constraints on evolution of Earth's mantle from rare gas systematics. Nature 303:762–766

Lee JY, Marti K, Severinghaus JP, Kawamura K, Yoo HS, Lee JB, Kim JS (2006) A redetermination of the isotopic abundances of atmospheric Ar. Geochim Cosmochim Acta 70:4507

Merrihue C, Turner G (1966) Potassium-argon dating by activation with fast neutrons. J Geophys Res 71:2852

Moreira M, Kunz J, Allègre CJ (1998) Rare gas systematics in Popping Rock : isotopic and elemental compositions in the upper mantle. Science 279:1178

Nier A (1950) A redetermination of the relative abundances of the isotopes of carbon, nitrogen, oxygen, argon, and potassium. Phys Rev 77:789

Ozima M, Kudo K (1972) Excess argon in submarine basalts and an earth-atmosphere evolution model. Nature 239:23

Pujol M, Marty B, Burgess R, Turner G, Philippot P (2013) Argon isotopic composition of Archean atmosphere probes early Earth geodynamics. Nature 498:87

Sarda P, Staudacher T, Allègre CJ (1985) 40Ar/36Ar in MORB glases : constraints on atmosphere and mantle evolution. Earth Planet Sci Lett 72:357

Steiger RH, Jäger E (1977) Subcommission on geochronology: convention on the use of decay constants in geo-and cosmochronology. Earth Planet Sci Lett 36:359

von Weizsäcker CF (1937) Über die Möglichkeit eines dualen-Zerfalls von Kalium. Physik Z 38:623

Arsenic

Monica Vasiliu and David A. Dixon
Department of Chemistry, University of Alabama, Tuscaloosa, AL, USA

Element Data
Atomic Symbol: As
Atomic Number: 33
Atomic Weight: 74.9216
Isotopes and Abundances: ^{75}As 100%
1 Atm Melting Point: 1090 K
1 Atm Boiling Point: 887 K (sublimes)
Common Valences: +5, +3, and −3
Ionic Radii: (+V) 46, (+III) 69, and (−III) 222 ppm
Pauling Electronegativity: 2.18
First Ionization Energy: 947.0 kJ/mol
Chondritic (CI) Abundance: 1.86 ppm
Silicate Earth Abundance: 0.05 ppm
Crustal Abundance: 2.1 ppm
Seawater Abundance: 0.0026 ppm
Core Abundance: 5 ppm

Properties

Arsenic (Emsley 1991, 2001; Anthoni 2006; Anders and Grevesse 1989; McDonough 2005), a metalloid, has three allotropic forms: yellow, black, and gray. The most common form is a shiny, gray, brittle, metallic-looking crystalline solid. The less common yellow form is a crystalline solid which is produced when vapors of arsenic are cooled suddenly. It tarnishes rapidly in air and when heated does not melt, but sublimes although it can be forced to melt as well. When arsenic is heated in air, it reacts with oxygen to form arsenic oxide forming a blue flame with a garlic-like odor.

History and Use

Arsenic was certainly known to the ancient civilizations under different forms, but the credit for its discovery goes to alchemist Albert the Great (Albertus Magnus, 1193–1280).

Arsenic is a well-known poison, being used in insecticides or in rat poisons. Arsenic can be used in making special types of glass and as a wood preservative. When combined with gallium, it is a III–V direct bandgap semiconductor with a zinc blende crystal structure with uses in integrated circuits, light-emitting diodes, as well as optical windows. It is also used in bronzing and pyrotechnics and for hardening shot. Arsine (AsH_3) gas, which is extremely toxic, is used as a dopant gas in the microchip industry. Surprisingly, arsenic compounds can have medicinal applications.

Geochemical Behavior

A small amount of arsenic is found in its native state as microcrystalline masses. Arsenic is usually found as ores, and the most common ones are arsenopyrite (FeAsS), orpiment (As_2S_3), and realgar (As_4S_4) which are obtained as a by-product of the mining purification of a metal. The world production is 50,000 t/year in the form of oxides which is far more than industry needs.

Volcanoes release about 3,000 t/year of arsenic into the atmosphere, and microorganisms release up to 20,000 t/year of volatile methylarsines as well. The largest atmospheric emissions are the 80,000 t/year of arsenic released from burning fossil fuels.

Biological Utilization and Toxicity

Arsenic is one of the most toxic elements found, but at the same time, some scientists believe that it might be essential to human diet in very low doses. In very small doses, arsenic stimulates metabolism and boosts the formation of red blood cells. Prolonged exposure to inorganic arsenic can cause various health effects from irritation of the stomach and intestines, decrease in the production of white and red blood cells, lung irritation, and skin changes due to DNA damage leading to improved chances of developing cancer (skin, lung, liver, and lymphatic). Organic arsenic is not as harmful as inorganic arsenic compounds. Humans can be exposed to arsenic through food, water, and air or even through skin contact with soil or water that contains high levels of arsenic. High levels of arsenic are found in fish because they can absorb arsenic from water. A lethal dose of arsenic oxide is about 100 mg. An example of the use of arsenic as a poison is the play and movie, "Arsenic and Old Lace" from the late 1930s and early 1940s. Arsenic poisoning, whether accidental or explicit, has been attributed to the deaths of many important historical figures.

References

Anders E, Grevesse N (1989) Abundances of the elements: meteoritic and solar. Geochim Cosmochim Acta 53:197–214. http://meteorites.wustl.edu/goodstuff/chondritic_abundances.htm

Anthoni JF (2006) The chemical composition of seawater in. http://www.seafriends.org.nz/oceano/seawater.htm

Emsley J (1991) The elements, 2nd edn. Clarendon Press, Oxford

Emsley J (2001) Nature's building blocks an A-Z guide to the elements. Oxford University Press, Oxford

McDonough WF (2005) Compositional model for the earth's core. In: Carlson RW (ed) The mantle and core. Elsevier, Oxford, pp 547–568. http://www.knowledgedoor.com/2/elements_handbook/element_abundances_in_the_earth_s_core.html

Astatine

Monica Vasiliu and David A. Dixon
Department of Chemistry, University of Alabama, Tuscaloosa, AL, USA

Element Data
Atomic Symbol: At
Atomic Number: 85
Atomic Weight: (210)
Isotopes (radioactive): ^{210}At, ($t_{1/2}$ = 8.1 h), ^{211}At, ($t_{1/2}$ = 7.2 h)
1 Atm Melting Point: 575 K (estimate)
1 Atm Boiling Point: 610 K (estimate)
Common Valences: +5, +1, −1
Ionic Radii: (+V) 57, (−I) 227 ppm
Pauling Electronegativity: 2.2
First Ionization Potential: 899.0 kJ/mol
Chondritic (CI) Abundance:
Silicate Earth Abundance:
Crustal Abundance: trace amount in some minerals
Seawater Abundance: –
Core Abundance:

Properties

Astatine (Emsley 1991, 2001) is a reactive, radioactive nonmetal element which resembles iodine. The properties of astatine are not well established. It has been not extensively studied because all its isotopes have short half-lives. Much of what is known about astatine has been estimated from its

position in the periodic table, below iodine, and by studying its chemistry in extremely dilute solutions.

History and Use

In 1931 a group of chemists led by Fred Allison reported that they had detected the previously unknown element below iodine in the periodic table. They decided to call it alabamine, after Alabama, but their claim was a mistake. In 1940, three chemists (Dale R. Corson, Kenneth R. Mackenzie, and Emilio Segre) working at the University of California at Berkeley found evidence of element 85 at the end of an experiment they were conducting in a cyclotron. They reported this discovery but were unable to continue research on the element due to World War II and the Manhattan Project. In 1947, they named the new element astatine because there are no stable isotopes for the element and in Greek the word for unstable is "astatos."

Geochemical Behavior

Astatine actually appears in the Earth's crust for a short time from decay of radioactive isotopes of uranium and thorium. Astatine is usually synthesized in very small amounts in nuclear reactions, for example, neutron bombardment of ^{209}Bi produces ^{211}At. No more than 10^{-6} g of astatine has ever been synthesized in the laboratory.

Biological Utilization and Toxicity

Astatine is a highly radioactive element.

References

Emsley J (1991) The elements, 2nd edn. Clarendon Press, Oxford
Emsley J (2001) Nature's building blocks an A-Z guide to the elements. Oxford University Press, Oxford

Atmophile Elements

Daniele L. Pinti
GEOTOP, Research Center on the Dynamics of Earth System, Université du Québec à Montréal, Montréal, QC, Canada

Synonyms

Volatile elements

Definition

In the Goldschmidt geochemical classification, *atmophile* (literally "gas-loving") are those elements that are extremely volatile, i.e., they form gases or liquids at the surface of the Earth, and they are usually concentrated in the terrestrial atmosphere and hydrosphere. The atmophile elements are Hydrogen (H), Carbon (C), Nitrogen (N), and noble gases, namely Helium (He), Neon (Ne), Argon (Ar), Krypton (Kr), Xenon (Xe), and Radon (Rn).

Overview

Victor Moritz Goldschmidt, Swiss mineralogist and geologist is considered the father of geochemistry. His major achievement is the so-called Goldschmidt geochemical classification of the elements. The Goldschmidt geochemical classification of elements groups the chemical elements according to their preferred host phases within the Earth into lithophile (rock-loving), siderophile (iron-loving), chalcophile (sulfur-loving), and atmophile (gas-loving). For this reason, elements from each group are concentrated in specific terrestrial reservoirs. Strictly speaking, the atmophile elements are H, C, N, He, Ne, Ar, Kr, Xe, and Rn. These elements are those able to form gases or liquids. They are concentrated mainly in the Earth's atmosphere and hydrosphere. Atmophile elements are also called "volatile elements." However, this last term might bring to confusion with the planetary science classification of the chemical elements. In this classification, "volatile" is any chemical element and chemical compound with low boiling points (< 1100 K) that is associated with a planet's or moon's crust (i.e., K, Rb, S, etc.) and/or a planetary atmosphere (i.e., C, N, ammonia, noble gases, halogens). For this reason, it is often believed that halogens are atmophile elements, being concentrated in the atmospheres of the giant planets. However, for the Goldschmidt geochemical classification of elements, halogens are nonmetallic lithophile elements, forming on Earth salty minerals found in seawater and in pegmatites.

Atmophiles in Earth's Atmosphere

Atmophile elements are stable except for Radon (^{222}Rn) which is radioactive and decays rapidly with a half-life of 3.82 days.

Oxygen is a major component of the present-day atmosphere (20.9435 vol% in air; Gatley et al. 2008), but it is not considered an atmophile element in the Goldschmidt geochemical classification of elements. Oxygen is mainly present in the Earth's crust as oxide and silicate minerals and thus it is commonly considered a lithophile element. Its accumulation

in the Earth's atmosphere at the end of the Archean era is likely the result of a complex interplay between oxygen sources (production from photosynthesis) and sinks (burial of organics, volcanic gas oxidation, etc.) (e.g., Catling 2015).

The recent discover of molecular O_2 in the coma of the comet 67P/Churyumov–Gerasimenko by the Rosetta instrumentation (Bieler et al. 2015; Mousis et al. 2016) might call for a redefinition of oxygen as an atmophile element in celestial bodies.

Carbon has a double geochemical behavior. It behaves as an atmophile element when forms compounds with oxygen as carbon dioxide (CO_2), the fourth more abundant gas in the present-day Earth's atmosphere (406 ppm), or carbon monoxide (CO) emitted in the atmosphere by volcanoes with a short residence time of a few months. Carbon behaves also as a siderophile element and is one of the candidate light elements proposed to account for the density deficit of the Earth's core (Zhang and Yin 2012). Hydrogen occurs mainly as water (H_2O) in the hydrosphere and in the present atmosphere as water vapor.

Nitrogen forms molecular N_2 with a strong triple covalent bond that makes it mostly unreactive, as noble gases, and thus it is mainly partitioned into the atmosphere. Nitrogen can occur in silicate rocks, mainly as ammonium (NH_4^+), replacing K^+ ions in mica and feldspars (Pinti and Hashizume 2011). Although atmospheric nitrogen is cycled in the modern ocean by microorganisms through three dominant metabolic processes, namely fixation ($N_2 \rightarrow NH_3$), nitrification ($NH_3 \rightarrow NO_3^-$), and denitrification ($NO_3^- \rightarrow N_2$) (Sigman et al. 2009), the resulting concentration in the atmosphere is assumed constant (78.048 volume % in air). Kasting (1993) suggested that nitrogen partial pressure in the atmosphere was close to 1 atm since the formation of the secondary atmosphere of the Earth. More recently, Marty et al. (2013) suggested that the partial pressure of N_2 of the Archean atmosphere was lower than 1.1 bar, possibly as low as 0.5 bar from the analysis of nitrogen and argon isotopes in fluid inclusions trapped in 3.0- to 3.5-billion-year-old hydrothermal quartz.

Finally, noble gases have their outer electron shell filled, making them chemically inert as well as volatile elements per excellence. They are typically present at very low concentrations in the Earth's atmosphere with argon being the most abundant (0.9340 volume % in air). Although rare, the elemental and isotopic abundance of noble gases has been pivotal for the understanding of the origin and evolution of the hydrosphere-atmosphere system on Earth (e.g., Marty 2012) and Mars (e.g., Atreya et al. 2013). Helium has two stable isotopes of masses 3 and 4, respectively. The ^{3}He which is abundant in the Earth's mantle is a primordial noble gas of solar origin. Together with mantle neon ^{3}He could be the only remnant of the Presolar Nebula or PSN-derived primitive atmosphere of the Earth. The primitive atmosphere of the Earth, as those of Venus and Mars, have been stripped almost totally by strong solar winds during the first phases of the Sun formation, the so-called *T-Tauri stage*. This is the name of a class of young stars very bright and emanating powerful stellar winds.

^{4}He is radiogenic and mainly derived from the decays of ^{238,235}U and ^{232}Th in the Earth's crust, as for ^{40}Ar which has been accumulated since the Earth's formation by the decay of ^{40}K contained in the crust. It was believed that argon, krypton, and xenon were mainly of secondary origin, brought on Earth by chondritic bodies. Indeed, when the terrestrial abundance of these gases (and C, N) is compared with the solar abundance and that of carbonaceous chondrites, the Earth's atmosphere and mantle Ar, Kr, and Xe abundance match closely that of chondrites, except for Xe which is depleted by a factor of ~20 relative to Kr (Marty 2012). This Xe depletion known under the synonym of "*Missing Xenon*" has been generally interpreted as indicative of a small contribution of cometary volatiles having low Xe/Ar ratios (Dauphas 2003), although alternative views have been recently proposed (see ▶ "Earth's Atmosphere" entry for details).

Based on recent measurements of volatiles in the coma of the comet 67P/Churyumov–Gerasimenko by the Rosetta onboard instrumentation, it has been suggested that cometary C, N, and water makes less than 1% of their total respective inventories on Earth (Marty et al. 2016), most of them having been contributed by wet asteroids. However, ^{36}Ar could be up to 90% of cometary origin and it suggests that the terrestrial atmosphere could contain a significant, possibly dominant, fraction of cometary heavier noble gases (Ar, Kr, and Xe), which might have been delivered during the Terrestrial Late Heavy Bombardment around 4 Ga ago (Marty et al. 2016).

Summary

Atmophile elements *sensu stricto* are those which have an affinity for gaseous/fluid phases, enriched in the atmosphere and hydrosphere of the Earth. Volatile elements include the atmophiles but extend to all elements having a low boiling point and which, at certain conditions, can occur in planetary atmospheres such as the halogens in the outer layers of the giant planets.

Although occurring in notable amounts in the Earth's atmosphere, oxygen is not considered an atmophile element. Oxygen forms silicate minerals and thus it occurs mainly in crusts and mantles of telluric planets. Its occurrence in the commonness molecular form O_2 in primitive bodies such as comets might change our vision on this element. N, C, H, and noble gases are believed to have been brought on Earth by wet planetesimals such as asteroids and comets. This event took place after the Earth's core formation with possible additional contributions of volatile to Earth during the Terrestrial Late Heavy Bombardment, 4 Ga ago.

Cross-References

- Argon
- Argon Isotopes
- Carbon
- Earth's Atmosphere
- Geochemical Classification of Elements
- Helium
- Helium Isotopes
- Hydrogen
- Krypton
- Neon
- Neon Isotopes
- Nitrogen
- Nitrogen Cycle
- Noble Gases
- Oxygen
- Radon
- Xenon

References

Atreya SK et al (2013) Primordial argon isotope fractionation in the atmosphere of Mars measured by the SAM instrument on curiosity and implications for atmospheric loss. Geophys Res Lett 40:5605–5609

Bieler A and 33 others (2015) Abundant molecular oxygen in the coma of comet 67P/Churyumov-Gerasimenko. Nature 526:678–681

Dauphas N (2003) The dual origin of the terrestrial atmosphere. Icarus 165:326–339

Gatley DP, Herrman S, Kretzschmar H-J (2008) A twenty-first century molar mass for dry air. HVAC&R Res 14:655–662

Kasting JF (1993) Earth's early atmosphere. Science 259:920–926

Marty B (2012) The origins and concentrations of water, carbon, nitrogen and noble gases on Earth. Earth Planet Sci Lett 313–314:56–66

Marty B, Zimmermann L, Pujol M, Burgess R, Philippot P (2013) Nitrogen isotopic composition and density of the Archean atmosphere. Science 342:101–104

Marty B, Avice G, Sano Y, Altwegg K, Balsiger H, Hässig M, Morbidelli A, Mousis O, Rubin M (2016) Origins of volatile elements (H, C, N, noble gases) on Earth and Mars in light of recent results from the ROSETTA cometary mission. Earth Planet Sci Lett 441:91–102

Mousis O, Ronnet T, Brugger B, Ozgurel O, Pauzat F, Ellinger Y, Maggiolo R, Wurz P, Vernazza P, Lunine JI, Luspay-Kuti A, Mandt KE, Altwegg K, Bieler A, Markovits A, Rubin M (2016) Origin of molecular oxygen in comet 67P/Churyumov–Gerasimenko. Astrophys J Lett 823:L41

Pinti DL, Hashizume K (2011) Early life record from nitrogen isotopes. In: Golding DS, Glikson M (eds) Earliest life on Earth: habitats, environments and methods of detection. Springer, Dordrecht, pp 183–205

Sigman DM, Kash KL, Casciotti KL (2009) Ocean process tracers: nitrogen isotopes in the ocean. In: Steele JH, Turekian KK, Thorpe SA (eds) Encyclopedia of ocean science, 2nd edn. Elsevier, Amsterdam

Zhang Y, Yin Q-Z (2012) Carbon and other light element contents in the Earth's core based on first-principles molecular dynamics. Proc Natl Acad Sci 109:19579–19583

Atmospheric Evolution

Colin Goldblatt
School of Earth and Ocean Sciences,
University of Victoria, Victoria, BC, Canada

Definition

Earth's atmosphere has evolved as volatile species cycle between the atmosphere, ocean, biomass, and the solid Earth. The geochemical, biological, and astrophysical processes that control atmospheric evolution are reviewed from an "Earth Systems" perspective, with a view not only to understanding the history of Earth but also to generalizing to other solar system planets and exoplanets.

Introduction

The evolution of Earth's atmosphere has been a function of the cycling of volatile species between the atmosphere, ocean, biomass, and the solid Earth. The composition of the atmosphere largely determines the climate, thus whether life can thrive, and the rate of many geochemical processes. Atmospheric evolution is an inherently interdisciplinary problem, requiring an "Earth system" approach; it is replete with feedback processes and neither a single branch of science nor study of any single part of the Earth is sufficient to make progress.

In the preface to *The Biosphere*, a visionary work of what would now be Earth system science, Vernadsky (1926) wrote

> Historically, geology has been viewed as a collection of events derived from insignificant causes, a string of accidents. This of course ignores the scientific idea that geological events are planetary phenomena and that the laws governing these events are not peculiar to Earth alone.

This review proceeds from that paradigm, with a focus on process and mechanism applicable to the evolution of Earth's atmosphere that are generalizable to other atmospheres, either comparison planets in our solar system or other inhabited planets.

Indeed, as we enter the age of exoplanets, understanding the evolution of Earth's atmosphere gains greater meaning. The practical method of remotely determining the geochemistry of a planet, and potentially detecting life, is a spectroscopic analysis of the planetary atmosphere (Lovelock 1965; Hitchcock and Lovelock 1967). Interpreting whether a remotely detected atmospheric composition implies life requires an understanding the range of compositions that an inhabited planet atmosphere could have, and Earth history is the biggest sampling of this parameter space available.

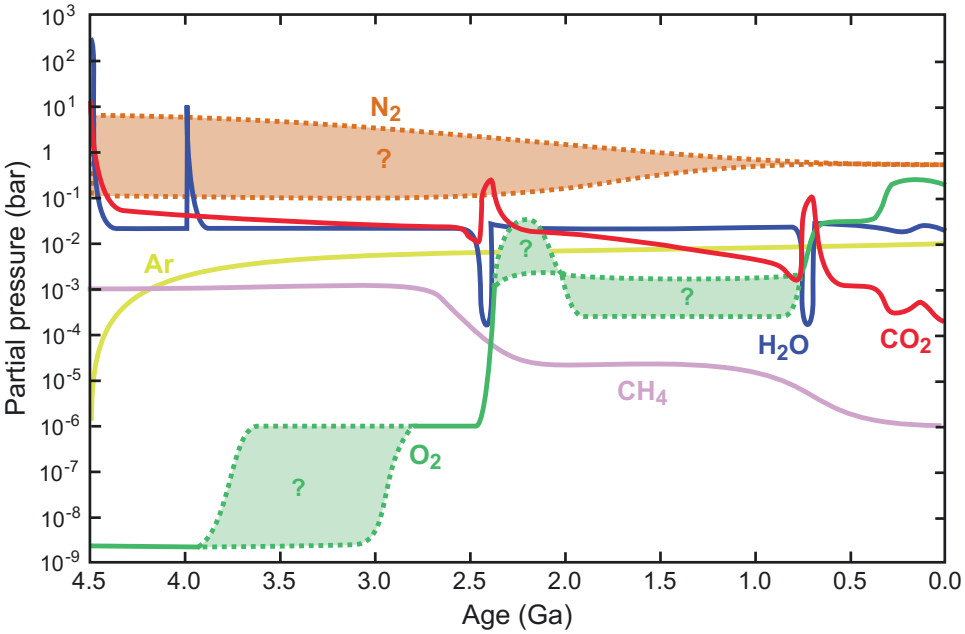

Atmospheric Evolution, Fig. 1 The evolution of Earth's atmosphere (an artist's conception). Uncertainties of a factor of a few are implied; smooth lines mostly correspond to lack of theory and constraints. Snowball Earth periods likely involve two or three glacials and interglacials but are shown as one for simplicity

The structure of this review is to first introduce the role of the atmosphere in maintaining climate, then treat atmospheric gasses beginning with the most abundant: nitrogen, oxygen, carbon dioxide, and then water. Trace species are treated with the more abundant gas that they are most closely linked to. Figure 1 gives a schematic summary of atmospheric evolution.

The Atmosphere and Climate

A Climate Primer

On timescales relevant to atmospheric evolution, Earth's atmosphere is in energy balance: energy in equals energy out. Solar energy incident on Earth (F_{solar}) dominates over the transfer of accretional and radiogenic heat to the surface by four orders of magnitude (342 Wm^{-2} versus 82 mWm^{-2}), so the Sun is the driver of climate. A fraction of the incident sunlight is reflected back to space by clouds, molecules, or the surface, referred to as the planetary albedo (α_p), around 0.3 for Earth today. Some sunlight is absorbed by water vapor in the lower atmosphere, but the bulk is absorbed at the surface. The result is that the atmosphere is heated from the base. Convection, therefore, dominates the lowest layer of the atmosphere, the troposphere, with temperature decreasing with height as rising air expands and cools. Above the top of this layer (the tropopause), vertical motions are minimal and the temperature structure is set by the balance of radiative absorption and emission. This layer is the stratosphere. Today, temperature increases in the stratosphere (a "temperature inversion") due to strong absorption of UV light by ozone.

Were Earth airless, radiative emission to space would equal surface emission and planetary temperature would be trivial to calculate. Surface emission approximates a black-body and would balance absorbed solar radiation averaged over the surface: $(1-\alpha_p)F_{\text{solar}} = \sigma T_{\text{surf}}^4$, where σ is the Stefan-Boltzmann constant and T_{surf} is the surface temperature, giving $T_{\text{surf}} = 255$ K.

Earth, of course, has an atmosphere which imparts a greenhouse effect, meaning that thermal emission to space for a given surface temperature is less than the black-body flux. This greenhouse effect occurs as infrared radiation is absorbed in the atmosphere by gases ("greenhouse gases") or particles (e.g., clouds), which then emit radiation both upward and downward. Given that the atmosphere is colder than the surface, the total thermal radiation to space is less in the presence of greenhouse absorption than it would be without.

For greenhouse gases at climatically relevant levels, it is fundamental to note that the strength of the greenhouse effect is proportional to the logarithm of gas abundance (Fig. 2). This relates to the absorption spectra of real gasses; see an excellent review of the greenhouse effect by Pierrehumbert (2011) for an explanation. Arising from this is the common misunderstanding that methane is an inherently strong greenhouse gas. It is actually a rather weak infrared absorber; however, its low abundance *in the present-day atmosphere,* 300 times lower than carbon dioxide, means that adding a fixed number of moles of carbon as CH_4 rather than CO_2 will give a larger forcing.

The Faint Young Sun Paradox

The amount of solar energy incident on Earth has increased by 30% through Earth history due to stellar evolution, yet it does not appear that Earth was substantially colder in the past

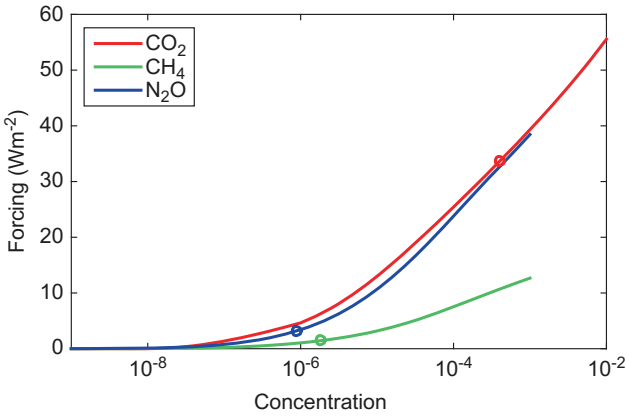

Atmospheric Evolution, Fig. 2 Greenhouse gas forcing (change in net flux at the tropopause) relative to zero concentration of that gas (Byrne and Goldblatt 2014b)

(Sagan and Mullen 1972). This is the so-called Faint Young Sun Paradox (FYSP), which substantially motivates the study of atmospheric evolution from a paleoclimate perspective: the past atmospheric composition must have been very different in order to keep Earth warm.

Primary evidence for temperate early Earth climate comes from the ubiquity of fluvial successions and subaqueously deposited strata in the Archean, compared to a dearth of glacial features (Nisbet 1987). Whereas regional glaciation recurs every ~100 Myr during the Phanerozoic, Precambrian glaciation is rare: low-latitude "Snowball Earth" glaciation in the Cryogenian (Neoproterozoic) and Siderian (Palaeoproterozoic) and regional glaciations in the Ediacaran (Neoproterozoic) and Mesoarchean (Evans 2003, Paul Hoffman, private communication).

Given lower insolation, temperate climate requires either a much stronger greenhouse effect or a lower planetary albedo, or both. Most attention has focused on greenhouse gases, with likely contributions from carbon dioxide (Owen et al. 1979) and methane (Haqq-Misra et al. 2008) and many other possible contributors (Byrne and Goldblatt 2014a). Clouds could contribute to a stronger greenhouse effect if there were more high clouds, or reduce the albedo if there were less low clouds (Goldblatt and Zahnle 2011).

See Feulner (2012) for a recent review of the FYSP.

Nitrogen

Nitrogen is present in the atmosphere as dinitrogen (N_2), the dominant background gas, and as more reactive and radiatively active species, primarily nitrous oxide (N_2O) and ammonia (NH_3). Nitrogen is a major element in life and thus has a fast biological cycle. There is also a slow geological cycle which determines atmospheric N_2 levels, which has only recently begun to be elucidated.

An understanding of the biological N cycle (Entry ▶ Nitrogen Cycle) underpins all theory of N evolution. In summary: for nitrogen to be bioavailable, it must be chemically reduced (fixed) from N_2 to ammonium (NH_4^+). Fixation is dominated by organisms; there is a metabolic cost to N-fixation, but this is selected for when N is a limiting nutrient. In oxic conditions (in confined oxygen oases in the Neoarchean, then widespread from the Paleoproterozoic onward), NH_4^+ may be returned to N_2 via nitrification and denitrification. If denitrification is incomplete, nitrous oxide (N_2O) is produced, then returned to N_2 by atmospheric photolysis. Under widespread anoxia (Meoarchean and earlier, and often in the Neoarchean), the major destruction pathway for (NH_4^+) would be outgassing of ammonia from the ocean followed by atmospheric photolysis (Entry ▶ Earth's Atmosphere). Evolution of the N cycle is reviewed by Stüeken et al. (2016).

Dinitrogen

Dinitrogen dominates Earth's atmosphere ($pN_2 = 0.78$ bar at present) and is subject to slow geologic cycling, making variations in the N_2 inventory likely. Until recently, atmospheric N_2 had generally been thought of as constant, with the implicit assumption that the biological cycle was entirely closed. However, a small leakage of fixed N from the ocean to the geosphere drives a whole Earth N cycle, just as organic carbon burial drives a large part of the coupled carbon-oxygen cycle. Recent whole-Earth nitrogen budgets have shown that there is more nitrogen in the silicate-Earth than in the atmosphere and that this nitrogen is necessarily of atmospheric origin and fixed biologically. This calls for a cycle of nitrogen between the atmosphere and the crust and mantle, operating over billions of years. Variations in the size of the atmospheric N_2 inventory by a factor of two or three are expected but are very poorly constrained at present (Goldblatt et al. 2009; Johnson and Goldblatt 2015).

Table 1 shows Earth's nitrogen reservoirs. The total nitrogen inventory is consistent with a chondritic source with ~10% retention. Nitrogen in the core is assumed to be inaccessible to the rest of the Earth system, leaving dominant exchangeable reservoirs to be the mantle (a few times the present atmospheric inventory), continental crust (around half the present atmospheric inventory), and the atmosphere itself. Understanding of the evolution of the atmospheric reservoir must, therefore, emerge from understanding the history of exchange with the crust and mantle.

The most important way that nitrogen enters rocks is as NH_4^+, which substitutes well for potassium ions (K^+) in silicate rocks, as they have the same change and a similar ionic radii. Organic nitrogen in sedimentary rock is an additional source, and this may be transferred to silicate-bound NH_4^+ during hydrothermal alteration, diagenesis, or

Atmospheric Evolution, Table 1 Earth system nitrogen reservoirs, after Johnson and Goldblatt (2015). The "high N" mantle reservoir is quite uncertain. The core is likely a large N reservoir, but is excluded as it is not thought to exchange with the atmosphere after core-mantle segregation

Reservoir	Size (10^{18} kg N)
Biomass (live and dead)	**9.3×10^{-4}**
Land	1.3×10^{-4}
Ocean	8.0×10^{-4}
Ocean	**2.4×10^{-2}**
Atmosphere	**4.0**
Ocean crust	0.47± 0.20
Sedimentary	0.41 ± 0.20
Igneous (altered)	0.061 ± 0.007
Continental crust	**2.0 ± 0.16**
Upper crust	
Sedimentary	0.76 ± 0.06
Metamorphic	0.72 ± 0.13
Volcanic	0.017 ± 0.020
Felsic intrusive	0.31 ± 0.04
Mafic intrusive	0.0036 ± 0.0015
Lower crust	0.18 ± 0.06
Mantle	**24.2 ± 16**
MORB source	7.2 ± 5.9
High N	17 ± 15
TOTAL	**30.2 ± 16**

metamorphosis. The geological N cycle and budget were recently reviewed by Johnson and Goldblatt (2015).

Nitrogen concentrations in continental crust rocks have increased with time. Upper crust concentrations from tills are 66 ± 100 ppm for the Neoarchean and Palaeoproterozoic and 290 ± 165 ppm for the Neoproterozoic to present day (Johnson and Goldblatt 2017). This change implies net drawdown from the atmosphere.

Mantle nitrogen is of subducted origin (Marty 1995), with a return flux via mantle outgassing. This is evident from noble-gas systematics, specifically the relationship between N and Ar (which has a similar solubility to N). Nitrogen abundance does not correlate with the primordial Ar isotope, ^{36}Ar, indicating that most primordial nitrogen has been outgassed. Rather, it correlates well with ^{40}Ar, the radiogenic daughter product of ^{40}K. This correlation suggests a mantle inventory a few times the size of the atmospheric reservoir (Marty 1995; Marty and Dauphas 2003). Given that K is lithophile (incompatible with mantle rock, preferentially entering melt and thus residing in the crust), the association of N with K requires that the mantle N is of subduction origin (Marty 1995, Marty and Dauphas 2003). Given the source species is NH_4^+, biological fixation of atmospheric N_2 is necessarily invoked (Goldblatt et al. 2009).

While the size and source of the mantle reservoir are evident, there are presently neither constraints on its age, nor on the balance of N subduction and outgassing through time. Present day rates suggest a slow net transfer of N to the mantle (Li and Bebout 2005; Li et al. 2007; Goldblatt et al. 2009), with a mantle N lifetime of billions of years (Goldblatt et al. 2009). Nitrogen transfer into the subduction zone depends on how much NH_4^+ can substitute into ocean crust and on how much nitrogen is retained in sediments; both of these may have been higher in the past when the deep ocean was anoxic. Some proportion of the subducted nitrogen returns to the atmosphere through arc volcanoes, depending on the temperature gradient of the subduction zone (Bebout et al. 1999). Assessing the nitrogen transfer across subduction zones is challenging because of the need to fully account for geological nitrogen entering the system, and atmospheric contamination makes estimating the gas flux outward hard. Nonetheless, modern studies do call for net subduction (Li and Bebout 2005, Li et al. 2007, Goldblatt et al. 2009).

In developing a theory of atmospheric N_2 evolution, primary uncertainties remain. At the end of accretion and differentiation of Earth, was the N in the mantle or atmosphere? How has the rate of N subduction changed through time, and how has it been balanced by mantle outgassing? A first-order understanding of the N_2 evolution, and thus the evolution of atmospheric mass, is only presently being developed: histories of increasing or decreasing atmospheric di-nitrogen, or of local maxima and minima, are all permissible.

Reactive N Species

Ammonia and nitrous oxide are both potent greenhouse gases and may have played a role in keeping early Earth warm. Indeed, ammonia is one of the best greenhouse gases, absorbing strongly in the 10 μm water vapor window (Sagan and Mullen 1972; Byrne and Goldblatt 2014a), and nitrous oxide is of similar strength to CO_2 (Roberson et al. 2011; Byrne and Goldblatt 2014a). They would require concentrations of 0.8 and 5 ppmv, respectively, in a 1 bar atmosphere to give a 10 Wm^{-2} radiative forcing and counter 20% of the 50Wm^{-2} radiative deficit from the faint young Sun (Byrne and Goldblatt 2014a).

Ammonia was the original proposal to resolve the Faint Young Sun Paradox (Sagan and Mullen 1972). However, this was predicated on a highly reducing Archean atmosphere, which is no longer supported. Ammonia is very soluble in seawater and photochemically unstable (Kuhn and Atreya 1979) so long-term, high concentrations would have been difficult to support, though the presence of an organic haze could enhance the photochemical lifetime of ammonia (Sagan and Chyba 1997). A trace amount could be sustained by a balance of nitrogen fixation followed by ocean outgassing and photochemical destruction.

Nitrous oxide is the product of partial denitrification. This could be favored in anoxic and sulfidic oceans, which may have been the norm in the Proterozoic, as copper limitation may have prevented the formation of the nitric oxide synthase (NOS) enzyme which transitions N_2O to N_2, possibly giving

N_2O fluxes 20 times the modern rate (Buick 2007). However, reduced atmospheric oxygen leads to faster photolysis of N_2O, making concentrations above 1 ppmv difficult to support (Roberson et al. 2011).

Oxygen and Ozone

Di-oxygen (O_2) is the second most abundant gas in the modern atmosphere (21%), and ozone (O_3) is a photochemical product of this. The atmospheric evolution of these are interwoven; producing ozone requires a sufficient oxygen inventory, whereas the formation of the stratospheric ozone layer provided photochemical shielding to the troposphere, allowing oxygen concentrations to rise towards modern levels. The evolution of these two gases must, therefore, be discussed together.

The di-oxygen in Earth's atmosphere is a biological product, formed during oxygen producing (oxygenic) photosynthesis, and it is able to accumulate in the atmosphere only in the absence of consumption of organic matter by aerobic respiration. The oxygen and organic carbon cycles are thus intrinsically linked. Oxygen is highly reactive (it will oxidize volcanic gases, crustal rocks, organic carbon, and so on), so the oxygen evolution must further be considered in the context of the global redox budget.

After introducing the record of redox evolution of Earth, the processes determining oxygen levels are described, so as to place oxygen evolution in the context of the development of these Earth system processes.

The History of O

Oxygen evolution has occurred in a number of steps. There is ample evidence, described below, for a "Great Oxidation" of the Earth, a geologically rapid transition from a reducing to an oxidizing atmosphere, early in the Paleoproterozoic. Oxygen levels are inferred to be parts per million or less prior to this and up to a percent afterward. Proterozoic oxygen levels were likely a fraction of a percent. The next major transition was in the Neopro-terozoic, when oxygen reached several percent, and near modern levels were achieved in the Devonian. The Great Oxidation represents by far the most profound change in geochemistry in Earth history and is the focus here.

Oxygen oxidizes; thus there is an excellent record from which this history has been elucidated. Traditional indicators of oxygen levels use the redox state of minerals in the sedimentary record (Holland 1984). Iron is one of the most important redox-sensitive elements, with two oxidation states: a reduced species Fe^{2+} (ferrous), which is water soluble, and an oxidized species Fe^{2+} (ferric), which is insoluble. Two classical oxygen indicators derive from this and serve as tutorial examples. Redbeds are detrital sedimentary rocks (commonly sandstones), which contain a red ferric oxide cement formed through subaerial alteration in an oxidizing atmosphere; they are found since 2.3 Ga. Banded iron formations are ocean sediments containing alternating layers of chert and either magnetite or haematite. These are formed distant from any iron source, so require long-range transport of iron in the ocean. This, in turn, requires a reduced ocean such that iron is soluble. Banded iron formations occur mostly before 2.4 Ga (Holland 1984; Isley and Abbott 1999). Other classical redox indicators include detrital grains of reduced minerals common in Archean sediments (requiring a reduced atmosphere) and changes in the mineralogy of paleosols (see Holland 1984, for a wide-ranging discussion). The ensemble of these is sufficient that it has long been possible to identify a change from a reducing to an oxidizing atmosphere around the Archean-Proterozoic boundary.

Twenty-first-century work has constrained oxygen evolution via numerous isotope systems. The defining modern indicator of the Great Oxidation comes from sulfur isotopes (Farquhar et al. 2000). The sulfur isotope record prior to 2.4 Ga is characterized by anomalies from the expected mass dependent trend in triple-isotope measurements, the so-called "mass-independent fractionation" of sulfur isotopes (MIF-S), whereas this feature is absent in younger sediments. The anomalies are photochemically generated. They require (1) a sufficient flux volcanic sulfur to the atmosphere; (2) the absence of an ozone layer, which would provide photochemical shielding; and (3) a reducing atmosphere, which allows multiple exit pathways for sulfur such that isotopic heterogeneity can be preserved (Zahnle et al. 2006). The existence of the MIF-S record thus constrains Archean oxygen to a maximum of part per million levels (Pavlov and Kasting 2002; Zahnle et al. 2006).

The currently prevailing interpretation of Proterozoic oxygen history is (1) the Great Oxidation event in the earliest Paleoproterozoic, which is coeval with low-latitude glaciation; (2) peak levels for a couple of hundred million years in the Paleoproterozoic; (3) a decrease to a fraction of a percent, which is maintained for most of the Proterozoic (Lyons et al. 2014); then (4) a second oxygenation to perhaps 1% of modern levels in the Neoproterozoic. The exact time of the Neoproterozoic oxidation is not well constrained, but it may well occur coeval with another set of low-latitude glaciations in the Cryogenian. The first large metazoa in the fossil record, which likely required percent O_2, appear in the Ediacaran (Och and Shields-Zhou 2012). The Paleoproterozoic peak in oxygen is linked to abundant organic carbon burial causing an oxygen source, which is required to explain the Lomagundi carbon isotope excursion. Mesoproterozoic oxygen levels are constrained by a variety of trace metal systems to a fraction of a percent, and imply an anoxic, ferruginous, and locally euxinic ocean, for much of the Proterozoic (Lyons et al. 2014).

A most remarkable aspect of the 2.4 Ga Great Oxidation is how late it is. There are numerous lines of evidence for the origin of oxygen-producing photosynthesis several hundred

million years earlier (see Lyons et al. 2014, for a recent discussion). The motivating question becomes: why was the rise of atmospheric oxygen delayed following the advent of oxygen production?

Sources and Sinks of Atmospheric Oxygen

The oxygen cycle begins with a fast biological cycle, closed either within the biosphere or by atmospheric chemistry. A slow geologic cycle involves burial and subsequent oxidative weathering of organic carbon.

It is a common misconception to simply equate atmospheric oxygen to oxygen production by photosynthesis. The problem is, of course, that in the presence of abundant oxygen, the vast majority of the carbon fixed (reduced from CO_2 to organic carbon, and represented schematically as CH_2O) is oxidized on short timescales by aerobic respiration:

$$CO_2 + H_2O \underset{\text{aerobic respiration}}{\overset{\text{oxygenic photosynthesis}}{\rightleftharpoons}} CH_2O + O_2 \qquad (1)$$

That is, the modern oxygen production cycle is largely closed by biology. A long-term source of oxygen to the atmosphere requires burial of organic carbon in sediments and sedimentary rock, leaving the O_2 in the atmosphere. Oxidation of organic carbon during weathering is, equivalently, a sink for atmospheric oxygen. The reservoir of sedimentary organic carbon is 1×10^{21} mol, implying a time-integrated oxygen source of ~30 times the atmospheric inventory (Catling and Claire 2005).

Where high oxygen, aerobic respiration, and closure of the oxygen production by biology is one end member, the other end member is anoxia, wherein fermentation and methanogenesis decompose organic matter and ultimately closure of the cycle is via atmospheric chemistry. Net methanogenesis can be represented schematically

$$CH_2O \rightarrow \tfrac{1}{2}CO_2 + \tfrac{1}{2}CH_4 \qquad (2)$$

so the net effect of photosynthetic production and decay of organic matter is

$$\tfrac{1}{2}CO_2 + H_2O \rightarrow O_2 + \tfrac{1}{2}CH_4 \qquad (3)$$

That is given anoxia, there should be a large and stoichiometrically balanced flux of oxygen and methane from the biosphere to the atmosphere. The closure of the system is by net methane oxidation, which is photochemically mediated:

$$\tfrac{1}{2}CH_4 + O_2 \rightarrow H_2O + \tfrac{1}{2}CO_2 \qquad (4)$$

The rate of net methane oxidation has a nonlinear dependence on oxygen and ozone levels (described below). High atmospheric methane is expected.

An additional, and important, net source of oxygen is hydrogen escape to space (Hunten and Donahue 1976). High in the atmosphere, any hydrogen bearing compounds may be photolyzed, freeing hydrogen atoms light enough to escape Earth's gravity. For Earth-like, hydrogen-poor, atmospheres the rate-limiting step is upward diffusion of hydrogen-bearing compounds from the homopause (the level at which the atmosphere ceases to be well mixed, ~100 km for Earth). The escape flux thus depends directly on both the total hydrogen mixing ratio at the homopause and on gravity (the latter because diffusion upwards is a buoyancy flux). Because water condenses at atmospheric temperatures, it is scarce at the homopause, and methane likely contributed the most hydrogen for escape (Catling et al. 2001). Schematically hydrogen escape can be represented

$$\begin{aligned} CH_4 &\rightarrow 4H(\textit{to space}) + C \\ C + O_2 &\rightarrow CO_2 \end{aligned} \qquad (5)$$

The oxygen source arises as two moles of oxygen are produced for each mole of methane (Eqs. 1–3) but only one oxygen is used associated with hydrogen escape (Eq. 6). Taking a representative methane mixing ratio of 100ppmv, for the first half of Earth history, the oxygen flux would be 0.7×10^{12} mol $yr.^{-1}$ and the total oxygen source is 1.6×10^{21} mol, equivalent to 50 times the modern atmospheric oxygen inventory (Catling et al. 2001; Catling and Claire 2005).

Major oxygen sinks arise from the oxidation of crustal rocks and volcanic gases. Catling and Claire (2005) estimate the excess of oxidized iron (Fe^{3+}) and sulfate in rocks and sediments to be equivalent to a time-integrated oxygen sinks of around 2.5×10^{21} mol and 0.5×10^{21} mol respectively, together 100 times the present atmospheric O_2 inventory.

Mass balance requrires that time-integrated oxygen sources and sinks balance: oxidized reservoirs (atmospheric O2 and, dominantly, the oxidized crust) are balanced by a combination of burial of organic carbon and hydrogen escape.

Photochemistry, Ozone, and a Model for the Great Oxidation

Ozone, O_3, is a photochemical product of O_2, so the generation of a stratospheric ozone layer is intimately connected to the rise of oxygen as a major atmospheric gas. Establishment of an ozone layer requires a threshold level of oxygen. Once established, the ozone layer provides photochemical shielding of the troposphere, thus reducing the efficiency of methane oxidation and facilitating the accumulation of atmospheric oxygen. Thus, the formation of the ozone layer is the mechanism of the Great Oxidation (Goldblatt et al. 2006).

The reaction sequence for ozone production (Chapman 1930, Entry ▶ Ozone and Stratospheric Chemistry) is

$$O_2 + h\nu(\lambda < 240\,\text{nm}) \rightarrow O + O \quad (6)$$

$$O + O + M \rightarrow O_3 + M \quad (7)$$

$$O_3 + h\nu(\lambda < 320\,\text{nm}) \rightarrow O_2 + O \quad (8)$$

$$O_3 + O \rightarrow 2O_2 \quad (9)$$

Ozone production requires sufficient oxygen levels to produce odd oxygen via Eq. 6. In photochemical models, some ozone production can be seen at ~1 ppm O_2, whereas a modern-like ozone layer forms at 1% of present oxygen levels (Kasting and Donahue 1980).

Methane oxidation rates, as with much atmospheric chemistry, depend on the availability of OH^- radicals. The main source of OH^- is photolysis of water vapor which, given the decrease in atmospheric temperature with altitude, is found dominantly in the troposphere. The existence of the ozone layer and consequent UV shielding of the troposphere reduces tropospheric OH^- availability and slows down much of the atmospheric chemistry.

Thus, with an ozone layer, the effective rate constant for methane oxidation is lower, which drastically changes the dynamics of oxygen. Given the same stoichiometrically balanced flux of methane and oxygen from the biosphere, the oxygen level necessarily should increase so that the photochemical sink balances the source. Equivalently, the lifetime of oxygen is extended.

Two rather distinct stable states of oxygen exist: a low oxygen stable state with around a part per million oxygen and a high oxygen stable state of near a percent. There is a very nonlinear transition between these: the Great Oxidation (Goldblatt et al. 2006).

Carbon Dioxide

Carbon has a variety of valence states; in the atmosphere, carbon dioxide (CO_2) is the main oxidized species and methane (CH_4) the main reduced species. Carbon dioxide has likely been the dominant greenhouse gas throughout Earth history, with methane a popular candidate for second place. In terms of both budget and processes, there is a fundamental split between the cycles of inorganic (oxidized) and organic (reduced) carbon. The main link between these is oxygenic photosynthesis, reversed in oxidizing conditions by aerobic respiration (Eq. 1) or in anaerobic conditions by methanogenesis and subsequent atmospheric methane oxidation (Eqs. 2 and 4). The link between organic carbon and oxygen is so strong that atmospheric methane and the organic carbon budget are considered alongside oxygen (section "Sources and Sinks of Atmospheric Oxygen").

Atmospheric Evolution, Table 2 Global carbon budget. Atmospheric CO_2 was 403 ppmv at the time of writing. Mantle reservoirs are from Anderson and Poland (2017) and Le Voyer et al. (2017), but method-dependent uncertainties are a factor of a few. Other reservoirs from Kump et al. (2009) and Wallmann and Aloisi (2012) (error for rock sedimentary reservoirs is not stated, but will be non-trivial)

Reservoir	Size (10^{12} kg C)
Biomass (live)	**600**
Land	600
Ocean	6
Soils and sediment	**4100**
Organic	1600
Inorganic (carbonate)	2500
Ocean (inorganic)	**39,000**
Atmosphere	**870**
Methane	1.7
Carbon dioxide	868
Methane hydrates	**2400 ± 1200**
Sedimentary rock	$\mathbf{7.5 \times 10^7}$
Organic	1.5×10^7
Inorganic (carbonate)	6×10^7
Mantle	$\mathbf{(7.0 \pm 1.7) \times 10^8}$
MORB source	$(3.8 \pm 1.5) \times 10^8$
OIB source	$(3.2 \pm 0.8) \times 10^8$
TOTAL	$\mathbf{\sim 7.8 \times 10^8}$

The carbon budget is given in Table 2. Carbon dioxide is a minor species today, but the vast size of geological reservoirs of inorganic carbon make a much higher inventory in the deep past easy to motivate. Indeed, the carbon dioxide inventory of Venus' atmosphere is essentially equivalent to the geological C on Earth (see section "Comparative Planetology"). On Earth, the inorganic carbon (limestone) reservoirs are largely biogenic. On shorter timescales, the intermediate-sized ocean reservoirs provide rapidly exchangeable carbon; this has dominated CO_2 change through Quaternary glacial cycles.

Atmospheric carbon dioxide is controlled by a hierarchy of processes, depending on the timescale. On subannual timescales, higher rates of photosynthesis during the summer and respiration during the winter, especially from northern hemisphere land biota, give a hemispheric annual cycle of 10 ppm. On annual to centennial timescales, the dominant processes changing CO_2 now are anthropogenic fossil fuel burning and cement production (CHAPTER-REF?), which are increasing CO_2 by 2 ppm per year (https://scripps.ucsd.edu/programs/keelingcurve/). More generally, annual to millennial control on CO_2 is via ocean carbonate chemistry (changes in the speciation of inorganic carbon in the ocean) (Ridgwell and Zeebe 2005; Zeebe and Wolf-Gladrow 2001). This, in turn, is very heavily modulated by life and, on $\gtrsim 10^5$yr timescales, by geological activity. Presence of widespread and cumulatively vast deposits of biogenic calcium carbonate rock throughout

Earth history provides a prima facie case for the combined role of life, ocean chemistry, and geology in controlling CO_2.

Control of CO_2 by Ocean Chemistry

Carbon dioxide readily dissolves in seawater. The equilibrium dissolved carbon dioxide is given by Henry's Law

$$[CO_2] = k_H CO_2 \tag{10}$$

There is a similar amount of dissolved molecular CO_2 in the ocean as atmospheric CO_2. Once in solution, however, the total amount of dissolved inorganic carbon (DIC) partitions between CO2, H2CO3 (carbonic acid), HCO_3^- (bicarbonate ion), and CO_3^{2-} (carbonate ion). For Henry's law, only the dissolved CO_2 matters (i.e., that is all the atmosphere "sees") so the sum of these species, the DIC, is 50 times larger than dissolved CO_2 alone. The equation for the partitioning are

$$CO_2 + H_2O \rightleftharpoons H_2CO_3 \tag{11}$$

$$\begin{aligned} H_2CO_3 &\rightleftharpoons H^+ + HCO_3^- \\ HCO_3^- &\rightleftharpoons H^+ + CO_3^{2-} \end{aligned} \tag{12}$$

which give three equations with five unknowns. Two more constraints are needed. First is that DIC is a conserved quantity (conservation of mass of carbon atoms):

$$\mathrm{DIC} = [CO_2] + [H_2CO_3] + [HCO_3^-] + [CO_3^{2-}] \tag{13}$$

The second conserved quantity is alkalinity, which accounts for conservation of charge. Ions in the ocean may, conceptually, be split into two groups. First, those from the dissolution of salts and strong acids; negative changer from Cl~ and others *almost* balances positive charge from Na^+, Mg^{2+}, Ca^{2+}, and others. These are referred to as conservative ions. Second, alkalinity is the net negative charge provided by species which exchange protons at $pH > 4.5$, which balances the net charge from conservative ions. For instructive purposes (in terms of the equations above), we can define alkalinity

$$\mathrm{Alk} = [HCO_3^-] + [CO_3^{2-}] \quad (\ldots - [H^+] + \ldots) \tag{14}$$

The first two terms on the right-hand side are the "carbonate alkalinity," which dominate. The bracketed term is small, but included to show, conceptually, how the Eq. 12 are balanced. In the real ocean, borate contributes at percent levels and there are additional minor contributing species.

Zeebe and Wolf-Gladrow (2001) provide an excellent textbook description of these processes.

Specifying any two parameters in the carbonate system (Eqs. 12–14) is sufficient to determine the whole system. DIC and alkalinity are the conserved quantities and have clear physical meaning (total carbon and charge balance), so make the most sense to use. Figure 3 shows the partitioning of carbon between different reservoirs. What should be immediately obvious is that pCO_2 – hence the contribution of inorganic carbon to the greenhouse effect – cannot be determined directly from the DIC: knowledge of alkalinity as needed. That is, ocean chemistry is fundamental to the abundance of the dominant noncondensible greenhouse gas in Earth's atmosphere.

Calcium Carbonate Formation

Ocean chemistry is linked to sediments and sedimentary rock via the formation and dissolution of $CaCO_3$:

$$Ca^{2+} + CO_3^{2-} \rightleftharpoons CaCO_3 \tag{15}$$

This has important consequences for pCO_2 and climate on millennial and longer timescales.

The position of solution with respect to equilibrium in Eq. 15 can be expressed as the calcite saturation, Ω_{calc}

$$\Omega = \frac{[Ca^{2+}][CO_3^{2-}]}{k_{sp}} \tag{16}$$

As an approximation, carbonates will decompose when $\Omega_{calc} < 1$ whereas formation requires supersaturation, perhaps $\Omega_{calc} \approx 30$ for chemical precipitation (also referred to as authigenic formation) or Ω_{calc} of 1–3 for biologically mediated formation. Variation in $[CO_3^{2-}]$ dominates over variation in $[Ca^{2+}]$, hence the ratio of alkalinity to DIC has a controlling influence on $CaCO_3$ precipitation: a high alkalinity to DIC ratio gives high $[CO_3^{2-}]$ and therefore high Ω_{calc}.

Calcium carbonate formation removes two units of alkalinity for each unit of DIC. The immediate effect, therefore, is to shift the partitioning of DIC away from $[CO_3^{2-}]$ and toward $[CO_2]$, consequently reducing the system's propensity to precipitate more calcite and increasing atmospheric pCO_2. On longer timescales, however, it is more important to think of this process as removing inorganic carbon from the atmosphere-ocean system, to be discussed further below.

Carbonate sediments are ubiquitous throughout the geological record. Their relatively continual formation places an empirical constraint on Ω_{calc}, implying that there have only been minor variations in the ratio of alkalinity to DIC through most of Earth history (Walker 1983). The fundamental question of what operates this control remains somewhat open. The amount of limestone ($CaCO_3$ in sedimentary rock) is vast: 5×10^{21} mol (Table 2). Were this in the atmosphere, Earth would have a 42 bar CO_2 atmosphere and a surface far too hot for life. The role of limestone

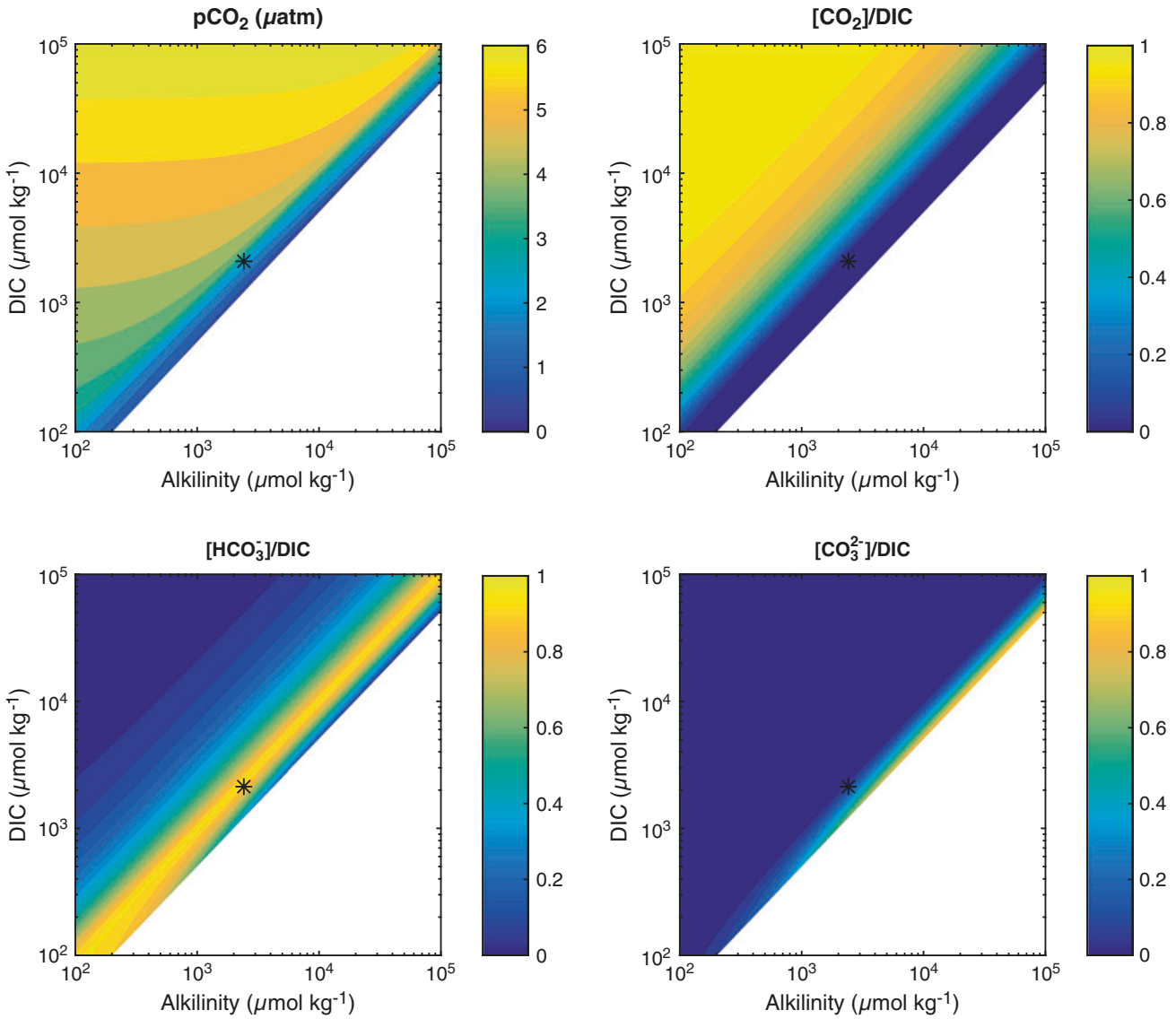

Atmospheric Evolution, Fig. 3 Atmospheric carbon dioxide and dissolved species concentrations as a function of DIC and Alk. There is a tendency to think of the total amount of carbon in the atmosphere-ocean determining the strength of the CO_2 greenhouse, but quite clearly alkalinity exerts equal leverage. Figures made with the Zeebe code (Zeebe and Wolf-Gladrow 2001)

formation – which is biologically controlled on Earth – in maintaining habitable conditions is evident.

Geological Control of Alkalinity: The Carbonate-Silicate Thermostat

An ocean of pure water would not mediate carbonate deposition. Rather fortunately in this regard, Earth's ocean is impure, containing dissolved ions from the chemical weathering of crustal rocks. As alkalinity balances the overabundance of cations among these salts, the cation flux determines long-term rates of carbonate deposition.

Weathering of crustal silicate rocks can be represented with the following series of reactions, using simplified stoichiometry. Atmospheric CO_2 dissolves and hydrates to become carbonic acid, which reacts with silicate rock (represented $CaSiO_3$):

$$2(CO_2 + H_2O \rightarrow H_2CO_3) \tag{17}$$

$$CaSiO_3 + 2H_2CO_3 \rightarrow Ca^{2+} + 2HCO_3^- + SiO_2 + H_2O \tag{18}$$

Two units of CO_2 are removed from the atmosphere and two units of both DIC and Alk are added to the ocean for each unit of silicate weathered. Given that CO_2 exchange between atmosphere an ocean is rapid, DIC will be removed by gas

flux to the atmosphere. Increasing Alk then dominates in the ocean, and a shift in DIC from bicarbonate to carbonate ions causes carbonate deposition,

$$2HCO_3^- \rightarrow CO_3^{2-} + CO_2 + H_2O \quad (19)$$

$$Ca^{2+} + CO_3^{2-} \rightarrow CaCO_3 \quad (20)$$

removing two units of both alkalinity and DIC from the ocean. The net stoichiometry of all of these is

$$2CO_2 + 2H_2O + CaSiO_3 \rightarrow SiO_2 + CO_2 + 2H_2O + CaCO_3 \quad (21)$$

$$CO_2 + CaSiO_3 \rightarrow SiO_2 + CaCO_3$$

This system is known as the Urey reactions (Urey 1952). Thus, silicate weathering followed by carbonate deposition leads to removal of inorganic carbon from the atmosphere-ocean system.

In a seminal paper, Walker et al. (1981) described a negative feedback on the long-term climate of Earth. Carbon dioxide is a greenhouse gas, so higher atmosphere-ocean carbon should result in a warmer planet and faster reaction rates. Likewise, a warmer planet would have higher rainfall which would enhance weathering. Warming would lead to carbon dioxide draw-down, providing a negative feedback on global temperatures. The WHAK feedback (known for Walker, Hays, and Kasting) remains the dominant paradigm for temperature regulation on Earth.

Its utility notwithstanding, there are various nuances and complications of the behavior of this system, such that one should look beyond the idea of a set point temperature toward which Earth is regulated. These include system dynamics, the mechanics of weathering, and the role of life.

Any dynamical model (there are many) will ultimately balance a volcanic CO_2 source with weathering-motivated carbonate deposition. Decreasing outgassing rate or increasing the reaction coefficient for weathering will then give a colder steady state; decrease these far enough and glaciation will ensue. Cold temperatures curtail weathering, atmospheric CO_2 accumulates and Earth warms; thus limit-cycle behavior can emerge (Mills et al. 2011; Abbot 2016).

Weathering does not occur uniformly. Rates are highest where there is fresh volcanic rock, young mountains, and warm and wet conditions. Fifty percent of global chemical weathering occurs on 9% of the surface (Hartmann et al. 2009). Broadly, felsic rock (e.g., granite) is less susceptible to weathering than mafic rock (e.g., basalt) (Ibarra et al. 2016), so weathering can be dominated by fresh exposures of mafic, volcanic rock. Today, basalts are responsible for 30–35% of the global CO_2 sink by weathering, dominated by tropical volcanic island arcs (Dessert et al. 2003). In the past, migration of large igneous provinces (flood basalts) through the humid tropics may have been responsible for major cooling; hypothesis attributes Cenozoic cooling (Kent and Muttoni 2013) and the Neoproterozoic snowball (Goddéris et al. 2003) to this mechanism, for example. For much of the continental interiors, where there is little variation in elevation, chemical weathering is limited by the availability of fresh rock and is not temperature dependence; only in mountainous areas, where exposure of fresh rock is rapid, are weathering rates temperature dependent (West et al. 2005).

Life is deeply implicated in the control of alkalinity, and therefore atmospheric CO_2. In soils, pCO_2 is elevated above atmospheric levels by respiration (Berner et al. 1983). Furthermore, fungal hyphae and plant roots penetrate rock, excreting organic acids which enhance weathering. The evolution of lichens (probably in Neoproterozoic time), a symbiosis of algae which provide a photosynthetic source of carbon and energy, and fungus which extracts nutrients, may have marked the beginning of very efficient, photosynthetically driven, enhancement of the weathering (Berner 1992). The evolution of nonvascular plants (mosses) in the Ordovician, and vascular plants in the Devonian further enhanced alkalinity supply by a factor of 2–10 (Lenton et al. 2012). Enhanced weathering has been linked to various glaciations (e.g., Berner 1997; Royer 2006; Lenton et al. 2012). In the ocean, organisms precipitate $CaCO_3$ at much lower Q than authigenic precipitation (Zeebe and Wolf-Gladrow 2001). The biota thus causes atmospheric CO_2 to be lower than it would be on an otherwise equivalent but sterile planet.

Proxy Constraints on, and History of, Atmospheric CO_2

With CO_2 as the main noncondensible greenhouse gas and a fainter Sun in the past, simple theoretical treatment of silicate-weathering feedback would call for pCO_2 to be high in the Archean and decrease over time to modern values. Since the proposal of high CO_2 as the resolution to the faint young Sun problem, there has been a consistent mismatch between climate model estimates of how much CO_2 should be required, and proxy estimates of how much is in the atmosphere.

For the Neoarchean and Proterozoic, paleosol constraints have been used for some decades. Soils are necessarily in contact with the atmosphere, so can be used as an atmospheric proxy. The absence of siderite can be used to exclude very high pCO_2 (Rye et al. 1995). Models can be used to quantify pCO_2, e.g., Sheldon (2006) suggests $23^{\times 3}_{\div 3}$ times the present level, but key parameters (e.g., soil formation rate) are very poorly constrained, making such model interpretations very challenging.

Recently, calcium isotopes have been used to more directly constrain the carbonate system via [Ca]/Alk; still, this does not uniquely constrain pCO_2, and a supplemental assumption about pH is necessary. A nominal assumption of pH of

7 would give around 30,000 ppmv CO_2. However, if another carobonate system parameter can be determined independently, then an actual constraint on pCO_2 will be available (Blattler et al. 2017).

For the Phanerozoic, a variety of proxies exist and give a somewhat consistent picture: pCO_2 decreases from around 5000 ppmv in the Silurian to less than 1000 ppmv in the Carboniferous, then varies between a few hundred and a few thousand ppmv until the present day (Royer 2006).

Water

Water is unique among Earth's atmospheric gases in that the control on its abundance is physical: equilibrium between vapor and a large condensed reservoir known as "the ocean." This physical control is via the saturation vapor pressure: the amount of vapor in equilibrium with a condensed reservoir depends exponentially on temperature. At the mean surface temperature of $\overline{T}_s = 15°\mathrm{C}$, the saturation vapor pressure of water is 1.7 kPa, implying that water comprises just under 2% of the atmosphere. In reality, it is somewhat less: the atmosphere cools with height, so the saturation vapor pressure decreases strongly with altitude, and in general, the atmosphere is subsaturated with water vapor. Spatial variations are important: Earth's warm tropics are very moist and the cold polar regions quite dry; water vapor is not well-mixed.

Water vapor content has changed by several orders of magnitude, covarying with temperature. In times when Earth was much colder, for example during Paleo- and Neoproterozoic Snowball Earth episodes with $\overline{T}_s \approx -40°\mathrm{C}$, the corresponding saturation vapor pressure was 100 times lower than today. During hyperthermal periods, such as the Cretaceous warm period with $\overline{T}_s \approx 30°\mathrm{C}$, the corresponding saturation vapor pressure was 2.5 times higher than today. Over these range of temperatures, which characterize most of Earth history, the expectation is that water vapor has varied by more than two orders of magnitude, between a trace to a minor constituent of the atmosphere.

Based on these arguments, three qualitatively different atmospheric water inventories, corresponding to different climate states, can be inferred to have existed through Earth history: cold and dry, with trace water in equilibrium with an ice surface (snowball Earth); intermediate climate with strong meridional gradients of temperature and water vapor, so that water is a minor (percent level) constituent in the tropics but trace at the poles (e.g., present day); and warm and moist in equilibrium with a warm ocean, small meridional temperature gradients, and water vapor as a minor constituent throughout.

When water becomes a major constituent, there are further qualitative changes to system behavior: transition to a hot and water-dominated atmosphere occurs above a threshold solar constant. That is, a liquid water ocean is stable only up to a limit on the energy supplied to the planet, after which a "runaway greenhouse" occurs, the ocean evaporates, and the atmosphere becomes water dominated (Simpson 1927; Komabayashi 1967; Ingersoll 1969). Given a water vapor column of 30 kgm^{-2}, corresponding to a saturated atmosphere with a surface temperature of 300 K, the atmosphere is optically thick at all thermal wavelengths. Consequently, only radiation from the atmosphere can reach space, and none from the surface, limiting outgoing thermal radiation. If more energy is absorbed by the planet, there will be a nonlinear transition of the atmosphere as the entire ocean evaporates (see reviews by Nakajima et al. 1992, Goldblatt and Watson 2012). Modern calculations of the radiation limit in clear-sky conditions give 283 Wm^{-2}, which corresponds to the sunlight that would be absorbed by a cloud-free planet at Earth's orbit (Goldblatt et al. 2013). Clouds are net reflectors, so increase the threshold insolation to at least 1.1 times the present solar constant (Leconte et al. 2013; Wolf and Toon 2014; Popp et al. 2016). As the solar constant increases, Earth will transition to a water-dominated atmosphere in around a billion years. Likewise, Venus receives 1.9 times the sunlight that Earth does, and the composition of the Venusian atmosphere is consistent with a postrunaway state. Whether Venus had oceans which evaporated at some point in the past, or never condensed any, is model dependent (Hamano et al. 2013).

Additionally, impact energy could be sufficient to evaporate the oceans and give a water-dominated atmosphere. This undoubtedly occurred during accretion. During the end-Hadean late heavy bombardment, statistics indicate that there would have been zero to four impacts sufficient to evaporate the oceans (Zahnle et al. 2007). The timescale of an impact-generated steam atmosphere would be a few thousand years (Zahnle et al. 2007). Likewise, early in the evolution of a planetary system, tidal heating of the planet could induce a runaway greenhouse (Barnes et al. 2013).

Discussion

Atmospheric Homeostasis, Vernadsky's "Biosphere," and the Gaia Hypothesis

The most remarkable observation of Earth history is the continual lineage of a single genesis of life spanning four billion years. Indeed, deep in the Archean record, the evidence for life is in general commensurate with the maximum that could be expected, given the preservation of the sedimentary record (Nisbet and Sleep 2001). Life requires temperature to be in a somewhat limited range, by necessity maintained for the entire length of the record. Three alternate explanations for this long-term homeostasis may be offered: luck,

abiological regulation, or an explanation based on the action of life itself.

Luck is a somewhat irrefutable option. Further disentanglement becomes difficult due to observer bias: our position as observers of this history is contingent on history itself: conditions must have been such that the long evolution to organisms with the science of geology and printing presses to make encyclopedia could occur. Our ability to pose the question requires continual habitability, so the observation itself is bias; such is the *weak anthropic principle* (Watson 1999).

Abiological regulation is supported by evidence of chemical feedback processes contributing to climate regulation, with the negative feedback on temperature via the silicate weathering and carbonate deposition cycle (Walker et al. 1981) the seminal contribution. A purely abiological model would have these geochemical mechanisms regulate temperature to a level at which life is plausible, allowing life to adapt to the environment. There is little doubt that this represents part of the explanation, but the entanglement of life in these geochemical mechanisms, enhancing both weathering and carbonate deposition, makes isolation to only abiological processes rather difficult. Life and nonlife processes are deeply entwined on Earth.

Biological control was a part of Vernadsky's original enunciation of the biosphere. Vernadsky (1926) described the biosphere as composing both living and nonliving parts, the atmosphere being the type example of the latter. He saw life as the dominant geological force, and that the planetary scale influence of life has increased with time – i.e., that the biota controlled the atmospheric composition, and that the control has become stronger has evolved to increasing complexity and dominance. Written in Russian and French, Vernadsky's original and visionary work on the biosphere was largely lost to anglophone science until David Langmuir's 1970's translation circulated in the late twentieth century and was eventually published in 1998 (but see also Vernadsky 1945).

In Western science, biological regulation was proposed by Lovelock (1972) with the *Gaia hypothesis:* "homoeostasis by and for the biosphere." A modern statement of this is "Organisms and their environment evolve as a single, self-regulating system" (Lovelock 2003). Thus, not only are organisms selected for their environmental fitness but are selected for their ability to modify the environment in beneficial ways (Lenton 1998).

It is plain that biology is deeply and intimately involved in the control of Earth's atmospheric composition. The question of whether this has directionality – whether the biota regulates – is probably the single most important open question in the study of atmospheric evolution of Earth. Significant theoretical development is needed and, ultimately, experiments to detect life on planets outside the solar system may provide the sample size to resolve the question empirically.

Comparative Planetology

Science progresses best with a sample size greater than one. Thus, as in seeking to understand the evolution of our own atmosphere, much is to be learnt from looking outward. In our solar system, primary comparisons are to our neighbors, Venus and Mars and further information come from including the giant planet moons (nomenclature and orbit type – planet, moon, dwarf planet – do not affect the geophysics).

The first, and obvious issue, is whether or not a planet actually has an atmosphere. Earth, Venus, Mars, and Titan do, whereas Ganymede, Calisto, Io, Mercury, and many smaller bodies do not. Presence of an atmosphere may be empirically determined via the "cosmic shoreline": a power law relating threshold insolation to escape velocity to the fourth power. Stellar energy drives atmospheric loss, whereas planetary mass holds the atmosphere down (Zahnle and Catling 2017).

Venus is the most Earth-like planet, with similar size and bulk composition. Venusian atmosphere has a 90 bar surface pressure (Earth is 1 bar), with a composition of 97.5% CO_2 and 3.5% N_2 and a surface temperature of 700 K. There is no ocean and water is only a trace atmospheric constituent.

Venus' current atmosphere is understood on the basis that it experienced a runaway greenhouse in the past (Walker 1975). The present insolation at Venus' orbit is well in excess of the runaway greenhouse limit, so if a Venusian ocean ever condensed after accretion, it later evaporated. Much of the hydrogen from the water was lost to space, evidenced by strong enrichment of D/H relative to Earth (Donahue et al. 1982). The timescale for loss of an Earth-size ocean via hydrodynamic escape is a few hundred million years (Watson et al. 1981). Accumulation of oxygen, however, may throttle hydrogen escape (Wordsworth and Pierrehumbert 2014), and extensive hydration of the surface rocks is another potential sink for water (Matsui and Abe 1986).

The carbon reservoir in Venus' atmosphere is of comparable size to the carbon stored in carbonate and organic carbon rocks on Earth. If there was an ocean on Venus, carbonates would have most likely been deposited, but these would have thermally decomposed during the runaway greenhouse (the equivalent process is used in industrial cement manufacture in lime kilns on Earth).

Venus gives two primary lessons that pertain to Earth. First, is contingency in planetary evolution. Venus' present state is only possible to understand through the presence of atmospheric water in the past, even though it is absent today. Second, is Earth's future: solar constant increases with time, so Earth should reach the runaway greenhouse threshold in a billion years. Venus' past informs us directly or what Earth's future: the end of the world will be a runaway greenhouse, lime-kiln, inferno.

Mars, by contrast, has a rather feeble atmosphere: 0.006 bar of CO_2, supporting a mean surface temperature around 220 K. Mars' mass and insolation are such that it is only marginally on the atmospheric side of the cosmic shoreline. Yet, there is abundant evidence in Mars' geological record for liquid water in the first billion years of the solar system, despite a dimmer Sun. It is not obvious whether early Mars was always warm, or only episodically so (Wordsworth 2016), but almost any solution requires both a thicker atmosphere and much stronger greenhouse effect in the past.

Mars and Venus together provide two primary lessons pertinent to Earth. First, that major variations in planetary atmosphere mass and composition, and thus climate, through time are the norm for terrestrial planets. Long-term consistency of any of these should be seen as an exceptional result, requiring exceptional evidence and explanation. Second, both have CO_2 dominated atmospheres which can be explained by photochemical equilibrium without any biology in stark contrast to Earth, whose atmospheric composition is to a large extent a biological construct. Life's alteration of Earth is of first order importance.

Outlook

Humanity is in the midst of a great age of discovery, as planets around other stars are discovered and characterized: "the age of exoplanets." Life has had a dominant role in altering the atmospheric composition of Earth, distinguishing us significantly from uninhabited planets. The composition of exoplanet atmospheres will soon be able to be determined remotely via spectroscopy, making *atmospheric analysis* the viable method of detecting life on other planets via *their influence on the atmosphere* (Lovelock 1965; Hitchcock and Lovelock 1967; Sagan et al. 1993). Life detection will require the detection of atmospheric disequilibrium and the exclusion of any abiotic cause. There is, however, no simple formula for what the composition of an atmosphere should be, so determining whether an observed atmosphere represents a living planet will only be achievable through a deep understanding of the processes determining atmospheric composition. Understanding Earth's atmospheric evolution is thus fundamental to learning our place in the universe.

Cross-References

- Argon
- Calcium Isotopes
- Carbon
- Carbon cycle
- Carbonate Minerals and the CO_2-Carbonic Acid System
- Chemical Weathering
- Earth's Atmosphere
- Earth's continental crust
- Earth's core
- Henry's Law
- Iron
- Mantle Geochemistry
- Nitrogen
- Nitrogen Cycle
- Ocean Biochemical Cycling and Trace Elements
- Oxygen
- Ozone and Stratospheric Chemistry
- Paleoclimatology
- Paleoenvironments
- Paleoproductivity
- Paleotemperatures
- Potassium
- Subduction Zone Geochemistry
- Sulfur Isotopes

References

Abbot DS (2016) Analytical investigation of the decrease in the size of the habitable zone due to a limited CO2 outgassing rate. Astrophys J 827(2):117. https://doi.org/10.3847/0004-637X/827/2/117

Anderson KR, Poland MP (2017) Abundant carbon in the mantle beneath Hawaii. Nat Geosci 10(9):704–708. https://doi.org/10.1038/ngeo3007

Barnes R, Mullins K, Goldblatt C, Meadows VS, Kasting JF, Heller R (2013) Tidal Venuses: triggering a climate catastrophe via tidal heating. Astrobiology 13(3):225–250. https://doi.org/10.1089/ast.2012.0851

Bebout GE, Ryan JG, Leeman WP, Bebout AE (1999) Fractionation of trace elements by subduction-zone metamorphism – effect of convergent-margin thermal evolution. Earth Planet Sci Lett 171(1):63–81

Berner RA (1992) Weathering, plants, and the long-term carbon cycle. Geochim Cosmochim Acta 56(8):3225–3231. https://doi.org/10.1016/0016-7037(92) 90300-8

Berner RA (1997) The rise of plants and their effect on weathering and atmospheric CO2. Science 276(5312):544–546. https://doi.org/10.1126/science.276.5312.544

Berner RA, Lasaga AC, Garrels RM (1983) The carbonate-silicate geochemical cycle and its effect on atmospheric carbon dioxide over the past 100 million years. Am J Sci 283:641–683

Blattler CL, Kump LR, Fischer WW, Paris G, Kasbohm JJ, Higgins JA (2017) Constraints on ocean carbonate chemistry and p. Nat Geosci 10(January):41–45. https://doi.org/10.1038/NGEO2844

Buick R (2007) Did the Proterozoic 'Canfield Ocean' cause a laughing gas greenhouse? Geobiology 5:97–100

Byrne B, Goldblatt C (2014a) Radiative forcings for 28 potential Archean greenhouse gases. Clim Past 10(3):1779–1801. https://doi.org/10.5194/cp-10-1779-2014

Byrne B, Goldblatt C (2014b) Radiative forcing at high concentrations of wellmixed greenhouse gaases. Geophys Res Lett 41(1):152–160. https://doi.org/10.1002/2013GL058456

Catling DC, Claire MW (2005) How Earth's atmosphere evolved to an oxic state: a status report. Earth Planet Sci Lett 237(1–2):1–20

Catling DC, Zahnle KJ, Mckay CP (2001) Biogenic methane, hydrogen escape, and the irreversible oxidation of early earth. Science 293:839–843. https://doi.org/10.1126/science.1061976

Chapman S (1930) On ozone and atomic oxygen in the upper atmosphere. London, Edinburgh Dublin Philos Mag J Sci 10:369–383
Dessert C, Dupre B, Gaillardet J, Francois LM, Allegre CJ (2003) Basalt weathering laws and the impact of basalt weathering on the global carbon cycle. Chem Geol 202:257–273. https://doi.org/10.1016/j.chemgeo.2002.10. 001
Donahue TM, Hoffman JH, Hodges RR, Watson AJ (1982) Venus was wet—a measurement of the ratio of deuterium to hydrogen. Science 216(4546):630–633. https://doi.org/10.1126/science.216
Evans DAD (2003) A fundamental Precambrian—Phanerozoic shift in Earth's glacial style? Tectonophysics 375:353–385
Farquhar J, Bao H, Thiemens M (2000) Atmospheric influence of Earth's earliest sulfur cycle. Science 289(August):756–758
Feulner G (2012) The faint young sun problem. Rev Geophys 50(2):1–30. https://doi.org/10.1029/2011RG000375
Goddéris Y, Donnadieu Y, Nédélec A, Dupré B, Dessert C, Grard A, Ramstein G, François LM (2003) The Sturtian 'snowball' glaciation: fire and ice. Earth Planet Sci Lett 211(1–2):1–12. https://doi.org/10.1016/S0012-821X(03)00197-3
Goldblatt C, Watson AJ (2012) The runaway greenhouse: implications for future climate change, geoengineering and planetary atmospheres. Phil Trans Roy Soc A 370(1974):4197–4216. https://doi.org/10.1098/rsta.2012. 0004
Goldblatt C, Zahnle KJ (2011) Clouds and the faint young sun paradox. Clim Past 7(1):203–220. https://doi.org/10.5194/cp-7-203-2011
Goldblatt C, Lenton TM, Watson AJ (2006) Bistability of atmospheric oxygen and the great oxidation. Nature 443(7112):683–686. https://doi.org/10.1038/nature05169
Goldblatt C, Claire MW, Lenton TM, Matthews AJ, Watson AJ, Zahnle KJ (nov 2009) Nitrogen-enhanced greenhouse warming on early earth. Nat Geosci 2(12):891–896. https://doi.org/10.1038/ngeo692
Goldblatt C, Robinson TD, Zahnle KJ, Crisp D (jul 2013) Low simulated radiation limit for runaway greenhouse climates (supplementary). Nat Geosci 6(8):661–667. https://doi.org/10.1038/ngeo1892
Hamano K, Abe Y, Genda H (may 2013) Emergence of two types of terrestrial planet on solidification of magma ocean. Nature 497(7451):607–610. https://doi.org/10.1038/nature12163
Haqq-Misra JD, Domagal-Goldman SD, Kasting PJ, Kasting JF (2008) A revised, hazy methane greenhouse for the Archean earth. Astrobiology 8(6):1127–1137. https://doi.org/10.1089/ast.2007.0197
Hartmann J, Jansen N, Dürr HH, Kempe S, Köhler P (2009) Global CO2-consumption by chemical weathering: what is the contribution of highly active weathering regions? Glob Planet Change 69(4):185–194. https://doi.org/10.1016/j.gloplacha.2009.07.007
Hitchcock DR, Lovelock JE (1967) Life detection by atmospheric analysis. Icarus 7(2):149–159
Holland HD (1984) The chemical evolution of the atmosphere and oceans. Princeton University Press, Princeton, NJ
Hunten DM, Donahue TM (1976) Hydrogen loss from the terrestrial planets. Annu Rev Earth Pl Sc 4:265–292. https://doi.org/10.1146/annurev.ea.04. 050176.001405
Ibarra DE, Caves JK, Moon S, Thomas DL, Hartmann J, Chamberlain CP, Maher K (2016) Differential weathering of basaltic and granitic catchments from concentration discharge relationships. Geochim Cosmochim Acta 190:265–293. https://doi.org/10.1016/j.gca.2016.07.006
Ingersoll AP (1969) The runaway greenhouse: a history of water on Venus. J Atmos Sci 26:1191–1198
Isley AE, Abbott DH (1999) Plume-related mafic volcanism and the deposition of banded iron formation. J Geophys Res 104(B7):15461–15477
Johnson BW, Goldblatt C (2015) The nitrogen budget of Earth. Earth Sci Rev 148:150–173. https://doi.org/10.1016/j.earscirev.2015.05.006
Johnson BW, Goldblatt C (2017) A secular increase in continental crust nitrogen during the Precambrian. Geochem Persp Lett 4:24–28. https://doi.org/10.7185/geochemlet.1731
Kasting JF, Donahue TM (1980) The evolution of the atmospheric ozone. J Geophys Res 85:3255–3263
Kent DV, Muttoni G (2013) Modulation of late cretaceous and Cenozoic climate by variable drawdown of atmospheric pCO2 from weathering of basaltic provinces on continents drifting through the equatorial humid belt. Clim Past 9(2):525–546. https://doi.org/10.5194/cp-9-525-2013
Komabayashi M (1967) Discrete equilibrium temperatures of a hypothetical planet with the atmosphere and the hydrosphere of a one component–two phase system under constant solar radiation. J Meteor Soc Japan 45:137–139
Kuhn WR, Atreya SK (1979) Ammonia photolysis and the greenhouse effect in the primordial atmosphere of the earth. Icarus 37:207–213
Kump LR, Kasting JF, Crane RG (2009) The earth system, 3rd edn. Pearson, Upper Saddle River, NJ
Le Voyer M, Kelley KA, Cottrell E, Hauri EH (2017) Heterogeneity in mantle carbon content from CO2-undersaturated basalts. Nat Commun 8:14062. https://doi.org/10.1038/ncomms14062
Leconte J, Forget F, Charnay B, Wordsworth R, Pottier A (2013) Increased insolation threshold for runaway greenhouse processes on earth-like planets. Nature 504(7479):268–271. https://doi.org/10.1038/nature12827
Lenton TM (1998) Gaia and natural selection. Nature 394(6692):439–447. https://doi.org/10.1038/28792
Lenton TM, Crouch M, Johnson M, Pires N, Dolan L (2012) First plants cooled the Ordovician. Nat Geosci 5(2):86–89. https://doi.org/10.1038/ngeo1390
Li L, Bebout GE (2005) Carbon and nitrogen geochemistry of sediments in the central American convergent margin: insights regarding subduction input fluxes, diagenesis, and paleoproductivity. J Geophys Res 110:B11202. https://doi.org/10.1029/2004JB003276
Li L, Bebout GE, Idleman BD (2007) Nitrogen concentration and δ15N of altered oceanic crust obtained on ODP legs 129 and 185: insights into alteration-related nitrogen enrichment and the nitrogen subduction budget. Geochim Cosmochim Acta 71(9):2344–2360. https://doi.org/10.1016/j.gca.2007.02.001
Lovelock JE (1965) A physical basis for life detection experiments. Nature 207(4997):568–570
Lovelock JE (1972) Gaia as seen through the atmosphere. Atmos Environ 6:579–580
Lovelock JE (2003) The living earth. Nature 426(December):769–770
Lyons TW, Reinhard CT, Planavsky NJ (2014) The rise of oxygen in Earth's early ocean and atmosphere. Nature 506(7488):307–315. https://doi.org/10.1038/nature13068
Marty B (1995) Nitrogen content of the mantle inferred from N2–Ar correlation in oceanic basalts. Nature 377:326–329
Marty B, Dauphas N (2003) The nitrogen record of crust–mantle interaction and mantle convection from Archean to present. Earth Planet Sci Lett 206:397–410. https://doi.org/10.1016/S0012-821X(02)01108-1
Matsui T, Abe Y (1986) Evolution of an impact-induced atmosphere and magma ocean on the accreting earth. Nature 319:303–305. https://doi.org/10.1038/319303a0
Mills B, Watson AJ, Goldblatt C, Boyle R, Lenton TM (2011) Timing of Neoproterozoic glaciations linked to transport-limited global weathering. Nat Geosci 4(12):861–864. https://doi.org/10.1038/ngeo1305
Nakajima S, Hayashi Y-Y, Abe Y (1992) A study of the "runaway greenhouse effect" with a one-dimensional radiative–convective model. J Atmos Sci 49:2256–2266
Nisbet EG (1987) The young earth: an introduction to Archaean geology. Allen & Unwin, London
Nisbet EG, Sleep NH (2001) The habitat and nature of early life. Nature 409:1083–1091

A

Och LM, Shields-Zhou GA (2012) The Neoproterozoic oxygenation event: environmental perturbations and biogeochemical cycling. Earth Sci Rev 110:26–57
Owen T, Cess RD, Ramanathan V (1979) Enhanced CO2 greenhouse to compensate for reduced solar luminosity on early earth. Nature 277(5698):640–642
Pavlov AA, Kasting JF (2002) Mass-independent fractionation of sulfur isotopes in Archean sediments: strong evidence for and anoxic Archean atmosphere. Astrobiology 2(1):27–41
Pierrehumbert RT (2011) Infrared radiation and planetary temperature. Phys Today 64(1):33–38
Popp M, Schmidt H, Marotzke J (2016) Transition to a moist greenhouse with CO2 and solar forcing. Nat Commun 7:10627. https://doi.org/10.1038/ncomms10627
Ridgwell AJ, Zeebe RE (2005) The role of the global carbonate cycle in the regulation and evolution of the earth system. Earth Planet Sci Lett 234(3–4):299–315. https://doi.org/10.1016/j.epsl.2005.03.006
Roberson AL, Roadt J, Halevy I, Kasting JF (2011) Greenhouse warming by nitrous oxide and methane in the Proterozoic eon. Geobiology 9:313–320. https://doi.org/10.1111/j.1472-4669.2011.00286.x
Royer DL (2006) CO2-forced climate thresholds during the Phanerozoic. Geochim Cosmochim Acta 70(23):5665–5675. https://doi.org/10.1016/j.gca.2005.11.031
Rye R, Kuo PH, Holland HD (1995) Atmospheric carbon dioxide concentrations before 2.2 billion years ago. Nature 378:603–605
Sagan C, Chyba C (1997) The early faint sun paradox: organic shielding of ultraviolet-labile greenhouse gases. Science 276(1997):1217–1221. https://doi.org/10.1126/science.276.5316.1217
Sagan C, Mullen G (1972) Earth and Mars: evolution of atmospheres and surface temperatures. Science 177(4043):52–56
Sagan C, Thompson WR, Carlson R, Gurnett D, Hord C (1993) A search for life on earth from the Galileo spacecraft. Nature 365:715–721. https://doi.org/10.1038/365715a0
Sheldon ND (2006) Precambrian paleosols and atmospheric CO2 levels. Precambrian Res 147(1–2):148–155. https://doi.org/10.1016/j.precamres.2006.02.004
Simpson GC (1927) Some studies in terrestrial radiation. Mem Roy Met Soc 11:69–95
Stüeken EE, Kipp MA, Koehler MC, Buick R (2016) The evolution of Earth's biogeochemical nitrogen cycle. Earth Sci Rev 160:220–239. https://doi.org/10.1016/j.earscirev.2016.07.007
Urey HC (1952) On the early chemical history of the earth and the origin of life. Proc Natl Acad Sci U S A 38(4):351. https://doi.org/10.1073/pnas. 38.4.351
Vernadsky VI (1926) Biosphere. Scientific Chemistry–Technical Publishing, Leningrad
Vernadsky VI (1945) The biosphere and the noösphere. Am Sci 33:1–12
Walker JCG (1975) Evolution of the atmosphere od Venus. J Atmos Sci 32:1248–1256
Walker JCG (1983) Possible limits on the composition of the Archean Ocean. Nature 302:518–520
Walker JCG, Hays PB, Kasting JF (1981) A negative feedback mechanism for the long-term stabilisation of the Earth's surface temperature. J Geophys Res 86(C10):9776–9782
Wallmann K, Aloisi G (2012) The global carbon cycle: geological processes. In: Knoll AH, Canfield DE, Konhauser KO (eds) Fundamentals of Geobiology. Wiley-Blackwell, Oxford, pp 20–35
Watson AJ (1999) Co-evolution of Earth's environment and life: goldilocks, Gaia and the anthropic principle. In: Craig GY, Hull JH (eds) James Hutt. – present and future, vol 150. Geological Society, London, pp 75–88
Watson AJ, Donahue TM, Walker JCG (1981) The dynamics of a rapidly escaping atmosphere: applications to the evolution of earth and Venus. Icarus 48:150–166
West AJ, Galy A, Bickle M (2005) Tectonic and climatic controls on silicate weathering. Earth Planet Sci Lett 235:211–228
Wolf ET, Toon OB (2014) Delayed onset of runaway and moist greenhouse climates for earth. Geophys Res Lett 41:167–172. https://doi.org/10.1002/2013GL058376.Received
Wordsworth RD (2016) The climate of early Mars. Annu Rev Earth Planet Sci 44(1):381–408. https://doi.org/10.1146/annurev-earth-060115-012355
Wordsworth R, Pierrehumbert RT (2014) Abiotic oxygen dominated atmospheres on terrestrial habitable zone planets. Astrophys J Lett 785:L20. https://doi.org/10.1088/2041-8205/785/2/L20
Zahnle KJ, Catling DC (2017) The cosmic shoreline: the evidence that escape determines which planets have atmospheres, and what this may mean for Proxima Centauri b. Astrophys J 843(2):122. https://doi.org/10.3847/1538-4357/aa7846
Zahnle KJ, Claire M, Catling D (2006) The loss of mass-independent fractionation in sulfur due to a Palaeoproterozoic collapse of atmospheric methane. Geobiology 4(4):271–283
Zahnle KJ, Arndt N, Cockell C, Halliday AN, Nisbet EG, Selsis F, Sleep NH (2007) Emergence of a habitable planet. Space Sci Rev 129(1–3):35–78
Zeebe RE, Wolf-Gladrow D (2001) CO2 in seawater: equilibrium, kinetics, isotopes. Elsevier, Amsterdam

Atomic Absorption, Inductively Coupled Plasma Optical Emission Spectroscopy, and Infrared Spectroscopy

Michael A. Rutzke
College of Agriculture and Life Sciences Nutrient Analysis Lab, Cornell University, Ithaca, NY, USA

Definition

Analytical spectroscopy is about measuring and recording the observations that occur when matter (atoms, ions, and molecules) interacts with or is exposed to thermal heating and/or electromagnetic radiation (light).

Introduction

The interactions that occur when matter interacts with electromagnetic radiation in the infrared and microwave range (thermal heating) and/or the visible range (light) allow us to identify the chemical species in a sample and to investigate their structures and physicochemical properties. This is possible because matter emits photons with energies equal to the energy differences between the initial and the final states that occur after stimulation of the matter. A stimulating source can be thermal, electrical, chemical, physical, or electromagnetic. This chapter will focus on stimulations (excitation) due to electromagnetic and thermal heating. These excited transitions are quantized – meaning atoms, ions, and molecules exist only in discrete states associated

with specific energies. Because each atom, ion, or molecule has a unique pattern of discrete energy states, we can use these properties to determine their presence and abundance and to measure their physicochemical properties. This information allows us to understand better the structure and physicochemical properties of geological material.

Electromagnetic radiation has many useful properties including velocity, wavelength, amplitude (intensity), polarization, and phase, but of these analytical spectroscopy is based on variation in the wavelength (or equivalently, frequency) of light.

Atomic spectroscopy utilizes the electromagnetic spectrum from 130 nm (ultraviolet, UV) through the visible spectrum up to 800 nm (infrared, IR). Atomic spectroscopy is simple because we are dealing with the energy released from a single atom, where each element gives a different emission pattern. An example of an emission spectra is shown in Fig. 1.

By comparison, the spectra obtained when one does molecular spectroscopy are more complicated because molecules contain two or more atoms. Molecular spectroscopy uses the electromagnetic spectrum from 800 nm to 1 mm. Molecular spectroscopy is a very popular technique used by organic chemists and geochemists as well. This branch of spectroscopy characterizes and measures vibrational and rotational energies in a molecule. It can also be used to measure the bond strengths of atoms in a molecule.

Basic Principles of Spectroscopy

The wavelength of light (λ, in m) is directly determined using a Michelson interferometer or a grating. The frequency (v, in s^{-1}) of the wave is determined by dividing the speed of light (3×10^8 m/s) by the wavelength.

$$v = \frac{c}{\lambda}$$

The total kinetic energy of a system is the summation of the electronic energy, vibrational energy, rotational energy, and the translational (thermal) energy.

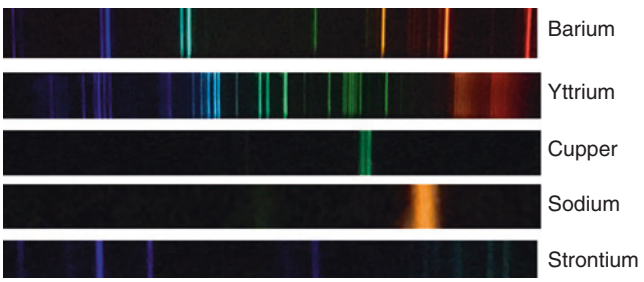

Atomic Absorption, Inductively Coupled Plasma Optical Emission Spectroscopy, and Infrared Spectroscopy, Fig. 1 Examples of ICP-OES spectra for 5 different metals. (Photograph taken by Michael B. Rutzke)

The Maxwell-Boltzmann equation, given below, predicts the ratio of the excited states of the electronic, vibrational, or rotational energy to those in the ground state as a function of the temperature.

$$\frac{N_b}{N_a} = \left(\frac{g_b}{g_a}\right) e^{-\frac{\Delta E}{kT}}$$

where $\frac{N_b}{N_a}$ is the ratio of excited atoms to ground-state atoms, g_b is the number of excited states having equal energy, and g_a is the number of ground states having equal energy. The ratio $\frac{g_b}{g_a}$, known as the degeneracy, is typically 2–3; T is the absolute temperature in degrees Kelvin. k is the Boltzmann constant: $k = 8.617 \times 10^{-5}$ eV/K when ΔE is in volts. When ΔE is in Joules then the Boltzmann constant K is (1.381×10^{-23} J/K).

$$\Delta E = \frac{1240}{\lambda}$$

ΔE is in eV when λ is in nm. The ratio of excited- to ground-state atoms ($\frac{N_b}{N_a}$) in Na, which has a degeneracy of 2 and which emits 589.0 nm light at 2,500 K, is 1.14×10^{-4}. At 5,000 K, the ratio is 1.5×10^{-2}. Because of the exponential relationship, doubling the temperature increases the number of excited Na atoms by 128 times.

In Zn, which has a degeneracy of 3 and which emits 213.9 nm light at 2,500 K, the ratio of excited- to ground-state atoms is 6.17×10^{-12}. At 5,000 K, the ratio is 4.27×10^{-6}, a 705,000-fold increase in excited Zn atoms for a doubling of the temperature.

Since ΔE is inversely proportional to the wavelength, the number of atoms or molecules in the excited state will be dramatically higher with elements or molecules emitting radiation at longer wavelengths and with increasing temperature. This is why it is important to use a high-temperature excitation source for emission spectroscopy when analyzing elements emitting with short wavelengths.

Atomic Spectroscopy

Atomic Absorption Spectroscopy (AAS)

In March of 1952, Alan Walsh invented the popular technique known as atomic absorption spectroscopy. This was a major breakthrough in analytical chemistry for the analysis of elements. Prior to the invention of AAS, most elemental analysis was done using flame atomic emission spectroscopy (AES) or slow and labor-intensive chemical methods (Dawson and Price 1999). AAS had the ability to analyze about 50 elements in complex matrixes with minimum sample preparation one element at a time.

Atomic Absorption, Inductively Coupled Plasma Optical Emission Spectroscopy, and Infrared Spectroscopy,
Fig. 2 Schematic diagram of an atomic absorption spectrometer

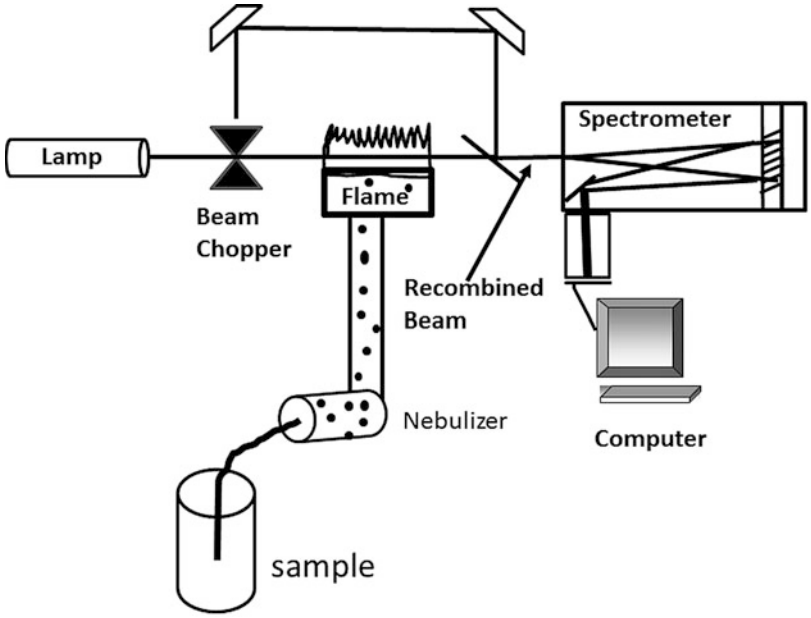

AAS is an analytical method based on the absorption of discrete wavelengths of light by adequately spaced free atoms in the gaseous ground state. The wavelength coverage for this technique is generally for elements that absorb UV and visible light. The concept is rather simple. Adequately spaced free atoms in the gaseous ground state absorb very narrow absorption lines from a radiating light source (lamp) emitting at that specific wavelength. The detector records a decrease in signal from the lamp that is dependent on the concentration of the element in the sample.

There are basically two ways to generate free well-spaced atoms for AAS. (1) The most popular method uses a nebulizer to aspirate the sample into a flame. This is referred to as flame AAS or (2) to vaporize the sample using a graphite tube that is heated with electricity. This is referred to as thermal vaporization. This method is very sensitive and uses about 1–200 μl of sample but is prone to matrix interferences. Matrix interferences occur when the composition of the calibration standards and the sample behaves differently in the flame. This can result in the atomization rate of the sample and standard to be different.

AAS instrumentation is rather simple (Fig. 2). Flame AAS uses a nebulizer (similar to a paint sprayer) which converts the sample into very fine mist that is mixed with air and usually acetylene to produce a hot flame about 2,500 K. At this temperature, most compounds can be degraded to individual elements, producing adequately spaced free atoms in the gaseous ground state. The beam from the lamp passes through a rotating beam chopper that is synchronized with the electronics and serves as the reference beam. This mechanism alternately routes the beam around the flame or allows the beam to pass through the flame where some of the beam of light is absorbed by the sample. The two beams of light are recombined and pass into a spectrometer to a detector. The readout is then processed by a computer.

The amount of radiation absorbed by the analyte element is given by *Beer's law*:

$$A = \log\left(\frac{I_o}{I}\right)$$

where A is the absorbance, I_o is the intensity of radiation incident on the flame, and I is the intensity of radiation exiting the flame. The concentration of the element of interest is directly proportional to the absorption.

In some circumstances, the elements in the flame will reform more stable compounds. For example, when samples containing Ca are heated in the flame, the Ca will combine with PO_4^{-2} to form calcium pyrophosphate which will not dissociate at this flame temperature. Also refractory elements such as Al, Mo, Ti, W, and Zr, in the presence of the flame, can combine with oxygen to form thermally stable oxides. The flame is prone to chemical and matrix interferences (West et al. 1973; Boss et al. 1989).

Flame Emission Spectroscopy

It is possible to operate the AAS instrument in emission mode (flame AES). At these low temperatures, only elements of low excitation temperatures can be measured as predicted by the Maxwell-Boltzmann equation. These include the elements of Na, K, Ca, Sr, and a few others.

In flame emission spectroscopy, most samples are introduced as an aerosol. Many of the elements in the sample upon coming in contact with the hot flame (2,400 K) quickly become desolated, vaporized, and atomized. Thermal

collisions with these hot gasses cause the valance electrons of free elements to be excited. When the excited electrons relax to a lower energy state or ground state, they emit light. The emitted light then passes into a spectrometer and is digitally processed by a computer.

In general, AAS is less prone to spectral interferences than emission spectroscopy, but both AAS and AES are prone to chemical interferences and matrix interferences. AAS is a good technique for the determination of a single element in a sample if the standards and samples are closely matched and the flame parameters are optimized for that element.

Inductively Coupled Plasma Optical Emission Spectroscopy (ICP-OES)

Background and History of Development of Inductively Coupled Plasma Optical Emission Spectroscopy (ICP-OES) Technology

The modern ICP-OES used today was first explored by Velmer Fassel and Stanley Greenfield in 1962. The lower power (1–2 kW) design by Fassel eventually became the instrument of choice (Montaser 1998).

The first generation of commercial ICP-OES instruments was introduced in 1974. These instruments were an ideal substitute for the popular flame AAS and flame AES spectrometers. This is because the ICP-OES has multielement determination capabilities, is more sensitive, and is less prone to matrix interferences (Dubuisson et al. 1998; Larson et al. 1975; West et al. 1973). The ICP-OES torch operates at temperatures up to about 7,000 K. At this temperature, the entire sample including calcium pyrophosphate and metal oxides is dissociated. Also at this temperature, there are enough energies of excitation for elements emitting from 135 nm to be analyzed.

Principles of Inductively Coupled Plasma Optical Emission Spectroscopy

Unlike flame AES, which combusts fuel to create the high temperature for excitation, ICP-OES uses an inductive-coupling process to heat argon to 10,000 K. This is the temperature of the surface of the sun. This process is similar to the heating of water in a microwave oven, which involves the radiative transfer of microwave energy to the water molecules. In the case of the ICP-AES radio frequency, energy is transferred to electrons which are accelerated in the magnetic field.

The ICP-OES uses an inert argon plasma between 6,000 and 10,000 K which quickly desolvates, vaporizes, and atomizes the sample. The plasma torch consists of three open-ended concentric quartz or ceramic tubes centered in a metal coil termed the load coil. A stream of argon flows through the middle and outer tube. A radio frequency (RF) power is applied to the load coil creating a magnetic field oscillating at 27 or 40 MHz. The collisions of the electrons with argon neutrals produce Joule heating and create secondary argon ions and electrons. The process converts 1% of the argon stream to ions. At this point, the plasma is stable and self-sustaining for as long as the RF field is applied. The concentration of argon ions in the central channel which is in contact with the sample is about 0.1%. Fig. 3 shows the components of the plasma.

Thermal Equilibrium Models and Excitation Mechanisms

The ICP-OES is a useful analytical tool because it operates at steady state. This means that the plasma has a continuously stable and reproducible output. The observation zone of the ICP-OES is about 7,000°K, which at this temperature dramatically increases the ratio of the element in the excited state to the ground state as compared with a flame. But in addition unlike other excitation sources, the ratio of the elements in the excited state to ground state is much higher in the ICP plasma than what the Boltzmann equation predicts. As a result, the emission observed is also increased over what would be expected at this temperature. There is general agreement that excitation is dependent primarily on the number and temperature of the electrons. The electrons when accelerated in a magnetic field acquire enough kinetic energy to excite the analyte upon collision. It is believed that electron impact is the primary excitation mechanism in the observation zone of the plasma (Hasegwa et al. 1992; Heiftje et al. 1985).

The ICP-OES plasma can be configured in one of the two ways shown in Fig. 4: radial viewing or axial viewing. In normal operation, samples are introduced as an aerosol. Figure 3 shows a picture and diagram of a ICP-OES plasma. Figure 4 shows how the chemical state of the sample changes as it travels through the plasma. The light emitted from the ICP is then transferred into a spectrometer where the signals are recorded and then processed by a computer. The two most popular spectrometers use a Rowland circle or an Echelle design. The main differences between manufacturers of ICP-OES are the design, of the spectrometer, the type of detector used, the RF field used (27 or 40 MHz), and the operating system.

The ICP-OES does suffer from spectral interferences (see Fig. 5). This is the result of the spectrometer not having a high enough resolution to separate the peaks. These interferences can be corrected for by measuring the interfering element at another wavelength, developing a mathematical equation to define the interference and then subtracting it out.

In a radial-viewed plasma, the matrix effects are much less than flame AAS or AES because the plasma is hot enough to atomize and vaporize all the sample. The axially viewed ICP-AES is about ten times more sensitive than the radial-viewed ICP-OES but unfortunately exhibits worse matrix interferences (Brenner and Zander 2000). This is most noticeable when

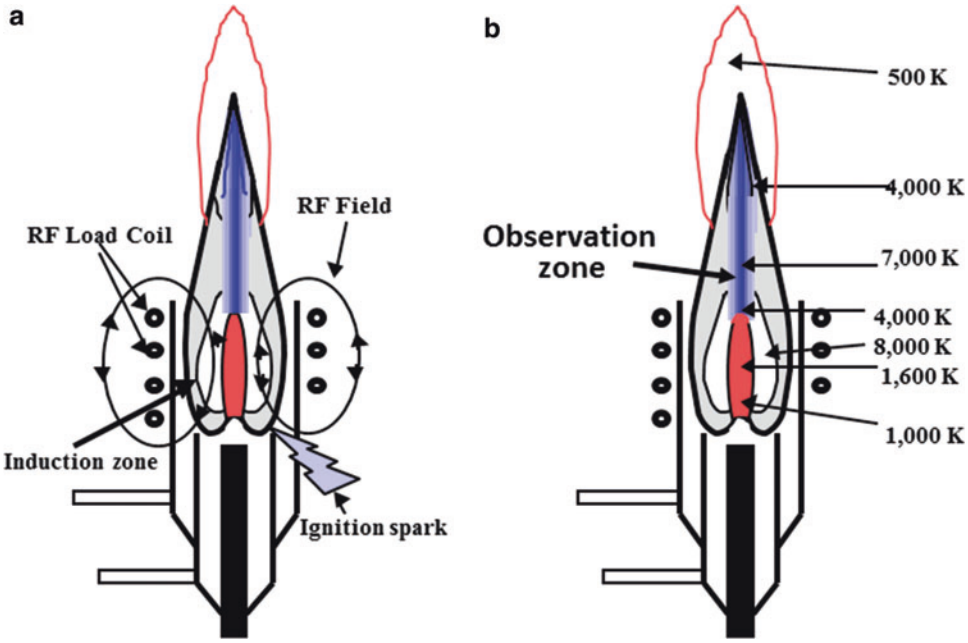

Atomic Absorption, Inductively Coupled Plasma Optical Emission Spectroscopy, and Infrared Spectroscopy, Fig. 3 The ICP plasma: (**a**) the process by which the plasma is formed and sustained and (**b**) the temparature distribution of the plasma (From Miller 2010 with permission of Springer)

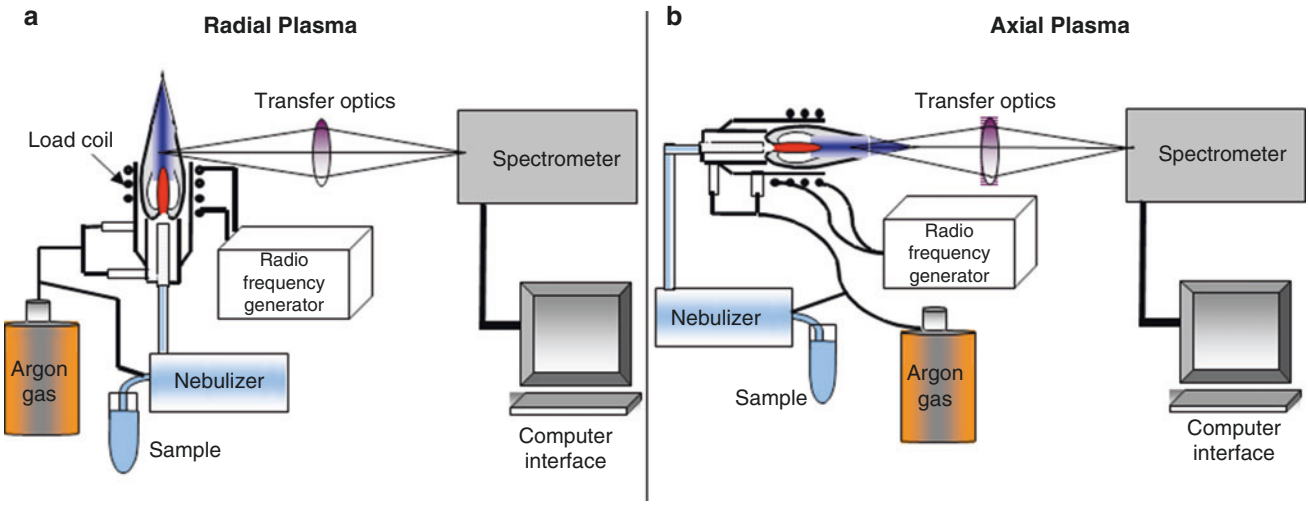

Atomic Absorption, Inductively Coupled Plasma Optical Emission Spectroscopy, and Infrared Spectroscopy, Fig. 4 Major components and typical layour of (**a**) radially viewed ICP-AES instrument and (**b**) axially viewed ICP-AES instrument (From Miller 2010 with permission of Springer)

samples contain high concentrations (500–1,000 ppm) of Ca, Na, Mg, K, or La. These elements reduce or enhance the emission intensities from trace elements, including Zn, Cd, Mn, Fe, Cr, and Ni by as much as 17%. Emission from easily ionized elements, like K, Li, and Na, is enhanced by other easily ionized elements, and these elements also show self-enhancement. Self-enhancement results when the ratio of the analyte signal to analyte concentration increases with increasing analyte concentration. This results in positive curvature when analyte emission is plotted against analyte concentration.

Over all, the ICP-OES continues to be a popular technique for the analysis of geological materials.

Molecular Spectroscopy

In addition to translational energy and energy of excited electrons that form the basics of atomic spectroscopy, energy is also stored in molecules through their vibration and rotational states.

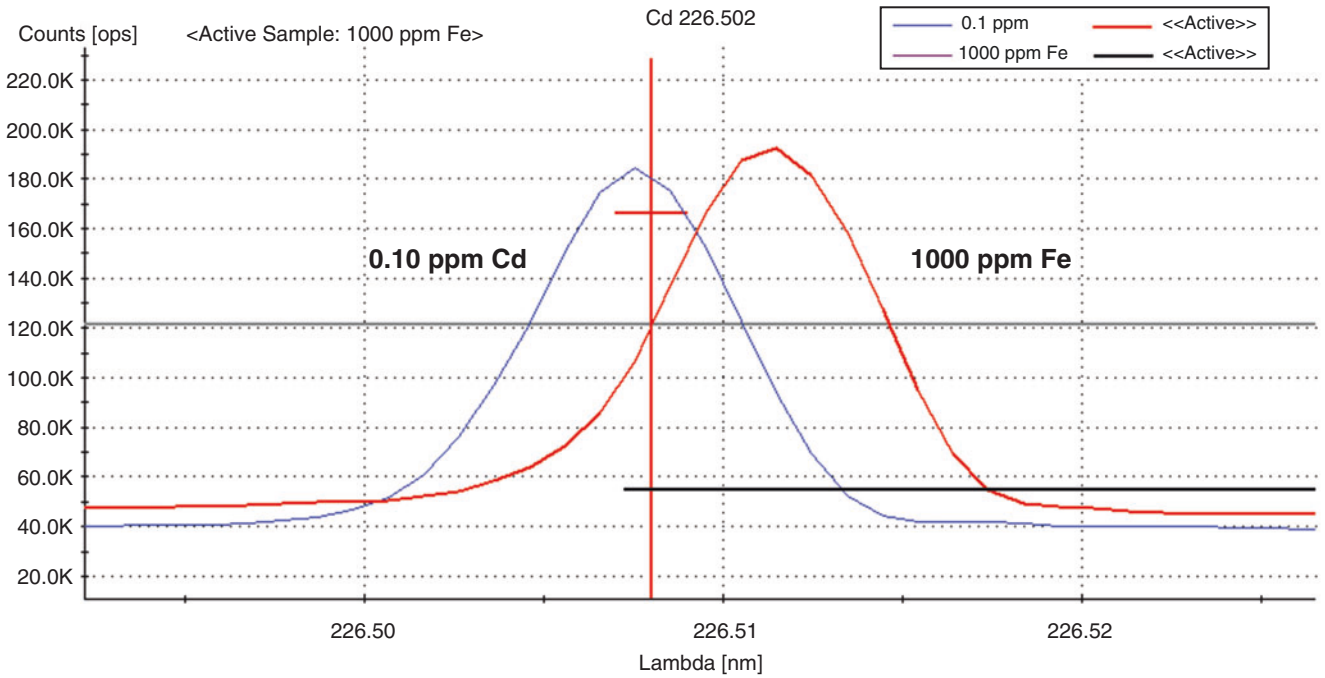

Atomic Absorption, Inductively Coupled Plasma Optical Emission Spectroscopy, and Infrared Spectroscopy, Fig. 5 A 1000 ppm Fe interfering with Cd analysis

Infrared (IR) radiation was discovered serendipitously by Sir William Herschel in 1800. He noticed that light after passing through a prism could heat a blackened thermometer outside the zones of the red visible spectrum. This demonstrated that there is radiation we can't see with our eyes.

Infrared (IR) spectroscopy is a very broad field that usually measures the absorption of the wavelengths of radiation between 0.75 and 200 μm in solids, liquids, and gasses (Wehling 2010). Unlike atomic spectroscopy which reports in wavelengths, IR spectroscopy displays are usually reported in wavenumbers ($\tilde{\nu}$, in cm^{-1}), which is the number of wavelengths per unit distance. The wavenumber range would be 13.333 cm^{-1} (0.75 μm) to 50.0 cm^{-1} (200 μm) (http://www.impublications.com/wavenumber-wavelength-converter). The wavenumber has the advantage in that the energy is linearly proportional to wavenumber while it is inversely proportional to wavelength. The disadvantage is that wavenumber often has two meanings ($\tilde{\nu} = \frac{1}{\lambda}$ or $\nu = \frac{c}{\lambda}$), and the one used must be clearly stated.

$$E = \frac{hc}{\lambda} = hc\tilde{\nu}$$

where E is the energy of the system, h is Planck's constant, ν is the frequency, and $\tilde{\nu}$ is the vibrational frequency (cm^{-1}).

The IR spectrum is complex because a molecule has many degrees of freedom to absorb energy. Each atom (n) in the molecule has ($3n$) degrees of freedom. The total degrees of freedom of a molecule is given by the product of the number of atoms (n) times the number of directions each atom can move in space. This corresponds to the Cartesian coordinates (X, Y, Z). The degrees of freedom in a molecule include three degrees of freedom for translation, three degrees of freedom for rotation of a nonlinear, or two degrees of freedom of rotation for a linear molecule. The remaining degrees of freedom are for vibrational energies. The vibrational degrees of freedom for a linear molecule is $3n - 5$. In this case, you subtract the three degrees of freedom for translation and the two degrees of freedom for rotation. In the case of a nonlinear molecule to calculate the vibrational degrees of freedom, you subtract the three degrees of freedom for translation and the three degrees of freedom for rotation. The equation is $3n - 6$.

When matter is exposed to quantized bands of IR radiation, the radiation will be absorbed by the molecule, increase the energies of vibrations of the atoms in the molecule, and also cause the molecule's rotational energy to increase.

The two types of molecular vibrations are stretching and bending. There are two types of stretching motions: symmetrical and asymmetrical. In symmetrical stretching, the distance between the atoms increases or decreases equally. Asymmetrical stretching involves the simultaneous vibration of two adjacent bonds that increase or decrease unequally. The bending vibration consists of a change in the bond angle between bonds with a common atom or group of atoms. These bending movements include rocking, scissoring, wagging, and twisting. The only vibrations of molecules observed in the IR are those that have a rhythmic change in their dipole moment.

Factors Affecting the Frequency of Vibration

A molecular vibration can be thought of as a harmonic oscillator. The following equation helps explain the factors that govern the energy levels of the vibration.

$$E = \frac{h}{2\pi}\left(v + \frac{1}{2}\right)\sqrt{\frac{f(m_1 + m_2)}{m_1 m_2}} \text{ and } \widetilde{\nu}$$
$$= \frac{1}{2\pi c}\sqrt{\frac{f(m_1 + m_2)}{m_1 m_2}}$$

where v is the vibrational quantum number, $\widetilde{\nu}$ = the vibrational frequency (cm^{-1}) h = Planck's constant, c = speed of light in cm/sec, f = force constant of the bond (dynes/cm), and m_1 and m_2 are the masses of the individual atoms involved in the vibration. This equation shows that the vibration energy and the frequency of vibration are proportional to the square root of the strength of the bond and inversely proportional to the square root of the reduced mass $\left(\frac{m_1 m_2}{m_1 + m_2}\right)$ of the molecular system in grams (Wehling 2010).

IR spectroscopy is useful to geologists because it can help them identify the structure of molecules. For example, a = C–H stretch occurs at 3,078 cm^{-1}. A coupled C = C–C = C occurs at 1,640 cm^{-1}. Because most molecules have a unique pattern, it is possible to identify unknown compounds with the aid of standards. These spectra can also be used to measure bond strengths. For example, the force f for a single bond is 5×10^5 dynes per cm, a double bond is 1×10^6 dynes per cm, and a triple bond is 1.5×10^6 dynes per cm.

IR Instrumentation

There are basically two types of instruments used. In the 1980s, IR spectrometers were double-beam dispersive grating spectrometers. They were similar to UV/VIS absorption spectrometers adapted for IR absorption. Most instruments used today are Fourier transform infrared spectroscopy (FTIR) (see Fig. 6). The principle of operation is as follows. The polychromatic IR beam after leaving the IR source strikes a beam splitter sending half the light to a stationary mirror and the other half of the light to a moveable mirror. The mirrors are originally adjusted so the path length of the recombined beams is equal at the detector. When the moveable mirror is moved, the path length of the beam changes. As the beam passes back through the beam splitter, it recombines with the beam from the stationary mirror. The recombined ray will develop constructive and destructive interference patterns and then pass through the sample where the sample absorbs its characteristic frequencies. These interactions generate a pattern of fluctuating optical interference fringes producing what is termed an interferogram. The interferogram is imaged on to a detector like a CCD camera which converts it to a digital electrical signal which is then processed by a computer using a mathematical equation to construct the image.

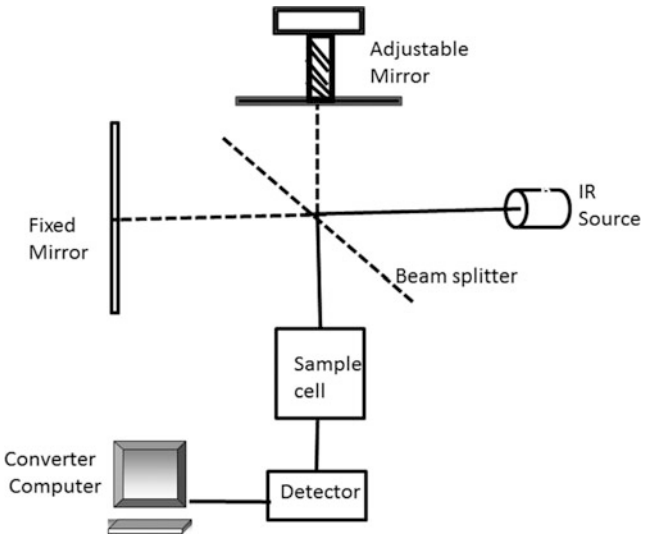

Atomic Absorption, Inductively Coupled Plasma Optical Emission Spectroscopy, and Infrared Spectroscopy, Fig. 6 Fourier transform infrared spectroscopy (FTIR)

Summary

The fields of atomic and molecular spectroscopies continue to contribute greatly to geology by determining the concentration and composition of components that make up geological materials. The instrumentation used today is well established and reliable.

Cross-References

- Analytical Techniques
- Geochemical Reference Materials
- Organic Geochemistry
- Trace Elements

References

Boss CB, Fredeen KJ (1989) ICP-AES methodology. In: Concepts, instrumentation, and techniques in inductively coupled plasma atomic emission spectrometry. The Perkin-Elmer Corporation, Norwalk

Brenner IB, Zander AT (2000) Axially and radially viewed inductively coupled plasmas – a critical review. Spectrochim Acta Part B 55:1195–1240

Dawson JB, Price JW (1999) Alan Walsh his influence on the development of atomic spectroscopy in the UK. Spectrochim Acta B 54(14):201–2015

Dubuisson C et al (1998) Comparison of ionic line-based internal standardization with axially and radially viewed inductively coupled

plasma atomic emission spectrometry to compensate for sodium effects on accuracy. J Anal At Spectrom 13:1265–1269
Hasegwa T et al (1992) Fundamental properties of inductively coupled plasmas. In: Montaser A, Golightly DW (eds) Inductively coupled plasmas in atomic spectrometry, 2nd edn. VCH, New York, pp 429–430
Heiftje GM et al (1985) A steady-state approach to excitation mechanisms in the ICP. Spectrochim Acta 40B:167–176
Larson GF et al (1975) Inductively coupled plasma – optical emission analytical spectrometry – study of some interelement effects. Anal Chem 47:238–243
Montaser A (1998) The science of a revolutionary chemist and spectroscopist: Velmer A. Fassel. Appl Spectrosc 52(11):406A–426A
West AC et al (1973) Lateral diffusion interferences inflame atomic absorption and emission spectrometry. Anal Chem 45:1586–1159

Further Reading

Miller DD, Rutzke MA (2010) Atomic absorption spectroscopy and inductively coupled plasma-mass spectrometry. In: Nielsen SS (ed), 4th edn. Springer, New York, PP 421–442
Robinson JW (1966) Atomic absorption spectroscopy, 1st edn. Marcell Decker. Inc, New York, pp 1–103
Robinson JW et al (2014a) Introduction to spectroscopy. In: Robinson JW (ed) Undergraduate instrumental analysis, 7th edn. CRC press, Boca Raton, pp 61–112
Robinson JW et al (2014b) Infrared, near-infrared and Raman spectroscopy. In: Robinson JW (ed) Undergraduate instrumental analysis, 7th edn. CRC press, Boca Raton, pp 243–264
Robinson JW et al (2014c) Atomic absorption spectroscopy. In: Robinson JW (ed) Undergraduate instrumental analysis, 7th edn. CRC press, Boca Raton, pp 441–505
Silverstein RM et al (1981) Infrared spectrometry. In: Silverstein RM et al (eds) Spectrometric identification of organic compounds, 4th edn. Wiley, New York, pp 95–111
Wehling RL (2010) Infrared spectroscopy. In: Nielsen SS (ed), 4th edn. Springer, New York, pp 409–420

Atomic Number, Mass Number, and Isotopes

Russell S. Harmon
North Carolina State University, Raleigh, NC, USA

Definitions

The primary building blocks of atoms are protons, neutrons, and electrons. It is convenient to describe the composition of an atom in terms of the number of protons and neutrons in its nucleus (Fig. 1). The term *atomic number*, conventionally denoted by the symbol *Z*, indicates number of protons present in the nucleus of an atom, which is also equal to the number of electrons in an uncharged atom. The number of neutrons is represented by the *neutron number* (*N*). Because the mass of these nuclear particles is each approximately equal to one unified atomic mass unit (u), the sum of the protons plus neutrons is designated as the *mass number* (*A*). The mass of the electron is more than 1800 times smaller than the proton mass and, therefore, can be neglected in calculating the mass number. For any element, the mass number is equal to the atomic weight rounded off to the nearest integer value.

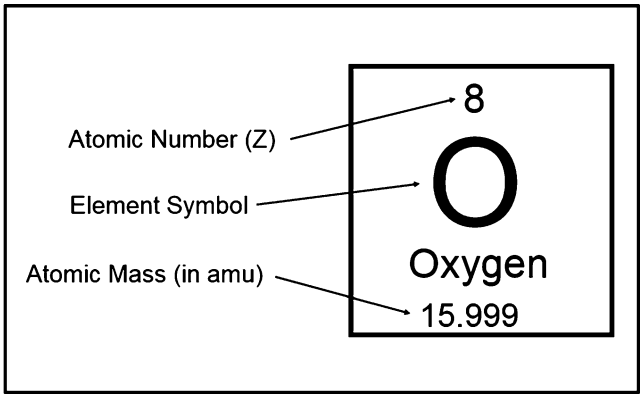

Atomic Number, Mass Number, and Isotopes, Fig. 1 Atomic number as displayed in the periodic table of the elements

Nuclear Structure and Stability

The proton has a positive charge that is equal in magnitude, but opposite in polarity, to the charge of an electron. The number of protons defines how many extranuclear electrons an atom can have under conditions of electronic neutrality. It is the number of electrons and their distribution about the nucleus that determines the chemical properties of an atom, whereas it is the composition of the nucleus that is responsible for the phenomenon of radioactivity. The modern periodic table of the elements is based on the fact that the properties of the elements are repetitive functions of their atomic number.

The term *nuclide* denotes any of the more than 1300 different atomic species characterized by a distinct combination of protons and neutrons, only about 270 of which are stable (i.e., non radioactive). The nuclear composition of any nuclide can be represented by the relationship $A = Z + N$. The two numbers Z and A completely describe any nuclear configuration, which can be conveniently written by means of a shorthand notation consisting of the chemical symbol of the element, with Z written as a subscript and A written as a superscript. For example, consider the element nickel (Ni), which has an atomic number of 28 and consists of five naturally occurring isotopes of masses 58, 60, 61, 62, and 64. Therefore, the notation ${}_{28}{}^{61}\mathrm{Ni}$ identifies the particular nuclide of nickel with 28 protons, an equal number of electrons, and 33 neutrons. Variation in A and at constant value of Z accounts for the occurrence of *isotopes*; nuclides with similar chemical characteristics but different masses depend on physical properties (e.g., ${}^{14}\mathrm{N}$ and ${}^{15}\mathrm{N}$), like diffusion rate. Approximately three-quarters of naturally occurring elements are mixtures of two or more isotopes. Nuclides having the

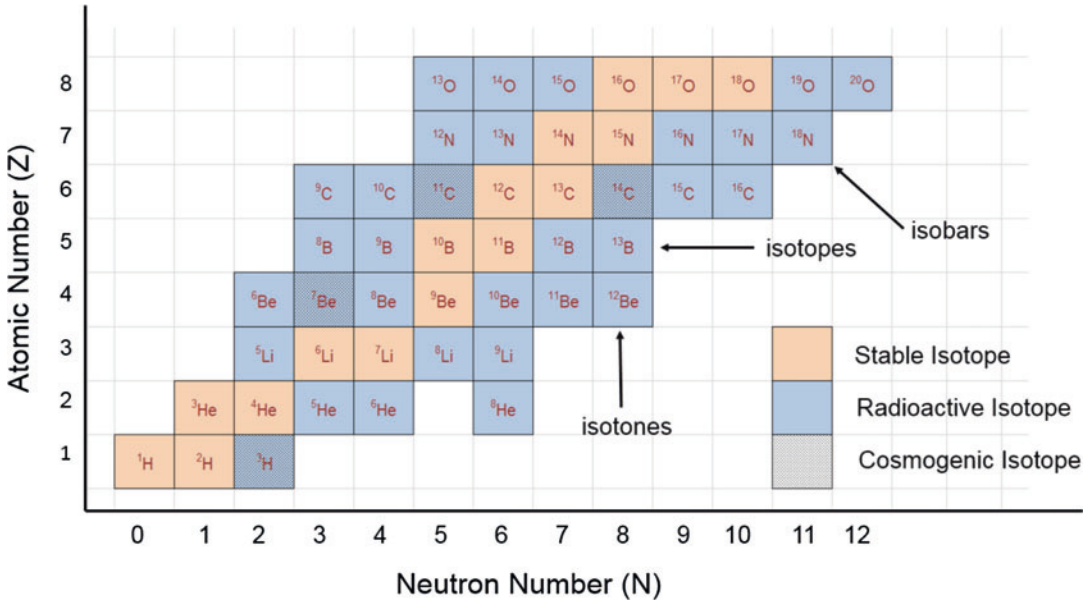

Atomic Number, Mass Number, and Isotopes, Fig. 2 Partial chart of the nuclides. Stable isotopes are shown in *orange* shading and radioactive isotopes in *blue* shading, and cosmogenic isotopes are denoted by the *stippled* pattern overlay

same A, but different Z, are called *isotones* (^{9}Be and ^{10}B), whereas nuclides having the same A, but different Z and N, are called *isobars* (e.g., ^{3}H and ^{3}He). As illustrated in Fig. 2, which is a plot of atomic number against neutron number, almost all elements occur in nature as mixtures of two or more isotopes. In some cases, this mixture includes cosmogenic isotopes that exist only because they are produced in the Earth's atmosphere, soil, or rock as a consequence of in situ interactions of high-energy cosmic rays with atomic nuclei (Fig. 2). *Atomic weight* is a term commonly used in physics, chemistry, and engineering to indicate the average mass of a chemical element, in unified atomic mass units.

Certain combinations of protons and neutrons produce stable nuclei, whereas other nuclear configurations are unstable and ultimately revert to a stable state through the process of radioactive decay. Nuclear stability is attained for low atomic numbers when the number of protons is approximately equal to the number of neutrons (i.e., at $Z/N \approx 1$). Above calcium ($Z = 20$), no stable nuclide exists with equal numbers of protons and neutrons, for as Z increases, the repulsive Coulombic forces increase at a greater rate than the attractive nuclear forces. Thus, the presence of additional neutrons is required to increase the average distance between protons within the nucleus and, thereby, reduce the Coulombic force according to the inverse-square law. For the heaviest stable nuclei, the Z/N ratio is >1.5. However, there is a limit to the number of excess neutrons that a nucleus can contain and remain stable. Beyond ^{209}Bi, the heaviest stable nuclide, with 83 protons and 126 neutrons, a neutron excess introduces instability and leads to beta decay (i.e., a type of radioactive decay in which a neutron is transformed into a proton, or vice versa, inside an atomic nucleus with the emission of an electron or positron or by electron capture). Such a process is known as *nuclear transmutation*, as the original element becomes a new chemical element as a consequence of the decay process (e.g., $_{53}{}^{131}\mathrm{I} \rightarrow_{54}{}^{131}\mathrm{I} + \mathrm{e}^{-} + \bar{\nu}_e$). Beyond ^{209}Bi, no combination of protons and neutrons is stable, and for A above ~230, there is an increasing instability relative to alpha decay.

The cosmic abundance of the elements varies systematically with atomic number. Only 12 elements, all with $Z < 27$, exhibit appreciable abundance (H, He, O, C, Ne, Fe, N, Si, Mg, S, Ar, Ca). Elements with a low atomic number (<40) exhibit an exponential decay in abundance, whereas elements of higher atomic number are of relatively constant abundance. The relative abundance of elements above 28 is less variable than elements of lower atomic number. Notably, elements of even neutron number and atomic number are more abundant than adjacent elements of odd atomic number. Additionally, certain combinations of neutrons and protons in the nucleus – 2, 8, 28, 50, 82, and 126 (called *magic numbers*) – produce particularly stable nuclear configurations that are characterized by high nuclide natural abundance and a large number of stable isotopes or isotones relative to neighboring nuclides. These observations provide strong support for a nuclear shell model, analogous to the well-known extranuclear electron shell model, on which *magic numbers* represent the number of particles required to give complete shell occupancy.

Summary

The atomic number designates the number of protons in an element's nucleus and because that determines its electronic structure, its chemical behavior. The mass number of a nuclide is equal to the number of protons and neutrons in the nucleus; variation in the number of the latter produces results in different isotopes of that element.

Cross-References

- ▶ Cosmic Elemental Abundances
- ▶ Nucleosynthesis
- ▶ Periodic Table
- ▶ Radioactivity
- ▶ Unified Atomic Mass Unit, Avogadro Constant, and Mole

References

Faure G (1977) Principles of isotope geology, 2nd edn. Wiley, New York. 464 pp

Loveland WD, Morrissey DJ, Seaborg GT (2005) Modern nuclear chemistry. Wiley, New York. 644 pp

White WM (2013) Geochemistry. Wiley, New York. 672 p

Authigenesis

Norbert Clauer
Laboratoire d'Hydrologie et de Géochimie de Strasbourg, CNRS - Université de Strasbourg, Strasbourg, France

Definition

Often used by sedimentologists and low-temperature mineralogists and geochemists to describe in situ (on site) mineral precipitation in "soft" rocks, "authigenesis" is derived from Greek "indigenous." Generally, it results from a discrete and long-lasting process that involves pore fluids of local origin or introduced from elsewhere. However, authigenesis occurs not only in sediments and at low-temperature (<150 °C), that is to say under diagenetic conditions. Its consequences can be very important economically; for instance, industrial clay and metal deposits, as well as mineral precipitation related to hydrocarbon maturation and trapping, may result from authigenic processes.

Some Complementary Aspects of the Definition

Based on the above definition, authigenesis can occur at any time after sediment deposition, depending on the reactivity of the mineral components (organics are also able to interfere or even contribute, but they will not be considered here) that interact with fluids of local or remote origin. In turn, this definition excludes mineral crystallization from massive high-temperature recrystallized or metasomatic concentrations. Fairbridge and Bourgeois (1978) segmented authigenesis into (1) an early occurrence immediately after sediment deposition (= syndiagenetic), (2) a continental weathering of sediments in contact with the atmosphere after initial burial (= epidiagenetic), and (3) a deep-burial episode of host sediments (= anadiagenetic).

In fact, the meaning of "authigenesis" depends mainly on what the user wants to highlight of a mineral crystallization at a given sediment site or even of tectono-thermally affected metasediments that are basically excluded from the above, somewhat restrictive definition. In fact, metasediments can also host authigenic minerals with the difference that the fluids responsible for in situ mineral crystallization were activated by a remote tectonic or igneous activity. In a broad sense, authigenesis can last for millions of years and induce any mineral precipitation at a given time in a sedimentary or low-grade metamorphic environment (Fairbridge 1981). It is also to be kept in mind that discrete authigenic reactions are dependent on chemical (chemistry of interacting fluids, mineral reactivity, biological contribution) and physical (rock porosity, fluid temperature, water/rock ratio) conditions during mineral crystallization, and that they may determine economic impacts.

Where to Expect Authigenesis and of Which Minerals?

In Continental Aerial Environments

Authigenesis occurring during subaerial exposure of varied rock types to atmosphere results from weathering processes driven by rainwater infiltration or runoff. Precipitation of chemical elements removed from outcropping rocks by surface and subsurface fluids that are often acidic favors nearby or remote mineral precipitation that might clog up the pore system of the host rocks. Various types of authigenic clays have been reported during continental weathering (Wilson 1999; Velde and Meunier 2008), the removed elements also generating massive authigenic duricrusts typical for semiarid regions that may host authigenic hematite and goethite nodules (Ramanaidou et al. 1996). The nature of such crusts depends on the major constitutive elements: calcretes

consisting mainly of calcium are the most common; when iron is included they become ferricretes or silcretes when silica is most incorporated. The climate is naturally a determining driving force of these authigenic precipitations: humid climates accelerate weathering and even dissolution of the most fragile rock-constitutive minerals, and they favor elemental release as solutes into the associated fluids, whereas seasonal evaporation is needed to agglomerate the elements into crusts (Girard et al. 2002).

In Marine Environments

Oceans are the most favorable places for varied authigenic mineralization, in fact wherever local conditions are in chemical disequilibrium. About 30–40 years ago, glauconite authigenesis was very extensively studied (e.g., Odin 1988). Along the western African Coast, it resulted from deposition of continental ferrous smectite that was oxidized and supplied with potassium in situ to trend towards glauconite. Useful as stratigraphic markers, glauconite grains represent the classic example of clay authigenesis in oceans that was also described at other places such as the oceanic ridges with local advective supply of hydrothermal fluids. There, original authigenic nontronite (= Fe-smectite; Bailey 1980) can also be changed into glauconite by addition of potassium, sometimes together with Mn-oxides precipitating in the black smokers of spreading centers (e.g., Hess et al. 1991). Pacific deep-sea red clays also host authigenic minerals, such as phillipsite, a zeolite of sedimentary origin involving volcanic rocks (Honnorez 1978; Clauer 1982), as well as Fe-Mn crusts and nodules in the eastern Atlantic and southern Pacific oceans (e.g., Glasby et al. 2015). These nodules were once the topic of extensive exploration and even of deep-sea mining projects (e.g., Sharma 2015). Metal authigenesis was also described in present-day Red Sea deposits by direct metallic precipitation from overlying acidic brines and in situ crystallization of pyrite framboids (Fig. 1a; Pierret et al. 2000) and other metal-type minerals (e.g., Anschutz and Blanc 1995).

In Buried Sediments

After deposition, sediments are progressively buried, which modifies their physical and chemical characteristics, including those of their pore system. Temperature increases, pore space is reduced, and pore waters are expelled, all inducing new conditions altering the detrital mineral and organic components, which favors precipitation on site of new minerals. For instance, pyrite "balls" crystallized on site in "nests" built by detrital minerals of Triassic sandstones at 2000-m depth in the eastern Paris Basin, before some were wrapped by an authigenic illite veil of a later generation (Fig. 1b; Blaise et al. 2016). Their idiomorphic shape testifies for on-site formation, even if under conditions different than those of the Suakin Depth of the Red Sea (Fig. 1a).

Paleocene Atlantic Ocean sediments drilled during the Deep Sea Drilling Project contain fuzzy, flake-like detrital smectite crystals that interacted with their pore system after deposition. Probably in thermodynamic disequilibrium with the initial depositional environment, the smectite particles were dissolved progressively and replaced in situ by diagenetic, lath-like authigenic crystals, surprisingly of the same smectite type (Clauer et al. 1990).

Combined with concomitant alteration of the initial detrital particles, authigenic processes can last for long times, especially when sediment burial is slow. Interestingly, the intensity of illite authigenesis differs in interlayered shaly and sandy units of a sedimentary sequence, partly because there is less pore fluid and a different chemistry, in the former than in the latter layers at similar depths (e.g., Clauer and Lerman 2012). Illite is an excellent tracer of hydrocarbon maturation in shaly source rocks and trapping in sandy or carbonate reservoirs, both buried at several thousands of meters (Pevear 1999). For instance, illite precipitated in situ at the same time in oil reservoirs located about 500 km apart in the North-Sea Viking Graben, of stratigraphically different sandstones buried at different depths (Clauer and Liewig 2013). Detailed observation may even show successive illite authigenic episodes in the same host rocks, the initial covering quartz grains as "palisades" and the second growing "fibers" into the pore space (Fig. 1c) that literally form a fiber "meadow" on detrital quartz grains (Fig. 1d).

Authigenesis of another clay is of importance for economical reasons, namely, that of kaolinite for the porcelain industry. Of course, kaolinite concentrations are not always authigenic, deriving also from continental weathering followed by river transport and deposition, or from hydrothermal cooling related to late magmatic events (e.g., Murray 1988). However, numerous studies in northwestern Spain have identified kaolinite authigenesis in sediments and plutonic basement rocks (Galán and Martín Vivaldi 1972). Authigenesis of uraninite has probably an even more important economical impact. Numerous studies of illite authigenesis in uranium-bearing Proterozoic sediments from Canada and Australia helped understanding of the combined precipitation of illite and uraninite. For instance, the description of successive episodes of hydrothermal illite authigenesis in the sedimentary cover and in main faults of the underlying basement allowed reconstruction of the evolution pattern of major uranium deposits of Australia (Clauer et al. 2015). Illite authigenesis was the signature of the major episodes of uranium concentration, whereas illite was lacking during episodes of minor uraninite recrystallization into coffinite.

In Volcanic Ash Beds

Volcanic ash layers sandwiched in sediment accumulations witness volcanic episodes. Those of the East Slovak Basin

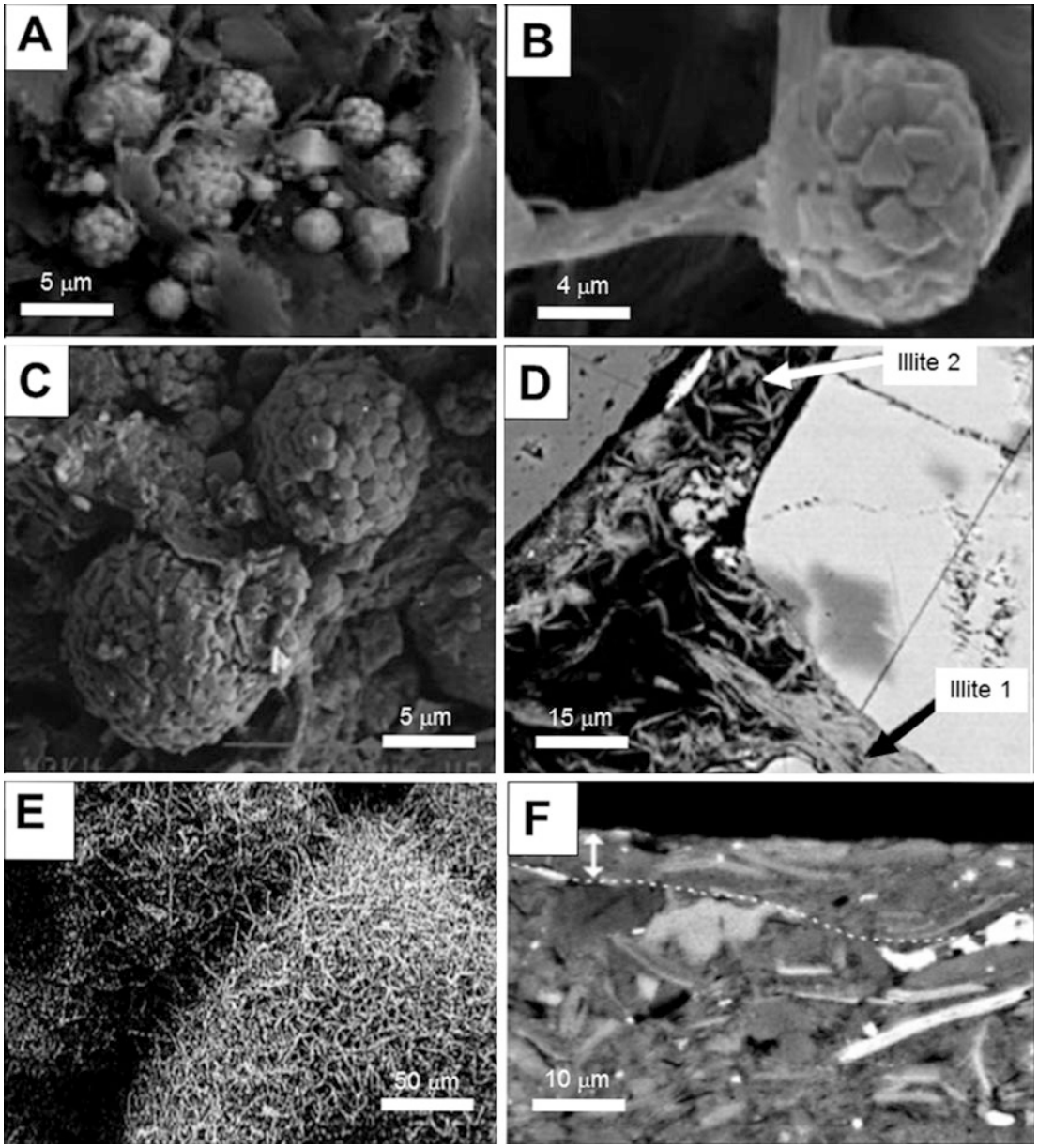

Authigenesis, Fig. 1 (**a**) Authigenic pyrite framboids in a "nest" of detrital clay particles from a Triassic sandstone of the Paris Basin; (**b**) Authigenic pyrite framboid wrapped in a younger authigenic illite veil (both from Blaise et al. 2016); (**c**) Authigenic pyrite framboid from Suakin Depth of the Red Sea due to rain out from brines above (from Pierret et al. 2000); (**d**) Two authigenic illite generations grown in the pore system of an oil reservoir. Illite 1 grew as a "palisade" on quartz grains, while illite 2 fibers grew into the pore space (from Clauer and Lerman 2012); (**e**) Authigenic illite fibers grown into the pores between quartz grains. The black dot to the left top is the impact of a removed quartz grain, the pore spaces are the black holes to the lower left and upper right (unpublished, courtesy of J. Cocker, ARAMCO); (**f**) Side micro-picture of a fracture in a gouge with illite authigenesis: in the upper part between the void on the top and the dashed line, the authigenic illite fibers are thinner and more flexible than those of detrital origin below the dashed line (from Laurich et al. 2014)

showed that the original volcanic glass was altered progressively after deposition into an authigenic smectite (Kováč et al. 1997). Further addition of potassium by interstitial fluids from surrounding shales progressively modified this smectite into illite (Honty et al. 2004). In fact, illitization did not start at the same time in most of the regionally scattered bentonite beds and did not last the same time interval (Clauer et al. 2014a). The main driving force of illitization and probably of other authigenic processes is the changing chemical composition of the interacting fluid, coupled with the temperature increase resulting from progressive burial (Clauer et al. 2014b).

In Hydrothermal Environments

Authigenesis was also described in rocks percolated by hydrothermal fluids driven by close or remote tectonic activities. For instance, gouges represent plausible locations where illite authigenesis is expected in tectono-thermal contexts. These gouges are characterized by an intense grinding of their components but also by significant fluid flow. Recent ultra-fine observations of such gouge volumes have identified authigenic illite crystals as small as a few nanometers along shear zones representing favorable channels for circulation of the migrating fluids (Fig. 1e; Laurich et al. 2014).

Fluids flowing in gouges originated necessarily away from where their interactions are visible. This aspect becomes somewhat controversial in the case of illite authigenesis, as its precipitation is clearly contemporaneous with an identified tectonic activity (for instance in case of rifting) but located sometimes far from this activity. In Triassic sandstones from Paris Basin, illite authigenic crystals provided similar to identical isotopic ages at varied places in the basin (Blaise et al. 2016) despite widely dispersed locations, sometimes within faults. The fact that illitization was contemporaneous with major adjustments of the basement connects the authigenesis process to fluids released by tectono-thermal events from within or outside the basin. This connection is again of economic importance as the described illite authigenesis also relates to varied authigenic metal deposits next to the outcropping plutonic basement in the center of the Paris Basin and on its western side (Cathelineau et al. 2012).

Authigenesis at Crystal Scale

Mineralogical, crystallographic, chemical, and isotopic studies of authigenic illite from bentonite beds of the East Slovak Basin were privileged for a time, because the lack of detrital crystals in these rocks ensures that the observation and analysis of illite is not hindered or obscured. Studies of separated nanometer-sized illite crystals (<0.02 μm) defined an authigenic process with nucleation and crystal growth (e.g., Środoń et al. 1992; Eberl et al. 1998). Illitization was described as successive pulses of variable duration in the entire basin, with changing intensities at similar temperatures (Clauer et al. 2014a).

Summary: "Authigenesis" Needs to be Precisely Defined for Any Use

In the previous entry of authigenesis in this Encyclopedia of Geochemistry, Fairbridge (1999) questioned *sensu stricto* mineral authigenesis when interacting with "deep burial interstitial fluids that reflect more or less remote source rocks from which they have been expelled." There is nothing to argue about this statement except that it incites thinking that in situ minerals crystallized from remote fluids are not authigenic. This conceptual discrimination may raise debates that can be avoided by defining precisely the meaning of the somewhat ambivalent authigenic wording because of its potential wide applicability.

In summary, authigenesis is a discrete, often long-lasting process that favors new mineral crystallization on site, by involving the associated detrital minerals, especially those altered by the interacting fluids that can be local or derived from distance. And last but not least, mineral authigenesis can have very important economical consequences, especially if it involves metals and/or hydrocarbons.

Cross-References

- ▶ Clay Minerals
- ▶ Diagenesis
- ▶ Fluid Inclusions
- ▶ Hydrocarbons
- ▶ Hydrothermal Alteration
- ▶ Hydrothermal Solutions
- ▶ Low-Temperature Geochemistry
- ▶ Mineral Genesis
- ▶ Ore Deposits
- ▶ Oxidation-Reduction Reactions and Eh-pH (Pourbaix) Diagrams
- ▶ Petroleum

References

Anschutz P, Blanc G (1995) Chemical mass balances in metalliferous deposits from the Atlantis II Deep, Red Sea. Geochim Cosmochim Acta 59:4205–4218

Bailey SW (1980) Structure of layer silicates. In: Brindley GW, Brown G (eds) Crystal structure of clay minerals and their identification, Monograph, vol 5. Mineralogical Society, London, pp 28–39

Blaise T, Clauer N, Cathelineau M, Boiron MC, Techer I, Boulvais P (2016) Reconstructing fluid-flow events in lower-Triassic sandstones of the eastern Paris Basin by elemental tracing and isotopic dating of nanometric illite crystals. Geochim Cosmochim Acta 176:157–184

Cathelineau M, Boiron MC, Fourcade S, Ruffet G, Clauer N, Belcourt O, Coulibaly Y, Banks DA, Guillocheau F (2012) A major late Jurassic fluid event at the basin/basement unconformity in western France: $^{40}Ar/^{39}Ar$ and K-Ar dating, fluid chemistry, and related geodynamic context. Chem Geol 322–323:99–120

Clauer N (1982) Strontium isotopes of tertiary phillipsites from the Southern Pacific: timing of the geochemical evolution. J Sediment Petrol 52:1003–1009

Clauer N, Lerman A (2012) Thermal history analysis of sedimentary basins: an isotopic approach to illitization. In: Harris ND, Peters K (eds) Thermal history analysis of sedimentary basins: methods and case histories, Society of economic paleontologists and minerlogists, Special publication, vol 11. Springer, New York, pp 125–146

Clauer N, Liewig N (2013) Episodic and simultaneous illitization in oil-bearing Brent Group and fulmar formation sandstones from the

northern and southern North Sea based on illite K-Ar dating. Am Assoc Pet Geol Bull 97:2149–2171
Clauer N, O'Neil JR, Bonnot-Courtois C, Holtzapffel T (1990) Morphological, chemical, and isotopic evidence for an early diagenetic evolution of detrital smectite in marine sediments. Clay Clay Miner 38:33–46
Clauer N, Honty M, Fallick AE, Šucha V (2014a) Regional illitization in bentonite beds from East Slovak Basin based on isotopic characteristics (K-Ar, $\delta^{18}O$ and δD) of illite-type nanoparticles. Clay Miner 49:165–194
Clauer N, Williams LB, Fallick AE (2014b) Genesis of nanometric illite crystals elucidated by light-element (hydrogen, lithium, boron and oxygen) isotope tracing, and K-Ar and Rb-Sr dating. Chem Geol 383:26–50
Clauer N, Mercadier J, Patrier P, Laverret E, Bruneton P (2015) Relating unconformity-type uranium mineralization of the alligator rivers uranium field (Northern Territory, Australia) to the regional Proterozoic tectono-thermal activity: an illite K-Ar dating approach. Precambrian Res 269:107–121
Eberl DD, Drits VQ, Środoń J (1998) Deducing growth mechanisms for minerals from the shapes of crystal size distributions. Am J Sci 298:499–533
Fairbridge RW (1981) In: Frye K (ed) Encyclopedia of mineralogy. Hutchinson and Ross, Stroudsburg, pp 31–33
Fairbridge RW (1999) Authigenesis. In: Marshall CP, Fairbridge RW (eds) Encyclopedia of geochemistry. Kluwer, Boston/Dordrecht, pp 26–27
Fairbridge RW, Bourgeois J (eds) (1978) Encyclopedia of sedimentology. Dowden, Hutchinson and Ross, Stroudsburg. 901p
Galán E, Martín Vivaldi JL (1972) Genetic classification of the Spanish kaolin deposits and their typology. In: Serratosa JM (ed) Proceedings of the 1972 international clay conference. CSIC, Madrid, pp 737–748
Girard JP, Freyssinet P, Morillon AC (2002) Oxygen isotope study of Cayenne duricrust paleosurfaces: implications for past climate and lateritization processes over French Guiana. Chem Geol 191:329–343
Glasby GP, Li J, Sun Z (2015) Deep-sea nodules and Co-rich Mn crusts. Mar Georesour Geotechnol 33:72–78
Hess J, Bender M, Schilling JG (1991) Assessing seawater/basalt exchange of strontium isotopes in hydrothermal processes on the flanks of mid-ocean ridges. Earth Planet Sci Lett 103:133–142
Honnorez J (1978) Generation of phillipsites by palagonitization of basaltic glass in sea water and the origin of K-rich deep-sea sediments. In: Sand LB, Mumpton FA (eds) Natural zeolites, occurrence, properties, use. Pergamon Press Ltd., London, pp 245–248
Honty M, Uhlík P, Šucha V, Caplovicová M, Francù J, Clauer N, Biron A (2004) Smectite-to-illite alteration in salt-bearing bentonites (the East Slovak Basin). Clay Clay Miner 52:533–551
Kováč M, Bielik M, Lexa J, Pereszlényi M, Šefara J, Túnyi I, Vass D (1997) The Western Carpathian intramontane basins. In: Grecula P, Hovorka D, Putiš M (eds) Geological evolution of the Western Carpathians. Geological Survey of Slovak Republic, Bratislava, pp 43–64
Laurich B, Urai JL, Desbois G, Vollmer C, Nussbaum C (2014) Microstructural evolution of an incipient fault zone in Opalinus Clay: insights from an optical and electron microscopic study of ion-beam polished samples from the main fault in the Mt-Terri Underground Research Laboratory. J Struct Geol 67:107–128
Murray HH et al (1988) Kaolin minerals: their genesis and occurrences. In: Hydrous phyllosilicates, Reviews in mineralogy, vol 19. Mineralogical Society of America, Washington, DC, pp 67–89
Odin GS (ed) (1988) Green marine clays, Developments in sedimentology, vol 45, 1st edn. Elsevier, Amsterdam. 444p
Pevear DR (1999) Illite and hydrocarbon exploration. Proc Natl Acad Sci 96:3440–3446
Pierret MC, Blanc G, Clauer N (2000) Sur l'origine de la pyrite framboïdale dans les sédiments de la fosse Suakin (Mer Rouge). C R Acad Sci 330:31–38
Ramanaidou E, Nahon D, Decarreau A, Melfi AJ (1996) Hematite and goethite from duricrusts developed by lateritic chemical weathering of Precambrian banded iron formations, Minas Gerais, Brazil. Clay Clay Miner 44:22–31
Sharma R (2015) Environmental issues of deep-sea mining. Procedia Earth Planet Sci 11:204–211
Środoń J, Elsass F, McHardy WJ, Morgan DJ (1992) Chemistry of illite-smectite inferred from TEM measurements of fundamental particles. Clay Miner 27:137–158
Velde BB, Meunier A (2008) The origin of clays in soils and weathered rocks. Springer, Berlin. 405p
Wilson MJ (1999) The origin and formation of clay minerals in soils: past, present and future perspectives. Clay Miner 34:7–25

B

Barium

William M. White
Department of Earth and Atmospheric Sciences, Cornell University, Ithaca, NY, USA

Element Data
Atomic Symbol: Ba
Atomic Number: 56
Atomic Weight: 132.9054 g/mol
Isotopes and Abundances: ^{130}Ba 0.11%, ^{132}Ba 0.10%, ^{134}Ba 2.42%, ^{135}Ba 6.59%, ^{136}Ba 7.85%, ^{137}Ba 11.23%, ^{138}Ba 71.70%
1 Atm Melting Point: 727 °C
1 Atm Boiling Point: 1845 °C
Common Valences: 2+
Ionic Radii: 149 pm (6-fold)
Pauling Electronegativity: 0.89
First Ionization Energy: 502.9 kJ/mol
Chondritic (CI) Abundance: 2.42 ppm
Silicate Earth Abundance: 6.6 ppm
Crustal Abundance: 390 ppm
Seawater Abundance: 30 to 150 nmol/kg
Core Abundance: ~0

Properties

Barium derived its English name from the Greek *barys*, meaning heavy. It is the heaviest stable alkaline earth and unusually abundant for an element with such a high atomic number. Barium, Pb, and Te are the only elements heavier than Zr (atomic number 40) with CI chondritic abundances greater than 2 ppm (Palme (in press), ▶ "Cosmic Elemental Abundances," this volume). This is due in large part to the unusual abundance of ^{138}Ba, which has a magic number of neutrons (82). In pure form, Ba is a silvery, slightly golden metal, but, as is the case with other alkaline earths, it tarnishes quickly upon exposure to the atmosphere.

History and Use

German-Swedish chemist Carl Scheele first recognized that barite (barium sulfate) contained an unrecognized chemical element in 1774. Barium was subsequently isolated and named by English chemist Humphry Davy in 1808.

The uses of barium are quite limited. In the late nineteenth and early twentieth century, it was used to produce oxygen in the Brin process. At present, the most common use of barium, in the form of barium sulfate, is as a component of drilling fluids ("mud") in the petroleum and natural gas industry to increase fluid density. Because of its insolubility, low toxicity, and strong X-ray absorption, barium sulfate is also used as a radiocontrast agent in medical X-ray gastrointestinal procedures. Barium has more limited uses in paints, plastics, alloys, glasses and optics, fireworks and flares, and fluorescent lamps. Barite ($BaSO_4$) is the principal source of industrial barium.

Geochemical Behavior

Barium is a refractory element with a 50% nebular condensation temperature of 1455 K. It is also a lithophile element and consequently its abundance in the silicate Earth relative to other such elements should be the same as in chondritic meteorites. As a consequence of its large ionic radius, it is a highly incompatible element and one of the large ion lithophile elements that cannot be readily accommodated in most igneous minerals. Biotite, alkali feldspar, and apatite are principal exceptions and the principal hosts of Ba in granitic rocks. As a result, Ba is strongly concentrated in the Earth's continental crust relative to the mantle. Barium is also a

W. M. White (ed.), *Encyclopedia of Geochemistry*,
https://doi.org/10.1007/978-3-319-39312-4

relatively fluid-mobile element and abundances in igneous rocks are readily disturbed by weathering and metamorphism. High concentrations of Ba relative to fluid-immobile incompatible elements such as Th and La in subduction-related magmas provide evidence of the role fluids as well as subducted sediments in such magmatism (Kay 1980; Plank (2016), ▶ "Subduction Zone Geochemistry," this volume).

Barite is a common but minor component of many sedimentary rocks and hydrothermal deposits. Witherite ($BaCO_3$) is a rare mineral associated with low temperature hydrothermal deposits. Benitoite ($BaTiSi_3O_9$) is a very rare mineral occurring in association with blueschist facies metamorphic rocks.

In the oceans, Ba is present as the Ba^{2+} ion and has a nutrient-like distribution with low concentrations (35–45 nM) in surface waters and higher concentrations (~100–200 nM) in deep water, and an average concentration of 110 nM (Chan et al. 1976, 1977; DeBaar et al. (in press), ▶ "Ocean Biochemical Cycling and Trace Elements," this volume). However, Ba is not bioutilized nor does it appear to be taken up by phytoplankton. Rather it appears that Ba is precipitated as barite in microenvironments associated with decaying organic matter and opal in surface waters, despite general undersaturation (Bishop 1988; McManus et al. 1998). Absorption on particulate matter may also contribute to Ba removal in surface waters. Barium is then partially remobilized in deep water. As is true for nutrients, this results in Pacific and Indian deep waters, which are relatively old, being richer in Ba than the young deep waters of the Atlantic Ocean. While Ba is cycled internally in the ocean, its residence time is long, ~10,000 years (Chan et al. 1976), compared to bioutilized elements, although much shorter than conservative elements.

Despite partial redissolution in deep water, barite is a common component of marine sediments. Marine sediment Ba concentrations vary from several hundred ppm to over 2500 ppm and are highest beneath regions of high biological productivity. Dymond et al. (1992) suggested Ba in sediments might make a useful proxy for paleoproductivity; however, McManus et al. (1998) showed that under suboxic diagenetic conditions, which are common where biological productivity is high, Ba can be mobilized and diffuse out of sediments. Ba/Ca ratios in corals have been used to reconstruct changes in the upwelling of nutrient-rich deep waters and coastal waters (e.g., Lea et al. 1989; LaVigne et al. 2016).

Barium Isotopes

^{138}Ba is produced by radioactive decay of ^{138}La, but the fraction of radiogenic ^{138}Ba is almost always trivial as a consequence of very high $^{138}Ba/^{138}La$ ratio in terrestrial and meteoric materials and the long half-life of ^{138}La (~10^{11} years). Thus, there have been very few studies of this decay system, with the focus instead on Ce isotopes as ^{138}Ce is also produced by ^{138}La decay. Andreasen and Sharma (2007) and Carlson found that carbonaceous chondrites are slightly enriched in r-process (rapid neutron capture) nuclides ^{135}Ba and ^{137}Ba produced in supernovae compared to the Ba in ordinary chondrites and terrestrial materials. Moynier et al. (2015) found small mass-dependent fractionations among chondrite components, but found that all whole-rock terrestrial igneous and meteorite samples were isotopically identical within 50 ppm per atomic mass unit. More recently, Seibert and Munker (2017) reported small but significant variations in $\delta^{134/137}Ba$ in subduction-related volcanics.

Several studies have found significant mass-dependent fractionation of Ba isotopes in seawater, with $\delta^{138/134}Ba$ in deep waters 0.3–0.4‰ lower than surface waters (Horner et al. 2015; Hsieh and Henderson 2017) as a consequence of preferential incorporation of absorption of light isotopes on particulates in surface waters. This process maintains seawater $\delta^{138/134}Ba$ that is several tenths of per mil heavier than river water (Cao et al. 2016; Hsieh and Henderson 2017).

Biological Utilization and Toxicity

Barium has no known biological function and is toxic; ingestion or exposure can lead to a large number of adverse health effects including serious adverse neurological, cardiovascular, and gastrointestinal effects. Toxicity likely results from its biochemical similarity to potassium and consequent interference with potassium ion regulation. The no-observed-adverse-effect level (NOAEL) in humans is estimated to be 0.21 mg barium/kg body weight per day (Choudhury and Cary 2001). Because of its insolubility, barite represents a lesser hazard than other forms of Ba.

Summary

Society has found only limited uses for Ba, but it has proved quite useful to geochemists in understanding a range of phenomena including subduction zone volcanism and ocean circulation. The limited studies of Ba isotopes to date suggest that they have potential as a tracer of the carbon cycle and ocean in both modern and ancient oceans.

Cross-References

▶ Alkali and Alkaline Earth Metals
▶ Atomic Number, Mass Number, and Isotopes
▶ Chondrites

▶ Geochemical Classification of Elements
▶ Incompatible Elements
▶ Large-Ion Lithophile Elements
▶ Lithophile Elements
▶ Meteorites
▶ Nucleosynthesis
▶ Ocean Biochemical Cycling and Trace Elements
▶ Stable Isotope Geochemistry
▶ Subduction Zone Geochemistry
▶ Trace Elements

References

Andreasen R, Sharma M (2007) Mixing and homogenization in the early solar system: clues from Sr, Ba, Nd, and Sm isotopes in meteorites. Astrophys J 665(1):874

Bishop JKB (1988) The barite-opal-organic carbon association in oceanic particulate matter. Nature 332:341–343. https://doi.org/10.1038/332341a0

Cao Z, Siebert C, Hathorne EC, Dai M, Frank M (2016) Constraining the oceanic barium cycle with stable barium isotopes. Earth Planet Sci Lett 434:1–9. https://doi.org/10.1016/j.epsl.2015.11.017

Carlson RW, Boyet M, Horan M (2007) Chondrite barium, neodymium, and samarium isotopic heterogeneity and early Earth differentiation. Science 316(5828):1175–1178. https://doi.org/10.1126/science.1140189

Chan LH, Edmond JM, Stallard RF, Broecker WS, Chung YC, Weiss RF, Ku TL (1976) Radium and barium at GEOSECS stations in the Atlantic and Pacific. Earth Planet Sci Lett 32:258–267

Chan LH, Drummond D, Edmond JM, Grant B (1977) On the barium data from the Atlantic GEOSECS expedition. Deep-Sea Res 24:613–649

Choudhury H, Cary R (2001) Barium and barium compounds. World Health Organization concise international chemical assessment document 33. World Health Organization, Geneva. Retrieved from http://apps.who.int/iris/bitstream/10665/42398/1/9241530332.pdf

Dymond J, Suess E, Lyle M (1992) Barium in deep-sea sediment: a geochemical proxy for paleoproductivity. Paleoceanography 7(2):163–181. https://doi.org/10.1029/92PA00181

Horner TJ, Kinsley CW, Nielsen SG (2015) Barium-isotopic fractionation in seawater mediated by barite cycling and oceanic circulation. Earth Planet Sci Lett 430:511–522. https://doi.org/10.1016/j.epsl.2015.07.027

Hsieh Y-T, Henderson GM (2017) Barium stable isotopes in the global ocean: tracer of Ba inputs and utilization. Earth Planet Sci Lett 473:269–278. https://doi.org/10.1016/j.epsl.2017.06.024

Kay RW (1980) Volcanic arc magmas: implications of a melting-mixing model for element recycling in the crust-upper mantle system. J Geol 88(5):497–522. https://doi.org/10.2307/30066081

LaVigne M, Grottoli AG, Palardy JE, Sherrell RM (2016) Multi-colony calibrations of coral Ba/Ca with a contemporaneous in situ seawater barium record. Geochim Cosmochim Acta 179:203–216. https://doi.org/10.1016/j.gca.2015.12.038

Lea DW, Shen GT, Boyle EA (1989) Coralline barium records temporal variability in equatorial Pacific upwelling. Nature 340(6232):373–376

McManus J, Berelson WM, Klinkhammer GP, Johnson KS, Coale KH, Anderson RF, Kumar N, Burdige DJ, Hammond DE, Brumsack HJ, McCorkle DC, Rushdi A (1998) Geochemistry of barium in marine sediments: implications for its use as a paleoproxy. Geochim Cosmochim Acta 62(21):3453–3473. https://doi.org/10.1016/S0016-7037(98)00248-8

Moynier F, Pringle EA, Bouvier A, Moureau J (2015) Barium stable isotope composition of the Earth, meteorites, and calcium–aluminum-rich inclusions. Chem Geol 413:1–6. https://doi.org/10.1016/j.chemgeo.2015.08.002

Plank T (2014) The chemical composition of subducting sediments. In: Turekian KK, Holland HD (eds) Treatise on geochemistry, vol 4, 2nd edn. Elsevier, Oxford, pp 607–629. https://doi.org/10.1016/B978-0-08-095975-7.00319-3

Siebert C, Munker C (2017) Barium isotope fractionation during subduction zone processes. Presented at 2017 Goldschmidt conference, Paris

Beryllium

Jeffrey G. Ryan
School of Geosciences, University of South Florida, Tampa, FL, USA

Element Data

Atomic Symbol: Be
Atomic Number: 4.
Atomic Weight: 9.01218.
Stable Isotope: ^{9}Be (9.0121822 amu): 100%; Relevant Radioisotopes: ^{10}Be ($t_{1/2} \approx 1.38$ Ma), ^{7}Be ($t_{1/2} \approx 53.28$ days)
1 Atm Melting Point: 1287 °C
1 Atm Boiling Point: 2471 °C
Valence: +2.
Ionic Radius: 0.41 Å (tetrahedral); 0.59 Å (octahedral)
Pauling Electronegativity: 1.57
First Ionization Potential: 9.322
CI Chondritic Abundance: 0.025 ppm
Continental Crust: 1.9 ppm
Silicate Earth: 0.07 ppm
Seawater: 0.0018 pg/g
Core Abundance: ~0
(Earthref.org 2016; McDonough 2004; Palme et al. 2014)

Properties

Beryllium, the lowest atomic number alkaline earth element, is a steel-gray, brittle, lightweight metal. It is most commonly encountered in a small number of silicate and oxide minerals and occurs as a low abundance, lithophile trace element in most geologic systems.

History and Use

Beryllium was discovered by Louis-Nicolas Vauquelin in 1798 in the oxide form via extraction from emerald and beryl. In 1828, Friedrich Wohler and Antoine Bussy independently isolated Be metal via reaction between potassium and $BeCl_2$. As a low density, high-strength metal, Be is commonly used in metal alloys, in particular in beryllium copper, which is used in non-sparking tools, golf clubs, springs, as well as in a range of structural applications in aircraft, spacecraft, and satellites. It is transparent to X-rays and as such is used as X-ray window material in analytical instruments such as electron microprobes. Its small thermal neutron capture cross-section makes it useful as a moderator in nuclear reactors (Trujillo et al. 2011).

Geochemical Behavior

Beryllium abundances in the solar system and in meteorites are low, consistent with its origins as an element that was not formed during the Big Bang, and is destroyed by nucleosynthetic processes in the interiors of stars. Beryllium forms only via late-stage cosmic ray spallation reactions in the interstellar medium (Stegman and Walker 1992; Shearer 2002). During nebular condensation, Be is incorporated into early, Ca-Al rich phases as a refractory trace element (Lauretta and Lodders 1997). In terms of its geochemical behavior, Be shows systematics less like those of alkaline earth elements and more like that of Al (Grew 2002). In aqueous systems, Be is consistently low in abundance, albeit with some variation: Be abundances in ridgecrest hydrothermal fluids are enriched by a factor of 10^3 over seawater (0.09–0.8 ng/g vs. 0.2 pg/g Be; Measures and Edmond 1982), though even enriched hydrothermal solutions are 10^3 times lower in Be than terrestrial rocks.

Be abundances in mid-ocean ridge basalts (MORBs) and basalts from volcanic arcs range from 0.1 to 1.0 ppm; basalts from intraplate settings are an order of magnitude higher in Be, ranging from 0.8 to >10 ppm (Ryan and Langmuir 1988; Ryan 2002; Ryan and Kyle 2004). Differentiated arc lavas, marine sediments, and crustal rocks range from 1 to 3 ppm Be (Ryan 2002), consistent with recent estimates for Be in the continental crust (e.g., Rudnick and Gao 2014). During magmatic and hydrothermal processes, Be shows strong similarities in its mineral/melt distribution patterns to neodymium, with an inferred partition coefficient, D_{Be}, between 0.03 and 0.06 for basaltic melting and crystallization; however, in terms of ionic radius, Be^{2+} is closest to Al^{3+} and appears to substitute for Al in crystal lattices. D_{Be} is ≈0.3 for plagioclase, 0.05 for pyroxene, and <0.003 for olivine in basalts, while in more siliceous magmas D_{Be} approaches 1.0 for all phases (Monaghan et al. 1988; Brenan et al. 1998; Ryan 2002). The most economically significant beryllium mineral is beryl ($Be_3Al_2[Si_6O_{18}]$), which is found commonly in pegmatites and less frequently in metamorphic associations. Emerald, aquamarine, and morganite are, respectively, deep green, pale blue–green, and pink gem varieties of beryl. Other beryllium minerals of note are chrysoberyl ($BeA1_2O_4$), bertrandite ($Be_4Si_2O_7(OH)_2$), and phenakite (Be_2SiO_4) (Grew 2002).

Isotopic Systematics

Beryllium has only one stable isotope, ^{9}Be. However, the cosmogenic radionuclides ^{10}Be and ^{7}Be have become important as tracers for a wide variety of geologic, environmental, and cosmochemical processes. Variations in atmospherically produced ^{10}Be, which is concentrated in sediments at the Earth's surface, have been used to study marine sedimentary processes (i.e., the dating of sediments and studies of sedimentary rates or rates of growth for marine Mn nodules); soil development and erosion; and climate change, while ^{7}Be is used to trace short-term (<1 year duration) processes at the Earth's surface (Bierman et al. 2002; Morris et al. 2002; Kaste et al. 2002). In situ ^{10}Be production and decay rates have been used to estimate weathering rates on bare rock surfaces, as well as to estimate cosmic ray exposure ages (and thereby solar system travel times) for silicate meteorites (Morris et al. 2002). Significant ^{10}Be abundances have also been observed in fresh, zero-age lavas from several volcanic arcs and are believed to reflect chemical inputs to arc source regions from subducted marine sediments (Tera et al. 1986).

Biological Utilization and Toxicity

Beryllium compounds are generally toxic to humans. Inhalation of Be or its compounds can lead to chronic beryllium disease, a debilitating lung disorder, with no minimum "safe" level for exposure (Taylor et al. 2003).

Cross-References

- ▶ Alkali and Alkaline Earth Metals
- ▶ Beryllium Isotopes
- ▶ Cosmogenic Nuclides
- ▶ Lithophile Elements
- ▶ Nucleosynthesis
- ▶ Partitioning and Partition Coefficients
- ▶ Trace Elements

References

Bierman PR, Caffee MW, Davis PT, Marsella K, Pavich M, Colgan P, Mickelson D, Larsen J (2002) Rates and timing of earth surface processes from in situ-produced cosmogenic Be-10. In: Grew E (ed) Beryllium: mineralogy, petrology and geochemistry, Reviews in mineralogy and geochemistry, vol 50. Mineralogical Society of America, Washington, DC, pp 147–205

Brenan JM, Neroda E, Lundstrom CC, Shaw HF, Ryerson FJ, Phinney DL (1998) Behavior of boron, beryllium and lithium during melting and crystallization: constraints from mineral-melt partitioning experiments. Geochim Cosmochim Acta 62:2129–2141

Earthref.org (2016) Geochemical Earth Reference Model (GERM). https://earthref.org/GERM/

Grew ES (2002) Mineralogy, petrology and geochemistry of beryllium: an introduction and list of beryllium minerals. In: Grew E (ed) Beryllium: mineralogy, petrology and geochemistry, Reviews in mineralogy and geochemistry, vol 50. Mineralogical Society of America, Washington, DC, pp 1–76

Kaste JM, Norton SA, Hess CT (2002) Environmental chemistry of beryllium-7. In: Grew E (ed) Beryllium: mineralogy, petrology and geochemistry, Reviews in mineralogy and geochemistry, vol 50. Mineralogical Society of America, Washington, DC, pp 271–289

Lauretta DS, Lodders K (1997) The cosmochemical behavior of beryllium and boron. Earth Planet Sci Lett 146:315–327

McDonough W (2004) Compositional model of the Earth's core, Chapter 3.16. In: Treatise on geochemistry. Elsevier, Amsterdam, pp 559–577

Measures CI, Edmond JM (1982) The geochemical cycle of 9Be: a reconnaissance. Earth Planet Sci Lett 66:101–110

Monaghan MC, Klein J, Measures CI (1988) The origin of ^{10}Be in island arc volcanic rocks. Earth Planet Sci Lett 89:288–298

Morris JD, Gosse J, Brachfield S, Tera F (2002) Cosmogenic 10-Be and the solid earth: studies in geomagnetism, subduction zone processes, and active tectonics. In: Grew E (ed) Beryllium: mineralogy, petrology and geochemistry, Reviews in mineralogy and geochemistry, vol 50. Mineralogical Society of America, Washington, DC, pp 207–270

Palme H, Lodders K, Jones A (2014) Solar system abundances of the elements, Chapter 2.2. In: Holland HD, Turekian KK (eds) Treatise on geochemistry. Elsevier, Amsterdam, pp 15–36

Rudnick RL, Gao S (2014) Composition of the continental crust, Chapter 4.13. In: Holland HD, Turekian KK (eds) Treatise on geochemistry. Elsevier, Amsterdam, pp 1–51

Ryan JG (2002) Trace element systematics of beryllium in natural materials. In: Grew E (ed) Beryllium: mineralogy petrology and geochemistry, Reviews in mineralogy and geochemistry, vol 50. Mineralogical Society of America, Washington, DC, pp 121–145

Ryan JG, Kyle PR (2004) Lithium and lithium isotope variations in intraplate mantle sources: insights from McMurdo Group lavas (Mt. Erebus) and other intraplate volcanic rocks. Chem Geol 212:125–142

Ryan JG, Langmuir CH (1988) Beryllium systematics in young volcanic rocks: implications for ^{10}Be. Geochim Cosmochim Acta 52:237–244

Shearer CK (2002) Behavior of beryllium during solar system and planetary evolution: evidence from planetary materials. In: Grew E (ed) Beryllium: mineralogy petrology and geochemistry, Reviews in mineralogy and geochemistry, vol 50. Mineralogical Society of America, Washington, DC, pp 78–120

Stegman G, Walker TP (1992) Production of Li, Be, and B in the early galaxy. Astrophys J 385:L13–L16

Taylor TP, Ding M, Ehler DS, Foreman TM, Kaszuba JP, Sauer NN (2003) Beryllium in the environment: a review. J Environ Sci Health A Tox Hazard Subst Environ Eng 38(2):439–469

Tera F, Brown L, Morris J, Sacks IS, Klein J, Middleton R (1986) Sediment incorporation in island-arc magmas: inferences from ^{10}Be. Geochim Cosmochim Acta 50:535–550

Trujillo M, Hobart D, Smith J (2011) Beryllium. In: Periodic table of the elements. Online resource. Los Alamos National Laboratory. http://periodic.lanl.gov/4.shtml

B

Beryllium Isotopes

Paul R. Bierman[1] and Eric W. Portenga[2]

[1]Department of Geology, University of Vermont, Burlington, VT, USA

[2]Department of Geography and Geology, Eastern Michigan University, Ypsilanti, MI, USA

Definition

Beryllium (atomic number 4) has twelve isotopes, but only three are routinely measured: ^{7}Be, ^{9}Be, and ^{10}Be. ^{9}Be is a stable isotope that is found naturally in geological materials typically at $\mu g\ g^{-1}$ levels and is considered in the ▶ Beryllium chapter. ^{7}Be is a short-lived radionuclide ($t_{1/2} = 53$ days) and ^{10}Be is a long-lived radionuclide ($t_{1/2} = 1.38$ Myr) produced both in the atmosphere and in earth materials by cosmic-ray interactions. ^{10}Be produced in the atmosphere is termed "meteoric" ($^{10}Be_m$), whereas *in situ* ^{10}Be ($^{10}Be_i$) is produced within geological materials primarily within the uppermost few meters of Earth's surface (Lal 1988). Although both ^{7}Be and ^{10}Be have been used in geological, geomorphological, and geographical studies, we focus here on ^{10}Be. We consider both $^{10}Be_i$ and $^{10}Be_m$; $^{10}Be_i$ has been used to solve many more problems in Earth Science than $^{10}Be_m$, and our review reflects this.

^{7}Be Production, Delivery, and Analysis

^{7}Be is produced in the atmosphere by spallation reactions and delivered to Earth's surface with precipitation and as dry fallout. It is particle-reactive and thus sorbed to particle surfaces and incorporated in grain coatings which are stable at neutral and basic pH. As a result, ^{7}Be is often used to monitor very short-term sediment transport down hillslopes and in drainage networks (Wallbrink and Murray 1993) and as a tracer of air movement in the atmosphere and water movement in the oceans. ^{7}Be is usually measured by decay counting, but recently it has been measured by accelerator mass spectrometry (AMS). Because of ^{7}Be's very short half-life in comparison to ^{10}Be, it is of limited utility in studying all but the shortest near-surface processes and thus not

considered further in this review. We refer the reader to other papers for more information on ^{7}Be (e.g., Kaste et al. 2002; Landis et al. 2012).

^{10}Be Production and/or Delivery

Primary cosmic rays, mostly protons, enter Earth's atmosphere where many are deflected by Earth's magnetosphere. Protons that penetrate the atmosphere interact with atmospheric gases by spallation reactions, producing a variety of cosmogenic nuclides (e.g., ^{14}C, ^{7}Be, ^{10}Be$_{m}$) as well as a cascade of secondary neutrons that attenuate with increasing atmospheric depth and interact with rock and sediment at Earth's surface (Lal and Peters 1967); as a result, the production of ^{10}Be$_{i}$ at Earth's surface varies with latitude and elevation (Lal 1988). Production rates of ^{10}Be$_{i}$ have been estimated using both models and empirical measurements made in surfaces of otherwise known age (Borchers et al. 2016). These rates are scaled to different latitudes and elevations using a variety of schemes, both model-based and empirical (e.g., Lal 1991; Stone 2000). The delivery rate of ^{10}Be$_{m}$ depends on atmospheric production, mixing, rainout by precipitation, and dry fallout (Graly et al. 2011; Heikkilä et al. 2008) and has been estimated by measurements of samples from otherwise dated surfaces (Reusser et al. 2010).

^{10}Be$_{i}$ production decreases with depth in earth surface materials according to the material density and the attenuation length of cosmic ray neutrons (160 g cm^{-2}; Gosse and Phillips 2001); the only nuclide production at depths greater than a few meters is by muons which have many times longer attenuation lengths than neutrons and induce little nuclide production relative to spallogenic production of ^{10}Be$_{i}$ (Heisinger et al. 1997). ^{10}Be$_{i}$ accumulates in rock and soil on landscapes, and nuclide production is eventually balanced by nuclide loss due both to radioactive decay and surface erosion.

Sample Selection, Preparation, and Measurement

The near-ubiquity of the mineral quartz (SiO_2) in rocks at Earth's surface, its simple chemical formula, and its resistance to physical and chemical weathering make it an ideal mineral from which ^{10}Be$_{i}$ can be isolated and measured. Weak acid etches and sometimes heavy-liquid density separations remove carbonate and nonquartz minerals so as to isolate and purify quartz (Kohl and Nishiizumi 1992), which is dissolved in HF after ^{9}Be-carrier solution is added. Anion- and cation-exchange column chemistry isolates beryllium from solution (Corbett et al. 2016). ^{10}Be$_{m}$ can be removed from any substrate using either acid leaching or total fusion (Barg et al. 1997; Stone 1998).

AMS is required for ^{10}Be measurements because it can reliably separate the common isobar, ^{10}B. ^{10}Be/^{9}Be ratios of process blanks (e.g., only ^{9}Be-carrier) are measured and used for background correction. All ratio measurements are normalized to standard materials with consensus ^{10}Be/^{9}Be ratios; the nominal ratios of standards have changed over time in part because of changes in the accepted half-life of ^{10}Be (Nishiizumi et al. 2007); thus, most ^{10}Be data published prior to 2008 require recalculation. It is assumed that purified quartz contains no ^{9}Be; however, some samples include naturally occurring ^{9}Be which must be quantified or calculations will be inaccurate (Portenga et al. 2015).

Applications of In Situ ^{10}Be

Exposure Dating

The concentration of ^{10}Be$_{i}$ in rock and sediment exposed at Earth's surface can be used to calculate a duration of rock exposure – an exposure age – if the following assumptions are met: (1) the surface has not eroded since initial exposure, (2) the surface has not been buried after initial exposure, and (3) the exposed surface did not inherit any ^{10}Be$_{i}$ from one or more prior periods of exposure. Exposure ages are useful because they allow dating of landforms which cannot be dated by other means; primarily, exposure ages have been measured on boulders to date ice cap, ice sheet, and alpine glacial moraines around the world. Interpretation of boulder ages as the age of the underlying moraine is not always straightforward because both the boulders and the moraines on which they sit erode, lowering measured exposure ages. Alternatively, boulders can carry ^{10}Be$_{i}$ from prior periods of exposure; in this case, calculated exposure ages can overestimate the age of the landform (Briner et al. 2016; Heyman et al. 2011).

Paleoseismic studies have benefited from ^{10}Be$_{i}$ measurements. Fault scarps have been directly dated and the dates used to calculate rates of offset (Bierman et al. 2014). Numerical ages of offset surfaces have been determined using ^{10}Be$_{i}$ and those surfaces then used as strain gauges (Matmon et al. 2005). Rock falls likely related to paleo-earthquakes have been dated (Rinat et al. 2014) as have precariously balanced rocks which, through the application of numerical models, have been used to constrain maximum prior ground motion (Balco et al. 2011).

Terraces, both riverine and coastal, have been dated with ^{10}Be$_{i}$ using several different approaches. For bedrock strath terraces, outcrops can be dated directly (Reusser et al. 2006) and incision rates calculated. For alluvial terraces, depth

profiles can be measured and the inherited $^{10}Be_i$ estimated from samples collected at depth (Anderson et al. 1996).

Erosion Rate Estimates

If a rock outcrop surface has experienced constant erosion as it is exhumed through the uppermost few meters of Earth's surface, the production of ^{10}Be in that rock is balanced by nuclide loss through radioactive decay and erosion (Lal 1991). Thus, the rate of rock erosion can be deduced from the measured $^{10}Be_i$ concentrations, which are inversely proportional to erosion rate. Important assumptions inherent in this method are that (1) the erosion rate is constant in time, (2) the rock surface from which a sample is collected has a simple exposure history and has not been episodically buried for any significant amount of time prior to sample collection, and (3) erosion is by granular disintegration of the rock surface and not by removal of decimeter-scale rinds or slabs. Measuring $^{10}Be_i$ in outcrop samples gives erosion rates for points on a landscape and may not be representative of regional landscape erosion. Landscape-wide erosion rates have been derived by measuring $^{10}Be_i$ in sand collected from stream channels, a technique that assumes that the $^{10}Be_i$ in river sand is representative of $^{10}Be_i$ eroded from all quartz-bearing lithologies upstream of the sample collection site (Brown et al. 1995).

The bedrock and fluvial sediment techniques of measuring erosion rates have been used to assess landscape dynamics in a variety of landscapes around the world (Portenga and Bierman 2011). For example, $^{10}Be_i$ erosion rates have been used to assess landscape stability and relief generation (Bierman et al. 2014), infer uplift along tectonic, climate, and vegetation gradients (e.g., Olen et al. 2016), to understand passive margin escarpment retreat (Vanacker et al. 2007), and to assess the impact of human land use on landscapes (Portenga et al. 2016; Reusser et al. 2015).

Techniques have been devised to measure paleo-erosion rates of river catchments (Schaller et al. 2004). Deriving paleo-erosion rates relies on knowing the burial age of sediment from which quartz is extracted and the accumulation rate of sediment overlying any given sample. With this knowledge, the amount of $^{10}Be_i$ lost to radioactive decay can be determined as well as the amount of $^{10}Be_i$ produced during sample burial.

Landscape History and Sediment Tracing

$^{10}Be_i$ can also be used to infer landscape histories and to trace the movement of sediment across Earth's surface and the source of such sediment. In Greenland, Nelson et al. (2014) measured $^{10}Be_i$ in both glacial and fluvial sediment and used the measured concentrations to suggest that most of the sediment shed from Greenland today originated from under the ice sheet and not from deglaciated areas outside the ice margin. Bierman et al. (2016) used Nelson et al.'s results in conjunction with $^{10}Be_i$ measurements in quartz isolated from 7.5 Myr of marine sediment off the coast of Greenland to demonstrate a long history of erosion and ice cover on the continent. Perg et al. (2003) used $^{10}Be_i$ concentrations to identify the source of sediment in the littoral zone along California's Pacific coast, whereas Nichols et al. (2007) did the same in the Mojave Desert working out a sediment budgets for an arid region sediment system and thereby calculating sediment residence times (many kyr) and virtual sediment velocity (dm/yr) down desert piedmonts.

In many landscapes, erosion rates calculated from the measured concentration of $^{10}Be_i$ in river sediment are compared to the present-day rate of sediment export from watersheds to assess the impact of human land use. Such comparisons often show contemporary rates of sediment yield exceed long-term rates of sediment generation (Hewawasam et al. 2003) although there are situations where contemporary sediment yield is lower than long-term rates (Kirchner et al. 2001) likely because infrequent but large-magnitude sediment transport events are missing from the contemporary record.

By sampling rock and saprolite below soil cover, $^{10}Be_i$ has been used to estimate soil production functions – the rate at which rock weathers to soil parent material under different thicknesses of regolith. Such functions have been defined so far in North America and Australia and typically show the highest soil production rates at intermediate depths of regolith cover (Heimsath et al. 2009).

Applications of Meteoric ^{10}Be

$^{10}Be_m$ is typically present in concentrations orders of magnitude higher than the concentration of $^{10}Be_i$ and was thus measured more frequently during the early years of AMS. Initial applications of $^{10}Be_m$ were focused on estimating erosion rates and ages of soils (Pavich et al. 1984). Soon, improvements in AMS detection limits and questions about the retention of $^{10}Be_m$ in soils (Monaghan et al. 1983) slowed the pace of $^{10}Be_m$ research. Since 2010, $^{10}Be_m$ has undergone a renaissance, with numerous different applications.

$^{10}Be_m$ has been used to estimate the rate at which fine-grained soil moves down hillslopes. McKean et al. (1993) developed the first interpretive model that allowed $^{10}Be_m$ measured in hillslope soils to be interpreted as a sediment transport rate. His work in California was followed by similar sampling and analysis in the eastern United States which examined slope-aspect dependence of sediment transport and production in Pennsylvania (West et al. 2013) as well as comparing $^{10}Be_m$ to $^{10}Be_i$ in soils of the southern Appalachian Mountains (Jungers et al. 2009).

In the absence of quartz-bearing lithologies, some suggest that landscape dynamics may be assessed by normalizing measured concentrations of $^{10}Be_m$ to that of the reactive phase of ^{9}Be, both of which are adhered to the surfaces of sediment grains in streams (von Blackenburg et al. 2012). This technique requires representative concentration estimates of $^{10}Be_m$ in sediment grain coatings, ^{9}Be in parent bedrock sources, ^{9}Be weathered from minerals and adhered to sediment grain coatings, and ^{9}Be weathered from minerals and dissolved in stream water. Making such estimates is not trivial and may require many measurements collected over the course of many years. The ratio of $^{10}Be_m$ to ^{9}Be dissolved in sea water has been used as a proxy for terrigenous mass fluxes to global oceans (von Blackenburg and Bouchez 2014). Data from these studies suggest that late-Cenozoic global climate change has not significantly altered the magnitude of continental weathering processes on a global scale.

Human impacts on landscapes have been examined using $^{10}Be_m$. Brown et al. (1988) used $^{10}Be_m$ measurements in fluvial sediment to develop a mass and isotope balance approach, termed the erosion index, to understand land-use impacts in the eastern North America at the watershed scale. More recently, Reusser and Bierman (2010) used $^{10}Be_m$ as a sediment tracer to show downstream dilution of sediment released from a mega-landslide exacerbated by deforestation, and Portenga et al. (2017) paired measurements of $^{10}Be_m$ with bulk sediment luminescence to identify sediment sources and trace sediment transport in a gully-affected landscape.

$^{10}Be_m$ has been used at the plate tectonic scale to understand better the source and timescale of melt generation and igneous rock formation in subduction zones and to show that sediment can be subducted to mantle depths. Down-going oceanic slabs are covered with a mantle of marine sediment rich in $^{10}Be_m$. This hydrous material either melts or releases $^{10}Be_m$ in solution such that it enters magma. If transit times are short enough (less than several ^{10}Be half-lives), ^{10}Be can be measured in rock samples collected at Earth's surface (Morris et al. 2002).

Summary and Conclusions

Advances in ^{10}Be isotope extraction, analysis, and data interpretation over the last three decades have allowed Earth Scientists to study the processes that shape Earth's surface over hundreds to tens of thousands of years. Few other geological techniques operate over centennial-millennial timescales; thus, ^{10}Be bridges the knowledge gap between periods of historical observation and geological timescales. The examples of ^{10}Be applications in Earth Sciences presented above are by no means a comprehensive summary of the literature. What these examples do illustrate, however, is the wide variety of questions and topics that can be addressed with ^{10}Be. In time, this broadening of applications and consideration of new and different approaches beyond simple exposure ages, and erosion rates will allow an even greater understanding of the Earth system.

Cross-References

- Atomic Number, Mass Number, and Isotopes
- Beryllium
- Boron
- Cosmogenic Nuclides
- Geochronology and Radiogenic Isotopes
- Incompatible Elements
- Low-Temperature Geochemistry
- Soils
- Subduction Zone Geochemistry
- Trace Elements

References

Anderson RS, Repka JL, Dick GS (1996) Explicit treatment of inheritance in dating depositional surfaces using in situ ^{10}Be and ^{26}Al. Geology 24:47–51

Balco G, Purvance MD, Rood DH (2011) Exposure dating of precariously balanced rocks. Quat Geochronol 6(3–4):295–303

Barg E, Lal D, Pavich MJ, Caffee MW, Southon JR (1997) Beryllium geochemistry in soils: evaluation of $^{10}Be/^{9}Be$ ratios in authigenic minerals as a basis for age models. Chem Geol 140(3–4):237–258

Bierman PR, Coppersmith R, Hanson K, Neveling J, Portenga EW, Rood DH (2014) A cosmogenic view of erosion, relief generation, and the age of faulting in southern Africa. GSA Today 24(9):4–10

Bierman PR, Shakun JD, Corbett LB, Zimmerman SR, Rood DH (2016) A persistent and dynamic East Greenland Ice Sheet over the past 7.5 million years. Nature 540(7632):256–260

Borchers B, Marrero S, Balco G, Caffee M, Goehring B, Lifton N, Nishiizumi K, Phillips F, Schaefer J, Stone J (2016) Geological calibration of spallation production rates in the CRONUS-Earth project. Quat Geochronol 31:188–198

Briner JP, Goehring BM, Mangerud J, Svendsen JI (2016) The deep accumulation of ^{10}Be at Utsira, southwestern Norway: implications for cosmogenic nuclide exposure dating in peripheral ice sheet landscapes. Geophys Res Lett 43:9121–9129

Brown L, Pavich MJ, Hickman RE, Klein J, Middleton R (1988) Erosion of the eastern United States observed with ^{10}Be. Earth Surf Process Landf 13:441–457

Brown ET, Stallard RF, Larsen MC, Raisbeck GM, Yiou F (1995) Denudation rates determined from the accumulation of in situ-produced ^{10}Be in the luquillo experimental forest, Puerto Rico. Earth Planet Sci Lett 129:193–202

Corbett LB, Bierman PR, Rood DH (2016) An approach for optimizing in situ cosmogenic ^{10}Be sample preparation. Quat Geochronol 33:24–34

Gosse JC, Phillips FM (2001) Terrestrial in situ cosmogenic nuclides: theory and application. Quat Sci Rev 20(14):1475–1560

Graly JA, Reusser LJ, Bierman PR (2011) Short and long-term delivery rates of meteoric ^{10}Be to terrestrial soils. Earth Planet Sci Lett 302(3):329–336

Heikkilä U, Beer J, Alfimov V (2008) Beryllium-10 and beryllium-7 in precipitation in Dubendorf (440 m) and at Jungfraujoch (3580 m), Switzerland (1998–2005). J Geophys Res Atmos 113(D11):D11104

Heimsath AM, Fink D, Hancock GR (2009) The "humped" soil production function: eroding Arnhem Land, Australia. Earth Surf Process Landf 34:1674–1684

Heisinger B, Niodermayer M, Hartmann FJ, Korschinek G, Nolte E, Morteani G, Neumaier S, Patitjean C, Kubik P, Synal A, Ivy-Ochs S (1997) In-situ production of radionuclides at great depths. Nucl Inst Methods Phys Res B 123:341–346

Hewawasam T, von Blackenburg F, Schaller M, Kubik P (2003) Increase of human over natural erosion rates in tropical highlands constrained by cosmogenic nuclides. Geology 31(7):597–600

Heyman J, Stroeven AP, Harbor JM, Caffee MW (2011) Too young or too old: evaluating cosmogenic exposure dating based on an analysis of compiled boulder exposure ages. Earth Planet Sci Lett 302(1-2):71–80

Jungers MC, Bierman PR, Matmon A, Nichols K, Larsen J, Finkel R (2009) Tracing hillslope sediment production and transport with in situ and meteoric ^{10}Be. J Geophys Res Earth Surf 114(F04020):1–16

Kaste JM, Norton SA, Hess CT (2002) Environmental chemistry of Beryllium-7. Rev Mineral Geochem 50(1):271–289

Kirchner JW, Finkel RC, Riebe CS, Granger DE, Clayton JL, King JG, Megahan WF (2001) Mountain erosion over 10 yr, 10 k.y., and 10 m.y. time scales. Geology 29(7):591–594

Kohl CP, Nishiizumi K (1992) Chemical isolation of quartz for measurement of in-situ -produced cosmogenic nuclides. Geochim Cosmochim Acta 56:3583–3587

Lal D (1988) In situ-produced cosmogenic isotopes in terrestrial rocks. Annu Rev Earth Planet Sci 16:355–388

Lal D (1991) Cosmic ray labeling of erosion surfaces; in situ nuclide production rates and erosion models. Earth Planet Sci Lett 104(2–4):424–439

Lal D, Peters B (1967) Cosmic ray produced radioactivity on the earth. In: Sitte K (ed) Handbuch der Physik. Springer, New York, pp 551–612

Landis JD, Renshaw CE, Kaste JM (2012) Measurement of ^{7}Be in soils and sediments by gamma spectroscopy. Chem Geol 91:175–185

Matmon A, Schwartz DP, Finkel R, Clemmens S, Hanks T (2005) Dating offset fans along the Mojave section of the San Andreas fault using cosmogenic ^{26}Al and ^{10}Be. Geol Soc Am Bull 117(5–6):795

McKean JA, Dietrich WE, Finkel RC, Southon JR, Caffee MW (1993) Quantification of soil production and downslope creep rates from cosmogenic ^{10}Be accumulations on a hillslope profile. Geology 21(4):343–346

Monaghan MC, Krishnaswami S, Thomas JH (1983) ^{10}Be concentrations and the long-term fate of particle-reactive nuclides in five soil profiles from California. Earth Planet Sci Lett 65:51–60

Morris J, Valentine R, Harrison T (2002) ^{10}Be imaging of sedment accretion and subduction along the northeast Japan and Costa Rica convergent margins. Geology 30(1):59–62

Nelson AH, Bierman PR, Shakun JD, Rood DH (2014) Using in situ cosmogenic ^{10}Be to identify the source of sediment leaving Greenland. Earth Surf Process Landf 39(8):1087–1100

Nichols KK, Bierman P, Matmon A (2007) Deconvolving semi-arid landscape histories: insights from cosmogenic nuclides. Quat Int 167–168(3):305

Nishiizumi K, Imamura M, Caffee MW, Southon JR, Finkel RC, McAninch J (2007) Absolute calibration of ^{10}Be AMS standards. Nucl Inst Methods Phys Res B 258(2):403–413

Olen S, Bookhagen B, Strecker MR (2016) Role of climate and vegetation density in modulating denudation rates in the Himalaya. Earth Planet Sci Lett 445:57–67

Pavich MJ, Brown L, Klein J, Middleton R (1984) ^{10}Be accumulation in a soil chronosequence. Earth Planet Sci Lett 68:198–204

Portenga EW, Bierman PR (2011) Understanding Earth's eroding surface with 10Be. GSA Today 21(8):4–10

Perg LA, Anderson RS, Finkel RC (2003) Use of cosmogenic radionuclides as a sediment tracer in the Santa Cruz littoral cell, California, USA. Geology 31:299–302

Portenga EW, Bierman PR, Duncan C, Corbett LB, Kehrwald NM, Rood DH (2015) Erosion rates of the Bhutanese Himalaya determined using in situ-produced ^{10}Be. Geomorphology 233:112–126

Portenga EW, Rood DH, Bishop P, Bierman PR (2016) A late Holocene onset of Aboriginal burning in southeastern Australia. Geology 44(2):131–134

Portenga EW, Bishop P, Rood DH, Bierman PR (2017) Combining bulk sediment OSL and meteoric ^{10}Be fingerprinting techniques to identify gully initiation sites and erosion depths. J Geophys Res Earth Surf 122:513

Reusser LJ, Bierman PR (2010) Using meteoric ^{10}Be to track fluvial sand through the Waipaoa River basin, New Zealand. Geology 38(1):47–50

Reusser L, Bierman P, Pavich M, Larsen J, Finkel R (2006) An episode of rapid bedrock channel incision during the last glacial cycle, measured with ^{10}Be. Am J Sci 306(2):69–102

Reusser L, Graly J, Bierman P, Rood D (2010) Calibrating a long-term meteoric ^{10}Be accumulation rate in soil. Geophys Res Lett 37(19)

Reusser L, Bierman P, Rood D (2015) Quantifying human impacts on rates of erosion and sediment transport at a landscape scale. Geology 43(2):171–174

Rinat Y, Matmon A, Arnold M, Aumaître G, Bourlès D, Keddadouche K, Porat N, Morin E, Finkel RC (2014) Holocene rockfalls in the southern Negev Desert, Israel and their relation to Dead Sea fault earthquakes. Quat Res 81(2):260–273

Schaller M, von Blanckenburg F, Hovius N, Veldkamp A, van den Berg MW, Kubik PW (2004) Paleoerosion rates from cosmogenic Be-10 in a 1.3 Ma terrace sequence: Response of the river Meuse to changes in climate and rock uplift. J Geol 112(2):127–144

Stone J (1998) A rapid fusion method for separation of beryllium-10 from soils and silicates. Geochim Cosmochim Acta 62(3):555–561

Stone JO (2000) Air pressure and cosmogenic isotope production. J Geophys Res Solid Earth 105(B10):23753–23759

Vanacker V, von Blackenburg F, Hewawasam T, Kubik PW (2007) Constraining landscape development of the Sri Lankan escarpment with cosmogenic nuclides in river sediment. Earth Planet Sci Lett 253:402–414

von Blackenburg F, Bouchez J (2014) River fluxes to the sea from the ocean's ^{10}Be/^{9}Be ratio. Earth Planet Sci Lett 387:34–43

von Blackenburg F, Bouchez J, Wittmann H (2012) Earth surface erosion and weathering from the ^{10}Be (meteoric)/^{9}Be ratio. Earth Planet Sci Lett 351–352:295–305

Wallbrink PJ, Murray AS (1993) Use of fallout radionuclides as indicators of erosion processes. Hydrol Process 7(3):297–304

West N, Kirby E, Bierman P, Slingerland R, Ma L, Rood D, Brantley S (2013) Regolith production and transport at the Susquehanna Shale Hills Critical Zone Observatory, part 2: insights from meteoric ^{10}Be. J Geophys Res Earth Surf 118(3):1877–1896

Biogenic Methane

Dariusz Strąpoć
Geoservices, Schlumberger, Roissy, France

Definition

Biogenic methane is generated via a process called microbial methanogenesis, which is uniquely performed by methanogenic Archaea, the methanogens, namely several subbranches of Euryarchaeota on the 16S rRNA-based phylogenetic tree of life, i.e., *Methanomicrobiales, Methanosarcinales, Methanococcales, and Methanobacteriales* (Pace 2009). Microbial methanogenesis is the main terminal process of subsurface anaerobic organic-matter biodegradation (Head et al. 2003). Therefore, methanogenesis is important in the global carbon cycle, contributing to the terminal mineralization of organic matter. Figure 1 provides a summary of processes (biological and thermochemical) and substrates (organic and inorganic) for methane generation in nature and clarifies associated terminology. Accepted synonyms: microbial methane.

Methanogenic Pathways

The predominant biogenic methane generation pathways are CO_2-reducing and acetoclastic methanogenesis. Some environmental conditions, such as variations in salinity and pH or substrate specificity, can promote other methanogenic

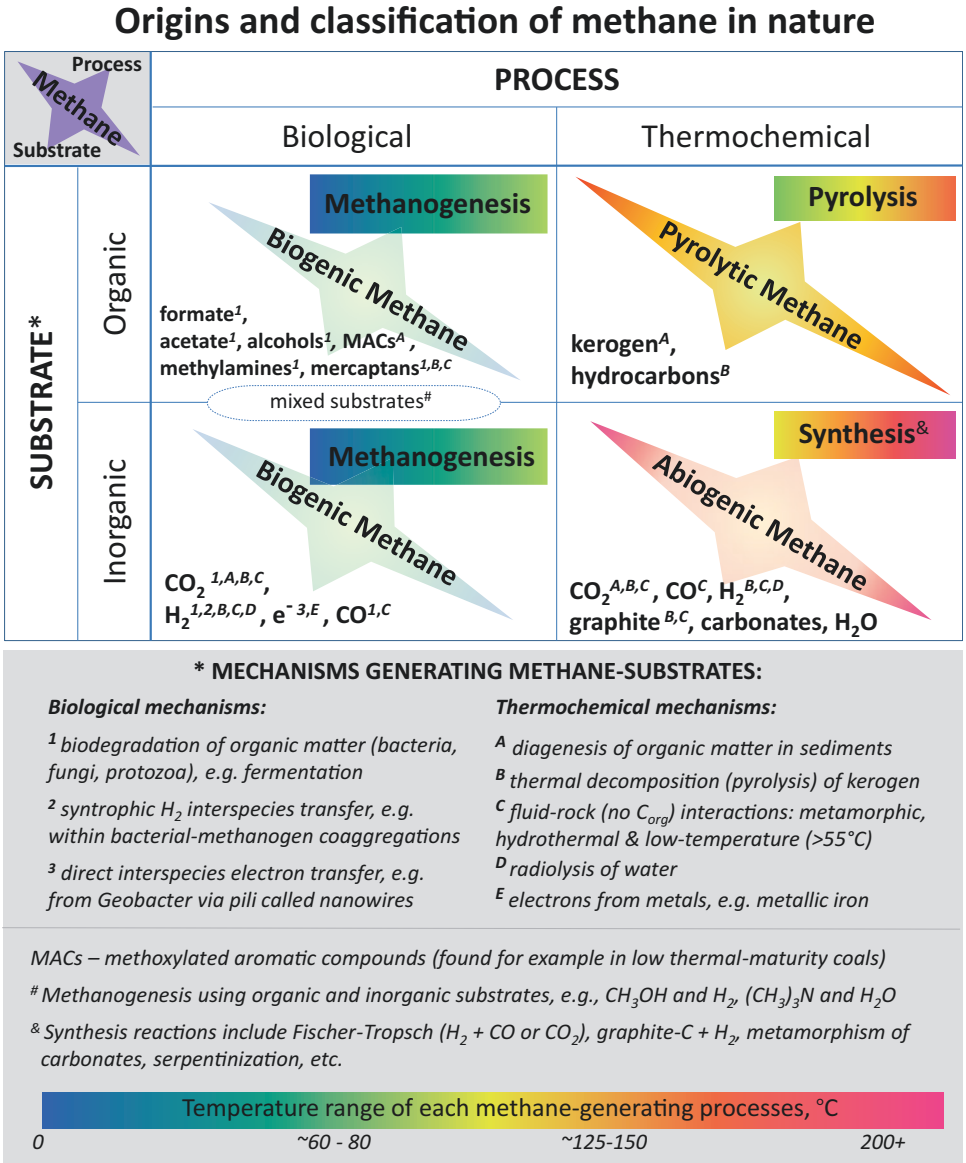

Biogenic Methane, Fig. 1 Classification and proposed nomenclature of methane according to its process of origin (X-axis) and directly utilized substrates (Y-axis; schematic explanation in the upper left corner field). The grey box below the diagram explains (i) origins of substrates for methanogenesis (1–2 and A–C), (ii) other subscripts, and (iii) temperature range used as the *color bar* behind each of the three processes (methanogenesis, pyrolysis, and synthesis). Despite small overlaps, all three processes have characteristic temperature ranges. Note that biogenic methane can be generated from inorganic substrates produced by thermal mechanisms and, conversely, methane can be also produced thermally from biologically formed substrates (pyrolytic methane). The term "thermogenic methane" has been replaced by "pyrolytic methane." The latter term both points to a thermal origin and refers to the substrate of organic carbon. Additionally, the pyrolysis or cracking process (thermal breakdown of larger organic molecules) is, in essence, directly opposite to synthesis, another thermochemical process, which forms abiogenic methane (the lower right field)

pathways, including methanol-utilizing pathway (Strąpoć et al. 2010a). In CO_2-reduction methanogenesis, the reaction $CO_2 + 4H_2 \rightarrow CH_4 + 2H_2O$ provides energy. This pathway utilizes: (i) Ni/Fe-containing hydrogenases (Thauer et al. 2010) coupled with coenzyme F_{420} (Mills et al. 2013) and (ii) sulfide- or heterosulfide-bound coenzymes CoB and CoM (for schematic illustration of all major methanogenic pathways and involved enzymes see Fig. 1 in Borrel et al. 2013). In acetoclastic methanogenesis, methanogens split and disproportionate an acetate molecule into one methane and one carbon-dioxide molecule ($CH_3COOH \rightarrow CH_4 + CO_2$). Methanol-utilizing methanogenesis can proceed via two reactions: $4CH_3OH \rightarrow 3CH_4 + CO_2 + 2H_2O$ or $CH_3OH + H_2 \rightarrow CH_4 + H_2O$.

Laboratory geochemical studies have also reported the ability of methanogens to utilize a wider variety of substrates, typically containing methyl groups (e.g., methylsulfides or methylamines), formate, and alcohols other than methanol. See Table 1 in Whitman et al. (2006) for a list of methanogenic reactions with standard free energies. Some methanogens can also convert carbon monoxide (CO) to methane (e.g., *Methonosarcina acetivorans* Moran et al. 2008). Although some methanogens are universalists and able to utilize a wide variety of substrates [e.g., *Methanosarcina barkeri* can use CO_2/H_2, acetate, methanol, methylamines (Hutten et al. 1980)], others are specialists limited to one substrate, e.g., acetate (*Methanosaeta*), methanol (*Methanolobus* or extremothermophilic *Methanopyrus*), or two substrates, e.g., CO_2 or formate (*Methanocospusculum*). Further advancements in understanding microbial methanogenesis have been enhanced by full genome sequencing, e.g., of an obligate methylotroph *Methanococcoides methylutens* (Guan et al. 2014) and studies on functional genomics (Lupa 2010). Comprehensive textbook resources include Ferry's (1993) *Methanogenesis: Ecology, Physiology, Biochemistry & Genetic*s and Whitman et al.'s (2006) *Prokaryotes*.

Additionally, Mayumi et al. (2016) recently discovered that methoxylated aromatic compounds (e.g., methoxybenzenes and -benzoates) can be used as a sole substrate by a methanol-/methylamines-utilizing *Methermicoccus shengliesis*. This means that methanogens can directly and independently of bacterial consortia utilize methoxy groups attached to aromatic rings within a kerogen structure, e.g., of low thermal-maturity coals. This implies that other relatively reactive moieties (not only methoxy groups) containing N, O, and S heteroatoms attached to kerogen structure could possibly serve as direct methanogenic substrates.

In most ecological niches abundant in organic carbon, methanogenic substrates are generated by organic-matter-degrading anaerobic or facultative bacteria, e.g., fermenters, within specific microbial consortia. Fermentative bacteria and methanogens often form syntrophic partnerships, in which methanogenic removal of bacterial by-products maintains thermodynamically favorable reactions or prevents fouling of the system. A classic example is the H_2 interspecies transfer between propionate-oxidizing *Pelotomaculum thermopropionicum* and CO_2-reducing *Methanothermobacter thermoautotrophicus* (Ishii et al. 2005) within cellular coaggregations. In guts of termites and other arthropods, H_2 for methanogens is symbiotically provided by anaerobic protozoa (i.e., ciliates) that possess H_2-producing organelles – hydrogenosomes (Wrede et al. 2012). Anaerobic H_2-producing representatives of another Kingdom of Eukaryotes, Fungi, also form syntrophic relationships with methanogens, e.g., in rumens of herbivores (Bauchop and Mountfort 1981) or within shallow coal beds (Guo et al. 2017).

Syntrophic bacteria can also donate electrons directly to the methanogens via interspecies extracellular electron transfer using pili termed nanowires, e.g., from ethanol-metabolizing *Geobacter metallireducens* assisting *Methanosaeta* or *Methanosarcina harudinacea* with CO_2-reduction ($8H^+ + 8e^- + CO_2 \rightarrow CH_4 + 2H_2O$) (Rotaru et al. 2014; Kouzuma et al. 2015). In turn, the *Geobacter* requires the by-products of its ethanol metabolism (electrons and acetate) to be harvested and converted to methane by the methanogen partner. The high efficiency of microbial conversion of electrical current to methane could be utilized as temporary energy storage (Cheng et al. 2009). Electromethanogenesis (or bioelectrosynthesis if molecules other than methane are synthesized by a microbe, e.g., formate by *Methanococcus maripaludis*) can be associated with metal corrosion (Deutzmann et al. 2015) and is often observed in petroleum facilities (Uchiyama et al. 2010).

Methanogenic substrates may also originate from inorganic processes, e.g., CO_2 from thermolysis of carbonates, H_2 from water radiolysis (Blair et al. 2007), olivine serpentinization (Sleep et al. 2004), or other low-temperature reactions between water and minerals (e.g., spinels; Mayhew et al. 2013; see Fig. 1). Such reactions involve mafic rocks or carbonates and include minerals such as calcite, dolomite, siderite, serpentine, ferrous hydroxide, olivine, talc, and graphite (Sherwood Lollar et al. 1993). Additionally, recent experiments show that even at low temperatures (above about 50 °C), H_2 can be generated from water-mafic rock reactions (e.g., Mayhew et al. 2013). Such abiotic H_2 supply allows CO_2-reducing methanogen to thrive in some extreme environments. Certain methanogens (including specific thermophiles) are known to be lithoautotrophs (e.g., *Methanobacterium thermoautotrophicum*, Zeikus et al. 1980) that obtain energy and synthesize their biomass from inorganic substrates such as CO_2 and H_2. These CO_2-reducing lithoautotrophic methanogens fix carbon following the reductive acetyl-CoA pathway (Berg et al. 2010). However, there are also lithoheterotrophic CO_2-reducing

methanogens, which require organic molecules as a carbon source, e.g., *Methanothermobacter tenebrarum* requires acetate (Kouzuma et al. 2017).

Ecology of Microbial Methanogenesis

Methanogens originated during the Archaean era before 2.5 Ga ago or even as early as 3.5 Ga ago (Ueno et al. 2006) prior to Earth's oxygenation, when biogenic methane was an important component of the atmosphere (Izon et al. 2017). After the atmosphere's oxygenation, methanogens retracted to and became widespread in a variety of anoxic environments, some of which (e.g., hydrothermal vents or deep lithosphere) resemble early Earth environments. Different methanogens thrive over a wide range of temperature, pressure, nutrient supply, salinity, and pH. The minimum requirements for microbial methanogenesis include: (i) anoxic conditions (very low/no O_2); (ii) low levels of other electron acceptors (oxidizers) such as sulfate, nitrate, and multivalent metals [e.g., Fe(III), Mn(IV)], and (iii) a supply of one or more methanogenic catabolic substrates (see section on "Methanogenic Pathways"). Among methanogens, there are halophiles (*Methanohalophilus mahii*; Paterek and Smith 1988) and hyperthermophiles, which are able to thrive at temperatures up to 122 °C (*Methanopyrus kandleri*, Takai et al. 2008) at pressures simulating deep subsurface (20–40 MPa).

Typical environments of significant active biogenic methane generation are marshes and lake and sea floor sediments (Colwell et al. 2008), permafrost (Kraev et al. 2017), hydrate or clathrate intervals (Milkov 2005), seafloor hydrothermal vents or smokers (*Methanocaldococcus indicus*, L'Haridon et al. 2003; *Methanocaldococcus jannaschii*, Ver Eecke et al. 2012), terrestrial hot springs, and onshore sediments beneath ice sheets (Wadham et al. 2012). Over geological time, methanogen ecological versatility within near-surface environments led to their perseverance in sedimentary basins and fractured crystalline lithosphere down to ~3–4 km (Inagaki et al. 2015; Moser et al. 2005). Methanogens are also common colonizers of biota and inhabit animal digestive tracts (i.e., rumen) or guts of arthropods such as termites. Anthropogenic accumulations of organic matter, i.e., dump sites and wastewater treatment plants (e.g., Rotaru et al. 2014), have become another common niche for methanogens.

Intriguingly, methane has been detected on other planetary bodies as well, i.e., Mars or Saturn's largest moon – Titan. Models show that since 3.5 Ga ago approximately 360 thousands of viable objects (minimum 3 m diameter) or $120*10^6$ t of rocks got transferred from Earth to Mars (and 60 times more the other way) (Worth et al. 2013). Yet, it remains to be proven that such a violent, long trip and "transplantation" can be survived by any microbe. Probability of transfer of any viable objects from Earth or from Mars to the Jovian or Saturnian moons in the last 3.5 Ga was from very low to zero (Worth et al. 2013).

Biogenic Methanogenesis in the Subsurface

Evidence of past and present-day subsurface biogenic methane generation is found throughout the world in a wide range of sediments and rocks. Primary biogenic methane, derived from thermally immature organic matter, can be generated at significant rates down to ~3 km depth, corresponding roughly with 60–80 °C (e.g., Zeikus et al. 1980; Head et al. 2003), depending on the local geothermal gradient. However, viable methanogens have been found even deeper, e.g., a *Methanobacterium* inhabiting a fault down to 5 km (Moser et al. 2005). As the burial progresses, small fractions of this biogenic methane (~10 moles or ~0.25 m^3 of methane at surface conditions per cubic meter of sedimentary rock on average, Strąpoć et al. 2017) can remain adsorbed on kerogen and clay minerals (despite competitiveness with water and CO_2 molecules as modeled by Jin and Firoozabadi 2014) and get buried within rocks to beyond geopasteurization temperatures where microbial cells disintegrate. Primary biogenic methane preservation is documented within boreholes drilled into sedimentary basins worldwide, based on isotopic and molecular characteristics of recovered gas. Presence of methane at concentrations greater than >99% of total hydrocarbon gases and with $\delta^{13}C_{methane} < -60‰$ is diagnostic and has been found even in low-TOC rocks (shales and siltstones) or sandstones that are devoid of petroleum. Such consistent presence of primary biogenic methane has been observed (Inagaki et al. 2015) even down to depths of 10 km (Strąpoć et al. 2017; Jacquet et al. 2017), in cases where neither pyrolytic nor abiogenic methane overwhelmed the system.

Pyrolytic methane is also generated from organic material in sufficiently buried or heated formations. This pyrolytic methane often migrates or leaks and therefore mixes with pre-existing primary biogenic methane retained in surrounding formations. The two types of methane can be distinguished, and their mixing ratio can be estimated using diagnostic isotopic signatures (see following section and silty shale 1 on Fig. 2). The preservation of the primary biogenic methane, during burial below the habitable lithosphere, and its mixing with pyrolytic methane, is also clearly illustrated by modeling gas evolution in a passive coastal margin such as the northern coast of the Gulf of Mexico (Archer et al. 2012; see also associated video simulation at http://geosci.uchicago.edu/~archer/spongebob_passive/del13.movie.gif).

Secondary biogenic methane generation occurs when pyrolytic hydrocarbons generated from kerogen are expelled from organic-rich formations and migrate towards shallower,

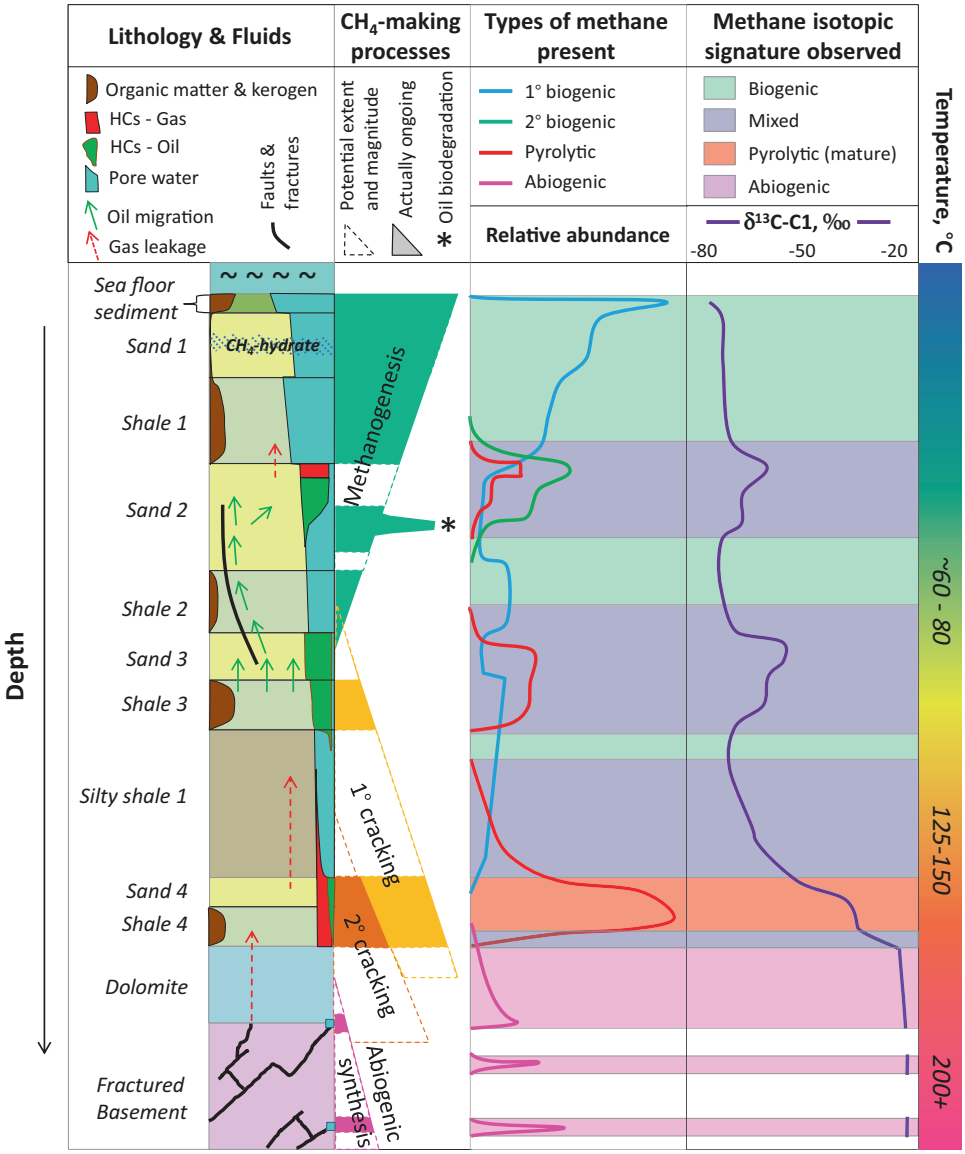

Biogenic Methane, Fig. 2 Schematic depth profile of a subseafloor sedimentary column above igneous basement used to illustrate methane-forming processes, distribution of types of methane, and observed $\delta^{13}C$ of bulk methane present. Each process requires favorable conditions (i.e., temperature) and presence of substrate (e.g., organic matter) to be active. Estimated temperature range is the same as on Fig. 1. Methanogenesis requires habitable conditions and a substrate, e.g., note a spike of activity of secondary biogenic methane generation in a water-oil transition zone in Sand 2, which experienced a charge of hydrocarbons from deeper and hotter intervals. Also, observe the presence of primary biogenic methane below habitable temperatures adsorbed on sediments as a result of burial history (below Shale 2). If a subsequent charge of thermally generated hydrocarbons arrives, a mixed signature and origin of methane is observed (e.g., via leakage in Silty shale 1). Pyrolytic methane can be derived from thermolysis of kerogen (Shales 3 and 4) or secondary cracking of oil and gas (in Sand 4 and Shale 4). Finally, abiogenic methane can be synthesized via metamorphic reactions (e.g., in fractured ultramafic basement) and mix by leaking with other types of methane (see bottom of Shale 4)

cooler, and more porous formations inhabited by microbial methanogenic consortia. Biodegradation of such migrated oil or gas occurs within the oil-water or water-gas transition zones leading to the secondary biogenic methane generation (Fig. 2). This process leaves behind biodegraded oil (so-called heavy oil, e.g., in Bohai Bai, China, Qiang et al. 2016) or, in extreme cases, a recalcitrant tar-like residue rich in asphaltenes, e.g., Canadian oil sands (Aitken et al. 2004).

Alternatively, secondary biogenic methane can be generated from biodegradation of the kerogen itself, e.g., within shallow coals or organic-rich shales. Specifically, rock formations previously geopasteurized and subsequently exposed to lower temperatures and depths via erosional or tectonic uplift can be recolonized by microbial consortia. The recolonization occurs via contact with or access by meteoric or shallower pore waters containing microbial consortia, e.g., via outcrops of highly fractured coals and shales, and diluting the prohibitively high salinity of basinal brines (Strąpoć et al. 2008; Martini et al. 2008). Multiple biogenic methane reactivation events in the same formation have been documented as well. For example, alternating burial and uplift-erosion events in the Black Warrior Basin (Pashin 2007) exposed coal to freshwater recharge and led to the recolonization by microbial consortia.

Accumulations of Biogenic Methane

Methanogenesis would likely occur in any rock formation, provided that at some time in geologic history it fulfilled the minimum requirements: delivery/accommodation of methanogens (can be as small as 0.4 μm, Strąpoć et al. 2008)

and of substrate for energy and for biomass. Microbial methanogenesis has been extremely widespread across geologic time and space within the lithosphere. Additionally, over geologic time scales biogenic methane can migrate laterally and vertically or leak from its parent formation and accumulate elsewhere, e.g., sandstone channels above coal beds in Alberta basin (Bachu and Michael 2003). In the case of seafloor sediments on continental shelves, large amounts of predominantly biogenic methane are locked in the methane hydrates or clathrates (Archer 2007), a vast organic carbon pool spread out worldwide. In the high latitudes on shore, large amounts of methane are trapped within or beneath the permafrost.

As a result, some of the accumulations of biogenic methane are preserved in significant volumes and are exploited as an energy resource. Examples include widespread biogenic coalbed methane (CBM) accumulations (see Strąpoć et al. 2011, for global review), specifically, the Powder River and San Juan Basins in the USA (Formolo et al. 2008) and the Sydney Basin in Australia (Faiz and Hendry 2006), among others. Examples of significant biogenic methane accumulations in shale formations include the Western Canada Sedimentary Basin (Cokar et al. 2010) and the Illinois and Michigan Basins in USA (Martini et al. 2008; Strąpoć et al. 2010b). In addition to these so-called unconventional CBM and shale gas accumulations, biogenic methane also commonly occurs in more conventional reservoirs where more porous and permeable rocks, such as sandstone, are capped by a seal rock, e.g., the Cook Inlet Basin, where the Beluga field-reservoir consists of reworked fluvial sediment with sufficient dispersed organic matter as a substrate for methanogenesis (Strąpoć et al. 2010a). Recent discoveries of vast and economically significant accumulations of biogenic methane include the Levant Basin, in the eastern Mediterranean (~$1x10^{12}$ m^3 or 37 Tcf, Durham 2013; basin models by Wygrala et al. 2014 and Schneider et al. 2016), offshore Myanmar (Pinyo et al. 2016), northern Adriatic (Belopolsky et al. 2012), in the Qaidam Basin in China (lacustrine sediments), and in Hangzhou Bay (last two ~2.3×10^{11} m^3 or 8 Tcf; Pang et al. 2005; Li and Lin 2010), among others. The scale of these accumulations confirms and elucidates the importance of biogenic methane as a large pool of organic carbon. Our estimates of the biogenic methane pool size within the lithosphere, including methane hydrates, are similar or higher than another large organic carbon pool on Earth: the soil (~1500 pG or $1500*10^{15}$ g, Scharlemann et al. 2016).

Fate of Biogenic Methane and Impact on Climate

A large fraction of the subsurface-generated biogenic methane leaks or migrates, reaching near-surface sediments and eventually might be released to the atmosphere. Methane hydrates and permafrost provide a large volume-buffer storage of methane. However, the stability of these mostly biogenic methane storages can be very sensitive to climatic changes. Destabilization of methane hydrates, e.g., due to other climate drivers, such as astronomical cycles, have been shown to have a positive feedback on the climate warming, e.g., during the Paleocene-Eocene Thermal Maximum (Archer 2007) or Early Jurassic (Kemp et al. 2005) but could also respond to current anthropogenic climate warming caused by greenhouse gas emissions. In general, leaking methane is anaerobically or aerobically oxidized to CO_2 by microbes within shallow sediments, water columns (Carini et al. 2005), or soils. A fraction of carbon from the leaking methane is incorporated into biomass (e.g., in wetlands, Segarra et al. 2015, even up to 85% in shallow coastal sediments of Gulf of Mexico, Coffin et al. 2015).

Half of any methane leaking all the way to the atmosphere is oxidized to CO_2 within the first 9 years. Currently, at approximately 1.8 vol. ppm with preindustrial estimates of 0.4–0.8 vol. ppm, methane is a very potent greenhouse gas, absorbing 24 times more heat than CO_2 (Wuebbles and Hayhoe 2002). Biogenic methane contributes approximately two-thirds of global emissions of methane to the atmosphere, about half of which is anthropogenically induced: livestock guts (rumen, Hook et al. 2010), waste deposition or processing sites, and rice paddies. The natural sources are dominated foremost by wetlands, followed by termites and oceanic degassing (Bousquet et al. 2006). Climate warming may convert vast permafrost areas rich in organic carbon into additional high-methane-flux wetlands (Camill 2005) and, on slightly longer time scales (~millennial), destabilize global methane hydrates (Archer 2007). Furthermore, human activity adds industrial methane emissions to the atmosphere with the main sources being the fossil fuel industry (16% of global emissions) and incomplete burning of biomass and biofuels (Bousquet et al. 2006).

Stable Isotopic Composition of Methane

The stable isotopic composition of methane can be used to determine if the gas is biogenic or was generated via thermochemical processes (pyrolysis or abiogenic synthesis, Fig. 1). The stable isotopic composition of C and H in methane is expressed as two ratios, ^{13}C to ^{12}C and ^{2}H (or D – deuterium) to ^{1}H. These ratios are expressed relatively to the international standards (primary reference or scale-defining materials, Brandt et al. 2014) via the delta notation, $\delta^{13}C$ and $\delta^{2}H$, respectively. Biogenic methane is strongly depleted in ^{13}C relative to the standard and relative to other nonbiological methane sources. Whereas $\delta^{13}C$ of biogenic methane ranges from −120‰ to −50‰ (typically −80‰ to −60‰; Fig. 2), abiogenic methane or pyrolytic methane

derived from subsurface thermal defragmentation of kerogen and/or hydrocarbons ranges from −50‰ to −20‰. δ^2H, on the other hand, helps to distinguish methanogenic pathways, specifically the main ones including CO_2-reduction versus methanol- and acetate-utilizing (acetoclastic) pathways. The latter two are characterized by δ^2H more negative than −300‰, whereas the CO_2-reduction one by δ^2H similar in range to the pyrolytic methane (between −250‰ and −150‰, Whiticar 1999).

Abiogenic methane typically has isotopically distinct signatures (both C and H enriched in heavy isotope). However, as a caution, the final observed isotopic signature of methane depends on: (i) the isotopic composition of the substrate (e.g., $\delta^{13}C_{CO2}$ in subsurface can vary between −30‰ and +20‰, typically −10‰ to +10‰); (ii) the isotopic fractionation factor, which could depend on enzymatic pathway but also on temperature (e.g., $\varepsilon^{13}C_{CO2\text{-}CH4}$ for CO_2-reducing methanogens typically is between 60‰ and 80‰ or $\alpha^{13}C_{CO2\text{-}CH4}$ 1.060–1.080, Conrad 2005, but can be as low as 10‰ under hyperthermophilic and in situ pressure conditions, Takai et al. 2008) or other environmental stress;, and, finally, (iii) methane-alteration processes, such as mixing, diffusive transport (Prinzhofer and Pernaton 1997), and microbial oxidation at shallower depths (e.g., microbial anaerobic methane oxidation, Biddle et al. 2012; Segarra et al. 2015), with the latter two processes promoting $^{12}CH_4$ over $^{13}CH_4$.

Thermochemical Methanogenesis

Certain conditions in nature lead to generation of methane without involving methanogens. These thermochemical processes could be either (i) thermal decomposition of organic matter (e.g., kerogen or hydrocarbons) called pyrolysis or (ii) hydrothermal and metamorphic methane-synthesizing mineral-fluid interactions (e.g., during serpentinization or H_2 reaction with graphite, Sherwood Lollar 1993) or via Fischer-Tropsch type reactions at higher pressure and temperature regimes in deep lithosphere (Horita and Berndt 1999; Fig. 1). Additionally, there are synthetic and industrial methods of obtaining methane, e.g., Fischer-Tropsch synthesis from syngas (H_2 + CO) or photocatalysis from: (i) CO_2 via UV-illuminated rhodium particles (Zhang et al. 2017) or (ii) CO using iron molecular catalyst and visible light (Rao et al. 2017), both at ambient temperatures.

Summary

Biogenic methane is formed by microbial methanogens (methanogenic *Archaea*) using a variety of substrates, alone or in syntrophy with bacteria, fungi, or protozoa, in a variety of anoxic environments or microenvironments, ranging in scale from worldwide sedimentary basins and fractured upper lithosphere to the guts of termites or corroded petroleum pipeline. Adaptability and versatility of methanogens contributed to their omnipresence in anoxic environments throughout geologic time and led to widespread accumulations of biogenic methane within the lithosphere. Examples include methane hydrates, background primary biogenic methane in worldwide sedimentary basins, and economically important shallow coalbed methane or recently discovered vast conventional reservoirs. About two-thirds of global methane emissions to the atmosphere are of biogenic origin and half of those are linked to anthropogenic activities such as farming and waste management. From the early stages of life on Earth, microbial methanogenesis acted as a conduit between inorganic and organic carbon pools. Biogenic methane within the lithosphere is a significant fraction of the global organic carbon pool and can impact both short- and long-term carbon and climate cycles.

Cross-References

- ▶ Biogeochemistry
- ▶ Carbon Cycle
- ▶ Gas hydrates

References

Aitken CM, Jones DM, Larter SR (2004) Anaerobic hydrocarbon biodegradation in deep subsurface oil reservoirs. Nature 431:291–294

Archer D (2007) Methane hydrate stability and anthropogenic climate change. Biogeosci Discuss 2007(4):993–1057, European Geosciences Union

Archer DE, Buffett BA, McGuire PC (2012) A two-dimensional model of the passive coastal margin deep sedimentary carbon and methane cycles. Biogeosciences 9:2859–2878

Bachu S, Michael K (2003) Possible controls of hydrogeological and stress regimes on the producibility of coalbed methane in Upper Cretaceous-Tertiary strata of the Alberta basin, Canada. AAPG Bull 87:1729–1754

Bauchop T, Mountfort DO (1981) Cellulose fermentation by a rumen anaerobic fungus in both the absence and the presence of rumen methanogens. Appl Environ Microbiol 42:1103–1110

Belopolsky A, Tari G, Craig J, Iliffe J (2012) New and emerging plays in the eastern Mediterranean: an introduction. Pet Geosci 18:371–372

Berg IA, Kockelkorn D, Ramos-Vera WH, Say RF, Zarzycki J, Hügler M, Alber BE, Fuchs G (2010) Autotrophic carbon fixation in archaea. Nat Rev Microbiol 8:447–460

Biddle JF, Cardman Z, Mendlovitz H, Albert DB, Lloyd KG, Boetius A, Teske A (2012) Anaerobic oxidation of methane at different temperature regimes in Guaymas Basin hydrothermal sediments. Intl Soc Microbiol Ecol J 6:1018–1031

Blair CC, D'Hondt S, Spivack AJ, Kingsley RH (2007) Radiolytic hydrogen and microbial respiration in subsurface sediments. Astrobiology 7:951–970

Borrel G, O'Toole PW, Harris HMB, Peyret P, Brugere J-F, Gribaldo S (2013) Phylogenomic data support a seventh order of methylotrophic methanogens and provide insights into the evolution of methanogenesis. Genome Biol Evol 5:1769–1780

Bousquet P, Tyler SC, Peylin P, Van Der Werf GR, Prigent C, Hauglustaine DA, Dlugokencky EJ, Miller JB, Ciais P, White J, Steele LP, Schmidt M, Ramonet M, Papa F, Lathière J, Langenfelds RL, Carouge C, Brunke E-G (2006) Contribution of anthropogenic and natural sources to atmospheric methane variability. Nature 443:439–443

Brandt WA, Coplen TB, Vogl J, Rosner M, Prohaska T (2014) Assessment of international reference materials for isotope-ratio analysis (IUPAC Technical report). Pure Appl Chem 86:425–467

Camill P (2005) Permafrost thaw accelerates in boreal peatlands during late-20th century climate warming. Clim Change 68:135–152

Carini S, Bano N, LeCleir G, Joye SB (2005) Aerobic methane oxidation and methanotroph community composition during seasonal stratification in Mono Lake, California (USA). Environ Microbiol 7:1127–1138

Cheng S, Xing D, Call DF, Logan BE (2009) Direct biological conversion of electrical current into methane by electromethanogenesis. Environ Sci Technol 43:3953–3958

Coffin RB, Osburn CL, Plummer RE, Smith JP, Rose PS, Grabowski KS (2015) Deep sediment-sourced methane contribution to shallow sediment organic carbon: Atwater Valley, Texas-Louisiana Shelf, Gulf of Mexico. Energies 8:1561–1583

Cokar M, Kallos MS, Huang H, Larter SR, Gates ID (2010) Biogenic gas generation from shallow organic-matter-rich shales. Can Soc Unconv Gas/Soc Petrol Eng 135323, 13p

Colwell FS, Boyd S, Delwiche ME, Reed DW, Phelps TJ, Newby DT (2008) Estimates of biogenic methane production rates in deep marine sediments at Hydrate Ridge, Cascadia Margin. Appl Environ Microbiol 74:3444–3452

Conrad R (2005) Quantification of methanogenic pathways using stable carbon isotopic signatures: a review and a proposal. Org Geochem 36:739–752

Deutzmann JS, Sahina M, Spormanna AM (2015) Extracellular enzymes facilitate electron uptake in biocorrosion and bioelectrosynthesis. MBio 6:e00496-15

Durham LS (2013) Levant Basin brings potential to new areas. AAPG Explor, May 2013. http://archives.aapg.org/explorer/2013/05may/ace_levant0513.cfm

Faiz M, Hendry P (2006) Significance of microbial activity in Australian coal bed methane reservoirs – a review. Bull Can Petrol Geol 54:261–272

Ferry JG (1993) Methanogenesis: Ecology, physiology, biochemistry & genetics. Ferry JG (ed). Chapman & Hall, New York, 536p

Formolo M, Martini A, Petsch S (2008) Biodegradation of sedimentary organic matter associated with coalbed methane in the Powder River and San Juan Basins, U.S.A. Int J Coal Geol 76:86–97

Guan Y, Ngugi DK, Blom J, Ali S, Ferry JG, Stingl U (2014) Draft genome sequence of an obligately methylotrophic methanogen, *Methanococcoides methylutens* isolated from marine sediment. Genome Announc 2(6):e01184-14

Guo H, Zhang J, Han Q, Huang Z, Urynowicz MA, Wang F (2017) Important role of fungi in the production of secondary biogenic coalbed methane in China's Southern Qinshui Basin. Energy Fuel 31:7197–7207

Head IM, Jones DM, Larter SR (2003) Biological activity in the deep subsurface and the origin of heavy oil. Nature 426:344–352

Hook SE, Wright A-DG, McBride BW (2010) Methanogens: methane producers of the rumen and mitigation strategies. Archaea 2010:11, Article ID 945785

Horita J, Berndt ME (1999) Abiogenic methane formation and isotopic fractionation under hydrothermal conditions. Science 285:1055–1057

Hutten TJ, Bongaerts HC, van der Drift C, Vogels GD (1980) Acetate, methanol and carbon dioxide as substrates for growth of *Methanosarcina barkeri*. Antonie Van Leeuwenhoek 46:601–610

Inagaki F, Hinrichs K-U, Kubo Y et al (2015) Exploring deep microbial life in coal-bearing sediment down to ~2.5 km below the ocean floor. Science 349:420–424

Ishii S, Kosaka T, Hori K, Hotta Y, Watanabe K (2005) Coaggregation facilitates interspecies hydrogen transfer between *Pelotomaculum thermopropionicum* and *Methanothermobacter thermautotrophicus*. Appl Environ Microbiol 71:7838–7845

Izon G, Zerkle AL, Williford KH, Farquhar J, Poulton SW, Claire MW (2017) Biological regulation of atmospheric chemistry en route to planetary oxygenation. Proc Natl Acad Sci U S A 114:E2571–E2579

Jacquet B, Strąpoć D, Khan S, Inan Villegas E, Albrecht H, Okoh B, McKinney D (2017) Persistence of biogenic methane and its mixing with thermogenic fluids: observations and consequences. IMOG2017, abstract P216

Jin Z, Firoozabadi A (2014) Effect of water on methane and carbon dioxide sorption in clay minerals by Monte Carlo simulations. Fluid Phase Equilib 382:10–20

Kemp DB, Coe AL, Cohen AS, Schwark L (2005) Astronomical pacing of methane release in the Early Jurassic period. Nature 437:396–399

Kouzuma A, Kato S, Watanabe K (2015) Microbial interspecies interactions: recent findings in syntrophic consortia. Front Microbiol 6:8, Article 477

Kouzuma A, Tsutsumi M, Ishii S, Ueno Y, Abe T, Watanabe K (2017) Non-autotrophic methanogens dominate in anaerobic digesters. Nature Sci Rep 7:1510. https://doi.org/10.1038/s41598-017-01752-x

Kraev G, Schulze E-D, Yurova A, Kholodov A, Chuvilin E, Rivkina E (2017) Cryogenic displacement and accumulation of biogenic methane in frozen soils. Atmosphere 8:19

L'Haridon S, Reysenbach A-L, Banta A, Messner P, Schumann P, Stackebrandt E, Jeanthon C (2003) *Methanocaldococcus indicus* sp. nov., a novel hyperthermophilic methanogen isolated from the Central Indian Ridge. Int J Syst Evol Microbiol 53:1931–1935

Li Y-L, Lin C-M (2010) Exploration methods for late Quaternary shallow biogenic gas reservoirs in the Hangzhou Bay area, eastern China. AAPG Bull 94:1741–1759

Lupa B (2010) Functional genomics of methanogens. In: Timmis KN, McGenity TJ, van der Meer JR, de Lorenzo V (eds) Handbook of hydrocarbon and lipid microbiology. Springer, Berlin, pp 501–508

Martini AM, Walter LM, McIntosh JC (2008) Identification of microbial and thermogenic gas components from Upper Devonian black shale cores, Illinois and Michigan basins. AAPG Bull 92:327–339

Mayhew LE, Ellison ET, McCollom TM, Trainor TP, Templeton AS (2013) Hydrogen generation from low-temperature water–rock reactions. Nat Geosci 6:478–484

Mayumi D, Mochimaru H, Tamaki H, Yamamoto K (2016) Methane production from coal by a single methanogen. Science 354:222–225

Milkov AV (2005) Molecular and stable isotope compositions of natural gas hydrates: a revised global dataset and basic interpretations in the context of geological settings. Org Geochem 36:681–702

Mills DJ, Vitt S, Strauss M, Shima S, Vonck J (2013) De novo modeling of the F420-reducing [NiFe]-hydrogenase from a methanogenic archaeon by cryo-electron microscopy. Elife 2:e00218. https://doi.org/10.7554/eLife.00218

Moran JJ, House CH, Vrentas JM, Freeman KH (2008) Methyl sulfide production by a novel carbon monoxide metabolism in *Methanosarcina acetivorans*. Appl Environ Microbiol 74:540–542

Moser DP, Gihring TM, Brockman FJ, Fredrickson JK, Balkwill DL, Dollhopf ME, Sherwood Lollar B, Pratt ML, Boice E, Southam G, Wagner G, Baker BJ, Pfiffner SM, Lin L-H, Onstott TC (2005) *Desulfotomaculum* and *Methanobacterium* spp. dominate a 4- to 5-kilometer-deep fault. Appl Environ Microbiol 71:8773–8763

Pace NR (2009) Mapping the tree of life: progress and prospects. Microbiol Mol Biol Rev 73:565–576

Pang X, Zhao W, Su A, Li S (2005) Geochemistry and origin of the giant Quaternary shallow gas accumulations in the eastern Qaidam Basin, NW China. Org Geochem 36:1636–1649

Pashin JC (2007) Hydrodynamics of coalbed methane reservoirs in the Black Warrior Basin: key to understanding reservoir performance and environmental issues. Appl Geochem 22:2257–2272

Paterek JR, Smith PH (1988) Methanophilus mahii gen. nov., sp. nov., a methylotrophic halophilic methanogen. Int J Syst Bacteriol 38:122–123
Pinyo K, Wooding S, Masdakom M (2016) Unlocking the mystery of Zawtika biogenic gas accumulations, offshore Gulf of Moattama, Myanmar. International petroleum technology conference, Bangkok, 14–16 Nov 2016, IPTC-18832-MS, 21p
Prinzhofer A, Pernaton E (1997) Isotopically light methane in natural gas: bacterial imprint or diffusive fractionation? Chem Geol 142:193–200
Qiang J, Fuqi C, Yang G, Liang C (2016) Restricted access genetic types and accumulation models for biogenic gases in Bohai Bay Basin, eastern China. Bull Can Petrol Geol 64:24–46
Rao H, Schmidt LC, Bonin J, Robert M (2017) Visible-light-driven methane formation from CO_2 with a molecular iron catalyst. Nature. https://doi.org/10.1038/nature23016
Rotaru A-E, Malla Shrestha P, Liu F, Markovaite B, Chen S, Nevin KP, Lovley DR (2014) Direct interspecies electron transfer between *Geobacter metallireducens* and *Methanosarcina barkeri*. Appl Environ Microbiol 80:4599–4605
Scharlemann JPW, Tanner EVJ, Hiederer R, Kapos V (2016) Global soil carbon: understanding and managing the largest terrestrial carbon pool. Carbon Manage 5:81–91
Schneider F, Dubille M, Montadert L (2016) Modeling of microbial gas generation: application to the eastern Mediterranean "Biogenic Play". Geol Acta 14:403–417
Segarra KEA, Schubotz F, Samarkin V, Yoshinaga MY, Hinrichs K-U, Joye SB (2015) High rates of anaerobic methane oxidation in freshwater wetlands reduce potential atmospheric methane emissions. Nat Commun 6, Article 7477
Sherwood Lollar B, Frape SK, Weise SM, Fritz P, Macko SA, Welhan JA (1993) Abiogenic methanogenesis in crystalline rocks. Geochim Cosmochim Acta 57:5087–5097
Sleep NH, Meibom A, Fridriksson T, Coleman RG, Bird DK (2004) H2-rich fluids from serpentinization: geochemical and biotic implications. Proc Natl Acad Sci U S A 101:12818–12823
Strąpoć D, Picardal FW, Turich C, Schaperdoth I, Macalady JL, Lipp JS, Lin Y-S, Ertefai TF, Schubotz F, Hinrichs K-U, Mastalerz M, Schimmelmann A (2008) Methane-producing microbial community in a coal bed of the Illinois basin. Appl Environ Microbiol 74:2424–2432
Strąpoć D, Ashby M, Wood L, Levinson R, Huizinga B (2010a) Significant contribution of methyl/methanol-utilizing methanogenic pathway in a subsurface biogas environment. In: Whitby C, Skovhus TL (eds) Applied microbiology and molecular biology in oil field systems, Part 4. Springer, Netherlands, pp 211–216
Strąpoć D, Mastalerz M, Drobniak A, Schimmelmann A, Hasenmueller NR (2010b) Geochemical constraints on the origin and volume of gas in the New Albany Shale (Devonian – Mississippian), eastern Illinois basin. AAPG Bull 94:1713–1740.
Strąpoć D, Mastalerz M, Dawson K, Macalady JL, Callaghan AV, Wawrik B, Turich C, Ashby M (2011) Biogeochemistry of microbial coal-bed methane. Annu Rev Earth Planet Sci 39:617–656
Strąpoć D, Jacquet B, Torres O, Khan RMS, Inan Villegas E, Albrecht H, Okoh B, McKinney D (2017) Deep biogenic methane and drilling-associated gas artifacts: impact and consequences on characterization of petroleum fluids. In preparation for AAPG Bull
Takai K, Nakamura K, Toki T, Tsunogai U, Miyazaki M, Miyazaki J, Hirayama H, Nakagawa S, Nunoura T, Horikoshi K (2008) Cell proliferation at 122°C and isotopically heavy CH4 production by a hyperthermophilic methanogen under high-pressure cultivation. Proc Natl Acad Sci U S A 105:10949–10954
Thauer RK, Kaster AK, Goenrich M, Schick M, Hiromoto T, Shima S (2010) Hydrogenases from methanogenic archaea, nickel, a novel cofactor, and H2 storage. Annu Rev Biochem 79:507–536
Uchiyama T, Ito K, Mori K, Tsurumaru H, Harayama S (2010) Iron-corroding methanogen isolated from a crude-oil storage tank. Appl Environ Microbiol 76:1783–1788
Ueno Y, Yamada K, Yoshida N, Maruyama S, Isozaki Y (2006) Evidence from fluid inclusions for microbial methanogenesis in the early Archaean era. Nature 440:516–519
Ver Eecke HC, Butterfield DA, Huber JA, Lilley MD, Olson EJ, Roe KK, Evans LJ, Merkel AY, Cantin HV, Holden JF (2012) Hydrogen-limited growth of hyperthermophilic methanogens at deep-sea hydrothermal vents. Proc Natl Acad Sci U S A 100:13674–13679
Wadham JL, Arndt S, Tulaczyk S, Stibal M, Tranter M, Telling J, Lis GP, Lawson E, Ridgwell A, Dubnick A, Sharp MJ, Anesio AM, Butler CEH (2012) Potential methane reservoirs beneath Antarctica. Nature 488:633–637
Whiticar MJ (1999) Carbon and hydrogen isotope systematics of bacterial formation and oxidation of methane. Chem Geol 161:291–314
Whitman WB, Bowen TL, Boone DR (2006) The methanogenic bacteria. Prokaryotes 3:165–207
Worth RJ, Sigurdsson S, House CH (2013) Seeding life on the Moons of the outer planets via lithopanspermia. Earth Planet Astrophys. arXiv:1311.2558 [astro-ph.EP], p 13
Wrede C, Dreier A, Kokoshka S, Hoppert M (2012) Archaea in symbioses. Archaea 2012:11, Article ID 596846
Wuebbles D, Hayhoe K (2002) Atmospheric methane and global change. Earth Sci Rev 57:177–210
Wygrala B, Rottke W, Kornpihl D, Neumaier M, Al-Balushi A, Marlow L (2014) Assessment of controlling factors in mixed biogenic and thermogenic petroleum systems – a case study from the Levantine Basin. AAPG Search & Discovery Article #10636. Adapted from poster presentation given at AAPG Annual Convention and Exhibition, Houston, 6–9 Apr 2014, 3p
Zeikus JG, Ben-Bassat A, Hegge PW (1980) Microbiology of methanogenesis in thermal, volcanic environments. J Bacteriol 143:432–440
Zhang X, Li X, Zhang D, Qiang Su N, Yang W, Everitt HO, Liu J (2017) Product selectivity in plasmonic photocatalysis for carbon dioxide hydrogenation. Nat Commun 8, Article 14542

B

Biogeochemistry

Hilairy Ellen Hartnett
School of Earth and Space Exploration and School of Molecular Sciences, Arizona State University, Tempe, AZ, USA

Definition

Biogeochemistry is the scientific discipline that explores the physical, chemical, biological, and geological processes that control the composition of and changes to Earth's surface environments.

Introduction

A fundamental premise within biogeochemistry is that the influence of life, in particular microbial life, is so pervasive that Earth's surface geochemistry cannot be understood

without considering the biological components and processes (Schlesinger and Bernhardt 2013). Indeed, no surface environment on Earth has been demonstrated to be uninhabitable. The key biogeochemical processes involve elements that are necessary for or are affected by metabolism – especially C, H, N, O, S, but also many other major and trace elements. Biogeochemistry addresses both biotic and abiotic reactions and involves both organic and inorganic species. The science of biogeochemistry spans the marine, aquatic, terrestrial, and atmospheric sciences, it operates over a wide range of temporal and spatial scales, and it involves significant complexity due to the interactions and feedbacks among the many elemental cycles. Biogeochemistry regularly looks both backwards through the historical and geological records to understand underlying cycles and patterns but also strives to make predictions about future changes in Earth elemental cycles. Given that Earth is fundamentally an inhabited planet, biogeochemistry also has implications for understanding the controls on the distribution of life on other planets. Increasingly, biogeochemistry also examines the role of humans in altering elemental cycles and the coevolution of humans and their environment in the future.

Spatial and temporal scales in biogeochemistry. A fundamental challenge in biogeochemistry is that the relevant spatial and temporal scales range over many orders of magnitude – from the submicron-scale cells and nanometer-scale molecules that operate on the millisecond timescales of chemical reactions, to planetary-scale elemental cycles that operate over centuries to millennia. A single biogeochemical process, for example, photosynthesis, can exhibit day-to-night (diel) patterns, seasonal (summer/winter) variations, interannual (climatic) trends, and very long-term (glacial/interglacial) cycles. Evolutionary timescales are also relevant as the photosynthetic biochemistry has evolved over billions of years of Earth history. Many biogeochemical patterns, for example, seasonal variations, may be difficult to discern without detailed process studies that examine both shorter and longer temporal scales. At very long time frames, patterns found Earth's rock record have such long integration times that it is difficult to determine specific causative processes. For example, the seemingly rapid rise in atmospheric O_2 at ~2.5 billion years ago was likely a result of both slow secular H_2 loss from the Earth's mantle and the rapid biological production of O_2 via photosynthesis (Lyons et al. 2014). Steady-state approximations are often appropriate for processes and cycles that operate on long time scales (e.g., the carbonate-silicate weathering cycle that controls atmospheric CO_2 on geologic time scales; Berner et al. 2003) but non-steady-state conditions (e.g., the rapid increase in CO_2 over the last 200 years which is not balanced by rock weathering) are also possible.

Thermodynamic considerations. Biogeochemistry is based in the fundamental physical laws of thermodynamics. Chemical reactions tend toward equilibrium (energy minimization), and biological processes cannot subvert this. All biological reactions are thermodynamically favorable ($\Delta G_r < 0$); although, they may be kinetically inhibited. Biology can overcome kinetic barriers through enzymatic reactions, but it cannot force reactions to "run uphill." Biological systems take advantage of favorable redox gradients to gain energy from their environment; they must have continuous input of energy in order to maintain their reduced carbon molecules or their very biomass will tend (albeit, perhaps slowly) toward equilibrium. The evolutionary revolution of photosynthesis, whereby organisms harvest solar energy as photons, allowed biology to capture additional energy beyond that supplied geochemically, which could then be used to fix CO_2 into organic molecules.

Stoichiometry is another fundamental principle within biogeochemistry – the concept that the elemental composition of molecules can be extended to explain the elemental composition of biomass, communities, and even ecosystems. The classical Redfield ratio (C:N:P::106:16:1) in phytoplankton (Redfield 1958) describes the C:N:P content of phytoplankton; that same elemental ratio is reflected in the nutrient content of the surface ocean. Like a limiting reagent in a chemical reaction, ecological stoichiometry posits that availability of limiting nutrients control ecosystem structure and function (Sterner and Elser 2002). The Redfield ratio concept has been extended to include larger organisms and beyond C, N, and P to include other major elements (e.g., Ca, S) and a host of trace elements (e.g., Fe, Mo, Ni, etc.). It has been demonstrated that often Fe is a limiting nutrient in marine systems because algae require Fe for photosynthesis. Different organisms can have different stoichiometric ratios depending not only on their food sources but also on the plasticity of their metabolisms and the range of metal cofactors their enzymes utilize.

Coupled biogeochemical cycles. Biogeochemistry fundamentally addresses the global cycles of biologically relevant elements, especially carbon, oxygen, nitrogen, hydrogen, and sulfur, but also such elements as calcium, iron, silicon, mercury, and many others. Importantly, each cycle is considered a closed loop and the science of biogeochemistry seeks to determine how they are related and how they interact.

Carbon is centrally important for all life on Earth and thus the cycling of carbon is at the heart of biogeochemistry. Carbon exists in organic and inorganic forms, it has a wide range of stable redox states, and it can exist in in solid, dissolved, and gaseous phases. The fundamental biological processes that produce and consume organic carbon are

$$\text{Photosynthesis: } CO_2 + H_2O \rightarrow \text{organic carbon } (\text{“}CH_2O\text{”}) + O_2, \text{ and}$$
$$\text{Respiration: } O_2 + \text{organic carbon } (\text{“}CH_2O\text{”}) \rightarrow CO_2 + H_2O.$$

In these equations, the complex organic matter produced that includes proteins, carbohydrates, and lipids is

abbreviated as "CH_2O," a very rough approximation of the stoichiometry of a carbohydrate. The respiration equation assumes aerobic respiration, but the process can also proceed through a range of anaerobic metabolisms. Of course, this abbreviated organic matter also contains N, P, S, and trace metals in addition to C, H, and O. The full stoichiometric equations for photosynthesis and respiration allow the interactions of coupled elemental cycles to be examined. For example, plants require nitrate or ammonium and the amount of O_2 produced during photosynthesis varies depending on which N species is utilized. Respiration reactions also reflect significant biogeochemical complexity. Aerobic respiration of N-containing organic matter will generate ammonia (which can be subsequently oxidized to nitrate in the presence of O_2). Anaerobic carbon oxidation by NO_3^{2-} (e.g., denitrification) generates N_2 but can also produce a range of other species (NH_4^+, NO, N_2O, and NO_2^-) depending on the specific consortia of organisms present. The biogeochemical cycling of carbon also includes an inorganic cycle that is tied to the biological production of carbonate ($CaCO_3$) shells, abiotic carbonate precipitation in soils, and the weathering of carbonate rocks. The speciation of dissolved CO_2 and carbonate in water is a primary control on the pH of natural waters, and the coupling of the organic and inorganic carbon cycles is critical for understanding the sources and fate of CO_2 in the atmosphere. Humans are influencing the carbon cycle directly through the production of CO_2 from fossil fuels and indirectly via the downstream impacts on biological and geochemical cycling of this added C. There are many documented examples of carbon cycle feedbacks between human activities and biogeochemical systems. In coastal marine systems, increased CO_2 is contributing to ocean acidification, and lower pH is causing decalcification of organisms like oysters and mussels; this in turn is affecting shellfish productivity (Barton et al. 2012). In terrestrial systems, recent work has demonstrated that plants grown under elevated CO_2 are nitrogen poor relative to plants grown under ambient CO_2; this has significant implications for the nutritional value of future food crops (Huang et al. 2015; Sardans et al. 2017).

Nitrogen and phosphorus each have relatively small, rapidly cycling pool coupled to a large, but slowly cycling geologic reservoir (the atmosphere and crustal rock for N and P, respectively). Both the N and P cycles are tightly coupled to the carbon and oxygen cycles (Ingall and Jahnke 1994; Galloway et al. 2008). The global nitrogen cycle is coupled to photosynthesis and respiration, but also depends on nitrogen fixation (the conversion of N_2 gas to ammonium, NH_4^+, or nitrate, NO_3^{2-}) which occurs naturally through a bacterial process or due to lightning. Like carbon, nitrogen has a wide range of stable forms and redox states; one of which, N_2O, is a potent greenhouse gas and a catalyst of stratospheric ozone destruction. The global phosphorus cycle is somewhat simpler in that P is a rock derived element and its global cycle, unlike that of carbon and nitrogen has no source through biological fixation. Rivers convey the dominant flux of P from the land to the ocean, and on long time scales P is buried in marine sediments and returned to land via rock uplift.

Human activity has a profound and direct impact on both N and P cycles. Human N_2 fixation via industrial fertilizer production and fossil fuel burning now rivals natural N_2 fixation rates. Humans have directly enhanced P fluxes from the land to the ocean through the mining phosphate rocks for industrial use and fertilizer production. Geologic (rock-derived) P is a nonrenewable resource and current rates of P mining are unsustainable in the long term, suggesting P scarcity could become a significant foodsecurity issue by the latter half of the twenty-first century (Vaccari and Strigul 2011; Neset and Cordell 2012). Pollutant nitrogen and phosphorus from agricultural runoff and other waste is increasing coastal primary production rates and causing eutrophication (oxygen depletion due to excess organic matter production and subsequent decomposition). Recent work has shown that eutrophication also causes coastal waters to be more susceptible to ocean acidification since CO_2 produced by decomposition further decreases the oceans ability to buffer CO_2 from the atmosphere (Cai et al. 2011). Ecosystems respond rapidly and strongly to increases in N and P; as humans continue to alter the N and P cycles, it is important for biogeochemists to understand and predict how CO_2 in the atmosphere may respond to alterations in the biosphere and changes in N and P.

Atmospheric, terrestrial, and marine biogeochemistry. Atmospheric processes can affect climate due to changes in the concentration of greenhouse gases. Changes in atmospheric trace gas composition can affect ozone (O_3) levels and sulfate aerosols. The atmosphere also influences primary productivity though the deposition of nutrients, including: nitrogen oxides (NO, NO_2^-, $NO_3^=$), ammonia and ammonium (NH_3 and NH_4^+), and sulfate $\left(SO_4^=\right)$ on the Earth surface. In the lower atmosphere (troposphere), important processes include the conversion of N_2 to fixed nitrogen species (e.g., NO, NOx), uptake and release of CO_2, and the accumulation and consumption of O_2. In the upper atmosphere (stratosphere), the important processes are reactions that consume ozone (O_3), and reactions that affect sulfate aerosols which have a cooling effect on Earth's climate. The loss of stratospheric ozone in particular has been linked to human activity and the production of halogenated trace gases; this ozone loss (through the chemical cycling of NO) leads to increased UV radiation which causes cancer and cataracts in humans and may decrease primary production in the southern ocean. Human impacts on the atmosphere are quite pronounced because the atmosphere mixes rapidly, and many species are reactive on short time scales.

On land, the biogeochemical processes of rock weathering and soil development are important for nutrient supply and for carbon cycling. Nutrients and CO_2 are in turn key requirements for primary production. Land plants account for 50% of global net primary production (~60 Tg C $year^{-1}$; Schlesinger and Bernhardt 2013). Most of the organic carbon produced is delivered as plant detritus to soils where it is decomposed relatively efficiently back to CO_2. Soil C has a continuum of turnover times, with small rapidly cycling pools (months), is dominated by pools with turnover times of decades to millennia. Traditionally, these are defined as fast, slow, and passive. Agricultural activities have increased decomposition rates and thus move soil organic carbon back into the atmospheric CO_2 pool.

Marine biogeochemical cycles are dominated by algal production and microbial consumption. Marine primary production is about equal in magnitude to terrestrial primary production (~51 Tg C $year^{-1}$; Schlesinger and Bernhardt 2013). Like terrestrial production, the majority (~95%) of the marine production is rapidly decomposed by bacteria and converted to CO_2. However, the small amount of organic carbon that escapes degradation can be exported from the surface ocean to be buried in marine sediments. Decomposition in the sediments also consumes organic carbon and ultimately less than ~1% of marine primary production is permanently buried. This small burial flux, however, is the key to maintaining our atmospheric oxygen concentrations. Each mole of organic carbon atom that is buried was originally produced via photosynthesis along with an equimolar amount of oxygen. If that carbon escapes reoxidation, the oxygen produced with that organic carbon contributes to the atmosphere oxygen pool. This leads to a long-term negative feedback between the carbon and oxygen cycles. Low oxygen conditions promote carbon burial by inhibiting decomposition, and over long time scales oxygen can build up in the atmosphere. High O_2 leads to the more efficient oxidation of organic matter, reducing carbon burial and consuming atmospheric O_2 (Berner et al. 2003).

Models. Given the vast range in temporal and special scales as well as the range of ecosystems and metabolisms encompassed by biogeochemistry, conceptual models and numerical models are critical tools for exploring rates and processes. The simplest models are 1D mass-balance or box models with inventories for each box or reservoir and fluxes into and out of (and between) each box. These can be one or two box models or more complex models with many boxes. The most complex models are fully dynamic, 3D global circulation models (GCM) that conserve motion and mass and have parameterized chemical reactions for each species of interest. Biogeochemical modules that dynamically trace a wide range of elements and processes have been developed to run on top of these GCMs. Such coupled models are computationally intensive, but they allow us to faithfully reproduce past patterns in elemental cycles and they are necessary if we want to make predictions about future biogeochemical cycles.

Summary

Biogeochemistry and the science of global change. As Earth enters the Anthropocene (the epoch in which humans have become a dominant force on the Earth), the influence of humans on the planet's chemistry is clear. Human activities alter the cycling of C, N, P, and many other elements in the atmosphere, in soils, and in aquatic and marine environments. Biogeochemistry not only reveals changes in Earth's biological systems and patterns in the past it also provides a context for understanding change in the future. As the human population grows and the level of development improves for many countries, we have the potential to deplete resources, pollute waterways, and increase atmospheric greenhouse gases, or we can use the tools that biogeochemistry provides to develop an understanding of the connections and feedbacks among human activities and global biogeochemical cycles. The science of global change is ultimately a transdisciplinary one that must integrate biogeochemistry with human-systems science to help us to make informed, sustainable decisions about how we manage our environments and utilize resources to attain a thriving, positive future.

Cross-References

- ▶ Anthropogenic CO_2
- ▶ Atmospheric Evolution
- ▶ Carbon
- ▶ Carbon Cycle
- ▶ Chemical Weathering
- ▶ Equilibrium
- ▶ Geochemical Thermodynamics
- ▶ Iron
- ▶ Kinetics of Geochemical Processes
- ▶ Nitrogen
- ▶ Nitrogen Cycle
- ▶ Organic Geochemistry
- ▶ Organic Matter Degradation and Preservation
- ▶ Oxygen
- ▶ Ozone and Stratospheric Chemistry
- ▶ Phosphorus
- ▶ Soils
- ▶ Stoichiometry

References

Barton A, Hales B, Waldbusser GG, Langdon C, Feely RA (2012) The Pacific oyster, *Crassostrea gigas*, shows negative correlation to naturally elevated carbon dioxide levels: implications for near-term ocean acidification effects. Limnol Oceanogr 57:698–710

Berner RA, Beerling DJ, Dudley R, Robinson JM, Wildman RA (2003) Phanerozoic atmospheric oxygen. Annu Rev Earth Planet Sci 31:105–134

Cai W-J, Hu X, Huang W-J, Murrell MC, Lehrter JC, Lohrenz SE, Chou W-C, Zhai W, Hollibaugh JT, Wang Y, Zhao P, Guo X, Gundersen K, Dai M, Gong G-C (2011) Acidification of subsurface coastal waters enhanced by eutrophication. Nat Geosci 4:766–770

Galloway JN, Townsend AR, Erisman JW, Bekunda M, Cai Z, Freney JR, Martinelli LA, Seitzinger SP, Sutton MA (2008) Transformation of the nitrogen cycle: recent trends, questions, and potential solutions. Science 320:889–892

Huang W, Houlton BZ, Marklein AR, Liu J, Zhou G (2015) Plant stoichiometric responses to elevated CO_2 vary with nitrogen and phosphorus inputs: evidence from a global-scale meta-analysis. Sci Rep 5:18225. https://doi.org/10.1038/srep18225

Ingall E, Jahnke R (1994) Evidence for enhanced phosphorus regeneration from marine sediments overlain by oxygen depleted waters. Geochim Cosmochim Acta 58:2571–2575

Lyons TW, Reinhard CT, Planavsky NJ (2014) The rise of oxygen in Earth's early ocean and atmosphere. Nature 506:307–315

Neset T-SS, Cordell D (2012) Global phosphorus scarcity: identifying synergies for a sustainable future. J Sci Food Agric 92:2–6

Redfield AC (1958) The biological control of chemical factors in the environment. Am Sci 46:205–221

Sardans J, Grau O, Chen HYH, Janssens IA, Ciais P, Piao S, Peñuelas J (2017) Changes in nutrient concentrations of leaves and roots in response to global change factors. Glob Chang Biol 23: 3849–3856

Schlesinger WM, Bernhardt E (2013) Biogeochemistry, an analysis of global change. Academic, Waltham

Sterner R, Elser J (2002) Ecological stoichiometry: the biology of elements from molecules to the biosphere. Princeton University Press, Princeton

Vaccari DA, Strigul N (2011) Extrapolating phosphorus production to estimate resource reserves. Chemosphere 84:792–797

Biological Pump

Sarah L. C. Giering[1] and Matthew P. Humphreys[2]
[1]Ocean Biogeochemistry and Ecosystems, National Oceanography Centre, Southampton, UK
[2]Ocean and Earth Science, University of Southampton, Southampton, UK

Definition

The biological pump is the collection of marine biogeochemical processes that convert dissolved inorganic matter in the surface ocean into biomass and transport this to the ocean interior, where the biomass is returned to its original dissolved inorganic forms.

Introduction

The concentrations of elements vary throughout the global ocean. Concentrations of dissolved inorganic carbon (DIC – the sum of the aqueous CO_2 (<1%), bicarbonate (~90%), and carbonate ion (~10%) concentrations) and nutrients are greater in deep waters relative to the near-surface, and in older water masses relative to younger ones. Some trace metals, on the other hand, have higher concentrations in surface waters. The biological pump is an important process that contributes to these gradients.

The biological pump begins in the sunlit upper ocean, called the euphotic zone. Here, photosynthesizing organisms convert DIC and nutrients into biomass, in the form of particular organic matter (e.g., carbohydrates, lipids, and proteins) and biominerals (e.g., calcium carbonate and silica). This biomass is constantly reworked in a complex web of trophic interactions, and is mostly converted back into an inorganic form within the surface ocean. However, a fraction of the organic matter is "exported" from the surface ocean into the deeper interior. There, these particles may dissolve or be processed by the resident biota, ultimately converting them back into their inorganic forms ("remineralization"). Most remineralization occurs in the upper 1000 m of the water column, although a fraction of the organic matter also reaches the deeper waters and seafloor sediments.

Export

"Export flux" is the rate per unit area at which biomass exits the surface ocean through a reference depth. A fixed reference depth of 100 m is often used for studies that are based on modeling or remote sensing. A dynamic reference depth, such as the base of either the mixed layer or the euphotic zone, is more appropriate to capture particle dynamics and compare export across different ecosystems (Buesseler and Boyd 2009). The ratio of export flux to primary production is called "export efficiency." Three processes can drive export from the surface layer: sinking, active transport, and physical transport.

Sinking

The euphotic zone overlaps with the surface mixed layer, which is physically separated from the interior ocean by a density gradient sustained by winds and air-sea heat and freshwater fluxes. Nevertheless, a fraction of the organic matter passes through this density gradient in the form of sinking particles or through active transport. Sinking particles are a major pathway for biomass transfer to depth. These particles range in diameter from a few micrometers to several centimeters, and particles >0.5 mm across are called "marine snow." Each particle's sinking speed is determined by its

density and drag, with larger particles generally sinking faster. The incorporation of biominerals, such as biogenic silica produced by diatoms, increases density and can thus increase the sinking speed. Large particles are produced primarily through aggregation, which occurs through "coagulation" or biologically mediated repackaging (Burd and Jackson 2009). Coagulation requires particles to stick together to form a larger particle. "Stickiness" is currently not well understood but may be mediated by cell shape (e.g., whether plankton cells have spines or form chains) and the presence of exopolymers (e.g., transparent exopolymer particles) (Burd and Jackson 2009). Aggregation can further occur through feeding and repackaging by larger zooplankton and fish, which results in growth (i.e., biomass accumulation) and the production of fecal pellets (Steinberg and Landry 2017). The sinking of carcasses, in particular those of jellyfish and mammals, could be a significant contributor to export, but remains poorly quantified.

Active Transport

Larger zooplankton and fish export organic matter through vertical migration (Steinberg and Landry 2017). Many larger zooplankton feed in the mixed layer at night and retreat to a depth of several hundred meters during the day, in a process called "diel vertical migration." While resting at depth, migrating animals continue to respire, excrete, and release fecal material, and may die. Migrating animals thus actively export organic matter. The fraction of total export driven by diel vertical migration could be up to 40% (Brierley 2014). On seasonal timescales, some zooplankton species transport organic matter deeper still as they overwinter at over 1 km depth (Steinberg and Landry 2017). There is an additional nondiurnal contribution to active transport by krill, fish, and marine mammals.

Physical Transport

Physical transport can occur in areas of deep water formation, such as in the subpolar North Atlantic and the Southern Ocean. There, cold air takes up heat from warm, poleward-flowing surface waters, thus increasing their density and allowing them to sink to depths of up to 4 km. In the subtropical gyres, wind-driven downwelling can subduct surface waters into the interior (Carlson et al. 2010; Fontela et al. 2016). On smaller spatial scales, export via "detrainment" (i.e., the "mixed layer pump") can occur where stratification is unstable. A prominent example occurs during the onset of spring stratification at high latitudes (Dall'Olmo and Mork 2014). Rising air temperatures allow weak stratification to develop, promoting surface layer carbon fixation through phytoplankton production. During this time, unstable weather conditions (e.g., strong winds) can induce short-term mixed layer deepening, thus mixing the new biomass to greater depth. Once stratification strengthens again, this biomass remains isolated from the surface ocean. Export through detrainment has occurred if the biomass is not mixed back to the surface (or "entrained") during subsequent mixing events. These different types of vertical water mass transport can carry nonsinking organic matter and biominerals into the deep ocean.

Remineralization and Transfer

Most exported biomass is converted back into a dissolved inorganic form in the interior ocean through a set of processes together called remineralization. The remineralization rate, coupled with the vertical and horizontal transport, thus influences the distribution of dissolved inorganic matter, as well as its residence time in the interior ocean.

Sinking is the most effective export process for transporting biomass beyond a few hundred meters' depth, as active and physical transport are often restricted to the upper water column. Sinking particles can also penetrate density gradients and thus travel through different water masses, potentially reaching the seafloor. The "transfer efficiency" quantifies the fraction of organic matter exported from the surface layer that subsequently reaches a deeper reference depth (typically chosen between 500 and 2000 m).

Vertical Profiles

For sinking particles, transfer efficiency is a function of sinking speed and remineralization rate: fast remineralization and slow sinking retains matter near the surface ocean, while slow remineralization and fast sinking allow organic matter to be transported much deeper. Assuming that remineralization rate (r) and sinking speed (v) are constant with depth, flux (F_z) at a depth (z) can be calculated from a reference flux (F_{z0}) as:

$$\mathrm{F_z} = \mathrm{F_{z0}e^{-(rz)/v}} \tag{1}$$

Observations of particle flux profiles suggest that particle flux is better described by an empirical power-law function known as the "Martin curve" (Martin et al. 1987):

$$\mathrm{F_z} = \mathrm{F_{z0}(z/z_0)^{-b}} \tag{2}$$

This power-law function implies that particle sinking speeds increase, and/or remineralization rates decrease, with depth. For carbon, "Martin's coefficient" b varies regionally with a global average of 0.86, while other elements have different values due to varying remineralization and transfer rates (Boyd et al. 2017).

As particles sink, they undergo transformation: remineralization and dissolution returns biomass into its dissolved components, while adsorption onto sinking particles removes

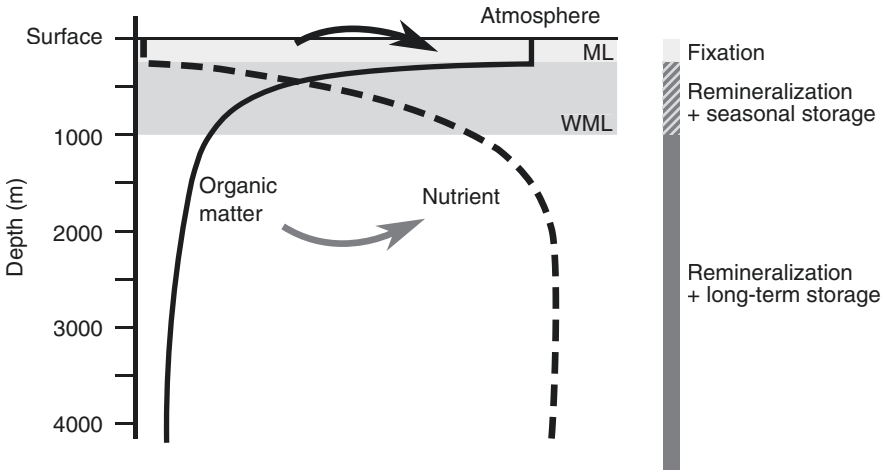

Biological Pump, Fig. 1 Idealized depth profiles of organic matter (solid line) and inorganic nutrients (dashed line). Mixed layer (ML) and winter mixed layer (WML) are illustrated by the green and blue areas, respectively. "Long-term" refers to time scales of up to about 1000 years. Arrows indicate fixation (black) and remineralization (gray)

dissolved elements from the water and transports these to the sediments. The unique combination of chemical and biological processes affecting each element thus drives its distinct vertical profile.

Depletion of an element in the surface layer indicates biological uptake, and such elements can limit primary production (they are "bio-limiting"). These elements are rapidly remineralized near the surface ocean, leading to increased concentrations of their dissolved form at depth ("nutrient-type profile"; Fig. 1). Prominent examples are N, P, Si, Fe, Cd, and Zn (Johnson et al. 2017). Elements that follow the nutrient-type profiles but only show slight surface depletion are called "bio-intermediates," such as Sr which is only used by relatively rare planktonic organisms. Other bio-intermediate examples are C, Ba and Ca.

The adsorption of ions onto sinking particles removes dissolved elements from the water column. This process is more pronounced in surface waters, where particle concentrations are high, and in older, deeper water masses. Adsorption results in decreasing concentrations with depth ("scavenged profile"), with examples being Pb, Mn, Sn, and Co. Short residence times of reactive elements (less than the ocean mixing time) further means that their source of origin influences their distribution, leading to unique depth profiles. Elements whose residence time is longer than the ocean mixing time show nearly uniform concentrations throughout the ocean and have a "conservative profile." Examples are Na, Mg, and Ca (Johnson et al. 2017).

Remineralization

Remineralization occurs via metabolic processes and dissolution. Exported organic matter provides the main energy source for organisms living beneath the sunlit surface. While microbes are principally responsible for remineralization, much of the rapid decrease in organic matter fluxes in the region just below the surface ocean (Fig. 1) is attributed to zooplankton (Giering et al. 2014). Zooplankton fragment large, fast-sinking particles into slow-sinking or suspended particles, thus facilitating shallow microbial remineralization. The metabolic requirements of microbes and zooplankton therefore determine the rate and processes responsible for remineralization.

Metabolic requirements vary for different elements, driving vertical decoupling. Compounds and elements that are essential to life are preferentially metabolized, so the majority of these are remineralized near the ocean surface. Remineralization is thus faster for macronutrients than for metals and approximately follows N > organic C > P > metals (Boyd et al. 2017).

Fresh aggregates are characterized by a high amount of labile compounds, such as essential amino acids and polyunsaturated fatty acids. Deep-sea organisms preferentially metabolize these labile compounds. Therefore, as organic matter "ages" (i.e., is processed), its lability decreases, and the contribution of saturated fatty acids and heterotrophic biomarkers increases (Lee et al. 2004). Eventually, the complex compounds are degraded into their inorganic forms and released as metabolic waste products. Organic nitrogen is converted to ammonia and then to nitrate by nitrifying bacteria. Organic phosphorus is excreted as phosphate. Organic carbon undergoes extensive reworking but is eventually respired as DIC.

Biominerals such as calcium carbonate and biogenic silica are produced along with organic matter. As they have little metabolic value to the deep-sea biota, their remineralization is determined by abiotic dissolution. The silica cycle illustrates how the biological pump influences elemental distributions in the ocean. The appearance of diatoms, which have high silicon requirements, led to a drop in silicic acid concentrations from ~1 mM to today's concentrations of ~70 uM, and resulted in a nutrient-type distribution for the past 50–100 million years (De La Rocha 2007).

Biological Carbon Pump

The biological carbon pump transports 5–20 Gt carbon annually from the surface into the interior ocean (Henson et al. 2011), and keeps, according to models, the atmospheric CO_2 concentration much lower than without ocean biology (Parekh et al. 2006). However, its effect on surface layer CO_2 uptake differs depending upon the type of particulate material produced in the surface ocean.

The soft-tissue pump converts DIC into organic matter in the surface layer. This acts as a sink for atmospheric CO_2: More CO_2 can be added to the water, through air-sea exchange, to replace the DIC that was converted into organic matter. The carbonate "counter" pump converts DIC into particulate inorganic carbon (i.e., $CaCO_3$) through near-surface calcification. Although this process also takes up DIC from the seawater, it reduces the total alkalinity of seawater (Wolf-Gladrow et al. 2007). Alkalinity controls the capacity for seawater to store DIC. The loss of alkalinity during calcification results in a reduction of the DIC storage capacity that is greater than the uptake of DIC. The net effect of calcification is therefore to drive the sea surface towards being a source of CO_2 to the atmosphere.

In the context of the biological carbon pump, the appropriate reference depth for export is the base of the winter mixed layer, because of the effect on isolation time from the atmosphere. DIC produced through remineralization above this depth will be mixed back up to the surface during the winter, where it is back in contact with the atmosphere, and thus promotes CO_2 outgassing. DIC produced beneath the winter mixed layer is considered to be isolated from the atmosphere until upwelling brings it back to the surface. The final isolation time depends on the location of particle export and depth of remineralization, and can be on the order of whole-ocean mixing (i.e., about 1000 years).

Global Pattern

While there is still much uncertainty about the absolute magnitude of export, remineralization, and transfer, general global patterns have been identified (Henson et al. 2012; Siegel et al. 2014). Export flux is typically higher at high latitudes, in the equatorial Pacific, and in upwelling regions (Fig. 2a). Where

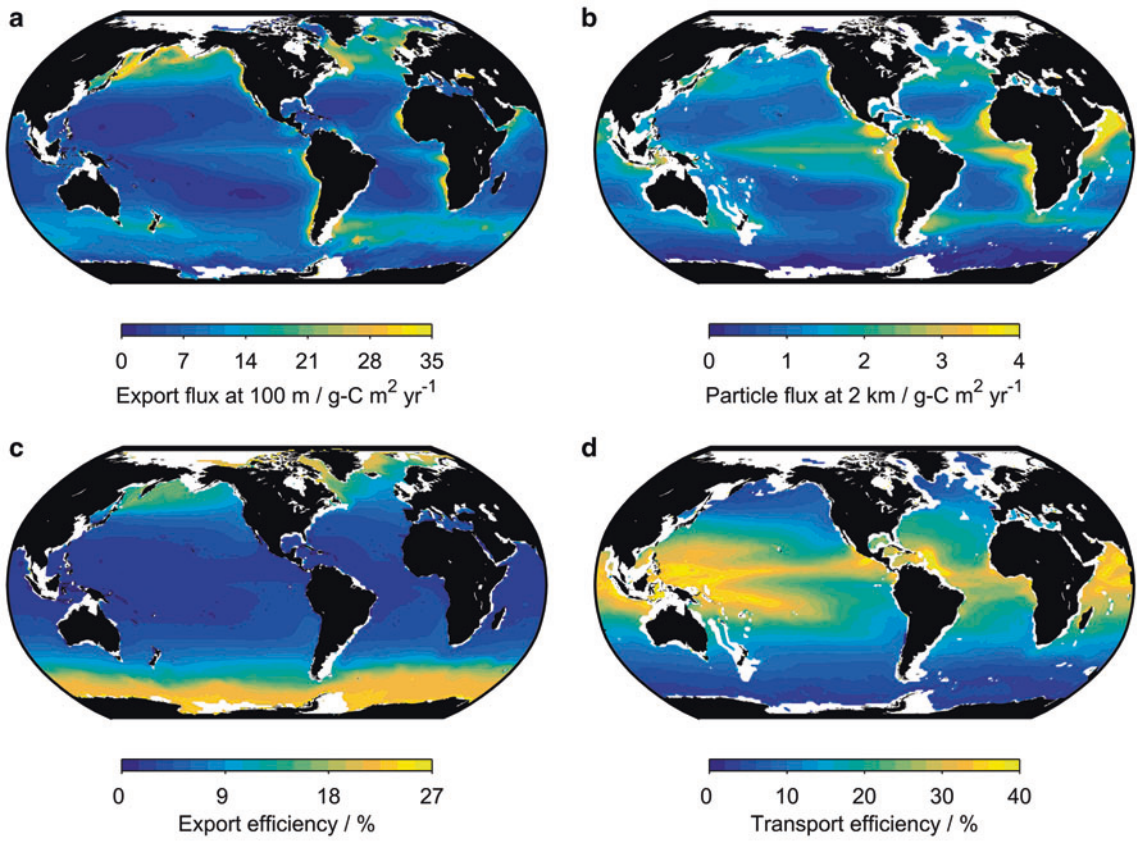

Biological Pump, Fig. 2 Global map of satellite-derived estimates of (**a**) export flux at 100 m depth, (**b**) particle flux at 2000 m depth, (**c**) export efficiency (flux at 100 m depth/depth-integrated primary production), and (**d**) transfer efficiency (flux at 2000 m/flux at 100 m) (Redrawn from Henson et al. 2012). These maps show the approximate global patterns of each variable, but uncertainties for exact values at any specific location are high

primary production is strongly seasonal, export flux peaks during and after the phytoplankton bloom and is lowest during winter (Siegel et al. 2014). High-latitude regions can have high export efficiencies (Fig. 2c), while low-latitude systems generally retain a large fraction of the organic matter in the surface ocean. Inversely, transport efficiency has been shown to increase towards the tropics (Fig. 2d), leading to highest annual deep particle fluxes near the equator (Fig. 2b) (Henson et al. 2012).

Climate and Bioengineering

Various "geo-engineering" techniques have been proposed to offset the impacts of the anthropogenic increase in atmospheric CO_2. Some aim to increase the ocean's capacity to take up and store carbon by enhancing the biological carbon pump. For example, iron addition could promote carbon fixation in areas where iron limits primary production, like the Southern Ocean. Experiments have confirmed that this approach can boost primary production, thus enhancing CO_2 uptake (Lampitt et al. 2008). However, for long-term CO_2 storage, the newly produced organic carbon must be transported below the winter mixed layer. An artificially fertilized, diatom-dominated bloom in the Southern Ocean exported more than half of its biomass to deeper than 1000 m, providing successful long-term DIC storage (Smetacek et al. 2012). However, little carbon was exported to the ocean interior in a similar experiment in the Subantarctic Atlantic Ocean, despite a short-term increase in primary production near the surface (Martin et al. 2013). This spatial variability in efficiency, coupled with concerns about disruptive effects on ecosystems, has led to skepticism that this technique could mitigate the adverse effects of anthropogenic CO_2 (Strong et al. 2009).

Summary

Through the biological pump, dissolved inorganic matter is converted into biomass in the surface ocean, and exported to the interior via sinking, active transport or physical transport. At depth, this biomass is processed (fragmented and/or repackaged) by deep-sea organisms and remineralized. Essential elements are remineralized near the surface ocean and thus have "nutrient-type" vertical profiles (increasing concentration with depth). Non-essential elements exhibit a variety of profiles including decreasing concentrations with depth ("scavenged") and uniform distributions ("conservative"). The storage of carbon in the interior ocean sustained by the biological carbon pump plays an important role in regulating the atmospheric CO_2 concentration. The biological pump thus sustains life in the deep sea and drives the spatial distributions of many elements throughout the global ocean.

Cross-References

- ▶ Anthropogenic CO_2
- ▶ Biogeochemistry
- ▶ Carbon
- ▶ Carbon Cycle
- ▶ Carbonate Compensation Depth
- ▶ Carbonate Minerals and the CO_2-Carbonic Acid System
- ▶ Dissolved Organic Matter (DOM)
- ▶ Iron
- ▶ Marine Sediment
- ▶ Nitrogen Cycle
- ▶ Nutrients
- ▶ Ocean Biochemical Cycling and Trace Elements
- ▶ Ocean Salinity, Major Elements, and Thermohaline Circulation
- ▶ Organic Matter Degradation and Preservation
- ▶ Phosphorus
- ▶ Silicon
- ▶ Solubility

References

Boyd PW, Ellwood MJ, Tagliabue A, Twining BS (2017) Biotic and abiotic retention, recycling and remineralization of metals in the ocean. Nat Geosci 10:167–173. https://doi.org/10.1038/ngeo2876

Brierley AS (2014) Diel vertical migration. Curr Biol 24:R1074–R1076. https://doi.org/10.1016/j.cub.2014.08.054

Buesseler KO, Boyd PW (2009) Shedding light on processes that control particle export and flux attenuation in the twilight zone of the open ocean. Limnol Oceanogr 54:1210–1232. https://doi.org/10.4319/lo.2009.54.4.1210

Burd AB, Jackson GA (2009) Particle aggregation. Ann Rev Mar Sci 1:65–90. https://doi.org/10.1146/annurev.marine.010908.163904

Carlson CA, Hansell DA, Nelson NB et al (2010) Dissolved organic carbon export and subsequent remineralization in the mesopelagic and bathypelagic realms of the North Atlantic basin. Deep Sea Res II Top Stud Oceanogr 57:1433–1445. https://doi.org/10.1016/j.dsr2.2010.02.013

Dall'Olmo G, Mork KA (2014) Carbon export by small particles in the Norwegian Sea. Geophys Res Lett 41:2921–2927. https://doi.org/10.1002/2014GL059244

De La Rocha CL (2007) The biological pump. In: Heinrich DH, Karl KT (eds) Treatise on geochemistry. Pergamon, Oxford, pp 1–29

Fontela M, García-Ibáñez MI, Hansell DA et al (2016) Dissolved organic carbon in the North Atlantic Meridional overturning circulation. Sci Rep 6:26931. https://doi.org/10.1038/srep26931

Giering SLC, Sanders R, Lampitt RS et al (2014) Reconciliation of the carbon budget in the ocean's twilight zone. Nature 507:480–483. https://doi.org/10.1038/nature13123

Henson SA, Sanders R, Madsen E et al (2011) A reduced estimate of the strength of the ocean's biological carbon pump. Geophys Res Lett 38:L04606. https://doi.org/10.1029/2011GL046735

Henson SA, Sanders R, Madsen E (2012) Global patterns in efficiency of particulate organic carbon export and transfer to the deep ocean. Glob Biogeochem Cycles 26:1–14. https://doi.org/10.1029/2011GB004099

Johnson et al (2017) Periodic table of elements in the ocean. http://www.mbari.org/science/upper-ocean-systems/chemical-sensor-group/periodic-table-of-elements-in-the-ocean/

Lampitt RS, Achterberg EP, Anderson TR et al (2008) Ocean fertilization: a potential means of geoengineering? Philos Trans Ser A 366:3919–3945. https://doi.org/10.1098/rsta.2008.0139
Lee C, Wakeham S, Arnosti C (2004) Particulate organic matter in the sea: the composition conundrum. AMBIO J Hum Environ 33:565–575. https://doi.org/10.1579/0044-7447-33.8.565
Martin JH, Knauer GA, Karl DM, Broenkow WW (1987) VERTEX: carbon cycling in the northeast Pacific. Deep Sea Res 34:267–285. https://doi.org/10.1016/0198-0149(87)90086-0
Martin P, van der Loeff MR, Cassar N et al (2013) Iron fertilization enhanced net community production but not downward particle flux during the Southern Ocean iron fertilization experiment LOHAFEX. Glob Biogeochem Cycles 27:871–881. https://doi.org/10.1002/gbc.20077
Parekh P, Dutkiewicz S, Follows MJ, Ito T (2006) Atmospheric carbon dioxide in a less dusty world. Geophys Res Lett 33:L03610. https://doi.org/10.1029/2005GL025098
Siegel DA, Buesseler KO, Doney SC et al (2014) Global assessment of ocean carbon export by combining satellite observations and food-web models. Glob Biogeochem Cycles 28:181–196. https://doi.org/10.1002/2013GB004743
Smetacek V, Klaas C, Strass VH et al (2012) Deep carbon export from a Southern Ocean iron-fertilized diatom bloom. Nature 487:313–319. https://doi.org/10.1038/nature11229
Steinberg DK, Landry MR (2017) Zooplankton and the ocean carbon cycle. Annu Rev Mar Sci 9:413–444. https://doi.org/10.1146/annurev-marine-010814-015924
Strong A, Chisholm S, Miller C, Cullen J (2009) Ocean fertilization: time to move on. Nature 461:347–348. https://doi.org/10.1038/461347a
Wolf-Gladrow DA, Zeebe RE, Klaas C et al (2007) Total alkalinity: the explicit conservative expression and its application to biogeochemical processes. Mar Chem 106:287–300. https://doi.org/10.1016/j.marchem.2007.01.006

Biomarker: Assessment of Thermal Maturity

Kenneth E. Peters[1,2] and J. Michael Moldowan[3]
[1]Schlumberger, Mill Valley, CA, USA
[2]Department of Geological Sciences, Stanford University, Stanford, CA, USA
[3]Biomarker Technologies, Inc., Rohnert Park, CA, USA

Definition

Thermal maturity consists of temperature/time-driven disproportionation reactions that convert sedimentary organic matter into light and heavy fractions of petroleum and finally into hydrocarbon gas and pyrobitumen or graphite. Different geochemical scales commonly used to describe the extent of thermal maturation include vitrinite reflectance (R_o), programmed pyrolysis (e.g., Rock-Eval) T_{max} and production index, and biomarker maturity ratios (e.g., Peters et al. 2005).

Introduction

Geochemists divide thermal maturation into three stages: diagenesis, catagenesis, and metagenesis. Temperature and vitrinite reflectance values at the transitions between these stages vary depending on the burial heating rate and type of organic matter and are thus only approximate. Diagenesis consists of chemical, physical, and biological changes in the organic matter during and after sediment deposition and lithification at temperatures below ~80 °C (R_o <0.6%). Diagenesis occurs prior to thermogenic oil and hydrocarbon gas generation but can include formation of microbial methane. Catagenesis includes thermal alteration of organic matter during burial at ~80–150 °C (R_o ~0.6–2.0%), which may require millions of years. The depth interval of catagenesis corresponds to the oil window or principal zone of oil formation. Metagenesis cracks organic molecules to gas and pyrobitumen at ~150–200 °C (R_o ~2.0–4.0%), prior to greenschist metamorphism (>200 °C). Because common thermal maturity parameters are measured using irreversible reactions, uplifted petroleum source rocks may show higher maturity than expected based on their present-day burial depth.

Vitrinite reflectance is a popular maturity parameter based on organic petrography or rock samples (e.g., Peters and Cassa 1994). Vitrinite phytoclasts are fine particles of higher-plant organic matter that are rare or absent in some rocks, so biomarkers or other parameters are required to assess their maturity (Peters et al. 2005). Because R_o cannot be determined on oil samples or rock extracts, geochemists commonly describe their thermal maturity in terms of equivalent R_o, which can be inferred from biomarkers or other compounds, such as methylphenanthrenes (Peters et al. 2005), or calculated based on time-temperature burial history (e.g., Sweeney and Burnham 1990).

Certain biomarker stereoisomer ratios are among the most common measures of thermal maturity because, unlike R_o and other parameters, biomarkers are nearly ubiquitous in crude oil and sedimentary rock. Stereoisomers have the same molecular formula and the same bonds between atoms but different spatial arrangements of the atoms around each asymmetric carbon atom. Asymmetric carbon atoms are surrounded by four different substituents, thus allowing mirror-image molecules having the same molecular formula, such as L or D amino acids (Fig. 1). Stereoisomers include enantiomers (mirror-image structures having one or more asymmetric carbon atoms) and diastereomers (epimers), which differ at certain asymmetric centers, but may be identical at others.

Methods and General Approach

Gas chromatography-mass spectrometry (GC-MS) generates mass chromatograms, which detect steranes and other

biomarkers by focusing on the principal mass fragment ion that is diagnostic for that class of biomarkers (e.g., Fig. 2; m/z 217 for steranes). The following discussion focuses on steranes as examples of key biomarkers used to assess thermal maturity. Steranes in sediments and petroleum originate from sterols in once-living organisms (Peters et al. 2005). Three asymmetric centers in sterols (C-14, C-17, and C-20) are always in the "biological" configuration: 14α,17α(H),20R, i.e., αα20R. During thermal maturation, the biological configuration can undergo stereoisomerization to more stable "geological" configurations by formation of a carbocation and migration of a hydrogen ion. The biological and three key geological stereoisomers are readily quantified by gas chromatography-mass spectrometry (m/z 217; Fig. 2, far right). Two common sterane maturity ratios are: (1) 100 × αα20S/(αα20S + αα20R), also called %20S, and (2) 100 × (ββ20S+ββ20R)/(ββ20S+ββ20R+αα20S+αα20R), also called %ββ. X = H, CH_3, C_2H_5, and other groups. These ratios are normally measured for the C_{29} sterane homolog, which is called stigmastane (X = C_2H_5).

However, sterane homologs at C_{27}, C_{28}, C_{29}, and C_{30} in oil or extract samples can interfere with each other on mass chromatograms, resulting in inaccurate assessment of stereoisomer ratios. Gas chromatography-mass spectrometry-mass spectrometry (GC-MS-MS) eliminates interference among homologs by means of precursor-product (also called

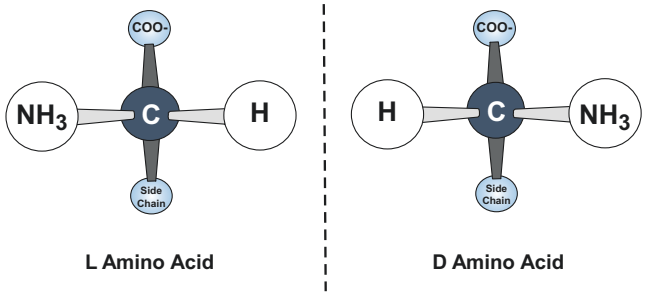

Biomarker: Assessment of Thermal Maturity, Fig. 1 Inversion of one asymmetric carbon atom (epimerization) in an amino acid results in a type of stereoisomer called an enantiomer, which is a molecule having a nonsuperimposable mirror image (indicated by *dashed line*). Nearly all living organisms have amino acids in the L configuration. In molecules having more than one asymmetric center, inversion of all asymmetric centers leads to the enantiomer (mirror image). Inversion of one or more, but not all asymmetric centers, yields a diastereomer. Biomarkers in petroleum and source rock extracts have many asymmetric centers and therefore many diastereomers and enantiomers are possible for each

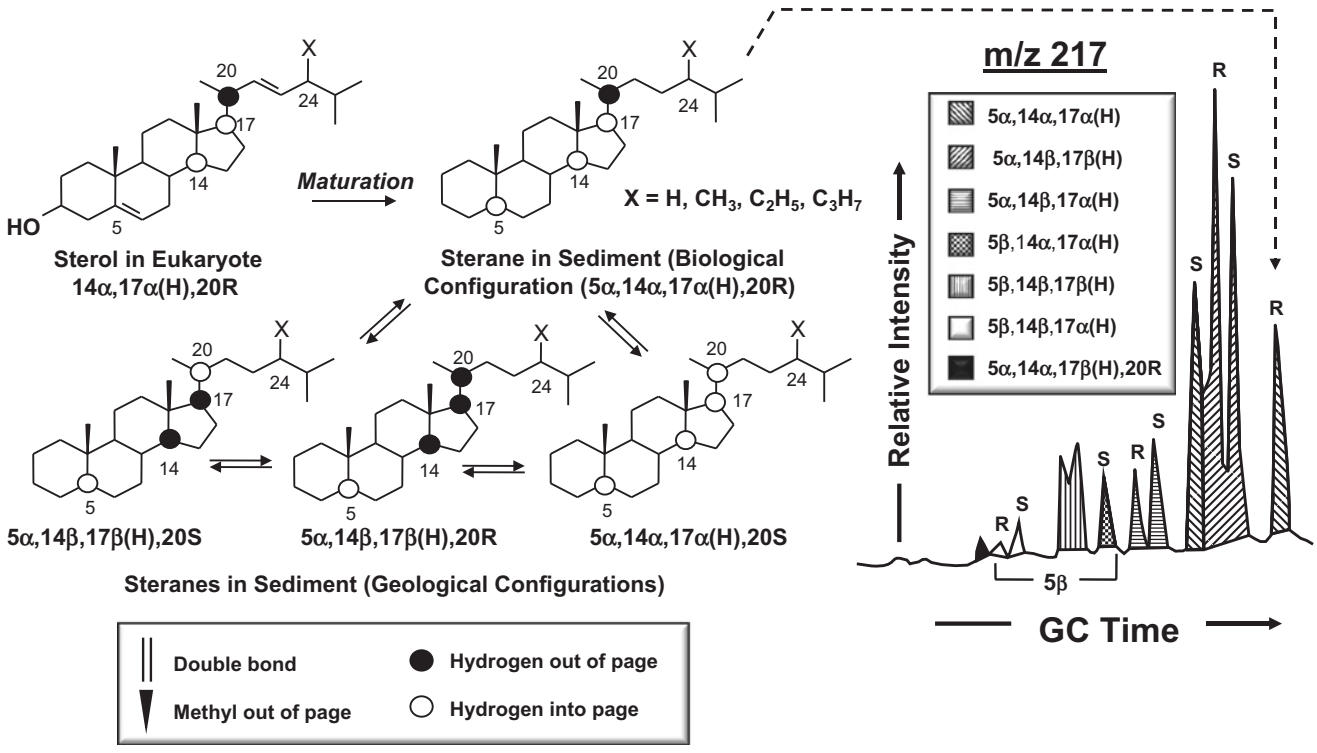

Biomarker: Assessment of Thermal Maturity, Fig. 2 Steranes in petroleum originate from sterols in once-living organisms (*top left*). During early diagenesis, steranes retain the original biological stereochemistry at positions C-14, C-17, and C-20 (αα20R). During catagenesis, steranes undergo stereoisomerziation at these and other positions, resulting in some proportion of thermally more stable geological stereioisomers (mass chromatogram at *right*; Seifert and Moldowan 1979). The extent of each reaction varies depending on the specific atomic geometry at each asymmetric center but can also be influenced by temperature and catalysis by minerals

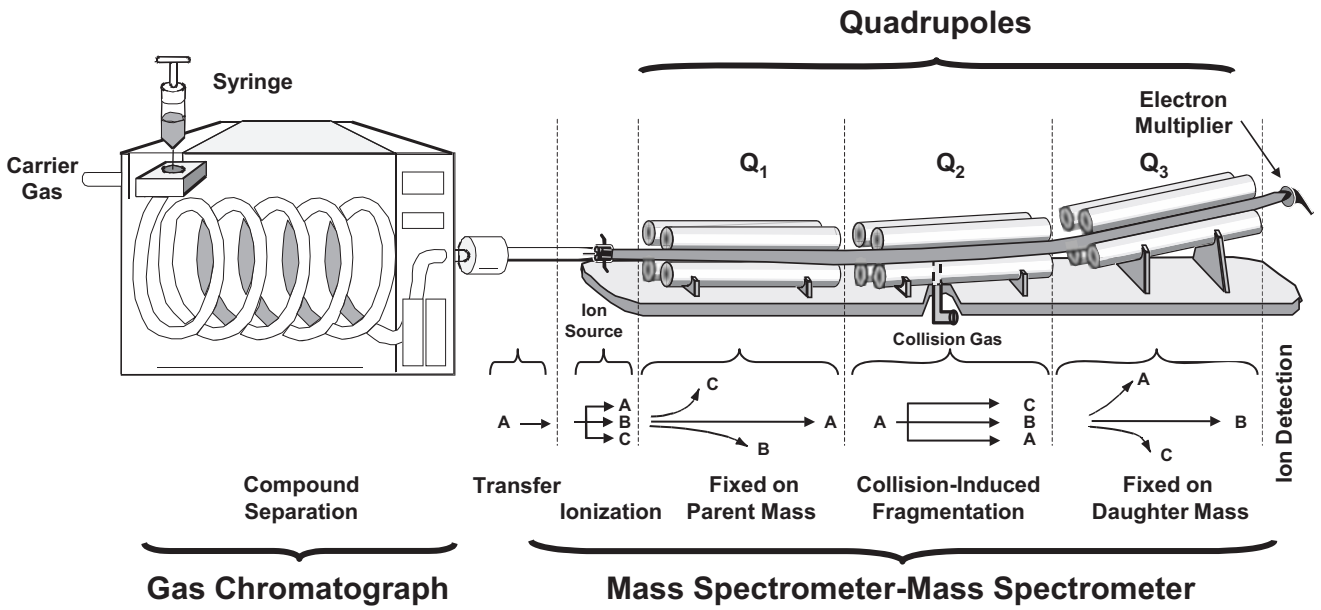

Biomarker: Assessment of Thermal Maturity, Fig. 3 Schematic view of a gas chromatograph equipped with a triple-quadrupole mass spectrometer consisting of three sets of quadrupole rods (GC-MS-MS; not to scale). Three quadrupoles allow highly selective precursor-product detection (e.g., only product ion B from precursor compound A). The gas chromatograph separates compound A, which undergoes ionization in the ion source at 70 eV. The first quadrupole (Q1) focuses the molecular ion of A, which is the precursor of additional ion products by collision-induced fragmentation in Q2. Q3 focuses the diagnostic product ion B, thus removing interference by other ions created in Q2

parent-daughter) ion monitoring. For example, C_{29} steranes can be monitored using triple-quadrupole mass spectrometry (Fig. 3) by allowing only ions having a precursor mass (M+) of m/z 400 to enter the second or collision quadrupole for further fragmentation. The third quadrupole focuses only on the appropriate product mass for steranes (m/z 217), thus resulting in a mass chromatogram that is unique for C_{29} steranes (Fig. 4).

Parameters

Various saturated and aromatic biomarker ratios can be used to assess thermal maturity of crude oils or source rock extracts (Peters et al. 2005). Most ratios are expressed as the product (B) divided by the reactant (A) plus the product, i.e., B/(B + A). These ratios are based on two reaction types: (1) stereoisomerization at asymmetric carbon atoms in saturated biomarkers and (2) cracking and/or aromatization, including so-called side-chain scission reactions in aromatic biomarkers. It is more likely that relative stability of the short versus long side-chain compounds is the basis for these cracking parameters. Relative stability is the basis for several other saturated biomarker maturity parameters, such as C_{23} tricyclic terpane/C_{30}-hopane, diasteranes/steranes, Ts/Tm [18α-trisnorneohopane/17α-trisnorhopane, usually presented as Ts/(Ts + Tm)], and 18α,30-norneohopane/17α-30-norhopane [abbreviated as C_{29}Ts/C_{29}Hop or C_{29}Ts/(C_{29}Ts + C_{29}Hop)]. The latter two and many other maturity parameters are not stereoisomerizations but are based on the relative kinetic and/or thermodynamic stability of the components toward C─C bond cracking. Thus, Ts/(Ts + Tm) progresses from zero in immature samples to one (or 100%) at late oil-window maturity due to greater relative stability of Ts compared to Tm. Such parameters, termed irreversible, become important for maturity estimation from before the peak to the end of the oil window, a maturity range in which sterane and hopane stereoisomer ratios have maximized at some value between zero and one.

Stereoisomerization ratios are preferred because the reactant in thermally-immature sediments is 100% in the biological configuration, whereas the product geological configurations are absent. In reality, even stereoisomer ratios cannot be described strictly by simple conversion of A to B. For this reason, kinetics derived for these presumed reactions cannot be reliably used to calibrate basin and petroleum system models (Walters et al. 2012). Four of the most commonly used ratios are based on isomerization of hydrogen atoms around asymmetric carbon atoms at C-20 [%20S/(20S + 20R)] and C-14 and C-17 [%ββ/(ββ + αα)] in the steranes, C-22 in the hopanes [%22S/(22S + 22R)], and both C-17 and C-21 in the hopanes [%ββ/(ββ + βα + αβ)], as indicated in Fig. 5. Other saturated biomarker maturity parameters supplement these isomerization ratios, such as the moretane/17α-hopane [17ß,21α/17α,21ß].

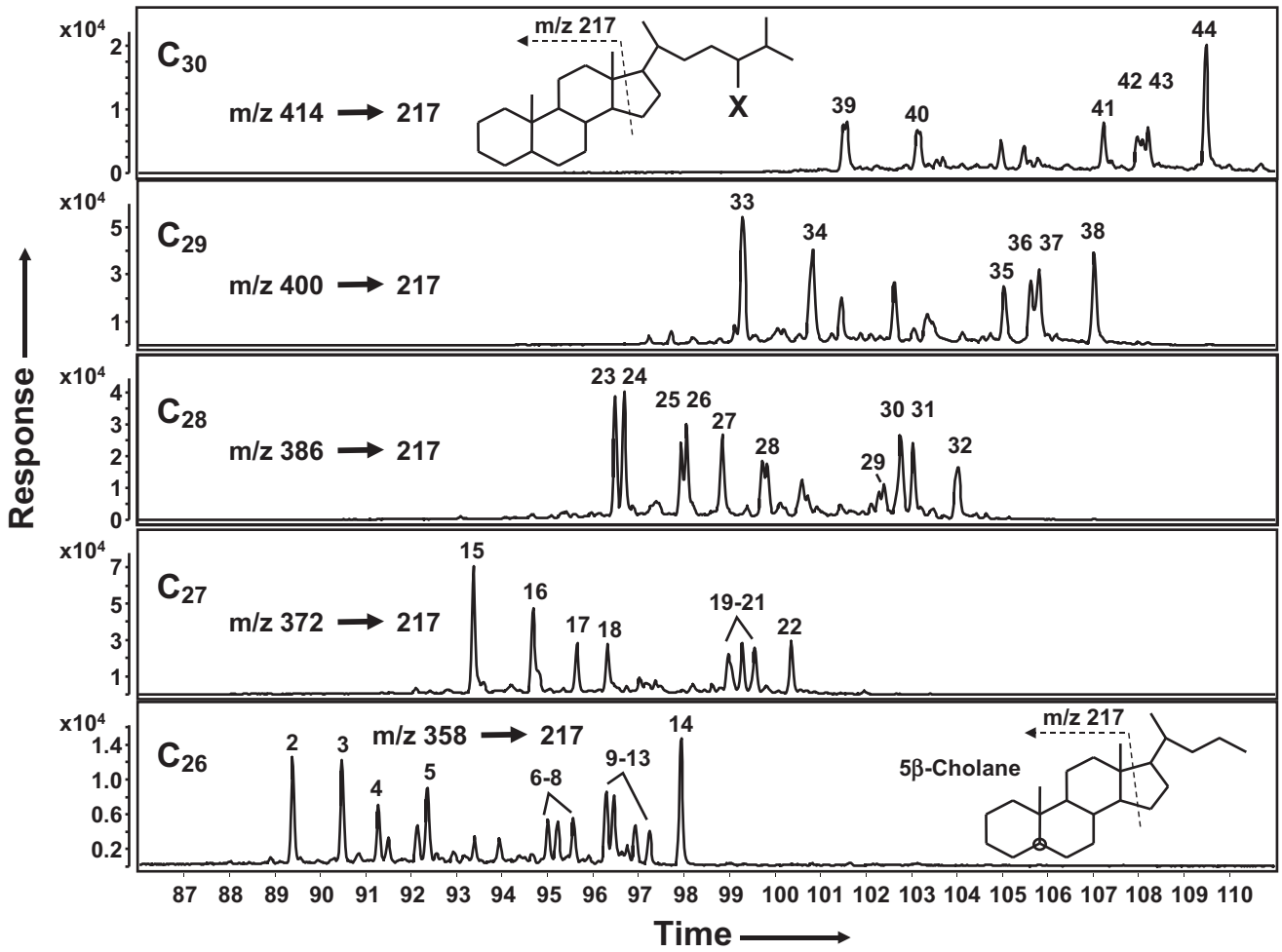

Biomarker: Assessment of Thermal Maturity, Fig. 4 Gas chromatography-mass spectrometry-mass spectrometry (GC-MS-MS) of a crude oil mixture (Stanford-1) in precursor-product mode (M+ → m/z 217) differentiates sterane epimers by carbon number, thus reducing interference seen in GC-MS. Stanford-1 is a blend of several oil samples and some pure synthetic compounds blended to include most biomarkers in crude oils derived from source rocks deposited in various depositional environments. *Dashed arrows* in the upper inset identify the m/z 217 product ion. X = H, CH_3, C_2H_5, and C_3H_8 for the C_{27} to C_{30} homologs (precursor ion, M+ = m/z 372, 386, 400, and 414, respectively). 5β-Cholane (*lower right*) is a C_{24} sterane not abundant in crude oil that is used as an internal standard to quantify peaks. Peaks 35–38 (Table 1) can be used to generate two C_{29} sterane stereoisomer ratios used to assess the thermal maturity of crude oil and source rock extracts (Fig. 5): %20S/(20S + 20R) and % ββ/(ββ + αα). Peaks 23–26 were recently identified in Peters et al. (2014)

Another biomarker cracking ratio is based on the conversion of monoaromatic (MA) to triaromatic (TA) steroids (Fig. 5). The TA/(MA + TA) ratio is less commonly applied for maturity assessment than isomerization ratios because (1) quantification of aromatic steroids can be difficult and (2) thermally immature samples may not start with 100% of the presumed reactant. Some additional aromatic maturity parameters are based on ratios of aromatic steroids with short versus long side chains (commonly described as side-chain cleavage reactions). These aromatic steroid side-chain scission parameters are similar to Ts/Tm in that they extend the application of biomarker maturity estimates from the middle to well into the late-oil window, where stereoisomeriztion ratios are ineffective.

Data Interpretation

Biomarker ratios can be used to assess the relative thermal maturity of crude oils and source rock extracts, particularly when the samples are genetically related based on oil-oil or oil-source rock correlation using source-related biomarker and stable carbon isotope ratios (Peters et al. 2005). Figure 6 shows the relative thermal maturity of nine genetically related crude oils based on two C_{29} sterane stereoisomer ratios from GC-MS-MS.

Assessment of thermal maturity relative to the oil window or vitrinite reflectance using biomarker ratios (Fig. 5) is not as straightforward as relative maturity assessment (Fig. 6). All relationships between reaction extent and the stage of oil

Biomarker: Assessment of Thermal Maturity, Table 1 Identification of biomarker peaks from Fig. 4, including peaks 35–38 that are used to generate two C_{29} sterane stereoisomer ratios in Fig. 5 and 6. Peaks are quantified using the C_{24} sterane 5β-cholane internal standard (peak 1 not shown in Fig. 4), which is measured from the m/z 330 to 217 precursor-product transition with calibration using the Stanford-1 external standard (Peters et al. 2005)

Peak	Identification	Carbon number
1	5β-Cholane	24
2	13β,17α(H)-24-Nordiacholestane 20S	26
3	13β,17α(H)-24-Nordiacholestane 20R	26
4	13β,17α(H)-27-Nordiacholestane 20S	26
5	13β,17α(H)-27-Nordiacholestane 20R	26
6	5α,14α,17α(H)-24-Norcholestane 20S	26
7	5α,14β,17β(H)-24-Norcholestane 20R	26
8	5α,14β,17β(H)-24-Norcholestane 20S	26
9	5α,14α,17α(H)-24-Norcholestane 20R	26
10	5α,14α,17α(H) + αββ(H)-21-Norcholestane	26
11	5α,14α,17α(H)-27-Norcholestane 20S	26
12	5α,14β,17β(H)-27-Norcholestane 20R	26
13	5α,14β,17β(H)-27-Norcholestane 20S	26
14	5α,14α,17α(H)-27-Norcholestane 20R	26
15	13β,17α(H)-Diacholestane 20S	27
16	13β,17α(H)-Diacholestane 20R	27
17	13α,17β(H)-Diacholestane 20S	27
18	13α,17β(H)-Diacholestane 20R	27
19	5α,14α,17α(H)-Cholestane 20S	27
20	5α,14β,17β(H)-Cholestane 20R	27
21	5α,14β,17β(H)-Cholestane 20S	27
22	5α,14α,17α(H)-Cholestane 20R	27
23	13β,17α(H)-Diaergostane 20S,24R	28
24	13β,17α(H)-Diaergostane 20S,24S	28
25	13β,17α(H)-Diaergostane 20R,24S	28
26	13β,17α(H)-Diaergostane 20R,24R	28
27	13α,17β(H)-Diaergostane 20S,24R + 20S,24S	28
28	13α,17β(H)-Diaergostane 20R,24S + 20R,24R	28
29	5α,14α,17α(H)-Ergosstane 20S,24R + 20S,24S	28
30	5α,14α,17α(H)-Ergosstane 20R,24R + 20R,24S	28
31	5α,14β,17β(H)-Ergostane 20S,24R + 20S,24S	28
32	5α,14α,17α(H)-Ergostane 20R,24R + 20R,24S	28
33	13β,17α(H)-Diastigmastane 20S,24R + 20S,24S	29
34	13β,17α(H)-Diastigmastane 20R,24R + 20R,24S	29
35	5α,14α,17α(H)-Stigmastane 20S,24R + 20S,24S	29
36	5α,14β,17β(H)-Stigmastane 20R,24R + 20R,24S	29
37	5α,14β,17β(H)-Stigmastane 20S,24R + 20S,24S	29
38	5α,14α,17α(H)-Stigmastane 20R,24R + 20R,24S	29
39	13β,17α(H)-24-Dia-*n*-propylcholestane 20S,24R + 20S,24S	30
40	13β,17α(H)-24-Dia-*n*-propylcholestane 20R,24R + 20R,24S	30
41	5α,14α,17α(H)-24-*n*-Propylcholestane 20S,24R + 20S,24S	30
42	5α,14β,17β(H)-24-*n*-Propylcholestane 20R,24R + 20R,24S	30
43(40)	5α,14β,17β(H)-24-*n*-Propylcholestane 20S,24R + 20S,24S	30
44(41)	5α,14α,17α(H)-24-*n*-Propylcholestane 20R,24R + 20R,24S	30

generation or vitrinite reflectance (R_o) are approximate. Readers are cautioned against inferring equivalent R_o from a single biomarker ratio. Reflectance inferred from multiple biomarker ratios may show variations of ±0.1% R_o.

The most reliable approach to assess thermal maturity from Fig. 5 is to start by using stereoisomer ratios based on fast reactions (e.g., C_{32} hopane %22S/(22S + 22R). For example, if a sample achieved the endpoint for %22S/(22S + 22R) (~60%), this nominally represents maturity equivalent to at least the beginning of the oil window (R_o ~0.6%). All samples in Fig. 6 have achieved endpoint for this ratio. Next, proceed to the ratio for a slower reaction, such as C_{29} sterane %20S/(20S + 20R). If the endpoint for %20S/(20S + 20R) has been achieved, then proceed to an even slower reaction, such as C_{29} sterane %ββ/(ββ + αα). If this ratio did not achieve endpoint (~70%) for a sample (e.g., sample H in Fig. 6), then the thermal maturity is bracketed by the endpoints for %20S/(20S + 20R) and %ββ/(ββ + αα)], which approximately corresponds to the peak of the oil window or R_o ~0.9% (Fig. 5). If the sample achieved endpoint for %ββ/(ββ + αα), e.g., sample I in Fig. 6, then further assessment requires use of ratios from even slower reactions such as mono- or triaromatic side-chain cleavage parameters: MA(I)/MA(I + II) or TA(I)/TA(I + II), which are based on stereoisomerization. We do not recommend that maturity assessment begin with ratios based on such slow reactions, because (1) reactions controlling these ratios are complex and the initial amounts of reactant and product may not be 100% and 0%, respectively and (2) these robust ratios may not even respond at low maturity, thus resulting in no systematic trend. Nevertheless, ratios for these slow reactions can show systematic variations with maturity in some cases and it is preferable to consider as many biomarker maturity parameters as possible to corroborate interpretations.

Supporting Analyses

Perhaps the most straightforward biomarker maturity parameters rely simply on biomarker concentrations in oil and rock extract samples. Biomarker concentrations can be measured by GC-MS or GC-MS-MS by introducing calibration factors determined through analysis of an external standard, where the abundance of the ion being measured for each biomarker (e.g., m/z 217 for steranes by GC-MS or the m/z 400 → 217 transition for C_{29}-steranes by GC-MS-MS) is calculated based on its known concentration in the standard. Biomarker concentrations steadily decrease from a maximum before the beginning of the oil window to zero at or before the end of the oil window, depending on which biomarker is being measured. One such biomarker concentration that is commonly used in this way is that of the ααα20R-C_{29}-sterane (sometimes named stigmastane) when

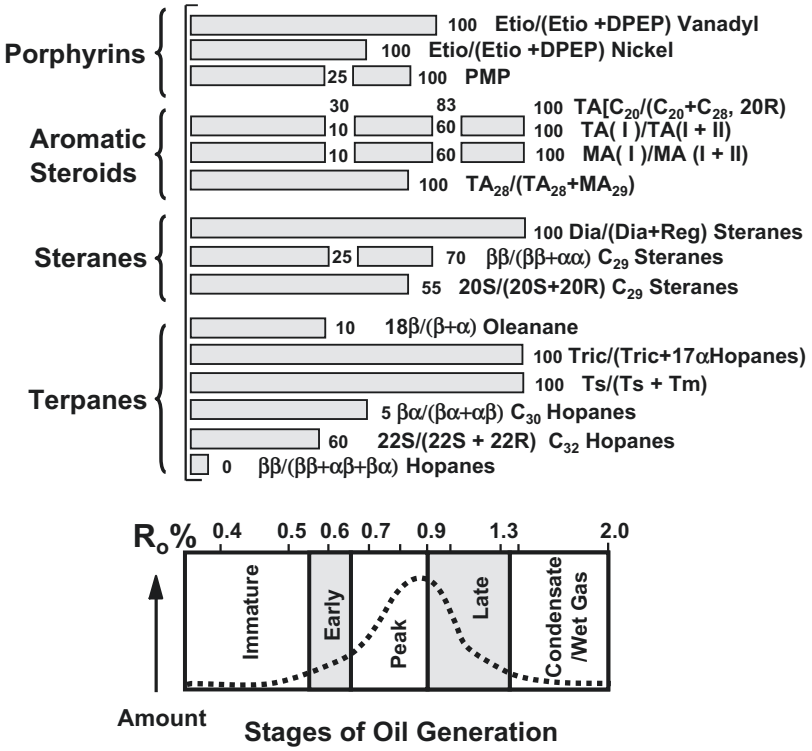

Biomarker: Assessment of Thermal Maturity, Fig. 5 Approximate ranges of some biomarker maturity parameters relative to equivalent vitrinite reflectance (R_o) and the oil generation window (modified from Peters and Moldowan 1993). *Solid bars* show the range for each ratio relative to the stages of oil generation. Each ratio reaches a constant percentage indicated at the end of the bar, which normally does not change with further maturity. This ratio is the maximum value for most of the parameters, except 18ß/(18α + 18ß)-oleanane, ßα/(αß + ßα)-hopanes (C_{30}) and ßß/(ßß + αß + ßα)-hopanes, where 10, 5, and 0 are minimum values, respectively. Intermediate values are shown for a few ratios within the bars to indicate earlier stages of maturity (Reprinted with permission by ChevronTexaco Exploration and Production Technology Company, a division of Chevron U.S.A. Inc.)

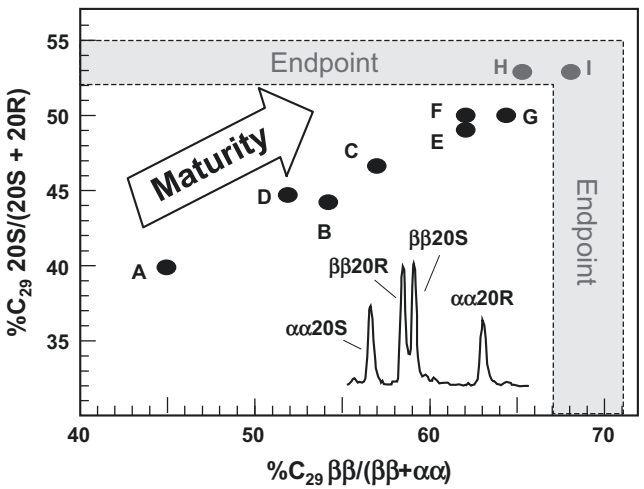

Biomarker: Assessment of Thermal Maturity, Fig. 6 Relative thermal maturity for nine genetically related crude oil samples based on two C_{29} sterane stereoisomer ratios. Inset shows peaks used for the C_{29} sterane ratios from GC-MS-MS analysis (m/z 400 → 217; peaks 35–38 in Fig. 4). The %20S and %ββ ratios require two and four peaks, respectively. Sample A is the least mature. Sample G is less mature than samples H and I. Sample I is more mature than H because it has achieved endpoint for both ratios. Complete maturity assessment of sample I requires additional biomarker ratios that respond at higher levels of thermal maturity

plotted versus the sum of the concentrations of two diamondoids; 3- and 4-methyldiamantanes (Dahl et al. 1999). Diamondoid concentrations are measured by adding deuterated diamondoids to the oil or extract sample before analysis (diamondoid methods and applications are reviewed by Moldowan et al. 2015). This method accounts for maturity from the beginning of the oil window extending into the gas window, i.e., from R_o ~0.6 to 4.0% or more. The ααα20R-C_{29}-sterane reaches negligible concentrations at approximately the maturity where oil begins to crack to gas and pyrobitumen is being formed. On the other hand, the diamondoids are thermally very stable and actually become more concentrated after significant oil cracking begins. Thus, Fig. 7 can be used to determine relative maturities of oil samples both within and far beyond oil-window maturity.

Additional maturity measurements help to validate biomarker maturity assessments. For example, vitrinite reflectance or programmed pyrolysis T_{max} and production index for rock samples help to verify biomarker interpretations based on the corresponding rock extracts. Nonbiomarker maturity parameters, such as the methylphenanthrene index (Radke and Welte 1983), can be used to corroborate biomarker assessment of oil maturity.

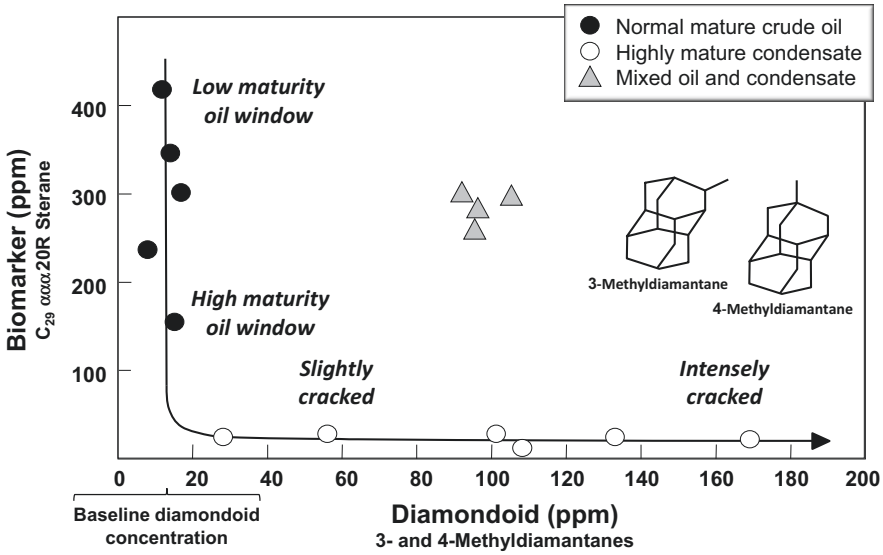

Biomarker: Assessment of Thermal Maturity, Fig. 7 The biomarker-diamondoid method can be used to assess thermal maturity of crude oil or source rock extract samples. Oil samples having maturities within the oil window show significant C_{29} sterane (stigmastane) concentrations and low concentrations of diamondoids (3- and 4-methyldiamantanes). Diamondoids increase rapidly from baseline concentrations after significant oil cracking begins. Oil samples showing mixed maturity signals, i.e., elevated stigmastane and elevated 3- and 4-methyldiamantane concentrations (*triangles*), represent mixtures of both oil-window (e.g., black oil) and postmature components (e.g., light oil or condensate) that result from multiple charge events in the petroleum reservoir (Figure adapted from Dahl et al. (1999))

Summary

In general, the relative thermal maturity of genetically related oil or source-rock extract samples can be readily assessed using various biomarker maturity ratios. Maturity ranking may not be possible for samples that are contaminated, heavily biodegraded, or so highly mature that specific biomarkers are low (<3–5 ppm) or absent. However, highly mature samples can still be evaluated using the quantitative biomarker-diamondoid method. Estimates of maturity relative to the oil window or vitrinite reflectance using biomarker ratios may not be as straightforward as relative maturity assessment. Biomarker maturity ratios are limited in the effective maturity ranges that they cover. Therefore, the most reliable maturity assessments are based on multiple biomarker ratios from progressively slower reactions, which bracket the maturity of each oil or rock extract sample. Stereoisomer ratios are preferred because the initial amount of reactant in the biological configuration is 100%, while that of the product is 0%.

Cross-References

- Biogenic Methane
- Biomarkers: Petroleum
- Carbon Isotopes
- Dissolved Organic Matter (DOM)
- Gas Chromatography–Mass Spectrometry (GC–MS)
- Geochemical Thermodynamics
- Kinetics of Geochemical Processes
- Laboratory Simulations of Organic Geochemical Processes at Elevated Temperatures
- Oil-Oil and Oil-Source Rock Correlations
- Organic Matter Degradation and Preservation
- Organic Matter in Fossils
- Petroleum
- Precambrian Organic Matter
- Programmed Temperature Pyrolysis

References

Dahl J, Moldowan JM, Peters KE, Claypool GE, Rooney MA, Michael GE, Mello MR, Kohnen ML (1999) Diamondoid hydrocarbons as indicators of natural oil cracking. Nature 399:54–57

Moldowan JM, Dahl JE, Zinniker D, Barbanti SM (2015) Underutilized advanced geochemical technologies for oil and gas exploration and production-1.The diamondoids. J Pet Sci Eng 126:87–96

Peters KE, Cassa MR (1994) Applied source rock geochemistry. In: Magoon LB, Dow WG (eds) The petroleum system – from source to trap, American association of petroleum geologists memoirs, vol 60, pp 93–117

Peters KE, Moldowan JM (1993) The biomarker guide. Prentice-Hall, Englewood Cliffs. 363 p

Peters KE, Walters CC, Moldowan JM (2005) The biomarker guide. Cambridge University Press, Cambridge, UK. 1155 p

Peters KE, Moldowan JM, LaCroce MV, Kubicki JD (2014) Stereochemistry, elution order, and molecular modeling of four diaergostanes in petroleum. Org Geochem 76:1–8

Radke M, Welte DH (1983) The methylphenanthrene index (MPI). A maturity parameter based on aromatic hydrocarbons. In: Bjorøy M,

Albrecht C, Cornford C, de Groot K, Eglinton E, Galimov E, Leythaeuser D, Pelet R, Rullkötter J, Speer G (eds) Advances in organic geochemistry, vol 1981. Wiley, New York, pp 504–512
Seifert WK, Moldowan JM (1979) The effect of biodegradation on steranes and terpanes in crude oils. Geochim Cosmochim Acta 43:111–126
Sweeney JJ, Burnham AK (1990) Evaluation of a simple model of vitrinite reflectance based on chemical kinetics. Am Assoc Pet Geol Bull 74:1559–1570
Walters CC, Lillis PG, Peters KE (2012) Molecular indicators of geothermal history. In: Harris NB, Peters KE (eds) Analyzing the thermal history of sedimentary basins: methods and case studies, SEPM special publication, vol 103, pp 17–28

Biomarkers: Coal

Achim Bechtel[1] and Wilhelm Püttmann[2]
[1]Department of Applied Geoscience and Geophysics Petroleum Geology, Montanuniversitaet Leoben, Leoben, Austria
[2]Institute for Atmospheric and Environmental Sciences, Department of Environmental Analytical Chemistry, Goethe University, Frankfurt am Main, Germany

Definition

Biomarkers. Complex organic compounds which retained structural similarities to biological precursors identified in living organisms.

Lipids. Small molecules that originate from biochemical subunits, including fats, waxes, sterols, etc. These molecules can be extracted by organic solvents.

Coal. Combustible black sedimentary rock formed by humification of plant materials. According to increased maturation, coals are classified as lignites, subbituminous coals, bituminous coals, and anthracites, respectively.

Introduction

Organic geochemical methods have become important tools for the reconstruction of paleovegetation, environmental changes, and transformation processes of organic matter during diagenesis. The application of gas chromatography and mass spectrometry techniques on extractable organic matter (i.e. lipids) from low-rank coals or compounds released during pyrolysis has been used to gain information about coal-forming vegetation. Biomarkers were successfully used for the taxonomical differentiation of plant families. Effects of humification, microbial activity, and diagenetic pathways on biomarker composition have been derived from coal-bearing sequences subjected to increased thermal maturation.

Lipids (especially hydrocarbons) are minor constituents in lignite and subbituminous coals. However, their composition provides information on paleovegetation and paleoclimate, especially if combined with the results of paleontological studies. The diagnostic biomarkers decrease in intensity with increasing maturity, and they largely disappear in butuminous coals. Instead information about thermal transformation processes (diagenetic pathways) of biomarkers can be derived from these coals.

Biomarkers and Paleovegetation

Besides pollen assemblages, changes in paleovegetation are reflected by biomarker composition of coals. Several attempts have been made to interpret *n*-alkane distribution patterns in terms of floral changes. However, the potential outcomes are controversially discussed. More specifically, terpenoids were found to contain diagnostic biomarkers for the reconstruction of the coal-forming vegetation.

Terpenoids (isoprenoids) represent the largest and most diverse class of biomolecules among the compounds produced by plants. Plants employ terpenoid metabolites for a variety of basic functions in growth and development but use the majority of terpenoids for more specialized chemical interactions and protection in the abiotic and biotic environment. They defend many species of plants, animals, and microorganisms against predators, pathogens, and competitors. Based on the number of isoprene units, the terpenoid biomarkers are subdivided into sesquiterpenoids, diterpenoids, and triterpenoids.

n-Alkane Distribution

Different types of plants produce leaf wax *n*-alkanes with differing carbon chain lengths. Leaf wax of vascular plants (grasses, sedges, trees, and shrubs) is dominated by long chain (C_{29}–C_{31}) *n*-alkanes, whereas *Sphagnum* leaf wax is characterized by medium chain length (C_{23}–C_{25}) *n*-alkanes (Nott et al. 2000; Pancost et al. 2002). The potential of using biomarker *n*-alkanes as surface moisture proxies by comparing changes in the ratios of *n*-alkanes with already observed changes in water table depths and humification indices in a peat core from Minden Bog in southeastern Michigan (USA) has been documented by Nichols et al. (2006).

Recently, the combination of hydrogen isotopic compositions of low (C_{23}, C_{25}) and high molecular weight (C_{31}, C_{33}) *n*-alkanes with *n*-alkane ratios revealed differences in hydrology and the relative contribution of aquatic to terrestrial plants in a Quaternary peat bog of northwestern China (Seki et al. 2009).

Sesquiterpenoids

Sesquiterpenoids (C_{15}) include more than 2,500 compounds. Besides the origin of several bicyclic

sesquiterpanes (i.e., drimane) through biodegradation or thermal cleavage of pentacyclic triterpenes, the occurrence of mono- and bicyclic sesquiterpanes in crude oils derived from terrestrial sources has been reported (Alexander et al. 1983; Philp 1985).

Monocyclic bisabolanes and biosynthetically related compounds (cuparene (**I;** Fig. 1) and α-cedrene (**II;** Fig. 1); Otto and Wilde 2001) have been identified in a fossil resin and montane wax derived from conifers of the family Cupressaceae (Grantham and Douglas 1980). Besides this well-established

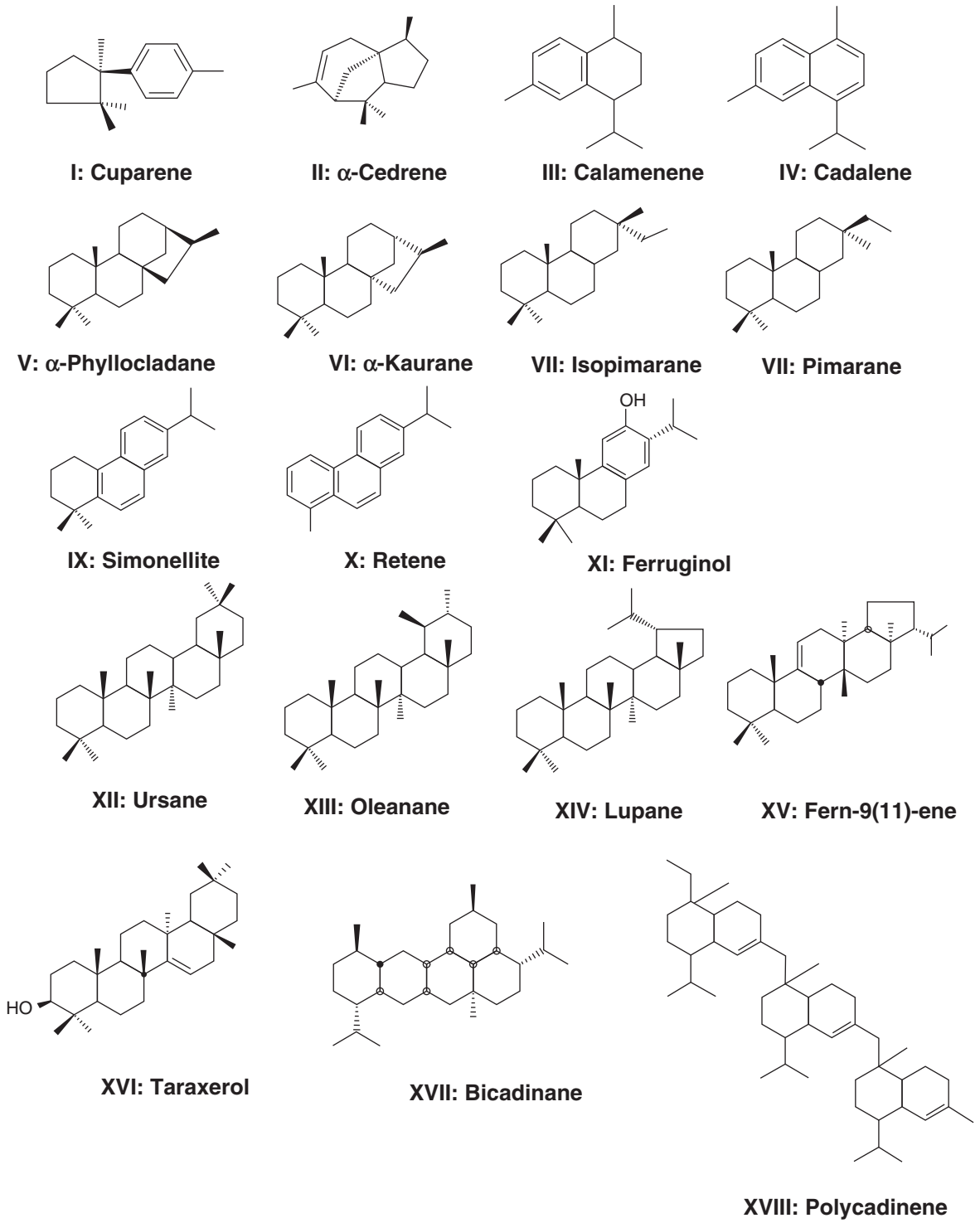

Biomarkers: Coal, Fig. 1 Terpenoid compounds of different structural types discussed in the text

precursor/product relationship, sesquiterpenoids are less specific for the identification of contributions of different gymnosperm families.

Bicyclic sesquiterpenoids are widely distributed in higher plants, and related hydrocarbons were found in oils and source rocks. Cadinanes are common constituents of conifers. However, these sesquiterpenoids are also known as catagenic products of polycadinenes, biomarkers specific for the angiosperm family Dipterocarpaceae (van Aarssen et al. 1990). Based on the identification of cadalane-type **(III, IV;** Fig. 1) sesquiterpenoids in fossil resins of the Oligo/Miocene *Taxodium*-rich oxbow lake clays, the origin of these sesquiterpenoids from Taxodiaceae was concluded (Otto et al. 1997; Vávra and Walther 1993).

Diterpenoids

Tetracyclic diterpenoid hydrocarbons include the phyllocladane- (**V;** Fig. 1) and kaurane-type (**VI;** Fig. 1) compounds (Fig. 2). They have been proposed as biomarkers for the Podocarpaceae and Araucariaceae families, respectively (Noble et al. 1985). The determination of the diagenetic molecular signatures of extant representatives of Araucariaceae through artificial maturation by confined pyrolysis confirmed the predominance of saturated tetracyclic diterpenoids including phyllocladanes and kauranes (Lu et al. 2013). However, the identification of phyllocladanes in Upper Carboniferous coals suggested their synthesis already in the ancient conifers of the order Voltziales (Schulze and Michaelis 1990). The occurrence of phyllocladanes in *Taxodium* peat from the Okefenokee swamp (Georgia, USA) and in the Miocene Oberpfalz coal (Germany), built up by Taxodiaceae-dominated vegetation, provided evidence for the correlation of phyllocladanes and Taxodiaceae (Dehmer 1989). Phyllocladanes may, therefore, originate from different conifer families. Only in Pinaceae, phyllocladanes have not been found (Otto and Wilde 2001). Therefore, a significant contribution of Pinaceae to peat formation can be excluded based on the predominance of tetracyclic diterpenoids in the hydrocarbon fractions.

Tricyclic diterpenoids may provide complimentary information about the peat-forming vegetation. Isopimaranes (**VII;** Fig. 1) and pimaranes (**VIII;** Fig. 1) are common constituents of conifers (Fig. 2a). They have been detected in recent species of Pinaceae, Cupressaceae, and Taxodiaceae (Otto and Wilde 2001). Recently, the higher pimarane/16α (H)-phyllocladane ratios in Lower and Middle Miocene lignites in comparison to Upper Miocene coals of Serbia were interpreted to imply a higher contribution of Pinaceae to coal formation, consistent with palynological data (Stojanović and Životić 2013).

Additional indication about the role of Pinaceae is based on abietane-type compounds. Diterpenoids of the abietane type (Fig. 2a) have been identified in many sediments and coals (Simoneit et al. 1986). As abietic acid only occurs in Pinaceae species, their diagentic products simonellite (**IX;** Fig. 1) and retene (**X;** Fig. 1) were often referred to as biomarkers for Pinaceae. However, abietane-type diterpenoids in the geosphere may also derive from phenolic derivatives. The phenolic abietane ferruginol (**XI;** Fig. 1) has been described in most conifer families, especially Cupressaceae, Taxodiaceae, and Podocarpaceae, but seems to be absent in Pinaceae (Otto and Wilde 2001). Therefore, only nonaromatic abietanes can be considered as diagenetic products of abietic acid, specific for conifers of the Pinaceae family.

Triterpenoids

Deciphering precise precursor/product relationships for triterpenoids often suffers from largely unknown compound transformation routes, as well as the occurrence of nonspecific precursors in higher land plants (Regnery et al. 2013).

For example, oxygenated pentacyclic triterpenoids of the ursane (**XII,** Fig. 1), oleanane (**XIII;** Fig. 1), and lupane (**XIV;** Fig. 1) types occur in almost all angiosperm taxa (Fig. 2b), and their attribution to individual plant families is difficult (Medeiros and Simoneit 2007). With respect to lupanes (Fig. 2b), only correlation with angiosperms of the Betulaceae family is convincing, since the lupane precursors betulin, lupeol, and betulinic acid are the dominant pentacyclic constituents of *Betula* bark (Hayek et al. 1989). Betulin is also found in the bark of other genera belonging to the Betulaceae family, including *Alnus*, *Corylus*, and *Carpinus* (Hayek et al. 1990).

Based on pollen assemblages in several lignite deposits, ferns are considered to significantly contribute to peat formation. The presence of des-A-fernenes (Loureiro and Cardoso 1990), as well as fernenes of either Δ^7, Δ^8, or $\Delta^{9(11)}$ (**XV;** Fig. 1) (Paull et al. 1998), are considered as characteristic biomarkers. Fern-8-enes (C_{29}–C_{31}) and fern-9(11)-enes (C_{29}–C_{30}) have been identified in the aliphatic hydrocarbon fraction of Late Triassic subbituminous coals, mudstones, and plant fossils from the Telford Basin, Australia. These hydrocarbons were found to be related to pteridosperms (seed ferns) of the genus *Dicroidium* (Paull et al. 1998). However, fernenes have also been found in modern sediments where the input from ferns has been excluded (i.e., deep-sea sites, Antarctic saline lake; Peters et al. 2005). Previous paleobotanical studies on coals from Euramerican Pennsylvanian (Late Carboniferous) coal basins indicate a major change in coal-swamp floras, especially at the Westphalian–Stephanian (≈Kasimovian–Gzhelian) boundary. Biomarker studies at the Westphalian/Stephanian of the Saar–Nahe Basin (Germany) revealed that aromatized arborane/fernane derivatives are prominent constituents of the extracts of cordaitean macrofossils and can therefore be regarded as biomarkers for this group of gymnosperms (Auras et al. 2006).

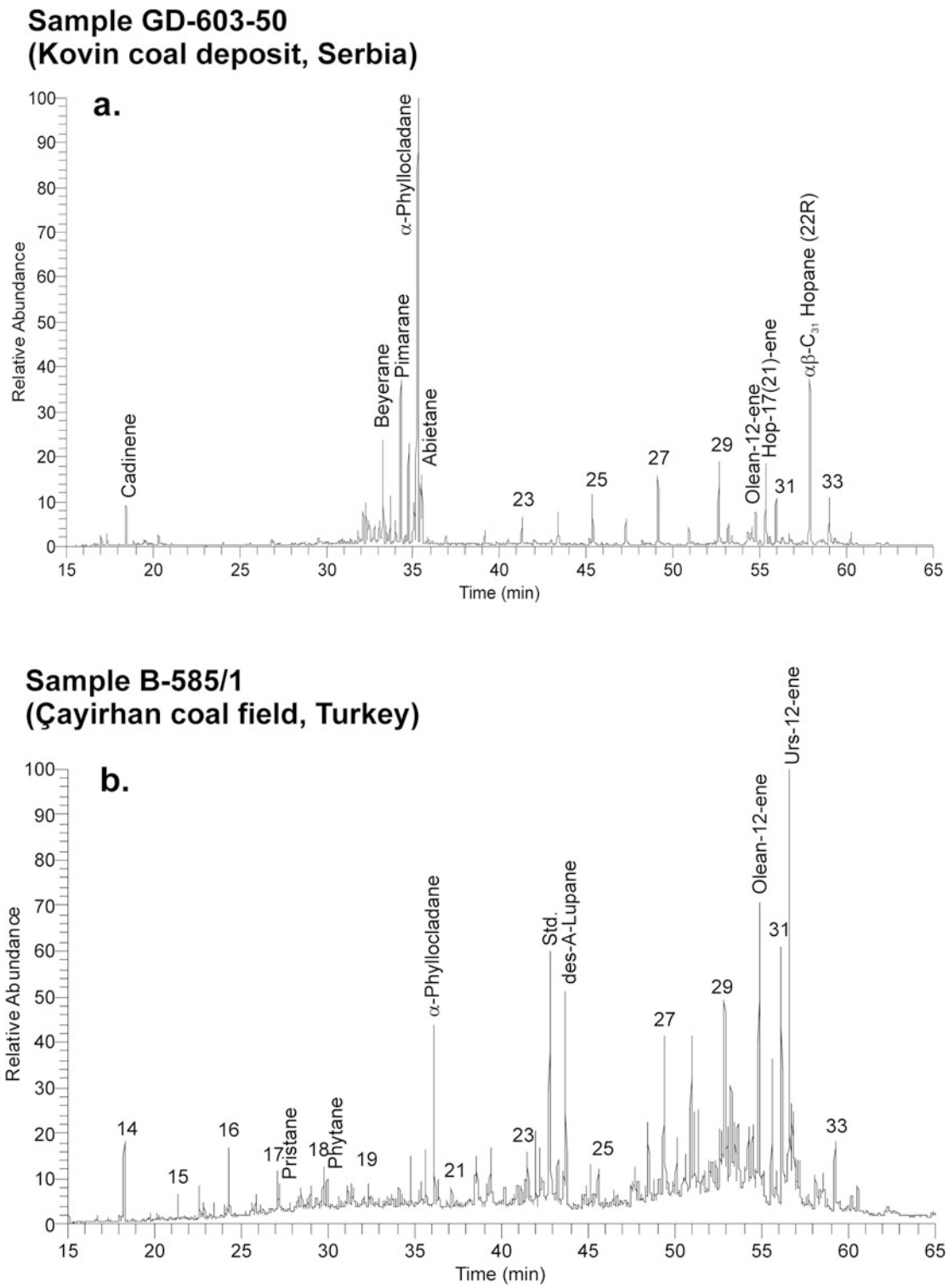

Biomarkers: Coal, Fig. 2 Gas chromatograms (total ion current) of the saturated hydrocarbon fractions of (**a**) one Upper Miocene lignite sample from the Kovin deposit (Serbia), dominated by hydrocarbons derived from resinous compounds of conifers, and of (**b**) Middle Miocene lignite from the Çayirhan coal field (Turkey), containing high contents of angiosperm-derived triterpenoid hydrocarbons. *n*-Alkanes are labeled according to their carbon number. *Std* Standard (deuterated *n*-tetracosane) (**b** adopted from Bechtel et al. 2014)

In surface sediments and sediment cores from the Angola and Cape basins (southeast Atlantic), high concentrations of taraxerol (**XVI;** Fig. 1) have been found corresponding with maxima in the relative abundance of pollen from mangrove trees. Therefore, Versteegh et al. (2004) concluded that taraxerol can be used as a lipid biomarker for mangrove input. Taraxerol was also found to be the main component in the examined mangrove sediments in coastal areas of the Bragança peninsula in North Brazil (Koch et al. 2003). However, taraxer-14-ene has been suggested as a marker for Ericaceae based on biomarker data recovered from a peat deposited in a Dutch ombrotrophic bog (Pancost et al. 2002).

Cadalane-Type Biopolymers

Polymers of cadalanes (i.e., bicadinanes (**XVII;** Fig. 1), polycadinenes (**XVIII,** Fig. 1)) have been found in the angiosperm dammar resins of the family Dipterocarpaceae, a tropical hardwood (van Aarssen et al. 1990). These resins were identified to be responsible for much of the crude oil found in Southeast Asia and Australia (Murray et al. 1994).

Biomarkers and Paleoclimate

In several studies it was found that an alternance of humid and dry periods is reflected and the aquatic plant *n*-alkane proxy Paq (Ficken et al. 2000; Nott et al. 2000; Nichols et al. 2006) were used to estimate the relative contributions of mosses and aquatic macrophytes vs. higher plants, the former predominating in humid periods. In addition $n\text{-}C_{27}/n\text{-}C_{31}$ could be used to estimate the relative contributions of shrubs and trees vs. herbaceous plants to peat formation (López-Dias et al. 2013). Alterations in the chain length distributions of plant wax *n*-alkanes in lacustrine and peat deposits have been further related to differences in growing season temperatures of the source regions (Zheng et al. 2009).

Recently, the distribution of bacterial branched glycerol dialkyl glycerol tetraethers (brGDGTs) has been investigated from 96 peatlands around the world with a broad mean annual air temperature (MAAT) and pH range (Naafs et al. 2017). It could be shown that the degree of cyclisation of brGDGTs is positively related to pH, and the degree of methylation of brGDGTs is positively correlated with MAAT. Based on the peat-specific calibrations (Naafs et al. 2017), the potential exists to use brGDGTs in peats and lignite to reconstruct terrestrial climate during the Cenozoic.

The presence of biomarker characteristic for plant families of specific climatic requirements is useful as paleoclimatic proxy. Such reconstructions are limited by the scarcity of source-specific plant biomarkers. The increasing relative abundance of biomarkers from gymnosperms versus angiosperms in low-rank coals is suggested to reflect cooler and drier climatic conditions during periods of peat accumulation. The retene/cadalene ratio has been used to reconstruct changes in the paleoflora and paleoclimate during Jurassic in the Paris Basin (France). In this study, the increase in the retene/cadalene ratio around the *cordatum* Zone was interpreted to reflect the rising proportion of Pinaceae indicating an increase in aridity at the end of the Lower Oxfordian (Hautevelle et al. 2006).

A significant change in the ratios of diterpenoids specific for gymnosperms versus angiosperm-derived triterpenoids has been obtained from studies on numerous lignites and subbituminous coals throughout the Cenozoic of central Europe (Fig. 3; Bechtel et al. 2005, 2008). Conifer biomarkers were found to predominate in Upper Oligocene and younger coal seams, whereas Eocene coals are derived from angiosperm-dominated vegetation. The results are in agreement with paleobotanical records, indicating that broad-leaved evergreen vegetation extended to almost 60°N during the Paleocene and Eocene. At the end of the Eocene, a decrease in both mean annual range of temperature and mean annual temperature resulted in northern European vegetation represented by temperate deciduous and coniferous forests (Wolfe 1980).

Stable carbon isotopes on cellulose from tree rings and fossil wood have been used to reconstruct changes in Earth's carbon cycle (Arens et al. 2000; Feng and Epstein 1995). Besides that, $\delta^{13}C$ values of tree ring cellulose reflect changes in humidity and air temperature (Hemming et al. 1998). However, the reconstruction of paleoclimate based on carbon isotope ratios of coal and fossil wood requires the correction for the effects of species variations (especially with respect to gymnosperm versus angiosperm contributions) and for microbial activities (Fig. 3; Bechtel et al. 2008). The interfering processes can be resolved by combining detailed molecular information on wood and coal composition with stable isotope data (Poole et al. 2006).

Recently, the stable isotope composition of leaf wax *n*-alkanes in coals and sediments was used to decipher environmental changes. In most studies, $\delta^{13}C$ values have been interpreted with respect to changes in the contribution of C3 versus C4 plants during the Cenozoic (Makou et al. 2007). Relatively little attention has been given to the fact that $\delta^{13}C$ values may be influenced by changing gymnosperm/angiosperm contributions. The analysis of hydrogen isotope composition of leaf wax lipids is a promising tool to reconstruct hydrological changes during Earth's history (Sachse et al. 2012). δD most likely records the hydrogen isotopic composition of plant growth water and thus may act as a proxy for local aridity (Seki et al. 2009).

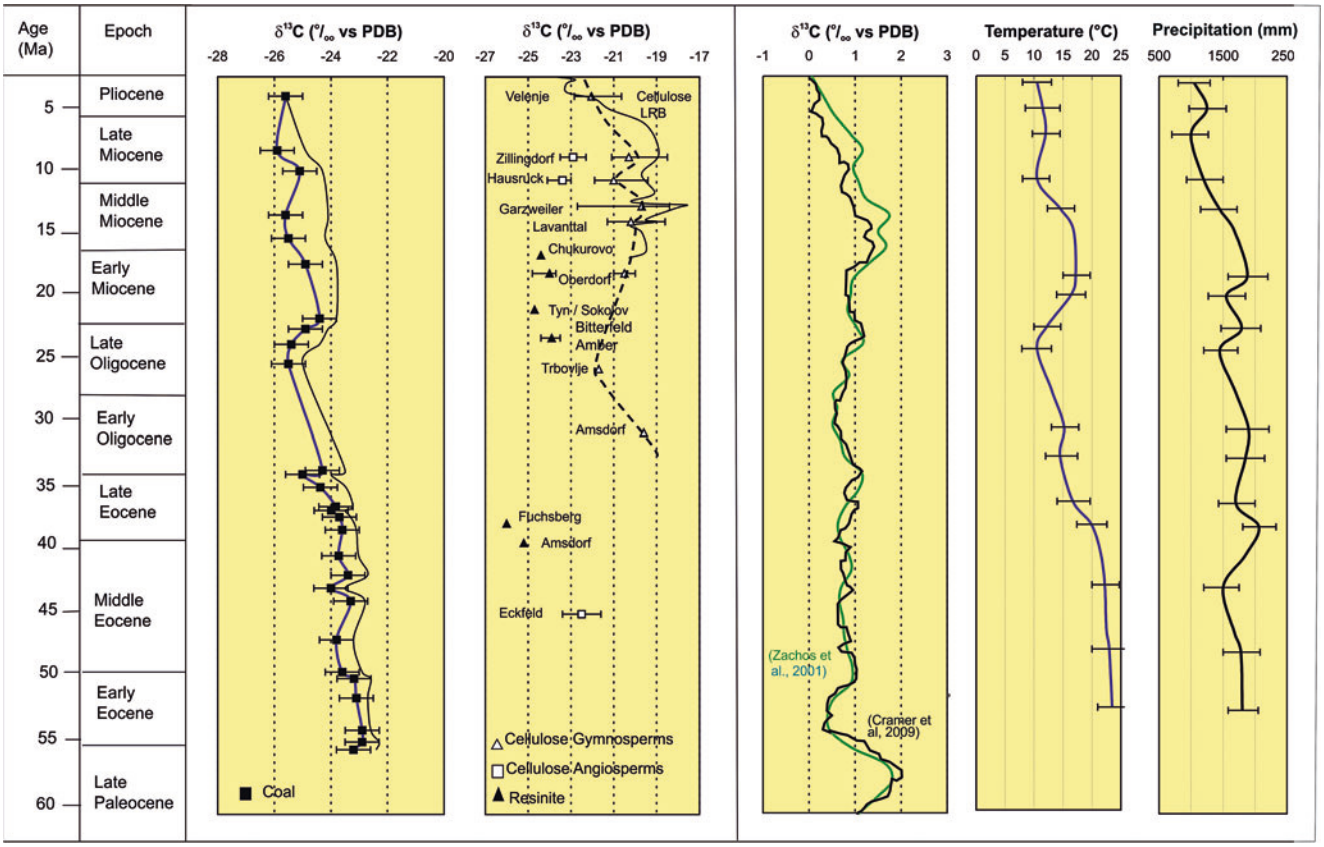

Biomarkers: Coal, Fig. 3 Variation of $\delta^{13}C$ of terrestrial organic matter during the Cenozoic of central Europe corrected for the effect of liptinite and hopanoid contents, gelification index and varying contributions of angiosperms to peat formation on $\delta^{13}C$ of coal (*thin solid line*), as well as after additional correction for the effect of changing $\delta^{13}C$ values of atmospheric CO_2 on $\delta^{13}C$ of C3 plants (*bold line*), $\delta^{13}C$ of fossil wood, extracted wood cellulose (Data from the Lower Rhine Basin according to Jordan 1995), and resinites, carbon isotope records from benthic foraminifera (Zachos et al. 2001; Cramer et al. 2009), as well as estimates about the variability of mean annual temperatures and precipitation in central Europe during the Tertiary based on compilations of paleobotanical data (Blumenstengel et al. 1996; Bruch 1998; Eissmann 1994; Haas et al. 1998; Kolcon and Sachsenhofer 1999; Krutzsch et al. 1992) (Figure modified according to Bechtel et al. 2008)

Biomarkers and the Environment of Peat and Coal Deposition

The biomarker composition of peat, lignite, and coal provides not only insight into the paleovegetation contributing to the organic matter accumulated in the deposits but also to the environmental conditions during the deposition of organic matter.

The pristane/phytane ratio is among the most widely used molecular parameter for reconstruction of the paleodepositional environments in both marine and terrestrial environments. An explanation for the usability of this ratio as a parameter for the reconstruction of redox conditions during deposition of sediments was provided by Didyk et al. (1978). According to their explanation, phytol originating from the phytyl side chain of chlorophyll is oxidized in sediments under aerobic conditions to phytenic acid, which is decarboxylated to pristene. The pristene is subsequently hydrated to pristane. Under anaerobic conditions phytol is at first hydrated to dihydrophytol und subsequently further reduced to phytane. According to this concept after diagenesis of the organic matter, high pristane/phytane ratios indicate oxidizing conditions during sediment deposition, while low ratios will result when reducing conditions prevailed. The concept has been shown to be valid for many sediments and also crude oils (Didyk et al. 1978). However, an additional bacterial origin of acyclic isoprenoids must be considered (Tornabene et al. 1979), and also tocopherols were recognized as possible sources of pristane in sediments (Goossens et al. 1984). Due to the knowledge about multiple sources of pristane and phytane, ten Haven et al. (1987) argued for a restricted usability of the pristane/phytane ratio as an indicator for paleoenvironmental conditions of sediment deposition. However, the conflicts regarding the usability of the pristane/phytane ratio as indicator for paleoenvironmental conditions are largely related to the marine environment. Later, also for the terrestrial environment, concern about the assumption that chlorophyll is the common source for pristane and phytane

arose when phospholipids of archaeol were detected in methanogenic archaebacterial biomass (Tomoaia-Cortisel et al. 1992). Upon cleavage of the ether bonds of archaeol, one would expect the formation of phytane during diagenesis (Pancost and Sinnighe Damste 2003). Since methanogenic archaea are known to be active in peat, archaeol has to be considered as additional source of phytane in peat bogs, and the pristane/phytane ratio during diagenesis would be depending on the methanogenic activity in the former peat bog. Archaeol was additionally detected in the marine environment as constituent of anaerobic methanotrophic archaea with the particular attribute to provide a very light carbon isotopic signature of $\delta^{13}C = -104.29‰$ (Orphan et al. 2001).

However, by use of compound specific carbon isotopic measurements ($\delta^{13}C$) on individual compounds, it should therefore be possible to distinguish whether phytane is coming from phytol ($\delta^{13}C \sim -29‰$) or from archaeol originating either from methanotrophic archaea with $\delta^{13}C \sim -100‰$ (Orphan et al. 2001) or from archaeol originating from methanogenic archaea, which has not been analyzed yet with respect to its carbon isotopic composition. In case that the biomass of methanogens and methanotrophs would contribute significantly to the total organic matter in peat, one would expect lower $\delta^{13}C$ values for phytane than for pristane, originating in the terrestrial environment preferentially from the chlorophyll of higher land plants. The pristane/phytane ratio in coal might consequently reflect both the paleo-redox conditions during deposition of former peat bogs and the intensity of methane formation and oxidation during deposition and early diagenesis.

In only very few studies of coals, the $\delta^{13}C$ values have been determined simultaneously on pristane and phytane. In 12 coal samples from the Eocene Fushun Basin in NE China, the $\delta^{13}C$ values of pristane and phytane were on average −27,37‰ and −28,22‰, respectively (Strobl et al. 2014). Phytane is only by 0.85‰ more depleted in ^{13}C compared to pristane which argues for a similar precursor (i.e., chlorophyll) for both compounds. Schwarzbauer et al. (2013) determined $\delta^{13}C$ values of both pristane and phytane on 34 Late Paleozoic coals from all over the world, and on average phytane was by 1.07‰ more depleted in ^{13}C than pristane which confirms the dominating origin of both compounds from chlorophyll but also a minor contribution of methanogens and methanotrophs to the total biomass.

For the terrestrial environment, numerous examples have been provided showing the usefulness of the pristane/phytane ratio for the reconstruction preferentially of paleo-redox conditions in peats, lignites, and subbituminous and bituminous coals.

In three seams of middle Eocene subbituminous coals from Markushegy (Hungary), the values of the pristane/phytane ratio varied from values of 0.6 to 4.8 with decreasing ratios in the uppermost parts of the seams and in the shaly layers, which is in agreement with the establishment of reducing conditions due to increasing levels of the (ground)water table (Bechtel et al. 2007). Moreover, the pristane/phytane ratio provided a significant correlation with the abundance of inertinite macerals present in the coals, supporting the assumption that inertinite macerals in peat deposits and mires are formed preferentially under dry and oxic conditions under participation of fungi (Moore et al. 1996).

In solvent extracts of samples from the Upper Oligocene Trbovlje coal seam from Slovenia, the pristane/phytane ratio has been shown to correlate inversely with the amount of hop-17(21)-ene (Bechtel et al. 2004). This also confirms the influence of redox conditions during deposition of peat on the pristane/phytane ratio since hop-17(21)-ene is most likely originating from anaerobic (iron-reducing) bacteria (Wolff et al. 1992,) which can be expected to become more active in the peat together with intensifying anaerobic conditions.

In bituminous coals from the Saar-Nahe Basin,the pristane/phytane ratio increased significantly in coal seams of the Upper Carboniferous approaching to the Permian in accordance with the well-known shift to a drier climate (Vliex et al. 1994).

These examples show that the pristane/phytane ratio is a useful parameter for the reconstruction of paleo-redox conditions in peat, lignite, and subbituminous coals. However, several studies have shown that at higher rank of coals (approximately >0.5% vitrinite reflectance (Rm)), a maturity effect superimposes the redox effect on the pristane/phytane ratio. Among the first application of the pristane/phytane ratio in coal studies was reported by Radke et al. (1980), showing that in a set of 26 hard coals from the Ruhr district (Germany), covering a wide rank range (0.63–1.7% Rm), the pristane/phytane ratio varies significantly depending on the rank of the coal. In the range of 0.63–0.88% Rm, pristane/phytane ratio increases from values of 8 to 10 followed by a decrease from values of approximately 10 to 1 concomitant with further increasing rank of coals from 0.88% to 1.7% Rm. This observation is explained by an asynchronous formation of pristane and phytane from kerogen with pristane being generated earlier and phytane later during coalification. The tendency of increasing pristane/phytane ratios up to a rank of 0.8% Rm and decreasing pristane/phytane ratios together with further increase of the rank was later confirmed on Pennsylvanian coals from the Kittanning formation in Eastern Ohio, USA (Dzou et al. 1995). In their study absolute amounts of both compounds were determined, and results have shown that the phytane concentration remained largely constant over the rank range from 0.5% to 1.8% Rm, while changes in the pristane/phytane ratio were mostly attributed to concentration variations of pristane.

Biomarkers for Carbon Cycling in Peat Bogs

Approximately 30% of the global terrestrial carbon is stored in peat bogs dominated by *Sphagnum moss* and is thus an

important factor in the global carbon cycle (Smith et al. 2004). Ten percent of the total methane flux to the atmosphere has been suggested to originate from peat bogs (Smith et al. 2004). However, methane oxidation is well known to reduce the potential atmospheric methane emissions from both peatlands (Kip et al. 2010) and freshwater wetlands (Segarra et al. 2015). In ombrotrophic peat bogs, methanogens grow heterotrophically on acetate or other multi-carbon substrates and are expected to have $\delta^{13}C$ values similar to those of the used carbon source (Pancost et al. 2000a). The analysis of preferentially *Sphagnum* peat cores from ombrotrophic bogs taken from four northern European sites revealed the presence of archaeol and *sn*-2-hydroxyarchaeol which were suggested to be appropriates biomarker for methanogens (Pancost et al. 2011). Lim et al. (2012) proposed later the use of archaeol as biomarker for the methanogen biomass in water-saturated soil. The carbon isotopic composition of the archaeol and *sn*-2-hydroxyarchaeol was not determined in these studies, but both compounds revealed to be useful biomarkers. However, Pancost et al. (2000a) could find in two Holocene peat bogs from the Netherlands and Ireland neither molecular nor isotopic evidence for the activity of aerobic methane-oxidizing bacteria (methanotrophs) indicating the need for research to find additionally appropriate biomarkers for methane-oxidizing bacteria in peat deposits. Anaerobic methane oxidation is well known from the marine environment and generally coupled to sulfate reduction being available in high abundance (Pancost et al. 2000b; Orphan et al. 2001). However, the importance of both aerobic and anaerobic methane oxidation is also well known in peatlands and has been reviewed by Smemo and Yavitt (2011).

According to Fig. 4 in peat-forming wetlands, the zone of anaerobic methane oxidation is covered by a zone of aerobic methane oxidation, and both zones might migrate within the soil profile depending on the variation of the amount of precipitation over time. Possible electron acceptors for the anaerobic methane oxidation are sulfate, humic matter, and ferric iron, with sulfate being in general less available in peat-forming environments. In case that iron(III) is used as electron acceptor, iron(II) will be generated which can be reoxidized upon lowering of the water table. Humic substances might serve in this process as chelators for iron(III) which makes it available for iron reduction (Lipson et al. 2010). The internal recycling of iron(III) might be an effective process supporting the anaerobic methane oxidation. However, so far quantification of the proportion of anaerobic versus aerobic methane oxidation in peat-forming environments is not possible, and the knowledge of specific biomarkers might help to solve this problem.

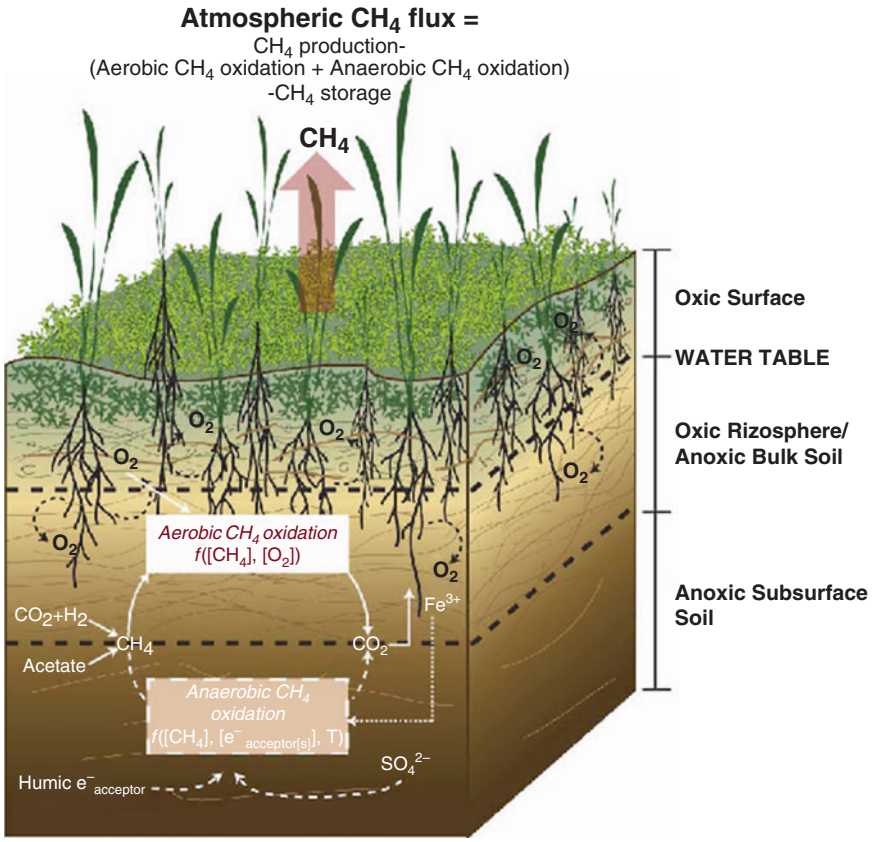

Biomarkers: Coal, Fig. 4 Conceptual model of CH_4 cycling in the profile of *Sphagnum* sp. and *Carex* sp. covered peat-forming wetland indicating the relationship between water table depth, plant rooting zone, and redox status. *Solid boxes* and *arrows* represent known processes and controls of CH_4 fluxes, *dashed black arrows* represent O_2 fluxes from plant roots, and *dashed white boxes* and *arrows* represent recently quantified or hypothesized processes and controls. Factors controlling net atmospheric CH_4 flux rates from peatland ecosystems are illustrated by the equation at the *top* of the figure (Adopted from Smemo and Yavitt 2011; licensed under CC BY 3.0)

To establish biomarkers for methane oxidizing bacteria in peat deposits, van Winden et al. (2010) carried out incubation experiments with $^{13}CH_4$ and *Sphagnum* moss spp. It was not possible to identify an unambiguous biomarker for methanotrophs in peat moss, but particularly hopenes (hop-17(21)-ene and 2-methylhop-17(21)-ene) provided high degrees of ^{13}C-labeled incorporation into the individual lipid molecules. However, pure cultures of methanotrophs contained no hop-17(21)-ene but diploptene instead, leading to the conclusion that hop-17(21)-ene can be generated from diploptene through isomerization under acidic conditions (van Winden et al. 2012). Kip et al. (2010) carried out laboratory experiments with *Sphagnum* mosses from pools, lawns, and hummocks in nine *Sphagnum*-dominated peatlands from all over the world and tested their capacity to oxidize methane. A symbiosis between mosses and methanotrophs developed in all experiments, and ^{13}C labeling of methane has shown that methane-derived carbon was incorporated not only into hopanoids but also into steroidal plant lipids.

Zheng et al. (2014) investigated Holocene sediments from the Tibetan Plateau and used archaeol and *sn*-2-hydroxyarchaeol as biomarkers for methanogens. Lower concentrations of both compounds in the interval from 6 to 4 ka were interpreted as a result of lower methanogenic activity during this period associated with drier environmental conditions. In this profile also diploptene and the stable carbon isotopic composition ($\delta^{13}C$) of diploptene have been determined, and increasing amounts of diploptene were associated with decreasing $\delta^{13}C$ values of the diploptene supporting that the additional (light) diploptene might come from the biomass of methanotrophs. More recently, several bacteriohopanepolyols and further functionalized hopanoids in *Sphagnum* peat from Bissendorf Moor, Germany, have been reported to be biomarkers for aerobic methane-oxidizing bacteria (Talbot et al. 2016), but these compounds will not survive progressing diagenesis and will undergo further changes during coalification. The influence of potential electron acceptors (nitrate, sulfate, and ferric iron) on anaerobic methane oxidation has been studied by sealed incubation experiments using peat from Michigan Hollow (Gupta et al. 2013). The results have shown that these inorganic electron acceptors were not involved in the redox processes, and a putative organic electron acceptor has been suggested to be responsible for the anaerobic methane oxidation observed in the experiments (Gupta et al. 2013). In peat bogs, the availability of sulfate and nitrate is generally low and their contribution to anaerobic methane oxidation expected to be low, but iron(III) is available as possible electron acceptor and due to internal oxidation–reduction cycles iron (and also manganese) might be recycled for reuse in the anaerobic oxidation of methane (Smemo and Yavitt 2011). Further studies should be carried out, therefore, for the identification of biomarkers indicative for iron-reducing bacteria in the peatland environment.

Biomarkers and Thermal Maturity of Coals

The thermal maturity or rank of coals has for a long time been determined preferentially by the use of optical methods such the determination of the mean random vitrinite reflectance (Rm) or by the use of fluorescence light microscopy. An attempt to determine the thermal maturity of coals based on parameters derived from the composition of compounds extractable from coals by organic solvents has been reported by Radke et al. (1980). The development of glass capillary columns made it possible to separate all methylphenanthrene (MP) isomers present in coal extracts into individual peaks and revealed changing relative intensities of the compounds with the rank in a set of 24 Upper Carboniferous coals from the Ruhr area in Germany. Radke et al. (1982) developed the so-called methylphenanthrene index (MPI-1) according to the following equation:

$$\mathrm{MPI\ 1} = 1.5(2\text{-MP} + 3\text{-MP})/\mathrm{P} + 1\text{-MP} + 9\text{-MP}$$

with P phenanthrene, *2*-MP 2-methylphenanthrene, *3*-MP 3-methylphenanthrene, *1*-MP 1-methylphenanthrene, and *9*-MP 9-methylphenanthrene.

A linear correlation was observed in the rank range represented by vitrinite reflectance values ranging from approximately 0.6% to 1.5% Rm which allowed the determination of a "calculated vitrinite reflectance" (Rc) using equation $\mathrm{Rc} = 0.63 \times \mathrm{MPI\ 1} + 0.42$.

Moreover, the methylphenanthrene ratio (MPR) (representing the relative intensities of 2-MP/1-MP) revealed a linear correlation with the measured vitrinite reflectance of the coals.

Having more data points available from further coal samples of other provinces (Tertiary and Cretaceous age), the correlation equation slightly changes to $\mathrm{Rc} = 0.60 \times \mathrm{MPI\ 1} + 0.40$ for coals in the rank range of 0.65–1.35% Rm, and a further correlation between the MPI 1 and the Rm was defined for coals of higher rank (>1.35% Rm) from which also an equation for the calculation of the vitrinite reflectance was proposed: $\mathrm{Rc} = -0.61 \times \mathrm{MPI\ 1} + 2.30$ (Radke et al. 1982).

The change of the distribution pattern of phenanthrene and four of its methylphenanthrene isomers was explained to result from different reactivity at the ring carbon. At lower rank (~0.65% Rm), the isomers 1-MP and 9-MP dominate quantitatively over 2-MP and 3-MP since these positions at the phenanthrene ring are favored for methylation. With increasing rank (up to 1.35% Rm), rearrangement reactions occur leading to an increasing abundance of the thermodynamically more stable isomers 2-MP and 3-MP. Upon further

increase of the coal rank (>1.35% Rm) and under the influence of the associated higher temperatures, the MPI-1 is lowered continuously due to demethylation of methylphenanthrenes under formation of the parent compound phenanthrene (Radke et al. 1982). In principal, this explanation has recently been confirmed by the estimation and application of thermodynamic properties of aqueous phenanthrene and methylphenanthrene isomers at higher temperature (Dick et al. 2013). Ab initio quantum chemical calculations (DFT) led to the identification of possible transition states and to the determination of activation energies for reactions of the compounds in aqueous solutions, and according to the data the MPR, defined as the ratio 2-MP/1-MP, was suggested to be more closely related to thermal maturity than MPI-1 (Szczerba and Rospondek 2010).

Further studies revealed that the MPI-1 is a robust chemical maturation indicator but can be affected by organic matter type in coals and sediments (Radke et al. 1984, 1986). Apart from the MPI-1, additional maturity parameters for sediments and rank parameters for coals based on relative proportions of alkylated naphthalenes, phenanthrenes, and dibenzothiophenes have been developed, and the influence of organic matter type on each parameter has been tested (Radke et al. 1986). The alkylated naphthalenes revealed to be particularly useful for the maturity assessment of type II_B kerogens, while the alkylated phenanthrenes are more appropriate as rank parameters for type III kerogen including coal.

Kvalheim et al. (1987) applied multivariate analysis methods (principal component analysis followed by factor rotation) to the relative proportions of phenanthrene and the methylphenanthrene isomers obtained from 15 coals from different provinces covering different ages from Cretaceous to Carboniferous and a wide rank range from 0.53% to 1.29% Rm. The results have shown that the variation of rank correlates rather with the distribution of the methylphenanthrene isomers and less with the relative abundance of the phenanthrene. Therefore, they proposed to apply the methylphenanthrene distribution factor (MPDF) as an alternative maturity indicator, MDPF = (2−MP + 3−MP)/(2−MP + 3−MP + 1−MP + 9−MP), with the following linear regression equation: Rc = − 0.166 + 2.2423 × MPDF.

Boreham et al. (1988) investigated the aromatic hydrocarbon compositions of 94 coals and sediments with terrestrial organic matter from eight Australian basins and ages ranging from Tertiary to Carboniferous. MPI-1 values and MPDF values were calculated from the peak areas in the gas chromatograms. From the linear regression analysis at reflectance levels ranging from 0.3% to 1.7% Rm, the relationship between Rm (%) and MPI-1 results in a significant correlation coefficient of $r = 0.84$ and the following equation for the determination of the calculated vitrinite reflectance, Rc = 0.7 × MPI-1 + 0.22, which differs from the relationship proposed previously by Radke et al. (1982). The correlation coefficient between Rm and the simultaneously determined MPDF value was much lower ($r = 0.64$), but the formula for the linear regression line between MPDF and Rm was similar to the formula proposed by Kvalheim et al. (1987). For higher rank levels (>1.7% Rm), the following equation results: Rc = −0.55 × MPI-1 + 3.0 which also differs from the equation proposed by Radke et al. (1982). Attempts to explain the observed changes in the regression equation for the calculation of Rc from MPI-1 values using coals from different basins and ages have later been provided by Heppenheimer et al. (1992) showing that one of the methylphenanthrene isomers (1-MP) is increased significantly in relation to the other isomers and explained this observation by the abundance of coniferous resinite contributing retene, pimanthrene (1,7-dimethylphenanthrene), and 1-MP as diagenetic products of abietic acid and pimaric acid to the aromatic hydrocarbon fraction. Thereby, 1-MP is added to the distribution profile of the MPs expectable according to the usual isomerization and methylation reactions. Norgate et al. (1999) investigated the aromatic hydrocarbon composition of 22 Eocene bituminous coals from the Buller Coalfield, New Zealand. The calibration of the measured MPI-1 values and vitrinite reflectance values provided the following equation for the calculated vitrinite reflectance: Rc = 1.1 × MPI-1 + 0.07 ($R^2 = 0.71$). The calibration values in this equation differ significantly from the values determined in previous studies (Radke et al. 1982; Boreham et al. 1988). The deviation is explained by the fact that the investigated set of Buller coals is partly composed of perhydrous coals with a higher hydrogen/carbon atomic ratio compared to coals of similar rank which results in a lowering of the MPI-1 values (Norgate et al. 1999). Nevertheless, considering the aforementioned exceptions, the MPI-1 parameter has been established as a reliable maturity/rank parameter for coals and sediments with type III kerogen.

Summary

Based on the relative contents of sesqui-, di-, and triterpenoids in coal, the contribution of gymnosperms versus angiosperms to peat formation can be deduced. The occurrence of some of the terpenoid biomarkers is diagnostic for specific plant families (e.g., Cupressaceae, Betulaceae, ferns, mangrove trees, Dipterocarpaceae) in the peat-forming vegetation. However, deciphering precise precursor/product relationships often suffers from largely unknown compound transformation routes, as well as the occurrence of non-specific precursors in higher land plants.

Biomarkers characteristic for plant families of specific climatic requirements are regarded as useful paleoclimatic proxies. Based on the peat-specific calibration of the effects of changing pH and air temperature on the distribution of brGDGTs, there is a clear potential to use these biomarkers in

peat and lignite to reconstruct past terrestrial climate. Stable carbon isotopes on cellulose have also been used to reconstruct changes in Earth's carbon cycle, as well as in humidity and air temperature. Interfering processes (i.e., species variations, microbial activities), inhibiting the reconstruction of paleoclimate based on carbon isotope ratios of coal and fossil wood, can be overcome by combining molecular information of coal composition with stable isotope data. Recently, the stable isotope (C, H) composition of leaf wax *n*-alkanes in coals and sediments was used to decipher changes in paleovegetation, atmospheric CO_2 content, and humidity.

The pristane/phytane ratio is a valuable parameter for the reconstruction of paleo-redox conditions of lignites and subbituminous coals of lower rank. Due to the maturity effect and potentially different precursors, pristane/phytane ratios should be only applied to coals of identical rank and if both isoprenoids show similar $\delta^{13}C$ values. The $\delta^{13}C$ values of biomarkers originating from archaea and bacteria are useful to identify their specific role in the carbon cycling in peat and the contribution of wetland to methane emission.

The thermal maturity of coals can be successfully assessed by the isomerization of methylphenanthrenes. Different correlation equations have been postulated in order to relate the ratios in the relative proportions of methylphenanthrene isomers to vitrinite reflectance data. Significant correlations have been found in the range of 0.6–1.7% Rm.

Cross-References

- ▶ Biomarker: Assessment of Thermal Maturity
- ▶ Carbon Cycle
- ▶ Carbon Isotopes
- ▶ Coal
- ▶ Compound-Specific Isotope Analysis
- ▶ Gas Chromatography–Mass Spectrometry (GC–MS)
- ▶ Hydrocarbons
- ▶ Hydrogen Isotopes
- ▶ Kerogen
- ▶ Organic Geochemistry
- ▶ Organics: Sources and Depositional Environments
- ▶ Paleoclimatology
- ▶ Paleoenvironments
- ▶ Peat

References

Alexander R, Kagi RI, Woodhouse GW, Volkman JK (1983) The geochemistry of some biodegraded Australian oils. APEA J 23:53–63

Arens NC, Jahren AH, Amundson R (2000) Can C3 plants faithfully record the carbon isotopic composition of atmospheric carbon dioxide? Paleobiology 261:137–164

Auras S, Wilde V, Scheffler K, Hoernes S, Kerp H, Püttmann W (2006) Aromatized arborane/fernane hydrocarbons as biomarkers for cordaites. Naturwissenschaften 93:616–621

Bechtel A, Markic M, Sachsenhofer RF, Jelen B, Gratzer R, Püttmann W (2004) Paleoenvironment of the upper Oligocene Trbovlje coal seam (Slovenia). Int J Coal Geol 57:23–48

Bechtel A, Sachsenhofer RF, Zdravkov A, Kostova I, Gratzer R (2005) Influence of floral assemblage, facies and diagenesis on petrography and organic geochemistry of the Eocene Bourgas coal and the Miocene Maritza East lignite (Bulgaria). Org Geochem 36:1498–1522

Bechtel A, Hamor-Vido M, Sachsenhofer RF, Reischenbacher D, Gratzer R, Püttmann W (2007) The middle Eocene Markushegy subbituminous coal (Hungary): paleoenvironmental implications from petrographical and geochemical studies. Int J Coal Geol 72:33–52

Bechtel A, Gratzer R, Sachsenhofer RF, Gusterhuber J, Lücke A, Püttmann W (2008) Biomarker and carbon isotope variation in coal and fossil wood of Central Europe through the Cenozoic. Palaeogeogr Palaeoclimatol Palaeoecol 262:166–175

Bechtel A, Karayiğit AI, Sachsenhofer RF, Inaner H, Christanis K, Gratzer G (2014) Spatial and temporal variability in vegetation and coal facies as reflected by organic petrological and geochemical data in the Middle Miocene Çayirhan coal field (Turkey). Int J Coal Geol 134–135:46–60

Blumenstengel H, Krutzsch W, Volland L, Knoth W, Knuth G (1996) Revidierte Stratigraphie tertiärer Ablagerungen im südlischen Sachsen-Anhalt Teil 1: Raum Halle-Merseburg. Hallesches Jahrbuch der Geowissenschaften. Reihe B, Beiheft, Landesamt für Geologie und Bergwesen, Sachsen-Anhalt, Halle/Saale 1:101 pp

Boreham CJ, Crick IH, Powell TG (1988) Alternative calibration of the Methylphenanthrene index against vitrinite reflectance: application to maturity measurements on oils and sediments. Org Geochem 12:289–294

Bruch A (1998) Palynologische Untersuchungen im Oligozän Sloweniens – Paläoumwelt und Paläoklima im Ostalpenraum. Tübinger Mikropaläontol Mitt 18:1–193

Cramer BS, Toggweiler JR, Wright JD, Katz ME, Miller KG (2009) Ocean overturning since the Late Cretaceous: inferences from a new benthic foraminiferal isotope compilation. Paleoceanography 24:PA4216. https://doi.org/10.1029/2008PA001683

Dehmer J (1989) Petrographical and organic geochemical investigation of the Oberpfalz brown coal deposit, West Germany. Int J Coal Geol 11:273–290

Dick JM, Evans KA, Holman AI, Jaraula CMB, Grice K (2013) Estimation and application of the thermodynamic properties of aqueous phenanthrene and isomers of methylphenanthrenes at high temperature. Geochim Cosmochim Acta 122:247–266

Didyk BM, Simoneit BRT, Brassell SC, Eglinton G (1978) Organic geochemical indicators of paleoenvironmental conditions of sedimentation. Nature 272:261–222

Dzou LIP, Noble RA, Senftle JT (1995) Maturation effects on absolute biomarker concentration in a suite of coals and associated vitrinite concentrates. Org Geochem 23:681–697

Eissmann L (1994) Leitfaden der Geologie des Präquartärs im Saale-Elbe-Gebiet. DEUQUA-Tagung 1994, Leipzig. Altenberger Naturwiss Forsch 7:11–53

Feng X, Epstein S (1995) Carbon isotopes of trees from arid environments and implications for reconstructing atmospheric CO_2 concentration. Geochim Cosmochim Acta 59:2599–2608

Ficken KJ, Li B, Swain DL, Eglinton G (2000) An *n*-alkane proxy for the sedimentary input of submerged/ floating freshwater aquatic macrophytes. Org Geochem 31:745–749

Goossens H, de Leeuw JW, Schenk PA, Brassell SC (1984) Tocopherols as likely precursors of pristane in ancient sediments an crude oils. Nature 312:440–442

Grantham PJ, Douglas AG (1980) The nature and origin of sesquiterpenoids in some tertiary fossil resins. Geochim Cosmochim Acta 44:1801–1810

Gupta V, Smemo KA, Yavitt JB, Fowle D, Branfireum B, Basiliko N (2013) Stable isotopes reveal widespread anaerobic methane oxidation across latitude and peatland type. Environ Sci Technol 47:8273–8279

Haas M, Daxner-Höck G, Decker K, Kolcon I, Kovar-Eder J, Meller B, Sachsenhofer RF (1998) Palaeoenvironmental studies in the Early Miocene lignite opencast mine Oberdorf, N Voitsberg, Styria, Austria. In: Steininger FF (ed) The Early Miocene lignite deposit of Oberdorf N Voitsberg, 140. Jahrbuch Geologische Bundesanstalt, Wien, pp 413–424

Hautevelle Y, Michels R, Malartre F, Trouiller A (2006) Vascular plant biomarker as proxies for palaeoflora and palaeoclimatic changes at the Dogger/Malm transition of the Paris Basin (France). Org Geochem 37:610–625

Hayek EWH, Jordis U, Moche W, Sauter F (1989) A bicentennial of betulin. Phytochemistry 28:2229–2242

Hayek EWH, Krenmayr P, Lohninger H, Jordis U, Moche W, Sauter F (1990) Identification of archaeological and recent wood tar pitches using gas chromatography/mass spectrometry and pattern recognition. Anal Chem 62:2038–2043

Hemming DL, Switsur VR, Waterhouse JS, Heaton THE, Carter AH (1998) Climate variation and the stable carbon isotope composition of tree ring cellulose: an intercomparison of *Quercus robur*, *Fagus sylvatica* and *Pinus silvestris*. Tellus 50B:25–33

Heppenheimer H, Steffens K, Püttmann W, Kalkreuth W (1992) Comparison of resinite related aromatic biomarker distributions in Cretaceous-Tertiary coals from Canada and Germany. Org Geochem 18:273–287

Jordan M (1995) δ^{13}C-Markierungen in Jahrringen fossiler Baumstämme – miozäne Klimazeugen aus der Niederrheinischen Bucht. Hundt Druck GmbH, Köln

Kip N, van Winden JF, Pan Y, Bodrossy L, Reichart G-J, Smolders AJP, Jetten MSM, Sinninge Damste JS, Op den Caop HJM (2010) Global prevalence of methane oxidation by symbiotic bacteria in peat-moss ecosystems. Nat Geosci 3:617–621

Koch BP, Rullkötter J, Lara RJ (2003) Evaluation of triterpenols and sterols as organic matter biomarkers in a mangrove ecosystem in northern Brazil. Wetl Ecol Manag 11:257–263

Kolcon I, Sachsenhofer RF (1999) Petrography, palynology and depositional environment of the early Miocene Oberdorf lignite seam (Styrian Basin, Austria). Int J Coal Geol 41:275–308

Krutzsch W, Blumenstengel H, Kiesel Y, Rüffle L (1992) Paläobotanische Klimagliederung des Alttertiärs (Mitteleozän bis Oberoligozän) in Mitteldeutschland und das Problem der Verknüpfung mariner und kontinentaler Gliederungen (klassische Biostratigraphien – paläobotanisch-ökologische Klimastratigraphie – Evolutions-Stratigraphie der Vertebraten). N Jb Geol Paläontol 186:137–253

Kvalheim OM, Christy AA, Telnaes N, Bjorseth A (1987) Maturity determination of organic matter in coals using the methylphenanthrene distribution. Geochim Cosmochim Acta 51:1883–1888

Lim KLH, Pancost RD, Hornibrook ERC, Maxfield PJ, Evershed RP (2012) Archaeol: an indicator of methanogenesis in water-saturated soils. Archaea 2012. https://doi.org/10.1155/2012/896727

Lipson DA, Jha M, Raab TK, Oechel WC (2010) Reduction of iron (III) and humic substances plays a major role in anaerobic respiration in an Arctic peat soil. J Geophys Res Biogeosci 115:G00I06. https://doi.org/10.1029/2009JG001147

López-Dias V, Urbanczyk J, Blanco CG, Borrego AG (2013) Biomarkers as paleoclimate proxies in peatlands in coastal high plains in Asturias, N Spain. Int J Coal Geol 116–117:270–280

Loureiro MRB, Cardoso JN (1990) Aromatic hydrocarbons in the Paraiba Valley oil shale. Org Geochem 15:351–359

Lu Y, Hautevelle Y, Michels R (2013) Determination of the molecular signature of fossil conifers by experimental palaeochemotaxonomy – part 1: the Araucariaceae family. Biogeosciences 10:1943–1962

Makou MC, Hughen KA, Xu L, Sylva SP, Eglinton TI (2007) Isotopic records of tropical vegetation and climate change from terrestrial vascular plant biomarkers preserved in Cariaco Basin sediments. Org Geochem 38:1680–1691

Medeiros PM, Simoneit BRT (2007) Gas chromatography coupled to mass spectrometry for analyses of organic compounds and biomarkers as tracers for geological, environmental, and forensic research. J Sep Sci 30:1516–1536

Moore TA, Shearer JC, Miller SL (1996) Fungal origin of oxidized plant material in the Palangkaraya peat deposit, Kalimantan Tengah, Indonesia: implications of 'inertinite' formation in coal. Int J Coal Geol 30:1–23

Murray AP, Padley D, McKirdy DM, Booth WE, Summons RE (1994) Oceanic transport of fossil dammar resin: the chemistry of coastal resinites from South Australia. Geochim Cosmochim Acta 58:3049–3059

Naafs BDA, Inglis GN, Zheng Y, Amesbury MJ, Biester H et al (2017) Introducing global peat-specific temperature and pH calibrations based on brGDGT bacterial lipids. Geochim Cosmochim Acta 208:285–301

Nichols JE, Booth RK, Jackson ST, Pendall EG, Huang Y (2006) Paleohydrologic reconstruction based on n-alkane distributions in ombrotrophic peat. Org Geochem 37:1505–1513

Noble RA, Alexander R, Kagi RI, Knox J (1985) Tetracyclic diterpenoid hydrocarbons in some Australian coals, sediments and crude oils. Geochim Cosmochim Acta 49:2141–2147

Norgate CM, Boreham CJ, Wilkins AJ (1999) Changes in hydrocarbon maturity indices with coal rank and type, Buller Coalfield, New Zealand. Org Geochem 30:985–1010

Nott CJ, Xie S, Avsejs LA, Maddy D, Chambers FM, Evershed RP (2000) *n*-Alkane distributions in ombrotrophic mires as indicators of vegetation change related to climatic variation. Org Geochem 31:231–235

Orphan VJ, House CH, Hinrichs KU, McKeegan KD, DeLong EF (2001) Methano-consuming archaea revealed by direct coupled isotopic and phylogenetic analysis. Science 293:484–487

Otto A, Wilde V (2001) Sesqui-, di-, and triterpenoids as chemosystematic markers in extant conifers – a review. Bot Rev 67:141–238

Otto A, Walther H, Püttmann W (1997) Sesqui- and diterpenoid biomarkers in *Taxodium*-rich Oligocene oxbow lake clays, Weisselster basin, Germany. Org Geochem 26:105–115

Pancost RD, Sinninge Damsté JS (2003) Carbon isotopic compositions of prokaryotic lipids as tracers of carbon cycling in diverse settings. Chem Geol 195:29–58

Pancost RD, Sinninghe Damsté JS, de Lint S, van der Maarel MJEC, Gottschal JC, TMMS Party (2000a) Biomarker evidence for widespread anaerobic methane oxidation in Mediterranean sediments by a consortium of methanogenic archaea and bacteria. Appl Environ Microbiol 66:1126–1132

Pancost RD, van Geel B, Baas M, Sinnighe-Damsté JS (2000b) Delta^{13}C values and radiocarbon dates of microbial biomarkers as tracers for carbon recycling in peat deposits. Geology 28:663–666

Pancost RD, Baas M, van Geel B, Sinninghe Damsté JS (2002) Biomarkers as proxies for plant inputs to peats: an example from a subboreal ombrotrophic bog. Org Geochem 33:675–690

Pancost RD, McClymont EL, Bingham EM, Roberts Z, Charman DJ, Hornibrook ERC, Blundell A, Chambers FM, Lim KLH, Evershed

RP (2011) Archeol as a methanogen biomarker in ombrotrophic bogs. Org Geochem 42:1279–1287
Paull R, Michaelsen BH, McKirdy DM (1998) Fernenes and other triterpenoid hydrocarbons in *Dicroidium*-bearing Triassic mudstones and coals from South Australia. Org Geochem 29:1331–1343
Peters KE, Walters C, Moldowan JM (2005) The biomarker guide, 2nd edn. Cambridge University Press, Cambridge, UK
Philp RP (1985) Fossil fuel biomarkers. Applications and spectra. Methods Geochem Geophys 23:1–294
Poole I, Dolezych M, Kool J, van der Burgh J, van Bergen PF (2006) Do stable carbon isotopes of brown coal woods record changes in Lower Miocene palaeoecology? Palaeogeogr Palaeoclimatol Palaeoecol 236:345–354
Radke M, Schaefer RG, Leythaueser D, Teichmüller M (1980) Composition of soluble organic matter in coals: relation to rank and liptinite fluorescence. Geochim Cosmochim Acta 44:1787–1800
Radke M, Wilsch H, Leythaueser D, Teichmüller M (1982) Aromatic components of coal: relation of distribution pattern to rank. Geochim Cosmochim Acta 46:1831–1848
Radke M, Leythaeuser D, Teichmüller M (1984) Relationship between rank and composition of aromatic hydrocarbons for coals of different origins. Org Geochem 6:423–430
Radke M, Welte HD, Willsch H (1986) Maturity parameters based on aromatic hydrocarbons: influence of organic matter type. Org Geochem 10:51–64
Regnery J, Püttmann W, Koutsodendris A, Mulch A, Pross J (2013) Comparison of the paleoclimatic significance of higher plant biomarker concentrations and pollen data: a case study of lake sediments from the Holsteinian interglacial. Org Geochem 61:73–84
Sachse D, Billault I, Bowen GJ, Chikaraishi Y, Dawson TE, Feakins SJ, Freeman KH, Magill CR, McInerney FA, van der Meer MTJ, Polissar P, Robins RJ, Sachs JP, Schmidt H-L, Sessions AL, White JWC, West JB, Kahmen A (2012) Molecular paleohydrology: interpreting the hydrogen-isotopic composition of lipid biomarkers from photosynthesizing organisms. Annu Rev Earth Planet Sci 40:221–249
Schulze T, Michaelis W (1990) Structure and origin of terpenoid hydrocarbons in some German coals. Org Geochem 16:1051–1058
Schwarzbauer J, Littke R, Meier R, Strauss H (2013) Stable carbon isotope ratios of aliphatic biomarkers in late Paleozoic coals. Int J Coal Geol 107:127–140
Segarra KEA, Schubotz F, Samarkin V, Yoshinga MY, Hinrichs K.U, Joye SB (2015) High rates of anerobic methane oxidation in freshwater wetlands reduce potential atmospheric methane emissions. Nat Commun 8. https://doi.org/10.1038/ncomms8477
Seki O, Meyers PA, Kawamura K, Zheng Y, Zhou W (2009) Hydrogen isotopic ratios of plant wax *n*-alkanes in a peat bog deposited in northeast China during the last 16 kyr. Org Geochem 33:671–677
Simoneit BRT, Grimalt JO, Wang TG, Cox RE, Hatcher PG, Nissenbaum A (1986) Cyclic terpenoids of contemporary resinous plant detritus and of fossil woods, ambers, and coal. Org Geochem 10:877–889
Smemo KA, Yavitt JB (2011) Anaerobic oxidation of methane: an underappreciated aspect of methane cycling in peatland ecosystems. Biogeosciences 8:779–793
Smith LC, MacDonalds GM, Velicjko AA, Beilman DW, Borisowa OK, Frey KE, Krementski KV, Sheng Y (2004) Siberian peatlands: a net carbon sink and global methane source since the early. Holocene Sci 303:353–356
Stojanović K, Životić D (2013) Comparative study of Serbian Miocene coals – insights from biomarker composition. Int J Coal Geol 107:3–23
Strobl SAI, Sachsenhofer RF, Bechtel A, Meng Q (2014) Paeleoenvironment of the Eocene coal seam in the Fushun basin (NE China): implications from petrography and organic geochemistry. Int J Coal Geol 134–135:24–37
Szczerba M, Rospondek MJ (2010) Controls on distributions of methylphenanthrenes in sedimentary rock extracts: critical evaluation of existing geochemical data from molecular modelling. Org Geochem 41:1297–1311
Talbot HM, McClymont EL, Inglis GN, Evershed RP, Pancost RD (2016) Origin and preservation of bacteriohopanepolyol signatures in Sphagnum peat from Bissendorf Moor (Germany). Org Geochem 97:95–110
ten Haven HL, de Leeuw JW, Rullkötter J, Sinninghe Damste JS (1987) Restricted utility of the pristane/phytane ratio as a paleoenvironmental indicator. Nature 330:641–643
Tomoaia-Cortisel M, Chifu E, Zsako J, Mocanu, Quin PJ, Kates M (1992) Monolayer properties of archaeol and caldarchaeol polar lipids of a methanogenic archaebacterium, *Methanospirillum hungatei*, at the air/water interface. Chem Phys Lipids 63:131–138
Tornabene TG, Langworthy TA, Holzer G, Oro J (1979) Squalenes, phytanes and other isoprenoids as major neutral lipids of methanogenic and thermoacidophilic Archarbacteria. J Mol Evol 13:73–83
van Aarssen BGK, Cox H, Hoogendoorn NP, de Leeuw JW (1990) A cadinene biopolymer in fossil and extant dammar resin as a source for cadinanes and biocadinanes in crude oils from South East Asia. Geochim Cosmochim Acta 54:3021–3031
van Winden JF, Kip N, Reichart GJ, Jetter MSM, Po den Camp HJM, Sinninghe Damste JS (2010) Lipids of symbiotic methane oxidizing bacteria in peat moss studied using stable carbon isotopic labelling. Org Geochem 41:1040–1044
van Winden JF, Talbot HM, Vleeschouwer FD, Reichart G-J, Sinninge Damste JS (2012) Variation of methanotroph-related proxies in peat deposits from Misten Bog, Hautes-Fagnes, Belgium. Org Geochem 53:73–79
Vávra N, Walther H (1993) Chemofossilien aus dem Harz von *Cunninghamia miocenica* ETTINGSHAUSEN (Taxodiaceae, Oligo/Miozän). N Jb Geol Paläont 11:693–704
Versteegh GJM, Schefuß E, Dupont L, Marret F, Sinnighe Damsté JS, Jansen JHF (2004) Taraxerol and *Rhizophora* pollen as proxies for tracking past mangrove ecosystems. Geochim Cosmochim Acta 68:411–422
Vliex M, Hageman HW, Püttmann W (1994) Aromatized arborane/fernane hydrocarbons as molecular indicators of floral changes in the Upper Carboniferous/Lower Permian strata of the Saar/Nahe Basin, southwestern Germany. Geochim Cosmochim Acta 58:4689–4702
Wolfe JA (1980) Tertiary climates and floristic relationships at high latitudes in the northern hemisphere. Palaeogeogr Palaeoclimatol Palaeoeol 30:313–323
Wolff GA, Ruskin N, Marshall JD (1992) Biogeochemistry of an early diagenetic concretion from the Birchi Bed (L. Lias, W. Dorset, U.K.) Org Geochem 19:431–444
Zachos J, Pagani M, Sloan L, Thomas E, Billups K (2001) Trends, rhythms, and aberrations in global climate 65 Ma to present. Science 292:686–693
Zheng YH, Zhou WJ, Xie SC, Yu XF (2009) A comparative study of n-alkane biomarkers and pollen records: an example from southern China. Chin Sci Bull 54:1065–1072
Zheng Y, Singarayer JS, Cheng P, Yu X, Liu Z, Valdes PJ, Pancost RD (2014) Holocene variations in peatland methane cycling associated with the Asian summer monsoon system. Nat Commun 5. https://doi.org/10.1038/ncomms5631

Biomarkers: Petroleum

Meng He[1], J. Michael Moldowan[2] and Kenneth E. Peters[3,4]
[1]Department of Geological and Environmental Sciences, Stanford University, Stanford, CA, USA
[2]Biomarker Technologies, Inc., Rohnert Park, CA, USA
[3]Schlumberger, Mill Valley, CA, USA
[4]Department of Geological Sciences, Stanford University, Stanford, CA, USA

Definition

Biomarkers	Biomarkers or biological markers are the complex organic compounds which are comprised of carbon, hydrogen, and other elements. Biomarkers are usually found in oil, bitumen, rocks, and sediments, and they usually show little changes in terms of molecule structure from their parent organic molecules in living organisms.
Petroleum	Petroleum is a complex mixture of liquid, gas, and solid hydrocarbons with small amounts of other substances and may include crude oil, natural gas, and natural asphalt that form naturally in sedimentary rocksfrom the remains of organisms.

Introduction

The term "biomarker" refers to a molecular fossil, which is an organic chemical that can be identified as originating from a particular biologically synthesized organic molecule. It is distinct from the broader term, "biosignature," which is used in the context of the search for evidence of extraterrestrial life and refers to any evidence of life (Biosignatures Workshop 2000). Biomarkers in geological environment, e.g., in sediments, rocks, and soil extracts, are unambiguously related to enzymatic synthesis in living organisms (Eglinton et al. 1964; Eglinton and Calvin 1967). Lipids, proteins, and carbohydrates are three main macromolecules of living organisms, and are also the potential biomarkers. Lipids include fats and waxes. They are the most probable candidates for evidence of extraterrestrial life due to their preservation in sediments over long periods. Most lipids on Earth come from cellular components. Lipids are known for their stability in sediments and for having a wide variety of diagnostic structural signatures (Engle and Macko 1993). In contrast, proteins and carbohydrates can be rapidly recycled by other living systems and consequently are extremely poorly preserved in sediments over geological timescales (Nagy 1982). Typically, biomarkers undergo a little or no structural change during diagenesis at a low temperature and they inherit most of the carbon skeleton from their original natural products (compounds produced by living organisms). This structural similarity explains why biomarkers can be used as "molecular fossils."

Treibs (1936) first defined the biomarker concept by his pioneering work on the identification of porphyrins in crude oil and their origin from chlorophyll in plants (Fig. 1). Biomarkers have a presence in both the biosphere and geosphere. Biomarkers and their products include most of the organic materials in the geosphere that are amenable to mass spectrometric analysis. Biomarkers have a variety of applications and are used extensively in exploration for petroleum resources (Peters et al. 2005). They are a powerful tool for paleoenvironmental interpretation in Earth history (Eglinton 1964; Eglinton and Calvin 1967; Summons and Walter 1990). Biomarkers can reveal (1) genetic relationships between an oil sample and the potential source rock, (2) geological age, (3) the lithology of the source (carbonate vs. shale vs. coal, etc.), (4) depositional environments (lacustrine, hypersaline, fluvial-deltaic, and marine) of the source rock, and (5) thermal maturity of the source rock and petroleum during petroleum generation (Peters and Moldowan 1993).

Petroleum consists largely of components derived from lipids and can be stable in the subsurface for billions of years (Peters et al. 2005). Since petroleum forms under a variety of geological conditions, each petroleum sample tends to have a unique biomarker fingerprint. The composition of petroleum varies widely due to origination from (1) different source rocks deposited in different depositional environments; (2) the thermal regime during burial, maturation, and oil generation; and (3) different migration pathways and in-reservoir alterations. In addition, the constituents of petroleum undergo changes in chemical structure due to biodegradation or weathering. However, relative to some other compound classes in petroleum, biomarkers are more resistant to biodegradation.

Analytical Methods for Biomarkers

The principle methods of analyzing the biomarkers in petroleum are gas chromatography-mass spectrometry (GC-MS) or gas chromatography-mass spectrometry-mass spectrometry (GC-MS-MS). Analyses are typically performed on the saturated hydrocarbon fraction or the aromatic hydrocarbon fraction, which are the most abundant in petroleum. Isotope ratio gas chromatography-mass spectrometry (IRGC-MS) will be another important research tool widely used in both academia and the oil industry, which can help geochemists interpret the biosynthetic origin of organic compounds, reconstruct ancient geological environment, identify the thermal maturity of the oil, and build the correlation between oil and source rock samples. It can also predict the characteristics

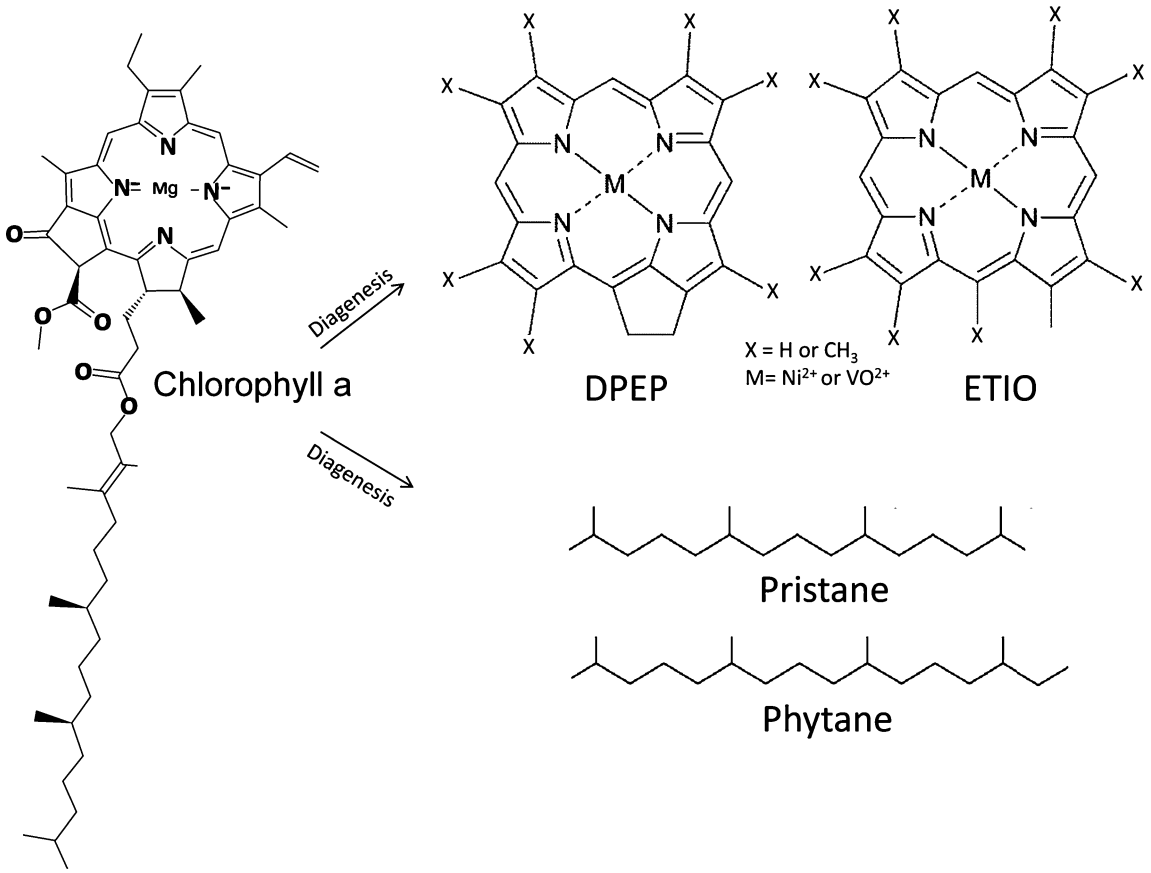

Biomarkers: Petroleum, Fig. 1 Chlorophyll a is a pigment used by most photosynthetic organisms to release chemical energy during photosynthesis. The molecular structure of chlorophyll a is composed of a chlorin ring (four nitrogen atoms surround a central magnesium atom), several said chains, and a hydrocarbon tail. The tetrapyrrole ring and phytyl side chain in chlorophyll a can be converted to several biomarkers during sedimentary burial and thermal maturation, including deoxophylloerythroetioporphyrins (DPEP), etioporphyrins (ETIO), pristane, and phytane. X is hydrogen or an alkyl group and M is commonly nickel (Ni^{2+}) or vanadyl (VO^{2+}) in petroleum

of a source by the carbon isotope fractionation on individual hydrocarbons, which were generated by the source rocks through geological processes. In certain circumstances, it is only possible by using IRGC-MS instead of other methods to detect excess carbon isotopic fractionation compared to that which might be available from abiotic synthesis, and determine what source rocks are present and the level of exposure to thermal stress in mixtures of highly degraded or thermally altered hydrocarbons. Certainly, this would be an added piece of information for petroleum exploration.

Since petroleum is an extremely complex natural mixture of hydrocarbons, its chemical characterization remains an extremely challenging task to analytical scientists. Concentrations of individual biomarkers in petroleum typically range from <1 to 500 ppm, making them some of the most abundant, structurally defined compounds. To increase the accuracy of biomarker analysis, a series of separations is typically conducted before the analysis. First, silica-gel chromatography is applied to separate oil into saturates and aromatics. Second, the zeolite ZSM-5 or other molecular sieves might be used to remove normal alkanes (*n*-alkanes or paraffins) from the saturate fraction. Before removing normal alkanes, saturate fractions can be spiked with internal standards and then subjected to gas chromatography-mass spectrometry (GC-MS), which is the widely-used method to generate accurate analytical profiles for chemical fingerprinting of petroleum (Seifert and Moldowan 1979). The rapid development of organic geochemistry and its important application in petroleum exploration since the 1960s was mainly due to the application of GC-MS, especially after its computerization in the late 1970s. The commercial availability of GC-MS and associated data systems in the mid-1970s helped scientists extend biomarkers studies with a wide variety of purposes. GC-MS is routinely used to analyze biomarkers in whole oils or more commonly, the saturated and aromatic hydrocarbon fractions of oils. Modern GC capillary columns with nonpolar stationary phases are sufficient to resolve many biomarkers, including epimers. A mass spectrometer is used for detection, providing molecular "fingerprints" that identify the eluting compounds. In other words, gas chromatography

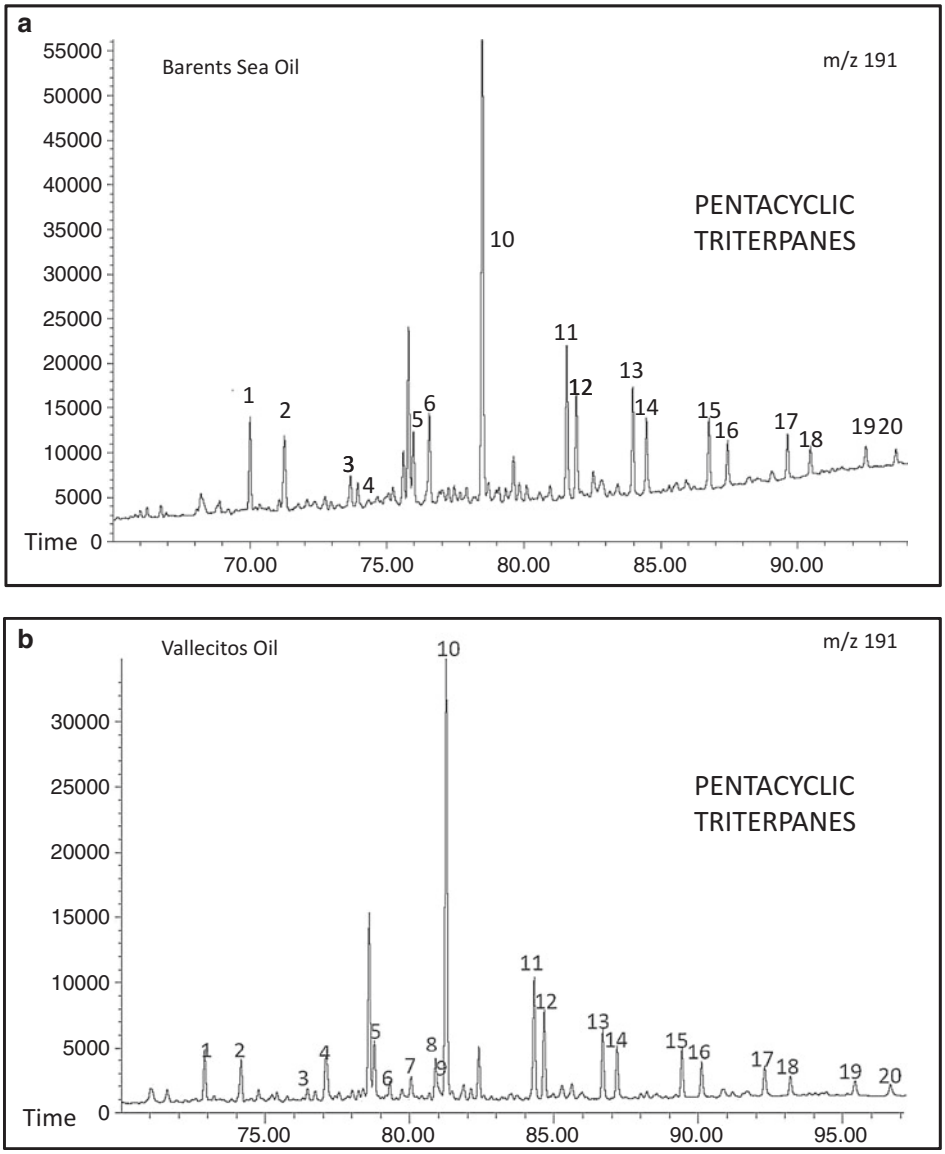

Biomarkers: Petroleum, Fig. 2 (**a**) Terpane mass chromatograms (m/z 191) for the crude oils from Barents Sea Basin. (**b**) Terpane mass chromatograms (m/z 191) for the crude oils from Vallecitos syncline in California

(GC) is used for biomarker analysis to provide the significant advantage of separating the different structures of biomarkers while a mass spectrometer (MS) can be accurately used to detect and identify those different structures. Electron ionization (typically 70 eV) is the most commonly used ionization technique, where classes of biomarkers yield characteristic ion fragments. For example, all hopanes and most other triterpanes and diterpanes yield a characteristic ion with mass-to-charge ratio (m/z) of 191 (Fig. 2a, b; Table 1), while steranes yield characteristic ions with m/z 217 (Fig. 3; Table 1). The m/z 217 ion is diagnostic for all steranes. Since the biomarkers with complicated structure and low concentrations require more sensitive and precise analysis in the biomarker studies, the development of analytical methodologies and combinations between these methods become very important for applications of the biomarker in both sediments and petroleum. To enhance sensitivity, the biomarkers (terpanes) in branched, cyclic, and aromatic fractions are analyzed by selected ion recording-gas chromatography mass spectrometry (SIR-GCMS). Figures 2a, b and 3 show SIM mass chromatograms for terpanes (m/z 191) and steranes (m/z 217) in saturated hydrocarbon fractions of the Barents Sea Basin (He et al. 2012) and Vallecitos Syncline in the western part of the San Joaquin Basin (He et al. 2014). The biomarker distributions of the Barents Sea oils show characteristics of sourcing from a marine shale, such as high C_{26}/C_{25} tricyclic terpane ratios, low $C_{19}/(C_{19} + C_{23})$, low C_{22}/C_{21}, high C_{24}/C_{23}, and low C_{29}/C_{30} hopane ratios. Characteristic distribution of extended homohopane homologs (relatively low C_{33}, C_{34}, and C_{35} homohopane peaks) on the m/z

Biomarkers: Petroleum, Table 1 Identification of labeled biomarker peaks shown in Figs. 2a, b, and 3

Peak ID	Sterane m/z = 217	Peak ID	Terpane m/z = 191
1	C_{27} βα 20S diacholestane	1	Ts 18α(H)-trisnorhopane
2	C_{27} βα 20R diacholestane	2	Tm 17α(H)-trisnorhopane
3	C_{28} βα 20S diasterane 24S	3	C_{28} 17α,18α,21β(H)-bisnorhopane
4	C_{28} βα 20S diasterane 24R	4	C_{29} 25-nor-hopane
5	C_{28} βα 20R diasterane 24S	5	C_{29} Ts 18α(H)-norneohopane
6	C_{28} βα 20R diasterane 24R	6	C_{30} 17α(H)-diahopane
7	C_{27} αα 20S cholestane	7	C_{29} normoretane
8	C_{27} ββ 20R cholestane + C29 βα 20S diastigmastane	8	18α-oleanane
9	C_{27} ββ 20S cholestane	9	18β-oleanane
10	C_{27} αα 20R cholestane	10	C_{30} 17α(H) hopane
11	C_{29} βα 20R diastigmastane	11	C_{31} 22S 17α homohopane
12	C_{28} αα 20S ergostane	12	C_{31} 22R 17α homohopane
13	C_{28} αα 20S ergostane	13	C_{32} 22S 17α bishomohopane
14	C_{28} ββ 20R ergostane	14	C_{32} 22R 17α bishomohopane
15	C_{28} ββ 20S ergostane	15	C_{33} 22S 17α trishomohopane
16	C_{28} αα 20R ergostane	16	C_{33} 22R 17α trishomohopane
17	C_{29} αα 20S stigmastane	17	C_{34} 22S 17α tetrakishomohopane
18	C_{29} ββ 20R stigmastane	18	C_{34} 22R 17α tetrakishomohopane
19	C_{29} ββ 20S stigmastane	19	C_{35} 22S 17α pentakishomohopane
20	C_{29} αα 20R stigmastane	20	C_{35} 22R 17α pentakishomohopane

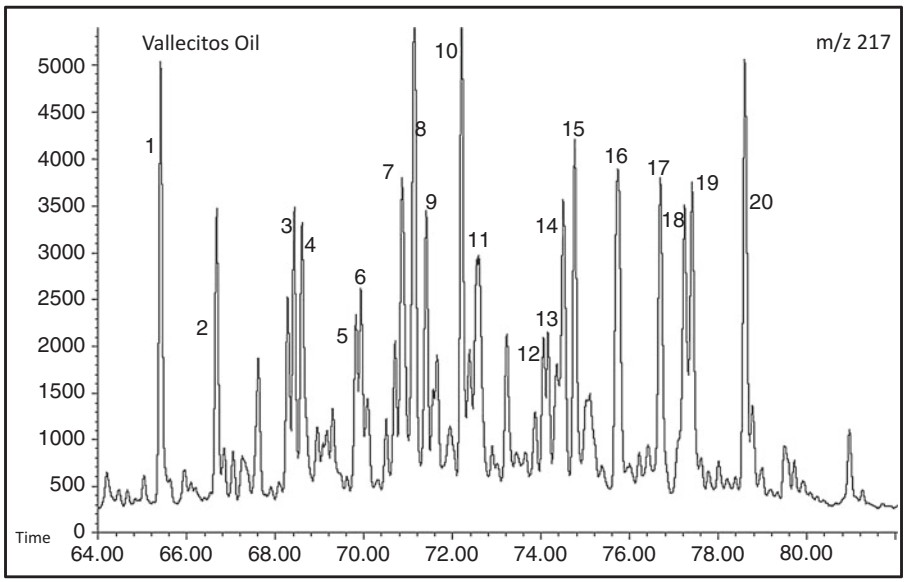

Biomarkers: Petroleum, Fig. 3 Sterane mass chromatograms (m/z 217) for the crude oil from Vallecitos syncline in California

191 ion chromatogram (Fig. 2a) indicates that the source rock was deposited under dysoxic to oxic depositional conditions. The Kreyenhagen oil samples have slightly different biomarker distributions on the m/z 191 ion chromatogram (Fig. 2b). The biomarker analysis indicates little terrigenous organic matter input, and a clay-rich source rock (shale) by the ratio of C_{29}hopaneover C_{30} hopane ($C_{29}/C_{30} < 0.6$). The extended homohopane distribution of Kreyenhagen oil, a decrease in the concentration of extended homohopane homologs C_{31} to C_{35} with poor preservation of C_{35} homohopane, indicates that Eocene Kreyenhagen source rocks in the San Joaquin Basin were deposited in a dysoxic to the oxic open marine environment.

Since the mass spectrometer has high sensitivity, specificity, and capability to precisely elucidate the molecular structure of a particular compound, it has been widely used as the most powerful detector for gas chromatography. Mass fragmentography serves as a satisfactory tool for obtaining specific fingerprints for classes and homologous series of compounds which were originally identified by traditional

chemical structure elucidation techniques, such as nuclear magnetic resonance (NMR), X-ray crystallography, and GC coelution with authentic standards. Gas chromatography-mass spectrometry-mass spectrometry (GC–MS-MS) in the parent-daughter mode reduces interference and thus allows more definitive genetic oil-oil or oil-source rock correlations and thermal maturity assessments than is possible using conventional GC-MS. GC-MS resolves and identifies many of the major saturated and aromatic biomarkers, but the detection of steranes by GC-MS is often problematic due to the co-elution of specific sterane isomers and homologous series. Quantitative metastable reaction monitoring (MRM-GCMS) using a double focusing magnetic sector mass spectrometer and GC-MS-MS using other multisector mass spectrometer systems, such as a triple quadrupole have been used to analyze steranes (regular steranes, such as cholestanes, ergostanes and stigmastanes, diasteranes, dinosteranes), as well as certain terpanes (bicadinanes, tetracyclic polyprenoids, terrestrial diterpanes), since these GC-MS-MS methods resolve the co-elution problems. This type of biomarker analysis has enriched the application of biomarker science. By the use of GC-MS-MS many additional biomarkers have been found and well-studied to enhance the possibilities of understanding ancient depositional environments besides improving petroleum correlation studies. It is supposed that many biomarkers remain to be discovered. The development of the GC-MS is responsible for the growth of biomarker analysis and GC-MS-MS further refines the detection of biomarkers by eliminating interfering compounds.

The compound specific isotope analysis (CSIA) is another breakthrough applied in recent biomarker studies. The CSIA could be thought as a new analytical method that opens new insight and applications based on the GC-MS and GC-MS-MS. CSIA requires fairly precise separation of the compounds and high-resolution analysis to attain accurate measurements, but it is a key to extend a wide range of biomarker analysis of petroleum and source rock extracts. It can be both challenging and encouraging to develop more sensitive identification tools of biomarker analysis, particularly for petroleum with relatively low concentrations of biomarkers at high maturity levels or when severely altered by secondary alteration processes.

Biosynthesis of Biomarker Precursors

A landmark paper by Alfred Treibs (Treibs 1936) demonstrated an organic origin of petroleum when he showed the link between chlorophyll in photosynthetic autotrophs and porphyrins in petroleum (Fig. 1). This work marked the birth of organic geochemistry and laid foundations for the field of biomarker research. Chlorophylls from plants are the most abundant tetrapyrroles in the biosphere. Other tetrapyrroles include hemes in the blood of many animals. Tetrapyrroles preserved in sediments are so complex that they can only have come from chlorophylls or hemes. As discussed above, biomarkers encode abundant information about ancient biodiversity, sediment depositional environment, types of ancient organic matter, and food chain associations. While porphyrins are the first recognized biomarkers, those derived from terpenes by diagenesis are overwhelmingly the most commonly recognized and utilized today.

In general, lipids are a complex variety of organic compounds that are defined by their insolubility and immiscibility in water. Lipids have several biological functions such as constructing cell membranes, storing energy and as signaling molecules. The two main categories of the hydrocarbon skeletons of lipids produced in biosynthesis are: (1) acetogenic lipids having straight normal or simple branched (e.g., iso-, anteiso-) hydrocarbon chains built from C_2 (acetate) subunits; (2) polyisoprenoids, which are built from C_5 (isoprene) subunits by C─C covalent bonds, and are not readily broken down or depolymerized. Importantly, many features of naturally occurring lipids, such as stereochemistry and nonrandom distribution, cannot be explained by abiogenic synthesis. The biosignatures of these compounds can be recognized since abiotic synthesis produces a composition which is out of balance and different from what biotic synthesis produces.

The normal alkanes (*n*-alkanes) are the most abundant individual hydrocarbons in petroleum. Most are biosynthetically produced as functionalized compounds, such as fatty acids, and then converted into *n*-alkanes in diagenesis at a moderate temperature. While Fischer-Tropsch synthesis, which is an abiotic process, is also able to produce these straights-chain hydrocarbons with functionality (McCollom et al. 1998), the distribution of such abiotically produced *n*-alkanes is dramatically different from those produced by biotic synthesis. Fischer-Tropsch synthesis products show a smooth distribution of *n*-alkanes, as expected from abiotic synthesis. In contrast to biogenic synthesis, there is no outstanding excess or lack of any particular homolog such those distributions usually produced by enzymatic synthesis. The key factors which most likely control the distribution of the homologs in abiogenic synthesis lie in the conditions of the synthesis, namely as temperature, pressure, and catalysis.

Petroleum shows multiple expressions of biological synthesis. As discussed above, several *n*-alkanes have a relatively high abundance above the envelope of *n*-alkane peaks shown on the *n*-alkane distribution of the petroleum composition and indicate preferential biosynthesis of their precursors. Fatty acids are almost entirely even carbon-numbered, and if exposed to oxidative depositional conditions they yield predominantly odd carbon-numbered alkanes; whereas predominantly reducing conditions results in predominantly even carbon-numbered alkanes. The combined envelope of *n*-alkanes in an oil sample can, therefore, be considered a type of biosignature, but individual *n*-alkanes are generally not considered biomarkers in themselves. The isoprenoids, such as pristane and phytane, are the

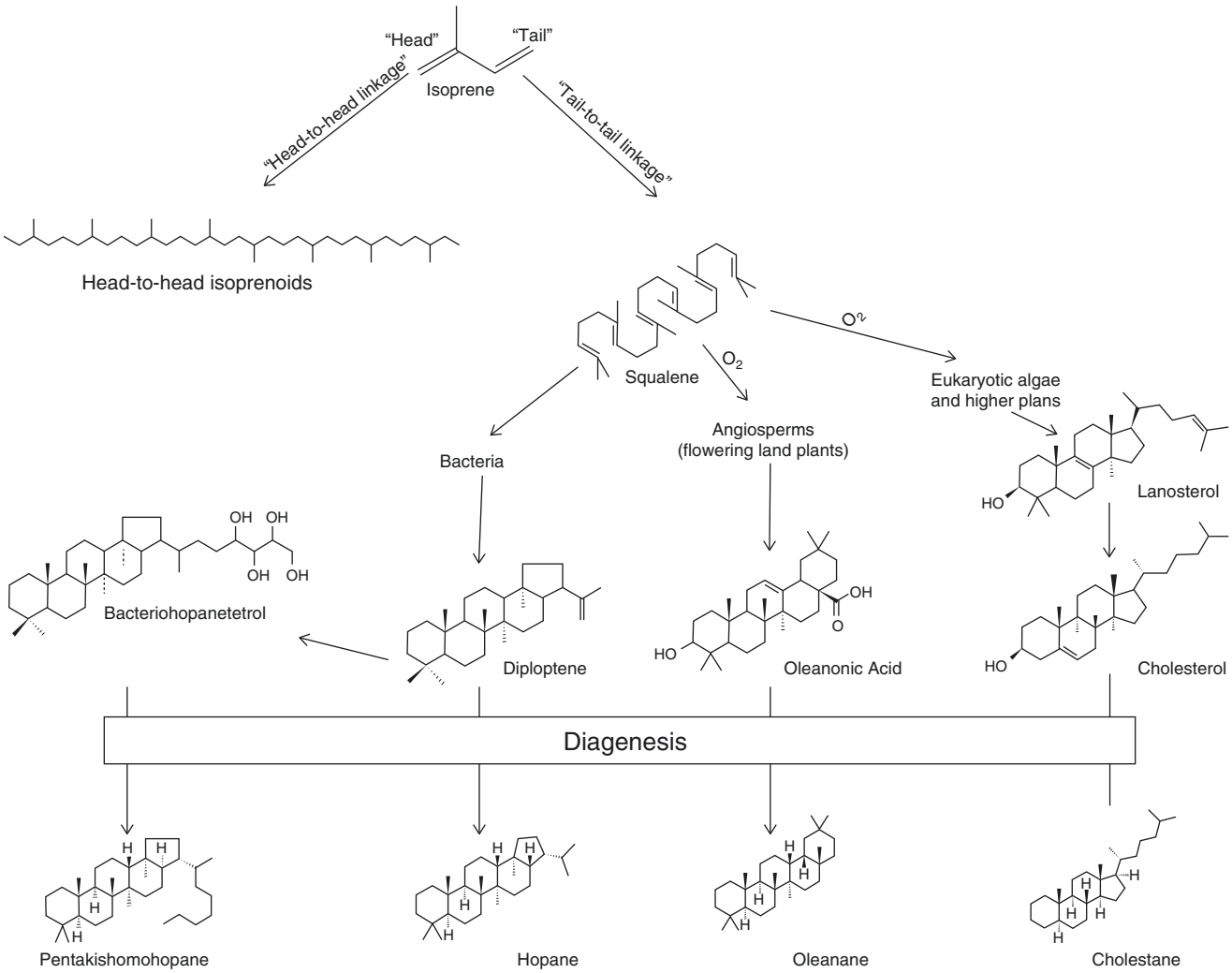

Biomarkers: Petroleum, Fig. 4 Isoprene is an unsaturated pentahydrocarbon and it is produced biologically in animals, plants, and humans. The isoprene skeleton can be found in naturally occurring compounds called terpenes (known as isoprenoids), which can be viewed as multiples of isoprene subunits. The isoprenoids are derived from isoprene. Squalene is composed of six isoprene subunits linked head-to-tail except between the third and fourth subunits where they are linked tail to tail. Biosynthetic modification of squalene in living organisms yields various hopanoids and steroids, which can be further altered during burial to form some of the common biomarkers found in petroleum

classical biomarkers having structures with regularly repeating isopentenyl subunits (Fig. 4). Pristane and phytane are often the most abundant biomarkers in a petroleum sample. Branched hydrocarbons in petroleum show a greater relative abundance than those formed by Fischer-Tropsch synthesis and is another feature showing the biological attribute of petroleum. In fact, the positions of single methyl groups in simple methyl-branched alkanes indicate a positional preference along the carbon chain at the two and three positions, and those positions may have their own biological functions as a key biosignature, most likely due to the link between these lipids and primitive living organisms (Kenig et al. 1995).

Many biomarkers have taxon specificity and are important because they can be used to identify the organic inputs from various domains, kingdoms, families, and even individual species. Most precursors that give rise to biomarkers (e.g., steroids and pentacyclic triterpenoids) have a common biosynthetic precursor -squalene- a C_{30} acyclic isoprenoid composed of six isoprene units (Fig. 4). Under anaerobic conditions, bacteria can cyclize squalene to produce diploptene, which is a pentacyclic triterpenoid. Diploptene can then be biosynthetically modified to yield many other biomarker precursors in organisms. When these organisms die, their remains may be deposited in surficial sediments.

Most functional groups, such as hydroxyl groups and isolated double bonds, are lost or chemically reduced when these compounds undergo sedimentary burial. However, biomarkers in the geosphere commonly retain the carbon skeletons of their

biological precursors. For example, the addition of D-pentose to diploptene during biosynthesis yields C_{35}-bacteriohopanetetrol, which is a structural component of bacterial cell membranes. The defunctionalized product, C_{35} hopane (pentakishomohopane), is common in rock extracts and petroleum. The hopanoids (e.g., hopanes, hopene, and benzohopanes) are generated mainly from hopane polyols, which can be found in bacterial membranes, and have a general application in petroleum as biomarkers for aerobic bacteria (Fig. 4). Since the principal biological function of the most abundant petroleum biomarkers (steranes and hopanes) is as cell-membrane constituents, many biomarkers only appear after catagenesis, the process of kerogen breakdown by heating to generate petroleum. The heating necessary for catagenesis usually occurs by sufficiently deep burial of the rock containing the kerogen, but other processes can also result in catagenesis, such as volcanic intrusions and heating by hydrothermal vents.

Most organisms can biologically synthesize the acyclic molecule, squalene, which can be cyclized into the pentacyclic triterpene, hopane, by cyclase (Fig. 4). In bacteria, its derivative, hopene, can be further converted to bacteriohopane by adding a 5-carbon chain derived from the sugar ribose (Flesch and Rohmer 1988). Because bacteria constitute such a large fraction of Earth's biomass, hopane molecules with their persistency and thermodynamic stability have been said to comprise the most abundant large-molecule repository of carbon on Earth (Ourisson and Albercht 1992). Hundreds of hopanoids products can be further produced by degradation and by rearrangement of hopene (C_{30}) and bacteriohopane (C_{35}) through catalytic and thermal effects during diagenesis and catagenesis. Hopanoid products have been well identified in soils, sediments, other organic matter, and oil (Ourisson et al. 1984). However, even though the postdepositional degradation and rearrangement can alter the biochemistry (usually does not completely erase it), hopanoids have a fixed stereochemistry derived from enzymatic synthesis. They can still be recognized as biomarkers although they are partially altered.

Unlike prokaryotes, such as bacteria, eukaryotes are unicellular or multicellular organisms, including algae, protozoa, fungi, plants, and animals, whose cells contain a membrane-bound nucleus and complex organelles. Eukaryotic organisms use oxygen to synthesize tetracyclic triterpenes, precursors to the steroids instead of other triterpenoids (Fig. 4). Lanosterol is a precursor for many sterols. Cholesterol is one of the most common sterols in plants and animals and is the precursor for cholestane in petroleum. Prokaryotic hopanoids and eukaryotic steroids are key structural elements in prokaryotic and eukaryotic cellular membranes, which could explain the ubiquity and relative abundance of their hopane and sterane products in petroleum. Higher land plants synthesize many other biochemicals from squalene, including oleanolic acid and β-amyrin, to name a couple that can be precursors for the oleanane in petroleum (Fig. 4).

Archea possesses a cell wall and has a unique way of joining isoprenoids to form a "head-to-head" linkage (Fig. 4). This unique pattern of the isoprenoid linkage appears to be Archea-specific, reflecting a distinctly ancestral chemical differentiation from bacteria and eukaroytes, the other two domains of life (Chappe et al. 1982).The long hydrocarbon chains with head-to-head linkage could possibly include the short side hydrocarbon chains and rings. Archea uses acyclic isoprenoids to make phospholipids, which may help archean membranes from leaking at high temperature. Archea, bacteria, and photosynthetic eukaryotes are known to produce smaller isoprenoid chains, like pristane and phytane. Although acyclic isoprenoids play a significant role in forms of life and can be useful to indicate even very primitive life, they are not taxon-specific for tracking any particular domain due to their various original sources.

Biomarkers as Source and Environmental Indicators

Biomarkers are useful in petroleum exploration and production geochemistry because they carry information about organic matter input, depositional environment, age, and thermal history of the petroleum source rock, as well as the extent of alteration of petroleum in the reservoir rocks (Peters et al. 2005). For example, diagenesis and catagenesis of chlorophyll yields three common constituents in petroleum: porphyrins, and the acyclic diterpanes, pristane, and phytane (Fig. 1). Some porphyrins can be related to specific organisms in the source-rock depositional environment.

Certain steranes and triterpanes in petroleum and rock extracts are also diagnostic for specific biota. Dinoflagellates produce the dinosteranes. 24-*n*-Propylcholestane indicates input from marine Chrysophyte algae (Moldowan et al. 1990). Highly branched isoprenoids are derived from diatoms. Saturated equivalents of botyrococcene (botryococcane) are produced by the freshwater green algae *Botryococcusbraunii*. Botryococcane in petroleum from Minas Field in Indonesia indicates that it originated from a source rock that was deposited in a lacustrine environment conducive to Botryococcus blooms (Moldowan and Seifert 1980). Oleananes, lupanes, and taraxeranes are biomarkers of flowering plants and are also present in the source rock (Ekweozor and Udo 1988; Moldowan et al. 1994). Bicadinanes are derived from dipterocarpaceae tree resins (Cox et al. 1986). Retene, cadalene, and tetracyclic diterpanes indicate conifer input to the source rock (Noble et al. 1985).

An abundance of C_{35}-homohopanes in petroleum (relative to C_{31}-C_{34}-homohopanes) indicates source rocks deposited under anoxic conditions. High abundance of 28, 30-bisnorhopane in petroleum also indicates a reducing environment. 30-Norhopanes (the C_{29}/C_{30}-hopane ratio) have been widely used as a proxy for carbonate source rock. Oil

from carbonate source rock usually has a relatively low diasterane/sterane ratio and high concentrations of 2-α-methylhopanes (Summons et al. 1999). The pristane/phytane ratio can be used to support inferences about the redox conditions of the depositional environment (ten Haven et al. 1988). High concentrations of gammacerane in oils originate from tetrahymanol, which is a triterpanoid produced by anaerobic green-sulfur bacteria in source rocks, often deposited under hypersaline conditions and a stratified water column (Sinninghe Damste et al. 1995). Isorenieratane in petroleum originates from isorenieratene in green sulfur bacteria, which are anoxygenic phototrophs (Summons and Powell 1987). Thus, isorenieratane in petroleum and rock extracts indicates photic zone anoxia when the source rock was deposited.

Kerogen represents ~90% of the organic carbon in sedimentary rocks. Functionalized forms of biomarkers may still occur in extracts from thermally immature petroleum source rocks and low-maturity petroleum, but the defunctionalized saturate and aromatic biomarkers dominate under thermal conditions associated with oil generation. Hopanoids in the geosphere occur insignificant amounts, which is as much or more than the total mass of organic carbon in living organisms. Depending on the depositional setting, the sterol concentration may be more or less than that of the hopanoids. Some biomarkers contain heteroatoms. For example, sulfur can be incorporated into biomarkers during early burial under anoxic, marine conditions. Nitrogen and metals, such as vanadium and nickel, are common in low-maturity petroleum that contains porphyrins. Oxygen can be introduced into biomarkers as acid groups during microbial biodegradation.

Age-Diagnostic Biomarkers

Biomarkers can reveal the age of the source rock (Peters and Moldowan 1993). Steranes and hopanes occur in old Precambrian rocks and in much younger Tertiary rocks. Therefore, their presence in petroleum yields little information about the age of the source rock. However, some precursors originated with the evolution of new biota during the Phanerozoic and can be used as age-diagnostic biomarkers. Age-diagnostic biomarkers are important because they help to identify the origin of petroleum that may have migrated many kilometers from its source rock. Some compounds in petroleum and rock extracts cannot be identified as biomarkers based only on their chemical structures. For example, crude oils with abundant odd-carbon numbered *n*-alkanes in the range *n*-C_{11} to *n*-C_{19} and low amounts of pristane, phytane, and *n*-alkanes above *n*-C_{20} may have originated from *Gloeocapsomorpha prisca*, an extinct green algae that flourished during the early Paleozoic.

Gloeocapsomorpha prisca is the main contributing organism to many lower Paleozoic hydrocarbon source rocks. Evidence of *G. prisca* rarely occurs in post-Ordovician sediments. Source rocks enriched by *G. prisca* and oil derived from them show a distinctive geochemical characteristic of saturated fractions dominated by *n*-alkanes up to C_{19} with a pronounced odd-carbon number predominance. This particular alkane distribution suggests that oil might have been generated from source rocks of Ordovician or lower Paleozoic age. It is predominated by compounds with less than 20 carbons and with a strong odd-carbon predominance for *n*-alkanes (*n*C_{15}, *n*C_{17}, *n*C_{19}). The distribution of *n*-alkanes and low presence of the isoprenoids pristane and phytane results from source facies dominated by a single organism, *Glaecapsamorpha prisca* (*G. prisca*), which proliferated in carbonate banks of the Ordovician.

Sterane biomarkers are derived from steroids which are important constituents of eukaryotic cell-membranes. Steroids have been synthesized by various organisms from Precambrian to present times. C_{28}- and C_{29}-steranes are common constituents from green algae and C_{27}-steranes are prevalent in red algae in marine environment. However, these associations are not exclusive of all species of these groups. Regular steranes consist primarily of C_{27}, C_{28}, and C_{29} carbon numbers. Moldowan et al. (1985) and Grantham and Wakefield (1988) recognized that the ratio of C_{28} to C_{29} steranes varies with the geological age of marine source rocks and that the regular C_{28}/C_{29}-sterane ratio can be used to assess age of oils generated from marine source rocks. Variation in the C_{28}/C_{29} ratio is interpreted to be the result of diversification of sterane-producing organisms, including diatoms, coccolithophores, and dinoflagellates in the Jurassic and Cretaceous periods, particularly those that generate C_{28} compounds over geological time. Caution was emphasized by Peters et al. (2005) in using this ratio without other support due to the certain exceptions, such as land plant sources which have a high concentration of C_{29}-steranes.The ratio of C_{28}/C_{29} regular steranes is best suited for discriminating Palaeozoic from Tertiary sources and is only applicable to open marine organic facies.

Eukaryotic steroids are the most common biomarkers in geological record. The C_{30}-sterane 24-*n*-prophylcholestane (24-*npc*) derived from marine algae is commonly used as an indicator of ancient marine sedimentary depositional environments. The 24-*n*-propylcholestanes are diagnostic markers for marine algae of the older Sarcinochrysidales and brown tide algae (Moldowan et al. 1990). These C_{30}-steranes first appeared in Phanerozoic and their source algae evolved between Early Ordovician and Devonian. The 24-isopropyl/24-*n*-propylcholestanes ratio is used to assess the age of marine source rocks or oils generated from a marine source, particularly for Late Proterozoic (Vendian) to Ordovician sources. The modern precursors of 24-isopropylcholestane are found almost exclusively in marine porifera (sponges) referred to as Demospongiae (McCaffrey et al. 1994). Marine Chrysophyte algae biosynthesizes the 24-*n*-propylcholesterols, which are

related to the 24-*n*-propylcholestanes (Moldowan et al. 1990). The Demospongiae were proposed as the precursors of 24-isopropylcholestane based on the prevalence of 24-isopropylcholesterols in their natural products (McCaffrey et al. 1994). High concentrations of 24-isopropylcholestane (relative to 24-*n*-propylcholestane) were found in some Vendian-Cambrian rock extracts and petroleum, implying that sponges or related organisms were relatively more abundant in Vendian-Cambrian than at other geological times (McCaffrey et al. 1994). High 24-isopropylcholestane ratios appear to result from input of stomatoporids, the dominant reef-building organisms during Late Proterozoic and Early Cambrian. The stomatoporids may have a relationship to modern Porifera (sponges) containing abundant sterols having the 24-isopropylcholestane skeleton.

Dinoflagellates are single-celled eukaryotes whose nucleus lacks histones and having chromosomes that remain condensed throughout the cell division cycle.They are a major part of the marine microplankton flora, which has been around at least since the Late Proterozoic. Dinosterols (natural lipid precursors) and related compounds occur abundantly in modern dinoflagellates although dinosterols have been detected at low abundances in a few of marine diatom species. Consequently, dinosterane, the corresponding saturate hydrocarbon, is a specific marker for dinoflagellates. A relationship between cyst-forming dinoflagellates and pre-Triassic ancestors was constructed by molecular fossil evidence provided by Moldowan and Talyzina (1998). It has been shown in many studies that dinoflagellates are an important source of Mesozoic and Cenozoic marine oil and gas and they are widely accepted as important oil-generating algae. Dinosteranes and triaromatic dinosteroids are used to distinguish marine Jurassic or younger sources, where they occur abundantly and ubiquitously, from marine Paleozoic oils or extracts where they are much less abundant or absent, while Triassic abundances and occurrences are intermediate in magnitude and frequency. Thus, abundant dinosteranes or triaromatic dinosteroids suggest a Triassic or younger age of crude oils and rock extracts.

Tracking of dinosteranes and dinosteroids biomarkers in fossils has been valuable for documenting time-dependent changes in the fossil record. Although the pre-Triassic record contains only equivocal occurrences of dinoflagellates, comparative ultrastructural and molecular phylogenetic evidence from acritarchs (organic-walled microfossils thought to be algal cysts or resting stages) indicates a possible Precambrian origin for the lineage. Thus, it has often been proposed that the dearth of Paleozoic fossil dinoflagellates was due to a lack of preservation or recognition and that the relatively sudden appearance of dinoflagellates in the Mesozoic is an artifact of the record. However, new evidence from a detailed analysis of fossil records and from the biogeochemical records indicates that dinoflagellates did indeed undergo a major evolutionary radiation in the early Mesozoic. Moldowan et al. (1996) reported that triaromatic dinosteroids, which are derived almost exclusively from dinoflagellates, have not been detected in samples from Carboniferous and Permian, but occur sporadically in pre-Carboniferous rocks enriched in acritarchs. A combined dinoflagellate and acritarch species count appears to mirror the occurrence of the dinosteroids. Moldowan and Talyzina (1998) suggested that abundant triaromatic dinosteroids in some Paleozoic rocks and even Proterozoic strata could be related to marine acritarchs, potentially derived from dinoflagellates, which are potentially primary producers in Paleozoic oceans. This might indicate that dinoflagellates could have existed long before the appearance of dinoflagellate cyst fossils in the Triassic.

The C_{26}-sterane, 24-norcholestane, has also been demonstrated to be a useful constraint on geological age and depositional environment (Holba et al. 1998). The 24-norcholestanes are more abundant in oils and rocks younger than Paleozoic even though the source of the 24-norcholestanes is still unproven. The oldest occurrence of 24-norcholestanes probably has a dinoflagellate origin. According to the study by Moldowan and Talyzina (1998) acritarchs that are dinoflagellate ancestors were present as far back as the Early Cambrian. The 24-norcolestanes, along with 24-nordiacholestanes, are used to assess the age of source rocks and oils generated from both marine and non-marine sources. They are best suited for separating Tertiary from Cretaceous, and older than Cretaceous sources. There is still a debate on the relationship between 24-norcholestanes and specific modern taxa because traces of 24-norcholesterol have been observed in both living marine algae and invertebrates, suggesting an origin in eukaryotes which may or may not have prokaryotic symbionts. 24-Norsterols or 24-norsteranes (derived from 24-norsterols in diagenesis) may originate from dinoflagellates in temperate and tropical areas (Rampen et al. 2007). The presence of 24-norcholestane in recent sediment extracts and diatom blooms (Nichols et al. 1990), ancient diatomaceous sediments (Suzuki et al. 1993), and petroleum generated from siliceous sources indicates that diatoms may also be a source of 24-norsteroids. However, in recent studies both diatoms and dinoflagellates are now believed to generate the 24-norcholestanes found in both sediments and petroleum. The temporal evolution and expansion of both dinoflagellates and diatoms can explain the observed stepwise increases in 24-norcholestane concentrations in the sediment record and provide a rationale for their use as age-diagnostic biomarkers.

Highly-branched isoprenoids (HBIs) alkanes and alkenes with 25 carbons have been reported to occur widely in both recent and ancient sediments. These compounds are useful paleoenvironmental biomarkers. Generation of HBIs has been most likely controlled by some environmental factors, but a detailed understanding of these remains unclear. These unusual highly branched hydrocarbons have only been observed in

certain diatoms indicating that organic matter in the sediments includes diatoms. Diatoms (Bacillariophyta) are unicellular eukaryotic algae and they use water and light to stimulate their photosynthesis. Diatoms exhibit a great diversity within marine environments including benthic, planktonic, marine, and freshwater species that produce C_{25} HBIs. Diatoms are believed to have originated in the Jurassic and became dominant in Cretaceous and younger periods. In order to determine the timing of the origin of the HBI biosynthetic pathway, Sinninghe Damste et al. (2004) studied the fossil record. They believed that HBI biosynthesis evolved in the Upper Turonian (~90 Ma) according to their data in the study. It also has been observed that the HBI first occurred in sediments of Upper Turonian from the Guyana Basin (French Guyana) in the Canje Formation. There is no occurrence of C_{25} HBIs earlier than Upper Turonian, whereas C_{25} HBIs have widespread occurrence in younger marine sediments (Younger than Upper Turonian age). The HBI occurrence in petroleum shows the great similarity to how the HBI biosynthetic pathway evolved (Peters et al. 2005). For example, the petroleum from the Maracaibo Basin (Venezuela) has a Cenomanian/Turonian age of source rock. Also, it has been documented as the oldest petroleum containing the C_{25} HBI alkane above the detection limit. The close match between sediments and petroleum makes the C_{25} HBI a probable candidate of age-related biomarker. It could be inferred that petroleum containing the C_{25} HBI alkane must be sourced by sedimentary rocks with an age of Upper Turonian or younger. Thus, highly branched isoprenoids with high concentrations of C_{25} HBIs (more than 100 ppm as a detection limit) indicates a Late Cretaceous or younger marine source. HBIs are present in most of the modern coastal sediments and are very common in many lake sediments.

The oleananes are probably derived from pentacyclic triterpenes in angiosperms (flowering plants) (Moldowan et al. 1994). The earliest fossil of angiosperms are found in Early Cretaceous rocks. Therefore, the presence of oleanane suggests that organic matter has been sourced from land plants, specifically angiosperms (Philp and Gilbert 1986) of mid-Cretaceous age or younger. A nonzero oleanane index in these samples indicates some contribution from land plants (angiosperms) to the source rocks where these oils were generated. Angiosperms diversified and spread rapidly in the Late Cretaceous (Moldowan et al. 1994) and came to dominate the terrestrial biota by the end of the Cretaceous. Thus, oleanane is present, though in some cases in reduced quantities, in a majority of crude oil samples from the Cretaceous reservoirs in the world. Higher concentration of oleanane strengthens an interpretation of a tertiary source; the source rock most likely has tertiary age if oleanane is greater than 20% of the sum of oleanane + αβ-hopane. At low concentrations (i.e., less than 3% of the C_{30}-αβ-hopane peak), other compounds unrelated to oleanane can be mistakenly identified as oleanane. The presence of oleanane does not rule out a pre-mid-Cretaceous source because oils generated from older strata could have migrated through post-mid-Cretaceous strata. If the post-mid-Cretaceous strata are immature and rich in biomarkers, compounds such as oleanane can be entrained by the migrating oil. Conversely, the absence of oleanane does not rule out a post-mid-Cretaceous source. Highly mature material or sources dominated by marine organic matter will have low concentrations of oleanane.

Several considerations must be kept in mind when using age-related biomarkers to assess the age of source rock and petroleum samples. In general, it is recommended to look at more than one age-related biomarker to improve the confidence in the age identification. Age-related biomarkers are also affected by source facies, biodegradation, secondary processes in the reservoirs, and maturity. It is not easy to build the relationship between a biomarker parameter ratio and the source rock maturity because many factors such as heating rate, source rock lithofacies, and source rock organic facies (kerogen type) could variously impact identification of that relationship. As a result, it always happens that the exact maturity (i.e., vitrinite reflectance equivalent) associated with a given value for a biomarker parameter ratio could vary from basin to basin with different depositional settings. Most significantly, the concentrations of biomarkers in petroleum dramatically decrease with increasing thermal maturity, and many age-related biomarkers would reach their terminal values. Hence, any given biomarker parameter ratio is applicable within its own limitations.

Biomarker Stereochemistry

Stereochemistry refers to a way in which the atoms of a molecule are spatially arranged. Biological compounds have stereochemistries that give them the capability of fulfilling specific functions in organisms, such as membrane stabilization. The vast majority of biomarkers have some kind of stereospecificity. Spatial arrangement is the key concept in understanding chirality and stereochemistry. Molecules display their own spatial preference based on the kinetics and energetics of their formation. Enzymatic synthesis plays an important role by placing constraints on the three-dimensional shape of the biosynthesized natural products, since only specific molecular shapes are biologically active. Therefore, molecules with a unique spatial arrangement of atoms in three-dimensional space have different chemical-physical properties from molecules having exactly the same composition (empirical formula). Chirality has received wide attention in organic chemistry and also is an important biosignature of biomarkers. It helps to explain the physical and theoretical reasons behind the biomarker structure and is related to the origin of biomarkers via enzyme-assisted synthesis. A molecule with a chiral center has a non-superimposable mirror image. In reality, a carbon atom with four different surrounding atoms bonded to it is treated as

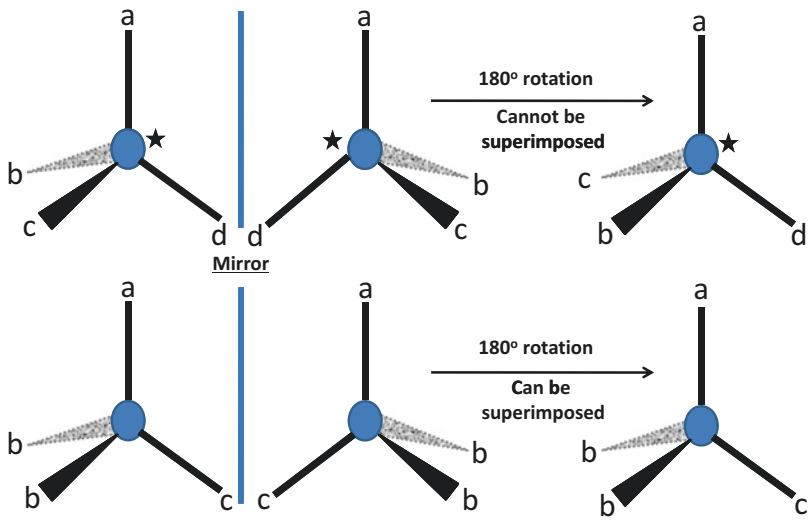

Biomarkers: Petroleum, Fig. 5 It is shown the comparison of chiral and achiral molecules. The center atom is commonly carbon atom in petroleum, a, b, c, and d are different either atoms or atom groups attached to the carbon atom. The chiral molecule has a stereocenter which is designated with an asterisk. Rotation of its mirror image does not generate the original structure. In contrast, the mirror image of the achiral molecule can be superimposed on the original structure after the 180° rotation

chiral molecules if it cannot be superimposed upon itself after 180° rotation (Fig. 5). Many biomarkers, such as steranes and hopanes, have multiple chiral centers which can be preserved through diagenesis. They have multiple quaternary asymmetric carbon atoms (carbon atoms bonded to four different groups) in their carbon backbone structures, which allow them to be recognized by the mass spectrometry. Epimerization is the process during which one asymmetric carbon center is converted to its chiral counterpart. With relatively mild diagenetic conditions, biomarkers with asymmetric centers (tertiary asymmetric carbon atoms bonded to only one hydrogen atom), such as acyclic isoprenoids and amino acids, generate a racemic mixture, a 50:50 mixture of enantiomers, of both the biologically and geologically produced antipodes via epimerization.

Isomers are molecules that have the same chemical formula but a different structural arrangement of atoms in space. Many different types of isomers are important in organic geochemistry. Molecules are identical in a two-dimensional view but can be differentiated stereochemically in three dimensions can be designated as enantiomers, diastereomers, or epimers. Usually biosynthesis produces one isomer exclusively, known as homochirality; for example, amino acids are biosynthesized exclusively as the L-enantiomer rather than the D-enantiomer. Internal rotational and vibrational energies cause these molecules to twist and writhe in space instead of being static. In general, lipids having carbon atoms as asymmetric centers (centers with four different groups attached by four single bonds) are biosynthesized as one or the other antipode.

However, once organisms die, the biological configurations of these compounds may not be stable in the biosphere and geosphere. Certain asymmetric centers can be inverted during diagenesis. As a result, amino acids in ancient organic matter containing tend to epimerize into a racemic mixture (50:50 mixtures) of Land D amino acids. Biomarkers encode valuable information about diagenetic and thermal conditions by suffering postmortem stereochemical changes. Enantiomers receiveless attention during biomarker analysis, because it is not easy to resolve them by the available analytical technology. However, compounds with multiple asymmetric centers can be resolved as diastereomers due to the inversion of some of the asymmetric centers. Asymmetric centers carrying a hydrogen atom (tertiary carbon centers) tend to invert but asymmetric quaternary carbon centers (carbon atom bound to four different groups other than hydrogen) cannot. Inversion at asymmetric centers is called stereoisomerization. During the process of the stereoisomerization, the formation of thermodynamically more stable geological epimers from less-stable biological epimers takes place. However, it does not usually generate a 50:50 mixture of the two configurations because some of the multiple asymmetric centers are involved and some of them are not free to invert. It is impossible for quaternary centers to complete the stereoisomerization during diagenesis, and disruption of these centers may lead to rearranging and destroying the base molecular structure. Acyclic isoprenoids readily isomerize very early in their burial and steroids can form pairs of diastereoisomers at former sites of unsaturation (double bonds). Certain hydrogen atoms at ring junctions are prone to isomerize and even the whole steroid backbone can rearrange. This backbone rearrangement is particularly catalyzed in the presence of acidic clays in the enclosing sediment. Whereas such rearrangements are often suppressed in the carbonate sediments due to the different type of diagenesis in carbonate rocks. Thus, stereoisomerization reactions can be used not only as thermal maturity indicators but also as depositional environment indicators.

Thermal maturity describes the extent of heat-driven reactions that convert sedimentary organic matter into petroleum. Petroleum is a complex mixture of metastable products that

evolve toward greater thermodynamic stability during maturation. Exploration success for petroleum can be improved by identifying areas within sedimentary basins where thermal maturity is favorable for the occurrence of crude oil. Thermal stress parameters are the most commonly utilized parameters for evaluating the maturity of organic matter. The effect of temperature leads to conversion of relatively unstable compounds to thermodynamic more stable compounds based on either rearrangement or decomposition. The mechanism of rearrangement or decomposition proceeds via aromatization, dealkylation, isomerization, and alkylation, and these chemical changes can be enhanced by catalytic activity.

Organic matter from bacterial and plant debris in sediments is generally converted into kerogen and bitumen by means of biological, physical, and chemical alterations and without pronounced effects of temperature during diagenesis. After progressive diagenesis, catagenesis and metagenesis can commence upon deep burial and organic matter is converted into petroleum and, ultimately, to gas and graphite (Peters et al. 2005). Since the changes are progressive during the long geological periods of burial in the sediments, most biomarkers comprise mixtures dominated by the most thermodynamically stable stereoisomers. For example, during the thermal process, cleavage and reformation of the bonds result in two configurations where the asymmetric center is with or without an attachment to a ring. Therefore, with increasing maturity, these reactions lead to the enrichment of the thermodynamically more stable isomers. The extents of such conversions can be used as maturity indicators.

Summary

Petroleum occurs naturally in complex mixtures. It contains more than 20,000 hydrocarbon compounds having a broad structural and chemical diversity. Those compounds are predominantly comprised of aliphatic hydrocarbons, aromatic hydrocarbons, and many other constituents with heteroatoms (N, O, S) and with different volatilities.

Biomarkers are important compounds in petroleum, whose basic structure provides an unambiguous link with formerly-living organisms. Their basic molecular structures are primarily inherited from the parent organic molecules with little or no change.

Further, their structures undergo few changes during diagenesis and catagenesis. The most important biomarkers are hydrocarbons. Crude oils exhibit different biomarker fingerprints. The high specificity of some biomarkers in petroleum and source rocks toward specific classes of organisms and different types of depositional environments allows the interpretation of paleoenvironmental conditions at the time of sedimentation, thermal maturity, type of organic matter in the source rock, and genetic relationships between petroleum and source rocks. In addition, biomarker analysis can also provide important information about migration pathways from the source rock to the reservoir based on oil-to-oil and oil-to-source rock correlation. Biomarkers provide information of great importance in forensic investigations to determine the source of spilled oil, differentiate and correlate oils, and monitor the degradation process and weathering of oils because they resist biodegradation and weathering.

Cross-References

- ▶ Biomarker: Assessment of Thermal Maturity
- ▶ Biopolymers and Macromolecules
- ▶ Carbon
- ▶ Carbon Isotopes
- ▶ Compound-Specific Isotope Analysis
- ▶ Gas Chromatography–Mass Spectrometry (GC–MS)
- ▶ High-Resolution Mass Spectrometry
- ▶ History of Geochemistry
- ▶ Hydrocarbons
- ▶ Hydrogen
- ▶ Kerogen
- ▶ Natural Gas
- ▶ Nuclear Magnetic Resonance
- ▶ Oil-Oil and Oil-Source Rock Correlations
- ▶ Organic Geochemistry
- ▶ Organics: Sources and Depositional Environments
- ▶ Petroleum
- ▶ Porphyrins

References

Biosignature Workshop (2000) sponsored by NASA, University of California, San Diego, 3–5 Mar 2000

Chappe B, Albrecht P, Michaelis W (1982) Polar lipids of archaebacteriain sediments and petroleums. Science 217:65–66

Cox HC, DeLeeuw JW, Schenck PA, van Koningsveld H, Jansen JC, van de Graaf B, van Geerestein J, Kanters JA, Jans WH (1986) Bicadinane, a C_{30} pentacyclic isoprenoid hydrocarbon found in crude oil. Nature 319:316–318

Eglinton G, Calvin M (1967) Chemical fossils. Sci Am 261:32–43

Eglinton G, Scott PM, Besky T, Burlingame AL, Calvin M (1964) Hydrocarbons of biological origin from an one-billion-year-old sediment. Science 145:263–264

Ekweozor CM, Udo OT (1988) The oleananes: origin, maturation, and limits of occurrence in Southern Nigeria sedimentary basins. In: Mattavelli L, Novelli L (eds) Advances in organic geochemistry 1987. Organic geochemistry, vol 13. Pergamon Press, London, pp 131–140

Engle MH, Macko SA (eds) (1993) Organic geochemistry: principles and applications. Plenum Press, New York, p 861

Flesch G, Rohmer M (1988) Prokaryotic hopanoids: the biosynthesis of thebacteriohopane skeleton. Formation of isoprenic units from two distinct acetate pools and a novel type of carbon/carbon linkage between a triterpene and D-ribose. Eur J Biochem 175:405–411

Grantham PJ, Wakefield LL (1988) Variations in the sterane carbon number distributions of marine source rock derived crude oils through geological time. Org Geochem 12:61–73
He M, Moldowan MJ, Peters K, Rovenskaya A (2012) Oil families and their inferred source rocks in Barents Sea and northern Timan-Pechora Basin, Russia. Am Assoc Pet Geol Bull 96:1121–1146
He M, Graham SA, Scheirer AH, Peters K (2014) A basin modeling and organic geochemistry study in the Vallecitos syncline, San Joaquin Basin, California. Mar Pet Geol 49:15–34
Holba AG, Tegelaar EW, Huizinga BJ, Moldowan JM, Singletary MS, McCaffrey MA, Dzou LIP (1998) 24-Norcholestanes as age-sensitive molecular fossils. Geology 26:783–786
Kenig E, SinninghеDamste JS, Kock-van Dalen AC, Rijpstra WIC, Huc AY, de Leeuw JW (1995) Geochim Cosmochim Acta 59:2999–3015
McCaffrey MA, Moldowan JM, Lipton PA et al (1994) Paleoenvironmental implications of noval C_{30} steranes in Precambrian to Cenozoic age petroleum and bitumn. Geochim Cosmochim Acta 58:529–532
McCollom TM, Ritter G, Simoneit BRT (1998) Lipid synthesis underhydrothermal conditions by Fischer-Tropsch-type reactions. Orig Life Evol Biosph 28:1–14
Moldowan JM, Seifert WK (1980) First discovery of botryococcane in petroleum. J Chem Soc Chem Commun 1980:912–914
Moldowan JM, Talyzina NM (1998) Biogeochemical evidence for dinoflagellate ancestors in the Early Cambrian. Science 281:1168–1170
Moldowan JM, Seifert WK, Gallegos EJ (1985) Relationship between petroleum composition and depositional environment of petroleum source rocks. Am Assoc Pet Geol Bull 69:1255–1268
Moldowan JM, Fago FJ, Lee CY, Jacobson SR, Watt DS, Slougui NE, Jeganathan A, Yong DC (1990) Sedimentary 24-n-propylcholestanes, molecular fossils diagnostic of marine algae. Science 247:309–312.
Moldowan JM, Dahl J, Huizinga BJ (1994) The molecular fossil record of oleanane and its relation to angiosperms. Science 265:768–771
Moldowan JM, Dahl J, Jacobson SR, Huizinga BJ, Fago FJ, Shetty R, Watt DS, Peters KE (1996) Chemostratigraphic reconstruction of biofacies: molecular evidence linking cyst-forming dinoflagellates with pre-Triassic ancestors. Geology 24:159–162
Nagy B (1982) Search for biochemical fossils on Earth and non-biological organic molecules on Jupiter, Saturn and Titan. Naturwissenschaften 69:301–310
Nichols PD, Palmisano AC, Rayner MS, Smith GA, White D (1990) Occurrence of novel C_{30} sterols in Antarctic sea-ice diatom communities during a spring bloom. Org Geochem 15:503–508
Noble RA, Alexander AR, Kagi RI, Knox J (1985) Tetracyclic deterpenoid hydrocarbons in some Australian coals, sediments and crude oils. Geochim Cosmochim Acta 49:2141–2147
Ourisson G, Albercht P (1992) Hopanoids. 1. Geohopanoids: the most abundant natural products on Earth? Acc Chem Res 25:398–402
Ourisson G, Albrecht P, Rohmer M (1984) The microbial origin of fossil fuels. Sci Am 251:44–51
Peters KE, Moldowan JM (1993) The biomarker guide interpreting molecular fossils in petroleum and ancient sediments. Prentice Hall, Englewood Cliffs, 363pp
Peters KE, Walters CC, Moldowan JM (2005) The biomarker guide, 2nd edn. Cambridge University Press, Cambridge, Part 1 and 2, 1155pp
Philp RP, Gilbert TD (1986) Biomarker distributions in Australian oils derived from terrigenous source material. Org Geochem 10:73–84
Rampen SW, Schouten S, Panoto FE, Muyzer G, Campbell CN, Fehling J, SinninghеDamste JS (2007) On the origin of 24-norcholestanes and their use as age-diagnostic biomarkers. Geology 35:419–422
Seifert WK, Moldowan JM (1979) The effect of biodegradation on steranes and terpanes in crude oils. Geochim Cosmochim Acta 43:111–126
Sinninghe Damste JS, Kenig F, Koopmans MP, Koster J, Schouten S, Hayes JM, de Leeuw JW (1995) Evidence for gammacerane as an indicator of water column stratification. Geochim Cosmochim Acta 56:1391–1900
Sinninghe Damste JS, Muyzer G, Abbas B, Rampen SW, Masse G, Allard WG, Belt ST, Robert JM, Rowland SJ, Moldowan JM, Barbanti SM, Fago FJ, Denisevich P, Dahl J, Trindade LF, Schouten S (2004) The rise of the rhizosolenid diatoms. Science 304:584–587
Summons RE, Powell TG (1987) Identification of arylisoprenoids in a source rock and crude oils: biological markers for the green sulfur bacteria. Geochim Cosmochim Acta 51:557–566
Summons RE, Walter MR (1990) Molecular fossils and microfossils of prokaryotes and protists from Proterozoic sediments. Am J Sci 290-A:212–244
Summons RE, Jahnke LL, Hope JM, Logan GA (1999) 2-Methylhopanoids as biomarkers for cyanobacterial oxygenic photosynthesis. Nature 400:554–557
Suzuki N, Sampei Y, Koga O (1993) Norcholestane in Miocene Onnagawa siliceous sediments, Japan. Geochim Cosmochim Acta 57:4539–4545
ten Haven HL, de Leeuw JW, SinninghеDamste JS, Schenck PA, Palmer SE, Zumberge JE (1988) Application of biological markers in the recognition of paleo-hypersaline environments. In: Kelts K, Fleet A, Talbot M (eds) Lacustrine petroleum source rocks. Special publication, vol 40. Blackwell, Geological Society, London, pp 123–130
Treibs A (1936) Chlorophyll and hemin derivatives in organic mineral substances. Angew Chem 49:682–686

Biopolymers and Macromolecules

Markus Kleber[1] and Patrick Reardon[2]
[1]Department of Crop and Soil Science, Oregon State University, Corvallis, OR, USA
[2]Nuclear Magnetic Resonance Facility, Oregon State University, Corvallis, OR, USA

Definition

A *polymer* is "a chemical compound or mixture of compounds formed by polymerization and consisting essentially of repeating structural units" (Merriam-Webster 2017). As the original meaning of the term polymer does not include any reference to molecular size, Staudinger and Fritschi (1922) introduced the word *macromolecule* to describe large covalently bonded organic chain molecules containing more than 10^3 atoms. By convention, the term macromolecule is reserved for organic molecules; it does not cover inorganic geopolymers such as obsidian. The official definition (IUPAC 2006) of the term macromolecule regards a molecule as having a high relative molecular mass if the addition or removal of one or a few of the units has a negligible effect on the molecular properties. Also, when a molecule has a high molecular mass *and* comprises the multiple repetitions of units derived from molecules of low relative molecular mass, it may be described as either macromolecular or

polymeric. *Supramolecular assemblies* of amphiphilic subunits share the element of monomer repetition and the element of potentially large molecular size, but here the monomers are not covalently linked. Size, biological functionality, and shape of supramolecular assemblies in geosystems depend on the presence and ionic composition of the supporting aqueous phase.

Types of Macromolecules in Geosystems

Biomacromolecules include a wide range of species such as cellulose, hemicellulose, lignin, protein, DNA, RNA, resins, glycogen, and many others. Many of these macromolecules play important roles in geophysical systems. These roles can be separated into four broad categories based on the propensity of the respective molecule to maintain some form of biogeochemical functionality in the environment: (i) providers of energy, carbon, nutrients, and biophysical functionality, (ii) conservation of information and signaling, (iii) extracellular catalysis, and (iv) residuum with no obvious biological function.

Biomacromolecules as a Source of Energy, Carbon, and Nutrients

Globally, two major biomacromolecule production environments can be distinguished. (a) In terrestrial systems, vascular plants predominate and consist largely of carbon-rich biomacromolecules such as cellulose, lignin, and tannin (Table 1). A detailed description of these compounds has been offered by Kögel-Knabner (2002). Dead plant matter from the shoot is dropped on the soil surface, while root derived debris and exudates enter the subsurface mineral soil. Mesofauna, fungi, bacteria, and archaea constitute the decomposer community involved in the conversion of dead plant matter to smaller intermediate compounds and ultimately to end products such as CO_2, HCO_3^-, and CH_4. Terrestrial systems receive variable amounts of rainwater which percolates through the soil and so generates a constant vertical removal vector for all soluble organic compounds, requiring those organisms who wish to feed on such compounds to be alert, selective, and efficient. Because terrestrial systems are overwhelmingly aerobic environments, fungi specialized on producing O_2 – requiring oxidative enzymes are particularly important for decomposition processes. (b) In the oceans, phytoplankton produce a nitrogen – rich biomass (Table 1), where bacteria and archaea recycle the constituents of dead organisms in the water column. Any debris that escape degradation sink to the underlying sea floor, where the scarcity of oxygen means degradation can only continue with the help of electron acceptors (such as nitrate, sulfate) that allow for lesser energy yields than oxygen. Vascular plants and their unique macromolecular constituents (lignin, tannin, crystalline cellulose) are largely absent, as are the fungal decomposers that are specialists on such materials.

As long as oxygen is present, microbial decomposition is vigorous in both terrestrial and marine systems and even organic debris encapsulated in aggregates or adsorbed to mineral surfaces will eventually be mineralized (Hedges and Oades 1997). Preservation of organic debris over geological time scales requires the absence or profound impediment of prokaryotic life. For instance, deep burial of anoxic sediments may lead to elevated pressure and temperature and thus prevent decomposer activity.

Biomacromolecules as Information Carriers

The nucleic acids, DNA and RNA, are the primary information carrying macromolecules.Nucleic acids are normally protected from the extracellular environment inside cells or the capsid of viruses. However, they can be found in the environment as the result of cell lysis or excretion by live cells (Lorenz and Wackernagel 1994). In the environment, nucleic acids are subject to degradation by nucleases, which is a relatively rapid process. DNA is degraded in aquatic

Biopolymers and Macromolecules, Table 1 Relative composition of vascular plants, algae, bacteria, and fungi, modified after Kleber et al. (2007)

	Vascular plants	Algae	Bacteria	Fungi
	% dry matter			
Lignin	5–30			
Cellulose	15–60			
Hemicellulose	10–30			
N-containing compounds	2–15	24–50	50–60	14–52
Lipids	Minor	2–10	10–35	1–42
Noncellulosic carbohydrates	Minor	40	4–32	8–60
	Ratio			
C:N ratio	20–50 (tree leaves) 25–80 (herbaceous plants)	6	5–8	≈10

systems with a half-life of minutes to hours. In contrast, rapid binding to soil minerals can result in persistence of nucleic acids for many hours, days, or weeks (Lorenz and Wackernagel 1994). Organisms in the soil can utilize this genetic information when they take up the nucleic acids by transformation. Transformation of environmental DNA has been implicated in gene transfer and the emergence of antibiotic resistance in the environment (Berglund 2015). Proteins can also carry information, albeit not genetic in nature. Signal peptides are often used in quorum sensing, a mechanism that is thought to coordinate activities between groups of microorganism (Miller and Bassler 2001; Hibbing et al. 2010).

Biomacromolecules as Catalysts

Proteins account for the majority of catalytic macromolecules in the extracellular environment. As polymers of amino acids, these macromolecules incorporate a wide range of functional groups, such as amines, carboxylic acids, and aromatics. The wide range of functional groups in proteins contributes to their varied functions and behavior. Most catalytically active proteins (or enzymes) fold into complex three-dimensional structures that form an active site where important functional groups are optimally positioned to carry out catalysis. Denaturation or unfolding of an enzyme typically results in its loss of function. RNA is also capable of carrying out catalytic function (Fedor and Williamson 2005), with the ribosome being one of the most important examples. However, the extent to which RNA contributes to soil catalytic processes has not been fully determined.

Proteins can associate with soil mineral surfaces resulting in various outcomes (Gianfreda et al. 2011). In some cases, binding of proteins to minerals has resulted in loss of catalytic activity, implying that either the active site has been occluded or the protein has unfolded. In other cases, proteins bound to minerals have retained their catalytic activity and have also been found to have improved thermal stability (Huang et al. 2005). These and similar observations have suggested the hypothesis that mineral association by proteins results in their reduced degradation and extended persistence in the environment (Burns et al. 2013). The hypothesis is further supported by the observation of mineral associated proteins preserved in the environment for time periods in excess of four million years (Demarchi et al. 2016). Yet, it is important to note that not all minerals will reduce protein degradation. Reactive metal oxides, such as birnessite, have been shown to readily degrade proteins (Reardon et al. 2016; Russo et al. 2009). In another case (Johnson et al. 2006), the phyllosilicate montmorillonite was observed to cleave a pathogenic prion protein, although the pathogenic subunit remained intact and infective. This is particularly interesting, because montmorillonites generally are thought to bind and preserve protein (Gougeon et al. 2003), rather than contribute to its degradation. Thus, while many protein mineral interactions result in thermal stabilization, and perhaps protection from degradation, this is not true of all such interactions. Biophysical properties of the particular proteins involved in the interaction and the local environmental conditions likely contribute to these interactions and the resulting outcomes.

The tendency of proteins to interact with soil minerals, regardless of the eventual outcome of these interactions, has complicated their study (Quiquampoix and Burns 2007). Their wide range of biophysical properties results in complex interactions with minerals and involve an array of molecular level forces (Norde 2008). Thus, a given mineral can exhibit strong affinity for one protein but modest affinity for another. Further, environmental conditions, such as pH, can have a significant influence on affinity (Reardon et al. 2016). Many studies of soil protein require extraction of protein from the mineral for subsequent downstream analysis. However, the complexity of these interactions can hamper protein extraction. Methods intended to extract total protein from minerals have been developed; however, the actual efficiency of extraction is typically well below 100% (Chourey et al. 2010; Wu et al. 2014; Keiblinger et al. 2012).

Residual Carbon: Macromolecularity as a Condition for Persistence

The realization that molecular complexity and degree of polymerization are linked to slow decomposition can be traced back to the early decades of the twentieth century (Waksman 1936) and received strong support from the work of Martin and coworkers (Haider and Martin 1975; Haider and Trojanowski 1975; Martin and Haider 1971; Martin et al. 1982). These scientists introduced ^{14}C into the molecular structure of phenolic acids and artificially prepared phenolic polymers. This allowed them to identify the molecular origin of the carbon in the $^{14}CO_2$ that evolved during decomposition of these molecules. In a seminal publication, Haider and Martin (1975) showed how linkage into polymeric structures was able to retard the decomposition of organic carbon in 12-week incubation experiments. As a result, macromolecularity has long been considered one of the major factors determining the persistence of organic C in geosystems. This perception contributed to attempts to predict the persistence of organic C based on the molecular properties of organic substrates (reviewed by Derenne and Largeau 2001). One significant outcome of this view is the traditional model of kerogen formation (Fig. 1) as the result of initial depolymerization followed by partial recondensation of decomposition fragments into operationally defined "humic substances" (Hedges 1988).

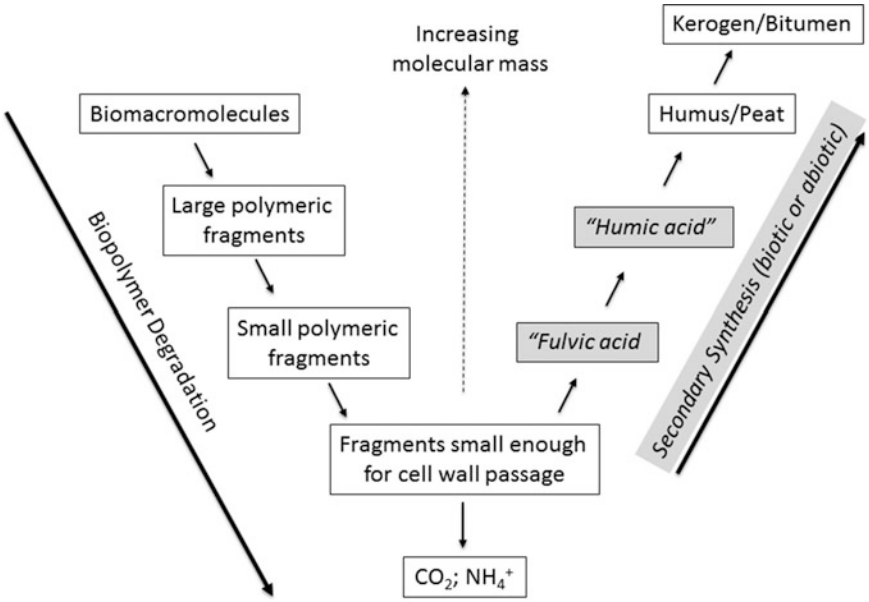

Biopolymers and Macromolecules, Fig. 1 Classic view of the biopolymer degradation and abiotic condensation pathways (Modified after Hedges 1988). *Gray shadowing*: fraction or mechanism currently debated. Fulvic acid and humic acid are operationally defined fractions obtained by an alkaline extraction procedure, their actual physical existence in geosystems has not been verified in observations using independent methodology. While demonstrable in laboratory settings, secondary synthesis of small fragments into larger, operationally defined "humic substances" has so far not been shown to be of quantitative relevance for organic matter accumulation in geosystems

Two major developments have altered this view. The advent of supramolecular chemistry inspired Wershaw (1993) to conceptualize decaying organic matter as a collection of relatively small amphiphilic molecules assembled into micellar or hemimicellar associations held together by noncovalent interactions among the component molecules, a view that has steadily gained traction (Kleber et al. 2007; Piccolo 2001; Sutton and Sposito 2005). Concomitantly, analytical techniques such as solid state nuclear magnetic resonance spectrometry (SS-NMR) and synchrotron spectromicroscopy (STXM-NEXAFS) have allowed the community to observe the chemical characteristics of organic compounds in situ and independent of operational extraction procedures. This has led to the development of alternate models to explain the survival of fragmented organic matter without the need for a recondensation step. The biodegradation/sorption model proposed by Hedges and Keil (1999) posits that some degradation intermediates escape microbial uptake and are leached into the soil where they partition between the aqueous phase and the surrounding mineral surfaces. These organic materials escape remineralization due to protective sorption/aggregation without the need to invoke spontaneous condensation reactions. Based on in situ observations using modern spectrometric techniques (Keiluweit et al. 2012; Kelleher and Simpson 2006; Lehmann et al. 2008; Masoom et al. 2016; Myneni et al. 1999), this concept has since been further refined into the soil continuum model (Lehmann and Kleber 2015), which conceptualizes soil organic matter as a continuum of progressively decomposing organic compounds whose persistence depends on interactions with the mineral phase. Recent evidence for the ability of mesofauna and symbiotic microorganisms to decompose even industrial polymers (Yang et al. 2014, 2015, Yoshida et al. 2016) emphasizes the insight of Jenkinson (1981) that "in the long run, no fraction of organic matter can withstand decomposition" and that the molecular peculiarities associated with kerogen formation (Vandenbroucke and Largeau 2007) arise from the combined effects of exclusion of decomposer organisms, anoxia, heat, and pressure following burial and not as a consequence of polymerization reactions during humus or peat formation.

Summary

Biomacromolecules are synthesized by organisms to perform numerous functions inside and outside of the cell. Historically, emphasis was placed on the decomposition, alteration, and persistence of macromolecules in geosystems. The concepts and pathways involved in the early stages of macromolecule transformations are currently revised based on new information made available by innovative methods for in situ observation of chemical processes at the submicron scale. Extracellular functions of biomacromolecules such as catalysis, signaling, and transfer of genetic information are receiving increasing attention and constitute an exciting realm of future research.

Cross-References

- Analytical Techniques
- Clay Minerals
- Kerogen
- Nuclear Magnetic Resonance
- Organic Geochemistry
- Organic Matter Degradation and Preservation
- Soils

References

Berglund B (2015) Environmental dissemination of antibiotic resistance genes and correlation to anthropogenic contamination with antibiotics. Infect Ecol Epidemol 5:28564

Burns RG, DeForest JL, Marxsen J, Sinsabaugh RL, Stromberger ME, Wallenstein MD, Weintraub MN, Zoppini A (2013) Soil enzymes in a changing environment: current knowledge and future directions. Soil Biol Biochem 58:216–234

Chourey K et al (2010) Direct cellular lysis/protein extraction protocol for soil metaproteomics. J Proteome Res 9:6615–6622

Demarchi B et al (2016) Protein sequences bound to mineral surfaces persist into deep time. elife 5:e17092

Derenne S, Largeau C (2001) A review of some important families of refractory macromolecules: composition, origin and fate in soils and sediments. Soil Sci 166:833–847

Fedor MJ, Williamson JR (2005) The catalytic diversity of RNAs. Nat Rev Mol Cell Biol 6:399–412

Gianfreda L, Rao MA, Mora M (2011) Enzymatic activity as influenced by soil mineral and humic colloids and its impact on biogeochemical processes. Handbook of Soil Science Resource of Management and Environmental Impacts, Second Edition, CRC Press, Taylor & Francis, Boca Raton, Fl., Chapter 5, pp. 1–24

Gougeon R et al (2003) Polypeptide adsorption on a synthetic montmorillonite: a combined solid-state NMR spectroscopy, X-ray diffraction, thermal analysis and N_2 adsorption study. Eur J Inorg Chem 7:1366–1372

Haider K, Martin JP (1975) Decomposition of specifically C14 labeled benzoic and cinnamic acid derivatives in soil. Soil Sci Soc Am J 39:657–662

Haider K, Trojanowski J (1975) Decomposition of specifically C-14-labeled phenols and dehydropolymers of coniferyl alcohol as models for lignin degradation by soft and white rot fungi. Arch Microbiol 105:33–41

Hedges JI (1988) Polymerization of humic substances in natural environments. In: Frimmel FH, Christman RF (eds) Humic substances and their role in the environment. Wiley, Chichester, pp 45–58

Hedges JI, Keil RG (1999) Organic geochemical perspectives on estuarine processes: sorption reactions and consequences. Mar Chem 65:55–65

Hedges JI, Oades JM (1997) Comparative organic geochemistries of soils and marine sediments. Org Geochem 27:319–361

Hibbing ME, Fuqua C, Parsek MR, Peterson SB (2010) Bacterial competition: surviving and thriving in the microbial jungle. Nat Rev Microbiol 8:15–25

Huang PM, Wang MK, Chiu CY (2005) Soil mineral-organic matter-microbe interactions: impacts on biogeochemical processes and biodiversity in soils. Pedobiologia 49:609–635

IUPAC (2006) Compendium of chemical terminology, 2nd edn. (the "Gold Book"). Compiled by A. D. McNaught and A. Wilkinson XML on-line corrected version: (2006-) created by M. Nic, J. Jirat, B. Kosata; updates compiled by A. Jenkins: Blackwell, Oxford (1997)

Jenkinson DS (1981) The fate of plant and animal residues in soil. In: Greenland DJ, MHB H (eds) The chemistry of sol processes. Wiley, Chichester, pp 505–561

Johnson CJ, Phillips KE, Schramm PT, McKenzie D, Aiken JM, Pedersen JA (2006) Prions adhere to soil minerals and remain infectious. PLoS Pathog 2:e32: 296–302

Keiblinger KM, Wilhartitz IC, Schneider T, Roschitzki B, Schmid E, Eberl L, Riedel K, Zechmeister-Boltenstern S (2012) Soil metaproteomics – comparative evaluation of protein extraction protocols. Soil Biol Biochem 54:14–24

Keiluweit M, Bougoure JJ, Zeglin LH, Myrold DD, Weber PK, Pett-Ridge J, Kleber M, Nico PS (2012) Nano-scale investigation of the association of microbial nitrogen residues with iron (hydr)oxides in a forest soil O-horizon. Geochim Cosmochim Acta 95:213–226

Kelleher BP, Simpson AJ (2006) Humic substances in soils: are they really chemically distinct? Environ Sci Technol 40:4605–4611

Kleber M, Sollins P, Sutton R (2007) A conceptual model of organo-mineral interactions in soils: self-assembly of organic molecular fragments into zonal structures on mineral surfaces. Biogeochemistry 85:9–24

Kögel-Knabner I (2002) The macromolecular organic composition of plant and microbial residues as inputs to soil organic matter. Soil Biol Biochem 34(2):139–162

Lehmann J, Kleber M (2015) The contentious nature of soil organic matter. Nature 528:60–68

Lehmann J, Solomon D, Kinyangi J, Dathe L, Wirick S, Jacobsen C (2008) Spatial complexity of soil organic matter forms at nanometre scales. Nat Geosci 1:238–242

Lorenz MG, Wackernagel W (1994) Bacterial gene transfer by natural genetic transformation in the environment. Microbiol Rev 58:563–602

Martin JP, Haider K (1971) Microbial activity in relation to soil humus formation. Soil Sci 111:54–63

Martin JP, Zunino H, Peirano P, Caiozzi M, Haider K (1982) Decomposition of 14C-labeled lignins, model humic acid polymers, and funal melanins in allophanic soils. Soil Biol Biochem 14:289–293

Masoom H et al (2016) Soil organic matter in its native state: unravelling the most complex biomaterial on Earth. Environ Sci Technol 50:1670–1680

Merriam-Webster ndW (2017) "Polymer" (9 May 2017)

Miller MB, Bassler BL (2001) Quorum sensing in bacteria. Annu Rev Microbiol 55:165–199

Myneni SCB, Brown JT, Martinez GA, Meyer-Ilse W (1999) Imaging of humic substance macromolecular structures in water and soils. Science 286:1335–1337

Norde W (2008) My voyage of discovery to proteins in flatland ... and beyond. Colloids Surf B-Biointer 61:1–9

Piccolo A (2001) The supramolecular structure of humic substances. Soil Sci 166:810–832

Quiquampoix H, Burns RG (2007) Interactions between proteins and soil mineral surfaces: environmental and health consequences. Elements 3:401–406

Reardon PN, Chacon SS, Walter ED, Bowden ME, Washton NM, Kleber M (2016) Abiotic protein fragmentation by manganese oxide: implications for a mechanism to supply soil biota with oligopeptides. Environ Sci Technol 50(7):3486–3493

Russo F, Johnson CJ, Johnson CJ, McKenzie D, Aiken JM, Pedersen JA (2009) Pathogenic prion protein is degraded by a manganese oxide mineral found in soils. J Gen Virol 90:275–280

Staudinger H, Fritschi J (1922) Über die Hydrierung des Kautschuks und über seine Konstitution. Helv Chim Acta 5:785–806

Sutton R, Sposito G (2005) Molecular structure in soil humic substances: the new view. Environ Sci Technol 39:9009–9015

Vandenbroucke M, Largeau C (2007) Kerogen origin, evolution and structure. Org Geochem 38:719–833
Waksman SA (1936) Humus. Origin, chemical composition and importance in nature. Williams and Wilkins, Baltimore
Wershaw RL (1993) Model for humus in soils and sediments. Envion Sci Technol 27:814–816
Wu X, Xiong E, Wang W, Scali M, Cresti M (2014) Universal sample preparation method integrating trichloroacetic acid/acetone precipitation with phenol extraction forcrop proteomic analysis. Nat Protoc 9:362–374
Yang J, Yang Y, Wu W-M, Zhao J, Jiang L (2014) Evidence of polyethylene biodegradation by bacterial strains from the guts of plastic-eating waxworms. Environ Sci Technol 48:13776–13784
Yang Y, Yang J, Wu WM, Zhao J, Song YL, Gao LC, Yang RF, Jiang L (2015) Biodegradation and mineralization of polystyrene by plastic-eating mealworms: part 2. Role Gut Microorgan Environ Sci Technol 49:12087–12093
Yoshida S, Hiraga K, Takehana T, Taniguchi I, Yamaji H, Maeda Y, Toyohara K, Miyamoto K, Kimura Y, Oda K (2016) A bacterium that degrades and assimilates poly(ethylene terephthalate). Science 351:1196–1199

Bismuth

Cristiana L. Ciobanu and Nigel J. Cook
School of Chemical Engineering, The University of Adelaide, Adelaide, SA, Australia

Element Data
Atomic Symbol: Bi
Atomic Number: 83
Atomic Weight: 208.9804
Isotopes and Abundances: Bi^{209} (100%) – several other isotopes are short-lived intermediate products of U^{238} (Bi^{210} and Bi^{214}), U^{235} (Bi^{211} and Bi^{213}), and Th^{232} (Bi^{212}) decay. Bi^{209} is a rare primordial isotope, discovered in 2003, that decays via α-decay with a half-life greater than a billion times the age of the universe.
1 Atm Melting Point: 544.52 °C
1 Atm Boiling Point: 1837 °C
Common Valences: +3 (0, +5)
Ionic Radii: 3+: 101 pm
Pauling Electronegativity: 2.02
First Ionization Potential: 703 kJ mol^{-1}
Chondritic (CI) Abundance: 0.11 ppm
Silicate Earth Abundance: 0.003 ppm
Crustal Abundance: 0.025 ppm
Seawater Abundance: 0.015 μg/l
Core Abundance: ~0.03 ppm
Ahrens and Erlank (1969), Angino and Long (1979), Norman (1998), Palme and O'Neill (2014)

Properties

Bismuth is a brittle, diamagnetic, reddish white metal which tarnishes to a brassy color and is a poor conductor of heat and electricity. Chemically, bismuth is similar to metalloids antimony and arsenic, albeit with greater metallic character. The metal burns upon heating with oxygen to give the oxide Bi_2O_3 (Bi_2O_5 is unstable).

Bismuth is most commonly found in the +3 oxidation state in minerals, rarely as Bi^{5+}. Bismuth readily forms chloride ($BiCl_5^{2-}$ and $BiCl_6^{3-}$), oxide, and hydroxide complexes, notably $Bi(OH)_{3(aq)}$ (Tooth et al. 2013; Etschmann et al. 2016). Bismuth is the most ionic of the Group VA elements and tends to form strong bases in aqueous solutions.

Bismuth is a moderately volatile chalcophile element and is typically enriched in sulfide-bearing meteorites. A subordinate lithophile character is reported but remains poorly documented.

History and Use

Known since ancient times [from the German, *Weisse Masse* (white mass), later *Wismuth*, or possibly via Arabic *bi ismid* (having the properties of antimony), and translated in the sixteenth century to the New Latin name *bisemutum*].

Bismuth has a remarkably low toxicity relative to lead, and bismuth alloys are increasingly used instead of lead in a variety of applications, including water pipes, ceramic glazes, fishing weights, solders, and gunshot. More than half the annual production of bismuth (13,600 tonnes in 2015; USGS 2016) is, however, used for manufacture of compounds for the cosmetics, pigment, and, increasingly, pharmaceutical industries. Bismuth-based compounds, notably tellurides and selenides alloyed with antimony and, most recently, sodium bismuthinides, have attracted considerable interest as thermoelectric materials and topological insulators on account of their semiconducting properties.

Bismuth production, sufficient to meet world demand, comes largely as a by-product of lead (and in China, also tungsten) mining. Two mines, one each in Bolivia and China, have exploited bismuth ore. China and Vietnam are currently the world's most important suppliers.

Geochemical Behavior

Bismuth concentrations in most rock types are low, around or below minimum limits of detection. The element is, however, typically enriched in felsic rocks (~0.9 ppm in rhyolite,

0.27 ppm in granites), although concentrations tend to vary from example to example. Concentrations are an order of magnitude lower in mafic or intermediate rocks. It is therefore unsurprising that the greatest concentrations of bismuth minerals are found in pegmatites associated with granites, in hydrothermal deposits associated with granites, and in skarn deposits formed via intrusive-related metasomatism. Concentrations of bismuth in sedimentary rocks vary; they are highest in recent pelagic sediments (0.56 ppm) and shales (0.26 ppm) and low in sand- and limestones (averaging 0.03 ppm). Coals are typically relatively enriched in bismuth (average 5 ppm). Metamorphic rocks appear typically low in bismuth.

Mineralogy

Bismuth is one of a number of elements (the others are Cu, Ag, As, Se, Ag, Sb, Te, Pb, and U) which build an anomalously large number of distinct minerals in which it is an essential component. Bismuth is second only to tellurium in terms of mineralogical diversity (Christy 2015).

Bismuth is found as native metal but more commonly as a relatively large number of sulfides, the most abundant of which is the mineral bismuthinite (Bi_2S_3). Bismuthinite forms a solid solution with stibnite (Sb_2S_3). There are currently around 210 approved bismuth minerals. Bismuth sulfosalts (and selenosalts) (Moëlo et al. 2008) are a particularly diverse group and make up around half this number. Among the most common sulfosalts of bismuth are bismuthinite derivatives, lillianite homologues, and cosalite. These may contain lead, copper, and/or silver and can be classified into a number of homologous series on the basis of related crystal structures (Makovicky 1997, 2006). Additional bismuth sulfosalts are described and named each year. Other primary bismuth minerals include Te- and/or Se-bearing chalcogenides (e.g., tetradymite, Bi_2Te_2S), also making up an extensive homologous series of structurally related species (Lind and Lidin 2003; Cook et al. 2007; Ciobanu et al. 2009a), and bismuthides (e.g., maldonite, Au_2Bi). Secondary bismuth species include oxides (most common: bismite, Bi_2O_3), carbonates (most common bismutite, $Bi_2(CO_3)O_2$), and less abundant vanadates, molybdates, arsenates, and tungstates. There are three bismuth silicates (all rare). Bismuth can also substitute into common sulfide minerals, notably galena (via the coupled substitution $2Pb^{2+} \rightleftharpoons M^{+} + (Bi,Sb)^{3+}$ where M is typically Ag). Bismuth also substitutes into the copper Cu-(Fe)-sulfides bornite, chalcocite, and chalcopyrite (at up to concentrations of hundreds or even thousands of ppm; Cook et al. 2011). Since bismuth can cause copper to become brittle, copper concentrates containing greater than statutory concentrations of bismuth may be liable to severe financial penalties when sold to smelter.

Economic Geology and Mining

Apart from pegmatites, bismuth is most commonly found in polymetallic sulfide ore deposits of hydrothermal origin, associated with silver, copper, lead, zinc, tin, and sometimes molybdenum and tungsten.

Bismuth has a low melting point relative to most other metals. The role of bismuth melts has been demonstrated in a number of ore deposits, notably to scavenge gold from hydrothermal fluids and contribute to its concentration in ore. Empirical and experimental evidence for the scavenging of gold by bismuth melts (Tooth et al. 2011) help explain the strong association often observed between gold and bismuth minerals in skarns and some "orogenic" gold deposits, as well as the presence of gold in some bismuth minerals (Ciobanu et al. 2009b).

Biological Utilization and Toxicity

There is no natural biological utilization. Considered as a "green" heavy metal, the replacement of lead by bismuth in some applications is seen as a way to mitigate environmental problems caused by heavy metal pollution. Bismuth has low toxicity to humans, and a number of bismuth-based drugs have been developed as treatments for various health conditions. In high concentrations, bismuth may however be damaging to health (Yang and Sun 2011).

Cross-References

- ▶ Chalcophile Elements
- ▶ Elements: Metalloids
- ▶ Ore Deposits

References

Ahrens L, Erlank AJ (1969) Bismuth. In: Wedepohl KH (ed) Handbook of geochemistry. Springer, New York, pp 83-A-1–83-O-1

Angino EE, Long DT (eds) (1979) The geochemistry of bismuth. Dowden, Hutchinson and Ross, Stroudsberg. 689 pp

Christy AG (2015) Causes of anomalous mineralogical diversity in the periodic table. Mineral Mag 79:33–49

Ciobanu CL, Pring A, Cook NJ, Self P, Jefferson D, Dima G, Melnikov V (2009a) Chemical-structural modularity in the tetradymite group: a HRTEM study. Am Mineral 94:517–534

Ciobanu CL, Cook NJ, Pring A, Brugger J, Danushevsky L, Shimizu M (2009b) 'Invisible gold' in bismuth chalcogenides. Geochim Cosmochim Acta 73:1970–1999

Cook NJ, Ciobanu CL, Wagner T, Stanley CJ (2007) Minerals of the system Bi-Te-Se-S related to the tetradymite archetype: review of classification and compositional variation. Can Mineral 45:665–708

Cook NJ, Ciobanu CL, Danyushevsky LV, Gilbert S (2011) Minor and trace elements in bornite and associated Cu–(Fe)-sulfides: a LA-ICP-MS study. Geochim Cosmochim Acta 75:6473–6496
Etschmann BE, Liu W, Pring A, Grundler PV, Tooth B, Borg S, Testemale D, Brewe D, Brugger J (2016) The role of Te(IV) and Bi (III) chloride complexes in hydrothermal mass transfer: an X-ray absorption spectroscopic study. Chem Geol 425:37–51
Lind H, Lidin S (2003) A general structure model for Bi-Se phases using a superspace formalism. Solid State Sci 5:47–57
Makovicky E (1997) Modular crystal chemistry of sulphosalts and other complex sulphides. EMU Notes Mineral 1:237–271
Makovicky E (2006) Crystal structures of sulfides and other chalcogenides. Rev Mineral Geochem 61:7–125
Moëlo Y, Makovicky E, Mozgova NN, Jambor JL, Cook NJ, Pring A, Paar W, Nickel EH, Graeser G, Karup-Møller S, Balić-Žunić T, Mumme WG, Vurro V, Topa D, Bindi L, Bente K, Shimizu M (2008) Sulfosalt systematics: a review. Report of the sulfosalt subcommittee of the IMA Commission on Ore Mineralogy. Eur J Mineral 20:7–46
Norman NC (1998) Chemistry of arsenic, antimony, and bismuth. Springer, Netherlands. 484 pp, ISBN 978-0-7514-0389-3
Palme H, O'Neill HSC (2014) 3.1 – Cosmochemical estimates of mantle composition. In: Turekian HDHK (ed) Treatise on geochemistry, 2nd edn. Elsevier, Oxford, pp 1–39
Tooth B, Ciobanu CL, Green L, O'Neill B, Brugger J (2011) Bi-melt formation and gold scavenging from hydrothermal fluids: an experimental study. Geochim Cosmochim Acta 75:5423–5443
Tooth B, Etschmann E, Pokrovski GS, Testemal D, Hazemann J-L, Grundler PV, Brugger J (2013) Bismuth speciation in hydrothermal fluids: an X-ray absorption spectroscopy and solubility study. Geochim Cosmochim Acta 101:156–172
USGS (2016) http://minerals.usgs.gov/minerals/pubs/commodity/bismuth/mcs-2016-bismu.pdf
Yang N, Sun H (2011) Bismuth: environmental pollution and health effects. Encyclopedia of environmental health. Reference module in Earth systems and environmental sciences. Elsevier, pp 414–420. ISBN: 978-0-12-409548-9

Black Shales and Sapropels

Kay-Christian Emeis
Department of Earth Sciences, Hamburg University, Hamburg, Germany

Synonyms

Bituminous rock; Organic-rich shale; Sapropelites

Definition

Black shales are organic carbon-rich sediments or sedimentary rocks. Black shales are important source rocks of fossil fuels (petroleum and natural gas) (Tissot and Welte 1984) and in some cases host economically viable metal accumulations (Vine and Tourtelot 1970). Sapropels are a geologically young analogue of black shales and offer high-resolution archives to decipher the interplay of paleoclimate and paleoceanography with biogeochemical and biological conditions in marine black shale depositional environments of the more distant geological past (Emeis and Weissert 2009).

Characteristics

Black shales and sapropels represent paleoenvironmental conditions that caused an unusually efficient transfer of mainly marine nonliving biomass into the geosphere and thus have been a key regulation on the global carbon cycle throughout Earth history. The sequestration of organic carbon in the geosphere is a small sink in the contemporaneous global carbon cycle (estimated at 0.2*10^15 g C annually), but this small flux has over Earth history accumulated an enormous amount of organic carbon in the geological sediment record (estimated at 1.2*10^22 g C). The long-term organic carbon sink for CO_2 is of the same magnitude as chemical weathering in regulating atmospheric CO_2. The fossil reduced carbon (in the form of kerogen, insoluble organic matter dispersed in sediment, originating from buried remains of marine plankton or land plants) is a minor constituent in most sedimentary deposits (constituting between 0.0 and 0.5 percent by weight), but organic carbon concentrations in black shales and their variants commonly exceed 1% by weight and can reach up to 50%. Such organic-rich sediments and sedimentary rocks are typically fine-grained (sand-silt-clay or mud) and dark, and the organic matter is interspersed in a matrix of clastic or biogenic origin. Enrichment of metals is commonly associated with high sulfide concentrations.

Black shale depositional environments range from lakes to the open ocean but cluster in:

(a) Open-ocean settings where the biological productivity in the sea surface was high (recent analogues are upwelling areas)
(b) Young ocean basins dissected by sills with impeded deepwater recharge (a recent analogue is the Black Sea)
(c) Hemipelagic settings over continental margins that lead to concentrations of allochthonous organic matter (of marine and also of terrestrial provenance) by physical transport
(d) Vast epeiric seas created during periods of high global sea level and warm climates in Earth history (no large recent analogue)

Such environments are conducive to enhance organic carbon burial via two interlinked controls that regulate the rate of organic carbon sequestration in marine environments:

biological productivity in the sea (or lake) surface fueled by nutrients originating from enhanced weathering of continents and oxygen depletion in deep waters or in oceanic oxygen-minimum zones preventing settling and sedimenting organic matter from being oxidized. In the Mesozoic Era (252 to 66 million years ago), extended (up to several million years duration) periods of coeval deposition of black shales in all ocean basins are thought to represent global oceanic anoxic events (Schlanger and Jenkyns 1976).

The interplay between climate, oceanography, and biogeochemistry in the origin of black shales is exceptionally well preserved in sapropels – layers of organic-rich sediments intercalated in late Cenozoic sediments of the Mediterranean realm (and in some other silled basins) (Rohling et al. 2015). Here, changes in the climate and hydrology of the Mediterranean Sea and its North African catchment, predominantly related to insolation-driven changes in African monsoon runoff into the Eastern Mediterranean (Rossignol-Strick et al. 1982) but also linked to global sea level/ice sheet fluctuations (Grimm et al. 2015), caused a dramatic change in the oxygenation of Eastern Mediterranean deep waters. Deepwater ventilation was inhibited when warming and freshening of Eastern Mediterranean sea surface layers caused stratification of the water column; the aging deep waters then became anoxic from continued mineralization of organic matter, leading to enhanced preservation of organic carbon (over a few thousand to ten thousand years). Increased surface water productivity likely contributed to sapropel deposition in some cases although there are differences between sapropels, and it can be hard to distinguish between increased productivity and preservation (Rohling et al. 2015).

References

Emeis K-C, Weissert H (2009) Tethyan–Mediterranean organic carbon-rich sediments from Mesozoic black shales to sapropels. Sedimentology 56:247–266

Grimm R, Maier-Reimer E, Mikolajewicz U, Schmiedl G, Müller-Navarra K, Adloff F, Grant K, Ziegler M, Lourens L, Emeis K (2015) Late glacial initiation of Holocene eastern Mediterranean sapropel formation. Nat Commun 6(7099):1–12

Rohling EJ, Marino G, Grant K (2015) Mediterranean climate and oceanography, and the periodic development of anoxic events (sapropels). Earth Sci Rev 143:62–97

Rossignol-Strick M, Nesteroff V, Olive P, Vergnaud-Grazzini C (1982) After the deluge; Mediterranean stagnation and sapropel formation. Nature 295:105–110

Schlanger SO, Jenkyns HC (1976) Cretaceous anoxic events: causes and consequences. Geologie en Mijnbouw 55:179–184

Tissot BP, Welte DH (1984) Petroleum formation and occurrence. Springer-Verlag, Berlin/Heidelberg/New York/Tokyo

Vine JD, Tourtelot EB (1970) Geochemistry of black shale deposits – a summary report. Econ Geol 65:253–272

Boron

Christophe Lécuyer
Laboratoire de Géologie de Lyon, LGL-TPE, CNRS UMR 5276, Université Claude Bernard Lyon 1 and Institut Universitaire de France, Lyon, France

Element Data
Atomic Symbol: B
Atomic Number: 5
Atomic Weight: [10.806, 10.821]
Isotopes and Abundances: ^{10}B: 19.9 ± 7%, ^{11}B: 80.1 ± 7
1 Atm Melting Point: 2,350 °C
1 Atm Boiling Point: 4,000 °C
Common Valences: +3
Ionic Radii: atomic radius = 87 pm, covalent radius = 84 pm
Pauling Electronegativity: 2.04
First Ionization Potential: 800.6 kJ.mol^{-1}
Chondritic (CI) Abundance: 0.78 ppm (16.9 ± 2.2 atoms/10^{6}Si)
Silicate Earth Abundance: 0.26 ± 0.04 ppm
Crustal Abundance: 17 ppm
Seawater Abundance: 4.5 ppm
Core Abundance: ~0

Properties

Boron is a metalloid with a rhombohedral crystal structure. This element belongs to the group 13 and period 2 of the periodic table (Fig. 1). Boron has sixteen known isotopes of which two are stable, ^{10}B and ^{11}B, of relative atomic mass 10.01293695(41) and 11.00930536(45) (source of data: National Institute of Standards and Technology): http://www.nist.gov/pml/data/comp.cfm. Geochemists measure the relative variations in the ^{11}B/^{10}B of terrestrial and extraterrestrial materials as per mil deviations from the isotopic composition of a synthetic boric acid (international reference: NIST SRM-951a; Atom%: ^{11}B = 80.173 ± 0.013; ^{10}B = 19.827 ± 0.013) according to Catanzaro et al. (1970):

$$\delta^{11}B = \left(\frac{{}^{11}B/{}^{10}B_{\text{sample}}}{{}^{11}B/{}^{10}B_{\text{reference}} - 1} \right) \times 10^3 \qquad (1)$$

The electronic configuration of boron is $1s^2 2s^2 2p^1$ while valence states are possibly +4, +3, +2, and +1, the oxidation

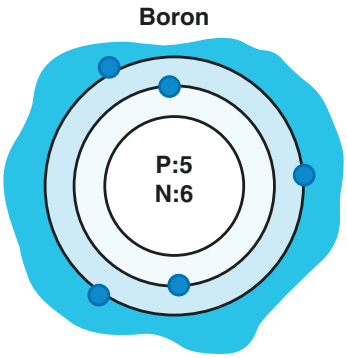

Boron, Fig. 1 Schematic illustration of the atomic configuration of ^{11}B

state +3 being by far the most common one. Its nonbonded atomic radius is 1.92 Å, its covalent radius is 0.84 Å, along with a strong electronegativity of 2.04 on the Pauling scale and an electron affinity of 26.989 kJ.mol^{-1} (Coursey et al. 2010; Haynes 2015). Amorphous and β-rhombohedral boron have a density of 2,350 kg.m^{-3} while the α-rhombohedral phase has a density of 2,460 kg.m^{-3}. Boron, as the metalloid element, does not react with water under standard conditions. Boron salts, however, are soluble in water, with boric acid H_3BO_3 showing a solubility of 57 g.L^{-1}, borax having a solubility of 25.2 g.L^{-1}, and boron trioxide (B_2O_3) having a solubility of 22 g.L^{-1}. Boron has a specific heat capacity of 1,026 J.kg^{-1}.K^{-1}.

History and Use

The name Boron originates from the Arabic word "buraq" and the Persian word "burah"; however, the English word "Boron" resulted from a combination of the words "borax" (the main boron ore) and "carbon" that indicates both its natural source and resemblance to carbon. In nature, boron does not occur in its elemental form but is bound to oxygen. According to Wisniak (2005), boron compounds such as borax ($Na_2[B_4O_5(OH)_4].8H_2O$) may have been known for about 6,000 years, Babylonians most likely being the first to have used borax brought from the Far East followed by Egyptians, Chinese, Tibetans, and Arabians. Borax has been used to decorate Chinese pottery dated to the third century. In Europe, as early as in the twelfth century, borax was used by silversmiths to strip precious metals such as gold. Medical prescriptions have been recorded in Coptic Papyruses describing a borax-based recipe for the treatment of eye diseases (Travis and Cocks 1984).

In 1702, Wilhelm Homberg transformed borax into a snow-white powder known today as metaboric acid (HBO_2). The element itself was discovered independently in June, 1808, by the English chemist Sir Humphry Davy and French chemists Joseph-Louis Gay-Lussac and Louis Jacques Thénard. Davy (1808) obtained boron by electrolysis while Gay-Lussac and Thénard (1808) isolated the element through a reduction of boric acid (H_3BO_3) with potassium. Neither of these discoveries allowed boron to be truly purified as synthesized compounds contained less than 50 wt% of boron. Boron was isolated and purified with better chemical yields by Moissan (1895), who reduced boric anhydride (B_2O_3) with magnesium in a thermite-type chemical reaction. Weintraub (1911) was the first to obtain a high-level of purity (near 99%), but pure boron phases were not obtained until the late 1950s. Pure boron is either dark brownish gray (amorphous powder or poorly crystallized phase) or silver-gray in color with a metallic, lustrous brilliance (polycrystalline phase).

Natural Abundance

Boron is a lithophile element according to Goldschmidt's classification (Goldschmidt 1926), meaning that it forms very strong covalent bonds with oxygen and thus commonly occurs in silicate mineral phases despite its low crustal abundance (≈10 ppm).

Ordinary and carbonaceous chondrites contain indistinguishable amounts of boron, together ranging from 0.3 to 1.4 ppm (Shaw et al. 1988; Zhai and Shaw 1994). This range was obtained by analyses of 36 fragments of meteorites by gamma-ray neutron activation analysis. CI chondrites contain 0.78 ppm of boron on average (Lodders 2010). The boron content of carbonaceous chondrites results from a weighted linear combination of the matrix (0.69 ppm) and chondrules (0.23 ppm; Zhai and Shaw 1994). The mean boron content of the matrix of carbonaceous chondrites has been used to calculate a normalized Solar System abundance of 16.9 ± 2.2 atoms/10^{6}Si. Large variations in $\delta^{11}B$, from −50 ± 10‰ to +40 ± 10‰, were documented for chondrules (Chaussidon 1995) whereas more restricted variation ($\delta^{11}B = 25 \pm 15‰$) has been observed for the Allende CV3 meteorite. Chaussidon and Robert (1995) suggested that these variations in boron isotope composition reflect synthesis of boron in the presolar cloud via spallation processes involving nebular hydrogen and cosmic rays. These isotopic heterogeneities are at least partly preserved in chondrules that formed at early stages in the evolution of the solar system. Cosmic ray spallation can explain the greater abundance of the heavy isotope of boron, as for lithium.

Menard et al. (2013) estimated a primitive mantle B concentration of 0.26 ± 0.04 ppm, based on analyses of peridotite xenoliths from Mongolia and Russia and fresh lavas from the active volcano of Piton de la Fournaise, Réunion Island. Mid-ocean ridge basalts contain 0.5 to 1.3 ppm of boron, as determined by ion microprobe (Chaussidon and Jambon 1994), and upper continental crust contains an average boron concentration of 17 ppm (Rudnick and Gao 2005).

In seawater, with pH of ~8, boron occurs as trigonal boric acid H_3BO_3 (≈90%) and tetrahedral borate ion $B(OH)_4^-$ (≈10%; relative abundance of these species is from Hemming and Hanson 1992). Average seawater abundance is 4.5 ppm; consequently it is the 11th most abundant element (Brown et al. Open University 1989) dissolved in seawater (O_2 gas excluded), showing conservative vertical profiles and similar contents in Earth's oceans. Its abundance and homogenous distribution in seawater is also related to its long residence time of about 10 to 14 My calculated by Broecker and Peng (1982), Lemarchand et al. (2000), and Simon et al. (2006). Spivack and Edmond (1987) suggested a longer residence time of 20 My, based on the ratio of the total amount of dissolved boron in the oceans and the global average river input, and assuming that the boron cycle is at steady state.

River water contains low concentrations of dissolved boron, ranging from 1 to 200 ppb, with an average value of 10.2 ppb. Global variations in the B concentrations of lake waters are very large and, not surprisingly, the concentrations are higher in more saline lakes. For example, boron concentrations of Dead Sea surface waters range from 38 to 44 ppm (Vengosh et al. 1991), whereas in fresher lakes in Australia, boron concentrations range from 0.3 to 17 ppm (Vengosh et al. 1991).

Minerals and Ores

Several silicate minerals contain abundant tetrahedral boron (e.g., danburite, $CaB_2Si_2O_8$; datolite, $CaBSiO_4(OH)$) or trigonal boron (grandidierite, $(Mg,Fe)Al_3BSiO_9$), each of these phases occurring as an accessory mineral in metamorphic rocks. Tourmaline (rhombohedral), by far the most abundant borosilicate, has the generalized formula of $(X)(Y_3)(Z_6)T_6O_{18}(BO_3)_3V_3W$ (Hawthorne 1996).

However, the most common sources of boron are boron salts (borax, kernite or rasorite, ulexite, and colemanite) deposited during the evaporation of water bodies (e.g., saline lakes) in a volcanic context (Fig. 2). The most important mines are in Turkey (Mustafakemalpascha Mine, West-Anatolia), California (city of Boron, Kern County; Rio Tinto Boron Mine, Fig. 3), Chile (Atacama Desert), Argentina (Tincalayu, Sijes, and Porvenir), Russia (Dalnegorsk), Tibet, and Italy (Siena Province). In these occurrences, the primary B-rich minerals are kernite or rasorite ($Na_2B_4O_7.4H_2O$), borax ($Na_2[B_4O_5(OH)_4].8H_2O$), ulexite ($NaCaB_5O_6(OH)_6.5H_2O$),

Boron, Fig. 2 Borax crystals

Boron, Fig. 3 Rio Tinto Boron Mine (35°02'34.63"N – 117°40'21.19"0), city of Boron, Kern County, California, USA. GoogleEarth® satellite view (15 km above sea level)

and colemanite ($Ca_2B_6O_{11}.5H_2O$). Italy was the first country exploiting boron ores, as early as 1830, and the present-day annual world production is about one million tons of B_2O_3 (source: USGS).

Geochemical Behavior

Birth of oceanic lithosphere and its recycling in subduction zones constitute two important geological processes responsible for chemical and heat exchange between Earth's mantle and oceanic crust. In subduction zones, the creation of volcanic island arcs constitutes an opportunity to identify and quantify the respective amounts of fluids and solids that exchange between the mantle wedge and the subducted slab. Island-arc magmas are commonly interpreted as resulting from the partial melting of the mantle wedge metasomatized by liquids (aqueous fluids, silicate melts) or solids (sediments, altered oceanic basalts) derived from the subducted lithospheric plate. Those "contaminants" are also considered to play a significant role in generating the geochemical "signatures" of arc magmas (Gill 1981). As emphasized by Straub and Layne (2002) and Rosner et al. (2003), boron is a highly mobile element toward the aqueous phase along with an incompatible behavior during processes of partial melting. Moreover, boron is highly concentrated in oceanic sediments and hydrothermally altered oceanic crust compared to fresh rocks derived from upper mantle melting. Consequently, boron can be considered as a key tracer of slab contribution to island-arc volcanic rocks (Morris et al. 1990; Ryan and Langmuir 1993; Leeman and Sisson 1996; Bebout et al. 1999). Moreover, the hydrothermally altered oceanic crust and the subducted sediments constitute two geochemical reservoirs of highly contrasted boron isotope compositions.

The main dissolved boron species in waters are the neutral trigonal boric acid and the tetrahedral borate anion (Culberson and Pytkowicz 1967; Felmy and Weare 1986). Boric acid acts as an electron acceptor in aqueous solution, accepting a hydroxide ion from water to form $B(OH)_4^-$. The molar proportions of the dissolved boron species are strongly dependent upon pH. At pH above 7, boric acid is the dominant species whereas borate ions prevail under acidic conditions. The two boron species coexist in most natural surface waters. High concentrations in solutions (>0.1 M of boric acid), and at slightly acidic (pH = 6) to alkaline (pH = 11) pH, can lead to the formation of polymeric species such as $B_3O_3(OH)_4^-$, $B_5O_6(OH)_4$, $B_3O_3(OH)_5^{2-}$, and $B_4O_5(OH)_4^{2-}$ (Choi and Chen 1979).

Boron has a strong affinity with water because its salts have high-solubility products. The temperature dependence of the solubility product (K_{sp}) of minerals, based on experiments, can be expressed by the following equation:

$$\ln K_{sp} = (-\Delta H^o/R).(1/T) + \Delta S^o/R \quad (2)$$

where ΔH^o and ΔS^o are the standard enthalpy and entropy of the chemical reaction, T the temperature, and R the gas constant. In the case of boron salts such as borax, its dissociation in water is expressed as follows:

$$Na_2B_4O_5(OH)_4.8H_2O \Leftrightarrow B_4O_5(OH)_4^{2-} + 2Na^+ + 8H_2O \quad (3)$$

According to the mass action law, the corresponding solubility product of borax is:

$$K_{sp} = [Na^+]^2.\left[B_4O_5(OH)_4^{2-}\right] \quad (4)$$

Its temperature dependence has been determined experimentally as follows:

$$\ln K_{sp} = -16.10^3/T + 47.7 \quad (5)$$

For example, at the mean temperature at Earth's surface, near 15 °C, the K_{sp} of borax is $10^{-3.43}$.

In the oceans, borate ions are absorbed by clays, explaining the high concentrations of B in shales deposited on the seafloor. At seafloor spreading centers, seawater interacts with oceanic crust at temperatures ranging from a few tens of degrees to 450 °C. At temperatures >350 °C, boron is leached from basalts and gabbros whereas at temperatures <150 °C, boron is trapped within clays such as smectites (Seyfried et al. 1984). The net flux of boron from the oceanic crust to the oceans was estimated at $2.3.10^{14}$ kg B.year^{-1} (Simon et al. 2006).

In contrast with the low boron concentrations in river water (mean concentration of 10 ppb), high concentrations of dissolved boron have been documented in some hydrothermal waters linked to active volcanoes. Hot spring waters in Japan have boron contents ranging from 0.35 to 200 ppm (Musashi et al. 1991) while they vary within a more narrow range (0.4 to 9 ppm) in Iceland (Aggarwal et al. 2000). Geysers from Yellowstone National Park, Wyoming, USA, have boron concentrations of 35 to 730 ppb (Gemery-Hill et al. 2007).

Boron compounds are released to water in municipal sewage from perborates in detergents and in wastewaters from coal-burning power plants, copper smelters, and industries using boron (e.g., metallurgy). Borate levels from 1 to 10 ppm, far higher than the natural background of a few ppb, have been measured in runoff waters from areas where boron-rich fertilizers or herbicides are used (e.g., Butterwick et al. 1989). Xiao et al. (2013) reviewed the potential use of boron isotopes to track pollution of surface and groundwaters. Sodium perborate is the main source of water pollution resulting from human activity, and it is synthesized by

decomposition of sodium tetraborate decahydrate (a type of borax) by the following reaction:

$$Na_2B_4O_7.10H_2O + 2NaOH + H_2O + 4H_2O_2 \rightarrow 4(NaBO_3.4H_2O) \quad (6)$$

Biological Utilization and Toxicity

The highest naturally occurring concentrations of boron are observed in soils developed from marine evaporites and clays. It is very difficult to remove boron from soils except by leaching with huge amounts of boron-free water.

As early as 1910, boron was recognized as an essential element in the functioning of the higher plants (Agulhon 1910; Warington 1923). Boron is a micronutrient required for the growth and development of vascular plants, marine algae, diatoms, and cyanobacteria (Dembitsky et al. 2002). Boron as H_3BO_3 is absorbed by plant roots from soil water, then stored in roots, stalks, and cell walls of many plants. Boron also plays a key role in maintaining the structural integrity of plasma plant cell membranes (Hu and Brown 1997). Boron deficiency in soils is responsible for a yellowing of plant leaves. Plants contain from a few ppb and up to 400 ppb, the highest concentrations corresponding to aquatic plants. Plants are able to adapt, through genetic responses, to high concentrations of boron in soils.

Boron is generally not considered poisonous to animals; however, exposure to high levels of boron in diets could negatively affect general metabolism or even can be lethal. For example, Sisk et al. (1988) reported that goats that ingested 3.6 g of boron fertilizer per kg of body weight developed diarrhea, weakness, ataxia, and signs of depression and died, usually within a few hours. Human exposure to boron, typically as borates or boric acid, can occur through ingestion of food and water, or through use of pesticides containing boron compounds (and inhalation of boron-containing powders or dusts), or by use of boron-rich cosmetics, or medical preparations. The primary health effects associated with inhalation exposure of humans to boron are acute respiratory inflammation. Human beings ingest about 2 mg of add a blank boron per day, largely in fruits, green vegetables, nuts, beans, and drinking water. Boron does not accumulate in soft tissues but in bones where it assists in maintaining healthy bones, thus a boron deficiency can contribute to the development of arthritis. Boron has been also recognized as useful to healthy brain functions such as memory and hand-eye coordination. In excess, boric acids and borates are toxic for most living organisms. Poisoning of human beings may result either by accidental ingestion or an excessive use of boric acid ointment for the treatment of burns (Pfeiffer et al. 1945). Normal levels of boron in soft tissues, urine, and blood generally range from less than 0.05 ppm to no more than 10 ppm. In cases of boron poisoning of human beings, the concentration of boric acid in brain and liver tissues has been measured at as high as 2,000 ppm (Moseman 1994).

Summary

Boron compounds such as borax have been known and used by humans of different cultures for several thousand years. In early times, the uses of borax were diverse, in the decoration of potteries, the cleaning of precious metals such as gold, or even medical prescriptions for the treatment of eye diseases. The most important modern use of boron is in the production of borosilicate glasses used as thermal shock-resistant containers as well as the manufacturing of high-quality optical glasses for telescopes. Boron also forms hard alloys (BC and BN) with nitrogen and carbon. In nuclear power plants, the light stable isotope of boron (^{10}B) is employed as a neutron absorber due to its high neutron cross-section. Despite its relative low abundance in solid Earth's envelopes, the affinity of boron for aqueous solutions and the large magnitudes in isotopic fractionation that take place between minerals and fluids make it a powerful geochemical tracer. The resulting highly contrasted isotopic compositions of reservoirs that constitute its natural geochemical cycle allow the possibility of quantifying water-rock interactions. In combination with lithium, it is also useful to calculate the amounts of recycled hydrothermally altered rocks and sediments in subduction zones.

Cross-References

- ▶ Acid–Base Reactions
- ▶ Boron Stable Isotopes
- ▶ Chondrites
- ▶ Lithophile Elements
- ▶ Ocean Biochemical Cycling and Trace Elements
- ▶ Solubility
- ▶ Water

References

Aggarwal J, Palmer MR, Bullen TD, Arnorsson S, Ragnarsdottir KV (2000) The boron isotope systematics of Icelandic geothermal waters: 1. Meteoric water charged system. Geochim Cosmochim Acta 64:579–585

Agulhon H (1910) Présence et utilité du bore chez les végétaux. Ann Inst Pasteur (Paris) 24:321–329

Bebout GE, Ryan JG, Leeman WP, Bebout AE (1999) Fractionation of trace elements by subduction-zone metamorphism – effect of convergent margin thermal evolution. Earth Planet Sci Lett 171:63–82

Broecker WS, Peng T-H (1982) Tracers in the sea. Lamont-Doherty Geol. Observation. Eldigo Press, Palisades. 690 pp
Brown J, Colling A, Park D, Phillips J, Rothery D, Wright J (1989) Seawater: its composition, properties and behaviour. The Open University. Pergamon Press, Oxford, p 165
Butterwick L, de Oude N, Raymond K (1989) Safety assessment of boron in aquatic and terrestrial environments. Ecotoxicol Environ Saf 17:339–371
Catanzaro EJ, Champion CE, Garner EL, Marinenko G, Sappenfield KM, Shields WR (1970) Standard reference materials: boric acid; Isotopic, and assay standard reference materials. U.S. National Bureau of Standards. Special publication 206–17, 70 pp
Chaussidon M (1995) Isotope geochemistry of boron in mantle rocks, tektites and meteorites. CR Acad Sci Paris 321:455–472
Chaussidon M, Jambon A (1994) Boron content and isotopic composition of oceanic basalts: geochemical and cosmochemical implications. Earth Planet Sci Lett 121:277–291
Chaussidon M, Robert F (1995) Nucleosynthesis of 11B-rich boron in the presolar cloud recorded in meteoric chondrules. Nature 374:337–339
Choi W-W, Chen KY (1979) Evaluation of boron removal by adsorption on solids. Environ Sci Technol 13:189–196
Coursey JS, Schwab DJ, Tsai JJ, Dragoset RA (2010) Atomic weights and isotopic compositions. National Institute of Standards and Technology, Gaithersburg
Culberson C, Pytkowicz RM (1967) Effect of pressure on carbonic acid, boric acid and the pH of seawater. Science 157:59–61
Davy H (1808) Electro-chemical researches, on the decomposition of the Earths; with observations on the metals obtained from the alkaline earths, and on the amalgam procured from ammonia. Phil Trans R Soc London 98:333–370
Dembitsky VM, Smoum R, Al-Quntar AA, Ali HA, Pergament I, Srebnik M (2002) Natural occurrence of boron-containing compounds in plants, algae and microorganisms. Plant Sci 163:931–942
Felmy A, Weare JH (1986) The prediction of borate mineral equilibria in natural waters: application to Searles Lake, California. Geochim Cosmochim Acta 50:2771–2783
Gay-Lussac JL, Thénard LJ (1808) Sur la décomposition et la recomposition de l'acide boracique. Ann Chim Phys 68:169–174
Gemery-Hill PA, Shanks WCIII, Balistrieri LS, Lee GK (2007) Geochemical data for selected drivers, lake waters, hydrothermal vents, and subaerial geysers in Yellowstone National Park. In: Morgan LA (ed) Integrated geoscience studies in the greater Yellowstone area: volcanic, tectonic, and hydrothermal processes in the Yellowstone Geoecosystem: U.S. Geological Survey professional paper. U.S. Department of the Interior Reston, Vinginia. 1717, pp 365–426
Gill JB (1981) Orogenic Andesites and plate tectonics. Springer, New York, p 390
Goldschmidt VM (1926) Geochemische Verteilungsgesetze der Elemente. Skrifter Norske Videnskaps – Akad, Oslo. (I) Mat. Natur
Hawthorne FC (1996) Structural mechanisms for light-element variations in tourmaline. Can Mineral 34:123–132
Haynes WM (2015) CRC handbook of chemistry and physics, 95th edn. CRC Press/Taylor and Francis, Boca Raton
Hemming NG, Hanson GN (1992) Boron isotopic composition and concentration in modern marine carbonates. Geochim Cosmochim Acta 56:537–543
Hu H, Brown PH (1997) Absorption of boron by plant roots. Plant Soil 193:49–58
Leeman WP, Sisson VB (1996) Geochemistry of boron and its implications for crustal and mantle processes. In: Reviews in mineralogy, vol 33. Minenalogical Society of America Chantillly, Virginia, pp 645–707
Lemarchand D, Gaillardet J, Lewin E, Allègre CJ (2000) The influence of rivers on marine boron isotopes and implications for reconstructing past ocean pH. Nature 403:951–954
Lodders K (2010) Solar system abundances of the elements. In: Goswami A, Reddy BE (eds) Principles and perspectives in cosmochemistry. Astrophysics and space science proceedings. Springer, Berlin/Heidelberg, pp 379–417
Menard G, Vlastélic I, Ionov DA, Rose-Koga EF, Piro J-L, Pin C (2013) Precise and accurate determination of boron concentration in silicate rocks by direct isotope dilution ICP-MS: insights into the B budget of the mantle and B behavior in magmatic systems. Chem Geol 354:139–149
Moissan H (1895) Etude du bore amorphe. Ann Chim Phys 6:296–320
Morris JD, Leeman WP, Tera F (1990) The subducted component in island arc lavas: constraints from Be isotopes and B-Be systematics. Nature 344:31–36
Moseman RF (1994) Chemical disposition of boron in animals and humans. Environ Health Perspect 102:113–117
Musashi M, Oi T, Ossaka T, Kakihana H (1991) Natural boron isotope fractionation between hot spring water and rock in direct contact. Isotopenraxis 27:163–166
Pfeiffer CC, Hallman LF, Gersh I (1945) Boric acid ointment – a study of possible intoxication in the treatment of burns. J Am Med Assoc 128:266–274
Rosner M, Erzinger J, Franz G, Trumbull RB (2003) Slab-derived boron isotope signatures in arc volcanic rocks from the Central Andes and evidence for boron isotope fractionation during progressive slab dehydration. Geochem Geophys Geosyst. https://doi.org/10.1029/2002GC000438
Rudnick RL, Gao S (2005) Composition of the continental crust. In: Rudnick RL (ed) Treatise on geochemistry, The crust, vol 3. Elsevier-Pergamon, Oxford, pp 1–64
Ryan JG, Langmuir CH (1993) The systematics of boron abundances in young volcanic rocks. Geochim Cosmochim Acta 57:1489–1498
Seyfried WE, Janecky DR, Mottl MJ (1984) Alteration of the oceanic crust: implications for geochemical cycles of lithium and boron. Geochim Cosmochim Acta 48:557–569
Shaw DM, Higgins MD, Hinton RW, Truscott MG, Middleton TA (1988) Boron in chondritic meteorites. Geochim Cosmochim Acta 52:2311–2319
Simon L, Lécuyer C, Maréchal C, Coltice N (2006) Modelling the geochemical cycle of boron: implications for the long-term $\delta^{11}B$ evolution of seawater and oceanic crust. Chem Geol 225:61–76
Sisk DB, Colvin BM, Bridges CR (1988) Acute, fatal illness in cattle exposed to boron fertilizer. J Am Vet Med Assoc 193:943–945
Spivack AJ, Edmond JM (1987) Boron isotopic exchange between seawater and the oceanic crust. Geochim Cosmochim Acta 51:1033–1043
Straub SM, Layne GD (2002) The systematics of boron isotopes in Izu arc front volcanic rocks. Earth Planet Sci 198:25–39
Travis NJ, Cocks EJ (1984) The tincal trail – a history of borax. Harrap, London
Vengosh A, Kolodny Y, Starinsky A, Chivas AR, McCulloch MT (1991) Coprecipitation and isotopic fractionation of boron in modern biogenic carbonates. Geochim Cosmochim Acta 55:2901–2910
Warington K (1923) The effect of boric acid and borax on the broad bean and certain other plants. Ann Bot 37:629–672
Weintraub E (1911) On the properties and preparation of the element boron. J Ind Eng Chem 3:299–301
Wisniak J (2005) Borax, boric acid, and boron – from exotic to commodity. Indian J Chem Technol 12:488–500
Xiao J, Xiao Y-K, Jin Z-D, He M-Y, Liu C-Q (2013) Boron isotope variations and its geochemical application in nature. Aust J Earth Sci 60:431–447
Zhai M, Shaw DM (1994) Boron cosmochemistry. Part I: boron in meteorites. Meteoritics 29:607–615

Boron Stable Isotopes

Gavin L. Foster[1], Christophe Lécuyer[2] and Horst R. Marschall[3,4]
[1]Ocean and Earth Science, National Oceanography Centre Southampton, University of Southampton, Southampton, UK
[2]Laboratoire de Géologie de Lyon, LGL-TPE, CNRS UMR 5276, Université Claude Bernard Lyon 1 and Institut Universitaire de France, Lyon, France
[3]Department of Geology and Geophysics, Woods Hole Oceanographic Institution, Wood Hole, MA, USA
[4]Institut für Geowissenschaften, Goethe-Universität Frankfurt, Frankfurt am Main, Germany

Properties

Boron, a group 13 metalloid, has two natural occurring stable isotopes, ^{11}B (11.00930536[45]) and ^{10}B (10.01293695[41]), with relative abundances of 0.199(7) and 0.801(7), respectively, and hence occurs approximately in a 4:1 ratio (source of data: National Institute of Standards and Technology, http://www.nist.gov/pml/data/comp.cfm). Numerous radioisotopes of boron also occur with masses from ^{7}B to ^{17}B, but their half-lives are all <1 s. As with other stable isotopic systems, natural isotope variation is described using delta notation, i.e., the per mil variation from the ^{11}B/^{10}B ratio of the synthetic boric acid international reference material NIST SRM-951 (atom%: ^{11}B = 80.173 ± 0.013; ^{10}B = 19.827 ± 0.013; Catanzaro et al. 1970). This can be described by the following equation:

$$\delta^{11}B = \left(\frac{{}^{11}B/{}^{10}B_{\text{sample}}}{{}^{11}B/{}^{10}B_{\text{reference}}} - 1 \right) \times 10^3 \qquad (1)$$

In natural systems, boron is almost exclusively found bound to oxygen in either tetrahedral (e.g., borate ion, $B(OH)_4^-$) or trigonal complexes (e.g., boric acid, $B(OH)_3$). Natural fractionation of the two isotopes is governed principally by their distribution between such complexes, with a tendency for ^{11}B to be incorporated preferentially in the stronger bonded trigonal molecules (e.g., boric acid in seawater). Boron is very soluble and hence fluid mobile and exhibits a dynamic speciation at low temperature. These features, coupled with its relatively light mass (10.806–10.821) and the large mass difference between its isotopes (~10%), combine to cause a very wide range in natural isotopic compositions (from −50 ‰ to +60 ‰; Barth 1993; Fig. 1).

History and Use

F.W. Aston made the first determinations of the isotopic composition of naturally occurring boron in 1920 using what was then known as a "positive ray spectrograph" and what is now known as mass spectrometry (Aston 1920). Due to its utility in tracing low-temperature geochemical processes, relative to other nongaseous stable isotope systems (e.g., Li, Ca, Cu, Co, etc.), boron isotope research in the Earth sciences has a relatively long history with the first measurement of natural materials in the early 1960s (e.g., McMullen et al. 1961). Like many isotopic systems, technological developments have led the expansion in the use of boron isotopes as a geochemical tracer with significant growth in the 1980s with the improvement and development of thermal ionization techniques (e.g., Zeininger and Heumann 1983), and a more recent expansion with plasma-based analytical methods in the 2000s for both bulk and in situ measurements (e.g., Lécuyer et al. 2002; Foster 2008; Fietzke et al. 2010).

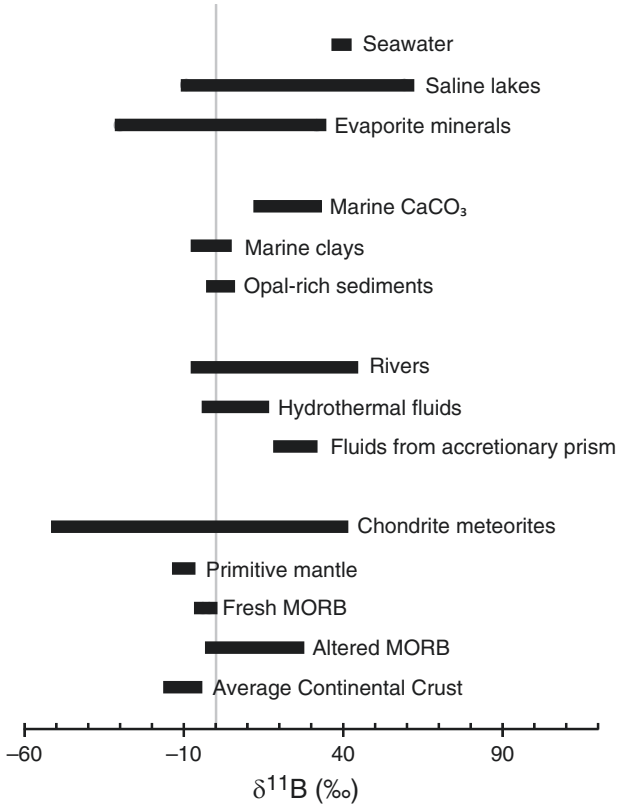

Boron Stable Isotopes, Fig. 1 Boron isotopic composition of some terrestrial and extraterrestrial materials (Sources are either as in text or from Barth 1993)

Geochemical and Isotopic Behavior

Figure 1 shows the large range (>100 ‰) of δ^{11}B observed in terrestrial and extraterrestrial materials. The building blocks of the terrestrial planets, the carbonaceous chondrites, have a relatively low boron concentration (~0.8 μg/g; Lodders

2010), and chondrules exhibit an isotopic variation that spans nearly the entire range of observed values in terrestrial materials (from −50 ± 10 ‰ to +40 ± 10 ‰; Fig. 1; Chaussidon 1995), while more restricted variations ($\delta^{11}B$ = +25 ± 15 ‰) have been observed in the Allende CV3 meteorite. This is thought to be the result of the synthesis of B via spallation processes involving nebular hydrogen and cosmic rays (Chaussidon and Robert 1995). This process also offers an explanation of why ^{11}B is more abundant than ^{10}B, in a similar fashion to lithium.

In contrast to the chondrites, the boron content of the Earth's mantle is relatively low (~0.3 μg/g; Menard et al. 2013), and its isotopic composition is ≈−10 ‰ (Chaussidon and Marty 1995). Unaltered (i.e., fresh) mid-ocean ridge basalts (MORB) have ~1 μg/g B with a $\delta^{11}B$ in the range −10 to −2 ‰ (e.g., Spivak and Edmond 1987). Alteration through reaction with seawater increases their B content (up to 120 μg/g) and drives the $\delta^{11}B$ up (−2 to +26 ‰; Smith et al. 1995). The mean $\delta^{11}B$ of the continental crust is hard to define but is most likely in the range −15 to −5 ‰ (Ishikawa and Nakamura 1993). Tourmaline is the most common boron-bearing mineral (borosilicate) in the continental crust and has $\delta^{11}B$ values ranging from −30 ‰ to +37 ‰ reflecting the nature of the fluids and rock types it is associated with (Marschall and Jiang 2011). The isotopic composition of the common ores of boron (hydrated sodium and calcium borates such as borax, kernite or rasorite, ulexite, and colemanite) depends on the nature of their parent fluid. Borates from marine evaporite deposits have $\delta^{11}B$ values that range from +18 ‰ to +32 ‰, in average much higher than those measured in nonmarine evaporation borates (−30 ‰ $< \delta^{11}B <$ +12 ‰), thus reflecting their highly isotopically contrasted source reservoirs, which are seawater (today $\delta^{11}B$ = +39.6 ‰; Foster et al. 2010) and the continental crust ($\delta^{11}B \approx$ −15 to −5 ‰), respectively.

The isotopic composition of boron is also fractionated in the terrestrial weathering environment with ^{10}B preferentially retained in secondary clays (Schmitt et al. 2012). As a consequence, river water has low boron concentrations (1 to <40 ng/g) and has a $\delta^{11}B$ (−6 to +43 ‰) that is typically heavier than average continental crust (Lemarchand et al. 2002). The flux-weighted mean $\delta^{11}B$ of riverine boron supply to the oceans is +10 ‰ (Lemarchand et al. 2002). Freshwater lakes have variable boron contents (0.3 to 44 μg/g) and also exhibit a wide range in $\delta^{11}B$ from −4.4 to +59 ‰ (Vengosh et al. 1991). Additional fractionations can occur in the terrestrial realm through the uptake and fractionation of boron in plants (Xu et al. 2015).

Boron has a long residence time in the oceans (10–20 million years; Simon et al. 2006) and is both uniform in concentration (4.5 μg/g; Lee et al. 2010) and isotopic composition ($\delta^{11}B$ = 39.61 ‰; Foster et al. 2010). Boron is also supplied to the ocean via hydrothermal fluids with $\delta^{11}B$ = −2.5 to +14.5 ‰ and fluids expelled from accretionary prisms (+25 ± 5 ‰; Smith et al. 1995). Since the boron isotopic composition of the ocean is significantly heavier than these inputs (Fig. 1), other processes must operate that preferentially remove ^{10}B to isotopically enrich the remaining boron. Three major sinks have been recognized: (1) the alteration of oceanic crust (see above; Smith et al. 1995), (2) the adsorption of boron onto clays such that marine clays have $\delta^{11}B$ = −6 to +2.8 ‰ (Ishikawa and Nakamura 1993), and (3) coprecipitation of boron in calcium carbonate and biogenic silica (Fig. 1; Ishikawa and Nakamura 1993).

The magnitude of fractionation via adsorption to clays and coprecipitation with calcium carbonate is a well-described function of pH (Palmer et al. 1987; Zeebe and Wolf-Gladrow 2001). This pH sensitivity arises because of the pH dependency of speciation of aqueous boron species: at low pH, trigonal boric acid ($B(OH)_3$) dominates, and at high pH, boron is predominantly in the tetrahedral borate ion ($B(OH)_4^-$) complex (Fig. 2). Due to the structural differences between the two aqueous forms of boron found in seawater, there is a large isotopic fractionation between them, with ^{11}B preferentially incorporated into boric acid. The isotopic exchange between these species can be described by the reaction:

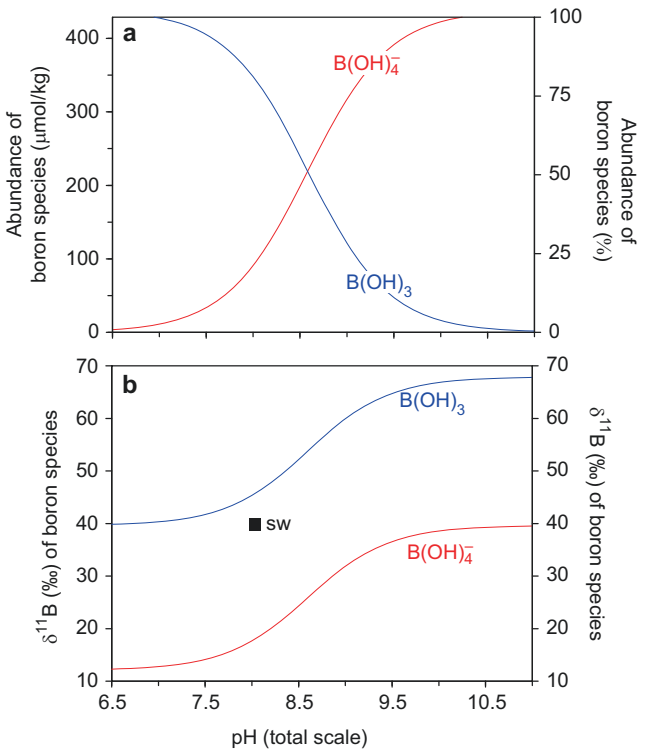

Boron Stable Isotopes, Fig. 2 The variation of concentration (**a**) and isotopic composition (**b**) of borate ion ($B(OH)_4^-$) and boric acid ($B(OH)_3$) with changing seawater pH (total scale) at typical surface ocean conditions (T = 25 °C, S = 35 psu). Also shown in (**b**) is the $\delta^{11}B$ of total boron in seawater (39.61 ‰; Foster et al. 2010)

$$^{10}B(OH)_3 + {}^{11}B(OH)_4^- \Leftrightarrow {}^{11}B(OH)_3 + {}^{10}B(OH)_4^-, \quad (2)$$

with the isotopic fractionation, α_B (also written $^{11-10}K_B$ and α_{B4-3}), given as:

$$\alpha_B = \frac{{}^{11}_{10}R_{B(OH)_3}}{{}^{11}_{10}R_{B(OH)_4^-}}, \quad (3)$$

where $^{11/10}R$ is the $^{11}B/^{10}B$ ratio of each dissolved species. At any given pH, the sum of total boron in seawater and its $\delta^{11}B$ can be described by the following reaction:

$${}^{11}_{10}R_{B_{sw}} \times [B]_{sw} \Leftrightarrow {}^{1110}R_{B(OH)_3} \times [B(OH)_3] + {}^{11}_{10}R_{B(OH)_4^-} \times [B(OH)_4^-]. \quad (4)$$

It follows therefore that as the abundance of each species changes with pH so does their isotopic composition (Fig. 2). There have been numerous attempts to define α_B, and recent direct measurements place its value in seawater at 1.0272 ± 0.0006 to 1.0260 ± 0.0010 at 25 °C (Klochko et al. 2006; Nir et al. 2015). At present, the temperature sensitivity of α_B is uncertain, but it is likely to be small (Rae et al. 2011). It has been experimentally determined and observed through isotopic measurements of natural materials that both boron absorbed to clays (e.g., Palmer et al. 1987) and boron coprecipitated with $CaCO_3$ are isotopically lighter than seawater (Sanyal et al. 2000; Fig. 1). This arises due to the preferential absorption of the charged and isotopically light borate ion species to clay particles in seawater and to the growing surfaces of $CaCO_3$. The latter behavior forms the basis of the boron isotope pH proxy (see below and Foster and Rae 2016).

Applications to Geochemical Studies

Boron Isotopes as a Tracer of Human Activities

Xiao et al. (2013) reviewed the potential use of boron isotopes to track pollution of surface and groundwaters. Sodium perborate is the main source of boron pollution in water resulting from human activity. The synthesis of sodium perborate operates through the decomposition of sodium tetraborate decahydrate (a kind of borax) as follows:

$$Na_2B_4O_7.10H_2O + 2NaOH + H_2O + 4H_2O_2 \rightarrow 4(NaBO_3.4H_2O) \quad (5)$$

As this chemical reaction does not involve any boron isotope fractionation (e.g., Barth 1998), the product of this reaction preserves the isotopic composition of its source, making it possible to track boron pollution in natural waters under the condition that reservoirs involved have distinct $\delta^{11}B$ values.

Warner et al. (2014) also recently proposed the use of boron isotopes to trace contamination of groundwater and rivers by hydraulic fracturing fluids (HFF) from oil and gas operations. Distinct boron isotopic fingerprints for HFF relate to either the process of hydraulic fracking liberating the light isotope from clay surfaces, boron associated with the liberated hydrocarbons or trapped brine, and/or from chemical additives to the fluid.

Phase Partitioning

Fractionation of Boron Isotopes Between Mineral and Fluid: The Case of Tourmaline

Boron isotopes are valuable to track processes of mass transfer between Earth's surficial and rock reservoirs. Both the solubility of most boron-bearing minerals and the incompatible behavior of this element during magmatic processes enable its isotopic composition to fingerprint dehydration and water-rock interaction during lithospheric subduction, metamorphic reactions, and magmatic activity along with associated hydrothermal circulations. Tourmaline is a mineral of predominant interest as it is stable over a wide range of pressure and temperature. The fractionation of boron in tourmaline relative to the aqueous fluids in which it forms was first identified to be temperature dependent by Palmer et al. (1992) and more recently defined as $\Delta^{11}B(\text{tourmaline-aqueous fluid}) = -4.20(10^3.T^{-1}) + 3.52$, by Meyer et al. (2008), with no dependence on pressure (at least between 200 and 500 MPa). These experimentally determined tourmaline-fluid isotope fractionation factors are employed, for example, to quantify the evolution of fluids involved in the genesis of large ore deposits (e.g., Bast et al. 2014).

Fractionation of Boron Isotopes Between $CaCO_3$ and Seawater: The $\delta^{11}B$-pH Proxy

The pH of the ocean, like its CO_2 content, is determined by the ratio of total alkalinity (the charge balance, TA) to the sum of dissolved inorganic carbon species (DIC): as the CO_2 content of the water increases, its pH decreases. Reconstructions of ocean pH in the past therefore offer the ability to trace the CO_2 content of the oceans through time. This is useful because (i) the partitioning of CO_2 between the ocean and the atmosphere is thought to govern atmospheric CO_2 change on glacial-interglacial timescales, and (ii) on a global-scale, the CO_2 content of the oceans determines the CO_2 content of the atmosphere, thereby allowing pH reconstructions to constrain the CO_2 content of the ancient atmosphere (e.g., Martínez-Botí et al. 2015).

The boron isotopic composition of marine $CaCO_3$ is well-defined proxy of ocean pH because it is predominantly the borate ion that is incorporated into the growing $CaCO_3$ (Hemming and Hanson 1992) resulting in the $\delta^{11}B$ of $CaCO_3$ ($\delta^{11}B_c$) varying as a strong function of pH (at pH = 8.2, +0.1 pH units = +1 ‰ $\delta^{11}B$), as defined by Zeebe and Wolf-Gladrow (2001):

$$\mathrm{pH} = \mathrm{p}K_B^* - \log\left(-\frac{\delta^{11}B_{sw} - \delta^{11}B_c}{\delta^{11}B_{sw} - \alpha_B\delta^{11}B_c - \varepsilon_B}\right). \quad (6)$$

where $\delta^{11}B_{sw}$ is the boron isotopic composition of seawater, α_B is defined above and $\varepsilon_B = (\alpha_B - 1) * 1000$. pK_B^* is the dissociation constant of boron in seawater which is a function of temperature, pressure, and salinity.

Although biogenic marine $CaCO_3$ largely conforms to this simple inorganic model a number of complications arise. For instance, life processes in some, but not all (e.g., Rae et al. 2011), $CaCO_3$ secreting organisms modify either the pH around themselves or internally in the calcifying space (e.g., coral; McCulloch et al. 2012), such that $\delta^{11}B$ of the marine carbonate is offset from the $\delta^{11}B$ of borate ion ($\delta^{11}B_{borate}$). The existence of such "vital effects" therefore requires species-specific calibrations to account for the $\delta^{11}B_c \neq \delta^{11}B_{borate}$ and allow pH to be reconstructed (e.g., Henehan et al. 2013).

Despite these limitations, $\delta^{11}B$ in carbonates can reconstruct past pH with a typical accuracy of around ±0.02 pH units, and under favorable conditions, this translates into reconstructions of ancient atmospheric CO_2 with an uncertainty of ±20 ppm (Foster 2008).

Tracing the Recycling of Subducted Oceanic Crust

Island-arc magmas are commonly interpreted as resulting from the partial melting of the mantle wedge metasomatized by liquids (aqueous fluids, silicate melts) or solids (sediments, altered oceanic basalts) derived from the subducted lithospheric plate. Those "contaminants" are also considered to play a significant role in generating the geochemical "signatures" of arc magmas. As emphasized by Rosner et al. (2003), boron is a highly mobile element in the aqueous phase with an incompatible behavior during processes of partial melting. Moreover, boron is highly concentrated in oceanic sediments and hydrothermally altered oceanic crust compared to fresh rocks derived from upper mantle melting. Consequently, boron can be considered as a key tracer of slab contribution to island-arc volcanic rocks. Moreover, the hydrothermally altered oceanic crust and the subducted sediments constitute two geochemical reservoirs of highly contrasted boron isotope compositions. As a result, $\delta^{11}B$ values of volcanic arc rocks reflect their relative contributions during their petrogenesis, albeit modified by fractionation that occurs during dehydration of the subducted slab (Leeman et al. 2004).

Summary

The stable isotopes of boron exhibit a very wide range in natural and extraterrestrial materials. This is virtue of their light mass, large mass difference between ^{11}B and ^{10}B, and the geochemical behavior of B itself. As a consequence, however, the boron isotope system has great utility in the Earth sciences, and the use of boron to trace low-temperature geochemical and extraterrestrial processes has a long history and is continuing to grow.

Cross-References

- Acid–Base Reactions
- Boron
- Carbonate Minerals and the CO_2-Carbonic Acid System
- Carbon Cycle
- Chemical Weathering
- Chondrites
- Clay Minerals
- Earth's Oceanic Crust
- Hydrothermal Alteration
- Hydrothermal Solutions
- Lithophile Elements
- Ocean Biochemical Cycling and Trace Elements
- Ocean Salinity, Major Elements, and Thermohaline Circulation
- Solubility
- Subduction Zone Geochemistry

References

Aston FW (1920) The mass-spectra of chemical elements. Philos Mag 39:611–625

Barth S (1993) Boron isotope variations in nature: a synthesis. Geol Rundsch 82:640–651

Barth S (1998) Application of boron isotopes for tracing sources of anthropogenic contamination in groundwater. Water Resour 32:685–690

Bast R, Scherer EE, Mezger K, Austheim H, Ludwig T, Marschall HR, Putnis A, Lowen K (2014) Boron isotopes in tourmaline as a tracer of metasomatic processes in the Bamble sector of Southern Norway. Contrib Mineral Petrol 168:1069

Catanzaro EJ, Champion CE, Garner EL, Marinenko G, Sappenfield KM, Shields WR (1970) Boric assay; isotopic, and assay standard reference materials. https://www.google.co.uk/url?sa=t&rct=j&q=&esrc=s&source=web&cd=2&ved=0ahUKEwiBn8Wi7OvPAhWhJ8A

KHbXzAxsQFggjMAE&url=https%3A%2F%2Fwww.nist.gov%2Fdocument-10540&usg=AFQjCNE_2yV4zQHmpOjae2B7dz2xOVTPEw&sig2=85gz67j2R_NdoNe0gp7Vsg
Chaussidon M (1995) Isotope geochemistry of boron in mantle rocks, tektites and meteorites. Comptes Rendus de l'Academie des Sciences Paris 321:455–472
Chaussidon M, Marty B (1995) Primitive boron isotope composition of the mantle. Science 269:383–386
Chaussidon M, Robert F (1995) Nucleosynthesis of ^{11}B-rich boron in the presolar cloud recorded in meteoritic chondrules. Nature 374:337–339
Fietzke J, Heinemann A, Taubner I, Bohm F, Erez J, Eisenhauer A (2010) Boron isotopic ratio determination in carbonates via LA-MC-ICP-MS using soda-lime glass standards as reference materials. J Anal At Spectrom 25:1953–1957
Foster GL (2008) Seawater pH, pCO_2 and [CO_3^{2-}] variations in the Caribbean Sea over the last 130 kyr: a boron isotope and B/Ca study of planktic foraminifera. Earth Planet Sci Lett 271:254–266
Foster GL, Rae JWB (2016) Reconstructing Ocean pH with boron isotopes in foraminifera. Annu Rev Earth Planet Sci 44:207–237
Foster GL, Pogge von Strandmann PAE, Rae JWB (2010) Boron and magnesium isotopic composition of seawater. Geochem Geophys Geosyst 11:Q08015. https://doi.org/10.1029/2010GC003201
Hemming NG, Hanson GN (1992) Boron isotopic composition and concentration in modern marine carbonates. Geochim Cosmochim Acta 56:537–543
Henehan MJ, Rae JWB, Foster GL, Erez J, Prentice KC, Kurcera M, Bostock HC, Martinez-Boti MA, Milton JA, Wilson PA, Marshall B, Elliott T (2013) Calibration of the boron isotope proxy in the planktonic foraminifera *Globigerinoides ruber* for use in palaeo-CO_2 reconstruction. Earth Planet Sci Lett 364:111–122
Ishikawa T, Nakamura E (1993) Boron isotope systematics of marine sediments. Earth Planet Sci Lett 117:567–580
Klochko K, Kaufman AJ, Yoa W, Byrne RH, Tossell JA (2006) Experimental measurement of boron isotope fractionation in seawater. Earth Planet Sci Lett 248:261–270
Lécuyer C, Grandjean P, Reynard B, Albarede F, Telouk P (2002) ^{11}B/^{10}B analysis of geological materials by ICP-MS Plasma 54: application to the boron fractionation between brachiopod calcite and seawater. Chem Geol 186:45–55
Lee K, Kim T-W, Byrne RH, Millero FJ, Feely RA, Liu Y-M (2010) The universal ratio of boron to chlorinity for the North Pacific and North Atlantic oceans. Geochim Cosmochim Acta 74:1801–1811
Leeman WP, Tonarini S, Chan LH, Borg LE (2004) Boron and lithium isotopic variations in a hot subduction zone – the southern Washington Cascades. Chem Geol 212:101–124
Lemarchand D, Gaillardet J, Lewin E, Allegre CJ (2002) Boron isotope systematics in large rivers: implications for the marine boron budget and paleo-pH reconstruction over the Cenozoic. Chem Geol 190:123–140
Lodders K (2010) Solar system abundances of the elements. In: Goswami A, Reddy BE (eds) Principles and perspectives in cosmochemistry. Astrophysics and space science proceedings. Springer, Berlin/Heidelberg, pp 379–417
Marschall HR, Jiang SY (2011) Tourmaline isotopes: no element left behind. Elements 7:313–319
Martinez-Boti MA, Foster GL, Chalk TB, Rohling EJ, Sexton PF, Lunt DJ, Pancost RD, Badger MPS, Schmidt D (2015) Plio-Pleistocene climate sensitivity evaluated using high-resolution CO_2 records. Nature 518:49–54
McCulloch MT, Falter J, Trotter J, Montagna P (2012) Coral resilience to ocean acidification and global warming through pH up-regulation. Nat Clim Chang 2:623–627
McMullen CC, Gragg CB, Thode HG (1961) Absolute ratio B^{11}/B^{10} in Searles Lake borax. Geochim Cosmochim Acta 23:147–149
Menard G, Vlastélic I, Ionov DA, Rose-Koga EF, Piro J-L, Pin C (2013) Precise and accurate determination of boron concentration in silicate rocks by direct isotope dilution ICP-MS: insights into the B budget of the mantle and B behavior in magmatic systems. Chem Geol 354:139–149
Meyer C, Wunder B, Meixner A, Romer RL, Heinrich W (2008) Boron-isotope fractionation between tourmaline and fluid: an experimental re-investigation. Contrib Mineral Petrol 156:259–267
Nir O, Vengosh A, Harkness JS, Dwyer GS, Lahav O (2015) Direct measurement of the boron isotope fractionation factor: reducing the uncertainty in reconstructing ocean paleo-pH. Earth Planet Sci Lett 414:1–5
Palmer MR, Spivack AJ, Edmond JM (1987) Temperature and pH controls over isotopic fractionation during adsorption of boron on marine clay. Geochim Cosmochim Acta 51:2319–2323
Palmer MR, London D, Morgan GB, Babb HA (1992) Experimental determination of fractionation of ^{11}B/^{10}B between tourmaline and aqueous vapour: a temperature and pressure dependent isotopic system. Chem Geol 101:123–129
Rae JWB, Foster GL, Schmidt DN, Elliott T (2011) Boron isotopes and B/Ca in benthic foraminifera: proxies for the deep ocean carbonate system. Earth Planet Sci Lett 302:403–413
Rosner M, Erzinger J, Franz G, Trumbull RB (2003) Slab-derived boron isotope signatures in arc volcanic rocks from the Central Andes and evidence for boron isotope fractionation during progressive slab dehydration. Geochem Geophys Geosyst 4(8). https://doi.org/10.1029/2002GC000438
Sanyal A, Nugent M, Reeder RJ, Bijma J (2000) Seawater pH control on the boron isotopic composition of calcite: evidence from inorganic calcite precipitation experiments. Geochim Cosmochim Acta 64:1551–1555
Schmitt A-D, Vigier N, Lemarchand D, Millot R, Stille P, Chabaux F (2012) Processes controlling the stable isotope compositions of Li, B, Mg and Ca in plants, soils and waters: a review. Compt Rendus Geosci 344:704–722
Simon L, Lécuyer C, Maréchal C, Coltice N (2006) Modelling the geochemical cycle of boron: implications for the long-term δ^{11}B evolution of seawater and oceanic crust. Chem Geol 225:61–76
Smith HJ, Spivack AJ, Staudigel H, Hart SR (1995) The boron isotopic composition of altered oceanic crust. Chem Geol 126:119–135
Spivack AJ, Edmond JM (1987) Boron isotope exchange between seawater and the oceanic-crust. Geochim Cosmochim Acta 51:1033–1043
Vengosh A, Chivas AR, McCulloch MT, Starinsky A, Kolodny Y (1991) Boron isotope geochemistry of Australian salt lakes. Geochem Cosmochim Acta 55:2591–2606
Warner NR, Darrah TH, Jackson RB, Millot R, Kloppmann W, Vengosh A (2014) New tracers identify hydraulic fracturing fluids and accidental releases from oil and gas operations. Environ Sci Technol 48 (21):12552–12560
Xiao J, Xiao Y-K, Jin Z-D, He M-Y, Liu C-Q (2013) Boron isotope variations and its geochemical application in nature. Aust J Earth Sci 60:431–447
Xu Q, Dong Y, Zhu H, Sun A (2015) Separation and analysis of boron isotope in high plant by thermal ionisation mass spectrometry. Int J Anal Chem 2015:6. Article ID 364242. https://doi.org/10.1155/2015/364242
Zeebe R, Wolf-Gladow DA (2001) CO_2in seawater: equilibrium, kinetics, isotopes. Elsevier, Amesterdam
Zeininger H, Heumann KG (1983) Boron isotopic ratio measurement by negative thermal ionization mass spectrometry. Int J Mass Spectrom Ion Process 48:377–380

Bromine

Hélène Bureau
Institut de Minéralogie, de Physique desMatériaux et de Cosmochimie (IMPMC), Sorbonne Universités – UPMCUniv. Paris 06, CNRSUMR 7590, MuséumNational d'Histoire Naturelle, Paris, France

Element Data
Atomic Symbol: Br
Atomic Number: 35
Atomic Weight: 79.901–79.907
Stable Isotopes: ^{79}Br: 50.5–50.8%
^{81}Br: 49.2–49.5%
1 Atm Melting Point: 266 K
1 Atm Boiling Point: 332.7 K
1 Atm of Nebular Condensation[a]: 546 K
Valence State: $4s^2p^5$
Common Valences: −1, 0, +1, +3, +5
Common Ions: Br^-, BrO^-, BrO_3^-, BrO_4^-
Ionic Radius[a]: 196 pm
Pauling Electronegativity: 2.96
First Ionization Potential: 1139.9 kJ/mol
Chondritic (CI) Abundance [b]: 3.26 ppm
Silicate Earth Abundance [cb]: 50–75 ppb
Crustal Abundance[d]: 0.88 ppm
Oceanic Crust[e]: 0.17 ppm
Depleted Mantle[e]: 0.02 ppm
Seawater Abundance[f]: ~67 ppm
Evaporites[g]: 151 ppm
Sediments + Pore Water[h]: 97 ppm
Troposphere[i]: 0.016 ppbv
Core Abundance[j]: ~0.7 ppm
from: [a]J. Meija et al. (2016) [b]Jambon et al. 1995; [c]McDonough and Sun; [d]Rudnick and Gao 2003; [e]Schilling et al. 1980; [f]Bruland and Lohan 2003; [g]Hay et al. 2006; [h]Knaugh (1998); [i]Warneck 2000; [j]McDonough, 2005.

Properties

Bromine is the third halogen element located in the group XVII of the periodic table with an electronic configuration of [Ar] $3d^{10}$ $4s^2$ $4p^5$. It has 35 protons and has two stable isotopes. Bromine is a minor component on Earth, mostly concentrated in the hydrosphere (oceans). There is an increasing interest in geochemistry to study Br because of its high volatility during volcanic eruptions, as Br contributes to the destruction of the stratospheric ozone. It is also considered as an excellent tracer of geochemical processes such as recycling processes in subduction zones.

History and Use

The etymology of Br derives from the Greek "bromos" meaning stench due to a pungent, irritating odor. Bromine was discovered in 1826, simultaneously by Antoine-Jérôme Balard in Montpellier, France, and by Carl Löwig in Heidelberg, Germany, thought it was used during antiquity as the main ingredient of the Tyrian purple famous pigment derived from snails' secretions.

Bromine does not occur as a free element in nature; it is naturally concentrated in bromide salts present in evaporites and ore deposits, in seawater, and therefore easily workable for human uses. Traces of Br are also found in crustal and mantle rocks. Gaseous Br species such as bromoform organobromides and other Br-radicals are present as traces in the atmosphere and stratosphere.

Bromine compounds are commonly used in agricultural chemicals, in pesticides, in chemical intermediates such as disinfectants for swimming pools. Silver bromide AgBr is a chemical used in film photography. Bromine compounds are also used in lamps, dyestuffs, and cosmetics. Halons are flame-retardants in fire extinguishers, and they are added to furniture foam, plastic casings for electronics, and textiles to make them less flammable.

Isotopes

Bromine has two stable isotopes (^{79}Br, ^{81}Br), both having similar abundances. Variations in Br isotope data are reported in the standard delta notation:

$$\delta^{81}\mathrm{Br} = \frac{\left(\frac{^{81}\mathrm{Br}}{^{79}\mathrm{Br}}\right)\mathrm{sample} - \left(\frac{^{81}\mathrm{Br}}{^{79}\mathrm{Br}}\right)\mathrm{standard}}{\left(\frac{^{81}\mathrm{Br}}{^{79}\mathrm{Br}}\right)\mathrm{standard}} * 1000$$

The composition of the ocean water is used as the reference and defined as SMOB for Standard Mean Ocean Bromine analog to SMOC for chlorine. Bromine isotopes have not yet been intensely investigated because of technical difficulties (Eggenkamp 2014). Bromine isotope signatures allow for predicting the equilibrium fractionation between different oxidation states of Br oxyanions. Up to now they have been measured to study seawater, pore fluids, brines, and evaporates.

Mineralogy and Geochemistry

All halogen elements are characterized by the s^2p^5 outer shell configuration, with one missing electron in the last electron shell.

Elemental Br can be produced as a liquid or gaseous diatomic molecule Br_2. It commonly occurs as aqueous monovalent ions or salts, such as NaBr and AgBr in which the bromine atom has a −1 charge and oxidation number. They have the same face-centered cubic crystalline structure than NaCl. Bromine is always found associated with chlorine or iodine. Bromine forms numerous interesting covalent compounds as well, including two oxides: BrO_2 and Br_2O. Due to a large ionic radius, Br is incorporated in rock-forming minerals as traces.

Geochemistry of Bromine in Terrestrial Reservoirs

From a geochemical point of view, Br is classified as a lithophile element (McDonough and Sun 1995); it is considered as volatile with a nebular condensation temperature of 546 K (Lodders 2003). Br exhibits a similar geochemical behavior than Cl and I in most igneous processes, and differs from fluorine (strongly lithophile). Bromine is depleted compared to chondritic material in the bulk silicate Earth such as Cl and I (McDonough and Sun 1995). Halogen abundances decrease with respect to their size F<Cl<Br<I; Br natural abundances are low, ranging from ppb to several ppm, depending on the contexts.

Quantifying the distribution of Br in the deep Earth's major reservoirs is still difficult today due to the challenge of analyzing very low Br abundances and due to the limited access to natural deep mantle samples. Recent studies have attempted to constrain the geochemical behavior of bromine in igneous processes and bromine global cycling. The initial Br content for the Earth is still unknown, such as its origin that could be from a solar, a chondritic, or a cometary source or from a combination of the latter (Marty 2012). The bulk silicate Earth content would range from 0.05 to 0.075 ppm wt. when the CI chondrites (volatile-rich meteorites) contain 3.26 ppm wt. Br, but these calculations are based on the composition of mid ocean ridge basalts and on the assumption that Br/Cl has a constant value for the whole mantle, which may not be true.

Bromine in Upper Crust, Oceans, and Atmosphere

The chemistry of Br in the stratosphere is the object of strong attention because it is roughly 45 times more effective than chlorine for destroying ozone (Daniel et al. 1999). While the presence of Br in the atmosphere mostly results from anthropic activity (agricultural pesticides, biomass burning, automobiles, etc.), there are also natural sources such as seawater ice and seawater evaporation, cyanobacterias, phytoplankton, volcanic activity, etc. Bromine reacts with ozone and reduces its production through chain reactions as long as it is present as a reactive species (von Glasow and Crutzen 2014).

Similarly to the other halogen elements Br is strongly concentrated in Earth's differentiated crust, sediments, and hydrosphere.

Oceans are the major superficial reservoirs for Br, where marine phytoplankton and sea ice algae are the main source of bromoform and dibromomethane involved in ozone depletion. The role of organisms is determinant for Br chemistry also in terrestrial ecosystems forming organo-bromine compounds in soils (Vainikka and Hupa 2012).

Evaporites are the principal mineral sources for Br, and they are mined for Br commercial exploitation. They result from the evaporation of seawater and/or terrestrial lake waters. Although bromide salts (NaBr, KBr) are not present as individual minerals in evaporates, Br is concentrated in halite NaCl.

Bromine is significantly present in fluid inclusions from crustal minerals and is used to determine the origins of ore forming brines and to map hydrothermal processes (Leisen et al. 2012).

Bromine in Igneous Processes and in the Mantle

Bromine is found as traces in apatite, amphibole, biotite (e.g., O'Reilly and Griffin 2000; Teiber et al. 2013), in phengite, lawsonite (Pagé et al. 2016), and in serpentine-group minerals (Sumino et al. 2010; John et al. 2011; Kendrick et al. 2013).

The difficulty of measuring trace amounts of bromine in igneous samples explains that trace element geochemistry of Br in the mantle is currently poorly constrained. Halogens are thought to play a central role in the evolution of magmatic systems and associated ore deposits (e.g., Liu et al. 2014).

The magmatic abundances of Br are determined from analysis of volcanic glasses where Bromine is ranging from tens of ppb to a few ppm (Schilling et al. 1980; Jambon et al. 1995; Kendrick et al. 2012a; Kendrick et al. 2012b).

Bromine is expected to be incompatible during partial melting and differentiation. Br, Cl, and I are not strongly fractionated during partial melting or fractional crystallization and are expected to behave similarly in magmas; therefore, halogen ratios Br/Cl and Br/I provide crucial information on halogen sources, crystallization, degassing, and contamination processes (Pyle and Mather 2009; Aiuppa et al. 2009).

A few experimental studies probe Br behavior in silicate melts. The measured solubility of Br in hydrous silicate melts is similar to that of Cl and can reach a few wt.% in hydrous silicic melts (Bureau and Métrich 2003). Partitioning results show that Br concentration in silicate melts in equilibrium with aqueous vapor decreases together with pressure (Bureau et al. 2000; Bureau et al. 2010) that highlights the strong volatility of Br compared to Cl. The global volcanic bromine input to the atmosphere is very difficult to measure; estimates

would range from 5 to 15 Gg/a HBr (Pyle and Mather 2009). HBr and BrO have been measured in volcanic plumes in significant amounts (e.g., Bobrowski et al. 2003; Aiuppa et al. 2005; Kutterolf et al. 2015). Furthermore, HBr, the most common Br species released by volcanoes, reacts in plumes where it is converted into BrO, (Oppenheimer et al. 2006) meaning that volcanic vents should be regarded not only as passive providers of bromine but as "reaction vessels" (Mather 2016).

Bromine is recycled in the Earth's mantle with sediments, altered oceanic crust, and serpentinites. These last are transferred at depth where major fluid-rock interactions occur. Bromine is successively stored and released during serpentinization and deserpentization processes (John et al. 2011). It is a conservative fluid tracer. The Br content found in the arc-volcanic material may be highly influenced by the fluid release of deserpentinizing slabs as evidenced by Br/Cl, F/Cl, and I/Cl ratios that are used to understand their transfers and cycling in subduction settings (e.g., Kendrick et al. 2012b; Pagé et al. 2016). Deep Br-rich marine pore fluids are also found in exhumed peridotites, showing that Br is preserved in the down going hydrous peridotite that retained the pore fluids in a closed system up to at least 100 km (Sumino et al. 2010).

There is a real debate about potential deep recycling of Br. Is all Br subducted finally mobilized in arc magmatism (e.g., Kendrick et al. 2012b), is it retained within the subcontinental lithospheric mantle (Broadley et al. 2016), or is it cycling across the whole mantle? Experiments show that although most of the Br is mobilized by fluids escaping the down going slabs, a significant part of Br could be subducted deeper in the mantle (Bureau et al. 2010), implying that high pressure melts are ideal deep vectors and potential repositories. Indeed, Br speciation in hydrous melts at high pressure (7.6 GPa) indicates that Br anions form NaBr complexes in the hydrous melts and possibly BrOH complexes (Cochain et al. 2015).

Hydrous high pressure mineral phases may transfer bromine and other halogen in the deep mantle. The deep recycling of Br is also supported by the presence of Br-rich fluid inclusions trapped in diamonds (Johnson et al. 2000; Burgess et al. 2002).

Biological Utilization and Toxicity

In pharmacology, potassium bromide KBr is used as a sedative and can treat epilepsy. Bromine is mostly known as a toxic and corrosive reddish brown liquid/vapor. It is very reactive and poisonous, causing burns. Dibromide (Br_2) and a wide variety of organobromine compounds are used in industry. Among organobromine compounds, "halons" for haloalkanes, consisting of alkanes linked with halogens such as organobromides (i.e., bromomethane CH_3Br bromochloromethane, CH_2BrCl bromochlorodifluoromethane, CF_2ClBr, etc.), have been intensively produced, and they have a particularly harmful bad effect on the atmosphere chemistry. Therefore, organobromine is now a significant pollutant substance, and some uses are being phased out.

Summary and Conclusions

In geochemistry, determination of Br abundances combined with those of other halogen elements Cl, F, and I is extremely useful to understand how element transfer and store at depth. The geodynamical cycle of Br is linked to the cycle of water, fluids being efficient vectors for Br transport. The study of Br helps to understand hydrothermal geology, ore deposition processes, fluid–rock reactions, and subduction recycling. But today, the storage of bromine in the deep reservoirs is totally indeterminate. Further investigation would be useful to better constrain the extent of Br heterogeneity in the mantle and its cycling. Experimental studies (i.e., partitioning of Br between minerals from mantle rocks) would certainly help to determine if bromine is possibly stored at depth or not and to characterize the real bromine abundance of the Earth.

Cross-References

- ▶ Chlorine
- ▶ Fluorine
- ▶ Halogens
- ▶ Iodine
- ▶ Ocean Biochemical Cycling and Trace Elements
- ▶ Ozone and Stratospheric Chemistry

References

Aiuppa A, Federico C, Franco A, Giudice G, Gurrieri S, Inguaggiato S, Luizzo M, McGonicle AJS, Valenza M (2005) Emission of bromine and iodine from Mount Etna volcano. Geochem Geophys Geosyst 6(8):8

Aiuppa A, Baker DR, Webster JD (2009) Halogens in volcanic systems. Chem Geol 263:1–18

Bobrowski N, Hönninger G, Galle B, Platt U (2003) Detection of bromine monoxide in a volcanic plume. Nature 423:273–276

Broadley MW, Ballentine CJ, Chavrit D, Dallai L, Burgess R (2016) Sedimentary halogens and noble gases within Western Antarctic xenoliths: implications of extensive volatile recycling to the sub continental lithospheric mantle. Geochim Cosmochim Acta 176:139–156

Bruland KW, Lohan MC (2003) Controls of trace metals in seawater. Pergamon, Oxford, pp 23–47

Bureau H, Métrich N (2003) An experimental study of bromine behavior in water-saturated silicic melts. Geochim Cosmochim Acta 67(9):1689–1697

Bureau H, Keppler H, Métrich N (2000) Volcanic degassing of bromine and iodine: experimental fluid/melt partitioning data and applications to stratospheric chemistry. Earth Planet Sci Lett 183:51–60

Bureau H, Foy E, Raepsaet C, Somogyi A, Munsch P, Simon G, Kubsky S (2010) Bromine cycle in subduction zones through in situ br monitoring in diamond anvil cells. Geochim Cosmochim Acta 74:3839–3850

Burgess R, Layzelle E, Turner G, Harris JW (2002) Constraints on the age and halogen composition of mantle fluids in Siberian coated diamonds. Earth Planet Sci Lett 197:193–203

Cochain B, Sanloup C, de Grouchy C, Crépisson C, Bureau H, Leroy C, Kantor I, Irifune T (2015) Bromine speciation in hydrous silicate melts at high pressure. Chem Geol 404:18–26

Daniel JS, Solomon S, Portmann RW, Garcia RR (1999) Stratospheric ozone destruction: the importance of bromine relative to chlorine. J Geophys Res 104(D):23871–23880

Eggenkamp HGM (2014) The geochemistry of stable chlorine and bromine isotopes. Springer, Heidelberg. 172pp

Hay WW, Migdisov A, Balukhovsky AN, Wold CN, Flögel S, Söding E (2006) Evaporites and the salinity of the ocean during the Phanerozoic: implications for climate, ocean circulation and life. Palaeogeogr Palaeoclimatol Palaeoecol 240:3–46

Jambon A, Déruelle B, Dreibus G, Pineau F (1995) Chlorine and bromine abundance in MORB: the contrasting behavior of the Mid-Atlantic Ridge and East Pacific Rise and implications for chlorine geodynamic cycle. Earth Planet Sci Lett 126:101–117

John T, Scambelluri M, Frische M, Barnes JD, Bach W (2011) Dehydration of subducting serpentinite: implications for halogen mobility in subduction zones and the deep halogen cycle. Earth Planet Sci Lett 308:65–76

Johnson LH, Burgess R, Turner G, Milledge HJ, Harris JW (2000) Noble gas and halogen geochemistry of mantle fluids: comparison of African and Canadian diamonds. Geochim Cosmochim Acta 64:717–732

Kendrick MA, Kamenetsky VS, Phillips D, Honda M (2012a) Halogen systematics (Cl, Br, I) in Mid-Ocean Ridge Basalts: a Macquarie Island case study. Geochim Cosmochim Acta 81:82–93

Kendrick MA, Woodhead JD, Kamenetsky VS (2012b) Tracking halogens through the subduction cycle. Geology 40:1075–1078

Kendrick MA, Honda M, Pettke T, Scambelluri M, Phillips D, Giuliani A (2013) Subduction zone fluxes of halogens and noble gases in seafloor and forarc serpentinites. Earth Planet Sci Lett 365:86–96

Knaugh LP (1998) Salinity history of the Earth's early ocean. Nature 395:554–555

Kutterolf S, Hansteen TH, Freundt A, Wehrmann H, Appel K, Krüger K, Pérez W (2015) Bromine and chlorine emissions from Plinian eruptions along the Central American Volcanic Arc: from source to atmosphere. Earth Planet Sci Lett 429:234–246

Leisen M, Boiron MC, Richard A, Dubessy J (2012) Determination of Cl and Br concentrations in individual fluid inclusions by combining microthermometry and LA-ICPMS analysis: implications for the origin of salinity in crustal fluids. Chem Geol 330–331:197–206

Liu W, Etschmann B, Testemale D, Hazemann JL, Rempel K, Müller H, Brugger J (2014) Gold transport in hydrothermal fluids: competition among the CL-, Br-, HS- and NH3(aq) ligands. Chem Geol 376:11–19

Lodders K (2003) Solar system abundances and condensation temperatures of the elements. Astrophys J 591:1220–1247

Marty B (2012) The origins and concentrations of water, carbon, nitrogen and noble gases on Earth. Earth Planet Sci Lett 313–314:56–66

Mather TA (2016) Volcanism and the atmosphere: the potential role of the atmosphere in unlocking the reactivity of volcanic emissions. Phil Trans R Soc A 366:4581–4595

McDonough WF (2005) Compositional model for the Earth's core. In: Carlson RW (ed) The mantle and Core. Elsevier, Oxford, pp 547–568

McDonough WF, Sun SS (1995) The composition of the Earth. Chem Geol 120:223–253

Meija J, Coplen TB, Berglund M, Brand WA, De Bièvre P, Gröning M, Holden NE, Irrgeher J, Loss RD, Walczyk T, Prohaska T (2016) Isotopic compositions of the elements 2013 (IUPAC technical report). Pure Appl Chem 88:293–306. http://www.nist.gov/pml/data/comp.cfm

O'Reilly SY, Griffin WL (2000) Apatite in the mantle: implications for metasomatic processes and high heat production in Phanerozoic mantle. Lithos 53:217–232

Oppenheimer C, Tsanev VI, Braban CF, Cox RA, Adams JW, Aiuppa A, Bobrowski N, Demelle P, Barcaly J, McGonicle AJS (2006) BrO formation in volcanic plumes. Geochim Cosmochim Acta 70:2935–2941

Pagé L, Hattori K, De Hoog JCM, Okay AI (2016) Halogen (F, Cl, Br, I) behaviour in subducting slabs: a study of lawsonite blueschists in western Turkey. Earth Planet Sci Lett 442:113–142

Pyle DM, Mather TA (2009) Halogens in igneous processes and their fluxes to the atmosphere and oceans from volcanic activity: a review. Chem Geol 263:110–121

Rudnick RL, Gao S (2003) Composition of the continental crust. Treatrise Geochem 3:1–64

Schilling BG, Bergeron MB, Evans R (1980) Halogens in the mantle beneath the North Atlantic. Philos Trans R Soc Lond A 297:147–178

Sumino H, Burgess R, Mizukami T, Wallis SR, Holland G, Ballentine CJ (2010) Seawater-derived noble gases and halogens preserved in exhumed mantle wedge peridotite. Earth Planet Sci Lett 294:163–172

Teiber H, Marks MAW, Wenzel T, Siebel W, Altherr R, Markl G (2013) The distribution of halogens (F, Cl, Br) in granitoid rocks. Chem Geol 374–375:92–109

Vainikka P, Hupa M (2012) Review on bromine in solid fuels. Part 1: natural occurrence. Fuels 95:1–14

von Glasow R, Crutzen PJ (2014) Tropospheric halogen chemistry. In: Treatrise in geochemistry, vol 4, 2nd edn. Elsevier, Netherlands, pp 1–67

Warneck P (2000) Chemistry of the natural atmosphere, 2nd edn. Academic, London. 927 pp

C

Cadmium

Monica Vasiliu and David A. Dixon
Department of Chemistry, University of Alabama, Tuscaloosa, AL, USA

Element Data
Atomic Symbol: Cd
Atomic Number: 48
Atomic Weight: 112.411
Isotopes and Abundances: ^{106}Cd 1.25%, ^{108}Cd 0.89%, ^{110}Cd 12.51%, ^{111}Cd 12.81%, ^{112}Cd 24.13%, ^{113}Cd 12.22%, ^{114}Cd 28.72%, ^{116}Cd 7.47%
1 Atm Melting Point: 594.1 K
1 Atm Boiling Point: 1038 K
Common Valences: +2, +1
Ionic Radii: (+II) 103 ppm, (+I) 114 ppm
Pauling Electronegativity: 1.69
First Ionization Energy: 867.8 kJ/mol
Chondritic (CI) Abundance: 686 ppb
Silicate Earth Abundance: 0.04 ppm
Crustal Abundance: 0.11 ppm
Seawater Abundance: 0.11 ppb
Core Abundance: 0.15 ppm

Properties

Cadmium (Emsley 1991, 2001; Anthoni 2006; Anders and Grevesse 1989; McDonough 2005) is a lustrous, silvery-white metal with a bluish tinge on the surface and tarnishes in air. It is very ductile and malleable and is soft enough to be cut with a knife. Cadmium is soluble in acids but not in alkaline solutions. In many ways, cadmium is similar to zinc but forms more complex compounds.

Cadmium was not considered to be radioactive until 1970 when, as a surprise, ^{113}Cd was shown to be an α-emitter with a very long half-life (9×10^{15} years). The consequence of this radioactivity is negligible as only one atom is lost per minute in a 10 g piece of cadmium metal.

History and Use

At the beginning of the 1800s, apothecaries made zinc oxide by heating a naturally occurring form of zinc carbonate called cadmia, also named calamine. Sometimes the resulting product was yellow instead of being pure white. And Friedrich Stromeyer of Göttingen University traced the discoloration to a component in the mineral that he could not identify. In 1817, he separated a brown oxide, purified unknown element, and named it cadmium after the mineral from which it came. Karl Meissner in Halle, and Karl Karsten in Berlin, working on the same problem, reported their discovery of cadmium 1 year later. A significant amount of research led to the conclusion that cadmium is present in all zinc ores but has no effect on the performance of zinc compounds. Cadmium was partly removed when zinc metal was smelted because cadmium is more volatile than zinc and was lost in the atmosphere.

Cadmium is a poison and is known to cause birth defects and cancers so its use is more limited. Around 80% of the cadmium that is produced is used in rechargeable Ni-Cd batteries. These batteries are slowly being phased out and replaced with nickel hydride batteries. The remainder of the cadmium is mainly used for pigments (yellow, orange, and red), coatings, and plating and as stabilizers for plastics.

W. M. White (ed.), *Encyclopedia of Geochemistry*,
https://doi.org/10.1007/978-3-319-39312-4

Cadmium films about 0.05 mm thick were used to electroplate steel to protect it against corrosion. It is still used today to protect critical components of airplanes and oil platforms. Cadmium absorbs neutrons and is used in rods in nuclear reactors to control atomic fission.

Geochemical Behavior

Cadmium is naturally occurring in the Earth's crust and always occurs in combination with zinc. The only mineral containing significant quantities of cadmium is greenockite (cadmium sulfide). It is also present is small amounts in sphalerite (ZnS) in which CdS is a significant up to 3% impurity. Almost all commercially produced cadmium is obtained as a by-product of zinc, lead, or copper extractions and refining.

Naturally, a cadmium is released into the environment with half being released into rivers through weathering rocks and some released into the air by forest fires and volcanoes. The remainder of the released cadmium is from human activities including manufacturing. In some cases, cadmium is washed onto soil used to grow crops and to feed animals.

Biological Utilization and Toxicity

Cadmium is toxic, carcinogenic, and teratogenic. On average the human intake is 0.05 mg/day, but it accumulates and stays in the body for around 30 years; the human body stores about 50 mg of cadmium.

Before the dangers of cadmium were fully understood, welders and some other metal workers were at risk of becoming ill. For example, in 1966 welders working on the Severn Road Bridge in England became ill from breathing cadmium fumes.

Although it has not been proven, there are suggestions that cadmium could be essential for some species, as it can stimulate metabolism. Marine organisms absorb cadmium rapidly so that little cadmium is found in the surface layers of the oceans.

Cadmium can never be totally excluded from the diet and can be found in food like offal, shellfish, and rice. Some fungi such as the mushroom *Amanita muscaria* and other food crops (lettuce, spinach, cabbage, and turnip) have the ability to absorb cadmium. Smoking adds to the body burden because tobacco plants absorb it as well.

Cross-References

► Zinc

References

Anders E, Grevesse N (1989) Abundances of the elements: meteoritic and solar. Geochim Cosmochim Acta 53:197–214. http://meteorites.wustl.edu/goodstuff/chondritic_abundances.htm

Anthoni JF (2006) The chemical composition of seawater. http://www.seafriends.org.nz/oceano/seawater.htm

Emsley J (1991) The elements, 2nd edn. Clarendon Press, Oxford

Emsley J (2001) Nature's building blocks an A-Z guide to the elements. Oxford University Press, Oxford

McDonough WF (2005) Compositional model for the earth's core. In: Carlson RW (ed) The mantle and core. Elsevier, Oxford, pp 547–568. http://www.knowledgedoor.com/2/elements_handbook/element_abundances_in_the_earth_s_core.html

Caesium

Gray E. Bebout
Department of Earth and Environmental Sciences, Lehigh University, Bethlehem, PA, USA

Element Data
Atomic Symbol: **Cs**
Atomic Number: **55**
Atomic Weight: 132.90545 u
Isotopes and Abundances: ^{133}Cs, ~100%
1 Atm Melting Point: 28.5 °C
1 Atm Boiling Point: 670.8 °C
Common Valences: 1+
Ionic Radii: 12-fold: 188 pm
Pauling Electronegativity: 0.79
First Ionization Energy: 375.4 kJ/mol
Chondritic (CI) Abundance: 0.188 ppm
Silicate Earth Abundance: 7.7 ppb
Crustal Abundance: 2 ppm
Seawater Abundance: 2 nmol/kg
Core Abundance: ~0

Properties

Caesium, a reactive silvery-gold metal belonging to the group IA on the periodic table, is one of the alkali elements and considered as a "lithophile" element as defined by Goldschmidt. Caesium, atomic number 55, has a standard atomic weight of 132.90545 and an electronic configuration of [Xe]6 s^1. The lone 6 s electron is relatively easily removed; this first ionization potential of Cs is 375.4 kJ/mol. Caesium is highly ionic in character and the ionic radius of Cs^{1+} is

188 pm in 12-fold coordination. Caesium has a 1 atm melting point of 28.5 °C. Caesium has only one naturally occurring isotope, the stable ^{133}Cs. However, there are 40 known isotopes of Cs, with atomic masses of 112–151. The longest-lived radioisotope of Cs is ^{135}Cs, with a half-life of 2.3 million years. All but three of the other radioisotopes of Cs have half-lives of less than 2 weeks, many of them well under 1 h.

Caesium nearly always is bonded by electrostatic forces as Cs^{+1} with various anions and it is, in general, highly soluble in aqueous solutions, for example, during weathering and in the oceans. Caesium, with an ionic radius similar to that of K^+, tends to show geochemical behavior similar to that of K^+ and therefore in silicate rocks to occur in greatest concentrations in K-rich minerals such as illite (a clay mineral), muscovite and biotite (both micas; phengite is a Si-rich muscovite), and alkali feldspars. Concentrations of Cs in silicate minerals are ordinarily at trace levels in the ppm range, commonly lower than 100 ppm but in some rocks as high as 100 s of ppm (see, for example, the ion microprobe analyses of coexisting metamorphic minerals in Bebout et al. 2007, 2013). In the crust, it is a main constituent in nonabundant minerals such as pollucite, a tectosilicate (zeolite group mineral), and lepidolite (a Li-rich mica), both found in Li-rich pegmatites.

History and Uses

Caesium was discovered, along with Rb, by Gustav Kirchhoff and Robert Bunsen in 1860 by spectroscopic study of mineral waters. Its name derives from the Latin *caesius*, meaning sky blue, referring to the color of its emission spectrum. "Caesium" is the name adopted by the International Union of Pure and Applied Chemistry while the American Chemical Society uses "Cesium," which is also common usage in North America. Nonradioactive Cs is used in drilling fluids in the oil industry (the largest current use) and also in atomic clocks and various electronics applications.

The radioactive isotope ^{137}Cs has been used as a tracer in hydrologic studies, in applications similar to those of ^{3}H; both of these isotopes are produced largely by nuclear testing. With the initiation of nuclear testing in 1945, Cs isotopes were released into the atmosphere where it is absorbed readily into solution and is returned to the surface of the earth as a component of radioactive fallout. ^{137}Cs is a particularly dangerous fission product because of its high yield during fission, moderate half-life (30.17 years), high-energy decay pathway, and chemical reactivity. Because of these properties, ^{137}Cs is a major contributor to the total radiation released during nuclear accidents. Despite its prevalence in spent nuclear fuel and nuclear waste, ^{137}Cs is extremely rare. Its half-life is too short for it to persist from natural fission sources, and on earth it is a synthetic isotope only, presently showing decline in concentration in surface reservoirs due to the cessation of major nuclear bomb testing.

Abundances

The solar system abundance of Cs is estimated at 0.371 Atoms/10^6 Si; (Lodders et al. 2009), based on study of meteorites. The bulk Earth Cs concentration is believed to be 0.035 ppm (McDonough 2003) and Hofmann and White (1982) estimated a concentration of 7.7 ppb in the primitive mantle. Seawater contains 2 nmol/kg of Cs and shows concentrations as high as 368 nmol/kg of seawater in seafloor hydrothermal fluids (Palmer and Edmond 1989). Caesium concentration in the continental crust is estimated as being near 2 ppm, with greater amounts (4.9 ppm) concentrated in the more felsic upper continental crust (Rudnick and Gao 2014) and 2.2 and 0.3 ppm concentrations in the middle and lower continental crust, respectively. Fresh NMORB contains ~0.01 ppm and is enriched by up to ~20X during seafloor alteration (see Bebout 2014 and references therein), with Cs enrichments showing strong correlation with enrichments of K and Rb (see Bebout 2014). Seafloor sediments can contain far greater concentrations of Cs, with the GLOSS (global subducting sediment) composition containing ~3.5 ppm or about 350X the concentration in fresh NMORB (see Plank 2014).

General Behavior in Fluid/Melt-Mineral Systems

Caesium is commonly thought of as belonging to the group of large-ion lithophile elements (LILE), along with K, Rb, Sr, and Ba, and showing the most similarity in behavior with K and Rb. It shows strong incompatibility during melting in the mantle and is partitioned into basaltic melts. Its great tendency to partition into fluids and melts is reflected in its tendency to be enriched in late-stage differentiation products in more felsic igneous systems. Economically important Cs deposits are commonly in pegmatitic systems reflecting this late-stage differentiation. During metamorphism of sedimentary rocks, Cs concentrations are largely governed by reactions involving phyllosilicates capable of housing this element as highly coordinated atoms in interlayer sites. However, Cs has shown some tendency to become mobilized in H_2O-rich fluids, during devolatilization reactions, to a greater extent than other LILE and charged molecules residing in these sites (e.g., K^+, Rb^+, and NH_4^+ see Bebout et al. 1999, 2007). Although significant loss of Cs to fluids can occur during low- to medium-grade metamorphism, and during

partial melting reactions, significant fractions of the protolith Cs can be retained even during partial melting, including those that result in destabilization of its preferred mineral host, the micas. Caesium, on the average, shows somewhat greater tendency than K^+ and Rb^+ to be mobilized into aqueous fluids and depleted in devolatilizing rocks, thus whole-rock Rb/Cs and K/Cs can be strongly increased by devolatilization (see the discussion of Rb and Cs on Earth by McDonough et al. 1992; also see Rudnick and Gao 2014). In seafloor basaltic rocks, Cs concentrations are enriched along with K during hydrothermal alteration and, as for metasedimentary rocks, strongly influenced in their behavior by the abundance of potassic mineral phases, particularly the clays and micas.

Subduction Zone Cycling of Caesium

Subduction of Cs, along with Rb^+ and NH_4^+ is strongly tied to the stability and reactions involving K-rich micas such as phengite (Si-rich muscovite). In subduction zones with typical relatively "cool" thermal structure, much of the LILE inventory in both sedimentary and basaltic rocks could be retained to depths beneath volcanic arcs (and perhaps beyond, into the deeper mantle; see Bebout et al. 2013). Figure 1 illustrates the strong dependence of Cs retention in subducted sediments on the thermal structure of the subduction zone. On this figure, whole-rock (Fig. 1a; data from Bebout et al. 1999) and phengite (Fig. 1b; data obtained using an ion microprobe; see Bebout et al. 2007) Rb/Cs are plotted against metamorphic grade in the Catalina Schist paleo-accretionary complex, exposed on Santa Catalina Island, California. From the left to the right on this diagram, rocks experienced increasingly warmer P-T paths during their subduction into this evolving paleo-margin (all at pressures of ~8–11 kb, corresponding to ~24–33 km depths). The increase in Rb/Cs, with increasing grade, is associated with loss of Cs at relatively constant Rb concentration.

Caesium enrichments in volcanic lavas are one characteristic of these rocks believed to reflect additions to mantle-wedge melting regions by aqueous fluids or silicate melts derived in subducting slabs (Elliott 2003). In Fig. 2 (from Bebout 2014), element concentrations in arc volcanic rocks and in mid-ocean ridge basalts are normalized to concentrations in the primitive Earth mantle. High- and ultrahigh-pressure metamorphic rocks, representing deeply subducted oceanic slab sections (oceanic crust and overlying sediment), contain a complementary record of Cs release, mobility during devolatilization reactions, and metasomatic enrichment in metabasaltic and metaultramafic rocks (Bebout 2014).

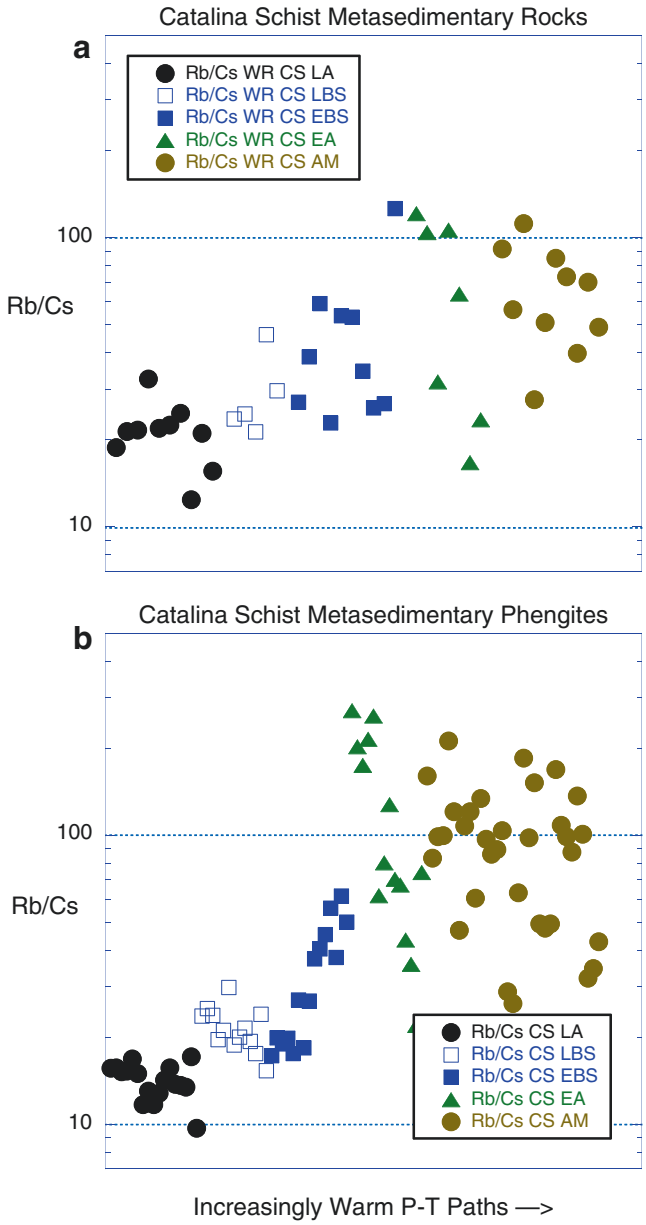

Caesium, Fig. 1 Ratio of Rb to Cs concentration in whole-rock samples (**a**) and phengites (siliceous white micas; **b**) in subduction-zone-metamorphosed sedimentary rocks in the Catalina Schist (from Bebout et al. 1999, 2007). From *left* to *right* on this diagram, the metamorphic units experienced increasingly higher-temperature P-T paths during prograde metamorphism in the evolving paleo-subduction zone (*LA* lawsonite-albite, *LBS* lawsonite blueschist, *EBS* epidote blueschist, *EA* epidote amphibolite, *AM* amphibolite). Bebout et al. (2007) presented Cs and Rb concentrations in all coexisting minerals in these samples, demonstrating the strong partitioning of both elements into phengite. Also showing whole-rock (and phengite) losses was (**B**), which like Cs is highly concentrated in the micas. In these rocks, Ba^{+2} also is strongly concentrated in the phengite (at considerably higher concentrations of 1000 s of ppm) but does not show evidence of loss across this range in grade

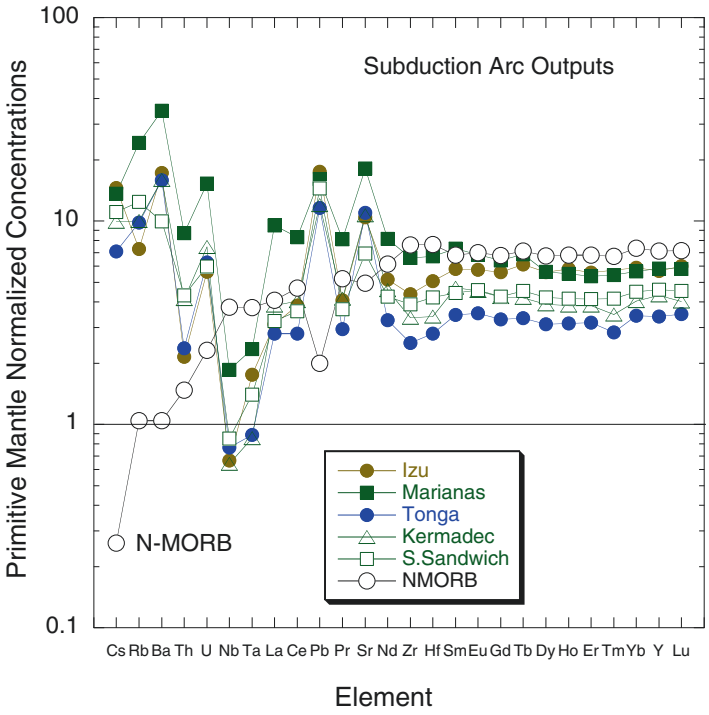

Caesium, Fig. 2 Chemical characteristics of subduction zone outputs: erupted lavas. Data are normalized to primitive mantle from Hofmann (1988). Data for arc basalt outputs are from Elliott (2003). Note the large enrichments in Cs in arc lavas, relative to mid-ocean ridge basalts, accompanied by enrichments in Rb and Ba. These enrichments are generally attributed to additions to mantle-wedge arc magma source regions by hydrous fluids or silicate melts derived in subducting slabs and overlying sediments

Caesium Behavior During Partial Melting in the Continental Crust

Partial melting in the continental crust shows a tendency to similarly disrupt the Rb/Cs of metasedimentary rocks, as related to the preferential loss of Cs, relative to Rb, during partial melting. Figure 3a shows the apparent effect of partial melting reactions (at pressures of 4–8 kb; corresponding to ~12–24 km depths) on Rb and Cs concentrations, and Rb/Cs, in the Ivrea Zone, Italy (data from Bea and Montero 1999). Figure 3b shows the change in the concentrations of the two elements, and Rb/Cs, as related to a series of partial melting reactions experienced at pressures of 2–4 kb (corresponding to ~6–12 depths) and now exhibited in Zones 1–3 at Mt. Stafford, Australia (from Palya et al. 2011). Rubidium shows only very modest change but Cs shows considerable loss, producing the increase in Rb/Cs. In such rocks, partial melting reactions can be driven by infiltration by H_2O-rich fluids (H_2O-saturated melting) or can involve partial or complete breakdown of hydrous mineral phases such as the micas, the latter in many cases the dominant mineral hosts for both Rb and Cs. In rocks experiencing complete mica breakdown, these elements can be partly retained in feldspars, particularly the alkali feldspars. A combination of devolatilization and partial melting, and ascent of relatively low Rb/Cs felsic magmas to shallow levels, likely contributes to the elevated Rb/Cs of middle and lower continental crust, ~30 and ~37, respectively, as compared with the Rb/Cs of upper continental crust (~17; see Rudnick and Gao 2014).

Biological Utilization and Toxicity

Caesium has no biological role, although it can to some extent replace potassium in the body because of the chemical similarity of the two elements and can be uptaken by plants affected by potassium nutrition (White and Broadley 2000; Fujiwara 2013). Ingestion of any caesium compound is in general to be avoided; however, it is unlikely that humans would be exposed to enough ^{133}Cs to experience health effects that can be related to this stable isotope. Because of the similarity in behavior of caesium with potassium, the radioactive isotopes ^{134}Cs and ^{137}Cs (present in the biosphere in small amounts as a result of radiation leaks) are very toxic. Both isotopes emit beta radiation and gamma radiation. ^{137}Cs is also used in some medical applications (e.g., brachytherapy).

Summary

Caesium, of interest to researchers in many scientific fields, shows strong similarity in behavior with potassium but also some intriguing differences in behavior compared with this

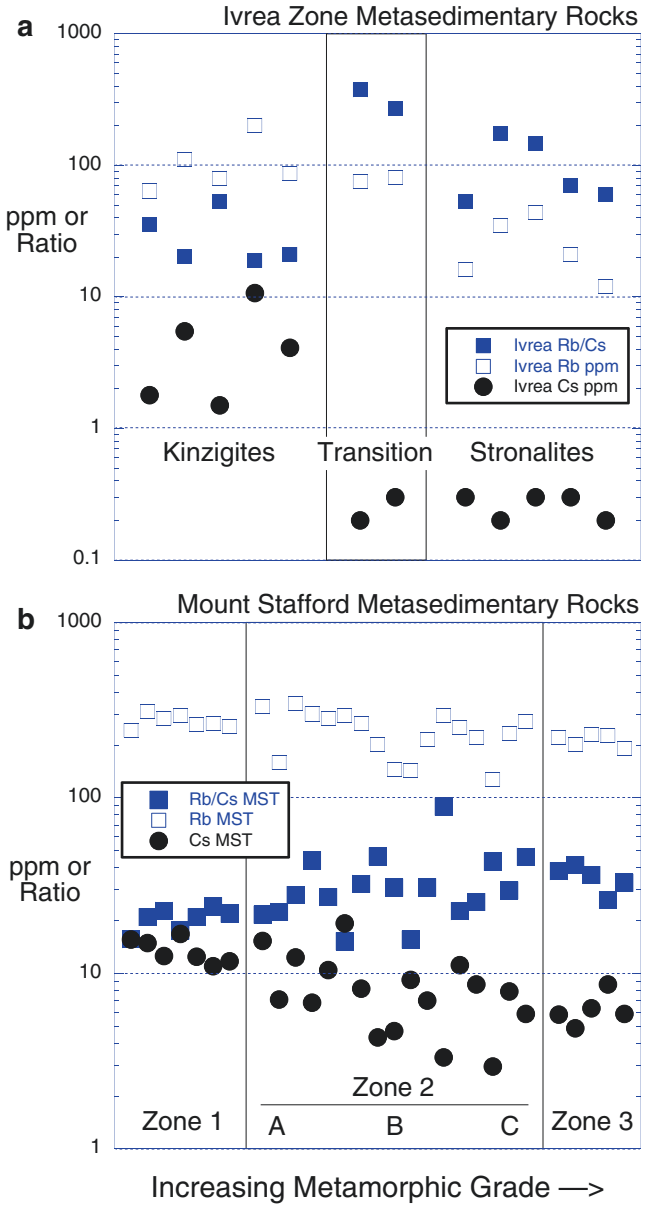

Caesium, Fig. 3 Caesium and Rb concentrations, and Rb/Cs, in whole-rock metasedimentary samples experiencing partial melting reactions at middle to deep levels of the continental crust. (**a**) Data for migmatites of the Ivrea Zone, Italy (Val Strona di Omegna), investigated by Bea and Montero (1999). (**b**) Data for metasedimentary rocks exposed at Mt. Stafford (North-Central Australia), from Palya et al. (2011). On both diagrams, metamorphic grade increases from left to right (see the labeled zones described in detail by Bea and Montero (1999), and Palya et al. 2011)

and other LILE. It is a trace element in most environments of interest to humans, but it serves as an extremely useful tracer of a large number of processes in the hydrosphere, biosphere, and lithosphere. Because of the hazards associated with radioactive ^{137}Cs, caesium receives attention in not only the scientific community but also from the medical community and more broadly in society.

Cross-References

- Clay Minerals
- Earth's Continental Crust
- Fluid–Rock Interaction
- Geochemical Classification of Elements
- Hydrothermal Alteration
- Large-Ion Lithophile Elements
- Metamorphic Reactions and Processes
- Partial Melting
- Radioactivity
- Rubidium
- Subduction Zone Geochemistry

References

Bea F, Montero P (1999) Behavior of accessory phases and redistribution of Zr, REE, Y, Th, and U during metamorphismand partial melting ofmetapelites in the lower crust: an example from the Kinzigite formation of Ivrea-Verbano, NW Italy. Geochim Cosmochim Acta 63:1133–1153

Bebout GE (2014) 4.20. Chemical and isotopic cycling in subduction zones. In: Rudnick RL (ed) Treatise on geochemistry: the crust, vol 4, 2nd edn. Elsevier, Amsterdam, pp 703–747

Bebout GE, Ryan JG, Leeman WP, Bebout AE (1999) Fractionation of trace elements during subduction-zone metamorphism: impact of convergent margin thermal evolution. Earth Planet Sci Lett 171:63–81

Bebout GE, Bebout AE, Graham CM (2007) Cycling of B, Li, and LILE (K, Cs, Rb, Ba, Sr) into subduction zones: SIMS evidence from micas in high-P/T metasedimentary rocks. Chem Geol 239:284–304

Bebout GE, Agard P, Kobayashi K, Moriguti T, Nakamura E (2013) Devolatilization history and trace element mobility in deeply subducted sedimentary rocks: SIMS evidence from Western Alps HP/UHP suites. Chem Geol 342:1–20

Elliott T (2003) Tracers of the slab. In: Eiler J (ed) Inside the subduction factory, Geophysical Monograph, vol 138. American Geophysical Union, Washington, DC, pp 23–45

Fujiwara T (2013) Cesium uptake in rice: possible transporter, distribution, and variation, Chapter 4. In: Nakanishi TM, Tanoi K (eds) Agricultural implications of the Fukushima nuclear accident. Springer, New York, pp 29–35

Hofmann AW (1988) Chemical differentiation of the earth: the relationship between mantle, continental crust, and oceanic crust. Earth Planet Sci Lett 90:297–314

Hofmann AW, White WM (1982) Ba, Rb, and Cs in the Earth's mantle. Z Naturforsch A 38(2):256–266

Lodders K, Palme H, Gail HP (2009) Abundances of the elements in the solar system, Chapter 4.4. In: Trümper JE (ed) Landolt Börnstein, new series, vol VI/4B. Springer, Berlin/Heidelberg/New York, pp 560–630

McDonough WF (2003) Compositional model for the Earth's core. In: Carlson RW (ed) Treatise on geochemistry: the mantle and core, vol 2, 1st edn. Elsevier, Amsterdam, pp 547–568

McDonough WF, Sun S-S, Ringwood AE, Jagoutz E, Hofmann AW (1992) Potassium, rubidium, and caesium in the Earth and Moon and the evolution of the mantle of the Earth. Geochim Cosmochim Acta 56:1001–1012

Palmer MR, Edmond JM (1989) Cesium and rubidium in submarine hydrothermal fluids: evidence for recycling of alkali elements. Earth Planet Sci Lett 95:8–14

Palya AP, Buick IS, Bebout GE (2011) Storage and mobility of nitrogen in the continental crust: evidence from partially melted metasedimentary rocks at Mount Stafford, North-Central Australia. Chem Geol 281:211–226
Plank T (2014) 4.17. The chemical composition of subducting sediments. In: Rudnick RL (ed) Treatise on geochemistry: the crust, vol 4, 2nd edn. Elsevier, Amsterdam, pp 607–629
Rudnick RL, Gao S (2014) 4.1. Composition of the continental crust. In: Rudnick RL (ed) Treatise on geochemistry: the crust, vol 4, 2nd edn. Elsevier, Amsterdam, pp 1–51
White PJ, Broadley MR (2000) Mechanisms of caesium uptake by plants. New Phytol 147:241–256

Calcium

Christophe Lécuyer
Laboratoire de Géologie de Lyon, LGL-TPE, CNRS UMR 5276, Université Claude Bernard Lyon 1 and Institut Universitaire de France, Lyon, France

Element Data
Atomic Symbol: Ca
Atomic Number: 20
Atomic Weight: 40.078(4)
Isotopes and Abundances: ^{40}Ca, 96.941(156)%; ^{42}Ca, 0.647(23)%; ^{43}Ca, 0.135(10)%; ^{44}Ca, 2.086(110)%; ^{48}Ca, 0.187(21)%
1 Atm Melting Point: 840 °C
1 Atm Boiling Point: 1,484 °C
Common Valences: +2
Ionic Radii: 6-fold: 114 pm
Pauling Electronegativity: 1.00
First Ionization Potential: 589.83 kJ.mol^{-1}
Chondritic (CI) Abundance: 9,110 ppm (59,820 atoms/10^6 Si)
Silicate Earth Abundance: 25,300 ppm
Crustal Abundance: 41,500 ppm
Seawater Abundance: 412 to 420 ppm
Core Abundance: ~0

Properties

Calcium is a metal (alkaline earth) with a silvery color and a cubic crystal structure. This element belongs to group 2 and period 4 of the periodic table (Fig. 1). Calcium has 25 known isotopes of which 5 are stable (source of data: National Institute of Standards and Technology: http://www.nist.gov/pml/data/comp.cfm).

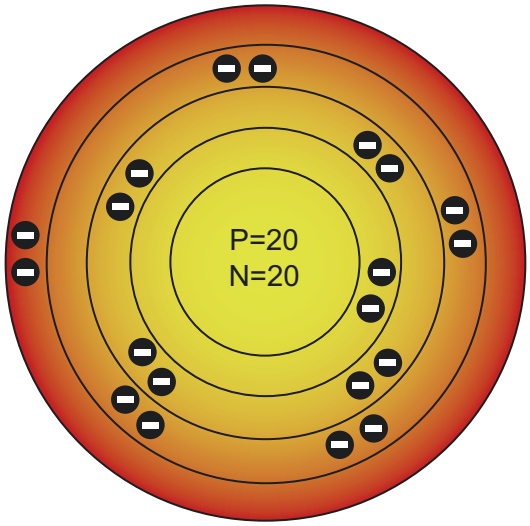

Calcium, Fig. 1 Schematic illustration of the atomic configuration of ^{40}Ca

Geochemists measure the relative variations in the ^{44}Ca/^{40}Ca of terrestrial and extraterrestrial materials that result mainly from chemical equilibrium and kinetic effects. Some of this variation also results from the β decay of ^{40}K (decay constant = 4.962×10^{-10} year^{-1}) to ^{40}Ca (Dickin 2005). For example, ^{40}K–^{40}Ca measurements were performed to quantify the contribution of crustal silicates to the marine calcium cycle (Caro et al. 2010).

The electron configuration of calcium is $1s^2 2s^2 2p^6 3s^2 3p^6 4s^2$, while its valence state is +2, forming ionic bonds with nonmetal elements. Its nonbonded atomic radius is 197 pm; its covalent radius is 174 pm, along with a strong electronegativity of 1.00 on the Pauling scale and an electron affinity of 2.369 kJ.mol^{-1} (Coursey et al. 2010; Haynes 2015). Calcium has a density of 1,550 kg.m^{-3} at 20 °C. Calcium salts are more or less soluble in water; indeed, at 25 °C, the solubility products of calcite (trigonal $CaCO_3$), aragonite (orthorhombic $CaCO_3$), gypsum ($CaSO_4.2H_2O$), anhydrite ($CaSO_4$), and antarcticite ($CaCl_2.6H_2O$) are $10^{-8.48}$, $10^{-8.34}$, $10^{-4.58}$, $10^{-4.36}$, and $10^{-4.09}$, respectively. Hydroxyapatite, the biomineral constituting the skeleton of vertebrates, has a much lower solubility product of $10^{-54.45}$ (Fig. 2). Calcium is also characterized by a specific heat capacity of 653 J.kg^{-1}.K^{-1}.

History and Use

The name calcium originates from the Latin word “calx” that means “the ashy remaining substance after burning,” i.e., the “lime.” In nature, calcium does not occur in its elemental form but bounds to oxygen or halogens (fluorite CaF_2). Calcium compounds, such as quick lime (CaO), slaked

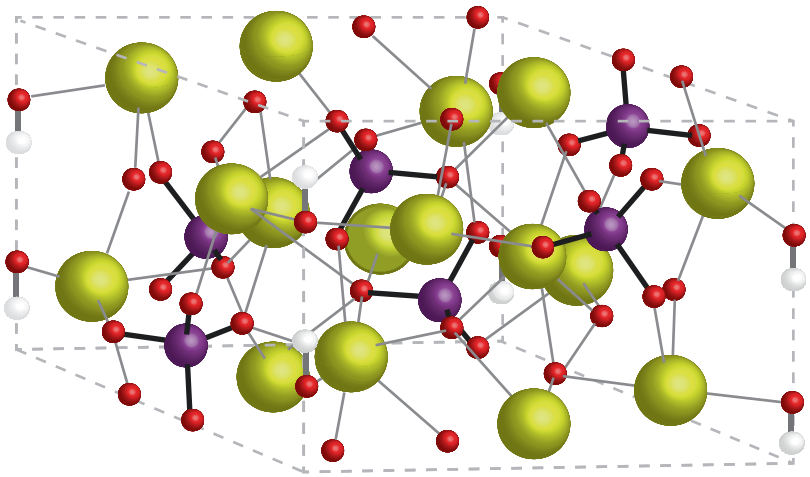

Calcium, Fig. 2 Crystal lattice of hydroxyapatite. Atomic symbols: *Yellow* calcium, *dark gray* carbon, *red* oxygen, *white* hydrogen, *purple* phosphorus

lime ($Ca(OH)_2$), limestone ($CaCO_3$), gypsum ($CaSO_4.2H_2O$), anhydrite ($CaSO_4$), and hydroxyapatite ($Ca_5(PO_4)_3(OH)$), have all been known and used by human beings for several thousands of years. The Romans heated calx (limestone) to produce a decarbonation reaction leaving calcium oxide as the solid residue. While gypsum is a common component of wallboard for buildings and concrete for the construction of highways and bridges, it has also been used for centuries in the field of fine arts. Alabaster, which is the translucent variety of gypsum, is a sought-after mineral used for ornamental stonework and sculptures. Anhydrite is commonly used to produce industrial sulfuric acid.

Despite the use of calcium compounds for centuries, the element calcium was not isolated and identified until electricity was under control. Calcium as a metal species was first isolated by Sir Humphry Davy (1808). Calcium forms alloys with magnesium, aluminum, copper, and lead. Calcium bromide ($CaBr_2$), a white powder, has many uses and is present in fire retardants, drilling fluids, cooling agents in freezing mixtures, food preservatives, and medication for the treatment of anxiety. Quicklime (CaO) is, for example, used in water purification devices for drinking water production. Calcium favors the growth of symbiotic and nonsymbiotic nitrogen-fixing bacteria, which are critical for the growth of legumes.

Natural Abundance

Calcium is a lithophile element according to Goldschmidt's classification (Goldschmidt 1926); it is one of the most important rock-forming element (after Si, Al, and Na) at the Earth's surface with a crustal abundance of 41,500 ppm. Several minerals, rare to common, contain from ≈8 to 40 mol% of Ca (Table 1).

CI meteorites contain 9,110 ppm on average (Palme et al. 2014). In most chondrites, calcium is hosted by diopside ($CaMgSi_2O_6$), chlorapatite ($Ca_5(PO4)_3Cl$), and merrillite ($Ca_9Na(Mg,Fe)(PO_4)_7$) and also occurs in minor amounts in feldspars or orthopyroxene. Despite the strong lithophile property of calcium as mentioned above, it may occur as sulfides such as oldhamite ((Ca,Mg,Fe)S) in the reduced sulfide-rich enstatite chondrites. It is also worth noting that calcite, dolomite, and gypsum have been observed in Cl and C2 chondrites.

Calcium, Table 1 Molar content of calcium in the most common of Earth's crust minerals and biominerals

Mineral	Chemical formula	Ca mol%
Calcite, aragonite	$CaCO_3$	40.04
Dolomite	$CaMg(CO_3)_2$	21.73
Anhydrite	$CaSO_4$	29.44
Gypsum	$CaSO_4.2H_2O$	25.47
Anorthite	$CaAl_2Si_2O_8$	14.41
Wollastonite	$CaSiO_3$	34.50
Diopside	$CaMgSi_2O_6$	18.51
Hydroxyapatite	$Ca_5(PO_4)_3(OH)$	07.98
Fluorite	CaF_2	51.33
Antarcticite	$CaCl_2.6H_2O$	26.67

Of special interest are the calcium-aluminum-rich inclusions (CAIs), considered to belong to the first solid grains that condensed in the nebular disc surrounding the protosun. Pb-Pb dating of these CAIs indicates that they formed 4,568.2 My ago, the oldest age obtained for any solar system object so far (Bouvier and Wadhwa 2010).

Palme and O'Neill (2014) have estimated the upper primitive mantle CaO content at 3.78 wt%. Mid-ocean ridge basalts contain between 11.39 and 11.46 wt% of CaO according to measurements of fresh basaltic glass (Gale et al. 2013; White and Klein 2014). Wedepohl (1995) calculated that the CaO content of the bulk continental crust is close to 5.5 wt‰. The upper continental crust contains an average CaO concentration of 3.59 ± 0.2 wt% (Rudnick and Gao 2005).

Seawater calcium abundance is in the range 412–420 ppm; consequently it is the fifth most abundant element after Cl,

Na, Mg, and S (Bruland et al. 2014) dissolved in seawater (O_2 gas excluded). The calcium content increases from the ocean surface down to depths of 2,000–3,000 m and then decreases again down to the seafloor (de Villiers 1998). The calcium content was found to be closely related to carbonate alkalinity according to the temperature and pH dependence of calcium carbonate solubility in seawater. However, de Villiers (1998) observed that the deep ocean contains higher amounts of dissolved calcium than predicted by the thermodynamics of calcium carbonate dissolution. The Ca excess occurring at these intermediate depths could correspond to the calcium contribution from hydrothermal systems located at the axis of mid-ocean ridges (de Villiers 1998).

Dissolved calcium abundance and its rather homogeneous distribution in seawater are related to its relative high residence time close to 1 My. Consequently Ca is considered as a "conservative" element in seawater.

The world's average polluted river water contains 14.7 ppm of calcium, with anthropogenic contributions corresponding to 9% of the total concentration. The main non-anthropogenic calcium fluxes to rivers result from the dissolution of calcium and magnesium carbonates (≈70% of the total flux), evaporites such as gypsum or anhydrite (≈10% of the total flux), and Ca-feldspars or Ca-pyroxenes hosted by basaltic or ultrabasic rocks (≈20% of the total flux).

Most lakes contain from a few ppm to a few dozens of ppm of dissolved calcium. The highly alkaline saline Mono Lake, USA, has only a $[Ca^{2+}] \approx 6$ mg.L^{-1} for a pH of 9.8 and a salinity S of 81 g.L^{-1} (Domagalski et al. 1990). Acid lakes are generally characterized by higher concentrations of dissolved calcium, typically in the range 50–100 ppm (Lake Ontario, Canada).

Geochemical Cycling

The long-term (My scale) calcium geochemical cycle is basically defined by four reservoirs, which are (1) the upper continental crust, (2) the marine biomass made of calcifying organisms, (3) the marine sediments, and (4) the oceanic crust. Connecting fluxes are contributed by (1) the rivers; (2) the dissolution and precipitation of sediments (carbonates and sulfates); (3) the primary production of calcifying organisms with the most important planktonic producers being the coccolithophores, the foraminifera, and the euthecosomatous pteropods (Fabry et al. 2008); and (4) the seawater-basalt interactions associated with hydrothermal activity located at mid-ocean ridges.

The two net input Ca fluxes to the oceans are the river and hydrothermal fluxes. The first one is obtained by multiplying the world river flux (3.74×10^{16} kg of water per year) by the average river Ca content of 14.7 ppm, which gives a calcium flux of 5.5×10^{11} kg.year^{-1}. The second flux corresponds to the release of dissolved calcium at mid-ocean ridges during the hydrothermal alteration of clinopyroxene (diopside; (Ca, Mg)Si_2O_6) into amphibole (tremolite; $Ca_2Mg_5(Si_8O_{22})(OH)_2$) (6) and Ca-plagioclase (anorthite; $CaAl_2Si_2O_8$) into Na-plagioclase (albite; $NaAlSi_3O_8$).

This hydrothermal flux was estimated close to 1×10^{11} kg of Ca per year (Alt et al. 1986; Bednarz and Schmincke 1989). Consequently, the total input flux to the oceans is about 6.5×10^{11} kg.year^{-1}.

Assuming that the calcium geochemical cycle is close to steady state, output fluxes from the oceans to other solid reservoirs should more or less balance the net input flux estimated above. A first output flux is the precipitation of calcium carbonate in the tensile fractures that develop in the oceanic crust during its off-axis cooling.

Alt and Teagle (1999) calculated a flux of about 1.4×10^{11} kg Ca.year^{-1}. A second flux corresponds to the subduction of sediments that operates at a rate of 0.5 km^3. year^{-1} with a present-day carbon content of 8,200 ppm. These data allow the calculation of an average carbon flux of 1.2×10^{10} kg.year^{-1}. The biogenic contribution to this C flux is evaluated at 15% of the total sedimentary flux, thus corresponding to a Ca flux of 1.7×10^{11} kg Ca.year^{-1}.

Consequently, the difference between the net input and output flux is 3.4×10^{11} kg Ca.year^{-1}. Such an apparent "missing output Ca flux" could be explained by the oceanic primary productivity involving the calcifying organisms. Indeed, the dissolution of carbonated skeletons from dead organisms does not match the rate of calcification in the oceans. According to Langer et al. (1997), the total present-day $CaCO_3$ production in the world oceans is 3.27×10^{12} kg. year^{-1}, which corresponds to a flux of 1.31×10^{12} kg Ca. year^{-1}. A part of this flux could have contributed to the progressive integration of carbonates into the upper continental crust through the accumulation of carbonates in passive margins. The amount of Ca trapped into carbonates (limestones and dolomites) (Taylor and McLennan 1985) was estimated close to 1.8×10^{20} kg Ca. The apparent "missing output flux of Ca" from the oceans could be thus explained by the storage of carbonates in passive margins during the last 530 My (≈ the Phanerozoic) at a rate of 3.4×10^{11} kg of Ca.year^{-1}.

It is also worthy to note that the budget of Ca^{2+} in the oceans is linked to the carbon cycle through the dissolution and precipitation (8) of carbonates. One mole of carbon is trapped during carbonate precipitation, but one mole is released as CO_2. The dissolution of $CaCO_3$ tends to buffer the pH of the oceans when atmospheric pCO_2 is rising.

Strong connections operate between Earth's climate modes and geochemical cycles. Such relationships are evidenced by secular variations in seawater chemistry over the Phanerozoic, which have been recorded in the composition of marine evaporites (halite) and biogenic carbonates

such as corals and foraminifera. The "greenhouse" climatic conditions of both Jurassic and Cretaceous were characterized by low molar Mg/Ca ratios (≈1) that favored the precipitation of calcitic cements (the so-called "calcite" seas), while the "icehouse" Tertiary has been a period of high Mg/Ca ratios (from 3 to 5) that produced inorganic aragonite cements in the so-called "aragonite" seas (Gothmann et al. 2015).

On the continents, massive precipitation of calcium carbonates (travertines) may occur associated with geothermal waters. In most cases, geothermal waters originate from meteoric waters that infiltrate the continental crust through fissures and cracks and that are heated up at the contact of magma chambers beneath volcanoes or slowly cooling plutonic rocks such as granites. Carbonate precipitation then occurs as a result of the degassing of carbon dioxide when calcium concentrations higher than 100 $mg.L^{-1}$.

Biological Utilization and Toxicity

Calcium is of primordial importance for the growth of skeletons of many invertebrates (e.g., mollusks, foraminifera, coccolithophores, corals, bryozoans) and all vertebrates. Calcium ions are the most important messengers between cells in living organisms. Calcium oxalates, such as weddellite ($Ca(C_2O_4).2(H_2O)$) and whewellite ($Ca(C_2O_4).(H_2O)$), are present in soils and play an important role in the availability of nutrients to plant roots (Graustein et al. 1977).

In the oceans, phytoplankton developed the remarkable ability to regulate the concentration of Ca^{2+} in the intracellular cytosol. Over geological times, most taxonomic groups were thus able to cope with variations in seawater chemistry (Müller et al. 2015). For example, coccolithophores were abundant during the Cretaceous, a warm period most likely characterized by high levels in seawater dissolved calcium abundance (Müller et al. 2015).

Calcifying marine organisms is commonly considered to be highly sensitive to a decrease in oceanic pH because calcification rates are expected to decrease. However, in situ observations, laboratory experiments, and paleontological records indicate that numerous marine organisms are capable of adjusting their physiological functions to deal with an increase in seawater acidity (Findlay et al. 2009). For example, McCulloch et al. 2012) have shown that cold-water scleractinian corals have a strong resilience to oceanic acidification.

Calcium is the most abundant of the metallic elements in the human body. The average adult body contains about 1 kg of calcium, 99% of which is located in the hydroxyapatite mineral constituting the skeleton. While old bone is regularly eliminated by osteoclasts, new bone is mineralized by osteoblasts in fibroblasts that secrete and mineralize the bone matrix. The mineralized extracellular matrix is mainly composed of type I collagen and osteocalcin (a noncollagenous protein), matrix Gla protein, osteopontin, bone sialoprotein, bone morphogenetic proteins (BMPs), transforming growth factor-beta (TGF-β), and hydroxyapatite.

If calcium is crucial for living organisms including human beings, intake of calcium in excess may provoke arterial calcification and may also increase the risk of cardiovascular diseases in elderly persons. Even healthy kidneys have a restricted capability for eliminating excessive calcium derived from the diet. So high calcium intakes in adults should be avoided since they have relatively limited or no positive consequences for bone mineral density (Anderson and Klemmer 2013).

Summary

This lithophile element is one of the most important rock-forming elements of the Earth. The budget of Ca^{2+} in the oceans is linked to the carbon cycle through dissolution and precipitation of $CaCO_3$.

Calcium is a critical component of skeletons of many invertebrates and all vertebrates, and its ions are the most important messengers between cells, resulting in Ca being the most abundant of the metallic elements in the human body.

Cross-References

- ▶ Acid–Base Reactions
- ▶ Alkali and Alkaline Earth Metals
- ▶ Carbonate Minerals and the CO2-Carbonic Acid System
- ▶ Calcium Isotopes
- ▶ Carbon Cycle
- ▶ Carbonate Compensation Depth
- ▶ Carbonate Minerals and the CO2-Carbonic Acid System
- ▶ Carbonate Compensation Depth
- ▶ Chondrites
- ▶ Geochemical Thermodynamics
- ▶ Lithophile Elements
- ▶ Ocean Biochemical Cycling and Trace Elements
- ▶ Refractory Inclusions in Chondritic Meteorites
- ▶ Solubility
- ▶ Sulfate Minerals

References

Alt JC, Teagle DA (1999) The uptake of carbon during alteration of ocean crust. Geochim Cosmochim Acta 63:1527–1535

Alt JC, Honnorez J, Laverne C, Emmermann R (1986) Hydrothermal alteration of a 1 km section through the upper oceanic crust, Deep Sea Drilling Project Hole 504B: mineralogy, chemistry and evolution of

seawater-basalt interactions. J Geophys Res Solid Earth 91:10309–10335
Anderson JJ, Klemmer PJ (2013) Risk of high dietary calcium for arterial calcification in older adults. Forum Nutr 5:3964–3974
Bednarz U, Schmincke HU (1989) Mass transfer during sub-seafloor alteration of the upper Troodos crust (Cyprus). Contrib Mineral Petrol 102:93–101
Bouvier A, Wadhwa M (2010) The age of the Solar System redefined by the oldest Pb–Pb age of a meteoritic inclusion. Nat Geosci 3:637–641
Bruland KW, Middag R, Lohan MC (2014) 8.2 – controls of trace metals in seawater A2 – Holland, Heinrich D. In: Turekian KK (ed) Treatise on geochemistry, 2nd edn. Elsevier, Oxford, pp 19–51
Caro G, Papanastassiou DA, Wasserburg GJ (2010) ^{40}K-^{40}Ca isotopic constraints on the oceanic calcium cycle. Earth Planet Sci Lett 296:124–132
Coursey JS, Schwab DJ, Tsai JJ, Dragoset RA (2010) Atomic weights and isotopic compositions. National Institute of Standards and Technology, Gaithersburg
Davy H (1808) The Bakerian lecture: on some new phenomena of chemical changes produced by electricity, particularly the decomposition of the fixed alkalies, and the exhibition of the new substances which constitute their bases; and on the general nature of alkaline bodies. Phil Trans R Soc London 98:1–44
de Villiers S (1998) Excess dissolved Ca in the deep ocean: a hydrothermal hypothesis. Earth Planet Sci Lett 164:627–641
Dickin AP (2005) Radiogenic isotope geology. Cambridge University Press, Cambridge. 492 pp
Domagalski JL, Eugster HP, Jones BF (1990) Trace metal geochemistry of Walker, Mono, and Great Salt Lakes. Fluid-Miner Interactions 2:315–353
Fabry VJ, Seibel BA, Feely RA, Orr JC (2008) Impacts of ocean acidification on marine fauna and ecosystem processes. ICES J Mar Sci 65:414–432
Findlay HS, Wood HL, Kendall MA, Spicer JI, Twitchett RJ, Widdicombe S (2009) Calcification, a physiological process to be considered in the context of the whole organism. Biogeosci Discuss 6:2267–2284
Gale A, Dalton CA, Langmuir CH, Su Y, Schilling J-G (2013) The mean composition of ocean ridge basalts. Geochem Geophys Geosyst 14(3):489–518
Goldschmidt VM (1926) Geochemische Verteilungsgesetze der Elemente. VII: Die Gesetze der Krystallochemie. Skrifter Norske Videnskaps Akad, Oslo, (I) Mat. Natur. K1, Oslo
Gothmann AM, Stolarski J, Adkins JF, Schoene B, Dennis KJ, Schrag DP, Mazur M, Bender ML (2015) Fossil corals as an archive of secular variations in seawater chemistry since the Mesozoic. Geochim Cosmochim Acta 160:188–208
Graustein WC, Cromack K, Sollins P (1977) Calcium oxalate: occurrence in soils and effect on nutrient and geochemical cycles. Science 198:1252–1254
Haynes WM (2015) CRC handbook of chemistry and physics, 95th edn. CRC Press & Taylor and Francis, Boca Raton
Langer MR, Silk MT, Lipps JH (1997) Global Ocean carbonate and carbon dioxide production; the role of reef Foraminifera. J Foram Res 27:271–277
McCulloch M, Trotter J, Montagna P, Falter J, Dumbar R, Freiwald A, Försterra G, López Correa M, Maier C, Rüggeberg A, Taviani M (2012) Resilience of cold-water scleractinian corals to ocean acidification: boron isotopic systematics of pH and saturation state up-regulation. Geochim Cosmochim Acta 87:21–34
Müller MN, Barcelos e Ramos J, Schulz KG, Riebesell U, Kazmierczak J, Gallo F, Mackinder L, Li Y, Nesterenko PN, Trull TW, Hallegraeff GM (2015) Phytoplankton calcification as an effective mechanism to prevent cellular calcium poisoning. Biogeosci Discuss 12:6493–6501
Palme H, O'Neill HSC (2014) 3.1 – Cosmochemical estimates of mantle composition. In: Turekian HDHK (ed) Treatise on geochemistry, 2nd edn. Elsevier, Oxford, pp 1–39
Palme H, Lodders K, Jones A (2014) 2.2 – solar system abundances of the elements A2. In: Holland HD, Turekian KK (eds) Treatise on geochemistry, 2nd edn. Elsevier, Oxford, pp 15–36
Rudnick RL, Gao S (2005) Composition of the continental crust. In: Rudnick RL (ed) Treatise on geochemistry, The crust, vol 3. Elsevier-Pergamon, Oxford, pp 1–64
Taylor SR, McLennan SM (1985) The continental crust: its composition and evolution. An examination of the geochemical record preserved in sedimentary rocks. Blackwell Scientific Publications, Oxford. 312 pp
Wedepohl KH (1995) The composition of the continental crust. Geochim Cosmochim Acta 59:1217–1232
White WM, Klein EM (2014) 4.13 – composition of the oceanic crust. In: Holland HD, Turekian KK (eds) Treatise on geochemistry, 2nd edn. Elsevier, Oxford, pp 457–496

Calcium Isotopes

Juraj Farkaš
Department of Earth Sciences, School of Physical Sciences, University of Adelaide, Adelaide, South Australia, Australia
Department of Geochemistry, Czech Geological Survey, Prague, Czech Republic

Introduction

Calcium (Ca) is the fifth most abundant element and dissolved ion, respectively, in the Earth's crust and the oceans. Ca is also an essential nutrient for marine and terrestrial organisms where it regulates metabolic processes (i.e., calcium homeostasis) as well as the production of skeletal structures (i.e., bones and calcitic shells). Importantly, Ca has six naturally occurring isotopes (^{40}Ca, ^{42}Ca, ^{43}Ca, ^{44}Ca, ^{46}Ca, and ^{48}Ca), where ^{40}Ca is the most abundant and also produced by the radioactive decay of potassium ^{40}K with a half-life of ~1.277 billion years (Byr). Due to its numerous isotopes and a high mobility in near-surface environments, Ca represents a valuable tracer for earth system processes and biogeochemical pathways. The isotope studies of Ca are thus relevant for a better understanding of global elemental cycles and mutual interactions between lithosphere, hydrosphere, and biosphere. In this contribution, we present the stable Ca isotope variations as delta values ($\delta^{44/40}$Ca, in per mil) normalized to NIST 915a; and the radiogenic ^{40}Ca isotope anomalies are expressed as epsilon units (εCa, in parts per ten thousand).

The global biogeochemical cycle of Ca is tightly linked to other major elemental cycles, including the global carbon (C) cycle, which is facilitated through processes such as continental weathering, hydrothermal exchange at

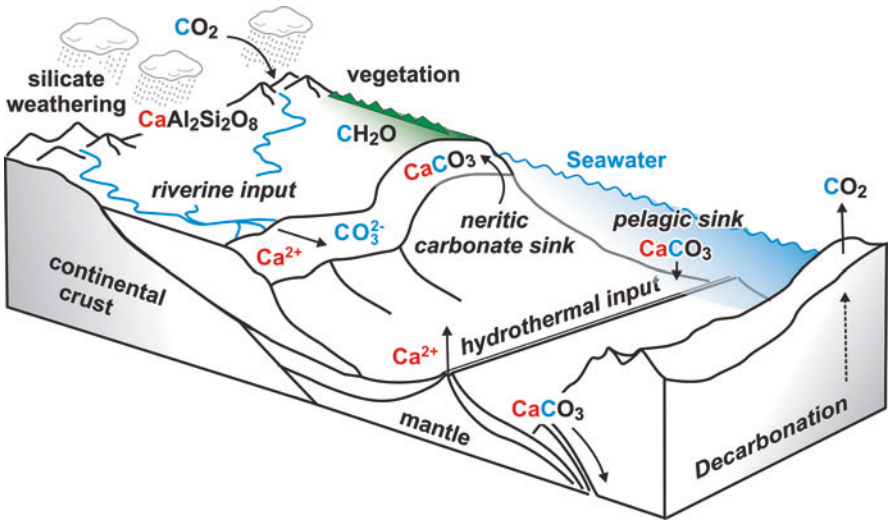

Calcium Isotopes, Fig. 1 A schematic diagram showing the links between the global Ca and C cycles in the earth surface environments, including the main sources and sinks of Ca^{2+} and C O_3^{2-} ions in the modern oceans (Modified after Husson et al. 2015)

mid-ocean ridges, and/or the formation and deposition of marine carbonates (see Fig. 1). The majority of Ca delivered to the oceans by rivers is primarily derived from the dissolution of continental crust, which contains Ca-bearing carbonate and silicate minerals, expressed by simplified chemical formulas $CaCO_3$ and $CaAl_2Si_2O_8$, respectively. Although carbonates are more soluble, it is the dissolution of silicates that consumes carbon dioxide (CO_2) from the atmosphere, which in turn regulates the Earth's climate over geological time, according to the following simplified reaction (cf., Berner and Berner 1997):

$$\begin{aligned} &CaAl_2Si_2O_8\ (\text{silicate}) + CO_2\ (\text{gas}) \\ &\quad \Rightarrow CaCO_3\ (\text{carbonate}) + Al_2O_3 + 2SiO_2 \end{aligned} \qquad (1)$$

A reversed process of this reaction is the "decarbonation" of limestones in the subduction zones, where the increasing temperature decomposes carbonate minerals and liberates CO_2 gas which can be then reintroduced back into the atmosphere via volcanic systems (see Fig. 1). The tight coupling between the global Ca and C cycles in terrestrial and marine environments highlights the importance of Ca isotope studies for a better understanding of the global C cycle and its role in the modulation of atmospheric CO_2 levels.

Stable Calcium Isotope Variations and Global Ca Cycle

The stable, or mass-dependent, isotope fractionation of Ca in nature is expressed as delta (δ) notation based on the measured isotope ratios of $^{44}Ca/^{40}Ca$ (or alternatively also $^{44}Ca/^{42}Ca$) in a sample relative to a standard, according to the following relation:

$$\delta^{44/40}Ca = \left(\frac{\left(^{44}Ca/^{40}Ca\right)_{\text{sample}}}{\left(^{44}Ca/^{40}Ca\right)_{\text{standard}}} - 1 \right) \cdot 10^3 \qquad (2)$$

where the reported delta values ($\delta^{44/40}Ca$) are in "per mil" (‰, parts per thousand), and here normalized to a standard NIST 915a. The recent compilation of $\delta^{44/40}Ca$ values from major geological and biological reservoirs (Fantle and Tipper 2014) shows an overall range of about 4 ‰ for various terrestrial and marine samples (see Fig. 2; $n > 2600$ measurements), where the isotopically heaviest Ca reservoir on Earth is the ocean water ($\delta^{44/40}Ca \approx 1.9$ ‰). In contrast, the isotopically lightest Ca is associated with vegetation (i.e., terrestrial plants) and/or biologically precipitated marine carbonates (i.e., calcitic and aragonitic shells). This points to a critical role of organisms and the biosphere in fractionating the stable Ca isotopes in the Earth's surface environments, due to a preferential incorporation of lighter Ca isotopes by plants and animals, which is a common feature of the stable isotope systems of other bioessential elements including carbon (Hoefs 2015). Nevertheless, pure abiotic processes such as (i) the inorganic precipitation of $CaCO_3$ and $CaSO_4$ minerals due to an oversaturation of natural waters, and/or (ii) the adsorption of dissolved Ca^{2+} ions on clays and exchangeable sites of particles can also lead to a significant fractionation of stable Ca isotopes at low temperatures (Fantle and Tipper 2014 and references therein).

The magnitude of stable Ca isotope fractionation in nature diminishes with an increasing temperature (being proportional to $1/T^2$ at high temperatures), and thus igneous silicate Ca reservoirs exhibit much narrower range of $\delta^{44/40}Ca$ values (about 2 ‰) compared to marine carbonates and/or the organically complexed Ca (see Fig. 2). Nevertheless, recent studies of Ca isotope fractionation in high-temperature

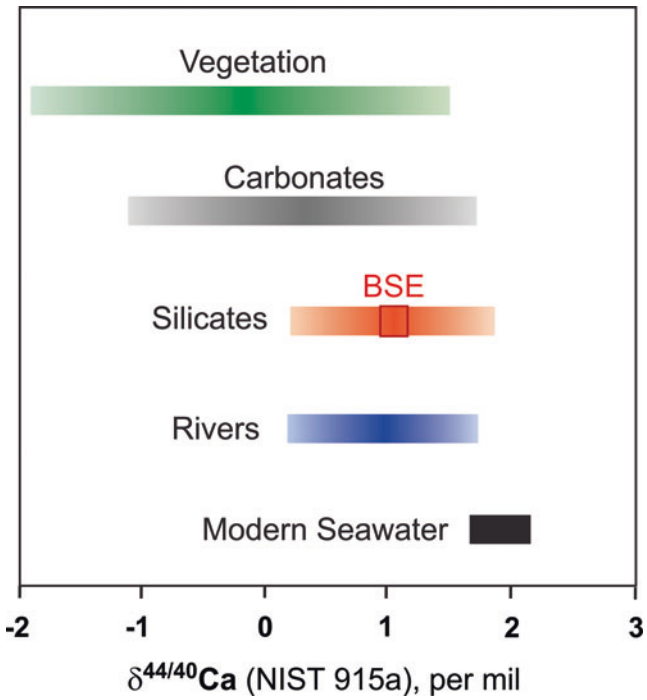

Calcium Isotopes, Fig. 2 A compilation of the published Ca isotope data from terrestrial samples (more than 2600 measurements) presented on a common delta scale: $\delta^{44/40}$Ca relative to NIST 915a (Modified after Fantle and Tipper 2014). *BSE* Bulk Silicate Earth (After Huang et al. 2010)

geological settings revealed systematic behavior of the $\delta^{44/40}$Ca proxy in certain igneous rocks and silicate minerals (Schiller et al. 2016 and references therein). Specifically, there is a general coupling between Ca isotopes and Ca and Mg contents in ultramafic rocks (i.e., dunite, peridotite, komatiite), where $\delta^{44/40}$Ca values become higher (i.e., heavier) with decreasing CaO and increasing MgO contents, but such trend has not been documented for felsic and mafic rocks (Schiller et al. 2016 and references therein). Complementary to this isotopically heavy Ca source in ultramafic rocks is the isotopically light Ca present in serpentinized slab mantle rocks, suggesting that perhaps dehydration of slab-mantle serpentinite can produce fluids with high $\delta^{44/40}$Ca that could be then imparted to ultramafic rocks via metasomatisms (Schiller et al. 2016 and references therein). Moreover, the Ca isotope analysis of mineral separates from mantle xenoliths and/or granitic rocks revealed systematic differences in $\delta^{44/40}$Ca signatures of individual minerals, which have been interpreted to reflect either a high temperature equilibrium isotope fractionation or isotope effects generated by igneous differentiation processes (Schiller et al. 2016 and references therein). Overall, the average $\delta^{44/40}$Ca of silicate rocks is close to 1 ‰, which is also our best estimate for the Ca isotope composition of the *bulk silicate Earth* (BSE), the latter constrained by the analysis of mineral separates from mantle xenolithes and bulk mafic rocks (cf., DePaolo 2004; Huang et al. 2010).

Apart from the unanticipated and relatively large (up to 0.8 ‰) high-temperature fractionation of Ca isotopes in the Earth's mantle, another intriguing and currently unresolved aspect of the terrestrial Ca isotope cycle is the fact the mean $\delta^{44/40}$Ca signature of the global riverine Ca flux of about 0.9 ‰ overlaps with that of the silicate Ca reservoir ($\delta^{44/40}$Ca of ~1 ‰) but is systematically higher than the mean $\delta^{44/40}$Ca of carbonates ($\delta^{44/40}$Ca of ~0.6 ‰; Fantle and Tipper 2014). This finding is unexpected considering that previous studies suggested that the majority (>75%) of Ca in the global riverine flux should be derived from carbonates (Gaillardet et al. 1999; Berner and Berner 2012). Hence, one would expect that the mean $\delta^{44/40}$Ca signature of the global riverine flux to be much lower and closer to carbonate sources, i.e., somewhere between 0.6 and 0.7 ‰, based on a simple isotope mass-balance constraints using available data (cf., Fantle and Tipper 2014). Accordingly, either the current estimates of silicate vs. carbonate contributions of Ca to the global riverine flux are incorrect (i.e., the silicate-derived Ca contribution is underestimated), or there is an ongoing fractionation of Ca isotopes during the weathering and transport of Ca^{2+} ions that shifts the riverine $\delta^{44/40}$Ca to higher values relative to those observed in the source rocks (Fantle and Tipper 2014).

Radiogenic Calcium Isotopes in Geological Reservoirs

The radiogenic, or mass independent, isotope variation of ^{40}Ca in nature is expressed as an epsilon (ε) notation in parts per ten thousand (10^4), relative to the Earth's mantle reservoir, according to the following relation (Marshall and DePaolo 1982):

$$\varepsilon_{Ca} = \left[\left({}^{40}Ca/{}^{n}Ca \right)_{sample} / \left({}^{40}Ca/{}^{n}Ca \right)_{mantle} - 1 \right] \cdot 10^4 \quad (3)$$

where n is 44 or 42, and the Ca isotope ratios of sample and mantle are after an "internal normalization" following an exponential law for the correction of an instrumental fractionation during the isotope analysis. The radiogenic isotope of calcium, ^{40}Ca, is the product of radioactive decay of potassium ^{40}K, with a half-life of 1.277 billion years; however, only about 89.5% of the ^{40}K decay results in the production of ^{40}Ca and the remaining 10.5% produce ^{40}Ar. Due to the relatively short half-life of ^{40}K compared to the age of the Earth, minerals and rock that crystallized in Precambrian and had high initial K/Ca ratios (e.g., the continental crust containing K-rich minerals like potassium feldspar and biotite) can accumulate significant amount of the radiogenic ^{40}Ca over time, thus yielding positive epsilon ε_{Ca} values.

The potential of a radiogenic ε_{Ca} tracer for the earth system evolution studies has been explored by Kreissig and Elliott (2005) to distinguish between two possible end-member scenarios for the early crustal growth (i.e., "steady-state" vs. "continuous" growth models) and concluded that Ca isotope data provide little support for the "steady-state" model. However, this study also found that the radiogenic Ca isotope proxy is not a robust tracer of crustal growth due to its sensitivity to secondary processes such as potassium metasomatism and/or the Ca isotope exchange during metamorphic events. More recent studies, performed both in laboratory (Ryu et al. 2011) and natural settings (Farkaš et al. 2011; Hindshaw et al. 2011), applied the ε_{Ca} proxy to investigate the weathering processes in granitic rocks and the associated release of a radiogenic ^{40}Ca from K-rich minerals (i.e., feldspar and biotite), with implications for mineral weathering, soil formation, and the sources of bioavailable Ca^{2+} for plants at base-poor granitic sites.

Future Directions in Ca Isotope Research

Aside from the abovementioned problem regarding the unexpectedly high $\delta^{44/40}Ca$ in the global riverine flux, compared to what is anticipated based on the estimates of carbonate vs. silicate partitioning of Ca in the world's rivers (Fantle and Tipper 2014), there are also unresolved issues related to the interpretation of Ca isotope variability observed in igneous rocks (Schiller et al. 2016 and references therein) and marine sedimentary archives (Fantle and Tipper 2014); the latter relevant for the reconstructions of past changes in the oceanic Ca cycle. Numerous studies aimed to constrain the Ca isotope evolution of seawater over different time intervals (e.g., Heuser et al. 2005; Farkaš et al. 2007; Payne et al. 2010; Blättler et al. 2011), using various marine archives such as bulk carbonate sediments, calcitic shells, marine barite, and phosphate. As pointed out by Fantle and Tipper (2014), such different approaches and recording phases have led to some conflicting results and uncertainties in terms of the reconstructed $\delta^{44/40}Ca$ evolution of the past seawater. Since then, more work has been done on Ca isotopes in the marine Ca cycle, particularly with the emphasis on "deep times" including Paleozoic and Neoproterozoic (e.g., Blättler and Higgins 2014; Kasemann et al. 2014; Du Vivier et al. 2015; Husson et al. 2015; Farkaš et al. 2016), yet the uncertainty with respect to the reconstructed $\delta^{44/40}Ca$ of paleo-seawater remains, and thus a more systematic research towards a better understanding of a marine $\delta^{44/40}Ca$ proxy in different mineral archives and depositional environments (e.g., *open* vs. *restricted* settings) is currently of a high priority. First pioneering studies addressing these issues have been recently performed, specifically Holmden et al. (2012a) investigated the effects of submarine groundwater (SGD) and a "local elemental cycling" on the marine $\delta^{44/40}Ca$ proxy in a modern shallow-lagoon environment; and Hinojosa et al. (2012) utilized a "multiple-archive" approach (i.e., based on marine carbonates and phosphates) to constrain the Ca isotope composition of paleo-seawater. More work following these directions is needed, including laboratory-controlled precipitation and culturing experiments (cf., Tang et al. 2008), to realize the full potential of the Ca isotope proxy for the paleoceanographic and earth system evolution studies.

Finally, due to the different residence times of Ca and C in the oceans (i.e., 10^6 vs. 10^5 years, respectively), the marine $\delta^{44/40}Ca$ and $\delta^{13}C$ proxies are expected to respond differently to perturbations in the oceanic Ca and C cycles, assuming that these occurred in an "open ocean" settings (cf., Holmden et al. 2012b; Farkaš et al. 2016). Hence, any positive or negative $\delta^{13}C$ excursion recorded in marine archives should recover much faster compared to a time needed for the recovery of a possible accompanying $\delta^{44/40}Ca$ excursion, due to an order of magnitude longer residence time of Ca in the oceans compared to C. Accordingly, future detail studies that will use a coupled $\delta^{44/40}Ca$ and $\delta^{13}C$ proxy approach might help to clarify if the observed C isotope excursions in marine carbonates are indeed an evidence of past changes in the *global* marine C cycle, or rather reflect diagenetic and/or *local* scale processes. The latter involving a locally enhanced bioproductivity and/or a mixing of different water masses (e.g., seawater, groundwater) and carbonate sediments (i.e., facies migration) within a basin, linked to eustatic sea-level fluctuations (cf., Holmden et al. 2012b; Husson et al. 2015; Farkaš et al. 2016).

Advances in Ca Isotope Analysis

Analytical challenges associated with a precise and accurate measurements of stable and radiogenic Ca isotopes have been recognized by the community for decades (cf., Boulyga 2010; Fantle and Tipper 2014), and it was really the development of a new generation of mass spectrometers (both TIMS and MC ICP MS) over the last ca. 10–15 years which opened up the possibilities to fully explore the research potential of Ca isotopes. Although, most of the instrumental and analytical issues are now resolved and well understood, the main limitation for a rapid expansion of the field of the Ca isotope biogeochemistry lies in the relatively time-consuming sample preparation (i.e., chemical purification of Ca) and the necessity for a longer analytical runs (i.e., ca. 1.5 h for TIMS). Fortunately, recent advances in semiautomated sample purification systems (cf., Romaniello et al. 2015; Husson et al. 2015) promise to significantly speed up this sample preparation step, thus allowing a higher and more efficient sample throughput, and possibly also a more rapid expansion of the field in the near future.

Summary and Conclusions

Calcium is the fifth most abundant element in the Earth's crust, and due to its numerous isotopes (^{40}Ca, ^{42}Ca, ^{43}Ca, ^{44}Ca, ^{46}Ca, and ^{48}Ca), it is also a valuable isotope tracer in many geological and biological systems. The natural variations in the Ca isotope composition can be produced by either mass-depended fractionation processes (i.e., $\delta^{44/40}$Ca and $\delta^{44/42}$Ca variations) or via a radioactive decay of potassium ^{40}K, which generates radiogenic ^{40}Ca isotopes (i.e., ε_{Ca} variations). Thus far, available studies documented approximately 4 per mil variation in $\delta^{44/40}$Ca in different terrestrial and marine samples, where the largest anomalies towards light Ca are produced due to a biological cycling of Ca both on land (i.e., plants, vegetation) and in the oceans (i.e., marine carbonates). In contrast, the isotopically heaviest Ca reservoir on Earth is the ocean water, which is thus complementary to the isotopically light Ca accumulated in marine carbonates. Relatively large Ca isotope variations (>0.5 per mil) have been documented in terrestrial igneous rocks, including ocean island basalts, granites, and mantle-derived rocks; thus implying that Ca isotopes can be also significantly fractionated during high-temperature processes.

Importantly, the biogeochemical cycle of Ca on Earth is tightly linked with the global C cycle and therefore the atmospheric CO_2, via processes such as continental weathering of carbonate/silicate rocks, hydrothermal reactions at mid-ocean ridges and off-axis centers, and the precipitation of shallow- and deep-water marine carbonates. Future detail Ca isotope studies on marine carbonate archives could thus help to better understand the functioning of the global C cycle and the origin of C isotope anomalies recorded in marine carbonate sediments.

Cross-References

- ▶ Alkali and Alkaline Earth Metals
- ▶ Calcium
- ▶ Carbonate Minerals and the CO_2-Carbonic Acid System
- ▶ Carbon Cycle
- ▶ Carbon Isotopes
- ▶ Geochronology and Radiogenic Isotopes
- ▶ Stable Isotope Geochemistry

References

Berner RA, Berner EK (1997) Silicate weathering and climate. In: Ruddiman WF (ed) Tectonic uplift and climate change. Plenum Press, New York, pp 313–327

Berner RA, Berner EK (2012) Global environment: water, air, and geochemical cycles. Princeton University Press, Princeton, p 488

Blättler CL, Higgins JA (2014) Calcium isotopes in evaporites record variations in Phanerozoic seawater SO_4 and Ca. Geology 42:711–714

Blättler CL, Jenkyns HC, Reynard LM, Henderson GM (2011) Significant increases in global weathering during Oceanic Anoxic Events 1a and 2 indicated by calcium isotopes. Earth Planet Sci Lett 309:77–88

Boulyga SF (2010) Calcium isotope analysis by mass spectrometry. Mass Spectrom Rev 29:685–716

DePaolo DJ (2004) Calcium isotopic variations produced by biological, kinetic, radiogenic and nucleosynthetic processes. Rev Mineral Geochem 55:255–288

Du Vivier ADC, Jacobson A, Lehn G, Selby D, Hurtgen MT, Sageman BB (2015) Ca isotope stratigraphy across the Cenomanian-Turonian OAE 2: links between volcanism, seawater geochemistry, and the carbonate fractionation factor. Earth Planet Sci Lett 416:121–131

Fantle MS, Tipper ET (2014) Calcium isotopes in the global biogeochemical Ca cycle: implications for development of a Ca isotope proxy. Earth Sci Rev 129:148–177

Farkaš J, Böhm F, Wallmann K, Blenkinsop J, Eisenhauer A, van Geldern R, Munnecke A, Voigt S, Veizer J (2007) Calcium isotope record of Phanerozoic oceans: implications for chemical evolution of seawater and its causative mechanisms. Geochim Cosmochim Acta 71:5117–5134

Farkaš J, Déjeant A, Novák M, Jacobsen SB (2011) Calcium isotope constraints on the uptake and sources of Ca^{2+} in a base-poor forest: a new concept of combining stable ($\delta^{44/42}$Ca) and radiogenic (εCa) signals. Geochim Cosmochim Acta 75:7031–7046

Farkaš J, Frýda J, Holmden C (2016) Calcium isotope constraints on marine carbon cycle and $CaCO_3$ deposition during the late Silurian (mid-Ludfordian) positive d13C excursion. Earth Planet Sci Lett. (in press). https://doi.org/10.1016/j.epsl.2016.06.038

Gaillardet J, Dupre B, Louvat P, Allegre CJ (1999) Global silicate weathering and CO_2 consumption rates deduced from the chemistry of large rivers. Chem Geol 159:3–30

Heuser A, Eisenhauer A, Böhm F, Wallmann K, Gussone N, Pearson PN, Nägler TF, Dullo WC (2005) Calcium isotope ($\delta^{44/40}$Ca) variations of Neogene planktonic foraminifera. Paleoceanography 20:PA2013

Hindshaw RS, Reynolds B, Wiederhold JG, Bourdon B (2011) Calcium isotopes in a proglacial weathering environment: Damma Glacier, Switzerland. Geochim Cosmochim Acta 75:106–118

Hinojosa JL, Brown ST, Chen J, DePaolo DJ, Paytan A, Shen SZ, Payne JL (2012) Evidence for end-Permian Ocean acidification from calcium isotopes in biogenic apatite. Geology 40:743–746

Hoefs J (2015) Stable isotope geochemistry. Springer, Berlin, p 389

Holmden C, Papanastassiou DA, Blanchon P, Evans S (2012a) $\delta^{44/40}$Ca variability in shallow water carbonates and the impact of submarine groundwater discharge on Ca-cycling in marine environments. Geochim Cosmochim Acta 83:179–194

Holmden C, Panchuk K, Finney S (2012b) Tightly coupled records of Ca and C isotope changes during the Hirnantian glaciation event in an epeiric sea settings. Geochim Cosmochim Acta 98:94–106

Huang S, Farkaš J, Jacobsen SB (2010) Calcium isotope fractionation between clinopyroxene and orthopyroxene from mantle peridotites. Earth Planet Sci Lett 292:337–344

Husson JM, Higgins JA, Maloof AC, Schoene B (2015) Ca and Mg isotope constraints on the origin of Earth's deepest δ^{13}C excursion. Geochim Cosmochim Acta 160:243–266

Kasemann SA, Pogge von Strandmann PAE, Prave AR, Fallick AE, Elliott T, Hoffmann KH (2014) Continental weathering following a Cryogenian glaciation: evidence from calcium and magnesium isotopes. Earth Planet Sci Lett 396:66–77

Kreissig K, Elliott T (2005) Ca isotope fingerprints of early crust-mantle evolution. Geochim Cosmochim Acta 69:165–176

Marshall BD, DePaolo DJ (1982) Precise age determinations and petrogenetic studies using K-Ca method. Geochim Cosmochim Acta 46:2537–2545

Payne JL, Turchyn AV, Paytan A, DePaolo DJ, Lehrmann DJ, Yu M, Wei J (2010) Calcium isotope constraints on the end-Permian mass extinction. Proc Natl Acad Sci 107:8543–8548

Romaniello SJ, Field MP, Smith HB, Gordon GW, Kim MH, Anbar AD (2015) Fully automated chromatographic purification of Sr and Ca for isotopic analysis. J Anal At Spectrom 30:1906–1912

Ryu JS, Jacobson AD, Holmden C, Lundstrom C, Zhang Z (2011) The major ion, $\delta^{44/40}$Ca, $\delta^{44/42}$Ca, and δ^{26}Mg geochemistry of granite weathering at pH = 1 and T = 25° C: power-law processes and the relative reactivity of minerals. Geochim Cosmochim Acta 75:6004–6026

Schiller M, Gussone N, Wombacher F (2016) High temperature geochemistry and cosmochemistry. In: Calcium stable isotope geochemistry. Springer, Berlin/Heidelberg

Tang J, Dietzel M, Böhm F, Köhler SJ, Eisenhauer A (2008) Sr^{2+}/Ca^{2+} and $^{44}Ca/^{40}Ca$ fractionation during inorganic calcite formation: II. Ca isotopes. Geochim Cosmochim Acta 72:3733–3745

Calorimetry

Masaki Akaogi
Department of Chemistry, Gakushuin University, Tokyo, Japan

Definition

In major areas in Earth Science, particularly geochemistry, petrology, and mineralogy, one of fundamental theoretical frameworks is thermodynamics which is expressed by thermodynamic functions: Gibbs energy, Helmholtz energy, enthalpy, entropy, heat capacity, etc. Calorimetry means experiments to measure heat changes which lead to the thermodynamic quantities. A calorimeter is an instrument used to measure the heat change associated with change of a substance. The heat change at a constant pressure is equal to enthalpy change. Calorimetric measurements are generally divided into two categories (Sorai 2004). The first one is measurement of heat capacity, and the second is measurement of heat of reaction.

Heat Capacity Measurement

The heat capacity is defined as absorbed heat energy divided by the associated temperature change in a substance, and customarily two different heat capacities are defined, C_p and C_v, relating to temperature change at constant pressure and to that at constant volume, respectively. The heat capacity is a function of intrinsic energy related to atomic motion or lattice vibration of the substance. At a temperature range between near 0 K and about room temperature, C_p is measured using adiabatic calorimetry and thermal relaxation calorimetry. The standard entropy at 298.15 K ($S^0_{298.15}$) of a pure crystalline substance is obtained by integrating C_p/T with T between 0 and 298.15 K. A latent heat of transition is also measured in the heat capacity measurement. For C_p measurement at temperature above room temperature, two methods can be adopted: differential scanning calorimetry up to about 2000 K and high-temperature drop calorimetry up to about 2500 K. Among the above techniques, the adiabatic calorimetry is most accurate but requires a sample of at least several grams, as well as in the high-temperature drop calorimetry. Instruments for differential scanning calorimetry and thermal relaxation calorimetry are commercially available and need a sample of only about 10–20 mg, though the methods are somewhat less accurate than the other two methods. However, it is generally not feasible to get a large amount of natural homogeneous samples or to synthesize pure materials of several grams, particularly at high pressure and high temperature.

Reaction Calorimetry

The second method of calorimetry used in Earth Science is reaction calorimetry, which is generally solution calorimetry to measure heat associated with dissolution of a substance in a solvent at a constant pressure, mostly atmospheric pressure. The experimental solution calorimetry is divided into two types: hydrofluoric acid solution calorimetry and high-temperature oxide melt solution calorimetry. In the former measurement, a sample is dissolved in HF at around 323 K, and in the latter a sample is dissolved in oxide melt such as lead borate and sodium molybdate at 1000–1100 K, in order to measure heat of solution of a substance. The heats of formation, transition, and reaction are calculated from the measured heats using thermochemical cycles. The heats of mixing of solid solutions and of glasses and heat associated with order-disorder transition can also be measured. Oxide melt solution calorimetry needs a sample of only several to several 10 mg and is widely used to various inorganic compounds including silicate minerals, metal oxides, hydrous phases, high-pressure phases, nanomaterials, etc.

Summary

Measurements of heat capacity and heat of reaction are fundamental experimental techniques to obtain the important thermodynamic quantities. A limited number of laboratories perform calorimetric measurements because the methods are specialized. For minerals and related inorganic substances of

geochemical, petrological, and mineralogical interests, calorimetrically measured data and derived data from them are summarized in several publications (e.g., Robie and Hemingway 1995; Navrotsky 1997, 2014).

Cross-References

- ▶ Enthalpy
- ▶ Entropy
- ▶ Equilibrium
- ▶ Free Energy
- ▶ Geochemical Thermodynamics
- ▶ Geothermometry and Geobarometry
- ▶ Heat Capacity
- ▶ Phase Equilibria

References

Navrotsky A (1997) Progress and new directions in high temperature calorimetry revisited. Phys Chem Minerals 24:222–241
Navrotsky A (2014) Progress and new directions in calorimetry: a 2014 perspective. J Am Ceram Soc 97:3349
Robie RA, Hemingway BS (1995) Thermodynamic properties of minerals and related substances at 298.15 K and 1 bar (10^5 Pascals) pressure and at higher temperatures. US Geol Surv 2131: 461pp
Sorai M (2004) Comprehensive handbook of calorimetry and thermal analysis. Wiley, London, 534 pp

Carbon

Adrian Jones
Department of Earth Sciences, University College London, London, UK

Element Data
Atomic Symbol: C
Atomic Number: 6
Atomic Weight: 12.0107
Isotopes and Abundances: ^{12}**C**: ~98.89%, ^{13}**C:** ~1.11%, ^{14}**C** $\sim 10^{-12}$
Atm Melting Point*: 3550 °C
1 Atm Boiling Point*: 4492 °C (101 kPa)
Common Valences: −4, 0, +2, +4
Ionic Radii: 30 pm (4+)
Pauling Electronegativity: 2.5
First Ionization Energy: 1086 kJmol^{-1}
(*continued*)

Chondritic (CI) Abundance: 3.65 wt%
Silicate Earth Abundance: 50–500 ppm
Crustal Abundance: ~1800 ppm
Seawater Abundance: ~28 ppm
Core Abundance: unknown 0.2–2%

Properties

Carbon has three isotopes, two are stable ^{12}C (98.89%) and ^{13}C (1.11%) plus a radioactive isotope ^{14}C ($\sim 10^{-12}$). The systematics of carbon isotopes yield important information about their environments and are discussed separately (Cross reference #1). ^{12}C is the standard which defines mass number 12 containing 6 protons, 6 neutrons, and 6 electrons.

The melting point of carbon is extremely high and varies with pressure*; in a carbon arc, it sublimes above ~5,530 °C, which is higher in temperature than any known metal. Consequently, carbon may have been the first element to condense from gas to solid in the protoplanetary nebula as nanodiamond or graphite, although oxidized forms are also abundant in the universe. The ability of hydrocarbons to bond with themselves is known as catenation and leads to more complex forms, such as cyclohexane, or even benzene. Hydrocarbons are hydrophobic. Some are abundant in the solar system as sampled widely in primitive undifferentiated meteorites like chondrites (Sephton 2002). Carbon-rich lakes of methane occur on Titan, and polycyclic aromatic hydrocarbons (PAHs) are abundant in nebulae. In carbonaceous chondrites, the average carbon abundance is 3.65 wt%, whereas in the bulk Earth estimates for carbon vary from 50 to 500 (Zhang and Zindler 1993; Marty 2012) and much of Earth's carbon from ~0.2 to 2 wt%, maybe in the core (Wood et al. 2013).

History and Use

Carbon (*from* Latin *carbo* meaning charcoal or coal), the element with atomic number 6, is the fourth most abundant element in the universe but is less abundant in the *differentiated* Earth. Carbon occurs naturally in pure elemental form, the two most famous crystalline allotropes of carbon are diamond (cubic, density 3.51 gcm^{-3}), the hardest known mineral, and graphite (hexagonal, density 2.266 gcm^{-3}), one of the softest and most refractory substances known. Other carbon allotropes of native carbon include crystalline lonsdaleite, chaoite, fullerenes, and graphene, plus several noncrystalline forms of glassy ("vitreous") carbon, nanofoam ("carbon aerogel"), and carbine (Hazen et al. 2013, Table 1).

In diamond, each carbon atom is bonded to four adjacent carbon atoms in tetrahedral coordination, with a C—C distance of ~1.54 A°, and C—C—C angles close to ideal 109.5°. This tetrahedral covalent bonding configuration reflects the hybridization of one 2 *s* and three 2*p* orbitals from each carbon atom to form four sp^3 orbitals. The framework structure of diamond leads to its superlative physical and chemical properties, including being the hardest known material (10 on *Moh's scale of hardness*). The absence of conduction electrons make diamond an insulator, yet paradoxically it is an excellent thermal conductor with ~five times better thermal conductivity than copper, which some jewellers can detect by touch. Diamond forms naturally at depths on Earth below ~150 km and is stable to temperatures and pressures greater than at the centre of the Earth (Oganov et al. 2013).

The optical properties of diamond feature the widest transparency of all known solids, extending from the UV (225 nm) to the far infrared, even at very high temperatures and radiation intensities. The combination of unique properties, including hardness and brilliance, have led to its preeminence as a gemstone. The best diamond gemstones are graded for qualities of the "four c's"; cut, color, clarity (absence of inclusions), and carat weight. One carat equals 1/5 g. The main impurity in "Type I" natural diamond is nitrogen, trapped in the lattice as single atoms, aggregates or clusters capable of changing color toward yellow and brown. The specific nitrogen residency in diamond provides a useful way of categorizing diamond, with nitrogen-free "Type II" diamond being the rarest (Cartigny 2005). A nitrogen-induced optical absorption in diamond around 270 nm has been identified in interstellar clouds. Diamond formed by shock during hypervelocity impact cratering usually contains the hexagonal polymorph called lonsdaleite, as at the 35 Ma Popigai impact crater in Siberia (Jones et al. 2016).

Since the 1950s, diamond synthesized at high pressures and temperatures (HPHT) replicates all of the mechanical properties of natural diamond suitable for industrial uses, but usually with different absorption and luminescence lines inherited from nickel and cobalt-rich metal solvents. Diamond can also be grown dynamically from low-pressure gas by chemical vapor deposition (CVD).

"Carbonado" is a variety of black or dark polycrystalline diamond, which is slightly porous, found only in Brazil and the Central African Republic, and possibly of nonterrestrial origin (Garai et al. 2006).

In graphite, graphene, fullerenes, and several types of amorphous and glassy carbon, the carbon atoms are covalently bonded in planar three-coordination, with typical C—C distances of ~1.42 A°, and C—C—C angles close to 120°. This trigonal coordination results from hybridization of carbon electrons where the *2 s* orbital mixes with two *2p* orbitals to form three sp^2 orbitals. Graphite is formed of electronically neutral, monatomic flat carbon layers, which bonds through relatively weak van der Waals attractions between the layers, separated by 3.41 A°. The layered structure leads to highly orientation-dependent or anisotropic properties and the weak interlayer bonding leads to uses as a lubricant and as pencil "lead." Graphite is highly refractory and its very high-temperature stability, >4,800 K, make it useful as a heater or in nuclear reactors as a neutron moderator.

Individual one atom-thick two-dimensional carbon layers when meticulously separated are known as graphene, a pure carbon allotrope ~200 times stronger than steel, with unique electronic and mechanical properties (Geim and Novoselov 2007) that can produce lightweight composite structures which can be transparent, flexible, and yet impermeable even to helium.

Geochemical Behavior

Carbon shows remarkable chemical flexibility with the ability to bond to itself and with more than 80 other elements, most commonly in 2-, 3-, and 4-coordination. Carbon has oxidation numbers ranging from −4 to +4 and can behave as a cation, as an anion, and as a neutral species in mineral phases with a spectacular variety of crystal structures, chemical bonding, and physical and chemical properties (Hazen et al. 2013). Carbon occurs in solids, liquids, and gases in variable amounts throughout the Earth, from the atmosphere and oceans to the crust-mantle and core, as both a major element and trace element. Carbon on Earth also moves, and is fundamental to life, it belongs to the boundary matter between living and nonliving matter, and is central to the science of organic chemistry. Carbon transforms and moves between near-surface reservoirs in the *carbon cycle* (Berner 2004) and carbon also moves deep below the surface through rocks over geological timescales, as studied by the Deep Carbon Observatory (https://deepcarbon.net) extending the biosphere on Earth to the deep subsurface (Colwell and D'Hondt 2013; Schrenk et al. 2013). Evidence for the connection between the Earth's conventional *carbon cycle* and the *deep carbon cycle* is provided in the form of volcanic degassing, where volatile gases deliver carbon as CO_2 to the atmosphere, and subducting plates return solid carbon back into the mantle; the carbon flux of this geological process is enormous but slow and is globally estimated to be largely in balance (Kelemen and Manning 2015).

Carbon Minerals

By far the most abundant carbon minerals in the Earth's crust are carbonates, whose crystal structures incorporate $(CO_3)^{2-}$ anions, with an equilateral triangle of oxygen atoms around the central carbon atom. Most C—O bond distances are

between 1.21 and 1.30 A^{O}, and O—C—O angles are ~120°. Two types of rhombohedral carbonates, calcite and dolomite ($CaMg(CO_3)_2$), account for at least 90% of crustal carbon as massive sedimentary and metamorphic formations (Reeder 1983). In the calcite structure ($CaCO_3$), each Ca^{2+} cation is coordinated to six $(CO_3)^{2-}$ groups and each $(CO_3)^{2-}$ group is coordinated to six Ca^{2+} cations.

Calcite appears most commonly in sedimentary rocks where it occurs as the principal mineral of limestone, and as natural cement in siliceous sandstone and shales. In the present day, calcite is deposited within shallow marine settings, but the distributions of carbonate minerals have varied through Earth history, principally as a consequence of evolving feedback between the geosphere and biosphere (Hazen et al. 2008). Calcite is also common in metamorphic rocks such as marble and calcareous gneiss. Calcite and other carbonate minerals also crystallize in unusual carbonate-rich igneous volcanic rocks called carbonatites (Jones et al. 2013). Approximately 200 of the ~300 known carbonate minerals also include water in their structure. These include mixed anionic forms such as carbonate sulfates, carbonate silicates, and carbonate phosphates. The common copper carbonates are also hydrous including highly colored varieties like green malachite and blue azurite, which form in the oxidized zones of copper deposits.

Carbides, such as cohenite $(Fe, Co, Ni)_3C$, are refractory materials formed where carbon bonds to a less electronegative element, represented by ~10 different naturally occurring minerals. These are scarce in the Earth's crust, but familiar from meteorites and may represent a significant volume fraction of carbon in Earth's deep interior especially the core (Wood et al. 2013).

Organic Carbon and Energy

Carbon forms a variety of minerals which incorporate organic molecules into their structure, including organic molecular crystals, carbon minerals with organic anions, clathrate silicates, and clathrate hydrates. These can have both biological and nonbiological origins. The water-based clathrates are also known as gas hydrates or clathrate hydrates, and are remarkable compounds which form at low temperatures (<0 °C) and elevated pressures (>6 MPa). They are widely distributed around the globe in deep-offshore marine environments and have attracted growing interest because of their enormous potential for methane-based energy. The unnamed main form of "methane ice," which occurs in oceans and deep permafrost regions, is a large cubic 3D H_2O framework with two types of cages partially filled with methane (CH_4) molecules holding on average ~0.17 moles of methane per mole of water, with a density close to 0.9 gcm^{-3} (Max 2003).

A major category of carbon materials concerns carbon deposits in the crust, which are related to energy resources, namely coal and hydrocarbons. Coals are combustible sedimentary rocks derived from organic matter and are composed primarily of carbon, plus other volatile elements like hydrogen, oxygen, sulfur, and nitrogen. The sequence of coal formation by *carbonization* occurs over long geological timescales, accompanied by burial, increasing in grade from peat to lignite, then subbituminous coal, bituminous coal, and finally anthracite. Mature coal deposits sometimes hold unusual crystalline hydrocarbon phases and other organic materials (Sephton and Hazen 2013).

Deep deposits of hydrocarbons represent perhaps the most economically important component of the deep carbon cycle. Most are considered to have a purely biological origin, but there are some challenges to this paradigm, which include similar methane-rich hydrocarbons observed to form in ultramafic rocks like serpentinites (Schrenk et al. 2013), suggesting that alternative nonbiogenic pathways to form hydrocarbon gas deposits are also possible.

Conventional natural oil and gas resources reside in sedimentary basins, and the hydrocarbons of interest consist entirely of carbon and hydrogen, forming a large number of organic compounds. Their empirical formulae differ between types of gaseous hydrocarbons in the series of linear structured hydrocarbons; the amount of bonded hydrogen decreases in the series of alkanes, alkenes, and alkynes, with self-bonding of carbon preventing saturation of the hydrocarbon by the formation of double or triple bonds. Liquid components of petroleum include a complex mixture primarily of linear and cyclic hydrocarbons from C_3 to C_{10}, as well as numerous other molecular species, while solid hydrocarbons include such broad categories as paraffin waxes (typically from C_{18} to C_{40}).

Summary

Carbon (atomic number 6) is the fourth most abundant element in the solar system. Its abundance on Earth is much less well known. It exists everywhere in the atmosphere and oceans, through the crust and mantle in the deep subsurface all the way to the core. A major global concerted effort is underway (the *Deep Carbon Observatory*) to quantify the reservoirs and fluxes of carbon below the surface, to find out how deep life can exist on our planet, and to evaluate how all this additional carbon impacts, if at all, on the measurable and observable *carbon cycle*.

Diamond is the most spectacular form of native elemental carbon. Used since ancient times as a gemstone, not only does it have brilliant optical properties and unmatched hardness, but sophisticated advances in synthesis, including low-pressure chemical vapor deposition (Roy 1987), are leading

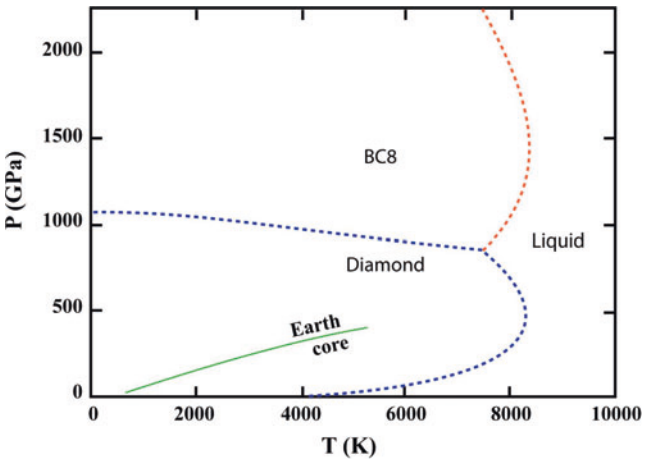

Carbon, Fig. 1 Phase diagram for elemental carbon at high temperatures and pressures

to new uses of diamond in industry. Diamond is also at the forefront of experimental research into defining the limits of extreme pressure and temperature. Two opposing diamonds are used to generate very high static pressures in the megabar range a small experimental device called a "diamond anvil cell," permitting simultaneous heating by laser to thousands of degrees (Lazor et al. 1992). Diamond is the deepest known mineral from Earth, and may also be the oldest, but it is currently impossible to date. By contrast 1-atom thick-layered carbon, graphene, was only isolated in 2004 and is emerging as an important industrial material.

Carbon exists in many forms on Earth, not just as allotropes some of which like diamond are actually rare, but also as hundreds of inorganic minerals and organic compounds or hydrocarbons. Dispersed carbon may also be present deep in the Earth as a nonstoichiometric component in high-pressure silicate minerals and dissolved as CO_2 in silicate melts (Ni and Keppler 2013).

Carbon is essential to life on Earth and can exist in gaseous, liquid, and solid forms. Its mobility in dissolved aqueous fluids is particularly important, not only in the oceans and hydrosphere but in the way tectonic plates are subducted at plate boundaries over geological time (Fig. 1).

Cross-References

- Carbon Cycle
- Carbon Isotopes
- Carbonate Minerals and the CO_2-Carbonic Acid System
- Hydrocarbons
- Meteorites
- Native Minerals
- Natural Gas
- Noble Gases
- Oil Shale
- Oil Seeps and Coastal Bitumen
- Oil-Oil and Oil-Source Rock Correlations
- Organic Geochemistry
- Presolar Grains
- Volcanic Gases

References

Berner RA (2004) The phanerozoic carbon cycle. Oxford University Press, Oxford, 158 pp
Cartigny P (2005) Stable isotopes and the origin of diamond. Elements 1:79–84
Colwell FS, D'Hondt S (2013) Nature and extent of the deep biosphere. In: Hazen RM, Jones AP, Baross JA (eds) Carbon in Earth. Review in mineral and geochemistry, vol 75, pp 547–574
Garai J, Haggerty SE, Rekhi S, Chance M (2006) Infrared absorption investigations confirm the extraterrestrial origin of carbonado diamonds. Astrophys J 653:L153–L156
Geim AK, Novoselov KS (2007) The rise of graphene. Nat Mater 6:181–191
Hazen RM, Papineau D, Bleeker W, Downs RT, Ferry JM, McCoy TJ, Sverjensky DA, Yang H (2008) Mineral evolutions. Am Mineral 93:1693–1720
Hazen RM, Downs RT, Jones AP, Kah L (2013) Carbon mineralogy and crystal chemistry. In: Hazen RM, Jones AP, Baross JA (eds) Carbon in Earth. Review in mineral and geochemistry, vol 75, pp 7–46
Jones AP, McMillan PF, Salzmann CG, Alvaro M, Nestola F, Prencipe M, Dobson D, Hazael R, Moore M (2016) Structural characterisation of natural diamond shocked to 60 GPa; implications for earth and planetary sciences. Lithos 265:214–221
Jones AP, Genge M, Carmody L (2013) Carbonate melts and carbonatites. In: Hazen RM, Jones AP, Baross JA (eds) Carbon in Earth. Review in mineralogy and Geochemistry, vol 75, pp 289–322
Kelemen PB, Manning CE (2015) Reevaluating carbon fluxes in subduction zones, what goes down, mostly comes up. Proc Natl Acad Sci 112:E3997–E4006
Lazor P, Shen G, Saxena SK (1992) Laser-heated diamond anvil cell experiments at high pressure: melting curve of nickel up to 700 kbar. Phys Chem Miner 20:86–90
Marty B (2012) The origins and concentrations of water, carbon, nitrogen and noble gases on earth. Earth Planet Sci Lett 313–314:56–66
Max MD (2003) Natural gas hydrate in oceanic and permafrost environments. Kluwer Academic, Dordrecht
Ni H, Keppler H (2013) Carbon in silicate melts. In: Hazen RM, Jones AP, Baross JA (eds) Carbon in Earth. Review in mineral and geochemistry, vol 75, pp 251–287
Oganov AR, Hemley RJ, Hazen RM, Jones AP (2013) Structure, bonding, and mineralogy of carbon at extreme conditions. In: Hazen RM, Jones AP, Baross JA (eds) Carbon in Earth. Review in mineral and geochemistry, vol 75, pp 47–77
Reeder RJ (ed) (1983) Carbonates: mineralogy and chemistry. Reviews in Mineralogy, vol 11
Roy R (1987) Diamonds at low pressure. Nature 325:17–18
Schrenk MO, Brazelton WJ, Lang SQ (2013) Serpentinization, carbon, and deep life. In: Hazen RM, Jones AP, Baross JA (eds) Carbon in Earth. Review in mineral and geochemistry, vol 75 pp 575–606
Sephton MA (2002) Organic compounds in carbonaceous chondrites. Nat Prod Rep 19:292–311
Sephton MA, Hazen RM (2013) On the origins of deep hydrocarbons. In: Hazen RM, Jones AP, Baross JA (eds) Carbon in Earth. Review in mineral and geochemistry, vol 75, pp 449–465

Wood BJ, Li J, Shahar A (2013) Carbon in the core: its influence on the properties of core and mantle. In: Hazen RM, Jones AP, Baross JA (eds) Carbon in Earth. Review in mineral and geochemistry, vol 75, pp 231–250
Zhang YZ, Zindler A (1993) Distribution and evolution of carbon and nitrogen in earth. Earth Planet Sci Lett 117:331–345

Carbon Cycle

Elizabeth A. Canuel[1] and Amber K. Hardison[2]
[1]Department of Physical Science, Virginia Institute of Marine Science, College of William & Mary, Gloucester Point, VA, USA
[2]Marine Science Institute, The University of Texas at Austin, Port Aransas, TX, USA

Definition

The biochemical and geochemical cycling of the organic and inorganic forms of carbon through Earth processes is referred to as the global carbon cycle. The carbon cycle considers the flow of carbon across four reservoirs: atmosphere; continental, including the biosphere, freshwaters, and soils; ocean; and geosphere (Fig. 1). Processes influencing the transfer of carbon between reservoirs occur over short (active) and long (geologic) timescales. The global carbon cycle is closely linked to the cycles of other elements (e.g., oxygen, nitrogen, phosphorus, and sulfur) because of the important role these elements play in biological and geological processes. Studies of the carbon cycle encompass contemporary, historical, and geologic timescales. Analyses of the rock and sediment records aim to understand how the carbon cycle has varied in the past in response to global transformations and earth system cycles and provide useful analogues for understanding future change. Ice cores provide a record of atmospheric concentrations of carbon dioxide (CO_2) and methane (CH_4) over the past 400,000 years. Interest in the carbon cycle has grown in recent decades due to increasing concentrations of atmospheric CO_2 from anthropogenic combustion of fossil fuels and associated effects on global climate change.

Inorganic Carbon

The main reservoirs of inorganic carbon in the Earth's crust are sedimentary rocks, which hold ~60,000,000 Pg (1 Pg = 10^{15} g) (Hedges and Keil 1995). This oxidized carbon occurs primarily as carbonate minerals (calcite and dolomite) in limestones (80%) and shales (14%) (Hunt 1996). These rock reservoirs are isolated from surficial processes by deep burial and only affect biological cycles on geologic timescales. In contrast, surficial reservoirs, although considerably smaller in size, are more dynamic on biological timescales. The largest of these "active" reservoirs is dissolved inorganic carbon (DIC) in seawater (~40,000 PgC) (Hedges and Keil 1995). Approximately 25% of all marine DIC is stored in the upper kilometer of ocean above the permanent thermocline (Hedges 1992) with most exchange between the atmosphere and ocean taking place in the mixed layer (25–200 m). DIC is also stored in the deep ocean, and exchange between the deep ocean carbon pool and the atmosphere through the process of upwelling occurs at ~1,000 year timescales. Other major reservoirs of inorganic carbon at the Earth's surface include soil carbonates (1,100 PgC) and atmospheric CO_2 (828 PgC).

At geologic timescales, inorganic carbon is transferred between the geosphere and atmosphere by geochemical (weathering) and geothermal (tectonic) processes (Eqs. 1 and 2). Rock weathering produces dissolved bicarbonate (HCO_3^-), which is delivered to the ocean by rivers and groundwater where it is precipitated as calcium carbonate ($CaCO_3$) and other carbonate minerals. There is a positive feedback between weathering and tectonics because subduction processes cause the outgassing of CO_2 from the mantle, thereby increasing atmospheric CO_2 and temperature. Tectonic processes also increase weathering by increasing the amount of land available to weathering through uplift and mountain building. These processes are summarized in the following equations with the forward reaction described on top and the reverse reaction on the bottom:

$$CO_2 + CaSiO_3 \underset{geochemical}{\overset{weathering}{\rightleftarrows}} CaCO_3 + SiO_2 \quad (1)$$

$$CO_2 + MgSiO_3 \underset{geochemical}{\overset{weathering}{\rightleftarrows}} MgCO_3 + SiO_2 \quad (2)$$

Organic Carbon

Organic carbon (OC) is present in both living and nonliving systems and ultimately fuels all of Earth's biogeochemical processes. Understanding the formation, cycling, and preservation of OC is essential for understanding the cycling of all bio-elements between living and nonliving reservoirs, the formation of economically important petroleum and coal deposits, and predicting how human activity may change the natural balance of these systems.

Much of the OC formed during photosynthesis or by chemosynthetic autotrophs is decomposed by heterotrophic organisms. Heterotrophic processes occur in the water column of marine and aquatic environments, as well as in sediments, soils, and rocks. Organic matter (OM) diagenesis

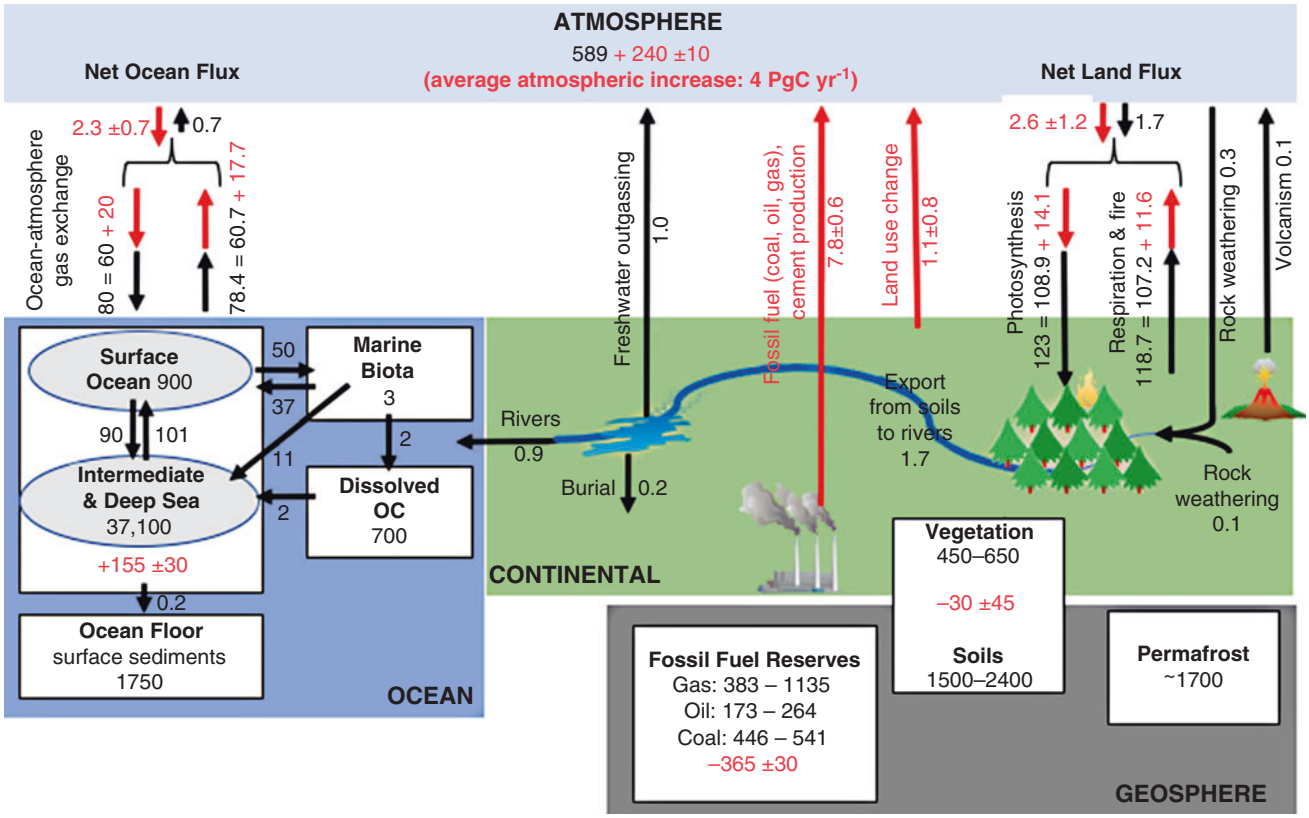

Carbon Cycle, Fig. 1 Simplified schematic of the global carbon cycle, with a focus on the relatively fast-cycling reservoirs. *Numbers* represent reservoir mass, also called "carbon stocks" in PgC and annual carbon exchange fluxes (in PgC year^{-1}). *Numbers* and *arrows* indicate reservoir mass and exchange fluxes estimated for the time prior to the Industrial Era (~1750). *Red* reservoir numbers denote cumulative changes of anthropogenic carbon over the Industrial Period 1750–2011. *Red arrows* and *numbers* indicate annual anthropogenic fluxes averaged from 2000 to 2009. By convention, a positive cumulative change means that a reservoir has gained carbon since 1750. Unless otherwise specified, these values pertain to total C, while values in the text are provided for organic and inorganic C pools (Figure adapted from Ciais et al. (2013) and references therein. *Symbols* courtesy of Integration and Application Network, University of Maryland Center for Environmental Science (ian.umces.edu/imagelibrary/))

occurs under low temperature (<50 °C) and low pressure and primarily through biological processes that occur in surface sediments. The OC preserved following diagenesis is subject to further alteration by the processes of catagenesis and metagenesis, which occur at higher temperatures and pressures and lead to the formation of petroleum and natural gas.

$$\underset{\text{oxidative weathering}}{\overset{\text{photosynthesis and organic burial}}{CO_2 + H_2O + \text{light} \rightleftarrows CH_2O + O_2}} \quad (3)$$

The major fluxes between organic pools are driven by marine and terrestrial primary production (Fig. 1). The active (surficial) pools of OC include soil humus, land and marine plant tissue, seawater dissolved OC (DOC), and surface marine sediments (Hedges and Keil 1995). Photosynthesis, the harvesting of light energy to convert inorganic carbon to reduced (organic) forms in the tissue of plants, is the primary mode of primary production. However, chemosynthesis by microbial organisms, which uses chemical energy rather than sunlight, is also important. The fixation of carbon by plants over the Earth's history accounts for the oxygen in the atmosphere; thus the cycles of carbon and oxygen are closely linked over geologic time. In fact, to maintain current atmospheric oxygen levels, rapid cycling of carbon in the surficial pools is required. These pools exchange on relatively short timescales (10^2–10^4 years). In contrast, OC that remains in the sedimentary system cycles slowly (~10^8 year). Over geologic time, sedimentary reservoirs only become exchangeable through uplift, followed by oxidative weathering of OC by exposure to the atmosphere (Eq. 3).

Global gross primary production on land (123 PgC year^{-1}) is dominated by nonwoody plant tissues such as leaves, grasses, and herbaceous plants (Schlesinger 1997). The highest gross terrestrial production and storage as biomass occurs in the tropics (56%), while polar regions are considerably less productive (0.5%; Taube 1992). Forests are the most productive continental biomes; deserts and tundra are the least productive, reflecting global patterns of temperature and

precipitation. Marine primary productivity (~50 PgC $year^{-1}$) is dominated by open water (pelagic) phytoplankton productivity because open water constitutes ~75% of the total ocean area. However, when normalized to area, coastal and upwelling areas together account for nearly two-thirds of the total oceanic productivity because a greater supply of nutrients is available to support phytoplankton in these areas. Other primary producers along the coasts (i.e., seagrass, marsh plants, macroalgae, mangroves) provide locally important sources of OC (Canuel and Hardison 2016).

Delivery of OC (as dissolved and particulate fractions) from the land to coastal marine environments by rivers accounts for 0.4 PgC $year^{-1}$ (Meybeck 1982). However, there remains considerable uncertainty in the ability to adequately quantify carbon exchange from land to the coastal ocean and in understanding the processes influencing the fate of terrigenous carbon in coastal sediments (Hedges and Keil 1995). Generally, the total annual riverine OC load to the ocean is proportional to annual total river flow, which is dominated by a small set of rivers that transport the bulk of the freshwater from land to sea (Schlesinger 1997). However, seasonal and annual/interannual variations in hydrology as well as large events such as storms and hurricanes influence the input, dispersion, and cycling of sediment OM in coastal environments, thus making it difficult to trace terrigenous OM. In addition, molecular and isotopic evidence suggests that OC in seawater and marine sediments is marine, rather than terrestrial, in source, suggesting that remineralization of terrestrial material must occur in rivers prior to delivery to the coastal ocean (Cole et al. 2007) or in the marine environment. Eaolian (air) OC flux from the land to the sea approximates 0.1 Pg C $year^{-1}$, but this estimate remains uncertain (Zafiriou et al. 1985).

Organic Matter Preservation and Geologic Processes

Only ~0.1% of global net primary production (NPP) is ultimately preserved within sediments; however, it is this OC that eventually becomes part of the sedimentary record and available to be transformed into fossil fuels. The remaining 99.9% of global NPP is remineralized to inorganic carbon, nutrients, and water. Remineralization represents a sink for oxygen, linking the global cycles of OC and oxygen. Microfauna, bacteria, and fungi (on land) are responsible for the breakdown of OM.

The rates and extent of decomposition are influenced by environmental, biological, and physical factors. There must be a sufficient supply of labile OM to be degraded, and the depth-integrated rate of OM remineralization in marine sediments correlates closely with carbon flux to the sediment surface (Henrichs 1993). Interestingly, the fraction of OC that is *not* remineralized is also highly correlated with the carbon flux to the sediment surface. Thus, the efficiency of OM decomposition appears to be lower in systems that receive the highest input of OC compared to systems with lower accumulation rates (Henrichs and Reeburgh 1983). Second, like most metabolic processes, decomposition rates are proportional to temperature, resulting in global patterns of decomposition rates (e.g., higher degradation rates in the tropics than in tundra systems) (Schlesinger 1997). Oxygen is also a controlling factor for decomposition. Recent evidence suggests that oxygen exposure time rather than oxygen concentration may be an important determinant of the extent to which OM is decomposed (Hartnett et al. 1998).

Physical and chemical "protection" of OM also plays a key role in controlling preservation. Protection by binding to inorganic ions, clays, and organic residues decreases the surface area of OM that is exposed to bacteria for degradation. This protection or encapsulation of OM explains why compounds that appear to be labile, or readily available for decomposition, have been found in sedimentary OC deposits. Preservation of OC occurs predominantly in anoxic marine sediments. More than 80% of preserved OC is located in deltaic-shelf environments associated with fine-grained sediments (Berner 1982), which supports the physical or chemical protection model since these sediments provide the most potential surface area with which OM can bind. This has likely been true for millions of years, as current petroleum deposits are found in areas that were formerly coastal, fine-grained sediments. Major depositional environments include lacustrine environments (open, closed lakes), peat swamps and coal, and continental margins, enclosed or silled basins, and the Black Sea (Hedges and Keil 1995).

Sedimentary rocks are the largest geologic reservoir of OC and make up ~99.5% of the total global OC. Sedimentary OC occurs primarily as kerogen, coal beds, and petroleum reservoirs, which ultimately come from biogenic processes or sources. Kerogen is amorphous, highly insoluble particulate OM that is thought to form by two pathways – selective preservation and geopolymerization – both of which occur under low temperature and pressure conditions. Petroleum, naturally occurring fluids (liquid and gases) that evolve from kerogen, is formed primarily from the remains of microbes (algae and bacteria) although some types of petroleum are formed from higher plants. In contrast, coal is a solid and is formed from the remains of higher plants. The most common type of coals, humic coals, is formed through the processes of peatification and coalification, which involve both biological and geochemical processes. The OC in ancient sedimentary rocks provides these economically important fossil fuels as well as a molecular record of life, which has allowed the construction of evolutionary trees and an understanding of the geologic timing of past events and the response of natural systems to tectonic, environmental, and biological change.

Summary

The global carbon cycle involves exchange of OC between surface and subsurface (buried) reservoirs on timescales of less than 1 year to millions of years. These fluxes are driven by the production and cycling of OC through biological, physical, and geological processes. The global OC cycle is intimately linked with other global cycles and is sensitive to human-induced perturbations. In 2016, concentrations of atmospheric CO_2 (~400 ppm) and CH_4 (1,834 ppb) reached a new milestone in human history, and the last time the Earth experienced atmospheric concentrations of CO_2 that were this high was during the Pliocene (~3 million years ago). Understanding changes in the size and composition of carbon reservoirs and changes in these reservoirs through space and time is essential for predicting Earth system responses to anthropogenic activities as well as responses in the associated cycles of other biologically important elements.

Cross-References

- Anthropogenic CO_2
- Atmospheric Evolution
- Biogeochemistry
- Coal
- Diagenesis
- Geochemistry
- Kerogen
- Nitrogen Cycle
- Organic Geochemistry
- Organic Matter Degradation and Preservation
- Oxygen
- Peat
- Petroleum
- Soils
- Sulfur Cycle

References

Berner RA (1982) Burial of organic carbon and pyrite sulfur in the modern ocean: its geochemical and environmental significance. Am J Sci 282:451–473

Canuel EA, Hardison AK (2016) Sources, ages, and alteration of organic matter in estuaries. Annu Rev Mar Sci 8:409–434

Ciais P, Sabine C, Bala G, Bopp L, Brovkin V, Canadell J, Chhabra A, DeFries R, Galloway J, Heimann M, Jones C, Le Quéré C, Myneni RB, Piao S, Thornton P (2013) Carbon and other biogeochemical cycles. In: Stocker TF, Qin D, Plattner G-K, Tignor M, Allen SK, Boschung J, Nauels A, Xia Y, Bex V, Midgley M (eds) Climate change 2013: the physical science basis, Contribution of Working Group I to the Fifth Assessment Report of the Intergovernmental Panel on Climate Change. Cambridge University Press, Cambridge, UK

Cole JJ, Prairie YR, Caraco NF, McDowell WH, Tranvik LJ, Striegl RG, Duarte CM, Kortelainen P, Downing JA, Middelburg JJ, Melack J (2007) Plumbing the global carbon cycle: integrating inland waters into the terrestrial carbon budget. Ecosystems 10:171–184

Hartnett HE, Keil RG, Hedges JI, Devol AH (1998) Influence of oxygen exposure time on organic carbon preservation in continental margin sediments. Nature 391:572–574

Hedges JI (1992) Global biogeochemical cycles: progress and problems. Mar Chem 39:67–93

Hedges JI, Keil RG (1995) Sedimentary organic matter preservation: an assessment and speculative synthesis. Mar Chem 49:81–115

Henrichs SM (1993) Early diagenesis of organic matter: the dynamics (rates) of cycling of organic compounds. In: Engel MH, Macko SA (eds) Organic geochemistry. Plenum Press, New York, pp 101–117

Henrichs SM, Reeburgh WS (1983) Anaerobic mineralization of marine sediment organic matter: rates and the role of anaerobic processes in the oceanic carbon economy. Geomicrobiology 5:191–237

Hunt JM (1996) Petroleum geochemistry and geology, 2nd Edition. W.H. Freeman and Company, New York

Meybeck M (1982) Carbon, nitrogen, and phosphorus transport by world rivers. Am J Sci 282:401–450

Schlesinger WH (1997) Biogeochemistry: an analysis of global change. Academic Press, San Diego, CA

Taube M (1992) Evolution of matter and energy. In: P. Craig and O. Hutzinger (eds) The Natural Environment and the Biogeochemical Cycles, Springer-Verlag, New York, pp 200

Zafiriou OC, Gagosian RB, Peltzer ET, Alford JB, Loder T (1985) Air-to-sea fluxes of lipids at Enewetak Atoll. Geophys Res 90(D1):2409–2423

Carbon Isotopes

Thomas Wagner[1], Clayton R. Magill[1] and Jens O. Herrle[2]
[1]Lyell Centre for Marine and Earth Science and Technology, Heriot-Watt University, Edinburgh, UK
[2]Institute of Geosciences, Goethe University Frankfurt, Frankfurt, Germany

Synonyms

$^{13}C/^{12}C$ ratios; Carbon isotope stratigraphy; Stable carbon isotopes

Definition

The stable carbon isotopes ^{12}C and ^{13}C comprise 98.89% and 1.11% respectively of the carbon on Earth (Craig 1953). Measurements of these isotopes are expressed as ratios to the more common ^{12}C in a sample ($^{13}C/^{12}C$) and reported in the $\delta^{13}C$ notation relative to the Vienna Pee Dee Belemnite (VPDB) standard in per mil (Coplen 1996). There is also an unstable nuclide – radiocarbon (^{14}C) – that is much rarer, with a natural abundance of ~1 part per trillion (Chanton et al. 2014).

Introduction and Main Applications

The stable carbon isotopes measured on the carbonate and organic carbon fractions in sediments or carbonate tests from planktonic and benthic organisms and molecular compounds (biomarkers) isolated from them are classical proxies in marine sciences. This chapter focusses on main applications of carbon isotopes in marine and climate sciences, which include reconstructions of the global carbon cycle, chemostratigraphy, tracing of water masses, and surface water productivity in the modern and past ocean, reconstructing early life, and likewise are relevant to applied forensic applications in numerous archaeological (sub)disciplines.

Carbon Isotopes

Isotopes are atoms with the same number of protons but different numbers of neutrons. Traditional nomenclature denotes isotopic species as ${}^{A}_{Z}\mathrm{E}$, in which Z is the element's atomic number (e.g., number of protons) and A is the mass number (i.e., sum of protons and neutrons). For example, carbon atoms always contain six protons ($n = 6$), but this atom can contain either six, seven, or eight neutrons ($m = 12$, 13, or 14, respectively). With this in mind, the characteristic atomic weight for any particular atom is the average of the relative mass contributions of the atom's isotopic species, which for carbon is equal to 12.0107 (Coplen 1996).

Isotopic Nomenclature and Fractionation Mechanisms

Selective relative enrichment (discrimination) of discrete isotopic species, such as ^{12}C and ^{13}C, between compounds or coexisting phases (e.g., gaseous vs. aqueous carbon dioxide) is called "fractionation." There are two main important types of isotope fractionation – equilibrium and kinetic. Equilibrium isotope fractionation occurs via isotopic exchange when there is a relative separation (discrimination) of isotopes between substances in chemical equilibrium as a result of the reduction in vibrational (zero point) energy when a more massive isotope (e.g., ^{13}C) is substituted for a less massive isotope (e.g., ^{12}C). As such, isotopic exchange reactions occur if the isotope distribution of two or more substances changes, with no change in reactants or products. In contrast, kinetic fractionation is the consequence of rate dependent, incomplete, or nonreversible reactions, such as distillation ("rain out") and biology processes (Chen and Marcus 2005). In such systems, reaction dynamics are sensitive to atomic mass in one or more of the reactants. For instance, products show disproportional incorporation of lighter isotopes compared with reactants because molecules with the heavier isotope form stronger bonds and have higher dissociation energies compared with molecules with lighter isotopes (Fig. 1a, b). Thus, the energy required to achieve molecular dissociation is much lower for ^{12}C–^{12}C bonds compared with ^{13}C–^{12}C bonds (Matsson et al. 2005).

Isotopic exchange reactions are well described by generic equilibrium dynamics:

$$aA_1 + bB_1 = aA_2 + bB_2$$

Here, subscripts 1 and 2 represent the respective abundances of the light and heavy isotopic species of substances A and B, such that the equilibrium constant for such a reaction would be:

$$K = \frac{\left({}^{A_2}/_{A_1}\right)^a}{\left({}^{B_2}/_{B_1}\right)^b}$$

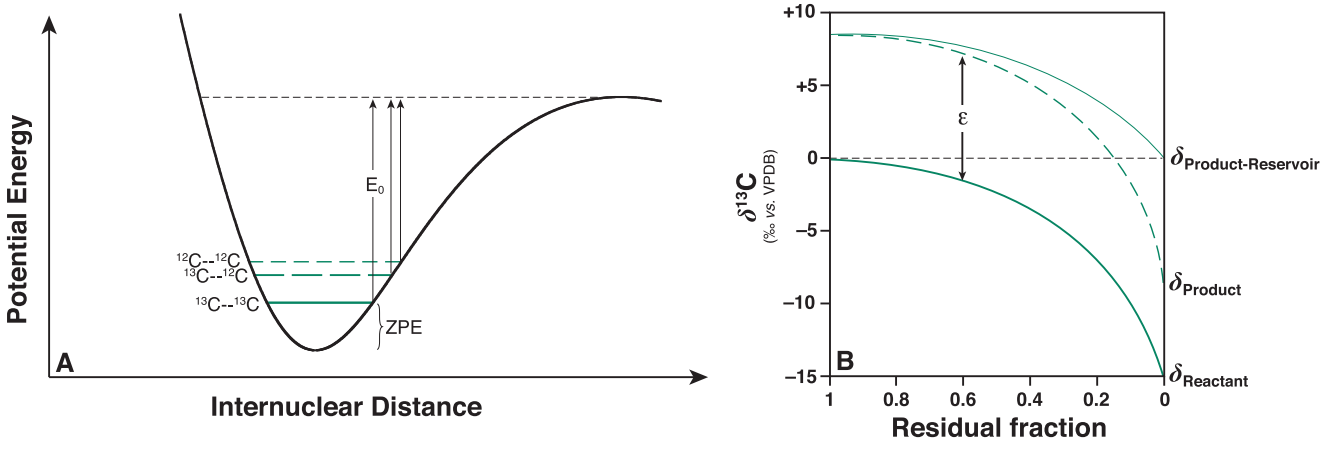

Carbon Isotopes, Fig. 1 (**a**) Schematic potential energy curve for the interaction of two carbon atoms in a stable molecule or amid two molecules in a solid/liquid. (**b**) Coeval $\delta^{13}C$ values of two discrete substances as a function of the residual fraction of the reactant for a Rayleigh process. ZPE (E_0) = Zero point energy

According to statistical mechanics, the equilibrium constant can be expressed by partition functions (Q) of these respective substances:

$$K = \frac{\left(Q_{A_2}/Q_{A_1}\right)}{\left(Q_{B_2}/Q_{B_1}\right)}$$

Accordingly, partition functions are defined by:

$$Q = \sum_i \left[g_i\, e^{(-E_i/kT)}\right]$$

where associated functions are summed for every potential level (E_i), g_i is equal to statistical weight of different i^{th} levels, k is the Boltzmann constant, and T is temperature in Kelvin (Stern et al. 1968).

The fractionation factor α mathematically describes isotopic discrimination, where $\alpha = R_A/R_B$. R is the isotopic ratio of interest (e.g., $^{13}C/^{12}C$), and A and B are discrete compounds or phases. The equilibrium constant (K) is related to the fractionation factor (α) by the equation $\alpha = K^{1/n}$, where n equals the number of atoms exchanged. For isotope exchange reactions involving a single atom, $K = \alpha_{A\text{-}B}$. As an example, consider exchange of ^{13}C and ^{12}C between carbon dioxide and Ca-carbonate:

$$^{13}CO_2 + Ca^{12}CO_3 < - - - > {}^{12}CO_2 + Ca^{13}CO_3$$

This reaction would have an isotopic fractionation factor for aragonite equal to (Emrich et al. 1970).

$$\alpha_{CaCO_3-CO_2} = \frac{\left(\frac{^{13}C}{^{12}C}\right)_{CaCO_3}}{\left(\frac{^{13}C}{^{12}C}\right)_{CO_2}} = +10.63 \text{ (at } 25^{*}C).$$

For calcite, which is common in many marine settings, the isotopic fractionation factors will be different (Romanek et al. 1992; Turner 1982).

Based on available experiments and theoretical data, $\alpha_{CaCO3\text{–}CO2}$ can be calculated from ambient temperature with the equation (Horita 2014):

$$10^3 \ln\alpha_{CaCO_3-CO_2} = -1.637\left(^{10^6}/_{T^2}\right) + 7.290$$

Note that the addition of 10^3 is convenient for conversion of fractionations into more customary per mil (‰) deviations, which are straightforward to compare with conventional delta (δ) values vis-à-vis epsilon values:

$$\varepsilon_{CaCO_3-CO_2} = 10^3(\alpha_{CaCO_3-CO_2} - 1) = 10^3\left(^{R_B}/_{R_A} - 1\right)$$

Delta (δ) notation is defined by the equation:

$$\delta_{SA}(‰) = 10^3\left(\frac{(R_{SA} - R_{ST})}{R_{ST}}\right)$$

where R is the isotope ratio and subscripts SA and ST represent sample and standard respectively.

Carbon isotope ratio measurements are compared to an international isotopic reference material called Vienna Peedee Belemnite (VPDB) with an R equal to 0.011237 (Coplen 1996). As such, a sample substance's measured $^{13}C/^{12}C$ ratio is used to calculate stable carbon isotope values ($\delta^{13}C$):

$$\delta^{13}C_{Sample} = 10^3\left(\frac{\left(\frac{^{13}C}{^{12}C}\right)_{Sample} - \left(\frac{^{13}C}{^{12}C}\right)_{VPDB}}{\left(\frac{^{13}C}{^{12}C}\right)_{VPDB}}\right)$$

In conjunction with the epsilon equation above, the stable carbon isotopic fractionation (α) between two substances can be calculated (*c.f.*, Table 1):

$$\alpha_{A-B} = {}^{R_B}/_{R_A} = {}^{(\delta^{13}C_A+1000)}/_{(\delta^{13}C_B+1000)}$$
$$\approx \delta^{13}C_A - \delta^{13}C_B = \Delta\delta^{13}C_{A-B}$$

Carbon Isotopic Measurements

Isotope ratio mass spectrometry (IRMS) provides measurements of the absolute abundance of stable carbon isotopes in natural or synthetic materials. Over the last few decades, advances in IRMS instrumentation now allow for accurate and highly precise stable carbon isotope measurements of bulk and molecular samples. Further, recent IRMS

Carbon Isotopes, Table 1 Comparison of $\delta^{13}C$, $\Delta\delta^{13}C_{A-B}$, α_{A-B}, and 1000 ln α_{A-B} values of two discrete materials with different ^{13}C abundances

$\delta^{13}C_A$	$\delta^{13}C_B$	$\Delta^{13}C_{A\text{-}B}$	$\alpha_{A\text{-}B}$	$10^3 \ln \alpha_{A\text{-}B}$
−20.0	0	−20.0	0.980	−20.2
−10.0	0	−10.0	0.990	−10.1
−5.0	0	−5.0	0.995	−5.0
−1.0	0	−1.0	0.999	−1.0
0	0	0	1.000	0
1.0	0	1.0	1.001	1.0
5.0	0	5.0	1.005	5.0
10.0	0	10.0	1.010	9.9
10.0	1.0	9.0	1.009	10.9
10.0	−1.0	11.0	1.011	8.9

technologies now support coupled instrumental techniques, which are configured to incorporate a range of differing peripheral (front-end) techniques such as elemental analysis (EA, Muccio and Jackson 2009), gas chromatography (GC; Sessions 2006), and high performance liquid chromatography (HPLC, Godin et al. 2007). Ultimately, these peripheral techniques use oxidation to convert diverse carbon compounds into carbon dioxide for IRMS detection (*c.f.*, Sessions 2006; Muccio and Jackson 2009). Following gasification, samples are compared to a reference gas calibrated with recognized international isotope reference materials (Table 2). This approach thus normalizes measured (raw) $\delta^{13}C$ values to a common reference scale shared between laboratories worldwide.

Current theoretical sensitivities of IRMS for combustion-interface carbon isotope measurements are about 0.025 nmol for samples with natural ^{13}C distribution abundances, although realized detection thresholds are much higher at 1–5 nmol (~50 ng of typical hydrocarbons [Sessions 2006]) for on-column injections. Precision of $\delta^{13}C$ values measured from samples with >5 nmol C is presently ca. 0.1–0.3‰ (1σ standard deviation). Comprehensive review of IRMS instrumentation and techniques are well beyond the scope of this chapter. The reader is directed toward recent literature reviews (c.f., Brand 2004; Sessions 2006; Muccio and Jackson 2009) and other contributions in this encyclopedia.

Carbon Isotopes, Table 2 Reported $\delta^{13}C$ values of NBS-reference materials against VPDB

Ref.	Material	$\delta^{13}C$
NBS-18	Carbonatite	−5.0
NBS-19	Marble	+1.9
NBS-20	Limestone	−1.1
NBS-21	Graohite	−28.1
NBS-22	0il	−30.0

Distribution of Carbon Isotopes in Nature

Stable carbon isotopic compositions are widely used as geochemical proxies to reconstruct changes in the global carbon cycle. Two main carbon reservoirs exist, the reduced biogenic organic carbon reservoir (organic matter) and the oxidized carbonate reservoir, covering a wide range of stable carbon isotopic signatures from less than −100‰ to greater than 10‰, depending on the carbon source (Figs. 2 and 3). The lowest $\delta^{13}C$ values are related to microbially produced methane (CH_4) (Grossman et al. 2002) in, e.g., gas-hydrate bearing sediments along continental slopes and related carbonate biohermes, marine seep systems, and Arctic permafrost (e.g., Claypool and Kvenvolden 1983; Whiticar 1999, and references therein). The highest values (>10‰) occur in dissolved inorganic carbon (DIC) associated with methanogenesis (Claypool and Kaplan 1974; Hudson 1977).

Differences in the organic carbon isotopic composition ($\delta^{13}C_{org}$), both at the bulk and the molecular level, are controlled by complex biosynthetic pathways, including the fractionation during the production of biomass, e.g., photosynthesis, in the marine and the terrestrial biosphere (e.g., Degens et al. 1968). Bulk organic carbon from terrestrial C3 plants, the most common type of vegetation on Earth, is lower in $\delta^{13}C$ with mean values of about −27‰. Bulk $\delta^{13}C_{org}$ values for marine algae scatter around −21‰. Terrestrial vegetation from arid climate zones utilizing the C4 and Crassulacean Acid Metabolism (CAM) photosynthetic pathway, mainly Savannah grasslands,

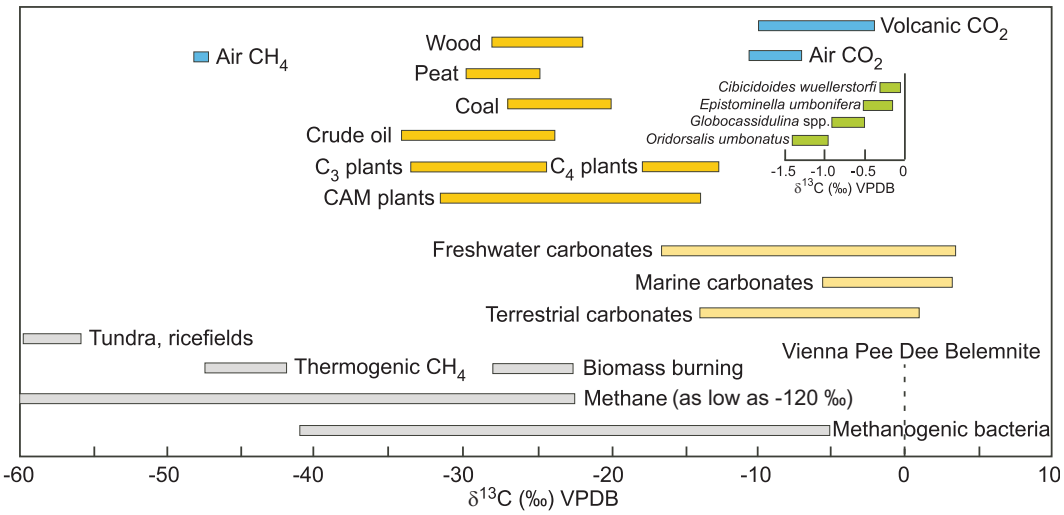

Carbon Isotopes, Fig. 2 Variations in stable carbon isotope ratios for different organic and inorganic sources in the modern environment and in sediments (Modified from Schidlowski and Aharon 1992; Wefer and Berger 1991)

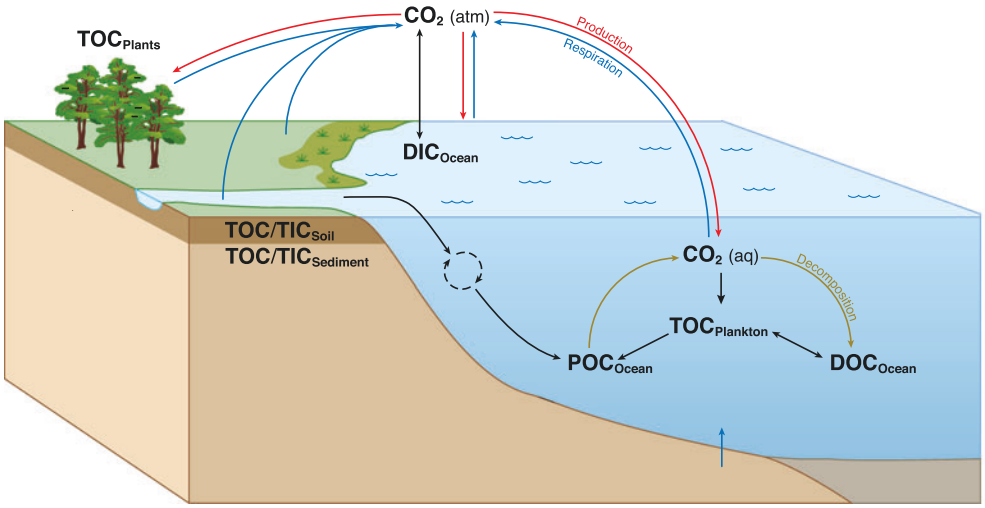

Reservoir	Size (GtC)	$\delta^{13}C$
CO_2 (atm)	750	–8‰
CO_2 (aq)	250	–9‰
DIC_{Ocean}	37500	+1‰
$TIC_{Sediment}$	125‡	+2‰
DOC_{Ocean}	750	–22‰
POC_{Ocean}	25	–22‰
$TOC_{Plankton}$	5	–28‰
$TOC_{Sediment}$	1750	–20‰
TOC_{Soil}	1500	–20‰
TOC_{Plants}	500	–24‰

‡Surface (<1 m)

Carbon Isotopes, Fig. 3 Carbon cycle dynamics along the land-river-ocean continuum (modified from Canuel et al. 2012). Average $\delta^{13}C$ values, reservoir sizes, and fluxes are also shown for reference (Siegenthaler and Sarmiento 1993; Hedges et al. 1997; Rabouille et al. 2001)

shows averaged bulk $\delta^{13}C_{org}$ values of about −12‰. Within all these organisms, at the molecular scale, most lipids are ^{13}C–depleted (lower $\delta^{13}C$ values) as compared to starch ($\Delta\delta^{13}C_{Starch–Lipid}$ = 6.0‰), sugars ($\Delta\delta^{13}C_{Sugar–Lipid}$ = 5.5‰), proteins ($\Delta\delta^{13}C_{Protein–Lipid}$ = 5.0‰), and therefore bulk biomass ($\Delta\delta^{13}C_{Bulk–Lipid}$ = 4.0‰), as a consequence of biochemical (enzymatic) differences during production and transport through an organism (Hobbie and Werner 2004; Bowling et al. 2008).

Carbon Isotopes and the Emergence of Life

Physiochemical and biological processes create distinctive carbon isotopic signatures in biogenic material that trace the occurrence of life. In consequence, $^{13}C/^{12}C$ variations in sedimentary geologic archives are often used to reconstruct the origin(s) and evolution of life because of its characteristic discrimination against heavier isotopes. For instance, numerous studies adopt $\delta^{13}C$ values of fossil organic matter (kerogen) in sedimentary rocks to resolve the antiquity of life as we understand it based on remarkably persistent kinetic isotope effects associated with enzymatic carboxylation reactions (e.g., photosynthetic assimilation via ribulose bisphosphate carboxylase) as compared to inorganic carbon species, such as carbon dioxide and (bi)carbonate (Schidlowski and Aharon 1992; Havig et al. 2017).

Other disciplines, including paleontology and archeological fields, similarly utilize characteristic carbon isotopic discriminations imparted by plants and higher animal-derived biomass in order to more fully understand the evolution of life and behavior. For example, many previous studies interpret $\delta^{13}C$ values of dental bioapatite derived from early humans with respect to vegetable versus meat-based dietary preferences during our species' evolution (Cerling et al. 2011; Sponheimer et al. 2013; Loftus et al. 2016). These same values also create an explicit link between our ancestors and their environments, which then can be contextualized by plant lipid $\delta^{13}C$ analyses of the matrix across an archeological horizon in order to shed light on community patterns, resource use, and (pre)historical behavior (Magill et al. 2016). The analysis of biochemical "residues" similarly provide new dimensions in archeological investigations of diverse materials, such as pottery (potsherds), soils, sediments, and biogenic remains in order to link lipid residues with their organic and environmental sources (Dudd and Evershed 1998; Dunne et al. 2016). Thus, combined bulk and molecular analyses are especially powerful because they can disentangle source-specific inputs within otherwise complex mixtures of lipids.

Carbon Isotopes in Shallow Seawater

The dissolved inorganic carbon (DIC) $\delta^{13}C$ of seawater ($\delta^{13}C_{DIC}$) is dynamically coupled to the global carbon cycle via the partitioning of the main carbon reservoirs between the ocean, atmosphere, and terrestrial biosphere (Fig. 3). $\delta^{13}C_{DIC}$ is not uniform in the modern ocean, nor constant over time (e.g., Sundquist and Visser 2004). The global seawater $\delta^{13}C_{DIC}$ composition is mainly controlled by three processes: photosynthesis, microbial decay of algal organic matter, and physical fractionation during gas exchange at the air-sea interface (Broecker and Maier-Reimer 1992). Marine surface

water is generally enriched in ^{13}C because photosynthesis of marine phytoplankton favors the light ^{12}C over the heavy ^{13}C, leading to lower $\delta^{13}C$ values for organic matter ($\delta^{13}C_{org}$) relative to ambient seawater $\delta^{13}C_{DIC}$ (Garlick 1974). This process is limited by the availability of nutrients, in particular nitrate and phosphate (Broecker and Peng 1982).

Most marine organisms exhibit $\delta^{13}C$ values in their carbonate shells, which were formed not in full equilibrium relative to ambient seawater (Fig. 1). The reason for this is manifold but metabolic effects, including the photosynthetic activity of algal symbionts, kinetic fractionation tied to growth rates, and carbonate ion concentrations are critical (McConnaughy 1989; Rohling and Cook 1999). These effects, together with species-specific differences, are summarized as 'vital effects' (e.g., Wefer and Berger 1991). Intriguingly, previous studies suggest that, if these vital effects are corrected for, isotopic mass-balance calculations can be used for reconstructions of biophysical factors, such as the concentration and the composition of Earth's atmospheric carbon dioxide (e.g., alkenones; Pagani 2014).

In most places, modern sea surface waters $\delta^{13}C_{DIC}$ is about 2–3‰ heavier than the deep-water values of about 0‰ due to biological activity in the photic zone (Kroopnick 1985; Raven and Falkowski 1999; Sarmiento and Gruber 2006). In addition, changes of the $\delta^{13}C_{DIC}$ in the ocean are influenced by increasing anthropogenic pCO_2 causing a decline in the ^{13}C content of DIC relative to ^{12}C – a phenomenon called the "Suess effect" (Keeling 1979; Quay et al. 1992).

Remineralization of organic matter and nutrients within thermocline subsurface water recycle isotopically light ^{12}C. Due to upwelling and wind-mixing of shallow waters, this light ^{12}C and nutrient-rich subsurface water can be remobilized back into the surface waters thereby stimulating primary productivity and influencing the carbon isotopic composition of calcareous shells (e.g. Broecker and Peng 1982).

Tracing of Seawater Masses, Surface Water Productivity, and Ecology

The $\delta^{13}C_{DIC}$ in water is widely used as a tracer for seawater masses. Although changes in surface water productivity and mixing influence $\delta^{13}C_{DIC}$, other processes, including water mass formation, respiration, ocean circulation, and vital effects, determine the $\delta^{13}C_{DIC}$ value and therefore can be used as tracers for water masses (e.g., Ravelo and Hillarie-Marcel 2007). Deep water captures the $\delta^{13}C$ signature from its surface water sources. North Atlantic Deep Water (NADW) has therefore relatively high $\delta^{13}C$ values (~1.11‰) whereas Antarctic Bottom Water (ABW) is relatively low (~0.4‰), reflecting the major differences in surface water $\delta^{13}C_{DIC}$ in both high latitude source regions (Kroopnick 1985). Variations in deep water $\delta^{13}C$ can, therefore, be used to trace the history of deep water currents. This approach is also referred to as "aging" of deep water (Rohling and Cook 1999), where the relative age of deep water provides a measure for ocean circulation.

The $\delta^{13}C$ difference between shallow and deep dwelling planktic foraminifera ($\Delta\delta^{13}C$) provides a well-established proxy for thermocline productivity and the depth of the shallow water mixed layer (e.g., Wefer et al. 1999). Increasing $\Delta\delta^{13}C$ values reflect more stratified surface water masses due to increasing contrasts between shallow and deep waters, and vice versa. A comparable approach is used to reconstruct productivity via changes in benthic foraminifera $\Delta\delta^{13}C$ of epifaunal and infaunal species (Zahn et al. 1986). Here, the $\delta^{13}C$ differences are mainly controlled by pore water geochemical gradients and the intensity of organic matter degradation, the latter being a function of organic matter supply (flux) to the sea floor (McCorkle et al. 1990). Large $\Delta\delta^{13}C$ values represent less organic matter flux, and thus less primary productivity, and vice versa. Benthic foraminifera $\Delta\delta^{13}C$ gradients can, however, be biased by the variability in new production of organic matter (fresh phytodetritus), which influences the stable isotope signal. This effect, constrained by variable primary productivity and organic matter fluxes at seasonal time scales, is referred to as the "Phytodetritus" or "Mackensen effect" (Mackensen et al. 1993). Furthermore, the carbon and oxygen isotopic composition of calcite tests of planktic foraminifera is used for reconstructing depth habitats and thus the ecology of extant and extinct species (e.g., Pearson et al. 1993).

Chemostratigraphy and Carbon Isotope Excursions (CIE)

The history of the global carbon cycle and climate through time is preserved in the carbon isotope record of marine and terrestrial sediments (Fig. 4). The application of organic and inorganic carbon isotope ratios as chemical fingerprints for stratigraphic correlations was pioneered in the late 1970s with the studies of Berger et al. (1978), Weissert et al. (1979), and Scholle and Arthur (1980), more recently summarized in Weissert et al. (2008), Saltzman and Thomas (2012), Wendler (2013), and Jarvis et al. (2015). The most robust Phanerozoic archives of marine carbon isotope signatures are from individual pristine preserved fossils and bulk carbonate from marine sediments (e.g., Joachimski and Buggisch 1993; Veizer et al. 1999; Grossman et al. 2008; Saltzman and Thomas 2012, and references therein). Carbon isotope fluctuations of several per mil are also reported from hemipelagic sediments, shallow water carbonates, and terrestrial sediments. Due to multiple local influences, however, they may differ in their absolute isotope values and ranges from their

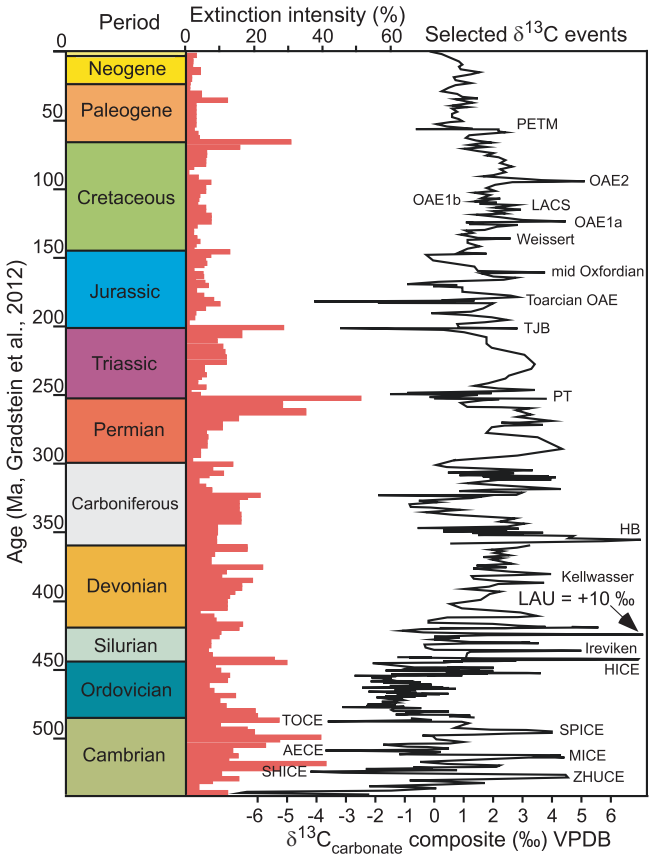

Carbon Isotopes, Fig. 4 Phanerozoic carbon isotope record, extinction events, and selected global events (CIEs) based on Gradstein et al. (2012) and references therein, Caplan and Bustin (1999), Munnecke et al. (2003), Wagner et al. (2007), Korte and Kozur (2010), and McAnena et al. (2013). Extinction intensity represents the fraction of genera that are present in each interval of time but do not exist in the following interval (Modified after Rohde and Muller (2005) and Sepkoski (2002). *PETM* Paleocene Eocene Thermal Maximum, *OAE* Oceanic Anoxic Events, *LACS* Late Aptian Cold Snap, *TJB* Triassic Jurassic Boundary, *PT* Perm-Trias Event, *HB* Hangenberg Event, *LAU* Lau Event, *HICE* Hirnantian Event, *TOCE* Top Cambrian Excursion, *SPICE* Steptoean Event, *MICE* Mingxinsi Event, *AECE* Archaeocyathids Event, *SHICE* Shiyantou Event, *ZHUCE* Zhujiaqing Event

corresponding pelagic sediment records, complicating their use in stratigraphic correlation across wider areas (Weissert and Breheret 1991; Saltzman and Thomas 2012; Jarvis et al. 2015).

The long-term trend in Earth's climate is interrupted by series of transient events, identified by distinct positive or negative carbon isotope excursions, CIEs (Fig. 4). These CIEs, combined with longer trends in the global carbon isotope record, are used in chemostratigraphy to identify chemical events (e.g., Zachos et al. 2001; Weissert et al. 1998), which can be correlated within and across shallow, hemipelagic, and pelagic marine and the terrestrial environments (e.g., Gröcke et al. 1999; Herrle et al. 2004). Well-documented examples of CIEs representing major perturbations of the global carbon cycle are reported from, e.g., the Mesozoic-Paleogene greenhouse (Paleocene–Eocene thermal maximum PETM, Early Jurassic and Cretaceous Oceanic Anoxic Events, OAEs, Jenkyns 2003), and the Paleozoic (Saltzman and Thomas 2012, Fig. 4). In contrast to the large Paleozoic fluctuations of >10‰, the Mesozoic and Cenozoic amplitudes are with >2‰ much smaller. Many CIEs coincide with widespread environmental perturbations including severe and short-term global warming (hyperthermal events), ocean acidification, shoaling of the carbonate compensation depth (CCD), enhanced marine organic carbon burial linked to widespread ocean anoxia, major crisis or extinction of biota on land and in the ocean, and sudden shifts in Earth's hydrological cycle and climate (e.g., Leckie 2009; Stanley 2010; Beerling and Woodward 2001). Understanding how the Earth system responded to and recovered from these past extreme events remains a major focal point of Earth Sciences, adding to the discussion on anthropogenically induced global warming (Stanley 2010).

The magnitude of 2 to >10‰ and rapidity of CIEs in the Phanerozoic, combined with evidence for massive environmental change, has stimulated intense interdisciplinary research about the underlying trigger and feedback mechanisms. Positive CIEs are reported for multimillion to orbital time scales and are, among other possible mechanisms (Fig. 4), commonly associated with periods of globally enhanced marine carbon burial, leading to the concept of Oceanic Anoxic Events (Schlanger and Jenkyns 1976, Scholle and Arthur 1980) and global cooling (e.g., Kuypers et al. 1999). Recent studies, combining geochemical with biotic data and biogeochemical modeling, have shown that global cooling can cause perturbations to marine ecosystems and biogeochemical cycles at scales comparable to those associated with global warming (McAnena et al. 2013). Sharp negative CIEs, either isolated within the chemostratigraphic record or in combination with positive CIEs, have been recorded throughout the Phanerozoic sedimentary record (e.g., Saltzman and Thomas 2012) and have become a focal point for Earth System research. Negative CIEs have been related to a large number of mechanisms, including rapid dissociation of metastable marine methane hydrate, build-up and release of isotopically "light" carbon in stratified epicontinental seas, thermogenic release of methane related to the placement of volcanic dykes into coal-bearing strata or thermal maturation of other organic-rich sediments, extensive biomass burning, mobilization of labile carbon pools from terrestrial permafrost, ventilation of marine dissolved organic carbon, and others (for further information on mechanisms see, e.g., Cohen et al. 2007; deConto et al. 2012). Correlations of smaller magnitudes of >1.0‰ within less than 100 kyrs have been successfully used in regional epicontinental settings of the late Cretaceous (Menegatti et al. 1998; Herrle et al. 2004; Jarvis et al. 2015). In contrast to the large amplitudes, the factors controlling small scale variations of <0.5‰ are far less understood. Among

others, coccolith distribution and depletion in marl–limestone alternations, diagenetic effects of pore waters, sedimentation, and cementation have been identified to play a role (Jarvis et al. 1988, 2015; Mitchell et al. 1997).

Processes Limiting the Use of C within Chemostratigraphy

Major processes affecting the absolute values in both organic and inorganic matter are surface water productivity (Arthur et al. 1988), input of organic matter from land (Jarvis et al. 2015), remineralization in the water column (Sinninghe Damste and Köster 1998), mineralogy, and carbonate and organic composition of the sediments (cements, carbonate producers such as calcareous nannofossils composition and abundances; Beltran et al. 2007; Jarvis et al. 2015), early and late diagenetic processes (Mitchell et al. 1997; Allan and Matthews 1982; and Immenhauser et al. 2003), CO_2 (Kump and Arthur 1999), and sea-level changes (Jenkyns 1996). Furthermore, it has been shown that mineralogy can impact on carbon isotopic stratigraphy (e.g., Swart 2008). Paired organic and inorganic carbon isotope records might help overcome this problem (Menegatti et al. 1998; Jarvis et al. 2015). Parallel shifts, in both organic and inorganic carbon isotopes, are often a robust signal in different marine records as it is documented for example for the early Aptian carbon isotope event. For this event, a consistent >4–6‰ shift is observed in organic and inorganic carbon isotopes from shallow marine Cretaceous Arctic marsh records and subtropical pelagic and shallow marine records (Menegatti et al. 1998; Herrle et al. 2015).

Besides the chemical and physical alteration of the carbon isotope signals, the impact of orbital forcing on the carbon cycle, which is most dominant within the 400 kyr cycle in the Cenozoic and Mesozoic $\delta^{13}C$ records (Pälike et al. 2006; Gale et al. 2011), can make correlations difficult if major $\delta^{13}C$ shifts of >2‰ are absent. Thus, instead of correlating single peaks, longer intervals (>0.5–1 Ma) are needed to be studied together with biostratigraphic and/or chronostratigraphic makers (Herrle et al. 2004). The absolute $\delta^{13}C$ values might be obscured but the form and shape of isotope profiles are a robust feature in many long- and short-term records (Herrle et al. 2015; Jarvis et al. 2015). Thus, using longer records, the form and the shape are the basis for a reliable high-resolution chemostratigraphic approaches (Jarvis et al. 2015).

Conclusions

Stable carbon isotopes are commonly used for a wide range of applications in marine sciences and climate research. Applications include reconstructions of the global carbon cycle including short-term perturbations, chemostratigraphy, and tracing of water masses and surface water productivity in the modern and past ocean. The development of carbon isotopes at the bulk sediment, foraminifera shell, and compound-specific (molecular) level, especially when combined with complementary evidence from biota, nutrients, ocean chemistry and redox, and modeling, has opened new pathways to unravel the complex interplay between fluctuations of main carbon pools between the atmosphere, the living biosphere, and carbon buried in the sediments, and their interactions with and impact on global climate at multiple temporal and spatial scales.

Cross-References

- Anthropogenic CO_2
- Archeological Geochemistry
- Biogenic Methane
- Biogeochemistry
- Carbon
- Carbon Cycle
- Carbonate Compensation Depth
- Carbonate Minerals and the CO_2-Carbonic Acid System
- Coal
- Compound-Specific Isotope Analysis
- Diagenesis
- Dissolved Organic Matter (DOM)
- Gas Chromatography–Mass Spectrometry (GC–MS)
- Gas Hydrates
- Gas Source Mass Spectrometry (GS-MS)
- Marine Sediment
- Ocean Biochemical Cycling and Trace Elements
- Ocean Salinity, Major Elements, and Thermohaline Circulation
- Organic Geochemistry
- Organic Matter Degradation and Preservation
- Organics: Sources and Depositional Environments
- Oxygen Isotopes
- Paleoenvironments
- Paleoproductivity
- Stable Isotope Geochemistry

References

Allan J, Matthews R (1982) Isotope signatures associated with early meteoric diagenesis. Sedimentology 29:797–817

Arthur MA, Dean WE, Pratt LM (1988) Geochemical and climatic effects of increased marine organic carbon burial at the Cenomanian/Turonian boundary. Nature 335:714–717

Beerling DJ, Woodward FI (2001) Vegetation and the terrestrial carbon cycle: modelling the first 400 million years. Cambridge University Press, Cambridge, UK

Beltran C, de Rafélis M, Minoletti F, Foucault A, Renard M, Sicre MA, Ezat U (2007) Coccolith δ18O and alkenone records in middle Pliocene orbitally-controlled deposits: high frequency temperature and salinity variations of sea surface water. Geochem Geophys Geosyst 8. https://doi.org/10.1029/2006GC001483

Berger WH, Killingley JS, Vincent E (1978) Stable isotopes in deep-sea carbonates: box core ERDC-92, west equatorial Pacific. Oceanol Acta 1:203–216

Bowling DR, Pataki DE, Randerson JT (2008) Carbon isotopes in terrestrial ecosystem pools and CO_2 fluxes. New Phytol 178(1):24–40

Brand WA (2004) Mass spectrometer hardware for analyzing stable isotope ratios. Handbook of stable isotope analytical techniques 1:835–856

Broecker WS, Maier-Reimer E (1992) The influence of air and sea exchange on the carbon isotope distribution in the sea. Glob Biogeochem Cycles 6:315–320

Broecker WS, Peng T-H (1982) Tracers in the sea. Eldigio Press, Palisades

Canuel EA, Cammer SS, McIntosh HA, Pondell CR (2012) Climate change impacts on the organic carbon cycle at the land-ocean interface. Ann Rev Earth Planet Sci 40:685–711

Caplan ML, Bustin RM (1999) Devonian-carboniferous Hangenberg mass extinction event, widespread organic-rich mudrock and anoxia: causes and consequences. Palaeogeogr Palaeoclimatol Palaeoecol 148:187–207

Chanton J, Zhao T, Rosenheim BE, Joye S, Bosman S, Brunner C, Yeager KM, Diercks AR, Hollander D (2014) Using natural abundance radiocarbon to trace the flux of petrocarbon to the seafloor following the Deepwater horizon oil spill. Environ Sci Technol 49(2):847–854

Chen WC, Marcus RA (2005) On the theory of the CO+ OH reaction, including H and C kinetic isotope effects. J Chem Phys 123(9):094307

Cerling TE, Mbua E, Kirera FM, Manthi FK, Grine FE, Leakey MG, Sponheimer M, Uno KT (2011) Diet of Paranthropus boisei in the early Pleistocene of East Africa. Proc Natl Acad Sci 108(23):9337–9341

Claypool GE, Kaplan IR (1974) The origin and distribution of methane in marine sediments. In: Kaplan IR (ed) Natural gases in marine sediments, Springer, New York, pp 99–139

Claypool GE, Kvenvolden KA (1983) Methane and other hydrocarbon gases in marine sediment. Annu Rev Earth Planet Sci 11(1):299–327

Cohen AS, Coe AL, Kemp DB (2007) The late Paleocene-early Eocene and Toarcian (early Jurassic) carbon-isotope excursions: a comparison of their timescales, associated environmental changes, causes and consequences. J Geol Soc London 164:1093–1108

Coplen TB (1996) New guidelines for the reporting of stable hydrogen, carbon and oxygen isotope ratio data. Geochim Cosmochim Acta 60:3359–3360

Craig H (1953) The geochemistry of the stable carbon isotopes. Geochim Cosmochim Acta 3:53–92

Damsté JSS, Köster J (1998) A euxinic southern North Atlantic Ocean during the Cenomanian/Turonian oceanic anoxic event. Earth Planet Sci Lett 158(3):165–173

DeConto R, Galeotti S, Pagani M, Tracy D, Schaefer K, Zhang T, Pollard D, Beerling DJ (2012) Past extreme warming events linked to massive carbon release from thawing permafrost. Nature 484:87–92

Degens ET, Guillard RRL, Sackett WM, Hellebust JA (1968) Metabolic fractionation of carbon isotopes in marine plankton. I. Temperature and respiration experiments. Deep-Sea Res 15:1–9

Dudd SN, Evershed RP (1998) Direct demonstration of milk as an element of archaeological economies. Science 282:1478–1481

Dunne J, Mercuri AM, Evershed RP, Bruni S, di Lernia S (2016) Earliest direct evidence of plant processing in prehistoric Saharan pottery. Nature Plants 3:16194

Emrich K, Ehhalt DH, Vogel JC (1970) Carbon isotope fractionation during the precipitation of calcium carbonate. Earth Planet Sci Lett 8(5):363–371

Gale AS, Bown PR, Caron M, Crampton J, Crowhurst SJ, Kennedy WJ, Petrizzo MR, Wray DS (2011) The uppermost Middle and Upper Albian succession at the Col de Palluel, Hautes-Alpes, France: an integrated study (ammonites, inoceramid bivalves, planktonic foraminifera, nannofossils, geochemistry, stable oxygen and carbon isotopes, cyclostratigraphy). Cretaceous Res 32:59–130

Garlick GD (1974) The stable isotopes of oxygen, carbon, and hydrogen in the marine environment. In: Goldberg ED (ed) The Sea, vol 5. Wiley, New York, pp 393–425

Gradstein FM, Ogg JG, Schmitz M, Ogg G (2012) The Geological Time Scale. Elsevier, Amsterdam

Godin JP, Fay LB, Hopfgartner G (2007) Liquid chromatography combined with mass spectrometry for ^{13}C isotopic analysis in life science research. Mass Spectrom Rev 26(6):751–774

Grossman EL, Cifuentes LA, Cozzarelli IM (2002) Anaerobic methane oxidation in a landfill-leachate plume. Environ Sci Technol 36(11):2436–2442

Grossman EL, Yancey TE, Jones TE, Bruckschen P, Chuvashov B, Mazzullo SJ, Mii HS (2008) Glaciation, aridification, and carbon sequestration in the Permo-Carboniferous: the isotopic record from low latitudes. Palaeogeogr Palaeoclimatol Palaeoecol 268:222–233

Gröcke DR, Hesselbo SP, Jenkyns HC (1999) Carbon-isotope composition of lower cretaceous fossil wood: ocean-atmosphere chemistry and relation to sea-level change. Geology 27:155–158

Havig JR, Hamilton TL, Bachan A, Kump LR (2017) Sulfur and carbon isotopic evidence for metabolic pathway evolution and a four-stepped Earth system progression across the Archean and Paleoproterozoic. Earth Sci Rev https://doi.org/10.1016/j.earscirev.2017.06.014

Hedges JI, Keil RG, Benner R (1997) What happens to terrestrial organic matter in the ocean? Org Geochem 27(5):195–212

Herrle JO, Kößler P, Friedrich O, Erlenkeuser H, Hemleben C (2004) High-resolution carbon isotope records of the Aptian to lower Albian from SE France and the Mazagan plateau (DSPD site 545): a stratigraphic tool for paleocanographic and paleobiologic reconstruction. Earth Planet Sci Lett 218:149–161

Herrle JO, Schröder-Adams CJ, Davis W, Pugh AT, Galloway JM, Fath J (2015) Mid-Cretaceous high Arctic stratigraphy, climate, and oceanic anoxic events. Geology 43(5):403–406

Hobbie E, Werner RA (2004) Intramolecular, compound-specific, and bulk carbon isotope patterns in C3 and C4 plants: a review and synthesis. New Phytol 161(2):371–385

Hoefs J (2009) Stable isotope geochemistry, vol 6. Springer, Berlin

Horita J (2014) Oxygen and carbon isotope fractionation in the system dolomite–water–CO_2 to elevated temperatures. Geochim Cosmochim Acta 129:111–124

Hudson J (1977) Stable isotopes and limestone lithification. J Geol Soc 133:637–660

Immenhauser A, Della Porta G, Kenter JAM, Bahamonde JR (2003) An alternative model for positive shifts in shallow-marine carbonate $\delta^{13}C$ and $\delta^{18}O$. Sedimentology 50:953–959

Jarvis I, Trabucho-Alexandre J, Gröcke DR, Ulicny D, Laurin J (2015) Intercontinental correlation of organic carbon and carbonate stable isotope records: evidence of climate and sea-level change during the Turonian (Cretaceous). The Depositional Record 1:53–90

Jarvis I, Carson GA, Cooper MKE, Hart MB, Leary PN, Tocher BA, Horne D, Rosenfeld A (1988) Microfossil assemblages and the Cenomanian – Turonian (late Cretaceous) oceanic anoxic event. Cretaceous Res 9:3–103

Jenkyns HC (1996) Relative sea-level change and carbon isotopes: data from the Upper Jurassic (Oxfordian) of central and Southern Europe. Terra Nova 8:1365–3121

Jenkyns HC (2003) Evidence for rapid climate change in the Mesozoic-Palaeogene greenhouse world. Phil Trans R Soc Lond, Series A 361:1885–1916

Joachimski MM, Buggisch W (1993) Anoxic events in the late Frasnian – causes of the Frasnian-Famennian faunal crisis? Geology 21:675–678

Keeling CD (1979) The Suess effect: ^{13}Carbon-^{14}Carbon interrelations. Environ Int 2:229–300

Korte C, Kozur HW (2010) Carbon–isotope stratigraphy across the Permian-Triassic boundary: a review. J Asian Earth Sci 39:215–235

Kroopnick P (1985) The distribution of ^{13}C of ΣCO_2 in the world oceans. Deep-Sea Res 32:5784

Kump LR, Arthur MA (1999) Interpreting carbon-isotope excursions: carbonates and organic matter. Chem Geol 161(1–3):181–198

Kuypers MMM, Pancost R, Shinninghe Damsté JS (1999) A large and abrupt fall in atmospheric CO_2 concentration during Cretaceous times. Nature 399:342–345

Leckie M (2009) Seeking a better life in the plankton. Proc Natl Acad Sci 106(34):14183–14184

Loftus E, Roberts P, Lee-Thorp JA (2016) An isotopic generation: four decades of stable isotope analysis in African archaeology. Azania 51 (1):88–114

Mackensen A, Hubberten HW, Bickert T, Fischer G, Fütterer DK (1993) The ^{13}C in benthic foraminiferal tests of Fontbotia wuellerstorfi (Schwager) relative to the ^{13}C of dissolved inorganic carbon in southern ocean deep water: implications for glacial ocean circulation models. Paleoceanography 8:587–610

Magill CR, Ashley GM, Domínguez-Rodrigo M, Freeman KH (2016) Dietary options and behavior suggested by plant biomarker evidence in an early human habitat. Proc Natl Acad Sci 113(11):2874–2879

Matsson O, Dybala-Defratyka A, Rostkowski M, Paneth P, Westaway KC (2005) A theoretical investigation of α-carbon kinetic isotope effects and their relationship to the transition-state structure of SN2 reactions. J Org Chem 70(10):4022–4027

McAnena A, Flogel S, Hofmann P, Herrle JO, Griesand A, Pross J, Talbot HM, Rethemeyer J, Wallmann K, Wagner T (2013) Atlantic cooling associated with a marine biotic crisis during the mid-cretaceous period. Nat Geosci 6:558–561

McConnaughy T (1989) ^{13}C and ^{18}O disequilibrium in biological carbonates: I. Patterns. Geochim Cosmochim Acta 53:151–162

McCorkle DC, Keigwin LD, Corliss BH, Emerson SR (1990) The influence of microhabitats on the carbon isotopic composition of deep-sea benthic foraminifera. Paleoceanography 5:161–185

Menegatti AP, Weissert H, Brown RS, Tyson RV, Farrimond P, Strasser A, Caron M (1998) High-resolution $\delta^{13}C$ stratigraphy through the early Aptian 'Livello Selli' of the alpine Tethys. Paleoceanography 13:530–545

Mitchell SF, Ball JD, Crowley SF, Marshall JD, Paul CRC, Veltkamp C (1997) Isotope data from cretaceous chalks and foraminifera: environmental or diagenetic signals? Geology 25:691–694

Muccio Z, Jackson GP (2009) Isotope ratio mass spectrometry. Analyst 134(2):213–222

Munnecke A, Samtleben C, Bickert T (2003) The Ireviken event in the lower Silurian of Gotland, Sweden – relation to similar Palaeozoic and Proterozoic events. Palaeogeogr Palaeoclimatol Palaeoecol 195:99–124

Pagani M (2014) 12.13 biomarker-based inferences of past climate: the Alkenone pCO_2 proxy. Treatise on Geochemistry. Elsevier, Oxford, pp 361–378

Pälike H, Norris RD, Herrle JO, Wilson PA, Coxall HK, Lear CH, Shackleton NJ, Tripati AK, Wade BS (2006) The heartbeat of the Oligocene climate system. Science 314:1894–1898

Pearson PN, Shackleton NJ, Hall MA (1993) Stable isotope paleoecology of middle Eocene planktonic foraminifera and integrated isotope stratigraphy, DSDP site 523, South Atlantic. J Foramin Res 23:123–140

Quay PD, Tilbrook B, Wong CS (1992) Oceanic uptake of fossil fuel CO_2: Carbon-13 evidence. Science 256:74–79

Rabouille C, Mackenzie FT, Ver LM (2001) Influence of the human perturbation on carbon, nitrogen, and oxygen biogeochemical cycles in the global coastal ocean. Geochim Cosmochim Acta 65 (21):3615–3641

Ravelo A, Hillarie-Marcel C (2007) The use of oxygen and carbon isotopes of foraminifera in paleoceanography. In: Hillaire-Marcel C, de Vernal A (eds) Proxies in late Cenozoic paleoceanography, Developments in marine geology, vol 1. Elsevier, Amsterdam, pp 735–764

Raven JA, Falkowski PG (1999) Oceanic sink for atmospheric CO_2. Plant Cell Environ 22(6):741–755

Rohde RA, Muller RA (2005) Cycles in fossil diversity. Nature 434:209–210

Rohling EJ, Cook S (1999) Stable oxygen and carbon isotopes on foraminiferal carbonate shells. In: Gupta BKS (ed) Modern Foraminifera. Kluwer, Dordrecht, pp 239–258

Romanek CS, Grossman EL, Morse JW (1992) Carbon isotopic fractionation in synthetic aragonite and calcite: effects of temperature and precipitation rate. Geochim Cosmochim Acta 56(1):419–430

Saltzman MR, Thomas E (2012) Carbon isotope stratigraphy. In: Gradstein FM, Ogg JG, Schmitz M, Ogg G (eds) The Geological Time Scale, vol 1. Elsevier, Amsterdam, pp 207–232

Sarmiento JL, Gruber N (2006) Ocean Biogeochemical Dynamics. Princeton University Press, Princeton, p 503

Schidlowski M. Aharon P., 1992. Carbon cycle and carbon isotopic record: geochemical impact of life over 3.8 Ga of earth history. In: Schidlowski, M. et al., Early organic evolution: implications for energy and mineral resources. Springer, Berlin: 147–175

Schlanger SO, Jenkyns HC (1976) Cretaceous oceanic anoxic events: causes and consequences. Geol Mijnb 55:179–184

Scholle PA, Arthur MA (1980) Carbon-isotope fluctuations in cretaceous pelagic limestones: potential stratigraphic and petroleum exploration tool. AAPG Bull 64:67–87

Sepkoski JJ (2002) A compendium of fossil marine animal genera. Bull Am Paleontol 363:560

Sessions AL (2006) Isotope-ratio detection for gas chromatography. J Sep Sci 29(12):1946–1961

Siegenthaler U, Sarmiento JL (1993) Atmospheric carbon dioxide and the ocean. Nature 365(6442):119–125

Sponheimer M, Alemseged Z, Cerling TE, Grine FE, Kimbel WH, Leakey MG, Lee-Thorp JA et al (2013) Isotopic evidence of early hominin diets. Proc Natl Acad Sci 110(26):10513–10518

Stanley SM (2010) Relation of Phanerozoic stable isotope excursions to climate, bacterial metabolism, and major extinctions. Proc Natl Acad Sci 107:19185–19189

Stern MJ, Spindel W, Monse EU (1968) Temperature dependences of isotope effects. J Chem Phys 48(7):2908–2919

Sundquist ET, Visser K (2004) The geologic history of the carbon cycle. Treatise in. Geochemistry 8:425–472

Swart PK (2008) Global synchronous changes in the carbon isotopic composition of carbonate sediments unrelated to changes in the global carbon cycle. Proc Natl Acad Sci 105:13741–13745

Turner JV (1982) Kinetic fractionation of carbon-13 during calcium carbonate precipitation. Geochim Cosmochim Acta 46(7):1183–1191

Veizer J, Ala D, Azmy K, Bruckschen P, Buhl D, Bruhn F, Carden GAF, Diener A, Ebneth S, Godderis Y, Jasper T, Korte C, Pawellek F, Podlaha O, Strauss H (1999) $^{87}Sr/^{86}Sr$, $\delta^{13}C$ and $\delta^{18}O$ evolution of Phanerozoic seawater. Chem Geol 161:37–57

Wagner T, Wallmann K, Herrle JO, Hofmann P, Stüsser I (2007) Consequences of moderate 25,000 year lasting emission of light CO_2 into the mid-Cretaceous ocean. Earth Planet Sci Lett 259:200–211
Wefer G, Berger WH (1991) Isotope paleontology: growth and composition of extant calcareous species. Mar Geol 100:207–248
Wefer G, Berger WH, Bijma J, Fischer G (1999) Clues to ocean history: a brief overview of proxies. In: Fischer G, Wefer G (eds) Use of proxies in paleoceanography. Springer, Berlin, p 68
Weissert H, Bréhéret JG (1991) A carbonate carbon-isotope record from Aptian-Albian sediments of the Vocontian trough (SE France). Bull Soc Geol Fr 162(6):1133–1140
Weissert H, Joachimski M, Sarnthein M (2008) Chemostratigraphy. Newsl Stratigr 42:145–179
Weissert H, Lini A, Föllmi KB, Kuhn O (1998) Correlation of early Cretaceous carbon isotope stratigraphy and platform drowning events: a possible link? Palaeogeogr Palaeoclimatol Palaeoecol 137:189–203
Weissert H, McKenzie JA, Hochuli P (1979) Cyclic anoxic event in the early Cretaceous Tethys ocean. Geology 7:147–151
Wendler I (2013) A critical evaluation of carbon isotope stratigraphy and biostratigraphic implications for late Cretaceous global correlation. Earth-Sci Rev 126:116–146
Whiticar MJ (1999) Carbon and hydrogen isotope systematics of bacterial formation and oxidation of methane. Chem Geol 161(1):291–314
Zachos J, Pagani M, Sloan L, Thomas E, Billups K (2001) Trends rhythms, and aberrations in global climate 65 Ma to present. Science 292:689–693
Zahn R, Winn K, Sarnthein M (1986) Venthic foraminiferal ^{13}C and accumulation rates of organic carbon: Uvigerina peregrine group and Cibicidoides wuellerstorfi. Paleoceanography 1:27–42

Carbonate Compensation Depth

Ryan J. Woosley
Department of Ocean Science, University of Miami, Rosenstiel School of Marine and Atmospheric Sciences, Miami, FL, USA

Definition

Calcifying organisms in the surface supply $CaCO_3$ to deep waters when they die, and their tests or shells fall through the water column. As a result of respiration, increasing pressure, and decreasing temperature, waters become increasingly undersaturated with respect to $CaCO_3$ with depth, allowing the tests to dissolve more readily. The depth in the water column at which the rate of calcium carbonate supplied from the surface equals the rate of dissolution is called the carbonate compensation depth (CCD). If the sea floor lies above the CCD, these $CaCO_3$ tests can accumulate in the sediments; if the sea floor lies below the CCD, $CaCO_3$ will be absent from the sediments. In this way, the CCD can be thought of as a "snowline" marking the separation between carbonate-rich sediments and carbonate-deficient sediments. This gives rise to an alternative definition of CCD as the depth at which the carbonate content of the sediments is 0% by weight. This is a more practical definition because measuring the carbonate content of sediments is much easier than measuring rates of supply and dissolution in the water column.

There are actually at least two different CCDs because there are two common crystalline polymorphs of $CaCO_3$ produced in the surface. Pteropods (cone-shaped mollusks) secrete the more soluble form, aragonite, while foraminifera (zooplankton) and coccolithophores (phytoplankton) secrete the more stable form, calcite. The aragonite compensation depth (ACD) is typically about 3,000 m shallower than the calcite compensation depth (Morse and Mackenzie 1990). Studies generally focus on the calcite compensation depth because it marks the complete dissolution of carbonates from the sediments. The system is further complicated by high-magnesium calcites, which are actually more soluble than aragonite, can also be produced as a by-product of osmoregulation (Woosley et al. 2012), and likely begin to dissolve shallower in the water column; however, very little is known about their contribution to the carbon cycle.

Factors Controlling CCD

The depth of the CCD is mainly controlled by two factors: the degree of undersaturation with respect to calcite or aragonite and the flux of $CaCO_3$ debris from the surface. The saturation state (Ω) is the ratio of the ion concentration product ($[Ca^{2+}][CO_3^{2-}]$) to the apparent solubility constant and represents how close the water is to thermodynamic equilibrium. Surface waters are generally supersaturated ($\Omega > 1$). The degree of supersaturation decreases with depth as a result of decreases in the solubility of the minerals with increasing pressure and decreasing temperature, as well as increased total CO_2 from remineralization of organic matter, until the water reaches saturation ($\Omega = 1$), a depth called the saturation horizon. Below the saturation horizon, the saturation state continues to decrease and the waters become undersaturated ($\Omega < 1$), allowing $CaCO_3$ to dissolve. At some depth at or below the saturation horizon, there is a rapid increase in the rate of dissolution; this is called the lysocline. Below the lysocline, the percent of $CaCO_3$ found in sediments decreases rapidly until the CCD is reached. The saturation horizon, lysocline, and CCD are shown schematically in Fig. 1. In a thermodynamically controlled ocean, the depth of the saturation horizon, lysocline, and CCD would all be very similar. But because the kinetics of $CaCO_3$ dissolution are complex and nonlinear, the lysocline and CCD can be 200–1000 m deeper than the saturation horizon. The majority of dissolution occurs at the sediment-water interface because $CaCO_3$

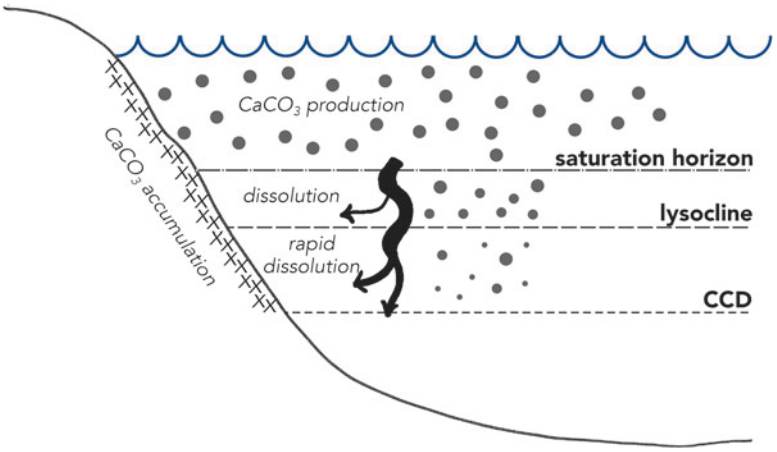

Carbonate Compensation Depth, Fig. 1 A schematic showing the relationship between the saturation horizon, lysocline, and carbonate compensation depth (CCD) in the ocean. The location of the three levels varies by location as a result of differences in $CaCO_3$ production at the surface and the degree of undersaturation at depth

particles generally fall through the water column faster than they can dissolve. There is some evidence of dissolution above the aragonite saturation horizon, which is thought to be dissolution of high-magnesium calcites.

Spatiotemporal Variability

The position of the CCD varies spatially as the result of differences in the magnitude and type of production at the surface and saturation state at depth. Specifically, the CCD is deeper in the Atlantic (~5,000 m) than in the Pacific and Indian (~3,500–4,500 m) due to a lower saturation state in the subsurface Pacific and Indian as a result of higher total CO_2 concentrations from organic matter remineralization. The CCD is also deeper in the tropics due to high productivity in the surface resulting in a higher flux of $CaCO_3$ to the deep and shallower near the continental margins due to increased organic matter remineralization decreasing the saturation state.

The position of the CCD also varies greatly (~2,000 m) over geologic time scales. This variability has major implications for the global carbon cycle because it determines how much carbon is stored long term (millions of years) in deep-sea sediments and how much is actively cycled through the ocean, atmosphere, and biosphere (~1,000-year time scales).

Buffering Anthropogenic CO_2

Currently, the uptake of anthropogenic CO_2 by the oceans is resulting in a decrease in pH and CO_3^{2-} concentration, a process termed ocean acidification. These changes to the inorganic carbon system cause the saturation horizon, and in turn the lysocline and CCD, to shoal. Lowering of the saturation state in the surface ocean may also lead to a decrease in $CaCO_3$ production at the surface and thus reduce the supply of $CaCO_3$ to sediments, causing the CCD to shoal. If the CCD shoals, carbonate sediments that were formally below the CCD will become exposed to corrosive waters and begin to dissolve. The dissolution of $CaCO_3$ consumes CO_2 according to the following reaction:

$$CO_2 + H_2O + CaCO_3 \rightarrow Ca^{2+} + 2HCO_3^{-}. \quad (1)$$

This reaction reflects the "neutralizing capacity" of the deep ocean by increasing the alkalinity (or buffering capacity) and will play a major role in returning atmospheric CO_2 concentrations to "natural" levels once fossil fuel burning ceases (Morse and Mackenzie 1990). However, this re-equilibration will take thousands of years (Broecker and Takahashi 2011).

Cross-References

- Biological Pump
- Calcium
- Carbonate Minerals and the CO2-Carbonic Acid System
- Dolomite and Dolomitization
- Earth's Oceanic Crust
- Fluid–Rock Interaction
- Organic Geochemistry

References

Broecker WS, Takahashi T (2011) Neutralization of fossil fuel CO_2 by marine calcium carbonate. In: Archer D, Pierrehumbert R (eds) The warming papers: the scientific Foundation for the climate change forecast. Wiley-Blackwell, Oxford, UK, pp 341–353

Morse JW, Mackenzie FT (1990) Geochemistry of sedimentary carbonates. Elsevier, Amsterdam, p 707

Woosley RJ, Millero FJ, Grosell M (2012) The solubility of fish-produced high magnesium calcite in seawater. J Geophys Res 117: C04018. https://doi.org/10.1029/2011JC007599

Carbonate Minerals and the CO_2-Carbonic Acid System

Abraham Lerman[1] and Fred T. Mackenzie[2]
[1]Department of Earth and Planetary Sciences, Northwestern University, Evanston, IL, USA
[2]Department of Oceanography, School of Ocean and Earth Science and Technology, University of Hawai'i at Manoa, Honolulu, HI, USA

Definition

Carbonic acid, H_2CO_3, forms from the dissolution of CO_2 in water and plays a key role in weathering, biological production, formation and deposition of sediments, and the carbon cycle. Carbonate minerals, primarily calcite, aragonite, and dolomite precipitating from these solutions, constitute the second most abundant class of sedimentary rocks.

Introduction

Carbonate rocks, consisting mainly of the minerals calcite ($CaCO_3$) and dolomite [$CaMg(CO_3)_2$], are the second most abundant class of sedimentary rocks, after terrigenous clastics, on land and on the ocean floor. The widespread occurrence of carbonate rocks in the geologic record is attributable to the following factors:

1. CO_2 gas has a relatively high solubility in water, higher than molecular oxygen and nitrogen.
2. CO_2 hydrolyzes in water, making the bicarbonate and carbonate anions (discussed in more detail in section "CO_2-Carbonic Acid-Carbonate System and Seawater") that react with divalent and monovalent metals.
3. Among the divalent cations, calcium combined with the carbonate anion makes a solid of low solubility.

Calcium is the fifth and carbon the 15th most abundant elements in the Earth's crust, and their presence in natural waters accounts for the formation of mineral $CaCO_3$ by inorganic and biogenic processes in many environments.

Twenty-seven carbonate minerals are listed in Table 1 to provide the reader with an appreciation of the wide variety of minerals in this mineral group. In terms of their abundance, calcites with Mg in their structure ($Ca_{1-x}Mg_xCO_3$) and aragonite ($CaCO_3$) are more abundant in the extant younger sedimentary mass, whereas dolomite and nearly pure calcite are more abundant in the geologically older sequences. Figure 1 shows the mass of calcite and dolomite in the preserved sedimentary carbonate mass. A long-standing and unresolved geologic problem is how much of the extant dolomite in the sedimentary record is of primary origin, that is, a direct precipitate from seawater, and how much is secondary formed from alteration of calcite and aragonite. Some scientists have proposed that both the calcite/dolomite preserved mass distribution and the original composition of inorganic and biogenic calcite and aragonite phases have varied cyclically during the Phanerozoic (the past 545 Ma) reflecting major changes in seawater composition during this eon (see, e.g., Mackenzie and Andersson 2013).

Ca-carbonates are primarily inorganic and biogenic products of the marine environment. $CaCO_3$ is a first precipitate in an evaporative sequence of seawater, and later precipitates are Na and K chlorides and sulfates. In continental waters, however, the anions HCO_3^- and CO_3^{2-} are usually more abundant than Cl^- and SO_4^{2-}, and the minerals precipitating are the various carbonates of Na, as shown in Table 1. Much of the information in this article is based on the books by Morse and Mackenzie (1990), Mackenzie and Lerman (2006), and Mackenzie and Andersson (2013).

CO_2-Carbonic Acid-Carbonate System and Seawater

This section presents some of the basic physical-chemical relationships relevant to understanding the behavior of CO_2 in aqueous solution in the Earth's surface environments. Readers are referred to the books by Broecker and Peng (1982), Morse and Mackenzie (1990), Mackenzie and Lerman (2006), Zeebe and Wolf-Gladrow (2001), and Millero (2013) for a detailed development of the subject material.

***Dissolution and Dissociation of CO_2 in Water*:** Dissolution of carbon dioxide in water is the first step that enables photosynthetic production of organic matter in aqueous environments, precipitation of carbonate minerals from aqueous solutions, and chemical weathering of the Earth's crust and sediments. Carbon dioxide dissolves in water and reacts with it producing negatively charged bicarbonate and carbonate ions. In pure water the electrical charges are balanced by the hydrogen ion or in natural or experimental more complex aqueous solutions by other metal cations and the hydrogen ion. Dissolution and dissociation of the gaseous species $CO_2(g)$ in water are represented by the following reactions:

$$CO_{2(g)} = CO_{2(aq)} \quad (1)$$

$$CO_{2(aq)} + H_2O_{(l)} = H_2CO_{3(aq)} \quad (2)$$

$$H_2CO_{3(aq)} = H^+_{(aq)} + HCO_{3\,(aq)} \quad (3)$$

$$HCO_3{}^-_{(aq)} = H^+_{(aq)} + CO_3{}^{2+}_{(aq)} \quad (4)$$

Carbonate Minerals and the CO_2-Carbonic Acid System, Table 1 Carbonate minerals[a,b]

	Mineral	Composition	Occurrence[b]
1	Calcite	$Ca_{1-x}Mg_xCO_3$, $0 \leq x \leq 0.25$	A major rock-forming mineral in sedimentary environments. Calcite is a common constituent of sedimentary rocks, limestone in particular, much of which is formed from the shells of dead marine organisms. Approximately 10% of sedimentary rock is limestone. Calcite is the primary mineral in metamorphic marble. It also occurs as a vein mineral in deposits from hot springs, and it occurs in caverns as stalactites and stalagmites. Calcite may also be found in volcanic or mantle-derived rocks such as carbonatites, kimberlites, or rarely in peridotites. Calcite is often the primary constituent of the shells of marine organisms, e.g., plankton (such as coccoliths and planktonic foraminifera), the hard parts of red algae, some sponges, brachiopods, echinoderms, some serpulids, most bryozoa, and parts of the shells of some bivalves (such as oysters and rudists) The largest documented single crystal of calcite originated from Iceland, measured 7 × 7 × 2 m and 6 × 6 × 3 m and weighed about 250 t
2	Aragonite	$CaCO_3$	Aragonite is the high pressure polymorph of calcium carbonate. As such, it occurs in high pressure metamorphic rocks such as those formed at subduction zones. Aragonite and calcite precipitate in hot springs as travertine deposits. Aragonite forms naturally in almost all mollusk shells, and as the calcareous endoskeleton of warm- and cold-water corals (Scleractinia). Several serpulids have aragonitic tubes. In some mollusks, such as pteropods, the entire shell is aragonite; in others, aragonite forms only discrete parts of a bimineralic shell (aragonite plus calcite). The nacreous layer of the aragonite fossil shells of some extinct ammonites forms an iridescent material called ammolite. Aragonite also forms in the ocean and in caves as inorganic precipitates called marine cements and speleothems, respectively. Aragonite is not uncommon in serpentinites where high Mg in pore solutions apparently inhibits calcite growth and promotes aragonite precipitation
3	Vaterite	$CaCO_3$	Vaterite occurs in mineral springs, organic tissue, gallstones, and urinary calculi. Vaterite can be produced as the first mineral deposits repairing natural or experimentally induced shell damage in some aragonite-shelled mollusks (e.g., gastropods). Subsequent shell deposition occurs as aragonite
4	Ikaite	$CaCO_3 \cdot 6H_2O$	At the Ikka Fjord, Greenland, Ikaite, occurs in spectacular towers growing out of the fjord floor toward the surface water, where they are naturally truncated by waves. The Ikaite towers are created as the result of a groundwater seep, rich in carbonate and bicarbonate ions, entering the fjord bottom. Ikaite has also been reported as occurring in high-latitude marine sediments in Antarctica, Sea of Okhotsk, and Saanich Inlet, British Columbia, Canada. In addition it has been reported in a deep sea fan off the Congo. The most recent occurrence has been reported by Dieckmann et al. (2008). Ikaite directly precipitates in sea ice in the Weddell Sea and throughout fast ice off Adélie Land, Antarctica
5	Monohydrocalcite	$CaCO_3 \cdot H_2O$	Monohydrocalcite has been observed in air conditioning systems, and in moonmilk deposits in caves, both probably formed from spray of carbonate-rich fluids. It is well known in Robe on the Limestone Coast of South Australia as a component of beach sands of Lake Fellmongery and Lake Butler, where it is believed to be formed from algal spume. Other lacustrine deposits include Lake Issyk-Kul, Lake Kivu, and Solar Lake, Sinai
6	Magnesite	$MgCO_3$	Magnesite occurs as veins in and an alteration product of ultramafic rocks, serpentinite, and other magnesium-rich rock types in both contact and regional metamorphic terrains. Magnesite is also present within the regolith above ultramafic rocks as a secondary carbonate within soil and subsoil, where it is deposited as a consequence of dissolution of magnesium-bearing minerals by carbon dioxide within groundwater
7	Barringtonite	$MgCO_3 \cdot 2H_2O$	Found with nesquehonite on the surfaces of olivine basalts
8	Nesquehonite	$MgCO_3 \cdot 3H_2O$	Bases of stalactites and incrustations, the remainder of which consisted of lansfordite. Anthracite coal deposit
9	Lansfordite	$MgCO_3 \cdot 5H_2O$	Small stalactites attached to carbonaceous shale
10	Pokrovskite	$MgCO_3 \cdot Mg(OH)_2 \cdot 0.5H_2O$	Alteration of ultramafic bodies of dunite and serpentinite
11	Artinite	$MgCO_3 \cdot Mg(OH)_2 \cdot 3H_2O$	Artinite is found along with hydromagnesite and other minerals as a low-temperature alteration product as veinlets or crusts in serpentinized ultrabasic rocks
12	Hydromagnesite	$4MgCO_3 \cdot Mg(OH)_2 \cdot 4H_2O$	Associated with the weathering products of magnesium containing minerals such as serpentine or brucite. It occurs as incrustations and vein or fracture fillings in ultramafic rocks and serpentinites. It occurs in hydrothermally altered dolomite and marble. It commonly appears in caves as speleothems and "moonmilk," deposited from water that has seeped through magnesium-rich rocks. It is the most common cave carbonate after calcite and aragonite
	Giorgiosite	$4MgCO_3 \cdot Mg(OH)_2 \cdot 4–6H_2O$	In white powdery crusts on lava

(*continued*)

Carbonate Minerals and the CO_2-Carbonic Acid System, Table 1 (continued)

	Mineral	Composition	Occurrence[b]
13	Dypingite	$4MgCO_3{\cdot}Mg(OH)_2{\cdot}5H_2O$	Alteration product in serpentines
14	Strontianite	$SrCO_3$	Strontianite is an uncommon low-temperature hydrothermal mineral formed in veins in limestone, marl, and chalk, and in geodes and concretions. It occurs rarely in hydrothermal metallic veins but is common in carbonatites
15	Witherite	$BaCO_3$	Witherite forms in low-temperature hydrothermal environments
16	Siderite	$FeCO_3$	Siderite is commonly found in hydrothermal veins and is associated with barite, fluorite, galena, and others. It is also a common diagenetic mineral in shales and sandstones, where it sometimes forms concretions, which can encase three-dimensionally preserved fossils. In sedimentary rocks, siderite commonly forms at shallow burial depths and its elemental composition is often related to the depositional environment of the enclosing sediments https://en.wikipedia.org/wiki/Lagoon
17	Dolomite	$CaMg(CO_3)_2$ or $Ca_{0.5}Mg_{0.5}CO_3$	A major sedimentary rock-forming mineral. Modern dolomite formation has been found to occur under anaerobic conditions in supersaturated saline lagoons. Vast deposits of dolomite are present in the geological record, but the mineral is relatively rare in modern environments
18	Ankerite	$Ca(Fe,Mg)(CO_3)_2$	Ankerite occurs with siderite in metamorphosed ironstones and sedimentary banded iron formations. It also occurs in carbonatites. In sediments it occurs as authigenic, diagenetic minerals and as a product of hydrothermal deposition
19	Natron	$Na_2CO_3{\cdot}10H_2O$	Geologically, the mineral natron and the historical natron are formed as transpiro-evaporite minerals, i.e., crystallizing during the drying up of salt lakes rich in sodium carbonate. The sodium carbonate is usually formed by absorption of carbon dioxide from the atmosphere by a highly alkaline, sodium-rich lake brine. Pure deposits of sodium carbonate decahydrate are rare, due to the limited temperature stability of this compound and due to the fact that the absorption of carbon dioxide usually produces mixtures of bicarbonate and carbonate in solution
20		$Na_2CO_3{\cdot}7H_2O$	*No known occurrences in nature*
21	Thermonatrite	$Na_2CO_3{\cdot}H_2O$	As efflorescences on soil in arid regions and in saline lakes
22	Natrite	Na_2CO_3	Locally abundant in deep drill holes in pegmatites occurring in differentiated alkaline massifs, in sodalite xenoliths associated with an intrusive alkalic gabbro-syenite complex
23	Nahcolite	$NaHCO_3$	In lava tunnels. It occurs as a hot spring and saline lake precipitate or efflorescence, in differentiated alkalic massifs, in fluid inclusions as a daughter mineral phase, and in evaporite deposits
24	Wegscheiderite	$Na_2CO_3{\cdot}3NaHCO_3$	As a replacement of trona in a lacustrine deposit. Lacustrine deposits
25	Trona	$Na_2CO_3{\cdot}NaHCO_3{\cdot}2H_2O$	Trona is found in alkaline saline lakes. Trona also occurs in magmatic environments, where it forms by autometasomatic reactions of late-magmatic fluids or supercritical fluid-melt mixtures with earlier crystallized rocks
26	Pirssonite	$Na_2CO_3{\cdot}CaCO_3{\cdot}2H_2O$	Lacustrine clay beds. In oil shales; in sediments of a salt pan
27	Gaylussite	$Na_2CO_3{\cdot}CaCO_3{\cdot}5H_2O$	Forms as an evaporite from alkali lacustrine waters. Also occurs rarely as veinlets in alkalic igneous rocks

[a]Morse and Mackenzie (1990), Mackenzie and Andersson (2013), Railsback (2002)
[b]Anthony et al. (1997–2003), Mindat (1993–2016), and Wikipedia articles by mineral name https://en.wikipedia.org/wiki/[mineralname]

Although aqueous uncharged CO_2 can include the species $H_2CO_{3(aq)}$, this species constitutes only a small fraction, about 1/400, of CO_2 in solution. As such the use of either $CO_{2(aq)}$ or $H_2CO_{3(aq)}$ for all of the aqueous species CO_2 is acceptable without a loss of meaning or accuracy (Millero 2013).

For each of the mass action Eqs. 1, 2, 3, and 4, one can write a thermodynamic equilibrium constant, using H_2CO_3* to represent both undissociated aqueous carbon species in solution – $H_2CO_{3(aq)}$ and $CO_{2(aq)}$ – which have values at 25 °C and 1 atm total pressure as follows (Morse and Mackenzie 1990):

$$K_o = \{H_2CO_3^*\}/P_{CO2} = 10^{-1.47} \quad (5)$$

$$K_1 = \{H^+\}\{HCO_3^-\}/\{H_2CO_3^*\} = 10^{-6.34} \quad (6)$$

$$K_2 = \{H^+\}\{CO_3^{2-}\}/\{HCO_3^-\} = 10^{-10.33} \quad (7)$$

where curly brackets designate thermodynamic activities of the chemical species (dimensionless quantities), and P_{CO2} is the partial pressure of CO_2, taken as an ideal gas and replacing its fugacity that is also dimensionless. The activities are also denoted as, for example, a_{H^+}, for the activity of the hydrogen ion, and a_{ion} for other species.

The activities of aqueous species and solids are referred to a standard state, chosen as a normal temperature and pressure

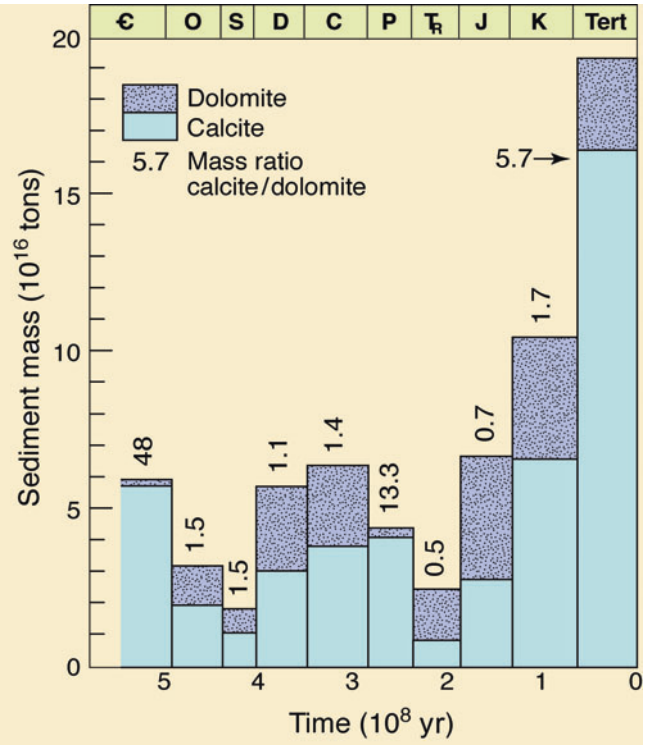

Carbonate Minerals and the CO_2-Carbonic Acid System, Fig. 1 Period-averaged preserved (extant) mass distribution of calcite and dolomite and mass ratio of calcite/dolomite through Phanerozoic time (After Mackenzie and Morse (1992))

(NTP) of 25 °C and 1 atm pressure, usually replaced by 298 K and 1 bar. Pure solids and solutes have an activity of 1 in a standard state. For solutes it is a 1 m (molal) solution, such that at infinite dilution the activity coefficient of the solute is equal to one. Thus, mass action equations written in terms of equilibrium constants are expressed as activities of the chemical species of interest and are a function of only pressure and temperature.

Because of the difficulties in determining the values of activity coefficients in seawater or compositional modifications of such, another standard state has been developed, that of the composition of seawater at the salinity $S = 35‰$ (g dissolved solids in 1 kg of solution; however, S in seawater is now taken as a dimensionless number because it is measured using a salinometer, which is based on electrical conductivity), 25 °C, and 1 atm total pressure. Thus for calculations of seawater CO_2-carbonic acid system chemistry, "apparent" or stoichiometric constants have been adopted and these vary with pressure, temperature, *and* composition (salinity). In seawater the mass action equations and the CO_2-carbonic acid system stoichiometric equilibrium constants (K-primes) have a similar formulation as the thermodynamic constants, but the expressions are written in terms of the concentrations of the dissolved inorganic carbon chemical species, have different values, and are functions of salinity as well as temperature and pressure. As an example, for an average seawater salinity of 35‰ and at a temperature of 25 °C and a total pressure of 1 bar (= ~1 atm), the stoichiometric constants and their values corresponding to Eqs. 5, 6, and 7 are Morse and Mackenzie (1990)

$$K'_0 = [H_2CO_3^*]/P_{CO2} = 2.84 \times 10^{-2} \quad (8)$$

$$K'_1 = [H^+][HCO_3]/[H_2CO_3^*] = 1.39 \times 10^{-6} \quad (9)$$

$$K'_2 = [H^+][CO_3^{2}]/[HCO_3] = 1.19 \times 10^{-9} \quad (10)$$

where brackets denote concentrations of the chemical species in mol per 1 kg seawater.

***Dissolved Inorganic Carbon*:** Because of the formation of the aqueous ions HCO_3^- and CO_3^{2-} from CO_2 in solution, the total concentration of dissolved inorganic carbon is the sum of all the inorganic carbon species, $CO_{2(aq)}$, HCO_3^-, and CO_3^{2-}. This parameter is termed dissolved inorganic carbon, to distinguish it from dissolved organic compounds, and it is usually denoted as ΣCO_2 or DIC:

$$DIC = CO_{2(aq)} + HCO_3^- + CO_3^{2-}. \quad (11)$$

The relative distribution of DIC chemical species is commonly shown as a function of pH in a plot known as a Bjerrum diagram (Fig. 2). The individual values of the three fractions of DIC (CO_2 plus H_2CO_3 as CO_2, HCO_3^- and CO_3^{2-}) are shown in the figure for different sets of conditions, as a function of the solution pH, between pH = 2 and 12, at two temperatures of 5 and 25 °C, and 1 bar total pressure and for seawater $S = 35‰$ and 1 and 300 bar total pressure. In a very dilute solution of zero ionic strength (Fig. 2a), HCO_3^- is the dominant DIC species over the pH range from roughly 6.5 to slightly more than 10. This is the range in pH of many natural waters. In addition, in dilute waters, lower temperature favors relatively higher concentrations of undissociated CO_2 and lower concentrations of the carbonate anion, CO_3^{2-}; that is, the equal concentration points of 50% shift to the left, toward lower pH values.

The effects of salt concentration and pressure on the distribution of the dissolved carbon species are shown in Fig. 2b. Notice first that HCO_3^- is still by far the dominant species in seawater over its pH range of slightly above 7 (deep ocean waters) to slightly above 8 (surface ocean waters). In addition, at 5 and 25 °C, the effect of a mean seawater salinity of 35‰ on the abundance of the various DIC species is pronounced: from a dilute solution of salinity 0–35‰, the abundance of the bicarbonate ion, HCO_3^-,

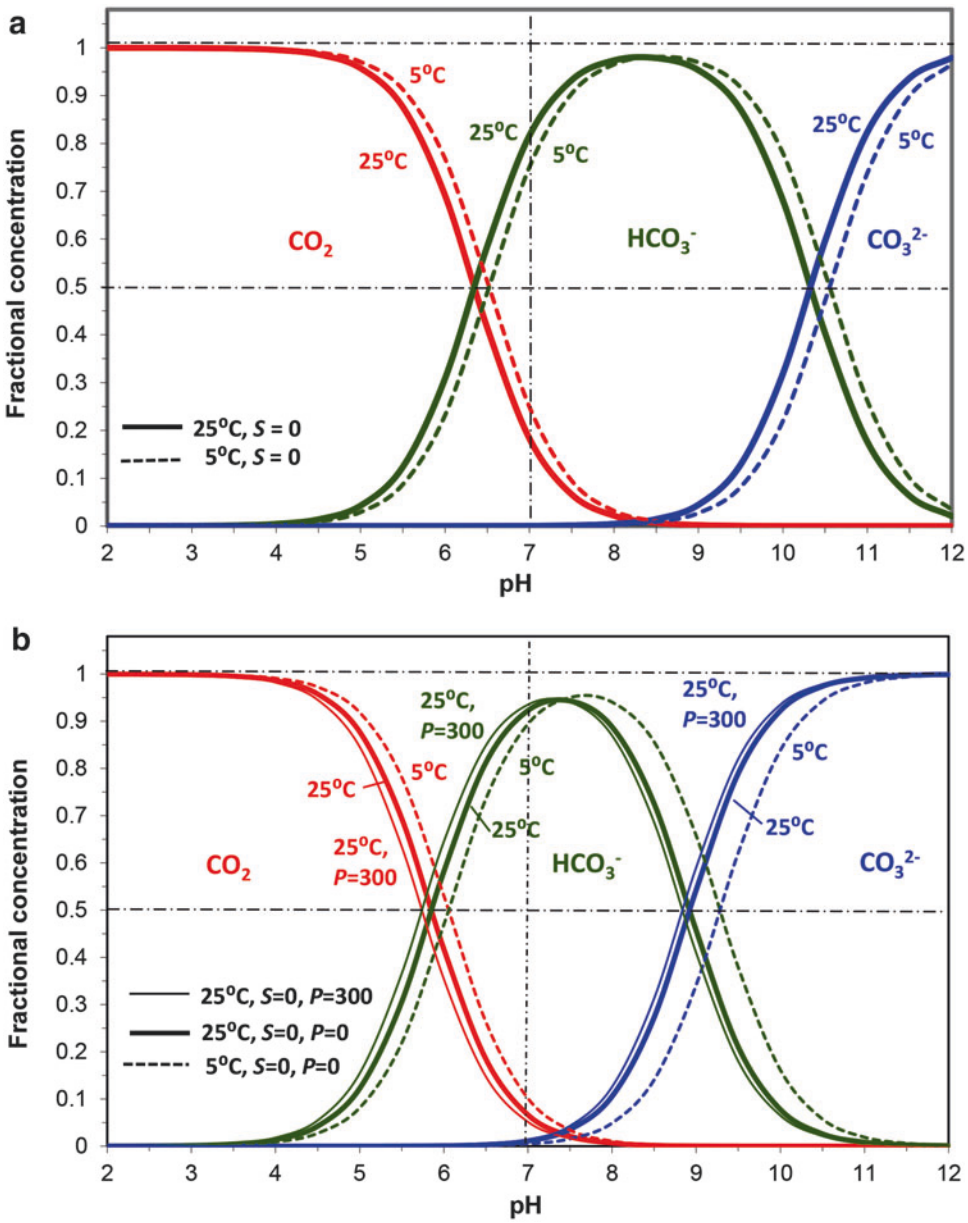

Carbonate Minerals and the CO_2-Carbonic Acid System, Fig. 2 Bjerrum diagram showing (**a**) Fractional concentrations of dissolved inorganic carbon species in pure water (salinity $S = 0‰$) as a function of pH at 5 ° and 25 °C. (**b**) Fractional concentrations of dissolved inorganic carbon species in seawater ($S = 35‰$) at 5 and 25 °C at atmospheric pressure, and at a pressure of 300 bar (After Mackenzie and Lerman (2006))

decreases at the expense of the other two species of $CO_{2(aq)}$ and CO_3^{2-}. However, the effect of pressure is small at a mean ocean water salinity of 35‰: a total pressure increase from atmospheric to 300 bars of pressure has only a small effect on the shift in the relative abundance of the DIC chemical species.

***Total Alkalinity*:** One other variable of the CO_2-carbonic acid system that is important to seawater carbon chemistry is that of total alkalinity. For seawater, the difference between the charges of the conservative cations and anions is equal to the algebraic sum of the charges of the H^+-dependent ions, and this difference is called the total alkalinity of the solution, denoted [TA]:

$$2[Ca^{2+}] + 2[Mg^{2+}] + [Na^+] + [K^+] - [Cl^-] - 2[SO_4^{2-}] = [HCO_3^-] + 2[CO_3^{2-}] + [B(OH)_4^-] + [OH^-] - [H^+] \quad (12)$$

and for the major species in seawater that contribute to the total alkalinity:

$$[TA] = [HCO_3^-] + 2[CO_3^{2-}] + [B(OH)_4^-] + [OH^-] - [H^+]. \quad (13)$$

The determination of TA and DIC in ocean waters is a powerful tool to use to trace water masses in the ocean and to obtain estimates of primary productivity and the dissolution

and precipitation of carbonate minerals. Also if the values of these two variables are known, the pH and pCO_2 of seawater can be calculated. Alternatively, the pH can be measured in solution instead of being calculated.

Saturation State: It is also possible to write reactions and equilibrium constants for the solution (dissolution) and precipitation of minerals in aqueous solutions. The carbonate minerals are especially important minerals found in the ocean as the skeletons and tests of marine organisms and as cements in marine sediments. Calcite (hexagonal $CaCO_3$), aragonite (orthorhombic $CaCO_3$), and dolomite [hexagonal $CaMg(CO_3)_2$] are important marine minerals. The latter mineral is not found in great abundance in modern environmental settings, but it is an important carbonate mineral found in ancient rocks deposited in the marine environment (Fig. 1). The mass action equation for both calcite and aragonite is written

$$CaCO_3 = Ca^{2+} + CO_3{}^{2-}, \tag{14}$$

and at 25 °C and 1 atm total pressure, the thermodynamic equilibrium constants are

$$K_{cal} = \left\{Ca^{2+}\right\}\left\{CO_3{}^{2-}\right\} = 10^{-8.46} \tag{15}$$

and

$$K_{arag} = \left\{Ca^{2+}\right\}\left\{CO_3{}^{2-}\right\} = 10^{-8.3} \tag{16}$$

and in seawater of $S = 35‰$ under the same P and T conditions

$$K'_{cal} = \left[Ca^{2+}\right]\left[CO_3{}^{2-}\right] = 10^{-6.37} \tag{17}$$

and

$$K'_{arag} = \left[Ca^{2+}\right]\left[CO_3{}^{2-}\right] = 10^{-6.19}. \tag{18}$$

Despite the two minerals having the same composition, they differ in their atomic structure, and thus the K values for the two minerals differ. These K values basically represent the solubilities of the two minerals. The larger K value for aragonite than for calcite implies that aragonite is a more soluble mineral than calcite and is unstable relative to calcite under the environmental conditions specified above. However for these minerals to dissolve, the aqueous solution in which the minerals are bathed must be undersaturated with respect to the two minerals. This implies that the product of the activities or concentrations of Ca^{2+} and $CO_3{}^{2,-}$, termed the ion activity product (*IAP*) or ion concentration product (*ICP*), respectively, in the solution must be smaller than the K values for the minerals; that is, the ratio of *IAP/K* or *ICP/K′* must be <1. In general, in a solution at equilibrium, $\Omega = 1$:

$$\Omega = IAP/K \text{or } ICP/K' = 1 \text{ at saturation.} \tag{19}$$

In a supersaturated solution $\Omega > 1$, and in an undersaturated solution, $\Omega < 1$.

Both calcite and aragonite contain other elements in minor or trace amounts, and this affects their solubilities. Strontium is especially important in aragonite and magnesium in calcite. Indeed Mg can be so plentiful in biogenically and inorganically produced calcite that a special term has been applied to the calcites containing more than about 4 wt.% Mg, the magnesian calcites, that generally have greater solubilities than pure calcite, and for some magnesian calcite compositions, even than aragonite. The general mass action equation and thermodynamic equilibrium constant for calcites with Mg in them is written as

$$Ca_{(1-x)}Mg_x(CO_3) = (1-x)Ca^{2+} + xMg^{2+} + CO_3{}^{2-} \tag{20}$$

and

$$K_{Mg-calcite} = \left\{Ca^{2+}\right\}^{(1-x)}\left\{Mg^{2+}\right\}^{(x)}\left\{CO_3{}^{2-}\right\} \tag{21}$$

where x is the mole fraction of $MgCO_3$.

For dolomite the mass action equation is

$$CaMg(CO_3)_2 = Ca^{2+} + Mg^{2+} + 2CO_3{}^{2-} \tag{22}$$

and

$$K_{dol} = \left\{Ca^{2+}\right\}\left\{Mg^{2+}\right\}\left\{CO_3{}^{2-}\right\}^2 = \sim 10^{-17}. \tag{23}$$

To our knowledge the K', that is, the stoichiometric constant, for dolomite has never been determined experimentally in seawater because of the difficulty in doing experiments involving this phase at low temperatures due to its slow reactivity in aqueous solution.

Thermodynamic and Thermophysical Data for Major Carbonate Minerals

This section discusses a number of fundamental thermophysical and thermodynamic data for the major sedimentary carbonate minerals calcite, aragonite, dolomite, and magnesite that are germane to their occurrences on Earth. Table 2 gives the molecular mass of each mineral, its molar volume, and density at ambient conditions (25 °C and 1 atm total pressure, rounded to 298 K and 1 bar). Also given are the coefficients of volume expansion as a function of temperature $\alpha_V = (1/V)(\partial V/\partial T)_P$ K^{-1}, and the coefficient of isothermal compressibility $\beta_T = -(1/V)(\partial V/\partial P)_T$ bar^{-1}.

Carbonate Minerals and the CO_2-Carbonic Acid System, Table 2 Thermophysical data for four carbonate minerals

Mineral phase	Molecular mass	V_0[a]	ρ[a]	α_V			β_T			β_{ad}[i]
	(g/mol)[a]	(cm^3/mol)	(g/cm^3)	T range (K)	(K^{-1})	Ref.	P range (kbar)	(bar^{-1})	Ref.	(bar^{-1})
$CaCO_3$ calcite	100.09	36.93	2.71	293–873	1.88E–05	[b]	2–12	1.39E–06	[d]	1.36E–06
				297–1,173	3.80E–06	[c]				
$CaCO_3$ aragonite	100.09	34.15	2.93	293–673	6.22E–05	[c]		1.55E–06	[d]	
				293–673	5.53E–05	[b]		1.45E–06	[e]	
$CaMg(CO_3)_2$ dolomite	184.40	64.34	2.87	297–973	2.28E–05	[c]		1.22E–06	[d]	1.05E–06
$MgCO_3$ magnesite	84.31	28.02	3.01	297–773	1.82E–05	[c]	0–60	8.71E–07	[f]	8.77E–07
							0–80	8.77E–07	[g]	
							0–20	6.83E–07	[h]	

[a]Robie and Hemingway (1995), density ρ from V and gram-formula mass of mineral
[b]Skinner (1966, p. 82)
[c]Fei (1995, p. 32)
[d]Birch (1966)
[e]Liu et al. (2005)
[f]Zhang and Reeder (1999)
[g]Ross (1997)
[h]Redfern et al. (1993)
[i]Bass (1995, p. 49)

The coefficient of adiabatic compressibility in Table 2 $\beta_{ad} = -(1/V)(\partial V/\partial P)_{ad}$ is related to β_T by the relationship $\beta_{ad} = \beta_T C_V/C_P$ bar^{-1}, where C_V and C_P are heat capacities of the mineral at constant volume and pressure, respectively, in J mol K^{-1}. Heat capacities at constant pressure, C_P, are given in Table 3 for different temperatures. Heat capacity at constant volume, C_V, is calculated from the thermodynamic relationship $C_P - C_V = TV\alpha_V{}^2/\beta_T$, where all the parameters are as defined above, and the ratios C_P/C_V for each mineral at different temperatures are given in Table 3.

The essential thermodynamic data that are needed for computation of mineral equilibria above the standard conditions of $T = 298$ K and $P = 1$ bar are summarized in Table 3 for temperatures from 298 to 900 K at 1 bar total pressure. The Gibbs standard free energy of formation of a mineral is designated $\Delta G_{T,1}$ (kJ/mol) and molar volume is $V_{T,1} = V_{0,1}[1 + \alpha_V(T - 298)]$($cm^3$/mol), where the coefficient of thermal expansion α is given in Table 3.

The equilibrium constant of a reaction, log K, is defined in terms of the Gibbs standard free energy change for the reaction, $\Delta G_{r\,T,1} = \Delta G_{T,1}$ (products) – $\Delta G_{T,1}$ (reactants), as

$$\log K_{T,P=1} = -\frac{\Delta G_{rT,1}}{2.3RT} \tag{24}$$

where ΔG in kJ mol^{-1} and $R = 8.314 \times 10^{-3}$ kJ mol^{-1} K^{-1}.

For solids at higher pressures, by integration of Eq. 24,

$$\log K_{T,P} - \log K_{T,1} = -\frac{\Delta V_{rT,1}(P-1)}{2.3RT} \tag{25}$$

where the values of $V_{T,1}$ of the individual minerals are given in Table 3, P is pressure in bars, and the gas constant $R = 83.14$ cm^3 bar mol^{-1} K^{-1}. If isothermal compressibility β_T of the reacting phases needs to be taken into account at pressures in the megabar range, then Eqs. 24 and 25 become:

$$\left(\frac{\partial \log K}{\partial P}\right)_T = -\frac{1}{2.3RT}\left(\frac{\partial \Delta G_{rT,1}}{\partial P}\right)_T = -\frac{\Delta V_{rT,1}(1-\beta_T P)}{2.3RT} \tag{26}$$

$$\log K_{T,P} - \log K_{T,1} = -\frac{\Delta V_{rT,1}}{2.3RT}\left((P-1) - \frac{\beta_T(P^2-1)}{2}\right) \tag{27}$$

Carbonate Mineral Stability in the System $CaCO_3$-$MgCO_3$

Determination of the univariant temperature-CO_2 curve for the calcite-dolomite-magnesite system was made by Harker and Tuttle (1955) at high to moderate temperatures and pressures. The order of decomposition with increasing temperature was shown to be magnesite, dolomite, and calcite. The location of the calcite-dolomite and dolomite-magnesite solvi along the $CaCO_3$-$MgCO_3$ binary join (Fig. 3) was established through the collective work of a number of investigators (e.g., Graf and Goldsmith 1955; Goldsmith and Heard 1961). The top of the calcite-dolomite solvus was located by Goldsmith and Heard (1961) at 1,075 °C, giving a composition of $Ca_{0.57.5}Mg_{0.42.5}CO_3$, a slightly calcium-rich phase. Note in Fig. 3 that the composition of calcite in terms of its Mg

Carbonate Minerals and the CO_2-Carbonic Acid System, Table 3 Thermodynamic data for four carbonate minerals at 298.15 $\leq T \leq$ 900 K and $P = 1$ atm ($\approx$1 bar). $\Delta G_{T,1}$ and C_p from Robie and Hemingway (1995). Others as explained in the text

T (K)	$\Delta G_{T,1}$ (kJ mol^{-1})				C_p J mol^{-1} K^{-1}				$V_{T,1}$ cm^3 mol^{-1}				C_p/C_v			
	cal	arag	dol	mag	cal	arag	dol	mag	cal	arag	dol	mag	cal	arag	dol	mag
298.15	−1128.5	−1127.4	−2161.30	−1029.5	83.47	82.31	157.51	76.09	36.93	34.15	64.34	28.02	1.035	1.323	1.046	1.044
300	−1128.0	−1126.9	−2160.30	−1029.0	83.82	82.55	158.06	76.44	37.14	34.79	64.78	28.17	1.035	1.332	1.046	1.044
400	−1101.6	−1100.2	−2105.70	−1000.9	97	92.67	183.54	90.57	37.21	35.00	64.93	28.22	1.041	1.425	1.053	1.050
500	−1075.6	−1073.6	*−2051.50*	−973.0	104.55	99.8	201.89	99.92	37.28	35.21	65.07	28.27	1.047	1.534	1.061	1.057
600	−1049.9	−1047.3	−1997.70	−945.3	109.88	105.76	215.66	107.38	37.35	35.42	65.22	28.33	1.055	1.657	1.070	1.064
700	−1024.4	−1021.2	−1944.40	−917.9	114.16	111.17	226.65	113.96	37.42	35.64	65.37	28.38	1.062	1.794	1.078	1.071
800	−999.0	−995.0	−1891.40	−890.7	117.88	116.28	236.08	120.06	37.49	35.85	65.51	28.43	1.069	1.948	1.086	1.078
900	−973.8	−969.1	−1838.70	−863.7	121.18	121.22	244.73	125.88	37.55	36.06	65.66	28.48	1.076	2.120	1.095	1.084

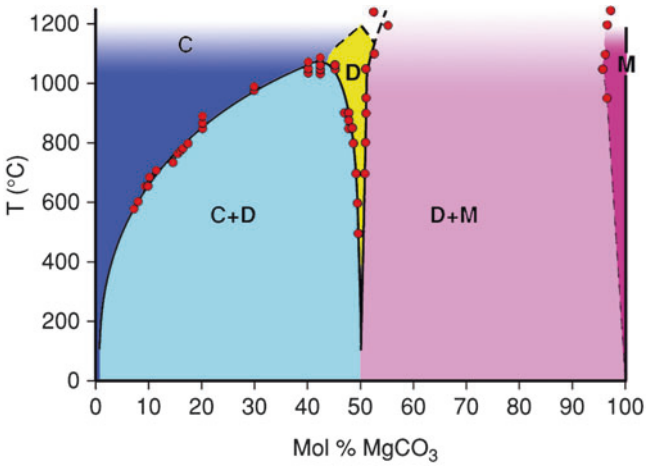

Carbonate Minerals and the CO_2-Carbonic Acid System, Fig. 3 Subsolvus relationships for the $CaCO_3$-$MgCO_3$ join. The top of the calcite-dolomite immisibility gap occurs at 1075 ºC. At this temperature, the phase composition is $Ca_{57.5}Mg_{42.5}(CO_3)_2$. *Dotted line* represents limit of detectable ordering in the dolomite structure. *C* calcite, *M* magnesite, and *D* dolomite (After Graf and Goldsmith (1958) and Goldsmith and Heard (1961); figure modified in Mackenzie and Andersson (2013))

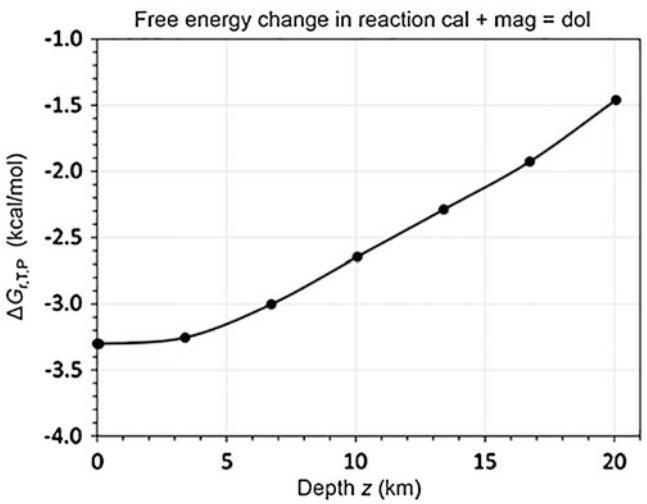

Carbonate Minerals and the CO_2-Carbonic Acid System, Fig. 4 Free energy change of the reaction calcite + magnesite = dolomite with increasing T and P

content at the Earth's surface temperature and pressure in equilibrium with dolomite contains only a couple of mol% Mg in solid solution. All calcites containing more Mg than this are unstable relative to nearly pure calcite $CaCO_3$. Calcium-rich, somewhat disordered dolomite, protodolomite, is commonly found in younger sediments and, with aging of the rock, progressively converts to a stoichiometric dolomite with distinct ordering (Land 1985).

From the Earth's surface and down the *P-T* gradient, dolomite is a more stable phase than calcite and magnesite. This is illustrated in Fig. 4 for the free energy of the reaction

$$CaCO_3 + MgCO_3 = CaMg(CO_3)_2,$$

where the value of $\Delta G_{r\ T,P}$ is <0, indicating that the dolomite phase is more stable than the two reactant phases (data in Table 3).

Stability of the Calcites: Calcites constitute major and very important biogenic and inorganic constituents of modern marine sediments, Pleistocene, and older rocks as skeletal clasts and cements. These phases can contain up to 25 mol% $MgCO_3$, and higher Mg content phases have been produced in the laboratory and observed sparingly in nature. Calcites with more than a few percent $MgCO_3$ are usually referred to as magnesian calcites or magnesium calcites (Mg calcites). Generally, for the same $MgCO_3$ content, calcites comprising the skeletons and tests of organisms have greater concentrations of sodium, sulfate, water, hydroxide, and bicarbonate and tend to have larger cell volumes and greater carbonate anion and cation positional disorder in their structure than natural or synthetic mineral phases. Chemical and microstructural heterogeneities especially characterize biogenic magnesian calcites, and dislocations and plane defects are common in their crystals. All of these characteristics may affect the thermodynamic and kinetic properties and reactivity of these phases in aqueous solution.

The solubility of calcites depends on their $MgCO_3$ content, in addition to other chemical constituents, and environmental parameters. The solubility of calcites can be expressed as a function of their $MgCO_3$ content and the ion activity product (*IAP*) of a solution in equilibrium with the solid (Plummer and Mackenzie 1974):

$$Ca_{1-x}Mg_xCO_3 = (1-x)Ca^{2+} + xMg^{2+} + CO_3{}^{2-} \quad (28)$$

$$IAP_{\text{calcite}} = K_{sp} = \{Ca^{2+}\}^{1-x}\{Mg^{2+}\}^{x}\{CO_3{}^{2-}\}, \quad (29)$$

where curly brackets in the latter expression denote the *activities* of the ions in aqueous solution, x is the mole fraction of $MgCO_3$ in the solid, and K_{sp} is the solubility product. For pure calcite, the mole fraction of $MgCO_3$ is zero. The generalized trend in solubility with $MgCO_3$ content of calcite phases at 25 °C and 1 atm total pressure appears reasonably well defined (Fig. 5) owing to the work of Plummer and Mackenzie (1974), Thorstenson and Plummer (1977), Walter and Morse (1984), Bischoff et al. (1987, 1993), and Busenburg and Plummer (1989). Bertram et al. (1991) have made estimates of the change in solubility with temperature demonstrating that as with pure calcite, the magnesian calcites have retrograde solubility (solubility decreases with increasing temperature).

The *thermodynamic solubility product* of pure calcite at 25 °C and 1 atm is about $10^{-8.46}$. The solubilities of the compositions of other calcites with Mg in them expressed in terms of IAP exhibit a minimum of around two mole percent $MgCO_3$, beyond which their solubility increases nearly linearly with increasing $MgCO_3$ content. There appear to be three recognizable trends in the solubility-composition data: one for abiotic solids that are well crystallized, compositionally homogeneous, and chemically pure (Fig. 5, curve 3), and the other for biogenic phases and abiotic solids that exhibit substantial lattice defects, carbonate positional disorder, and substitution of such foreign ions as sulfate and sodium (Fig. 5, curve 2). The third solubility-composition curve is that of Plummer and Mackenzie (1974) for biogenic materials subjected to minimal cleaning procedures in the laboratory before use in dissolution experiments designed to determine the solubilities of these phases (Fig. 5, curve 1). This curve may best reflect the effective solubility of the biogenic magnesian calcites in nature as a function of $MgCO_3$ content. It is this latter curve that is most used by scientists today when they report the saturation state of an aqueous solution with respect to a Mg-calcite composition.

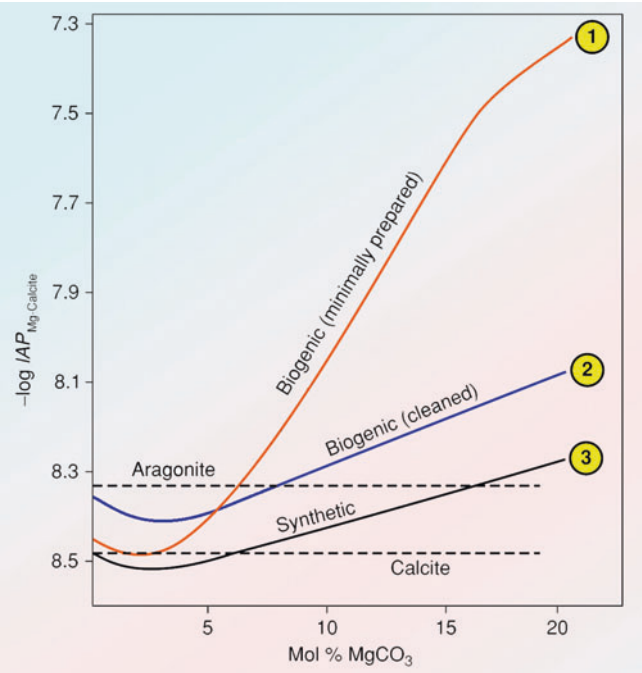

Carbonate Minerals and the CO_2-Carbonic Acid System, Fig. 5 Solubility of the magnesian calcites as a function of the $MgCO_3$ in the phase. See text for further explanation (After Bischoff et al. (1993); figure modified in Mackenzie and Andersson (2013))

Biogenic and some abiotic calcites are unstable in aqueous solutions relative to synthetic phases of similar $MgCO_3$ content. Their solubilities differ by roughly 0.15 pIAP units (pIAP = −log IAP), or about 4.6 kJ mol^{-1} (1.1 kcal mol^{-1}). This difference arises because of physical and chemical differences between the two types of solids. The complex microarchitecture, greater positional disorder of the $CO_3{}^{2-}$ anion group, and chemical impurity of the biogenic phases and some biogenic calcites result in higher solubilities of these solids. It is likely that the solubility-composition curve 3 for pure, compositionally homogeneous, and structurally well-ordered calcite phases represents the true metastable equilibrium solubility of magnesian calcites in aqueous solution at 25 °C and 1 atm.

Stability of Aragonite: The most abundant naturally occurring orthorhombic carbonate is aragonite, the dimorph of calcite. At near Earth surface pressure and temperature, aragonite is found as the biogenic component of many common invertebrate skeletons, as sediments derived from the physical and biological disintegration and erosion of these skeletons, as cements in modern marine sediments and Neogene limestones, in some carbonate cave deposits and travertine precipitated by hot springs, and often as a replacement mineral in igneous and metamorphic rocks and ore deposits (Speer 1983; Table 1). Although aragonite has larger cation sites, the phase is denser than calcite and hence is stable relative to calcite at elevated pressure and temperature (Fig. 6). The solubility product of aragonite at 25 °C and 1 atm is about $10^{-8.30}$. Aragonites exhibit only limited solid solution, primarily with Pb and Sr. Plumbian aragonites with up to 2.5 mol% are common, and strontian aragonites occurring in hot springs may contain up to 14 mol% $SrCO_3$ (Speer 1983). The limited solid solution of Sr is of importance because of the fact that the degree of

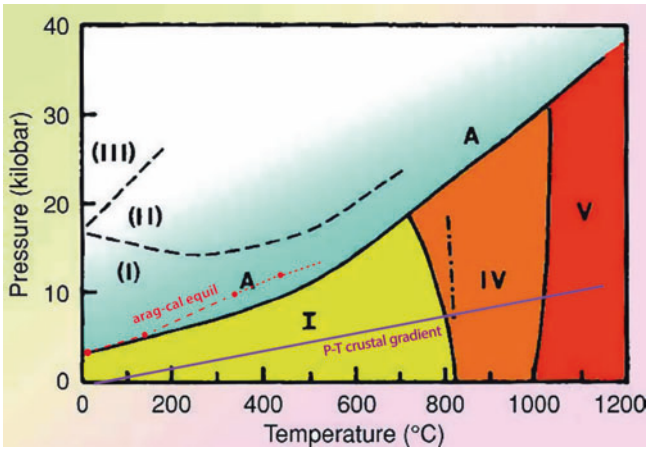

Carbonate Minerals and the CO_2-Carbonic Acid System, Fig. 6 Stability fields of aragonite and different polymorphs of calcite as a function of temperature and pressure. *A* aragonite, *I* through IV: calcite polymorphs with metastable fields shown by parentheses; *dash-dot line* at 800°C represents aragonite-calcite transition encountered on experimental cooling runs; *solid line* at lower temperature represents transition encountered on experimental heating runs (After Carlson (1980); figure modified in Mackenzie and Andersson (2013)). Calcite is the stable phase along the *P-T* gradient in Earth's crust. An equilibrium between aragonite and calcite, as shown by the *red dashed line*, would require pressures higher than those along the *P-T* gradient

solid solution varies among different groups of organisms having aragonitic shells, and the Sr content of some skeletal species has been used to obtain the Sr/Ca ratio or the temperature of the water from which the organism precipitated its skeleton.

Because aragonite is unstable relative to calcite at near Earth surface pressures and temperatures, with time and changes in environmental conditions, such as exposure to meteoric waters or burial in the subsurface, abiotic and biogenic aragonite can be converted to calcite or dolomite. Thus the original texture of the aragonite can be altered and the chemical and isotopic information contained in the phase lost. Rocks older than Neogene contain very little aragonite because of diagenetic reactions that lead to leaching of the components of the phase from the rock or its recrystallization to another mineral. Scant aragonite has been found in rocks as old as Pennsylvanian in age. The recrystallization process can lead to a loss of information concerning the environment of formation of a biogenic or abiotic aragonitic precipitate.

Stability of Dolomite: The mineral dolomite is a major constituent of especially ancient carbonate rocks. Dolomite was named in honor of Dieudonné Dolomieu (also known as Déodat Dolomieu), a geologist who worked in the Pyrenees and Alps in the eighteenth century and first described the mineral's characteristics and occurrence. Dolomite is distinguished from calcite and the other rhombohedral carbonates by its stoichiometry. Ideal dolomite has equal numbers of Ca and Mg atoms, and the Ca and Mg are segregated in distinct lattice planes. These planes are oriented normal to the *c*-axis, each alternating with *c*-normal trigonal CO_3 groups that are also in essentially planar orientation. For geologists, dolomite has been the center of an unending debate regarding its mode of formation in surface environments, its past abundance relative to other sedimentary carbonates, and its overall significance in the geologic record (e.g., Land 1985; Machel and Mountjoy 1986; Hardie 1987; McKenzie 1991; Mackenzie and Morse 1992; McKenzie and Vasconcelos 2009). The stability relations for dolomite in the $CaCO_3$-$MgCO_3$ system are shown in Fig. 4. In many aqueous solutions, including seawater, the solution is found to be oversaturated with respect to dolomite, but the phase does not spontaneously precipitate. This conundrum is probably at least in part a result of the kinetics of the dolomite precipitation reaction, which are very slow due to the difficulty in forming such a well-ordered phase from solution at near Earth surface *T* and *P*. Arvidson and Mackenzie (1997, 1999) have shown experimentally that increases in temperature and saturation state of a solution with respect to dolomite increase the rate of precipitation of dolomite. Field data tend to support the experimental observations since most unequivocal *primary* dolomite forming in the modern marine environment and that which is observed in the rock record has formed from compositionally modified seawater solutions with higher dolomite saturation states and at warmer temperatures than the global mean average of today.

Importance of Reaction of Calcium Silicate, Calcium Carbonate, and CO_2 in Earth History

The connection between the world of silicate minerals in the Earth's igneous crust and the sedimentary carbonates is represented by the reaction

$$CaSiO_3 + CO_2 = CaCO_3 + SiO_2, \qquad (30)$$

where $CaSiO_3$ is a shorthand notation for the silicate minerals containing the 1st (O), 2nd (Si), and 5th (Ca) most abundant elements by mass in the Earth's crust, CO_2 is gas, and the products are solid calcite and amorphous silica which recrystallizes to quartz with time. The reaction was introduced by Urey (1952), and it was known as the Urey reaction until Berner and Maasch (1996) produced evidence that the chemist and mining engineer Jacques-Joseph Ebelmen thought of this reaction in 1845–1847. Since then, the name has been deservedly changed to the Ebelmen-Urey reaction.

After the Earth had formed and was still hot, all the volatiles occurred as gases in the primordial atmosphere at about 700 K – above the critical temperature of water of 647.14 K and other gases, atmospheric pressure was 342 bar, comprising mostly H_2O, CO_2, N_2, HCl, and H_2S

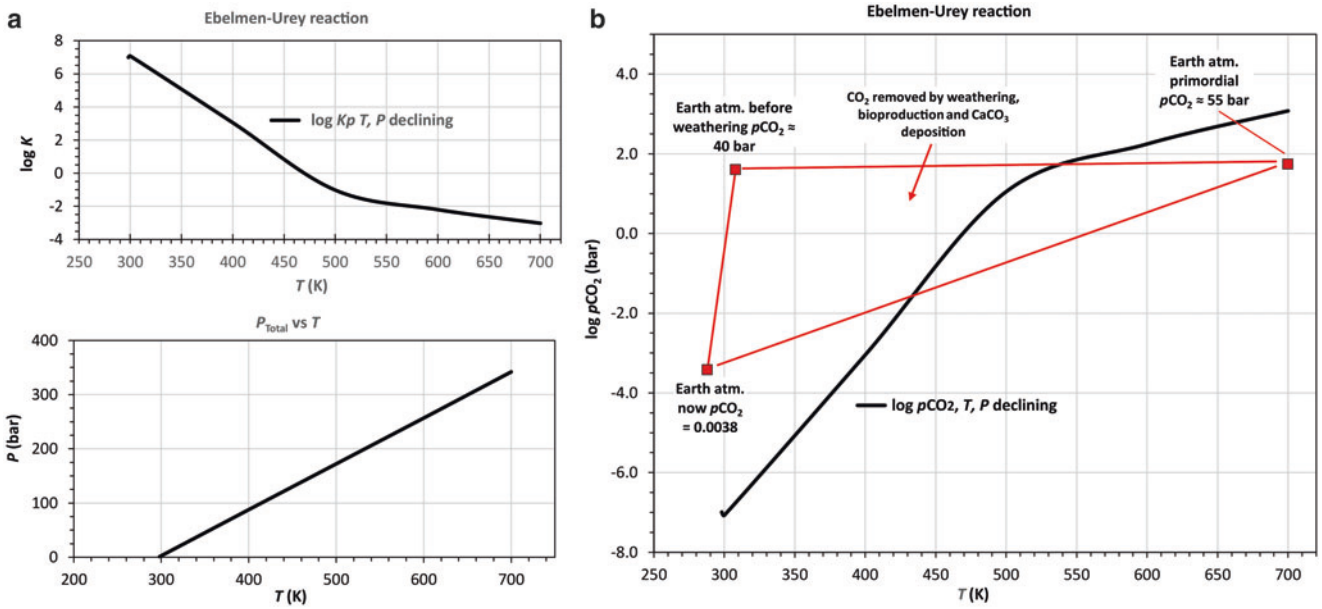

Carbonate Minerals and the CO_2-Carbonic Acid System, Fig. 7 (**a**) log K of reaction (30) at decreasing T (K), and P (bar). (**b**) Model decrease of atmospheric pressure P (bar) with decreasing temperature T (K). (**c**) p_{CO_2} from Eq. 31 calculated for atmospheric pressure P (bar) and T (K) decreasing as shown in (**b**). The triangular section of CO_2 decrease on the cooling Earth from Mackenzie and Lerman (2006)

(Mackenzie and Lerman 2006). As the Earth cooled, water condensed to liquid, and CO_2 and other gases dissolved in the primordial ocean. Subsequently, the weathering reactions, deposition of limestone, and biological production and burial of organic matter have further reduced the atmospheric CO_2 content. Two paths of the depletion of the atmosphere in CO_2 are schematically shown in Fig. 7 where they are compared to p_{CO_2} from the equilibrium constants of reaction (30):

$$\log K_{T,P} = \frac{a_{CaCO_3}\, a_{SiO_2}}{a_{CaSiO_3}\, p_{CO_2}} \tag{31}$$

where a are the activities of pure solids ($a > 1$ at $P > 1$ bar) and p_{CO2} is partial pressure of CO_2 ideal gas.

Log $K_{T,P}$ for reaction (30) at the T and P values of the crustal geothermal-geobaric gradient were computed from the data of Robie and Hemingway (1995), such as those cited in Table 3. For solids $CaSiO_3$ (wollastonite), $CaCO_3$ (calcite), and SiO_2 (glass), the molar volume change in the reaction, $\Delta V_{solid,T,P}$ is as given in (Eq. 27), using α_V (K^{-1}) and β_T (bar^{-1}) from Table 3. At the highest point of $T = 700$ K and $P = 342$ bar, the solid activities are: $a_{CaSiO_3} = 1.27, a_{CaCO_3} = 1.25$, and $a_{SiO_2} = 1.17$. For the solids, the volume change of the reaction is small, $\Delta V_{solids\ T,P} = 24$–$25$ cm^3 mol^{-1}. Much bigger volume change is associated with the reactant CO_2 that decreases from 24,666 cm^3 mol^{-1} at 298.15 K, 1 bar, to 178 cm^3 mol^{-1} at 700 K, 342 bar (NIST 2016). The equilibrium constant at a higher pressure is

$$\log K_{T,P} = \log K_{T,P=1} - \left(\frac{V_{sil} + V_{cal} - V_{wol} - V_{CO_2}}{2.303RT}\right)_{T,P} \times (P-1) \tag{32}$$

where V (cm^3 mol^{-1}) is molar volume at the temperature and pressure shown and gas constant $R = 83.14$ cm^3 bar mol^{-1} K^{-1}.

The relationships in Fig. 7c indicate that p_{CO_2} in the earlier Earth's atmosphere was lower than the equilibrium value of reaction (30–32) at the temperature above about 550 K. As the Earth cooled below 530–430 K, the equilibrium value of p_{CO_2} should be smaller that the atmospheric value. Under these conditions reaction (30) could be driven to the right and Ca-silicate converted to carbonate.

Accretion of the Earth, according to different models, might have lasted about 40 million years (Hanks and Anderson 1969; Wood et al. 2006). If life on Earth existed as early as 3.9 billion years B.P., the temperature of the atmosphere was likely to be below 50 °C or 325 K. This would imply that 325 K in Fig. 7c was reached some 600 million years after Earth's accretion, and most of the removal of atmospheric CO_2 by biological production and $CaCO_3$ formation occurred over a very long time stretch of Earth's history. In all, in the course of Earth's history 2.85×10^{20} kg CO_2 were removed

Carbonate Minerals and the CO_2-Carbonic Acid System, Table 4 Precipitation and dissolution rates of three major carbonate minerals

Precipitation $R_p = k_p(\Omega - 1)^n$ (Zhong and Mucci 1989)	Rate constant (k) (μmol m–2 h − 1)	Reaction order (n)
1. Calcite	$10^{-0.20}$	2.80
2. 15 mol% Mg-calcite	$10^{-0.20}$	2.80
3. Aragonite	$10^{1.00}$	2.36
Dissolution $R_d = k_d(1 - \Omega)^n$ (Walter and Morse 1985)	Rate constant (k) (μmol g–1 h−1)	
5. Calcite	$10^{2.82}$	2.86
6. 15 mol% Mg-calcite	$10^{2.62}$	3.34
7. Aragonite	$10^{2.89}$	2.48

from the atmosphere, leaving there 0.001% of the original mass, including the anthropogenic additions.

Carbonate Mineral Dissolution and Precipitation Rates

The relationships between the dissolution (R_d) and precipitation (R_p) rates of calcite, Mg-calcite, and aragonite at 25 °C in seawater are summarized in Table 4.

The dissolution rate is also a function of the pH. When a mineral dissolves in a partly closed system, such as in sediment pore water, of initially $\Omega < 1$, the solution can approach $\Omega = 1$ as dissolution progresses and the dissolution rate slows down. Mean dissolution rate $\overline{R}_d$ in the interval between the initial $\Omega < 1$ and final $\Omega = 1$ is:

$$\overline{R}_d = \frac{1}{1-\Omega}\int_{\Omega}^{1} k(1-\Omega')^n d\Omega' = \frac{k(1-\Omega)^n}{n+1} \quad \mu\text{mol g}^{-1}\text{h}^{-1} \tag{33}$$

The rates of dissolution of several carbonate minerals at 25 °C as function of pH are shown in Fig. 8. It should be noted that the rates are a strong function of pH, and that aragonite has the fastest dissolution rate and magnesite the slowest. There is also a considerable variation in the dissolution rate of the biogenic $CaCO_3$ phases (Fig. 9). The taxonomic nature of the carbonate-secreting organism evidently affects the crystal structure of the skeleton and hence its dissolution rate. Even though red algae particles of a Mg-calcite composition of ~20 mol% $MgCO_3$ are more soluble than the aragonitic green algal *Halimeda* sp., the rate of dissolution of the *Halimeda* is about 67% faster than that of the red algae. Pickett and Anderrson (2015) studied the dissolution rates of various biogenic Mg calcites in natural seawater at elevated pCO_2 values. They found that the rates increased with increasing Mg content, and that the relative dissolution rates were observed to be a function of both Mg content and

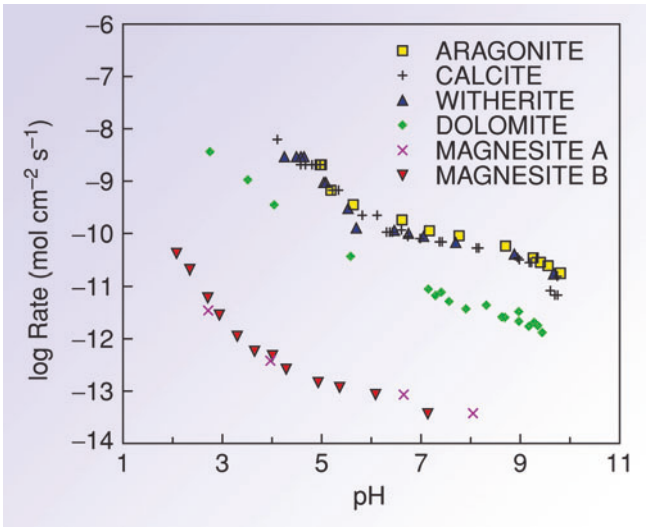

Carbonate Minerals and the CO_2-Carbonic Acid System, Fig. 8 Logarithmic rates of dissolution of several important carbonate minerals in distilled water at 25 °C and 1 atm as a function of pH. Notice the slower rates of dissolution for dolomite and especially magnesite. Also that aragonite dissolves faster than calcite (After Chou et al. (1989); figure modified in Mackenzie and Andersson (2013))

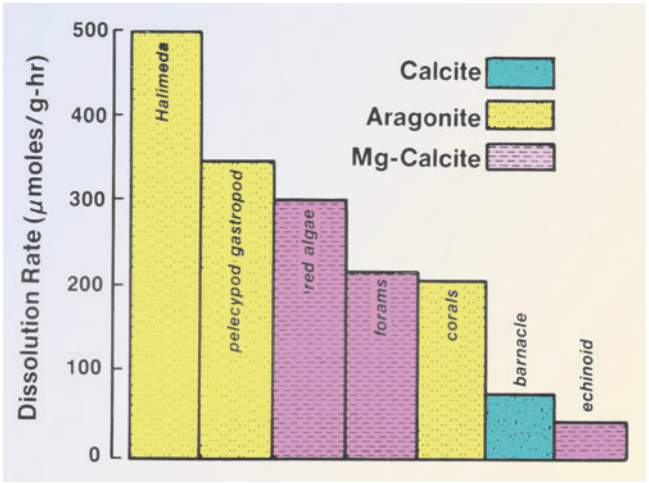

Carbonate Minerals and the CO_2-Carbonic Acid System, Fig. 9 Dissolution rates of disintegrated skeletons of various marine organisms of different carbonate mineralogies (After Walter and Morse (1985); figure modified in Mackenzie and Andersson (2013))

microstructure (surface area). Measured rates of dissolution increased with increasing pCO_2 treatment for all substrates and ranged from 2.5 to 18 umol g^{-1} h^{-1}.

CO_2-Carbonic Acid-Carbonate System of Ocean Waters

Discussion of the CO_2-carbonic acid-carbonate system of seawater is a treatise in itself (see, e.g., Broecker and Peng

1982; Andersson 2014). Here we look at two important aspects of the system in ocean water so the reader can gain an impression of the variables involved and their distribution and an appreciation of application of knowledge of the system to a major environmental problem, that of ocean acidification (OA).

Saturation State of Central Pacific Ocean Water Column: Surface ocean water is generally supersaturated with respect to the minerals aragonite and calcite ($CaCO_3$). Deeper-ocean waters are undersaturated with respect to aragonite and calcite, and the saturation depth is shallower for aragonite than that for calcite because aragonite is more soluble and hence $K'_{arag} > K'_{cal}$. The decrease in the degree of saturation with increasing depth is primarily due to an increase in CO_2 concentration due to bacterial decomposition of sinking organic matter and concomitant decrease in the CO_3^{2-}-ion concentration at the lower temperature of deep water and an increase in the value of K'_{cal} and K'_{arag} with increasing pressure. The depth where supersaturation changes to undersaturation varies among the major oceans (deepest in the Atlantic, shallower in the Indian, and shallowest in the Pacific oceans) and with latitude and location within an ocean (Broecker and Peng 1982; Morse and Mackenzie 1990).

Figure 10 shows generalized depth profiles of temperature, calcite and aragonite saturation states, dissolved inorganic carbon (DIC), total alkalinity, and dissolved calcium in waters of the Central Pacific. Notice the rapid decline with increasing depth of the degree of saturation of ocean water with respect to aragonite and calcite down to a depth of about 500 m and then the slow but steady decline to greater depths (Fig. 10b). The saturation depth of the more soluble aragonite is at about 500 m and that of calcite is at 3,000 m. The undersaturation of ocean waters at depth with respect to carbonate phases (Fig. 10b) accounts for the dissolution of $CaCO_3$ particles settling from the surface ocean layer and the return of calcium and total alkalinity to solution in this pump-like process. The increase in DIC with depth is mainly due to the microbial-mediated oxidation of organic matter sinking through the water column and at greater depth, the dissolution of $CaCO_3$.

It is of interest at this point to obtain a feel for how fast $CaCO_3$ dissolves in ocean waters and how quickly a hypothetical state of carbonate saturation in the oceanic water column might be reached. For the entire 5,500-m water column of Fig. 10, the average values of the degree of saturation are $\Omega_{cal} = 1.5$ and $\Omega_{ar} = 0.95$. However, below the saturation depth of 500 m for aragonite, the picture is very different: $\Omega_{ar} = 0.685$ from 500 to 5,500 m. To raise the degree of saturation with respect to aragonite to $\Omega_{ar} = 1.0$ within this depth range, total alkalinity (TA, Fig. 10c) would have to increase by a factor of 1.5. Equating this increase in TA as due to dissolution of $CaCO_3$ in ocean-floor carbonate sediments, the mass of the dissolved $CaCO_3$ would be 620 kg $CaCO_3/m^2$ or 21 cm/m^2 of solid $CaCO_3$. The mean rate of aragonite dissolution, using Eq. 7 in Table 4 for $\Omega_{ar} = 0.685$ and $\overline{R}_d$ from Eq. 33, is 6.91×10^{-3} kg yr^{-1}. The time to dissolve the mass of aragonite of 620 kg m^{-2} is

$$t = \frac{\text{Mass } CaCO_3 \text{ dissolved}}{\text{Dissolution rate}} = \frac{620 \text{ kg m}^{-2}}{6.91 \times 10^{-3} \text{kg year}^{-1}} \approx 90,000 \text{ year} \quad (34)$$

The preceding calculation assumes that Ω_{ar} rises in the course of aragonite dissolution from 0.685 to 1. The turnover time of the global ocean is much shorter ≥1,000 years, and this may assure that the undersaturation value is maintained at 0.685, making the dissolution rate in Eq. 33 faster. Therefore the time of dissolution of 620 kg aragonite/m^2 in Eq. 34, needed for the theoretical saturation, would be considerably shorter, about 26,000 years. If the dissolution rates determined in the laboratory (Table 4) hold in the ocean, the mass of $CaCO_3$ that is needed to bring the entire water column to saturation with respect to aragonite would be smaller than, or comparable to, the thickness of $CaCO_3$ deposited over such periods of time at an estimated rate of about 3 cm/10^4 years (Hay et al. 1988).

Ocean Acidification: Carbon dioxide is one of the concentration variables in the definition of DIC, where $DIC = HCO_3^- + CO_3^{2-} + CO_2$ (Eq. 11). CO_2 exchange between surface ocean water and the atmosphere is mainly controlled by the partial pressure difference of gaseous CO_2 between surface waters and the atmosphere and an exchange coefficient that is mainly a function of wind speed. Carbon dioxide is naturally exchanged between seawater and the atmosphere by physical factors and biological productivity that draws down CO_2 and respiration that produces CO_2, determining whether surface seawater acts as a source or sink of CO_2. Prior to the eighteenth century, the oceans appear to have been a net source of CO_2 that eventually was consumed in plant productivity on land (Lerman et al. 2011; Mackenzie et al. 2011). With the burning of fossil fuels of coal, oil, and gas and land use changes (mainly deforestation), the situation was reversed. CO_2 emissions to the atmosphere from these anthropogenic activities led to accumulation of CO_2 in the atmosphere, and in the early part of the twenty-first century, storage of 26% of the anthropogenic CO_2 emissions in ocean waters (Fig. 11). This has led to the second problem of anthropogenic CO_2 emissions – the first being global climate change – that of ocean acidification (OA).

As CO_2 from anthropogenic emissions of CO_2 have been absorbed by ocean waters, the pH has decreased, and consequently the CO_3^{2-}anion has decreased in concentration leading to a reduction in the carbonate saturation state of surface seawater:

$$2CO_2 + CO_3^{2-} + 2H_2O = 3HCO_3^- + H^+ \quad (35)$$

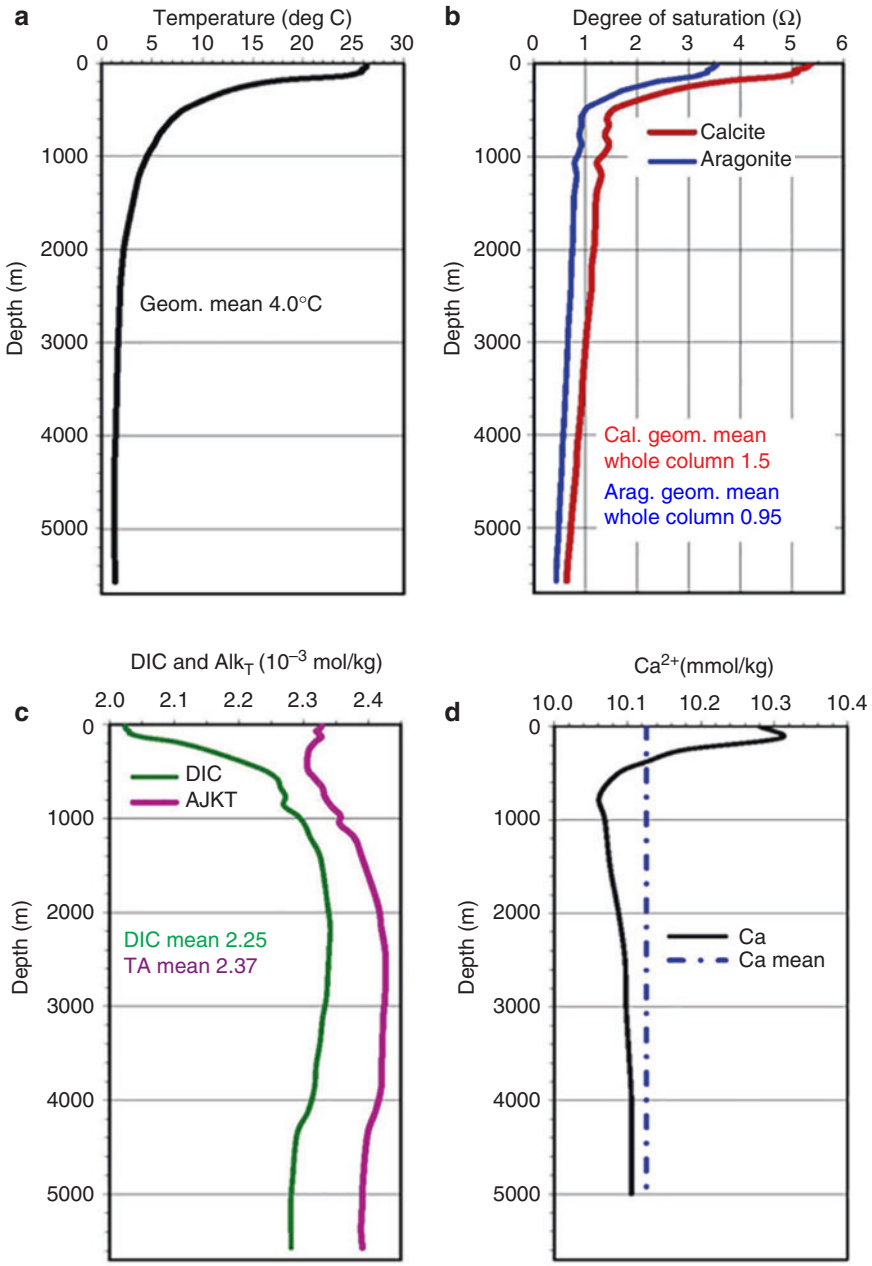

Carbonate Minerals and the CO_2-Carbonic Acid System, Fig. 10 Central Equatorial Pacific, W168.75°, S0° (WOCE Section P15S/14S, NOAA CGC-96, 6 March 1996, http://cdiac.ornl.gov/oceans/RepeatSections/clivar_p15s.html). Water depths calculated from pressure (Chapman 2006). (**a**) Temperature. (**b**) Degree of calcite and aragonite saturation (Ω) from *T*-*S*-*P* and carbonate-system parameters (Zeebe and Wolf-Gladrow 2001). (**c**) Dissolved inorganic carbon (DIC) and total alkalinity (TA). (**d**) Ca^{2+} concentration

Figure 12 shows the depth to which anthropogenic CO_2 has penetrated the oceans integrated over the time period 1800–1994. Notice in particular the "hot spot" of penetration in the high North Atlantic where North Atlantic deep water forms and sinks.

Experimental work and direct observations (e.g., Sabine et al. 2004; references in the legend of Fig. 11) have shown that lowering of the pH of seawater decreases the rate of calcification of a skeletal organism. This has been observed for pelagic and benthic foraminifera, coralline red algae, and of most concern, hermatypic corals, among others. In a world affected by OA, there is much concern for coral reefs and other carbonate ecosystems of the world as skeletal organisms' ability to calcify will be diminished. Also, with lowered seawater pH, particles produced by the disintegration of organism shells and tests will be more susceptible to dissolution in the more acidic seawater. It is possible that because of these two effects of anthropogenic CO_2 uptake by surface ocean waters, coral reefs will cease to accrete, and there will be net loss of $CaCO_3$ from their structural edifices. This implies potential loss of these structures as refuges for fish, barriers to storm surges, sources of beach sand, and an aesthetic environment for all to appreciate.

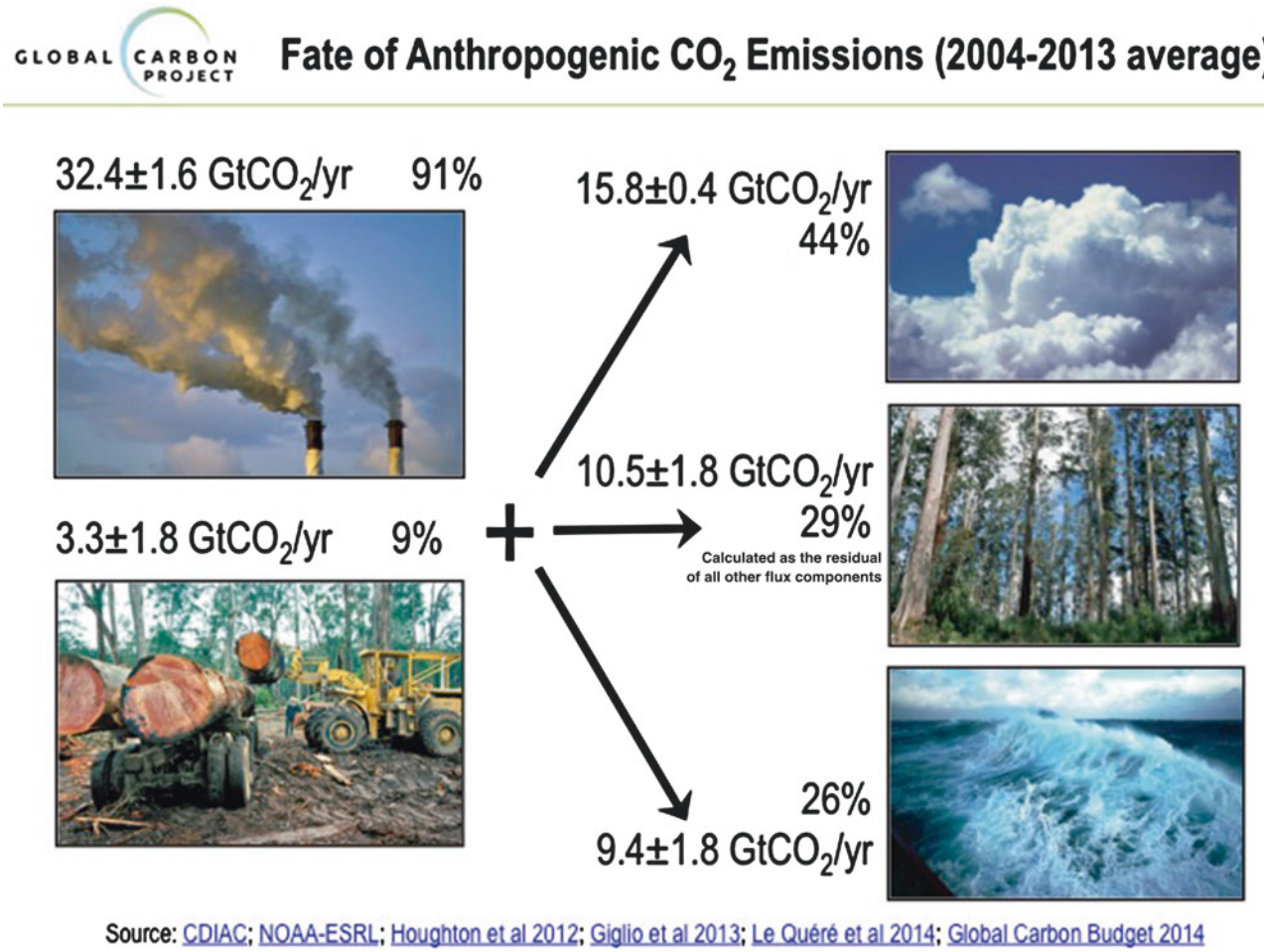

Carbonate Minerals and the CO_2-Carbonic Acid System, Fig. 11 Fate of anthropogenic CO_2 emissions from the fossil fuels of coal, oil, and gas and that of land use changes (deforestation). The sinks are the atmosphere, ocean waters, and by difference the land. Fossil-fuels have a lower $^{13}C/^{12}C$ ratio than CO_2 in the preindustrial atmosphere and their emissions dilute it (After Le Quere et al. (2015); see "Isotopes in Carbonates in Interpretation of Earth History" section)

Isotopes in Carbonates in Interpretation of Earth History

The heavier isotopes of an element are usually more abundant than the light ones (with the exception of ^{11}B and ^{7}Li among the common elements). Isotope concentrations in different materials are denoted as abundance ratios, $R = {}^{\text{heavy}}X/{}^{\text{light}}X$, in a sample relative to the ratio in a standard as

$$\delta X = \left(\frac{R_{\text{sample}}}{R_{\text{standard}}} - 1\right) \times 1000 \quad (‰)$$

For details of the notation of the isotope abundance, the reader may refer to such textbooks as Faure and Mensing (2004). An equilibrium constant of an isotope exchange reaction between two phases, X_1 and X_2, is usually denoted

$$\alpha_{1-2} = \frac{1 + \delta X_1}{1 + \delta X_2}$$

$$\ln \alpha_{1-2} = \ln \frac{1 + \delta X_1}{1 + \delta X_2} \approx \delta X_1 - \delta X_2$$

and the quantity $1000\ \ln\alpha_{1-2}$ is the fractionation factor of the isotope ratio $R = {}^{\text{heavy}}X/{}^{\text{light}}X$ between phases 1 and 2. Of the main components of $(Ca, Mg)CO_3$, calcium (atomic number $Z = 20$) has seven naturally occurring isotopes, one radioactive cosmogenic ^{41}Ca of half-life

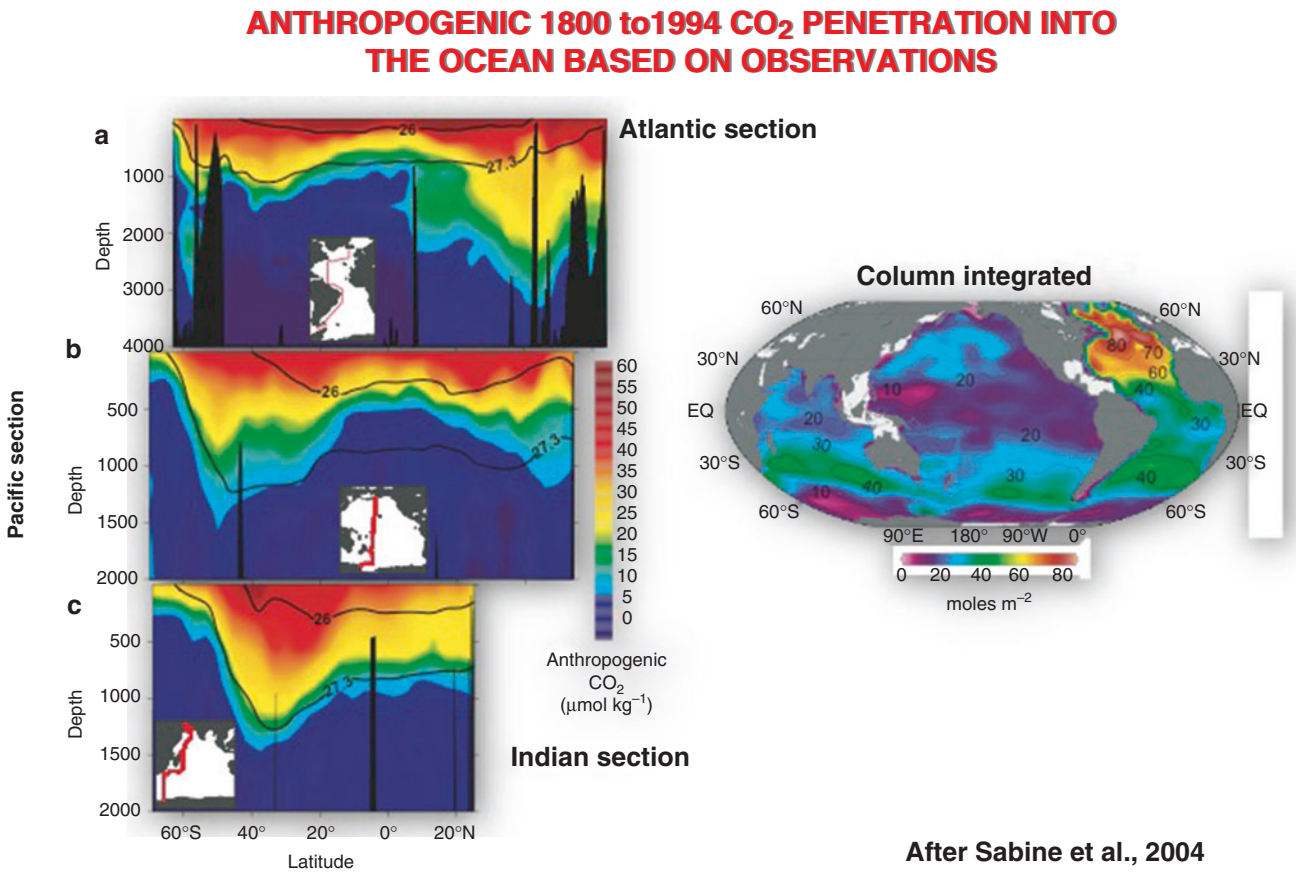

Carbonate Minerals and the CO_2-Carbonic Acid System, Fig. 12 Anthropogenic CO_2 penetration into the world's oceans from 1800 to 1994. Notice in particular the deep penetration and amount of anthropogenic carbon in waters of the region where the North Atlantic deep water forms and sinks (After Sabine et al. (2004))

Carbonate Minerals and the CO_2-Carbonic Acid System, Table 5 Stable isotopes of Ca, C, O, and Mg and their abundances in atomic %

Mass	% atomic abundance	Mass	% atomic abundance	Mass	% atomic abundance	Mass	% atomic abundance
^{40}Ca	96.941	^{12}C	98.93	^{16}O	99.757	^{24}Mg	78.7
^{42}Ca	0.647	^{13}C	1.07	^{17}O	0.038	^{25}Mg	10.13
^{43}Ca	0.135			^{18}O	0.205	^{26}Mg	11.17
^{44}Ca	2.086						
^{46}Ca	0.004						
^{48}Ca	0.187						

102,000 years, and six stable isotopes. Carbon ($Z = 6$) has two stable and one radioactive ^{14}C of half-life 5,730 years. Oxygen ($Z = 8$) and magnesium ($Z = 12$) each has three Table 5:

The most abundant isotope of calcium, ^{40}Ca, is also produced by decay of ^{40}K (Weatherill 1966). Fantle and Tipper (2014) have shown that for average bulk crustal rocks, the rate of ^{40}Ca addition from the decay of ^{40}K is less than 0.3‰ over 1 billion (10^9) years. Translating the addition rate of ^{40}Ca to Ca in the limestone and dolomite masses in Fig. 1, we use the following data: in carbonate rocks (Fig. 1), calcite makes 4.5×10^{20} and dolomite 2.1×10^{20} kg; mean K concentration in Eastern Kansas limestones of 0.22 wt.% K (Runnels and Schleicher 1956); ^{40}K atomic abundance fraction of K 1.17×10^{-4}; decay half-life of ^{40}K to ^{40}Ca 1.47×10^9 years; and ^{40}Ca atomic abundance fraction of Ca 0.97. Taking the limestones as pure $CaCO_3$ (40.0 wt.% Ca) and dolomites as $CaMg(CO_3)_2$ (21.7 wt.% Ca), the mass of Ca

Carbonate Minerals and the CO_2-Carbonic Acid System, Table 6 Fractionation factors of isotopic ratios

Isotopes (‰)	$\delta^{13}C/^{12}C$	$\delta^{18}O/^{16}O$	$\delta^{44}Ca/^{40}Ca$	$\delta^{26}Mg/^{24}Mg$
Inorganic precipitation	9.6–13.6[a), b)]	37–25[b)]	0.9–1.7 tidal dol[d)]	−0.7 to −1.3 [d)]
	5–17[d)]	28–29[c)]	0.2–0.7 dol Williston basin[d)]	−1.33 to −2.66[e)]
Modern seawater	0	0	1[f), i)], 1.81[h)], 1.7–2.1[j)]	+2.8[f)]
Biological mineralization	−8 to +2[k)]	−6 to +5[k)]	0.2–1.2[g)] var. taxa	+2[f)] coral
			−18 to −2.6[l)]	−3 to −1[f)] forams
Bioproduction of organic matter	−13 ± 4 C3 plants[n)]	27–43[m)]	−1.25 to +1.25[j)]	
	−27 ± 6 C4 plants[n)]			
Standards[o, p]	PDB, VPDB, VSMOW	PDB, VPDB, VSMOW	NIST SRM 915a NIST SRM 915b	DSM3 SRM980

[a]Emrich et al. (1970)
[b]O'Neil et al. (1969)
[c]Gussone et al. (2005)
[d]Farkaš et al. (2012)
[e]Saulnier et el. (2012)
[f]Chang et al. (2004)
[g]Böhm et al. (2006)
[h]Holmden et al. (2012)
[i]Fantle and DePaolo (2007)
[j]Fantle and Tipper (2014)
[k]Henkes et al. (2013)
[l]Zhu and Macdougall (1998)
[m]Tuthorn et al. (2014)
[n]O'Leary (1988), Mackenzie and Lerman (2006)
[o]Coplen (1995)
[p]Hippler et al. (2003)

in sedimentary carbonates is 2.24×10^{20} kg. The mass of ^{40}Ca in the carbonate reservoir is

$$\begin{aligned}&\left(2.24 \times 10^{23}\text{g Ca}/40.078\text{g Ca/mol}\right)\\&\quad\times\left(0.969\text{ mol fraction}^{40}\text{Ca}\right)\times\left(39.963\text{ g}^{40}\text{Ca/mol}\right)\\&\quad=2.17\times10^{20}\text{kg}.\end{aligned}$$

The result is that 82,000 kg ^{40}Ca/year are added to 2.17×10^{20} kg ^{40}Ca in the carbonate rocks in the sedimentary record. Thus the residence time of ^{40}Ca in carbonate rocks with respect to its production from $^{40}K - 2.17 \times 10^{20}$ kg/8.24×10^4 kg/year is very long, 2.6×10^{15} years, indicating that a change in the ^{40}Ca isotopic composition of carbonates is insignificant, in the absence of local strong K sources. The fractionation factors of the four isotopic ratios in some natural environments and processes are given in Table 6.

The main goals of studying the isotope fractionation in natural environments is to establish relationships between the fractionation and climate parameters, such as temperature or paleotemperature (Epstein et al. 1951, 1953), partial pressure of atmospheric CO_2, history of seawater, and diagenesis of carbonate sediments (references in Table 6 and others cited therein). The record of $\delta^{13}C$ in Phanerozoic carbonates and Cenozoic carbonates is shown in Fig. 13b. A number of long-term trends can be distinguished in the Phanerozoic (Lerman and Clauer 2007):

- A secular increase in the $\delta^{13}C$ during the 180 Ma from the Ordovician to the Carboniferous-Permian boundary broadly coincides with the emergence of higher plants and massive storage of organic carbon of lower $\delta^{13}C$ as coal in the Carboniferous.
- The next 100 Ma include glaciations of Gondwana near and above the Carboniferous-Permian boundary and a major extinction at the Permian-Triassic transition. This time represents a slightly declining trend, with much scatter, of the carbonate $\delta^{13}C$. However, some detailed $\delta^{13}C$ profiles across the Permian-Triassic boundary have provided internally consistent trends and information for the modeling of changes in atmospheric CO_2 and O_2 at that time (Berner 2006).
- From the Jurassic to the Miocene, a period from about 200 to 20 Ma, there is a slight increase in the $\delta^{13}C$, although it is smaller than an increase in the Paleozoic over a similar length of time. Within the Jurassic to the Miocene data, there are periods of elevated $\delta^{13}C$ values that lasted about 5–10 Ma and shorter periods of $\leq$1 Ma that are associated with oceanic anoxic events (Katz et al. 2005).
- The decrease in the $\delta^{13}C$ of carbonates at least during the last 30 Ma to the present represents a trend that may

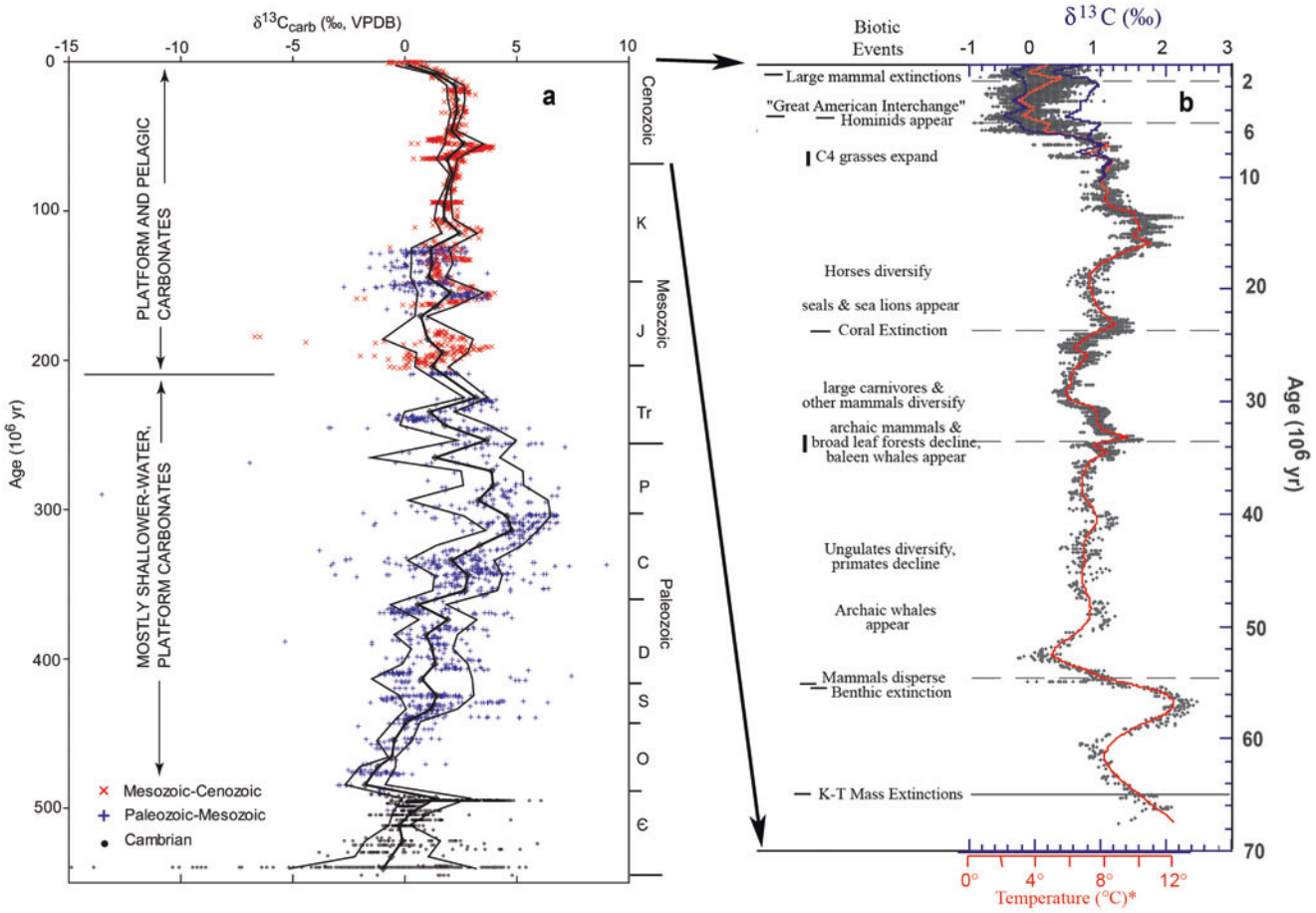

Carbonate Minerals and the CO_2-Carbonic Acid System, Fig. 13 (**a**) $\delta^{13}C$ values of Phanerozoic carbonates. Cambrian to Jurassic (*black* • and *blue* +) data from Veizer et al. (1999; courtesy of J. Veizer); Jurassic to Recent (*red* ×) from Katz et al. (2005). VPDB scale. Stratigraphic time scale from Gradstein et al. (2004). *Thick line*: consecutive 10-Ma-interval means (5-Ma in the most recent 10-Ma interval); *thin lines* are ±1 standard deviation (From Lerman and Clauer (2007)). (**b**) $\delta^{13}C$ values of Cenozoic carbonates (Modified from Zachos et al. (2001))

indicate a smaller biological fractionation between the carbonate carbon and organic carbon in the ocean. It has been variably proposed that a greater weathering of old organic matter has increased the delivery of isotopically lighter inorganic carbon forming from the remineralization of ^{13}C-depleted organic matter and it has been, consequently, one cause of the decreasing $\delta^{13}C$ values of marine carbonates. The rise of ^{13}C-enriched terrestrial grasses and the rapid radiation of ^{13}C-enriched diatoms also probably contributed to the depletion of ocean water in ^{13}C and hence to this trend in the carbon isotopes precipitated from the ^{13}C-depleted seawater (Katz et al. 2007). Finally in Fig. 13b, Zachos et al. (2001) relate the changes in $\delta^{13}C$ of the last 65 million years to the important biological, climatic, and orbital changes of the Earth.

Summary

Dissolved CO_2 in aqueous solution in the form of carbonic acid and carbonate ions has played a key role in processes at the Earth's surface over its entire history. Weathering reactions and subsequent precipitation of carbonate sediments together with biological production and burial of organic matter have removed 2.85×10^{20} kg of CO_2 from the atmosphere, leaving there 0.001% of the original mass. Cycling of CO_2 between dissolved forms in the ocean, gaseous form in the atmosphere, and carbonate sediments continues to exert a major control on Earth's climate. Dissolved carbonate exerts a major control on the pH of seawater and other natural waters. Burning of fossil fuels and other anthropogenic activities is increasing the amount of dissolved CO_2 in the ocean and reducing ocean pH,

threatening carbonate-secreting organisms such as corals. Carbonate minerals, primarily calcite and dolomite precipitating from these solutions, constitute the second most abundant class sedimentary rocks.

Cross-References

- Acid–Base Reactions
- Activity and Activity Coefficients
- Aqueous Solutions
- Atmospheric Evolution
- Calcium
- Carbon
- Carbon Cycle
- Carbon Isotopes
- Dolomite and Dolomitization
- Equilibrium Constant
- Formation and Evolution of the Earth
- Free Energy
- Geochemical Thermodynamics
- Heat Capacity
- Low-Temperature Geochemistry
- Magnesium
- Marine Sediment
- Ocean Biochemical Cycling and Trace Elements
- Solubility
- Standard States
- Strontium

Acknowledgments This work was supported by NOAA Hawaii Sea Grant, School of Earth and Ocean Science and Technology, University of Hawaii, and by Weinberg College of Arts and Sciences, Northwestern University. We thank Mr. Noah Howins, University of Hawaii, for help with the compilation of references cited.

References

Andersson AJ (2014) The oceanic $CaCO_3$ cycle. In: Holland HD, Turekian KK (eds) Treatise on geochemistry, vol 8. Elsevier, Oxford, pp 519–542

Anthony JW, Bideaux RA, Bladh KW, Nichols MC (2003) Handbook of mineralogy, Borates, Carbonates, Sulphates, vol 5. Mineralogical Society of America, Chantilly. http://www.handbookofmineralogy.org/

Arvidson RS, Mackenzie FT (1997) Tentative kinetic model for dolomite precipitation rate and its application to dolomite distribution. Aquat Geochem 2:273–298

Arvidson RS, Mackenzie FT (1999) The dolomite problem: control of precipitation kinetics by temperature and saturation state. Am J Sci 299:257–288

Bass JD (1995) Elasticity of minerals, glasses, and melts. In: Mineral physics and crystallography: a handbook of physical constants. American Geophysical Union, Washington, DC, pp 45–63

Berner RA (2006) Carbon, sulfur and O_2 across the Permian-Triassic boundary. J Geochem Explor 88:416–418

Berner RA, Maasch KA (1996) Chemical weathering and controls on atmospheric O_2 and CO_2: fundamental principles were enunciated by J. J. Ebelmen in 1845. Geochim Cosmochim Acta 60(9):1633–1637

Bertram MA, Mackenzie FT, Bishop FC, Bischoff WD (1991) Influence of temperature on the stability of magnesian calcites. Am Mineral 76:1889–1896

Bertram MA, Mackenzie FT, Bishop FC, Bischoff WD (1991) Influence of temperature on the stability of magnesian calcites. Am Mineral 76:1889–1896

Birch F (1966) Compressibility; elastic constants. In: Clark SP Jr (ed) Handbook of physical constants, Geological Society of America Memoir, vol 97. Geological Society of America, New York, pp 97–173

Bischoff WD, Mackenzie FT, Bishop FC (1987) Stabilities of synthetic magnesian calcites in aqueous solution: comparison with biogenic materials. Geochim Cosmochim Acta 51:1413–1423

Bischoff WD, Bertram MA, Mackenzie FT, Bishop FC (1993) Diagenetic stabilization pathways of magnesian calcites. Carbonates Evaporites 8:82–89

Böhm F, Gussone N, Eisenhauer A, Reynaud S, Paytan A, Bosellini F, Brachert T, Reitner J, Wörheide G, Dullo W-C (2006) Ca isotope fractionation of inorganic, biologically induced and biologically controlled calcium carbonates. Geophys Res Abstr 8:09686

Broecker WS, Peng T-H (1982) Tracers in the sea. Lamont-Doherty Geological Observatory, Columbia University, Palisades

Busenburg E, Plummer LN (1989) Thermodynamics of magnesian calcite solid-solutions at 25°C and 1 atm pressure. Geochimica et Coscochimica Acta 53:1189–1208

Carlson WD (1980) The calcite-aragonite equilibrium: effects of Sr substitution and anion orientational disorder. Am Mineral 65:1252–1262

Chang VT-C, Williams RJP, Makishima A, Belshawl NS, O'Nion RK (2004) Mg and ca isotope fractionation during $CaCO_3$ biomineralisation. Biochem Biophys Res Commun 323:79–85

Chapman R (2006) A sea water equation of state calculator. The Johns Hopkins Universisty. Applied Physics Laboratory, Laurel. http://fermi.jhuapl.edu/denscalc.html

Chou L, Garrels RM, Wollast R (1989) Comparative study of the kinetics and mechanisms of dissolution of carbonate minerals. Chem Geol 78:269–282

Coplen TB (1995) Discontinuance of SMOW and PDB. Nature 375:285

Emrich K, Ehhalt DH, Vogel JC (1970) Carbon isotope fractionation during the precipitation of calcium carbonate. Earth Planet Sci Lett 8:363–371

Epstein S, Buchsbaum R, Lowenstam HA, Urey HC (1951) Carbonate-water isotopic temperature scale. Geol Soc Am Bull 62:417–426

Epstein S, Buchsbaum R, Lowenstam HA, Urey HC (1953) Revised carbonate-water isotopic temperature scale. Geol Soc Am Bull 64:1315–1326

Fantle MS, DePaolo DJ (2007) Ca isotopes in carbonate sediment and pore fluid from ODP site 807A: the Ca^{2+}(aq)–calcite equilibrium fractionation factor and calcite recrystallization rates in Pleistocene sediments. Geochim Cosmochim Acta 71:2524–2546

Fantle MS, Tipper ET (2014) Calcium isotopes in the global biogeochemical ca cycle: implications for development of a ca isotope proxy. Earth-Sci Rev 129:148–177

Farkaš J, Chackrabati R, Jacobsen SB, Kump LR, Melezhik VA (2012) Chapter 7.10.3: Ca and Mg isotopes in sedimentary carbonates. In: Frontiers in Earth Sciences, vol 8. Springer, New York, pp 1467–1482

Faure G, Mensing TM (2004) Isotopes: principles and applications, 3rd edn. Wiley, Hoboken. xxv+897 pp

Fei Y (1995) Thermal expansion. In: Mineral physics and crystallography: a handbook of physical constants. American Geophysical Union, Washington, DC, pp 29–44
Goldsmith JR, Heard HC (1961) Subsolidus phase relations in the system $CaCO_3$–$MgCO_3$. J Geol 69:45–74
Gradstein FM, Ogg JG, Smith AG (2004) A Geologic Time Scale 2004. Cambridge University Press, New York
Graf DL, Goldsmith JR (1955) Dolomite-magnesian calcite relations at elevated temperatures and CO_2 pressures. Geochim Cosmochim Acta 7:109–128
Graf DL, Goldsmith JR (1958) The solid solubility of $MgCO_3$ in $CaCO_3$: a revision. Geochim Cosmochim Acta 13:218–219
Gussone N, Böhm F, Eisenhauer A, Dietzel M, Heuser A, Teichert BMA, Reitner J, Wörheide G, Dullo W-C (2005) Calcium isotope fractionation in calcite and aragonite. Geochim Cosmochim Acta 69 (18):4485–4494
Hanks TC, Anderson DL (1969) The early thermal history of the earth. Phys Earth Planet Inter 2:19–29
Hardie LA (1987) Perspectives on dolomitization: a critical review of some current views. J Sediment Petrol 57:166–183
Harker RI, Tuttle OF (1955) Studies in the system CaO-MgO-CO_2, part 2. Limits of solid solution along the join $CaCO_3$–$MgCO_3$. Am J Sci 253:274–282
Hay WW, Sloan JL II, Wold CN (1988) Mass/age distribution and composition of sediments on the ocean floor and the global rate of sediment subduction. J Geophys Res 93(B12):14,933–14,940
Henkes GA, Passey BH, Wanamaker AD Jr, Grossman EL, Ambrose WG Jr, Carroll ML (2013) Carbonate clumped isotope compositions of modern marine mollusk and brachiopod shells. Geochim Cosmochim Acta 106:307–325
Hippler D, Schmitt A-D, Gussone N, Heuser A, Stille P, Eisenhauer A, Nägler TF (2003) Calcium isotopic composition of various reference materials and seawater. Geostandards Newslett, Journal of Geostandards and Geoanalytical 27(1):13–19
Holmden C, Papanastassiou DA, Blanchon P, Evans S (2012) $\delta^{44/40}$Ca variability in shallow water carbonates and the impact of submarine groundwater discharge on ca-cycling in marine environments. Geochim Cosmochim Acta 83:179–184
Katz ME, Wright JD, Miller KG, Cramer BS, Fennel K, Falkowski PG (2005) Biological overprint of the geological carbon cycle. Mar Geol 217:323–338. (Falkowsi PG, Knoll AH (eds) Evolution of primary producers in the Sea, Chapter 18. Amsterdam, Elsevier, pp 405–430)
Katz ME, Fennel K, Falkowski PG (2007) Geochemical and biological consequences of phytoplankton evolution. In: Falkowski PG, Knoll A (eds) Evolution of aquatic photoautotrophs. Academic, pp 405–430
Land LS (1985) The origin of massive dolomite. J Geol 33:112–125
Le Quere C, Moriarty R, Andrew RM et al (2015) Carbon budget 2014. Earth Syst Sci Data 7:47–85
Lerman A, Clauer N (2007) Stable isotopes in the sedimentary record. Treatise Geochem 7:1–55
Lerman A, Guidry M, Andersson A, Mackenzie FT (2011) Coastal Ocean last glacial maximum to 2100 CO_2-carbonic acid-carbonate system: a modeling approach. Aquat Geochem 17:749–773
Liu L-g, Chen C-c, Lin C-C, Yang Y-j (2005) Elasticity of single-crystal aragonite by Brillouin spectroscopy. Phys Chem Miner 32:97–102
Machel HG, Mountjoy EW (1986) Chemistry and environments of dolomitization – a reappraisal. Earth-Sci Rev 23:175–222
Mackenzie FT, Andersson AJ (2013) The marine carbon system and ocean acidification during Phanerozoic time. Geochem Perspect 2:1–227
Mackenzie FT, Lerman A (2006) Carbon in the geobiosphere – Earth's outer Shell. Springer, Dordrecht. xxi+402 pp
Mackenzie FT, Morse JW (1992) Sedimentary carbonates through Phanerozoic time. Geochim Cosmochim Acta 56:3281–3295
Mackenzie FT, Lerman A, DeCarlo EH (2011) Coupled C, N, P, and O biogeochemical cycling at the land-ocean interface. In: Middleburg J, Laane R (eds) Treatise on coastal and estuarine science, vol 5. Elsevier, New York, pp 317–342
McKenzie JA (1991) The dolomite problem: an outstanding controversy. In: Muller DW, McKenzie JA, Weissert H (eds) Controversies in modern geology: evolution of geological theories in sedimentology, earth history and tectonics. Academic, London, pp 37–54
McKenzie JA, Vasconcelos C (2009) Dolomite Mountains and the origin of the dolomite rock of which they mainly consist: historical developments and new perspectives. Sedimentology 56(1): 205–219
Millero F (2013) Chemical oceanography, 4th edn. CRC Press/Taylor & Francis Group, Boca Raton. 547 pp
Mindat (1993–2016) http://www.mindat.org/
Morse JW, Mackenzie FT (1990) Geochemistry of sedimentary carbonates. Elsevier, New York. xvi + 707 pp
NIST (2016) Thermophysical properties of fluid systems. http://webbook.nist.gov/chemistry/fluid/
O'Leary MH (1988) Carbon isotopes in photosynthesis. Bioscience 38:328–335
O'Neil JR, Clayton RN, Mayeda TK (1969) Oxygen isotope fractionation in divalent metal carbonates. J Chem Phys 51(12):5547–5558
Pickett M, Anderrson AJ (2015) Dissolution rates of biogenic carbonates in natural seawater at different pCO2 conditions: a laboratory study. Aquat Geochem 21(6):459–485
Plummer LN, Mackenzie FT (1974) Predicting mineral solubility from rate data: application to the dissolution of magnesian calcites. Am J Sci 274:61–83
Railsback LB (2002) Patterns in the compositions, properties, and geochemistry of carbonate minerals. Department of Geology, University of Georgia, Athens. http://www.gly.uga.edu/railsback/Fundamentals/FundamentalsCarbs.html
Redfern SAT, Wood BJ, Henderson CMB (1993) Static compressibility of magnesite to 20 GPa: implications for $MgCO_3$ in the lower mantle. Geophys Res Lett 20(19):2099–2012
Robie RA, Hemingway BS (1995) Thermodynamic properties of minerals and related substances at 298.15 K and 1 bar (10^5Pascals) Pressure and at higher temperatures. USGS Bulletin 2131. iv+461 pp
Ross NA (1997) The equation of state and high-pressure behavior of magnesite. Am Mineral 82:682–688
Runnels RT, Schleicher JA (1956) Chemical composition of Eastern Kansas limestone. Kans Geol Surv Bull 119(3):1–18
Sabine CL, Feely RA, Gruber N, Key RM et al (2004) The oceanic sink for anthropogenic CO_2. Science 305(5862):367–371
Saulnier S, Rollion-Bard C, Vigier N, Chaussidon M (2012) Mg isotope fractionation during calcite precipitation: an experimental study. Geochim Cosmochim Acta 91:75–91
Skinner BJ (1966) Thermal expansion. In: Clark SP Jr (ed) Handbook of physical constants, Geological Society of America Memoir, vol 97. Geological Society of America, New York, pp 75–96
Speer JA (1983) Crystal chemistry and phase relations of orthorhombic carbonates. Rev Mineral 11:145–189
Thorstenson DC, Plummer LN (1977) Equilibrium criteria for two component solids reacting with fixed composition in an aqueous phase – example: the magnesian calcites. Am J Sci 277:1203–1223
Tuthorn M, Zech M, Ruppenthal M, Oelmann Y, Kahmen A, del Valle HF, Wilcke W, Glaser B (2014) Oxygen isotope ratios ($^{18}O/^{16}O$) of hemicellulose-derived sugar biomarkers in plants, soils and

sediments as paleoclimate proxy II: insight from a climate transect study. Geochim Cosmochim Acta 126:624–634
Urey HC (1952) The planets: their origin and development. Yale University Press, New Haven. xvii+245 pp
Veizer J, Ala D, Azmy K, Bruckschen P, Buhl D, Bruhn F, Carden GAF, Diener A, Ebneth S, Goddéris Y, Jasper T, Korte C, Pawellek F, Podlaha OG, Strauss H (1999) $^{87}Sr/^{86}Sr$, $\delta^{13}C$ and $\delta^{18}O$ evolution of Phanerozoic seawater. Chem Geol 161:59–88
Walter LM, Morse JW (1984) Reactive surface area of skeletal carbonate during dissolution: effect of grain size. J Sediment Petrol 54:1081–1090
Walter LM, Morse JW (1985) The dissolution kinetics of shallow marine carbonates in seawater: a laboratory study. Geochim Cosmochim Acta 49:1503–1513
Weatherill GW (1966) Radioactive decay constants and energies. In: Clark SP Jr (ed) Handbook of physical constants, Geological Society of America Memoir, vol 97. Geological Society of America, New York, pp 513–519
Wood BJ, Walter MJ, Wade J (2006) Accretion of the Earth and segregation of its core. Nature 441:825–833
Zachos J, Pagani M, Sloan L, Thomas E, Billups K (2001) Trends, rhythms, and aberrations in global climate 65 Ma to present. Science 292(5517):686–693
Zeebe RE, Wolf-Gladrow D (2001) CO_2 in seawater: equilibrium, kinetics, isotopes. Elsevier, Amsterdam. xiii+346 pp
Zhang J, Reeder RJ (1999) Comparative compressibilities of calcite-structure carbonates: deviations from empirical relations. Am Mineral 84:861–870
Zhong S, Mucci A (1989) Calcite and aragonite precipitation from seawater solutions of various salinities: precipitation rates and overgrowth compositions. Chem Geol 78(3):283–299
Zhu P, Macdougall JD (1998) Calcium isotopes in the marine environment and the oceanic calcium cycle. Geochim Cosmochim Acta 62 (10):1691–1698

Cerium

Catherine Chauvel
ISTerre, University Grenoble Alpes, CNRS, Grenoble, France

Element Data
Atomic Symbol: **Ce**
Atomic Number: **58**
Atomic Weight: 140.115 g/mol
Isotopes and Abundances: ^{136}Ce *0.186%*, ^{138}Ce 0.251%, ^{140}Ce 88.449%, and ^{142}Ce 11.114%
1 Atm Melting Point: 795 °C
1 Atm Boiling Point: 3443 °C
Common Valences: +3 and +4
Ionic Radii: 3+: 101 pm, 4+: 87 pm
Pauling Electronegativity: 1.12
(*continued*)

Chondritic (CI) Abundance: 0.6379 ppm
Silicate Earth Abundance: 1.675 ppm
Crustal Abundance: 63 ppm
Seawater Abundance: $\approx 1*10^{-6}$ ppm
Core Abundance: ~0

Properties

Cerium is a reactive and gray metal that tarnishes in air and burns when heated. It usually occurs in substitution to major elements in minerals.

History and Use

Cerium was discovered in Bastnäs (Sweden) in 1803 by J. J. Berzelius and W. Hissinger and was named after asteroid Ceres. Cerium is the most abundant of the lanthanide metals (also called rare earth elements), a group of 15 similar elements between lanthanum and lutetium in the periodic table and behaves cosmochemically as a refractory lithophile element.

Cerium has been used for a long time in industry: it is a key constituent of lighter flints; it provides special properties to some stainless steels; it is added to some special glasses and it is a key constituent of polishing powders. It is also used in catalytic converters.

Geochemical Behavior

Cerium is the most abundant rare earth element, but it is still rarely a constituent of mineral phases on Earth. Nevertheless, two common REE minerals exist: monazite ((Ce,La,Nd,Th)PO_4) and bastnäsite ((Ce,La,Y)CO_3F). During partial melting and fractional crystallization of magmas, it behaves as an incompatible element and is concentrated in melts. It is therefore enriched in basalts relative to their mantle source and enriched in continental crust relative to Earth's mantle. Together with the other REE, it is widely used in geochemistry to trace geological processes.

In contrast to other REE, Ce can have two valences: in the Earth's interior, it is almost exclusively in the +3 as most REE but can be in the +4 in oxidizing environments at the Earth's surface, and consequently, it can be decoupled from other REE in those environments. The decoupling is quantified as the Ce anomaly (Ce_N/Ce_N^*) with $Ce_N^* = 0.5La_N + 0.5Pr_N$ and all concentrations normalized to a reference reservoir that

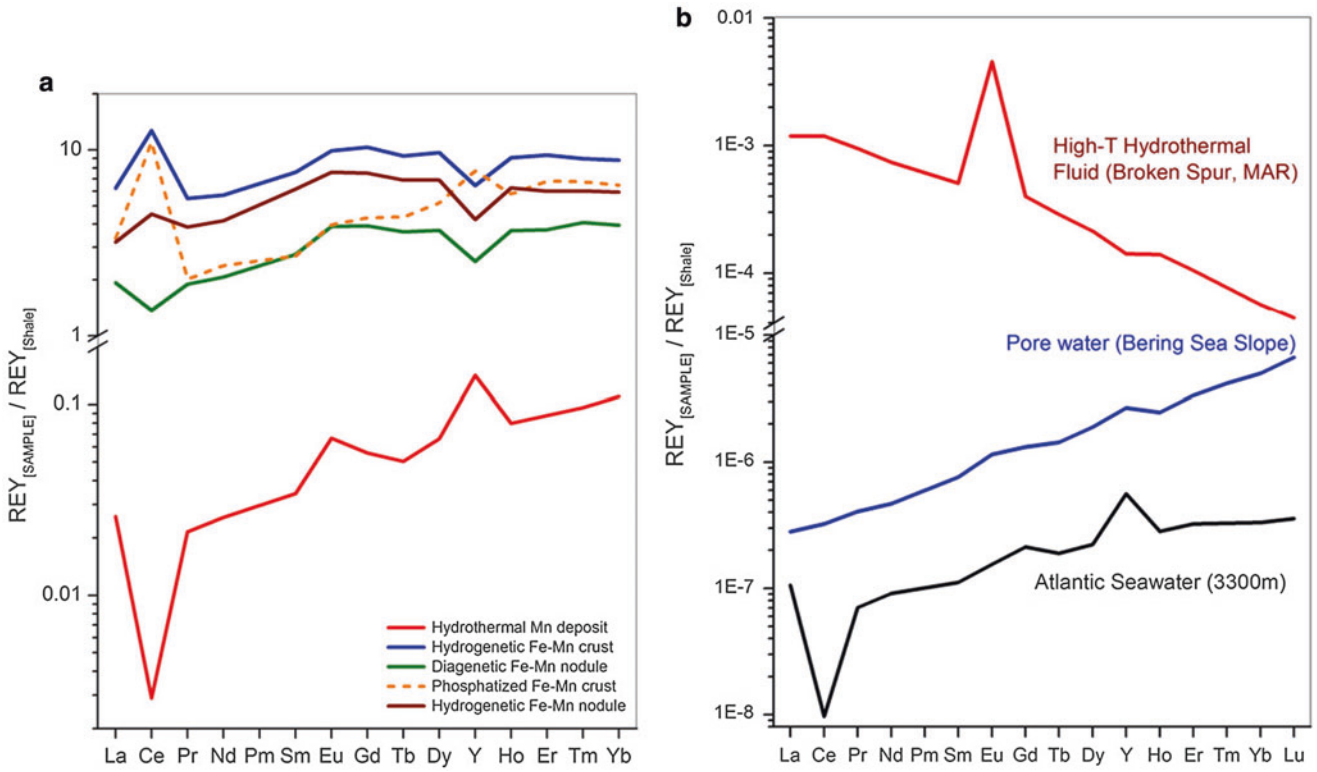

Cerium, Fig. 1 Typical patterns of (**a**) marine hydrothermal Fe–Mn deposits, diagenetic Fe–Mn nodules, hydrogenetic Fe–Mn nodules, hydrogenetic Fe–Mn crusts, and phosphatized hydrogenetic Fe–Mn crusts, and (**b**) high-temperature hydrothermal (black-smoker) fluids, seawater, and marine porewater (From Bau et al. (2014) and references therein)

can be the primitive mantle or another reservoir. During supergene weathering in tropical climates, negative cerium anomalies occur in altered soil materials, and precipitation of cerianite ($(Ce,Th)O_2$) leads to the formation of positive anomalies in other soil layers (Cotten et al. 1995). Similarly, seawater is characterized by a strong negative Ce anomaly, while Fe–Mn nodules have positive Ce anomalies (see Fig. 1) (Bau et al. 2014).

Geochronology and Isotope Geochemistry

Cerium has four isotopes, and one of them, ^{138}Ce (0.251%), is produced by the radioactive decay of ^{138}La with a half-life of ≈292.5 Ga. Because of the very long half-life and the analytical difficulties related to the low abundance of ^{138}Ce, the decay system has hardly been used in geochronology. However, with the arrival on the market of more precise and accurate mass spectrometers, new perspectives are now open.

In the field of isotope geochemistry, it could be an interesting tool to distinguish the type of sedimentary material involved in the source of island arc volcanic rocks. A pioneer study published by Bellot et al. (2015) demonstrates that coupling Ce and Nd isotopes could help distinguish hydrogenetic deposits from hydrothermal or detrital materials. As shown in Fig. 2, different types of sediment evolve on very different evolutionary paths as time goes past; in addition, distinct Ce isotopic compositions can be acquired within a relative short time (less than 200 Ma), an age that corresponds to the oldest subducted oceanic plate in the Pacific.

Coupled Ce and Nd isotopic studies of planetary materials and of early Earth rocks could also be very interesting because of the constraints it could provide on the nature of the material that accreted to form planets and on the nature of the dominant processes during the early stages of Earth evolution.

Biological Utilization and Toxicity

Cerium has no known biological role and has low to moderate level of toxicity.

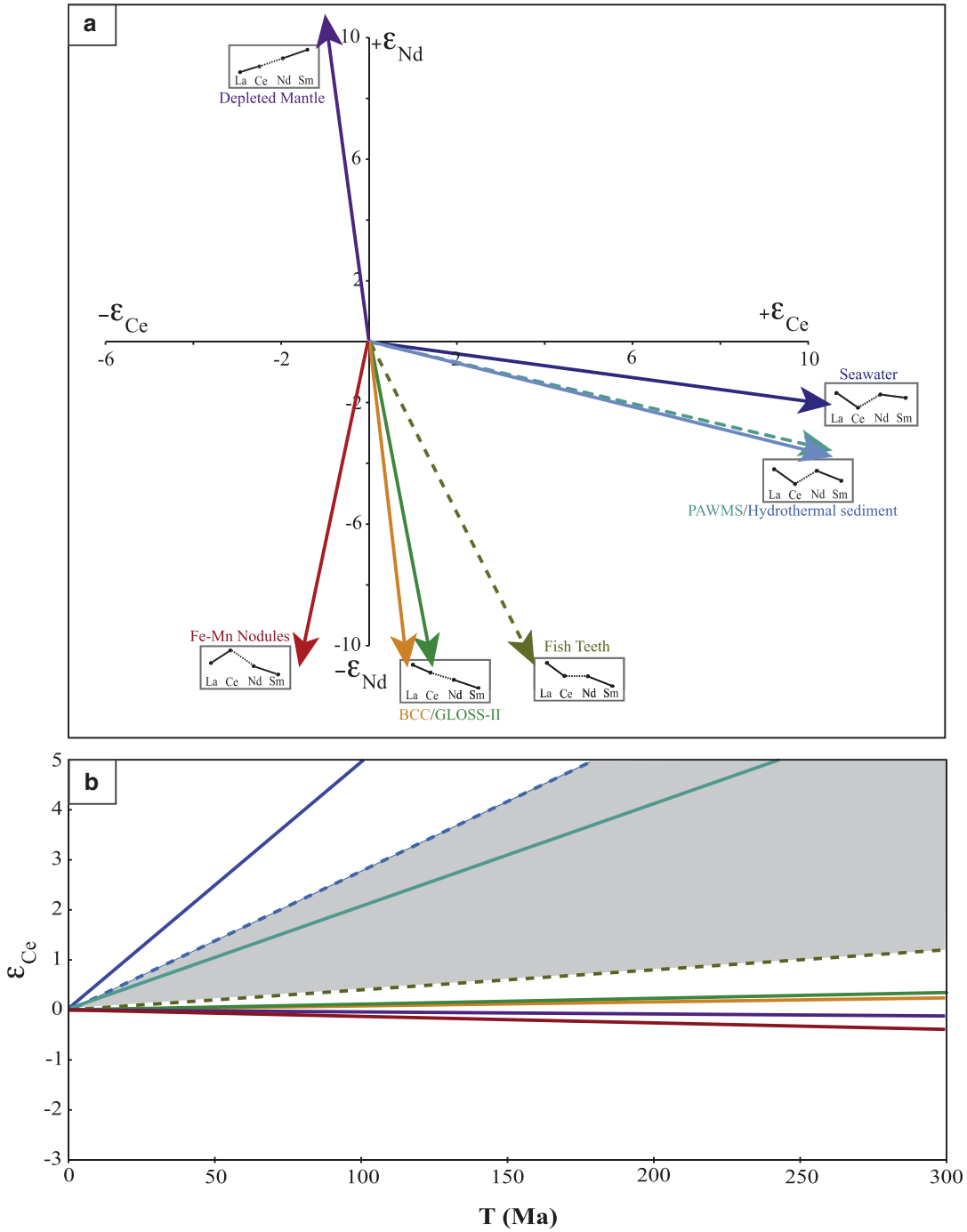

Cerium, Fig. 2 Schematic diagram showing the isotopic trajectories of various Earth reservoirs in Ce–Nd isotopic spaces. ε_{Ce} and ε_{Nd} measure the deviation in 10^4 of Ce and Nd isotopic compositions relative to chondritic references (i.e., $\varepsilon_{Ce} = ([^{138}Ce/^{142}Ce]/[^{138}Ce/^{142}Ce_{CHUR}] -1)*10^4$) (See Bellot et al. (2015) and references therein for further details)

Cross-References

- Chemical Weathering
- Ferromanganese Crusts and Nodules: Rocks That Grow
- Incompatible Elements
- Lanthanide Rare Earths
- Lanthanum
- Lithophile Elements
- Marine Sediment
- Ocean Biochemical Cycling and Trace Elements

▶ Oxidation-Reduction Reactions and Eh-pH (Pourbaix) Diagrams
▶ Supergene

References

Bau M, Schmidt K, Koschinsky A, Hein J, Kuhn T, Usui A (2014) Discriminating between different genetic types of marine ferro-manganese crusts and nodules based on rare earth elements and yttrium. Chem Geol 381:1–9

Bellot N, Boyet M, Doucelance R, Pin C, Chauvel C, Auclair D (2015) Ce isotope systematics of island arc lavas from the Lesser Antilles. Geochim Cosmochim Acta 168:261–279

Cotten J, Le Dez A, Bau M, Caroff M, Maury RC, Dulski P, Fourcade S, Bohn M, Brousse R (1995) Origin of anomalous rare-earth element and yttrium enrichments in subaerially exposed basalts: evidence from French Polynesia. Chem Geol 119:115–138

Chalcophile Elements

Sarah-Jane Barnes
Sciences de la Terre, Université du Québec à Chicoutimi, Chicoutimi, QC, Canada

Definition

The term chalcophile (derived from the Greek for copper-loving) was originally introduced by Goldschmidt (1923) to describe the group of elements that are concentrated in sulfide minerals in meteorites. Traditionally this group is defined as the elements Ag, As, Bi, Cd, Cu, Hg, In, Pb, S, Sb, Se, Te, Tl, and Zn. Goldschmidt classified the other elements in meteorites into two groups: those associated with Fe alloy as siderophile (iron loving) and those concentrated in silicates minerals as lithophile (rock loving). Subsequently Goldschmidt applied his classification to the whole Earth and modified it to include two new groups of elements: atmophile, those concentrated in the atmosphere and biophile elements, those concentrated by organic processes (Goldschmidt 1930).

Distribution in Terrestrial Rocks

Whereas the concepts outlined by Goldschmidt are useful, as is evidenced by the fact the terms, siderophile, chalcophile, and lithophile are in daily use by geochemists, the behavior of an element depends on the composition of the system, oxygen fugacity (fO_2), temperature, and pressure (Li and Audétat 2015); thus, its behavior may vary depending on the context. Lodders (2003) outlined the behavior of the elements during condensation of the elements to form the solar system, and under these low fO_2 conditions, the chalcophile group is restricted to Ag, Cd, Hg, In, Pb, S, Se, Te, and Zn. Low fO_2 conditions would also have prevailed during the segregation of the earth's core and consequently many elements behaved in a siderophile manner. Current estimates of the core composition show enrichment of up to 1000 times primitive mantle (Fig. 2) for elements such as the platinum-group elements (PGE; Ru, Rh, Pd, Os, Ir, Pt). In contrast at the oxygen fugacities found in the Earth's mantle and crust, Fe alloy is very rarely present and many elements that are siderophiles in meteorites and during core segregation partition into sulfide minerals rather than Fe alloy and thus behave as chalcophile elements.

The partition coefficients between sulfide droplets and mid-ocean ridge basalts (MORB) give an indication of how chalcophile each element is under crustal conditions (Fig. 1). Elements with partition coefficients between 1 and 10 may be described as slightly chalcophile (Zn, Mo, As, Sb, Tl, In, and

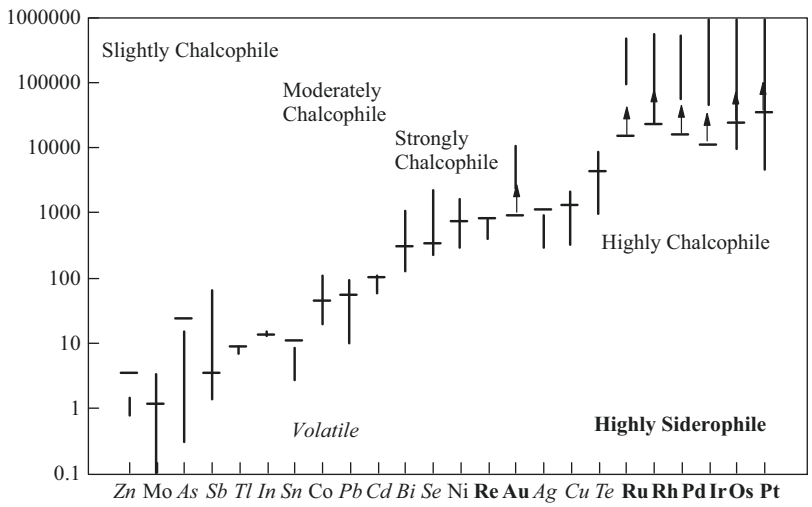

Chalcophile Elements, Fig. 1 Partition coefficients between mafic magma and sulfide liquid. — indicates partition coefficients between MORB and sulfide droplet; I indicates range of values from experiments conducted at *f*O2 between −2 FMQ +2; ↑ indicates minimum partition coefficients; italics indicates the element is volatile; bold indicates that the element is highly siderophile (Data from Barnes and Ripley (2016) and references therein, plus Li and Audétat (2015))

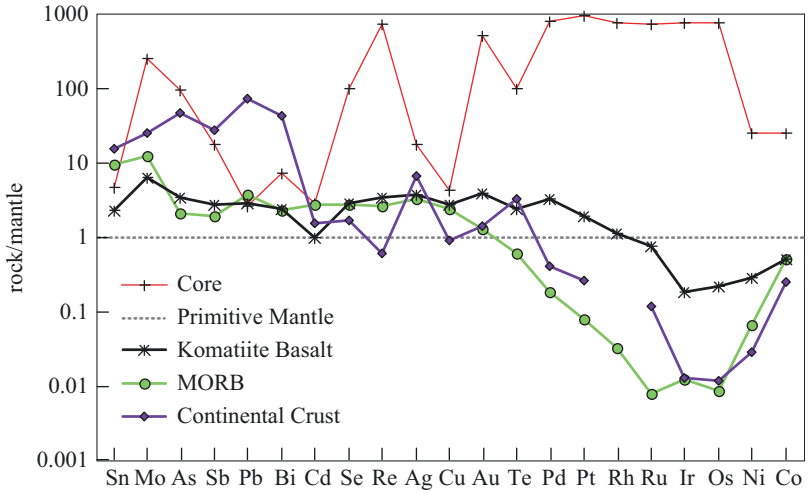

Chalcophile Elements, Fig. 2 Concentrations of chalcophile elements in the core, komatiitic basalt, MORB, and the continental crust normalized to primitive mantle and plotted in order of incompatibility with komatiitic basalt (Data for the core from McDonough and Sun (1995); mantle from Lyubetskaya and Korenaga (2007); MORB form Arevalo and McDonough (2010); continental crust from Rudnick and Gao (2003); komatiitic basalt from this work (median of 52 samples from the Cape Smith Fold Belt northern Quebec))

Sn,), those with partition coefficients in the range 20–100 as moderately chalcophile (Pb, Co, Cd), those with a partition coefficient in the 100–1000 range as strongly chalcophile (Bi, Se, Ni, Re), and those with partition coefficients above 1000 as highly chalcophile (Au, Cu, Te, Ru, Rh, Pd, Os, Ir, Pt).

Among the group that behave as highly chalcophile elements under crustal conditions are the PGE which together with Au and Re are commonly referred to as highly siderophile elements because of their very high partition coefficients into Fe alloy (Harvey and Day 2016 and references therein). The highly siderophile elements attract a great deal of interest because of their potential to investigate the early history of planetary formation. In particular the relatively high concentrations of the highly siderophile elements in the Earth's mantle suggest that it is not in equilibrium with the core and that, during late meteorite bombardment, highly siderophile elements were added to the mantle (Dale et al. 2012).

The behavior of the chalcophile elements during mantle melting can be considered by inspection of a mantle-normalized plot of average MORB and komatiitic basalts (Fig. 2). The elements are plotted in approximately decreasing normalized abundance in komatiitic basalt. For komatiitic basalt most of the chalcophile elements from Sn to Pt are present at the two to three times mantle concentrations. Moderately incompatible lithophile elements such as Sm are present in these rocks at similar to slightly higher levels (three to four times mantle); thus most of the chalcophile elements behave as incompatible elements and sulfide phases do not appear to control the behavior of the chalcophile elements at the high degrees of partial melting required to produce komatiitic basalts. In contrast the Ir-platinum-group elements (IPGE, Os, Ir, Ru, and Rh), Ni, and Co are present at less than one times mantle and behave as compatible elements.

The concentrations of the chalcophile elements in MORB show a wider range of values. Tin and Mo are present at close to ten times mantle, most of the chalcophile elements (As to Cu) show a lower degree of enrichment in the range of twice to three times mantle. Tellurium, Au, Ni, and Co are present at 0.1–1 times mantle exhibiting compatible behavior, and the PGE are extremely depleted at 0.01–0.1 times mantle. The variations in the behavior of the chalcophile elements in MORB are generally attributed to the presence of residual sulfides in the MORB source. The PGE exhibit extreme depletion because of their very high partition coefficients into sulfides, whereas the moderately chalcophile elements exhibit a much smaller degree of depletion because the sulfide phases will affect their bulk partition coefficients less (Patten et al. 2013). Tin and Mo at ten times mantle show an enrichment similar to incompatible lithophile elements, suggesting that the presence of sulfide phases has a negligible influence on these elements.

The average continental crust is depleted in most moderately to strongly chalcophile elements and like MORB is particularly depleted in PGE (Fig. 2). However it is enriched at 10–100 times mantle in the slightly to moderately chalcophile elements Sn to Pb and in the strongly chalcophile elements Bi and Ag (Fig. 2).

Naturally all of the chalcophile elements are concentrated into magmatic sulfide liquids when they segregated from mafic magmas, and the Ni and PGE ore deposits that form from the liquids are enriched in all of these elements (Barnes and Ripley 2016). Most of the chalcophile elements are enriched by a factor of 100–1000 relative to mafic magma Fig. 3. The slightly chalcophile elements are less enriched with enrichment factors of approximately 10 reflecting their lower partition coefficients (Figs. 1 and 3).

During crystallization of magma, the silicate liquid may become saturated in a magmatic-hydrothermal fluid.

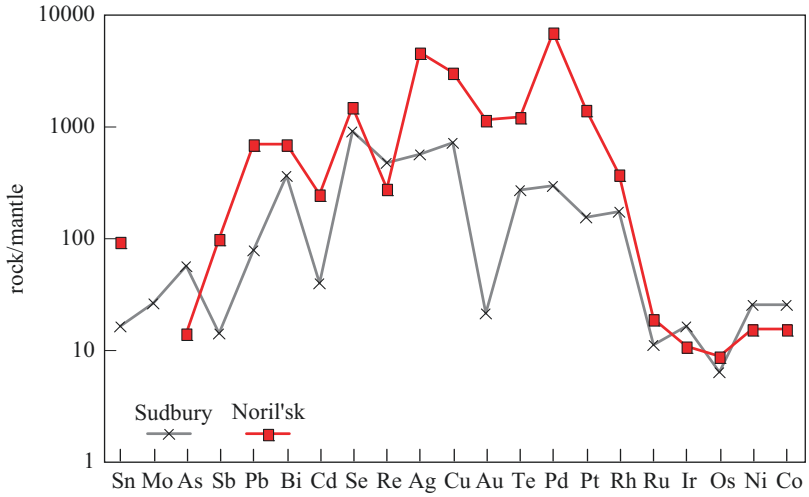

Chalcophile Elements, Fig. 3 Mantle-normalized concentrations of chalcophile elements from the two largest magmatic Ni-sulfide deposits, Sudbury and Noril'sk (Data from Dare et al. (2011) and Zientek et al. (1994))

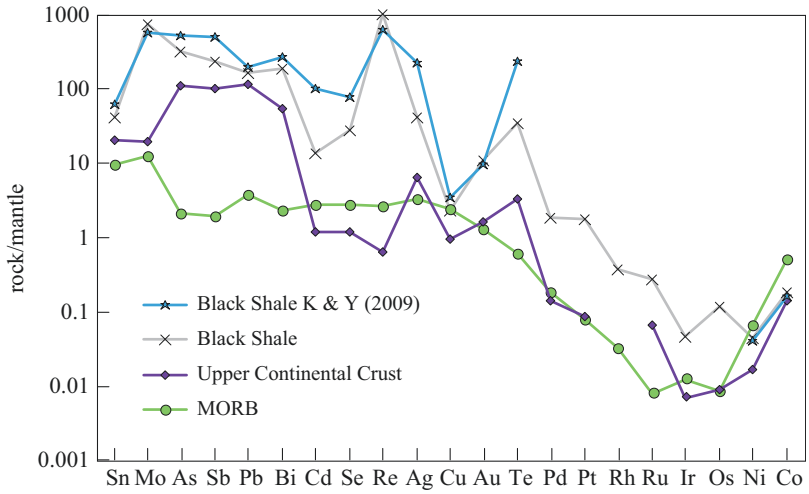

Chalcophile Elements, Fig. 4 Comparison of mantle-normalized concentrations of chalcophile elements in black shales with the upper continental crust and MORB (Data from Ketris and Yudovich (2009), this work of literature survey, Hu and Gao (2008), and Arevalo and McDonough (2010))

Some chalcophile elements and S partition into these fluids. For example, fluid inclusions from Cu-Mo porphyries are enriched in Cu, Mo, Zn, Ag, Tl Au, Pb, and Bi (John et al. 2010). The fluids then react with country rocks and the chalcophile elements are deposited along with sulfides as a result of the reactions (Keith et al. 1997; John et al. 2010; Richards 2011).

At low pressures the silicate magma or a magmatic-hydrothermal fluid may become saturated with a vapor. Some chalcophile elements preferentially partition into the vapor phase. Based on their condensation temperatures during the formation of the solar system, Lodders (2003) defined Hg, Tl, In, Cd, Se, S. Sn, Te, Pb, Bi, Sb, Ag, Cu, As, and Au as volatile. Volcanic gasses and sublimates have been found to be enriched in these elements (Hinkley et al. 1994; Zelenski et al. 2013). Another effect of the vapor is that magmatic sulfide droplets in the magma may lose S during magma degassing. The loss of S destabilizes the sulfides and some of the chalcophile elements partition into the vapor.

Black shales are also enriched in many chalcophile elements (Fig. 4). [Some black shales, such as those in southern China, show much greater degree of enrichment than the median (Xu et al. 2013).] Relative to the upper crust (a potential source of the clastic component of the shales), the median black shale is enriched by a factor of 2 to 10 for most of the elements (Ketris and Yudovich 2009). Molybdenum, Cd, Se, Ag, and Te show larger enrichments in the range of 30–100, and Re shows the most extreme degree of enrichment at 1000. Ketris and Yudovich (2009) did not provide estimates for the PGE. But based on a survey of the literature, the PGE are also enriched in black shales at approximately ten times crustal values (Fig. 4). The origin of the enrichment of the metals in black shales has been much debated with one school of thought favoring the precipitation of the metals from seawater in anoxic basins (Xu et al. 2013) and the

other school suggesting that the metals are derived from hydrothermal fluids (Orberger et al. 2003). Recently models involving both processes have become popular (Slack et al. 2015).

Over the past few years, the concentrations of chalcophile elements in pyrites from black shales have become the focus of intense study as a means of exploration for Au deposits (Large et al. 2011). In this model the chalcophile elements are precipitated by organic matter and pyrite and incorporated into the pyrite during diagenesis. During greenschist facies metamorphism, the pyrite recrystallizes and releases many of the chalcophile elements to metamorphic fluids which can migrate to low pressure zones where they precipitate Au and other chalcophile elements.

Summary

The chalcophile elements can be divided into slightly, moderately, strongly, and highly chalcophile based on their partition coefficients between silicate and sulfide melts. Some of the highly and strongly chalcophile elements (PGE, Au, Re) are also highly siderophile, and thus most of the budget of these elements is found in the Earth's core. The slightly chalcophile elements Sn, Mo, As, Sb, and Pb together with Bi are enriched in the continental crust. Black shales are an important reservoir of most chalcophile elements in the Earth's crust. MORB is slightly enriched in most chalcophile elements except the highly chalcophile elements. In the Earth's crust highly chalcophile elements are only found in significant quantities in magmatic sulfide deposits.

Cross-References

- Antimony
- Arsenic
- Bismuth
- Black Shales and Sapropels
- Cadmium
- Copper
- Earth's Core
- Geochemical Classification of Elements
- Indium
- Lead
- Mercury
- Meteorites
- Mid-Ocean Ridge Basalts (MORB)
- Ore Deposits
- Platinum Group Elements
- Selenium
- Siderophile Elements
- Silver
- Sulfur
- Tellurium
- Thallium
- Zinc

References

Arevalo R Jr, McDonough WF (2010) Chemical variations and regional diversity observed in MORB. Chem Geol 271:70–85

Barnes S-J, Ripley EM (2016) Highly siderophile and strongly chalcophile elements in magmatic ore deposits. Rev Mineral Geochem 81:725–774

Dale CW, Burton KW, Greenwood RC, Gannoun A, Wade J, Wood BJ, Pearson DG (2012) Late accretion on the earliest planetesimals revealed by the highly siderophile elements. Science 336:72–75

Dare SA, Barnes S-J, Prichard HM, Fisher PC (2011) Chalcophile and platinum-group element (PGE) concentrations in the sulphide minerals from the McCreedy East deposit, Sudbury, Canada, and the origin of PGE in pyrite. Mineral Deposita 46:381–407

Goldschmidt VM (1923) Geochemische Verteilungsgesetze der ElementeSkrifter utg. av det Norske Visenskaps-Akademii i Oslo I. Mat-Naturv Klasse 2:1–17

Goldschmidt V (1930) Geochemische Verteilungsgesetze und kosmische Häufigkeit der Elemente. Naturwissenschaften 18:999–1013

Harvey J, Day JM (2016) Highly siderophile and strongly chalcophile elements in high temperature geochemistry and cosmochemistry. Rev Mineral Geochem 81:774

Hinkley TK, Le Cloarec M-F, Lambert G (1994) Fractionation of families of major, minor, and trace metals across the melt-vapor interface in volcanic exhalations. Geochim Cosmochim Acta 58:3255–3263

Hu Z, Gao S (2008) Upper crustal abundances of trace elements: a revision and update. Chem Geol 253(3):205–221

John DA, Ayuso RA, Barton MD, Blakely RJ, Bodnar RJ, Dilles JH, Gray F, Graybeal FT, Mars JC, McPhee DK, Seal RR, Taylor RD, Vikre PG (2010) Porphyry copper deposit model, chap. B of Mineral deposit models for resource assessment: U.S. Geological Survey Scientific Investigations Report 2010-5070–B, p 169

Keith J, Whitney J, Hattori K, Ballantyne G, Christiansen E, Barr D, Cannan T, Hook C (1997) The role of magmatic sulphides and mafic alkaline magmas in the Bingham and Tintic mining districts, Utah. J Petrol 38:1679–1690

Ketris M, Yudovich YE (2009) Estimations of Clarkes for carbonaceous biolithes: world averages for trace element contents in black shales and coals. Int J Coal Geol 78:135–148

Large RR, Bull SW, Maslennikov VV (2011) A carbonaceous sedimentary source-rock model for Carlin-type and orogenic gold deposits. Econ Geol 106:331–358

Li Y, Audétat A (2015) Effects of temperature, silicate melt composition, and oxygen fugacity on the partitioning of V, Mn, Co, Ni, Cu, Zn, As, Mo, Ag, Sn, Sb, W, Au, Pb, and Bi between sulphide phases and silicate melt. Geochim Cosmochim Acta 162:25–45

Lodders K (2003) Solar system abundances and condensation temperatures of the elements. Astrophys J 591:1220–1247

Lyubetskaya T, Korenaga J (2007) Chemical composition of Earth's primitive mantle and its variance: 1. Method and results. J Geophys Res 112:B03211

McDonough WF, Sun S-S (1995) The composition of the Earth. Chem Geol 120:223–253

Orberger B, Pasava J, Gallien JP, Daudin L, Pinti DL (2003) Biogenic and abiogenic hydrothermal sulphides: controls of rare metal distribution in black shales (Yukon Territories, Canada). J Geochem Explor 78:559–563

Patten C, Barnes S-J, Mathez EA, Jenner FE (2013) Partition coefficients of chalcophile elements between sulphide and silicate melts and the early crystallization history of sulphide liquid: LA-ICP-MS analysis of MORB sulphide droplets. Chem Geol 358:170–188
Richards JP (2011) Magmatic to hydrothermal metal fluxes in convergent and collided margins. Ore Geol Rev 40:1–26
Rudnick RL, Gao S (2003) Composition of the continental crust. Treatise Geochem 3:1–64
Slack JF, Selby D, Dumoulin JA (2015) Hydrothermal, biogenic, and seawater components in metalliferous black shales of the Brooks Range, Alaska: synsedimentary metal enrichment in a carbonate ramp setting. Econ Geol 110:653–675
Xu L, Lehmann B, Mao J (2013) Seawater contribution to polymetallic Ni–Mo–PGE–Au mineralization in early Cambrian black shales of South China: evidence from Mo isotope, PGE, trace element, and REE geochemistry. Ore Geol Rev 52:66–84
Zelenski ME, Fischer TP, de Moor JM, Marty B, Zimmermann L, Ayalew D, Nekrasov AN, Karandashev VK (2013) Trace elements in the gas emissions from the Erta Ale volcano, Afar, Ethiopia. Chem Geol 357:95–116
Zientek ML, Likhachev AP, Kunilov VE, Barnes S-J, Meier AL, Carlson RR, Briggs PH, Fries TL, Adrian BM (1994) Cumulus processes and the composition of magmatic ore deposits: examples from the Talnakh District, Russia. In: Lightfoot PC, Naldrett AJ (eds) Proceedings of the Sudbury-Noril'sk symposium, Ontario Geological Survey, Special publication, vol 5, Ontario, pp 373–392

Chelation

Corey D. Pilgrim
Department of Chemistry, University of California, Davis, Davis, CA, USA

Definition

Chelation is the complexation process by which a metal ion is bound to more than one atom in a single ligand. The ligand in question is said to be polydentate and is described by how many bonds are formed to the metal (e.g., a bidentate ligand has two bonds or a tridentate ligand has three bonds). The term chelation uses the Greek root *chela*, which is descriptive of the claws of lobsters and crabs, and is used because the resulting chelate complexes look as if the metal ion is caught between the pincers of the ligand. The favorable process of the replacement of monodentate ligands with polydentate ligands is known as the "chelate effect."

Chelation plays a prominent role in both inorganic chemistry and geologic processes. Water-solvated metal ions do not exist as discrete species in solution; they order the solvent molecules around themselves in different spheres of interaction (Richens 1997). Usually, these water molecules orient such that the negatively charged end of the dipole is attracted to the positively charged metal ion. These solvent molecules are thus coordinating as monodentate ligands around the metal center. Most geochemically important coordination complexes involve the interaction between Lewis acids and Lewis bases, such that the electrons in the coordinating ligand are donating to the electron poor metal center. Chelation occurs when a ligand, with multiple sites that act as Lewis bases, replaces the monodentate ligands around the metal center. This can result in interesting complexes forming – as an example, carbonate is a geologically abundant, bidentate, hard Lewis base which likes to coordinate with metal centers (interestingly, it can even form tricarbonate complexes with the early actinides, Fig. 1a). Another example of a chelating ligand is the molecule ethylenediaminetetraacetate (EDTA). This ligand is a hexadentate ligand that can coordinate a metal center through the lone electron pairs found on the four oxygen and two nitrogen atoms (Fig. 1b). EDTA can fill all octahedral sites around a metal center, effectively surrounding the ion in a cage. EDTA is used medically to trap toxic metals that have been digested by humans. It is also used as a complexometric titrant to determine the metal ion content in mixed solutions. Replacement of lower coordination number ligands by these higher coordination number ligands is known as the chelate effect.

The chelate effect, the process of exchanging lower coordinated ligands for higher coordinated ones, is an entropically favored process. When the higher coordinating ligand displaces the lower coordinating ligand, more species are in solution, where there are then more available translational, vibrational, and rotational modes of freedom. This increases the entropy (ΔS) of the system through the increase in

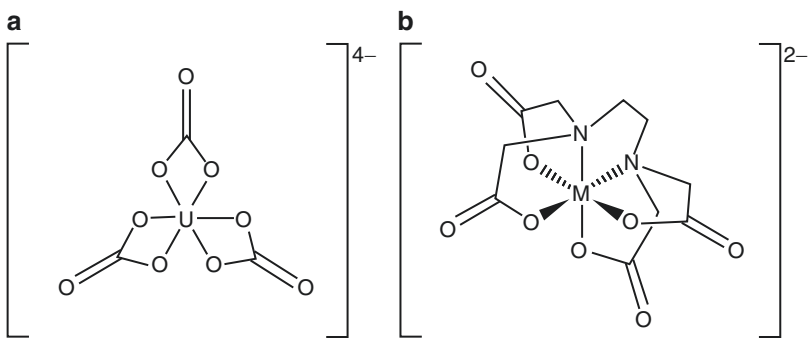

Chelation, Fig. 1 (**a**) Triscarbonato uranyl complex, with the axial "–yl" oxygens omitted for clarity. (**b**) Deprotonated ethylenediaminetetraacetate, chelated around a generic M^{2+} metal center

disorder. This process must overcome the enthalpy (ΔH) of the initial complex – the net gain in disorder must be greater than the change in the amount of energy that is stored in the coordinating bond between the Lewis acid–base pairs. When looking at coordination compounds, a few specific donor atoms have prevalence, most notably oxygen and nitrogen. The effects of replacing an oxygen – metal bond from a lower coordinating ligand with another oxygen – metal bond from a higher coordinating ligand are almost negligible, and the entropy of the exchange can be considered as the dominant thermodynamic process involved. However, a careful study of the enthalpy differences must be done if the donor atoms are different.

References

Richens DT (1997) The chemistry of aqua ions, 1st edn. Wiley, Chichester

Chemical Bonds

Barry R. Bickmore and Matthew C. F. Wander
Department of Geological Sciences, Brigham Young University, Provo, UT, USA

Definition

Linus Pauling famously described a chemical bond as "whatever is convenient to the chemist to define as a bond" (Pauling 1960). In the simplest terms, a chemical bond is merely an attraction between atoms in a substance containing an aggregation of two or more atoms. However, while all bonds are based on the attraction between positively charged protons and negatively charged electrons, quantum mechanical effects governing the spatial distribution of electrons give rise to a wide range of bond properties and a continuum of bond types. The standard types include covalent, metallic, ionic, hydrogen, and van der Waals bonds (Gillespie and Popelier 2001).

Traditional Valence Bonds

The strongest chemical bonds (covalent, metallic, and ionic) are sometimes called "valence bonds," due to the fact that they are formed when partially filled *valence atomic orbitals* combine to create molecular orbitals (Albright et al. 2013). The average spatial distribution of electrons (the electron probability density or electron density) around a free atom can be described in terms of atomic orbitals, which form three-dimensional standing wave patterns about the nucleus. As atoms approach one another, their atomic orbitals mix to create molecular orbitals, which form three-dimensional standing wave patterns about multiple nuclei. The resulting redistribution of the bonding electron density causes a net attraction between the atomic centers, but the bond properties depend strongly on the details of the redistribution (Gillespie and Popelier 2001). These details will be discussed here with reference to the *electronegativity* of the participating atoms. (*Electronegativity* is a single-parameter summary of the electron-attracting power of atoms.)

Ionic bonds form between atoms with widely different electronegativity values (metals with nonmetals). In these bonds, molecular orbitals concentrate most of the bonding electron density around the more electronegative atoms, resulting in some atoms with a net negative charge (anions) and others with a net positive charge (cations), which if sufficiently large can behave as separate ions. An ideal ionic bond would involve a cation and anion that can be treated as two point charges, but in real ionic systems, some sharing of valence electrons occurs, the molecular orbitals are not fully spherically symmetrical about the atomic centers, and there is always some orbital overlap, or sharing, of electrons. Therefore, even bonds between atoms with the most disparate electronegativity values are not considered fully ionic (Rohrer 2001).

Covalent bonds form between atoms with similar, high electronegativity values (nonmetals). Here molecular orbitals distribute, or share, the bonding electron density more or less evenly between the atoms involved, with an accumulation of electron density in the overlap region between atomic centers (Popelier 2000). Although fully ionic bonds do not exist, fully covalent bonds do exist between atoms of the same element. Given that covalent bonds involve atoms that tend to hold tightly to their valence electrons, the molecular orbitals form with their associated electron density concentrated very locally, around neighboring atoms. This makes the bonds very localized and directional, i.e., the angles between bonds to a given atom are relatively tightly constrained (Gillespie and Hargittai 1991).

Metallic bonds form between atoms with similar, low electronegativity values (metals). These atoms hold relatively weakly to their valence electrons, and the molecular orbitals formed spread out to encompass a very large number of atoms. Thus, metallically bonded systems are often described as positively charged atoms (nuclei + core electrons) held together by a "sea" of valence electrons shared between all the atoms. When so many atomic orbitals combine, a large number of closely spaced (in terms of energy) molecular orbitals become available, with a relatively small gap (or no

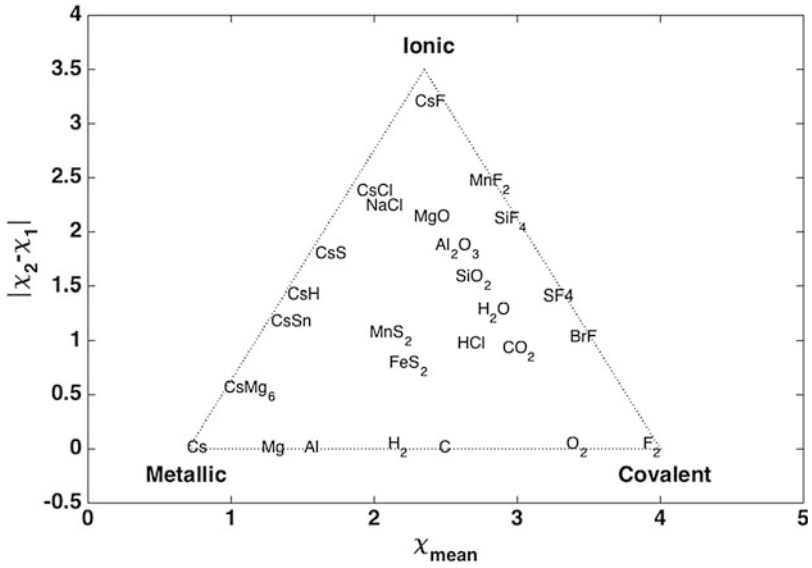

Chemical Bonds, Fig. 1 A van Arkel–Ketelaar triangle, illustrating the continuum of bond types between the ionic, covalent, and metallic limits. The *x*-axis represents the mean electronegativity (χ_{mean}) of the two atoms involved in the bonds in each of the substances plotted. The *y*-axis represents the difference in the two electronegativity values (χ_1–χ_2)

gap) between the filled and unfilled levels. This leads to the high thermal and electrical conductivity of metals, because a relatively small excitation of a bonding electron takes it into molecular orbitals that are comparatively empty and extend throughout the substance. The delocalization of the bonding electrons also results in considerably less directionality and force in the bonds, which explains the malleability of metallic solids (Burdett 1997; Rohrer 2001).

The different types of valence bonds form a continuum, in which the degree of ionicity can be roughly estimated in terms of electronegativity differences between atoms, and covalency/metallicity can be roughly estimated in terms of the average electronegativity of the bonded atoms (Rohrer 2001). Figure 1 shows a van Arkel–Ketelaar triangle, which schematically illustrates this point. However, bonding character can also be affected by factors such as pressure and temperature (Burdett 1997; Batsanov and Batsanov 2012).

One defining attribute of valence bonds is bond order. Bond order refers to the number of valence electron pairs involved in an individual bond, whether shared or transferred (IUPAC 1997; Brown 2002). (In cases where antibonding electron pairs exist, these are subtracted from the bond order.) The bond in an $F_{2(g)}$ molecule, for example, has a bond order of 1, because the electrons from two half-filled atomic orbitals are shared in one bonding molecular orbital. The electrons from three half-filled atomic orbitals are shared in $N_{2(g)}$ molecules, so the bond order is 3. In a $CsF_{(g)}$ molecule, an electron from a half-filled atomic orbital in Cs is transferred to a half-filled orbital on the F, creating an ionic bond with a bond order of 1. The orders of bonds incident to a given atom in a stable substance must sum to the atomic valence of the atom. The atomic valence is equivalent to the number of H atoms to which it can bond. Given that bond lengths are highly correlated with bond orders (Brown 2002), this creates stringent constraints regarding the combinations of bond lengths that are possible in a stable structure. Although atomic valence values are necessarily integers, bond orders can have non-integer values, especially in condensed phases with extended networks of valence bonds. For example, in corundum (α-Al_2O_3) Al has a valence of 3, while O has a valence of 2. The Al-O bonds have bond orders of ~0.5, so that each Al is bonded to six O atoms, and each O is bonded to four Al atoms. Non-integer orders for individual bonds are possible because molecular orbitals, which must contain an integral number of electrons, can encompass multiple atoms (Brown 2002; Albright et al. 2013).

At least for covalent bonds with integer bond orders, the force constants used to describe bond vibrations are proportional to the bond order (Johnston 1966). This gives rise to another defining attribute of bonds, i.e., the inverse relationship between bond length and strength.

Bonds can also profitably be characterized in terms of bond energy (E_{bond}), which is the average energy per mole of bonds released when molecules are separated into their constituent atoms. A similar quantity can be obtained from dividing the atomization energies of solids by the number of bonds per formula unit (Sanderson 1976). For a bond between two given elements, of a given bond order, E_{bond} values are relatively transferable. Therefore, it is possible to roughly estimate enthalpies of formation by summing bond energies. It is important to note that, for the same bond order, E_{bond} can vary by hundreds of kJ/mol for bonds between different elements. For example, the bond energy for the single bond in $F_{2(g)}$ is 158.67 kJ/mol, whereas that for

$Cs_{2(g)}$ is 43.919 kJ/mol and that for $CsF_{(g)}$ is 517.1 kJ/mol (Luo 2007). However, bond energies are not strictly proportional to bond order, although there is a relationship between the two.

Hydrogen Bonds as Valence Bonds

Hydrogen bonds (H-bonds) are the weaker of conjugate bonds formed between H and two or more highly electronegative atoms such as N, O, or F and are usually designated as X–H. . .X, where X represents the more electronegative atoms, the solid line represents a strong, polar covalent bond, and the dotted line represents an H-bond. The electron density involved in the strong bond is shifted toward the more electronegative atom, creating a dipole between the two atoms, resulting in a relatively weak electrostatic attraction between the positively charged H and any other electronegative atoms in the vicinity. Thus, the H is bonded strongly to one comparatively electronegative atom and much more weakly to one or more others. Due to the fact that H atoms have only one electron, along with their small size, shifting its electron density toward the anion results in a relatively high positive charge density.

Hydrogen bonds are often treated as simple electrostatic dipole interactions, rather than valence bonds, but in fact, it has been shown that even weak hydrogen bonds have some covalent character, so there is no reason to treat them as anything but weak valence bonds that may be assigned a bond order. In fact, when H-bonds are shorter, the adjacent stronger bonds become longer, as one would expect for a valence bond (Steiner and Saenger 1994; Steiner 2002).

The typical asymmetry of X–H. . .X bonds is likely to be a product of the small size of H atoms. Symmetric H-bonds, in which the two bonds to H have equal bond orders of 0.5, do exist. However, they are quite rare because bond order falls off exponentially with distance. Therefore, an X–H–X configuration with two 0.5 order bonds draws the X atoms considerably closer to one another than would typically be the case for nonbonded atoms, whereas an asymmetric X–H. . .X configuration results in a considerably longer X–X distance (Brown 2002). However, symmetric H-bonds become more common at high pressure (Steiner 2002), because X atoms are forced together by compression.

London Dispersion (van der Waals) Forces

London dispersion (van der Waals) forces originate due to oscillations in the instantaneous electron distribution around atoms. The average electron distribution is generally very symmetrically disposed about the nucleus, but at any given instant this may not be the case, creating a small dipole moment. As atoms approach one another, their oscillations synchronize to maximize attraction. This oscillation is correctly accounted for with electron correlation calculations and is in itself a type of standing wave behavior. A very weak molecular state is created in these cases, which explains why an attraction between filled shells is possible (Housden and Pyper 2007; Krapp and Frenking 2007). This is why noble gases, with filled valence shells, can condense into liquid at very low temperatures.

Bonds and the Distribution of Elements

A number of factors contribute to the distribution of the elements in the Earth, as described by the traditional *Goldschmidt classification* (Faure 1998), but one such factor has to do with bond energies. As noted above, bonds of the same order can vary widely in bond energy with the bond character. Elements with very low electronegativity (e.g., the alkali and alkali earth metals) favor highly ionic bonds with fractional bond orders (i.e., bond order < 1), so they naturally bond easily to O in network solids. Oxygen is the most abundant element in the Earth and the second-most electronegative, and some of the more electronegative elements, such as the halogens, often substitute for O. Therefore, these elements are classified as *lithophile* and are enriched in the crust and mantle. Some of the more electronegative elements, such as C and N, favor covalent bonds with one another, having high bond orders (1 or greater). This results in fewer bonds and discrete molecules rather than network solids. A number of elements with moderately high electronegativity favor covalent bonds with similar elements and low to moderate bond orders, so these tend to congregate in sulfides, and are classified as *chalcophile*. A number of metals with moderately low electronegativity favor metallic bonds with one another, with low bond orders. These tend to form metallic solids and are classified as *siderophile*, because they readily bond with Fe and are enriched in the core.

Summary and Conclusions

Chemical bonds can usefully be characterized in terms of bond order, bond energy, and bond type. Bond orders constrain suitable combinations of bond lengths incident to atoms in stable configurations, and bond energies for bonds of the same order vary widely as a function of bond type. It is impossible to classify a given chemical bond as exclusively one type, however, because van der Waals interactions are present between all neighboring atoms, and even in cases where van der Waals interactions dominate (e.g., noble gas dimers and condensed phases), molecular orbitals play some role. This is why there is a continuum between the

different bond types, based on the affinity for electrons of the bonded atoms. The relationships between bond order and bond energy for different atom pairs are one of the determining factors affecting the distribution of elements in the Earth.

Cross-References

- ▶ Ab Initio Calculations
- ▶ Atmophile Elements
- ▶ Chalcophile Elements
- ▶ Electronegativity
- ▶ Geochemical classification of elements
- ▶ Lithophile Elements
- ▶ Siderophile Elements

References

Albright TA, Burdett JK, Whangbo M-H (2013) Orbital interactions in chemistry. Wiley, Hoboken. 819 p

Batsanov SS, Batsanov AS (2012) Introduction to structural chemistry. Springer, Dordrecht. 542 p

Brown ID (2002) The chemical bond in inorganic chemistry: the bond valence model. Oxford University Press, New York. 278 p

Burdett JK (1997) Chemical bonds: a dialog. Wiley, Chichester. 166 p

Faure G (1998) Principles and applications of geochemistry. Prentice Hall, Upper Saddle River. 600 p

Gillespie RJ, Hargittai I (1991) The VSEPR model of molecular geometry. Allyn and Bacon, Boston. 248 p

Gillespie RJ, Popelier PLA (2001) Chemical bonding and molecular geometry: from Lewis structures to electron densities. Oxford University Press, Oxford. 268 p

Housden MP, Pyper NC (2007) The noble gas dimers as a probe of the energetic contributions of dispersion and short-range electron correlation in weakly-bound systems. Mol Phys 105: 2353–2361

IUPAC (1997) Compendium of chemical terminology. Blackwell Scientific Publications, Oxford

Johnston VHS (1966) Gas phase reaction rate theory. Ronald Press, New York. 372 p

Krapp A, Frenking G (2007) Is this a chemical bond? A theoretical study of $Ng_2@C_{60}$ (Ng = He, Ne, Ar, Kr, Xe). Chem Eur J 13: 8256–8270

Luo Y-R (2007) Comprehensive handbook of chemical bond energies. CRC Press, New York. 1657 p

Pauling L (1960) The nature of the chemical bond. Cornell University Press, Ithaca. 644 p

Popelier PLA (2000) Atoms in molecules: an introduction. Pearson Education, Essex. 164 p

Rohrer GS (2001) Structure and bonding in crystalline materials. Cambridge University Press, Cambridge. 540 p

Sanderson RT (1976) Chemical bonds and bond energy. Academic, New York. 218 p

Steiner T (2002) The hydrogen bond in the solid state. Angew Chem Int Ed 41:48–76

Steiner T, Saenger W (1994) Lengthening of the covalent O–H bond in O–H. . .O hydrogen bonds re-examined from low-temperature neutron diffraction data of organic compounds. Acta Crystallogr B50:348–357

Chemical Weathering

Jérôme Viers and Priscia Oliva
CNRS/IRD, Paul Sabatier University, Toulouse, France

C

Definition

Chemical weathering may be defined as the *spontaneous* and *irreversible* thermodynamic process that causes degradation of the mineral phases under the prevailing environmental conditions at the surface of the Earth. If one must differentiate the weathering in the continental and marine environments, chemical weathering is usually considered to be the solid/solution interactive process occurring in contact with the atmosphere. By extension, in the language of the specialists of the critical zone, chemical weathering may be defined as that set of processes which alter a rock into a layer of chemically and physically transformed superficial material (i.e., regolith) which is susceptible to evolve (soil or karst) with time following biogeochemical processes.

Introduction

While this process of chemical modification can be easily formalized by writing on paper, for example, the chemical reaction of dissolving a mineral (1), the reality is much more complex because it actually encompasses a set of chemical, physical, or biological complex interactions:

$$CaAl_2Si_2O_8 s + 4H^+ aq = Ca^{2+} aq + Al_2Si_2O_5(OH)_4 s \quad (1)$$

The physical process that causes the dissolution of calcium feldspar (1) is a process of hydrolysis corresponding to the replacement of a cation (Ca^{2+}) on the mineral surface by a proton (H^+). This first step in chemical weathering is the surface protonation of the mineral. The presence of protons in the etching solution is explained by chemical equilibria involving the distribution of CO_2 (atmospheric) between the aqueous and gaseous phases, e.g.:

$$CO_{2(g)} + H_2O = H^+ + HCO^-_{3(aq)} \quad (2)$$

In the conditions at the Earth's surface, chemical weathering processes occur mainly in contact with acidic solutions that result from natural acidification of rainwater in reaction (2) and subsequent acidification of solutions in the soil environment due to microbial activity (decomposition of organic matter) and root respiration (atmospheric CO_2 enrichment of the soil). In certain geological environments

(sulfide-rich volcanic or metamorphic formations), production of acid can be generated by the oxidative dissolution of sulfides such as:

$$FeS_2 s + 15/4 O_2 g + 7/2 H_2 O aq = 2SO_4^{2-} aq + Fe(OH)_3 s + 4H^+ aq \quad (3)$$

The principal reactions of chemical weathering are hydrolysis (1), oxidation (3), and the dissolution of ionic compounds. Chemical weathering processes in saline or alkaline environment exist but are very minor at the natural environment's surface conditions. The products of these reactions may be both dissolved compounds and secondary solid phases, which may be either well or poorly crystallized. The reaction is said to be incongruent when we have both aqueous and solid phases and congruent when having only dissolved compounds. The principal secondary minerals that form in the conditions at the surface across the critical zone are clay minerals or metal oxyhydroxides which are more stable from a thermodynamic perspective than are the primary minerals. Both secondary phases and residual primary minerals (inherent minerals) constitute soils mineralogical assemblage.

The products of chemical weathering can then be transported by surface water: we speak of transportation for dissolved compounds in solution (Ca^{2+}, HCO_3^-, small organic molecules, etc.) and particulate matter (or sediments) for either mineral or organic solid compounds. Geochemists have conventionally considered that the boundary between the dissolved phase and the particulate phase is defined by membranes filtration of water with the empirical pore diameter being 0.45 or 0.2 micrometers. Data on concentrations (dissolved and particulate) combined with the water discharges of rivers are therefore used to define, respectively, the chemical and physical erosion fluxes. This process of chemical weathering of rocks associated with their physical dismantling and potential material transport by inland waters is responsible for about 15 billion tons of sediment exported from the continents to the oceans annually (Milliman and Farnsworth 2011).

Chemical Weathering: A Major Geological Process

Chemical weathering is a fundamental "geological" process because it plays a major role in the global geodynamic of our planet; this role is complex because it occurs at highly variable scales of time and space.

- At the scale of the weathering front (a zone of transition between the rock and soil) or the soil itself, chemical weathering is accompanied by the release of nutrients (e.g., major elements such as K or Ca, and trace elements such as Fe or Co) essential to the functioning of the continental ecosystems. The soil which is a product of chemical weathering appears here as a fundamental natural resource, nonrenewable on the scale of humanity. It provides numerous economic functions (agricultural production, materials production in quarries, etc.), cultural (recreational, archaeological sites, etc.), or environmental (regulation of water flow, retention of contaminants, etc.). Yet in many parts of the world, soils are subjected to very high stressors (e.g., contamination, salinization, desertification, etc.) and are often irreversibly lost for any use by society.
- On a global scale, chemical weathering plays an important but complex role in regulating the climate of our planet. This role stems from the fact that the chemical weathering of silicate rocks consumes atmospheric CO_2 because the calcium and bicarbonate ions (produced in reactions (1) and (2) above) are carried to the ocean by rivers where they are precipitated (usually biologically) as calcium carbonate (4):

$$Ca^{2+} + HCO_3^- = CaCO_3 + H^+ \quad (4)$$

In the early 1980s, Walker et al. (1981) proposed a negative feedback loop between the climate and the chemical weathering of continental surfaces: an increase in the partial pressure of CO_2 (pCO_2) from the atmosphere induces an increase in air temperature and accelerates the hydrological cycle. This change of physical parameters enhances the chemical weathering of silicate rocks which in turn lowers pCO_2 and therefore regulates the Earth's climate.

However, the links between climate and weathering today appear much more complex than envisioned by Walker et al.; therefore, in recent decades, chemical weathering has undergone numerous studies conducted via different approaches.

The Different Approaches Used to Study Chemical Weathering

The chemical weathering processes can be studied in differing ways:

- They can be studied under controlled laboratory conditions. Many studies have been conducted to examine this process in conditions near to and far from thermodynamic equilibrium. These studies were intended to better understand the reactions occurring on the mineral surface during dissolution and thus gain a better understanding of the parameters controlling the kinetics of dissolution. They allowed the proposal of the empirical laws of chemical weathering (e.g., transition state theory; Berner 1995 and references therein) that revealed the importance of many factors: mineral surfaces, temperature, chemical affinity, proton activity, organic compound).

- Laboratory research on chemical weathering has a long history (about a century), and the nature of these involved processes is still undergoing debate within the scientific community. Most experiments in dissolution yield chemical weathering rates up to four orders of magnitude greater than those estimated from field studies. This discrepancy between the experimental and natural chemical weathering rates is called the "dissolution rate conundrum" (Maher et al. 2006). Under natural conditions, a progressive loss of reactive surface sites for silicate weathering over time is observed. It may be attributed to the inhibitory effect on mineral dissolution due to the presence of Al^{3+} or organic ligands in solution or to surface coating by the secondary phases precipitates in a natural context which are rare in dissolution experiments (Oelkers et al. 1994). Indeed, experimental conditions still remain far from natural circumstances (e.g., duration, fluid / mineral ratios, fluid composition) (White and Brantley 1995). The saturation state of the solution appears to be a key parameter as it controls the effects of microstructures and microtextures on chemical weathering (Chardon et al. 2006 and references therein).
- Chemical weathering processes can be studied in situ by considering the weathering products constituting the regoliths and soils. Mineralogical and/or chemical composition of the regolith represents an integrated view of all the processes that have occurred over time to form this regolith. One approach allows for the establishment of mass balances for chemical elements using references called invariant elements such as zirconium or titanium. This approach has the merit of being able to estimate the flow of chemical elements and, therefore, rates of loss or enrichment of elements throughout the soil profile. However, it often remains impossible to transform these fluxes into chemical erosion rates because the age of a given soil is often very difficult to narrow down.
- A third method is the "watershed" approach. This approach involves studying the fluxes of chemicals leaving the watersheds. These studies involve the hydrological and chemical monitoring of water during the course of continental surface drainage. This approach can be conducted on large river basins (Amazon, Congo, Lena, etc.) or small watersheds. The "large pool" approach offers the advantage of being inclusive of processes over large areas; the "small pool" approach offers the advantage of often working on more homogeneous systems (e.g., as for lithology) rendering the least complex object for study. Over watersheds of varying lithology, chemical erosion rates associated with silicate rocks may be understood by "direct" (Garrels and McKenzie 1967) or 'indirect' methods, the latter by the use of inverse methods of calculation (e.g. Gaillardet et al. 1999). All of these studies allowed highlighting of the roles of certain parameters on the weathering: mineralogy of exposed rocks, surface ages, precipitation/dissolution of clay minerals, presence of easily changeable accessory minerals, movement and time that water resides in the soil, physical erosion, vegetation, anthropogenic disturbance (fertilizer) (Oliva et al. 2003; Perrin et al. 2008).
- More recently, there are several works studying chemical weathering from numerical models (Duffy et al. 2014). These studies seek to examine/simulate chemical weathering occurring today (MacKenzie watershed, Beaulieu et al. 2011) or in the past (Goddéris et al. 2014). This is, for example, the case of the WITCH model based on the law of weathering kinetics (Beaulieu et al. 2011). In recent years, this type of model has been coupled with global dynamic models of vegetation because vegetation plays an important role with regard to the flow of water (in the soil and the soil interface/atmosphere). Vegetation plays a more direct role in the dissolution of minerals because of root activity and the release of organic acids in soil (Drever and Vance 1994). In the future, one challenge will be to model the effects on the evolution of biodiversity on the cycle of elements because vegetation is not only a sink or reservoir for carbon but is this for all of the other chemical elements (Mg, Si, Ca) (Chave 1999; Viers et al. 2005). Recent field and laboratory tests have also shown that the dissolution of phytoliths (siliceous particles produced in the plant and then recovered in the soil) showed faster dissolution kinetics than the secondary minerals (clay) and therefore could play an important role in the silicon cycle on the surface of the Earth (Derry et al. 2005; Fraysse et al. 2009). This is another poorly known effect of the role of vegetation on chemical erosion rates and more generally on the cycle of elements.

Unifying Natural and Experimental Chemical Weathering Rates

During the last decade, one of the major scientific questions circulating about chemical weathering was to understand the existing disparities between the field measurements of natural "chemical weathering rates" and the measurements carried out in the laboratory, the objective being to attempt unification of this dual information. The most significant results were obtained from multidisciplinary approaches in geochemistry and mineralogy (Ferrier et al. 2010) or by focusing on the molecular-level mineral-water interface by means of new observational tools and analyses of mineral surfaces with high resolution [e.g., Raman spectroscopy, high-resolution and energy-filtered TEM, in situ atomic force microscopy (AFM)] as defined in the publications of Hellmann et al. (2012) or Ruiz Agudo et al. (2012). These methods have identified the mechanisms of interface-coupled dissolution-reprecipitation mechanisms during chemical weathering. These results put into question the currently accepted leached-layer model of

chemical weathering (Oelkers et al. 2009; Schott et al. 2012) which involves preferential removal of weakly bonded cations (e.g., Na^+ and K^+) from the surface regions of silicates, which precedes the removal of the more strongly bonded cations (e.g., Al^{3+} and Si^{4+}) at acidic pH values resulting in apparent incongruent dissolution for silicate minerals.

Concurrently, Rasmussen et al. (2011) using a more traditional approach (measurement of the ground flux versus thermodynamic calculations on the basis of Na export) on a set of data very well documented across the Rio Icacos watershed were able to quantify the activation energies (E_a) for the weathering of feldspars comparable to those data given in the literature for the experimental dissolution of albite. These results indicate that to correctly quantify E_a dissolution from field data, certain parameters (i.e., water availability, erosion) rather neglected up to that point, must be considered. It's about the physicochemical and regolith soil data, particularly the availability of water to perform mineral weathering. Rasmussen et al. (2011) calculated an average apparent activation energy of 69 $kJ.mol^{-1}$ Na for positive annual water balance zones and 136 $kJ.mol^{-1}$ Na for water-limited locations, respectively. This suggests that water availability is the dominant factor limiting rate kinetics for albite weathering in the cool climate of the water-limited systems.

The Effect of Water Availability and Time Duration for the Presence of Water

The availability of water is proposed as the factor limiting the rate of chemical weathering in weathering systems by many authors (Maher 2010). Long transit times of water (>1 decade) are consistent with a kinetic control of the weathering by thermodynamics through the precipitation of secondary phases or activity of microorganisms, while the short times that water is present are synonymous with control by the processes of transport and hydrology. Thus, some authors consider that the dependence of chemical weathering on time, which is often considered to be the major parameter in the models of landform contour evolution, is in fact a result of mechanisms controlled by hydrological processes (water availability, time period that water is present, etc.). The concept of a hydrological thermostat ("hydrologic thermostat") was established to describe the role of hydrological processes in the regulation of chemical weathering and associated with the consumption of CO_2 (Maher and Chamberlain 2014). The flow (*runoff*) appears as the most relevant parameter to describe the flux of weathering in comparison with the temperature in many environments. The most important flow of weathering measured at present corresponds to the environments of volcanic islands (Goldsmith et al. 2010; Schopka et al. 2011) in which deeply circulating hydrological systems (table) can play a major role (Schopka and Derry 2012).

Summary and Conclusions

Numerous studies conducted over the past two decades on chemical weathering are related to its ability to remove CO_2 from the atmosphere because that can condition our Earth's climate (West 2012). Understanding the links between the climate and tectonics in the geological history of our planet inevitably involves taking the carbon cycle into account and thus, chemical weathering. Certainly the study of current systems helps to better establish some parametric laws between weathering and climate. However, the relationship between climate, tectonics, erosion, and the sets of potential feedback is still a major subject of study. The study of the role of mountain ranges and flood plains of major rivers in weathering (such as those currently in the Amazon watershed) will remain a preferred subject of study over the coming years (Moquet et al. 2011; Bouchez et al. 2012).

Cross-References

- ▶ Acid–Base Reactions
- ▶ Aqueous Solutions
- ▶ Earth's Atmosphere
- ▶ Carbon Cycle
- ▶ Clay Minerals
- ▶ Critical Zone
- ▶ Geochemical Thermodynamics
- ▶ Kinetics of Geochemical Processes
- ▶ Low-Temperature Geochemistry
- ▶ Oxidation-Reduction Reactions and Eh-pH (Pourbaix) Diagrams
- ▶ Oxide Minerals
- ▶ Silicate Minerals
- ▶ Soils
- ▶ Surface Geochemistry

Bibliography

Beaulieu E, Goddéris Y, Labat D, Roelandt C, Calmels D, Gaillardet J (2011) Modeling of water-rock interaction in the MacKenzie basin: competition between sulfuric and carbonic acids. Chem Geol 289:114–123

Berner RA (1995) Chemical weathering and its effect on atmospheric CO_2 and climate. In: White AF, Brantley SL (eds) Chemical weathering rates of silicate minerals, Reviews in mineralogy, vol 31. Mineralogical Society of America, Washington, DC, pp 565–583

Bouchez J, Gaillardet J, Lupker M, Louvat P, France-Lanord C, Maurice L, Armijos E, Moquet J-S (2012) Floodplains of large rivers: weathering reactors or simple solos? Chem Geol 332(333):166–184

Chardon D, Chevilotte V, Beauvais A, Grandin G, Boulangé B (2006) Planation, bauxites and epeirogeny: one or two paleosurfaces on the West African margin? Geomoph 82:273–282

Chave J (1999) Study of structural, successional and spatial patterns in tropical rain forests using TROLL, a spatially explicit forest model. Ecol Model 124:233–254
Derry LA, Kurtz AC, Ziegler K, Chadwick OA (2005) Biological control of terrestrial silica cycling and export fluxes to watersheds. Nature 433:728–731
Drever JI Vance GF (1994) Role of soil organic acids in mineral weathering process. In: Pittman ED, Lewan MD (eds) Organic acids in geological processes, Springer-Verlag, Berlin, 482pp
Duffy C, Shi Y, Davis K, Slingerland R, Li L, Sullivan PL, Goddéris Y, Brantley SL (2014) Designing a suite of models to explore critical zone function. Proc Earth Planet Sci 10:7–15
Ferrier KL, Kirchner JW, Riebe CS, Finkel RC (2010) Mineral-specific chemical weathering rates over millennial timescales: measurements at Rio Icacos, Puerto Rico. Chem Geol 277:101–114
Fraysse F, Pokrovsky O, Schott J, Meunier JD (2009) Surface chemistry and reactivity of plant phytoliths in aqueous solutions. Chem Geol 258:197–206
Gaillardet J, Dupré B, Louvat P, Allègre CJ (1999) Global silicate weathering and CO_2 consumption rates deduced from the chemistry of large rivers. Chem Geol 159:3–30
Garrels RM, Mackenzie FT (1967) Origin of the chemical compositions of some springs and lakes. Am Chem Soc Adv Chem Ser 67:222–242
Goddéris Y, Donnadieu Y, Le Hir G, Lefebvre V, Nardin E (2014) The role of paleogeography in the Phanerozoic history of atmospheric CO_2 and climate. Earth Sci Rev 128:122–138
Goldsmith ST, Carey AE, Johnson BM, Welch SA, Berry Lyons W, McDowell WH, Pigott JS (2010) Stream geochemistry, chemical weathering and CO_2 consumption potential of andesitic terrains, Dominica, lesser Antilles. Geochim Cosmochim Acta 74:85–103
Hellmann R, Wirth R, Daval D, Barnes JP, Penisson JM, Tisserand D, Epicier T, Florin B, Hervig RL (2012) Unifying natural and laboratory chemical weathering with interfacial dissolution-reprecipitation: a study based on the nanometer-scale chemistry of fluid-silicate interfaces. Chem Geol 294:203–216
Maher K (2010) The dependence of chemical weathering rates on fluid residence time. Earth Plan Sci Lett 294:101–110
Maher K, Chamberlain CP (2014) Hydrologic regulation of chemical weathering and the geologic carbon cycle. Science 342:1502–1504
Maher K, Steefel CI, DePaolo DJ, Viani BE (2006) The mineral dissolution rate conundrum: insights from reactive transport modelling of U isotopes and pore fluid chemistry in marine sediments. Geochim Cosmochim Acta 70:337–363
Milliman JD, Farnsworth KL (2011) River discharge to the coastal ocean: a global synthesis. Cambridge, Cambridge University Press, 392pp
Moquet J-S, Crave A, Viers J, Seyler P, Armijos E, Bourrel L, Chavarri E, Lagane C, Casimiro WSL, Pombosa R, Noriega L, Vera A, Guyot J-L (2011) Chemical weathering and atmospheric soil/CO_2 uptake in the Andean and foreland Amazon basins. Chem Geol 287:1–26
Oelkers EH, Schott J, Devidal JL (1994) The effect of aluminum, pH, and chemical affinity on the rates of aluminosilicate dissolution reactions. Geochim Cosmochim Acta 58:2011–2024
Oelkers EH, Golubev SV, Chairat C, Pokrovsky OS, Schott J (2009) The surface chemistry of multi-oxide silicates. Geochim Cosmochim Acta 73:4617–4634
Oliva P, Viers J, Dupré B (2003) Chemical weathering in granitic environments. Chem Geol 202:225–256
Perrin A-S, Probst A, Probst J-L (2008) Impact of nitrogenous fertilizers on carbonate dissolution in small agricultural catchments: implications for weathering CO_2 uptake at regional and global scales. Geochim Cosmochim Acta 72:3105–3123
Rasmussen C, Brantley S, deB Richter D, Blum A, Dixon J, White AF (2011) Strong climate and tectonic control on plagioclase weathering in granitic terrain. Earth Plan Sci Lett 301:521–530
Ruiz-Agudo E, Putnis CV, Rodriguez-Navarro C, Putnis A (2012) Mechanism of leached layer formation during chemical weathering of silicate minerals. Geology 40:947–950
Schopka HH, Derry LA (2012) Chemical weathering fluxes from volcanic islands and the importance of groundwater: the Hawaiian example. Earth Plan Sci Lett 339/340:67–78
Schopka HH, Derry LA, Arcilla CA (2011) Chemical weathering, river geochemistry and atmospheric carbon fluxes from volcanic and ultramafic regions on Luzon Island, the Philippines. Geochim Cosmochim Acta 75:978–1002
Schott J, Pokrovsky O, Spalla O, Devreux F, Gloter A, Mielczarski A (2012) Formation, growth and transformation of leached layers during silicate minerals dissolution: the example of wollastonite. Geochim Cosmochim Acta 98:259–281
Viers J, Barroux G, Pinelli M, Seyler P, Oliva P, Dupré B, Boaventura G (2005) The influence of the Amazonian floodplain ecosystems on the trace element dynamics of the Amazon River mainstem (Brazil). Sci Total Environ 339:219–232
Walker JCG, Hays PB, Kasting JF (1981) A negative feedback mechanism for the long-term stabilization of Earth's surface temperature. J Geophys Res 86:9776–9782
West AJ (2012) Thickness of the chemical weathering zone and implications for erosional and climatic drivers of weathering and for carbon-cycle feedbacks. Geology 40:811–814
White AF, Brantley SL (1995) Chemical weathering rates of silicate minerals: an overview. In: White AF, Brantley SL (eds) Chemical weathering rates of silicate minerals, Reviews in mineralogy, vol 31. Mineralogical Society of America, Washington, DC, pp 1–22

C

Chlorine

Mark A. Kendrick
Research School of Earth Sciences, Australian National University, Canberra, ACT, Australia

Element Data

Atomic Symbol: Cl
Atomic Number: 17
Atomic Weight: 35.453
Isotopes and Abundances: stable ^{35}Cl (75.76%) and ^{37}Cl (24.24%) and radioactive ^{36}Cl ($t_{1/2} = 301.3$ ka)
1 Atm Melting Point: 171.65 K
1 Atm Boiling Point: 239.11 K
Common Valences: −1, 1, 3, 5, 7
Ionic Radii: 1.8 Å
Pauling Electronegativity: 3.16
First Ionization Potential: 1256.2 kJ mol^{-1}
Chondritic (CI) Abundance: 680 ppm
Silicate Earth Abundance: 15–30 ppm
Crustal Abundance: 140–470 ppm
Seawater Abundance: 19,300 ppm
Core Abundance: <20 ppb?

Properties

Chlorine is a diatomic toxic green-yellow gas at room temperature with a bleach-like smell. However, Cl is characterized by an S^2P^5 outer electron shell configuration and is highly electronegative, meaning it rarely exists in its elemental form in nature. Chlorine most commonly forms the chloride ion with a valence of -1, but it can exist in a number of different valence states. Chloride forms strong ionic bonds in salts and substitutes for the OH group in many hydrous minerals. Hydrogen chloride [$HCl_{(g)}$] is a diatomic gas at room temperature and forms hydrochloric acid $HCl_{(aq)}$ when dissolved in water.

History and Use

Elemental $Cl_{2(g)}$ was first produced by the Swedish scientist Carl Wilhelm Scheele in 1774. Scheele isolated $Cl_2(g)$ by heating hydrochloric acid with the mineral pyrolusite (MnO_2) but believed the resulting gas was an oxide he named "dephlogisticated muriatic acid air." Later experiments showed that this gas would not decompose during reaction with charcoal, phosphorus, or ammonia, and by 1810 Sir Humphrey Davy concluded the gas was an element (Davy 1811). The name chlorine is derived from the Greek word chloros meaning green-yellow (Davy 1811).

Chloride in common salt has been used in cooking and food preservation since prehistoric times. Salt is produced commercially by the evaporation of seawater or mining. Chlorine gas is produced for industrial purposes by electrolysis of salt solutions or molten sodium or magnesium chloride. Chlorine is used to kill bacteria in drinking water and swimming pools and in the manufacture of a wide range of products including paper, paints, textiles, and plastics. PVC (polyvinyl chloride) alone is used extensively in the building and automotive industries. The high electronegativity of Cl means Cl or Cl compounds are used as oxidizing agents or in substitution reactions involved in the manufacture of many pharmaceuticals and some insecticides. In the past Cl was used to make chloroform ($CHCl_3$) which is a toxic but powerful anesthetic, chlorofluorocarbons (CFCs) were used as refrigerants and aerosol propellants before being linked to destruction of stratospheric ozone, and Cl gas was used as a highly toxic chemical weapon in World War 1.

Distribution in the Cosmos and on Earth

The solar photosphere contains 4.8 ppm Cl, making it the eighteenth most abundant element in the solar system (Lodders 2003). Chlorine is moderately volatile with a 50% condensation temperature of 954 K at 10^{-4} bar (Lodders 2003). Chlorine has a concentration of ~680 ppm in CI chondrites compared to an estimated concentration of ~15–30 ppm in the Earth's theoretical primitive mantle (McDonough and Sun 1995). Chlorine is depleted on Earth relative to other elements of similar volatility, and because Cl has a low compatibility in Fe-Ni alloys and is therefore expected to have a low concentration in the Earth's core, it is suggested that Cl was probably lost during Earth's accretion either with the early atmosphere or with crustal components removed by collisional erosion (Sharp and Draper 2013).

Chlorine is a strongly incompatible element and is concentrated in the Earth's surface reservoirs. Seawater with 1.9 wt. % Cl (~3.5 wt % salt) contains a bit less than half, and evaporites with up to 60 wt. % Cl contain about a quarter of the total Cl in the Earth's surface reservoirs (Schilling et al. 1978).

Chlorine has a residence time of 100s of Myr in seawater, suggesting a constant concentration; however, depending on the amount of Cl stored in evaporites, seawater salinities could have been very different (more saline) in the distant geological past (Hay et al. 2006). Sedimentary formation waters have salinities that commonly range from ~1 up to ~30 wt. % salt, but can include even higher salinities (Hanor 1994). Average continental crust has been variably estimated to contain 130–470 ppm Cl compared to ~1–5 ppm Cl in the depleted mantle (Rudnick and Gao 2003; Shimizu et al. 2016). Primitive mid-ocean ridge and ocean island basalt glasses contain ~30–2000 ppm Cl (Schilling et al. 1978; Michael and Cornell 1998; Kendrick et al. 2015). The average Cl content of altered ocean crust is not well constrained but could be as high as 100–500 ppm (Sano et al. 2008). High concentrations of Cl are common in metamorphic environments characterized by low fluid-rock ratios, and parts of the oceanic crust and lithosphere contain amphibole and serpentine with wt. % levels of Cl (Sharp and Barnes 2004; Kendrick et al. 2013; Kendrick 2017). The long-term exchange of Cl between the Earth's mantle and surface reservoir over time is an area of active research.

Significance in Geochemistry

Chlorine is undersaturated in typical submarine basaltic lavas and behaves as a lithophile element in the mantle. However, $HCl_{(g)}$ is degassed from subaerial volcanoes and has a significant influence on climate and ozone depletion (Kutterolf et al. 2013). Chloride is the dominant anion in geofluids, including magmatic fluids exsolved in the crust. Chloride acts as an important ligand enabling the transport of metals in hydrothermal solution (Yardley, 2005).

In sedimentary environments with a high water-rock ratio, fluid chlorinity is often considered to be conservative and can be used to infer a fluid source or migration pathway. In some cases the movement of saline formation waters (oil field brines) is linked with hydrocarbon migration. In higher-temperature metamorphic environments with lower fluid-rock ratios, the concentration of Cl in a geofluid is not conservative. Fluid salinity provides important evidence for hydrothermal phase separation and the Cl content of metamorphic minerals track the involvement of saline fluids in metamorphic processes (Kendrick 2017).

Chlorine Isotopes

Chlorine stable isotope ratios reported relative to standard mean ocean chloride vary by ~10 ‰ on Earth. Chondrites and samples from the terrestrial mantle typically have δ^{37}Cl of slightly less than seawater (0 ‰), suggesting that Cl was isotopically uniform in the inner solar nebular (Sharp et al. 2013). Minor variations in mantle δ^{37}Cl, including maximum δ^{37}Cl of up to +3 ‰, have been attributed to the subduction of sediments (John et al. 2010). However, the majority of materials from the Earth's surface including sediments have δ^{37}Cl of less than seawater, and the mechanisms for isotope fractionation are not well understood (Barnes and Straub 2010). The Moon exhibits much greater variation in δ^{37}Cl with maximum values of +25 ‰ attributed to fractionation during lunar degassing of metal-halides from anhydrous magmas at low atmospheric pressures (Sharp et al. 2010). The short-lived ^{36}Cl isotope ($t_{1/2}$ = 301.3 ka) is used in dating groundwater and cosmogenic exposure dating of landforms formed by lava flows or glacial erosion surfaces ranging from tens of thousands of years to about 1 Ma (Ivy-Ochs and Kober 2008).

Biological Utilization and Toxicity

Chlorine gas is a respiratory irritant, and it can be detected by a bleach-like odor at concentrations of less than 1 ppm; it causes immediate chest pain, vomiting, and shortness of breath at concentrations of ~30 ppm; and is fatal within minutes at concentrations of more than ~1000 ppm (About Chlorine 2016). In contrast, chloride is the dominant anion enabling cellular level electrochemistry, meaning that Cl is an essential element for life.

Cross-References

- ▶ Chlorine Isotopes
- ▶ Chondrites
- ▶ Cosmic Elemental Abundances
- ▶ Cosmogenic Nuclides
- ▶ Evaporites
- ▶ Fluid Inclusions
- ▶ Halide Minerals
- ▶ Halogens
- ▶ Hydrothermal Alteration
- ▶ Hydrothermal Solutions
- ▶ Hydrothermal Vents
- ▶ Mid-Ocean Ridge Basalts (MORB)
- ▶ Ocean Biochemical Cycling and Trace Elements
- ▶ Oceanic Island Basalts
- ▶ Subduction Zone Geochemistry

References

About Chlorine. Retrieved May 2016, The Chlorine Institute. Available at: http://chlorineinstitute.org/stewardship/about-chlorine

Barnes JD, Straub SM (2010) Chorine stable isotope variations in Izu Bonin tephra: implications for serpentinite subduction. Chem Geol 272(1–4):62–74

Davy H (1811) On a combination of oxymuriatic gas and oxygene gas. Philos Trans R Soc Lond 101:155–162

Hanor JS (1994) Origin of saline fluids in sedimentary basins. In: Parnell J (ed) Geofluids: origin, migration and evolution of fluids in sedimentary basins, Geological society special publication. Geological Society, London, pp 151–174

Hay WW, Migdisov A, Balukhovsky AN, Wold CN, Flögel S, Söding E (2006) Evaporites and the salinity of the ocean during the Phanerozoic: implications for climate, ocean circulation and life. Palaeogeogr Palaeoclimatol Palaeoecol 240(1–2):3–46

Ivy-Ochs S, Kober F (2008) Surface exposure dating with cosmogenic nuclides. Quat Sci J 57(1–2):179–209

John T, Layne GD, Haase KM, Barnes JD (2010) Chlorine isotope evidence for crustal recycling into the Earth's mantle. Earth Planet Sci Lett 298(1–2):175–182

Kendrick MA (2017) Halogens in seawater, marine sediments and the altered oceanic lithosphere. In: Harlov DE, Aranovich LY (eds) The role of halogens in terrestrial and extraterrestrial processes. Springer, Berlin. In press

Kendrick MA, Honda M, Pettke T, Scambelluri M, Phillips D, Giuliani A (2013) Subduction zone fluxes of halogens and noble gases in seafloor and forearc serpentinites. Earth Planet Sci Lett 365:86–96

Kendrick MA, Jackson MG, Hauri E, Phillips D (2015) The halogen (F, Cl, Br, I) and H_2O systematics of Samoan lavas: assimilated seawater, EM2 and high 3He/4He components. Earth Planet Sci Lett 410:197–209

Kutterolf S, Hansteen TH, Appel K, Freundt A, Krüger K, Pérez W, Wehrmann H (2013) Combined bromine and chlorine release from large explosive volcanic eruptions: a threat to stratospheric ozone? Geology 41(6):707–710

Lodders K (2003) Solar system abundances and condensation temperatures of the elements. Astrophys J 591:1220–1247

McDonough WF, Sun S-s (1995) The composition of the earth. Chem Geol 120:223–253

Michael PJ, Cornell WC (1998) Influence of spreading rate and magma supply on crystallization and assimilation beneath mid-ocean ridges: evidence from chlorine and major element chemistry of mid-ocean ridge basalts. J Geophys Res Solid Earth 103(B8): 18325–18356

Rudnick RL, Gao S (2003) Composition of the continental crust. In: Treatise of geochemistry. Elsevier, Amsterdam, pp 1–64

Sano T, Miyoshi M, Ingle S, Banerjee NR, Ishimoto M, Fukuoka T (2008) Boron and chlorine contents of upper oceanic crust: basement samples from IODP Hole 1256D. Geochem Geophys Geosyst 9(12): Q12O15
Schilling JG, Unni CK, Bender ML (1978) Origin of chlorine and bromine in the oceans. Nature 273:631–636
Sharp ZD, Barnes JD (2004) Water-soluble chlorides in massive seafloor serpentinites: a source of chloride in subduction zones. Earth Planet Sci Lett 226(1–2):243–254
Sharp ZD, Draper DS (2013) The chlorine abundance of earth: implications for a habitable planet. Earth Planet Sci Lett 369–370:71–77
Sharp ZD, Shearer CK, McKeegan KD, Barnes JD, Wang YQ (2010) The chlorine isotope composition of the moon and implications for an anhydrous mantle. Science 329(5995):1050–1053
Sharp ZD, Mercer JA, Jones RH, Brearley AJ, Selverstone J, Bekker A, Stachel T (2013) The chlorine isotope composition of chondrites and earth. Geochim Cosmochim Acta 107:189–204
Shimizu K, Saal AE, Myers CE, Nagle AN, Hauri EH, Forsyth DW, Kamenetsky VS, Niu Y (2016) Two-component mantle melting-mixing model for the generation of mid-ocean ridge basalts: implications for the volatile content of the Pacific upper mantle. Geochim Cosmochim Acta 176:44–80
Yardley BWD (2005) 100th anniversary special paper: metal concentrations in crustal fluids and their relationship to ore formation. Econ Geol 100(4):613–632

Chlorine Isotopes

Magali Bonifacie
Institut de Physique du Globe de Paris, Sorbonne Paris Cité, Université Paris Diderot, Paris, France

Introduction

Chlorine has 24 isotopes with mass numbers ranging from ^{28}Cl to ^{51}Cl. There are only two stable isotopes: ^{35}Cl and ^{37}Cl with respective proportions of 75.76% and 24.24% (Berglund and Wieser 2011). The longest-lived radioactive isotope is ^{36}Cl (half-life of 301,000 years); all other isotopes having half-lives of less than 1 h. Variations of the chlorine isotope ratio ($R = {}^{37}Cl/{}^{35}Cl$) are expressed in the δ-notation with $\delta^{37}Cl = \left(R_{sample}/R_{standard} - 1\right) * 1000$. The international reference standard for chlorine is the terrestrial ocean Standard Mean Ocean Chloride (SMOC), with $\delta^{37}Cl = 0$ ‰ (Godon et al. 2004a; Kaufmann et al. 1984).

History and Overview

Chlorine undergoes volatile and incompatible behavior during silicate melting and is water soluble. For these reasons, geological processes (including partial melting, magma degassing, hydrothermal activity, and weathering) have mostly concentrated Cl at the Earth's surface, particularly in the ocean, evaporites, and crustal brines. The most common and stable oxidation state of chlorine is -I, with chloride (Cl^-) being the main anion of most geological fluids.

Chlorine stable isotopic variations in geological samples were first reported in formation waters from the Gulf of Mexico (Kaufmann et al. 1984). Since then, chlorine stable isotopes have been used as a tool for tracing the origin and fate of fluids and rocks from the Earth's surface and interior (e.g., fluid movement in sedimentary basins, magma degassing, cycling of the subducted lithosphere into the mantle). Excluding volcanic fumaroles, the large majority of terrestrial samples analyzed to date have δ^{37} Cl between −2 and +2 ‰ (Fig. 1) requiring precise analytical methods to be able to identify and interpret small variations.

Stable Chlorine Isotope Measurements

Though chlorine isotopic compositions were, in the 1990s, measured via thermal ionization mass spectrometry (TIMS), δ^{37}Cl measurements are now mostly performed via gas source isotope ratio mass spectrometry (GS-IRMS) on gaseous methyl chloride. This requires prior precipitation of soluble chlorides Cl^- into $AgCl_{(s)}$, followed by the formation of $CH_3Cl_{(g)}$, via AgCl reaction with excess $CH_3I_{(g)}$ (Eggenkamp 1994). This method allows to reach the best precision on δ^{37}Cl measurements that are typically about ± 0.04 ‰ and ± 0.3 ‰ (1σ) when using either dual-inlet (Godon et al. 2004a; Bonifacie et al. 2005) or continuous-flow (Sharp et al. 2007) introduction modes. The determination of δ^{37}Cl of silicate bulk rocks and minerals requires an additional step of Cl extraction from the silicate network, usually made via pyrohydrolysis (Bonifacie et al. 2007a), before AgCl precipitation. Only recently, δ^{37}Cl values of rocks and minerals have been determined in situ with secondary ion mass spectrometry (SIMS) in Cl-rich terrestrial basaltic to andesitic glasses (Godon et al. 2004c; John et al. 2010; Layne et al. 2009) or melt inclusions (Manzini et al. 2017) but also in some extraterrestrial samples as chondritic sodalites (Sharp et al. 2007) or Cl-rich apatites from the Moon or Martian meteorites (Boyce et al. 2015; Sharp et al. 2010b; Williams et al. 2016). However, the uncertainty associated with δ^{37}Cl measurements by SIMS is still relatively large ± 0.5 ‰ (1σ) for samples with percent-level Cl (Williams et al. 2016) and larger for lower Cl-content samples.

Chlorine Isotope Fractionations

Many physical and chemical processes are likely to segregate isotopes of a single element according to their mass and following either thermodynamic equilibrium laws or kinetic processes. Theoretical studies based on ab initio calculations

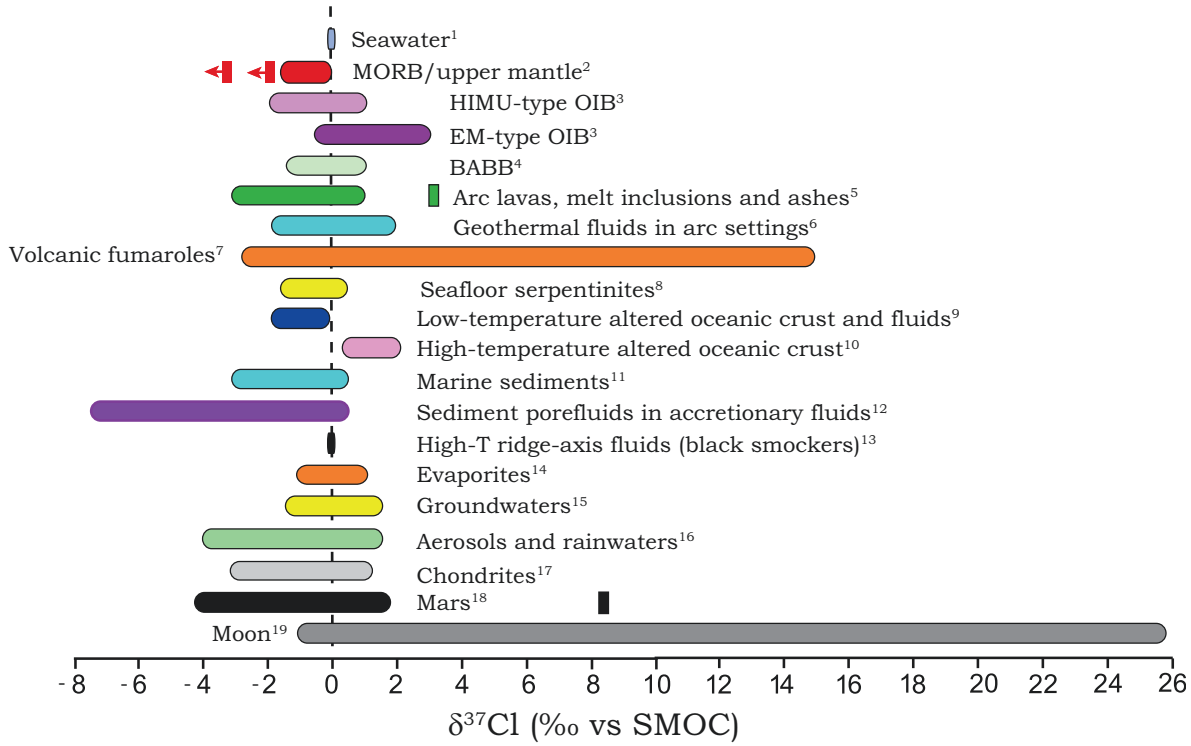

Chlorine Isotopes, Fig. 1 Chlorine isotope variations in terrestrial and extraterrestrial reservoirs. (1) Kaufman et al. (1984), Godon et al. (2004a). (2) Bonifacie et al. (2007a, 2008a), Sharp et al. (2007), Layne et al. (2009). (3) John et al. (2010). (4) Layne et al. (2009). (5) Barnes et al. (2009), Barnes and Straub (2010), Manzini et al. (2017). (6) Li et al. (2015), Chiaradia et al. (2014), Rodriguez et al. (2016). (7) Sharp et al. (2010a), Rizzo et al. (2013), Rodriguez et al. (2016). (8) Bonifacie et al. (2008b), Barnes and Sharp (2006). (9 and 10) Bonifacie et al. (2007a, 2007b), Barnes and Cisneros (2012). (11) Barnes and Straub (2010). (12) Godon et al. (2004b). (13) Bonifacie et al. (2005). (14) Eastoe et al. (2007). (15) Eastoe et al. (2001), Kaufmann et al. (1993), Stotler et al. (2010). (16) Koehler and Wassenaar (2010). (17) Bonifacie et al. (2007a), Sharp et al. (2007, 2013). (18) Williams et al. (2016). (19) Sharp et al. (2010b), Boyce et al. (2015)

have reported equilibrium fractionations between different Cl-bearing molecules of geochemical or environmental importance including chloride salts (e.g., NaCl, KCl, RbCl), gas-phase molecules (such as HCl and Cl_2 or molecule of interest in atmosphere as ClO, $ClONO_2$), dissolved species, and $FeCl_2$ and $MnCl_2$ as analogs for Cl-bearing silicates (Czarnacki and Hałas 2012; Richet et al. 1977; Schauble et al. 2003). Their main conclusions are (i) Cl isotope equilibrium fractionations are limited to only a few per mil when Cl is under –I oxidation state (the majority of geological samples) with fractionation decreasing with increasing temperature, (ii) the magnitude of fractionation is predicted to increase with the increasing oxidation state of Cl (e.g., ClO_4 is 75 ‰ enriched relative to chloride at 25 °C), and (iii) silicates are predicted to be enriched compared to coexisting brines (from about 2 ‰ to 3 ‰ at 25 °C). Experimental work to constrain equilibrium fractionations have been limited to chloride salt precipitation (Eggenkamp et al. 2016; confirming the theoretical predictions of less than 0.5 ‰ fractionations at 22 °C) or gaseous HCl in equilibrium with aqueous chloride (Sharp et al. 2010a; confirming the predicted ~1.5 ‰ gas enrichment at 50 °C). On the other hand, kinetic fractionations are suggested to occur at low temperature during processes such as (i) diffusion (^{35}Cl diffusing faster than ^{37}Cl; Desaulniers et al. 1986; Eggenkamp and Coleman 2009; Richter et al. 2006), (ii) ion filtration (this process results from a fluid flow forcing solute ions such as Cl^- through a negatively charged low-permeability medium/membrane such as clays – ^{35}Cl being more efficiently repelled than ^{37}Cl, the solution passing through the membrane is enriched in ^{37}Cl, and the solution on the inflow side is Cl-enriched but ^{37}Cl depleted; (Campbell 1985; Phillips and Bentley 1987)), or (iii) HCl dynamically escaping from an acid solution (Sharp et al. 2010a). Eggenkamp (2014) presents a detailed and up-to-date review of the aforementioned and other known Cl isotope fractionations.

Key Research Findings and Applications as a Geochemical Tracer

Multiple studies have used $\delta^{37}Cl$ values to trace the origin of salinity and the hydrodynamic history of saline fluids found in the continental crust, brines in sedimentary basins (e.g.,

Eastoe et al. 2001; Kaufmann et al. 1993), or crystalline waters from old cratons (e.g., Shouakar-Stash et al. 2007; Stotler et al. 2010). In contrast to most chemical tracers that are prone to changes upon water-rock interactions, chlorine is mainly conservative, therefore Cl isotopes are used to identify fluid circulation in sedimentary basins and quantify diffusion in aquifers (e.g., Eggenkamp 1994; Giunta 2015; Lavastre et al. 2005).

Over the last decade, δ^{37}Cl values have been increasingly used to constrain the source and/or degassing of terrestrial and extraterrestrial rocks and magmas. Notably, since chlorine isotopes are thought to not fractionate during high-temperature dehydration of the subducting slab (Bonifacie et al. 2008b; Selverstone and Sharp 2013), δ^{37}Cl is used to better constrain the deep-Earth cycling of halogens and the origin of mantle chemical heterogeneity. Since the work constraining the Cl composition of the depleted mantle (Bonifacie et al. 2008a; Sharp et al. 2007), several studies have used δ^{37}Cl values for tracing the source of ocean island basalts (Halldórsson et al. 2016; John et al. 2010), back-arc basalts (Layne et al. 2009; Barnes et al. 2009), or arc magmas (e.g., Barnes and Straub 2010; Barnes et al. 2009).

Chlorine shows a unique combination of geochemical properties that can inimitably trace the history of magmas from their origin through their differentiation, degassing, and interactions with meteoric or hydrothermal fluids. Notably, chlorine is among the last volatiles degassed (mainly as HCl) from magmas, is chemically nonreactive (unlike most other main volatile elements), and is highly hydrophilic. Fumaroles, geothermal waters, and rocks of various arc volcanoes have been investigated in order to trace the source of magmas [for instance, the Poas volcano (Rodríguez et al. 2016; Sharp et al. 2010a), the Soufrière de Guadeloupe (Li et al. 2015), or the Mount Etna (Rizzo et al. 2013) or along an active arc setting (e.g., Barnes et al. 2009; Chiaradia et al. 2014; Li et al. 2015)]. Some studies also presented a time-related evolution of δ^{37}Cl in springwaters and fumaroles to test their relevance for volcanic surveillance (Li et al. 2015; Rodríguez et al. 2016). In parallel, the highly ^{37}Cl-enriched apatites of lunar basalts (with δ^{37}Cl up to +25 ‰) have been explained as resulting from the degassing of metal halides from an anhydrous mantle (Sharp et al. 2010a) or alternatively from the degassing of a lunar magma ocean early in the Moon's history (Boyce et al. 2015).

Summary and Future Directions

Because of the unique characteristics of chlorine when compared to most other abundant and geochemically important volatiles or mobile elements on Earth, δ^{37}Cl are increasingly used to reveal the origin and fate of terrestrial and extraterrestrial reservoirs. However, before reaching their full potential as a geochemical tracer, there is still a need of strengthening our fundamental knowledge on Cl isotope systematics (mainly further determination of isotopic fractionations between Cl species in various conditions and improvements of analytical methods in order to determine precise δ^{37}Cl on Cl-poor samples). Another promising aspect is the recent advance in measuring bromine stable isotope compositions in low Br-content geological samples (Louvat et al. 2016). Because Br shares most chemical characteristics with Cl (although slightly more reactive), the coupled used of Cl and Br stable isotopes should undoubtedly unravel important features of the halogen geodynamics.

Cross-References

- Ab Initio Calculations
- Bromine
- Chlorine
- Gas Source Mass Spectrometry (GS-MS)
- Halogens
- Hydrothermal Solutions
- Mantle Geochemistry
- Ocean Biochemical Cycling and Trace Elements
- Stable Isotope Geochemistry

References

Barnes JD, Cisneros M (2012) Mineralogical control on the chlorine isotope composition of altered oceanic crust. Chem Geol 326–327:51–60. https://doi.org/10.1016/j.chemgeo.2012.07.022

Barnes JD, Sharp ZD (2006) A chlorine isotope study of DSDP/ODP serpentinized ultramafic rocks: insights into the serpentinization process. Chem Geol 228:246–265. https://doi.org/10.1016/j.chemgeo.2005.10.011

Barnes JD, Straub SM (2010) Chorine stable isotope variations in Izu Bonin tephra: implications for serpentinite subduction. Chem Geol 272:62–74. https://doi.org/10.1016/j.chemgeo.2010.02.005

Barnes JD, Sharp ZD, Fischer TP, Hilton DR, Carr MJ (2009) Chlorine isotope variations along the Central American volcanic front and back arc. Geochem Geophys Geosyst 10. https://doi.org/10.1029/2009GC002587

Berglund M, Wieser M (2011) Isotopic compositions of the elements 2009 (IUPAC technical report). Pure Appl Chem. 397–410. https://doi.org/10.1351/PAC-REP-10-06-02

Bonifacie M, Charlou JL, Jendrzejewski N, Agrinier P, Donval JP (2005) Chlorine isotopic compositions of high temperature hydrothermal vent fluids over ridge axes. Chem Geol 221:279–288. https://doi.org/10.1016/j.chemgeo.2005.06.008

Bonifacie M, Jendrzejewski N, Agrinier P, Coleman M, Pineau F, Javoy M (2007a) Pyrohydrolysis-IRMS determination of silicate chlorine stable isotope compositions. Application to oceanic crust and meteorite samples. Chem Geol 242:187–201. https://doi.org/10.1016/j.chemgeo.2007.03.012

Bonifacie M, Monnin C, Jendrzejewski N, Agrinier P, Javoy M (2007b) Chlorine stable isotopic composition of basement fluids of the eastern flank of the Juan de Fuca Ridge (ODP Leg 168). Earth Planet Sci Lett 260:10–22. https://doi.org/10.1016/j.epsl.2007.05.011

Bonifacie M, Jendrzejewski N, Agrinier P, Humler E, Coleman M, Javoy M (2008a) The chlorine isotope composition of Earth's mantle. Science 319:1518–1520. https://doi.org/10.1126/science.1150988

Bonifacie M, Busigny V, Mével C, Philippot P, Agrinier P, Jendrzejewski N, Scambelluri M, Javoy M (2008b) Chlorine isotopic composition in seafloor serpentinites and high-pressure metaperidotites. Insights into oceanic serpentinization and subduction processes. Geochim Cosmochim Acta 72:126–139. https://doi.org/10.1016/j.gca.2007.10.010

Boyce JW, Treiman AH, Guan Y, Ma C, Eiler JM, Gross J, Greenwood JP, Stolper EM (2015) The chlorine isotope fingerprint of the lunar magma ocean. Sci Adv 1:e1500380–e1500380. https://doi.org/10.1126/sciadv.1500380

Campbell D (1985) Fractionation of stable chlorine isotopes during transport through semipermeable membranes. The University of Arizona, Vasa

Chiaradia M, Barnes JD, Cadet-Voisin S (2014) Chlorine stable isotope variations across the quaternary volcanic arc of Ecuador. Earth Planet Sci Lett 396:22–33. https://doi.org/10.1016/j.epsl.2014.03.062

Czarnacki M, Hałas S (2012) Isotope fractionation in aqua -gas systems: Cl 2 -HCl-Cl −, Br 2 -HBr-Br − and H 2 S-S 2−. Isot Environ Health Stud 48:55–64. https://doi.org/10.1080/10256016.2011.616269

Desaulniers DE, Kaufmann RS, Cherry JA, Bentley HW (1986) 37Cl-35Cl variations in a diffusion-controlled groundwater system. Geochim Cosmochim Acta 50:1757–1764. https://doi.org/10.1016/0016-7037(86)90137-7

Eastoe CJ, Long A, Land LS, Kyle JR (2001) Stable chlorine isotopes in halite and brine from the gulf coast basin: brine genesis and evolution. Chem Geol 176:343–360. https://doi.org/10.1016/S0009-2541(00)00374-0

Eastoe CJ, Peryt TM, Petrychenko OY, Geisler-Cussey D (2007) Stable chlorine isotopes in Phanerozoic evaporites. Appl Geochem 22:575–588. https://doi.org/10.1016/j.apgeochem.2006.12.012

Eggenkamp HGM (1994) The geochemistry of chlorine isotopes. Thesis. Utrecht University

Eggenkamp HGM (2014) The geochemistry of stable chlorine and bromine isotopes, Advance in isotope geochemistry. Edited by Springer, p 172

Eggenkamp HGM, Coleman ML (2009) The effect of aqueous diffusion on the fractionation of chlorine and bromine stable isotopes. Geochim Cosmochim Acta 73:3539–3548. https://doi.org/10.1016/j.gca.2009.03.036

Eggenkamp HGM, Bonifacie M, Ader M, Agrinier P (2016) Experimental determination of stable chlorine and bromine isotope fractionation during precipitation of salt from a saturated solution. Chem Geol 433:46–56. https://doi.org/10.1016/j.chemgeo.2016.04.009

Giunta T (2015) Contraintes sur la géochimie isotopique du Chlore et du Brome dans les eaux de sub-surface. Thesis. Paris Diderot – Institut de Physique du Globe

Godon A, Jendrzejewski N, Eggenkamp HGM, Banks DA, Ader M, Coleman ML, Pineau F (2004a) A cross-calibration of chlorine isotopic measurements and suitability of seawater as the international reference material. Chem Geol 207:1–12. https://doi.org/10.1016/j.chemgeo.2003.11.019

Godon A, Jendrzejewski N, Castrec-Rouelle M, Dia A, Pineau F, Boulégue J, Javoy M (2004b) Origin and evolution of fluids from mud volcanoes in the Barbados accretionary complex. Geochim Cosmochim Acta 68:2153–2165. https://doi.org/10.1016/j.gca.2003.08.021

Godon A, Webster JD, Layne GD, Pineau F (2004c) Secondary ion mass spectrometry for the determination of δ37Cl Part II. Intercalibration of SIMS and IRMS for aluminosilicate glasses. Chem Geol 207:291–303. https://doi.org/10.1016/j.chemgeo.2004.04.003

Halldórsson SA, Barnes JD, Stefánsson A, Hilton DR, Hauri EH, Marshall EW (2016) Subducted lithosphere controls halogen enrichments in the Iceland mantle plume source. Geology 44:679–682. https://doi.org/10.1130/G37924.1

John T, Layne GD, Haase KM, Barnes JD (2010) Chlorine isotope evidence for crustal recycling into the Earth's mantle. Earth Planet Sci Lett 298:175–182. https://doi.org/10.1016/j.epsl.2010.07.039

Kaufmann RS, Long A, Bentley H, Davis S (1984) Natural chlorine isotope variations. Nature 309:338–340

Kaufmann RS, Frape S, McNutt R, Eastoe CJ (1993) Chlorine stable isotope distribution of Michigan basin formation waters. Appl Geochem 8:403–407

Koehler G, Wassenaar LI (2010) The stable isotopic composition (37Cl/35Cl) of dissolved chloride in rainwater. Appl Geochem 25:91–96. https://doi.org/10.1016/j.apgeochem.2009.10.004

Lavastre V, Jendrzejewski N, Agrinier P, Javoy M, Evrard M (2005) Chlorine transfer out of a very low permeability clay sequence (Paris Basin, France): 35Cl and 37Cl evidence. Geochim Cosmochim Acta 69:4949–4961. https://doi.org/10.1016/j.gca.2005.04.025

Layne GD, Kent AJR, Bach W (2009) δ^{37}Cl systematics of a backarc spreading system: the Lau basin. Geology 37:427–430. https://doi.org/10.1130/G25520A.1

Li L, Bonifacie M, Aubaud C, Crispi O, Dessert C, Agrinier P (2015) Chlorine isotopes of thermal springs in arc volcanoes for tracing shallow magmatic activity. Earth Planet Sci Lett 413:101–110. https://doi.org/10.1016/j.epsl.2014.12.044

Louvat P, Bonifacie M, Giunta T, Michel A, Coleman M (2016) Determination of bromine stable isotope ratios from saline solutions by "wet plasma" MC-ICPMS including a comparison between high- and low-resolution modes, and three introduction systems. Anal Chem 88:3891–3898. https://doi.org/10.1021/acs.analchem.6b00062

Manzini M, Bouvier A-S, Barnes JD, Bonifacie M, Rose-Koga EF, Ulmer P, Métrich N, Bardoux G, Williams J, Layne GD, Straub S, Baumgartner LP, John T (2017) SIMS chlorine isotope analyses in melt inclusions from arc settings. Chem Geol. https://doi.org/10.1016/j.chemgeo.2016.12.002

Phillips FM, Bentley HW (1987) Isotopic fractionation during ion filtration. Geochim Cosmochim Acta 51:683–695

Richet P, Bottinga Y, Javoy M (1977) A review of hydrogen, carbon, nitrogen, and chlorine stable isotope fractionation among gaseous molecules. Annu Rev Earth Planet Sci 5:65–110

Richter FM, Mendybaev RA, Christensen JN, Hutcheon ID, Williams RW, Sturchio NC, Beloso AD (2006) Kinetic isotopic fractionation during diffusion of ionic species in water. Geochim Cosmochim Acta 70:277–289. https://doi.org/10.1016/j.gca.2005.09.016

Rizzo AL, Caracausi A, Liotta M, Paonita A, Barnes JD, Corsaro RA, Martelli M (2013) Chlorine isotope composition of volcanic gases and rocks at Mount Etna (Italy) and inferences on the local mantle source. Earth Planet Sci Lett 371:134–142. https://doi.org/10.1016/j.epsl.2013.04.004

Rodríguez A, Eggenkamp HGM, Cruz MM, van Bergen MJ (2016) Chlorine isotope and Cl–Br fractionation in fluids of Poás volcano (Costa Rica): insight into an active volcanic–hydrothermal system. J Volcanol Geotherm Res 325:70–85. https://doi.org/10.1016/j.jvolgeores.2016.05.020

Schauble EA, Rossman GR, Taylor HPJ (2003) Theoretical estimates of equilibrium chlorine-isotope fractionations. Geochim Cosmochim Acta 67:3267–3281. https://doi.org/10.1016/S0016-7037(00)01375-3

Selverstone J, Sharp ZD (2013) Chlorine isotope constraints on fluid-rock interactions during subduction and exhumation of the Zermatt-Saas ophiolite. Geochem Geophys Geosyst 14:4370–4391. https://doi.org/10.1002/ggge.20269

Sharp ZD, Barnes JD, Brearley AJ, Chaussidon M, Fischer TP, Kamenetsky VS (2007) Chlorine isotope homogeneity of the mantle, crust and carbonaceous chondrites. Nature 446:1062–1065. https://doi.org/10.1038/nature05748

Sharp ZD, Barnes JD, Fischer TP, Halick M (2010a) An experimental determination of chlorine isotope fractionation in acid systems and applications to volcanic fumaroles. Geochim Cosmochim Acta 74:264–273. https://doi.org/10.1016/j.gca.2009.09.032

Sharp ZD, Shearer CK, McKeegan KD, Barnes JD, Wang YQ (2010b) The chlorine isotope composition of the moon and implications for an anhydrous mantle. Science 329:1050–1053. https://doi.org/10.1126/science.1192606

Sharp ZD, Mercer JA, Jones RH, Brearley AJ, Selverstone J, Bekker A, Stachel T (2013) The chlorine isotope composition of chondrites and Earth. Geochim Cosmochim Acta 107:189–204

Shouakar-Stash O, Alexeev SV, Frape SK, Alexeeva LP, Drimmie RJ (2007) Geochemistry and stable isotopic signatures, including chlorine and bromine isotopes, of the deep groundwaters of the Siberian platform, Russia. Appl Geochem 22:589–605. https://doi.org/10.1016/j.apgeochem.2006.12.005

Stotler RL, Frape SK, Shouakar-Stash O (2010) An isotopic survey of δ^{81}Br and δ^{37}Cl of dissolved halides in the Canadian and Fennoscandian shields. Chem Geol 274:38–55. https://doi.org/10.1016/j.chemgeo.2010.03.014

Williams JT, Shearer CK, Sharp ZD, Burger PV, Cubbin FMMC, Santos AR, Agee CB, Keegan KDMC (2016) The chlorine isotopic composition of Martian meteorites 1: chlorine isotope composition of Martian mantle and crustal reservoirs and their interactions. 19:1–19. https://doi.org/10.1111/maps.12647

Chondrites

Sara Russell
Department of Earth Sciences, The Natural History Museum, London, UK

Definition

Chondrites are the most common type of *meteorites*, making up around 80% of all known meteorite falls. Chondrites are stony meteorites and most are dark brown, gray, and/or black in color. Chondrites are accreted material from nebular components formed within the dusty cloud that circulated around the young Sun. They avoided igneous differentiation and so contain approximately solar proportions of the elements. Therefore, they likely originated on minor planets (mainly asteroids) which were not large enough to generate heat to melt. Most chondrites preserve an original texture from the time of their accretion. This texture consists of ~mm sized spherical silicate balls called chondrules surrounded by a submicron sized material called matrix (Fig. 1). In some chondrites, metal and/or sulfides are common and in some can be found refractory inclusions, including calcium-aluminum-rich inclusions (CAIs). Less heated chondrites typically contain primordial organic material and presolar grains that formed around ancient ancestral stars.Organic material can be complex and includes polyaromatic hydrocarbons. More details about chondrites and their classification can be found in Krot et al. (2013); Scott and Krot (2013); and Grady et al. (2014).

Alteration of Chondrites

As well as classifications of chemical class, chondrites are classified according to the degree of alteration (aqueous interaction and/or heating) they experienced on their parent asteroid. This is called the petrological scale and chondrites are numbered from 1 to 6 (Van Schmus and Wood 1967). According to this classification scheme, petrological types 2 and 1 show increasing amounts of aqueous alteration from 2 to 1, and types 3 to 6 show increasing amounts of changes due to heating. Type 1 chondrites only rarely contain anhydrous minerals; typically silicates have been entirely transformed to clays. Type 2 chondrites contain visible chondrules but also abundant phyllosilicate minerals. Type 3 chondrites are petrologically pristine, with clearly defined chondrules composed of anhydrous olivine, pyroxene, metal, and minor minerals, and containing glass in chondrule mesostasis. A continuum exists from type 3 to type 6 chondrites that have lost almost all their petrological texture and chondrules are barely visible. Meteorites that have been completely melted but retain a chondritic bulk composition are occasionally termed "Type 7 chondrites."

Chondrites are often affected by shock processing, most commonly while on their parent body. This can result in the formation of veins and mineralogical effects such as planar deformation features. A classification system for shock in ordinary chondrites was devised by Stoffler et al. (1991).

Another process that can affect chondrites, especially finds rather than falls, is terrestrial *weathering*. The most obvious effects of terrestrial weathering are oxidation of native iron to form oxides. Weathering also affects bulk chemistry and the silicate mineralogy of the sample, with CCs most easily affected (Bland et al. 2006).

Classification

Chondrites are cateogorized according to their chemical and isotopic properties, with the three main types or *classes* being ordinary chondrites, carbonaceous chondrites, and enstatite chondrites (Fig. 1).There are rare chondrites that do not fit into these classes: the Rumuruti type chondrites (R chondrites) and the Kakangari type chondrites (K chondrites). Additionally, a few chondrites do not fall into any of these types and are classified as ungrouped. These classes are further subdivided into *groups*, as outlined below. In addition, the chondrite is assigned a *petrologic type*, which is an indication of the type of asteroidal processing it has experienced.

Ordinary Chondrites (OC): Ordinary chondrites are the most common type of meteorite and around 95% of all chondrite falls are OCs. OCs are composed of chondrules rich in olivine and pyroxene, with minor silicates, oxides, sulfides,

and metal, surrounded by fine grained matrix that is composed of chondrule-like fragments and sometimes amorphous material. Ordinary chondrites are typically petrological types 3–6. They contain metal in the form of Fe-Ni in varying proportions. Ordinary chondrites are further subdivided into three groups, H, L, and LL, according to their metal content and composition of silicates. H chondrites contain 15–20% free metal (a Fe-Ni alloy) and the olivine composition is $Fa_{16–20}$; L chondrites contain 7–11% free metal and their olivine composition is $Fa_{21–25}$; LL chondrites contain 3–5% free metal and olivine of $Fa_{26–32}$. Ordinary chondrites have oxygen isotope compositions distinct from terrestrial samples (Fig. 2). The JAXA Hayabusa mission returned material from an S type asteroid, which is remarkably similar to LL chondrite material (Nakamura et al. 2011). Therefore, S type asteroids are likely to be the source of most ordinary chondrites.

Chondrites, Fig. 1 The Parnallee meteorite that fell in India in 1857. This type 3 ordinary chondrite (LL) contains distinct rounded chondrules surrounded by a fine grained matrix. Natural History Museum specimen number BM 34792. The specimen is approximately 16 cm across

Carbonaceous Chondrites (CC): Although a minor contribution to known meteorites, carbonaceous chondrites have been extensively studied as they have suffered on minimal heating while on their parent bodies, and their petrological types are usually 1–3. The term carbonaceous is misleading; they typically contain no more than a few percent carbon and often much less. Carbonaceous chondrites are exceptionally diverse in texture and chemistry. The CCs are divided into classes, represented by a letter that usually refers to the type specimen of that class.

CV meteorites, which contain large chondrules of up to several mm in size and rather abundant white CAIs (around 5 vol%) which are irregular or rounded in shape and can be up to cm in size.

CK meteorites contain textural and oxygen isotope similarities to the CV meteorites, but they are more oxidized. CK are the only carbonaceous chondrites that are mostly typically metamorphosed, with petrological types 4–6 most common. Some researchers believe CV and CK are the same or related group (e.g., Greenwood et al. 2010).

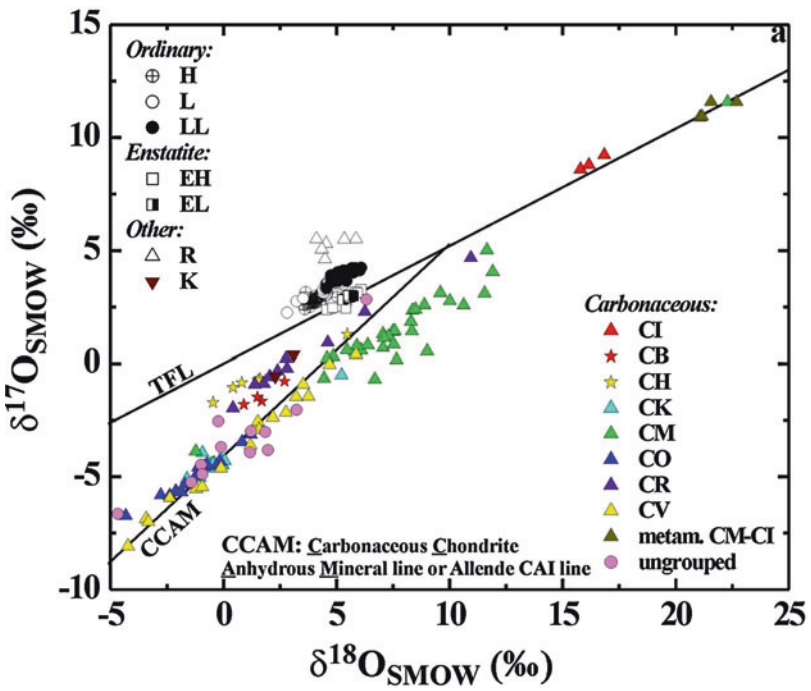

Chondrites, Fig. 2 Oxygen isotope composition of chondrites. On a three-isotope oxygen diagram, $^{17}O/^{16}O$ ratio vs. $^{18}O/^{16}O$ ratio, both normalized to the Standard Mean Ocean Water value, chondrite groups occupy distinct regions. CCs typically plot below the terrestrial fractionation line; most non-CCs above it. $\delta^{17,18}O = [(^{17,18}O/^{16}O)_{sample}/(^{17,18}O/^{16}O)_{SMOW}-1] \times 1{,}000$ (From Scott and Krot 2013)

CO chondrites have a similar bulk chemistry to CVs and a similar abundance of CAIs, but both chondrules and CAIs in these meteorites are much smaller, around ~100 μm typically.

CM chondrites contain small chondrules and abundant matrix (around 50%). They are nearly always petrological type 2 and have experienced significant aqueous alteration.

CI chondrites have been extensively aqueously altered, which has destroyed much of their original texture and mineralogy. These chondrites have no (or very rare) chondrules and consist almost entirely of water-formed minerals such as phyllosilicates, sulfides, carbonates, and oxides. CIs are the most chemically primitive chondrites, and their bulk composition resembles that of the Sun, apart from volatile species such as H and He (e.g., Lodders 2003).

CR chondrites contain large chondrules similar in size to those in CV chondrites, but they only rarely contain CAIs. Iron nickel metal is abundant. Matrix makes up around 50% of the rock.

CH chondrites are very enriched in metal, have very small chondrules (~20 microns), and also contain CAIs. CH chondrites are exceptional among meteorite groups in that they do not contain true matrix, but instead the chondrules are closely packed. They are highly depleted in volatile elements.

CB chondrites contain large amounts of metal and are subdivided into two chemically similar textural types. CBa meteorites have extremely large chondrules (>cm in size), large metal grains, and are depleted in CAIs. CBb meteorites contain smaller chondrules (mm in size) and contain CAIs.

The CR, CB, and CH chondrites contain geochemical similarities to each other (e.g., they all have elevated $^{15}N/^{14}N$ compared to other chondrite groups) and are referred to as a clan.

Carbonaceous chondrites are darker in color than most other meteorites, and spectroscopically they resemble some C type or related asteroids such as G, B, or D. These asteroids are therefore the likely source for carbonaceous chondrites. Carbonaceous chondrites may preferentially originate in the outer regions of the main asteroid belt. There have been suggestions in the literature that CI chondrites may have a cometary source (e.g., Gounelle et al. 2010).

Enstatite chondrites (EC): Enstatite chondrites are highly reduced rocks that are rich in Fe, Ni-metal, and sulfides. Enstatite ($MgSiO_3$) is common, and Fe is almost absent in silicates. ECs are divided into two groups: the EH meteorites that contain chondrules around 0.2 mm in diameter and high abundance of metal and EL meteorites that contain larger chondrules (~0.5 mm) and less free metal. Enstatite chondrites have similar isotopic compositions to the Earth (Fig. 2). They are spectrally similar to many E-type asteroids.

Kakangari type chondrites (K): These are matrix-rich chondrites that are highly reduced.

Rumuruti type chondrites (R): Rumurutiite meteorites are enriched in matrix and are very oxidized with essentially no free metal.

Oxygen Isotopes

Measurements of the ratios of the three stable isotopes of oxygen (^{16}O, ^{17}O, and ^{18}O) are an essential tool in understanding the relationships between meteorite classes and groups (Fig. 2). On a graph of $^{17}O/^{18}O$ as a function of $^{18}O/^{16}O$, most terrestrial objects fall on a mass-related fractionation line of slope ~0.5, whereas meteorites fall off this line, with each group occupying a distinct oxygen isotope field. Meteorites with similar oxygen isotopic composition may have formed on the same or related asteroids, whereas differences may indicate an origin on separate parent bodies (e.g., Clayton 1993).

Ages of Chondrites

While the exact timing of accretion of chondrites has not been measured, age dates for many chondritic components have been reported, with Pb-Pb data giving the most accurate absolute ages. CAIs have ages of around 4567 Myr while chondrules tend to give similar or younger ages by a few Myr (e.g., Connelly et al. 2012). A minimum age of the accreted parent body can be determined from the age of alteration products that formed on the asteroid; for example, Mn-Cr isotopic data suggests that chondrites accreted and carbonates formed ~3Myr after the formation of the constituents of chondrites (e.g., Fujiya et al. 2011).

Summary and Conclusions

Chondrites are an invaluable tool for the geochemist, as they provide information about the original material from which terrestrial planets accreted. There is a great diversity in geochemistry, isotope compositions, and texture among chondrites, which likely reflects a diversity among the asteroids that are the source of most chondrites. Increased astronomical observations along with recent and upcoming sample return missions are helping us to refine our understanding of the sources of chondrites.

Cross-References

- ▶ Chemical Weathering
- ▶ Chondrules
- ▶ Meteorites
- ▶ Oxygen Isotopes
- ▶ Refractory Inclusions in Chondritic Meteorites

References

Bland PA, Zolensky M, Benedix G, Sephton M (2006) Weathering of chondritic meteorites. In: Lauretta D, McSween HP (eds) Meteorites and the early solar system II. University of Arizona Press, Tucson
Clayton RN (1993) Oxygen isotopes in meteorites. Annu Rev Earth Planet Sci 21:115–149
Connelly JN, Bizzarro M, Krot AN, Nordlund A, Wielandt D, Ivanova MA (2012) The absolute chronology and thermal processing of solids in the solar protoplanetary disk. Science 297:1678–1683
Fujiya W, Sugiura N, Hotta H, Ichimura K, Sano Y (2011) Evidence for the late formation of hydrous asteroids from young meteoritic carbonates. Nat Commun 3:627
Gounelle M, Spurny P, Bland PA (2010) The orbit and atmospheric trajectory of the Orgueil meteorite from historical records. Meteorit Planet Sci 41:135–150
Grady MM, Pratesi G, Cecchi VM (2014) Atlas of meteorites. Cambridge University Press, New York
Greenwood RC, Franchi IA, Kearsley AT, Alard O (2010) The relationship between CK and CV chondrites. Geochim Cosmochim Acta 74:1684–1705
Krot AN, Keil K, Goodrich C, Weisberg MK, Scott ERD (2013) Classification of meteorites. In: Davis AM, Holland HD, Turekian KK (eds) Meteorites and cosmochemical processes, Treatise on geochemistry, vol 1. Elsevier, Oxford, pp 1–63
Lodders K (2003) Solar system abundances and condensation temperatures of the elements. Astron J 591:1220–1247
Nakamura T, Noguchi T, Tanaka M et al (2011) Itokawa dust particles: a direct link between S-type asteroids and ordinary chondrites. Science 333:1113–1116
Scott ERD, Krot AN (2013) Chondrites and their components. In: Davis AM, Holland HD, Turekian KK (eds) Meteorites and cosmochemical processes, Treatise on geochemistry, vol 1. Elsevier, Oxford, pp 65–137
Stoffler D, Keil K, Scott ERD (1991) Shock metamorphism of ordinary chondrites. Geochim Cosmochim Acta 55:3845–3867
Van Schmus WR, Wood JA (1967) A chemical-petrologic classification for the chondritic meteorites. Geochim Cosmochim Acta 31:747–765

Chondrules

Rhian Jones
School of Earth and Environmental Sciences, The University of Manchester, Manchester, UK

Definition

Chondrules are the most abundant component of chondrite meteorites. The term chondrule comes from the ancient Greek word for the kernel of a grain of wheat, χονδρος (chondros), which chondrules roughly resemble in size and shape. Chondrules are rounded, millimeter, or submillimeter stone particles. They are among the oldest solid materials in the solar system. Shapes and textures of chondrules indicate that they formed from molten droplets which were floating freely in the gas of the protoplanetary disk at the time of cooling and solidification. After formation, chondrules accreted with other materials to form asteroids, from which chondrite meteorites are derived. There is debate about the heating process that melted chondrules and the environment in which they formed. Properties of chondrules can be used to infer physical and chemical conditions within the protoplanetary disk in the first few million years of solar system history.

Chemistry and Mineralogy of Chondrules

Chondrules constitute up to 80% by volume of ordinary (O) and enstatite (E) chondrites and approximately 50% of carbonaceous (C) chondrites (Scott and Krot 2014, Zanda 2004). This high abundance has been used to estimate that chondrules made up about 10^{24} g of material in the early solar system (Desch et al. 2012), and thus they provide an important record of materials that remain from the protoplanetary disk environment. The description of chondrules presented here considers only the primary properties of chondrules, i.e., properties that pertain to their formation and history prior to incorporation into the asteroid parent bodies of their host chondrites. Most chondrites have undergone secondary processing after accretion to their parent asteroids, to varying degrees, including aqueous alteration, heating that resulted in metamorphism, and/or shock resulting from impacts. Primary properties of chondrules must often be deduced by considering the nature of any alteration and disentangling effects that may have altered or erased primary signatures. Chondrules occur in all chondrite groups except for the CI chondrites, which have undergone complete aqueous alteration of the initially anhydrous assemblage, to the extent that any chondrules that were originally present have been obliterated.

The basic chemical and mineralogical properties of individual chondrules are similar, but they differ in detail. Chondrule chemistry varies widely both within and among chondrite groups and classes (Jones et al. 2005; Jones 2012). Average major element contents for bulk chondrules (Fe, Mg, Si, Ca, Al) are similar to solar or CI chondrite abundances, and there is little fractionation among refractory elements (e.g., Ca, Al, Ti, Mg, rare earth elements). However, bulk compositions of individual chondrules are variable, for example, within a single chondrite the ratio of refractory elements to Si can vary by about a factor of 3, and the Fe/Si ratio can vary by more than an order of magnitude. Abundances of moderately volatile elements (e.g., Mn, Na, K, S) are also highly variable among individual chondrules.

In all chondrite groups, there is a range of chondrule textures (Connolly and Desch 2004; Lauretta et al. 2006; Jones 2012; Scott and Krot 2014) (Fig. 1). The dominant silicate minerals are olivine ($(Mg,Fe)_2SiO_4$) and pyroxene

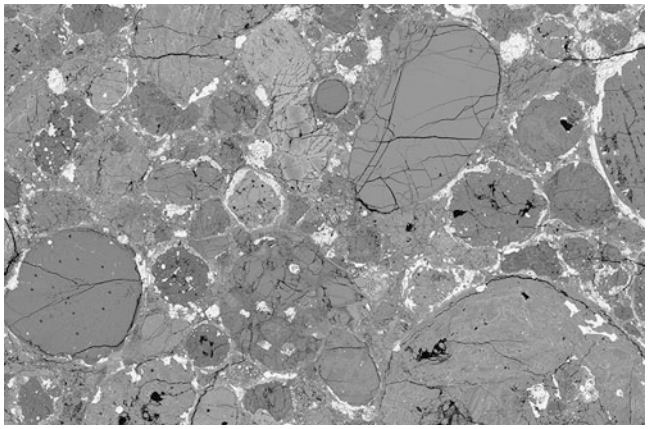

Chondrules, Fig. 1 The Semarkona ordinary chondrite: back-scattered electron image, ~9 mm across. Chondrules are round or have rounded outlines. Individual chondrules have different textures, as well as different chemical compositions. The most abundant minerals are olivine and pyroxene, for which darker shades of *gray* correspond to higher Mg/(Mg + Fe) ratio. *White* grains are metal and/or sulfide (Image by J. Lewis)

($(Mg,Fe,Ca)_2Si_2O_6$): individual chondrules have varying ratios of olivine/pyroxene, from 100% olivine to 100% pyroxene, and an interstitial feldspathic phase that may be crystalline feldspar ($CaAl_2Si_2O_8$-$NaAlSi_3O_8$) or glass. Chondrules also contain varying amounts of Fe-Ni metal and/or sulfide minerals. In most chondrules, olivine and pyroxene grains have regular crystal forms: these chondrules are described as having porphyritic textures. Olivine and pyroxene can also show a range of morphologies that are a function of growth rate including hopper morphologies, elongate barred grains (usually bars of olivine), radiating needles, and cryptocrystalline textures. Two common types of chondrules are defined based on their textures and chemical characteristics (Brearley and Jones 1998). Type I chondrules are chemically reduced: olivine and pyroxene have a high atomic Mg/(Mg + Fe) ratio, commonly around 0.99, and they contain abundant metallic iron, commonly kamacite ($Fe_{\sim 0.95}Ni_{\sim 0.05}$). Type II chondrules are more oxidized: olivine and pyroxene have lower atomic Mg/(Mg + Fe) ratios than type I chondrules, and olivine and pyroxene grains usually show strong growth zoning (igneous zoning), e.g., Mg/(Mg + Fe) ratios from around 0.8 to 0.7 in ordinary chondrites. Compared with type I chondrules, type II chondrules contain less metallic iron but more iron sulfide (typically troilite, FeS), and they have higher abundances of moderately volatile elements than type I chondrules (Na, Mn, P, S).

The majority of olivine and pyroxene grains in chondrules crystallized from melt as the droplet cooled. There is also a population of identifiable grains called relict grains which were inherited from previous generations of chondrules and did not melt during the heating event (Jones 2012). These include MgO-rich olivine (forsterite) in type II chondrules and relict grains of MgO-rich olivine in type I chondrules. Relict grains termed dusty olivine are grains of FeO-rich olivine that were incorporated into type I chondrules. During the heating event that melted the type I chondrule, the FeO-rich olivine grain underwent reduction, and small blebs of Fe metal precipitated which give the grain a dusty appearance in transmitted or reflected light. Chemical compositions and oxygen isotope compositions of relict grains are consistent with formation in previous generations of chondrules and provide evidence that there were multiple heating episodes in the chondrule-formation region. Further evidence for repeated heating is found in igneous rims on chondrules: these represent a second episode of heating that melted a dusty rim that was deposited after the host chondrule solidified.

There are significant differences in the chondrule populations among the different chondrite classes and groups (Jones 2012). These include properties such as mean chondrule sizes and the distribution of different textural types of chondrules. There are chemical differences between chondrules of similar textural type that occur in different chondrite groups, and abundances of relict grains in chondrules of the same textural type vary among chondrite groups. Also, chondrules from O, C, and E chondrites have different oxygen isotope compositions. Differences in chondrule properties specific to individual chondrite groups indicate that the disk was chemically heterogeneous and that chondritic asteroids accreted from localized batches of materials.

Oxygen Isotope Compositions of Chondrules

Oxygen isotope compositions of early solar system materials are an important record of relationships among different components of chondrites, as well as among different chondrite groups. In an oxygen three-isotope diagram ($\delta^{17}O$ vs. $\delta^{18}O$, where $\delta^n O = [(^nO/^{16}O)_{sample}/(^nO/^{16}O)_{SMOW} - 1]^*10^3$ and SMOW = standard mean ocean water), mass-dependent isotopic fractionation results in a distribution of compositions along a line of slope 0.52, an example of which is the terrestrial fractionation line, TFL. Oxygen isotope compositions of chondrules in O, E, and C chondrites lie above, along, and below TFL, respectively (Clayton 2003; Krot et al. 2006; Yurimoto et al. 2008; Scott and Krot 2014). Chondrules have significantly higher values of $\delta^{17}O$ and $\delta^{18}O$ than calcium-aluminum inclusions (CAIs), which have $\delta^{18}O$ values around −40‰, close to values inferred for the sun. For bulk chondrules, $\delta^{18}O$ values are typically in the range −10 to +7‰. Oxygen isotope compositions of chondrules in C chondrites lie on arrays that have a slope close to one on the oxygen three-isotope diagram, which indicates mixing of

isotopic reservoirs that were related by non-mass-dependent processes. Isotopic self-shielding, possibly within the protoplanetary disk or in its precursor molecular cloud, could have led to an isotopically heavy ice component that evaporated in the region of chondrule formation and became incorporated into chondrule materials (Clayton 2003; Krot et al. 2006; Yurimoto et al. 2008).

Chondrule Precursor Material

Since chondrules are solidified melt droplets, the precursor material from which they formed has largely been erased during melting. Relict grains are a direct record of precursor material that would have been present as grains tens of micrometers across in the precursor assemblage. The remainder of the precursor material was probably a fine-grained mixture of silicates, metal, and sulfide grains (e.g., Jones et al. 2005), although in chondrule-formation models that involve collisions between molten planetesimals, the predominant precursor material would have been molten. Matrix in chondritic meteorites consists of a fine-grained assemblage of silicate, oxide, metal, and sulfide materials (Scott and Krot 2014), but it is not chemically equivalent to material needed for chondrule precursors. Chondrules and matrix show chemical complementarity in that their combined chemistry is similar to solar abundances, suggesting that each chondrite group formed in a chemical reservoir of broadly solar composition, after condensation of refractory, common, and moderately volatile elements.

A group of chondrules described as aluminum-rich chondrules spans the compositional gap between CAIs and the common ferromagnesian chondrules (Connolly and Desch 2004). Relict fragments of CAIs are observed in these chondrules (Krot et al. 2009). Oxygen isotope compositions of chondrules from C chondrites also show clear relationships to CAIs and other types of refractory inclusions. Hence, fragments of CAIs are plausible components of chondrule precursor material.

Thermal Histories of Chondrules

Thermal histories of chondrules have been deduced from their textures and mineralogy, as well as from analogue experiments (Desch and Connolly 2004; Hewins et al. 2005; Lauretta et al. 2005; Jones et al. 2005; Desch et al. 2012). The ambient temperature prior to heating was below the temperature at which sulfur condensed from the solar nebula gas, <400 °C. Peak temperatures for chondrule formation were close to the temperature of complete melting of the chondrule material, around 1500–1600 °C. The duration of heating at the peak temperature was short, seconds to minutes, in order to retain moderately volatile elements such as Na and S that would evaporate during an extended period of melting. Retention of Na also requires a high gas density. After melting, chondrules cooled at rates that range from around five to several hundreds of degrees per hour. These cooling rates are constrained by laboratory experiments that reproduce chondrule textures, as well as considerations such as the development of igneous growth zoning in olivine and dissolution rates of relict grains. The wide range of cooling rates is responsible for production of different chondrule textures because morphologies of olivine and pyroxene grains are a function of growth rate, which is a function of undercooling. Chondrule cooling rates are significantly slower than cooling rates that would result from black-body radiation of isolated molten droplets into free space, indicating that they formed in a gas of higher density (Alexander and Ebel 2012).

Ages of Chondrules

Chondrules formed within the first few million years of solar system history. Absolute ages of chondrules determined by high-precision Pb-Pb radiometric dating range from 4567 to 4565 Ma (see Krot et al. 2009; Wadhwa 2014). Ages are also measured based on chronometers that use extinct short-lived radioisotopes that were present in the early solar system, such as ^{26}Al which decays to ^{26}Mg with a half-life of 0.75 My. Most ^{26}Al ages for chondrules are within 1–3 million years after the CAI formation age (4567 Ma) (Krot et al. 2009; Desch et al. 2012; Kita and Ushikubo 2012). Hence, chondrule formation appears to have begun contemporaneously with CAI formation and persisted throughout the time period when planetesimals were accreting. Most measured chondrule ages are younger than the time scales of differentiation on the earliest planetesimals (Wadhwa 2014). It is possible that chondrule formation occurred prior to formation of those bodies and that earlier generations of chondrules no longer exist because the bodies in which they were incorporated have been melted.

Chondrules in the metal-rich CB and CH chondrite groups differ from other O, C, and E groups. Chondrules in the CB_a chondrites are unusually large (up to cm sized), whereas those in the CB_b and CH chondrites are small (mean diameters 0.5 and <0.1 mm, respectively). These meteorites have a high proportion of non-porphyritic chondrules (Scott and Krot 2014). They likely formed in a large impact plume that resulted from a collision involving a metal-rich body. Ages of chondrules in CB chondrites are significantly younger than typical chondrules in most chondrite groups, 4563 Ma, so they probably formed after the nebular gas had dissipated (Desch et al. 2014; Wadhwa 2014).

Chondrule-Formation Models

Chondrule-formation models must take into account the chemical, isotopic, and physical properties of chondrules and the constraints those properties impose. A variety of models has been proposed to account for the rapid heating and cooling events that chondrules experienced, but no single model is clearly preferred. Models include heating in a shock front as a result of gas drag combined with radiant heat, heating in the X-wind that lofted chondrules above the nebular midplane in the magnetocentrifugal outflow, lightning within the disk, collisions involving partially or completely molten planetesimals, and collisions involving solid planetesimals (e.g., Connolly and Desch 2004; Desch et al. 2012; Johnson et al. 2015). For the shock model, chondrule formation could have occurred in the bow shock of a planetesimal moving through the disk in an eccentric orbit or in the shock front associated with gravitational instabilities in the disk. A chondrule-formation process has not been detected directly in astronomical observations of protoplanetary disks around young stellar objects.

Summary

Chondrules formed from partially to fully molten liquid droplets that solidified into approximately spherical, (sub) millimeter-sized beads. They formed within one to three million years of the formation of the first solids in the solar system. Chondrules have approximately chondritic chemical compositions and consist predominantly of olivine, pyroxene, a feldspathic phase, metal, and sulfide. Chemical, isotopic, and physical properties of chondrules vary among the different chondrite groups. Chondrule cooling rates inferred from their textures and mineralogy are between a few to several hundred degrees per hour. Models for the mechanism that resulted in chondrule formation include heating within shock fronts and collisions between either solid or partially molten planetesimals during the early stages of formation of the solar system.

Cross-References

- ▶ Aluminum
- ▶ Chondrites
- ▶ Experimental Mineralogy and Petrology
- ▶ Geochronology and Radiogenic Isotopes
- ▶ Iron
- ▶ Meteorites
- ▶ Mineralogy
- ▶ Refractory Inclusions in Chondritic Meteorites
- ▶ Silicate Melts
- ▶ Silicate Minerals

References

Alexander CMO'D, Ebel DS (2012) Questions, questions: can the contradictions between the petrologic, isotopic, thermodynamic, and astrophysical constraints on chondrule formation be resolved? Meteorit Planet Sci 47:1157–1175

Brearley AJ, Jones RH (1998) Chondritic meteorites. In: Papike JJ (ed) Planetary materials. Reviews in mineralogy, vol 36. Mineralogical Society of America, Chantilly, pp 3-1–3-398

Clayton RN (2003) Oxygen isotopes in meteorites. In Davis AM (ed) Meteorites, comets and planets. Treatise on geochemistry, vol 1. Elsevier, Oxford, pp 129–142

Connolly HC Jr, Desch SJ (2004) On the origin of the "kleine Kügelchen" called chondrules. Chem Erde 64:95–125

Desch SJ, Morris MA, Connolly HC, Boss AP (2012) The importance of experiments: constraints on chondrule formation models. Meteorit Planet Sci 47:1139–1156

Hewins RH, Connolly HC Jr, Lofgren GE, Libourel G (2005) Experimental constraints on chondrule formation. In Krot AN, Scott ERD, Reipurth B (eds) Chondrites and the protoplanetary disk. Astronomical Society of the Pacific conference series, 341. Astronomical Society of the Pacific, San Francisco, pp 286–316

Johnson BC, Minton DA, Melosh HJ, Zuber MT (2015) Impact jetting as the origin of chondrules. Nature 517:339–341

Jones RH (2012) Petrographic constraints on the diversity of chondrule reservoirs in the protoplanetary disk. Meteorit Planet Sci 47:1176–1190

Jones RH, Grossman JN, Rubin AE (2005) Chemical, mineralogical and isotopic properties of chondrules: clues to their origins. In Krot AN, Scott ERD, Reipurth B (eds) Chondrites and the protoplanetary disk. Astronomical Society of the Pacific conference series, 341. Astronomical Society of the Pacific, San Francisco, pp 251–285

Kita NT, Ushikubo T (2012) Evolution of protoplanetary disk inferred from ^{26}Al chronology of individual chondrules. Meteorit Planet Sci 47:1108–1119

Krot AN, Yurimoto H, McKeegan KD, Leshin L, Chaussidon M, Libourel G, Yoshitake M, Huss GR, Guan Y, Zanda B (2006) Oxygen isotopic compositions of chondrules: implications for evolution of oxygen isotopic reservoirs in the inner solar nebula. Chem Erde 66:249–276

Krot AN, Amelin Y, Bland P, Ciesla FJ, Connelly J, Davis AM, Huss GR, Hutcheon ID, Makide K, Nagashima K, Nyquist LE, Russell SS, Scott ERD, Thrane K, Yurimoto H, Yin Q-Z (2009) Origin and chronology of chondritic components: a review. Geochim Cosmochim Acta 73:4963–4997

Lauretta DS, Nagahara H, Alexander CMO'D (2006) Petrology and origin of ferromagnesian silicate chondrules. In: Lauretta DS, McSween HY (eds) Meteorites and the early solar system II. University of Arizona Press, Tucson, pp 431–459

Scott ERD, Krot AN (2014) Chondrites and their components. In Davis AM (ed) Meteorites and cosmochemical processes, 2nd edn. Treatise on geochemistry, vol 1. Elsevier, Oxford, pp 65–137

Wadhwa M (2014) Solar system time scales from long-lived radioisotopes in meteorites and planetary materials. In Davis AM (ed) Meteorites and cosmochemical processes, 2nd edn. Treatise on geochemistry, vol 1. Elsevier, Oxford, pp 397–418

Yurimoto H, Krot AN, Choi BG, Aléon J, Kunihiro T, Brearley AJ (2008) Oxygen isotopes of chondritic components. In: MacPherson GJ (ed) Oxygen in the solar system. Reviews in mineralogy, vol 68. Mineralogical Society of America, Chantilly, pp 141–186

Zanda B (2004) Chondrules. Earth Planet Sci Lett 224:1–17

Chromium

Monica Vasiliu and David A. Dixon
Department of Chemistry, University of Alabama, Tuscaloosa, AL, USA

Element Data
Atomic Symbol: Cr.
Atomic Number: 24.
Atomic Weight: 51.9961.
Isotopes and Abundances: ^{50}Cr 4.35%, ^{52}Cr 83.79%, ^{53}Cr 9.50%, ^{54}Cr 2.36%.
1 Atm Melting Point: 2130 ± 20 K.
1 Atm Boiling Point: 2945.
Common Valences: 2, 3, 4, 6.
Ionic Radii: (+II) 84, (+III) 64, (+IV) 56, (+VI) 44 ppm.
Pauling Electronegativity: 1.66.
First Ionization Potential: 6.76 eV.
Chondritic (CI) Abundance: 2660 ppm.
Silicate Earth Abundance: 2625 ppm.
Crustal Abundance: ~100 ppm.
Seawater Abundance: 0.2 ppb.
Core Abundance: 0.90%.

Properties

Chromium (Emsley 1991, 2001; Anthoni 2006; Anders and Grevesse 1989; McDonough 2005) is a lustrous, brittle, hard, and very corrosion-resistant metal. It has a silver-gray color with a blue tinge and it can be highly polished. It does not tarnish in air, but when heated it burns forming the green chromic oxide. Chromium is unstable in oxygen as it immediately reacts to form a thin oxide layer that is impermeable to oxygen and protects the metal below. Chromium dissolves in HCl and H_2SO_4 but not in H_3PO_4. None of the natually occurring chromium isotopes are radioactive.

History and Use

Chromium was discovered in 1797 by Louis Nicolas Vauquelin while experimenting with a material known as Siberian red lead, the mineral crocoite ($PbCrO_4$). He produced chromium oxide by mixing crocoite with hydrochloric acid. Although he believed a method for isolating chromium didn't yet exist, Vauquelin showed in 1798 that he was able to obtain metallic chromium by simply heating chromium oxide in a charcoal oven.

Chromium can be polished to form a very shiny surface and is often plated to other metals to form a protective and attractive covering. Chromium is added to steel to harden it and to form stainless steel, an iron-based alloy that contains at least 10% chromium. Other chromium-steel alloys are used to make armor plate, safes, ball bearings, and cutting tools. Chromium compounds are also used to anodize aluminum, a process which coats aluminum with a thick, protective layer of oxide. Chromite, chromium's primary ore, is used to make molds for the firing of bricks because of its high melting point, moderate thermal expansion, and stable crystal structure.

Crocoite or lead chromate is also known as chrome yellow and has been used as a yellow pigment in paints. Chromic oxide (Cr_2O_3), also known as chrome green, is the ninth most abundant compound in the Earth's crust and is a widely used green pigment. Ruby (variety of corundum, Al_2O_3) and emerald (variety of beryl, $Be_3Al_2(SiO_3)_6$) owe their colors to chromium compounds. Potassium dichromate ($K_2Cr_2O_7$) is used in the tanning of leather, while other chromium compounds are used as mordants (materials which permanently fix dyes to fabrics). Chromium(IV) oxide (CrO_2) is used to manufacture magnetic tape.

Geochemical Behavior

Chromium is not found free in nature and is found mainly as chromite. This ore is found in many places including South Africa, India, Kazakhstan, and Turkey. Chromium metal is usually produced by reducing chromite with carbon in an electric-arc furnace or reducing chromium(III) oxide with aluminum or silicon.

Chromium enters the air, water, and soil in the chromium (III) and chromium(VI) oxidation states through natural processes and human activities. Most of the chromium in air will eventually settle and end up in waters or soils. Chromium in soils strongly attaches to soil particles and as a result it will not move toward groundwater. In water, chromium will absorb on sediment and become immobile. Only a small part of the chromium that ends up in water will eventually dissolve.

The main human activities that increase the concentrations of chromium(III) are steel, leather, and textile manufacturing. The main human activities that increase chromium(VI) concentrations are chemical, leather, and textile manufacturing and electro painting, as industrial examples. These applications will mainly increase concentrations of chromium in water. Through coal combustion, chromium will also end up in air, and through waste disposal, chromium will end up in soils.

Sodium dichromate is a corrosion inhibitor and was added to the Columbia River water used to cool the nuclear reactors, which produced plutonium for nuclear weapons at the

Hanford site in Washington, USA. Some of this material spilled or leaked from pipes leading to soil contamination. Large holes of at least 26 m deep and more than 5000 m^2 at the top were dug down to the groundwater. Approximately two million tons of contaminated soil containing an estimated 129 tons of concentrated chromium was removed and transported to a lined landfill at Hanford. The most contaminated soil is mixed with cement to prevent additional leaching. This led to the reduction of risk to a key salmon spawning region in the Columbia River.

Biological Utilization and Toxicity

Chromium(III) is an essential trace element for organisms including humans, who consume approximately 1 mg a day, because it can disrupt the sugar metabolism pathway, for example, leading to heart conditions, when the daily dose is too low (Vincent 2013). Like other metals that organisms require in trace amounts, chromium can be quite toxic, especially chromium(VI) (chromates (CrO_4^{2-})), which can alter genes, for example, causing cancer. Humans can be exposed to chromium through breathing, eating, or drinking and skin contact with chromium or chromium-containing compounds. The level of chromium in air and water is generally low; however, conytaminated well water may contain the dangerous hexavalent chromium(VI). Food consumption is the main route of chromium(III) uptake, as chromium(III) occurs naturally in many vegetables, fruits, meats (kidneys), yeasts, and grains (brewer's yeast, wheat germ). Various methods of food preparation and storage may alter the chromium content of food; for example, food stored in steel tanks or cans can absorb chromium.

Crops contain biological control systems that arrange the chromium uptake to be low enough not to cause any harm, but when the amount of chromium in the soil rises, this can lead to higher concentrations in crops. Acidification of soil can also influence chromium uptake by crops. Plants usually absorb only chromium(III). This may be the essential kind of chromium, but when concentrations exceed a certain value, negative impacts on animal health can still occur.

Chromium is not known to accumulate in the bodies of fish, but high concentrations of chromium, due to the disposal of metal products in surface waters, can damage the gills of fish that swim near the point of disposal. In animals, chromium can cause respiratory problems, a lower ability to fight disease, birth defects, infertility, and tumor formation.

Cross-References

- ▶ Chromium Isotopes
- ▶ Transition Elements

References

Anders E, Grevesse N (1989) Abundances of the elements: Meteoritic and solar. Geochimica et Cosmochimica Acta 53:197–214. http://meteorites.wustl.edu/goodstuff/chondritic_abundances.htm

Anthoni JF (2006) The chemical composition of seawater in. http://www.seafriends.org.nz/oceano/seawater.htm

Emsley J (1991) The elements, 2nd edn. Clarendon Press, Oxford

Emsley J (2001) Nature's building blocks an A-Z guide to the elements. Oxford University Press, Oxford

McDonough WF (2005) Compositional model for the Earth's core. In: Carlson RW (ed) The Mantle and Core. Elsevier, Oxford, pp. 547–568. http://www.knowledgedoor.com/2/elements_handbook/element_abundances_in_the_earth_s_core.html

Vincent JB (2013) The bioinorganic chemistry of chromium. Wiley, Chichester, p 1213

Chromium Isotopes

Devon B. Cole[1], Xiangli Wang[1], Liping Qin[2], Noah J. Planavsky[1] and Christopher T. Reinhard[3]

[1]Department of Geology and Geophysics, Yale University, New Haven, CT, USA

[2]Department of Earth and Space Science, China University of Science and Technology, Hefei, Hubei, China

[3]School of Earth and Atmospheric Science, Georgia Institute of Technology, Atlanta, GA, USA

Definition

Chromium has four naturally occurring stable isotopes (^{50}Cr, ^{52}Cr, ^{53}Cr, and ^{54}Cr) with natural abundances of 4.35%, 83.79%, 9.50%, and 2.36%, respectively. Among these, ^{50}Cr, ^{52}Cr, and ^{54}Cr are nonradiogenic, while ^{53}Cr is the radiogenic product of ^{53}Mn, an extinct nuclide with a half-life of 3.7 Myr. Chromium isotope variations in terrestrial samples are reported using the ratio $^{53}Cr/^{52}Cr$, expressed in conventional delta notation ($\delta^{53}Cr$) relative to NIST SRM 979, a metallic Cr standard from the National Institute of Standards and Technology. In meteorite samples, the ratio $^{54}Cr/^{52}Cr$ is sometimes used to report nuclear synthetic anomalies (conventionally reported in epsilon notation). Chromium isotopes have a wide range of applications in cosmochemistry, geochemistry, and environmental remediation efforts.

Introduction

The earliest work on Cr isotopes was largely focused on cosmochemical processes, namely the application of the short-lived ^{53}Mn-^{53}Cr radiochronometer to date early solar system events (e.g., Birck and Allègre 1984). Other early

work was been driven by the need to monitor hexavalent Cr as an environmental contaminant, which has resulted in a well-developed framework for understanding low-temperature mass-dependent Cr isotope systematics. Building on this foundation, there has been a surge of recent work focused on using Cr isotopes as a paleoredox proxy. Most recently, work has also focused on improving our understanding of Cr cycling on the modern Earth surface and on developing a global isotope mass balance for the Cr system. Given the broad scope of Cr isotope work, we will touch only briefly on each of the primary applications for the system and then highlight aspects of the Cr system that have drawn recent attention.

Methods

Chromium isotopes can be measured either by thermal ionization mass spectrometry (TIMS) or by multicollector inductively coupled plasma source mass spectrometry (MC-ICP-MS). Typically a tracer containing known concentrations of two isotopes (most commonly ^{50}Cr and ^{54}Cr) is added to samples prior to sample preparation. This method, known as the "double-spike" method, can be used to correct for any fractionation during sample preparation or analysis based on the known and measured ^{50}Cr/^{54}Cr ratio. Due to isobaric interferences with ^{51}V, ^{49}Ti, and ^{56}Fe, and the relatively small range of Cr isotopic variation seen in nature, chemical purification of samples is required prior to analysis. This is typically accomplished via column chromatography using cation or anion exchange methods (e.g., Schoenberg et al. 2008; Yamakawa et al. 2009), followed by additional column purification to remove remaining Fe, Ti, and V. Analysis on TIMS is relatively straightforward – Cr is ionized at ~1200–1400 °C, which is below the temperatures required to efficiently ionize Fe. Interferences during MC-ICP-MS analysis can be much more problematic, in particular polyatomic interferences associated with the use of Ar as a plasma gas. These require the measurement of Cr on the "shoulder," instead of in the center of a flat peak as is typical of most systems. Additionally, these analyses typically must be conducted with a high mass resolution instrument in order to distinguish Cr and Fe peaks (Weyer and Schwieters 2003).

Cosmochemistry

Early work on chromium isotope systematics in natural materials focused on mass-independent effects, i.e., radiogenic effects on ^{53}Cr, and nucleosynthetic effects on ^{54}Cr. Mass-independent Cr isotopic composition are typically expressed in ε notation (deviation of the isotopic ratio of the sample from the standard multiplied by 10,000). In contrast to mass-dependent measurements, measured isotope ratios are corrected for the mass-dependent fractionations that occur naturally and during sample preparation and instrumental analysis by assuming a natural ratio for two isotopes (often least affected by mass-independent effects) of the same element. In the case of Cr, ^{50}Cr and ^{52}Cr are usually used for normalization.

The decay product of short-lived nuclide ^{53}Mn (half-life 3.7 Myr) is ^{53}Cr (Kaye and Cressy 1965). Due to the relatively short half-life, the change in parent/daughter ratio was extremely large during the early evolution of the solar system, and thus short-lived nuclide systems are sensitive to tracking events during this period. Further, because the parent isotope is extinct, examination of the change in daughter isotopes (differentiation between Mn and Cr leads to varying Mn/Cr ratio and thus different ^{53}Cr ingrowth) can further provide age information. ^{53}Mn-^{53}Cr is one of the few short-lived chronometers that have achieved prominence (Birck and Allègre 1985, 1988; Rotaru et al. 1992; Lugmair and Shukolyukov 1998), which is partially due to the relatively high abundances of both Mn and Cr in many solar system objects. These applications are explored further by McKeegan and Davis (2014) and Qin and Wang (2017).

In a second application of mass-independent fractionation, anomalies in ^{54}Cr/^{52}Cr relative to terrestrial rocks have been reported for both bulk meteorites and individual meteorite components (Birck and Allègre 1984; Papanastassiou 1986; Rotaru et al. 1992; Podosek et al. 1997; Trinquier et al. 2008; Qin et al. 2011). These are thought to be the result of incomplete mixing of nuclides synthesized in different nucleosynthetic sources with distinct isotopic signatures. Such isotope anomalies have been found for a range of other elements in addition to Cr (further discussed by Qin and Carlson (2016)). These isotope anomalies have been very useful for identifying the sources of materials accreted into the early solar nebula. Anomalies at the whole meteorite scale are especially useful for understanding heterogeneity in the solar nebula, can act as fingerprints of specific meteorites, and can be used to probe the genetic relationship between different meteorite groups.

High-Temperature Terrestrial Settings

Mass-dependent fractionation of Cr under high-T settings is much less constrained compared to that under low-T settings. This limits the application of Cr isotopes to trace geological and planetary processes. Such studies are also important for constraining the Cr isotope inventories of major terrestrial reservoirs, which often serve as the basis for the application of Cr isotopes in low-T settings. An early study by Schoenberg et al. (2008) found a limited variation in the Cr isotopic

composition of different types of igneous rocks and marine sediments, and the bulk silicate earth (BSE) value of δ^{53}Cr was therein estimated to be -0.124 ± 0.101‰. These authors argued for a homogeneous mantle source and limited Cr isotopic fractionation during partial melting and magma differentiation (Schoenberg et al. 2008). Chondrites show a similarly limited range of variations (Qin and Carlson 2016; Bonnand et al. 2016b; Schoenberg et al. 2016). A recent Cr isotopic study by Xia et al. (2017) on mantle xenoliths from various locations showed much larger variation (δ^{53}Cr ranging from -1.36‰ to 0.75‰), than found by Schoenberg et al. (2008). Although some of the variations are likely due to secondary processes such as metasomatism and these results suggest some mantle heterogeneity, the variation is mainly caused by interaction of mantle peridotites with silicate melts long before they were brought to the surface. This study also confirmed that partial melting does not lead to significant Cr isotopic fractionation. The most recent estimate of the BSE value is -0.14 ± 0.12‰ (Xia et al. 2017), in concert with the previously determined value (Schoenberg et al. 2008). Studies on subducted continental and oceanic crusts showed that dehydration does not fractionation Cr isotopes, probably due to limited dissolution of Cr(III) in the fluids or limited amounts of fluid generated (Shen et al. 2015; Wang et al. 2016a). However, serpentinized oceanic crusts have been shown to be significantly isotopically heavier than BSE (Wang et al. 2016a; Xia et al. 2017) and the missing isotopically light source warrants future studies.

Further insights on high-T Cr isotopic behavior can be gained from the study of intermineral isotopic fractionation of mantle minerals. Based on first-principle calculations, Moynier et al. (2011) made theoretical estimations of Cr isotopic fractionation between co-existing minerals under conditions of planetary core-mantle segregation. The differences between most Cr(II) and Cr(0)-bearing minerals are minor at high temperatures, but the difference between those with Cr(III) and Cr(0) can be much larger. Farkaš et al. (2013) observed that chromites of different origins all have slightly heavier Cr isotopic compositions (with an average δ^{53}Cr value of -0.079 ± 0.129‰) than the BSE value. This finding was confirmed in a later study by Shen et al. (2015). Lunar mare basalts show Cr isotopic variation correlated with MgO content, likely due to spinel crystallization (Bonnand et al. 2016a). More modeling and laboratory observations are needed to further characterize mineral-scale Cr isotope heterogeneity.

Environmental Applications

Chromium has two major species in the natural surface environment – trivalent and hexavalent – denoted as Cr(III) and Cr(VI), respectively. Cr(VI) is carcinogenic and soluble in aquatic solution, while Cr(III) is sparingly soluble and can act as a micronutrient (Bartlett and Kimble 1976, 1979; Rai et al. 1987, 1989; Fendorf 1995). The major source of Cr (VI) to the environment is from industrial activities such as electrical plating and leather tanning (e.g., Megharaj et al. 2003), although geogenic pollution can also occur in areas covered with Cr-rich ultramafic bedrocks (e.g., Bartlett and James 1979; Oze et al. 2007).

The reduction of Cr(VI) to insoluble Cr(III) can remove Cr(VI) from groundwater (e.g., Cheung and Gu 2007; Dhal et al. 2013). Natural attenuation (Palmer and Puls 1994), active remediation (e.g., the use of permeable reactive barriers (Blowes et al. 1997, 2000; Puls et al. 1999; Wilkin et al. 2005) and biostimulation (Oliver et al. 2003; Cheung and Gu 2007; Dhal et al. 2013)) has been used to remove potentially dangerous levels of Cr(VI) from groundwater. Cr isotopes are a key tool used to monitor the effectiveness of these techniques. Light isotopes are preferentially reduced (and removed from groundwater) relative to heavy ones, leading to systematically increasing δ^{53}Cr in the remaining Cr(VI) thereby creating a means to track the extent of reduction and removal of Cr from this soluble pool (e.g., Ellis et al. 2002; Basu and Johnson 2012). The preferential reduction of light isotopes is linked to weaker chemical bonds in lower mass isotopes (Urey 1947; Bigeleisen 1965).

Numerous laboratory and field studies have been conducted to determine the fractionation factor during reduction (α). The α values determined in the lab range from as high as 0.9996 (-0.04‰) to as low as 0.9920 (-8‰) (see Qin and Wang 2017 for a more detailed review), in contrast to the narrower range observed in the field, which range from ca. 0.3‰ to ca. -2‰ (Berna et al. 2010; Izbicki et al. 2012). Lower fractionations derived from field studies likely result from a diffusion-reaction process, where Cr(VI) must diffuse into isolated reduction zones and the isotopically fractionated Cr(VI) can then diffuse back into solution (e.g., Clark and Johnson 2008). This systematic change in δ^{53}Cr during reduction can be described by a Rayleigh distillation model whereby groundwater δ^{53}Cr will become increasingly heavy as mobile Cr (VI) is reduced (e.g., Ellis et al. 2002; Scott et al. 2004; Abe and Hunkeler 2006).

Interpretation of Cr isotope data from field samples requires a clear understanding of several nonredox-dependent processes. Significantly, adsorption of Cr(VI) to mineral surfaces does not induce Cr isotope fractionation (Ellis et al. 2004) and therefore does not interfere with the use of Cr isotopes in tracking reduction. However, isotope exchange between remaining Cr(VI) and previously formed Cr(III) (Altman and King 1961) can lead to large isotope fractionations (Schauble et al. 2004; Wang et al. 2015). The

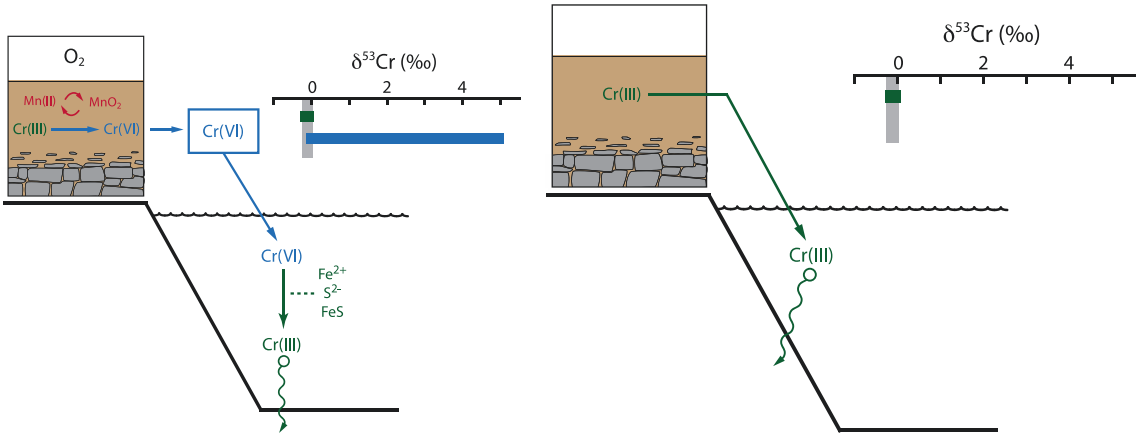

Chromium Isotopes, Fig. 1 Schematic of Cr cycle as a paleobarometer for atmospheric oxygen level. Large Cr isotope fractionations are expected in an oxic world (left hand side), while limited fractionations are expected in an anoxic world

timescale and impact of isotope exchange depends on the Cr concentrations and the relative masses of dissolved Cr (VI) and exposed Cr(III). Therefore, field conditions must be taken into account to assess uncertainties related to isotope exchange when using groundwater δ^{53}Cr to detect and quantify the extent of Cr(VI) reduction. Furthermore, additional complications can arise from solubilization of Cr(III) by organic ligands and reoxidation of previously formed Cr (III) (e.g., Bartlett and James 1979; Buerge and Hug 1998), which are still poorly understood. In sum, the Cr isotope system is useful redox proxy that can move forward our understanding of hexavalent Cr contamination. However, potential complications regarding isotope exchange, ligand mobilization, and oxidation continue to pose challenges and offer future research opportunities.

Cr Isotopes as a Paleoredox Proxy

More recently, Cr isotopes have emerged as a tracer of Earth's atmospheric oxygenation (e.g., Frei et al. 2009, 2013; Crowe et al. 2013; Planavsky et al. 2014; Cole et al. 2016; Gilleaudeau et al. 2016). The simplest application of Cr isotopes as a paleoredox proxy relies on the basic idea that variability of δ^{53}Cr in sedimentary rocks requires mobile Cr (VI) on Earth's surface and that the oxidation of Cr(III) to Cr (VI), via Mn oxides, requires free oxygen. The isotopic variability of this mobile pool has been demonstrated in modern riverine and marine systems (e.g., Bonnand et al. 2013; Frei et al. 2014; Scheiderich et al. 2015; Wu et al. 2017; D'Arcy et al. 2016; Farkaš et al. 2013; Novak et al. 2014), while the potential to record these signals in sedimentary archives has also been demonstrated in modern systems (e.g., Reinhard et al. 2014; Gueguen et al. 2016; Pereira et al. 2016; Wang et al. 2016b). Oxidized and mobile Cr(VI) is isotopically enriched, while residual soils are isotopically depleted. Using this framework, a lack of variability in the δ^{53}Cr sedimentary record should be indicative of very low surface oxygen levels, not capable of inducing oxidative Cr cycling, while the onset of variability in the δ^{53}Cr record should mark a shift to oxidative terrestrial weathering of Cr and an oxidized surface environment (Fig. 1).

Initial paleoredox Cr isotope studies have focused on reconstructing this record of Earth's oxygenation using banded iron formations (BIFs) and ironstones as an archive for Cr (Frei et al. 2009; Planavsky et al. 2014). These sediments can provide an ideal sedimentary archive as they are likely to develop large authigenic (seawater-derived) Cr enrichments with little detrital input and should be well rock-buffered and therefore resistant to later diagenetic influence. Unfortunately, these formations are not common throughout the rock record, and while they indicate a shift to an oxidizing Earth surface by the early Neoproterozoic, these records lack necessary temporal resolution. Significantly however, the oxygen level at which surface Cr oxidation can proceed has been suggested as ~0.1% and 1% present atmospheric levels (PAL), based on kinetics of Mn oxidation and the lack of available Fe(II) in order to prevent reduction, respectively (Crowe et al. 2013; Planavsky et al. 2014). These estimates are below theoretical and experimental estimates for the minimum oxygen needs of the earliest complex animals (Sperling et al. 2013; Mills et al. 2014). As such, understanding the timing of this shift to and Earth system capable of the terrestrial oxidative weathering of Cr has major implications for understanding the rise of complex life and the relationship between biologic innovation and environmental factors.

A number of other sedimentary archives also have the potential to record shifts in the δ^{53}Cr record, including organic-rich black shales and carbonates, which are both

ubiquitous throughout the rock record. Work on shales has demonstrated that these sediments are capable of recording modern marine variability in δ^{53}Cr values in the recent sedimentary record (e.g., Reinhard et al. 2014; Gueguen et al. 2016), and this archive has been expanded into deep time, providing increased resolution in understanding the transition to an oxidizing Earth surface, just prior to the earliest evidence of complex life (Cole et al. 2016). Additional work on shales from the Cretaceous shows a negative δ^{53}Cr excursion, coincident with Ocean Anoxic Event II, suggesting that with new developments in our understanding of the Cr mass balance there is also potential to track marine redox changes in the sedimentary record (Wang et al. 2016c).

Others have focused on investigating δ^{53}Cr isotopes in carbonates, both in laboratory experiments and in modern settings, as well as in deep time records. Laboratory work has suggested that moderate fractions are possible during carbonate precipitation when Cr(VI) is incorporated in to the crystal lattice (Tang et al. 2007; Rodler et al. 2015). These abiogenic fractionations were observed to be ~0.3‰, while biogenic uptake can vary much more significantly, ranging from −0.5 to 0.3‰ in corals, and showing species-dependent variations in foraminiferal calcification (Rodler et al. 2015; Pereira et al. 2016; Wang et al. 2016b). Further, there has not yet been an investigation of Cr(III) incorporation into carbonates and the fractionations that could be associated with this process. Despite these complexities, the currently observed abiogenic fractionations are small enough that abiogenic carbonates could potentially record a shift in Earth's redox state (e.g., Frei et al. 2011; Gilleaudeau et al. 2016). Gilleaudeau et al. (2016) reported both unfractionated and some fractionated δ^{53}Cr values from bulk carbonate analyses as ~1.1 Ga, which if primary, would suggest oxygen levels above ~0.1–1% PAL by the late Mesoproterozoic. However, carbonate rocks can be susceptible to later diagenetic alteration, and trace metal signatures are frequently diagenetic in origin as these lithologies are somewhat poorly rock-buffered (e.g., Brand and Veizer 1980; Jahn and Cuvellier 1994).

In sum, the Cr isotope system, even in its relatively nascent state as a paleoredox proxy, has proven a sensitive and useful tool in shaping our understanding of Earth's redox evolution. With further developments in our understanding of modern systems, the Cr mass balance, and sedimentary archives, this system is poised to provide many new high-resolution insights into the redox story of Earth's oceans and atmosphere through time.

Summary and Conclusions

Chromium isotopes are now an established system being routinely measured in a wide range of applications. Work in this system has revealed important new insights in the fields of cosmochemistry, environmental remediation and monitoring procedures, and most recently in reconstructing Earth's redox evolution, which has been a major contribution to the ongoing debate about the relationship between environmental factors and the evolution of life on this planet.

Cross-References

- ▶ Chromium
- ▶ Paleoenvironments

References

Abe Y, Hunkeler D (2006) Does the Rayleigh equation apply to evaluate field isotope data in contaminant hydrogeology? Environ Sci Technol 40:1588–1596

Altman C, King EL (1961) The mechanism of the exchange of chromium (III) and chromium(VI) in acidic solutions. J Am Chem Soc 83:2825–2830

Bartlett R, James B (1979) Behavior of chromium in soils: III. Oxidation. J Environ Qual 8:31–35

Bartlett R, Kimble J (1976) Behavior of chromium in soils: II. Hexavalent forms. J Environ Qual 5:383–386

Basu A, Johnson TM (2012) Determination of hexavalent chromium reduction using Cr stable isotopes: isotopic fractionation factors for permeable reactive barrier materials. Environ Sci Technol 46:5353–5360

Berna EC, Johnson TM, Makdisi RS, Basu A (2010) Cr stable isotopes as indicators of Cr (VI) reduction in groundwater: a detailed time-series study of a point-source plume. Environ Sci Technol 44:1043–1048

Bigeleisen J (1965) Chemistry of isotopes. Science 147:463

Birck J-L, Allègre CJ (1984) Chromium isotopic anomalies in Allende refractory inclusions. Geophys Res Lett 11:943–946

Birck J-L, Allègre CJ (1985) Evidence for the presence of 53Mn in the early solar system. Geophys Res Lett 12:745

Birck J-L, Allègre CJ (1988) Manganese chromium isotope systematics and development of the early solar system. Nature 331:579–584

Blowes DW, Ptacek CJ, Jambor JL (1997) In-situ remediation of Cr (VI)-contaminated groundwater using permeable reactive walls: laboratory studies. Environ Sci Technol 31:3348–3357

Blowes DW, Ptacek CJ, Benner SG, McRae CW, Bennett TA, Puls RW (2000) Treatment of inorganic contaminants using permeable reactive barriers. J Contam Hydrol 45:123–137

Bonnand P, James RH, Parkinson IJ, Connelly DP, Fairchild IJ (2013) The chromium isotopic composition of seawater and marine carbonates. Earth Planet Sci Lett 382:10–20

Bonnand P, Parkinson IJ, Anand M (2016a) Mass dependent fractionation of stable chromium isotopes in mare basalts: implications for the formation and the differentiation of the Moon. Geochim Cosmochim Acta 175:208–221

Bonnand P, Williams H, Parkinson I, Wood B, Halliday A (2016b) Stable chromium isotopic composition of meteorites and metal–silicate experiments: implications for fractionation during core formation. Earth Planet Sci Lett 435:14–21

Brand U, Veizer J (1980) Chemical diagenesis of a multicomponent carbonate system – 1: trace elements. J Sediment Res 50: 1219–1236

Buerge IJ, Hug SJ (1998) Influence of organic ligands on chromium (VI) reduction by iron(II). Environ Sci Technol 32:2092–2099

Cheung K, Gu J-D (2007) Mechanism of hexavalent chromium detoxification by microorganisms and bioremediation application potential: a review. Int Biodeterior Biodegrad 59:8–15

Clark SK, Johnson TM (2008) Effective isotopic fractionation factors for solute removal by reactive sediments: a laboratory microcosm and slurry study. Environ Sci Technol 42:7850–7855

Cole DB, Reinhard CT, Wang X, Gueguen B, Halverson GP, Gibson T, Hodgskiss MSW, McKenzie NR, Lyons TW, Planavsky NJ (2016) A shale-hosted Cr isotope record of low atmospheric oxygen during the Proterozoic. Geology 44:555

Crowe SA, Dossing LN, Beukes NJ, Bau M, Kruger SJ, Frei R, Canfield DE (2013) Atmospheric oxygenation three billion years ago. Nature 501:535–538

D'Arcy J, Babechuk MG, Døssing LN, Gaucher C, Frei R (2016) Processes controlling the chromium isotopic composition of river water: constraints from basaltic river catchments. Geochim Cosmochim Acta 186:296–315

Dhal B, Thatoi H, Das N, Pandey B (2013) Chemical and microbial remediation of hexavalent chromium from contaminated soil and mining/metallurgical solid waste: a review. J Hazard Mater 250:272–291

Ellis AS, Johnson TM, Bullen TD (2002) Chromium isotopes and the fate of hexavalent chromium in the environment. Science 295:2060

Ellis AS, Johnson TM, Bullen TD (2004) Using chromium stable isotope ratios to quantify Cr (VI) reduction: lack of sorption effects. Environ Sci Technol 38:3604–3607

Farkaš J, Chrastny V, Novak M, Cadkova E, Pasava J, Chakrabarti R, Jacobsen SB, Ackerman L, Bullen TD (2013) Chromium isotope variations ($\delta^{53/52}$Cr) in mantle-derived sources and their weathering products: implications for environmental studies and the evolution of $\delta^{53/52}$Cr in the Earth's mantle over geologic time. Geochim Cosmochim Acta 123:74–92

Fendorf SE (1995) Surface reactions of chromium in soils and waters. Geoderma 67:55–71

Frei R, Gaucher C, Poulton SW, Canfield DE (2009) Fluctuations in Precambrian atmospheric oxygenation recorded by chromium isotopes. Nature 461:250–253

Frei R, Gaucher C, Døssing LN, Sial AN (2011) Chromium isotopes in carbonates – a tracer for climate change and for reconstructing the redox state of ancient seawater. Earth Planet Sci Lett 312:114–125

Frei R, Gaucher C, Stolper D, Canfield DE (2013) Fluctuations in late Neoproterozoic atmospheric oxidation – Cr isotope chemostratigraphy and iron speciation of the late Ediacaran lower Arroyo del Soldado Group (Uruguay). Gondwana Res 23:797–811

Frei R, Poiré D, Frei KM (2014) Weathering on land and transport of chromium to the ocean in a subtropical region (Misiones, NW Argentina): a chromium stable isotope perspective. Chem Geol 381:110–124

Gilleaudeau G, Frei R, Kaufman A, Kah L, Azmy K, Bartley J, Chernyavskiy P, Knoll A (2016) Oxygenation of the mid-Proterozoic atmosphere: clues from chromium isotopes in carbonates. Geochem Perspect Lett 2:178–187

Gueguen B, Reinhard CT, Algeo TJ, Peterson LC, Nielsen SG, Wang X, Rowe H, Planavsky NJ (2016) The chromium isotope composition of reducing and oxic marine sediments. Geochim Cosmochim Acta 184:1–19

Izbicki JA, Bullen TD, Martin P, Schroth B (2012) Delta Chromium-53/52 isotopic composition of native and contaminated groundwater, Mojave Desert, USA. Appl Geochem 27:841–853

Jahn B-M, Cuvellier H (1994) Pb–Pb and U–Pb geochronology of carbonate rocks: an assessment. Chem Geol 115:125–151

Kaye J, Cressy P (1965) Half-life of manganese-53 from meteorite observations. J Inorg Nucl Chem 27:1889–1892

Lugmair GW, Shukolyukov A (1998) Early solar system timescales according to ^{53}Mn-^{53}Cr systematics. Geochim Cosmochim Acta 62:2863–2886

McKeegan KD, Davis AM (2014) Early solar system chronology. In: Turekian KK, Holland HD (eds) Treatise on geochemistry, 2nd edn. Elsevier, Oxford/San Diego, pp 431–460

Megharaj M, Avudainayagam S, Naidu R (2003) Toxicity of hexavalent chromium and its reduction by bacteria isolated from soil contaminated with tannery waste. Curr Microbiol 47:0051–0054

Mills DB, Ward LM, Jones C, Sweeten B, Forth M, Treusch AH, Canfield DE (2014) Oxygen requirements of the earliest animals. Proc Natl Acad Sci U S A 111:4168–4172

Moynier F, Yin Q-Z, Schauble E (2011) Isotopic evidence of Cr partitioning into Earth's core. Science 331:1417–1420

Novak M, Chrastny V, Čadková E, Farkas J, Bullen T, Tylcer J, Szurmanova Z, Cron M, Prechova E, Curik J (2014) Common occurrence of a positive δ^{53}Cr shift in Central European waters contaminated by geogenic/industrial chromium relative to source values. Environ Sci Technol 48:6089–6096

Oliver DS, Brockman FJ, Bowman RS, Kieft TL (2003) Microbial reduction of hexavalent chromium under vadose zone conditions. J Environ Qual 32:317–324

Oze C, Bird DK, Fendorf S (2007) Genesis of hexavalent chromium from natural sources in soil and groundwater. Proc Natl Acad Sci U S A 104:6544–6549

Palmer CD, Puls RW (1994) Natural attenuation of hexavalent chromium in ground water and soils. U.S. Environmental Protection Agency Ground Water Issue. EPA/540/5-94/505, Washington DC, pp 1–12

Papanastassiou DA (1986) Chromium isotopic anomalies in the Allende meteorite. Astrophys J 308:L27–L30

Pereira NS, Voegelin AR, Paulukat C, Sial AN, Ferreira VP, Frei R (2016) Chromium-isotope signatures in scleractinian corals from the Rocas Atoll, Tropical South Atlantic. Geobiology 14:54–67

Planavsky NJ, Reinhard CT, Wang X, Thomson D, McGoldrick P, Rainbird RH, Johnson T, Fischer WW, Lyons TW (2014) Low mid-Proterozoic atmospheric oxygen levels and the delayed rise of animals. Science 346:635–638

Podosek FA, Ott U, Brannon JC, Neal CR, Bernatowicz TJ (1997) Thoroughly anomalous chromium in Orgueil. Meteorit Planet Sci 32:617–627

Puls RW, Paul CJ, Powell RM (1999) The application of in situ permeable reactive (zero-valent iron) barrier technology for the remediation of chromate-contaminated groundwater: a field test. Appl Geochem 14:989–1000

Qin L, Carlson RW (2016) Nucleosynthetic isotope anomalies and their cosmochemical significance. Geochem J 50:43–65

Qin L, Wang X (2017) Chromium isotope geochemistry. Rev Mineral Geochem 82:379–414

Qin L, Carlson RW, Alexander CMOD (2011) Correlated nucleosynthetic isotopic variability in Cr, Sr, Ba, Sm, Nd and Hf in Murchison and QUE 97008. Geochim Cosmochim Acta 75:7806–7828

Rai D, Sass BM, Moore DA (1987) Chromium(III) hydrolysis constants and solubility of chromium(III) hydroxide. Inorg Chem 26:345–349

Rai D, Eary L, Zachara J (1989) Environmental chemistry of chromium. Sci Total Environ 86:15–23

Reinhard CT, Planavsky NJ, Wang X, Fischer WW, Johnson TM, Lyons TW (2014) The isotopic composition of authigenic chromium in anoxic marine sediments: a case study from the Cariaco Basin. Earth Planet Sci Lett 407:9–18

Rodler A, Sánchez-Pastor N, Fernández-Díaz L, Frei R (2015) Fractionation behavior of chromium isotopes during coprecipitation with

calcium carbonate: implications for their use as paleoclimatic proxy. Geochim Cosmochim Acta 164:221–235
Rotaru M, Birck J-L, Allègre CJ (1992) Clues to early solar system history from chromium isotopes in carbonaceous chondrites. Nature 358:465–470
Schauble E, Rossman GR, Taylor HP Jr (2004) Theoretical estimates of equilibrium chromium-isotope fractionations. Chem Geol 205:99–114
Scheiderich K, Amini M, Holmden C, Francois R (2015) Global variability of chromium isotopes in seawater demonstrated by Pacific, Atlantic, and Arctic Ocean samples. Earth Planet Sci Lett 423:87–97
Schoenberg R, Zink S, Staubwasser M, Von Blanckenburg F (2008) The stable Cr isotope inventory of solid Earth reservoirs determined by double spike MC-ICP-MS. Chem Geol 249:294–306
Schoenberg R, Merdian A, Holmden C, Kleinhanns IC, Haßler K, Wille M, Reitter E (2016) The stable Cr isotopic compositions of chondrites and silicate planetary reservoirs. Geochim Cosmochim Acta 183:14–30
Scott K, Lu X, Cavanaugh C, Liu J (2004) Optimal methods for estimating kinetic isotope effects from different forms of the Rayleigh distillation equation. Geochim Cosmochim Acta 68:433–442
Shen J, Liu J, Qin L, Wang SJ, Li S, Xia J, Ke S, Yang J (2015) Chromium isotope signature during continental crust subduction recorded in metamorphic rocks. Geochem Geophys Geosyst 16:3840–3854
Sperling EA, Halverson GP, Knoll AH, Macdonald FA, Johnston DT (2013) A basin redox transect at the dawn of animal life. Earth Planet Sci Lett 371–372:143–155
Tang Y, Elzinga EJ, Jae Lee Y, Reeder RJ (2007) Coprecipitation of chromate with calcite: batch experiments and X-ray absorption spectroscopy. Geochim Cosmochim Acta 71:1480–1493
Trinquier A, Birck J-L, Allègre CJ, Göpel C, Ulfbeck D (2008) ^{53}Mn-^{53}Cr systematics of the early solar system revisited. Geochim Cosmochim Acta 72:5146–5163
Truex M, Vermeul V, Fruchter J (2009) Treatability testing of an in situ bio-stimulation barrier for nitrate and chromium treatment. 2009 Waste Management Symposium - WM2009/WM'09: HLW, TRU, LLW/ILW, Mixed, Hazardous Wastes and Environmental Management - Waste Management for the Nuclear Renaissance, United States
Urey HC (1947) The thermodynamic properties of isotopic substances. J Chem Soc (Resumed) 562–581
Wang X, Johnson TM, Ellis AS (2015) Equilibrium isotopic fractionation and isotopic exchange kinetics between Cr (III) and Cr (VI). Geochim Cosmochim Acta 153:72–90
Wang X, Planavsky NJ, Reinhard CT, Zou H, Ague JJ, Wu Y, Gill BC, Schwarzenbach EM, Peucker-Ehrenbrink B (2016a) Chromium isotope fractionation during subduction-related metamorphism, black shale weathering, and hydrothermal alteration. Chem Geol 423:19
Wang X, Planavsky NJ, Hull PM, Tripati AE, Zou HJ, Elder L, Henehan M (2016b) Chromium isotopic composition of core-top planktonic foraminifera. Geobiology 15:51–64
Wang X, Reinhard CT, Planavsky NJ, Owens JD, Lyons TW, Johnson TM (2016c) Sedimentary chromium isotopic compositions across the Cretaceous OSE2 at Demerara Rise Site 1258. Chem Geol 429:85–92
Weyer S, Schwieters J (2003) High precision Fe isotope measurements with high mass resolution MC-ICPMS. Int J Mass Spectrom Ion Process 226:355–368
Wilkin RT, Su C, Ford RG, Paul CJ (2005) Chromium-removal processes during groundwater remediation by a zerovalent iron permeable reactive barrier. Environ Sci Technol 39:4599–4605
Wu W, Wang X, Reinhard CT, Planavsky NJ (2017) Chromium isotope systematics in the Connecticut River. Chem Geol 456:98
Xia J, Qin L, Shen J, Carlson RW, Ionov DA, Mock TD (2017) Chromium isotope heterogeneity in the mantle. Earth Planet Sci Lett. https://doi.org/10.1016/j.epsl.2017.1001.1045
Yamakawa A, Yamashita K, Makishima A, Nakamura E (2009) Chemical separation and mass spectrometry of Cr, Fe, Ni, Zn, and Cu in terrestrial and extraterrestrial materials using thermal ionization mass spectrometry. Anal Chem 81:9787–9794

Clapeyron's Equation

Masaki Akaogi
Department of Chemistry, Gakushuin University, Tokyo, Japan

Definition

We consider here that a substance changes from a reactant phase to a product phase and that both the phases are in equilibrium at pressure (P) and temperature (T). Clapeyron's equation expresses the stability relation between the reactant and product phases and gives a dP/dT slope of equilibrium phase boundary between the reactant and the product as a function of P and T. This equation is one of the most important equations for understanding thermodynamic stability relations in geochemical, petrological, and mineralogical processes. For example, when α-quartz SiO_2 is in equilibrium with coesite at certain P, T conditions, Clapeyron's equation gives the slope of the equilibrium quartz-coesite transition boundary in a P-T space where quartz is stable at relatively lower P and higher T and coesite at relatively higher P and lower T.

Clapeyron's Equation

When reactant and product phases are in equilibrium at P and T, and changes of entropy (ΔS) and volume (ΔV) accompany with the reaction at P and T, Clapeyron's equation is given as:

$$dP/dT = \Delta S/\Delta V \quad (1)$$

If the reaction reaches equilibrium state, $\Delta H = T\Delta S$, where ΔH is enthalpy of reaction. Therefore, Eq. 1 is rewritten as:

$$dP/dT = \Delta H/T\Delta V \quad (2)$$

Note that ΔS, ΔV, and ΔH are entropy, volume, and enthalpy changes at the P, T conditions considered. In principle, the values of ΔS, ΔV, and ΔH cannot be assumed as constants along the equilibrium phase boundary, and

therefore the slope is not constant. However, in solid-solid phase transitions in limited P, T ranges, ΔS, ΔV, and ΔH may generally be approximated as constants, resulting in a constant slope. In reactions involving vapor or liquid phase, the boundary is generally curved, because the vapor or liquid phase has higher entropy and is more compressible than the solid phase. Several textbooks on thermodynamics show a simple derivation of Clapeyron's equation from thermodynamic principles (e.g., Richet 2001).

It should be noted that Clapeyron's equation is applicable to the first-order phase transitions but cannot be applied to the second-order transitions in which both ΔS and ΔV are zero. Clapeyron's equation is useful for understanding stability relations of a substance and for constructing phase diagrams by combining with Schreinemaker's rule.

Summary

Clapeyron's equation is widely used in thermodynamics for materials of geochemical, petrological, and mineralogical interests. One of important applications of Clapeyron's equation in the fields is to evaluate dP/dT slopes of phase transition boundaries in silicates at high pressure and high temperature. In particular, dissociation reaction of spinel-type $(Mg,Fe)_2SiO_4$ to perovskite-type $(Mg,Fe)SiO_3$ and (Mg,Fe)O, called the post-spinel transition, which occurs at 660 km depth in the Earth's mantle, has a phase boundary with a negative dP/dT slope. The transition with the negative Clapeyron slope provides substantial resistance for subduction of slabs, resulting in significant effects on mantle dynamics and geochemical evolution of the mantle (e.g., Christensen 1995).

Cross-References

- ▶ Enthalpy
- ▶ Entropy
- ▶ Equilibrium
- ▶ Experimental Mineralogy and Petrology
- ▶ Free Energy
- ▶ Geochemical Thermodynamics
- ▶ Geothermometry and Geobarometry
- ▶ Mantle Geochemistry
- ▶ Phase Equilibria

References

Christensen U (1995) Effects of phase transitions on mantle convection. Annu Rev Earth Planet Sci 23:65–87

Richet P (2001) The physical basis of thermodynamics. Kluwer/Plenum Publishers, New York, 442 pp

Clay Membranes

Ian C. Bourg
Department of Civil and Environmental Engineering and Princeton Environmental Institute, Princeton University, Princeton, NJ, USA

C

Definition

Clay membranes are clay-rich media (soils, sediments, or sedimentary rocks) that exhibit partial restriction of solute migration relative to that of water, i.e., semipermeable membrane properties.

Geochemical Importance

Clay membrane properties have the potential to significantly modulate the groundwater hydrology of clay-rich media, at least in some cases. They have been studied as a potential cause of erratic fluid pressures in sedimentary formations and, also, because of their potential impacts on well-bore stability, chemico-osmotic consolidation, water and nutrient fluxes in soils, and waste isolation using natural and engineered clay barriers (Takeda et al. 2014).

Phenomenology

Clay membranes give rise to two geochemical phenomena: hyperfiltration and osmosis. Hyperfiltration occurs when a hydraulic pressure gradient drives water flow across a clay membrane. For solutes that exhibit restricted migration through the membrane, the solute concentration of the permeate is depleted by a dimensionless factor σ known as the osmotic efficiency or solute reflection coefficient.

Osmosis occurs when a clay membrane separates two aqueous reservoirs with different concentrations of a solute. The associated gradients in chemical potential give rise to a diffusive flux of solute toward the dilute reservoir and of water toward the concentrated reservoir. If the porous medium separating the two reservoirs partially restricts solute migration relative to that of water, a net flux of solution (the osmotic flux) occurs toward the concentrated reservoir.

Reported values of σ in fine-grained sedimentary rocks range from 0 to 0.5, with a tendency of σ to increase with decreasing permeability and salinity (Takeda et al. 2014). Values of σ up to ~1.0 have been reported in compacted smectite or bentonite samples, with a strong dependence on salt concentration, counterion valence, and compaction (Kemper and Rollins 1966; Malusis et al. 2012).

Fundamental Basis

Porous media exhibit semipermeable membrane properties if their pores are sufficiently narrow that steric or electrostatic effects significantly hinder solute migration. In clay membranes, the predominant mechanism is the partial exclusion of anions from the electrical double layer (EDL), the region of interfacial water where electrolyte ions screen the negative surface charge of the clay particles. Anion exclusion restricts the migration of anions through the clay membrane and, therefore, that of cations because of the electroneutrality requirement.

Theories of the structure of the electrical double layer, such as the Gouy-Chapman model, predict that anion exclusion has a characteristic length scale d_a equal to twice the Debye length (Tournassat and Appelo 2011). At room temperature in a 0.1 M NaCl electrolyte, d_a equals ~2 nm on each pore wall, suggesting that anions are almost completely excluded from pores narrower than ~4 nm. The anion exclusion thickness d_a varies with the inverse square root of ionic strength and decreases significantly in the presence of multivalent cations.

In clay-rich sedimentary rocks, the largest pore-width mode observed by nitrogen adsorption or mercury intrusion porosimetry is often on the order of ~10 nm. This value is consistent with the observation that the anion-accessible pore space equals roughly half of the total pore space in many clay-rich rocks. Together, these observations suggest that most fine-grained sedimentary rocks have the potential to behave as clay membranes, particularly in aqueous chemistry conditions where the Debye length is large (low salinity, Na^+ as the predominant exchangeable cation) and where pores are small (low porosity, high content of smectite clay).

Mathematical Formulation

At the macroscopic scale, solution volumetric flux $\mathbf{J}_v$ (m s^{-1}) and solute molar flux relative to solution $\mathbf{J}^d{}_s$ (mol m^{-2} s^{-1}) in clay membranes are commonly described using the following pair of equations derived from non-equilibrium thermodynamics:

$$\mathbf{J}_v = L_{11}\nabla P + L_{12}\nabla \mu_s \tag{1}$$

$$\mathbf{J}^d{}_s = L_{21}\nabla P + L_{22}\nabla \mu_s \tag{2}$$

where $L_{12} = L_{21}$ based on Onsager's reciprocity rule. The most appropriate formulation of the L_{ij} parameters is not entirely settled, however, as noted below. One possible formulation yields the following expressions for $\mathbf{J}_v$ and for the net solute flux $\mathbf{J}_s = c_s\mathbf{J}_v + \mathbf{J}^d{}_s$ (Malusis et al. 2012; Takeda et al. 2014):

$$\mathbf{J}_v = -(\mathrm{k}/\mu)\left(\Delta P - \sigma\nabla\prod\right) \tag{3}$$

$$\mathbf{J}_s = (1-\sigma)c_s\mathbf{J}_\mathbf{v} - D_e\nabla c_s \tag{4}$$

where k is the intrinsic permeability of the porous medium (m^2), μ is the dynamic viscosity of the solution (Pa s), P is pressure (Pa), Π is osmotic pressure (Pa), D_e is the effective diffusion coefficient of the solute in the porous medium (m^2 s^{-1}), and c_s is solute concentration (mol m^{-3}). The osmotic pressure gradient ideally is given by Van't Hoff's relation: $\Pi = \nu RTc_s$, where R is the ideal gas constant (Pa m^3 mol^{-1} K^{-1}), T is absolute temperature (K), and ν is the number of constituents in the solute (e.g., $\nu = 2$ for NaCl).

Unresolved Issues

Several incompletely resolved issues exist in the study of clay membrane properties, particularly with regard to the choice of formulation for the L_{ij} parameters in Eqs. 1 and 2 (Bader and Kooi 2005; Malusis et al. 2012). For example, the common assumption that $\mathbf{J}_v$ is accurately described by Darcy's law if $\nabla\mu_s = 0$ yields an advective coefficient $L_{11} = \mathrm{k}/\mu$. The definition of the reflection coefficient can then be used to write $\sigma = -L_{12}/c_sL_{11}$, which yields $L_{12} = -\sigma\,(\mathrm{k}/\mu)\,c_s$. This formulation (used in Eq. 3) describes the osmotic flux of solution as an advective phenomenon (dependent on k) even though its fundamental origin is a difference in the diffusive fluxes of water and solute.

A second unresolved issue is whether a full characterization of clay membrane behavior requires two parameters: the reflection coefficient σ describing the tendency of the solute to resist *advection* through the membrane and an additional coefficient σ_d describing the tendency of the solute to resist *diffusion* through the membrane (Katchalsky and Curran 1965). Geochemical studies have often used the simplifying assumption $\sigma_d = \sigma$ while noting that the validity of this assumption is not entirely settled (Bader and Kooi 2005; Malusis et al. 2012).

A third important conceptual question is the manner in which Eqs. 1 and 2 should be solved in clay membranes of non-negligible thickness, where $\mathbf{J}_v$ and $\mathbf{J}^d{}_s$ are not inherently at steady state. Existing schemes rely on treating σ as invariant with time (Takeda et al. 2014), despite strong evidence that σ can vary significantly with time if salt diffusion and cation exchange occur in the membrane (Shackelford and Lee 2003).

A fourth important question is whether membrane efficiency (σ) can be correlated with other properties of the porous medium (Malusis et al. 2012). Experimental results suggest possible correlations with salinity, in agreement with the strong salinity dependence of EDL thickness, and permeability, in agreement with the expected sensitivity of both permeability and membrane efficiency to the width and connectivity of the largest pores (Takeda et al. 2014). Relatively little progress has been made on relating these results to the microstructure of clayey media, because of the difficulty of precisely characterizing the pore networks that control σ in these media and because the microstructure itself, in some cases, is sensitive to salinity (Tournassat and Appelo 2011).

Summary

Clay membrane behavior is relatively widely observed in sedimentary rocks and compacted clay barriers. Observations of this behavior reflect conditions where flow in a clay-rich medium is controlled by pores with a pore width on the order of ~10 nm or less. The osmotic efficiency of clay membranes decreases significantly with increasing salinity, pore width, and counterion valence. Significant conceptual questions remain unanswered with regard to the geochemical modeling of clay membranes.

Cross-References

- ▶ Clay Minerals
- ▶ Diffusion
- ▶ Soils

References

Bader S, Kooi H (2005) Modelling of solute and water transport in semi-permeable clay membranes: comparison with experiments. Adv Water Resour 28:203–214

Katchalsky A, Curran PF (1965) Biophysics. Harvard University Press, Cambridge, MA, 248 pp

Kemper WD, Rollins JB (1966) Osmotic efficiency coefficients across compacted clays. Soil Sci Soc Am Proc 30:529–534

Malusis MA, Shackelford CD, Maneval JE (2012) Critical review of coupled flux formations for clay membranes based on non-equilibrium thermodynamics. J Contam Hydrol 138–139:40–59

Shackelford CD, Lee J-M (2003) The destructive role of diffusion on clay membrane behavior. Clay Clay Miner 51:186–196

Takeda M, Hiratsuka T, Manaka M, Finsterle S, Ito K (2014) Experimental examination of the relationships among chemico-osmotic, hydraulic, and diffusion parameters of Wakkanai mudstones. J Geophys Res Solid Earth 119

Tournassat C, Appelo CAJ (2011) Modelling approaches for anion-exclusion in compacted Na-bentonite. Geochim Cosmochim Acta 75:3698–3710

Clay Minerals

Josh Wimpenny
Nuclear and Chemical Sciences Division, Lawrence Livermore National Laboratory, Livermore, CA, USA

C

Definition

Clay minerals are a diverse group of minerals that are fine grained and crystalline and ultimately form from the aqueous alteration of primary igneous minerals at or near the surface of the Earth. They have a layered structure, commonly consisting of repeating sheets of Si tetrahedra and Al octahedra. The wide diversity of clay minerals stems from the way that these sheets stack together and the identity of ions that commonly substitute into the clay mineral structure. Due to their unique layered structure and their effectiveness as ion exchangers, the formation of clay minerals can have a significant impact over the chemical and isotopic compositions of solid and fluid phases during weathering.

Introduction

Clay minerals are a highly diverse and abundant group of minerals that derive from the interaction of water with rock in the Earth's crust. Because clay minerals are often found in the clay-size fraction of sediments and soils (i.e., below 2 μm), the terms "clay" and "clay minerals" are often used interchangeably. However, the term clay minerals refers to a distinct group of minerals with a layered structure, rather than having grain-size significance.

Clay minerals are comprised of repeating aluminosilicate layers (or sheets), and the way that these sheets stack together helps to control their physical properties and chemical composition. Clay minerals form in a range of conditions (pH, temperature, pressure), and clay-rich sediments result from a range of different formation mechanisms, from solid-state alteration to dissolution and neoformation, to detrital inheritance (Singer 1980). Due to their layered structures, large surface area, and prevalence in the Earth's crust, the formation of clay minerals can have a significant impact over the chemical and isotopic composition of crustal rocks, sediments, and soils, and understanding how and when clay minerals have formed can shape our understanding of past weathering regimes and changes in the Earth's climate. Furthermore, the alteration of primary silicate minerals and formation of clay minerals have a significant impact on the chemical and isotopic composition of crustal fluids, including rivers, lakes,

and groundwaters, and, ultimately, help to control the past chemical composition of the Earth's oceans.

The unique physical and chemical properties of clay minerals mean that understanding how and why they form is critical in our understanding of natural processes, such as changes in past climate and crustal cycling, as well as facilitating our development of natural resources such as aquifers and oil and gas fields. Our utilization of clay minerals goes further still. Clay minerals are currently directly involved in many industrial applications and find their way into our homes where they are used on a daily basis, from ceramics to building materials to the production of paper, as well as in major engineering projects such as dams and landfill sites. Clay minerals are found in a wide range of environments, from soils and weathering profiles, to hydrothermal systems, to lake and estuaries and deep sea sediments. The ubiquitous occurrence of clay minerals on Earth has even helped to guide our ongoing exploration of the solar system. Recently, the Mars rover Curiosity was sent to a clay-rich region of the red planet because of the link between formations of clay minerals with liquid water. The finding of clay minerals on Mars suggests a distant past with a once water-rich environment that could have harbored life.

In this summary of clay mineralogy, we will discuss (i) the basics of clay mineralogy, (ii) the most common types of clay minerals and their uses, (iii) the ion exchange processes and their significance in influencing the chemical composition of rivers and the oceans, and (iv) the human uses for clay minerals.

Clay Mineral Structure and Ion Exchange

The basic structure of clay minerals consists of repeating sequences of Si-O tetrahedra (T) and Al-O octahedra (O) that form layers or sheets that bind together by sharing oxygens (Merkel et al. 2005). In tetrahedral coordination, the central cation is surrounded by four oxygen atoms, while in octahedral coordination, the central cation is surrounded by six oxygen atoms. The distinctive clay mineralogies and their chemical and physical properties are, to a first order, controlled by how these sheets of Si tetrahedra and Al octahedra stack together. For this reason, clay minerals are often described by the ratio of T:O layers in their structure. For example, the kaolin group of clay minerals is comprised of tightly packed alternating T-O units and so is called 1:1 clay minerals. Another common group of clay minerals, the mica group, consists of repeating T-O-T units and so is referred to as 2:1 clay minerals. The 2:1 clay minerals are some of the most common in the crust and include the highly abundant mineral smectite, vermiculite, and illite. The layer of oxygen atoms that bound the basal tetrahedral layer in a 2:1 clay mineral is often referred to as the siloxane layer (e.g., Sposito et al. 1999), and the characteristic spacing between adjacent tetrahedral layers is called the interlayer (Drever 1988).

While the basic structure of clay minerals is dominated by Si and Al, clay minerals can contain significant quantities of other cations due to structural substitution reactions. The most common is the replacement of Si^{4+} in the tetrahedral sheet by Al^{3+}, with a limit to ~15% substitution (Krauskopf and Bird 1967), and replacement of Al^{3+} in the octahedral sheet, in which both the identity of the exchanging cation and the amount of substitution can vary. The most common cations that exchange into the octahedral sheet are Mg^{2+}, Fe^{2+}, and Ca^{2+}. In these isomorphic substitutions, the charge of the replacing cation is less important than the length of the cation-oxygen bond. For this reason, these substitutions often result in a charge imbalance, which is typically negative and is considered to be permanent (Odom 1984; Drever 1988; Appelo and Postma 2005; Merkel et al. 2005). An example is the substitution of Mg^{2+} for Al^{3+} in the octahedral layer of pyrophyllite, resulting in the formation of the common smectite group mineral montmorillonite. This isomorphic substitution of cations into structural layers can be significant; in the case of montmorillonite, the clay can contain upward of 3 Wt % Mg (Mermut and Cano 2001). Isomorphic substitutions are not common in all clay minerals; they do not occur to any significance in the kaolin group minerals, and as a consequence, these minerals do not develop a significant charge imbalance.

Where isomorphic substitutions do occur, the resulting negative structural charge is balanced by adsorption of freely exchangeable positively charged cations from solution (e.g., Mg^{2+}, Ca^{2+}, Na^{+}, and H^{+}). Adsorption of cations onto clay minerals is typically described as occurring in one of two ways: inner-sphere or outer-sphere adsorption (e.g., Sposito et al. 1999; Strawn and Sparks 1999). Outer-sphere complexes contain a water molecule in between constituent ions of the complex, which are solvated (Sposito et al. 1999; Appelo and Postma 2005). Outer-sphere complexation usually occurs on the basal planes, or interlayer, of the clay mineral (Strawn and Sparks 1999). Inner-sphere complexation occurs when the water molecule is expelled and covalent bonding can occur (Appelo and Postma 2005).

There is a general order of chemical affinity for adsorption of cations from solution. Typically the divalent cations (e.g., Mg^{2+}, Ca^{2+}) have a stronger affinity for adsorption than the monovalent cations (e.g., Na^{+}, K^{+}). However, within cations of the same charge, those that have the smallest hydrated ionic radii typically have the strongest adsorption affinity. Adsorbed ions are commonly incorporated into the clay interlayer region where they electrostatically bond to the siloxane layers on the basal plane of Si-tetrahedral layers (Odom 1984; Drever 1988; Strawn et al. 2004; Merkel et al. 2005). This ensures net charge neutrality across the clay mineral structure. The uptake of exchangeable cations is

usually more important where there is the greatest charge imbalance, i.e., where isomorphic substitution has occurred, and the capacity for electrostatic uptake is greatest. The capacity of clay minerals for ion exchange or adsorption (the cation exchange capacity or CEC) is dependent on pH and the type of ions that already occupy exchange sites. In general, the expandable clay minerals such as smectite and vermiculite have higher CEC values than non-expandable minerals such as kaolinite and illite (Ma and Eggleton 1999).

Minerals in which substitution reactions do not occur and interlayer expansion is not important (e.g., kaolinite) can still be important adsorbing agents. Other important adsorption sites include surface hydroxyl sites that form at edge sites where the clay structure has been interrupted (Papelis and Hayes 1996) or silanol sites which can be amphoteric (Peacock and Sherman 2005).

Common Clay Minerals

As described, there is a diverse range of clay minerals, but they have, in general, similar structural components. In the following the main groups of clay minerals will be described, from the simple phases similar to layered double hydroxides to expandable clay minerals such as the smectite group. Basic physical properties of the main clay groups are given in Table 1, while chemical formulas of clay minerals from each group are given in Table 2. Illustrations of the structure of kaolin, smectite, and mica group minerals are shown in Fig. 1.

Gibbsite, Brucite, and Layered Double Hydroxides (LDH)

These minerals differ from what are typically thought of as phyllosilicates, because they do not consist of layers of both Si tetrahedra and Al octahedra, instead being more analogous to the octahedral sheet itself. The structure of these minerals is two closely packed layers of hydroxyl ions (hence layered double hydroxides) with cations in octahedral coordination between the two sheets (Drever 1988). In the case of brucite, this octahedral cation is Mg^{2+}, and each Mg^{2+} is coordinated by 6 OH^- ions, while each OH- ions is coordinated to 3 Mg^{2+} ions. In this way the charges balance with the formula Mg $(OH)_2$, and all of the octahedral sites are filled. In the case of gibbsite, the octahedral cations are Al^{3+}. Because Al is trivalent, it cannot be coordinated in the same way as Mg^{2+} without resulting in a charge imbalance. Hence in gibbsite every third octahedral site is left empty so it has a formula Al $(OH)_3$. Clay minerals in which the octahedral vacancies are all filled (e.g., brucite) are called trioctahedral, while those in which only two out of three octahedral sites are occupied are called dioctahedral.

The dioctahedral mineral gibbsite is particularly relevant to further discussion, not only because of its analogous structure to the octahedral sheet in most phyllosilicates but because of its capacity for swelling and uptake of cations and anions into structural sites and the interlayer. By definition the dioctahedral clay minerals have one void in the octahedral layer that has potential to be filled, albeit the radius of the void limits the cation size. In simple minerals such as gibbsite, the voids have easy access for small cations including Li^+ and Mg^{2+}. The uptake of Li^+ into the octahedral vacancy in gibbsite would result in a charge imbalance; hence Li also takes its accompanying counterion such as Cl^-. Experiments have shown that reaction of LiCl solutions with gibbsite results in appreciable uptake of Li, and large swelling of the clay layers, as significant anions are required to maintain charge balance (e.g., Fogg and O'Hare 1999; Wimpenny et al. 2015). This interlayer expansion is an important quality

Clay Minerals, Table 1 Physical characteristics of clay mineral groups (Data taken from Drever 1988 and Appelo and Postma 2005)

	Kaolin group	Smectite group	Mica group	Chlorite
Structure	T-O (1:1)	T-O-T (2:1)	T-O-T (2:1)	T-O-T-(O) (2:2)
Layer charge	<0.01	0.5–1.2	1.4–2	variable
Unit layer	7A	Ranges depending on interlayer: 14A to 17A	10A	14A
Cation exchange capacity (CEC) meq/100 g	1–10	80–150	10–40	<10

Clay Minerals, Table 2 Examples and formulas of common clay minerals based on mineral group

Group	Mineral	Formula
Kaolin/ serpentine group	Kaolinite	$Al_2Si_2O_5(OH)_4$
	Serpentine	$Mg_3Si_2O_5(OH)_4$
Smectite	Pyrophyllite	$Al_2Si_4O_{10}(OH)_2$
	Talc	$Mg_3Si_4O_{10}(OH)_2$
	Montmorillonite	$(Na,Ca)_{0.33}(Mg,Al)_2(Si_4O_{10})(OH)_2.nH2O$
	Saponite	$Ca_{0.25}(Mg,Fe)_3((AlSi)_4O_{10})(OH)_2.nH2O$
	Hectorite	$Na_{0.3}(Mg,Li)_3(Si_4O_{10})(F,OH)_2$
	Beidellite	$(Na,Ca_{0.5})_{0.3}Al_2((Si,Al)_4O_{10})(OH)_2.nH2O$
Mica	Muscovite	$KAl_2(AlSi_3O_{10})(OH)_2$
	Phlogopite	$KMg_3(AlSi_3O_{10})(OH)_2$
	Paragonite	$NaAl_2(AlSi_3O_{10})(OH)_2$
Chlorite	Clinochlore	$Mg_5Al(AlSi_3O_{10})(OH)_8$
	Chamosite	$(Fe^{2+},Mg,Al,Fe^{3+})_6((Al,Si)_4O_{10})(OH,O)_8$

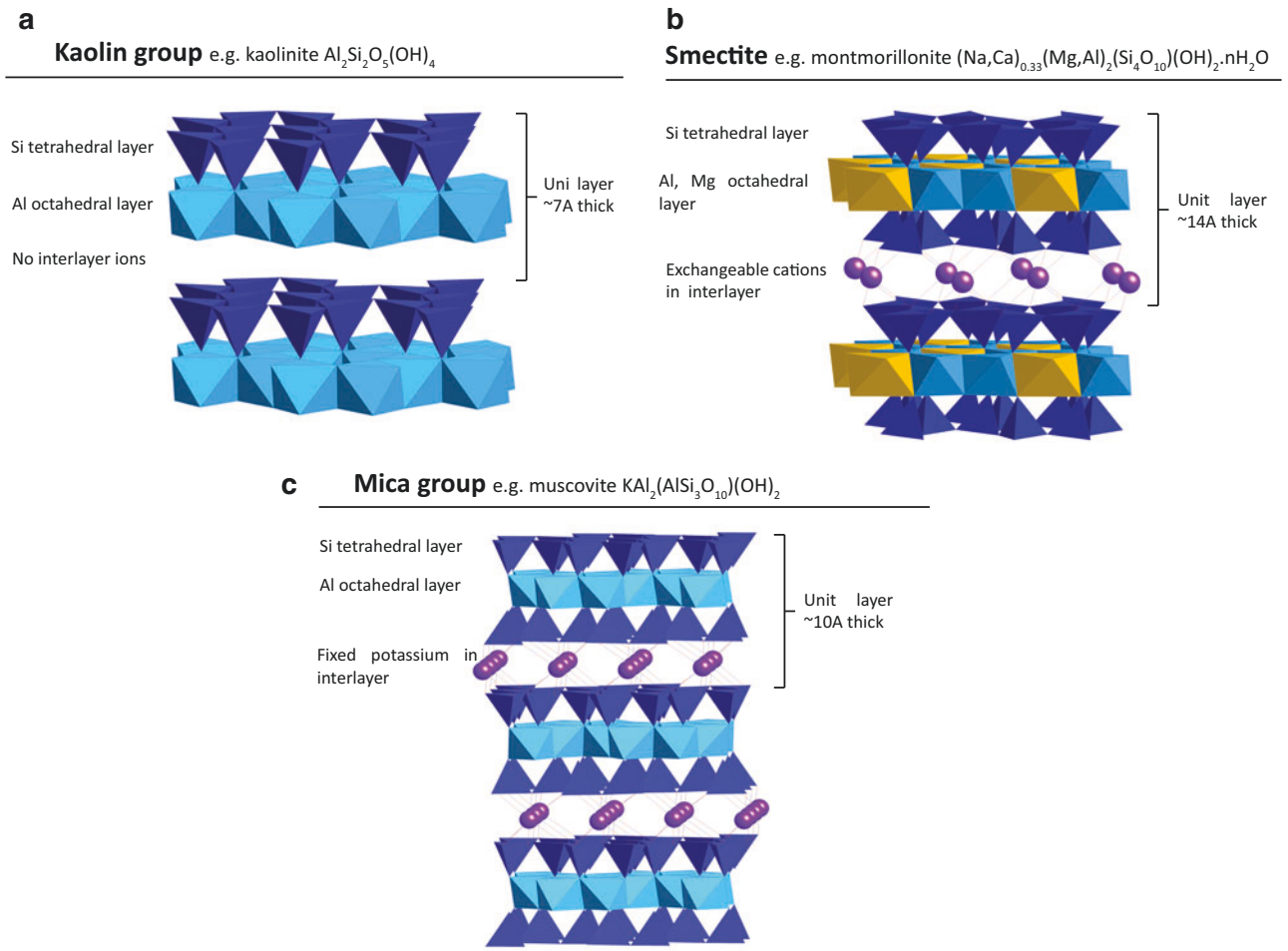

Clay Minerals, Fig. 1 Structure of the three major clay mineral groups: (**a**) kaolin, (**b**) smectite, and (**c**) mica. Figures show the stacking of Si tetrahedra and Al octahedra and characteristic basic spacing

of clay minerals that can have implications not only for the bulk clay chemical composition but also on the chemical composition of the fluid phase in which the clay is reacting (e.g., rivers and seawater).

Kaolin Group

Kaolin group minerals are one of the most common clay minerals during weathering and are particularly prone to formation in warm, humid climates (Dixon 1989). Kaolin minerals are all 1:1 phyllosilicates, with a unit structure comprising a single Si-tetrahedral sheet bonded to a single Al-octahedral sheet (analogous to gibbsite) by sharing oxygen atoms between adjacent Si and Al atoms (Murray 1991; Angove et al. 1997). These 1:1 layers stack together by hydrogen bonding and van der Waals forces. The way that these aluminosilicate layers stack together determines the distinct kaolin group minerals. For example, halloysite differs from kaolinite by having a layer of water molecules between the T-O unit layers. These minor differences can affect the dominant clay form; while kaolinite typically forms plates, halloysite forms characteristic nanotubes (Tan et al. 2015). Isomorphic exchange can occur in kaolin group minerals, but these reactions are not common, and minimal charge deficit is associated with the structure. One of the most common ions to be incorporated into structural sites in kaolinite is iron, although levels are still typically low (less than a Wt %), and it is difficult to tell whether the Fe is actually structurally incorporated into the clay, or is an artifact of a mixed kaolinite-smectite (Dixon 1989). In addition to isomorphic exchange being relatively unimportant, the bonding between the 1:1 layers in kaolin minerals is relatively strong, so that interlayer exchange cannot occur (Angove et al. 1997). The low-layer charge and no interlayer mean that the cation exchange capacity of kaolinite is much lower than expandable clays such as smectites (see later), typically ~1–10 $cmol_c/kg$ (Drever 1988). Any limited sorption capacity of kaolinites is usually caused by broken bonds at the layer edge (Bolland et al. 1976; Ma and Eggleton 1999) and the presence of

pH-dependent functional groups on the clay surface and edge sites (Papelis and Hayes 1996; Strawn et al. 2004; Merkel et al. 2005).

Smectite Group

The smectite group clay minerals are 2:1, or T-O-T, phyllosilicates. As described this means that they have two octahedral sheets bounding a single tetrahedral layer. Other common 2:1 phyllosilicates will be described later on and include micas and chlorite, although there are important structural differences between these minerals and smectite.

Due to the common occurrence of isomorphic substitution into the phyllosilicate structural layers in 2:1 clay minerals, there are a wide range of smectite group clays found in nature. For this reason, we will start with the simplest case, in which the tetrahedral and octahedral sheets are pure. If the octahedral sheet is similar to gibbsite ($Al(OH)_3$), the resulting clay mineral is called pyrophyllite and has the formula $Al_2Si_4O_{10}(OH)_2$. If the octahedral sheet is similar to brucite ($Mg(OH)_2$), the resulting clay mineral is called talc and has the formula $Mg_3Si_4O_{10}(OH)_2$ (Drever 1988). Common smectite group clay minerals and their chemical formula are shown in Table 2. Changes in their chemical composition relative to these end-member compositions result directly from isomorphic exchange, i.e., exchange of trivalent cations for Si^{4+}, divalent cations for Al^{3+}, and/or monovalent cations for Mg^{2+}.

A key property of smectite clay minerals that differentiate them from kaolin and other 2:1 group clay minerals is the relative expandability of the interlayer and the fact that the interlayer can be hydrated. The uptake of exchangeable cations results from the relative charge imbalance caused by isomorphic exchange into structural layers. The most common exchangeable cations in smectite minerals are Mg^{2+}, Ca^{2+}, Fe^{2+}, Na^{+}, and H^{+}, although other cations will also exchange (Odom 1984). Although many smectites contain abundant amounts of Mg^{2+}, the amount of Mg and Ca in the interlayer is usually very similar, and smectite minerals with both Mg and Ca are usually very common. The amount of water that can be incorporated into the smectite will depend on the identity of the interlayer species, for example, where Mg or Ca^{2+} is present, two layers of water molecules can be incorporated and the smectite will expand to ~14A (Drever 1988). In contrast, a smectite in which Na is the dominant cation in the interlayer can expand by up to 10 times its original size. In fact the swelling of Na-rich smectites can cause complete dissociation of individual smectite crystals, resulting in dispersion and the formation of a colloidal-like solution with an increased viscosity. For this reason, Na montmorillonites are in high demand in the oil industry as drilling muds (Murray 1991). Ultimately, the cation exchange capacity (CEC) of a smectite mineral will of course depend on its chemical composition, but is usually in the range of 70–130 meq/100 g (Odom 1984; Murray 1991). Most of this CEC is caused by charge deficiency resulting from structural substitution reactions (Odom 1984).

Vermiculites

Vermiculite is a mineral similar in structure to the smectite group minerals but has a greater charge across the interlayer. As a result, the interlayer is less readily expandable than in smectite minerals, and the amount of cation exchange is lower, although because of the higher charge, the CEC of vermiculite is greater than in most smectites.

Mica Group

Mica group clay minerals are also 2:1 clay mineral similar to smectites. However, the isomorphic substitution in mica group clay minerals typically occurs in the tetrahedral layer, where Si^{4+} is replaced by Al^{3+}. The resulting charge deficit is accounted for by incorporation of K+ into the interlayer. Because the charge deficit is derived from the tetrahedral layers, the K is held very tightly in the interlayer (Krauskopf and Bird 1967) and is generally not exchangeable. Common mica group minerals include muscovite, phlogopite, and biotite (see Table 2). Mica group minerals are also commonly referred to as illite. Most natural illites are actually mixed layers of muscovite-like minerals and smectite-like minerals (Drever 1988). Illites make up the bulk of ancient shales, and illitization reactions are common during late diagenesis of siliciclastic materials (Drever 1988; Milliken 2003).

Chlorite Group

Chlorite consists of a 2:1-layered structure similar to the structure of smectite and illite. However, a major difference in the structure of chlorite is that a structural charge imbalance remains even after uptake of exchangeable cations. In chlorites the negative charge is compensated for by the formation of a brucite-like layer within the interlayer region (Velde and Meunier 2008). This brucite-like layer is bonded to the basal tetrahedral layers by coulomb attraction and can be rich in Mg, Al, or Fe (Bailey 1972). Hence the structure of chlorite is essentially 2:1:1 or 2:2 (Drever 1988). Most chlorites are trioctahedral, containing Mg in both the structural octahedral layer and in the interlayer sheet. However, Fe-rich chlorites also exist and occur commonly in iron-ore deposits. Chlorites form in nature via diagenesis of mafic and ultramafic rocks at low- to medium-grade metamorphic conditions, or from the alteration of volcanic rocks. Chlorites have also been synthesized in the laboratory from hydrothermal alteration of montmorillonite and Al or Mg hydroxides (Slaughter and Milne 2013).

Clay Mineral Formation

Clay minerals ultimately form from the alteration of primary silicate minerals. These primary phases form from the crystallization of magma at high temperature and a range of pressures in the Earth's crust. After crystallization and cooling, these primary minerals may be exposed to surface conditions through uplift and erosion. In the low-temperature and low-pressure environment of the Earth's surface, minerals derived from igneous processes are unstable, with those minerals forming at highest temperature, such as olivine, being the least stable at surface conditions. Clay minerals are either direct or indirect alteration products of these unstable primary phases, forming through incomplete (or incongruent) weathering. The relative insolubility of aluminum compounds such as Al oxide (Appelo and Postma 2005) is a major reason that clay minerals are so ubiquitous throughout the crust.

The type of clay mineral that forms during weathering will be dependent on many factors including the type of primary mineral or rock that is being weathered, the fluid composition, the pH and temperature of that fluid, the water-rock contact time, and the influence of biological agents (Galan and Ferrell 2013). While clay minerals are more stable than primary igneous minerals at the Earth's surface, clay minerals themselves can continue to alter during weathering. With increasing intensity of alteration (i.e., temperature and water-rock contact time), clay minerals will tend to change from containing higher amounts of structural Si and other cations to containing higher concentrations of Al, for example, the transition from montmorillonite to kaolinite to gibbsite (Appelo and Postma 2005). Thus aluminum oxide minerals such as gibbsite are typically a product of the more extreme weathering environments.

Continuing alteration of clay minerals can often be associated with a change in the environment (e.g., solution composition, temperature and runoff, pH) such as that associated with a change in climate or progressive burial. This is most easily observed in weathering profiles such as in the study of laterites, which contain distinct layers with different clay mineralogies, caused by abrupt change in climate and subsurface processes such as a fluctuating water table. The formation processes of clay minerals are diverse, ranging from newly formed clays by direct precipitation from solution to solid-state alteration in which the previous clay mineral structure is retained in the new form (e.g., transformation by ion exchange) or in which structural reorganization takes place (e.g., during diagenesis). This diversity in formation mechanism is intuitive if we consider that clay minerals are found in a wide range of environments within the Earth's crust and subjected to changing chemical and physical conditions. A more detailed consideration of clay mineral formation mechanisms follows:

Direct Precipitation or Neoformation

The classic way to envisage the formation of a new mineral is via direct crystallization from a solution, which can also be termed direct precipitation or neoformation. This mechanism requires that a solution has a pH, temperature, and dissolved solid content that promotes precipitation of a new mineral. Based on knowledge of these parameters, it is possible to calculate how stable a mineral phase is in a solution by calculation of its saturation state. Such calculations can provide information about whether a mineral is more likely to dissolve or precipitate in a solution, i.e., whether it is undersaturated or oversaturated. It is important to realize that simply because a certain mineral is oversaturated in solution, it will not necessarily precipitate. The type of clay mineral that forms via neoformation will be dependent on many factors including precursor mineralogy, climate, drainage, and weathering time (Eberl et al. 1984). For example, a classic study in Hawaii, where the bedrock is all basalt, shows that different clay minerals predominantly form in different microclimates (Eberl et al. 1984 and references within). In this case, smectite formed on the drier part of the island, while gibbsite formed where rainfall was much higher. Thus clay minerals that are comprised of soluble cations such as Mg and Ca will only form where these cations can accumulate, such as in dry climates or regions where drainage is poor. In contrast, clay minerals that comprise mostly insoluble elements such as gibbsite will form where rainfall is high and drainage is good so Al will accumulate (Eberl et al. 1984).

At the extreme high-temperature end of the scale, clay minerals can form directly from magma-derived fluids. These fluids originate from deeper in the crust (e.g., a cooling magma chamber) and interact with crustal rocks, stripping out silica and aluminum and forming clay minerals at temperatures up to 450 °C (Kerr 1955). Hydrothermal alteration will typically cause clay formation on a limited scale, restricted to contact metamorphic zones in which temperature is elevated (>50 °C). The clay minerals that form will be controlled not only by temperature but also on the environment of formation, for example, a hydrothermal vent on the seafloor versus a continental extensional setting such as the Basin and Range in western United States.

Diagenesis and Solid-State Alteration

Solid-state alteration can take place either by ion exchange or by alteration of the structural layers in a clay mineral (Eberl et al. 1984). For example, the interlayer leaching of potassium from the interlayer of an illite will result in vermiculite formation (Wilson 1999); this is a common process in soils where the alteration of micas and chlorite can progress in sequence through vermiculite, smectitic mixed layers, degraded smectite, and finally amorphous compounds such as allophane (Chamley 2013). Such a progression is usually observed as one moves from the base to the top of a soil

profile. Other common solid-state alteration phases include products of igneous rock weathering such as that experienced by basaltic lavas or large-scale granitic intrusions. Typically the type of clay mineral formed will depend on the precursor igneous mineralogy and fluid composition and residence time. For example, plagioclase feldspar is typically replaced by kaolinite (e.g., Nesbitt et al. 1997), particularly in more intense weathering regimes where more mobile cations like Mg, Ca, and Na are removed from the rock. In humid tropical environments, highly altered weathering profiles called laterites develop on crustal rocks, for example, the Deccan traps flood basalts in India. Here clay minerals such as kaolinite replace the primary mineralogy, and as weathering progresses, all primary igneous textures are lost, suggesting that both transformation and neoformation of clay minerals occur.

As clay minerals are buried within the Earth's crust, they undergo transformation induced by changes in the pressure and temperature. Notably these changes in PT conditions will progressively expel water from a clay mineral structure and cause a decrease in porosity. In summarizing diagenetic alteration of clay minerals, authors have typically invoke a number of stages of alteration that will ultimately depend on the type of clay protolith. With progressive burial (i.e., increasing PT conditions), there is initial compaction, loss of interlayer cations and water, and a decrease in porosity (Segonzac 1970; Aoyagi and Kazama 1980), although recirculation of water can still occur and can cause retrograde or reverse weathering reactions to occur. In alkaline environments rich in K and Na, the diagenesis of dioctahedral smectite can result in the formation of mixed layer illite-smectite minerals. This reaction usually proceeds at ~60 °C (Perry and Hower 1970), and while the initial distribution of illite and smectite layers is random but with increasing temperature and pressure and increased illite proportion, the distribution of the illite-smectite layers becomes ordered. The reaction is thought to occur as increasing amounts of Al^{3+} substitute into the Si-tetrahedral layer of smectite. This results in an increasing charge across the interlayer, and interlayer K^{+} becomes dehydrated, i.e., resulting in the formation of illite (or mica). The identity of the clay mineral that forms from diagenetic reaction will depend on the chemical composition of the precursor mineral and fluid phases. For example, the burial of trioctahedral smectite (i.e., Mg^{2+}-rich montmorillonite) usually results in the formation of chlorite minerals (Galan and Ferrell 2013), while the diagenesis of kaolinite can result in transformation to a more ordered form called dickite, although dickite can also form from K feldspar and other Al-rich silicate minerals.

Further burial and compaction results in complete dehydration with the mixed layer smectite-illites converted to illite and chlorite. These reactions are not usually reversible. At even higher metamorphic grade, the chlorite and illite become ordered, and particle sizes increase to above what is typically considered to be clay sized (<2 μm).

Detrital Inheritance

While neoformation and solid-state alteration are the two main mechanisms by which clay minerals form, a third mechanism can account for large-scale clay deposits; this accumulation of clay minerals from disparate sources is often termed detrital inheritance. Inheritance is an important mechanism because of the stability of the clay mineral group at the Earth's surface, meaning reaction rates are slow and clay minerals can survive physical and/or chemical weathering in their original location and transport to a new accumulation zone. An obvious location for detrital inheritance is in soil profiles that have directly formed from weathering of a sedimentary sequence.

An important region of clay mineral inheritance is on the seafloor, where continental sediments are deposited via outflow from rivers and from aerial deposition. Riverine transport is one of the most important mechanisms, and accumulation of continental detritus, including abundant clay minerals, is common at the continental margin. As one would expect, the clay mineralogy of oceanic sediments usually corresponds to the dominant mineralogy and climate of the adjacent continental region (Eberl et al. 1984; Thiry 2000). Thus kaolin minerals are more common in the tropics, while illite and chlorite are more common at high latitudes, possibly due to their production during glacial weathering (Thiry 2000). As one moves further from the continent, the dominant clay mineralogy changes depending on clay settling time, which is related to the ease with which a clay mineral flocculates. Far out from the continental margin on the abyssal plain, the rate of clay mineral sedimentation is incredibly slow (cm per 1000 years). Here the sediment accumulation is comprised of mixed calcareous ooze and detrital clay minerals that are fine-grained Aeolian sediments and volcanic ash.

While all three mechanisms are important in the formation of clay mineral-rich sediments, they are not mutually exclusive processes; often they work in tandem, and it can be difficult to discern one process from another, i.e., at what point does transformation become neoformation? For example, detrital clay minerals often undergo ion exchange processes in the oceans; the exchange of Ca^{2+} in clay minerals for Mg^{2+} in seawater is such an effective process that it has implications for long-term CO2 drawdown, carbon storage, and climate change (Gislason et al. 1996).

Clay Mineral Isotope Geochemistry

Investigating the isotopic fractionation of stable isotope systems is an established technique within geochemistry that can provide a wide range of useful information about the

formation and chemical evolution of clay minerals. The fractionation of stable isotope systems is mass dependent and is also controlled by temperature (Urey 1947) and the bonding environment (Bigleisen and Mayer 1947). The isotopic composition of a clay mineral will depend on the isotopic composition of the precursor mineral and the fluid phase from which the clay forms. It will also be dependent on the temperature of the system (less fractionation at higher T) and whether the clay mineral forms in a system at equilibrium, or through a unidirectional or kinetic process. Furthermore, isotopic compositions can be altered post-formation in environments where the chemical properties of an element might change (e.g., change in redox conditions between Fe^{2+} and Fe^{3+}), or during re-equilibration at higher temperatures. For example, studies of O and H isotopes in clay minerals provide useful information about the conditions of clay formation and subsequent post-formation processes, because many clay minerals tend to retain their initial O and H isotopic compositions unless subjected to diagenetic or metamorphic conditions (Sheppard and Gilg 1996). For example, detrital clay minerals in the oceans often retain their continental H and O isotope signatures (Sheppard and Gilg 1996). The unique layered structure of clay minerals and importance of ion exchange and adsorption mean that careful isotopic analyses of clay minerals can also shed light on recent fluid interactions by isolating and examining the isotopic composition of interlayer ions in minerals such as smectite. Isotopic analyses have shown that interlayer cations and water rapidly exchange with fluid phases, meaning the interlayer reservoir can be isotopically distinct to the composition of the structural sheets (e.g., Savin and Epstein 1970; Wimpenny et al. 2015).

While the stable isotope systems of H, C, N, and O have been well established for many decades, advancing technology means a wide range of stable isotopic systems from Li all the way up to U can now be studied, many of which are influenced by clay mineral formation. The utility of these isotope systems varies, from understanding global weathering processes (e.g., Li, Mg), to tracing nutrient use (e.g., Fe isotopes), to understanding the transport and distribution of potentially toxic heavy metals (e.g., Cr, Cd, Hg). In all cases, to understand the geochemistry and isotopic composition of these elements in waters and sediments from the Earth's crust requires understanding of the way clay minerals influence their mass budget during weathering and, because their uptake and incorporation into clays usually occurs with an isotopic preference, how the formation of phyllosilicates influences their isotopic composition. Through a combination of field studies and experimental work, an increasing understanding of isotopic behavior has been gained detailing the sense and isotopic fractionation factor associated with elemental uptake or sorption into clay minerals.

While stable isotope systems can provide useful information about general clay mineral formation processes, radiogenic isotope systems can potentially provide information about when and from what parent material the clay mineral formed or originated. A problem with utilizing clay minerals as a dating tool is that they have often undergone burial and diagenesis which could influence the meaning of any obtained age (i.e., what event are we dating?). However certain chronometers such as the Ar-Ar and Rb-Sr systems have proved successful in dating clay mineral formation, particularly in the study of illite formation (e.g., Kelley 2002). For example, Clauer et al. (1997) used both Ar-Ar and Rb-Sr dating techniques to assess the timing of diagenetic illite formation in a sandstone reservoir rock from the North Sea.

Regardless of whether age dating results in reliable age determination, radiogenic isotope systems can also provide useful information about clay provenance. This is because different rock types often have different radiogenic isotopic compositions due to differences in age and/or the way elements partition into different minerals. Thus two different potential source terrains for an inherited clay sediment can be distinguished based upon their radiogenic isotopic composition. It is also important to understand the radiogenic isotopic characteristics of clay minerals when interpreting water-rock interactions. For example, the rubidium ion (Rb^+) commonly substitutes for K^+ in micaceous minerals due to similarity in ionic radius and charge. The relatively high concentration of Rb in micas means that their Rb/Sr ratio is also elevated, and because ^{87}Rb decays to ^{87}Sr over time, these minerals can develop highly radiogenic $^{87}Sr/^{86}Sr$ ratios. In glacial rivers where interlayer leaching of biotite is an important process, the Sr isotopic signal delivered to rivers is often far more radiogenic than the bedrock. This has important consequences for the evolution of Sr isotopes in the ocean during the Cenozoic.

Clay Minerals in the Solar System

The search for life outside of own planet has important implications for how we understand our own origin and the origin of life throughout the universe. Though we do not understand exactly how life on Earth started, we know that liquid water is a key prerequisite for life to begin, develop, and ultimately thrive over geological time. Thus the search for life, or past signs that life was once present, hinges on the ability to identify regions that have once known liquid water. As has already been discussed, clay minerals form due to the interaction of primary igneous minerals with water and are the most ubiquitous alteration minerals on Earth. Of the many planets and moons in our solar system, one of the most

promising places to look for the presence of clay minerals is on our neighbor, Mars. This comes from two lines of evidence: orbital observations from probes and satellites and pieces of Martian crust in the meteorite record.

Orbital observations (e.g. Ehlmann et al. 2008, 2011) have identified a diverse range of clay minerals on Mars surface with the most common clay minerals being Fe-Mg smectites and chlorite. The abundance of chlorite suggests the clays formed in closed system environments at temperatures ranging from ambient to hydrothermal (~400 °C). From these observations and stratigraphic relationships upon Mars, some estimates of the relative timing of clay formation have been made, with the most important period of clay mineral formation occurring between 4.1 and 3.1 billion years ago. These observations suggest that earlier in this period (4.1–3.7By), there was widespread hydrothermal alteration in the subsurface of Mars and, due to the presence of sedimentary structures, the presence of liquid water at the surface, if only as a short-lived phenomenon. As time progressed (3.7–3.1By), the formation of clay minerals is hypothesized to have declined, perhaps because heat sources for hydrothermal alteration (e.g., impacts, volcanism) also declined at this time. Younger terrains (<3.1By) are dominated by crystalline materials. These observations are indicative of Mars being water rich early in its history and transitioning to being increasingly arid.

Unfortunately, we cannot study the Martian crust here on Earth because a sample return mission from Mars is, as yet, not possible due to its extreme technical difficulty and prohibitive cost. Further investigation of Mars surface, the presence of clay minerals, and the possibility of discovering life can be addressed in one of two ways: the study of the Martian meteorite record and sending a remote controlled lander onto Mars surface. While a growing number of Martian meteorites have been identified, they are not ideal rocks in which to look for these chemical signatures. They are derived from impact so have been altered both during impact and ejection from Mars and on entry to the Earth's atmosphere. But perhaps more fundamentally, we have no control over where they came from; from remote observations, it is clear that some locations on Mars are more promising as once having known the presence of water.

These problems can be avoided by sending a rover to make remote measurements on Mars surface, with the caveat that instruments on a rover are far less sophisticated than instruments found in laboratories on Earth. In NASA's recent Mars Science Laboratory (MSL) mission, the rover Curiosity was sent to Gale Crater, an area where hydrated clay minerals and sulfates had been identified from orbit (Ehlmann et al. 2008; Ehlmann et al. 2011; Grotzinger et al. 2014). Recently, Curiosity traversed an area of Gale Crater, encountering sandstones and mudstones interpreted to have a fluvial origin (Grotzinger et al. 2015). Detailed analysis of a mudstone layer identified around 20% saponitic smectite, probably formed by aqueous alteration of primary olivine in a lacustrine environment. These initial analyses by Curiosity point to an environment that could conceivably have been habitable to basic life once in Mars history.

C

Clay Mineral Uses

There are a wide range of uses for clay minerals based on their unique mineralogical properties including grain size, surface area, adsorption, color, plasticity, and fire strength (Murray 1991). A brief summary of clay mineral uses is given in the following:

Kaolinites

They are relatively soft (1.5 on Mohs scale) so it is not abrasive and can be used in many industrial applications without causing degradation of machines. They are used in ceramics because they fire to a white color and don't shrink after firing (Murray 2000). The fact that kaolinite is highly dispersible and particles form micron-sized platelets that orient on coated surfaces means they are used to provide a sheened or glossy finish for paper. Calcining kaolinite drives off the hydroxyl groups from the structure. This meta-kaolin has dielectric properties and so has been used as a filler in electric wiring. Kaolinites have a diverse range of applications although their exact use will differ depending on specific properties of the deposit. For example, only kaolinites with the correct color can be used for ceramics. Kaolinites are used as the raw material for the production of fiberglass (Murray 1991) due to the health risks of asbestos.

Smectites

The high-charge, surface area, and cation exchange capacity mean smectites are highly absorbent. When mixed with water, the swelling properties of the clay give the fluid a high viscosity. The largest swelling properties are exhibited by Na montmorillonites. These can expand by up to ten times their original size when immersed in water (Murray 1991). These smectites can yield large volumes of drilling mud. While other smectite minerals such as Ca montmorillonite can be treated to exchange Ca for Na in the interlayer and increase the cation exchange properties and swelling volume, these clays are less useful than naturally occurring Na bentonite. High-swelling clays such as Na bentonites are also commonly used where water barriers are necessary, e.g., in the construction of dams, containment of chemicals in toxic waste dumps, landfill, and nuclear waste disposal sites. Blends of Ca and Na smectites are also typically used as absorbents in animal waste products such as cat litter.

Micas

The most commercially useful micas are muscovite and phlogopite. Both phlogopite and muscovite mica are used as electrical insulators. Dry ground mica has a wide variety of uses from dry wall filler, to an additive to paint, to a reinforcement material in plastics. Ground mica is also used in drilling mud for oil and gas wells where it prevents loss of circulation by filling cracks and reducing porosity in the well. Wet ground mica is used in pearlescent paints and the cosmetic industry where it is incorporated into a range of products from lipstick and nail polish to moisturizing lotion.

Mixtures of shale and chlorite are commonly used in construction, particularly in the production of bricks and cement (Virta 2013, USGS).

Summary

Clay minerals are ubiquitous in the weathering environment. Their diversity in chemical composition and unique physical and chemical properties stems from their layered structure and the ability to take up exchangeable ions from solution. Because clay minerals form from alteration of primary rocks and minerals near the surface of the Earth, they have a direct influence over the chemical evolution of the crust and provide a critical control over the chemical and isotopic composition of river and groundwaters that ultimately feed the oceans. For this reason, characterizing how elements and isotopic systems behave during incorporation into clay minerals will ultimately help us understand large-scale processes such as the impact of climate change, or tectonic shifts on past ocean chemistry. The association between clay minerals and water means that the presence of clay minerals can also guide our exploration of the solar system and the search for life on other worlds. Finally, understanding the physical and chemical properties of clay minerals has practical benefits to society; clay minerals are used widely in industry from drilling mud in oil field exploration to building supplies and plastics to uses around our homes such as in paints and coatings on paper. The utility of clay minerals stems from their unique physical and chemical properties; furthering our understanding of these minerals will both enhance future scientific studies and have important industrial implications.

Cross-References

- ▶ Chemical Weathering
- ▶ Clay Membranes
- ▶ Diagenesis
- ▶ Fluid–Rock Interaction
- ▶ Silicate Minerals

Acknowledgments Prepared by LLNL under Contract DE-AC52-07NA27344.

References

Angove MJ, Johnson BB, Wells JD (1997) Adsorption of cadmium (II) on kaolinite. Colloids Surf A Physicochem Eng Asp 126(2): 137–147

Aoyagi K, Kazama T (1980) Transformational changes of clay minerals, zeolites and silica minerals during diagenesis. Sedimentology 27(2):179–188

Appelo CAJ, Postma D (2005) Geochemistry, groundwater and pollution. CRC Press, Leiden

Bailey SW (1972) Determination of chlorite compositions by X-ray spacings and intensities. Clay Clay Miner 20(6):381–388

Bigeleisen J, Mayer MG (1947) Calculation of equilibrium constants for isotopic exchange reactions. J Chem Phys 15(5):261–267

Bolland MDA, Posner AM, Quirk JP (1976) Surface charge on kaolinites in aqueous suspension. Soil Res 14(2):197–216

Chamley H (2013) Clay sedimentology. Springer Science & Business Media, Berlin

Clauer N, Srodon J, Francu J, Sucha V (1997) K-Ar dating of illite fundamental particles separated from illite-smectite. Clay Miner 32(2):181–196

Dixon JB (1989) Kaolin and serpentine group minerals. In: Minerals in soil environments, SSSA Book series, vol 1. SSSA, Madison. 2:467–526

Drever JI (1988) The geochemistry of natural waters, vol 437. Prentice Hall, Englewood Cliffs

Eberl DD, Farmer VC, Barrer RM (1984) Clay mineral formation and transformation in rocks and soils [and discussion]. Philos Trans R Soc Lond A 311(1517):241–257

Ehlmann BL, Mustard JF, Fassett CI, Schon SC, Head JW III, Des Marais DJ, . . . Murchie SL (2008) Clay minerals in delta deposits and organic preservation potential on Mars. Nat Geosci, 1(6): 355–358

Ehlmann BL, Mustard JF, Murchie SL, Bibring JP, Meunier A, Fraeman AA, Langevin Y (2011) Subsurface water and clay mineral formation during the early history of Mars. Nature 479(7371):53–60

Fogg AM, O'Hare D (1999) Study of the intercalation of lithium salt in gibbsite using time-resolved in situ X-ray diffraction. Chem Mater 11(7):1771–1775

Galan E, Ferrell RE (2013) Genesis of clay minerals. In: Handbook of clay science, vol 5. Elsevier, Amsterdam, p 83

Gislason SR, Arnorsson S, Armannsson H (1996) Chemical weathering of basalt in Southwest Iceland; effects of runoff, age of rocks and vegetative/glacial cover. Am J Sci 296(8):837–907

Grotzinger JP, Sumner DY, Kah LC, Stack K, Gupta S, Edgar L, . . . Milliken R (2014) A habitable fluvio-lacustrine environment at Yellowknife Bay, Gale Crater, Mars. Science 343(6169): 1242777

Grotzinger JP, Gupta S, Malin MC, Rubin DM, Schieber J, Siebach K, . . . Calef F (2015) Deposition, exhumation, and paleoclimate of an ancient lake deposit, Gale crater, Mars. Science 350(6257): aac7575

Kelley S (2002) K-Ar and Ar-Ar dating. Rev Mineral Geochem 47(1):785–818

Kerr PF (1955) Hydrothermal alteration and weathering. Geol Soc Am Spec Pap 62:525–546

Krauskopf KB, Bird DK (1967) Introduction to geochemistry, vol 721. McGraw-Hill, New York

Ma C, Eggleton RA (1999) Cation exchange capacity of kaolinite. Clay Clay Miner 47(2):174–180

Merkel BJ, Planer-Friedrich B, Nordstrom D (2005) Groundwater geochemistry. In: A practical guide to Modeling of natural and contaminated aquatic systems, vol 2. Springer, Berlin
Mermut AR, Cano AF (2001) Baseline studies of the clay minerals society source clays: chemical analyses of major elements. Clay Clay Miner 49(5):381–386
Milliken KL (2003) Late diagenesis and mass transfer in sandstone shale sequences. In: Treatise on geochemistry, vol 7. Elsevier, Amsterdam, pp 159–190
Murray HH (1991) Overview – clay mineral applications. Appl Clay Sci 5(5):379–395
Murray HH (2000) Traditional and new applications for kaolin, smectite, and palygorskite: a general overview. Appl Clay Sci 17(5): 207–221
Nesbitt HW, Fedo CM, Young GM (1997) Quartz and feldspar stability, steady and non-steady-state weathering, and petrogenesis of siliciclastic sands and muds. J Geol 105(2):173–192
Odom IE (1984) Smectite clay minerals: properties and uses. Philos Trans R Soc Lond A 311(1517):391–409
Papelis C, Hayes KF (1996) Distinguishing between interlayer and external sorption sites of clay minerals using X-ray absorption spectroscopy. Colloids Surf A Physicochem Eng Asp 107:89–96
Peacock CL, Sherman DM (2005) Surface complexation model for multisite adsorption of copper (II) onto kaolinite. Geochim Cosmochim Acta 69(15):3733–3745
Perry E, Hower J (1970) Burial diagenesis in Gulf Coast pelitic sediments. Clay Clay Miner 18(3):165–177
Savin SM, Epstein S (1970) The oxygen and hydrogen isotope geochemistry of clay minerals. Geochim Cosmochim Acta 34(1):25–42
Segonzac GD (1970) The transformation of clay minerals during diagenesis and low-grade metamorphism: a review. Sedimentology 15(3–4):281–346
Sheppard SMF, Gilg HA (1996) Stable isotope geochemistry of clay minerals. Clay Miner 31(1):1–24
Singer A (1980) The paleoclimatic interpretation of clay minerals in soils and weathering profiles. Earth Sci Rev 15(4):303–326
Slaughter M, Milne I (2013) The formation of chlorite-like structures from montmorillonite. Clay Clay Miner 1960:114–124
Sposito G, Skipper NT, Sutton R, Park SH, Soper AK, Greathouse JA (1999) Surface geochemistry of the clay minerals. Proc Natl Acad Sci 96(7):3358–3364
Strawn DG, Sparks DL (1999) The use of XAFS to distinguish between inner-and outer-sphere lead adsorption complexes on montmorillonite. J Colloid Interface Sci 216(2):257–269
Strawn DG, Palmer NE, Furnare LJ, Goodell C, Amonette JE, Kukkadapu RK (2004) Copper sorption mechanisms on smectites. Clay Clay Miner 52(3):321–333
Tan D, Yuan P, Annabi-Bergaya F, Dong F, Liu D, He H (2015) A comparative study of tubular halloysite and platy kaolinite as carriers for the loading and release of the herbicide amitrole. Appl Clay Sci 114:190–196
Thiry M (2000) Palaeoclimatic interpretation of clay minerals in marine deposits: an outlook from the continental origin. Earth Sci Rev 49(1):201–221
Urey HC (1947) The thermodynamic properties of isotopic substances. J Chem Soc (Resumed). 562–581
Velde BB, Meunier A (2008) The origin of clay minerals in soils and weathered rocks: with 23 tables. Springer Science & Business Media, Berlin
Virta RL (2013) Common clay and shale. Min Eng 2013(July):36–37
Wilson MJ (1999) The origin and formation of clay minerals in soils: past, present and future perspectives. Clay Miner 34(1):7
Wimpenny J, Colla CA, Yu P, Yin QZ, Rustad JR, Casey WH (2015) Lithium isotope fractionation during uptake by gibbsite. Geochim Cosmochim Acta 168:133–150

Coal

Stephen F. Greb[1], Cortland F. Eble[1] and James C. Hower[2]
[1]Kentucky Geological Survey, University of Kentucky, Lexington, KY, USA
[2]Center for Applied Energy Research, University of Kentucky, Lexington, KY, USA

Definition

Coal is a naturally occurring sedimentary carbonaceous rock composed of at least 50% organic matter by weight, and 70% carbonaceous material by volume, mostly from the diagenesis (chemical and physical alteration) of plant material in buried peat (Schopf 1956, 1966; Alpern and DeSousa 2002). Coal is a solid hydrocarbon. It is a rock that can burn. Coal does not have a distinct chemical formula, although it is dominated by complexly bound C, H, O, N, and S. Coal has an organic matrix but also contains inorganic (mineral) and fluid components. The chemical variability in coal is a result of (1) variability in the soils and weathered surfaces upon which the peat accumulated, (2) different types of plants and plant remains in peat, different types of peat mires, (3) the depositional history of the peat mire, (4) the syndepositional environments lateral to the peat which contributed inorganic sediment to the mire, (5) burial environments and history, (6) the long diagenetic history in which the peat was altered to coal, and (7) the exhumation history in which the coal was brought back to the surface or near-surface.

Coal Origins

Coal is physically, chemically, and thermally altered peat. *Peat* is partially decayed plant material, mineral matter, and water, which accumulates in anoxic swamps or mires (peat-forming wetlands). Peats generally have organic contents greater than 75%, inorganic mineral contents less than 25%, and water contents of 75–90% (Schopf 1966; Jarrett 1983; Clymo 1987; Alpern and deSousa 2002). Because they represent buried organic material, peats are natural carbon sinks and are an important component of the global carbon cycle (Gorham 1991; Yu et al. 2011). The plant material in peat varies, but in general, consists of organic compounds and plant tissues (wood, cortical tissues, roots, leaf cuticles, spores, pollens, etc.) which are composed of carbohydrates (mainly cellulose), lignins, proteins, lipids, waxes, and resins. Summaries of the chemistry of these tissues can be found in Bouška (1981), Given (1984), de Leeuw and Largeau (1993), and Krevelen (1993). The plants also contain inorganic

constituents, which are the precursors of some of the mineral matter in coal (see "Mineral Content").

The breakdown of plant parts through microbial and chemical activity while the peat is accumulating is termed *peatification.* Peatification involves oxidation, fermentation, gelification, methanogenesis, and humification, among other processes. Anaerobic transformation of carbon occurs through fermentation, which results in formation of low-molecular weight, acids, alcohols, and carbon dioxide (CO_2). In methanogenesis, bacteria convert cellulose (and other carbohydrates) into biogenic methane (CH_4). *Humification* is the physical and biochemical breakdown of plant tissues into humic substances (Stach et al. 1982; Krevelen 1993; Mitsch and Gosselink 2000). Most of the cellulose in plant debris is broken down by fungi and bacteria during peatification and only small amounts survive into low-rank coalification. Lignins, sporopollenins, cutans, suberans (periderm), resins, and algaenans are also degraded but can survive peatification and humification into coalification as different types of macerals (Stach et al. 1982; Given 1984; Teichmüller 1989; de Leeuw and Largeau 1993; Krevelen 1993; Hatcher and Clifford 1997). Biomarkers from organic compounds of these plant tissues have also been detected from organic geochemistry of the hydrocarbon fractions of the soluble organic matter of coals (Hatcher et al. 1982; Tissot and Welte 1984; Bustin et al. 1985).

Peat Mires

Not all peats form coal. Those peats which have a chance to become coal beds generally must be widespread, thick, and accumulate for thousands of years (or more). For thick peats to accumulate, plant production and plant-part accumulation must be greater than the rate of organic decay. Organic decay is slowed in most peats by maintaining waterlogged, anaerobic, acidic conditions. Maintenance of high water tables requires precipitation or groundwater contributions in excess of evaporation. Hence, climate plays a significant role in peat accumulation. Additionally, for thick peats to accumulate they must be protected from significant clastic sediment input or oxygenation (Moore and Shearer 2003; Clymo 1987; Stach et al. 1982).

Peat accumulates in a variety of different types of wetlands including bogs, fens, mires, and swamps. Two broad divisions based on chemistry and hydrology are (1) rheotrophic (minerotrophic) and (2) ombrotrophic (Mitsch and Gosselink 2000; Moore 1989; Clymo 1987). Rheotrophic peat-forming wetlands are groundwater sourced and tend to fill depressions in the landscape, while ombrotrophic mires are rainwater sourced and build up above the landscape (Fig. 1). These basic distinctions have profound influence on the resulting precursor peat chemistry, because topography-filling rheotrophic peats can be intermittently inundated by flood waters containing dissolved and suspended inorganic

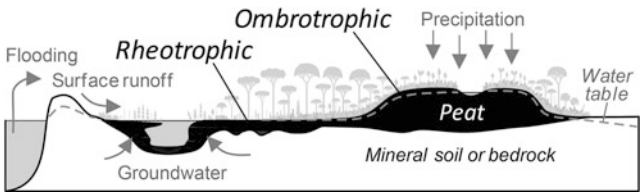

Coal, Fig. 1 Two broad subdivisions of peat, the precursors of coal

sediment, the precursors of mineral matter and much of the ash in coals. In contrast, ombrotrophic peats which build up above the level of bounding lakes or rivers are more sheltered from water-born sediment influx and receive only wind-born detrital minerals. Such peats will produce coals with low ash yields (Eble and Grady 1993; Neuzil et al. 1993; Staub 1991; Cecil et al. 1985). Different types of peat may grade into each other and succeed each other through time.

Peat Accumulation and Preservation

In order for thick peats to accumulate and be preserved, space must be generated for preservation. Relative to the accumulation and burial of peat, accommodation space can be generated (1) below the peat through compaction of underlying sediments or tectonic subsidence; (2) within the peat through biochemical processes resulting in auto-compaction; and (3) above the peat through base-level or sea-level rise. Optimal conditions for thick peat accumulation are when the rates of peat accumulation keep pace with the net rate of subsidence, sea-level change, and sedimentation (McCabe 1984; Butler et al. 1988; Diessel 1992; Bohacs and Suter 1997; Holz et al. 2002).

Peats Through Geologic Time

Time is another variable relative to coal. The oldest mires, and therefore oldest true peats, were in the Late Devonian, following the evolution of vascular plants on land. Although coals occur in rock strata from the Devonian Period through the Neogene Period, they are more common at certain times than others, because of changing global climatic and tectonic conditions. Also, plants have evolved through time, resulting in changes to the vegetative components of peats and the coals they form (Collinson and Scott 1987; Cross and Phillips 1990; Greb et al. 2006a). Different plants have different rates of decomposition and provide different chemical constituents (lignins, resins, etc.) to peat. Most plants contain inorganic elements which contribute to mineral matter in the peat and ultimately the coal formed from the peat. For example, Permian-age coals from southern continents (Australia, India) have higher inertinite (see "Coal Macerals") contents than Carboniferous-age coals from Europe and North America, because the precursor peats had different flora accumulating under different climates (Hunt and Smyth 1989; Taylor et al. 1989).

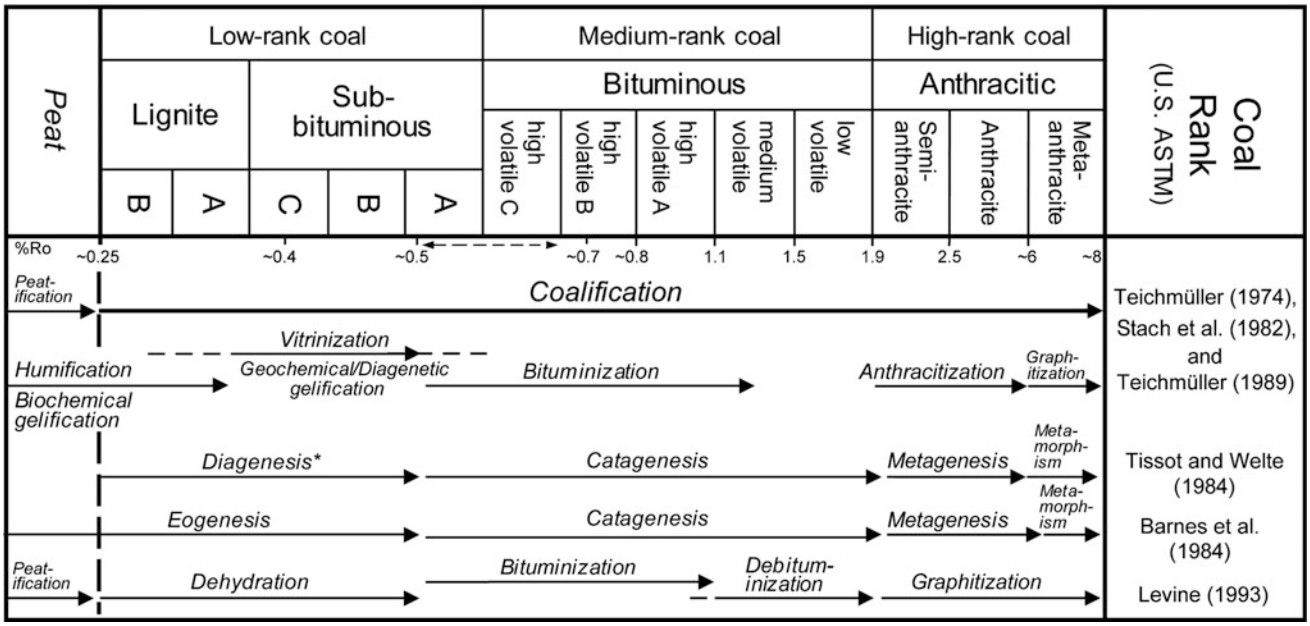

Coal, Fig. 2 Diagram showing stages of coalification cited in different reports relative to their approximate US coal rank (Note the term *diagenesis* was used by Tissot and Welte (1984) for the initial stages of coalification but in many reports it is used synonymously with the entire coalification process. %Ro vitrinite reflectance in oil. %Ro data from Teichmüller and Teichmüller (1982). In the US classification system, vitrinite reflectance values overlap between subbituminous A and high volatile bituminous C ranks, which is shown here as a *dashed line*)

Coalification

Coalification is the process by which peat is transformed into coal. The increasing alteration of coal is classified by rank (see next section). Coalification involves the breakdown of the original plant components in peat and the preservation of other more resistant plant components followed by reorganization of the biopolymers and geopolymers that survive (Hatcher and Clifford 1997). Historically, several processes were used to describe the transformation of peat and its constituent plant parts into coal and its components (Stach et al. 1982; Teichmüller 1974, 1989 in Fig. 2). More recent explanations have subdivided coalification into a series of stages relative to thermal maturation of source rocks (Tissot and Welte 1984; Barnes et al. 1984; Levine 1993; in Fig. 2). These stages approximate different processes which dominate coalification at different temperatures, although in some cases, they are overlapping. These processes are discussed further under *coal rank.*

Not included in Fig. 2, are alterations to coal chemistry which may accompany igneous intrusions, hydrothermal fluids, and natural exhumation of deeply buried coal to the surface where it can be introduced (again) to near-surface and surface processes. A *telogenesis* stage is sometimes added to the coalification tract to include these processes (Barnes et al. 1984; Bustin et al. 1985). The diagenesis of coal is irreversible. Once a coal reaches its highest rank, it remains at that rank; however, minerals and elements within the coal may be oxygenated or react with minerals in groundwater during exhumation and telogenesis.

Coal Classification: Rank, Grade, and Types

Different countries and, in some cases, industries classify coal in different ways. Three general means of classification are based around parameters of (1) rank, (2) grade or quality, and (3) type or macroscopic and microscopic characterization.

Coal Rank

Coal rank is the terminology used to classify coal based on its relative coalification. In general, increasing coalification results in the loss of moisture and compounds rich in hydrogen and oxygen and the relative enrichment of carbon. Krevelen (1993) provides a good summary of different global classification schemes and the parameters upon which they are based. In the US classification scheme, calorific value is used to subdivide low-rank through medium-rank coals, and volatile matter or fixed carbon content is used for higher medium rank and high-rank coals (Fig. 3, ASTM 2014). Calorific value is a measure of the amount of energy produced from coal when it is combusted. Volatile matter is a measure of the nonwater gases formed from a coal sample during heating under oxygen-free conditions. Fixed carbon is a calculated value of the amount of nonvolatile carbon remaining

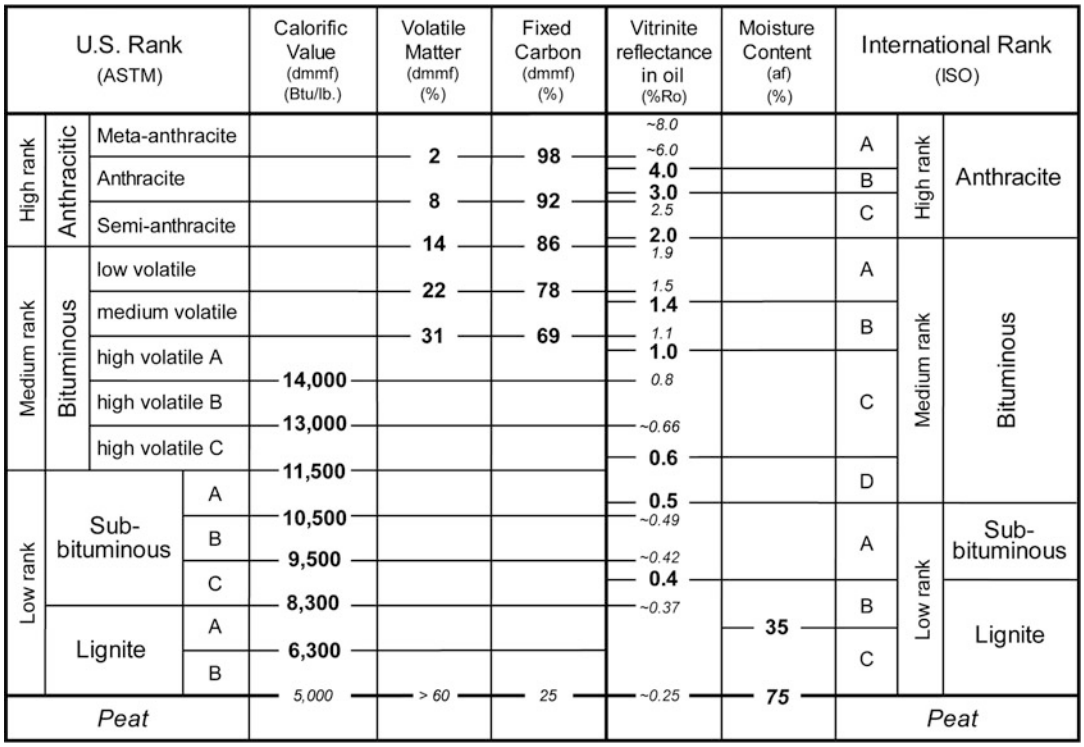

Coal, Fig. 3 Comparison of US and international rank subdivisions of coal. Critical values of defining parameters (calorific value, volatile matter, fixed carbon) for the US system (ASTM 2014) and defining parameters (vitrinite reflectance, moisture content) for the international system (ISO 2005) are shown in *bold*. Typical vitrinite reflectance values for US coal ranks and for the peat-lignite subdivision also shown for comparison (Data from Teichmüller and Teichmüller 1982). In the US classification system, vitrinite reflectance values overlap between subbituminous A and high volatile bituminous C ranks (Data from ASTM 2014; Schweinfurth and Finkelman 2003; ISO 2005; Diessel 1992; Given 1984; Stach et al. 1982). *dmmf* dry, mineral-matter-free basis, *af* ash-free basis)

in a coal sample after combustion of the sample. In the international system, moisture content is used to subdivide low-rank coals, while the reflective properties of vitrinite (a coal maceral discussed in a following section) are used to subdivide medium- and high-rank coals (Fig. 3, ISO 2005).

Ash yield and the percentage of vitrinite reflectance are used for further subdivisions and modifiers. Vitrinite reflectance can be used to compare the two classifications (Fig. 3).

Lignites are the lowest rank of coals. They are brown in color and have an earthy, crumbly texture. The boundary between what is termed peat and what is termed lignite is transitional, but having 75% or less moisture content (weight %) is a common parameter for lignite (UNECE 1998; Alpern and DeSousa 2002; ISO 2005). The dominant processes during the lignite stage of coalification are physical compaction, dewatering (dehydration stage in Fig. 2), and biogeochemical gelification (Fig. 2). Moisture content decreases dramatically from peat to lignite and subbituminous ranks as the coal is compacted by increasing burial. Additional moisture is lost through the loss of methoxyl ($–OCH_3$), hydroxyl (–OH), carboxyl (COOH–), and carbonyl (C=O) functional groups. Compaction from moisture loss is also associated with increasing hardness and development of fracture or joint sets in the coal called cleats (Taylor et al. 1998; Mukhopadhyay and Hatcher 1993; Krevelen 1993; Levine 1993; Teichmüller 1989; Given 1984; Hatcher et al. 1982; Stach et al. 1982). The carbon structure of lignites is dominated by catechol-like carbon rings (Hatcher and Clifford 1997). Catechols have two hydroxyl groups linked to an aromatic carbon (benzene-like) ring.

Subbituminous coals are the second division of low-rank coals (Figs. 2 and 3). In appearance and physical properties they are transitional between lignites and bituminous coals. Subbituminous C coals in the US rank system are brown and earthy like lignites, whereas subbituminous A coals are gray to black and shiny like bituminous coals. During coalification of subbituminous coals, moisture loss continues, but biochemical gelification is replaced by geochemical gelification, also termed vitrinization (Fig. 2). Vitrinization involves homogenization, compression, decarboxylation (loss of –COOH), and dewatering (dehydration) of low-rank huminite macerals to form vitrinite macerals (Mukhopadhyay and Hatcher 1993; Krevelen 1993; Teichmüller 1989; Given 1984; Stach et al. 1982; Schopf 1948). Continued loss of oxygen-bearing functional groups transforms the carbon structure of subbituminous coals from catechol-like structures

to phenols and alkylated phenols (Hatcher and Clifford 1997). Phenols have one hydroxyl group linked to a carbon ring.

In the transition from subbituminous B to A and bituminous C rank (US rank system), the color of coal changes, from brown to black. This color change is caused by chemical (diagenetic) gelification of humic substances and marks the beginning of the bituminization or catagenesis stage of coalification (Fig. 2). Bituminization involves the generation and entrapment of hydrocarbons from thermal processes, depolymerization of the coal matrix, and increased hydrogen bonding (Teichmüller 1974, 1989; Stach et al. 1982; Bustin et al. 1985; Levine 1993).

Bituminous coals are black, shiny, and generally hard. Bituminous coals begin with abundant volatile matter (high volatile bituminous coals) but with increased rank, volatile matter is lost (medium volatile and low volatile bituminous coals). In the high volatile bituminous rank, bituminization continues and transforms the molecular phase of the coal from a water-based to bitumen-based system (Teichmüller 1989; Levine 1993). The high volatile bituminous rank is approximately equivalent to the oil-forming window of hydrocarbon generation in source rocks (Teichmüller 1974, 1989; Hunt 1979; Levine 1993; Mukhopadhyay and Hatcher 1993). Coalification from the uppermost high volatile A through low volatile ranks is dominated by thermal degradation and repolymerization (cracking) of the molecular components of the coal and expulsion of low-molecular weight hydrocarbons, especially thermogenic methane. This is the thermogenic gas window in coals (Teichmüller 1974, 1989; Tissot and Welte 1984; Barnes et al. 1984; Bustin et al. 1985; Levine 1993; Mukhopadhyay and Hatcher 1993). Thermogenic gas is generated at burial temperatures of 150–220 °C (Hood et al. 1975; Quigley and Mackenzie 1988; Stolper et al. 2014).

At the bituminous stage of coalification, aromaticity increases through the condensation of phenols to heterocyclic aromatic compounds and benzene-like structures (Hatcher and Clifford 1997).

High volatile bituminous coals (high volatile B and C) are classified using gross calorific value in the US system. Calorific value, however, does not systematically change above the high volatile A bituminous rank, so other parameters are used to classify higher rank coals. Medium volatile and low volatile bituminous ranks in the US system are defined based on volatile matter or fixed carbon (Fig. 3, ASTM 2014). The international system uses vitrinite reflectance to subdivide bituminous coals (Fig. 3, ISO 2005).

Anthracitic coals are high rank coals (Figs. 2 and 3). They are shiny (glassy) and break with a conchoidal fracture. The anthracitic rank is characterized by a sharp decrease in hydrogen content and the H/C ratio. From the semianthracite to anthracite rank, coalification involves condensation of small aromatic ring to larger ordered structures (Stach et al. 1982; Krevelen 1993; Levine 1993). Most coals do not reach anthracitic rank, which requires high heat, generally considered to be greater than 200–250 °C (Bostick 1979; Hunt 1979; Price 1983), from very deep burial, tectonic metamorphism, or contact metamorphism. It is commonly thought that further heating would transform meta-anthracite coal to graphite, a crystalline form of carbon. However, the activation energy for the formation of graphite may be too high to be formed in nature by heating alone, and significant strain energy appears to be required to produce natural graphite from anthracitic coals (Wilks et al. 1993; Bustin et al. 1995; Bustin 1999).

Heat related to burial depth and geothermal fluids is considered the leading cause for coal rank changes (Teichmüller 1989; Daniels et al. 1990; Hower and Gayer 2002; Ruppert et al. 2010). The maximum heat achieved and the duration of that heating event are important factors in maturation and rank changes (Lopatin 1971; Bostick 1979; Teichmüller 1989).

Coal Grade

Coal grade is generally an economic or technological classification reflecting the relative quality of a coal for a particular use. For example, the grade of coals used to generate steam in electric power utilities (called *steam coals*) usually is a reference to a coal's ability to combust with minimal leftover material and minimal emitted pollutants, based on government regulation. Likewise, coal used to produce steel, referred to as metallurgical coal, or *met-coal*, has very specific grade requirements. The coal must be very low in ash (generally $<10\%$) and sulfur ($<1\%$), have volatile matter contents between about 20% and 30%, and have a favorable balance of volatile and inert components. Element concentrations are important as well, as certain elements (e.g., phosphorous) are deleterious (e.g., Zimmerman 1979; Stach et al. 1982). In many cases, different coals are blended to achieve the grade and quality needed for a specific use.

Coal Types

The term "type" relative to coal description and classification unfortunately has many different uses (e.g., O'Keefe et al. 2013), but in coal science, type refers to the general appearance of a coal, which is based on the manner in which the coal (or parts of the coal) was deposited. Shearer and Moore (1999) provide a brief summary of maceral-based and botanical-based type classifications. Stach et al.'s (1982) classification (based in part on Stopes 1919; Schopf 1960) has two types: humic and sapropelic. *Humic* coals are banded coals and are most abundant. The humic type is divided into four lithotypes (vitrain, clarain, durain, and fusain) based on appearance (Table 1). A single humic coal bed may contain all four lithotypes. *Sapropelic* coals are nonbanded coals that form in standing water (ponds, lakes) within peatlands. Sapropelic coals are subdivided into cannel and boghead coals, based on whether the dominant organic material is pollen and spores (cannel), or algae (boghead) (Table 1).

Coal, Table 1 Coal types and their dominant microlithotypes and maceral content. Many different types of macerals can be found in microlithotypes, and many microlithotypes can be found in lithotypes

Coal type	Lithotype (macroscopic)	Appearance	Dominant microscopic components	
			Microlithotype	Macerals
Humic (banded)	Vitrain	Bright, black, shiny and brittle bands, usually with fissures. Tends to break into small cubes	Vitrite	Vitrinite/huminite
	Clarain	Semi-bright (between vitrain and clarain), black, and very finely (mm-scale) interlayered bands of vitrain, durain, and sometimes fusain	Clarite, clarodurite	Vitrinite/ huminite, inertinite
	Durain	Dull, black to gray-black bands with rough surface. Bands have less fissures than vitrain. Tends to break into lumps	Durite, durolaclarite	Inertinite, vitrinite/huminite
	Fusain	Silky lustre, black to gray-black, fibrous bands. Soft and friable, sometimes like charcoal	Inertite, vitrinertite	Inertinite, vitrinite/huminite
Sapropelic (nonbanded)	Cannel	Dull to greasy lustre, black, very hard nonbanded coal. Breaks with conchoidal fracture	Liptite	Sporinite (a liptinite group maceral)
	Boghead	Similar to cannel but brownish	Liptite	Alginite (a liptinite group maceral)

Data from Stach et al. (1982)

Sapropelic coals are far less common than humic coals and may occur as layers or benches, within an otherwise humic coal. Further subdivisions of sapropelic coals are shown in Hutton and Hower (1999).

Relative to geochemistry, different coal types begin with different weight percentages of carbon (C), hydrogen (H), and oxygen (O). For example, humic coals are initially rich in oxygen and poor in hydrogen, whereas sapropelic boghead coals are rich in hydrogen and poor in oxygen. Ratios of H/C to O/C change along different paths for sapropelic and humic coals through medium volatile bituminous rank (Krevelen 1952, 1993; Tissot and Welte 1984; Levine 1993).

Different countries and industries may have their own "type" classification and in some cases, existing classifications are added, or subdivided further, based on local or regional needs. For example, Hagemann and Hollerbach (1980) subdivided German lignite classes into four lithotypes based on texture and the ratio between ground mass and identifiable plant remains, and varieties of lithotypes based on color and hue, evidence of gelification, the presence of organic inclusions, and surface texture.

Coal Microlithotypes

Each coal type is composed of microlithotypes (Table 1). *Microlithotypes* are microscopic associations of macerals (see next section) with a minimum band width of 50 microns (ICCP 1963). Microlithotypes can be mono-, bi-, or trimaceralic depending whether they contain one, two, or three of the maceral groups. A fourth microlithotype group, termed carbominerite, can also be identified for microlithotypes which contain more than 25% mineral matter. Humic coal lithotypes commonly consist of vitrite, clarite, vitrinertite, duroclarite, or inertite microlithotypes. Sapropelic coal lithotypes tend to consist of liptite, vitrinertoliptite, and durite microlithotypes (ICCP 1963; Stach et al. 1982; O'Keefe et al. 2013). End-member microlithotypes (vitrite, liptite, and inertite) represent coal that is dominantly (>95%) composed of vitrinite, liptinite, and inertinite, respectively. Coal with varying proportions of different macerals is classified accordingly to their composition. For example, the bimacerite clarite is composed of >95% vitrinite and liptinite, while durite is composed of >95% inertinite and liptinite.

The chemistry of micolithotypes can influence the physical behavior of coals (e.g., Suárez-Ruiz and Crelling 2008). For example, the relative composition of inertinites from microlithotypes can be used as an indicator of coke strength in coking coals (Brown et al. 1964). It also influences the ability to grind (Hower et al. 1987; Moore and Shearer 1999) and break (Esterle et al. 2002), which influence coal processing for electrical and commercial uses.

Coal Macerals

Macerals are microscopic components of coal that are distinguished and classified based on petrographic properties, observed in reflected light on polished surfaces. They are the building blocks of microlithotypes. Macerals represent the altered remains and byproducts of the original plant material and are analogous to the sediment grains and cements that compose a clastic sedimentary rock. The current maceral classification and the plant parts from which they originate are shown in Fig. 4.

Low-rank Macerals			Higher-rank Macerals			Origin
Group	Subgroup	Maceral	Group	Subgroup	Maceral	
Huminite	Humotelinite	Texinite →	Vitrinite	Telovitrinite	Telinite	Plant cell walls (with visible structure)
		Ulminite →			Collotelinite	Plant cell walls (gelified, structureless)
	Humotelinite	Attrinite →		Detrovitrinite	Vitrodetrinite	Small particles of attritus (huminitic particles)
		Densinite →			Collodetrinite	Mottled groundmass (originally attritus)
	Humocollinite	Corpohuminite →		Gelovitrinite	Corpogelinite	Primary and secondary cell infillings from humic gels
		Gelinite			Gelinite	Crack infillings of amorphous humic matter
Liptinite		Sporinite			Sporinite	Outer membranes of plant spores and pollen
		Cutinite			Cutinite	Outer coatings (cuticles) of leaves, roots, stems
		Suberinite			Suberinite	Suberinized cell walls of cork in bark and roots
		Resinite			Resinite	Plant resins, balsams, latexes, fats, and waxes
		Alginite			Alginite	Algae (mostly planktonic)
		Bituminite			Bituminite	Amorphous degraded material of algal or bacterial origin
		Exsudatinite*			Exsudatinite	Secondary crack-filling material after oil generation
		Liptodetrinite			Liptodetrinite	Mechanically degraded particles and residues of liptinites
		Chlorophyllinite			X	Chlorophyll-derived material in peat through lignite rank
Inertinite		Fusinite			Fusinite	Fusinization of plant cell walls (fires, decarboxylation, etc.)
		Semifusinite			Semifusinite	Weakly humified and dehydrated plant tissues
		Funginite			Funginite	Fungal spores, sclerotia, and other fungal tissues
		Secretinite			Secretinite	Oxidation of resin and possibly humic gels
		Macrinite			Macrinite	Dehydrated flocculated humic matrix substances
		Inertodetrinite			Inertodetrinite	Fusinization of tiny varied inertinite precursors
		X			Micrinite	Secondary coalification residues of liptinitic substances

Coal, Fig. 4 Terminology of macerals and their suspected origins. *Arrows* show direct relationship between low rank maceral and higher rank macerals (Data from ICCP 1971, 1998, 2001; Stach et al. 1982; Scott 2002; Sýkorová et al. 2005; Pickel et al. 2017)

Macerals were originally defined based on their relative reflectance in incident light (Stopes 1935). They are classified intro three broad groups: liptinites, vitrinites, and inertinites. For low-rank coals, the precursor of vitrinite is referred to as huminite. Different macerals have different coalification tracks, or different rates at which hydrogen, carbon, and oxygen contents change in the macerals with rank, although in general, macerals increase in aromaticity from liptinite to vitrinite to inertinite, and aromaticity increases within each maceral group with rank. Different macerals also have different volatility. Vitrinite, liptinite, and a portion of semifusinite tend to be volatile, while inertinite macerals tend to be inert. Also, some macerals may be more likely to be associated with mineral matter. For example, fusain contains many pores, which are often filled with mineral matter (Masterlerz and Bustin 1993; Krevelen 1993; Given 1984; Stach et al. 1982).

Huminite-Vitrinite

Huminite and vitrinite group macerals are largely derived from woody and structurally resistant plant tissues (Fig. 4). Huminite group macerals in low-rank coals are the precursors of vitrinite macerals in higher-rank coals and vitrinite group macerals are the dominant macerals in most humic medium- and high-rank coal beds. These macerals are defined by structural features representing the degree of gelification of the precursor plant material. They have high oxygen contents and low carbon contents relative to the other maceral groups, but carbon content increases with rank (Sýkorová et al. 2005; ICCP 1998; Stach et al. 1982).

Huminite and vitrinite macerals increase in aromaticity through coalification, which influences their reflectivity. Vitrinite macerals are gray in reflected light, but their reflectance increases uniformly through coalification, providing a parameter that can be used to measure rank in coal (Fig. 2), and thermomaturity in organic-rich shales containing particles of vitrinite and bitumen. Bitumen is a thermomaturation product of kerogen in organic-rich petroleum source rocks (Hunt 1979; Tissot and Welte 1984; Teichmüller 1989; Littke 1999).

Inertinite

Inertinite group macerals are the oxidized remains of woody and other plant tissues, as well as humic gels and coprolites (Fig. 4). Different macerals in the inertinite group are defined based on the presence or absence of original plant structure. The term implies that these macerals are chemically more inert than other macerals, particularly in carbonization (making coke for steel) processes. They tend to be carbon-rich and hydrogen-poor. The carbon content depends on the origin of the maceral and extent of desiccation or redox processes it underwent during peatification. Inertinite macerals are highly reflective and appear white in reflected light, but they become difficult to distinguish petrographically at anthracite rank because all macerals have the same high reflectance by that stage of coalification (Stach et al. 1982; Teichmuller 1989; ICCP 2001).

Liptinite

Liptinite group macerals are black or brown in reflected white light and fluoresce under blue or ultraviolet light. They are

derived from cutans (waxes), resins, spores, and pollens in plants (Fig. 4) and as such, they tend to be hydrogen rich. Liptinites are involved in two coalification jumps. The first occurs in high volatile bituminous B and C coals when they begin to expulse liquids. The second occurs at or near the boundary of high volatile and medium volatile coals, where they lose their fluorescent properties, and their reflectance becomes similar to vitrinite (Stach et al. 1982; Teichmüller 1974, 1989; Pickel et al. 2017).

Coal Molecular Structure

There is no singular molecular chemical model for coal because coals are chemically and physically microheterogenous, both between different coals and within individual coals. Coals are aromatic (consist chiefly of aromatic [pentagonal rings] of carbon) compounds, and more than 100 molecular models have been proposed for the "basic" coal molecule. Mathews and Chaffie (2012), Mathews et al. (2011), and Marzec (2002) provide summaries of these models. Most modern models illustrate coal as a complex macromolecular network, which changes with rank. Levine (1993) summarized the macromolecular coal model as a (1) three-dimensional macromolecular matrix fraction composed mostly of single or polycyclic aromatic carbon structures fringed by H- and O-bearing functional groups and cross-linked by H- and O- bridge structures; and a (2) molecular fraction formed by tightly bound oils and asphaltenes of medium- to high-molecular weight and lower molecular weight compounds either physically entrapped or loosely bound to the matrix. The lower molecular weight fraction includes H_2O, CH_4, and CO_2, which change with rank.

Mineral Content

Coal is also comprised of minerals, separate or entrapped within the organic coal matrix. Mineral matter occurs as nonmineral inorganics and discrete inorganic crystalline and noncrystalline particles or masses. The minerals in a coal may have originated in the original peat (detrital, authigenic, biogenic) or may have been introduced, remobilized, or transformed within the coal at any time during post-peat coalification (Table 2). More than 120 minerals and inorganic compounds have been documented in coals worldwide (Schweinfurth and Finkelman 2003; Ward 2002; Vassilev and Vassileva 1996; Finkelman 1981). Table 3 shows some of the minerals which have been reported from coal.

Minerals in coal commonly occur as single crystals or concentrations of crystals within the coal matrix or in voids (fractures, cleats, rotted roots, etc.) within the coal. Authigenic minerals (Table 2) tend to be very fine grained (microns) and embedded in the coal matrix, often occurring within cell-sized voids of individual macerals. In contrast, diagenetic minerals (Table 2) tend to be coarser crystalline, macroscopic concentrations in cleat and fracture fills. This distinction is significant as cleat-filling minerals are generally easier to remove from coal prior to utilization than authigenic minerals (Rao and Gluskoter 1973; Mackowsky 1982; Renton 1982; Ward 1989; Krevelen 1993). The amount, particle size, and type of mineral matter in coal influence a wide variety of uses, including combustion for steam for electrical energy production and the production of metallurgical coke to make steal. Understanding mineral components is not only important for the practical processes and maintenance of combustion equipment but also chemical reactions during combustion, and the resultant composition of emissions and solid residues, especially in countries where the chemical composition of the emissions or residues is regulated.

Silicate Minerals

The most common minerals in coal are silicates, especially quartz and assorted clays (Table 3). Quartz is a common detrital mineral in flood waters and can also be deposited in peats from wind-blown sediment and volcanic ash falls (e.g., Neuzil et al. 1993; Ruppert et al. 1993). Biogenic opaline quartz accumulates from plant phytoliths and in sponge spicules in peat (Andrejko et al. 1983; Davis et al. 1984; Ruppert et al. 1993). Although most quartz in coal is syngenetic, diagenetic quartz-filling cleats are also reported in high-rank coals (Ward 2002; Spears 1987; Renton 1982).

Feldspars are minor mineral constituents in coals. Most feldspars are detrital in origin. Micas are rare, but detrital micas, which were weathered by acidic peat waters, may be the source for many clays, especially chlorite, in coal beds (Staub and Cohen 1978; Davis et al. 1984; Vassilev and Vassileva 1996).

Clay minerals are the most common silicate minerals in coal, and total clays often constitute the majority of mineral matter in coal. Kaolinite and illite are two of the most common clays in coals, but different types of clays are common in different coals in different basins (Table 3). Clays are common constituents of flood waters, so are common detrital additions to peats. Authigenic clays in peat can be sourced from (1) inorganic constituents in the original plant material, which become amorphous inorganics in the peat, which in turn, are altered to clays (Renton et al. 1979); (2) weathering of volcanic ash (Stach et al. 1982; Ward 2002); (3) from altered detrital muscovite (Staub and Cohen 1978; Davis et al. 1984); and from leaching and alteration of bedrock and underlying soil materials (Spears 1987). Kaolinite is favored in acidic peats, whereas smectite-dominated mixed layer clays dominate in neutral pH conditions. Smectite can

Coal, Table 2 Terminology used to describe the relative timing of mineral formation, deposition, or emplacement in peat and coal, and some of the sources and processes involved

Timing of mineral emplacement				Source/Origin		Dominant processes and products
Non-mineral inorganics	Higher Rank Coals ← Lignite ← Peat	Syngenetic (Primary)	*Early (During peat accumulation)*	Authigenic	Peat pore fluids	Dissolved salts and other inorganics in peat pore waters
Inorganic mineral particles (Crystalline and non-crystalline)					Biogenic	Inorganic elements in organic compounds in peat
				Allogenic Detrital	Clastic Epiclastic	Aqueous: Sediment deposited in peat from adjacent waters
						Aeolian: Air-born dust and sediment in peat
					Ash falls	Deposition of volcanic ash in peat
			Both Early and Late	Authigenic	Biogenic	Inorganic components of plants (e.g. pytholiths) and animals (e.g. spicules) produced through biologic/metabolic activity
					Chemical precipitates (pore filling)	Alteration of detrital and biogenic minerals in peat
						Bacterial reduction of sulfates sourced from peat processes and from marine flood waters
			Late (after burial)			Pre-compactional minerals formed from soluble ions during biochemical gelification at low temperatures
		Diagenetic (Secondary)		Epigenic	Chemical precipitates and transformations (cleat filling)	Transformation of minerals in coal through interactions with fluids and gases produced by coalification processes or from geothermal fluids at increasing burial temperatures and pressures
						Remobilization of minerals and ions in coal and fluids with increasing heat, pressure, and fluid chemical evolution, resulting in mineral deposition in cleats and fractures
						Metamorphism from igneous intrusions or geologic metamorphism at higher anthracitic ranks
		Telogenetic (Tertiary)			Chemical precipitates	Oxidation of minerals in coal at the surface after exhumation
						Mineralogical reactions associated with burning coal at the surface after exhumation

From data in Mackowsky (1982), Ward (2002). A telogenesis stage is added here to show processes at the surface which can precipitate minerals in coal

later be transformed to illite during diagenesis. Kaolinite and illite can also be formed by diagenetic transformations and are common in cleat and fracture fills in coal beds (Rao and Gluskoter 1973; Renton et al. 1979; Renton 1982; Spears 1987; Vassilev and Vassileva 1996).

Carbonate Minerals

Siderite, calcite, dolomite, and ankerite are common, and sometimes abundant constituents of the mineral fraction of coals (Table 3). In anaerobic, alkaline peat sediments, iron can accumulate as siderite (Postma 1977, 1982; Shotyk et al. 1992), possibly from CO_2 released by organic decay (Gould and Smith 1979; Ward 1989). Concretionary masses of calcite in coal beds, called coal balls, are found in some coal basins. Many coal balls preserve the cellular structure of plants in the peats in which they formed so are early syngenetic (e.g., Stopes and Watson 1909; Phillips 1980; Scott et al. 1996). Syngenetic dolomite may be introduced to peats if peats are

buried by marine waters (Stach et al. 1982). Carbonates can also be diagenetic. Calcite, and to a lesser extent, dolomite and ankerite are common fracture- and cleat-filling minerals formed in medium- and high-rank coals (Rao and Gluskoter 1973; Mackowsky 1982; Ward 1989, 2002). Some cleat-filling calcite cements may also result from telogenesis and precipitation from meteoric groundwater during exhumation (e.g., Kolker and Chou 1994).

Sulfide and Sulfate Minerals

Sulfur occurs in three forms in coal: (a) organic sulfur from the organic compounds in the coal; (b) sulfide minerals; and (c) sulfate minerals (usually hydrous iron and calcium sulfates) produced by oxidation of pyritic sulfides. At least 24 sulfate minerals and 19 sulfide minerals have been identified in coals (Ward 1989, 2002; Casagrande 1987; Davis 1982; Finkelman 1981). Pyrite and marcasite are the most

Coal, Table 3 Some of the minerals found in coals. Occurrence and abundance varies within and between coal beds. Not all minerals are found in all coals

Silicates		Carbonates	Sulfides
Amphibole $(Ca,Na)_{2-3}(Mg,Fe,Al)_5(Al,Si)_8O_{22}(OH)_2$ Epidote $Ca_2Al_2(Fe^{3+},Al)(SiO_4)(Si_2O_7)O(OH)$ Homeblende $Ca_2(Mg,Fe,Al)_5(AI,Si)_8O_{22}(OH)_2$ Kyanite Al_2SiO_5 **► Quartz-Chalcedony SiO_2** Pyroxene-Enstatite $MgSiO_3$ Pyroxene-Augite $(Ca,Na)(Mg,Fe^{2+},Al,Fe^{3+},Ti)(Si,AI)_2O_6$ Staurolite $Fe^{2+}{}_2Al_9O_8(SiO_4)_4(O,OH)_2$ Tourmaline $(Na,Ca)(Mg,La,Fe,Mn)_3Al_6(BO_3)_3Si_6O_{18}(OH)_4$ ○ Zircon $ZrSiO_4$		Alstonite $BaCa(CO_3)_2$ Ankerite $Ca(Fe^{2+},Mg,Mn)CO_3$ Aragonite $CaCO_3$ **► Calcite $CaCO_3$** Dawsonite $NaAICO_3(OH)_2$ ○ Dolomite $CaMg(CO_3)_2$ **►Siderite $FeCO_3$** Strontianite $SrCO_3$ Witherite $BaCO_3$	○ Chalcopyrite $CuFeS_2$ ○ Galena PbS Greigite $Fe^{2+}Fe^{3+}{}_2S_4$ ○ Marcasite FeS_2 Millerite NiS **► Pyrite FeS_2** Pyrrhotite $Fe_{(1-x)}S$ ○ Sphalerite $(Zn,Fe)S_2$ Stibnite SbS
Clay Minerals		Oxidesand Hydroxides	Sulfates
► Chlorite $(Mg_5Al)(AlSi_3)O_{10}(OH)_8$ **► Kaolinite $Al_2Si_2O_5(OH)_4$** **► lllite $KAl_2(AlSi_7)O_{20}(OH)_4$** **► Interstratified (mixed-layer) clays** **► Smectite (Montmorillonlite) $(1/2Ca, NA)_{0,7}(Al, Mg, Fe)_4[(Si, Al)_4O_{10}]_2(OH)_2•nH_2O$**		○ Anatase-Rutile TiO_2 Boehmite Al•O•H Brucite $Mg(OH)_2$ Corundum Al_2O_3 Diaspore AlO(OH) Gibbsite $Al(OH)_3$ Goethite-Limonite $Fe(OH)_3$ Hematite Fe_2O_3 Magnetite $Fe^{2+}Fe^{3+}O_4$ Portlandite $Ca(OH)_2$ Spinel $MgAl_2O_4$	Alunite $KAl_3(SO_4)_2(OH)_6$ Anhydrite $CaSO_4$ ○ **Barite $BaSO_4$** Bassanite $CaSO_4•{}_{1/2}H_2O$ Bloedite $Na_2Mg(SO_4)_2$ Celestite $SrSO_4$ Coquimbite $Fe_2(SO_4)_3•9H_2O$ Glauberite $Na_2Ca(SO_4)_2$ Gypsum $CaSO_4•2H_2O$ Hexahydrite $MgSO_4•{}_6H_2O$ Jarosite $(Na,K)Fe_3(SO_4)_2(OH)_6$ Melanterite $FeSO_4•{}_7H_2O$ Natrojarosite
Feldspars			
○ Plagioclase-Albite $NaAlSi_3O_8$ ○ Plagioclase-Anorthite $CaAl_2Si_2O_8$ ○ Orthoclase-Microcline $KAlSi_3O_8$ ○ o Sanidine $(K,Na)AlSi_3O_8$	**Legend** **► Major minerals** ○ Minor minerals Rare minerals		
Zeolites		Phosphates	
○ **Analcime $NaAlSi_2O_6•H_2O$** Clinoptilolite-Heulandite $(Na,K,Ca)_{2-3}Al_3(Al,Si)_2Si_{13}O_{36}•12H_2O$		○ Apatite $Ca_5F(PO_4)_3(OH,F,CI)$ ○ Crandallite	

(*continued*)

Coal, Table 3 (continued)

Laumontite $Ca(AlSi_2O_6)_2•4H_2O$ Mordenite $(Ca,Na_2,K_2)Al_2Si_{10}O_{24}•7H_2O$		(Y)$CaAl_3(PO_4)_2(OH)_5·H_2O$ ○ Florencite $(Ce)Al_3(PO_4)_2(OH)_6$ ○ Gorceixite $BaAl_3(PO_4)_2(OH)_5•H_2O$ ○ Goyazite $SrAl_3(PO_4)_2(OH)_5•H_2O$ ○ Monazite $(Ce,La,Y,Th,Nd)PO_4$ ○ Xenotime $(Y,Er)PO_4$	$NaFe_3(SO_4)_2(OH)_6$ Rozenite $FeSO_4•_4H_2O$ Szomolnokite $FeSO_4•H_2O$ Thenardite Na_2SO_4 Tschermigite $NH_4Al(SO_4)_2•12H_2O$
	Other	Phosphates	Halides
	Chromite $FeCr_2O_4$ ○ **Clausthalite PbSe** Corundum Al_2O_3 Crocoite $PbCrO_4$	○ Apatite $Ca_5F(PO_4)_3(OH,F,Cl)$ ○ Crandallite (Y)$CaAl_3(PO_4)_2(OH)_5·H_2O$ ○ Florencite $(Ce)Al_3(PO_4)_2(OH)_6$ ○ Gorceixite $BaAl_3(PO_4)_2(OH)_5•H_2O$ ○ Goyazite $SrAl_3(PO_4)_2(OH)_5•H_2O$ ○ Monazite $(Ce,La,Y,Th,Nd)PO_4$ ○ **o** Xenotime $(Y,Er)PO_4$	Chlorine-Halite NaCl Sylvite KCl

From data in Rao and Gluskoter (1973), Finkelman (1981), Mackowsky (1982), Renton (1982), Vassilev and Vassileva (1996, 2000), Hower et al. (1999), Ward (2002), Schweinfurth and Finkelman (2003)

common sulfide minerals in coal (Table 3). These may be authigenic or diagenetic. Authigenic pyrite can form in peat while the peat is accumulating, or in peats buried by marine waters (e.g., Casagrande 1987). Authigenic pyrite may occur as single crystals or clusters of crystals in individual macerals of coal. Diagenetic (epigenetic) pyrite tends to fill veins and cleats in coal and be more coarsely crystalline (Rao and Gluskoter 1973; Mackowsky 1982; Vassilev and Vassileva 1996). Additional diagenetic sulfide minerals include sphalerite, galena, and chalcopyrite, especially from coals which have encountered hydrothermal fluids (Mackowsky 1982; Finkelman 1981, 1985). Many of the sulfate minerals found in coal (e.g., coquimbite, jarosite, melanterite, rozenite, szomolmokite) result from exposure of sulfide minerals in coal at the surface (e.g., Rao and Gluskoter 1973).

Pyrite (FeS_2) breaks down with potentially deleterious consequences in many parts of the coal mining and utilization cycle. Weathering of mined exposures of coal and high-sulfur stratum, or abandoned spoil piles with significant pyrite concentrations, can result in acid-mine drainage (ARC 1969; NRC 1990; Brady et al. 1998; Greb et al. 2006b; Finkelman and Greb 2008). In boilers and furnaces, pyrite breaks down into elemental iron and sulfur, which can lead to corrosion and fouling. Each element combines with oxygen to form oxides. Iron oxide becomes part of the bottom or fly ash. Sulfur dioxide (SO_2) is emitted in the gas stream, which can react with water vapor to form sulfurous acid (H_2SO_3), which oxidizes to sulfuric acid (H_2SO_4), a major component of acid rain (EIA 1997, 2001; U.S. EPA 2004; Greb et al. 2006b). Many different types of mitigation are employed to

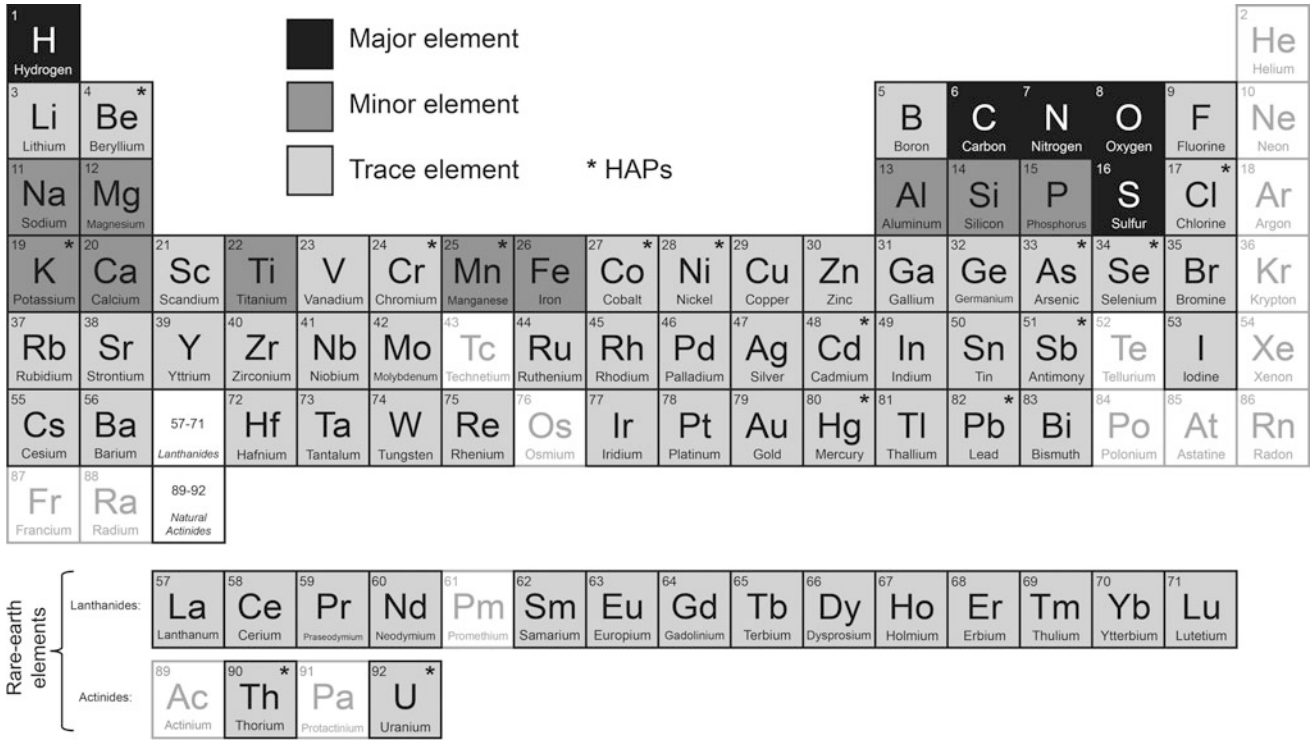

Coal, Fig. 5 Periodic table of naturally occurring elements, showing the elements reported from coal. Not all elements are found in all coals (After Schweinfurth and Finkelman 2003, Fig. 9)

remove or reduce pyrite from mined coal and to reduce or limit sulfurous emissions during and following combustion. Many techniques are also available for limiting acid-mine drainage from mine sites, and from mitigating drainage from mine sites which were abandoned before modern regulations in developed countries.

Major, Minor, and Trace Elements

Figure 5 shows the elements that have been reported in coal. Although coal does not have a unique chemical structure, the major elements (more than 1%) in the coal matrix are carbon (C), hydrogen (H), oxygen (O), nitrogen (N), and sulfur (S) (Fig. 5). The relative percentage of carbon increases with rank, while oxygen and hydrogen decrease with rank. Major elements are mostly organically associated, although they are found in inorganic (mineral) associations as well. Minor elements (1.0–0.01%) in coal are Na, Mg, Al, Si, P, K, Ca, Ti, Mn, and Fe (Fig. 5). Most of the minor elements are associated with the mineral constituents in coal, although phosphorus (P) is also organically associated. Minor elements are relatively common in coal but do not occur in all coal seams and occur in different concentrations in different seams (Finkelman 1981, 1985; Schweinfurth and Finkelman 2003; Swain 2013).

Trace elements (Fig. 5) are elements which occur in concentrations of 100 parts per million or smaller. Not all coals contain these elements, and concentrations of these elements vary greatly among and within coal beds. Similar to mineral matter, trace elements may be introduced during peatification or at any stage of coalification. Most appear to be syngenetic. From the peat through lignite stage of coalification, fresh cations may be introduced from groundwater and by ion exchange with carboxyl acids or their salts. Organic acids in peat and low-rank coals provide a large capacity for ion-exchange and complexation of metal ions into organometallic compounds (Rashid 1974; Nissenbaum and Swain 1976; Miller and Given 1986; Given and Miller 1987; Mitsch and Gosselink 2000; Li et al. 2010). Some trace elements are also epigenetic and are introduced with epigenetic minerals.

An important aspect of trace elements is their chemical association. Trace elements can be organically bound to the coal matrix or associated with mineral matter. The elements B, Be, Ga, Ge, and Sb are usually organically bound. The elements As, Cr, Ni, Se, Ti, U, and V, among others, may be either organically bound or occur in mineral matter, depending on the coal. Most of the other trace elements in coal shown in Fig. 5 are associated with mineral matter (Gluskoter et al. 1977; Miller and Given 1986; Given and Miller 1987; Goodarzi 1988; Finkelman 1995; Swaine

2013). In fact, some elements tend to have associations with certain minerals. For example, Cr, Hf, Rb, Ti, and Zr are commonly associated with aluminosilicate minerals like micas, feldspars, and clays (e.g., Suárez-Ruiz and Crelling 2008). Be, Cr, Mn, and Ni are commonly associated with the clay mineral chlorite. As, Cd, Co, Hg, Ni, Sb, and Se are commonly associated with the sulfide minerals pyrite and marcasite (e.g., Schweinfurth and Finkelman 2003). Understanding the chemical association of trace elements in a coal can aid in (1) determining if the elements can be or need to be removed or diminished from the coal prior to utilization, (2) where the elements will end up (emissions, solid residues) during and following coal utilization, and (3) determining the best mechanisms for mitigating any potential technological or environmental issues an element may have in the utilization process based on best practices and regulations.

Of the trace elements which can occur in coal, there are 15 which are listed as hazardous air pollutants (HAPS) by the US EPA (Fig. 5) although currently, mercury (Hg) is the only element of the 15 regulated and monitored from coal-fired power plant emissions in the United States (U.S. EPA 1998, 2016a). Many of the other HAPS (As, Cd, Co, Hg, Pb, some Se, and Sb) are commonly associated with sulfide minerals (see previous section), so removal of (or at least reducing) sulfide minerals from the coal prior to combustion in preparation plants aids in mitigation.

Coal Utilization

The majority of chemical testing of coal beds is conducted to (1) determine how a particular bed will react during its prospective use; (2) what and how much solid, particulate, and gaseous products may be produced from its use; and (3) address any technological or environmental issues resulting from coal utilization. Globally, coal is mostly combusted to generate steam to provide electrical power. Hence, much of the geochemical analysis of coal is aimed at understanding combustion characteristics and potential environmental issues of coal combustion. Environmental issues depend on the coal, the local environment (climate, pH, moisture, etc.), combustion technology, and the type of pollution control systems used in the process. A variety of coal-combustion emissions (SO_2, NO_x, etc.) are regulated in developed countries (e.g., U.S. EPA 1998). Concerns about CO_2 emissions and global climate change have also sparked limits on carbon emissions in some countries (Houghton et al. 1990; UN 1998; Stocker et al. 2013; U.S. EPA 2016b; EU 2016). Other than emissions, the chemistry of solid combustion residues and by-products is also important for determining potential by-product uses or for mitigating potential groundwater issues related to disposal of combustion residues in landfills (Adriano et al. 1980; U.S. EPA 1999, 2015; Izquierdo and Querol 2012). More information and references concerning environmental chemistry and issues of coal utilization, including various emissions, and solid residues, can be found at government agencies charged with their regulation and in Greb (2006).

Coal also has *nonfuel* uses. The principle nonfuel use of coal is to make metallurgical coke, which is used to make steel. A by-product of metallurgical coke are coal tars, which can be used to produce a wide array of aromatic chemicals. The pitch fraction of the tar can also be used to make an array of specialty carbon materials such as graphite and carbon fibers. Coal can also be gasified to make synthesis gases and other chemicals and can be liquefied to make synthetic fuels (Miura 2000; Schobert and Song 2002). More information about the commercial chemistry of coal and coal by-products can be found in Bouška (1981), Given (1984), Berkowitz (1985), and Krevelen (1993).

Conclusions

Coal is a complex material composed of an organic matrix, as well as inorganic and fluid constituents. Coal is diagenetically altered peat. Much of the chemistry of a particular coal is inherited from its peat precursor, but overprinted by its diagenetic history. This results in variability between and within coal beds. Coal chemistry changes with rank, which is largely a function of burial and thermal diagenesis. Variability in coal composition can generally be seen and analyzed at different scales, from the whole seam or benches of a seam, to bands in the seam (type), to microscopic bands and associations (microlithotype), to macerals (microscopic particles), to sub-maceral elemental composition. Understanding a coal's composition requires an understanding of a particular coal from its genesis as peat, through its geologic history to exhumation and exposure. How detailed the analysis of a particular coal is, generally depends on the coal's end use. Most chemical analyses on coals are done to determine parameters which influence the technological utilization of the coal, and to plan for any environmental or regulatory considerations of that particular use. Such considerations involve more than the coal itself, but also the equipment used and regulations, which vary considerably around the globe.

Cross-References

- ▶ Acid–Base Reactions
- ▶ Authigenesis
- ▶ Biogenic Methane

- Biomarkers: Coal
- Biopolymers and Macromolecules
- Carbon
- Carbon Cycle
- Diagenesis
- Geochemistry
- Hydrogen
- Biopolymers and Macromolecules
- Mineral Genesis
- Natural Gas
- Nitrogen
- Organic Geochemistry
- Organics: Sources and Depositional Environments
- Oxygen
- Peat
- Petroleum
- Sulfate Minerals
- Sulfide Minerals
- Sulfur
- Trace Elements

References

Adriano DC, Page AL, Elsewi AA, Chang AC, Staughan I (1980) Utilization and disposal of fly ash and other coal residues in terrestrial ecosystems: a review. J Environ Qual 9:333–334

Alpern B, de Sousa ML (2002) Documented international enquiry on solid sedimentary fossil fuels; coal: definitions, classifications, reserves-resources, and energy potential. Int J Coal Geol 50(1):3–41

Andrejko MJ, Cohen AD, Raymond R (1983) Origin of mineral matter in peat. In: Raymond R, Andrejko MJ (eds) Mineral matter in peat, its occurrence, form, and distribution. Los Alamos National Laboratory, Los Alamos, pp 3–24

Appalachian Regional Commission (1969) Acid mine drainage in Appalachia: Congressional house document no. 91-180, v. I, II, and III, Washington, DC

ASTM (2014) D388-12 Standard classification of coal by rank. ASTM International, West Conshohocken, v. 5.06–Gaseous fuels; Coal and coke; Bioenergy and industrial chemicals from biomass: 396–402

Barnes MA, Barnes WC, Bustin RM (1984) Diagenesis 8. Chemistry and evolution of organic matter. Geosci Can 11(3):102–114

Berkowitz N (1985) The chemistry of coal. Coals science and technology, vol 7. Elsevier, New York

Bohacs K, Suter J (1997) Sequence stratigraphic distribution of coaly rocks: fundamental controls and paralic examples. Am Assoc Pet Geol Bull 81(10):1612–1639

Bostick NH (1979) Microscopic measurement of the level of catagenesis of solid organic matter in sedimentary rocks to aid exploration for petroleum and to determine former burial temperatures a review. SEPM Spec Publ 26:17–43

Bouška V (1981) Geochemistry of coal. Coal science and technology, vol 1. Elsevier, New York

Brady BC, Kania T, Smith WM, Hornberger RJ (eds) (1998) Coal mine drainage prediction and pollution prevention in Pennsylvania. Pennsylvania Department of Environmental Protection, Harrisburg

Brown HR, Taylor GH, Cook AC (1964) Prediction of coke strength from the rank and petrographic composition of Australian coals. Fuel 43:43–54

Bustin RM (1999) Coal origins and diagenesis. In: Marshall CP, Rhodes WF (eds) Encyclopedia of geochemistry. Kluwer, Boston, pp 90–92

Bustin RM, Barnes MA, Barnes WC (1985) Diagenesis 10. Quantification and modelling of organic diagenesis. Geosci Can 12(1):4–21

Bustin RM, Ross JV, Rouzaud JN (1995) Mechanisms of graphite formation from kerogen: experimental evidence. Int J Coal Geol 28(1):1–36

Butler J, Marsh H, Goodarzi F (1988) World coals: genesis of the world's major coalfields in relation to plate tectonics. Fuel 67(2):269–274

Casagrande DJ (1987) Sulphur in peat and coal. In: Scott AC (ed) Coal and coal-bearing strata–recent advances. Geological Society, London, Special Publications 32(1):87–105

Cecil CB, Stanton RW, Neuzil SG, Dulong FT, Ruppert LF, Pierce BS (1985) Paleoclimate controls on late Paleozoic sedimentation and peat formation in the central Appalachian Basin (USA). Int J Coal Geol 5(1):195–230

Clymo RS (1987) Rainwater-fed peat as a precursor of coal. In Scott AC (ed) Coal and coal-bearing strata–recent advances. Geological Society, London, Special Publications 32(1):17–23

Collinson ME, Scott AC (1987) Implications of vegetational change through the geological record on models for coal-forming environments. In Scott AC (ed) Coal and coal-bearing strata–recent advances. Geological Society, London, Special Publications 32(1):67–85

Cross AT, Phillips TL (1990) Coal-forming through time in North America. Int J Coal Geol 16(1):1–46

Daniels EJ, Altaner SP, Marshak S, Eggleston JR (1990) Hydrothermal alteration in anthracite from eastern Pennsylvania: implications for mechanisms of anthracite formation. Geology 18(3):247–250

Davis A (1982) Sulfur in coal. Earth and Mineral Science Letters 51:1–18

Davis A, Russell SJ, Rimmer SM, Yeakel JD (1984) Some genetic implications of silica and aluminosilicates in peat and coal. Int J Coal Geol 3(4):293–314

De Leeuw JW, Largeau C (1993) A review of macromolecular organic compounds that comprise living organisms and their role in kerogen, coal, and petroleum formation. In: Engel M, Macko SA (eds) Organic geochemistry. Springer, New York, pp 23–72

Diessel CFK (1992) Coal formation and sequence stratigraphy. Springer, Berlin

Eble CF, Grady WC (1993) Palynologic and petrographic characteristics of two middle Pennsylvanian coal beds and a probable modern analogue. In: Cobb JC, Cecil CB (eds) Modern and ancient coal-forming environments. Geological Society of America, Special Paper 286:119–138

Energy Information Administration (1997) Effects of title IV of the Clean Air Act Amendments of 1990 on utilities: an update: U.S. Department of Energy, Washington, DC, EIA-0582

Energy Information Administration (2001) Reducing emissions of sulfur dioxide, nitrogen oxides, and mercury from electric power plants: U.S. Department of Energy, Office of Integrated Analysis and Forecasting, Washington, DC

Esterle JS, Kolatschek Y, O'Brien G (2002) Relationship between in situ coal stratigraphy and particle size and composition after breakage in bituminous coals. Int J Coal Geol 49(2):195–214

European Union (EU) (2016) Climate action. Website, http://ec.europa.eu/clima/index_en.htm. Accessed Jan 2016

Finkelman RB (1981) Modes of occurrence of trace elements in coal. U.S. Geological Survey Open-File Report, OFR-81-99

Finkelman R B (1985) Mode of occurrence of accessory sulfide and selenide minerals in coal. In: Cross AT (ed) Neuviene Congress

International de Stratigraphic et de Geologic du Carbonifere. Compte Rendu. 4:407–412
Finkelman RB (1995) Mode of occurrence of environmentally-sensitive trace elements in coal. In: Swaine DJ, Goodarzi F (eds) Environmental aspects of trace elements in coal. Springer, New York, Energy and the Environment 2:24–50
Finkelman R, Greb S (2008) Environmental and health impacts [of coal], Chapter 10. In: Suárez-Ruiz I, Crelling JC (eds) Applied coal petrology-the role of petrology in coal utilization. Elsevier Publications, Amsterdam, pp 263–287
Given PH (1984) An essay on the organic geochemistry of coal. In: Gorbaty ML, Larsen JW, Wender I (eds) Coal science, v.3. Academic, New York: 63–252
Given PH, Miller RN (1987) The association of major, minor and trace inorganic elements with lignites. III. Trace elements in four lignites and general discussion of all data from this study. Geochim Cosmochim Acta 51(7):1843–1853
Gluskoter HJ, Ruch RR, Miller WG, Cahill RA, Dreher GB (1977) Trace elements in coal: occurrence and distribution. Illinois State Geological Survey, Circular, Urbana 499
Goodarzi F (1988) Elemental distribution in coal seams at the Fording coal mine, British Columbia, Canada. Chem Geol 68:129–154
Gorham E (1991) Northern peatlands: role in the carbon cycle and probable responses to climatic warming. Ecol Appl 1(2):182–195
Gould KW, Smith JW (1979) The genesis and isotopic composition of carbonates associated with some Permian Australian coals. Chem Geol 24:137–150
Greb SF (2006) Coal and the environments references: Kentucky Geological Survey, University of Kentucky. Website, http://www.uky.edu/KGS/coal/coal_reference.htm. Accessed Jan 2016
Greb SF, DiMichele WA, Gastaldo RA (2006a) Evolution and importance of wetlands in earth history. In: Greb SF, DiMichele WA (eds) Wetlands through time. Geological Society of America Special Paper 399:1–40
Greb SF, Eble CF, Peters DC, Papp AR (2006b) Coal and the environment. American Geological Institute, Environmental Education Series, Alexandria
Hagemann HW, Hollerbach A (1980) Relationship between the macropetrographic and organic geochemical composition of lignites. Phys Chem Earth 12:631–638
Hatcher PG, Clifford DJ (1997) The organic geochemistry of coal: from plant materials to coal. Org Geochem 27(5):251–274
Hatcher PG, Breger IA, Szeverenyi N, Maciel GE (1982) Nuclear magnetic resonance studies of ancient buried wood–II. Observations on the origin of coal from lignite to bituminous coal. Org Geochem 4(1):9–18
Holz M, Kalkreuth W, Banerjee I (2002) Sequence stratigraphy of paralic coal-bearing strata: an overview. Int J Coal Geol 48(3):147–179
Hood ACCM, Gutjahr CCM, Heacock RL (1975) Organic metamorphism and the generation of petroleum. Am Assoc Pet Geol Bull 59(6):986–996
Houghton JT, Jenkins GJ, Ephraums JJ (eds) (1990) Report prepared for intergovernmental panel on climate change by working group I. Cambridge University Press, Cambridge
Hower JC, Gayer RA (2002) Mechanisms of coal metamorphism: case studies from Paleozoic coalfields. Int J Coal Geol 50(1):215–245
Hower JC, Graese AM, Klapheke J (1987) Influence of microlithotype composition on Hardgrove grindability for selected eastern Kentucky coals. Int J Coal Geol 7:227–244
Hower JC, Ruppert LF, Eble CF (1999) Lanthanide, yttrium, and zirconium anomalies in the Fire Clay coal bed, Eastern Kentucky. Int J Coal Geol 39:141–153
Hunt JM (1979) Petroleum geochemistry and geology. W.H. Freeman and Co, San Francisco, 617p
Hunt JW, Smyth M (1989) Origin of inertinite-rich coals of Australian cratonic basins. Int J Coal Geol 11(1):23–46
Hutton AC, Hower JC (1999) Cannel coals: implications for classification and terminology. Int J Coal Geol 41(1):157–188
International Committee for Coal and Organic Petrology (ICCP) (1998) The new vitrinite classification (ICCP system 1994). Fuel 77:349–358
International Committee for Coal and Organic Petrology (ICCP) (2001) The new inertinite classification (ICCP system 1994). Fuel 80:459–471
International Committee for Coal Petrology (ICCP) (1963) International handbook of coal petrography, 2nd edn. Centre National de la Recherche Scientifique, Academy of Sciences of the USSR, Paris, Moscow
International Committee for Coal Petrology (ICCP) (1971) International handbook of coal petrology, first supplement to, 2nd edn. Centre National de la Recherche Scientifique, Paris
ISO (International Organization for Standardization) (2005) Classification of coal. ISO (International Organization for Standardization), 11760. 1st edition, Geneva
Izquierdo M, Querol X (2012) Leaching behaviour of elements from coal combustion fly ash: an overview. Int J Coal Geol 94:54–66
Jarrett PM (ed) (1983) Testing of peats and organic soils. Symposium Proceedings, Toronto, Canada, June 23, 1982, ASTM Committee D-18 on Soil and Rock, ASTM Special Technical Publication 820
Kolker A, Chou CL (1994) Cleat-filling calcite in Illinois Basin coals: trace-element evidence for meteoric fluid migration in a coal basin. J Geol 102(1):111–116
Krevelen DW van (1952) Some chemical aspects of coal genesis and coal structure. In: Troisième Congres pour l'avancement des études de stratigraphie et de géologie du Carbonifère, Heelen, Compte Rendu 1:359–363
Krevelen DW van (1993) Coal: typology, physics, chemistry, constitution, 3rd edn. Elsevier, New York
Levine JR (1993) Coalification: the evolution of coal as source rock and reservoir rock for oil and gas. In: Law BE, Rice, DD (eds) Hydrocarbons from coal. American Association of Petroleum Geologists, Studies in Geology, 38:39–77
Li Z, Ward CR, Gurba LW (2010) Occurrence of non-mineral inorganic elements in macerals of low-rank coals. Int J Coal Geol 81(4):242–250
Littke R (1999) Coal: Vitrinite reflectance and maturity. In: Marshall CP, Rhodes WF (eds) Encyclopedia of geochemistry. Kluwer, Boston, p 96
Lopatin NV (1971) Temperature and geologic time as factors in coalification (in Russian). Akad Nauk SSSR Izv Ser Geol 3:95–106
Mackowsky M-T (1982) Minerals and trace elements occurring in coal. In: Stach E, Mackowsky M-T, Teichmüller M, Taylor GH, Chandra D, Teichmüller R (eds) Stach's textbook of coal petrology, 3rd edn. Gebrüder Borntraeger, Berlin, pp 153–171
Marzec A (2002) Towards an understanding of the coal structure: a review. Fuel Process Technol 77:25–32
Mastalerz M, Bustin RM (1993) Variation in maceral chemistry within and between coals of varying rank: an electron microprobe and micro-FTIR investigation. J Microsc 171(2):153–166
Mathews JP, Chaffee AL (2012) The molecular representations of coal–a review. Fuel 96:1–14
Mathews JP, Van Duin AC, Chaffee AL (2011) The utility of coal molecular models. Fuel Process Technol 92(4):718–728
McCabe PJ (1984) Depositional environments of coal and coal-bearing strata. In: Rahmani RA, Flores, RM (eds) Sedimentology of coal and coal-bearing sequences. International Association of Sedimentologists, Special Publication 7:13–42

Miller RN, Given PH (1986) The association of major, minor and trace inorganic elements with lignites. I. Experimental approach and study of a North Dakota lignite. Geochim Cosmochim Acta 50(9):2033–2043
Mitsch WJ, Gosselink JG (2000) Wetlands, 3rd edn. Wiley, New York
Miura K (2000) Mild conversion of coal for producing valuable chemicals. Fuel Process Technol 62(2):119–135
Moore PD (1989) The ecology of peat-forming processes: a review. Int J Coal Geol 12(1):89–103
Moore TA, Shearer JC (1999) Coal: types and characteristics. In: Marshall CP, Rhodes WF (eds) Encyclopedia of geochemistry. Kluwer, Boston, pp 92–96
Moore TA, Shearer JC (2003) Peat/coal type and depositional environment – are they related? Int J Coal Geol 56(3):233–252
Mukhopadhyay PK, Hatcher PG (1993) Composition of coal. In: Law BE, Rice DD (eds) Hydrocarbons from coal. American Association of Petroleum Geologists, Studies in Geology 38:79–118
National Research Council (1990) Surface mining effects: committee on ground water recharge in surface-mined areas. Water Science and Technology Board, National Research Council, National Academy Press, Washington, DC
Neuzil SG, Supardi SG, Cecil CB, Kane JS, Soedjono K (1993) Inorganic geochemistry of domed peat in Indonesia and its implication for the origin of mineral matter in coal. In: Cobb JC, Cecil CB (eds) Modern and ancient coal-forming environments. Geological Society of America, Special Paper 286:23–44
Nissenbaum A, Swaine DJ (1976) Organic matter-metal interactions in recent sediments: the role of humic substances. Geochim Cosmochim Acta 40(7):809–816
O'Keefe JM, Bechtel A, Christanis K, Dai S, DiMichele WA, Eble CF, Esterle JS, Mastalerz M, Raymond AL, Valentim BV, Wagner NJ, Ward CR, Hower JC (2013) On the fundamental difference between coal rank and coal type. Int J Coal Geol 118:58–87
Pickel W, Kus J, Flores D, Kalaizidis S, Christanis K, Cardott BJ, Misz-Kennan M, Rodrigues S, Hentschel A, Hamor-Vido M, Crosdale P, Wagner N, ICCP (2017) Classification of liptinite – ICCP system 1994. Int J Coal Geol 169:40–61
Phillips TL (1980) Stratigraphic and geographic occurrences of permineralized coal-swamp plants-Upper Carboniferous of North America and Europe. Biostratigraphy of fossil plants: 25–92
Postma D (1982) Pyrite and siderite formation in brackish and freshwater swamp sediments. Am J Sci 282(8):1151–1183
Postma D (1977) The occurrence and chemical composition of recent Fe-rich mixed carbonates in a river bog. J Sediment Petrol 47:1089–1098
Price LC (1983) Geologic time as a parameter in organic metamorphism and vitrinite reflectance as an absolute paleogeothermometer. J Pet Geol 6(1):5–37
Quigley TM, Mackenzie AS (1988) The temperatures of oil and gas formation in the sub-surface. Nature 333(6173):549–552
Rao CP, Gluskoter HJ (1973) Occurrence and distribution of minerals in Illinois coals. Circular, 476. Illinois State Geological Survey, Urbana
Rashid MA (1974) Absorption of metals on sedimentary and peat humic acids. Chem Geol 13(2):115–123
Renton JJ (1982) Mineral matter in coal. In: Meyers RA (ed) Coal structures. Academic, New York, pp 283–326
Renton JJ, Cecil CB, Stanton R, Dulong F (1979) Compositional relationships of plants and peats from modern peat swamps in support of a chemical coal model. In: Donaldson AC, Presley MW, Renton JJ (eds) Carboniferous coal short course and guidebook, vol 3. West Virginia Geologic and Economic Survey, Morgantown, pp 43–56
Ruppert LF, Neuzil, SG, Cecil CB, Kane JS (1993) Inorganic constituents from samples of domed and lacustrine peat, Sumatra, Indonesia. In: Cobb JC, Cecil CB (eds) Modern and ancient coal-forming environments. Geological Society of America Special Paper 286:83–96
Ruppert LF, Hower JC, Ryder RT, Levine JR, Trippi MH, Grady WC (2010) Geologic controls on thermal maturity patterns in Pennsylvanian coal-bearing rocks in the Appalachian basin. Int J Coal Geol 81:169–181
Schobert HH, Song C (2002) Chemicals and materials from coal in the 21st century. Fuel 81:15–32
Schopf JM (1948) Variable coalification; the processes involved in coal formation. Econ Geol 43(3):207–225
Schopf JM (1956) A definition of coal. Econ Geol 51(6):521–527
Schopf JM (1960) Field description and sampling of coal beds. U.S. Geological Survey, Bulletin 1111-B, 70 p
Schopf JM (1966) Definitions of peat and coal and of graphite that terminates the coal series (graphocite). J Geol 74(5):584–592
Schweinfurth SP, Finkelman RB (2003) Coal–a complex natural resource: an overview of factors affecting coal quality and use in the United States. Circular, 1143. U.S. Geological Survey, Urbana
Scott AC (2002) Coal petrology and the origin of coal macerals: a way ahead? Int J Coal Geol 50(1):119–134
Scott AC (1989) Observations on the nature and origin of fusain. Int J Coal Geol 12(1):443–475
Scott AC, Mattey DP, Howard R (1996) New data on the formation of Carboniferous coal balls. Rev Palaeobot Palynol 93:317–331
Shearer JC, Moore TA (1999) Coal: organic petrography. In: Marshall CP, Rhodes WF (eds) Encyclopedia of geochemistry. Kluwer, Boston, pp 87–90
Shotyk WH, Nesbitt W, Fyfe WS (1992) Natural and antropogenic enrichments of trace metals in peat profiles. Int J Coal Geol 20:49–84
Spears DA (1987) Mineral matter in coals, with special reference to the Pennine Coalfields. In: Scottt AC (ed) Coal and coal-bearing strata–recent advances. Geological Society, London, Special Publications 32:171–185
Stach E, Mackowsky M-T, Teichmüller M, Taylor GH, Chandra D, Teichmüller R (1982) Stach's textbook of coal petrology. Gebrüder Borntraeger, Stuttgart
Staub JR (1991) Comparisons of central Appalachian carboniferous coal beds by benches and a raised Holocene peat deposit. Int J Coal Geol 18(1):45–69
Staub JR, Cohen AD (1978) Kaolinite enrichment beneath coals; a modern analog, Snuggedy swamp, South Carolina. J Sediment Petrol 48:203–210
Stocker TF, Qin D, Plattner G-K, Tignor M, Allen SK, Boschung J, Nauels A, Xia Y, Bex V, Midgley PM, IPCC (eds) (2013) Climate change 2013: the physical science basis. Cambridge University Press, Cambridge
Stolper DA, Lawson M, Davis CL, Ferreira AA, Neto ES, Ellis GS, Lewan MD, Martini AM, Tang Y, Schoell M, Sessions AL (2014) Formation temperatures of thermogenic and biogenic methane. Science 344(6191):1500–1503
Stopes M (1919) On the four visible ingredients in banded bituminous coal. Proc R Soc Lond B9:470–487
Stopes MC (1935) On the petrology of banded bituminous coals. Fuel 14:4–13
Stopes MC, Watson DMS (1909) On the present distribution and origin of the calcareous concretions in coal seams, known as "coal balls". Phil Trans R Soc Lond B 200:167–218
Suárez-Ruiz I, Crelling JC (eds) (2008) Applied coal petrology–the role of petrology in coal utilization. Elsevier Publications, New York
Swaine DJ (2013) Trace elements in coal. Butterworth-Heinemann, Boston
Sýkorová I, Pickel W, Christanis K, Wolf M, Taylor GH, Flores D (2005) Classification of huminite–ICCP system 1994. Int J Coal Geol 62:85–106

Taylor GH, Liu SY, Diessel CFK (1989) The cold-climate origin of inertinite-rich Gondwana coals. Int J Coal Geol 11(1):1–22
Taylor GH, Teichmüller M, Davis A, Diessel CFK, Littke R, Robert P (1998) Organic petrology. Gebrüder Borntraeger, Berlin/Stuttgart
Teichmüller M (1974) Generation of petroleum-like substances in coal seams as seen under the microscope. In: Tissot BP, Bienner F (eds) Advances in geochemistry. Éditions Technip, Paris. Proceedings of the 6th international meeting on organic geochemistry, Rueil-Malmaison, 18–21 Sept, pp 379–408
Teichmüller M (1989) The genesis of coal from the viewpoint of coal petrology. Int J Coal Geol 12:1–87
Teichmüller M, Teichmüller R (1982) Fundamentals of coal petrology. In: Stach E, Mackowsky M-T, Teichmüller M, Taylor GH, Chandra D, Teichmüller R (eds) Stach's textbook of coal petrology. Gebrüder Borntraeger, Stuttgart: 5–108
Tissot B, Welte DH (1984) Petroleum formation and occurrence, 2nd edn. Springer, Berlin
U.S. Environmental Protection Agency (1997) Mercury study report to Congress-, v. 1, Executive summary: Office of Air Quality, Planning, and Standards, and Office of Research and Development, Washington, DC, EPA-452/R-97-003
U.S. Environmental Protection Agency (1999) Report to Congress–wastes from the combustion of fossil fuels. Office of Solid Waste and Emergency Response, Washington, DC, EPA 530-S-99-010, Executive Summary, 1 and 2
U.S. Environmental Protection Agency (2004) Acid rain program, 2003 progress report: Washington, D.C., EPA 430-R-04-009, 17 p.
U.S. Environmental Protection Agency (2015) Final rule: disposal of coal combustion residuals from electric utilities. http://www.epa.gov/coalash/coal-ash-rule. Accessed Jan 2016
U.S. Environmental Protection Agency (EPA) (2016a) Mercury and air toxics standards. http://www3.epa.gov/mats/. Accessed Jan 2016
U.S. Environmental Protection Agency (EPA) (2016b) Climate change. http://www3.epa.gov/climatechange/. Accessed Jan 2016
U.S. Environmental Protection Agency (US EPA) (1998) Study of hazardous air pollutant emissions from electric utility steam generating units–Final report. U. S. Environmental Protection Agency, Office of Air Quality, Research Triangle Park, North Carolina, EPA-453/R-98-004a, volumes 1 and 2, varied pagination
United Nations (1998) Kyoto protocol to the United Nations framework convention on climate change, Dec. 10, 1997, U.N. Doc FCCC/CP/1997/7/Add.1, 37 I.L.M. 22. UN, Geneva
United Nations Economic Commission for Europe (UN-ECE) (1998) International classification of in-seam coals. UN Economic Commission for Europe, Committee on Sustainable Energy, Geneva
Vassilev SV, Vassileva CG (1996) Occurrence, abundance and origin of minerals in coals and coal ashes. Fuel Process Technol 48(2):85–106
Vassilev SV, Eskenazy GM, Vassileva CG (2000) Contents, modes of occurrence and origin of chlorine and bromine in coal. Fuel 79(8):903–921
Ward CR (1989) Minerals in bituminous coals of the Sydney basin (Australia) and the Illinois basin (U.S.A.) Int J Coal Geol 13:455–479
Ward CR (2002) Analysis and significance of mineral matter in coal seams. Int J Coal Geol 50(1):135–168
Wilks KR, Mastalerz M, Bustin RM, Ross JV (1993) The role of shear strain in the graphitization of a high-volatile bituminous and an anthracitic coal. Int J Coal Geol 22:247–277
Yu Z, Beilman DW, Frolking S, MacDonald GM, Roulet NT, Camill P, Charman DJ (2011) Peatlands and their role in the global carbon cycle. EOS Trans Am Geophys Union 92(12):97–98
Zimmerman RE (1979) Evaluation and testing the coking properties of coal. Miller Freeman Publications, San Francisco

Cobalt

Olivier Pourret and Michel-Pierre Faucon
UniLaSalle, Beauvais Cedex, France

Element Data
Atomic Symbol: **Co**
Atomic Number: **27**
Atomic Weight: 58.933195 g/mol
Isotopes and Abundances: ^{59}Co 100%
1 Atm Melting Point: 1495 °C
1 Atm Boiling Point: 2927 °C
Common Valences: 2+, 3+
Ionic Radii: 65 pm (2+, 6-fold coordination)
Pauling Electronegativity: 1.88
First Ionization Energy: 7.88 eV
Chondritic (CI) Abundance: 513 ppm[a]
Silicate Earth Abundance: 102 ppm[a]
Crustal Abundance: 26.6 ppm[b]
Seawater Abundance: ~3–300 pmol/kg[c]
Core Abundance: 0.25%[d]
[a]Palme et al. (2014)
[b]Rudnick and Gao (2014)
[c]Bruland et al. (2014)
[d]McDonough (2014)

Properties

Cobalt (chemical symbol, Co) is a d-block transition metal, bluish white. It appears in the first long period of the periodic table between iron and nickel. Cobalt shares many chemical and physical properties with these two elements. Naturally occurring Co consists of a single stable isotope: ^{59}Co, whereas ^{60}Co is an artificial isotope that is an important γ-ray source. Cobalt has two main oxidation states (2+ and 3+). The common oxidation state for simple compounds is Co^{2+}. Depending upon geometry and environment, Co ionic radii vary between 56 pm and 90 pm. Cobalt is a transitional, compatible, and siderophile (chalcophile and lithophile in the Earth's crust) element, has a high melting point of 1495 °C, and is ferromagnetic. Cobalt has an electronegativity of 1.88 on the Pauling scale and displays a first ionization potential of 7.88 eV. More details can be found in Blackman (2006), Raveau and Seikh (2012), and Haynes (2015).

History and Use

Cobalt has been utilized by the society since the Bronze Age, mainly to impart a rich blue color to glass and ceramics. Its name derives from the German word kobald (goblin or evil spirit) and Greek word cobalos (mine), because Co minerals fooled miners with their bright colors. However, it was only isolated as a pure metal by Swedish chemist Brandt in 1735. Demand for Co remained subdued until the turn of the twentieth century and the development of cobalt-chromium alloys. Indeed, the demand for Co increased considerably after the Second World War, driven by the use of high-purity Co in jet engines and gas turbines. Cobalt demand has further accelerated in the past 30 years. Indeed, it reflects the increased use of Co as an essential constituent of materials used in high-technology industries including rechargeable batteries, superalloys, and catalysts. Cobalt, like Fe, can be magnetized and so is used to make magnets. It is alloyed with Al and Ni to make particularly powerful magnets. Other alloys of Co are used in jet turbines and gas turbine generators, where high-temperature strength is important. Cobalt metal is sometimes used in electroplating because of its attractive appearance, hardness and resistance to oxidation, and thus corrosion. Cobalt salts have been used for centuries to produce brilliant blue colors in paint, porcelain, glass, and pottery. Cobalt is one of the elements defined as a critical metal to clean energy over the next 5–15 years, because of its use in lithium ion batteries: each electric-powered vehicle will demand 9.4 kg of Co (Crundwell et al. 2011). Although Co does not get a ton of press, it is a pretty important metal in this day and age. The artificial radionuclide ^{60}Co is widely used in cancer treatment, as a tracer, and for radiotherapy.

Geochemical Behavior

Cobalt is often associated with Ni, Ag, Pb, Cu, and Fe-Mn ores, from which it is most frequently obtained as a by-product (Gunn 2014). The main known ore deposits are found in Katanga (Democratic Republic of Congo) (Decrée et al. 2015), whereas some recent discoveries evidenced that central Pacific Ocean may have Co-rich deposits (i.e., manganese nodules and Co-rich ferromanganese crusts) (Josso et al. 2017) at relatively shallow depths. Almost 50% of the world's cobalt supply in 2014 was mined in the Democratic Republic of Congo. Mining and smelter activities in Katanga have contaminated soil, water, and urban environments (Pourret et al. 2016).

Cobalt forms a number of minerals: cobaltite [CoAsS], skutterudite [$CoAs_{3-x}$], erythrite [$Co_3(AsO_4)_2.8H_2O$], spherocobaltite [$CoCO_3$], and heterogenite [CoO(OH)]. It is widely distributed in igneous and sedimentary rocks and minerals. Cobalt is also present in meteorites (i.e., iron-nickel metal contains a few tenths of a percent cobalt). Its average content in the Earth's crust is approximately 25–30 ppm, though widely distributed, stands only 33rd in order of abundance, and is less common than all other transition metals except scandium. It is, however, more dispersed in the crust than either of those elements, and concentrated mineral deposits are consequently rare. The average Co contents of CI chondrites estimated in a few studies are quite consistent, ranging from 500 ppm to 513 ppm. The bulk Earth has a Co content of 880 ppm, lower than that in the metallic core (0.25%). Cobalt contents in the bulk continental crust vary significantly from 15 ppm to 30 ppm. In particular, Co is most abundant in ultramafic rocks with an average concentration of 110 ppm. During differentiation of a basaltic magma, most of Co enters the ferromagnesian minerals. Cobalt content of these minerals depends on the total number of Fe-Mg lattice sites and is independent of the Fe/Mg ratio. Cobalt is strongly coherent with Mg in granitic rocks and behaves like Mg in its partition relations between metamorphic minerals. The acceptance of both Co and Mg is more selective at lower grades of metamorphism. These aspects have been further reviewed by Gunn (2014), McDonough (2014), Palme et al. (2014), and Rudnick and Gao (2014).

Cobalt is also a naturally occurring element in air, soil, plants, and water. The mean concentration of Co in the open ocean is very low (~40 pmol/kg) which in part reflects its short residence time. Co^{2+} is the principal aquatic species in seawater (Bruland et al. 2014). There has been considerable speculation on its mode of uptake in deep-sea manganese nodules and crusts. Cobalt tends to be associated with either Mn or Fe oxyhydroxides (Brown and Calas 2012). Cobalt may substitute as exchangeable Co^{2+} in marine manganates and then be oxidized to Co^{3+} by Mn^{4+}, whereas Co^{3+} may substitute for Fe^{3+} in Fe oxyhydroxide minerals. Cobalt may also be incorporated in birnessite as Co(II) at pH 7 and Co(III) above pH 8. The aqueous speciation and chemistry of Co in terrestrial environments is now an important focus of research, as the solution speciation of Co has a critical influence on its biological activity in the environment. Although there is a lack of comprehensive data on aqueous Co concentrations in soil porewaters, groundwater, and surface waters, natural Co concentrations vary mostly from 0.006 μg/L to 0.43 μg/L (Gaillardet et al. 2014). Cobalt is considered as moderately mobile with a mobility 10 times less than that of Na. Cobalt chemistry is dominated by the Co(II) oxidation state in the aqueous phase of terrestrial environments primarily due to the extremely low solubility of Co(III). There is no universal agreement on the importance of Co (II) complexation in the solution phase of terrestrial environments and, furthermore, on the nature of the major binding inorganic and organic ligands. The kinetics of Co (II) complexation to, and dissociation from, natural organic

complexing ligands are such that the speciation of Co is likely to significantly diverge from estimates based on thermodynamic equilibrium calculations. As a result, an accurate understanding of Co bioavailability, toxicity, and transport in terrestrial aquatic environments will only be achieved when thermodynamics can be reconciled with reaction kinetics.

Biological Utilization and Toxicity

Cobalt is an essential trace element in life and plays an important role in biochemical reactions essential for life, notably in the coenzyme cobalamin (Co chelated to four N atoms at the center of a porphyrin-like structure, Chivers 2014). Cobalamin has a complex biochemistry, and there is a number of cobalamin-dependent enzymes. Cobalamin-dependent enzymes influence nodulation and N_2 fixation in legume plants that can be used to supply nitrogen in crops (Underwood 1977). Cobalt deficiency affects nodule development, function, and nitrogen fixation. Cobalamin, also called vitamin B-12, is essential for human and animal health, nutrition, and growth. The amount needed is very small. Dietary Co intake is estimated to range 5–40 μg/day in the general human population (Simonsen et al. 2012).

Understanding the factors which affect Co uptake by plants across a range of soil types is essential for food quality as well as for possible remediation of contaminated sites. The relevant pedogenic processes contributing to Co uptake from soils by plants includes total, extractable, and exchangeable soil Co concentrations, pH and other soil chemical parameters, microbial variations, as well as anthropogenic inputs. In soils, Co is fixed by Mn-oxides in a non-extractable form, and its bioavailability is inversely proportional to the Mn content of the soil (Collins and Kinsela 2010).

High and frequent Co exposures can affect nervous system and cause an *axonopathy* (Flora 2014). Chronic inhalational intake of cobalt dust can lead to diffuse-inflammatory reactions of the bronchial mucosa and chronic respiratory tract disorders (Banza et al. 2009; Cheyns et al. 2014). In large doses, some Co forms are carcinogenic. Some plant species, also called metallophytes, have adapted to natural and contaminated Co-rich soils (Faucon et al. 2007). Among these metallophytes, some are able to hyperaccumulate Co in plant shoots (>300 ppm, without toxicity symptoms and growth inhibition) (Lange et al. 2017).

Summary

Cobalt production hugely increases in the last decade as the global demand for Co increases. However, its exploitation becomes a new urgent environmental issue, especially in region such as Democratic Republic of Congo. Cobalt has been suggested to be a potentially dangerous pollutant, and the United States Environmental Protection Agency classifies Co in the priority list of environmental risk elements. A better understanding of Co biogeochemical behavior may support to assess the risk to the environment and to human health and to assist in developing new remediation tools.

Cross-References

- ▶ Complexes
- ▶ Copper
- ▶ Ferromanganese Crusts and Nodules: Rocks That Grow
- ▶ Manganese
- ▶ Ore Deposits
- ▶ Siderophile Elements
- ▶ Trace Elements
- ▶ Transition Elements

References

Banza CLN, Nawrot TS, Haufroid V, Decrée S, De Putter T, Smolders E, Kabyla BI, Luboya OS, Ilunga AN, Mutombo AM, Nemery B (2009) High human exposure to cobalt and other metals in Katanga, a mining area of the Democratic Republic of Congo. Environ Res 109:745–752

Blackman AG (2006) Cobalt: inorganic & coordination chemistry. In: Encyclopedia of inorganic chemistry. Wiley, Chichester

Brown GE, Calas G (2012) Section 18. Mineral-water interfaces as driving forces for metal concentration: the example of cobalt trapping by Mn-Oxides. Geochem Perspect 1:667–669

Bruland KW, Middag R, Lohan MC (2014) 8.2 – controls of trace metals in seawater. In: Holland HD, Turekian KK (eds) Treatise on geochemistry, 2nd edn. Elsevier, Oxford, pp 19–51

Cheyns K, Banza Lubaba Nkulu C, Ngombe LK, Asosa JN, Haufroid V, De Putter T, Nawrot T, Kimpanga CM, Numbi OL, Ilunga BK et al (2014) Pathways of human exposure to cobalt in Katanga, a mining area of the D.R. Congo. Sci Total Environ 490:313–321

Chivers PT (2014) Chapter 14 Cobalt and nickel. In: Maret W, Wedd A (eds) Binding, transport and storage of metal ions in biological cells. The Royal Society of Chemistry, Cambridge, UK, pp 381–428

Collins RN, Kinsela AS (2010) The aqueous phase speciation and chemistry of cobalt in terrestrial environments. Chemosphere 79:763–771

Crundwell FK, Moats MS, Ramachandran V, Robinson TG, Davenport WG (2011) Extractive metallurgy of nickel, cobalt and platinum group metals. Elsevier, Amsterdam

Decrée S, Pourret O, Baele J-M (2015) Rare earth element fractionation in heterogenite (CoOOH): implication for cobalt oxidized ore in the Katanga Copperbelt (Democratic Republic of Congo). J Geochem Explor 159:290–301

Faucon MP, Shutcha MN, Meerts P (2007) Revisiting copper and cobalt concentrations in supposed hyperaccumulators from SC Africa: influence of washing and metal concentrations in soil. Plant Soil 301:29–36

Flora SJS (2014) Chapter 22 – Metals. In: Aronson JK (ed) Side effects of drugs annual. Elsevier, Amsterdam, pp 297–322

Gaillardet J, Viers J, Dupré B (2014) 7.7 – trace elements in river waters. In: Holland HD, Turekian KK (eds) Treatise on geochemistry, 2nd edn. Elsevier, Oxford, pp 195–235
Gunn G (2014) Critical metal handbook. Wiley, Chichester
Haynes WM (2015) CRC handbook of chemistry and physics, 96th edn. CRC Press, Boca Raton
Josso P, Pelleter E, Pourret O, Fouquet Y, Etoubleau J, Cheron S, Bollinger C (2017) A new discrimination scheme for oceanic ferromanganese deposits using high field strength and rare earth elements. Ore Geol Rev 87:3–15
Lange B, van der Ent A, Baker AJM, Echevarria G, Mahy G, Malaisse F, Meerts P, Pourret O, Verbruggen N, Faucon M-P (2017) Copper and cobalt accumulation in plants: a critical assessment of the current state of knowledge. New Phytol 213:537–551
McDonough WF (2014) 3.16 – compositional model for the Earth's core. In: Holland HD, Turekian KK (eds) Treatise on geochemistry, 2nd edn. Elsevier, Oxford, pp 559–577
Palme H, Lodders K, Jones A (2014) 2.2 – solar system abundances of the elements. In: Holland HD, Turekian KK (eds) Treatise on geochemistry, 2nd edn. Elsevier, Oxford, pp 15–36
Pourret O, Lange B, Bonhoure J, Colinet G, Decrée S, Mahy G, Séleck M, Shutcha M, Faucon M-P (2016) Assessment of soil metal distribution and environmental impact of mining in Katanga (Democratic Republic of Congo). Appl Geochem 64:43–55
Raveau B, Seikh MM (2012) Cobalt oxides: from crystal chemistry to physics. Wiley, Weinheim
Rudnick RL, Gao S (2014) 4.1 – composition of the continental crust. In: Turekian HD, Holland KK (eds) Treatise on geochemistry, 2nd edn. Elsevier, Oxford, pp 1–51
Simonsen LO, Harbak H, Bennekou P (2012) Cobalt metabolism and toxicology – a brief update. Sci Total Environ 432:210–215
Underwood EJ (1977) 5 – cobalt. In: Underwood EJ (ed) Trace elements in human and animal nutrition, 4th edn. Academic, New York, pp 132–158

Colloids

Jean-François Boily
Department of Chemistry, Umeå University, Umeå, SE, Sweden

Definition

Colloids are (in)organic (poly)molecular particles in which at least one dimension is of the order ~1–1000 nm in length. They may occur as individually dispersed and/or aggregated particles of a given substance suspended in another substance. They cannot be separated by conventional forms of filtration or centrifugation.

Introduction

Colloidal suspensions consist of particles of one phase (solid, liquid, gas) in a second continuous phase. Particles are ~1–1000 nm (or even ~10 μm) wide in at least one direction, can be amorphous or crystalline, and be composed of inorganic, organic, or biological materials. Colloids of interest to Earth Sciences can be dispersed in solids, liquids, and gases, with representative examples shown in Table 1. Notable examples of colloids of biogeochemical importance include clays, fine silt, condensed Al(III) and Fe(III) (oxyhydr)oxides, as well as humic substances. Biocolloids are of organic nature and can include bacteria, viruses, protozoae, including macromolecular breakdown products and exudates.

Colloids, Table 1 Colloidal systems according to states of matter[a]

Dispersed phase	Dispersing medium	Colloidal system	Examples
Gas	Liquid	Foam	Gas bubbles in water and magmas
	Solid	Solid foam	Pumice
Liquid	Gas	Liquid aerosol	Fog
	Liquid	Emulsion	Water-in-oil emulsions
	Solid	Gel	Fluid inclusions
Solid	Gas	Solid aerosol	Atmospheric mineral "dust"
	Liquid	Sol, suspensions	Mineral particles in aquatic environments
	Solid	Solid sol	Opals

[a]After Yariv and Cross (1979)

In contrast to dissolved substances in homogeneous solutions, colloids can undergo Brownian motion due to collisions with molecules of the host medium. Many can also scatter light (Tyndall effect) when suspended in light-transparent media. Stable colloidal suspensions, namely those that do no settle effectively, are stabilized by strong solvation forces from the dispersing medium, thus effectively overcoming gravitational forces. Destabilized colloids can however agglomerate and settle if this fine balance of forces is compromised. Note that "flocculation," "agglomeration," and "coagulation" are terms that are often used interchangeably in the literature. Still, "coagulation" can be more specifically used to refer to the near irreversible aggregation of tightly packed colloids into a "coagulum," while "flocculation" can pertain to loose and open colloidal aggregates that can be readily dispersed by external forces.

Because colloids can expose reactive functional groups capable of removing molecules from the host medium, they can play key roles in the (bio)geochemical cycling of elements and mass transport in nature. For instance, the biogeochemical cycling of elements can be strongly coupled to the occurrence and reactivity of high specific surface area iron (oxyhydr)oxide colloids (Raiswell and Canfield 2012). Colloidal transport through waterways of Earth's surface or through porous/fissured media of Earth's upper crust represents an additional important vector affecting mass transport.

In this article an overview of representative colloids and colloidal processes of central interest to Earth Sciences is presented. It briefly highlights settings from Earth's atmosphere and low-temperature environments to those relevant to magmatic settings.

Colloidal Suspension Properties

Colloids form (i) chemically by *condensation* of new phases from molecular units (e.g., hydrolysis and precipitation of Al(III)), or (ii) by physical or chemical *comminution* (dispersion) of host materials into smaller fragments. As these are materials with high surface area to bulk mass ratios, surfaces play a determining role on the behavior of colloids. These particles can then be subjected several forces that can even overcome gravitational forces and suspend particles temporarily or indefinitely, namely with suspension times from seconds to years. The concept of colloidal stability ratio (W) accounts suspension stability in terms of the the ratio of the rates of diffusion-controlled to interaction force-controlled interparticle collision (*cf.* Hunter 1981). In thermodynamic parlance, the total Gibbs free energy of colloidal suspensions can be given by a balance of attractive and repulsive contribution (Fig. 1; Moore et al. 2015):

$$\Delta G_{\text{total}} = \Delta G_{\text{repulsive}} + \Delta G_{\text{attractive}} \quad (1)$$

Each of these latter terms can be broken into components referring to distinct physicochemical phenomena including solvation, electrostatic (electric double layers), steric, polymer flocculation, and hydrophobic contributions.

In vacuum or inert air, van der Waals attractive force can drive aggregation as a means to minimize surface energies of colloidal particles. These energies can however also be decreased via adsorption of solvents, such as water, which in turn form *excluded volumes* that hinder particle-particle collisions. Adsorption reactions involving potential-determining ions and counterions (e.g., Na^+ and Cl^-) can also generate an electric double layer (EDL) repelling charged particles from one another. The magnitude and sign of the EDL potential as well as its thickness affect colloidal stability. This is classically expressed by DLVO theory (Derjaguin, Landau, Verway and Overbeek (Verwey and Overbeek 1948) by accounting for the interplay of electrostatic repulsion of the EDL and of van der Waals attraction between particles. Stable colloidal suspensions thus result from dominant electrostatic repulsion between particles. Stability may however be compromised by changes in salinity because weakly- to non-binding ions (e.g., Na^+, Cl^-) can effectively contract EDL thickness. This can be accounted by the Debye screening length (Hunter 1981), which can range from

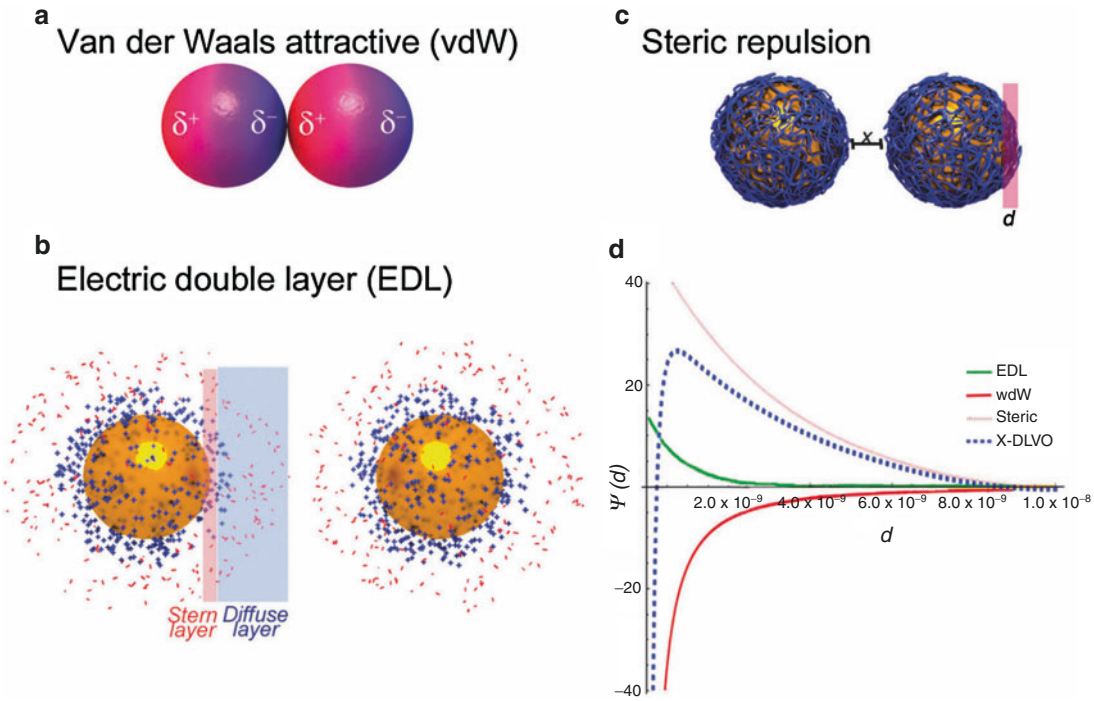

Colloids, Fig. 1 Colloidal interactions. (**a**) Van der Waals attractive forces. (**b**) Electric double layer formed at charged particle surfaces. (**c**) Steric repulsion caused by sorbed macromolecules. (**d**) Potential energy distance curve (DLVO, *blue dashed*) broken down for contributions from van der Waals (*red*), electric double layer (*green*), and steric (*pink*). (Taken from Moore et al. (2015)

~300 nm at 0.001 M to ~11 nm at 0.7 M, the latter being close to seawater. Thus, when fluvial colloids are discharged into estuarine environments, or when water evaporates from a colloidal suspension, the contraction of the EDL enables attractive to van der Waals forces to drive particle flocculation and sedimentation. At the same time, colloidal stability can be compromised by changes in pH or binding of foreign species (e.g., metal ions, natural organic matter) affecting the magnitude and sign of EDL potentials, and therefore electrostatic contributions to colloidal stability.

Additionally, adsorption of polymeric-like molecules, such as possibly natural organic matter, can present possibilities for *steric stabilization*. Particle-particle interactions can be inhibited by an an osmotic pressure effect driving water molecules between interpenetrating polymeric units of approaching particles. Loss of degrees of freedom of polymers between particles also result in a lost of entropy, and thus induce a thermodynamically unfavorable condition for colloidal stability.

Examples of Colloids on Earth

Colloids are of widespread occurrence in terrestrial environments. Predominant forms of sedimentary rocks (shales, sandstones and limestones) in fact cover ~73% of modern-day continents and can be made up of considerable portions of colloidal particles. In soils, they can be generated by the physicochemical breakdown of host rock, or by precipitation from aqueous solution (e.g., via hydrolysis of Al(III) and Fe(III)). Gravitation of colloids from upper soil horizons to accumulative horizons in the lower portion of soils is an additional process contributing to mass transfer across soil profiles. Likewise, the transport of colloids in porous or fissured environments of Earth's upper crust is key to the understanding on nutrient, metal, radionuclide and contaminant transport.

Sedimentation of colloidal suspensions in open waterways can be strongly affected by particle density, size, and water movement. For instance, while an important quantitity of matter collected by rivers is deposited as sediments at estuaries, fines such as clays, silt, and organic matter are transported further to oceans. Additionally, particles may remain in suspension or be resuspended by wave, tidal, and flood activities in spite of favorable physicochemical conditions for flocculation.

Opals are another example of sedimentary deposits consisting of colloidal particles. These mineraloids can be refered as *colloidal crystals* and consist of (hexagonal, cubic) close-packed colloidal particles of hydrated SiO_2 spheres of ~150–300 nm in size. They can form from evaporated silica-rich solutions that have leached through sandstones. Subsequent compaction and partial dehydration of the silica spheres produce opals with various degrees of organisation, with gemstone-like attributes.

Gas bubbles represent another form of colloidal entity strongly relevant to Earth sciences. Bubbles expelled by biotic, diagenetic, and igneous processes can be dispersed in the form of a foam. Water-based foams can, for instance, reduce the permeability of porous media, such as soils and sediments. Air bubbles can also be captured in freezing soils or (sea) water (Deville 2017), which are in turn used for tracking paleoclimates. Nucleation and growth of bubbles in magmas are also key to understand explosive in relation to effusive volcanic eruptions. Gas bubbles in pumice, a vecicular volcanic glass, are also viewed as colloids (Table 1).

Finally, the atmosphere can also be considered as a colloidal system. Colloids in these systems are more often refered to as solid or liquid aerosols. A notable example is water droplet formation from the condensation of atmospheric water vapor (*e.g.*, fog, cloud, mist, droplets), and with droplet sizes in the ~1–100 100 μm range. Atmospheric mineral dust particles ejected from volcanoes, blown from deserts, and, more recently, produced by industry play integral parts to atmospheric processes, and most notably in ice nucleation (Hoose and Möhler 2012). Deposition of iron-bearing particles to the oceans is, moreover, a key input to ocean productivity and biogeochemistry (Tagliabue et al. 2017).

Summary

Colloids are inorganic and organic fines of diverse compositions and sources. They are of widespread occurrence in continental, oceanic, and atmospheric environments. The high surface-to-bulk mass ratio of these particles is especially responsible for their large chemical reactivity and for their important roles in the biogeochemical cycling of elements in nature and even in atmospheric processes.

Cross-References

- ▶ Aqueous Solutions
- ▶ Chemical Weathering
- ▶ Earth's Atmosphere
- ▶ Entropy
- ▶ Equilibrium
- ▶ Fluid–Rock Interaction
- ▶ Geochemical Thermodynamics
- ▶ Laboratory Simulations of Organic Geochemical Processes at Elevated Temperatures
- ▶ Low-Temperature Geochemistry
- ▶ Marine Sediment
- ▶ Surface Geochemistry
- ▶ Volcanic Gases
- ▶ Water

References

Deville S (2017) Freezing colloids: observations, principles, control, and use. Springer, Switzerland

Hoose C, Möhler O (2012) Heterogeneous ice nucleation on atmospheric aerosols: a review of results from laboratory experiments. Atmos Chem Phys 12:9817–9854

Hunter RJ (1981) Zeta potential in colloid science: principles and applictions. Academic Press, New York

Moore TL et al (2015) Nanoparticle colloidal stability in cell culture media and impact on cellular interactions. Chem Soc Rev 44:6287–6305. https://doi.org/10.1039/C4CS00487F

Raiswell R, Canfeild DE (2012) The iron biogeochemical cycle past and present. Geochem Perspect 1:1–217

Tagliabue A, Bowie AR, Boyd PW, Buck KN, Johnson KS, Saito MA (2017) The integral role of iron in ocean biogeochemistry. Nature 543:51–59. https://doi.org/10.1038/nature21058

Verwey EJW, Overbeek JTG (1948) Colloidal dispersions. Cambridge University Press, New York

Yariv S, Cross H (1979) Geochemistry of colloid systems: for earth scientists. Springer-Verlag, Berlin, Heidelberg

Complexes

Jay R. Black
School of Earth Sciences, The University of Melbourne, Melbourne, VIC, Australia

Synonyms

Aqueous species; Coordination complex; Ion pair

Definition

Complexes are compounds that form in solutions due to interactions between ions or neutral molecules forming coordinating bonds between them. Coordination complexes commonly form between positively charged cations (e.g., Ca^{2+}, Mg^{2+}, Na^{+} and Cu^{2+}), which act as a central atom and are bound to negatively charged anion species (e.g., Cl^{-}, SO_4^{2-}, HCO_3^{-} and F^{-}) or neutral species (e.g., H_2O and NH_3), also referred to as ligands. The types of bonds that form may be ionic due to Coulombic forces or covalent due to sharing of electrons between atoms or other types of interactions such as dipole-dipole interactions (See entries ▶ "Chemical Bonds" and ▶ "Van der Waals Force"). Ligands that form more than one bond with a central metal atom, thus occupying more than one coordination site, are called chelates (See entry ▶ "Chelation"). Many organic ligands act as chelates forming multiple bonds with a metal, such as porphyrin a ring shaped tetradendate ligand which binds metals in the center via 4 bonds (See entry ▶ "Porphyrins"). Complexes that form with more than one metal center are referred to as multi- or polynuclear complexes (Stumm and Morgan 1996).

Complex Formation and Coordination Chemistry

A general chemical reaction for complex formation can be written with an acidic electron accepting group (the metal) and a basic electron donating group (the ligand), much in the same sense as that of acid–base chemistry (See entry ▶ "Acid–Base Reactions") but defined as:

$$mM^{i+} + nL^{j-} = (M_mL_n)^{(mi+nj)} \quad (1)$$

where, M is a metal of charge i + and L is a ligand of charge j-, m and n being stoichiometric constants.

In aqueous solutions metals will form a coordination complex with water molecules, which form an inner sphere of hydration of varying coordination depending upon the metals type (See entry ▶ "Aqueous solutions"). For instance, at most ionic strengths Mg^{2+} forms an octahedrally coordinated inner sphere complex with 6 molecules of H_2O ($Mg(H_2O)_6^{2+}$, see Bock et al. 1994), whereas, Li^{+} forms a tetrahedrally coordinated inner sphere complex with 4 molecules of H_2O ($Li(H_2O)_4^{+}$, see Rudolph et al. 1995) (Fig. 1). The water molecules bound to the inner sphere of a complex are often omitted, for instance, $Mg^{2+}_{(aq)}$ would refer to the $Mg(H_2O)_6^{2+}$ complex and the subscript (aq) is commonly used to designate an aqueous complex. Thus, a knowledge of coordination chemistry is needed to understand the chemical environment of an aqueous complex.

Inner-Sphere and Outer-Sphere Complex Formation

The inner sphere constitutes ligands that are directly bonded to the metal center in the inner coordination environment. Beyond the coordination environment of the inner sphere of a complex the solvent or solutes may also be ordered around a complex forming an outer sphere coordination environment due to electrostatic interaction between the central cation and solvated anions or dipole-dipole interactions with water. As the types of interactions leading to the formation of an outer sphere complex are often weaker than inner sphere interactions, the structure of the outer sphere is often not considered until higher ionic strengths are reached where ion pairing becomes more important (See entry ▶ "Debye-Hückel Equation"). However, considering the second solvation sphere of an aqueous complex is often important in order to accurately predict the vibrational spectra of the complex (e.g., $Li(H_2O)_4^{+}.4H_2O$, Fig. 1; Pye et al. 1996). Inner and outer

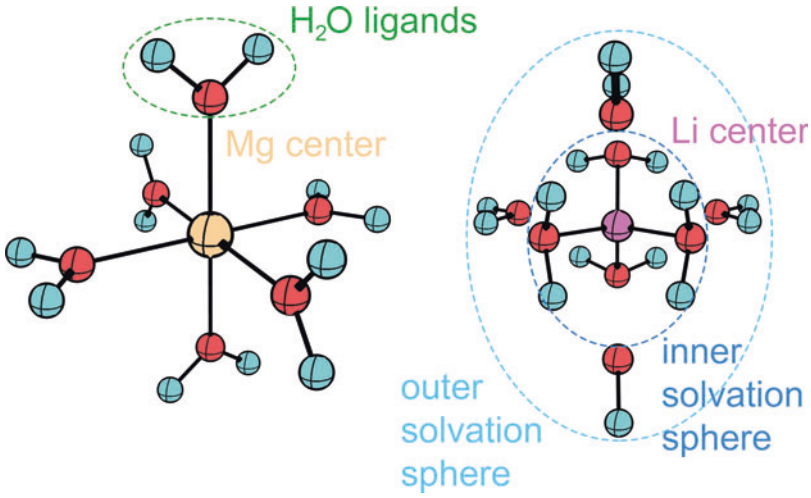

Complexes, Fig. 1 Molecular models of aqueous complexes of octahedral $Mg(H_2O)_6^{2+}$ (on the *left*) and tetrahedral $Li(H_2O)_4^{+}.4H_2O$ (on the *right*) showing both the inner sphere and outer sphere solvation of the lithium ion

sphere complexes are also important to the complex structure that forms at mineral surfaces at the water-mineral interface where a minerals surface charge affects the adsorption of aqueous metals and ligands forming surface complexes (See entries ▶ "Surface Geochemistry" and ▶ "Gouy-Chapman Theory").

For example, sulphate may form an outer-sphere complex with magnesium or ion pair (Eq. 2). As the concentration of sulphate in solution increases it may exchange with a water bound to the inner sphere of the hexaaquomagnesium complex, thus going from being bound as an outer-sphere complex to a inner-sphere complex or contact ion pair (Eq. 3):

$$\left[Mg(H_2O)_6\right]^{2+} + SO_4^{2-} = \left[Mg(H_2O)_6\right].SO_4 \qquad (2)$$

$$\left[Mg(H_2O)_6\right].SO_4 = \left[MgSO_4(H_2O)_5\right] + H_2O \qquad (3)$$

The ligand-exchange reactions shown in Eqs. 2 and 3 simplify the solvation structure, as the sulfate ligand may also be solvated and bound as an outer-sphere complex via it's solvation sphere. Rates of ligand exchange between the inner and outer spheres are often quite rapid in aqueous solution (See entry ▶ "Kinetics of Geochemical Processes").

Complex Speciation and Stability

The addition of many solutes and ligand types to an aqueous solution may lead to various metal complexes forming in solution, the distribution of these complexes or aqueous species is known as the aqueous or complex speciation of the solution. Simply varying the pH of an aqueous solution may lead to the formation of various metal hydrolysis products (i.e., the formation of soluble metal hydroxides and oxide complexes). The hydrolysis of cations has been reviewed in detail by Baes and Mesmer (1976). Complex speciation affects many environmental processes from the solubility of minerals (See entry ▶ "Solubility"), to the transport of metals in hydrothermal fluids and their eventual deposition as an ore deposit (See entries ▶ "Hydrothermal Solutions" and ▶ "Ore Deposits").

The thermodynamic stability of aqueous complexes can be measured and is defined by an equilibrium constant for reactions such as those represented by Eq. 1 (See entry ▶ "Equilibrium constant"). Ligand substitution reactions can be written in a stepwise or cumulative manner and formation constants defined as K (Eqs. 4, 5, and 6) or β (Eq. 7), respectively:

Stepwise complex formation and constants:

$$M^+ + L^- \overset{K_1}{=} ML^0 \text{ where } K_1 = \frac{\left[ML^0\right]}{\left[M^+\right]\left[L^-\right]} \qquad (4)$$

$$ML^0 + L^- \overset{K_2}{=} ML_2^- \text{ where } K_2 = \frac{\left[ML_2^-\right]}{\left[ML^0\right]\left[L^-\right]} \qquad (5)$$

$$ML_{(n-1)}^{(2-n)} + L^- \overset{K_n}{=} ML_n^{(1-n)} \text{ where } K_n = \frac{\left[ML_n^{(1-n)}\right]}{\left[ML_{(n-1)}^{(2-n)}\right]\left[L^-\right]} \qquad (6)$$

Cumulative complex formation and constant:

$$M^+ + nL^- \overset{\beta_n}{=} ML_n^{(1-n)} \text{ where } \beta_n = \frac{\left[ML_n^{(1-n)}\right]}{\left[M^+\right]\left[L^-\right]^n} \qquad (7)$$

The cumulative formation constant is related to the stepwise formation constant by the expression:

$$\beta_n = K_1 \cdot K_2 \ldots \cdot K_n \qquad (8)$$

The concentration of aqueous complexes as defined by the formation constants above (Eqs. 4, 5, 6, and 7) does not account for species activity, which is affected by the ionic strength of a solution where ion pairing increases with increasing ionic strength (See entries ▶ "Activity and Activity Coefficients" and ▶ "Debye-Hückel Equation").

Complex stability is affected by the strength of bonds which form, and as metals can be treated as hard or soft Lewis acids and ligands as hard or soft Lewis bases, the stability and reactions between complexes can be treated similarly to Lewis acid–base chemistry (Pearson 1963; Stumm and Morgan 1996) (See entry ▶ "Acid–Base Reactions"). Pearson's HSAB (Hard Soft Acid Base) principles can be used to determine the relative strength of bonds that form between metals and ligands (Liu et al. 2014; Pearson 1963).

Temperature and pressure of a system also affect complex stability. With increasing temperature the dielectric constant of water decreases making it less polarizable, which leads to a decrease in the coordination number of waters solvating an ion (Seward and Driesner 2004). Increasing pressure in a system may also lead to change in coordination environment of a complex due to changes in the solvent structure again leading to a dehydration of an ion (Seward and Driesner 2004). These changes in ion hydration and solvent structure inherently lead to a change in water activity affecting the water-rock interactions and complex formation and stability at higher temperatures and pressures.

Complex Speciation in the Environment

The formation of aqueous complexes affects many natural processes, from mineral solubility to metal transport in hydrothermal solutions. Formation waters occurring deep within the aquifers of sedimentary basins range in composition from fresh to extremely saline, and their composition can affect the diagenesis of minerals within the basin (See entry ▶ "Diagenesis"). Hydrothermal fluids found much deeper in the Earth's crust and potentially originating from the mantle or other sources can vary in composition significantly (See entry ▶ "Hydrothermal Solutions"). Hydrothermal fluids can transport high concentrations of various metals through complexation with ligands such as Cl^-, HS^- and OH^-. For example, the formation of gold complexes in hydrothermal solutions containing Cl^-, Br^-, HS^- and $NH_{3(aq)}$ ligands (Liu et al. 2014), where Au^+ preferentially binds with HS^- ligands to form a $Au(HS)_2^-$ complex.

The chemistry of Earth's oceans is affected by the complex speciation between a number of dissolved metals and ligands found in seawater. For instance, the ionic strength (I) of seawater (I = c. 0.69 m) leads to significant ion pairing and formation of complexes of $MgHCO_3^+$, $MgCO_3^0$, $MgSO_4^0$, $NaHCO_3^0$, $NaCO_3^-$, $NaSO_4^-$, $CaHCO_3^+$, $CaCO_3$, $CaSO_4^0$ and KSO_4^- in excess of 0.01 millimolal in solution. The pH of seawater is influenced by this complex speciation and in particular the equilibrium established between the bicarbonate (HCO_3^-) and carbonate (CO_3^{2-}) ligands, dissolved CO_2 and various metals (See entry ▶ "Carbon Cycle").

Understanding complex speciation is important to contaminant transport in shallow groundwater environments where toxic or radioactive metals have been mobilized in surface and groundwaters. For example, the persistence of methylmercury complexes (e.g., CH_3Hg^+, CH_3HgS^-, $(CH_3)_2Hg^0$, CH_3HgOH^0 and CH_3HgCl^0) in the environment, of which the neutral complexes are highly mobile increasing their bioavailability (Stumm and Morgan 1996).

Summary and Conclusions

Complex formation and speciation is important to understanding the distribution and transport of metals in the environment. The formation of aqueous complexes affects the solubility of minerals and transport of dissolved solutes in the environment from the Earth's oceans to formation waters in sedimentary basins and hydrothermal fluids. Complex stability is affected by the concentration and type of ligands available to bond with metals, as well as the temperature and pressure of a system. Further information about complex formation, structure and bonding can be found in most inorganic chemistry text books discussing crystal field theory and ligand field theory (e.g., Shriver and Atkins 1999).

Cross-References

- ▶ Acid–Base Reactions
- ▶ Activity and Activity Coefficients
- ▶ Aqueous Solutions
- ▶ Chelation
- ▶ Chemical Bonds
- ▶ Debye-Hückel Equation
- ▶ Diagenesis
- ▶ Equilibrium Constant
- ▶ Gouy-Chapman Theory
- ▶ Hydrothermal Solutions
- ▶ Kinetics of Geochemical Processes
- ▶ Ore Deposits
- ▶ Porphyrins
- ▶ Surface Geochemistry
- ▶ Van der Waals Force

References

Baes CF, Mesmer RE (1976) The Hydrolysis of Cations. Wiley, New York, 489 pp

Bock CW, Kaufman A, Glusker JP (1994) Coordination of water to magnesium cation. Inorganic Chemistry 33:419–427

Liu W, Etschmann B, Testemale D, Hazemann J-L, Rempel K, Müller H, Brugger J (2014) Gold transport in hydrothermal fluids: competition among the Cl^-, Br^-, HS^- and $NH_{3(aq)}$ ligands. Chemical Geology 376:11–19

Pearson RG (1963) Hard and soft acids and bases. Journal of the American Chemical Society 85:3533–3540

Pye CC, Rudolph W, Poirier RA (1996) An ab Initio investigation of lithium ion hydration. The Journal of Physical Chemistry 100:601–605

Rudolph W, Brooker MH, Pye CC (1995) Hydration of lithium ion in aqueous solution. The Journal of Physical Chemistry 99:3793–3797

Seward TM, Driesner T (2004) Chapter 5, Hydrothermal solution structure: experiments and computer simulations. In: Palmer DA, Fernández-Prini RJ, Harvey AH (eds) Aqueous Systems at Elevated Temperatures and Pressures: Physical Chemistry in Water, Steam and Hydrothermal Solutions. Elsevier, Amsterdam, pp 149–182

Shriver DF, Atkins PW (1999) Inorganic Chemistry, 3rd edn. Oxford University Press, Oxford, 763 pp

Stumm W, Morgan JJ (1996) Aquatic Chemistry: Chemical Equilibria and Rates in Natural Waters, 3rd edn. Wiley, New York, 1022 pp

Compound-Specific Isotope Analysis

Yi Ge Zhang
Department of Oceanography, Texas A&M University, College Station, TX, USA

Definition

Compound-specific isotope analysis (CSIA), as opposed to bulk analysis, determines the isotopic signatures (for example, $^{13}C/^{12}C$, D/H, $^{15}N/^{14}N$, $^{18}O/^{16}O$) at the molecular level. The separation and purification of organic compounds can be achieved by gas chromatography (GC) or liquid chromatography (LC). The analysis of stable isotopes requires an isotope ratio mass spectrometry (IRMS).

Analytical Methods: GC-IRMS

Traditionally, CSIA refers only to the stable isotope measurements of the molecules separated by GC. The system usually consists of a GC, a chemical reaction interface, and an IRMS (Sessions 2006; Summons 2000). Individual compounds are separated by the GC, followed by quantitative conversion at the interface, and continuous-flow isotopic analysis using the IRMS. The interface either diverts or removes the interfering compounds such as the solvents and H_2O.

Early CSIA focused on stable carbon isotopes (Hayes et al. 1989; Matthews and Hayes 1978). Organic molecules can be rapidly and quantitatively combusted to CO_2, done by metal oxides (e.g., CuO, NiO) with the presence of catalysts (e.g., Pt) at high temperature (900–1200 °C). The oxidizing reagents are regenerated by flushing the combustion reactor with O_2 after analysis (Merritt et al. 1995). The solvent peak is usually diverted by backflushing the reactor with a He flow. And the impurities in the CO_2 stream (H_2O, S, and N oxides) are removed by Nafion™, a selectively permeable membrane of the sulfonated fluoropolymer (Leckrone and Hayes 1997), and by passing the combusted gas through the elemental copper at a lower temperature. CO_2 is then analyzed in a gas source IRMS, which usually consists of an electron-impact ionization source, a magnetic-sector analyzer, and several Faraday cup detectors which receive analog signals of the ion currents.

Compound-specific nitrogen isotope measurement is also based on combustion/reduction, which produces NO_x then reduced to N_2 (Merritt and Hayes 1994). Notably, a bacterial method which could be used to convert organic N to N_2O significantly reduces the amount of N required for accurate measurements (Sigman et al. 2001). Hydrogen isotope analysis is usually achieved by pyrolysis using carbon-lined reactors heated to > 1440 °C (Burgoyne and Hayes 1998). In the IRMS ion source, H_2 reacts to form H_3^+ and therefore the "H_3-factor" must be determined and corrected for (Sessions et al. 2001). Oxygen isotope measurements also rely on pyrolysis and reduction, which transfers O from organic material to CO.

Recent Developments

GC-IRMS has greatly expanded our ability to analyze compound-specific isotopes on GC-amenable molecules. However, many higher molecular weight, more complex compounds cannot be directly vaporized in the traditional GC. Further, the process of combustion/pyrolysis destroys the position-specific isotope signatures. Nonetheless, recent efforts have made interesting developments to tackle these issues.

Compound Separations Without a GC

A large number of nonvolatile biochemical such as nucleic acids, proteins, polar lipids, and carbohydrates cannot be separated by the traditional GC. To tackle this problem, a variety of offline preparative procedures (e.g., prep LC) were developed to fraction-collect and purify the compounds of interest, for further "bulk" analysis. The stable isotope

measurements can be achieved on the conventional elemental analyzer (EA)-IRMS or the spooling wire microcombustion (SWiM-IRMS)(Sessions et al. 2005) and nano-EA-IRMS (Polissar et al. 2009), both of which significantly reduce the quantities needed for isotope ratio monitoring. For example, the precision on the SWiM-IRMS is about 0.4‰ for ~2 μg C (Pearson et al. 2016).

High-Temperature GC-IRMS

An alternative approach to volatize the larger compounds is to increase the temperature of the GC oven, from ~320 °C to a maximum of ~450 °C. Studies have shown that if connections are all air-tight by using metal ferrules, high-temperature resistant components as well as sensitive systems that discriminates the analytes from high column bleeding, the GC-MS system can detect *n*-alkanes with more than 100 carbon atoms (Sutton and Rowland 2012). Measuring these high molecular weight compounds on GC-IRMS is being experimented as this entry is written in 2016.

Site-Specific Isotope Measurements

The conversion of C, H, N, or O to analyte gases is required by CSIA based on the traditional gas source IRMS. The isotopic value, however, is an average over all elemental positions within its molecular structure. Intramolecular variations in isotopic signatures are missing in this approach.

Innovations in the technology, including the utilizations of high-sensitivity detectors capable to quantify low-intensity multiply substituted ion beams using both improved IRMS (Eiler et al. 2013) or IR absorption spectroscopy (Ono et al. 2014). Position-specific intramolecular isotopic distributions are now being reported from several molecules, including ethane (Webb et al. 2013) and propane (Piasecki et al. 2016).

Selected Applications in Geoscience

The Alkenone-$\delta^{13}C$ Method for pCO_2

One of the earliest applications of CSIA was to measure the $\delta^{13}C$ of biomarkers associated with photosynthesis, such as porphyrins (Hayes et al. 1989; Popp et al. 1989) and alkenones (Jasper and Hayes 1990), as a proxy for atmospheric CO_2 levels. This methodology stems through the isotopic fractionation models of C3 plants during photosynthesis (Farquhar et al. 1982, 1989). Compared with the traditional bulk organic carbon measurements, CSIA provides isotopic evidence from the substance with a clear photosynthetic origin. Alkenones are then favored over porphyrins because they are only produced by a few species of the haptophyte algea in the modern ocean (Conte et al. 1994).

The alkenone-^{13}C based pCO_2 estimates have covered most of the Cenozoic era, which reveals a long-term decline of the greenhouse gas forcing from the Paleogene into the Neogene (Pagani et al. 2005; Zhang et al. 2013). Specific time intervals are also targeted, with pCO_2 often found to be tightly coupled to major climate change events (Bijl et al. 2010; Pagani et al. 2011). Alkenone-derived reconstructions largely agree with other proxy-based CO_2 estimates (Palmer et al. 2010), but occasionally show low sensitivity to CO_2 changes (Badger et al. 2013). Efforts are being made to constrain the physiology of the haptophyte algae and how they are going to affect carbon isotope fractionations (Bolton et al. 2016; Henderiks and Pagani 2007).

^{13}C–Depleted Biomarkers and Methane Cycling

CSIA is widely used to trace biogeochemical processes (Freeman et al. 1990). For example, massive amount of methane produced in the deep ocean are oxidized anaerobically before they can reach the sea surface. Anaerobic oxidation of methane (AOM) has been suggested by geochemical data in the 1970s (Reeburgh 1976). However, for a long time the microorganisms responsible for this process could not been identified. In 1999, Hinrichs et al. noticed that the biomarkers associated with archaea in a gas hydrate site offshore of northern California are extremely depleted in ^{13}C. The $\delta^{13}C$ of these biomarkers, including archaeol, hydroxyarchaeol, and *sn*-2-hydroxyarchaeol, ranges between −100 and −110‰, indicating that the carbon source of the archaea has a methenotrophic origin (Hinrichs et al. 1999). Later, microscopic evidence was provided to confirm the role of archaea in the AOM process, and showed that a consortium of archaea and sulfate reducing bacteria that commonly perform sulfate reduction – anaerobic methane oxidation in marine sediment (Boetius et al. 2000).

Summary

Compound-specific isotope analysis has broad utilities in tracing sources and revealing the biogeochemical processes that involves isotopic fractionation. The field has greatly expanded from measuring carbon isotopes of GC-amendable compounds to employing a variety of approaches to separate and purify compounds, including those that cannot be separated by the traditional GC, for isotope measurements of C, N, H, O, S, and other light elements. Position-specific isotope analysis is also being explored that adds a whole new dimension to CSIA. CSIA is widely applied in organic geochemistry, biogeochemistry, geobiology, paleoclimatology, forensic geoscience, and petroleum science and technology.

Cross-References

- Atmospheric Evolution
- Biogeochemistry
- Carbon Cycle
- Carbon Isotopes
- Gas Chromatography–Mass Spectrometry (GC–MS)
- Hydrogen Isotopes
- Natural Gas
- Nitrogen Isotopes
- Organic Geochemistry
- Oxygen Isotopes
- Paleoclimatology
- Porphyrins
- Stable Isotope Geochemistry

References

Badger MPS, Schmidt DN, Mackensen A, Pancost RD (2013) High-resolution alkenone palaeobarometry indicates relatively stable pCO_2 during the Pliocene (3.3–2.8 ma). Phil Trans R Soc A 371(2001):20130094

Bijl PK, Houben AJP, Schouten S, Bohaty S, Sluijs A, Reichart GJ, Damste JSS, Brinkhuis H (2010) Transient middle eocene atmospheric CO_2 and temperature variations. Science 330:819–821

Boetius A, Ravenschlag K, Schubert CJ, Rickert D, Widdel F, Cleseke A, Amann R, Jorgensen BB, Witte U, Pfannkuche O (2000) A marine microbial consurtium apparently mediating anaerobic oxidation of methane. Nature 407:623–626

Bolton CT, Hernandez-Sanchez MT, Fuertes M-A, Gonzalez-Lemos S, Abrevaya L, Mendez-Vicente A, Flores J-A, Probert I, Giosan L, Johnson J, Stoll HM (2016) Decrease in coccolithophore calcification and CO_2 since the middle Miocene. Nat Commun 7:10284

Burgoyne TW, Hayes JM (1998) Quantitative production of H_2 by pyropysis of gas chromatographic effluents. Anal Chem 70:5136–5141

Conte M, Volkman JK, Eglinton G (1994) Lipid biomarkers of the haptophyta. In: Green JC, Leadbeater BSC (eds) The haptophyte algae. Clarendon Press, Oxford, pp 351–377

Eiler JM, Clog M, Magyar P, Piasecki A, Sessions AL, Stolper D, Deerberg M, Schlueter H-J, Schwieters J (2013) A high-resolution gas-source isotope ratio mass spectrometer. Int J Mass Spectrom 335:45–56

Farquhar GD, O'Leary MH, Berry JA (1982) On the relationship between carbon isotope discrimination and the intercellular carbon dioxide concentration in leaves. Aust J Plant Physiol 9:121–137

Farquhar GD, Ehleringer JR, Hubick KT (1989) Carbon isotope discrimination and photosynthesis. Annu Rev Plant Physiol Plant Mol Biol 40:503–537

Freeman KH, Hayes JM, Trendel J-M, Albrecht P (1990) Evidence from carbon isotope measurements for diverse origins of sedimentary hydrocarbons. Nature 343:254–256

Hayes JM, Freeman KH, Popp BN, Hoham CH (1989) Compound-specific isotopic analyses: a novel tool for reconstruction of ancient biogeochemical processes. Org Geochem 16:1115–1128

Henderiks J, Pagani M (2007) Refining ancient carbon dioxide estimates: significance of coccolithophore cell size for alkenone-based pCO_2 records. Paleoceanography 22:PA3202

Hinrichs KU, Hayes JM, Sylva SP, Brewer PG, DeLong EF (1999) Methane-consuming archaebacteria in marine sediments. Nature 398:802–805

Jasper JP, Hayes JM (1990) A carbon isotope record of CO_2 levels during the late quaternary. Nature 347:462–464

Leckrone KJ, Hayes JM (1997) Efficiecy and temperature dependence of water removal by membrane dryers. Anal Chem 1997:911–918

Matthews DE, Hayes JM (1978) Isotope-ratio-monitoring gas chromatography mas spectrometry. Anal Chem 50:1465–1473

Merritt DA, Hayes JM (1994) Nitrogen isotopic analysis by isotope-ratio-monitoring gas chromatography-mass spectrometry. J Am Soc Mass Spectrom 5:387–397

Merritt DA, Freeman KH, Ricci MP, Studley SA, Hayes JM (1995) Performance and optimization of a combustion interface for isotope ratio monitoring gas chromatography/mass spectrometry. Anal Chem 67:2461–2473

Ono S, Wang DT, Gruen DS, Sherwood Lollar B, Zahniser MS, McManus BJ, Nelson DD (2014) Measurement of a doubly substituted methane isotopologue, $^{13}CH\ ^{3}D$, by tunable infrared laser direct absorption spectroscopy. Anal Chem 86:6487–6494

Pagani M, Zachos JC, Freeman KH, Tipple B, Bohaty S (2005) Marked decline in atmospheric carbon dioxide concentrations during the Paleogene. Science 309:600–603

Pagani M, Huber M, Liu ZH, Bohaty S, Henderiks J, Sijp W, Krishnan S, DeConto R (2011) The role of carbon dioxide during the onset of Antarctic glaciation. Science 334:1261–1264

Palmer MR, Brummer GJ, Cooper MJ, Elderfield H, Greaves MJ, Reichart GJ, Schouten S, Yu JM (2010) Multi-proxy reconstruction of surface water pCO_2 in the northern Arabian Sea since 29 ka. Earth Planet Sci Lett 295:49–57

Pearson A, Hurley S, Shah Walter SR, Kusch S, Lichtin S, Zhang YG (2016) Stable carbon isotope ratios of intact GDGTs indicate heterogeneous sources to marine sediments. Geochim Cosmochim Acta 181:18–35

Piasecki A, Sessions AL, Lawson M, Ferreira AA, Santos Neto EV, Eiler JM (2016) Analysis of the site-specific carbon isotope composition of propane by gas source isotope ratio mass spectrometer. Geochim Cosmochim Acta 188:58–72

Polissar PJ, Fulton JM, Junium CK, Turich CC, Freeman KH (2009) Measurement of ^{13}C and ^{15}N isotopic composition on nanomolar quantities of C and N. Anal Chem 81:755–763

Popp BN, Takigiku R, Hayes JM, Louda JW, Baker EW (1989) The post-Paleozoic chronology and mechanism of ^{13}C depletion in primary marine organic matter. Am J Sci 289:436–454

Reeburgh WS (1976) Methane comsumption in Cariaco trench waters and sediments. Earth Planet Sci Lett 28:337–344

Sessions AL (2006) Isotope-ratio detection for gas chromatography. J Sep Sci 29:1946–1961

Sessions AL, Burgoyne TW, Hayes JM (2001) Correction of H_3^+ contributions in hydrogen isotope ratio monitoring mass spectrometry. Anal Chem 73:192–199

Sessions AL, Sylva SP, Hayes JM (2005) Moving-wire device for carbon isotopic analyses of nanogram quantities of nonvolatile organic carbon. Anal Chem 77:6519–6527

Sigman DM, Casciotti KL, Andreani M, Barford C, Galanter M, Bohlke JK (2001) A bacterial method for the nitrogen isotopic analysis of nitrate in seawater and freshwater. Anal Chem 73:4145–4153

Summons R (2000) Compound-specific isotope analysis. In: Marshall CP, Fairbridge RW (eds) Encyclopedia of geochemistry. Springer, Amsterdam, Netherlands, p 100

Sutton PA, Rowland SJ (2012) High temperature gas chromatography-time-of-flight-mass spectrometry (HTGC-ToF-MS) for high-bioling compounds. J Chromatogr A 1243:69–80

Webb M, Wang Y, Braams BJ, Bowman JM, Miller TF III (2013) Equilibrium clumped-isotope effects in doubly substituted isotopologues of ethane. Geochimi Cosmochimi Acta 197:14–26

Zhang YG, Pagani M, Liu Z, Bohaty SM, DeConto R (2013) A 40-million-year history of atmospheric CO_2. Phil Trans R Soc A 371:20130096

Copper

Xingcheng Liu and Xiaolin Xiong
Guangzhou Institute of Geochemistry, Chinese Academy of Sciences, Guangzhou, China

Element Data
Atomic Symbol: Cu
Atomic Number: 29
Atomic Weight: 63.546 u
Isotopes and Abundances: ^{63}Cu 69.15%, ^{65}Cu 30.85%
1 Atm Melting Point: 1084.6 °C
1 Atm Boiling Point: 2562 °C
Common Valences: 2+, 1+
Ionic Radii: 1+: fourfold: 60 pm, sixfold: 77 pm; 2+: Fourfold: 57 pm, sixfold: 73 pm
Pauling Electronegativity: 1.9
First Ionization Energy: 745.5 kJ mol^{-1}
Chondritic (CI) Abundance: 131 ppm
Silicate Earth Abundance: 20–30 ppm
Crustal Abundance: 27 ppm
Seawater Abundance: 0.4–5 nmol/kg
Core Abundance: 125 ppm

Properties

Copper (Cu) is a reddish metal with an atomic number 29, standard atomic weight of 63.546, and melting point of 1357.8 K at 1 atm. It was moderately volatile during the Earth formation by accretion of solid material condensed from the solar nebula. As a siderophile element, it partitioned into the core during the separation of metallic core from molten silicate mantle. In the silicate Earth, it behaves as a chalcophile element and usually forms stable sulfides; chalcopyrite ($CuFeS_2$) is the most common copper-bearing sulfide. In nature, copper is the 26th most abundant element in the Earth's crust, with concentrations ranging from 26 ppm in the lower continental crust to 28 ppm in the upper continental crust; the concentration in the oceanic crust is lower at 44 ppm. Concentrations in MORB range from 60 to 80 ppm, in arc basalts from 50 to 100 ppm, and in oceanic island basalts from 80 to 120 ppm (White 2013).

History and Use

Cu was the first metal people learned to smelt and this discovery ended the Stone Age in many parts of the world. The discovery that alloying it with tin produced bronze, a stronger metal, led to the Bronze Age.

Due to its high electrical conductivity, tensile strength, ductility, creep resistance, corrosion resistance, low thermal expansion, and high thermal conductivity, copper is extensively used in building construction, power generation and transmission, electronic product manufacturing, and the production of industrial machinery and transportation vehicles nowadays (Doebrich 2009). Besides the pure metal, copper is often alloyed with zinc, tin, gold, and nickel in industrial applications.

The US Geological Survey estimates the global mine production and consumption of Cu is over 18 and 20 million metric tons in 2015, respectively. Major producing countries include Chile, China, and Peru.

Geochemical Behavior: Magmatic Processes

Copper dissolves in silicate melts (natural magmas) dominantly as Cu^{1+} and perhaps in very minor amounts as Cu^{2+}. Copper is believed to dissolve in silicate melts mainly as $CuO_{0.5}$. The solubility of Cu in sulfur-free silicate melts increases with increasing temperature and increasing oxygen fugacity (Liu et al. 2015 and references therein). Zajacz et al. (2012, 2013) also suggest that Cu dissolves in silicate melts dominantly as Cu–O complex, while Cu–S and Cu–Cl complexes are not significant; thus, its solubility is enhanced only slightly by the presence of chlorine (Cl) and sulfur (S) in the melts.

In magmatic evolution, the geochemical behavior of Cu is controlled by the partition coefficients between silicate minerals, Fe–Ti oxides, sulfides, and magmas. The partition coefficients (given in Table 1) suggest that Cu is highly incompatible in silicate minerals (generally <0.2), incompatible to moderately compatible in Fe–Ti oxides, and highly compatible in sulfides. It should be noted that the partition coefficients are generally controlled by compositions of silicate melts, temperature, pressure, and oxidation state. Thus it's important to know the chemical and physical environmental conditions while applying the partition coefficients to predict the geochemical behavior of Cu.

Geochemical Behavior: Hydrothermal Processes

In contrast, the behavior of Cu in fluids (volatile phases) is a different story. The presences of S and Cl significantly enhance the solubility of Cu in the geological fluids. According to direct Cu K-edge X-ray absorption near-edge structure (XANES) spectra, Berry et al. (2006) suggest that Cu^{+} is stable in high-temperature brines in synthetic

Copper, Table 1 Partition coefficients of Cu between mineral and silicate melts

Minerals	Liu et al.	F & C	Lee et al.	A & P	Recommended
Olivine	0.04–0.20	0.06–0.21	0.03–0.16	0.02–0.07	0.1
Orthopyroxene	0.04–0.24	0.15–0.82	0.03		0.1
Clinopyroxene	0.04–0.45		0.04	0.01–0.07	0.2
Garnet	0.01–0.06		0.004		0.04
Amphibole	0.04–0.20		0.05		0.1
Plagioclase	0.02–0.12				0.08
Spinel	0.18–1.3		0.22		0.5
Fe–Ti oxides	0.2–1.8			0.17–0.63	1
Sulfides	L & A	K & W	Zajacz et al.	M & B	
MSS (pyrrhotite)	280–42,000		50–9400		
Sulfide liquid	800–4600	38–675		1060–2130	

Data are from Liu et al. (2014, 2015); F & C, Fellows and Canil (2012); Lee et al. (2012); A & P, Audétat and Pettke (2006); L & A, Li and Audétat (2012, 2015); K & W, Kiseeva and Wood (2013); Zajacz et al. (2013); M & B, Mungall and Brenan (2014).
MSS monosulfide solid solution.

fluid inclusions. In addition, Cu typically occurs as $CuCl_2^-$ ($\pm Cu(HS)_2^-$) in natural hydrothermal systems, in which the partition coefficients of Cu between volatile phases and silicate melts range from dozens to several hundreds (Simon and Ripley 2011; Pokrovski et al. 2013). This means that Cu will be transported into brines or vapors from ascending magma in magmatic–hydrothermal processes if the magmatic aqueous fluids are present. The mass transfer of Cu from magmas to volatile phase(s) is the most important process in the development of a porphyry Cu deposit (Audétat and Simon 2012, and references therein).

Ore Deposits

Most copper is extracted from ore deposits as copper sulfides. Porphyry Cu deposits and sediment-hosted Cu deposits contain most portions of the world's Cu resources. Porphyry ore deposits supply over 70% of the world's copper. They dominantly formed above subduction zones and most of them are genetically related to intermediate to felsic calc-alkaline magmas, which provide metals and fluids (e.g., H_2O, CO_2, Cl, and S) for the ore formation. However, the most important controlling factor(s) is still debated.

Individual copper deposits may contain millions of tons of copper and generally are developed by using open-pit mining methods (Doebrich 2009).

Natural Waters

Copper exists in natural waters mainly as Cu^{2+} and is readily complexed by hydroxyl and carbonate. Surface water concentrations of dissolved Cu are 63.55 ppt in the open ocean and 1.48 ppb in the rivers (global average) (Bruland et al. 2014; Gaillardet et al. 2014). The Cu^{2+} in surface waters is buffered by a strong Cu-binding class of organic ligands, called L_1, which chelates nearly 99.8% Cu^{2+} and reduces the Cu^{2+} concentration to a nontoxic condition for phytoplankton. Without organic complexation, the dominant species of Cu would be $Cu(CO_3)^0$ and approximately a factor of 20 lower than the total dissolved concentration (Bruland et al. 2014 and references therein).

Biological Utilization and Toxicity

$Cu^{2+}$and Cu^+ can participate in a wide spectrum of interactions with proteins to drive diverse structures and biochemical reactions. As life evolved, more complex roles for Cu arose, concurrent with the elaboration of mechanisms to tightly regulate acquisition and distribution of Cu and provide protection against Cu toxicity (Festa and Thiele 2011). It is an essential and required trace element in plants and animals but can be toxic to some microorganisms at relatively low concentrations. Defects in Cu homeostasis lead to human disease. On the other hand, excess Cu intake induces toxicity for human.

Summary

Humans have been using copper for several thousands of years. As an industrial material, it is significant and widely used in modern society. As a trace element in Earth, it also provides insight into the crust–mantle differentiation, the formation of ore deposits, and the redox history of magmas.

Cross-References

- Chalcophile Elements
- Copper Isotopes
- Ore Deposits
- Partitioning and Partition Coefficients
- Sulfide Minerals

References

Audetat A, Pettke T (2006) Evolution of a porphyry-Cu mineralized magma system at Santa Rita, New Mexico (USA). J Petrol 47 (10):2021–2046

Audétat A, Simon A (2012) Magmatic controls on porphyry copper deposits. Soc Econ Geol Spec Publ 16:573–618

Berry AJ, Hack AC, Mavrogenes JA, Newville M, Sutton SR (2006) A XANES study of Cu speciation in high-temperature brines using synthetic fluid inclusions. Am Mineral 91(11–12):1773–1782

Bruland KW, Middag R, Lohan MC (2014) 8.2 – controls of trace metals in seawater. In: Turekian HDHK (ed) Treatise on geochemistry, 2nd edn. Elsevier, Oxford, pp 19–51

Doebrich J (2009) Copper–A metal for the ages: U.S. Geological Survey fact sheet 2009–3031, 4 p. Available at http://pubs.usgs.gov/fs/2009/3031/

Fellows SA, Canil D (2012) Experimental study of the partitioning of Cu during partial melting of Earth's mantle. Earth Planet Sci Lett 337:133–143

Festa RA, Thiele DJ (2011) Copper: an essential metal in biology. Curr Biol 21(21):R877–R883

Gaillardet J, Viers J, Dupré B. 7.7 – trace elements in river waters. In: Turekian HDHK (ed) Treatise on geochemistry, 2nd edn. Elsevier, Oxford, pp 195–235

Kiseeva ES, Wood BJ (2013) A simple model for chalcophile element partitioning between sulphide and silicate liquids with geochemical applications. Earth Planet Sci Lett 383:68–81

Lee C-TA, Luffi P, Chin EJ, Bouchet R, Dasgupta R, Morton DM, Le Roux V, Yin Q-Z, Jin D (2012) Copper systematics in arc magmas and implications for crust-mantle differentiation. Science 336 (6077):64–68

Li Y, Audétat A (2012) Partitioning of V, Mn, Co, Ni, Cu, Zn, As, Mo, Ag, Sn, Sb, W, Au, Pb, and Bi between sulfide phases and hydrous basanite melt at upper mantle conditions. Earth Planet Sci Lett 355:327–340

Li Y, Audétat A (2015) Effects of temperature, silicate melt composition, and oxygen fugacity on the partitioning of V, Mn, Co, Ni, Cu, Zn, As, Mo, Ag, Sn, Sb, W, Au, Pb, and Bi between sulfide phases and silicate melt. Geochim Cosmochim Acta 162:25–45

Liu X, Xiong X, Audétat A, Li Y, Song M, Li L, Sun W, Ding X (2014) Partitioning of copper between olivine, orthopyroxene, clinopyroxene, spinel, garnet and silicate melts at upper mantle conditions. Geochim Cosmochim Acta 125:1–22

Liu X, Xiong X, Audetat A, Li Y (2015) Partitioning of Cu between mafic minerals, Fe-Ti oxides and intermediate to felsic melts. Geochim Cosmochim Acta 151:86–102

Mungall J, Brenan J (2014) Partitioning of platinum-group elements and Au between sulfide liquid and basalt and the origins of mantle-crust fractionation of the chalcophile elements. Geochim Cosmochim Acta 125:265–289

Pokrovski GS, Borisova AY, Bychkov AY (2013) Speciation and transport of metals and metalloids in geological vapors. Rev Mineral Geochem 76(1):165–218

Simon AC, Ripley EM (2011) The role of magmatic sulfur in the formation of ore deposits. Rev Mineral Geochem 73(1):513–578

White WM (2013) Geochemistry. Wiley-Blackwell, Oxford, UK

Zajacz Z, Candela PA, Piccoli PM, Wälle M, Sanchez-Valle C (2012) Gold and copper in volatile saturated mafic to intermediate magmas: Solubilities, partitioning, and implications for ore deposit formation. Geochim Cosmochim Acta 91:140–159

Zajacz Z, Candela PA, Piccoli PM, Sanchez-Valle C, Wälle M (2013) Solubility and partitioning behavior of Au, Cu, Ag and reduced S in magmas. Geochim Cosmochim Acta 112:288–304

C

Copper Isotopes

Paul Savage
Department of Earth and Environmental Sciences, University of St Andrews, St Andrews, UK

Synonyms

Copper stable isotopes; Cu isotopes

Introduction

Copper has two stable isotopes, ^{63}Cu and ^{65}Cu, with relative abundances of 69.15% and 30.85%, respectively. A transition metal, Cu is moderately siderophile and strongly chalcophile (around 2/3 of Earth's Cu is thought to be stored in its core). Copper is redox-sensitive and is present in three oxidation states in terrestrial environments: native Cu^0, Cu^+ and Cu^{2+}. Copper is both economically important and an essential micronutrient. For all these reasons, isotopic variations of Cu have the potential to inform us of processes, sources, and phenomena in all disciplines of the geosciences. A more detailed review of the myriad applications of Cu isotopes is given by Moynier et al. (in press).

Analysis

As with many other stable isotope systems, accurate, precise, and routine measurement of Cu isotope ratio was made possible with the advent of Multi-collector Inductively-Coupled-Plasma Mass Spectrometry (MC-ICPMS) and precisions of <50 ppm are now attainable. This is usually by solution analysis, whereby copper is isolated from a dissolved sample using ion exchange chromatography (Marechal et al. 1999); however, some in-situ laser ablation isotope analyses has been made (Ikehata and Hirata 2013). Variations in Cu isotopes are represented using the delta notation as $\delta^{65}Cu$ in permil (‰; Eq. 1), relative to the pure Cu standard NIST976:

$$\delta^{65}\mathrm{Cu} = \left[\frac{\left(^{65}\mathrm{Cu}/^{63}\mathrm{Cu}\right)_{\mathrm{sample}}}{\left(^{65}\mathrm{Cu}/^{63}\mathrm{Cu}\right)_{\mathrm{NIST976}}} - 1\right] \times 1000 \qquad (1)$$

(N.B. while this standard is still utilized in Cu isotope analysis, it is now commercially unavailable and a number of replacements have been characterized, e.g., Moeller et al. 2012; however, δ^{65}Cu values should remain relative to NIST976 using a precalibrated standard, to allow for direct comparison of all Cu isotope data).

Meteorites

The chondritic meteorites display significant variability in Cu isotope abundances. Carbonaceous chondrites (CC) define the largest range, from CI (0.02 ± 0.12) to CV (-1.45 ± 0.04) and each group has a distinct average (Fig. 1; Luck et al. 2003). Ordinary chondrites (OC) define a smaller range; nevertheless, the groups H, L, and LL again have distinct δ^{65}Cu, becoming more enriched in ^{65}Cu with decreasing Fe content (Fig. 1). Both CC and OC δ^{65}Cu

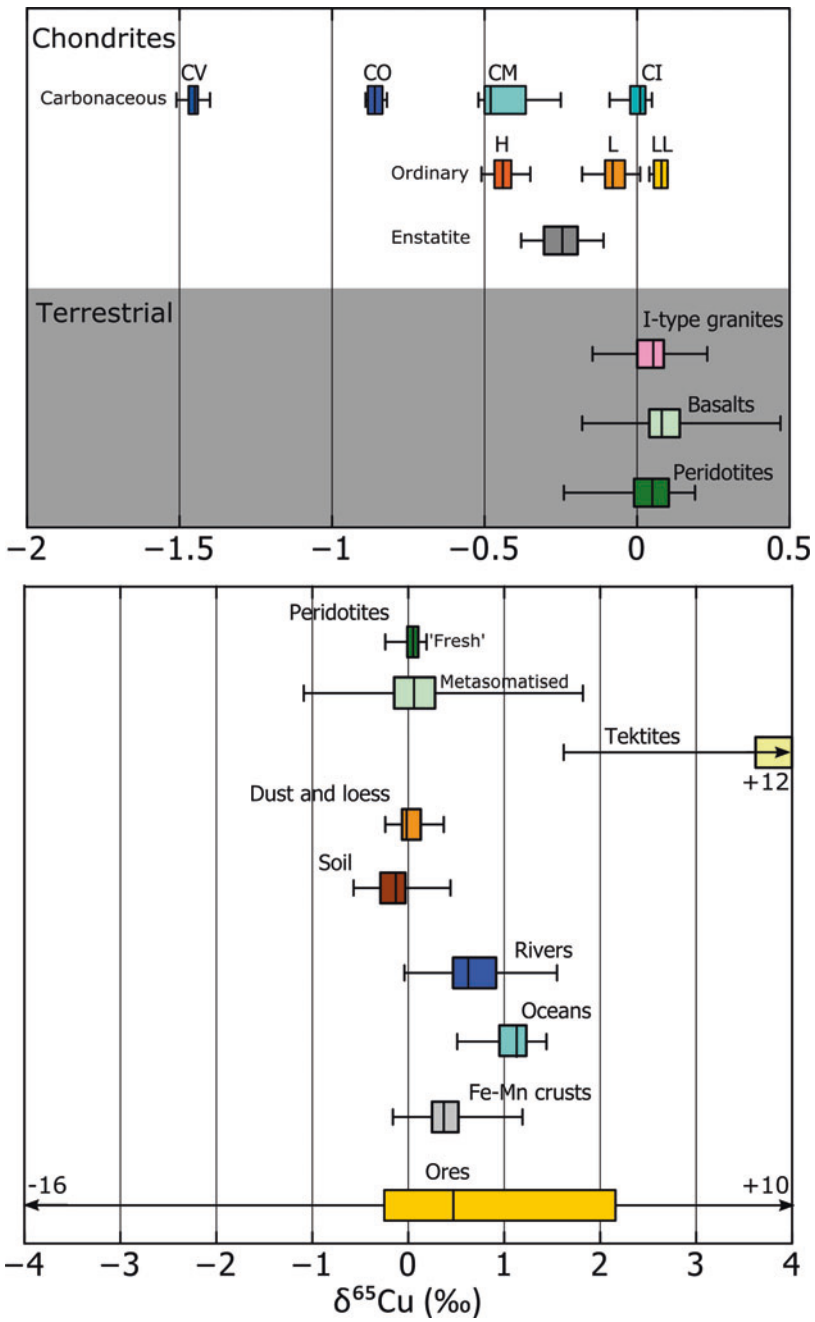

Copper Isotopes, Fig. 1 *Box* and *whisker plot* showing representative ranges of various Cu isotope reservoirs – see text for data sources. *Top panel* – high-temperature and extra-terrestrial samples. *Bottom panel* – impact-generated and critical zone (low temperature) samples

values vary systematically with oxygen isotope anomaly ($\Delta^{17}O$), which Luck et al. (2003) interpreted as revealing the presence of two, possibly three, distinct Cu isotope reservoirs in the early solar system, which mixed in varying proportions by nebula processing. Unlike carbonaceous and ordinary, enstatite chondrite groups (EH and EL) have similar Cu isotope compositions, which fall in the middle of the primitive meteorite range (-0.25 ± 0.09; Fig. 1). Savage et al. (2015a) used these data, in part, to define the bulk Earth $\delta^{65}Cu$ based on the observation that for many other isotope systems, enstatite chondrites and terrestrial materials appear identical.

In terms of iron meteorites, the first Cu isotope analyses by Luck et al. (2005) showed that IIIAB (magmatic), IA, and IIICD (silicate-bearing) iron meteorites showed similar, limited compositional ranges which broadly fell within the chondrite array ("magmatic" irons are thought to represent the cores of asteroids, and "silicate-bearing" possibly represent impact-generated melt-pools). A subsequent study by Bishop et al. (2012) showed that the silicate-bearing irons' Cu isotope and $\Delta^{17}O$ compositions correlate – as with the chondrites. The same could be true for the magmatic irons; as these meteorites have no silicates (and thus minimal oxygen to measure), Bishop et al. (2012) suggested that their Cu isotope compositions could instead be used to indicate genetic links with other meteorites. Most recently, large (negative) Cu isotope variations (-5.84 to -0.24) have been measured in the volatile element-poor IVB meteorites (Chen et al. 2016). These meteorites have high Ni/Cu ratios, and these negative enrichments are interpreted as resulting from variable exposure to galactic cosmic rays, whereby neutron capture forms excesses of ^{63}Ni, which decays quickly to ^{63}Cu.

Igneous Rocks

Two recent estimates of the copper isotope composition of the bulk silicate Earth (BSE; i.e. the mantle and crust) place it at 0.07 ± 0.10 and 0.06 ± 0.20 (Savage et al. 2015a; Liu et al. 2015, respectively). Both estimates were based on representative suites of mantle peridotites and ultra-mafic and mafic mantle-derived melts (e.g. komatiites, mid-ocean ridge basalts, ocean-island basalts) and are identical within error. Copper isotopes do not appear to fractionate greatly as a result of magmatic differentiation, even in systems where sulfide fractionation is occurring (Savage et al. 2015b). There appears to be a small enrichment (+0.1 ‰) in heavy Cu as differentiation approaches rhyolitic compositions, which agrees with the few analyses of I-type granites available in the literature (Li et al. 2009; Fig. 1). Metasomatism appears to have a strong effect on Cu isotope compositions, as evinced by much larger Cu isotope variations seen in metasomatized peridotites (Savage et al. 2015b; Liu et al. 2015; Fig. 1). This raises the possibility that Cu isotopes could be used to characterize the nature of a metasomatic agent.

Planetary Accretion and Differentiation

Savage et al. (2015a) noted that the Cu isotope composition of BSE is heavy compared to estimates for bulk Earth and suggested that fractionation occurred during Earth's differentiation. This isotope difference could reflect metal-silicate equilibration during core formation; however, experiments performed by Savage et al. (2015a), as well as analyses of individual metal, silicate, and sulphide grains from iron meteorites (Williams and Archer 2011) suggest that metal-hosted Cu is isotopically heavier than co-evolving silicates. This seems to rule out core formation as explaining the positive $\Delta^{65}Cu_{BSE\text{-}bulk\ Earth}$ ($\delta^{65}Cu_{BSE} - \delta^{65}Cu_{bulk\ Earth}$), as an isotopically heavier core implies a negative $\Delta^{65}Cu_{BSE\text{-}bulk\ Earth}$. Savage et al. (2015a) argued that either 1) the $\Delta^{65}Cu_{BSE\text{-}bulk\ Earth}$ implies that the majority of mantle Cu was delivered post-core formation, by a CI-like impactor (cf. Schonbachler et al. 2010); or 2) this missing light Cu is stored in sulfides, either in the mantle or a reservoir that was subsequently admixed into the core. Further experimental constraints on the partitioning behavior of Cu isotopes are required, but there is great potential for Cu isotopes to reveal information about the formation of Earth and other rocky bodies.

Impact-Driven Loss of Cu

Some of the largest Cu isotope variations measured in natural samples are recorded in tektites, glasses formed by high-energy (i.e., meteorite) impact events. Values up to 12.5 ‰ have been measured in tektites from the across the globe (Fig. 1; Moynier et al. 2010; Rodovská et al. 2015), which have been interpreted as an effect of kinetic isotope fractionation – whereby the lighter isotope can escape to the gas phase more easily – in a diffusion-limited regime. Anomalously high Cu isotope compositions have also been measured in lunar soils (Moynier et al. 2006; Herzog et al. 2009), caused by micro-meteorite "gardening" and, potentially, lunar basalts (~0.5 ‰). Because igneous processes do not fractionate Cu isotopes resolvably, the isotopically heavy composition of the latter sample group relative to Earth could be induced by volatile Cu loss, reflecting the violent nature of the Moon's birth (Day and Moynier 2014).

Low Temperature Environments

Mechanical weathering (to form dust, loess, clastic sediments) does not appear (as would be expected) to fractionate Cu isotopes – with aeolian dust samples showing limited Cu isotope variation and compositions close to BSE (Fig. 1;

Dong et al. 2013). However, compared to that seen in high-temperature terrestrial settings, a much wider range of Cu isotope compositions have been measured in such systems affected by chemical weathering and biological activity that occur in the "critical zone".

Weathering/leaching of primary Cu-bearing minerals generally involves oxidation (from Cu^{+} to Cu^{2+}) and results in the release of isotopically heavier Cu (by ~0.5–4.0 ‰) relative to the source. This has been shown via experiments (Fernandez and Borrok 2009) as well as measurements of soils and corresponding pore waters (Fig. 1; Mathur et al. 2012). Acid mine drainage solutions also have relatively heavy Cu isotope compositions, thought to be related to the oxidation of the source Cu (Kimball et al. 2009). These observations have been corroborated by ab initio calculations (Fujii et al. 2013). Biological utilization of Cu can also involve oxidation (i.e. through the reductase enzyme in the plant root system), and where this occurs, the biologically-complexed Cu is heavier than the source (Jouvin et al. 2012).

Redox reactions are thought to be the main control over the extremely large range of Cu isotope compositions seen in ore minerals. Specifically, "primary" (igneous) ore minerals have compositions close to that of BSE (~0.0 ± 0.5 ‰), whereas supergene ores show huge variability (−16.5 to +10 ‰; Mathur et al. 2009; Fig. 1). These large variations are likely due to multiple cycles of oxidation and reduction in the supergene environment, although Rayleigh fractionation, kinetic effects, and complexing ligand (Fujii et al. 2013) could also play a role.

Most Cu in the "critical zone" is organically complexed or sorbed onto the surface of Fe (oxy)-hydroxides (Vance et al. 2009). In regards to organically complexed Cu, experiments show that this pool is isotopically heavier than the free Cu ion and that the magnitude of isotope fractionation between the two pools increases as the stability constant of the complex increases (e.g. Ryan et al. 2014) – again, corroborated by ab initio calculations (Sherman 2013). Like organic complexation, sorbtion onto Fe-oxides causes a positive isotope effect, with the sorbed Cu showing around a 1 ‰ enrichment compared to the free metal pool (Pokrovsky et al. 2008).

Vegetation also has an impact on Cu isotopes in the critical zone. In general, plant material has an isotopically light Cu isotope composition compared to the surface pool. In a study by Weinstein et al. (2011) on lentil plants, light Cu was seen to be preferentially transferred up the plant, such that the youngest leaves were isotopically lighter than the root system. Comparison experiments between Strategy I plants (which involve a reduction step during Cu utilization) and Strategy II (no reduction), reveal that the latter have lighter isotope compositions than the former, identifying the importance of the reduction step in controlling Cu isotope compositions under Strategy I (Jouvin et al. 2012; Ryan et al. 2013). Any organic-rich soil horizon should therefore be isotopically light, and this has been observed in natural settings where decaying plant material was present (e.g., Bigalke et al. 2011).

In summary, weathering and Cu bio-utilization in the critical zone release isotopically heavy Cu to the solution – via oxidation of primary minerals, organic complexation, and/or preferential storage of light Cu in biomass. This suggests that the riverine and ocean Cu isotope compositions should be heavier than the continents – and this is indeed the case. Measurements of the isotope composition of dissolved riverine Cu give an average composition of ~0.7 ‰ (Fig. 1; Vance et al. 2008) and, given that riverine input dominates oceanic Cu, this will be close to average ocean δ^{65}Cu. The recent study of Little et al. (2014) modeled both the elemental and isotopic ocean Cu cycle and revealed a missing, isotopically heavy, Cu sink. One explanation could be that ^{65}Cu is preferentially sorbed on Mn-Fe oxides (e.g. Pokrovsky et al. 2008); however, Little et al. (2014) went on to measure such samples and found that they were isotopically light (~0.2 ‰; Fig. 1) relative to the oceans. This issue, as of writing, remains unresolved.

Biomedical Applications

The application of traditionally geochemical techniques to biomedicine is a new and exciting topic (Albarède 2015). Copper plays a vital role in the human body, thus Cu isotopes may be extremely important in this new field. Arguably the most promising application for Cu isotopes is in the early detection of some cancers. In patients with cancer, blood serum Cu is known to be anomalously high; however, changes in serum [Cu] are typically too ambiguous to be usable as a biomarker. However, Telouk et al. (2015) found a significant difference in the Cu isotope composition of blood serum from cancer patients compared to healthy patients, which, in their pilot study, was more explicit than the canonical cancer biomarker.

Cross-References

- ▶ Chalcophile Elements
- ▶ Chemical Weathering
- ▶ Copper
- ▶ Formation and Evolution of the Earth
- ▶ Inductively Coupled Plasma Mass Spectrometry (ICP-MS)

References

Albarède F (2015) Metal stable isotopes in the human body: a tribute of geochemistry to medicine. Elements 11:265–269

Bigalke M, Weyer S, Wilcke W (2011) Stable Cu isotope fractionation in soils during oxic weathering and podzolization. Geochim Cosmochim Acta 75:3119–3134

Bishop MC, Moynier F, Weinstein C, Fraboulet JG, Wang K, Foriel J (2012) The Cu isotopic composition of iron meteorites. Meteorit Planet Sci 47:268–276

Chen H, Moynier F, Humayun M, Bishop MC, Williams J (2016) Cosmogenic effects on Cu isotopes in IVB iron meteorites. Geochim Cosmochim Acta 182:145–154

Day JM, Moynier F (2014) Evaporative fractionation of volatile stable isotopes and their bearing on the origin of the Moon. Philos Transact A 372:20130259

Dong S, Weiss DJ, Strekopytov S, Kreissig K, Sun Y, Baker AR, Formenti P (2013) Stable isotope ratio measurements of Cu and Zn in mineral dust (bulk and size fractions) from the Taklimakan Desert and the Sahel and in aerosols from the eastern tropical North Atlantic Ocean. Talanta 114:103–109

Fernandez A, Borrok DM (2009) Fractionation of Cu, Fe and Zn isotopes during weathering of sulfide-rich rocks. Chem Geol 264:1–12

Fujii T, Moynier F, Abe M, Nemoto K, Albarède F (2013) Copper isotope fractionation between aqueous compounds relevant to low temperature geochemistry and biology. Geochim Cosmochim Acta 110:29–44

Herzog GF, Moynier F, Albarède F, Berezhnoy AA (2009) Isotopic and elemental abundances of copper and zinc in lunar samples, Zagami, Pele's hairs, and a terrestrial basalt. Geochim Cosmochim Acta 73:5884–5904

Ikehata K, Hirata T (2013) Evaluation of UV-fs-LA-MC-ICP-MS for precise in situ copper isotopic microanalysis of cubanite. Anal Sci 29:1213–1217

Jouvin D, Weiss D, Mason T, Bravin M, Louvat P, Zhao F, Ferec F, Hinsinger P, Benedetti M (2012) Stable isotopes of Cu and Zn in higher plants: evidence for Cu reduction at the root surface and two conceptual models for isotopic fractionation processes. Environ Sci Technol 46:2652–2660

Kimball BE, Mathur R, Dohnalkova AC, Wall AJ, Runkel RL, Brantley SL (2009) Copper isotope fractionatin in acid mine drainage. Geochim Cosmochim Acta 73:1247–1263

Li W, Jackson S, Pearson NJ, Alard O, Chappell BW (2009) The Cu isotopic signature of granites from the Lachlan Fold Belt, SE Australia. Chem Geol 258:38–49

Little SH, Vance D, Walker-Brown C, Landing WM (2014) The oceanic mass balance of copper and zinc isotopes, investigated by analysis of their inputs, and outputs to ferromanganese oxide sediments. Geochim Cosmochim Acta 125:673–693

Liu S-A, Huang J, Liu J, Woerner G, Yang W, Tang Y-J, Chen Y, Tang L, Zheng J, Li S (2015) Copper isotopic composition of the silicate Earth. Earth Planet Sci Lett 427:95–103

Luck JM, Othman DB, Barrat JA, Albarède F (2003) Coupled ^{63}Cu and ^{16}O excesses in chondrites. Geochim Cosmochim Acta 67:143–151

Luck JM, Othman DB, Albarède F (2005) Zn and Cu isotopic variations in chondrites and iron meteorites: early solar nebula reservoirs and parent-body processes. Geochim Cosmochim Acta 69:5351–5363

Maréchal C, Télouk P, Albarède F (1999) Precise analysis of copper and zinc isotopic compositions by plasma-source mass spectrometry. Chem Geol 156:251–273

Mathur R, Titley S, Barra F, Brantley S, Wilson M, Phillips A, Munizaga F, Maksaev V, Vervoort J, Hart G (2009) Exploration potential of Cu isotope fractionation in porphyry copper deposits. J Geochem Explor 102:1–6

Mathur R, Jin L, Prush V, Paul J, Ebersole C, Fornadel A, Williams JZ, Brantley S (2012) Cu isotopes and concentrations during weathering of black shale of the Marcellus formation, Huntingdon County, Pennsylvania (USA). Chem Geol 304:175–184

Moeller K, Schoenberg R, Pedersen R-B, Weiss D, Dong S (2012) Calibration of the new certified reference materials ERM-AE633 and ERM-AE647 for copper and IRMM-3702 for zinc isotope amount ratio determinations. Geostand Geoanal Res 36(2): 177–199

Moynier F, Albarede F, Herzog GF (2006) Isotopic composition of zinc, copper and iron in lunar samples. Geochim Cosmochim Acta 70:6103–6117

Moynier F, Koeberl C, Beck P, Jourdan F, Telouk P (2010) Isotopic fractionation of Cu in tektites. Geochim Cosmochim Acta 74:799–807

Moynier F, Vance D, Fujii T, Savage PS (2017) The isotope geochemistry of zinc and copper. In: Teng F-Z, Watkins J, Dauphas N (eds), Reviews in mineralogy and geochemistry, vol 82, Non-traditional stable isotopes, pp 543–600. https://doi.org/10.2138/rmg.2017.82.13

Pokrovsky OS, Viers J, Emnova EE, Kompantseva EI, Freydier R (2008) Copper isotope fractionation during its interaction with soil and aquatic microorganisms and metal oxy(hyd)oxides: possible structural control. Geochim Cosmochim Acta 72:1742–1757

Rodovská Z, Magna T, Kato C, Savage PS, Moynier F, Žák K (2015) Zinc and copper isotopes in central European tektites and sediments from the Ries impact area – implications for material sources and loss of volatile elements during tektite formation. In: 46th lunar and planetary science conference, vol 1832, p 1951

Ryan BM, Kirby JK, Degryse F, Harris H, McLaughlin MJ, Scheiderich K (2013) Copper speciation and isotopic fractionation in plants: uptake and translocation mechanisms. New Phytol 199:367–378

Ryan BM, Kirby JK, Degryse F, Scheiderich K, McLaughlin MJ (2014) Copper isotope fractionation during equilibration with natural and synthetic ligands. Environ Sci Technol 48:862–866

Savage P, Moynier F, Chen H, Shofner G, Siebert J, Badro J, Puchtel IS (2015a) Copper isotope evidence for large-scale sulphide fractionation during Earth's differentiation. Geochem Perspect Lett 1:53–64

Savage P, Moynier F, Harvey J, Burton K (2015b) The behavior of copper isotopes during igneous processes. In: AGU conference, San Francisco

Schonbachler M, Carlson RW, Horan MF, Mock TD, Hauri EH (2010) Heterogeneous accretion and the moderately volatile element budget of Earth. Science 328:884–887

Sherman DM (2013) Equilibrium isotopic fractionation of copper during oxidation/reduction, aqueous complexation and ore-forming processes: predictions from hybrid density functional theory. Geochim Cosmochim Acta 118:85–97

Telouk P, Puisieux A, Fujii T, Balter V, Bondanese VP, Morel A-P, Clapisson G, Lamboux A, Albarède F (2015) Copper isotope effect in serum of cancer patients. A pilot study. Metallomics 7:299–308

Vance D, Archer C, Bermin J, Perkins J, Statham PJ, Lohan MC, Ellwood MJ, Mills RA (2008) The copper isotope geochemistry of rivers and the oceans. Earth Planet Sci Lett 274:204–213

Vance D, Teagle DAH, Foster GL (2009) Variable quaternary chemical weathering fluxes and imbalances in marine geochemical budgets. Nature 458:493–496

Weinstein C, Moynier F, Wang K, Paniello R, Foriel J, Catalano J, Foriel J (2011) Cu isotopic fractionation in plants. Chem Geol 286:266–271

Williams HM, Archer C (2011) Copper stable isotopes as tracers of metal-sulphide segregation and fractional crystallisation processes on iron meteorite parent bodies. Geochim Cosmochim Acta 75:3166–3178

Cosmic Elemental Abundances

Herbert Palme
Forschungsinstitut und Naturmuseum Senckenberg, Frankfurt am Main, Germany

Definition

The average chemical composition of the solar system is identical to the composition of the Sun, representing more than 99.8% of the mass of the solar system. Solar abundance data obtained from absorption spectroscopy and complemented by the more accurate chemical data on CI chondrites, a small group of meteorites with solar abundances of non-volatile elements, define the *solar system element abundances*, which are known to within a few percent for most elements. Many stars have compositions similar to the average solar system composition, justifying the term cosmic element abundances. Solar system abundances are, however, much better known than the more loosely defined cosmic element abundances.

The Concept of Cosmic Abundances

Three lines of evidence lead to the concept of cosmic abundances. (1) Since about 1920, it is possible to determine the abundances of most chemical elements in the photosphere of the Sun by using the absorption lines in the solar emission spectrum. Although this only allows determining the composition of the outer 200 km of the Sun, it is believed that the interior of the Sun has essentially the same composition. The same procedure can be applied to stars. Thus the chemical composition of numerous stars is known. (2) Undifferentiated or chondritic meteorites come from planetesimals that were never fully molten. These meteorites have compositions not very different from that of the solar photosphere. A precise match, i.e., agreement of most elements within the error bars between solar abundances and meteoritic abundances, is found for one specific group of meteorites, the CI chondrites. The agreement is for all elements heavier than oxygen and excluding the very volatile rare gases. Other groups of undifferentiated or chondritic meteorites deviate somewhat from the solar or CI abundances. (3) The Big Bang produced hydrogen (H), helium (He), and some lithium (Li), about 13.8 billion years ago. All other chemical elements were made later in stars by nuclear reactions. As a result the heavy element abundances in the universe increase continually with time. The parameter [Fe/H] of a star is called metallicity. It is the logarithm of the ratio of iron atoms divided by hydrogen atoms divided by the same ratio in the Sun. The metallicity of the 4.67 billion-year-old Sun is 1, and stars older than the Sun have metallicities lower than 1 and younger stars above 1. The relative abundances of metals (all elements heavier than H and He in the jargon of astronomers) are in most stars very similar to those in the Sun. This element pattern is in agreement with nucleosynthetic calculations. An important parameter is the stability of a nucleus or its binding energy. Elements with even mass or atomic number gaining stability from pairing energy of neutrons and/or protons are more stable and therefore more abundant than elements with uneven mass or atomic numbers. This is visible in Fig. 1, displaying the abundances of elements in the Sun versus atomic number.

The convergence of solar-observed photospheric abundances, measured meteoritic abundances, and calculations of nucleosynthesis to a single more or less constant element pattern is a strong indication for well-defined solar system abundances, which when extended to other stars become cosmic abundances. The only variable is the metallicity, the ratio of heavy elements to hydrogen, which continually increases with time.

Historical Background

During the 1920s and 1930s of the last century, Victor Moritz Goldschmidt and his colleagues measured and compiled chemical data of terrestrial rocks, meteorites, and individual phases of meteorites. Based on these data Goldschmidt set up a cosmic abundance table. Goldschmidt realized that most meteorites should be representative of average cosmic matter because they have not been affected by melting and crystallization, whereas the crust of the Earth, a product of mantle melting, is not representative of the Earth's bulk composition. Goldschmidt calculated the average concentrations of elements in cosmic matter by using a weighted mean of element abundances in meteorite phases: metal (2 parts), sulfide (1 part), and silicates (10) parts.

The German physicist Joseph von Fraunhofer (1787–1826) was the first to observe dark lines in the spectrum of the light emitted from the Sun. Some 50 years later, G. Kirchhoff (1824–1887) recognized that these lines are characteristic of chemical elements, and he correctly concluded that the outer cooler layers of the Sun absorb radiation from the hotter underlying parts. At the beginning of the twentieth century, C.H. Payne made the first attempts to

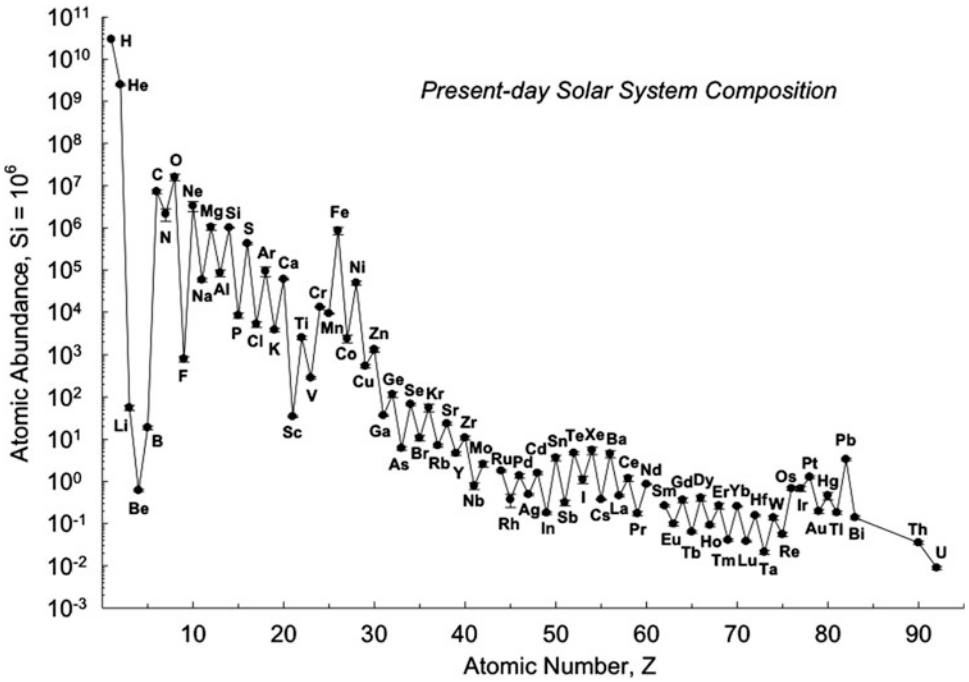

Cosmic Elemental Abundances, Fig. 1 Elemental solar system abundances as function of atomic number normalized to 10^6 Si atoms. The preponderance of H and He is obvious. The stability of ^{56}Fe and the higher stability of elements with even atomic numbers are clearly visible (Figure is from Lodders et al. 2009)

quantify the information contained in stellar and solar absorption lines. She recognized the large abundance of H in stars and gave the first estimates of the chemical composition of stellar atmospheres. Later N. H. Russell published the elemental abundances of 56 elements in the solar photosphere.

Goldschmidt's and Russell's lists had most of the major features of the solar system abundances as we know them today: the dominance of H and He; the strong decrease in abundance with increasing atomic number; the very low abundances of Li, Be, and B; and the pronounced abundance peak at ^{56}Fe (see Fig. 1).

Later compilations took into account improved analytical data of meteorites and of the solar photospheric spectrum (see Lodders et al. 2009 and Palme et al. 2014 for references).

Abundances of Elements in the Sun and in Meteorites

In Table 1, we have listed elemental abundances of the Sun and compare them to the abundances in CI chondrites which closely match the solar abundances for heavy elements. Solar and meteoritic abundances are calculated relative to 10^{12} hydrogen atoms, the scale used in astronomy. The Table is from Palme et al. (2014), and from Lodders et al. (2009). The solar abundances listed here are very similar to those in Asplund et al. (2009).

Table 2 contains the abundances of elements by mass in CI meteorites, chiefly the Orgueil meteorite. The table is from Palme et al. (2014), largely based on earlier compilations (Lodders et al. 2009). In the last column data are converted to atoms and normalized to 10^6 atoms of Si. The conversion from the astronomical scale (A_{ast}) based on 10^{12} H atoms to the meteoritical scale (A_{met}) based on 10^6 atoms of Si is according to Palme et al. (2014):

$$\log A_{ast} = \log A_{met} + 1.533$$

The CI chondrites match the solar element abundances within analytical uncertainties. Other groups of chondritic meteorites deviate somewhat from the solar composition. This is demonstrated in Fig. 2, where several abundance ratios are plotted for members of the major chondrite classes and compared with solar abundance ratios.

The major chondrite classes shown in Fig. 2 are carbonaceous chondrites with CI, CM, CO, and CV groups; ordinary chondrites with H, L, and LL groups; and enstatite chondrites with EH and EL groups. These are the most populated chondrite groups (e.g., Krot et al. 2003).

The element ratios plotted in Fig. 2 are representative of different cosmochemical components. Each of these

Cosmic Elemental Abundances, Table 1 Solar photospheric abundances and meteorite-derived solar system abundances

		Solar photosphere	s.d. dex	Meteorite (CI)	s.d. dex	Sun/meteorite N_{sun}/N_{met}
1	H	12		8.24	0.04	5.70E + 03
2	He	10.925	0.02	1.31		3.86E + 09
3	Li	1.10	0.10	3.28	0.04	0.01
4	Be	1.38	0.09	1.32	0.03	1.10
5	B	2.70	0.17	2.81	0.04	0.78
6	C	8.39	0.04	7.42	0.04	9.44
7	N	7.86	0.12	6.28	0.06	38.2
8	O	8.73	0.07	8.42	0.04	2.09
9	F	4.56	0.30	4.44	0.06	1.32
10	Ne	8.05	0.10	−1.1		1.40E + 09
11	Na	6.30	0.03	6.29	0.04	1.03
12	Mg	7.54	0.06	7.55	0.02	0.98
13	Al	6.47	0.07	6.45	0.03	1.06
14	Si	7.52	0.06	7.53	0.01	1.01
15	P	5.46	0.04	5.45	0.03	1.01
16	S	7.14	0.01	7.18	0.02	0.92
17	Cl	5.50	0.30	5.25	0.06	1.79
18	Ar	6.50	0.10	−0.48		9.61E + 06
19	K	5.12	0.03	5.10	0.04	1.05
20	Ca	6.33	0.07	6.32	0.03	1.12
21	Sc	3.10	0.10	3.07	0.03	1.09
22	Ti	4.90	0.06	4.93	0.03	1.25
23	V	4.00	0.02	3.98	0.03	1.04
24	Cr	5.64	0.01	5.66	0.02	0.96
25	Mn	5.37	0.05	5.50	0.03	0.75
26	Fe	7.45	0.08	7.47	0.02	0.94
27	Co	4.92	0.08	4.89	0.02	1.06
28	Ni	6.23	0.04	6.22	0.03	0.99
29	Cu	4.21	0.04	4.27	0.06	0.86
30	Zn	4.62	0.15	4.65	0.02	0.98
31	Ga	2.88	0.10	3.10	0.03	0.61
32	Ge	3.58	0.05	3.61	0.04	0.94
33	As			2.32	0.04	
34	Se			3.37	0.03	
35	Br			2.56	0.06	
36	Kr	3.28	0.08	−2.25		3.41E + 05
37	Rb	2.60	0.10	2.39	0.03	1.63
38	Sr	2.92	0.05	2.90	0.03	1.04
39	Y	2.21	0.02	2.19	0.02	1.10
40	Zr	2.58	0.02	2.56	0.02	1.06
41	Nb	1.42	0.06	1.43	0.04	0.96
42	Mo	1.92	0.05	1.96	0.04	0.93
44	Ru	1.84	0.07	1.79	0.02	1.13
45	Rh	1.127	0.12	1.08	0.02	1.14
46	Pd	1.66	0.04	1.67	0.02	0.97
47	Ag	0.94	0.30	1.22	0.04	0.52
48	Cd	1.77	0.11	1.73	0.03	1.09
49	In	<1.50	UL	0.78	0.02	5.97
50	Sn	2.00	0.30	2.09	0.06	0.81
51	Sb	1.00	0.30	1.04	0.06	0.94
52	Te			2.20	0.03	0.01
53	I			1.57	0.08	0.03
54	Xe	2.27	0.08	−1.92		1.56E + 04

(*continued*)

Cosmic Elemental Abundances, Table 1 (continued)

		Solar photosphere	s.d. dex	Meteorite (CI)	s.d. dex	Sun/meteorite N_{sun}/N_{met}
55	Cs			1.10	0.03	0.08
56	Ba	2.17	0.07	2.20	0.02	0.94
57	La	1.14	0.03	1.20	0.01	0.86
58	Ce	1.61	0.06	1.60	0.01	0.96
59	Pr	0.76	0.04	0.78	0.01	0.86
60	Nd	1.45	0.05	1.47	0.01	0.96
62	Sm	1.00	0.05	0.96	0.01	1.09
63	Eu	0.52	0.04	0.53	0.01	0.95
64	Gd	1.11	0.05	1.07	0.01	1.09
65	Tb	0.28	0.10	0.34	0.01	0.89
66	Dy	1.13	0.06	1.15	0.01	0.98
67	Ho	0.51	0.10	0.50	0.01	1.05
68	Er	0.96	0.06	0.94	0.01	1.03
69	Tm	0.14	0.04	0.14	0.01	0.72
70	Yb	0.86	0.10	0.94	0.01	1.37
71	Lu	0.12	0.08	0.11	0.01	0.89
72	Hf	0.88	0.08	0.73	0.01	1.42
73	Ta			−0.15	0.04	1.34
74	W	1.11	0.15	0.67	0.04	2.75
75	Re			0.28	0.02	0.52
76	Os	1.45	0.11	1.37	0.02	1.21
77	Ir	1.38	0.05	1.34	0.02	1.10
78	Pt	1.74	0.30	1.64	0.02	1.29
79	Au	1.01	0.18	0.82	0.05	1.52
80	Hg			1.19	0.18	0.06
81	Tl	0.95	0.20	0.79	0.05	1.45
82	Pb	2.00	0.06	2.06	0.03	0.88
83	Bi			0.67	0.04	0.21
90	Th	<0.08	UL	0.08	0.03	1.04
92	U	<−0.47	UL	−0.52	0.03	1.11

s.d. standard deviation, *dex* decimal exponent on a $\log_{10}$ scale, e.g., a s.d. of 0.1 dex indicates an uncertainty of about 25%

Cosmic Elemental Abundances, Table 2 Solar system abundances based on CI meteorites

Element		Mean CI abundance (by mass)		Estimated accuracy in (%)	Atoms per 1.00E + 06 atoms of Si
1	H	1.97	%	10	5.13E + 06
2	He	0.00917	ppm		0.601
3	Li	1.45	ppm	10	54.8
4	Be	0.0219	ppm	7	0.638
5	B	0.775	ppm	10	18.8
6	C	3.48	%	10	7.60E + 05
7	N	0.295	%	15	5.53E + 04
8	O	45.90	%	10	7.53E + 06
9	F	58.2	ppm	16	804
10	Ne	0.00018	ppm		0.0023
11	Na	4962	ppm	9	5.67E + 04
12	Mg	9.54	%	4	1.03 E + 06
13	Al	0.840	%	6	8.17E + 04
14	Si	10.70	%	3	1.00E + 06
15	P	985	ppm	8	8.34 + 03
16	S	5.35	%	5	4.38E + 05
17	Cl	698	ppm	15	5.17E + 03
18	Ar	0.00133	ppm		0.0096

(*continued*)

Cosmic Elemental Abundances, Table 2 (continued)

Element		Mean CI abundance (by mass)		Estimated accuracy in (%)	Atoms per 1.00E + 06 atoms of Si
19	K	546	ppm	9	3.67E + 03
20	Ca	0.911	%	6	5.97E + 04
21	Sc	5.81	ppm	6	33.9
22	Ti	447	ppm	7	2.43E + 03
23	V	54.6	ppm	6	281
24	Cr	2623	ppm	5	1.32E + 04
25	Mn	1916	ppm	6	9.15 + 03
26	Fe	18.66	ppm	4	8.77E + 05
27	Co	513	ppm	4	2.28E + 03
28	Ni	1.091	%	7	4.83E + 04
29	Cu	133	ppm	14	549
30	Zn	309	ppm	4	1.24E + 03
31	Ga	9.62	ppm	6	36.2
32	Ge	32.6	ppm	9	118
33	As	1.74	ppm	9	6.10
34	Se	20.3	ppm	7	67.53
35	Br	3.26	ppm	15	10.7
36	Kr	5.22E − 5	ppm		1.64E − 4
37	Rb	2.32	ppm	8	7.13
38	Sr	7.79	ppm	7	23.3
39	Y	1.46	ppm	5	4.31
40	Zr	3.63	ppm	5	10.4
41	Nb	0.283	ppm	10	0.800
42	Mo	0.961	ppm	10	2.66
44	Ru	0.690	ppm	5	1.79
45	Rh	0.127	ppm	5	0.337
46	Pd	0.560	ppm	4	1.38
47	Ag	0.201	ppm	9	0.489
48	Cd	0.674	ppm	7	1.49
49	In	0.0778	ppm	5	0.168
50	Sn	1.63	ppm	15	3.35
51	Sb	0.145	ppm	14	0.300
52	Te	2.28	ppm	7	4.56
53	I	0.53	ppm	20	1.05
54	Xe	1.74E − 4	ppm		3.48E − 4
55	Cs	0.188	ppm	6	0.371
56	Ba	2.42	ppm	5	4.63
57	La	0.2414	ppm	3	0.4561
58	Ce	0.6194	ppm	3	1.160
59	Pr	0.09390	ppm	3	0.1749
60	Nd	0.4737	ppm	3	0.8621
62	Sm	0.1536	ppm	3	0.2681
63	Eu	0.05883	ppm	3	0.1016
64	Gd	0.2069	ppm	3	0.3453
65	Tb	0.03797	ppm	3	0.06271
66	Dy	0.2558	ppm	3	0.4132
67	Ho	0.05644	ppm	3	0.08982
68	Er	0.1655	ppm	3	0.2597
69	Tm	0.02609	ppm	3	0.04054
70	Yb	0.1687	ppm	3	0.2559
71	Lu	0.02503	ppm	3	0.03755
72	Hf	0.1065	ppm	3	0.1566
73	Ta	0.015	ppm	10	0.0218

(*continued*)

Cosmic Elemental Abundances, Table 2 (continued)

Element		Mean CI abundance (by mass)		Estimated accuracy in (%)	Atoms per 1.00E + 06 atoms of Si
74	W	0.096	ppm	10	0.137
75	Re	0.0400	ppm	5	0.0554
76	Os	0.495	ppm	5	0.683
77	Ir	0.469	ppm	5	0.640
78	Pt	0.925	ppm	5	1.24
79	Au	0.148	ppm	12	0.197
80	Hg	0.35	ppm	50	0.41
82	Tl	0.140	ppm	11	0.184
82	Pb	2.62	ppm	8	3.32
83	Bi	0.110	ppm	9	0.138
90	Th	0.0300	ppm	7	0.0339
92	U	0.00810	ppm	7	0.00893

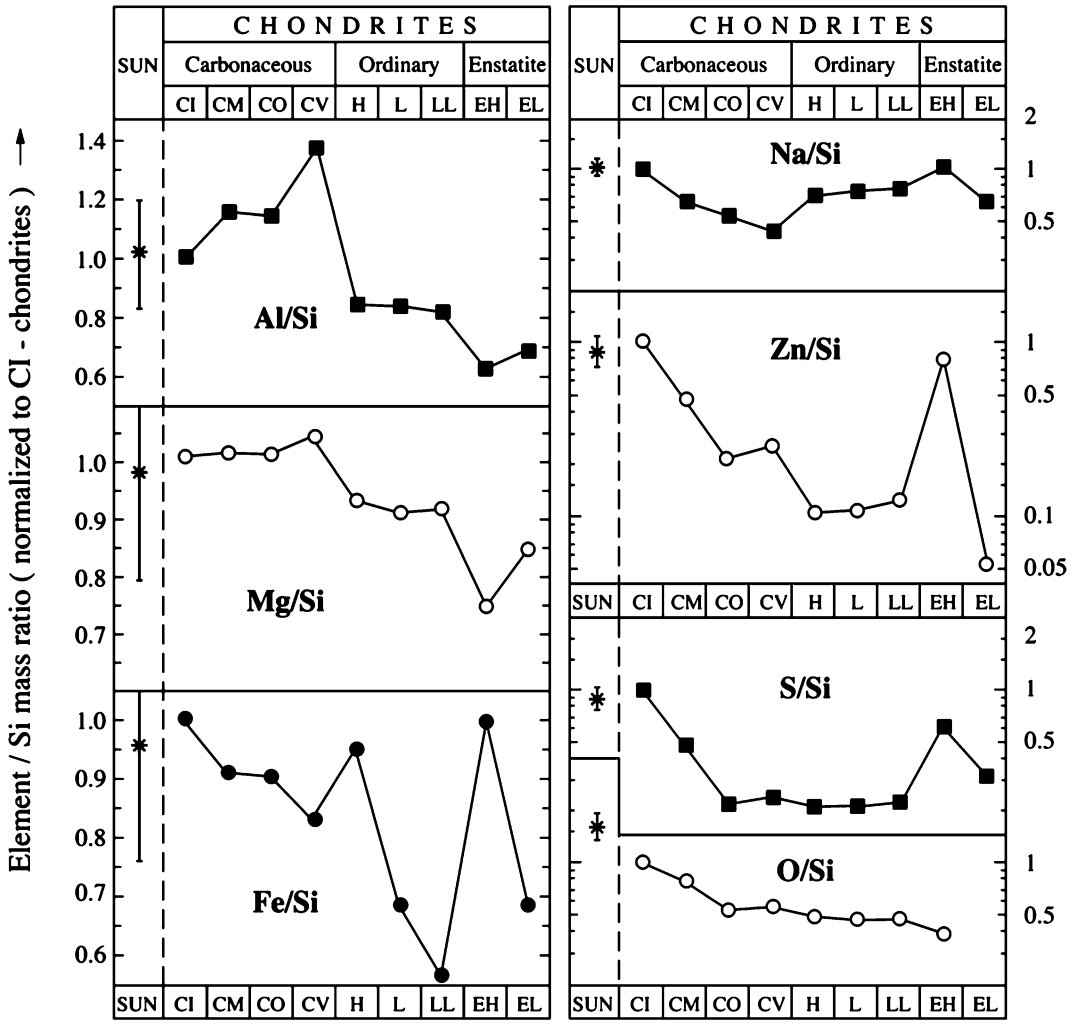

Cosmic Elemental Abundances, Fig. 2 Element/Si mass ratios of characteristic elements in various groups of chondritic (undifferentiated) meteorites. The refractory component is represented by Al; Mg represents the Mg silicates, Fe the metal component, and Na, Zn, and S the moderately volatile elements. Only CI chondrites fit with photospheric abundances indicated on the left side (Figure is from Lodders et al. 2009)

components has a characteristic formation temperature indicated by condensation temperatures of elements and phases involved. Condensation temperatures are calculated by assuming thermodynamic equilibrium between solids and a cooling gas of solar composition (see Lodders 2003, for details). The various cosmochemical components are in order of decreasing condensation temperatures:

Refractory component: The first phases to condense from a cooling gas of solar composition are Ca,Al-oxides, and silicates associated with many trace elements, such as the REE (rare earth elements), Zr, Hf, and Sc, and additionally refractory metals, e.g., W, Os, and Ir. The refractory component makes up about 5% of the total condensable matter. Variations in, e.g., Al/Si and Ca/Si ratios of bulk chondrites may be ascribed to the incorporation of variable amounts of early condensed refractory phases.

Mg silicates: The major fraction of condensable matter is associated with the three most abundant elements heavier than oxygen: Si, Mg, and Fe. In the relatively reducing environment of the solar nebula, Fe condenses almost entirely as metal alloy (FeNi), while Mg and Si form forsterite (Mg_2SiO_4) which converts to enstatite ($MgSiO_3$) at lower temperatures by reaction with gaseous SiO. Variations in Mg/Si ratios of bulk meteorites are produced by the incorporation of various amounts of early-formed forsterite.

Metallic iron condenses as a FeNi alloy at about the same temperature as forsterite, the sequence depending on total pressure. Variations in the concentrations of Fe and other siderophile elements in meteorites are produced by the incorporation of variable fractions of metal.

Moderately volatile elements have condensation temperatures between those of Mg silicates and FeS (troilite). The most abundant element of the moderately volatile elements is sulfur. The amount and the relative abundances of these elements in meteorites are probably the result of removal of volatiles during condensation.

Highly volatile elements have condensation temperatures below FeS and above water ice The group of highly volatile elements comprises elements with very different geochemical affinities, such as the chalcophile Pb and the lithophile I. Similar processes as those invoked for the depletion of moderately volatile elements are responsible for variations in these elements. In addition, heating on small parent bodies may lead to loss of highly volatile elements by evaporation.

Ultra volatile elements have condensation temperatures below that of water ice. This group includes H, C N, O, and the noble gases.

In summary, Fig. 2 gives some indication for the range of elemental variations in chondritic meteorites. We assume that minor compositional variations among chondritic meteorites are produced by nebular processes that occurred before accretion of planetesimals. Planetary melting processes, such as core formation or partial melting, lead to rocks with completely different compositions.

The bulk composition of the terrestrial planets is essentially solar with similar numbers of Mg, Si, and Fe atoms and about one tenth of Al atoms. This characteristic composition prevails, with more or less variability in kilometer-sized asteroids, meter-sized chondritic meteorites, submillimeter- to millimeter-sized micrometeorites, micrometer-sized interplanetary dust particles, and sub-micrometer-sized particles, possibly interstellar dust. The major variables are the ratio of metallic to oxidized Fe and variations in the depletion of volatile elements.

Summary

The abundance pattern of chemical elements in the Sun and many other stars is determined by the Big Bang making H and He and by later production of heavy elements in the interior of stars, a process that is still active. The pattern of heavy, non-volatile elements in unmelted, chondritic meteorites is the same as in the Sun, with one group of meteorites the CI chondrites fitting best. Other undifferentiated, chondritic meteorites have compositions deviating somewhat from solar. These meteorites were modified by solar nebula processes before planetesimal accretion. The solar system abundances, a combination of solar photospheric and meteoritic abundances, are known to within a few percent for each element. Extension to other stars leads to heavy element cosmic abundances which are less well known.

Cross-References

- ▶ Chondrites
- ▶ Formation and Evolution of the Earth
- ▶ Meteorites

References

Asplund M, Grevesse N, Sauval J, Scott P (2009) The chemical composition of the Sun. Annu Rev Astron Astrophys 47:481–522

Krot AN, Keil K, Goodrich CA, Scott ERD, Weisberg MK (2003) Classification of meteorites. In: Davis AM, Holland HD, Turekian KK (eds) Meteorites, comets and planets, Treatise on geochemistry, vol Vol. 1. Elsevier, Oxford, pp 83–128

Lodders K (2003) Solar system abundances and condensation temperatures of the elements. Astrophys J 591:1220–1247

Lodders K, Palme H, Gail HP (2009) Abundances in the solar system., Chap. 4.4. In: Trümper JE (ed) Landolt-Börnstein, new series, vol VI/4B. Springer, Berlin/Heidelberg/New York, pp 560–598

Palme H, Lodders K, Jones A (2014) Solar system abundances of the elements. In: Holland HD, Turekian KK (eds) Treatise on geochemistry, vol 2, 2nd edn. Elsevier, Oxford, pp 15–36

Cosmogenic Nuclides

Rainer Wieler
Department of Earth Sciences, Institute of Geochemistry and Petrology, ETH Zürich, Zürich, Switzerland

Definition

Cosmogenic nuclides are produced when primary or secondary particles of the galactic (or in some cases also the solar) cosmic radiation interact with atomic nuclei in extraterrestrial or terrestrial material. Cosmogenic nuclides are observable mainly for noble gas isotopes and radioactive nuclides, whose abundances in the target materials are otherwise extremely low. In this article, we discuss production and applications of cosmogenic nuclides in meteorites and other extraterrestrial samples (Wieler 2002; Eugster et al. 2006; Herzog and Caffee 2014) as well as in terrestrial samples (Gosse and Phillips 2001; Dunai 2010; Granger et al. 2013). In solid matter, the cosmic-ray flux has a mean attenuation length of roughly 50 cm. Hence, cosmogenic nuclides in meteorites are primarily used to determine exposure ages, i.e., the time spent as meter sized or smaller body in interplanetary space before falling on Earth or in some cases also the residence time in the uppermost few meters of their larger parent body. Cosmogenic nuclides in terrestrial rocks allow determining ages or erosion rates of geologic surfaces and nuclides produced in the atmosphere and subsequently being deposited in terrestrial archives provide records of, e.g., past solar activity and geomagnetic field variations.

Introduction

On Earth, cosmogenic nuclides are produced both in the atmosphere and in situ in solid samples at the Earth's surface. Cosmogenic radionuclides produced in the atmosphere (together with contributions from nuclear power plants and nuclear bombs) are used to study atmospheric dynamics and the hydrological cycle. Nuclides produced in the atmosphere will eventually also be deposited in the geosphere or hydrosphere as "meteoric nuclides." Meteoric nuclides which found their way into archives such as ice or sediment cores allow us to determine the past flux of the cosmic radiation entering the Earth's atmosphere. Such archives are therefore used to investigate the physics of the sun, the heliosphere, and the geomagnetic field. Meteoric radionuclides also allow us to study processes near the Earth's surface such as subduction of oceanic crust or sediment dynamics. A particularly important cosmogenic nuclide produced in the atmosphere is ^{14}C, which ultimately may find its way into organic matter. The nuclide ^{14}C is the basis of the most widely used radiometric dating method. On the Earth's surface, the cosmic-ray flux is several orders of magnitude lower than in interplanetary space. Production rates and concentrations of cosmogenic nuclides produced at the Earth's solid surface are thus much lower than in meteorites, which presents considerable analytical challenges. Nevertheless, cosmogenic radionuclides and noble gases produced in situ in terrestrial surface rocks have become a very widely used tool in Earth surface sciences, allowing, e.g., to determine the time since a rock has been exposed on the Earth's surface or long-term erosion rates of landscapes.

Production of Cosmogenic Nuclides

Cosmogenic nuclides are produced either when target atoms interact with high-energy cosmic-ray particles (mainly between 100 MeV–10 GeV) or when they capture low-energy neutrons ("thermal" or "epithermal" neutrons, i.e., ~0.025 eV and 0.5 eV–0.1 MeV, respectively). A detailed account of cosmogenic nuclide production is given by Gosse and Phillips (2001). Primary cosmic-ray particles (mostly protons and alpha particles) need to be distinguished from secondary particles, the latter being created in the cascade of nuclear reactions initiated by primary particles. Secondary particles include high-energy protons and neutrons as well as thermal and epithermal neutrons. On the Earth also secondary cosmic-ray muons are of some importance. These can be considered as heavier brothers of the electron with a half-life on the order of a microsecond. In meteorites production by primary and secondary particles is important (Eugster et al. 2006; Herzog and Caffee 2014). In contrast, the cosmogenic nuclide production in terrestrial rocks is largely dominated by secondary neutrons, since hardly any cosmic-ray protons arrive at the Earth's surface. Muon-induced reactions become important at depths below several meters, because the mean attenuation length of muons in matter is much larger than that of neutrons. As discussed further down, the analysis of several cosmogenic nuclides in the same or adjacent samples will often allow us to constrain the "shielding" of a meteorite sample during cosmic-ray exposure, i.e., the size of the meteorite before it becomes ablated upon passage through the Earth's atmosphere and the depth of the sample within this "meteoroid." This is because production rates of different cosmogenic nuclides vary with depth in different ways. Analyses of several nuclides are also used to better constrain exposure and erosional histories of terrestrial samples. Most widely studied nuclides are the rare isotopes of helium, neon and argon (^{3}He, ^{21}Ne, ^{38}Ar) and the radioactive nuclides ^{10}Be ($T_{1/2}$ = 1.387 Ma), ^{14}C (5730 a), ^{26}Al (0.717 Ma), ^{36}Cl (0.301 Ma) and ^{53}Mn (3.74 Ma). Complete lists of nuclides measured in meteorites and terrestrial samples are given by Eugster et al. (2006) and Dunai (2010), respectively.

In meteorites, important parameters governing production rates are energy-dependent particle fluxes at the sample site, energy-dependent cross sections of all important reactions, and the major target element composition of the sample (e.g., Leya and Masarik 2009). The particle flux depends on the primary cosmic-ray proton flux, which varies with the solar cycle but usually is assumed to be constant over longer time scales. The flux seen by a sample also depends on its shielding and on the composition of the meteorite as a whole. A high Fe concentration, for example, leads to a higher production of secondary neutrons, while neutrons are more efficiently slowed down in meteorites relatively rich in H and C. Production rates are usually considerably higher from target elements with only a slightly higher mass than the product nuclide. For example, the production of ^{21}Ne from Mg is about 2.5–3 times higher than that from Si and some two orders of magnitude higher than that from Fe (Leya and Masarik 2009). A good knowledge of the major target element composition of a given sample is thus a prerequisite for an accurate production rate estimate.

Production rates on the Earth depend largely on the shielding of a sample by the atmosphere (i.e., the sample's altitude) and the modulation of the primary proton flux by the Earth's magnetic field (the geomagnetic latitude). For example, at a given latitude, production rates at sea level are some 15–20 times lower than at 4000 m altitude, and at the equator, production rates are ~2.5 times lower than at latitudes >60° (Lal 1991; Balco et al. 2008; Lifton et al. 2014). This is because near the poles virtually all cosmic-ray protons reach the upper atmosphere unhindered by the Earth's magnetic field, whereas at lower latitudes lower energy protons will be deflected (Gosse and Phillips 2001; Beer et al. 2012). For the relatively short-lived nuclide ^{14}C (which is also produced in situ in rocks) and for samples with high erosion rates, the position of the geomagnetic poles in the past (polar wandering) may have to be considered. For longer-lived nuclides, it is usually assumed that the average position of the geomagnetic poles coincides with the geographic poles, as these nuclides integrate production over at least several ten thousand years unless erosion rates are very high (see below). Time-integrated production rates of a sample will crucially depend on the rock's erosion history, as a sample now at the immediate rock surface will in the past have been shielded by overlying material. The production rate in the past will therefore have been lower than the present day surface value, and this effect will be more pronounced with higher erosion rates (Lal 1991; Gosse and Phillips 2001; Dunai 2010, see Fig. 1). This is the reason why cosmogenic nuclides very often are used to constrain erosion rates rather than exposure ages.

Models to calculate production rates in meteorites are based on large libraries of measured cross sections for proton- and neutron-induced reactions as well as nuclear model codes used to extend or interpolate measured data (Leya and Masarik 2009). This needs especially to be done for neutron-induced reactions to compensate for the many gaps in the measured data. The spectra of primary and secondary protons and neutrons as function of meteorite radius and sample depth are calculated by nuclear codes using Monte Carlo techniques (Leya and Masarik 2009). The primary galactic cosmic-ray proton flux is calibrated by fitting modelled concentrations of radionuclides (e.g., ^{10}Be) to measured values in well-studied meteorites, for which the preatmospheric geometry can be reliably reconstructed and which have exposure ages long enough for the radionuclide concentration to have reached its equilibrium value, where production and radioactive decay match (in practice after some 4–5 half-lives of the nuclide). Figure 2 shows modelled production rates of ^{21}Ne (P21) as a function of depth in spherical meteorites of H-chondritic composition and radii between 10 and 500 cm. The increase of P21 from the meteorite surface up to depths varying between ~15 and 40 cm reflects the development of the cascade of secondary protons and neutrons. At large depths, the decrease of P21 approximately reflects the mean attenuation length of the cosmic-ray flux of ~50 cm.

Because meteorites suffer large ablation losses or split into multiple fragments upon atmospheric passage, preatmospheric meteorite size and sample depth will hardly ever be known a priori. However, analyses of several cosmogenic nuclides on the same sample (or a series of samples) combined with model calculations may allow one to constrain the shielding of a given sample and hence its production rates.

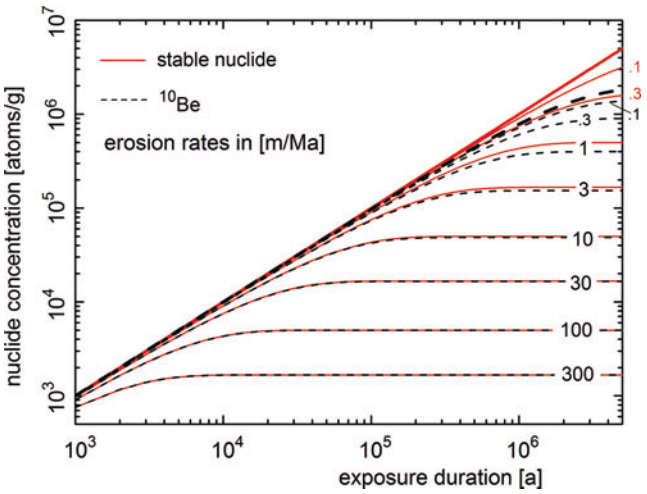

Cosmogenic Nuclides, Fig. 1 Nuclide concentrations at the top of eroding surfaces. Exposure duration in years since onset of erosion with constant rate [m/Ma]. *Red solid lines* are valid for stable nuclides, *dashed lines* for ^{10}Be. The two *thick lines* represent non-eroding surfaces. A hypothetical production rate of 1 atom per gram per year is adopted; hence concentrations need to be multiplied with the actual local production rate. Concentrations of ^{10}Be are only sizably affected due to radioactive decay for erosion rates not exceeding ~3 m/Ma. In eroding surfaces also stable nuclides reach a steady-state concentration which depends on the erosion rate (Figure adapted from Lal (1991) and Dunai (2010))

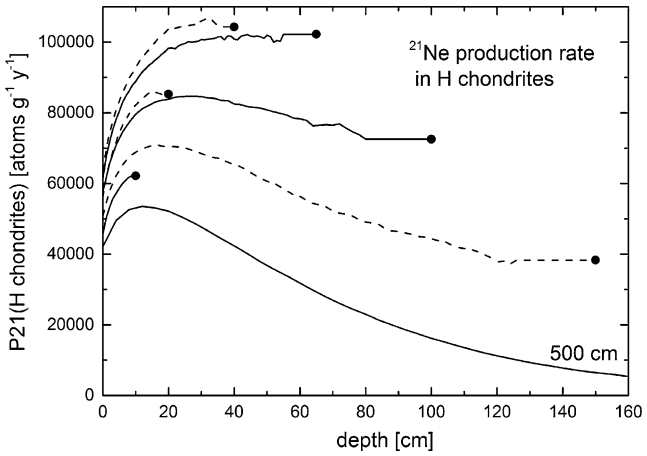

Cosmogenic Nuclides, Fig. 2 Production rate of ^{21}Ne in meteorites of H-chondritic composition with radii of 10, 20, 40, 65, 100, 150, and 500 cm, calculated with the nuclide production model by Leya and Masarik (2009). Wiggles near the centers of the meteorites are the result of poor statistics in the model calculations due to relatively low volumes considered

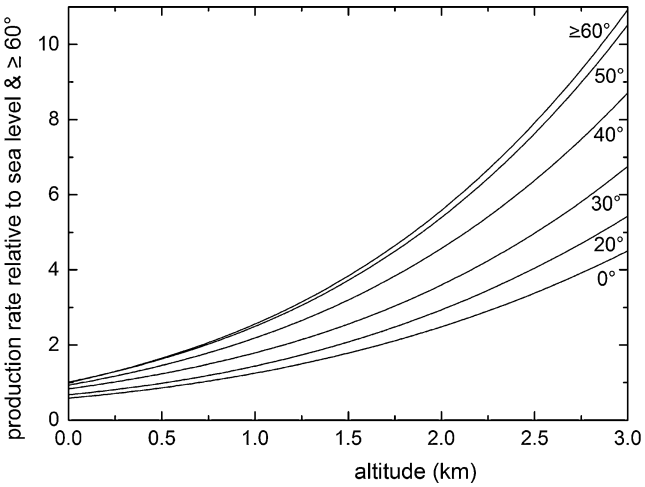

Cosmogenic Nuclides, Fig. 3 Cosmogenic nuclide production rates relative to values at sea level and high latitude (≥60°, SLHL) according to the classical scaling scheme proposed by Lal (1991). Production rates at 3000 m altitude and high latitude are ~11 times higher than the SLHL values; production rates at sea level and the equator are ~60% of the SLHL values. Other scaling schemes are mentioned in the text

A widely used shielding parameter is the ratio ^{22}Ne/^{21}Ne, which decreases with increasing shielding, since production of ^{21}Ne by secondary neutrons is higher than that of ^{22}Ne. Other shielding indicators are based on ratios of a stable to a radioactive nuclide, which may vary little over a certain shielding range (Herzog and Caffee 2014). If the radionuclide can be assumed to be in saturation, the production rate of the stable nuclide can be determined. A well-known such combination is ^{26}Al-^{21}Ne. The combination of radioactive ^{81}Kr with stable Kr isotopes even yields shielding-corrected exposure ages by a single Kr isotope analysis (e.g., Leya et al. 2015). None of these shielding corrections is perfect, however. They may be valid over a limited size and depth range only, some of them require multiple analyses and analytical precision is often also a problem. ^{81}Kr concentrations, for example, are very low, and in many cases, also corrections for non-cosmogenic stable Kr isotopes are very substantial. In summary, production rates usually have considerable uncertainties, in favorable cases perhaps 10%, but often 20% or more.

A major issue when studying cosmogenic nuclide production at the Earth's surface is proper "scaling" of production rates determined at one geographical location to altitude and latitude of any sample site of interest. In contrast to meteorites, the moment in time when a sample at the Earth's surface had been freshly exposed to cosmic rays can independently be deduced in favorable cases (Dunai 2010; Granger et al. 2013). For example, the eruption age of a lava flow can be determined by radiometric dating. Production rates of cosmogenic nuclides at the sample site can then be deduced, although care is required to properly assess potential erosion of the calibration sample or effects such as episodic cover by snow or vegetation. Also partial shielding from cosmic rays by surrounding mountains, other obstacles or inclined surfaces need to be considered (Gosse and Phillips 2001; Dunai 2010). Fortunately, topographic shielding is only significant in "rather spectacular" landscapes (Dunai 2010), because the angular cosmic-ray flux seen by a sample strongly decreases towards the horizon. For relatively young samples, also the paleopole positions may have to be taken into account. In the case of in situ ^{14}C, it may not even be necessary to know the actual exposure age of a sample. Similar to production rate determinations of radionuclides in meteorites, it may suffice if one reliably can assume the sample to have been exposed for longer than some four or five half-lives of ^{14}C, i.e., for more than ~25 ka. Potential uplift of a calibration sample – leading to increasing production rates with time – should hardly be a concern, since suitable calibration samples mostly have rather low exposure ages in order to minimize uncertainties due to erosion. By convention, production rates determined at a calibration site are scaled to sea level and high latitude (>60°) as described in the next paragraph, and these "SLHL" values are reported. At 60°or higher, production rates will not increase with latitude any further.

Scaling schemes are largely based on measured neutron fluxes in the atmosphere. Figure 3 shows scaling factors according to the classical study by Lal (1991). A recent model uses analytical approximations to fluxes of cosmic-ray neutrons as well as protons and muons modeled by Monte Carlo techniques (Lifton et al. 2014). Various online calculators and computer codes are available to scale production rates to latitude and altitude of samples of interest (Vermeesch 2007; Balco et al. 2008; Lifton et al. 2014). It is highly recommended to always report the scaling scheme

used in a particular study. Dunai (2010) provides a checklist of further information recommended to be reported. Because pressure regimes are not identical to standard atmospheric values everywhere on Earth, corrections for such persistent anomalies may be required. The best-known case is Antarctica, where today pressures at all elevations are a few ten hPa lower than standard values and production rates accordingly some 25–30% higher (Stone 2000). When calculating exposures ages of antarctic samples, it is usually assumed that this anomaly has persisted over millions of years.

Production rates of cosmogenic nuclides in the atmosphere are also calculated with physical models. Required proton and neutron flux spectra are obtained with extensive computer codes (Masarik and Beer 2009; Kovaltsov and Usoskin 2010; Beer et al. 2012). Similar to the Earth's surface, production rates increase with geomagnetic latitude. However, because of atmospheric mixing, concentrations of atmosphere-derived cosmogenic nuclides in terrestrial archives such as ice cores depend much less on the latitude than is the case for in situ produced nuclides.

Analytical Aspects

Cosmogenic noble gases are measured by noble gas mass spectrometry; radionuclides are mostly analyzed by accelerator mass spectrometry (AMS) (Christl et al. 2014). For routine analyses of meteorites, often whole-rock samples are measured, whereas mineral separates are the rule in terrestrial studies, with quartz being the most important by far. A major reason for this is that meteoric radionuclides can be removed in a controlled way from quartz by etching off grain surface layers (Kohl and Nishiizumi 1992). Meteoric ^{10}Be in an untreated quartz separate is orders of magnitude more abundant than in situ produced ^{10}Be. Noble gases are usually extracted by heating samples in single or multiple steps, sometimes combined with in vacuo crushing, e.g., to partly remove or correct for non-cosmogenic ^{3}He or ^{21}Ne (Niedermann 2002). Preparation for radionuclide analyses of rock samples requires several steps of chemical treatment, first to obtain clean mineral separates (Kohl and Nishiizumi 1992) and next to extract the nuclides (Gosse and Phillips 2001). Similar procedures – though nuclide and sample specific – are used for meteoric radionuclide separation from terrestrial archives (Beer et al. 2012). Cosmogenic and non-cosmogenic noble gases can usually not be separated quantitatively from each other, or in many cases are not separated at all, e.g., in meteorite analyses. Corrections for non-cosmogenic contributions may be minor in many cases, e.g., for meteorites with low concentrations of primordial or solar-wind-implanted noble gases, but often non-cosmogenic noble gases are the limiting factor deciding whether or not concentrations of cosmogenic noble gases in a sample may be determined. This is particularly a problem for terrestrial samples and is the main reason why often much lower exposure ages can be determined with radionuclides than with noble gases. On the other hand, stable noble gas isotopes are useful to determine very old exposure ages in very slowly eroding arid landscapes.

Cosmogenic Nuclides in Extraterrestrial Samples

Two classical applications of cosmogenic nuclides in meteorites are to determine their cosmic-ray exposure age and their terrestrial age, i.e., the time they spent in interplanetary space as roughly meter-sized objects and the time they fell on Earth and became essentially shielded from cosmic rays by the atmosphere. Exposure ages longer than ~5–6 Ma (some 4–5 half-lives of ^{10}Be) are determined with stable noble gas isotopes, often together with radionuclide analyses to constrain shielding of and hence production rate in a sample, as explained above. With some exceptions, exposure ages of stony meteorites fall in the range of below one Ma to about hundred Ma, whereas iron meteorites often have exposure ages of several hundred Ma, with a highest value of some two Ga (Marti and Graf 1992; Herzog and Caffee 2014). Figure 4 shows the exposure age distribution of the H chondrites, one of the largest stony meteorite classes.

In arid areas meteorites weather only slowly, hence terrestrial ages of meteorites from hot deserts are often in the ten to several ten thousand year range, whereas many meteorites found in Antarctica have been on Earth since several hundred

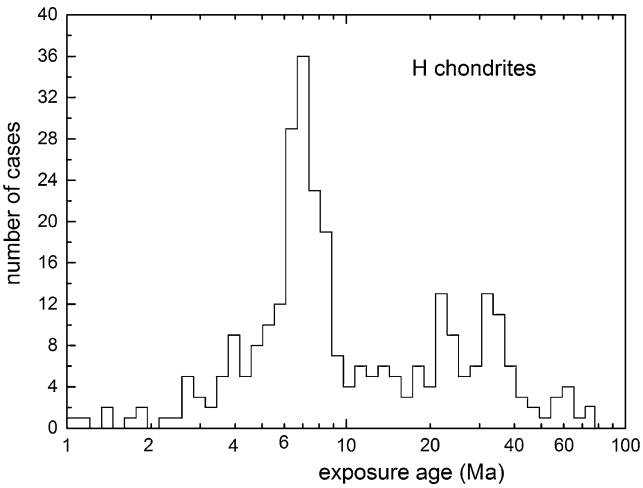

Cosmogenic Nuclides, Fig. 4 Cosmic-ray exposure age distribution of H chondrites (Graf and Marti 1995). About 45% of all H chondrites show an exposure age of 7–8 Ma, indicating one (or perhaps two) major collision(s) in the asteroid belt 7–8 Ma ago. Minor peaks at ~24 Ma and 33 Ma are the result of further major collisions in the asteroid belt. Exposure age distributions of other meteorite classes are shown by Herzog and Caffee (2014). Often also these histograms show a clustering of ages typical for the respective class

thousand years, with the highest reported values being ~3 Ma (Jull 2006; Herzog et al. 2015). Terrestrial ages are determined with radionuclides of suitable half-lives. An additional noble gas analysis may confirm that the exposure age of the sample had been long enough to bring the radionuclide concentration in saturation at the time of fall. Carbon-14 is the main nuclide used for stony meteorites; ^{36}Cl is used for iron meteorites and for stony meteorites with long terrestrial ages. Also pairs of radionuclides are used for shielding corrections, e.g., ^{14}C–^{10}Be or ^{36}Cl–^{41}Ca (Jull 2006; Herzog et al. 2015). The atmosphere can be assumed to completely shield a fallen meteorite from further cosmogenic nuclide production, since production rates on Earth are very much lower than in space.

Meteorites from the asteroid belt are delivered to Earth through resonances, for example, the 3:1 mean-motion resonance with Jupiter. A meteorite with a semimajor axis of ~2.5 astronomical units will complete three orbits in the time Jupiter revolves around the sun once. Such resonances result in chaotic eccentricities and inclinations, and the meteorite may collide with the Earth within one Ma or so (Wisdom 1987; Gladman et al. 1997). Since most meteorites have much longer exposure ages, they must therefore spend most of their lifetime as meter-sized bodies in the asteroid belt. After having been released from larger parent bodies by a collision, they slowly move towards a resonance largely due to non-gravitational forces, e.g., the Yarkovsky effect, the anisotropic emission of infrared photons (Bottke et al. 2002).

Cosmic-ray exposure ages are important to evaluate whether meteorites may be paired or source paired, i.e., whether they belonged to the same meteoroid prior to breakup in the atmosphere or were ejected from their parent body by the same event, respectively. Identification of paired meteorites is especially important for the numerous desert finds. Identical terrestrial ages are a further pairing criterion, and in some cases, short-lived cosmogenic radionuclides (half-lives on the order of months or years) provide evidence for a (common) recent fall date. Care is required not to overinterpret cosmogenic nuclide data, however. Identical exposure ages of two meteorites are by far not a sufficient pairing criterion by themselves. For example, about 20% of all H chondrites – belonging to many hundred different falls - have an exposure age of about 7–8 Ma (Fig. 4). On the other hand, the 7–8 Ma H chondrites indeed very likely originate from one (or perhaps two) major collisions in the asteroid belt (Graf and Marti 1995).

By now, exposure age distributions of most major meteorite classes are known, and it is clear that different classes have different distributions (Herzog and Caffee 2014). Most of them show clusters similar to the 7–8 Ma peak in the H chondrite histogram. This means that a small number of collisions produced a very large fraction of the known meteorites, which indicates that we sampled only a tiny portion of the potential meteorite parent bodies in the asteroid belt (Wieler and Graf 2001).

Sometimes, exposure ages derived for different samples of the same meteorite or by different nuclides in the same sample are clearly discrepant. This often indicates a "complex" exposure history, which means that not all cosmogenic nuclides were acquired during the recent exposure stage prior to fall but that some of them testify of earlier irradiations in different settings (Herzog and Caffee 2014). For example, a meteorite may have been broken up on its way to Earth. Particularly interesting are complex exposure histories where the first stage happened near the surface of the parent body. In such cases, cosmogenic nuclides allow us to study the dynamics of the parent body regolith. This can often only be done with stable noble gas nuclides, as radionuclides potentially acquired on the parent body may have completely decayed during the transfer of the meteorite to Earth. Differences in nominal cosmic-ray exposure ages indicate that different samples from a regolith breccia had spent variable times near the surface of their parent body (perhaps at different depths) before compaction into the present-day meteorite (Wieler 2002). Complex exposure histories are also reported for single grains or single chondrules in some meteorites, which contain sometimes orders of magnitude higher concentrations of cosmogenic noble gases than the parent meteorite as a whole. It remains controversial whether this indicates – at least in some cases – an irradiation by a high fluence of solar energetic particles from the very early sun (Woolum and Hohenberg 1993) or simply a prolonged irradiation by galactic cosmic rays in the parent body regolith (Roth et al. 2011). Most lunar meteorites contain cosmogenic noble gases acquired on the parent body, indicating a shallow excavation depth (Herzog and Caffee 2014; Herzog et al. 2015). In contrast, martian meteorites show hardly any signs of a parent body exposure, hence must have been excavated from larger depths (Herzog and Caffee 2014). Also in situ analyses of cosmogenic nuclides by spacecraft have a considerable potential to study the evolution of the morphology of planetary surfaces, in essence similar to what is now routinely done on Earth (e.g., Farley et al. 2014).

Not only noble gases and radionuclides but essentially the isotopes of all other elements are also produced by cosmic-ray interactions. Until recently, however, the resulting shifts in isotopic composition have in most cases remained unnoticed. Exceptions were gadolinium and samarium which both contain isotopes with very large cross sections for thermal neutron capture. These elements have been used to study the depositional history of the lunar regolith with samples from Apollo drill cores (Russ et al. 1972; Hidaka and Yoneda 2007) and cosmic-ray exposure histories of large meteorites (Bogard et al. 1995). The very high precision of present-day analyses now reveal tiny isotopic anomalies in several other elements as results of cosmic-ray effects. Some of these elements are important for cosmochemistry, and the cosmogenic isotopic shifts are large enough to require a proper

correction. The foremost example is tungsten, measured to date early solar system events by the Hf-W method (Kleine et al. 2009). Cosmic rays modify not only the abundances of the radiogenic isotope ^{182}W (from decay of ^{182}Hf) but also W isotopes used to correct for instrumental mass fractionation (or sometimes to study potential primordial isotopic anomalies). The effects are largest in samples with long exposure ages, especially lunar samples and iron meteorites (Leya et al. 2000). The knowledge of an exposure age alone does often not permit a proper correction, however, because the magnitude of isotopic shifts may also substantially depend on the shielding of the sample. Isotopes of platinum are an excellent monitor to correct tungsten isotopes in iron meteorites for cosmic-ray effects, because W and Pt are both modified by thermal and epithermal neutrons (Kruijer et al. 2013).

Cosmogenic Nuclides in Terrestrial Rocks

Considerably later than in meteoritics in situ produced cosmogenic nuclides also became an important tool in Earth surface sciences. This delay is due to the fact that nuclide concentrations on Earth are orders of magnitude lower than in meteorite samples. Yet, since the late 1980s terrestrial applications proliferate and led to what is often called a revolution in Earth surface science. Publication and citation rates of Earth science studies involving cosmogenic nuclides increased by orders of magnitude in the past 20–25 years (Dunai 2010). Cosmogenic nuclides allow us to study and quantify processes and timescales in geomorphology in a qualitatively new way.

Two major applications are dating the ages of geologic surfaces (exposure dating) and determinations of erosion or denudation rates. The two questions are often intertwined, as is illustrated in Fig. 1. Concentrations of stable nuclides (e.g., ^{21}Ne) and the radionuclide ^{10}Be ($T_{1/2} = 1.38$ Ma) in a sample presently at the immediate surface of the Earth are shown as a function of exposure duration and for different (time-independent) erosion rates. A hypothetical production rate of 1 atom per gram per year is adopted. Concentrations as displayed therefore need to be multiplied with the actual local production rate at a sample site. The concentration of a stable nuclide in a non-eroding surface increases linearly with time, but in an eroding surface, also stable nuclides will eventually reach equilibrium. The higher the erosion rate, the sooner the equilibrium concentration will be reached and the lower it will be. This is because the cosmic-ray neutron flux seen by the sample had always been lower than the present-day value at the very surface as long as it was shielded by overlying material (Lal 1991). For erosion rates larger than some 3 m/Ma, radioactive decay has no discernible additional effect on the ^{10}Be concentration. For very high erosion rates of 300 m/Ma (0.3 mm/a), erosional saturation is reached already after some 7000 a, whereas for low erosion rates of 0.3 m/Ma, stable nuclides will not have reached their steady-state concentrations even after ~5 Ma and ^{10}Be hardly so. The figure also illustrates that with a single nuclide, essentially only a minimum exposure age (assuming no erosion) or a maximum erosion rate (assuming an infinite exposure age) can be determined. Analyses of two nuclides with different half-lives (e.g., ^{10}Be and stable ^{21}Ne or ^{10}Be and ^{26}Al) in principle allow the determination of both erosion rate and exposure age. Such data pairs also permit to recognize "complex" exposure histories, i.e., when a sample already contained "inherited" nuclides from a previous exposure stage under a different geometry or when a sample had been buried for a certain time (Lal 1991; Granger 2006; Dunai 2010). However, analytical uncertainties often limit the accuracy of erosion rate/exposure age data pairs.

Some of the numerous studies using in situ produced cosmogenic nuclides to determine exposure ages and erosion rates are reviewed, e.g., by Morris et al. (2002), Dunai (2010), Balco (2011) and Granger et al. (2013). Classical examples include dating of glacial moraines and other glacially overprinted landscapes, studies of other erosional surfaces such as river terraces or slowly eroding desert landscapes, and dating of lava flows or fault scarps induced, e.g., by earthquakes. Careful fieldwork is obviously crucial, and sampling strategies need to take into account the specific requirements for cosmogenic nuclide studies.

Cosmogenic radionuclides may not only allow us to derive the time when a rock became exposed to the cosmic radiation but also the moment a sample became completely shielded from cosmic rays. This can occur when sediments are washed into caves or when rocks are covered by water, ice, sediment deposits, volcanic flows, etc. The principle of "burial dating" is somewhat analogous to terrestrial age determinations of meteorites with cosmogenic radionuclides, except that in the terrestrial case, two radionuclides with different half-lives are required (Granger 2006; Dunai 2010). If the concentration ratio of the two nuclides at the time the sample became buried can be assumed to be known, the measured ratio will yield the burial duration. Well suited is the couple ^{10}Be-^{26}Al, since their preburial concentration ratio can often reliably be assumed to be close to the production rate ratio. While for samples that experienced a simple exposure history followed by a rapid burial, the burial event can be dated, for samples that experienced repeated episodes of exposure and burial, cosmogenic nuclides can only provide a lower limit for the total near-surface exposure (Granger 2006).

Cosmogenic nuclides do not only constrain erosion rates at a specific site but can also be used to derive erosion rates averaged over entire river catchments (von Blanckenburg 2005; Portenga and Bierman 2011; Willenbring et al. 2013). This is done by analyzing sediment samples from active river channels at the low end of a catchment of interest. To obtain accurate results, several conditions need to be fulfilled (Dunai 2010). These include that (i) erosion rates in the catchment are constant over

the period reflected by a nuclide studied, i.e., mass wasting processes did not contribute significantly to the overall erosion, (ii) all lithologies in the catchment are equally well represented in the sample analyzed (often a quartz grain separate), and (iii) transit times of sediments through the catchment are short compared to the erosional timescale. Even if not all these conditions are met, however, the method may still usefully constrain catchment wide erosion rates, though with limited accuracy (Dunai 2010). Relevant production rates averaged over the entire catchment are derived either from digital elevation models or – more simply – are taken to be equal to the production rate at the mean altitude (and latitude) of a catchment.

Catchment-wide erosion rates in the past are reflected in cosmogenic nuclide concentrations in sediment cores (Schaller et al. 2002; Charreau et al. 2011; Savi et al. 2014). These data may require a – sometimes large – correction for in situ nuclide production after sediment deposition. Limited knowledge of variables such as the extent of the paleo source region may also lead to considerable uncertainties, but the method can provide important data not to be obtained otherwise (Granger et al. 2013).

Meteoric ^{10}Be (and ^{14}C)

The two most important cosmogenic nuclides produced in the atmosphere and eventually incorporated into solid or liquid inventories are ^{14}C and ^{10}Be. Here we concentrate on meteoric ^{10}Be but also discuss ^{14}C in tree rings independently dated by dendrochronology. Beryllium-10 is produced mainly from atmospheric nitrogen and oxygen, ^{14}C from nitrogen, with a production maximum at ~10–12 km altitude (Masarik and Beer 2009; Kovaltsov and Usoskin 2010; Beer et al. 2012). Carbon-14 atoms combine with oxygen to form CO_2 , the major fraction of which becoming dissolved in the ocean while a smaller part quickly gets incorporated into plants. This carbon cycle is explained in more detail by Beer et al. (2012) and an understanding of its basics is required to properly use ^{14}C as dating tool or environmental tracer. Beryllium-10 atoms get adsorbed on aerosol particles which are deposited at the Earth's surface typically within less than a year (Morris et al. 2002; Beer et al. 2012). About two orders of magnitude more ^{10}Be is produced in the atmosphere than in situ in rocks. Therefore, in terrestrial samples, meteoric ^{10}Be usually completely dominates in situ produced ^{10}Be and needs to be removed carefully when the latter is of interest, as discussed above. The large amounts of meteoric ^{10}Be require, on the other hand, much lower sample sizes than in situ studies, or – alternatively – can be detected even when strongly diluted, e.g., upon subduction and recycling of sediment at convergent margins (Morris et al. 2002).

Because intensity and energy spectrum of the cosmic radiation entering the Earth's atmosphere are influenced by both the heliospheric and the geomagnetic fields, analyses of meteoric ^{10}Be in ice cores and ^{14}C in tree rings provide a paleo-cosmic-ray record, which is used to investigate the physics of the sun, the heliosphere, and the geomagnetic field in the past several ten thousand to several hundred thousand years (Beer et al. 2012). High solar activity leads to stronger cosmic-ray attenuation and hence lower nuclide production and vice versa. Six "Grand minima" (several consecutive solar cycles with very low activity maxima such as the "Maunder Minimum" in the seventeenth century) are recorded both in ^{14}C and ^{10}Be records over the last 1200 years. Such minima occur in clusters, and four clusters in the past ~7.5 ka are revealed by the ^{10}Be data (Steinhilber et al. 2010). The ^{14}C and ^{10}Be records over the last 10 ka agree very well with each other, which means that the observed variations are indeed caused by periodic changes in the cosmic-ray intensity in the past and are not a "transport" effect, i.e., caused by variations in atmospheric transport processes of ^{14}C and ^{10}Be or ocean storage of ^{14}C (Beer et al. 2012).

To derive solar magnetic field intensity changes over timescales of more than a few hundred years, variations in radionuclide concentrations caused by variations in the geomagnetic field need to be corrected for, as the latter dominate the overall variability on these timescales. This can be done by conventional paleomagnetic techniques, e.g., by measuring the magnetic properties of dated samples. A second method is to combine ^{14}C and ^{10}Be data, which helps to reduce the effects of noise in the data. While this is far from trivial, the overall agreement between the two different paleofield reconstructions in the past 50 ka is satisfying (Beer et al. 2012). Beryllium-10 data from ice or sediment cores (sometimes stacked data from many cores) are also used to derive the geomagnetic field intensity in the past several ten thousand to several hundred thousand years (Frank et al. 1997; Beer et al. 2012). Even the Brunhes-Matuyama magnetic field reversal ~780 ka ago has been observed in the Epica Dome C ice core in Antarctica (Raisbeck et al. 2006).

Meteoric ^{10}Be is also used to date sediments, for example, ferromanganese crusts at ocean floors. Beryllium-10 in sediments is used to derive paleodenudation rates over millions of years and catchment-wide modern erosion rates (Willenbring and von Blanckenburg 2010a, b; von Blanckenburg et al. 2012; Granger et al. 2013). In these cases, also the concentration of the non-cosmogenic stable ^{9}Be isotope needs to be determined. One of the first applications of meteoric ^{10}Be has been its use as tracer of subduction zone processes: cosmogenic ^{10}Be found in island-arc volcanic rocks and other mantle-derived rocks has been recycled from marine sediments incorporated into arc lavas during subduction (Morris et al. 2002). In such studies, ^{10}Be is also combined with U-series studies to better constrain timescales and mechanisms of the transfer from the slab to the mantle.

Beer et al. (2012) give an overview of further applications of radionuclides in studies of the atmosphere, hydrosphere,

and geosphere. Such work includes analyses of many nuclides not discussed so far, with a wide range of half-lives, e.g., Tritium, ^{36}Cl, ^{39}Ar, ^{81}Kr, ^{85}Kr, and ^{129}I. Some of these nuclides are predominantly anthropogenic, produced during nuclear bomb testing or deriving from nuclear power or reprocessing plants.

Summary

Cosmogenic nuclides are very widely studied in cosmochemistry and geochemistry. They allow us to study the transport of meteorites from their parent bodies to Earth and sometimes their previous history near the parent body surface. Cosmogenic nuclides are a tool to judge whether different meteorite specimens, e.g., found in a desert, may belong to a common fall or may have been released from their parent body by the same event. While in the past mostly bulk meteorite samples were analyzed, more recently much attention is given to single phases, such as individual chondrules or calcium-aluminum-rich inclusions. It is still debated whether or not such studies allow us to recognize irradiation of meteoritic matter by an intense flux of solar particles in the early solar system. Analytical advances also allow us to analyze cosmogenic nuclides in other tiny samples such as single presolar grains in meteorites, interplanetary dust particles, and material from sample return missions, e.g., from the regolith of the asteroid Itokawa sampled by the Japanese Hayabusa probe. Since some three decades, cosmogenic nuclides are having a tremendous impact in Earth surface sciences. Fields such as geomorphology, glaciology, paleoseismology, or volcanology profit from the unprecedented possibility to quantify geomorphic processes and timescales. Progress is driven by continuous analytical developments, allowing, in particular, the analysis of ever smaller amounts of cosmogenic radionuclides by new generations of accelerator mass spectrometers. Apart from cosmogenic nuclides produced in situ in rock samples, meteoric radionuclides – produced in the atmosphere before being deposited at the Earth's surface – have long since been and continue to be important tools in paleoclimatology and paleomagnetic studies. More recently, the potential of meteoric radionuclides as tracers and as tools to study large scale erosion has been recognized. A continuing challenge in many applications of cosmogenic nuclides in cosmochemistry and geochemistry is a reliable and accurate determination of relevant production rates. Further progress depends on both theoretical and experimental work.

Cross-References

- ▶ Beryllium Isotopes
- ▶ Meteorites

References

Balco G, Stone JO, Lifton NA, Dunai TJ (2008) A complete and easily accessible means of calculating surface exposure ages or erosion rates from ^{10}Be and ^{26}Al measurements. Quat Geochronol 3:174–195

Balco G. (2011) Contributions and unrealized potential contributions of cosmogenic-nuclide exposure dating to glacier chronology, 1990–2010. Quaternary Science Reviews 30:3–27

Beer J, McCracken K, von Steiger R (2012) Cosmogenic radionuclides - theory and applications in the terrestrial and space environments. Springer, Berlin/Heidelberg

Bogard DD, Nyquist LE, Bansal BM, Garrison DH, Wiesmann H, Herzog GF, Albrecht AA, Vogt S, Klein J (1995) Neutron-capture ^{36}Cl, ^{41}Ca, ^{36}Ar, and ^{150}Sm in large chondrites: evidence for high fluences of thermalized neutrons. J Geophys Res Planets 100:9401–9416

Bottke WF, Vokrouhlický D, Rubinkam DP, Broz M (2002) The effect of Yarkovsky thermal forces on the dynamical evolution of asteroids and meteoroids. In: Bottke WF et al (eds) Asteroids III. University of Arizona Press, Tucson, pp 395–408

Charreau J, Blard PH, Puchol N, Avouac JP, Lallier-Vergès E, Bourlès, D, Braucher R, Gallaud, A, Finkel R, Jolivet M, Chen Y, Roy P (2011) Paleo-erosion rates in Central Asia since 9 Ma: A transient increase at the onset of Quaternary glaciations? Earth Planet Sci Lett 304:85–92

Christl M, Wieler R, Finkel RC (2014) Measuring one atom in a million billion with mass spectrometry. Elements 10:330–332

Dunai TJ (2010) Cosmogenic nuclides – principles, concepts and applications in the earth surface sciences. Cambridge University Press, Cambridge, MA, 187pp

Eugster O, Herzog GF, Marti K, Caffee MW (2006) Irradiation records, cosmic ray exposure ages, and transfer times of meteorites. In: auretta DS, McSween HY (eds) Meteorites and the early solar system II. University Arizona Press, Tucson, pp 829–851

Farley KA et al (2014) In situ radiometric and exposure age dating of the Martian surface. Science 343:1247166

Frank M, Schwarz B, Baumann S, Kubik PW, Suter M, Mangini A (1997) A 200 kyr record of cosmogenic radionuclide production rate and geomagnetic field intensity from ^{10}Be in globally stacked deep-sea sediments. Earth Planet Sci Lett 149:121–129

Gladman BJ, Migliorini F, Morbidelli A, Zappalà V, Michel P, Cellino A, Froeschlé C, Levison HF, Bailey M, Duncan M (1997) Dynamical lifetimes of objects injected into asteroid belt resonances. Science 277(5323):197–201

Gosse JC, Phillips FM (2001) Terrestrial in situ cosmogenic nuclides: theory and application. Quaternary Sci Rev 20:1475–1560

Graf T, Marti K (1995) Collisional history of H chondrites. J Geophys Res Planets 100:21247–21263

Granger DE (2006) A review of burial dating methods using ^{26}Al and ^{10}Be. In: Siame LL, Bourlès DL, Brown ET (eds) In situ-produced cosmogenic nuclides and quantification of geological processes. Geological Society of America Special Paper 415:1–16

Granger DE, Lifton NA, Willenbring JK (2013) A cosmic trip: 25 years of cosmogenic nuclides in geology. Geol Soc Am Bull 125:1379–1402

Herzog GF, Caffee MW (2014) Cosmic-ray exposure ages of meteorites. In: Davis AM (ed) Treatise in geochemistry, 2nd edn. Elsevier, Oxford, pp 419–454

Herzog GF, Caffee MW, Jull AJT, (2015) Cosmogenic nuclides in antarctic meteorites. In: Righter K, Corrigan CM, McCoy TJ, Harvey RP (eds) 35 seasons of U.S. Antarctic meteorites (1976–2010): a pictorial guide to the collection. American geophysical union, special publication series. Wiley, Hoboken, 320pp

Hidaka H, Yoneda S (2007) Sm and Gd isotopic shifts of Apollo 16 and 17 drill stem samples and their implications for regolith history. Geochim Cosmochim Acta 71:1074–1086

Jull AJT (2006) Terrestrial ages of meteorites. In: Lauretta DS, McSween HY (eds) Meteorites and the early solar system II. University Arizona Press, Tucson, pp 889–905
Kleine T, Touboul M, Bourdon B, Nimmo F, Mezger K, Palme H, Jacobsen SB, Yin QZ, Halliday AN (2009) Hf-W chronology of the accretion and early evolution of asteroids and terrestrial planets. Geochim Cosmochim Acta 73:5150–5188
Kohl CP, Nishiizumi K (1992) Chemical isolation of quartz for measurement of in-situ produced cosmogenic nuclides. Geochim Cosmochim Acta 56:3583–3587
Kovaltsov GA, Usoskin IG (2010) A new 3D numerical model of cosmogenic nuclide Be-10 production in the atmosphere. Earth Planet Sci Lett 291:182–188
Kruijer TS, Fischer-Gödde M, Kleine T, Sprung P, Leya I, Wieler R (2013) Neutron capture on Pt isotopes in iron meteorites and the Hf-W chronology of core formation in planetesimals. Earth Planet Sci Lett 361:162–172
Lal D (1991) Cosmic ray labeling of erosion surfaces: in situ nuclide production rates and erosion models. Earth Planet Sci Lett 104:424–439
Leya I, Masarik J (2009) Cosmogenic nuclides in stony meteorites revisited. Meteoritics Planet Sci 44:1061–1086
Leya I, Wieler R, Halliday AN (2000) Cosmic-ray production of tungsten isotopes in lunar samples and meteorites and its implications for Hf-W cosmochemistry. Earth Planet Sci Lett 175:1–12
Leya I, Dalcher N, Vogel N, Wieler R, Caffee MW, Welten KC, Nishiizumi K (2015) Calibration of cosmogenic noble gas production based on ^{36}Cl-^{36}Arages. Part 2. The ^{81}Kr-Kr dating technique. Meteorit Planet Sci 50:1863–1879
Lifton N, Sato T, Dunai TJ (2014) Scaling in situ cosmogenic nuclide production rates using analytical approximations to atmospheric cosmic-ray fluxes. Earth Planet Sci Lett 386:149–160
Marti K, Graf T (1992) Cosmic-ray exposure history of ordinary chondrites. Annu Rev Earth Planet Sci 20:221–243
Masarik J, Beer J (2009) An updated simulation of particle fluxes and cosmogenic nuclide production in the Earth's atmosphere. J Geophys Res Atmos 114: Article Number D11103
Morris JD, Gosse J, Brachfeld S, Tera F (2002) Cosmogenic ^{10}Be and the solid earth: studies in geomagnetism, subduction zone processes, and active tectonics. Rev Mineral Geochem 50:207–270
Niedermann S (2002) Cosmic-ray-produced noble gases in terrestrial rocks: dating tools for surface processes. Rev Min Geochem 47:731–784
Portenga EW, Bierman PR (2011) Understanding Earth's eroding surface with ^{10}Be. GSA Today 21: 4–10
Raisbeck GM, Yiou F, Cattani O, Jouzel J (2006) Be-10 evidence for the Matuyama-Brunhes geomagnetic reversal in the EPICA Dome C ice core. Nature 444:82–84
Roth ASG, Baur H, Heber VS, Reusser E, Wieler R (2011) Cosmogenic helium and neon in individual chondrules from Allende and Murchison: implications for the precompaction exposure history of chondrules. Meteoritics Planet Sci 46:989–1006
Russ GP, Burnett DS, Wasserburg GJ (1972) Lunar neutron stratigraphy. Earth Planet Sci Lett 15:172–186
Savi S, Norton KP, Picotti V, Akcar N, Delunel R, Brardinoni F, Kubik P, Schlunegger F (2014) Quantifying sediment supply at the end of the last glaciation: Dynamic reconstruction of an alpine debris-flow fan. Geol Soc Am Bull 126:773–790
Schaller M, von Blanckenburg F, Veldkamp A, Tebbens LA, Hovius N, Kubik PW (2002) A 30 000 yr record of erosion rates from cosmogenic ^{10}Be in Middle European river terraces. Earth Planet Sci Lett 204:307–320
Steinhilber F, Abreu JA, Beer J, McCracken KG (2010) Interplanetary magnetic field during the past 9300 years inferred from cosmogenic radionuclides. J Geophys Res-Space Phys 115: Article Number A 01101
Stone J (2000) Air pressure and cosmogenic isotope production. J Geophys Res-Solid Earth 105:23753–23759
Vermeesch P (2007) CosmoCalc: an Excel add-in for cosmogenic nuclide calculations. Geochem Geophys Geosyst 8:Q08003
Von Blanckenburg F (2005) The control mechanisms of erosion and weathering at basin scale from cosmogenic nuclides in river sediment. Earth Planet Sci Lett 237:462–479
von Blanckenburg F, Bouchez J, Wittmann H (2012) Earth surface erosion and weathering from the ^{10}Be (meteoric)/^{9}Be ratio. Earth Planet Sci Lett 351:295–305
Wieler R (2002) Cosmic-ray-produced noble gases in meteorites. Rev Mineral Geochem 47:125–170
Wieler R, Graf T (2001) Cosmic ray exposure history of meteorites. In: Peucker-Ehrenbrink B, Schmitz B (eds) Accretion of extraterrestrial matter throughout Earth's history. Kluwer, New York, pp 221–240
Willenbring JK, von Blanckenburg F (2010a) Long-term stability of global erosion rates and weathering during late-Cenozoic cooling. Nature 465:211–214
Willenbring JK, von Blanckenburg F (2010b) Meteoric cosmogenic Beryllium-10 adsorbed to river sediment and soil: applications for earth-surface dynamics. Earth Sci Rev 98:105–122
Willenbring JK, Codilean AT, McElroy B (2013) Earth is (mostly) flat: Apportionment of the flux of continental sediment over millennial time scales. Geology 41:343–346
Wisdom J (1987) Chaotic dynamics in the solar system. Icarus 72:241–275
Woolum DS, Hohenberg C (1993) Energetic particle environment in the early solar system – extremely long pre-compaction meteoritic ages or an enhanced early particle flux. In: Levy EH, Lunine JI (eds) Protostars and planets III. University Arizona Press, Tucson, pp 903–919

Critical Points

William H. Casey[1] and Peter A. Rock[2]
[1]Department of Chemistry and Department of Earth and Planetary Sciences, University of California, Davis, CA, USA
[2]College of Math and Physical Sciences, Department of Chemistry, University of California, Davis, CA, USA

Definition

The point in phase space where the distinction between liquid and vapor disappears.

Elaboration

If you heat water in a closed volume, the temperature and pressure are initially fixed by equilibrium between a liquid and vapor. Beyond a certain temperature and pressure, however, the meniscus that separates the two phases disappears, and they become indistinguishable. If one draws a curve in

Prof. Peter A. Rock is deceased.

P-V space that identifies the region where both a liquid and vapor coexist, the *critical point* lies at the maximum where the slope is zero:

$$\left(\frac{\partial P}{\partial V}\right)_{T=T_c} = 0 \quad \text{and} \quad \left(\frac{\partial^2 P}{\partial V^2}\right)_{T=T_c} = 0 \qquad (1)$$

As this point is approached, the two phases, gas and liquid, begin to closely resemble one another on a molecular scale. The critical point for pure water is at 374.2 °C and 218.3 atm.

Near the critical point, the structure of these phases is very sensitive to small changes in temperature and pressure, and these changes are reflected in the macroscopic properties. Density, for example, changes considerably with small variations in pressure and temperature because the relative proportions of the two phases, liquid and vapor, fluctuate widely.

To illustrate the sensitivity of fluid properties near the critical point, consider that the critical point for pure CO_2 is at 31.8 °C and 72.9 atm, which are easily accessible in a laboratory. At these conditions a change in pressure of 1 part in 50,000 causes the CO_2 fluid density to increase by 10%. The density of critical CO_2 is 0.5 g/cm^3 so that 1 torr of CO_2 corresponds to an inch-thick layer. This one-inch-thick layer of CO_2 exhibits a 10% greater density at the bottom of the column than at the top simply due to the weight of the gas.

Likewise, the enthalpy of vaporization goes to zero at the critical point, and it can be seen that the isothermal compressibility

$$\beta \equiv -\frac{1}{V}\left(\frac{\partial V}{\partial P}\right)_T \qquad (2)$$

becomes infinite at the critical point. Correspondingly, the heat capacity, C_p, for the substance reaches large values near the critical point. Near-critical fluids also exhibit curious properties, such as critical opalescence, where light scatters into a dazzling display as the fluid reaches a certain molecular density because the molecular structures reach a characteristic length similar to the wavelength of visible light. Stated differently, the refractive index varies widely near the critical point along with the other bulk properties.

Addition of other components, such as CO_2, NaCl, or H_2, to H_2O dramatically affects the critical point of the solution. For these systems, a curve of critical points is defined in *P-T-X* space (*X is* a composition variable) that is generally nonlinear. The critical curve for the CO_2-H_2O system, for example, is a saddle with two maxima near end-member compositions and a minimum at intermediate values. The critical point for a saturated NaCl-H_2O mixture is at almost 600 °C and approximately 390 bars pressure, significantly higher than the value for pure H_2O.

Understanding the thermodynamic properties of mixed volatile fluids (e.g. CO_2-H_2O; H_2-H_2O) is important for predicting phase assemblages in rocks, for interpreting the compositions of fluid inclusions in minerals, and for predicting the effect of volatile gases on magma. Establishing these thermodynamic properties has been a major success in geochemistry during the last 50 years, and thermodynamic models have recently been extended to 6.0 GPa and 1200 °C based upon molecular-dynamic estimates of the dielectric constant of water (Sverjensky et al. 2014).

Cross-References

- ▶ Geochemical Thermodynamics
- ▶ Hydrothermal Vents
- ▶ Phase Equilibria

References

Sverjensky DA, Harrison B, Azzolini D (2014) Water in the deep earth: the dielectric constant and the solubilities of quartz and corundum to 60 kb and 1200 °C. Geochim Cosmochim Acta 129:125–145

Critical Zone

Justin B. Richardson
Dept. of Earth and Atmospheric Sciences, Cornell University, Ithaca, NY, USA

Synonyms

Earth's critical zone

Definition

The critical zone, the near-surface terrestrial environment from the bottom of circulating groundwater to the top of vegetation, hosts the complex interactions involving rock, soil, water, air, and living organisms that regulate life-sustaining resources.

Introduction

The term "critical zone" was first applied to the surface terrestrial environment by Dr. Gail Ashley (1998) in a presentation at the Geological Society of America. In her work, Dr. Ashley introduced the concept of the critical zone when

she wrote that a "holistic approach is needed to understand the three-dimensional complex linkages involving physical, chemical, and biological processes" and a study of geologic and surface processes that are "crucial for life" (Ashley 1998). In 2001, the United States National Research Council's Committee on Basic Research Opportunities in the Earth Sciences noted the future importance of the critical zone concept as integrative of disciplines and required to address interconnected problems (NRC 2001). The National Research Council defined the critical zone as "*the heterogeneous, near surface environment in which complex interactions involving rock, soil, water, air and living organisms regulate the natural habitat and determine availability of life sustaining resources*." Brantley et al. (2007) provided an alternative definition of the critical zone as "*the fragile skin of the planet defined from the outer extent of vegetation down to the lower limits of groundwater*," and many others have followed. In all definitions, the critical zone is recognized as a location of complex biogeochemical and physical processes that supports the terrestrial biosphere (Fig. 1) (White and Sharkey 2016). Study of the structure and function of the critical zone explicitly includes study of processes evolving at all timescales from that of the geologist to that of the meteorologist, and explicitly includes atmospheric (i.e., climate), geologic (e.g., volcanic, tectonic), and biologic (e.g., microbes, plants, organisms, humans) changes throughout Earth's deep and recent history (NRC 2001). Critical zone science can provide information for sustainable adaptation to human perturbations (e.g., intensive land use and climate change).

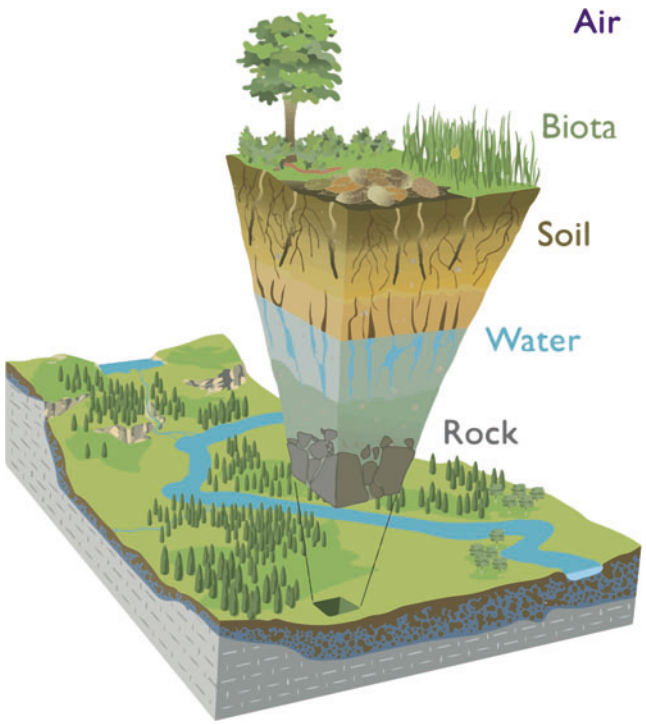

Critical Zone, Fig. 1 An illustration of the Critical zone conceptual model modified from Chorover et al. (2007) (Artwork by R. Kindlimann)

Essential Concepts

The critical zone paradigm is a new integration of existing fields of natural sciences (Fig. 1). One of the essential aspects of this paradigm is that the term "critical" reflects that nearly all terrestrial life, including humans, depends on the critical zone (Giardino and Houser 2015; NRC 2001), establishing a clear link between Earth's surface processes and geosystems with humans (Brantley et al. 2007; Richter and Billings 2015). Land use and climatic impacts are affecting processes that govern biomass productivity, soil formation, geochemical cycling of elements, and water resources (Hooke et al. 2012). For this reason, it is essential for developing predictive abilities of how attributes, processes, and outputs of the critical zone will respond to projected climate and land-use changes. Some of the central scientific concepts that have been investigated through critical zone science are: (1) formation and distribution of weathered bedrock, (2) sustainability of water and soil resources, (3) tracing the movement of energy and reactive material, and (4) integration of processes across spatial and time scales and with respect to anthropogenic uses and perturbations.

Understanding the biological, chemical, and physical properties controlling bedrock and surficial deposit weathering is a central topic for critical zone science and for parallel efforts in geobiology and geochemistry (Pope 2015). The formation of weathered bedrock has been investigated by Earth scientists for more than 170 years (see Ebelmen 1845; Gilbert 1909). Critical zone science has generated renewed interest in the distribution, structure, and residence of weathered rock, features whose spatial distribution are generally considered to be difficult to measure (Holbrook et al. 2014). The architecture of the weathered bedrock of the critical zone has been shown to be a combination of tectonic, topographic, and weathering processes combined (e.g., Brantley and Lebedeva 2011; St. Clair et al. 2015). Weathering of bedrock may influence sustainability issues, in particular, the feedback between weathering rates and atmospheric CO_2 concentrations (Raymo 1989). Bedrock composition can also directly control the aboveground ecosystem. Hahm et al. (2014) found differences in forest productivity were directly linked to major and minor element composition of the underlying bedrock. The architecture and distribution of fractures is not only important for element cycling, but is also key for reservoirs of materials and energy in the critical zone. For example, the thickness and structure of the weathered bedrock in the critical zone controls many hydrologic properties such as water table elevation, plant-available water, and discharge rates to streams and rivers (Brooks et al. 2015).

Soil and water sustainability is a fundamental component of critical zone science. Much of the framework of critical zone science is built upon principal themes of soil science (e.g., state factor model of Hans Jenny 1941) and hydrology (e.g., subsurface and surface flow by Freeze 1972). Critical zone science focuses on soil sustainability through estimating soil formation rates (e.g., soil formation on a hillslope by Riggins et al. 2011), modeling nutrient cycling (e.g., soil-vegetation cycling rates in a temperate forest by Kraepiel et al. 2015), and quantifying erosion and denudation rates (e.g., sediment transport from following a storm by Foster and Anderson 2016). In addition, water sustainability is considered through snowpack (e.g., snow accumulation in the southern Sierra Nevada by Kirchner et al. 2014), belowground water storage (e.g., water table recharge along a hillslope by Dralle et al. 2014), surface and subsurface flow (e.g., depth of preferential flow rates through soils by Thomas et al. 2013), plant-availability (e.g., plant ecohydrological strategies in seasonally dry ecosystems by Vico et al. 2015), and evapotranspiration losses (e.g., evapotranspiration along an elevation gradient in southern Sierra Nevada mountains by Goulden et al. 2012). While many of these efforts run parallel with traditional soil and hydrological sciences, their integration with other disciplines for broader theoretical understanding and quantitative modeling is pivotal for critical zone science. For an example of greater integration, Bales et al. (2011) observed that during severe droughts in the Sierra Nevada Mountains, California, the majority of water lost from soils and trees can be sourced from water stored in weathered bedrock. In addition, Wilson et al. (2016) linked tillage practices in agroecosystems with soil erosion, which influences crop productivity, carbon storage, and net income from a parcel of land. Critical zone science has built upon existing soil and water sustainability concepts with greater integration as a holistic system (Richter and Billings 2015).

Tracing the movement of material and energy is important for quantifying and modeling local and global critical zone processes, particularly those that are reactive. The movement of materials through soil and unconsolidated material has been a topic of concern for many disciplines. Materials of interest include nutrients (e.g., Davis et al. 2014), inorganic colloids (e.g., Trostle et al. 2016), organic carbon (e.g., Stielstra et al. 2015), trace metals and metalloids (e.g., Ma et al. 2011), and pollutants (e.g., Ma et al. 2014). The movement of these materials through the critical zone controls natural phenomena such as chemical weathering, erosion, nutrient cycling, and anthropogenic issues, such as acid-mine drainage, eutrophication of surface waters, atmospheric CO_2 concentrations, and contamination of drinking water (Li et al. 2017). Studies of material movement range from empirical studies and process-based models to quantify their movement. Li et al. (2017) described four areas in which reactive transport models may substantially contribute to critical zone science as testable hypotheses: (1) evapotranspiration-chemical weathering controlled by reactive gases, (2) water availability-chemical weathering-atmospheric CO_2-temperature linkages at the global scale, (3) soil moisture influences on carbon stabilization in soil, and (4) plant root controls on soil formation and function. Understanding the movement of energy in the critical zone is important for investigating thermodynamic controls from climate on physical, biological, and chemical processes. Rasmussen et al. (2011) proposed the structure and evolution of the critical zone can be described using climatic and biotic forcings as a single environmental energy and mass transfer (EEMT) parameter with energy flux units (e.g., J m−2 s−1). This concept has many potential applications and may be applied across any chosen spatial and temporal scales. Further coupling the movement of materials and energy are current areas of study with many future implications for understanding the critical zone.

Linking critical zone processes across time and spatial scales is a principal goal of critical zone science. Many chemical reactions occur at molecular microsystems (mineral surfaces, root surfaces, macropores, rock fractures), and critical zone scientists are working to measure their effect on larger scale processes (soil formation, hillslopes development, watersheds ecosystem services). For example, Brantley et al. (2011) notes that as rocks and minerals weather, their size decreases and surface area increases, exerting a control on the rate of chemical weathering in the soil profile with potential influences at the watershed scale in Puerto Rico and Pennsylvania. Moreover, mechanisms occurring in a soil profile or at an acre scale can be coupled with regional and global scale estimates. In addition to size and spatial scales, the other most arduous endeavors for Earth Scientists has been linking short-term processes (hours, days, years) with longer-term changes (decades, centuries, and millennia). Monitoring efforts have been fundamental for quantifying short- and long-term biogeochemical and physical processes of the critical zone. For example, a short-term observation may be daily monitoring for peak streamflow during melt season in a snow-dominated watershed (Chen et al. 2016). As a long-term example, Richter et al. (2000) observed that the impact of atmospheric nitrogen was dominant in biological nitrogen fixation over 40 years, by comparing soils collected and archived from 1962 through 1997 at the Calhoun Experimental Forest. Coupled numerical models, such as Flux-Penn State Integrated Hydrologic Model (Flux-PIHM) (Shi et al. 2013) and Terrestrial Integrated Modeling System (TIMS) (Niu et al. 2014), are the leading edge on combining processes over multiple time scales to evaluate the relative influences of different critical zone parameters, and hold out the capacity to support predictions of critical zone processes in the past and future. Furthermore, coupled numerical models are capable of using contemporary processes to

investigate changes over geologic time scales (thousands to millions of years).

Current Investigations

The critical zone is studied at a number of Critical Zone Observatories (CZOs), where multiple scientific communities work in tandem to understand coupled processes, through both field and theoretical approaches. Teams of researchers monitor surface and subsurface water, meteorological conditions, soil properties, and vegetation. In addition, researchers undertake sampling campaigns of vegetation, soils, sediments, regolith, and bedrock. Information generated through monitoring and from sampling campaigns is synthesized to investigate complex systems at CZOs.

While individual CZOs each develop novel approaches to quantify critical zone processes, observatories aim to complete comparable measurements as a network. A key aspect is to use common measurements in which sampling is guided by overarching hypotheses and further developed to reflect site conditions, but materials and methods are implemented in a similar manner across the CZO network (White et al. 2015). Although cross-CZO data comparisons are a substantial goal, many lines of inquiry are site-specific and utilize approaches based on the principal of "best technique and sampling design" at each individual CZO. Thus, even though CZOs are individual entities, data is collected to be comparable with local, regional, and global monitoring efforts. Cross-CZO comparisons that are generalizable across space and time may be modeled using common measurement data and are paramount for creating integrated processes theories needed to expand predictive modeling (i.e., Earth-casting) (White et al. 2015; Richter and Billings 2015).

The United States National Science Foundation (NSF) has funded 10 CZOs across the United States and nine of these still receive funding (White et al. 2015). The NSF CZO program began in 2007 with support of three CZOs: Susquehanna-Shale Hills CZO in Pennsylvania, the Southern Sierra CZO in California, and the Boulder Creek CZO in Colorado. In 2009, three additional observatories were added: Luquillo Mountains CZO in Puerto Rico, Christina River Basin CZO in Delaware and Pennsylvania, and the Jemez River Basin/Santa Catalina Mountains CZO in Arizona and New Mexico. In 2013, four new observatories were selected for funding: Eel River CZO in northern California; Reynolds Creek CZO in Idaho; the Intensively Managed Landscape CZO in Illinois, Iowa, and Minnesota, and the Calhoun CZO in northern South Carolina. Measurements at the NSF-funded CZOs include a common set of variables that quantify Critical zone architecture and evolution, fluxes across the Critical zone boundaries, and changes in storage of the major critical zone reservoirs. The CZOs have recognized that many of the details of overarching science questions can best be addressed if a core set of variables is measured across the CZOs, and if those core measurements are made using the same or readily comparable methods. In 2014, the CZO National Office was created to spur network level research and outreach activities.

There have been many international projects to conduct critical zone research globally. Although some observatories worldwide are not called CZOs, scientists across the international research communities have adopted the framework and nomenclature of "critical zone science," because the paradigm is compelling for addressing environmental sustainability and accelerating interest in Earth surface sciences (White et al. 2015; Richter and Billings 2015). International CZOs and similar projects have identified objectives of determining changes to the critical zone in response to human pressures, and each program has its own approach and strategy. The European Commission funded SoilTrEC in 2009. The SoilTrEC network consisted of four CZOs: Koilaris River Basin in Crete, Damma Glacier in Switzerland, Slavka Forest in the Czech Republic, and in Fuchsenbigl, Austria. Germany has also established the TERENO network, a set of four observatories: Eifel/Lower Rhine Valley, Harz/Central German Lowland, Northeastern German Lowland, and Bavarian Alps/pre-Alps Observatories. Additional CZOs in France and through a United Kingdom-China partnership are in development. Through internationally funded meeting and workshops, there are 60 countries conducting research at 21 funded CZOs as of 2015 (White et al. 2015).

Conclusions

Critical zone science is a new paradigm focusing on integration of existing fields of natural sciences: a systems approach needed to understand the three-dimensional complex linkages involving physical, chemical, and biological processes at the Earth's surface. The term "critical" reflects that nearly all terrestrial life depends on the critical zone. Critical zone science aims to develop predictive abilities, which are essential to understand the past and future effects of climate and land-use. The central scientific concepts investigated through critical zone science are the formation of weathered bedrock, water and soil resources, the movement of energy and reactive material, and integration of natural processes across spatial and time scales. The critical zone is studied at Critical Zone Observatories (CZOs), where multiple scientific communities monitor and conduct sampling campaigns to synthesize the complex interactions systems. Critical zone research is conducted globally as international research communities have adopted the framework and nomenclature to renew interest in Earth surface processes and their sustainability.

Cross-References

- Anthropogenic CO_2
- Biogeochemistry
- Carbon Cycle
- Chemical Weathering
- Earth's Atmosphere
- Earth's Continental Crust
- Geochemical Thermodynamics
- Geochemistry
- Hydrologic Cycle
- Kinetics of Geochemical Processes
- Low-Temperature Geochemistry
- Nutrients
- Water

References

Ashley GM (1998) Where are we headed? "Soft" rock research into the new millennium. Geo Soc Am Ab/Pro 30:A-148

Bales RC, Hopmans JW, O'Geen AT, Meadows M, Hartsough PC, Kirchner P, Hunsaker CT, Beaudette D (2011) Soil moisture response to snowmelt and rainfall in a Sierra Nevada mixed-conifer forest. Vadose Zone J 10:786–799

Brantley SL, Lebedeva M (2011) Learning to read the chemistry of regolith to understand the critical zone. Annu Rev Earth Planet Sci 39:387–416

Brantley SL, Goldhaber MB, Ragnarsdottir KV (2007) Crossing disciplines and scales to understand the critical zone. Elements 3:307–314

Brantley SL, Buss HL, Lebedeva M, Fletcher RC, Ma L (2011) Investigating the complex interface where bedrock transforms to regolith. Appl Geochem 26:S12–S15. https://doi.org/10.1016/j.apgeochem.2011.03.017

Brooks PD, Chorover J, Fan Y, Godsey SE, Maxwell RM, McNamara JP, Tague C (2015) Hydrological partitioning in the critical zone: recent advances and opportunities for developing transferable understanding of water cycle dynamics. Water Resour Res 51:6973–6987

Chen X, Kumar M, Wang R, Winstral A, Marks D (2016) Assessment of the timing of daily peak streamflow during the melt season in a snow-dominated watershed. J Hydrometeorol 17:2225–2244

Chorover J, Kretzschmar R, Garcia-Pichel F, Sparks DL (2007) Soil biogeochemical processes within the critical zone. Elements 3:321–326

Davis CA, Ward AS, Burgin AJ, Loecke TD, Riveros-Iregui DA, Schnoebelen DJ, Just CL, Thomas SA, Weber LJ, St. Clair MA (2014) Antecedent moisture controls on stream nitrate flux in an agricultural watershed. J Environ Qual 43:1494–1503. https://doi.org/10.2134/jeq2013.11.0438

Dralle DN, Boisramé G, Thompson SE (2014) Spatially variable water table recharge and the hillslope hydrologic response: analytical solutions to the linearized hillslope Boussinesq equation. Water Resour Res 50:8515–8530

Ebelmen JJ (1845) Sur les produits de la décomposition des espèces minérales de la famille des silicates. In Annales des Mines 7:66

Foster MA, Anderson RS (2016) Assessing the effect of a major storm on 10 BE concentrations and inferred basin-averaged denudation rates. Quat Geochronol 34:58–68

Giardino JR, Houser C (2015) Introduction to the Critical zone. In: Principles and Dynamics of the Critical zone, vol 19, Elsevier, Amsterdam, Netherlands, pp 1–14

Gilbert GK (1909) The convexity of hilltops. J Geol 17:344–350

Goulden ML, Anderson RG, Bales RC, Kelly AE, Meadows M, Winston GC (2012) Evapotranspiration along an elevation gradient in California's Sierra Nevada. J Geophys Res Biogeo 117(G3)

Hahm WJ, Riebe CS, Lukens CE, Araki S (2014). Bedrock composition regulates mountain ecosystems and landscape evolution. Proceedings of the National Academy of Sciences, 111:3338-3343

Holbrook WS, Riebe CS, Elwaseif M, Hayes JL, Basler-Reeder K, Harry DL, Malazian A, Dosseto A, Hartsough PC, Hopmans JW (2014) Geophysical constraints on deep weathering and water storage potential in the Southern Sierra Critical zone Observatory. Earth Surf Process Landf 39:366–380

Hooke RL, Martín-Duque JF, Pedraza J (2012) Land transformation by humans: a review. GSA Today 22:4–10

Jenny H (1941) Factors of soil formation: a system of quantitative pedology. McGraw-Hill Book Company, Inc., New York

Kirchner PB, Bales RC, Molotch NP, Flanagan J, Guo Q (2014) LiDAR measurement of seasonal snow accumulation along an elevation gradient in the southern Sierra Nevada. California Hyd Earth Sys Sci 18:4261–4275. https://doi.org/10.5194/hess1842612014

Kraepiel AML, Dere AL, Herndon EM, Brantley SL (2015) Natural and anthropogenic processes contributing to metal enrichment in surface soils of central Pennsylvania. Biogeochemistry 123:265–283

Li L, Maher K, Navarre-Sitchler A, Druhan J, Meile C, Lawrence C, Moore J, Perdrial J, Sullivan P, Thompson A, Jin L, Bolton EW, Brantley SL, Dietrich WE, Mayer KU, Steefel CL, Valocci A, Zachara J, Kocar B, Mcintosh J, Tutolo BM, Kumar M, Sonnenthal E, Bao C, Beisman J (2017) Expanding the role of reactive transport models in critical zone processes. Earth Sci Rev 165:280–301

Ma L, Jin L, Brantley SL (2011) Geochemical behaviors of different element groups during shale weathering at the Susquehanna/Shale Hills Critical zone Observatory. Appl Geochem 26:S89–S93. https://doi.org/10.1016/j.apgeochem.2011.03.038

Ma L, Konter J, Herndon E, Jin L, Steinhoefel G, Sanchez D, Brantley S (2014) Quantifying an early signature of the industrial revolution from lead concentrations and isotopes in soils of Pennsylvania, USA. Anthropocene 7:16–29

Niu GY, Paniconi C, Troch PA, Zeng X, Durcik M, Huxman T (2014) An integrated modeling framework of catchment-scale ecohydrological processes: 1. Model description and tests over an energy-limited watershed. Ecohydrolog 7:427–439. https://doi.org/10.1002/eco.1362

NRC, National Research Council (2001) Basic research opportunities in earth sciences. National Academies Press, Washington, DC

Pope GA (2015) Regolith and weathering (rock decay) in the critical zone. In: Principles and dynamics of the critical zone, vol 19, Elsevier, Amsterdam, Netherlands, pp 113–146

Rasmussen C, Troch PA, Chorover J, Brooks PD, Pelletier JD, Huxman TE (2011) An open system framework for integrating critical zone structure and function. Biogeochemistry 102:15–29. https://doi.org/10.1007/s10533-010-9476-8

Raymo ME (1989) Geochemical evidence supporting T.C. Chamberlin's theory of glaciation. Geology 19(4):344–347

Richter DD, Billings SA (2015) 'One physical system': Tansley's ecosystem as Earth's critical zone. New Phytol 206:900–912

Richter DD, Markewitz D, Heine PR, Jin V, Raikes J, Tian K, Wells CG (2000) Legacies of agriculture and forest regrowth in the nitrogen of old-field soils. For Ecol Manag 138:233–248

Riggins SG, Anderson RS, Anderson SP, Tye AM (2011) Solving a conundrum of a steady-state hillslope with variable soil depths and production rates, Bodmin Moor, UK. Geomorphology 128:73–84. https://doi.org/10.1016/j.geomorph.2010.12.023

Shi Y, Davis KJ, Duffy CJ, Yu X (2013) Development of a coupled land surface hydrologic model and evaluation at a critical zone observatory. J Hydrometeorology 14:1401–1420

St. Clair J, Moon S, Holbrook WS, Perron JT, Riebe CS, Martel SJ, Carr B, Harman C, Singha K, Richter DD (2015) Geophysical imaging reveals topographic stress control of bedrock weathering. Science 350:534–538. https://doi.org/10.1126/science.aab2210

Stielstra CM, Lohse KA, Chorover J, McIntosh JC, Barron-Gafford GA, Perdrial JN, Litvak M, Barnard HR, Brooks PD (2015) Climatic and landscape influences on soil moisture are primary determinants of soil carbon fluxes in seasonally snow-covered forest ecosystems. Biogeochemistry 123:447–465. https://doi.org/10.1007/s10533-015-0078-3

Thomas EM, Lin H, Duffy CJ, Sullivan PL, Holmes GH, Brantley SL, Jin L (2013) Spatiotemporal patterns of water stable isotope compositions at the Shale Hills Critical zone Observatory: Linkages to subsurface hydrologic processes. Vadose Zone J 12:1–16

Trostle KD, Ray Runyon J, Pohlmann MA, Redfield SE, Pelletier J, McIntosh J, Chorover J (2016) Colloids and organic matter complexation control trace metal concentration-discharge relationships in Marshall Gulch stream waters. Water Resour Res 52:7931–7944

Vico G, Thompson SE, Manzoni S, Molini A, Albertson JD, Almeida-Cortez JS, Fay PA, Feng X, Guswa AJ, Liu H, Wilson TG (2015) Climatic, ecophysiological, and phenological controls on plant ecohydrological strategies in seasonally dry ecosystems. Ecohydrology 8:660–681

White T, Sharkey S (2016) Critical zone Oxford bibliography. Oxford Bibliographies. https://doi.org/10.1093/OBO/9780199363445-0055

White T, Brantley S, Banwart S, Chorover J, Dietrich W, Derry L, Lohse K, Anderson S, Aufdendkampe A, Bales R, Kumar P (2015) The role of critical zone observatories in critical zone science. Dev Earth Sur Proc 19:15–78

Wilson CG, Wacha KM, Papanicolaou AN, Sander HA, Freudenberg VB, Abban BK, Zhao C (2016) Dynamic assessment of current management in an intensively managed agroecosystem. J Contemp Water Res Edu 158:148–171

Crystal Chemistry

Dana T. Griffen
Geology Department, Brigham Young University, Provo, UT, USA

Definition

Crystalline materials consist of periodically repeating arrays of atoms with compositions that can be represented by definite chemical formulas (which may be variable within certain compositional limits). Crystal chemistry addresses the interdependence of crystallography and chemistry and the attendant consequences and phenomena. Thus, crystal chemistry is concerned with the symmetry and dimensions of the unit cell, the positions of atoms within the unit cell, the kinds of atoms found at each crystallographic site, and relationships with similar phases through such phenomena as solid solution, exsolution, polymorphism, and so forth. For earth scientists, the crystals of interest are minerals. Although the boundaries between crystal chemistry, materials science, and certain areas of solid-state physics and solid-state chemistry are quite blurry, we shall approach the subject from the viewpoint of geology – that is, mineralogical crystal chemistry.

Originally published in: Marshall CP, Fairbridge RW (eds) Encyclopedia of Geochemistry, Springer Netherlands, 1999.

Stereochemistry

Atoms

Virtually everything of interest in crystal chemistry is related in some way to the spatial and chemical relationships among atoms or ions in a crystal. (The terms "cation" and "anion" are used hereafter to suggest atoms with lesser or greater electronegativity, respectively. No implication of fully ionic charges or fully ionic bonds is intended. Ionic size is discussed under ▶ ionic radii.) In general, ions may be viewed as soft spheres, with cations smaller than anions and surrounded by them; the number of ions bonded to a cation or anion is the coordination number. That the coordination numbers of cations should depend on their sizes relative to the surrounding anions and that bond lengths should equal the sums of the ionic radii are ideas formalized early in the twentieth century. They were stated in the first of five rules by Linus Pauling (1929), and these came to be known as Pauling's rules. For decades, they were taken as the basis for understanding inorganic crystal structures. Because they are often cited even in current literature, it is worthwhile to consider them as relevant concepts that are discussed in the paragraphs below.

Coordination Polyhedra

Imagining cations surrounded by anions leads to the concept of coordination polyhedra, envisioned by connecting the anions about a cation (Gibbs 1982). Figure 1 illustrates this concept using the crystal structure of the common mineral, titanite ($CaTiSiO_5$). Figure 1a is a "ball-and-stick" depiction of the structure and has the advantage of showing the positions of each atom; even so, it is somewhat confusing, and the coordination numbers and geometric relationships can be extracted only by careful study. Figure 1b is a polyhedral drawing, anions are assumed to be at each corner of each polyhedron, cations are presumed to lie within (although not necessarily at the precise center of) each polyhedron, and the coordination numbers and geometric relationships are immediately obvious. For atoms that have large coordination numbers and/or irregular coordination polyhedra, such as the Ca atoms in titanite, it is often advantageous to show them simply as independent spheres.

The frequent occurrence of 3-, 4-, 6-, 8-, and 12-coordination in crystalline solids leads to the recognition of regular coordination polyhedra (see Table 1 and Fig. 2). "Regular coordination" need not mean geometrically ideal, indeed, coordination polyhedra are most often distorted in

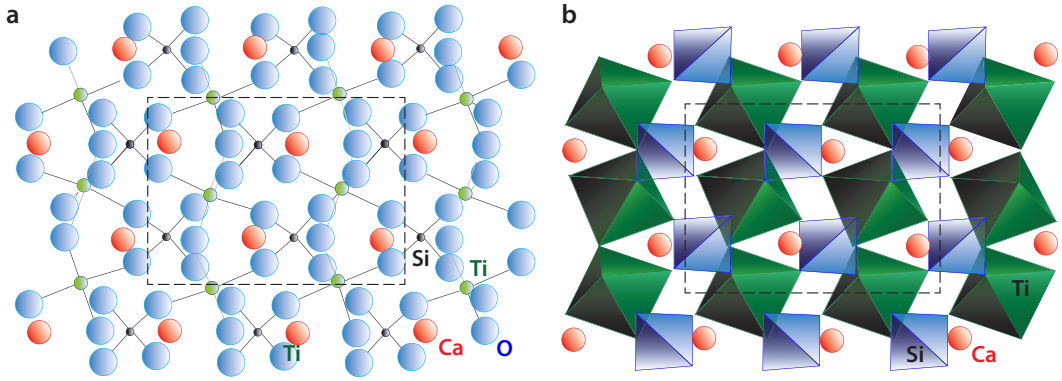

Crystal Chemistry, Fig. 1 (**a**) The crystal structure of titanite ($CaTiSiO_5$) represented as a "ball-and-stick" illustration. (**b**) The same crystal structure represented as a polyhedral diagram with the SiO_4 tetrahedra and TiO_6 octahedra shaded; the Ca polyhedra are irregular, and the Ca atoms are left as independent spheres for clarity

some way, but it implies representation by some type of regular solid. Coordination numbers such as 5, 7, 9, and 10 do occur, although much less frequently for cations with radii below about 1.0 Å, and with some exceptions, no attempt is made to represent these by polyhedra with simple shapes.

Figure 2e, f look very similar, but note that the triangles of anions on the top are rotated 60° with respect to one another. Figure 2e represents hexagonal close packing of anions (the layer sequence is . . .ABABA. . .), and Fig. 2f represents cubic close packing (. . .ABCABC. . .). Many minerals have crystal structures that are based on one of the two types of close packing. For example, olivine is based on a distorted hexagonal close packed array of oxygens with Si in some of the tetrahedral interstices and Mg or Fe^{2+} in some of the octahedral interstices; the pyroxene structure is based on very distorted cubic close packing.

Polyhedral Arrangements

Representing crystal structures, or parts thereof, as assemblages of linked polyhedra not only simplifies envisioning the structure but leads to crystallochemically useful ways of classifying minerals. Silicates, for example, are classified on the basis of tetrahedral polymerization – that is, the extent to which tetrahedra are linked (or "share corners") in the structure. (See ► Silicate Minerals)

Consideration of the extent to which corners can be shared, that is, the number of cations bonded to an anion, leads to another important crystallochemical principle. Pauling's second rule states that the sum of electrostatic bond strengths reaching an anion is equal to the charge (oxidation number) of the anion with the sign reversed. Electrostatic bond strength is defined as

$$\mathrm{EBS} = \frac{\mathrm{cationoxidationnumber}}{\mathrm{cationcoordinationnumber}} \qquad (1)$$

Crystal Chemistry, Table 1 The regular coordination polyhedra

Type	No. of corners	No. of edges
Triangle	3	3
Tetrahedron	4	6
Octahedron	6	12
Cube	8	12
Cuboctahedron	12	24

and is the proportion of the formal charge of the cation allotted to each coordinating anion. The rule seems a reasonable requirement, and there are many structures for which it works perfectly. Consider the common garnet, grossular, $Ca_3Al_2Si_3O_{12}$. There is only one crystallographically unique oxygen atom, and it is bonded to one Si, one Al, and two Ca atoms, which are 4-, 6-, and 8-coordinated, respectively. The bond strengths are therefore

$$\mathrm{EBS_{Si}} = \frac{4}{4} = 1; \quad \mathrm{EBS_{Al}} = \frac{3}{6} = \frac{1}{2}; \quad \mathrm{EBS_{Ca}} = \frac{2}{8} = \frac{1}{4}$$

Thus,

$$\sum \mathrm{EBS} = 1 + \frac{1}{2} + 2\left(\frac{1}{4}\right) = 2$$

which is the oxidation number of oxygen with the sign reversed.

Very often, Pauling's second rule fails, however. Sometimes the failure is minor, in that the deviations in Σ EBS are not large, and the average over the anions is correct. In other cases, the deviations are quite large. The problem is that the rule tacitly assumes that all of the bond lengths about a cation are identical, and this is most often not the case. Because shorter bonds are obviously stronger than longer ones for the same cation–anion pair, dividing the oxidation number by the

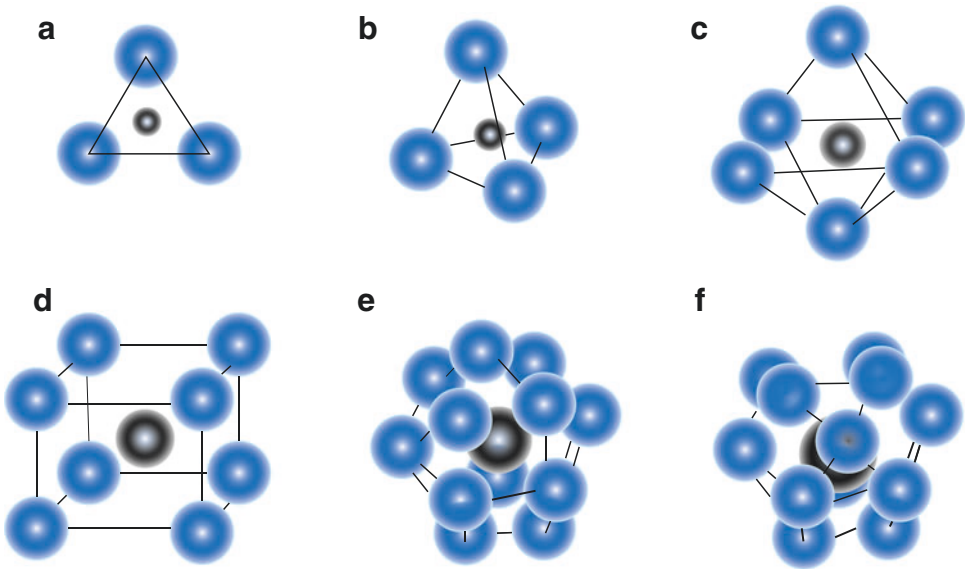

Crystal Chemistry, Fig. 2 Regular coordination polyhedra. (**a**) Triangular coordination. (**b**) Tetrahedral coordination. (**c**) Octahedral coordination. (**d**) Cubic coordination. (**e**, **f**) Two types of 12-coordination, one based on hexagonal close packing (**e**) and one on cubic close packing (**f**)

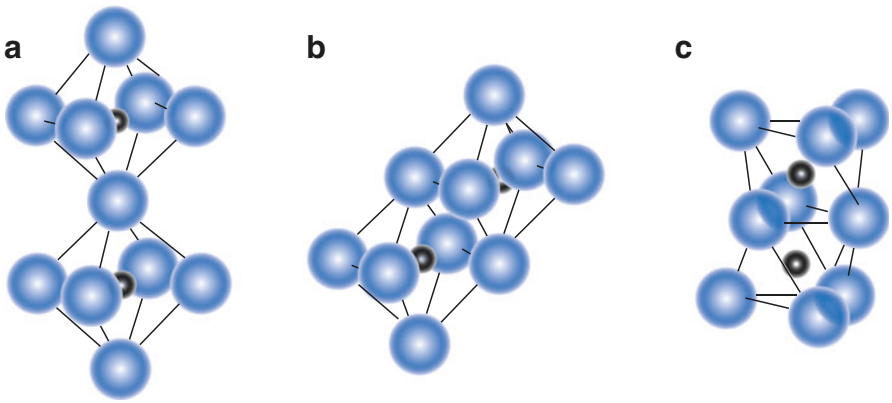

Crystal Chemistry, Fig. 3 The effects on cation–cation distances of sharing polyhedral elements. (**a**) Shared octahedral corner (one anion). (**b**) Shared octahedral edge (two anions). (**c**) Shared octahedral face (three anions)

coordination number does not yield a proper bond strength. A popular approach to "correcting" this problem has been the development of empirical bond-strength–bond-length relationships of the form

$$s = \mathrm{e}^{(r-r_0)/B} \tag{2}$$

or

$$s = \left(\frac{r}{r_0}\right)^{-N} \tag{3}$$

where s is often called bond valence, r is bond length, and r_0, B, and N are adjustable parameters (e.g., Brown and Shannon 1981). Using this approach, it is generally possible to obtain bond–valence sums that are very close to the oxidation number of the anion. It also facilitates the recognition of hydroxyls in a structure that has been refined by X-ray diffraction; the bond–valence sum about a hydroxyl should be close to 1 rather than 2. Even using a refinement such as the bond–valence approach, the sums are often not quite perfect, for the same reasons that the first rule of Pauling lacks rigor: Variations in bond strength, like variations in bond length, result not only from the ionic effects assumed by the models but also from the effects of covalence.

Shared Polyhedral Elements

Figure 3 shows pairs of octahedra sharing a corner (i.e., one anion), an edge (two anions), and a face (three anions). It is evident that the cation–cation distance decreases in the order shared corner-edge-face. The third and fourth of Pauling's rules state that the sharing of polyhedral edges and (particularly) faces tends to decrease the stability of a structure and that this effect is largest for small, highly charged cations, which tend not to share polyhedral elements with one another. The usual rationale is based on cation–cation repulsions, which, it will be seen from Fig. 3, increase as edges and faces are shared.

The sharing of polyhedral elements is extremely common, however. It is true that the size and charge of the cations have an

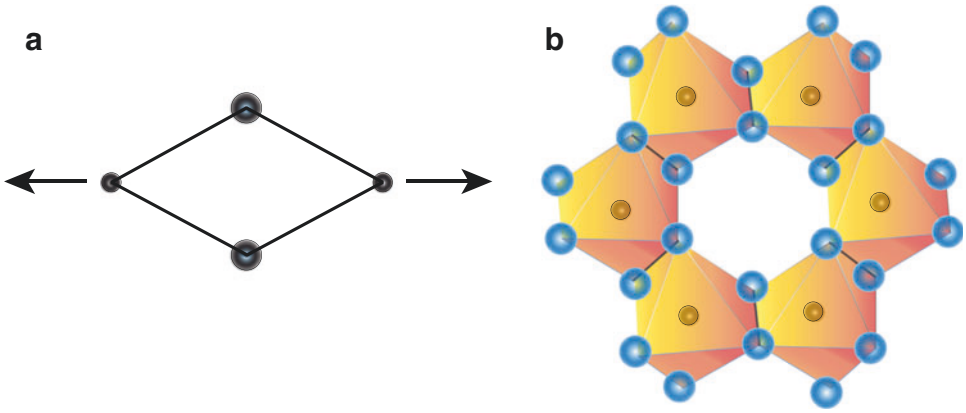

Crystal Chemistry, Fig. 4 (**a**) The direction in which the shortening of shared polyhedral edges increases the cation–cation distances, thereby reducing cation–cation repulsion. (**b**) A part of the octahedral sheet in muscovite. The shared octahedral edges are shown by heavy *lines*

effect (e.g., SiO_4 tetrahedra never share faces, although BeO_4 tetrahedra are known to), but the sharing of octahedral edges occurs in many minerals (olivines, pyroxenes, amphiboles, micas, and many more), and octahedral faces are even shared in some (e.g., corundum, hematite, and dumortierite). In the case of shared edges, one structural compensation that occurs is that the shared edges tend to shorten, thereby lengthening the cation–cation distance and perhaps positioning the anions so as to increase the negative charge density between the cations (Fig. 4a). Figure 4b shows part of a sheet of octahedra in muscovite. Note that the shared octahedral edges (heavy lines) are shorter than the unshared edges. In the case of shared faces, not only do edges shorten, but the cations typically move away from the shared face if it is opposite to an unshared face.

Pauling's fifth and last rule is known as the rule of parsimony and states that the number of essentially different kinds of constituents in a crystal structure tends to be small. If "constituents" are interpreted as coordination polyhedra, and if "essentially different kinds" means that differently distorted polyhedra with the same number of anions are considered "the same kind," then this rule is acceptable, although of doubtful practical significance. Consider this example: Anorthite contains eight symmetrically unique sites containing Si, eight containing Al, and eight containing Ca. Each of the Si sites is geometrically somewhat different from all of the others, and the same is true for each Al and each Ca site. Twenty-four unique kinds of coordination polyhedra are not a small number. Nevertheless, if it is conceded that all of the tetrahedral (Si and Al) sites are very similar, as are all of the Ca sites, then there are only two kinds of "constituents" in anorthite – tetrahedra of oxygens with either Si or Al in the centers and an irregular Ca polyhedron.

Why Are Some Structures Stable While Others Do Not Occur?

Pauling's rules served for many years as the basis for rationalizing the steric details of crystal structures. Even with the recognition of their important limitations, they have proven too useful to crystal chemists to be abandoned altogether. Nonetheless, they and the various modifications and amendments that have been added over the years are tools for rationalization of what is observed, not for prediction of what might be observed. At least two kinds of crystallochemical predictions are of interest: (1) Given a certain type of structure, what are the limits of chemical substitution that the structure will tolerate, and (2) given a certain proposed stoichiometry, what kinds of crystal structures are stable? The first is perhaps the easier to approach, because the atomic substitutions envisioned will impose roughly predictable variations on bond lengths, nonbonded distances, and interatomic bond angles, and there is a substantial body of literature documenting the acceptable ranges of values for these sorts of parameters. The second question is more interesting and much more difficult to deal with. Recent and current research, both on the general question and on predictions for specific minerals and other inorganic compounds, has focused on bond topology (connectivity, particularly of the strongest bonds in a structure), the predictive use of bond–valence theory, the application of molecular orbital theory (at various levels of approximation, applied both qualitatively and quantitatively) to "molecular" fragments of crystal structures, band theory, experimental methods such as vibrational spectroscopy (Berry and Vaughan 1985), Landau theory (Tolédano and Tolédano 1987), and others.

Crystallography and Crystal Symmetry

By definition, a crystal consists of an arrangement of atoms that is periodically repeated in three dimensions. The smallest parallelepiped that possesses within both the symmetry and stoichiometry of the overall arrangement is called the unit cell, and the entire crystal consists of unit cells related to one another by translation alone. The corners of the unit cell are surrounded by identical groups of atoms, and form a lattice, the definition of which is an array of points in space arranged such that each one has an identical and indistinguishable environment. There may be other points that are surrounded

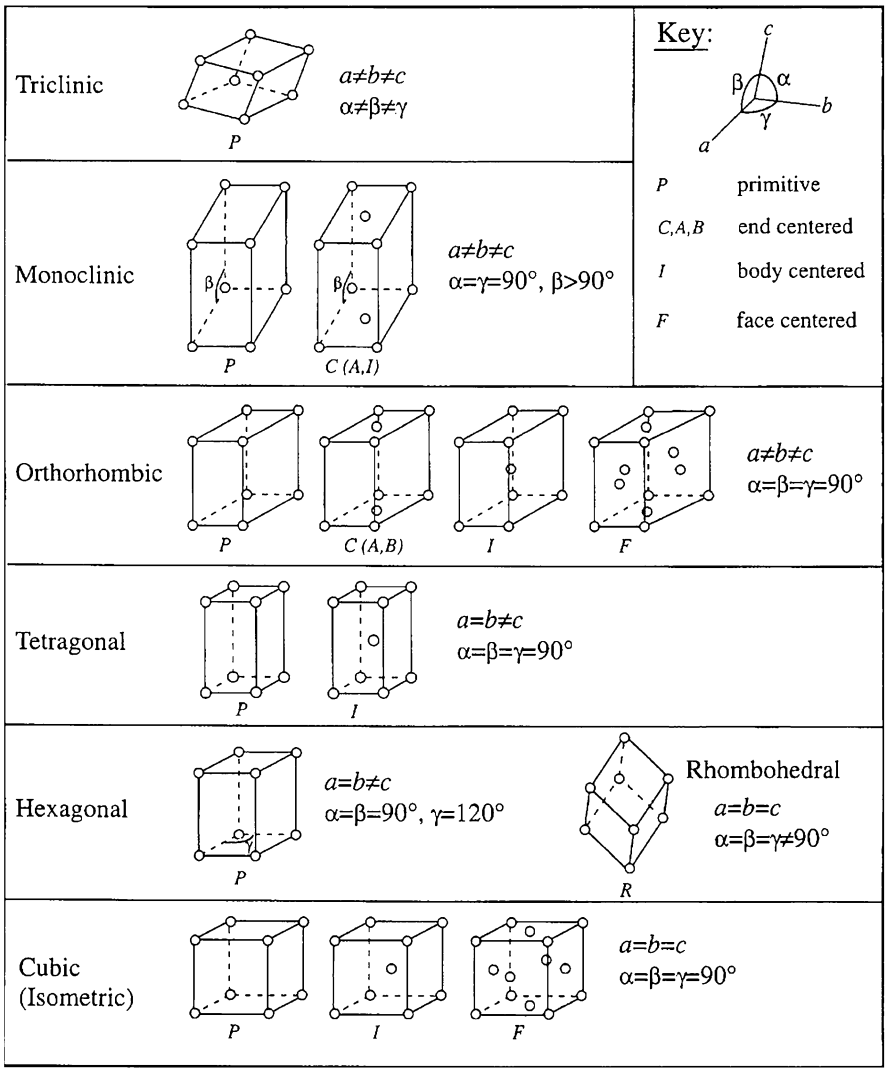

Crystal Chemistry, Fig. 5 The 14 Bravais lattices, arranged by crystal system

by groups of atoms identical to those around the corners of the unit cell; if so, the lattice is referred to as a centered lattice, and if not it is called a primitive lattice. Combining both primitive and centered lattices, there are only 14 symmetrically unique possibilities. These are called the Bravais lattices, after Auguste Bravais (1811–1863), and they are illustrated in Fig. 5. Note that each lattice is represented in Fig. 5 by a single unit cell, the edges of which define three crystallographic axes a, b, and c separated by three interaxial angles α, β, and γ.

Rotational Symmetry

Consideration of the data in Fig. 5 reveals that each type of lattice can be mapped into itself by at least one symmetry operation. Depending upon the arrangement of the atoms about the lattice points, this will be true also of the unit cells (i.e., of the entire crystal structure). Although it is easy to conceive of an atomic arrangement that would yield no symmetry, there are very few minerals that fall into that category; the overwhelming majority show symmetry of some sort.

Rotational symmetry elements are lines (axes of symmetry) around which an arrangement of atoms may be rotated so as to exactly reproduce itself. Proper rotation axes are those that map right-handed objects into right-handed objects, and improper rotation axes map right-handed objects into left-handed ones. Proper symmetry operations are represented symbolically by Arabic numerals, and improper symmetry operations are represented by Arabic numerals with a bar over them. The constraints imposed by the definition of a lattice (given above) limit the types of rotations that may occur in a crystal structure (and in the resulting macroscopic crystal) to those shown in Table 2. It can be shown that the sixfold rotoinversion is equivalent to a triad with a mirror plane perpendicular to it (symbolized $3/m$), but $\overline{6}$ is usually used. The symbol m (rather than $\overline{2}$) is used for a mirror plane.

Crystal Classes

Not only are the types of rotational symmetry in crystals limited but so are the compatible combinations of symmetry elements. First, it is possible for a crystalline atomic arrangement or a macroscopic crystal to have only one kind of rotational symmetry. If there are two symmetrically different kinds, however, then there must also be a third that is symmetrically distinct from the other two. Symmetrically distinct or different here means that the operation of any one of the symmetry elements does not map the other two into each other. Among these three symmetry elements, all may be proper, or one can be proper and two improper. Given these constraints, there are only 32 permissible groups of symmetry elements (including those groups made up of but a single symmetry element), and these are called the crystal classes or crystallographic point groups. They are a subset of the infinite set of noncrystallographic point groups that are not restricted to one-, two-, three-, four-, and sixfold symmetry. The 32 crystal classes are given in Table 3. The symbols in the table are called Hermann–Mauguin symbols, and they specify the particular symmetry required for the class. A fuller explanation is beyond the scope of this article but may be found in any introductory text on mineralogy or crystallography or in Hahn (1987).

Table 3 also lists the defining symmetry for each of the crystal systems; this is the minimum symmetry that must be possessed by a crystal to place it in a particular crystal system.

Crystal Chemistry, Table 2 Permissible rotational symmetry operations

Symbol	Names	Rotation angle
1	Onefold rotation axis monad	0°, 360°
2	Twofold rotation axis diad	180°
3	Threefold rotation axis triad	120°
4	Fourfold rotation axis tetrad	90°
6	Sixfold rotation axis hexad	60°
$\overline{1}$	Center of symmetry inversion center	0° or 360° + inversion
$\overline{2} = m$	Mirror plane of reflection	180° + inversion
$\overline{3}$	Threefold rotoinversion bar-three	120° + inversion
$\overline{4}$	Fourfold rotoinversion bar-four	90° + inversion
$\overline{6}$	Sixfold rotoinversion bar-six	60° + inversion

Symmetry is a more rigorous requirement for membership in a crystal system than is the geometry of the unit cell (Fig. 5). To illustrate, it is possible to superimpose on a cubic lattice a periodic arrangement of atoms that negates all of the inherent symmetry of the lattice; thus one would have a metrically cubic unit cell with no symmetry, and it would belong to the triclinic system. Although this is highly unlikely, because the non-cubic arrangement of atoms would impose asymmetrical atomic interactions that would lower the symmetry of the lattice, it does sometimes happen that experimental measurements of a unit cell (by, e.g., X-ray diffraction) show it to be within experimental error of the geometry of a higher crystal system than the atomic arrangement allows.

The external symmetry of a macroscopic crystal is completely described by the rotational symmetry elements of the 32 crystal classes. For the crystal chemist, the more interesting issue is the symmetry of the arrangement of atoms, and this sometimes involves symmetry elements that combine both rotation and translation.

Translational Symmetry Elements

Figure 6a shows a set of footprints. It is obvious that there is some symmetrical relationship between the set of right footprints and the set of left ones, but it is more complicated than a simple reflection. Figure 6b shows the symmetry relationship to be a reflection followed by a translation of one-half the repeat distance parallel to the mirror plane. This is called a glide plane, and the glide plane that relates successive tetrahedra in the pyroxene chain is shown in Fig. 6c, d. Because the translation component of the glide plane is parallel to the *c* crystallographic axis in the case of pyroxenes, it is called a *c*-glide; the other axial glide planes are *a*-glides and *b*-glides. Two other types of glide planes may be found in some atomic arrangements: diagonal glides, in which the glide component is one-half the vector sum of two axial translations, and diamond glides, in which the glide component is one-fourth the vector sum or difference of either two or three of the axial translations; they are labeled *n*-glides and *d*-glides, respectively.

The final type of translational symmetry element is the screw axis, which is a rotation (two-, three-, four-, or sixfold) followed by a translation. Figure 7 illustrates a screw axis.

Crystal Chemistry, Table 3 The 32 crystal classes

System	Minimum symmetry			Hermann-Mauguin symbols for crystal classes				
Triclinic	None	1	$\overline{1}$					
Monoclinic	1 diad[a]	2	m	$\frac{2}{m}$				
Orthorhombic	3 ⊥ diads[a]	222	mm^2	$\frac{2}{m}\,\frac{2}{m}\,\frac{2}{m}$				
Tetragonal	1 tetrad[a]	4	$\overline{4}$	$\frac{4}{m}$	422	4 mm	$\overline{4}$2m	$\frac{4}{m}\,\frac{2}{m}\,\frac{2}{m}$
Hexagonal	1 hexad[a]	6	$\overline{6}$	$\frac{6}{m}$	622	6 mm	$\overline{6}$m2	$\frac{6}{m}\,\frac{2}{m}\,\frac{2}{m}$
(Trigonal)	(1 triad[a])		3	$\overline{3}$	32	3 m	$\overline{3}\,\frac{2}{m}$	
Cubic	4 triads[a]		23	$\frac{2}{m}\overline{3}$	432	$\overline{4}$32	$\frac{4}{m}\overline{3}\,\frac{2}{m}$	

[a]May include a permissible combination of proper and improper axes

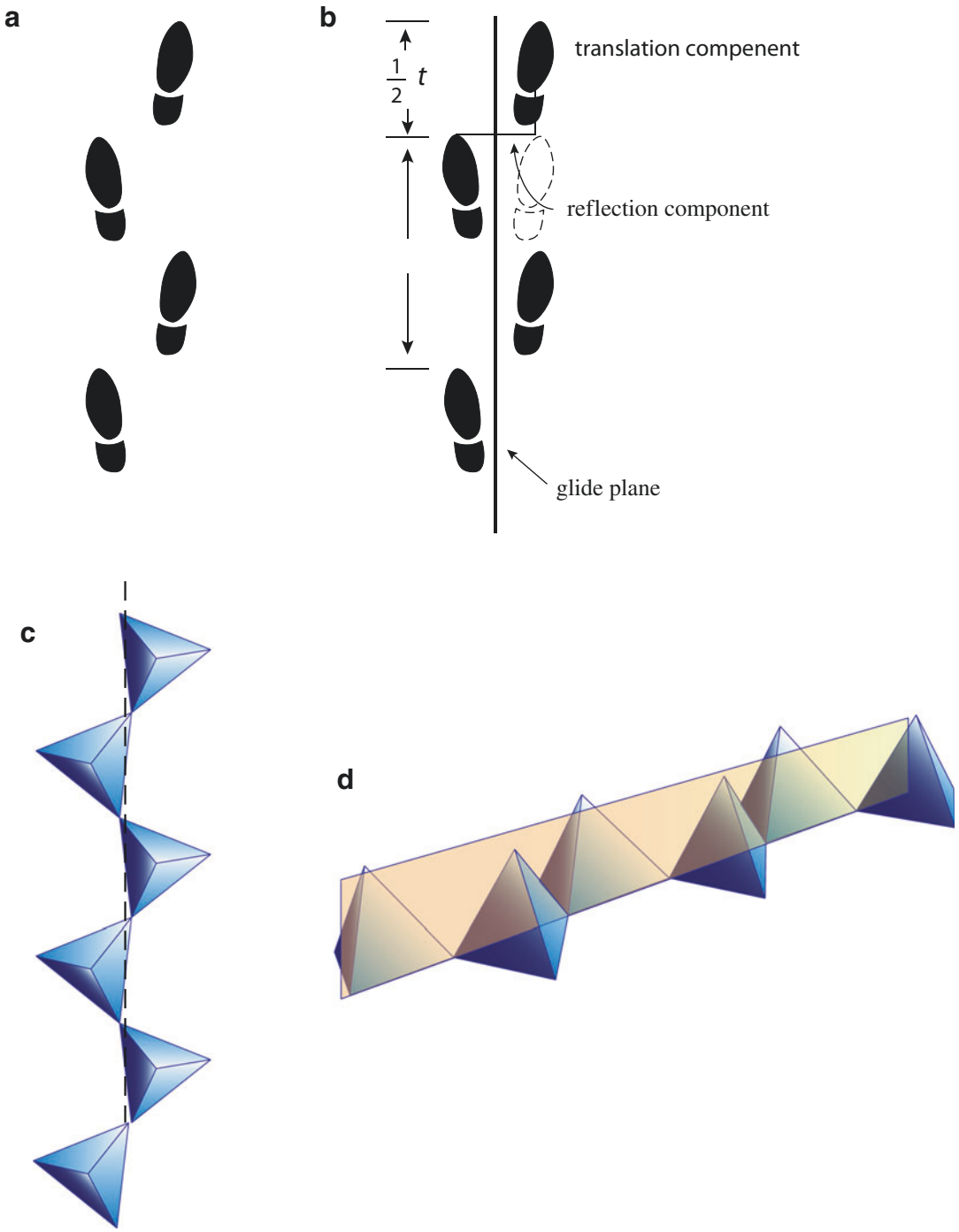

Crystal Chemistry, Fig. 6 (**a**) Although there is clearly some symmetry relationship between the right and left footprints, it is not pure reflection. (**b**) A reflection followed by a translation of one-half the repeat distance parallel to the mirror plane is called a glide reflection, and the symmetry element is a glide plane. (**c**) The tetrahedral chain of Si-containing tetrahedra in pyroxene (diopside, in this case). Oxygen atoms are implied at the corners of the tetrahedra. The chain runs parallel to the *c* crystallographic axis, so this is a *c*-glide (*dashed*). (**d**) The *c*-glide in diopside seen in perspective

The types of possible screw axes are 2_1, 3_1, 3_2, 4_1, 4_2, 4_3, 6_1, 6_2, 6_3, 6_4, and 6_5. If the subscript is less than one-half of the Arabic numeral representing the rotation, the screw axis is right-handed (i.e., a rotation to the right followed by translation); if it is greater than one-half of the rotation numeral, the screw axis is left-handed; if it is equal to one-half of the rotation numeral, the screw axis is neutral, because right- and left-handed rotations yield identical results. Table 4 shows the translation distances, in fractions of the repeat distance along the axis, for each type of screw axis.

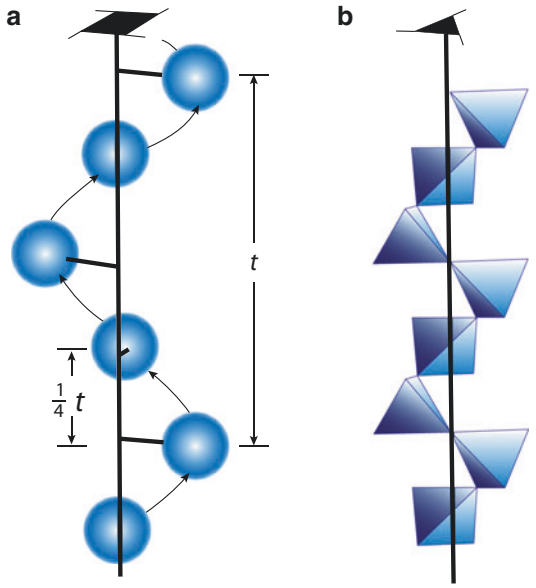

Crystal Chemistry, Fig. 7 (**a**) A schematic 4_1 screw axis consisting of successive 90° right-handed rotations followed by translations of one-fourth the repeat distance parallel to the rotation axis. (**b**) The helical chain of tetrahedra found in quartz; tetrahedra are related by a 3_2 screw axis

Crystal Chemistry, Table 4 Translational components of screw axes

Rotation	Translation[a]			
	$\frac{c}{2}$	$\frac{c}{3}$	$\frac{c}{4}$	$\frac{c}{6}$
180°	2_1			
120°		3_1, 3_2		
90°	4_2		4_1, 4_3	
60°	6_3	6_2, 6_4		6_1, 6_5

[a]2_1 screw axes may be in other directions than parallel to *c*, depending on crystal system. All three-, four-, and sixfold screw axes are parallel to *c*; in the cubic system, a fourfold screw axis parallel to *c* requires one parallel to *a* and *b* as well

Space Groups

The combination of 14 Bravais lattices, 32 crystal classes, and glide planes and screw axes leads to 230 unique combinations of crystallographic symmetry elements that describe the symmetry of crystals on the atomic level (Burns and Glazer 1990). They are called space groups and are enumerated, diagrammed, and thoroughly explained in Hahn (1987). The determination of the space group of a particular mineral does not specify its atomic arrangement (i.e., crystal structure) but places limitations and requirements on the possible locations of atoms. For example, although tremolite and sanidine have entirely different crystal structures, they crystallize in the same space group and therefore possess identical symmetry properties.

The notation used for space groups provides the type of Bravais lattice, the crystal system, the crystal class, and the translational symmetry elements present and is best understood by analyzing an example. The space group of the clinopyroxenes, such as diopside, is *C*2/*c*. The first letter, always in upper case, is the Bravais lattice type – a *C*-centered lattice in this case. 2/*c* is the crystal class with translational symmetry elements replacing rotational symmetry elements, if applicable; in this case, a *c*-glide replaces the mirror plane that is normal to the diad. Thus the crystal class is 2/*m* and the crystal is monoclinic, but the atoms that would be related by a mirror plane are instead related by a glide operation.

Crystallochemical Phenomena

Polymorphism and Phase Transformations

Polymorphism is the existence of two or more different crystal structures with identical chemical compositions. (Technically, if only two structures exist for a given composition, they should be referred to as dimorphs, but the almost universal practice is to call them polymorphs.) Transformations between phases provide important information about the conditions of formation or the thermobaric history of a rock, and they can be described in several different ways (Price and Ross 1992; Hazen and Finger 1982):

1. Transformations in which atomic bonds are broken and rearranged (i.e., in which the topology is changed) are called reconstructive transformations. They are generally sluggish, often leading to the metastable persistence of phases under conditions of thermodynamic instability (Lasaga and Kirkpatrick 1981). For example, Al_2SiO_5 exists as the minerals kyanite, andalusite, and sillimanite, all of which have fields of stability in pressure–temperature (P–T) space and each of which possesses a quite different bond topology; nevertheless, all of these can be found in rocks that have been exposed at the Earth's surface, because the energy required to break and reform the bonds is unavailable under ambient conditions. Transformations that involve only shifts in atomic positions without the breaking of bonds leave bond topology unchanged and are called displacive transformations. These phase transitions are typically rapid and easily reversible. A good example is the β–α quartz transformation, which occurs around 573 °C at atmospheric pressure. When that temperature is reached from either above or below, the atomic transformation occurs immediately, regardless of the rate of temperature change; thus, β-quartz does not exist in rocks under surface conditions.
2. Another way of characterizing phase transformations is to examine changes in coordination polyhedra. If the number of anions around a cation changes as a result of the transition, then it is a change in primary coordination. Again, the Al_2SiO_5 polymorphs provide an example, and the change is apparent if the coordination numbers are written as upper

left superscripts in the chemical formulas: Kyanite is $^{[6]}Al^{[6]}Al^{[4]}SiO_5$, andalusite is $^{[6]}Al^{[5]}Al^{[4]}SiO_5$, and sillimanite is $^{[6]}Al^{[4]}Al^{[4]}SiO_5$. If no primary coordination numbers change, but the dispositions of polyhedra are altered (i.e., if the numbers and/or types of atoms in the second coordination sphere change), then this is a change in secondary coordination. The transition between quartz and tridymite, wherein all Si atoms in both phases are tetrahedrally coordinated, but the arrangements of tetrahedra are quite different, is of this type. If coordination numbers do not change, but the chemical species within polyhedra are rearranged, then the change is an ordering transformation. For example, two polymorphs of $KAlSi_3O_8$ are sanidine and microcline; they differ in the way in which Al and Si are ordered within the available tetrahedral sites.

3. Phase transformations can also be defined in thermodynamic terms based on the behavior of derivatives of the Gibbs free energy (G), defined as

$$G - H - \mathrm{TS} \tag{4}$$

where H is enthalpy, T is temperature, and S is entropy. Molar volume and entropy are first derivatives of G, and heat capacity, compressibility, and thermal expansion coefficient are second derivatives. If the first derivatives of G are discontinuous at the transformation temperature, the transformation is a first-order transition. If the first derivatives are continuous but the second derivatives are discontinuous, the transformation is of second order. If the second derivatives (particularly heat capacity, C_P) tend to infinity at the transition temperature, it is called a lambda transformation. Reconstructive transformations tend to be first order, displacive transformations are often second order, and the α–β quartz transition may be a lambda transformation.

4. If the new phase nucleates at discrete locations in the host phase and grows from these, the transformation is called a discontinuous phase transition. If, on the other hand, the transformation occurs simultaneously throughout the host by structural modulation of the parent atomic arrangement, the transformation is a continuous phase transition.

A single example of the information available from the study of phase transformations must suffice. Consider the Ca-poor clinopyroxene, pigeonite. At high temperature, it crystallizes in space group $C2/c$, so that all of the tetrahedral chains (see Fig. 6c, d) are identical. As the temperature decreases, the site in which the small amount of Ca present is concentrated contracts, causing different rotations in what had previously been two symmetrically identical tetrahedral chains. This yields symmetrically different SiA and SiB chains and lowers the symmetry to $P2_1/c$. The transformation is rapid and displacive. Because either chain in the $C2/c$ structure can become the SiB chain in the $P2_1/c$ structure, the "choice" is made differently in different parts of the crystal, and when the microdomains of consistent "choice" meet, they are out of phase with one another. This antiphase domain texture can be observed by transmission electron microscopy and provides information on the thermal history of the sample.

C

Solid Solution and Exsolution

Many minerals exist in ranges of compositions that are limited by three factors:

1. The crystal structures of all compositions exhibited by a mineral must be topologically identical (i.e., they may differ only by small distortions).
2. The atoms (or ions) that substitute for one another must have roughly the same radii.
3. Electrostatic neutrality must be retained by the substitutions.

If all three requirements are met and a range of compositions is in fact observed, the mineral is said to exhibit solid solution. The requirement for similarity in radii is important but only approximate; a rule of thumb often stated is that the radii should be within 15% of each other. Electrostatic neutrality may be maintained either by substituting ions that have identical oxidation numbers or by substituting ions in combination with one another (coupled substitutions) so that overall neutrality is maintained.

Consider, for example, the feldspars. The plagioclase feldspars consist of the solid solution series $NaAlSi_3O_8$–$CaAl_2Si_2O_8$ (albite to anorthite). The crystal structures are topologically identical; the effective ionic radii of Na and Ca in 7-coordination are 1.12 Å and 1.06 Å, respectively; and the substitution $Na^+Si^{4+} \leftrightarrow Ca^{2+}Al^{3+}$ meets the requirement for electrostatic neutrality. Thus, to a first approximation, the plagioclase feldspars display a complete solid solution series between the two end members. The alkali feldspars are those with compositions between albite and $KAlSi_3O_8$ (compositionally called orthoclase, although it can exist in several polymorphs). Like Na, K is monovalent, but its radius is 1.46 Å. At high temperature, atomic vibrations make the effective sizes of Na and K similar, and complete solid solution occurs. As temperature decreases, however, the size difference becomes important, and at low temperatures, there is only limited solid solution; that is, a small amount of K can substitute in crystals of albite-rich composition, and a small amount of Na can substitute in crystals of K-rich composition. Between the K and Ca end members, solid solution is even more restricted.

If alkali feldspar crystallizes at high temperature as a homogenous phase in a magma, and then the temperature is slowly lowered (as, e.g., in a cooling pluton), the feldspar becomes unstable because of the substantial crystallographic

strains required to accommodate both K and Na in the same lattice. The result is a solid-state migration of K and Na, which separate into regions of high K and regions of high Na concentration. If the bulk composition is nearer the K end member, then a K-rich feldspar becomes the host to exsolution "stringers" or lamellae of an Na-rich phase; if it is nearer the Na end member, then the reverse occurs. Although feldspars have been used for illustration, solid solution is extremely common for many important mineral families, and exsolution occurs when solid solution behavior for end members differs significantly over the temperature range experienced by the mineral.

Other Phenomena

Among the many other phenomena that arise from the crystal chemistry of minerals are color, elastic and vibrational properties, ordering of atomic species in preferred crystallographic sites, polytypism, twinning, compositional zoning, hydration and surface phenomena, and others. Space does not permit more than this brief enumeration, but the bibliographic listings include works that delve into all of these areas and more (Boisen and Gibbs 1985; Burdett 1995; Deer et al. 2013; Griffen 1992; Kieffer and Navrotsky 1985; Jaffe 1988; Vaughan and Pattrick 1985).

Cross-References

- ▶ Atomic Absorption, Inductively Coupled Plasma Optical Emission Spectroscopy, and Infrared Spectroscopy
- ▶ Crystal Chemistry
- ▶ Crystal Field Theory
- ▶ Diffusion
- ▶ Dolomite and Dolomitization
- ▶ Electron Probe Microanalysis (EPMA)
- ▶ Geochemical Thermodynamics
- ▶ Ionic Radii
- ▶ Kinetics of Geochemical Processes
- ▶ Mineral Defects
- ▶ Mineralogy
- ▶ Phase Equilibria
- ▶ Solid Solution/Exsolution
- ▶ Stoichiometry
- ▶ Surface Geochemistry
- ▶ X-Ray Diffraction

References

Berry FJ, Vaughan DJ (eds) (1985) Chemical bonding and spectroscopy in mineral chemistry. Chapman and Hall, New York. 325 pp
Boisen MB Jr, Gibbs GV (1985) Mathematical crystallography, Reviews in Mineralogy, vol 15. Mineralogical Society of America, Washington, DC. 460 pp
Brown ID, Shannon RD (1981) The bond–valence method: an empirical approach to chemical structure and bonding. In: O'Keefe M, Navrotsky A (eds) Structure and bonding in crystals, vol 2. Academic, New York, pp 1–31
Burdett JK (1995) Chemical bonding in solids. Oxford University Press, New York. 319 pp
Burdett JK, McLarnen TM (1984) An orbital interpretation of Pauling's rules. Am Mineral 69:601–621
Burns G, Glazer AM (1990) Space groups for solid state scientists. Academic, San Diego. 343 pp
Deer WA, Howie RA, Zussman J (2013) An introduction to the rock-forming minerals. The Mineralogical Society, London. 498 pp
Gibbs GV (1982) Molecules as models for bonding in silicates. Am Mineral 67:421–450
Griffen DT (1992) Silicate crystal chemistry. Oxford University Press, New York. 442 pp
Hahn T (ed) (1987) International tables for crystallography, vol A. D. Reidel Publishing Company, Dordrecht. 878 pp
Hazen RM, Finger LW (1982) Comparative crystal chemistry: temperature, pressure, composition, and the variation of crystal structure. Wiley, New York. 231 pp
Jaffe HW (1988) Crystal chemistry and refractivity. Cambridge University Press, Cambridge. 335 pp
Kieffer SW, Navrotsky A (eds) (1985) Microscopic to macroscopic, Reviews in mineralogy, vol 14. Mineralogical Society of America, Washington, DC. 428 pp
Lasaga AC, Kirkpatrick RJ (eds) (1981) Kinetics of geochemical processes, Reviews in mineralogy, vol 8. Mineralogical Society of America, Washington, DC. 398 pp
Megaw HD (1973) Crystal structures: a working approach. Saunders, Philadelphia. 563 pp
Pauling L (1929) The principles determining the structure of complex ionic crystals. J Am Chem Soc 51:1010–1026
Price GD, Ross NL (eds) (1992) The stability of minerals. Chapman and Hall, London. 368 pp
Putnis A, McConnell JDC (1980) Principles of mineral behaviour. Elsevier, New York. 257 pp
Tolédano J, Tolédano P (1987) The Landau theory of phase transitions. World Scientific Publishing Co., Singapore. 451 pp
Vaughan DJ, Pattrick RAD (eds) (1985) Mineral surfaces. Chapman and Hall, London. 370 pp

Crystal Field Theory

Hans Keppler
Bayerisches Geoinstitut, University of Bayreuth, Bayreuth, Germany

Crystal field theory is a model describing the interaction between the electric charges of a cation and the surrounding anions. A more sophisticated version of this model, which includes covalent bonding effects, is the ligand field theory. Very frequently, however, the terms crystal field theory and ligand field theory are used synonymously. Crystal field

Originally published in: Marshall CP, Fairbridge RW (eds) Encyclopedia of Geochemistry, Springer Netherlands, 1999.

theory can be used to extract thermodynamic properties (crystal field stabilization energies) from optical spectra of minerals and other substances. By considering crystal field stabilization energies, many features of the geochemistry of transition metals can be explained.

The basic idea of crystal field theory is related to the fact that the charge distribution of the d- and f-orbitals in cations is not spherically symmetrical. This means that the repulsive electrostatic forces between the electrons in these orbitals and the surrounding anions (ligands) depend on the relative orientations of the anions. This is shown schematically in Fig. 1. If one considers the charge density of d-orbitals in the *xy*-plane of a Cartesian coordinate system, the d_{xy} orbital has maximum charge density (maximum probability to find an electron) between the coordinate axes. The $d_{x^2-y^2}$ orbital, on the other hand, has the maximum charge in the direction of the coordinate axes. If the cation is surrounded by six anions in octahedral coordination, these anions can be grouped in the directions of the coordinate axes (four in the *xy*-plane, one in $+z$, and one in $-z$ direction), as shown in Fig. 1. Obviously, the electrostatic repulsion between these anions and the $d_{x^2-y^2}$ orbital will be stronger than the repulsion between the anion and the d_{xy} orbital. Therefore, the energy of an electron in the $d_{x^2-y^2}$ orbital will be higher than in the d_{xy} orbital. In vacuum or in a spherically symmetrical field, however, the energies of these orbitals are equal – they are said to be degenerate. Therefore, the effect of the electrical field of the anions is to split the d-orbitals into groups of different energies. The magnitude of this splitting is called the crystal field splitting Δ. A detailed analysis shows that an octahedral field splits the five d-orbitals into two levels, the t_{2g} level (d_{xy}, d_{xz}, d_{yz} orbital) and the e_g level ($d_{x^2-y^2}$, d_{z^2} orbital). The magnitude of the splitting follows the so-called center of gravity rule, which means that the average energy of the five orbitals must equal the energy of the orbitals in a spherically symmetric field. This condition is only fulfilled if relative to a spherically symmetrical field the t_{2g} levels are lowered in energy by $2/5\Delta$ while the e_g levels are raised by $3/5\Delta$. This situation is schematically depicted in Fig. 2.

The type and magnitude of the crystal field splitting depend on the geometry of the coordination polyhedron. It can be shown, for example, that in a tetrahedral environment, the effect of the crystal field splitting is opposite to the octahedral case, i.e., the energies of d_{xy}, d_{xz}, and d_{yz} are raised, while the energies of $d_{x^2-y^2}$ and d_{z^2} are lowered. Other things being equal, the magnitude of the crystal field splitting in a tetrahedral field will be 4/9 of that in an octahedral field. Furthermore, if the symmetry of the coordination polyhedron is lower than cubic, i.e., if the coordination tetrahedron or octahedron is distorted, additional splittings of energy levels can be induced. For example, $d_{x^2-y^2}$ and d_{z^2} orbitals no longer

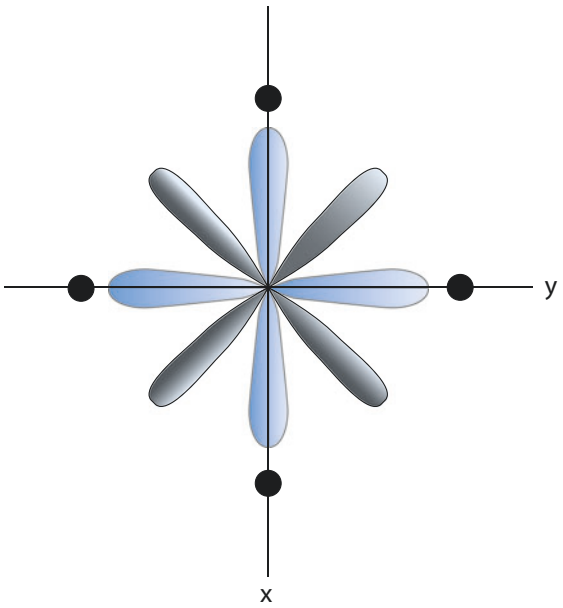

Crystal Field Theory, Fig. 1 Orientation of the $d_{x^2-y^2}$ (*light blue*) and d_{xy} (*dark*) orbitals of a cation relative to the *xy*-plane of a Cartesian coordinate system. The positions of anions surrounding the cation in octahedral coordination are indicated as *black dots*. Four of these anions are in the *xy*-plane, one is above in $+z$, and one below in $-z$ direction

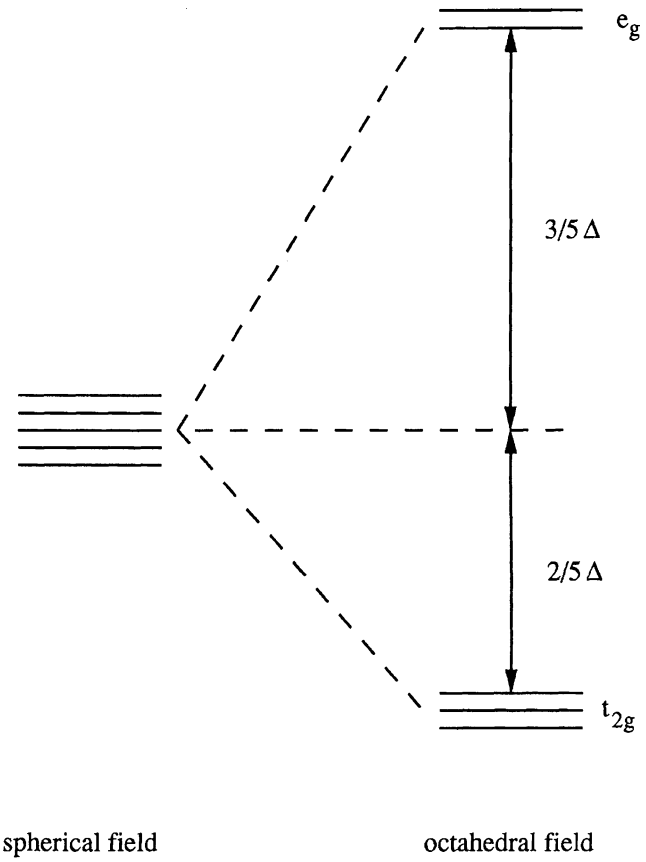

Crystal Field Theory, Fig. 2 Splitting of the energies of d-orbitals in an octahedral environment. Δ is the crystal field splitting

need to have the same energy in a distorted octahedral or tetrahedral environment.

Crystal field theory was originally derived for cations in a crystal lattice (Bethe 1929). However, exactly the same formalism can be applied to cations in liquids (silicate melts, aqueous solutions) and even gases. The effects described by crystal field theory are almost completely due to interactions within the first coordination shell, so that the medium and long-range order in the phase considered is not important.

The splitting of d-orbital levels by interaction with the charges in the first coordination sphere has important consequences if the d-orbital shell is not completely filled. Consider, for example, an ion with three d-electrons, such as Cr^{3+}, in an octahedral environment. In the ground state of the ion, the three electrons will occupy the d_{xy}, d_{xz}, and d_{yx} orbitals (the t_{2g} level, Fig. 2). The $d_{x^2-y^2}$ and d_{z^2} orbitals are empty. This has the following consequences:

1. Relative to Cr^{3+} in a spherically symmetric electrostatic field, the energy of the octahedrally coordinated Cr^{3+} ion will be lowered. Since the t_{2g} level is lowered by $2/5\Delta$ and there are three electrons in this level, this effect stabilizes the octahedral Cr^{3+} by $6/5\Delta$. This energy is called the crystal field stabilization energy (CFSE). CFSE is often in the order of the free energy of chemical reactions (several 10 or 100 kJ/mol). In the case of ions which have very large CFSE, such as octahedral Cr^{3+} or Ni^{2+}, one can often predict the direction of a reaction or the approximate value of an equilibrium constant by considering the CFSE of the ions in the phases involved. Such considerations have been very fruitful for predicting the partitioning of transition metal ions between different sites in a crystal (e.g., tetrahedral and octahedral sites in spinel) as well as for predicting the partitioning between different phases (minerals and silicate melts). However, it is important to note that the CFSE amounts only to a maximum of 20–30% of the total bonding energy, which means that other effects can also be important.
2. Since the three electrons in Cr^{3+} occupy those orbitals which have the weakest interaction with the anions, while the orbitals that are closest to the anions are empty the effective ionic radius of octahedral Cr^{3+} is lower than expected for a spherically symmetrical charge distribution. Crystal field theory can therefore explain irregularities in the ionic radii of transition metal ions.
3. If the Cr^{3+} ion interacts with electromagnetic radiation, electrons can be promoted from the t_{2g} into the e_g level. This gives rise to absorption bands in the near-infrared, visible, and ultraviolet region of the electromagnetic spectrum. These spectra can be used to detect the oxidation state and coordination number of transition metals. Moreover, the crystal field splitting and crystal field stabilization energy can easily be obtained from such spectra. A fully quantitative interpretation of the spectra requires a modification of the simple electrostatic model of crystal field theory that allows for some covalent bonding effects. This model is often called ligand field theory. Covalent bonding implies that the electrons are not completely localized at the cation any more, but they can be "smeared out" over the anions. This effect will reduce the interelectronic repulsion, because the average distance between the electrons increases. The Racah parameter B is a measure for interelectronic repulsion and can be obtained from optical absorption spectra. If there is some covalent bonding, the Racah parameter will be reduced relative to the value for the free ion in vacuum. In order to obtain both the crystal field splitting and the Racah parameter from spectroscopic data, the Tanabe–Sugano diagrams (Tanabe and Sugano 1954) are used which are plots of the energies of the possible states of an ion as a function of Δ and B.

If the d-electron levels are completely filled, the CFSE is zero, and no optical absorption due to transitions within the d-orbital levels can occur. Ions with incompletely filled f-orbitals (lanthanides and actinides) are in principle subjected to crystal field effects. These effects, however, are relatively small, since the f-electrons are strongly shielded from the surrounding electrostatic fields. Therefore, crystal field theory is primarily a tool for understanding the chemistry and geochemistry of transition metal ions which contain partially filled d-orbitals.

A special situation can arise, for example, for octahedrally coordinated cations having four d-electrons, such as Cr^{2+} or Mn^{3+}. In these cations, three electrons will occupy the t_{2g} level, while one electron is in the e_g level, i.e., either in the $d_{x^2-y^2}$ or the d_{z^2} orbital (see Fig. 2). In an undistorted octahedron, the energies of the $d_{x^2-y^2}$ orbital and the d_{z^2} orbital are identical. This means that there are two possible ground states (states with lowest energy) of the ion, depending on which one of the two e_g orbitals contains an electron. This is often expressed by saying that the ground state of these ions is degenerate. However, if the octahedron is slightly distorted, the degeneracy is lifted, since then the two orbitals will have different energy. Since the e_g electron can then reside in the orbital with the lower energy ($d_{x^2-y^2}$ or d_{z^2}, depending on the type of distortion), generally this effect will lower the total energy of the system. Therefore, the coordination polyhedron of ions with a degenerate ground state, such as octahedral Cr^{2+} or Mn^{3+}, will always be distorted. This is known as the Jahn–Teller effect. As a consequence of this effect, cations such as Cr^{2+} or Mn^{3+} will prefer the more distorted sites in

crystal structures, if several sites of approximately equal size are available.

In most coordination environments, the crystal field splitting is small compared to the energy necessary to cause spin pairing of electrons. This means that if five electrons are present in an octahedrally coordinated cation, three will occupy the t_{2g} and two the e_g-level (Fig. 2). Any additional electrons will then enter these orbitals with antiparallel spin. However, in some cases the crystal field splitting can become so large that spin pairing is induced. In this case, up to six electrons will first enter the t_{2g} level, and only after that the e_g level can be filled with additional electrons. This means that for some cations, two different electronic configurations are possible, depending on the magnitude of the crystal field splitting: the high-spin configuration (where the vectorial sum of the electron spins is maximum) for low Δ and the low-spin configuration for high Δ. Certain ligands, such as sulfide, can cause Δ to be very large; therefore, many transition metal sulfides are in the low-spin state. Oxides and silicates under normal conditions are in the high-spin state. It is possible, however, that they convert into the low-spin state at extreme pressures prevailing in the lower mantle. Since the high-spin to low-spin transition changes the configuration of the outer electron shell, this could completely change the geochemical behavior of the elements involved.

A good introduction into the theoretical background of crystal field theory is the book by Figgis (1966). Symmetry aspects are discussed by Cotton (1971). Geochemical applications can be found in Burns (1985, 1993) and Rossman (1988).

Cross-References

- ▶ Atomic Absorption, Inductively Coupled Plasma Optical Emission Spectroscopy, and Infrared Spectroscopy
- ▶ Crystal Chemistry
- ▶ Free Energy
- ▶ Geochemical Thermodynamics
- ▶ Mineral Defects
- ▶ Mineralogy
- ▶ Solid Solution/Exsolution
- ▶ Transition Elements

References

Bethe H (1929) Termaufspaltung in Kristallen. Ann Phys 3:133–206
Burns RG (1985) Thermodynamic data from crystal field spectra. Rev Mineral 14:277–316
Burns RG (1993) Mineralogical applications of crystal field theory, 2nd edn. Cambridge University Press, Cambridge. 551 pp
Cotton FA (1971) Chemical applications of group theory, 2nd edn. Wiley, New York. 386 pp
Figgis BN (1966) Introduction to ligand fields. Wiley, New York. 351 pp
Rossman GR (1988) Optical spectroscopy. Rev Mineral 18:207–254
Tanabe Y, Sugano S (1954) On the absorption spectra of complex ions. J Phys Soc Jpn 9:753–779

D

Debye-Hückel Equation

Jay R. Black
School of Earth Sciences, The University of Melbourne, Melbourne, VIC, Australia

Definition

Named after Peter Debye (1884–1966) and Erich Hückel (1896–1980) for their work pioneering the understanding of aqueous electrolyte solutions, the Debye-Hückel equation defines the activity coefficient (γ) of an aqueous ion as a function of the ionic strength of solution. Models that incorporate Debye-Hückel's theory and equations enable geochemists to predict the complex speciation of solutes in aqueous solutions from thermodynamic principles (See ▶ "Activity and Activity Coefficients"; ▶ "Aqueous Solutions"; ▶ "Complexes"; ▶ "Geochemical Thermodynamics").

Debye-Hückel Models

There are a number of theoretical expressions of the Debye-Hückel model, the primitive Debye-Hückel model describes long-range Coulombic forces between dissolved ions where the solvent acts as a structureless dielectric continuum and solutes are defined as hard spheres with a charge at the center (See "Electrolyte Theory"). Coulombic interactions between dissolved ions tend to promote ordering of negatively charged anions around positively charged cations, and vice versa, leading to a decrease in the thermodynamic free energy of the system (See ▶ "Free Energy") compared to if the dissolved ions were distributed randomly in solution. If ions are considered to be point charges then Coulombic interactions between ions will lead to a Boltzmann distribution of ions around one another and the Debye-Hückel limiting law is defined as:

$$\log_{10}\gamma_i = -Az_i^2\sqrt{I} \quad (1)$$

where A is a constant that is dependent on temperature and pressure, z_i is the charge on the ion (i) and I is the ionic strength defined by the equation:

$$I = \frac{1}{2}\sum_i m_i z_i^2 \quad (2)$$

where, m_i is the molal concentration of the ion (i). Equation 1 is only valid for very low ionic strengths ($I < 10^{-3}$ molal) due to the assumption of ions being point charges. The Debye-Hückel model can be extended to higher ionic strengths by considering that ions have a finite diameter, yielding the equation:

$$\log_{10}\gamma_i = \frac{-Az_i^2\sqrt{I}}{1 + B\mathring{a}\sqrt{I}} \quad (3)$$

where B is a constant that is dependent on temperature and pressure and $\mathring{a}$ is the distance of closest approach equivalent to the hydrated radius of the ion in Angstroms.

Equation 3 is generally valid for $I <= 0.1$ molal for monovalent ions, but lower ionic strengths for multi-valent ions and mixed electrolyte solutions. The parameter $\mathring{a}$ can be varied for different ionic species, as would be expected due to different ionic complexes having different hydrated radii, however doing so violates the assumption of the Debye-Hückel model that all ions are hard-spheres of the same diameter and thermodynamic relationships can no longer be satisfied (See ▶ "Geochemical Thermodynamics"). As such, some variations of Eq. 3 assume the $B\mathring{a}$ term is constant regardless of ion type, e.g., where $B\mathring{a} = 1$ it is known at the Güntelberg equation. Varying $\mathring{a}$ for different ions is often used in the implementation of the Debye-Hückel model in various thermodynamic databases for geochemical modeling programs (e.g., WATEQ: Truesdell and Jones 1974; EQ3/6: Wolery and Jarek 2003).

W. M. White (ed.), *Encyclopedia of Geochemistry*,
https://doi.org/10.1007/978-3-319-39312-4

At higher ionic strengths the primitive Debye-Hückel models become inaccurate due a number of effects and underlying assumptions. Real solutes are not hard-spheres with a central charge and the hydration state of ions can change with increasing ionic strength and vary between different ionic complexes (i.e., different values for $\mathring{a}$). Ion association (See ▶ "Complexes") becomes increasingly important at higher ionic strengths and hard-core effects become important (Pitzer 1973). Attempts to expand the Debye-Hückel model further to account for ion association at higher ionic strengths have included an extra ionic strength dependent term:

$$\log_{10}\gamma_i = \frac{-Az_i^2\sqrt{I}}{1 + B\mathring{a}\sqrt{I}} + bI \quad (4)$$

where b is a constant that may or may not be ion specific. Various expansions of the Debye-Hückel equation of this nature are collectively referred to as specific ion interaction theory, one form of which is the Davies (1962) equation.

Care must be taken when computing the value for the constant A depending upon whether the form of the Debye-Hückel model being used is written as ln γ or $\log_{10}\gamma$ and similarly care must be taken with the units of the constant A being on the same length scale used for parameter $\mathring{a}$. Analytical expressions for the constants A and B from 25 °C to 600 °C and 0.001–5 kbar pressure can be found in Helgeson and Kirkham (1974).

Model Comparison to Experiments

Activity coefficients for individual ions cannot be measured, as such, measured values for the mean activity coefficient of NaCl (γ_{NaCl}) at various ionic strengths are plotted in Fig. 1 (Robinson and Stokes 1965; Haynes 2015–2016) and compared to calculations using the Debye-Hückel models presented here (Eqs. 1, 2, 3, and 4). Since Eqs. 1, 3 and 4 calculate activity coefficients for individual ionic species (Na^+ and Cl^-), the mean activity coefficient is determined using the following equation:

$$\gamma_{NaCl} = \sqrt{\gamma_{Na^+}\gamma_{Cl^-}} \quad (5)$$

At high enough dilutions Debye-Hückel models fit measured activity coefficients for solutes very well, however, the monotonic decrease of the activity coefficient predicted by Eqs. 1 and 3 with increasing ionic strength is no longer observed in solutions of high ionic strength ($I >$ c. 1.2 molal) where the activity coefficient exponentially increases (Fig. 1). Debye-Hückel models such as that presented in Eq. 4 can be empirically fit to experimental data (e.g., Fig. 1).

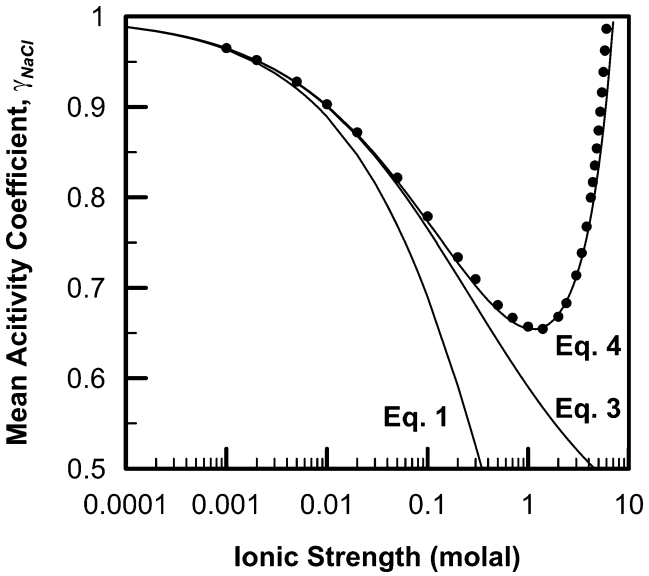

Debye-Hückel Equation, Fig. 1 Mean activity coefficients for NaCl at 25 °C as a function of ionic strength. Experimental data plotted as circles (Robinson and Stokes 1965; Haynes 2015–2016). Results using Eqs. 1, 2, 3, and 4 and with Eq. 5 are plotted as lines using: $\mathring{a}_{Na} = 4$; $\mathring{a}_{Cl} = 3.5$; $b_{Na} = 0.075$; $b_{Cl} = 0.015$ (Truesdell and Jones 1974)

Summary and Conclusion

The Debye-Hückel equation and models derived from the underlying electrolyte theory allow geochemists to model the behavior of ionic solutes in dilute aqueous solutions. The expanded version of the Debye-Hückel equation presented in Eq. 4 fits experimental data for NaCl up to much higher ionic strengths (close to the solubility limit for NaCl, Fig. 1). However, the most successful specific ion interaction theory models expanding on the Debye-Hückel equation are those of Pitzer (1973). Pitzer's equations account for secondary and tertiary ion-pair interactions through a virial expansion of the Debye-Hückel model and can successfully model systems containing single and multiple electrolytes to high ionic strengths. For further reading see Pitzer (1973) and implementation of the Pitzer equations to geochemical modeling (Wolery and Jarek 2003).

Cross-References

- ▶ Activity and Activity Coefficients
- ▶ Aqueous Solutions
- ▶ Complexes
- ▶ Free Energy
- ▶ Geochemical Thermodynamics

References

Davies CW (1962) Ion association. Butterworths, London. 190 pp
Haynes WM (2015–2016) CRC handbook of chemistry and physics, 96th edn. Taylor and Francis GroupLLC, Boca Raton
Helgeson HC, Kirkham DH (1974) Theoretical prediction of the thermodynamic behavior of aqueous electrolytes at high pressures and temperatures: II. Debye-Hückel parameters for activity coefficients and relative partial molal properties Am J Sci 274:1199–1261
Pitzer KS (1973) Thermodynamics of electrolytes. I. Theoretical basis and general equations. J Phys Chem 77:268–277
Robinson RA, Stokes RH (1965) Electrolyte solutions, 2nd edn., revised. Butterworths, London. 571 pp
Truesdell AH, Jones BF (1974) WATEQ, a computer program for calculating chemical equilibria of natural waters. J Res US Geol Surv 2:233–248
Wolery TW, Jarek RL (2003) Software User's manual EQ 3/6, Version 8.0. Sandia National Laboratories/U.S. Department of Energy Report. 376 pp

Density Functional Theory

David A. Dixon
Department of Chemistry, University of Alabama, Tuscaloosa, AL, USA

Definition

Density functional theory is an approach to solving the Schrödinger equation for the motion of electrons in molecules (as well as atoms) based on the concept that the energy is a functional of the density. In principle, it is an exact theory if the density and the functional are known. In practice, the exact form of the functional is not known. This method is another way to solve the Schrödinger equation for the electronic motion of electrons in atoms and molecules in addition to molecular orbital theory. It has been extensively applied to both molecules and solids and is probably the most common method in use today for electronic structure calculations.

Overview

Density functional theory (DFT) can be used to determine the ground state energy of the system as well as to predict a wide range of properties including structures, spectra, energetics, and charge distributions (Parr and Wang 1989; Dreizler and Gross 1990; Labanowski and Andzelm 1991; Seminario and Politzer 1995; Laird et al. 1996; Springborg 1997; Sholl and Steckel 2009). Rather than solving the Schrödinger equation explicitly as in molecular orbital theory, one uses a theorem (Hohenberg and Kohn 1964) which states that the exact energy is a functional of the density ρ. This means there is a one-to-one correspondence between the electronic energy and the electron density. The foundation for the use of DFT methods in computational geochemistry was the realization that the external potential is determined, within an additive constant, by the electron density (Kohn and Sham 1965). Since the wave function is a functional of the electron density, it follows that the density also determines the ground state wave function and all other electronic properties of the system. Because ρ determines N (the number of electrons) and v (the external potential) and hence all the properties of the electronic ground state, we can write the energy to explicitly depend on v:

$$E_v[\rho] = T[\rho] + V_{ne}[\rho] + V_{ee}[\rho] = \int \rho(r)v(r)dr + F_{HK}[\rho] \quad (1)$$

where

$$F_{HK}[\rho] = T[\rho] + V_{ee}[\rho] \quad (2)$$

We write $V_{ee}[\rho] = J[\rho] + E_{xc}[\rho]$, where $J[\rho]$ is the classical repulsion and $E_{xc}[\rho]$ is a nonclassical term referred to as the "exchange-correlation energy." The first and second terms correspond to the kinetic energy of the electrons and to the classical Coulomb electronic-nuclear attraction term, respectively. The $E_{ne}[\rho]$ and $J[\rho]$ terms are given by their classical expressions (Eqs. 3 and 4), and the factor of ½ in the $J[\rho]$ functional allows for the integration over all space for both variables:

$$E_{ne}[\rho] = \sum_a \int \frac{Z_a \rho(r)}{|R_a - r|} dr \quad (3)$$

$$J[\rho] = \frac{1}{2} \iint \frac{\rho(r)\rho(r')}{|r - r'|} dr dr' \quad (4)$$

The last term, E_{xc} the exchange-correlation energy, contains all of the many-body contributions to the energy. If the form of this term were known exactly, then one could solve for the total energy using Eq. 1, but, the exact form of this term is not known, so it is necessary to use some approximation for E_{xc}. The last term contains the exchange energy $K[\rho]$ and the correlation energy. For a noninteracting uniform electron gas, $T[\rho]$ and $K[\rho]$ are given by Eqs. 5 and 6:

$$T[\rho] = C_F \int \rho^{\frac{5}{3}}(r) dr \quad (5)$$

$$K[\rho] = -C_x \int \rho^{\frac{4}{3}}(r) dr \quad (6)$$

with the coefficients C_F and C_x given by

$$C_F = \frac{3}{10}\left(3\pi^2\right)^{\frac{2}{3}} \tag{7}$$

$$C_x = \frac{3}{4}\left(\frac{3}{\pi}\right)^{\frac{1}{3}} \tag{8}$$

The second Hohenberg-Kohn theorem provides the energy variational principle, $E_0[\rho_0] < \mathrm{E}_0[\rho]$ for $\rho_0 \neq \rho$; the exact energy for the ground state is obtained for $\rho_0 = \rho$. This is analogous to the variational principle for wave functions from molecular orbital theory.

Although DFT has been around since the mid-1960s, it is only recently (since ~ 1990) that its application to chemical, including geochemical, problems has become popular. This was because of the development of new approaches to solve the DFT equations implemented in software used by chemists coupled with exchange-correlation functionals that could be applied for use in chemical molecular problems. In addition, DFT works very well for many chemical systems with a reduced computational cost. For about the same cost of doing a Hartree-Fock calculation, DFT usually includes a significant fraction of the electron correlation energy. Note that DFT is *not* a Hartree-Fock method, nor is it (strictly speaking) a post-Hartree-Fock method. The wave function is constructed in a different way (the spin and spatial parts are different to those developed in Hartree-Fock theory), and the resulting orbitals are often referred to as "Kohn-Sham" orbitals.

The computer programs that actually solve the DFT equations have much in common with Hartree-Fock electronic structure programs, and chemical theorists initially adapted their Hartree-Fock programs to perform DFT computations, although there were a number of codes that were developed just for DFT. Like Hartree-Fock, the DFT equations must be solved self-consistently, making DFT another type of self-consistent field (SCF) method. Instead of focusing on wave functions and orbitals, DFT focuses on the electron density, although molecular DFT calculations usually employ orbitals to get the density. As it includes an approximate treatment of electron correlation, it should be more accurate than Hartree-Fock theory. There are many different variations of DFT, depending on the particular treatment of correlation and exchange, i.e., the choice of the exchange-correlation functional. The main drawback of DFT is that as the exact form of the exchange-correlation functional is not known, improvements to the functional are not straightforward. This contrasts with other *ab initio* electronic structure methods, where one can keep improving the results until the electronic Schrödinger equation is solved exactly. The reason DFT is broadly used is that it tends to give very accurate results much more cheaply than many competing MO-based methods, especially for molecules containing transition metals.

Functionals

The two input computational parameters for the solution of the Schrödinger equation for a system using DFT are the exchange-correlation functional and the functions used to represent the electrons, the one-particle basis set. At the present time, there is no formal systematic way of choosing the functional, and the most popular ones in the literature have been derived by careful comparison with experiment as well as meeting the formal criteria for a functional (Scuseria and Staroverov 2005). Examples of commonly used functionals are given in Table 1. The selected examples of DFT exchange-correlation functionals consist of (1) local spin density approximation (LSDA), (2) generalized gradient approximations (GGA), (3) meta GGA (mGGA), (4) hybrid GGA (HGGA), and (5) hybrid meta GGA (HmGGA) functionals. We note that Perdew and coworkers have called the hierarchy of functionals the "Jacob's ladder of functionals"(Perdew and Schmidt 2001; Tao et al. 2003; Perdew et al. 2005). The first level of approximation usually used is the local density approximation, and this is usually taken as Slater exchange together with the correlation energy of the uniform electron gas. This functional depends only on the density. The LSDA for the exchange-correlation functional in DFT is well known for its accuracy in predicting properties such as lattice parameters and bulk moduli in metallic systems. However, the LSDA results for electronic properties are of lower quality, because of intrinsic deficiencies, including missing self-interaction corrections and the absence of the derivative discontinuity in the exchange-correlation potential.

The functional can be improved by incorporating gradient (nonlocal) corrections to the exchange and correlation energy (GGA). A third type of functional, called hybrid GGA (HGGA), is a gradient-corrected functional that includes some components of HF exact exchange. For molecules, hybrid exchange-correlation functionals often show improvement in the prediction of energetics over those from GGA functionals because the hybrid functionals help to delocalize the exchange hole. Hybrid functionals have proven to be equally good at predicting a range of physical properties, but such calculations in the solid state are computationally expensive due to the need to calculate Hartree-Fock exchange (Kudin et al. 2002). Commonly used GGAs are B88P86, PBE, and PW91. B3LYP is the most commonly used HGGA by a wide margin.

Weak interactions such as those involving van der Waals interactions or hydrogen bonding are important for geochemical applications. As hydrogen bonding has some electrostatic

Density Functional Theory, Table 1 Selected DFT exchange-correlation functionals

Method	Exchange	Correlation	Type
B1B95	(Becke 1996)	(Becke 1996)	HmGGA
B1LYP Adamo and Barone 1997	(Becke 1996)	Lee-Yang-Parr (Lee et al. 1988)	HGGA
B3LYP	(Becke 1993)	Lee-Yang-Parr (Lee et al. 1988)	HGGA
B972	Wilson-Bradley-Tozer's modified B97 (Wilson et al. 2001)	Wilson-Bradley-Tozer's modified B97 (Wilson et al. 2001)	HGGA
B98	Becke 98 (Schmider and Becke 1998)	Becke 98 (Schmider and Becke 1998)	HGGA
BLYP	(Becke 1988)	Lee-Yang-Parr (Lee et al. 1988)	GGA
BMK	(Boese and Martin 2004)	(Boese and Martin 2004)	HGGA
B88P86	(Becke 1988)	(Perdew 1986)	GGA
CAMB3LYP (Yanai et al. 2004)	(Becke 1988)	Lee-Yang-Parr (Lee et al. 1988)	HGGA[a]
G96LYP	Gill 1996	Lee et al. 1988	GGA
HCTH407	Hamprecht, Cohen, Tozer, Hand (Hamprecht et al. 1998) (Boese et al. 2000) (Boese and Handy 2001)	Hamprecht, Cohen, Tozer, Hand (Hamprecht et al. 1998) (Boese et al. 2000) (Boese and Handy 2001)	GGA
HSE1PBE	Heyd-Scuseria-Ernzerhof (Heyd et al. 2003, 2005) (Heyd and Scuseria 2004) (Krukau et al. 2006)	Perdew-Burke-Ernzerhof (Perdew et al. 1996)	HGGA
LCBP86 (Iikura et al. 2001)	(Becke 88)	(Perdew 1986)	GGA[a]
LCωPBE (Vydrov and Scuseria 2006)	Perdew-Burke-Ernzerhof (Perdew et al. 1996)	Perdew-Burke-Ernzerhof (Perdew et al. 1996)	HGGA[a]
M06	Minnesota 06 (Zhao and Truhlar 2008)	Minnesota 06 (Zhao and Truhlar 2008)	HmGGA
mPW1PW91	Barone's modified PW91 (Adamo and Barone 1998)	Perdew-Wang 91 (Perdew and Wang 1992)	HGGA
O3LYP/OLYP	Handy's OPTX (Cohen and Handy 2001; Handy and Cohen 2001)	Lee-Yang-Parr (Lee et al. 1988)	HGGA/ GGA
PBE/PBE1PBE	Perdew-Burke-Ernzerhof (Perdew et al. 1996)	Perdew-Burke-Ernzerhof (Perdew et al. 1996)	GGA/HGGA
PBEhPBE/PBEh1PBE	98 Revised PBE (Ernzerhof and Perdew 1998)	Perdew-Burke-Ernzerhof (Perdew et al. 1996)	GGA/ HGGA
PKZB	Perdew, Kurth, Zupan, Blaha (Perdew et al. 1999)	Perdew, Kurth, Zupan, Blaha (Perdew et al. 1999)	GGA
PW91	Perdew-Wang 91 (Perdew and Wang 1992; Burke et al. 1997)	Perdew-Wang 1991 (Perdew and Wang 1992)	GGA
SVWN5	(Slater 1974)	VWN functional (Vosko et al. 1980)	LSDA
τ-HCTH(hyb)	τ-dependent of HCTH (Boese and Handy 2002)	τ-dependent of HCTH (Boese and Handy 2002)	mGGA (HGGA)
TPSS	Tao-Perdew-Staroverov-Scuseria (Tao et al. 2003)	Tao-Perdew-Staroverov-Scuseria (Tao et al. 2003)	mGGA
TPSSh	Tao-Perdew-Staroverov-Scuseria (Staroverov et al. 2003)	Tao-Perdew-Staroverov-Scuseria (Staroverov et al. 2003)	HmGGA
VSXC	(van Voorhis and Scuseria 1997, 1998)	(van Voorhis and Scuseria 1997, 1998)	mGGA
ωB97(X, X-D) (Chai, Head-Gordon, 2008)	(Becke 1997)	(Becke 1997)	HGGA[a]
X3LYP (Xu and Goddard 2004)	(Becke 1988) (Perdew-Wang 1992)	Lee-Yang-Parr (Lee et al. 1988)	HGGA

[a]Long range corrected exchange correlation functional.

D

or dipolar component, a number of functionals can provide reasonable hydrogen bond energies, although if there are a large number of such interactions, the total error may not be small. On the other hand, most common DFT functionals do not handle dispersion corrections properly. One approach is to add in a set of atom-pairwise empirically based corrections as developed by Grimme and coworkers, the –D3 correction, for example (Grimme 2006; Grimme et al. 2010). Another approach is to add on a more formally developed correction based on the electron density a van der Waals nonlocal functional, which is added to commonly used exchange and correlation components, such as the VV10 functional (Vydrov and Van Voorhis 2009, 2010). These different types of corrections have been evaluated (Hujo and Grimme 2011, 2013; Mardirossian and Head-Gordon 2014).

The use of approximate exchange-correlation functionals allows one to solve the density functional equation exactly for an approximate energy expression, whereas molecular orbital methods solve an exact expression for the energy approximately. An advantage of many DFT functionals without exact exchange is that they formally scale as N^3 as compared to the N^4 scaling of Hartree-Fock theory and the N^5–N^7 scaling of common correlation methods. Thus, DFT methods, if derived without the inclusion of Hartree-Fock exchange, are computationally much cheaper than Hartree-Fock-based methods and exhibit a much better scaling with the size of the molecule. In fact, the Hartree-Fock method is a special case of DFT with the exchange term computed exactly and the correlation term equal to zero.

Other Features of DFT

An important use of DFT is to predict spectroscopic properties. The prediction of infrared and Raman vibrational spectra including intensities for molecules follows the second derivative methods developed for molecular orbital theory. UV-vis spectra can be calculated using time-dependent density functional theory (TD-DFT) (Bauernschmitt and Ahlrichs 1996; Casida et al. 1998). Nuclear magnetic resonance chemical shifts can be calculated using the gauge invariant atomic orbital (GIAO) approach (Wolinski et al. 1990) with density functional theory (Schreckenbach and Ziegler 1995, 1996, 1997). It is also possible to include relativistic effects in the zeroth-order regular approximation (ZORA) for the NMR chemical shifts (Wolff and Ziegler 1998; Wolff et al. 1999; Autschbach and Ziegler 2004).

As DFT developed as a broad-based chemical tool for predicting structures and energetics, there has been a continued development of the method for providing insights into chemical bonding and reactivity. This approach is often called conceptual DFT (Geerlings et al. 2003, 2014; De Proft et al. 2014). For example, it provides formal definitions of hardness and softness, the basis of hard-soft acid/base theory as well as electronegativity.

Solid State and Plane Waves

DFT calculations on solids are done with periodic boundary conditions. Plane waves are usually used rather than the Gaussian-type orbitals used in molecular calculations although the latter can be used in solid-state calculations. Plane waves are used in the electronic structure because they fit more naturally with the Bloch states and they are expanded in Wannier functions. In addition, they do not have the problems that Gaussian orbitals have in calculating diffuse parts of the wave function. The periodic calculations can be performed using the projector augmented wave (PAW) method, which deals with the full wave functions and allows the treatment of all elements in the periodic table (Blöchl 1994). Such calculations usually employ pseudopotentials so that calculations are only performed on the valence electrons as the contracted size of the inner shell orbitals makes it difficult to calculate these electronic states using plane waves. Ultrasoft pseudopotentials (Vanderbilt 1990) are broadly used and, for example, allow first-row transition metal elements to be dealt with in an economical manner.

Several approaches to improving the quality of band gaps including LSDA + U, which relies on LSDA-optimized lattice parameters, and many-body perturbation theory in the framework of the Green's function (GW) method have been developed (Grossman et al. 2001; Onida et al. 2002). Although these approaches predict improved band gaps, just like hybrid functionals, they are computationally demanding and are usually applied only to small systems. By using a screened hybrid functional that includes nonlocal Hartree-Fock exchange but decomposes the Coulomb operator into short-range and long-range components, such as that in the HSE functional (Heyd et al. 2003), it is possible to accurately and efficiently predict semiconductor and insulator band gaps (Prodan et al. 2007).

Conclusions

Density functional theory is an important tool for predicting the properties of geochemical systems based on their electronic structure. It is important to choose a properly benchmarked exchange-correlation functional together with an appropriate basis set. DFT can provide a broad

range of structural, energetic, and spectroscopic predictions that can be used to obtain detailed insights into geochemical systems at the molecular level. DFT is currently the most popular computational electronic structure method for geochemical applications, especially for predictions in the solid state or at extended interfaces. DFT can also provide qualitative insights into molecular reactivity through the use of conceptual DFT.

Cross-References

► Ab Initio Calculations

References

Adamo C, Barone V (1997) Toward reliable adiabatic connection models free from adjustable parameters. Chem Phys Lett 274:242–250

Adamo C, Barone V (1998) Exchange functionals with improved long-range behavior and adiabatic connection methods without adjustable parameters: the mPW and mPW1PW models. J Chem Phys 108:664–675

Autschbach J, Ziegler T (2004) Calculation of heavy-nucleus chemical shifts: relativistic all-electron methods. In: Kaupp M, Buhl M, Malkin VG (eds) Calculation of NMR and EPR parameters: theory and application. Wiley-VCH & Co, Weinheim, pp 249–264

Bauernschmitt R, Ahlrichs R (1996) Treatment of electronic excitations within the adiabatic approximation of time dependent density functional theory. Chem Phys Lett 256:454–464

Becke AD (1988) Density-functional exchange-energy approximation with correct asymptotic behavior. Phys Rev A 38:3098–3100

Becke AD (1993) Density-functional thermochemistry. III. The role of exact exchange. J Chem Phys 98:5648–5652

Becke AD (1996) Density-functional thermochemistry. IV. A new dynamical correlation functional and implications for exact-exchange mixing. J Chem Phys 104:1040–1046

Becke AD (1997) Density-functional thermochemistry. V. Systematic optimization of exchange-correlation functionals. J Chem Phys 107:8554–8560

Blöchl PE (1994) Projector augmented-wave method. Phys Rev B 50:17953–17979

Boese AD, Handy NC (2001) A new parametrization of exchange-correlation generalized gradient approximation functionals. J Chem Phys 114:5497–5503

Boese AD, Handy NC (2002) New exchange-correlation density functionals: the role of the kinetic-energy density. J Chem Phys 116:9559–9969

Boese AD, Martin JML (2004) Development of density functionals for thermochemical kinetics. J Chem Phys 121:3405–3416

Boese AD, Doltsinis NL, Handy NC, Sprik M (2000) New generalized gradient approximation functionals. J Chem Phys 112:1670–1678

Burke K, Perdew JP, Wang Y (1997) Derivation of a generalized gradient approximation: the PW91 density functional. In: Dobson JF, Vignale G, Das MP (eds) Electronic density functional theory: recent progress and new directions. Plenum, New York, pp 81–121

Casida ME, Jamorski C, Casida KC, Salahub DR (1998) Molecular excitation energies to high-lying bound states from time-dependent density-functional response theory: characterization and correction of the time-dependent local density approximation ionization threshold. J Chem Phys 108:4439–4449

Chai J-D, Head-Gordon M (2008) Systematic optimization of long-range corrected hybrid density functionals. J Chem Phys 128:084106. (15pages)

Cohen AJ, Handy NC (2001) Dynamic correlation. Mol Phys 99:607–615

De Proft F, Ayers PW, Geerlings P (2014) Chapter. 7. The conceptual density functional theory perspective of bonding. In: Frenking G, Shaik S (eds) The chemical bond: fundamental aspects of chemical bonding. Wiley, New York, pp 233–265

Dreizler RM, Gross EKU (1990) Density functional theory. An approach to the quantum many-body problem. Springer, Berlin

Ernzerhof M, Perdew JP (1998) Generalized gradient approximation to the angle- and system-averaged exchange hole. J Chem Phys 109:3313–3320

Geerlings P, De Proft F, Langenaecker W (2003) Conceptual density functional theory. Chem Rev 103:1793–1873

Geerlings P, Fias S, Boisdenghien Z, De Proft F (2014) Conceptual DFT: chemistry from the linear response function. Chem Soc Rev 43:4989–5008

Gill PMW (1996) A new gradient-corrected exchange functional. Mol Phys 89:433–445

Grimme S (2006) Semiempirical GGA-type density functional constructed with a long-range dispersion correction. J Comput Chem 27:1787–1799

Grimme S, Antony J, Ehrlich S, Krieg H (2010) A consistent and accurate ab initio parametrization of density functional dispersion correction (DFT-D) for the 94 elements H-Pu. J Chem Phys 132:154104

Grossman JC, Rohlfing M, Mitas L, Louie SG, Cohen ML (2001) High accuracy many-body calculational approaches for excitations in molecules. Phys Rev Lett 86:472–475

Hamprecht FA, Cohen A, Tozer DJ, Handy NC (1998) Development and assessment of new exchange-correlation functionals. J Chem Phys 109:6264–6271

Handy NC, Cohen AJ (2001) Left-right correlation energy. Mol Phys 99:403–412

Heyd J, Scuseria GE (2004) Assessment and validation of a screened Coulomb hybrid density functional. J Chem Phys 120:7274–7280

Heyd J, Scuseria GE, Ernzerhof M (2003) Hybrid functionals based on a screened Coulomb potential. J Chem Phys 118:8207–8215. Erratum: J Chem Phys 2006, 124, 219906

Heyd J, Peralta JE, Scuseria GE, Martin RL (2005) Energy band gaps and lattice parameters evaluated with the Heyd-Scuseria-Ernzerhof screened hybrid functional. J Chem Phys 123:174101. (8 pages)

Hohenberg P, Kohn W (1964) Inhomogeneous electron gas. Phys Rev 136:B864–B871

Hujo W, Grimme S (2011) Performance of the van der Waals density functional VV10 and (hybrid) GGA variants for thermochemistry and noncovalent interactions. J Chem Theory Comput 7:3866–3871

Hujo W, Grimme S (2013) Performance of non-local and atom-pairwise dispersion corrections to DFT for structural parameters of molecules with noncovalent interactions. J Chem Theory Comput 9:308–315

Iikura H, Tsuneda T, Yanai T, Hirao K (2001) Long-range correction scheme for generalized-gradient-approximation exchange functionals. J Chem Phys 115:3540–3544

Kohn W, Sham LJ (1965) Self-consistent equations including exchange and correlation effects. Phys Rev 140:A1133–A1138
Krukau AV, Vydrov OA, Izmaylov AF, Scuseria GE (2006) Influence of the exchange screening parameter on the performance of screened hybrid functionals. J Chem Phys 125:224106. (4 pages)
Kudin KN, Scuseria GE, Martin RL (2002) Hybrid density-functional theory and the insulating gap of UO2. Phys Rev Lett 89:266402. (4 pages)
Labanowski J, Andzelm JW (eds) (1991) Density functional methods in chemistry. Springer, New York
Laird BB, Ross RB, Ziegler T (eds) (1996) Chemical applications of density functional theory, ACS symposium series, vol 629. American Chemical Society, Washington
Lee C, Yang W, Parr RG (1988) Development of the Colle-Salvetti correlation-energy formula into a functional of the electron density. Phys Rev B 37:785–789
Mardirossian N, Head-Gordon M (2014) wB97X-V: a 10-parameter, range-separated hybrid, generalized gradient approximation density functional with nonlocal correlation, designed by a survival-of-the-fittest strategy. Phys Chem Chem Phys 16:9904–9924
Onida G, Reining L, Rubio A (2002) Electronic excitations: density-functional versus many-body Green's-function approaches. Rev Mod Phys 74:601–659
Parr RG, Wang W (1989) Density-functional theory of atoms and molecules. Oxford Science, New York
Perdew JP (1986) Density-functional approximation for the correlation energy of the inhomogeneous electron gas. Phys Rev B 33:8822–8824
Perdew JP, Schmidt K (2001) Jacob's ladder of density functional approximations for the exchange-correlation energy. AIP Conf Proc 577:1–20
Perdew JP, Wang Y (1992) Accurate and simple analytic representation of the electron gas correlation energy. Phys Rev B 45:13244–13249
Perdew JP, Burke K, Ernzerhof M (1996) Generalized gradient approximation made simple. Phys Rev Lett 77:3865–3868. Errata. Phys Rev Lett 1997, 78, 1396
Perdew JP, Kurth S, Zupan A, Blaha P (1999) Accurate density functional with correct formal properties: a step beyond the generalized gradient approximation. Phys Rev Lett 82:2544–2547
Perdew JP, Ruzsinszky A, Tao J, Staroverov VN, Scuseria GE, Csonka GI (2005) Prescription for the design and selection of density functional approximations: more constraint satisfaction with fewer fits. J Chem Phys 123:062201. (9 pages)
Prodan ID, Scuseria GE, Martin RL (2007) Covalency in the actinide dioxides: systematic study of the electronic properties using screened hybrid density functional theory. Phys Rev B 76:033101. (4 pages)
Schmider HL, Becke AD (1998) Optimized density functionals from the extended G2 test set. J Chem Phys 108:9624–9631
Schreckenbach G, Ziegler T (1995) Calculation of NMR shielding tensors using gauge-including atomic orbitals and modern density functional theory. J Phys Chem 99:606–611
Schreckenbach G, Ziegler T (1996) The calculation of NMR shielding tensors based on density functional theory and the frozen-core approximation. Int J Quantum Chem 60:753–766
Schreckenbach G, Ziegler T (1997) Calculation of NMR shielding tensors based on density functional theory and a scalar relativistic Pauli-type Hamiltonian. The application to transition metal complexes. Int J Quantum Chem 61:899–918
Scuseria GE, Staroverov VN (2005) Chapter 24. Development of approximate exchange-correlation functionals. In: Dykstra CE, Frenking G, Kim KS, Scuseria GE (eds) Theory and applications of computational chemistry: the first 40 years. Elsevier, Amsterdam, pp 669–724
Seminario JM, Politzer P (eds) (1995) Modern density functional theory: a tool for chemistry. Elsevier, Amsterdam
Sholl DS, Steckel JA (2009) Density functional theory: a practical introduction. Wiley, New York
Slater JC (1974) Quantum theory of molecules and solids. McGraw-Hill, New York, p 4
Springborg M (ed) (1997) Density-functional methods in chemistry and materials science. Wiley, Chichester
Staroverov VN, Scuseria GE, Tao J, Perdew JP (2003) Comparative assessment of a new nonempirical density functional: molecules and hydrogen-bonded complexes. J Chem Phys 119:12129–12137
Tao J, Perdew JP, Staroverov VN, Scuseria GE (2003) Climbing the density functional ladder: nonempirical meta-generalized gradient approximation designed for molecules and solids. Phys Rev Lett 91:146401. (4 pages)
Vanderbilt D (1990) Soft self-consistent pseudopotentials in a generalized eigenvalue formalism. Phys Rev B 41:7892–7895
Voorhis TV, Scuseria GE (1997) Exchange energy functionals based on the density matrix expansion of the Hartree-Fock exchange term. Mol Phys 92:601–608
Voorhis TV, Scuseria GE (1998) A novel form for the exchange-correlation energy functional. J Chem Phys 109:400–410; Erratum 2008, 129, 219901
Vosko SH, Wilk L, Nusair M (1980) Accurate spin-dependent electron liquid correlation energies for local spin density calculations: a critical analysis. Can J Phys 58:1200–1211
Vydrov OA, Scuseria GE (2006) Assessment of a long range corrected hybrid functional. J Chem Phys 125:234109. (9 pages)
Vydrov OA, Van Voorhis T (2009) Nonlocal van der Waals density functional made simple. Phys Rev Lett 103:063004. (4 pages)
Vydrov OA, Van Voorhis T (2010) Nonlocal van der Waals density functional: the simpler the better. J Chem Phys 133:244103. (9 pages)
Wilson PJ, Bradley TJ, Tozer DJ (2001) Hybrid exchange-correlation functional determined from thermochemical data and ab initio potentials. J Chem Phys 115:9233–9242
Wolff SK, Ziegler T (1998) Calculation of DFT-GIAO NMR shifts with the inclusion of spin-orbit coupling. J Chem Phys 109:895–905
Wolff SK, Ziegler T, van Lenthe E, Baerends EJ (1999) Density functional calculations of nuclear magnetic shieldings using the zeroth-order regular approximation (ZORA) for relativistic effects: ZORA nuclear magnetic resonance. J Chem Phys 110:7689–7698
Wolinski K, Hinton JF, Pulay P (1990) Efficient implementation of the gauge-independent atomic orbital method for NMR chemical shift calculations. J Am Chem Soc 112:8251–8260
Xu X, Goddard WA III (2004) The X3LYP extended density functional for accurate descriptions of nonbond interactions, spin states, and thermochemical properties. Proc Natl Acad Sci USA 101:2673–2677
Yanai T, Tew D, Handy N (2004) A new hybrid exchange-correlation functional using the coulomb-attenuating method (CAM-B3LYP). Chem Phys Lett 393:51–57
Zhao Y, Truhlar DG (2008) The M06 suite of density functionals for main group thermochemistry, thermochemical kinetics, noncovalent interactions, excited states, and transition elements: two new functionals and systematic testing of four M06-class functionals and 12 other functionals. Theor Chem Accounts 120:215–241

Diagenesis

Isabel P. Montañez[1] and Laura J. Crossey[2]
[1]Department of Earth and Planetary Sciences, University of California, Davis, CA, USA
[2]Department of Earth and Planetary Sciences, University of New Mexico, Albuquerque, NM, USA

Synonyms

Diagenesis classified by setting and evolutionary stage of sedimentary basins: Eogenetic or *eodiagenesis* (near surface and shallow burial), *mesogenetic* or *mesodiagenesis* (deeper burial), and *telogenetic* or *telodiagenesis* (uplifted succession) (Choquette and Pray 1970).

Diagenesis classified by process: Syndiagenesis (biogeochemical processes at the sediment-water interface through shallow burial), *anadiagenesis* (dominantly physicochemical processes under deeper burial or orogenic conditions), and *epidiagenesis* (biogeochemical processes associated with fluid flow during uplift) (Fairbridge 1967).

Catagenesis (late, deep-burial diagenesis, referred by some as "burial metamorphism" as it incorporates the earliest stage of metamorphism).

Definition

Diagenesis is the sum total of physical, chemical, and biological processes that occur in sediments and sedimentary rocks from immediately after deposition through to the metamorphic realm. No universal definition exists for diagenesis and the term has evolved since it was defined nearly 150 years ago (de Segonzac 1968). It is generally agreed that diagenetic processes occur under Earth surface conditions (~0–30 °C and 1 bar of pressure) to temperatures of ≤250 °C and pressures of up to 2.5 kb (7 km) involving a broad range of fluid compositions from fresh water to concentrated brines (Fig. 1). Diagenesis involves both the conversion of sediments into sedimentary rock and the subsequent changes that occur prior to entering the metamorphic realm. There is no distinct boundary between the culmination of diagenesis and the onset of metamorphism nor between early diagenesis and weathering. The process of diagenetic conversion begins at the sediment-water interface in marine and terrestrial depositional sites, which have sufficient accommodation space to accumulate and preserve sediments, and continues to influence mineral and organic matter throughout its burial in sedimentary basins and associated tectonic history. Given the high reactivity of many minerals and organic matter within sediments and sedimentary rocks and the evolving nature of pore fluid temperature and chemistry, diagenesis is a continually active process with a protracted history of physical and chemical processes that lead to dissolution, chemical transformation of mineral components, precipitation of new mineral cements, and maturation of organic matter. Many resources such as coal, oil, gas, and ore deposits result from diagenetic processes.

D

The Diagenetic Cycle

The diagenetic cycle begins immediately following deposition on the ocean, lake, or channel/floodplain floor and continues through shallow- to deep-burial, and for many sediments ends with exposure above sea- or base-level where erosion, chemical weathering, and other diagenetic processes take place. Water and organic matter decomposition are the agents of diagenesis providing the fuel for the chemical and microbial processes that act on newly deposited detrital siliciclastic materials and chemically precipitated minerals, such as carbonates, amorphous silica, and evaporites (Ali et al. 2010). The course of diagenesis is dictated by sedimentary factors such as particle size and mineralogic composition, fluid-rock ratio, fluid chemistry and flow rates, organic matter content, the presence of microbial communities, as well as environmental conditions (temperature, fluid chemistry, pressure). In turn, diagenetic processes can change the chemical properties of the pore fluids over time, causing additional changes to mineralogy, fluid composition, and petrologic properties. Figure 1 summarizes many aspects of diagenesis. Figure 2 places these processes in a schematic cross section and provides a framework for the conditions under which diagenesis occurs.

- The ***early diagenetic realm*** (eogenesis or eogenetic zone, Fig. 2) occurs during burial to a few hundred meters and involves changes to the sediment, organic matter it hosts, and the interstitial fluids (pore water) by surface-related processes under near surface temperatures (≤30 °C). Diffusion of gases (e.g., oxygen, carbon dioxide, hydrogen sulfide, and methane) can also influence the geochemical environment. Early diagenesis typically involves dewatering of fine-grained sediments by gravitational compaction, bioturbation by burrowing organisms, dissolution of unstable minerals, diffusion of dissolved cations (e.g., Ca^{2+}, Mg^{2+}, Fe^{2+}, Mn^{2+}, Sr^{2+}), anionic species and gases (e.g., SO_4^{2-}, HCO_3^-, O_2, CO_2, CH_4, H_2S) through the sediment, bacterial decomposition of organic matter, transformation (neomorphism or recrystallization) of

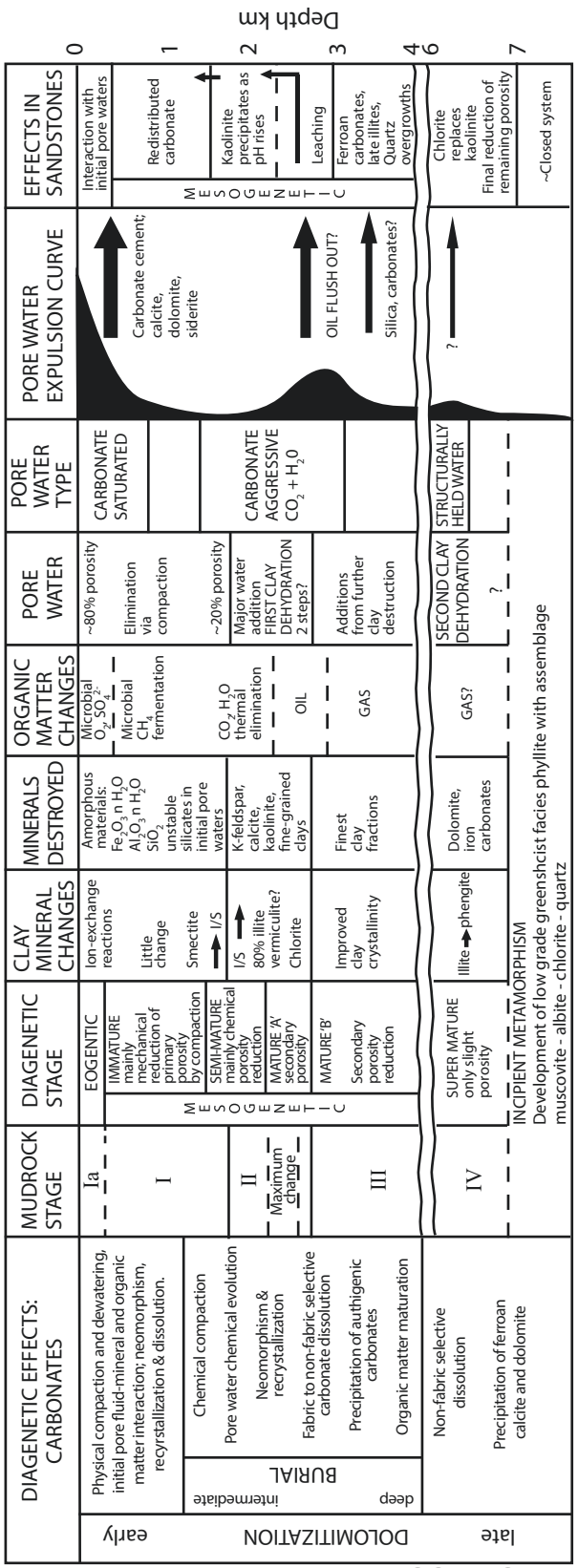

Diagenesis, Fig. 1 Matrix illustrating different aspects of diagenesis. The matrix is arranged with increasing depth (temperature) toward the bottom, and different sedimentary components in the columns (Modified from Burley et al. (1985))

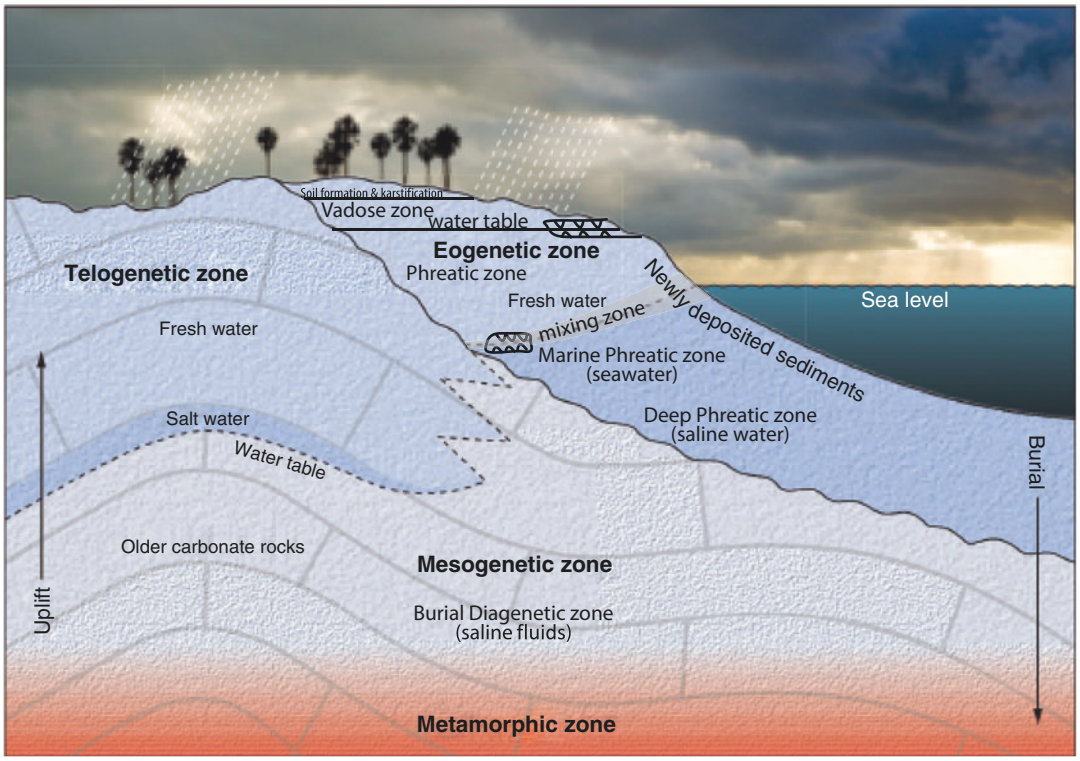

Diagenesis, Fig. 2 Summary of diagenetic realms. Sediments deposited in Earth surface environments pass through the diagenetic cycle post deposition, which can include the eogenetic zone (early diagenetic realm), the mesogenetic zone (burial diagenetic realm), and the telogenetic zone (exposure) (Modified from Ali et al. (2010))

unstable minerals, and precipitation of authigenic carbonates, oxides, hydroxy-oxides, aluminosilicates, sulfates, and sulfides. Sedimentation rate controls the degree of physical compaction and dewatering of sediments as well as the depths of bioturbation and cation/molecule diffusion rates. Most early diagenetic chemical reactions are driven by the reactivity of metastable minerals (e.g., amorphous silica, aragonite, high Mg-calcite, dolomite) or phyllosilicates. Many early diagenetic processes involve the kinetic boost by bacteria, referred to as bacterial mediation. Empirical studies of the early diagenetic realm involve outcrop studies and coring of marine and lake sediments and analysis of sediment mineralogy, texture, and grain size distribution, pore-water chemistry, and in recent years, the composition of associated microbial communities.

- Sediments continue to undergo geochemical modification in the ***burial diagenetic realm*** (mesogenesis or mesogenetic zone, Fig. 2) involving processes that are no longer directly related to the surface including chemical compaction (pressure solution), dissolution, precipitation of authigenic minerals (i.e., cementation), and organic matter maturation. This diagenetic realm is commonly partitioned into the intermediate burial (between 500 and 2000 m depth) and deep burial ($\geq$ 2 km) zones. Elevated temperature and pressure play a major role in driving the physicochemical reactions in the burial diagenetic realm. The chemical composition of pore waters evolves with depth, typically becoming more saline, due to fluid-rock interactions such as dewatering of clays and dissolution of buried evaporites. Maturation of organic matter releases organic acids and contributes toward lowering pH and changing redox conditions of interstitial fluids (Surdam and Crossey 1987; Harrison and Thyne 1992). Consequently, minerals, which were initially stable in the shallow diagenetic realm, become metastable with burial driving dissolution and precipitation of authigenic minerals such as calcite, dolomite, anhydrite, silica, zeolites, and clay mineral transformations. Overall, cementation is thought to dominate over dissolution in the burial diagenetic realm (Ali et al. 2010).
- Exposure of sedimentary rocks above base level by tectonic uplift (telogenesis) or sea-level fall exposes them to atmospheric processes and physical erosion and chemical weathering. Meteoric (fresh, dilute) waters can penetrate deeply into exposed or tectonically uplifted sedimentary rocks through permeable units or fracture porosity and develop extensive karst and dissolution features in carbonate-dominated successions (telogenetic zone, Fig. 2).

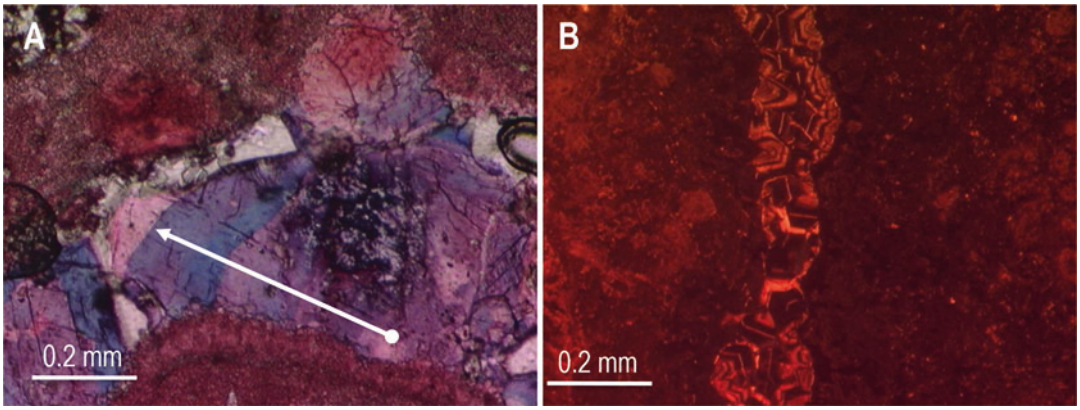

Diagenesis, Fig. 3 Photomicrographs of carbonate. (**a**) Stained (Alizarin *Red* and potassium ferricyanide) thin section showing calcite cement sequence (paragenesis) in a calcite spar cement that occludes a primary pore developed between grains (*pink*); thin marine cement and freshwater cement rims (*pink* staining are developed on grains. *White* triangular cement lining pores are dolomite. (**b**) Cathdoloumінescent zoning in calcite cement occluding porosity in a fracture (or between grains). The alternating bright luminescent and nonluminescent banding of the cement records the migration of multiple generations of calcite-precipitating fluids

- Tectonic forces and sea level fluctuations lead to cycling of sediments and sedimentary rocks between the diagenetic realms resulting in multiple cycles of dissolution, cementation, mineral transformation, and recystallization until a steady state or equilibrium is reached. The extent and nature of diagenesis will reflect the reactivity of the initial sediment, its fluid-rock interaction history including fluid-rock ratios and exposure time to each diagenetic zone.
- Where multiple diagenetic events have influenced a sedimentary rock, the paragenetic sequence of these events (Fig. 3) can be reconstructed by integrating microscope (thin sections to scanning electron microscopy) and geochemical studies of the sedimentary rocks and their fluid inclusion waters as well as associated organic matter. Diagenetic transformation of sedimentary rocks can substantially impact their porosity and permeability and in turn their fluid conduit and aquifer or reservoir potential (Montañez 1997).

Methods Applied to Study of Siliciclastic and Carbonate Rocks

Petrographic study of thin sections employing the optical microscope forms the basis for understanding the composition (mineralogy), spatial and textural relationships between detrital grains, authigenic minerals, and pore geometries (Fig. 3). Optical examination is aided by specialized preparation (impregnation of the rock with colored epoxy to highlight porosity) and staining techniques for recognition of specific carbonate minerals (Fig. 3a) and feldspars as well as calcite cements of differing Fe^{2+} concentration (Nelson and Read 1990; also see Humphries (1992) for a guide to thin section preparation methods). Cathodoluminescence study of thin sections (Fig. 3b) is commonly used to further identify textures and to define a paragenetic sequence for a given sample or suite of samples. A paragenesis is the sequence in which different minerals or generations of a given mineral (e.g., calcite) were precipitated. Carbonate cements exhibit varying shades of brown, red, yellow, and orange under cathodoluminescence due to incorporation of varying amounts of Fe^{2+} and Mn^{2+} into the crystal lattice. Cathodoluminescent zoning in carbonate cements reflects the Mn^{2+} to Fe^{2+} ratio of a given generation of carbonate cement, and in turn that of the fluid from which it precipitated. Authigenic feldspar overgrowths and cements are nonluminescent, whereas detrital cores and grains exhibit blue luminescence. Discrete generations of carbonate cements typically are identified by their coupled staining and cathodoluminescence (Fig. 3).

X-ray diffraction (XRD) is the preferred method for structural identification of fine-grained minerals, particularly in mudrocks. Moore and Reynolds (1989) provide a summary of preparation and analysis: Brindley and Brown (1984) and Newman (1987) provide detailed descriptions of clay minerals.

Geochemical analysis may include elemental and isotopic (both stable and radiogenic) approaches. While a comprehensive survey of all methods is beyond the scope of this overview, several common techniques will be mentioned. Electron microbeam techniques are powerful tools for in situ chemical and mineralogical examination of sedimentary rocks of all types. Scanning electron microscopy (SEM) is widely used to understand three-dimensional morphology, pore geometries, sequence of mineral growth, and more recently, microbe/mineral interactions (Banfield and Nealson 1997). Electron microprobe analysis (EMPA) provides quantitative chemical analyses of phases typically of 10 micron and greater size though specialized instruments may target smaller regions. This tool is generally restricted to major and minor element analysis. The secondary ion microprobe (SIMS) has gained

wide use in geoscience applications (see review in Stern 2009) and provides quantitative trace element and stable isotopic analyses in spatial context. Methods involving laser ablation in tandem with inductively coupled plasma mass spectrometry are providing new approaches to both elemental and isotopic analysis of sedimentary materials with excellent opportunities for application to diagenesis research (see examples in Rasbury et al. 2012). Integration of petrographic features with elemental and isotope analysis (carbon, oxygen, sulfur, and nitrogen) of authigenic phases, at times coupled with fluid inclusion study, has been effective in understanding conditions of formation and paleofluid composition in some cases (see summaries in Sharp 2007). Banner (2004) provides a comprehensive overview of applications of radiogenic isotopes to sedimentary systems.

Carbonate Diagenesis

Carbonates are minerals with a structural CO_3^{2-} group and Ca^{2+}, Mg^{2+}, or a combination of these two elements. Weight percent Fe^{2+}, Mn^{2+}, and Sr^{2+} occur in less common carbonates. Most carbonate sediments form in marine settings commonly with coexisting polymorphs of aragonite and low- ($\leq$5% $MgCO_3$) to high-Mg calcite (5–20% $MgCO_3$), as well as rarely dolomite (Moore 1989). Terrestrial carbonates form as low-Mg calcite and siderite in lacustrine, wetland, and spring deposits, low-Mg calcite and sphaerosiderites in soils, and low- to high-Mg calcite and aragonite in travertines and cave speleothems. This entry focuses on marine carbonates given their prevalence in the modern and geologic record; see reviews by Ford and Pedley (1996) and Capezzuoli et al. (2014) for freshwater carbonates.

Carbonate mineralogy in the marine realm is determined thermodynamically by mineral stability (solubility) and kinetically by substrate mineralogy, biological effects, differences in precipitation rates, and the presence/absence of organic compounds and inorganic inhibitors (e.g., SO_4^{2-}, PO_4^{3-}, Mg^{2+}) (Burton 1993). Biological effects include microbial mediation and vital effects. With the exception of low-Mg calcite, all of these carbonate mineralogies are thermodynamically metastable (high Mg-calcite, aragonite, non-stoichiometric dolomite) at Earth surface conditions and will convert to stable low-Mg calcite or stoichiometric dolomite during subsequent exposure to evolved marine pore waters, introduction of meteoric fluids, and/or interaction with saline brines during burial (Walter 1985).

Early Diagenetic Realm

For shallow-water carbonates, extensive diagenesis occurs proximal to the sediment-fluid or atmosphere interface due to repeated flushing by seawater or freshwater (eogenetic zone, Fig. 2). Their metastable mineralogy makes them highly susceptible to post-depositional mineralogical and geochemical alteration as the pore fluid chemistry evolves with fluid mixing and chemical reactions (Moore 1989; James and Choquette 1990). Diagenesis at the sediment-seawater interface begins with boring by endolithic algae, sponges, and fungi, which replace primary skeletal carbonate with clay-size carbonate precipitates (micrite), a process called micritization. Within the first few centimeters to meters of burial, dissolution of high-Mg calcite and aragonite releases bicarbonate (HCO_3^-) that along with fluid CO_2 degassing promotes neomorphism and recrystallization of grains, carbonate cementation, and calcite overgrowths on biotic templates. Neomorphism involves the molecular-scale replacement of an unstable phase of carbonate by thermodynamically more stable low-Mg calcite. Recrystallization of grains and early cements involves the wholesale dissolution of the original carbonate and simultaneous precipitation of a more stable phase resulting in a possible volume change and loss of original textures. Recrystallization occurs in both carbonates and siliciclastic deposits. These early diagenetic processes lead to preservation of much of the original fabric and retard compaction in shallow-water marine carbonates. Dissolution of aragonitic fossils and matrix creates secondary moldic or vuggy porosity.

In contrast to shallow-water carbonates, the predominance in deep-sea sediments of stable low-Mg calcite causes delay in dissolution and cementation. The presence of small amounts of calcite overgrowths and cements on shells and shell recrystallization indicates localized regions of carbonate dissolution and diffusion/advection to areas of calcite cementation (Moore 1989). Oxidation of organic matter buried with carbonate sediments provides HCO_3^- to pore fluids for carbonate precipitation. Pore water profiles of the oxygen ($\delta^{18}O$) and calcium ($\delta^{44}Ca$) isotopic composition and trace element concentrations are used to model the rates of carbonate recrystallization in deep-sea sediments (Fantle et al. 2010). Gravitational compaction of deep-sea sediments in the shallow burial realm (within the first 200 m of burial) is a major influence on lithification and leads to substantial loss of porosity (from ~80% to $\leq$50–60%).

The diagenetic evolution of carbonate sediments, which were deposited on the slopes surrounding shallow-water carbonate platforms, falls between that of deep-sea sediments and shallow-water marine carbonates. This reflects the mixing of a pelagic low-Mg calcite source with a platform-shed source of reactive aragonite and high-Mg calcite as well as overall higher concentrations of organic matter (Swart 2015). Thus, periplatform carbonates may undergo extensive dissolution and cementation during initial burial making them more resistant to compaction than deep-sea sediments.

Meteoric diagenesis: The vast majority of carbonates are deposited during sea level highstands when shallow water platforms are inundated (Ali et al. 2010). These carbonates

are subsequently exposed to freshwater, which is undersaturated with respect to carbonates, during subsequent drop in base level whether driven by eustasy or tectonic uplift (telo- or epidiagenesis). Meteoric diagenesis occurs over a series of near-surface (eogenetic) diagenetic zones (Fig. 2) including soil formation and karstification and vadose, phreatic, and mixing zones (see reviews by Moore 1989; James and Choquette 1990). Overall, freshwater reactions with metastable carbonates result in extensive stabilization (through neomorphism or recrystallization) of carbonate grains, superimposed generations of dissolution and low-Mg calcite cementation, as well as substantial redistribution of pore space. The degree of diagenetic alteration is dictated by the reactivity of the initial mineralogy, the pore fluid chemistry, fluid-rock ratios, and flow rates.

Diagenesis in the freshwater undersaturated vadose zone is characterized by seepage flow through intergranular porosity and conduit flow through solution-enlarged fissures (Fig. 2). Vadose waters are typically CO_2-charged and chemically aggressive given exchange with the atmosphere and with soil-formed CO_2. Rapid conduit flow leads to extensive, non-mineral selective dissolution. Rates of calcite precipitation are far slower than fluid flow rates, thus as dissolution proceeds fluids become oversaturated with respect to low-Mg calcite and precipitate cements down-flow (Moore 1989). Freshwater that percolates slowly through the vadose zone by diffuse flow promotes mineral-controlled diagenesis, which is controlled by the differing solubilities of the carbonate polymorphs. Aragonite is 1.5 times more soluble than low-Mg calcite at a given temperature, whereas high-Mg calcite, whose solubility increases with Mg content, can be up to an order of magnitude more soluble than low-Mg calcite (Walter 1985). Dissolution of more soluble carbonate under the slow diffuse flow rates leads to oversaturation with respect to low-Mg calcite proximal to the site of dissolution driving widespread fabric-retentive neomorphism, recrystallization, and precipitation of vadose calcite cements (e.g., pendant and meniscus cements, crystal silt, fine crystalline equant cements unevenly lining primary porosity). The end-product can be wholesale transformation of metastable carbonates to thermodynamically stable low-Mg calcite while retaining much primary texture and fabric. This conversion process, however, is slow (on the order of 10^6 year) reflecting the overall low water-rock ratios of the vadose zone.

The water table (Fig. 2) delineates the boundary between the vadose and underlying saturated phreatic zone. High flow rates and turbulent exchange at the water table promotes CO_2 dissolution into water or high CO_2 degassing rates making this region a dynamic zone of dissolution and low-Mg cementation (Moore 1989; James and Choquette 1990). The phreatic zone hosts the bulk of dissolution and cementation by freshwater. Exposure of marine carbonates due to sea level fall leads to deep penetration of meteoric water given that the freshwater phreatic lens will develop to depths of ~40 times the height of the water table above sea level (Ghyben–Herzberg principle). Diagenetic processes in the shallow phreatic zone are orders of magnitude faster than in the vadose zone reflecting overall higher flow rates and fluid-rock ratios. In this zone, low-Mg calcite cements form isopachous rims of equant to bladed crystals on grains and within moldic porosity and microspar cements partially to fully occlude porosity. Relatively rapid flow rates lead to large-scale transport of dissolved carbonate and Ca^{2+} down-flow resulting in extensive dissolution updip and cementation downdip.

Mineralogic stabilization within the phreatic zone (Fig. 2) occurs rapidly (10^4–10^5 year) relative to the vadose zone. Once stabilized, subsequent diagenetic modification is limited to minor cementation within conduits that focus fluid flow. The mixing zone (Fig. 2), at the interface between the freshwater phreatic zone and the underlying deep phreatic zone with saline continental or marine interstitial fluids, is a chemically active region given that physical and diffusive mixing of waters leads to nonlinear changes in carbonate mineral saturation. The mixing zone is a region of abundant secondary porosity and subsurface karst development (e.g., Boulder zone in the Tertiary Florida aquifer or the ceynotes of the Yucatan Peninsula). The different zones of meteoric diagenesis have characteristic stable (O and C) isotopic and trace element signatures that when coupled with stratigraphic and petrographic studies have been used to reconstruct the diagenetic history of carbonate successions. The reader is directed to Moore (1989) and Swart (2015) for a comprehensive review of the geochemistry of meteoric diagenesis. The deep phreatic zone (Fig. 2) is a shallow burial locale of substantially slower diagenesis given the slow fluid flow rates and low fluid-rock ratios. Low-Mg calcite and dolomite cements that form in this zone are typically large and blocky reflecting their slow growth rates under very low saturation states.

The meteoric diagenetic realm is dynamic with fluctuations in base level, whether driven by eustasy or tectonics, that induce repeated large-scale vertical migration of the marine, vadose, phreatic, and mixing zones through a sedimentary succession over time (Read and Horbury 1993). Throughout Earth history, sea level has fluctuated 10 s to 100 s of m over a spectrum of timescales (10^4–10^7 -year) driven by orbitally forced waxing and waning of ice sheets, atmospheric pCO_2 variability, and tectonic and mantle processes. These shifts in the meteoric diagenetic zones impart a mineralogic and geochemical signature that is characteristic of the magnitude of relative sea-level fluctuations and the climate regime under which they occurred (Read and Horbury 1993). Zonation in low-Mg calcite cements, discernible petrographically under transmitted light or by cathodoluminescence (Fig. 3) as well as by their geochemical compositions (Fe, Mn, Mg,

concentrations and $\delta^{18}O$ and $\delta^{13}C$ isotopic compositions), record changes in fluid conditions (redox, temperature, salinity) through time from which the spatial migration of the near-surface diagenetic zones can be reconstructed (Niemann and Read 1988; Nelson and Read 1990). In many cases, zoned phreatic cements capture multiple cycles of fluid change within a pore providing a strip chart of the eustatic fluctuations that affected a given carbonate succession (Read and Horbury 1993) even when deeply eroded by post-depositional processes (Bishop et al. 2009).

Intermediate-to-Deep Burial Diagenetic Realm

Ultimately, most sedimentary deposits are buried sufficiently (>1 km) by overlying sediments and rocks that they are introduced to the intermediate-to-deep-burial diagenetic realm (herein referred to as "burial diagenetic" or mesogenetic zone). The burial diagenetic zone (Fig. 2) begins proximal to the liquid oil window in hydrocarbon source rocks (Machel 2005). Formation temperatures are elevated above ~50 °C reaching conditions of over 100–200 °C, which enhances diagenetic reactions. The burial diagenetic realm is characterized by further chemical compaction and dissolution, mineral stabilization, and precipitation of cements. Depending on the clay mineral content and previous cementation history, chemical compaction can become a predominant process with the degree of pressure solution influenced by pore-water composition, mineralogy, degree of previous cementation, and the presence of organic matter. Grains or primary marine cements or earlier diagenetic precipitates, which were not previously stabilized, become thermodynamically metastable in the deep subsurface due to changing fluid conditions driving further recystallization and mineral replacement, including widespread dolomite replacement of limestone host rocks (Machel 2005).

Interstitial (formation) fluids in the deep-burial diagenetic environment range from brackish (< 35 weight percent) to hypersaline reflecting their interaction history with sedimentary rocks, including evaporites and siliciclastics, along their flow path and mixing with organic-rich fluids, which formed during hydrocarbon maturation. Fluid flow rates vary from near stagnant to moderately fast if an external hydraulic gradient is established by regional groundwater flow systems or dewatering of shale basins. At temperatures proximal to and within the oil window (~80–120 °C), thermal maturation of organic matter (decarboxylation) and other mineral reactions occurring in situ or in shale basins introduce organic-acid, CO_2-rich brines that can lead to extensive non-fabric-specific dissolution (Montañez 1994, 1997; Machel 2005). As these fluids evolve down-flow through wholesale dissolution and pressure solution, they become saturated and precipitate Fe- and Mg-rich calcite cements and Ca-rich dolomites (Montañez 1994). Dolomite, anhydrite, and silica (chert) replacement of limestones is common in the deep-burial diagenetic realm. Exposure of evaporite-rich deposits to hydrocarbon-bearing fluids at elevated temperatures promotes thermochemical sulfate reduction, which produces significant amounts of H_2S and water and precipitation of low-Mg calcite and pyrite, and possibly saddle dolomite (Swart 2015). At temperatures <80–100 °C, bacterial sulfate reduction dominates when dissolved sulfate is exposed to hydrocarbons.

Ultimately, tectonic processes may uplift deeply buried carbonate successions and expose them to meteoric conditions. For those carbonates, which were previously stabilized and lithified in near-surface to deep-burial diagenetic zones, the extent of dissolution and cementation in this telogenetic zone (Fig. 2) will be greatly reduced. Rather, diagenesis will occur as karstification and development of fluid conduits associated with fractures and joints.

Dolomitization

The origin of dolomite, particularly early diagenetic dolomite, remains elusive despite over a century of empirical and experimental studies. This reflects that dolomite ($CaMg(CO_3)_2$) is rare in modern environments but very common in ancient carbonate successions. Furthermore, constraints on the chemical and hydrologic conditions of dolomite formation are limited and the kinetics of dolomite precipitation are poorly understood (Machel 2004). Although seawater is ~1000 times oversaturated with respect to dolomite, it rarely forms in the marine realm given the need for a source and mechanism of steady Mg^{2+} supply (Swart 2015) and mechanism to overcome kinetic inhibitors (e.g., SO_4^{2-}). Thus, dolomite precipitation (i.e., primary dolomite) and replacement of $CaCO_3$ (i.e., dolomitization) at earth surface conditions require a mechanism to raise the saturation state of dolomite and provide the necessary high fluid-rock ratios for steady Mg^{2+} supply. Highly evaporative environments (arid climate tidal flats) and refluxing of evaporatively sourced brines through shallow-water carbonates (Montañez and Read 1992a), possibly in mafic parent-material or seasonally very dry soils (Capo et al. 2000) and fluids in which the alkalinity is increased by oxidation of organic matter provide such a mechanism for "early" dolomitization (Fig. 1; Machel 2004; Swart 2015). The fluid mixing zone at the interface between the freshwater phreatic lens and underlying deep phreatic zone has been invoked as a locale of dolomite formation (Fig. 2) given that fluid mixing leads to undersaturation with respect to calcite but high supersaturation with respect to dolomite. Dolomite, however, is absent from most modern-day mixing zones and ancient examples have been contested (Machel 2004; Swart 2015). Bacterial mediation is likely involved in the precipitation of many near surface dolomites (Vasconcelos et al. 1995), in particular in highly evaporative environments and/or organic-rich deposits. Early formed dolomites are typically poorly ordered and Ca-rich

(non-stoichiometric) and volumetrically minimal. These disordered and Ca-rich dolomites undergo stepwise recrystallization throughout burial, becoming more ordered and stoichiometric with time and with exposure to dolomitizing fluids (Montañez and Read 1992b). Progressive recrystallization overprints their original geochemical signature although a memory of the primary composition can be preserved.

Extensive dolomitization, however, likely occurs in the intermediate- (100 s m) to deep-burial realm (up to 1000s of m) (Fig. 1). This reflects the elevated temperatures needed to overcome kinetic inhibitors, the very high fluid-rock ratios, the hydrologic plumbing to provide the Mg^{2+} and CO_3^{2-} supply, and the time required to produce volumetrically large (massive) dolomites (Machel 2004). Normal seawater may be capable of extensive dolomitization at slightly elevated temperatures (50–80 °C) and moderate depths (few 100 meters) in regions of large-scale thermal circulation through isolated carbonate platforms (Kohout convection). Regional or basinwide dolomitization, however, likely develops through multiple generations of dolomite replacement of limestones and precipitation of dolomite cements (Montañez 1992, 1994). Hydrologic models invoked for regional dolomitization, in addition to thermal convection, include tectonically induced flow of basinal brines, funneled compaction flow, and rapid upward advection of hydrothermal fluids along faults (summarized in Machel 2004), although the latter process is likely limited in spatial scope. Integration of stratigraphy, petrographic (textures and cathodoluminescent zoning) features, and geochemical compositions of dolomite and its fluid inclusion waters has been effectively used to unravel the paragenesis of multigeneration massive dolomites (e.g., Montañez 1994) and to reconstruct the hydrology of dolomitizing environments (studies summarized in Machel 2004; Swart 2015; and Montañez 1992, 1994). Massive dolomites (dolostones) in the subsurface tend to have higher porosities than limestones making them excellent reservoirs (Montañez 1997). Enhanced porosity is attributed to (1) a 12% porosity increase during replacement given the smaller molar volume of dolomite relative to calcite, (2) dissolution of original calcite during burial dolomitization or during subsequent migration of low pH brines, and/or (3) thermochemical sulfate reduction.

Siliciclastic (Sandstones and Mudrock) Diagenesis

The diagenesis of siliciclastic grains encompasses the full range of grain sizes found in sedimentary systems. Siliciclastic systems usually are composed of a primary population of detrital grains and primary porosity. A summary of the controls on initial composition of clastic grains may be found in Johnsson (1993). Common physical diagenetic changes in siliciclastic sediments include compaction, bioturbation, and tectonic deformation. All three of these processes may result in the rearrangement of primary grains, hence influence the porosity and permeability of the unconsolidated sediment. Compaction acts to reduce primary porosity, and may reduce both inter- and intragranular volume. Deformation may result in crushing of primary grains as well as cross-cutting fractures in lithified rocks. Chemical diagenetic changes in siliciclastic systems involve fluid-rock interaction and result in mineral precipitation, dissolution, or recrystallization. Examples include recrystallization of metastable or unstable phases, precipitation of new, authigenic phases as grain replacement or intergranular cement, and dissolution of unstable phases resulting in secondary porosity. While many cements and mineral reactions appear to result from predictable, equilibrium processes, it is common for siliciclastic sediments and rocks to be in an overall state of chemical disequilibrium due to the presence of a wide range of primary constituents and the relatively low temperatures (hence slow reaction rates) particularly during early diagenesis. Figure 1 highlights some important depth-related changes in clastic rocks. Original grain composition, increasing temperature and pressure, the hydrodynamic conditions, and the presence of reactive organic matter all play an important role in determining the extent of diagenetic modification.

Early Diagenesis

During early diagenesis, the precipitation of carbonate minerals (especially, calcite, ankerite, and siderite), quartz, and aluminosilicates such as kaolinite, smectite and illite predominate. If oxidizing conditions are encountered (as through active meteoric recharge in the near-surface (eogenetic) environment), oxides and hydroxides of iron and manganese may form as well (these include ferrihydrite, goethite, limonite, todorokite, and pyrolusite). High water throughput or excess acidity during early diagenesis may also result in selective dissolution of primary grains (especially carbonates) or alteration of lithic and feldspar grains to produce secondary porosity in addition to authigenic clays. Some primary clastic assemblages, for example, volcanic materials including glass, result in high pH conditions that foster the formation of zeolites in addition to clay minerals. An extensive theoretical treatment of early diagenesis is provided in Berner (1980).

Burial Diagenesis

During burial, shales undergo dewatering including compaction-driven expulsion and loss of water from dehydration of silicates (clay minerals). In sandstones, authigenic growth of quartz (commonly as syntaxial overgrowths on existing clean quartz grain surfaces), kaolinite (often accompanying detrital feldspar alteration), smectite, illite, and calcite dominates. At greater depths, mixed-layer clays become

more illitic and chlorite, dolomite, and ankerite are more common. Detrital feldspars alter toward more sodic compositions (albitization). The geochemistry of authigenic phases, as well as of fluid inclusions within these minerals, provides information on the burial conditions.

Novel Approaches to Studying Diagenesis

The study of carbonate diagenesis is experiencing a rejuvenation with the introduction of new visualization, geochemical proxy and modeling approaches. Although petrographic and SEM study coupled with geochemical analysis of carbonate and siliciclastic rocks have become fundamental tools for reconstructing diagenetic pathways and environments, a new suite of stable (boron, sulfur, magnesium, calcium, lithium) and radiogenic (Sr, Nd, U) isotopes are being applied to carbonates to reconstruct paleo-seawater pH, oxygenation, and temperature as well as to place constraints on past carbon, sulfur, and magnesium cycling, weathering rates, and crystallization rates. Such studies have implications for the evolution of pCO_2 and pO_2 and life-environment interactions. With the advent of better methods for determination of trace element concentrations and their isotopic compositions through applications of ICP-MS, the use of trace metals as paleo-redox and paleoproductivity proxies has led to a rich literature (Lyons et al. 2014; Tribovillard et al. 2006; Gill et al. 2011; Jones and Manning 1994). Of particular interest for diagenetic studies is clumped isotope paleothermometry (Δ_{47}), which uniquely permits independent measurements of carbonate cement precipitation temperatures in carbonate and siliciclastic sedimentary rocks and the $\delta^{18}O_{fluid}$ in which they formed. Although the application of clumped isotope thermometry to diagenetic studies is only beginning, initial results show promise for constraining diagenetic conditions and the evolution of fluid-flow conduits (Huntington et al. 2011; Budd et al. 2013). These applications of sedimentary geochemistry require assessment of separate diagenetic effects from primary signals in rocks across the broadest range of time scales. A surge in computational power over the past two decades is permitting the integration of sedimentology, petrography, geochemistry, geodynamics, and structural geology into forward modeling of the diagenetic evolution of sedimentary successions and the impact of diagenesis on their petrophysical properties and hydrologic potential (e.g., Whitaker et al. 2014; Agar and Geiger 2015).

Summary

Diagenetic modification of freshwater and marine carbonates and siliciclastic deposits by physical and chemical processes is a dynamic process that begins immediately following deposition (0–30 °C) through to the metamorphic realm (~250 °C). Sediments are converted to sedimentary rocks, and permeability and porosity develop by the integrated effects of dissolution, cementation, mineral overgrowth, neomophism, and recrystallization. The extent of diagenetic modification is governed by the original grain composition and reactivity, temperature and pressure, hydrodynamic conditions, and the presence of reactive organic matter. Bacterial mediation is an important component of carbonate and siliciclastic diagenesis.

The diagenetic cycle includes the early (eogenetic) through burial (mesogenetic) diagenetic realms as well as the telogenetic zone associated with tectonic uplift or sea-level exposure of sedimentary rocks. Although dolomite has been shown to form at Earth's surface conditions with microbial mediation, extensive dolomitization occurs in the burial realm where kinetic inhibitors are overcome and elevated temperatures and high fluid-rock ratios promote the process. Maturation of sedimentary hosted organic matter through the diagenetic cycle has produced the world's coal, oil, and gas deposits. Modern diagenetic studies are coupling new visualization, geochemical proxy, and modeling approaches with fundamental petrographic and geochemical tools in order to (1) quantitatively constrain the diagenetic history of carbonate and siliciclastic successions, (2) assess the potential of sedimentary rocks as archives of past surface conditions, and (3) reconstruct the evolution of petrophysical properties and hydrologic conduits in sedimentary units, as well as their resource potential.

Cross-References

► Fluid–Rock Interaction

References

Agar SM, Geiger S (2015) Fundamental controls on fluid flow in carbonates: current workflows to emerging technologies. In: Agar SM, Geige S (eds) Fundamental controls on fluid flow in carbonates: current workflows to emerging technologies. Geological Society of London, London, UK, no. 406. pp 1–59

Ali SA, Clark WJ, Moore WR, Dribus JR (2010) Diagenesis and reservoir quality. Oilfield Rev 22(Summer Issue):1–27

Banfield JF, Nealson KH (eds) (1997) Geomicrobiology: interactions between microbes and minerals. Reviews in mineralogy, 35. The Mineralogical Society of America, Washington, DC, 448 p

Banner JL (2004) Radiogenic isotopes: systematics and applications to earth surface processes and chemical stratigraphy. Earth Sci Rev 65:141–194

Berner RA (1980) Early diagenesis: a theoretical approach, vol 1. Princeton University Press, Princeton

Bishop JW, Montañez IP, Gulbranson EL, Brenckle PL (2009) The onset of mid-Carboniferous glacio-eustasy: sedimentologic and diagenetic constraints, Arrow Canyon, NV. Palaeogeogr Palaeoclimatol Palaeoecol 276:217–243

Brindley G, Brown G (1984) Chrystal structures of clay minerals and their X-ray identification. Mineral Soc Monogr 5:504 p
Budd DA, Frost EL III, Huntington KW, Allwardt PF (2013) Syndepositional deformation features in high-relief carbonate platforms: long-lived conduits for diagenetic fluids. J Sediment Res 83:14–38
Burley S, Kantorowicz JD, Waugh B (1985) Clastic diagenesis. Sedimentology 18:189–226
Burton EA (1993) Controls on marine carbonate cement mineralogy: review and reassessment. Chem Geol 105:163–179
Capezzuoli E, Gandin A, Pedley M (2014) Decoding tufa and travertine (fresh water carbonates) in the sedimentary record: the state of the art. Sedimentology 61:1–21
Capo RC, Whipkey CE, Blachere JR, Chadwick O (2000) Pedogenic origin of dolomite in a basaltic weathering profile, Kohala Peninsula, Hawaii. Geology 28:271–274
Choquette PW, Pray LC (1970) Geologic nomenclature and classification of porosity in sedimentary carbonates. Bull Am Assoc Pet Geol 54:207–250
de Segonzac DG (1968) The birth and development of the concept of diagenesis (1866–1966). Earth Sci Rev 4:153–201
Fairbridge RW (1967) Phases of diagenesis and authigenesis. In: Larsen G, Chilinger GV (eds) Diagenesis in sediments. Elsevier, Amsterdam, pp 19–89
Fantle MS, Maher KM, DePaolo DJ (2010) Isotopic approaches for quantifying the rates of marine burial diagenesis. Rev Geophys 48:1–48
Ford ND, Pedley HM (1996) A review of tufa and travertine deposits of the world. Earth Sci Rev 41:117–175
Gill BC, Lyons TW, Young SA, Kump LR, Knoll AH, Saltzman MR (2011) Geochemical evidence for widespread euxinia in the later Cambrian ocean. Nature 469:80–83
Harrison W, Thyne G (1992) Predictions of diagenetic reactions in the presence of organic acids. Geochim Cosmochim Acta 56:565–586
Humphries DW (1992) The preparation of thin sections of rocks, minerals, and ceramics. Oxford University Press, Oxford, 83 p
Huntington KW, Budd DA, Wernicke BP, Eiler JM (2011) Use of clumped-isotope thermometry to constrain the crystallization temperature of diagenetic calcite. J Sediment Res 81:656–669
James NP, Choquette PW (1990) Limestones – the meteoric diagenetic environment. In: McIlreath IA, Morrow DA (eds) Diagenesis reprint series 4. Geoscience Canada, Geological Association of Canada, St. John's, NL A1B 3X5 Canada, pp 35–73
Johnsson MJ (1993) The system controlling the composition of clastic sediments. Geol Soc Am Spec Pap 284:1–20
Jones B, Manning DA (1994) Comparison of geochemical indices used for the interpretation of palaeoredox conditions in ancient mudstones. Chem Geol 111:111–129
Larsen G, Chilingar GV (eds) (1983) Diagenesis in sediments and sedimentary rocks, 2. Developments in sedimentology 25B. Elsevier, Amsterdam, 563 p
Lyons TW, Reinhard CT, Planavsky NJ (2014) The rise of oxygen in earth's early ocean and atmosphere. Nature 506:307–315
Machel HG (2004) Concepts and models of dolomitization: a critical reappraisal. In: Braithwaite CJR, Rizzi G, Darke G (eds) The geometry and petrogenesis of dolomite reservoirs. Geological Society of London, London, no. 235. pp 7–63
Machel HG (2005) Investigations of burial diagenesis in carbonate hydrocarbon reservoir rocks. Geosci Can 32:103–128
Montañez IP (1992) Controls of eustasy and associated diagenesis on reservoir heterogeneity in Lower ordovician, upper knox carbonates, appalachians. In: Candelaria MP, Reed CA (eds) Paleokarst, karst related diagenesis, and reservoir development: examples from ordovician-devonian age Strata of West Texas and the Mid-Continent, Permian basin section SEPM special publication, SEPM (Society for Sedimentary Geology), Tulsa, OK no. 92-33. pp 165–181
Montañez IP (1994) Late diagenetic dolomitization of Lower Ordovician Upper Knox Carbonates: a record of the hydrodynamic evolution of the southern Appalachian Basin. Am Assoc Pet Geol Bull 78:1210–1239
Montañez IP (1997) Secondary porosity and late diagenetic cements of the Upper Knox Group, central Tennessee region: a temporal and spatial history of fluid flow conduit development within the Knox regional aquifer. In: Montañez IP, Gregg JM, Shelton K (eds) Basinwide fluid flow and associated diagenetic patterns: integrated petrologic, geochemical and hydrologic considerations, SEPM special publication, no. 57. pp 101–117
Montañez IP, Read JF (1992a) Eustatic control on early dolomitization of cyclic peritidal carbonates: evidence from the early ordovician upper knox group. Appalachians Geol Soc Amer Bull 104:872–886
Montañez IP, Read JF (1992b) Fluid-rock interaction history during stabilization of early dolomites of the upper knox group (early ordovician). Appalachians J Sediment Petrol 62:753–778
Moore CH (1989) Carbonate diagenesis; porosity evolution and diagenesis in a sequence stratigraphic framework, Developments in sedimentology, vol 46. Elsevier, Amsterdam, 321 p
Moore DM, Reynolds RC (1989) X-ray diffraction and the identification and analysis of clay minerals 378. Oxford University Press, Oxford
Nelson WA, Read JF (1990) Updip to downdip cementation and dolomitization patterns in a Mississippian aquifer. Appalachians J Sediment Petrol 60:379–396
Newman ACD (1987) Chemistry of clays and clay minerals, Mineralogical society monograph, vol 6. Wiley, New York, 480 p
Niemann JC, Read JF (1988) Regional cementation from unconformity-recharged aquifer and burial fluids, Mississippian Newman Limestone, Kentucky. J Sediment Petrol 58:688–705
Rasbury ET, Hemming S, Riggs N (2012) Mineralogical and geochemical approaches to provenance. Geological Society of America special paper 487
Read JF, Horbury AD (1993) Eustatic and tectonic controls on porosity evolution beneath sequence-bounding unconformities and parasequence disconformities on carbonate platforms. In: Horbury AD, Robinson AG (eds) Diagenesis and basin development: studies in geology, vol #36. American Association of Petroleum Geologists, Tulsa, pp 155–197
Sharp Z (2007) Principles of stable isotope geochemistry. Pearson Education, Upper Saddle River, 344 p
Stern RA (2009) Introduction to secondary ion mass spectrometry (SIMS) in geology. In: Fayek M (ed) Secondary ion mass spectrometry in the earth sciences, Mineral. Association of Canada, Short Course Series, 41, pp 1–18
Surdam RC, Crossey LC (1987) Integrated diagenetic modeling: a process-oriented approach for clastic systems. Annual Rev Earth Planet Sci 15:141–170
Surdam RC, Crossey LJ, Hagen ES, Heasler HP (1989) Organic-inorganic interactions and sandstone diagenesis. Amer Assoc Petrol Geol Bull 73:1–23
Swart PK (2015) The geochemistry of carbonate diagenesis: the past, present and future. Sedimentology 62:1233–1304
Tribovillard N, Algeo TJ, Lyons T, Riboulleau A (2006) Trace metals as paleoredox and paleoproductivity proxies: an update. Chem Geol 232:12–32
Vasconcelos C, McKenzie JA, Bernasconi S, Grujic D, Tien AJ (1995) Microbial mediation as a possible mechanism for natural dolomite formation at low temperatures. Nature 377:220–222
Walter LM (1985) Relative reactivity of skeletal carbonates during dissolution: implications for diagenesis. In: Schneidermann N, Harris PM (eds) Carbonate cements. SEPM special publication, no. 36. Tulsa, pp 3–16
Whitaker FF, Felce GP, Benson GS, Amour F, Mutti M, Smart PL (2014) Simulating flow through forward sediment model stratigraphies: insights into climatic control of reservoir quality in isolated carbonate platforms. Pet Geosci 20:27–40

Diffusion

Yan Liang
Department of Earth, Environmental and Planetary Sciences, Brown University, Providence, RI, USA

Definition

Diffusion arises from random motions of particles in a fluid or solid. Here the particles can be neutral molecules or atoms, or charged cations or anions. The particle that diffuses through a medium or substance is called diffusant. Diffusion is a microscopic kinetic phenomenon that results in intermingling and homogenization of the chemical components in a substance. It is part of the mixing process that is not accounted for by the bulk flow or advection of the chemical system. The word "diffusion" originates from the Latin word "diffundere" which means to pour out or spread out.

Fick's Laws of Diffusion

The spreading of diffusant in a medium can be quantified by applying the laws of diffusion which are established through observations of natural phenomenon and laboratory diffusion experiments. During diffusion, random motions of the particles in a chemically heterogeneous phase will redistribute its constituent from regions of high concentration to low concentration, which eventually leads to homogenization of the phase. The amount of materials that move perpendicular through a unit cross-section area by diffusion or random motions of the particles in the medium is called diffusive flux. According to Fick's first law of diffusion, the diffusive flux for a component of interest, $\mathbf{J_i}$, is proportional to the concentration gradient of the component in the system. For one-dimensional diffusion, this can be written as

$$\mathbf{J_i} = -D_i \frac{\partial c_i}{\partial x}, \tag{1}$$

where D_i is the diffusion coefficient or diffusivity of component i; c_i is the concentration of component i; and $\partial c_i/\partial x$ is the concentration gradient of component i along the x direction. The diffusive flux has the units of mass per unit area per unit time. The concentration has the units of mass per unit volume. The diffusion coefficient has the units of length-squared per unit time, for example, $m^2\ s^{-1}$. The diffusive flux is a vector (along x direction in this case) and the negative sign in Eq. 1 is to ensure that material diffuses from regions of high concentration to low concentration, that is, along the direction of decreasing concentration gradient.

Fick's first law of diffusion was postulated by Adolf Fick in 1855, drawing on the analogy between the spreading of a solute in a solvent to Fourier's law for the diffusion of heat by conduction and Ohm's law for the flow of electric current in a conductor (Tyrrell 1964; Narasimhan 2004). It was based on observations of diffusion in a binary solution (salt and water in Fick's case). The term interdiffusion has also been used to describe diffusion in a binary liquid or solid (e.g., diffusion of salt in water or Fe-Mg diffusion in olivine). The diffusion coefficient obtained from a binary diffusion experiment is called the interdiffusion coefficient. Fick's first law has been used to define the diffusion coefficient and to study steady-state diffusion along a concentration gradient.

Fick's second law of diffusion is a statement of mass conservation for diffusive mass transfer in a medium. In one dimension, the diffusion equation can be written as

$$\frac{\partial c_i}{\partial t} = \frac{\partial}{\partial x}\left(D_i \frac{\partial c_i}{\partial x}\right), \tag{2}$$

where t is the diffusion time. When density variation in the system is small, the concentration in Eq. 2 can be replaced by the weight or molar fraction. This practice has been routinely used in studies of diffusion in silicate melts and crystals. When the diffusion coefficient is independent of concentration or spatial coordinate, the diffusion equation takes on the simple expression:

$$\frac{\partial c_i}{\partial t} = D_i \frac{\partial^2 c_i}{\partial x^2}. \tag{3}$$

For diffusion in three-dimensional isotropic media, the diffusion equation takes on the more general form in a Cartesian coordinate:

$$\frac{\partial c_i}{\partial t} = D_i\left(\frac{\partial^2 c_i}{\partial x^2} + \frac{\partial^2 c_i}{\partial y^2} + \frac{\partial^2 c_i}{\partial z^2}\right) = D_i \nabla^2 c_i, \tag{4}$$

where ∇^2 is the Laplacian operator. For diffusion in an axisymmetric sphere, the diffusion equation takes on the special form:

$$\frac{\partial c_i}{\partial t} = D_i\left(\frac{\partial^2 c_i}{\partial r^2} + \frac{2}{r}\frac{\partial c_i}{\partial r}\right), \tag{5}$$

where r is the radial coordinate. Equation 5 can be used to model diffusion in and around mineral grains and fluid or melt inclusions. Equations 2, 3, 4, and 5 are partial differential equations. Their solutions depend on the initial and boundary conditions. Analytical solutions to Eqs. 3, 4, 5, and 6 subject to various initial and boundary conditions can be found in the treatise *The Mathematics of Diffusion* (Crank 1975). For a variable diffusion coefficient, the diffusion

equation can be solved numerically using a finite difference method (Crank 1975).

Fick's laws of diffusion were originally developed for diffusion in fluids. These laws are directly applicable to diffusion in isotropic media such as melts, glasses, and minerals of isometric crystal system. The diffusion coefficient in an isotropic medium is independent of direction or orientation and can be treated as a scalar. For diffusion in anisotropic media, such as minerals of crystal systems other than isometric, the diffusion coefficient will depend on the direction of diffusion in the crystals. Diffusivities measured along different directions in the crystal may be different depending on the symmetry of the crystal. For example, for oxygen diffusion in quartz, Giletti and Yund (1984) found that diffusivities of oxygen parallel and perpendicular to the c axis of quartz differ by two orders of magnitude. Diffusion modeling in such systems may be simplified by using two diffusivities in the cylindrical coordinate:

$$\frac{\partial c_i}{\partial t} = D_{\perp c}\left(\frac{\partial^2 c_i}{\partial r^2} + \frac{1}{r}\frac{\partial c_i}{\partial r}\right) + D_{\parallel c}\frac{\partial^2 c_i}{\partial z^2}, \tag{6}$$

where $D_{\perp c}$ and $D_{\parallel c}$ are diffusivities perpendicular and parallel to the c axis of quartz. Equation 6 can be used to model diffusion in hexagonal, tetragonal, and trigonal crystal systems. For diffusion in orthorhombic crystal systems, diffusion coefficients measured along three orthogonal directions are needed to completely describe a diffusive flux. Shea et al. (2015) presented an example of three-dimensional numerical modeling of anisotropic Fe-Mg diffusion in olivine, which is a mineral in the orthorhombic crystal system. In general, a full description of the direction-dependent diffusivity for diffusion in anisotropic media requires a symmetric second order tensor (Nye 1985). In practice, due to the lack of sufficient diffusion data and complicated geometry of the crystals, simplifications are made in diffusion modeling of anisotropic minerals, for example, by using Eq. 2 or 5 with a single diffusion coefficient (Zhang 2010; Shea et al. 2015). A list of diffusion tensors for different crystal systems can be found in Nye (1985) and Zhang (2010).

Types of Diffusion

Depending on the chemical state of the system, the nature of the diffusants, the initial and boundary conditions, and simplifications involved, several types of diffusion can be identified: self diffusion, chemical diffusion, multicomponent diffusion, effective binary diffusion, thermal diffusion, and grain boundary diffusion.

Self diffusion or tracer diffusion takes place when the system of interest is at chemical, but not isotopic, equilibrium. There is no concentration or chemical potential gradient of any elements in the system. Self diffusivity of an element or component is determined by labeling some of the atoms in the diffusant using isotopic tracers, hence the name tracer diffusion. For example, to determine the self diffusivity of Mg in an olivine crystal, one can deposit a thin layer of ^{26}Mg-spiked olivine on the surface of the crystal and follow the spread of ^{26}Mg in the olivine grain.

Chemical diffusion or multicomponent diffusion takes place when the system of interest is out of chemical equilibrium. Many geological systems are made of two or more components. A silicate magma, for example, typically has seven or more major oxide components. Diffusion in such systems is referred to as multicomponent diffusion or chemical diffusion. During chemical diffusion, the concentration gradient of one component may affect the diffusive flux of another component. Lars Onsager generalized Fick's laws of diffusion in binary fluids to multicomponent systems by considering the rate of entropy production which can be written as a sum of scalar products between diffusive fluxes and driving forces for diffusion (e.g., de Groot and Mazur 1962; Hasse 1969). The driving force for chemical diffusion at a constant temperature and pressure is the chemical potential gradient. Since chemical potential of a component in a multicomponent substance (μ_i) is a function of temperature, pressure, and concentration, it is convenient to express diffusive fluxes in terms of concentration gradients of the components in the system. For a binary fluid, for example, Fick's first law can be written as

$$\mathbf{J_i} = -L_i\frac{\partial \mu_i}{\partial x} = -\left(L_i\frac{\partial \mu_i}{\partial c_i}\right)\frac{\partial c_i}{\partial x}, \tag{7}$$

where L_i is the phenomenological coefficient for diffusion. The term in the parentheses is identified as the diffusion coefficient. According to Onsager (1945), the diffusive flux of a given component in a multicomponent liquid can be expressed as a linear combination of concentration gradients of the independent components in the system. In a volume-fixed frame of reference, the one-dimensional diffusive flux of component i in an n component fluid or melt at constant temperature and pressure is given by (Onsager 1945):

$$\mathbf{J_i} = -\sum_{j=1}^{n-1} D_{ij}\frac{\partial c_j}{\partial x}, \tag{8}$$

where D_{ij} are elements of an $(n-1)$ by $(n-1)$ diffusion matrix with component n taken as the dependent variable. The index i in Eq. 8 takes on integers $1, 2, \ldots, n-1$. The diffusive flux of the dependent component n is constrained by the requirement of total flux conservation. The latter depends on the choice of reference frame. An important property of the diffusion matrix is that its eigenvalues are positive, which is

a prerequisite for stable solutions of the diffusion equations. For a ternary system, there are two independent components. The diffusion equations for the independent components 1 and 2 are

$$\frac{\partial c_1}{\partial t} = D_{11}\frac{\partial^2 c_1}{\partial x^2} + D_{12}\frac{\partial^2 c_2}{\partial x^2}, \tag{9a}$$

$$\frac{\partial c_2}{\partial t} = D_{21}\frac{\partial^2 c_1}{\partial x^2} + D_{22}\frac{\partial^2 c_2}{\partial x^2}, \tag{9b}$$

where D_{11} and D_{22} are the diagonal terms and D_{12} and D_{21} are the off-diagonal terms of the 2 × 2 diffusion matrix. For diffusion in an n component system, the diffusion equation for component i is

$$\frac{\partial c_i}{\partial t} = \sum_{j=1}^{n-1} D_{ij}\frac{\partial^2 c_j}{\partial x^2}. \tag{10}$$

Equations 9 and 10 are coupled diffusion equations because of the presence of the off-diagonal terms. A peculiar consequence of coupled diffusion is uphill diffusion, which happens when the spreading direction of a diffusant is in the opposite direction of its own concentration gradient (i.e., the diffusant can migrate from regions of low concentration to high concentration). Uphill diffusion is a transient phenomenon. It occurs when the net diffusive flux produced by concentration gradients of all other components in Eq. 10 is larger than and has the opposite sign relative to the diffusive flux produced by the concentration gradient of the component of interest. Examples of uphill diffusion in molten silicates can be found in Zhang et al. (1989), Watson and Baker (1991), Liang et al. (1996), Richter et al. (1998), and Guo and Zhang (2016). When elements of the diffusion matrix are constant and uniform, analytical solutions to the coupled diffusion equations can be constructed from solutions to the equivalent binary cases using the method of linear transformation (Toor 1964; Gupta and Cooper 1971). Exact solutions for multicomponent diffusion in ternary systems were derived by Fujita and Gosting (1956) and Kirkaldy (1958) for one-dimensional semi-infinite diffusion couples. A recent summary with additional examples can be found in Liang (2010).

Numerical values of the diffusion matrix depend on the choice of the dependent variable, units of concentration, and the frame of reference for the diffusive fluxes. The volume-fixed frame of reference is most suitable for studying chemical diffusion in the laboratory. For diffusive mass transfer in geological systems, mass-fixed frame of reference is most convenient. The difference between the two frames of reference is whether the sum of the volume fluxes or the mass fluxes is set to zero. For a general treatment of multicomponent diffusion, including coordinate transformation, the reader is referred to the textbooks or monographs by de Groot and Mazur (1962), Katchalsky and Curran (1967), Hasse (1969), Tyrrell and Harris (1984), Miller et al. (1986), Kirkaldy and Young (1987), and Kondepudi and Prigogine (1998). Relevant reviews or summaries in the geochemical literature include Anderson (1981), Lasaga (1998), and Liang (2010).

Effective binary diffusion is a simplified treatment of chemical diffusion in multicomponent fluids or solids. Here the multicomponent system is treated as a pseudo-binary system in which the component of interest is taken as the independent variable and all other components are taken together as the dependent variable (Cooper 1968). The diffusive flux of the component of interest (i) is assumed to follow a relation similar to Fick's first law of diffusion for binary fluids,

$$\mathbf{J_i} = -D_i^E\frac{\partial c_i}{\partial x}, \tag{11}$$

where D_i^E is the effective binary diffusion coefficient of component i. The diffusive flux defined by Eq. 11 is equivalent to that defined by Eq. 8 if the effective binary diffusion coefficient is given by (Cooper 1968):

$$D_i^E = \sum_{j=1}^{n-1} D_{ij}\frac{\partial c_j}{\partial c_i}. \tag{12}$$

Most diffusion coefficients for chemical diffusion in fluids, melts, and crystals reported in the geochemical literature were obtained using the effective binary approximation (see reviews by Watson and Baker 1991; Zhang et al. 2010). Unlike the diffusion matrix for a multicomponent system, the effective binary diffusion coefficients depend on the direction of diffusion in composition space, that is, they are sensitive to the specific diffusion experiments from which they are derived. This is shown by the composition derivatives in Eq. 12 and verified by many laboratory studies of chemical diffusion in molten silicates. For diffusion in a confined system or finite geometry, $\partial c_j/\partial c_i$ in Eq. 12 may change its sign during diffusion (Watson and Baker 1991; Liang 2010), and the effective binary diffusion coefficient may also vary as a function of time. Since D_i^E must be positive for the diffusion equation to be stable, Eq. 11 cannot be used to model uphill diffusion without additional assumptions (Richter 1993; Zhang 1993). For a detailed discussion on the usefulness and limitations of effective binary diffusion and its relation to multicomponent diffusion, the reader is referred to Cooper (1968), Liang (2010), and Zhang (2010).

Relationship between self diffusion and chemical diffusion Self diffusivity is a measure of the intrinsic mobility of the diffusing species. In the presence of chemical potential or

concentration gradient in a binary system, the intrinsic diffusivity for component 1 (D_1^I) is related to the self diffusivity of component 1 (D_1) through the expression

$$D_1^I = \left(1 + \frac{d\ln\gamma_1}{d\ln X_1}\right) D_1, \tag{13}$$

where γ_1 is the activity coefficient and X_1 is the molar fraction of component 1 in the binary system. The term in the parentheses is called the thermodynamic factor, which is identical to that for component 2 in the binary system. For chemical diffusion in a simple binary fluid or solid, the interdiffusion coefficient ($\tilde{D}$) is related to the intrinsic diffusion coefficients of the two components through Darken's equation

$$\tilde{D} = X_2 D_1^I + X_1 D_2^I = (X_2 D_1 + X_1 D_2)\left(1 + \frac{d\ln\gamma_1}{d\ln X_1}\right). \tag{14}$$

A comparable expression for interdiffusion of two counter ion species in a binary crystal or fluid is given by the expression (Helfferich and Plesset 1958; Barrer et al. 1963):

$$\tilde{D} = \frac{D_1 D_2 (X_1 Z_1^2 + X_2 Z_2^2)}{D_1 X_1 Z_1^2 + D_2 X_2 Z_2^2}\left(1 + \frac{d\ln\gamma_1}{d\ln X_1}\right), \tag{15}$$

where Z_1 and Z_2 are charge numbers of the two ions. When the abundance of component 1 is much smaller than that of component 2 ($X_1 << X_2$), the interdiffusion coefficient in Eq. 14 or 15 is mostly determined by the self diffusivity of component 1. Generalizations of Eqs. 14 and 15 to multicomponent geological fluids or solids can be found in Cooper (1965), Lasaga (1979), and Liang et al. (1997). In all cases, the diffusion matrix can be written as a product of a kinetic matrix and a thermodynamic matrix. Elements of the kinetic matrix are functions of self diffusivities of the components in the system, while elements of the thermodynamic matrix depend on activity-composition relationships of the components. Darken's equation and its generalizations have been used to study chemical diffusion in molten silicates and selected minerals (Chakraborty 2010; Ganguly 2010; Liang 2010).

Thermal diffusion is a general case of chemical diffusion in that the flow of heat drives a flow of matter. This transport phenomenon is often referred to as the "Soret effect" after the Swiss chemist Charles Soret. The driving force for thermal diffusion involves temperature gradient. For a multicomponent fluid, the diffusive flux for an independent component takes on a more general form (e.g., de Groot and Mazur 1962; Hasse 1969). With concentration in mass fraction, the diffusive flux for component 1 in a binary fluid is written as the sum of two parts – one proportional to the concentration gradient and the other proportional to the temperature gradient:

$$\mathbf{J}_1 = -\rho D_1 \left[\frac{\partial w_1}{\partial x} + S_T w_1 (1 - w_1)\frac{\partial T}{\partial x}\right], \tag{16}$$

where ρ is the density of the fluid; w_1 is the mass fraction of component 1 in the fluid; D_1 is the diffusion coefficient of component 1; and S_T is the Soret coefficient. The product $D_1 S_T$ is called the thermal diffusion coefficient, designated as D_T. The Soret coefficient or thermal diffusion coefficient can be either positive or negative, depending on the response of the component to the imposed temperature gradient. While the concentration gradient serves to homogenize a fluid, the presence of a temperature gradient across the fluid can result in mass separation. This is a key difference between thermal diffusion and chemical diffusion and can be demonstrated by setting the diffusive flux to steady state (i.e., $\mathbf{J}_1 = 0$ in a confined system). Equation 16 then is reduced to

$$\frac{dw_1}{dT} = -w_1(1 - w_1)S_T. \tag{17}$$

For steady-state thermal diffusion across molten silicates, it has been observed in the laboratory that SiO_2, Na_2O, and K_2O migrate towards the hot end (negative S_T), whereas CaO, MgO, FeO, and TiO_2 concentrate towards the cold end (positive S_T) of diffusion charges (Walker et al. 1981; Lesher 1986; Richter et al. 2009).

Grain boundary diffusion is a general case of diffusion in crystalline solids in which the boundaries between neighboring grains and dislocation pipes within the crystals serve as fast-pathways or short-circuits for the spreading of diffusant. Diffusion in polycrystalline materials is multipath and consists of both lattice diffusion (also called volume diffusion) and grain boundary diffusion. The mathematical treatment of diffusion in polycrystalline materials generally requires two independent diffusivities, one for diffusion in the crystal lattice and the other for diffusion along grain boundaries or dislocation pipes (Fisher 1951; Whipple 1954; Suzuoka 1961; Le Claire 1963). The structure of grain boundaries are relatively open compared to the structure of the crystal lattice. Diffusion along grain boundaries is typically orders of magnitude faster than diffusion within the crystal lattice. The grain boundary diffusivity is comparable to the diffusivity in the melt as the temperature approaches the melting temperature of the solid (Mishin et al. 1997). During diffusion, a particle may spend some fraction of time in the crystal lattice and the rest of the time in the grain boundary, wandering back and forth between the lattice and the grain boundary. Depending on their relative contributions to the bulk or net transport of diffusants through the polycrystalline material, three types or regimes of grain boundary diffusion are identified in the absence of grain boundary migration (Harrison 1961): A, B, and C. Types A and C are endmember cases in which volume diffusion is either dominant or insignificant, respectively,

whereas Type B is the intermediate regime and also the most complicated case of grain boundary diffusion. Type C diffusion happens when the diffusion time is too short for appreciable contribution of lattice diffusion, and the net mass transport of diffusants through the polycrystals can be solely accounted for by diffusion along grain boundaries. Type A diffusion is dominant when the diffusion time is long and the volume diffusivity (D_L) is large such that the diffusion length in the solid is much larger than the average grain size (d), that is,

$$\sqrt{D_L t} >> d. \tag{18}$$

The bulk diffusive flux in the polycrystalline material can be modeled by Fick's first law of diffusion (Eq. 1) with an effective diffusion coefficient (D_{eff}) that is a weighted average of diffusivities for the lattice and grain boundary diffusion (Hart 1957):

$$D_{eff} = f_{gb} D_{gb} + \left(1 - f_{gb}\right) D_L, \tag{19}$$

where D_{gb} is the grain boundary diffusivity; f_{gb} is the volume fraction of grain boundaries in the polycrystals. f_{gb} is proportional to the ratio between the grain boundary width and the average grain size. The boundary width is reasoned to be very small, on the order of several interatomic distances. Hence, grain boundary diffusion is more effective for diffusive mass transfer in fine-grained solids (larger f_{gb}) at low temperatures (smaller D_L). Type B regime is observed when significant concentration zoning is present in the crystals. The diffusion length in the crystal is smaller than the grain size. Depending on temperature, diffusion time, and grain size, the three regimes of grain boundary diffusion may coexist in different parts of a system. During grain growth or recrystallization, grain boundaries migrate in polycrystalline solids. The classification of grain boundary diffusion also depends on the grain boundary migration velocity. For additional reading on grain boundary diffusion, including mathematical treatment and summary of diffusion data in silicate and oxide minerals, the reader is referred to the review articles by Joesten (1991), Mishin et al. (1997), Watson and Baxter (2007), and Dohmen and Milke (2010).

Diffusion Coefficients

Diffusion is a thermally activated process. In general, both self diffusion and chemical diffusion coefficients in a substance or medium vary systematically with temperature, pressure, and composition. For a given composition, the diffusion coefficient of a component (D) in the medium follows the Arrhenius equation:

$$D = D_0 \exp\left(-\frac{E_a + PV_a}{RT}\right), \tag{20}$$

where D_0 is the pre-exponential factor for diffusion (in $m^2\ s^{-1}$); E_a is the activation energy for diffusion (in J mol^{-1}); V_a is the activation volume for diffusion (in $m^3\ mol^{-1}$); T is the temperature (in K); P is the pressure (in Pa); and R is the gas constant (8.314 J $mol^{-1}\ K^{-1}$). D_0 is related to the vibration frequency and jumping distance of the diffusing species in the medium. The sum $E_a + PV_a$ in the Arrhenius equation is called the activation enthalpy for diffusion (H_a). The linearized version of the Arrhenius equation can be used to determine the diffusion parameters (D_0, E_a, and V_a):

$$\ln D = \ln D_0 - \frac{E_a + PV_a}{RT}. \tag{21}$$

A set of diffusion coefficients of a component in the medium measured at a constant pressure but different temperatures generally defines a straight line in the plot of ln D against the reciprocal of the temperature (Fig. 1). Such a diagram is referred to as the Arrhenius plot or Arrhenius diagram. The intercept of the line is ln D_0 and the slope of the line in the Arrhenius plot is $-H_a/R$. The larger the activation energy for diffusion, the stronger the dependence of diffusion on temperature. The activation enthalpy obtained through a set of

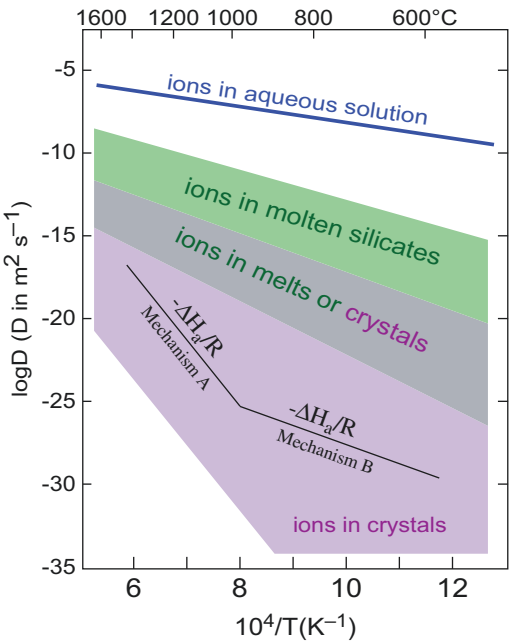

Diffusion, Fig. 1 Arrhenius plot illustrating the ranges of diffusivities of various cations and anions in aqueous solutions, molten silicates, and crystals. The change in the slope in this diagram may indicate a change in diffusion mechanism (A vs. B) (Modified from Watson and Baxter (2007) by E. Bruce Watson)

diffusion data collected at a constant pressure is often called the activation energy in the literature, which may cause confusion. Care should be exercised when comparing activation energies measured at different pressures. Deviation from the straight line in the Arrhenius plot, such as a change in the slope (black lines in Fig. 1), often suggests either a change in diffusion mechanism or inaccurate diffusion data. A family of straight lines is established in the Arrhenius plot if diffusion coefficients are measured over a range of pressures and temperatures. A comprehensive compilation of diffusivities and diffusion parameters for self diffusion and chemical diffusion of cations, anions, volatile species, and noble gases in silicate melts and crystals can be found in the monograph *Diffusion in Minerals and Melts* (Zhang and Cherniak 2010). A few first order features are highlighted below.

Depending on physical state of the substance and diffusing species, values of activation energy for diffusion in earth and planetary materials vary greatly. In general, diffusivities of ions (cations and anions) in aqueous solutions are considerably larger than those in molten silicates which, in turn, are larger than those in silicate or oxide minerals. Activation energies for diffusion in the minerals are generally larger than those for diffusion in the melts with which the minerals may reside (e.g., olivine and pyroxene vs. basalts, feldspars vs. rhyolites). Figure 1 is from Watson and Baxter (2007) and illustrates the enormous ranges of diffusivity and activation enthalpy for diffusion of cations and anions in geological fluids, melts, and minerals, from ~40 kJ mol^{-1} for interdiffusion in supercritical aqueous solution (Wark and Watson 2004) up to ~800 kJ mol^{-1} for tetravalent Hf diffusion in zircon (Cherniak et al. 1997a). Figure 2 highlights both the complexity and systematics of the Arrhenius relations for monovalent (H, Li, Na, and K), divalent (Ca and O), tetravalent (Ti and Si) ions and molecules (H_2O and Ar) in quartz under nominally anhydrous conditions. The general trends of increasing activation energy and decreasing diffusivity with increasing ionic charge and size are also observed for diffusion in other minerals and silicate melts, although exceptions are abundant. For example, diffusivities of trivalent REE in diopside and zircon vary systematically as a function of ionic radius (Cherniak et al. 1997b; Van Orman et al. 2001), whereas diffusivities of REE in enstatite and plagioclase appear to be insensitive to the size of REE (Cherniak 2003; Cherniak and Liang 2007).

Few studies have focused on the effect of pressure on cation diffusion in minerals and melts, as pressure has a negligible effect on diffusion under crustal conditions. However, pressure may play an important role in modulating diffusion rate under mantle conditions. For example, diffusivities of network-forming cations, such as Si and Al, in

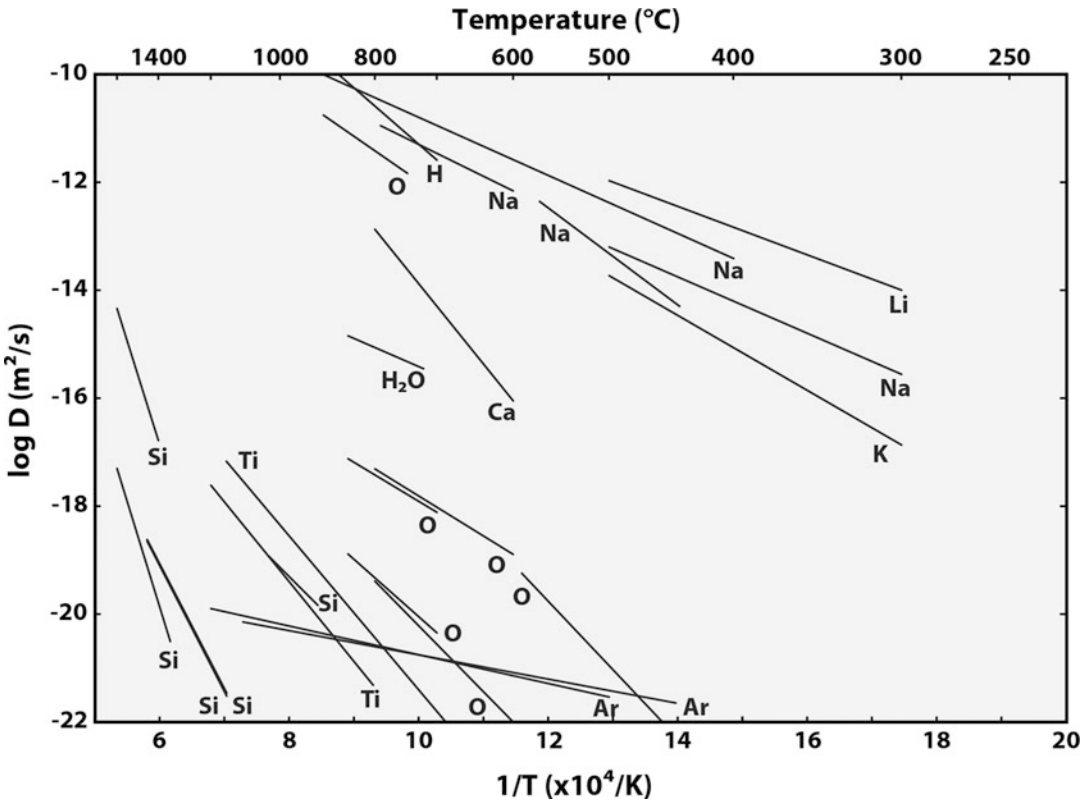

Diffusion, Fig. 2 Diagram summarizing Arrhenius relations for diffusion of various cations, anions (oxygen), and Ar in quartz under nominally anhydrous conditions (Adapted from Brady and Cherniak 2010)

highly polymerized melts increase with the increase of pressure (an apparent negative activation volume), which are attributed to changes in the melt structure with pressure (Kushiro 1983; Poe et al. 1997). Activation volumes (V_a) for cation diffusion in minerals are generally positive and range from less than 10^{-6} m^3 mol^{-1} to 20×10^{-6} m^3 mol^{-1} (Béjina et al. 2003; Chakraborty 2010). At 1200 °C, trivalent REE diffusivities in diopside (V_a ~10×10^{-6} m^3 mol^{-1}, Van Orman et al. 2001) and garnet ($V_a = 10 \times 10^{-6}$ to 20×10^{-6} m^3 mol^{-1}, Van Orman et al. 2002; Carlson 2012; Bloch et al. 2015) decrease by one and two orders of magnitude, respectively, when the pressure is increased from 1 to 4 GPa. The diffusion of divalent cations (Fe-Mg, Mn, and Ni) in garnet and olivine depends moderately on pressure ($V_a = 4\sim8 \times 10^{-6}$ m^3 mol^{-1}, Béjina et al. 2003; Holzapfel et al. 2007; Chakraborty 2010). Since diffusion coefficients decrease with the decrease of temperature and the increase of pressure, simultaneous changes in temperature and pressure along a geotherm can significantly reduce temperature-induced variations in diffusivity (Holzapfel et al. 2007; Watson and Baxter 2007; Liang 2017). Holzapfel et al. (2007) gave an example of Fe-Mg diffusion in olivine along a *P-T* path in the upper mantle. According to their calculation, the diffusivity of Fe-Mg in olivine increases from ~10^{-25} to 10^{-15} m^2 s^{-1} in the lithosphere (50–150 km depth) and then decreases gradually through the asthenosphere. Near the bottom of the upper mantle (400 km) the Fe-Mg diffusion coefficient is reduced to 10^{-16} m^2 s^{-1}. Without the competing effect of pressure, the Fe-Mg diffusivity in olivine would monotonically increase in the asthenospheric part of the upper mantle. Similar variations in diffusivity with depth are also expected for cation diffusion in other mantle minerals (Watson and Baxter 2007).

Diffusion in oxides and silicate crystals depends on diffusion mechanism and defect chemistry (Watson and Baxter 2007; Chakraborty 2008, 2010; Cherniak and Dimanov 2010; Van Orman and Crispin 2010). The mechanisms of diffusion in minerals are complicated and still not well understood in many cases. Because natural minerals typically are solid solutions and contain vacancies and impurities of various sizes and valences, diffusion of an ion in a mineral may take more than one mechanism. For the same ion, its diffusion mechanism in one mineral may not necessarily be the same as in another mineral. For example, Li diffusion in olivine follows two pathways: a fast path through interstitial sites and a slow path through octahedral sites in olivine (Dohmen et al. 2010), whereas Li diffusion in zircon appears to follow one mechanism (Cherniak and Watson 2010; Trail et al. 2016). When vacancies are involved, diffusion in minerals can be broadly divided into two regimes: a high temperature or intrinsic regime where diffusivity is proportional to vacancy abundance in the minerals, and a low temperature or extrinsic regime where the vacancy abundance is low and does not contribute significantly to the overall diffusion. For Fe-bearing minerals, vacancy abundance is sensitive to oxygen fugacity. Measured diffusivities then depend on oxygen fugacity (e.g., Fe-Mg diffusion in olivine, Chakraborty 2010). The activation enthalpy for diffusion in the intrinsic regime is higher than that for diffusion in the extrinsic regime. The two regimes of diffusion are illustrated as mechanisms A and B in Fig. 1. Diffusion in minerals also depends on mineral composition. Cation diffusion in feldspars, for example, is very sensitive to feldspar compositions: Mg, Pb, Sr, and Nd diffusivities in anorthite are one to two orders of magnitude smaller than those in oligoclase (Giletti and Casserly 1994; Cherniak and Watson 1994; Cherniak 1995, 2003; Van Orman et al. 2014). Finally, the presence of water and H species in minerals enhances oxygen diffusion but generally has very little effect on cation diffusion in minerals (Watson and Baxter 2007). Figure 3 is a broad-brush summary of cation and anion diffusion in minerals commonly observed in the earth and planetary materials (Brady and Cherniak 2010). The general trends and variations in diffusivities highlight the importance of mineral composition, mineral structure, temperature, and oxygen fugacity on diffusion in minerals.

Diffusion in silicate melts depends strongly on melt composition and melt structure (Watson and Baker 1991; Lesher 2010; Liang 2010; Zhang et al. 2010). Chemical diffusivities for cations in silicate melts are typically measured with metal oxides as independent components. In general, diffusivities decrease with the increase of SiO_2 and the decrease of alkali and water contents in the melt. For example, diffusivities of oxide components (including total water) decrease by over an order of magnitude from basalt to rhyolite, whereas the diffusivity of Li_2O only decreases by a factor of two and the diffusivity of CO_2 appears to be insensitive to melt composition (Watson and Baker 1991; Richter et al. 2003; Zhang and Ni 2010). Figure 4 displays an example of chemical diffusion between a basaltic melt and a rhyolitic melt (Richter et al. 2003). The steep gradients on the high SiO_2 or rhyolite side of the diffusion couple are due to the composition-dependent diffusivity in the melt, and can be reproduced by allowing the effective binary diffusion coefficients of the oxides to vary by factors of ~10–20 across the diffusion couple (Richter et al. 2003).

It has been demonstrated experimentally that isotopes of a number of elements (Li, Mg, Ca, K, Fe, and Ge) can be fractionated from each other during self diffusion, chemical diffusion, and thermal diffusion in aqueous solutions, molten silicates, iron-nickel alloys, as well as minerals such as pyroxene (e.g., Richter et al. 1999, 2003, 2006, 2009, 2014, 2016; Watkins et al. 2011, 2014; Watson et al. 2016). Richter and coworkers quantified this effect by relating diffusivity ratio of two isotopes to the reciprocal of their mass ratio through an empirical kinetic parameter β:

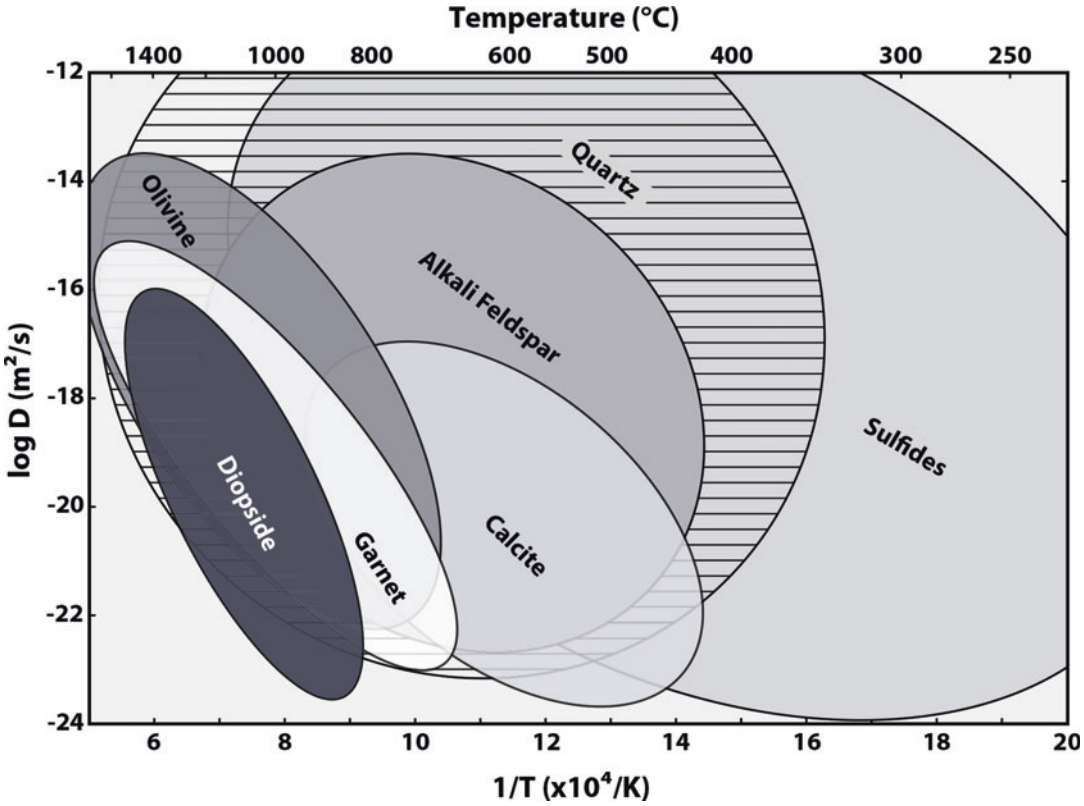

Diffusion, Fig. 3 Schematic Arrhenius diagram showing the approximate ranges of measured diffusion coefficients and temperatures for all elements (except H, He, Ar, and Li) in several common minerals or mineral groups (Adapted from Brady and Cherniak 2010)

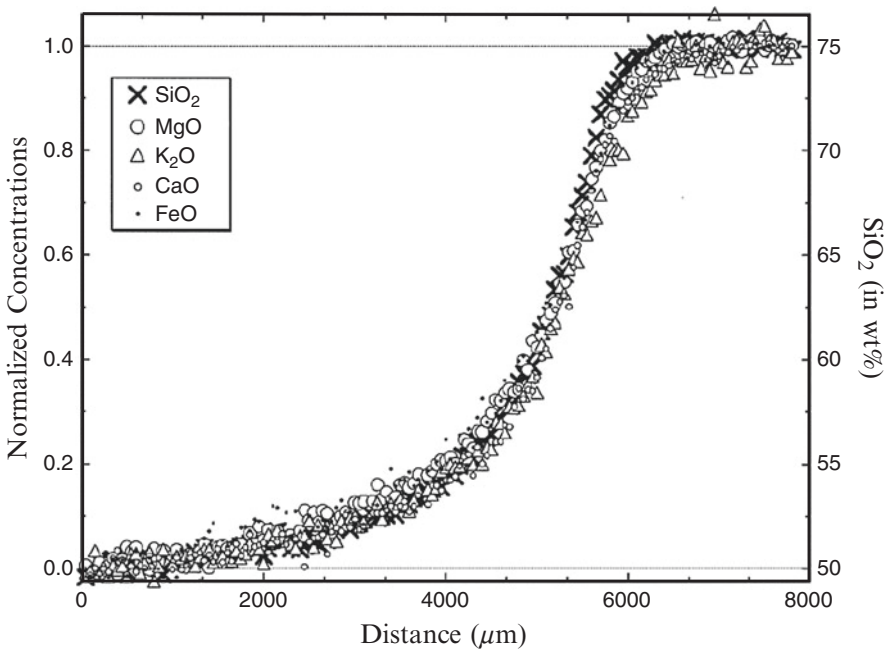

Diffusion, Fig. 4 Variations of selected oxide abundances across a basalt-rhyolite diffusion couple. The diffusion experiment was conducted at 1450 °C and 1.3 GPa for 15.7 h. At the start of the experiment, compositions of the basalt (left) and rhyolite (right) are homogeneous and shown as thin gray lines. The measured concentration profiles are shown as open circles. The small dots are calculated diffusion profiles using composition-dependent effective binary diffusion coefficients (Adapted from Richter et al. 2003)

$$\frac{D_1}{D_2} = \left(\frac{M_2}{M_1}\right)^{\beta}, \tag{22}$$

where D is the diffusivity and M is the mass of isotope 1 or 2 of the element of interest. While the experimentally determined β values in silicate melts are small for cations (0.215 for Li, but <0.1 for Ca, Mg, Fe and Si), they give rise to kinetic isotope fractionations that are larger compared to the precision with which isotope ratios are routinely measured. The values of {\beta} in minerals are often larger than in melts (e.g., ~0.3 for Li in pyroxene), while they are much smaller for salts diffusing in water. But in every case the light isotope diffuses slightly faster than the heavy isotope. Compilations of β values in aqueous solutions, melts, and minerals can be found in Richter et al. (2009) and Watkins et al. (2017). Isotope fractionation by diffusion is becoming a powerful tool for identifying diffusion-dominated mass transfer process in natural samples and as a result there is a growing interest in its geochemical applications. Some examples involving measurements and diffusion modeling of both isotopic ratio and element concentration profiles in natural settings can be found in Teng et al. (2006), Chopra et al. (2012), Sio et al. (2013), and Richter et al. (2014, 2016), among others.

Methods for Measuring Diffusion Coefficients

Diffusion coefficients for earth and planetary materials reported in the literature are mostly obtained from laboratory experiments. The methods for measuring diffusivities vary considerably, depending on physical state of the matter (fluid, melt, glass, or solid) and availability of analytical methods. Regardless of experimental complexity and sophistication, the basic idea of all diffusion experiments remain the same: Given an initial perturbation in concentration or isotopic ratio on the surface or in part of the specimen of interest, monitor the spread of the diffusant in the specimen as a function of diffusion time by measuring concentration and/or isotopic ratio profile(s) in the experimental charge using a suitable analytical instrument, and retrieve diffusion coefficient(s) from the measured concentration profiles using solutions to diffusion equations pertinent to the experimental setup. For the convenience of mathematical treatment of diffusion data, diffusion experiments are typically arranged in an effective one-dimensional geometry using one of the three setups or methods: diffusion couple method, thin source method, and constant source method. In the diffusion couple method, two rods or slabs of uniform but different composition starting materials are juxtaposed against each other in a capsule. In the thin source method, a thin film of diffusant is deposited on the surface of a polished specimen. In the constant source method, concentration of the diffusant at the surface or interface of the specimen of interest is kept constant during the course of diffusion. The diffusion couple method has been widely used to study self diffusion and chemical diffusion in molten silicates. This method has also been used to study chemical diffusion in minerals (e.g., garnet, olivine, and spinel) that have relatively fast diffusion rates on the laboratory time scale (the high temperature region labeled "ions in melts or crystals" in Fig. 1). The thin source method has been more frequently used to study diffusion in solids (minerals and glasses). The constant source method has been used to study diffusion of trace elements in either melts or minerals. This method has also been used to study diffusional loss or gain of diffusant in mineral grains in spherical geometry. The length of diffusion profile and the abundance of diffusant largely determine the analytical method used in a diffusion study (e.g., electron microprobe, ion microprobe, laser-ablation inductively coupled mass spectrometry, Rutherford backscatter spectroscopy, and nuclear reaction analysis). Depending on diffusivity and experimental run duration (minutes to a month), typical diffusion lengths range from 100s ~1000s microns for diffusion in melts (e.g., basalt-rhyolite interdiffusion) to 10s microns ~ less than 100 nanometers for diffusion in minerals (e.g., Fe-Mg diffusion in olivine; REE diffusion in pyroxene). Experimental studies of diffusion in fluids at elevated temperatures and pressures are more challenging and require special setups and capsules (e.g., the differential solubility and diffusion cell of Watson and Wark 1997; Wark and Watson 2004). A common practice in laboratory diffusion measurements is the time series study, in which a set of diffusion experiments is carried out at the same temperature and pressure but for different annealing times. Diffusion coefficients obtained from a time series study should be identical to within experimental uncertainty if diffusion is the sole mass transfer mechanism. To determine activation energy and activation volume for diffusion, diffusion experiments are conducted over a range of temperatures and pressures. Diffusivities obtained from such experiments can be used to extract diffusion parameters for the Arrhenius equation (Eq. 20). Finally, it is worth noting that diffusivities in fluids, melts, and crystals can be calculated theoretically through atomistic simulations. Computer simulations can extend the temperature and pressure ranges beyond those accessible in the laboratory, making it a powerful tool for studying thermodynamic and transport properties (including diffusivity) of earth and planetary materials. So far, atomistic simulations have been mainly used to study diffusion of major elements in simple but geologically relevant materials and the results are promising. For detailed summaries of various methods used in diffusion studies, the reader is

referred to the review articles by Ryerson (1987), Cherniak et al. (2010), de Koker and Stixrude (2010), and Watson and Dohmen (2010).

Diffusion Length and Closure Temperature

Diffusion length is a measure of the length scale of a region that is affected by the spread of diffusant. The diffusion length, L_D, scales with the square root of diffusion time and is given by the simple expression:

$$L_D = \sqrt{Dt}. \tag{23}$$

For diffusion coefficients $D = 10^{-6}$, 10^{-11}, and 10^{-19} $m^2\,s^{-1}$, which are within the ranges for diffusion in fluids, melts, and solids (Fig. 1), the diffusion lengths are 5.6 km, 18 m, and 1.8 mm, respectively, for a diffusion time of one million years. Depending on time scales of geological processes, concentration variations in mineral grains may not be effectively homogenized by diffusion. Indeed, zoning patterns preserved in mineral grains offer valuable information on time scales of geological processes, such as magma residence time, magma ascent rates, and cooling rates (Dohmen et al. 2017). During cooling, the diffusivity decreases with temperature and time, and the diffusion length may be estimated using a time-integrated diffusivity:

$$L_D = \left[\int_0^t D(t)dt\right]^{\frac{1}{2}}. \tag{24}$$

With decreasing temperature, concentration profiles in the interiors of the mineral grain become progressively insensitive to variations in mineral surface concentration. In terms of diffusional loss or gain, the mineral effectively ceases diffusive exchange with its surrounding at some lower temperature limit. This lower temperature limit is called the closure temperature (Dodson 1973). At closure temperature, the diffusion length defined by Eq. 24 is comparable to mineral grain size. By considering diffusional loss to a large reservoir along a prescribed cooling curve, Dodson (1973, 1986) obtained an equation for the mean closure temperature (T_c) for an element in a mineral grain of effective radius d,

$$\frac{E_a}{RT_c} = G + \ln\frac{D_0RT_c^2}{E_a\dot{s}d^2}, \tag{25}$$

where $\dot{s}$ is the absolute value of cooling rate at the closure temperature; G is the spatial average of the closure function and depends on geometry of the mineral ($G = 4.0066$ for sphere, 3.29506 for cylinder, and 2.15821 for plane sheet). The closure temperature decreases with the decrease of the product of cooling rate and the square of the effective diffusion radius. The geometric function, G, in Dodson's equation was modified by Ganguly and Tirone (1999) to include the "memory effect" that arises from situations when diffusion has not affected the center of the crystal (i.e., cases of fast cooling and/or large grain size). In his original derivation, Dodson (1973) used a cooling curve along which the reciprocal of the temperature increases linearly as a function of time. Generalization of Dodson's equation can be made to other heating-cooling-upwelling scenarios (Gardés and Montel 2009; Watson and Cherniak 2013; Liang 2017) and to two minerals in a closed system (Powell and White 1995; Liang 2015). Combined with geothermometers and isotopic dating, closure temperatures can be used to constrain thermal history of igneous and metamorphic rocks (Mueller et al. 2010).

Summary

Diffusion is a kinetic phenomenon that arises when there are gradients in concentration, chemical potential or temperature in a substance. Many geological processes are rate-limited by diffusion. Fick's laws of diffusion form the basis for quantifying diffusion kinetics in earth and planetary materials. The types of diffusion that are important to understand diffusion kinetics include self diffusion, chemical diffusion, multicomponent diffusion, effective binary diffusion, thermal diffusion, and grain boundary diffusion. Diffusion is a thermally activated process. Diffusion coefficients for geologically relevant fluids, melts, and solids vary enormously and systematically. The temperature- and pressure-dependent diffusivities follow the Arrhenius equation. Diffusion in silicate melts and crystals also depends on composition and structure of the melts and the crystals. Methods for measuring diffusion coefficients depend on physical state of the matter and availability of analytical methods. Atomistic simulations are becoming a powerful tool for diffusion studies and have the potential to significantly improve our knowledge and understanding of diffusion of earth and planetary materials at temperatures and pressures inaccessible in the laboratory. The field of diffusion studies is expanding owing to the continuing improvement and development of experimental, computational, and analytical methods, theories for diffusion, and numerical models for diffusion-related mass transfer. Because the diffusion equations are time-dependent, they can be used to infer rates and time scales of geological processes. There is a growing interest in applying diffusion data and models to field observations of earth and planetary materials. Indeed, diffusion is a cornerstone that connects several branches of the earth and planetary sciences.

Cross-References

- Activation Parameters: Energy, Enthalpy, Entropy, and Volume
- Activity and Activity Coefficients
- Analytical Techniques
- Aqueous Solutions
- Crystal Chemistry
- Electron Probe Microanalysis (EPMA)
- Experimental Mineralogy and Petrology
- Fugacity
- Geothermometry and Geobarometry
- Ion Microprobe
- Ionic Radii
- Kinetics of Geochemical Processes
- Laser Ablation – Inductively Coupled Plasma Mass Spectrometry
- Magmatic Process Modeling
- Mass Transfer
- Metamorphic Reactions and Processes
- Mineral Defects
- Mineralogy
- Silicate Melts
- Silicate Minerals
- Trace Elements

References

Anderson AC (1981) Diffusion in electrolyte mixtures. Rev Mineral 8:211–260

Barrer RM, Bartholomew RF, Rees LVC (1963) Ion exchange in porous crystals. Part II. The relationship between self- and exchange-diffusion coefficients. Phys Chem Solids 24:309–317

Béjina F, Jaoul O, Liebermann RC (2003) Diffusion in minerals at high pressure: a review. Phys Earth Planet Inter 139:3–20

Bloch E, Ganguly J, Hervig R, Cheng W (2015) ^{176}Lu-^{176}Hf geochronology of garnet I: experimental determination of diffusion kinetics of Lu^{3+} and Hf^{4+} in garnet, closure temperatures and geochronological implications. Contrib Mineral Petrol 169:12

Brady JB, Cherniak DJ (2010) Diffusion in minerals: an overview of published experimental diffusion data. In: Zhang Y, Cherniak DJ (eds) Diffusion in minerals and melts. Reviews in mineralogy and geochemistry. Mineralogical Society of America, Chantilly, Virginia, vol 72. pp 899–920

Carlson WD (2012) Rates and mechanism of Y, REE, and Cr diffusion in garnet. Am Mineral 97:1598–1618

Chakraborty S (2008) Diffusion in solid silicates: a tool to trace time-scales of processes comes of age. Annu Rev Earth Planet Sci 36:153–190

Chakraborty S (2010) Diffusion coefficients in olivine, wadsleyite and ringwoodite. In: Zhang Y, Cherniak DJ (eds) Diffusion in minerals and melts. Reviews in mineralogy and geochemistry. Mineralogical Society of America, Chantilly, Virginia, vol 72. pp 603–640

Cherniak DJ (1995) Diffusion of lead in plagioclase and K-feldspar: an investigation using Rutherford backscattering and resonant nuclear reaction analysis. Contrib Mineral Petrol 120:358–371

Cherniak DJ (2003) REE diffusion in feldspar. Chem Geol 193:25–41

Cherniak DJ, Dimanov A (2010) Diffusion in pyroxene, mica and amphibole. In: Zhang Y, Cherniak DJ (eds) Diffusion in minerals and melts. Reviews in mineralogy and geochemistry. Mineralogical Society of America, Chantilly, Virginia, vol 72. pp 641–690

Cherniak DJ, Liang Y (2007) Rare earth element diffusion in natural enstatite. Geochim Cosmochim Acta 71:1324–1340

Cherniak DJ, Watson EB (1994) A study of strontium diffusion in plagioclase using Rutherford backscattering spectroscopy. Geochim Cosmochim Acta 58:5179–5190

Cherniak DJ, Watson EB (2010) Li diffusion in zircon. Contrib Mineral Petrol 160:383–390

Cherniak DJ, Hanchar JM, Watson EB (1997a) Diffusion of tetravalent cations in zircon. Contrib Mineral Petrol 127:383–390

Cherniak DJ, Hanchar JM, Watson EB (1997b) Rare-earth diffusion in zircon. Chem Geol 134:289–301

Cherniak DJ, Hervig R, Koepke J, Zhang Y, Zhan D (2010) Analytical methods in diffusion studies. In: Zhang Y, Cherniak DJ (eds) Diffusion in minerals and melts. Reviews in mineralogy and geochemistry. Mineralogical Society of America, Chantilly, Virginia, vol 72. pp 107–170

Chopra R, Richter FM, Watson EB, Scullard CR (2012) Magnesium isotope fractionation by chemical diffusion in natural settings and in laboratory analogues. Geochim Cosmochim Acta 88:1–18

Cooper AR (1965) Model for multi-component diffusion. Phys Chem Glasses 6:55–61

Cooper AR (1968) The use and limitations of the concept of an effective binary diffusion coefficient for multi-component diffusion. In: Wachtman JB, Franklin AD (eds) Mass transport in oxides. NBS special publication. Mineralogical Society of America, Chantilly, Virginia, vol 296. pp 79–84

Crank J (1975) The mathematics of diffusion. Clarendon, Oxford

de Groot SR, Mazur P (1962) Non-equilibrium thermodynamics. Dover, New York

de Koker N, Stixrude L (2010) Theoretical computation of diffusion in minerals and melts. In: Zhang Y, Cherniak DJ (eds) Diffusion in minerals and melts. Reviews in mineralogy and geochemistry. Mineralogical Society of America, Chantilly, Virginia, vol 72. pp 971–996

Dodson MH (1973) Closure temperature in cooling geochronological and petrological systems. Contrib Mineral Petrol 40:259–274

Dodson MH (1986) Closure profiles in cooling systems. Mater Sci Forum 7:145–154

Dohmen R, Milke R (2010) Diffusion in polycrystalline materials: grain boundaries, mathematical models, and experimental data. In: Zhang Y, Cherniak DJ (eds) Diffusion in minerals and melts. Reviews in mineralogy and geochemistry. Mineralogical Society of America, Chantilly, Virginia, vol 72. pp 921–970

Dohmen R, Kasemann SA, Coogan L, Chakraborty S (2010) Diffusion of Li in olivine. Part I: experimental observations and a multi species diffusion model. Geochim Cosmochim Acta 74:274–292

Dohmen R, Faak K, Blundy JD (2017) Chronometry and speedometry of magmatic processes using chemical diffusion in olivine, plagioclase and pyroxene. In: Teng F-Z, Dauphas N, Watkins JM (eds) Non-traditional stable isotopes. Reviews in mineralogy and geochemistry. Mineralogical Society of America, Chantilly, Virginia, vol 82. pp 535–575

Fisher JC (1951) Calculation of diffusion penetration curves for surface and grain boundary diffusion. J Appl Phys 22:74–77

Fujita H, Gosting LJ (1956) An exact solution of the equations for free diffusion in three-component systems with interacting flows, and its use in evaluation of the diffusion coefficients. J Am Chem Soc 78:1099–1106

Ganguly J (2010) Cation diffusion kinetics in aluminosilicate garnets and geological applications. In: Zhang Y, Cherniak DJ (eds) Diffusion in minerals and melts. Reviews in mineralogy and geochemistry. Mineralogical Society of America, Chantilly, Virginia, vol 72. pp 559–601

Ganguly J, Tirone M (1999) Diffusion closure temperature and age of a mineral with arbitrary extent of diffusion theoretical formulation and applications. Earth Planet Sci Lett 170:131–140

Gardés M, Montel J-M (2009) Opening and resetting temperatures in heating geochronological systems. Contrib Mineral Petrol 158:185–195

Giletti BJ, Casserly JED (1994) Strontium diffusion kinetics in plagioclase feldspars. Geochim Cosmochim Acta 58:3785–3793

Giletti BJ, Yund RA (1984) Oxygen diffusion in quartz. J Geophys Res 89:4039–4046

Guo C, Zhang Y (2016) Multicomponent diffusion in silicate melts: SiO_2-TiO_2-Al_2O_3-MgO-Na_2O-K_2O system. Geochim Cosmochim Acta 195:126–141

Gupta PK, Cooper AR Jr (1971) The [D] matrix for multicomponent diffusion. Physica 54:39–59

Harrison LG (1961) Influence of dislocation on diffusion kinetics in solids with particular reference to the alkali halides. Trans Faraday Soc 57:1191–1199

Hart EW (1957) On the role of dislocations in bulk diffusion. Acta Metall 5:597–597

Hasse R (1969) Thermodynamics of irreversible processes. Dover, New York

Helfferich F, Plesset MS (1958) Ion exchange kinetics. A nonlinear diffusion problem. J Chem Phys 28:418–424

Holzapfel C, Chakraborty S, Rubie DC, Frost DJ (2007) Effect of pressure on Fe-Mg, Ni and Mn diffusion in $(Fe_xMg_{1-x})_2SiO_4$ olivine. Phys Earth Planet Inter 162:186–198

Joesten R (1991) Grain-boundary diffusion kinetics in silicate and oxide minerals. In: Gangule J (ed) Diffusion, atomic ordering, and mass transport. Springer, New York, pp 345–395

Liang Y, Richter FM, and Watson EB (1996) Diffusion in silicate melts: II. Multicomponent diffusion in CaO-$_{Al2O3}$-$_{SiO2}$ at 1500°C and 1 GPa. Geochim Cosmochim Acta 60, 5021-5035

Katchalsky A, Curran PF (1967) Nonequilibrium thermodynamics in biophysics. Harvard University Press, Cambridge, MA

Kirkaldy JS (1958) Diffusion in multicomponent metallic systems: I. Phenomenological theory for substitutional solid solution alloys. Can J Phys 36:899–906

Kirkaldy JS, Young DJ (1987) Diffusion in condensed state. Wiley, New York

Kondepudi D, Prigogine I (1998) Modern thermodynamics: from heat engines to dissipative structures. Wiley, New York

Kushiro I (1983) Effect of pressure on the diffusivity of network-forming cations in melts of jadeitic compositions. Geochim Cosmochim Acta 47:1415–1422

Lasaga AC (1979) Multicomponent exchange and diffusion in silicates. Geochim Cosmochim Acta 43:455–469

Lasaga AC (1998) Kinetic theory in the Earth sciences. Princeton University Press, Princeton

Le Claire AD (1963) The analysis of grain boundary diffusion measurments. Br J Appl Phys 14:351–356

Lesher CE (1986) Effects of silicate liquid composition on mineral-liquid element partitioning from Soret diffusion studies. J Geophys Res 91:6123–6141

Lesher CE (2010) Self-diffusion in silicate melts: theory, observations and applications to magmatic systems. In: Zhang Y, Cherniak DJ (eds) Diffusion in minerals and melts. Reviews in mineralogy and geochemistry. Mineralogical Society of America, Chantilly, Virginia, vol 72. pp 269–309

Liang Y (2010) Multicomponent diffusion in molten silicates: theory, experiments, and geological applications. In: Zhang Y, Cherniak DJ (eds) Diffusion in minerals and melts. Reviews in mineralogy and geochemistry. Mineralogical Society of America, Chantilly, Virginia, vol 72. pp 409–446

Liang Y (2015) Simple models for closure temperature of a trace element in cooling bi-mineralic systems. Geochim Cosmochim Acta 165:35–43

Liang Y (2017) Effect of pressure on closure temperature of a trace element in cooling petrological systems. Contrib Mineral Petrol 172:8

Liang Y, Richter FM, Chamberlin L (1997) Diffusion in silicate melts: III. Empirical models for multicomponent diffusion. Geochim Cosmochim Acta 61:5295–5312

Miller DG, Vitagliano V, Sartorio R (1986) Some comments on multicomponent diffusion: negative main term diffusion coefficients, second law constrains, solvent choices, and reference frame. J Phys Chem 90:1509–1519

Mishin Y, Herzig C, Bernardini J, Gust W (1997) Grain boundary diffusion: fundamentals to recent developments. Int Mater Rev 42:155–178

Mueller T, Watson EB, Harrison TM (2010) Applications of diffusion data to high-temperature earth systems. In: Zhang Y, Cherniak DJ (eds) Diffusion in minerals and melts. Reviews in mineralogy and geochemistry. Mineralogical Society of America, Chantilly, Virginia, vol 72. pp 997–1038

Narasimhan TN (2004) Fick's insights on liquid diffusion. Eos 85:499–501

Nye JF (1985) Physical properties of crystals. Clarendon, Oxford

Onsager L (1945) Theories and problems of liquid diffusion. Ann N Y Acad Sci 46:241–265

Poe BT, McMillan PF, Rubie DC, Chakraborty S, Yarger J, Diefenbacher J (1997) Silicon and oxygen self-diffusivities in silicate liquids measured to 15 Gigapascals and 2800 Kelvin. Science 276:1245–1248

Powell R, White L (1995) Diffusive equilibration between minerals during cooling: an analytical extension to Dodson's equation for closure in one dimension. Geol J 30:297–305

Richter FM (1993) A method for determining activity-composition relations using chemical diffusion in silicate melts. Geochim Cosmochim Acta 57:2019–2032

Richter FM, Liang Y, Minarik WG (1998) Multicomponent diffusion and convection in molten MgO-Al_2O_3-SiO_2. Geochim Cosmochim Acta 62:1985–1991

Richter FM, Liang Y, and Davis AM (1999) Isotope fractionation by diffusion in molten oxides. Geochim Cosmochim Acta 63, 2853–2861

Richter FM, Davis AM, DePaolo DJ, Watson EB (2003) Isotope fractionation by chemical diffusion between molten basalts and rhyolite. Geochim Cosmochim Acta 67:3905–3923

Richter FM, Mendybaev RA, Christensen JN, Hutcheon ID, Williams RW, Sturchio NC, Beloso Jr AD (2006) Kinetic isotope fractionation during diffusion of ionic species in water. Geochim. Cosmochim. Acta, 70:277–289

Richter FM, Watson EB, Mendybaev RA, Dauphas N, Geory B, Watkins J, Valley J (2009) Isotope fractionation of the major elements of molten basalt by chemical and thermal diffusion. Geochim Cosmochim Acta 73:4250–4263

Richter FM, Watson EB, Chaussidon M, Mendybaev RA, Ruscitto D (2014) Lithium isotope fractionation by diffusion in minerals. Part 1: pyroxenes. Geochim Cosmochim Acta 126:352–370

Richter FM, Chaussidon M, Mendybaev RA, Kite E (2016) Reassessing the cooling rate and geologic setting of Martian meteorites MIL 03346 and NWA 817. Geochim Cosmochim Acta 182:1–23

Ryerson FJ (1987) Diffusion measurements: experimental methods. Methods Exp Phys 24A:89–130

Shea T, Costa F, Krimer D, Hammer JE (2015) Accuracy of timescales retrieved from diffusion modeling in olivine: a 3D perspective. Am Mineral 100:2026–2042

Sio CK, Dauphas N, Teng F-Z, Chaussidon M, Helz RT, Roskosz M (2013) Discerning crystal growth from diffusion profiles in zoned olivine by in situ Mg-Fe isotopic analyses. Geochim Cosmochim Acta 123:302–321

Suzuoka T (1961) Lattice and grain boundary diffusion in polycrystals. Trans Jpn Inst Met 2:25–32

Teng F-Z, McDonough WF, Rudnick RL, Walker RJ (2006) Diffusion-driven extreme lithium isotopic fractionation in country rocks of the Tin Mountain pegmatite. Earth Planet Sci Lett 243:701–710
Toor HL (1964) Solution of the linearized equation of multicomponent mass transfer: I. AIChE J 10:448–455
Trail D, Cherniak DJ, Watson EB, Harrison TM, Weiss BP, Szumila I (2016) Li zoning in zircon as a potential geospeedometer and peak temperature indicator. Contrib Mineral Petrol 171:25
Tyrrell HJV (1964) The origin and present status of Fick's diffusion law. J Chem Educ 41:397–400
Tyrrell HJV, Harris KR (1984) Diffusion in liquids. Butterworths, London
Van Orman JA, Crispin KL (2010) Diffusion in oxides. In: Zhang Y, Cherniak DJ (eds) Diffusion in minerals and melts. Reviews in mineralogy and geochemistry. Mineralogical Society of America, Chantilly, Virginia, vol 72. pp 757–825
Van Orman JA, Grove TL, Shimizu N (2001) Rare earth element diffusion in diopside: influence of temperature, pressure, and ionic radius, and an elastic model for diffusion in silicates. Contrib Mineral Petrol 141:687–703
Van Orman JA, Grove TL, Shimizu N, Layne GD (2002) Rare earth element diffusion in a natural pyrope single crystal at 2.8 GPa. Contrib Mineral Petrol 142:416–424
Van Orman JA, Cherniak DJ, Kita N (2014) Magesium diffusion in plagioclase: dependence on composition, and implications for thermal resetting of the ^{26}Al-^{26}Mg early solar system chronometer. Earth Planet Sci Lett 385:79–88
Walker D, Lesher CE, Hays JF (1981) Soret separation of lunar liquid. Proc Lunar Planet Sci 12B:991–999
Wark DA, Watson EB (2004) Interdiffusion of H_2O and CO_2 in metamorphic fluids at ~490 to 690 °C and 1 GPa. Geochim Cosmochim Acta 68:2693–2698
Watkins JM, DePaolo DJ, Ryerson FJ, Peterson BT (2011) Influence of liquid structure on diffusive isotope separation in molten silicates and aqueous solutions. Geochim Cosmochim Acta 75:3103–3118
Watkins JM, Liang Y, Richter FM, Ryerson FJ, DePaolo DJ (2014) Diffusion of multi-isotopic chemical species in molten silicates. Geochim Cosmochim Acta 139:313–326
Watkins JM, DePaolo DJ, Watson EB (2017) Kinetic fraction of non-traditional stable isotopes by diffusion and crystal growth reaction. In: Teng F-Z, Dauphas N, Watkins JM (eds) Non-traditional stable isotopes. Reviews in mineralogy and geochemistry. Mineralogical Society of America, Chantilly, Virginia, vol 82. pp 85–125
Watson EB, Baker DR (1991) Chemical diffusion in magmas: an overview of experimental results and geochemical applications. In: Perchuk LL, Kushiro I (eds) Physical chemistry of magmas. Springer, New York, pp 120–151
Watson EB, Baxter EF (2007) Diffusion in solid-Earth systems. Earth Planet Sci Lett 253:307–327
Watson EB, Cherniak DJ (2013) Simple equations for diffusion in response to heating. Chem Geol 335:93–104
Watson EB, Dohmen R (2010) Non-traditional and emerging methods for characterizing diffusion in minerals and minerals aggregates. In: Zhang Y, Cherniak DJ (eds) Diffusion in minerals and melts. Reviews in mineralogy and geochemistry. Mineralogical Society of America, Chantilly, Virginia, vol 72. pp 61–105
Watson EB, Wark DA (1997) Diffusion of dissolved SiO_2 in H_2O at 1 GPa, with implications for mass transport in the crust and upper mantle. Contrib Mineral Petrol 130:66–80
Watson HC, Richter FM, Liu A, Huss GR (2016) Iron and nickel isotope fractionation by diffusion, with applications to iron meteorites. Earth Planet Sci Lett 451:159–167
Whipple RTP (1954) Concentration contours in grain boundary diffusion. Philos Mag 45:1225–1236
Zhang Y (1993) A modified effective binary diffusion model. J Geophys Res 98:11901–11920
Zhang Y (2010) Diffusion in minerals and melts: theoretical background. In: Zhang Y, Cherniak DJ (eds) Diffusion in minerals and melts. Reviews in mineralogy and geochemistry. Mineralogical Society of America, Chantilly, Virginia, vol 72. pp 5–59
Zhang Y, Cherniak DJ (2010) Diffusion in minerals and melts. Reviews in mineralogy and geochemistry, vol 72. Mineralogical Society of America, Chantilly
Zhang Y, Ni H (2010) Diffusion of H, C, and O components in silicate melts. In: Zhang Y, Cherniak DJ (eds) Diffusion in minerals and melts. Reviews in mineralogy and geochemistry. Mineralogical Society of America, Chantilly, Virginia, vol 72. pp 171–225
Zhang Y, Walker D, Lesher CE (1989) Diffusive crystal dissolution. Contrib Mineral Petrol 102:492–513
Zhang Y, Ni H, Chen Y (2010) Diffusion data in silicate melts. In: Zhang Y, Cherniak DJ (eds) Diffusion in minerals and melts. Reviews in mineralogy and geochemistry. Mineralogical Society of America, Chantilly, Virginia, vol 72. pp 311–408

Dissolved Organic Matter (DOM)

Hilairy Ellen Hartnett
School of Earth and Space Exploration and School of Molecular Sciences, Arizona State University, Tempe, AZ, USA

Definition

Dissolved organic matter is a heterogeneous class of water-soluble compounds that contain reduced (organic) carbon from a variety of biological and geological sources with a wide range of chemical reactivity. Dissolved organic matter is a key component in the biogeochemical cycling of carbon.

Introduction

Dissolved organic matter (DOM) is operationally defined as any organic matter that is able to pass through a filter. It is described in contrast to particulate organic matter (POM) retained on the filter. Traditionally, glass fiber filters with a nominal pore size of 0.7 μm were the standard. Currently, smaller-sized filters (0.2 μm) are often used because they are readily available and they remove most bacteria, which can degrade a DOM sample. DOM is derived from many sources both external and internal to an aquatic system. Dissolved organic matter is a complex mixture of organic molecules made up of carbon, hydrogen, and oxygen as well as the heteroatoms nitrogen, phosphorous, and sulfur; thus DOM comprises dissolved organic carbon, nitrogen, phosphorous, and sulfur. This heterogeneity makes it difficult to define DOM composition. Dissolved organic matter is an important component of the global carbon cycle and is among the most reactive pools of organic material at Earth's surface.

(Hedges 2002; Hansell and Carlson 2015). In marine systems, DOM is the primary currency of the microbial loop as it provides a food and energy source to microbes. DOM also forms complexes with trace metals making the metals more soluble and more bioavailable. In addition, in freshwater systems, DOM influences aqueous geochemistry by contributing to acidification in low-alkalinity, weakly buffered systems; it can also impart color, taste, and odor to drinking water.

Marine dissolved organic carbon concentrations range from very low values in the deep ocean (~40 μM) to very high values (>300 μM) in coastal regions. Pore water DOM values tend to be higher as particulate organic matter (POM) decomposition within sediments can release DOM. In freshwater systems, DOM ranges from 40 to1000 μM and can reach mM levels in the most carbon-rich systems (e.g., wetlands, bogs, and swamps). The reactivity or bioavailability of DOM describes how well this carbon pool can support the growth of microorganisms. Due to its diverse molecular composition DOM can be highly reactive or quite recalcitrant.

Sample Collection and Bulk Quantification

The choice of filter for DOM sampling is important. Glass fiber filters and silver membrane filters are easily cleaned but suffer from large pore sizes and very high cost, respectively. Membrane filters, especially nitrocellulose and polypropylene filters, are inexpensive but often cause significant sample contamination because they leach carbon and are difficult to clean. Polyethersulfone filters (PES, Supor™) are membrane filters that can be cleaned with deionized water and are available with small pore sizes. The choice of filter is dictated by the specific needs of the sample and the environment in which it is collected. Ideally samples should be collected and stored in ashed (500 °C, 4 h) glass containers and stored cold and in the dark to reduce biological modifications of the sample. If samples are to be stored for long periods, acidification or freezing will reduce post-filtration alteration.

Bulk quantification of DOM is achieved by converting the organic molecules to CO_2 followed by infrared detection of the CO_2 molecule. The method requires (1) complete removal of inorganic carbon from the sample and then (2) complete oxidation of the reduced organic carbon. Inorganic carbon removal is achieved by reducing pH to <2, converting carbonate and bicarbonate to carbon dioxide, and sparging to remove CO_2 gas. The oxidation of organic carbon can be achieved by UV (light) or by persulfate (wet chemical), but most modern DOM analyzers rely on oxidation by high-temperature combustion (HTC). The HTC methods generally employ a platina-alumina catalyst and temperatures of ~720 °C, followed by nondispersive infrared detection of the CO_2. Dissolved organic nitrogen (the DOM molecules that contain N in addition to C, H, and O) can be quantified separately via HTC followed by chemiluminescent detection of the NO formed during oxidation.

In the 1980s, DOM analytical methods were plagued by uncertainty surrounding analytical blanks. A broad community intercomparison revealed that careful attention to sample collection and handling techniques, as well as a commitment to uniform use of standard reference materials, allows routine, high-precision (CV ~ 3–5%), accurate measurement of DOM concentrations down to <35 μM (Sharp et al. 2002).

Characterization

The specific molecular composition of DOM is important for understanding its reactivity and fate in the environment. The direct analysis of DOM composition can be challenging due to low concentrations of individual DOM components and the sheer number of molecules represented; however, great advances have been made in the last 20 years. Improvements in isolation and extraction techniques have helped the low concentration problem, but all methods isolate only a fraction of the DOM pool. It is important to recognize that no individual analysis technique can detect 100% of the carbon in a sample at the molecular level. Thus, multiple methods must be applied to fully characterize the classes of carbon compounds present or to quantify all the molecules in a sample. Biological and environmental samples are especially complex (Kujawinski 2011; Moran et al. 2016).

DOM is comprised of a wide range of biomolecules and organic moieties ranging from large bio- and geopolymers to low molecular weight monomers. A single natural dissolved organic matter sample can be comprised of thousands of different molecules (Sleighter and Hatcher 2007). The dominant classes of biomolecules include proteins and nucleic acids, carbohydrates (sugars), lipids (fatty acids, sterols, and alkenes), pigments, and an array of smaller primary and secondary metabolites. In marine systems, fresh, algal-derived DOM reflects the relative distribution of the biomolecules in plankton biomass; however, microbial and photochemical degradation of DOM rapidly obscures the molecular composition because partially degraded molecules become unrecognizable and difficult to classify. In the deep ocean, a majority of the DOM cannot be classified as individual biomolecules because they have been partially degraded and no longer fall into a given analytical window. In terrestrial aquatic systems, similar biomolecules predominate, but there are also significant contributions from degraded, soil-derived carbon and from land plants (lignin, as well as humic and fulvic acids). Dissolved organic matter can also include geological and anthropogenically derived compounds (i.e., petroleum-derived compounds, PAHs, pesticides, detergents and surfactants, pharmaceuticals, and other emerging contaminants).

Analytical methods that have been applied to characterize DOM at the molecular level include spectrophotometric and optical techniques, nuclear magnetic resonance (NMR) spectroscopy, 2D gas chromatography, and a wide array of mass spectrometry techniques with a variety of ionization techniques. Stable carbon and radiocarbon isotope analyses of DOM are also possible and reveal information about carbon source, reactivity, and fate in the environment. Mass spectrometry can be applied to both extracted and derivatized components as well as to bulk DOM. High-resolution mass spectrometry (e.g., FT-ICR MS and ToF-MS techniques) is an especially exciting field as it is now possible to identify virtually all of the molecules present in a given sample. This capability enables true proteomics and metabolomics analyses in complex environmental samples.

Optical techniques for DOM characterization are gaining popularity because they require little sample preparation, they are nondestructive, and they can characterize different pools of organic carbon. These techniques include UV-Vis absorbance and fluorescence spectroscopy. Some compound classes of the dissolved organic matter can absorb light (colored dissolved organic matter, CDOM); these molecules affect light penetration and therefore primary production. Only certain classes of organic molecules, generally those that are aromatic or highly conjugated, are also fluorescent (fDOM). Absorbance spectroscopy can be used to characterize the aromatic fraction of the DOM (e.g., specific UV absorbance at 240 nm, $SUVA_{254}$), which is related to humic content. Fluorescence is emerging as a powerful tool to characterize aromatic/humic components of the DOM as well as moieties that contain tryptophan-like and tyrosine-like fluorescence (Fellman et al. 2010). Modeling approaches (PARAFAC) have been developed that quasi-quantify contributions of different fluorescent components (Stedmon and Bro 2008). It is not yet well known what fraction of the DOM is comprised by CDOM and fDOM, and further research is required to determine how the reactivity of CDOM and fDOM relates to the bulk DOM reactivity.

Importance to the Carbon Cycle and Current Questions

Dissolved organic matter plays a major role in the carbon cycle. The marine DOM pool holds ~700 Pg of carbon, roughly equivalent to the atmospheric pool. This DOM is a fundamental component of the Earth's active carbon cycle, and the wide range in molecules present means that some fractions are labile and readily degraded by microbes, while other fractions are recalcitrant and can persist for thousands of years. The DOM pool is also in dynamic equilibrium with particulate organic carbon (POC), and the sorption of DOM to particles provides a measure of protection from microbial degradation. The specific mechanism of this sorptive protection is not well known.

Questions remain as to what controls DOM accumulation and removal in marine and terrestrial systems and how microbial and abiotic processes affect DOM composition. Terrestrial carbon, once thought to be highly refractory (non-labile), has been shown to be reactive on short timescales (days to weeks) in estuaries. Surface ocean carbon in excess of deep ocean concentrations holds a modern radiocarbon signature (recently produced) but seems to be semi-labile, possibly due to the more limited microbial diversity in surface waters relative to that in deep waters and coastal regions. DOM in surface waters can also be photooxidized which may influence the lability of the DOM. The vast, deep ocean pool of DOM is old, but small additions of labile and semi-labile material do occur upon solubilization of sinking biogenic POM, and this labile carbon may have a "priming" effect that induces DOM degradation. The complexity of dissolved organic carbon is enormous, and our understanding of the detailed cycling of dissolved organic carbon is still quite limited. New approaches that link microbial ecology with high-resolution geochemical analyses and informatics data are necessary to achieve predictive understanding of DOM cycling (Moran et al. 2016).

Summary

Dissolved organic matter is a complex mixture of organic molecules that occupies a central role in Earth's surface carbon cycle. The complexity of DOM composition has made it difficult to characterize at the molecular level, and we are only beginning to understand the interactions among microbes, metabolisms, and dissolved organic matter cycling.

Cross-References

- ▶ Analytical Techniques
- ▶ Biogeochemistry
- ▶ Biological Pump
- ▶ Biomarker: Assessment of Thermal Maturity
- ▶ Biopolymers and Macromolecules
- ▶ Carbon Cycle
- ▶ Carbon Isotopes
- ▶ Complexes
- ▶ Gas Chromatography–Mass Spectrometry (GC–MS)
- ▶ High-Resolution Mass Spectrometry
- ▶ Lipids (Bacteria and Archaea)
- ▶ Nitrogen Cycle
- ▶ Nuclear Magnetic Resonance
- ▶ Organic Geochemistry
- ▶ Phosphorus

References

Fellman JB, Hood E, Spencer RGM (2010) Fluorescence spectroscopy opens new windows into dissolved organic matter dynamics in freshwater ecosystems: a review. Limnol Oceanogr 55:2452–2462

Hansell DA, Carlson CA (eds) (2015) Biogeochemistry of marine dissolved organic matter, 2nd edn. Academic Press, San Diego

Hedges JI (2002) Why dissolved organics matter. In: Hansell DA, Carlson CA (eds) Biogeochemistry of marine dissolved organic matter. Elsevier, London, pp 1–33

Kujawinski EB (2011) The impact of microbial metabolism on marine dissolved organic matter. Annu Rev Mar Sci 3:567–599

Moran MA, Kujawinski EB, Stubbins A, Fatland R, Aluwihare LI, Buchan A, Crump BC, Dorrestein PC, Dyhrman ST, Hess NJ, Howe B, Longnecker K, Medeiros PM, Niggemann J, Obernosterer I, Repeta DJ, Waldbauer JR (2016) Deciphering ocean carbon in a changing world. Proc Natl Acad Sci 113:3143–3151

Sharp JH, Carlson CA, Peltzer ET, Castle-Ward DM, Savidge KB, Rinker KR (2002) Final dissolved organic carbon broad community intercalibration and preliminary use of DOC reference materials. Mar Chem 77:239–253

Sleighter RL, Hatcher PG (2007) The application of electrospray ionization coupled to ultrahigh resolution mass spectrometry for the molecular characterization of natural organic matter. J Mass Spectrom 42:559–574

Stedmon CA, Bro R (2008) Characterizing dissolved organic matter fluorescence with parallel factor analysis: a tutorial. Limnol Oceanogr Meth 6:572–579

Dolomite and Dolomitization

Jennifer A. Roberts
Department of Geology, University of Kansas, Lawrence, KS, USA

Definition

Dolomite is a trigonal–rhombohedral, ordered Ca, Mg carbonate mineral ($CaMg(CO_3)_2$) occurring primarily in sedimentary and metamorphic rocks. Dolomitization is the process in which Mg ions replace Ca ions in a calcium carbonate mineral.

Crystal Structure and Geochemistry

The crystal structure of dolomite is similar to calcite with Mg ions substituting for Ca in every other layer. To accommodate this substitution, due to differences in bond lengths between Ca–CO_3 and Mg–CO_3 (238 pm versus 208 pm, respectively), CO_3 in the Mg layer is uniformly rotated about the threefold axis relative to calcite (Reeder and Wenk 1983).

Stoichiometric dolomite (50:50 $CaCO_3$:$MgCO_3$) is part of a solid solution between calcite ($CaCO_3$), magnesite ($MgCO_3$), and ankerite ($FeCO_3$). Iron substitution as well as Mg substitution greater than ~10 mol% will lead to disordering and expansion of the unit cell (Antao et al. 2004; Carmichael and Ferry 2008). These disordered phases are thermodynamically metastable and over time, and with diagenetic alteration, through dissolution/re-precipitation are replaced by more ordered phases.

Dolomite stoichiometry can be measured using atomic absorption spectroscopy, inductively coupled plasma, and electron microprobe. Crystal structure and ordering of dolomite can be identified using X-ray diffraction (XRD) techniques; however, determination of stoichiometry requires the use of empirical curves that relate dolomite to calcite d_{104} to account for unit cell changes with substitution of $MgCO_3$ (e.g., Zhang et al. 2010). In mixed mineralogy samples and in samples where dolomite is in low abundance, XRD may not give unequivocal results of stoichiometry and ordering (e.g., Gregg et al. 2015), and techniques such as transmission electron microscopy (Fig. 1) with selected area electron diffraction (Zhang et al. 2010; Zhang et al. 2012a; Zhang et al. 2012b; Roberts et al. 2013), laser scanning Raman spectroscopy (e.g., Sun et al. 2014), synchrotron-based energy-dispersive X-ray diffraction, and infrared spectroscopy (Rodriguez-Blanco et al. 2015) may help confirm these results.

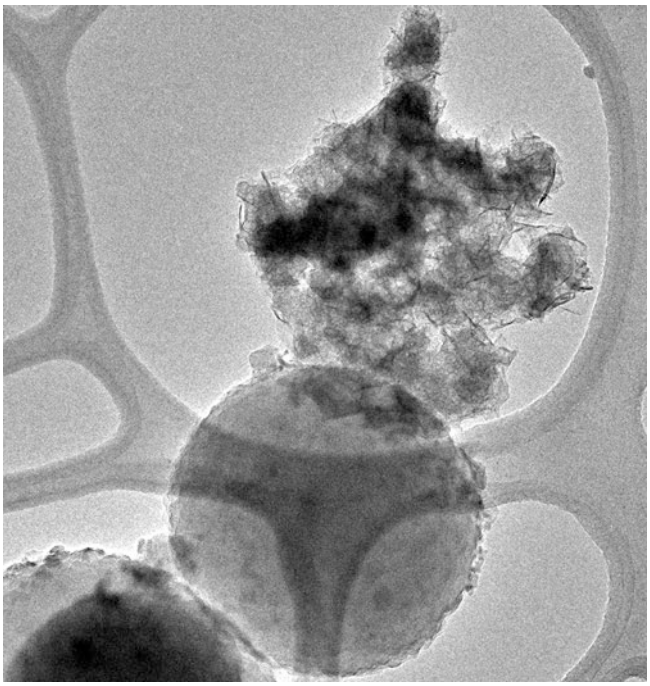

Dolomite and Dolomitization, Fig. 1 Dolomite precipitates abiotically at 25 °C on a carboxylated, polystyrene sphere in seawater approximating Silurian conditions (see Roberts et al. 2013 for experimental conditions). Sphere is 0.8 μm in diameter

Kinetics of Precipitation

Stoichiometric, ordered dolomite readily forms at temperatures above 100 °C (Arvidson and Mackenzie 1999); however, changes in temperature and solution chemistry significantly influence the stoichiometry of precipitated phases. Thermodynamic constants and isotopic fractionation factors have been developed for dolomite at high temperatures (80–250 °C; Baker and Kastner 1981; Sibley et al. 1987; Li et al. 2015) and extrapolated to lower temperatures where laboratory synthesis is hindered by slow reaction kinetics (e.g., Land 1998). Kinetic inhibition of dolomite precipitation at low temperature is attributed to lack of persistent solution supersaturation, low Mg:Ca ratios, sulfate inhibition, Mg-dehydration barrier, and lack of nucleation sites or critical nuclei (e.g., Baker and Kastner 1981; Hardie 1987; Zhong and Mucci 1989; Slaughter and Hill 1991; Brady et al. 1996; Arvidson and Mackenzie 1999; Wright and Wacey 2004).

There are many reports of microbially facilitated dolomite at low temperature (<80 °C) in which kinetic barriers such as solution supersaturation, sulfate inhibition, Mg desolvation, and nucleation sites are attributed to microbial metabolism and surfaces (e.g., Vasconcelos et al. 1995; Warthmann et al. 2000; Mazullo 2000; van Lith et al. 2003; Moreira et al. 2004; Roberts et al. 2004; Wright and Wacey 2004; Wright and Wacey 2005; Braissant et al. 2007; Bontognali et al. 2008; Sánchez-Román et al. 2008; Sánchez-Román et al. 2009; Kenward et al. 2009; Bontognali et al. 2010; Krause et al. 2012; Kenward et al. 2013; Meister et al. 2007; Petrash et al. 2015). These reports link microorganisms to dolomite formation; however, few studies have identified definitive mechanisms by which microbial activity or surfaces facilitate nucleation and subsequent precipitation at low temperature. Enhanced Mg incorporation into the calcite crystal structure has been linked abiotically to dissolved sulfide, which sorbs onto crystal surfaces and facilitates Mg dehydration (Zhang et al. 2012b). Dolomite and Mg-calcite precipitation has been linked also to exopolymeric substances found in microbial biofilms (Bontognali et al. 2008; Krause et al. 2012) in which carboxyl groups associated with these surfaces or other organic matter complex and dehydrate Mg (e.g., Zhang et al. 2012a; Roberts et al. 2013). Many of these reports are of disordered phases, although there are reports of ordered, stoichiometric dolomite forming at low temperature (e.g., Roberts et al. 2004; Kenward et al. 2009; Kenward et al. 2013; Roberts et al. 2013).

Geological Significance and Occurrence

A long-standing conundrum in the geosciences is the so-called dolomite problem. Modern dolomite is scarce and rarely forms on Earth today due to slow reaction kinetics (<50 °C); however, ancient low-temperature dolomite formed in large quantities in Precambrian oceans and throughout the Phanerozoic from so-called calcite seas, apparently dependent upon secular variation of seawater geochemistry (Hardie 1987). Temporal changes in seawater Mg:Ca ratios, pCO_2, and dissolved sulfate concentrations contribute to thermodynamic favorability of aragonite ($CaCO_3$) versus calcite ($CaCO_3$) and dolomite (Wilkinson and Given 1986). Ancient dolomite formed through both primary precipitation and replacement (dolomitization) of $CaCO_3$, presumably by Mg-rich fluids. In modern systems, primary dolomite is constrained to hypersaline environments, such as lagoons (e.g., Vasconcelos and McKenzie 1997) and sabkha environments (e.g., Wright and Wacey 2005), and evidence of ongoing dolomitization of $CaCO_3$ in low-temperature settings has not been reported.

Large-scale models of carbonate dolomitization, including mixing of seawater and groundwater, reflux dolomitization by mesohaline brines, and (hydro)thermal circulation of seawater, have varying evidence of their contributions to dolomitization (e.g., Machel 2004). These models underpin the prevalence of dolomite as a prolific petroleum reservoir. Its utility as a reservoir is attributed to the fact that dolomite preserves its porosity more readily with burial than other carbonate units (Schmoker and Halley 1982; Sun 1995) due to the increased resistance to mechanical and chemical compaction of dolomite compared to calcite (Gale et al. 2010).

History and Use

Giovanni Arduino, an Italian geologist, is credited with the first identification of the mineral now known as dolomite in 1779 (McKenzie and Vasconcelos 2009); however, Déodat de Dolomieu is credited with recognizing the mineral that makes up the mountains now known as the Dolomite Mountains of Northern Italy (de Dolomieu 1791; Zenger et al. 1994).

In addition to its utility as a petroleum reservoir, dolomite is also used as a paleothermometer and a tracer of seawater geochemistry. It is mined and used as a source of Mg and a pH buffer in soils and is used as a flux for smelting and ceramics.

Summary

Extensive research has been performed on kinetics of dolomite precipitation and dolomitization reactions. These efforts further refine models of large-scale dolomite formation that are found in ancient rock.

Cross-References

- ▶ Calcium
- ▶ Carbonate Compensation Depth
- ▶ Crystal Chemistry
- ▶ Diagenesis
- ▶ Fluid–Rock Interaction
- ▶ Kinetics of Geochemical Processes
- ▶ Low-Temperature Geochemistry
- ▶ Magnesium
- ▶ Mineralogy
- ▶ Ocean Biochemical Cycling and Trace Elements
- ▶ Petroleum

References

Antao S, Mulder W, Hassan I, Crichton W, Parise J (2004) Cation disorder in dolomite, $CaMg(CO_3)_2$, and its influence on the aragonite + magnesite ↔ dolomite reaction boundary. Am Mineral 89:1142–1147

Arvidson R, MacKenzie F (1999) The dolomite problem: control of precipitation kinetics by temperature and saturation state. Am J Sci 299:257–288

Baker P, Kastner M (1981) Constraints on the formation of sedimentary dolomite. Science 213:214–216

Bontognali T, Vasconcelos C, Warthmann R, Dupraz C, Bernasconi S, McKenzie J (2008) Microbes produce nanobacteria-like structures, avoiding cell entombment. Geology 36:663–666

Bontognali T, Vasconcelos C, Warthmann R, Bernasconi S, Dupraz C, Strohmenger C, McKenzie J (2010) Dolomite formation within microbial mats in the coastal sabkha of Abu Dhabi (United Arab Emirates). Sedimentology 57:824–844

Brady P, Krumhans J, Papenguth J (1996) Surface complexation clues to dolomite growth. Geochim Cosmochim Acta 60:727–731

Braissant O, Decho W, Dupraz C, Glunk C, Przekop K, Visscher P (2007) Exopolymeric substances of sulfate-reducing bacteria: interactions with calcium at alkaline pH and implication for formation of carbonate minerals. Geobiology 5:401–411

Carmichael S, Ferry A (2008) Formation of replacement dolomite in the latemar carbonate buildup, dolomite, Northern Italy: part 2. Origin of the dolomitization fluid and the amount and duration of fluid flow. Am J Sci 308:885–904

de Dolomieu D (1791) Sur un genre de pierres calcaires trespeu effervescentes avec les acides et phosphorescentes par la collision. J Phys 39:3–10

Gale J, Lander R, Reed F, Laubach S (2010) Modeling fracture porosity evolution in dolostone. J Struct Geol 32:1201–1211

Gregg J, Bish D, Kaczmarek S, Machel H (2015) Mineralogy, nucleation and growth of dolomite in the laboratory and sedimentary environment: a review. Sedimentology 62:1749–1769

Hardie L (1987) Dolomitization: a critical view of some current views. J Sediment Petrol 57:166–183

Kenward P, Goldstein R, González L, Roberts J (2009) Precipitation of low-temperature dolomite from an anaerobic microbial consortium: the role of methanogenic Archaea. Geobiology 7:556–565

Kenward P, Goldstein R, González L, Fowle D, Ueshima M, Roberts J (2013) Ordered, low-temperature dolomite mediated by carboxyl-group density of microbial cell walls. AAPG Bull 97:2113–2125

Krause S, Liebtrau V, Gorb S, Sanchez-Roman M, McKenzie M, Treude T (2012) Microbial nucleation of Mg-rich dolomite in exopolymeric substances under anoxic modern seawater salinity: new insight into an old enigma. Geology 40:587–590

Land L (1998) Failure to precipitate dolomite at 25°C from dilute solution despite 1000-fold oversaturation after 32 years. Aquat Geochem 4:361–368

Li W, Beard BL, Li C, Xu H, Johnson C (2015) Experimental calibration of Mg isotope fractionation between dolomite and aqueous solution and its geological implications. Geochim Cosmochim Acta 157:164–181

Machel H (2004) Concepts and models of dolomitization: a critical reappraisal. Geol Soc Lond, Spec Publ 235:7–63

Mazullo S (2000) Organogenic dolomitization in peritidal to deep sea sediments. J Sediment Res 70:10–23

McKenzie J, Vasconcelos C (2009) Dolomite Mountains and the origin of the dolomite rock of which they mainly consist: historical developments and new perspectives. Sedimentology 56:205–219

Meister P, McKenzie J, Vasconcelos C, Bernasconi S, Frank M, Guthjahrs M, Schrag M (2007) Dolomite formation in the dynamic deep biosphere: results from the Peru margin. Sedimentology 54:1007–1031

Moreira N, Walter W, Vasconcelos C, McKenzie J, McCall P (2004) Role of sulfide oxidation in dolomitization: sediment and pore-water geochemistry of a modern hypersaline lagoon system. Geology 32:701–704

Petrash D, Lalonde S, Gonzalez-Arismendi G, Gordon R, Gingras M, Konhauser K (2015) Can Mn-S cycling drive sedimentary dolomite formation? A hypothesis. Chem Geol 404:27–40

Reeder R, Wenk H (1983) Structure refinements of some thermally disordered dolomites. Am Mineral 68:769–776

Roberts J, Bennett P, Macpherson G, González L, Milliken K (2004) Microbial precipitation of dolomite in groundwater: field and laboratory experiments. Geology 32:277–280

Roberts J, Kenward P, Fowle D, González L, Goldstein R, Moore D (2013) Surface chemistry allows for precipitation of dolomite at low temperature. PNAS 110:14540–14545

Rodriguez-Blanco J, Shaw S, Benning L (2015) A route for the direct crystallization of dolomite. Am Mineral 100:1172–1181

Sánchez-Román M, Vasconcelos C, Schmid T, Dittrich M, McKenzie J, Zenobi R, Rivadeneyra M (2008) Aerobic microbial dolomite at the nanometer scale: implications for the geologic record. Geology 36:879–882

Sánchez-Román M, McKenzie J, de Luca Rebello Wagner A, Rivadeneyra M, Vasconcelos C (2009) Presence of sulfate does not inhibit low-temperature dolomite precipitation. Earth Planet Sci Lett 285:131–139

Schmoker J, Halley R (1982) Carbonate porosity versus depth: a predictable relation for South Florida. AAPG Bull 66:2561–2570

Sibley D, Dedoes R, Bartlett T (1987) The kinetics of dolomitization. Geology 15:1112–1114

Slaughter M, Hill R (1991) The influence of organic matter in organogenic dolomitization. J Sediment Petrol 61:296–303

Sun S (1995) Dolomite reservoirs: porosity evolution and reservoir characteristics. AAPG Bull 79:186–204

Sun J, Wu Z, Cheng H, Zhang Z, Frost R (2014) A Raman spectroscopic comparison of calcite and dolomite. Spectrochim Acta A Mol Biomol Spectrosc 117:158–162

van Lith Y, Warthmann R, Vasconcelos C, McKenzie J (2003) Sulfate-reducing bacteria induce low-temperature Ca dolomite and high-Mg calcite formation. Geobiology 1:71–79

Vasconcelos C, McKenzie J (1997) Microbial mediation of modern dolomite precipitation and diagenesis under anoxic conditions

(Lagoa Vermelha, Rio de Janeiro, Brazil). J Sediment Res 67:378–390
Vasconcelos C, McKenzie J, Bernasconi S, Grujic D, Tien A (1995) Microbial mediation as a possible mechanism for natural dolomite formation at low temperatures. Nature 377:220–222
Warthmann R, van Lith Y, Vasconcelos C, McKenzie J, Karpoff A (2000) Bacterially induced dolomite precipitation in anoxic culture experiments. Geology 28:1091–1094
Wilkinson B, Given K (1986) Secular variation in abiotic marine carbonates: constraints on Phanerozoic atmospheric carbon dioxide contents and oceanic Mg/Ca ratios. J Geol 94:21–33
Wright D, Wacey D (2004) Sedimentary dolomite: a reality check. In: Braithwaite C, Rizzi G, Darke G (eds) The geometry and petrogenesis of dolomite hydrocarbon reservoirs, Special publication, vol 235. Geological Society, pp 65–74
Wright D, Wacey D (2005) Precipitation of dolomite using sulfate-reducing bacteria from the Coorong region, South Australia: significance and implications. Sedimentology 28:987–1008
Zenger D, Bourrouilh-Le Jan F, Carozzi A (1994) Dolomieu and the first description of dolomite. In: Purser B, Tucker M, Zenger D (eds) Dolomites: a volume in honour of dolomieu, IAS special publication, vol 21, New York, pp 21–28
Zhang F, Xu H, Konishi H, Roden E (2010) A relationship between d104 value and composition in the calcite-disordered dolomite solid-solution series. Am Mineral 95:1650–1656
Zhang F, Xu H, Konishi H, Shelobolina E, Roden E (2012a) Polysaccharide-catalyzed nucleation and growth of disordered dolomite: a potential precursor of sedimentary dolomite. Am Mineral 97:556–567
Zhang F, Xu H, Konishi H, Kemp J, Roden E (2012b) Dissolved sulfide-catalyzed crystallization of Ca-Mg carbonates and implications for the formation mechanism of sedimentary dolomite. Geochim Cosmochim Acta 97:148–165
Zhong S, Mucci A (1989) Calcite and aragonite precipitation from seawater solutions of various salinities: precipitation rates and overgrowth compositions. Chem Geol 78:283–299

Dysprosium

Scott M. McLennan
Department of Geosciences, Stony Brook University, Stony Brook, NY, USA

Element Data
Atomic Symbol: Dy
Atomic Number: 66
Atomic Weight: 162.500(1)
Isotopes and Abundances: ^{156}Dy, 0.056(3)%; ^{158}Dy, 0.095(3)%; ^{160}Dy, 2.329(18)%; ^{161}Dy, 18.889(42)%; ^{162}Dy, 25.475(36)%; ^{163}Dy, 24.896(42)%; and ^{164}Dy, 28.260(54)%
1 Atm Melting Point: 1412 °C
(*continued*)

1 Atm Boiling Point: 2567 °C
Common Valences: +3
Ionic Radii: 91.2 pm (CN6), 102.7 pm (CN8), and 122.8 pm (CN12)
Pauling Electronegativity: 1.22
First Ionization Energy: 573.02 kJ mol^{-1}
Chondritic (CI) Abundance: 0.254 ppm
Silicate Earth Abundance: 0.566 ppm
Crustal Abundance: 3.7 ppm
Seawater Abundance: 1.06 ppt
Core Abundance: ~0

Properties

Dysprosium (Dy), from the Greek *dysprositos* (hard to access), is a soft, ductile, dense (8.551 g cm^{-3}), bright silvery metal. Its electronic configuration is [Xe]4f^{10}6s^{2}. It is stable at room temperature and readily dissolves in mineral acids. It is a group 3 or IIIB inner transition element, with +3 being its only valence state in geological environments, and is one of the lanthanide rare earth elements (REE). In geochemical terminology, it is grouped with heavy rare earth elements (HREE; Gd-Lu). Dysprosium has seven natural, stable isotopes, listed above with their abundances.

More than 270 minerals contain lanthanides as essential structural constituents, but those with Dy as a major component are restricted to Y and HREE varieties, such as xenotime [$Y(PO_4)$], bastnäsite [$REE(CO_3)F$], allanite [$(REE,Ca,Y)_2(Al,Fe^{2+},Fe^{3+})_3(SiO_4)_3(OH)$], and britholite [$(REE,Ca)_5(SiO_4,PO_4)_3(OH,F)$]. In addition, Dy may be enriched in ion adsorption lateritic kaolinite–halloysite clay deposits that are mined for REE.

Details of properties, mineralogy, history, and uses of Dy were compiled from Goonan (2011), Chakhmouradian and Wall (2012), Zaimes et al. (2015), Gschneidner Jr (2016), Hammond (2016), and Meija et al. (2016a, b).

History and Use

Dysprosium was discovered in 1886 by Paul Émile Lecoq de Boisbaudran but not isolated until about 1950. Its major use is as a component for neodymium magnets. Due to a relatively high thermal absorption cross section, Dy_2O_3–nickel ceramic metals (cermets) have been used in nuclear reactor cooling rods. Other uses include as components in lasers, magnets, metallic coatings, ionizing radiation dosimeters, transducers, and infrared radiation sources.

Geochemical Behavior

The fundamental importance of Dy in geochemistry is that it is one of the small trivalent rare earth elements, among the most useful trace elements in all areas of geochemistry and cosmochemistry due to their coherent and systematic behavior as a group, largely a consequence of the "lanthanide contraction."

Dysprosium is typically a trace element in most rocks and minerals. It is classified geochemically and cosmochemically as a highly refractory lithophile element with a 50% $T_{condensation}$ of 1659 K at 10^{-4} bars (Lodders 2003). In most igneous systems, Dy is incompatible with bulk partition coefficients, $D < 1$. In aqueous systems, Dy normally has very low fluid/rock partition coefficients ($\ll 1$). As a result, Dy contents of clastic sediments typically reflect their average provenance abundances.

In seawater, Dy has very low concentrations (~ppt) and residence times (~740 year) with speciation dominated by Dy^{3+}, $DyCO_3^+$, and $Dy(CO_3)_2^-$. In other aqueous systems (e.g., magmatic, hydrothermal), Dy can reach ppm levels due to elevated temperatures, pH effects, and complexing with various ligands (e.g., F^-, Cl^-, OH^-).

Concentration and residence time data are from compilations in Taylor and McLennan (2009) and Nozaki (2001).

Biological Utilization and Toxicity

There are no documented biological uses for Dy, but in China REE have been added to fertilizers and to stock feed to promote growth. REE (including Dy^{3+}) likely substitute for Ca^{2+} in biological materials and processes. REE concentrations (including Dy) in human tissues and fluids are very low (tens of ppb to <ppb levels, respectively) due to very low concentrations in natural waters and low uptake rates throughout the food chain (Bulman 2003). At low levels of ingestion, there are no established toxic effects that pose a threat to human health.

Cross-References

- Incompatible Elements
- Lanthanide Rare Earths
- Lithophile Elements
- Trace Elements
- Transition Elements

References

Bulman RA (2003) Metabolism and toxicity of the lanthanides. In: Sigel A, Sigel H (eds) Metal ions in biological systems, Vol. 40, the lanthanides and their interrelations and Biosystems. Marcel Dekker, Basel, pp 683–703

Chakhmouradian AR, Wall F (2012) Rare earth elements. Elements 8:333–376

Goonan TG (2011) Rare earth elements – end use and recyclability. US Geol Surv Sci Invest Rpt 2011–5094. 15pp

Gschneidner KA Jr (2016) Physical properties of the rare earth metals. In: Haynes WM (ed) CRC handbook of chemistry and physics, 96th edn. CRC Press, Boca Raton, pp 4-115–4-120

Hammond CR (2016) The elements. In: Haynes WM (ed) CRC handbook of chemistry and physics, 96th edn. CRC Press, Boca Raton, pp 4-1–4-42

Lodders K (2003) Solar system abundances and condensation temperatures of the elements. Astrophys J 591:1220–1247

Meija J, Coplen TB, Berglund M, Brand WA, De Bièvre P, Gröning M, Holden NE, Irrgeher J, Loss RD, Walczyk T, Prohaska T (2016a) Atomic weights of the elements 2013. Pure Appl Chem 88:265–291. (IUPAC Technical Report)

Meija J, Coplen TB, Berglund M, Brand WA, De Bièvre P, Gröning M, Holden NE, Irrgeher J, Loss RD, Walczyk T, Prohaska T (2016b) Isotopic compositions of the elements 2013. Pure Appl Chem 88:293–306. (IUPAC Technical Report)

Nozaki Y (2001) Rare earth elements and their isotopes in the ocean. In: Steele JH et al (eds) Encyclopedia of ocean sciences. Academic, London, pp 2354–2366

Taylor SR, McLennan SM (2009) Planetary crusts: their composition, origin and evolution. Cambridge University Press, Cambridge. 378 pp

Zaimes GG, Hubler BJ, Wang S, Khanna V (2015) Environmental life cycle perspective on rare earth oxide production. ACS Sustain Chem Eng 3:237–244

E

Earth's Atmosphere

Daniele L. Pinti
GEOTOP, Research Center on the Dynamics of Earth System, Université du Québec à Montréal, Montréal, QC, Canada

Definition

The Earth's atmosphere is the outer layer of our planet. This layer contains gases, commonly referred to as *air*.

Overview

The atmosphere is retained by the Earth's gravity, although some of it is lost to outer space through thermal escape, known as *Jeans escape*. By volume, dry air contains 78.08% N_2, 20.94% O_2, 0.933% Ar, and 409 ppmv CO_2 (CO_2 data from the Mauna Loa Observatory, April 2017 at https://www.esrl.noaa.gov/gmd/ccgg/trends/monthly.html). The noble gases He, Ne, Kr, and Xe, together with CH_4 and H_2O (as water vapor), occur in trace concentrations (see Table 1). The total mass of the atmosphere is approximately 5.15×10^{18} kg, mainly concentrated in the first layer, called the *troposphere*, which extends from the topographic surface of the planet to 12 km above it.

The atmosphere is divided into five layers, from the surface to outer space: the troposphere (0–12 km), the stratosphere (12–50 km), the mesosphere (50–80 km), the thermosphere (80–700 km), and the exosphere (700–10,000 km). The exosphere merges with the solar wind. The current chemical composition of the atmosphere is the result of several extraterrestrial volatile sources – wet asteroids and comets – deeply modified by the activity of life. Due to these latter processes, the Earth's atmosphere can be classified as *habitable*. The most apparent effect of biological activity on Earth is the progressive accumulation of molecular oxygen (O_2) since the end of the Archean and the formation of the ozone (O_3) layer.

How the atmosphere formed has fascinated philosophers, scholars, and scientists for centuries, since ancient Greece. The advent of cosmochemistry and isotope geochemistry in the twentieth century provided valuable contributions to understanding how the Solar system formed and how rocky planets acquired their atmospheres and oceans. However, recent discoveries made by the Rosetta mission on comet 67P/Churyumov–Gerasimenko might revolutionize our theories of the Earth's formation and the evolution of its differentiated geochemical reservoirs.

History of the Origins

One of the first treatises on the physics of the atmosphere is *Meteorologica* by **Aristotle** (384–322 BC), the title of which comes from the ancient Greek μετέωρον (metéōron, "high in the sky"). In this work, Aristotle attempted to describe everything of a physical nature in the sky. One of the philosophical thoughts of Aristotle was that earthquakes resulted from winds within the Earth caused by the Earth's own heat, as well as heat from the Sun. Volcanoes, he thought, marked the points at which these winds finally escaped from inside the Earth into the atmosphere (Aristotle and Lee 1952). Prior to Aristotle, **Anaximander of Miletus** (611–549) speculated that the Earth began as fluid, some of which dried to become solid earth and some of which evaporated to become the atmosphere.

This vision, in which the atmosphere was derived from the degassing of the interior of the Earth, lasted for centuries. In one of the first treatises of geology, *Mundus subterraneus, quo universae denique naturae divitiae*, the German Jesuit and scholar **Athanasius Kircher** (1602 – 1680) illustrated the interior of the Earth with a central core from which conduits extend to the surface, with intermediate cavities (*pyrophylacies*) filled with fluids and gases. The conduits

W. M. White (ed.), *Encyclopedia of Geochemistry*,
https://doi.org/10.1007/978-3-319-39312-4

Earth's Atmosphere, Table 1 Twenty-first century elemental composition of dry air by volume (Data modified after Gatley et al. 2008)

Constituent (chemical symbol)	Volume %
Nitrogen (N_2)	78.0818
Oxygen (O_2)	20.9435
Argon[a] (Ar)	0.9332
Carbon dioxide[b] (CO^b)	0.0385
Subtotals	99.9970
Neon (Ne)	0.001818
Helium (He)	0.000524
Methane (CH_4)	0.00015
Krypton (Kr)	0.000114
Hydrogen (H_2)	0.00005
Nitrous oxide (N_2O)	0.00003
Xenon (Xe)	0.0000087
Subtotals	0.0026947
Eight trace gases, including CO, O_3, SO_2, NO_2, NH_3, and H_2O	0.0003053
Total	100.0000

Notes: Because Gatley et al. (2008) assumed that increases in CO_2 result from combustion and respiration processes, and the increase is perfectly correlated with a decrease in O_2, then the volume % of O_2 in the 2016 dry air should be 20.9417

[a]The amount of CO_2 reported was measured in 2008. The present-day value (April 28th 2017) is 409.48 ppmv (Mauna Loa Observatory at https://www.esrl.noaa.gov/gmd/ccgg/trends/monthly.html)

[b]NASA continues to use 0.9340 as the volume % for argon, as calculated at the beginning of the twentieth century

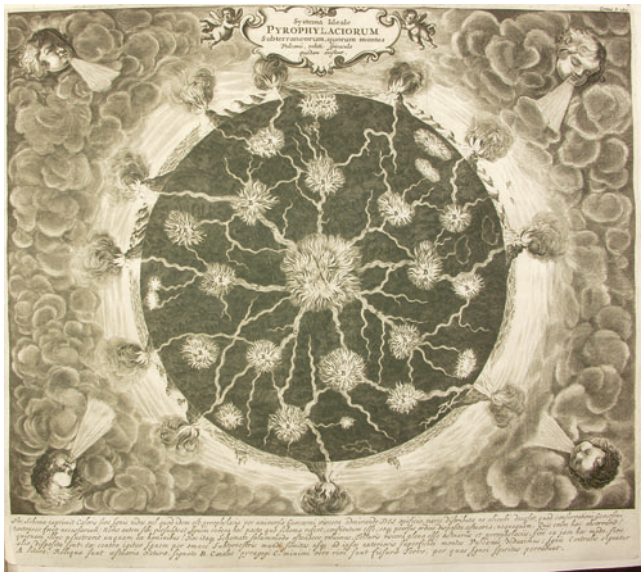

Earth's Atmosphere, Fig. 1 Kircher's vision of the *Mundus Subterraneus* and its interior, in which conduits extend to the surface, with intermediate cavities (pyrophylacies) filled with fluids and gases (From Kircher 1678)

were thought to reach the surface to form volcanoes from which the internal fire escaped to the atmosphere (Fig. 1) (Kircher 1678).

In 1833, the French physicist **André-Marie Ampère** concluded that the Earth's atmosphere resulted from the reduction of oxygenated bodies by metals, leading to the release of nitrogen originally combined with oxygen, also explaining the origin of oxygen in the atmosphere.

Mid-twentieth century, American geologist **William W. Rubey** (1951) wrote a seminal paper entitled *Geological History of Seawater. An attempt to state the problem,* in which he attempted to resolve the origin of the atmosphere and the oceans.

He noticed that the most common volatiles – H_2O, CO_2, Cl, N, and S – are too abundant in the atmosphere, hydrosphere, biosphere, and in ancient sediments to be produced by the weathering of the continental masses, which he assumed to be constant. For example, he estimated that only one hundredth of the 1.37×10^{21} kg of H_2O present in the hydrosphere and atmosphere could be derived from silicate rock weathering. Continents growth throughout the Hadean and Archean eons, reaching the present volume somewhere at the end of the Archean or in the Proterozoic, (e.g., Hawkesworth and Kemp 2006). The supply of volatiles from rock weathering would therefore be even lower than that estimated by Rubey. Furthermore, it is now recognized that the terrestrial mantle contains at least five times the amounts of hydroxides as the global ocean mass in high-pressure mineral phases, such as ringwoodite (Pearson et al. 2014), so any hypothesized source of water on Earth must be able to explain the occurrence of a total water amount of ~8–9 $\times 10^{21}$ kg.

Rubey (1951) noticed that the amount of volatiles "in excess" of those possibly formed by rock weathering was similar to the combined amounts found in gases escaping from volcanoes, fumaroles, hot springs, and in gases trapped in igneous rocks. He concluded that during the crystallization of melts, water and carbon dioxide were preferentially partitioned in the residual melt and then released during the last stages of magma differentiation. Intrusive rocks might have been the main sources of these volatiles, escaping to the atmosphere through hot springs. Again, the hypothesis of a volatile source from the interior of the Earth prevailed.

Modern Theories of Earth's Atmosphere Formation

The hypothesis that the volatiles forming the atmosphere and hydrosphere were degassed from the Earth's interior became even stronger with the advent of noble gas geochemistry. In 1969, American geochemist Harmon Craig and colleagues found ^{3}He anomalies in seawater samples taken at the proximity of the East Pacific Rise (Clarke et al. 1969). In the same year, anomalous helium isotopic compositions (^{3}He/^{4}He ratios) were found in the volcanic gases of Kamkatcha

(Mamyrin et al. 1969). Mamyrin and his colleagues argued that the high $^{3}He/^{4}He$ ratios found was due to ^{3}He production from decay of tritium released during Russian tests. Later tritium measurements in the area dismissed this hypothesis.

^{3}He is a primordial isotope (of solar origin) trapped in the mantle during Earth's accretion from the protosolar nebula (PSN hereafter). It is extremely rare in the atmosphere and the hydrosphere. The presence of ^{3}He in seawater was a clear indication that volatiles are still degassing from the mantle, mainly at the mid-ocean ridges (presently, the ^{3}He flux at MOR is 4 ± 1 atoms $cm^{-2}s^{-1}$; Craig et al. 1975) and in minor amount in back-arc basins (0.6–1.6 atoms $cm^{-2}s^{-1}$; Lan et al. 2010). This degassing is the residual of a catastrophic degassing event which took place within 50–100 Ma of the Earth's formation (Marty 1989; Kunz et al. 1998). This hypothesis was reached after the discovery of the extinct radionuclides, particularly the ^{129}I-^{129}Xe system (e.g., Butler et al. 1963). ^{129}Xe is produced by ^{129}I, a short-lived nuclide with a half-life of 16 Ma. ^{129}Xe, normalized to the primordial ^{130}Xe isotope, is less abundant in the atmosphere ($^{129}Xe/^{130}Xe = 6.496$; Ozima and Podosek 1983) than in the mantle basalts ($^{129}Xe/^{130}Xe \leq 8.2$; Moreira et al. 1998). This means that atmospheric ^{129}Xe was outgassed from the mantle when the parent element was still present, and the two reservoirs were then essentially isolated from each other. Residual ^{129}I in the mantle would have continued to produce ^{129}Xe, creating the isotopic difference between the two reservoirs. This model is consistent with that of the evolution of $^{40}Ar/^{36}Ar$ in the atmosphere (e.g., Sarda et al. 1985). Like ^{3}He, ^{36}Ar is a primordial isotope. ^{40}Ar, present in negligible amounts at the time of terrestrial accretion, has been produced by the decay of ^{40}K, present in the continental crust throughout the Earth's history. The $^{40}Ar/^{36}Ar$ ratio in the atmosphere evolved from nearly zero (2×10^{-4}) to the present-day value of 298.6 by addition of radiogenic ^{40}Ar. All models which take continental crust growth into account predict that more than 80% of the ^{36}Ar was degassed very early in the Earth's history, while ^{40}Ar slowly built up in the atmosphere (Hamano and Ozima 1978; Turner 1989).

If the idea that the atmosphere was derived from volatiles added during Earth's accretion and then degassed from its interior is basically correct; the source of these volatiles is still not completely clear. The Earth's atmosphere, also made up of gases such as oxygen that were added more recently by the activity of life, does not have a solar composition, except for ^{3}He (and possibly ^{20}Ne; see below). The primary atmospheres enveloping the rocky planets were stripped by powerful stellar winds during the first phases of young Sun activity, known as the T-Tauri stage, and only survived in the giant planets of the Solar system. Earth retained a small amount of hydrogen and helium (^{3}He). Indeed, primitive magmatic rocks show $^{3}He/^{4}He$ ratios of up to 60 times (Stuart et al. 2003) the atmospheric ratio ($Ra = 1.382 \times 10^{-6}$; Sano et al. 2013), clearly indicating the occurrence of solar ^{3}He in the Earth's interior. These values are lower than the expected solar ratio of 108 Ra (Geiss et al. 1995), because of the ubiquitous atmospheric contamination of terrestrial rocks.

There is still debate as to whether ^{20}Ne on Earth is also from the PSN (Sarda et al. 1988). ^{20}Ne excesses over ^{22}Ne compared to the ratio in the present atmosphere ($(^{20}Ne/^{22}Ne)_{air} = 9.80$; Ozima and Podosek 1983) were measured in deep CO_2 well gases ($^{20}Ne/^{22}Ne$ up to 11.85 ± 0.04; Ballentine and Holland 2008) and in magmatic rocks from the lower, non-degassed mantle ($^{20}Ne/^{22}Ne$ up to 13 ± 0.7; Matsumoto et al. 1997). More recently, Yokochi and Marty (2004) gave a more precise value of 13.0 ± 0.2 for the Kola plume, while Mukhopadhyay (2012) gave a closer value of 12.88 ± 0.06. ^{20}Ne excesses could either be accounted for by protosolar Ne ($^{20}Ne/^{22}Ne = 13.8$; Benkert et al. 1993; $= 13.4$; Heber et al. 2007) trapped during the accretion of planetesimals or solar wind-implanted (SWI)-Ne ($^{20}Ne/^{22}Ne = 12.5$; Wieler 2002; Raquin et al. 2008). This latter Ne component is mainly recorded in gas-rich meteorites and may have been produced on the meteorite surface by irradiation by the solar wind.

Models of solar system dynamics suggest that the Earth formed in a region of the nascent Solar system too energetic to permit the trapping of volatile elements in the planetary embryos (Fig. 2). The accreting material was essentially dry (e.g., Wanke and Gold 1981). In his model, Javoy (1997) assumed that the Earth was made almost entirely of enstatite chondrites, the driest objects in the solar system, consisting of

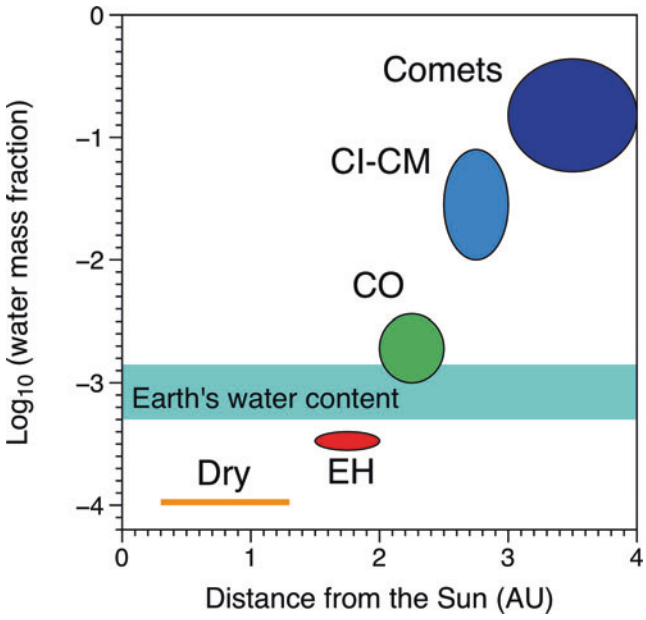

Earth's Atmosphere, Fig. 2 Water content (as a mass fraction of the planetary body) in different objects of the solar system, compared to the Earth's water content, including the mass of the global oceans and five times this mass in the terrestrial mantle ($8–9 \times 10^{21}$ kg) (Redrawn from Dauphas and Morbidelli (2014))

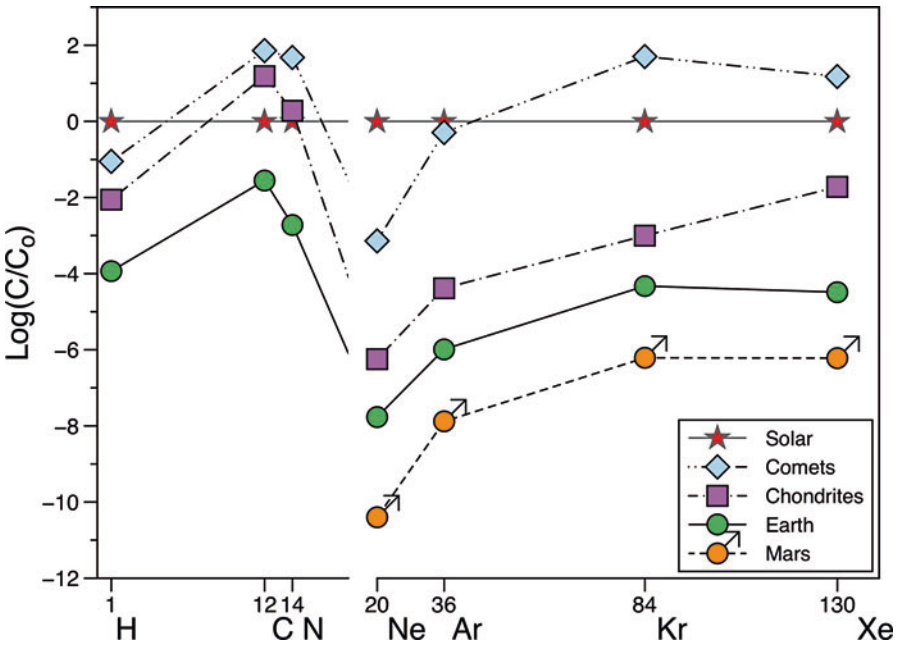

Earth's Atmosphere, Fig. 3 Major volatile (HCN) and noble gas abundances in different objects of the solar system (Mars, CI-CM type chondrites, and comets) compared to abundances in the Earth's atmosphere (labeled "Earth"). Abundances are reported as the logarithm of the ratio of the abundances, normalized to the solar composition. Comet abundances are derived from noble gas-trapping experiments in amorphous ice (calculated at 55 K) (Owen and Bar-Nun 1995). Note the split in the X-axis for clarity (Data are from Dauphas and Morbidelli (2014))

only 0.01% water (Fig. 2). Drake and Righter (2002) suggested an unknown primitive meteoritic material as the building blocks of the Earth, something between ordinary and enstatite chondrites, and almost entirely dry. In conclusion, when the Earth arrived at the waning stages of accretion, it was basically depleted in any sort of volatile.

This ascertainment led to the late veneer theory (Chou 1978). Basically, wet bodies, akin to carbonaceous chondrites, brought the main volatiles and water to a dry proto-Earth at the end of accretion and after core formation (Wanke and Gold 1981). The late veneer theory also elegantly resolved another conundrum: the presence of platinum group elements (PGE) in the mantle. Indeed, it is expected that these highly siderophile elements (HSE) were all drained into the core during the differentiation of the Earth. In order to explain the mantle excesses of PGE, Morgan et al. (1981) postulated the need for a chondritic veneer (C1 type). The mass of chondritic material added to a dry proto-Earth was estimated to range between 0.12% and 0.74% of the whole mantle (Morgan et al. 1981; Dauphas and Marty 2002; Wang and Becker 2013). We will see in the last section that the late veneer did not contribute substantially to the volatile inventory of the hydrosphere-atmosphere, which was instead contributed by chondritic planetary bodies during the Earth's building stages.

Asteroids or Comets: The Long-Standing Controversy

The development of cosmochemistry and isotope geochemistry in the second half of the twentieth century provided a great deal of help in refining the model of Earth's atmosphere and hydrosphere formation.

By looking at the total atmospheric inventory of major gaseous species and noble gases, a complex formation scenario is revealed. In Fig. 3, the total inventories of ^{1}H, ^{14}N, ^{12}C, ^{20}Ne, ^{36}Ar, ^{84}Kr, and ^{130}Xe in the present-day Earth atmosphere, on Mars' surface, in volatile-rich carbonaceous chondrites (CI-CM class meteorites), and in comets are normalized to their solar abundances (data from Dauphas and Morbidelli 2014). Because noble gases are chemically inert, their abundances and isotopic ratios should provide solid constraints on the cosmic reservoirs from which the volatiles originated.

The major volatile elements (H, C, N) in the Earth's atmosphere are one to two orders of magnitude lower than in the chondrites and comets but show a similar pattern. However, the cometary pattern shows a slight enrichment in N with respect to C compared with the present-day Earth's atmosphere (i.e., the C/N ratio in comets is lower than on Earth; Fig. 3). Primordial noble gas isotopes are also depleted in the Earth's atmosphere compared with the other reservoirs, with mass-dependent depletion; Ne being the most depleted and Xe the least depleted compared to the solar abundance. The patterns of Mars and Earth are identical and very close to that of chondrites, except for Xe, which is depleted compared to that in chondrites. This is known as the *missing Xe problem*. Comets are more depleted in Ne and more enriched in Kr than Earth, but they show Xe depletion, like Mars and Earth. It is important to note that the cometary abundances reported in Fig. 3 (and in Dauphas and Morbidelli 2014) are those derived from noble gas-trapping experiments in amorphous ice (calculated at 55 K) (Owen and Bar-Nun 1995). The recent

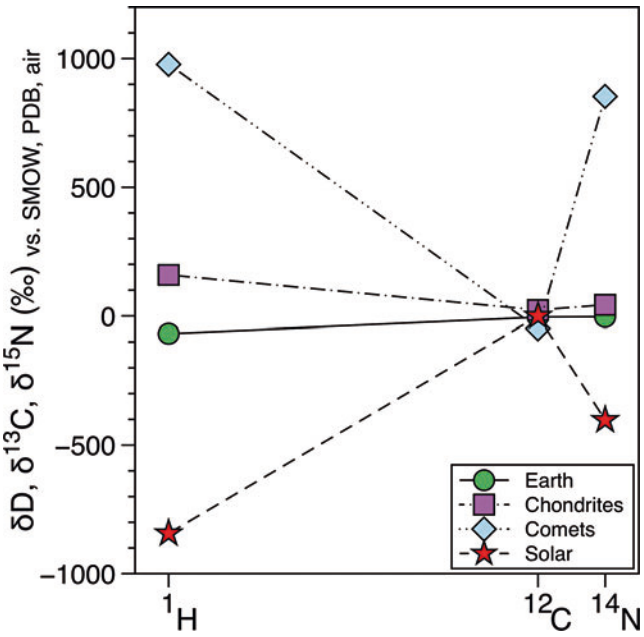

Earth's Atmosphere, Fig. 4 Isotopic composition of major volatiles (HCN) in comets, CI-CM chondrites, and solar compared to those in the Earth (Redrawn from Dauphas and Morbidelli (2014))

Rosetta mission on comet 67P/Churyumov–Gerasimenko only allowed ^{36}Ar to be measured (Marty et al. 2016).

The similarity of the noble gas abundance patterns between the Earth and chondrites suggests that chondrites could be the main external carrier of volatiles (including water) on Earth. This is also supported by similar isotopic ratio patterns of major volatiles (R = ^{2}H/1H, ^{13}C/^{12}C, ^{15}N/^{14}N), as reported in Fig. 4 in delta notation ($\delta i(‰) = [R_{reservoir}/R_{std}]\text{-}1) \times 1000$, where the reference standard (std) is V-SMOW for H, PDB for C, and air for N). The isotopic composition of H, C, and N of Earth and of chondrites (data compiled from Dauphas and Morbidelli 2014) are comparable (Fig. 4), while clearly different from that of comets (except for C). Mars is not reported because its atmospheric isotopic composition is strongly fractionated toward higher values by massive loss of the hydrosphere-atmosphere system (Atreya et al. 2013).

These simple observations suggest that volatile-rich chondrites, such as carbonaceous chondrites, are the main carrier of water and of the atmophile elements on Earth. However, the depletion of Xe (the so-called *missing Xe problem*) calls for a possible contribution from comets. There are numerous hypotheses to explain the missing Xe, such as hidden reservoirs on Earth (in clays (Bernatowicz et al. 1984); in high-pressure phases in the mantle (Sanloup et al. 2005; Dewaele et al. 2016); in the core (Lee and Steinle-Neumann 2006)) or the progressive escape of Xe ions from the early Earth atmosphere, possibly through the interaction with UV light from the young Sun (Pujol et al. 2011). However, the contribution of cometary xenon cannot be excluded. Based on missing Xe, Dauphas (2003) calculated a maximum cometary mass accreted to the Earth of 3×10^{18} kg (i.e., 0.00005% of the Earth's mass). Comets could only have contributed 2–3% the total water budget on Earth by mass ($8–9 \times 10^{21}$kg).

There are two other convincing pieces of evidence that major volatiles and some of the noble gases were brought to Earth by chondritic bodies rather than by comets: the isotopic signature of the oceanic water on Earth and the very recent analysis of volatiles form the coma of the 67P/Churyumov–Gerasimenko comet (Marty et al. 2016).

The water molecule has two elements, H and O. Hydrogen has two stable isotopes (^{1}H and ^{2}H, or D for deuterium), and oxygen has three stable isotopes (^{16}O, ^{17}O, and ^{18}O). The major hydrogen reservoir in the universe is atomic or molecular hydrogen. The isotopic composition of water in several objects of our Solar system, such as comets, chondrites, or planets, shows a systematic enrichment in deuterium, which can be determined by measuring the ^{2}H/^{1}H or D/H ratio (e.g., Robert 2001a) (Fig. 5).

Models of the PSN evolution indicate that once they had entered the nebula, interstellar ice grains vaporized, and the D/H ratio of the resulting deuterium-rich water vapor was lowered through isotopic exchange with molecular hydrogen. Water vapor successively condensed into microscopic icy grains, with decreasing D/H ratios, the closer they were to the Sun. This isotopic gradient reflects the fact that the closer to the Sun, the higher the temperature and the faster the isotopic exchange between water and molecular hydrogen. The D/H heliocentric gradient predicts that the D/H ratio for water condensed at Earth's distance (1 AU) from the Sun should be ~80×10^{-6} or $\delta D = -490‰$ depleted compared the global ocean (V-SMOW = 155.67×10^{-6} or $\delta D = 0‰$ by definition) (Robert 2001a; Fig. 5). The water isotopic composition of the bulk Earth is only slightly depleted compared to the global ocean ($149 \pm 3 \times 10^{-6}$ or $\delta D = -43‰$; Lécuyer et al. 1998) and is very different from the PSN value of $21 \pm 5 \times 10^{-6}$. Giant planets (which have primary atmospheres of solar composition) have D/H ratios ranging from 21 ± 8 to $65 \pm 2 \times 10^{-6}$ (δD from −865 to −580‰), while long period comets from the Oort cloud have D/H ratios much higher than bulk Earth (average D/H of $296 \pm 25 \times 10^{-6}$ or $\delta D = +900‰$; Robert 2001a, b; Hartogh et al. 2011).

Conversely, carbonaceous chondrites show an average D/H of $149 \pm 6 \times 10^{-6}$ ($\delta D = -43‰$; data compiled by Pinti 2005), which encompasses the bulk Earth value (Fig. 5). Antarctic micrometeorites (which have a CM-CR carbonaceous chondrite composition; Kurat et al. 1994) show an average value of $154 \pm 16 \times 10^{-6}$ or $\delta D = -11‰$ (Engrand et al. 1999, data compiled by Pinti 2005; Fig. 5).

The comparison of D/H ratios of water supports the hypothesis that chondrites are the main carrier of volatiles on Earth. However, defenders of the theory of cometary

E

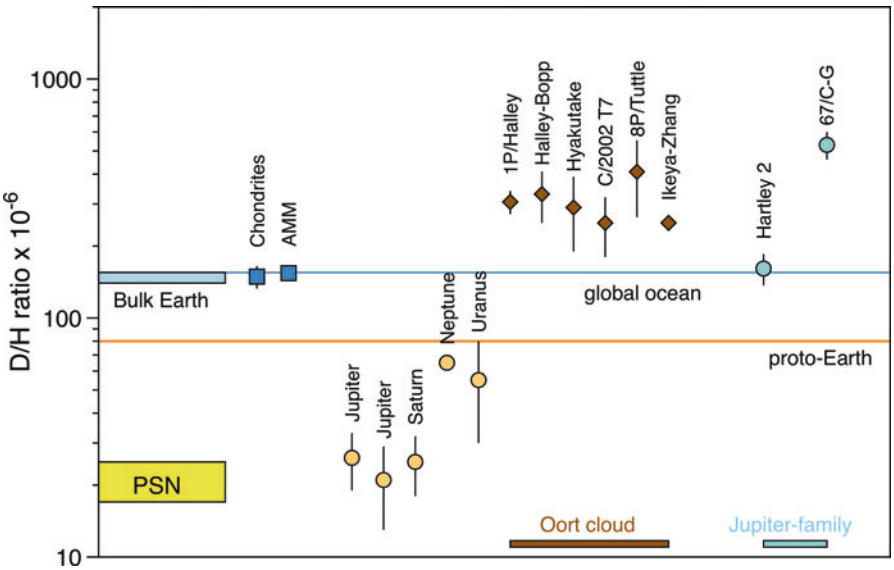

Earth's Atmosphere, Fig. 5 Variation in the D/H ratio in the solar system. Proto-Earth is the expected initial D/H ratio in the region where the Earth formed, based on isotopic exchange models between molecular H and water (Robert 2001a). The bulk Earth value range is from Lécuyer et al. (1998). Gaseous planets, protosolar nebula (PSN) and Oort cloud comet D/H ratios are compiled by Robert (2001b) and Hartogh et al. (2011). Chondrite and Antarctic Micrometeorite (AMM) data are from a literature compilation in Pinti (2005). D/H for the 67P/Churyumov–Gerasimenko comet is from Altwegg et al. (2015)

contribution to water and volatiles on Earth contested that comets formed within the Solar system, in the Kuiper belt (the short-period Jupiter-family comets), are the best candidate to have contributed to the Earth's wetness. Most of the data available are from Oort cloud comets that might have condensed water from the outer Solar system, where isotopic exchange is slow and deuterium is enriched in the water phase. The measurement of a "terrestrial" D/H ratio of $161 \pm 24 \times 10^{-6}$ or $\delta D = +34‰$ in the Jupiter family comet, 103P/Hartley 2, by the Herschel telescope refueled the debate (Hartogh et al. 2011). However, very recent D/H data obtained by in situ coma measurement of the Jupiter family 67P/Churyumov–Gerasimenko comet by the ROSINA mass spectrometer onboard the ROSETTA orbiter seems to have settled the controversy regarding the origin of water. Indeed 67P/Churyumov–Gerasimenko is a short-period comet, presumably originating from the Kuiper belt and yet has the highest D/H ratio among comets. Altwegg et al. (2015) measured a D/H of $530 \pm 70 \times 10^{-6}$ or $\delta D = +2400‰$ in the 67P/Churyumov–Gerasimenko comet (i.e., three times higher than in the bulk Earth; Fig. 5).

More interestingly, the first measurements of noble gas ^{36}Ar, together with major volatiles H, C, and N in the coma of 67P/Churyumov–Gerasimenko comet, allowed to calculate the contribution of chondritic versus cometary material to the Earth volatile inventory (Fig. 6; Marty et al. 2016). Figure 6 reports the $^{36}Ar/H_2O$ (a), $^{36}Ar/N$ (b), and $^{36}Ar/C$ (c, d) versus D/H mixing diagrams between cometary and chondritic (asteroidal) end-members (after Marty et al. 2016). Bulk Earth and Earth surface (hydrosphere + atmosphere) volatile compositions are also reported. From the mixing curves, the cometary % of H, C, and N are estimated to vary from less than 1% for H_2O and C to less than 10% for N. On the other hand, 10 to 90% of ^{36}Ar, and by extension the other heavy noble gases, Kr and Xe, could be of cometary origin. To reconcile these findings with a general model where carbonaceous chondrite material brought the main volatiles to Earth, Marty et al. (2016) suggested that 10% of cometary material could have been added during the Late Heavy Bombardment (LHB), bringing argon, but not substantially affecting the original amounts of major volatiles, brought much earlier by asteroids of chondritic composition.

Timing and Processes of the Earth's Atmosphere Formation

The major volatiles composing the early atmosphere and hydrosphere reservoirs on Earth were brought by asteroids of chondritic composition very early during the accretion of the Earth. There are several lines of evidence suggesting this scenario. First, models of Solar system formation indicate that only a few wet asteroids of carbonaceous chondrite composition, formed originally in the outer asteroid belt, were able to deliver water in the inner Solar system during the waning phases of the Earth's accretion (~70% of the Earth's mass accreted) (Morbidelli et al. 2000). Planetary formation models are also able to simulate the migration of wet planetary embryos from distances of up to 5 AU into the Earth's orbit, delivering water (Raymond et al. 2006). Volatiles added to the planet were partitioned preferentially into melt during the magma ocean episode (complete melt of the planet at the end of its accretion) or during the melt of its surface by the successive impacts. Volatiles, including water, were thus incorporated into the interior of the planet. This process would have been brief and happened very early in the history of the Earth. A model of catastrophic mantle degassing and secondary atmosphere formation based on ^{129}I-^{129}Xe

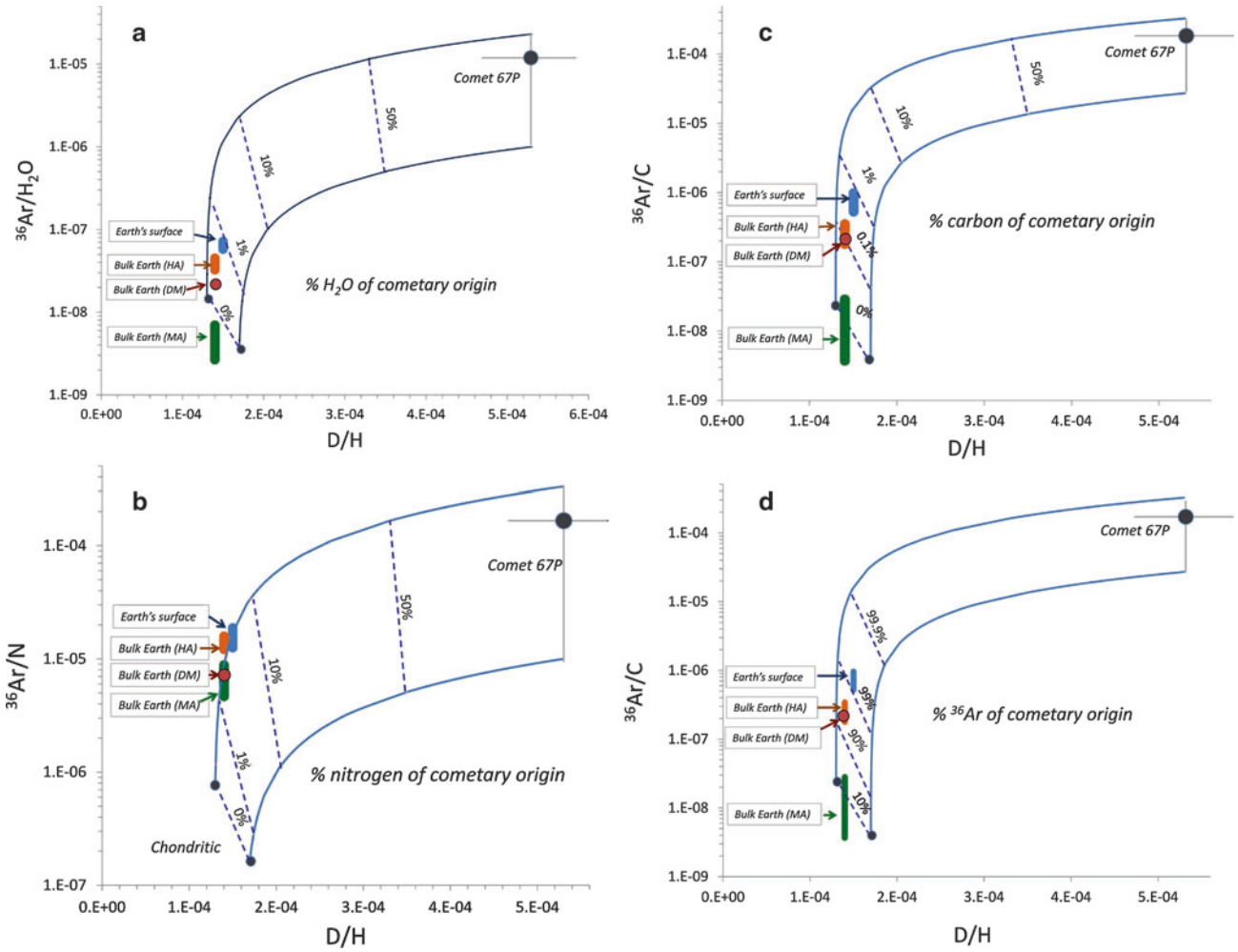

Earth's Atmosphere, Fig. 6 $^{36}Ar/H_2O$ (a), $^{36}Ar/N$ (b), and $^{36}Ar/C$ (c, d) versus D/H mixing diagrams, between cometary and chondritic (asteroidal) end-members. Bulk Earth composition, labeled differently, is from various literature sources (see Marty et al. (2016) for details on bibliographic references). Solid curves represent hyperbolic mixing lines between cometary and chondritic end-members, the curvature factor calculated using known elemental and isotopic compositions of the end-members. *Dotted lines* and associated numbers represent the percentages of volatiles of cometary origin in the mixture (From Marty et al. (2016))

indicated that mantle degassing was likely produced within the first 50 Ma after the Solar system formation (e.g., Kunz et al. 1998; Avice and Marty 2014), which is also the minimum age of the formation of the Earth (30–60 Ma) based on ^{82}Hf-^{182} W systematics (e.g., Kleine et al. 2002; Yin et al. 2002). Consequently, the delivery of volatiles must precede this episode of massive degassing. The impact of a Mars-sized object colliding with the Earth 50–100 Ma after the Solar system formation (Canup and Asphag 2001) could have been the trigger of the catastrophic volatile degassing, including water, from the terrestrial interior (Sleep et al. 2001; Pinti 2005).

The amount of carbonaceous chondrite material added to the mass of the Earth would have had to have been approximately 4% of the Earth's mass (Albarède et al. 2013) (Fig. 7) to explain the entire volatile inventory of the Earth (H, C, Ne, Ar, Kr, and halogens). N and Xe are more depleted on Earth than other volatiles and would require a much smaller amount of chondritic material to be added, equivalent to that of the late veneer (Fig. 7). To reconcile these diverging views, Marty (2012) suggested that the missing N is now partitioned into the core. The missing Xe could be related to late cometary contributions (Dauphas 2003) or to Xe-specific atmospheric loss through geological periods of time (Pujol et al. 2011). Mass balance results reported in Fig. 7 also place strong constraints on the timing of volatile delivery to Earth. Excesses of PGE in the mantle require a smaller contribution of chondritic (or cometary) material, probably less than 0.5%, while volatiles require 4% of accreted mass. To reconcile the volatile and PGE mass balances, we need to assume that volatiles were mainly brought prior to core differentiation. In this case, the accompanying PGE would have been totally segregated into the core, leaving the mantle depleted in these HSEs. The timing of core formation is highly variable and

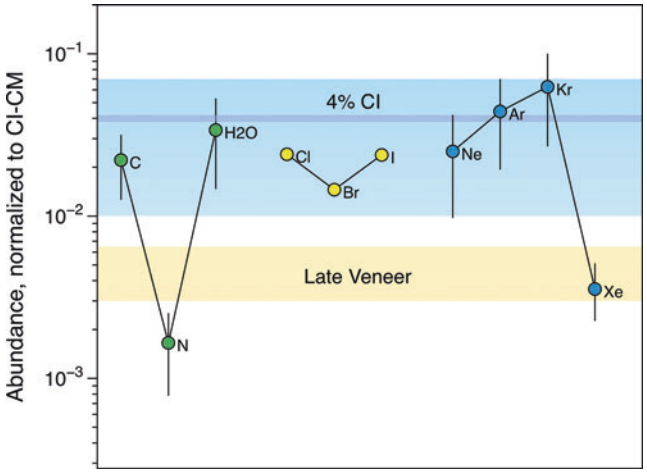

Earth's Atmosphere, Fig. 7 Comparison of the CI-normalized concentrations of terrestrial volatile elements (amounts in the mantle + surface), with the amounts predicted by the conventional late veneer assumption (*pale brown*) and by the addition of 4% CI chondrites (*blue*) (Redrawn from Albarède et al. (2013))

isotopic model dependent. It varies from 30−≥60 Ma after Solar system formation based on ^{182}Hf-^{182}W systematics and possibly terminating within 80–200 Ma after Solar system formation, based on coupled Hf-W and Pb-Pb systems (Nimmo and Kleine 2015). Successive delivery of PGE by 0.5–1% of chondritic material and a smaller percentage of cometary material during a late veneer episode or even during the Late Heavy Bombardment could explain the current PGE excesses in the mantle (Dauphas and Marty 2002) and a late delivery of cometary Ar (and possibly Xe) without considerably affecting the inventory of major volatiles (Marty and Meibom 2007; Marty et al. 2016).

Summary

Resolving the origin of the Earth's atmophile elements has been an intriguing scientific problem for centuries. Development of geochemistry as an Earth science and planetary discipline, particularly isotope geochemistry (noble gases, radiogenic isotopes, and extinct radionuclides) and cosmochemistry, has been an exceptional tool for deciphering between different theories. If the scientific community generally accepts the fact that water and volatiles were brought to Earth by planetary bodies assimilated to CI-CM class carbonaceous chondrites, numerous questions remain unresolved. Among them we can mention, the mechanisms and timing of Earth's ingassing and successive degassing, and the relative contribution to Earth's volatile budget of the late veneer during the LHB compared to the early delivery from wet asteroids. If new volatile data from the ROSETTA mission seem to support the hypothesis of a chondritic origin of the main volatiles on Earth (the D/H ratio dismisses comets as the water carriers to Earth), a new line of questioning is also opened on the origin of the trace gases, particularly the heavier noble gases, Ar, Kr, and Xe. This points out of the importance of in situ measurements or home return samples in future space missions to asteroids (Osirix-Rex, Hayabusa 2) and comets, so as to obtain precise and pristine isotopic data to constrain a univocal mechanism and timing of atmophile arrival to our planet to form a stable atmosphere-hydrosphere system.

Cross-References

- Argon Isotopes
- Atmophile Elements
- Atmospheric Evolution
- Carbon
- Formation and Evolution of the Earth
- Helium Isotopes
- Hydrogen
- Krypton
- Neon Isotopes
- Nitrogen
- Noble Gases
- Water
- Xenon

References

Albarède F, Ballhaus C, Blichert-Toft J, Lee C-T, Marty B, Moynier F, Yin Q-Z (2013) Asteroidal impacts and the origin of terrestrial and lunar volatiles. Icarus 222:44–52

Altwegg K et al (2015) 67P/Churyumov-Gerasimenko, a Jupiter family comet with a high D/H ratio. Science 347

Aristotle, Lee HDP (1952) Meteorologica. Harvard University Press, Cambridge, MA

Atreya SK et al (2013) Primordial argon isotope fractionation in the atmosphere of Mars measured by the SAM instrument on curiosity and implications for atmospheric loss. Geophys Res Lett 40:5605–5609

Avice G, Marty B (2014) The iodine–plutonium–xenon age of the moon–earth system revisited. Phil Trans R Soc A 372:20130260

Ballentine CJ, Holland G (2008) What CO_2 well gases tell us about the origin of noble gases in the mantle and their relationship to the atmosphere. Philos Transact A Math Phys Eng Sci 366:4183–4203

Benkert J-P, Baur H, Signer P, Wieler R (1993) He, ne, and Ar from the solar wind and solar energetic particles in lunar ilmenites and pyroxenes. J Geophys Res Planets 98:13147–13162

Bernatowicz TJ, Podosek FA, Honda M, Kramer FE (1984) The atmospheric inventory of xenon and noble gases in shales: the plastic bag experiment. J Geophys Res Solid Earth 89:4597–4611

Butler WA, Jeffery PM, Reynolds JH, Wasserburg GJ (1963) Isotopic variations in terrestrial xenon. J Geophys Res 68:3283–3291

Canup RM, Asphaug E (2001) Origin of the moon in a giant impact near the end of the Earth's formation. Nature 412:708–712

Chou CL (1978) Fractionation of Siderophile elements in the Earth's upper mantle. Proceedings of 9th lunar and planetary Science Conference, vol 1, pp 219–230

Clarke WB, Beg MA, Craig H (1969) Excess 3He in the sea: evidence for terrestrial primordial helium. Earth Planet Sci Lett 6:213–220
Craig H, Clarke WB, Beg MA (1975) Excess ^{3}He in deep water on the East Pacific rise. Earth Planet Sci Lett 26:125–132
Dauphas N (2003) The dual origin of the terrestrial atmosphere. Icarus 165:326–339
Dauphas N, Marty B (2002) Inference on the nature and the mass of Earth's late veneer from noble metals and gases. J Geophys Res Planets 107:5129. https://doi.org/10.1029/2001JE001617
Dauphas N, Morbidelli A (2014) 6.1 - Geochemical and Planetary Dynamical Views on the Origin of Earth's Atmosphere and Oceans. In: Holland HD, Turekian KK (eds) Treatise on Geochemistry, 2nd edn. Elsevier, Oxford, pp 1–35
Dewaele A, Worth N, Pickard CJ, Needs RJ, Pascarelli S, Mathon O, Mezouar M, Irifune T (2016) Synthesis and stability of xenon oxides Xe_2O_5 and Xe_3O_2 under pressure. Nat Chem 8:784–790
Drake M, Righter K (2002) Determining the composition of the Earth. Nature 416:39–44
Engrand C, DeLoule E, Robert F, Maurette M, Kurat G (1999) Extraterrestrial water in micrometeorites and cosmic spherules from Antarctica: an ion microprobe study. Meteorit Planet Sci 34:773–786
Gatley DP, Herrmann S, Kretzschmar H-J (2008) A twenty-first century molar mass for dry air. HVAC&R Research 14:655–662
Geiss J, Gloeckler G, Von Steiger R (1995) Origin of the solar wind from composition data. Space Sci Rev 72:49–60
Hamano Y, Ozima M (1978) Earth-atmosphere evolution model based on Ar isotopic data. In: Alexander Jr EC, Ozima M (eds.), Terrestrial rare gases. Japan Societies Press, Hakone, Kanagawa, Japan, pp 155–171
Hartogh P, Lis DC, Bockelee-Morvan D, de Val-Borro M, Biver N, Kuppers M, Emprechtinger M, Bergin EA, Crovisier J, Rengel M, Moreno R, Szutowicz S, Blake GA (2011) Ocean-like water in the Jupiter-family comet 103P/Hartley 2. Nature 478:218–220
Hawkesworth CJ, Kemp AIS (2006) The differentiation and rates of generation of the continental crust. Chem Geol 226:134–143
Heber VS, Wiens RC, Reisenfeld DB, Allton JH, Baur H, Burnett DS, Olinger CT, Wiechert U, Wieler R (2007) The genesis solar wind concentrator target: mass fractionation characterised by neon isotopes. In: von Steiger R, Gloeckler G, Mason GM (eds) The composition of matter. Springer, New York, pp 309–316
Javoy M (1997) The major volatile elements of the earth: their origin, behavior, and fate. Geophys Res Lett 24:177–180
Kircher A (1678) Athanasii Kircheri Mundus Subterraneus Athanasii Kircheri Mundus Subterraneus. Apud Joannem Janssonium à Waesberge & filios, Amsterdam
Kleine T, Munker C, Mezger K, Palme H (2002) Rapid accretion and early core formation on asteroids and the terrestrial planets from Hf-W chronometry. Nature 418:952–955
Kunz J, Staudacher T, Allègre CJ (1998) Plutonium-fission xenon found in Earth's mantle. Science 280:877–880
Kurat G, Koeberl C, Presper T, Brandstätter F, Maurette M (1994) Petrology and geochemistry of Antarctic micrometeorites. Geochim Cosmochim Acta 58:3879–3904
Lan TF, Sano Y, Yang TF, Takahata N, Shirai K, Pinti DL (2010) Evaluating earth degassing in subduction zones by measuring helium fluxes from the ocean floor. Earth Planet Sci Lett 298:317–322
Lécuyer C, Gillet P, Robert F (1998) The hydrogen isotope composition of seawater and the global water cycle. Chem Geol 145:249–261
Lee KKM, Steinle-Neumann G (2006) High-pressure alloying of iron and xenon: "Missing" Xe in the Earth's core? Journal of Geophysical Research: Solid Earth 111:B02202
Mamyrin BA, Tolstikhin IN, Anufriev GS, Kamenskyi IL (1969) Anomalous isotopic composition of helium in volcanic gases. Dokl Akad Nauk SSSR 1197. (in Russian)
Marty B (1989) Neon and xenon isotopes in MORB – implications for the earth-atmosphere evolution. Earth Planet Sci Lett 94:45–56
Marty B (2012) The origins and concentrations of water, carbon, nitrogen and noble gases on earth. Earth Planet Sci Lett 313–314:56–66
Marty B, Meibom A (2007) Noble gas signature of the late heavy bombardment in the Earth's atmosphere. eEarth 2:43–49
Marty B, Avice G, Sano Y, Altwegg K, Balsiger H, Hässig M, Morbidelli A, Mousis O, Rubin M (2016) Origins of volatile elements (H, C, N, noble gases) on earth and Mars in light of recent results from the ROSETTA cometary mission. Earth Planet Sci Lett 441:91–102
Matsumoto T, Honda M, McDougall I, Yatsevich I, O'Reilly SY (1997) Plume-like neon in a metasomatic apatite from the Australian lithospheric mantle. Nature 388:162–164
Morbidelli A, Chambers J, Lunine JI, Petit JM, Robert F, Valsecchi GB, Cyr KE (2000) Source regions and timescales for the delivery of water to the earth. Meteorit Planet Sci 35:1309–1320
Moreira M, Kunz J, Allègre C (1998) Rare gas systematics in popping rocks: isotopic and elemental compositions in the upper mantle. Science 279:1178–1180
Morgan JW, Wandless GA, Petrie RK, Irving AJ (1981) Composition of the earth's upper mantle – I. Siderophile trace elements in ultramafic nodules. Tectonophysics 75:47–67
Mukhopadhyay S (2012) Early differentiation and volatile accretion recorded in deep-mantle neon and xenon. Nature 486:101–104
Nimmo F, Kleine T (2015) Early differentiation and core formation: processes and timescales. In: Badro J, Walter M (eds) The early earth: accretion and differentiation, Geophysical Monograph series, vol 212. American Geophysical Union, Washington, DC, pp 83–102
Owen T, Bar-Nun A (1995) Comets, impacts, and atmospheres. Icarus 116:215–226
Ozima M, Podosek FA (1983) Noble gas geochemistry. Cambridge University Press, Cambridge
Pearson DG, Brenker FE, Nestola F, McNeill J, Nasdala L, Hutchison MT, Matveev S, Mather K, Silversmit G, Schmitz S, Vekemans B, Vincze L (2014) Hydrous mantle transition zone indicated by ringwoodite included within diamond. Nature 507:221–224
Pinti DL (2005) The origin and evolution of the oceans. In: Gargaud M, Barbier B, Martin H, Reisse J (eds) Lectures in astrobiology. Springer, Berlin, pp 83–112
Pujol M, Marty B, Burgess R (2011) Chondritic-like xenon trapped in Archean rocks: a possible signature of the ancient atmosphere. Earth Planet Sci Lett 308:298–306
Raquin A, Moreira MA, Guillon F (2008) He, ne and Ar systematics in single vesicles: mantle isotopic ratios and origin of the air component in basaltic glasses. Earth Planet Sci Lett 274:142–150
Raymond SN, Quinn T, Lunine JI (2006) High-resolution simulations of the final assembly of Earth-like planets I: terrestrial accretion and dynamics. Icarus 183:265–282
Robert F (2001a) The origin of water on Earth. Science 293: 1056–1058
Robert F (2001b) L'origine de l'eau dans le Système Solaire telle que est enregistrée par son rapport isotopique D/H. In: Gargaud M, Despois D, Parisot J-P (ed) L'environnement de la Terre primitive. Presses Universitaires de Bordeaux, Bordeaux, France, pp 79–89
Rubey WW (1951) Geologic history of seawater: an attempt to state the problem. GSA Bull 62:1111–1147
Sanloup C, Schmidt BC, Perez EMC, Jambon A, Gregoryanz E, Mezouar M (2005) Retention of xenon in quartz and Earth's missing xenon. Science 310:1174–1177
Sano Y, Marty B, Burnard P (2013) Noble gases in the atmosphere. In: Burnard P (ed) The Noble gases as geochemical tracers. Springer, Berlin, pp 17–31
Sarda P, Staudacher T, Allègre CJ (1985) ^{40}Ar/^{36}Ar in MORB glasses: constraints on atmosphere and mantle evolution. Earth Planet Sci Lett 72:357–375
Sarda P, Staudacher T, Allegre CJ (1988) Neon isotopes in submarine basalts. Earth Planet Sci Lett 91:73–88

E

Sleep NH, Zahnle K, Neuhoff PS (2001) Initiation of clement surface conditions on the earliest Earth. Proc Nat Acad Sci USA 98: 3666–3672
Stuart FM, Lass-Evans S, Godfrey Fitton J, Ellam RM (2003) High 3He/4He ratios in picritic basalts from Baffin Island and the role of a mixed reservoir in mantle plumes. Nature 424:57–59
Turner G (1989) The outgassing history of the Earth's atmosphere. J Geol Soc Lond 146:147–154
Wang Z, Becker H (2013) Ratios of S, se and Te in the silicate earth require a volatile-rich late veneer. Nature 499:328–331
Wanke H, Gold T (1981) Constitution of terrestrial planets [and discussion]. Philos Trans R Soc A Math Phys Eng Sci 303:287–302
Wieler R (2002) Cosmic-ray-produced Noble gases in meteorites. Rev Mineral Geochem 47:125–170
Yin Q, Jacobsen SB, Yamashita K, Blichert-Toft J, Telouk P, Albarède F (2002) A short timescale for terrestrial planet formation from Hf-W chronometry of meteorites. Nature 418:949–952
Yokochi R, Marty B (2004) A determination of the neon isotopic composition of the deep mantle. Earth Planet Sci Lett 225:77–88

Earth's Continental Crust

Roberta L. Rudnick
Department of Earth Science, University of California, Santa Barbara, CA, USA
Department of Geology, University of Maryland, College Park, MD, USA

Definition

The continental crust is typically defined as that portion of the outer rocky layer of the Earth that extends vertically from the surface (subaerial or submarine) to the Mohorovicic discontinuity (or Moho) and laterally to the slope break on continental shelves (Cogley 1984).

Introduction

The continental crust has an average thickness of around 35 km (Hacker et al. 2015; Huang et al. 2013), considerably thicker than oceanic crust, which averages 6.5 km in thickness (White and Klein 2014). The lower density and greater thickness of the continental crust compared to oceanic crust causes it to ride higher on the mantle; consequently, a large proportion (70% by area) is exposed above sea level. Data for the physical properties of the continental crust are given in Table 1.

The continental crust is arguably the best-studied and understood region of the solid Earth, given that we live on the continental crust, that our species evolved on the continents, and that nearly all of the resources required to sustain our civilization derive from it. It thus has an importance disproportionate to its mass, which is only ~0.5% of the silicate portion of the Earth. Despite this proximity, however, there are still first-order questions about the continental crust for which no consensus answers exist. What is the average composition of the continental crust, and how might that composition changed over time? When and how did the continental crust form? How has the volume of continental crust changed over Earth history? What was the nature of the earliest crust on Earth, and how did that crust, which is no longer preserved, compare to the continental crust of today? Each of these major questions are addressed, in turn.

Composition and Structure

While the composition of the upper continental crust is derived by study of rocks exposed at Earth's surface, the structure and composition of the crust at depth have generally been inferred from geophysical data (specifically, seismic and heat flow data, e.g., Christensen and Mooney 1995; McLennan and Taylor 1996; Rudnick and Fountain 1995; Wedepohl 1995). Seismic refraction studies generally divide the crust into layers, varying in number from two to six (see compilations in Pasyanos et al. 2014; Rudnick and Fountain 1995). In general, geochemical models for the crust composition divide the crust into either two or three layers, comprising the upper and lower (e.g., Hacker et al. 2011; Taylor and McLennan 1985; Wedepohl 1995) or upper, middle, and lower continental crust (Gao et al. 1998; Hacker et al. 2015; Rudnick and Fountain 1995). In two-layer crust models the upper crust is generally considered the heat-producing layer, which does not extend below the upper 1/3 of the crust; the one exception is the study of Wedepohl (1995), which splits the crust into roughly equal proportions of upper and lower crust. In reality, it's unlikely that the crust is truly layered, and these hypothetical layers are used as a matter of convenience because many seismic refraction profiles report layers, and also to allow discussion of different portions of the crust.

The upper crust is the most accessible portion of the continental crust, and hence, its composition is the best constrained. Estimates of the composition of the upper continental crust are based on widescale surface sampling (e.g., Eade and Fahrig 1971, 1973; Gao et al. 1998; Shaw et al. 1967, 1976; Togashi et al. 2000), and analyses of fine-grained sediments or sedimentary rocks such as shales (Haskin and Haskin 1966; McLennan and Taylor 1980; Nance and Taylor 1976, 1977), loess (Chauvel et al. 2014; Park et al. 2012; Peucker-Ehrenbrink and Jahn 2001; Sauzéat et al. 2015; Taylor et al. 1983), and river sediments (Kamber et al. 2005), which provide natural averages for relatively insoluble trace elements in the crust that is exposed to weathering and erosion (see summary of methods in Rudnick and Gao 2003). In addition, the fine-grained matrices of glacial diamictites have recently been utilized to determine the major and trace element composition of the upper continental crust (Chen

Earth's Continental Crust, Table 1 Physical parameters of different portions of the continental crust

Units	Density g/cm^3	Thickness km	Mass $\times 10^{21}$ kg	Total Mass %	Total Thickness %	Elevation m
Sed	2.25	1.5	0.7	3.4	4.3	
UC	2.76	11.6	6.7	32.5	33.6	
MC	2.88	11.4	6.9	33.5	33.0	
LC	3.05	10	6.3	30.6	29.0	
Total		34.5	20.6	100	100	
Average	2.87					800

Sed is uppermost sedimentary layer, *UC* upper crust, *MC* middle crust, *LC* lower crust
Data from Huang et al. (2013)

et al. 2016; Gaschnig et al. 2016), following on from the original approach of Goldschmidt (1933). Table 2 provides examples of these estimates of the upper continental crust.

All estimates of upper crust composition are felsic (SiO_2 = 66 to 70 wt.%, 1.6 to 2.5 wt.% MgO) with significant heat-producing element (HPE: K, Th, and U) concentrations (average heat production varies from 1.3 to 1.8 $\mu W\ m^{-3}$). The compositional estimate derived from river sediments and glacial diamictites shows the influence of chemical weathering (i.e., depletion of relatively soluble elements such as Mg, Ca, Na, Sr, and Mo), as both sample the uppermost crust (upper 1–2 m) that has experienced significant chemical modification due to weathering (Gaschnig et al. 2016; Kamber et al. 2005; Li et al. 2016). This strongly weathered signature probably does not extend through the entire upper continental crust. Excluding the elements thus influenced, all major element estimates fall within a factor of 1.7 of each other, and many trace element estimates fall within a factor of two. For three elements listed in the table (e.g., Br, Rh, Te), there is only one estimate of average upper crust composition, and our knowledge of the upper crustal abundances of these elements should be considered preliminary, at best. For some of the trace elements that show more than a factor of two difference between estimates, the variability reflects an outlier composition. For example, the Shaw et al. (1967, 1976, 1986) estimates for C, Sc, Cr, Cu, and Bi are all considerably lower than other estimates for these elements and may reflect the limitations of their study, as they describe: "few sampling areas, inadequate sampling within areas, lack of stratigraphic control" (Shaw et al. 1976). When these outliers are eliminated, all of the remaining estimates for these elements fall within a factor of two of each other. Other outliers are likely related to analytical issues (e.g., the La estimate of Eade and Fahrig 1973; the Nb and Ta estimates of Shaw et al. 1976; and the Sn estimate of Taylor and McLennan 1985), as discussed in Rudnick and Gao (2003). Similarly, the Ru value in Rudnick and Gao (2003), which derives from Peucker-Ehrenbrink and Jahn (2001), may be an analytical artifact (see discussion in Park et al. 2012). Elimination of these compromised values brings the overall variability of different estimates generally to within a factor of two. The exceptions include Be, B, S, Cl, Ni, V, As, Se, Mo, Sb, I, Ba, some of the heavy rare earth elements (HREE), Re, Hg, Tl, the platinum group elements (PGEs), and the elements mentioned above for which there is only a single estimate.

Estimates for the composition of the middle continental crust (that part of the crust between the upper and lower crust, generally defined seismically, see Huang et al. 2013; Rudnick and Fountain 1995) are based on the geochemistry of amphibolite-facies rocks (Gao et al. 1998; Huang et al. 2013; Shaw et al. 1994; Weaver and Tarney 1984) or granulites, corrected for loss of K, Rb, Cs, Th, and U that is associated with high-grade metamorphism (Rudnick and Fountain 1995). The values published in Rudnick and Gao (2003) are mostly averages of previous studies, with some exceptions noted by them. The estimates range from intermediate to felsic compositions (SiO_2 = 62 to 69 wt.%, Table 3), with magnesium numbers (Mg#'s = 100*Mg/(Mg + Fe_T), where "T" denotes all Fe as ferrous iron) that overlap with but range to higher values than observed in upper crustal estimates. Relative to the upper crust, there are very few trace element estimates yet made for the middle crust, and of those available, there is much greater variability among the estimates. Heat production ranges from 0.75 to 1.36 $\mu W\ m^{-3}$ and is generally below that of upper crust estimates. The middle crust is currently the least well-documented portion of the crust from a geochemical perspective.

In contrast to the middle crust, there have been a large number of investigations into the composition of the lower continental crust, though some of these lump middle and lower crust together (e.g., Hacker et al. 2011, 2015; Taylor and McLennan 1985), making direct comparison of compositions potentially misleading. Table 4 presents a subset of lower crustal compositions from the literature (see also Table 7 of Rudnick and Gao 2003). Many investigations use measured seismic velocities of the deep crust (i.e., that crust below the upper crust) and ultrasonic wave speeds of different types of deep crustal rocks determined in the laboratory to infer rock type, and combine these with geochemical data for granulite-facies rocks to derive lower crustal composition (e.g., Rudnick and Fountain 1995; Christensen and Mooney 1995; Wedepohl 1995; see review of methods by Rudnick and Gao 2003 and more recently, Huang et al. 2013). An alternative approach is to calculate equilibrium mineralogy and wave

Earth's Continental Crust, Table 2 Selected compositional estimates for average upper continental crust, along with minimum and maximum values for each element

	Units	1 Shaw et al. (1967, 1976, 1986)	2 Fahrig and Eade (1968) and Eade and Fahrig (1973)	3 Condie (1993)	4 Gao et al.[a] (1998)	5 Wedepohl[b] (1995)	6 Taylor and McLennan (1985, 1995)	7 Togashi et al. (2000)	8 Rudnick and Gao (2003)	9 Kamber et al. (2005)	10 Hu and Gao (2008)	11 Gaschnig et al.[c] (2016) and Chen et al. (2016)	Others[d]	Max/min All	Max/min Outliers removed
SiO_2	wt.%	66.8	66.2	67.0	67.97	66.8	65.89	67.53	66.62	68.5		70.4		1.07	
TiO_2	wt.%	0.54	0.54	0.56	0.67	0.54	0.50	0.62	0.64	1.38		0.7		2.76	
Al_2O_3	wt.%	15.05	16.11	15.14	14.17	15.05	15.17	14.67	15.4	17.6		14.6		1.24	
FeO_T[e]	wt.%	4.09	4.41	4.76	5.33	4.09	4.49	4.85	5.04	7.1		5.5		1.74	
MnO	wt.%	0.07	0.08		0.10	0.07	0.07	0.11	0.10	0.14		0.1		2.00	
MgO[f]	wt.%	2.30	2.23	2.45	2.62	2.30	2.20	2.53	2.48	1.6		2.0		1.65	1.65
CaO[f]	wt.%	4.24	3.44	3.64	3.44	4.24	4.19	3.90	3.59	1.1		1.4		3.78	1.23
Na_2O[f]	wt.%	3.56	3.95	3.55	2.86	3.56	3.89	2.72	3.27	0.8		1.6		4.88	1.45
K_2O	wt.%	3.19	2.91	2.76	2.68	3.19	3.39	2.42	2.80	1.6		3.6		2.31	
P_2O_5	wt.%	0.15	0.16	0.12	0.16	0.15	0.20	0.12	0.15	0.18		0.2		1.67	
Mg#		50.1	47.4	47.9	46.7	50.1	46.6	48.2	46.7	28.5		39.3			
Li	μg/g	22			20	[22]	20		21	28.2	41	31.3	30.5	2.05	
Be	μg/g	1.3			1.95	3.1	3		2.1	1.92	1.9	2.34		2.38	
B	μg/g	9.2			28	17	15		17		47			5.11	
C[g]	μg/g	290			3290	3240								11.34	1.02
N	μg/g					83			83				150	1.81	
F	μg/g	500			561	611			557					1.22	
S	μg/g	600			309	953			621					3.08	
Cl	μg/g	100			142	640			370				631	6.40	
Sc[g]	μg/g	7	12	13.4	15	[7]	13.6[h]	16	14	16.5	14	12.1		2.36	1.38
V	μg/g	53	59	86	98	[53]	107[h]	110	97	120	106	74		2.26	
Cr	μg/g	35	76	112	80	[35]	85[h]	84	92	65	73	53		3.20	2.11
Co[g,i]	μg/g	12		18	17	[12]	17[h]	15	17.3	22.4	15	11.8		1.90	
Ni[i]	μg/g	19	19	60	38	[19]	44[h]	38	47	31.6	34	26.3		3.16	3.16
Cu[g,i]	μg/g	14	26		32	[14]	25	25	28	32.4	27	20.2		2.31	1.58
Zn[i]	μg/g	52	60		70	[52]	71	74	67	73	75	73		1.44	1.44
Ga	μg/g	14			18	[14]	17		17.5	19.1	18.6	18.2		1.36	
Ge	μg/g				1.34	1.4	1.6		1.4		1.3	1.66		1.28	
As	μg/g				4.4	2	1.5	6.8	4.8		5.7			4.53	
Se	μg/g				0.15	0.083	0.05		0.09					3.00	
Br	μg/g					1.6			1.6						
Rb	μg/g	110	85	83	82	110	112	85	84	80	94	110		1.40	
Sr[f]	μg/g	316	380	289	266	[316]	350	225	320	142		91.5		4.15	1.69

Y	µg/g	21	21	24	17.4	[21]	22	26	21	32		33.2		1.91	
Zr	µg/g	237	190	160	188	[237]	190	135	193	199		220		1.76	
Nb[g]	µg/g	26		9.8	12	[26]	12[h]	9	12	15	11.6	12.7		2.89	1.67
Mo[f]	µg/g				0.78	1.4	1.5		1.1		0.6	0.3		5.00	2.50
Ru[j]	ng/g								0.34			0.079	0.030	11.33	2.63
Rh	ng/g												0.018		
Pd	ng/g				1.46		0.5		0.52			0.80	0.53	2.92	
Ag	ng/g				55	55	50		53					1.10	
Cd	ng/g	75			79	102	98		90		60	110		1.83	
In	ng/g					61	50		56		66	62		1.32	
Sn[k]	µg/g				1.73	2.5	5.5		2.1	2.8	2.2	2.5		3.18	1.62
Sb	ng/g				300	310	200	610	400		750	418		3.75	
Te	ng/g										27				
I	ng/g					1.4			1.4				218	156	
Cs	µg/g				3.55	5.8	4.6[h]	5.5	4.9	5.4	4.9	4.3		1.63	
Ba	µg/g	1070	730	633	678	668	550	458	624	396		731		2.70	
La[l]	µg/g	32.3	71	28.4	34.8	[32.3]	30	21.7	31	32.5		37		3.27	1.68
Ce	µg/g	65.6		57.5	66.4	[65.7]	64	46.4	63	71.1		73		1.57	
Pr	µg/g					6.3	7.1	5.54	7.1	8.5		8.54		1.54	
Nd	µg/g	25.9		25.6	30.4		26	20.8	27	32.9		33.3		1.60	
Sm	µg/g	4.61		4.59	5.09	4.7	4.5	4.28	4.7	6.88		6.84		1.61	
Eu	µg/g	0.937		1.05	1.21	0.95	0.88	1.07	1.0	1.57		1.37		1.78	
Gd	µg/g			4.21		2.8	3.8	3.65	4.0	6.36		6.05		2.27	
Tb	µg/g	0.481		0.66	0.82	[0.5]	0.64	0.70	0.7	0.99		0.98		2.06	
Dy	µg/g	2.9				[2.9]	3.5	3.94	3.9	5.89		5.57		2.03	
Ho	µg/g	0.62				[0.62]	0.8	0.72	0.83	1.22		1.13		1.97	
Er	µg/g						2.3	2.39	2.3	3.37	2.3	3.27		1.47	
Tm	µg/g						0.33	0.39	0.30	0.51	0.37	0.51		1.70	
Yb	µg/g	1.47		1.91	2.26	[1.5]	2.2	2.57	2.0	3.25	2.34	3.07		2.21	
Lu	µg/g	0.233		0.32	0.35	[0.27]	0.32	0.4	0.31	0.49	0.36	0.48		2.10	
Hf	µg/g	5.8		4.3	5.12	[5.8]	5.8	4.1	5.3	5.3		6.50		1.59	
Ta[g]	µg/g	5.7		0.79	0.74	1.5	1.0[h]	0.72	0.88	1.12	0.92	0.94		7.92	2.08
W	µg/g				0.91	1.4	2		1.9	1.6	1.4	1.10		2.20	
Re	ng/g						0.4		0.198			0.25	0.176	2.27	
Os	ng/g						0.05		0.031			0.059		1.90	
Ir	ng/g	0.02					[0.02]		0.022			0.036	0.022	1.80	
Pt	ng/g								0.5			0.8	0.599	1.60	
Au	ng/g	1.81			1.24		[1.8]		1.5					1.46	
Hg	ng/g	96			12.3	56			50					7.80	
Tl	µg/g	0.52			1.55	0.75	0.75		0.9	0.42	0.55	0.69		3.69	
Pb[i]	µg/g	17	18	17	18	17	17[h]	16.9	17	20.4		15.8		1.29	1.14

(*continued*)

Earth's Continental Crust, Table 2 (continued)

	Units	1 Shaw et al. (1967, 1976, 1986)	2 Fahrig and Eade (1968) and Eade and Fahrig (1973)	3 Condie (1993)	4 Gao et al.[a] (1998)	5 Wedepohl[b] (1995)	6 Taylor and McLennan (1985, 1995)	7 Togashi et al. (2000)	8 Rudnick and Gao (2003)	9 Kamber et al. (2005)	10 Hu and Gao (2008)	11 Gaschnig et al.[c] (2016) and Chen et al. (2016)	Others[d]	Max/min All	Max/min Outliers removed
Bi[g]	ng/g	35			230	123	130		160		230	240		6.86	1.95
Th	μg/g	10.3	10.8	8.6	8.95	[10.3]	10.7	8.3	10.5	11.1		11.3		1.36	
U	μg/g	2.45	1.5	2.2	1.55	[2.5]	2.8	2.32	2.7	3.27	2.6	2.66		2.18	
Heat production	$\mu W/m^3$	1.65	1.41	1.43	1.27	1.66	1.79	1.41	1.7	1.80		1.81			

Major elements recast to 100% anhydrous
Mg# = molar 100*Mg/(Mg + Fe_T)
[a]Calculated on a sedimentary rock-free carbonate basis
[b]Wedepohl's upper crust is largely derived from the Canadian Shield composites of Shaw et al. (1967, 1976). Values taken directly from Shaw et al. are shown in brackets
[c]Preferred values from Table 4 of Gaschnig et al. (2016), except for Be, Ga, In, Sn, and Tl data, which come from preferred values of Table 5 in the same reference
[d]Values taken from studies of individual elements: Li value from Sauzeat et al. (2015); N value from Johnson and Goldblatt (2015); platinum group elements and Re from Park et al. (2012)
[e]Total Fe as FeO
[f]Values of Kamber et al. (2005) and Gaschnig et al. (2016) reflect depletion due to chemical weathering of surficial layer
[g]Values of Shaw et al. are outliers
[h]Value from McLennan (2001)
[i]Values of Kamber et al. (2005) elevated due to anthropogenic input
[j]Value in Rudnick and Gao is analytical artifact
[k]Value in Taylor and McLennan is analytical artifact
[l]Value in Eade and Fahrig is an analytical artifact; see text for discussion of each of these outliers

Earth's Continental Crust, Table 3 Selected compositional estimates for average middle continental crust, along with the ratio of minimum and maximum values for each element

	Units	1 Weaver and Tarney (1984)	2 Shaw et al. (1994)*	3 Rudnick and Fountain (1995)	4 Gao et al. (1998)	5 Rudnick and Gao (2003)	6 Others[a]	Max/min All
SiO_2	wt.%	68.1	69.4	62.4	64.6	63.5		1.11
TiO_2	wt.%	0.31	0.33	0.72	0.67	0.69		2.35
Al_2O_3	wt.%	16.33	16.21	15.96	14.08	15.0		1.16
FeO_T[b]	wt.%	3.27	2.72	6.59	5.45	6.02		2.43
MnO	wt.%	0.04	0.03	0.10	0.11	0.10		3.51
MgO	wt.%	1.43	1.27	3.50	3.67	3.59		2.88
CaO	wt.%	3.27	2.96	5.25	5.24	5.25		1.78
Na_2O	wt.%	5.00	3.55	3.30	3.48	3.39		1.52
K_2O	wt.%	2.14	3.36	2.07	2.52	2.30	1.82	1.84
P_2O_5	wt.%	0.14	0.15	0.10	0.19	0.15		1.88
Mg#		43.8	45.5	48.6	54.5	51.5		
Li	μg/g		20.5	7	16	12		2.93
Be	μg/g				2.29	2.29		
B	μg/g		3.2		17	17		5.31
C	μg/g				3520			
N	μg/g							
F	μg/g				524	524		
S	μg/g				20	20		
Cl	μg/g				182	182		
Sc	μg/g		5.4	22	15	19		4.07
V	μg/g		46	118	95	107		2.57
Cr	μg/g	32	43	83	69	76		2.59
Co	μg/g		30	25	18	22		1.67
Ni	μg/g	20	18	33	34	33.5		1.89
Cu	μg/g		8	20	32	26		4.00
Zn	μg/g		50	70	69	69.5		1.40
Ga	μg/g			17	18	17.5		1.06
Ge	μg/g				1.13	1.13		
As	μg/g				3.1	3.1		
Se	ng/g				0.064	0.064		
Br	μg/g							
Rb	μg/g	74	92	62	67	65		1.48
Sr	μg/g	580	465	281	283	282		2.06
Y	μg/g	9	16	22	17.0	20		2.44
Zr	μg/g	193	129	125	173	149		1.54
Nb	μg/g	6	8.7	8	11	10		1.83
Mo	μg/g		0.3		0.60	0.60		2.00
Ru	ng/g							
Rh	ng/g							
Pd	ng/g				0.76	0.76		
Ag	ng/g				48	48		
Cd	ng/g				61	61		
In	ng/g							
Sn	μg/g				1.30	1.30		
Sb	ng/g				280	280		
Te	ng/g							
I	ng/g							
Cs	μg/g		0.98	2.4	1.96	2.2		2.45
Ba	μg/g	713	1376	402	661	532		3.42
La	μg/g	36	22.9	17	30.8	24		2.12

(*continued*)

Earth's Continental Crust, Table 3 (continued)

	Units	1 Weaver and Tarney (1984)	2 Shaw et al. (1994)*	3 Rudnick and Fountain (1995)	4 Gao et al. (1998)	5 Rudnick and Gao (2003)	6 Others[a]	Max/min All
Ce	μg/g	69	42.1	45	60.3	53		1.64
Pr	μg/g			5.8		5.8		
Nd	μg/g	30	18.3	24	26.2	25		1.64
Sm	μg/g	4.4	2.8	4.4	4.74	4.6		1.69
Eu	μg/g	1.09	0.78	1.5	1.20	1.4		1.92
Gd	μg/g		2.11	4.0		4.0		1.90
Tb	μg/g	0.41	0.28	0.58	0.76	0.7		2.71
Dy	μg/g		1.54	3.8		3.8		2.47
Ho	μg/g			0.82		0.82		
Er	μg/g			2.3		2.3		
Tm	μg/g	0.14				0.32		2.29
Yb	μg/g	0.76	0.63	2.3	2.17	2.2		3.65
Lu	μg/g	0.1	0.12	0.41	0.32	0.4		4.10
Hf	μg/g	3.8	3.3	4.0	4.79	4.4		1.45
Ta	μg/g		1.8	0.6	0.55	0.6		3.27
W	μg/g				0.60	0.60		
Re	ng/g							
Os	ng/g							
Ir	ng/g							
Pt	ng/g				0.85	0.85		
Au	ng/g				0.66	0.66		
Hg	ng/g				7.9	7.9		
Tl	μg/g				0.27	0.27		
Pb	μg/g	22	9.0	15.3	15	15.2		2.44
Bi	ng/g				0.17	0.17		
Th	μg/g	8.4	6.4	6.1	6.84	6.5	4.86	1.73
U	μg/g	2.2	0.9	1.6	1.02	1.3	0.97	2.44
Heat production	$\mu W/m^3$	1.36	0.97	1.03	0.97	1.00	0.75	

Major elements recast to 100% anhydrous
Mg# = molar 100*Mg/(Mg + FeT)
[a]Values taken from studies of individual elements: K, Th, and U from Huang et al. (2013)
[b]Total Fe as FeO
*Taken from the Wawa average of Table 3 in Shaw et al. with Fe_2O_3 converted to FeO and major elements re-normalized to 100%

speeds for granulite-facies rocks as a function of pressure and temperature to infer lithology and composition (Behn and Kelemen 2003; Hacker et al. 2011, 2015).

In nearly every seismic survey, the velocity of the continental crust increases with depth (see summaries in Christensen and Mooney 1995; Pasyanos et al. 2014; Rudnick and Fountain 1995). Temperature and pressure also increase with depth, and while P-wave velocities decrease with increasing temperature by $\sim -4 \times 10^{-4}$ km s^{-1} $°C^{-1}$, they increase with pressure (2×10^{-4} km s^{-1} MPa^{-1}; see references in Rudnick and Fountain 1995 for the temperature and pressure derivatives). Nevertheless, the in situ velocity of a given rock will either stay approximately the same (in areas of low heat flow) or will decrease (in areas of high heat flow) with depth in the crust (see Fig. 1 of Rudnick and Fountain 1995). Therefore, the increasing seismic velocity with depth reflects either metamorphic recrystallization, causing an increase in the bulk and shear moduli ($V_p = \sqrt{\frac{\kappa + \frac{4}{3}\mu}{\rho}}$, where K is the bulk modulus, μ is the shear modulus, and ρ is the density) and/or increasingly mafic compositions with depth, as seismic velocity increases with decreasing SiO_2 for rocks of a given metamorphic grade (Fig. 1). Despite this correlation between composition and seismic velocities, the latter may vary by over 10% for a given bulk composition depending on mineralogy (Fig. 1). Moreover, metapelitic rocks (metamorphosed mudstones and shales) show a huge range in seismic velocities, depending upon the original proportion of clay to quartz in the sample and the amount of melt

Earth's Continental Crust, Table 4 Selected compositional estimates for average lower continental crust, along with ratios of the minimum and maximum for each element

	Units	1 Weaver and Tarney (1984)	2 Rudnick and Fountain (1995)	3 Wedepohl (1995)	4 Gao et al.[a] (1998)	5 Taylor and McLennan[b] (1985), 1995	6 Rudnick and Gao (2003)	7 Hacker et al.[b] (2011)	8 Hacker et al. (2015) felsic	9 Hacker et al. (2015) mafic	10 Others[c]	Max/min All
SiO_2	wt.%	62.9	53.4	59.0	59.8	54.3	53.4	64.4	61.9	48.6		1.33
TiO_2	wt.%	0.5	0.82	0.85	1.04	0.97[d]	0.82	0.7	0.78	1.4		2.00
Al_2O_3	wt.%	16.0	16.9	15.8	14.0	16.1	16.9	14.8	16.1	18.1		1.29
FeO_T[e]	wt.%	5.4	8.57	7.47	9.30	10.6	8.57	6.1	6.52	10.44		1.73
MnO	wt.%	0.08	0.10	0.12	0.16	0.22	0.10	0.1	0.11	0.18		2.19
MgO	wt.%	3.5	7.24	5.32	4.46	6.28	7.24	2.5	3.14	6.87		2.90
CaO	wt.%	5.8	9.59	6.92	6.20	8.48	9.59	3.4	5.77	10.11		2.97
Na_2O	wt.%	4.5	2.65	2.91	3.00	2.79	2.65	2.8	3.92	2.85		1.48
K_2O	wt.%	1.0	0.61	1.61	1.75	0.64[d]	0.61	1.5	1.54[f]	1.22[f]	1.82	2.98
P_2O_5	wt.%	0.19	0.10		0.21		0.10	0.1	0.21	0.23		2.30
Mg#		53.4	60.1	55.9	46.1	51.4	60.1	42.2	46.2	54.0		
Li	μg/g		6	13	13	11	13	7			8	2.17
Be	μg/g			1.7	1.1	1.0	1.4					1.70
B	μg/g			5	7.6	8.3	2					4.15
C	μg/g			588	2900							4.93
N	μg/g			34			34				17	2.00
F	μg/g			429	703		570					1.64
S	μg/g			408	231		345					1.77
Cl	μg/g			278	216		250				322	1.49
Sc	μg/g		31	25	26	35[d]	31	21.8				1.42
V	μg/g		196	149	185	271[d]	196	84				2.33
Cr	μg/g	88	215	228	123	219[d]	215	51				4.47
Co	μg/g		38	38	36	33[d]	38	23.5				1.62
Ni	μg/g	58	88	99	64	156[d]	88	31				3.19
Cu	μg/g		26	37	50	90	26	14				6.43
Zn	μg/g		78	79	102	83	78	71				1.44
Ga	μg/g		13	17	19	18	13	19				1.48
Ge	μg/g			1.4	1.24	1.6	1.3					1.29
As	μg/g			1.3	1.6	0.8	0.2					8.11
Se	ng/g			170	170	50	200					4.00
Br	μg/g			0.28			0.3					1.07
Rb	μg/g	11	11	41	56	12[d]	11	41	14	17		5.05
Sr	μg/g	569	348	352	308	230	348	206	320	289		1.71
Y	μg/g	7	16	27	18	19	16	25	20.6	21		1.70
Zr	μg/g	202	68	165	162	70	68	156	127	72		2.43

(*continued*)

Earth's Continental Crust, Table 4 (continued)

	Units	1 Weaver and Tarney (1984)	2 Rudnick and Fountain (1995)	3 Wedepohl (1995)	4 Gao et al.[a] (1998)	5 Taylor and McLennan[b] (1985), 1995	6 Rudnick and Gao (2003)	7 Hacker et al.[b] (2011)	8 Hacker et al. (2015) felsic	9 Hacker et al. (2015) mafic	10 Others[c]	Max/min All
Nb	μg/g	5	5.0	11	10	6.7[d]	5	10	7.1	4.9		2.31
Mo	μg/g			0.6	0.54	0.8	0.6					1.47
Ru	ng/g						0.75					
Rh	ng/g											
Pd	ng/g				2.78	1	2.8					2.80
Ag	ng/g			80	51	90	65					1.77
Cd	ng/g			101	97	98	100					1.04
In	ng/g			52		50	50					1.04
Sn	μg/g			2.1	1.34	1.5	1.7					1.57
Sb	ng/g			30	90	200	100					6.67
Te	ng/g											
I	ng/g			140			140				11	12.73
Cs	μg/g		0.3	0.8	2.6	0.47[d]	0.3	0.2[f]				8.60
Ba	μg/g	757	259	568	509	150	259	390	419	204		3.79
La	μg/g	22	8	27	29	11	8	19	20	8		3.60
Ce	μg/g	44	20	53	53	23	20	53	46	19		2.79
Pr	μg/g			7.4		2.8	2.4	8	5.1	2.5		3.37
Nd	μg/g	19	11	28	25	13	11	26	22	13		2.55
Sm	μg/g	3.3	2.8	6.0	4.65	3.17	2.8	5.4	4.1	2.9		2.14
Eu	μg/g	1.18	1.1	1.6	1.39	1.17	1.1	1.6	1.1	1.1		1.45
Gd	μg/g		3.1	5.4		3.13	3.1	4.6	3.7	3.5		1.74
Tb	μg/g	0.43	0.48	0.81	0.86	0.59	0.48	0.8	0.66	0.52		1.80
Dy	μg/g		3.1	4.7		3.6	3.1	3.4	3.1	3.6		1.52
Ho	μg/g		0.68	0.99		0.77	0.68	0.68	0.61	0.75		1.62
Er	μg/g		1.9			2.2	1.9	2	1.6	2		1.38

Tm	μg/g	0.19				0.32	0.24					1.32
Yb	μg/g	1.2	1.5	2.5	2.29	2.2	1.5	2.5	1.5	1.8		1.67
Lu	μg/g	0.18	0.25	0.43	0.38	0.29	0.25	0.5	0.24	0.3		2.08
Hf	μg/g	3.6	1.9	4.0	4.2	2.1	1.9	3.3	3.5	1.7		2.48
Ta	μg/g		0.6	0.8	0.6	0.7[d]	0.6	0.4	0.42	0.34		2.47
W	μg/g			0.6	0.51	0.6[d]	0.6					1.17
Re	ng/g					0.4	0.18					2.22
Os	ng/g					0.05	0.049					1.02
Ir	ng/g					0.13	0.05					2.60
Pt	ng/g				2.87		2.7					1.06
Au	ng/g				1.58	3.4	1.6					2.16
Hg	ng/g			21	6.3		14					3.33
Tl	μg/g			0.26	0.38	0.23	0.32					1.65
Pb	μg/g	13	4	12.5	13	5.0[d]	4	14	10.2	5.3		3.50
Bi	ng/g			37	380	38	200					10.27
Th	μg/g	0.42	1.2	6.6	5.23	2.0[d]	1.2	5.6	1.26	0.75	4.86	8.80
U	μg/g	0.05	0.2	0.93	0.86	0.53[d]	0.2	0.7	0.29	0.25	0.97	4.85
Heat production	$\mu W/m^3$	0.12	0.19	0.85	0.75	0.34	0.19	0.71	0.29	0.22		

Major elements recast to 100% anhydrous
Mg# = molar 100*Mg/(Mg + Fe_T)
[a]Model CEC3
[b]Combined middle and lower crust
[c]Values taken from studies of individual elements: K, Th, and U from Huang et al. (2013); Li from Teng et al. (2008); N from Johnson and Goldblatt (2015); Cl and I from Muramatsu and Wedepohl (1998, mixing 62% felsic granulite with 38% mafic granulite; nb that lower crust represents approximately 50% of total crust)
[d]Value from McLennan (2001)
[e]Total Fe as FeO
[f]Corrected value from misprint in published paper, via personal communication from the author

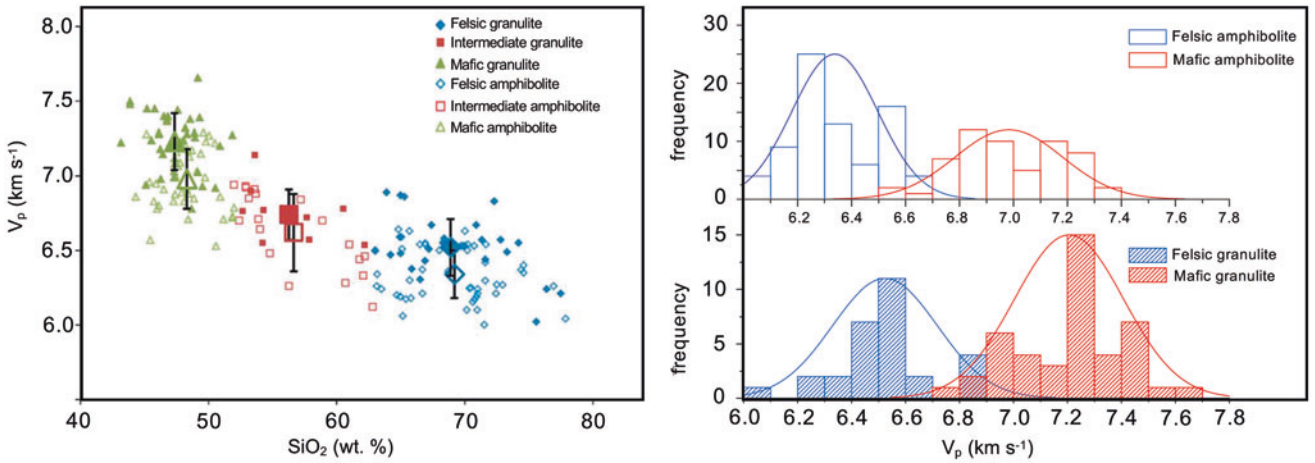

Earth's Continental Crust, Fig. 1 (**a**) Correlation between SiO_2 content and laboratory measured room-temperature ultrasonic velocities of amphibolite- and granulite-facies rocks of different bulk composition: mafic = 45 to 52 wt.% SiO_2, intermediate = 52 to 63 wt.% SiO_2, felsic >63 wt.% SiO_2. (**b**) Histograms of the same data shown in panel **a** (Modified from Huang et al. 2013)

extraction they experienced during metamorphism. The elastic properties of quartz, the second-most common crustal mineral, are also quite unusual with respect to most crustal minerals, causing further uncertainty (Abers and Hacker 2016). Thus, constraining the proportion of metasedimentary rocks in the lower crust from seismic velocity is difficult (Rudnick and Fountain 1995).

This ambiguity in using seismic velocities to infer rock type forms the cornerstone of one of the current debates regarding the composition of the deep crust. Whereas most studies using seismic velocities to infer deep crustal composition have concluded that the crust becomes more mafic with depth (Christensen and Mooney 1995; Huang et al. 2013; Rudnick and Fountain 1995; Wedepohl 1995), an alternative hypothesis (driven by the relamination scenario, which is described in the next section) is that the lower crust is composed of relatively felsic rock types, including metapelites (Hacker et al. 2011, 2015). Heat flow data currently provide only broad constraints on the composition of the deep crust: heat production must decrease with increasing depth (see Jaupart and Mareschal 2014, for a recent review), and a felsic lower crust produces a surface heat flow that is at the upper bounds of those permitted by heat flow data (Hacker et al. 2011).

As can be seen from Table 4, the different compositional models for average lower crust vary from mafic to intermediate (48.6 to 64.4 wt.% SiO_2, MgO = 2.5 to 7.2 wt.%, and Mg# = 46 to 60). Interestingly, the two studies that consider the lower crust as the lower ⅔ to ½ of the crust fall at different ends of the compositional spectrum: the Taylor and McLennan (1985) lower crust is the most mafic (54 wt.% SiO_2, 6.3 wt.% MgO), whereas the Hacker et al. (2011) lower crustal model is the most felsic (64 wt.% SiO_2, 2.5 wt.% MgO). Heat production varies by a factor of seven among all models listed in Table 4, with the least radioactive crust being the relatively felsic composition of Weaver and Tarney (1984), who used the extremely HPE-depleted Scourian granulites to represent the lower crust.

Composition of the Bulk Continental Crust and Implications for Its Formation

The bulk continental crust is estimated, by all who have undertaken such an exercise, to be "intermediate" in composition (see Rudnick and Gao 2003 for the most recent review on the methods used to estimate crust composition and Hacker et al. (2015) and Huang et al. (2013) for updated perspectives on its average composition). If cast in terms of an igneous rock type, the bulk crust would be called "andesitic," sensu lato, in that all estimates have between 57 and 65 wt.% SiO_2 (Table 5). This intermediate composition distinguishes the continental crust from all other planetary crusts recognized in our solar system, which are dominated by basalt (Fegley 2014; McCoy and Nittler 2014; McSween and McLennan 2014). The significance of an "andesitic" continental crust on Earth is twofold: (1) it points to more protracted processes of crust formation on Earth compared to other planets, as andesite, unlike basalt, is not a primary melt of peridotitic mantle, and (2) the majority of andesites on Earth are generated in subduction zones (indeed, the type locality for andesite is the Andes), suggesting a link between generation of the continental crust and subduction, one of the defining processes of plate tectonics on Earth (e.g., Taylor 1977).

Despite the overall andesitic bulk composition of the continental crust, andesite (or its intrusive equivalent, diorite) is not a particularly common rock type within the crust, and the average andesitic composition reflects the fact that the continental crust is a mixture of a wide array of rock types, particularly mafic igneous rocks such as basalts and gabbros

Earth's Continental Crust, Table 5 Selected compositional estimates for average bulk continental crust, along with ratios of maximum/minimum values for each element

	Units	1 Taylor (1964)	2 Weaver and Tarney (1984)	3 Shaw et al. (1986)	4 Christensen and Mooney (1995)	5 Rudnick and Fountain (1995)	6 Wedepohl (1995)	7 Gao et al.[a] (1998)	8 Taylor and McLennan (1985, 1995)	9 Rudnick and Gao (2003, 2014)	10 Hacker et al. (2011)	11 Hacker et al.[b] (2015) most mafic	12 Hacker et al.[b] (2015) most felsic	13 Others[c]	Max/min
SiO_2	wt.%	60.4	63.9	64.5	62.4	60.1	62.8	64.2	57.1	60.6	65.2	56.0	65.4		1.17
TiO_2	wt.%	1.0	0.6	0.7	0.9	0.7	0.7	0.8	0.9	0.72	0.7	1.1	0.7		1.83
Al_2O_3	wt.%	15.6	16.3	15.1	14.9	16.1	15.4	14.1	15.9	15.9	15.0	16.7	15.7		1.18
FeO_T[d]	wt.%	7.3	5.0	5.7	6.9	6.7	5.7	6.8	9.1	6.7	5.8	8.7	5.3		1.83
MnO	wt.%	0.12	0.08	0.09	0.10	0.11	0.10	0.12	0.18	0.10	0.10	0.17	0.1		2.22
MgO	wt.%	3.9	2.8	3.2	3.1	4.5	3.8	3.5	5.3	4.7	2.5	5.2	2.4		2.17
CaO	wt.%	5.8	4.8	4.8	5.8	6.5	5.6	4.9	7.4	6.4	3.4	7.1	4.3		2.17
Na_2O	wt.%	3.2	4.2	3.4	3.6	3.3	3.3	3.1	3.1	3.1	3.0	3.2	3.7		1.42
K_2O	wt.%	2.5	2.1	2.4	2.1	1.9	2.7	2.3	1.3	1.8	1.9	1.75	2.21		2.69
P_2O_5	wt.%	0.24	0.19	0.14	0.20	0.20		0.18		0.1	0.1	0.2	0.2		2.41
Mg#		48.7	50.5	50.1	44.8	54.3	54.3	48.3	50.9	55.3	43.5	51.5	44.9		
Li	μg/g	20				11	18	17	13	17	13				1.82
Be	μg/g	2.8					2.4	1.7	1.5	1.9					1.87
B	μg/g	10		9.3			11	18	10	11					1.92
C	μg/g	200					1990	3120							15.6
N	μg/g	20					60			56				120	3.00
F	μg/g	625					525	602		553					1.19
S	μg/g	260					697	283		404					2.68
Cl	μg/g	130					472	179		244				448	3.63
Sc	μg/g	22		13		22	16	19	30	21.9	19				2.31
V	μg/g	135		96		131	98	128	230	138	89				2.58
Cr	μg/g	100	56	90		119	126	92	185	135	65				3.30
Co	μg/g	25		26		25	24	24	29	26.6	21.3				1.36
Ni	μg/g	75	35	54		51	56	46	105	59	31				3.39
Cu	μg/g	55		26		24	25	38	75	27	19				3.95
Zn	μg/g	70		71		73	65	81	80	72	69				1.25
Ga	μg/g	15				16	15	18	18	16	18				1.21
Ge	μg/g	1.5					1.4	1.25	1.6	1.3					1.28
As	μg/g	1.8					1.7	3.1	1.0	2.5					3.07
Se	ng/g	50					120	130	50	130					2.60
Br	μg/g	2.5					1.0			0.88					2.83
Rb	μg/g	90	61	76		58	78	69	37[e]	49	55	39	41		2.31
Sr	μg/g	375	503	317		325	333	285	260	320	246	276	385		2.04

(*continued*)

Earth's Continental Crust, Table 5 (continued)

	Units	1 Taylor (1964)	2 Weaver and Tarney (1984)	3 Shaw et al. (1986)	4 Christensen and Mooney (1995)	5 Rudnick and Fountain (1995)	6 Wedepohl (1995)	7 Gao et al.[a] (1998)	8 Taylor and McLennan (1985, 1995)	9 Rudnick and Gao (2003, 2014)	10 Hacker et al. (2011)	11 Hacker et al.[b] (2015) most mafic	12 Hacker et al.[b] (2015) most felsic	13 Others[c]	Max/min
Y	μg/g	33	14	26		20	24	17.5	20	19	24	22	18		2.36
Zr	μg/g	165	210	203		123	203	175	100	132	169	120	148		2.10
Nb	μg/g	20	13	20		8[f]	19	11	8[f]	8	11	7.4	8.1		2.70
Mo	μg/g	1.5					1.1	0.65	1.0	0.8					2.31
Ru	ng/g						0.1			0.57					5.70
Rh	ng/g						0.06								
Pd	ng/g						0.4	1.74	1	1.5					4.36
Ag	ng/g	70					70	52	80	56					1.54
Cd	ng/g	200					100	80	100	80					2.50
In	ng/g	100					50		50	50					2.00
Sn	μg/g	2.0					2.3	1.5	2.5	1.7					1.69
Sb	ng/g	200					300	200	200	200					1.50
Te	ng/g						5								
I	ng/g	500					800			700				119	1.60
Cs	μg/g	3.0				2.6	3.4	2.8	1.5[e]	2	2				1.70
Ba	μg/g	425	707	764		390	584	614	250	456	473	329	534		3.06
La	μg/g	30	28			18	30	31.6	16	20	23	17	23		1.98
Ce	μg/g	60	57			42	60	60.0	33	43	56	36	49		1.82
Pr	μg/g	8.2					6.7		3.9	4.9	8	4.5	5.5		2.10
Nd	μg/g	28	23			20	27	27.4	16	20	26	19	23		1.75
Sm	μg/g	6	4.1			3.9	5.3	4.84	3.5	3.9	5.1	3.9	4.1		1.71
Eu	μg/g	1.2	1.09			1.2	1.3	1.27	1.1	1.1	1.4	1.1	1.1		1.28
Gd	μg/g	5.4					4.0		3.3	3.7	4.4	3.8	3.6		1.64
Tb	μg/g	0.9	0.53			0.56	0.65	0.82	0.60	0.6	0.8	0.66	0.59		1.70
Dy	μg/g	3					3.8		3.7	3.6	3.5	3.9	3.0		1.30

Ho	µg/g	1.2					0.80		0.78	0.77	0.73	0.84	0.61		1.97
Er	µg/g	2.8					2.1		2.2	2.1	2.1	2.3	1.7		1.65
Tm	µg/g	0.48	0.24				0.30		0.32	0.28					2.00
Yb	µg/g	3.0	1.5			2.0	2.0	2.2	2.2	*1.9*	2.3	2.1	1.6		1.96
Lu	µg/g	0.50	0.23			0.33	0.35	0.35	0.30	0.30	0.4	0.33	0.24		2.17
Hf	µg/g	3	4.7	5		3.7	4.9	4.71	3.0	3.7	4.0	3.1	4		1.67
Ta	µg/g	2		4		0.7[f]	1.1	0.6	0.8[e]	0.7	0.6	0.54	0.52		7.69
W	µg/g	1.5					1.0	0.7	1.0	1				0.7	2.18
Re	ng/g						0.4		0.4	0.19					2.13
Os	ng/g						0.05		0.05	0.041					1.21
Ir	ng/g						0.05		0.10	0.037					2.67
Pt	ng/g						0.4	1.81		0.5					4.53
Au	ng/g	4					2.5	1.21	3.0	1.3					3.31
Hg	ng/g	80					40	9		30				2.9	8.89
Tl	µg/g	0.45					0.52	0.39	0.36	0.50					1.44
Pb	µg/g	12.5	15	20		12.6	14.8	15	8.0	11	15	9.5	11.7		2.50
Bi	µg/g	0.17					0.085	0.27	0.06	0.18					4.43
Th	µg/g	9.6	5.7	9		5.6	8.5	7.1	4.2	5.6	7.3	4.29	4.20		2.29
U	µg/g	2.7	1.3	1.8		1.4	1.7	1.2	1.1	1.3	1.4	1.13	1.09		2.48
Heat production	µW/m^3	1.6	0.93	1.32		0.93	1.28	1.01	0.7	0.89	1.05	0.85	0.88		

Major elements recast to 100% anhydrous

[a]Model CEC[3]

[b]This paper presents several compositional models based on differing assumptions regarding matching composition to seismic velocities and heat flow constraints; shown here are the end-member compositions

[c]Values taken from studies of individual elements: N concentration from Johnson and Goldblatt (2015); Cl and I concentrations from Muramatsu and Wedephohl (1998); W concentration from König et al. (2011); Hg concentration from Canil et al. (2015)

[d]Total Fe as FeO

[e]Updated by McLennan (2001)

[f]Updated by Barth et al. (2000)

and felsic igneous rocks such as rhyolites and granites (Hacker et al. 2015; Rudnick and Fountain 1995). Indeed, many have argued that andesites themselves result from mixing of basalt and rhyolite (e.g., Eichelberger 1975; Kent et al. 2010; Reubi and Blundy 2009), though crystal fractionation is also an important process in generating evolved igneous rocks (Keller et al. 2015; Lee and Bachmann 2014; Yanagi and Yamashita 1994), and there is ongoing debate regarding the relative importance of partial melting versus crystal fractionation in generating evolved igneous rock types. Assuming that crust grows by mass transfer from the mantle via melt intrusion, and because the primary melt of mantle peridotite is basalt (or more Mg-rich lavas such as picrites or komatiites), processes in addition to mantle melting must have modified the crust. This mismatch between crustal building-blocks (mantle-derived basalts) and the crustal edifice (andesitic crust) has been termed the "andesite paradox" (Kelemen et al. 2003a) or the "crust composition paradox" (Rollinson 2008).

Processes that have been suggested to solve the crust composition paradox include weathering, slab melting, and preferential recycling of mafic to ultramafic rocks from the continental lithosphere into the mantle (see reviews of Hacker et al. 2015; and Rudnick 1995). Each of these processes is addressed, in turn.

The weathering hypothesis, whereby soluble elements such as Mg are lost from the continents, are taken up in altered oceanic crust, and then preferentially recycled back into the mantle when that crust subducts (Albarède 1998; Anderson 1982; Lee et al. 2008; Liu and Rudnick 2011), serves to deplete Mg (and possibly other soluble elements) from basaltic crust. The fact that most rocks of the continental crust have oxygen (Simon and Lecuyer 2005) and lithium (Liu and Rudnick 2011; Teng et al. 2004) isotopic compositions that are offset from those of primary mantle-derived magmas in the direction expected for a weathered regolith is prima facie evidence that weathering played a role in generating the continental crust that we see today. Estimates for the mass of continental crust lost to chemical weathering vary from >20% (Lee et al. 2008) to between 15% and 65% (Liu and Rudnick 2011).

Whereas the thermal structure of the majority of modern subduction zones is cool enough that melting within the slab is primarily confined to the water-laden sedimentary layer ± uppermost volcanic rocks (van Keken et al. 2011), this may not have been the case in the ancient past (although the question of when subduction initiated is very much an ongoing debate, as discussed below). In particular, higher heat flow expected in the Archean due to greater heat production may have led to dehydration melting of subducted, hydrated basaltic crust, generating Na-rich granitic rocks, the so-called tonalite-trondhjemite-granodiorites (TTGs, Martin 1986) that may then interact with mantle wedge peridotite before they cross the Moho (Martin and Moyen 2002). In this scenario, the igneous flux across the Moho is not basaltic, but rather tonalitic.

Removal of mafic lower continental crust may happen through a variety of processes that involve density sorting (see Hacker et al. 2011; Lee 2014). One popular hypothesis is that mafic to ultramafic lithologies that may be present in the deep crust may be denser than underlying mantle (e.g., if the crust is thickened so that eclogite forms) and can be lost from the base of the crust through density foundering (Arndt and Goldstein 1989; Herzberg et al. 1983; Jull and Kelemen 2001; Kay and Kay 1991), which is often referred to erroneously as "delamination." A more recent hypothesis suggests that subduction of compositionally stratified continental or differentiated arc crust leads to density segregation as the buoyant upper layers underplate the overlying crust, while the denser, deeper sections founder into the convecting mantle (the "relamination" hypothesis of Hacker et al. 2011; Kelemen and Behn 2016). Estimates for the cumulative mass of continental crust lost to lower crustal recycling vary from 0.3 to 4 times the present mass of the continental crust (Table 6).

Tectonic Setting of Crust Formation

Creation of continental crust is fundamentally an igneous process, as the crust grows by mass addition of melts from the mantle. Today, mantle melting occurs mainly in three distinct plate tectonic settings: rifts, where melts are generated due to adiabatic melting; convergent margins, where hydrous fluids/melts from the subducting slab flux the overlying mantle wedge; and intraplate settings, which are often attributed to mantle plumes. Debate centers on which tectonic environments have been most important in generating the crust that we see today.

Many workers have cited the similarity between the trace element composition of the continental crust and convergent margin magmas, such as the significant depletions in Nb and Ta relative to La (Fig. 2 the elements are plotted on this figure in order of bulk partition coefficients during adiabatic mantle melting) and enrichments in Pb relative to neighboring elements, as evidence that most continental crust formed above subduction zones (e.g., Barth et al. 2000; Hawkesworth and Kemp 2006; Kelemen 1995; Rudnick 1995). Such anomalies in multielement plots are iconic features of convergent margin magmas and are attributed to retention of Nb and Ta in the slab (possibly due to the presence of a Ti-bearing phase such as rutile) and enrichment of more soluble elements such as Pb and Sr in slab fluids and/or melts (Elliott 2003; Kelemen et al. 2003b). Using the magnitude of Nb depletion relative to La, mass balance between different end-member compositions have been used to suggest that 80–95% of the present continental crust formed in subduction zones (Barth et al. 2000; Hawkesworth and Kemp 2006).

Earth's Continental Crust, Table 6 Estimates of the amount of lower continental crust recycled into the mantle

References	% of juvenile crust lost to foundering	Proportion of present crustal masses lost to foundering	Region	Basis
Gao et al. (1998)	50–71%	1.0–2.4	Dabie-Sulu, China	Trace element mass balance
Ducea (2002)	50–60%	1.0–1.5	Sierra Nevada, CA	Petrological mass balance
Plank (2005)[a]	25–60%	0.3–1.5	Global	Th/La ratio mass balance
Lee et al. (2007)	60–75%	1.5–3	Sierra Nevada, CA	Petrological mass balance
Clift et al. (2009)[b]	30–43%	0.4–0.8	Global	Compilation of regional studies
Jagoutz and Schmidt (2013)	52–74%	1.1–2.9	Kohistan arc	Petrological mass balance
Tang et al. (2015)	65–80%	2–4	Global	Eu/Eu[a] mass balance

[a]Minimum estimate
[b]For orogenic plateaus only and assuming crust formation for the past 2.5 to 4.5 Ga, density of foundered crust = 3200 kg/m^3, and mass of present-day crust is 2.06 × 10^{22} kg (Huang et al. 2013)

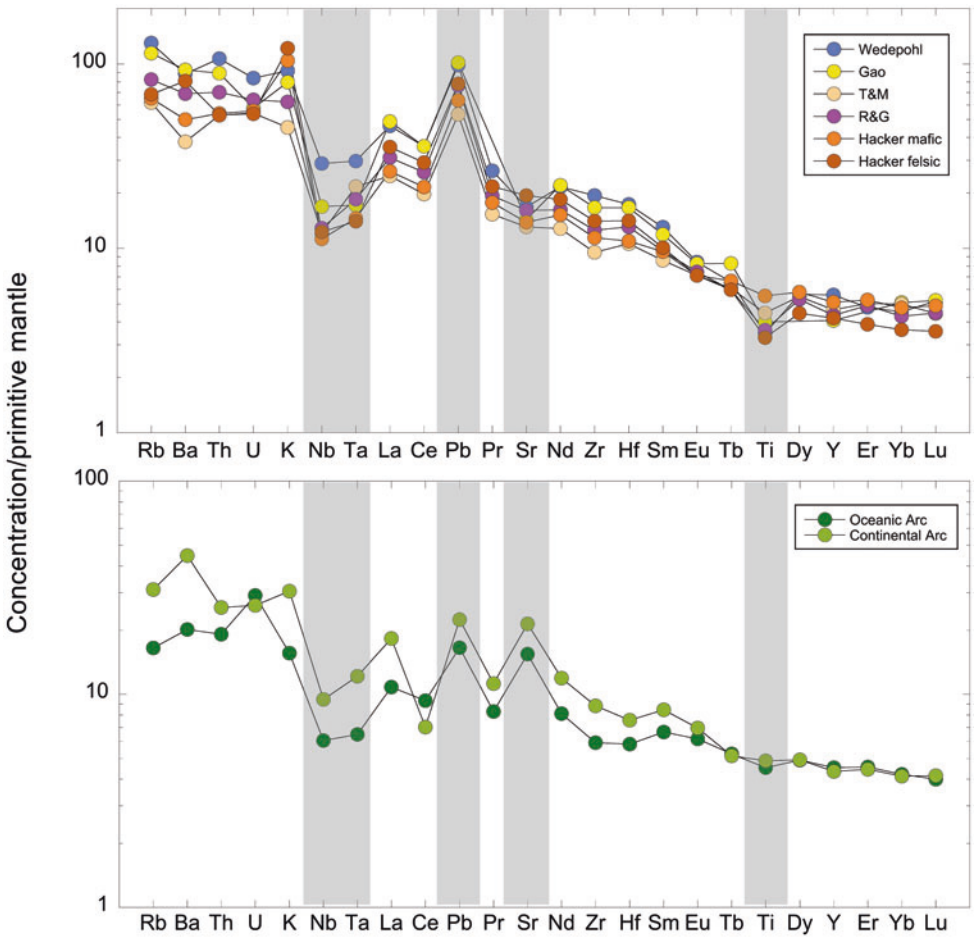

Earth's Continental Crust, Fig. 2 Primitive mantle-normalized trace element abundances of (**a**) different compositional models of the bulk continental crust (Wedepohl 1995; Gao et al. 1998; Taylor and McLennan 1985; Rudnick and Gao 2003; Hacker et al. 2015 showing the mafic and felsic end-members). (**b**) Average primitive arc lavas from oceanic and continental settings (From Kelemen et al. 2003b). Vertical *gray bars* highlight, from *left* to *right*: Nb and Ta (depleted in continental crust and arc lavas), Pb (enriched in both), Sr (enriched in arcs but not bulk crust), and Ti (depleted in bulk crust and variable in arc lavas). Mantle-normalizing values are from McDonough and Sun (1995)

By contrast, Albarède (1998) and Stein and Hofmann (1994), citing the apparent episodicity in crustal growth (discussed below), suggest that much of the continental crust formed in intraplate settings by "superplume" or "mantle overturn" events, respectively. They explained the similarities between the trace element composition of the continental crust and convergent margin magmas as being due to later reprocessing of original plume-generated crust in subduction zones. A more recent hypothesis regarding the role of plumes in generating episodic continental crustal

growth was proposed by Arndt and Davaille (2013) whereby large mantle plumes displaced material from the upper mantle and accelerated subduction to generate new crust.

It is worth noting that estimates of the trace element composition of the bulk continental crust, while similar to one another and to convergent margin magmas, also show differences with the latter. For example, subduction zone magmas are typically enriched in Sr relative to Nd (also attributed to slab fluids and/or melts), yet the bulk continental crust does not show such an enrichment (Fig. 2). This lack of Sr enrichment, and perhaps even Sr depletion, in the continental crust may be due, in part, to chemical weathering, as Sr is highly soluble and is preferentially lost from the continents (e.g., Gaschnig et al. 2016; Goldstein 1989; Rudnick 1995). Strontium depletion may also be generated by removal of plagioclase-bearing residues or cumulates from the base of the crust, as plagioclase incorporates Sr relative to Nd. Indeed, Tang et al. (2015) presented evidence that the bulk continental crust possesses a negative Eu anomaly (Eu/Eu*) ("Eu/Eu* = $Eu_N/(Sm_N*Gd_N)^{1/2}$, where "N" signifies concentrations normalized to chondrite"), which they attributed to this process. In addition, Plank (2005) noted that the high Th/La ratio seen in arc lavas is inherited from subducted terrigenous sediments and is not generated through subduction. She suggested that the continental crust attained a high Th/La due to intracrustal melting, followed by removal of the low Th/La residue. So, whereas the overall pattern of trace elements within the continental crust is similar to that of convergent margin magmas, there are also notable differences that must relate to the signature of crustal recycling superimposed on the original igneous composition, just as the major element composition of the bulk crust requires return of mafic materials to the mantle.

Finally, it is also worth noting that arc-like trace element signatures (light rare earth element (LREE) enrichment, Nb and Ta depletion, Sr and Pb enrichment) can also be generated in intraplate settings by melting of thickened mafic crust. An example of such magmas has been documented in Iceland (Willbold et al. 2009) and may be an analogy for crust formation during the Archean. Indeed, if most of the continental crust formed in the Archean (see below), modern plate tectonic settings may bear little relevance to the environment in which much of the continental crust formed, as discussed in the next section.

Temporal Evolution of the Continental Crust

The continental crust today is the product of billions of years of evolution involving mantle melting, igneous differentiation (e.g., crystal fractionation, crustal melting, and crustal assimilation), fluid and melt transfer in subduction zones, weathering, metamorphism, and crustal recycling, which may occur via both subduction and foundering, as described above. A number of lines of evidence point to a fundamental change in the composition of the upper continental crust at the Archean-Proterozoic (A-P) boundary (i.e., 2500 Ma) (Fig. 3), which may signal a shift in the processes by which continental crust formed. Evidence for this change is seen in the compositions of fine-grained terrigenous sedimentary rocks (Fig. 3a, b), in the composition of Archean chemical sediments, and the composition of magmatic rocks (Fig. 3c, d), and surface exposures of igneous rocks, as discussed below.

Taylor and McLennan (1985) summarized the evidence for crustal compositional change contained within the insoluble trace element concentrations in fine-grained terrigenous sedimentary rocks such as shales, mudstones, and their metamorphosed equivalents. This includes a decrease in first-row transition elements (e.g., Sc, Cr, Co, Ni) and an increase in incompatible element concentrations (e.g., Th, La) as well as Eu anomalies of shales at the A-P boundary. Figure 3a shows how Th/Sc increases in fine-grained terrigenous sedimentary rocks across the A-P boundary, which is due to both an increase in Th and a decrease in Sc concentrations. Th is a highly incompatible trace element while Sc is a compatible trace element, so this change reflects a change from relatively mafic to felsic crust across the A-P boundary. Later studies of shales and glacial diamictites have confirmed these compositional changes (e.g., Condie 1993; Gaschnig et al. 2016; McLennan and Taylor 1991; Tang et al. 2016).

The composition of chemical sedimentary rocks (banded iron formations, carbonates, and cherts) provide insights into the chemical composition of the ancient oceans, which, like the modern ocean, reflect a mixture of inputs from continental weathering (rivers) and hydrothermal vents, and outputs through exchange with oceanic crust. Veizer and Compston (1976) noted that the $^{87}Sr/^{86}Sr$ ratio of Archean carbonates are similar to values expected for the Archean mantle and suggested that this low ratio arose from weathering of an Archean continental crust that was dominated by greenstone belt basalts. Later studies attributed the low $^{87}Sr/^{86}Sr$ in Archean carbonates to the influence of hydrothermal vents. However, Kamber (2010) suggested that the observed Sr and Eu concentrations and Nd isotopes observed in Archean chemical sediments do not match those expected from mixing between hydrothermal vents and rivers draining evolved continents. He instead suggested that these rather enigmatic compositions reflect the weathering of widespread mafic to ultramafic volcanic surfaces on subaerial oceanic plateaus.

Studies of surface exposures of igneous rocks also suggest a compositional change of the upper continental crust at the A-P boundary. Using geologic maps and measured stratigraphic sections, Condie (1993) observed that greenstone belts show an increase in the proportion of felsic volcanic rocks and graywackes, whereas komatiites drop to almost zero at the A-P boundary. He also observed a systematic

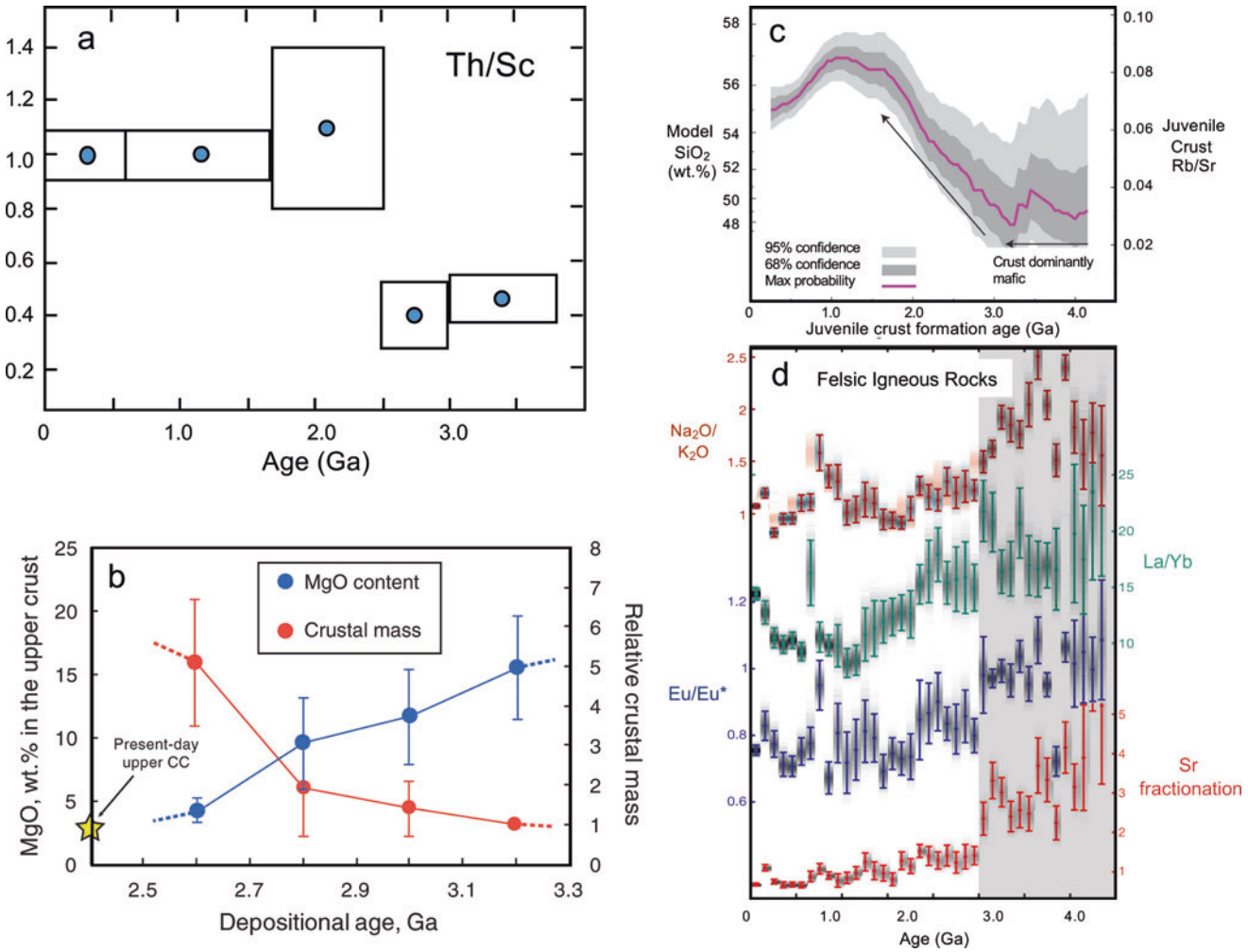

Earth's Continental Crust, Fig. 3 Illustration of various lines of evidence for a compositional change in the composition of the continental crust across the Archean-Proterozoic (A-P) boundary. (**a**) Average Th/Sc ratio in fine-grained sedimentary rocks (Modified from Taylor and McLennan 1985). Because both Th and Sc are insoluble elements, the values reflect the average composition of the crust exposed to weathering and erosion for a given time period. Boxes represent time interval under consideration and 95% confidence interval of mean. (**b**) Changing average MgO concentration of upper continental crust as a function of time, inferred from Ni/Co and Cr/Zn ratios in fine-grained sedimentary rocks. Also shown is inferred change in crustal mass based on addition of TTGs to original mafic crust (From Tang et al. (2016). (**c**) Changing Rb/Sr ratio of juvenile crust and correlated SiO_2 as a function of time based on data for over 13,000 igneous rocks (Modified from Dhuime et al. 2015). (**d**) Changes in the geochemistry of felsic igneous rocks as a function of time, based on data for over 70,000 igneous rocks (Modified from Keller and Schoene 2012)

change during the Archean, with Late Archean upper crust having lower Mg, Cr, Ni, Co, and Eu/Eu* and higher K, Rb, Ba, Th, U, and HREE compared to that of the Early Archean. These findings are consistent with a shift from more mafic to more felsic crust within the Archean and across the A-P boundary. Comparing shales to surface exposures of igneous rocks in the Archean, he found that the shales, on average, lack HREE depletion and are more enriched in Fe, V, and Sc compared to the surface exposures and hypothesized that the source of the shales, which had since eroded away, was dominated by basalt and komatiite with little HREE-depleted TTGs. This finding is supported by an inferred drop in average upper crustal MgO content from ~15 wt.% in the Early Archean, to ~4 wt.% in the Late Archean based on transition metal ratios in fine-grained sedimentary rocks (Tang et al. 2016, Fig. 3b). It remains an open question whether this change in MgO reflects a vertical or temporal change in upper crust composition.

Dhuime et al. (2015) used initial Sr isotope ratios and Nd model ages of igneous rocks to calculate the Rb/Sr ratio of juvenile crust at the time of mantle extraction. Because Rb/Sr ratio increases systematically with SiO_2 concentration, they used these results to estimate the average SiO_2 concentration of newly generated continental crust over time (Fig. 3c). They found that both Rb/Sr and SiO_2 increased dramatically around 3.0 Ga, which they attributed to the start of plate tectonics.

Keller and Schoene (2012) used statistical sampling of over 70,000 dated igneous rocks compiled from geochemical databases and other sources to examine secular trends in the compositional data. They found that continental basalt compositions record a gradual decrease in mantle melt fraction but with an abrupt change occurring at the A-P boundary. Likewise, felsic igneous rocks also show a rather abrupt change in composition at the A-P boundary from high Na/K, La/Yb, Eu/Eu* (typical of TTGs) to lower ratios (Fig. 3d). Keller and Schoene attributed these changes to decreasing mantle temperature and changing continental crustal thickness at the A-P boundary and inferred that the Archean crust was originally thick and mafic. Melting in its deeper sections produced TTGs followed by recycling of the residues to leave a relatively thin and felsic crust in Archean regions today. Keller and Schoene's interpretations suggest that the deep continental crust, as well as the upper continental crust, was more mafic in the Archean than in the post-Archean.

Most recently, Lee et al. (2016) suggested that the first significant peak seen in detrital zircon dates, at ~2.8 Ga (see next section), may reflect the transition from a mafic crust where the magmas are not generally saturated in zircon, to a felsic crust that grew abundant zircon. Because production of copious amounts of felsic magmas requires water (e.g., Arndt 2013; Campbell and Taylor 1985), they also suggested that this transition may mark the evolution from stagnant lid tectonics to plate tectonics, which provides a ready mechanism by which to carry water to depth.

Crustal Growth

One of the most persistent debates concerning the continental crust is the question of how the volume of the crust may have changed through time. Did continents form early and remain more or less in steady state as new additions were balanced by subtraction due to recycling (e.g., Armstrong 1981, 1991)? Or has the volume of continental crust increased over Earth history (e.g., Dhuime et al. 2012; McCulloch and Bennett 1994; Taylor and McLennan 1985)? If the latter, what is the shape of the growth curve? Fig. 4 shows a recent compilation of crustal growth curves by Cawood et al. (2013). While there is far from a consensus on this topic, the burgeoning information being gleaned from zircons, particularly detrital zircons harvested from terrigenous sedimentary rocks, points to significant generation of felsic continental crust in the mid- to Late Archean.

Zircons are particularly powerful recorders of geologic history because their crystallization age can be determined precisely via U-Pb dating (see reviews by Scherer et al. 2007; Schoene 2014), and they contain relatively high concentrations of Hf. Decay of ^{176}Lu to ^{176}Hf (half-life = ~37.5 Ga,

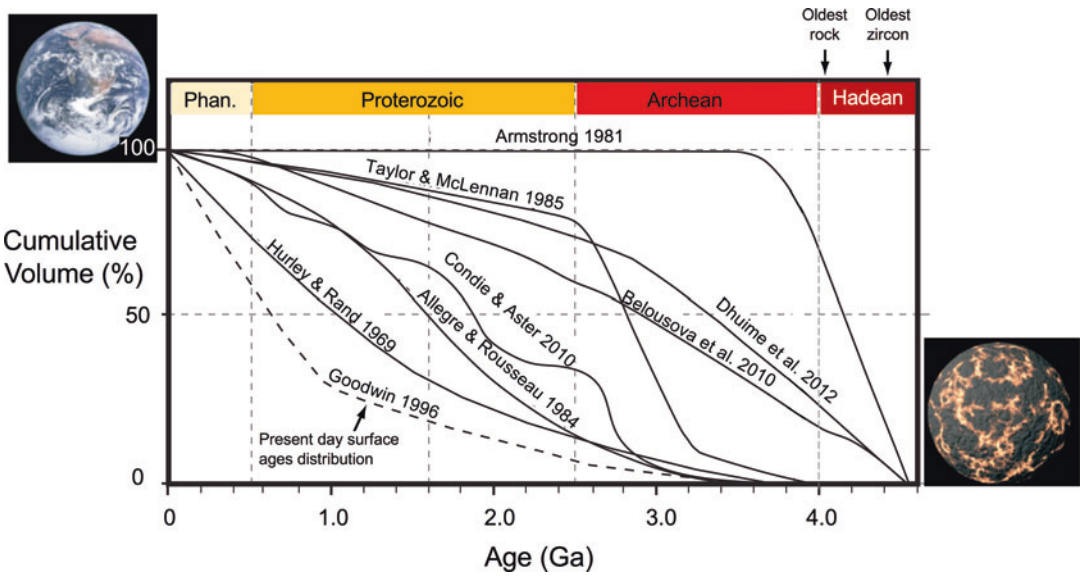

Earth's Continental Crust, Fig. 4 A selection of continental crustal growth or preservation curves, compiled by Cawood et al. (2013). The curves of Goodwin (1996) and Hurley and Rand (1969) are based on the present-day surface Rb-Sr and K-Ar dates and represent minima, as they do not take into consideration isotopic resetting due to metamorphism. The curve of Condie and Aster (2010) is based on a combination of U-Pb dates of zircons from both orogenic granites for which Nd whole rock data exist and U-Pb dates of detrital zircons for which Hf isotope data exist, as well as map distributions of dated rocks. The Allègre and Rousseau (1984) curve is based on Sm-Nd model ages in shales, while the curves of Belousova et al. (2010) and Dhuime et al. (2012) are different takes on Lu-Hf model ages of detrital zircons. The remaining curves (Armstrong 1981; Taylor and McLennan 1985) are based on concepts about how the crust may have grown (Modified from Cawood et al. 2013)

Scherer et al. 2001; Söderlund et al. 2004) and the relatively low Lu/Hf ratio of zircon means that mantle derivation ages (or model ages) can be determined for each zircon, provided that the Lu/Hf ratio of the pre-existing crustal reservoir and the Hf isotope mantle evolution curve can be approximated (see Kemp and Hawkesworth 2014; Payne et al. 2016; Vervoort and Kemp 2016 for recent reviews of the methods and potential pitfalls involved). In particular, with the widespread application of in situ analytical methods such as secondary ion mass spectrometry (SIMS) and laser ablation inductively coupled multi-collector plasma mass spectrometry (LA-MC-ICP-MS), both U-Pb dates and Hf isotopes can be determined for the same zone within a given zircon (zircons frequently contain different domains grown at different times, Fig. 5), or even for the same volume (e.g., employing laser ablation split-stream methods, Fisher et al. 2014; Kylander-Clark et al. 2013; Yuan et al. 2008) to ensure a direct match between U-Pb date and Hf isotope model age. Finally, oxygen isotopes of the zircons can be used to identify zircons derived, in part or in whole, from pre-existing crust, which will generally have non-mantle-like $\delta^{18}O$ values. In this way, zircons that crystallized from magmas that contain components of older continental crust can be identified, in order to infer the proportions of juvenile to pre-existing crust and define crustal growth curves (Kemp et al. 2006). The results from analyses of thousands of zircons suggest that most (~60–75%) of the continental crust formed by the end of the Archean, possibly by processes other than subduction zone magmatism. Assuming that it is difficult for the zircon record to be completely obliterated by crustal recycling because weathering and erosion disperse detrital zircons, the results also suggest that only a small fraction of present-day continental crust (20–25%) was present at the start of the Archean at about 3.8 Ga. In these discussions, it is important to note, as pointed out by Lee et al. (2016) that the U-Pb zircon record is mostly a record of felsic crust, as zircon is not saturated in mafic melts. In addition, detrital zircons (and their associated sedimentary rocks) can only be generated if crust is exposed above sea level. It is conceivable that evolved crust submerged below the oceans could have been efficiently recycled in the Hadean without leaving a trace. However, based on the evidence for dominantly mafic crust in the Archean cited above, this scenario is unlikely.

A striking feature of the age distribution of continental crust is the well-defined peaks in U-Pb zircon dates (Fig. 6). These peaks appear in zircons from both terrigenous sediments and igneous rocks and are found on all continents. Given the very large number of near-concordant U-Pb dates for zircons from the continental crust (several hundred thousand), the peaks appear to be robust and are unlikely to be an artifact of incomplete sampling. Yet the significance of these peaks is debated. One school of thought interprets the peaks as episodes of enhanced crustal growth, possibly driven by superplume events or slab avalanches in the mantle (Arndt and Davaille 2013; Condie 1998; Parman 2015). This interpretation is supported by peaks at similar time intervals in Os model ages in mantle peridotites and platinum-group alloy grains from ophiolites, which may date continental crust extraction events (Pearson et al. 2007). An alternative interpretation suggests that crustal preservation may be uneven (Gurnis and Davies 1986) and that the U-Pb peaks may represent zircon growth and preservation during supercontinent formation (Condie and Aster 2010; Hawkesworth et al. 2010, 2013; Kemp et al. 2006). This interpretation is supported by the apparent absence of corresponding peaks in Lu-Hf model ages from the same zircons (Voice et al. 2011), including those that have been filtered using oxygen isotopes to identify only zircons from juvenile crustal additions (Dhuime et al. 2012; Kemp et al. 2006). If the Lu-Hf model age distributions prove robust (see caveats in Payne

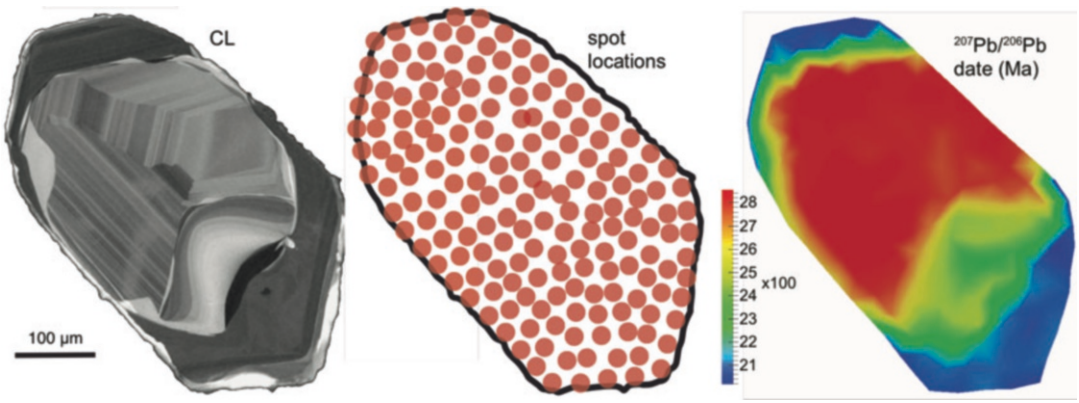

Earth's Continental Crust, Fig. 5 Example of a complexly zoned zircon crystal from a granite from Cameroon. *Left*: cathodoluminescence image, *right*: $^{207}Pb/^{206}Pb$ age map; *center* panel shows the position of the individual laser spot analyses that were used to create the map on the right. The analyses reveal a ~2.8 Ga igneous core with oscillatory zoning that was partially resorbed and overgrown in the latest Archean, earliest Paleoproterozoic. The outer rim grew around 2.1 Ga (Modified from Cottle and Stearns 2017)

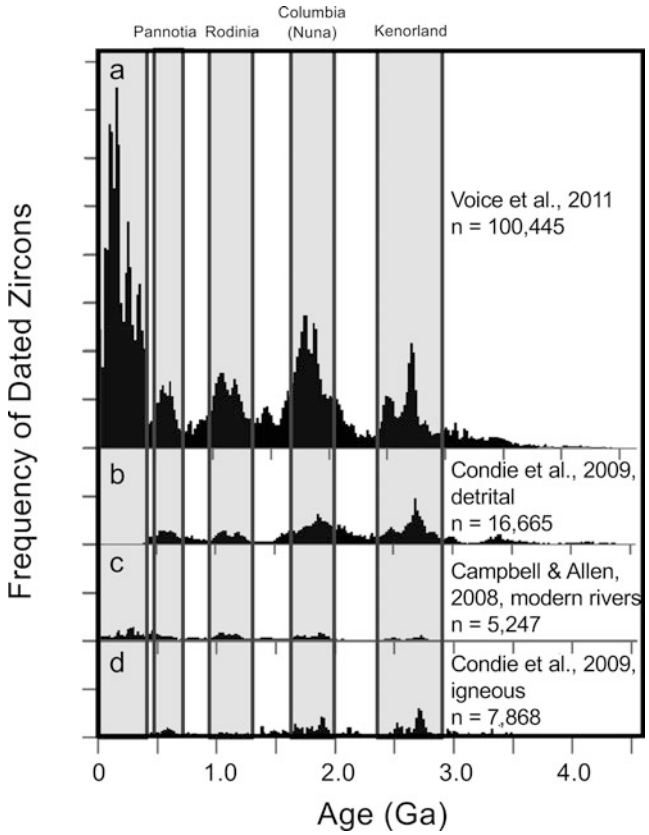

Earth's Continental Crust, Fig. 6 U-Pb dates of zircons from detrital terrigenous sedimentary rocks and granites. (**a**) Detrital zircons that are less than 5% discordant, from Voice et al. (2011); (**b**) detrital zircons <10% discordant, from Condie et al. (2009); (**c**) detrital zircons from global modern river sediments, from Campbell and Allen (2008); (**d**) zircons for orogenic granites that are <5% discordant, from Condie et al. (2009). Vertical *gray bars* delineate the statistically significant peaks and proposed times of supercontinent formation (labels at *top*) (Modified from Voice et al. 2011)

et al. 2016), they indicate that crustal growth was a far more continuous process than the U-Pb zircon age peaks suggest.

Earth's Earliest Crust

The oldest known indigenous minerals found on Earth are Hadean detrital zircons from Mt. Narryer and the Jack Hills, Western Australia (Compston and Pidgeon 1986; Froude et al. 1983), which date back to 4.4 Ga (Wilde et al. 2001). Since their discovery, these tiny grains have been the subject of intense scientific scrutiny in order to divine the nature of the Hadean Earth, for which we have no rock record (see review by Harrison 2009). Key features suggest that these zircons crystallized from hydrous, relatively low-temperature granitic melts: encapsulation of mineral inclusions of typical granitic composition (e.g., quartz, muscovite, K-feldspar, hornblende, Hopkins et al. 2008; Maas et al. 1992), fractionated oxygen isotopes, indicating incorporation of materials that experienced low temperature alteration in the presence of liquid water (Mojzsis et al. 2001; Wilde et al. 2001), and low Ti-in-zircon temperatures indicative of relatively evolved melt compositions (Fu et al. 2008; Watson and Harrison 2005). These results have been interpreted to suggest that the Hadean Earth was temperate, with liquid water, and possibly also widespread continents created by plate tectonics (Harrison 2009; Mojzsis et al. 2001; Wilde et al. 2001). Most recently, isotopically light carbon isotopes measured in graphite contained within a 4.1 Ga zircon suggests the possibility of a biosphere at this time (Bell et al. 2015), and remnant magnetism has even been detected in the Hadean zircons, leading to the suggestion that the Hadean Earth possessed a magnetic field (Tarduno et al. 2015), though debate exists regarding the veracity of this signal (cf. Cottrell et al. 2016; Weiss et al. 2015).

Origins alternative to a wet granite source for the zircons have also been proposed. For example, the zircons may have crystallized during differentiation of impact melts, as zircons from the Sudbury impact melt sheet also record low Ti-in-zircon temperatures (e.g., Darling et al. 2009; Kenny et al. 2016). Or the Hadean zircons may have crystallized during the final stages of differentiation of basaltic melts (e.g., Rollinson 2008). Various lines of argument have been mustered to counter these arguments. Perhaps the most compelling evidence lies in the presence of muscovite inclusions, which, after quartz, are the second most abundant inclusion observed (Hopkins et al. 2008). Muscovite does not crystallize during basalt differentiation and has not been recognized in impact melts. Moreover, the trace element compositions of the zircons are distinct from those formed in late-stage differentiates of basalt (Grimes et al. 2007).

Although the weight of evidence supports crystallization of the Jack Hills zircons from hydrous granitic melts, the degree to which these rare crystals indicate the presence of widespread continental crust and the operation of plate tectonics is open to debate. Harrison (2009) made the case that the inferred low geotherm determined from thermobarometry of the mineral inclusions (Hopkins et al. 2008) could only reasonably exist on a hotter Hadean Earth if there were subduction zones, which are characterized by exceedingly low temperatures in the modern Earth and, by analogy, the Hadean Earth. However, others have suggested that it is unlikely that widespread Hadean continental crust could be obliterated with nary a trace. For example, the rarity of detrital zircons having Hadean U-Pb ages is hard to explain if such widespread felsic crust existed (Belousova et al. 2010; Voice et al. 2011). Moreover, Lu-Hf model ages for the most ancient zircons typically fail to exhibit evidence for significant volumes of Hadean continental crust (Kemp et al. 2010, 2015; Vervoort et al. 1996). In addition, the evidence reviewed above for a dominantly mafic crust in the Archean does not

support the presence of widespread granitic crust in the Archean or Hadean. Finally, one of Armstrong's (1991) strongest arguments for very early differentiation of Earth's crust is the comparison with other rocky planets in our solar system, all of which show evidence of early crust formation (e.g., Taylor and McLennan 2009). It is indeed quite likely that such differentiation occurred on Earth but that the earliest crust was dominated by basalts and komatiites, consistent with the higher mantle temperatures at that time, and with the basaltic compositions of other ancient planetary crusts (Taylor and McLennan 2009).

In addition to the Hadean zircons, evidence for the nature of the earliest crust comes from some of the oldest rocks on Earth: the 4.0 Ga Acasta gneisses in the Great Slave Craton, Canada, the 3.8-3.9 Ga rocks of southwest Greenland, and unusual, ~3.8 Ga ortho-amphibole-bearing amphibolites and associated TTGs of the Nuvvuagittuq Greenstone Belt, Canada.

The oldest dated rocks are tonalitic gneisses – the Acasta gneisses from the Slave Craton, Northwest Territories, Canada, which have U-Pb zircon ages dating back to 4.03 Ga (Bowring and Williams 1999). Several lines of evidence suggest that the original tonalitic magmas derived from pre-existing mafic to ultramafic crust. Whole rock ^{142}Nd isotope data for the Acasta gneisses that deviate from that of the bulk Earth have been interpreted to reflect their derivation from a ~4.3 Ga precursor mafic crust (Roth et al. 2014 and references therein). Likewise, Hf isotope compositions of zircons from a 4.02 Ga Acasta gneiss indicate its derivation from mafic to ultramafic crust, with no evidence for earlier granitic continental crust (Reimink et al. 2016).

The Itsaq gneiss complex and Isua supracrustal belt in southwestern Greenland were recognized early on as containing some of Earth's most ancient rocks, dating to at least 3.7 Ga (Moorbath et al. 1972, 1973). They form the largest continuous track of early Archean rocks yet recognized. More recent work shows these rocks to have formed as far back as ~3.9 Ga (Nutman et al. 1996, 1997). The Itsaq gneisses are highly deformed amphibolite facies rocks comprised of ~80% gray gneisses dating to >3.8 Ga, 10% supracrustal, mafic, and ultramafic rocks formed at ≥3.87 to 3.6 Ga and 10% somewhat younger (≤3.65 Ga) granites (Nutman et al. 1997). By contrast, the Isua supracrustal belt is comprised of less deformed amphibolite-facies chemical (BIF, cherts, and carbonates) and clastic sedimentary rocks interbedded with bimodal (mafic-felsic) volcanic rocks that form a least two distinct stratigraphic units dating to 3.7 Ga and ≥3.8 Ga (Nutman et al. 1997) and contain what may be the oldest microbial mats (Nutman et al. 2016). The SW Greenland rocks record both positive (Boyet et al. 2003; Caro et al. 2003; Harper and Jacobsen 1992) and negative ^{142}Nd isotopic anomalies (Rizo et al. 2012), indicating their derivation from rocks that originally differentiated in the Hadean.

The most recently recognized ancient crust occurs in the Nuvvuagittuq Greenstone Belt, in the Minto Block of the northern Superior Province, which crops out on the eastern shore of Hudson Bay in northern Quebec. The lithological assembly comprises chemical sedimentary rocks (quartz-magnetite rocks, ferruginous quartz-pyroxene rocks), quartz-biotite schists containing clasts of quartzite and mafic rocks (Cates and Mojzsis 2007), ultramafic sills, as well as unusual cummingtonite-bearing amphibolites (O'Neil et al. 2008). The oldest dated rocks in the assemblage are felsic schists, interpreted to be volcanic in origin with U-Pb zircon dates of 3.77 (Augland and David 2015) to 3.82 Ga (David et al. 2009). The amphibolites generally have lower ^{142}Nd/^{144}Nd than bulk Earth and correlate with Sm/Nd ratios to yield an isochron of 4280 Ma (O'Neil et al. 2008), which has been interpreted, with some controversy (e.g., Roth et al. 2013), to represent the age of the belt. Irrespective of this debate, multiple lines of evidence suggest the derivation of the Nuvvuagittuq igneous rocks from mantle that experienced melt depletion early in the Hadean (Roth et al. 2013; O'Neil et al. 2016). Most recently, coupled ^{142}Nd and ^{143}Nd isotopic studies of much younger granitoids in the region point to their derivation from extensive Hadean mafic crust (O'Neil and Carlson 2017).

Summary

Earth is the only planet in our solar system that has a compositionally highly evolved crust – the continental crust – that contains a significant fraction of Earth's most strongly incompatible elements, including the heat-producing elements K, Th, and U. All estimates agree that the present-day continental crust has an average "andesite" composition and is vertically stratified. The upper continental crust is evolved (66–70 wt.% SiO_2), and its composition is the best constrained of any portion of the crust, with average estimates for major element concentrations falling within 70% of one another and most trace element concentration estimates falling within a factor of two. The average compositions of the middle and lower crust are much less constrained and the subject of debate (mafic or intermediate?), but surface heat flow observations require they be depleted in heat-producing elements. An average andesitic crust composition cannot be generated by single-stage melting of mantle peridotite. Multiple processes likely helped to transform original basaltic crust to the crust present today, including weathering and erosion, melting of subducted or foundered basaltic rocks, and density foundering and/or "relamination."

A number of lines of evidence point to a fundamental change in the bulk continental crust composition in the Late Archean from dominantly mafic to felsic by 2.5 Ga. Such a transformation may signal the onset of widespread plate

tectonics as a ready means to generate voluminous granitic magmas, though hydrous, K-rich granites existed in the Hadean, as inferred from Hadean-aged detrital zircons. The timing of growth of the continental crust is a topic of major debate. Early crust formation must have occurred in response to a cooling Earth, but it is likely that this crust was dominantly basaltic, with minor TTGs, but thick enough to rise above sea level locally. Growth of volumetrically significant felsic continental crust likely occurred in the Late Archean. Prominent peaks in U-Pb zircon dates are observed on all continents, but the interpretation of these peaks is uncertain: they may represent periods of enhanced crust formation or preservation.

Acknowledgments Peter van Keken, Gray Bebout, Ralf Halama, and Sujoy Mukhopadhyay all provided help in tracking down compositional estimates for the continental crust or other data. John Cottle kindly provided the beautiful zircon images in Fig. 5. Mike Free, Allison Greaney, and Ming Tang provided comments that helped me to clarify different parts of the original manuscript. I appreciate review comments from Kent Condie, Bruno Dhuime, Brad Hacker, Chris Hawkesworth, and Scott McLennan. I am grateful for support of my research from the National Science Foundation over the past two decades. Finally, I thank Bill White for being exceedingly patient while the writing of this entry was delayed due to my move across a continent.

References

Abers GA, Hacker BR (2016) A MATLAB toolbox and Excel workbook for calculating the densities, seismic wave speeds, and major element composition of minerals and rocks at pressure and temperature. Geochem Geophys Geosyst. https://doi.org/10.1002/2015GC006171

Albarède F (1998) The growth of continental crust. Tectonophysics 296:1–14

Allègre CJ, Rousseau D (1984) The growth of the continent through geological time studied by Nd isotope analysis of shales. Earth Planet Sci Lett 67:19–34. https://doi.org/10.1016/0012-821X(84)90035-9

Anderson AT (1982) Parental basalts in subduction zones: implications for continental evolution. J Geophys Res 87:7047–7060

Armstrong RL (1981) Radiogenic isotopes: the case for crustal recycling on a near-steady-state no-continental-growth Earth. Phil Trnas R Soc Lond A 301:443–472

Armstrong RL (1991) The persistent myth of crustal growth. Aust J Earth Sci 38:613–630

Arndt NT (2013) The formation and evolution of the continental crust. Geochem Perspect 2(3):405–533. https://doi.org/10.7185/geochempersp.2.3

Arndt N, Davaille A (2013) Episodic Earth evolution. Tectonophysics 609:661–674. https://doi.org/10.1016/j.tecto.2013.07.002

Arndt NT, Goldstein SL (1989) An open boundary between lower continental crust and mantle: its role in crust formation and crustal recycling. Tectonophys 161:201–212

Augland LE, David J (2015) Protocrustal evolution of the Nuvvuagittuq Supracrustal Belt as determined by high precision zircon Lu-Hf and U-Pb isotope data. Earth Planet Sci Lett 428:162–171. https://doi.org/10.1016/j.epsl.2015.07.039

Barth M, McDonough WF, Rudnick RL (2000) Tracking the budget of Nb and Ta in the continental crust. Chem Geol 165:197–213

Behn MD, Kelemen PB (2003) The relationship between seismic P-wave velocity and the composition of anhydrous igneous and meta-igneous rocks. Geochem Geophys Geosys 4:1041. https://doi.org/10.1029/2002GC000393

Bell EA, Boehnke P, Harrison TM, Mao WL (2015) Potentially biogenic carbon preserved in a 4.1 billion-year-old zircon. Proc Natl Acad Sci U S A 112(47):14518–14521. https://doi.org/10.1073/pnas.1517557112

Belousova EA, Kostitsyn YA, Griffin WL, Begg GC, O'Reilly SY, Pearson NJ (2010) The growth of the continental crust: constraints from zircon Hfisotope data. Lithos 119:457–466. https://doi.org/10.1016/j.lithos.2010.07.024

Bowring SA, Williams IS (1999) Priscoan (4.00-4.03 Ga) orthogneisses from northwestern Canada. Contrib Mineral Petrol 134(1):3–16

Boyet M, Blichert-Toft J, Rosing MT, Storey M, Telouk P, Albarede F (2003) 142Nd evidence for early Earth diferentiation. Earth Planet Sci Lett 214:427–442. https://doi.org/10.1016/S0012-821X(03)00423-0

Campbell IH, Allen CM (2008) Formation of supercontinents linked to increases in atmospheric oxygen. Nat Geosci 1(8):554–558. https://doi.org/10.1038/ngeo259

Campbell IH, Taylor SR (1985) No water, no granites – no oceans, no continents. Geophys Res Lett 10:1061–1064

Canil D, Crockford PW, Rossin R, Telmer K (2015) Mercury in some arc crustal rocks and mantle peridotites and relevance to the moderately volatile element budget of the Earth. Chem Geol 396:134–142. https://doi.org/10.1016/j.chemgeo.2014.12.029

Caro G, Bourdon B, Birck JL, Moorbath S (2003) Sm-146-Nd-142 evidence from Isua metamorphosed sediments for early differentiation of the Earth's mantle. Nature 423(6938):428–432. https://doi.org/10.1038/nature01668

Cates NL, Mojzsis SJ (2007) Pre-3750 Ma supracrustal rocks from the Nuvvuagittuq supracrustal belt, Northern Quebec. Earth Planet Sci Lett 255(1–2):9–21. https://doi.org/10.1016/j.epsl.2006.11.034

Cawood PA, Hawkesworth CJ, Dhuime B (2013) The continental record and the generation of continental crust. Geol Soc Am Bull 125(1–2):14–32. https://doi.org/10.1130/b30722.1

Chauvel C, Garcon M, Bureau S, Besnault A, Jahn BM, Ding ZL (2014) Constraints from loess on the Hf-Nd isotopic composition of the upper continental crust. Earth Planet Sci Lett 388:48–58. https://doi.org/10.1016/j.epsl.2013.11.045

Chen K, Walker RJ, Rudnick RL, Gao S, Gaschnig RM, Puchtel IS, Tang M, Hu Z-C (2016) Platinum-group element abundances and Re-Os isotopic systematics of the upper continental crust through time: evidence from glacial diamictites. Geochim Cosmochim Acta 191:1–16. https://doi.org/10.1016/j.gca.2016.07.004

Christensen NI, Mooney WD (1995) Seismic velocity structure and composition of the continental crust: a global view. J Geophys Res 100(B7):9761–9788

Clift PD, Vannucchi P, Morgan JP (2009) Crustal redistribution, crust-mantle recycling and Phanerozoic evolution of the continental crust. Earth-Sci Rev 97(1–4):80–104. https://doi.org/10.1016/j.earscirev.2009.10.003

Cogley JG (1984) Continental margins and the extent and number of the continents. Rev Geophys Space Phys 22:101–122

Compston W, Pidgeon RT (1986) Jack Hills, evidence of more very old detrital zircons in western. Aust Nat 321(6072):766–769. https://doi.org/10.1038/321766a0

Condie KC (1993) Chemical composition and evolution of the upper continental crust: contrasting results form surface samples and shales. Chem Geol 104:1–37

Condie KC (1998) Episodic continental growth and supercontinents: a mantle avalanche connection? Earth Planet Sci Lett 163(1–4):97–108. https://doi.org/10.1016/s0012-821x(98)00178-2

Condie KC, Aster RC (2010) Episodic zircon age spectra of orogenic granitoids: the supercontinent connection and continental growth. Precambrian Res 180(3–4):227–236. https://doi.org/10.1016/j.precamres.2010.03.008

Condie KC, Belousova E, Griffin WL, Sircombe KN (2009) Granitoid events in space and time: constraints from igneous and detrital zircon age spectra. Gondwana Res 15(3–4):228–242. https://doi.org/10.1016/j.gr.2008.06.001

Cottle JM, Stearns MA (2017) Application of single shot laser ablation split stream to accessory phase petrochronology. In: Macrostructural geochronology; lattice to atom-scale records of planetary evolution. American Geophysical Union Monograph, Washington, DC

Cottrell RD, Tarduno JA, Bono RK, Dare MS, Mitra G (2016) The inverse microconglomerate test: further evidence for the preservation of Hadean magnetizations in metasediments of the Jack Hills, Western Australia. Geophys Res Lett 43(9):4215–4220. https://doi.org/10.1002/2016gl068150

Darling J, Storey C, Hawkesworth C (2009) Impact melt sheet zircons and their implications for the Hadean crust. Geology 37(10):927–930. https://doi.org/10.1130/g30251a.1

David J, Godin L, Stevenson R, O'Neil J, Francis D (2009) U-Pb ages (3.8-2.7 Ga) and Nd isotope data from the newly identified Eoarchean Nuvvuagittuq supracrustal belt, superior Craton, Canada. Geol Soc Am Bull 121(1–2):150–163. https://doi.org/10.1130/b26369.1

Dhuime B, Hawkesworth CJ, Cawood PA, Storey CD (2012) A change in the geodynamics of continental growth 3 billion years ago. Science 335(6074):1334–1336. https://doi.org/10.1126/science.1216066

Dhuime B, Wuestefeld A, Hawkesworth CJ (2015) Emergence of modern continental crust about 3 billion years ago. Nat Geosci 8(7):552–555. https://doi.org/10.1038/ngeo2466

Ducea MN (2002) Constraints on the bulk composition and root foundering rates of continental arcs: a California arc perspective. J Geophys Res-Solid Earth 107(B11)

Eade KE, Fahrig WF (1971) Chemical evolutionary trends of continental plates – a preliminary study of the Canadian Sheild. Canadian Geological Survey, Ottawa

Eade KE, Fahrig WF (1973) Regional, lithological, and temporal variation in the abundances of some trace elements in the Canadian Shield. Canadian Geological Survey, Ottawa

Eichelberger JC (1975) Origin of andesite and dacite – evidence of mixing of magmas at Glass Mountain in California and at other circum-Pacific volcanoes. Geol Soc Am Bull 86(10):1381–1391. https://doi.org/10.1130/0016-7606(1975)86<1381:ooaade>2.0.co;2

Elliott T (2003) Tracers of the slab. In: Eiler J (ed) Inside the subduction factory, Geophysical monograph, vol 138. American Geophysical Union, Washington, DC, pp 23–45

Fahrig WF, Eade KE (1968) The chemical evolution of the Canadian Shield. Geochim Cosmochim Acta 5:1247–1252

Fegley B (2014) Venus. In: Davis AM (ed) Planets, asteroids, comets and the solar system, Treatise on geochemistry, vol 2. Elsevier, Oxford, pp 127–148

Fisher CM, Vervoort JD, DuFrane SA (2014) Accurate Hf isotope determinations of complex zircons using the "laser ablation split stream" method. Geochem Geophys Geosyst 15(1):121–139. https://doi.org/10.1002/2013gc004962

Froude DO, Ireland TR, Kinny PD, Williams IS, Compston W, Williams IR, Myers JS (1983) Ion micropre identification of 4,11-4,200 Myr-old terrestiral zircons. Nature 304(5927):616–618. https://doi.org/10.1038/304616a0

Fu B, Page FZ, Cavosie AJ, Fournelle J, Kita NT, Lackey JS, Wilde SA, Valley JW (2008) Ti-in-zircon thermometry: applications and limitations. Contrib Mineral Petrol 156(2):197–215. https://doi.org/10.1007/s00410-008-0281-5

Gao S, Luo T-C, Zhang B-R, Zhang H-F, Han Y-W, Hu Y-K, Zhao Z-D (1998) Chemical composition of the continental crust as revealed by studies in East China. Geochim Cosmochim Acta 62:1959–1975

Gaschnig RM, Rudnick RL, McDonough WF, Kaufman AJ, Valley JW, Hu Z-C, Gao S, Beck ML (2016) Compositional evolution of the upper continental crust through time, as constrained by ancient glacial diamictites. Geochim Cosmochim Acta 186:316–343

Goldschmidt VM (1933) Grundlagen der quantitativen Geochemie. Fortschr Mienral Kirst Petrog 17:112

Goldstein SL (1989) Decoupled evolution of Nd and Sr isotopes in the continental crust and the mantle. Nature 336:733–738

Goodwin AM (1996) Principles of Precambrian geology. Academic, London

Grimes CB, John BE, Kelemen PB, Mazdab FK, Wooden JL, Cheadle MJ, Hanghoj K, Schwartz JJ (2007) Trace element chemistry of zircons from oceanic crust: a method for distinguishing detrital zircon provenance. Geology 35(7):643–646. https://doi.org/10.1130/g23603a.1

Gurnis M, Davies GF (1986) Apparent episodic crustal growth arising from a smoothly evolving mantle. Geology 14:396–399

Hacker BR, Kelemen PB, Behn MD (2011) Differentiation of the continental crust by relamination. Earth Planet Sci Lett 307(3–4):501–516. https://doi.org/10.1016/j.epsl.2011.05.024

Hacker BR, Kelemen PB, Behn MD (2015) Continental lower crust. In: Jeanloz R, Freeman KH (eds) Annu Rev Earth Planet Sci 43:167–205

Harper CL, Jacobsen SB (1992) Evidence from coupled ^{147}Sm-^{143}Nd and ^{146}Sm-^{142}Nd systematics for very early (4.5 Gyr) differentiation of the Earth's mantle. Nature 360:728–732

Harrison TM (2009) The Hadean crust: evidence from >4 Ga zircons. Annu Rev Earth Planet Sci 37:479–505. https://doi.org/10.1146/annurev.earth.031208.100151

Haskin MA, Haskin LA (1966) Rare earths in European shales: a redetermination. Science 154:507–509

Hawkesworth CJ, Kemp AIS (2006) Evolution of the continental crust. Nature 443(7113):811–817. https://doi.org/10.1038/nature05191

Hawkesworth CJ, Dhuime B, Pietranik AB, Cawood PA, Kemp AIS, Storey CD (2010) The generation and evolution of the continental crust. J Geol Soc 167(2):229–248. https://doi.org/10.1144/0016-76492009-072

Hawkesworth C, Cawood P, Dhuime B (2013) Continental growth and the crustal record. Tectonophysics 609:651–660. https://doi.org/10.1016/j.tecto.2013.08.013

Herzberg CT, Fyfe WS, Carr MJ (1983) Density constraints on the formation of the continental Moho and crust. Contrib Mineral Petrol 84:1–5

Hopkins M, Harrison TM, Manning CE (2008) Low heat flow inferred from >4 Gyr zircons suggests Hadean plate boundary interactions. Nature 456(7221):493–496. https://doi.org/10.1038/nature07465

Hu ZC, Gao S (2008) Upper crustal abundances of trace elements: revision and update. Chemi Geol 253(3–4):205–221. https://doi.org/10.1016/j.chemgeo.2008.05.010

Huang Y, Chubakov V, Mantovani F, Rudnick RL, McDonough WF (2013) A reference Earth model for the heat-producing elements and associated geoneutrino flux. Geochem Geophys Geosyst 14(6):2003–2029. https://doi.org/10.1002/ggge.20129

Hurley PM, Rand JR (1969) Pre-drift continental nuclei. Science 164:1229–1242

Jagoutz O, Schmidt MW (2013) The composition of the foundered complement to the continental crust and a re-evaluation of fluxes in arcs. Earth Planet Sci Lett 371:177–190. https://doi.org/10.1016/j.epsl.2013.03.051

Jaupart C, Mareschal J-C (2014) Constraints on crustal heat production from heat flow data. In: Rudnick RL (ed) The crust, Treatise on geochemistry, vol 4. Elsevier, Oxford, pp 53–72

Johnson B, Goldblatt C (2015) The nitrogen budget of Earth. Earth-Sci Rev 148:150–173. https://doi.org/10.1016/j.earscirev.2015.05.006

Jull M, Kelemen PB (2001) On the conditions for lower crustal convective instability. J Geophys Res 106(4):6423–6446

Kamber BS (2010) Archean mafic-ultramafic volcanic landmasses and their effect on ocean atmosphere chemistry. Chem Geol 274(1–2):19–28. https://doi.org/10.1016/j.chemgeo.2010.03.009

Kamber BS, Greig A, Collerson KD (2005) A new estimate for the composition of weathered young upper continental crust from

E

alluvial sediments, Queensland, Australia. Geochim Cosmochim Acta 69(4):1041–1058. https://doi.org/10.1016/j.gca.2004.08.020
Kay RW, Kay SM (1991) Creation and destruction of lower continental crust. Geol Rundsch 80:259–278
Kelemen PB (1995) Genesis of high Mg# andesites and the continental crust. Contrib Mineral Petrol 120:1–19
Kelemen PB, Behn MD (2016) Formation of lower continental crust by relamination of buoyant arc lavas and plutons. Nat Geosci 9:197–205. https://doi.org/10.1038/NGEO2662
Kelemen PB et al (2003a) Along-strike variation in lavas of the Aleutian island arc: implications for the genesis of high Mg# andesite and the continental crust. In: Eiler J (ed) Inside the subduction factory, AGU monograph, vol 138. Washington, DC, pp 293–311
Kelemen PB, Hanghoj K, Greene A (2003b) One view of the geochemistry of subduction-related magmatic arcs, with an emphasis on primitive andesite and lower crust. In: Rudnick RL (ed) The crust, Treatise on geochemistry, vol 3. Elsevier, Amsterdam, pp 593–659
Keller CB, Schoene B (2012) Statistical geochemistry reveals disruption in secular lithospheric evolution about 2.5 Gyr ago. Nature 485(7399):490–493. https://doi.org/10.1038/nature11024
Keller CB, Schoene B, Barboni M, Samperton KM, Husson JM (2015) Volcanic-plutonic parity and the differentiation of the continental crust. Nature 523(7560):301–307. https://doi.org/10.1038/nature14584
Kemp AIS, Hawkesworth CJ (2014) Growth and differentiation of the continental crust from isotope studies of accessory minerals. In: Rudnick RL (ed) The crust, vol 4. Elsevier, Oxford, pp 379–421
Kemp AIS, Hawkesworth CJ, Paterson BA, Kinny PD (2006) Episodic growth of the Gondwana supercontinent from hafnium and oxygen isotopes in zircon. Nature 439(7076):580–583
Kemp AIS, Wilde SA, Hawkesworth CJ, Coath CD, Nemchin A, Pidgeon RT, Vervoort JD, DuFrane SA (2010) Hadean crustal evolution revisited: new constraints from Pb-Hf isotope systematics of the Jack Hills zircons. Earth Planet Sci Lett 296(1–2):45–56. https://doi.org/10.1016/j.epsl.2010.04.043
Kemp AIS, Hickman AH, Kirkland CL, Vervoort JD (2015) Hf isotopes in detrital and inherited zircons of the Pilbara Craton provide no evidence for Hadean continents. Precambrian Res 261:112–126. https://doi.org/10.1016/j.precamres.2015.02.011
Kenny GG, Whitehouse MJ, Kamber BS (2016) Differentiated impact melt sheets may be a potential source of Hadean detrital zircon. Geology 44(6):435–438. https://doi.org/10.1130/g37898.1
Kent AJR, Darr C, Koleszar AM, Salisbury MJ, Cooper KM (2010) Preferential eruption of andesitic magmas through recharge filtering. Nat Geosci 3(9):631–636. https://doi.org/10.1038/ngeo924
König S, Munker C, Hohl S, Paulick H, Barth AR, Lagos M, Pfander J, Buchl A (2011) The Earth's tungsten budget during mantle melting and crust formation. Geochim Cosmochim Acta 75(8):2119–2136. https://doi.org/10.1016/j.gca.2011.01.031
Kylander-Clark ARC, Hacker BR, Cottle JM (2013) Laser-ablation split-stream ICP petrochronology. Chem Geol 345:99–112. https://doi.org/10.1016/j.chemgeo.2013.02.019
Lee CTA (2014) Physics and chemistry of deep continental crust recycling. In: Rudnick RL (ed) The crust, vol 4. Elsevier, Oxford, pp 423–456
Lee C-TA, Bachmann O (2014) How important is the role of crystal fractionation in making intermediate magmas? Insights from Zr and P systematics. Earth Planet Sci Lett 393:266–274. https://doi.org/10.1016/j.epsl.2014.02.044
Lee CTA, Morton DM, Kistler RW, Baird AK (2007) Petrology and tectonics of Phanerozoic continent formation: From island arcs to accretion and continental arc magmatism. Earth Planet Sci Lett 263 (3–4):370–387
Lee CTA, Morton DM, Little MG, Kistler R, Horodyskyj UN, Leeman WP, Agranier A (2008) Regulating continent growth and composition by chemical weathering. Proc Natl Acad Sci U S A 105(13):4981–4986
Lee CTA, Yeung LY, McKenzie NR, Yokoyama Y, Ozaki K, Lenardic A (2016) Two-step rise of atmospheric oxygen linked to the growth of continents. Nat Geosci 9(6):417–424. https://doi.org/10.1038/ngeo2707
Li S, Gaschnig RM, Rudnick RL (2016) Insights into chemical weathering of the upper continental crust from the geochemistry of ancient glacial diamictites. Geochim Cosmochim Acta 176:96–117. https://doi.org/10.1016/j.gea.2015.12.012
Liu X-M, Rudnick RL (2011) Constraints on continental crustal mass loss via chemical weathering using lithium and its isotopes. Proc Natl Acad Sci U S A 108(52):20873–20880. https://doi.org/10.1073/pnas.1115671108
Maas R, Kinny PD, Williams IS, Froude DO, Compston W (1992) The Earth's oldest known crust – a geochronological and geochemical study of the 3900-4200 Ma old detrital zircons from Mt. Narryer and Jack Hills, Western Australia. Geochimica Et Cosmochimica Acta 56(3):1281–1300. https://doi.org/10.1016/0016-7037(92)90062-n
Martin H (1986) Effect of steeper Archean geothermal gradient on geochemistry of subduction-zone magmas. Geology 14:753–756
Martin H, Moyen JF (2002) Secular changes in tonalite-trondhjemite-granodiorite composition as markers of the progressive cooling of Earth. Geology 30(4):319–322
McCoy TJ, Nittler LR (2014) Mercury. In: Davis AM (ed) Meteorites, comets and planets, Treatise on geochemistry, vol 2. Elsevier, Oxford, pp 119–126
McCulloch MT, Bennett VC (1994) Progressive growth of the Earth's continental crust and depleted mantle: geochemical constraints. Geochim Cosmochim Acta 58:4717–4738
McDonough WF, Sun S-S (1995) Composition of the earth. Chem Geol 120:223–253
McLennan SM (2001) Relationships between the trace element composition of sedimentary rocks and upper continental crust. Geochem Geophys Geosyst 2:art. no.-2000GC000109
McLennan SM, Taylor SR (1980) Th and U in sedimentary rocks: crustal evolution and sedimentary recycling. Nature 285:621–624
McLennan SM, Taylor SR (1991) Sedimentary-rocks and crustal evolution – tectonic setting and secular trends. J Geol 99(1):1–21
McLennan SM, Taylor SR (1996) Heat flow and the chemical composition of continental crust. J Geol 104:396–377
McSween HY Jr, McLennan SM (2014) Mars. In: Davis AM (ed) Meteorites, comets and planets, Treatise on geochemistry, vol 2. Elsevier, Oxford, pp 251–300
Mojzsis SJ, Harrison TM, Pidgeon RT (2001) Oxygen-isotope evidence from ancient zircons for liquid water at the Earth's surface 4,300 Myr ago. Nature 409(6817):178–181. https://doi.org/10.1038/35051557
Moorbath S, Gale NH, Pankhurst RJ, McGregor VR, Onions RK (1972) Further rubidium-strontium age determinations on very early Precambrian rocks of Godthaab district, West Greenland. Nat Phys Sci 240(100):78–82
Moorbath S, Onions RK, Pankhurst RJ (1973) Early Archaean age for Isua iron formation, West Greenland. Nature 245(5421):138–139. https://doi.org/10.1038/245138a0
Muramatsu Y, Wedepohl KH (1998) The distribution of iodine in the earth's crust. Chem Geol 147(3–4):201–216. https://doi.org/10.1016/s0009-2541(98)00013-8
Nance WB, Taylor SR (1976) Rare-Earth element patterns and crustal evolution. 1. Australian post-Archean sedimentary-rocks. Geochim Cosmochim Acta 40(12):1539–1551. https://doi.org/10.1016/0016-7037(76)90093-4
Nance WB, Taylor SR (1977) Rare-Earth element patterns and crustal evolution. 2. Archean sedimentary-rocks from Kalgoorlie, Australia. Geochim Cosmochim Acta 41(2):225–231. https://doi.org/10.1016/0016-7037(77)90229-0

Nutman AP, McGregor VR, Friend CRL, Bennett VC, Kinny PD (1996) The Itsaq Gneiss Complex of southern west Greenland; the world's most extensive record of early crustal evolution (3900-3600 Ma). Precambrian Res 78(1–3):1–39. https://doi.org/10.1016/0301-9268(95)00066-6

Nutman AP, Bennett VC, Friend CRL, Rosing MT (1997) ~ 3710 and >3790 Ma volcanic sequences in the Isua (Greenland) supracrustal belt; structural and Nd isotope implications. Chem Geol 141(3–4):271–287. https://doi.org/10.1016/s0009-2541(97)00084-3

Nutman AP, Bennett VC, Van Kranendonk MJ, Chivas AR (2016) Rapid emergence of life shown by discovery of 3,700-million-year-old microbial structures. Nature. https://doi.org/10.1038/nature19355

O'Neil J, Carlson RW (2017) Building Archean cratons from Hadean mafic crust. Science 355:1199–1202

O'Neil J, Carlson RW, Francis D, Stevenson RK (2008) Neodymium-142 evidence for hadean mafic crust. Science 321(5897):1828–1831. https://doi.org/10.1126/science.1161925

O'Neil J, Rizo H, Boyet M, Carlson RW, Rosing MT (2016) Geochemistry and Nd isotopic characteristics of Earth's Hadean mantle and primitive crust. Earth Planet Sci Lett 442:194–205. https://doi.org/10.1016/j.epsl.2016.02.055

Park JW, Hu ZC, Gao S, Campbell IH, Gong HJ (2012) Platinum group element abundances in the upper continental crust revisited – new constraints from analyses of Chinese loess. Geochim Cosmochim Acta 93:63–76. https://doi.org/10.1016/j.gca.2012.06.026

Parman SW (2015) Time-lapse zirconography: imaging punctuated continental evolution. Geochem Perspect Lett 1:43–52. https://doi.org/10.7185/geochemlet.1505

Pasyanos ME, Masters TG, Laske G, Ma ZT (2014) LITHO1.0: an updated crust and lithospheric model of the earth. J Geophys ResSolid Earth 119(3):2153–2173. https://doi.org/10.1002/2013jb010626

Payne JL, McInerney DJ, Barovich KM, Kirkland CL, Pearson NJ, Hand M (2016) Strengths and limitations of zircon Lu-Hf and O isotopes in modelling crustal growth. Lithos 248:175–192. https://doi.org/10.1016/j.lithos.2015.12.015

Pearson DG, Parman SW, Nowell GM (2007) A link between large mantle melting events and continent growth seen in osmium isotopes. Nature 449(7159):202–205. https://doi.org/10.1038/nature06122

Peucker-Ehrenbrink B, Jahn B-M (2001) Rhenium-osmium isotope systematics and platinum group element concentations: loess and the upper continental crust. Geochem Geophys Geosyst 2:2001GC000172

Plank T (2005) Constraints from Th/La on sediment recycling at subduction zones and the evolution of the continents. J Petrol 46:921–944

Reimink JR, Davies JHFL, Chacko T, Stern RA, Heaman LM, Sarkar C, Schaltegger U, Creaser RA, Pearson DG (2016) No evicence for Hadean continental crust within Earth's oldest evovled rock unit. Nat Geosci. https://doi.org/10.1038/ngeo2786

Reubi O, Blundy J (2009) A dearth of intermediate melts at subduction zone volcanoes and the petrogenesis of arc andesites. Nature 461(7268):1269–1273. https://doi.org/10.1038/nature08510

Rizo H, Boyet M, Blichert-Toft J, O'Neil J, Rosing MT, Paquette JL (2012) The elusive Hadean enriched reservoir revealed by Nd-142 deficits in Isua Archaean rocks. Nature 491(7422):96–U109. https://doi.org/10.1038/nature11565

Rollinson H (2008) Secular evolution of the continental crust: implications for crust evolution models. Geochem Geophys Geosyst 9. https://doi.org/10.1029/2008gc002262

Roth ASG, Bourdon B, Mojzsis SJ, Touboul M, Sprung P, Guitreau M, Blichert-Toft J (2013) Inherited Nd-142 anomalies in Eoarchean protoliths. Earth Planet Sci Lett 361:50–57. https://doi.org/10.1016/j.epsl.2012.11.023

Roth ASG, Bourdon B, Mojzsis SJ, Rudge JF, Guitreau M, Blichert-Toft J (2014) Combined Sm-147,Sm-146-Nd-143,Nd-142 constraints on the longevity and residence time of early terrestrial crust. Geochem Geophys Geosyst 15(6):2329–2345. https://doi.org/10.1002/2014gc005313

Rudnick RL (1995) Making continental crust. Nature 378:571–578

Rudnick RL, Fountain DM (1995) Nature and composition of the continental crust: a lower crustal perspective. Rev Geophys 33(3):267–309

Rudnick RL, Gao S (2003) The composition of the continental crust. In: Rudnick RL (ed) The crust, vol 3. Elsevier, Amsterdam, pp 1–64

Sauzéat L, Rudnick RL, Chauvel C, Garçon M, Tang M (2015) New perspectives on the Li isotopic composition of the upper continental crust and its weathering signature. Earth Planet Sci Lett 428:181–192. https://doi.org/10.1016/j.epsl.2015.07.032

Scherer E, Munker C, Mezger K (2001) Calibration of the lutetium-hafnium clock. Science 293(5530):683–687. https://doi.org/10.1126/science.1061372

Scherer EE, Whitehouse MJ, Munker C (2007) Zircon as a monitor of crustal growth. Elements 3(1):19–24. https://doi.org/10.2113/gselements.3.1.19

Schoene B (2014) U-Pb geochronology. In: Rudnick RL (ed) The crust, vol 4. Elsevier, Oxford, pp 341–378

Shaw DM, Reilly GA, Muysson JR, Pattenden GE, Campbell FE (1967) An estimate of the chemical composition of the Canadian Precambrian shield. Can J Earth Sci 4:829–853

Shaw DM, Dostal J, Keays RR (1976) Additional estimates of continental surface Precambrian shield composition in Canada. Geochim Cosmochim Acta 40:73–83

Shaw DM, Cramer JJ, Higgins MD, Truscott MG (1986) Composition of the Canadian Precambrian shield and the continental crust of the earth. In: Dawson JB, Carswell DA, Hall J, Wedepohl KH (eds) The nature of the lower continental crust, vol 24. Geol Soc London, London, pp 257–282

Shaw DM, Dickin AP, Li H, McNutt RH, Schwarcz HP, Truscott MG (1994) Crustal geochemistry in the Wawa-Foleyet region, Ontario. Can J Earth Sci 31(7):1104–1121

Simon L, Lecuyer C (2005) Continental recycling: the oxygen isotope point of view. Geochem Geophys Geosyst 6:Q08004. https://doi.org/10.1029/2005GC000958

Söderlund U, Patchett JP, Vervoort JD, Isachsen CE (2004) The Lu-176 decay constant determined by Lu-Hf and U-Pb isotope systematics of Precambrian mafic intrusions. Earth Planet Sci Lett 219(3–4):311–324. https://doi.org/10.1016/s0012-821x(04)00012-3

Stein M, Hofmann AW (1994) Mantle plumes and episodic crustal growth. Nature 372:63–68

Tang M, Rudnick RL, McDonough WF, Gaschnig RM, Huang Y (2015) Europium anomalies constrain the mass of recycled lower continental crust. Geology 43(8):703–706. https://doi.org/10.1130/g36641.1

Tang M, Chen K, Rudnick RL (2016) Archean upper crust transition from mafic to felsic marks the onset of plate tectonics. Science 351(6271):372–375. https://doi.org/10.1126/science.aad5513

Tarduno JA, Cottrell RD, Davis WJ, Nimmo F, Bono RK (2015) A Hadean to Paleoarchean geodynamo recorded by single zircon crystals. Science 349(6247):521–524. https://doi.org/10.1126/science.aaa9114

Taylor SR (1964) Abundance of chemical elements in the continental crust – a new table. Geochim Cosmochim Acta 28:1273–1285

Taylor SR (1977) Island arc models and the composition of the continental crust. In: Talwani M, Pitmann WC III (eds) Island arcs, deep sea trenches and back-arc basins, vol 1. American Geophysical Union, Washington, DC, pp 325–336

Taylor SR, McLennan S (1985) The continenal crust: its composition and evolution. Blackwell, Oxford

Taylor SR, McLennan SM (1995) The geochemical evolution of the continental crust. Rev Geophys 33:241–265

Taylor SR, McLennan SM (2009) Planetary crusts their composition, origin and evolution. Cambridge University Press, Cambridge
Taylor SR, McLennan SM, McCulloch MT (1983) Geochemistry of loess, continental crustal composition and crustal model ages. Geochim Cosmochim Acta 47:1897–1905
Teng FZ, McDonough WF, Rudnick RL, Dalpe C, Tomascak PB, Chappell BW, Gao S (2004) Lithium isotopic composition and concentration of the upper continental crust. Geochim Cosmochim Acta 68(20):4167–4178
Teng FZ, Rudnick RL, McDonough WF, Gao S, Tomascak PB, Liu YS (2008) Lithium isotopic composition and concentration of the deep continental crust. Chem Geol 255(1–2):47–59. https://doi.org/10.1016/j.chemgeo.2008.06.009
Togashi S, Imai N, Okuyama-Kusunose Y, Tanaka T, Okai T, Koma T, Murata Y (2000) Young upper crustal chemical composition of the orogenic Japan arc. Geochem Geophys Geosyst 1. https://doi.org/10.1029/2000GC000083
van Keken PE, Hacker BR, Syracuse EM, Abers GA (2011) Subduction factory: 4. Depth-dependent flux of H2O from subducting slabs worldwide. J Geophys ResSolid Earth 116. https://doi.org/10.1029/2010jb007922
Veizer J, Compston W (1976) SR-87-SR-86 in Precambrian carbonates as an index of crustal evolution. Geochim Cosmochim Acta 40(8):905–914. https://doi.org/10.1016/0016-7037(76)90139-3
Vervoort JD, Kemp AIS (2016) Clarifying the zircon Hf isotope record of crust-mantle evolution. Chem Geol 425:65–75. https://doi.org/10.1016/j.chemgeo.2016.01.023
Vervoort JD, Patchett PJ, Gehrels GE, Nutman AP (1996) Constraints on early Earth differentiation from hafnium and neodymium isotopes. Nature 379(6566):624–627. https://doi.org/10.1038/379624a0
Voice PJ, Kowalewski M, Eriksson KA (2011) Quantifying the timing and rate of crustal evolution: global compilation of radiometrically dated detrital zircon grains. J Geol 119(2):109–126. https://doi.org/10.1086/658295
Watson EB, Harrison TM (2005) Zircon thermometer reveals minimum melting conditions on earliest Earth. Science 308(5723):841–844. https://doi.org/10.1126/science.1110873
Weaver BL, Tarney J (1984) Empirical approach to estimating the composition of the continental crust. Nature 310:575–577
Wedepohl H (1995) The composition of the continental crust. Geochim Cosmochim Acta 59:1217–1239
Weiss BP, Maloof AC, Tailby N, Ramezani J, Fu RR, Hanus V, Trail D, Watson EB, Harrison TM, Bowring SA, Kirschvink JL, Swanson-Hysell NL, Coe RS (2015) Pervasive remagnetization of detrital zircon host rocks in the Jack Hills, Western Australia and implications for records of the early geodynamo. Earth Planet Sci Lett 430:115–128. https://doi.org/10.1016/j.epsl.2015.07.067
White WM, Klein EM (2014) Composition of the oceanic crust. In: Holland HD, Turekian KK (eds) Treatise on geochemistry, vol 4, 2nd edn. Elsevier, Oxford, pp 457–495
Wilde SA, Valley JW, Peck WH, Graham CM (2001) Evidence from detrital zircons for the existence of continental crust and oceans on the earth 4.4 Gyr ago. Nature 409(6817):175–178
Willbold M, Hegner E, Stracke A, Rocholl A (2009) Continental geochemical signatures in dacites from Iceland and implications for models of early Archaean crust formation. Earth Planet Sci Lett 279(1–2):44–52. https://doi.org/10.1016/j.epsl.2008.12.029
Yanagi T, Yamashita K (1994) Genesis of continental-crust under island-arc conditions. Lithos 33(1–3):209–223. https://doi.org/10.1016/0024-4937(94)90061-2
Yuan HL, Gao S, Dai MN, Zong CL, Gunther D, Fontaine GH, Liu XM, Diwu C (2008) Simultaneous determinations of U-Pb age, Hf isotopes and trace element compositions of zircon by excimer laser-ablation quadrupole and multiple-collector ICP-MS. Chem Geol 247(1–2):100–118. https://doi.org/10.1016/j.chemgeo.2007.10.003

Earth's Core

William F. McDonough
Department of Geology, University of Maryland, College Park, MD, USA

Definition

The composition of the Earth's core is essentially 85% Fe, 5% Ni, and ~10% other, by weight. The details are more complicated, with the "other" being a light element component, which results in the core having on average a lower mean atomic number than that of iron. Birch (1952, 1964) recognized a 10% difference in the density of the outer core relative to an iron-nickel alloy at core pressure and temperature conditions. Anderson and Isaak (2002) recommend that the core density deficit is between 3% and 7%. Both the liquid outer core (~95% by mass) and solid inner core (~5%) contain a fraction of a light element (nominally in a ~2/1 proportion, respectively).

Properties

For more than a century the Earth has been described as having a metallic core surrounded by a silicate shell. A brief history of this topic is given in McDonough (2014). Emil Wiechert in 1897 first subdivided the Earth's interior into these two main components and later, his graduate student Beno Gutenberg, using seismological data, established the core-mantle boundary (CMB) at 2900 km depth, which is within uncertainty the accepted depth for the boundary. First-order physical aspects of the core are listed in Table 1 and are based on fundamental constraints derived from seismology, geodetics of the planets, mineral physics, and experimental studies, with limited additional constraints from geochemistry and cosmochemistry. Seismology reveals that the CMB is more than half an Earth's radius. The outer core (OC) is liquid (absence of a shear-wave) and the inner core (IC) is solid (given observation of PKJKP waves (i.e., P-waves in mantle and OC that converts to an S-wave in IC then back to P-wave as it leaves the IC). Geodesy documents the coefficient of the planet's moment of inertia (i.e., a dense core surrounds a less dense silicate shell) and libration confirms the liquid state of the outer core. Thermodynamic analysis and experimental studies document the conditions of melting and crystallization of Fe-Ni alloys at core conditions and set the upper temperature limits at the inner-outer core boundary. Meteorites confirm that Fe and Ni are chemical partners and their ratios

Earth's Core, Table 1 Physical properties of the Earth's core

Mass	Value (±)	Units	Ref	(% Planet)
Earth	5. 97218(60) × 10^{24}	kg	Chambat et al. (2010)	100%
Inner core	9.68 × 10^{22}	kg	Yoder (1995)	1.6%
Outer core	1.84 × 10^{24}	kg	Yoder (1995)	30.7%
Core	1.93 × 10^{24}	kg	Yoder (1995)	32.3%
Mantle	4.015 × 10^{24}	kg	Chambat et al. (2010), Yoder (1995), Huang et al. (2013)	67.7%
Crust (ocean + continental)	2.73(48) × 10^{22}	kg	Huang et al. (2013)	0.46%
Inner core to core (%)				5.0%
Radius				
Inner-outer core boundary	1220 ± 10	km	Masters and Shearer (1995)	19%
Core-mantle boundary	3483 ± 5	km	Masters and Shearer (1995)	55%
Mean radius of the Earth	6371.23 (0.01)	km	Chambat et al. (2010)	100%
Volume				
Inner core	7.61 × 10^{9}	km^3		0.7%
Outer core	1.69 × 10^{11}	km^3		16%
Bulk core	1.77 × 10^{11}	km^3		16%
Silicate Earth	9.14 × 10^{11}	km^3		84%
Earth	1.083 × 10^{12}	km^3		100%
Density				
Outermost inner core (solid)	12,830	kg/m^3	Masters and Gubbins (2003)	
Innermost outer core (liquid)	12,010	kg/m^3	Masters and Gubbins (2003)	
Inner-outer core Δ density	820 (180)	kg/m^3	Masters and Gubbins (2003)	
Average outer core density	11,160 (60)	kg/m^3	Masters and Gubbins (2003)	
Average inner core density	13,070 (260)	kg = m^3	Masters and Gubbins (2003)	
CMB (Core-mantle boundary)				
Peak-to-peak topography	<3	km	Sze and van der Hilst (2003)	
CMB ellipticity	~0.2	km	Sze and van der Hilst (2003)	
Thermal and pressure data				
Top of outer core	4000 ± 500	K	Tsuchiya et al. (2016), Fischer (2016)	137 GPa
Top of inner core	5700 ± 550	K	Tsuchiya et al. (2016), Fischer (2016)	330 GPa
Outer core adiabatic gradient	0.55 (0.1)	K/km	Tsuchiya et al. (2016)	
Heat flow across CMB	5–15	TW	Tsuchiya et al. (2016)	
Moment of inertia constants				
Equatorial moment of inertia (I)	0.3299765	Ma^2	Yoder (1995)	
Mean moment of inertia (I)	0.330690 (9)	MR^2_0	Chambat et al. (2010)	

in primitive and iron meteorites inform us of their initial proportions in the Earth.

The maximum in the Earth's gravitational acceleration occurs at just above the CMB, where being close to the high density core has its greatest effect on the gravity field. Consequently, "g" (i.e., acceleration of gravity) increases in roughly linear fashion from center to CMB (i.e., approximately a uniform density sphere) and then remains between 9.8 and 10.5 m/s^2 from the surface to the CMB. The Earth's dynamic figure for the gravitational field is known to six significant figures and in combination with seismological constraints indicates that the excess ellipticity of the CMB is slight (~0.2 km) and that the CMB surface topography is smooth at long-wavelength being on the order of 1–3 km of peak-to-peak topographic amplitude (Table 1).

Formation

The core's origin dates back to the formation of the planet, with planet accretion occurring via accumulation and agglomeration of increasing size of particles and later planetesimals. Our solar system owes it origin to a supernova (or multiple supernovae) where the mass and momenta of the supernova combined with a fragment of an interstellar gas-dust cloud to rotate, collapse, condense, and centrally concentrate mass, internally controlled by a balance of gravitational and centripetal forces. Because of its mass the Sun, and to a lesser extent Jupiter, dominated accretion and condensation of the inner rocky planets, which formed relatively early (a few 10^6 years) and grew by the accretion of material flowing into and less so out of their respective feeding zone (first few AU surrounding the Sun).

Growth by accretion of a planet does not require differentiation of the body into a core and mantle, although differentiation likely occurred in stages during growth and included accretion of predifferentiated planetismals. For the Earth, it is likely that as accretion progressed the proto-Earth at some point reach melting temperatures for metallic liquids (lower than that for silicate liquids) and because of the large density contrasts (i.e., silicates being ~3000 and iron metal being ~7900 kg/m^3 at surface conditions) gravitational separation of a metallic core quickly ensued. The mean time of formation of the bulk of the Earth's core is, however, an open question with best estimates being between 30 and 60 Ma (million years) after the formation of the solar system (an age established by the oldest dated materials in the solar system, Hf-W isotope systematics of iron meteorites, and the age of Moon formation; more about this topic later). Note, timing of core formation can be considered as the mean age (or mean lifetime), which is a scaling time reflecting when much of the mass of metallic atoms were separated. The initial mass associated with core formation was likely significant and rapidly separated. Subsequent additions to the core might have followed some exponentially decreasing mass versus time function.

A second constraint on the time of core formation comes from understanding the origin of the Moon and the dating of its oldest rocks. This constraint is based on the fact that the Moon possesses a bulk composition that approximates that of the Earth's mantle (i.e., they share the same oxygen isotopic composition to six significant figures), with a bit more iron in the Moon (Young et al. 2016). The Moon's origin is often ascribed to being due to a giant impact (collision) between a nearly completely formed Earth and a Mars sized impactor (Mars is ~10% by mass the size of the Earth, whereas the Moon's mass is 7.346×10^{22} kg, which is 1.2% of the mass of the Earth) (Canup 2012; Cuk and Stewart 2012). Alternative scenarios for the moon-forming event(s) allow for a series of lesser, but still substantial, impacts that also satisfy the observational constraints (Cuk et al. 2016). The material ejected during this event coalesced into a corotating accretion disk around the Earth, possessed only a small fraction of metal from the Earth's core or the impactor, and subsequently accreted to form the Moon. The general features of this model (Canup 2012; Cuk and Stewart 2012; Cuk et al. 2016) are consistent with hydrodynamic models of accretion that seek to reconcile the angular momentum of the Earth-Moon system and isotopic constraints.

Major questions about the composition of the Earth's core, its age, the age of the inner core, present conditions, and dynamics of its formation remain unresolved. Debate focuses on the following questions for which we have limited observational constraints:

Formation Conditions and Composition

- What was the integrated composition of material feeding the Earth (i.e., chondrites)?
- What is the temperature and pressure evolution of planet growth and core formations?
- What was the integrated fO_2, fH_2, and fS_2 (gas fugacity) of core formation?
- How did the redox state of core formation evolve (early to late evolution)?
- Was segregation and sinking of metal from silicate an equilibrium process throughout the mantle or only for a portion thereof?
- Was core separation accomplished in the presence a magma ocean or not?
- Did the process of giant impact collision coalesce and emulsify the cores of the Earth and its impactor and re-establish metal-silicate equilibrium?
- What is the duration and timing of core formation (e.g., ^{182}Hf-^{182}W. isotope system)?
- How much S, C, N, and H (i.e., volatile elements) are in core?
- How much O, Si, and Mg (i.e., major elements) are in core?
- Are there radioactive elements in the core and if so, how much?

Inner-Outer Core

- When did the inner core start to form?
- What is the crystal structure of the inner core?
- How much and what is (are) the light element(s) in the inner core?
- How much and what is (are) the light element(s) in the outer core?
- Does enrichment of buoyant, light-element-rich liquids, produced at the inner-outer core boundary, drive compositional convection and the geodynamo?
- To what degree does crystallization of the inner core drive compositional convection?

Many unknowns remain and detailed constraints on the core's composition come almost exclusively from the chemical and isotopic composition of the silicate Earth and meteorites.

Building Compositional Models of the Planet and Core

Our view of planetary compositional modeling is explicitly informed by the compositions of chondrites, the most primitive rocks of the solar system. Chondritic meteorites, which make up the bulk of the meteoritic material (~95% of the falls), fell to the Earth during historical times and thus shape our view of the building blocks of the planets (Engel and

McDonough 2016). CI1 carbonaceous chondrites have the most primitive composition of the various chondrites and closely match the spectroscopically derived composition of the solar photosphere for all but H, C, N, O, and the noble gases (McDonough 2016). [Note, that the chondrite type is CI and the metamorphic grade is 1, hence CI1.] The element abundance curve for the solar photosphere, for at least the dozen most abundant elements, is the same as that for other stars in the galaxy and nearby galaxies. Thus, the principles developed below are applicable for exoplanet building too.

As building blocks, chondrites provide the basis for compositional models that can plausibly describe what is in the Earth's core. Some proposed models of the Earth's composition fall outside of the observed range for chondrites, with enrichments in refractory elements and stronger depletions in volatile element abundances than seen in chondrites (Fig. 1) (McDonough 2014). Element classification (i.e., volatile versus refractory) is defined in terms of half-mass condensation temperatures of an element during cooling of a nebular accretion disk and precipitation into common mineral phases. Given the plausible range of volatile and refractory element abundances in different groups of chondrites that accreted to form the Earth, it is not possible to uniquely define the planet's composition. Moreover, while chondrites represent a compositional guide, the Earth is unlikely to match the composition of any specific, single chondrite. The standard rules for planet building are as follows:

- Use orbital and seismic constraints, if available, to define the physical state
- Use chemical and isotopic data from chondritic (i.e., primitive) meteorites and the solar photosphere
- Assume chondritic proportions for the refractory elements and model their absolute abundances based on chemical trends observed for mantle samples (basalts and peridotites),
- Model the absolute abundances of Mg, Fe, Si, and O; these are the major elements, which are nonrefractory elements, and constitute >90% by mass of the rocky planets
- Recognize a chemical gradient in solar system (e.g., rocky planets versus the gas giants)
- Model the relative and absolute abundances of the nonrefractory elements in the planet

Model core compositions are estimated by subtracting the composition of the silicate Earth from the composition of the bulk planet. The relative distribution of lithophile elements (those that tend to bond with oxygen and are excluded from the core) versus siderophile elements (those that tend to bond with iron and are dominantly stored in the core) in the crust and mantle define the composition of the silicate Earth. For refractory elements, including lithophile and siderophile, their relative proportions in the planet are the same as in chondrites (i.e., the lithophiles have constant ratios at ±10% or better, constant ratios of siderophiles are at ±15% or better, and ratios of lithophile to siderophile have uncertainties at circa ±25%, with the greater difference for the latter being due to variations in the proportion of metal to silicate in chondrites). Therefore, if we can predict the abundance of one refractory element in the Earth, we can predict the planetary inventory of all 37 refractory elements, which include: Be, Al, Ca, Sc, Ti, V, Sr, Y, Zr, Nb, Ba, REE, Hf, Ta, Th, and U (these are the lithophiles); and Mo, Ru, Rh, W, Re, Os, Ir, and Pt (these are the siderophiles, with V showing both behavior). How and why elements are distributed between the core (mostly siderophile) and the surrounding silicate shell (lithophile) depends on the conditions of pressure, temperature, and redox state during core formation. The conditions of core formation are critical to establishing its final composition.

Among the dozen most common elements in the solar system, the rocky planets are variably depleted in the most

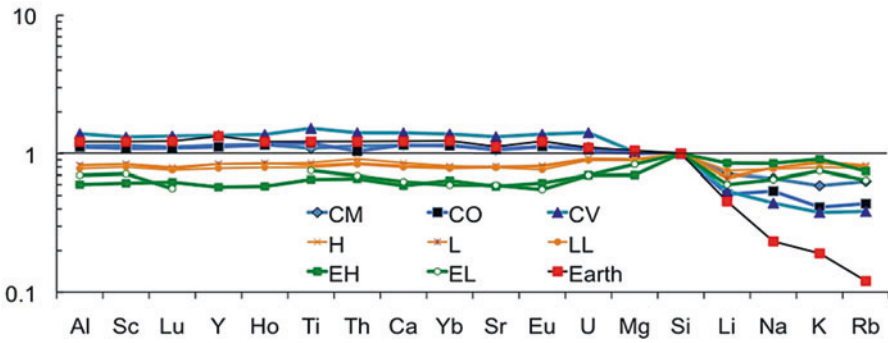

Earth's Core, Fig. 1 Chondrite normalize compositions for carbonaceous chondrites (CM, CO, CV subtypes), ordinary chondrites (H, L, and LL subgroups), enstatite chondrites (EH and EL subgroups) and the Earth. The figure is double normalized with all compositional models plotted as having the same Si content, which corrects for differing amounts of highly volatile element contents (i.e., H, C, N, O). Normalizing reference frame assumes a CI1 chondrites composition. Data for the chondrites are from Wasson and Kallemeyn (1988) and McDonough (2014)

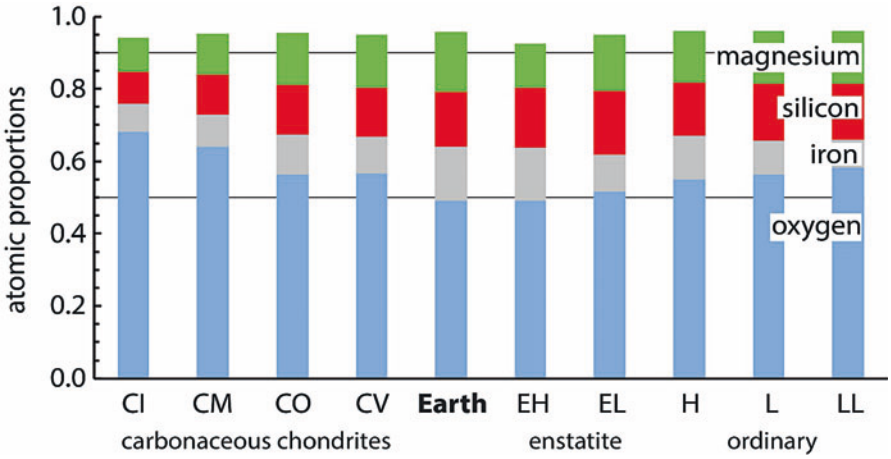

Earth's Core, Fig. 2 Atomic proportions of O, Fe, Si, and Mg in chondrites and the Earth. Data sources listed in Fig. 1. The O context is ≥50% in the chondrites and the total atomic fraction for these four elements in all of these materials adds up to >90%

volatile constituents (i.e., the gases: H, He, C, N, O, Ne, Ar). The remaining common elements are O, Fe, Si, and Mg, which constitute between 90% and 95% the mass of the Earth, Mars, and Venus roughly in the mass proportion 30:30:20:20 (or in the approximate atomic proportions of 50:15:15:15), respectively (Fig. 2). The high density and small radius of Mercury indicates that it likely has a much higher proportion of iron than the other rocky planets. Compositional models for the Earth, other terrestrial planets, and exoplanets with bulk density in the range 3000–6000 kg/m^3 will be dictated by mixtures of metal and silicate. The silicates are predominately a bimineralic mix of olivine and pyroxene at pressures equivalent to the Earth's upper mantle. At the seismically define base of the Transition Zone (i.e., 660 km depth, ~22 GPa), olivine disproportionates into bridgmanite (Mg-Fe silicate perovskite) and ferro-periclase, whereas the pyroxene component (which in the upper mantle has gradually dissolved into a majoritic garnet) converts to bridgmanite and Ca perovskite over a broader range of pressures (i.e, ~19–24 GPa).

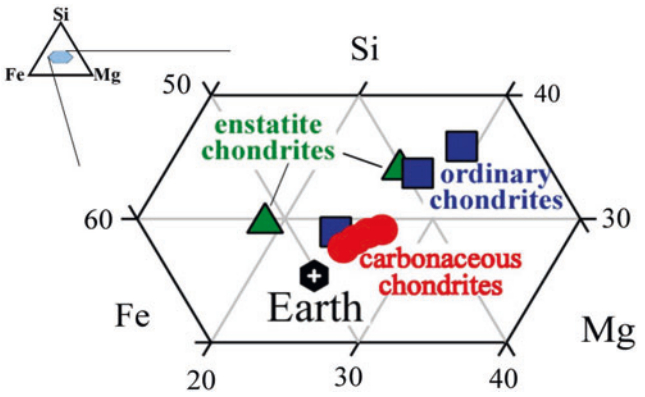

Earth's Core, Fig. 3 The compositional space for the chondrites and the Earth in a tetrahedral volume plotted from the apices of Si, Mg, Fe, and O, with the data plotted onto the surface of the Si-Fe-Mg plane. Data sources listed in Fig. 1. The Earth's composition falls outside of the field of the known chondrites. This model composition for the Earth is acceptable given observations of the spatial variations in rates of olivine to pyroxene crystallization in accretion disks (See text for further details)

A big unknown in predicting the bulk composition of a planet is establishing the proportion of olivine to pyroxene accreted by the body, which is indicated by its Mg/Si ratio. There is no fixed Mg/Si ratio for chondrites and thus there is no chondritic constraint (Fig. 3). Olivine has a 2:1 molar Mg/Si content, whereas pyroxene's molar ratio is 1:1. Astromineralogical observations of accretion disks reveal radial variations in the proportion of olivine to pyroxene, some with inner disk regions being richer in olivine relative to the disk wide composition (van Boekel et al. 2004), whereas other have more olivine in the outer part of the circumstellar disk; differences in disk mineralogy may relate to type of star (e.g., T Tauri vs. Herbig Ae/Be stars) (Bouwman et al. 2010). Likewise, one can also envisage disk evolution in time with temperature decreasing as the disk cools leading to decreasing Mg/Si (less olivine ppt with time). Moreover, crystallinity scales radially, with inner disk regions (a few AU) having higher abundances of large grains and generally higher crystallinity as compared to outer disk regions, suggesting grain growth occurs more rapidly in the inner disk regions (D'Alessio et al. 2005; Sargent et al. 2009). Thus, planetary modelers must acknowledge that there is no fixed Mg/Si value for a planet.

After O, Fe, Si, and Mg, the next most abundant elements in chondrites and rocky planets are Al, Ca, and Ni and together these seven elements, plus S, make up >98% by mass of these solid bodies. Both Ca and Al are refractory elements, and their planetary weight ratio is 1.1 (atomic ratio is 0.72), equal to that of chondrites, but their absolute abundances in the Earth are model dependent; these elements are exclusively lithophile and thus concentrate in only the silicate portion of the Earth. Nickel and sulfur are both nonrefractory elements and are partitioned into both the core and mantle, with Ni being dominantly siderophile (>90% of the Earth's

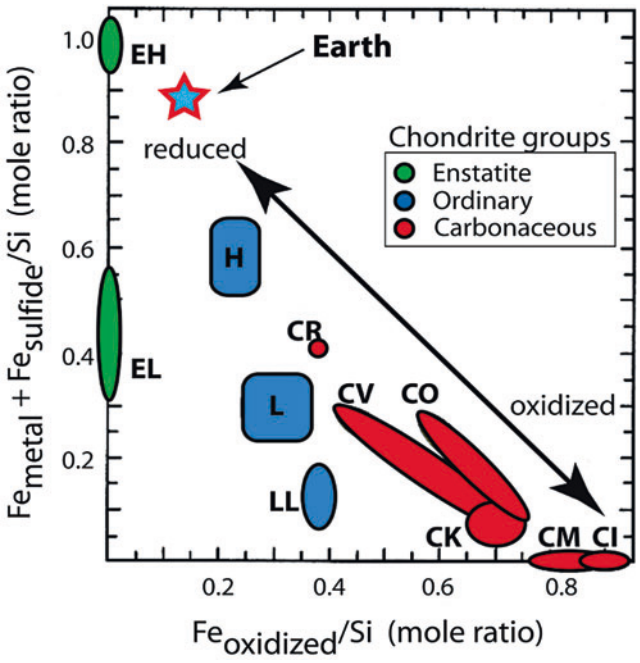

Earth's Core, Fig. 4 A plot of the oxidized iron to Si content of chondrites versus the metallic and sulfur-bearing content to Si content of chondrites. This diagram is also referred to as a Urey-Craig diagram. The Earth plots intermediate to the highly reduced enstatite chondrites and the less reduced ordinary chondrites. The CM and CI chondrites have nearly (or all) iron as oxidized, with no metallic iron

Ni is hosted in the core) and sulfur is the definition of what is a chalcophile element (>95% of the Earth's sulfur is in the core) (McDonough 2014).

The ratio of metals to oxides is a basic feature used to classify chondrites. The chondrites, carbonaceous (highly oxidized), ordinary (an intermediate redox state), and enstatite (highly reduced state) can be divided into subgroups of high, low, and low-low iron contents. Therefore, the amount of Fe relative to O, Si, and Mg in chondrites and planets can vary considerably. The redox state of a planet can be readily established by determining the Mg # (atomic Mg/(Mg + Fe)) of mantle silicates in combination with a value for the mass proportion of metallic to silicate shells. The Earth with 90% of its iron in metallic state is a reduced body with a redox state intermediate between ordinary and enstatite chondrites (Fig. 4).

Importantly, there are a number of critical element ratios for the nonrefractory elements that are relatively constant in chondrites and, if these element pairs have similar condensation temperatures, then these fixed ratios can be used to place compositional constraints on the bulk planet. The fixed chondritic ratios of Fe/Ni (17.4 ± 0.5) and Ni/Co (20.5 ± 0.6) constrains the planetary and core abundances of Ni and Co, given well established values for the mantle. To this end, a major advance was made when Thibault and Walter (1995) and Li and Agee (1996) identified the pressure dependence partitioning of Ni relative to Co and found that at mid-mantle conditions the relative partitioning of these two elements approached 1, with both the core and mantle having chondritic Ni/Co values. This finding was fundamental as the silicate Earth and core are assumed to have a mass balance in these ratios.

The initial growth of Earth and core-mantle segregation is often consider in terms of occurring under conditions of homogeneous or heterogeneous accretion, with the former model assuming that the accreting materials had a fixed, constant composition throughout planetary growth, while latter model models envisages significant changes in the composition of material that accretes to the Earth as it grew (see also discussion in McDonough (2014)). These different models seek to explain the siderophile element composition of the mantle. For the most part models of homogeneous accretion require a continuous and restricted set of physical and chemical conditions to achieve the present composition of the core and mantle, whereas heterogeneous accretion models allow for a range of probable conditions envisaged in an evolving proto-planetary disk, including temporal variations in redox conditions and the relative proportions of volatile to refractory materials.

Given an average condition for temperature, pressure, and oxygen fugacity of core formation we can construct models for the core that fit the existing constraints and match compositional models of the silicate Earth and chondrites. The abundance, absolute and relative, of various redox sensitive siderophile elements (e.g., W, V, Cr, Nb, Mn, Mo, and others) in the silicate Earth further define the relative silicate-metal partitioning of elements during core formation (Badro et al. 2015; Badro et al. 2014; Corgne et al. 2008; Fischer et al. 2015; Rubie et al. 2015). At this stage there remains one further consideration before estimating the composition of the core, and that is identifying the chemical identity of the element(s) accounting for its density deficit.

Finally, an important constraint on core formation came from the observation that the primitive mantle abundances of the highly siderophile elements (i.e., those with metal/silicate partition coefficients of 10^4 and greater and include the platinum group metals (Ru, Rh, Pd, Os, Ir, Pt), Re and Au) are in chondritic proportions and are enriched in the mantle at concentration levels well beyond that expected for their known metal/silicate partition coefficients (Kimura et al. 1974). Following a range of experimental studies it has been demonstrated that that the relative metal/silicate partitioning behavior of the highly siderophile elements are 10^4 and greater and that the relative differences between different member of this element group would result in grossly non-chondritic ratios for the Re-Os-Pt isotope system, which is not observed (Brenan et al. 2016; Day et al. 2016). Thus, the mantle signature requires the addition of a late veneer of

added chondritic material, with a mass contribution equivalent to about 0.5% to <1% the mass of the mantle (Day et al. 2016).

Core Composition and Its "Light Element(s)"

Table 2 presents a model for the composition of the Earth, its core, and the silicate Earth. The core model was constructed as the difference based on estimates of the bulk silicate Earth and the bulk planet compositions. The core composition proposed here has a mixture of O, Si, and S that accounts for the density deficit (3–7%). The relative proportions of O and Si in the core were established by metal/silicate partitioning (Badro et al. 2015; Fischer et al. 2015; Rubie et al. 2011). Assuming the core's mean atomic number to be 23 (Birch 1964), the absolute proportions of O and Si is then fixed. By way of comparison, McDonough (2014) proposed two end-member models, with one model containing Si and S and no O as the light elements and the other model contains O and S and no Si. Other compositional models are presented for comparison in Table 1 in Hirose et al. (2013), where they have sorted the different models in terms of simple single light element versus multiply, mixed light element models. One should view all of these models as acceptable, given the available constraints.

Let me start by saying that I do not know what is (are) the light element(s) in the core. The issue has dogged our science for half of a century and will continue to do so for some time. Words of caution are needed before discussing further the composition of the core. My bias as a geochemist states that observations on the composition of the silicate Earth and the range of compositions in chondrites defines the recipe that must be matched by experimental studies to define the P-T-fO_2-Xi (i.e., pressure, temperature, oxygen fugacity, and compositional) space for metal-silicate equilibrium during core formation. Models describing the dynamics of core formation and its final composition are probability positions and need to be recognized as such. As a second cautionary note, the periodic table is not a one-stop shopping table, if it is argued that a minor or trace element is in the core, then other elements in the same column are likely there too in some proportional relationship (e.g., Cr: Mo and W, Mn: Re, V: Nb and Ta). This principle is fundamental chemistry reflecting the importance of outer orbital electrons in controlling the partitioning behavior of elements. Thirdly, all partition coefficients (D-values) go to 1 as temperature goes to infinity and thus metal-silicate fractionation becomes muted at higher temperature conditions. Finally, appeals to adding specific elements into the core are also understandably done so to explain the power driving the geodynamo; resolving the energy equation for the geodynamo is intractable and will be so for some time.

The identity of the light element(s) in the core is elusive. Many suggestions have been published over the decades (e.g., H, C, N, O, Mg, Si, S). In general, any element with a lower atomic number than $_{26}$Fe is a likely candidate. Assuming Birch's law

$$V_\phi = \left(\frac{K}{\rho}\right)^{0.5}; \; V_p = M_\rho + B + A(T - T_0)(\rho - \rho^*) \quad (1)$$

where Vϕ is hydrodynamic or bulk sound velocity, V_P is compressional wave velocity, κ is bulk modulus, ρ is density, M and B are room temperature coefficients of Birch's law, and A and ρ^* account for its temperature dependence (see also Sakamaki et al. (2016))], one can predict the mean atomic weight of the mantle or core. Recently, Helffrich (2015) reported a similar relationship between sound speed and molecular weight using a hard sphere model for liquids. In addition, Poirier (1994), Anderson and Isaak (2002) and Badro et al. (2014) present simple graphical models to determine the amount (in wt%) of light element mixture in the core that scales as a function of core temperature. The model presented in Table 2 uses these principles to constrain the proportion of O and Si in the core. The S content of the core is established on cosmochemical grounds (Dreibus and Palme 1996) and constraints from the modeling of the bulk silicate Earth (McDonough and Sun 1995).

Chemical and physical observations are useful for developing plausible models for the nature and amount of a light element(s) in the core. Lithophile elements like O, Si, and Mg, in addition to Fe, are the most abundant elements in the Earth and can be readily defended as being dissolved in a core forming metallic liquid. Likewise, the gases of H-C-N-O are abundant in the solar system and would have been abundant in the nebular disk. The rocky planets might have had a dense surrounding atmosphere, particularly early in their evolution, which increases the solubility of these gases in a magma ocean and the potential for partitioning these elements into a core forming metallic melt. Thus, models invoking H, C, and/or N as constituents of the core cannot be dismissed. On the other hand, however, the Earth, and potentially the rest of the terrestrial planets in the solar system, is volatile depleted, as documented by its Rb-Sr, K-Ar, K-U, and He-Ne-Ar isotopic systems and total radiogenic heat production. Therefore, the Earth's volatile depletion curve establishes the limit of 2% (by mass) of sulfur in the core. Overall, chemistry offers guidelines, but a few constraints in eliminating competing core compositional models. Physical observations provide the best limits on acceptable core models.

The small addition of the lightest elements (e.g., H and C) is appealing because they offer considerable leverage in lowering the mean atomic weight of the core. It is noteworthy that the core composition reported in Table 2 posits significant amounts of C and H in the core given the Earth's volatility

Earth's Core, Table 2 Composition of the Earth, silicate Earth, and core in weight percent and atomic proportions

wt%	Earth	Silicate Earth	Core	Atomic prop.	Earth	Silicate Earth	Core
Fe	31.9	6.26	85.5	Fe	0.148	0.024	0.750
O	30.4	44	2	O	0.493	0.581	0.061
Si	15.3	21	4	Si	0.142	0.158	0.070
Mg	15.4	22.8	0	Mg	0.164	0.198	0
Ni	1.83	0.196	5.10	Ni	0.008	0.001	0.043
Co	0.090	0.0105	0.249	Co	0.0004	0.00004	0.002
Ca	1.71	2.53	0	Ca	0.011	0.013	0
Al	1.59	2.35	0	Al	0.015	0.018	0
S	0.650	0.025	1.9	S	0.005	0.0002	0.029
Cr	0.43	0.263	0.75	Cr	0.002	0.001	0.007
Na	0.18	0.27	0	Na	0.002	0.002	0
P	0.072	0.009	0.02	P	0.001	0.0001	0.0003
Mn	0.08	0.105	0.03	Mn	0.0004	0.0004	0.0003
C	0.073	0.012	0.2	C	0.002	0.0002	0.008
H	0.026	0.01	0.06	H	0.007	0.002	0.029
Total	99.7	99.8	99.8	Total	1.000	1.000	1.000

Absolute and relative proportions of O and Si in the core were established by metal/silicate partitioning and fixing the core's mean atomic number to 22.9 (c.f. Birch 1964)

curve (McDonough 2014). However, their appeal is diminished if their addition to the core also comes with consequences for the mantle (e.g., limited metal-silicate fractionation for H and C during core formation). Compositional models for the mantle have proposed a range of H and C abundances (Dasgupta and Hirschmann 2010; Halliday 2013; Marty 2012) and variable estimates for the contents of H and C in the core and some model compositions proposed for the Earth's core suggest abundant carbon (Wood 1993) or hydrogen (Williams and Hemley 2001) for consideration.

Considerable attention has been paid to models with O, Si, or both as likely light element candidates (Badro et al. 2015; Fischer et al. 2015; Li and Fei 2014; Ringwood 1984). Based on the differences in the silicon isotopic composition of chondrites and the Earth, Fitoussi and Bourdon (2012) and Fitoussi et al. (2016) proposed that the Earth core contains some 4–7 wt% Si, with the range taking into account metal-silicate isotopic fractionation at presumed core separation temperatures. Initially, the presence of silicon and oxygen in the core was considered an either or condition, whereas today many have found a range of acceptable conditions of core formation that result in iron alloys with mixed amounts of silicon and oxygen. More recent models suggest that Mg may have once been present as a light element in the core (Badro et al. 2016; O'Rourke and Stevenson 2016). This suggestion is permitted given that Mg is one of the four most abundant elements in the Earth. Moreover, these authors note that as the core cools down it exsolves MgO (or Mg silicate) and this reaction is exothermic and thus provides a power source for driving the geodynamo. Alternatively, Hirose et al. (2017) have suggested that exsolution of SiO_2 from the outer core is another potential power source for the geodynamo. The present-day situation we face is that there are many competing models to explain the core composition and potentially also energy sources for driving the core's dynamo.

Power to Drive the Geodynamo and Radioactive Elements in the Core

The geodynamo is produced in the outer core and demands power for its operation. Several papers have considered the presence of radioactive, heat producing elements (i.e., HPE = K, Th, and U) in the Earth's core, as they provide power to drive the core's dynamo. There is no compelling experimental or geochemical constraint that requires HPE in the core. Moreover, doing so often requires incorporation of other lithophile elements for which there is no supporting evidence for their depletion in the silicate Earth.

The energy budget of the core does not require HPE, as alternative energy sources (e.g., oxide exsolution, see above) may also provide the needed power. In addition, unknowns in understanding the generation and maintenance of a geodynamo are great, which includes being able to describe accurately the core's energy equation.

As is the case with the discussion of the light element in the core, so too for the presence of radioactive elements in the core: there are big unknowns. Thus, one should not confuse the conditions of what is plausible and what is needed.

Potassium: Incorporation of K in the core has been considered by numerous workers (Corgne et al. 2007; Li and Fei 2014; Watanabe et al. 2014) and generally found that a few to a couple tens of μ g/g of K, or less, can be accommodated in the core. Using ab initio calculations Lee et al. (2004)

suggested that the metallization of potassium at pressure, due to s-to d-orbital transitions, as a mechanism for alloying potassium with Fe. Both Cs and Rb, larger alkali metals, would undergo similar orbital transitions, but at lower pressures. There is no evidence, however, that Rb is anomalously depleted in the mantle with respect to the planetary volatility curve, contrary to an expectation from the pressure-dependent metallization process.

Uranium and thorium: Wheeler et al. (2006) and Malavergne et al. (2007) show that under core segregation conditions U remains strongly lithophile and is for the most part excluded from the core. Similarly, thorium has not been found to partition into a core forming metal phase; it is understood to be wholly lithophile. An additional constraint on the abundance and relative distribution of Th and U in the bulk silicate Earth comes from Pb isotope studies. The κ_{Pb} ratio (i.e., the time integrated Th/U ratio derived from the $^{208*}Pb/^{206*}Pb$ ratio) of the silicate Earth is comparable to that of chondrites at ±25% (Andersen et al. 2015; Castillo 2016; Elliott et al. 1999; Galer and O'Nions 1985; Kumari et al. 2016; Paul et al. 2003), consistent with negligible amounts of Th and U in the Earth's core. Studies on the partitioning of thorium between metal and silicate demonstrate that it is wholly lithophile in its behavior.

The Age of Core-Mantle Separation

Age of core formation is constrained by the ^{182}Hf-^{182}W isotope system ($t_{1/2}$ of 9 Ma) and known to be on the order of 30–150 million years after the age of solar system formation (Kleine et al. 2002; Kleine et al. 2009; Yin et al. 2002). The solar system formation age ($t_0 = 4568$ Ga) is established mostly from the absolute system, U-Pb isotopes, and the relative system $^{26}Al/^{26}Mg$ isotopes ($t_{1/2}$ of 0.7 Ma), as applied to the earliest condensates, which are high temperature, refractory materials (i.e., CAIs, calcium alumina inclusions) found as inclusions in chondritic meteorites (Brennecka et al. 2015; Connelly et al. 2012; MacPherson et al. 2012). Together these isotopic systems indicate that the bulk of Earth's accretion occurred some 10^6–10^7 years after t_0 and core formation followed as accretion progressed, including some modification during and following the Moon-forming impact event.

The current core formation paradigm posits segregation of sinking metal diapirs that chemically interact with the immediately surrounding silicate (liquid or solid) during or following a magma ocean(s) environment of the early Earth. The degree of metal-silicate equilibrium occurring during descent of these diapirs is unknown. However, as metal aggregates ponds and then begin to sink the potential for chemical exchange becomes less efficient as the length scale increases. Chemical consequences of a large Moon-forming impact event introduces other unknowns, for which we do not know whether or not the impactor's core merged, emulsified in the mantle, or otherwise superimposed additional complications on the core's composition (Nakajima and Stevenson 2015).

Hafnium and tungsten readily and effectively separate between the metallic (core) and silicate Earth (planet minus the core), with Hf hosted nearly exclusively in the silicate Earth and W almost wholly (90%) in the core. Due to the solar system initiating supernova, the solar system (and hence the Earth) inherited a fraction of live ^{182}Hf (Lugaro et al. 2014) that decayed into ^{182}W and consequently the age of core formation reflects the competing processes of metal segregation versus ^{182}Hf decay.

Chronologically, what has been established recently is that small bodies, as represented by groups of iron meteorites, accreted and differentiated quickly (i.e., 0–5 Ma after t_0) (Kruijer et al. 2014). During the waning stages of small-body accretion (t_0 + 3–5 million years), and when radiogenic heating from the $^{26}Al/^{26}Mg$ isotope system was running out of energy, the formation of chondritic bodies occurs, which are the most primitive and undifferentiated planetesimals in the solar system. Hence, the preservation of chondritic parent bodies represents a waning stage of accretion of small bodies. It is likely that Earth's formation occurred throughout this sequence and beyond and consequently its inventory of ^{182}W was shared between the core and mantle, revealing that the amount of ^{182}W in the silicate Earth establishes a lower limit to core formation age, while the timing of Moon formation sets the upper limit. Our present estimate is the silicate Earth has a $\mu^{182}W$ isotopic composition of zero (it is the reference point for the isotope system and units are expressed as deviations in parts in 10^6), chondrites are approximately −200 and the Earth's core is slightly more negative (~−220) (Walker 2016).

Inner Core and Its Age of Crystallization

The inner core is <2% the mass of the Earth and 5% the mass of the core. It is slightly smaller than the Earth's moon and is at about the temperature of the Sun's surface. The ICB (inner-outer core boundary) surface provides a constraint for estimating the temperature at the center of the Earth. An upper temperature limit is obtained from the melting temperature of Fe at relevant temperatures and pressures (~6200 K, 330 GPa) and an assumed conductive thermal gradient (Fischer 2016). Experimental challenges associated with determining the melting curve of iron and the upper temperature limit of the ICB are formidable; there is a range of 1500 K at 330 GPa for the Fe-alloy melting curves (Fischer 2016). Nonetheless, given the potential light element candidates and their influence on melting point depression, an ICB temperature of 5700 ± 550 K covers the range of estimates (Fischer 2016).

The inner core has about half the density deficit relative to that of the outer core (Anderson and Isaak 2002; Jephcoat and Olson 1987; Masters and Gubbins 2003); proportionally, one might intuit that this translates to approximately half the amount of light element. The phase diagram dictates that the inner core crystallization temperature will be lower than that for pure iron due to freezing point depression. Thus, an estimate of the temperature of the ICB depends on one's estimate for the light element composition of the outer core, which is a concatenation of unknowns.

Compositional estimates for the inner core are not forthcoming, as the unknowns are great, and come with considerable nonuniqueness (Antonangeli et al. 2010; Badro et al. 2007; Sakamaki et al. 2016). We know that its solid, likely in an hcp (hexagonal close packed) structure, there is 820 ± 180 kg/m^3 density increase across the ICB (Masters and Gubbins 2003), it has a density deficit, and it is anisotropic (polar vs equatorial wave speed). The inner core may be undergoing thermal convection (Cottaar and Buffett 2012), which may explain its seismic anisotropy.

Solidification of the inner core produces latent heat and results in a buoyant, residual liquid enriched in light elements. The Coriolis force from the Earth's rotation, combined with a heated, compositionally buoyant fluid, gives this ascending fluid the power to generate a magnetic field. In addition, heat extracted from the core by the mantle, as the planet cools, gives rise to the core's thermal convection. In combination with rotational forces, the thermal and compositional effects are the most probable energy sources driving the geodynamo.

When did inner core crystallization begin? This question hinges greatly on understanding the thermal history of the core. There are many unknowns that contribute to this question and most are active areas of research accompanied by considerable debate, these include: the thermal and electrical conductivity of core materials (where there is an ongoing debate over the factor of 2 difference in the assumed values for these parameters), the initial and present day core temperature, heat flow across the CMB (see Table 1), and whether there are (and how much) radioactive elements in the core. Debates on these topics will continue for some time as technical and computational challenges are great, including understanding the energy budget needed to drive the geodynamo.

For about a decade there were models that proposed early inner core crystallization, as early as 4.5 Ga. Models of early inner core growth were nearly exclusively based on anomalous ^{186}Os-^{188}Os and ^{187}Os-^{188}Os isotopic compositions in basalts whose source region experience core additions; the origins of these anomalies came from decays in the Re-Os and Pt-Os isotope systems and parent daughter fractionation due to inner core crystallization (Walker 2016). More recently, however, corroborating ^{182}W isotopic evidence of this core-mantle exchange process occurring was not found in these basalts and thus the model of early inner core growth based on isotopic evidence has been abandoned (Walker 2016).

Geophysical estimates for the age of the inner core are based on a full understanding of the core's energy equation and usually includes a trade-off between internal heat production and heat dissipation across the core-mantle boundary. Labrosse et al. (2001) examined the question assuming a role for heat generation from potassium, modeling up to 200 μg/g K in the core, and showed that core crystallization might have started anytime from the Archean to nearly the present depending on how much potassium is in the core. Later, addressing this issue following the recently revised thermal and electrical conductivity values for the core, Gomi et al. (2013) and Labrosse (2015) concluded that the amount of potassium in the core plays less of a role in establishing the initiation of inner-core crystallization, but that the core cooling rate is significant. From these analyses a young age (circa ~05 Ga) for initiation of inner core is favored. Alternatively, estimates of an inner core having begun crystallization from 1.5 to 0.5 billion years ago are common (Labrosse et al. 2001). Overall, there are few constraints regarding the physical state and evolution of the core and inner core system, leaving us with open questions about when the inner core began to crystallize, the heat flux across the core-mantle boundary, and the power budget for the geodynamo.

Summary

The Earth's core comprises the innermost 3483 km of the planet. Both the inner solid core and outer liquid core consist of about 85% iron and 5% nickel with $\leq$10% other elements including lighter elements O, Si, and/or S as well as most of the inventory of highly siderophile elements such as the platinum group elements and gold. A metallic liquid core had likely formed within the first 30–60 million years of solar system history. The solid inner core has grown by crystallization of the outer core, a process that may have begun as recently as 0.5–1.5 billion years ago.

Cross-References

- ▶ Chondrites
- ▶ Cosmic Elemental Abundances
- ▶ Formation and Evolution of the Earth
- ▶ Fugacity
- ▶ Giant Impact Hypothesis
- ▶ Heat-Producing Elements (HPEs)
- ▶ Iron
- ▶ Iron Meteorites

- ▶ Lithophile Elements
- ▶ Nickel
- ▶ Partitioning and Partition Coefficients
- ▶ Siderophile Elements
- ▶ Sulfur

References

Andersen MB, Elliott T, Freymuth H, Sims KWW, Niu Y, Kelley KA (2015) The terrestrial uranium isotope cycle. Nature 517: 356–359

Anderson OL, Isaak DG (2002) Another look at the core density deficit of Earth's outer core. Phys Earth Planet Inter 131:19–27

Antonangeli D, Siebert J, Badro J, Farber DL, Fiquet G, Morard G, Ryerson FJ (2010) Composition of the Earth's inner core from high-pressure sound velocity measurements in Fe-Ni-Si alloys. Earth Planet Sci Lett 295:292–296

Badro J, Brodholt JP, Piet H, Siebert J, Ryerson FJ (2015) Core formation and core composition from coupled geochemical and geophysical constraints. Proc Natl Acad Sci USA 112:12310–12314

Badro J, Cote AS, Brodholt JP (2014) A seismologically consistent compositional model of Earth's core. Proc Natl Acad Sci USA 111:7542–7545

Badro J, Fiquet G, Guyot F, Gregoryanz E, Occelli F, Antonangeli D, d'Astuto M (2007) Effect of light elements on the sound velocities in solid iron: Implications for the composition of Earth's core. Earth Planet Sci Lett 254:233–238

Badro J, Siebert J, Nimmo F (2016) An early geodynamo driven by exsolution of mantle components from Earth's core. Nature 536:326–328

Birch F (1952) Elasticity and Constitution of the Earth's Interior. J Geophys Res 57:227–286

Birch F (1964) Density and Composition of Mantle and Core. J Geophys Res 69:4377–4388

Bouwman J, Lawson WA, Juhasz A, Dominik C, Feigelson ED, Henning T, Tielens AGGM, Waters LBFM (2010) The protoplanetary disk around the M4 Star Recx 5: Witnessing the influence of planet formation? Astrophys J Lett 723:L243–L247

Brenan JM, Bennett NR, Zajacz Z (2016) Experimental results on fractionation of the highly siderophile elements (HSE) at variable pressures and temperatures during planetary and magmatic differentiation. In: Harvey J, Day JMD (eds) Highly siderophile and strongly chalcophile elements in high-temperature geochemistry and cosmochemistry, vol 81. Mineralogical Society of America, Washington, DC, pp 1–88

Brennecka GA, Budde G, Kleine T (2015) Uranium isotopic composition and absolute ages of Allende chondrules. Meteorit Planet Sci 50:1995–2002

Canup RM (2012) Forming a Moon with an Earth-like composition via a Giant Impact. Science 338:1052–1055

Castillo PR (2016) A proposed new approach and unified solution to old Pb paradoxes. Lithos 252:32–40

Chambat F, Ricard Y, Valette B (2010) Flattening of the Earth: Further from hydrostaticity than previously estimated. Geophys J Int 183:727–732

Connelly JN, Bizzarro M, Krot AN, Nordlund A, Wielandt D, Ivanova MA (2012) The absolute chronology and thermal processing of solids in the solar protoplanetary disk. Science 338:651–655

Corgne A, Keshav S, Fei YW, McDonough WF (2007) How much potassium is in the Earth's core? New insights from partitioning experiments. Earth Planet Sci Lett 256:567–576

Corgne A, Keshav S, Wood BJ, McDonough WF, Fei YW (2008) Metal-silicate partitioning and constraints on core composition and oxygen fugacity during Earth's accretion. Geochim Cosmochim Acta 72:574–589

Cottaar S, Buffett B (2012) Convection in the Earth's inner core. Phys Earth Planet Inter 198:67–78

Cuk M, Stewart ST (2012) Making the Moon from a fast-spinning earth: a giant impact followed by resonant despinning. Science 338:1047–1052

Cuk M, Hamilton DP, Lock SJ, Stewart ST (2016) Tidal evolution of the Moon from a high-obliquity, high-angular-momentum Earth. Nature 539:402–406

DAlessio P, Merin B, Calvet N, Hartmann L, Montesinos B (2005) WWW database of models of accretion disks irradiated by the central star. Rev Mex Astron Astrofis 41:61–67

Dasgupta R, Hirschmann MM (2010) The deep carbon cycle and melting in Earth's interior. Earth Planet Sci Lett 298:1–13

Day JMD, Brandon AD, Walker RJ (2016) Highly siderophile elements in Earth, Mars, the Moon, and Asteroids. In: Harvey J, Day JMD (eds) Highly Siderophile and Strongly Chalcophile Elements in High-Temperature Geochemistry and Cosmochemistry, vol 81. Mineralogical Society of America, pp 161–238

Dreibus G, Palme H (1996) Cosmochemical constraints on the sulfur content in the Earth's core. Geochim Cosmochim Acta 60: 1125–1130

Elliott T, Zindler A, Bourdon B (1999) Exploring the kappa conundrum: the role of recycling in the lead isotope evolution of the mantle. Earth Planet Sci Lett 169:129–145

Engel K, McDonough WF (2016) Geochemical models of the Earth and the crustal geoneutrino flux. In: Ludhova L (ed) Geo-neutrino. Open Academic Press

Fischer RA (2016) Melting of Fe alloys and the thermal structure of the core. In: Terasaki H, Fischer RA (eds) Deep Earth: physics and chemistry of the lower mantle and core. John Wiley & Sons, Inc., Washington, DC, pp 3–12

Fischer RA, Nakajima Y, Campbell AJ, Frost DJ, Harries D, Langenhorst F, Miyajima N, Pollok K, Rubie DC (2015) High pressure metal-silicate partitioning of Ni, Co, V, Cr, Si, and O. Geochim Cosmochim Acta 167:177–194

Fitoussi C, Bourdon B (2012) Silicon isotope evidence against an enstatite chondrite Earth. Science 335:1477–1480

Fitoussi C, Bourdon B, Wang XY (2016) The building blocks of Earth and Mars: a close genetic link. Earth Planet Sci Lett 434:151–160

Galer SJG, O'Nions RK (1985) Residence time of thorium, uranium and lead in the mantle with implications for mantle convection. Nature 316:778–782

Gomi H, Ohta K, Hirose K, Labrosse S, Caracas R, Verstraete MJ, Hernlund JW (2013) The high conductivity of iron and thermal evolution of the Earth's core. Phys Earth Planet Inter 224: 88–103

Halliday AN (2013) The origins of volatiles in the terrestrial planets. Geochim Cosmochim Acta 105:146–171

Helffrich G (2015) The hard sphere view of the outer core. Earth Planets Space 67:73

Hirose K, Labrosse S, Hernlund J (2013) Composition and State of the Core. Annu Rev Earth Planet Sci 41:657–691

Hirose K, Morard G, Sinmyo R, Umemoto K, Hernlund JW, Helffrich G, Labrosse S (2017) Crystallization of silicon dioxide and compositional evolution of the Earth's core. Nature 543:99–102

Huang Y, Chubakov V, Mantovani F, Rudnick RL, McDonough WF (2013) A reference Earth model for the heat-producing elements and associated geoneutrino flux. Geochem Geophys Geosyst 14:2003–2029

Jephcoat A, Olson P (1987) Is the inner core of the Earth pure iron. Nature 325:332–335

Kimura K, Lewis RS, Anders E (1974) Distribution of gold and rhenium between nickeliron and silicate melts. Geochim Cosmochim Acta 38:683,781

Kleine T, Munker C, Mezger K, Palme H (2002) Rapid accretion and early core formation on asteroids and the terrestrial planets from Hf-W chronometry. Nature 418:952–955
Kleine T, Touboul M, Bourdon B, Nimmo F, Mezger K, Palme H, Jacobsen SB, Yin QZ, Halliday AN (2009) Hf-W chronology of the accretion and early evolution of asteroids and terrestrial planets. Geochim Cosmochim Acta 73:5150–5188
Kruijer TS, Touboul M, Fischer-Godde M, Bermingham KR, Walker RJ, Kleine T (2014) Protracted core formation and rapid accretion of protoplanets. Science 344:1150–1154
Kumari S, Paul D, Stracke A (2016) Open system models of isotopic evolution in Earth's silicate reservoirs: implications for crustal growth and mantle heterogeneity. Geochim Cosmochim Acta 195:142–157
Labrosse S (2015) Thermal evolution of the core with a high thermal conductivity. Phys Earth Planet Inter 247:36–55
Labrosse S, Poirier JP, Le Mouel JL (2001) The age of the inner core. Earth Planet Sci Lett 190:111–123
Lee KKM, Steinle-Neumann G, Jeanloz R (2004) Ab-initio high-pressure alloying of iron and potassium: implications for the Earth's core. Geophys Res Lett 31, L11603, https://doi.org/10.1029/2004GL019839
Li J, Agee CB (1996) Geochemistry of mantle-core differentiation at high pressure. Nature 381:686–689
Li J, Fei Y (2014) Experimental constraints on core composition. In: Carlson RW (ed) Treatise on geochemistry: the mantle. Elsevier, New York, pp 527–557
Lugaro M, Heger A, Osrin D, Goriely S, Zuber K, Karakas AI, Gibson BK, Doherty CL, Lattanzio JC, Ott U (2014) Stellar origin of the Hf-182 cosmochronometer and the presolar history of solar system matter. Science 345:650–653
MacPherson GJ, Kita NT, Ushikubo T, Bullock ES, Davis AM (2012) Wellresolved variations in the formation ages for Ca-Al-rich inclusions in the early solar system. Earth Planet Sci Lett 331:43–54
Malavergne V, Tarrida M, Combes R, Bureau H, Jones J, Schwandt C (2007) New high-pressure and high-temperature metal/silicate partitioning of U and Pb: implications for the cores of the Earth and Mars. Geochim Cosmochim Acta 71:2637–2655
Marty B (2012) The origins and concentrations of water, carbon, nitrogen and noble gases on Earth. Earth Planet Sci Lett 313:56–66
Masters G, Gubbins D (2003) On the resolution of density within the Earth. Phys Earth Planet Inter 140:159–167
Masters TG, Shearer PM (1995) Seismic models of the Earth: elastic and anelastic. In: Ahrens TJ (ed) Global Earth Physics. American Geophysical Union, Washington, DC, pp 88–103
McDonough WF (2014) Compositional models for the Earth's core. In: Carlson RW (ed) Treatise on geochemistry: the mantle, 2nd edn. Elsevier, New York, pp 559–576
McDonough WF (2016) The composition of the lower mantle and core. In: Terasaki H, Fischer R (eds) Deep Earth: physics and chemistry of the lower mantle and core. AGU-Wiley, Washington, DC, pp 145–159
McDonough WF, Sun SS (1995) The Composition of the Earth. Chem Geol 120:223–253
Nakajima M, Stevenson DJ (2015) Melting and mixing states of the Earth's mantle after the Moon-forming impact. Earth Planet Sci Lett 427:286–295
O'Rourke JG, Stevenson DJ (2016) Powering Earth's dynamo with magnesium precipitation from the core. Nature 529:387–389
Paul D, White WM, Turcotte DL (2003) Constraints on the Th-232/U-238 ratio (kappa) of the continental crust. Geochem Geophys Geosyst 4
Poirier JP (1994) Light-elements in the Earth's outer core: a critical-review. Phys Earth Planet Inter 85:319–337
Ringwood AE (1984) The Bakerian lecture, 1983: the Earth's core – its composition, formation and bearing upon the origin of the Earth. P Roy Soc Lond a Mat 395:1–46
Rubie DC, Frost DJ, Mann U, Asahara Y, Nimmo F, Tsuno K, Kegler P, Holzheid A, Palme H (2011) Heterogeneous accretion, composition and core-mantle differentiation of the Earth. Earth Planet Sci Lett 301:31–42
Rubie DC, Jacobson SA, Morbidelli A, O'Brien DP, Young ED, de Vries J, Nimmo F, Palme H, Frost DJ (2015) Accretion and differentiation of the terrestrial planets with implications for the compositions of early-formed Solar System bodies and accretion of water. Icarus 248:89–108
Sakamaki T, Ohtani E, Fukui H, Kamada S, Takahashi S, Sakairi T, Takahata A, Sakai T, Tsutsui S, Ishikawa D, Shiraishi R, Seto Y, Tsuchiya T, Baron AQR (2016) Constraints on Earth's inner core composition inferred from measurements of the sound velocity of hcp-iron in extreme conditions. Sci Adv Vol. 2, no. 2, e1500802. https://doi.org/10.1126/sciadv.1500802
Sargent BA, Forrest WJ, Tayrien C, McClure MK, Li A, Basu AR, Manoj P, Watson DM, Bohac CJ, Furlan E, Kim KH, Green JD, Sloan GC (2009) Silica in protoplanetary disks. Astrophys J 690:1193–1207
Sze EKM, van der Hilst RD (2003) Core mantle boundary topography from short period PcP, PKP, and PKKP data. Phys Earth Planet Inter 135:27–46
Thibault Y, Walter MJ (1995) The influence of pressure and temperature on the metal-silicate partition-coefficients of nickel and cobalt in a model-C1 chondrite and implications for metal segregation in a deep magma ocean. Geochim Cosmochim Acta 59:991–1002
Tsuchiya T, Kawai K, Wang X, Ichikawa H, Dekura H (2016) Temperature of the Lower Mantle and Core based on ab initio mineral physics data. In: Terasaki H, Fischer R (eds) Deep Earth: physics and chemistry of the lower mantle and core. American Geophysical Union, Washington, DC, pp 13–30
van Boekel R, Min M, Leinert C, Waters LB, Richichi A, Chesneau O, Dominik C, Jaffe W, Dutrey A, Graser U, Henning T, de Jong J, Kohler R, de Koter A, Lopez B, Malbet F, Morel S, Paresce F, Perrin G, Preibisch T, Przygodda F, Scholler M, Wittkowski M (2004) The building blocks of planets within the "terrestrial" region of protoplanetary disks. Nature 432:479–482
Walker RJ (2016) Siderophile elements in tracing planetary formation and evolution. Geochem Perspect 5:1–142
Wasson JT, Kallemeyn GW (1988) Compositions of chondrites. Philos Trans R Soc A Math Phys Eng Sci 325:535–544
Watanabe K, Ohtani E, Kamada S, Sakamaki T, Miyahara M, Ito Y (2014) The abundance of potassium in the Earth's core. Phys Earth Planet Inter 237:65–72
Wheeler KT, Walker D, Fei YW, Minarik WG, McDonough WF (2006) Experimental partitioning of uranium between liquid iron sulfide and liquid silicate: Implications for radioactivity in the Earth's core. Geochim Cosmochim Acta 70:1537–1547
Williams Q, Hemley RJ (2001) Hydrogen in the deep Earth. Annu Rev Earth Planet Sci 29:365–418
Wood BJ (1993) Carbon in the core Earth planet. Sci Lett 117:593–607
Yin QZ, Jacobsen SB, Yamashita K, Blichert-Toft J, Telouk P, Albarede F (2002) A short timescale for terrestrial planet formation from Hf-W chronometry of meteorites. Nature 418:949–952
Yoder CF (1995) Astrometric and geodetic properties of the Earth and the solar system. In: Ahrens TJ (ed) Global Earth Physics. American Geophysical Union, Washington, DC, pp 1–31
Young ED, Kohl IE, Warren PH, Rubie DC, Jacobson SA, Morbidelli A (2016) Oxygen isotopic evidence for vigorous mixing during the Moon-forming giant impact. Science 351:493–496

E

Earth's Oceanic Crust

Michael Perfit
Department of Geological Sciences, University of Florida, Gainesville, FL, USA

Definition

Oceanic crust is the outermost solid layer of the lithospheric tectonic plates under the oceans that covers much of the Earth's surface. It has a distinctive basaltic composition characterized by rocks that have relatively low concentrations of potassium and other highly incompatible trace elements (those typically excluded from minerals that comprise the mantle). Not including a sedimentary cover of variable thickness and composition, the oceanic crust consists of three layers: (1) a relatively thin uppermost volcanic layer of basaltic lavas known as mid-ocean ridge basalts (MORB) erupted on the seafloor; (2) a thicker layer of more coarsely crystalline, intrusive basaltic dikes that feed the volcanic layer; and (3) a thick lowermost layer of intrusive coarse-grained gabbros that mostly represent minerals that have settled out of slowly cooled melt bodies and lenses in a crystal mush zone below ridge crests.

Introduction

Nearly three-quarters of Earth's surface lies beneath the oceans and marginal seas where most of the oceanic crust has been formed by magmatic processes at mid-ocean ridges (MOR) and near-ridge seamounts. However, there are some regions where significant volumes of crust have formed locally such as at intraplate hotspot volcanoes, back-arc basins, and oceanic plateaus that will not be discussed here. Oceanic crust formed at MOR is primarily basaltic in composition and thin (~3–10 km thick) compared to continental crust that has an average thickness of 35–40 km and a roughly andesitic composition (Taylor and McLennan 1985; Rudnick 1995). In-situ sampling of the oceanic crust has largely been restricted to surface lava flows by dredging, drilling, remotely operated vehicles and human-occupied submersibles. Therefore, in order to estimate the bulk composition of the entire oceanic crust, these surficial samples have been augmented by dredging steep faults, several deep drill holes, investigations of ophiolite complexes (fragments of oceanic and back-arc crust and upper mantle that have been thrust upon to continents), and comparisons of the seismic structure of the oceanic crust with laboratory determinations of seismic wave velocities in known rock types. Integration of observations and analysis of oceanic rocks on the seafloor and exposed above sea level, combined with geophysical information, provides us with a reasonable view of Earth's oceanic crustal composition. Here the focus is on the composition of rocks that comprise the crust formed at MOR with the understanding that there is a range of compositions associated with other oceanic magmatic environments (e.g., intraplate hotspots, island arcs).

Seismic investigations of the seafloor have determined that the thickness of oceanic crust averages about 6–7 km at fast- and intermediate-spreading rate ridges, but typically is much thinner at slow-spreading MOR where the crust exhibits greater variation in thickness and is remarkably complex compared to crust formed at magmatically robust fast-spreading centers (Cannat 1996; Dunn and Forsyth 2007). In general, seismic layers 2a and 2b form the top 2 km of the oceanic crust and are comprised of extrusive basaltic lava flows and intrusive dikes that serve as conduits that supply the magma erupted on the seafloor. Compared to basalts erupted in other tectonic environments, mid-ocean ridge basalts (MORB) have rather limited compositions. However, they are far from being a homogeneous group, reflecting their diverse sources and melting conditions, as well as the magmatic processes that cause them to differentiate into different rock types (Melson et al. 1976; Langmuir et al. 1992; Perfit and Chadwick 1998; Arevalo and McDonough 2010; O'Neill and Jenner 2012; Gale et al. 2013). The lower and thicker part of the crust (~5 km thick) consists of a wide variety of coarse-grained plutonic rocks that range in composition from ultramafic cumulate rocks to a wide variety of cumulate and isotropic gabbros and even to silica-rich plagiogranites (Coogan 2014). Although detailed surficial sampling and mapping has been completed at a large number of MOR and some sampling has been carried out along steep escarpments and rifts in the crust (tectonic windows), only very limited direct sampling of the deep oceanic crust has been accomplished. Consequently, there are significant uncertainties about the detailed internal structure and overall composition of the crust.

Composition of the Upper Oceanic Crust: Major Elements

The chemical characteristics of MORB provide critical information about their origin (source) and petrologic evolution (Langmuir et al. 1992; Rubin and Sinton 2007; Rubin et al. 2009). Deciphering the magmatic history of MORBMid-ocean ridge basalts (MORB) suites can be relatively straightforward and provides information about the mantle without the complexities that arise, for example, when magmas transit through thick, old continental crust or where subducted sediments contaminate mantle sources beneath island arcs. Slight differences in oceanic mantle sources and the extents and

depths of melting of these sources, however, are known to generate "parental melts" with compositions that differ within individual ridge segments and relative to spreading rates (e.g., Klein and Langmuir 1987). Variations in the amounts of FeO, Na_2O (Fig. 1), and K_2O (Fig. 2) at specific MgO contents reflect the effects of source composition and/or extents and depths of mantle melting.

Although as a global rock type MOR lavas are thought to be relatively homogeneous, significant differences in major element compositions also occur on both large (ridges with different spreading rates) and small (adjacent ridge segments) spatial scales as well as over short-time intervals (decades) (Langmuir et al. 1986; Reynolds et al. 1992; Perfit et al. 1994; Perfit and Chadwick 1998; Smith et al. 2001; Rubin and Sinton 2007; Rubin et al. 2009; Goss et al. 2010). Both the most primitive (high MgO wt%) and evolved (low MgO, high SiO_2) tend to erupt at discontinuities in the linear ridge segments such as transform faults and overlapping spreading centers where magma mixing and recharge are limited.

To eliminate some of the complexities of different sources and amounts and depths of melting, Fig. 3 shows only the compositional variation of lavas (glasses) from a limited region of the northern East Pacific Rise. As observed in many other ridges, MORB can range in composition from rare picrites with high MgO contents to ferrobasalts and FeTi (iron-titanium) basalts containing lower MgO concentrations and high concentrations of FeO and TiO_2. The pronounced iron-enrichment trend with decreasing MgO contents (Fig. 3 bottom) is primarily related to fractional crystallization as magmas cool. It is this trend together with their low alkali contents that classifies MORB as belonging to what is known as the subalkaline "tholeiitic magmatic suite." Hence MORB are sometimes also known as ocean floor tholeiites. More

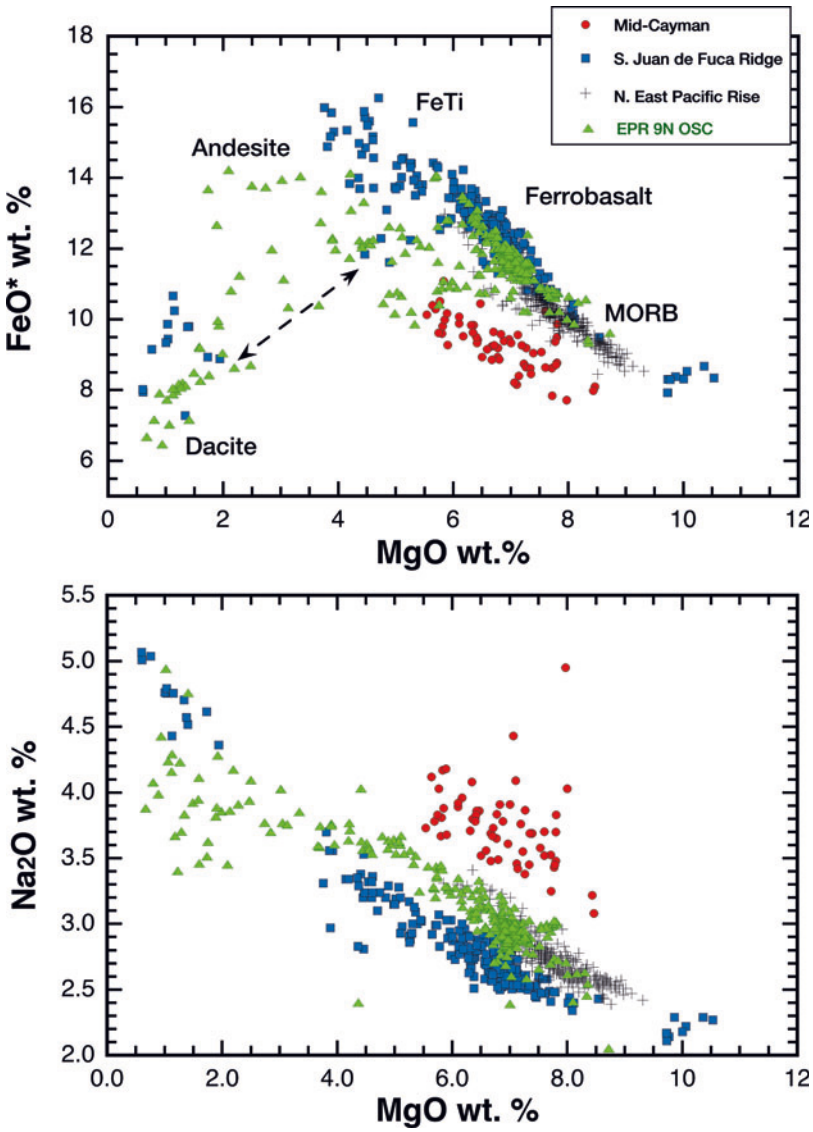

Earth's Oceanic Crust,
Fig. 1 Major element diagram showing the variation of MgO wt% versus FeO (total) wt% (*top*) and Na_2O wt% (*bottom*) in quenched glass from lavas from three mid-ocean ridges that have different spreading rates. Basalts from more slowly spread ridges have relatively higher Na_2O and lower FeO. Volcanic rock names are shown adjacent to their typical range of compositions in *top diagram*. The general elemental trends with decreasing MgO are primarily due to fractional crystallization for typical MORB suites. The variations in FeO and Na_2O at any given MgO reflect different extents and integrated depths of melting (Klein and Langmuir 1987; Langmuir et al. 1992; Gale et al. 2013; White and Klein, 2015)

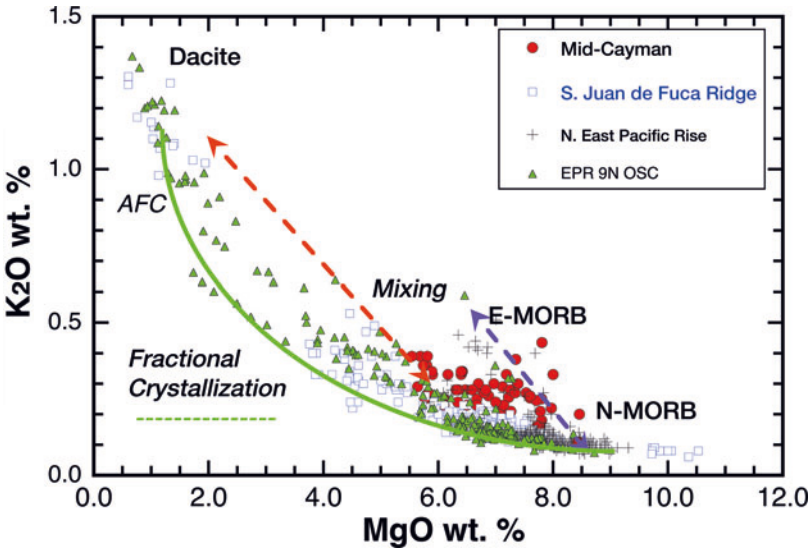

Earth's Oceanic Crust, Fig. 2 Variations in K_2O wt% versus MgO wt % in MORB from different MOR. Differences in K_2O in lavas with high MgO (e.g., parental N-MORB vs. E-MORB) arise from differences in the K_2O in their mantle source and/or extents of melting of the source. Potassium is an incompatible element in MOR magmatic systems and as such also exhibits large increases in concentration with decreasing MgO as a consequence of fractional crystallization (typical fractional crystallization path shown as *green curve*). Dacite lava compositions reflect additional enrichments from crustal assimilation coupled with fractional crystallization (*AFC*) (Data from Wanless et al. 2010). Some variability may also be due to mixing between N- and E-MORB melts (*purple dashed line*) or between highly evolved, low-MgO magmas and evolved basalts (*red dashed line*) (Modified from Karson et al. 2015)

rarely, and almost exclusively, found on fast- and intermediate-spreading rate ridges, are even more differentiated, silica-enriched lavas that include low-potassium MOR basaltic andesites, andesites (icelandites), dacites, and rhyodacites. They have low MgO (<4 wt%) concentrations and SiO_2 contents that range from 52 wt% to more than 70 wt% (Fig. 3 top).

Composition of the Upper Oceanic Crust: Trace Elements

MORB are similar to tholeiitic basalts erupted on oceanic islands like Iceland, the Galápagos, and the Hawaiian Islands in that they are composed of about 50 wt% silica (SiO_2) and lesser amounts of the oxides of magnesium, iron, calcium, and aluminum. However, MORB differ from ocean island basalts (OIBOcean island basalts (OIB)) and oceanic arc basalts in their distinct trace element and isotopic chemical characteristics (Sun et al. 1979; Sun and McDonough 1989; White and Klein 2014). In comparison to other magmatic/tectonic environments, MORB contain very low abundances of K_2O and trace elements such as cesium, rubidium, barium, (large ion lithophile elements), uranium, thorium, niobium, the LREE, and volatile elements. These elements are all considered to be highly incompatible in typical mantle mineral assemblages, and their low concentrations indicate MORB mantle was depleted in these elements by previous melting events. The trace element abundances in MOR lavas relative to an accepted value of "primitive mantle" show the differences in MORB types (Fig. 4). So-called normal mid-ocean ridge basalts, or N-MORB, are those with very low concentrations of highly incompatible trace elements and consequently are characterize as "depleted" relative to basalts from continents, island arcs, or ocean islands. On normalized elemental abundance diagrams, N-MORB exhibit characteristic smooth concave-down patterns reflecting their incompatible element depleted nature. MORB containing slightly greater concentrations of highly incompatible elements, including K_2O, are termed "enriched" or E-MORB (Figs. 3 and 4). In some localities, samples have been recovered that are even more depleted than N-MORB and are consequently classified as D-MORB (Gale et al. 2013).

Differences in the absolute abundances of elements are commonly related to the amount of crystal fractionation that magmas experience during cooling. In contrast, the relative abundances of elements, reflected in the slope of the elemental patterns, are generally considered to reflect source composition and/or extents of melting of different mantle sources (or mixing between different MORB types). Relatively enriched MORB are volumetrically minor on most normal ridge segments but can comprise a significant proportion of the crust around regions influenced by plume magmatism such as the Galapagos Islands, the Azores, and Iceland (e.g., White and Schilling 1978; Schilling 1985; White et al., 1993).

Isotopic investigations have conclusively shown that values of the radiogenic isotopes of strontium, neodymium, hafnium, and lead in N-MORB are consistent with their

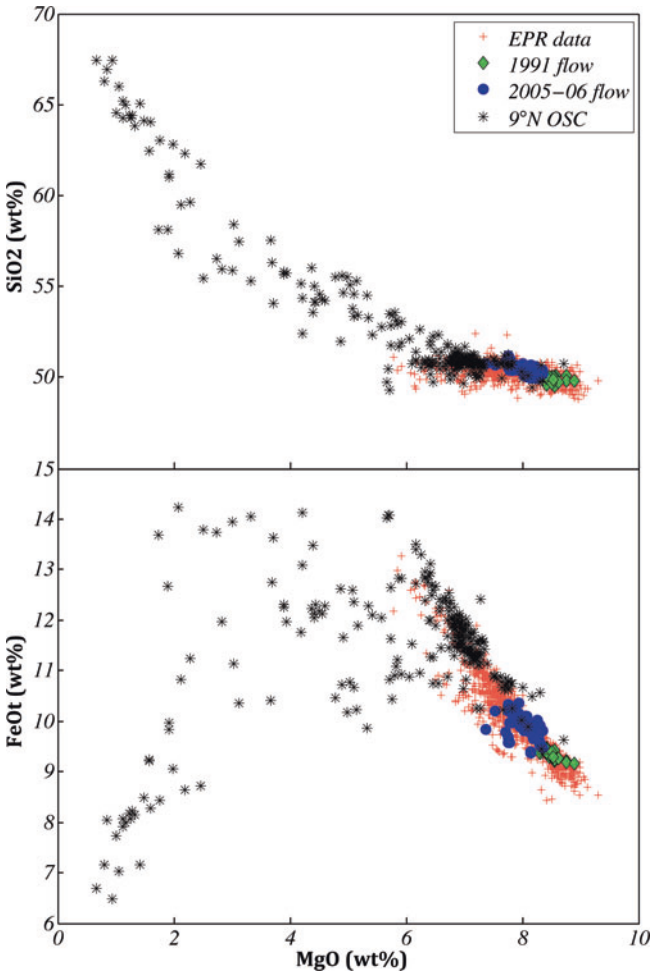

Earth's Oceanic Crust, Fig. 3 Major element variation diagrams of MORB glasses from 9 to 10° N on the East Pacific Rise (*EPR*) as an example of the range of compositions along a fast-spread MOR (Perfit et al. 2012). The plot shows the compositions in ~1600 lavas erupted between 9° 17′ N and 10° N (*red crosses*) compared to those from an Overlapping Spreading Center (OSC) at 9° N (*black asterisks*). The general compositional trends in the basalt data (MgO > ~6 wt%, SiO_2 < 52 wt%) are primarily due to the effects of low to moderate pressure fractional crystallization. Highly evolved andesites and dacites, exemplified by those erupted at around 9° N (Wanless et al. 2010; *asterisks*), are a result of extreme fractional crystallization coupled with crustal assimilation (AFC) along a propagating limb of the OSC, as well as a component of magma mixing between high-SiO_2 magmas and relatively evolved basaltic liquids. Also shown are the composition of lavas from 9° 50′ N that erupted in 1991 and again in 2005–2006 showing the relatively restricted compositional variations that characterize individual MOR eruptions. There are, however, distinct differences in the compositions of lavas erupted in 1991 (*green diamonds*) versus 2005–2006 (*blue circles*) that reflect magma cooling and mixing during the ~15 years between eruptions at the same locality (Goss et al. 2010)

incompatible element-depleted characteristics and indicate this depletion occurred via one or more episodes of partial melting of upper mantle sources beginning more than 2 billion years ago (Hart 1971; Zindler and Hart 1986; Hofmann 1988; White and Klein 2014). E-MORB, on the other hand, have obtained their geochemical characteristics from mantle that has been enriched in incompatible trace elements relatively recently in Earth history (Schilling 1985; Hofmann 1997; Stracke 2012).

The geochemical characteristics of MORB have been used to decipher the composition of their mantle source(s), how much mantle melting occurred, and at what temperatures and pressures (Langmuir et al. 1986, 1992; Putirka et al. 2011; Stracke 2012; Gale et al. 2013). It has been clearly shown that different MOR segments have distinctive chemical characteristics that can be related to differences in regional mantle sources and melting (Schilling et al. 1983; Graham et al. 1992; Michael 1995). On a much smaller scale, detailed geochemical investigations of lavas have documented the dominant effects of fractional crystallization and magma mixing on MORB geochemistry (e.g., Rhodes et al. 1979; Perfit and Fornari 1983; Perfit et al. 1983; Langmuir et al. 1992; Frey et al. 1993; Perfit and Chadwick 1998; Wanless et al. 2010; Rubin 2014). High melt supply at fast-spreading ridges leads to greater degrees of differentiation and homogenization of parental magmas in shallow magma chambers or lenses. At slower-spreading ridges where magma supply is low, episodic magma accumulation in deeper, poorly connected, and more insulated melt reservoirs produces less differentiated and more heterogeneous lavas (Rubin and Sinton 2007; Rubin et al. 2009).

Recent examinations of trace element systematics in MORB and mineralogic reactions in gabbros and xenoliths enclosed in some lavas have indicated that other magmatic processes such as reactive porous flow, in situ crystallization, and frequently replenished, open system magma chambers likely occur in the magma chambers or crystal-melt mush zones beneath ridge axes (Langmuir 1989; Ridley et al. 2006; Kvassnes and Grove 2008; Lissenberg and Dick 2008; Lissenberg et al. 2013; Coogan and O'Hara 2015). The greatest extents of chemical diversity occur at MOR discontinuities such as environments proximal to transform faults, propagating rift tips, and overlapping spreading centers where highly differentiated FeTi basalts are common and iron-rich andesites and dacites are often found (Perfit et al. 1983; Sinton et al. 1983; Rubin and Sinton 2007; Wanless et al. 2010). This is largely due to extensive fractional crystallization coupled with some crustal assimilation (AFC- assimilation fractional crystallization) in crustal magma chambers as a consequence of the relatively cooler thermal regimes and magmatic processes associated with ridge propagation and/or proximity to transform faults.

High-resolution sampling has also documented the inherent short-term and spatial variability of MOR eruptions (Perfit et al. 1996; Smith et al. 2001; Stakes et al. 2006; Bergmanis et al. 2007; Rubin and Sinton 2007; Goss et al. 2010). Significant geochemical differences in closely spaced dikes from

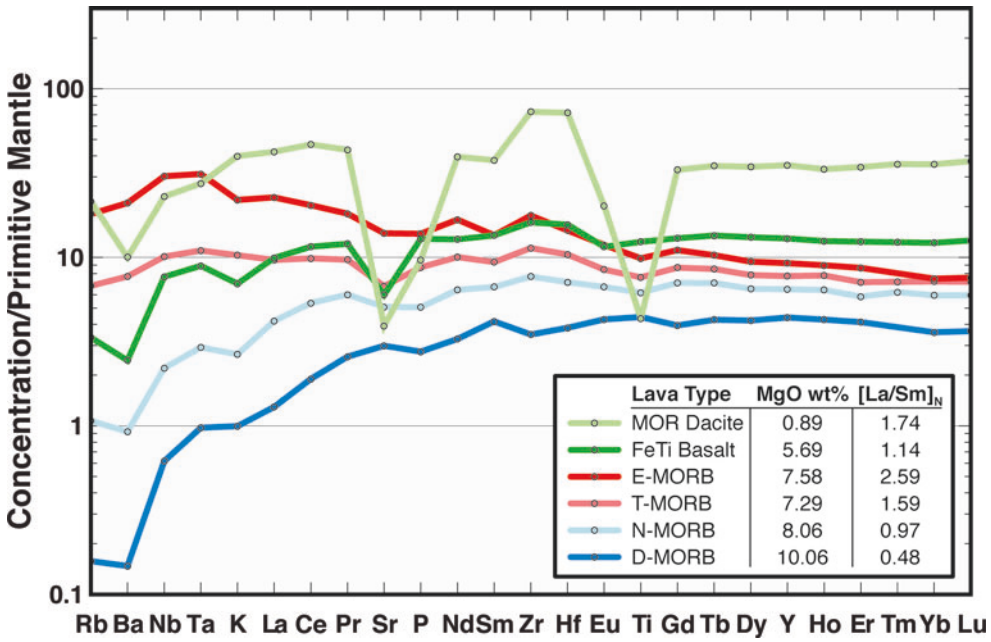

Earth's Oceanic Crust, Fig. 4 Incompatible trace element abundances are commonly used to chemically characterize different types of MORB and to provide information about magmatic processes and sources. Concentrations of incompatible elements (on X-axis) plotted on this primitive mantle-normalized diagram (Values from Sun and McDonough 1989) show the variations in trace element "patterns" for representative E-MORB (enriched), N-MORB (normal), and D-MORB (depleted). Transitional varieties are sometimes referred to as T-MORB. The degrees of enrichment (e.g., increased La/Sm) in MORB show good correlations with K_2O contents (see Fig. 2) and K/Ti ratios. E-MORB have strong enrichments in elements that are the most incompatible during mantle melting (elements on far *left*) relative to the middle to heavy rare earth elements and may be the result of melting enriched mantle source or smaller extents of melting. Highly differentiated N-MORB (low-MgO) FeTi and dacite lavas exhibit overall enrichments of incompatible elements but also some significant elemental depletions (e.g., Sr, P, Eu, Ti) due to their compatibility in minerals crystallizing out of more evolved magmas. All samples shown are from the 8°–10° N segment of the EPREast Pacific Rise (EPR) including the D-MORB from the Siqueiros Transform (From Karson et al. 2015)

sheeted dike complexes that presumably fed overlying lava flows are also consistent with the short-term temporal and spatial variability in ridge magmatic systems (Stewart et al. 2002, 2003; Pollock et al. 2009).

MOR Dikes

Dikes that comprise seismic layer 2b in the oceanic crust have compositions and mineralogies similar, although not identical, to the overlying MORB lavas they supply. Basaltic dikes have been recovered together with lavas at a few tectonic windows and from a few deep-drilling sites. Where unaltered, dikes have major element compositions that, for the most part, overlap the composition of spatially associated lavas (Stewart et al. 2002, 2003; Pollock et al. 2009; Sano et al. 2011). Dikes tend to have coarser textures than lavas, as a consequence of their intrusive nature where cooling rates can be much slower than magma extruded on the seafloor. Ubiquitous patchy, hydrothermal metamorphism of both the lowermost lavas in layer 2a and the sheeted dike complex complicates direct comparisons between the geochemistry of lavas and dikes in some instances.

Gabbroic Layer

The middle to lower portions of the oceanic crust (seismic layer 3) are composed of a complex and varied assemblage of coarse-grained, gabbroic, and ultramafic plutonic rocks. These materials primarily formed by slow cooling and crystallization of melts stored in mushy magma chambers or melt sills (mixtures of crystals and melt) located at depths of ~1–4 km below the seafloor. Unlike crystal-poor volcanic lavas on the seafloor, and the dikes that feed them, these plutonic rocks are comprised of crystalline minerals that reflect the physical and chemical conditions under which they formed. Mafic and ultramafic plutonic rocks constitute the bulk of the oceanic crust (>60% by volume). Most of the gabbroic rocks have mineralogies dominated by plagioclase, olivine, pyroxenes, and minor spinel (Fig. 5). In more evolved rock types, hornblende and Fe-Ti oxides are more prevalent and olivine and spinel less so.

Various magmatic processes that occur in crustal magma chambers such as fractional crystallization coupled with crystal settling and accumulation form cumulate plutonic rock types, commonly exhibiting igneous layering, such as dunites rich in accumulated olivine, anorthosites rich in plagioclase,

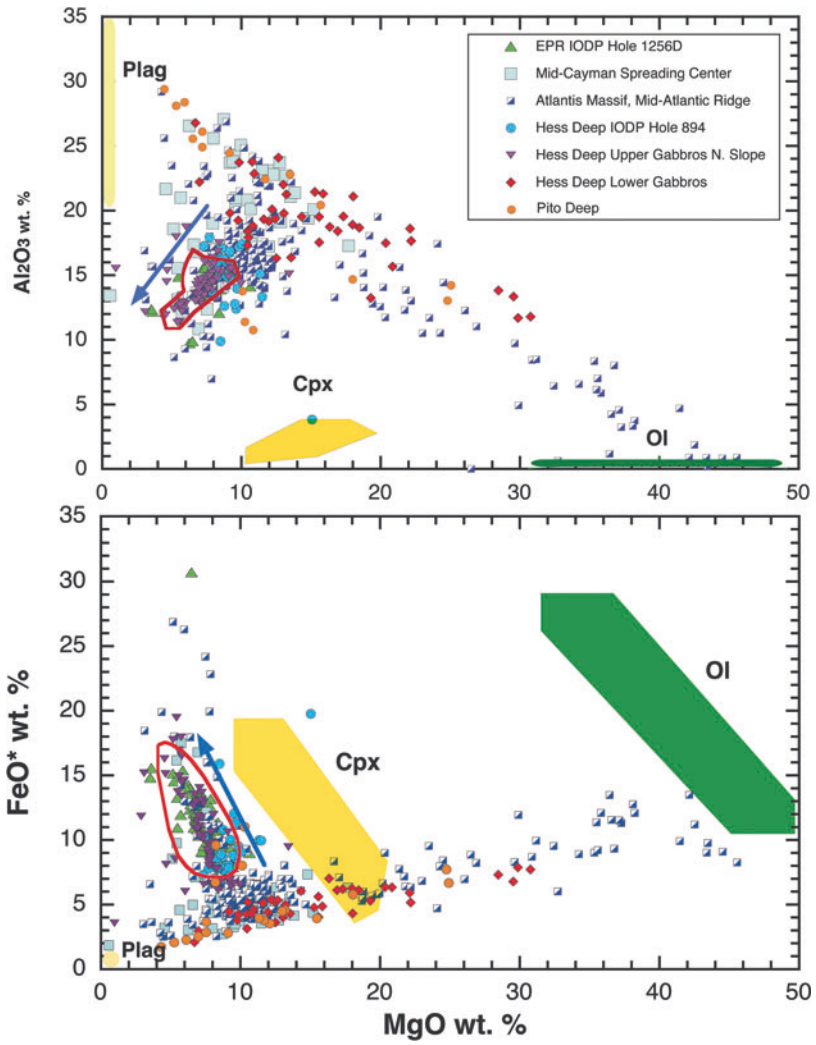

Earth's Oceanic Crust, Fig. 5 Major element variations in gabbros, from various ocean floor localities compared to lavas and dikes from Hess Deep and Pito Deep rifts in the southern Pacific. Overall, gabbros exhibit a much wider compositional range than lavas and dikes due to accumulation of crystals during their formation. MgO-rich olivine gabbros and troctolites have trends that project toward magnesian olivine (*Ol*) compositions (*green field*) whereas high Al_2O_3, low MgO gabbros project toward calcic plagioclase (*Plag*) compositions (*yellow field*). Some more evolved upper crustal gabbros (e.g., IODP Hole 894 from Hess Deep and IODP Hole 1256 from the EPR) have compositions similar to lavas and dikes from Hess Deep (*red outlined field*). These more evolved gabbros, including ferrogabbros, follow the same differentiation trends observed in the lavas and dikes (*blue arrow*) due to low-pressure fractional crystallization (Modified from Karson et al. 2015)

and pyroxenites rich in pyroxenes. Various combinations of these mineral phases form a range of rock types including troctolite, olivine-gabbro, gabbronorite, and ferrogabbros, collectively referred to as gabbroic rocks. Rare silica- and plagioclase-rich intrusive bodies, commonly found in the upper parts of layer 3, are collectively known as plagiogranites.

On the seafloor, plutonic rocks are only exposed on slow- and ultraslow-spread ridges where major faulting has removed the overlying upper crustal units exposing core complexes or where deeply rifted crustal sections provide tectonic escarpments. Along segments of the melt-poor, ultraslow-spread Southwest Indian and Gakkel ridges, serpentinized peridotites (altered mantle rocks) are exposed directly on the seafloor with minor amounts of gabbro (Dick et al. 2003; Cannat et al. 2006). Only the uppermost portions of the plutonic section, away from tectonic windows have been penetrated and sampled by crustal drilling (Coogan et al. 2002; Coogan 2014; Karson et al. 2015). Despite their abundance and importance in constructing oceanic crust, the paucity of exposures and difficulties in recovering gabbros in situ on the seafloor limit our understanding of their origins and overall compositions.

Gabbroic rocks recovered from the oceans display a much greater compositional variation than their spatially related dikes and lavas (Fig. 5). Whereas the major element trends in the lava and dike compositions primarily reflect the differentiation and evolution of primitive liquids via crystal fractionation and magma mixing, the spread in gabbro data mainly reflects crystal accumulation within MORMid-ocean ridges (MOR) magma chambers and crystal mush zones as well as the addition of melts that permeate and react with the cumulate minerals. For example, elemental trends toward high Al_2O_3 and low FeO and MgO contents in plutonic rocks reflect the accumulation of calcic plagioclase in many of the troctolites, gabbros, and anorthositic gabbros whereas more mafic samples with high MgO contents primarily show the effects of magnesian olivine accumulation (Fig. 5).

Gabbroic rocks recovered from the seafloor exhibit a large range of trace element abundances, particularly the highly

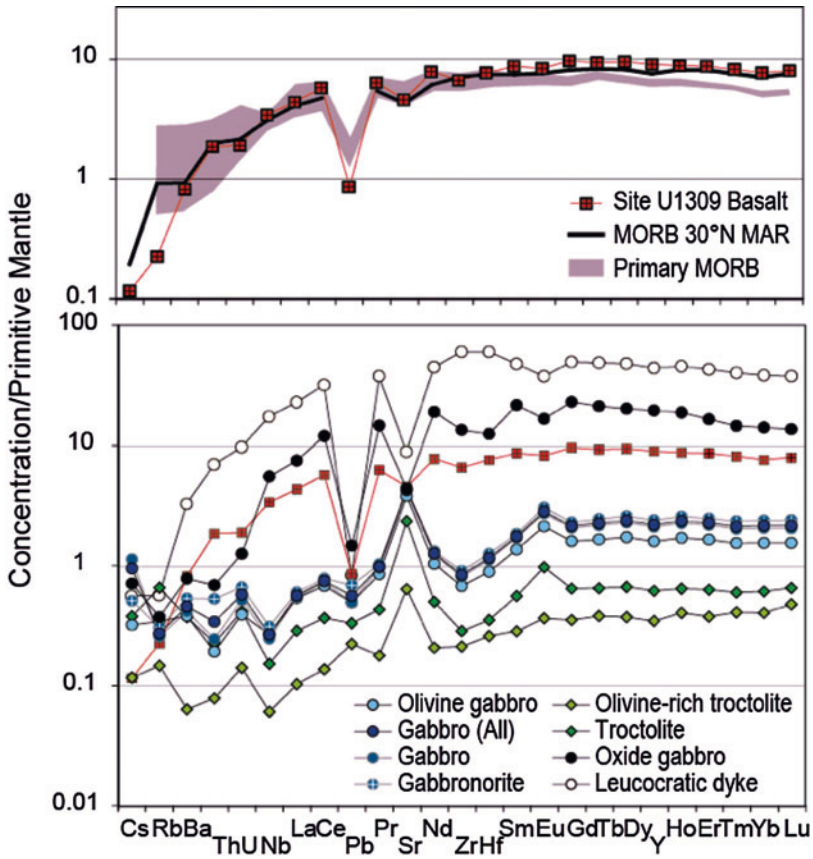

Earth's Oceanic Crust, Fig. 6 Normalized trace element concentration diagram showing the relative abundances of incompatible trace elements in gabbros (*lower plot*) from the Atlantis Massif (IODP Site U1309) relative to spatially associated MORB from the MAR (*upper diagram*). The primitive mantle-normalized values are mean values for different types of gabbroic rocks corresponding to the range of compositions shown in Fig. 5. Excluding the highly differentiated oxide gabbro and leucocratic dike, the gabbroic rocks are unlike MORB, characterized by variable but overall low abundances of incompatible trace elements and anomalously high concentrations of Sr and Eu relative to the REE indicative of their cumulate nature. Incompatible trace element pattern for a typical MORB (*red*) from the Mid-Atlantic Ridge is shown relative to the gabbros (*lower plot*) highlighting the differences between intrusive rocks and erupted basalts (From Godard et al. 2009)

incompatible elements that correspond to their varied major element compositions (Fig. 6). The trace element abundances partly reflect the concentrations in parental melts but are also largely dependent on the proportion of cumulus phases (including accessory phases) and intercumulus melts. Chondrite-normalized REE patterns vary from very LREE-depleted troctolites to slightly LREE-enriched ferrogabbros and plagiogranites (e.g., Dick et al. 2000; Coogan et al. 2002; Godard et al. 2009; Gillis et al. 2013; Coogan 2014). Relative to primitive mantle concentrations, some cumulate gabbros have low incompatible element and REE abundances with characteristic positive Sr- and Eu-anomalies – indicative of plagioclase accumulation (Fig. 6). The most evolved ferrogabbros exhibit elevated incompatible element contents and negative Sr- and Eu-anomalies indicative of plagioclase removal from evolving magmas, consistent with their relatively low Al_2O_3 contents. Relatively few gabbros have trace element patterns that mimic those in dikes and lavas. Because the compositions of gabbroic rocks reflect the variable proportions of accumulated phases and different amounts of interstitial melt, they cannot be directly related to mantle-derived melts. However, detailed mineralogic studies suggest many gabbros have experienced complex crystal-melt reactions within crystal mush zones in the lower crust (Natland and Dick 2001; Gao et al. 2007; Suhr et al. 2008; Lissenberg et al. 2013; Coogan 2014).

Bulk Composition of the Oceanic Crust

Because oceanic crust has been incompletely sampled and is heterogeneous on a small scale, it is difficult to determine its bulk chemical composition with confidence. However some estimates have recently been made of the compositions of the volcanic and plutonic layers (Arevalo and McDonough 2010; Gale et al. 2013; Coogan 2014; White and Klein 2014) that, together with their relative volumes, allow some constraints to be placed on the bulk unaltered composition of the oceanic crust. However, one needs to be aware that it is uncertain what proportion of the oceanic crust has been chemically modified by the pervasive hydrothermal alteration associated with submarine volcanism focused at the ridge crest and low-temperature submarine weathering that occurs as crust moves away from the magmatic portion of ridges (Ridley et al. 1994; Alt 1995; Alt 2004; Staudigel 2013). Basically, the interaction of seawater with oceanic igneous rocks in low-temperature (<100 °C), off-axis hydrothermal recharge environments results in increased oxidation and alkali fixation, an increase in volatiles and some large ion lithophile elements (e.g., Rb, K, Cs), and a depletion of Ca, Sr, S that is sometimes associated with depletions in Mg, Si, Co, and Ni (Alt 1995). In deeper regions of the crust where temperatures are higher (>150 °C) and fluid flow may be more restricted, there are significant gains in Na, Mg, H_2O, and CO_2 and

losses in S, Ca, Si, alkalis, and Au. Where temperatures are even higher (>350 °C), which typically occurs in focused or diffuse reaction zones in the dikes and upper gabbros beneath hydrothermal vents and stockwork zones, significant depletion of liable trace metals (e.g., Cu, Zn, Co, Fe) occurs along with the stripping of S and alkalis (Alt 1995). A study of an in situ section of crust drilled at IODP hole 1256D showed significant depletions (> ~8% relative to fresh MORB) in Au, As, Se, S, Cu, Zn, and Pb in the lower portions of the dike layer and uppermost gabbroic samples. However, the same elements are commonly enriched in altered rocks at higher levels in the crust beneath zones of high-temperature venting (Patten et al. 2016). In sections of the upper crust dominated by hydrothermal fluid-rock interactions, major element enrichments and depletions are quite variable and difficult to generalize (Ridley et al. 1994). Overall, the extent of alteration and elemental exchange in the oceanic crust can be highly variable depending on the temperature of the circulating seawater or hydrothermal fluids and the water to rock ratio. Although alteration of the upper portions of the crust clearly plays an important role in determining the bulk composition of the oceanic crust, the overall effects and volume of crust affected are uncertain.

Summary

The composition of the oceanic crust is roughly basaltic; however, an accurate estimate of the bulk composition is difficult to make for many of the reasons discussed above (also see Rubin et al. 2009). Reasonable estimates of the composition of the bulk, unaltered oceanic crust might be made by using two methods. First, one can take a mass-balance approach by determining the compositions and volumetric proportions of the various rocks that comprise the crust but the current state of our knowledge of the lower crust precludes any precision.

Alternatively, one can estimate the composition of primary, mantle-derived magmas that crystallized and differentiated to form the different crustal lithologies observed. Current estimates of primary MOR mantle melts are still somewhat speculative and debatable (Kinzler and Grove 1993). High-MgO lavas that have compositions comparable to some high-pressure melting experiments of likely mantle source rocks include rare picritic lavas and magnesian glasses that have been recovered from a few ocean floor locales (Elthon 1979; van Heerden and le Roex 1988; Natland 1989; Perfit et al. 1996; Wendt et al. 1999). MgO contents for those rocks range from ~10 wt% to over 15 wt% and could have been primary or near-primary mantle melts. But are they representative of the composition of the oceanic crust as a whole? The range of their observed compositions likely reflects variations in source composition, extents of melting, types of melting and minor effects of crustal differentiation. Consequently, the estimates are not very precise and the bulk composition of the oceanic crust remains controversial and a focus of current investigations.

Cross-References

- ▶ Fractional Crystallization and Assimilation
- ▶ Hydrothermal Vents
- ▶ Incompatible Elements
- ▶ Lanthanide Rare Earths
- ▶ Large-Ion Lithophile Elements
- ▶ Lithophile Elements
- ▶ Mantle Geochemistry
- ▶ Mid-Ocean Ridge Basalts (MORB)
- ▶ Mineralogy
- ▶ Volcanism

References

Alt JC (1995) Subseafloor processes in mid-ocean ridge hydrothermal systems. In: Humphris SE, Zierenberg RA, Mullineaux LS, Thompson RE (eds) Seafloor hydrothermal systems: physical, chemical, biological, and geological interactions, Geophysical monograph, vol 91. American Geophysical Union, Washington, DC, pp 85–114

Alt JC (2004) Alteration of the upper oceanic crust: mineralogy, chemistry and processes. In: Davis EE, Elderfield H (eds) Hydrogeology of the oceanic lithosphere. Cambridge University Press, Cambridge, pp 495–533

Arevalo R, McDonough WF (2010) Chemical variations and regional diversity observed in MORB. Chem Geol 271(1):70–85

Bergmanis EC, Sinton JM, Rubin KH (2007) Eruptive history and magma reservoir dynamics on the East Pacific rise at 17° 30′ N. Geochem Geophys Geosyst 8(12). https://doi.org/10.1029/2007GC001742

Cannat M (1996) How thick is the magmatic crust at slow spreading oceanic ridges? J Geophys Res 101:2847–2857

Cannat M, Sauter D, Mendel V, Ruellan E, Okino K, Escartin J, Baala M (2006) Modes of seafloor generation at a melt-poor ultraslow-spreading ridge. Geology 34:605–608

Coogan LA (2014) The lower oceanic crust. In: Holland H, Turekian K (eds) Treatise on geochemistry, Reference module in earth systems and environmental sciences, Vol. 4: the crust, 2nd edn. Elsevier, Oxford, pp 497–541. https://doi.org/10.1016/B978-0-08-095975-7.00316-8

Coogan LA, O'Hara MJ (2015) MORB differentiation: in situ crystallization in replenished-tapped magma chambers. Geochim Cosmochim Acta 158:147–161

Coogan LA, Gillis KM, MacLeod CJ, Thompson GM, Hékinian R (2002) Petrology and geochemistry of the lower oceanic crust formed at the East Pacific rise and exposed at Hess deep: a synthesis and new results. Geochem Geophys Geosyst. https://doi.org/10.1029/2001/GC000230

Dick HJB, Natland JH, Alt JC et al (2000) A long in situ section of the lower oceanic crust: results of ODP Leg 176 drilling at the Southwest Indian ridge. Earth Planet Sci Lett 179:31–51

Dick HJB, Lin J, Schouten H (2003) An ultraslow-spreading class of ocean ridge. Nature 426:405–412

E

Dunn RA, Forsyth DW (2007) Crust and lithospheric structure – seismic structure of mid-ocean ridges. Treatise Geophys 1:419–443
Elthon D (1979) High magnesia liquids as the parental magma for ocean floor basalts. Nature 278:514–518
Frey FA, Walker N, Stakes D, Hart SR, Nielsen R (1993) Geochemical characteristics of basaltic glasses from the AMAR and FAMOUS axial valleys, Mid-Atlantic Ridge (36°–37° N): petrogenetic implications. Earth Planet Sci Lett 115(1):117–136
Gale A, Dalton CA, Langmuir CH, Su Y, Schilling J-G (2013) The mean composition of ocean ridge basalts. Geochem Geophys Geosyst 14:489–518. https://doi.org/10.1029/2012GC004334
Gao Y, Hoefs J, Hellebrand E, Von Der Handt A, Snow JE (2007) Trace element zoning in pyroxenes from ODP hole 735B gabbros: diffusive exchange or synkinematic crystal fractionation? Contrib Mineral Petrol 152:429–442. https://doi.org/10.1007/s00410-006-0158-4
Gillis KM, Snow JE, Klaus A et al (2013) Primitive layered gabbros from fast-spreading lower oceanic crust. Nature. https://doi.org/10.1038/nature12778
Godard M, Awaji S, Hansen H-E et al (2009) Geochemistry of a long in-situ section of intrusive slow-spread lithosphere: results from IODP site U1309 (Atlantis Massif, 30° N Mid-Atlantic Ridge). Earth Planet Sci Lett 279:110–122
Goss AR, Perfit MR, Ridley WI et al (2010) Geochemistry of lavas from the 2005–2006 eruption at the East Pacific Rise, 9° 46′ N–9° 56′ N: implications for ridge crest plumbing and decadal changes in magma chamber compositions. Geochem Geophys Geosyst 11:Q05T09. https://doi.org/10.1029/2009GC00297
Graham DW, Jenkins WJ, Schilling JG, Thompson G, Kurz MD, Humphris SE (1992) Helium isotope geochemistry of mid-ocean ridge basalts from the South Atlantic. Earth Planet Sci Lett 110(1):133–147
Hart SR (1971) The geochemistry of basaltic rocks. In: Carnegie Institution of Washington yearbook, vol 70. Carnegie Institution, Washington, DC, pp 353–355
Hofmann AW (1988) Chemical differentiation of the Earth: the relationship between mantle, continental crust and oceanic crust. Earth Planet Sci Lett 90:297–314
Hofmann AW (1997) Mantle geochemistry: the message from oceanic volcanism. Nature 385(6613):219–229
Karson JA, Kelley DS, Fornari DJ, Perfit MR, Shank TM (2015) Discovering the deep: a photographic atlas of the seafloor and ocean crust. Cambridge University Press, Cambridge, UK. 430 p
Kinzler R, Grove T (1993) Corrections and further discussion of the primary magmas of mid-ocean ridge basalts, 1 and 2. J Geophys Res 98:22339–22347
Klein EM, Langmuir CH (1987) Global correlations of ocean ridge basalt chemistry with axial depth and crustal thickness. J Geophys Res 92:8089–8115
Kvassnes AJ, Grove TL (2008) How partial melts of mafic lower crust affect ascending magmas at oceanic ridges. Contrib Mineral Petrol 156(1):49–71
Langmuir CH (1989) Geochemical consequences of in situ crystallization. Nature 340(6230):199–205
Langmuir CH, Bender JF, Batiza R (1986) Petrologic and tectonic segmentation of the East Pacific Rise, 5° 30′–14° 30′ N. Nature 322:422–426
Langmuir CH, Klein EM, Plank T (1992) Petrological systematics of mid-ocean ridge basalts: constraints on melt generation beneath ocean ridges. In: Phipps-Morgan J, Blackman DK, Sinton J (eds) Mantle flow and melt generation at Mid-Ocean ridges, Geophysical monograph series, vol 71. American Geophysical Union, Washington, DC, pp 183–280
Lissenberg CJ, Dick HJB (2008) Melt–rock reaction in the lower oceanic crust and its implications for the genesis of mid-ocean ridge basalt. Earth Planet Sci Lett 271(1):311–325
Lissenberg CJ, MacLeod CJ, Howard KA, Godard M (2013) Pervasive reactive melt migration through fast-spreading lower oceanic crust (Hess Deep, equatorial Pacific Ocean). Earth Planet Sci Lett 361:436–447
Melson WG, Vallier TL, Wright TL, Byerley G, Nelen J (1976) Chemical diversity of abyssal volcanic glass erupted along Pacific, Atlantic and Indian Ocean Sea-floor spreading centers. In: Sutton GH, Manghnani MH, Moberly R (eds) The geophysics of the Pacific Ocean basin and its margins. American Geophysical Union, Washington, DC, pp 351–367
Michael PJ (1995) Regionally distinctive sources of depleted MORB: evidence from trace elements and H_2O. Earth Planet Sci Lett 131(3):301–320
Natland JH (1989) Partial melting of lithologically heterogeneous mantle: inferences from crystallization histories of magnesian abyssal tholeiites from the Siqueiros fracture zone. In: Saunders AD, Norry MJ (eds) Magmatism in the ocean basins, Geological Society of London special publication, vol 42. Geological Society of London, London, pp 41–70
Natland JH, Dick HJB (2001) Formation of the lower ocean crust and the crystallization of gabbroic cumulates at a very slowly spreading ridge. J Volcanol Geotherm Res 110(3–4):191–233
O'Neill HSC, Jenner FE (2012) The global pattern of trace-element distributions in ocean floor basalts. Nature 491(7426):698–704
Patten CGC, Pitcairn IK, Teagle DAH, Harris M (2016) Mobility of Au and related elements during the hydrothermal alteration of the oceanic crust: implications for the sources of metals in VMS deposits. Mineral Deposita 51:179–200
Perfit MR, Chadwick WW Jr (1998) Magmatism at mid-ocean ridges: constraints from volcanological and geochemical investigations. In: Buck WR, Delaney PT, Karson JA, Lagabrielle Y (eds) Faulting and magmatism at mid-ocean ridges. American Geophysical Union, Washington, DC, pp 59–115
Perfit MR, Fornari DJ (1983) Geochemical studies of abyssal lavas recovered by DSRV ALVIN from the eastern Galapagos rift – Inca transform – Ecuador rift: II. Phase chemistry and crystallization history. J Geophys Res 88:10530–10550
Perfit MR, Fornari DJ, Malahoff A, Embley RW (1983) Geochemical studies of abyssal lavas recovered by DSRV ALVIN from the eastern Galapagos rift – Inca transform – Ecuador rift: III. J Geophys Res 88:10551–10572
Perfit MR, Fornari DJ, Smith MC, Bender JF, Langmuir CH, Haymon RM (1994) Small-scale spatial and temporal variations in mid-ocean ridge crest magmatic processes. Geology 22:375–379
Perfit MR, Fornari DJ, Ridley WI, Kirk PA, Casey J, Kastens KA, Edwards M, Shuster R, Paradis S (1996) Recent volcanism in the Siqueiros transform fault: picritic basalts and implications for MORB magma genesis. Earth Planet Sci Lett 141:91–108
Perfit MR, Wanless VD, Ridley WI, Klein E, Smith MC, Hinds JS, Kutza S, Fornari DJ (2012) EPR ISS lava geochemistry – 2 decades of comprehensive sampling and 2 eruptions. Oceanography 25(1):89–93
Pollock MA, Klein EM, Karson JA, Coleman DS (2009) Compositions of dikes and lavas from the Pito deep rift: implications for accretion at superfast spreading centers. J Geophys Res 114(B3). https://doi.org/10.1029/2007JB005436
Putirka K, Ryerson FJ, Perfit M, Ridley WI (2011) Mineralogy and composition of the oceanic mantle. J Petrol 52(2):279–313
Reynolds JR, Langmuir CH, Bender JF, Kastens KA, Ryan WB (1992) Spatial and temporal variability in the geochemistry of basalts from the East Pacific rise. Nature 359(6395):493–499
Rhodes JM, Dungan MA, Blanchard DP, Long PE (1979) Magma mixing at mid-ocean ridges: evidence from basalts drilled near 22 N on the Mid-Atlantic Ridge. Tectonophysics 55(1–2):35–61
Ridley WI, Perfit MR, Jonasson IR, Smith MF (1994) Chemical pathways of alteration in oceanic volcanics: a detailed study at the

Galapagos fossil hydrothermal field. Geochim Cosmochim Acta 58:2477–2494
Ridley WI, Perfit MR, Fornari DJ, Smith MC (2006) Magmatic processes in developing oceanic crust revealed in a cumulate xenolith collected at the East Pacific Rise, 9° 50′ N. Geochem Geophys Geosyst 7:Q12O04. https://doi.org/10.1029/2006GC001316
Rubin KH (2014) Mid-Ocean ridge magmatism and volcanism. In: Harff J, Meschede M, Petersen S, Thiede J (eds) Encyclopedia of marine geosciences. Springer, Dordrecht, pp 1–21. https://doi.org/10.1007/978-94-007-6644-0_28-3
Rubin KH, Sinton JM (2007) Inferences on mid-ocean ridge thermal and magmatic structure from MORB compositions. Earth Planet Sci Lett 260:257–276
Rubin KH, Sinton JM, Maclennan J, Hellebrand E (2009) Magmatic filtering of mantle compositions at mid-ocean-ridge volcanoes. Nat Geosci 2(5):321–328
Rudnick RL (1995) Making continental crust. Nature 378:571–577
Sano T, Sakuyama T, Ingle S, Rodriguez S, Yamasaki T (2011) Petrological relationships among lavas, dikes, and gabbros from Integrated Ocean drilling program hole 1256D: insight into the magma plumbing system beneath the East Pacific Rise. Geochem Geophys Geosyst 12(6):Q06013. https://doi.org/10.1029/2011GC003548
Schilling J-G (1985) Upper mantle heterogeneities and dynamics. Nature 314:62–67
Schilling J-G, Zajac M, Evans R et al (1983) Petrologic and geochemical variations along the Mid-Atlantic Ridge from 29° N to 73° N. Am J Sci 283:510–586
Sinton JM, Wilson DS, Christie DM, Hey RN, Delaney JR (1983) Petrologic consequences of rift propagation on oceanic spreading ridges. Earth Planet Sci Lett 62:193–207
Smith MC, Perfit MR, Fornari DJ et al (2001) Magmatic processes and segmentation at a fast spreading mid-ocean ridge: detailed investigation of an axial discontinuity on the East Pacific Rise crest at 9° 37′ N. Geochem Geophys Geosyst 2:1–32. https://doi.org/10.1029/2000GC000134
Stakes DS, Perfit MR, Tivey MA et al (2006) The cleft revealed: geologic, magnetic and morphologic evidence for construction of upper oceanic crust along the southern Juan de Fuca Ridge. Geochem Geophys Geosyst 7:Q04003. https://doi.org/10.1029/2005GC001038
Staudigel H (2013) Chemical fluxes from hydrothermal alteration of the oceanic crust. In: Treatise of geochemistry, vol 4, Holland, pp 583–606
Stewart MS, Klein EM, Karson JA (2002) The geochemistry of dikes and lavas from the north wall of the Hess Deep Rift: insights into the four-dimensional character of crustal construction at fast-spreading mid-ocean ridges. J Geophys Res 107(B9):2181. https://doi.org/10.1029/2000JB000051
Stewart MA, Klein EM, Karson JA, Brophy JG (2003) Geochemical relationships between dikes and lavas at the Hess Deep Rift: implications for magma eruptibility. J Geophys Res 108(B4):2184. https://doi.org/10.1029/2001JB001622
Stracke A (2012) Earth's heterogeneous mantle: a product of convection-driven interaction between crust and mantle. Chem Geol 330–331:274–299
Suhr G, Hellebrand E, Johnson K, Brunelli D (2008) Stacked gabbro units and intervening mantle: a detailed look at a section of IODP Leg 305, Hole U1309D. Geochem Geophys Geosyst 9. https://doi.org/10.1029/2008GC002012
Sun S-S, McDonough WF (1989) Chemical and isotopic systematics of oceanic basalts: implications for mantle composition and processes. In: Saunders AD, Norry MJ (eds) Magmatism in the ocean basins, Geological Society of London special publication, vol 42. Geological Society of London, London, pp 313–345
Sun S-S, Nesbitt RW, Sharaskin AY (1979) Geochemical characteristics of mid-ocean ridge basalts. Earth Planet Sci Lett 44:119–138
Taylor SR, McLennan SM (1985) The continental crust: its composition and evolution. Blackwell, Oxford, UK, p 312
van Heerden LA, le Roex AP (1988) Petrogenesis of picrite and associated basalts from the southern Mid-Atlantic Ridge. Contrib Mineral Petrol 100:47–60
Wanless VD, Perfit MR, Ridley WI, Klein EM (2010) Dacite petrogenesis on mid-ocean ridges: evidence for crustal melting and assimilation. J Petrol 51:2377–2410
Wendt JI, Regelous M, Niu Y, Hékinian R, Collerson KD (1999) Geochemistry of lavas from the Garrett transform fault: insights into mantle heterogeneity beneath the eastern Pacific. Earth Planet Sci Lett 173:271–284
White WM, Klein EM (2014) Composition of the oceanic crust. In: Holland HD, Turekian KK (eds) Treatise on geochemistry, 2nd edn. Elsevier, Oxford, pp 457–496. https://doi.org/10.1016/B978-0-08-095975-7.00315-6
White WM, Schilling J-G (1978) The nature and origin of geochemical variation in Mid-Atlantic Ridge basalts from the Central North Atlantic. Geochim Cosmochim Acta 42(10):1501–1516
White WM, McBirney AR, Duncan RA (1993) Petrology and geochemistry of the Galápagos Islands: portrait of a pathological mantle plume. J Geophys Res 98(B11):19533–19563. https://doi.org/10.1029/93JB02018
Zindler A, Hart S (1986) Chemical geodynamics. Annu Rev Earth Planet Sci 14:493–571

Electron Probe Microanalysis (EPMA)

Stuart Kearns
School of Earth Sciences, University of Bristol, Bristol, UK

Definition

A microanalytical technique yielding quantitative major and minor elemental analysis from solid materials using an electron source and X-ray spectrometers.

The technique of electron probe microanalysis (EPMA) was developed in the 1950s, primarily the outcome of a PhD thesis by Castaing (1951). In the following decade, it became established as the preferred method to characterize the in situ chemistry of very small volumes of mainly inorganic materials, including minerals. The instrument, often referred to as the "microprobe" or sometimes simply the "probe," works by firing a beam of electrons accelerated to high potential (1–30 kV) and focused to a small convergent spot which strikes a flat, usually polished sample. Atoms within the sample undergo inner shell ionization resulting in characteristic X-ray emission. These X-rays are detected and measured by X-ray spectrometers, and their count rates are compared to known standards to yield a primary intensity ratio – the *k*-ratio. As both the incoming electron beam and outgoing X-rays are subject to other interaction events, the *k*-ratio needs to be corrected for matrix effects to yield a quantitative analysis.

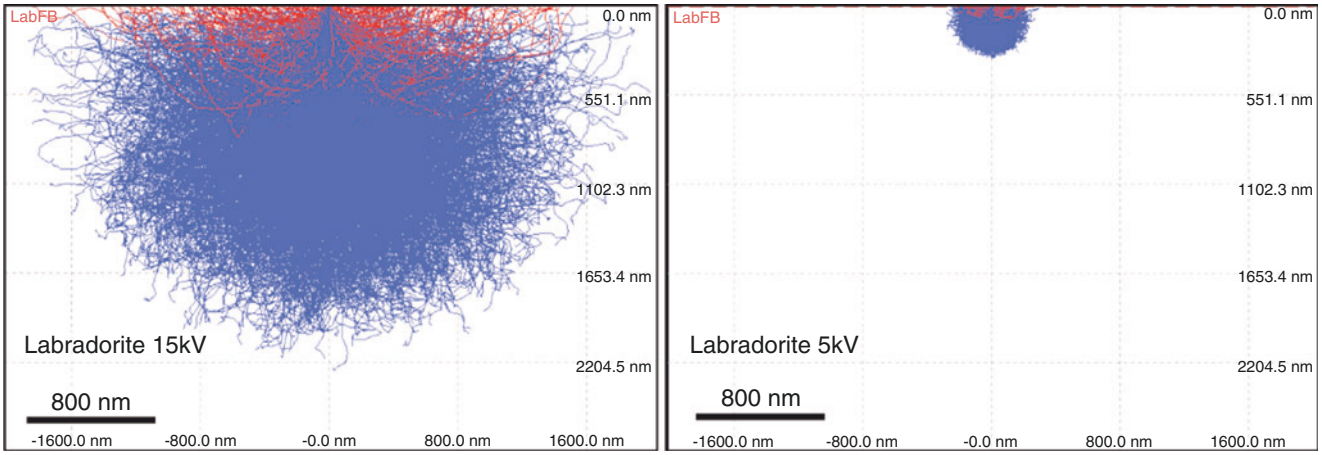

Electron Probe Microanalysis (EPMA), Fig. 1 Monte Carlo simulation for labradorite plagioclase at 15 kV and 5 kV accelerating voltage. Electron interaction volume is shown (red lines display emitted backscattered electron trajectories). Generated using Casino (Hovington et al. 1997)

Electron Source

The electron gun is supplied as one of three options –a tungsten filament, lanthanum hexaboride (LaB6), and thermal Schottky Field Emission Gun (FEG). All three sources have been used extensively in scanning electron microscopes (SEM). EPMA has traditionally utilized the tungsten filament as it offers sufficient longevity and good stability, critical for quantitative analysis. Technology advances now mean that both LaB6 and FEG can also supply a very stable beam with the benefit of higher beam brightness yielding a smaller spot size and therefore the promise of higher resolution analysis, with the FEG offering the highest. EPMA instruments include a scan generator and electron detectors such that standard SEM images can be acquired.

Analytical Resolution

The analytical resolution can be determined from Monte Carlo simulation of the electron beam interaction and X-ray emission. The volume of material excited is much greater than that for either secondary electron (SE) or backscattered electron (BSE) yields. It is strongly dependent on both the beam voltage and sample properties, importantly density (Fig. 1).

Typically silicate minerals will yield excitation volumes of several cubic micrometers using a 20 kV electron beam. At 5 kV when the beam penetration is maybe only a few hundred nanometers, submicron resolution is achievable. However, at such low voltage, only low energy X-rays, whose critical excitation potential is exceeded, can be detected.

X-ray Spectrometers

The microprobe usually consists of one Energy Dispersive Spectrometer (EDS) and multiple wavelength dispersive spectrometers (WDS) around the electron column. The EDS benefits from parallel detection of all X-rays. Contrastingly each WDS has a limited wavelength range (depending on its diffracting crystal d-spacing) but benefits from much greater resolution and better peak to background ratio (Fig. 2).

WDS operates on the basis of diffraction of X-ray photons by a crystal of known d-spacing according to Bragg's Law – as the angle of incidence changes, it detects X-rays of varying wavelengths in a serial fashion.

Today's EDS consists of a silicon drift detector (SDD) with the older Si (Li) detectors slowly being replaced. The SDD offers much higher throughput such that it can operate at high beam currents without excessive deadtime – a limitation of Si (Li) detectors. As such, SDD is an ideal accompaniment to WDS on a microprobe. Additionally, to the delight of laboratory managers, the SDD only requires Peltier cooling; the constant necessity to replenish the liquid nitrogen dewers of Si(Li) detectors is no longer needed.

A modern addition to the standard detectors is a soft X-ray emission spectrometer (Terauchi et al. 2012) based on a diffraction grating which offers spectacular resolution improvement in the <1 kV X-ray range. Other detectors usually associated with the SEM, e.g., cathodoluminescence and electron backscatter diffraction are occasionally added to microprobes.

Quantitative Analysis

The conversion of the emitted X-ray signals into a quantitative analysis requires firstly measurement of a set of primary standards containing known concentrations of each of the elements of interest. The derived *k*-ratio from the unknown is then subject to an iterative matrix correction algorithm to take account of the effects of Rayleigh scattering, Compton scattering, and photoelectric absorption. The relationship

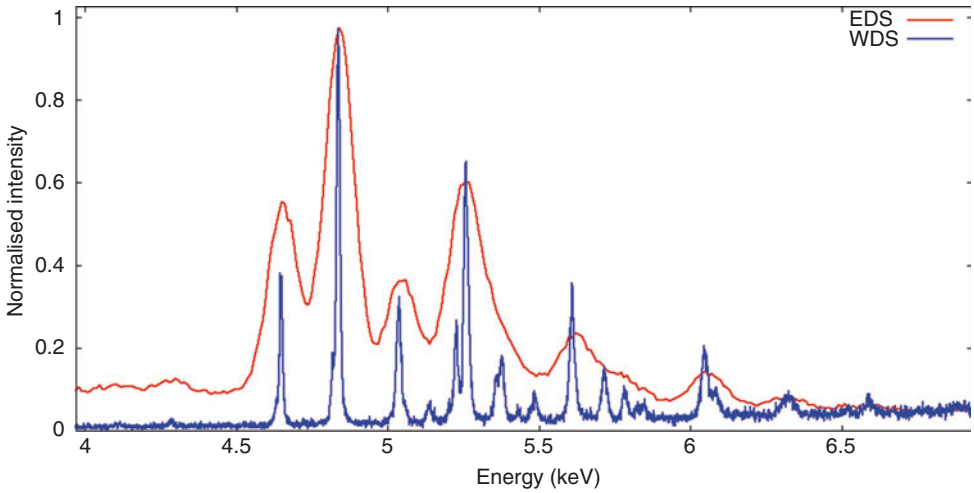

Electron Probe Microanalysis (EPMA), Fig. 2 Comparison of Energy dispersive (red) and wavelength dispersive (blue) spectra of LREEs from a monazite recorded under identical operating conditions

between the X-ray intensity and the elemental composition is established using the phi-rho-z method – an integral as a function of mass depth provided the depth distribution of ionizations is known. Several models to predict this function are available, e.g., the double Gaussian model, X-Phi (Merlet 1994). The calculation is performed online and yields a quantitative analysis with elemental concentrations expressed as atomic or weight percents. We would expect an accuracy of better than 2% on samples of known concentration.

As the wavelengths of X-rays increase so the uncertainty becomes greater; absorption effects are larger for "soft" X-rays and the correction factors increase. Consequently at low accelerating potentials, selection of primary standard materials as compositionally similar to the unknowns as possible, and measured under the same operating conditions, is required to yield the best quantitative results (Bastin and Heijligers 2004). Routinely in earth sciences, oxygen is assumed to have a fixed stoichiometry and is rarely analyzed directly – EPMA cannot readily distinguish between varying valence states.

The X-ray spectrum includes a continuum of "*bremsstrahlung*" – literally a braking radiation which forms a background of variable intensity. This must be measured and subtracted from the characteristic peak intensity. The detection limits of EPMA may be defined as 3 standard deviations of the background count rate. Typically, minimum detection limits are in the range 100–500 ppm but in cases where multiple WD spectrometers are assigned to a single element and long count times and high beam currents are employed, less than 10 ppm of some elements may be detectable (e.g., analysis of Ti in quartz, Wark and Watson 2006).

X-ray Mapping

If the beam is scanned across a sample surface, and spectrometers record the X-ray intensity as the scan progresses, a map of that X-ray, and therefore element distribution, can be collected (Wuhrer and Moran 2014). The X-ray signal is subject to the same matrix effects as with spot analyses, but quantitative element maps can be produced. Using EDS, it is now commonplace to acquire a full ED spectrum for each pixel on an image permitting complex phase mapping. As WDS signals are serially collected, a single element is mapped on each spectrometer. As with quantitative analysis the background intensity needs to be subtracted especially when mapping multiphase samples. This can either be measured directly or estimated using a mean atomic number calculation (Donovan and Tingle 1996).

Sample Preparation and Materials

It is imperative that samples are clean, flat, and polished and, as most earth science materials are dielectric, are rendered conductive by application of a coating of conductive material, typically carbon or alternatively, gold, silver, or aluminum. Many materials (especially those containing water or hydroxyl) suffer from beam damage, often a result of phonon excitation. For this reason, a range of optimal operating conditions exist depending upon the task in question. For example, rhyolitic glasses suffer from alkali migration during beam exposure; this is mitigated by using a defocused beam and low beam currents (2–5 nA) (Morgan and London 2005). Time-dependent intensity calculation can be used to restore the intensity back to that expected at $t = 0$ (e.g., halogen analysis in apatites, Goldoff et al. 2012).

Conclusions

Since the 1950s, EPMA has developed into a mature technique and continues to play an important role in the chemical characterization of minerals and glasses. Modern advances offer the prospect of better light element analysis,

quantification of smaller volumes of material, and improved X-ray mapping systems. EPMA occupies a unique analytical niche and compliments many other techniques such as XRF, XRD, SEM, SIMS, LA-ICPMS.

References

Bastin GF, Heijligers HJM (2004) Quantitative electron probe microanalysis of nonconducting specimens: science or art? Microsc Microanal 10:733–738

Castaing R (1951) Application of electron probes to local chemical and crystallographic analysis. PhD thesis, University of Paris. [English translation by P Duwez and DB Wittry, California Institute of Technology, 1955]

Donovan JJ, Tingle TN (1996) An improved mean atomic number background correction for quantitative microanalysis. Microsc Microanal 2:1–7

Goldoff B, Webster JD, Harlov DE (2012) Characterization of fluor-chlorapatites by electron probe microanalysis with a focus on time-dependent intensity variation of halogens. Am Mineral 97:1103–1115

Hovington P, Drouin D, Gauvin R (1997) CASINO: a new era of Monte Carlo code in C language for the electron beam interaction – Part I: description of the program. Scanning 19:1–14

Merlet C (1994) An accurate computer program for quantitative electron probe microanalysis. Mikrochim Acta 114/115:363–376

Morgan G, London D (2005) Effect of current density on the electron microprobe analysis of alkali aluminosilicate glasses. Am Mineral 90:1131–1138

Terauchi M, Takahashi H, Handa N, Murano T, Koike M, Kawachi T, Imazono T, Koeda M, Nagano T, Sasai H, Oue Y, Yonezawa Z, Kuramoto S (2012) Ultrasoft-X-ray emission spectroscopy by using a newly designed WDS spectrometer attached to a transmission electron microscope. J Electron Microsc 61:1–8

Wark D, Watson EB (2006) TitaniQ; a titanium-in-quartz geothermometer. Contrib Mineral Petrol 152:743–754

Wuhrer R, Moran K (2014) Quantitative X-ray mapping, scatter diagrams and the generation of correction maps to obtain more information about your material. IOP Conf Ser Mater Sci Eng 55:012021

Electronegativity

Barry R. Bickmore and Matthew C. F. Wander
Department of Geological Sciences, Brigham Young University, Provo, UT, USA

Definition

Electronegativity is a measure of the electron attracting power of an atom, or group of atoms, in a molecule. Several electronegativity scales exist, based on different physical properties, but all of them are highly correlated. Electronegativity is used for a variety of purposes in chemistry, providing both an intuitive concept with which to rationalize chemical trends and values that are highly correlated with a number of chemical and physical properties.

Introduction

Electronegativity is one of the most ambiguously defined but useful concepts commonly employed in chemistry. In 1806, Humphry Davy posited that the chemical affinity between two substances was related to the degree of difference in their electrical properties, i.e., their ability to obtain and hold positive or negative charge. Avogadro expanded upon it and gave similar suggestions in 1809, when he envisioned a relative scale on which all simple substances could be ranked, calling it the scale of "oxygenicity." Over the next few years, Jacob Berzelius constructed a similar ranking, calling it the scale of "electronegativity." As theories of atomic structure progressed, the term came to mean the ability of an atom to attract and hold electrons (Jensen 1996). Linus Pauling was the first to create a quantitative scale of electronegativity, based on thermochemical data (Pauling 1932). Since then, a number of electronegativity scales have been proposed, with precise definitions based on various types of chemical and spectroscopic data, and the concept has been extended to encompass groups of atoms or even entire molecules. The fact that there is no unique definition of electronegativity has caused some to question the usefulness of the concept (Bergmann and Hinze 1996), but all these scales are highly correlated, implying they all are based on a fundamental atomic characteristic.

In this entry, we explore the origin of some of the most commonly used electronegativity scales and their applications.

Electronegativity Scales

Pauling (1932) created the first numerical electronegativity scale based on the dissociation energies of single bonds. He noted that there was considerable evidence for the proposition that the energies of normal covalent, single bonds are additive. In other words, if there are two molecules A_2 and B_2, internally held together by covalent single bonds, the dissociation energy of the molecule AB (E_{AB}) will be approximately equal to the mean of the dissociation energies of A_2 and B_2 (E_{AA} and E_{BB}). However, this is not the case when AB is ionically bonded; instead, the dissociation energy of AB is larger than the average of the other two by some amount Δ_{AB}. Pauling represented this using Eq. 1.

$$E_{AB} = \frac{E_{AA} + E_{BB}}{2} + \Delta_{AB} \tag{1}$$

Pauling constructed his electronegativity scale to follow the definition in Eq. 2, where χ_A and χ_B represent the electronegativity values of elements A and B, respectively.

$$\Delta_{AB} = (\chi_A - \chi_B)^2 \tag{2}$$

Thus, the difference in electronegativity values is related to the polarity of the bond between the two atoms, with the more electronegative atom attracting the bonding electrons to a greater extent than the other. Pauling rationalized bond polarity in terms of his valence-bond theory, in particular the resonance between the states AB, A^-B^+, and A^+B^-. That is, the relative electronegativity of the two atoms determines the degree to which some resonance states are favored over the others in the molecule. The calibration of the Pauling electronegativity scale is somewhat arbitrary, in that it is based on the assignment of $\chi = 4.0$ for F (Malito 1995). The scale has since been updated and expanded several times, based on larger sets of thermochemical data (e.g., Allred 1961).

In the Pauling definition, electronegativity is conceived as an intrinsic property of an atom, but its definition is tied to the energies of bonds between atoms. Allred and Rochow (1958), in contrast, developed an alternative scale in which electronegativity is more closely tied to a physical, though oversimplified, picture of the atom itself. Here, electronegativity is conceived as the electric force experienced by an electron on the "surface" of an atom, proportional to the force of attraction between an atomic core (nucleus + core electrons) and a valence electron in terms of a simple Coulomb's Law calculation. Specifically, the Allred-Rochow electronegativity (χ_{AR}) is proportional to the effective nuclear charge (Z_{eff}), obtained by applying Slater's rules (Slater 1930), and inversely proportional to the squared covalent radius (r_{cov}), as shown in Eq. 3, where e is the charge on an electron. The values obtained are then scaled to be comparable to the 4-point Pauling scale (Malito 1995).

$$\chi_{AR} \propto \frac{Z_{eff}e}{r_{cov}^2} \tag{3}$$

This physical picture is oversimplified, in that r_{cov} is a very rough approximation of the distance of valence electrons from the nucleus, and orbital shapes are not taken into account. Furthermore, Allred-Rochow electronegativity values can be problematic, due to the difficulty in obtaining accurate Z_{eff} and the fact that the covalent radii of transition metals lead to lower electronegativity values than other scales.

Although the Allred-Rochow scale is based on an oversimplified physical depiction of the atom, one of its advantages is that it makes a very direct link between electronegativity and its definition as the relative ability of an atom to attract electrons. The Pauling scale, in contrast, is linked to the definition more indirectly via bond dissociation energies. Another scale, the Mulliken-Jaffe electronegativity scale is similar to the Allred-Rochow scale, in that it has a direct connection to the ability of an atom to attract electrons, but the former has the advantage of being based on precisely measurable quantities. Mulliken-Jaffe electronegativity values (χ_{MJ}) are calculated by taking the arithmetic mean of an atom's first ionization energy (the energy required to remove the most loosely bound electron from the neutral atom to make a positively charged ion) and its electron affinity (the energy released when the neutral atom captures one extra electron to make a negatively charged ion). This produces a value in energy units, which is often subsequently scaled to be comparable to Pauling electronegativity values (Malito 1995).

Several other electronegativity scales are commonly used, but all of them are highly correlated with one another, especially among main group elements. Certainly this indicates that all of the precise definitions used are based on highly related atomic and molecular characteristics, but the particular definition employed determines how useful electronegativity values will be for a given application.

Electronegativity and Chemical Context

If the purpose of an electronegativity scale is to provide insight about trends in chemical reactivity, then viewing electronegativity as an intrinsic property of a certain element, rather than a property of an atom in a particular chemical environment, may prove too inflexible for some purposes.

One obvious deficiency is that electronegativity values are often presented as an unchanging property of a given element, when in fact the relative attraction of an atom for electrons should depend strongly on the oxidation state. Electronegativity values for individual oxidation states of some elements have been reported, and, at least for some definitions, there is no a priori reason why they should not be. The main obstacle, in these cases, is usually a paucity of available data for the less common oxidation states (Malito 1995).

Even for a given oxidation state of an element, electronegativity should vary somewhat with chemical context, due to the competition for electrons among all the atoms in a particular neighborhood. For example, all else being equal, the carbon atom in a trifluoromethyl group ($R–CF_3$) must hold its electrons more tightly, with respect to the rest of the molecule, than that in a methyl group ($R–CH_3$), because its association with fluorine would decrease its polarizability. Organic chemists, therefore, commonly assign "group electronegativity" values based on several methods (Mullay 1987).

Finally, the assignment of electronegativity scales to the noble gases has been particularly difficult. For those scales that attempt it, widely varying answers are obtained. While these elements are able to undergo chemical reactivity, their special natures make them difficult to analyze with such a simple model.

Electronegativity Equalization

Some of these methods for calculating group electronegativity rely on the principle of "electronegativity equalization," which

has received strong support from density functional theory (Mullay 1987). That is, as atoms come together and electron density is redistributed toward the more electronegative elements, the electronegativity values of the atoms change with their atomic charge, until all the atoms in a system have equal electronegativity values. In Sanderson's electronegativity equalization method, for example, the final electronegativity of all atoms is taken as the geometric mean of the atomic electronegativity values, and atomic partial charges are assumed to vary linearly with electronegativity (Sanderson 1983).

Sanderson was able to accurately calculate many bond dissociation energies with this method, but it presents certain problems for large molecules and condensed phases. If all atoms in a molecule have the same electronegativity value, for example, and partial charge on atoms of the same element is linked only to their electronegativity, then it follows that all atoms of the same element in a system must have the same partial charge. This contradicts the argument presented above about the behavior of methyl and trifluoromethyl groups, at least if they exist in the same molecule. Therefore, others have developed partial equilibration schemes to more adequately deal with proximity effects (Mullay 1987). Several of these schemes have been implemented to estimate partial charges in molecular mechanics calculations (Oliferenko et al. 2006).

Applications

The utility of the electronegativity concept is that it condenses complex atomic characteristics in a way that correlates with important chemical properties in an intuitively understandable manner. One can readily imagine how a property like electronegativity would affect the behavior of atoms in a molecule, so a model meant to predict some chemical behavior based on correlation with a quantity derived from electronegativity values often also provides a simple, intuitive rationale for that behavior. For instance, the distribution of charge around the atoms in a compound would obviously affect the energies of available orbitals, so it is no surprise that atomic charges calculated from electronegativity equalization correlate well with chemical shifts in X-ray photoelectron spectroscopy data (Bergmann and Hinze 1996). Charge distribution obviously affects bond energies (Pauling 1932), so it is no surprise that the ionic character of a bond is an important predictor of equilibrium constants for acid dissociation reactions (Li 2000; Bickmore et al. 2004). Similar arguments can be made for the relationships between electronegativity and stretching force constants, bond lengths, and many other properties (Bergmann and Hinze 1996).

Summary and Conclusions

The definition of electronegativity, the power of an atom to attract electrons, may be somewhat vague, but it has nevertheless proven to be an extremely useful concept in chemistry and geochemistry. Certainly we have available more rigorous theoretical constructs, like quantum mechanics, but given the difficulty in applying rigorous theory in some contexts, simpler, more intuitive constructs are warranted for creating models of chemical behavior. Furthermore, intuitive concepts like electronegativity are useful as a means to facilitate fluent thinking about chemical problems (Brown 2003).

Although electronegativity is usually presented as an invariant atomic property, it nevertheless depends strongly on the chemical context. Oxidation state and the electronegativity of surrounding atoms, for instance, both affect the attraction of a particular atom for electrons. In fact, it has been shown that the electronegativity values of atoms in a compound at least partially equilibrate with one another, and several electronegativity equilibration schemes have proven useful for calculating on-the-fly atomic charges for molecular simulations.

Cross-References

- ▶ Chemical Bonds
- ▶ Equilibrium Constant

References

Allred AL (1961) Electronegativity values from thermochemical data. J Inorg Nucl Chem 17:215–221

Allred AL, Rochow EG (1958) A scale of electronetativity based on electrostatic force. J Inorg Nucl Chem 5:264–268

Bergmann D, Hinze J (1996) Electronegativity and molecular properties. Angew Chem Int Ed Engl 35:150–163

Bickmore BR, Tadanier CJ, Rosso KM, Monn WD, Eggett DL (2004) Bond-valence methods for pK_a prediction: critical reanalysis and a new approach. Geochim Cosmochim Acta 68:2025–2042

Brown TL (2003) Making truth: metaphor in science. University of Illinois Press, Urbana. 215 p

Jensen WB (1996) Electronegativity from Avogadro to Pauling. Part I. Origins of the electronegativity concept. J Chem Educ 73:11–20

Li Y-H (2000) A compendium of geochemistry: from solar nebula to the human brain. Princeton University Press, Princeton. 475 p

Malito J (1995) A plethora of electronegativity scales. Chim Oggi Chem Today 13:57–64

Mullay J (1987) Estimation of atomic and group electronegativities. Struct Bond 66:1–25

Oliferenko AA, Pisarev SA, Palyulin VA, Zefirov NS (2006) Atomic charges via electronegativity equalization: generalizations and perspectives. Adv Quantum Chem 51:139–156

Pauling L (1932) The nature of the chemical bond IV. The energy of single bonds and the relative electronegativity of atoms. J Am Chem Soc 54:3570–3582

Sanderson RT (1983) Polar Covalence. Academic, New York. 240 p

Slater JC (1930) Atomic shielding constants. Phys Rev 36:57–64

Elements: Metalloids

David A. Dixon and Monica Vasiliu
Department of Chemistry, University of Alabama, Tuscaloosa, AL, USA

Definition

The metalloids comprise a group of main group elements found along the stair-step line that divides metals (transition metals and other metals) and the nonmetals. The metalloids usually include B (Group 13) in the first row, Si (Group 14) in the second row, Ge (Group 14) and As (Group 15) in the third row, Sb (Group 15) and Te (Group 16) in the fourth row, and At (Group 17) in the fifth row.

Overview

The metalloid are main group elements that are at the border of solids that are metallic (itinerate electrons that are shared freely among the atoms) in contrast to those that are covalent with chemical bonds. Note that as one proceeds down the Periodic Table, the metalloids move to the right in the Table.

The metalloids exhibit mixed properties as they are solids and may even look metallic but may not conduct electricity and heat in the same way as a metal. For example, silicon looks like a metal as it is shiny, but it is not malleable like a metal, and is a poor conductor of heat and electricity. The metalloids can exhibit different crystal structures. For example, white tin is a metallic conductor with a tetragonal crystal structure, whereas below 13 °C, it is known as gray tin and forms a powder with the diamond crystal structure and is a poor conductor. A number of the metalloids are semiconductors as they have intermediate conductivity which is temperature dependent. The ability of the metalloids to conduct electricity and heat is far better than the nonmetals, for example, diamond, which are insulators. As such, the metalloids play a major role in the electronics industry, and modern society is built around the properties of the metalloids and their compounds.

These elements can be quite toxic and are associated with ore formation and hydrothermal chemistry. Thus, compounds of the metalloids play an important role in geochemistry as their compounds make up much of the Earth's surface, for example, the critical role of silicon oxides in geochemical systems. As another example, there is an important role for boron in geochemical systems, and boron isotope fractionation factors play an important role in understanding paleoclimates as the equilibrium constant for the isotope exchange reaction

$$^{10}B(OH)_3(aq) + {}^{11}B(OH)_4^-(aq) \leftrightarrow {}^{11}B(OH)_3(aq) + {}^{10}B(OH)_4^-(aq)$$

is the basis for a method commonly used to infer the pH of the ancient oceans and, hence, the PCO_2 of the ancient atmosphere (Hemming and Hanson 1992; Spivack et al. 1993; Sanyal et al. 1995; Rustad et al. 2010).

Silicon is the most abundant of the metalloids on Earth, and it is the second most abundant element in the Earth's crust after oxygen. Tellurium is the least abundant among the nonradioactive metalloids, and it is one of the rarest stable elements on Earth with an abundance similar to platinum.

Because the metalloid elements are in different columns in the Periodic Table, the properties and reactivity of these elements are quite different from each other due to having different numbers of valence electrons. Boron with three valence electrons forms trivalent molecules with an empty 2p orbital which often makes its compounds good Lewis acids, electron pair acceptors. Boron also forms electron-deficient bonds in compounds such as the boron hydrides. Silicon with four valence electrons forms tetravalent compounds but can expand its valency up to six, for example, SiF_6^{2-} which is important in the fluoridation of water (Jagtap et al. 2012; Urbansky 2002). Germanium with four valence electrons is also tetravalent and like silicon can expand its valency up to six. Arsenic with five valence electrons forms both trivalent and pentavalent compounds as does antimony. The pentafluorides of As (AsF_5) and Sb (SbF_5) are very strong Lewis acids (Christe et al. 2000; Dagani 2003), and SbF_5 with FSO_3H is the basis of magic acid, a super Brönsted acid (Olah et al. 2009). Tellurium can form divalent, tetravalent, and hexavalent compounds. Little is known about the chemistry of astatine, but as it is in the halogen column with seven valence electrons, it would be expected to be able to form mono-, tri-, penta-, and heptavalent compounds.

Conclusions

Metalloids have properties of both metals and nonmetals. Metalloids are solids under standard conditions and can appear to be metallic in appearance, but they are brittle and generally form alloys with metals. They usually do not conduct heat or electricity that well in many forms. Some of the metalloids (silicon and germanium) are semiconductors making them useful in chips for the semiconductor industry. Other metalloids are often used as dopants for semiconductor manufacturing. Because of the variation in the number of valence electrons, the chemistry of these elements can be very different. Overall compounds containing the metalloids are mostly nonmetallic in their properties.

References

Christe KO, Dixon DA, McLemore DK, Wilson WW, Sheehy J, Boatz JA (2000) On a quantitative scale for Lewis acidity and recent progress in polynitrogen chemistry. J Fluor Chem 101:151–153

Dagani R (2003) Feast for Fluorine Aficionados. Chem Eng News Mar 3, pp. 44–49

Hemming NG, Hanson GN (1992) Boron isotopic composition and concentration in modern marine carbonates. Geochim Cosmochim Acta 56:537–543

Jagtap SM, Yenkie K, Labhsetwar N, Rayalu S (2012) Fluoride in drinking water and defluoridation of water. Chem Rev 112:2454–2466

Olah GA, Prakash S, Molnar A, Sommer J (2009) Superacid chemistry, 2nd edn. Wiley, New York

Rustad JR, Bylaska EJ, Jackson VE, Dixon DA (2010) Calculation of boron-isotope fractionation between $B(OH)_3$(aq) and $B(OH)_4^-$(aq). Geochim Cosmochim Acta 74:2843–2850

Sanyal A, Hemming NG, Hanson GN, Broecker WS (1995) Evidence for a higher pH in the glacial ocean from boron isotopes in *Foraminifera*. Nature 373:234–236

Spivack AJ, You C-F, Smith HJ (1993) *Foraminiferal* boron isotope ratios as a proxy for surface ocean pH over the past 21-myr. Nature 363:149–151

Urbansky ET (2002) Fate of fluorosilicate drinking water additives. Chem Rev 102:2837–2854

Enthalpy

Carl O. Moses
Provost and Vice President for Academic Affairs, Grand View University, Des Moines, IA, USA

Enthalpy (from the Greek root for "heat"), H, is a thermodynamic function that provides a measure of the energy in a system. Enthalpy is fundamentally important to geochemistry owing to its relationship to heat capacity (see ▶ Geochemical Thermodynamics), its role in defining and giving the temperature dependence of free energy (see ▶ Free Energy), and its relationship to the entropy of the system's surroundings (see ▶ Entropy). The conditions under which H represents a system's energy are different from those under which internal energy, U (see ▶ Geochemical Thermodynamics), represents the energy of the same system. In fact, U is the basis for the definition of enthalpy, $H \And \equiv 6; U + PV$, so a brief background discussion of U is warranted.

The first law of thermodynamics (Eq. 1), in which q is heat and w is work, is the basis for measuring energy changes.

$$\Delta U = q + w \tag{1}$$

Measuring changes in U entails partitioning the work term into P-V (pressure-volume) work ($w = -P\,\mathrm{d}\,V$) and another form of work (e.g., electrical work, w_e) that can be measured to give the energy change for the process in question (Eq. 2).

$$\Delta U = q + w_e - \int P\,\mathrm{d}V \tag{2}$$

Because q cannot be measured, calorimeters are well insulated so that processes are as adiabatic as possible ($q \to 0$). In principle, one could measure $\int P\,\mathrm{d}V$, but it is generally more practical to make $\mathrm{d}V = 0$ (i.e., a constant volume process) so that Eq. 2 yields $\Delta U = w_e$. Such measurements are called constant volume calorimetry (see ▶ Calorimetry).

An alternative measurement of the energy in a system is obtained if P is held constant. In the adiabatic limit, Eq. 2 gives, under constant pressure conditions,

$$\begin{aligned} \Delta U &= w_e - P\Delta V \\ &= w_e - \left(PV_f - PV_i\right), \end{aligned} \tag{3}$$

where the subscripts f and i denote the final and initial states, respectively, of the system. Because V is a state function, the potentials PV_f and PV_i depend only on the states and are independent of the means by which the system is transformed from initial to final state. Similarly, $\Delta U = U_f - U_i$, and rearranging Eq. 3 gives $(U_f + PV_f) - (U_i + PV_i) = w_e$. Thus, the constant pressure calorimetric measurement is $w_e = \Delta(U + PV)$ or $w_e = \Delta H$. Because the difference between constant volume and constant pressure conditions is so fundamental, it is convenient to use U and $H = U + PV$ to obtain different measures of energy in the system. In general, the enthalpy function is more relevant to geochemical processes than internal energy because very few natural systems operate at constant volume.

Differentiating the definition of enthalpy gives

$$\mathrm{d}H = \mathrm{d}U + P\,\mathrm{d}V + V\,\mathrm{d}P. \tag{4}$$

Equation 1 can be written $\mathrm{d}U = q - P\,\mathrm{d}V$, excluding all forms of work besides P-V work, so Eq. 4 can be rewritten as $\mathrm{d}H = q + V\,\mathrm{d}P$, an alternative statement of the first law. Another first law statement is obtained from Eq. 4 when the state function entropy, S, is introduced (see ▶ Entropy), and Eq. 1 written $\mathrm{d}U = T\,\mathrm{d}S - P\,\mathrm{d}V$: $\mathrm{d}H = T\,\mathrm{d}S + V\,\mathrm{d}P$.

By convention, the enthalpy of elements in the standard state (usually 298 K, 1 bar) is 0. For compounds or elements in a state other than the standard state, the standard state enthalpy of formation (from the standard state elements), Δ^0_f, represents the energy of making the bonds of the compound and, therefore, stored in those bonds. For example, graphite, the standard state form of elemental carbon, has

Originally published in: Marshall CP, Fairbridge RW (eds) Encyclopedia of Geochemistry, Springer Netherlands, 1999

$\Delta H^0_f = 0$, while for diamond, $\Delta H^0_f = 1.9$ kJ/mol, indicating that converting the planar trigonal bonds of a mole of graphite into the tetrahedral bonds of diamond requires 1.9 kJ. Thus, the diamond bonds are "stronger" than those of graphite by that amount. Note that, although diamond is a polymorph of elemental carbon, it is not the standard state form, so its ΔH^0_f is nonzero.

Generally, a convenient notation includes a subscript on ΔH^0, where the superscript 0 denotes standard state, which indicates the process (e.g., chemical reaction, phase transition) for which the enthalpy change is calculated:

$$\Delta H^0_{\text{process}} = \sum \nu_i \Delta H^0_{f,i},$$

where the ν_i are the stoichiometric coefficients of the constituents of the system in the final state (e.g., reaction products, $\nu_i > 0$) or the initial state (e.g., reactants, $\nu_i < 0$). For example, the evaporation of liquid water, $H_2O_{(l)} = H_2O_{(g)}$, involves an enthalpy change given by $\Delta H^0_{\text{evap}} = \Delta H^0_{f,} H_2O_{(g)} - \Delta H^0_{f,H\ 2}O_{(l)} = (-241.8) - (-285.8) = 44$ kJ/mol at 298 K. Because $\Delta H^0_{\text{evap}} > 0$, it is said to be an endothermic process, one in which the final state (water vapor) has greater energy than the initial state. Equation 4 shows that, at constant pressure, this energy must be in the form of heat. Another example: the enthalpy change for the quartz-fayalite-magnetite O_2-buffer reaction, $3Fe_2SiO_{4(fay)} + O_2(g) = 2Fe_3O_{4(mag)} + 3SiO_{2(qtz)}$ is given by

$$\Delta H^0_{\text{QFM}} = \left(2\Delta H^0_{f,\text{mag}} + 3\Delta H^0_{f,\text{qtz}}\right) - \left(3\Delta H^0_{f,\text{fay}} + 0\right) = -529.9\,\text{kJ/mol}$$

at 298 K. For this reaction, $\Delta H^0_{\text{QFM}} < 0$, indicating an exothermic process that releases energy to the surroundings (as heat at constant pressure) and yielding a final state with less energy than the initial state.

Like most properties of condensed phases (solids and liquids), enthalpy has only a weak pressure dependence, but the pressure dependence for gases can be quite strong. The differential expression of the isothermal pressure dependence of enthalpy, $(\partial H/\partial P)_T$ can be inverted to give $-(\partial T/\partial P)_H(\partial H/\partial T)_P$. At constant pressure, Eq. 4 shows that $dH = q$ or $dH = dq$. Because constant pressure heat capacity is defined as $C_P = (\partial q/\partial T)_P$ (see ▶ Geochemical Thermodynamics), we have the isobaric (constant pressure) temperature dependence of enthalpy: $(\partial H/\partial T)_P = C_P$. Thus the isothermal pressure dependence of enthalpy becomes $-(\partial H/\partial P)_H C_P$. Finally, the isenthalpic pressure dependence of temperature, $(\partial T/\partial P)_H$, is known as the Joule-Thomson coefficient, μ_{JT}, so we have $(\partial H/\partial P)_T = -\mu_{JT} C_p$.

Enthalpy is temperature dependent in both gases and condensed phases. If C_p is independent of T over the temperature range of interest, i.e., $C_p \neq f(T)$), integration of $(\partial H/\partial T)_P = C_p$ gives the simple relationship $\Delta H = C_P \Delta T$ or $H_{T2} = H_{T1} + C_P \Delta T$. If, however, $C_p = f(T)$, an analytical function for the T dependence of C_p must be substituted and integrated.

Another important relationship can be derived for the temperature dependence of enthalpy, this one for isochoric (constant volume) temperature dependence, $(\partial H/\partial T)_V$; although we will not pursue the complete derivation here. The isobaric thermal expansivity, α, is given by $(1/V)(\partial V/\partial T)_P$, and the isothermal compressibility, k, is given by $-(1/V)(\partial V/\partial T)_T$. If we begin by writing a total differential for $H = f(T, P)$, $dH = (\partial H/\partial P)_T\, dP + (\partial H/\partial T)_P\, dT$, we can derive $(\partial H/\partial T)_V = [1 - (\alpha\mu_{JT}/k)]C_p$.

E

Cross-References

- ▶ Activation Parameters: Energy, Enthalpy, Entropy, and Volume
- ▶ Chelation
- ▶ Entropy
- ▶ Equilibrium
- ▶ Free Energy
- ▶ Geochemical Thermodynamics
- ▶ Kinetics of Geochemical Processes

References

Anderson GM, Crerar DA (1993) Thermodynamics in geochemistry. The equilibrium model. Oxford University Press, New York. 588 pp

Atkins PW (1986) Physical chemistry, 3rd edn. W. H. Freeman, New York. 857 pp

Nordstrom DK, Munoz JL (1994) Geochemical thermodynamics, 2nd edn. Blackwell, Cambridge. 493 pp

Robie RA, Hemingway BS, Fisher JR (1978) Thermodyna mic properties of minerals and related substances at 298.15 K and 1 Bar (10^5Pascals) pressure and at higher temperatures, US Geological Survey bulletin, vol 1452. US Government Printing Office, Washington, DC, p 456

Entropy

Carl O. Moses
Provost and Vice President for Academic Affairs, Grand View University, Des Moines, IA, USA

Introduction and Definition

The Greek word εντροπε refers to a property that indicates the direction of change. In thermodynamics, the entropy function, *S,* provides the criteria for predicting the direction

Originally published in: Marshall CP, Fairbridge RW (eds) Encyclopedia of Geochemistry, Springer Netherlands, 1999

of spontaneous natural processes and the equilibrium state of a system. Entropy is a state function, which means that its value is determined by the state of a system and is independent of the process or path by which the system arrived at its state.

Background and Framework

The need for a function such as entropy arises from the fact that the zeroth and first laws of thermodynamics (see ▶ "Geochemical Thermodynamics") fail to explain the direction of natural processes. The zeroth law introduces the concept of thermal equilibrium and provides a basis for temperature measurements, while the first law is a statement of the conservation of energy principle and the interconvertibility of heat (q) and work (w). Heat exchange and work contribute to changes in the internal energy (U) of a system. The first law gives us a tool for meeting one of the principal objectives of thermodynamics: keeping track of energy changes in a system (Eq. 1).

$$\Delta U = q + w \tag{1}$$

A system is a region whose boundaries can be specified. A system's surroundings only include those entities with which it actually interacts, and we define the sum of the system and its surroundings as a thermodynamic universe (not the same as the cosmologic Universe; thermodynamics does not presume to apply on such vast scales). Accordingly, a universe is itself an isolated system (one that does not interact with its surroundings). We can quantify an extensive property (one that depends on the amount of substance present) of a universe by adding the contribution from the system of interest and the contribution from the system's surroundings. For example, $\sum S = S^{\text{univ}} = S^{\text{sys}} + S^{\text{surr}}$.

The Thermodynamic Concept of Entropy

As important as it is to quantify the conservation of energy principle, the first law cannot explain why natural processes proceed spontaneously in one direction only. For example, why is heat spontaneously transferred from a warm object to a colder object, and why do we never observe the cold object to transfer some of its heat spontaneously to the warmer object? One of the earliest statements of the second law, attributed to Rudolph Clausius, holds that there exists no process in which the sole result is the transfer of heat from a cooler to a hotter body. Another early statement, attributed to William Thomson, Lord Kelvin, holds that there exists no process in which the sole result is the complete conversion of heat absorbed by a system into work. Clausius' statement emphasizes the unidirectional nature of natural spontaneous processes while Kelvin's emphasizes the idea that energy is degraded when it is transferred as heat, so not all of the absorbed heat is available for work. The interconvertibility of heat and work is thus asymmetrical. Because energy is conserved. Kelvin's degradation of energy requires a quantity (a potential) into which energy can be converted but not recovered, which is Clausius' unidirectional change.

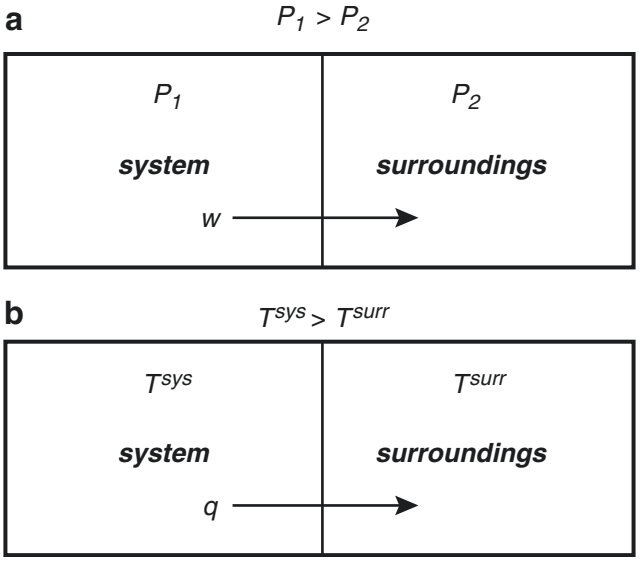

Entropy, Fig. 1 (**a**) In response to a pressure gradient, the system transfers energy to its surroundings by expanding and, thereby, doing work on the surroundings. The heavy line encloses a universe, and the system is separated from its surroundings by a movable or deformable partition. (**b**) In response to a temperature gradient, the system transfers energy to its surroundings as heat. As in (**a**), the heavy line encloses a universe, but here the system is separated from its surroundings by a rigid, unmovable wall

Consider a mechanical analog that provides a basis for analyzing the second law (Fig. 1a). The apparatus is enclosed by rigid unmovable walls and is well insulated, so it is a universe. Energy will be transferred from the system to its surroundings as the system's volume expands against the lower pressure of the surroundings. The amount of work done by the system on its surroundings is proportional to the change in volume of the system: $w \propto -\Delta V$. Pressure gives the magnitude of the proportionality (higher pressure yields greater work for a given volume change), hence $w = -P\Delta V$.

Decompression may be carried out reversibly or irreversibly (Fig. 2). The irreversible process takes place by, for example, a combination of isothermal and isobaric steps. The changes in P, T, and V are finite, and derivatives relating P, T, V, and U (e.g., dP/dT) are undefined. ΔV or ΔU can be calculated from the P and T coordinates of any pair of intermediate states along the path using an equation of state, relying on the fact that V and U are state functions and $\Delta V = V_f - V_i$ and $\Delta U = U_f - U_i$, regardless of the sequence of

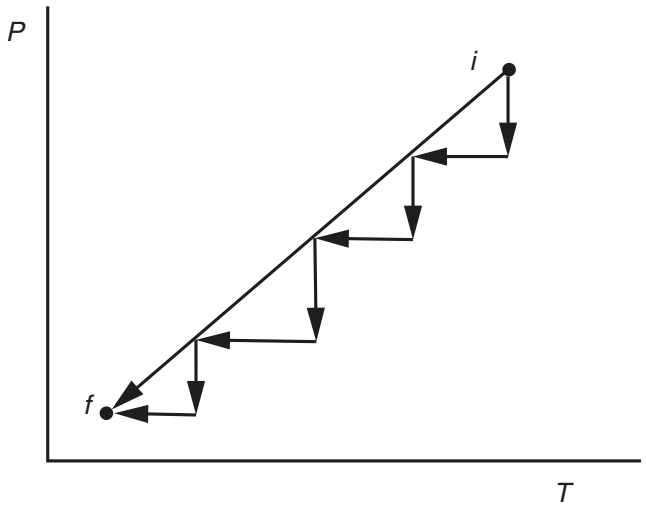

Entropy, Fig. 2 Decompression of the system in Fig. 1a, from initial state *i* to final state *f,* in *P-T* coordinates. There is one reversible path (*the diagonal arrow*); an irreversible path, comprising one set of the infinite number of irreversible steps between *i* and *f,* is also shown

steps (*f* and *i* denote final and initial states, respectively). During an isothermal decompression step, the system must absorb heat from the surroundings ($q^{sys} > 0$), while during an isobaric cooling step, the system must transfer heat to the surroundings ($q^{sys} < 0$). For irreversible processes, $w = \Delta U - q$ depends on the net heat exchange between system and surroundings, so the work depends on the character of the path rather than the change in state of the system. Because we can know ΔV_j and P_j for each j step of the irreversible process, we can calculate w_j for each step, and the total work is given by $w_{irrev} = -\Sigma P_j \Delta V_j$.

If we make the isothermal and isobaric steps increasingly smaller, $\Delta P \rightarrow dP$, $\Delta T \rightarrow dT$ (accordingly, $\Delta V \rightarrow dV$ and $\Delta U \rightarrow dU$, the behavior of the system approaches reversibility. The reversible process is continuous, and derivatives like dP/dT are defined. As a consequence of the infinitesimal size of the steps, $q \rightarrow 0$. The reversible behavior of the system is singular, because there can be only one path in which the steps are infinitely small. Now, $w_{rev} = \Delta U$ because no heat is exchanged between system and surroundings, but w is no less dependent on path than before because we have stipulated a very specific path. As the steps become infinitesimal, the summation used for the total work becomes an integral, so $w_{rev} = -\int_i^f P\, dV$, and $dw_{rev} = -P dV$. Because no heat is exchanged, all of the energy of the system is available for work, so $w_{max} = w_{rev}$ and for any arbitrary process, $w \leq w_{rev}$.

Now consider a universe in which the system is separated from its surroundings by a unmovable diathermal wall (one that readily permits heat exchanges but does not permit work; Fig. 1b). If heat is transferred in infinitesimal increments (dq) by allowing the temperature of the system and its surroundings to differ only very slightly, the heat transfer can be made reversible. This energy transfer is completely analogous to the case of the pressure gradient, but now energy is transferred down the gradient as heat rather than work, entropy change is the quantity analogous to volume change, and in place of $w \propto -\Delta V$, we have $q_{rev}^{sys} \pi \Delta S^{sys}$. Because higher temperatures yield greater heat transfer for a given entropy change, T determines the magnitude of the proportionality between the heat transfer and the entropy change, and $dq_{rev}^{sys} = T\, dS^{sys}$. Whether applied to the system or to the surroundings, the defining expression for entropy holds that entropy is the state function whose differential is given by the reversible transfer of heat divided by temperature (Eq. 2).

$$dS = \frac{dq_{rev}}{T} \tag{2}$$

We might similarly say that volume is the state function whose differential is given by work divided by pressure [$dV = (-dw_{rev}/P$]. Both expressions emphasize the relationships between energy changes as work or heat and corresponding changes in volume (energy/pressure) or entropy (energy/temperature). A given amount of work (heat) creates a larger volume (entropy) change in a system of lower pressure (temperature).

Because work and heat are both potentials, dw and dq correspond to the potential gradients P dV and T d*S,* and PV and TS are potentials. With entropy defined and work restricted to volume changes, the first law may be written as $dU = T\, dS - P\, dV$ (each of *U, S,* and *V* is measured for the system), a form that is sometimes called the first part of the second law of thermodynamics.

The Clausius Inequality

Reversibility means that a transfer of energy between the system and its surroundings can be reversed without changing the state of the surroundings. At every stage of the process, the system and its surroundings are in equilibrium. Reversibility is an idealization, but one that can be approached very closely in many systems often well within the limits of measurement error; it is a pragmatically viable concept. In the reversible heat transfer example above, the heat transferred from the system to the surroundings was exactly balanced by the heat gain in the surroundings. We can write $dq_{rev}^{sys} = -dq_{rev}^{surr}$ or $dq_{rev}^{sys}/T = -dq_{rev}^{surr}/T$, so $dS^{sys} = -dS^{surr}$. We conclude that $dS^{univ} = dS^{sys} + dS^{surr} = 0$ for a reversible process.

What if we carry out the heat transfer irreversibly? In this case, the process could not be reversed without causing a definite change in the state of the surroundings. Because no change results to the state of the surroundings in a reversible process, the change in the state of the surroundings must be larger for an irreversible process than for a reversible one.

From the point of view of the system, therefore, $dq^{sys}_{irrev} < dq^{sys}_{rev}$ (generally, $dq^{sys} \leq dq^{sys}_{rev}$, just as we concluded for work in the previous section), which means that $dq^{sys}_{irrev}/T < dq^{sys}_{rev}/T$ and $dq^{sys}_{irrev}/T < dS^{sys}$. Generally, $dq^{sys}/T \leq dS^{sys}$; the "<" condition applies to irreversible processes, while the "=" condition applies to reversible processes. Because S is a state function, $\oint dS^{sys} = 0$, where the $\oint$ denotes a loop integral and implies a path from state A to state B to state A (i.e., a cycle in which the final state is congruent with the initial state). Accordingly, $\oint dq^{sys}_{rev}/T = 0$, but generally,

$$\oint \frac{dq^{sys}}{T} \leq 0. \tag{3}$$

If we take a system from an initial state i to a final state f by an arbitrary process, which may be reversible or irreversible, and then return it to i by a reversible process, we can write:

$$\oint \frac{dq^{sys}}{T} = \int_i^f \frac{dq^{sys}}{T} + \int_f^i \frac{dq^{sys}_{rev}}{T}.$$

The second term on the right hand side is equivalent to $-\int_i^f dS^{sys} = -\Delta S^{sys}$ (switching the limits of integration while changing the sign is legitimate only for a state function), so:

$$\oint \frac{dq^{sys}}{T} = \oint_i^f \frac{dq^{sys}}{T} - \Delta S^{sys}. \tag{4}$$

By combining Eqs. 3 and 4,

$$0 \geq \int_i^f \frac{dq^{sys}}{T} - \Delta S^{sys},$$

or

$$\Delta S^{sys} \geq \int_i^f \frac{dq^{sys}}{T}, \tag{5}$$

which is the Clausius, or fundamental, inequality. In an isolated system, $dq^{sys} = 0$ always, and because an isolated system is the same as a universe, the Clausius inequality leads to $\Delta S^{univ} \geq 0$, which is the second part of the second law. A spontaneous process in a universe must be irreversible (i.e., caused by an internal potential gradient), so $\Delta S^{univ} > 0$. For a universe at equilibrium (no internal gradients), $\Delta S^{univ} = 0$. The second part of the second law provides the criterion for the direction of spontaneous processes (the direction that yields an increase in the entropy of a universe) and the criterion for equilibrium (the state in which the entropy of a universe remains constant). There are no known processes that cause a decrease in the entropy of a universe. Energy must be conserved, but S^{univ} is a very different sort of function because it is conserved only under the special conditions of the equilibrium state; if there are internal gradients, entropy will be generated!

Using the Second Law Entropy Criteria for Direction and Equilibrium

Only the sum of ΔS^{sys} and ΔS^{surr} must be ≥ 0, so it is possible for $dS^{sys} \leq 0$. For a spontaneous process, any decrease in S^{sys} must be accompanied by an offsetting increase in S^{surr}, and at equilibrium, where $dS^{univ} = 0$, $dS^{sys} = -dS^{surr}$ (including the possibility that both dS^{sys} and dS^{surr} are zero). Because the second law criteria for direction and equilibrium are expressed only in terms of dS^{univ}, it seems that we need to know something about both dS^{surr} and dS^{sys} in order to use those criteria.

Because TS^{sys} represents a potential quantity unavailable for doing work, we define free energy as the net energy available for doing work. With two measures of the total energy in a system (internal energy, U, and enthalpy, H; see ▶ "Enthalpy"), there are two measures of free energy: $A \equiv U - TS^{sys}$ and $G \equiv H - TS^{sys}$ (see ▶ "Free Energy"). For our present purposes, we will concentrate on G, which is called Gibbs free energy. In differential form and under isothermal conditions ($dT = 0$),

$$dG = dH - T\,dS^{sys}. \tag{6}$$

Each quantity in Eq. 6 is a property of the system. Is there a way to use free energy to determine the direction of spontaneous processes or equilibrium?

For an arbitrary (reversible or irreversible) isothermal process, $dS^{surr} = dq^{surr}/T = -dq^{sys}/T$. Summing the contributions to dS^{univ} from the system and the surroundings and referring to the second part of the second law,

$$dS^{univ} = dS^{sys} - \frac{dq^{sys}}{T} \geq 0. \tag{7}$$

With Eq. 7 we can express dS^{univ} in terms of quantities measured for the system, but we need a proxy for dq^{sys} because we cannot measure q. Under constant pressure conditions, $dq^{sys} = dH$, so we can write $dS^{sys} - dH/T \geq 0$, identifying $-dH/T$ with dq^{surr} and dS^{surr}. With this identity and the result of dividing Eq. 6 by $-T$, we have an expression that is congruent with $dS^{univ} = dS^{surr} + dS^{sys}$ (Eq. 8; an analogous expression can be established for A and U).

$$\frac{-dG}{T} = \frac{-dH}{T} + dS \tag{8}$$

Equation 8, in which G, H, and S are all properties of the system, is one of the most important equations in chemical thermodynamics, and it allows us to translate the second law criteria for direction and equilibrium into free energy terms: $-\mathrm{d}G/T \geq 0$. Spontaneous processes lead to minimizing G ($\mathrm{d}G < 0$), and at equilibrium, $\mathrm{d}G = 0$.

Measuring Entropy

For entropy to be a useful function, we need a way to measure it. From Eq. 2, a system heated from an initial temperature T_i to a final temperature T_f, must undergo an entropy change given by:

$$\Delta S^{\mathrm{sys}} = \int_{T_i}^{T_f} \frac{\mathrm{d}q_{\mathrm{rev}}^{\mathrm{sys}}}{T}.$$

If we treat T_i as a reference temperature (T_{ref}), we define a scale of entropy measurements, and for any T,

$$S_T^{\mathrm{sys}} = S_{T_{\mathrm{ref}}}^{\mathrm{sys}} + \int_{T_{\mathrm{ref}}}^{T} \frac{\mathrm{d}q_{\mathrm{rev}}^{\mathrm{sys}}}{T}.$$

Given that constant pressure heat capacity C_p is defined as $(\partial q/\partial T)_{\mathrm{P}}$ (see ▶ "Heat Capacity"), we have:

$$S_T^{\mathrm{sys}} = S_{T_{\mathrm{ref}}}^{\mathrm{sys}} + \int_{T_{\mathrm{ref}}}^{T} \frac{C_P \mathrm{d}T}{T}. \tag{9}$$

If $C_p \neq f(T)$, Eq. 9 gives $S_T^{\mathrm{sys}} = S_T^{\mathrm{sys}} + C_p \ln(T/T_{\mathrm{ref}})$. Over temperature ranges for which $C_p = f(T)$, we need at temperature-dependent expression for C_p that is integrated in Eq. 9. If the temperature range spans a phase transition, an entropy change $\Delta S_{\mathrm{trans}}^{\mathrm{sys}} = \Delta H_{\mathrm{trans}}/T_{\mathrm{trans}}$ must be added to Eq. 9. A rational choice for T_{ref} is 0 K, so a complete expression for the entropy of a gas (i.e., $T > T_{\mathrm{boil}}$) is:

$$S_T^{\mathrm{sys}} = S_0^{\mathrm{sys}} + \int_0^{T_{\mathrm{melt}}} \frac{C_P^{\mathrm{solid}} \mathrm{d}T}{T} + \frac{\Delta H_{\mathrm{melt}}}{T_{\mathrm{melt}}} + \int_{T_{\mathrm{melt}}}^{T_{\mathrm{boil}}} \frac{C_P^{\mathrm{liquid}} \mathrm{d}T}{T} + \frac{\Delta H_{\mathrm{vap}}}{T_{\mathrm{boil}}} + \int_{T_{\mathrm{boil}}}^{T} \frac{C_P^{\mathrm{gas}} \mathrm{d}T}{T}$$

For a liquid ($T_{\mathrm{melt}} < T < T_{\mathrm{boil}}$), the last two terms are not needed, and the second integration is carried from T_{melt} to T; for a solid ($T < T_{\mathrm{melt}}$), the last four terms are not needed, and the first integration is carried from 0 to T. In practice, C_p data for the lowest temperatures ($<\sim$10 K) are extrapolated from a function like aT^3, which is fitted to C_p data for temperatures up to ~50 K.

The third law of thermodynamics holds that all pure substances have the same entropy at $T = 0$ K. Thus, for all pure substances, S_0^{sys}, the reference entropy, is the same. For convenience, we use $S_0^{\mathrm{sys}} = 0$. The so-called absolute entropies of substances, S_T^{sys}, are given the symbol S_T^0 and have units of energy/temperature/amount (e.g., J/K/mol).

Values of S_T^0, based on calorimetric and heat capacity measurements, are tabulated and can be used to calculate standard state entropy changes, ΔS_R^0, for reactions. Entropy changes in processes are calculated from:

$$\Delta S_{\mathrm{process}}^0 = \sum \nu_j \Delta S_{T,j}^0,$$

where the ν_j are the stoichiometric coefficients of the constituents of the system in the final state (e.g., reaction products, $\nu_j > 0$) or the initial state (e.g., reactants, $\nu_j < 0$). The subscript R may be substituted by a more informative subscript denoting the specific process in question (e.g., melt or boil). Note that S_T^0 is not the same as $\Delta S_f{}^0$. By convention, the ΔG_f^0 for an element in the standard state (usually 298 K, 1 bar) is 0, as are ΔH_f^0 and ΔS_f^0. Absolute entropy gives the entropy change for a substance from 0 K to T, so $S_T^0 > 0$. Furthermore, for a nonelement, S_T^0 includes the entropy of formation, ΔS_f^0, of that substance plus the absolute entropies of its constituent elements. For example, at 298 K, graphite, the standard state form of elemental carbon, has $\Delta H_f^0 = \Delta G_f^0 = \Delta S_f^0 = 0$, while for diamond, $\Delta H_{f,\mathrm{dia}}^0 = 1.9$ kJ/mol and $\Delta G_{f,\mathrm{dia}}^0 = 2.9$ kJ/mol. The difference, 1 kJ/mol, is the potential $-T\Delta S_{f,\mathrm{dia}}^0$, so $\Delta S_{f,\mathrm{dia}}^0 = -3.36$ J/mol/K. Note that $\Delta S_{f,\mathrm{dia}}^0 = S_{\mathrm{dia}}^0 - S_{\mathrm{gra}}^0 = (2.38 - 5.74)$ J/mol/K. Values of ΔS_f^0 are not usually tabulated. In calculating ΔS_R^0, this distinction is transparent. For the graphite = diamond transition,

$$\begin{aligned}\Delta S_R^0 &= S_{\mathrm{dia}}^0 - S_{\mathrm{gra}}^0 = (2.38 - 5.74)\,\mathrm{J/mol/K} \\ &= \Delta S_{f,\,\mathrm{dia}}^0 - \Delta S_{f,\,\mathrm{gra}}^0 = -3.36 - 0\,\mathrm{J/mol/K}\end{aligned}$$

It is important to recognize, however, that the distinction matters in calculations of ΔS_f^0 for nonelements, which are in turn required with values ΔH_f^0 of in calculations of ΔG_f^0.

Clapeyron Equation

Entropy has practical utility beyond providing criteria for the direction of spontaneous change and equilibria. If we remove the isothermal constraint used in deriving Eq. 6 and substitute $\mathrm{d}H = T\,\mathrm{d}S + V\,\mathrm{d}P$, we have:

$$\mathrm{d}G = V\,\mathrm{d}P - S\,\mathrm{d}T \tag{10}$$

(see ▶ "Free Energy" for more discussion of the derivation of Eq. 10). Then, if we define chemical potential, μ, as the partial molar Gibbs free energy of a substance j, $\mu_j = (\delta G/\delta n_j)_{T,P,nk \neq j}$ (the subscripts denote constant pressure, temperature, and composition; see ▶ "Free Energy"

and ▶ Geochemical thermodynamics), Eq. 10 can be rewritten in terms of $\mu(P,T)$: $\mu_j = \overline{V}_j^0\,dP - \overline{S}_j^0\,dT$, where the overbar on $\overline{V}_j$ and $\overline{S}_j^0$ denotes a molar quantity. At equilibrium, two coexisting phases (A and B) must have the same μ. Accordingly, $\mu_A = \mu_B$, and $\overline{V}_A^0\,dP - \overline{S}_A^0\,dT = \overline{V}_B^0\,dP - \overline{S}_B^0\,dT$. After collecting like terms, we have:

$$\frac{dP}{dT} = \frac{\Delta S_R^0}{\Delta V_R^0} \tag{11}$$

Equation 12 is the Clapeyron equation, which is the basis for deriving the equations for phase boundaries in P-T coordinates ($P = f(T)$). Note that ΔS_R^0 and ΔV_R^0 are taken to be molar quantities. No assumptions or approximations are involved in the derivation of Eq. 12, so it is exact and applies to all phase changes (see section "Clapeyron Equation").

The Molecular Basis of Entropy

From the thermodynamic point of view, there is no need to establish a molecular basis for any process; all that is necessary is to account for the energy changes. From this perspective, the idea that entropy is the state function given by Eq. 2 is sufficiently powerful and leads to many other useful relationships. A somewhat deeper measure of understanding can, however, be acquired by inquiring into the molecular basis of entropy.

The fundamental proposition of statistical thermodynamics is that a system contains a very large number of molecules, the average properties of which determine the behavior or state of the system. The goal, then, is to calculate the average properties. The most basic property of a molecular system is the distribution of molecules among the system's energy levels, which are quantized according to the rules of quantum mechanics. The lowest energy level is the ground state of a molecule; all other states have higher energy. The configuration of a system expresses how many molecules are in each state. There are W different ways to organize N molecules into a given configuration:

$$W = \frac{N!}{n_0!n_1!n_2!\ldots},$$

where n_j represents the number of molecules in state j, and $j = 0$ represents the ground state. The most probable configuration of a system is the one with the largest W subject to the constraints $\Sigma n_j = N$ and $\Sigma n_j \varepsilon_j = E$ (ε_j is the energy of state j) so that the number of molecules N and the total energy E of the system are fixed. For the most probable configuration, W is denoted by W^* and each n_j by n_j^*. The Boltzmann distribution gives the ratio of each n_j^* to N as a function of the discrete (quantized) ε_j :

$$\frac{n_j^*}{N} = \frac{\exp(-\varepsilon_j/kT)}{q},$$

where k is the Boltzmann constant (1.381×10^{-23}J/K), and q is the molecular partition function, $\Sigma_j \exp(-\varepsilon_j/kT)$. Deriving and interpreting partition functions for different modes of molecular motion and different systems is one of the principal tasks of statistical thermodynamics.

For the sake of brevity, we will assume that macroscopic thermodynamic systems are ergodic (properties averaged over a very large number of identical systems are the same as the properties of one such system averaged over a long period of time) and bypass the development of canonical ensembles, but the reader is cautioned that the ergodic hypothesis and our assumption are untested. The total energy term, E, used above is the difference between the internal energy of a system at T and U_0, the system's internal energy at $T = 0$, so the most probable configuration gives $U - U_0 = n_j^* \varepsilon_j$. By differentiation, we obtain an expression for changes in U with contributions from changes in U_0, changes in the energy states of the system, and changes in the distribution of molecules among the energy states (Eq. 12).

$$dU = dU_0 + \sum n_j^*\,d\varepsilon_j + \sum \varepsilon_j\,dn_j \tag{12}$$

We observe that reversible work changes internal energy by altering the energy levels of a system but does not alter the n_j^* distribution of molecules in the levels, so we identify $dw_{rev} = dU_0 + \sum n_j^*\,d\varepsilon_j$. On the other hand, reversible heat transfers change the distribution without altering the levels, so we identify $dq_{rev}^{sys} = T dS^{sys} = \Sigma \varepsilon_j\,dn_j$, or:

$$dS^{sys} = \left(\frac{1}{T}\right)\sum \varepsilon_j\,dn_j. \tag{13}$$

Under isothermal conditions, N is fixed, so $\Sigma dn = 0$ on its own. If molecules shift from low energy levels ε_{low} to high energy levels ε_{high}, however, and $dn_{low} < 0$ and $dn_{high} > 0$ (in fact, $dn_{low} = -dn_{high}$). Accordingly, $\varepsilon_{low} dn_{low} < 0$ and $\varepsilon_{high} dn_{high} > 0$. Because of the energy difference, $|\varepsilon_{low}\,dn_{low}| < |\varepsilon_{high}\,dn_{high}|$ so $\Sigma \varepsilon_j\,dn_j > 0$ and $T dS^{sys} > 0$. If we define entropy as being proportional to W^*,

$$S = k \ln W^*, \tag{14}$$

we can derive the established identity (Eq. 13) by another route beginning with Eq. 14. That derivation is beyond the scope of this article, but we conclude that it validates the definition in Eq. 14. If we increase the temperature of

the system, more energy levels become accessible, so the number of ways to distribute molecules among those energy levels and still satisfy the constraints increases. Accordingly, W^* and S also increase. Decreasing temperature yields lower values of W^* and S. In the limit of $T \rightarrow 0$ K, the only accessible energy level is the ground state, so $\lim_{T \rightarrow 0} W^* = 1$. It follows that $\lim_{T \rightarrow 0} S = 0$, which is consistent with our earlier discussion of the third law and absolute entropies.

Cross-References

- Activation Parameters: Energy, Enthalpy, Entropy, and Volume
- Chelation
- Enthalpy
- Equilibrium
- Free Energy
- Fugacity
- Geochemical Thermodynamics
- Henry's Law
- Kinetics of Geochemical Processes
- Solid Solution/Exsolution

References

Anderson GM, Crerar DA (1993) Thermodynamics in geochemistry. The equilibrium model. Oxford University Press, New York. 588 pp
Atkins PW (1986) Physical chemistry, 3rd edn. W. H. Freeman, New York. 857 pp
Denbigh K (1971) The Principles of chemical equilibrium, 3rd edn. Cambridge University Press, Cambridge. 494 pp
McGlashan ML (1966) The use and misuse of the laws of thermodynamics. J Chem Educ 43:226–232
McGlashan ML (1979) Chemical thermodynamics. Academic, New York. 345 pp
Nordstrom DK, Munoz JL (1994) Geochemical thermodynamics, 2nd edn. Blackwell Scientific Publications, Cambridge. 493 pp

Epigenesis

Jamie J. Wilkinson
Department of Earth Sciences, Natural History Museum, London, UK
Department of Earth Science and Engineering, Imperial College, London, UK

Definition

Epigenesis is a term derived from the Greek (epi+genesis = after formation) that is primarily used to describe a geological process involving the addition, modification, and/or removal of minerals from a rock subsequent to its formation. It typically refers to a *metasomatic* process that has, as well as transforming the mineral assemblage, modified the chemical composition and even textural properties of the bulk rock via the addition or removal of elements. The term may be applied in geomorphology to the formation of glacial valleys, in soil science to soil formation, and in sedimentology to the process of formation of a mineral, texture, or structure subsequent to compaction – thus partly synonymous with *diagenesis*. However, it is most commonly used in geochemistry in relation to the formation of mineral deposits – in particular those formed from *hydrothermal solutions* such as sediment-hosted mineral deposits (Brown 2014; Ramanaidou and Wells 2014; Wilkinson 2014) and volcanogenic massive sulfide deposits (Franklin et al. 1981).

Epigenetic Mineral Deposits

The early subdivision of mineral deposits into those that formed by *syngenesis* (process of formation similar to that which formed the enclosing rock and, in modern usage, also implying a temporal connection) and *epigenesis* (introduced into a preexisting rock) recognized the fundamental difference in mineral deposit morphology that can result from these end-member processes (Lindgren 1913). The morphology is important for mineral exploration and mining because different methods are used to recognize and mine ore from *syngenetic* deposits that are lenticular and conformable with stratigraphic units (described as *stratiform*) and *epigenetic* deposits that may have tabular, pipelike, or irregular geometries that are contained within specific stratigraphic units (*stratabound)* or crosscut stratigraphy. In sedimentary ore systems, there is overlap in the usage of terms, with *syngenesis* often considered synonymous with *early diagenesis* and *epigenesis* with *late diagenesis* (or *epidiagenesis*; particularly in the USA). *Syndiagenesis* has been used as a term by economic geologists to separate the stages of syngenesis and epigenesis (e.g., Bartholomé et al. 1972; Boast et al. 1981). In carbonate sedimentology, *syndiagenesis* is broadly synonymous with *eogenesis*.

Epigenetic deposits may form in two general ways: either by infiltration of fluids into intergranular porosity with precipitation of ore and gangue minerals in pore space and by replacement of existing grains or by infiltration of fluids along fracture permeability or brecciated zones with precipitation of minerals to form veins or breccia cements. Gradations between the two end-members frequently occur, where mineralization spreads into the wall rocks surrounding vein systems or into breccia clasts. Replacement can be either highly selective, preserving primary rock components such as fossils or primary rock-forming minerals and textures, or may be texturally destructive so that primary features are obscured.

Controversy Regarding the Syngenetic or Epigenetic Origin of Mineral Deposits

The distinction between syngenesis and epigenesis is not straightforward and has led to extensive debate in the literature surrounding the processes responsible for the formation of certain types of mineral deposits, such as sediment-hosted Pb-Zn deposits (e.g., Leach et al. 2005). *Syngenesis*, as applied to sediment-hosted or volcanogenic massive sulfide deposits, implies that ore-forming processes occurred near the water-sediment interface, effectively in connection with the hydrosphere and biosphere. By contrast, *epigenesis* can have occurred tens or hundreds of millions of years after rock lithification, potentially at significant burial depths, and possibly at high temperatures. Clearly, the processes involved in the transport and precipitation of ore-forming elements in such contrasting regimes are very different. The relative timing of ore formation also has major implications for mineral exploration: syngenetic deposits are likely to be found in a specific stratigraphic interval in a particular terrane, whereas epigenetic deposits could be found in any suitably receptive rocks that are older than the hydrothermal system involved. In a number of cases, both genetic models have been proposed for the same ore deposits, with perhaps the best-known examples being the Proterozoic sediment-hosted Zn-Pb deposits of the McArthur Basin in Australia (Large et al. 1998; Perkins and Bell 1998) and the Carboniferous deposits of the Irish Midlands orefield (Hitzman and Beaty 1996; Wilkinson et al. 2005). The principal arguments for the timing of mineralization are based on geological relationships and textural observations – whether the ore minerals form stratigraphically conformable sedimentary layers that can be accounted for by deposition from suspension in water or if they can be shown to transgress stratigraphic contacts and replace preexisting minerals in the rock. Unfortunately, where a mineral deposit is subject to post-formation diagenetic, tectonic, or metamorphic overprinting, remobilization of minerals can obscure primary depositional textures and generate secondary "epigenetic" characteristics. Thus, because of the ambiguity often present in such observations, research efforts increasingly utilize isotope geochemistry or geochronology to distinguish between syngenesis and epigenesis (e.g., Hnatyshin et al. 2015).

Mineral Systems with Syngenetic and Epigenetic Components

Other complications include the fact that syngenetic deposits can also have epigenetic components in the form of vein, breccia, and/or alteration "feeder" zones that underlie the main deposit, such as in sedimentary-exhalative (SEDEX) deposits (Leach et al. 2005) or volcanic-hosted massive sulfide deposits (Franklin et al. 1981). These reflect the upward passage of buoyant hydrothermal fluids into the ore-forming environment and so are an intrinsic part of the overall hydrothermal system. The temporal relationship between the metasomatic process and rock lithification implicit in the term *epigenesis* is also subject to ambiguity when the host rocks are carbonate rich. Such rocks lithify very quickly, potentially at the seafloor (Bathurst 1970); as a result, strictly epigenetic processes and textures can be generated, although the processes are effectively operating within the syngenetic domain (e.g., Wilkinson and Hitzman 2014).

Summary

Epigenesis has wide usage in the geoscience literature but is most commonly applied in the description of mineral deposits. Because it describes a genetic process that may not be easily constrained from the rock record, and because it also represents an "end-member" of a spectrum of linked processes, its usage is quite commonly controversial. For more details on distinctions between the usage of "epigenesis," "diagenesis," and "syngenesis" in the context of mineral deposits, see Misra (2000).

Cross-References

- ▶ Diagenesis
- ▶ Hydrothermal Solutions
- ▶ Ore Deposits

References

Bartholomé P, Evrard P, Katekesha F, Lopez-Ruiz J, Ngongo M (1972) Diagenetic ore-forming processes at Kamoto, Katanga, Republic of the Congo. In: Amstutz GC, Bernard AJ (eds) Ore in sediments. Springer, New York, pp 21–41

Bathurst RGC (1970) Problems of lithification in carbonate muds. Proc Geol Assoc 81:429–440

Boast AM, Coleman ML, Halls C (1981) Textural and stable isotopic evidence for the genesis of the Tynagh base metal deposit, Ireland. Econ Geol 76:27–55

Brown AC (2014) Low-temperature sediment-hosted copper deposits. In: Holland HD, Turekian KK (eds) Treatise on geochemistry, Geochemistry of mineral deposits, vol 13, 2nd edn. Elsevier, Amsterdam, pp 251–272

Franklin JM, Sangster DM, Lydon JW (1981) Volcanic-associated massive sulfide deposits. In: Skinner BJ (ed) Economic geology 75th anniversary volume. Lancaster Press, Pennsylvania, pp 485–626

Hitzman MW, Beaty DW (1996) The Irish Zn-Pb-(Ba) orefield. In: Sangster DF (ed) Carbonate-hosted lead-zinc deposits, Special publication, vol 4. Society of Economic Geologists, Littleton, pp 112–143

Hnatyshin D, Creaser RA, Wilkinson JJ, Gleeson SA (2015) Re-Os dating of pyrite confirms an early diagenetic onset and extended duration of mineralization in the Irish Zn-Pb orefield. Geology 43:143–146

Large RR, Bull SW, Cooke DR, McGoldrick PJ (1998) A genetic model for the HYC deposit, Australia: based on regional sedimentology, geochemistry, and sulphide–sediment relationships. Econ Geol 93:1345–1368
Leach DL, Sangster DF, Kelley KD, Large RR, Garven G, Allen C R, Gutzmer J, Walters S (2005) Sediment-hosted lead-zinc deposits: a global perspective. Econ Geol (100th Anniversary Volume, 1905–2005):561–607
Lindgren W (1913) Mineral deposits, vol 11, 1st edn. McGraw-Hill Book Company, New York, pp 140–165
Misra K (2000) Understanding mineral deposits, vol 4. Springer, Netherlands, pp 228–237
Perkins WG, Bell TH (1998) Stratiform replacement lead-zinc deposits: a comparison between Mount Isa, Hilton, and McArthur River. Econ Geol 93:1190–1212
Ramanaidou ER, Wells MA (2014) Sedimentary hosted iron ores. In: Holland HD, Turekian KK (eds) Treatise on geochemistry, Geochemistry of mineral deposits, vol 13, 2nd edn. Elsevier, Amsterdam, pp 313–356
Wilkinson JJ (2014) Sediment-hosted zinc-lead mineralization: processes and perspectives. In: Holland HD, Turekian KK (eds) Treatise on geochemistry, Geochemistry of mineral deposits, vol 13, 2nd edn. Elsevier, Amsterdam, pp 219–250
Wilkinson JJ, Hitzman MW (2014) The Irish Zn-Pb Orefield: the view from 2014. In: Archibald SM, Piercey SJ (eds) Current perspectives in zinc deposits. Irish Association of economic geology, Dublin, pp 59–73
Wilkinson JJ, Everett CE, Boyce AJ, Gleeson SA, Rye DM (2005) Intracratonic crustal seawater circulation and the genesis of sub-seafloor Zn-Pb mineralization in the Irish orefield. Geology 33:805–808

Equilibrium

Heinz Gamsjäger
Leoben, Austria

Definition

Equilibrim is the condition toward which a system will change in the absence of constraints. In a chemical system it is the state with the minimum Gibbs Free Energy.

The state of equilibrium is a common feature of all branches of physical science. It plays an important role when either chemical, mechanical, or electromagnetic phenomena are described. Three examples emphasizing chemical applications must suffice. Analytical and preparative chemists use equilibrium considerations to select the temperature and concentration ranges best suited for their work. Chemical and metallurgical processes are often designed on the basis of equilibrium calculations. Moreover, equilibrium models for the distribution of species in natural waters are frequently applied by geochemists.

Heinz Gamsjager is deceased.
Originally published in: Marshall CP, Fairbridge RW (eds) Encyclopedia of Geochemistry, Springer Netherlands, 1999

As originally demonstrated by Gibbs, the concept of equilibrium is described in an entirely general way by classical thermodynamics (Gibbs 1875). Let us consider the contemporary treatment also based on the second law and using modern nomenclature given by McGlashan (1979):

> If a spontaneous process occurs in an isolated system (L) consisting of one or more phases α, β, ..., the entropy S^{Σ} of the system increases. If nothing is happening, the entropy remains constant and the isolated system is said to be in a state of equilibrium.

In an isolated system the quantities internal energy U^{Σ}, volume V^{Σ} and the total amount of substance n^{Σ} are kept constant. Expressing the entropy variation by its time derivative $\partial S/\partial t$, the statement can be cast into a mathematical relation where the inequality and equality signs refer to spontaneous process and equilibrium respectively:

$$\left(\partial S^{\Sigma}/\partial t\right)_{U^{\Sigma},V^{\Sigma},n^{\Sigma}} \geqslant 0 \tag{1}$$

The definition $\partial S^{\Sigma}/\partial t = 0$ includes metastable equilibria, provided no change is detected during the period and with the instruments of observation. Thus, a mixture of methane and air at ambient temperatures is metastable unless it is lighted, whereupon it burns and transforms into the even more stable state of flue gas.

Other, sometimes more convenient, sets of independent variables are obtained from Eq. 1 simply by applying the rules of differentiation. By this method, the extensive quantity U is successively transformed into the likewise extensive quantities H (enthalpy), A (Helmholtz function), and G (Gibbs function). Now, the conditions for chemical as well as thermal, hydrostatic, diffusive, etc. equilibrium can be derived from Eq. 1 or one of its alternative forms (McGlashan 1979). It is easy to carry out and study chemical reactions at constant thermodynamic temperature T and pressure p; consequently, Eq. 2 is the most important from the viewpoint of chemistry.

$$\left(\partial G^{\Sigma}/\partial t\right)_{T,p,n^{\Sigma}} \leqslant 0 \tag{2}$$

It can be shown that the general homogeneous reaction:

$$aA + bB \rightleftharpoons cC + dD \tag{3}$$

is in a state of equilibrium when the chemical potentials μ satisfy the following equation:

$$c\mu_C + d\mu_D - a\mu_A - b\mu_B = 0 \tag{4}$$

This result can easily be generalized to systems, composed of more than one phase, in which two or more simultaneous reactions occur.

Once a system has attained chemical equilibrium the concentrations of the chemical species involved no longer change, on a macroscopic level it has chemically come to a rest. On the molecular level, the reactions are still going on, however, as can be demonstrated by spiking an equilibrated system with an isotopic tracer.

Cross-References

- ▶ Activation Parameters: Energy, Enthalpy, Entropy, and Volume
- ▶ Chemical Bonds
- ▶ Clapeyron's Equation
- ▶ Enthalpy
- ▶ Entropy
- ▶ Equilibrium Constant
- ▶ Fluid–Rock Interaction
- ▶ Free Energy
- ▶ Fugacity
- ▶ Geochemical Thermodynamics
- ▶ Gibbs-Duhem Equation
- ▶ Henry's Law
- ▶ Kinetics of Geochemical Processes
- ▶ Metamorphic Reactions and Processes
- ▶ Partitioning and Partition Coefficients
- ▶ Phase Equilibria

References

Gibbs JW (1875) On the equilibrium of heterogeneous substances. In: The collected works of J. Willard Gibbs, vol I: Thermodynamics. Yale University Press, New Haven, p 56. Reprinted 1948

McGlashan ML (1979) Chemical thermodynamics. Academic, London, 345 pp

Equilibrium Constant

Erich Königsberger
Chemical and Metallurgical Engineering and Chemistry, School of Engineering and Information Technology, Murdoch University, Murdoch, WA, Australia

Definition

The *standard equilibrium constant*, $K^{\ominus}(T)$, for a chemical reaction is a dimensionless quantity defined by

$$K^{\ominus}(T) = \exp\{-\Delta_r G^{\ominus}(T)/RT\},$$

where $\Delta_r G^{\ominus}(T)$ is the change in the standard molar Gibbs energy due to the reaction. The value of $K^{\ominus}(T)$ depends on the choice of the standard state, which must be specified. The standard equilibrium constant is, like all standard thermodynamic quantities, independent of pressure and composition (Ewing et al. 1994; Cohen et al. 2008).

Introduction

The following definitions and examples are based on recommendations by the Commission on Thermodynamics of the International Union of Pure and Applied Chemistry (Ewing et al. 1994), cf. also the recommendations given in IUPAC's *Green Book* (Cohen et al. 2008). Further details can be found in textbooks on Chemical Thermodynamics (e.g., McGlashan 1979).

According to IUPAC, *all* standard chemical potentials and standard equilibrium constants are defined in terms of an arbitrarily chosen standard pressure. Alternative definitions with explicit pressure dependencies of these quantities are possible for reactions in *condensed* phases (e.g., Wood and Battino 1990). This, however, requires different relationships for reactions in condensed and gaseous phases, because for the latter the standard thermodynamic quantities are usually defined for a standard pressure of 1 bar.

It should be emphasized that other choices can be made as well. For instance, fixed-temperature and fixed-pressure standard states have been proposed for aqueous solutions (Nordstrom and Munoz 1986, p. 186).

Equilibrium Condition

Consider a chemical reaction written as

$$\sum_{\mathrm{B}} \nu_{\mathrm{B}} \mathrm{B} = 0, \tag{1}$$

where each ν_{B} represents the stoichiometric coefficient of the substance B in the balanced reaction; the sign is positive for products and negative for reactants.

The Gibbs energy, $G(T,p,\xi)$, of the reacting system (1) is defined as

$$G(T,p,\xi) = \sum_{\mathrm{B}} n_{\mathrm{B}}(\xi)\mu_{\mathrm{B}}(T,p,\xi),$$

where $n_{\mathrm{B}}(\xi)$ is the amount of substance B and $\mu_{\mathrm{B}}(T,p,\xi)$ denotes the chemical potential of substance B which depends on temperature, pressure, and the extent of reaction, ξ. Chemical equilibrium will be attained when G assumes a minimum

with respect to ξ at constants T and p. The extent of reaction is defined by

$$n_{\mathrm{B}}(\xi) = n_{\mathrm{B}}(0) + \nu_{\mathrm{B}}\xi, \tag{2}$$

where $n_{\mathrm{B}}(0)$ denotes the initial amount of substance B. Hence, the condition of equilibrium for reaction (1) is given by

$$\frac{\partial G}{\partial \xi} = \sum_{\mathrm{B}} \frac{\partial n_{\mathrm{B}}}{\partial \xi}\mu_{\mathrm{B}} + \sum_{\mathrm{B}} n_{\mathrm{B}}\frac{\partial \mu_{\mathrm{B}}}{\partial \xi} = 0. \tag{3}$$

According to the Gibbs-Duhem equation, the second sum in Eq. 3 is identically equal to zero. Consequently, by the use of Eq. 2,

$$\sum_{\mathrm{B}} \nu_{\mathrm{B}}\mu_{\mathrm{B}}(T, p, \xi^{\mathrm{eq}}) = 0, \tag{4}$$

where ξ^{eq} denotes the extent of reaction at chemical equilibrium.

Standard Equilibrium Constant

The standard equilibrium constant $K^{\ominus}(T)$ for reaction (1) is a dimensionless quantity defined by

$$RT\ln K^{\ominus}(T) = -\sum_{\mathrm{B}} \nu_{\mathrm{B}}\mu_{\mathrm{B}}^{\ominus}(T) = -\Delta_{\mathrm{r}}G^{\ominus}(T) \tag{5}$$

where $\mu_{\mathrm{B}}^{\ominus}(T)$ denotes the standard chemical potential of substance B and $\Delta_{\mathrm{r}}G^{\ominus}(T)$ is the standard Gibbs energy of reaction (1).

Combination of Eqs. 4 and 5 yields

$$RT\ln K^{\ominus}(T) = \sum_{\mathrm{B}} \nu_{\mathrm{B}}\left\{\mu_{\mathrm{B}}(T, p, \xi^{\mathrm{eq}}) - \mu_{\mathrm{B}}^{\ominus}(T)\right\}. \tag{6}$$

Evaluation of the differences

$$\left\{\mu_{\mathrm{B}}(T, p, \xi) - \mu_{\mathrm{B}}^{\ominus}(T)\right\}$$

between the chemical potential of substance B and its standard chemical potential for the same temperature and state of aggregation will be discussed below.

Standard Chemical Potential

Since a variation of temperature, pressure, or composition changes the values of thermodynamic quantities, it is important to define a reference value of each quantity to which such changes, which can be measured or calculated easily, may be referred. Suitable reference values, known as standard thermodynamic quantities, can be obtained from the standard chemical potential by the usual mathematical operations (cf., e.g., McGlashan 1979).

The standard chemical potential is defined in terms of a specified state of aggregation, a specified temperature, and an arbitrarily chosen but specified standard pressure. For a solute substance in a solution, an arbitrarily chosen but specified standard molality is required too. Consequently, all standard thermodynamic quantities, including standard equilibrium constants, are independent of pressure and composition, but they remain functions of temperature.

The recommended value of the standard pressure $p^{\ominus}$ is 10^5 Pa (1 bar). If the value of $p^{\ominus}$ changes from $p_1^{\ominus}$ to $p_2^{\ominus}$, then the change in the standard chemical potential is given by one of the following three equations:

1. For a gaseous substance B, whether pure or mixed,

$$\mu_{\mathrm{B}}^{\ominus}(\mathrm{g}, T, p_2^{\ominus}) - \mu_{\mathrm{B}}^{\ominus}(g, T, p_1^{\ominus}) = RT\ln\left(p_2^{\ominus}/p_1^{\ominus}\right).$$

2. For a substance B in a condensed phase (cd), whether pure or mixed, or for a solvent substance B in a solution

$$\mu_{\mathrm{B}}^{\ominus}(\mathrm{cd}, T, p_2^{\ominus}) - \mu_{\mathrm{B}}^{\ominus}(\mathrm{cd}, T, p_1^{\ominus}) = \int_{p_1^{\ominus}}^{p_2^{\ominus}} V_{\mathrm{B}}^{*}(\mathrm{cd}, T, p)\,\mathrm{d}p,$$

where $V_{\mathrm{B}}^{*}(\mathrm{cd}, T, p)$ is the molar volume of the pure substance B.

3. For a solute substance B in a solution

$$\mu_{\mathrm{B}}^{\ominus}(\mathrm{solute}, T, p_2^{\ominus}) - \mu_{\mathrm{B}}^{\ominus}(\mathrm{solute}, T, p_1^{\ominus}) = \int_{p_1^{\ominus}}^{p_2^{\ominus}} V_{\mathrm{B}}^{\infty}(\mathrm{solute}, T, p)\,\mathrm{d}p,$$

where $V_{\mathrm{B}}^{\infty}(\mathrm{solute}, T, p)$ is the partial molar volume of the solute B at infinite dilution.

For example, if $p^{\ominus}$ increases from 10^5 Pa to 101,325 Pa (1 atm), then, for a gaseous substance, the standard chemical potential increases by about 0.013 RT and the standard molar entropy decreases by about 0.013 R. For condensed phases, however, the same variation in the standard pressure will result in a negligible difference in the standard thermodynamic quantities compared with the current uncertainties in these data.

The recommended value of the standard molality $m^{\ominus}$ is 1 mol kg^{-1}.

In the following three sections, definitions are given for the standard chemical potential of a substance B in the following states of aggregation: pure or mixed gas phase, pure or mixed condensed phase or solvent substance in a solution, and solute substance in a solution. Using these definitions, methods for the calculation and measurement of the differences

$\{\mu_B(T,p,\xi) - \mu_B^{\ominus}(T)\}$, and hence of the standard equilibrium constant, can be derived.

Gaseous Systems

The standard chemical potential of a gaseous substance B, whether pure or mixed, is defined by the relation

$$\mu_B(g,T,p,x) - \mu_B^{\ominus}(g,T) = RT\ln(f_B/p^{\ominus}), \tag{7}$$

where x denotes the set of mole fractions x_B, x_C, $\cdots$ of B, C, $\cdots$ and f_B is the fugacity of B defined by

$$f_B = (x_B p)\exp\left\{\int_0^p \left(\frac{V_B}{RT} - \frac{1}{p}\right) dp\right\}, \tag{8}$$

where $V_B = V_B(g, T, p, x)$ is the (partial) molar volume of B. Consequently, the fugacity has the same dimension as pressure. Since the integral in Eq. 8 vanishes for a perfect gas, the fugacity is sometimes used as a measure of the deviation of the gas or gaseous mixture from perfection. For an expression of the fugacity in terms of the virial equation of state see, e.g., Ewing et al. (1994) or McGlashan (1979). As the symbol f_B is also used for the activity coefficient of substance B referenced to Raoult's law, the fugacity is sometimes denoted as $\tilde{p}_B$ (Cohen et al. 2008).

The standard equilibrium constant for a reaction in the gas phase is derived by combining Eqs. 6 and 7:

$$K^{\ominus}(g,T) = \prod_B (f_B/p^{\ominus})^{\nu_B} = \lim_{p\to 0} \prod_B (x_B p/p^{\ominus})^{\nu_B}.$$

The second form of this equation, which follows from Eq. 8, provides the most direct method of determining $K^{\ominus}(g, T)$ experimentally and is useful when the partial molar volumes $V_B(g, T, p, x)$ are not known. At least at low to moderate pressures, the extrapolation to zero pressure is often not necessary. In practice the quantity

$$K_p(g,T,p,x) = \prod_B (x_B p)^{\nu_B}$$

which has the dimension of $(\text{pressure})^{\Sigma_B \nu_B}$ is often used. However, K_p varies with pressure and composition and should be clearly distinguished from the dimensionless standard equilibrium constant $K^{\ominus}(g, T)$.

Condensed Phases

The standard chemical potential of a substance B in a condensed phase, whether pure or mixed, is defined by the relation

$$\mu_B^{\ominus}(cd,T) = \mu_B^*(cd,T,p) + \int_p^{p^{\ominus}} V_B^* \, dp, \tag{9}$$

where $\mu_B^*(cd,T,p)$ and $V_B^*(cd,T,p)$ are the chemical potential and the molar volume of the pure substance B, respectively.

The activity coefficient f_B of a substance B in a liquid or solid mixture is a dimensionless quantity defined by

$$\mu_B(cd,T,p,x) - \mu_B^{\ominus}(cd,T) = RT\ln(x_B f_B) - \int_p^{p^{\ominus}} V_B^* \, dp, \tag{10}$$

where x denotes the set of mole fractions x_B, x_C, $\cdots$ of B, C, $\cdots$ in the mixture. The (relative) activity of B in a mixture is a dimensionless quantity given by

$$a_B = x_B f_B. \tag{11}$$

It follows from the definitions of a_B and f_B that

$$\lim_{x_B\to 1} a_B = \lim_{x_B\to 1} f_B = 1.$$

A mixture of substances B, C, $\cdots$ is called an ideal mixture when $a_B = x_B$, $a_C = x_C$, $\cdots$ or $f_B = 1, f_C = 1, \cdots$.

The standard equilibrium constant for a reaction in a condensed phase is given by

$$K^{\ominus}(cd,T) = \prod_B (x_B f_B)^{\nu_B} \exp\left[-\int_p^{p^{\ominus}} \sum_B \frac{\nu_B V_B^*}{RT} dp\right]. \tag{12}$$

The pressure integral in Eq. 12 is often neglected, especially when $p \approx p^{\ominus}$. Then, the quantity

$$K_{xf}(cd,T,p) = \prod_B (x_B f_B)^{\nu_B}$$

is a good approximation to $K^{\ominus}(cd, T)$, whereas the quantity

$$K_x(cd,T,p,x) = \prod_B (x_B)^{\nu_B}$$

usually varies strongly with composition and is therefore a poor approximation to $K^{\ominus}(cd, T)$ because only few real mixtures are even approximately ideal.

Solutions

A solution is a special description of a mixture for which it is convenient to distinguish between the solvent A, usually present in excess, and the solutes B, C, $\cdots$.

The standard chemical potential $\mu_B^{\ominus}$ of a solute substance B in a solution of B, C, $\cdots$ in a solvent substance A is defined by

$$\mu_B^{\ominus}(\text{solute}, T) = \{\mu_B(\text{solute}, T, p, m) - RT \ln (m_B/m^{\ominus})\}^{\infty} + \int_p^{p^{\ominus}} V_B^{\infty} \, dp, \tag{13}$$

where m denotes the set of molalities m_B, m_C, $\cdots$ of B, C, $\cdots$ in the solvent A, $m^{\ominus}$ is the standard molality, $V_B^{\infty} = V_B^{\infty}(\text{solute}, T, p)$ is the partial molar volume of B at infinite dilution, and ∞ denotes the limit at infinite dilution, i.e., $\sum_B m_B \to 0$. In Eq. 13, both terms inside $\{\cdots\}^{\infty}$ diverge as $m_B \to 0$, but their difference remains finite.

The activity coefficient $\gamma_{m,B}$ of a solute B in a solution is a dimensionless quantity given by

$$\mu_B(\text{solute}, T, p, m) - \mu_B^{\ominus}(\text{solute}, T) = RT \ln\left(m_B \gamma_{m,B}/m^{\ominus}\right) - \int_p^{p^{\ominus}} V_B^{\infty} \, dp.$$

The (relative) activity a_B of a solute B in a solution is a dimensionless quantity given by

$$a_B = m_B \gamma_{m,B}/m^{\ominus}.$$

It follows from the definitions of a_B and $\gamma_{m,B}$ that

$$(a_B m^{\ominus}/m_B)^{\infty} = \lim_{\Sigma_B m_B \to 0} \gamma_{m,B} = 1.$$

A solution of solutes B, C, $\cdots$ in a solvent A is called an ideal-dilute solution when $a_B = m_B/m^{\ominus}$, $a_C = m_C/m^{\ominus}$, $\cdots$ or $\gamma_{m,B} = 1$, $\gamma_{m,C} = 1$, $\cdots$.

The definition of the standard chemical potential of the solvent A in a solution is identical with the definition (9) of the standard chemical potential of any substance B in a condensed phase. The activity a_A of the solvent A is defined by relations analogous to Eqs. 10 and 11.

Since the solvent A is treated differently from the solutes B, C, $\cdots$, the expression for a chemical reaction in a solution may be written in the form

$$\nu_A A + \sum_B \nu_B B = 0.$$

The standard equilibrium constant then takes the form

$$K^{\ominus}(\text{solution}, T) = (a_A)^{\nu_A} \prod_B (a_B)^{\nu_B} \exp\left[-\int_p^{p^{\ominus}} \frac{\nu_A V_A^* + \Sigma_B \nu_B V_B^{\infty}}{RT} dp\right]. \tag{14}$$

The pressure integral in Eq. 14 is often neglected, especially when $p \approx p^{\ominus}$. Then, the quantity

$$K_a(\text{solution}, T, p) = (a_A)^{\nu_A} \prod_B (a_B)^{\nu_B}$$

varies with pressure but may still be a good approximation to $K^{\ominus}$. The solvent term, which is close to unity for sufficiently dilute solutions, is also often omitted. Then, the quantity

$$K_{m\gamma}(\text{solution}, T, p, m) = \prod_B \left(m_B \gamma_{m,B}/m^{\ominus}\right)^{\nu_B}$$

varies with composition but may still be a good approximation to $K^{\ominus}$. The quantity

$$K_m(\text{solution}, T, p, m) = \prod_B (m_B)^{\nu_B},$$

which has the dimension of $(\text{molality})^{\Sigma_B \nu_B}$, is sometimes used in practice; however, it should be clearly distinguished from the dimensionless quantity $K^{\ominus}$ (solution, T). The dependence of K_m on solution composition may be severe, especially for aqueous electrolyte solutions.

In many experimental studies on complex formation and solubility, the solution composition has been kept essentially constant by adding an "inert" electrolyte (constant ionic medium method). Also, some natural waters maintain a rather constant composition, such as surface seawater. For reactions involving minor species B at $p = p^{\ominus}$, a so-called stoichiometric equilibrium constant may be defined as

$$K_{st}(\text{solution}, T, m_C) = \lim_{\Sigma_B m_B \to 0} \prod_B (m_B)^{\nu_B}, \quad m_{C \neq B} = \text{constant}.$$

The quantity K_{st}, which has the dimension of $(\text{molality})^{\Sigma_B \nu_B}$, varies with solution composition and is only valid for a particular set of $m_{C \neq B}$.

For any solution at $p = p^{\ominus}$, Eq. 14 can be written in the form

$$K^{\ominus}(\text{solution}, T) = \lim_{\Sigma_B m_B \to 0} \prod_B (m_B/m^{\ominus})^{\nu_B}.$$

This equation provides the most direct method of determining $K^{\ominus}$ (solution, T) experimentally and is useful when the activity a_A for the solvent and the activity coefficients $\gamma_{m,B}$, $\gamma_{m,C}$, $\cdots$ for the solutes are not known.

E

Effect of Temperature on the Equilibrium Constant

The standard molar enthalpy of substance B, $H_B^\ominus$, is given by the Gibbs-Helmholtz equation:

$$H_B^\ominus = \mu_B^\ominus - T\mathrm{d}\mu_B^\ominus/\mathrm{d}T = -RT^2\mathrm{d}(\mu_B^\ominus/RT)/\mathrm{d}T.$$

(cf. McGlashan 1979). Remember that all standard quantities are functions of temperature only. Then, by the use of Eq. 5, van't Hoff's Eq. 15 is obtained:

$$\mathrm{d}\ln K^\ominus/\mathrm{d}T = \sum_B \nu_B H_B^\ominus/RT^2 = \Delta_r H^\ominus/RT^2. \quad (15)$$

Integration of Eq. 15 yields

$$\ln K^\ominus(T_2) - \ln K^\ominus(T_1) = \int_{T_1}^{T_2} \left\{\Delta_r H^\ominus(T)/RT^2\right\}\mathrm{d}T. \quad (16)$$

Thus, if the value of $K^\ominus$ is known for a temperature T_1, its value at another temperature T_2 can be calculated, provided that the standard enthalpy of reaction, $\Delta_r H^\ominus(T)$, is known over the temperature range T_1 to T_2. Usually, the standard molar heat capacities at constant pressure, $C_{p,B}^\ominus$, have been measured and tabulated (e.g., as coefficients of a power series in T), and $\Delta_r H^\ominus(T_0)$ is known at some reference temperature T_0 (which may be outside the range T_1 to T_2). Since

$$\Delta_r H^\ominus(T) - \Delta_r H^\ominus(T_0) = \int_{T_0}^{T} \sum_B \nu_B C_{p,B}^\ominus(T)\,\mathrm{d}T,$$

Eq. 16 can be rewritten as

$$\ln K^\ominus(T_2) - \ln K^\ominus(T_1) = \Delta_r H^\ominus(T_0)(T_2 - T_1)/RT_1T_2 + \int_{T_1}^{T_2}\left\{\int_{T_0}^{T}\sum_B \nu_B C_{p,B}^\ominus(T)\mathrm{d}T\right\}\left(1/RT^2\right)\mathrm{d}T.$$

Examples

In practice, many chemical reactions involve more than one phase. Then, the expressions for the standard equilibrium constant are appropriate combinations of those given above for reactions in a single phase (an illustrative example is presented by Ewing et al. 1994).

Standard equilibrium constants can be defined and also determined experimentally for electron-transfer reactions, proton-transfer reactions (e.g., standard acidity constant, $K_A^\ominus$), water dissociation (standard ionization constant, $K_w^\ominus$), complex formation (standard stability constant), dissolution of solid electrolytes (standard solubility product, $K_s^\ominus$), etc. (cf. McGlashan 1979).

Cross-References

- ▶ Equilibrium
- ▶ Free Energy
- ▶ Geochemical Thermodynamics

References

Cohen ER, Cvitaš T, Frey JG, Holmström B, Kuchitsu K, Marquardt R, Mills I, Pavese F, Quack M, Stohner J, Strauss HL, Takami M, Thor AJ (2008) Quantities, units and symbols in physical chemistry, IUPAC Green Book, 3rd edn, 2nd printing. IUPAC & RSC Publishing, Cambridge

Ewing MB, Lilley TH, Olofsson GM, Rätzsch MT, Somsen G (1994) Standard quantities in chemical thermodynamics. Pure Appl Chem 66:533–552

McGlashan ML (1979) Chemical thermodynamics. Academic, London

Nordstrom DK, Munoz JL (1986) Geochemical thermodynamics. Blackwell, Palo Alto

Wood SE, Battino R (1990) Thermodynamics of chemical systems. Cambridge University Press, Cambridge

Erbium

Scott M. McLennan
Department of Geosciences, Stony Brook University, Stony Brook, NY, USA

Element Data

Atomic Symbol: Er
Atomic Number: 68
Atomic Weight: 167.259(3)
Isotopes and Abundances: ^{162}Er, 0.139(5)%; ^{164}Er, 1.601(3)%; ^{166}Er, 33.503(36)%; ^{167}Er, 22.869(9)%; ^{168}Er, 26.978(18)%; and ^{170}Er, 14.910(36)%
1 Atm Melting Point: 1529 °C
1 Atm Boiling Point: 2868 °C
Common Valences: +3
Ionic Radii: 89.0 pm (CN6), 100.4 pm (CN8), and 121.4 pm (CN12)
Pauling Electronegativity: 1.24
First Ionization Energy: 589.30 kJ mol^{-1}
Chondritic (CI) Abundance: 0.166 ppm
Silicate Earth Abundance: 0.370 ppm
Crustal Abundance: 2.2 ppm
Seawater Abundance: 1.09 ppt
Core Abundance: ~0

Properties

Erbium (Er), named after the Swedish village of Ytterby, is a soft, malleable, dense (9.066 g cm^{-3}), bright silvery-white metal. Its electronic configuration is $[Xe]4f^{12}6s^2$. It is stable at room temperature and readily dissolves in mineral acids. It is a group 3 or IIIB inner transition element, with +3 being its only valence state in geological environments, and is one of the lanthanide rare earth elements (REE). In geochemical terminology, it is grouped with heavy rare earth elements (HREE; Gd-Lu). Erbium has six natural, stable isotopes, listed above with their abundances.

More than 270 minerals contain lanthanides as essential structural constituents, but those with Er as a major component are restricted to Y and HREE varieties, such as xenotime [$Y(PO_4)$], bastnäsite [$REE(CO_3)F$], allanite [$(REE,Ca,Y)_2(Al,Fe^{2+},Fe^{3+})_3(SiO_4)_3(OH)$], and britholite [$(REE,Ca)_5(SiO_4,PO_4)_3(OH,F)$]. In addition, Er may be enriched in ion adsorption lateritic kaolinite-halloysite clay deposits that are mined for REE.

Details of properties, mineralogy, history, and uses of Er were compiled from Goonan (2011), Chakhmouradian and Wall (2012), Zaimes et al. (2015), Gschneidner (2016), Hammond (2016), and Meija et al. (2016a, b).

History and Use

Erbium was discovered in 1843 by Carl Gustaf Mosander, but early naming is somewhat confused as the names erbium and terbium were switched in 1864; it was first isolated as a metal in 1934. Erbium oxide has a distinctive pink color and so is used as a colorization additive to glass, cubic zirconia jewelry, and glazes on ceramics. Due to the Er ion 2940 nm emission, it is also used to produce Er:YAG lasers, commonly used for certain types of cosmetic and dental surgeries. Erbium-doped fiber amplifiers (EDFA) can be used to amplify modulated laser beams and accordingly are used in fiber-optic systems.

Geochemical Behavior

The fundamental importance of Er in geochemistry is that it is one of the small trivalent rare earth elements, among the most useful trace elements in all areas of geochemistry and cosmochemistry due to their coherent and systematic behavior as a group, largely a consequence of the "lanthanide contraction."

Erbium is typically a trace element in most rocks and minerals. It is classified geochemically and cosmochemically as a highly refractory lithophile element, with a 50% $T_{condensation}$ of 1659 K at 10^{-4} bars (Lodders 2003). In most igneous systems, Er is incompatible with bulk partition coefficients, $D < 1$. In aqueous systems, Er normally has very low fluid/rock partition coefficients ($\ll 1$). As a result, Er contents of clastic sediments typically reflect their average provenance.

In seawater, Er has very low concentrations (~ppt) and residence times (~2420 year) with speciation dominated by Er^{3+}, $ErCO_3^+$, and $Er(CO_3)_2^-$. In other aqueous systems (e.g., magmatic, hydrothermal), Er can reach ppm levels due to elevated temperatures, pH effects, and complexing with various ligands (e.g., F^-, Cl^-, OH^-).

Concentration and residence time data are from compilations in Taylor and McLennan (2009) and Nozaki (2001).

Biological Utilization and Toxicity

There are no documented biological uses for Er, but in China REE have been added to fertilizers and to stock feed to promote growth. REE (including Er^{3+}) likely substitute for Ca^{2+} in biological materials and processes. REE concentrations (including Er) in human tissues and fluids are very low (tens of ppb to <ppb levels, respectively) due to very low concentrations in natural waters and low uptake rates throughout the food chain (Bulman 2003). At low levels of ingestion, there are no established toxic effects that pose a threat to human health.

Cross-References

- ▶ Incompatible Elements
- ▶ Lanthanide Rare Earths
- ▶ Lithophile Elements
- ▶ Trace Elements
- ▶ Transition Elements

References

Bulman RA (2003) Metabolism and toxicity of the lanthanides. In: Sigel A, Sigel H (eds) Metal ions in biological systems, vol 40, The lanthanides and their interrelations and biosystems. Marcel Dekker, Basel, pp 683–703

Chakhmouradian AR, Wall F (eds) (2012) Rare earth elements. Elements 8:333–376

Goonan TG (2011) Rare earth elements – end use and recyclability. US Geol Surv Sci Invest Rpt 2011–5094. 15pp

Gschneidner KA Jr (2016) Physical properties of the rare earth metals. In: Haynes WM (ed) CRC handbook of chemistry and physics, 96th edn. CRC Press, Boca Raton, pp 4-115–4-120

Hammond CR (2016) The elements. In: Haynes WM (ed) CRC handbook of chemistry and physics, 96th edn. CRC Press, Boca Raton, pp 4-1–4-42

Lodders K (2003) Solar system abundances and condensation temperatures of the elements. Astrophys J 591:1220–1247

Meija J, Coplen TB, Berglund M, Brand WA, De Bièvre P, Gröning M, Holden NE, Irrgeher J, Loss RD, Walczyk T, Prohaska T (2016a) Atomic weights of the elements 2013. Pure Appl Chem 88:265–291. (IUPAC Technical Report)
Meija J, Coplen TB, Berglund M, Brand WA, De Bièvre P, Gröning M, Holden NE, Irrgeher J, Loss RD, Walczyk T, Prohaska T (2016b) Isotopic compositions of the elements 2013. Pure Appl Chem 88:293–306. (IUPAC Technical Report)
Nozaki Y (2001) Rare earth elements and their isotopes in the ocean. In: Steele JH et al (eds) Encyclopedia of ocean sciences. Academic, London, pp 2354–2366
Taylor SR, McLennan SM (2009) Planetary crusts: their composition, origin and evolution. Cambridge University Press, Cambridge. 378pp
Zaimes GG, Hubler BJ, Wang S, Khanna V (2015) Environmental life cycle perspective on rare earth oxide production. ACS Sustain Chem Eng 3:237–244

Europium

Matthias Willbold
School of Earth, Atmospheric and Environmental Sciences, University of Manchester, Manchester, UK

Element Data
Atomic Symbol: Eu
Atomic Number: 63
Atomic Weight: 151.965 g/mol
Isotopes and Abundances: ^{151}Eu 47.8%, ^{153}Eu 52.2%
1 Atm Melting Point: 822 °C
1 Atm Boiling Point: 1529 °C
Common Valences: 3+, 2+
Ionic Radii: Eu $^{3+}$ 109 pm (sixfold), 121 pm (eightfold); Eu $^{2+}$ 131 pm (sixfold), 139 pm (eightfold)
Pauling Electronegativity: 1.2
First Ionization Potential: 5.6704 eV
Chondritic (CI) Abundance: 0.056 µg/g
Silicate Earth Abundance: 0.166 µg/g
Crustal Abundance: 1.1 µg/g
Seawater Abundance: <~0.3 pg/g
Core Abundance: ~0

Properties

Europium is a silvery-white rare-earth element with a pale yellow tint (Greenwood and Earshaw 1997). It is a ductile metal and has the second lowest melting point and the lowest density of all rare-earth elements (Haynes 2016). Europium metal is commercially produced by isolation from rare-earth element-bearing minerals such as bastnäsite and more rarely monazite. Currently, the Bayan Obo iron ore deposit (China) is one of the most important sources of bastnäsite worldwide (Wu 2008).

Europium is the most reactive element of all rare-earth elements, and it readily oxidizes in air and water to form colorful Eu(III) compounds. Although predominantly occurring in the trivalent state, it is the only rare-earth element that occurs in the divalent state under reducing conditions. Divalent Eu is highly reducing and has an ionic radius and coordination number similar to that of Ca^{2+} (calcium), Sr^{2+} (strontium), and Ba^{2+} (barium). Many Eu compounds exhibit phosphorescence properties.

History and Use

Europium was discovered in 1890 by Paul Émile Lecoq de Boisbaudran. It was first isolated in 1901 by Eugène-Anatole Demarçay who named it after Europe. Commercial use of Eu is limited and centered on its phosphorescence characteristics. Europium has been used as a dopant in laser crystals and as a fluorescent material in cathode ray tube television sets and fluorescent lamps.

Geochemical Behavior

Europium is a refractory, lithophile element (Goldschmidt 1930; Lodders 2003) and is concentrated in the silicate fraction of terrestrial planets, i.e., the Earth's mantle and crust. It is classified as a trace element. The redox-sensitive property of Eu makes it a useful geochemical tracer. In oxidized magmatic systems, it exists – like most other rare-earth elements – as a trivalent ion rendering it incompatible in rock-forming minerals. Under reducing magmatic conditions, Eu is compatible in feldspar because Eu $^{2+}$ can substitute for divalent alkaline earth elements in its crystal lattice. This geochemical characteristic can lead to relative enrichment of Eu in feldspar-rich rocks. When compared to other rare-earth elements of similar geochemical properties (samarium and gadolinium), rocks with an overabundance of Eu relative to a reference material (most commonly a chondritic meteorite or an average mid-ocean ridge basalts composition) are said to have a positive Eu anomaly, while those with a deficiency are referred to as having a negative Eu anomaly.

Being an important rock-forming mineral in crustal lithologies, fractional crystallization of feldspar in magmatic systems has a significant effect on the distribution of Eu within the crust of the Earth, the Moon, and other planetary bodies. Feldspar-rich lithologies and geochemical reservoirs, such as the lower continental crust on Earth or the lunar highland terrains, exhibit large positive Eu

anomalies, while the Earth's upper continental crust and the lunar mare basalts comprise complementary negative Eu anomalies (Rudnick and Gao 2014; Taylor and McLennan 2010). This makes Eu the most heterogeneously distributed rare-earth element within the crust. The dichotomy of Eu distribution in the Earth's continental crust has recently been used to trace recycled upper and lower continental crust materials in enriched mantle reservoirs (Willbold and Stracke 2010).

In chondritic meteorites, negative Eu anomalies have been measured in some chondrules and interpreted as the result of rare-earth element gas-solid fractionation at reducing conditions within the solar nebula (Pack et al. 2004).

In aquatic environments, enrichment of Eu relative to other rare-earth elements can only occur in reduced hydrothermal systems (Klinkhammer et al. 1994; Olivarez and Owen 1991). Experimental data suggest that in hydrothermal fluids Eu exists in the divalent form, which exhibits higher solubility than trivalent rare-earth elements (Bau 1991; Haas et al. 1995).

In seawater, Eu only occurs in trivalent form (Goldstein and Hemming 2014; Piper and Bau 2013). Like other rare-earth elements, Eu complexes have a low solubility in seawater. Europium has an average residence time in the oceans of up to 820 years (Alibo and Nozaki 1999; Li 1982).

Both naturally occurring isotopes of Eu can be regarded as stable. ^{151}Eu has recently been found to undergo α-decay to ^{147}Pm, albeit with an extremely long half-life of 4.6×10^{18} years (Casali et al. 2014). Natural mass-dependent variations of Eu isotopes have so far only been reported for two calcium-aluminum inclusions from a carbonaceous chondrite (Moynier et al. 2006).

Biological Utilization and Toxicity

Europium is not known to have a biological role and is not classified as a toxic or harmful element in the environment. Owing to its susceptibility to oxidation, metal powder of Eu can ignite in air at temperatures >150 °C and may thus present a fire and explosion hazard.

Summary

The unique geochemical property of Eu to change valence state depending on ambient redox conditions can be used to understand the magmatic history of igneous rocks and meteoritic components, investigate crustal evolution and mantle recycling models, constrain the sources of sedimentary rocks and water masses, as well as to study hydrothermal systems and their deposits.

Cross-References

- Barium
- Calcium
- Chondrites
- Chondrules
- Earth's Continental Crust
- Mantle Geochemistry
- Gadolinium
- Hydrothermal Alteration
- Lanthanide Rare Earths
- Lithophile Elements
- Mid-Ocean Ridge Basalts (MORB)
- Oxidation-Reduction Reactions and Eh-pH (Pourbaix) Diagrams
- Trace Elements
- Samarium
- Solubility

References

Alibo DS, Nozaki Y (1999) Rare earth elements in seawater: particle association, shale-normalization, and Ce oxidation. Geochim Cosmochim Acta 63:363–372

Bau M (1991) Rare-earth element mobility during hydrothermal and metamorphic fluid-rock interaction and the significance of the oxidation state of europium. Chem Geol 93:219–230

Casali N, Nagorny SS, Orio F, Pattavina L, Beeman JW, Bellini F, Cardani L, Dafinei I, Domizio SD, Vacri MLD, Gironi L, Kosmyna MB, Nazarenko BP, Nisi S, Pessina G, Piperno G, Pirro S, Rusconi C, Shekhovtsov AN, Tomei C, Vignati M (2014) Discovery of the^{151} Eu α-decay. J Phys G Nucl Part Phys 41(7):075101. https://doi.org/10.1088/0954-3899/41/7/075101

Goldschmidt VM (1930) Geochemische Verteilungsgesetze und kosmische Häufigkeiten der Elemente. Naturwissenschaften 18 (47–49):999–1013

Goldstein SL, Hemming SR (2014) Long-lived isotopic tracers in oceanography, paleoceanography, and ice-sheet dynamics. In: Holland HD, Turekian KK (eds) Treatise on geochemistry, vol 8, 2nd edn. Elsevier, Amsterdam/Oxford/Waltham, pp 453–483

Greenwood NN, Earshaw A (1997) Chemistry of the elements. Pergamon Press, Oxford

Haas JR, Shock EL, Sassani DC (1995) Rare earth elements in hydrothermal systems: estimates of standard partial molal thermodynamic properties of aqueous complexes of the rare earth elements at high pressures and temperatures. Geochim Cosmochim Acta 59:4329–4350

Haynes WM (2016) Handbook of chemistry and physics. CRC Press, New York

Klinkhammer GP, Elderfield H, Edmond JM, Mitra A (1994) Geochemical implications of rare earth element patterns in hydrothermal fluids from mid-ocean ridges. Geochim Cosmochim Acta 58:5105–5113

Li Y-H (1982) A brief discussion on the mean oceanic residence time of elements. Geochim Cosmochim Acta 46:2671–2675

Lodders K (2003) Solar system abundances and condensation temperatures of the elements. Astrophys J 591:1220–1247

Moynier F, Bouvier A, Blichert-Toft J, Telouk P, Gasperini D, Albarède F (2006) Europium isotopic variations in Allende CAIs and the nature of mass-dependent fractionation in the solar nebula. Geochim

E

Cosmochim Acta 70(16):4287–4294. https://doi.org/10.1016/j.gca.2006.06.1371
Olivarez AM, Owen RM (1991) The europium anomaly of seawater: implications for fluvial versus hydrothermal REE inputs to the oceans. Chem Geol 92:317–328
Pack A, Shelley JMG, Palme H (2004) Chondrules with peculiar REE patterns: implications for solar nebular condensation at high C/O. Science 303:997–1000
Palme H, O'Neill HSC (2014) Cosmochemical estimates of mantle composition. In: Holland HD, Turekian KK (eds) Treatise on geochemistry, vol 3, 2nd edn. Elsevier, Amsterdam/Oxford/Waltham, pp 1–39
Palme H, Lodders K, Jones A (2014) Solar system abundances of the elements. In: Holland HD, Turekian KK (eds) Treatise on geochemistry, vol 2, 2nd edn. Elsevier, Amsterdam/Oxford/Waltham, pp 15–36
Piper DZ, Bau M (2013) Normalized rare earth elements in water, sediments, and wine: identifying sources and environmental redox conditions. Am J Anal Chem 04(10):69–83. https://doi.org/10.4236/ajac.2013.410A1009
Rudnick RL, Gao S (2014) Composition of the continental crust. In: Holland HD, Turekian KK (eds) Treatise on geochemistry, vol 4, 2nd edn. Elsevier, Amsterdam/Oxford/Waltham, pp 1–51
Taylor SR, McLennan SM (2010) Planetary crusts – their composition, origin and evolution. Cambridge University Press, Cambridge
Willbold M, Stracke A (2010) Formation of enriched mantle components by recycling of upper and lower continental crust. Chem Geol 276:188–197
Wu C (2008) Bayan Obo Controversy: carbonatites versus Iron Oxide-Cu-Au-(REE-U). Resour Geol 58(4):348–354. https://doi.org/10.1111/j.1751-3928.2008.00069.x
Zheng X-Y, Yang J, Henderson GM (2015) A Robust procedure for high-precision determination of rare earth element concentrations in seawater. Geostand Geoanal Res 39(3):277–292. https://doi.org/10.1111/j.1751-908X.2014.00307.x

Evaporites

John Warren
Petroleum Geoscience Prog., Chulalongkorn University, Bangkok, Thailand

Synonyms

Bittern salts; Marine salts

Definition

A widely accepted definition of an evaporite is "A salt rock originally precipitated from a saturated surface or near-surface brine in hydrologies driven by solar evaporation" (Warren 2016).

How Evaporite Salts Form

Evaporites are the resultant mineral precipitates accumulating in and around an increasingly saline residual brine undergoing evaporation, which has reached a state of supersaturation with respect to a particular mineral salt or salts. This simple definition encompasses a broad range of naturally precipitated salts and includes alkali earth carbonates as well as some halide salts (see also halide salts).

Brine Chemistry and Evolution

The mother brine that precipitates a suite of evaporite salts can be either marine or nonmarine. Sometimes the source of an ancient evaporite salt can be inferred from the chemical proportions of the ions in the deposited salt sequence (Figs. 1 and 2).

Marine Brine

When seawater evaporates, a predictable suite of primary evaporite salts crystallizes from increasingly concentrated hypersaline waters (Fig. 1). Today, the chemical makeup and the proportion of the major ions in seawater are near constant in all the world's oceans and are dominated by Na and Cl, with lesser amounts of SO_4, Mg, Ca, K, CO_3, and HCO_3 (Fig. 1a). Using the brine classification of Eugster and Hardie (1978), modern seawater is a Na–(Mg)–Cl–(SO_4) solution, with a density of ~1.03 g/cc and a salinity around 35 ‰. By the time a modern seawater brine attains the bittern stage (defined by the onset of the potassium and magnesium salts), it has become a Mg–SO_4–Cl brine (Fig. 1a). The first mineral to precipitate in the seawater evaporation series is $CaCO_3$, usually as aragonite. This begins in mesohaline waters when the brine reaches twice the concentration of seawater (40–60 ‰) and achieves a density ≈1.10 g/cc. As the brine continues to concentrate and approaches four to five times the concentration of seawater, that is 130–160 ‰, gypsum precipitates from penesaline waters, with densities around 1.13 g/cc. At 10–12 times the original seawater concentration (340–360 ‰) and densities around 1.22 g/cc, halite drops out of supersaline marine waters.

After halite, the bittern salts (potassium or magnesium sulfates/chlorides) precipitate from supersaline waters with concentrations more than 70–90 times that of the original seawater. Brine density by this stage is more than 1.30 g/cc, while brine viscosity and feel approach that of olive oil. Because magnesium and sulfate, along with chloride, are the major ionic components of a modern seawater bittern, carnallite ($KMgCl_3 \cdot 6(H_2O)$) and epsomite ($MgSO \cdot 7H_2O$) are the dominant bittern precipitates (Fig. 1b). In contrast, sylvite (KCl), not carnallite, was a significant primary bittern salt at different times in the Phanerozoic when seawater contained lesser amounts of dissolved Mg and SO_4. The varying proportion of magnesium relative to calcium and sulfate in Phanerozoic seawater was likely controlled by rates of rock–fluid interactions. Proportions varied according to the rate of

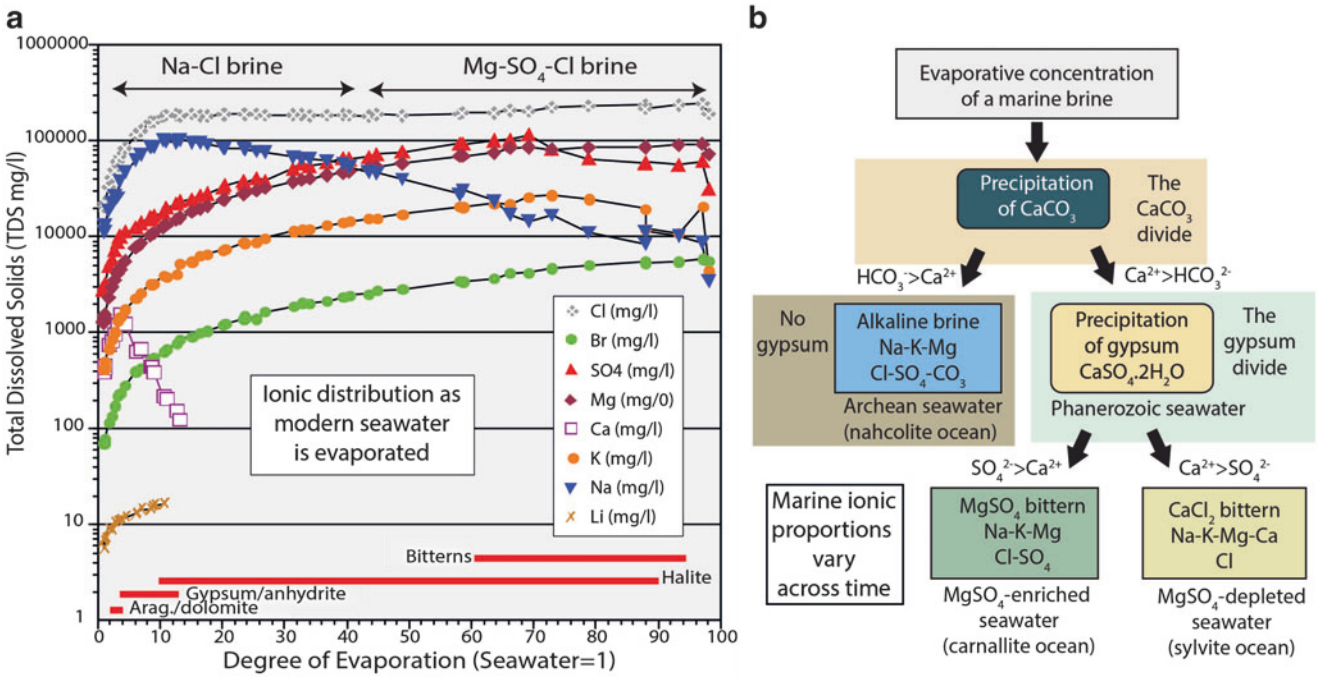

Evaporites, Fig. 1 Chemical evolution of marine brine. (**a**) Changes in ionic proportions due to sequential precipitation of aragonite, gypsum, halite and bittern salts as modern seawater is evaporated to 100 times its original concentration (in part, after McCaffrey et al. 1987; Warren 2016). (**b**) Chemical divides and the evolution of three major brine types in a framework of geological time (in part after Hardie 1990)

creation of newly formed oceanic crust at mid-ocean ridges or varying extents of epeiric seaways and associated rates of dolomitization (Holland et al. 1996; Lowenstein et al. 2014). Further back in time, in the early Archean, when the atmosphere was hotter, lacked oxygen, and contained high levels of CO_2 and CH_4, the typical marine evaporites were aragonite, nahcolite ($NaHCO_3$), and trona ($Na_2CO_3 \cdot NaHCO_3 \cdot 2H_2O$), along with halite, with little or no primary gypsum. Given the vast age of these sediments, the chemically aggressive Archean atmosphere, and the inherent high reactivity of most mineral salts in the subsurface, only silicified or baritized pseudomorphs of Archean evaporite salts remain (Sugitani et al. 2003; Lowe and Tice 2004).

Nonmarine Brine

More diverse, less predictable suites of evaporite minerals precipitate during evaporation of continental waters. In nonmarine settings, rivers and groundwaters source most of the ions that ultimately deposit as evaporite salts. Unlike marine-derived brines, evaporating continental waters do not draw on the near-isochemical reservoir that is the ocean. So, in closed nonmarine hydrologies, the composition of nonmarine brines and the resulting evaporite suite depends on lithologies leaching in the surrounding drainage basin (Eugster and Hardie 1978; Eugster 1980). Flow through limestone aquifers in hydrologically closed basins produces inflow waters rich in Ca and HCO_3, dolomite dissolution generates more Mg, while igneous and metamorphic matrices tend to yield silica-rich Ca–Na–HCO_3 waters. Pyritic shale and other sulfide-rich sediment under today's oxidizing atmosphere contribute sulfate ions, whereas basic and ultrabasic rocks tend to produce alkaline Mg–HCO_3 mother waters. In all, Eugster and Hardie (1978) distinguished five major water types in what they termed "hydrologically closed" continental evaporite basins (Fig. 2a):

I. Ca–Mg–Na–(K)–Cl
II. Na–(Ca)–SO_4–Cl
III. Mg–Na–(Ca)–SO_4–Cl
IV. Na–CO_3–Cl
V. Na–CO_3–SO_4–Cl waters

As any one of these waters concentrates within a particular evaporite basin, it deposits a characteristic suite of evaporite minerals (Fig. 2b). Early precipitates are the alkaline earth carbonates: low-magnesian calcite, high-magnesian calcite, aragonite, and dolomite. Mineralogy of initial precipitates depends on Mg/Ca ratio in the parent brine. Subsequent evaporation pathway (types I, II, and III) of a continental brine is controlled by relative proportions of calcium, magnesium, and bicarbonate ions in inflow waters. That is, early carbonate precipitation sets up geochemical divides that then control subsequent geochemical and mineralogical (Fig. 2a).

Archean seawater, which due to much higher levels of CO_2 in the atmosphere, had a chemical makeup much like a type

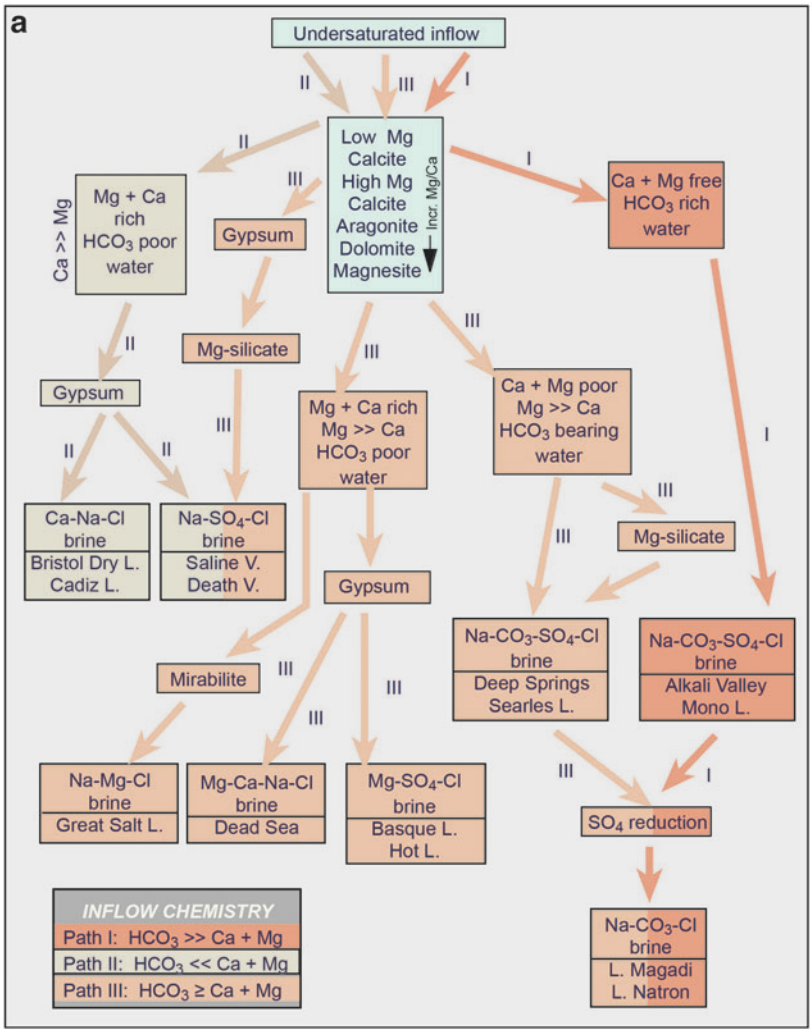

b

Brine Type	Saline Mineral	
Ca-Mg-Na-(K)-Cl	Antarcticite	$CaCl_2.6H_2O$
	Bischofite	$MgCl_2.6H_2O$
	Carnallite	$MgCl_2.KCl.6H_2O$
	Halite	NaCl
	Sylvite	KCl
Na-(Ca)-SO_4-Cl	Tachyhydrite	$CaCl_2.2MgCl_2.12H_2O$
	Glauberite	$CaSO_4.Na_2SO_4$
	Gypsum	$CaSO_4.2H_2O$
	Halite	NaCl
	Mirabilite	$Na_2SO_4.10H_2O$
	Thenardite	Na_2SO_4
Mg-Na-(Ca)-SO_4-Cl	Bischofite	$MgCl_2.6H_2O$
	Bloedite	$Na_2SO_4.MgSO_4.4H_2O$
	Epsomite	$MgSO_4.7H_2O$
	Glauberite	$CaSO_4.Na_2SO_4$
	Gypsum	$CaSO_4.2H_2O$
	Halite	NaCl
	Hexahydrite	$MgSO_4.6H_2O$
	Kieserite	$MgSO_4.H_2O$
	Mirabilite	$Na_2SO_4.10H_2O$
	Thernadite	Na_2SO_4
Na-CO_3-Cl	Halite	NaCl
	Nahcolite	$NaHCO_3$
	Natron	$Na_2CO_3.10H_2O$
	Thermonatrite	$NaCO_3.H_2O$
	Trona	$NaHCO_3.Na_2CO_3$
Na-CO_3-SO_4-Cl	Burkeite	$Na_2CO_3.2Na_2SO_4$
	Halite	NaCl
	Mirabilite	$Na_2SO_4.10H_2O$
	Nahcolite	$NaHCO_3$
	Natron	$Na_2CO_3.10H_2O$
	Thernadite	Na_2SO_4
	Thermonatrite	$NaCO_3.H_2O$

Evaporites, Fig. 2 Nonmarine brine evolution pathways (After Eugster and Hardie 1978). (**a**) Hydrologic classification and brine evolution pathways of concentrating nonmarine waters (*L* lake, *V* valley). (**b**) Listing of major evaporite minerals associated with the different brine types

I brine, tended to precipitate trona and nahcolite, along with some halite but no gypsum (Lowe and Fisher-Worrell, 1999; Sugitani et al. 2003). Thermally dependent type I pathways explain widespread occurrence of nahcolite in saline lacustrine deposits of the Eocene in the USA and China. At that time, atmospheric CO_2 levels were significantly higher than today. During the Eocene climatic optimum, atmospheric CO_2 ranged between 680 and 1260 ppm, compared to current levels around 400 ppm (Jagniecki et al. 2015).

Genetic Mechanism and Salt Texture

For a water molecule to escape into the vapor phase in an evaporitic setting, and so increase the salinity of the residual brine lake, or pore water in a sabkha, the molecule must (1) absorb heat energy, (2) be located near the liquid surface, (3) be moving in the proper direction, (4) have sufficient energy to overcome liquid-phase intermolecular forces, and (5) pass through the surface tension interface.

Simple physics (rate and intensity) of molecular escape during solar evaporation largely controls the hydrological nature of the remaining brine. Brine bodies, either as perennial surface waters or as shallow capillary pore brines, are where various evaporite salts crystallize. Precipitative textures preserved in an accumulating salt bed are the result of concentration levels in the brine and its hydrological setting/stability. In combination, relative brine density and specific heat capacity of adjacent brine masses control density and thermal stratification in saline brine bodies located at or near the earth's surface. Subsequent burial and interaction with other regional shallow and deep phreatic hydrologies control later textural evolution (Warren 2016).

Specific heat, or heat capacity, is the amount of heat needed to raise 1 g of a substance by 1 °C. For a given amount of heat

input, a unit volume of hypersaline water will show a greater increase in temperature than a less saline water. Given the same degree of insolation, this means density-stratified water columns tend to be heliothermic, with the lower, denser bottom brine layer being warmer than the somewhat less saline, less dense, upper water layer (Fig. 3). The condition of a warmer lower water and a cooler upper water is known as heliothermality. The level in a water column where a marked change in temperature occurs in the water column is called the thermocline, and in a density-stratified brine, mass corresponds to the halocline, sometimes also referred to as the chemocline. The combination of high temperature, high salinity, and lowered oxygen in the lower brine mass of a heliothermal brine system means only a specialized biota can survive in these waters, often with a specialized bacterial population occurring in waters just above a saline thermocline (Warren 2011).

Holomixis allows deposition of a consistent salt layer across the whole basin floor, beneath both shallow and deep brine columns. Density stratification allows evaporitic salts to crystallize only in the upper water mass or at the brine–brine interface, so bottom nucleation tends to occur on the shallower lake floor, where it lies above the halocline. That is, long-term (ectogenic) column stratification means bottom nucleation of salts can only occur where the upper salt-saturated brine mass intersects the sediment bottom, with pelagic settling of salts occurring deeper out in the depositional basin. Bottom growth of crystals cannot occur on the deeper bottom beneath a density-stratified system as there is no mechanism to drive ongoing supersaturation in the lower water mass. For the same reason, constant brine reflux driving sinking of a dense brine into sediments below the flow of the evaporite basin can only proceed in significant volumes if the overlying brine mass is holomictic. Deposition of capillary salts (sabkha deposits) occurs in sub-aerial settings, wherever the saline capillary zone intersects the land surface.

When salts are accumulating beneath a holomictic brine mass, the nature of bottom nucleates is controlled by the stability of the overlying brine column (Fig. 3a). When the overlying column is deep (>30–100 m), then, other than areas on the deep bottom of local phreatic outflows, there is no widespread hydrochemical mechanism to drive fluctuations in bottom-brine chemistry. The resulting deep bottom precipitates tend to be monomineralogic crystal clusters, possibly encased by re-transported material washed in from the shallower surrounds (Fig. 3a). In contrast, when the overlying brine column is shallow (<30 m and typically <5–10 m), then the chemistry and stability of the brine varies on a shorter-term (daily weekly) basis, so more layered bottom nucleates can accumulate as layered to laminated salt beds. In addition, all evaporite sediments can be mechanically reworked by process sets that also typify siliciclastic and carbonate sediments (Fig. 3b).

World-Scale Depositional Associations

At the world scale, most ancient evaporites are marine and were deposited in either of two large-scale settings that at times merged into one another, namely, (1) platform evaporites and (2) basinwide evaporites (Fig. 4).

Platform Evaporites

Platform evaporites are made up of stratiform beds, usually <50 m thick and composed of stacked <1–5 m thick parasequences or evaporite cycles, with a variably present restricted marine carbonate at its cycle base (Table 2). Salts were deposited as mixed evaporitic mudflat and saltern evaporites, sometimes with local accumulations of bitterns. Typically, platform salts were deposited in laterally extensive (>50–100 km wide), hydrographically isolated, subsea level marine-seepage seaways known as salterns or in evaporitic mudflats made up of a mosaic of sabkhas and salinas (Warren 2016). These regions had no same-scale modern counterparts and extended as widespread depositional sheets across large portions of marine platform areas, which passed seaward across a sub-aerial seepage barrier into open marine sediments. In marine-margin epeiric settings, such as the Jurassic Arab/Hith and Permian Khuff cycles of the Middle East or the Cretaceous Ferry Lake Anhydrite in the Gulf of Mexico, these platform evaporites are intercalated with shoalwater marine-influenced carbonate shelf/ramp sediments, which in turn pass basinward across a sub-aerial sill into open marine carbonates. Landward, they pass into arid zone continental siliciclastics or carbonate mudflats.

Platform evaporite deposition occurred in pericontinental or intracratonic (epicontinental) settings, at times of low-amplitude sea level changes, which typify greenhouse eustasy. Platform evaporites cannot survive in the high-amplitude, high-frequency sea level changes of icehouse eustasy. The 100 m + amplitude oscillations of icehouse times mean sea level falls off the shelf edge every 100,000 years, so any evaporite that had formed on the platform is sub-aerially exposed and leached. Fourth-order high-amplitude icehouse eustatic cycles also tend to prevent laterally continuous carbonate sediment barriers forming at the top of the shelf to slope break, and so icehouse evaporite systems tend not to be hydrographically isolated (drawdown) at the platform scale. Rather icehouse eustasy favors nonmarine evaporites as the dominant style, along with small ephemeral marine-margin salt bodies.

Platform evaporite successions may contain halite beds, especially in intracratonic basinwide settings, but in peri-platform settings are typically dominated by 5–40 m thick Ca-sulfate beds intercalated with normal marine platform carbonates. The lateral extent of these epeiric platform salts, like the Khuff Anhydrite with its area of 1,206,668 km^2, constitutes some of the most aerially extensive evaporite beds ever deposited.

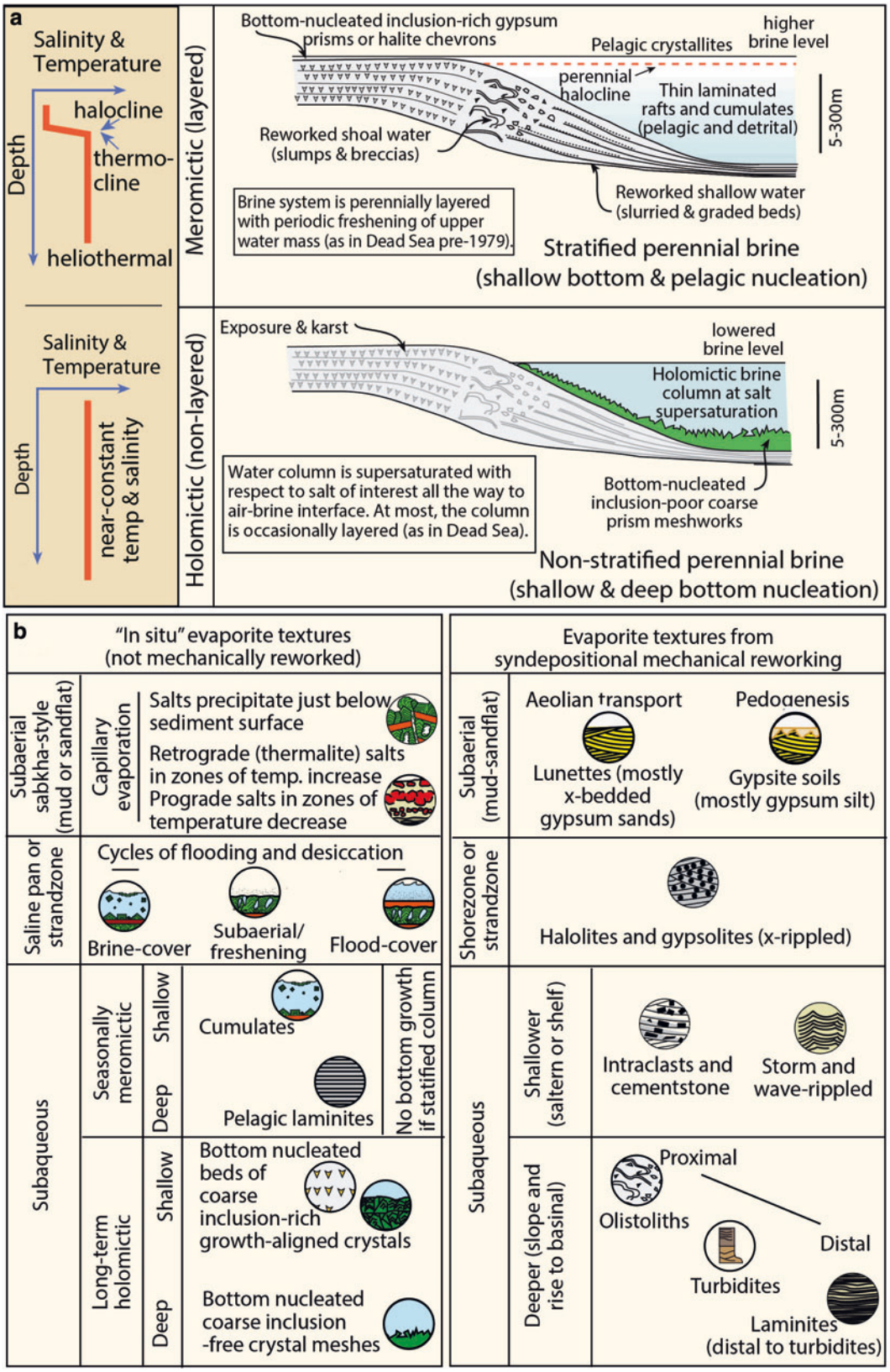

Evaporites, Fig. 3 Textures are controlled by hydrology (After Warren 2016). (**a**) Inter-relationships between brine stratification, stability and depositional texture. (**b**) When brine column is stratified, bottom nucleation is restricted to shallower areas, when holomictic, bottom nucleated growth possible over whole basin floor

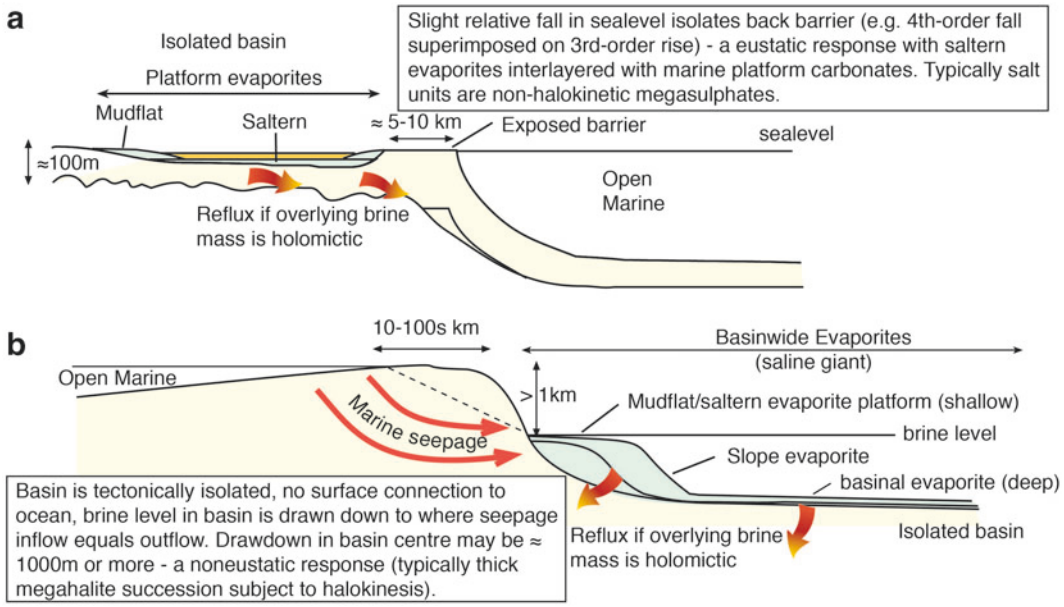

Evaporites, Fig. 4 Schematic cross sections of ancient evaporite settings that have no modern counterparts. (**a**) Platform evaporites. (**b**) Basinwide evaporites

Basinwide Evaporites

Basinwide evaporites are made up of thick evaporite units >50–100 m thick made up of varying combinations of deep-water and shallow water evaporites. They retain textural evidence of different but synchronous depositional settings, including mudflat, saltern, slope, and basin (Fig. 4). When evaporite deposition took place, the whole basin was evaporitic, holomictic, and typically saturated with the same mineral phase across vast areas of the basin floor (as when today in the Dead Sea basin, but within its more limited lateral scale, halite forms decimeter-thick chevron-dominated beds on the saline-pan floor and coarse inclusion-poor crystal meshworks on the deep basin floor). Basinwide successions are usually dominated by thick massive salt beds (generally more than 100 m thick), which are made up of stacked thick halite beds, but can also contain substantial volumes of thick-bedded Ca-sulfate and evaporitic carbonate, as in the intracratonic basinwide accumulations of the Delaware and Otto Fiord Basins.

Some basinwide systems (mostly marine-fed intracratonic) also entrain the larger accumulations of the world's potash salts, even though our only Quaternary examples of economic potash are continental systems (Warren 2010). Owing to inherent purity and thickness of the deposited halite, many halite-dominant basinwide beds are also remobilized via loading or tectonics into various halokinetic geometries (Hudec and Jackson 2007).

Basinwide evaporite deposits require tectonically and hydrologically isolated widespread subsea level depressions that are not currently present on the world's surface. They were last active in the Late Miocene, in association with soft-suture collision basins tied to the Alpine–Himalaya orogenic belt and to Middle Miocene basins developed in the early rift stages of the Red Sea. Basinwide systems will be active again in the future at sites and times of appropriate plate–plate interaction, when two continental plates are nearby and the intervening floor at or near a plate-edge rift or suture is both subsea level and hydrographically isolated.

Lacustrine (Nonmarine) Evaporites

Quaternary continental playa/lacustrine is constructed of stratiform salt units, with the greater volume of saline sediment accumulating in lower, more saline portions of the lacustrine landscape. Beds are usually dominated by nodular gypsum and displacive halite, deposited in widespread evaporitic mudflats and saltpans, rather than as bedded bottom-nucleated layers on the subaqueous floors of perennial brine lakes. In ancient counterparts, the total saline lacustrine thickness ranged from meters to hundreds of meters, with lateral extents measured in tens to hundreds of kilometers. Lacustrine salt beds are separated vertically and usually surrounded by deposits of lacustrine muds, alluvial fans, ephemeral streams, sheet floods, eolian sands, and redbeds. As today, ancient lacustrine salts accumulated in endorheic or highly restricted discharge basins, with perennial saline water masses tending to occur in the drainage sumps of steep-sided drainage basins (Warren 2010, 2016). Saline lake basins accumulating gypsum, or more saline salts like halite or glauberite, typically have a shallow water table in peripheral saline mudflat area and so are dominated by sabkha textures.

The lowermost part of the lacustrine depression or sump is typified by ephemeral ponded brine pan deposits rather than permanent saline waters with subaqueous textures lacking evidence of drawdown and exposure.

Across the Quaternary, less-saline perennial saline lake beds tend to occur during more humid periods in the same continental lacustrine depressions where saline pan beds form today (e.g., Lake Magadi, Great Salt Lake, Lake Urmia). On a smaller scale, in some modern saline lake basins, parts of the lake floor can be permanently located below sea level (Northern Basin in the Dead Sea, Lake Assal). In some modern saline sumps dominated by mudflats, a perennial saline lake water mass can be located toward the edge of a more central salt-flat zone, forming a "moat" facies (Salar de Atacama, Salar de Uyuni, Lake Magadi, Lake Natron). These permanent saline water "moat" regions are typically created where fresher inflows come in contact with saltier beds of the lake center, dissolve them, and so form water-filled peripheral depressions.

As mentioned earlier, saline lacustrine evaporite mineralogies depend on compositions of inflowing waters (Fig. 1); suitable settings can accumulate thick sequences of nonmarine salts such as trona, glauberite, and thenardite, as well as more typical sequences of halite, gypsum, and anhydrite. High-water stage perennial saline lacustrine sediments tend to be carbonate-rich or silica-rich (diatomaceous) laminites. Ancient examples of large saline lacustrine deposits include the Eocene Green River Formation of Wyoming and the Permian Pingdiquan Formation of the Junggar Basin, China. Evaporites deposited in a supra-sealevel lacustrine basin (especially Neogene deposits) have numerous same-scale quaternary analogs, unlike the more voluminous ancient marine platform and basinwide evaporites.

Summary

Evaporites are sedimentary salts precipitated at or just below the earth's surface in arid hydrologies where the concentration of the mother brine is driven by solar evaporation. Inflow brines can be either nonmarine (continental) or marine (seawater supplied). The largest modern evaporite settings are continental endorheic sumps with base levels that may be hundreds to thousands and meters above sea level. The largest ancient evaporite basins were marine, with vast expanses of bedded salt accumulating in seawater-seepage fed, sub-sealevel basins. Ancient marine evaporite basins were of two types, (a) platform evaporite systems and (b) basinwide evaporite systems. Platform evaporite systems typify epeiric and intracontinental seaways during times of basin restriction in arid settings when the earth was in greenhouse climate mode. Basinwide evaporite systems are tectonically induced and accumulated large volumes of salt at times of plate tectonic-scale continent–continent proximity in both extensional (early rift) and compressional (suture basins) plate-scale settings. Platform and basinwide settings require hydrographical isolation of the evaporite basin, that is, no long-term surface connection to waters of the open ocean, but typically had an ongoing marine seepage (drawdown) connection. Because of the continual seepage connection to the large isochemical of the ocean, volumes of salt found in ancient marine evaporite basins are much larger than any continental lacustrine evaporite system (modern or ancient). Because of the earth's current icehouse mode, and a lack of appropriate zones of continent–continent proximity, there are no regions on the earth's surface where large-scale platform or basinwide hydrologies are currently active. The last time a basinwide system was active was across the various Messinian (Late Miocene) basins of the Mediterranean, while the last time a widespread set of bedded platform evaporite salts accumulated was during the Eocene in the Middle East.

Cross-References

- ▶ Aqueous Solutions
- ▶ Carbonate Minerals and the CO2-Carbonic Acid System
- ▶ Halide Minerals
- ▶ Heat Capacity
- ▶ Ocean Biochemical Cycling and Trace Elements
- ▶ Sulfate Minerals

References

Eugster HP (1980) Geochemistry of evaporitic lacustrine deposits. Annu Rev Earth Planet Sci 8:35–63

Eugster HP, Hardie LA (1978) Saline lakes. In: Lerman A (ed) Lakes; chemistry, geology, physics. Springer, New York, pp 237–293

Hardie LA (1990) The roles of rifting and hydrothermal $CaCl_2$ brines in the origin of potash evaporites: an hypothesis. Am J Sci 290:43–106

Holland HD, Horita J, Seyfried W (1996) On the secular variations in the composition of Phanerozoic marine potash evaporites. Geology 24:993–996

Hudec MR, Jackson MPA (2007) Terra infirma: understanding salt tectonics. Earth Sci Rev 82:1–28

Jagniecki EA, Lowenstein TK, Jenkins DM, Demicco RV (2015) Eocene atmospheric CO_2 from the nahcolite proxy. Geology 43:1075–1078

Lowe DR, Fisher-Worrell G (1999) Sedimentology, mineralogy, and implications of silicified evaporites in the Kromberg formation, Barberton Greenstone Belt, South Africa. In: Lowe DR, Byerly GR (eds) Geologic evolution of the Barberton Greenstone Belt, South Africa, Special paper, vol 329. Geological Society of America, pp 167–188

Lowe DR, Tice MM (2004) Geologic evidence for Archean atmospheric and climatic evolution: fluctuating levels of CO2, CH4, and O2 with an overriding tectonic control. Geology 32:493–496

Lowenstein T, Kendall B, Anbar AD (2014) Chapter 8.21. The geologic history of seawater, treatise on geochemistry, 2nd edn. Elsevier, pp 569–621

McCaffrey MA, Lazar B, Holland HD (1987) The evaporation path of seawater and the coprecipitation of Br − and K+ with halite. J Sediment Petrol 57:928–937
Sugitani K, Mimura K, Suzuki K, Nagamine K, Sugisaki R (2003) Stratigraphy and sedimentary petrology of an Archean volcanic-sedimentary succession at Mt. Goldsworthy in the Pilbara Block, Western Australia: implications of evaporite (nahcolite) and barite deposition. Precambrian Res 120:55–79
Warren JK (2010) Evaporites through time: tectonic, climatic and eustatic controls in marine and nonmarine deposits. Earth Sci Rev 98:217–268
Warren JK (2011) Evaporitic source rocks: mesohaline responses to cycles of "famine or feast" in layered brines, Doug Shearman memorial volume, IAS special publication number, vol 43, Wiley-Blackwell, pp 315–392
Warren JK (2016) Evaporites: A Compendium. Springer, Berlin, 1854 p. ISBN 978-3-319-13511-3

Experimental Mineralogy and Petrology

Charles A. Geiger[1] and Tatsuhiko Kawamoto[2]
[1]Department of Chemistry and Physics of Materials, Section Mineralogy, University of Salzburg, Salzburg, Austria
[2]Institute for Geothermal Sciences, Graduate School of Science, Kyoto University, Kyoto, Japan

Definition

Experimental mineralogy and petrology is an Earth science discipline that models or simulates mineralogical, petrological, and geochemical processes within the laboratory in order to understand the physical and chemical properties of minerals, rocks, melts, and fluids and their interactions. For example, most of Earth's interior and that of other planets are not accessible to direct study. Thus, various types of high-pressure and high-temperature experiments are carried out in order to obtain an understanding of deep Earth and planetary structure and behavior.

History and Introduction

The field of experimental mineralogy and petrology, which constitutes a part of the geological or Earth sciences, can be traced back for at least 200 years. The Scottish geologist Sir James Hall (1761–1832) is considered to be the father of experimental petrology. His laboratory experiments on the melting and crystallization of basaltic magmas were decisive in resolving the debate between the Plutonist and Neptunist schools of geologists in the late eighteenth and early nineteenth centuries and in favor of the former. His results illustrated the power of laboratory investigations for a scientific field that was field orientated and observational. The publication of N.L. Bowen's well-known book *The Evolution of the Igneous Rocks* in 1928, which was largely based on his pioneering laboratory melting investigations on simple model silicate systems at the Geophysical Laboratory of the Carnegie Institute of Washington, D.C., proved the necessity of experimentation in understanding the diversity of igneous rocks found in Earth. It was not until the last half of the twentieth century, though, that experimental mineralogy and petrology became an integral part of geology departments at universities.

The main, but not only, goal of experimental mineralogy and petrology is to model or simulate certain conditions within the laboratory in order to understand the physical and chemical properties of minerals, rocks, melts, and fluids and their interactions. As such, it is closely linked to the field of geochemistry and also partly geophysics. Most of Earth's interior and that of other planets are not accessible to direct study. Thus, it is necessary to simulate conditions or model geochemical or geophysical processes in order to gain a more complete understanding of these bodies. In addition, experimental mineralogical studies can have technical applications relating it, in part, to the fields of inorganic and physical chemistry, solid-state physics, and materials science.

The physicist Percy Bridgman (1882–1962), a foremost scientist in high-pressure research and a Noble prize recipient, developed methods to reach conditions up to 2 GPa in 1905 while a student at Harvard University. Since then, studies have increased greatly in variety and complexity with technical advances so great and wide-ranging that it is presently possible to make experiments in the laboratory between pressures of 0.01 Pa and 100 GPa on mm-size samples using various large-volume presses (Fig. 1) and up to 500 GPa on micrometer-size samples with a small hand-sized diamond anvil cell (DAC, Fig. 2). Accessible temperatures range from those of liquid helium (~3 K) for SQUID magnetic susceptibility measurements in the DAC up to 6,000 K using focused laser heating in the same device. Hence, it is now technically possible to simulate the full range of pressure-temperature (*P-T*) conditions encountered on and within Earth, other rocky planets, and extraterrestrial bodies as well the large gaseous planets to substantial depths.

Phase Equilibrium Experiments: The Mineralogy and Petrology of the Earth

Traditionally, phase equilibrium studies have played the central role in experimental mineralogy and petrology. They normally consider the *P-T-X* stability relations, where *X* represents the composition of the system under study, namely, a mineral, mineral assemblage (i.e., rock), melt, or

fluid phase. In most experiments, a sample, either synthetic or natural in nature, is held for a certain length of time at the desired *P-T* condition in some device, quenched to ambient conditions, and the experimental products are examined. Normally, the assumption is made that chemical equilibrium was achieved at the *P* and *T* of the experiment and it is preserved in the quenched state. The chemical and structural state of the different phases from a series of experiments can then be characterized and a *P-T* phase diagram, for example, constructed. Hence, various solid-state mineral reactions, melting relations, solid phase transitions, fluid-rock interactions, or changes in chemical and physical properties can be described. In the 1980s, in situ experiments using the DAC and simple optical observation were made, which is possible because of the transparency of diamond. Intense synchrotron radiation can be used for in situ experiments using large-volume multi-anvil type (Fig. 1) or toroidal-cell-type devices, and the DAC (Fig. 2). X-ray diffraction, absorption, and fluorescence measurements are possible.

Phase equilibrium studies are coupled to the field of chemical thermodynamics. The stability of a given phase with respect to another phase or phase assemblage is a function of the *P-T-X* conditions of the system. Thermodynamic analysis enables experimental results to be extrapolated outside of the *P-T* conditions under study and also to extract thermodynamic properties of the participating phases.

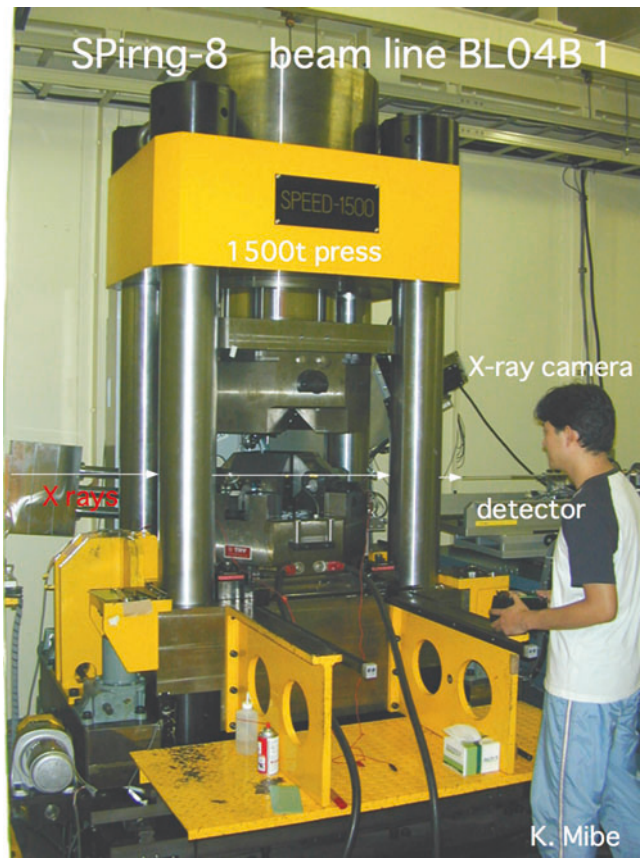

Experimental Mineralogy and Petrology, Fig. 1 A large volume 1,500-ton Kawai-type multi-anvil press used in connection with synchrotron radiation at the SPring-8 facility, Japan, in order to study various processes in situ at high *P* and *T*. (Kawamoto et al. 2012, Proceedings of the National Academy of Sciences, U. S. A., 109, 18695)

Some important areas involving phase equilibrium study have involved or are:

i. The determination of phase diagrams showing *P-T* stability relations for key minerals and their reactions in Earth's crust and upper mantle. Here, cold-seal (for $P < 0.5$ GPa) and solid-media piston-cylinder (for $P < 5$ GPa) devices are often used. Various mineral geothermometers and geobarometers have also been calibrated. They can be used, as with phase diagrams, to determine paleo *P-T* conditions experienced by buried rocks, which have been returned to Earth's surface in a metamorphic cycle, for example, to understand tectonic events of the crust.

ii. In terms of igneous petrology, laboratory studies made in the 1950s at relatively low pressures and temperatures ($P < 0.5$ GPa and $T < 750$ °C) showed that most natural granitic bodies are the products of partial melting processes in the continental crust and were not formed by fluid-related metasomatic processes, as had been advanced by some field geologists.

iii. To understand the mineralogy of the deeper mantle, experiments using various multi-anvil devices and the DAC over the past 50 years have been made. They show that Earth's transition zone, located between seismic discontinuities at 400 and 670 km depth, consists largely of β-Mg_2SiO_4 (wadsleyite) or γ-Mg_2SiO_4 (ringwoodite) and a compositionally complex garnet solid solution containing a majorite component [$Mg_3(Mg,Si)Si_3O_{12}$]. The 400 km discontinuity is related to the relatively sharp phase transition of upper-mantle olivine (Mg_2SiO_4) to β-Mg_2SiO_4. Experiments using the DAC and multi-anvil devices have shown that below the 670 km discontinuity, in the lower mantle, $MgSiO_3$ bridgmanite and magnesiowüstite [(Mg,Fe)O] are stable. The former phase is considered the most abundant silicate in Earth. At even higher *P* and *T* conditions, DAC experiments led to the discovery of a new phase called post-bridgmanite, which is thought be a main constituent of the D″ layer at the mantle-core boundary.

iv. DAC experiments at extreme *P* and *T* are now being made on the system Fe–O–S with or without H, for example, in order to better understand the nature of Earth's Fe-rich outer and inner core.

Fluid, Melt, and Rheological Behavior at High Pressure and Temperature

Research has been carried out to study the phase relations and thermodynamic behavior of single or multicomponent fluids

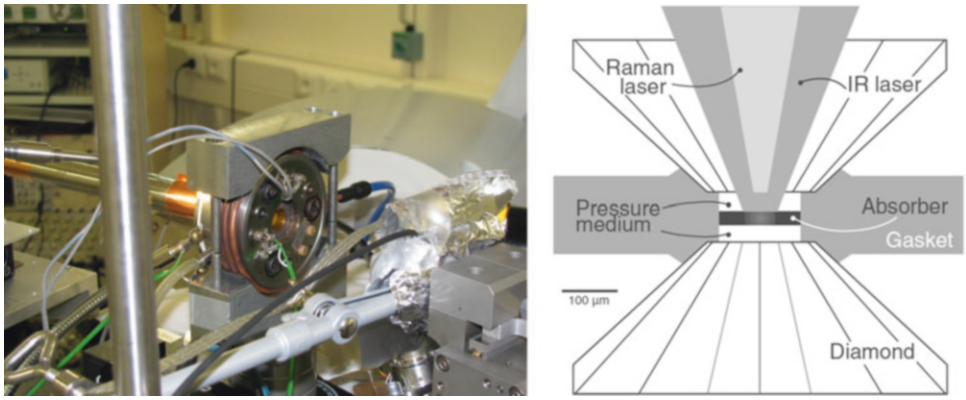

Experimental Mineralogy and Petrology, Fig. 2 (*left*) Externally heated Bassett-type hydrothermal diamond anvil cell (DAC) setup used for high-*P* and high-*T* investigations in connection with synchrotron radiation at the Soleil facility, France. The cell size is 75 mm in diameter. (Kawamoto et al. 2014, Earth, Planets and Space, v. 66, 61). (*right*) Schematic figure showing just the two diamond anvils. Between the diamond faces, a sample is enclosed in NaCl, for example, which serves as the pressure-transmitting medium and thermal insulator. Here, focused heating is done internally using an IR laser, and Raman and synchrotron X-ray measurements can be made (Uts et al. 2013, Reviews of Scientific Instruments, v. 84, 103904)

(e.g., H_2O, H_2O–CO_2, H_2O–CO_2–CH_4). Equations of state have been developed that describe *P*-*V*(volume)-*T* relations to extreme conditions. In addition, much work over the years has been made to understand mineral or rock phase relations with fluids at high *P* and *T*. Research has showed that water is soluble in silicate melts as molecular H_2O and OH^-. Starting in the 1960s, the critical endpoints between SiO_2 and aqueous fluids were determined at 1 GPa, and it was determined that those between H_2O and various natural rocks occurred at higher pressures. The compositions of basaltic and high-Mg andesitic partial melts derived from mantle peridotite in the presence of H_2O were determined at 1 GPa in the 1990s. At pressures greater than 3 GPa, partial melts of hydrous peridotite are more mafic in composition than those obtained by anhydrous melting. Experiments also showed that the composition of aqueous fluids changes with pressure. Those coexisting with forsterite (Mg_2SiO_4) and enstatite ($MgSiO_3$) are relatively silica rich from 1 to 2 GPa, but they become more mafic than enstatite in composition at 3 GPa and are close to peridotite composition from 3 and 5 GPa. The interpretation is that the solvus between melt and aqueous fluid in the peridotite-H_2O system closes at pressures greater than 3 GPa.

More recently, the critical endpoints between various natural rock compositions and aqueous fluids have been studied in situ with multi-anvil devices using synchrotron X-ray radiography. The second critical endpoints are located at 2.5 GPa and 700 °C for pelite-H_2O, 2.9 GPa and 800 °C for high-Mg andesite-H_2O, 3.4 GPa and 900 °C for basalt-H_2O, and 3.8 GPa and 1,000 °C for peridotite-H_2O. These results are significant because beyond the endpoints, there is no phase separation between silicate melt and aqueous fluid. Only a single fluid phase exists.

The solubility of minerals in aqueous fluids has also been investigated in situ using the DAC via simple visual observation or using synchrotron X-ray fluorescence. The results agree with those obtained using the larger devices. Finally of note, the solubility of hydrogen in nominally anhydrous minerals (e.g., olivine, pyroxene, garnet, plagioclase, wadsleyite, ringwoodite, bridgmanite) coexisting with free aqueous fluids, as well as the hydrogen partitioning behavior between minerals and silicate melts, has been determined from high-*P* and high-*T* quenched experiments. It has been argued through these investigations that Earth's mantle possibly contains several "oceans of water" relative to its hydrosphere.

The physical processes governing melt generation, segregation, and extraction, from an initially solid source, are important in understanding magma genesis and transport. Experimental studies have determined the amount of melt that must be present and under which physical conditions, before it can separate from a crystalline matrix. Mg-rich silicate melts, which are difficult to quench from high *P* and *T*, can be studied using the "floating-bead method" with laser heating, with which it is possible to make forsterite (Mg_2SiO_4) glass. Laboratory measurements have shown that some silicate melts are more compressible than their equivalent crystalline materials and that at some elevated pressure, a crossover point occurs such that melts will have negative buoyancy and crystals will float even under hydrous conditions. Investigations have also focused on measuring the macroscopic physical properties, such as density and viscosity, of silicate- and oxide-based melts for both model and natural composition systems. High-pressure compression experiments on some crystalline silicates have shown that pressure-induced amorphization can be achieved without heating or melting. Hence, the realm between the amorphous state of glass, having only short-range order, and crystalline materials, having long-range translational

symmetry, may not be as widely separated as previously believed.

Rheological studies have been made on the deformational properties of Earth materials and in the presence or absence of a fluid and differential stress. Using synchrotron X-rays, deformation experiments in large-volume multi-anvil apparatus have been carried out at controlled strain rates at high-*P* and high-*T* conditions. High-pressure experiments to investigate the conversion of olivine to β-Mg_2SiO_4 have been undertaken to understand the physical properties of subducting lithosphere. The metastable persistence of olivine beyond its equilibrium pressure stability in relatively cool subducted slabs, followed by a sudden transition to β-Mg_2SiO_4, has been proposed as a mechanism for triggering deep-focus earthquakes.

Rock physics and fracture-mechanics investigations, often undertaken by the engineering community, have now also found a place within the Earth sciences. Deformation and textural studies of polymineralogic rocks, highlighting their anisotropic physical properties, are important for interpreting seismic profiles of the lower crust and upper mantle. The lattice preferred orientation of olivine is used as a hydrometer and also to determine stress conditions in the upper mantle. Fracture mechanics studies, concerning the strength and ductility of crustal rocks, are undertaken to better understand, for example, the cause of earthquakes generated in active fault zones.

Low-Temperature Mineral Solubility and Kinetic and Diffusion Studies

At low *P-T* conditions, with *T* less than roughly 300 °C, solubility measurements of minerals in H_2O can be made. The results can be used to extract thermodynamic data for phases that are not stable at high temperatures or where the kinetics of growth are slow, and, hence, thermodynamic equilibrium is not reached. These experiments are designed to understand, for example, near surface geological processes and hydrosphere-lithosphere interactions. Studies have been undertaken to model seawater-basalt interactions occurring at ocean spreading centers and to understand the processes causing submarine sulfide precipitation and ore-forming reactions.

Phase equilibrium work is complemented by atomic diffusion studies of minerals, glasses, and melts and kinetic studies of reactions. Experiments investigating the rates of cation or anion diffusion in minerals at different *P* and *T* conditions have been done and interpreted using the theory of chemical kinetics. In these studies, atomic diffusion coefficients have been determined for important rock-forming crystals such as olivine and garnet to better understand their compositional zoning. It is possible to estimate the cooling histories of some rocks and meteorites using such data.

The study of crystalline point defects in minerals is important in kinetic-related experiments, as it is in investigations of electrical and thermal conductivity behavior. Impedance spectroscopy and EMF measurements using oxygen-sensitive solid electrolytes are used in studies of point defects and electrical conductivity.

Mineral Physics and Experimental Measurement Techniques

Mineral physics is a scientific field related to experimental mineralogy and petrology that largely focuses on the physical properties of minerals often, but not only, at extreme *P-T* conditions. The fields of geophysics and mineralogy have merged, in part, creating the field of high-*P* mineral physics. Investigations employ an ever-increasing variety of techniques to study condensed matter properties. Diffraction measurements often use synchrotron radiation. In addition, infrared, Raman, Mössbauer, nuclear magnetic resonance (NMR), X-ray absorption (i.e., EXAFS and XANES), UV/VIS optical absorption, electron paramagnetic resonance, and neutron spectroscopies are being used routinely.

Magic-angle spinning NMR work has been made on glasses synthesized in the laboratory to determine their local properties such as the type of polyhedral coordination units that are present and their degree of polymerization. Some NMR measurements can even be made directly at high *T* in the stability field of the melt phase. Raman and IR spectroscopy are used in DAC experiments at high-*P* and high-*T* conditions. Inelastic synchrotron X-ray scattering measurements are made to study the electronic state of various elements and their oxygen coordination behavior at high pressures.

The determination of density and bulk modulus and its pressure derivatives (equations of state) of mantle phases and silicate melts is needed for the interpretation of seismic velocity profiles measured in Earth. They are used in models that attempt to understand early Earth differentiation and Earth structure with depth. The elastic constants at room temperature of most of the important rock-forming silicates have been measured by ultrasonic and Brillouin methods. They, together with diffraction measurements made in the DAC, allow the density and bulk moduli of minerals to be determined. X-rays at synchrotron facilities permit, further, both the *P* and *T* effects on the elastic properties and sound wave velocities to be measured. The results are important because density and sound velocity properties of minerals can be compared with geophysical seismic measurements through the whole Earth to analyze mantle structure and its mineralogical composition with depth.

Other measurement techniques that are being employed include electron back-scattered diffraction to determine

single-crystal orientations. Computer tomography is used to make nondestructive analyses of the 3D distributions of minerals, melts, and pore spaces in both natural and synthetic rocks. Very minute sections of experimental charges retrieved from laser-heated high-*P* and high-*T* DAC experiments can be excised using focused ion beams for careful transmission electron microscopy examination that indicate reaction and melting features.

Crystallographers and mineral physicists have contributed knowledge to other fields concerned with crystal chemistry and chemical bonding behavior such as inorganic and physical chemistry and solid-state physics. An emphasis is being placed on understanding the atomistic scale behavior of Earth materials (e.g., minerals, melts, fluids) and their relationship to macroscopic properties and under different, often extreme, *P-T-X* environments.

Mineral Synthesis

The discipline of mineral synthesis is also an important, but often overlooked, part of experimental mineralogy and petrology. The growth or production of single crystals, mineral assemblages, or glasses in the laboratory are invaluable for other investigations. For example, compositionally simple end-member and solid-solution minerals, which cannot be found in nature, have been synthesized for calorimetric measurements to determine their thermodynamic properties. These thermodynamic data have been used to construct geothermobarometers and calculate various *P-T* positions of mineral reactions and complement those calibrated in phase equilibrium experiments. Single crystals are grown for crystal-chemical study using different spectroscopic and diffraction techniques. Polycrystalline nano-diamonds are synthesized directly from graphite at high *P* and *T*, and they are harder than single crystal diamond. They can be used, for example, to generate the highest pressures in large-volume multi-anvil devices.

Present and Future Developments

Today, there is an extensive and impressive arsenal of experimental techniques available for investigating the chemical and physical properties of Earth and planetary materials. Traditional methods used in experimental mineralogy and petrology of just 30 years ago largely involved optical microscope examination, X-ray powder diffraction measurements, and chemical analysis using the electron microprobe. Technical developments have made it possible to make measurements on continually smaller amounts of material and at higher spatial resolutions. The development and construction of large national and international research facilities has increased. Dedicated third-generation synchrotron sources, characterized by extremely intense radiation, and advanced neutron spallation sources are permitting new condensed matter experiments unimaginable 30 years ago. Novel experiments and measurements on minerals and other materials are being made, and investigations are of increasing complexity and cost and sometimes involve teams of specialists and researchers.

Applied research, though not discussed here, is becoming more widespread, and collaborations between mineral physicists and material scientists and condensed matter physicists are increasing. Experimentalists are needed to apply their expertise to solve environmental problems in such areas as radioactive waste disposal, pollution control and cleanup and in finding ways to reduce atmospheric CO_2 by storage in underground reservoirs and through CO_2 binding by forming carbonate minerals. Here, the field of experimental mineralogy and petrology strongly overlaps that of geochemistry.

Concomitant with these experimental developments, there has been an increase in theoretical and computer studies (computational or theoretical mineralogy). Molecular dynamic simulations, empirically based static lattice energy, lattice dynamic, and ab initio quantum mechanical calculations are being applied in a variety of mineralogical, geochemical, and geophysical studies. Experimentalists can use these calculations to guide their avenues of research and to interpret their results. Calculations can be used to plan experiments and to predict certain behavior, but ultimately it is in the laboratory or in nature where they must be tested.

Summary

The field of experimental mineralogy and petrology has become extremely diverse encompassing many different approaches and areas of research. The principles of physics and chemistry are of increasing importance in many areas of the Earth sciences. Developments point to the breakdown of traditional borders both within the Earth sciences and between it and other scientific disciplines. The synergy generated by closer collaboration between different scientific disciplines is spawning new methods and types of experiments and is providing an evermore quantitative and comprehensive understanding of a variety of Earth processes.

Cross-References

- ▶ Fluid–Rock Interaction
- ▶ Formation and Evolution of the Earth
- ▶ Fractional Crystallization and Assimilation

- ▶ Geochemical Thermodynamics
- ▶ Geothermometry and Geobarometry
- ▶ Kinetics of Geochemical Processes
- ▶ Magmatic Process Modeling
- ▶ Partial Melting
- ▶ Partitioning and Partition Coefficients.
- ▶ Phase Equilibria

References

Henderson GS, Neuville DR, Downs RT (eds) (2014) Spectroscopic methods in mineralogy and material sciences. Reviews in mineralogy and geochemistry. Mineralogical Society of America and Geochemical Society, vol 78. Minerological Society of America, Chantilly, 800 pp

Holloway JR, Wood BJ (1988) Simulating the earth: experimental geochemistry. Unwin Hyman, Boston. 196 pp

Kawamoto T, Kanzaki M, Mibe K, Matsukage KN, Ono S (2012) Separation of supercritical slab-fluids to form aqueous fluid and melt components in subduction zone magmatism. Proc Natl Acad Sci USA 109:18695

Kawamoto T, Mibe K, Bureau H, Reguer S, Mocuta C, Kubsky S, Thiaudière D, Ono S, Kogiso T (2014) Large ion lithophile elements delivered by saline fluids to the sub-arc mantle. Earth Planets Space 66:61

Miletich R (ed) (2005) Mineral behaviour at extreme conditions, European Mineralogical Union – notes in mineralogy, vol 7, McLean. 488 pp

Oelkers EH, Schott J (eds) (2009) Thermodynamics and kinetics of water-rock interaction, Reviews in Mineralogy and Geochemistry, vol 70. Mineralogical Society of America and Geochemical Society, Chantilly. 569 pp

Uts I, Glazyrin K, Lee KKM (2013) Effect of laser annealing of pressure gradients in a diamond-anvil cell using common solid pressure media. Rev Sci Instrum 84. 103904 pp

F

Ferromanganese Crusts and Nodules: Rocks That Grow

Kira Mizell[1,2] and James R. Hein[1]
[1]Pacific Coastal and Marine Science Center, U.S. Geological Survey, Santa Cruz, CA, USA
[2]Department of Ocean Sciences, University of California, Santa Cruz, Santa Cruz, CA, USA

Synonyms

Cobalt crusts; Cobalt-rich ferromanganese crusts; Fe-Mn crusts; Fe-Mn nodules; Ferromanganese crusts; Ferromanganese nodules; Iron-manganese crusts; Iron-manganese nodules; Polymetallic crusts; Polymetallic nodules

Definition

Ferromanganese (Fe-Mn) crusts and nodules are marine sedimentary mineral deposits, composed mostly of iron and manganese oxides. They precipitate very slowly from seawater, or for nodules also from deep-sea sediment pore waters, recording the chemical signature of these source waters as they grow. Additional elements incorporate via sorption processes onto the Fe-Mn oxides, including rare and valuable metals that can reach concentrations that are economically valuable.

Introduction

Fe-Mn crusts and nodules occur throughout the global ocean, from the flanks of seamounts to the abyssal plains of the deep ocean. Unique compared to other marine rocks, Fe-Mn mineral deposits actually grow over time. They grow extremely slowly by precipitation of metals from seawater onto seamount rock outcrops for Fe-Mn crusts, and for nodules by precipitation from both seawater and bottom-sediment pore waters around nuclei at the sediment surface. Although the deposits are composed mainly of iron and manganese oxide minerals, their unique formation allows for the acquisition and concentration of numerous other elements, many of which are economically valuable, including critical metals, platinum group metals, and the rare earth elements. The concentrations of metals vary with water depth and geographic location. Fe-Mn crusts and nodules are excellent archives for paleoceanographic conditions and are used extensively to understand Earth's geologic history. The study of Fe-Mn deposits is therefore very active as scientists probe them at a molecular level for paleoceanographic and element mass-balance studies, and scientists, governments, and companies pursue them from the level of global- to local-scale distributions to understand and quantify their valuable metal contents.

Formation and Composition

Mechanism of Chemical Sedimentation

Fe oxyhydroxide and Mn oxide are the dominant minerals that compose Fe-Mn crusts and nodules, and additional metals are sorbed onto these main phases (see "Mineralogy" section below for further information). When seawater is the sole source of the metals, which is true for all crusts and some nodules, the deposit is called hydrogenetic. Elements dissolved in seawater are derived predominantly from land via rivers and wind-blown dust, which then dissolve to various degrees forming ions and complexes. Another source of elements to seawater is hydrothermal venting that occurs along the 89,000 kilometers (km) of oceanic spreading centers and volcanic arcs, which is the source of most manganese and some iron dissolved in seawater. When metals are supplied from the pore waters of seafloor sediments, the deposits are called diagenetic. Metals in the pore-fluid are derived from diagenetic oxidation-reduction (redox) reactions that occur in

W. M. White (ed.), *Encyclopedia of Geochemistry*,
https://doi.org/10.1007/978-3-319-39312-4

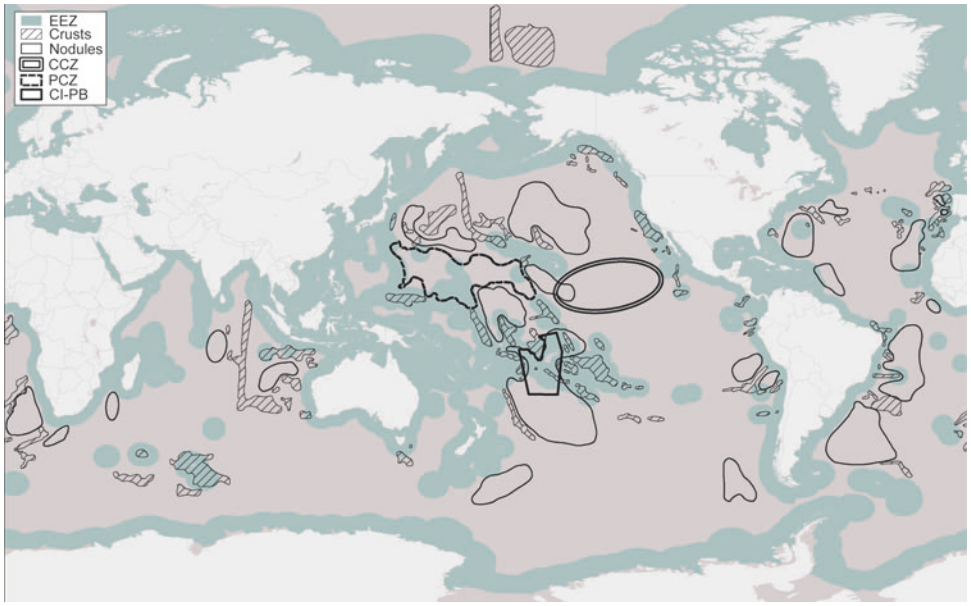

Ferromanganese Crusts and Nodules: Rocks That Grow, Fig. 1 Map of global distribution of Exclusive Economic Zones (EEZ; *teal* shading), areas beyond national jurisdictions (*gray*), and global permissive areas for ferromanganese crust (*diagonal line fill*) and abyssal plain nodules (*thin outline*). Areas of high economic interest, the Clarion-Clipperton Zone, Prime Crust Zone, and Cook Islands-Penryhn Basin (CCZ, PCZ, CI-PB, respectively) are marked by unique outlines as indicated in the legend. Notes: (1) designation of an area as permissive indicates the possibility, not certainty, of economically valuable deposits (2) small patches of scattered nodules occur in regions not indicated on this figure

the sediment layers, then diffuse upward and are incorporated into the Mn and Fe minerals forming at the seabed. Only nodules have input of diagenetically produced metals, and some nodule fields receive metals predominantly from that source (i.e., Peru Basin; Fig. 1) but most have a mixed hydrogenetic and diagenetic origin. Sediment pore fluids can be the dominant source of Ni, Cu, Mn, and Li, while seawater is the dominant source of Co, Te, platinum group metals (PGM), rare earth elements plus Y (REY), and others (Hein and Koschinsky 2014).

Charged ions dissolved in seawater then sorb onto the surface of the Fe and Mn oxides according to charge as designated by a first-order electrochemical model. Cations sorb onto the Mn oxide, which has a strong negative surface charge at seawater pH. In contrast, the negative and neutral element complexes dissolved in seawater sorb onto the slightly positively charged surface of Fe oxyhydroxide (Koschinsky and Hein 2003). Elements can undergo outer-sphere (weak) sorption or inner-sphere (strong) sorption. In the latter, covalent bonds are formed that tightly hold the metals to the main Fe and Mn minerals. Many of the metals that are highly enriched in Fe-Mn deposits are oxidized to an immobile state on the surface of the Fe and Mn minerals accompanying inner-sphere sorption (Hein and Koschinsky 2014). For example, Co^{2+}, Ce^{3+}, and Tl^{+} oxidize to Co^{3+}, Ce^{4+}, and Tl^{3+}, respectively, on the surface of the Mn oxide while Te^{4+} and Pt^{2+} may oxidize to Te^{6+} and Pt^{4+} on the surface of the Fe oxyhydroxide.

Structure and Texture

Hydrogenetic precipitation of Fe-Mn crusts produce strata (layers) with complex structures determined by changes over time in seawater composition, growth rates, bottom current activity, and location, including water depth. These layers begin at the substrate rock and stack on top of one another along a vertical growth axis. Layers have unique chemical compositions and are visually distinguishable, allowing for evaluation of crust growth through time (Fig. 2). Layers range from dense and massive to friable and loosely consolidated, and textures are most commonly laminar, columnar, and botryoidal (mamillary).

Fe-Mn nodules grow by mineral precipitation in concentric layers around a minute nucleus that is commonly composed of a fragment of an older nodule, rock fragment, or even a shark's tooth (Fig. 2). Like crusts, the layers are distinct in chemical composition, texture, and appearance, but in this case, they are aligned along the radial growth axis. Although nodules typically sit at the sediment surface and therefore grow both hydrogenetically and diagenetically, individual layers tend to be uniform around the circumference. Therefore, the nodules must rotate as they grow causing near-equal exposure to seawater and sediment pore waters.

Growth Rates

Fe-Mn crusts accrete/precipitate at average rates of 1–5 mm per million years (mm/Ma), and crusts with slower growth

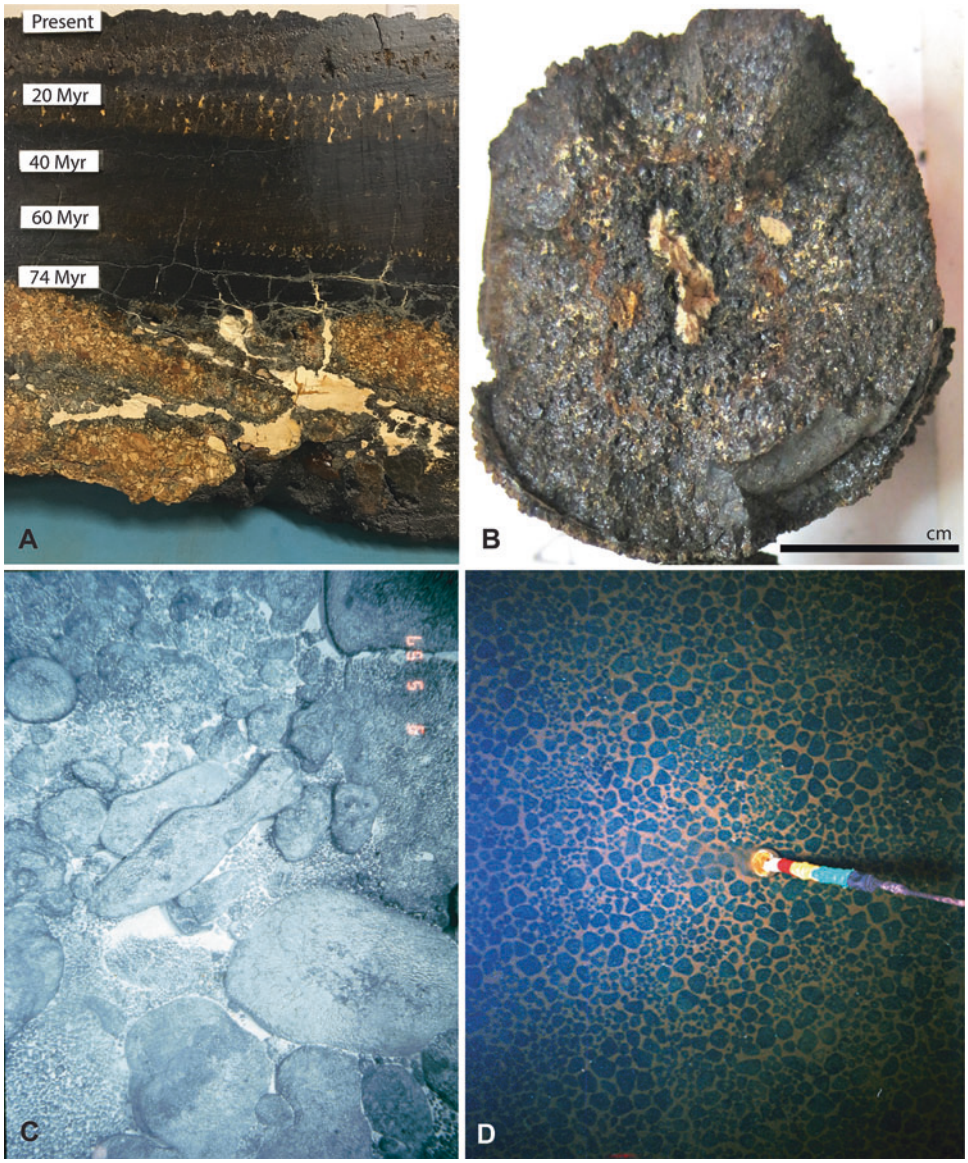

Ferromanganese Crusts and Nodules: Rocks That Grow, Fig. 2 Representative photographs of ferromanganese crusts and nodules: (**a**) cross-section of crust CD29-2 collected during cruise F7-86-HW from Karin Ridge, Central Pacific (168°42′N, 168°14′W) at a water depth of 2,180 m; approximate ages for each crust layer are labeled in million years (Myr) ago (Klemm et al. 2005; Nielsen et al. 2009); (**b**) interior of a nodule from Cook Islands-Penrhyn Basin with small mudstone nucleus; scale bar represents 1 cm (sample ID: CK-76-1 STN-11 FFG-14A; Hein et al. 2015); (**c**) seafloor paved with Fe-Mn crust from Horizon Guyot in the Johnston Island EEZ, Central Pacific, 2,000 m water depth; (**d**) seafloor image of Cook Islands nodule field, 5,009 m water depth, taken during a Japanese research cruise in 2000 (Photograph 0447, JICA/MMAJ 2001)

F

rates contain higher concentrations of sorbed metals. If bottom currents do not keep the seamounts free of sediment, small amounts of sinking particles can be incorporated into the crusts. Incorporation of these particles in large enough quantities can increase the growth rates. Hydrogenetic nodules also grow remarkably slowly, at rates similar to those of Fe-Mn crusts, whereas purely diagenetic nodules grow at rates up to 250 mm/Ma. Because most nodules form by hydrogenetic and diagenetic precipitation, they grow at intermediate rates of several tens of mm/Ma (Hein and Koschinsky 2014). Despite average nodule growth rates being thousands of times slower than the average sediment accumulation rate, nodules persist at the sediment surface. There have been several proposals to describe the mechanism for keeping nodules at the seabed (e.g., Halbach et al. 1988), although the actual process remains a mystery.

Mineralogy

Fe-Mn crusts are composed predominantly of nano-structured vernadite ($MnO_{2-x}•xH_2O$; also called δ-MnO_2 and turbostratically disordered birnessite) and X-ray amorphous Fe oxyhydroxides (FeO(OH); feroxyhyte, ferrihydrite, and goethite) as determined by electron diffraction. The crusts contain minor amounts of detrital minerals, such as quartz and feldspar, that are deposited as sinking particulate from the water column. Older layers of thick crusts contain carbonate fluorapatite ($Ca_5(PO_4,CO_3)_3(F,Cl)$), a secondary phosphate mineral that formed by replacement and precipitation in crust pore spaces long after the Mn and Fe minerals precipitated from seawater. Fe-Mn nodules are also composed predominantly of hydrogenetic vernadite, as well as 10 Å manganates (todorokite, buserite, asbolan), and occasionally diagenetic birnessite, a 7 Å manganate. Mixed-origin and

Ferromanganese Crusts and Nodules: Rocks That Grow, Table 1 Hygroscopic water-free metal contents and contained metal tonnages for Fe-Mn deposits and comparison with land-based resources

	Prime crust zone[a]	CCZ nodules[a]	Prime crust zone[b]	Global terrestrial reserve base[c]	CCZ nodules[b]
Element	Mean	Mean	Mean	Mean	Mean
Fe	16.8	6.16	1,266	230,000	1300
Mn	22.8	28.4	1,714	5,200	**5,992**[d]
Cu	0.10	1.07	7.4	1,000+	226
Ni	0.42	1.30	32	150	**274**
Co	0.67	0.21	**50**	13	**44**
Li	3.3	131	0.02	14	2.8
Mo	463	590	3.5	19	12
Te	60	3.6	**0.45**	0.05	**0.08**
Zr	559	307	4.2	77[e]	6.5
Pt	477	128	0.004	0.08[f]	0.003

[a]Fe through Co in wt.%, Li through Zr in ppm, Pt in ppb
[b]Total nodule tonnage used is 21,100 million dry tonnes and total crust tonnage used is 7,533 million dry tonnes (From Hein and Koschinsky 2014); units are in million tonnes
[c]USGS 2009 reserve base includes resources that are currently economic (reserves), marginally economic, and subeconomic (U.S. Geological Survey 2009); units are in million tonnes
[d]Metals highlighted in bold are those with greater tonnages than terrestrial reserve base
[e]Zr as ZrO_2
[f]Total platinum group metals

diagenetic nodules contain lesser amounts of Fe oxyhydroxide, as well as minor amounts of detrital material, and authigenic minerals that formed in the sediment from alteration of other materials (alteration products of volcanic glass are particularly common). As discussed above regarding fluid source, mineral crystal structure can also influence metal concentrations. The tunnel structure of todorokite, for example, enables the acquisition of large amounts of Ni, Cu, and other diagenetic elements, such as Li, whereas the more common hydrogenetic manganese oxide, vernadite, is a phyllomanganate that has a layered structure and tends to accumulate more Co (Post 1999). Lead, which sorbs onto Fe oxyhydroxides (Koschinsky and Hein 2003), occurs in much higher concentrations in hydrogenetic deposits because the Fe minerals are much more abundant in Fe-Mn crusts than in diagenetic-influenced nodules.

Metal Concentration

In addition to the subequal iron and manganese contents, the concentrations of other metals in Fe-Mn deposits are variable based on their seawater composition, growth rates, water depth, etc., as discussed above. Mineralogy can also have an influence, as is the case for cobalt and many other rare metals that are adsorbed onto vernadite, which is more abundant in crusts than nodules (Hein and Koschinsky 2014). The rare metals Te and Pt are also more highly concentrated in crusts than nodules because they are sorbed onto and ultimately bonded to the more abundant iron oxyhydroxide in crusts. For diagenetic nodules or those of mixed origin, Mn concentrations are much higher than in crusts, and the metals of greatest economic interest are Ni, Cu, Co, Li, Mo, and REY. Additional trace elements of note for crusts and nodules can be seen in Table 1.

Geologic Setting and Distribution

Crusts

Fe-Mn crusts form pavements on rock surfaces and coat pebbles and cobbles throughout the global ocean where these substrates have been kept free of sediment for millions of years. The primary setting for crust growth is the flanks of extinct submarine volcanoes (seamounts, guyots), ridges, and plateaus, of which there are more than 100,000 throughout the global ocean. This co-occurrence with seamounts allows crusts to grow at a wide range of water depths from 400 to 7,000 meters (m), and the maximum thickness of the crust is proportional to the age of the seamount. Crust thickness varies from less than 1 mm to about 260 mm. In ocean basins that host fewer seamounts, the Atlantic and Indian Oceans, crusts are also associated with oceanic spreading centers and their accompanying hydrothermal activity. Hydrothermally influenced crusts obtain increased concentrations of Fe or Mn, mostly to the lowermost layers, which dilute the trace and rare metals. Therefore, Fe-Mn crusts of economic interest occur distant from hydrothermal sources and from continental margins. Based on these criteria, and the fact that the oldest seamounts occur in the equatorial NW Pacific, the area with the thickest and most metal-rich crusts of greatest economic interest occurs there (Fig. 1), which is called the prime crust zone (PCZ; Hein et al. 2009). However, thick and metal-rich crusts occur at other locations, including in the Atlantic Ocean

on deep-water seamounts in the marginal areas, especially east of New England, west of the Iberian Peninsula, the Rio Grande Rise, and ridges in the SE Atlantic.

Nodules

Fe-Mn nodules occur as abundant individual rocks on the surface of or partially buried in sediment that blankets abyssal plains throughout the global ocean, which occupy water depths of about 3,500 to 6,500 m. Specifically, nodules form where sedimentation rates remain less than 10 mm per thousand years (mm/ka), and abyssal plain sedimentation rates are usually low in areas distant from continents where biological productivity is low and in areas that remain below the carbonate compensation depth but also near continental margins that are bordered by a deep-sea trench, arid climate, or have a wide continental shelf. Nodules are generally golf-ball size with average diameters of 1–12 cm, but they can vary in diameter from millimeters (micronodules) to 20 cm. The size of nodules maximizes with increasing diagenetic input of metals, whereas the economic value is greatest in areas of moderate primary productivity in surface waters, which allows both hydrogenetic and diagenetic growth (ISA 2010). Therefore, despite nodule fields being vast and relatively common, nodule size, density, and metal content can vary greatly. To date, the regions confirmed to have the greatest concentrations of metal-rich nodules are: the NE Pacific Clarion Clipperton Zone (CCZ; Fig. 1) that extends from offshore Mexico to as far west as the longitude of Hawaii, the central South Pacific Penrhyn Basin, the NE Pacific Peru Basin, and the Central Indian Ocean Basin. In general, fewer large abyssal plains exist in the Atlantic and Indian Oceans compared to the Pacific because their topography is dominated by midocean ridge systems. Other areas may possess nodule fields, but more exploration is needed.

Economic Potential

Regional-Scale Metal Grade and Tonnage

Due to the high demand for metals as technology advances and population increases, the metal content in Fe-Mn deposits is attractive as a potentially minable ore. To estimate the potential economic value of Fe-Mn crust and nodule deposits, first-principle calculations are made using average element concentration data from many individual samples and estimated tonnages based on observed nodule densities and total area of the deposit. Here, one major well-known deposit for crusts (PCZ) and two for nodules (CCZ and Cook Islands-Penrhyn Basin; CI-PB) will be discussed, but numerous other studies characterize additional deposits (e.g., Sudhakar 1989).

In the CCZ, the Mn nodule field covers an area of about 9 million square km that contains on average about 6 kilograms (dry weight) of nodules per square meter (kg/m^2) of seabed but can reach up to 44 kg/m^2 (Hein et al. 2015; Fig. 1). Using these figures, it is estimated that about 21,100 million dry tonnes of nodules occur within the CCZ. That tonnage of nodules would provide nearly 6,000 million tonnes of Mn. To put this amount into perspective, it is possible to compare it with the terrestrial reserve base (TRB), which includes resources that are currently economic (reserves), marginally economic, and subeconomic (U.S. Geological Survey 2013). There is more Mn in the nodules from the CCZ than the entire TRB of Mn (Hein and Koschinsky 2014; Hein et al. 2013; Table 1). The tonnage of Ni, Co, Te, and Y in CCZ nodules exceeds that of the TRB by 2, 3, 1.4, and 4 times, respectively. Other elements add up to a significant percentage of the TRB: Mo – 63%, Li – 19%, and total REY as oxides – 11%.

The Cook Islands-Penrhyn Basin (CI-PB) nodule field hosts 8.86 million tonnes (dry weight) of nodules; this high tonnage is largely due to the high abundance of nodules which average 14.4 kg/m^2 (dry weight); the maximum nodule abundance recorded is 58 kg/m^2 (Hein et al. 2015; Fig. 1). CI-PB nodules have significantly more Co and Te than the TRB; for Te, this is true even if only the high tonnage belt (>25 kg/m^2) is considered. The CI-PB nodules also contain about 25% of the TRB of Ni, 28% of Nb, 27% of Mn, and 10–12% of REY, Mo, Ti, and V. In addition, the complement of heavy REY (Eu-Lu) of the total REY content averages 17% (maximum 24%; Hein et al. 2015), which contrasts significantly with the <1% heavy REY complement in the large land-based carbonatite-hosted REY deposits (Hein et al. 2013) – it is the heavy REY that are most needed for high-tech applications.

For Fe-Mn crusts, 7,533 million dry tonnes of crust are estimated to reside in the PCZ (Hein and Koschinsky 2014; Fig. 1). Although PCZ crusts only amount to 36% of the tonnage of CCZ nodules, they have ~1,700 times more Tl, 9 times more Te, 3.8 times more Co, and 3.4 times more Y than the TRB (Table 1). Additional metals in PCZ crusts as a percent of the total TRB are Bi 46%, Mn 33%, Ni 21%, Mo 18%, V 13%, Nb 13%, total REY as oxides 11%, W 11%, Ti 10%, Th 8%, PGM 5%, and Cu 0.7% (Hein et al. 2013; Table 1). Although calculations illustrate that significant tonnages of metals occur in marine Fe-Mn deposits, it should be noted that not all the nodules and crusts in any one deposit will be recovered, as is also true for the metals that make up the TRB.

Exploration and Mining Progress

Some Fe-Mn deposits occur relatively close to the coasts of countries and are therefore hosted within their 200 nautical mile Exclusive Economic Zone (EEZ; Fig. 1). Within these EEZs, countries have full jurisdiction over the exploration and exploitation of marine mineral deposits. An example is the CIs nodules, which encompasses 1,977,000 km^2 and is currently the only country with a public tender for exploration contracts for nodules (Hein et al. 2015).

Many Fe-Mn deposits, however, occur outside the EEZs known as the area beyond national jurisdictions, or simply "The Area" (Fig. 1). To manage this, the United Nations, through the Convention of the Law of the Sea Treaty (UNCLOS), established the International Seabed Authority (ISA) as an independent agency that would oversee development of mineral resources in The Area. The ISA has 166 member states plus the European Union and receives applications by government agencies and industry for exclusive rights for exploration in specific areas. As of May 2016, there are 17 confirmed or pending contracts for exploration areas for nodules, 16 of which are within the CCZ and 1 within the Central Indian Ocean Basin, and 5 exploration contracts for crusts, 4 in the PCZ and 1 in the SW Atlantic Ocean.

There is as yet no mining in The Area and exploration encompasses resource delineation and evaluation, baseline data collection, and study of environmental impacts; however, exploitation regulations are currently under development by the ISA. The global demand for metal continues to rise as population increases and technological needs grow while terrestrial ore grades diminish and mines are closed. The promising metals grades in Fe-Mn deposits, especially nodules which are easier to harvest at the sediment surface then are crusts, will thus continue to be evaluated for their resource potential, and the likelihood of mining them will certainly increase if environmental impacts are deemed acceptable and viable mining technologies are engineered.

Summary and Conclusions

Fe-Mn mineral deposits are extensive in the deep ocean wherever low sediment accumulation is maintained. Fe-Mn crusts grow ubiquitously on rock outcrops throughout the global ocean whereas Fe-Mn nodules are expansively developed on the abyssal plains. Both crusts and nodules are composed predominantly of Fe and Mn oxide minerals that precipitate from cold seawater and/or deep-sea sediment porewaters and acquire abundant metals and other elements via sorption on the main Fe and Mn minerals as controlled by these source waters. Both Fe-Mn deposit types record the history of the waters they precipitated from, and crusts especially serve as one of the most important records of oceanographic events that have occurred over the past 70 million years. Metals essential to many emerging technologies are enriched in these nonrenewable Fe-Mn deposits to the extent that they are considered a potential resource for mining in the near future. Twenty-two contracts for exploration for nodules and crusts have already been signed or are pending with the International Seabed Authority (ISA). A set of environmental and other exploitation regulations are currently under development by the ISA and expectations are that they will be finalized within the next 3–4 years.

Cross-References

- ▶ Authigenesis
- ▶ Carbonate Compensation Depth
- ▶ Copper
- ▶ Diagenesis
- ▶ Earth's Oceanic Crust
- ▶ Fluid–Rock Interaction
- ▶ Geochemical Exploration
- ▶ Iron
- ▶ Lanthanide Rare Earths
- ▶ Lithium
- ▶ Low-Temperature Geochemistry
- ▶ Manganese
- ▶ Mineralogy
- ▶ Natural Gas
- ▶ Nickel
- ▶ Ocean Biochemical Cycling and Trace Elements
- ▶ Ore Deposits
- ▶ Oxidation-Reduction Reactions and Eh-pH (Pourbaix) Diagrams
- ▶ Oxide Minerals
- ▶ Paleoenvironments
- ▶ Platinum
- ▶ Surface Geochemistry
- ▶ Tellurium
- ▶ Trace Elements
- ▶ Transition Elements
- ▶ X-Ray Diffraction

References

Halbach P, Friedrich G, von Stackelberg U (eds) (1988) The manganese nodule belt of the Pacific Ocean – geological environment nodule formation, and mining aspects. F. Enke, Stuttgart, p 254

Hein JR, Conrad TA, Dunham RE (2009) Seamount characteristics and mine-site model applied to exploration- and mining-lease-block selection for cobalt-rich ferromanganese crusts. Mar Georesour Geotechnol 27:160–176

Hein JR, Koschinsky A (2014) Deep-ocean ferromanganese crusts and nodules, Chap. 11. In: Holland HD, Turekian KK (eds) Treatise on geochemistry, vol 13. Elsevier, Oxford, pp 273–291

Hein JR, Mizell K, Koschinsky A, Conrad TA (2013) Deep-ocean mineral deposits as a source of critical metals for high- and green-technology applications: comparison with land-based resources. Ore Geol Rev 51:1–14

Hein JR, Spinardi F, Okamoto N, Mizell K, Thorburn D, Tawake A (2015) Critical metals in manganese nodules from the Cook Islands EEZ, abundances and distributions. Ore Geol Rev 68:97–116

ISA (2010) A geological model of polymetallic nodule deposits in the clarion-Clipperton fracture zone, ISA technical study, vol 6. International Seabed Authority, Kingston, p 105

JICA/MMAJ (2001) Report on the cooperative study project of the Deep Sea mineral resources in selected offshore area of the SOPAC region, vol 1: sea area of the Cook Islands. Japan International Cooperation Agency and Metal Mining Agency of Japan, p 322

Klemm V, Levasseur S, Frank M, Hein JR, Halliday AN (2005) Osmium isotope stratigraphy of a ferromanganese crust. Earth Planet Sci Lett 238:42–48
Koschinsky A, Hein JR (2003) Uptake of elements from seawater by ferromanganese crusts: solid phase association and seawater speciation. Mar Geol 198:331–351
Nielsen SG, Mar-Gerrison S, Gannoun A, LaRowe D, Klemm V, Halliday AN, Burton KW, Hein JR (2009) Thallium isotope evidence for a permanent increase in marine organic carbon export in the early Eocene. Earth Planet Sci Lett 278:297–307
Post JE (1999) Manganese oxide minerals: crystal structures and economic and environmental significance. Proc Natl Acad Sci USA 96 (Colloquium Paper):3447–3454
Sudhakar M (1989) Ore grade manganese nodules from the central Indian Basin: an evaluation. Mar Min 8:201–214
U.S. Geological Survey (2009) Mineral commodity summaries 2009. U.S. Geological Survey. 195 p
U.S. Geological Survey (2013) Mineral commodity summaries 2013. U.S. Geological Survey. 198 p

Fick's Law

Isao Sakaguchi
National Institute for Materials Science, Tsukuba, Ibaraki, Japan

Definition

Fick's First Law

It is considered that the concentration gradient of elements in mineral and rock resulted from an evidence of diffusion, and the nonequilibrium state was frozen in them. The mobile element found the concentration gradient in material is useful as the tracer to estimate the timescale. The tracer diffuses in a manner to decrease the concentration gradient from the material surface. In such cases, the flux density of species, *i*, in the three dimensions is given by

$$J_i = -D_i \rho \nabla C_i \tag{1}$$

where D_i is the diffusion coefficient, ρ is the density, and ∇C_i is the mass fraction concentration gradient. In one dimension, Eq. 1 becomes

$$J_i = -D_i \rho \left(\frac{\partial C_i}{\partial x} \right) \tag{2}$$

Fick's Second Law

Equation 2 is written with the consideration of the conservation of mass. It can be shown that

$$\frac{\partial C_i}{\partial t} = \frac{\partial}{\partial x} \left(D_i \frac{\partial C_i}{\partial x} \right) \tag{3}$$

where t is time. This is known as Fick's second law. If D is independent at the position, Eq. 3 is written as

$$\frac{\partial C_i}{\partial t} = D_i \frac{\partial^2 C_i}{\partial x^2} \tag{4}$$

Equation 4 is solved with the boundary condition, and then the solution is given the concentration of tracer "species, *i*," in the solid as a function of the distance, x, and time, t. In the experiment of elemental diffusion in the solid, the following boundary conditions are considered.

Solution of Constant Concentration on the Surface

First is that the surface x = 0 is maintained at a constant concentration during the diffusion annealing.

$$C(x,t) = C_l \text{ for } 0 \le t \le \infty$$

$$C(0,t) = C_l \text{ at } t > 0$$

$$C(x,t) = C_l \text{ as } x \to \infty$$

The solution to Eq. 4 satisfying above condition is

$$C(x,t) - C_l = (C_o - C_l) erfc \left[\frac{x}{2\sqrt{Dt}} \right] \tag{5}$$

where *erfc* is the complementary error function. Above boundary condition is achieved in the diffusion experiment of gas–solid exchange at high temperature. For example, above solution is usually used to calculate the diffusion coefficient of oxygen tracer (^{18}O) in oxide materials.

Solution of Thin Film Source

Second boundary condition used a thin film as tracer source deposited on the material. Above state is the boundary condition for one of the simplest solutions to Fick's second law. If the thin film source on the material is heated so that the tracer diffuses, the tracer composition will be given by:

$$C(x,t) = \frac{\alpha}{2\sqrt{Dt}} exp \left(\frac{-x^2}{4Dt} \right) \tag{6}$$

where α is the total amount of tracer. This is called the "thin film solution" and it holds for a film thickness less than $\sqrt{Dt}$. The diffusion experiments satisfying the boundary condition are usually carried out to determine the diffusion coefficient of cation in materials.

F

Summary

Fick's law is a basic law to understand diffusion phenomena.

Cross-References

- ▶ Diffusion
- ▶ Free Energy
- ▶ Geochemical Thermodynamics
- ▶ Mass Transfer

References

Crank J (1980) The mathematics of diffusion, 2nd edn. Oxford University Press, Oxford. 424pp

Shewmon P (2016) Diffusion in solids, 2nd edn. Springer. 238 pp

Fission Track Analysis

Stuart N. Thomson
Department of Geosciences, University of Arizona, Tucson, AZ, USA

Definition

Fission track analysis is the study of microscopic linear traces of radiation damage in minerals and natural glass formed by radioactive decay of the ^{238}U isotope of uranium by spontaneous fission. The constant accumulation rate of fission tracks provides a means to date geologic materials, and the gradual fading of fission tracks (annealing) at elevated temperatures over geologic time can be used to elucidate host rock thermal histories.

Introduction: What Are Fission Tracks?

Radioactive decay of natural uranium occurs by two processes: alpha and beta decay to stable isotopes of lead – the basis of U-Pb, (U-Th)/He, and U-series dating – and by natural spontaneous fission. The latter process is restricted almost exclusively to the ^{238}U isotope of uranium and occurs with a probability almost two million times lower than U to Pb alpha decay. The energy released by spontaneous fission propels two fission fragments in opposite directions, which in an insulating solid such as a crystal lattice forms a metastable linear zone of damage known as a *fission track*. The most widely accepted model for fission track formation is the ion explosion spike mechanism (Fleischer et al. 1965) whereby the positively charged fission fragments strip electrons from atoms in the lattice leaving behind a trail of positively charged ions that mutually repel one another. Newly formed fission tracks are generally assumed to have the same initial length, typically 10–20 μm long and 5–10 nm in diameter, dependent on the composition and density of the medium in which they form.

Revealing Fission Tracks

Fission tracks were first observed using transmission electron microscopy by Silk and Barnes (1959). A few years later Price and Walker (1962) discovered fission tracks could be enlarged by means of selective chemical etching, allowing routine observation using optical microscopy. Chemical etchants preferentially attack the fission track relative to the surrounding undamaged bulk material (Fleischer et al. 1975; Wagner and Van den haute 1992). To avoid externally sourced fission tracks, etching is done on the polished internal surface of mineral grains mounted in an etchant-resistant medium such as epoxy resin (apatite) or FEP Teflon (zircon).

Fission Track Dating

Spontaneous fission of ^{238}U occurs at a known constant rate, meaning fission tracks can be used to date geologic materials (Price and Walker 1963). Fission track dating was first applied successfully to natural glass (Fleischer and Price 1964) and today is most commonly applied to apatite and zircon. Fission decay follows the exponential radioactive decay law, whereby the concentration of daughter product, in this case the number of spontaneous fission tracks per unit area (track density), is dependent on (1) the time of residence of parent isotope ^{238}U in the material, (2) the concentration of ^{238}U, (3) the rate of ^{238}U radioactive decay by spontaneous fission, and (4) the assumption that fission tracks are not removed following their formation.

Track Counting and Density Measurement

Fission track densities are typically measured manually with a tally counter using an optical research microscope at around 1250x magnification under either transmitted and reflected light (Fig. 1). Recent development of automated counting systems using digital image track recognition algorithms offers potential for faster, more reliable track counting (Gleadow et al. 2009).

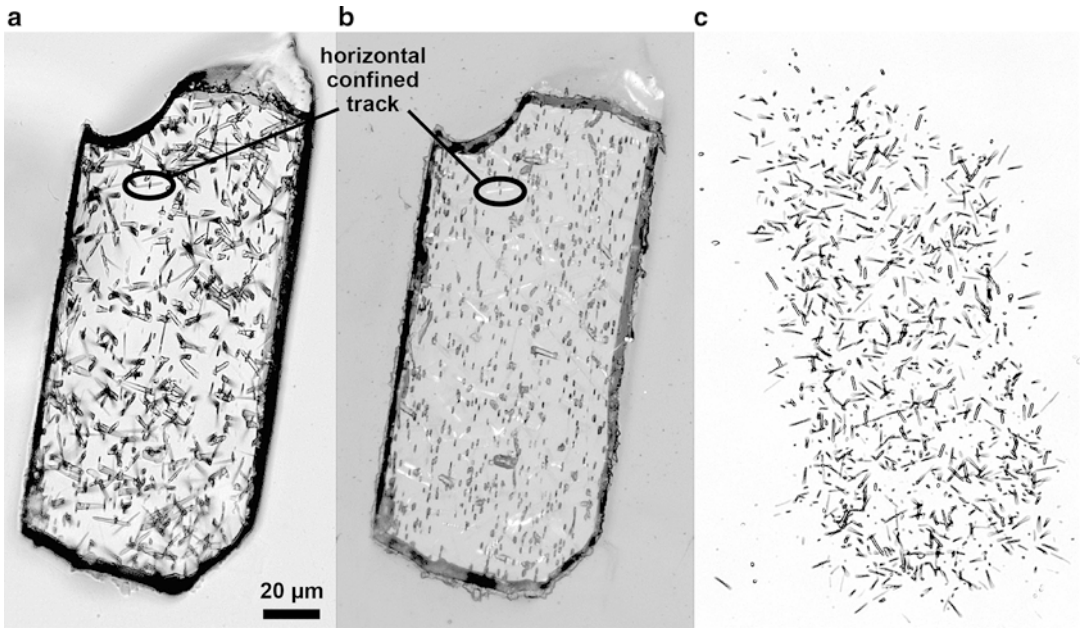

Fission Track Analysis, Fig. 1 (**a**) Transmitted light photomicrograph of etched spontaneous fission tracks in a polished apatite grain from the Sierra Nevada Batholith, California. A horizontal confined track is *circled* (see section "Fission Track Annealing"). (**b**) Same crystal viewed with reflected light highlighting etch pits (where tracks intersect surface). (**c**) Etched induced fission tracks in mica derived from the same apatite crystal using the external detector method

Dating Methods and Determination of ^{238}U Concentration

To measure the ^{238}U concentration for fission track dating, a sample can be exposed to a dose of thermal neutrons (neutrons with low kinetic energy) to induce fission in the rarer ^{235}U isotope of uranium (Price and Walker 1963). Since the present-day terrestrial isotopic ^{238}U/^{235}U ratio is effectively constant, then if the total thermal neutron dose is known, the concentration of ^{238}U can be determined from the density of ^{235}U-induced fission tracks. The ratio of spontaneous to induced fission track density (equivalent to the ratio of daughter to parent isotopes) can be used to calculate a fission track age, t, according to the basic fission track age equation first proposed by Fleischer and Price (1964):

$$t = \frac{1}{\lambda_D} \ln\left\{1 + \left(\frac{\lambda_D}{\lambda_f}\right)\left(\frac{\rho_s}{\rho_i}\right) I\sigma\phi_{th}QG\right\} \qquad (1)$$

where $\lambda_D = {}^{238}$U total decay constant (1.55125×10^{-10} year^{-1}), $\lambda_f = {}^{238}$U spontaneous fission decay constant (~8.46×10^{-17} year^{-1}), $I =$ isotopic ratio of ^{235}U/^{238}U = 0.00725268, $\sigma =$ thermal neutron cross section for ^{235}U (580.2×10^{-24} cm^{-2}), $\phi_{th} =$ total thermal neutron fluence (n.cm^{-2}), $Q =$ a track etching and recognition efficiency factor with a value = 1 if spontaneous and induced tracks are etched and observed under the same conditions, and $G =$ a geometry factor with ideal value of 0.5 to account for spontaneous tracks being formed on both sides of a polished internal surface, whereas induced tracks are only produced from the one side remaining after polishing.

Sample handling procedures for fission track dating fall into two broad groups (Hurford and Green 1982): (1) grain population methods, where two mineral aliquots are measured, one for spontaneous tracks and another for induced tracks, and (2) grain-by-grain methods where spontaneous and induced tracks are analyzed from the same mineral grain. Grain-by-grain methods are generally favored as they allow full assessment of age and uranium concentration variation between grains within a sample. The most popular procedure is the *external detector method*. It involves counting spontaneous tracks on the internal surface of mineral grains contained in a sample mount. An external detector (usually a low uranium mica sheet) is then placed firmly against the etched surface of the mounted grains. During neutron irradiation, induced fission fragments from the polished grain are recorded as etchable tracks in the mica. Etched induced mica tracks can be matched to each mineral grain through the use of an automated microscope stage (Fig. 1c). External mica detectors are also used to estimate total neutron fluence by measuring induced track density in a mica placed against a standard dosimeter glass with known uranium concentration. The induced track density, ρ_d, is related to the total thermal neutron fluence by the expression

$$\phi_{th} = B.\rho_d \qquad (2)$$

where B is a constant that can be evaluated by metal activation monitors (Hurford and Green 1981). One issue with the external detector method is that spontaneous and induced tracks are measured on materials with different track etching and recognition efficiencies. To minimize this difference, spontaneous tracks are only counted in crystals in the optimum orientation of minimum bulk etching rate to match the low bulk etching rate of the cleaved mica surface. In both apatite and zircon, this is the plane parallel to the crystallographic c-axis.

This issue can be avoided by using an age-standard approach known as the *zeta age calibration* (Hurford and Green 1983; Hurford 1990). This was originally motivated by uncertainties in the true value of the ^{238}U spontaneous fission decay constant and difficulties accurately measuring the neutron fluence. Instead, the constants and problematic parameters in Eq. 1 are combined in to a zeta calibration factor $\zeta = I\sigma B/\lambda_f$ (where B comes from Eq. 2). Using a suitable age standard (typically minerals from quickly cooled rocks with precise, homogeneous age determined by other dating techniques from several different laboratories, Hurford 1990), Eq. 1 can be rearranged to determine a zeta value. To account for natural statistical dispersion, at least 20–30 zeta values from different age standards and irradiations are required for a robust calibration. If the etching procedure and track recognition for the age standard and unknown are the same, the factor, Q, can be ignored. Because track recognition, Q, varies between analysts and the B value varies between different irradiation facilities, a zeta value is unique to a particular user for any specific laboratory and irradiation facility.

Laser ablation inductively coupled mass spectrometry (LA-ICP-MS) has recently emerged as an alternative method to measure ^{238}U concentration for fission track dating (Hasebe et al. 2004). Ages have been reported using both an absolute determination of ^{238}U concentration by reference to a standard glass (Gleadow and Seiler 2015) and using a modified zeta calibration approach, with reference to an age standard (Chew and Donelick 2012).

Fission Track Annealing

Fission tracks fade or anneal when heated to relatively low near-surface temperatures over geologic time (Fleischer et al. 1964). Conceptual annealing models (e.g., Green et al. 1986) and observation of unetched fission track annealing in apatite (Li et al. 2012) indicate a two-stage annealing process. In the first main phase, tracks shorten from both ends. Once the track reaches about half its original length, a secondary phase of track segmentation occurs, leaving unetchable gaps preventing full revelation. Shorter annealed tracks have less chance of intersecting any polished surface; thus annealing leads to lower track density and hence a reduction in age (Laslett et al. 1982).

Precise evaluation of fission track annealing is achieved by measuring track length reduction in so-called *confined tracks* that are within 15° of horizontal (Laslett et al. 1982). These are complete fission tracks situated fully below the polished surface that can be revealed by etching if they intersect a track or crack that penetrates the etched surface (Fig. 1). Track length reduction has been studied in numerous laboratory heating experiments resulting in a number of predictive annealing models (Laslett et al. 1987; Carlson et al. 1999; Ketcham et al. 2007 for apatite; Tagami et al. 1998; Rahn et al. 2004 for zircon). For a fixed amount of track length reduction, experimental data shows annealing has an Arrhenius relationship (a positive dependence between log time and inverse temperature) that can be extrapolated to geologic time.

Annealing rate is also correlated with several other measurable kinetic parameters. These include crystal orientation and apatite crystal chemistry (primarily Cl concentration) (Green et al. 1986), as well as apatite bulk etching characteristics, measured using the parameter *Dpar* – the diameter of a track etch-pit parallel to the c-axis (Burtner et al. 1994) – and alpha-decay radiation damage in zircon (Rahn et al. 2004). In apatite no parameter fully describes annealing rate variability, but Cl concentration or *Dpar* are effective for about 90% of commonly encountered apatite compositions (Donelick et al. 2005). These annealing models, plus data from deep boreholes (e.g., Gleadow and Duddy 1981), reveal that significant fission track annealing in apatite starts at about 60 °C, with full annealing at ca. 125 °C, although high Cl concentration or large *Dpar* apatite grains may retain tracks up to ca. 160 °C. This range of temperatures is known as the *partial annealing zone* (PAZ). Other minerals have different annealing temperatures (see Wagner and Van den haute 1992). For example, zircon shows higher annealing temperatures (ca. 180–340 °C), but this remains less well quantified owing to complexities related to variable etching and radiation damage (Rahn et al. 2004).

Thermal History Modeling

A valuable property of fission tracks is that they form continuously over time and have effectively constant initial length (ca. 16 μm and ca. 11 μm for spontaneous tracks in apatite and zircon, respectively). Thus, each track experiences its own unique annealing history dependent on when it formed during the full thermal history of its host mineral. Measuring horizontal confined track length distributions is thus a powerful interpretative tool for evaluating sample thermal histories.

Using the annealing models outlined above, computer techniques can be used to predict such fission track length distributions, as well as age, from any given thermal history (a so-called *forward* approach), allowing manual comparison to measured data (Green et al. 1989). More efficient and

statistically robust *inverse* algorithms have since been developed, whereby measured data are tested against the predictions of many computer-generated time-temperature paths, with the most likely thermal histories chosen using statistical goodness-of-fit tests. Two currently popular public-domain applications using this method are HeFTy (Ketcham 2005) and QTQt (Gallagher 2012).

Summary

Fission track analysis, coupled with more recently developed techniques such as (U-Th)/He and cosmogenic nuclide dating, has helped transform our understanding of upper crustal thermal histories and geologic processes. It has been at the forefront of understanding the erosion processes behind the shaping of mountain belts, as well as long-term landscape evolution in non-orogenic settings. Other popular applications include sedimentary basin analysis and hydrocarbon generation, the timing and rates of extensional unroofing, sedimentary provenance discrimination, and conventional dating of volcanic ash and archaeological samples. Extensive reviews of these and other applications are provided by Gallagher et al. (1998), Bernet and Spiegel (2004), Galbraith (2005), Reiners and Ehlers (2005), Braun et al. (2006), and Lisker et al. (2009).

Current progress in fission track analysis includes LA-ICP-MS and electron microprobe to determine uranium concentrations, image analysis techniques for improved track recognition, and integration with other techniques to obtain multiple dates from single mineral grains. Future perspectives include improvements to empirical annealing models, particularly for zircon, and more fully understanding the atomic-scale physical process of track formation and annealing.

Cross-References

- ▶ Geochronology and Radiogenic Isotopes
- ▶ Laser Ablation – Inductively Coupled Plasma Mass Spectrometry
- ▶ Radioactivity
- ▶ Uranium

References

Bernet M, Spiegel C (2004) Detrital Thermochronology: provenance analysis, exhumation, and landscape evolution of mountain belts, Geological Society of America special publication, vol 378. Geological Society of America, Boulder

Braun J, Van der Beek P, Batt G (2006) Quantitative Thermochronology: numerical methods for the interpretation of Thermochronological data. Cambridge University Press, New York

Burtner RL, Nigrini A, Donelick RA (1994) Thermochronology of lower cretaceous source rocks in the Idaho-Wyoming thrust belt. Bull Am Assoc Petrol Geol 78:1613–1636

Carlson WD, Donelick RA, Ketcham RA (1999) Variability of apatite fission-track annealing kinetics: I. Experimental results. Am Mineral 84:1213–1223

Chew DM, Donelick RA (2012) Combined apatite fission-track and U-Pb dating by LA-ICP-MS and its application in apatite provenance analysis. In: Sylvester P (ed) Quantitative mineralogy and microanalysis of sediments and sedimentary rocks. Mineralogical Association of Canada. Short Course, Québec, pp 219–248

Donelick RA, O'Sullivan PB, Ketcham RA (2005) Apatite fission-track analysis. Rev Mineral Geochem 58:49–94

Fleischer RL, Price PB (1964) Glass dating by fission fragment tracks. J Geophys Res 69:331–339

Fleischer RL, Miller DS, Price PB, Symes EM (1964) Fission-track ages and track-annealing behavior of some micas. Science 143:349–351

Fleischer RL, Price PB, Walker RM (1965) Ion explosion spike mechanism for formation of charged-particle tracks in solids. J Appl Phys 36:3645–3652

Fleischer RL, Price PB, Walker RM (1975) Nuclear tracks in solids: principles and applications. University of California Press, Berkeley

Galbraith RF (2005) Statistics for fission track analysis. Chapman and Hall/CRC, Boca Raton

Gallagher K (2012) Transdimensional inverse thermal history modeling for quantitative thermochronology. J Geophys Res 117:B02408

Gallagher K, Brown RW, Johnson C (1998) Fission track analysis and its application to geological problems. Annu Rev Earth Planet Sci 26:519–572

Gleadow AJW, Duddy IR (1981) A natural long-term track annealing experiment for apatite. Nucl Tracks 5:169–174

Gleadow AJW, Seiler C (2015) Fission track dating and thermochronology. In: Rink WJ, Thompson JW (eds) Encyclopedia of scientific dating methods. Springer, Dordrecht

Gleadow AJW, Gleadow SJ, Belton DX, Kohn BP, Krochmal MS (2009) Coincidence mapping a key strategy for automated counting in fission track dating. In: Lisker F, Ventura B, Glasmacher UA (eds) Thermochronological methods: from Palaeotemperature constraints to landscape evolution models, Geological Society of London special publication, vol 324. Geological Society, London, pp 25–36

Green PF, Duddy IR, Gleadow AJW et al (1986) Thermal annealing of fission tracks in apatite.1. A qualitative description. Chem Geol 59:237–253

Green PF, Duddy IR, Laslett GM, Hegarty KA (1989) Thermal annealing of fission tracks in apatite. 4. Quantitative modelling techniques and extension to geological timescales. Chem Geol Isot Geosci Sect 79:155–182

Hasebe N, Barbarand J, Jarvis K et al (2004) Apatite fission-track chronometry using laser ablation ICP-MS. Chem Geol 207:135–145

Hurford AJ (1990) Standardization of fission track dating calibration: recommendation by the fission track working group of the I.U.G.S. Subcommission on geochronology. Chem Geol 80:171–178

Hurford AJ, Green PF (1981) A reappraisal of neutron dosimetry and uranium-238 lamda-f values in fission-track dating. Nucl Tracks Radiat Meas 5:53–61

Hurford AJ, Green PF (1982) A users' guide to fission track dating calibration. Earth Planet Sci Lett 59:343–354

Hurford AJ, Green PF (1983) The zeta age calibration of fission-track dating. Isot Geosci 1:285–317

Ketcham RA (2005) Forward and inverse modeling of low-temperature thermochronometry data. Rev Mineral Geochem 58:275–314

Ketcham RA, Carter A, Donelick RA et al (2007) Improved modeling of fission-track annealing in apatite. Am Mineral 92:799–810

Laslett GM, Kendall WS, Gleadow AJW, Duddy IR (1982) Bias in measurement of fission-track length distributions. Nucl Tracks Radiat Meas 6:79–85
Laslett GM, Green PF, Duddy IR, Gleadow AJW (1987) Thermal annealing of fission tracks in apatite. 2. A quantitative analysis. Chem Geol 65:1–13
Li W, Lang M, Gleadow AJW et al (2012) Thermal annealing of unetched fission tracks in apatite. Earth Planet Sci Lett 321–322:121–127
Lisker F, Ventura B, Glasmacher UA (2009) Thermochronological methods: from Palaeotemperature constraints to landscape evolution models, Geological Society of London special publication, vol 324. Geological Society, London
Price PB, Walker RM (1962) Chemical etching of charged-particle tracks in solids. J Appl Phys 33:3407–3412
Price PB, Walker RM (1963) Fossil tracks of charged particles in mica and the age of minerals. J Geophys Res 68:4847–4862
Rahn MK, Brandon MT, Batt GE, Garver JI (2004) A zero-damage model for fission-track annealing in zircon. Am Mineral 89:473–484
Reiners PW, Ehlers TA Low-temperature thermochronology: techniques, interpretations, and applications, Reviews in mineralogy and geochemistry, vol 58. Mineralogical Society of America. 622 p
Silk ECH, Barnes RS (1959) Examination of fission fragment tracks with an electron microscope. Philos Mag 4:970–972
Tagami T, Galbraith RF, Yamada R, Laslett GM (1998) Revised annealing kinetics of fission tracks in zircon and geological implications. In: Van den Haute P, De Corte F (eds) Advances in fission-track geochronology. Kluwer, Dordrecht, pp 99–112
Wagner GA, Van den haute P (1992) Fission-track dating. Kluwer, Dordrecht

Fluid Inclusions

Robert J. Bodnar
Department of Geosciences, Virginia Tech, Blacksburg, VA, USA

Definition

Fluid inclusions. Small, usually microscopic, droplets of fluid that are trapped in crystals during their initial growth or post-growth during healing of fractures in the mineral.

Introduction

Fluid inclusions are small droplets of fluid that are trapped in minerals. Those trapped during growth of the crystal are referred to as primary fluid inclusions, whereas those trapped along fractures that develop and heal long after the crystal has formed are termed secondary inclusions. Pseudo-secondary inclusions are inclusions that form along a healed fracture that develops and heals during the continued growth of the crystal.

During the past three-quarter century, fluid inclusions have evolved from being viewed as curious artifacts contained in minerals to become one of the most commonly used tools to constrain temperatures and pressures attending geologic processes, and for characterizing the compositions of fluids involved in those processes. Fluid inclusions range in size from submicron to several tens to hundreds of microns in diameter and typically contain on the order of 10^{-13}–10^{-6} g of fluid (Roedder 1984). In practice, most fluid inclusions that are studied are those that are optically resolvable using a conventional petrographic microscope, and range from a few to several tens of microns in maximum dimension.

The presence of fluid inclusions in minerals has been known for at least two millennia, as Pliny the Elder (Gaius Plinius Secundus) described features thought to be fluid inclusions in his volume *Natural History* that was written in about 75 AD. In ~400 AD, the Latin poet Claudius Claudianus wrote a poem entitled "On a crystal enclosing a drop of water" that is thought to describe a large fluid inclusion in a quartz crystal. Numerous other reports of large, macroscale fluid inclusions in minerals (today known as enhydros) appeared during the following centuries, but the first detailed scientific description of fluid (and melt) inclusions was in a classic paper by H. C. Sorby (1858). The paper was published by the Geological Society of London, and such publications were first presented as lectures in an adversarial setting with friends and opponents of the speaker lined up on opposite sides of the lecture hall. After Sorby's talk, the President of the Society at the time is reported to have commented that it was the least plausible paper he had ever heard presented – how could one understand the formation of mountains from such tiny features in the rock? Sorby responded that ". . . there is no necessary connection between the size of an object and the value of a fact, and that, though the objects I have described [fluid inclusions] are minute, the conclusions to be derived from the facts are great."

Information Available from Fluid Inclusions

Fluid inclusions have the potential to provide information concerning temperatures, pressures, compositions, and densities of fluids associated with various geological events or processes. However, certain requirements must be met for fluid inclusions to provide reliable information concerning the physical and chemical conditions of formation. These requirements, which are commonly referred to as Roedder's (or Sorby's) rules, state that (1) the fluid inclusion traps a single, homogeneous phase, (2) the inclusion represents a constant volume (isochoric) system, and (3) nothing has been added to or lost from the inclusion following trapping, i.e., it remains a closed system. Fluid inclusions that do not meet one or more of these requirements fail to

record and preserve information on original trapping conditions. Adherence to Roedder's rules is confirmed by examining a group of inclusions that were all trapped at the same time (referred to as a fluid inclusion assemblage; Goldstein and Reynolds 1994). If the inclusions were all trapped at the same time, they would have all formed at the same temperature and pressure, and all would have trapped a fluid of the same composition. As such, all inclusions in the FIA would show similar phase behavior when observed at room temperature and similar temperatures of phase changes during heating and/or cooling. A wide range in room temperature phase ratios or microthermometric behavior could result from trapping mixtures of two or more fluids, from loss (or gain) of material following inclusion formation, or a change in the fluid inclusion volume following trapping. In many cases, the cause of the variability cannot be determined, but, in all cases, the fluid inclusion data should be discarded if any of Roedder's rules are violated. Unfortunately, much of the fluid inclusion data in the literature is of questionable quality because the researchers did not follow the FIA protocol when collecting and evaluating data.

Temperature

Although many geothermometers are available to constrain temperatures of geologic processes, none of the mineralogical or isotope-based geothermometers offer the temperature or temporal resolution offered by fluid inclusions. A single fluid "event" such as the formation of a growth zone in a crystal or healing of a fracture in a mineral can often be determined to ±1–5 °C using fluid inclusions. For example, Roedder (1974, see also Roedder 1984, Fig. 15.6) examined temperature (and salinity) fluctuations during the precipitation of a single, large sphalerite (ZnS) crystal from the Creede, Colorado, mining district. He identified 21 distinct growth zones in the crystal, and the temperature of formation of each growth zone could be constrained to within ≈±1 °C by fluid inclusions, even though the entire crystal precipitated over the range 200–270 °C. Each growth zone likely took 10^2–10^3 years to precipitate – thus, fluid inclusions provide a temporal resolution that is typically 2–4 orders of magnitude better than is possible with more conventional geothermometers that constrain temperatures with a resolution of hundreds of thousands to tens of millions of years.

Pressure

Fluid inclusion microthermometric data, combined with phase equilibrium data for the fluid in the inclusion and/or an equation of state to estimate the pressure-volume-temperature-composition (PVTX) properties of the fluid, allow pressures of fluid inclusion formation to be determined (Roedder and Bodnar 1980). The most reliable pressures are obtained when fluid inclusions are trapped from boiling or immiscible fluids, as evidenced by coexisting liquid-rich and vapor-rich fluid inclusions within the same fluid inclusion assemblage. In this case, the pressure at trapping is equal to the pressure in the inclusion at the homogenization temperature, and this pressure in turn may be determined from PVTX data. Alternatively, if the fluid inclusions are trapped in a single fluid phase field, the pressure of trapping may be determined from the intersection of the isochore corresponding to the measured homogenization temperature with some other relevant phase boundary. One example is when fluid and melt inclusions are trapped simultaneously on the water-saturated solidus in a silicate melt - water system, i.e., granite water. In this case, the intersection of the fluid inclusion isochore with the H_2O-saturated solidus provides both the pressure and temperature of fluid (and melt) inclusion formation (Lecumberri-Sanchez et al. 2015).

Fluid Density

Fluid inclusions provide the only direct method to determine densities of fluids associated with ancient geologic processes. Assuming that either experimental data or an equation of state is available for the fluid composition in the inclusion, the density of the fluid may be determined using the measured homogenization temperature (and pressure). Density information obtained from fluid inclusions provide a valuable source of information to develop and test fluid flow models that simulate fluid flow in magmatic-hydrothermal systems (Weis et al. 2014).

Fluid Composition

Among the information available from fluid inclusions, and which is not available from any other source, is the composition of the fluid associated with various geological processes. Over the past half century, techniques for determining compositions of fluid inclusions have advanced significantly. In the late 1950s, it was only possible to determine bulk salinities of fluid inclusions based on microthermometry or from bulk analyses of fluid inclusion-bearing samples. While bulk analysis often provided very precise results, most natural samples contain multiple generations of primary and secondary inclusions, and each of these different generations may have contained fluids with very different compositions. Starting in the late 1970s and continuing today, various techniques were introduced that allowed analysis of individual fluid inclusions. Raman spectroscopy proved to be an important tool to determine the compositions of volatile components and daughter minerals in fluid inclusions, and today it is possible to quantitatively determine compositions of many different types of fluid inclusions by Raman analysis (Frezzotti et al. 2012).

The most significant advance in fluid inclusion research in recent decades has been the development and application of laser ablation inductively coupled plasma mass spectrometry (LA-ICP-MS) to determine major, minor, and trace element

compositions of individual fluid inclusions (Günther et al. 1998). Before introduction of LA-ICP-MS analysis in fluid inclusion research, it was only possible to infer concentrations of a few major elements (such as Na, Cl, K) from phases observed in fluid inclusions at room temperature and/or from observations during heating or cooling of the inclusions. Today, it is possible to measure major, minor, and trace element abundances (representing 4–6 orders of magnitude range in concentrations) in fluid inclusions as small as 5–10 μ. These data have revolutionized our understanding of ore-forming processes by providing direct evidence on the concentrations of metals in ore-forming fluids (Roedder and Bodnar 1997). A recent review of the current status of laser ablation microanalysis to studies of hydrothermal systems is provided by Wagner et al. (2016).

Synthetic Fluid Inclusions

While the underlying physical and chemical principles that govern the interpretation of natural fluid inclusions are robust and supported by theoretical and empirical models, in many cases the assumptions involved were taken "on faith." Then, in the early 1980s, it was recognized that synthetic fluid inclusions could be trapped under carefully controlled and known experimental conditions (Sterner and Bodnar 1984), and these inclusions could then be studied to test the many assumptions involved in fluid inclusion interpretation, such as assumptions related to isochoric (constant-volume) behavior, trapping of single, homogeneous phases, etc. Moreover, because it was quickly confirmed that the synthetic fluid inclusions did indeed record and preserve the trapping conditions (temperature, pressure, fluid composition), it became apparent that synthetic fluid inclusions could be used to determine fluid PVTX properties and could be employed to examine the conditions under which fluid inclusions might violate the requirements imposed by Roedder's rules. This has led to hundreds of studies in labs worldwide and resulted in major advances in our understanding of fluid inclusion trapping and subsequent modifications and has significantly increased the amount of experimental PVTX data available to interpret results obtained from natural inclusions.

Post-Entrapment Changes

Early workers recognized that, in some cases, fluid inclusions violated one or more of Roedder's rules (Larson et al.1973), but the mechanisms responsible were poorly understood. Starting in the 1970s and continuing today, numerous workers have investigated the various types of reequilibration, and the causes, that fluid inclusions experience after trapping. A review of the various reequilibration processes associated with fluid inclusions is provided by Bodnar (2003). Bodnar et al. (1989) showed that the internal overpressure required to cause fluid inclusions in quartz to change volume is mostly a function of inclusion size and, to a lesser extent, inclusion shape, with rounded, equant inclusions less susceptible to reequilibration compared to more irregularly shaped inclusions. Sterner and Bodnar (1989) reequilibrated synthetic fluid inclusions in quartz along various PT paths simulating those followed by metamorphic rocks during exhumation. The results showed that the textures and distribution of homogenization temperatures following reequilibration showed systematic variations and characteristics that permit PT paths of natural inclusions to be inferred based on textural and microthermometric characteristics. Vityk and Bodnar (1995) similarly reequilibrated inclusions in quartz along various PT paths and observed that inclusions reequilibrated along a compressional path in which the internal pressure in the inclusion was less than the confining pressure developed an annular texture that was remarkably similar to textures of natural inclusions from the Himalayan Mountains that had been interpreted to have reequilibrated during compressional loading. Similarly, Vityk and Bodnar (1998) showed that the distribution of fluid inclusion homogenization temperatures on histograms varies in a systematic manner as a function of the mode and duration of the reequilibration event.

Experimental studies have documented the extent to which fluid inclusion compositions might change in response to a changing external physical and chemical environment. It has long been speculated that hydrogen easily diffuses out of fluid inclusions, thus changing the oxidation state in the inclusion. This process was thought to be responsible for the observation that solid phases, such as sulfides, sulfates, iron oxides, etc. that contain elements that occur in multiple oxidation states in crustal environments, often fail to dissolve when the inclusions are heated. This interpretation was supported by experimental studies in which chalcopyrite-bearing fluid inclusions were heated under pressure in the presence of a high hydrogen gas pressure, thus causing hydrogen to diffuse into the fluid inclusions (Mavrogenes and Bodnar 1994). Before the experiment the chalcopyrite phase did not dissolve during heating. However, following the experiment, the chalcopyrite did dissolve when heated and observed under the microscope because the addition of hydrogen had lowered the oxidation state of the fluid. Similarly, Hall et al. (1991) showed that diffusion of hydrogen into fluid inclusions resulted in a D/H isotopic composition that was 65‰ too low to be in isotopic equilibrium with the surrounding mineral assemblage. In addition to hydrogen, other recent experiments have documented the apparent ease with which some elements, such as Cu, Na, Li, and Ag, diffuse out of inclusions following formation (Zajacz et al. 2009). Diamond and Tarantola (2015) conducted experiments under non-

isotropic stress and found that some inclusions became dismembered and produced irregularly shaped inclusions surrounded by planar arrays of tiny inclusions. These workers observed that deformed inclusions preserve their pre-deformation concentration ratios of gases to electrolytes but have lost some H_2O. Significantly, the results suggest that the orientation of the maximum principal compressive stress at the time of deformation can be obtained from these data and that the density of newly formed inclusions records the maximum pressure during deformation.

Summary and Conclusions

During the last few decades, significant advances have been made in our ability to quantitatively analyze individual fluid inclusions by Raman spectroscopy and laser ablation ICPMS. In the next years, it is likely that much progress will be made in determining the stable and radiogenic isotopic compositions of fluids in individual fluid inclusions. This revolutionary advance will allow workers to better determine sources of fluids using, for example, D/H and $^{18}O/^{16}O$ ratios of water in fluid inclusions (Dublyanksy and Spötl 2009). Similarly, Pb and Sr isotopic compositions of individual fluid inclusions (Pettke et al. 2012) will allow determination of the "ages" of fluids and their host phases and contribute to our understanding of the timing and duration of ore-forming processes.

Cross-References

- Aqueous Solutions
- Crystal Chemistry
- Diffusion
- Experimental Mineralogy and Petrology
- Geothermometry and Geobarometry
- Hydrogen
- Hydrogen Isotopes
- Hydrothermal Solutions
- Laser Ablation – Inductively Coupled Plasma Mass Spectrometry
- Metamorphic Reactions and Processes
- Ore Deposits
- Oxygen Isotopes
- Phase Equilibria
- Raman Microspectroscopy

References

Bodnar RJ (2003) Reequilibration of fluid inclusions. In: Samson I, Anderson A, Marshall D (eds) Fluid inclusions: analysis and interpretation, Mineralogical association of Canada, short course, vol 32, pp 213–230

Bodnar RJ, Binns PR, Hall DL (1989) Synthetic fluid inclusions. VI. Quantitative evaluation of the decrepitation behavior of fluid inclusions in quartz at one atmosphere confining pressure. J Metamorph Geol 7:229–242

Diamond LW, Tarantola A (2015) Interpretation of fluid inclusions in quartz deformed by weak ductile shearing: reconstruction of differential stress magnitude and pre-deformation fluid properties. Earth Planet Sci Lett 417:107–119

Dublyanksy YV, Spötl C (2009) Hydrogen and oxygen isotopes of water from inclusions in minerals: design of a new crushing system and on-line continuous flow isotope mass spectrometric analysis. Rapid Commun Mass Spectrom 23:2605–2613

Frezzotti ML, Tecce F, Casagli A (2012) Raman spectroscopy for fluid inclusion analysis. J Geochem Explor 112:1–20

Goldstein RH, Reynolds TJ (1994) Systematics of fluid inclusions in diagenetic minerals. Society for sedimentary geology short course notes, SEPM, Tulsa, 199 pp

Günther D, Audétat A, Frischknecht R, Heinrich CA (1998) Quantitative analysis of major, minor and trace elements in fluid inclusions using laser ablation inductively coupled plasma mass spectrometry. J Anal At Spectrom 13(4):263–270

Hall DL, Bodnar RJ, Craig JR (1991) Evidence for post-entrapment diffusion of hydrogen into peak metamorphic fluid inclusions from the massive sulfide deposits at Ducktown, Tennessee. Am Mineral 76:1344–1355

Larson LT, Miller JD, Nadeau JE, Roedder E (1973) Two sources of error in low temperature inclusion homogenization determination, and corrections on published temperatures for the East Tennessee and Laisvall deposits. Econ Geol 68:113–116

Lecumberri-Sanchez P, Steele-MacInnis M, Weis P, Driesner T, Bodnar RJ (2015) Salt precipitation in magmatic-hydrothermal systems associated with upper-crustal plutons. Geology 43(12):1063–1066

Mavrogenes JA, Bodnar RJ (1994) Hydrogen movement into and out of fluid inclusions in quartz: experimental evidence and geologic implications. Geochim Cosmochim Acta 58:141–148

Pettke T, Oberli F, Audétat A, Guillong M, Simon AC, Hanley JJ, Klemm LM (2012) Recent developments in element concentration and isotope ratio analysis of individual fluid inclusions by laser ablation single and multiple collector ICP-MS. Ore Geol Rev 44:10–38

Roedder E (1974) Changes in ore fluid with time, from fluid inclusion studies at Creede. In: 4th international association on the genesis of ore deposits (IAGOD) symposium, Varna. Proceedings, vol 2, pp 179–185

Roedder E (1984) Fluid inclusions. Rev Mineral 12, Mineralogical Society of America, 644 pp

Roedder E, Bodnar RJ (1980) Geologic pressure determinations from fluid inclusion studies. Annu Rev Earth Planet Sci 8:263–301

Roedder E, Bodnar RJ (1997) Fluid inclusion studies of hydrothermal ore deposits. In: Barnes HL (ed) Geochemistry of hydrothermal ore deposits, 3rd edn. Wiley, New York, pp 657–698

Sorby HC (1858) On the microscopical structure of crystals, indicating the origin of minerals and rocks. Q J Geol Soc Lond 14:453–460

Sterner SM, Bodnar RJ (1984) Synthetic fluid inclusions in natural quartz I. Compositional types synthesized and applications to experimental geochemistry. Geochim Cosmochim Acta 48:2659–2668

Sterner SM, Bodnar RJ (1989) Synthetic fluid inclusions: VII. Reequilibration of fluid inclusions in quartz during laboratory-simulated metamorphic uplift. J Metamorph Geol 7:243–260

Vityk MO, Bodnar RJ (1995) Textural evolution of synthetic fluid inclusions in quartz during re-equilibration, with applications to tectonic reconstruction. Contrib Mineral Petrol 121:309–323

Vityk MO, Bodnar RJ (1998) Statistical microthermometry of synthetic fluid inclusions in quartz during decompression. Contrib Mineral Petrol 132:149–162

Wagner T, Fusswinkel T, Wälle M, Heinrich CA (2016) Microanalysis of fluid inclusions in crustal hydrothermal systems using laser ablation methods. Elements 12:323–328

Weis P, Driesner T, Coumou D, Geiger S (2014) Hydrothermal, multiphase convection of H_2O-NaCl fluids from ambient to magmatic temperatures: a new numerical scheme and benchmarks for code comparison. Geofluids 14:347–371

Zajacz Z, Hanley JJ, Heinrich CA, Halter WE, Guillong M (2009) Diffusive reequilibration of quartz-hosted silicate melt and fluid inclusions: are all metal concentrations unmodified? Geochim Cosmochim Acta 73:3013–3027

Fluid–Rock Interaction

William E. Glassley[1], Laura J. Crossey[2] and Isabel P. Montanez[1]

[1]Department of Earth and Planetary Sciences, University of California, Davis, CA, USA

[2]Department of Earth and Planetary Sciences, University of New Mexico, Albuquerque, NM, USA

Definition

Throughout the Earth's crust there is chemical and mineralogical evidence that fluids are present as rocks evolve. Those fluids, which are mainly aqueous, chemically interact with the minerals present to modify the mineral chemistry or completely change the assemblage of minerals that compose the rock. This process is called *fluid–rock interaction* and is the subject of a broad body of research and technological development activity.

Introduction and Concepts

Fluid–rock interaction is the process in which solutions, which are usually aqueous, and the rock material with which they are in contact, chemically react to achieve a state that approaches thermodynamic equilibrium. The tendency to approach equilibrium is driven by chemical thermodynamics and is manifest as the tendency to develop assemblages of co-existing minerals and dissolved aqueous species that possess the lowest free energy for the chemical components in the total system. The rate at which equilibrium is approached is controlled by reaction kinetics. These processes occur in all regions of the Earth where aqueous solutions are found, which usually is restricted to those portions of the Earth where temperatures are between 0 °C and ~ 800 °C and pressures are between 0.1 MPa and ~ 3 GPa. To theoretically predict the products of these interactions and to quantitatively interpret the mineralogical and chemical evolution of geologic systems through time, data must be available on the thermodynamic properties of minerals and dissolved species over this range of physical conditions and on the rates at which minerals dissolve and precipitate (the rates at which speciation reactions occur in solution are usually considered to be instantaneous).

The principal mechanism whereby fluid–rock interaction takes place is dissolution and precipitation of mineral phases. Minerals with which water is in contact will dissolve, if the solution is undersaturated in the mineral phase, and minerals will precipitate if the solution is supersaturated with those phases, although the actual chemical pathway may be mediated by microbial activity at low temperature conditions. Also important in fluid–rock interaction are ion exchange processes at mineral surfaces (sorption effects), which involve exchange of ions between water and crystallographic sites in mineral structures. The rates at which these various mechanisms occur are strong functions of temperature, surface area (and number of available sites, in the case of ion exchange), pH, water composition, and ionic strength. Reaction rates are also influenced by whether the system is far from equilibrium, reaction rates being significantly higher when systems are far from equilibrium. These processes are primarily expressed on the pore scale, where the fluid and minerals are in intimate contact (Steefel et al. 2015 and other papers in that volume).

In general, rates for silicate and oxide mineral dissolution and precipitation are in the range of 10^{-10}–10^{-15} mol/cm^2 surface area/s at 25 °C. These rates are many orders of magnitude slower than other rate processes that influence water composition, such as salt dissolution or precipitation and ion exchange. Hence, for processes in which short time scales (seconds to hours) are important, silicate mineral dissolution and precipitation must be considered a second order effect in controlling water composition; ion exchange processes and salt dissolution or precipitation would be expected to control water chemistry. For longer-term concerns (months to years), the influence of silicate mineral saturation state becomes paramount.

Within the near-surface environment, fluid–rock interaction, often with the participation of microbial communities, controls the development of soils, the quality of water in streams, rivers and aquifers, and the chemistry of the oceans and ocean sediments (Holland 1984) and is thus an important influence in establishing the overall state of the environment. Soils represent the chemical products that form when minerals in igneous, metamorphic, and sedimentary rocks are hydrated, oxidized, and carbonated under low temperature conditions in which the water is in contact with atmospheric gases and influenced by diurnal and seasonal temperature cycles and biological activity. In this case, carbonates, oxides and hydroxides of iron, and clays (hydrated alumino-silicates) tend to be the thermodynamically stable reaction products. However, rigorous thermodynamic equilibrium is often not achieved due to the low temperatures, and hence low reaction

rates, characteristic of this environment. This is usually indicated by the metastable persistence of preexisting mineral phases and structural and compositional irregularities in many of the minerals that form during weathering. Those mineral phases that form during weathering often have a large capacity for exchanging ions and can readily influence the composition of water that may flow through them. The chemical compositions of waters in streams, rivers, and aquifers thus reflect both the effects of mineral dissolution and precipitation during weathering of preexisting rocks and the effects of ion exchange with the minerals that formed as a result of weathering. The chemical composition of the ocean reflects the time-integrated result of these near-surface rock–water interaction processes, modified by atmospheric interactions, the effects of seawater alteration of oceanic crust, and marine sedimentation (Holland 1984).

Interaction of fluids with rock at deeper levels in the crust is strongly influenced by the elevated temperatures and higher pressures found at depth and is an integral part of metamorphic recrystallization. As temperatures and pressures increase, reaction rates also increase, thus tending to generate mineral assemblages that are locally in chemical equilibrium. The total fluid volume present during metamorphism has been difficult to estimate but is expected to diminish as pore volumes and fracture permeability drop to very low values (ca. microdarcies) at the high pressures achieved tens of kilometers into the crust. Nevertheless, the presence of a wide variety of ore deposits, pegmatitic bodies, fluid inclusions, and mineral segregations and veins, all of which formed as a result of fluid–rock interaction (see Ilton and Eugster 1990, and other papers in that volume), requires at least the episodic presence of significant volumes of water-rich fluids at elevated temperatures and pressures.

Fluid–rock interaction associated with magmatic processes has been well documented through field and isotopic studies. In general, emplacement of magma bodies in the crust results in strong thermal gradients that drive convective flow of high temperature aqueous solutions. These fluids are a combination of solutions derived from the rocks that enclose the magma bodies and fluids derived from the crystallizing magma. Relatively rapid flow of these complex solutions around the magma body transports the fluids along temperature gradients and into other rock units. This results in extensive dissolution and precipitation, as the hot fluids interact with a range of rocks under different temperature and pressure conditions. Systems such as these tend to generate highly altered rock systems which are preserved in geologic environments as chemically evolved ("metasomatized") lithologic units in which extensive mass transfer is recorded (often called skarns) or, in those cases where active systems extend to the Earth's surface, are expressed as hot springs, geysers, and other expressions of hydrothermal and geothermal activity (Glassley 2014).

The primary methods for establishing the source regions for fluids involved in crustal processes, and their ages, is via studies of stable and radiogenic isotope systems (e.g., Craig 1963; Giggenbach 1992; Ivanovich and Harmon 1992; Seal 2006; Kennedy and van Soest 2007). Tritium, ^{3}He, ^{14}C, and ^{36}Cl are among the radiogenic isotope systems commonly used to date groundwaters or to establish the recharge rates or residence times of groundwaters. To obtain information about ion exchange, and dissolution and precipitation processes in aqueous systems, the systematics of the U-Th decay chain are often used. This system contains numerous daughter isotopes of varying half-lives and chemical properties. Disequilibrium in this decay chain can provide information about the exchange rates of ions and the chemical behavior of the local fluid–rock system. Oxygen, hydrogen, carbon, and sulfur isotope systems are often used to examine the extent to which evaporation has influenced near-surface fluid–rock systems, to determine whether biological sources played a role in the evolution of the fluid–rock system, and to determine whether mixing of fluids from different sources has occurred. Isotopic ratios involving these elements can also be used to evaluate reaction progress and the state of fluid–rock equilibrium and, in some cases, the temperature at which isotopic equilibrium was achieved, for rock systems that have experienced conditions typical of intermediate and deep crustal levels.

Practical Aspects of Fluid–Rock Interaction

Practical aspects of fluid–rock interaction include the important role these processes play in maintaining the quality of water resources (Manahan 1994). Through exchange and sorption of metals and other dissolved constituents onto their surfaces, clays and zeolites in geologic materials strongly influence overall water quality. Conversely, degradation of this capacity in aquifers that are naturally rich in clays and zeolites can result when aquifers are invaded by solutions that either diminish the abundance of these minerals or which overwhelm the available exchange sites of these minerals. Sea water incursion in regions of severe groundwater exploitation or leakage of contaminants from underground storage facilities are examples of processes that can diminish the exchange capacity of minerals that contribute to maintaining water quality.

Active Research Areas

The ability to rigorously simulate all aspects of fluid–rock interaction is a rapidly expanding field of research. Conceptual models of these processes, the mathematical constructs that rigorously describe them, and the computer codes to carry

out the calculations have rapidly evolved, although they are still limited by insufficient information about reaction mechanisms and processes that occur at mineral surfaces (Steefel et al. 2015). Nevertheless, a broad spectrum of efforts is being pursued to refine and apply existing capabilities (see papers in Lichtner et al 1996; Steefel et al. 2005). Molecular simulation of, and experiments on, interactions at mineral surfaces and within pores is an active research area. Simulations of rock–water interaction under conditions of fluid flow, often termed reactive transport, are playing a large role in establishing how mineral assemblages, individual lithologic units, and large sedimentary basins and petroleum reservoirs evolve through time. These capabilities are important because they are required for understanding the geologic and environmental consequences resulting from change due to the temporal variability of natural processes and those effects resulting from human activity such as CO_2 disposal (Al-Khoury and Bundschuh 2014).

The primary limitation in these efforts is an insufficient database for conducting the simulations. The database limitations stem from insufficient measurements of thermodynamic properties and rate constants for complex mineral phases and a dearth of experimental studies of processes at mineral surfaces and in complex isotope systems. The magnitude of this problem is greatest for conditions at high temperatures and pressures, although data at standard temperature and pressure are also inadequate.

Another area of active research is in establishing the characteristics of aqueous fluids at elevated temperatures and pressures. From theoretical considerations of the solubilities of mineral phases, it is clear that aqueous solutions with significant amounts of dissolved species should be present during recrystallization in metamorphic environments. Observations from fluid inclusion studies (e.g., Roedder 1984) document the common presence of such water-rich solutions, some of which are highly concentrated brines with total dissolved solids exceeding 40% by weight of the aqueous phase, thus supporting the theoretical considerations. However, such solutions are not miscible with fluids that are predominantly $H_2O - CO_2$ (Duan et al. 1995), which are often the two most abundant components in crustal fluids. Thus, it is expected that rock–water interaction during metamorphism may, in many cases, actually involve co-existing fluid phases, one of which is a concentrated brine, the other an $H_2O - CO_2$ solution. The relative abundances of these solutions remain unknown but can be expected to vary from region to region. The role such fluids play in mass transport in the crust, and methods for identifying their respective effects, have yet to be established.

Advances in the understanding of the role of microbial activity in subsurface environments have expanded interdisciplinary research in geomicrobiology and biogeochemistry. Genetic, geochemical, and genomic approaches have led to a greater understanding of how microbes (and microbial communities) depend on, and shape, their geochemical environments. Geomicrobiological effects on water–rock interaction include modification of chemical gradients, changes in fluid and gas composition, as well as modifying reaction rates. Early efforts focused on geochemical links to metabolic processes in hydrothermal ecosystems (Brock 1978), while more recently interdisciplinary efforts have covered a wide range of subsurface environments (Newman and Banfield 2002; Reysenbach and Shock 2002; Hinman 2013).

Summary and Conclusions

Fluid–rock interaction is a common process within the Earth that affects mineral compositions and mineral assemblages in rocks through numerous thermodynamically driven pathways. These interactions can provide a history of the diagenetic and metamorphic processes rocks experience and have an important influence on the specific mineral assemblages and mineral compositions that are stable at any given set of conditions. From a practical perspective, fluid–rock interaction can play an important role in establishing water quality in a region. Fluid–rock interaction also is important in considerations involving CO_2 disposal and contaminant transport in the subsurface. Current research areas include isotopic systematics of fluid–rock systems, computer simulations of fluid–rock interaction, and the kinetics that control the rates of these processes.

Cross-References

- ▶ Acid–Base Reactions
- ▶ Aqueous Solutions
- ▶ Diagenesis

References

Al-Khoury R, Bundschuh J (2014) Computational models for CO_2 sequestration and compressed air energy storage. CRC Press, Boca Raton. 533pp

Brock TD (1978) Thermophilic microorganisms and life at high temperatures. Springer, New York. 465pp

Craig H (1963) The isotopic geochemistry of water and carbon in geothermal areas. In: Tongiorgi E (ed) Nuclear geology in geothermal areas, Spoleto. Consiglio Nazionale delle Ricerche, Laboratorio di Geologia Nucleare, Pisa, pp 17–53

Duan Z, Moller N, Weare JH (1995) Equation of state for the NaCl-H_2O–CO_2 system: prediction of phase equilibria and volumetric properties. Geochim Cosmochim Acta 59:2869–2882

Giggenbach WF (1992) Isotopic shifts in waters from geothermal and volcanic systems along convergent plate boundaries and their origin. Earth Planet Sci Lett 113:495–510

Glassley WE (2014) Geothermal energy, 2nd edn. CRC Press, Boca Raton. 381 pp

Hinman N (2013) Water-rock interaction and life. Procedia Earth Planet Sci 7:354–359
Holland HD (1984) Chemical evolution of the atmosphere and oceans. Princeton University Press, Princeton. 582 pp
Ilton ES, Eugster HP (1990) Partitioning of base metals between silicate, oxides and a chloride-rich hydrothermal fluid. Part I. Evaluation of data derived from experimental and natural assemblages. Geochem Soc Spec Publ 2:157–169
Ivanovich M, Harmon RS (1992) Uranium-series disequilibrium: application to earth, marine, and environmental sciences. Oxford University Press, New York. 914 pp
Kennedy BM, van Soest MC (2007) Flow of mantle fluids through the ductile lower crust: helium isotope trends. Science 318:1433–1436
Lichtner PC, Steefel CI, Oelkers EH (1996) Reactive transport in porous media, Reviews in mineralogy, vol 34. Mineralogical Society of America, Washington, DC, p 438
Manahan SE (1994) Environmental chemistry, 6th edn. Lewis Publishers, Boca Raton. 811 pp
Newman DK, Banfield JF (2002) Geomicrobiology: how molecular-scale interactions underpin biogeochemical systems. Science 296:1071–1077
Reysenbach AL, Shock E (2002) Merging genomes with geochemistry in hydrothermal systems. Science 296:1077–1082
Roedder E (1984) Fluid inclusions. Rev Mineral 12. 644pp
Seal RR II (2006) Sulfur isotope geochemistry of sulfide minerals. Rev Mineral Geochem 61:633–677
Steefel CI, DePaolo DJ, Lichtner PC (2005) Reactive transport modeling: an essential tool and a new research approach for the Earth sciences. Earth Planet Sci Lett 240:539–558
Steefel CI, Emmanuel S, Anovitz LM (2015) Pore-scale geochemical processes, Reviews in mineralogy and geochemistry, vol 80. The Mineralogical Society of America, Chantilly. 491 p

Fluorine

Kenneth T. Koga and Estelle F. Rose-Koga
Laboratoire Magmas et Volcans, Université Blaise Pascal – CNRS, Clermont-Ferrand, France

Element Data
Atomic Symbol: F
Atomic Number: 9
Atomic Weight: 18.998 g/mol
Isotopes and Abundances: ^{19}F 100%
1 Atm Melting Point: −219.67 °C
1 Atm Boiling Point: −188.11 °C
Common Valences: −1
Ionic Radii: 130 (III), 131 (IV), and 133 (VI), in pm (coordination number)
Pauling Electronegativity: 3.98
First Ionization Potential: 17.4428 eV
Chondritic (CI) Abundance: 60.7 μg.g^{-1}
Silicate Earth Abundance: two estimates – 18 ± 8 and 25 ± 10 μg.g^{-1}
(*continued*)

Continental Crust Abundance ~ 550 μg.g^{-1}
Oceanic Crust Abundance 130 ~ 1000 (est. 400) μg.g^{-1}
Seawater Abundance: 1.3 μg.g^{-1}
Core Abundance: considered as 0

Properties

In its elemental form, fluorine exists as a diatomic molecule of highly toxic, corrosive, pale yellow gas with a pungent smell in ambient conditions. As the most electronegative element, fluorine is reactive and commonly found in nature as ionic compounds bonded to metal cations or hydrogen. Fluorine can dissolve into solution forming F^- ions.

History and Use

Fluorite (CaF_2) has been known and used in the metal smelting process to lower the melting temperature of metal ores since the sixteenth century. It was then known as *fluores* or *flusse*. The element was later isolated in 1886 (Moissan 1886), 330 years after fluorite was first described by Agricola (1556). Today, 6.2 million metric tons of fluorite is mined for industrial use (British Geological Survey 2010–2014 report) in metallurgy, ceramics, and chemistry, with applications including the production of aluminum, fluorocarbons, and fluorine gas. For example, fluorine is used to separate uranium in the nuclear power industry and to produce high-performance plastics such as polytetrafluoroethylene (PTFE, commonly known as Teflon®) and the Gore-Tex® membrane.

Geochemical Behavior

Fluorine plays an important role in geochemical and biogeochemical systems, despite its relative low overall abundance on Earth and in the cosmos. For example, fluorine can exert a significant control on the behavior and composition of magmas, the composition of hydrothermal fluids, and the transport of ore metals in the crust. The distribution of fluorine in various geological samples is therefore of interest in geochemical investigations, including tracing the evolution and source of hydrothermal fluids active in ore deposit formation, metamorphism and subsolidus alteration, and tracking subduction-related mantle to crust mass transfer.

Fluorine has a strong tendency to bond with silica and other cations and is therefore considered a lithophile element. Reflecting this characteristic, a dominant fraction of F on Earth, ~99%, is estimated to exist in the solid earth. However, fluorine is also referred to as a magmatic volatile element, as it

is found as HF gas in volcanic edifices and fumaroles. A small quantity of F is found in surface waters. On the contrary, F is thought to play a role in forming ligands and increasing metal solubility in high-temperature fluids (hydrothermal fluids, diagenetic formation waters, metasomatic fluids).

Considerable effort has been put into the advancement of analytical techniques to accurately determine the fluorine content of geological materials. Such analytical techniques include anion chromatographic column, selective electrode, neutron activation, electron microprobe, ion probe (SIMS), and irradiated rare-gas analysis (Hanley and Koga in prep).

Abundances

Fluorine, having the single isotopic species $^{19}_{9}F$, was produced by nucleosynthesis in stars and supernovae predating the sun, through neutrino spallation of ^{20}Ne and hydrogen-helium burning involving ^{14}N, ^{18}F, ^{18}O, and ^{15}N (Woosley and Haxton 1988; Forestini et al. 1992). At the time of the formation of the solar system, F is considered to have been moderately volatile with a 50% condensation temperature of 734 K for fluorapatite (Lodders et al. 2009). The solar abundance has been assessed by measurements of volatile element-rich CI chondrites and spectrometry of the sun's photosphere. While heavier halogen elements tend to be less abundant, the lightest halogen, fluorine, is notably less abundant than the heavier element Cl. In addition, F is 3–4 orders of magnitude less abundant than neighboring elements, namely, C, N, O, and Ne, due to a small probability of production and its destruction in supernovae (Clayton 2003).

Meteoritic F abundances vary by a factor of 20; CI and EH chondrites show higher abundances among the different chondrite classes (i.e., CM, CO, CV, H, and L, while EL and LL show the highest abundances; Wasson and Kallemeyn 1988). Fluorine contents of the Moon, Mars, and Vesta are also reported. The Moon's mantle is reported as 5.3 ppm F, based on glass samples (approximately 30% of Earth mantle). Bulk F abundance for Mars is 21 $\pm$ 13 ppm, estimated from shergottite meteorites (Taylor 2013). The eucrite parent body, Vesta, probably contains some volatile elements since F-rich apatites have been found in this class of meteorites.

The abundance of trace elements in the Earth's mantle is commonly assessed through compositional correlations among primitive basalt, peridotite xenoliths, and chondritic meteorites. The modeled F content of the bulk silicate earth (BSE) ranges from 18 to 25 ppm, with different estimates agreeing within reported uncertainty. Mid-ocean ridge basalt (MORB) are derived from a depleted mantle source with F contents ranging from 6 to 22 ppm. Limited data on the bulk F content of mantle xenoliths shows significant variability from 7 to 400 ppm (Hanley and Koga in prep).

Laboratory experiments show that F has a stronger affinity to silicate melt than to metals, metal alloys, and sulfides (e.g., Mungall and Brenan 2003). Based on a comparison of chondritic and BSE abundances, F abundance in the core is negligible (McDonough 2003).

Seawater, representing only 0.02% of Earth's mass, is a negligible F reservoir as it contains less than 1% of the total F budget of the bulk earth. The preferred mean abundance of F in seawater is 1.3 ppm. Fluorine in river water is reported as 10–20 ppb. Formation water in sedimentary basins and well waters in crystalline basements typically ranges from 0.5 to 10 ppm (Hanley and Koga in prep). Hydrofluoric acid is present in high-temperature volcanic gases, with concentrations typically in the range of 100–300 ppm, in which F is the least abundant of the six elements (H, C, O, S, Cl, and F) constituting volcanic gas (Symonds et al. 1994).

Fluorine abundance in the bulk continental crust is estimated as 553 ppm; this value is a volumetric average of upper (611 ppm) and lower crustal (429 ppm) average abundances. The upper continental crust is enriched in fluorine, relative to the lower continental crust, by a factor of 1.4–2.3 (Rudnick and Gao 2003).

Fluorine contents in magmatic rocks are in the 100s to 1000s of ppm range. Highly fractionated peraluminous and peralkaline granitoids, and some basaltic rocks, show the highest abundances, as F is generally concentrated into magmas during crystal fractionation. In addition, F is incorporated into silicate melt by bonding to Si and Al, resulting its higher solubility in felsic than mafic melts (Dalou et al. 2015).

During the weathering of volcanic products, glass devitrification results in mobilization of F (e.g., Stix et al. 1995). F is particularly rich in phosphatic shales, caliche (nitrate) deposits (up to ~4000 ppm; Batista et al. 2005), and evaporites.

Fluorine can be locally concentrated in mantle as halides and hydroxyl minerals. Carbonatites from Ol Doinyo Lengai, Tanzania, contain between 1.2 and 3.5 wt% F, occurring as immiscible halide melt (Teague et al. 2011); halide melt inclusions in magmatic minerals are found in intrusive carbonatites (Saint-Honoré, Quebec, Canada). Furthermore, fluoride melt has been reported in peridotite xenoliths (Klemme 2004). Similarly, F-rich micas and amphiboles are reported from various mantle nodules (e.g., up to 8 wt% F for phlogopite found in peridotite nodules).

Mineralogical Hosts

There are 427 naturally occurring fluorine-hosting minerals registered in the IMA inventory, in which halides, oxyhalides, silicates, and other groups are listed. Nearly all silicate minerals with hydroxyl (OH^-) sites can potentially have F-bearing species, such as mica, amphibole, apatite, and

norbergite. Fluorite (CaF_2) contains 48.7 wt% F. Up to a few weight percent, F can be found in micas, amphiboles, and apatites (e.g., 4.5 wt% phlogopite, 4.6 wt% fluororichterite, 3.8 wt% fluorapatite). Trace quantities of F can be incorporated into minerals without crystallographic site accommodation because of its similar ionic size to oxygen. For example, olivine and orthopyroxene in mantle peridotites are reported to contain 2.9–30.3 and 12–30 ppm, respectively (Beyer et al. 2012).

Biological Utilization and Toxicity

The teeth of some sharks are enameloid (in contrast to common dentin), which consists of fluorapatite, contrary to hydroxyapatite in human teeth. The lattice parameters of enameloid are close to those of the geological fluorapatite single crystal, with enameloid F content being 3.1 wt%, similar to the F content of geological fluorapatite (3.64 wt%; Enax et al. 2012). Incorporation of F in benthic foraminifera shells ranges from 0.00016 to 0.0016 F/Ca by weight, a maximum of 650 ppm F (Rosenthal et al. 1997). Corals contain 700 ~ 1200 ppm F.

In low concentrations, fluoride (F^-) strengthens the teeth and bones of vertebrates, and less than 2 ppm is added to toothpaste and drinking water in some countries. The human body contains on average 3 mg of F^-.

Elemental fluorine is highly toxic. Studies have found that a single ingestion of just 0.1–0.3 mg F/kg (i.e., milligrams of F for every kilogram of body weight) can cause the first symptoms of poisoning, including nausea, vomiting, abdominal pain, and diarrhea. Ingested fluoride is transformed in the stomach to hydrofluoric acid, which has a corrosive effect on the epithelial lining of the gastrointestinal tract. Fluoride consumed in excess is an endocrine disruptor that can affect bones, brain, thyroid gland, pineal gland, and even blood sugar levels (Akiniwa 1997).

Cross-References

- Chemical Weathering
- Chlorine
- Chlorine Isotopes
- Chondrites
- Cosmic Elemental Abundances
- Halide Minerals
- Halogens
- Hydrothermal Solutions
- Lithophile Elements
- Magmatic Process Modeling
- Meteorites
- Nucleosynthesis
- Ore Deposits
- Silicate Minerals
- Volcanic Gases

References

Agricola G (1556) De re metallica (translated version, Hoover HC, and Hoover LH (1912) De re metallica. Dover, New York)

Akiniwa K (1997) Re-examination of acute toxicity of fluoride. Fluoride 30:89–104

Batista MJ, Bidovec M, Demetriades A, De Vivo B, De Vos W, Duris M, Gilu-cis A, Gregorauskiene V, Halamic J, Heitzmann P, Lima A, Jordan G, Klaver G, Klein P, Lis J, Locutura J, Marsina K, Mazreku A, O'Connor PJ, Olsson SÅ, Ottesen R-T, Petersell V, Plant JA, Reeder S, Salpeteur I, Sandström H, Siewers U, Steenfelt A, Tarvainen T (2005) Geochemical atlas of Europe. In: Salminen R (ed) Part 1: background information, methodology and maps. Geological Survey of Finland, Espoo

Beyer C, Klemme S, Wiedenbeck M, Stracke A, Vollmer C (2012) Fluorine in nominally fluorine-free mantle minerals: experimental partitioning of F between olivine, orthopyroxene and silicate melts with implications for magmatic processes. Earth Planet Sci Lett 337:1–9

Clayton D (2003) Handbook of isotopes in cosmos, hydrogen to gallium. Cambridge University Press, Cambridge

Dalou C, Le Losq C, Mysen BO, Cody GD (2015) Solubility and solution mechanisms of chlorine and fluorine in aluminosilicate melts at high pressure and high temperature. Am Mineral 100:2272–2283. https://doi.org/10.2138/am-2015-5201

Enax J, Prymak O, Raabe D, Epple M (2012) Structure, composition, and mechanical properties of shark teeth. J Struct Biol 178:290–299

Forestini M, Goriely S, Jorissen A (1992) Fluorine production in thermal pulses on the asymptotic giant branch. Astron Astrophys 261:157–163

Hanley, Koga (in prep.) Halogens in terrestrial and cosmic geochemical systems: abundances, geochemical behaviors and analytical methods. In: Harlov D (ed) The role of halogens in terrestrial and extraterrestrial geochemical processes: surface, crust, and mantle. Springer, Berlin/Heidelberg

Klemme S (2004) Evidence for fluoride melts in Earth's mantle formed by liquid immiscibility. Geology 32:441

Lodders K, Palme H, Gail HP (2009) Abundances of the elements in the solar system. In: Astronomy and astrophysics. Springer, Berlin, pp 560–630

McDonough WF (2003) Compositional model for the Earth's Core. In: Holland HD, Turrekian KK (eds) Treatise on geochemistry, vol 2. Elsevier, Amsterdam, pp 547–568

Moissan H (1886) Sur la décomposition de l'acide fluorhydrique par un courant électrique. C R Hebd Seances Acad Sci 103:202–205

Mungall JE, Brenan JM (2003) Experimental evidence for the chalcophile behavior of the halogens. Can Mineral 41:207–220

Rosenthal Y, Boyle EA, Slowey N (1997) Temperature control on the incorporation of magnesium, strontium, fluorine, and cadmium into benthic foraminiferal shells from little Bahama Bank: prospects for thermocline paleoceanography. Geochim Cosmochim Acta 61:3633–3643

Rudnick RL, Gao S (2003) Composition of the continental crust. In: Holland HD, Turekian KK (eds) Treatise on geochemistry, vol 3. Elsevier, Amsterdam, pp 1–64

Stix J, Layne GD, Spell TL (1995) The behavior of light lithophile and halogen elements in felsic magma: geochemistry of the post-caldera Valles Rhyolites, Jemez Mountains Volcanic Field, New Mexico. J Volcanol Geotherm Res 67:61–77

Symonds RB, Rose WI, Bluth GJ, Gerlach TM (1994) Volcanic-gas studies; methods, results, and applications. Rev Mineral Geochem 30(1):1–66
Taylor GJ (2013) The bulk composition of Mars. Chem Erde-Geochem 73:401–420
Teague AJ, Hanley J, Seward TM, Reutten F (2011) Trace-element distribution between coexisting aqueous fumarole condensates and natrocarbonatite lavas at Oldoinyo Lengai volcano, Tanzania. Geol Soc Am Spec Pap 478:159–172
Wasson JT, Kallemeyn GW (1988) Compositions of chondrites. Philos Trans R Soc A Math Phys Eng Sci 325:535–544
Woosley SE, Haxton WC (1988) Supernova neutrinos, neutral currents and the origin of fluorine. Nature 334:45–47

Formation and Evolution of the Earth

Francis Albarède
Laboratoire de Géologie de Lyon, Ecole Normale Supérieure de Lyon, Lyon Cedex 7, France

Definition

Planet Earth is the largest rocky object of the inner Solar System. It formed some 4.5 billion years ago through accretion of smaller bodies, protoplanets, and planetesimals, which themselves had accreted from solids that condensed from the same nebula of gas and dust that formed the Sun. It has evolved since then through the segregation of the atmosphere, the oceans, the crust, the mantle, and the core, and, most peculiarly of all, of a biosphere.

Introduction

The Earth harbors a number of familiar characteristics, obviously life, but also a conspicuous ocean and an oxygen-rich atmosphere. The strong dichotomy between ocean and subaerial continents, which allows weathering and steady fluxes of nutrients to the ocean surface, a product of plate tectonics, is another distinctive feature of our planet. Only Mercury and Venus are closer to the Sun, whereas Mars is the last stop on the way to the outer Solar System, which is dominated by gaseous planets made of elements or compounds that condense at very low temperature, such as hydrogen, helium, and methane. The purpose of this article is to summarize our current understanding of the formation of our home planet, why it is so unique, and which processes and features allowed it to evolve through time into the modern Planet Earth. A strong caveat is that the scientific fields, which deal with these topics, are still evolving very fast. New fundamental observations are made each year and new concepts keep emerging. What was considered ground truth a decade ago is now being challenged, which should invite us to be modest when it comes to assessing the present state of the art.

The Formation of the Solar System

The best accepted model of the Solar System is the Solar Nebula hypothesis formulated by Immanuel Kant in 1755 and formally detailed by Pierre-Simon Laplace in 1796 (Fig. 1). In the beginning, 4.68 billion years ago, was a cloud of gas and dust. This cloud can be described by its mass, chemical composition, and rotational kinetic energy, which physicists usually deal by talking of angular momentum. These quantities are referred to as "conservative": mass does not change spontaneously in a closed system, while angular moment only changes under the effect of torques, such as those provided by tides. We know that today such nebular clouds are still formed from shreds torn off from very large dying stars, called the Asymptotic Giant Branch red-giant stars, and injected with material expelled from exploding supernovae.

Nebular gas is dominated by hydrogen (Fig. 2), but contains minute amounts of other elements, helium as well as heavier elements produced in older stars by nucleosynthesis. Gas collapses under its own weight, attracted, not toward the center of gravity, as this would violate the principle of angular momentum conservation, but vertically onto the midplane. The center of gravity remains nevertheless the locus of maximum mass accumulation and becomes the core of the newborn star. In the process, gravitational energy is changed into thermal agitation, the contracting cloud become extremely hot. The core of the Solar Nebula becomes dense and hot, enough to beam out large amounts of energy in the form of UV and X-ray light. This energy is strong enough to blow off all the nebular hydrogen and helium and chop off the outer edge of the collapsing cloud beyond 20 AU. A star at this

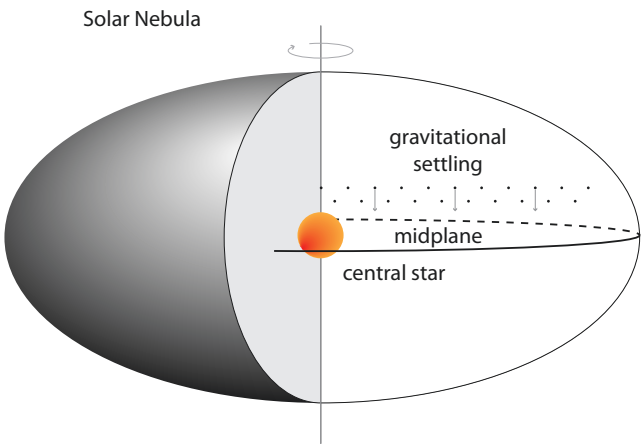

Formation and Evolution of the Earth, Fig. 1 The spinning and collapsing Solar Nebula. Because orbital angular momentum is conserved, material sedimentation takes place in the midplane

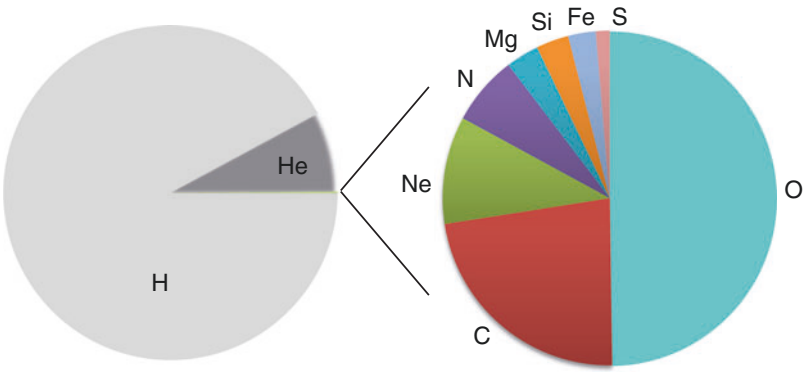

Formation and Evolution of the Earth, Fig. 2 The composition of the solar photosphere is dominated by H and He. The fraction of Si in the total Sun is 3.5×10^{-5}. Material used to form rocky planets, therefore, represents a very small fraction of the total nebular gas

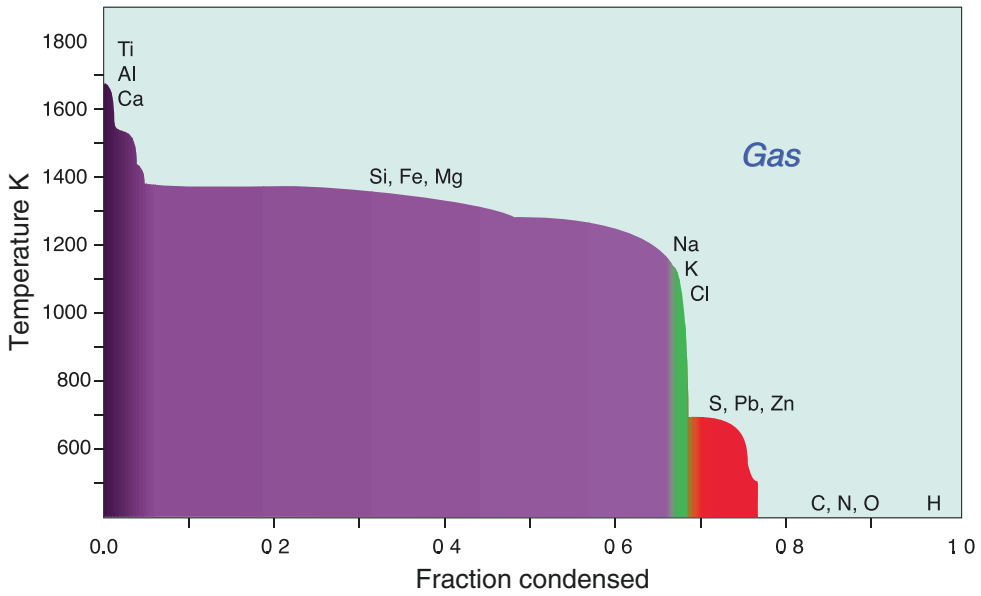

Formation and Evolution of the Earth, Fig. 3 Sequence of element condensation from the nebular gas as a function of the mass fraction of element condensed. Vertical segments represent condensation gaps with falling temperatures not affecting the fraction condensed. Condensation proceeds by stages separated by gaps, from ultrarefractory material (Ti, Al, Ca), planetary core and silicate mantle (Si, Fe, Mg), alkali elements (Na, K), sulfur-loving elements (S, Pb, Zn), and finally the most volatile elements, C, N, O. Hydrogen comes in at a very late stage. Planetary objects depleted in Zn and K, such as the Moon and the Earth, are therefore unlikely to have reached the condensation threshold for C, N, O, and H

stage is known by the name of the first example identified by astronomers, the star T in the Taurus constellation or T-Tauri. Further collapse of T-Tauri stars leads to the formation of a "true" star, in which central temperatures are high enough for the nuclear fusion of hydrogen into helium to be ignited. Observations of infrared radiations emitted by T-Tauri stars and blocked by the surrounding nebular disk led astronomers to conclude that this phase last less than 5 million years (Wyatt 2008).

The inner Solar System being hotter than its outer counterpart, gas and dust were lost before the primordial nebular material was fully condensed. Elements which condense at high temperatures (> 1300 K), such as aluminum, titanium, and magnesium, are called refractory, whereas those only condensing at lower temperatures (< 700 K), such as carbon, nitrogen, and hydrogen, but also sulfur and zinc, are referred to as volatiles (Fig. 3). The composition of the Solar Nebula is known in two ways, first by the spectroscopic analysis of the Sun's outer layer, the photosphere, second by measuring the elemental and isotopic abundances of the least transformed objects in the accessible Solar System. The Earth, Moon, and Mars were processed by impacts, and by internal and external geological processes, so in order to represent the nebular composition, excluding gases, cosmochemists turn to undifferentiated meteorites known as chondrites. These are aggregates of small beads of melted material (chondrules) cemented by a matrix of various fragments and debris and low-temperature condensates. Pre-solar grains may also be

present, although at < 0.1% level. Carbonaceous chondrites show evidence of a minimal deficit of the most volatile elements relative to the solar photosphere.

Condensation of the nebular gas to dust is probably the best understood part of Solar System history. Hydrogen makes up more than 98% of the gas, so the total pressure will be controlled by the dynamic expansion of the rotating nebular disk, its radiative cooling, and photoevaporation of the elements by stellar radiations. The rest of the elements are largely controlled by the respective thermodynamic properties of the gaseous and condensed phases. Upon cooling, condensation takes place in four stages (Fig. 3), first the ultrarefractory elements (Ti, Al, Ca), then the refractory elements, which account for most of the solid planetary interiors (Si, Fe, Mg), the moderately volatile elements, notably alkali elements (Na, K) and sulfur-loving (chalcophile) elements (Zn, S), and finally the elements involved in atmospheres and oceans (C, N, O, H). All these stages are separated by temperature intervals with little or no condensation.

The Formation of the Earth-Moon System

The standard planetary formation scenario can be divided into four main stages (Morbidelli et al. 2012). The first, and probably the least understood, stage takes the material from the dust, formed by the initial gas condensation. Dust grains can only stick together through weak van der Waals forces unless they are glued by shocks. Even objects of the size of a pebble bounce off each other upon collision. Passed this "bouncing barrier," aggregates continue to grow until they form kilometer-sized planetesimals. The myriads of planetesimals orbiting around the Sun sweep their orbit clean of dust and rocky debris; they collide and quickly form a smaller number protoplanets, with a typical size of 1000 km. This is the *runaway* growth stage. When too little material is left to sweep, planetary growth slows down and the large planetesimals gain control by perturbing the orbit of smaller objects: this is the *oligarchic* growth phase, at the end of which few protoplanets are left drifting in a medium still rich in planetesimals. The last, *chaotic* phase, lasts for a few tens of Ma: the combination of gravity fields of the Sun and Jupiter, the largest planet in the Solar System, perturbs the orbit of protoplanets and planetesimals. When a planetary object enters some resonance, i.e., when it returns to the same orbital position after an integer number of revolutions, gravitational pumping quickly builds up, orbits become increasingly elliptical, and the object is ejected from its orbit into the Sun, the inner Solar System where it can be captured by a resident planet, or lost from the Solar System. The number of planets quickly decreases to its current value and smaller objects are swept out of their original orbits over a time scale of about 150 Ma. Planetary orbits are not truly stable. Even giant planets can shift inward and then outward (the Grand Tack (Walsh et al. 2011)) and displace some large objects from their original orbit, which is a popular, yet not universally accepted, interpretation of the Late Heavy Bombardment of the inner Solar System some 700 Ma after its formation (the Nice model) (Gomes et al. 2005).

This well-structured picture has recently been blurred by new observations. First, isotopic analyses of oxygen implanted by the solar wind into metal grains at the surface of the Moon found it to be extremely enriched in the ^{16}O isotope relative to the rest of the Solar System (Hashizume and Chaussidon 2005). The difference is simply much too large relative to isotopic variations of other elements in the Solar System and cannot be explained by processes taking place within the nebula. This observation has been confirmed by the excess ^{16}O found in the solar wind implanted in material sent by NASA's Genesis mission (McKeegan et al. 2011) and by observations on a particular kind of refractory inclusions in chondrites showing FUN (Fractionation and Unknown Nuclear) effects (Krot et al. 2014) (Fig. 4). The suggestions that ^{16}O anomalies was produced by isotope-dependent photodissociation (self-shielding) of carbon monoxide generated controversy over the last 15 years (Clayton 2002; Lyons and Young 2005; Thiemens 2006). Rapid recombination of CO self-shielding products (Navon and Wasserburg 1985) led Yurimoto and Kuramoto (2004) and Lyons and Young (2005) to suggest that capture of anomalous oxygen upon freezing and transport of ice from the outer into the inner Solar System was responsible for isotopic heterogeneities. The strongly correlated concentrations of water and other volatile elements (e.g., K, Zn, Cd, Tl) in chondrites (Albarede et al. 2013) does not support a peculiar role for ice. The nucleosynthetic significance of ^{16}O anomalies became much more intelligible when they were found to correlate with nucleosynthetic excesses of some neutron-rich isotopes, notably chromium-54 and titanium-50 (Trinquier et al. 2007; Trinquier et al. 2009; Warren 2011), and even with the abundance of the stable isotopes of elements such as Cu, Zn, and Si (Fitoussi and Bourdon 2012; Luck et al. 2005; Luck et al. 2003). At least three unrelated components took part in the making of the Solar Nebula, the Sun itself, the inner Solar System, dominated by ordinary chondrites, and the outer Solar System, home of the carbonaceous chondrites and comets. Further down, we will explain how the low content of water and other volatiles in ordinary chondrites relative to carbonaceous chondrites is key to the understanding of the presence of water in the Earth.

The infant Earth drew heat from three sources of energy. First, as soon as a planet radius exceeds about 2000 km, conversion of gravitational energy by accretion of dust, asteroids, planetesimals, and planetary embryos into heat becomes very efficient, to the point that large amounts of material are molten and even vaporized. Second, internal differentiation,

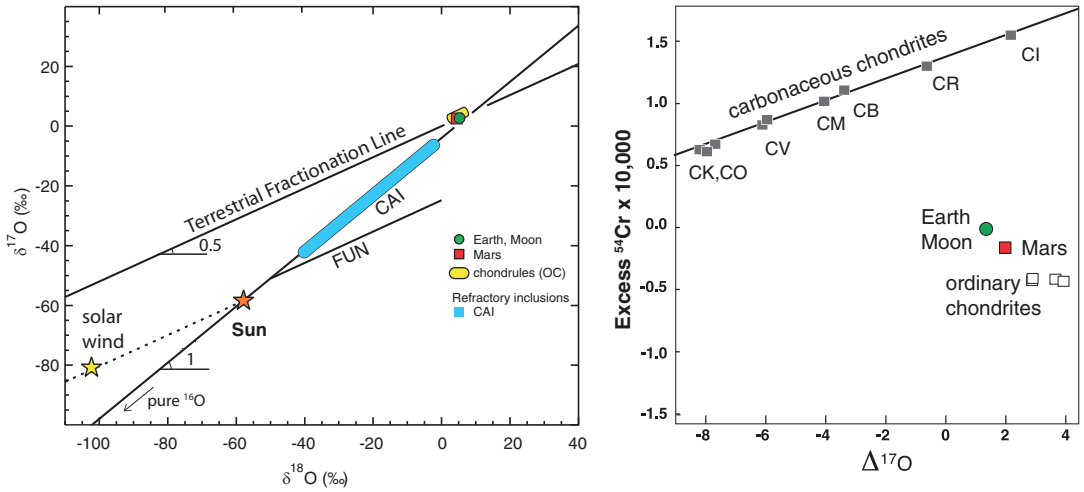

Formation and Evolution of the Earth, Fig. 4 The Solar Nebula is isotopically heterogeneous and must have formed from unrelated masses of interstellar gases. Left: oxygen isotope relationships in the inner Solar System (Krot et al. 2014). Thermodynamic processes, whether magmatic or environmental, produce an effect on the 18O/16O, which is twice the effect on 17O/16O, and hence moves oxygen isotopes on straight lines with a slope of 0.5 (Terrestrial Fractionation Line, FUN inclusions, solar wind). The elevation of a data point above the Terrestrial Fractionation Line is noted Δ17O and signals a nucleosynthetic origin different for the Earth and other material. The existence of a straight line with a slope of 1 on which the refractory calcium and aluminum-rich inclusions (CAI) found in chondrites demonstrates the existence of an excess of pure 16O in the Sun relative to the Earth. Right: the correlation of the excess of 54Cr with Δ17O in chondrites demonstrates the nucleosynthetic origin of both 16O and 54Cr excesses (Trinquier et al. 2007). Correlations of Δ17O with 65Cu/63Cu and 66Zn/64Zn in chondrites reinforce the conclusions that the Solar Nebula incorporated unrelated nucleosynthetic components

and in particular the segregation of the Earth's metallic core, liberates over the entire planet the equivalent of 2000 K heating. Third, stellar-derived short-lived aluminium-26, which decays into ^{26}Mg with a half-life of 0.7 Ma in releasing huge amounts of energy, was incorporated into the innermost regions of Solar Nebula, while the outer Solar System seems to have received only small amounts of it (van Kooten et al. 2016).

These heat sources drove melting of terrestrial planets and planetary embryos, which allowed dense iron and nickel to sink into planetary cores and left an outer shell of material known as a magma ocean. The fate of the magma ocean depends on the radius of the planet. If the planet is large, say the size of the Earth, and therefore its gravity strong, the surface of the molten layer solidifies as crystals of dense minerals, olivine and pyroxene, which quickly founders into the magma and the magma ocean crystallizes in a very short time (<1 Ma). For a small planet like the Moon, the gravity field is weak, buoyant crystals of a mineral known as plagioclase float to the surface and form as a thick blanket insulating the magma ocean from fast cooling (Fig. 5). Abundant plagioclase is responsible for the silvery shine of the lunar highlands. It is believed that under such conditions, the lunar magma ocean may have persisted for over 100–200 Ma (Elkins-Tanton et al. 2011; Nemchin et al. 2009).

The chronology of the lunar giant impact and of late accretion is not fully resolved, and as it ties into the origin

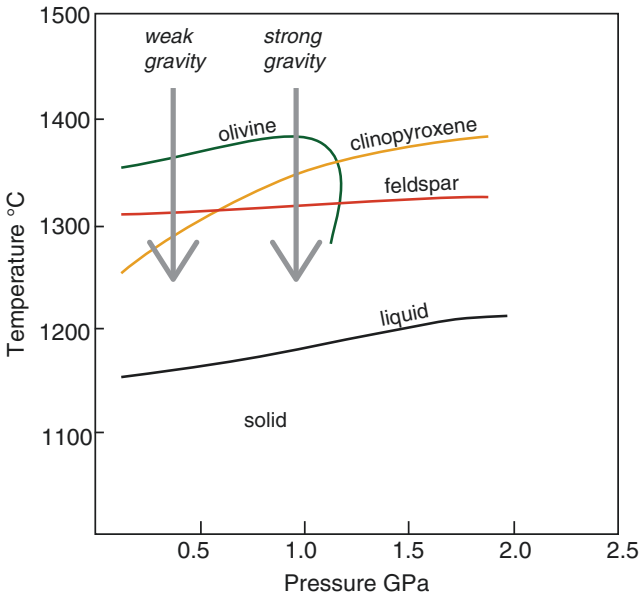

Formation and Evolution of the Earth, Fig. 5 Effect of gravity and, therefore, planetary size on the sequence of magma crystallization. At pressures in excess of 0.5 GPa (about 15 km in the Earth, and 90 km in the Moon), the first minerals to crystallize are olivine and pyroxene. These minerals are dense and sink in the magma, which keeps the magma largely exposed and causes fast cooling. In contrast, at pressures less than 0.5 GPa, plagioclase feldspar steps in at an earlier stage. This mineral is less dense than its parent melt and floats to the surface, creating an insulating blanket and slowing down magma crystallization. The lunar highlands and meteorites known as cumulate eucrites (likely from Vesta) illustrate how such a process can control the differentiation of small planets

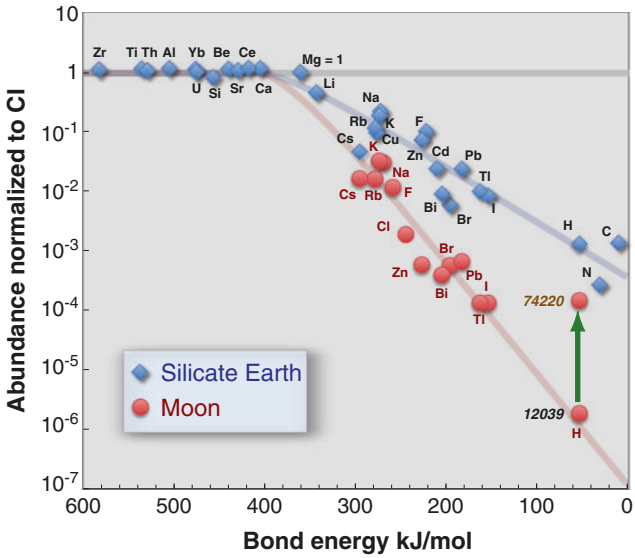

Formation and Evolution of the Earth, Fig. 6 Abundance of elements in the Earth and Moon normalized to carbonaceous chondrites and to Mg = 1. The bond-energy scale (Luo 2007) adopted in this plot (Albarède et al. 2015) is different from the 50% condensation temperature T50 (e.g., (Lodders 2003) calculated from the standard cooling sequence of the Solar Nebula. For the Earth, T50 can be calculated in kelvins by multiplying the value of bond energy by ~3 (e.g., T50 ~ 700 K for Zn). The lack of hydrogen and helium in the gas of the lunar disk in the aftermath of the Giant Lunar Impact makes T50 irrelevant. The Moon is clearly depleted in all volatile elements except in pyroclastic glasses produced by lava fountaining, such as "orange glass" 74220

of the terrestrial ocean, neither is the origin of water and volatiles in the Earth (Fig. 6). In the legacy of Apollo missions in the 1970s was the dry character of the Moon. Beyond manifest evidence that the Moon has no ocean, common hydrous minerals (amphiboles, micas) so conspicuous in terrestrial magmas are totally absent from the lunar basalts and other rocks or subordinate (apatite). The idea of a dry Moon was recently challenged when substantial amounts of water were found in melt droplets encased in olivine crystals present in blebs of pyroclastic lavas, a form of lavas produced by lava fountains (Hauri et al. 2011).

Are those new observations enough to discard the old theory of a dry Moon? Not yet. Water is made of two elements, oxygen and hydrogen. But outside of the biological world, water does not really hold the status of a "magic" component. In all the objects of the inner Solar System, hydrogen, and therefore water, shares a common trend with other volatile elements such as C and N, but also of less volatile elements such as S, Zn, K, and Na. Clearly, the Earth is depleted in all the volatile elements and the Moon is even more depleted than the Earth. Potassium which condenses at 1000 K is three times more depleted in the Moon, zinc which condenses at 700 K about 250 times, so what should we think about water which condenses at 180 K (Albarede 2009)? If pyroclastic lunar melts contain large amounts of water and other volatile elements, this property is not common to all lunar material indiscriminately.

This problem of water in the Moon is actually tightly connected to the question of water in the Earth and we are now going to discuss why. We focus on water primarily because of the ocean and the role of aqueous chemistry in the emergence of life. As indicated before, however, hydrogen abundances are strongly correlated with the abundance of other volatile elements. The question of water in terrestrial planets can be formulated in two different ways: (1) Were volatile elements initially present in planetary material but subsequently lost by shocks and gravitational escape? Or (2) Does the depletion pattern common to all the objects in the Solar System indicate that nebular gas was blown off before it cooled down to volatile condensation temperature? Solution (1) faces a very tough challenge because volatile elements with light masses should be more depleted than their heavier counterparts. Examining families of elements with related properties provides a strong clue: alkali elements sodium (M = 23) and cesium (M = 133) are not depleted to very different extents, nor are halogens Cl (M = 35) and iodine (M = 125). In general, depletion patterns are not related to mass.

Solution (2) faces a very different problem: if potassium, an element which condenses at 1000 K, is depleted by a factor of 6 in the Earth relative to the nebular composition, what are the chances that the Earth contains any water, which condenses at 180 K, at all? Given the broad gaps in condensation temperatures indicated above, the answer is clearly "none." Most elements condense and vaporize from the cooling nebular cloud in a temperature interval smaller than 100 K (Larimer 1973) and their abundances would be expected to "toggle" between condensation to no-condensation status. The broad range of temperature inferred from the abundance of moderate volatile elements, such as Zn, Rb, Mn, Li, in the Earth (>700 K; Palme and O'Neill 2003) calls for late addition of material variably depleted in volatile elements. Water in particular must have been added after the primordial condensation was completed. A similar response can be given for other volatile elements such as S, N, and C. Although water is found on Earth in the form of a conspicuous liquid ocean, most scientists would also argue that more inconspicuous water, worth more than an oceanic mass, is also present in the mantle.

This problem is addressed with the important concept of Late Veneer. At any given point in the history of the Solar System, material is left over with orbits that will eventually cross the Earth's orbit in the form of dust and grains (the modern equivalent being the shooting stars), asteroids such as the one ramming into the Earth killing dinosaurs and most living organisms 65 million years ago, and protoplanets such as Theia, which is widely believed to have caused the Lunar Giant Impact and left the Earth and Moon close to their modern configuration (Fig. 7). Today, the Earth's

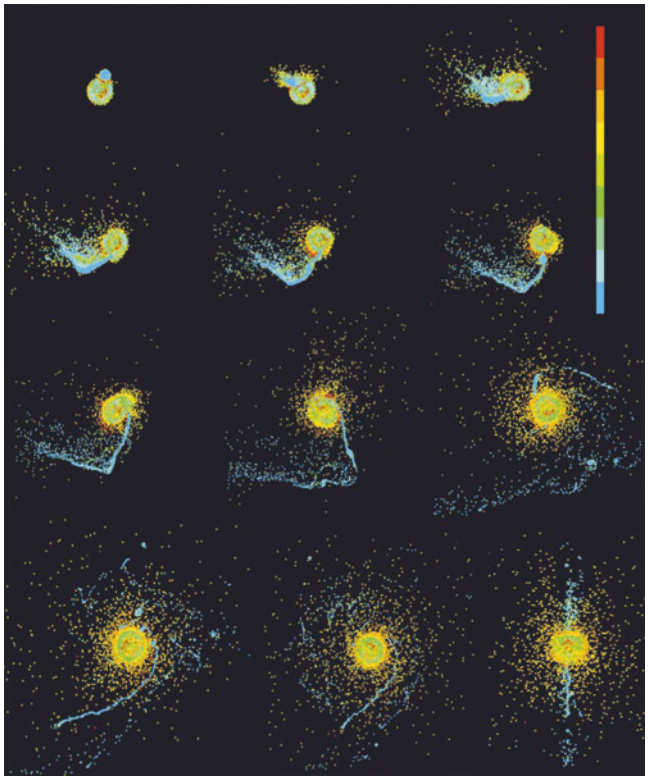

Formation and Evolution of the Earth, Fig. 7 The Lunar Giant Impact (Canup and Asphaug 2001). Theia, a Mars-size impactor (in blue in the upper left corner), obliquely collides with the proto-Earth. Scattered material is rapidly collected by the Earth or placed into orbit as a pre-lunar disk (in blue in the lower right corner). Colors refer to material temperature. Snapshots at time t = 0.3, 0.7, 1.4, 1.9, 3, 3.9, 5, 7.1, 11.6, 17, and 23 h

Formation and Evolution of the Earth, Table 1 Radioactive systems mentioned in the text and their half-lives

Parent	Character	Daughter	Character	Half-life $T_{1/2}$
^{26}Al	Lith	^{26}Mg	Lith	0.73×10^6 a
^{182}Hf	Lith	^{182}W	Sider	8.9×10^6 a
^{146}Sm	Lith	^{142}Nd	Lith	103×10^6 a
^{235}U	Lith	^{207}Pb	Chalc, lith	710×10^6 a
^{238}U	Lith	^{206}Pb	Chalc, lith	4.47×10^9 a
^{232}Th	Lith	^{208}Pb	Chalc, lith	14×10^9 a
^{87}Rb	Lith	^{87}Sr	Lith	49.7×10^9 a

Lith lithophile, *Chalc* chalcophile, *Sider* siderophile

neighborhood is relatively clean and safe, although some resonances with Jupiter may occasionally break asteroids and send the fragments flying across the Solar System as they did 160 (Bottke et al. 2007) or 420 (Nesvorný et al. 2007) Ma ago. Observations strongly support this concept: upon core segregation, iron-loving elements (siderophile) and in particular those of the platinum group family (PGEs, such as osmium, rhodium, etc.) are completely segregated into the metal phase. The overlying mantle should be left with barely a whiff of PGEs. Observations on ultramafic rocks and basalts show, however, that platinum and its kin are present in the mantle (Morgan 1986; Walker 2009). In addition, their relative proportions coincide with chondritic proportions, whereas if PGEs had been left behind by core-mantle segregation, elements should have strongly been fractionated from each other. All these observations can be reconciled with the Earth's growth history, if 0.4% chondritic material or more was added after the last major event of metal/silicate fractionation. This last added fraction is known as the Late Veneer.

The Late Veneer hypothesis (Chou 1978) has gained momentum as the prevailing mechanism for bringing water and other volatile elements, as well as the highly siderophile elements discussed above, to the Earth. Water can therefore be seen as "extraterrestrial." The older assumption that comets were the water carrier lost favor, largely because of their excessive deuterium abundance (Owen and Bar-Nun 1995; Robert et al. 2000). The "dry" character of the Moon is in keeping with Platinum Group Elements being some 40 times less concentrated in the lunar mantle indicating a much smaller contribution of Late Veneer relative to the Earth (Day et al. 2010). The stark contrast between the amount of Late Veneer brought to the two planetary bodies suggests that the Earth acquired its water and volatile elements by collision with a single object (Bottke et al. 2010) resembling one of the Jupiter's moons, Ganymede.

What was the timing of the events? The oldest age on the Moon was found in a zircon from a breccia (**4417 ± 6 Ma)** (Nemchin et al. 2009.) Our understanding of the chronology was greatly influenced by the extinct radioactivity of the isotope 182 of hafnium, which decays to the isotope 182 of tungsten with a half-life ($T_{1/2}$) of about 9 Ma (Table 1). Upon planetary melting, tungsten is preferentially hosted in the Earth's metallic core, whereas hafnium remains in the mantle. The ^{182}Hf-^{182} W is therefore an excellent chronometer of core/mantle segregation. It has been found that the Earth's core segregated some 30 Ma after the formation of the Solar Nebula (Kleine et al. 2002; Yin et al. 2002), while the lack of a significant excess of ^{182}W in the Moon relative to the Earth suggests that the Lunar Giant Impact took place after all radioactive ^{182}W disappeared, about 40–60 Ma later (Touboul et al. 2015). Such a late formation age of the Moon is based on Hf and W abundances in the terrestrial and lunar mantles, and on how well constrained the value of 0.4% of Late Veneer may be, two assumptions that are both the subject of variable opinions in the field of planetary geochemistry. How early the Moon formed is still a subject of active discussion. Can we now date the arrival of the Late Veneer? Although some scientists still believe that water and volatiles were accreted to the Earth at a very early stage, the case for a later event is based on multiple observations. The long-lived ^{235}U-^{207}Pb, ^{238}U-^{206}Pb, and ^{87}Rb-^{87}Sr chronometers suggest major events fractionating volatiles from

refractory elements at 100–150 Ma, and it is difficult to believe that these events are disconnected from the Late Veneer imprint.

What about the terrestrial atmosphere? It has long been pointed out that the distribution of rare gases (He, Ne, Ar, Kr, Xe) in the atmosphere is very different from solar abundances, which led earlier scientists to suggest that the terrestrial atmosphere is "secondary" and cannot have been outgassed from the mantle. The relative abundances of the stable isotopes of the rare gas xenon also are different in the atmosphere and the mantle (Caffee et al. 1999; Holland and Ballentine 2006), which confirms that the atmosphere cannot be simply accounted for by outgassing or mantle volatiles (Allegre et al. 1983). Again the extinct radioactivity of iodine-129 ($T_{1/2} = 15.6$ Ma) and plutonium-244 ($T_{1/2} = 80$ Ma) as measured by the relative proportions of their daughter xenon isotopes ^{129}Xe and $^{131\text{-}136}$Xe suggest an apparent age of the atmosphere of about 100 Ma after the formation of the Solar System (Ozima and Podosek 1999). If the Earth's atmosphere built up from small planetary objects brought from the outer Solar System, an initial composition rich in carbon dioxide (now stored as carbonates) and nitrogen is expected, very similar to the atmosphere of Venus.

The Early Earth

After the formation of the Earth-Moon system, the Earth was left with a partially molten mantle, a magma ocean occupying the top of the mantle and possibly another ocean at the bottom (Labrosse et al. 2007). For lack of relevant observations, the thermal regime of our planet at that stage is very poorly understood. Upward crystallization of the upper magma ocean gave most of the mid-mantle the geochemical character of a solid cumulate depleted in the most fusible elements, such as alkali elements, aluminum, and titanium, but also trace elements such as rare-earth elements and heat-producing uranium and thorium. Upward segregation of a liquid enriched in incompatible elements, very similar to the lunar basalt component dubbed "KREEP" to emphasize its high abundances in potassium, rare-earth elements, and phosphorus, may have been accompanied by the formation of a buoyant crust, for the composition of which we have very little evidence. Although mass balance between the primordial mantle, the crust, and the residual mantle may be satisfactorily worked out at the first-order for most elements, the geochemical pathways and processes that severely depleted the terrestrial upper mantle in incompatible elements and heat sources over geologic times and led to continental crust segregation remain poorly understood in detail.

A related issue is why the Earth was apparently the only planet to "go plate tectonics." The two main dynamic modes of terrestrial planets are (Schubert et al. 2001) (Fig. 8):

1. The stagnant lid regime, in which steady lithosphere, unbroken, cold, and solid overlies the convective mantle (Davaille and Jaupart 1993). The solid lithosphere thermally insulates the mantle and heat produced in the planetary interior can only be lost by conduction, a very inefficient cooling mechanism.
2. Plate tectonics, in which solid lithospheric plates yield under their own weight as they cool then founder into the mantle. This process is known as subduction. New lithosphere must therefore be created by upwelling of hot and partially molten upper mantle. The site at which new crust is created is called mid-ocean ridges. This process brings very hot material at the surface and acts very efficiently to cool the mantle. Many believe that the terrestrial dynamo and its external manifestation, the terrestrial magnetic field, owe their existence to the enhanced cooling provided by plate tectonics.

To some extent, plate tectonics prevailed in the Earth due to the presence of water, which decreases the viscosity of the mantle (Hirth and Kohlstedt 1996). But the exact mechanisms

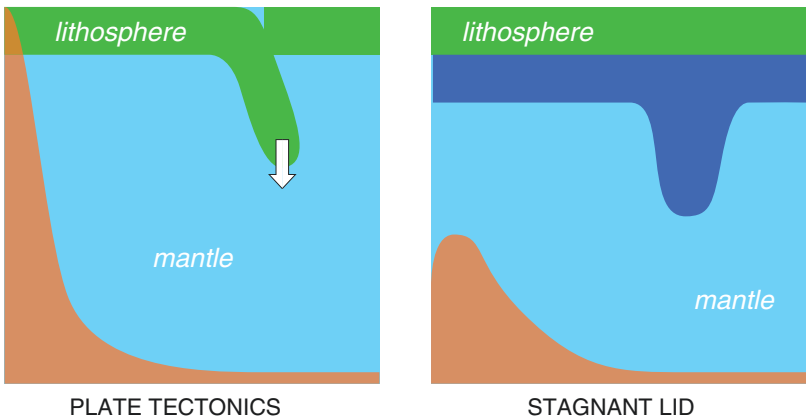

Formation and Evolution of the Earth, Fig. 8 The contrasting geodynamic regimes of Earth (left) and Mars (right). In the Earth, the abundance of water makes the lithosphere less resistant to gravitational pull and the mantle less viscous: plate tectonics is the stable regime and enhances planetary cooling. In Mars, the paucity of water and weaker gravity makes the lithosphere stable and act as a thermally insulating blanket

that allowed tectonic plates to form remain largely enigmatic. Two factors are thought to be primordial. First, mantle material obeys a nonlinear rheology (rocks only yield above a particular threshold). Second, by reducing grain size and damaging crystalline structures, shear helps localize deformation and cause plates to break (Bercovici and Ricard 2014).

The time at which tectonic plates appeared is better constrained thanks to the presence of very ancient granites, the hallmark of continental crust and plate tectonics. When extracted from the mantle, most primary basalts are saturated in magnesian olivine, the cardinal mantle mineral, but olivine irreversibly reacts with granitic liquids; granites cannot therefore be primary mantle melts and their presence indicates the remelting of basaltic rocks instead and the presence of water in the source. Such a process is known to take place within terrestrial subduction zones and, exceptionally, in Iceland, where the basaltic piles are hydrothermally altered upon infiltration of meteoric water. In most other oceanic islands, granites are very rare and reduced to isolated outcrops. In planetary materials such as lunar rocks, they occur as rare and small fracture-filling exudates. In contrast, granites and their metamorphic and sedimentary derivatives are major components of the continental crust. Ancient granites are best traced by zircon (zirconium silicate $ZrSiO_4$), a tiny but ubiquitous mineral, which crystallizes at high temperature and is extremely resistant to mechanical and chemical erosion. Abundant detrital zircons is a sure sign of the presence of granites in the watershed and therefore of continental crust. In addition to Zr, zircon contains substantial amounts of uranium, which makes this mineral the epitome of precise and reliable chronometers. It also hosts sizeable amounts of hafnium, a nearly perfect isomorph of zirconium, which allows the ^{176}Lu-^{176}Hf chronometer to be implemented and model ages of crustal residence to be calculated. In the Yilgarn craton, Western Australia, the ~3 Ga old Jack Hills conglomerate was found to contain a huge variety of detrital zircons, some of them as old as 4.1 Ga and up to 4.38 Ga (Harrison et al. 2005; Kemp et al. 2010; Wilde et al. 2001). Zircon crystals from Jack Hills also contain mineral inclusions that are all characteristic of granitic rocks, typically feldspars and micas. The presence of granitic rocks as early as 4.3 Ga and of a suite of granites at 4.1 Ga attests to the existence of some early form of continental crust and therefore of active plate tectonics less than 500 Ma after the formation of the Earth. Venus and its complete resurfacing about 1 Ga ago should be taken as a caveat (Phillips et al. 1992): we know very little about the geology of the first planet aeon. Although the view that plate tectonics started early in the Earth's history has gained momentum, it has also been suggested that it could have started at a much later stage.

Two unusual types of rocks are only found in the Archean crust, with rare exceptions. The first type is known as komatiites (Fig. 9), lavas that represent some sort of "superbasalts" melted at great depth in the mantle and erupted at temperatures in the order of 1500 °C, much higher than modern basalts (Arndt et al. 2008). Komatiites have been related to either mantle plumes or to subduction zones, and attest that the mantle was much hotter in the Archean than today. Such high temperatures reflect that the radioactive isotopes of potassium, uranium, and thorium were more abundant several billion years ago than today (Fig. 10). Another major group of Archean rocks, awkwardly designated as the tonalite-trondhjemite-granite or TTG assemblage (Fig. 11), has peculiar geochemical characteristics indicative of a mantle source enriched in incompatible elements. The

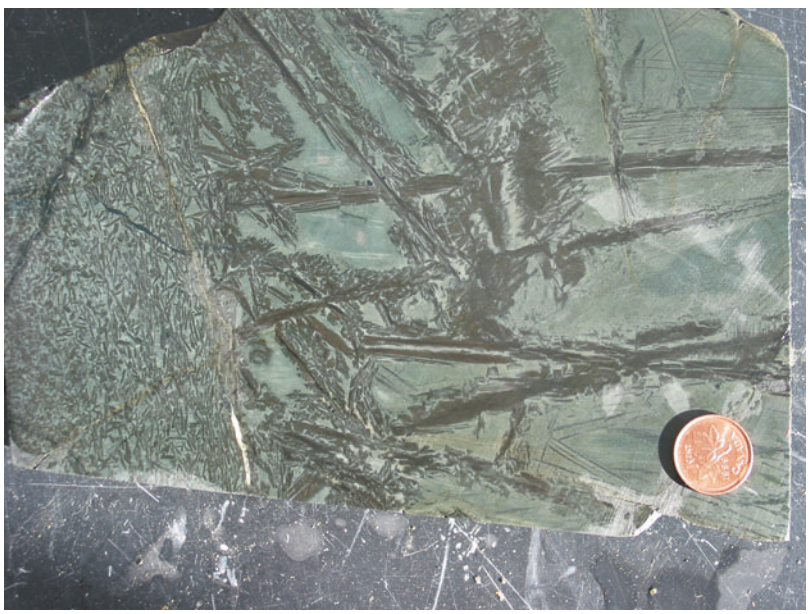

Formation and Evolution of the Earth, Fig. 9 Archaean komatiite from South Africa (courtesy of Nicholas T. Arndt) attest to extremely hot mantle sources. The eruption temperature of these lavas may have reached 1500 °C. Very rapid cooling rates induced the growth of long olivine crystals which gives the rock its fern-like appearance

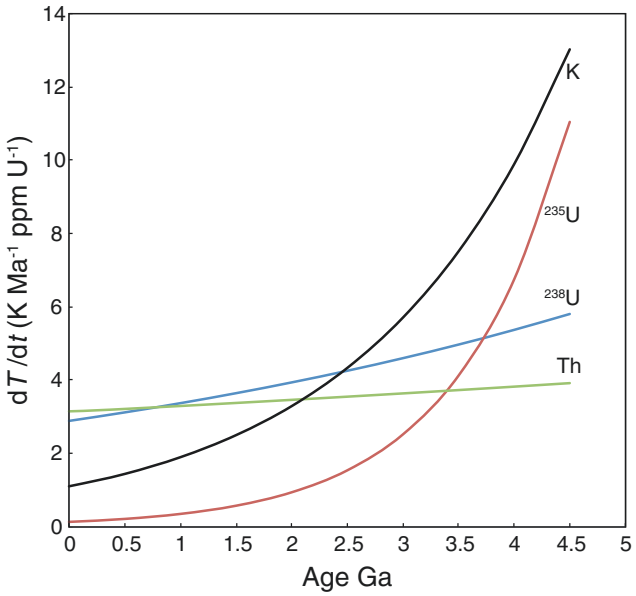

Formation and Evolution of the Earth, Fig. 10 Contribution of naturally occurring radioactive isotopes to the radioactive heating of the Earth through time. The curves represent the rate dT/dt of heating per Ma by radioactivity for a typical terrestrial rock containing today 1 part per million of uranium and 1% potassium (K/U = 10,000)

structure of Archean continents typically show TTG nuclei stitched to each other by komatiite-rich lineaments, referred to as greenstone belts. So, although the early Earth had gone the plate-tectonics way, the differences between Archean and modern geodynamics were fairly conspicuous.

An additional characteristic of the early Earth was continental elevation above sea level. Continental crust is significantly less dense than the ambient mantle and makes continental plates thick and buoyant. The Earth is therefore characterized by a strong dichotomy of elevations: plates capped with continental crust rise like icebergs above the sea surface. Today, they emerge above sea level, in contrast with oceanic plates, such as the Pacific plate, which are submerged by deep oceans and form oceanic abyssal plains. Such a dichotomy does not exist on other terrestrial planets (the contrast between the northern and southern hemispheres of Mars is believed to be inherited from a large impact) and is a sure indication of an active plate tectonics regime. Archean subaerial sediments such as river sandbars and braided channel deposits of mud flats are very uncommon (Eriksson et al. 2005; Long 2011). Most volcanic eruptions seem to have occurred under shallow water (Arndt 1999).

How Does the Mantle-Crust System Evolve?

Before discussion starts, a caveat must be born in mind. We walk on the Earth's surface only and the geologist can only scratch the top layers of the upper crust, which is, on average,

Formation and Evolution of the Earth, Fig. 11 The tonalite-trondhjemite-(TTG) granite association dominates continental crust in Archean terranes (Canada, courtesy Martin Guitreau). Here the color contrast between rocks of variable silica contents underlines the strong deformation of the whole crustal segment

35–40 km thick. Decreeing that a particular surface sample is representative of the lower crust requires detailed investigations with usually ambiguous conclusions. Volcanic eruptions raise rock fragments known as xenoliths, from the deep crust and the upper mantle to the surface. The depth at which the rock was torn off from the wall by the rising magma is usually assessed through thermodynamic models. The persistence of radiogenic isotope excesses in xenoliths (Bedini et al. 2004) indicates that, even at mantle depth, thermodynamic equilibrium may not be achieved. Faults, such as transform faults along mid-ocean ridges, exhume deep-seated material but often at the price of intense chemical and mechanical transformation. Most geologists would agree that we have a reasonably good sampling of the continental crust and the subcontinental lithospheric mantle. In contrast, we do not have access to samples from the convective mantle and we must rely on inferences from basalts and from rare samples of

intensely transformed peridotites collected along mid-ocean ridges.

For the sake of illustration, let us represent the Earth the "mantle" and the "crust" by two boxes exchanging material through magmatic activity, crustal foundering, and subduction (Fig. 12). Mantle peridotites partially melt by decompression under mid-ocean ridges. The partial melts, known as basalt, form a ~ 5 km thick oceanic crust, which, on average, remains on top of the oceanic plate for a geologically short ride of about 60 Ma. The crust and overlying sediments are sent back to the mantle at subduction zones, where they melt with partial melts being a major contributor to new continental crust and to ocean island material (Allegre et al. 1983; Hofmann and White 1982). The process is complex and involves fluxing of the subduction zone by fluids and foundering of deep crust into the mantle. The overall consequence is, however, that material extracted as basalt at mid-ocean ridges is partly allocated to the continental crust and partly returned to the mantle. Likewise, the subaerial upper crust is eroded, both chemically and mechanically with the product of erosion ending up in the oceanic crust, while some fraction of the lower crust founders into the mantle. Such a model describes well what drives the simplest model of crust formation and mantle-crust interactions.

A first major enigma is that of the initial state of the mantle-crust system. Isotopic anomalies associated with extinct radioactivities, such as that of ^{146}Sm (which produces ^{142}Nd with $T_{1/2} = 103$ Ma) and ^{182} W ($T_{1/2} = 9$ Ma), have been detected in early Archean rocks, which shows that the mantle did not start as a homogeneous medium (Caro et al. 2003; Boyet and Carlson 2006; Bennett et al. 2007; Willbold et al. 2011). The existence of a primordial crust is accepted by many, but its composition was certainly very different from the modern continents, and overall the conclusions still rest on shaky grounds. As attested to by the restriction of TTG to

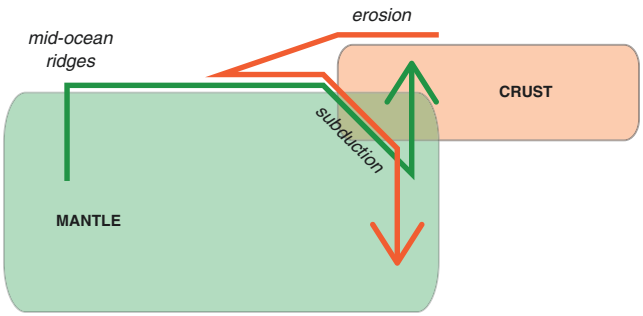

Formation and Evolution of the Earth, Fig. 12 The two-box representation of the mantle-crust system. Magmas erupted at mid-ocean ridges and oceanic islands are transported by plate tectonics to subduction zones. Erosion of continental crust, both chemical and mechanical, also brings material as sediments to the ocean floor and then to subduction zones. Both types of material are processed as orogenic magmas, which are incorporated to the crust, while the residue sinks into the mantle

Archean times, it took almost 2 billion years to remove the enrichment of the upper mantle in incompatible elements and turn it into the modern depleted upper mantle source of mid-ocean ridge and subduction zone magmas (Blichert-Toft and Albarède 2008). It took about the same time for komatiites to disappear as a prominent magma type (Arndt et al. 2008). Both the occurrence of TTG and komatiites, and their unusual compositions and geological settings relative to modern rocks attest to a particular thermal regime prevailing in the Archean. This is expressed by saying that "the Earth relaxed its initial conditions." The nature and composition of the mantle-crust system were reshaped by mantle convection, its surface expression plate tectonics, and by crustal growth.

The mantle-crust system never reached a true thermal and chemical steady-state because radioactive heat production strongly decreases through time (Fig. 9) and also because continental crust grows from the mantle. The idea that, although some crust may have existed from start, its volume increased through time and its composition evolved toward the more mature composition familiar to us is widely accepted. Many models of crustal growth still struggle with three major issues: (1) Was crustal growth continuous or episodic? The presence of very distinctive age provinces on continents, such as 3.3, 3.0, 2.7, 1.8, 1.0, 0.6, 0.3 Ga (Condie and Aster 2010; Condie and Aster 2013; Gastil 1960) (Fig. 13), suggests so, but alternative explanations have been put forward. The answer to this question has far-reaching consequences: subduction being a continuous process, episodic crustal growth would therefore call for episodic extraction of crustal material by mantle plumes rather than reprocessing of normal oceanic crust. (2) Was crustal growth faster in the past than today? It seems that, although a huge peak in crustal growth took place at about 2.7 Ga ago, continents never ceased to grow. (3) What fraction of continental crust gets recycled into the mantle? These questions are an active field of research and there is no indication that we may be nearing a consensus on any of them. We will see that the additional question of when continents rose above sea level (Flament et al. 2008) has huge consequences for rise of oxygen and the evolution of life (Campbell and Allen 2008; Pons et al. 2013).

The respective role of mid-ocean ridges and subduction zone, the two sides of the interface between the mantle and the crust, appears very clearly in the trace element and isotope geochemistry of modern basalts. Elemental fractionation prevailing at mid-ocean ridge is controlled exclusively by magmatic processes, whereas dehydration at subduction zones imparts a strong signature of hydrous process to the erupting magmas and indirectly to continental crust.

So far, we have assumed that the mantle and the crust behave as homogeneous boxes with relatively uniform properties. Isotope geochemistry demonstrates that, actually, the mantle is composed of different petrological units with

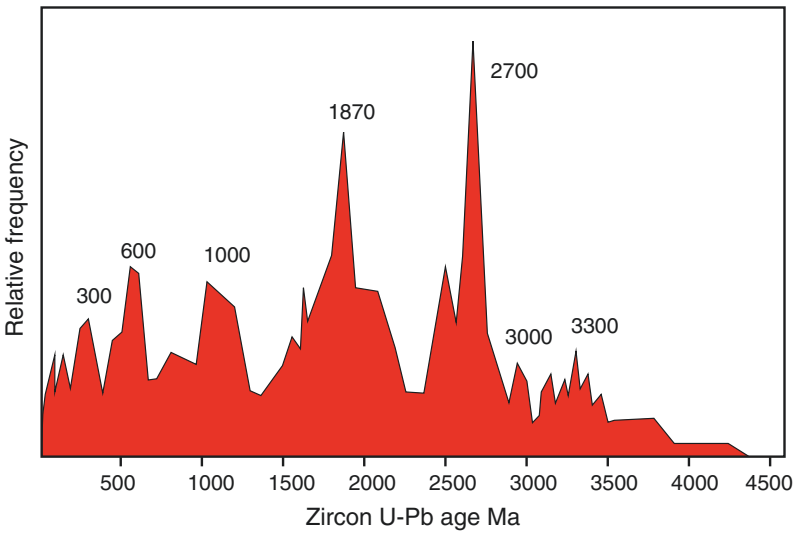

Formation and Evolution of the Earth, Fig. 13 Histogram of zircon U-Pb ages (Condie and Aster 2013). The database includes several thousands of zircon crystals from granites and river sediments. Although the concept was established in 1960, this database unambiguously demonstrates that crustal growth is episodic (although some believe that preservation may still play a role (Hawkesworth et al. 2009))

identifiable properties, known as geochemical components (Hofmann 1997; White 1985; Zindler and Hart 1986). For instance, the depleted mantle, which prevails in mid-ocean ridge basalts, is largely a residue from previous episodes of upper mantle melting. In contrast, the HIMU component, frequent in some oceanic islands, betrays the recycling of ancient oceanic crust, and the rare EM2 component the presence of continental debris in the source of basaltic rocks (see entries on mantle geochemistry and oceanic island basalts). In spite of vigorous convection, the mantle is not well mixed at all scales. Mixing results from the combination of mechanical stirring, which stretches and refolds layers of different compositions, e.g., peridotites and basalt, like in a marble cake (Allègre and Turcotte 1986; Olson et al. 1984; Tackley and Xie 2002) (Fig. 14), and molecular diffusion of elements from one layer to the next (Hofmann and Hart 1978). Stirring can be undone, at least as a thought experiment, in contrast with diffusion, which spontaneously increases entropy. The mantle is stirred in two ways (Agranier et al. 2005). First, three-dimensional velocity gradients associated with chaotic mantle convection creates streaks and tendrils in the entire volume. Second, fringe velocity gradients in the mantle penetrated by subducting plates efficiently perturb the original large-scale patterns of mantle geochemistry. Oceanic crust entering the mantle at subduction zones can be seen as a steady source of heterogeneities with length scales typical of those associated with lithospheric plates, while mantle convection progressively stretches and folds these heterogeneities and decreases their length scales. In contrast to mechanical stirring, which acts over long distances (1 meter to 1000s of kilometers), diffusion only acts locally (<1 m over billions of years). At mantle temperatures, it erases the original details of petrology and keeps isotopic chronometers open, thereby obliterating most of the local information, such as ages and original equilibration temperature, pressure, and composition

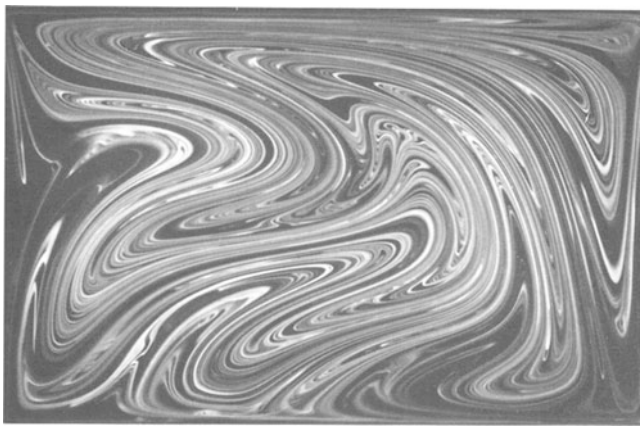

Formation and Evolution of the Earth, Fig. 14 Mechanical stirring reduces initial heterogeneities by stretching and refolding without destroying them (Ottino 1989)

conditions geochemists would hope to retrieve from the study of hand samples (Bedini et al. 2004; Hofmann and Hart 1978).

One of the major challenges of geochemistry has been the faint but unmistakable evidence that some parts of the mantle are poorly mixed and keep some record of the original chemistry of the planet. Historically, the strongest case was made by rare gases, and in particular by the presence of ^{3}He and solar neon, which are still present in basalts originating at great depth, like in Hawaii and Iceland. Once helium is outgassed from a volcano, it is rapidly lost to space because it is too light to be bound to the Earth's gravity field. Helium-3 is no more "primordial" than any other stable isotope of any element, but its excesses in basalts attest to the irreversible outgassing of primordial material from the mantle by magmatic activity. Thirty-year-old evidence from ^{3}He and other rare gases that the lower mantle was poorly mixed and still

contains material that avoided processing by mid-ocean ridges over the entire geological history is extremely strong (Graham 2002). It is in particular well established that the mantle source of hot-spot basalts (Iceland, Hawaii) has been much less outgassed than the source of mid-ocean ridge basalts. Likewise, excesses of tungsten-182 have now been found in large flood basalts, which entail that some mantle domains have been preserved since the formation of the Earth (Rizo et al. 2016).

To sum up this part, the Earth still remembers its original state inherited from accretion and magma ocean differentiation, but is well on its way to some sort of steady state controlled by continental crust extraction and recycling at subduction zones.

The Early Evolution of the Ocean and the Atmosphere

We will finally address how the evolution of the deep Earth affected the ocean and the atmosphere. Let us first describe their current state. An extraterrestrial traveler to Planet Earth would be first struck by the abundance of oxygen in the atmosphere and quickly conjecture that it originated from primordial CO_2 by removal of carbon and wonder where carbon went over the ages. The answer is clearly that a process known as oxygenic photosynthesis dissociates CO_2, with reduced carbon being buried in sediments and sent to the mantle by plate tectonics. Of course, would our visitor say, plankton receives light from the Sun and takes on the job. But, plankton also needs phosphate, a critical nutrient, and a lot of it, about one atom of P for 105 atoms of C: if carbon is lost to sediment, so is phosphorus (Delaney 1998). In addition, decades of careful investigations show that the oceanic crust acts as sink for phosphorus, not as a source (Wheat et al. 2003). How is the level of phosphorus maintained at the surface of the ocean? Still another miracle of plate tectonics! Water vapor produced by the ocean condenses as rain, which, combined with atmospheric CO_2, dissolves surface rocks and liberates ions, including phosphate, into the rivers. Without erosion, the terrestrial food chain as well as the marine one would collapse for lack of phosphorus. An additional effect of erosion is the control of ocean pH: reaction of rain and CO_2 with exposed crustal material liberates carbonates, while cations such as Na, Ca, and Mg are transported to the sea. The balance of negative and positive charges condition the dissolution of carbonates (HCO_3^- and CO_3^{2-}) and therefore buffer the pH of the ocean. Such conditions were never met on Mars which died a planet with a long-gone and rather acidic hydrosphere with sulfates as a prominent sediment. Although river-like morphologies show that some water was undoubtedly present at the surface of the young Mars, the paucity of hydrous minerals demonstrated by orbital spectrometers or observed in Martian meteorites is not in favor of a "wet Mars."

Can we try to guess how the ocean-atmosphere would function in a "water world" with very little emerged continental surface? Oceanic abysses would not be covered with as much sediments like they are today; carbonates and clays would necessarily be scarce. Planktonic life energized by sunlight could not function for lack of phosphorus replenishment and life should be segregated at the sediment-ocean interface or around hydrothermal vents, probably powered by chemotrophic organisms.

It is in this context that the Great Oxygenation Event (GOE) must be understood. By 2.4 Ga, several major changes occurred that would irreversibly change the face of the Earth. Banded iron formations formed by oxidation of dissolved ferrous iron and precipitation as ferric minerals disappeared. Minerals sensitive to atmospheric oxidation, such as uranium dioxide and pyrite, disappeared from the sedimentary record. Probably the strongest evidence of the GOE is the disappearance at 2.4 Ga of photolytic reactions between UV light and atmospheric SO_2 of volcanic origin and the rather brutal transition to the shielding of the atmosphere by the ozone layer, which itself attests to the presence of a high level of oxygen in the troposphere after that date. Evidence of photolytic reactions prior to the GOE rests on mass-independent effects (MIF = mass-independent fractionation) on sulfur isotope abundances measured by the excess of ^{33}S abundances predicted from ^{32}S and ^{34}S (Fig. 15) (Farquhar et al. 2000).

Many explanations have been claimed to account for the GOE. An internal geodynamic cause is unlikely because the event was essentially completed in less than 100 Ma. The most appealing interpretation rests on strontium isotopes (Flament et al. 2008). Radiogenic strontium-87 is produced by the slow decay of rubidium-87. The Rb/Sr is much smaller in the mantle relative to the crust, so that the apparent excess of radiogenic ^{87}Sr is also smaller in mantle material. Until 2.4 Ga, the ^{87}Sr excess of seawater recorded through time by marine carbonates is similar to that of the mantle, but suddenly increases at that time to track the ^{87}Sr excess of the crust. Such a spectacular shift signals the rise of continental crust above sea level, the onset of subaerial weathering, and the rapid drawdown of atmospheric CO_2. It seems that the GOE marked the emergence of permanently emerged continental surfaces, the beginning of a sustainable nutrient cycle, notably a rich supply of phosphates to the ocean (Pons et al. 2013). The prevalence of conditions favorable to oxygenic photosynthesis, which allowed carbon and oxygen to be dissociated, allowed organic carbon to be incorporated into seafloor sediments and subsequently dragged down to the mantle by sedimentation, leaving oxygen to accumulate in the atmosphere. By that time terrestrial atmosphere was on its way, the ocean could become oxygenated, oxygen could oxidize atmospheric methane, and the greenhouse effect be kept in check (Fig. 16).

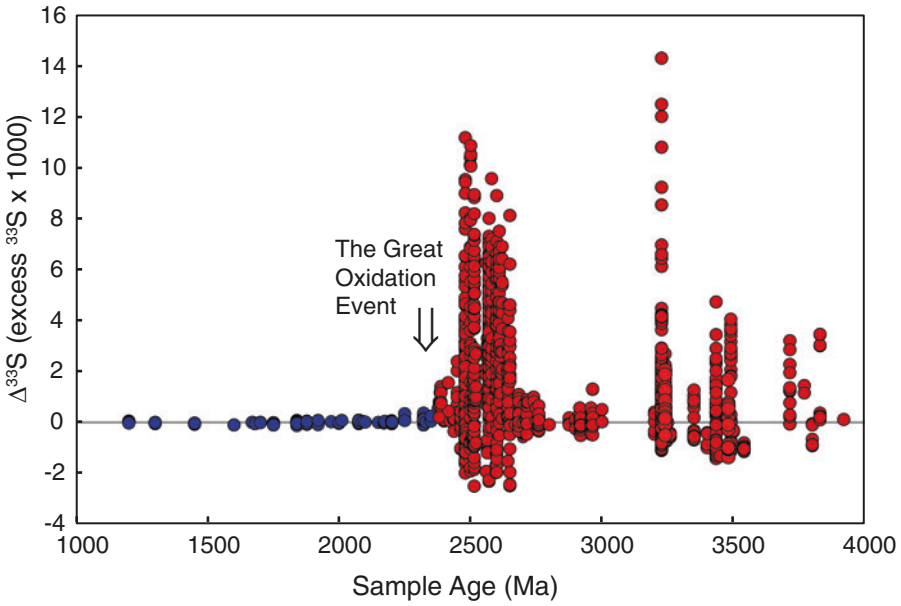

Formation and Evolution of the Earth, Fig. 15 Sulfur isotope evidence for the end of SO_2 photolytic destruction in the atmosphere and the rise of atmospheric oxygen. Before atmosphere was protected by the ozone layer, excess ^{33}S was produced by the effect of UV on volcanic SO_2 emissions into the atmosphere (courtesy James Farquhar)

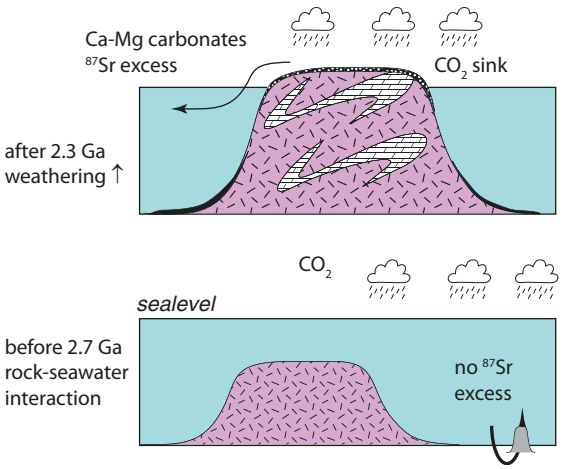

Formation and Evolution of the Earth, Fig. 16 A probable cause for the rise of atmospheric oxygen during the ~2.35-Ga-old Great Oxygenation Event (Pons et al. 2013). Release of radiogenic 87Sr into the ocean, as attested to by its capture by marine carbonates, indicates the onset of vigorous subaerial erosion of continental crust by CO2 and rainwater. The rise of continents above sea level, allowed the rapid drawdown of atmospheric CO2 and a supply of abundant phosphates to the ocean, which favored strong oxygenic photosynthesis. Sedimentation of reduced carbon on the seafloor and its subsequent removal by subduction triggered the sudden rise in atmospheric oxygen

Conclusion

Although the Earth formed under the control of physical processes common to all the terrestrial planets, it is unique with respect to multiple characters: it possesses a strong magnetic field, a prominent hydrosphere with a surface ocean, and its geodynamic regime is plate tectonics, which allowed a continent–ocean duality to emerge and a slowly evolving separation of a granitic crust from the residual upper mantle. The rather large size of our planet suppressed crystallization of a plagioclase-rich buoyant boundary layer and allowed the terrestrial magma ocean to vanish relatively fast. Water comes up as a remarkable "gift" from the outer Solar System. All these defining characters are inherited from the accretion stage and seem to have contributed to the emergence of life: the magnetic field protected the atmosphere, the hydrosphere fostered life for most of its history; plate tectonics divided the surface into subaqueous and subaerial expanses, each with a particular role with respect to life; the rise of continents allowed the rise of atmospheric oxygen.

Summary

4.56 Ga ago, Earth's material condensed from heterogeneous stellar residues, collectively known as the Solar Nebula, around the central star, our Sun. The Earth itself is the end product of very many collisions of planetesimals and protoplanets, the last of which, the Moon, accreted a few tens of Ma after condensation started. The Earth was born depleted in volatiles, which were later added to our planet by colliding water-rich bodies originating in the outer Solar System. Abundant water caused the interior of the Earth to develop a geodynamic regime of plate tectonics, leading to a strong dichotomy between continents and deep ocean basins and allowed life to appear. Oxygenation of the atmosphere some 2.4 Ga ago is attributed to thriving life and marks the rise of continents above sea level.

Cross-References

- Atmospheric Evolution
- Biogeochemistry
- Chondrites
- Earth's Continental Crust
- Earth's Core
- Geochronology and Radiogenic Isotopes
- Giant Impact Hypothesis
- Hydrogen
- Mantle Geochemistry
- Ocean Biochemical Cycling and Trace Elements
- Meteorites
- Mid-Ocean Ridge Basalts (MORB)
- Nutrients
- Oceanic Island Basalts
- Phosphorus
- Precambrian Geochemistry
- Strontium Isotopes
- Tungsten Isotopes

References

Agranier A, Blichert-Toft J, Graham DW, Debaille V, Schiano P, Albarède F (2005) The spectra of isotopic heterogeneities along the Mid-Atlantic Ridge. Earth Planet Sci Lett 238:96–109

Albarede F (2009) Volatile accretion history of the terrestrial planets and dynamic implications. Nature 461:1227–1233

Albarede F, Ballhaus C, Blichert-Toft J, Lee C-T, Marty B, Moynier F, Yin Q-Z (2013) Asteroidal impacts and the origin of terrestrial and lunar volatiles. Icarus 222:44–52

Albarède F, Albalat E, Lee C-TA (2015) An intrinsic volatility scale relevant to the Earth and Moon and the status of water in the Moon. Meteorit Planet Sci 50:568–577

Allègre CJ, Turcotte DL (1986) Implications of a two-component marble-cake mantle. Nature 323:123–127

Allegre CJ, Staudacher T, Sarda P, Kurz M (1983) Constraints on the evolution of the Earth's mantle from rare-gas systematics. Nature 303:762–766

Arndt N (1999) Why was flood volcanism on submerged continental platforms so common in the Precambrian? Precambrian Res 97:155–164

Arndt NT, Lesher CM, Barnes SJ (2008) Komatiite. Cambridge University Press, Cambridge

Bedini R-M, Blichert-Toft J, Boyet M, Albarède F (2004) Isotopic constraints on the cooling of the continental lithosphere. Earth Planet Sci Lett 223:99–111

Bennett VC, Brandon AD, Nutman AP (2007) Coupled 142Nd-143Nd isotopic evidence for Hadean mantle dynamics. Science 318:1907–1910

Bercovici D, Ricard Y (2014) Plate tectonics, damage and inheritance. Nature 508:513–516

Blichert-Toft J, Albarède F (2008) Hafnium isotopes in Jack Hills zircons and the formation of the Hadean crust. Earth Planet Sci Lett 265:686–702

Bottke WF, Vokrouhlický D, Nesvorný D (2007) An asteroid breakup 160 Myr ago as the probable source of the K/T impactor. Nature 449:48–53

Bottke WF, Walker RJ, Day JMD, Nesvorny D, Elkins-Tanton L (2010) Stochastic late accretion to Earth, the Moon, and Mars. Science 330:1527–1530

Boyet M, Carlson RW (2006) A new geochemical model for the Earth's mantle inferred from ^{146}Sm-^{142}Nd systematics. Earth Planet Sci Lett 250:254–268

Caffee MW, Hudson GU, Velsko C, Huss GR, Alexander EC, Chivas AR (1999) Primordial noble cases from Earth's mantle: identification of a primitive volatile component. Science 285:2115–2118

Campbell IH, Allen CM (2008) Formation of supercontinents linked to increases in atmospheric oxygen. Nat Geosci 1:554–558

Canup RM, Asphaug E (2001) Origin of the Moon in a giant impact near the end of the Earth's formation. Nature 412:708–712

Caro C, Bourdon B, Birck JL, Moorbath S (2003) 146Sm–142Nd evidence from Isua metamorphosed sediments for early differentiation of the Earth's mantle. Nature 423:428–432

Chou CL (1978) Fractionation of siderophile elements in the Earth's upper mantle. Proc Lunar Planet Sci Conf 9:219–230

Clayton RN (2002) Solar system: self-shielding in the solar nebula. Nature 415:860–861

Condie KC, Aster RC (2010) Episodic zircon age spectra of orogenic granitoids: the supercontinent connection and continental growth. Precambrian Res 180:227–236

Condie KC, Aster RC (2013) Refinement of the supercontinent cycle with Hf, Nd and Sr isotopes. Geosci Front 4:667–680

Davaille A, Jaupart C (1993) Transient high Rayleigh number thermal convection with large viscosity variation. J Fluid Mech 253(1):141

Day JMD, Walker RJ, James OB, Puchtel IS (2010) Osmium isotope and highly siderophile element systematics of the lunar crust. Earth Planet Sci Lett 289:595–605

Delaney M (1998) Phosphorus accumulation in marine sediments and the oceanic phosphorus cycle. Glob Biogeochem Cycles 12:563–572

Elkins-Tanton LT, Burgess S, Yin Q-Z (2011) The lunar magma ocean: reconciling the solidification process with lunar petrology and geochronology. Earth Planet Sci Lett 304:326–336

Eriksson PG, Catuneanu O, Sarkar S, Tirsgaard H (2005) Patterns of sedimentation in the Precambrian. Sediment Geol 176:17–42

Farquhar J, Bao HM, Thiemens M (2000) Atmospheric influence of Earth's earliest sulfur cycle. Science 289:756–758

Fitoussi C, Bourdon B (2012) Silicon isotope evidence against an enstatite chondrite earth. Science 335:1477–1480

Flament N, Coltice N, Rey PF (2008) A case for late-Archaean continental emergence from thermal evolution models and hypsometry. Earth Planet Sci Lett 275:326–336

Gastil G (1960) The distribution of mineral dates in space and time. Am J Sci 258:1–35

Gomes R, Levison HF, Tsiganis K, Morbidelli A (2005) Origin of the cataclysmic late heavy bombardment period of the terrestrial planets. Nature 435:466–469

Graham DW (2002) Noble gas isotope geochemistry of mid-ocean ridge and ocean island basalts; characterization of mantle source reservoirs. In: Porcelli D, Wieler R, Ballentine C (eds) Rev Mineral Geochem: Noble gases in geochemistry and cosmochemistry. Mineralogical Society of America, Washington, DC, pp 247–318

Harrison TM, Blichert-Toft J, Müller W, Albarede F, Holden P, Mojzsis SJ (2005) Heterogeneous Hadean hafnium: evidence of continental crust at 4.4 to 4.5 Ga. Science 310:1947–1950

Hashizume K, Chaussidon M (2005) A non-terrestrial 16O-rich isotopic composition for the protosolar nebula. Nature 434:619–622

Hauri EH, Weinreich T, Saal AE, Rutherford MC, Van Orman JA (2011) High pre-eruptive water contents reserved in lunar melt inclusions. Science 333:213–215

Hawkesworth C, Cawood P, Kemp T, Storey C, Dhuime B (2009) Geochemistry: a matter of preservation. Science 323:49–50

F

Hirth G, Kohlstedt DL (1996) Water in the oceanic upper mantle: implications for rheology, melt extraction and the evolution of the lithosphere. Earth Planet Sci Lett 144:93–108
Hofmann AW (1997) Mantle geochemistry: the message from oceanic volcanism. Nature 385:219–229
Hofmann AW, Hart SR (1978) An assessment of local and regional isotopic equilibrium in the mantle. Earth Planet Sci Lett 38:44–62
Hofmann AW, White WM (1982) Mantle plumes from ancient oceanic crust. Earth Planet Sci Lett 57:421–436
Holland G, Ballentine CJ (2006) Seawater subduction controls the heavy noble gas composition of the mantle. Nature 441:186–191
Kemp AIS, Wilde SA, Hawkesworth CJ, Coath CD, Nemchin A, Pidgeon RT, Vervoort JD, DuFrane SA (2010) Hadean crustal evolution revisited: new constraints from Pb-Hf isotope systematics of the Jack Hills zircons. Earth Planet Sci Lett 296:45–56
Kleine T, Münker C, Mezger K, Palme H (2002) Rapid accretion and early core formation on asteroids and the terrestrial planets from Hf–W chronometry. Nature 418:952–955
Krot AN, Nagashima K, Wasserburg GJ, Huss GR, Papanastassiou D, Davis AM, Hutcheon ID, Bizzarro M (2014) Calcium-aluminum-rich inclusions with fractionation and unknown nuclear effects (FUN CAIs): I. Mineralogy, petrology, and oxygen isotopic compositions. Geochim Cosmochim Acta 145:206–247
Labrosse S, Hernlund J, Coltice N (2007) A crystallizing dense magma ocean at the base of the Earth's mantle. Nature 450:866–869
Larimer JW (1973) Chemistry of the solar nebula. Space Sci Rev 15:103–119
Lodders K (2003) Solar system abundances and condensation temperatures of the elements. Astrophys J 591:1220–1247
Long DGF (2011) Architecture and depositional style of fluvial systems before land plants: a comparison of Precambrian, early Paleozoic, and modern river deposits. In: Davidson SK, Leleu S, North CP (eds) From river to rock record: the preservation of fluvial sediments and their subsequent interpretation. Society for Sedimentary Geology, Tulsa, pp 37–61
Luck JM, Othman DB, Barrat JA, Albarède F (2003) Coupled 63Cu and 16O excesses in chondrites. Geochim Cosmochim Acta 67:143–151
Luck J-M, Othman DB, Albarede F (2005) Zn and Cu isotopic variations in chondrites and iron meteorites: early solar nebula reservoirs and parent-body processes. Geochim Cosmochim Acta 69:5351–5363
Luo Y-R (2007) Comprehensive handbook of chemical bond energies. CRC Press, Boca Raton
Lyons JR, Young ED (2005) CO self-shielding as the origin of oxygen isotope anomalies in the early solar nebula. Nature 435:317–320
McKeegan KD, Kallio APA, Heber VS, Jarzebinski G, Mao PH, Coath CD, Kunihiro T, Wiens RC, Nordholt JE, Moses RW, Reisenfeld DB, Jurewicz AJG, Burnett DS (2011) The oxygen isotopic composition of the sun inferred from captured solar wind. Science 332:1528–1532
Morbidelli A, Lunine JI, Obrien DP, Raymond SN, Walsh KJ (2012) Building terrestrial planets. Annu Rev Earth Planet Sci 40:251–275
Morgan JW (1986) Ultramafic xenoliths: clues to Earth's late accretionary history. J Geophys Res 91:12375–12387
Navon O, Wasserburg G (1985) Self-shielding in O_2—a possible explanation for oxygen isotopic anomalies in meteorites? Earth Planet Sci Lett 73:1–16
Nemchin A, Timms N, Pidgeon R, Geisler T, Reddy S, Meyer C (2009) Timing of crystallization of the lunar magma ocean constrained by the oldest zircon. Nat Geosci 2:133–136
Nesvorný D, Vokrouhlický D, Bottke WF, Gladman B, Häggström T (2007) Express delivery of fossil meteorites from the inner asteroid belt to Sweden. Icarus 188:400–413
Olson P, Yuen DA, Balsiger D (1984) Mixing of passive heterogeneities by mantle convection. J Geophys Res 89:525–436
Ottino JM (1989) The kinematics of mixing: stretching, chaos, and transport. Cambridge University Press, Cambridge
Owen T, Bar-Nun A (1995) Comets, impacts, and atmospheres. Icarus 116:215–226
Ozima M, Podosek FA (1999) Formation age of Earth from I-129/I-127 and Pu-244/U-238 systematics and the missing Xe. J Geophys Res Solid Earth 104:25493–25499
Palme H, O'Neill HSC (2003) Cosmochemical estimates of mantle composition. In: Carlson RW (ed) Treatise on geochemistry, The mantle and core, vol 2. Elsevier, Amsterdam, pp 1–38
Phillips RJ, Raubertas RF, Arvidson RE, Sarkar IC, Herrick RR, Izenberg N, Grimm RE (1992) Impact craters and Venus resurfacing history. J Geophys Res Planets 97:15923–15948
Pons ML, Fujii T, Rosing M, Quitté G, Télouk P, Albarède F (2013) A Zn isotope perspective on the rise of continents. Geobiology 11:201–214
Rizo H, Walker RJ, Carlson RW, Horan MF, Mukhopadhyay S, Manthos V, Francis D, Jackson MG (2016) Preservation of Earth-forming events in the tungsten isotopic composition of modern flood basalts. Science 352:809–812
Robert F, Gautier D, Dubrulle B (2000) The solar system D/H ratio: observations and theories. Space Sci Rev 92:201–224
Schubert G, Turcotte DL, Olson P (2001) Mantle convection in the Earth and planets. Cambridge University Press, Cambridge
Tackley PJ, Xie S (2002) The thermochemical structure and evolution of Earth's mantle: constraints and numerical models. Phil Trans R Soc Lond A 360:2593–2609
Thiemens MH (2006) History and applications of mass-independent isotope effects. Annu Rev Earth Planet Sci 34:217–262
Touboul M, Puchtel IS, Walker RJ (2015) Tungsten isotopic evidence for disproportional late accretion to the Earth and Moon. Nature 520:530–533
Trinquier A, Birck J-L, Allegre CJ (2007) Widespread ^{54}Cr heterogeneity in the inner solar system. Astrophys J 655:1179–1185
Trinquier A, Elliott T, Ulfbeck D, Coath C, Krot AN, Bizzarro M (2009) Origin of nucleosynthetic isotope heterogeneity in the solar protoplanetary disk. Science 324:374–376
van Kooten EM, Wielandt D, Schiller M, Nagashima K, Thomen A, Larsen KK, Olsen MB, Nordlund Å, Krot AN, Bizzarro M (2016) Isotopic evidence for primordial molecular cloud material in metal-rich carbonaceous chondrites. Proc Natl Acad Sci 113:2011–2016
Walker RJ (2009) Highly siderophile elements in the Earth, Moon and Mars: update and implications for planetary accretion and differentiation. Chem Erde-Geochem 69:101–125
Walsh KJ, Morbidelli A, Raymond SN, O'Brien DP, Mandell AM (2011) A low mass for Mars from Jupiter/'s early gas-driven migration. Nature 475:206–209
Warren PH (2011) Stable-isotopic anomalies and the accretionary assemblage of the Earth and Mars: a subordinate role for carbonaceous chondrites. Earth Planet Sci Lett 311:93–100
Wheat GC, McManus J, Mottl MJ, Giambalvo E (2003) Oceanic phosphorus imbalance: magnitude of the mid-ocean ridge flank hydrothermal sink. Geophys Res Lett 30. https://doi.org/10.1029/2003GL017318
White WM (1985) Sources of oceanic basalts: radiogenic isotopic evidence. Geology 13:115–118
Wilde SA, Valley JW, Peck WH, Graham CM (2001) Evidence from detritical zircons for the existence of continental crust and oceans on the Earth 4.4 Gyr ago. Nature 409:175–178
Willbold M, Elliott T, Moorbath S (2011) The tungsten isotopic composition of the Earth/'s mantle before the terminal bombardment. Nature 477:195–198
Wyatt MC (2008) Evolution of debris disks. Annu Rev Astron Astrophys 46:339–383

Yin Q, Jacobsen SB, Yamashita K, Blichert-Toft J, Télouk P, Albarède F (2002) A short timescale for terrestrial planet formation from Hf-W chronometry of meteorites. Nature 418:949–952
Yurimoto H, Kuramoto K (2004) Molecular cloud origin for the oxygen isotope heterogeneity in the solar system. Science 305:1763–1766
Zindler AW, Hart SR (1986) Chemical geodynamics. Annu Rev Earth Planet Sci 14:493–571

Fractional Crystallization and Assimilation

Frank Spera and Melissa Scruggs
Department of Earth Science, University of California Santa Barbara, Santa Barbara, CA, USA

Definitions

Fractional crystallization is one of the most important petrogenetic processes contributing to the compositional diversity of magmas and associated igneous rocks of the Earth's continental and oceanic crust. N.L. Bowen, one of the guiding lights of modern petrology, brought this mechanism to the fore in the early part of the twentieth century. A multicomponent silicate liquid (melt) undergoes fractional crystallization when crystals precipitated from the melt do not remain in equilibrium with residual melt during crystallization. This may occur, for example, by physical separation of crystals from melt (e.g., by gravitative settling or floatation of crystals) or by sluggish crystal-melt reaction kinetics (nucleation and growth) without physical separation. Fractional crystallization in multicomponent silicate liquids is complex compared to crystallization in unary systems because the composition of removed crystals is generally different than the starting liquid composition. The only exception is when the bulk composition of the system resides at a thermodynamic invariant point. Because the composition of precipitated crystals is generally different from melt, residual melt will be compositionally distinct from parental (pre-crystallization) melt. Consequently, residual melt will evolve toward one with lower concentrations of the oxide components that are removed by crystallization. A detailed example of how mid-ocean basaltic melt, the dominant melt composition on Earth, changes upon closed-system fractional crystallization is presented below using the MELTS algorithm (Ghiorso and Sack 1995; Ghiorso and Gualda 2015). Fractional crystallization also leads to the strong enrichment of the incompatible trace elements that do not partition into crystalline phases. A quantitative example is presented below. Because there are very small isotopic fractionations of high atomic mass elements such as Sr, Nd, and U during crystallization, closed-system fractional crystallization produces very small, generally negligible, isotopic fractionations. Exceptions are for light elements such as hydrogen or oxygen although the effects are relatively small especially for oxygen.

Assimilation or magma contamination is compositional modification of preexisting magma by addition of material derived from country rock surrounding the magma body. Unlike fractional crystallization that operates in closed-system magma bodies, assimilation requires a flow of material across the magma body-country rock boundary and hence constitutes prima facie evidence of open-system behavior. Since country rock is practically always at a different temperature (generally lower) than the invaded magma, assimilation implies that heat is exchanged across the country rock-magma boundary. Assimilation can proceed by the addition of initially sub-solidus roof or wall rock or by the addition of partial melt generated in the country rock with subsequent transfer of country rock partial melt (or some fraction thereof) into the magma body by porous media percolative flow and/or flow in fractures. Such country rock fractures may be preexisting or may form due to thermal stresses associated with steep thermal gradients along the magma-country rock boundary. Assimilation differs from magma mixing, which is also an open-system process leading to magma contamination, in that the energy required for heating and partial melting of country rock in assimilation derives from the latent heat of crystallization and cooling within the magma body. In contrast, when magma contamination occurs by replenishment (magma mixing), heat may be transferred from recharge to resident magma or vice versa depending on the specific enthalpy (enthalpy per unit mass) of the two mixing end-members in their initial (premixed) state.

AFC is an acronym for *assimilation and fractional crystallization*. The AFC model adopts the approximation that the heat generated by fractional crystallization (enthalpy of crystallization plus the sensible heat from magma cooling) is available to heat up and potentially melt or partially melt host country rock. To model the extent of assimilation and its geochemical implications, an energy balance is explicitly considered along with constraints from mass balance and phase equilibria. In early models of AFC, the energetic requirements were modeled using the mass ratio of fractionation products (cumulates) to assimilated country rock set ab initio to a constant, and phase equilibria was approximated using heuristics. In modern models (e.g., Bohrson et al. 2014), partial melt generation is explicitly linked at each step to production of fractionated solids (cumulates), and thermodynamic methods are used to compute phase equilibria, energy balance, and trace element partitioning self-consistently for magma treated as an open multiphase-multicomponent system that may interact by material and energy exchange with its environment.

RAFC is an acronym for recharge, assimilation, and fractional crystallization. This set of processes describes the open-system evolution of a magma body that exchanges heat and mass with its surroundings. RAFC equilibrium models are developed by adding magma replenishment or recharge to AFC models in a thermodynamically self-consistent manner. Recharge magma is in internal thermodynamic equilibrium before addition to the magma body. Typically, the elementary step of magma mixing is accomplished isobarically and isenthalpically, and the mixing magmas are brought to thermodynamic equilibrium by maximization of the system entropy. The mixing process generates a hybrid magma that represents a unique thermodynamic state in which the composition and amount of all phases in equilibrium (solids, liquids, and fluids) as well as temperature is determined. Interestingly, the postmixing temperature does not necessarily lie between the initial temperatures of the mixing magmas. There are cases, specifically when one or both of the mixing magmas are phyric, for which the final (postmixing) magma temperature is lower than either of the mixing magmas. Assimilation can also be considered an isenthalpic-isobaric process with the post-assimilation state being one that maximizes the system entropy. In contrast, during isobaric fractional crystallization when temperature is fixed, the Gibbs free energy is minimized to obtain the phase equilibria solution. A model to perform these calculations is presented elsewhere (Bohrson et al. 2014).

Historical Development of Fractional Crystallization

Fractional crystallization is a fundamental process by which natural silicate melts (liquids) chemically evolve from an initial parental melt to a derived melt of different composition. The use of the word "evolve" harkens back to the early part of the twentieth century when N. L. Bowen, considered by many to be the founder of modern igneous petrology, first used the term in a petrological context. Bowen was influenced by its usage in biology, specifically the concept of Darwinian evolution whereby one species descends or evolves from a pre-existing one. Even today, petrologists use the phrase "liquid line of descent" to describe the sequence of melts that arise as crystalline solids are physically or chemically segregated from parental melt by the process of closed-system fractional crystallization. N.L. Bowen uniquely and masterfully blended many years of experimental investigation based on the physical chemistry and thermodynamics of high-temperature multiphase-multicomponent silicate systems with field observations on the rocks and rock-forming minerals to provide the conceptual infrastructure for modern igneous petrogenesis. His seminal ideas have ramifications for the search for mineral deposits, for the exploitation of geothermal energy, and for the origin and evolution of Earth's oceanic and continental crust and upper mantle.

Although Bowen focused on crystal fractionation as the essential mechanism driving the compositional variety of igneous rocks, he also discussed the role of assimilation, magma mixing, liquid immiscibility, and Soret separation as additional, but secondary, effects. Nowadays, due to detailed study of the trace element and isotopic geochemistry of magmas and a more comprehensive understanding of their phase equilibria and crystallization products, it is recognized that many magma bodies do not evolve strictly as closed chemical systems. When magma bodies behave as open systems, the processes of contamination via assimilation of country rock en masse or assimilation of melt derived by partial melting of country rock and the effects of magma replenishment by addition of recharge magma must be considered. The reheating of previously crystallized magma by fresh replenishment magma recharge to generate large volumes of invariant-point like melts may also be important. RAFC processes can occur concurrently, serially, or episodically in many different combinations that are not known a priori; much of modern petrogenesis involves the use of petrological, geochemical, isotopic, and geochronological tools in combination with field observations to elucidate the relative importance of RAFC phenomena in a geologically referenced spatial and temporal context. Complicated cycles of crystallization followed reheating and partial melting, assimilation, further crystallization. and magma replenishment may be the rule rather than the simpler closed-system monotonic behavior envisioned by Bowen and his cohorts. Nevertheless, the tremendous insights illuminated by N. L. Bowen by a half-century of research stand today as both a towering achievement and pillar upon which modern petrology has been built. Every student of igneous petrology should study his famous treatise of 1928, *The Evolution of Igneous Rocks* (Bowen 1928), not only for its vast insight into the petrogenesis of igneous rocks but also as an multifaceted example of the power of both inductive and deductive scientific reasoning based on sound thermodynamic principles and what might be called petrologic common sense based on careful observation in the field and in the laboratory. The fiftieth year anniversary of his classic treatise was celebrated in a publication edited by one of the mid-century geologists whose own work was emblematic of the Bowen tradition (Yoder 1979).

Styles of Closed-System Crystallization

Crystallization occurs along a continuous spectrum from equilibrium crystallization to perfect fractional crystallization. In equilibrium crystallization (EC), residual melt and precipitated solids remain in equilibrium throughout crystallization. At fixed pressure and temperature, the state of magma (i.e., the composition and amounts of coexisting phases) is determined by minimization of the Gibbs free energy. Because equilibrium is maintained, all coexisting phases are homogeneous: crystals are not compositionally zoned since crystal-melt equilibrium is maintained as magma cools and crystallizes. In contrast, during perfect fractional crystallization (PFC), each

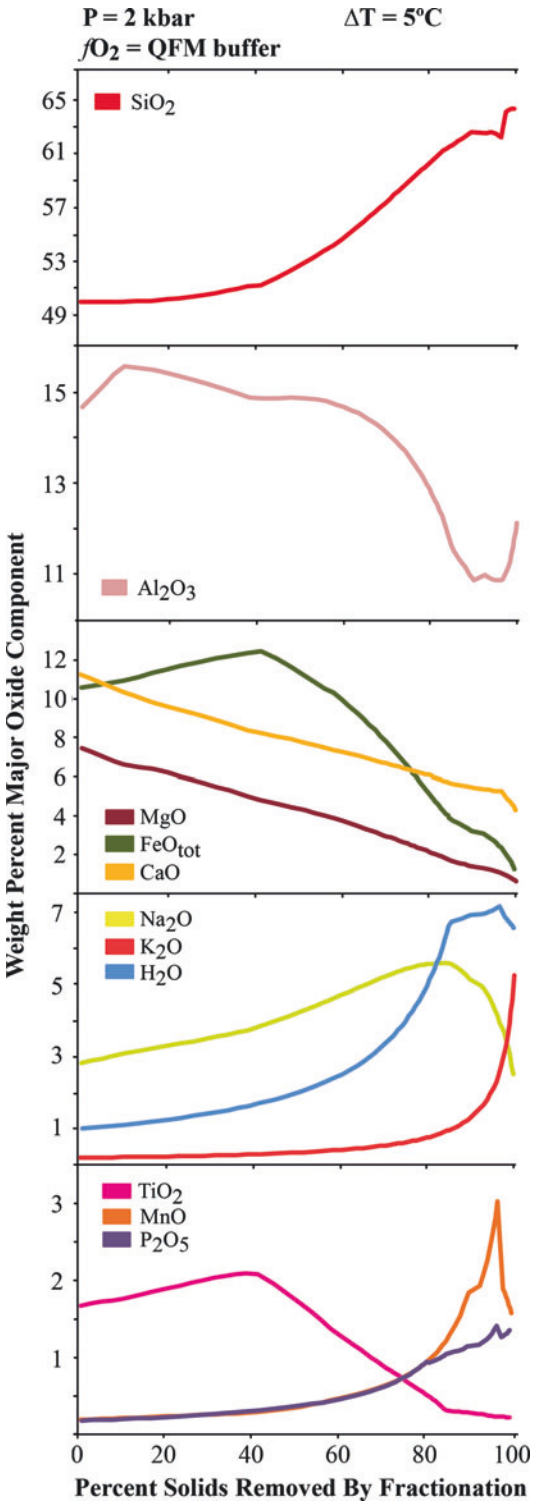

Fractional Crystallization and Assimilation, Fig. 1 The composition of residual melt in terms of the major oxide components SiO_2, TiO2, Al_2O_3, FeO_T, MnO, MgO, CaO, Na_2O, K_2O, P_2O_5, and H_2O versus the total (all phases) percent solids removed by fractional crystallization is portrayed in this sequence of diagrams. The starting composition is average MORB with one weight percent H_2O. Crystallization proceeds isobarically at 0.2 GPa (about 5 km depth on Earth) along the QFM oxygen buffer (see text). A few especially noteworthy features include (1) silica in the melt begins to rise significantly in concentration only after 40% crystallization; (2) The alkaline earth metal oxides MgO and CaO decrease monotonically, linearly, and similarly from high to low values; (3) the alkali oxides and water behave similarly until about 80% crystallization at which point behaviors diverge, and Na_2O increases early on because the plagioclase crystallizing is relatively calcic; (4) the minor element oxides titania, MnO, and P_2O_5 show diverse trends controlled by their degree of incompatibility with respect to specific accessory phases being removed by fractionation. No two melt chemical evolution trajectories are the same because the path depends on the initial conditions as well as the style (see text) of fractionation. Results presented here are generated using the rhyolite-MELTS algorithm (see text)

infinitesimal increment of solid that forms is immediately sequestered from the liquid: no further reaction between solid and melt occurs. In both EC and PFC, the melt changes composition as the mass of precipitated crystals increases in response to changing system conditions. However the extent of liquid compositional variation in PFC is greater than in EC because the reactive part of the system in PFC is solely the residual melt: earlier formed solids are completely removed from the liquid and hence cannot react with residual liquid. In EC by contrast, precipitated solids remain in equilibrium with liquid throughout the crystallization process.

In natural systems the style of crystallization is neither perfect fractional crystallization (PFC) nor equilibrium crystallization (EC). Perhaps the most reasonable model is one that may be termed finite-mass fractional crystallization or batch crystallization (BC). Note that PFC can be considered infinitesimal-mass fractional crystallization, an extreme form of BC. In BC, one considers the following scenario. Starting in the liquid state, a finite mass of solid forms by equilibrium crystallization (e.g., magma is cooled by extraction of heat). This finite batch of solid in equilibrium with remaining liquid is then removed (fractionated) from the system either physically (e.g., gravitative settling) or because of the inability of the precipitated solids to stay in chemical equilibrium with residual melt by reaction (e.g., slow solid-liquid reaction kinetics aided by sluggish diffusion in crystals compared to the liquid). The residual liquid then undergoes a second increment of solid removal. This crystallization-fractionation process is repeated until no liquid remains. To carry out BC one needs to specify the magnitude of the mass increment removed. As this mass increment approaches zero, BC approaches PFC. The composition of residual liquid does not continuously vary in composition during BC; instead there is a finite sequence of liquid compositions. The array of liquid compositions depends on the mass of the crystal batch removed at each step. In nature, the batch masses may vary depending on a myriad of (often covert) factors, and hence the (discontinuous) liquid line of descent will not necessarily follow a smooth trend on classical Harker diagrams.

As an illustration, Fig. 1 portrays the major element chemical evolution of melt, expressed in terms of metal oxides (e.g., SiO_2, Al_2O_3, TiO_2, etc.), for closed-system PFC of basaltic melt. This

example starts with a melt of average mid-ocean ridge basalt (MORB) composition at a pressure of 0.2 GPa and depicts how residual liquid evolves as crystals are removed. The oxygen fugacity during crystallization is fixed along an oxygen buffer defined by the assemblage quartz-fayalite and magnetite (QFM buffer) at each temperature. The state of the system is computed discretely at five-degree temperature decrements and, in this case, very closely approximates PFC.Melt composition in terms of the major oxide components is shown as a function of the total mass of removed (fractionated) crystals in the figure. The liquidus temperature at 0.2 GPa along the QFM buffer is 1170 °C where a Ca-rich monoclinic pyroxene first precipitates. This is followed by precipitation of plagioclase feldspar (An_{76} at 1148 °C), olivine (Fo_{77} at 1133 °C), cubic spinel at 1088 °C, orthorhombic pyroxene (En_{66} at 1068 °C), and the hexagonal phosphate mineral apatite at 953 °C. The melt becomes water saturated at 908 °C and the rhombohedral oxide ilmenite crystallizes at 883 °C. The magma is 99.9 wt% crystallized at 818 °C. The melt composition trajectory as a function of mass fractionated is easy to rationalize by noting the composition of the bulk solid being removed during the PFC closed-system evolution. Note that each oxide component exhibits a unique trajectory; some are monotonic, others are not. Some exhibit maxima or minima. Some vary smoothly and some more abrupt. The particular behavior of the liquid line of descent in general is a function of starting composition, pressure, oxygen buffer, and whether EC, BC, or PFC is the crystallization process. In the example shown, PFC is most applicable.

Fig. 2 shows the concentration of the trace element Ni in melt undergoing different styles of solid fractionation including equilibrium crystallization, four examples of batch crystallization each of unique mass batch decrement and perfect fractional crystallization. The partition coefficient, defined $K_{sm}^{Ni} = C_{Ni}^{solid}/C_{Ni}^{liquid}$, is treated as a constant equal to K_{sm}^{Ni}=1.5 throughout the crystallization process for all cases. In reality, the partition coefficient should be recomputed at each step to reflect the phase proportions that are being removed at each temperature. Here we neglect this to

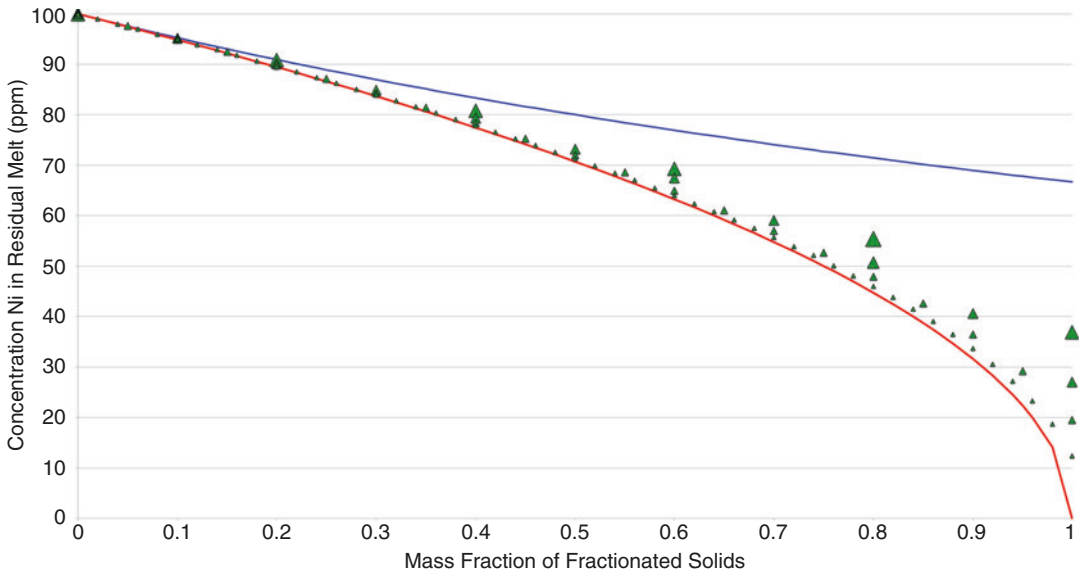

Fractional Crystallization and Assimilation, Fig. 2 Illustrative (hypothetical) example of the effects of fractionation style on the concentration of Ni in a silicate liquid undergoing closed-system fractionation. In this example (for all cases), the partition coefficient of Ni between solid and liquid is 1.50, and the initial a concentration of Ni in the liquid is 100 parts per million (ppm). Six examples illustrating the style of fractionation are depicted. The coordinates of the plot are concentration of Ni in residual liquid (ppm) versus the mass fraction of fractionated solid. The uppermost blue curve portrays equilibrium crystallization (EC) during which, by definition, solid remains in chemical potential equilibrium with liquid during crystallization. Because the partition coefficient is > 1, Ni is concentrated in the solid relative to the liquid and hence the concentration of Ni in the liquid decreases as solid precipitates. The lower red curve pertains to perfect fractional crystallization (PFC). In PFC, solid is removed from further reaction with liquid immediately upon crystallization. Liquid undergoes rapid depletion in Ni. The triangle symbols depict four examples of batch crystallization (BC). In BC, the mass of the (constant) decrement must be specified; the liquid takes on discrete values for the concentration of Ni defined only for discrete values of the mass of solid removed. The concentrations of Ni in residual liquid for the four cases are shown as green triangles. The size of the triangle scales with the mass decrement based on the mass fraction of removed solids in the order: 0.2 (*largest triangles*), 0.1, 0.05, 0.02 (*smallest triangles*). Note that the BC model, with 50 discrete mass decrements of removed solid each equal to 0.02, comes closest to PFC whereas the BC model with only five discrete removal events is closer to the EC path. That is, as the batch mass decrement increases, the concentration of Ni in residual melt approaches the EC limit and as the batch mass decrement becomes small, PFC is approached. In all cases, note that BC generates a discrete series of liquid compositions. It would be incorrect to represent the batch models using continuous curves because the concentration of Ni in the liquid is only *defined* for discontinuous values of the mass fraction of solids removed. The values depend critically on the mass decrement

schematically illustrate how the style of FC affects the trace element composition of residual melt during closed-system FC. The concentration of Ni in the residual melt decreases as the mass fraction of solid precipitated from the liquid increases in all cases but the quantitative details vary with fractionation process. The variation in the concentration of Ni in the melt is least dependent on the fraction of solid removed for equilibrium crystallization and most dramatically different for perfect fractional crystallization. Batch crystallization closely approximates perfect fractional crystallization when the mass decrement is small, whereas batch crystallization more closely resembles equilibrium crystallization when the mass decrement is large. Because equilibrium crystallization and perfect fractional crystallization are continuous processes, concentration of Ni in residual melt varies *continuously* from its starting value of 100 ppm to its final value as solid, always enriched in Ni relative to coexisting liquid, is removed. In contrast, because batch crystallization is a discrete process, the concentration of Ni in the melt is defined at integral multiples of the mass fraction decrement. Batch crystallization and perfect fractional crystallization, which is simply batch crystallization with an infinitesimal decrement, converge as the mass decrement becomes small. The difference in melt trace element concentration between BC and PFC depends on the partition coefficient for a fixed mass decrement: the difference between the trace element concentration of residual liquid in BC relative to PFC grows as the partition coefficient increasingly deviates from unity.

Models of RAFC

The recent trend in modeling the evolution of magmatic systems is based the concept that magmas evolve during ascent and storage as open-system multicomponent-multiphase geochemical reactors. Because magmas are high-temperature systems, a reasonable approximation is to assume that chemical potential equilibrium prevails locally at the scale of decimeters subject to the global constraints imposed by the transport of heat and matter across the boundaries of the magma body by assimilation and recharge. The evolution of the magma body then depends explicitly on the flow of mass and heat across the magma body considered as one subsystem in a larger composite supersystem of country rock + recharge reservoir + magma body. By adopting a magma body-centric view, the coupling of heat and material transport between all subsystems can be defined once relative masses are specified, thereby enabling a self-consistent solution to the "magma body as open-system" problem. Recent examples of this approach include Spera and Bohrson (2004), Bohrson and Spera (2007), Smith and Asimow (2005), and Bohrson et al. (2014). These models use the MELTS computation engine developed by Ghiorso and collaborators over the past 35 years.

Summary

About 30 cubic kilometers of magma is erupted or emplaced at shallow levels in the crust or uppermost mantle each year on Earth primarily at divergent (MORB) and convergent (IAM) plate boundaries and at intraplate locations (OIB). Magma originates mainly by partial melting in the Earth's upper mantle, which is predominantly peridotitic (a mixture of olivine, orthopyroxene, clinopyroxene, and garnet) although pods of eclogite (clinopyroxene plus garnet) and perhaps even crustal sediments or associated sedimentary rocks (varying mineralogy depending on bulk composition) are involved as well. The latter two sources are delivered to the mantle by subduction. The mixing or homogenization time for the Earth's mantle taken as a whole is of the order of or exceeds the age of the Earth. This explains why parental mafic magmas erupting today vary in trace element and isotopic composition; major elements also vary but differences are subtler. Once sufficient liquid forms such that melt buoyancy overcomes viscous forces impeding melt segregation and ascent, melt begins its journey to the Earth's surface or its crustal emplacement site provided the minimum principal stress is oriented horizontally or subhorizontally. The ascent of mafic magma occurs primarily by the upward propagation of vertical or subvertical melt-filled cracks with typical widths of 1–5 m. It is during ascent and post-emplacement that recharge (mixing of different magma batches), assimilation, and crystallization – the primary means of magma evolution – takes place. These processes, sometimes encapsulated by the acronym RAFC, are prima facie evidence for magma bodies behaving as open systems subject to heat loss and matter exchange. Styles of crystallization can be modeled based on the accurate calculation of phase relations using the methods of classical macroscopic thermodynamics. In order to quantify the style, additional assumptions regarding the extent of "communication" between solids precipitated and residual liquid must be made. The end-member possibilities for crystallization are equilibrium crystallization for which precipitated solids remain in equilibrium with melt throughout the crystallization interval to perfect (infinitesimal batch) fractional crystallization such that precipitated solid is chemically isolated from residual liquid. The most realistic style generally falls between these extremes and is called batch crystallization. Batch crystallization is determined using the mass balance relations of equilibrium crystallization applied to finite-mass batch decrements of solid removal. Batch crystallization can be combined with the thermodynamics of open-system assimilation and magma mixing (recharge) to develop open-system models for the evolution of magmatic systems.

In addition to the generation of basaltic melts by partial melting of eclogitic or peridotitic mantle, partial melting of crustal rocks is also a significant petrological mechanism.

Although not well constrained, it is likely that lower continental crust is approximately mafic (gabbroic) in composition on average. Partial melting of lower crust will generate intermediate to silicic composition melts, which due to their chemical buoyancy, tend to migrate upward. Stagnation within the crust leads to cooling and fractionation of these magmas to give residual liquids that are further enriched in silica (65–75 wt%) and other light components (e.g., Al_2O_3 and the alkalis). These silicic magmas can either crystallize at depth to produce granites such as the majestic batholithic rocks of California's Sierra Nevada Range or, when crustal stress fields are suitably oriented, ascend to the surface to give rise to supervolcanoes that erupt vast quantities of very differentiated melt to form the great rhyolitic ignimbrite deposits such as at Yellowstone National Park in the USA. Finally, upper crustal magmas may also originate by partial or total melting of upper crustal rocks. The upper crust is chemically quite heterogeneous. If mantle-derived mafic liquids solidify at shallow depths, mantle-derived heat would be available to melt or partially melt upper crustal materials. There is some geochemical evidence to suggest that some especially aluminous granites called S-type granites may originate in this manner.

Cross-References

- ▶ Entropy
- ▶ Experimental Mineralogy and Petrology
- ▶ Free Energy
- ▶ Geochemical Thermodynamics
- ▶ Incompatible Elements
- ▶ Kinetics of Geochemical Processes
- ▶ Magmatic Process Modeling
- ▶ Mid-Ocean Ridge Basalts (MORB)
- ▶ Nickel
- ▶ Oceanic Island Basalts
- ▶ Oxidation-Reduction Reactions and Eh-pH (Pourbaix) Diagrams
- ▶ Subduction Zone Geochemistry
- ▶ Trace Elements
- ▶ Volcanism

References

Bohrson WA, Spera FJ (2007) Energy-constrained recharge, assimilation, and fractional crystallization (EC-RAFC): a visual basic computer code for calculating trace element and isotope variations of open-system magmatic systems. Geochem Geophys Geosyst 8:Q11003

Bohrson W, Spera F, Ghiorso M, Brown G, Creamer J, Mayfield A (2014) Thermodynamic model for energy-constrained open system evolution of crustal magma bodies undergoing simultaneous recharge, assimilation and crystallization: the magma chamber simulator. J Petrol 55:1685–1718

Bowen NL (1928) The evolution of the igneous rocks. Princeton University Press, Princeton

Ghiorso MS, Gualda GR (2015) An H_2o-Co_2 mixed fluid saturation model compatible with rhyolite-MELTS. Contrib Mineral Petrol. https://doi.org/10.1007/s00410-015-1141-8

Ghiorso MS, Sack RO (1995) Chemical mass transfer in magmatic processes. IV. A revised and internally consistent thermodynamic model for the interpolation and extrapolation of liquid–solid equilibria in magmatic systems at elevated temperatures and pressures. Contrib Mineral Petrol 119:197–212

Smith PM, Asimow PD (2005) Adiabat_1ph: a new public front-end to the MELTS, pMELTS, and pHMELTS models. Geochem Geophys Geosyst 6(1):1525–2027

Spera FJ, Bohrson W (2004) Open-system magma chamber evolution: an energy-constrained geochemical model incorporating the effects of concurrent eruption, recharge, variable assimilation and fractional crystallization. J Petrol 45(12):2459–2480

Yoder HS (ed) (1979) The evolution of the igneous rocks. Fiftieth anniversary perspectives. Princeton University Press, Princeton. x + 588 pp

Free Energy

Carl O. Moses
Provost and Vice President for Academic Affairs, Grand View University, Des Moines, IA, USA

Natural processes tend to increase the amount of entropy in a universe (a thermodynamic universe is an isolated system not the cosmological universe), but they also tend to minimize the system's energy (see ▶ Geochemical Thermodynamics). Some processes can be regarded as end-members. For example, the mixing of two ideal gases is driven entirely by the maximization of entropy and entails no energy change. On the other hand, a ball rolls down a hill under the influence of energy minimization without any entropy change. If we wish to analyze processes such as chemical reactions in which both energy and entropy play a role, we need to determine how entropy maximization and energy minimization interact, and we accomplish this task by defining free energy. Free energy is the concept that embodies much of the geochemical motivation for studying thermodynamics because it provides an indication of the direction of a reaction. When used to calculate an equilibrium constant for a reaction, it also indicates the equilibrium composition of a system.

According to the second law of thermodynamics, the entropy of a system, S^{sys}, or more precisely a potential quantity, TS^{sys}, represents a dissipation of the system's energy from a form that is available for work to a form that is useless. Entropy is always produced when energy is transferred as heat, and the identity $dq_{rev}^{sys} = T dS^{sys}$ defines entropy

Originally published in: Marshall CP, Fairbridge RW (eds) Encyclopedia of Geochemistry, Springer Netherlands, 1999

(rev denotes a reversible process and sys indicates that the heat transfer dq is measured from the point of view of the system; see ▶ Entropy). The system's energy is measured as either internal energy, U, or enthalpy, H (see ▶ Enthalpy). Energy is frequently defined as the ability to work, and in the absence of entropy, U or H could be converted completely into useful work, such as the work of making and breaking bonds in a chemical reaction. A consequence of the second law, however, is that U and H are partitioned into a "lost" potential TS^{sys} and a "net" potential that is actually available for work. That net potential is called free energy, and two types of free energy are defined on the basis of the two measures of energy (Eq. 1).

$$\begin{aligned} A &\equiv U - TS^{sys}, \quad \text{Helmholtz free energy} \\ G &\equiv H - TS^{sys}, \quad \text{Gibbs free energy} \end{aligned} \tag{1}$$

Because constant pressure calorimetry is more pertinent than constant volume calorimetry to geochemical processes (most of which do not take place in rigidly confined vessels), H and G are more generally useful in geochemistry than U and A. The remainder of this entry focuses on G, but analogous expressions can be derived for A.

Gibbs free energy changes (Eq. 2) can be obtained by differentiating (1) and substituting $dH = T\,dS^{sys} + VdP$ (see ▶ Enthalpy).

$$\begin{aligned} dG &= dH - T\,dS^{sys} - S^{sys}\,dT \\ dG &= V\,dP - S^{sys}\,dT \end{aligned} \tag{2}$$

T and P are called "natural" variables of G, and we can say that G is a "characteristic" function of T and P, $G_{char} = f(T,P)$.

The second law of thermodynamics stipulates $dS^{univ} \geq 0$. Thus, S^{univ} is the basis of criteria for spontaneity or the direction of natural processes ($dS^{univ} > 0$) and for equilibrium ($dS^{univ} = 0$). No processes reduce S^{univ}; only "local" entropy changes (e.g., ΔS^{sys}) may be <0. These criteria are based on properties of a universe, but they can be translated into properties of the system of interest, yielding $\Delta G \leq 0$ (see ▶ Entropy). For all spontaneous processes, $\Delta G < 0$, corresponding to our expectations that spontaneous processes minimize energy and that the more stable of two states is the one with the lower energy. Free energy is, therefore, the appropriate system parameter for evaluating the direction of reactions or the stability of states (or phases). The equilibrium state is characterized by the absence of energy gradients, so $\Delta G = 0$.

It is frequently convenient to use the partial molar Gibbs free energy or chemical potential, μ (Eq. 3).

$$\mu_j = \left(\frac{\partial G}{\partial n_j}\right)_{T,P,n_{k\neq j}} \tag{3}$$

The chemical potential of substance j is the dependence of G for the system containing j on the amount of j (n_j, number of moles of j), with T, P, and composition (constituents k other than j) held constant.

The composition of a system, expressed in terms of activities of the constituents (see ▶ Activity and Activity Coefficients), is given by the mass-action expression Q (Eq. 4), which gives the product of each component's activity (a, raised to the power of its stoichiometric coefficient, ν; $\nu_{product} > 0$ and $V_{reactant} < 0$).

$$Q = \prod a_j^{\nu_j} \tag{4}$$

For example, the mass-action expression for the relative stability of albite and kaolinite in aqueous solution,

$$NaAlSi_3O_{8(alb)} + H^+ + \tfrac{9}{2}H_2O = \tfrac{1}{2}Al_2Si_2O_5(OH)_{4(kaol)} + Na^+ + 2H_4SiO_4^0$$

where the 0 superscript denotes an uncharged aqueous solute, would be:

$$Q = \frac{a_{kaol}^{1/2} a_{Na^+} \times a_{H_4SiO_4^0}^2}{a_{alb} a_{H^+} \times a_{H_2O}^{9/2}} \tag{5}$$

If we can assume that the solid phases are pure and that the aqueous solution is sufficiently dilute for the liquid water to behave as if it were pure, then those activities go to 1 (pure substances are in the standard state and have unit activity). With those assumptions, the mass-action expression simplifies to:

$$Q = \frac{a_{Na^+} \times a_{H_4SiO_4^0}^2}{a_{H^+}} \tag{6}$$

The free energy change of a reaction in any arbitrary state, ΔG_R, or the standard state free energy change of a reaction, $\Delta G^0{}_R$, are both molar quantities (energy/mol). The standard state is a carefully defined reference state for a substance or an assemblage of substances (a reaction system) at a given temperature, pressure, and system composition. The dependence of ΔG_R on composition (Eq. 7) uses Q as the compositional variable to correct the reference value for the actual composition of the system:

$$\Delta G_R = \Delta G_R^0 + RT \ln Q \tag{7}$$

As noted above, $\Delta G_R = 0$ at equilibrium. Also at equilibrium, the composition of the system assumes a singular mass-action ratio, whose value depends on T and P, and which is called the equilibrium constant, K. Thus, at equilibrium, Eq. 7 gives the important relationship between K and $\Delta G^0{}_R$ (Eq. 8):

F

$$\Delta G_R^0 = -RT\ln K$$
$$\Delta G_R^0 = -2.303\,RT\log K \quad (8)$$

Calculations of free energies are based on enthalpy and entropy measurements. Standard state enthalpies of formation, ΔH^0_f, and absolute entropies, S^0_T, based on calorimetric and heat capacity measurements, are tabulated and can be used to calculate standard state enthalpy changes, ΔH^0_R, and entropy changes, ΔS^0_R, for reactions. ΔG^0_R can then be calculated from $\Delta H^0_R - T\Delta S^0_R$ (Eq. 2). Similarly, $\Delta G^0_f = \Delta H^0_f - T\Delta S^0_f$, and it is more common, and usually more convenient, to calculate ΔG^0_R from tabulated values of ΔG^0_f. By convention, the ΔG^0_f for an element in the standard state (usually 298 K, 1 bar) is 0, as are ΔH^0_f and ΔS^0_f. For compounds or elements in a state other than the standard state, the standard state free energy of formation (from the standard state element), ΔG^0_f, represents the energy of making the bonds of the compound, ΔH^0_f, less the energy expended in the isothermal heat transfer accompanying the formation, $T\Delta S^0_f$. For example, at 298 K, graphite, the standard state form of elemental carbon, has $\Delta H^0_f = \Delta G^0_f = \Delta S^0_f = 0$, while for diamond, $\Delta H^0_f = 1.9$ kJ/mol and $\Delta G^0_f = 2.9$ kJ/mol. The difference, 1 kJ/mol, is the potential $-T\Delta S^0_{f,\text{dia}}$, so $\Delta S^0_{f,\text{dia}} = -3.36$ J/mol/K. Note that $\Delta S^0_{f,\text{dia}} = S^0_{\text{dia}} - S^0_{\text{gra}} = (2.38–5.84)$ J/mol/K (see ▶ Entropy for a discussion of the difference between S^0_T and ΔS^0_f).

The free energy change is calculated from:

$$\Delta G^0_{\text{process}} = \sum \nu_j \Delta G^0_{f,j}$$

where ν_j is the stoichiometric coefficient of the constituents of the system in the final state (e.g., reaction products, $\nu_j > 0$) or the initial state (e.g., reactants, $\nu_j < 0$). The subscript R may be substituted by a more informative subscript denoting the specific process in question. For example, the evaporation of liquid water, $H_2O_{(l)} = H_2O_{(g)}$, involves a free energy change given by:

$$\Delta G^0_{\text{evap}} = \Delta G^0_{f,H_2O_{(g)}} - \Delta G^0_{f,H_2O_{(l)}}$$
$$= (-228.6) - (-237.1) = 8.5\,\text{kJ/mol}$$

at 298 K. Because $\Delta G^0_{\text{evap}} > 0$, evaporation of water is not spontaneous at 298 K; $\Delta G^0_f, H_2O_{(l)} < \Delta G^0_f, H_2O_{(g)}$, so $H_2O_{(l)}$, is more stable than $H_2O_{(g)}$. The equilibrium constant for the evaporation of water at 298 K is thus:

$$\log K = \frac{-8500}{2.303(8.314)298.15} \approx -1.5 (K < 1),$$

and the equilibrium partial pressure of water vapor (i.e., the vapor pressure for water) at 298 K is ~ 32 mb.

Another example: the free energy change for the quartz-fayalite-magnetite O_2-buffer reaction, $3Fe_2SiO_{4(\text{fay})} + O_{2(g)} = 2Fe_3O_{4(\text{mag})} + 3SiO_{2(\text{qtz})}$ is given by:

$$\Delta G^0_{\text{QFM}} = \left(2\Delta G^0_{f,\text{mag}} + 3\Delta G^0_{f,\text{qtz}}\right) - \left(3\Delta G^0_{f,\text{fay}} + 0\right)$$
$$= -463.7\,\text{kJ/mol at 298 K}$$

The (fay + $O_{2(g)}$) assemblage is less stable than the (mag + qtz) assemblage, and for this reaction, $\Delta G^0_{\text{QFM}} < 0$, indicating a spontaneous process, for which we expect $K > 1$. Indeed,

$$\log K = \frac{463\,700}{2.303(8.314)298.15} \approx 81.2.$$

Accordingly, the equilibrium partial pressure of O_2 in the QFM buffer system at 298 K is $\sim 10^{-81.2}$ bar.

A total differential equation based on $G_{\text{char}} = f(T, P)$ gives:

$$dG = \left(\frac{\partial G}{\partial P}\right)_T dP + \left(\frac{\partial G}{\partial T}\right)_P dT$$

Comparison with Eq. 2 allows the immediate derivation of the isothermal pressure dependence and the isobaric (constant pressure) temperature dependence of G, respectively (Eq. 9); molar values, denoted by the overbar, are used here).

$$\left(\frac{\partial \overline{G}_i}{\partial P}\right)_T = \overline{V}_i \left(\frac{\partial \overline{G}_i}{\partial T}\right)_P = -\overline{S}_i \quad (9)$$

Accordingly, of two phases initially at equilibrium, the phase with the smaller molar volume will be more stable at higher pressures, while the phase with the larger molar entropy will be more stable at higher temperatures. The relationships in Eq. 9 apply equally well to reactions:

$$\left(\frac{\partial \Delta G^0_R}{\partial P}\right)_T = \Delta V^0_R \left(\frac{\partial \Delta G^0_R}{\partial T}\right)_P = -\Delta S^0_R \quad (10)$$

The overbar is not needed for the expressions in Eq. 10, because ΔY^0_R, where $Y = G, V, S$, is taken to be a molar quantity.

Correcting ΔG^0_R for pressure changes requires integrating the first expression in Eq. 10, giving:

$$\Delta G^0_{R,P} = \Delta G^0_{R,P_{\text{ref}}} + \Delta V^0_R (P - P_{\text{ref}}) \quad (11)$$

as long as $\Delta V^0_R \neq f(P)$. For condensed phases (solids and liquids), the pressure dependence of volume changes is usually very weak, even over large ranges of P. Clearly, however, the pressure dependence of volume is quite strong for gases. For this reason, the standard state of condensed phases is usually defined at a given temperature and pressure (i.e., both T and P are allowed to vary in the standard state), but for gases, the standard state is defined at a given temperature but for a single pressure (i.e., T may vary but P is fixed in the

standard state). All of the pressure dependence of G, and thus K, for gases is accounted for by the variation of fugacity with pressure (Eq. 12).

$$\mu_j = \mu_j^0 + RT\ln f_j \tag{12}$$

When calculating the pressure dependence of $\Delta G^0{}_R$ for a reaction in which one of the constituents is a gas, the gas itself is excluded from the calculation of $\Delta V^0{}_R$. In the QFM example above, therefore,

$$\Delta V_R^0 = \left(2\overline{V}_{\text{mag}} + 3\overline{V}_{\text{qtz}}\right) - \left(3\overline{V}_{\text{fay}}\right) = 17.9\,\text{cm}^3/\text{mol}$$

(1.79 J/bar/mol) at 298 K.

The second expression in Eq. 10 can be integrated to give the temperature dependence of $\Delta G^0{}_R$ (Eq. 13), which assumes that the temperature range between T and T_{ref} is narrow enough for $\Delta S^0{}_R$ to be effectively constant).

$$\Delta G_{R,T}^0 = \Delta G_{R,T_{\text{ref}}}^0 - \Delta S_R^0(T - T_{\text{ref}}) \tag{13}$$

In fact, the temperature dependence of the function G/T is of more interest, owing to the mathematics of deriving the temperature dependence of K. The Gibbs-Helmholtz equation gives the temperature dependence of G/T and can be applied directly to reactions (Eq. 14):

$$\left(\frac{\partial(G/T)}{\partial T}\right)_P = \frac{-H}{T^2}\left(\frac{\partial(\Delta G/T)}{\partial T}\right)_P = \frac{-\Delta H}{T^2} \tag{14}$$

From Eq. 8,

$$R\ln K = \frac{-\Delta G_R^0}{T}$$

and substituting that result into Eq. 14 gives:

$$\left(\frac{\partial \ln K}{\partial T}\right)_P = \frac{\Delta H_R^0}{RT^2}$$

the van't Hoff equation, which can be integrated to correct K for T.

The application of free energy to problems in geology and environmental science is constrained, as is the application of any thermodynamic concept, by two important considerations. First, free energy and the equilibrium constant provide no insight into the time required for a system to achieve equilibrium or the process by which equilibrium is attained. Reaction rates and reaction mechanisms fall in the domain of chemical kinetics. Second, open systems (e.g., fluid-rock systems in which fluids may be imported to or exported from the system) are not amenable to straightforward thermodynamic evaluation. Despite these important limitations, free energy has proved exceedingly useful in answering geologically relevant questions, such as whether a postulated reaction can occur (using the criterion of direction, $\Delta G^0{}_R < 0$) or determining the equilibrium composition of a system (using K, which is derived from the zero gradient equilibrium criterion, $\Delta G_R = 0$).

Cross-References

- Activation Parameters: Energy, Enthalpy, Entropy, and Volume
- Activity and Activity Coefficients
- Clapeyron's Equation
- Debye-Hückel Equation
- Electronegativity
- Enthalpy
- Entropy
- Equilibrium
- Geochemical Thermodynamics
- Gibbs-Duhem Equation
- Kinetics of Geochemical Processes
- Mass Transfer
- Solid Solution/Exsolution
- Standard States

References

Anderson GM, Crerar DA (1993) Thermodynamics in geochemistry. The equilibrium model. Oxford University Press, New York. 588 pp

Atkins PW (1986) Physical chemistry, 3rd edn. W.I. Freeman, New York. 857 pp

Nordstrom DK, Munoz JL (1994) Geochemical thermodynamics, 2nd edn. Blackwell Scientific Publications, Cambridge, MA. 493 pp

Robie RA, Hemingway BS, Fisher JR (1978) Thermodynamic properties of minerals and related substances at 298.15 K and 1 bar (10^5 Pascals) pressure and at higher temperatures. US Geol Surv Bull 1452:456

Fugacity

Christopher A. Colla and William H. Casey
Department of Chemistry and Department of Earth and Planetary Sciences, University of California, Davis, CA, USA

Definition

The thermodynamic pressure of a gas.

Introduction

The concept of fugacity was defined by G. N. Lewis, one of the most prominent American physical chemists in the early twentieth century (Rock 1983 and Laidler 1993). Lewis defined a ratio of fugacities to yield thermodynamic activities, and fugacity is the pressure if the gases both satisfy the ideal gas law and if the standard-state fugacity is defined for a total pressure of 1 bar (10^5 Pa). Pressure could not be used directly to define activities because some real gases deviate from behavior described by the ideal gas law. The choice of a standard-state fugacity of 1 bar total pressure, however, means that activities vary with total pressure, which is circumvented by geochemists who define standard states at elevated pressures for geochemical calculations. This concept is central to geochemistry because the conditions in the Earth deviate considerably from 1 bar (10^5 Pa) and 298 - K. Oxygen fugacities, for example, are an expression of the redox behavior of the Earth's crust and mantle (e.g., Ballhaus et al. 1990).

Elaboration

When introducing activities, it is useful to reprise the sequence employed in most introductory chemistry courses. Here, vapor-pressure measurements play a central role, and the thermodynamic activity is defined as a ratio of pressures by either Henry's law (if the component is treated as a solute) or Raoult's law (if the component is treated as a solvent): $a_i \equiv \frac{P_i}{P_i^o}$ where P_i^o is the pressure of the pure component. An ideal solution satisfies Raoult's law: $\frac{P_i}{P^o} = X_i$ where X is mole fraction. Deviations from this linear relation arise from chemical interactions among the components that cannot be treated using random-mixing statistics. These deviations indicate nonideality, interactions between components that yield an appreciable excess Gibbs energy of mixing and a pressure ratio that deviates from Raoult's Law.

In the case of Raoult's Law, P_i^o is a directly measurable quantity – it is the vapor pressure that would exist, for example, above a bottle of the pure solid or liquid purchased from a stockroom. Again using the most basic approach:

$$\mu_{\text{ideal}} - \mu^o_{\text{Henrian or Raoultian}} = RT\ln\left(\frac{P_i}{P^o_{i,\,\text{Henrian or Raoultian}}}\right) \tag{1}$$

In the case of Henry's law, the P_i^o value is not directly measurable but is estimated by extrapolating the variation of pressure with composition to the point where the solution is diluted to the extreme condition of the pure material. There is no reagent bottle that can be purchased that has this pressure over pure material. Practically this means drawing a line between P_i and X_i until the intercept is reached where $X_i = 1$. This intercept is now a *hypothetical* vapor pressure that would exist if the pure substance retained the same structure that it had at infinite dilution, when it satisfied Henry's law.

There are two simplifications that are never explained in these introductory chemistry courses. First, deviations from Raoult's law may arise because the gases do not behave ideally even at 1 bar (10^5 Pa). Thus the behavior of some compositions must be adjusted to account for interactions among the various gas molecules. The second simplification is more important to geochemists. Lewis defined the standard state, P^o, at the temperature of interest (which can vary), but only at a *total* pressure of 1 atm or 10^5 Pascals. Thus adjustments must be made if the total pressure deviates from this standard-state condition.

To accommodate the first difficulty, G. N. Lewis defined activity to be a ratio of *fugacities*, from the Latin word that means the tendency to flee (as in *tempus fugit*):

$$a_i \equiv \frac{f_i}{f_i^o}$$

with the caveat that $f_i \rightarrow P_i$ as pressure is reduced, since all gases behave ideally if the pressures are low enough. The ratio can also be derived from statistical mechanics (see Dill and Bromberg 2010, pp. 211–242). This first difficulty, the nonideality of gases, can be accounted by correcting the measured pressure using a model of interactions that recaptures the behavior of a perfect gas (see Nordstrom and Munoz 1994, pp. 131–136).

The second difficulty, the defined standard state at 1 bar pressure, can be adjusted either by allowing the activity to vary, which is illustrated in Table 1, or by moving the standard state to a new pressure, which is probably more convenient to geochemists (Lewis and Randall 1961). Chemical potentials relate to thermodynamic activities by an integration from a defined endpoint. At fixed temperature from a standard, or reference, state that is denoted by the superscript '^{o}' to another (nonstandard) state:

$$\int_{\mu_i=\mu^o}^{\mu_i} d\mu_i = \int_{a_i=a^o}^{a_i} RT\ d\ln(a_i) \tag{2}$$

Fugacity, Table 1 The vapor pressure of H_2O over the pure liquid differs with the total pressure at 298 K. These differences lead to a varying activity (column 3) even if the vapor behaves like an ideal gas because the standard state fugacity (or pressure) is defined at 1 bar total pressure (Adapted from Randall and Sosnick (1928) and Garrels and Christ (1965))

Total pressure (Pa)	Fugacity (Pa)	Activity of water
101,325	3166.41	1
1.013×10^7	3406.54	1.0757
2.027×10^7	3665.93	1.1576
3.040×10^7	3943.56	1.2454
4.053×10^7	4241.46	1.3394
5.066×10^7	4560.63	1.4402
6.080×10^7	4902.10	1.5481
7.093×10^7	5267.88	1.6637
8.106×10^7	5660.01	1.7874
9.119×10^7	6079.50	1.9200
1.013×10^8	6528.36	2.0618

or:

$$\mu_i - \mu_i^o = RT\ln\left(\frac{a_i}{a_i^o}\right) \tag{3}$$

Any fixed pressure could be used as a standard state, and activities that differ only in pressure are related by the equations:

$$\int_{\text{State1}}^{\text{State2}} d\ln(a_i) = \frac{1}{RT}\int_{P_1}^{P_2} \overline{V}_i \, \mathrm{dP} \tag{5}$$

where in general, $\overline{V}_i$ depends on both P and T. We can set $a_{i,1} = 1$ for any convenient value of P and refer all $a_{i,2}$ values to that new standard state (see Anderson and Crerar 1993).

Conclusions

The concept of fugacity is central to the use of thermodynamic activities to estimate the equilibrium state of materials in the Earth. It leads directly to definitions of standard states that are particularly important to geochemists because they treat variations in temperatures and pressures that span well beyond the range treated by most chemists.

Cross-References

- Activity and Activity Coefficients
- Equilibrium
- Geochemical Thermodynamics
- Gibbs-Duhem Equation
- Standard States

References

Anderson GM, Crerar DA (1993) Thermodynamics in geochemistry. Oxford University Press, New York. 588 pp

Ballhaus C, Berry RF, Green DH (1990) Oxygen fugacity controls in the Earth's upper mantle. Nature 348:437–440

Dill KA, Bromberg S (2010) Molecular driving forces: statistical thermodynamics in biology, chemistry, physics, and nanoscience, 2nd edn. Garland Science, London/New York. 756 pp

Garrels RM, Christ CL (1965) Solutions, minerals and equilibria. Freeman Cooper and Company, San Francisco. 450 pp

Laidler KJ (1993) The world of physical chemistry. Oxford University Press, New York. 476 pp

Lewis GL, Randall M (1961) Thermodynamics. Revised by Pitzer KS, Brewer L. McGraw-Hill, New York. 724 pp

Nordstrom DK, Munoz JL (1994) Geochemical thermodynamics, 2nd edn. Blackwell Scientific Publications, Cambridge, MA. 494 pp

Randall M, Sosnick B (1928) Gaseous solutions. J Am Chem Soc 50:967–980

Rock PA (1983) Chemical thermodynamics. University Science Books, Mill Valley. 548 pp

G

Gadolinium

Scott M. McLennan
Department of Geosciences, Stony Brook University, Stony Brook, NY, USA

Element Data
Atomic Symbol: Gd
Atomic Number: 64
Atomic Weight: 157.25(3)
Isotopes and Abundances: ^{152}Gd, 0.20(3)%; ^{154}Gd, 2.18(2)%; ^{155}Gd, 14.80(9)%; ^{156}Gd, 20.47(3)%; ^{157}Gd, 15.65(4)%; ^{158}Gd, 24.84(8)%; and ^{160}Gd, 21.86(3)%
1 Atm Melting Point: 1313 °C
1 Atm Boiling Point: 3273 °C
Common Valences: +3
Ionic Radii: 93.8 pm (CN6), 105.3 pm (CN8), and 124.6 pm (CN12)
Pauling Electronegativity: 1.20
First Ionization Energy: 593.39 kJ mol^{-1}
Chondritic (CI) Abundance: 0.204 ppm
Silicate Earth Abundance: 0.454 ppm
Crustal Abundance: 3.3 ppm
Seawater Abundance: 0.739 ppt
Core Abundance: ~0

Properties

Gadolinium (Gd), named after the geologist and chemist Johan Gadolin, is a malleable, ductile, moderately dense (7.901 g cm^{-3}), bright silvery-white metal. Its electronic configuration is [Xe]4f^{7}5d^{1}6s^2. Stable in dry air at room temperature, it oxidizes at elevated relative humidity and readily dissolves in mineral acids. It is a group 3 or IIIB inner transition element, with +3 being its only valence state in geological environments, and is one of the lanthanide rare earth elements (REE). In geochemical terminology, it is grouped with heavy rare earth elements (HREE; Gd-Lu). Gadolinium has six natural, stable isotopes and one long-lived radioisotope (^{152}Gd; $t_{1/2} = 1.081 \times 10^{14}$ years; alpha decaying to ^{148}Sm) occurring in nature, listed above with their abundances. ^{157}Gd is notable in having the highest thermal neutron absorption cross section (259,000 barns) of any stable nuclide.

More than 270 minerals contain lanthanides as essential structural constituents, but those with Gd as a major component are restricted to minerals such as gadolinite-Y [$Y_2FeBe_2(Si_2O_{10})$], xenotime [$Y(PO_4)$], bastnäsite [REE(CO_3)F], allanite [$(REE,Ca,Y)_2(Al,Fe^{2+},Fe^{3+})_3(SiO_4)_3(OH)$], and britholite [$(REE,Ca)_5(SiO_4,PO_4)_3(OH,F)$].

Details of properties, mineralogy, history, and uses of Gd were compiled from Goonan (2011), Chakhmouradian and Wall (2012), Zaimes et al. (2015), Gschneidner (2016), Hammond (2016), and Meija et al. (2016a, b).

History and Use

Gadolinium was identified spectroscopically in the minerals gadolinite and cerite in 1880 by Jean Charles Galissard de Marignac and first isolated as a metal in 1886. Gadolinium has numerous highly specialized commercial uses. For example, due to its high neutron absorption cross section, it is used both in nuclear reactor control rods and in nuclear medicine. Gadolinium's phosphorescent properties make it useful in X-ray imaging devices, and its room temperature paramagnetic properties make it useful as a component in magnetic resonance imaging.

Geochemical Behavior

The fundamental importance of Gd in geochemistry is that it is one of the small trivalent rare earth elements, among the

W. M. White (ed.), *Encyclopedia of Geochemistry*,
https://doi.org/10.1007/978-3-319-39312-4

most useful trace elements in all areas of geochemistry and cosmochemistry due to their coherent and systematic behavior as a group, largely a consequence of the "lanthanide contraction."

Gadolinium is typically a trace element in most rocks and minerals. It is classified geochemically and cosmochemically as a highly refractory lithophile element, with a 50% $T_{condensation}$ of 1659 K at 10^{-4} bars (Lodders 2003). In most igneous systems, Gd is incompatible with bulk partition coefficients, $D < 1$. In aqueous systems, Gd normally has very low fluid/rock partition coefficients ($\ll 1$). As a result, Gd contents of clastic sediments typically reflect their average provenance.

In seawater, Gd has very low concentrations (~ppt) and residence times (~520 year) with speciation dominated by Gd^{3+}, $GdCO_3^+$, and $Gd(CO_3)_2^-$. In other aqueous systems (e.g., magmatic, hydrothermal), Gd can reach ppm levels due to elevated temperatures, pH effects, and complexing with various ligands (e.g., F^-, Cl^-, OH^-).

Concentration and residence time data are from compilations in Taylor and McLennan (2009) and Nozaki (2001).

Biological Utilization and Toxicity

There are no documented biological uses for Gd, but in China REE have been added to fertilizers and to stock feed to promote growth. REE (including Gd^{3+}) likely substitute for Ca^{2+} in biological materials and processes. REE concentrations (including Gd) in human tissues and fluids are very low (tens of ppb to <ppb levels, respectively) due to very low concentrations in natural waters and low uptake rates throughout the food chain (Bulman 2003). At low levels of ingestion, there are no established toxic effects that pose a threat to human health.

Cross-References

- ▶ Incompatible Elements
- ▶ Lanthanide Rare Earths
- ▶ Lithophile Elements
- ▶ Trace Elements
- ▶ Transition Elements

References

Bulman RA (2003) Metabolism and toxicity of the lanthanides. In: Sigel A, Sigel H (eds) Metal ions in biological systems, vol 40, the lanthanides and their interrelations and biosystems. Marcel Dekker, Basel, pp 683–703

Chakhmouradian AR, Wall F (eds) (2012) Rare earth elements. Elements 8:333–376

Goonan TG (2011) Rare earth elements – end use and recyclability. US Geol Surv Sci Invest Rpt, 2011–5094. 15pp

Gschneidner KA Jr (2016) Physical properties of the rare earth metals. In: Haynes WM (ed) CRC handbook of chemistry and physics, 96th edn. CRC Press, Boca Raton, pp 4-115–4-120

Hammond CR (2016) The elements. In: Haynes WM (ed) CRC handbook of chemistry and physics, 96th edn. CRC Press, Boca Raton, pp 4-1–4-42

Lodders K (2003) Solar system abundances and condensation temperatures of the elements. Astrophys J 591:1220–1247

Meija J, Coplen TB, Berglund M, Brand WA, De Bièvre P, Gröning M, Holden NE, Irrgeher J, Loss RD, Walczyk T, Prohaska T (2016a) Atomic weights of the elements 2013. Pure Appl Chem 88:265–291. (IUPAC Technical Report)

Meija J, Coplen TB, Berglund M, Brand WA, De Bièvre P, Gröning M, Holden NE, Irrgeher J, Loss RD, Walczyk T, Prohaska T (2016b) Isotopic compositions of the elements 2013. Pure Appl Chem 88:293–306. (IUPAC Technical Report)

Nozaki Y et al (2001) Rare earth elements and their isotopes in the ocean. In: Steele JH (ed) Encyclopedia of ocean sciences. Academic, London, pp 2354–2366

Taylor SR, McLennan SM (2009) Planetary crusts: their composition, origin and evolution. Cambridge University Press, Cambridge. 378pp

Zaimes GG, Hubler BJ, Wang S, Khanna V (2015) Environmental life cycle perspective on rare earth oxide production. ACS Sustain Chem Eng 3:237–244

Gallium

Munir Humayun
Department of Earth, Ocean and Atmospheric Science, Florida State University, Tallahassee, FL, USA

Element Data
Atomic Symbol: Ga
Atomic Number: 31
Atomic Weight: 69.723 ± 1 g/mol
Isotopes and Abundances: ^{69}Ga 60.1%;^{71}Ga 39.9%
1 Atm Melting Point: 29.8 °C
1 Atm Boiling Point: ~2,400 °C
Common Valences: +3
Ionic Radii Values: 47 pm (fourfold); 62 pm (sixfold)
Pauling Electronegativity: 1.81
First Ionization Energy: 174.6 kJ/mol
Chondritic (CI) Abundance: 9.5 ± 0.3 μg/g
Silicate Earth Abundance: 4.0 μg/g
Crustal Abundance: 17.5 μg/g
Seawater Abundance: ~1.2 pg/g
Core Abundance: <1 μg/g

Properties

Gallium does not occur as a native metal and forms very few minerals like gallite ($CuGaS_2$), but widely occurs in nature as

a trace constituent substituted for Al. Gallium metal is prepared as a by-product of aluminum production from bauxite ore and from Zn ores (e.g., sphalerite). Synthetically prepared metallic Ga is a soft, silvery white metal and has a melting point below human body temperature so it can be readily melted in one's hand. Liquid gallium is one of a few substances (like water) that expand on solidification. Of all elements, Ga has the largest temperature range over which it is liquid.

Gallium has two stable isotopes, ^{69}Ga and ^{71}Ga, and about 20 known radioactive isotopes (Gross and Thoennessen 2012), all of which have half-lives <80 h and have found no geochemical applications.

History and Use

Before its eventual discovery and isolation, the existence of gallium was predicted by the Russian chemist Dmitri Mendeleev as "eka-aluminium," the element below Al, in his new periodic table in 1871. It was discovered spectroscopically in 1875 by the French chemist, Paul Emile Lecoq de Boisbaudran, in a sphalerite sample and subsequently isolated by electrolysis. Lecoq de Boisbaudran named the new element from Latin *Gallia*, the land of the Gauls, i.e., France.

The low melting point (29.78 °C) for metallic Ga allows it to be liquid near room temperature, while its low first ionization potential (5.1 eV) makes it easy to ionize, so it is widely used as an ion source in Ga ion guns for focused ion beam (FIB) slicing in transmission electron microscopy and for imaging in secondary ion mass spectrometry. Gallium readily alloys with many metals, finding use in low-melting alloys like galinstan, a eutectic alloy (m.p. −19 °C) of Ga, In, and Sn used in thermometers to replace toxic mercury. It is alloyed with δ-plutonium in nuclear weapons.

Neutrinos react with ^{71}Ga to form ^{71}Ge that can be radiochemically detected. Gallium metal is used in the SAGE (http://www.inr.troitsk.ru/eng/ebno.html) neutrino detector. Gallium trichloride is used in the GALLEX (https://www.mpi-hd.mpg.de/lin/research_history.de.html) neutrino detector.

Gallium's principal use is in semiconductors as gallium arsenide (GaAs) and gallium nitride (GaN). It finds use in optoelectronics, e.g., in light-emitting diodes (LEDs), and GaN is used in 405 nm diode lasers in Blu-ray disks. Gallium also finds important applications in photovoltaic (PV) cells as Cu-In-Ga-Se (CIGS), which is a solid solution of $CuInSe_2$ and $CuGaSe_2$, with the general formula $[Cu(In_xGa_{1-x})Se_2]$. The bandgap of CIGS can be varied from 1.04 to 1.68 eV by varying the ratio of In to Ga in the solid solution, leading to some of the highest efficiency solar PV cells (http://www.solarpowerworldonline.com/2014/01/cigs-solar-cells-simplified/).

Cosmochemical Behavior

Gallium, an odd Z element, is less abundant (9.5 ppm) than the neighboring elements of Zn (312 ppm) or Ge (32.7 ppm) in type I carbonaceous chondrites (CI). The nuclear statistical equilibrium process that creates the Fe peak elements mainly produces the stable isotopes of Ga. The astrophysical s-process contributes ~5% to the abundance of Ga, with an even smaller contribution from the r-process (Clayton 2003). In the first recent study of Ga isotopic variations, Kato et al. (2014) reported variations in δ^{71}Ga of −0.27 ‰ for eight samples of chondrites relative to terrestrial samples.

Gallium is a moderately volatile element during gas to solid or gas to liquid condensation or evaporation processes occurring in the solar nebula. While pure Ga metal has a high boiling point (2,400 °C), Ga forms volatile chlorides in a gas of solar composition. Thus, Ga condenses at 968 K (10 Pa total pressure) in Fe-Ni alloy, being more volatile than Cu or As but less volatile than Ge or Zn (Lodders 2003). As a moderately volatile element, Ga is depleted relative to CI abundances and the major elements in other chondrites and in all differentiated meteorites. In bulk chondrites, the abundances of Ga are highest in the enstatite chondrites, both EH (16 μg/g) and EL (11 μg/g) chondrites. The ordinary chondrites have a narrow range of Ga contents (5–6 ppm) independent of their metal abundances, because these chondrites are oxidized enough that much of their Ga inventory is in their silicate fraction. The depletion of Ga is evident in the successive order of Ga contents of carbonaceous chondrites: CI > CM > CO > CV > CR ~ CH > CB (Wasson and Kallemeyn 1988). The metal of CR and CB chondrites is depleted in Ga, with depletion factors relative to Ni and CI chondrites of 0.1–0.01 in CR metal (Humayun 2012). Gallium has a higher diffusivity in Fe-Ni metal than Ni (Righter et al. 2005) making it useful in determining cooling rates of metallic grains in chondrites (Humayun 2012).

Gallium is also moderately siderophile, partitioning into iron meteorites (Fig. 1) and into planetary cores. In metallic liquids, the partition coefficient of Ga between liquid Fe-FeS and solid Fe metal is close to unity, similar to that of Ge. The partition coefficient varies with increasing alloying by light elements like C, Si, P, and S driving the Ga into the solid metal. A notable exception occurs when oxygen is the alloying element, since Ga readily forms an oxide in an Fe-FeO-FeS liquid, Ga is systematically more incompatible in the solid metal with increasing mole fraction of oxygen dissolved in the metallic liquid relative to its behavior in pure Fe-FeS liquids (Chabot et al. 2015). Although Ga has chalcogenic properties, it is not detectable in meteoritic troilite, leaving metal and silicate as its major hosts.

Due to its volatility, Ga content varies in the parental materials from which the iron meteorites differentiated. This makes Ga (and Ge) useful in classifying iron meteorites into

chemical groups (Goldstein et al. 2009). The Ga contents span nearly three orders of magnitude in irons, with "magmatic" irons (e.g., IIAB, IIIAB, IVA, IVB), thought to represent asteroidal cores, having small ranges of Ga and Ni and "non-magmatic" irons (e.g., IAB, IIE), thought to represent smaller pools of iron formed by incipient differentiation, having larger ranges of Ga and Ni contents (Fig. 1).

The Ga that remains in the mantle (as Ga_2O_3) behaves similarly to Al, being moderately incompatible. This aspect of Ga makes the Ga/Al ratio a useful indictor of planetary origin for basaltic meteorites. Figure 2 is a plot of Ga vs. Al for a selection of planetary and asteroidal basalts. The order of depletion (largely controlled by volatility) is Mars<Earth<Moon<4 Vesta<angrites, with about two orders of magnitude decrease in the Ga/Al ratio in angrites relative to CI chondrites. Lunar rocks exhibit a convex upward pattern with basalts being positively correlated and anorthosites being negatively correlated with Al due to the low partition coefficient of Ga in plagioclase. The Ga/Al ratio of planetary basalts is sufficiently unique to a meteorite group that it is used in identifying basaltic meteorites.

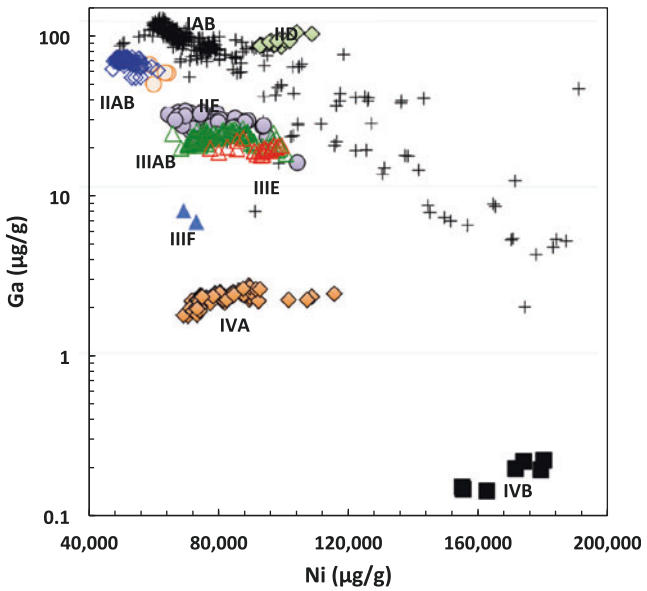

Gallium, Fig. 1 Gallium vs. Ni in iron meteorites (Campbell and Humayun 2005; Wasson et al. 2007)

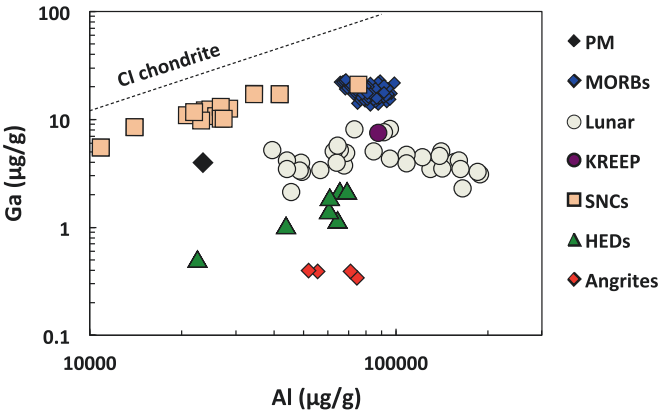

Gallium, Fig. 2 Gallium vs. Al in planetary and asteroidal basaltic rocks. PM, the silicate Earth composition; MORBs, mid-ocean ridge basalts; KREEP, enriched lunar composition; SNCs, martian meteorites; HEDs, Vestan meteorites (sources: Mittlefehldt et al. 1998; McDonough and Sun 1995; Jenner and O'Neill 2012; Wänke et al. 1976; Yang et al. 2015)

Geochemical Behavior

Gallium is a volatile siderophile element. Its siderophile character is intermediate between that of Fe and that of Si, while Al is not siderophile. The fact that Ga is less siderophile than Fe forms a useful property in tracking redox variations in core formation processes. The partitioning of Ga between mantle and core is dependent on pressure, temperature, and the nature of the light element in the core. Blanchard et al. (2015) found that the abundance of Ga in the Earth's mantle could be accounted for by formation of the core in a deep (>1,300 km) magma ocean if 5% of a combination of O and Si was present in the core. This process puts very little Ga into the core in contrast to iron meteorites, which contain a significant inventory of Ga.

Gallium is concentrated in Al-rich minerals in the crust. During partial melting of the mantle, Ga, like Al, is incompatible in most phases, including garnet, but is compatible in spinel (Davis et al. 2013).

Gallium contents in soils follow those of Al, due to the low solubility of both elements. The overall average abundance of Ga in a global compilation of 1,600 soils was ~21 ppm (Bowen 1982). Bauxite deposits formed by intense weathering concentrate Ga in Al-oxide ores with a mean Ga/Al ratio 2.7×10^{-4} (Schulte and Foley 2013), similar to the crustal value. Like Ge, Ga is known to be concentrated in coals and in coal ashes perhaps due to the presence of Ga-porphyrins (Bennett and Czechowski 1980).

Aqueous Geochemistry

The tendency of Ga^{+3} ions to form insoluble hydroxides in solution, similar to Al, results in very low abundances of Ga in natural waters. The solution species as a function of pH and temperature have been worked out from 25°C to 300 °C, with $Ga(OH)^{+2}$ and $Ga(OH)_2^{+}$ dominating at pH < 4 and Ga $(OH)_4^{-}$ dominating in more basic solutions. Gallium solubility increases with increasing temperature. Experimental studies of Ga solubility show that it is least soluble around a pH of 4 and becomes more soluble in either acidic or basic solution

(Benezeth et al. 1997; Diakonov et al. 1997). Since seafloor hydrothermal fluids have pH ~ 4, the Ga abundances are likely to be very low, although little is known about Ga in hydrothermal fluids at present.

During chemical weathering, Ga is preferentially leached from weathering residues relative to Al so that its abundance in stream waters is an order of magnitude higher than in the source rocks (Shiller and Frilot 1996). In fresh water, like Al, Ga may be complexed by organic ligands that enhance its solubility in rivers and streams (Shiller and Frilot 1996). Since the total inventory of Ga (or Al) that is removed by weathering from soils is negligible, even intense weathering residues like laterites and bauxites, still retain a Ga/Al ratio close to that of bedrocks.

Gallium is present in seawater at average concentrations of ~17 pmol/kg (~1.2 pg/g), with a profile similar to that of Al (Johnson 2016). Net sinks include clay minerals, with a Ga/Al ratio of pelagic clays (2.40×10^{-4}) being nearly identical to those of upper continental crust (2.35×10^{-4}) and in Mn oxides that exhibit a higher Ga/Al ratio of 9.7×10^{-4}. Figure 3 shows vertical profiles for Ga and Al in the Pacific Ocean (Orians and Bruland 1988), together with a dashed curve that shows the Ga abundance expected from the Al concentration using a crustal Ga/Al ratio. The Ga/Al ratio in seawater (15×10^{-3}) is over an order of magnitude higher than the crustal ratio, implying that Ga is scavenged less efficiently than Al. While the overall profile of Ga is similar to that of Al, there are key differences including a peak at intermediate depths (100–300 m) and a flatter profile than that of Al. The peak in Ga concentration at intermediate water depths is attributed to dissolution of aeolian dust. The overall patterns of both Al and Ga are determined by aeolian dust input to the surface water followed by scavenging on particles at depth that removes Al more than Ga. Inputs from sediments at the bottom of the ocean is thought to create the increase in Ga at depth. The concentration of Ga in surface waters is variable and has a small seasonal dependence (Orians and Bruland 1988; Johnson 2016).

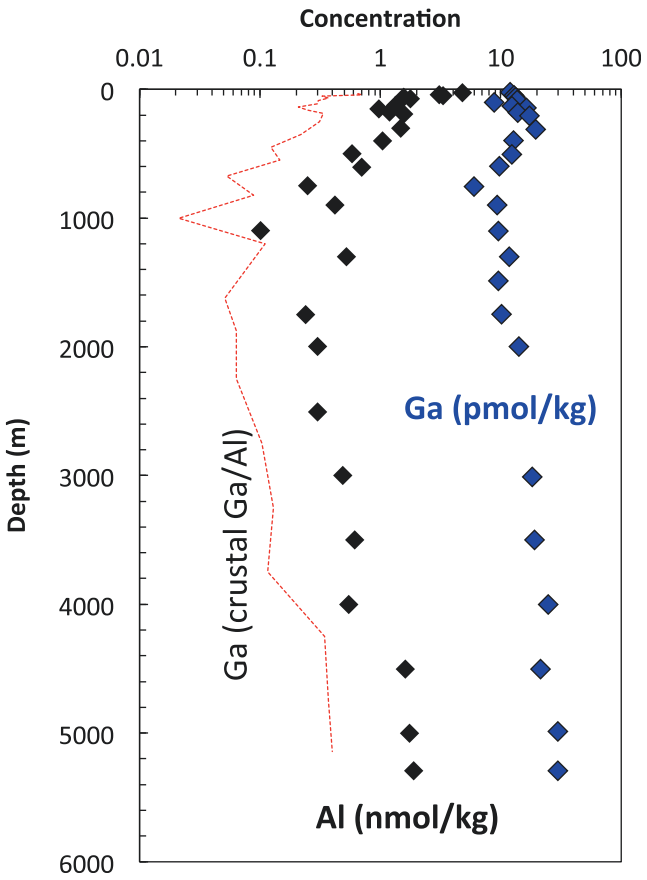

Gallium, Fig. 3 Vertical profiles of Ga (pmol/kg) and Al (nmol/kg) in Pacific seawater (Orians and Bruland 1988). The *dashed line* is the calculated Ga abundance from the Al profile and a crustal Ga/Al ratio

Gallium abundance in river waters is very low. A significant portion (20–90%) of the Ga transported is on Fe colloids (1–100 kDa) obtained by ultrafiltration of river water (Dupre et al. 1999). Organic colloids (including humic acids) do not appear to be important in the transport of Ga or Al. The abundance of Ga obtained in dialysis samples of river water has abundances of ~5–15 pg/g, which is higher than seawater (~1 pg/g) indicating that loss of Ga in estuaries must be significant.

Biological Utilization and Toxicity

Gallium is mainly nontoxic, but serves no essential nutrient function unlike neighboring Cu and Zn or the toxic As. Because it is not redox sensitive during biological uptake, occurring exclusively as Ga^{+3}, and insoluble like Al^{+3}, Ga^{+3} finds little function in biochemical processes. In biological systems, Ga^{+3} substitutes for Fe^{+3}-binding proteins, e.g., transferrin, lactoferrin, and bacterial siderophores. The radioisotope, ^{67}Ga (3.26 days half-life), is used in radioisotope imaging (radiopharmacology) of inflammation, tumors, and osteomyelitis. Ga^{+3} finds some use in medical applications as an antimicrobial agent where it can substitute for Fe^{+3} in some bacteria (e.g., *Pseudomonas*) shutting down microbial respiration (Chitamber 2010).

Cross-References

- Aluminum
- Earth's Core
- Elements: Metalloids
- Germanium
- Indium
- Meteorites
- Ocean Salinity, Major Elements, and Thermohaline Circulation

- ▶ Siderophile Elements
- ▶ Trace Elements
- ▶ Water
- ▶ Zinc

References

Benezeth P, Diakonov II, Pokrovski GS, Dandurand J-L, Schott J, Khodakovsky IL (1997) Gallium speciation in aqueous solution. Experimental study and modeling: part 2. Solubility of α-GaOOH in acidic solutions from 150 to 250°C and hydrolysis constants of gallium (III) to 300°C. Geochim Cosmochim Acta 61:1345–1357

Bennett R, Czechowski F (1980) Gallium porphyrins in bituminous coal. Nature 283:465–467

Blanchard I, Badro J, Siebert J, Ryerson FJ (2015) Composition of the core from gallium metal-silicate partitioning experiments. Earth Planet Sci Lett 427:191–201

Bowen HJM (1982) Chapter 12, Boron, aluminum, gallium, indium thallium. In: Environmental chemistry, vol 2. Royal Society of Chemistry, London, pp 159–161

Campbell AJ, Humayun M (2005) Compositions of group IVB iron meteorites and their parent melt. Geochim Cosmochim Acta 69:4733–4744

Chabot NL, Wollack EA, Humayun M, Shank EM (2015) The effect of oxygen as a light element in metallic liquids on partitioning behavior. Meteorit Planet Sci 50:530–546

Chitamber CR (2010) Medical applications and toxicities of gallium compounds. Int J Environ Res Public Health 7:2337–2361

Clayton DD (2003) Handbook of isotopes in the Cosmos: hydrogen to gallium. Cambridge University Press, Cambridge, UK. 326 pp

Davis FA, Humayun M, Hirschmann MM, Cooper RS (2013) Experimentally determined mineral/melt partitioning of first-row transition elements (FRTE) during partial melting of peridotite at 3 GPa. Geochim Cosmochim Acta 104:232–260

Diakonov II, Pokrovski GS, Benezeth P, Schott J, Dandurand J-L, Escalier J (1997) Gallium speciation in aqueous solution. Experimental study and modeling: part 1. Thermodynamic properties of Ga $(OH)_4^-$ to 300°C. Geochim Cosmochim Acta 61:1333–1343

Dupre B, Viers J, Dandurand J-L, Polve M, Benezeth P, Vervier P, Braun J-J (1999) Major and trace elements associated with colloids in organic-rich river waters: ultrafiltration of natural and spiked solutions. Chem Geol 160:63–80

Goldstein JI, Scott ERD, Chabot NL (2009) Iron meteorites: crystallization, thermal history, parent bodies, and origin. Chem Erde 69:293–325

Gross JL, Thoennessen M (2012) Discovery of gallium, germanium, lutetium, and hafnium isotopes. At Data Nucl Data Tables 98:983–1002

Humayun M (2012) Chondrule cooling rates inferred from diffusive profiles in metal lumps from the Acfer 097 CR2 chondrite. Meteorit Planet Sci 47:1191–1208

Jenner FE, O'Neill HSC (2012) Analysis of 60 elements in 616 ocean floor basaltic glasses. Geochem Geophys Geosyst 13:Q02005. https://doi.org/10.1029/2011GC004009

Johnson K (2016) Periodic table of elements in the ocean. Monterey Bay Aquarium Research Institute. Available at http://www.mbari.org/science/upper-ocean-systems/chemical-sensor-group/periodic-table-of-elements-in-the-ocean. Accessed 18 Jan 2016

Kato C, Foriel J, Moynier F (2014) Isotopic study of gallium in terrestrial and meteoritic samples. In: 77th annual meeting of the Meteoritical Society, Abstract #5209

Lodders K (2003) Solar system abundances and condensation temperatures of the elements. Astrophys J 591:1220–1247

McDonough WF, Sun S-S (1995) The composition of the Earth. Chem Geol 120:223–253

Mittlefehldt DW, McCoy TJ, Goodrich CA, Kracher A (1998) Non-chondritic meteorites from asteroidal bodies. In: Papike JJ (ed) Planetary materials, Reviews in mineralogy, vol 36. 195 pp

Orians KJ, Bruland KW (1988) The marine geochemistry of dissolved gallium: a comparison with dissolved aluminum. Geochim Cosmochim Acta 52:2955–2962

Righter K, Campbell AJ, Humayun M (2005) Diffusion of trace elements in FeNi metal: applications to zoned metal grains in chondrites. Geochim Cosmochim Acta 69:3145–3158

Schulte RF, Foley NK (2013) Compilation of gallium resource data for bauxite deposits. US Geol Surv 004Fpen File Rep 2013–1272. https://pubs.usgs.gov/of/2013/1272/pdf/ofr2013-1272.pdf

Shiller AM, Frilot DM (1996) The geochemistry of gallium relative to aluminum in California streams. Geochim Cosmochim Acta 60:1323–1328

Wänke H, Palme H, Kruse H, Baddenhausen H, Cendales M, Dreibus G, Hofmeister H, Jagoutz E, Palme C, Spettel B, Thacker R (1976) Chemistry of lunar highland rocks: a refined evaluation of the composition of primary matter. Proc Lunar Sci Conf 7:3479–3499

Wasson JT, Kallemeyn GW (1988) Compositions of chondrites. Philos Trans R Soc Lond A 325:535–544

Wasson JT, Huber H, Malvin DJ (2007) Formation of IIAB iron meteorites. Geochim Cosmochim Acta 71:760–781

Yang S, Humayun M, Righter K, Jefferson G, Fields D, Irving AJ (2015) Siderophile and chalcophile element abundances in shergottites: implications for Martian core formation. Meteorit Planet Sci 50:691–714

Gas Chromatography–Mass Spectrometry (GC–MS)

Patricia M. Medeiros
Department of Marine Sciences, University of Georgia, Athens, GA, USA

Definition

Gas chromatography-mass spectrometry (GC-MS) is one of the so-called hyphenated analytical techniques. It is actually two techniques that are combined to form a single method for analyzing mixtures of organic chemicals. Gas chromatography separates the components of a mixture, and mass spectrometry characterizes each of the components individually. The combination of the two techniques allows for both qualitative and quantitative evaluations of a sample containing a number of organic compounds. The uses for GC-MS are numerous, including chemical, geological, environmental, and forensic research.

Introduction

Structure elucidation of organic compounds has been carried out by organic chemists since the early 1900s.

Chromatography is an analytical technique used to separate mixtures of chemicals into individual components, and it was first employed in the separation of plant pigments (chlorophyll, carotenes, and xanthophylls) in 1901 (Ettre 2001). Chromatographic methods evolved, especially in the mid-twentieth century with the development of new techniques.

Gas chromatography (GC) was first described in 1952 with the separation of a mixture of small carboxylic acids (James and Martin 1952). A gas chromatograph uses a flow-through column, through which different chemical constituents of a sample pass in a gas stream (carrier gas, *mobile phase*) at different rates depending on their chemical and physical properties and their interaction with a specific column filling, called the *stationary phase*. The function of the stationary phase in the column is to separate different components, causing each one to exit the column at a different time. Other parameters that can be used to alter the time of retention are the carrier gas flow rate, column length, and temperature. At first, packed-columns were used; however, the power of GC was substantially improved by the introduction of wall-coated open-tubular capillary columns, initially glass but superseded by more durable fused-silica capillary columns in 1976. This was considered a major advance in the development of GC (Niessen 2001). As the chemicals exit the column, they are detected electronically.

Mass spectrometry (MS) is an analytical technique used to identify and quantify different chemicals present in a sample by measuring the mass-to-charge ratio and abundance of gas-phase ions. The history of mass spectrometry started in 1912 when the first mass spectra of compounds, such as Ne, N_2, CO_2, and $COCl_2$, were obtained (Thomson 1913). The first commercial instruments dedicated to organic analysis were built during World War II, with the major application at that time in petrochemistry (Niessen 2001).

In a typical MS procedure, a sample (solid, liquid, or gas) is ionized, for example by bombarding it with electrons (electron ionization – EI). This may cause some of the sample's molecules to break into charged fragments. These ions are then separated according to their mass-to-charge ratio, typically by accelerating and subjecting them to a magnetic or electric field or measuring the time taken to reach the detector: ions of the same mass-to-charge ratio will undergo the same amount of deflection. There are currently four main types of analyzers: magnetic sector, ion trap, quadrupole (Q), and time of flight (ToF), though these are often combined into tandem configurations such as a QToF. The mass resolution (accuracy to which masses can be separated) of the analyzer types varies, generally with quadrupoles being lowest, ion traps being intermediate, and ToF and magnetic sector being the highest (4 decimal place or better). The ions are detected by a mechanism capable of recognizing charged particles. The atoms or molecules in the sample can be identified by correlating theoretical masses to the identified masses or through a characteristic fragmentation pattern.

In 1958, the first online GC-MS instruments were introduced. In the early 1960s, the development of affordable and miniaturized computers has helped in the simplification of the use of this instrument, as well as allowed for great improvements in the amount of time it took to analyze a sample. The major breakthrough in GC-MS occurred in 1968 with the introduction of the first data-processing units. In 1981, fused-silica capillary columns were first applied for GC-MS, and today, it is the most widely used column in GC-MS analysis (Fig. 1a).

GC-MS Analysis

When GC is combined with MS, a powerful analytical tool is created. The instruments are coupled using a heated transfer line which the latter part of the column passes through and ends at the entrance to the MS ion source where compounds eluting from the column are converted to ions. Complex mixtures of chemicals may be separated, identified, and quantified. This makes it ideal for the analysis of the hundreds of relatively low molecular weight compounds found in environmental and biological materials. As a gas-phase separation method, GC requires the analytes to be volatilized prior to their separation. Therefore, in order for a compound to be analyzed by GC-MS, it must be sufficiently volatile and thermally stable. Samples are usually analyzed as organic solutions, consequently solid materials of interest (e.g., soils, sediments, tissues, etc.) need to be solvent-extracted and the extract subjected to "wet chemical" procedures (e.g., fractionation, concentration, derivatization) before GC-MS analysis. Thermal extraction and pyrolysis techniques for analyzing solid samples are also commonly used in geochemical analyses, and while more often utilized with GC-FID, they can also be coupled with GC-MS for characterization of the evolved organic fractions (e.g., Horsfield et al. 2015).

For liquid sample analysis, a known volume of the analyte is injected into a heated injector port commonly at 250–300 °C (GC inlet), usually using a microsyringe. A carrier gas (usually Helium) sweeps the vaporized analyte molecules through the column. Separation occurs by a combination of kinetic, physical, and chemical interactions with the stationary phase filling, resulting in the various components eluting at different times. The time at which each component reaches the outlet, the retention time (RT), is defined as the time from when the injection is made (time zero) to when elution occurs. As the instrument runs, a computer software generates a graph called *chromatogram* (Fig. 1b). The x-axis shows the RT, and the y-axis shows the intensity (abundance) of the signal.

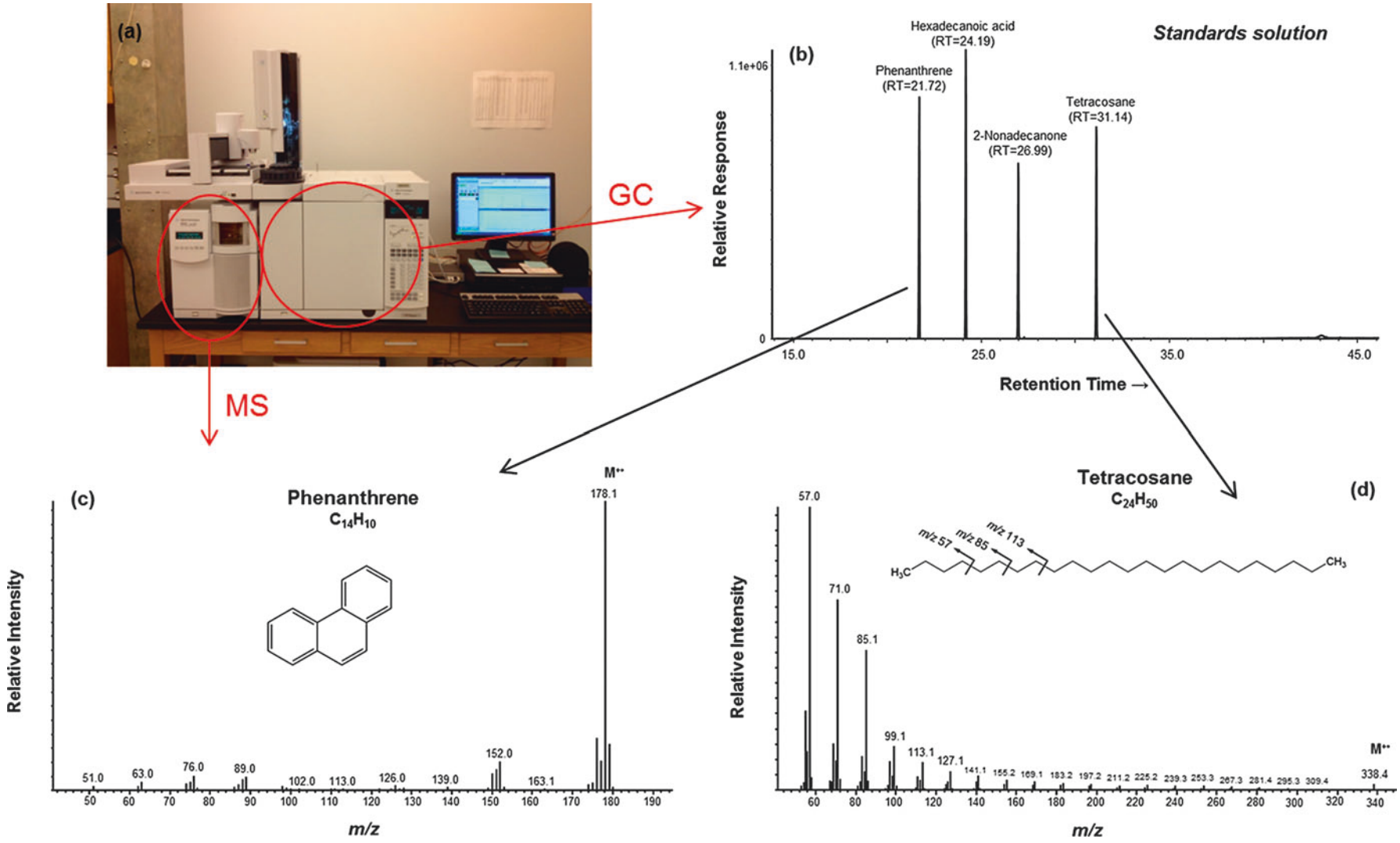

Gas Chromatography–Mass Spectrometry (GC–MS), Fig. 1 (**a**) GC-MS equipment in an environmental chemistry lab; **(b)** GC-MS data (chromatogram) for a standard solution containing phenanthrene ($C_{14}H_{10}$), hexadecanoic acid ($C_{16}H_{32}O_2$), 2-nonadecanone ($C_{19}H_{38}O$), and tetracosane ($C_{24}H_{50}$) with their respective retention times (RT); Mass spectra showing the molecular ion ($M^{+\cdot}$) and characteristic fragmentation patterns of **(c)** phenanthrene and **(d)** tetracosane. *m/z* = mass-to-charge ratio

The most frequently used methods for ion production are electron ionization (EI) and chemical ionization (CI). In geochemical applications, EI is primarily applied. A beam of electrons (e^-) at a known electron voltage (eV) ionizes the sample molecules resulting in the loss of one electron, producing a molecular ion represented by $M^{+\bullet}$ (a radical cation). Due to a large amount of energy imparted to the molecular ion, it usually fragments producing further smaller ions. The mass of the fragment divided by the charge is called mass-to-charge ratio (*m/z*). Since most fragments have charge of +1, the *m/z* usually represents the molecular mass of the fragment or the entire compound in the case of $M^{+\bullet}$.

Following ionization, the positively charged ions are accelerated into a mass analyzer (filter), which separates them according to their *m/z* ratios. After the ions are separated, they enter a detector where their outputs are amplified (by an electron multiplier or photomultiplier) to boost the signal. The detector sends information to a computer that records all of the data produced and converts the electrical impulses into visual displays called *mass spectrum* (Fig. 1c, d). In a mass spectrum, the x-axis represents the *m/z* ratios and the y-axis represents the signal intensity for each of the fragments detected. Because the mass spectrum produced by a given chemical at the same eV (most commonly 70 eV) is essentially the same every time and the fragmentation pattern is characteristic for that chemical, it represents the "fingerprint" for that molecular structure. This information may be then used to identify compounds of interest (often using library databases such as NIST or Wiley) and to help elucidate the structure of unknown components of mixtures. Quantification of individual compounds can be done by comparing the area of each identified peak on a given chromatogram to that of an internal standard, which is added in a known amount from a standard solution. Semiquantification can be conducted when internal standards are not present. The detection limits of GC-MS systems range from nanogram (10^{-9} g) to femtogram (10^{-15} g).

In a GC-MS, the collection of data can be performed in one of the two ways: full scan and selected ion monitoring (SIM). The full scan mode targets a broad range of mass fragments, typically from *m/z* 50 to *m/z* 600, and it is useful in determining unknown compounds in a sample. In contrast, SIM only monitors selected ions associated with a specific substance. This is a fast and efficient analysis, especially if the analyst has previous information about a sample or is only looking for a few specific substances.

GC-MS for Biomarker Elucidations

Structure elucidations of natural compounds by GC-MS were the major breakthrough in developing biomarker geochemistry, initially for petroleum exploration research and then for organic geochemistry in general. In geochemistry, biomarkers are defined as compounds derived from biological sources (i.e., plant, microbes, and animals) that retain some, if not all, of the structural characteristics of their parent precursor molecule after being preserved in the geological record or released into the environment. Hence, they can be traced back to their biological (natural) origin. Current instrumentation and derivatization methods extended the biomarker concept into other disciplines such as environmental, food, and forensic applications where natural as well as synthetic (anthropogenic) compounds are encountered.

Petroleum Exploration

In petroleum geochemistry, biomarkers or "molecular fossils" have had extensive applications as organic matter source, maturity, and alteration indicators. Whole oil screening by GC-MS is commonly undertaken to assess hydrocarbon distributions and identify samples for further more intensive geochemical investigations. Hydrocarbon profiles can be used to infer source matter, e.g., *Gloecapsomorpha prisca* in early Paleozoic oils through their distinctive odd over even *n*-alkane distributions (e.g., Reed et al. 1986; Fowler 1992), while the ratio of the isoprenoids pristane to phytane is used to infer redox conditions in the depositional environment, and the ratio of the polyaromatic hydrocarbon phenanthrene and its methyl homologues can be used as a maturity proxy (Peters et al. 2005). Due to the extremely complex nature of the biomarker distributions, the chromatographic separation can be problematic with many coelutions of diagnostic components, with tandem mass spectrometry (GC-MS/MS) being utilized for the greatest level in specificity.

Environmental Impacts and Forensic Applications

More recently, these compounds have been extensively utilized in fossil fuel pollution studies (e.g., Volkman et al. 1992; Aboul-Kassim and Simoneit 1996; Medeiros and Bícego 2004). Assessment of the environmental impact in the short- and long-term of crude oil spills such as the Exxon Valdez, MV Braer, Erika, and more recently the Deepwater Horizon relied greatly on the quantification of organic pollutants using GC-MS (e.g., Hostettler and Kvenvolden 1994; Webster et al. 1997; Rosenbauer et al. 2010; Natter et al. 2012; Babcock-Adams et al. 2017). GC-MS is also a key forensic tool in correlating sources of pollution to an incident. The Erika spill in 1999, for instance, was followed by many other oil tankers illegally cleaning their tanks at sea in the area. Through the use of GC-MS analyses, it was possible not only to differentiate numerous sources of residues in the region but also to accomplish the unambiguous correlation of residues from the Erika spill (Mazeas and Budzinski 2002).

Anthropogenic Impacts on Geological Matrices

Unfortunately for geochemical research anthropogenic contamination of geological samples, whether in the environment, during collection or in storages can overprint the indigenous biological compounds (e.g., Brocks 2011). Identification of these contaminants by GC-MS and subsequent methodologies for quantifying their pervasiveness allow more accurate determination and hence interpretation of original biomarkers from ancient materials (e.g., Brocks et al. 2008; John et al. 2017).

Paleoclimatology

Lipid biomarkers are compounds that can be traced to a particular biological source and, as such, provide numerous paleoecological and paleoclimatological proxies (Eglinton and Eglinton 2008). For example, higher plants produce high-molecular weight (C24–C36) *n*-alkanoic acids as part of their cuticular waxes, and these compounds can be preserved in sediments for thousands of years (Eglinton and Eglinton 2008; Bush and McInerney 2013). Measures such as average chain length (ACL) and carbon preference index (CPI) provide valuable information on past ecosystems, climates, and postdepositional processes (Bush and McInerney 2013). GC-MS analyses also provide a valuable screening tool prior to compound-specific isotope analysis (CSIA) of leaf wax compounds to ensure the fractionated extracts are of measurable concentration and free of coeluting compounds that could affect the isotopic value processes (Sachse et al. 2004).

Modern Environmental Studies

The application of biomarkers as tracers has been used extensively in determining sources, transport, and transformation products of organic matter in aquatic, soil, and atmospheric samples. For instance, higher plant biomarkers, such as diterpenoids and lignin phenols, have been used to trace terrestrial inputs in both coastal marine and open-ocean waters (Simoneit 1977; Goñi et al. 1997); phospholipid fatty acids (PLFA) patterns have become popular as a way of acquiring a view of the microbial community in soil samples (Medeiros et al. 2006b); biomass burning biomarkers such as levoglucosan, mannosan, and galactosan (decomposition products of burning of cellulose and hemicellulose) demonstrated their usefulness to be used as tracers of wildfires in the atmosphere (Simoneit et al. 1999; Medeiros et al. 2006a).

Conclusions

The coupling of GC and MS in the 1960s was a major development, first in the petrochemistry field and then for organic geochemistry in general. The elucidation of biomarkers allowed for their applications as molecular tracers for numerous processes in geological and environmental studies using natural and anthropogenic compounds. The number of novel compounds identified as well as the applications of biomarker tracers is expected to keep increasing. The utilities of GC-MS for contemporary interdisciplinary sciences will also continue to expand, especially as the analytical instrument capabilities develop further with increased sensitivities, ease of operation, lower maintenance, better separation technology, and improved ionization efficiencies. The current increasing use of related techniques such as GC-IRMS, GC × GC-MS, and GC-MS/MS is further advancing the utilization of hyphenated techniques.

Cross-References

- Analytical Techniques
- Biomarkers: Petroleum
- Compound-Specific Isotope Analysis
- High-Resolution Mass Spectrometry
- Hydrocarbons
- Lipids (Bacteria and Archaea)
- Marine Sediment
- Organic Geochemistry
- Organics: Sources and Depositional Environments
- Paleoclimatology
- Soils

References

Aboul-Kassim TAT, Simoneit BRT (1996) Lipid geochemistry of superficial sediments from the coastal environment of Egypt. I. Aliphatic hydrocarbons – characterization and sources. Mar Chem 54:135–158

Babcock-Adams L, Chanton JP, Joye SB, Medeiros PM (2017) Hydrocarbon composition and concentrations in the Gulf of Mexico sediments in the 3 years following the Macondo well blowout. Environ Pollut 229:329–338

Brocks JJ (2011) Millimeter-scale concentration gradients of hydrocarbons in Archean shales: live-oil escape or fingerprint of contamination? Geochim Cosmochim Acta 75:3196–3213

Brocks JJ, Grosjean E, Logan GA (2008) Assessing biomarker syngeneity using branched alkanes with quaternary carbon (BAQCs) and other plastic contaminants. Geochim Cosmochim Acta 72:871–888

Bush RT, McInerney FA (2013) Leaf wax *n*-alkane distributions in and across modern plants: implications for paleoecology and chemotaxonomy. Geochim Cosmochim Acta 117:161–179

Eglinton TI, Eglinton G (2008) Molecular proxies for paleoclimatology. Earth Planet Sci Lett 275(1–2):1–16

Ettre LS (2001) The predawn of paper chromatography. Chromatographia 54:409–414

Fowler MG (1992) The influence of *Gloecapsomorpha prisca* on the organic geochemistry of oils and organic-rich rocks of late Ordovician age from Canada. In: Schidlowski M, Golubic S, Kimberley MK, McKirdy DM, Trudinger PA (eds) Early organic evolution: implications for mineral and energy resources. Springer, Berlin, pp 336–356

Goñi MA, Ruttenberg KC, Eglinton TI (1997) Sources and contribution of terrigenous organic carbon to surface sediments in the Gulf of Mexico. Nature 389:275–278
Horsfield B, Leistner F, Hall K (2015) Microscale sealed vessel pyrolysis. In: Grice K (ed) Principles and practice of analytical techniques in geosciences. Royal Society of Chemistry, Oxfordshire, UK
Hostettler FD, Kvenvolden KA (1994) Geochemical changes in crude oil spilled from the Exxon Valdez supertanker into Prince William sound, Alaska. Org Geochem 21:927–936
James AT, Martin AJ (1952) Gas-liquid partition chromatography: the separation and micro- estimation of volatile fatty acids from formic acid to dodecanoic acid. Biochem J 50:679–690
John DL, Medeiros PM, Babcock-Adams L, Walker SE (2017) Cambrian trilobites as archives for Anthropocene biomarkers and other chemical compounds. Anthropocene 17:99–106
Mazeas L, Budzinski H (2002) Molecular and stable carbon isotopic source identification of oil residues and oiled bird feathers sampled along the Atlantic coast of France after the Erika oil spill. Environ Sci Technol 36:130–137
Medeiros PM, Bícego MC (2004) Investigation of natural and anthropogenic hydrocarbon inputs in sediments using geochemical markers. I. Santos, Brazil. Mar Pollut Bull 49:761–769
Medeiros PM, Conte MH, Weber JC, Simoneit BRT (2006a) Sugars as source indicators of biogenic organic carbon in aerosols collected above the Howland experimental Forest, Maine. Atmos Environ 40:1694–1705
Medeiros PM, Fernandes MF, Dick RP, Simoneit BRT (2006b) Seasonal variations in sugar contents and microbial community in a ryegrass soil. Chemosphere 65:832–839
Natter M, Keevan J, Wang Y, Keimowitz AR, Okeke BC, Son A, Lee M-K (2012) Level and degradation of deepwater horizon spilled oil in coastal marsh sediments and pore water. Environ Sci Technol 46:5744–5755
Niessen WMA (2001) Principles and instrumentation of gas chromatography-mass spectrometry. In: Current practice of gas chromatography-mass spectrometry, Chromatography science series, vol 86. Marcel Dekker, New York, pp 1–30
Peters KE, Walters CC, Moldowan JM (2005) The biomarker guide. Volume 1, Cambridge University Press, Cambridge, 471 p
Reed JD, Illich HA, Horsfield B (1986) Biochemical evolutionary significance of Ordovician oils and their sources. Org Geochem 10:347–358
Rosenbauer RJ, Campbell PL, Lam A, Lorenson TD, Hostettler FD, Thomas B, Wong FL (2010) Reconnaissance of Macondo-1 well oil sediment and tarballs from the northern Gulf of Mexico shoreline, Texas to Florida. USGS – A preliminary report to the U.S. Coast Guard, 22 p
Sachse D, Radke J, Gleixner G (2004) Hydrogen isotope ratios of recent lacustrine sedimentary *n*-alkanes record modern climate variability. Geochim Cosmochim Acta 68(23):4877–4889
Simoneit BRT (1977) Diterpenoid compounds and other lipids in deep-sea sediments and their geochemical significance. Geochim CosmochimActa 41:463–476
Simoneit BRT, Schauer JJ, Nolte CG, Oros DR, Elias VO, Fraser MP, Rogge WF, Cass GR (1999) Levoglucosan, a tracer for cellulose in biomass burning and atmospheric particles. Atmos Environ 33:173–182
Thomson JJ (1913) Rays of positive electricity and their application to chemical analysis. Longman's Green, London
Volkman JK, Holdworth DG, Neill GP, Bavor HJ Jr (1992) Identification of natural, anthropogenic and petroleum hydrocarbons in aquatic sediments. Sci Total Environ 112:203–219
Webster L, Angus L, Topping G, Dalgarno EJ, Moffat CF (1997) Long-term monitoring of polycyclic aromatic hydrocarbons in mussels (*Mytilus edulis*) following the Braer oil spill. Analyst 122:1491–1495

Gas Hydrates

Rajnish Kumar[1] and Praveen Linga[2]
[1]Department of Chemical Engineering, Indian Institute of Technology, Chennai, India
[2]Department of Chemical and Biomolecular Engineering, National University of Singapore, Singapore, Singapore

Definition

Gas hydrates are nonstoichiometric crystalline compounds in which hydrogen-bonded water molecules (host) create cavities that enclose a gaseous molecule or low molecular weight hydrocarbon (guest). The guest molecule inside the cavities rotates freely as there is no chemical bonding between the host water molecules and the enclosed guest molecule. Unlike crystalline ice which exists below 0 °C, solid crystals of gas hydrate are stable above or below 0 °C. Methane (CH_4) is the most common guest molecule. Methane hydrates are found in many subsea and permafrost regions on earth. Methane hydrates represent a highly concentrated form of methane; a cubic meter of methane hydrate may contain as much as 170 m^3 of methane at standard temperature-pressure condition along with 0.84 m^3 of (potable) water. An estimated 99% of worldwide gas hydrate occurs in ocean (marine) sediments at water depths ranging from 300 m to greater that 2500 m. Key challenges in exploiting this resource are locating gas hydrate reservoirs, obtaining extensive reservoir mapping and developing viable (safe and economical) production strategies for eventual natural gas production.

Introduction

The proven hydrocarbon reserves are roughly 235,000 million tons of oil and 200 trillion cubic meters of natural gas (BP 2013). Global oil production data show that crude oil production from the existing fields has already peaked and will decline significantly in years to come. At the current level of consumption, these reserves are sufficient to meet more than 50 years of global production of oil and natural gas. Coal as a fossil fuel is undesirable in CO_2 constrained world. Natural gas is the cleanest burning fossil fuel and there is an increasing effort to locate their existence in nature for exploitation. As a result, a new solid component of gas and water has emerged in the field of unconventional energy sources and is known as clathrate of natural gas commonly called as gas hydrate (Makogon 1965; Buffett 2000).

Estimates of gas hydrate deposits vary over several orders of magnitude but the energy contained in the gas hydrate accumulations is believed to be more than that of all the fossil

fuels combined (Makogon et al. 2007). The promise of this untapped energy source is such that it is prompting many governments and industry groups to set up national gas hydrate programs with countries like the USA, Japan, India, China, and Korea largely in the mix. Most of these countries may not have conventional resources of natural gas and for these economies, investing on natural gas hydrate "resources estimation" and "production" is a key strategy.

This article discusses the origin and distribution of gas hydrate deposits around the world, takes a look at the geochemical aspects and some of the early hydrate studies working toward the development and production of gas from gas hydrate deposits. A brief discussion on natural destabilization of natural gas hydrate is also given.

Structure and Characteristics of Gas Hydrates

Entrapment of guest molecules, such as methane or carbon dioxide by hydrogen-bonded water molecules at subambient temperature and moderate pressure, produces solid crystalline gas hydrates which physically resemble ice. Gas hydrates belong to a class of compounds known as clathrates (Davidson 1973; Englezos 1993; Sloan and Koh 2008). These are caged structures with varying sizes which further recombine to produce well-defined unit crystals as shown in Fig. 1.

Three most common structures, which have been found in nature and synthesized in laboratory setup at suitable conditions, are Structures I and II, which bear cubic symmetry and structure H which is hexagonal. Structure I typically forms by small gaseous guests molecules like CO_2, CH_4 (molecular diameter roughly 0.4–0.5 nm). Structure II type hydrates are formed by relatively larger gases or lower hydrocarbon liquids (molecular diameter roughly 0.5–0.7 nm) with water and are observed generally in areas of active hydrocarbon flux (deep-sea seeps). Structure II type hydrates are also formed by smaller gaseous molecules like H_2 and N_2 (molecular diameter roughly 0.3–0.4 nm) though at slightly higher pressure (Davidson et al. 1984). Larger hydrocarbon molecules which are too big to fit into the large cages of Structure II hydrates form Structure H type hydrates, however, not without the help of a gaseous molecule which by itself may form Structure I type hydrate. Figure 1 shows in detail the different type of cages formed for each structure, the respective number of cages per unit structure, and the number of water molecules needed for unit structure of each.

Gas Hydrate Resources

Ingredients for hydrate formation, water (host), and natural gas (guest) along with right pressure and temperature are simultaneously required for hydrate formation. Thus, unlike conventional natural gas resources, gas hydrate only occurs in sediments which exist at a suitable pressure and temperature conditions. However, gas hydrate deposits may not be always present within the gas hydrate stability zone. The key limiting factor in gas hydrate formation in most locations is the lack of adequate amounts of gas and in some cases a relative shortage of free water in sediments which limits gas hydrate formation. More than 99% of the hydrocarbon gases present in the natural hydrates are methane. Carbon isotopic compositions of methane from natural gas hydrate samples have

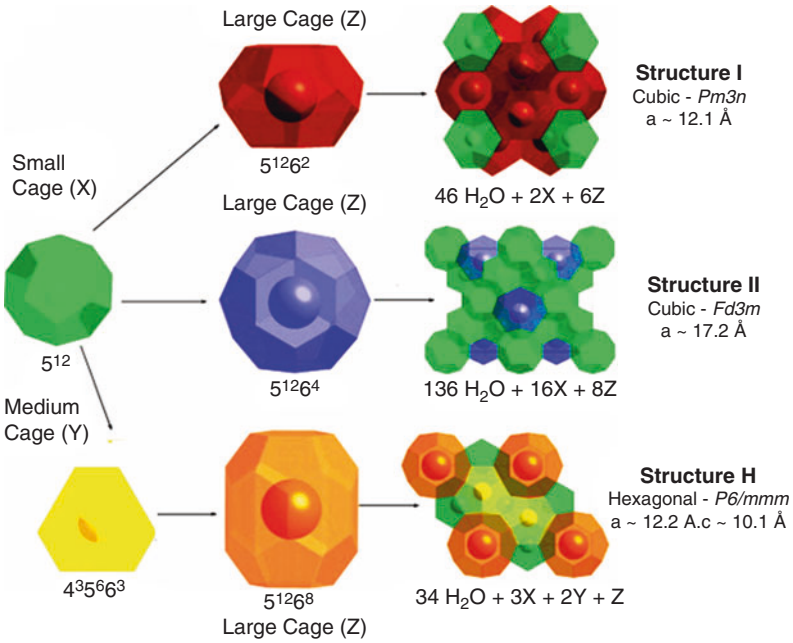

Gas Hydrates, Fig. 1 Three common clathrate hydrate structures, including the constituent cavities (Adapted from Strobel et al. 2009)

conclusively proved that source of methane in the subsea environment is microbial degradation of organic matters as methane is the only hydrocarbon generated in significant amounts. It is estimated that about 98–99% of the world's gas hydrates are concentrated within marine sediments and the rest beneath permafrost. Figure 2 shows the distribution of gas hydrate confirmed occurrences (marked with star) where hydrates were directly identified by taking out hydrate samples from the sea bed or it was inferred based on indirect measurement techniques discussed in the next section.

Moridis and Collett (2004) proposed a classification system for potential reservoirs. It does not distinguish between permafrost and marine gas hydrates, focusing instead on the association with mobile gas/fluids and concentration of the deposits. Classes 1–3 assume that the gas hydrate is contained with host sediment of high reservoir quality (sand-rich). Class 4 generally equates to gas hydrate within marine muds.

Class 1: Highly saturated deposits at the base of gas hydrate stability and underlain by free gas
Class 2: Deposits overlying a zone of mobile fluids
Class 3: Gas hydrate bearing layer with no mobile fluid above or below
Class 4: Generally marine deposits that are poorly saturated and for which there are no apparent lateral or vertical seals

Boswell and Collett (2006) suggested a distribution of natural gas hydrates based on the lithology of the host sediment. The pyramid shaped representation serves a dual purpose; it not only gives the quantity of such resource it also estimates the quality of these resources in terms of its ease of exploitation and commercialization. Boswell and Collett (2011) suggests that 10^5 TCF as an order of magnitude estimate of potential resources within resource grade deposits in marine settings. In comparison, the gross estimate for proven free natural gas is roughly 7×10^3 TCF (Fig. 3).

Locating Gas Hydrate Zones

Locating gas hydrate deposits has always been a major challenge; Bottom Simulating Reflector (BSR) was initially the primary tool in locating the presence of gas hydrates. BSRs are indicators of the base of the stability zone for a GHD (Gas Hydrate Deposit). However, gas hydrates have been sampled in many places even without the presence of a BSR. Inferences can also be made regarding the distribution and concentration of gas hydrates by systematic analysis of seismic data. Exploration approaches that integrates geological and geophysical methods and that focus on direct indicators of concentrated gas hydrate occurrence such as strong amplitude anomalies and intervals of increased velocity have shown great promise worldwide (Saeki et al. 2008; Boswell et al. 2016). 3D seismic data along with data from borehole logs have been used to outline the extent of GHDs in various places such as the Japanese and the Indian margins (Collett et al. 2009).

Production of Methane from Gas Hydrates

Exploitation of natural gas (or methane) from marine gas hydrate is quite different from the conventional gas production. Gas production from hydrate deposits goes through a

Gas Hydrates, Fig. 2 Global Map of Gas Hydrate occurrence as inferred from direct sampling or geophysical surveys (Map is a copyright of Encyclopedia Britannica, Inc.)

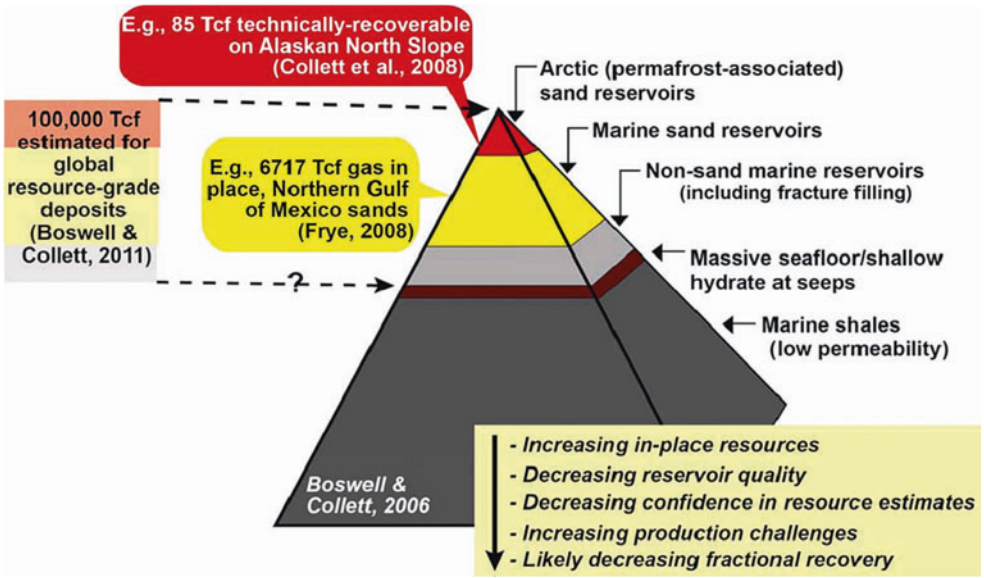

Gas Hydrates, Fig. 3 Gas hydrate resource pyramid (Adapted from Boswell and Collett 2006)

phase change from solid hydrate to liquid water and gaseous methane. Furthermore, hydrates being a crystalline solid releases a significant amount of energy during its formation and requires a sustained supply of energy during dissociation. Coupled with the mass transfer limitations, this becomes a multiphase heat and mass transfer controlled process which requires significant understanding at lab scale and pilot scale from the process engineering point of view. Existing technology employed in conventional oil and gas fields along with recent understanding from fracking of shale oil is a good starting point to identify the right tools and processes required for energy production from gas hydrate deposits. Production of natural gas from marine hydrate deposits are even more complicated compared to permafrost deposits.

Figure 4 explains the possible production scenario through simplified schematic. In essence, the three methods shown are thermal stimulation (supply of heat to dissociate hydrates), depressurization (reduction of pressure to dissociate the hydrates), and the injection of chemicals (shift the thermodynamic stability to dissociate hydrates). There is a body of work that summarizes the production strategies, challenges, production models, economics, and feasibility of production of energy from hydrates (Moridis et al. 2009, 2011; Chong et al. 2016; Yin et al. 2016).

An alternative approach similar to chemical injection is to inject a greenhouse gas like CO_2 into hydrate sediments; with this approach CH_4 gas could be extracted without coproduction of water. An added advantage of one such approach is that CO_2 would be sequestered as gas hydrate. It is a well-known fact that the thermodynamic condition for stable CO_2 hydrate is milder than that of methane hydrate. Methane recovery from hydrates through this approach has been studied at lab scale, bench scale, and pilot scale. A field trial has also been done by ConocoPhillips; however from the geochemist view point following questions still remains

1. Can CO_2 alone replace methane form large as well as small cages?
2. Can 100% methane be recovered from one such approach, if not? How to maximize methane recovery at the shortest possible time?
3. How do we ensure diffusion of CO_2 in the solid hydrate and enhance the kinetics of replacement?
4. Will the left-over hydrate would be as stable as pure methane hydrate? In other words, can CO_2 be sequestrated in an environmentally sustainable manner? This aspect is essential to safeguard the future emission of these greenhouse gases.

Challenges Faced During Extraction of Methane (Field Trials)

There is still a long way to go before commercial production from gas hydrates becomes a reality. Recovery factor and technoeconomic deliberations will be the key to successfully commercializing gas production from gas hydrates. A number of field trials have already been carried out across the world in order to validate the proof of concept of production of gas from gas hydrates. There are several challenges that have arisen from these field studies and these issues need to be addressed before we can move on from "methane hydrate resources" to "methane reserves."

In Mallik Production Research Program, a 6-day production test successfully demonstrated the proof of concept of producing gas from gas hydrates using the depressurization

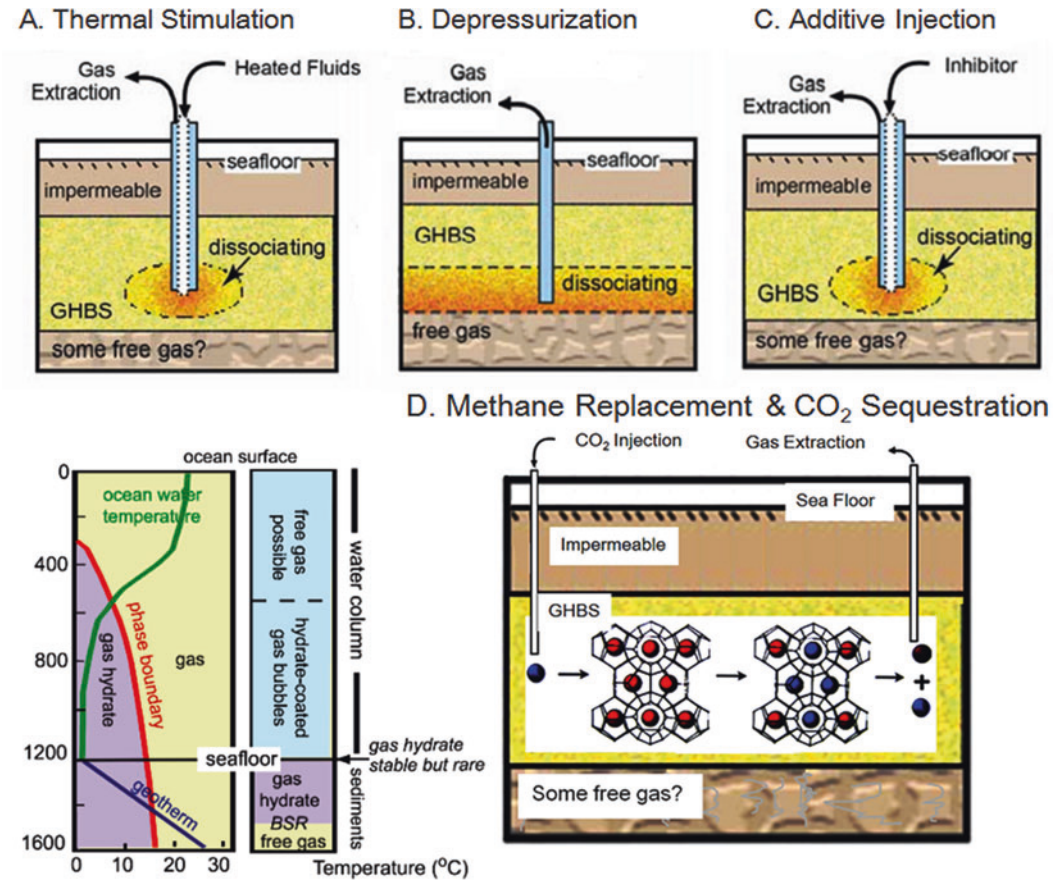

Gas Hydrates, Fig. 4 Different methods for producing gas from gas hydrates (Adapted from Ruppel 2007, 2011)

method. One of the achievements was to successfully maintain a sustained gas flow rates (2000–4000 m^3/day) throughout the course of the program. However, handling of sand during gas production was the biggest bottleneck which culminated in an abrupt halt in gas production. Thus, long production test could not be achieved. During the Nankai trough field trial by Japan, some of these problems were handled with better mechanical designs.

The contribution of gas hydrates to global warming and the greenhouse effect has become a major societal concern. However, natural destabilization (not due to human intervention) of gas hydrate is not a great concern as these hydrates have existed for millions of years. Moreover, there can't be a runaway effect as hydrate dissociation is an endothermic process. So-called global warming induced by either human interference or otherwise may gradually allow these hydrates to dissociate, released methane may further contribute to global warming. Zander et al. (2017) give a detailed discussion on the hazards of gas hydrate exploitation. There is a need to look at techniques for the production of gas from gas hydrates which avoid reservoir subsidence. One such technique which is being widely looked at the moment is the methane release via substitution of CO_2. This process, if found suitable, may also alleviate the excess production of sand and water as encountered during the field trial runs via depressurization. This process of methane replacement by CO_2 injection was pilot tested in the Iġnik Sikumi Field by Conoco Phillips in the Prudhoe Bay area of Alaska in 2012 (Boswell et al. 2017).

Current Status of Natural Gas Hydrate Exploitation

There have been some major developments in the area of gas hydrates research in the last few years with some countries successfully managing to extract a steady stream of gas from natural gas hydrate deposits. In 2012, the DOE in partnership with Conoco Phillips conducted an expedition in the Prudhoe Bay region of Alaska. They used the CO_2 injection method to ensure a steady stream of gas output. However, if the recovered methane was actually due to CO_2 replacement or due to thermal stimulation is still a big question.

In order to prove the feasibility of the depressurization method to extract methane from gas water hydrates at the subsea level, Japan Oil, Gas, and Metals National Corporation

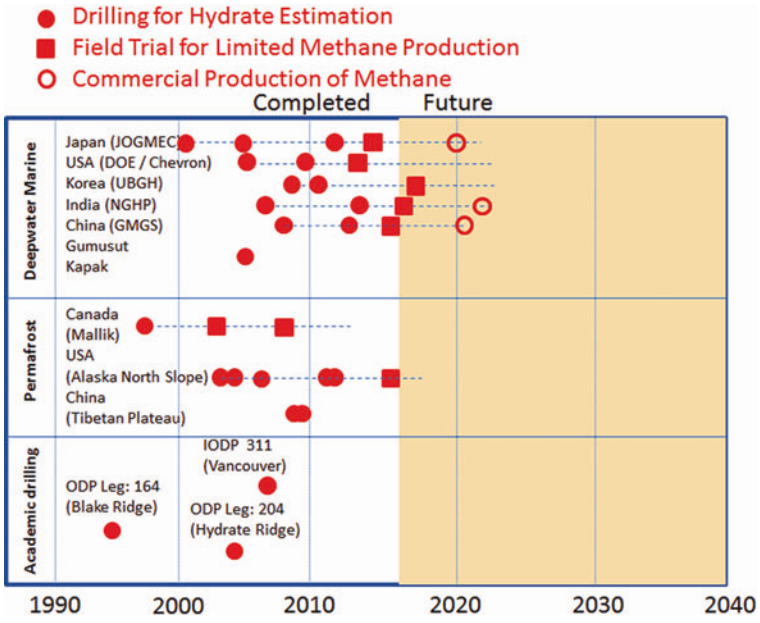

Gas Hydrates, Fig. 5 Natural gas hydrates research, development, and exploitation; past, present, and future (Based on the data available from the US Geological Survey)

(JOGMEC) conducted its first offshore methane hydrate production test off the coast of Honshu Island in March, 2013. JOGMEC succeeded in producing methane gas from the hydrate bearing sediments on March 12, 2013, after lowering the bottom hole pressure in the production well from 13.5 MPa to 4.5 MPa. Approximately, 120,000 cubic meters of gas was produced when production was stopped due to an increase in sand production. More recently China from a production site southeast of Hong Kong have extracted 230,000 cubic meters of methane in a month long trial.

Figure 5 shows the road map of proper exploitation of gas hydrate resource. The targets for next 5 years and beyond that can be identified as

- Drilling and identification of deep-water gas hydrate deposits for methane recovery by countries currently not active.
- More deep-water and permafrost field trials. One field trial each from China and Japan has just been concluded in the year 2017. India, China, and Japan are poised to do multiple field trials in next 5 years.
- Large-scale experimentation in the CO_2 injection method for extracting methane from gas hydrates.
- Small-scale production of methane from gas hydrates in order to meet local demands in remote areas such as the Alaskan North Slope (Ruppel 2011).

Summary and Conclusions

Natural gas hydrates are potentially one of the largest sources of unconventional natural gas,Gas hydrates which is the cleanest burning fossil fuel on earth. Given the widespread geographical distribution, production of methane from natural gas hydrates is going to be on potential options for curtailing the anthropogenic source of CO_2 in the atmosphere. Apart from the extraction of methane from the vast hydrate resource, potentially huge amount of CO_2 can be sequestered in an environmentally sustainable manner. However, there is a need for further laboratory and field tests, which employ better technologies to overcome some of the known problems and maintain continuous production over a sustained longer duration of time.

Cross-References

- ▶ Anthropogenic CO_2
- ▶ Carbon Cycle
- ▶ Carbon Isotopes
- ▶ Crystal Chemistry
- ▶ Geochemical Thermodynamics
- ▶ Hydrocarbons
- ▶ Kinetics of Geochemical Processes
- ▶ Natural Gas
- ▶ Organic Geochemistry

References

Boswell R, Collett TS (2006) The gas hydrates resource pyramid. Fire in the ice, vol 6(3). US Department of Energy, Office of Fossil Energy, National Energy Technology Laboratory, pp 5–7. https://www.netl.doe.gov/File%20Library/Research/Oil-Gas/methane%20hydrates/HMNewsFall06.pdf

Boswell R, Collett TS (2011) Current perspectives on gas hydrate resources. Energy Environ Sci 4:1206–1215

Boswell R, Bünz S, Collett TS, Frye M, Fujii T, McConnell D, Meinert J, Pecher I, Reichel T, Ryu BJ, Shelander D, Shin KS (2016) Introduction to special section: exploration and characterization of gas hydrates. Interpretation 4(1):SAi–SAii. https://doi.org/10.1190/INT-2016-0103-SPSEINTRO.1
Boswell R, Schoderbek D, Collett TS, Ohtsuki S, White M, Anderson BJ (2017) The Iġnik Sikumi field experiment, Alaska North Slope: design, operations, and implications for CO_2–CH_4 exchange in gas hydrate reservoirs. Energy Fuel 31(1):140–153
British Petroleum (2013, June) BP statistical review of world energy. Retrieved from http://www.rrojasdatabank.info/bpworld2013.pdf
Buffett BA (2000) Clathrate hydrates. Annu Rev Earth Planet Sci 28:477–507
Chong ZR, Yang SHB, Babu P, Linga P, Li XS (2016) Review of natural gas hydrates as an energy resource: prospects and challenges. Appl Energy 162:1633–1652
Collett TS, Johnson AH, Knapp CC, Boswell R (2009) Natural gas hydrates: a review. AAPG Spec Vol. https://doi.org/10.1306/13201101M891602
Davidson DW (1973) Clathrate hydrates. In: Water in crystalline hydrates aqueous solutions of simple nonelectrolytes. Springer, New York, pp 115–234
Davidson DW, Handa YP, Ratcliffe CI, Tse JS, Powell BM (1984) The ability of small molecules to form clathrate hydrates of structure I. Nature 311:142–143
Englezos P (1993) Clathrate hydrates. Ind Eng Chem Res 32:1251–1274
Makogon YF (1965) A gas hydrate formation in the gas saturated layers under low temperature. Gazov Promst 5:14–15
Makogon YF, Holditch SA, Makogon TY (2007) Natural gas-hydrates – a potential energy source for the 21st century. J Pet Sci Eng 56:14–31
Moridis GJ, Collett TS (2004) Strategies for gas production from hydrate accumulations under various geologic conditions. Report LBNL-52568. Lawrence Berkeley National Laboratory, Berkeley
Moridis GJ, Collett TS, Boswell R, Kurihara M, Reagan M, Koh CA, Sloan ED (2009) Toward production from gas hydrates: current status, assessment of resources, and simulation-based evaluation of technology and potential. SPE Reserv Eval Eng 12(5):745–771
Moridis GJ, Collett TS, Pooladi-Darvish M, Hancock S, Santamarina C, Boswell R, Kneafsey T, Rutqvist J, Kowalsky MB, Reagan MT, Sloan ED, Sum AK, Koh CA (2011) Challenges, uncertainties, and issues facing gas production from gas-hydrate deposits. SPE Reserv Eval Eng 14(1):76–112
Ruppel C (2007) Tapping methane hydrates for unconventional natural gas. Elements. https://doi.org/10.2113/gselements.3.3.193
Ruppel C (2011) Methane hydrates and the future of natural gas. MITEI natural gas report, supplementary paper on methane hydrates, 4. http://publications.iodp.org/proceedings/311/
Saeki T, Fujii T, Inamori T, Kobayashi T, Hayashi M, Nagakubo S, Takano O (2008) Extraction of methane hydrate concentrated zone for resource assessment in the Eastern Nankai Trough, Japan. Offshore Technol Conf. https://doi.org/10.4043/19311-MS
Sloan ED Jr, Koh CA (2008) Clathrate hydrates of the natural gases, 3rd edn. CRC Press, Boca Raton
Strobel TA, Hester KC, Koh CA, Sum AK, Sloan ED (2009) Properties of the clathrates of hydrogen and developments in their applicability for hydrogen storage. Chem Phys Lett 478(4):97–109
Yin Z, Chong ZR, Tan HK, Linga P (2016) Review of gas hydrates dissociation kinetic models for energy recovery. J Nat Gas Sci Eng 35:1362–1387
Zander T, Choi JC, Vanneste M, Berndt C, Dannowski A, Carlton B, Bialas J (2017) Potential impacts of gas hydrate exploitation on slope stability in the Danube deep-sea fan, Black Sea. Mar Pet Geol. https://doi.org/10.1016/j.marpetgeo.2017.08.010. In press

Gas Source Mass Spectrometry (GS-MS)

Masahiko Honda[1] and Allan R. Chivas[2,3]
[1]Research School of Earth Sciences, The Australian National University, Canberra, ACT, Australia
[2]GeoQuEST Research Centre, School of Earth and Environmental Sciences, University of Wollongong, Wollongong, NSW, Australia
[3]Department of Earth Sciences, University of Adelaide, Adelaide, SA, Australia

Synonyms

Electron bombardment mass spectrometry; Electron impact mass spectrometry

Definition

Gas source mass spectrometry (GS–MS) is the technique and instrumentation used to measure elemental and isotopic compositions of particular elements; these principally include light-element stable isotopes (H, C, N, O, and S) and noble gases (or rare gases) (He, Ne, Ar, Kr, and Xe). GS-MS instrumentation is composed of (1) an ion source for ionizing these gases, (2) an analyzer for separating ions on the basis of the ratio of ionized mass (m) to charge (z), and (3) a detector for counting ions. Figure 1 presents a typical mass spectrometer dedicated for the analyses of stable isotopes.

Introduction

To ionize these elements or gaseous compounds containing elements of interest for isotope analyses, Nier (1947) designed an electron bombardment-type ionization source. A similar type of ion source is still used in modern instruments. As shown in Fig. 2, gases are positively ionized in an ion box (or chamber; the ion source) by thermal electrons, with typical electron energies of 70–100 eV emitted from a hot tungsten (in some cases rhenium) filament, under vacuum ($<10^{-5}$ Pa). To improve ionization efficiencies, source magnets with a few hundred gauss are applied. A repeller plate is used to control the gradient of electrons/ions within the ion box to maximize ionization processes. A range of several kilovolts, relative to a zero plate, is applied to an ion box to accelerate ions produced inside the ion box. Half plates are used as a lens to converge and to extract ions.

For GS-MS, a magnetic sector mass analyzer is commonly utilized. In some cases a quadrupole mass analyzer and/or a time of flight (TOF) mass analyzer are used. For a magnetic sector mass analyzer, ions produced inside the ion box with

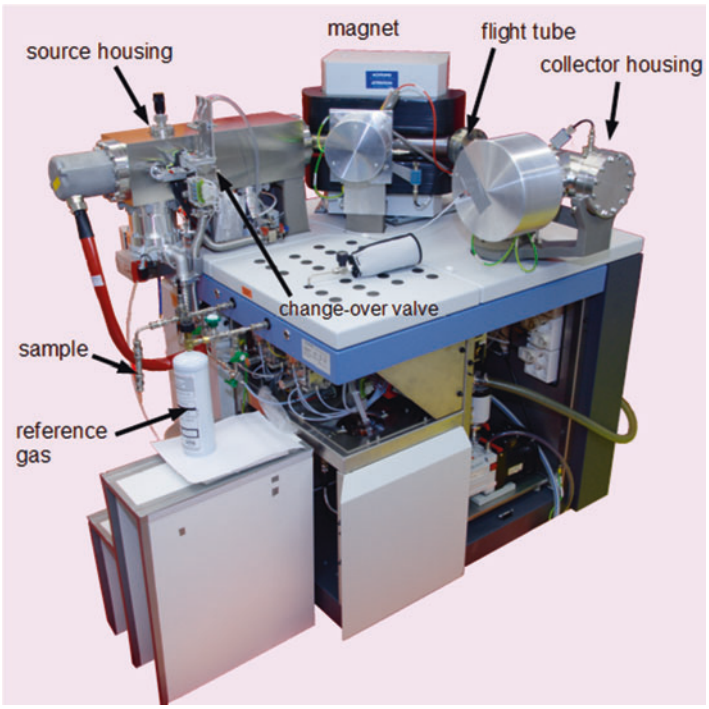

Gas Source Mass Spectrometry (GS-MS), Fig. 1 A stable isotope mass spectrometer (Thermo Scientific MAT 253) at the University of Wollongong. This instrument is configured with a dual inlet (note the position of the sample gas and a reference gas). Some features are not evident in the photograph. For example, the collector housing contains six Faraday collectors set to m/z of 44, 45, 46, 47, 48, and 49 to perform clumped-isotope analyses of prepared CO_2. The capillaries above the change-over valve are electropolished nickel. For scale, the benchtop is 0.87 × 1.04 m

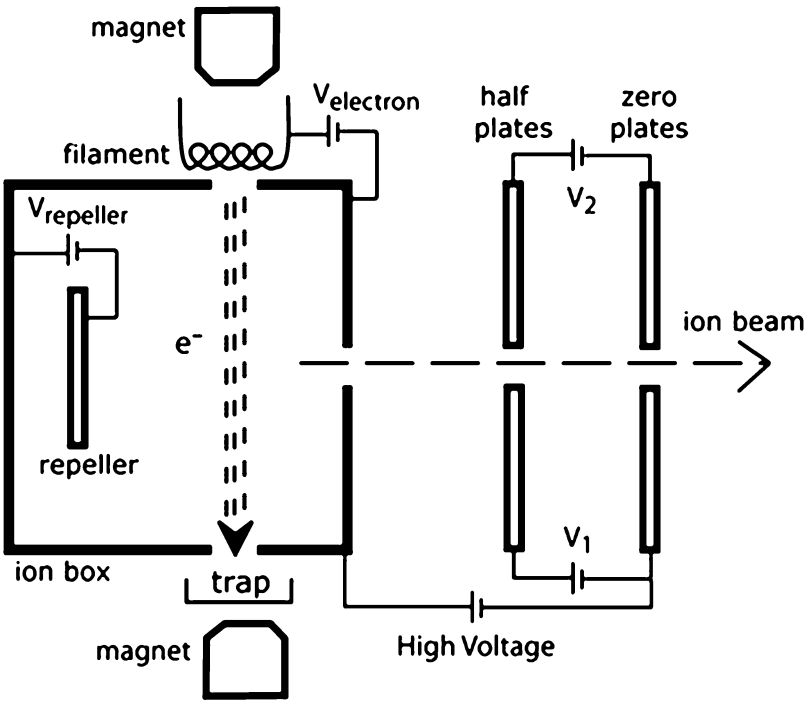

Gas Source Mass Spectrometry (GS-MS), Fig. 2 Nier-type electron ionization source for stable isotopes and noble gases (from Mabry et al. 2012). As an approximate scale, the length of the ion box, in various instruments, is commonly about 3 cm

certain kinetic energy, determined by acceleration voltage, travel along a flight tube and enter into a uniform magnetic field (normally a few thousand gauss) where ions (m/z) are deflected by the magnetic field (named as Lorentz force), which is balanced with the centrifugal force. As a function of magnetic field strength and accelerating voltage, the ions with a certain m/z will have a unique trajectory, and ions having different m/z are separated from each other, and arrive at respective focal points. When the ion beam is high ($>10^{-13}$amp), a Faraday cup is used to directly detect ion current using the Faraday amplifier with feedback resistors of $10^{11,\ 12,\ \text{or}\ 13}$ Ω. With a 10^{13} Ω Faraday amplifier a background of 10^{-18} amp can be obtained. When the ion beam is expected to be even lower, a secondary electron multiplier is used. Combining with an ion-pulse counting method, ion beams as low as 10^{-20} amp can be detected.

Stable Isotope Mass Spectrometry

In stable isotope geochemistry (q.v.), GS-MS is appropriate to the isotopic analysis of hydrogen (using H_2 as the analyte or working gas), carbon and oxygen (as CO_2), nitrogen (as N_2), sulfur (as SO_2 or SF_6), and less commonly to Cl (as CH_3Cl), silicon (as SiF_4), Se (as SeF_6), and Br (as CH_3Br). The isotopic ratios of the latter three elements may also be measured by other techniques, such as multicollector inductively coupled plasma mass spectrometry (MC-ICP-MS). A good reference to all aspects of the field of stable isotope geochemistry is the monograph by Hoefs (2015), and Brand (2004) describes the principles and practice of mass spectrometry.

Accordingly, much of the effort in conventional stable isotope analysis is concerned with producing appropriate pure and isotopically unfractionated working gases from geological materials. Modern systems include online preparation accessories attached directly to the mass spectrometer inlet, so that gas production, extraction, and purification and mass spectrometry are integrated and fully automated. There are many individually different gas-extraction protocols, for samples of water, air, organic matter, carbonates, silicates, phosphates, sulfates, sulfides; some procedures remain difficult to automate and involve extensive wet chemical preparation offline, that is, well away from the mass spectrometer.

Among the simplest and, probably most widespread procedure, remains the (now commonly automated) production of CO_2 from carbonate minerals using as little as 5–100 μg $CaCO_3$, by reaction with phosphoric acid (McCrea 1950), enabling the mass spectrometric analysis of both oxygen and carbon isotopes. Particularly small samples of gas may be liberated from spatially selected volumes within minerals by laser ablation heating and/or reaction within an evacuated cell.

The most commonly used inlet system to the mass spectrometer is a dual inlet (DI), where rapid cycling (alternating introduction) of a sample gas and a reference gas allows their comparison and provides highly precise analyses (to about 0.01 per mil of the normalized ratio between two or more isotopes of a given element). The sample and reference gas are introduced in individual geometrically matched stainless-steel capillaries of about a meter length and internal diameter of about 0.1 mm that cause each gas to enter the mass spectrometer under a viscous flow regime that precludes isotopic fractionation. The two capillaries are crimped so that these flows are balanced for both gases. The gases are usually pressure-balanced and then alternated through a change-over valve so that a uniform dynamic flow is maintained; at any time, one gas is entering the mass spectrometer source while the other is flowing to waste. The commonly determined ratios are $^{2}H/^{1}H$, $^{13}C/^{12}C$, $^{15}N/^{14}N$, $^{18}O/^{16}O$, $^{34}S/^{32}S$, $^{37}Cl/^{35}Cl$, and $^{30}Si/^{28}Si$. Some elements have more than two stable isotopes, and specialized applications, such as the search for non-mass-dependent isotopic fractionation, require measurement of additional isotopes. Thus, for example, $^{17}O/^{16}O$ as well as $^{18}O/^{16}O$ (using O_2 as the working gas) and $^{33}S/^{32}S$ and $^{36}S/^{32}S$ may be measured (using SF_6), the latter requiring quantification of all four stable isotopes of sulfur, ^{32}S, ^{33}S, ^{34}S, and ^{36}S.

A further inlet type is also common, namely the continuous flow (CF) inlet. This allows smaller gas samples (nanomoles to picomoles) to be measured, swept into the mass spectrometer source in a stream of helium, after gas chromatographic purification. There is no internal standardization as can be achieved with dual-inlet comparison, although reference materials are introduced at suitable intervals, as if samples, within each analytical session. The precision of CF analyses is less, commonly 0.2–0.5 per mil, than for the DI mode. However, the addition of automated preparation systems permits rapid analysis of bulk organic matter and the separation of individual organic compounds (i.e., compound-specific analysis) by gas or liquid chromatography, prior to their combustion or pyrolysis and analysis of their H, C, N, O, and S isotopes.

The precision of stable isotopic ratios is also enhanced by the universal use of multicollector Faraday cups applied in both DI and CF modes, as this allows simultaneous collection of all the isotopes of a given species. For example, the molecular ions of CO_2 have masses (m/z) of 44, 45, 46, 47, 48, and 49, given that oxygen has m/z of 16, 17, or 18 and carbon 12 or 13. Measurement of masses 44, 45, and 46 provides sufficient information to calculate the ratios $^{13}C/^{12}C$ and $^{18}O/^{16}O$ for most terrestrial samples. Accordingly, mass spectrometers equipped with three appropriately spaced collectors for these masses are the norm. The new field of clumped-isotope geochemistry (Eiler 2007) calculates the paleotemperature of carbonates by measurement of the relative abundance of $^{13}C^{18}O^{16}O$ (i.e., m/z of 47), so that specialized mass spectrometers with up to six collectors are required, as all masses of CO_2 are monitored, with masses 48 and 49, used as indicators of contamination.

The stable isotopic analyses of all materials are normalized to a set of internationally agreed values for reference materials that are available for distribution through the International Atomic Energy Agency (IAEA) in Vienna. Each laboratory is asked to use these sparingly and to establish and calibrate its own working standards for routine analyses (see the section on ▶ "Stable Isotope Geochemistry").

Noble Gas Mass Spectrometry

In contrast to the relatively abundant stable isotopes, noble gasNoble gases abundances in natural samples are minute and analyses of noble gas abundance of $10^{-22} \sim 10^{-12}$ mol are required. To fulfill this requirement, Reynolds (1956) deployed a glass noble gas mass spectrometer operated in

static mode (retaining all sample gases by isolating the system from the vacuum pumps). In addition, in order to reduce the background of noble gases and their interferences in a mass spectrometer, ultra-high ($<10^{-7}$ Pa) and clean vacuum is required, which can be achieved by baking the system in excess of 350 °C. Now that specialty steels and a variety of more exotic metals are more common, all-metal noble gas mass spectrometers are commercially available. In some cases, the nitrogen isotopes from minute amounts of gas from geological samples (for example, mantle-derived samples) are analyzed by a noble gas mass spectrometer in static mode.

In order to measure noble gas elemental and isotope abundances in geological (solid or fluid) samples, it is necessary to equip a dedicated sample handling system online to a noble gas mass spectrometer. Because helium permeates through normal glass, an all-metal sample handling system is usually used. The system consists of (1) gas extraction, (2) gas purification, (3) noble gas separation, and (4) standard pipettes.

In order to extract noble gases from solid samples, samples are heated by a high temperature furnace, as high as 2,000 °C as required in the case of graphitization of diamonds to extract noble gases, for bulk analyses or laser light for localized analyses. Vacuum crushing techniques to release inclusion-hosted noble gas components are also commonly used. Fluid samples collected in the field and stored in copper tubes (with both ends clamped) or lead glass containers are connected to the sample handling system for further processing. The gas purification section to remove active gas species, such as water and carbon dioxide, includes a bulk getter containing titanium-zirconium foils held at temperature higher than 600 °C, a low temperature (<400 °C) getter comprising titanium-aluminum alloys, and a titanium sublimation pump. After the gas purification, noble gases are physically adsorbed on an activated charcoal trap held at below 10 K. It is ideal to analyze each noble gas species separately to overcome the problem of isotope fractionation caused by the existence of other abundant noble gas species (for example, He in a Ne fraction, Ar in a Kr fraction). Noble gases are sequentially desorbed, starting with He, for isotopic analysis with a mass spectrometer. Effective separation of He from Ne, Ne from Ar, Ar from Kr, and Kr from Xe are attained at approximately 50 K, 125 K, 200 K, and 250 K, respectively. To calibrate instrumental sensitivity and mass discrimination (instrument-induced isotope fractionation that occurs mainly during the ionization processes in the ion box), it is necessary to install standard gas pipette tanks, which deliver aliquots of known amounts and isotopic compositions of noble gases and atmospheric noble gases are commonly used for this purpose. Data sets, performed by peak-jumping or multicollection, comprise the data acquisition time and peak intensity after subtraction of noise level. In order to compensate for the pumping action of noble gases by ionization in a mass spectrometer, the initial intensity when the gas was first introduced into the mass spectrometer is calculated by extrapolating the intensity back to the initial gas inlet time (T zero). In contrast to abundant stable isotope analyses with 0.01 per mil level precision, for noble gases analyses at per mil level precision is at best achievable.

In the 2010s, some commercial manufacturers launched multicollector noble gas mass spectrometers, which revolutionized applications in the cosmo-geo-sciences. Analyses of noble gas isotopes by multicollector systems have substantially improved precision and accuracy of measurements. For example, using a high-sensitivity, multicollector noble gas mass spectrometer, high precision measurements of atmospheric Ar isotopic ratios were undertaken, and atmospheric Ar isotope compositions were reevaluated. Similarly, $^{40}Ar/^{39}Ar$ geochronology analyses conducted on a multicollector mass spectrometer have produced significantly enhanced (by a factor of 10) precision levels. This capability is particularly well suited to high precision $^{40}Ar/^{39}Ar$ dating of young (<100 ka) basalts. In addition, a high mass resolution (~1,800), multicollector noble gas mass spectrometer is commercially available and this enables separation of the majority of isobaric interferences (e.g., hydrocarbons, hydrides, chlorides) relating to noble gas isotopes. For example, partial separation of $^{20}Ne^{1}H$ from ^{21}Ne makes it possible to precisely determine ^{21}Ne abundances in the atmosphere. Precise analyses (better than 0.5%) of Kr and Xe isotopes achieved by high mass resolution, multicollector noble gas mass spectrometers have demonstrated the existence of nonatmospheric isotope compositions in some terrestrial reservoirs which may directly link to early differentiation processes of the Earth.

Summary

Gas source mass spectrometry had its origins 70 years ago. Modern machines utilize the same principles although there have been significant advances in precision owing to multiple ion-beam collection, ion detection and amplification, and electronic stability. Substantial automation of both measurement and, in some cases, extraction of useable gases from geological, biological, atmospheric, and hydrological materials has led to higher productivity and analysis of smaller samples. The technique continues to be the principal analytical tool applied to both light-element stable isotope and noble gas geochemistry. It is anticipated that, utilizing multicollector noble gas mass spectrometers, the area of noble gas cosmo-geochemistry will continue to advance significantly in the next decade.

Cross-References

► Argon Isotopes
► Atmophile Elements

- ▶ Carbon Isotopes
- ▶ Chlorine Isotopes
- ▶ Compound-Specific Isotope Analysis
- ▶ Earth's Atmosphere
- ▶ Helium Isotopes
- ▶ Hydrogen Isotopes
- ▶ Neon Isotopes
- ▶ Nitrogen Isotopes
- ▶ Noble Gases
- ▶ Oxygen Isotopes
- ▶ Paleotemperatures
- ▶ Silicon Isotopes
- ▶ Stable Isotope Geochemistry
- ▶ Sulfur Isotopes
- ▶ Xenon Isotopes

References

Brand WA (2004) Mass spectrometer hardware for analysing stable isotope ratios. In: de Groot PA (ed) Handbook of stable isotope analytical techniques, vol 1. Elsevier, Amsterdam, pp 835–856

Eiler JM (2007) "Clumped-isotope" geochemistry – the study of naturally-occurring, multiply-substituted isotopologues. Earth Planet Sci Lett 262:309–327

Hoefs J (2015) Stable isotope geochemistry, 7th edn. Springer International, Switzerland

McCrea JM (1950) On the isotopic chemistry of carbonates and a paleotemperature scale. J Chem Phys 18:849–857

Mabry J, Burnard P, Blard P-H, Zimmermann L (2012) Mapping changes in helium sensitivity and peak shape for varying parameters of a Nier-type noble gas ion source. J Anal At Spectrom 27:1012–1017

Nier AO (1947) A mass spectrometer for isotope and gas analysis. Rev Sci Instrum 18:398–411

Reynolds JH (1956) High sensitivity mass spectrometer for noble gas analysis. Rev Sci Instrum 27:928–934

Geochemical Classification of Elements

Cin-Ty Lee
Department of Earth Science MS-126, Rice University, Houston, TX, USA

Definition

Geochemists classify elements in various ways based on their abundance, behavior, and distribution in the Earth.

Introduction

Elements can be qualitatively classified into **major** (>0.4 wt%), **minor** (0.1–0.4 wt%), and **trace** elements (<0.1 wt%). Major elements are those that define the primary structure of a given phase, which can be a mineral, liquid, or vapor. Major elements are abundant enough that they dictate a system's physical properties, including the assemblage of phases. Trace elements are not essential to the structure of a phase and do not directly influence the properties of a phase or system. Instead, trace elements occur passively as dissolved constituents or in the form of minor amounts of accessory phases. The distribution of elements on Earth is heterogeneous, ranging from the scale of hundreds to thousands of kilometers in the form of the Earth's layered structure (core, mantle, crust, ocean, and atmosphere) down to the scale of millimeters or less in the form of mineral grains or living organisms. Thus, although >99% of the bulk Earth, which includes the crust, mantle, and metallic core, is composed of Fe, O, Mg, Si, S, Ni, Ca, and Al, in order of decreasing abundance by weight, much of the Fe and almost all the Ni are sequestered in the core, whereas most of the Earth's O is locked up in the mantle and crust in the form of oxides (O makes up nearly 50% by weight of the mantle). The same element can be a major element in one geologic environment and a trace element in another. For example, during certain petrogenetic processes, an element initially occurring at trace levels can become concentrated enough to be a major or minor element. Cu ore deposits or Li-rich pegmatites are examples where elements normally in trace abundances can locally become quite enriched. Other examples are H, N, and C, which are trace elements in the mantle but major constituents of the oceans, atmosphere, and life. Redistribution of elements throughout the Earth, a process called differentiation, is dominantly controlled by the formation and physical segregation of silicate liquids, aqueous fluids, and gases, which serve as potential carriers of all elements of the periodic table.

Exactly how elements are spatially redistributed in a planetary body depends on their chemical behaviors and how they partition into different phases during geologic and biochemical processes. Chemical behavior of elements is dictated by the "stability" of the outer electrons. Elements whose outermost electron shells are nearly filled tend to readily attract electrons (high electronegativity), forming anions in chemical bonds. Elements with only partially filled outer shells tend to donate electrons (low electronegativity) and become cations in chemical bonds. Elements with very different electronegativities (opposite ends of the periodic table) tend to transfer electrons between atoms, resulting in ionic bonds. In contrast, elements with similar electronegativities tend to share electron clouds in chemical bonds (covalent bonds), making such bonds very strong. Most of the rocks on Earth are silicates, which are composed of complexes of silica tetrahedra (SiO_4^{4-}), where the similar electronegativities of Si and O result in significant degree of covalent character. Cations on the left side of the periodic table (alkali and alkali Earth metals), such as Mg^{2+}, Ca^{2+}, Na^{+}, and K^{+}, generate ionic bonds with the O^{2-} anions

making up the apices of the silica tetrahedra to form, for example, the silicate minerals that make up most of the Earth's mantle (olivine, Mg_2SiO_4) and crust (feldspar, e.g., $CaAl_2Si_2O_8$ and $NaAlSi_3O_8$). Elements with filled energy shells, such as the noble gases, tend to be chemically inert.

Partitioning Classifications

The efficiency to which an element partitions into a particular phase is controlled to first order by charge and ionic radius (cations are smaller and anions are larger than their respective atomic radii). During melting, elements can be classified into **compatible** or **incompatible** relative to the solid phase, that is, an incompatible element preferentially partitions into the melt phase, whereas a compatible element partitions into the solid phase. A cation becomes incompatible in a particular crystallographic site when excess electrostatic and strain energy is generated due to charge imbalance or when an ion is too big or too small for a particular crystallographic site (Wood and Blundy 2003). These effects are manifested as general trends in partitioning behavior as a function of ionic radii for a given charge. For any given mineral/melt pair, there is an optimum ionic radii for maximum compatibility (Wood and Blundy 2003). In the case of the rare earth elements in most mantle minerals, the heavy rare earths typically exhibit maximum compatibility because the lighter rare earths are too large. This variation in ionic radius, known as the "lanthanide contraction" of the f-orbital shell, thus manifests itself as a distinct decrease in compatibility toward the left-hand side of the periodic table for the rare earth elements.

Most of the high mass trace metals, such as Sr, Rb, and Ba, and the rare earth elements tend to be incompatible during mantle melting because of their large cationic radii. First-row transition metals, with ionic radii more similar to the cation crystallographic sites in mantle minerals, tend to be compatible (Ni and Co) or moderately incompatible (Sc, V, Mn) during melting (Canil 2004). Some highly charged transition metals, such as high field strength elements Ti, Zr, and Nb, are highly incompatible in common silicates due to charge imbalance. Some elements, however, can be highly compatible in a given phase, but exhibit overall incompatible behavior during melting if that phase represents a minor constituent in the rock. For example, Cu is highly compatible in sulfide, but because sulfides are low in abundance in typical mantle rocks, Cu behaves effectively as an incompatible element during mantle melting (Lee et al. 2012).

Partitioning behavior for a given element is rarely ever a constant due to many factors: (1) effective oxidation, which is controlled by the oxygen fugacity of the environment, (2) temperature, (3) pressure, (4) mineral composition, and (5) melt or fluid composition, which changes complexation behavior. An example of redox effects is seen in the difference in partitioning behaviors between Eu^{2+} and Eu^{3+} and between V^{2+} and V^{3+} (Canil 1997). An example of the influence of mineral composition is the effect of coupled substitutions. The presence of Al^{3+} as a major element in a pyroxene can enhance the compatibility of rare earth elements (+3) by providing a means of charge balance. Bridgmanite, a lower-mantle mineral with perovskite structure, can enhance the compatibility of Fe^{3+} if Al^{3+} is contained in its structure (Frost et al. 2004). The subsolidus transformation of wadsleyite or ringwoodite, which contains minimal Al^{3+}, to bridgmanite has been suggested to lead to disproportionation of Fe^{2+} into Fe^0 and Fe^{3+}, the latter dissolving into bridgmanite.

Another important quantity is the charge to ionic radius ratio, known as the **ionic potential**. Elements with high ionic potential are referred to as **high field strength elements** (HFSEs) and include Ti^{4+}, Zr^{4+}, Nb^{5+}, Ta^{5+}, and Hf^{4+}. Elements with low ionic potential are often referred to as **large ion lithophile elements** (LILEs) in the geochemical community. LILEs include Na^+, K^+, Rb^+, Cs^+, Sr^{2+}, and Ba^{2+}. Low ionic potential elements readily form inner sphere aquo-complexes in aqueous solutions because they are large enough to be surrounded and coordinated to water molecules (Langmuir 1997). This makes LILEs soluble in aqueous solutions. The high charge of HFSE and rare earth element cations reduces electron shielding within their outermost electron shell, resulting in significant reduction in ionic radii. Because of their small cationic radii and high charge, H is expelled from the solvation shell, preventing such elements from forming aquo-complexes and rendering them relatively insoluble in water (Langmuir 1997). Only by complexing with other anions, such as halides and oxyanions, can such elements become more soluble in water. These are the reasons why geochemists generally consider LILEs **fluid mobile** and HFSEs **fluid immobile**, but even fluid immobile elements can become mobile under certain conditions.

Geochemical Classifications

Elements are often categorized based on their general geochemical behaviors even though an element's chemical behavior depends strongly on variables such as temperature, pressure, and chemical environment; the latter of which can dictate an element's valence state and ability to form complexes. These classifications broadly follow Goldschmidt's original classifications (Goldschmidt 1937) with the addition of organophile and fluid-mobile elements.

Lithophile elements ("rock loving") are preferentially partitioned into silicate minerals. These include cations that commonly form oxides, such as Ca, Mg, Mn, Ti, Na, K, the rare earth elements, U, Th, Si, and Fe in its oxidized states.

Siderophile elements ("iron loving") are those that are preferentially partitioned into the metallic core, typically in the form of alloys with Fe. Elements exhibiting metallic behavior include the noble metals (Pt, Pd, Ir, Ru, Rh, and Os) as well as W, Ni, and Co. Some elements in their reduced states or at high enough pressures to impart metallic behavior can alloy with Fe metal; these include Si, C, and some high field strength elements like Nb. Sulfur may dissolve in the core as a sulfide complex and, under these conditions, is also considered siderophile.

Chalcophile elements are those that commonly form sulfide-type minerals. These include Cu, Pb, Zn, Cd, Mo, Hg, Sb, Sn, Tl, Te, As, as well as noble metals.

Atmophile elements are those that readily form volatile compounds at relatively low temperatures (<300 K), many of which are preferentially concentrated in planetary atmospheres. Atmophile elements include C, O, H, N, S, and the noble gases.

Organophile elements are those that form or associate with organic compounds (hydrocarbon molecules) in biochemical and biogeochemical processes. These include C, H, N, S, and P, but also include various metal-organic complexes. Many metals, such as U, V, Ge, Pb, and Mo, can complex with organic molecules, generating organic-rich sediments with high metal contents.

Fluid-mobile elements are those that readily dissolve in fluids, typically water-rich fluids. Elements with high solubility in water tend to be low field strength elements, such as the alkali and alkali Earth group elements, which readily form inner sphere aquo-complexes or highly electronegative elements, such as the halogens. High field strength elements, in the absence of complexation, tend to be insoluble. Transition metals tend to have lower solubilities, but the presence of anions in the water can greatly enhance their solubilities through complexation. For example, noble metals and high field strength elements can become more soluble if complexed with certain halogens or oxyanions. Introduction of carbonate ions into fluids or silicate melts can also enhance solubilities of certain elements.

It is important to recognize that elements can behave in different ways. Obviously, oxygen in its molecular form can be atmophile, but it also forms oxides and dominantly behaves as a lithophile element in the presence of metals. Elements like Ge can be lithophile, organophile, chalcophile, and siderophile, depending on oxidation state and chemical environment (Fig. 1).

Cosmochemical Classifications

There is a cosmochemical classification of elements that is primarily used to describe the temperature interval over which elements condense from a gaseous state to a solid or liquid state during nebular condensation and planetary accretion. These classifications are based on theoretical condensation temperatures calculated from a nebula with a solar composition and a pressure of 10^{-4} bar (at the 50% condensation

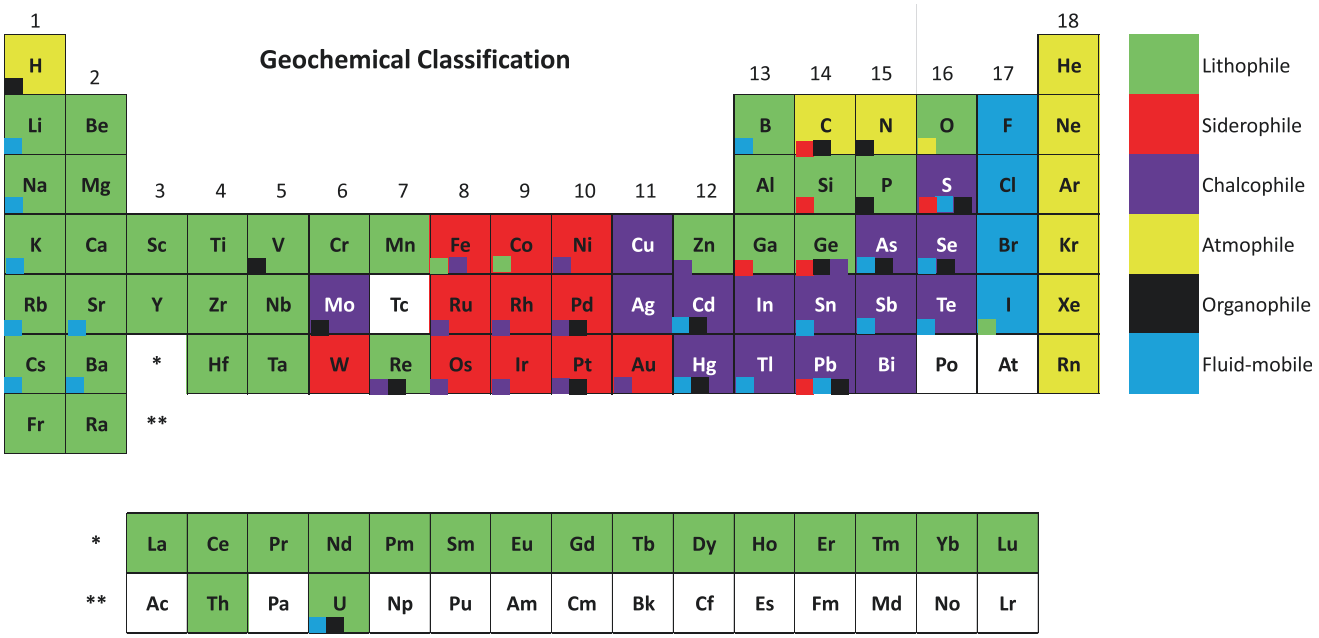

Geochemical Classification of Elements, Fig. 1 Cosmochemical classification of elements: Cosmochemical classification of elements based on 50% condensation temperatures at 10^{-4} bar using data from Lodders and Fegley (1998)

level) and are most applicable in the study of meteorites, impact processes, and planetary accretion (Lodders and Fegley 1998):

Highly refractory (>1700 K) – Re, Os, W, Zr, and Hf
Refractory (1500–1700 K) – Al, Sc, Ca, Ti, most rare earth elements, Th, and U
Moderately refractory (1300–1500 K) – Be, Mg, Si, Cr, Fe, Co, Ni, Nb, Ce, Yb, Pt, and Pd
Moderately volatile (1100–1500 K) – Cu, Ba, Mn, Sr, P, and Au
Volatile (700–1100 K) – Na, K, B, S, Rb, Cs, Ga, Sn, and Se
Highly volatile (<700 K) – Pb, Zn, Tl, In, Bi, O, C, N, H, and noble gases

The use of these classifications should generally be restricted to cosmochemical processes or during the high temperatures of planetary accretion instead of for differentiation within an already condensed planetary body. For example, refractory elements, in a cosmochemical sense, can be siderophile, lithophile, or even chalcophile during planetary differentiation. Care must also be taken when using the terms atmophile and volatile. For example, Pb and Zn are considered highly volatile from a cosmochemical perspective, but would not be considered atmophile. Nevertheless, under unusual situations, such as during a meteorite impact or volcanic processes, Pb and Zn can be volatilized briefly into the atmosphere before recondensing out of the atmosphere upon cooling. Ge can be volatile in a cosmochemical sense, but can be lithophile or siderophile in a geochemical sense (Fig. 2).

Using Elements in Geochemistry and Cosmochemistry

Major elements are best used for determining how phase assemblages evolve during petrogenesis of rocks. Compatible and moderately compatible trace elements can also be used to evaluate phase assemblages. Together, major elements and moderately incompatible to compatible trace elements can be powerful tools for unraveling the mineralogy of the source regions of magmas. Incompatible trace elements are less diagnostic of mineralogy because effects of fractionation strongly accentuate changes in incompatible trace element abundances. For example, continental crust is highly enriched in incompatible elements owing to extreme magmatic differentiation. Contamination of mantle-derived magmas with small amounts of continental crust or fluids can lead to significant changes in trace element signatures with only minor change in major element systematics. Because some trace element systems are associated with radioactive isotopic systems, a full understanding of the geochemical behavior of parent and daughter elements is critical for interpreting isotopic evolution of the Earth.

Because many factors influence element partitioning, some elements can be used to track various intensive variables, such as temperature, pressure, and oxygen fugacity, when used judiciously. For example, rare earth element partitioning between solid and melt and at subsolidus conditions can be used indirectly as a qualitative barometer by signaling the presence of high-pressure minerals (garnet) or as a quantitative thermobarometer with proper calibration (Liang et al. 2013). Variations in the oxidation state of Fe,

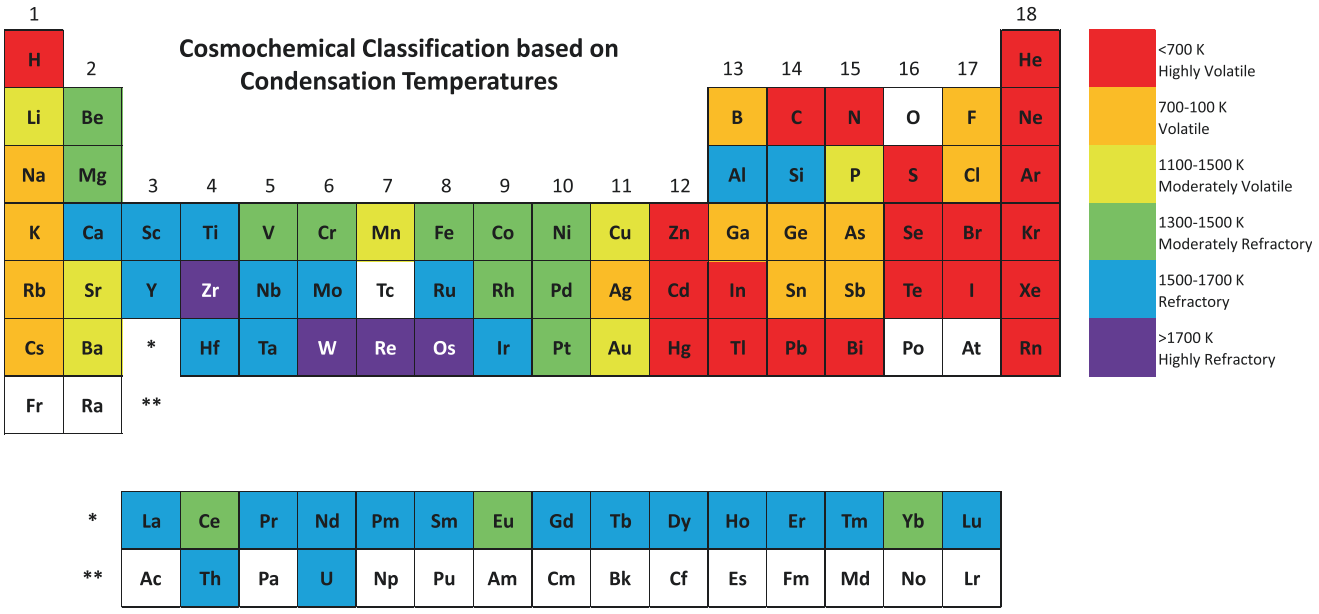

Geochemical Classification of Elements, Fig. 2 Geochemical classification of elements

Eu, and Ce influence their geochemical behaviors, allowing them to be used for tracking oxygen fugacity in the mantle, crust, oceans, and atmosphere through time.

Finally, elemental abundances provide first-order constraints on how different reservoirs interact and how elements are cycled through these reservoirs. For example, the abundance of an element in the ocean may shed light on the element's residence time, that is, elements in high abundance tend to be soluble and have long residence times (Na and Cl), whereas elements in low abundance tend to be insoluble and have short residence times (e.g., rare earth elements). Temporal variations in seawater composition have been used to reconstruct past variations in climate, ocean circulation, and weathering (Holland 1984). Similar approaches can be applied to better understand magma chamber dynamics.

Summary

The elements of the periodic table provide many different ways of investigating how the Earth system operates. In many cases, however, the study of major and trace elements is often treated separately. Many of the most interesting advances in geochemistry have come from a holistic understanding of the periodic table.

Cross-References

- ▶ Atmophile Elements
- ▶ Chalcophile Elements
- ▶ Chemical Bonds
- ▶ Complexes
- ▶ Earth's Core
- ▶ Electronegativity
- ▶ High Field Strength Elements
- ▶ Large-Ion Lithophile Elements
- ▶ Lithophile Elements
- ▶ Noble Gases
- ▶ Oxidation-Reduction Reactions and Eh-pH (Pourbaix) Diagrams
- ▶ Partitioning and Partition Coefficients
- ▶ Periodic Table
- ▶ Siderophile Elements
- ▶ Solubility
- ▶ Trace Elements
- ▶ Transition Elements

References

Canil D (1997) Vanadium partitioning and the oxidation state of Archaean komatiite magmas. Nature 389:842–845

Canil D (2004) Mildly incompatible elements in peridotites and the origins of mantle lithosphere. Lithos 77:375–393

Frost DJ, Liebske C, Langenhorst F, McCammon CA, Tronnes RG, Rubie DC (2004) Experimental evidence for the existence of iron-rich metal in the Earth's lower mantle. Nature 428:409–412

Goldschmidt VM (1937) The principles of the distribution of chemical elements in minerals and rocks. J Chem Soc, London 140:655–673

Holland HD (1984) The chemical evolution of the atmosphere and oceans. Princeton University Press, Princeton

Langmuir D (1997) Aqueous environmental geochemistry. Prentice Hall, Upper Saddle River

Lee C-TA, Luffi P, Chin EJ, Bouchet R, Dasgupta R, Morton DM, Le Roux V, Yin Q-Z, Jin D (2012) Copper systematics in arc magmas and implications for crust-mantle differentiation. Science 336:64–68

Liang Y, Sun C, Yao L (2013) A REE-in-two-pyroxene thermometer for mafic and ultramafic rocks. Geochim Cosmochim Acta 102:246–260

Lodders K, Fegley JB (1998) The planetary Scientist's companion. Oxford University Press, Oxford

Wood BJ, Blundy JD (2003) Trace element partitioning under crustal and uppermost mantle conditions: the influences of ionic radius, cation charge, pressure, and temperature. Treatise Geochem 2:395–424

G

Geochemical Exploration

John F. H. Thompson
Department of Earth and Atmospheric Sciences, Cornell University, Ithaca, NY, USA

Definition

Geochemical exploration, or exploration geochemistry, is a Geochemical explorationspatial sampling and analysis methodology used extensively in the search for mineral resources and routinely for petroleum. The approach is based on the natural dispersion of elements, minerals, and compounds from exposed or concealed mineral or petroleum deposits, whether by physical, chemical, or biological processes. Dispersion generates geochemical footprints significantly larger than the source deposit. Detection of concentrations of elements or minerals above what is expected or defined as background, and definition of the dispersion pattern, can lead to the discovery of new resources of economic interest. A similar methodology can be used to document contamination or pollution from anthropogenic sources, this approach usually being considered part of environmental geochemistry.

Background

Chemical sampling of soils and plants began in Russia and Scandinavia in the 1930s but was developed as exploration geochemistry to support mineral exploration when analytical techniques became routinely available, especially for trace element analysis, in the postwar period (Hawkes 1957; Ginzburg 1960; Kyser et al. 2015). Extensive use of exploration geochemistry in the 1960s and 1970s, particularly in

northern countries, led to a series of important publications (e.g., Levinson 1980; Govett 1981–1984). Throughout this period, and subsequently in the 1980s and 1990s, the use of geochemical surveys expanded in the search for different types of mineral deposit in a wide range of geological, surficial, and environmental settings. Over time, the focus expanded from trying to detect partially exposed deposits to include terrains where potential mineral deposits may exist beneath cover sequences at considerable depth (Cameron et al. 2005; Kelley et al. 2006). Geochemical exploration continues to advance with new approaches and improved analytical methods (Coker 2010).

Dispersion Processes

Mineral deposits represent natural concentrations of elements or minerals, which if proven to be economic may be termed an ore deposit (Arndt et al. 2017; Fig. 1). In some cases, formation of mineral deposits is concurrent with a significant chemical and mineralogical halo extending up to several kilometers from the deposit. The resulting geochemical pattern may contain specific trace elements related to the mineral deposit and complementary changes in secondary mineralogy. In some cases, the broad halo hosts distinct zones that change in character with increasing distance away from the principal mineral deposit. The processes that generated these geochemical haloes during formation of mineral deposits are termed primary dispersion by Kyser et al. (2015).

In contrast to primary dispersion, secondary dispersion typically occurs due to movement of elements in the near-surface environment relatively recently (1000s of years to a few million years ago), in most cases long after formation of the mineral deposit (Kyser et al. 2015). Secondary dispersion results from the presence of mineral deposits within a few hundred meters of the surface and therefore is an important discovery tool.

A variety of surface and near-surface processes may result in the dispersion of elements or minerals including:

1. Physical erosion and transport of minerals away from the mineral deposit in streams, glaciers, or during mass wasting. Minerals that are resistant under surface conditions may be transported tens of kilometers from their source. Other minerals may breakdown resulting in chemical transport of elements and precipitation or entrapment in secondary minerals or organic sites. Stream flow and other geomorphic processes may concentrate elements and minerals locally enhancing the dispersion pattern.
2. Physical and chemical movement of elements and minerals in soils that form above exposed or buried mineral deposits. The character and nature of the dispersion pattern in soils and regolith profiles are strongly influenced by climate, soil type, and topography. Dispersion can be on the hundreds of meters to kilometers in scale.
3. Chemical mobility in the subsurface may result from electrochemical reactions between conductive, sulfide-rich mineral deposits, wall rocks, and groundwater. The resulting subtle dispersion pattern may be detected at surface even where the mineral deposit is located tens or hundreds of meters below surface and in some cases when covered by overburden that is completely unrelated to the mineral deposit. In some environments, the sediments in lakes may accumulate elements that reflect regional dispersion from mineral deposits in the area.
4. Biological activity can release elements, e.g., through bacterially enhanced oxidation of sulfides, with subsequent transport of elements through plant root systems and

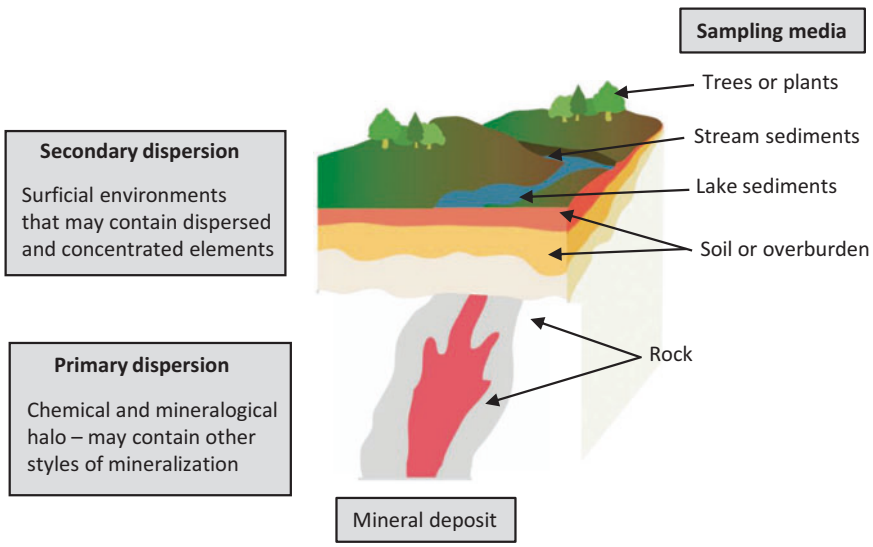

Geochemical Exploration, Fig. 1 Different types of media that can be sampled to detect a mineral deposit (in *red*) including those related to primary and secondary dispersion processes (Adapted from Kyser et al. 2015)

concentration in the various parts of trees and plants. The understanding and use of these dispersion processes is termed biogeochemistry (Dunn 2007).

Sampling Media and Methods

Based on the understanding of dispersion processes and their likely activity in different geologic, climatic, and topographic settings, geochemical exploration programs are designed to sample specific media that are most likely to display the distal geochemical signature of a desired mineral deposit, if present (Fig. 1). Media in widespread use include:

- Rocks sampled at surface or from drill core that are analyzed to detect variations in bulk chemistry (lithogeochemistry) resulting from mineralizing processes (Lawie 2009). Elevated levels of pathfinder elements in the rock or within specific minerals and the presence of characteristic mineral assemblages may be indicative of the outer zones of mineral deposits (e.g., Cooke et al. 2014).
- Stream sediments selected from hydromorphic sites that are most likely to collect heavy minerals and related elements. In some cases, large bulk samples are collected for bulk leaching (BLEG), while other techniques focus on specific size fractions or locations in stream beds.
- Soils form from the underlying bedrock and surface plant organic material with their character largely dependent on climate. If the bedrock is mineralized, soils will likely contain elements indicative of this mineralization. The geochemical signature may be significantly larger than the underlying mineralization due to chemical mobility at the water table or mass movement of soils. Soils form distinct horizons reflecting different climatic and topographic conditions, and the concentration of critical elements commonly varies among these horizons. Soil sampling therefore targets specific horizons during geochemical exploration using pits, augers, or overburden drills to reach the desired level. Particle size fractions and organic material have also been targeted for partial or selective leach extraction based on evidence to suggest that specific elements may reflect deeply buried mineralization (e.g., Cameron et al. 2005).
- Talus or scree may be sampled in mountainous or arid regions where soils are poorly developed. The fine fraction (<100 μm) sieved from talus material may contain elevated elements reflecting the presence of a mineral deposit beneath the talus.
- In glaciated terrains, overburden consisting of extensive glacial till masks local geology and hinders most conventional geochemical exploration approaches. In some regions with subdued topography, major esker systems can be preserved over hundreds of kilometers. Individual eskers may contain distinct suites of minerals that are characteristic of kimberlites, the host for diamonds, a considerable distance down-ice from the sample site. Sampling of specific size fractions and careful sample preparation are required. This approach was significant in the discovery of diamonds in the Northwest Territory, Canada.
- Organic-rich sediments in lakes that are abundant in glaciated terrains may contain enriched levels of elements indicative of mineralization in the region. Rapid sampling over large areas is possible using helicopters with floats. While useful as a first pass, the data can be ambiguous and other approaches are required to verify and define the presence of elements that may reflect mineralization.
- Trees and plants, particularly those with deep root systems, may concentrate elements indicative of buried mineralization. Selective sampling (e.g., bark, new growth, treetops, tree cores) of specific species has been found to generate the best signature, i.e., elevated concentrations of specific elements relative to background.
- In some regions, ants and termites build large mounds above extensive deep networks of small passageways. These mounds may include material from unexposed bedrock and therefore provide a medium for mineralogical and geochemical sampling.
- The importance of microbes in soils is well recognized. The recent development of genomic techniques allows the identification of specific species, that is, some cases may reflect geochemical conditions related to buried mineralization. The efficacy of this approach is still under investigation and development.
- Water wells for individual properties and communities provide access to local groundwater, and more extensive surveys of groundwaters and aquifers have been completed in some areas. Where documented, the chemistry of groundwaters varies considerably as result of interaction with rocks at local and potentially regional scales. The use of these data for mineral exploration has been considered, but there are few examples of direct relationships between water chemistry and mineralization and related successful application to mineral exploration.

Selection of an appropriate sampling medium and sampling technique is usually aided and tested by an orientation survey in the area of interest. This may be carried out over known mineralization, if available, but may be based on the relative response from different media, for example, different soil horizons.

Analytical Techniques

Over the last 20–30 years, there have been major advances in the available analytical techniques for analyzing samples of

bulk and selected mineralogical samples from geochemical exploration programs (Kyser et al. 2015). The detection limits have decreased markedly from ppm to ppb and, in some cases, ppt levels. At these levels, subtle and distal anomalous signatures may be detected with careful data analysis required to define background values (see below). Furthermore, many techniques now routinely provide multi-element data (30–45 elements) at relatively low costs. Commercial analytical laboratories commonly offer different packages each designed for different types of program (reconnaissance to detailed project scales), media, and geological environment or mineral deposit type. Isotopic analyses are also becoming more routinely available and are being used for geochemical exploration in selected settings.

Field work has also benefited from the development of handheld analytical tools that enable real-time analysis of soils and rocks at concentration levels that may be meaningful for exploration even with higher detection limits and lower precision than laboratory techniques. The most used tool for geochemical Short-wave infrared (SWIR) toolsX-ray fluorescence spectroscopy (XRF)analysis is portable X-ray fluorescence spectroscopy (XRF) (e.g., Hall and McClenaghan 2013), while portable short-wave infrared (SWIR) tools provide important mineralogical data.

Data Analysis and Interpretation

Interpretation of geochemical data (Grunsky 2010) requires careful data analysis, first and foremost to verify the quality of the data using quality control – quality assurance (QA/QC) procedures with blanks, duplicates, and standards. Assuming the data meets analytical standards, subsequent procedures may be used to level data from different programs and examine the influence of regional bedrock, topography, catchment basins, overburden types, and sampling media. The goal is to establish geochemical background levels for critical elements of interest for carefully defined regions with uniform characteristics and hence identify specific areas with geochemical values above background. These anomalous results may require follow-up sampling and application of other exploration techniques to define targets for detailed work and drill testing. Given the volume of multi-element data now routinely available, a variety of spatial and multivariate statistical techniques may be used to aid interpretation and seek anomalous results that are not immediately obvious from individual pathfinder elements. Lithogeochemical analysis of whole-rock geochemical data may directly identify distal metal signatures or can be used to define rock units and alteration of these units that may be indicative of mineralizing processes even in the absence of metal signatures.

Summary

Exploration geochemistry has been a critical component of mineral exploration for well over 50 years. Many discoveries of economic mineralization were made using geochemical exploration methods, although usually in conjunction with other methods. Approximately 40% of discoveries in the 1970–2000 period can be attributed at least partially to geochemical exploration (Schodde 2014), but the contribution appears to have declined somewhat in recent years due to the increased emphasis on exploration around existing mines and at depth (Arndt et al. 2017). New techniques and different media, decreasing detection limits, increasing multi-element and isotopic techniques at lower cost, and new portable technologies continue to offer improved ways to discover mineral deposits, particularly when integrated with other geological, geophysical, and remote-sensing exploration techniques.

Cross-References

- ▶ Biogeochemistry
- ▶ Chemical Weathering
- ▶ Ore Deposits
- ▶ Organic Geochemistry
- ▶ Soils

References

Arndt NT, Fontboté L, Hedenquist JW, Kesler SE, Thomspon, JFH, Wood D (2017) Future global mineral resources. Geochem Perspect 6, 171 pp

Cameron EM, Leybourne MI, Kelley DL (2005) Exploring for deposits under deep cover using geochemistry. Soc Econ Geol Newsl 63:9–15

Coker WB (2010) Future research directions in exploration geochemistry. Geochem: Explor Environ Anal 10:75–80

Cooke DR, Baker M, Hollings P, Sweet G, Chang Z, Danyushevsky L, Gilbert SD, Zhou T, White NC, Gemmell JB, Inglis S (2014) New advances in detecting the distal geochemical footprints of porphyry systems – epidote mineral chemistry as a tool for vectoring and fertility assessment. In: Kelley KD, Golden HC (eds) Building exploration capability for the 21st century. Society of Economic Geologists special publication 18. Society of Economic Geologists, Littleton, pp 127–152.

Dunn CE (2007) Biogeochemistry in mineral exploration. Elsevier, Amsterdam, 456 pp

Ginzburg II (1960) Principles of geochemical prospecting (translation from Russian by V. P. Sokoloff). Pergamon, New York/London, 311 pp. (Original published by Gosgeotekhizdat, Moscow, 1957, 298 pp)

Govett GJS (1981–1984) Handbook of exploration geochemistry, 6 vols. Elsevier, Amsterdam

Grunsky EC (2010) The interpretation of geochemical survey data. Geochem Explor Environ Anal 10:27–74

Hall GEM, McClenaghan MB (2013) Field portable XRF in exploration and mining. In: Paulen RC, McClenaghan MB (eds) New frontiers for exploration in glaciated terrain. Geological Survey of Canada Open File 7374, pp 75–81

Hawkes HE (1957) Principles of geochemical prospecting. U.S. Geol Surv Bull 1000-F:225–355
Kelley DL, Kelley KD, Coker WB, Caughlin B, Doherty ME (2006) Beyond the obvious limits of ore deposits: the use of mineralogical, geochemical, and biological features for remote detection of mineralization. Econ Geol 101:729–752
Kyser K, Barr J, Ihlenfeld C (2015) Applied geochemistry in mineral exploration and mining. Elements 11:241–246
Lawie DC (2009) New uses for old data; lithogeochemistry for classification, alteration and geometallurgy. Aust Inst Geosci Bull 50:47–52
Levinson AA (1980) Introduction to exploration geochemistry, 2nd edn. Applied Publishing, Wilmette, 923 pp
Schodde R (2014) The global shift to undercover exploration – how fast? How effective? SEG 2014 conference, Keystone, 30 Sept 2014. Available via MinEx Consulting. http://www.minexconsulting.com/publications/sep2014b.html

Geochemical Reference Materials

Thomas C. Meisel
General and Analytical Chemistry, Montanuniversität Leoben, Leoben, Austria

Definition

The ISO/REMCO Committee on reference materials defines reference materials (RMs) as "material, sufficiently homogeneous and stable with respect to one or more specified properties, which has been established to be fit for its intended use in a measurement process." This definition is accompanied by several notes. Note 2 states that properties can be quantitative or qualitative. Other notes relate to the use of RMs, which may include the calibration of a measurement system, assessment of a measurement procedure, assigning values to other materials, and quality control. Note 4 highlights the importance of using an RM independently of other processes: "An RM can only be used for a single purpose in a given measurement. For example, it cannot be used for both calibration and method validation in the same measurement process" (ISO Guide 30, 2015).

History and Production of Geochemical Reference Materials

In the field of geosciences, compared with other scientific fields, analytical (geo)chemists realized the need for matrix-matched geochemical reference materials in the first half of the twentieth century. The first large-scale interlaboratory study (Fairbairn et al. 1951) in the 1950s resulted in the production of a whole series of geochemical reference materials that have been used for calibration, method development, and validation and for quality control purposes in analytical geochemical laboratories ever since.

In the early days of the production and characterization of reference materials, compilations of data from large-scale interlaboratory studies were used to characterize the major, minor, and trace element and compound mass fractions. Emphasis for characterization studies was put on homogenous, easy to digest geological materials to reduce additional uncertainty components of the consensus value. The top ten most accessed geochemical reference materials on the GeoReM database (http://georem.mpch-mainz.gwdg.de), which is about 40% of all searches, are seven basalts (five as powder and two as glass), one andesite, and two synthetic glasses (NIST SRM 610 and 612). Unfortunately, this distribution does not reflect the current diversity of geochemical studies.

The nonconformity of the previous RM characterizations with modern metrological standards and the limited diversity of available reference materials have led the International Association of Geoanalysts (IAG) to produce certified reference materials (CRMs) according to ISO/REMCO ISO Guides 34 and 35 (ISO Guide 34 2009; ISO Guide 35 2006). The guides, based on internationally accepted metrological concepts valid for all types of CRMs, have been specifically adapted for the certification of geochemical reference materials (IAG protocol, Kane et al. 2003; Kane et al. 2007). The selection of competent laboratories providing data, a diversity of independent measurement principles, measurement uncertainties, and traceability statements are all integral parts of metrologically correct certificates.

Although for the latest geochemical reference materials, certified data for all rare earth elements are provided, and other scientifically and economically important elements such as Tl, Bi, In, Te, Se, Re, Au, and platinum group elements (Ru, Rh, Pd, Os, Ir, and Pt) as well as all halogens are not yet certified. Reasons for this unsatisfactory situation are the low natural abundance of these elements in the ng/kg and µg/kg range and the limited number of specialized laboratories capable of providing reliable data.

The development and certification of microanalytical reference materials for their trace element content as well as isotope amount ratio measurement and age determinations with SIMS and LA-ICP-MS is the most recent and challenging development in geochemical reference material production.

Cross-References

▶ Analytical Techniques
▶ Geochronology and Radiogenic Isotopes
▶ Halogens
▶ Lanthanide Rare Earths
▶ Platinum group elements

References

Fairbairn HW, Schlecht WG, Stevens RE, Dennen WH, Ahrens LH, Chayes F (1951) A cooperative investigation of precision and accuracy in chemical, spectrochemical, and modal analysis of silicate rocks. US Geol Surv Bull 980. 71p

ISO Guide 30 (2015) Reference materials – selected terms and definitions. ISO, Geneva

ISO Guide 34 (2009) General requirements for the competence of reference material producers. ISO, Geneva

ISO Guide 35 (2006) Reference materials – general and statistical principles for certification. ISO, Geneva

Kane JS, Potts PJ, Wiedenbeck M, Carignan J, Wilson S (2003) International association of geoanalysts' protocol for the certification of geological and environmental reference materials. Geostand Newslet 27:227–244

Kane JS, Potts PJ, Meisel T, Wiedenbeck M (2007) International Association of Geoanalysts' protocol for the certification of geological and environmental reference materials: a supplement. Geostand Geoanal Res 31:285–288

Geochemical Thermodynamics

William H. Casey[1] and Peter A. Rock[2]
[1]Department of Chemistry and Department of Earth and Planetary Sciences, University of California, Davis, CA, USA
[2]College of Math and Physical Sciences, Department of Chemistry, University of California, Davis, CA, USA

Definition

The transfer of energy between useful work and heat.

Introduction

Thermodynamics concerns the conversion of energy in the Earth. Length scales and times scales for Earth processes are so vast, and the mineral assemblages and fluids in nature are so complicated, that equilibrium thermodynamics is usually the starting point for any geochemical investigation. This point was established in the earliest days of modern science by the renowned physical chemist Jacobus Van't Hoff (1852–1911), who used the then newly established Gibbs Phase Rule to reconstruct the composition of ancient seawater from the mineral assemblages found in evaporite deposits (see Eugster 1971).

Peter A. Rock is deceased.

Laws of Thermodynamics

The laws of thermodynamics differ from most other scientific laws in that they are usually stated in terms of the *impossibility* of achieving certain types of energy transfers. The laws can be stated in terms of the operation of machines or in terms of the primary thermodynamic variables of temperature, energy, heat, work, and entropy. Here we do both:

First law: It is impossible to construct a device that operates in a cyclical manner and performs work without putting energy into the device.

Second law: Entropy increases in the universe. Or, stated differently, it is impossible to construct a device that can transfer energy as heat from a low-temperature reservoir to a higher-temperature reservoir without adding energy as work. It is impossible to construct a device that operates in a cyclical manner and takes in energy as heat from a high-temperature reservoir and performs work without, in some part of the cycle, discharging energy as heat to a low-temperature reservoir.

Third law: It is impossible to construct a device capable of decreasing the temperature of any macroscopic system to the absolute zero of temperature (0 K).

Stated in terms of the primary thermodynamic functions of temperature, energy, and entropy, the laws of thermodynamics can be stated succinctly as follows:

First law: The total energy is conserved (i.e., remains unchanged).

Second law: The total entropy increases.

Third law: The absolute (Kelvin) temperature remains above 0°.

These laws provide geochemists with (i) the conditions for the establishment of equilibrium in a system that includes chemical reactions, heat transfer, and mechanical strain; (ii) criteria to eliminate impossible processes; (iii) equations to convert thermodynamic data, such as the energy and entropy changes, into an equilibrium constant; and (iv) equations to predict the effects of changes in temperature, pressure, or composition on this reaction equilibrium.

The starting point in exploring thermodynamic laws is with knowledge of the experimental and thermodynamic properties of temperature, heat, work, energy, and entropy. Understanding work and heat is not difficult, but an understanding of temperature, energy, and entropy requires more effort.

Temperature

A device designed to measure temperature is called a thermometer, of which there are many types. Familiar examples are the liquid-in-glass capillary, thermocouples, and

resistance thermometers such as platinum wires and thermistors. All of these devices have a property that varies monotonically with temperature. The most fundamental thermometer, for example, is the constant-volume, ideal-gas thermometer, which is based on the fact that nonassociating gases obey the ideal-gas equation:

$$PV = nRT \tag{1}$$

in the limit as $P \rightarrow 0$ where P is the pressure of the gas, V is the volume, n is the number of moles of the gas, and R is the gas constant. With a constant-volume gas thermometer, we measure the temperature of a fixed reference point, such as the melting point of tin metal, as follows:

$$\begin{aligned} T &= (273.16\,\mathrm{K}) \lim_{P_{273.16\mathrm{K}} \rightarrow 0} \left[\frac{P_T}{P_{273.16\mathrm{K}}} \right] \\ &= (273.16\,\mathrm{K}) \left(\frac{nRT/V}{nR273.16/V} \right) \end{aligned} \tag{2}$$

We measure P_T, the pressure of n moles of the gas at temperature T for progressively smaller values of n. The resulting calculated values of temperature are extrapolated to zero pressure to obtain the thermodynamic temperature. The value of $P_{273.16\,K}$ is the corresponding measured pressure of the gas when the thermometer bulb is in contact with water at its triple point. The triple point of water is the single most important accessible reference point in thermometry and is assigned a temperature of exactly 273.16 K to preserve close numerical agreement with older temperature scales, such as the Celsius scale.

The temperature scale defined by Eq. 2 is an absolute scale where zero is the lowest possible temperature and all temperatures are positive. This scale is called the absolute Kelvin temperature scale, and temperatures are expressed as kelvins. Celsius temperatures are related to Kelvin temperatures via the equation

$$t/^{\circ}\mathrm{C} = T/K - 273.16 \tag{3}$$

The temperatures of fixed reference points obtained in the manner outlined above are, in turn, used to calibrate other more convenient thermometers.

Energy, Work, and Heat

Energy is an abstract mathematical concept that is quantified in terms of an energy function, U. Some other thermodynamic functions also are called energy functions (Gibbs energy, Helmholtz energy) and are chosen specifically as state functions that yield exact differentials in terms of experimentally convenient variables such at T and P.

Energy is not a thing. There are no meters capable of directly measuring energy, yet there are electric-current meters, gas-flow meters, volume meters, mass meters, pressure meters, length meters, time meters, and thermometers. These measureable properties are used to calculate energy changes. Determination of the amount of energy transferred from one system to another always involves measurements of the appropriate physical parameters followed by calculations involving the appropriate energy formulae.

The most significant mathematical property of the energy function is that of conservation. The principle of energy conservation amounts to the statement that, for any real process, the total amount of energy remains exactly the same at the end of the process as it was at the beginning. Energy can be transferred and transformed, but it cannot be created or destroyed. This conservation relates to the definition of a state function, which is also independent of path.

Work and heat are the only modes of energy transfer between systems. The transfer of energy as work requires the existence of an unbalanced force between a system and its surroundings. The transfer of energy as *heat* requires the existence of a temperature difference between the system and its surroundings. When a force F acts on a system and displaces the system by a differential amount dx, then the work done on the system is given by classical mechanics as

$$\delta w = -F dx \tag{4}$$

In general, the *work* done on a system depends on the path along which the process is carried out and must be specified (here from states $1 \rightarrow 2$):

$$w = -\int_1^2 \mathrm{F dx} \tag{5}$$

in order to calculate work: w. The minus sign in Eq. 5 is chosen to make work done on the system ($dx < 0$) a positive quantity. When the path must be specified before the integral in Eq. 5 can be evaluated, then the integral is called a line integral. If the work done is independent of the path, e.g., the work done in lifting a weight in a constant gravitational field

$$\begin{aligned} w &= -\int_1^2 F dx = \int_1^2 mg\, dh \\ &= mg(h_2 - h_1) \end{aligned} \tag{6}$$

then the force F is said to be conservative; in this case the formula $w = mg\Delta h$ is used to calculate the amount of energy.

A conservative force always can be expressed as the negative derivative of a potential energy, φ, with respect to the displacement:

$$F = -\frac{d\varphi}{dx} \tag{7}$$

and thus for a conservative force:

$$w = -\int F dx = \int_1^2 \frac{d\phi}{dx} \qquad dx = \int_1^2 d\phi = \phi_2 - \phi_1 \tag{8}$$

Note that if the force is conservative, then the work done depends only on the end states (initial and final) for the process and is thus path independent; this point is very important. These path-independent (state) functions and their manipulation lie at the core of thermodynamics.

If at any stage in the process energy is transferred as heat, then the force is not conservative, the value of w depends on the path, and we move from classical mechanics to thermodynamics. Energy added as heat to a system is taken as positive; and the SI unit of energy is the joule, J:

$$\begin{aligned} \text{energy} &= \text{force} \cdot \text{displacement} \\ &= \text{mass} \cdot \text{displacement} \cdot \text{acceleration} \end{aligned}$$

$$1\ \text{J} = (1\ \text{kg}) \cdot (1\ \text{m} \cdot \text{s}^{-2}) \cdot (1\ \text{m}) = 1\ \text{kg} \cdot \text{m}^2\text{s}^{-2} \tag{9}$$

For a general process involving both work and heat transfers, the first law of thermodynamics takes the form

$$dU = \delta q + \delta w \tag{10}$$

The energy function, U, is also called the internal energy and is a thermodynamic state function. The differential of a state function is said to be exact, because the value of $\Delta U = U_2 - U_1$ for the process is path independent, even if energy is transferred as heat in the process:

$$\int_1^2 dU = U_2 - U_1 = \Delta U = \int_1^2 dq + \int_1^2 dw = q + w \tag{11}$$

A key point to recognize is that for a given change (i.e., $1 \rightarrow 2$), the value of $U_2 - U_1$ is independent of path, whereas the values of q and w depend on the path. It is only the sum $q + w$ that is independent of path. This statement constitutes the *essence* of the first law of thermodynamics. If the process is adiabatic (i.e., $\delta q = 0$), then δw is exact, because $w = \Delta U$. If no work is done (i.e., $\delta w = 0$), then δq is exact (pure heat transfer), because $q = \Delta U$.

In summary, heat and work are modes of energy transfer, and energy cannot be created or destroyed; the energy of a system is characterized by its internal energy U. A system cannot *possess* heat or work; one can only perform work, that is, add energy by force gradients, and transfer heat.

Enthalpy and Heat Capacity

Much of the mineralogy that we observe at the Earth surface was formed by reactions at much higher temperatures, and these are slowly converted to minerals that are stable at low temperatures and in the presence of water. It is therefore desirable to have a thermodynamic function that describes the energy transferred as heat at a constant pressure but which does not depend on the path. Consider a process involving only pressure-volume work for which

$$w = -F\,dx = -\left(\frac{F}{A}\right)A\,dx = -P_{ext}\,dV \tag{12}$$

where P_{ext} denotes the externally applied pressure and we employ the definition of pressure $P =$ force/area $P = \frac{F}{A}$ and note that the volume element $dV =$ (area of the base)$\cdot$ (vertical displacement) $= A\,dx$. Combining Eqs. 11 and 12 yields

$$dU = \delta q - P_{ext}\,dV \tag{13}$$

We now define the enthalpy, H, a thermodynamic state function, as

$$H \equiv U + PV \tag{14}$$

From Eq. 14 we obtain by differentiation

$$dH = dU + PdV + VdP \tag{15}$$

Combining Eqs. 13 and 15 yields

$$dH = \delta q + VdP \tag{16}$$

or at constant pressure ($dP = 0$):

$$dH = \delta q_p \tag{17}$$

From Eq. 17 we see that the addition or removal of energy as heat from a system at constant P is equal to the change in enthalpy of the system.

The *heat capacity* of a system is a quantitative measure of the capacity of a system to take in energy as heat. The greater the heat capacity of a system, the smaller the change in temperature produced by the input of energy as heat. The heat capacity is necessarily positive and for a two-phase system (e.g., ice + liquid water) is infinite as long as both phases exist in equilibrium. The heat capacity, C_x, of a system

at constant x (where x is a thermodynamic state function, such as pressure) is defined as follows:

$$C_x = \lim_{\Delta T \to 0} \left(\frac{q_x}{\Delta T} \right) = C_x(x, T) \tag{18}$$

where $C_x(x,T)$ denotes that C_x is a function of both x and T. For a constant-pressure process we have from Eqs. 18 and 17:

$$C_p = \lim_{\Delta T \to 0} \left(\frac{q_p}{\Delta T} \right) = \lim_{\Delta T \to 0} \left(\frac{\Delta H}{\Delta T} \right)_P = \left(\frac{\partial H}{\partial T} \right)_P \tag{19}$$

Note also from Eq. 19 that

$$q_P = \int_1^2 C_P dT \tag{20}$$

A large heat capacity indicates that the system can take up substantial amounts of energy as heat owing to storage of the energy in the internal modes (translation, rotation, vibration, molecular dissociation) of the constituent particles. For example, the molar heat capacities of solid, liquid, and gaseous water over the temperature range 250–500 K are

$$\mathrm{H_2O(s)}: C_p = 37.66\ \mathrm{J \cdot K^{-1} \cdot mol^{-1}}$$
$$\mathrm{H_2O(l)}: C_p = 75.32\ \mathrm{J \cdot K^{-1} \cdot mol^{-1}}$$
$$\mathrm{H_2O(g)}: C_p = 30.54\ \mathrm{J \cdot K^{-1} \cdot mol^{-1}} + \left(1.03 \cdot 10^{-2} T\right)\ \mathrm{J \cdot K^{-2} \cdot mol^{-1}}$$

The roughly twofold greater heat capacity of liquid water relative to solid or gaseous water arises from the fact that a substantial (roughly half) of the heat energy input to liquid water is absorbed in breaking the hydrogen bonds in liquid water (≈20 kJ/mol). Ice absorbs energy as heat below its melting point without breaking any hydrogen bonds; ice is a completely hydrogen-bonded solid, whereas there are no hydrogen bonds in gaseous water.

Entropy

The concept of entropy and the science of thermodynamics have their origin in the fact that most naturally occurring processes involve the transfer of energy as heat. The first law of thermodynamics places no restrictions on energy transfers other than conservation and is completely silent about the direction of transfer. It is well known, however, that there are other restrictions on energy transfers. Some restrictions are:

(a) Heat always flows spontaneously from higher- to lower-temperature systems.
(b) Heat can be induced to flow from a lower- to a higher-temperature system only through the addition of energy as work.
(c) When a system undergoes a change in thermodynamic state, then the system and its surrounding (i.e., everything but the system) cannot both be restored exactly to their original states. All naturally occurring processes are in this sense irreversible.

A thermodynamically *reversible* process is defined as one for which the force and temperature differences between the system and the surroundings are never more than infinitesimal. A reversible process constitutes an ideal limiting case where the system can be restored to their original state and is thus of theoretical importance.

The second law of thermodynamics is fundamentally different from the first law in that it concerns the direction in which processes occur in nature. Rudolf Clausius, in 1865, chose the word *entropy* because it translates from the Greek as τρεπειυ (to a give direction), and the implicit connection of the second law with the passage of time has led to its characterization as "times arrow." The total entropy of the universe can only increase with time as the universe evolves to more probable distributions of mass and energy.

A mathematical statement of the second law of thermodynamics is as follows: for any change in defined thermodynamic states of a system, the change in entropy of the system, dS_{sys}, is

$$dS_{sys} \geq \frac{\delta q_{sys}}{T} \tag{21}$$

where T is the absolute thermodynamic temperature (K). The equality sign holds if the process is reversible, and the inequality sign holds if the process is irreversible. The function, S, the entropy, is a thermodynamic state function and has the units $\mathrm{J \cdot K^{-1}}$.

Suppose we have a system and its surroundings between which energy can be transferred. If the system undergoes a change in state, then the total entropy change is

$$dS_{tot} = dS_{sys} + dS_{sur} \tag{22}$$

If the process is adiabatic, then $\delta q_{sys} + \delta q_{sur} = 0$ and from Eq. 21 $dS_{sur} \geq 0$ and $dS_{sys} \geq 0$. Thus $dS_{tot} \geq 0$. The maximization of entropy provides the stability criterion for Gibbs energy and ultimately for our definition of equilibrium.

Suppose now that the system undergoes an isothermal process, $T = T_{\mathrm{sys}} = T_{\mathrm{sur}}$. From the second law, we have

$$\mathrm{dS_{sys}} \geq \frac{\delta q_{\mathrm{sys}}}{T} \text{ and } \mathrm{dS_{sur}} \geq \frac{\delta q_{\mathrm{sur}}}{T} \tag{23}$$

but $q_{\mathrm{sys}} = -q_{\mathrm{sur}}$ and thus $\Delta S_{\mathrm{tot}} \geq 0$. Note that in both cases there is net entropy production if the process is

irreversible, whereas the total entropy remains unchanged if the process is reversible.

All real processes involve some degree of irreversibility and thus lead to an increase in the total entropy of the universe. Unlike energy, entropy is not conserved, except in the hypothetical limiting case of a reversible process.

A thermodynamic system is said to be in an equilibrium state when it can no longer undergo any spontaneous, entropy-producing processes. The increase in total entropy that occurs in an irreversible process is a consequence of the failure to fully exploit the potential for doing work. When less than the maximum possible work is done in a process, net entropy is produced. The total entropy can never decrease, and, for a given energy and volume, a maximum in entropy indicates the most stable configuration, that is, equilibrium (see Dill and Bromberg 2011).

Entropy, like energy, is in essence an abstract mathematical concept. Because entropy is a state function:

$$\int_1^2 dS = S_2 - S_1 = \Delta S \tag{24}$$

For a given change in state (e.g., 1 → 2), the change in entropy of the system (but not the total entropy change, $\Delta S_{tot} = \Delta S_{sys} + \Delta S_{sur}$) is independent of the path that the system takes from state 1 to state 2.

Entropy is not a thing, and there are no entropy meters. Rather, entropy changes are calculated from measurable quantities, such as temperature, pressure, volume, and heat capacity. Entropy was described by the great thermodynamicist J. Willard Gibbs as a measure of the "mixed-up-ness" of a system, that is, the more disordered or random a system is, the higher is its entropy. Modern statistical mechanics relates this concept to the probability of accessible energy states (see Dill and Bromberg 2011).

Compared to the same pressure and temperature, liquids are more disordered than solids, and gases are more disordered than liquids. This result follows from the fact that the molecules of a gas have more freedom to move around than the molecules of a liquid. The same holds true for the molecules or ions of a liquid as compared to those of a solid. The melting of a solid involves an entropy increase of 8–40 J K^{-1} mol^{-1}. The temperature dependence of the entropy is found from Eqs. 21 and 18. From Eq. 21 we have for an isothermal pure heat transfer (i.e., $\delta w = 0$) at constant pressure $q_p = T\Delta S$. Substitution of this result into Eq. 19 yields

$$C_p = \lim_{\Delta T \to 0}\left(\frac{q_p}{\Delta T}\right) = T \lim_{\Delta T \to 0}\left(\frac{\Delta S}{\Delta T}\right)_p = T\left(\frac{\partial S}{\partial T}\right)_p \tag{25}$$

$$\text{Thus}: \left(\frac{\partial S}{\partial T}\right)_p = \frac{C_p}{T} \tag{26}$$

or

$$\Delta S = \int_1^2 \frac{C_p}{T} \mathrm{dT}\ (\text{at constant } P) \tag{27}$$

Because $C_p > 0$, the entropy of a substance always increases with increasing temperature at constant pressure. The increase in the entropy of a substance that undergoes an increase in temperature at fixed pressure is a consequence of the increased thermal randomness of the molecules at the higher temperature. A greater amount of energy is distributed over the same number of particles.

Entropies of solids can be determined using Eq. 27 and cryogenic calorimetry where the temperature of state 1 is near (but of course not at) absolute zero. These *third-law entropies* have been determined for a range of minerals, leading to important thermodynamic equations of state for describing the minerals in rocks (see Robie et al. 1978; Chase et al. 1986). They are referred to as "third-law entropies" because they employ the property that the entropy of a pure substance is zero at 0 K (the third law of thermodynamics).

Applications of the First and Second Laws of Thermodynamics

Combination of the first law with the second law yields

$$dU \leq TdS + \delta w \tag{28}$$

In applying Eq. 28 it is essential to include all of the relative work terms, of which there may be several. That is,

$$\delta w = \sum_i \delta w_i \tag{29}$$

as required by energy conservation. Some commonly encountered types of work are pressure-volume (expansion/compression) work, electrical work, surface area increases and decreases, and magnetic work.

Suppose we only have to deal with pressure-volume work and that the process occurs reversibly. In this special case Eq. 28 becomes

$$dU = TdS - PdV \tag{30}$$

Because U and S are state functions, we can compute the values of ΔU and ΔS along a reversible path between the given initial and final states of the actual process and equate the results for ΔU and ΔS for the system to those for the actual irreversible process. The values of q and w differ for the two paths, but not ΔU_{sys} or ΔS_{sys}.

Equation 28 is the differential equation used to calculate ΔU, which can be converted into more convenient stability criteria by choice of fixed variables. It expresses the change in the dependent variable in terms of changes in the independent variables S and V, that is, $U = U(S,V)$. The variables S and V are not convenient variables in geochemistry because they are difficult to control in the laboratory. More convenient variables for experimental work are pressure and temperature, which lead directly to a definition of the Gibbs energy via a Legendre transform of the combined first and second laws of thermodynamics. We can transform Eq. 30 into a differential equation with P and T as independent variables as follows:

$$\begin{aligned} &dU - TdS + PdV = 0 \\ &dU - TdS + PdV - SdT + VdP = -SdT + VdP \\ &d(U - TS + PV) = -SdT + VdP \end{aligned} \tag{31}$$

For compactness, we now define the thermodynamic energy state function, G, that can be used as stability criterion for system equilibrium in terms of the more convenient variables, T and P:

$$\begin{aligned} &G = U + \mathrm{PV} - \mathrm{TS} = H - \mathrm{TS} \\ &\text{where}: H = U + \mathrm{PV} \end{aligned} \tag{32}$$

The function G is called the Gibbs energy, or Gibbs free energy, after its creator, J. W. Gibbs, and plays a familiar role in geochemistry. From Eqs. 28 and 29 we have a combination of the first and second laws of thermodynamics:

$$dG = -SdT + VdP \tag{33}$$

which gives the differential equation for dG, where $G = G(T,P)$. Because dG is an exact differential, G is a state function, and from mathematics we can write

$$dG = \left(\frac{\partial G}{\partial T}\right)_p dT + \left(\frac{\partial G}{\partial P}\right)_T dP \tag{34}$$

Comparison of Eqs. 34 and 33 leads to

$$\left(\frac{\partial G}{\partial T}\right)_p = -S \tag{35}$$

$$\left(\frac{\partial G}{\partial P}\right)_T = V \tag{36}$$

Equation 35 is a restatement that the temperature dependence of the Gibbs energy is determined by the entropy, and Eq. 36 shows that the pressure dependence of the Gibbs energy is controlled by the volume. One could have employed a similar approach to achieve the Helmholtz free energy from the combined first and second laws of thermodynamics. The Helmholtz energy has as its natural variables temperature and volume rather than the natural variables of temperature and pressure of the Gibbs energy. Helmholtz free energies are used in cases where the volume is easily controlled, such as in computer simulations.

Because dG is an *exact* differential, it follows directly that the second cross partial derivatives are equal. This property is characteristic of an exact differential:

$$\left[\frac{\partial}{\partial P}\left(\frac{\partial G}{\partial T}\right)_P\right]_T = \left[\frac{\partial}{\partial T}\left(\frac{\partial G}{\partial P}\right)_T\right]_P \tag{37}$$

Substitution of Eqs. 35 and 36 into 37 yields

$$\left(\frac{\partial V}{\partial T}\right)_P = -\left(\frac{\partial S}{\partial P}\right)_T \tag{38}$$

Equation 38 is called a Maxwell relation after the early thermodynamicist James Clerk Maxwell (1831–1879) and is especially useful for computing changes in entropy with pressure when the equation of state (e.g., $V = V(T,P)$) for the system is known.

It is simple to illustrate the connection between the abstract thermodynamic functions and measurable properties of a mineral or solution if these measured properties are expressible as equations. For example, consider $S = S(T,P)$ from which we can write

$$dS = \left(\frac{\partial S}{\partial T}\right)_P dT + \left(\frac{\partial S}{\partial P}\right)_T dP \tag{39}$$

Substitution of Eqs. 26 and 38 into 39 yields

$$dS = \frac{C_p}{T} dT - \left(\frac{\partial V}{\partial T}\right)_P dP \tag{40}$$

One job of experimental petrologists is to evaluate equations of state that describe minerals and fluids as a function of temperature and pressure. Suppose we have a solid for which data on these properties had been accumulated and shown to be fit by equations of the form

$$C_p = n(a + bT) \qquad \text{and} \qquad V = nV_o(1 + \alpha T - \beta P) \tag{41}$$

where n is the number of moles and a, b, α, β, and v_o are constants characteristic of the particular solid. Substituting these two expressions into Eq. 40 yields

$$dS = n\left(\frac{a}{T} + b\right)dT - (nV_o\alpha)dP \tag{42}$$

which, on integration from P_1, T_1 to P_2 and T_2, yields for the entropy change of the substance:

$$\Delta S = n\left(a \ln \frac{T_2}{T_1}\right) + nb(T_2 - T_1) - nV_o\alpha(P_2 - P_1) \tag{43}$$

Partial Molar Thermodynamic Functions: Chemical Potential

A conspicuous feature of most rock-forming minerals is their capacity to change composition and to form solid solutions. Furthermore, aqueous solutions evolve considerably in composition along a flow path. Yet up to this point we restricted our treatment to a particular mass of substance of fixed composition. Mother Nature is not so kind.

If we allow the composition and/or the amount of the various chemical components to vary, then we must take this fact into account in our thermodynamic equations. In such case, the Gibbs energy of the system depends not only on T and P but also on the number of moles of the various components of the system (n_1, n_2, n_3,. . . . . .,n_c) where c is the total number of components. Thus:

$$G = G(T, P, n_1, n_2, n_3 \ldots n_c) \tag{44}$$

Because dG is an *exact* differential, we have from mathematics and the chain rule:

$$dG = \left(\frac{\partial G}{\partial T}\right)_{P, n_j} dT + \left(\frac{\partial G}{\partial P}\right)_{T, n_j} dP + \sum_{i=1}^{c} \left(\frac{\partial G}{\partial n_i}\right)_{T, P, n_{j \neq i}} dn_i \tag{45}$$

The notation $n_{j \neq i}$ denotes the set of all mole number except i itself. We now define the chemical potential of the i^{th} component, μ_i, of the system as

$$\mu_i \equiv \left(\frac{\partial G}{\partial n_i}\right)_{T, P, n_{j \neq i}} \tag{46}$$

The chemical potential of component i is thus its partial molar Gibbs energy.

Combination of Eqs. 45, 46, and 33 yields

$$\mathrm{dG} = -\mathrm{SdT} + \mathrm{VdP} + \sum_{i=1}^{c} \mu_i \mathrm{dn}_i \tag{47}$$

Equation 47 is the key equation for the analysis of thermodynamics of solutions and is an expression of the combined first and second laws of thermodynamics. Rearranged, it leads to a familiar form of the Gibbs-Duhem expression.

Another useful equation for solutions is obtained from Eq. 33:

$$\frac{\delta}{\delta n_i}(dG = -SdT + VdP)_{T, P, n_{j \neq i}}$$

or :

$$d\mu_i = -\overline{S}_i dT + \overline{V}_i dP_i \tag{48}$$

where :

$$\overline{S}_i = \left(\frac{\delta S}{\delta n_i}\right)_{T, P, n_{j \neq i}} \quad \text{and} \quad \overline{V}_i = \left(\frac{\delta V}{\delta n_i}\right)_{T, P, n_{j \neq i}}$$

where $\overline{S}_i = \left(\frac{\delta S}{\delta n_i}\right)_{T, P, n_{j \neq i}}$ and $\overline{V}_i = \left(\frac{\delta V}{\delta n_i}\right)_{T, P, n_{j \neq i}}$ are the partial molar entropy and the partial molar volume, respectively, of the ith component in the solution.

A Geochemical Example

A simple geochemical example would be making diamond from graphite at 298 K. Can we circumvent the very exploitive mining of kimberlite pipes by a clean industrial process at equilibrium? Experimental data reported in Robie et al. (1978) yield a change in the volume of the reaction:

$$\mathrm{C(diamond)} = \mathrm{C(graphite)} \tag{49}$$

of $\Delta V^o_{rxn} = +\ 0.1882$ J/mol and a value of ΔG^o_{rxn} (1 bar, 298 K) $= -2.9$ kJ/mol. At equilibrium the chemical potentials of carbon in each phase are equal. Because the activities of these solids are on the mole-fraction scale, and because they are pure, integration of this equation at constant temperature yields

$$\Delta G^o_{\mathrm{rxn}}(\mathrm{P}, 298\mathrm{K}) = 0 = \Delta G^o_{\mathrm{rxn}}(1\,\mathrm{bar}, 298\mathrm{K}) + \int_{1\,\mathrm{bar}}^{P} \Delta V_{\mathrm{rnx}} \mathrm{dP} \tag{50}$$

We use the approximation that ΔV^o_{rxn} is independent of pressure to rearrange the equation:

$$\frac{-\Delta G^{o}_{\mathrm{rxn}}(1\,\mathrm{bar}, 298\mathrm{K})}{\Delta V^{o}_{\mathrm{rxn}}(1\,\mathrm{bar}, 298\mathrm{K})} + 1 = P(\mathrm{bar}, 298K) \qquad (51)$$

The equilibrium pressure to make diamond from graphite is predicted to be 15.4 kbar, which is easily within the reach of commercial equipment or explosive shock-loading methods of synthesis. This example calculation does not tell one whether the reaction can be made to proceed; only that equilibration is possible at the stated conditions.

In summary, equilibrium thermodynamics allows geochemists to describe possible reactions that form and modify the mineral assemblages that make up rocks and soils. The tools are absolutely general and can be applied equally well to solutes in groundwater or the phase changes that account for seismic discontinuities in the deep crust and mantle. Thermodynamic truths are inescapable. The "no" of thermodynamics is absolute. The "yes" of thermodynamics is actually a "maybe" to be decided by the rates of the processes.

Conclusions

An understanding of geochemical thermodynamics allows scientists to make meaningful predictions about the chemical state of mineral and fluid assemblages in the Earth. It is the underpinning of all geochemistry.

Cross-References

- ▶ Activity and Activity Coefficients
- ▶ Enthalpy
- ▶ Entropy
- ▶ Equilibrium
- ▶ Fugacity
- ▶ Gibbs-Duhem Equation
- ▶ Standard States

References

Chase MW Jr, Davies CA, Downey JR Jr, Frurip DJ, McDonald RA, Syverud AN (1986) NIST Standard Reference Database 13. J Phys Chem Ref Data Monograph 9, 4th edition. (Janef Tables). 1961 pp

Dill KA, Bromberg S (2011) Molecular Driving Forces: Statistical Thermodynamics in Biology, Chemistry, Physics and Nanoscience, 2nd edn. Garland Science, London, p 756

Eugster HP (1971) The Beginnings of Experimental Petrology. Science 173:481–489

Robie RA, Hemingway BS, Fisher JR (1978) Thermodynamics properties of minerals and related substances at 298.15 K and 1 bar (10^5 Pascals) pressure and at higher temperatures. U.S. Geological Survey Bulletin 1452, 456 pp

Geochemistry

William M. White
Department of Earth and Atmospheric Sciences, Cornell University, Ithaca, NY, USA

Definition

As the term implies, geochemistry is a marriage between chemistry and geology, or more broadly geosciences or earth science, and it is arguably a subdiscipline of both. A better explanation of geochemistry is that it is applies chemistry and chemical principles to understanding the Earth and its cosmic environment and to using that understanding to better the human condition. The latter includes not only exploitation of resources but also safeguarding humans and the environment from the consequences of that exploitation.

Impact

Geochemistry has grown over the last 50 or 60 years to touch virtually every aspect of earth science. The contributions of geochemistry to this advance have been simply enormous. Much of this progress has come from innovation in analytical techniques and the ability to assess the nature of natural materials with evermore precision and on evermore finer scales. Geochemists have quantified the geologic time scale through analysis of radioactive and radiogenic isotopes. Through analysis of trace elements such as Ir and stable isotope ratios of C, O, and other elements, geochemists have been able to infer the causes of the crises and events that define that time scale (e.g., Alvarez et al. 1980). Geothermometers and geobarometers based on chemical thermodynamics are used to quantify the depths and temperatures at which magmas crystallize and at which the various metamorphic facies form. These can be combined with radiogenic isotope geochemistry to determine rates of geologic processes, such as magma crystallization, uplift, and erosion. Chemical and isotopic analysis of the components of meteorites provides some of the few hard constraints on how and when the solar system formed and with it the Earth. It is principally through isotope geochemistry that the timing and temperature swings of Louis Agassiz's ice ages have been determined and consequently their cause deduced. The evidence, albeit still controversial, that life was present on Earth by at least 3.8 billion years ago is not physical fossils, but carbon isotope ratios (Rosing et al. 1996). We have learned the atmosphere was barren of oxygen prior to 2.3 billion years ago, the so-called Great Oxidation Event (Holland 2006), and

that its present oxygen-rich nature is due to photosynthesis. Geochemistry is used to trace ocean circulation and biologic productivity, both now and in the past. Indeed, geochemistry is also used to unravel mantle convection patterns. Not surprisingly, instruments for chemical analysis have been key part of probes sent to other heavenly bodies, including Mercury, Venus, Mars, Vesta, Ceres, Jupiter, Saturn, and Pluto and their moons.

Problems such as water and soil pollution, acid rain, the ozone hole, and global warming and climate change are geochemical problems. Addressing these problems requires knowledge of geochemistry. Similarly, most of our nonrenewable resources, such as metal ores and petroleum, form through geochemical processes. Locating new sources of these resources requires geochemical approaches. This will be no less true in the carbon-free energy economy of the future as demand increases for scarce metals such as lithium, neodymium, dysprosium, and tellurium used in batteries, electric generators and motors, and photovoltaics.

Geochemistry has also contributed to archeology and understanding human history, particularly the period preceding written history. Techniques such as ^{14}C and U-Th decay series have been used to date everything from bones and artifacts to cave painting (Pike et al. 2012). Carbon and oxygen isotopes tell us about our ancestor's diet and environment, and the trace element and isotopic compositions of stone and metal tools and coins tell us about trade patterns.

Physicochemical Basis

In the nineteenth century, geochemistry, like geology, was more descriptive than quantitative. As chemists of the late nineteenth and earlier twentieth centuries such as Maxwell, Van't Hoff, Gibbs, Arrhenius, Lewis, and Randall laid the foundations of chemical thermodynamics and kinetics, geochemists such as F.W. Clarke and Victor Goldschmidt (Goldschmidt 1923, 1933) began to apply these approaches that eventually allowed deeper insights into geochemical processes.

Thermodynamics enables prediction of the equilibrium state of a system through analysis of energy and its transformations between chemical energy, heat, and work. In principle then, thermodynamics can predict which minerals will break down as a rock undergoes chemical weathering, which new minerals will replace them, and which elements will be carried away in solution. Thermodynamic magmatic process modeling can predict the sequence of minerals precipitating as magma of a given composition cools and how magma composition will consequently evolve. Thermodynamics can predict the metamorphic reactions and processes that will occur as igneous or sedimentary rocks experience elevated temperature and pressure. Perhaps more valuably, given the composition of a metamorphic rock, the temperature and pressure of metamorphism can be deduced from its constituent minerals and their compositions: something known as thermobarometry.

Before thermodynamics can be applied to geochemical problems, basic thermodynamic properties such as molar volume, entropy, enthalpy, heat capacity, compressibility, and the coefficient of thermal expansion must be determined for a vast array of natural substances. It was not until the second half of the twentieth century that the necessary data was available to allow geochemists such as Hal Helgeson (e.g., Helgeson 1968) and Ian Carmichael (Carmichael and Eugster 1987; Ghiorso et al. 1983) and their students to develop quantitative models to augment experimental approaches. Although this data set remains incomplete, much progress has been made and thermodynamics has become a routine tool across the breadth of geochemistry.

Geochemical systems are often not at equilibrium, particularly at surface temperatures, which limits the applicability of thermodynamics. Perhaps nothing better illustrates this than metamorphic assemblages equilibrated at lower crustal pressures and temperatures that persist in that state at the Earth's surface, or even more spectacularly the persistence on the surface of diamond, which is thermodynamically stable only at depths of 100 km or more (Kennedy and Kennedy 1976). Consequently, kinetics, which is the study of reaction rates and mechanisms, has an importance in geochemistry nearly equal to that of thermodynamics, and its importance and application in geochemistry has grown in tandem with thermodynamics. As opposed to the chemistry laboratory when reactions often occur in the gas or liquid phase in the restricted space of a beaker, geochemical scales are vast, and many solid-state geochemical reactions rates are limited by the rates at which reactants can be brought together by diffusion. Kinetics allows geochemists to understand under what circumstances equilibrium will or will not be achieved and how rapidly it is approached. As in thermodynamics, application of kinetics requires knowledge of fundamental properties such as activation energies and volumes and diffusion coefficients, and progress continues to be made on this front. Geochemical kinetics is applied on broader scales as well since, although it appears static, the Earth is a dynamic system. The oceans perhaps illustrate this best. Although their composition is nearly static over millions and tens of millions of years, this composition is maintained through constant fluxes from sources into the oceans and fluxes out of them. The carbon cycle is another illustration of this point. CO_2, which has been a key control on climate, has a residence time in the atmosphere of only about 4 years, as carbon cycles continually between the oceans, the atmosphere, the biosphere, and the soil. Shifts in carbon between these reservoirs have been responsible for climate change throughout Earth's

history (Berner 2006), just has it been doing since the industrial revolution.

Thermodynamics can be approached macroscopically – that is, one often need not know what occurs on the molecular or atomic level. Kinetics generally requires a more microscopic approach and some knowledge of the atomic/molecular nature of reactants to understand reaction fundamentals. In the last few decades, geochemistry has begun to approach problems from an even finer level, namely, the *ab initio* approach, which begins with calculations of atomic electronic and molecular orbitals. This requires enormous computational power but has already proved useful in a number of applications.

Breadth and Subdisciplines

Geochemistry can be divided into a variety of overlapping subfields. One such division is between applied geochemistry, on the one hand, and what could be called "pure" or "theoretical" geochemistry. The focus of the latter is understanding how the Earth works, how it has evolved, and how it operates as a chemical system. The focus of the former is to apply that understanding to finding and developing resources and avoiding or mitigating the environmental impacts of human activity. Occasionally, this flow of information reverses, and discoveries and techniques made by applied geochemists turn out to be useful in "pure" geochemistry.

Another division is between "low-temperature" and "high-temperature" geochemistry. The temperature of this divergence is not firmly established: certainly processes occurring at temperatures up to 100 °C or so would fall within the range of low-temperature geochemistry, while those at and above the temperatures of hydrothermal systems, 350–400 °C, would fall within the realm of high-temperature geochemistry. The latter is closely related to the fields of metamorphic and igneous petrology. Biogeochemistry and organic geochemistry are part of low-temperature geochemistry but are nevertheless distinct specialties. Isotope geochemistry is another distinct subfield and has applications in both low- and high-temperature geochemistry. The Earth is best understood, particularly its origins, in context of the solar system of which it is part and more broadly the universe in which its continuant elements have been created. These are the realms of cosmochemistry.

Low-Temperature Geochemistry

"Low-temperature geochemistry" is nearly synonymous with "environmental geochemistry," with the latter term having a more applied connotation. These fields focus on processes occurring in the oceans, in the atmosphere, and in the "critical zone," defined as Earth's permeable surface, from the top of the trees to the bottom of the groundwater zone, most of which involve reaction with, in, or mediated by water. The concept of the critical zone endeavors to acknowledge and integrate the complexity of the Earth's surface environment with the biological processes that strongly shape it: Vladimir Vernadsky's (1926) biosphere. They encompasses topics such as aquatic and groundwater chemistry, chemical oceanography, chemical weathering, mineral dissolution and precipitation, sedimentary chemistry and diagenesis, soil chemistry, atmospheric chemistry, and contaminant transport.

Current research on the critical zone involves learning about the kinetics of weathering reactions, including deducing exact reaction pathways and their dependence on factors such as temperature, rainfall, biota, rates of gas exchange, and anthropogenic disturbance (Brantley et al. 2006). Chemical components are also cycled within the critical zone, between solution, soils, colloids, and the biota, so that the residence time of weathering products within it can be considerable. This includes a continual cycling of nitrogen between N_2 and "fixed" nitrogen, which includes both oxidized and reduced forms such as NO_3^- and NH_4^-. This too is critical for life because, with the exception of some bacterial classes, autotrophs can only utilize fixed nitrogen.

Rivers carry the products of chemical weathering to the ocean; as Antoine Lavoisier noted, "The water of the sea results from a washing of the entire surface of the globe." Despite this continuous supply of salts, the saltiness, or salinity, of the oceans does not change substantially over time as salts are also continuously removed from the oceans and the concentrations of specific salts depend on the rate at which they are removed as well as the rate at which it is added. The major ions in seawater, Na, Ca, Mg, K, Cl, and SO_4, are always present in constant proportions to one and other and to total salinity, as was postulated by Forchhammer's Rule, and they all have very long residence times in seawater, hundreds of millions of years in some cases. Although the major element composition of seawater has been known since the nineteenth century, chemical oceanographers continue to improve understanding of the controls on it. For example, it was only with the discovery of deep-sea hydrothermal vents that it became clear that hydrothermal processes at mid-ocean ridges were the principal mechanism by which Mg is removed from seawater (Corliss et al. 1979). Although the general outlines of these processes have been known for sometime, the oceans are so vast and sampling is so limited; much of the detail is missing. Analytical advances and large-scale international sampling programs such as GEOTRACES in the last decade or two are greatly advancing knowledge of ocean chemistry, including the chemical speciation of key nutrients, such as Fe, and the distribution of anthropogenic contaminants such as Pb and Hg and radioisotopes (e.g., Boyle et al. 2015).

Sediments are the history book of the planet, and that history is recorded not only in sedimentary structures and

minerals but also in their chemistry. Studies of that chemistry have vastly expanded sedimentary petrology to reveal, for example, that while Earth's atmosphere first became oxidizing 2.3 billion years ago, it was only much later, perhaps 600 million years ago (Lyons et al. 2014), when that oxygen finally became abundant enough to support multicellular life and penetrated to the ocean's deep water (Xiao 2014).

Low-temperature processes are also responsible for many useful materials, such as evaporites, which are a primary source of halite, gypsum, Li, Mg, K, and other elements. Weathering and sorting produce deposits of high purity quartz sands, the raw material for silicon, and heavy mineral placers, a source of Zr, Cr, Ti, platinum group elements, Au, diamonds, etc. Sediments comprised of carbonate minerals such as limestone and its metamorphic equivalent, marble, are not only useful building materials in themselves but the source of lime, the key ingredient in cements and concrete, without which our cities would be very different. Contrasting oxidation states of the atmosphere and surface waters on the one hand and deep ocean water on the other in the Neoarchean and Paleoproterozoic resulted in oxidation–reduction reactions that produced banded iron formations, the major source of iron ore. A variety of U and other ore deposits also formed through oxidation–reduction reactions. Extreme weathering also produces useful deposits, including bauxite, the principal Al ore, lateritic Ni deposits, etc. Diagenetic brines are also capable of dissolving and subsequently precipitating metals as in Mississippi Valley-type ores or the Kupferschiefer of Germany and Poland.

While mining and refining metals has been key to the development of civilization, it also has and continues to impose a burden on society. The amount of mine waste generated annually is comparable to the amount of solids moved by natural geologic processes (Fyfe 1981). While this in itself can blight the landscape, the bigger problem is that this material is often toxic. The problem is particularly acute when the ores consist partly or wholly of sulfide minerals, which is often the case, particularly for so-called base metal ores such as Cu, Pb, and Zn. When exposed to oxygenated water, sulfide minerals quickly undergo oxic weathering, producing sulfuric acid.

The consequence of this is what is known as *acid mine drainage*, a classic example of which is the Rio Tinto in Andalusia, Spain, and ironically also the mine from which the huge multinational mining conglomerate Rio Tinto takes its name. Some 5000 years of mining of copper, silver, gold, and other metals as well as natural weathering have given the river a reddish hue due to the presence of dissolved iron. pH values of 2 and less extend 60 km downstream from the mine nearly to the estuary and tidal flat. Toxic levels of Cu, Zn, As, and Pb are found in sediments along the entire length of the river (Davis et al. 2000). Preventing future environmental problems and mitigating past ones requires a geochemical understanding of how metals and other elements in mine waste behave in the near-surface environment.

Biogeochemistry

Biogeochemistry is a subfield of low-temperature geochemistry that focuses on the interaction between life and its environment. The focus can range from the interaction of individual organisms with the soil and solutions surrounding them to the global scale of biogeochemical cycles, which considers the fluxes of elements and compounds between reservoirs such as the atmosphere, the ocean, the biosphere, etc.

The carbon cycle is an example of such a cycle and one of key importance given the control that atmospheric CO_2 exerts on climate. The residence time of CO_2 in the atmosphere is short, about 4 years, as it quickly cycles between the oceans, the biosphere, and soils. Of these reservoirs, the atmosphere is the smallest and the oceans the largest. Changes in the ocean–atmosphere carbon balance during Pleistocene ice ages reduced atmospheric CO_2 concentrations from 280 parts per million by volume (ppmv) to 180 ppmv, greatly amplifying the climate change induced by variations in Earth's orbit and rotation known as the Milankovitch cycles.

The above could be described as the exogenic or short-term carbon cycle. A deeper cycle also operates, but at a much slower rate. Weathering reactions such as

$$2H_2O + CO_2 + 2NaAlSi_3O_8 \rightharpoonup Al_2Si_2O_5(OH)_4 + 4SiO_2 + 2Na^+ + CO_3^{2-} \quad (1)$$

effectively convert atmospheric CO_2 to carbonate or bicarbonate ions, which are carried to the oceans by rivers and precipitated as calcium carbonate by marine organisms and ultimately buried in marine sediments. Variations in the rate of weathering have acted as one of the controls on atmospheric CO_2 and climate throughout the Phanerozoic (Berner 2006). In addition, some of the organic matter produced by marine phytoplankton is not respired but is buried along with marine sediment. Vastly more carbon is stored in sedimentary carbonate and organic carbon reservoirs than in all the exogenic reservoirs combined (e.g., Broecker 2012). These are slowly returned to the exogenic cycle when sediments are exhumed and weathered and organic carbon oxidized to CO_2. In addition, some carbonate in the oceanic crust and sediment is carried into the mantle in subduction zones where some of it undergoes decarbonation reactions with the CO_2 released through subduction zone volcanism. Some of it is carried into the deep mantle, but this too is ultimately returned to the atmosphere by volcanism, thus completing the cycle.

Fluxes into and out of these long-term reservoirs are not always in balance, leading to changes in atmospheric

composition. Fossil fuel burning since the industrial revolution has greatly accelerated loss from the sedimentary organic matter reservoir, and CO_2 has consequently increased from a preindustrial level of about 280 ppmv to a present (2016) level of $\gtrsim$400 ppmv. This increase, thus far at least, is small compared to variations in atmospheric CO_2 over Earth's history; those naturally driven changes, however, occurred far more slowly; the present rate of increase appears to be unprecedented.

The carbon cycle, because it involves photosynthesis and respiration, is closely linked to the oxygen and sulfur cycles, as well as to the behavior of redox-sensitive metals such as Fe, Mn, Mo, U, etc. and this has led to profound changes in the Earth's chemistry. There is considerable evidence that Earth's early atmosphere was quite different than the present one and was mostly likely dominated by CO_2 and N_2, similar to that of its sister planets. Photosynthesis, together with geologic burial of some fraction of the organic matter produced by that process, was responsible for the transition to the present N_2–O_2 composition (Holland 2006). A variety of geochemical and geological approaches have now established that molecular oxygen became a significant atmospheric component only in the Paleoproterozoic about 2.3–2.4 billion years ago, a time known as the Great Oxidation Event, although some free oxygen may have been present earlier in ocean surface waters (Farquhar et al. 2000; Kasting and Catling 2003).

Organic Geochemistry

Organic matter is an important part of the carbon cycle as the amount of carbon in soil and sediment organic matter vastly exceeds the amounts in the atmosphere and biosphere. Organic geochemistry is the study of nonliving organic matter in soil, water, air, and sediments and the reactions of those organic molecules under a broad range of Earth's surface and subsurface conditions. Oxidation by bacteria and other decomposers gives rise to the formation of oxygen-containing functional groups such as the hydroxyl and carboxyl group, which are polar, so that in the early stages of decomposition, the solubility of organic matter increases. Recent experimental work has also shown that simple organic molecules can be oxidized and reduced abiotically under hydrothermal conditions (300°C and 100 MPa) to produce similarly oxygenated functional groups (e.g., Shipp et al. 2013). Much of polar dissolved organic matter (DOC) consists of humic and fulvic acids that are rich in functional groups, notably amino and carboxylic acids, and that readily complex transition metals; consequently a substantial fraction of dissolved trace metals in natural waters may be complexed by these acids, enhancing their abundance as the solubility of these metals in natural aqueous solution is otherwise often quite limited.

Organic matter is also an important component of soils, where it plays an important role in soil fertility by releasing nutrients as it decomposes, stabilizing soil structure, increasing ion exchange capacity, and modulating porosity and water content. Recent advances in the past two decades have resulted in a paradigm shift as to the nature of soil organic matter and why it persists despite its thermodynamic instability (Kleber and Johnson 2010; Schmidt et al. 2011). Rather than recalcitrant condensates of biomolecules as previously thought, much of soil organic matter appears to consist of molecular aggregates of partially decomposed plant polymers loosely held together by entropic interactions and/or noncovalent bonds and that such aggregates are not inherently stable against decomposition (Kleber and Johnson 2010). Instead of molecular structure, environmental and biological factors, which remain poorly understood, appear to control the stability of soil organic matter (Schmidt et al. 2011).

Understanding how this organic matter is preserved in sediments and how it is transformed is an important part of organic geochemistry, not the least because the small fraction ultimately transformed to petroleum, gas, and coal is such an important energy resource. Even in aerobic environments, some organic matter survives, including some biomolecules or fragments of them that should be quite labile. Recent work suggests coprecipitation or chelation reactions result in macromolecular complexes between organic carbon and iron oxyhydroxide minerals that stabilize organic components and explain their survival (Lalonde et al. 2012).

The organic matter that does survive in sediments is transformed by bacterial and chemical processes that are part of the diagenetic process. The ultimate product of these processes is *kerogen*, the name given to the recalcitrant mixture of complex organic compounds that dominates the organic fraction in sediments. As sediments are buried, they experience progressively increasing temperature and pressure, and a number of new reactions, collectively called *catagenesis*, occur. During this process, kerogen disproportionates into comparatively simple hydrogen-rich molecules (hydrocarbons) and a hydrogen-depleted carbon-rich residue. As temperatures in the range of 100–150°C are reached, the so-called oil window, petroleum, a complex mixture of hydrocarbons, is produced. The petroleum is mobile and will migrate out of the source rock if a migration pathway exists. As temperatures approach and exceed 150°C, natural gas, a mixture of methane with some short-chain hydrocarbons such as ethane and propane, is produced in the *metagenesis* stage.

Despite changes occurring during diagenesis and catagenesis, some organic compounds in petroleum retain some of their original chemical structure and can be associated with specific classes of organisms; these are known as *biomarkers*. Biomarkers can be used to associate petroleum with the specific sedimentary source rocks and determine migration pathways (Peters et al. 2007), used to forensically

associate hydrocarbon pollution to specific sources (Briggs and Summons 2014), and in understanding the evolution of life (Eglinton and Eglinton 2008; Lalonde et al. 2012). Other organic compounds have proved useful for other paleoclimatology studies, including paleotemperature.

High-Temperature Geochemistry

High-temperature geochemistry focuses on magmatic, metamorphic, and hydrothermal processes occurring at temperatures well above those at the Earth's surface. In its broadest definition, high-temperature geochemistry includes igneous and metamorphic petrology and mineralogy. Among other ways, geochemistry expands these traditional topics by including study of trace elements, i.e., ones that are not stoichiometric components of the main igneous and metamorphic minerals. Studies of such elements, despite their inconsequential abundances, have proved invaluable to these fields in part because of their vast variation in abundances, orders of magnitude, in similar rock types, and because many elements are sensitive to factors to which major elements are insensitive, such as the extent of partial melting. Geochemistry also expands petrology's focus beyond the formation and evolution of rocks to the Earth's formation and the subsequent evolution of the continental crust and mantle.

Particularly when combined with geochronology and isotope geochemistry, described below, the geochemistry of igneous rocks has elucidated this evolution. Magmas produced from different tectonic environments usually have a distinctive chemical signature. For example, mid-ocean ridge basalts carry the signature of a mantle reservoir long ago depleted in "incompatible elements" – those elements that readily partition into a melt phase and hence transferred to the crust. In contrast, magmas produced in subduction zones carry a signature of having been produced from water- and oxygen-rich sources modified by fluids released by subducting oceanic crust and sediment (Plank 2016). Many intraplate magmas, including oceanic island basalts, carry yet a different signature – one of ancient re-enrichment in those incompatible elements concentrated in the Earth's crust (Jackson 2016). These magmas are often associated with mantle plumes, which can be traced to the deep mantle, which suggests the deep and shallow Earth are connected.

Geochemistry reveals that the continental crust has grown through time, apparently mainly, although not exclusively, through subduction-related volcanism (Rudnick, this volume). This growth has been uneven and pulsed (e.g., Condie and Aster 2010), but many details about the rate of continental growth remain obscure and debated, particularly during Earth's earliest history (e.g., Hawkesworth et al. 2010). Similarly, while plate tectonics has dominated crust–mantle evolution over the last three billion years, its importance before that remains debated (e.g., Condie and Pease 2008).

Many mineral deposits, which have enabled the development of human civilization since copper and bronze tools began to replace stone ones, are the consequence of high-temperature processes. These include magmatogenic ore deposits, including Cu–Ni sulfide deposits, platinum group element deposits, and chromite deposits, that formed as minerals or sulfide-rich immiscible melt droplets segregated within large magmatic intrusions as well as deposits of Li, Zr, rare earth elements, U, Th, Ta, Nb, Sn, Sb, and other metals that formed through extreme fractional crystallization of alkaline or silicic magmas or pegmatite veins related to them. Other important ore deposits, including those of base metals such as Cu, Zn, and Pb as well as precious ones such as Ag and Au, form through syngenetic hydrothermal processes usually associated with metamorphism, magmatism, or volcanism. These form when temperature, pressure, fluid composition, and oxidation state enable dissolution of metals from large volumes of rock, and subsequent change in these parameters results in their precipitation in much smaller volumes. Understanding the behavior these elements in magmatic and hydrothermal systems has significantly advanced our ability to identify future deposits and consequently insure the availability of these essential resources to future generations.

Isotope Geochemistry

Isotope geochemistry has two branches: radiogenic and stable. Radiogenic isotope geochemistry derives from the radioactive decay of isotopes of nine elements whose half-lives are long enough that they survive in measurable abundance on the Earth, yet short enough that they produce measurable isotopic variations in their radiogenic daughter elements. These half-lives range from 7×10^8 years to 4.5×10^{11} years. Variations in the relative abundances of radiogenic isotopes of a few shorter-lived nuclides that are now "extinct," such as ^{129}Xe, the product of ^{129}I (e.g., Mukhopadhyay 2012; Staudacher and Allègre 1982), and ^{142}Nd, the decay product of ^{146}Sm (Harper and Jacobsen 1992), and ^{182}W, the decay product of ^{182}Hf, have been studied in meteorites and Archean terrestrial rocks (Rizo et al. 2016). In addition, "cosmogenic" isotopes are produced by cosmic ray-induced nuclear reactions. Because the rate of radioactive decay is insensitive to external influences, this forms the basis of geochronology, determining the age of geologic events and thus the quantification of the geologic time scale, and, with the inclusion of the extinct radiogenic nuclides mentioned above, in early solar system chronology. Geochronology requires the rocks and minerals investigated to have been closed systems; even where this is not the case, variations in parent/daughter ratios produce variations in radiogenic isotope ratios that can be exploited as tracers.

Radiogenic isotope ratios are particularly valuable in understanding the composition and evolution of the Earth's mantle, which represents over half the Earth's mass and most of its volume. Basalts are the most common mantle sample but are a highly biased sample as a consequence of chemical fractionations occurring during partial melting and fractional crystallization. However, as Gast (1960) explained, radiogenic isotope ratios are not chemically fractionated, hence are identical to those ratios in the basalt source (or sources, including material assimilated during ascent).

Gast pointed out that differing behavior of parent and daughter elements in radioactive decay systems results, in time, in differences in the isotope ratios of terrestrial reservoirs, such as the crust and mantle. Thus radiogenic isotope ratios can be used to trace the evolution of these reservoirs. For example, Rb, Nd, and Hf partition preferentially into mantle melts and ultimately into the crust relative to Sr, Sm, and Lu. Consequently initial $^{87}Sr/^{86}Sr$ ratios will be lower and $^{143}Nd/^{144}Nd$ and $^{176}Hf/^{177}Hf$ higher in magmas that are new additions to the crust than in ones produced by remelting of crust, which allows the growth of continental crust to be traced through time (e.g., Allègre 1987; Hawkesworth et al. 2010).

Radiogenic isotope studies have demonstrated the existence of distinct reservoirs in the mantle (White 2015): a region, most likely the uppermost asthenospheric mantle, that is highly depleted in incompatible elements that gives rise to mid-ocean ridge basalts, the subcontinental lithospheric mantle, which is generally highly incompatible element-depleted but variably re-enriched in these elements by melts percolating into it from below, the mantle beneath island arc volcanoes which has been metasomatized by hydrous fluids and silicate melts from the subducting oceanic crust and sediment, and the deep mantle source of mantle plumes, which appears to consist of a mixture of relatively primitive material (most clearly evidenced in noble gas isotope ratios) and material recycled from the Earth's surface.

Elemental fractionation also occurs when the raw materials of glass or metal alloys are melted and smelted, which limits somewhat the use of elemental analysis in establishing provenance of archeological artifacts. Again, this is not the case for isotope ratios; hence, radiogenic isotope ratios including those of Pb, Nd, Os, and Sr as well as stable isotope ratios such as Sb, Sn, and B have been used to determine provenance in archeological geochemistry. Radiogenic isotope ratios are also useful tracers of groundwater (Jacobson and Wasserburg 2005) and ocean circulation, both past and present (e.g., Albarède et al. 1997; Godfrey et al. 2009).

Stable isotope geochemistry exploits isotopic fractionations that result from the effect of neutron mass on chemical bonding, diffusion, reaction rates, and the ability of molecules to transition between energy states. These effects are quite small and typically lead to a percent or less variation in the isotope ratios. Hydrogen is an exception with variations in the $^{2}H/^{1}H$ ratio often being tens of percent. Most of the focus of this field is on a handful of light elements: H, C, N, O, and S. Furthermore, since isotope fractionation decreases with the inverse square of temperature, the focus of stable isotope geochemistry is primarily on low-temperature processes at or near the Earth's surface. As a consequence of this temperature dependence, oxygen isotope fractionation between water and calcium carbonate shells of marine organisms provides useful paleothermometers (Urey et al. 1951) to, among other things, reveal the climatic swings of the Pleistocene (Imbrie 1985) which is certainly among stable isotope geochemistry's greatest contributions. In recent years this has been augmented through studies of hydrogen isotopes in Antarctic and Greenland ice sheets (Jouzel et al. 2007). Sulfur isotope geothermometry has been applied to the genesis of sulfide ore deposits; the end of mass-independent fractionation of sulfur isotopes 3.3 billion years ago records the initial oxidation of the atmosphere (Farquhar et al. 2000). Photosynthesis is the principal cause of variations in carbon isotope ratios, and all biogenic organic compounds are depleted in ^{13}C, typically in the range of 15–25 or more per mil. That petroleum carries this isotopic signature removes any doubt of its ultimate biological origin. That same signature is found in a subset of diamonds carrying deep mantle mineral inclusions, leading to the much more surprising inference that the carbon in them was derived from organic matter carried into the deep mantle (Walter et al. 2011). While photosynthetically produced compounds are depleted in ^{13}C, the remaining inorganic carbon in the system, such as the ocean, is necessarily enriched in this isotope. This has been exploited to trace both paleo-ocean circulation (Curry and Oppo 2005) and the biologic productivity and diversity through time, demonstrating the coupling of those to biogeochemical cycling and tectonics (Hannisdal and Peters 2011).

Stable isotope geochemistry has proved useful in archeology and paleontology as well. Carbon and nitrogen isotopes in bone collagen and apatite are widely used to determine food sources of ancient peoples and animals and, with caveats, can distinguish between marine diets and terrestrial ones and the extent of reliance on C_4 plants such as maize and sugarcane and C_3 plants, such as wheat, barley, etc. (e.g., Lee-Thorp 2008). Isotopic analysis of cooking residues on pottery has evolved from bulk isotopic analysis to analysis of specific compounds, such as lipids, providing insight not only into the diet of ancient peoples but their social interactions (Craig et al. 2015).

Several new exciting developments have occurred in stable isotope geochemistry over the past several decades (Eiler et al. 2014). One of these is, as in other fields of geochemistry, the development of new analytical techniques that allow more precise measurements and in situ measurements on very small samples. Another development is compound-specific isotopic analysis such as that mentioned in the preceding paragraph.

Another development is the extension of stable isotope geochemistry from a few light elements to nearly every polyisotopic element in the periodic table, including most of the transition metals as well as quite heavy ones such as U and Tl. Another advance is the development clumped isotopic analysis: the analysis of isotopes of pairs of elements, such as C and O, in individual isotopic species or isotopologues.

The noble gas isotopes are of particular interest because many are produced either by radioactive decay, secondary nuclear reactions triggered by radioactive decay, cosmic rays, or have experienced mass-dependent fractionation. Noble gas isotope geochemistry been applied to studies as diverse as fluids in the crust, ocean circulation, and erosion rates. Xenon isotopes produced by decay of the extinct radionuclides ^{129}I and ^{244}Pu provide clues to Earth's earliest history and the origin of its atmosphere.

Cosmochemistry

The Earth's formation is intimately linked to the formation of the Sun, its sister planets, and other objects in the solar system. Yet among these objects, the Earth is uniquely habitable. That habitability is in large measure a consequence of events occurring as the solar system formed – producing a rocky inner solar system planet with enough water and carbon to eventually sustain life and sufficient mass to hold on to volatile components over the eons. Earth's sister planets, Venus and Mars, formed from similar ingredients but evolved along different pathways. Much of what we know of how the solar system formed and planets developed comes from geochemical studies of meteorites – pieces of asteroids whose composition and mineralogy has been preserved over four and a half billion years. These studies, in conjunction with astronomical observations of young stars, have confirmed the nebular theory of Immanuel Kant.

Chondritic meteorites are composed of collections of the dust of the nebula from which the solar system, including the Earth, formed. They consist of high-temperature condensates such as calcium–aluminum inclusions or CAIs that formed as early as 4568.67 ± 0.17 Ma ago (Bouvier and Wadhwa 2010) and amoeboid olivine aggregates, chondrules, aggregations of dust melted during transient heating events, and fine-grained matrix which condensed at far lower temperatures, likely at a great distance from the Sun. Isotopic compositions of chondritic meteorites vary, most dramatically for oxygen (Clayton et al. 1976), likely reflecting a self-shielding of UV photodissociation of gas molecules in the nebula (Clayton 2002) and, subtlety in other elements, betraying incomplete mixing between nuclides synthesized by slow neutron capture in red giant stars and ones synthesized in rapid neutron and proton capture processes in supernova explosions (e.g., Burkhardt 2016), and the short-lived radionuclides must have been synthesized only shortly before solar system formation. And some chondrites preserve solids, such as SiC, graphite, diamond, and olivine (Mg_2SiO_4), which condensed from the outflow of those stars and supernovae, are preserved in the fine-grained matrix.

In contrast to chondrites, rocky achondrites and iron meteorites are remains of disrupted asteroid-sized planetesimals that melted and differentiated into iron cores and silicate mantles. NASA's DAWN spacecraft confirmed that some of these are from the asteroid Vesta, which apparently formed within the first few million years of solar system history.

In contrast to Vesta, formation of the Earth appears to have taken much longer, perhaps as long as 100 million years (Rudge et al. 2010). This process is generally thought to have culminated in a giant impact (Hartmann and Davis 1975), which formed the Moon. The great advantage of the impact model is that it explains the angular momentum constraints of the Earth–Moon system, and it is consistent with computer simulations that show that planets grow by collisions between progressively larger bodies. It is also consistent with the small size of the lunar core – the impact would have happened after the Earth's core had largely formed – and the general chemical similarity between the Earth and the Moon. But that same similarity is now seen as a problem – the two bodies are almost too similar, particularly in the isotopic compositions that vary between various solar system bodies, such as H, O, Fe, Si, Mg, K, Ti, Cr, and W. This requires very efficient mixing between material of the proto-Earth and the impactor (Elkins-Tanton 2013; Young et al. 2016), Theia, which in turn requires rather specific impact scenarios (e.g., Ćuk et al. 2016).

Summary

Study of the chemistry of natural materials and application of chemical principles to understanding natural processes has greatly advanced our understanding of the Earth and its neighbors. The range of topics to which geochemistry is applied is enormous ranging over, among others, formation of the solar system, geochronology, the evolution of life, plate tectonics, anthropogenic climate change, soil fertility, and ocean circulation. Advances in analytical techniques and our ability to model geochemical processes continue to push the frontiers of knowledge forward and reveal surprising details of how the Earth works.

Cross-References

- ▶ Ab Initio Calculations
- ▶ Achondrites
- ▶ Acid Deposition
- ▶ Analytical Techniques
- ▶ Anthropogenic CO_2
- ▶ Archeological Geochemistry

- Atmospheric Evolution
- Biogeochemistry
- Carbonate Minerals and the CO2-Carbonic Acid System
- Chemical Weathering
- Chondrules
- Critical Zone
- Diffusion
- Dissolved Organic Matter (DOM)
- Earth's Atmosphere
- Earth's Continental Crust
- Enthalpy
- Entropy
- Equilibrium
- Evaporites
- Formation and Evolution of the Earth
- Geochemical Thermodynamics
- Geochronology and Radiogenic Isotopes
- Geologic Time Scale
- Giant Impact Hypothesis
- Hydrothermal Alteration
- Iron Formations
- Iron Meteorites
- Kerogen
- Kinetics of Geochemical Processes
- Magmatic Process Modeling
- Metamorphic Reactions and Processes
- Meteorites
- Mid-Ocean Ridge Basalts (MORB)
- Ore Deposits
- Organic Geochemistry
- Ocean Biochemical Cycling and Trace Elements
- Oxidation-Reduction Reactions and Eh-pH (Pourbaix) Diagrams
- Ozone and Stratospheric Chemistry
- Paleoclimatology
- Refractory Inclusions in Chondritic Meteorites
- Soils
- Stable Isotope Geochemistry
- Subduction Zone Geochemistry
- Sulfide Minerals
- Trace Elements

References

Albarède F, Goldstein SL, Dautel D (1997) The neodymium isotopic composition of manganese nodules from the Southern and Indian oceans, the global oceanic neodymium budget, and their bearing on deep ocean circulation. Geochim Cosmochim Acta 61(6):1277–1291. https://doi.org/10.1016/S0016-7037(96)00404-8

Allègre CJ (1987) Isotope geodynamics. Earth Planet Sci Lett 86(2–4):175–203. https://doi.org/10.1016/0012-821X(87)90220-2

Alvarez LW, Alvarez W, Asaro F, Michel HV (1980) Extraterrestrial cause for the Cretaceous-Tertiary extinction. Science 208(4448):1095–1108. https://doi.org/10.1126/science.208.4448.1095

Berner RA (2006) GEOCARBSULF: a combined model for Phanerozoic atmospheric O_2 and CO_2. Geochim Cosmochim Acta 70(23):5653–5664. https://doi.org/10.1016/j.gca.2005.11.032

Bouvier A, Wadhwa M (2010) The age of the solar system redefined by the oldest Pb-Pb age of a meteoritic inclusion. Nat Geosci 3(9):637–641. https://doi.org/10.1038/ngeo941

Boyle EA, Anderson RF, Cutter GA, Fine R, Jenkins WJ, Saito M (2015) GEOTRACES GA-03 – the U.S. GEOTRACES North Atlantic transect. In: Deep sea research part II: topical studies in oceanography, vol 116. Elsevier, Amsterdam, p 342

Brantley SL, White TS, White A, Sparks D, Richter D, Pregitzer K, Derry L, Chorover J, Chadwick OA, April R, Anderson S, Amundson R (2006) Frontiers in exploration of the critical zone. National Science Foundation, Newark

Briggs DEG, Summons RE (2014) Ancient biomolecules: their origins, fossilization, and role in revealing the history of life. BioEssays 36(5):482–490. https://doi.org/10.1002/bies.201400010

Broecker W (2012) The carbon cycle and climate change: memoirs of my 60 years in science. Geochem Perspect 1(2):221–221

Burkhardt C, Borg LE, Brennecka GA, Shollenberger QR, Dauphas N, Kleine T (2016) A nucleosynthetic origin for the Earth's anomalous 142Nd composition. Nature 537(7620):394–398. https://doi.org/10.1038/nature18956

Carmichael ISE, Eugster HP (1987) Thermodynamic modeling of geological materials: minerals, fluids and melts. In: Ribbe PH (ed) Reviews in mineralogy, vol 17. Mineralogical Society of America, Washington, DC, p 499

Clayton RN (2002) Self-shielding in the solar nebula. Nature 415:860–861

Clayton RN, Onuma N, Mayeda TS (1976) A classification of meteorites based on oxygen isotope ratios. Earth Planet Sci Lett 30:10–18

Condie KC, Aster RC (2010) Episodic zircon age spectra of orogenic granitoids: the supercontinent connection and continental growth. Precambrian Res 180(3–4):227–236. https://doi.org/10.1016/j.precamres.2010.03.008

Condie KC, Pease V (2008) When did plate tectonics begin on planet Earth? In: GSA special papers, vol 440. Geologic Society of America, Boulder, p 294

Corliss JB, Dymond J, Gordon LI, Edmond JM, von Herzen RP, Ballard RD, Green K, Williams D, Bainbridge A, Crane K, van Andel TH (1979) Submarine thermal springs on the Galápagos rift. Science 203(4385):1073–1083. https://doi.org/10.1126/science.203.4385.1073

Craig OE, Shillito L-M, Albarella U, Viner-Daniels S, Chan B, Cleal R, Ixer R, Jay M, Marshall P, Simmons E, Wright E, Pearson MP (2015) Feeding Stonehenge: cuisine and consumption at the late Neolithic site of Durrington Walls. Antiquity 89(347):1096–1109. https://doi.org/10.15184/aqy.2015.110

Ćuk M, Hamilton DP, Lock SJ, Stewart ST (2016) Tidal evolution of the Moon from a high-obliquity, high-angular-momentum Earth. Nature advance online publication. https://doi.org/10.1038/nature19846

Curry WB, Oppo DW (2005) Glacial water mass geometry and the distribution of δ13C of ΣCO2 in the western Atlantic Ocean. Paleoceanography 20(1):PA1017. https://doi.org/10.1029/2004PA001021

Davis RA Jr, Welty TA, Borrego J, Morales AJ, Pendon GJ, Ryan GJ (2000) Rio Tinto estuary (Spain): 5000 years of pollution. Environ Geol 39(10):1107–1116. https://doi.org/10.1007/s002549900096

Eglinton TI, Eglinton G (2008) Molecular proxies for paleoclimatology. Earth Planet Sci Lett 275(1–2):1–16. https://doi.org/10.1016/j.epsl.2008.07.012

Eiler JM, Bergquist B, Bourg I, Cartigny P, Farquhar J, Gagnon A, Guo W, Halevy I, Hofmann A, Larson TE, Levin N, Schauble EA, Stolper D (2014) Frontiers of stable isotope geoscience. Chem Geol 372:119–143. https://doi.org/10.1016/j.chemgeo.2014.02.006

Elkins-Tanton LT (2013) Planetary science: Occam's origin of the moon. Nat Geosci 6(12):996–998. https://doi.org/10.1038/ngeo2026

Farquhar J, Bao H, Thiemens M (2000) Atmospheric influence of Earth's earliest sulfur cycle. Science 289(5480):756–758. https://doi.org/10.1126/science.289.5480.756

Fyfe W (1981) The environmental crisis: quantifying geosphere interactions. Science 213(4503):105–110

Gast PW (1960) Limitations on the composition of the upper mantle. J Geophys Res 65:1287–1297

Ghiorso MS, Carmichael ISE, Rivers ML, Sack RO (1983) The Gibbs free energy of mixing of natural silicate liquids; an expanded regular solution approximation for the calculation of magmatic intensive variables. Contrib Mineral Petrol 84:107–145

Godfrey LV, Zimmermann B, Lee DC, King RL, Vervoort JD, Sherrell RM, Halliday AN (2009) Hafnium and neodymium isotope variations in NE Atlantic seawater. Geochem Geophys Geosyst 10(8): Q08015. 10.1029/2009gc002508

Goldschmidt VM (1923) Geochemische Verteilungsgesetze der Elemente I. Skr utgivne af det Norske Vidensk Akad i Oslo I Matematisk-Naturvidenskapelig Klasse 2:1–17

Goldschmidt VM (1933) Grundlagen der quantitativen Geochemie. Fortschr Mineral Kristall Petrolgr 17:112–156

Hannisdal B, Peters SE (2011) Phanerozoic earth system evolution and marine biodiversity. Science 334(6059):1121–1124. https://doi.org/10.1126/science.1210695

Harper CL, Jacobsen SB (1992) Evidence from coupled ^{147}Sm-^{143}Nd and ^{146}Sm-^{142}Nd systematics for very early (4.5-Gyr) differentiation of the Earth's mantle. Nature 360:728–732

Hartmann WK, Davis DR (1975) Satellite-sized planetesimals and lunar origin. Icarus 24:504–515. https://doi.org/10.1016/0019-1035(75)90070-6

Hawkesworth CJ, Dhuime B, Pietranik AB, Cawood PA, Kemp AIS, Storey CD (2010) The generation and evolution of the continental crust. J Geol Soc 167(2):229–248. https://doi.org/10.1144/0016-76492009-072

Helgeson HC (1968) Evaluation of irreversible reactions in geochemical processes involving minerals and aqueous solutions—I. Thermodynamic relations. Geochim Cosmochim Acta 32(8):853–877. https://doi.org/10.1016/0016-7037(68)90100-2

Holland HD (2006) The oxygenation of the atmosphere and oceans. Philos Trans R Soc B 361(1470):903–915. https://doi.org/10.1098/rstb.2006.1838

Imbrie J (1985) A theoretical framework for the Pleistocene ice ages: William Smith lecture. J Geol Soc 142(3):417–432. https://doi.org/10.1144/gsjgs.142.3.0417

Jackson MG (2016) Oceanic Island basalts. In: White WM (ed) Encyclopedia of geochemistry: a comprehensive reference source on the chemistry of the Earth. Springer International Publishing, Cham, pp 1–5

Jacobson AD, Wasserburg GJ (2005) Anhydrite and the Sr isotope evolution of groundwater in a carbonate aquifer. Chem Geol 214(3–4):331–350. https://doi.org/10.1016/j.chemgeo.2004.10.006

Jouzel J, Masson-Delmotte V, Cattani O, Dreyfus G, Falourd S, Hoffmann G, Minster B, Nouet J, Barnola JM, Chappellaz J, Fischer H, Gallet JC, Johnsen S, Leuenberger M, Loulergue L, Luethi D, Oerter H, Parrenin F, Raisbeck G, Raynaud D, Schilt A, Schwander J, Selmo E, Souchez R, Spahni R, Stauffer B, Steffensen JP, Stenni B, Stocker TF, Tison JL, Werner M, Wolff EW (2007) Orbital and millennial Antarctic climate variability over the past 800,000 years. Science 317(5839):793–796. https://doi.org/10.1126/science.1141038

Kasting JF, Catling D (2003) Evolution of a habitable planet. Annu Rev Astron Astrophys 41(1):429–463. https://doi.org/10.1146/annurev.astro.41.071601.170049

Kennedy CS, Kennedy GC (1976) The equilibrium boundary between graphite and diamond. J Geophys Res 81(14):2467–2470. https://doi.org/10.1029/JB081i014p02467

Kleber M, Johnson MG (2010) Chapter 3. Advances in understanding the molecular structure of soil organic matter: implications for interactions in the environment. In: Donald LS (ed) Advances in agronomy, vol 106. Academic, San Diego, pp 77–142

Lalonde K, Mucci A, Ouellet A, Gelinas Y (2012) Preservation of organic matter in sediments promoted by iron. Nature 483(7388):198–200. https://doi.org/10.1038/nature10855

Lee-Thorp JA (2008) ON ISOTOPES AND OLD BONES*. Archaeometry 50(6):925–950. https://doi.org/10.1111/j.1475-4754.2008.00441.x

Lyons TW, Reinhard CT, Planavsky NJ (2014) The rise of oxygen in Earth's early ocean and atmosphere. Nature 506(7488):307–315. https://doi.org/10.1038/nature13068

Mukhopadhyay S (2012) Early differentiation and volatile accretion recorded in deep-mantle neon and xenon. Nature 486(7401):101–104

Peters KE, Walters CC, Moldowan JM (2007) The biomarker guide: volume 2, biomarkers and isotopes in petroleum systems and Earth history. Cambridge University Press, Cambridge

Pike AWG, Hoffmann DL, García-Diez M, Pettitt PB, Alcolea J, De Balbín R, González-Sainz C, de las Heras C, Lasheras JA, Montes R, Zilhão J (2012) U-series dating of Paleolithic art in 11 caves in Spain. Science 336(6087):1409–1413. https://doi.org/10.1126/science.1219957

Plank T (2016) Subduction zone geochemistry. In: White WM (ed) Encyclopedia of geochemistry: a comprehensive reference source on the chemistry of the Earth. Springer International Publishing, Cham, pp 1–9

Rizo H, Walker RJ, Carlson RW, Touboul M, Horan MF, Puchtel IS, Boyet M, Rosing MT (2016) Early Earth differentiation investigated through 142Nd, 182W, and highly siderophile element abundances in samples from Isua, Greenland. Geochim Cosmochim Acta 175:319–336. https://doi.org/10.1016/j.gca.2015.12.007

Rosing M, Rose MN, Bridgwater D, Thomsne HS (1996) Earliest part of Earth's stratigraphic record: a reappraisal of the >3.7 Ga Isua (Greenland) supracrustal sequence. Geology 24:43–46

Rudge JF, Kleine T, Bourdon B (2010) Broad bounds on Earth's accretion and core formation constrained by geochemical models. Nat Geosci 3(6):439–443. https://doi.org/10.1038/ngeo872

Schmidt MWI, Torn MS, Abiven S, Dittmar T, Guggenberger G, Janssens IA, Kleber M, Kogel-Knabner I, Lehmann J, Manning DAC, Nannipieri P, Rasse DP, Weiner S, Trumbore SE (2011) Persistence of soil organic matter as an ecosystem property. Nature 478(7367):49–56

Shipp J, Gould IR, Herckes P, Shock EL, Williams LB, Hartnett HE (2013) Organic functional group transformations in water at elevated temperature and pressure: reversibility, reactivity, and mechanisms. Geochim Cosmochim Acta 104:194–209. https://doi.org/10.1016/j.gca.2012.11.014

Staudacher T, Allègre CJ (1982) Terrestrial xenology. Earth Planet Sci Lett 60(3):389–406. https://doi.org/10.1016/0012-821X(82)90075-9

Urey HC, Lowenstam HA, Epstein S, McKinney CR (1951) Measurement of paleotemperatures and temperatures of the upper Cretaceous of England, Denmark, and the southeastern United States. Geol Soc Am Bull 62(4):399–416. https://doi.org/10.1130/0016-7606(1951)62[399:mopato]2.0.co;2

Vernadsky V (1926) Biosfera. Scientific Chemico-Technical Publishing, Leningrad

Walter MJ, Kohn SC, Araujo D, Bulanova GP, Smith CB, Gaillou E, Wang J, Steele A, Shirey SB (2011) Deep mantle cycling of oceanic crust: evidence from diamonds and their mineral inclusions. Science 334(6052):54–57. https://doi.org/10.1126/science.1209300

White WM (2015) Probing the Earth's deep interior through geochemistry. Geochemical Perspectives 4(2):95–251. https://doi.org/10.7185/geochempersp.4.2

Xiao S (2014) 6.10 – oxygen and early animal evolution A2 – Holland, Heinrich D. In: Turekian KK (ed) Treatise on geochemistry, 2nd edn. Elsevier, Oxford, pp 231–250
Young ED, Kohl IE, Warren PH, Rubie DC, Jacobson SA, Morbidelli A (2016) Oxygen isotopic evidence for vigorous mixing during the Moon-forming giant impact. Science 351(6272):493–496. https://doi.org/10.1126/science.aad0525

Geochronology and Radiogenic Isotopes

Jeff Vervoort
Geological Sciences, School of the Environment, Washington State University, Pullman, WA, USA

Definition

Geochronology is the science of determining absolute ages of geological events and Earth materials. It utilizes radioactive isotopes and the production and accumulation of radiogenic daughter isotopes naturally present on Earth. It can be applied to a wide range of samples including rocks, minerals, and some biological materials.

Introduction

Geochronology plays a critically important role in most fields of the Earth Sciences. Not only has geochronology provided an absolute time framework for the Earth and Solar System, but it has also provided important constraints on the rates and timing of diverse processes that have helped form and shape our planet. *Long-lived decay systems* (e.g., U-Pb, Sm-Nd, Lu-Hf, Rb-Sr, K-Ar, Re-Os; Table 1), with half-lives typically in the billions of years, have provided remarkably tight constraints on the absolute age of the solar system (e.g., Amelin and Ireland 2003), the age of Earth's oldest minerals (e.g., Wilde et al. 2001) and rocks (e.g., Bowring and Williams 1999), and the formation and modification ages of a wide variety of rocks throughout Earth's history. *Short-lived (extinct) radionuclides* (e.g., Al-Mg, Mn-Cr, I-Xe, Sm-Nd, Hf-W; Table 2) have half-lives ranging from less than a million years to tens of millions of years and have long since vanished from the solar system. Their daughter products have remained, however, and provide details on the timing of various processes during the early history of the solar system (e.g., Amelin and Ireland 2013), on core separation and moon formation (e.g., Kleine et al. 2002; Yin et al. 2002; Touboul et al. 2007), and on the differentiation of the silicate Earth and formation of Earth's early crust (e.g., ^{146}Sm-^{142}Nd, Boyet and Carlson 2005; O'Neil et al. 2008). *Intermediate short-lived radioactive daughters*, produced from the U-series decay chain (e.g., ^{234}U, ^{230}Th, ^{210}Pb; Table 3), have provided important constraints on a range of magmatic processes (e.g., Reid et al. 1997) and on refining climate records (e.g., Edwards et al. 1987). *Unstable cosmogenic nuclides* (e.g., ^{14}C, ^{36}Cl; Table 4), produced by interaction of cosmic rays with the atmosphere and solid Earth, have likewise provided important age constraints on the human timescale (e.g., ^{14}C, Beck et al. 2001) as well as on the timing of surficial processes on Earth (e.g., ^{36}Cl, Phillips et al. 1986).

In sum, geochronology has provided a detailed timeline for our solar system and planet from its very beginning through to processes operating today on a human timescale. This entry will discuss the long-lived decay systems. The short-lived decay systems are discussed elsewhere: extinct radionuclides are covered in chapters on Mg and Nd isotopes; U-series isotopes are discussed in uranium decay series; and cosmogenic isotopes are covered in the chapter on cosmogenic nuclides.

The long-lived decays are used in geochronology in two fundamentally different ways. For some of the decay systems – and with some mineral phases – there is little if any daughter isotope present when the rock or mineral forms allowing for an accurate calculation of radiogenic daughter accumulation over time. Two prominent examples of this are the U-Pb and K-Ar systems in zircon and hornblende (among many other phases), respectively. The second type is where

Geochronology and Radiogenic Isotopes, Table 1 List of some of the long-lived isotope systems used in geochronology

Parent	Daughter	Decay mode (β+)	λ	Half-life	Ratio	Reference
^{40}K	^{40}Ar	e.c, (β+)	5.757×10^{-11}y^{-1}	1.28×10^{9}yr	^{40}Ar/^{36}Ar	Renne et al. 2010 2011
^{87}Rb	^{87}Sr	β−	1.3968×10^{-11}y^{-1}	49.624×10^{9}yr	^{87}Sr/^{86}Sr	Rotenberg et al. 2012
^{147}Sm	^{143}Nd	α	6.54×10^{-12}y^{-1}	1.06×10^{11}yr	^{143}Nd/^{144}Nd	Lugmair and Marti 1978
^{176}Lu	^{176}Hf	β−	1.867×10^{-11}y^{-1}	3.6×10^{10}yr	^{176}Hf/^{177}Hf	Söderlund et al. 2004
^{187}Re	^{187}Os	β−	1.666×10^{-10}y^{-1}	4.161×10^{10}yr	^{187}Os/^{188}Os	Selby et al. 2007
^{190}Pt	^{186}Os	α	1.415×10^{-12}y^{-1}	4.899×10^{11}yr	^{186}Os/^{188}Os	Cook et al. 2004
^{232}Th	^{208}Pb	α, β−	4.948×10^{-11}y^{-1}	1.4×10^{10}yr	^{208}Pb/^{204}Pb	Jaffey et al. 1971
^{235}U	^{207}Pb	α, β−	9.8571×10^{-10}y^{-1}	7.033×10^{8}yr	^{207}Pb/^{204}Pb	Mattinson 2010
^{238}U	^{206}Pb	α, β−	1.55125×10^{-10}y^{-1}	4.47×10^{9}yr	^{206}Pb/^{204}Pb	Jaffey et al. 1971

Source: Table after White (2015)

there are abundant daughter isotopes present in the rock or mineral that cannot be unambiguously corrected for (e.g., Rb-Sr and Sm-Nd) and which require a different approach. These will be discussed separately below.

Fundamentals

Geochronology is based on the fundamental principle that an unstable (radioactive) nuclide will decay at a constant rate that is defined by the decay constant of that radionuclide and which depends only on the state of the nucleus and is independent of external factors such as temperature, pressure, or the past history of the nuclide. This fundamental principle can be applied in a number of different ways to determine "dates," or "ages," of various physical events and processes. [Note: Some geochronologists prefer to use "date" for what is measured and calculated for an individual rock or phase and "age" for the time that is assigned from all dates to a geological event. In reality (and probably much to the consternation of strict geochronology practitioners), however, "age" is widely used in both senses.]

Geochronology and Radiogenic Isotopes, Table 2 List of some of the intermediate decays of U and Th used in geochronology

Nuclide	Daughter	Half-life, yrs	Decay constant, yr-1	Series
^{234}U	^{230}Th	245,250	2.826×10^{-6}	^{238}U
^{231}Pa	^{227}Ac	32,670	2.116×10^{-5}	^{235}U
^{230}Th	^{226}Ra	75,690	9.158×10^{-6}	^{238}U
^{226}Ra	^{222}Rn	1600	4.332×10^{-4}	^{238}U
^{228}Ra	^{228}Ac	5.75	1.205×10^{-1}	^{232}Th
^{210}Pb	^{210}Bi	22.23	3.118×10^{-2}	^{238}U
^{210}Po	^{206}Pb	0.3789	1.829	^{238}U

Source: Table after White (2015). ^{234}U and ^{230}Th from Cheng et al. (2000); others are from Laboratoire National Henri Becquerel (www.nucleide.org)

Basic Equation of Radioactive Decay

All geochronology is based on the fundamental equation of radioactive decay,

$$\frac{dN}{dt} = -\lambda N \tag{1}$$

which states that the change in the number of radioactive atoms (dN) with time (dt) is proportional to the number of atoms present (N) and the decay constant (λ). The negative sign on λ indicates the numbers of radioactive atoms are decreasing with time.

Using this expression, the radiogenic decay equation can be derived.

$$N = N_0\, e^{-\lambda t} \tag{2}$$

This states that the number of radioactive parent isotopes present at a given time, N, is a function of the number present initially (N_0), the decay constant for that radionuclide, and time.

From this, an expression of the half-life of a particular radioactive isotope can be derived. By definition, this is the time when half of the radioactive nuclides have decayed to a daughter nuclide and is simply expressed as $N_0/N = 1/2$. Combining this with Eq. 2 gives the expression for the half-life of a radioactive isotope:

$$t_{1/2} = \frac{\ln 2}{\lambda} \tag{3}$$

It should be noted from this expression that the half-life can be calculated, provided the decay constant is known (and vice versa).

The radioactive decay of a parent isotope also produces a radiogenic daughter isotope (D^*), which is equal to the number of parent decays: $D^* = N_0 - N$. Substituting this into

Geochronology and Radiogenic Isotopes, Table 3 List of some of the short-lived and extinct isotope systems used in geochronology.

Radionuclide	Half-life, Ma	Decay	Daughter	Ratio	Initial abundance
^{10}Be	1.5	β–	^{10}B	^{10}Be/^{9}Be	7.5×10^{-4}
^{26}Al	0.72	β–	^{26}Mg	^{26}Al/^{27}Al	5.2×10^{-5}
^{36}Cl	0.301	β–	^{36}Ar, ^{36}S	^{36}Cl/^{35}Cl	1.6×10^{-4}
^{41}Ca	0.15	β–	^{41}K	^{41}Ca/^{40}Ca	1.5×10^{-8}
^{53}Mn	3.7	β–	^{53}Cr	^{53}Mn/^{55}Mn	1×10^{-5}
^{60}Fe	1.5	β–	^{60}Ni	^{60}Fe/^{56}Fe	5.8×10^{-8}
^{107}Pd	9.4	β–	^{107}Ag	^{107}Pd/^{108}Pd	5.9×10^{-4}
^{129}I	15.7	β–	^{129}Xe	^{129}I/^{127}I	1.2×10^{-4}
^{146}Sm	68	α	^{146}Nd	^{146}Sm/^{144}Sm	0.0094
^{182}Hf	9	β–	^{182}W	^{182}Hf/^{180}Hf	9.7×10^{-5}
^{244}Pu	82	α, SF	^{208}Pb, Xe	^{244}Pu/^{238}U	0.0068

Source: Table after White (2015)

Geochronology and Radiogenic Isotopes, Table 4 List of some of the important cosmogenic nuclides used in geochronology

Nuclide	Daughter	Half-life, years	Decay constant, yr.-1
^{3}H	^{3}He	12.33	5.62×10^{-2}
^{10}Be	^{10}Be	1.500×10^{6}	4.62×10^{-7}
^{14}C	^{14}N	5730	1.209×10^{-4}
^{26}Al	^{26}Mg	7.16×10^{5}	9.68×10^{-5}
^{32}Si	^{32}P	276	2.51×10^{-2}
^{36}Cl	^{36}Ar	3.08×10^{5}	2.25×10^{-6}

Source: Table after White (2015)

Eq. 2 gives the expression for the production of radiogenic daughters from a radioactive parent:

$$D^* = N\left(e^{\lambda t} - 1\right) \tag{4}$$

Geochronology Applications with No (or Correctible) Preexisting Daughter Nuclides

A simple application of this expression can be applied in the case where no daughter isotopes existed when the rock or mineral formed. We can call this "time 0" – the time when the material is effectively "closed" to movement of the elements of interest in or out of the system (i.e., becomes a closed system). In reality for most radioisotope decay systems, however, there are appreciable daughter nuclides present in the system at time 0, either from nucleosynthesis or from some prior decay. In this case, we need to subtract their presence from the total number of daughter isotopes,

$$D^* = D - D_0 = N\left(e^{\lambda t} - 1\right) \tag{5}$$

where D is the total number of daughter nuclides in the system of interest and D_0 is the number present at time 0.

Rearranging this equation to solve for t gives the expression:

$$t = \frac{\ln\left(\frac{D^*}{N} + 1\right)}{\lambda} \tag{6}$$

Thus, an age can be calculated using this expression by measuring N, the number of radioactive nuclides present today, and D*, the number of radiogenic daughter nuclides present. This assumes that neither N nor D has been lost or gained over the time of interest, and there are either no initial daughter nuclides present or that their abundance can be accurately calculated.

An example of this approach is the U/Pb system in zircon ($ZrSiO_4$) where – in the ideal case – no Pb isotopes were present when the zircon crystallized (referred to as "common" Pb) *or* that this common Pb can be accurately measured and corrected. In this case, the following expression can be used to determine an age using the ^{238}U to ^{206}Pb decay series (Table 1):

$$t_{^{206}Pb^*/^{238}U} = \frac{\ln\left(^{206}Pb^*/^{238}U + 1\right)}{\lambda^{238}U} \tag{6}$$

This is commonly called a U-Pb (or $^{206}Pb/^{238}U$) age and is widely used in U-Pb zircon geochronology. A similar approach can be used to calculate a U-Pb age using the ^{235}U to ^{207}Pb decay (Table 1). This is discussed further in the zircon geochronology section below.

The Isochron Method

For radiogenic isotope systems in most rocks and minerals, however, the amount of pre-existing daughter isotopes is large and cannot be accounted for unambiguously. In these cases, the so-called "isochron method" can be used to calculate an age. In practice, this method involves measuring both parent and daughter nuclides relative to a stable isotope of the daughter isotope.

Thus, the expression

$$D = D_0 + N\left(e^{\lambda t} - 1\right)$$

becomes:

$$\left(\frac{D}{D_r}\right)_p = \left(\frac{D}{D_r}\right)_i + \left(\frac{N}{D_r}\right)_p \left(e^{\lambda t} - 1\right) \tag{8}$$

where D_r is the reference isotope of the daughter element.

For the Rb-Sr isotope system (based on the ^{87}Rb to ^{87}Sr decay), this would be expressed in the following way, with ^{86}Sr as the commonly used reference isotope for Sr:

$$\left(\frac{^{87}Sr}{^{86}Sr}\right)_p = \left(\frac{^{87}Sr}{^{86}Sr}\right)_i + \left(\frac{^{87}Rb}{^{86}Sr}\right)_p \left(e^{\lambda t} - 1\right) \tag{9}$$

As written here, i denotes the initial isotope composition (e.g., at the crystallization or formation age) and p signifies the present time. A general expression for this is:

$$R_{(p)} = R_{(i)} + R_{p/d(p)}\left(e^{\lambda t} - 1\right) \tag{10}$$

For determining an age, however, this poses a problem in that there are now two unknowns: time (t) and the initial ratio, $R_{(i)}$. In these cases, the isochron method can be used to determine an age (t). This approach uses the isotope composition of a suite of rocks or minerals that are assumed to have had the same isotope composition at the time of formation.

This can then be expressed in two parallel equations for phases A and B:

$$R_{A(p)} = R_{A(i)} + R_{A\ p/d(p)}\left(e^{\lambda t} - 1\right) \tag{11}$$

$$R_{B(p)} = R_{B(i)} + R_{B\ p/d(p)}\left(e^{\lambda t} - 1\right) \tag{12}$$

The isochron approach assumes that all phases are in isotopic equilibrium at the time of their formation. If this is true, $R_{A(i)} = R_{B(i)}$ and, therefore, when taking the difference between these two equations, the initial isotope composition of both phases drops out of the equation. This leaves the expression:

$$R_{A(p)} - R_{B(p)} = \left[R_{A\ p/d(p)} - R_{B\ p/d(p)}\right]\left(e^{\lambda t} - 1\right) \tag{13}$$

For the Rb-Sr isotope system, this is expressed as

$$\left(\frac{^{87}Sr}{^{86}Sr}\right)_{A(p)} - \left(\frac{^{87}Sr}{^{86}Sr}\right)_{B(p)} = \left[\left(\frac{^{87}Rb}{^{86}Sr}\right)_{A(p)} - \left(\frac{^{87}Rb}{^{86}Sr}\right)_{B(p)}\right]\left(e^{\lambda t} - 1\right) \tag{14}$$

Defining the difference in isotopic composition between the two phases as Δ, and rearranging terms gives

$$\frac{\Delta\left(\frac{^{87}Sr}{^{86}Sr}\right)}{\Delta\left(\frac{^{87}Rb}{^{86}Sr}\right)} = \left(e^{\lambda t} - 1\right) \tag{15}$$

The expression on the left hand of the equation defines a slope on a $^{87}Sr/^{86}Sr$ vs. $^{87}Rb/^{86}Sr$ diagram as shown in Fig. 1.

Figure 1 shows the principle of the isochron method for the Rb/Sr isotope system. Starting with a simple case of a homogeneous magma cooling and solidifying, different phases forming in that rock at t = 0 will have the same Sr isotope composition (A in Fig. 1) but, because of varying partitioning of elements into these different phases, will have different Rb/Sr ratios (B). Over time, ^{87}Sr accumulates at the expense of ^{87}Rb due to its radioactive decay, thus resulting in an increase in $^{87}Sr/^{86}Sr$ ratios with time (C). A phase with more ^{87}Rb relative to ^{86}Sr will evolve to a higher $^{87}Sr/^{86}Sr$. At some later time (t) – if the system has been closed – these different mineral phases will define a line (D) whose slope is proportional to the age. In practice, multiple points are used to define the line and slope, which help to identify inherited components that were not in isotopic equilibrium with the rest of the rock and also to identify open-system behavior.

If a slope can be determined for a set of phases with the same starting isotope composition (and assuming a closed system), an isochron age can be calculated using the expression:

$$\text{slope} = \left(e^{\lambda t} - 1\right) \tag{16}$$

Rearranging this gives:

$$t = \ln(\text{slope} + 1)/\lambda \tag{17}$$

From this method, it is not only possible to determine an age, but also an initial isotope composition by determining the intercept of this regression line. This is the point where the parent/daughter ratio = 0 and, therefore, the isotope composition is time invariant (A in Fig. 1).

The isochron method was widely used to determine Rb-Sr ages from whole rocks (e.g., Moorbath et al. 1977) and, to a

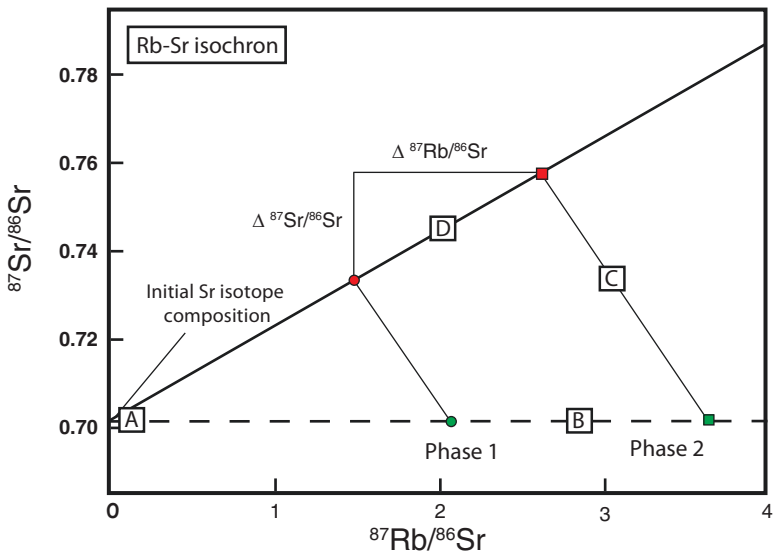

Geochronology and Radiogenic Isotopes, Fig. 1 Generalized Rb-Sr isochron diagram showing two phases with the same $^{87}Sr/^{86}Sr$ ratios at time = 0, but with different $^{87}Rb/^{86}Sr$ ratios. These phases will evolve at different rates as a function of their Rb/Sr ratios and, if the system has been closed over its history, will define a line, the slope of which corresponds to the time since the phases formed (t = 0). The significance of labels A-D is explained in the text

lesser extent, Sm-Nd (Hamilton et al. 1977), but is now recognized to suffer from some significant limitations: (1) in most cases, it is difficult (if not impossible) to assume that a suite of rocks (a sequence of lava flows, for example) indeed had identical isotope compositions at the time of their formation; (2) there is a likelihood of open-system behavior in many rocks for isotope systems with mobile elements such as in the Rb-Sr and K-Ar systems; and (3) there is generally a limited spread in parent/daughter ratios (especially for the Sm-Nd isotope system) for rocks that are truly cogenetic. In total, these problems violate the premise for determining an age using the isochron approach and, as a result, this method is now only rarely used to determine ages using bulk rock samples. The isochron method, however, has been used with somewhat better success for determining ages in internal (mineral) isochrons where there has been closed-system behavior such as in meteorites (e.g., Lugmair and Galer 1992) and with great success where there is a sufficiently large spread in parent/daughter ratios to overcome slight violations of the homogeneous initial isotope composition assumption (e.g., garnet Lu-Hf and Sm-Nd geochronology). These are discussed in greater detail below (section "Garnet Lu-Hf and Sm-Nd Geochronology"). The isochron method has also had important utility in K-Ar and $^{40}Ar/^{39}Ar$ dating (section "K-Ar and Ar-Ar Geochronology") as well as in Re-Os geochronology (e.g., Kendall et al. 2006).

Pb-Pb Isochrons

A variant on the isochron method is afforded by the dual decays of ^{238}U-^{206}Pb and ^{235}U-^{207}Pb. Both the ^{238}U and ^{235}U decays can be written in the standard radiogenic growth equation:

$$\left(\frac{^{206}Pb}{^{204}Pb}\right)_p = \left(\frac{^{206}Pb}{^{204}Pb}\right)_i + \left(\frac{^{238}U}{^{204}Pb}\right)_p \left(e^{\lambda_{238U}t} - 1\right) \quad (18)$$

$$\left(\frac{^{207}Pb}{^{204}Pb}\right)_p = \left(\frac{^{207}Pb}{^{204}Pb}\right)_i + \left(\frac{^{235}U}{^{204}Pb}\right)_p \left(e^{\lambda_{235U}t} - 1\right) \quad (19)$$

These equations are rarely, if ever, used in an isochron application for whole-rock compositions because of the mobility of U in Earth surface environments, but can be combined to determine whole-rock Pb-Pb ages. Rewriting these equations in terms of the radiogenic Pb added over an interval of time (e.g., $\Delta^{207}Pb/^{204}Pb = {}^{207}Pb/^{204}Pb_{(p)} - {}^{207}Pb/^{204}Pb_{(i)}$), substituting μ for the $^{238}U/^{204}Pb$ ratio, and incorporating the natural $^{238}U/^{235}U$ ratio, gives the following expressions.

$$\Delta\frac{^{206}Pb}{^{204}Pb}\Big)_p = \mu\left(e^{\lambda_{238U}t} - 1\right) \quad (20)$$

$$\Delta\frac{^{207}Pb}{^{204}Pb}\Big)_p = \frac{\mu}{137.88}\left(e^{\lambda_{235U}t} - 1\right) \quad (21)$$

These equations can then be combined to yield the following:

$$\Delta\frac{^{207}Pb}{^{206}Pb}\Big)_p = \frac{1}{137.88}\,\frac{\left(e^{\lambda_{235U}t} - 1\right)}{\left(e^{\lambda_{238U}t} - 1\right)} \quad (22)$$

[Note: The historic consensus $^{238}U/^{235}U$ value of 137.88 has been shown by recent determinations to be not invariant, sensu stricto, and these new determinations are lower than the value of 137.88. See Condon et al. (2010), Richter et al. (2010), Heiss et al. (2012) and Goldmann et al. (2015)].

It can be noted that combining these two equations eliminates the present-day U/Pb ratios and, therefore, what remains are only two variables, $\Delta^{207}Pb/^{206}Pb$ and time. This means that the age (or the $^{207}Pb/^{206}Pb$ ratio) is not affected by any change in the present day U/Pb ratio because it has been removed from the equation. Although $\Delta^{206}Pb/^{204}Pb$ and $\Delta^{207}Pb/^{204}Pb$ cannot be calculated unambiguously in whole rocks due to uncertainty in determining the initial Pb ratio (because of U mobility), $\Delta^{207}Pb/^{206}Pb$ can be calculated from the slope of a regression line drawn through a series of cogenetic samples on a $^{206}Pb/^{204}Pb$ and $^{207}Pb/^{204}Pb$ diagram (Fig. 2) in a way analogous to determining a Rb-Sr isochron date. Another important difference between this and a conventional isochron calculated with the parent isotope in the equation (e.g., Rb-Sr) is that initial Pb isotopic compositions cannot be determined from the intercept method (e.g., as can be done for isochron diagrams such as Rb-Sr) when the U/Pb ratio equals zero.

It should also be noted that Eq. 22 is a transcendental equation – time in this equation cannot be solved for directly. Rather, "t" is determined iteratively by estimating values for t, calculating a $\Delta^{207}Pb/^{206}Pb$ ratio, and comparing this to the calculated slope (Pb-Pb isochron application) or measured/calculated $^{207}Pb^*/^{206}Pb^*$ ratio, where the asterisk denotes just the radiogenic fraction (zircon application), until a solution has been made. This is easily now done in many software programs such as with solver in Excel.

The Pb-Pb whole-rock isochron approach is what was used by Claire Patterson (1956) to determine the first accurate estimate for the age of the Earth using a suite of meteorites (Fig. 2). $^{207}Pb/^{206}Pb$ ages are also widely used in zircon geochronology because of the very small amounts of ^{206}Pb and ^{207}Pb (i.e., "common Pb") present in zircon when it forms, requiring only small corrections. This means that the $^{207}Pb/^{206}Pb$ isotope ratios of the zircons can be used to determine ages. This is discussed further in the zircon U-Pb geochronology section below.

G

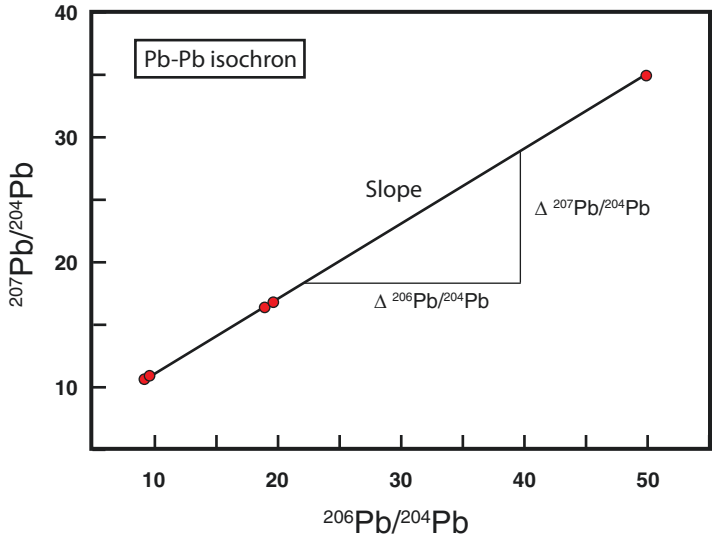

Geochronology and Radiogenic Isotopes, Fig. 2 A Pb-Pb isochron diagram showing a cogenetic series of samples defining a slope of $\Delta^{207}Pb/^{204}Pb/\Delta^{206}Pb/^{204}Pb$, which can be used to calculate an age. This diagram was drawn after a figure from Patterson (1956), who used these data to estimate an age of the Earth

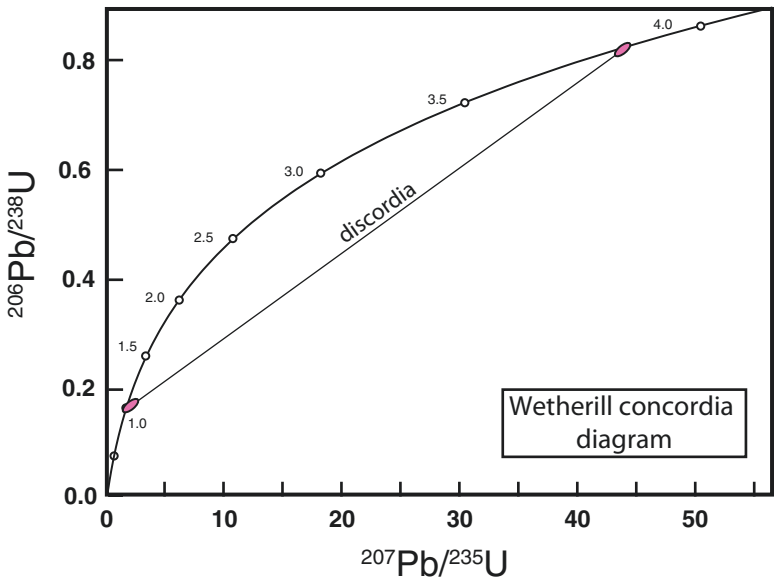

Geochronology and Radiogenic Isotopes, Fig. 3 The Wetherill Concordia diagram showing concordant points at 1.0 and 3.8 Ga and a Discordia line drawn between the two

Examples and Presentation

Zircon U-Pb Geochronology

Zircon U-Pb data are typically presented in two different ways that differ in how they represent the companion decays of ^{238}U-^{206}Pb and ^{235}U-^{207}Pb. The first of these to be used – and the more traditional presentation – is called the Wetherill concordia diagram (Fig. 3) named for its developer George Wetherill (Wetherill 1956). It plots the ratios of radiogenic daughter Pb to the parent U, for each system (e.g., $^{206}Pb^*/^{238}U$ and $^{207}Pb^*/^{235}U$, where the asterisk denotes radiogenic Pb). When zircon forms, it has no radiogenic Pb and, therefore, plots at the origin of the diagram (i.e., when $Pb^*/U = 0$). With time, radiogenic Pb accumulates corresponding to the U decays, resulting in increasing $^{206}Pb^*/^{238}U$ and $^{207}Pb^*/^{235}U$. Because of the differences in half-lives between ^{238}U and ^{235}U, radiogenic ^{206}Pb and ^{207}Pb accumulate at different rates throughout Earth's history. Early in Earth's history, when ^{235}U was still abundant, ^{207}Pb kept approximate pace with ^{206}Pb. Progressively over time, however, ^{235}U decreased dramatically in abundance, due to its short half-life (~ 0.7 Ga), resulting in progressively less ^{207}Pb production to the point today where ^{235}U is nearly extinct (^{235}U abundance ~0.7%) and radiogenic ^{207}Pb production is very small. The difference between the ^{238}U and ^{235}U decays, and their corresponding radiogenic Pb production rates, results in the characteristic curvature of the Pb growth curve. Equivalent $^{206}Pb^*/^{238}U$ and $^{207}Pb^*/^{235}U$ ages in this diagram define this curved Pb evolution line, referred to as Concordia; zircons that have been closed systems since formation will plot on this curve. These are referred to as concordant and are generally considered to yield reliable ages.

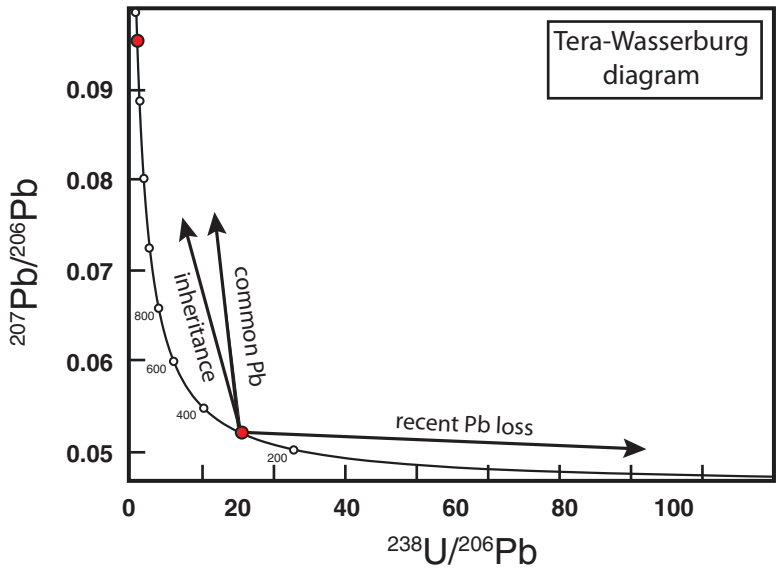

Geochronology and Radiogenic Isotopes, Fig. 4 The Tera-Wasserburg Concordia diagram. Arrows show the effects of inheritance of a ~ 1550 Ma zircon, common Pb, and recent Pb loss on a zircon with a crystallization age of 300 Ma

Disturbances and complexities in the U-Pb system, however, are common and can often be effectively illustrated by the Concordia diagram. These complexities generally take two forms: Pb loss (or, more rarely, gain) and multiple zircon growth components. In the case of the former, Pb loss will have lower Pb/U ratios and plot below Concordia. The loss of Pb from the zircon, if occurring in a discrete event, will plot along a straight line with an upper intercept on the concordia curve, representing no Pb loss, and a lower intercept, representing loss of all Pb from the zircon. This line is referred to as a "discordia" line. In this scenario, the upper intercept is taken to represent the crystallization age and the lower intercept is taken to represent the timing of Pb loss. Zircons plotting below Concordia are called normally discordant. In the more uncommon situation of zircons plotting above Concordia – due to Pb gain or U loss – these are called reversely discordant.

A second U-Pb diagram (called the Tera-Wasserburg concordia diagram; Fig. 4) plots $^{207}Pb/^{206}Pb$ vs. $^{238}U/^{206}Pb$ (Tera and Wasserburg 1972). There are some advantages of using this diagram. First, this diagram is less dependent on common Pb corrected Pb*/U ratios as is the case with the Wetherill Concordia diagram. Arrays of data points in this diagram, with variable uncorrected common Pb, can plot along linear arrays, whose upper intercept is taken to be the common Pb component and whose lower intercept is taken to be the crystallization age. This is useful for ^{204}Pb poor analyses and – especially – for microbeam methods (e.g., ion microprobe and LA-ICPMS) where quantitatively determining and removing a common Pb component is difficult. Finally, errors are only weakly correlated in this diagram allowing for a more rigorous assessment of any linearity in the data. A disadvantage of this diagram is that for old samples – whose analyses are close to concordia – it is difficult to identify a common Pb component, should it exist. In addition, it may be difficult to differentiate an inherited component from a common Pb component. Again this is particularly so for old samples.

The traditional way of presenting data – especially for data generated by ID-TIMS – is to use the Wetherill Concordia, which, for many users, may be more intuitive because it plots, on each axis, the ratio of the radiogenic daughter to the radioactive parent (i.e., $^{206}Pb^*/^{238}U$). U-Pb data generated by ion microprobe (e.g., SHRIMP) or by laser ablation ICPMS, however, typically measure $^{238}U/^{206}Pb$ and $^{207}Pb/^{206}Pb$ and calculate $^{235}U/^{207}Pb$ (which is not directly measured) from these two ratios and the natural $^{238}U/^{235}U$ ratio. As a result, many authors generating data with these methods plot their U-Pb data using the Tera-Wasserburg diagram as this plots the ratios actually being measured.

Despite the fact that the U-Pb system is widely considered to be the "gold standard" for geochronology – particularly for zircon and some other accessory phases – there are a number of potential factors that can complicate interpretations. For example, the U-Pb data shown in Fig. 5 can be produced in different ways. One way would be for zircon crystallizing from a rock at 3.8 Ga (A) and with subsequent variable Pb loss at 1.0 Ga (B,C). The discordia trend, however, could also be produced by mixing of two discrete age components. Using the example shown in Fig. 5, this could be produced by a rock crystallizing zircon at 3.8 Ga (A) and with magmatic or metamorphic overgrowths at 1.0 Ga (C, mixture at B). Alternatively, it could also be produced by the rock crystallizing at 1.0 Ga (C) but with some inheritance of 3.8 Ga zircons (A, mixture at B). In these two cases, the magmatic event (generally what we are most interested in dating) is very different and resolving between these two scenarios is not always straightforward. Fortunately, with modern in situ

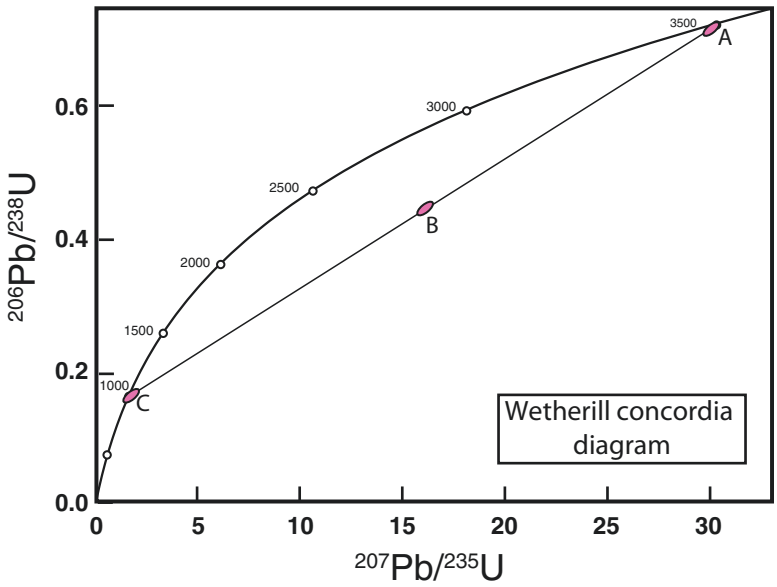

Geochronology and Radiogenic Isotopes, Fig. 5 A Wetherill Concordia diagram showing three hypothetical data points that can be explained by (1) Pb loss of 0%, 50% and 100% at 1.0 Ga from a zircon formed at 3.5 Ga or (2) mixing of components with ages of 3.5 and 1.0 Ga. See text for further explanation

analytical methods, integrated with cathodoluminescence imaging and informed by allied geochemical data such as Hf isotope compositions of the zircon zones, these different types of zircon growth can be resolved.

Both of these graphical methods have the ability to calculate upper and lower intercepts on discordia lines (when appropriate) as well as calculating concordia ages, which are weighted average ages of concordant analyses. In addition, weighted average $^{238}U/^{206}Pb$ and $^{207}Pb/^{206}Pb$ dates are commonly used for uniform populations of ages – typically $^{238}U/^{206}Pb$ for ages <1 Ga and $^{207}Pb/^{206}Pb$ for ages >1 Ga. The caveats with using these ages are that they can be affected by both Pb loss and inheritance, which can lead to spurious ages. The appropriate use of weighted ages can be generally informed by data plotted on the Concordia diagrams because these can help identify both Pb loss and inherited components in the populations by examination of the coupled U-Pb systematics.

For stand-alone ages, such as for detrital zircons, practitioners again typically use $^{238}U/^{206}Pb$ for dates < ~ 1 Ga and $^{207}Pb/^{206}Pb$ for dates > ~1 Ga. Data are commonly screened for potential complications on the basis of concordance; if a grain is >90% concordant (< 10% discordant based on the difference between the $^{238}U/^{206}Pb$ and $^{207}Pb/^{206}Pb$ dates), it is generally considered reliable. It is important to keep in mind that for detrital zircons the host rock is no longer present, making it difficult to determine the effect of ancient Pb loss or inheritance on the ages. Because this Pb loss trajectory can be parallel to Concordia, grains can have significant Pb loss or inheritance and still appear largely concordant based on the criteria described above.

The discussion above has focused on zircon because it is, by far, the most common phase used with the U-Pb system to determine dates. It is important to note, however, that the U-Pb system has been applied to other accessory phases with success and which have yielded complementary information to that obtained from zircon. Monazite U-Pb geochronology is chief among these other phases and has been used increasingly to determine ages of monazite growth during metamorphic events. Other phases include titanite, apatite, xenotime, and allanite (e.g., Ireland and Williams 2003; Woodhead et al. 2016). The challenge in many of these phases is the presence of higher amounts of common Pb, which can compromise the quantification of radiogenic Pb.

Monazite also has very high amounts of Th, which permits calculation of dates, based on the ^{232}Th-^{208}Pb decay scheme, to complement the U/Pb dates. In practice, however, the utility of the coupled U-Pb decays (e.g., in determining concordance, lead loss) generally outweighs the advantage of adding the Th-Pb chronometer and, therefore, the U-Pb systems are most widely used in monazite geochronology.

There are three primary analytical techniques that are routinely used in U-Pb geochronology of zircon and other accessory phases: ID-TIMS (isotope dilution-thermal ionization mass spectrometry), SIMS (secondary ionization mass spectrometry), and LA-ICPMS (laser ablation-inductively coupled plasma mass spectrometry). Each of these techniques has strengths and weaknesses – all have applications they are especially well suited for and others for which they are not. Description of these techniques has been discussed in detail elsewhere (e.g., Parish and Noble 2003; Ireland and Williams 2003; Kosler and Sylvester 2003). In general, however, it is useful here to briefly highlight their important features, strengths, and weaknesses as well as the applications to which they are most commonly applied.

Isotope dilution-thermal ionization mass spectrometry (ID-TIMS) involves complete dissolution of all of a zircon or zircon fragment, spiking the resulting solution with a

mixed U-Pb isotope tracer, separating Pb and U using ion chromatography, and analyzing these purified elements using thermal ionization mass spectrometry. In recent years, the technique of "chemical abrasion" (Mattinson 2005) has been added to this method (commonly called CA-ID-TIMS) which uses a combination of thermal annealing and partial dissolution of zircon with HF acid to remove radiation damaged domains, which are more subject to higher Pb loss, to greatly improve the concordance of the analysis. ID-TIMS offers, unquestionably, the highest precision measurements of the three techniques but has the poorest spatial resolution. This technique is best applied to simple zircons that have not been complicated by older inherited domains or younger overgrowths. It has been especially powerful in providing tight age constraints on the geological timescale by dating volcanic ash layers interbedded with sedimentary strata (e.g., Bowring and Schmitz 2003).

Secondary ionization mass spectrometry (SIMS) uses a primary beam of high-energy ions (typically O_2^- or $^{16}O^-$) that is focused onto a polished surface to produce a small volume of secondary ions that are then accelerated, focused, and analyzed by the mass spectrometer (e.g., Ireland and Williams 2003). The most common SIMS instrument for use in geochronology is the ion microprobe. The first of these instruments to be used for U-Pb geochronology was the SHRIMP (for Super High Resolution Ion Microprobe), later followed by the Cameca 1270 ion microprobe. These instruments use a large radius magnet and high resolution to separate and analyze the Pb and U (and Th) masses of interest. Typically a small (~30 μm; range 10–50 μm) primary ion beam ablates the surface of the target and consumes a pit (or spot) a few microns deep. Invariably these analyses are used in conjunction with cathodoluminescence (CL) and/or back scattered electron (BSE) images of the zircon grains, which provide essential information on the internal structure and growth domains of the zircon. In conjunction with the essentially nondestructive nature of the analysis, this technique affords unquestionably the highest spatial resolution and is particularly powerful in targeting specific domains of zircon crystals. These analyses, however, are not nearly as precise as the ID-TIMS measurements (Schmitz and Kuiper 2013).

Laser ablation-inductively coupled plasma mass spectrometry (LA-ICPMS) has seen an explosion of use in the last decade because it has brought the capability of U-Pb geochronology to many more laboratories through the acquisition of considerably lower cost instrumentation and with a technique that does not require low-blank clean chemical laboratories. This method uses a laser (typically a 193 or 213 nm) in conjunction with an inductively coupled plasma mass spectrometer. The laser is used to ablate the sample creating an aerosol, which is swept with carrier gases into the mass spectrometer's plasma where it is ionized, accelerated, and analyzed. Typical laser spot sizes are comparable to SIMS analyses (~30 μm), but the depth of the ablation pit – and, therefore, the ablated volume – is about an order of magnitude greater. Therefore, although this technique provides some spatial resolution, it is not as fine as it is for SIMS. The precision of individual spot analyses are comparable to SIMS, but this technique has had challenges with the normalization of U/Pb elemental fractionation during analysis and so it is currently limited to ~1–2% accuracy (the "so-called" 2% problem; Kosler et al. 2013).

The power of this technique is in its ability to produce a large throughput of relatively low-cost data with good spatial resolution and reasonable quality. This has been especially useful for applications requiring a large number of dates, such as detrital zircon U-Pb geochronology (e.g., Fedo et al. 2003), but also has allowed – owing to its greater access and lower cost – for the dating of many more rocks and minerals than would ever have been possible with ID-TIMS and SIMS alone. Although LA-ICPMS primarily began as a U-Pb zircon technique, it has also been successfully used for dating of monazite and other accessory phases (e.g., summary in Woodhead et al. 2016). In the last several years, the so-called "LASS" (laser ablation split stream) technique has been developed, which has been used to augment the U-Pb age data with other geochemical information. In this technique, the aerosol from the laser ablation is split into two mass spectrometers: one to analyze U-Pb to determine an age and the other to measure either isotopes (e.g., Hf isotopes in zircon, Yuan et al. 2008; Xie et al. 2008; Fisher et al. 2014a; Nd isotopes in monazite, Fisher et al. 2014b) or trace elements (Kylander-Clark et al. 2013). This has allowed for the integration of ages with isotopic or chemical data and has proved exceptionally useful in determining the source (e.g., Bauer et al. 2017) or petrogenesis (e.g., Kylander-Clark et al. 2013) of rocks as recorded by accessory phases. In sum, these three analytical techniques provide important complementary information and, for most applications, are much more powerful when used in concert rather than in isolation. In total, these techniques–and their integration–have solidified U-Pb as the pre-eminent geochronological tool.

K-Ar and Ar-Ar Geochronology

The K-Ar isotope system is based on the decay of ^{40}K to ^{40}Ar. This system has some advantages that make it particularly useful for geochronology. First, ^{40}K has one of the shortest half-lives (1.28×10^9 yr) of all the long-lived radioactive nuclides (Table 1). Second, K is a major element and is abundant in a wide variety of minerals. These factors make K-Ar (and $^{40}Ar/^{39}Ar$, described below) often the systems of choice for dating young geological events. But the K-Ar system is different from the others discussed here in a number of fundamental ways. First, ^{40}K has a branched decay with part of ^{40}K (~81%) decaying to ^{40}Ca by β^- decay and the rest (~19%) decaying to ^{40}Ar by electron capture. This branched

decay must be taken into account when calculating ages. Secondly, and more significantly for the ^{40}K-^{40}Ar decay, the parent nuclide is a lithophile element and is in a solid phase, whereas the daughter is a gas and is trapped in mineral phases and rocks rather than bound within crystallographic sites. This characteristic results in some significant challenges, but also confers some distinct advantages.

In an ideal case, we could imagine a mineral crystallizing from a magma and trapping neither atmospheric Ar nor radiogenic Ar from source or surrounding rocks. In this case, there would be no ^{40}Ar in the system at $t = 0$ and we could calculate an age directly from the measured $^{40}Ar/^{40}K$, in an analogous manner to calculating an age from $^{206}Pb/^{238}U$ ratio in zircon with no common Pb. In practice, however, trapped ^{40}Ar can exist in many cases (e.g., trapped atmospheric Ar by a sub-aerial lava flow, or ^{40}Ar present in source rocks from decay from K-rich minerals) and its presence needs to be corrected. Conversely, because Ar is a gas and not bound into crystal lattices, it can, and does, escape. This is an obvious disadvantage in the sense that loss of the radiogenic ^{40}Ar would result in anomalously young ages, but can also be used as a tool by utilizing the fact that Ar loss happens as a function of mineralogy, grain geometry, as well as the thermal history of the rock and mineral. This Ar loss is diffusion limited and is, therefore, quantifiable.

In practice, the K-Ar system is no longer widely used because, with K in a solid phase and Ar in the gas phase, it is difficult to determine the $^{40}K/^{40}Ar$ ratio precisely for calculating ages. To overcome this analytical hurdle, the $^{40}Ar/^{39}Ar$ approach was developed. In this technique, K-rich samples are irradiated in a nuclear reactor and ^{39}Ar is produced from ^{39}K present in the sample by neutron capture. The amount of ^{39}Ar produced is a function of the amount of K present in the target, the natural $^{40}K/^{39}K$ ratio, and the production factor of ^{39}Ar from ^{39}K in the reactor. In this way, ^{39}Ar can be used as a proxy for ^{40}K (and $^{40}Ar/^{39}Ar$ a proxy for $^{40}Ar/^{40}K$). The advantage of this technique is not only that $^{40}Ar/^{39}Ar$ can be measured more accurately but also that this ratio can be measured simultaneously in discrete gas fractions. In this technique, Ar is collected from samples as they are heated under vacuum. The $^{40}Ar/^{39}Ar$ ratio is then measured in these individual gas fractions (Fig. 6). In the case of a mineral grain, one would expect Ar to have been lost from the edges of the crystal, while the interior of the grain will have retained more of its Ar. Thus, as a grain is heated under vacuum, the first parts of the Ar released will likely come from the Ar pool that has already lost some Ar (and thus display lower $^{40}Ar/^{39}Ar$ ratios and younger apparent ages) and later fractions from Ar more tightly held by the mineral grain (and thus yielding higher $^{40}Ar/^{39}Ar$ ratios and older apparent ages closer to the true age). This technique, called step heating, has become a powerful technique in revealing the thermal history of rocks and minerals and for determining accurate ages for K-bearing minerals. In addition, the Ar isotope data can be plotted on an isochron diagram using $^{40}Ar/^{36}Ar$ on the ordinate and $^{39}Ar/^{36}Ar$ on the abscissa (again, where ^{39}Ar is a proxy for ^{40}K) or on an inverse isochron diagram where $^{36}Ar/^{40}Ar$ is on the ordinate and $^{39}Ar/^{40}Ar$ is on the abscissa. These diagrams are useful in identifying extraneous sources of Ar such as atmospheric or trapped Ar. All aspects of the $^{40}Ar/^{39}Ar$ method of dating are discussed in detail in McDougall and Harrison (1999).

In summary, several characteristics of the $^{40}Ar/^{39}Ar$ chronometer have contributed to its utility: the introduction and refinement of the $^{40}Ar/^{39}Ar$ method has improved determination of ages using the ^{40}K-^{40}Ar decay; the fact that this system is based on a major element present as a stoichiometric constituent in several rock-forming minerals makes it applicable to a wide variety of rock types; the relatively short half-

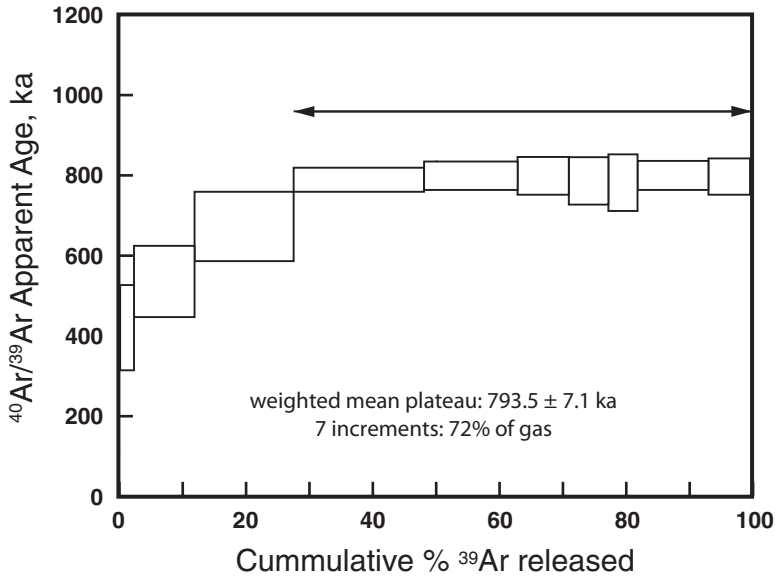

Geochronology and Radiogenic Isotopes, Fig. 6 An example of a $^{40}Ar/^{39}Ar$ age spectrum of a sample from a basaltic lava flow. Ten gas steps were released by successively raising the temperature in 50 °C increments. The plateau age in this example is calculated from seven contiguous steps comprising 72% of the gas released. The younger ages from gas released at lower temperatures are interpreted as Ar loss during weathering. Figure is from Singer 2007

life of ^{40}K allows this system to date young geological events; and Ar diffusion from the mineral lattice can be used to model the thermal history of a rock. These characteristics have contributed to making $^{40}Ar/^{39}Ar$ dating an exceptionally useful and diverse geochronological and thermochronological tool used widely throughout the geosciences.

Garnet Lu-Hf and Sm-Nd Geochronology

Garnet geochronology is an example of an effective use of the isochron method for determining reliable ages (Figs. 7, 8). This application utilizes both the Lu-Hf and Sm-Nd isotope systems (^{176}Lu to ^{176}Hf, $t_{1/2} = 36$ billion years; ^{147}Sm to ^{143}Nd, $t_{1/2} = 106$ billion years; Table 1) and provides constraints on the timing of garnet growth in the rock and, therefore, has been used to provide constraints on the timing of metamorphism by directly dating a major index mineral that is produced during metamorphism.

This chronometer utilizes garnet's ability to incorporate the parent elements Lu and Sm preferentially over their respective daughter elements (Hf, Nd) during growth, which results in highly elevated Lu/Hf and, to a lesser extent, Sm/Nd ratios in the garnet relative to the bulk rock. Whereas the bulk Earth has low $^{176}Lu/^{177}Hf$ and $^{147}Sm/^{144}Nd$ ratios (0.0336 and 0.1960, respectively; Bouvier et al. 2008), garnets often have parent/daughter ratios 2 to 3 orders of magnitude (or more) higher. Over time, these elevated parent/daughter ratios result in the growth of highly radiogenic Hf and Nd (i.e., elevated $^{176}Hf/^{177}Hf$ and $^{143}Nd/^{144}Nd$). Such high parent/daughter ratios and highly radiogenic Hf and Nd isotope compositions provide large leverage in regression of a line

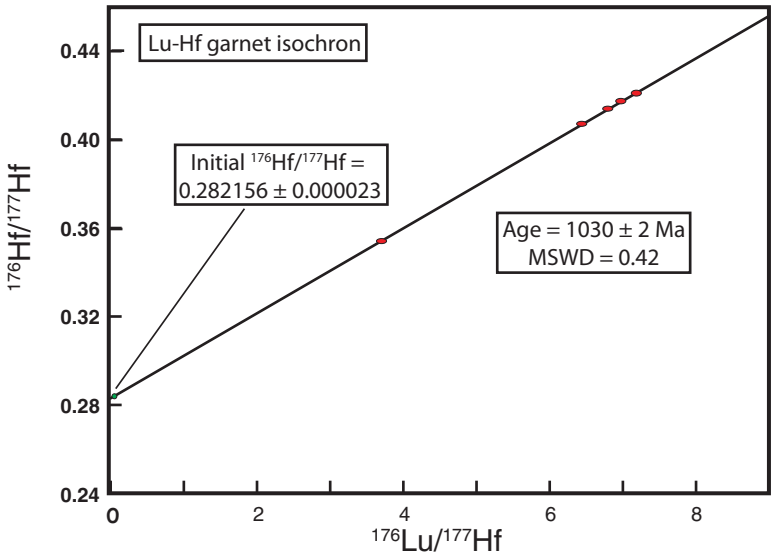

Geochronology and Radiogenic Isotopes, Fig. 7 Lu-Hf garnet isochron from a garnet granulite gneiss from the Virginia Grenville massif. The high Lu/Hf ratios (e.g., $^{176}Lu/^{177}Hf > 6$) in the garnet result in highly radiogenic Hf isotopic compositions ($^{176}Hf/^{177}Hf > 0.40$). This large range of parent/daughter ratios and Hf isotope compositions provide tight constraints for the regression line and result in a precise age

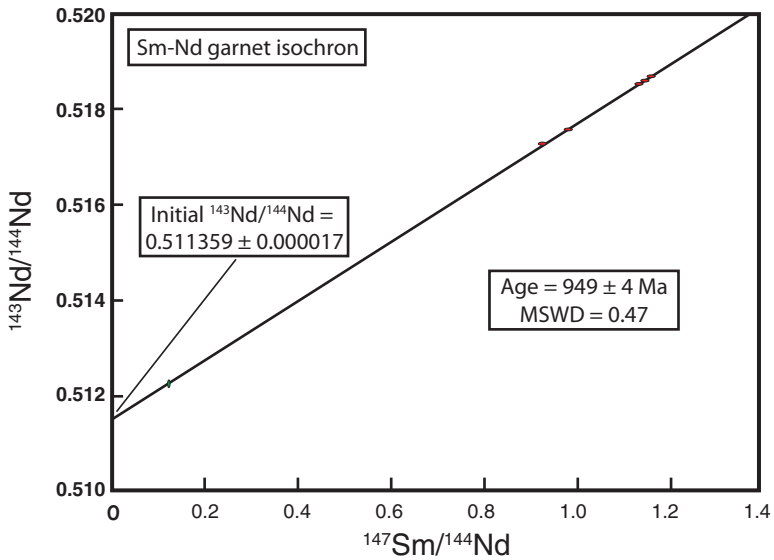

Geochronology and Radiogenic Isotopes, Fig. 8 Sm-Nd garnet isochron from the same garnet granulite gneiss as in Fig. 7. Note that this age, although tightly constrained as the Lu-Hf garnet age, is over 80 Ma younger. Johnson et al., (2017) have suggested this represents differences in the closure temperatures for the Lu-Hf and Sm-Nd isotope systems

through the data and, therefore, in a tightly constrained isochron age.

One of the major requirements for an accurate isochron age is that the system must be in isotopic equilibrium at time = 0. That is certainly not the case in the strict sense because the garnets are often riddled with inclusions, including zircon and other phases, which often do not have the same Hf isotopic composition as the garnet at the time the latter grew. The large radiogenic in-growth occurring during garnet growth, however, helps to compensate for initial isotopic heterogeneities that may have existed at the time of garnet growth and lessens the stringency of this isochron requirement. Initial Hf isotopic heterogeneity – particularly in robust, refractory, and Hf-rich inclusions like zircon – however, is still something to be vigilant about, especially for young rocks or rocks with a small range in Lu-Hf or Sm-Nd (e.g., Scherer et al. 2000). Fortunately, these inclusions can be effectively avoided, in many cases, using different dissolution and leaching strategies (e.g., Ankiewicz and Thirlwall 2003; Baxter and Scherer 2013; Cheng et al. 2008).

The coupled use of the Lu-Hf and Sm-Nd garnet chronometers can provide important information on the thermal conditions during metamorphic events. For example, the Lu-Hf and Sm-Nd isochrons shown in Figs. 7 and 8 are determined from the same mineral fractions and, despite both having tightly constrained ages, differ by over 80 Ma. This has been interpreted to represent different rates of diffusion of elements in these granulite-grade gneisses during prolonged heating during the Grenville orogeny (Johnson et al. 2017). Similar differences in Lu-Hf and Sm-Nd garnet dates from granulite terranes have been noted by Smit et al. (2013).

In summary, Lu-Hf and Sm-Nd garnet chronology is widely used for providing age constraints on garnet growth. When used in concert with other chronometers, such as monazite U-Pb geochronology, and also interpreted within the context of the petrography and mineral chemistry of the rock assemblage, it can be a very powerful tool in helping understand metamorphic histories and processes.

Tracer Isotopes and Model "Ages"

Radiogenic tracer isotope applications, by their very nature, include the element of time as recorded by the accumulation of the daughter isotope. In order to take full advantage of their utility, radiogenic tracer isotopes need to be placed in the proper temporal framework. In most cases, what is of most interest is the isotope composition of the rock or mineral at the time of formation rather than what it is at present. If there are independent constraints on the age of the rock or mineral, its isotopic composition at any time in the past can be calculated by subtracting the amount of radiogenic daughter atoms that had accumulated over the time interval of interest. For the Sm-Nd isotope system, this would be:

$$\left(\frac{^{143}Nd}{^{144}Nd}\right)_t = \left(\frac{^{143}Nd}{^{144}Nd}\right)_p - \left(\frac{^{147}Sm}{^{144}Nd}\right)_p \left(e^{\lambda t} - 1\right) \qquad (23)$$

where the subscript t is the time of interest and p signifies the present. What this equation shows is that the Nd isotope composition ($^{143}Nd/^{144}Nd$) at some time, t, can be calculated from the present-day $^{143}Nd/^{144}Nd$ and subtracting the amount of radiogenic ingrowth that has occurred over a given interval of time, which can be calculated from the $^{147}Sm/^{144}Nd$ ratio measured at present and the amount of time, t, that has elapsed.

If the *t* of interest is calculated at the time of formation (e.g., crystallization) of the rock, this is often denoted with the subscript "i" signifying the "initial" isotope ratio (e.g., $^{143}Nd/^{144}Nd_{(i)}$). Figure 9 shows the generalized evolutionary paths for chondritic (bulk silicate Earth), depleted mantle, and crustal reservoirs for the Sm-Nd isotope system, with a

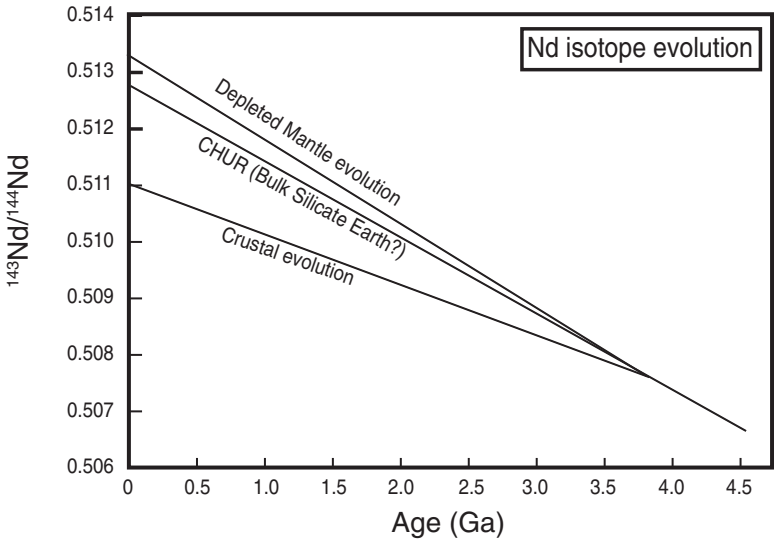

Geochronology and Radiogenic Isotopes, Fig. 9 Diagram showing model evolutionary paths for chondritic (bulk silicate Earth), depleted mantle, and crustal reservoirs for the Sm-Nd isotope system, with a hypothetical separation of the depleted mantle and a crustal reservoir from the bulk silicate Earth at ~3.8 Ga

hypothetical separation of the depleted mantle and a crustal reservoir from the bulk silicate Earth at ~3.8 Ga.

Radiogenic isotopes have also been used to calculate what has been called a "model age," which uses the trajectory of the radiogenic growth back into time to estimate the time of separation from a particular reservoir such as the depleted mantle (DM) or a chondritic Earth composition (e.g., CHUR or chondritic uniform reservoir). These are calculated in two basic ways. One is when there are no age constraints on the rock or mineral. In this case, the present-day parent/daughter ratio is used to calculate the trajectory back to the intersection with the estimated reservoir evolution. For a depleted mantle Nd model age, for example, this would be calculated with the following expression:

$$t_{CHUR} = \frac{1}{\lambda}\left[\frac{\frac{^{143}Nd}{^{144}Nd\ (\text{sample})} - \frac{^{143}Nd}{^{144}Nd\ (DM)}}{\frac{^{147}Sm}{^{144}Nd\ (\text{sample})} - \frac{^{147}Sm}{^{144}Nd\ (DM)}} + 1\right] \quad (24)$$

This method has been frequently used on sediments to calculate what has been called a "crustal residence" age, which is intended to estimate the *average* time the sources of the sediment have resided in the crustal reservoir (or the time since the precursor materials have been extracted from the mantle). A parallel expression can be written for the Lu-Hf isotope system. A graphical representation of chondritic (T_{CHUR}) and depleted mantle (T_{DM}) ages is shown in Fig. 10. Model ages have also been used effectively in the Re-Os system (see Shirey and Walker 1998, for a full discussion).

In many cases, however, there are independent constraints on the age of the rock or mineral. In such cases, the age and parent/daughter ratio are used to calculate the isotopic evolution back to the age of crystallization. From this point, a different trajectory often has to be assumed because the precursor evolution will be different from the rock or mineral that formed at that time. A clear example of this is for zircon Hf model ages, which have become increasingly common in detrital zircon studies because of the ability to measure both U-Pb and Hf isotopes on single zircon grains or spots of grains. In this case, the age and Lu/Hf ratio are used to calculate back to the age of the zircon. In the case of detrital zircons, however, there no longer is information on the rock from which that zircon was derived and a Lu/Hf ratio has to be assumed for its precursor rock. This assumed Lu/Hf ratio is then used to estimate the evolution path back to the reservoir of interest. This is shown diagrammatically in Fig. 11.

It is important to keep in mind, however, that there are many assumptions built into these calculations and even though these are commonly called model "ages," they are not ages at all in the quantitative sense. Rather, they are highly qualitative models to estimate a time of separation from a particular reservoir. The inherent uncertainty in these many assumptions should clearly be kept in mind in the interpretation of zircon Hf model ages. The limitations of model ages have been discussed in considerable depth in Vervoort and Kemp (2016).

Summary

In summary, geochronology is an essential part of Earth Sciences and has made profound contributions throughout virtually every aspect of this discipline for the simple reason that it provides information on timing and rates that is an integral part of Earth Sciences. Early applications of geochronology mostly involved employing one chronometer to answer a problem (e.g., using the Rb-Sr isotope system to

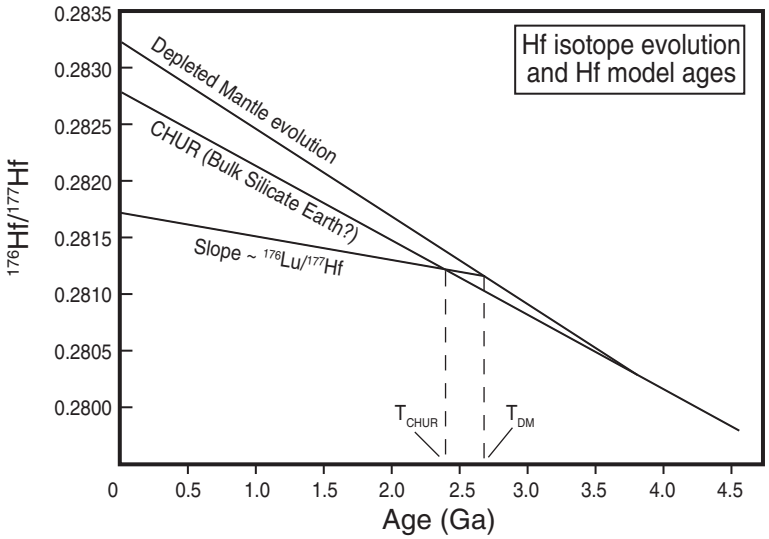

Geochronology and Radiogenic Isotopes, Fig. 10 Diagram showing model evolutionary paths for chondritic (bulk silicate Earth) and depleted mantle, and crustal reservoirs for the Lu-Hf isotope system, with a hypothetical separation of the depleted mantle from the bulk silicate Earth at ~3.8 Ga and separation of a crustal rock from the depleted mantle at 2.7 Ga. Also shown is a graphical representation of chondritic (T_{CHUR}) and depleted mantle (T_{DM}) Hf model ages

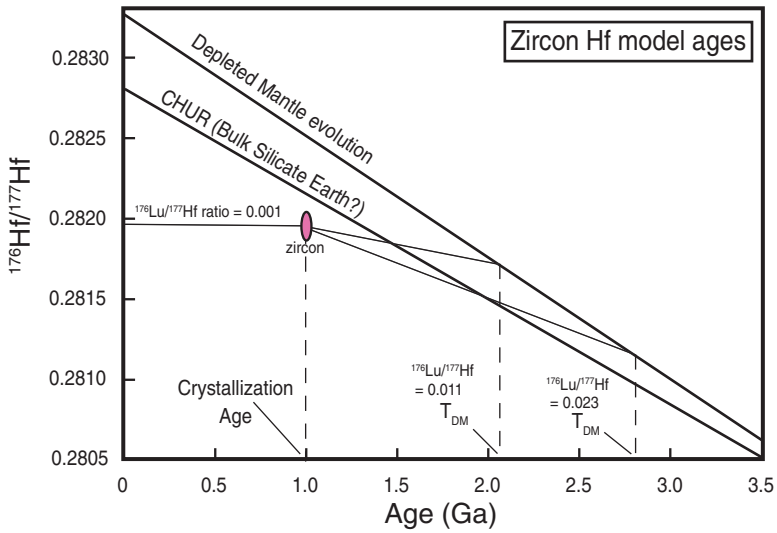

Geochronology and Radiogenic Isotopes, Fig. 11 Diagram showing the calculation of Hf model ages for a zircon with a crystallization age of 1.0 Ga. The Hf isotope composition of the zircon is calculated back to 1.0 Ga using the low Lu/Hf ratio of the zircon. Past that point, however, a precursor Lu/Hf needs to be assumed because the rock from which the zircon was derived no longer exists. A low Lu/Hf ratio, typical of an evolved precursor rock, would yield a model zircon Hf age of ~2.1 Ga, whereas a higher Lu/Hf ratio, typical of a more primitive precursor, would yield an older model age of ~2.8 Ga. This illustrates some of the uncertainty inherent in determining zircon Hf model ages (see Vervoort and Kemp 2016)

date a rock). It is becoming increasingly apparent, however, that each chronometer gives us a different set of information and, therefore, geochronology is much more powerful – and provides a more complete picture of past history – when used in concert with other chronometers. In addition, the information that these isotope systems provide is more meaningful when integrated with other isotope data (e.g., tracer isotopes) and also interpreted in the context of other geologic data from allied fields such as petrology, petrography, structural geology, tectonics, and geophysics.

Cross-References

- Argon Isotopes
- Argon
- Atomic Number, Mass Number, and Isotopes
- Chemical Weathering
- Compound-Specific Isotope Analysis
- Chondrites
- Cosmogenic Nuclides
- Diffusion
- Earth's Continental Crust
- Electron Probe Microanalysis (EPMA)
- Geothermal Systems
- Geochronology and Radiogenic Isotopes
- Geologic Time Scale
- Hafnium Isotopes
- Heat-Producing Elements (HPEs)
- Ion Microprobe
- Isotope Dilution
- Inductively Coupled Plasma Mass Spectrometry (ICP-MS)
- Laser Ablation – Inductively Coupled Plasma Mass Spectrometry
- Lead Isotopes
- Luminescence
- Mantle Geochemistry
- Neodymium Isotopes
- Radioactivity
- Strontium Isotopes
- Strontium Isotopes
- Thermal Ionization Mass Spectrometry
- Titanium
- Uranium
- Uranium Decay Series
- Zirconium

References

Amelin Y, Ireland TR (2003) Considerations in zircon geochronology by SIMS. In: Hanchar JM, Hoskin PWO (eds) Zircon. Reviews in mineralogy and geochemistry. Mineralogical Society of America, Chantilly, pp 215–242

Anczkiewicz R, Thirlwall MF (2003) Improving precision of Sm–Nd garnet dating by H_2SO_4 leaching – a simple solution to phosphate inclusions problem. In: Vance D, Mueller W, Villa IM (eds) Geochronology: linking the isotopic record with petrology and textures, Spec Publ – Geol Soc Lond, 220: 83–91

Bauer A, Fisher CM, Vervoort JD, Bowring SA (2017) Coupled zircon Lu–Hf and U–Pb isotopic analyses of the oldest terrestrial crust, the >4.03 Ga Acasta Gneiss Complex. Earth Planet Sci Lett 458:37–48

Baxter E, Scherer E (2013) Garnet geochronology: timekeeper of tectonometamorphic processes. Elements 9:433–438
Beck JW, Richards DA, Edwards RL (2001) Extremely large variations of atmospheric 14 C concentration during the last glacial period. Science 292:2453–2458
Bouvier A, Vervoort JD, Patchett PJ (2008) The Lu-Hf and Sm-Nd isotopic composition of CHUR: constraints from unequilibrated chondrites and implications for the bulk composition of terrestrial planets. Earth Planet Sci Lett 273(1–2):48–57
Bowring SA, Schmitz MD (2003) High-precision U-Pb zircon geochronology and the stratigraphic record. In: Hanchar JM, Hoskin PWO (eds) Zircon. Mineralogical Society of America, Chantilly, pp 305–326
Bowring SA, Williams IS (1999) Priscoan (4.00–4.03 Ga) orthogneisses from northwestern Canada. Contrib Mineral Petrol 134:3–16
Boyet M, Carlson RW (2005) ^{142}Nd evidence for early (>4.53 Ga) global differentiation of the silicate Earth. Science 309:576–581
Cheng H et al (2000) The half-lives of uranium-234 and thorium-230. Chem Geol 169:17–33
Cheng H, King RL, Nakamura RL, Vervoort JD, Zhao Z (2008) Coupled Lu–Hf and Sm–Nd geochronology constrains garnet growth in ultra-high-pressure eclogites from the Dabie orogen. J Metamorphic Geol 26:741–758
Condon DJ, McLean N, Noble SR, Bowring SA (2010) Isotopic composition (^{238}U/^{235}U) of some commonly used uranium reference materials. Geochim Cosmochim Acta 74:7127–7143
Cook DL, Walker RJ, Horan MF, Wasson JT, Morgan JW (2004) Pt-Re-Os systematics of group IIAB and IIIAB iron meteorites. Geochim Cosmochim Acta 68:1413–1431
Edwards RL, Chen JH, Ku TL, Wasserburg G (1987) Precise timing of the last interglacial period for mass spectrometric determination of Thorium-230 in corals. Science 236:1547–1553
Fedo CM, Sircombe KN, Rainbird RH (2003) Detrital zircon analysis of the sedimentary record. In: Hanchar JM, Hoskin PWO (eds) Zircon. Mineralogical Society of America, Chantilly, pp 277–303
Fisher CM, Vervoort J, Hanchar JM (2014a) Guidelines for reporting zircon Hf isotopic data by LA-MC-ICPMS and potential pitfalls in the interpretation of these data. Chem Geol 363:125–133
Fisher CM, Vervoort JD, DuFrane SA (2014b) Accurate Hf isotope determinations of complex zircons using the "laser ablation split stream" method. Geochem Geophys Geosyst 15:121–139
Goldmann A, Brennecka G, Noordmann J, Weyer S, Wadhwa M (2015) The uranium isotopic composition of the earth and the solar system. Geochim Cosmochim Acta 148:145–158
Hamilton PJ, O'Nions RK, Evenson NM (1977) Sm-Nd dating of Archean basic and ultrabasic volcanics. Earth Planet Sci Lett 36:263–268
Hiess J, Condon DJ, McLean N, Noble SR (2012) ^{238}U/^{235}U Systematics in Terrestrial Uranium-bearing minerals. Science 335:1610–1614
Ireland TR, Williams IS (2003) Considerations in Zircon Geochronology by SIMS. In Hanchar JM, Hoskin PWO (eds) Zircon. Mineralogical Society of America, Chintilly, pp. 215–241
Jaffey AH, Flynn KF, Glendenin LE, Bentley WC, Essling AM (1971) Precision measurements of half-lives and specific activities of ^{235}U and ^{238}U. Phys Rev C4:1889–1906
Johnson TA et al. (2017) Constraints on the timing and duration of the Grenville Orogeny. Geol Soc Am 49(3): Paper 10–18. https://doi.org/10.1130/abs/2017SE-290920
Kendall B, Creaser RA, Selby D (2006) Re-Os geochronology of post-glacial black shales in Australia: constraints on the timing of "Sturtian" glaciation. Geology 34:729–732
Kleine T, Münker C, Mezger K, Palme H (2002) Rapid accretion and early core formation on asteroids and the terrestrial planets from Hf-W chronometry. Nature 418:952–954
Kosler J, Sylvester PJ (2003) Present trends and the future of zircon in geochronology: laser ablation ICPMS. In: Hanchar JM, Hoskin PWO (eds) Zircon. Mineralogical Society of America, Chantilly, pp 243–275
Kosler J et al (2013) U-Pb detrital zircon analysis – results of an inter-laboratory comparison. Geostand Geoanal Res 37:243–259
Kylander-Clark ARC, Hacker BR, Cottle JM (2013) Laser-ablation split-stream ICP petrochronology. Chem Geol 345:99–112
Lugmair GW, Galer SJG (1992) Age and isotopic relationships among the angrites Lewis Cliff 86010 and Angra dos Reis. Geochim Cosmochim Acta 56:1673–1694
Lugmair GW, Marti K (1978) Lunar initial ^{143}Nd/^{144}Nd: differential evolution of the lunar crust and mantle. Earth Planet Sci Lett 39:349–357
Mattinson JM (2005) Zircon U–Pb chemical abrasion (CA-TIMS) method: combined annealing and multi-step partial dissolution analysis for improved precision and accuracy of zircon ages. Chem Geol 220:47–66
Marks NE, Borg LE, Hutcheon JD, Jacobsen B, Clayton RN (2014) Samarium–neodymium chronology and rubidium–strontium systematics of an Allende calcium–aluminum-rich inclusion with implications for 146Sm half-life. Earth Planet. Sci. Lett., 405: 15–24
Mattinson JM (2010) Analysis of the relative decay constants of ^{235}U and ^{238}U by multi-step CA-TIMS measurements of closed-system natural zircon samples. Chem Geol 275:186–198
McDougall I, Harrison TM (1999) Geochronology and thermochronology by the ^{40}Ar/^{39}Ar method. Oxford University Press, New York. 269 pp
Moorbath S, Allaart JH, Bridgewater D, McGregor VR (1977) Rb-Sr ages of early Archaean supracrustal rocks and Amitsog gneisses at Isua. Nature 270:43–45
O'Niel J, Carlson RL, Francis D, Stevenson RK (2008) Neodymium-142 evidence for Hadean mafic crust. Science 321:1828–1831
Parish RR, Noble S (2003) Zircon U-Th-Pb geochronology by isotope dilution – thermal ionization mass spectrometry (ID-TIMS). In: Hanchar JM, Hoskin PWO (eds) Zircon. Mineralogical Society of America, Chantilly, pp 183–213
Patterson CC (1956) Age of meteorites and the Earth. Geochim Cosmochim Acta 10:230–237
Phillips FM, Leavy BD, Jannik NO, Elmore D, Kubik PW (1986) The accumulation of cosmogenic chlorine-36 in rocks: a method for surface exposure dating. Science 231:41–43
Reid MR, Coath CD, Harrison TM, McKeegan KD (1997) Prolonged residence times for the youngest rhyolites associated with Long Valley Caldera; ^{230}Th-^{238} U ion microprobe dating of young zircons. Earth Planet Sci Lett 150(1–2):27–39
Renne P, Mundil R, Balco G, Min K, Ludwig KR (2010) Joint determination of ^{40}K decay constants and ^{40}Ar∗/^{40}K for the Fish Canyon sanidine standard, and improved accuracy for ^{40}Ar/^{39}Ar geochronology. Geochim Cosmochim Acta 74:5349–5367
Renne P, Balco G, Ludwig KR, Mundil R, Min K (2011) Response to the comment by W.H. Schwarz et al. on "Joint determination of 40K decay constants and ^{40}Ar∗/^{40}K for the Fish Canyon sanidine standard, and improved accuracy for ^{40}Ar/^{39}Ar geochronology" by P.R. Renne et al. (2010). Geochim Cosmochim Acta 75:5097–5100
Richter S, Eykens R, Kühn H, Aregbe Y, Verbruggen A, Weyer S (2010) New average values for the n(238U)/n(235U)isotope ratios of natural uranium standards. Int J Mass Spec 295:94–97
Rotenberg E, Davis D, Amelin Y, Ghosh S, Bergquist BA (2012) Determination of the decay-constant of ^{87}Rb by laboratory accumulation of ^{87}Sr. Geochim Cosmochim Acta 85:41–57
Scherer EE, Cameron KL, Blichert-Toft J (2000) Lu–Hf garnet geochronology: closure temperature relative to the Sm–Nd system and the effects of trace mineral inclusions. Geochim Cosmochim Acta 64:3413–3432
Schmitz MD, Kuiper KF (2013) High-precision geochronology. Elements 9:25–30
Selby D, Creaser RA, Stein HJ, Markey RJ, Hannah JL (2007) Assessment of the ^{187}Re decay constant by cross calibration of Re–Os molybdenite and U–Pb zircon chronometers in magmatic ore systems. Geochim Cosmochim Acta 71:1999–2013
Shirey SB, Walker RJ (1998) The Re-Os isotope system in cosmochemistry and high-temperature geochemistry. Ann Rev Earth Planet Sci 26(1):423–500

Singer BS (2007) Polarity transitions: radioisotopic dating. In: Gubbins D, Heeero-Bervera E (eds) Encyclopedia of geomagnetism and paleomagnetism. Springer, Dordrecht, pp 834–839
Smit MA, Scherer EE, Mezger K (2013) Lu-Hf and Sm-Nd garnet geochronology: chronometric closure and implications for dating petrological processes. Earth Planet Sci Lett 2013:222–233
Söderlund U, Patchett PJ, Vervoort JD, Isachsen CE (2004) The ^{176}Lu decay constant determined by Lu–Hf and U–Pb isotope systematics of Precambrian mafic intrusions. Earth Planet Sci Lett 219:311–324
Tera F, Wasserburg GJ (1972) U-Th-Pb systematics in three Apollo 14 basalts and the problem of initial Pb in lunar rocks. Earth Planet Sci Lett 14:281–304
Touboul M, Kleine T, Bourdon B, Palme H, Wieler R (2007) Late formation and prolonged differentiation of the Moon inferred from W isotopes in lunar metals. Nature 450:1206–1209
Vervoort JD, Kemp AIS (2016) Clarifying the zircon Hf isotope record of crust–mantle evolution. Chem Geol 425:65–75
Wetherill G (1956) Discordant uranium-lead ages. Trans Am Geophys Union 37:320–326
White WM (2015) Isotope geochemistry. John Wiley and Sons, Oxford. 496 pp.
Wilde SA, Valley JW, Peck WH, Graham CM (2001) Evidence from detrital zircons for the existence of continental crust and oceans on the Earth 4.4 Gyr ago. Nature 409:175–178
Woodhead JD, Horstwood MSA, Cottle JM (2016) Advances in isotope ratio determination by LA–ICP–MS. Elements 12:317–322
Xie LW, Zhang YB, Zhang HH, Sun JF, Wu FY (2008) In situ simultaneous determination of trace elements, U\Pb and Lu\Hf isotopes in zircon and baddeleyite. Chin Sci Bull 53: 1565–1573
Yin Q et al (2002) A short timescale for terrestrial planet formation from Hf-W chronometry of meteorites. Nature 418:949–951
Yuan H-L et al (2008) Simultaneous determinations of U–Pb age, Hf isotopes and trace element compositions of zircon by excimer laser-ablation quadrupole and multiple-collector ICP-MS. Chem Geol 247:100–118

Geologic Time Scale

Mark D. Schmitz
Department of Geosciences, Boise State University, Boise, ID, USA

Definition

The geologic time scale is the scientific reconstruction and representation of Earth's history from its rock record. The geologic time scale has its origins in the nineteenth-century recognition that through the application of the laws of superposition and fossil succession, a reproducible relative age order of rock strata could be assembled. The geologic time scale consists of two conceptual frameworks, one linked to the observable rock record of superposed sedimentary strata and their embedded physical, chemical, and fossil assemblage characters and the other tied to the theoretical construct of absolute time (Gradstein 2012). This rock versus time duality of the geologic time scale is manifested in the two distinct nomenclatures for *chronostratigraphic* and *geochronologic* age.

Time Scale Construction

In the Phanerozoic and the latest Precambrian, chronostratigraphic units are constructed from fossiliferous strata. The appearance, absence, acme, or coexistence of fossil organisms is variously used to construct a hierarchy of units, in the following order of increasing stratigraphic resolution: eonothem, erathem, system, series, and stage. The parallel geochronologic units are the eon, era, period, epoch, and age. Global chronostratigraphic units are developed and ratified through the efforts of the International Union of Geological Sciences (IUGS) International Commission on Stratigraphy (ICS) and its subcommissions. These units of the time scale are defined through boundary stratotypes, which preserve in a rock sequence the transition between two stages. The precise reference point for each stage boundary is established as a Global Stratotype Section and Point (GSSP), which comprises a set of primary and secondary correlation markers expressed within a stratigraphically complete interval of rock accumulation (Remane et al. 1996). The geologic time scale is thus defined by a series of GSSPs (Fig. 1).

Subsequent efforts to place this relative rock scale within an absolute time scale, notably first by Holmes (1913), have used a variety of radioisotopic dating methods based mainly upon K-Ar and U-Pb decay (Harland et al. 1982). Key criteria for precise and accurate age estimates are closed system behavior through geologic time, minimization or mitigation of initial daughter products in the dated minerals, precise and representative isotope ratio measurements, and accurately measured rate constants for the radioactive decay processes. The current standard methods for precise and accurate radioisotopic time scale calibration are the ^{238}U-^{206}Pb decay scheme measured by isotope dilution thermal ionization mass spectrometry in accessory minerals like zircon and the ^{40}Ar/^{39}Ar variant of ^{40}K decay as measured by multi-collector gas source mass spectrometry in sanidine feldspar (Schmitz 2012). Both methods provide numerical ages for geologically instantaneous event beds like volcanic tuffs or bolide ejecta with a relative precision and accuracy of *ca* 0.1% of the absolute age. Geologic time scale calibration involves the careful radioisotopic dating of these event beds within fossiliferous strata that also may record geochemical and geomagnetic correlation signals. In the Cenozoic and much of the Mesozoic, radioisotopic dating has been used to calibrate seafloor spreading models upon which the global magnetic polarity time scale has been constructed (Cande and Kent 1992; Ogg 2012). In the fossil-poor Precambrian, the geologic time scale is almost wholly dependent upon radioisotopic dates for establishing correlative strata and geochronologic intervals.

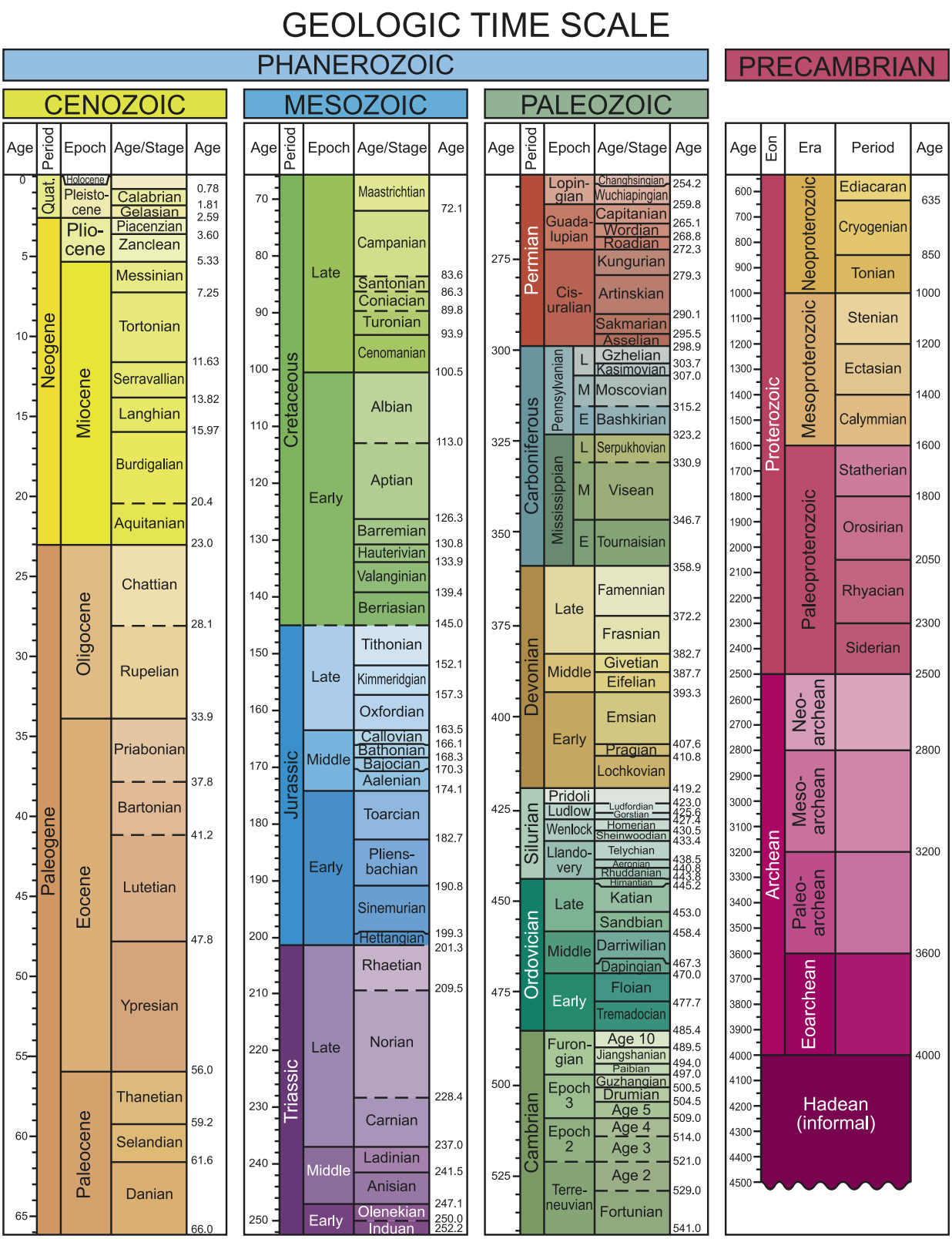

Geologic Time Scale, Fig. 1 Current global geologic time scale compiled by the 69 authors and contributors to *The Geologic Time Scale 2012* (Gradstein et al. 2012)

G

Chemostratigraphy

The use of geochemical signals in the stratigraphic record – chemostratigraphy – plays an important role in geologic time scale development, in tracking both endogenous (volcanism, weathering, biological productivity) and exogenous (cosmogenic ray flux, bolide impact) drivers for change in biogeochemical cycles and their associated geochemical excursions preserved in the rock record. Carbon isotope excursions are often found associated with major climatic and biological crises that accompany or even drive macroscopic lithological changes in the rock record. Where these excursions have been shown to be global and synchronous, they now provide important correlation markers (Halverson et al. 2010) and even define the GSSPs for some units of the geologic time scale (Aubry et al. 2007).

Cyclostratigraphy and Astrochronology

Geochemistry often elucidates rhythmic elemental or isotopic fluctuations within rock sequences that underlie the discipline of cyclostratigraphy. The causes of sedimentary cycles are varied, as are their megaannum to sub-annual periods. Most important to the geologic time scale are ca 20–400 kiloyear cycles corresponding to variations in the Earth's orbital and rotational parameters. Early attempts to identify within the rock record the rhythm of Earth's orbital variations and associated changes in incoming solar radiation began with Gilbert (1895), were placed on a quantitative astronomical footing by Milankovitch (1941), and reached fruition with the oxygen isotope records of Hays et al. (1976). When these cyclostratigraphic records are tuned to forward modeling of Earth's orbital motion (Berger et al. 1992; Laskar et al. 2011), the resulting astrochronology has provided a continuously calibrated time scale for the Neogene tied to the present day (Hinnov and Ogg 2007; Hilgen et al. 2012). Other cyclic records in deeper time provide floating astrochronologies that can be linked to the geologic time scale through both stratigraphic markers and radioisotopic dates (Pälike et al. 2006; Meyers et al. 2012). Extending astrochronology across the Paleogene and into the Mesozoic remains a primary goal for future refinement of the geologic time scale (Westerhold et al. 2008; Hilgen et al. 2010; Kuiper et al. 2008).

Summary

The geologic time scale provides a foundation for investigations of the correlation, causality, and rates of Earth processes in deep time. By pacing the tempo of biological and geological evolution, it reveals the interactions and feedbacks between Earth's complex systems. In bringing together stratigraphic and geochronologic records, it bridges the sedimentary, igneous, and metamorphic realms and allows paleogeographic and plate tectonic integration. Revision and refinement of the geologic time scale is an active endeavor facilitated by an interdisciplinary geoscientific community.

Cross-References

- ▶ Carbon Isotopes
- ▶ Geochronology and Radiogenic Isotopes
- ▶ Magnetism
- ▶ Radioactivity
- ▶ Thermal Ionization Mass Spectrometry

References

Aubry M-P, Ouda K, Dupuis C, Berggren WA, Van Couvering JA, The Members of the Working Group on the Paleocene/Eocene Boundary (2007) The Global Standard Stratotype-section and Point (GSSP) for the base of the Eocene Series in the Dababiya section (Egypt). Episodes 30:271–286

Berger A, Loutre M-F, Laskar J (1992) Stability of the astronomical frequencies over Earth's history for paleoclimate studies. Science 255:560–566

Cande S, Kent D (1992) A new geomagnetic polarity time scale for the Late Cretaceous and Cenozoic. J Geophys Res 97:13917–13951

Gilbert GK (1895) Sedimentary measurement of geological time. J Geol 3:121–127

Gradstein FM (2012) Chapter 1 – Introduction. In: Gradstein FM, Ogg JG, Schmitz MD, Ogg GM (eds) The geologic time scale. Elsevier, Boston, pp 1–29

Gradstein FM, Ogg JG, Schmitz MD, Ogg GM (eds) (2012) The geologic time scale. Elsevier, Boston, pp 115–126

Halverson GP, Wade BP, Hurtgen MT, Barovich KM (2010) Neoproterozoic chemostratigraphy. Precambrian Res 182: 337–350

Harland WB, Cox AV, Llewellyn PG, Pickton CAG, Smith AG, Walters R (1982) A geologic time scale. Cambridge University Press, Cambridge

Hays JD, Imbrie J, Shackleton NJ (1976) Variations in the Earth's orbit: pacemaker of the ice ages. Science 194:1121–1132

Hilgen FJ, Kuiper KF, Lourens LJ (2010) Evaluation of the astronomical time scale for the Paleocene and earliest Eocene. Earth Planet Sci Lett 300:139–151

Hilgen FJ, Lourens LJ, Van Dam JA, Beu AG, Boyes AF, Cooper RA, Krijgsman W, Ogg JG, Piller WE, Wilson DS (2012) Chapter 29 – the Neogene period. In: Gradstein FM, Ogg JG, Schmitz MD, Ogg GM (eds) The geologic time scale. Elsevier, Boston, pp 923–978

Hinnov LA, Ogg JG (2007) Cyclostratigraphy and the astronomical time scale. Stratigraphy 4:239–251

Holmes A (1913) The age of the Earth. Harper, London

Kuiper KF, Deino A, Hilgen FJ, Krijgsman W, Renne PR, Wijbrans JR (2008) Synchronizing rock clocks of Earth history. Science 320:500–504

Laskar J, Fienga A, Gastineau M, Manche H (2011) La2010: a new orbital solution for the long term motion of the Earth. Astron Astrophys 532. https://doi.org/10.1051/0004-6361/201116836

Meyers S, Siewert SE, Singer BS, Sageman BB, Condon DJ, Obradovich JD, Jicha BR, Sawyer DA (2012) Intercalibration of radioisotopic and astrochronologic time scales for the Cenomanian-Turonian boundary interval, Western Interior Basin, USA. Geology 40:7–10

Milankovitch M (1941) Kanon der Erdbestrahlung und seine Anwendung auf das Eiszeitenproblem. Royal Serbian Academy, Section of Mathematical and Natural Sciences, Belgrade

Ogg JG (2012) Chapter 5 – geomagnetic polarity time scale. In: Gradstein FM, Ogg JG, Schmitz MD, Ogg GM (eds) The geologic time scale. Elsevier, Boston, pp 85–113

Pälike H, Norris RD, Herrle JO, Wilson PA, Coxall HK, Lear CH, Shackleton NJ, Tripati AK, Wade BS (2006) The heartbeat of the Oligocene climate system. Science 314:1894–1898

Remane J, Bassett MG, Cowie JW, Gohrbandtm KH, Lane HR, Michelsen O, Wang N (1996) Revised guidelines for the establishment of global chronostratigraphic standards by the International Commission on Stratigraphy (ICS). Episodes 19:77–81

Schmitz MD (2012) Chapter 6 – radiogenic isotope geochronology. In: Gradstein FM, Ogg JG, Schmitz MD, Ogg GM (eds) The geologic time scale. Elsevier, Boston, pp 115–126

Westerhold T, Ro¨hl U, Raffi I, Fornaciari E, Monechi S, Reale V, Bowles J, Evans HF (2008) Astronomical calibration of the Paleocene time. Palaeogeogr Palaeoclimatol Palaeoecol 257:377–403

Geoneutrinos

William F. McDonough
Department of Geology, University of Maryland, College Park, MD, USA

Definition

Geoneutrinos are electron antineutrinos ($\overline{\nu}_e$) produced during beta-minus (β^-) decay and electron neutrinos (ν_e) produced during beta-plus (β^+) decay and electron capture of naturally occurring radionuclides. The generic versions of these decay schemes are

$$\text{beta} - \text{minus } (\beta^-) \text{ decay} \qquad {}^{A}_{Z}X \rightarrow {}^{A}_{Z+1}X' + e^- + \overline{\nu}_e$$

$$\text{beta} - \text{plus } (\beta^+) \text{ decay} \qquad {}^{A}_{Z}X \rightarrow {}^{A}_{Z-1}X' + e^+ + \nu_e$$

$$\text{electron capture} \qquad {}^{A}_{Z}X + e^- \rightarrow {}^{A}_{Z-1}X' + \nu_e$$

with mass number (A) being conserved, atomic number (Z) increasing or decreasing by one from the parent (X) to daughter (X′) element in the decaying nucleus and the production of a nuclear electron and electron antineutrino during β^- decay, nuclear positron and electron neutrino during β^+ decay, or only an electron neutrino during electron capture. Table 1 defines the elements in the Earth that undergo beta-minus (β^-) decay.

Geoneutrino Detection

Only four isotopes, two in the ^{232}Th decay chain (^{228}Ac and ^{212}Bi) and two in the ^{238}U chain (^{234}Pa and ^{214}Bi), emit electron antineutrinos with sufficient energies to be detected by present-day methods, which involves scintillation detection via the inverse beta decay mechanism (IBD). This process involves an electron antineutrino transiting a large volume (e.g., typically kiloton in scale), underground liquid scintillation detector and interacting with a free proton (hydrogen atom in the hydrocarbon scintillator) to produce a positron and a neutron $p + \overline{\nu}_e \rightarrow e^+ + n$. This reaction requires that the $\overline{\nu}_e$ possesses at least 1.806 MeV of energy to initiate the reaction. Consequently, inside the liquid scintillation detector, there are two flashes of light, the prompt flash associated with positron–electron annihilation, which occurs some several hundred picoseconds after the initial interaction, and the delayed flash from the neutron capture by a proton producing deuterium, with this latter flash generating 2.2 MeV of light and occurring approximately 30 cm and about 200 μm seconds further away. This highly synchronized event chain, which is only accessible to electron antineutrinos, eliminates most background and permits kiloton detectors to record at the feeble rate of about one event per month due to the incredibly weak interaction force and negligible interaction cross section (10^{-43} cm^2) of these neutrinos. The first detection of geoneutrino was reported in *Nature* in Araki et al. (2005), and to date only two detectors, KamLAND (1 kton) in Japan and Borexino (0.3 kton) in Italy, have reported on the Earth's flux (Gando et al. 2013; Agostini et al. 2015). The Earth is estimated to be radiating $\sim 3 \times 10^{25}$ antineutrinos per second to space, with an average surface flux of about ~6 million $\overline{\nu}_e$ cm^{-2} s^{-1} (Usman et al. 2015), although the surface flux varies considerably depending on if it is from the oceanic crust (low flux) or the continental crust (high flux). The dominant flux comes from potassium geoneutrinos and lesser amounts from U, Th, and Rb (Fig. 1); the remaining β^- decay schemes (including ^{235}U) contribute much less than 1% of the total flux. The Earth's flux of electron neutrinos from beta-plus (β^+) decay and electron capture has yet to be detected because of their low energies and weak signal as compared to the solar flux of electron neutrinos

Geoneutrinos, Table 1 Terrestrial beta-minus (β^-) decay scheme (Data from http://www.nndc.bnl.gov/chart/)

beta-minus (β^-) decay	Half-Life ($t_{1/2}$ years)	$\bar{\nu}$ E_{Max} (keV)	Branching fraction
Long-lived, naturally occurring			
$^{40}_{19}K \rightarrow {}^{40}_{20}Ca$	1.25E+09	1311	0.8928
$^{50}_{23}V \rightarrow {}^{50}_{24}Cr$	1.40E+17	254.6	0.17
$^{87}_{37}Rb \rightarrow {}^{87}_{38}Sr$	4.81E+10	282.2	1.00
$^{113}_{48}Cd \rightarrow {}^{113}_{49}In$	8.04E+15	322	1.00
$^{115}_{49}In \rightarrow {}^{115}_{50}Sn$	4.41E+14	497.49	1.00
$^{138}_{57}La \rightarrow {}^{138}_{58}Ce$	1.02E+11	255	0.344
$^{176}_{71}Lu \rightarrow {}^{176}_{72}Hf$	3.76E+10	1190.2	1.00
$^{187}_{75}Re \rightarrow {}^{187}_{76}Os$	4.33E+10	2.469	1.00
^{232}Th chain			
$^{228}_{88}Ra \rightarrow {}^{228}_{89}Ac$	5.750E+00	45.8	1.00
$^{228}_{89}Ac \rightarrow {}^{228}_{90}Th$	7.016E-04	**2134**	1.00
$^{212}_{82}Pb \rightarrow {}^{212}_{83}Bi$	1.214E-03	569.9	1.00
$^{212}_{84}Bi \rightarrow {}^{212}_{84}Po$	1.151E-04	**2252.1**	0.6406
$^{208}_{81}Tl \rightarrow {}^{208}_{82}Pb$	5.805E-06	1801.3	0.3594
^{235}U chain			
$^{231}_{90}Th \rightarrow {}^{231}_{91}Pa$	2.911E-03	391.6	1.00
$^{227}_{89}Ac \rightarrow {}^{227}_{90}Th$	2.177E+01	44.8	0.9862
$^{223}_{87}Fr \rightarrow {}^{223}_{88}Ra$	4.183E-05	1149.1	0.99994
$^{219}_{85}At \rightarrow {}^{219}_{86}Rn$	1.775E-06	1566	0.03
$^{215}_{83}Bi \rightarrow {}^{215}_{84}Po$	1.169E-06	2250	6.0E-05
$^{215}_{84}Po \rightarrow {}^{215}_{85}At$	5.644E-11	715	2E-05
$^{211}_{82}Pb \rightarrow {}^{211}_{83}Bi$	6.864E-05	1367	1.00
$^{211}_{83}Bi \rightarrow {}^{211}_{84}Po$	4.069E-06	574	0.0028
$^{207}_{81}Tl \rightarrow {}^{207}_{82}Pb$	9.069E-06	1418	1.00
^{238}U chain			
$^{234}_{90}Th \rightarrow {}^{234}_{91}Pa$	6.598E-02	273	1.00
$^{234}_{91}Pa \rightarrow {}^{234}_{92}U$	2.204E-06	**2197**	1.00
$^{218}_{84}Po \rightarrow {}^{218}_{85}At$	5.890E-06	260	0.0002
$^{218}_{85}At \rightarrow {}^{218}_{86}Rn$	4.753E-08	2881	0.001
$^{214}_{82}Pb \rightarrow {}^{214}_{83}Bi$	5.095E-05	1019	0.9998
$^{214}_{83}Bi \rightarrow {}^{214}_{84}Po$	3.784E-05	**3270**	0.9998
$^{210}_{81}Tl \rightarrow {}^{210}_{82}Pb$	2.472E-06	5482	0.0002
$^{210}_{82}Pb \rightarrow {}^{210}_{83}Bi$	2.220E+01	63.5	1.00
$^{210}_{83}Bi \rightarrow {}^{210}_{84}Po$	1.372E-02	1162.2	1.00
$^{206}_{80}Hg \rightarrow {}^{206}_{81}Tl$	1.582E-05	1308	1.90E-08
$^{206}_{81}Tl \rightarrow {}^{206}_{82}Pb$	7.111E-06	1532	1.32E-06

Red outline and bold numbers identify those β^- decays with sufficient energies to be detected by the inverse beta decay method.

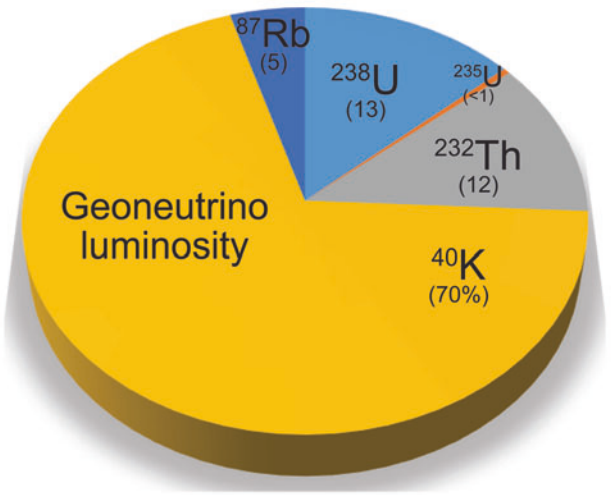

Geoneutrinos, Fig. 1 The relative luminosity of geoneutrino emission from the Earth

($\geq 10^5$ greater flux) from the proton–proton burning chain in the core of the Sun.

Constraining Earth's Composition and Terrestrial Heat Production

Geoneutrino studies will provide a quantitative measure of the amount of uranium and thorium inside the Earth. Based on these measurements and assuming negligible Th and U in the core and a K/U value for the silicate Earth (Arevalo et al. 2009), we can establish the planet's budget of the heat-producing elements (K, Th, and U provide more than 99% of its radiogenic power) and the absolute abundances of the refractory elements (e.g., Ca, Al, Th, and U) in the Earth. These data in turn provide critical constraints on the power driving plate tectonics, mantle convection, and the geodynamo. Estimates of the content of heat-producing elements in the continental crust, the most accessible part of the Earth, are 7 ± 1 TW (10^{12} W) (Huang et al. 2013), whereas estimates of the planetary production of radiogenic heat differ by a factor of 3 (~10 to 33 TW for the bulk silicate Earth (BSE)). Consequently, estimates of the production of radiogenic heat in the mantle vary by a factor of ~30 (subtracting 7 ± 1 (crustal estimate) from 10 ± 2 or 33 ± 3 low and high estimate of the BSE, respectively; see Šrámek et al. (2013) for details. Knowing the amount of radiogenic power in the mantle will in turn exclude end-member compositional models for the Earth and place significant limits on models defining the mode of mantle convection (Šrámek et al. 2016).

Future Studies

Geoneutrino research is an emerging field in the geosciences that has only recently completed its first decade of data taking. The detectors in Japan and Italy will soon be joined by the SNO+ detector (1 kton, expected to be counting in 2017) in Sudbury, Canada; the JUNO detector (20 kton, expected to be counting in 2020) in Jiangmen, China; and the Jinping detector (3 kton, expected to be counting in 2022) in Mianning County, Sichuan Province, China. The annual geoneutrino count rate at these detectors is low (measured at KamLAND at 14 events/year and Borexino at 4.2 and predicted at SNO+, 20; JUNO, 400; and Jinping, 100, with approximately 20% of the signal from Th and 80% from U), and so the total exposure time is significant for these experiments, as measurement uncertainties follow Poisson's statistics (Šrámek et al. 2016). Differences in count rates vary according to detector size, detector efficiency, and geologic setting. The convention is to report signal intensity in TNU (terrestrial neutrino units: given as one event per 10^{32} target nuclei (free protons) per year at 100% detection efficiency; Mantovani et al. (2004)), with the scaling between flux and TNU given as $C = \phi/R$ [$C_U = 7.6 \times 10^4$ cm^{-2} s^{-1} TNU^{-1} and $C_{Th} = 2.5 \times 10^4$ cm^{-2} s^{-1} TNU^{-1}] (Dye 2012). A recent projection for the year 2025, which was based on a reference BSE model and integrated counts from these detectors, yields a mantle flux of 8.2 ± 2.9 TNU (or 12 ± 4 TW) (Šrámek et al. 2016).

A proposal for an ocean-based detector (Hanohano: Hawaiian Anti-neutrino Observatory; said twice for added emphasis) has been put forth (Learned et al. 2007) for deployment at depth in the ocean, remote from nuclear reactors, and continental crust. Deploying such a detector in the Pacific Ocean, equidistant from Australia, South America, and the core–mantle boundary would offer the best mantle-only flux measurement. Šrámek et al. (2013) proposed that such a neutrino geoscope could be used to critically evaluate mantle structures such as the seismologically imaged LLSVPs (large low-shear-velocity provinces), which would generate tomographic images of the deep Earth based on north to south Pacific Ocean surveys. In addition, the promise of detector directionality is on the horizon (Tanaka and Watanabe 2014), where such imaging could potentially examine differences in mantle and core versus mantle-only signals (Dye 2010).

Finally, another form of neutrinos, called atmospheric electron neutrinos and electron antineutrinos, is produced from cosmic ray interactions with the atmosphere. These neutrinos can traverse the planet and ultimately be detected before leaving the Earth. Recently, Rott et al. (2015) showed that these neutrinos can probe the composition and density of the Earth as these neutrinos are sensitive to the Earth's electron density. These studies promise to bring insights into the Z/A state of the Earth's core and would be most sensitive to the amount of hydrogen in the core. Moreover, with greater sensitivity in future instrumentation, these measurements will place constraints on the nature of the light element mixture in the outer and inner core.

Cross-References

- Atomic Number, Mass Number, and Isotopes
- Heat-Producing Elements (HPEs)
- Potassium
- Radioactivity
- Thorium
- Uranium

G

References

Agostini M et al (2015) Spectroscopy of geoneutrinos from 2056 days of Borexino data. Phys Rev D 92:031101. https://doi.org/10.1103/PhysRevD.92.031101

Araki T et al (2005) Experimental investigation of geologically produced antineutrinos with KamLAND. Nature 436(7050):499–503

Arevalo R Jr, McDonough WF, Luong M (2009) The K/U ratio of the silicate Earth: insights into mantle composition, structure and thermal evolution. Earth Planet Sci Lett 278(3–4):361–369

Dye ST (2010) Geo-neutrinos and silicate earth enrichment of U and Th. Earth Planet Sci Lett 297(1–2):1–9

Dye ST (2012) Geoneutrinos and the radioactive power of the Earth. Rev Geophys 50:RG3007. https://doi.org/10.1029/2012RG000400

Gando A et al (2013) Reactor on-off antineutrino measurement with KamLAND. Phys Rev D 88:033001. https://doi.org/10.1103/PhysRevD.88.033001

Huang Y, Chubakov V, Mantovani F, Rudnick RL, McDonough WF (2013) A reference Earth model for the heat-producing elements and associated geoneutrino flux. Geochem Geophys Geosyst 14(6):2003–2029

Learned JG, Dye ST, Pakvasa S (2007) Hanohano: a Deep Ocean anti-neutrino detector for unique neutrino physics and geophysics studies. In: Proceedings of the twelfth international workshop on neutrino telescopes, Venice, pp. arXiv:0810.4975v1

Mantovani F, Carmignani L, Fiorentini G, Lissia M (2004) Antineutrinos from Earth: a reference model and its uncertainties. Phys Rev D 69:013001. https://doi.org/10.1103/PhysRevD.69.013001

Rott C, Taketa A, Bose D (2015) Spectrometry of the Earth using neutrino oscillations. Sci Rep 5:15225. https://doi.org/10.1038/srep15225

Šrámek O et al (2013) Geophysical and geochemical constraints on geoneutrino fluxes from Earth's mantle. Earth Planet Sci Lett 361(3–4):356–366

Šrámek O, Roskovec B, Wipperfurth SA, Xi Y, McDonough WF (2016) Revealing the Earth's mantle from the tallest mountains using the Jinping Neutrino Experiment. Sci Rep 6:33034. https://doi.org/10.1038/srep33034

Tanaka HKM, Watanabe H (2014) 6Li-loaded directionally sensitive anti-neutrino detector for possible geo-neutrinographic imaging applications. Sci Rep 4:4708. https://doi.org/10.1038/srep04708

Usman SM, Jocher GR, Dye ST, McDonough WF, Learned JG (2015) AGM2015: Antineutrino Global Map 2015. Sci Rep 5:13945. https://doi.org/10.1038/srep13945

Geothermal Systems

Adam J. Hawkins[1] and Jefferson W. Tester[1,2]
[1]Earth and Atmospheric Sciences, Cornell University, Ithaca, NY, USA
[2]School of Chemical and Biomolecular Engineering, Cornell University, Ithaca, NY, USA

Definition

Geothermal systems form a continuum having a wide range of geologic and thermal conditions depending on: (1) their depth and temperature (geothermal gradient); (2) the amount of natural steam and/or water they contain; and (3) the permeability and porosity of the geologic formation in which fluids flow. At one extreme are convective geothermal systems where nature provides sufficiently high temperatures, fluid content, and permeability to support convective fluid transport. At the other extreme are conduction dominated systems where fluid content and permeabilities are very low and reservoirs are at greater depth due to lower geothermal gradients. Although it is challenging to specify geologic conditions for each system, high-grade hydrothermal reservoirs are often contained in highly fractured volcanic rocks at or near tectonic plate boundaries. In contrast, conduction dominated systems are frequently associated with deeper sedimentary basins or basement rock formations that contain well-sealed fractures with very low permeability and porosity (Mock et al. 1997; Glassley 2010; IPCC 2011; Tester et al. 2012).

In this article, we focus on a class of geothermal systems dominated by convective circulation of subsurface fluids between cold, near-surface reservoirs and hot reservoirs.

Introduction

Heat sources in Earth's crust at depths ranging from roughly 2–5 km drive convective fluid circulation between cold shallow reservoirs and deeper hot reservoirs (Cathles 1977; Norton and Knight 1977; Hayba and Ingebritsen 1997). As dense, cold water in shallow reservoirs descends by gravity to reach a deeper heat source, fluid temperatures increase and densities decrease causing the fluid to rise buoyantly towards surface. In natural settings, fluid is then either discharged in surface features such as hot springs, geysers, and fumaroles or recirculated as it cools near ground surface. The circulation is further maintained by relatively continuous meteoric and/or oceanic recharge.

Geographic occurrences of geothermal systems are controlled by the distribution of heat sources in Earth's crust. Volcanic regions, such as subduction zones, spreading centers, and hot spots (i.e., an anomalous upwelling of mantle material to Earth's surface), frequently produce geothermal systems when sufficient fluid recharge and rock permeability are present. Additional geologic regions that produce geothermal systems are extensional and/or transtensional regions and regions with high radiogenic activity (such as radiating intrusive igneous rocks).

Geothermal systems have been utilized for thousands of years as a thermal heat source and for over a century for generating electricity and for district heating (see Stober and Bucher 2013 for a review of the history of geothermal utilization). Beginning in 1904 in Italy, steam from the hydrothermal Lardarello field in Tuscany was used to produce electric power. By 2015, total installed nameplate capacity worldwide reached over 12.5 GW_e (Bertani 2015; Matek 2015).

Direct thermal use of heating has been used for centuries. Today there are extensive geothermal district heating systems in Iceland, Paris, China, and other countries supplying several million homes and total installed capacity of direct geothermal utilization reached 70.3 GW_{th} in 2015 (Lund and Boyd 2015). In addition, the use of energy stored in shallow aquifers or conductive environments at low temperatures has been extensively utilized via geothermal heat pumps (IPCC 2011; Lund and Boyd 2015).

Additional interest in geothermal fluids arose due to the demand for concentrated chemical constituents frequently found within geothermal fluids. As far back as the early nineteenth century, boron was separated from geothermal fluids at the Larderello geothermal field in Italy (Armstead 1983; Burgassi 1999). Other potential coproduced commodities in geothermal fluids include lithium, zinc, silica, manganese, lead, gold, silver, and rare earth elements (Blake 1974; Harper and Thain 1992; Gallup 1998; Bourcier et al. 2005).

The chemical composition of geothermal fluids is highly variable and dependent largely upon fluid sources, water interactions with minerals comprising the reservoir, fluid phase separation, and fluid mixing. In general, geothermal fluids are frequently classified by the relative abundance of important components such as chloride, sulfate, and bicarbonate (Nicholson 1993). The relative abundance of certain constituents, including reactive components, are used to infer important characteristics of the geothermal system, such as heat source temperature, fluid sources, and the spatial distribution of fluid flow paths. "See the sections titled 'Primary Geothermal Fluids' and 'Secondary Geothermal Fluids' for a more detailed description of common chemical compositions."

Heat Sources

Shallow heat sources in Earth's crust develop as a result of magmatic emplacements, tectonic activity, and radiogenic

heat. Volcanic sources, such as subduction zones, spreading centers, and hot spots (i.e., an anomalous upwelling of mantle material to Earth's surface), produce high temperatures generally in the range of 150–300 °C at depths less than a few kilometers. Examples of geothermal energy exploitation in volcanic regions include Japan (subduction zone), The Great Rift Valley in Kenya (intra-continental rift), and Iceland (volcanic hot spot and divergent tectonic plate boundary).

Tectonic heat sources, such as those found in the Geysers region of California and throughout the Basin and Range of Nevada, typically result from extensional and/or transtenional regimes. Extension results in crustal thinning and, as a consequence, increases the geothermal gradient. Fluid flow paths are generated in regions of faulting which produce "damage zones" of high fluid permeability.

Isotopic decay of radiogenic elements in certain rocks can produce substantial heat fluxes. In Western Australia, for example, radiogenic heat is produced from isotopic decay of uranium, thorium, and potassium, which are found in igneous rock bodies at depth.

Fluid Sources

Geothermal fluids originate from several sources, including meteoric, oceanic, magmatic, metamorphic, and connate (see ▶ "Geothermal Systems," Fig. 1). In general, meteoric and oceanic recharge are considered the dominant source of geothermal fluids. As these source fluids migrate towards geothermal heat sources, several reactions alter their chemical state. Dissolution and precipitation can occur as source waters come into equilibrium with geothermal minerals. In addition, cation exchange reactions result in changes in the chemical composition of the descending and heated fluids.

Primary Geothermal Fluids

Geothermal fluids are considered "primary" fluids when they are at, or near, their heat source. These fluids are broadly grouped into three categories: Chloride waters, acid-sulfate waters, and high salinity waters.

The most common primary fluids found in deep high-temperature geothermal systems have near-neutral pH (at the temperature of measurement) with chloride as the dominant anion and is referred to as "chloride waters," but may also be referred to as "alkali-chloride" or "neutral-chloride" waters. Concentrations of chloride in chloride waters typically range from 1000 to 10,000 ppm. Other main constituents include sodium and potassium as the dominant cations with significant concentrations of silica and boron (Nicholson 1993).

Chlorides found in chloride waters are produced from magmatic fluids or through reactions with magmatic HCl

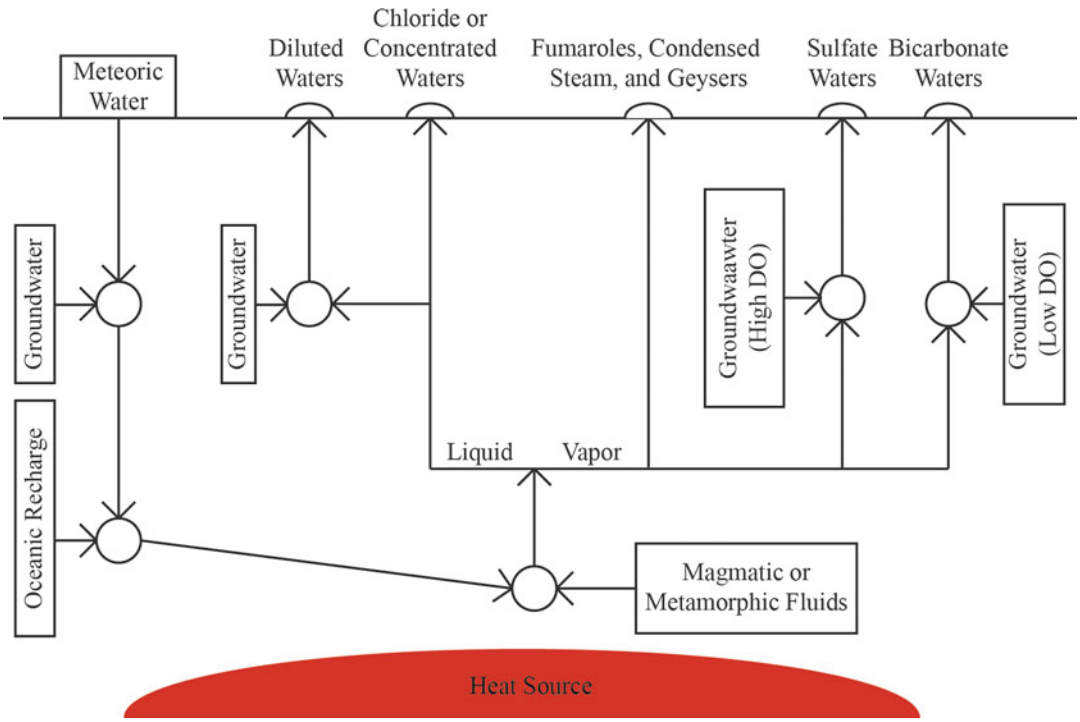

Geothermal Systems, Fig. 1 Schematic of fluid circulation through a geothermal system. Several potential sources, including meteoric, groundwater, oceanic, and magmatic/metamorphic form primary fluids near a heat source. As primary fluids rise buoyantly towards Earth's surface they form secondary fluids as they interact with rock minerals, undergo phase changes, and mix with near-surface waters

and rock-forming minerals. Chlorides in geothermal fluids from other sources, such as oceanic or dissolution of rock by meteoric water, are often classified separately as "high salinity waters" and are discussed later in this section. Concentrations of chloride in primary fluids depend on the lithology of their host rocks. For example, primary fluids in basalts and gabbros, in general, are relatively less rich in chloride whereas fluids in rhyolite and diorite are more concentrated. The variation results from deviations in each lithology's chlorine content. In basalts and gabbros, chlorine averages roughly 130 and 190 ppm, respectively, whereas rhyolites and diorites average roughly 330 and 335 ppm, respectively (Johns and Huang 1967).

Primary geothermal fluids with total dissolved solids (TDS) levels ranging from about 10,000–300,000 ppm are referred to as "high salinity waters." These fluids are produced mostly from oceanic recharge and evaporite dissolution in meteoric water, but might also form from connate water. Concentrations of TDS in these fluids can reach as high as 20–30 wt% as in Salton Sea, California, USA (Williams and McKibben 1989). These fluids can be heavily enriched in mineral commodities. In Salton Sea, California, USA, for example, high concentrations of several valuable commodities have been produced from geothermal wells, such as manganese (~500–700 ppm), lithium (~130–140 ppm), silicon (~180–200 ppm), and zinc (~200–350 ppm) as well as precious metals such as silver (~0.5–0.7 ppm), gold (~0.1 ppm), and platinum (~0.06 ppm) (Maimoni 1982).

Deep acid-sulfate waters form when HCl and SO_2 are transferred from a magmatic heat source to a circulating fluid. HCl and/or HSO_4 produce acidic conditions and such conditions have been found in many volcanic geothermal systems, particularly in andesitic rocks.

Secondary Geothermal Fluids

As primary fluids migrate towards Earth's surface they experience changes in their thermodynamic properties and chemical composition. In addition, they can be altered by mixing with shallow groundwater. As a result of these alterations the modified fluids are referred to as "secondary" geothermal fluids.

At depth, primary fluids may exist as a single phase liquid or gas, or a mixture of liquid and gas phases. When a liquid geothermal system encounters declining pressures, a vapor phase may appear. In addition, two phase flow may be encountered in the production well as fluid rises to ground surface Under hydrostatic conditions, geothermal liquid phase fluids between 200 and 250 °C boil at depths of roughly 200–500 m. Above 250 °C, the depth of boiling increases dramatically from roughly 500 m at 250 °C to roughly 1.5 km at 320 °C (Arnórsson et al. 2007). Under natural hydrostatic conditions, two-phases can exist within the reservoir. As a result of this phase separation, the residual liquid may be concentrated in TDS and the steam may contain high concentrations of hydrogen sulfide and carbon dioxide. The residual liquid component would be classified as a "concentrated" secondary geothermal fluid as the nonvolatile components of the primary geothermal fluid are concentrated due to liquid mass loss during vaporization.

If the steam phase is mixed into shallow groundwater, two different secondary geothermal fluids may be broadly classified. "Sulfate waters" will form if the shallow groundwater is rich in dissolved oxygen due to oxidation of sulfur by the reaction:

$$H_2S(g) + 2O_2(aq) = 2H^+(aq) + SO_4^{2-}(aq)$$

This reaction produces sulfate concentrations typically in the range 300–1300 ppm.

Sulfur oxidation also results in a reduction in pH which will reduce bicarbonate concentration as CO_2 is released from solution resulting in bicarbonate concentrations typically under ~1 ppm. At low pH, sulfate waters frequently contain high concentrations of dissolved metals such as aluminum (up to 7000 ppm), iron (up to 4500 ppm), manganese (up to 2500 ppm), chromium (up to 8.5 ppm), and arsenic (up to 15 ppm) (Hartley 1978). These high concentrations occur because lower pH (<~3–4) favors aqueous forms of these metals either through desorption or dissolution reactions.

In contrast, condensation of geothermal vapors in shallow groundwater that is depleted in dissolved oxygen will produce "bicarbonate waters" that are rich in bicarbonate (~300–2500 ppm) relative to sulfate waters (Nicholson 1993) by the reactions:

$$CO_2(g) + H_2O(l) = H_2CO_3(aq)$$

$$H_2CO_3(aq) = H^+(aq) + HCO_3^-(aq)$$

$$HCO_3^-(aq) = H^+(aq) + CO_3^{2-}(aq)$$

Because of the low redox potential of oxygen depleted groundwater, sulfur cannot be oxidized and the fluid remains high in total alkalinity. In these mixed fluids, bicarbonate, rather than CO_2, is the dominant species because it is the dominant species at near-neutral or mildly acidic pH.

"Dilute waters" can form when any primary geothermal fluid is diluted in near-surface groundwater. The term "dilute" is used to indicate the fact that primary geothermal fluids are typically concentrated in TDS relative to shallow groundwater and, as a consequence, dilute waters are typically lower in TDS relative to their primary fluid source. Identification of dilute waters can be an important task in the process of

geothermometry. For example, temperature estimates derived from the use of silica as a geothermometer assumes that the concentration of dissolved silica in sampled fluid is in equilibrium with precipitated silica (either as quartz or another polymorph) at the temperature of the reservoir at depth. In dilute waters, this assumption would lead to an underprediction of subsurface temperatures because shallow groundwater contains much lower concentrations of silica. Hot springs discharging dilute fluids can be identified by a negative correlation between surface fluid temperature and flow rate (Arnosson et al. 2007).

When primary or secondary geothermal fluids approach Earth's surface, they are either recirculated into the deep geothermal reservoir or they are discharge at ground surface either as hot springs (if liquid) or fumaroles (if gas). Fumaroles are direct releases of geothermal vapor and gasses at Earth's surface. Hot springs can consist of either primary geothermal fluids or secondary fluids, such as acid-sulfate waters, bicarbonate waters, dilute waters, and concentrated waters.

Geysers form when high confining pressures lead to pressure build up below ground surface. Once the confining pressure is overcome, a mix of liquid and gas is rapidly released and can cause streams of two-phase fluid to eject from Earth's surface as high as several tens of meters (Rinehart 1974).

Fluid-Rock Interactions

Dissolved constituents within geothermal fluids can be described as either conservative or reactive. Species that are highly soluble that tend to remain in solution, such as Cl, B, Br, As, and Cs, are considered conservative species because their fluid concentration is not heavily influenced by temperature dependent mineral-fluid equilibria nor do they readily participate in ion exchange processes. A notable exception would occur if the solution encountered another constituent that led to the precipitation of one or more of the soluble species. An example would be As precipitation in the presence of H_2S. In reality, chloride is the only truly conservative species as some other conservative species in geothermal fluids may participate in near-surface ion exchange reactions, particularly with clay minerals and iron oxides.

Reactive species, such as SiO_2, Na, K, Ca, and Mg, are subject to mineral-fluid equilibria that are dependent on the thermodynamic and mineralogical properties of the reservoir. The two most relevant types of fluid-rock reactions in geothermal systems are dissolution/precipitation reactions (e.g., SiO_2 and $CaCO_3$) and ion exchange reactions (e.g., Na and K). For many minerals of interest, solubility increases with increasing temperatures. For example, the concentration of a reactive species such as silica can be used to infer reservoir temperature based on the measured temperature dependence of silica solubility (Fournier and Potter 1982).

Retrograde solubility occurs when there is an inverse relationship between solubility and temperature. Calcite and gypsum, for instance, both have retrograde solubility and therefore will precipitate at higher temperatures. Solubility of calcite is also affected by the partial pressure of CO_2 and, as a consequence, calcite may precipitate as deep geothermal fluids migrate upwards and release CO_2 from solution. Calcium is not considered a reliable geothermometer, however, because calcite precipitation/dissolution reactions occur too rapidly. In contrast, silica precipitation/dissolution kinetics are very slow at low temperatures. Therefore, measured silica concentrations in nondiluted geothermal hot springs or in water samples taken from geothermal wells have been reliably used as a geothermometer.

Ion-exchange reactions, such as between Na in albite and K in potassium feldspar, are also temperature dependent and may therefore be used as an additional or alternative geothermometer. At high temperature, K is depleted in solution as potassium feldspar dominates over albite. The ratio of Na/K, therefore, is an indicator of reservoir temperature. Because this indicator is a ratio, it is sometimes a more reliable geothermometer than silica, particularly when geothermal fluids are mixed with shallow groundwater that is relatively low in Na and K concentration.

Several other geothermometers are utilized in geothermal systems such as additional liquid water ionic species (e.g., Na/Li, Li/Mg, K/Mg, Na-K-Ca, Na-K-Mg), isotopic tracers (e.g., ^{16}O vs. ^{18}O and ^{12}C vs. ^{13}C), and gas geothermometers (e.g., CO_2/H_2 and H_2/H_2). Which geothermometer is used depends largely upon the extent of fluid mixing, the temperature range, phase (gas or liquid), pH, and reaction kinetics. Examples of liquid water ionic geothermometers can be found in Fournier and Potter (1982), Fouillac and Michard (1981), Kharaka and Marina (1989), Giggenbach (1988), Fournier (1979), and Fournier and Truesdell (1973). Examples of isotopic geothermometers can be found in Arnórsson et al. (2000), Nuti et al. (1981), and Yokoyama et al. (1999). Examples of gas phase geothermometers can be found in D'Amore and Panichi (1980) and Arnórsson and Gunnlaugsson (1985).

A final group of chemical species useful in geothermal reservoir characterization are "applied tracers." In practice, a specific chemical tracer is introduced into a geothermal reservoir in an injection or monitoring well. A monitoring well or production well nearby can then be used to monitor these tracers as they appear at the surface. An important characteristic is the ability to measure extremely low concentrations (ideally less than 10 ppb). Commonly used tracers for geothermal reservoirs include salts, such as bromide and iodide; organic dyes, such xanthene, rhodamine, and fluorescein; radioactive tracers, such as Iodide-125; and polyaromatic sulfonates, such as naphthalene sulfonates (Adams and Davis (1991) and Rose et al. (2001)). The residence time

distribution (RTD) of fluid flowing through a geothermal reservoir can be determined by measuring the tracer concentration in production wells in response to a pulse or step change of tracer concentration in the injection well. The RTD is used to estimate attributes of the reservoir such as the reservoir volume and interwell connectivity.

Applied reactive tracers have long been proposed to infer geothermal reservoir properties such as temperature distribution (e.g., Robinson et al. 1988) and the fluid/rock surface area in-between two wells (e.g., Vetter and Crinchlow 1979). In recent field trials, reactive tracers have been shown to successfully characterize fluid permeability in a model geothermal reservoir (Hawkins et al. 2016, submitted).

Summary

Hydrothermal systems are produced when shallow heat sources drive convective circulation between cold shallow fluids and hot fluids at depth. The geochemistry of these systems is controlled by their fluid sources, fluid-rock interactions, phase separation, and dilution/concentration effects. Understanding these systems is important in quantifying the relative contribution from different fluid sources, estimating subsurface temperatures, controlling scaling, and evaluating the geothermal resource potential.

Cross-References

- ▶ Fluid–Rock Interaction
- ▶ Geothermometry and Geobarometry
- ▶ Hydrothermal Alteration
- ▶ Magmatic Process Modeling
- ▶ Ore Deposits
- ▶ Volcanic Gases
- ▶ Volcanism

References

Adams M, Davis J (1991) Kinetics of fluorescein decay and its application as a geothermal tracer. Geothermics 20:53–60

Armstead C (1983) Geothermal energy, 2nd edn. E. & F. N. Spon, London. 357 pp

Arnórsson S, Gunnlaugsson E (1985) New gas geothermometers for geothermal exploration calibration and application. Geochim Cosmochim Acta 49:549–1325

Arnórsson S, D'Amore F, Gerardo J (eds) (2000) Isotopic and chemical techniques in geothermal exploration. International Atomic Energy Agency, Vienna

Arnórsson S, Stefánsson A, Bjarnason J (2007) Fluid-fluid interactions in geothermal systems. Rev Mineral Geochem 65:259–312

Bertani R (2015) Geothermal power generation in the world 2010–2014 update report. In: Proceedings of the world geothermal congress, Melbourne, 19–25 April 2015

Blake R (1974) Extracting minerals from geothermal brines: a literature study. U.S. Bureau of Mines, Washington, DC

Bourcier W, Lin M, Nix G (2005) Recovery of minerals and metals from geothermal fluids. Lawrence Livermore National Laboratory, Livermore

Burgassi P (1999) Historical outline of geothermal technology in the Larderello region to the middle of the 20th century. In: Cataldi R, Hodgson S, Lund J (eds) Stories from a heated Earth. International Geothermal Association and the Geothermal Resources Council, Davis, pp 195–220

Cathles L (1977) An analysis of the cooling of intrusives by groundwater convection which includes boiling. Econ Geol 72:804–826

D'Amore F, Panichi C (1980) Evaluation of deep temperatures in hydrothermal systems by new gas geothermometer. Geochim Cosmochim Acta 44:549–556

Fouillac C, Michard G (1981) Sodium/lithium ratio in water applied to geothermometry of geothermal reservoirs. Geothermics 10:55–70

Fournier R (1979) A revised equation for the Na/K geothermometer. Geotherm Resour Counc Trans 3:221–224

Fournier R, Potter R (1982) A revised and expanded silica (quartz) geothermometer. Geotherm Resour Counc Trans 3:221–224

Fournier R, Truesdell A (1973) An empirical Na-K-ca geothermometer for natural waters. Geochim Cosmochim Acta 37:1255–1275

Gallup D (1998) Geochemistry of geothermal fluids and well scales, and potential for mineral recovery. Ore Geol Rev 12:225–236

Giggenbach W (1988) Geothermal solute equilibria: derivation of Na-K-Mg-Ca geoindicators. Geochim Cosmochim Acta 52:2749–2765

Glassley W (2010) Geothermal energy: renewable energy and the environment. CRC Press, Boca Raton

Harper R, Thain I (1992) Towards the efficient utilization of geothermal resources. Geothermics 21:641–651

Hartley R (1978) Pollution control guidance for geothermal energy development. Report no. EPA 600/7-78-101, p 130

Hawkins A, Fox D, Becker M, and Tester J (2016) Tracking subsurface temperature rise via thermally degrading tracer tests: field testing in a heterogeneous bedrock fracture. Manuscript submitted for publication

Hayba D, Ingebritsen S (1997) Multiphase groundwater flow near cooling plutons. J Geophys Res 102:12,235–12,252

IPCC (Intergovernmental Panel on climate change) (2011) Geothermal energy. In: Special report on renewable energy sources and climate change mitigation. Cambridge University Press, New York

Johns W, Huang W (1967) Distribution of chlorine in terrestrial rocks. Geochim Cosmochim Acta 31:35–49

Kharaka Y, Mariner R (1989) Chemical geothermometers and their application to formation waters from sedimentary basins. In: Naser N, McCollin T (eds) Thermal history of sedimentary basins. Springer, New York, pp 99–117

Lund J, Boyd T (2015) Direct utilization of geothermal energy 2015 worldwide review. In: Proceedings of the World Geothermal Congress, Melbourne, 19–25 April 2015

Maimoni A (1982) Minerals recovery from Salton Sea geothermal brines: a literature review and proposed cementation process. Geothermics 11:239–258

Matek B (2015) 2015 annual U.S. & global geothermal power production report. Geothermal Energy Association

Mock J, Tester J, Wright P (1997) Geothermal energy from the Earth: its potential impact as environmentally sustainable resource. Annu Rev Environ Resour 22:305–356

Nicholson K (1993) Geothermal fluids: chemistry and exploration techniques. Springer, Berlin

Norton D, Knight J (1977) Transport phenomena in hydrothermal systems: cooling plutons. Am J Sci 277:937–981

Nuti S, Calore C, Noto P (1981) Use of environmental isotopes as natural tracers in a reinjection experiment at Larderello. In: Proceedings of the 7th workshop on geothermal reservoir engineering. Stanford University, Stanford. December 1981

Rinehart J (1974) Geysers. Earth Space Sci News 55:1052–1062
Robinson B, Tester J, Brown L (1988) Reservoir sizing using inert and chemically reactive tracers. SPE Form Eval 3:227–234
Rose P, Benoit W, Kilbourn P (2001) The application of the polyaromatic sulfonates as tracers in geothermal reservoirs. Geothermics 30:617–640
Stober I, Bucher K (2013) History of geothermal energy use: from theoretical models to exploration and development. Springer, Berlin
Tester J, Drake E, Driscoll M, Golay M, Peters W (2012) Geothermal energy. In: Sustainable energy: choosing among options. MIT Press, Cambridge
Vetter O, Crichlow H (1979) Suggested solutions to injection problems. In: Injection, Injectivity and Injectability in geothermal operations: problems and possible solutions. U.S. Department of Energy: Division of Geothermal Energy, Costa Mesa/Norman
Williams A, McKibben M (1989) A brine interface in the Salton Sea Geothermal System, California: fluid geochemical and isotopic characteristics. Geochim Cosmochim Acta 53:1905–1920
Yokoyama T, Nakai S, Wakita H (1999) Helium and carbon isotopic compositions of hot spring gases in the Tibetan Plateau. J Volcanol Geotherm Res 88:99–107

Geothermometry and Geobarometry

Keith Putirka
Department of Earth and Environmental Sciences, California State University – Fresno, Fresno, CA, USA

Origins and Definitions

In its 1875 edition, *Encyclopaedia Britannica* described "natural philosophy" as "the science of energy"; by implication, thermometers and barometers, which measure the transfer of energy, are among the most fundamental of scientific instruments. Their development is traceable to the birth of science in the seventeenth century when, driven by curiosity about heat transfer, Santorre, Galileo, Sagredo, and Torricelli each constructed instruments to measure temperature (T) and pressure (P). These early instruments are in a liberal sense "geothermometers" and "geobarometers" as they were used to measure Earth's atmosphere, and mineral-bearing chemical reactions, in an age when mineralogy and chemistry were not distinct sciences. In geology, though, we invariably use these terms to refer to mathematical models that are used to estimate P and T of the solid Earth. And since P and T are usually interdependent, we often speak of "thermobarometers." Such "models" are invariably based on thermodynamic theory; they are usually analytic, i.e., involving equations that can be solved without recourse to differentiation, integration, or limits. An appropriate admonition from the statistician, George Box, is that "all models are wrong; some are useful." Models are simplifications of nature; none, however well known or successful, represent nature in some perfect, errorless sort of way. Many models, though, e.g., gravity, the ideal gas law, the covalent bond, etc., are nonetheless useful, allowing progress, in spite of inherent and unavoidable assumptions and flaws. But all models have limits, and to apprehend their regions of usefulness, error analysis during calibration and application is imperative.

The history of thermometry and barometry is indelibly tied to experiments of Boyle, Gay-Lussac, Charles, and others, whose work led to the ideal gas law ($PV = RT$). As we shall see, this law is central to most equations in physical chemistry, including geothermobarometers, and may be the single most influential equation ever devised. But while P-T estimates are now vital to discussions ranging from climate change to mantle convection, progress in the earth sciences was initially slow. Howard (1771) obtained a temperature estimate of a lava flow at Vesuvius (of 240 degrees, apparently on the Fahrenheit scale), by inserting a thermometer into crevices of a recent flow. Hall (1790, 1798) and Spallanzani (1789) would later measure the temperatures at which rocks melt, and their experimental studies would be advanced in the late 19th century (e.g., Joly 1891; Cusack 1896; Barus 1893; Doelter 1901; Day and Sossman 1911; see Young 2003). But the firm roots of geothermometry begin in the 20th century. Goldschmidt (1912) perhaps first introduced the term "geological thermometer," using thermodynamic data to chart the reaction: wollastonite = calcite + quartz (Q). But it would take several decades before thermobarometry would catch on, apparently beginning with Barth's (1934, 1951) calibration of feldspar thermometers and Bowen's (1940) development of the petrogenetic grid. Evans (2007) suggests that the delay may stem from a lack of thermodynamic data and this may be true for metamorphic systems (see Powell et al. 1998). But in igneous systems, experimental phase equilibria have proven to be the foundation on which thermobarometers have been based. We shall review how thermobarometers are developed and evaluated and how the resulting models can best be applied to understand natural systems.

Sources for Commonly Used Thermobarometers

There are far too many important and well-calibrated thermobarometers to summarize in anything but a massive tome. Several comprehensive reviews by Bohlen and Lindsley (1987), Spear (1993), Anderson (1996b), Anderson et al. (2008), Putirka (2008), and Putirka (2016a, b) provide context and access to important methods and models for metamorphic and igneous systems. To supplement these, and bring others up to date, we have: the Fe-Ti oxides (Ghiorso and Evans 2008; Buddington and Lindsley 1964; Anderson and Lindsley 1988), garnet-mica thermobarometers (Holdaway 2001; Wu et al. 2002; Wu and Zhao 2007; Caddick and Thompson 2008; Wu 2015), garnet + pyroxene thermobarometers (Powell 1985; Beyer et al. 2015), amphibole + plagioclase thermometers (Blundy and Holland 1990;

Holland and Blundy 1994), and recent calibrations of Ti-in-quartz (TitaniQ) and related accessory phase thermobarometers (Watson et al. 2006; Wark and Watson 2006; Ferry and Watson 2007; Hayden and Watson 2007; Thomas et al. 2010; Huang and Audetat 2012). In addition to these, mostly solid solution-based models, P estimates can be obtained from equations of state and fluid inclusion densities (Roedder 1965; Hansteen et al. 1998; Hansteen and Klugel 2008), which carry some fascinating potential to obtain P-T time (t) paths (Kohn 2014, 2016). And analytic expressions from all these works are complemented by computer-aided models, such as QUILF (Anderson et al. 1993), VOLATILECALC (Newman and Lowenstern 2002), THEMOCALC (Powell et al. 1998), and MELTS (Ghiorso and Sack 1995). The latter two can be used to estimate P-T positions of phase boundaries and so serve as an invaluable direct test of P-T estimates. In many of these models, though, whether analytic or computer enhanced, errors are not always well constrained and sometimes not identified at all. Without estimates of error, P-T estimates may not only be meaningless but misleading. Kohn and Spear (1991a, b) provide an outstanding summary of error sources and analysis, which are applicable to any thermobarometer or system.

An Illustration of Common Pitfalls: Controversy at the Bishop Tuff (BT)

Before reviewing equations and methods, the Ti-in-quartz (TitaniQ) thermobarometers (Wark and Watson 2006; Thomas et al. 2010), and their application to the Bishop Tuff (Wark et al. 2007; Wilson et al. 2012), illustrate some common pitfalls. The issues of calibration and application of Ti-in-qtz thermobarometers are general and can be carried over to other models and systems.

Wark and Watson (2006) present a thermometer, calibrated as: $\log C^{Q}_{\mathrm{Ti}} = 5.69 - 3765/T(K)$, where C^{Q}_{Ti} is the concentration of Ti-in-quartz in ppm. Using this model, Wark et al. (2007) obtain $T = 720$–810 °C for BT quartz grains, a range that closely matches that obtained by Fe-Ti oxides (714–818 °C; Hildreth and Wilson 2007). In Wark and Watson's (2006) experiments, quartz is co-saturated with rutile and glass and/or a fluid phase. Wark et al. (2007) reasonably posit that C^{Q}_{Ti} should be replaced by C^{Q}_{Ti}/a^{liq}_{Ti}, where a^{liq}_{Ti} is the activity of Ti in a liquid (or fluid), since Ti-in-quartz should be sensitive not just to T but to Ti contents of equilibrated phases. They define $a^{liq}_{Ti} = 1$ at rutile saturation (see Hayden and Watson 2007), and for the Bishop Tuff (not rutile saturated), they use $a^{liq}_{Ti} = 0.6$. Wark and Watson's (2006) experiments are also performed at 10 kbar and are applied to the BT assuming, based on molar volume arguments, that the P effect on the thermometer is small.

But Thomas et al. (2010) show that TitaniQ is indeed P sensitive and they derive a new Ti-in-quartz thermobarometer. The fun starts when Wilson et al. (2012) insert the apparently reliable Fe-Ti oxide temperatures into the new model to obtain $P = 9$ kbar, a value of which they reasonably reject, given the unlikelihood that BT quartz grains grew within the lower crust or upper mantle. Thomas and Watson (2012) counter that Fe-Ti oxide temperatures are too high and that a^{liq}_{Ti} might be closer to 0.3 rather than 0.6. Meanwhile, (a) Huang and Audetat (2012) are unable to reproduce the results of Wark and Watson (2006), and (b) Evans et al. (2016), using Roozeboom (1891)-type arguments, suggest that the Fe-Ti oxide T estimates at the BT are valid. Evans et al.'s (2016) tests are of interest. Roozeboom diagrams are tests of equilibrium. The most common geologic example is the Fe-Mg exchange coefficient ($K_{\mathrm{D}}^{\mathrm{Fe-Mg}}$) between olivine and liquid (Roeder and Emslie 1970). The general idea is that if two phases dissolve a similar component, then the concentrations of that component should vary monotonically in such phases, as P, T, and bulk composition varies (so that chemical potentials are equalized in each phase). Evans et al. (2016) show that Fe, Ti, Mg, and Mn in BT ilmenites, magnetites, and glasses co-vary in a way suggestive of equilibrium. So the Fe-Ti oxide temperatures, first invoked as a validity test for TitaniQ and then rejected due to conflict with the reformulated thermometer, are resurrected.

Lessons from the Bishop Tuff

There are difficulties related to the BT controversy that apply to any thermobarometer:

1. *Proper model calibration*. One problem is that none of the published C^{Q}_{Ti} thermobarometers are properly calibrated. Each are based on linear least squares regression methods that predict $\log_{10} C^{Q}_{Ti}$ when T is provided. But regression is not symmetric (see Putirka 2008 for an illustration); new regressions are needed to predict T when C^{Q}_{Ti} is given. In Wark and Watson's (2006) data, the $\log_{10} C^{Q}_{Ti}$ versus $1/T$ correlation is strong enough that this regression error is trivial (±2 °C), but on larger data sets, the problem is significant. Data from Wark and Watson (2006), Ostapenko et al. (2007; excluding their 500–750 °C data), Thomas et al. (2010), and Huang and Audetat (2012) yield

$$\frac{10^4}{T(^{\circ}C)} = 21.56 - 0.217P(\mathrm{kbar}) - 3.32\log_{10}\left[\frac{C^{Q}_{Ti}(\mathrm{ppm})}{a^{liq}_{TiO_2}}\right] \quad \text{(A)}$$

which reproduces T ±35 °C (a realistic error, typical of polybaric thermometers). Equation A yields T estimates for the Bishop Tuff that are 55 °C greater than those obtained

by rearranging a regression of $\log_{10} C_{\mathrm{Ti}}^{Q}$ using the same data. For a barometer, a proper regression of the data of Huang and Audetat (2012) yields

$$P(\mathrm{kbar}) = -29.53 - 0.0153T(^{\circ}C)\log_{10}\left[\frac{C_{Ti}^{Q}(\mathrm{ppm})}{a_{TiO_2}^{liq}}\right] + 0.0766T(^{\circ}C) \quad \text{(B)}$$

which reproduces P for all data (again excluding the Ostapenko et al. 500–750 °C data) to ±1.8 kbar. Equation B also yields reasonable P estimates (see Anderson et al. 2000) for the Bishop Tuff of 1.5 kbar, when $a_{TiO_2}^{liq} = 0.31, T(^{\circ}C) = 720$ and $C_{Ti}^{Q} = 48$ ppm. When other experimental data are used in the regression, the resulting barometers yield >4 kbar for the same conditions, regardless of regression method. Such comparisons, though, probably tell us less about experimental equilibrium or data quality and instead indicate that $a_{TiO_2}^{liq}$ may vary with P, T, and bulk composition. Ironically, $a_{TiO_2}^{liq}$ was introduced to apply TitaniQ to non-rutile saturated systems; but by being forced to estimate $a_{TiO_2}^{liq}$, we have drawn a useless circle.

2. *Single-phase thermobarometers have large errors*. Anderson and Smith (1995) show that Al-in-hornblende barometers are sensitive to T and composition and so are valid only under highly restrictive compositional and thermal limits (see Putirka 2016b for updated tests and Nimis and Taylor (2000) for an example based on clinopyroxene). Ti-in-quartz thermometry is no different. A useful Ti-in-quartz thermometer will await new experiments where Ti is measured in coexisting quartz and glass/fluid phases.
3. *Like validates like*. The only reliable tests for a thermometer or barometer are other thermometers and barometers; all other tests are inferential. The BT contains not just quartz and Fe-Ti oxides but two feldspars and a glass; four different thermometers from the latter agree within typical thermometer error (±30 °C), assuming $P = 2$ kbar and 5.5 wt. % H_2O in silicate liquids (Anderson et al. 2000). Temperature estimates need not agree, but such convergence is compelling evidence that we are approaching accurate magmatic temperatures for the BT. Lacking independent thermobarometers, Roozeboom (1891) diagrams are the next best tools, however indirect.
4. *Error must be expressly indicated*. The MELTS model yields quartz + two feldspar equilibrium for a BT liquid at 720–730 °C (Gardner et al. 2014), apparently validating the results of Fig. 1. But Scaillet and Evans (1999) show quartz saturation at 800–850 °C, at 5.5% H_2O and 2.2 kbar, for rhyolitic glasses that are not too different from those from BT. For any model, we must compare $T^{\mathrm{calculated}}$ versus T^{measured} to estimate error and accuracy; otherwise, model discrepancies, or agreements, cannot be judged.
5. *You cannot test an atomic clock with a wristwatch*. Huang and Audetat's (2012) results show that the Ti-in-quartz thermometer is a work in progress (Thomas et al. 2015 do not rectify the issues noted here). In contrast, Fe-Ti thermometers are well tested, both experimentally and in their application to natural systems. Interlaboratory tests are vital for any model, and it is too early to use TitaniQ as a test of Fe-Ti oxide thermometry.
6. *Errors on P-T estimates could be lower when averaged*. This precept assumes that error is random. To be sure, systematic error can affect experiments and our approach to natural samples (e.g., thermocouples may not measure the hot zone of a sample capsule; we may analyze un-equilibrated crystal compositions, instead of rims). But phases may approach equilibrium from different, random directions, and this sort of randomness may be quite important, as averaging appears to lead to more accurate P and T estimates (Powell and Holland 1994; Putirka et al. 1996; see Putirka 2016a). Moreover, if this were not the case, we would have no justification for using Fe-Mg exchange coefficients (e.g., Roeder and Emslie 1970) as we currently do, to test equilibrium. The issue is illustrated in Fig. 1: T estimates from the upper and lower stratigraphic sections of the BT cluster near 780 °C and 750 °C, respectively. That clustering, and t tests, indicate that the thermal contrasts are real. Thermal contrasts are also evident in Ti-in-quartz, which range from 722 °C for cores (48 ppm Ti) to 780 °C for rims (100 ppm Ti) using Eq. A. We might still be learning more about a_{Ti}^{liq} rather than absolute T, but TitaniQ may be immensely useful for translating quartz zoning patterns into *relative* T *estimates*, when other models delimit P, T, and a_{Ti}^{liq}. Used in this way, the intra-laboratory error of ±8 °C error (the standard error of estimate derived from Wark and Watson's (2006) data) might also be applicable, providing a powerful method to decipher geologic processes when using thermobarometers in concert. In the following sections, we will revisit some of these issues, first through theoretical foundations, and then some additional examples of model calibration and application.

Univariant and Multivariant Equilibria

Nearly all geothermobarometers involve heterogeneous equilibria – reactions that involve more than one phase (ice transforming to water), as opposed to homogenous equilibria where all chemical constituents of a "reaction" occur in a single phase (H_2O disassociating into OH^- and H^+). Bohlen and Lindsley (1987) provide a useful fivefold division of heterogeneous equilibria, which we will reduce to two: (a) multivariant equilibria – reactions that involve multiple phases, some of which exhibit solid solution. In the cases that interest us, the

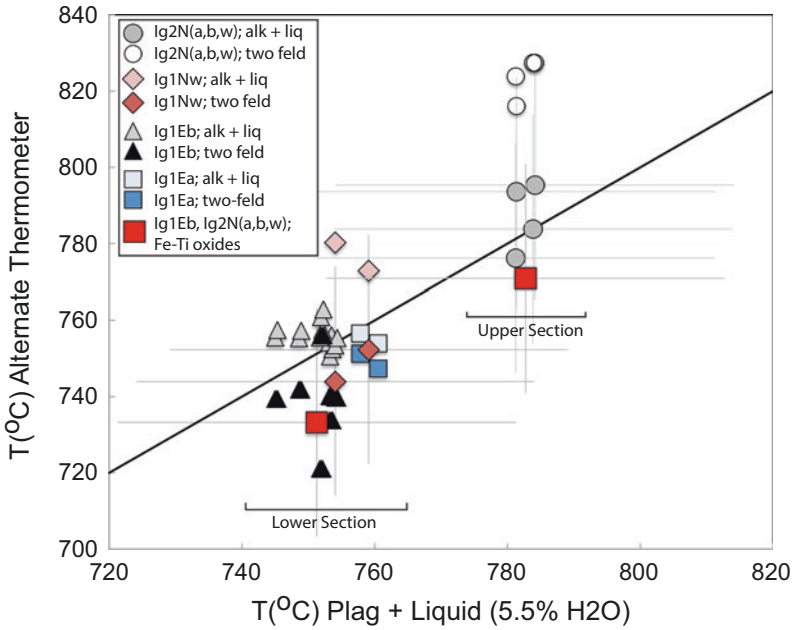

Geothermometry and Geobarometry, Fig. 1 A comparison of T estimates from plagioclase + liquid (Putirka 2008; Eq. 24a), alkali feldspar + liquid (Putirka 2008; Eq. 24b), two-feldspar (Putirka 2008; Eq. 27b), and Fe-Ti oxide thermometers (mean T of Fe-Ti estimates reported in Hildreth and Wilson (2007)). Feldspar compositions are from Chamberlain et al. (2014); silicate liquids are from Hildreth and Wilson (2007). We assume $P = 2$ kbar and that silicate liquids contain 5.5% H_2O (Anderson et al. 2000). The results are consistent with Gardner et al. (2014). It is not clear whether quartz (Q) should saturate at higher or lower T compared to plagioclase (Pl) or alkali feldspar (Af). Gardner et al. (2014) would place saturation as $T^{Af} > T^{Q} > T^{Pl}$, but the Pinatubo compositions of Scaillet and Evans (1999) are not very different, and their rhyolitic glasses have $T^{Pl,} > T^{Q} > T^{Af}$; in either case, quartz saturation temperatures should be similar to T estimates shown here

reactions do not go to completion. (b) Univariant equilibria: reactions that nominally involve pure phases, and usually go to completion – unless we are very lucky.

A classic example of case (b) is the system Al_2SiO_5. The polymorphs kyanite, sillimanite, and andalusite occupy different regions of P-T space (Fig. 2), separated by univariant curves. The term "univariant" herein means that if two or more pure phases are in equilibrium, then P and T cannot vary independently, so if one is specified, the other is determined. Geologists recognized the usefulness of such reactions very quickly. Iddings (1888) applied the quartz-tridymite transition to the origin of lithophysae at Obsidian Cliff, Yellowstone, while Barrow (1893) used the sillimanite-kyanite ["cyanite" in Barrow (1893)] transition in his classic study of contact metamorphism. Only one mathematical relationship is needed to evaluate univariant reactions, Clapeyron's (1834) equation:

$$\frac{dP}{dT} = \frac{\Delta H_r}{T\Delta V_r} = \frac{\Delta S_r}{\Delta V_r} \quad (1)$$

where ΔV_r, ΔH_r and ΔS_r are the volume, enthalpy, and entropy of reaction, respectively (e.g., $\Delta H_r = H^{products} - H^{reactants}$). Since only pure phases are involved, only P-T space is relevant. For an unalloyed barometer or thermometer, dP/dT (Fig. 2) should, respectively, approach either zero ($\Delta S_r \rightarrow 0$) or infinity ($\Delta V_r \rightarrow 0$). Few equilibria have such characteristics, but interdependency is not always disadvantageous. Sillimanite-bearing pelites and interbedded meta-sandstones containing albite (Ab), orthoclase (Or), and quartz (Q)

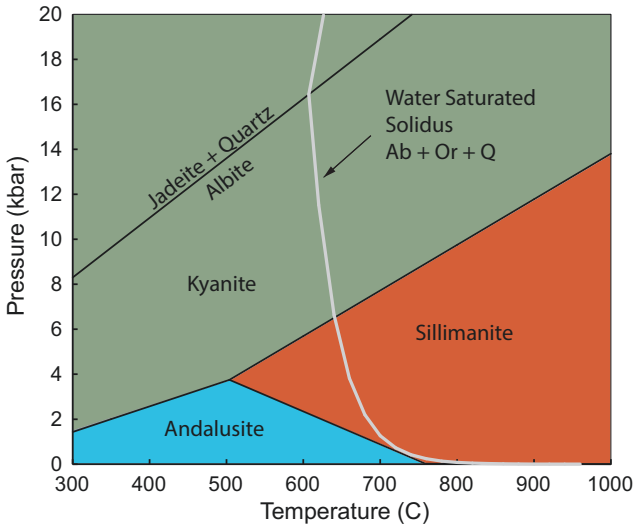

Geothermometry and Geobarometry, Fig. 2 P-T diagram showing aluminosilicate phase boundaries (Holdaway and Mukhopadhyay 1993), the albite + quartz = jadeite boundary (Holland 1980) and the water-saturated granite solidus (Johannes and Holtz 1996). Below the Ab + Q = Jd boundary, the granite solidus is P(kbar) = exp[(19.556–0.0276(T °C)]

that show no evidence of partial melting, must have *P-T* conditions that fall to the low-T side of the granite solidus (Ab + Or + Q = Liq), but within the sillimanite stability field, limiting the possible range of *P-T* conditions (Fig. 2). Similarly, equilibrated kyanite + albite defines, however, broadly a *P-T* window of stability (Fig. 2). A grand prize is awarded when phases that define a univariant curve or, better yet, an invariant point coexist; rocks containing both kyanite and andalusite must fall on the univariant curve that separates the two stability fields (Fig. 2). If all three aluminosilicates are at equilibrium, the system must have passed through the triple point: 3.75 kbar and 504 °C (Fig. 2). Lest any reader believe that the method was facile, the placement of the Al_2SiO_5 univariant boundaries consumed decades of work: from Althaus (1967), to Richardson et al. (1969), to Bohlen et al. (1991), to Holdaway and Mukhopadhyay (1993), the triple point fell from 6.5 to 3.75 kbar and 595 °C to 504 °C (~0.07 kbar/year and 3.7 °C/year). But as the number of phases in a lithologic system increases, so do the opportunities for improved *P-T* precision. It is thus possible to derive a rather dense fishing net of *P-T* curves (e.g., Caddick and Thompson 2008). As powerful as this method is, however, it is rare to obtain definite values of *P* and *T*, with specified errors. Multivariant equilibria offer such a prospect and will be the focus of the remainder of this review.

Thermodynamic Basis of Multivariant Equilibria

The theoretical basis of thermobarometry is what Anderson (1996a) calls the "most useful equation in thermodynamics":

$$-RTlnK_{\mathrm{eq}} = \Delta G_r^{o,T,P} \tag{2}$$

In Eq. 2, R is the gas constant, K_{eq} is the equilibrium constant (to be discussed forthwith), and $\Delta G_r^{o,\,T,\,P}$ is the Gibbs free energy difference between products and reactants (so $\Delta G_r^{o,T,P} = G^{o,T,P}_{\mathrm{products}} - G^{o,T,P}_{\mathrm{reactants}}$), as pure substances, at the P and T of interest. Some texts imply a 1 bar standard state, using $\Delta G_r^{o,T,\,1\,\mathrm{bar}}$. However, we follow what Castellan (1971, p. 358) refers to as the "rational system," which is convenient for understanding Eq. 2 and commonly used in geology. The superscript T in $\Delta G_r^{o,\,T,\,P}$ is the very same T as occurs in the $-RT\ln K_{\mathrm{eq}}$ term. To find a new value of K_{eq}, at some new T or P, it is necessary not only to insert a new value for T on the left-hand side of Eq. 2 but often (unless $\Delta G_r^{o,\,T,\,P}$ does not greatly change with P or T) to calculate a new $\Delta G_r^{o,\,T,\,P}$ at the P and T of interest as well. Textbooks have long presented Eq. 2 as if it were a Platonic form, falling ethereally out of some perfect realm. We will turn our heads to see how the shadows have been cast.

In the development of Eq. 2, revolutions and brilliant masterstrokes are rare. It has roots in Dalton's atomic hypothesis (ca. 1804), but the equilibrium constant had its birth much later, with Guldberg and Waage's (1864, 1879) work on a "law of mass action." Inspired by Berthelot, they posit that chemical reactions are driven by "chemical forces" that are proportional to mass, analogous to forces in Newtonian mechanics. Early experimenters knew that some reactions do not go to completion but rather stop partway, leaving an apparent stable assemblage of products and reactants. For chemical species A and B, reacting to form C and D, we can have:

$$\alpha\mathrm{A} + \beta\mathrm{B} = \gamma\mathrm{C} + \delta\mathrm{D} \tag{3}$$

where α, β, γ, and δ are stoichiometric coefficients, which give the numbers of chemical species involved in the balanced, chemical equilibrium. For Guldberg and Waage (1864), the idea was that a large mass of A and/or B creates a rightward-directed force to yield greater masses of C and D. Equilibrium is established when the two opposing forces are equal. The ideas of a chemical or an "affinity force" are now obsolete; today, we use molar concentrations instead of masses and speak of reaction rates instead of chemical forces. But the broad ideas are the same. Guldberg and Waage also hypothesized that to obtain the chemical forces, the masses of the species must be raised to some exponent; so for the forward reaction, the force would be $k_1A^xB^y$, where x, y, and k_1 are arbitrary constants, determined by experiment, and the reverse "force" would be $k_2C^wD^z$. The coefficients k_1 and k_2 are now called rate constants (so the reaction rate is $r_1 = k_1[A^xB^y]$). Guldberg and Waage (1864) did not yet recognize that the stoichiometric coefficients of Eq. 2 could serve as exponents. Lund (1965) credits August Horstman (1877) with this insight, and the idea would be demonstrated by Van't Hoff (1887) using the ideal gas law and Avogadro's idea that equal volumes of gases contain equal numbers of atoms. Guldberg and Waage (1879) applied this new idea, and so by 1879–1888, we approach a modern equilibrium constant – inspired from a theory of "chemical forces" that we no longer use and a theory of atoms that would not be widely accepted for another quarter century:

$$K_{eq}^{ideal} = \frac{(X_C)^{\gamma}(X_D)^{\delta}}{(X_A)^{\alpha}(X_B)^{\beta}} \tag{4a}$$

In Eq. 4a, terms such as $(X_C)^{\gamma}$ or $(X_A)^{\alpha}$ are, respectively, the mole fractions of C and A, X_C and X_A raised to an exponent equal to their stoichiometric coefficients γ and α. The molar concentrations, however, are only applicable when the chemical species do not interact (we say in this case that the system is "ideal"); more generally, we use activities:

$$K_{eq} = \frac{(a_C)^{\gamma}(a_D)^{\delta}}{(a_A)^{\alpha}(a_B)^{\beta}} \quad (4b)$$

where a_c is the activity of component C. For a geologic example:

$$2SiO_2{}^{liq} + 0.5Na_2O^{liq} + 0.5Al_2O_3{}^{liq} = NaAlSi_2O_6{}^{pyx} \quad (5)$$

where $NaAlSi_2O_6{}^{pyx}$ is jadeite (Jd) in pyroxene (pyx) and chemical species such as Na_2O^{liq} are oxides in a coexisting liquid. The equilibrium constant for Eq. 5, using Eq. 4b, is:

$$K_{\text{eq}} = \frac{a_{Jd}^{pyx}}{\left(a_{SiO_2}^{liq}\right)^2 \left(a_{Na_2O}^{liq}\right)^{0.5} \left(a_{Al_2O_3}^{liq}\right)^{0.5}} \quad (6)$$

and a_i^j is the activity of species i in phase j (so a_{Jd}^{pyx} is the activity of jadeite in pyroxene, and $a_{Na_2O}^{liq}$ is the activity of Na_2O in a coexisting silicate liquid). The idea of activity is another innovation from the late nineteenth century, formalized by Gilbert Lewis (1907). It is an effective concentration. For example, let us say that in the silicate liquid in Eq. 6, that Na_2O partially interacts with Fe_2O_3 or Cr_2O_3, in the liquid, perhaps forming $NaFe^{3+}O_2$ or $NaCrO_2$ molecular clusters. These Na-bearing clusters might not be equally available to participate in Eq. 6, thus reducing the amount of Na available to make jadeite. The effective concentration of Na_2O might thus be less than its molar concentration, $X_{Na_2O}^{liq}$. To count only that fraction of Na_2O available for Eq. 6, we use $a_{Na_2O}^{liq}$. The quantities $a_{Na_2O}^{liq}$ and $X_{Na_2O}^{liq}$ are related to one another by the activity coefficient λ_{Na_2O}, so that $a_{Na_2O}^{liq} = \lambda_{Na_2O} X_{Na_2O}^{liq}$ or, more generally,

$$a_i^j = \lambda_i X_i^j \quad (7)$$

where i is some chemical component in a solution of phase j. The limiting values of a_i^j are 0, when i is absent from solution, or 1 when the solution consists of pure i. The activity coefficient λ_i can range from 0 to any positive value. For $\lambda_i < 1$, component i is tied up as it interacts with other components in solution, as in the above example. For repulsive forces acting on component i in solution j, the effective concentration may be greater than X_i^{liq}, in which case $\lambda_i > 1$.

The concept of activity can also be related to Lewis' idea of fugacity, f_i, which measures the "tendency" of a chemical species i to "escape" from one phase and enter another (Lewis 1901). So activity can be defined as $a_i = \frac{f_i}{f_i^o}$ where f_i is measured in units of pressure and f_i^o is fugacity of i at a standard state. Because f_i^o can be defined at any P or T, a_i is not uniquely defined – even when P and T are fixed. For aqueous solutions, defining f_i^o is necessary since f_i is never equal to one; so $a_{\text{i}} = 1$ (a necessary condition for pure substances, as we shall see) only when $f_i = f_i^o$. For liquids and minerals, we can express concentrations as mole fractions, similar to pure substances, making the fugacity relationship unnecessary.

Activities are tied to "solution models," and some important examples are Raoult's (1884) law, where $a_i^j = X_i$, and Henry's law (dilute solutions, i.e., when X_{i} is small), where $a_i^j = \lambda_i X_i$ and λ_i does not depend upon composition. At high X_{i}, activity coefficients can be modeled as a function of composition, using Margules parameters (Nordstrom and Munoz 1986). For solid solutions, entropy of mixing is used to create a "mixing on sites" (MOS) model (see Nordstrom and Munoz 1986). But while the MOS model is accepted for minerals, nothing comparable has been developed for liquids. The activity model of Bottinga and Weill (1972), Nielsen and Drake (1979), and Nielsen and Dungan (1983) seems to describe mineral-liquid equilibria quite well but has not gained a stout following. The model is based on viscosity and spectroscopic observations (see Mysen 1991) where silicate melts are divided into network-forming (NF) cations, which are tetrahedrally coordinated units charge-balanced by K and Na, and network modifiers, which comprise all other cations. The MELTS model (Ghiorso et al. 2002) is currently the most utilized of igneous liquid activities. It employs a "regular solution" model, which means that volumes of mixing are zero and entropies of mixing are entirely configurational. MELTS is not only useful for interpolating experimental phase equilibria, but Stebbins (2016) shows that it successfully predicts compositional dependencies of Si activity, first noted by Ryerson (1985).

Equations 2, 4a, b and 7 are the basis of all multivariate geothermobarometers. P-T information comes from the fact that K_{eq} is not truly a constant, but varies with P and T, as is implicit in Eq. 2. To better understand Eq. 2, we can use:

$$\Delta G_r^{T,P} = \Delta G_r^{0,T,P} + RT\ln Q \quad (8)$$

In Eq. 8, $\Delta G_r^{T,P}$ is the Gibbs free energy difference between products and reactants as they actually exist in nature, at some P and T; with luck, nature approaches equilibrium where $\Delta G_r^{T,P} = 0$. In Eq. 8, we use Q (the "reaction quotient") instead of K_{eq}, because while it can be calculated in the same way, it is only equal to K_{eq} when $\Delta G_r^{T,P} = 0$. If $\Delta G_r^{T,P} \neq 0$, the concentrations of A, B, C, and D (Eq. 3) should spontaneously change until Q reaches the value of K_{eq} (but like diamond converting to graphite at 1 atm, energy barriers may prevent equilibrium from being achieved) and when this happens $\Delta G_r^{T,P} = 0$, we have Eq. 2.

The Meaning of K_{eq}

Equations 2 and 8 show that K_{eq} serves a unitary purpose: to account for all disturbances to equilibrium that result from

impurities; the term $RT\ln K_{eq}$ describes the free energy effect of *impure systems*. When all phases are pure, all activities are unity; Eq. 4b is equal to 1, and $-RTlnK_{eq} = 0$. For the case $\Delta G_r^{o,T,P} = 0$ (Eq. 8), then $\Delta G_r^{0,T,P} = 0$, which is why activities must be unified for standard states. In any case, if a system is not ideal, we can divide K_{eq} into ideal and nonideal parts:

$$K_{eq} = \frac{a_C^{\gamma} a_D^{\delta}}{a_A^{\alpha} a_B^{\beta}} = \frac{(\lambda_C X_C)^{\gamma}(\lambda_D X_D)^{\delta}}{(\lambda_A X_A)^{\alpha}(\lambda_B X_B)^{\beta}} = \left(\frac{X_C^{\gamma} X_D^{\delta}}{X_A^{\alpha} X_B^{\beta}}\right)\left(\frac{\lambda_C^{\gamma}\lambda_D^{\delta}}{\lambda_A^{\alpha}\lambda_B^{\beta}}\right) \quad (9)$$

where $K_{eq}^{ideal} = \left(\frac{X_C^{\gamma} X_D^{\delta}}{X_A^{\alpha} X_B^{\beta}}\right)$ and the nonideal part is $K_{\lambda} = \left(\frac{\lambda_C^{\gamma}\lambda_D^{\delta}}{\lambda_A^{\alpha}\lambda_B^{\beta}}\right)$; K_{λ} is the "excess" Gibbs free energy. With rearrangement, Eq. 2 thus becomes:

$$lnK_{eq} = \ln\left(\frac{X_C^{\gamma} X_D^{\delta}}{X_A^{\alpha} X_B^{\beta}}\right) + \ln\left(\frac{\lambda_C^{\gamma}\lambda_D^{\delta}}{\lambda_A^{\alpha}\lambda_B^{\beta}}\right) = -\frac{\Delta G_r^{0,T,P}}{RT} \quad (10)$$

To Construct a Thermobarometer

One avenue to develop a thermobarometer is to quantify how $\Delta G_r^{0,T,P} = 0$ varies with P and T. In 1883 Van't Hoff (1896) used the ideal gas law and concepts of heats of reaction to show that Guldberg and Waage's "law of mass action" should vary with temperature, creating his eponymous equation:

$$\frac{dlnK_{eq}}{dT} = \frac{-\Delta H_r^o}{RT^2} \quad \text{or} \quad \frac{dlnK_{eq}}{d\left(\frac{1}{T}\right)} = \frac{-\Delta H_r^o}{R} \quad (11)$$

where ΔH_r^o is the heat of reaction between pure substances at a reference P and T.

Josiah Willard Gibbs had already presented his ideas of chemical potential energy (Gibbs 1874–1878) – a work that was not immediately appreciated. But Van der Waals (1891) and Van Laar (1892) would later use Gibbs' ideas to derive Van't Hoff's equation (Eq. 11), and Van Laar (1892) would derive a P dependency for K_{eq}:

$$\frac{\mathrm{d}\ln K_{eq}}{\mathrm{dP}} = \frac{\Delta V_r^o}{RT} \quad (12)$$

where ΔV_r^o is the volume of reaction between pure substances at a reference P and T (see also Lewis 1899).

The key issue for us is that K_{eq} is a constant only when P and T are fixed. In igneous systems, we can use:

$$\Delta G_r^{o,T_{\mathrm{fus}},1bar} = \Delta H_r^{o,T_{\mathrm{fus}},1bar} - T\Delta S_r^{o,T_{\mathrm{fus}},1bar} \quad (13)$$

where T is the temperature of interest and T_{fus} can really be any reference T, but here it is the T of fusion of pure substances at 1 bar. A term such as $\Delta H_r^{o,T_{\mathrm{fus}},1\mathrm{bar}}$ is the heat of fusion of a pure substance at 1 bar. Values for $\Delta H_r^{o,T_{\mathrm{fus}},1\mathrm{bar}}$ and $\Delta S_r^{o,T_{\mathrm{fus}},1\mathrm{bar}}$ are nearly constant when heat capacities between products and reactants, ΔC_p, are close to zero. If ΔC_p is far from 0, then additional corrections are needed:

$$\Delta G_r^{o,T,1\ \mathrm{bar}} = \Delta H_r^{o,T_{\mathrm{fus}},1\mathrm{bar}} + \int_{T_{\mathrm{fus}}}^{T} \Delta C_p \mathrm{dT} - T\left[\Delta S_r^{o,T_{\mathrm{fus}},1\mathrm{bar}} + \int_{T_{\mathrm{fus}}}^{T} \frac{\Delta C_p}{T} dT\right] \quad (14)$$

For barometry, we need to define the P effects on $\Delta G_r^{0,T,P}$, which is

$$\Delta G_r^{o,T,P} = \Delta G_r^{o,T,1\ bar} + \int_{1\ bar}^{P} \Delta V_r^o dP \quad (15)$$

where ΔV_r^o is the molar volume difference between pure products and reactants at T. Adding Eqs. 14 and 15, we have

$$\Delta G_r^{o,T,P} = \Delta H_r^{o,T_{\mathrm{fus}},1\mathrm{bar}} + \int_{T_{fus}}^{T} \Delta C_p dT - T\left[\Delta S_r^{o,T_{fus},1bar} + \int_{T_{fus}}^{T} \frac{\Delta C_p}{T} dT\right] + \int_{P_o}^{P} \Delta V_r^o dP \quad (16)$$

The last integral in Eq. 15 is challenging because ΔV_r^o depends upon both P and T. Assuming ΔC_p = constant and constant values for differences in compressibility ($\Delta\beta = \beta^{\mathrm{products}} - \beta^{\mathrm{reactants}}$) and thermal expansion ($\Delta\alpha = \alpha^{\mathrm{products}} - \alpha^{\mathrm{reactants}}$) (see Putirka 1998), we obtain:

$$lnK_{eq} = \frac{A}{T} + B + Cln\left[\frac{T}{T_o}\right] + D\frac{P}{T} + E\frac{P^2}{T} + FP + GP^2 \quad (17)$$

where T_o is a reference temperature and $A = -\Delta H_r^{T_o}/R$, $B = \Delta S_r^{T_o}/R, C = \Delta C_p/R, D = -\Delta V_r^o/R$, $E = \Delta\beta\Delta V_r^o/2R$, $F = \Delta\alpha\Delta V_r^o/R$, and $G = \Delta\alpha\Delta\beta\Delta V_r^o/2R$. Experimental error on phase equilibria experiments, though, is such that $\Delta C_p \approx 0$ and $\Delta V_r^o \approx$ constant, so Eq. 17 can be simplified to:

$$lnK_{eq} = \frac{\Delta H_r^{o,T}}{RT} - \frac{\Delta S_r^{o,T}}{R} + \frac{P\Delta V_r^o}{RT} \quad (18)$$

G

Combining Eqs. 9 and 10 with Eq. 18, we have:

$$lnK_{eq} = lnK_{eq}^{ideal} + lnK_{\lambda} = ln\left(\frac{X_C^{\gamma}X_D^{\delta}}{X_A^{\alpha}X_B^{\beta}}\right) + ln\left(\frac{\lambda_C^{\gamma}\lambda_D^{\delta}}{\lambda_A^{\alpha}\lambda_B^{\beta}}\right) = \frac{A}{T} + B + D\frac{P}{T} \quad (19)$$

which we rearrange to obtain:

$$ln\left(\frac{X_C^{\gamma}X_D^{\delta}}{X_A^{\alpha}X_B^{\beta}}\right) = \frac{A}{T} + B + D\frac{P}{T} + ln\lambda_C^{\gamma} + ln\lambda_D^{\delta} - ln\lambda_A^{\alpha} - ln\lambda_B^{\beta} \quad (20)$$

In theory, we could use Eq. 20 as a thermometer or barometer if only we knew the values of $\Delta H_r^{T_o}$, $\Delta S_r^{T_o}$, and ΔV_r^o (which we will simply write as ΔH_r^o , ΔS_r^o , and ΔV_r^o) and could somehow derive values for the activity coefficients. We now have a rich database of thermodynamic data (Richet and Bottinga 1986; Berman 1988; Lange and Carmichael 1987; Berman 1988; Lange and Navrotsky 1992; Navrtosky 1995; Holland and Powell 1998). But compositional complexities are hidden within Eq. 9, and they are not trivial. So instead, we rearrange Eq. 20 to obtain a regression equation for barometry:

$$P = \in_1 + \in_2 T + \in_3 T ln\left(\frac{X_C^{\gamma}X_D^{\delta}}{X_A^{\alpha}X_B^{\beta}}\right) + \in_4 ln\lambda_C^{\gamma} + \in_5 ln\lambda_D^{\delta} - \in_6 ln\lambda_A^{\alpha} - \in_7 ln\lambda_B^{\beta} \quad (21)$$

And using T as the dependent variable, a useful regression equation for a thermometer is:

$$T = \frac{v_1 + v_2 P}{v_3 + v_4 ln\left(\frac{X_C^{\gamma}X_D^{\delta}}{X_A^{\alpha}X_B^{\beta}}\right) + v_5 ln\lambda_C^{\gamma} + v_6 ln\lambda_D^{\delta} - v_7 ln\lambda_A^{\alpha} - v_8 ln\lambda_B^{\beta}} \quad (22)$$

The coefficients $\in_i$ and v_i can be related to thermodynamic parameters as in Eqs. 18, 19, and 20. The use of Eq. 22, though, requires problematic nonlinear regression techniques, so it can be rearranged to:

$$\frac{10^4}{T} = aln\left(\frac{X_C^{\gamma}X_D^{\delta}}{X_A^{\alpha}X_B^{\beta}}\right) + b + cln\lambda_C^{\gamma} + dln\lambda_D^{\delta} + eln\lambda_A^{\alpha} + fln\lambda_B^{\beta} + gP \quad (23)$$

where coefficients a through g are empirical constants that may or may not approximate thermodynamic quantities (we usually regress on $10^4/T$ rather than $1/T$ to avoid obtaining values of a through g that are exceedingly small). Although empirical, Eq. 23 retains the natural mathematical relationships between T and its various dependent quantities.

Putting Theory into Practice (And the Problems Therein)

Clearly, a large ΔV_r^o provides a good barometer, while a large ΔS_r^o(or ΔH_r^o) provides a good thermometer. Essene (1982) suggests minimum values of $\Delta V_r^o \geq 0.2$J/bar and $\Delta S_r^o \geq 4$ kJ/mole for sub-solidus systems. But a good thermobarometer also requires phases that have very definite compositions. There may be no better illustration of this issue than the Al-in-hornblende barometer of Hammerstrom and Zen (1986) and attempts to expand this model to volcanic systems by Ridolfi and Renzulli (2011). The original data of Hammerstrom and Zen (1986) reveal very wide variations in Al-in-amphibole at low pressures. Such variation nearly encompasses the entire range of Al-in-hornblende observed at higher pressures (Putirka 2016b). Such wide compositional ranges may reflect amphibole solid solution traits, hypothetically illustrated in Fig. 3.

Figure 3 shows two components, A and B, in a solid and liquid solution; for each diagram, P and T are fixed (say, 1,050 °C and 2 kbar, although the specific values do not matter). In Fig. 3a, solid phase S_1 has limited solid solution and so has a very narrow G-x surface, compared to a coexisting liquid phase L_1. These G-x surfaces can move up or down as P and T change or even side to side if another component, say C (not shown), affects the mutual solubility of A and B in either S_1 or L_1. For the bulk composition X^o, its lowest Gibbs free energy is that of a mixture of S_1 and L_1 (G^{mix}), compared to the Gibbs free energy if it were completely solid (G^{solid}) or liquid (G^{liquid}) at the given P and T. In this hypothetical system, raising T would have the effect of lowering the G-x surface of L_1 relative to S_1, until that surface was everywhere lower than S_1; at this point, the system would be completely liquid. At temperatures where both solid and liquid are stable, the compositions of the coexisting phases are given by the common tangent to the curves S_1 and L_1 : X_B^S for the solid and X_B^L for the liquid. Although the tangent curve is mathematically a point, one can see that even small disturbances to equilibrium, due to very small changes in P, T, or X_B, can, in practice, lead to different compositions, X_B^S and X_B^L, as shown by the gray regions in Fig. 3a. Now compare these gray regions to Fig. 3b, where the two phases S_2 and L_2 exhibit much greater extents of solid solution. Aluminum contents of amphiboles may be analogous to Fig. 3b, and indeed, our uncertainty or lack of reproducibility in any experimental system may be limited by this effect. If this is the case for Al-based components in amphibole, then the very nature of solid solution may hamper

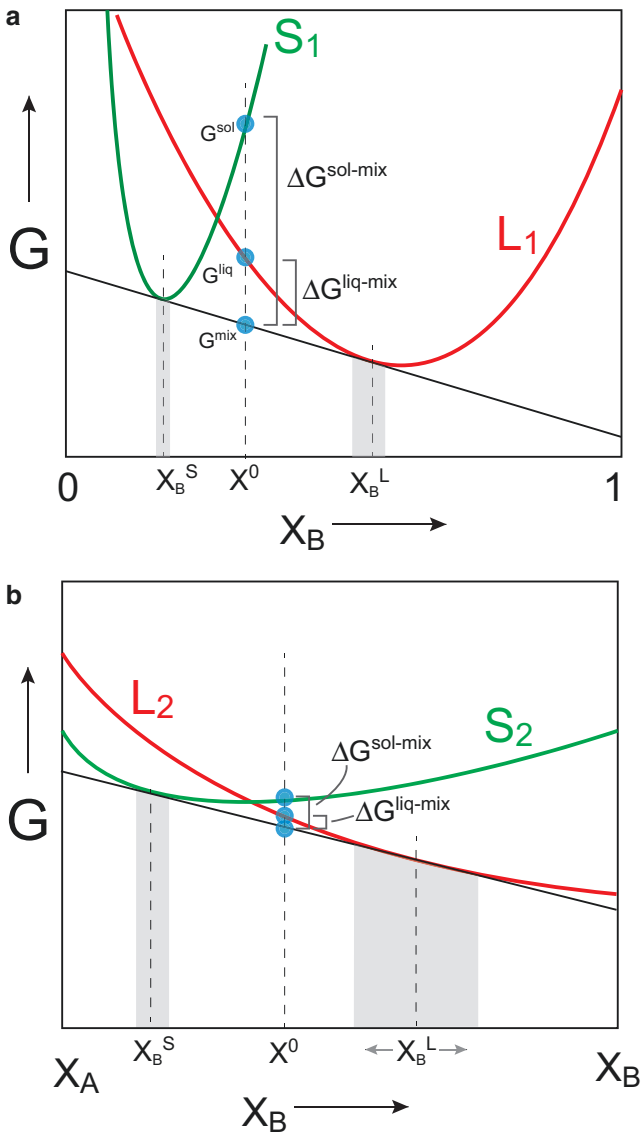

Geothermometry and Geobarometry, Fig. 3 Two diagrams illustrating hypothetical two-component (**a** and **b**) Gibbs free energy composition (or G-x) relationships, both at a fixed P and T. (**a**) illustrates hypothetical solid and liquid phases S_1 and L_1, which have narrower G-x surfaces compared to phases S_2 and L_2 in (**b**). The G-x surfaces can move up or down with changes in P and T and can also move side to side or change shape, depending upon how the compositions of other phases affect the mutual solubility of components A and B in the phases S and L. In both panels, an arbitrary bulk composition, X^o, has a lower Gibbs free energy (G^{mix}) if it decomposes into a mixture of S + L, compared to the Gibbs free energy it would have if it were completely liquid (G^{liq}) or solid (G^{sol}). The composition of the equilibrium solid and liquid phases, (X_B^S) and (X_B^L), is given by the common tangent in both panels. But in panel (b), due to the wider, flatter G-x surfaces, the equilibrium composition of the two phases is less sharply defined, as shown by the *gray* areas that surround the precise equilibrium compositions (given by *vertical dashed lines*). For solid solution behavior such as in panel (**b**), a variety of liquids may precipitate very similar solid phases, and because the Gibbs free energies, G^{mix}, G^{liq}, and G^{sol}, are closer together, crystals may move in or out of saturation, even without large changes in T or P. Calibrating a thermobarometer from phases that exhibit such solid solution behavior may be intrinsically challenging

attempts to find a unique equilibrium composition at a given P and T, and the nearness of G^{solid}, G^{liquid}, and G^{mix} may cause a crystalline phase to move in or out of equilibrium with just small changes in P, T, or X_B.

Using Calorimetric Data and Activity Models

In this section, we will take a critical look at the role of calorimetric data and activity models in the development of thermobarometry. One of the more precise thermometers for igneous systems is based on anorthite (An = $CaAl_2Si_2O_8$; Ab = $NaAlSi_3O_8$) crystallization, and the reaction can be written as (liq = liquid; pl = plagioclase; pyx = pyroxene):

$$CaO^{liq} + 2SiO_2{}^{pyx} + 2AlO_{1.5}{}^{liq} = CaAl_2Si_2O_8{}^{pl} \quad (24)$$

Eq. 24 can also be written as:

$$CaAl_2Si_2O_8{}^{liq} = CaAl_2Si_2O_8{}^{pl} \quad (25a)$$

or

$$0.5Ca_2Si_2O_6{}^{liq} + 0.25Si_4O_8{}^{pyx} + 0.5Al_4O_6{}^{liq} = CaAl_2Si_2O_8{}^{pl} \quad (25b)$$

Equation 25a is useful for describing the simple binary system investigated by Bowen (1913) and Eq. 25b uses the liquid components of MELTS (Ghiorso et al. 2002) (Tables 1, 2, and 3 show how to transform a set of conventional oxides, as in Eq. 24 into any set of equally numbered molecular components, as in Thompson 1982). The phase boundaries of the plagioclase crystallization loop (Fig. 4) can be computed using the following equations:

$$X_{Ab}^{liq} = \frac{exp\left[\frac{\Delta H_f^{An}}{R}\left(\frac{1}{T_f^{An}} - \frac{1}{T}\right)\right] - 1}{\frac{exp\left[\frac{\Delta H_f^{An}}{R}\left(\frac{1}{T_f^{An}} - \frac{1}{T}\right)\right]}{exp\left[\frac{\Delta H_f^{Ab}}{R}\left(\frac{1}{T_f^{Ab}} - \frac{1}{T}\right)\right]} - 1} \quad (26a)$$

$$X_{Ab}^{pl} = \frac{\exp\left[\frac{\Delta H_f^{An}}{R}\left(\frac{1}{T_f^{An}} - \frac{1}{T}\right)\right] - 1}{exp\left[\frac{\Delta H_f^{An}}{R}\left(\frac{1}{T_f^{An}} - \frac{1}{T}\right)\right] - exp\left[\frac{\Delta H_f^{Ab}}{R}\left(\frac{1}{T_f^{Ab}} - \frac{1}{T}\right)\right]} \quad (26b)$$

where terms such as X_{Ab}^{liq} and X_{Ab}^{pl} are the mole fractions of Ab in a binary Ab-An mixture of liquid or plagioclase, terms such as

Geothermometry and Geobarometry, Table 1 Express molecular components as a function of oxides

	SiO_2	TiO_2	$AlO_{1.5}$	FeO	MnO	MgO	CaO	$NaO_{0.5}$	$KO_{0.5}$	$PO_{2.5}$
1. SiO_2	1	0	0	0	0	0	0	0	0	0
2. TiO_2	0	1	0	0	0	0	0	0	0	0
3. Al_2O_3	0	0	2	0	0	0	0	0	0	0
4. Fe_2SiO_4	1	0	0	2	0	0	0	0	0	0
5. $MnSi_{0.5}O_2$	0.5	0	0	0	1	0	0	0	0	0
6. Mg_2SiO_4	1	0	0	0	0	2	0	0	0	0
7. $Ca_2Si_2O_6$	2	0	0	0	0	0	2	0	0	0
8. $NaSi_{0.5}O_{1.5}$	0.5	0	0	0	0	0	0	1	0	0
9. $KAlSiO_4$	1	0	1	0	0	0	0	0	1	0
10. $Ca_3(PO_4)_2$	0	0	0	0	0	0	3	0	0	2

In the above matrix, Ghiorso et al.'s (2002) melt components (SiO_2, Mg_2SiO_4, $Ca_2Si_2O_6$, et.) are in rows, and each component is expressed in terms of the number of oxides that make up each molecular component. For example, in row 5, the component $MnSi_{0.5}O_2$ is the sum of 1 unit of MnO and 0.5 units of SiO_2. All other row entries are zero

Geothermometry and Geobarometry, Table 2 Inverse of matrix of Table 1

	SiO_2	TiO_2	Al_2O_3	Fe_2SiO_4	$MnSi_{0.5}O_2$	Mg_2SiO_4	$Ca_2Si_2O_6$	$NaSi_{0.5}O_{1.5}$	$KAlSiO_4$	$Ca_3(PO_4)_2$
1. SiO_2	1	0	0	0	0	0	0	0	0	0
2. TiO_2	0	1	0	0	0	0	0	0	0	0
3. $AlO_{1.5}$	0	0	0.5	0	0	0	0	0	0	0
4. FeO	−0.5	0	0	0.5	0	0	0	0	0	0
5. MnO	−0.5	0	0	0	1	0	0	0	0	0
6. MgO	−0.5	0	0	0	0	0.5	0	0	0	0
7. CaO	−1	0	0	0	0	0	0.5	0	0	0
8. $NaO_{0.5}$	−0.5	0	0	0	0	0	0	1	0	0
9. $KO_{0.5}$	−1	0	−0.5	0	0	0	0	0	1	0
10. $PO_{2.5}$	1.5	0	0	0	0	0	−0.75	0	0	0.5

Geothermometry and Geobarometry, Table 3 Example of converting a liquid composition from weight % oxides to molecular components

Liquid composition	SiO_2	TiO_2	Al_2O_3	FeO	MnO	MgO	CaO	Na_2O	K_2O	P_2O_5
1. Weight %	50.25	2.8	14.59	12.96	0.2	5.2	10.17	2.69	0.94	0.74
	SiO_2	TiO_2	$AlO_{1.5}$	FeO	MnO	MgO	CaO	$NaO_{0.5}$	$KO_{0.5}$	$PO_{2.5}$
2. Cation proportions	0.836	0.035	0.286	0.180	0.003	0.129	0.181	0.087	0.020	0.010
3. Cation fractions	0.473	0.020	0.162	0.102	0.002	0.073	0.103	0.049	0.011	0.006
	SiO_2	TiO_2	Al_2O_3	Fe_2SiO_4	$MnSi_{0.5}O_2$	Mg_2SiO_4	$Ca_2Si_2O_6$	$NaSi_{0.5}O_{1.5}$	$KAlSiO_4$	$Ca_3(PO_4)_2$
4. MELT comp prop	0.255	0.020	0.075	0.051	0.002	0.036	0.047	0.049	0.011	0.003
5. MELT components	0.464	0.036	0.137	0.093	0.003	0.066	0.085	0.089	0.020	0.005

Row 1 is a liquid composition expressed in weight % of oxides. Row 2 provides oxides as cation proportions (only one cation per oxide unit), so the weight % of Al_2O_3, for example, is divided by the molecular weight of $AlO_{1.5}$. Row 3 is a renormalization of row 2 to provide a cation fraction (sum = 1). Row 4 gives the MELT components expressed as proportions; it is the product row matrix obtained by multiplying the row matrix Row 3 by the square matrix, Table 2, which converts the oxides to the molecular components shown in Tables 1 and 2. MELTS also calculates Si and Al as Si_4O_8 and Al_4O_6; to obtain these, use 4 atoms each of Si and Al in rows 1 and 3 of Table 1a. Row 5 is a renormalization of Row 4.

T_f^{An} are the fusion temperatures of pure An, and T is the T of the mixture in question. Equations 26a and 26b can be obtained from Bowen (1913) and Van Laar (1906); they are general and can be applied to any two-component system. In these equations, ΔH_f^{An} and ΔH_f^{Ab} are the heats of fusion of pure anorthite and pure albite at 1 atm. We can obtain these by regressing Bowen's (1913) experiments, using Eqn. 18 (where $\Delta V_r = 0$, since the experiments are performed at 1 atm) and (25a) and using $K_{eq}^{An-liq} = X_{An}^{pl}/X_{An}^{liq}$. This yields $\Delta H_f^{An} = 115$ kJ/mole and $\Delta H_f^{Ab} = 56$ kJ/mole, which, if inserted into Eqs. 26a and 26b, unsurprisingly fit Bowen's (1913) experiments quite well (Fig. 4b) – slightly better than Bowen's reported values of $\Delta H_f^{Ab} = 53$ and $\Delta H_f^{An} = 121$ kJ/mole.

Can we then use $\Delta H_f^{An} = 115$ kJ/mole (and $\Delta S_f^{An} = 63$ J/mole, from the same regression) in Eq. 18 to obtain a plagioclase thermometer? Despite Bowen's (1913) excellent

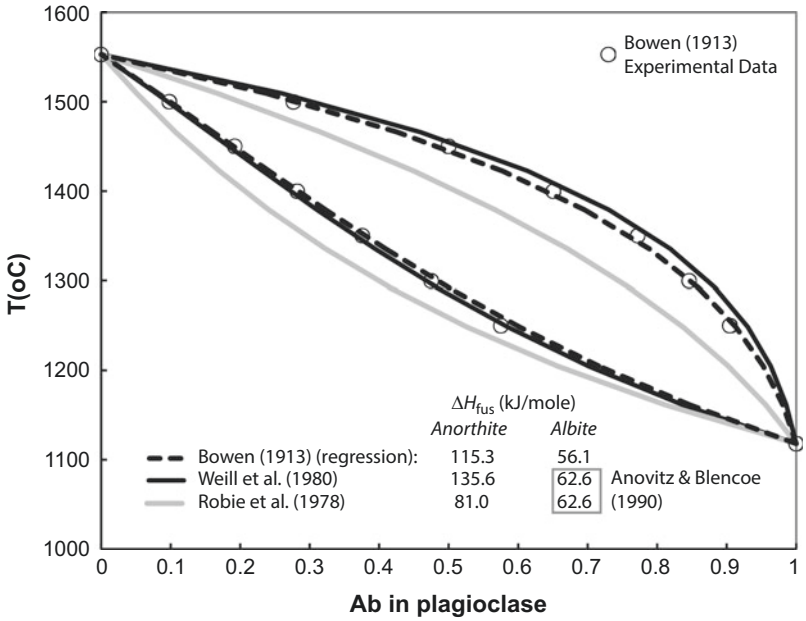

Geothermometry and Geobarometry, Fig. 4 The anorthite-albite (An-Ab) binary phase diagram. Experimental data (*circles*) are from Bowen (1913); the *dashed* phase loop is derived by regression of Eq. 18 using the Bowen (1913) data, to obtain heats of fusion for Ab and An (rather than Bowen's reported values, which are slightly different). For comparison, the phase loops using the Ab enthalpy of fusion of Anovitz and Blencoe (1999) and An enthalpies of fusion from Weill et al. (1980; *black curves*) and Robie et al. (1978; *gray curves*) are shown

experiments, calorimetric work yields different values for ΔH_f^{An} : Weill et al. (1980) and Richet and Bottinga (1986) obtain $\Delta H_f^{An} = 135.6$ and 134.0kJ/mole , respectively (identical within a ± 10 kJ/mole error); and Anovitz and Blencoe (1999) obtain $\Delta H_f^{Ab} = 62.6$kJ/mole . These estimates do not fit Bowen's (1913) data nearly as well (Fig. 4).

However, the misfit obtained using $\Delta H_f^{\mathrm{An}} = 135$kJ/mole may mean that we are using the wrong activity model $\left(K_{eq}^{An-liq} = X_{An}^{pl}/X_{An}^{liq}\right)$. We let $a_{An}^{pl} = X_{An}^{pl} = X_{CaO}^{pl}/\left[X_{CaO}^{pl} + X_{NaO_{0.5}}^{pl} + X_{KO_{0.5}}^{pl}\right]$. Instead, let us use Eq. 24, $K_{eq}^{An-liq} = a_{An}^{pl}/\left(X_{CaO}^{\mathrm{liq}}\left(X_{AlO_{1.5}}^{liq}\right)^2\left(X_{SiO_2}^{liq}\right)^2\right)$, and the Holland and Powell (1992) activity model, $a_{An}^{pl} = 16X_{Ca}^{pl}\left(X_{Al(T)}^{pl}\right)^2\left(X_{Si(T)}^{pl}\right)^2$, where X_{Ca}^{pl} is the fraction of Ca on the A site in plagioclase (effectively $\mathrm{Ca} = X_{CaO}^{pl}/\left[X_{CaO}^{pl} + X_{NaO_{0.5}}^{pl} + X_{KO_{0.5}}^{pl}\right]$) and $X_{Al(T)}^{pl}$ and $X^{pl}{}_{Si(T)}$ are the fractions of Al and Si on the tetrahedral sites (so $X_{Si(T)}^{pl} = X_{SiO_2}^{pl}/\left(X_{SiO_2}^{pl} + X_{AlO_{1.5}}^{pl}\right)$). This yields $\Delta H_f^{\mathrm{An}} = 139$kJ/mole for Bowen's (1913) data, which is within error of the Weill et al. (1980) and Richet et al. (1982) results.

Is this a victory for Holland and Powell? Not really. If our K_{eq} term and the activity models contained therein account for the free energy of mixing, then we should always recover the calorimetric value of ΔH_f^{An} – it should not change if we regress a different set of compositions. Table 4 shows regression results at 1 atm for anhydrous partial melting experiments performed on natural bulk compositions; each activity model yields a different value for ΔH_f^{An}, and for the natural data, the Holland and Powell (1992) model yields 19.6 kJ/mole.

Geothermometry and Geobarometry, Table 4 $\Delta H_{\mathrm{fus}}^{\mathrm{An}}$ (as $CaAl_2Si_2O_8$) in kJ/mole from regression (Eq. 18) using different activity models and experimental data (from Bowen 1913, and 1 bar anhydrous experiments on natural compositions)

Activity model for K_{eq}	Bowen (1913)	Natural data[a]
Ideal oxides[b]	152.7	35.2
Ghiorso and Sack (1995)[c]	89.1	45.7
Ghiorso et al. (2002)[d]	67.0	18.7
Nielsen and Drake (1979)[e]	300.4	**139.6**
Elkins-Tanton and Grove (1990)[f]	171.5	55.2
Holland and Powell (1992)[g]	**139.5**	19.6
H&P92 + N&D79[h]	287	124
Calorimetry[i]	**135 ± 9**	

[a]Experimentally equilibrated plagioclase + liquid, using natural bulk compositions; Anhydrous, 1 atm
[b]Activity of An $a(\mathrm{An}) = X_{CaO}{}^{pl}/(X_{CaO}{}^{pl} + X_{Na2O}{}^{pl} + X_{K2O}{}^{pl})$; $a(\mathrm{CaO})^{\mathrm{liq}} = X_{CaO}{}^{liq}$, $a(AlO_{1.5})^{liq} = X_{AlO1.5}{}^{liq}$, $a(SiO_2)^{liq} = X_{SiO2}{}^{\mathrm{liq}}$
[c]a(An) as in b; liquid components are as in Ghiorso and Sack (1995)
[d]a(An) as in b; liquid components are as in Ghiorso et al. (2002)
[e]a(An) as in b; liquid components are as in Nielsen and Drake (1979)
[f]Activities of liquid components as in b; a(An) as in Elkins-Tanton and Grove (1990)
[g]Activities of liquid components as in b; a(An) as in Holland and Powell (1992)
[h]The models of Holland and Powell (1992) and Nielsen and Drake (1979) are used together to define the activity of anorthite in plagioclase and the activity of melt components, respectively
[i]Calorimetric value for An heat of fusion, from Weill et al. (1980)

In contrast, Nielsen and Drake's (1979) activity model for liquid (liq) components (we revert back to $a_{An}^{pl} = X_{An}^{pl}$) yields 139 kJ/mole. Nielsen and Drake (1979), building on the work of Bottinga and Weill (1972), argue that silicate liquid cations fall into either network-forming (NF) sites, which consist of interconnected SiO_2, $NaAlO_2$, and $KAlO_2$ units, or "network-

modifying" (NM) sites, where NM = CaO + $AlO_{1.5}$ + FeO + MgO + MnO + $CrO_{1.5}$, and where NM cations disrupt the network. In Nielsen and Drake's (1979) model, $K_{eq}^{An-liq} = a_{An}^{pl} / \left(a_{CaO}^{liq}\left(a_{AlO_{1.5}}^{liq}\right)^2\left(a_{SiO_2}^{liq}\right)^2\right)$ where $a_{An}^{pl} = X_{An}^{pl} = X_{CaO}^{pl} / \left(X_{NaO_{0.5}}^{pl} + X_{KO_{0.5}}^{pl} + X_{CaO}^{pl}\right)$ and the activities of the liquid components are calculated as in Nielsen and Drake (1979): $a_{CaO}^{liq} = X_{CaO}^{liq}/\mathrm{NM}, a_{(AlO_{1.5})}^{liq} = \left(X_{(AlO_{1.5})}^{liq} - X_{(NaO_{0.5})}^{liq} - X_{(KO_{0.5})}^{liq}\right)/\mathrm{NM}$ and $a_{SiO_2}^{liq} = X_{SiO_2}^{liq} / \left(X_{SiO_2}^{liq} + X_{NaO_{0.5}}^{liq} + \mathrm{KO}_{0.5}^{liq}\right)$. And $a_{\mathrm{NaAlO_2}}^{\mathrm{liq}} = X_{\mathrm{NaO_{0.5}}}^{\mathrm{liq}} / \left(X_{NaO_{0.5}}^{liq} + X_{KO_{0.5}}^{liq} + X_{SiO_2}^{liq}\right)$.

What if we apply both Nielsen and Drake's (1979) and Holland and Powell's (1992) models? Then the 1 bar experiments using natural compositions yield $\Delta H_f^{\mathrm{An}} = 124\mathrm{kJ/mole}$, quite close to Bowen's (1913) original estimate but still short of the calorimetric value. But it is not clear that this represents a success, nor that the other activity models fail. MELTS successfully predicts plagioclase saturation temperatures for anhydrous liquids over a wide range of pressures (Putirka 2005). And while the very low ΔH_f^{An} values for some models would imply that they would make poor thermometers, this is not the case. In fact, the activity models have no impact upon thermometer calibration at all. Each of the models of Table 4, including one using simple cation fractions:

$$\frac{10^4}{T(K)} = 3.66 + 0.158\left[ln\left(\frac{X_{\mathrm{An}}^{\mathrm{pl}}}{X_{CaO}^{liq}\left(X_{AlO_{1.5}}^{liq}\right)^2\left(X_{SiO_2}^{liq}\right)^2}\right)\right] + 7.60\left[X_{KO_{0.5}}^{liq}\right] - 1.04\left[ln\left(X_{AlO_{1.5}}^{liq}\right)\right] - 0.013\left[ln\left(X_{NaO_{0.5}}^{liq}\right)\right] - 0.44\left[ln\left(X_{An}^{pl}\right)\right], \quad (27a)$$

yield thermometers that reproduce T for the anhydrous, 1 atm experimental data to within ±10–12 °C. The larger, often unappreciated issue is twofold: we do not understand activities well enough to fix the coefficients in Eq. 17 to theoretical values, and regression coefficients are sensitive to the kinds of parameters used in a model, the data used for regression, and the choice of independent variable. Regression analysis is a terrible way to determine thermodynamic parameters.

Worse still for activity modeling efforts, the two following equations show how some activity models, however justified by theory, actually impair our ability to predict T (or P). These two thermometers are calibrated using both anhydrous and hydrous data, at pressures of <3 kbar (low enough that we may ignore ΔV_r^o):

$$\frac{10^4}{T(K)} = 4.0 + 0.42\left[ln\left(\frac{X_{An}^{pl}}{X_{\mathrm{CaO}}^{liq}\left(X_{AlO_{1.5}}^{liq}\right)^2\left(X_{SiO_2}^{liq}\right)^2}\right)\right] - 2.92\left[X_{MgO}^{liq}\right] - 0.71\left[ln\left(X_{An}^{pl}\right)\right] + 0.2\left[C_{H_2O}^{liq}\right] \quad (27b)$$

$$\frac{10^4}{T(K)} = 6.13 + 0.19\left[ln\left(\frac{a_{An}^{pl}}{a_{CaO}^{liq}\left(a_{AlO_{1.5}}^{liq}\right)^2\left(a_{SiO_2}^{liq}\right)^2}\right)\right] - 6.24\left[a_{NaAlO_2}^{liq}\right] + 2.01\left[X_{Ab}^{pl}\right] + 0.26\left[C_{H_2O}^{liq}\right] \quad (27c)$$

As in Eq. 27a, all liquid components in Eqn. 27b, except for H_2O are cation fractions (X_i), (row 3 of Table 3), and $X_{An}^{pl} = X_{CaO}^{liq} / \left(X_{NaO_{0.5}}^{liq} + X_{KO_{0.5}}^{liq} + X_{CaO}^{liq}\right)$. In both equations, $C_{H_2O}^{liq}$ is the concentration of H_2O in a liquid, expressed in weight %. In Eq. 27c, all liquid components, except for H_2O, are as in Nielsen and Drake (1979), and a_{An}^{plag} is from Holland and Powell; X_{Ab}^{pl} is the cation fraction $X_{NaO_{0.5}}^{pl} / \left(X_{NaO_{0.5}}^{pl} + X_{KO_{0.5}}^{pl} + X_{CaO}^{pl}\right)$. The coefficients 0.42 and 0.19 in Eqs. 27b and 27c, respectively, translate to $\Delta H_f^{An} = 198$ and 438kJ/mole. No longer do the Holland and Powell (1992) and Nielsen and Drake (1979) activity models yield even remotely close approximations of calorimetric ΔH_f^{An}. Moreover, Holland and Powell's (1992) model does not save us from requiring a correction to the activity of An-in-plagioclase (the $\ln\left(X_{An}^{pl}\right)$ term), which is needed by both models to obtain the most precise T estimates possible. But finally, and most importantly, Eq. 27b actually *extrapolates better* than Eq. 27c, *providing better predictions of T for data not used in regression*. Both equations recover T for calibration data (n = 337; 850–1,244 °C, 1 atm to 3 kbar, and 0–8% H_2O) with comparable errors (±19 °C for Eq. 27a; ±21 °C for Eq. 27b). But Eq. 27b predicts T to ±55 °C for the test data, (n = 912) compared to ±67 °C for Eq. 27c (test data range from 1 atm to 27 kbar, 700–1,430 °C, and 0–19% H_2O). And Eq. 27b exhibits less systematic error: for a

regression of test data of $T^{predicted}$v . $T^{measured}$, Eq. 27b yields a slope and intercept of 0.99 and 25 °C, compared to a slope and intercept of 0.88 and 144 °C when $T^{predicted}$ is from Eq. 27c.

Summary

Part I: Guidelines for Calibration of a Thermobarometer

The above examples, of Ti-in-quartz, Al-in-hornblende, and plagioclase thermometry, reveal that thermodynamic theory provides the correct form of the equations needed for thermobarometry, but parameter coefficients are not easily defined. With this in mind, we end this section with guidelines for the calibration and application of geothermobarometers:

1. ***Select calibration data with care***. Bad data in a calibration will yield a bad model; the hallmarks of good data are those that are reproducible by other laboratories. There are no other simple or easy tests that allows one to say that one set of data are good and another are bad. A useful strategy is to look for data that are coherent (e.g., $\ln K_{eq}$ is highly correlated to $1/T$, as in Wark and Watson 2006) among multiple laboratories.
2. ***Use test data***. These are data that are not used for calibration. They are invaluable to calibrations, activity models, etc., as shown above for a plagioclase-liquid thermometer.
3. ***Use linear least squares when possible***. This approach allows error analysis on individual terms, and the regression-derived coefficients are certain to minimize error on the dependent variable. Nonlinear methods lack these qualities.
4. ***Isolate the quantity of interest (P or T) as the dependent variable***. As emphasized in Putirka (2008), and noted above, regression is not a symmetric method: errors reduced on y, in $y = mx + b$, will not minimize error on predictions of x, when rearranged. A new equation, using x as the dependent variable, is needed if x is to be calculated.
5. ***Use as few parameters as possible (and leverage tests)***. This is Occam's Razor, which has a statistical basis (Jefferys and Berger 1992), and is required by limits on experimental precision. For example, we know that ΔC_p is not zero, but terms such as $\ln\left[\frac{T}{T_o}\right]$ (Eqn. 17) rarely reduce error. Leverage plots from linear least squares are also useful, by allowing one to delete parameters that are controlled by just one or a few, possibly errant, data. Adding poorly supported terms can affect all other model coefficients, rendering a model less precise when used to predict P or T.

Part II: Guidelines for Applying Thermobarometers to Nature

Mineral compositions are important and powerful because of their often slow rates of diffusion at near-surface temperatures. A resistance to re-equilibration means that the samples we collect at the surface today preserve a P-T record of geologic processes of the past. But thermobarometers are based on ideas of equilibrium, and we sometimes need to infer or reconstruct an equilibrium state to infer P and T. In igneous systems, this is especially problematic because magma mixing, a ubiquitous process, mingles crystals with magmas from which they did not crystallize. The following guidelines may minimize the probability that our inferences of P and T go astray:

1. *Compare independent estimates of P and/or T*. Direct tests trump inferential ones, as shown above for the BT, keeping in mind that T (and P) estimates need not match, if minerals saturate at different temperatures (and pressures, e.g., Putirka and Condit 2003). This approach is no better illustrated than in Klügel and Klein (2005), who show that fluid inclusions and mineral-melt barometers yield convergent estimates for P of partial crystallization for the Madeira volcanic system. And Anderson (1996b) obtains P-T estimates of granitic rocks using both metamorphic and igneous equilibria. Putirka (2016b) also shows a convergence of amphibole and clinopyroxene barometers at some arcs. But also important are correlated estimates. In Hawaii, olivines yield higher temperatures than clinopyroxene, but the T contrast matches that predicted from phase equilibria (Putirka 1997), and the T ranges are remarkably similar (so we are apparently truly differentiating high and low T samples).
2. *Error should be well defined; averaged estimates are better*. Reported model errors, when quantified, are a *minimum estimate of actual error when predicting P or T in a natural system*, at least on individual estimates. Averaged P and T estimates are likely to be more accurate (Powell and Holland 1994). For example, Putirka et al. (1996) show that a clinopyroxene-liquid barometer has a precision of ±1.5–2.0 kbar for individual estimates but, when averaged, might be as low as ±0.7 kbar. This is evident in low P experiments where the models can yield negative pressures; but small negative estimates are not necessarily wrong. A series of clinopyroxenes, yielding pressures of, say −2 kbar to +3 kbar, can converge to a correct answer (1 kbar) in both experiments and in nature.
3. *Roozeboom diagrams and tests for equilibrium*. Lacking independent thermobarometers, tests for equilibrium are vital. Perhaps the single most successful example is the Fe-Mg exchange coefficient, developed by Roeder and Emslie (1970) for olivine + liquid equilibrium and

G

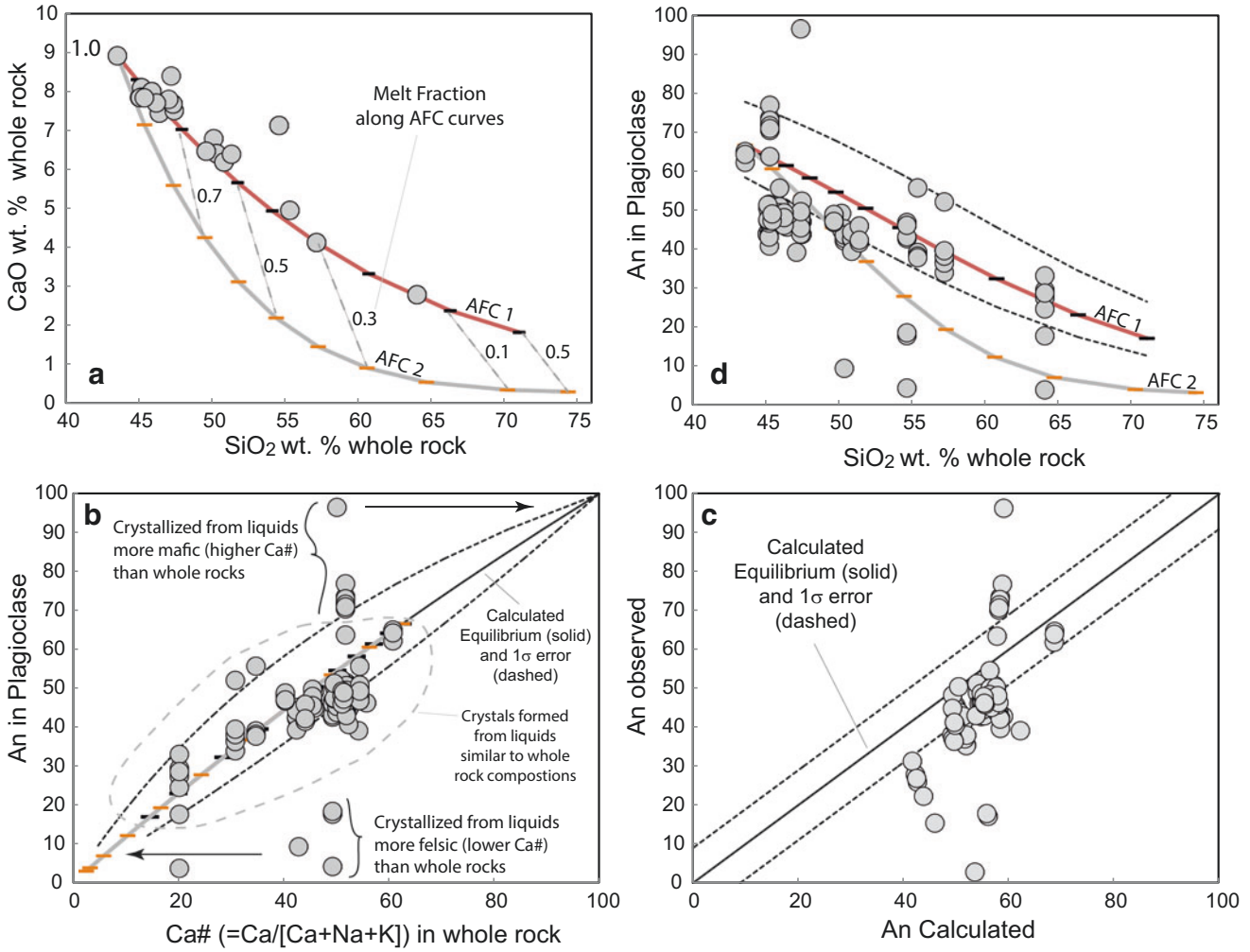

Geothermometry and Geobarometry, Fig. 5 An illustration of how to reconstruct equilibrium liquid compositions that would be paired with mineral compositions so as to predict *P* and *T* for igneous systems. (**a**) A variation diagram for whole-rock compositions from the Craters of the Moon Lava Field, ID (Putirka et al. 2009). The *gray* and *red curves* show AFC curves that use a primitive COM magma as a parent magma and an Idaho Batholith granite (AFC1) and a COM rhyolite xenolith (AFC2) as possible felsic end-members; hachures indicate melt fraction. (**b**) A Roozeboom-type diagram comparing Ca# for both Plagioclase and liquid. Ca# is the molar ratio $CaO/(CaO+NaO_{0.5}+KO_{0.5})$ in either a liquid or solid phase, and is equal to the An content in plagioclase. The solid *black line* is the inferred equilibrium ratio for Ca# determined from plagioclase-saturated experiments (LEPR); *dashed lines* show 1σ error. Some crystals are allowably in equilibrium with liquids that are similar to observed whole-rock compositions. (**c**) Shows a test of observed versus calculated An contents assuming that whole rocks act as liquids; *T* is calculated from model A of Putirka (2005), assuming *P* estimates in Putirka et al. (2009) and $H_2O = 0\%$. With these conditions, plagioclase An fractions (which are multiplied by 100 in the charts) are predicted using: $An = \exp(-2.13+3.74[X^{liq}_{AlO_{1.5}}]+13.97[X^{liq}_{CaO}]-25.44[KO^{liq}_{0.5}] - 31.6[P(kbar)]/T(K)+0.108[Mg\#^{liq}] + 829.9/T(K) + 157.96[KO^{liq}_{0.5}][X^{liq}_{AlO_{1.5}}] - 18.42[SiO^{liq}_2][X^{liq}_{CaO}])$. Clearly, plagioclase with very high and low An (**b** and **c**) must be derived from liquids with higher- and lower- than- observed $Ca\#^{liq}$ compared to whole rocks. Magma mixing homogenizes magma compositions, but mineral compositions at least partially preserve felsic and mafic end-member magma compositions. (**d**) Comparison of an contents with whole rock SiO_2; here, we use the bulk compositions generated along AFC1 in (**a**) to predict equilibrium An contents for such liquids using the equation just noted, with error bounds noted by dashed lines. The gray circles are the measured An contents compared to their host whole rock SiO_2. The *curve* AFC1 better describes the whole rock trend, but AFC2 can explain low An crystals. For example, plagioclase of <10% An content can equilibrate from liquids (along AFC2) that have 70–75% SiO_2. Whole rocks with such SiO_2 contents are not erupted at the COM, but low An crystals provide evidence that such high SiO_2 liquids existed prior to mixing with mafic magmas

employed in the Rhodes Diagram that compares the Mg# of Ol and liq (Putirka 2008). Through experiments and thermodynamic arguments, Roeder and Emslie showed that ΔH^o_r and ΔV^o_r are sufficiently small for the reaction between forsterite ($MgSi_{0.5}O_2$) and fayalite ($FeSi_{0.5}O_2$):

$$MgSi_{0.5}O_2 + FeO^{liq} = FeSi_{0.5}O_2 + MgO^{liq} \qquad (28a)$$

such that P and T do not affect K_{eq}:

$$K_{eq}^{ol-liq} = \frac{\left(a_{Fa}^{ol}\right)\left(a_{MgO}^{liq}\right)}{\left(a_{Fo}^{ol}\right)\left(a_{FeO}^{liq}\right)} \quad (28b)$$

To ease calculation, instead of using K_{eq} (Eq. 28b), Roeder and Emslie (1970) defined an exchange coefficient:

$$K_{D}^{ol-liq} = \frac{\left(X_{FeO}^{ol}\right)\left(X_{MgO}^{liq}\right)}{\left(X_{MgO}^{ol}\right)\left(X_{FeO}^{liq}\right)} \quad (28c)$$

Equation 28c is an approximation of Eq. 28b, where X_{Feo}^{ol} is a proxy for a_{Fa}^{ol}. Roeder and Emslie (1970) use only Fe^{2+} in liquid (FeO) in Eq. 28c, which removes the effect of oxygen fugacity (fO_2). Subsequent studies have shown that K_D^{ol-liq} is not greatly affected by composition or P (Putirka 2016b). This type of coefficient is something of a holy grail in petrology and is used for other igneous phases. If we let $X_{FeO}^{ol} = X_{FeOt}^{ol}$ (where FeO is total Fe, which introduces fO_2 sensitivity), then coefficients of the type $K_D^{\phi 1-\phi 2}$ (where ϕ_1 and ϕ_2 are coexisting, potentially equilibrated, phases) have similar values for a number of mineral-melt pairs, such as olivine (0.30; Roeder and Emslie 1970; Putirka 2016a), clinopyroxene (0.27; Putirka 2008), orthopyroxene (0.28; Beattie 1993), and amphibole (0.28; Putirka 2016b); the approach can even be applied to feldspars (0.55; Longhi et al. 1976).

The problem with this approach is that different equilibria can equilibrate at different rates. Due to higher expected rates of diffusion for Fe^{2+} and Mg^{2+}, compared to Al^{3+} (Brady and Cherniak 2010), for example, a clinopyroxene + liquid system may exhibit Fe-Mg exchange equilibrium, but not reflect equilibration with respect to the jadeite + liquid components that are used to estimate P. This approach is thus not a substitute for independent estimates of T and P although some experiments indicate that cooling rates might be obtained from systematic departures from equilibrium (Mollo et al. 2013a, b).

4. *Correcting igneous compositions and additional tests.* Igneous systems pose unique challenges to the application of thermobarometers since equilibrated crystals and liquids are easily separated from one another. Equilibrium tests can be applied to reconstruct possible equilibrium systems. Whole rock and plagioclase compositions from the Craters of the Moon (COM) Lava field (Putirka et al. 2009) provide an example. As a test of plagioclase + liquid equilibrium, we can use a Na-Ca exchange coefficient:

$$K_{D}^{pl-liq} = \frac{\left(X_{NaO_{0.5}}^{pl}\right)\left(X_{CaO}^{liq}\right)}{\left(X_{CaO}^{pl}\right)\left(X_{NaO_{0.5}}^{liq}\right)} \quad (29)$$

This coefficient ranges widely, but not systematically with P, or T, and except for H_2O, it is not affected by liquid or mineral compositions. Silicate liquids containing <0.5 wt. % H_2O yield a mean value of 0.84 ± 0.36, while hydrous systems (or systems at T<1,050 °C) yield a mean value somewhere between 0.38 ± 0.17 (n = 362) and 0.30 ± 0.09 (n = 313), depending upon which data are used.

The error on the coefficients (e.g., ±0.36) may seem broad, but the model is still effective. Figure 5a compares weight % values of CaO and SiO_2 for COM whole-rock compositions, with an assimilation-fractional crystallization (AFC 1) curve that explains their compositional variation (see Putirka et al. 2009). But Fig. 5b, making use of Eq. 29, reveals that not all plagioclase crystals formed from liquids that approximate observed whole-rock compositions. Figure 5c illustrates an independent test of the same idea: here we compare the observed An contents of plagioclase to those predicted to precipitate if the whole-rock compositions are liquids. Of course, magma mixing is a likely explanation for the discrepancy. But nonequilibrated plagioclase grains can tell us about pre-magma mixing conditions.

Figure 5d perhaps shows the issue more intuitively, where we again use Eq. 29 to compare plagioclase grains and whole rocks. Clearly, a given whole-rock composition can contain a wide range of plagioclase compositions – but it cannot be in equilibrium with all of them. Curve AFC2 shows how it might explain at least some of the dis-equilibrium plagioclase compositions (Fig. 5a). This curve does not reproduce whole-rock compositions, but the high SiO_2 liquids (70–75% SiO_2) produced along AFC2 have Ca# values that can produce the observed crystals with the lowest An content, which cannot be produced by liquids that look like the whole rocks themselves. A plausible explanation is that high SiO_2 liquids were indeed produced by a process like AFC2, but either were not erupted or were homogenized with mafic liquids to yield whole rocks with <64% SiO_2.

The key approach here is to explore a range of possible liquid compositions that are obtained by AFC, liquid lines of descent or mixing lines. These calculated liquids should simultaneously reproduce observed whole-rock compositions and yield mineral compositions that satisfy experimentally constrained conditions of equilibrium. A final test if possible, would be to compare multiple P and T estimates using such hypothetical liquids. When the convergences are numerous, such liquids and their calculated P-T conditions are likely to describe natural processes, rather than numerical accidents and so tell us something about Nature.

Cross-References

▶ Activity and Activity Coefficients
▶ Calorimetry

- Clapeyron's Equation
- Diffusion
- Enthalpy
- Entropy
- Equilibrium
- Equilibrium Constant
- Free Energy
- Fugacity
- Geochemical Thermodynamics
- Henry's Law
- Phase Equilibria
- Solid Solution/Exsolution
- Standard States

References

Althaus E (1967) The triple point andalusite-sillimanite-kyanite; an experimental and petrologic study. Contrib Mineral Petrol 16:29–44

Anderson GM (1996a) Thermodynamics of natural systems. Wiley, New York. 382 p

Anderson JL, Smith DR (1995) The effects of temperature and fO2 on the Al-in-hornblende barometer. Am Mineral 80:549–559

Anderson JL (1996b) Status of thermobarometry in granitic batholiths. Trans R Soc Edinb Earth Sci 87:125–138

Anderson DJ, Lindsley DH (1988) Internally consistent solution models for Fe- Mg-Mn-Ti oxides – Fe-Ti oxides. Am Mineral 73:714–726

Anderson DJ, Lindsley DH, Davidson PM (1993) QUILF – a Pascal program to assess equilibria among Fe-Mg-Mn-Ti oxides, pyroxenes, olivine, and quartz. Comput Geosci 19:1333–1350

Anderson AT, Davis AM, Lu F (2000) Evolution of Bishop Tuff rhyolite magma based on melt and magnetite inclusions and zoned phenocrysts. J Petrol 41:449–473

Anderson JL, Barth AP, Wooden JL, Mazdab F (2008) Thermometers and thermobarometers in granitic systems. In: Putirka KP, Tepley (eds) Minerals, inclusions and volcanic processes. Reviews in mineralogy and geochemistry, Mineralogical Society of America, Washington D.C. vol 69. pp 121–142.

Anovitz LM, Blencoe JG (1999) Dry melting of high albite. Am Mineral 84:1830–1842

Barrow G (1893) On an intrusion of muscovite-biotite gneiss in the south-eastern Highlands of Scotland, and its accompanying metamorphism. Q J Geol Soc 49:330–358

Barth TFW (1934) Temperaturen I lava- og magmamasser samt et nytt geologisk thermometer. Nature 8:187–192

Barth TFW (1951) The feldspar geologic thermometers. Neues Jb Mineral 82:143–153

Barus C (1893) High temperature work in igneous fusion and ebullition, chiefly in relation to pressure. U.S. Geological Survey Bulletin, vol 103. Government Printing Office, Washington, DC

Beattie P (1993) Olivine-melt and orthopyroxene-melt equilibria. Contrib Mineral Petrol 115:103–111

Berman RG (1988) Internally-consistent thermodynamic data for minerals in the system Na_2O-K_2O-CaO-MgO-FeO-Fe_2O_3-Al_2O_3-SiO_2-TiO_2-H_2O-CO_2. J Petrol 29:445–522

Beyer C, Frost DJ, Miyajima N (2015) Experimental calibration of a garnet-clinopyroxene geobarometer for mantle eclogites. Contrib Mineral Petrol 169:18

Blundy JD, Holland TJB (1990) Calcic amphibole equilibria and a new amphibole-plagioclase geothermometer. Contrib Mineral Petrol 104:208–224

Bohlen SR, Lindsley DH (1987) Thermometry and barometry of igneous and metamorphic rocks. Annu Rev Earth Planet Sci 15:397–420

Bohlen SR, Montana A, Kerrick DM (1991) Precise determination of the equilibria kyanite = silliaminate and kyanite = andalusite and a revised triple point for Al_2SiO_5 polymorphs. Am Mineral 76:677–684

Bottinga Y, Weill DF (1972) The viscosity of magmatic silicate liquids: a model for calculation. Am J Sci 272:438–475

Bowen NL (1913) The melting phenomena of the plagioclase feldspars. Am J Sci 35: 577–599

Bowen NL (1940) Progressive metamorphism of siliceous limestone and dolomite. J Geol 48:225–274

Brady JB, Cherniak DJ (2010) Diffusion in minerals: an overview of published experimental diffusion data. In: Zhang Y, Cherniak DJ (eds) Diffusion in minerals and melts. Reviews in mineralogy and geochemistry, Mineralogical Society of America, Washington D.C. vol 72. pp 899–920

Buddington AF, Lindsley DH (1964) Iron-titanium oxide minerals and synthetic equivalents. J Petrol 5:310–357

Caddick MJ, Thompson AB (2008) Quantifying the tectono-metamorphic evolution of politic rocks from a wide range of tectonic settings: mineral compositions in equilibrium. Contrib Mineral Petrol 156:177–195

Chamberlain KJ, Morgan DJ, Wilson CJN (2014) Timescales of mixing and mobilization in the Bishop Tuff magma body: perspectives from diffusion chronometry. Contrib Mineral Petrol 168. https://doi.org/10.1007/s00410-014-1034-2

Clapeyron E (1834) Memoir on the motive power of heat. J Ecole R Polytech 23:153–190, in Taylor's Scientific Memoirs, 14:153–190, article 15

Cusack R (1896) On the melting points of minerals. Proc R Ir Acad 4:399–413

Day AL, Sossman RB (1911) The melting points of minerals in light of recent investigations on the gas thermometer. Am J Sci 31:341–349

Doelter C (1901) Ueber die bestimmung der schmelzpunkte bei mineralien und gesteinen. Tschermaks Mineral Petrogr Mitt 20:210–232

Elkins LT, Grove TL (1990) Ternary feldspar experiments and thermodynamic models. Am Mineral 75:544–559

Essene EJ (1982) Geologic thermometry and barometry. In: Ferry JM (ed) Characterization of metamorphism through mineral equilibria. Reviews in mineralogy, vol 10. Mineralogical Society of America, Washington, DC, pp 153–206

Evans BW (2007) In: Wood BJS (Ser ed) Landmark papers: metamorphic petrology. Mineralogical society of Great Britain and Ireland, Middlesex, United Kingdom, vol 3, p 232

Evans BW, Hildreth W, Bachmann O, Scaillet B (2016) In defense of magnetite-ilmenite thermometry in the Bishop Tuff and its implications for gradients in silicic magma reservoirs. Am Mineral 101:469–482

Ferry JM, Watson EB (2007) New thermodynamic models and revised calibrations for the Ti-in-zircon and Zr-in-rutile thermometers. Contrib Mineral Petrol 154:429–437

Gardner JE, Befus KS, Gualda GAR, Ghiorso MS (2014) Experimental constraints on rhyolite-MELTS and the Late Bishop Tuff magma body. Contrib Mineral Petrol 168:1051. https://doi.org/10.1007/s00410-014-1051-1

Ghiorso MS, Sack RO (1995) Chemical mass transfer in magmatic processes IV. A revised and internally consistent thermodynamic mole for the interpolation and extrapolation of liquid-solid equilibria in magmatic systems at elevated temperatures and pressures. Contrib Mineral Petrol 119:197–212

Ghiorso MS, Hischmann MM, Reiners PW, Kress VC (2002) The pMelts: a revision of MELTS for improved calculation of phase relations and major element partitioning related to partial melting of the mantle to 3 GPa. Geochem Geophys Geosyst 3:1030

Ghiorso MS, Evans BW (2008) Thermodynamics of rhombohedral oxide solid solutions and a revision of the Fe-Ti two-oxide geothermometer and oxygen barometer. Am J Sci 308:957–1039

Gibbs JW (1874–1878) On the equilibrium of heterogeneous substances. Trans Connecticut Acad Arts Sci 111:101–524

Goldschmidt VM (1912) Die gesetze der gesteinsmetamorphose mit beispielen aus der geoloigie des sudlichen norwegens, Skrifter utgit av Videnskapsselskapet I Kristiania, I. Matematisk-Naturvidenskabelig Klasse 22

Guldberg CM, Waage P (1864) Studies concerning affinity. C.M. Forhandlinger: Videnskabs-Selskabet i Christiana, 35; Translator: EW Lund (1965). J Chem Educ 42:548–550

Guldberg CM, Waage P (1879) Ueber die chemische affinitat. J Prakt Chem 127:69–114

Hall J (1790) Observations on the formation of granite. Trans R Soc Edinb 3:8–12

Hall J (1798) Experiments on whinstone and lava. Trans R Soc Edinb 5:43–75

Hammerstrom JM, Zen E (1986) Aluminum in hornblende: an empirical igneous geobarometer. Am Mineral 71:1297–1313

Hansteen TH, Klugel A (2008) Fluid inclusion thermobarometry as a tracer for magmatic processes. In: Putirka KD, Tepley F (eds). Reviews in mineralogy and geochemistry, Mineralogical Society of America, Washington D.C. vol 69. pp 143–177

Hansteen TH, Klugel A, Schminke H-U (1998) Multi-stage magma ascent beneath the Canary Islands: evidence from fluid inclusions. Contrib Mineral Petrol 132:48–64

Hayden LA, Watson EB (2007) Rutile saturation in hydrous siliceous melts and its bearing on Ti-thermometer of quartz and zircon. Earth Planet Sci Lett 258:561–568

Hildreth W, Wilson CJN (2007) Compositional zoning of the Bishop Tuff. J Petrol 48:951–999

Holdaway MJ, Mukhopadhyay B (1993) A reevaluation of the stability relations of andalusite: thermochemical data and phase diagram for the aluminum silicates. Am Mineral 78:298–315

Holdaway MJ (2001) Recalibration of the GASP geobarometer in light of recent garnet and plagioclase activity models and versions of the garnet-biotite geothermometer. Am Mineral 86:1117–1129

Holland TJB (1980) The reaction albite = jadeite + quartz determined experimentally in the range 600–1200 °C. Am Mineral 65:129–134

Holland T, Powell R (1992) Plagioclase feldspars: activity-composition relations based upon Darken's quadratic formalism and Landau theory. Am Mineral 77:53–61

Holland T, Blundy J (1994) Non-ideal interactions in calcic amphiboles and their bearing on amphibole-plagioclase thermometry. Contrib Mineral Petrol 116:433–447

Holland TJB, Powell R (1998) An internally consistent thermodynamic data set for phases of petrological interest. J Metamorph Petrol 16:309–343

Horstman AF (1877) Ueber ein dissociationsproblem, Aus den Verhandlungen d. Naturhist.-Med., Heidelberg. In: Ostwald's Klassiker der Exakten Wissenschaften, Leipzig, Germany, vol 137. pp 42–55

Howard J (1771) Observations on the heat of the ground on Mount Vesuvius. Philos Trans (1683–1775) 61:53–54

Huang RF, Audetat A (2012) The titanium-in-quartz (Ttani Q) thermobarometer: a critical examination and re-calibration. Geochim Cosmochim Acta 84:75–89

Iddings JP (1888) Obsidian Cliff, Yellowstone National Park. Government Printing Office, Washington, DC

Jefferys WH, Berger JO (1992) Ockham's razor and Bayesian analysis. Am Sci 80:64–72

Johannes W, Holtz F (1996) Petrogenesis and experimental petrology of granitic rocks. Minerals and rocks, vol 22. Springer, Heidelberg, 335 p

Joly J (1891) On the determination of the melting points of minerals. Part I. The uses of the meldometer. Proc R Ir Acad (1889–1901), 2:38–64

Jones HC (1899) The modern theory of solutions: memoirs by Pfeffer, Van't Hoff, Arrhenius, and Raoult. Harper and Brothers Publishers, New York. 133 p

Klügel A, Klein F (2005) Complex magma storage and ascent at embryonic submarine volcanoes from the Madeira Archipelago. Geology 34:337–340

Kohn MJ (2014) "Thermoba-Raman-try": calibration of spectroscopic barometers and thermometers for mineral inclusions. Earth Planet Sci Lett 388:187–196

Kohn MJ (2016) Metamorphic chronology – a tool for all ages: past achievements and future prospects. Am Mineral 101:25–42

Kohn MJ, Spear FS (1991a) Error propagation for barometers 1: accuracy and precision of experimentally located end-member reactions. Am Mineral 76:128–137

Kohn MJ, Spear FS (1991b) Error propagation for barometers 2: application to rocks. Am Mineral 76:138–147

Lange RA, Carmichael ISE (1987) Densities of Na_2O-K_2O-CaO-MgO-FeO-Fe_2O_3-Al_2O_3-TiO_2-SiO_2liquids: new measurements and derived partial molar properties. Geochim Cosmochim Acta 51:2931–2946

Lange RA, Navrotsky A (1992) Heat capacities of Fe_2O_3-bearing silicate liquids. Contrib Mineral Petrol 110:311–320

Lewis GN (1899) The development and application of a general equation for free energy and physio-chemical equilibrium. Contributions from the chemical laboratory of Harvard College. Proc Am Acad Arts Sci 35:3–38

Lewis GN (1901) The law of physico-chemical change. Proc Am Acad Arts Sci 37:49–69

Lewis GN (1907) Outlines of a new system of thermodynamics chemistry. Contributions from the research laboratory of physical chemistry of the Massachusetts Institute of Technology, no. 17. Proc Am Acad Arts Sci 43:259–293

Longhi J, Walker D, Hays JF (1976) Fe and Mg in plagioclase. Proc Lunar Sci Conf 7:1281–1300

Lund EW (1965) Guldberg and Waage and the law of mass action. J Chem Educ 42:548–550

Mollo S, Putirka K, Iezzi G, Scarlato P (2013a) The control of cooling rate on titanomagnetite composition: implications for a geospeedometry model applicable to alkaline rocks from Mt. Etna volcano. Contrib Mineral Petrol 165:457–475

Mollo S, Putirka K, Misiti V, Soligo M, Scarlato P (2013b) A new test for equilibrium-based on clinopyroxene-melt pairs; clues on the solidification temperatures of Etnean alkaline melts at post-eruptive conditions. Chem Geol 352:92–100

Mysen BO (1991) Relations between structure, redox equilibria of iron, and properties of magmatic liquids. In: Perchuk LL, Kushiro I (eds) Physical chemistry of magmas. Advances in physical chemistry, Springer-Verlag, New York, vol 9. pp 41–98

Navrtosky A (1995) Thermodynamic properties of minerals. Mineral physics and crystallography: a handbook of physical constants. AGU reference shelf 2. American Geophysical Union, Washington, DC, pp 18–28

Newman S, Lowenstern JB (2002) VolatileCalc: a silicate melt-H_2O-CO_2 solution model written in Visual Basic for Excel. Comp Geosci 28:597–604

Nielsen RL, Drake MJ (1979) Pyroxene-melt equilibria. Geochim Cosmochim Acta 43:1259–1272

Nielsen RL, Dungan MA (1983) Low pressure mineral-melt equilibria in natural anhydrous mafic systems. Contrib Mineral Petrol 84:310–326

Nimis P, Taylor WR (2000) Single clinopyroxene thermobarometry for garnet peridotites. Part I. Calibration and testing of a Cr-in-Cpx barometer and an enstatite-in-cpx thermometer. Contrib Mineral Petrol 139:541–554

Nordstrom DK, Munoz JL (1986) Geochemical thermodynamics. Blackwell, Palo Alto, p 477
Ostapenko GT, Tarashchan AN, Mitsyuk BM (2007) Rutile-quartz geobarometer. Geochem Int 45:506–508
Powell, R (1985) Regression diagnostics and robust regression in geothermometer/geobarometer calibration: the garnet-clinopyroxene geothermometer revisited. J Metam Geol 3:231–243
Powell R, Holland T (1994) Optimal geothermometry and geobarometry. Am Mineral 79:120–133
Powell R, Holland TJB, Worley B (1998) Calculating phase diagrams involving solid solutions via non-linear equations, with examples using THERMOCALC. J Metamorph Geol 16:577–588
Putirka K (1997) Magma transport at Hawaii: inferences based on igneous thermobarometry. Geology 25:69–72
Putirka KD (1998) Garnet + liquid equilibrium. Contrib Mineral Petrol 131:273–288
Putirka K (2005) Igneous thermometers and barometers based on plagioclase + liquid equilibria: test of some existing models and new calibrations. Am Mineral 90:336–346
Putirka KD (2008) Thermometers and barometers for volcanic systems. In: Putirka KD, Tepley F (eds) Reviews in mineralogy and geochemistry, Mineralogical Society of America, Washington D.C. vol 69. pp 61–120
Putirka K (2016a) Cooling rates and mantle potential temperatures (Tp) for Earth, Moon, Mars and Vesta, from new models for Tp, oxygen fugacity, ferric-ferrous ratios, and olivine-liquid Fe-Mg exchange. Am Mineral 101:819–840
Putirka K (2016b) Amphibole thermometers and barometers for igneous systems, and some implications for eruption mechanisms of felsicmagmas at arc volcanoes. Am Mineral 101:841–858
Putirka K, Condit CD (2003) Cross section of a magma conduit system at the margin of the Colorado Plateau. Geology 31:701–704
Putirka K, Johnson M, Kinzler R, Walker D (1996) Thermobarometry of mafic igneous rocks based on clinopyroxene-liquid equilibria, 0–30 kbar. Contrib Mineral Petrol 123:92–108
Putirka K, Kuntz M, Unruh D, Vaid N (2009) Magma evolution and ascent at the Craters of the Moon and neighboring volcanic fields, southern ID, USA: implications for the evolution of polygenetic and monogenetic fields. J Petrol 50:1639–1665
Raoult FM (1884) The general law of the freezing of solvents. Ann Chim Phys 2:66–93
Richardson SW, Gilbert MC, Bell PM (1969) Experimental determination of kyanite-andalusite and andalusite-sillimanite equilibria; the aluminum silicate triple point. Am J Sci 267:259–272
Richet P, Bottinga Y (1986) Thermochemical properties of silicate glasses and liquids: a review. Rev Geogr 24:1–25
Ridolfi, F, Renzulli A (2011) Calcic amphiboles in calc-alkaline and alkaline magmas: thermobarometeric and chemometric empirical equations valid up to 1,130oC and 2.2 GPa. Contrib Mineral Petrol. https://doi.org/10.1007/s00410-011-0704-6
Robie RA, Hemingway BS, Fisher JR (1978) Thermodynamic properties of minerals and related substances at 298.15 K and 1 bar (105 Pascals) and at higher temperatures. U. S. Geological Survey bulletin, vol 1452. Government Printing Office, Washington, DC, 456 p
Roedder E (1965) Liquid CO_2 inclusions in olivine-bearing nodules and phenocrysts from basalts. Am Mineral 50:1746–1782
Roeder PL, Emslie RF (1970) Olivine-liquid equilibrium. Contrib Mineral Petrol 29:275–289
Roozeboom HWB (1891) Uber die loslichkeit von mischkrystallen, speziell zweier isomorpher korper. Z Phys Chem 8:504–530
Ryerson FJ (1985) Oxide solution mechanisms in silicate melts: systematic variations in the activity coefficient of SiO_2. Geochim Cosmochim Acta 49:637–650
Scaillet B, Evans BW (1999) The 15 June 1991 eruption of Mount Pinatubo. I. Phase equilibria and pre-eruption *P-T-fO_2-fH_2O* conditions of the dacite magma. J Petrol 40:381–411
Spallanzani AL (1789) Travels in the two Sicilies and some are parts of the Apennines. Translated from the original Italian, vol II. G.G. and J. Robinson, Paternoster-Row
Spear FS (1993) Metamorphic phase equilibria and pressure-temperature-time paths. Mineralogical Society of America monograph. Mineralogical Society of America, Washington, DC, 799 p
Stebbins JF (2016) Glass structure, melt structure and dynamics: some concepts for petrology. Am Mineral 101:753
Thomas JB, Watson EB, Spear FS, Shmella PT, Nayak SK, Lanzirotti A (2010) TitaniQ under pressure: the effect of pressure and temperature on the solubility of Ti in quartz. Contrib Mineral Petrol 160:743–759
Thomas JB, Watson EB (2012) Application of the Ti-in-quartz thermobarometer to rutile-free systems. Reply to: a comment on: 'TitanQ under pressure: the effect of pressure and temperature on the solubility of Ti in quartz' by Thomas et al. Contrib Mineral Petrol 164:369:374
Thomas JB, Watson EB, Spear FS, Wark DA (2015) TitaniQ recrystallized: experimental confirmation of the original Ti-in-quartz calibrations. Contrib Mineral Petrol 169. https://doi.org/10.1007/s00410-015-1120-0
Thompson JB (1982) Composition space: an algebraic and geometric approach. Rev Mineral 10:1–31
Van der Waals JD (1891) Die grosse des druckes bei koexistierenden phasen von mischungen, besonders bei salz- und saure-losungen. Z Phys Chem 8:189–214
Van Laar JJ (1892) Zur thermodynamic der elektrolytischen dissociation. Z Phys Chem 10:242–254
Van Laar JJ (1906) Uber den verlauf der schmezkurven bei festen losungen (oder isomorphen gemischen) in einem speziellen fall. Z Phys Chem 55:435–441
Van't Hoff JH (1887) Die Rolle des osmotischen Druckes in der Analogie zwischen Losungen und gasen. Z Phys Chem 1:481–508
Van't Hoff JH (1896) Studies in chemical dynamics (trans: Ewan T). Williams and Norgate, London, 286 p
Von Crustschoff K (1885) Ueber ein neues typisches zirkonfiihrendes Gestein. Mineral Petrogr Mitt 6:172–177
Von Crustschoff K, Hofmann A (1881) XXV Notizen. Mineral Petrogr Mitt 4:536–538
Wark DA, Watson EB (2006) TitaniQ: a titanium-in-quartz geothermometer. Contrib Mineral Petrol 152:743–754
Wark DA, Hildreth W, Spear FS, Cherniak DJ, Watson EB (2007) Pre-eruption recharge of the Bishop magma system. Geology 35:235–238
Watson EB, Wark DA, Thomas JB (2006) Crystallization thermometers for zircon and rutile. Contrib Mineral Petrol 151:413–433
Weill DF, Stebbins JF, Hon R, Carmichael ISE (1980) The enthalpy of fusion of anorthite. Contrib Mineral Petrol 74:95–102
Wilson CJN, Seward TM, Allan ASR, Charlier BLA, Bello L (2012) A comment on: 'TitaniQ under pressure: the effect of pressure and temperature on the solubility of Ti in quartz' by Jay B. Thomas, E. Bruce Watson, Frank S. Spear, Philip T. Shemella, Saroj K. Nayak and Antonio Lanzirotti. Contrib Mineral Petrol 164:359–368
Wu CM (2015) Revised empirical garnet-biotite-muscovite-plagioclase geobarometer in metapelites. J Metamorph Petrol 33:167–176
Wu CM, Zhao GC (2007) The metapelitic garnet-biotite-muscovite-aluminosilicate-quartz (GBMAQ) geobarometer. Lithos 97: 365–372
Wu CM, Wang X-S, Yang C-H, Geng Y-S, Liu F-L (2002) Empirical garnet-muscovite geothermometry in metapelites. Lithos 62:1–13
Young DA (2003) Mind over magma. Princeton University Press, Princeton. 686 p

Germanium

Louis A. Derry
Department of Earth and Atmospheric Sciences, Cornell University, Ithaca, NY, USA

Element Data
Atomic Symbol: Ge
Atomic Number: 32
Atomic Weight: 72.63
Isotopes and Abundances: ^{70}Ge 20.57%, ^{72}Ge 27.45%, ^{73}Ge 7.75%, ^{74}Ge 36.50%, Ge ^{76} 7.73%
1 Atm Melting Point: 983.3 °C
1 Atm Boiling Point: 2820 °C
Common Valences: 2+, 4+
Ionic Radii: Ge^{4+} IV: 39 pm, Ge^{4+} VI: 53 pm, Ge^{2+} VI: 73 pm
Pauling Electronegativity: 2.01
First Ionization Potential: 762 kJ mol^{-1}
Chondritic (CI) Abundance: 33.2 ppm
Silicate Earth Abundance: 1.1 ppm
Crustal Abundance: 1.3 ppm
Seawater Abundance: 5–160 pmol kg^{-1}
Core Abundance: 28–41 ppm

Properties

Germanium has an atomic number of 32 and atomic weight of 72.63. It is both siderophile and volatile, with an electronic structure $[Ar]3d^{10}4s^24p^2$. Under the older CAS or IUPAC nomenclature Ge was classified as either group IVA or IVB, an unfortunately confusing situation. The modern IUPAC classification for Ge is in Group number 14. It is normally found in two oxidation states, Ge^{II} and Ge^{IV}, with Ge^{IV} the most common under Earth surface conditions. Germanium has five stable isotopes, as well as radioactive ^{68}Ge and ^{71}Ge with half lives of 271 and 11 days, respectively. Ge forms stable halides, including hydrides, fluoride and chlorides. Generation of GeH_4 in the laboratory is a useful analytical technique.

History and Use

The existence of an element with properties between those of silicon and tin and an atomic mass of 73 was first predicted by Newlands in 1864, while Mendeleev made specific and generally accurate predictions of the properties of "eka-silicon" in 1872. Winkler (1886) isolated this element from a silver sulfide and named it in honor of his country.

The largest industrial uses of germanium are in catalyst production, optics, and semiconductor manufacturing (Höll et al. 2007). Ge is obtained commercially as a by-product of zinc production, typically by volatilization of GeF_4 or $GeCl_4$ from Zn and Ge-enriched flue dusts. Ge is also produced from coal fly ash.

Geochemical Behavior

The condensation temperature for Ge from the solar nebula into Fe alloy is estimated to be 885 K, making it one of the more volatile elements (Lodder 2003). As a consequence, the bulk Ge terrestrial abundance is approximately a factor of 2–3 below the chondritic value, i.e., ≈11–16 ppm. Experimental data on metal-silicate partitioning implies that Ge is strongly partitioned into the core (Righter et al. 2011), which retains 92–95% of terrestrial Ge. The mantle has [Ge] ≈ 1 ppm, and the continental crust is slightly enriched at ≈1.3 ppm. The geochemical behavior of germanium has long been recognized to be similar to that of silicon, where it embodies the "principle of camouflage" and readily substitutes into lattice positions occupied by Si (Goldschmidt 1937; Goldsmith 1950).

Germanium dioxide has close affinities to SiO_2. Hexagonal GeO_2 has a 4-coordinated β-quartz structure, while tetragonal GeO_2 forms a 6-coordinated stishovite structure. A number of germanate analogs of alumino-silicate minerals have been synthesized. Ge can readily substitute for Si in common mineral structures, where it appears to form mostly ideal solid solutions. It is useful to characterize Ge abundances by the Ge/Si ratio, typically near 1×10^{-6} mol mol^{-1} (μmol mol^{-1}) in most silicates. Ge/Si appears to vary with crystal structure, with lower values in quartz (<1 μmol mol^{-1}), intermediate values in feldspars and olivine (1.5–3 μmol mol^{-1}), and higher values in sheet silicates (micas and clays, 4–7 μmol mol^{-1}) (Kurtz et al. 2002). Partition coefficients for Ge with common mantle minerals are mostly within a factor of two of unity, and so Ge/Si ratios in melts should closely reflect their source regions (Le Roux et al. 2015).

Although GeS_2 is rare as a mineral phase, Ge is commonly enriched in sulfide minerals, notably in sphalerite and enargite (Bernstein 1985). Oxidized portion of sulfide ore bodies can contain high [Ge] in iron oxides. Ge also has an active organic chemistry. The majority of Ge in seawater is methylated (Lewis et al. 1985), while Ge is variably but often strongly enriched in coals.

In the oceans Ge/Si ratios are near a constant 0.7 μmol mol^{-1}, and thus exhibits nutrient-like depth profiles as does

silica. This ratio reflects a mixture between river inputs of dissolved Ge (present as germanic acid, Ge(OH)4) with Ge/Si $\approx$ 0.6 μmol mol^{-1}, and mid-ocean ridge hydrothermal systems with Ge/Si ≈10–20 μmol mol^{-1} (Froelich et al. 1985). The low Ge/Si of river waters relative to crustal sources implies the existence of an enriched reservoir, and soils with secondary clays commonly have high Ge/Si (Murnane and Stallard 1990; Kurtz et al. 2002). Silicate weathering reactions fractionate Ge/Si in a predictable way that can be used to quantify reaction pathways and yields (Lugolobi et al. 2010). Geothermal fluids can be extremely enriched in Ge, with Ge/Si up to ≈1000 μmol mol^{-1}. This enrichment results from both temperature effects on Ge solubility and Rayleigh fractionation related to quartz precipitation (Evans and Derry 2002).

The stable isotopic composition of germanium is commonly expressed as:

$$\delta^{74}Ge = \left[\frac{\left({}^{74}Ge/{}^{70}Ge\right)_{\text{sample}}}{\left({}^{74}Ge/{}^{70}Ge\right)_{\text{standard}}} - 1\right] \times 1000$$

Isotopic variations up to ≈7 ‰ have been reported to date, with the lowest values from hydrothermal minerals and the highest from marine biogenic silica (Rouxel et al. 2006; Belissont et al. 2014). A widely accepted Ge isotopic standard has not yet been established, with two solutions currently in use (JMC and Aldrich) that differ by 1.70 ± 0.22 ‰ (Luais 2007). Relative to the heavier JMC standard, magmatic iron meteorites thought to be representative of undifferentiated parent bodies have $\delta^{74}Ge = 1.77 \pm 0.22$‰, which is the current best estimate of the early solar system value (Luais 2007). Relative to the JMC standard the bulk silicate Earth (BSE) is estimated to have $\delta^{74}Ge = -0.4 \pm 0.2$‰, or 1.3 ± 0.2 relative the lighter Aldrich standard (Rouxel et al. 2006). This low value for the BSE may reflect the substantial loss of volatile Ge during planetary formation. Seawater has not been directly determined but based on data from marine sponges Rouxel et al. proposed that $\delta^{74}Ge_{sw} \geq 3.0$‰ relative to the Aldrich standard. Ab initio calculations support a moderately positive isotope fractionation factor ($\Delta_{min—Ge(OH)4}$) between aqueous $Ge(OH)_4$ and quartz, and strong negative fractionation between $Ge(OH)_4$ and sphalerite (Li et al. 2009), results that appear consistent with published data on hydrothermal minerals. Both Ge/Si and $\delta^{74}Ge$ ratios therefor appear promising as tracers of geothermal transport and mineralization processes.

Biological Utilization and Toxicity

Germanium is not toxic at typical environmental levels, and is taken up by siliceous marine organisms as well as terrestrial plants (Azam and Volcani 1981). Ge is not known to have a biological function. Inhibition of diatom growth has been noted at Ge/Si ≥ 0.01 mol/mol, but this ratio is four orders of magnitude higher than in natural waters. Renal function was negatively impacted in humans with high chronic exposure to GeO_2 via use as dietary supplements (Tao and Bolger 1997), but Ge does not appear to have carcinogenic or mutagenic activity, and appears to be "an element of rather low risk to man" (Gerber and Léonard 1997). Siliceous diatom frustrules have the same Ge/Si as the ambient seawater, and Ge is evidently not fractionated from Si by this major consumer of marine dissolve silica (Froelich et al. 1985). Consequently the residence time of inorganic Ge should be near that of silica, i.e., ≈15 kyr. In contrast, vascular plants fractionate germanium from silicon fairly strongly. While silica uptake varies significantly among plant groups, opal phytoliths from vascular plants generally have low Ge/Si (Delvigne et al. 2009). Biocycling of silica can be of considerable importance in terrestrial ecosystems, imparting a characteristic low Ge/Si signature to stream waters (Derry et al. 2005).

Environmental Significance

While germanium is not in itself normally a direct environmental concern, strong enrichment of Ge in sulfide ore bodies, in geothermal systems, and in coal ashes make it a potentially sensitive and unique tracer for inputs from these sources. Geothermal fluids have both high [Si] and high Ge/Si, and this signal can mix with ambient river waters. Simple mixing models of geothermal and "background" stream water can be used to quantify geothermal fluid fluxes in some systems (Evans et al. 2004). Coal fly and bottom ash are also strongly enriched in Ge, with Ge most enriched in the fine fraction of coal ash (Querol et al. 1995). Rivers in regions with a history of coal combustion commonly have Ge/Si ratios significantly elevated above background (Froelich et al. 1985). As a metalloid Ge has similar behavior to elements of concern such as arsenic (As) and antimony (Sb), and so Ge/Si anomalies have potential to be effective tracers of input of PM10 particulates and As and Sb arising from coal combustion.

Summary

Germanium is a siderophile, volatile element during planetary formation and is a trace element in both mantle and crustal rocks. It substitutes readily into lattice sites normally occupied by Si (tetrahedral coordination). Both Ge/Si and $\delta^{74}Ge$ ratios are useful tracers for weathering and geothermal processes, and also for inputs from sulfide mineralization and coal combustion.

Cross-References

- ▶ Coal
- ▶ Elements: Metalloids
- ▶ Hydrothermal Solutions
- ▶ Ocean Biochemical Cycling and Trace Elements
- ▶ Siderophile elements
- ▶ Silicon
- ▶ Stable Isotope Geochemistry
- ▶ Sulfide Minerals
- ▶ Zinc

References

Azam F, Volcani BE (1981) Germanium-silicon interactions in biological systems. In: Simpson TL et al (eds) Silicon and siliceous structures in biological systems. Springer, New York

Belissont R, Boiron M-C, Luais B, Cathelineau M (2014) LA-ICP-MS analyses of minor and trace elements and bulk Ge isotopes in zoned Ge-rich sphalerites from the Noailhac – Saint-Salvy deposit (France): insights into incorporation mechanisms and ore deposition processes. Geochim Cosmochim Acta 126: 518–540

Bernstein LR (1985) Germanium geochemistry and mineralogy. Geochim Cosmochim Acta 49:2409–2422

Delvigne C, Opfergelt S, Cardinal D, Delvaux B, Andre L (2009) Distinct silicon and germanium pathways in the soil-plant system: evidence from banana and horsetail. J Geophys Res Biogeosci 114: G02013. https://doi.org/10.1029/2008JG000899

Derry LA, Kurtz AC, Ziegler K, Chadwick OA (2005) Biological control of terrestrial silica cycling and export fluxes to watersheds. Nature 433:728–731

Evans MJ, Derry LA (2002) Quartz control of high germanium/silicon ratios in geothermal waters. Geology 30:1019–1022

Evans MJ, Derry LA, France-Lanord C (2004) Geothermal fluxes of alkalinity in the Narayani river system of Central Nepal. Geochem Geophys Geosyst 5:Q08011. https://doi.org/10.1029/2004GC000719

Froelich PN, Hambrick GA, Andreae MO, Mortlock RA, Edmond JM (1985) The geochemistry of germanium in natural waters. J Geophys Res 90:1133–1141

Gerber GB, Léonard A (1997) Mutagenicity, carcinogenicity and teratogenicity of germanium compounds. Mutat Res 387:141–146

Goldschmidt VM (1937) The principles of distribution of chemical elements in minerals and rocks. J Chem Soc 655–673. https://doi.org/10.1039/JR9370000655

Goldsmith JR (1950) Gallium and germanium substitutions in synthetic feldspars. J Geol 58(3):518–536

Höll R, Kling M, Schroll E (2007) Metallogenesis of germanium – a review. Ore Geol Rev 30:145–180

Kurtz AC, Derry LA, Chadwick OA (2002) Germanium-silicon fractionation in the weathering environment. Geochim Cosmochim Acta 66:1525–1537

Le Roux V, Dasgupta R, Lee C-T (2015) Recommended mineral-melt partition coefficients for FRTEs (Cu), Ga, and Ge during mantle melting. Am Mineral 100:2533–2544

Lewis BL, Froelich PN, Andreae MO (1985) Methyl germanium in natural waters. Nature 313:303–305

Li X, Zhao H, Liu Y (2009) Theoretical prediction for several important equilibrium Ge isotope fractionation factors and geological implications. Earth Planet Sci Lett 287:1–11

Lodder K (2003) Solar system abundances and condensation temperatures of the elements. Astrophys J 591:1220–1247

Luais B (2007) Isotopic fractionation of germanium in iron meteorites: significance for nebular condensation, core formation and impact processes. Earth Planet Sci Lett 262:21–36

Lugolobi F, Kurtz AC, Derry LA (2010) Germanium-silicon fractionation in a tropical, granitic weathering environment. Geochim Cosmochim Acta 74:1294–1308

Mendeleev D (1872) Die periodische Gesetsmäfsigkeit der chemischen Elemente. Annalen der Chemie und Pharmacie VIII:133–229. Translated from 1871 Russian original by F. Wreden

Murnane RJ, Stallard RF (1990) Germanium and silicon in rivers of the Orinoco drainage basin. Nature 344:749–752

Newlands JAR (1864) Relations between equivalents. Chem News 10:59–60

Querol X, Fernadez-Turiel JL, Lopez-Solder A (1995) Trace elements in coal and their behavior during combustion in a large power station. Fuel 74(3):331–343

Righter K, King C, Danielson L, Pando K, Lee CT (2011) Experimental determination of the metal/silicate partition coefficient of germanium: implications for core and mantle differentiation. Earth Planet Sci Lett 304:379–388

Rouxel O, Galy A, Elderfield H (2006) Germanium isotopic variations in igneous rocks and marine sediments. Geochim Cosmochim Acta 70:3387–3400

Tao S-H, Bolger PM (1997) Hazard assessment of germanium supplements. Regul Toxicol Pharmacol 25:211–219

Winkler C (1886) Germanium, Ge, ein neues, nicht-metallisches Element. Ber Dtsch Chem Ges 19:210–211

Giant Impact Hypothesis

Hidenori Genda
Earth-Life Science Institute (ELSI), Tokyo Institute of Technology, Tokyo, Japan

Definition

The giant impact hypothesis is one of the theories for the origin of the Moon. In this theory, a Mars-sized object hit Earth obliquely about 4.5 billion years ago, which ejected a lot of materials to form a disk around Earth. From this disk, a single huge moon was formed. Unlike the other hypotheses (the fission, capture, and binary accretion hypotheses), the giant impact hypothesis satisfies almost all physical and chemical constraints of the Moon (Stevenson 1987). Thus, the giant impact hypothesis is regarded as the leading theory for the origin of the Moon (e.g., Canup 2004).

Rise of Giant Impact Hypothesis

Before the 1970s, the fission, capture, and binary accretion hypotheses had been considered for the origin of the Moon. It is now known that these hypotheses have one or more crucial

difficulties in physically making the Moon and explaining the lunar chemical compositions (see review articles Boss 1986; Wood 1986). However, before the 1970s, the constraints on the origin of the Moon were not enough to verify these hypotheses. Thanks to Apollo missions, lunar samples returned to Earth revealed that the Moon had been covered entirely by a deep magma ocean. The lunar highlands crust was found to be made of anorthosites containing 75–95% plagioclase (Warren 1985). Anorthosite forms and floats as it crystallizes from denser magma ocean. The evidence of the lunar magma ocean is also supported by the positive europium (Eu) anomaly in lunar highlands crust and the negative Eu anomaly in lunar mare basalts (Warren 1985). Additionally, seismometers put on the Moon confirmed that it has no metallic iron core (or a tiny core even if it was). With these new constraints, scientists started to think of an alternative theory for the origin of the Moon.

Soon after the detailed analysis of the returned lunar samples, the idea that the Moon originated from oblique impacts ejecting material into Earth's orbit was independently proposed by both Hartmann and Davis (1975), and Cameron and Word (1976). Initially, these ideas were not taken seriously because of the claim that such a catastrophic event and extreme results seemed unlikely. However, 10 years later, the giant impact hypothesis emerged as the leading hypothesis after "The Origin of the Moon Conference" held in Kona, Hawaii, in 1984. A collection of papers from this meeting was published in the 1986 book titled *Origin of the Moon* (Hartmann et al. 1986).

After several series of hydrodynamic simulations of the lunar-forming giant impact (Canup 2004), it has been found that an oblique impact of a Mars-sized protoplanet (about 10% of the Earth's mass) onto the proto-Earth (almost fully-grown Earth) can eject a lot of materials to form a disk around Earth called "the proto-lunar disk," whose typical mass is about 2–3 lunar masses. It has also been confirmed that a single lunar-sized moon can be created from the proto-lunar disk (Ida et al. 1997). Since the energy released by the giant impact is enormous, the giant impact hypothesis naturally explains the formation of the lunar magma ocean, and volatile depletion (e.g., K, Na, and Zn) in the Moon. Since the impactor's mantle is selectively ejected, a metallic iron-depleted proto-lunar disk is formed, which leads to metallic iron depletion in the Moon. Impact angular momentum gives the current huge angular momentum of the Earth-Moon system. Therefore, nowadays, the giant impact hypothesis is the leading theory for the origin of the Moon.

Special or Common Event?

For a while after the giant impact hypothesis was first considered scientifically as the origin of the Moon, the event of the lunar-forming giant impact was thought to be a special event that Earth experienced only once. However, in the 1980s, planet formation theory based mainly on the analytical methods (Wetherill 1985) came to predict that occurrence of giant impacts during the growth of the terrestrial planets is not rare. This prediction was proven to be robust after direct *N*-body simulations in planet formation in the 1980s and 1990s, thanks to enormous development in computational performance (Kokubo and Ida 1998; Chambers and Wetherill 1998). The detailed processes in planet formation were revealed one after the other, and giant impacts are regarded as a natural consequence for terrestrial planet formations.

According to recent planet formation theory, planets are formed in a protoplanetary disk. In the disk, the building blocks of planets with kilometer-sized objects called planetesimals are formed through the accumulation of dust (Safronov 1969; Hayashi et al. 1985). Before the 1980s, it was thought that the Earth was formed through accretion of km-sized planetesimals from the beginning to the end, but the concept has completely changed. In the terrestrial planet region in our solar system, several tens of Mars-sized protoplanets form through accretion of planetesimals (e.g., Lissauer 1987; Kokubo and Ida 1998) and these protoplanets collide with each other to form Earth-sized planets such as the Earth and Venus (e.g., Chambers and Wetherill 1998; Agnor et al. 1999). Therefore, Earth and Venus should experience several giant impacts during their formation, especially the last giant impact onto Earth, as it created the Moon.

Hafnium-tungsten (Hf-W) dating suggests that the last giant impact on Earth happened more than 50 Myrs after the oldest age in our solar system, which was estimated from CAICa–Al-rich inclusion (CAI) (Ca–Al-rich inclusion) in meteorites (Touboul et al. 2007; Kleine et al. 2009). This timing is consistent with the duration time (~100 Myrs) of the giant impact stage deduced from numerical calculations (Kokubo and Genda 2010; O'Brien et al. 2014). Planet formation theory also predicts that Mars and Mercury experienced no giant impact or few giant impacts at most, and thus they are survivors of the protoplanets. This is also consistent with the early resetting time (~ several Myrs) of Hf-W chronometer in SNC meteorites that are thought to have come from Mars.

Recently, it has been thought that giant impacts happened not only on Earth, but also on other planets. Owing to its strangely high bulk density, Mercury has a huge metallic core (60–80 wt% in total mass) compared to the other terrestrial planets' cores (~ 30 wt%). A high-velocity giant impact onto proto-Mercury has the potential to extensively erode its mantle, resulting in a huge core (Benz et al. 2007). A giant impact would also be responsible for the formation of two small satellites orbiting Mars (Citron et al. 2015;

Rosenblatt et al. 2016), and the formation of huge satellite Charon orbiting Pluto (Canup 2005; Sekine et al. 2017). A giant impact of an Earth-sized object onto Uranus would tilt its obliquity up to 98 °. Thus, giant impacts were common during planet formation in our solar system. Even in extrasolar systems, configurations of observed super-Earths likely indicate giant impacts during their formation (Ogihara and Ida 2009).

Approaching Shadow

Since the giant impact hypothesis was proposed, the oxygen (O) isotopic composition of lunar materials has been revealed to be identical to that of the Earth's mantle within the analytical uncertainties (< 0.005‰) (Wiechert et al. 2001; Young et al. 2016). Chromium (Cr) and titanium (Ti) isotopic compositions were also recently revealed to be identical between the Earth and the Moon (Lugmair and Shukolyukov 1998; Zhang et al. 2012). However, there is clearly heterogeneity of isotopic compositions in our solar system because most types of meteorites, including SNC meteorites, have different isotopic compositions from those of the Earth-Moon system (Clayton 1993). This isotopic similarity casts a shadow over the giant impact hypothesis.

The simplest explanation for the isotopic similarity between the Earth and the Moon is that the Moon was formed mainly from Earth's mantle. However, in the canonical lunar-forming giant impact (i.e., collision of a Mars-sized impactor onto Earth), the proto-lunar disk is predominantly (> 60 wt%) composed of material originating from the impactor (Canup 2004), which is expected to have a different isotopic composition than Earth. Another explanation is that the impactor had an identical isotopic composition to Earth. It had been suggested that the impactor came from an orbit similar to that of Earth (Wood 1986), but it turned out that this was improbable given the degree of radial mixing expected during the giant impact stage (Pahlevan and Stevenson 2007). Therefore, if the isotopic similarity were the only constraint for the origin of the Moon, the fission or binary accretion hypothesis would be the most promising one. However, these hypotheses are physically unlikely and inconsistent with the other constraints (Stevenson 1987).

Postimpact isotopic equilibration by vigorous mixing between the proto-lunar disk and Earth's magma ocean via vapor materials was suggested as an explanation for the isotopic similarity (Pahlevan and Stevenson 2007). However, some weak points of this isotopic equilibration have been pointed out; angular momentum transfer in the proto-lunar disk involved in material mixing inhibits the isotopic equilibration (Melosh 2014), and Cr and Ti isotopic equilibration via the vapor phase is not achieved because of their refractory nature (Zhang et al. 2012).

In order to overcome this isotopic crisis, another type of giant impacts was proposed; the collision between a small impactor and a fast-spinning proto-Earth (Ćuk and Stewart 2012), and the collision between equal-sized planets half the mass of Earth (Canup 2012). These types of collisions naturally produce the proto-lunar disk whose isotopic composition is similar to the Earth. However, these collisions should have an excess of angular momentum, which is twice as much as that of the current Earth-Moon system. Ćuk and Stewart (2012) also argued that the excess of angular momentum could have been drained away through a resonance with the Sun, known as the evection resonance (Touma and Wisdom 1998), after the Moon formation. However, this resonance only seems to work in a narrow range of tidal parameters (Wisdom and Tian 2015). Thus, at this moment, the isotopic similarity between the Earth and the Moon has not yet been completely solved. A breakthrough in the giant impact hypothesis is needed, otherwise it seems another completely new idea for the origin of the Moon is needed.

Recent successive discoveries of water in lunar samples are also casting a shadow over the giant impact hypothesis. The discovery of water in lunar anorthosites (Hui et al. 2013) means that the Moon should have formed in a wetter environment than previously thought. The energy released by the giant impact is so huge that scientists have simply thought that volatiles should be enormously depleted. However, the detailed behavior of volatiles during the giant impact and in the proto-lunar disk has not been well investigated. More works with detailed chemical processes are clearly needed.

Summary

There are a lot of physical and chemical constraints for the origin of the Moon, including the comparatively huge mass ratio of the Moon to Earth (= 1/83), the current angular momentum of the Earth-Moon system, the lack of metallic iron core in the Moon, the similarity of chemical and isotopic compositions between the Moon and Earth's mantle, lunar volatile depletion (e.g., K, Na, and Zn), and formation of the lunar magma ocean. Although the giant impact hypothesis is not a perfect theory at this moment, it is a promising theory.

Cross-References

- ▶ Chromium Isotopes
- ▶ Europium
- ▶ Formation and Evolution of the Earth
- ▶ Mantle Geochemistry
- ▶ Oxygen Isotopes
- ▶ Tungsten Isotopes

References

Agnor CB, Canup RM, Levison HF (1999) On the character and consequences of large impacts in the late stage of terrestrial planet formation. Icarus 142:219–237

Benz W, Anic A, Horner J, Whitby JA (2007) The origin of mercury. Space Sci Rev 132:189–202

Boss AP (1986) The origin of the moon. Science 231:341–345

Cameron AGW, Ward WR (1976) The origin of the moon. Lunar and Planetary Science Conference, Houston, pp 120–122

Canup RM (2004) Dynamics of lunar formation. Annu Rev Astron Astrophys 42:441–475

Canup RM (2005) A giant impact origin of Pluto-Charon. Science 307:546–550

Canup RM (2012) Forming a moon with an earth-like composition via a Giant impact. Science 338:1052–1055

Chambers JE, Wetherill GW (1998) Making the terrestrial planets: *N*-body integrations of planetary embryos in three dimensions. Icarus 136:304–327

Citron RI, Genda H, Ida S (2015) Formation of Phobos and Deimos via a giant impact. Icarus 252:334–338

Clayton RN (1993) Oxygen isotopes in meteorites. Annu Rev Earth Planet Sci 21:115–149

Ćuk M, Stewart ST (2012) Making the moon from a fast-spinning earth: a giant impact followed by resonant despinning. Science 338:1047–1052

Hartmann WK, Davis DR (1975) Satellite-sized planetesimals and lunar origin. Icarus 24:504–514

Hartmann WK, Phillips RJ, Taylor GJ (eds) (1986) Origin of the moon. Houston, Lunar Planetary Science Institute, 781pp

Hayashi C, Nakazawa K, Nakagawa Y (1985) Formation of the solar system. In: Black DC, Matthews MS (eds) Protostars and planets II. University of Arizona Press, Tucson, pp 1100–1153

Hui H, Peslier AH, Zhang Y, Neal CR (2013) Water in lunar anorthosites and evidence for a wet early moon. Nat Geosci 6:177–180

Ida S, Canup RM, Stewart GR (1997) Lunar accretion from an impact-generated disk. Nature 389:353–357

Kleine T, Touboul M, Bourdon B, Nimmo F, Mezger K, Palme H, Jacobsen SB, Yin Q-Z, Halliday AN (2009) Hf–W chronology of the accretion and early evolution of asteroids and terrestrial planets. Geochim Cosmochim Acta 73:5150–5188

Kokubo E, Genda H (2010) Formation of terrestrial planets from protoplanets under a realistic accretion condition. Astrophys J 714: L21–L25

Kokubo E, Ida S (1998) Oligarchic growth of protoplanets. Icarus 131:171–178

Lissauer JJ (1987) Timescales for planetary accretion and the structure of the protoplanetary disk. Icarus 69:249–265

Lugmair GW, Shukolyukov A (1998) Early solar system timescales according to ^{53}Mn-^{53}Cr systematics. Geochim Cosmochim Acta 62:2863–2886

Melosh HJ (2014) New approaches to the Moon's isotopic crisis. Phil Trans R Soc A 372:20130168

O'Brien DP, Walsh KJ, Morbidelli A, Raymond SN, Mandell AM (2014) Water delivery and giant impacts in the "grand tack" scenario. Icarus 239:74–84

Ogihara M, Ida S (2009) N-body simulations of planetary accretion around M dwarf stars. Astrophys J 699:824–838

Pahlevan K, Stevenson DJ (2007) Equilibration in the aftermath of the lunar-forming giant impact. Earth Planet Sci Lett 262: 438–449

Rosenblatt P, Charnoz S, Dunseath KM, Terao-Dunseath M, Trinh A, Hyodo R, Genda H, Toupin S (2016) Accretion of Phobos and Deimos in an extended debris disc stirred by transient moons. Nat Geosci 9:581–583

Safronov VS (1969) Evolution of the protoplanetary cloud and formation of the Earth and Planets. Moscow. (Translation, 1972, NASA TT F-677)

Sekine Y, Genda H, Kamata S, Funatsu T (2017) The Charon-forming giant impact as a source of Pluto's dark equatorial regions. Nature Astronomy 1:0031

Stevenson DJ (1987) Origin of the moon – the collision hypothesis. Annu Rev Earth Planet Sci 15:271–315

Touboul M, Kleine T, Bourdon B, Palme H, Wieler R (2007) Late formation and prolonged differentiation of the moon inferred from W isotopes in lunar metals. Nature 450:1206–1209

Touma J, Wisdom J (1998) Resonances in the early evolution of the earth-moon system. Astron J 115:1653–1663

Warren PH (1985) The magma ocean concept and lunar evolution. Annu Rev Earth Planet Sci 13:201–240

Wetherill GW (1985) Occurrence of giant impacts during the growth of the terrestrial planets. Science 228:877–879

Wiechert U, Halliday AN, Lee D-C, Snyder GA, Taylor LA, Rumble D (2001) Oxygen isotopes and the moon-forming giant impact. Science 294:345–348

Wisdom J, Tian Z (2015) Early evolution of the earth-moon system with a fast– spinning earth. Icarus 256:138–146

Wood JA (1986) Moon over Mauna Loa: a review of hypotheses of formation of Earth's moon. In: Hartmann WK (ed) Origin of the moon. Lunar & Planetary Institute, Houston, pp 17–55

Young ED, Kohl IE, Warren PH, Rubie DC, Jacobson SA, Morbidelli A (2016) Oxygen isotopic evidence for vigorous mixing during the moon-forming giant impact. Science 351:493–496

Zhang J, Dauphas N, Davis AM, Leya I, Fedkin A (2012) The proto-earth as a significant source of lunar material. Nat Geosci 5:251–255

Gibbs-Duhem Equation

William H. Casey[1] and Peter A. Rock[2]

[1]Department of Chemistry and Department of Earth and Planetary Sciences, University of California, Davis, CA, USA

[2]College of Math and Physical Sciences, Department of Chemistry, University of California, Davis, CA, USA

Definition

The Gibbs-Duhem equation describes the relationship between simultaneous changes in temperature, pressure, and composition in a solution: $SdT - VdP + \sum_{i=1}^{c} n_i d\mu_i = 0$.

Introduction

Equilibrium thermodynamics plays a central role in geochemistry, much more than other physical disciplines, because of the immense time and length scales of geological processes, and the enormous range of temperatures and pressures. The

Peter A. Rock is deceased.

Gibbs-Duhem equation (GDE) considerably simplifies thermodynamic analysis of multicomponent solutions and is essential to derivation of the Gibbs phase rule.

Elaboration

The GDE places a restriction on the simultaneous variations in the intensive thermodynamic variables of a phase. For a phase with c components, for which the temperature T, the pressure P, and composition can be varied, the GDE has the form

$$SdT - VdP + \sum_{i=1}^{c} n_i d\mu_i = 0 \quad (1)$$

where n_i and μ_i are the numbers of moles and the chemical potential of the *ith* component and S and V are the total entropy and volume of the phase. Geochemists are familiar with a manifestation of the GDE as the phase rule. The GDE shows that, for the total of $c + 2$ intensive variables, namely, the c chemical potentials [μ_1, μ_2 ... μ_c] plus temperature and the pressure, only $c + 1$ of the variables can be independently varied. For a system involving p phases in equilibrium, such as an ensemble of minerals, there is a total of p GDEs of the form of Eq. 1, with one GDE for each phase. Thus, in an equilibrium, multiphase system of c components and p phases, there is a total $of f = c + 2 - p$ independent, intensive variables (or degrees of freedom, f).

The most common application of the GDE is for a solution phase at fixed T and P for which, from the general form of the GDE, we obtain

$$\sum_{i=1}^{c} n_i d\mu_i = 0 \quad (2)$$

Equation 2 is an expression of a partial-molar property of a solution where an extensive thermodynamic property is the sum of contributions from each component, so that the sum of derivatives equals zero.

The simplest case, for $c = 2$, we have

$$n_1 d\mu_1 + n_2 d\mu_2 = 0 \quad (3)$$

The chemical potential of a component is related to the thermodynamic *activity* of that component by: $d\mu_i = RT$ d ln (a_i). Thus Eq. 3 becomes

$$n_1 d\ln(a_1) + n_2 d\ln(a_2) = 0 \quad (4)$$

or, by dividing through by the total number of moles, n_1+n_2, an expression is reached on the mole-fraction concentration scale:

$$x_1 d\ln(a_1) + x_2 d\ln(a_2) = 0 \quad (5)$$

The form of the GDE represented by Eqs. 4 and 5 shows us that if we know (or can measure) the activity of one component in a solution over a composition range (say $0 \leq x_1 \leq 1$), then we can use Eq. 5 to calculate the activity of the other component over that range. Such an approach is a central application of the GDE to determine the activity of a component in a mixture that cannot be probed directly.

Thus the GDE is particularly useful for solutions composed of a nonvolatile solute in a volatile solvent, for example, a salt dissolved in water. If we measure the equilibrium vapor pressure of the water over the solution (which gives the activity of water) as a function of the concentration of dissolved salt, then we can calculate the activity of the dissolved salt by integration. Integration of Eq. 6 yields activities (or activity coefficients) as a function of composition. Such integrations require careful consideration of the limits of integration (Rock 1983). Using $a_i = x_i\gamma_i$, we have for the activity coefficient of the second component (γ_2):

$$\ln\gamma_2 = -\int_1^{\gamma_1} \frac{x_1}{x_2}\, d\ln(\gamma_1) \quad (6)$$

Summary and Conclusions

The GDE is essential to thermodynamic analysis, and a typical geochemical application would be to interpret the composition of coexisting phases in a rock, such as ion exchange among coexisting feldspars. It can also be employed for low-temperature studies where the activity of one component in a solid solution can be measured. For example, electrochemical cells can be constructed (Rock et al. 1994) where the activity of $CaCO_3$ in a solid can be sensed from the voltage. Two nearly identical electrochemical cells can then be constructed and wired together in series opposition so that one cell contains pure calcite, while the other contains a solid in which the activity of $CaCO_3$ is less than unity, such as a $Ca_xCd_{1-x}CO_3$ material. The resulting voltage of the tandem cells is related to the activity of $CaCO_3$ in the solid solution relative to pure calcite. The activity of $CdCO_3$ in the $Ca_xCd_{1-x}CO_3$ solid is then directly calculable via Eq. 6 using the values of x and the measured activities of $CaCO_3$, even though the $CdCO_3$ activity cannot be sensed directly.

Cross-References

- ▶ Activity and Activity Coefficients
- ▶ Equilibrium
- ▶ Geochemical Thermodynamics

► Gibbs-Duhem Equation
► Standard States

References

Rock PA (1983) Chemical Thermodynamics. University Science Books, Mill Valley
Rock PA, Casey WH, McBeath MM, Walling EM (1994) A new method for determining Gibbs energies of formation of metal-carbonate solid solutions: the $Ca_xCd_{1-x}CO_3$(s) system at 298 K and 1 bar. Geochim Cosmochim Acta 58:4281–4291

Gold

Monica Vasiliu and David A. Dixon
Department of Chemistry, University of Alabama, Tuscaloosa, AL, USA

Element Data
Atomic Symbol: Au
Atomic Number: 79
Atomic Weight: 196.96654
Isotopes and Abundances: ^{197}Au 100%
1 Atm Melting Point: 1337.58 K
1 Atm Boiling Point: 3080 K
Common Valences: +3, +1
Ionic Radii: (+III) 91; (+I) 137 ppm
Pauling Electronegativity: 2.54
First Ionization Potential: 9.23 eV
Chondritic (CI) Abundance: 140 ppb
Silicate Earth Abundance: 0.001 ppm
Crustal Abundance: 1.1 ppb
Seawater Abundance: 0.011 ppb
Core Abundance: 0.5 ppm

Properties

Gold (Emsley 1991, 2001; Anthoni 2006; Anders and Grevesse 1989; McDonough 2005) is a soft metal with a shiny yellow color in bulk. Micro and nanoparticles including colloidal gold can be black, red/ruby, or purple. Gold is a soft metal that is the most malleable and ductile metal and is mostly alloyed to give it more strength. Gold is unaffected by air, water, alkaline solutions, and acids except aqua regia (a mixture of nitric and hydrochloric acids) and selenic acid. Supercritical water (water heated under pressure to a temperature of about 374 °C) will dissolve gold as well. The most common gold compounds are auric chloride ($AuCl_3$) and chlorauric acid ($HAuCl_4$).

Although gold is considered to be a noble metal, it has a broad chemistry. For example, gold is a pseudohalogen as it has a large electron affinity leading to the formation of auric (Au^{-1}) compounds (Pyykkö 2002). The chemistry of gold is dominated by relativistic effects, and gold has been shown to be the most relativistic element with $Z < 100$ (Pyykkö 2004). In addition, gold compounds exhibit a bond length contraction due to relativity. The dominant relativistic effects in the atom are the contraction and stabilization of the 6 s orbital coupled with an expansion and destabilization of the 5d orbital.

History and Use

The name gold is the Anglo-Saxon word for the metal, and the symbol comes from the Latin “aurum” for gold. Gold has been known since prehistoric times, at least 3000 BC. Gold was probably one of the first metals to be worked because it was found as grains/particles or even nuggets in stream beds from which it was easily recovered. By 2000 BC, the Egyptians were already beginning to mine gold by following the veins of the metal in underground rocks. The death mask of Tutankhamen (died 1323 BC) was 100 kg of gold. The royal graves of ancient Ur (Iraq today), one of the earliest civilizations which flourished about 5000 years ago, contained skillfully worked gold objects.

Gold was easily separated from alloys and refined. The first pure gold coins were minted in Lydia (Turkey today) under King Croesus (ruled from about 561–547 BC).

For centuries, the lure of gold drove people to find ways of making gold, and alchemists spent much time searching for the “Philosopher’s Stone,” a key material that they hoped would transform basis metals like lead into gold.

Gold is used as bullion and in jewelry, glass, and electronics. The purity of gold has been measured in carats with pure gold being 24 carats, but it is very soft. Most gold is alloyed with silver or copper and 0.2% zinc to harden it. Jewelry consumes around 75% of all gold produced. Gold is also used for coinage, and it has been used as the standard for monetary systems in some countries.

Gold can be beaten into very thin sheets called “gold leaf” to be used in art, for decoration, and as an architectural ornament. Electroplating can be used to cover another metal with a very thin layer of gold. This is used in gears for watches, artificial limb joints, cheaper forms of jewelry, and electrical connectors. It is very useful for the protection of electrical copper components because gold is a good conductor of electricity but at the same time does not corrode. Thin gold wires are also used inside computer chips to produce circuits.

Colloidal gold is added to glass to color it red or purple, and metallic gold is applied as a thin film on windows of large buildings to reflect the heat of the Sun's rays, as gold has high infrared reflective properties. For the same reason, gold is used in space exploration systems.

Gold nanoparticles are being used as industrial catalysts. Vinyl acetate, used to make PVA (for glue, paint, and resin), is produced using a gold catalyst, for example.

Geochemical Behavior

Gold is one of the few elements to occur in its natural state. It is found in veins and alluvial deposits. Every year, about 1500 tons of gold are mined with two-thirds coming from South Africa and most of the rest from Russia. Gold is often extracted using a cyanide-based process which can lead to environmental issues due to the toxicity of the cyanide. Historically, gold was extracted using mercury which also had environmental and health effects.

Seawater contains 4 g of gold/10^6 tons of water. The concentration is so low that attempts to separate gold from seawater have failed.

Gold occurs mainly as a metal, sometimes as crystals, but more generally as grains, sheets, and flakes in other rocks. There are some gold ores as sylvanite, a combination of gold, silver, and tellurium. Mount Erebus, in Antarctica, the continuously erupting volcano, is unique among volcanoes because it emits gold dust.

There are some plants (Douglas fir, honeysuckle, and the mustard plant) that absorb gold from the soil in which they grow.

Biological Utilization and Toxicity

Inhalation of gold may cause irritation if exposure is prolonged or excessive. Gold may cause skin irritation and allergic reactions as well as eye irritation. Dentists sometimes use gold alloys in fillings, and a gold compound (Chrysotherapy) is used to treat some cases of arthritis.

References

Anders E, Grevesse N (1989) Abundances of the elements: meteoritic and solar. Geochim Cosmochim Acta 53:197–214. http://meteorites.wustl.edu/goodstuff/chondritic_abundances.htm

Anthoni JF (2006) The chemical composition of seawater. http://www.seafriends.org.nz/oceano/seawater.htm

Emsley J (1991) The elements, 2nd edn. Clarendon, Oxford

Emsley J (2001) Nature's building blocks an A-Z guide to the elements. Oxford University Press, Oxford

McDonough WF (2005) Compositional model for the earth's core. In: Carlson RW (ed) The mantle and core. Elsevier, Oxford, pp 547–568. http://www.knowledgedoor.com/2/elements_handbook/element_abundances_in_the_earth_s_core.html

Pyykkö P (2002) Relativity, gold, closed-shell interactions, and $CsAu{\cdot}NH_3$. Angew Chem Int Ed 41:3573–3578

Pyykkö P (2004) Theoretical chemistry of gold. Angew Chem Int Ed 43:4412–4456

Gouy-Chapman Theory

Garrison Sposito
Environmental Science, Policy and Management, University of California, Berkeley, CA, USA

G

Definition

Gouy-Chapman theory (Gouy 1910; Chapman 1913) is an electrostatic model of the spatial distribution of ions adsorbed, but not immobilized, by a charged particle surface reacting with an aqueous electrolyte solution. These ions are relatively free to move about while reacting with surface charge either by accumulation (positive adsorption) or depletion (negative adsorption) in the interfacial region. The fundamental question answered by Gouy-Chapman theory is how this "diffuse swarm" of adsorbed ions with given valence and radius will distribute itself near a particle of given charge and radius solely under the influence of coulomb forces between the ions and between them and the particle surface.

Introduction

The objective of Gouy-Chapman theory (Verwey and Overbeek 1999; Hunter 2001; Sposito 2004) is to calculate the spatial distribution of ions in the vicinity of a uniformly charged, molecularly smooth solid surface. This is accomplished by solving a nonlinear, second-order differential equation known as the Poisson-Boltzmann equation:

$$\frac{d^2\psi}{dx^2} + \frac{(1-2\nu)}{x}\frac{d\psi}{dx} = -\frac{1}{\varepsilon_0 D}\sum\nolimits_i Z_i F c_{i0} \exp\left(\frac{-Z_i F\psi}{RT}\right) \quad (1)$$

where $\psi(x)$ is the average electrostatic potential at a point x in a diffuse swarm of ions with differing valence Z_i ($i = 1, 2$, etc.); D is the dielectric constant of water; ε_0 is the permittivity of vacuum; F is the Faraday constant; c_{i0} is the concentration of ions of type i at a reference point far from the surface (bulk solution concentration of ion i), where $\psi \equiv 0$; R is the gas constant; and T is the absolute temperature. The coordinate x in Eq. 1 is measured along an axis perpendicular to the charged particle surface and extending into the aqueous

solution contacting it, with origin at the center of the particle. The particle surface may be planar ($\nu = ½$), cylindrical ($\nu = 0$), or spherical ($\nu = -½$) (Moon and Spencer 1988).

Equation 1 is subject to a charge-potential relationship, equivalent to Gauss's law in electrostatics, which acts as a boundary condition at the particle surface ($x = a$) (Hunter 2001):

$$\left(\frac{d\psi}{dx}\right)_{x=a} = -\frac{\sigma_p}{\varepsilon_0 D} \tag{2}$$

where σ_p is the net total particle charge, equal to the algebraic sum of the intrinsic surface charge, due to isomorphic substitutions in the particle structure and proton adsorption/desorption reactions, and the Stern layer charge, due to ions adsorbed in surface complexes (Sposito 2008). The distance a in Eq. 2, ranging typically from tens of nanometers to tens of micrometers, is equal to the distance from the center of the charged particle to its geometric surface plus the "distance of closest approach" of an ion to the geometric particle surface, $d_0/2$, equal to the sum of the crystallographic radius of the ion and the diameter of a water molecule (0.280 nm).

The derivation of Eq. 1 is based on three fundamental physical postulates (Carnie and Torrie 1984):

1. The charged particle surface is uniform and smooth, characterized by a charge density σ and by high symmetry, such that the electrostatic potential varies spatially only along a coordinate axis perpendicular to the particle surface, which is planar, cylindrical, or spherical.
2. Liquid water is modeled as a uniform continuum characterized solely by its dielectric constant.
3. The potential of mean force, which is the average energy required to move an ion from the reference point ($\psi \equiv 0$) to a point somewhere in the diffuse swarm near the particle surface, is proportional to $\psi(x)$.

The first two postulates imply that the molecular structure of both the solid particle surface and liquid water is neglected. The third postulate implies that short-range correlations among the ions in the swarm are neglected, with only long-range correlations arising from the coulomb force accounted for. However, regardless of its valence, an ion experiences non-coulombic, short-range repulsive interactions with other ions as it is moved along a path from the reference point to its place in the swarm, these interactions and the spatial correlations they produce coming as an effect of finite ion size. In addition, the accumulation of ions (counterions) near a particle surface of opposite charge sign allows the ions having the same charge sign as the surface (coions) to approach the surface more closely than they would otherwise because the repulsive effect of like charge is screened by the positively adsorbed counterions. These kinds of short-range spatial correlations are not reflected in the average electrostatic potential, which derives only from the Coulomb force.

The third postulate leads to a mathematical relationship between $c_i(x)$, the concentration of ions of type i at a point x, and the average electrostatic potential (Carnie and Torrie 1984):

$$RT\frac{d\ln c_i}{dx} = -Z_i F\frac{d\psi}{dx} \tag{3}$$

Eq. 2 states that ion concentration gradients in the diffuse swarm are produced by an average electrostatic force proportional to minus the gradient of the average electrostatic potential. [More generally, Eq. 2 is a relationship between the gradient of $\ln c_i(x)$ in the diffuse swarm and the average force acting on an ion of type i which produces the gradient, which by definition is proportional to minus the gradient of the potential of mean force (Carnie and Torrie 1984). In Gouy-Chapman theory, the potential of mean force is approximated by $Z_i F\psi$.] It follows that $c_i(x)$ has an explicit mathematical form obtained by integrating Eq. 2:

$$c_i(x) = c_{i0}\exp[-Z_i F\psi(x)/RT] \tag{4}$$

where the boundary condition on $c_i(x)$ at the reference point $\psi = 0$ is imposed. This expression appears on the right side of Eq. 1 as a term in a summation which is proportional to the net charge density in the ion swarm at a point x.

Gouy-Chapman Scaling

Equation 1 is not invariant in mathematical form under multiplication of either ψ or x by an arbitrary scale factor, which means that Gouy-Chapman theory must exhibit intrinsic scales of both the electrostatic potential and length (Sposito 2004). The intrinsic scale of electrostatic potential is RT/F (=25.7 mV at 298 K), which appears in the exponent on the right side of Eq. 1. After dividing both sides of Eq. 1 by this factor to define the dimensionless electrostatic potential, $y \equiv F\psi/RT$, the parameter:

$$\beta \equiv 2F^2/\varepsilon_0 DRT \tag{5}$$

emerges as the coefficient of c_{i0} in the summation on the right side. The product βc_{i0} has dimensions of inverse-length squared, leading to the definition of an intrinsic length scale as the inverse square root of the parameter:

$$\kappa_i^2 \equiv \beta c_{i0} \tag{6}$$

The value of κ_i^{-1} ranges from 1 to 30 nm at 298 K as the bulk solution concentration c_{i0} ranges from 0.1 to 100 mol m^{-3}, common in freshwaters, whereas $\kappa^{-1} \approx 0.36$ nm for standard seawater. Thus, nanometer length scales characterize the spatial variability of $\psi(x)$ as governed by Eq. 1, while millivolt potential scales characterize the magnitude of $\psi(x)$.

A second intrinsic length scale is associated with the boundary condition on $\psi(x)$ in Eq. 2. It involves the net total particle charge, σ_p (Sposito 2004):

$$\ell \equiv \varepsilon_0 DRT/F|\sigma_p| = 2F/\beta|\sigma_p| \tag{7}$$

Setting σ_p equal to the typical range of intrinsic surface charge for clay minerals and oxides (Sposito 2008), one finds that the minimal range of ℓ is between 0.05 and 0.25 nm, which is well below typical values for κ_i^{-1}. However, if intrinsic surface charge neutralization by ions adsorbed in the Stern layer reduces σ_p (in absolute value), the length scale ℓ can be larger than the upper limit of this minimal range. The physical significance of ℓ can be seen after dividing the boundary condition in Eq. 2 by the intrinsic electrostatic potential scale, RT/F, to derive the scaled boundary condition:

$$\left(\frac{dy}{dx}\right)_{x=a} = -\frac{\text{sgn}(\sigma_p)}{\ell} \tag{8}$$

where

$$\text{sgn}(\sigma) = \begin{cases} +1 & \sigma_p > 0 \\ -1 & \sigma_p < 0 \end{cases} \tag{9}$$

Equation 8 shows that ℓ defines an intrinsic length scale for the spatial variation of $\psi(x)$ at the particle surface: small values of ℓ imply sharp gradients of $\psi(x)$ at the particle surface.

Counterion Condensation and Coion Exclusion

Gouy-Chapman theory predicts a very high concentration of counterions near a planar charged surface, even at a relatively low net particle surface charge or bulk solution concentration (Verwey and Overbeek 1999; Sposito 2004). In quantitative terms, let $\varphi(x)$ be the fraction of the surface charge density σ_p at the point x that is screened by counterions occupying the region $x > a$. This fraction will depend on the surface charge density and the bulk solution concentration. Counterion condensation is said to exist if $\varphi(x)$ does not vanish as the bulk solution ion concentration goes to zero; that is, a fraction of the counterions remains very close to the charged surface even if the electrolyte solution which contacts it becomes infinitely dilute (Zimm and Le Bret 1983). Evidently, their electrostatic attraction to the charged surface is strong enough to prevent the counterions from drifting out into the bulk solution even as it decreases to zero concentration. Note that, in the context of Gouy-Chapman theory, even though compressed against the particle surface, the counterions remain mobile and do not form surface complexes.

For a diffuse swarm containing monovalent, positively charged counterions and monovalent, negatively charged coions, a quantitative description of condensation is given by the definition (Zimm and Le Bret 1983):

$$\begin{aligned} \varphi(x) &\equiv \left(F/|\sigma_p|\right)\int_a^x [c(s) - c_0]\, ds \\ &= \left(Fc_0/|\sigma_p|\right)\int_a^x \{\exp|y(s)| - 1\}\, ds \\ &= \frac{1}{2}\left(\kappa^2/\ell\right)\int_{|y_0(a)|}^{|y_0(x)|} \frac{[\exp|y| - 1]}{dy/dx}\, dy \end{aligned} \tag{10}$$

where y(x) is the scaled electrostatic potential and Eqs. 4, 5, 6, 7, and 8 have been applied to derive the final result. The limiting value of the right side of Eq. 10 as $k \downarrow 0$ can be shown to be (Zimm and Le Bret 1983)

$$\lim_{\kappa \downarrow 0} \varphi(x) = 1 - \{1 + [(1/2\ell)\ (x - a)]\}^{-1} \tag{11}$$

At 298 K, the numerator in Eq. 7, 2 F/β, has the value 1.781×10^{-11} C m^{-1}, leading to an estimate of $\ell = 0.178$ nm for $|\sigma_p| = 0.1$ C m^{-2}, which is typical of the intrinsic surface charge density for the planar surfaces of 2:1 clay minerals. With this value of ℓ, it follows from Eq. 11 that counterions within 1 nm of the particle surface screen about 75% of its charge. More generally, half the net particle surface charge is balanced by diffuse swarm counterions within the rather small distance 2ℓ ($0.10 < 2\ell < 0.50$ nm) from the particle surface, another reflection of the fact that small values of this intrinsic length scale signal sharp-negative gradients in the electrostatic potential (Eq. 8). However, this conclusion applies strictly to planar charged surfaces. The limit of $\varphi(x)$ as $k \downarrow 0$ is dependent on $|\sigma_p|$ for cylindrical particle surfaces, becoming equal to 0 below a certain absolute value of the net total particle charge (O'Shaughnessy and Yang 2005), and it is equal to 0 at any net total particle charge for spherical particle surfaces (Zimm and Le Bret 1983).

Coion exclusion refers to the pronounced depletion of ions by repulsion from a region near a particle surface having the same charge sign as the ions (Verwey and Overbeek 1999; Hunter 2001). Gouy-Chapman theory provides a mathematical model of coion exclusion through the parameter d_{ex}, the coion exclusion distance. For monovalent ions in a diffuse swarm (Pashley and Quirk 1997),

$$d_{ex} \equiv \int_a^{\infty} \left[1 - \frac{c(x)}{c_0}\right] dx + \frac{1}{2} d_0$$
$$= \int_{y(a)}^{0} \frac{\{1 - \exp[-|y|]\} dy}{dy/dx} + \frac{1}{2} d_0$$
$$= \frac{2}{\kappa} \{1 - \exp[-|y(a)|/2]\} + \frac{1}{2} d_0 \quad (12)$$

where y(x) is the scaled electrostatic potential, and a procedure like that used in developing Eq. 10 has been followed. By the definition of an integral, d_{ex} is a weighted sum of distance intervals within the diffuse swarm, the weighting factor being the fraction of coions not in the open interval (x, x + dx). In this sense, d_{ex} may be interpreted as an average distance from the surface of a charged particle over which coions are excluded. For calculated values of y(a) that are typical of planar 2:1 clay mineral surfaces and for typical values of the distance of closest approach, the exponential term in Eq. 12 is negligible (Sposito 2004) and d_{ex} closely equals twice the length scale, k^{-1}. If $0.1 < c_0 < 100$ mol m^{-3}, then, by Eq. 6, $0.033 < k < 1$ nm^{-1} at 298 K and, therefore, $2 < d_{ex} < 60$ nm (Sposito 1992).

These applications further illustrate the physical significance of the two intrinsic length scales of that arise in Gouy-Chapman theory. The scale factor k^{-1} is seen to provide a measure of coion exclusion, in that $2\,k^{-1}$ is approximately the average distance from a charged particle surface over which coions are effectively excluded from the interfacial region. The scale factor ℓ provides a measure of counterion accumulation, in that 2ℓ is the distance from a charged particle surface over which half the surface charge is screened by counterions in the limit of infinite dilution. This latter scale factor, intimately related to the magnitude of the net particle surface charge, gives a measure of the spatial extent or "thickness" of the diffuse swarm (Sposito 2004).

Validating Gouy-Chapman Theory

Equation 1 can be solved analytically for planar charged surfaces interacting with symmetric, 2:1, and 1:2 electrolyte solutions or their mixtures (Liu et al. 2013). Only approximate solutions of Eq. 1 are available for cylindrical and spherical charged surfaces, except under the condition that the electrostatic potential is small enough in absolute value to justify replacing each exponential term on the right side of Eq. 1 by the first two terms of its Maclaurin expansion, thereby linearizing the Poisson-Boltzmann equation (Sposito 2004). This is known as the Debye-Hückel approximation (Verwey and Overbeek 1999), equivalent in the present context to imposing the condition $\kappa\ell > 2$ on the two intrinsic length scales (Sposito 2004). This condition requires high bulk solution concentrations of the ions and/or low absolute values of the net particle surface charge.

The accuracy of Eq. 1 as a description of a diffuse swarm interacting in a dielectric continuum has been assessed by comparing its predictions of ion concentrations according to Eq. 4 with the results of Monte Carlo simulations of a swarm of monovalent hard-sphere ions immersed in a continuum dielectric fluid contacting a planar charged surface like that encountered for 2:1 clay minerals (Torrie and Valleau 1982). Figure 1 shows the concentration of cations (c_+) or anions (c_-), scaled by c_0, as calculated with Eq. 4, compared with those predicted by Monte Carlo simulation, both plotted against distance from the geometric particle surface scaled by $d_0 = 0.425$ nm. (In this application, the origin of the coordinate x was placed at the

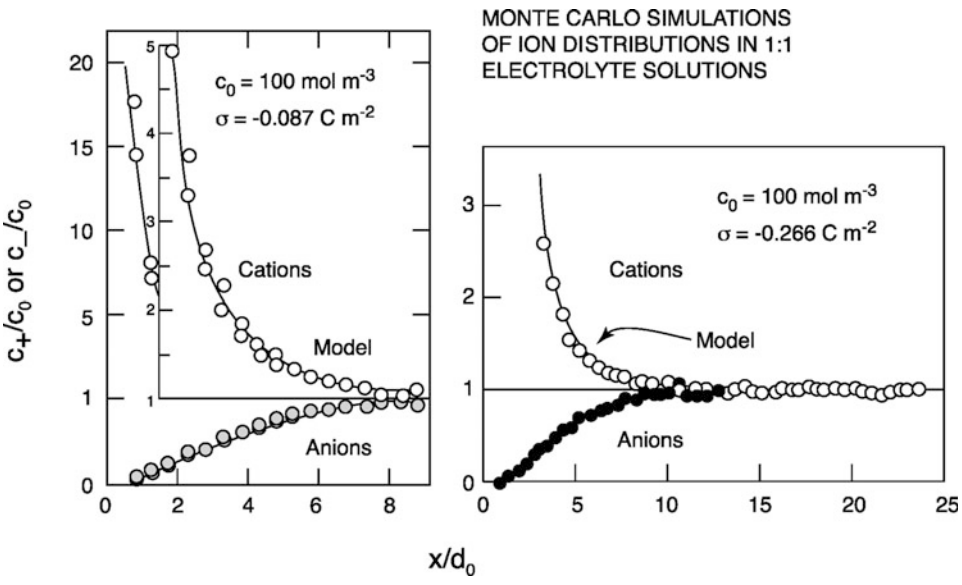

Gouy-Chapman Theory, Fig. 1 Comparison between Monte Carlo simulations (*circles*) of spatial ion distributions near a planar charged surface with the predictions of Gouy-Chapman theory (curves labeled "Model") (Reprinted with permission from Sposito, G. (2004) The surface chemistry of natural particles. Oxford, New York)

geometric particle surface instead of at the particle center, and $d_0/2$ was set equal to the ionic radius alone instead of the sum of the ionic radius and the diameter of a water molecule, thus allowing counterions to touch the geometric particle surface.) The bulk solution concentration is set at the upper end of the typical range for freshwaters, corresponding to $k \approx 1\ nm^{-1}$ at 298 K, while σ_p, here set equal to σ_0, the intrinsic surface charge density, takes on two values that bracket the normal range for smectites, corresponding to $\ell = 0.21$ and 0.085 nm, respectively, at 298 K. (Note that ℓ is far too small for $\kappa\ell$ to satisfy the condition required by the Debye-Hückel approximation.) Counterion condensation is apparent from the high concentration of cations (about 20 times larger than c_0) found at the distance of closest approach ($x = d_0/2$), even for $|\sigma|$ as low as $0.087\ C\ m^{-2}$. Similarly, coion exclusion is apparent in Fig. 1 by the anion concentration within about five ionic diameters of the particle surface lying well below the bulk solution concentration.

Thus Eq. 1 is thus validated for monovalent ions in a diffuse swarm for bulk solution concentrations up to 100 mol m^{-3}. Above this concentration, however, Gouy-Chapman theory is found to be inaccurate because of ion-ion correlation effects (Torrie and Valleau 1982; Carnie and Torrie 1984). Also because of these correlations, Eq. 1 proves to be inaccurate for bivalent ions at bulk solution concentrations as low as 5 mol m^{-3}. Gouy-Chapman theory overpredicts bivalent counterion concentrations (counterion condensation is overpredicted) while underpredicting monovalent coion concentrations in the presence of bivalent counterions (coion exclusion is also overpredicted); the latter counterion-coion correlations as described above can actually lead to a small positive coion adsorption (Torrie and Valleau 1982). Diffuse swarm models that go beyond Gouy-Chapman theory to include these correlations provide a much more accurate description of planar charged surfaces bearing adsorbed bivalent cations (Carnie and Torrie 1984; Blum and Henderson 1992; Attard 1996).

Summary

A net particle surface charge different from zero implies the existence of adsorbed ions in a diffuse swarm. Diffuse swarm species respond to surface charge by distributing themselves in order to screen it through counterion accumulation and coion exclusion. Screened particle charge, in turn, mediates the interparticle interactions in colloidal suspensions that determine their stability (Verwey and Overbeek 1999; Hunter 2001; Sposito 2008). Thus particle charge screening is the most important resultant chemical property of the diffuse swarm. Gouy-Chapman theory offers perhaps the simplest quantitative description of the spatial distribution of ions in a diffuse swarm through the Poisson-Boltzmann equation (Eq. 1), a nonlinear differential equation whose solution gives the spatial dependence of the average electrostatic potential in an adsorbed electrolyte solution modeled as a swarm of mobile hard-sphere ions immersed in a continuum dielectric medium contacting a charged particle surface that can be planar, cylindrical, or spherical.

Because they are not invariant under arbitrary scaling of the position coordinate, the Poisson-Boltzmann equation and its boundary value at the particle surface admit two intrinsic length scales (Eqs. 6 and 7):

k^{-1} Intrinsic length scale for spatial variability of $\psi(x)$ within the diffuse swarm

ℓ Intrinsic length scale for spatial variability of $\psi(x)$ at the particle surface

The intrinsic length scale ℓ provides a robust measure of the "thickness" of the electrical double layer comprising a diffuse swarm. Over the range of bulk solution concentrations that typify freshwaters, the dimensionless length ratios, $\kappa\ell$ and ka, where a locates the particle surface along a surface normal emanating from the center of the particle, give relative measures of electrostatic potential magnitude and colloidal particle size, respectively. Electrostatic potentials can be considered to be relatively small if the bulk solution concentration is sufficiently high and the net particle surface charge is very low (large $\kappa\ell$), whereas charged particles can be considered to be relatively small if the bulk solution concentration is sufficiently low (small ka).

Cross-References

- ▶ Clay Minerals
- ▶ Poisson-Boltzmann Equation
- ▶ Surface Geochemistry

References

Attard P (1996) Electrolytes and the electrical double layer. Adv Chem Phys 92:1–159

Blum L, Henderson D (1992) Statistical mechanics of electrolytes at interfaces. In: Henderson D (ed) Fundamentals of inhomogeneous fluids. Marcel Dekker, New York, pp 239–276

Carnie SL, Torrie GM (1984) The statistical mechanics of the electrical double layer. Adv Chem Phys 56:141–227

Chapman DL (1913) A contribution to the theory of electrocapillarity. Philos Mag 25:475–481

Gouy M (1910) Sur la constitution de la charge électrique a la surface d'un électrolyte. J Phys 9:457–468

Hunter RJ (2001) Foundations of colloid science. Oxford University Press, Oxford/New York

Liu X, Li H, Li R, Tian R (2013) Analytical solutions of the nonlinear Poisson-Boltzmann equation in mixture of electrolytes. Surf Sci 607:197–202

Moon P, Spencer DE (1988) Field theory handbook. Springer, New York
O'Shaughnessy B, Yang Q (2005) Manning-Oosawa counterion condensation. Phys Rev Lett 94:048302. (5 pp)
Pashley RM, Quirk JP (1997) Co-ion exclusion by clay surfaces: I. Equations for 1:1, 2:1, and 3:1 electrolyte solutions. Soil Sci Soc Am J 61:58–63
Sposito G (1992) The diffuse ion swarm in 1:1 electrolyte solutions. In: Güven N, Pollastro R (eds) Clay-water interface and its rheological applications. The Clay Minerals Society, Boulder, pp 127–155
Sposito G (2004) The surface chemistry of natural particles. Oxford University Press, Oxford/New York
Sposito G (2008) The chemistry of soils, 2nd edn. Oxford University Press, Oxford/New York
Torrie GM, Valleau JP (1982) Electrical double layers. 4. Limitations of the Gouy-Chapman theory. J Phys Chem 86:3251–3257
Verwey EJW, Overbeek JTG (1999) Theory of the stability of lyophobic colloids. Dover, New York
Zimm BH, Le Bret M (1983) Counter-ion condensation and system dimensionality. J Biomol Struct Dyn 1:461–471

H

Hafnium

Janne Blichert-Toft
Laboratoire de Géologie de Lyon, Ecole Normale Supérieure de Lyon, Université Claude Bernard Lyon 1, CNRS, Lyon, France

Element Data
Atomic Symbol: Hf
Atomic Number: 72
Atomic Weight: 178.49 g/mol
Isotopes and Abundances: ^{174}Hf 0.16%, ^{176}Hf 5.26%, ^{177}Hf 18.60%, ^{178}Hf 27.28%, ^{179}Hf 13.62%, ^{180}Hf 35.08%
1 Atm Melting Point: 2233 °C
1 Atm Boiling Point: 4603 °C
Common Valences: 4+
Ionic Radii: 6-fold: 78 pm (Hf^{4+})
Pauling Electronegativity: 1.3
First Ionization Energy: 658.5 kJ/mol
Chondritic (CI) Abundance: ~0.1 ppm
Silicate Earth Abundance: ~0.3 ppm
Crustal Abundance: 3.7 ppm
Seawater Abundance: ~0.5 pmol/kg
Core Abundance: 0

Properties

Hafnium's atomic number is 72, its standard atomic weight 178.49(2) g/mol, its density 13.31 g/cm^3, and its ionic radius between 0.58 and 0.83 Å depending on coordination state, with 0.78 Å for Hf^{4+} in sixfold coordination with oxygen, which is most common. Natural Hf has five stable isotopes (^{176}Hf, ^{177}Hf, ^{178}Hf, ^{179}Hf, and ^{180}Hf) and one very long-lived isotope (^{174}Hf with a half-life of 2×10^{15} years) with relative abundances of: ^{174}Hf = 0.16(1)%, ^{176}Hf = 5.26(7)%, ^{177}Hf = 18.60(9)%, ^{178}Hf = 27.28(7)%, ^{179}Hf = 13.62(2)%, and ^{180}Hf = 35.08(16)% (http://www.nist.gov/pml/data/comp.cfm). One of the stable isotopes (^{176}Hf) is radiogenic, produced, in part, by the beta decay of radioactive ^{176}Lu with a half-life of 37.12×10^9 years (Ga) and a decay constant λ^{176}Lu of $1.867 \pm 0.008 \times 10^{-11}$ year^{-1} (Scherer et al. 2001; Söderlund et al. 2004). Together, ^{176}Lu and ^{176}Hf provide the basis for the Lu-Hf chronometer. Over the age of the Earth and the Solar System (~4.5 Ga), ~3% of ^{176}Lu has decayed to ^{176}Hf and ~1% of ^{176}Hf is radiogenic with the rest being "common" Hf produced during nucleosynthesis. Hafnium also has a large number of unstable (radioactive or short-lived) isotopes with ^{182}Hf, now extinct for all practical intents and purposes, being the most pertinent to the field of earth and planetary sciences as its half-life of 8.9×10^6 years (Ma) and its beta decay product ^{182}W make it a powerful chronometer for dating silicate-metal segregation in the early Earth and other terrestrial bodies of the Solar System. Variations in ^{182}W have been observed in both meteorites and terrestrial materials and are described in the entry on ▶ Tungsten Isotopes, which covers the ^{182}Hf-^{182}W system.

In pure form, Hf is a silvery or steel gray, shiny, ductile, corrosion-resistant, transition metal of Group 4 (IVb) of the periodic table and has hexagonal crystal structure. It has oxidation states of 0 (the pure metal), 2+, 3+, and 4+, but in nature Hf is essentially exclusively tetravalent. Due to the lanthanide contraction of the rare earth elements in the sixth period of the periodic table, Zr and Hf have nearly identical ionic radii (Zr^{4+} being 0.79 Å compared with Hf^{4+} at 0.78 Å) resulting in the canonical terrestrial Zr/Hf ratio of ~34.3. Hafnium, therefore, substitutes readily for Zr in Zr minerals, first and foremost zircon ($ZrSiO_4$, where ~1–4% is Hf) and baddeleyite (ZrO_2, with ~0.1–2% Hf). It also substitutes in the Ti minerals rutile (TiO_2) and ilmenite ($FeTiO_3$) due to Ti and Hf having the same charge, and, like Zr, being in the same

W. M. White (ed.), *Encyclopedia of Geochemistry*,
https://doi.org/10.1007/978-3-319-39312-4

group in the periodic table. Owing to the similar properties of Zr and Hf (and Ti and Hf) and the much higher abundance of Zr (and Ti) in nature, Hf does not form any minerals of its own.

History and Use

Although the existence of Hf was predicted from the systematics of the periodic table of elements by Dmitri Mendeleev already back in 1869, the so-called missing element 72 was not discovered until 1922 by Dirk Coster, a Dutch physicist, and Georg Charles von Hevesy (also known as George Charles de Hevesy), a Hungarian Swedish chemist, at the Niels Bohr Institute in Copenhagen. Coster and de Hevesy used X-ray spectroscopy to study the arrangement of the outer electrons of atoms in samples of Zr ore. The electron structure of Hf had previously been predicted by Niels Bohr, and Coster and de Hevesy found a matching X-ray pattern. Their discovery, which at long last confirmed the existence of Hf, was published in *Nature* early the following year (Coster and de Hevesy 1923). The Latin name for Copenhagen is *Hafnia*, hence the name "hafnium" for the place where "the missing element 72" was finally discovered. Hafnium was the next-to-last stable element to be discovered, with Re, identified 2 years later in 1925, being the last. The reason it took over half a century to discover Hf after its existence had first been predicted, and why the analytical approach chosen was that of X-ray spectroscopy and not wet chemistry, is that Hf so closely resembles Zr chemically (because of having the same number of valence electrons, nearly the same ionic radius, and belonging to the same group in the periodic table) that it is extremely difficult to separate the two in the chemistry laboratory (although this was eventually accomplished the year after Hf's initial discovery by X-ray spectroscopy). The strong similarity of Hf and Zr, probably the two chemically most similar of all the elements in the periodic table, poses a major analytical challenge to Hf isotope geochemistry, but geochemists also take advantage of this property in Hf isotope studies coupled to zircon geochronology (see entry on ▶ Hafnium Isotopes).

Hafnium is extracted from the same sources as Zr, which are, primarily: (i) heavy mineral sand ore deposits of zircon, ilmenite, and rutile; (ii) pegmatites; and (iii) carbonatites. The production of Hf-free Zr is the main source of Hf. Hafnium-free Zr is needed for nuclear fuel rods because Zr, contrary to Hf, has a very small neutron capture cross-section, which makes it ideal as cladding material. Hafnium, with the exact opposite property, if present as impurities in the Zr, would offset the small neutron capture cross-section of Zr.

Hafnium mostly forms inorganic compounds in the oxidation state of 4+. Due to its refractory nature, Hf is responsible for the existence of several extreme compounds. Hafnium carbide (HfC) is the most refractory binary compound known, with a melting point of 3890 °C, while the mixed TaHf carbide Ta_4HfC_5 has the highest melting point (4215 °C) of any currently known compound. Hafnium nitride (HfN) is the most refractory of all known metal nitrides with a melting point of 3310 °C. Other Hf compounds include Hf chloride ($HfCl_4$), Hf fluoride (HfF_4), and Hf oxide (HfO_2).

The large thermal neutron capture cross-section of Hf makes it useful for neutron absorption in control rods in nuclear reactors and most of the Hf produced today is used for this purpose in nuclear power plants. Hafnium also is used in filaments and electrodes, while HfO_2 has found application in integrated circuits in semiconductors. Finally, together with other metals like Fe, Ti, Nb, Ta, and W, Hf is part of some superalloys used for special applications such as liquid propellants, and as a means of increasing corrosion resistance.

Another important use of Hf is in isotope geochemistry due to the decay of ^{176}Lu to ^{176}Hf. Owing to Hf's high first ionization potential, its isotopic composition is measured most practically by multicollector inductively coupled plasma mass spectrometry (MC-ICP-MS), the plasma source of which reaches temperatures of up to 6000–8000 °C. Since MC-ICP-MS was not developed until the mid 1990s, the routine exploitation of the Lu-Hf isotope system, as well as that of ^{182}Hf-^{182}W, as a chronometer and a tracer for dating and understanding the formation, evolution, and differentiation of the Earth, Moon, Mars, and other terrestrial materials of the Solar System, has only been possible for the last two decades. For details about the Lu-Hf isotope system, see entry on ▶ Hafnium Isotopes.

Geochemical Behavior

Hafnium is lithophile, strongly refractory, and incompatible. Due to its charge of 4+ in nature and its relatively small ionic radius, Hf is geochemically classified as a high field strength element together with Ti, Zr, Nb, Ta, and W. As a consequence of its high valence state it is highly insoluble in most aqueous solutions, although it does form a soluble fluoride complex. Hafnium is chemically similar to Zr and has similar incompatibility to Sm. Typical abundances of Hf in various rock types and meteorite groups can be found at http://earthref.org/GERMRD/e:72/. Here it suffices to mention just a few key illustrative examples such as CI chondrites (taken as representative of the Solar System and the bulk silicate Earth), which contain ~0.1 ppm Hf, Earth's core, which holds no Hf, komatiites with ~0.1–0.5 ppm Hf (though some range up to ~1.5 ppm), basalts with ~2–4 ppm Hf, tonalites-trondhjemites-granodiorites with ~4–5.5 ppm Hf, continental crust, including upper and lower crust, for which most average bulk crustal abundance estimates vary from ~3 to ~5 ppm

Hf, sediments, including Fe-Mn crusts and nodules, spanning a wide range of concentrations from a few ppm to tens of ppm of Hf, carbonates with ~0.5 ppm Hf, and seawater with ~0.5 pmol Hf/kg.

The similar incompatibility of Hf and Sm is demonstrated by the constant and chondritic Hf/Sm ratio of oceanic basalts of 0.75 ± 0.12 (Blichert-Toft et al. 1999, 2002), which is identical within error to the chondritic Hf/Sm ratio of 0.74 ± 0.03 that can be calculated from the data of Bouvier et al. (2008). While the Hf/Sm ratio is largely unaffected by magmatic processes such as melting, it is sensitive to fractionation by sedimentary processes and in particular zircon segregation. Zircon-rich clastic sediments have higher-than-chondritic Hf/REE ratios, whereas zircon-free pelagic, or hydrogenous, sediments have low Hf/REE ratios (Patchett et al. 1984; Plank and Langmuir 1998). Variable Hf/Sm in basalts, as well as in komatiites (Blichert-Toft et al. 2015), therefore betrays the presence of sedimentary material in their mantle source (White and Duncan 1996). The Hf/Sm ratio also attests to the role of ilmenite in planetary magmatic fractionation processes, such as recorded by some lunar rocks and Martian meteorites (Blichert-Toft et al. 1999; Bouvier et al. 2009).

Biological Utilization and Toxicity

Hafnium has no known biological utility and is not toxic.

Summary

In the context of the present *Encyclopedia of Geochemistry*, Hf, as part of both the long-lived, refractory, lithophile, incompatible, high-temperature Lu-Hf isotope system and the Hf/Sm ratio, the latter of which is remarkably constant in magmatic rocks but undergoes fractionation in the sedimentary cycle, has most interest as a tracer and a chronometer in geochemistry and cosmochemistry.

Cross-References

- ▶ Geochronology and Radiogenic Isotopes
- ▶ Hafnium Isotopes
- ▶ High Field Strength Elements
- ▶ Inductively Coupled Plasma Mass Spectrometry (ICP-MS)
- ▶ Lithophile Elements
- ▶ Lutetium
- ▶ Lanthanide Rare Earths
- ▶ Samarium
- ▶ Tungsten Isotopes
- ▶ Zirconium

References

Blichert-Toft J, Gleason JD, Télouk P, Albarède F (1999) The Lu-Hf isotope geochemistry of shergottites and the evolution of the Martian mantle-crust system. Earth Planet Sci Lett 173:25–39

Blichert-Toft J, Boyet M, Télouk P, Albarède F (2002) ^{147}Sm-^{143}Nd and ^{176}Lu-^{176}Hf in eucrites and the differentiation of the HED parent body. Earth Planet Sci Lett 204:167–181

Blichert-Toft J, Arndt NT, Wilson A, Coetzee G (2015) Hf and Nd isotope systematics of early Archean komatiites from surface sampling and ICDP drilling in the Barberton Greenstone Belt, South Africa. Am Mineral 100:2396–2411

Bouvier A, Vervoort JD, Patchett PJ (2008) The Lu–Hf and Sm–Nd isotopic composition of CHUR: constraints from unequilibrated chondrites and implications for the bulk composition of terrestrial planets. Earth Planet Sci Lett 273:48–57

Bouvier A, Blichert-Toft J, Albarède F (2009) Martian meteorite chronology and the evolution of the interior of Mars. Earth Planet Sci Lett 280:285–295

Coster D, Hevesy G (1923) On the missing element of atomic number 72. Nature 111:79

Patchett PJ, White WM, Feldmann H, Kielinczuk S, Hofmann AW (1984) Hafnium/rare earth element fractionation in the sedimentary system and crustal recycling into the Earth's mantle. Earth Planet Sci Lett 69:365–378

Plank T, Langmuir CH (1998) The chemical composition of subducting sediment and its consequences for the crust and mantle. Chem Geol 145:325–394

Scherer E, Münker C, Mezger K (2001) Calibration of the lutetium-hafnium clock. Science 293:683–687

Söderlund U, Patchett PJ, Vervoort JD, Isachsen CE (2004) The ^{176}Lu decay constant determined by Lu-Hf and U-Pb isotope systematics of Precambrian mafic intrusions. Earth Planet Sci Lett 219:311–324

White WM, Duncan RA (1996) Geochemistry and geochronology of the society islands: new evidence for deep mantle recycling. In: Basu A, Hart S (eds) Earth processes: reading the isotopic code, AGU geophysical monograph, vol 95. American Geophysical Union, Washington, DC, pp 183–206

H

Hafnium Isotopes

Janne Blichert-Toft
Laboratoire de Géologie de Lyon, Ecole Normale Supérieure de Lyon, Université Claude Bernard Lyon 1, CNRS, Lyon, France

Introduction

Hafnium consists of the five stable isotopes ^{176}Hf, ^{177}Hf, ^{178}Hf, ^{179}Hf, and ^{180}Hf. Of these, ~1% of ^{176}Hf is radiogenic (the rest being "common" Hf created during nucleosynthesis), produced by the beta decay of radioactive ^{176}Lu with a half-life of ~37 Ga. In addition, radioactive ^{182}Hf, with a half-life of 8.9 Ma, was present in the early Solar System, leading to variable abundances of its daughter ^{182}W in the Earth and in Solar System materials. Together, ^{176}Lu and ^{176}Hf constitute the long-lived Lu-Hf chronometer in which variations in

^{176}Hf resulting from the decay of ^{176}Lu, combined with variations in the Lu/Hf ratio of rocks and minerals, are used to date these rocks and minerals, track the chemical evolution and differentiation of the Earth, Moon, and other planetary bodies and materials of the Solar System, and constrain the nature of magma sources and the provenance of sediments.

History

The Lu-Hf isotope system with applications to tracer isotope geochemistry, cosmochemistry, and geochronology was pioneered in the early 1980s by Jon Patchett and co-workers (Patchett and Tatsumoto 1980a; Patchett and Tatsumoto 1980b; Patchett and Tatsumoto 1980c; Patchett et al. 1981; Patchett 1983a; White and Patchett 1984) using thermal ionization mass spectrometry (TIMS). They were inspired by Boudin and Deutsch (1970) whose first measurement of the ^{176}Lu decay constant held great promise for the Lu-Hf isotope system as a chronometer. However, as it turned out, because of its very low thermal ionization efficiency, the sheer quantity of Hf necessary for isotopic measurement by TIMS (several micrograms) posed a severe analytical challenge greatly limiting the type and number of samples that could be analyzed. Most crucially, extremely Hf-poor meteorites such as chondrites (~0.1 ppm Hf), used as a benchmark for the undifferentiated state of the Solar System and as a plausible composition for the bulk silicate Earth (BSE) (approximations justified by the refractory and lithophile nature of Lu and Hf), could not be analyzed, hence leaving the Lu-Hf isotope system without a baseline relative to which Earth and planetary evolution could be gauged. The Lu-Hf isotope system did not become a fully exploitable, routine geochemical tool until the advent in the mid-1990s of multi-collector inductively coupled plasma mass spectrometry (MC-ICP-MS), which combined the efficient ionization of Hf provided by the high-temperature (~6000–8000 °C) ICP source with the high precision of multi-collection (Walder and Freedman 1992; Blichert-Toft et al. 1997; Albarède et al. 2004). The Hf and Lu separation chemistry protocols needed for compatibility with this new technique, while still laborious, became significantly simpler and less time-consuming than those demanded by TIMS (Blichert-Toft et al. 1997; Blichert-Toft 2001; Münker et al. 2001; Connelly et al. 2006), and the amount of Hf required for high-precision isotopic analysis decreased by an order of magnitude from several micrograms to about a hundred nanograms. This led to a rapid increase in sample throughput and broadened the variety of rocks, meteorites, and minerals that could hereafter be targeted for Lu-Hf isotope analysis. The Hf sample size has since decreased even further to about ten nanograms in sync with MC-ICP-MS transmission increasing as new instrumental developments continue to render plasma source mass spectrometers ever more sensitive.

As a result of MC-ICP-MS, the Lu-Hf isotope system is today on a par with other routinely used long-lived radiogenic isotope systems, such as the Sm-Nd, Rb-Sr, and U-Th-Pb chronometers. Over the last two decades, (i) the Lu-Hf chondritic reference parameters, presumed representative of the bulk silicate Earth, have been established (Blichert-Toft and Albarède 1997; Bouvier et al. 2008; Iizuka et al. 2015); (ii) the ^{176}Lu decay constant, which was poorly defined prior to MC-ICP-MS, has been accurately and precisely determined (Scherer et al. 2001; Söderlund et al. 2004); (iii) Hf-poor samples, such as komatiites, have been analyzed in large numbers (see compilation in Blichert-Toft et al. 2015) shedding new light on early Earth evolution; and (iv) similarly Hf-poor but Lu-rich minerals, most notably garnet, have been put to use in the new powerful dating technique known as Lu-Hf garnet geochronology, which geologists use to unravel tectonic processes such as subduction, burial, and exhumation and the rates at which these mechanisms take place within the lithosphere (e.g., Duchêne et al. 1997; Blichert-Toft et al. 1999a; de Sigoyer et al. 2000; Scherer et al. 2000, to mention just the first few such successful garnet geochronology studies by MC-ICP-MS, which have since been followed by a whole field of diverse garnet dating applications). Moreover, (v) tiny but Hf-rich and highly refractory zircons can now be analyzed one at a time, whether by solution chemistry or laser ablation (e.g., Griffin et al. 2000; Harrison et al. 2005; Nebel-Jacobsen et al. 2005; Blichert-Toft 2008). Because zircon contains percent levels of Hf, incorporated directly into the crystal lattice by substitution with Zr, but only traces of Lu, leading to a very low Lu/Hf ratio (<0.005) and hence negligible radiogenic ingrowth, even over billions of years, the Hf isotopic composition of zircon is essentially frozen at the time of crystallization. Since zircons can be precisely dated by U-Pb geochronology, they provide a first-order record of the Hf isotopic evolution of the Earth's mantle and crust and in this way monitor crustal growth. Finally, (vi) Hf isotope systematics of magmas and sediments track their origins in the mantle or the crust, thereby portraying the timing and processes of planetary mantle-crust differentiation and, again, informing on crustal growth.

Geochemical Properties

Both Lu and Hf are lithophile and refractory elements. Because Lu is a heavy rare earth element (REE) with +3 valency and Hf is a high field strength element (HFSE) with +4 valency and properties very similar to those of Zr, the Lu/Hf ratio is readily fractionated by magmatic processes such as partial melting and fractional crystallization. This contrasts with the Sm-Nd isotope system, in which both the

parent and daughter elements are neighboring +3 charged light REE and therefore very difficult to fractionate from one another. Thus, owing to the different geochemical behavior between the REE and HFSE, there is generally stronger fractionation of the Lu/Hf than the Sm/Nd ratio, an important feature particularly manifested in minerals with affinities for REE, such as garnet and apatite. Another critical difference between these two otherwise very similar chronometers is that ^{176}Lu decays about three times faster than ^{147}Sm, rendering the Lu-Hf isotope system overall more time sensitive than the Sm-Nd isotope system by growing in larger and hence more easily resolvable, radiogenic isotopic differences in less time. The higher rate of ingrowth of ^{176}Hf compared to ^{143}Nd is particularly useful for identifying processes that lead to incongruence between the Lu-Hf and Sm-Nd isotope systems. Because the two systems usually are well correlated in the crust and the mantle, when they are not, their decoupling is telltale evidence of specific processes being at work.

The Lu-Hf and Sm-Nd isotope systems are often used in conjunction because of their broad geochemical similarities, including incompatible behavior during melting leading to their joint buildup in the melt over the residual solid. In addition, both the Lu-Hf and Sm-Nd isotope systems are, for the most part, resistant to perturbations and tend to preserve their isotopic records despite exposure to weathering, hydrothermal alteration, and metamorphic processes. The daughter elements of both systems, Hf and Nd, are relatively more incompatible than their respective parents, Lu and Sm, resulting in lower Lu/Hf and Sm/Nd in the melt than the residual solid. Over time, the melts and residual solids grow in isotopic signatures that are, respectively, less and more radiogenic than their source, and these differences in reservoir isotopic composition can be used to trace the nature of geological processes and the course of planetary differentiation and evolution. Because of the similar behavior during melting of the Lu-Hf and Sm-Nd isotope systems, the Hf and Nd isotope compositions of magmatic rocks are highly (positively) correlated, forming the so-called mantle, or terrestrial (mantle-crust), array (Fig. 1) (e.g., Patchett 1983b; Salters and Hart 1991; Johnson and Beard 1993; Blichert-Toft and Albarède 1997; Vervoort and Blichert-Toft 1999; Vervoort et al. 1999; Chauvel and Blichert-Toft 2001; Chauvel et al. 2008). Exceptions to this general correlation arise when zircon (with high affinity for Hf) and garnet (with high affinity for Lu) are involved, whether directly or indirectly.

^{176}Lu-^{176}Hf System Fundamentals

^{176}Lu disintegrates to ^{176}Hf by beta decay with a decay constant λ^{176}Lu of 1.867 ± 0.008 × 10^{-11} year^{-1} (Scherer et al. 2001; Söderlund et al. 2004) corresponding to a half-life of 37.12 Ga. For a review of the long path to finally arriving at an accurate determination of the ^{176}Lu decay constant, see Begemann et al. (2001) and Vervoort (2015). By convention, the reference stable isotope for the Lu-Hf isotope system is ^{177}Hf. When measuring the radiogenic ^{176}Hf/^{177}Hf ratio, as well as the stable ^{178}Hf/^{177}Hf and ^{180}Hf/^{177}Hf ratios, they are, likewise by convention, corrected for instrumental mass-dependent fractionation relative to the stable ^{179}Hf/^{177}Hf ratio, which is arbitrarily fixed at a value of 0.7325 (Patchett and Tatsumoto 1980b). Hafnium isotopic compositions are conveniently expressed in terms of the so-called epsilon (ε) notation, which is the deviation in parts per ten thousand of the Hf isotopic composition of a given sample from that of chondrites (i.e., the Solar System and bulk silicate Earth reference):

$$\varepsilon_{Hf} = \left[\frac{\left(^{176}Hf/^{177}Hf\right)_{\text{sample}} - \left(^{176}Hf/^{177}Hf\right)_{\text{chondrites}}}{\left(^{176}Hf/^{177}Hf\right)_{\text{chondrites}}}\right] \times 10,000$$

The original Hf solution standard used for Hf isotope analysis since the pioneering work of Jon Patchett and collaborators, which is still in use today, 35 years on, is the JMC-475 Hf standard, a Hf metal obtained from the Johnson Matthey Corporation and dissolved in hydrofluoric acid to produce the JMC-475 Hf standard solution (Patchett and Tatsumoto 1980b). This standard can still be obtained upon request from Dr Jeffrey Vervoort at Washington State University in Pullman (vervoort@wsu.edu) as long as stock remains.

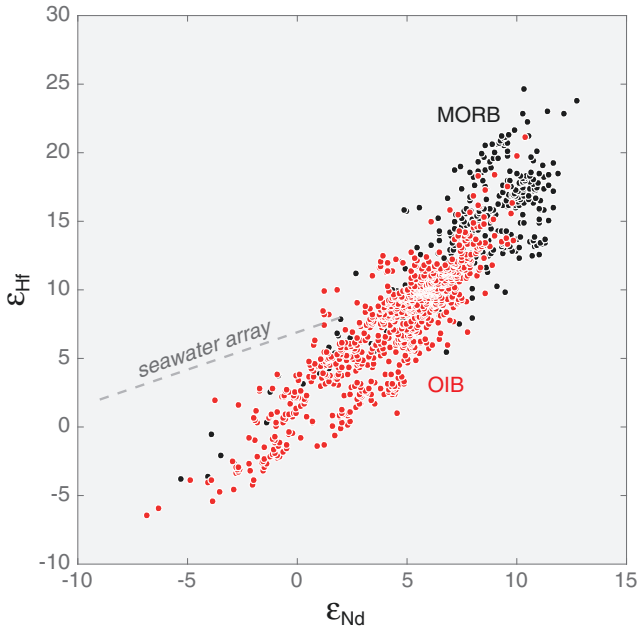

Hafnium Isotopes, Fig. 1 The mantle and seawater arrays in ε_{Hf}-ε_{Nd} space. *Black* symbols are mid-ocean ridge basalts (*MORB*) and *red* symbols are ocean island basalts (*OIB*). The respective slopes of the mantle and seawater arrays are 1.4 and 0.5

A true (accurate) $^{176}Hf/^{177}Hf$ value of the original JMC-475 Hf standard solution was determined by MC-ICP-MS to be 0.282163 ± 0.000009 (Blichert-Toft et al. 1997).

Isotopic Composition of CHUR and BSE

Usable Hf isotope compositions and Lu/Hf ratios of chondritic meteorites were first measured by Blichert-Toft and Albarède (1997). Their present-day $^{176}Hf/^{177}Hf$ and $^{176}Lu/^{177}Hf$ data accurately established the chondritic uniform reservoir (CHUR) reference parameters, which, due to the refractory, lithophile character of both Lu and Hf, are also taken as tenable values for the bulk silicate Earth (BSE). A decade later, with greatly improved analytical capabilities, Bouvier et al. (2008) redetermined the Lu-Hf CHUR/BSE parameters on unequilibrated chondrites, which exhibit less scatter. Most recently, Iizuka et al. (2015) measured the Lu-Hf CHUR/BSE parameters on refractory, low-Lu/Hf meteorite zircon. All three sets of reference parameters are listed in Table 1 and are all currently in use as they are indistinguishable within the associated analytical uncertainties and have calculated Solar System initial Hf isotopic compositions consistent within 1.2 ε units.

Blichert-Toft and Albarède (1997), based on mass balance constraints dictated by terrestrial and chondritic Hf and Nd elemental and isotopic compositions, postulated the existence of an enriched "hidden" reservoir, possibly early mafic crust either recycled into the deep mantle (Chase and Patchett 1988; Galer and Goldstein 1991) or lost to space by collisional erosion (e.g., Caro et al. 2008). Although a missing enriched reservoir is consistent with ^{146}Sm-^{142}Nd systematics between chondrites and the Earth (Boyet and Carlson 2005), it is now well understood that the isotopic compositions of a number of elements, such as ^{16}O and the neutron-rich ^{54}Cr and ^{50}Ti (e.g., Trinquier et al. 2009), vary among chondrite classes as well as between the Earth, Mars, and the Sun. It must further be kept in mind that CHUR is only a hypothetical reference and does not imply that the Earth is genetically related to any particular type of chondrite. Hence, if the underlying fundamental assumption that the Earth is chondritic does not hold up, the requirement of a missing reservoir is lifted. Consequently, the composition of the BSE and the degree to which it is chondritic is still an outstanding question (Caro et al. 2008).

The Seawater Array

The correlation between Hf and Nd isotopes in Fe-Mn crusts and nodules deviates from the terrestrial array toward highly radiogenic Hf for a given Nd isotopic composition forming what has become known as the "seawater array" (Fig. 1) and indicates that, in the ocean, Hf and Nd fractionate independently of the processes taking place in the mantle and the crust and, hence, provide a powerful tracer of the recycling of oceanic sediments into the mantle (White et al. 1986; Albarède et al. 1998). The Lu-Hf and Sm-Nd isotope systems are decoupled in the sedimentary system because zircon, which contains most of the Hf budget, is a heavy, refractory mineral that is deposited predominantly in fluvial or coastal settings, while most of the Lu budget (and that of the other REE) is contained in clays deposited in deeper water as pelagic sediment (Patchett et al. 1984). Furthermore, Hf in zircon is particularly unradiogenic and zircon is highly resistant to chemical weathering; thus, the dissolved load of rivers is more radiogenic than continents as a whole. Over time, the high-Lu/Hf fine-grained sediment resulting from this incongruent weathering develops unusually radiogenic Hf for a given Nd isotopic composition. This decoupling from the otherwise well-correlated Hf-Nd isotope array of terrestrial rocks arising from the "zircon effect" (Patchett et al. 1984; White et al. 1986; Blichert-Toft et al. 1999b) and defining a distinct separate array with a comparatively shallower slope (0.5 vs. 1.4 for the mantle array) is giveaway testimony to the presence in the source of high-$^{176}Hf/^{177}Hf$, low-$^{143}Nd/^{144}Nd$ rocks of Hf-depleted fine-grained sediment.

Lu-Hf Garnet Geochronology

The Lu-Hf isochron method is described in detail in Vervoort (2015) and will not be repeated here.

The proof of concept of the Lu-Hf garnet dating technique by MC-ICP-MS, which has upheld its early promise of great potential for accurate and precise chronology, was first demonstrated by Duchêne et al. (1997) and has since found multiple applications (Vervoort 2015 and references therein). Because Lu, but not Hf, partitions into garnet leading to high Lu/Hf ratios (inclusion-free garnet typically has Hf contents of 0.03–0.3 ppm, while Lu contents are of the order of 1–2 ppm), garnet is an ideal phase for high-precision

Hafnium Isotopes, Table 1 Currently accepted CHUR/BSE parameters for the Lu-Hf isotope system

Reference	$(^{176}Lu/^{177}Hf)_0$	$(^{176}Hf/^{177}Hf)_0$	$(^{176}Hf/^{177}Hf)_{4.568Ga}$[a]
Blichert-Toft and Albarède (1997)	0.0332 ± 0.0002	0.282772 ± 0.000029	0.279816 ± 0.000029
Bouvier et al. (2008)	0.0336 ± 0.0001	0.282785 ± 0.000011	0.279794 ± 0.000018
Iizuka et al. (2015)	0.0338 ± 0.0001	0.282793 ± 0.000011	0.279784 ± 0.000018

[a]Calculated using $\lambda^{176}Lu = 1.867 \times 10^{-11}$ year^{-1} (Söderlund et al. 2004)

chronometry. Garnet is usually combined with clinopyroxene, which contains relatively more Hf (about a factor of ten more than Lu) and less Lu than garnet and hence plots nearer the origin in an isochron diagram widely separated from garnet, thereby producing high-precision ages. The Lu-Hf garnet chronometer is used by geoscientists for dating petrological processes and duration of metamorphism, particularly in the context of subduction, burial, and exhumation and the rates at which these processes operate within the crust and the lithosphere. The so-called "garnet effect" further allows tracking the recycling of, especially, ancient garnet-bearing material into the mantle, such as delaminated lower crust or subcontinental lithospheric mantle foundering into the underlying mantle during continental breakup and with time giving rise to highly depleted Hf isotopic compositions accompanied by "normally" depleted Nd isotopic signatures (e.g., Hanan et al. 2004; Blichert-Toft et al. 2005). The Hf-Nd isotopic signature arising from the garnet effect is readily told apart from that due the zircon effect, despite both of them being characterized by unusually radiogenic Hf for a given Nd isotopic composition, by the former being far more radiogenic for both Hf and Nd than the latter.

Another reason why Lu-Hf garnet geochronology is powerful at keeping time is because of the high closure temperature of the Lu-Hf isotope system in garnet, which, although not well constrained, appears to be ~800 °C, making it particularly well suited for dating deep-seated rocks such as eclogites, peridotites, pyroxenites, granulites, and amphibolite-facies rocks. Since Lu-Hf garnet ages almost always are older than the corresponding Sm-Nd ages measured on the same mineral (e.g., Scherer et al. 2000; Bedini et al. 2004; Chin et al. 2015 and references therein), it can rather safely be deduced that the Lu-Hf system closes at a higher temperature than the Sm-Nd system.

Summary

MC-ICP-MS technology has made it possible over the last two decades to put the refractory Lu-Hf isotope system to full use on a routine basis as a tracer and a chronometer in geochemistry and cosmochemistry on a par with other isotope systems, to which it is largely complementary, such as the Sm-Nd, Rb-Sr, and U-Th-Pb systems. The ^{176}Lu decay constant has been determined, as have chondritic and bulk silicate Earth parameters with the caveat that Earth may not actually be chondritic; the Hf-Nd seawater array has been discovered, which allows the recycling of sediments into the mantle to be tracked closely over time; the development of a powerful dating technique based on garnet has shed new light on small- and large-scale petrological, metamorphic, and tectonics processes; Hf-poor samples, such as komatiites, can now be measured and have brought crucial insights into early Earth evolution; and single rather than batches of zircons are being analyzed, whether by solution or laser ablation protocols, monitoring crustal growth from the Hadean until today.

Cross-References

- ▶ Chondrites
- ▶ Geochronology and Radiogenic Isotopes
- ▶ Hafnium
- ▶ High Field Strength Elements
- ▶ Inductively Coupled Plasma Mass Spectrometry (ICP-MS)
- ▶ Lanthanide Rare Earths
- ▶ Lithophile Elements
- ▶ Lutetium
- ▶ Mantle Geochemistry
- ▶ Neodymium Isotopes
- ▶ Tungsten Isotopes
- ▶ Zirconium

References

Albarède F, Simonetti A, Vervoort JD, Blichert-Toft J, Abouchami W (1998) A Hf-Nd isotopic correlation in ferromanganese nodules. Geophys Res Lett 25:3895–3898

Albarède F, Télouk P, Blichert-Toft J, Boyet M, Agranier A, Nelson BK (2004) Precise and accurate isotopic measurements using multiple-collector ICPMS. Geochim Cosmochim Acta 68:2725–2744

Bedini R-M, Blichert-Toft J, Boyet M, Albarède F (2004) Isotopic constraints on the cooling of the continental lithosphere. Earth Planet Sci Lett 223:99–111

Begemann F, Ludwig KR, Lugmair GW, Min K, Nyquist LE, Patchett PJ, Renne PR, Shih C-Y, Villa IM, Walker RJ (2001) Call for an improved set of decay constants for geochronological use. Geochim Cosmochim Acta 65:111–121

Blichert-Toft J (2001) On the Lu-Hf isotope geochemistry of silicate rocks. Geostand Newslett 25:41–56

Blichert-Toft J (2008) The Hf isotopic composition of zircon reference material 91500. Chem Geol 253:252–257

Blichert-Toft J, Albarède F (1997) The Lu-Hf isotope geochemistry of chondrites and the evolution of the mantle-crust system. Earth Planet Sci Lett 148:243–258. Erratum (1998) Earth Planet Sci Lett 154: 349

Blichert-Toft J, Chauvel C, Albarède F (1997) Separation of Hf and Lu for high-precision isotope analysis of rock samples by magnetic sector-multiple collector ICP-MS. Contrib Mineral Petrol 127:248–260

Blichert-Toft J, Albarède F, Kornprobst J (1999a) Lu-Hf isotope systematics of garnet pyroxenites from Beni Bousera, Morocco: implications for basalt origin. Science 283:1303–1306

Blichert-Toft J, Frey FA, Albarède F (1999b) Hf isotope evidence for pelagic sediments in the source of Hawaiian basalts. Science 285:879–882

Blichert-Toft J, Agranier A, Andres M, Kingsley R, Schilling J-G, Albarède F (2005) Geochemical segmentation of the Mid-Atlantic Ridge north of Iceland and ridge-hot spot interaction in the North Atlantic. Geochem Geophys Geosyst 6. https://doi.org/10.1029/2004GC000788

Blichert-Toft J, Arndt NT, Wilson A, Coetzee G (2015) Hf and Nd isotope systematics of early Archean komatiites from surface sampling and ICDP drilling in the Barberton Greenstone Belt, South Africa. Am Mineral 100:2396–2411

H

Boudin A, Deutsch S (1970) Geochronology: recent development in the lutetium-176/hafnium-176 dating method. Science 168:1219–1220
Bouvier A, Vervoort JD, Patchett PJ (2008) The Lu–Hf and Sm–Nd isotopic composition of CHUR: constraints from unequilibrated chondrites and implications for the bulk composition of terrestrial planets. Earth Planet Sci Lett 273:48–57
Boyet M, Carlson RW (2005) Nd-142 evidence for early (>4.53 Ga) global differentiation of the silicate earth. Science 309:576–581
Caro G, Bourdon B, Halliday AN, Quitté G (2008) Super-chondritic Sm/Nd ratios in Mars, the Earth and the Moon. Nature 452:336–339
Chase CG, Patchett PJ (1988) Stored mafic/ultramafic crust and early Archean mantle depletion. Earth Planet Sci Lett 91:66–72
Chauvel C, Blichert-Toft J (2001) A hafnium isotope and trace element perspective on melting of the depleted mantle. Earth Planet Sci Lett 190:137–151
Chauvel C, Lewin E, Carpentier M, Arndt NT, Marini JC (2008) Role of recycled oceanic basalt and sediment in generating the Hf-Nd mantle array. Nat Geosci 1:64–67
Chin EJ, Lee C-TA, Blichert-Toft J (2015) Growth of upper plate lithosphere controls tempo of arc magmatism: constraints from Al-diffusion kinetics and coupled Lu-Hf and Sm-Nd chronology. Geochem Perspect Lett 1:20–32
Connelly JN, Ulfbeck DG, Thrane K, Bizzarro M, Housh T (2006) A method for purifying Lu and Hf for analyses by MC-ICP-MS using TODGA resin. Chem Geol 233:126–136
Duchêne S, Blichert-Toft J, Luais B, Télouk P, Lardeaux J-M, Albarède F (1997) The Lu-Hf dating of garnets and the ages of the Alpine high-pressure metamorphism. Nature 387:586–589
Galer SJG, Goldstein SL (1991) Early mantle differentiation and its thermal consequences. Geochim Cosmochim Acta 55:227–239
Griffin WL, Pearson NJ, Belousova E, Jackson SE, van Achterbergh E, O'Reilly SY, Shee SR (2000) The Hf isotope composition of cratonic mantle: LAM-MC-ICPMS analysis of zircon megacrysts in kimberlites. Geochim Cosmochim Acta 64:133–147
Hanan BB, Blichert-Toft J, Pyle DG, Christie DM (2004) Contrasting origins of the upper mantle revealed by hafnium and lead isotopes from the Southeast Indian Ridge. Nature 432:91–94. Corrigendum (2004) Nature 432: 653
Harrison TM, Blichert-Toft J, Müller W, Albarède F, Holden P, Mojzsis SJ (2005) Heterogeneous Hadean hafnium: evidence of continental crust at 4.4 to 4.5 Ga. Science 310:1947–1950
Iizuka T, Yamaguchi T, Hibiya Y, Amelin Y (2015) Meteorite zircon constraints on the bulk Lu-Hf isotope composition and early differentiation of the Earth. Proc Natl Acad Sci U S A 112:5331–5336
Johnson CM, Beard BL (1993) Evidence from hafnium isotopes for ancient sub-oceanic mantle beneath the Rio Grande rift. Nature 362:441–444
Münker C, Weyer S, Scherer E, Mezger K (2001) Separation of high field strength elements (Nb, Ta, Zr, Hf) and Lu from rock samples for MC-ICPMS measurements. Geochem Geophys Geosyst 2:art. no. 2001GC000183
Nebel-Jacobsen Y, Scherer EE, Münker C, Mezger K (2005) Separation of U, Pb, Lu, and Hf from single zircons for combined U-Pb dating and Hf isotope measurements by TIMS and MC-ICPMS. Chem Geol 220:105–120
Patchett PJ (1983a) Importance of the Lu-Hf isotope system in studies of planetary chronology and chemical evolution. Geochim Cosmochim Acta 47:81–91
Patchett PJ (1983b) Hafnium isotope results from mid-ocean ridges and Kerguelen. Lithos 16:47–51
Patchett PJ, Tatsumoto M (1980a) Hafnium isotope variations in oceanic basalts. Geophys Res Lett 7:1077–1080
Patchett PJ, Tatsumoto M (1980b) A routine high-precision method for Lu-Hf isotope geochemistry and chronology. Contrib Mineral Petrol 75:263–267
Patchett PJ, Tatsumoto M (1980c) Lu-Hf total-rock isochron for the eucrite meteorites. Nature 288:571–574
Patchett PJ, Kouvo O, Hedge CE, Tatsumoto M (1981) Evolution of continental crust and mantle heterogeneity: evidence from Hf isotopes. Contrib Mineral Petrol 78:279–297
Patchett PJ, White WM, Feldmann H, Kielinczuk S, Hofmann AW (1984) Hafnium/rare earth element fractionation in the sedimentary system and crustal recycling into the Earth's mantle. Earth Planet Sci Lett 69:365–378
Salters VJM, Hart SR (1991) The mantle sources of ocean ridges, islands and arcs: the Hf-isotope connection. Earth Planet Sci Lett 104:364–380
Scherer EE, Cameron KL, Blichert-Toft J (2000) Lu-Hf garnet geochronology: closure temperature relative to the Sm-Nd system and the effects of trace mineral inclusions. Geochim Cosmochim Acta 64:3413–3432
Scherer E, Münker C, Mezger K (2001) Calibration of the lutetium-hafnium clock. Science 293:683–687
de Sigoyer J, Chavagnac V, Blichert-Toft J, Villa IM, Luais B, Guillot S, Cosca M, Mascle G (2000) Dating the Indian continental subduction and collisional thickening in the northwest Himalaya: multichronology of the Tso Morari eclogites. Geology 28:487–490
Söderlund U, Patchett PJ, Vervoort JD, Isachsen CE (2004) The ^{176}Lu decay constant determined by Lu-Hf and U-Pb isotope systematics of Precambrian mafic intrusions. Earth Planet Sci Lett 219:311–324
Trinquier A, Elliott T, Ulfbeck D, Coath C, Krot AN, Bizzarro M (2009) Origin of nucleosynthetic isotope heterogeneity in the solar protoplanetary disk. Science 324:374–376
Vervoort JD (2015) Lu-Hf Dating: the Lu-Hf isotope system. Encyclopedia of scientific dating methods. Springer, Netherlands, pp 379–390
Vervoort JD, Blichert-Toft J (1999) Evolution of the depleted mantle: Hf isotope evidence from juvenile rocks through time. Geochim Cosmochim Acta 63:533–556
Vervoort JD, Patchett PJ, Blichert-Toft J, Albarède F (1999) Relationships between Lu-Hf and Sm-Nd isotopic systems in the global sedimentary system. Earth Planet Sci Lett 168:79–99
Walder AJ, Freedman PA (1992) Isotopic ratio measurement using a double focusing magnetic sector mass analyser with an inductively coupled plasma as an ion source. J Anal At Spectrom 7:571–575
White WM, Patchett PJ (1984) Hf-Nd-Sr isotopes and incompatible element abundances in island arcs: implications for magma origins and crust-mantle evolution. Earth Planet Sci Lett 67:167–185
White WM, Patchett PJ, Ben Othman D (1986) Hf isotope ratios of marine sediments and Mn nodules: evidence for a mantle source of Hf in seawater. Earth Planet Sci Lett 79:46–54

Halide Minerals

John Warren
Petroleum Geoscience Prog., Chulalongkorn University, Bangkok, Thailand

Definition

Halide minerals are a group of naturally occurring inorganic compounds that are salts of the halogen acids and encompass minerals with a dominant halide anion (F^-, Cl^-, Br^-, and I^-).

Complex halide minerals can also have polyatomic anions addition to, or that include, halides. With the notable exceptions of halite (rock salt), sylvite, carnallite, which are the result of the solar evaporation of a brine, and fluorite a widespread hydrothermal precipitate, halide minerals are typically rare and of very local occurrence. Most are fumarolic sublimates or alteration/weathering products tied to exposure to, or brine interaction with, various metalliferous ore deposits (Table 1).

Introduction

In the classification scheme pioneered by James Dana in the early 1800s, minerals are classified into eight major groups, based on the main type of cation present in the mineral structure, namely, (1) native elements; (2) sulfides; (3) oxides and hydroxides; (4) halides; (5) carbonates, nitrates, borates, and iodates; (6) sulfates, chromates, molybdates, and tungstates; (7) phosphates, arsenates, and vanadates; and (8) silicates.

Naturally occurring halide minerals are characterized by combinations with large, highly electronegative, monovalent anions, namely, fluorine (F^-), chlorine (Cl^-), bromine (Br^-), and iodine (I^-). These elements, collectively called the halogens, occur in row 17 (class VIIA) of the periodic table and are essential constituents of halide minerals in which they are ionically bonded with electropositive, metallic cations such as sodium (Na^+), potassium (K^+), calcium (Ca^{2+}) and various base and precious metals. The halides' ionic bonding and small ionic charge mean many of the resulting precipitates are brittle, translucent, and soluble in water. They also tend to possess low to moderate hardness, moderate to high melting temperatures, and to be poor conductors of heat and electricity. More than 80 halide minerals exist, and a selection covering most natural halide salts is listed in Table 1.

However, only three halide minerals – halite (NaCl), fluorite (CaF_2), and sylvite (KCl) – are common worldwide, two of them are evaporite salts (halite and sylvite) and are discussed in detail in that section of the encyclopedia, along with additional halides, sulfates, and carbonates, typical of evaporite deposits. The third, fluorite, is a relatively common hydrothermal precipitate. A fourth natural and locally common halide, cryolite (Na_3AlF_6), was formerly essential to the refining of aluminum ore, such as bauxite, and has a type occurrence at the former Ivigtut Mine, Greenland.

Compositionally and structurally, three broad categories of halide minerals are recognized. These three categories, which are also distinguishable in their modes of occurrence, encompass (1) simple halides, (2) halide complexes, and (3) oxyhydroxy-halides (Table 1).

Simple Halides

The simple halides are salts of the alkali, alkaline earth, and transition metals. Most are soluble in water, with the transition metal halides unstable upon exposure to air. Halite, sodium chloride (NaCl), is the most familiar example of a halide mineral; it often occurs with other evaporite minerals in enormous beds resulting from solar concentration of large accumulation of brines and trapped oceanic water in large shallow subsea-level isolated basins (see evaporites). Economically significant amounts of sylvite and other more complex chloride and sulfate salts are present in some such evaporite beds. Sylvite is the main source mineral for potash fertilizer, while halite is an essential feedstock to the world's chemical industries, is essential to human nutrition as table salt, and is widely used as a road deicer.

Fluorite, or calcium fluoride (CaF_2), another simple halide, is widespread in limestones that have been permeated by hydrothermal solutions containing the fluoride anion (Richardson and Holland 1979). Hence, it is a commonplace precipitate in Mississippi Valley-type (MVT) deposits and igneous skarns (Kendrick and Burnard 2013). Noteworthy deposits of fluorite occur in Mexico; Cumberland, England; and Illinois, Missouri, Kentucky, and Colorado in the United States. Other simple halide minerals such as sal ammoniac, ammonium chloride (NH_4Cl); lawrencite and ferrous chloride ($FeCl_2$); and molysite and ferric chloride ($FeCl_3$) occur in fumarolic vents and are highly unstable in air (Table 1). A few hydrothermal vein minerals in silver deposits, such as chlorargyrite and calomel, serve as minor and occasional ores of silver and mercury, respectively. A few double salts (e.g., carnallite and tachyhydrite) included among the simple halides have formed under evaporitic conditions similar to, but significantly more saline, than the brines that precipitate halite.

Halide Complexes

In the halide complexes, halide anions are tightly bound to a cation, usually aluminum; the resulting unit behaves as a single negative ion. The most common examples are the fluoroaluminates; cryolite, cryolithionite, thomsenolite, and weberite. Significant quantities of cryolite formerly were mined at Ivigtut, Greenland, and once used as flux in the recovery of aluminum from bauxite.

Oxyhydroxide Halides

Most oxyhydroxy-halides are rare and usually highly insoluble. Many have formed by the action of halide-bearing groundwater and thermal waters upon the oxidation products of previously existing sulfides: atacamite, matlockite,

Halide Minerals, Table 1 Natural halide minerals

Mineral Name	Mineral Properties: Formula, Mohs hardness, S.G., lustre, colour	Comments	References
Anarakite (see also herbertsmithite)	$ZnCu_3(OH)_6Cl_2$ (oxyhalide) 3–3.5, 3.8, vitreous to adamantine, light-green to blue-green	Alteration product of Cu mineralization in Triassic dolomites, near Anarak Iran, and syenitic porphyries and granites in Chile. Synthetic form of this salt exhibits properties of a quantum spin liquid and so shows constantly fluctuating scattered magnetic orientations	Adib and Ottemann 1972; Braithwaite et al. 2004
Antarcticite (see also sinjarite)	$CaCl_2.6H_2O$ (simple halide – hydrated) 2–3, 1.7, vitreous, deliquescent, colourless	Hydroscopic, cryogenic, precipitate in the hyperarid Don Juan pool, Wright Valley, Antarctica (type area). Also noted within fluid inclusions within quartz in pegmatite bodies in the Bushveld complex of South Africa and in association with halite, gypsum and celestine in brine pans in Bristol Dry lake, California	Torii and Ossaka 1965; Warren 2016
Atacamite	$Cu_2(OH)_3Cl$ ((oxyhalide) 3–3.5, 3.8, adamantine, various bright green shades, dark emerald green to black	Atacamite (minor ore product) forms in arid climates where copper minerals are exposed to oxidation or long-term arid-zone hydrothermal flushing, e. g. Chuquicamata, Mantos Blancos Cu-Ag deposit, Antofagasta, Atacama Desert. Atacamite is polymorphous with botallackite, clinoatacamite and paratacamite, and can be produced in in small amounts during biomineralisation	Cameron et al. 2007
Avogadrite	$(K,Cs)BF_4$ (Complex halide) n.d, 2.5-3.3, vitreous, colourless to white	Typically occurs as a sublimation product around volcanic fumaroles, as on Mt Vesuvius, Italy. Isostructural with baryte	Gaines et al. 1997
Bischofite	$MgCl_2.6H_20$ (simple halide – hydrated) 1.5-2, 1.6, vitreous, colourless, white, astringent bitter taste	Bittern precipitate from highly concentrated seawater brines. Significant amounts have precipitated in association with carnallite and sylvite in shallow subsurface salt beds in the Dallol depression, Ethiopia. (See evaporites)	Warren 2016
Bismoclite	(BiO)Cl (oxyhalide) 2–2.5, 7.8, vitreous to greasy, white, pale grey, yellowish brown	Bismuth salt, typically hosted in pegmatites in granites and greisen (is a member of matlockite mineral group). First described in 1937 from alluvium near bismuth-bearing pegmatites at Jackals Water, SW of Prieska, South Africa, also found at Bygoo, Australia and Tintic District Utah	Mountain 1937
Boleite	$KPb_{26}Ag_9Cu_{24}(OH)_{48}Cl_{62}$ (hydroxyhalide) 3–3.5, 5.1, vitreous to pearly, deep Prussian blue to indigo	Very minor ore product first described in 1973 from El Boleo Mine, Mexico. Worldwide, it occurs in association with numerous other secondary oxidation minerals in oxide zones, such as pseudoboleite, cumengite and diaboleite, all with similar crystal structures	Winchell and Rouse 1973
Botallackite	$Cu_2(OH)_3Cl$ (oxyhalide) Soft, 3.6, transparent to translucent, mountain green, bluish	Forms as alteration product in copper deposits exposed to weathering and salt water, type locality is Botallack mine, Cornwall, also Lubin Mine, Poland. Also reported from deep seafloor black smoker deposits, due to reaction of primary sulfide minerals with seawater and also found on copper bearing slag exposed to seawater. Botallackite is polymorphous with atacamite, clinoatacamite, and paratacamite	Hawthorne 1985
Bromargyrite	AgBr (Simple halide) 2.5, 6.5, adamantine, resinous, yellowish, greenish brown, bright green	Oxidation product of primary silver ore minerals, first described in 1859 for an occurrence in Plateros, Zacatecas, Mexico. Occurs in arid weathering environments along with native silver. Dimorphous with chlorargyite	Gaines et al. 1997

(*continued*)

Halide Minerals, Table 1 (continued)

Mineral Name	Mineral Properties: Formula, Mohs hardness, S.G., lustre, colour	Comments	References
Calomel	Hg_2Cl_2 (Simple halide) 1.5, 6.5, adamantine, colourless, dense white, greyish, yellowish white, brown. Insoluble in water	Secondary mercury salt that was result of alteration of Hg minerals in the oxidized zone of Hg deposits. For example, natural calomel is found together with native mercury, cinnabar, calcite, limonite, and clay at Moschellandsberg, Germany; Zimapán, Mexico; Avala, Serbia; and Brewster county, Texas, U.S.A. Mercuric chloride can be toxic but until the early 20th century, calomel was taken internally as a purgative or a laxative, and once used as disinfectant, as well as in the treatment of syphilis its previous internal usage once caused widespread mercury poisoning in the form of "pink Disease", with a mortality ratio of 1:10. Until 1954 it was also a common ingredient in teething powders in Britain	Korbel and Novik 2001
Carnallite	$KMgCl_3.6H_2O$ (simple halide – hydrated) 2.5, 1.6, resinous, dull to shining, milk-white to colourless, sometimes reddish from included Fe, Distinct highly bitter taste, soluble	Bittern precipitate from seawater brine. Ore for potassium and magnesium. Widespread precipitate in modern salt pans at the southern end of the Dead Sea. It is the dominant primary potassic bittern salt from the evaporation of modern seawater, which tends to be enriched in $MgSO_4$ compared to Palaeozoic seawater (see evaporites)	Warren 2016
Challacolloite	KPb_2Cl_5 (Simple halide) 2.3, 4.8, adamantine to greasy on exposure to air, colourless to white	Occurs as white fumarolic encrustations on lava, often intergrown with cotunnite. For example, at the Challacollo silver mine, Atacama Desert, northern Chile, at Vesuvius, Naples, Campania and in the La Fossa crater, Vulcano, Aeolian Archipelago, Sicily, Italy. Synthetic analogs, dosed with REE cations, are promising new laser host crystals	Schlüter et al. 2005
Chiolite	$Na_5Al_3F_{14}$ (complex halide) 3.5-4.0, 3.0, vitreous, colourless to snow-white	Pegmatite (cryolitic) veins in granites. For example, at Miass, Ilmen Mountains, Southern Ural Mountains, Russia. and the the Ivigtut cryolite deposit, southwestern Greenland. In the USA, occurs in the Morefield pegmatite mine, Amelia, Amelia Co., Virginia	Jacobini et al. 1981
Chlorargyrite	AgCl (simple halide) 2.5, 5.5, resinous, colourless, grey to violet	Secondary ore mineral, typically in oxidised zones of silver deposits, as in outcrops of Bonanza Ag-vein, Nevada, USA and Yinchangpo Pb-Zn-(Ag) deposit, Yunnan, China. Also known as cerargyrite and, when weathered in desert air, as "horn silver"	Gaines et al. 1997
Chlorocalcite	$KCaCl_3$ (simple halide) 2.5-3, 2.2, white, tinged violet, deliquescent	Typically found in active volcanic fumaroles as on Vesuvius, Campania, Italy, also in Mengye potash beds China and co-association with antarcticite in Bristol Dry Lake, California and at Stassfurt, 34 km south of Magdeburg, Saxony-Anhalt, Germany	Gaines et al. 1997
Chlormanganokalite	K_4MnCl_6 (complex halide) 2.5, 2.3, vitreous, champagne, lemon- to canary-yellow	Fumarolic precipitate in fissures and cavities in scoria blocks in Mt Vesuvius	Gaines et al. 1997
Chloroxiphite	$Pb_3CuO_2Cl_2(OH)_2$ (oxyhalide) 2.5, 6.8, adamantine, olive green to pistachio green	Typically formed as alteration product of Pb ore (as does the associated mendipite). Found in association with mendipite in the Mendip Hills, Somerset, England, and other areas where chloride-rich groundwaters flush Pb-ore	Finney et al. 1977; Siidra et al. 2008

(*continued*)

H

Halide Minerals, Table 1 (continued)

Mineral Name	Mineral Properties: Formula, Mohs hardness, S.G., lustre, colour	Comments	References
Coccinite	HgI_2 (simple halide) 2, 3.2, translucent, orange-red, volatile at room temperature, slightly soluble in water	Reported as secondary mineral from Broken Hill, New South Wales, and from a uranium mine in Thuringia and old mercury workings in the Rhineland-Palatinate in Germany. At the Thuringia deposit it is a sublimation product resulting from fires associated with pyrite-bearing, graptolitic slate	Witzke 1997
Cotunnite	$PbCl_2$ (simple halide) 2.5, 5.8, adamantine, colourless to white	Volcanic sublimate or as an alteration of galena in saline environments, also as an alteration product on leaden archeological objects or slag immersed in seawater. For example, on Vesuvius, Campania; in the Niccioleta mine, 40 km southwest of Siena; and along Baratti Beach, Tuscany, in slag. Also occurs in association with galena, cerussite, anglesite and matlockite in Caracoles, Chile and the Tolbachik volcano on the Kamchatka Peninsula, Russia	Gaines et al. 1997
Cryolite	Na_3AlF_6 (complex halide)2.5, 3.0, vitreous to greasy, colourless, white, pale brown, pink, smoky to black	Late stage precipitate in granitic (cryolitic) pegmatites, also occurs in tin-bearing alkalic granites; as vapor-phase mineral along fractures and in the groundmass of some fluorine-rich, topaz-bearing rhyolites; in pods in a carbonatite veins cutting fenitized biotite gneiss. Is also as a rare authigenic component of the marlstones and shales of the Green River Formation. Appears to disappear when immersed in water due to similar refractive indices. Was once an important ore feed for aluminum production (mined commercially at Ivigtut, Greenland)	Gaines et al. 1997
Cryolithionite	$Na_3Li_3Al_2F_{12}$ (complex halide) 2.5-3.0, 2.8, vitreous, colourless to white	Late stage precipitate in granitic (cryolitic) pegmatites as at Ivigtut and Arlsukfiord, West Greenland	Geller 1971
Cryptohalite	$(NH_4)_2SiF_6$ (complex halide) 2.5, 2.0, vitreous, colourless, grey, white	Formed as a sublimation product in fumaroles (Mt Vesuvius) and coal fires (Kateřina colliery, Radvanice, Eastern Bohemia, Czech Republic). It is a toxic salt, like all salts of fluorosilicic acid. Historically is was also called bararite, which is now considered a co-associated mineral, as is sal ammoniac	Klein and Dutrow 2008
Cumengeite	$Pb_{21}Cu_{20}Cl_{42}(OH)_{40}$ (oxyhalide) 2.5, 4.7, weakly vitreous, Indigo blue, can form distinctive "star-shaped" crystals	Secondary mineral formed through reaction of chloride ions with primary sulphides in the oxidized zone of some Pb-Cu deposits (Boleo Mine, Mexico) and exposed smelter slags (Larium, Greece)	Hawthorne and Groat 1986
Diaboleite	$Pb_2CuCl_2(OH)_4$ (oxyhalide) 2.5, 5.5, adamantine, deep blue	Occurs in association with manganese oxide ore, as a secondary mineral in lead and copper oxide ores and seawater exposed smelter slag (name means "distinct from boleite"). It is a low-temperature phase, that is stable under hydrothermal conditions at temperatures less than 100 to 170 °C. At higher temperatures, the first stable mineral to form is cumengeite	Hawthorne and Groat 1986; Winchell and Wenden 1968
Douglasite	$K_2Fe^{2+}Cl_4.2H_2O$ (hydrated complex halide) n.d., 2.1, vitreous, pale green, yellow-green, brownish red on exposure	Typically occurs as minor salt in a halite–potash deposit, Douglashall mine, Germany	Klein and Dutrow 2008
Embolite	Ag(Br, Cl) (simple halide) 1.5-2, 5.7, adamantine, resinous, yellowish green to greyish yellow	One of three natural minerals that contain bromine, others are idiobromite (Ag(Cl,Br,I) and bromyrite AgBr). Occurs as a weathering product of silver ore in the arid Broken Hill region, Australia and Chanarcillo region, Chile	Barclay and Jones 1971

(*continued*)

Halide Minerals, Table 1 (continued)

Mineral Name	Mineral Properties: Formula, Mohs hardness, S.G., lustre, colour	Comments	References
Erythrosiderite	$K_2Fe^{3+}Cl_5.H_2O$ (hydroxyhalide) N.d., 2.4, vitreous, translucent, ruby-red to red, soluble in water, deliquescent	Occurs as active fumarolic sublimates (highly hygroscopic) and associated with rinneite rims in some bedded salt deposits	Stewart 1963
Ferruccite	$NaBF_4$ (complex halide) 3.0, 2.5, translucent, colourless to white, soluble in water, bitter acid taste	Occurs as active fumarolic sublimate at Vesuvius, Campania, Vucano, Aeolian Islands, Italy and on volcanoes on the Kamchatka Peninsula, Russia	Brunton 1968
Fiedlerite	$Pb_3ClF(OH).H_2O$ (hydroxyhalide) 3.5, 5.9, transparent, colourless to white	Reaction of halide-bearing brines with Pb ore (Argent Pb-Zn Mine, Transvaal) or ancient smelter slag (Larium, Greece)	Merlino et al. 1994
Fluocerite	$(Ce,La)F_3$ (halide) 4–5, 5.9, vitreous, pale greenish yellow	Pegmatite REE association, hydrothermal veins in granite, as in the Zhanuzak area, Kent massif, Karaganda region, central Kazakhstan	Chistyakova and Kazakova 1969; Dill 2015
Fluorite (aka fluorspar)	CaF_2 (halide) 4, 3.2, vitreous, allochromatic: Purple, lilac, golden-yellow, green, colourless, blue, pink, champagne, brown	Widespread, typically a hydrothermal (vein) gangue associated with galena, sphalerite and barite ores in China, South Africa and Mexico also as cavity fill precipitates in MVT associations. Meta-evaporite igneous association at Dalnegors'k, Russia. Can be produced in small amounts during biomineralisation	Richardson and Holland 1979
Frankdicksonite	BaF_2 (halide) 2.5, 4.9, vitreous, colourless white	Extremely rare, occurs naturally as a hydrothermal precipitate in the Carlin gold deposit of Eureka County, Nevada as cubic crystals (0.1 - 4 mm) encased in quartz	Radkte and Brown 1974
Halite	NaCl, (halide) 2, 2.5, vitreous, colourless to white, als blue to red with impurities, salty taste	Worldwide it is the main evaporite salt produced by evaporation of seawater (See evaporite). Typically associated salts include sylvite, polyhalite, kieserite, carnallite, gypsum, anhydrite, dolomite. Can be produced in biomineralisation	Warren 2016
Hieratite	K_2SiF_6 (complex halide) 2.5, 2.7, vitreous, colourless, white to grey	Forming in active fumarolic sublimates, as in Italy, on Vulcano, Lipari Islands, and from Vesuvius, Campania. Can be produced in biomineralisation and was noted in the volcanic ash of the Eyjafjallajökull eruption, Iceland	Klein and Dutrow 2008; Gislason et al. 2011
Hydrohalite	$NaCl.2H_2O$ (hydrated halide) n.d. 1.6, vitreous, colourless, melts under own vapour pressure at $-0.1°C$ and converts to halite	Cryogenic precipitate in a saturated halite brines at cold temperatures ($\approx -5°C$), e.g. occurs naturally in Lake Bonney, Taylor Valley, Antarctica	Warren 2016; Starinsky and Katz 2003
Iodargyrite (aka Iodyrite)	AgI (halide) 1.5-2, 5.7, adamantine, resinous, colourless, pale yellow, greenish yellow	Silver ore. Naturally occurring mineral form of silver iodide formed in oxidized zoned of silver deposits, e.g. Broken Hill region Australia and Schöne Aussicht Mine in Wied Iron Spar district, Germany	Gaines et al. 1997; Gillard et al. 1997
Jarlite	$Na(Sr,Na)_7MgAl_6F_{32}(OH,H_2O)_2$ (hydrated complex halide) 4–4.5, 3.8, vitreous, colourless, grey to white	In vugs in cryolitic pegmatite veins along with with other fluorides as at Ivigtut, Greenland	Pauly et al. 1997
Kempite	$Mn_2(OH)_3Cl$ (oxyhalide) 3.5, 3, semi-transparent, emerald-green	Associated with platinum-group minerals in the Noril'sk Complex, and with the Korshunovskoye iron ores of the southern Siberian platform and in the Deep Copper Zone of the Sudbury Complex and in Alum Rock Canyon. California	Gaines et al. 1997; Saini-Eidukat et al. 1998
Laurionite	(Ag,Cu)I (halide) 3–3.5, 6.2, adamantine, Colourless to white	First documented at Larium, Greece, now known to be a natural mineral in the oxidized zone of some Pb–Zn–Cu–Ag deposits, especially in arid regions, e.g. Broken Hill region, Australia. Dimorphous with paralaurionite	Gaines et al. 1997

(*continued*)

H

Halide Minerals, Table 1 (continued)

Mineral Name	Mineral Properties: Formula, Mohs hardness, S.G., lustre, colour	Comments	References
Lawrencite	$(Fe,Ni)Cl_2$ (halide) soft, 3.2, translucent, green to brown, deliquescent	Forms in volcanic sublimates as at Mt Vesuvius, Italy and via terrestrial alteration of iron meteorites as in the Tazewell, Ovifak and Canyon Diablo meteorites	Buchwald and Clarke 1989
Lorettoite (chubutite)	$Pb_7O_6Cl_2$ (oxyhalide) 3, 7.7, adamantine, honey-yellow to reddish-yellow	Forms in oxidized lead ore zones, typically associated with ancient lead slags as at Larium, Greece, also at Loretto, Oklahoma. Probably discredited name as is manmade equivalent to chubutite	Gaines et al. 1997
Malladrite	Na_2SiF_6 (halide) n.d., 2.7, semi-transparent, pale rose, slightly soluble in water	Forms in volcanic sublimates, e.g. Vesuvius and the explosive ash cloud of the Eyjafjallajökull volcano when the meltwaters of the Eyjafjallajökull glacier mixed with hot magma. It Is a mineral with silica in the lattice but it is not a silicate	Zalkin et al. 1964; Gislason et al. 2011
Marshite	CuI (halide) 2.5, 5.6, transparent, colourless pale honey yellow to salmon red (on exposure)	Occurs as a rare mineral in the oxidized zone of Cu ores, as in the Broken Hill and Moonta mine regions, Australia and Chuquicamata porphyry Cu deposit, Atacama Desert, Chile	Barclay and Jones 1971; Garrett 1985
Matlockite	PbFCl (double halide) 2.5-3.0, 7.1, adamantine, colourless, pale yellow to yellow-orange	Forms in the oxide zone of some lead-bearing mineral deposits. Matlockite group consists of a number of minerals which share a similar crystal structure. The group includes bismuth, lead or calcium halides: bismoclite (BiO)Cl, daubréeite (BiO)(OH,Cl), laurionite PbCl(OH), paralaurionite PbCl(OH), rorisite CaFCl, zavaritskite (BiO)F and the eponymous matlockite	Pasero and Perchiazzi 1996
Mendipite	$Pb_3Cl_2O_{2.5}$ (oxyhalide) 2.5, 7.2, adamantine to pearly, colourless to white to brownish	Typically formed as alteration product (like chloroxiphite). Occurs in nodules Mendip Hills, Somerset, England, and other areas where chloride-rich groundwaters flush Pb-ore, as in the Broken Hill region, Australia	Symes and Embrey 1977; Gillard et al. 1997
Miersite	(Ag,Cu)I (Halide) 2.5, 5.6, adamantine, canary yellow	Rare mineral in the oxidized zone of some Pb–Zn–Cu–Ag deposits, especially in arid regions, e,g. Broken Hill region, Australia	Barclay and Jones 1971
Molysite	$FeCl_3$ (halide) Soft, 2.9, semitransparent, brownish red to yellow, very deliquescent	Rare, found as fumarolic sublimate as at Vesuvius and Vulcano, Lipari Islands, Italy. Toxic, highly corrosive and acidic. Co-associated minerals include; tridymite, hematite, anhydrite, halite	Gaines et al. 1997
Nantokite	CuCl (halide) 2.5, 4.1, adamantine, white, greyish to greenish on exposure	Forms a secondary mineral in hydrothermal copper-bearing deposits; rarely as volcanic sublimates, as in Carmen Bajo mine, Atacama, Dzhezkazgan, Kazakhstan. Also found in the Broken Hill and Cloncurry districts, Australia and the nitrate soils of the Atacama Desert	Gaines et al. 1997; Gillard et al. 1997
Pachnolite	$NaCaAlF_6.H_2O$ (hydrated complex halide) 3, 2.97, vitreous, colourless to white	Alteration product in cryolitic pegmatite veins along with other alkali aluminum fluorides, as at Ivigtut, Greenland and rare earth pegmatites in the Olary Block, Australia	Hawthorne and Ferguson 1983; Lottermoser and Lu 1997
Paralaurionite (rafaellite)	PbCl(OH) (oxyhalide) Soft, 6.1, sub-adamantine, colourless, white, pale greenish	Forms in lead-bearing slags exposed to seawater, as at Laurium, Greece, also occurs in alteration zones in some polymetallic ore deposits as at Higher Pitts mine, Mendip Hills and Argent Pb-Ab mine, South Africa	Merlino et al. 1993
Paratacamite	$Cu_2(OH)_3Cl$ (oxyhalide) 3, 3.7, vitreous, green to dark green	An oxidation product of other copper minerals, especially under arid, saline conditions as in Generosa Mine, Chile; also in fumarolic deposits and as a weathering product of sulphides in subsea black smoker deposits	Frondel 1950; Fleet 1975; Cameron et al. 2007

(*continued*)

Halide Minerals, Table 1 (continued)

Mineral Name	Mineral Properties: Formula, Mohs hardness, S.G., lustre, colour	Comments	References
Penfieldite	$Pb_2Cl_3(OH)$ (Oxyhalide) n.d, 5.8, adamantine to greasy, colourless to white, soluble in water	In oxidized hydrothermal lead deposits (Sierra Gordo District, Chile) and as an alteration product of lead-bearing slag immersed in seawater as at Laurium, Greece	Merlino et al. 1995
Prosopite	$CaAl_2(F,OH)_8$ (Complex halide) 4.5, 2.9, vitreous, weak, colourless, greyish white to blue	Disseminated precipitate in fluorine-rich granites, greisens, and granite pegmatites; more rarely in base-metal deposits, e.g., Ivigtut, Greenland; St. Peter's Dome near Pike's Peak, Colorado, USA; Mt Bischoff, Tasmania	Petersen 1986
Pseudoboleite	$Pb_5Cu_4Cl_{10}(OH)_8.2H_2O$ (hydroxyhalide) 2.5, 4.9, translucent, indigo blue	Secondary mineral precipitate formed through reaction of chloride with primary sulfides in the oxidized zone of Pb–Cu deposits as in the Amelia Mine, Boleo, Mexico and Larium Greece	Winchell and Rouse 1974
Ralstonite	$Na_xMg_xAl_{2-x}(F,OH)_6.H_2O$ (Hydroxyhalide) 4.5, 2.6, vitreous, colourless to milky white	Precipitates in some granite pegmatites and greisenized zones rich in fluorine; also in hydrothermal antimony deposit in silicified limestones, as in Ivigtut, Greenland and Mt Cleveland Tin mine, Tasmania and in volcanic caves	Pauly 1965; Forti 2005
Rinneite	$K_3NaFeCl_6$ (complex halide) 3, 2.3, adamantine silky, colourless, rose red to violet	Secondary mineral in marine saline evaporite deposits (see evaporites); in some salt diapirs, as in Sar Pohl diapir, southern Iran, or as a volcanic sublimate as at Mt. Vesuvius, Italy	Beattie and Moore 1982; Talbot et al. 2009
Sal Ammoniac	NH_4Cl (halide) 1.5-2, 1.5, vitreous, white to off-white, water soluble	Typically forms as encrustations formed by sublimation around volcanic vents as at Mt Vesuvius, also forms by alteration of guano and burning coals. Minor component of Alum stalactites in the Alum Cve, Italy. Named after fumarole occurrences at the Ancient Roman "Temple of Jupiter (Amun or Ammon)	Gaines et al. 1997; Forti 2005
Scacchite	$MnCl_2$ (halide) Soft, 3.0, transparent, colourless to rose red. deliquescent	Product of fumarolic activity as a Vesuvius Italy, also formed in the explosive ash cloud of the Eyjafjallajökull volcano when the meltwaters of the Eyjafjallajökull glacier mixed with hot magma	Gaines et al. 1997; Gislason et al. 2011
Sellaite	MgF_2 (halide) 5, 3.1, vitreous, colourless to white, slightly soluble in water	At its type locality, sellaite occurred within a bitumen-bearing dolomite-anhydrite rock within the moraine deposits of the Gebroulaz Glacier, France and Stassfurt salts, Germany. Also occurs in the Carrara Marble, granite pegmatites in Norway, fumarolic sublimates at Mt Vesuvius, and natrocarbonatites of the Oldoinyo Lengai volcano, Tanzania	Koritnig 1951; Raade and Haug 1981; Mangler et al. 2014
Sinjarite	$CaCl_2.2H_2O$ (hydrated halide) 1.8, 1.5, vitreous-resinous, light pink	Found in detritus in a wadi cutting across the Sinjar anticline, Iraq. Highly deliquescent. See also Antarcticite. Also present in hypersaline fluid inclusion in quartz in the meta-evaporites of the western Zambian copper Belt, Africa	Aljubouri and Alddabbagh 1980; Eglinger et al. 2014
Sylvite	KCl (halide) 2, 2, vitreous, colourless to white to red with iron oxides, soluble in water, salty taste with bitter overtones	Worldwide it is the main potash ore mineral in evaporite salt beds produced by evaporation of seawater (See evaporite) Can be produced in small amounts during bio-mineralisation and also occurs in sublimate in volcanic fumaroles as at Mt Vesuvius, Italy	Warren 2016
Tachyhydrite	$CaMg_2Cl_6.12H_2O$ (hydrated halide) 2, 1.7, vitreous, colourless, wax yellow to pale yellow, highly deliquescent, very sharp, bitter taste	Can be a minor component of marine evaporite deposits, especially in Aptian-age evaporites, where its relatively widespread occurrence is tied to $MgSO_4$-depleted world ocean chemistry (see evaporite)	Clark et al. 1980; Warren 2016

(*continued*)

Halide Minerals, Table 1 (continued)

Mineral Name	Mineral Properties: Formula, Mohs hardness, S.G., lustre, colour	Comments	References
Thomsenolite	$NaCaAlF_6.H_2O$ (complex halide) 2, 3, vitreous, colourless to white, reddish with iron oxides	Alteration product in cryolitic pegmatite veins along with other alkali aluminum fluorides, such as acuminite, as at Ivigtut, Greenland and in rare earth pegmatites as in the Olary Block, South Australia	Adhikesavalu et al. 1985; Lottermoser and Lu 1997
Villiaumite	NaF (halide) 2–2.5, 2.8, vitreous, carmine-pink to lavender-red, soluble in water	Occurs in nepheline syenite intrusives and pegmatites and in natrocarbonatites and nearby trona crusts in Lake Magadi. Toxic salt that can cause dental fluorosis in residents of African Rift valley	Stormer and Carmichael 1970; Mangler et al. 2014

nadorite, and diaboleite are examples. A few halide compounds such as fiedlerite, laurionite, and penfieldite have been documented as forming through the action of seawater upon ancient lead slags from the historic deposits at Laurium (Lavrion), Greece, although other natural occurrences are now known, since the initial documentation at Laurium. There are more than 300 and 70 minerals known from this locality, and many of them are halides (Kohlberger 1976).

Laurium was a mine for centuries, first for its silver ores starting with the Greeks under Peisistratus in the sixth century BC and then the Romans for the lead content of its ores (ending around 100 AD) (Jones 1982). Gangue rock, judged too poor in metals to be processed by the ancient miners, was dumped into the nearby ocean. Beginning in the nineteenth century, and periodically, the slag has been economically reprocessed (Skarpelis and Argyraki 2009). Related to this interest in reprocessing from this site, analysis of the slag rocks has yielded a wide variety of halide minerals, some unique, and many of which were created by exposure and interaction with halides in the seawater over the millennia since being dumped. Daily exposure to seawater, either by immersion or sea spray, altered exposed surfaces of low-grade lead ores and produced an unusual assortment of rare halide minerals. Purists do not consider many of these neo-formed minerals at Laurium to be true "natural" minerals as their creation was indirectly aided by anthropogenic activities, as are other halide minerals created by exposure to waters and brines in mined areas worldwide (Table 1).

Conclusions

Although halides are rare, they are nevertheless of great economic importance as fertilizer, in nutrition and chemical feedstock, and as ore of some metals.

Cross-References

- ▶ Alkali and Alkaline Earth Metals
- ▶ Chemical Bonds
- ▶ Evaporites
- ▶ Halogens
- ▶ Hydrothermal Solutions
- ▶ Silver

References

Adhikesavalu D, Cameron TS, Knop O (1985) Thomsenolite, $NaCaAlF_6.H_2O$: hydrogen bonding and comparison with pachnolite. Can J Chem 63:3322–3327

Adib D, Ottemann J (1972) Ein neues mineral, $(Cu,Zn)_2(OH)_3Cl$, aus der Kali-Kafi mine, Provinz Anarak, zentral Iran. Neues Jb Mineral Monat 9:335–338

Aljubouri ZA, Alddabbagh SM (1980) Sinjarite, a new mineral from Iraq. Mineral Mag 43:643–645

Barclay CJ, Jones JB (1971) The Broken Hill silver halides. J Geol Soc Aust 18:149–157

Beattie JK, Moore CJ (1982) Crystal and molecular structures of rinneite, sodium tripotassium hexachloroferrate(II), and hexa-amminecobalt(lll) hexachloroferrate(III). Comparison of iron-chloride distances in hexachloroferrates(lI) and -(III). Inorg Chem 21:1292–1295

Braithwaite RSW, Mereiter K, Paar WH, Clark AM (2004) Herbertsmithite, $Cu_3Zn(OH)_6Cl_2$, a new species, and the definition of paratacamite. Mineral Mag 68:527–539

Brunton G (1968) Refinement of the structure of $NaBF_4$. Acta Crystallogr 24:1703–1704

Buchwald VF, Clarke RS Jr (1989) Corrosion of Fe-Ni alloy by Cl-containing akaganéite (β-FeOOH): the Antarctic meteorite case. Am Mineral 74:663–664

Cameron E, Leybourne M, Palacios C (2007) Atacamite in the oxide zone of copper deposits in northern Chile: involvement of deep formation waters? Mineral Deposita 42:205–218

Chistyakova MB, Kazakova ME (1969) Fluocerite from Kazakhstan. Trudy Mineralog Muzeya Akademii Nauk SSSR 19: 236–238

Clark JR, Evans HT Jr, Erd RC (1980) Tachyhydrite, dimagnesium calcium chloride 12-hydrate. Acta Crystallogr 36:2736–2739

Dill HG (2015) Pegmatites and aplites. Their genetic and applied ore geology. Ore Geol Rev 69:417–561

Eglinger A, Ferraina C, Tarantola A, André-Mayer A-S, Vanderhaeghe O, Boiron M-C, Dubessy J, Richard A, Brouand M (2014) Hypersaline fluids generated by high-grade metamorphism of evaporites: fluid inclusion study of uranium occurrences in the western Zambian Copperbelt. Contrib Mineral Petrol 167:1–28

Finney JJ, Graeber EJ, Rosenzweig A, Hamilton RD (1977) The structure of chloroxiphite, $Pb_3CuO_2(OH)_2Cl_2$. Mineral Mag 41:357–361

Fleet ME (1975) The crystal structure of paratacamite, $Cu_2(OH)_3Cl$. Acta Crystallogr 31:183–187

Forti P (2005) Genetic processes of cave minerals in volcanic environments: an overview. J Cave Karst Stud 67(1):3–13. vol 67, pp 3–13
Frondel C (1950) On paratacamite and some related copper chlorides. Mineral Mag 29:34–45
Gaines RV, Skinner HCW, Foord EE, Mason B, Rosenzweig A (1997) Dana's new mineralogy: the system of mineralogy of James Dwight Dana and Edward Salisbury Dana, 8th edn. Wiley, New York, p 1819
Garrett DE (1985) Chemistry and origin of the Chilean nitrate deposits. Sixth International Symposium on Salt 1: 285–302
Geller S (1971) Refinement of the crystal structure of cryolithionite, $\{Na_3\}[Al_2](Li_3)F12$. Am Mineral 56:18–23
Gillard RD, Hart AD, Humphreys DA, Symes RF, Williams PA (1997) Compositions of silver halides from the Broken Hill district, New South Wales. Rec Aust Mus 49:217–228
Gislason SR, Hassenkam T, Nedel S, Bovet N, Eiriksdottir ES, Alfredsson HA, Hem CP, Balogh ZI, Dideriksen K, Oskarsson N, Sigfusson B, Larsen G, Stipp SLS (2011) Characterization of Eyjafjallajökull volcanic ash particles and a protocol for rapid risk assessment. Proc Natl Acad Sci 108:7307–7312
Hawthorne FC (1985) Refinement of the crystal structure of botallackite. Mineral Mag 49:87–89
Hawthorne FC, Ferguson RB (1983) The crystal structure of pachnolite. Can Mineral 21:561–566
Hawthorne FC, Groat LA (1986) The crystal structure and chemical composition of cumengeite. Mineral Mag 50:157–162
Jacobini C, Leble A, Rosseau JJ (1981) Détermination précise de la structure de la chiolite Na5Al3F14 etétude par R.P.E. de Na5Al3F14:Cr3+. J Solid State Chem 36:297–304
Jones JE (1982) The Laurion silver mines: a review of recent researches and results. Greece Rome 29:169–183
Kendrick M, Burnard P (2013) Noble gases and halogens in fluid inclusions: a journey through the earth's crust. In: Burnard P (ed) The Noble gases as geochemical tracers: advances in isotope geochemistry. Springer, Berlin/Heidelberg, pp 319–369
Klein C, Dutrow B (2008) The 23rd edition of the manual of mineral science. Wiley, Hoboken, p 675
Kohlberger W (1976) Minerals of the Laurium mines, Attica, Greece. Mineral Rec 7:114–125
Korbel P, Novik M (2001) The complete Encyclopedia of minerals. Books Grange, London, p 296
Koritnig S (1951) Ein beitrag zur geochemie des fluor: (Mit besonderer Berücksichtigung der Sedimente). Geochim Cosmochim Acta 1:89–116
Lottermoser BG, Lu J (1997) Petrogenesis of rare-element pegmatites in the Olary block, South Australia, part 1. Mineralogy and chemical evolution. Mineral Petrol 59:1–19
Mangler MF, Marks MAW, Zaitzev AN, Eby GN, Markl G (2014) Halogens (F, Cl and Br) at Oldoinyo Lengai volcano (Tanzania). Effects of magmatic differentiation, silicate–natrocarbonatite melt separation and surface alteration of natrocarbonatite. Chem Geol 365:43–53
Merlino S, Pasero M, Perchiazzi N (1993) Crystal structure of paralaurionite and its OD relationship with laurionite. Mineral Mag 57:323–328
Merlino S, Pasero M, Perchiazzi N (1994) Fiedlerite: revised chemical formula $[Pb_3Cl_4F(OH).H_2O]$, OD description and crystal structure refinement of the two MDO polytypes. Mineral Mag 58:69–78
Merlino S, Pasero M, Perchiazzi N, Gianfagna A (1995) X-ray and electron diffraction study of penfieldite: average structure and multiple cells. Mineral Mag 59:341–347
Mountain ED (1937) Two new bismuth minerals from South Africa. Mineral Mag 24:59–64
Pasero M, Perchiazzi N (1996) Crystal structure refinement of matlockite. Mineral Mag 60:833–836
Pauly H (1965) Ralstonite from Ivigtut, South Greenland. Am Mineral 50:1851–1864
Pauly H, Hawthorne FC, Burns PC, Ventura GD (1997) Jørgensenite, Na_2 (Sr, Ba)$_{14}Na_2A_{12}F_{64}$(OH, F)$_4$, a new aluminofluoride mineral from Ivigtut, Greenland. Can Mineral 35:175–179
Petersen OV (1986) On the prosopite, $CaAl_2F_24(OH)_4$, from Ivigtut. Neues Jb Mineral Monat 148:329–335
Raade G, Haug P (1981) Morphology and twinning of sellaite from Gjerdingen, Norway. Mineral Rec 12:231–232
Radkte AS, Brown GE (1974) Frankdicksonite, BaF2, a new mineral from Nevada. Am Mineral 59:885–888
Richardson CK, Holland HD (1979) Fluorite deposition in hydrothermal systems. Geochim Cosmochim Acta 43:1327–1335
Saini-Eidukat B, Rudashevsky NS, Polozov AG (1998) Evidence for hibbingite-kempite solid solution. Mineral Mag 62:251–255
Schlüter J, Pohl D, Britvin S (2005) The new mineral challacolloite, KPb2Cl5, the natural occurrence of a technically known laser material. Neues Jb Mineral Abh 182:95–101
Siidra OI, Krivovichev SV, Turner RW, Rumsey MS (2008) Chloroxiphite $Pb_3CuO_2(OH)_2Cl_2$: structure refinement and description in terms of oxocentred OPb_4 tetrahedra. Mineral Mag 72:793–798
Skarpelis N, Argyraki A (2009) Geology and origin of supergene ore at the Lavrion Pb-ag-Zn deposit, Attica, Greece. Resour Geol 59:1–14
Starinsky A, Katz A (2003) The formation of natural cryogenic brines. Geochim Cosmochim Acta 67:1475–1484
Stewart FP (1963) Data of geochemistry, chapter Y, marine evaporites. US Geologial Survey Professional Paper 440-Y: Y1–Y53
Stormer JC Jr, Carmichael ISE (1970) Villiaumite and the occurrence of fluoride minerals in igneous rocks. Am Mineral 55:126–134
Symes RF, Embrey PG (1977) Mendipite and other rare oxychloride minerals from the Mendip Hills, Somerset, England. Mineral Rec 8:298–303
Talbot CJ, Farhadi R, Aftabi P (2009) Potash in salt extruded at Sar Pohl diapir, southern Iran. Ore Geol Rev 35:352–366
Torii T, Ossaka J (1965) A new mineral, calcium chloride hexahydrate, discovered in Antarctica. Science 149:975–977
Warren JK (2016) Evaporites: a compendium. Springer, Berlin, p 1854. ISBN 978-3-319-13511-3
Winchell RE, Rouse RC (1973) The crystal structure of boleite – a mineral containing silver atom clusters. J Solid State Chem 6:86–92
Winchell RE, Rouse RC (1974) The mineralogy of the boleite group. Mineral Rec 5:280–287
Winchell RE, Wenden HE (1968) Synthesis and study of diaboleite. Mineral Mag 36:933–939
Witzke T (1997) New data on the mercury iodide mineral coccinite, HgI_2. Neues Jb Mineral Abh 172:505–510
Zalkin A, Forrester JD, Templeton DH (1964) The crystal structure of sodium fluosilicate. Acta Crystallogr 17

Halogens

Mark A. Kendrick
Research School of Earth Sciences, Australian National University, Canberra, ACT, Australia

Definition

The halogen group of elements includes the four stable elements, fluorine (F), chlorine (Cl), bromine (Br), and iodine (I), and the short-lived radioactive element astatine

(At) which exists only fleetingly in the Earth's crust (Chang 2016). The halogens occupy group 17 of the periodic table and are characterized by an S^2P^5 outer electron shell configuration enabling their characteristic ability to form halide anions in ionically bonded salts. The heavy halogens can exist in several valence states, however, the atomic radii of halogens and the ionic radii of the common halide ions, which have valences of −1, increase down the group (Table 1).

Properties

At room temperature, fluorine ($F_{2(g)}$) and chlorine ($Cl_{2(g)}$) are respectively toxic yellow and green-yellow diatomic gases. Exposure to concentrations of more than 25 ppm of either gas will cause significant irritation to eyes and respiratory system, and exposure to more than 1000 ppm is fatal within minutes. Bromine ($Br_{2(l)}$) is a toxic and corrosive red-brown liquid that can burn the skin. Iodine ($I_{2(s)}$) is a lustrous metallic gray solid that is a skin irritant and toxic if taken orally. The toxicity of the halogens derives from their highly reactive and oxidizing nature which enables them to generate acids and denature proteins. However, the halogens rarely occur in their molecular forms, and certain halogen compounds are essential for life. The hydrogen halides ($HF_{(g)}$, $HCl_{(g)}$, $HBr_{(g)}$, and $HI_{(g)}$) are diatomic gases at room temperature. They do not ionize in the gaseous phase, but disassociate to H^+ and a halide ion producing strong acids once dissolved in water.

Fluorine and iodine each have a single stable isotope (^{19}F and ^{127}I), whereas Cl and Br have two stable isotopes each: ^{35}Cl and ^{37}Cl have isotopic abundances of 75.76% and 24.24%, and ^{79}Br and ^{81}Br have isotopic abundances of 49.31% and 50.69%, respectively (Chang 2016). There are two geologically important radioactive halogen isotopes, ^{36}Cl with a half-life of 301.3 ka and ^{129}I with a half-life of 15.7 Myr (Chang 2016). Both isotopes are produced by cosmic rays at the Earth's surface and by nuclear processes in the Earth's crust; ^{36}Cl is produced by thermal neutron reactions with K, Ca, and ^{35}Cl, and ^{129}I is produced by fission of ^{238}U. There are several additional short-lived radioactive I isotopes produced by U fission including ^{131}I ($t_{1/2} = 8.0$ d; Chang 2016). The high mobility of I coupled with its role in the human thyroid means it constitutes a significant short-term hazard associated with radioactive waste. Radioactive ^{36}Cl decays to ^{36}Ar, whereas radioactive ^{129}I and ^{131}I decay to ^{129}Xe and ^{131}Xe, respectively (Chang 2016).

Contrasting Geochemical Behaviors

Fluorine is the most strongly electronegative element in the periodic table. The fluoride ion is smaller than the hydroxide (OH^-) and oxygen (O^{2-}) ions which have ionic radii of ~1.4 Å (cf. Table 1). Fluoride can substitute for O^{2-} in nominally anhydrous mafic minerals and behaves more compatibly in the Earth's mantle than the larger halogens (Dalou et al. 2012). Fluoride readily replaces the OH-group in many hydrous minerals and two F^- ions can substitute for carbonate (CO_3^{2-}) (Kendrick 2017). The high compatibility of F in a range of minerals means it has a low solubility in aqueous fluids (at surface conditions) and a concentration of only 1.3 ppm in seawater (Table 2). In comparison, the heavier halogens (Cl, Br, and I) all have similarly strong incompatibilities in the mantle (similar to K or Nb; Kendrick et al. 2013) and high solubilities in aqueous fluids. The heavy halogens are however fractionated from each other by the evaporation of seawater beyond the point of halite saturation, because Br and I are incompatible in halite, and Cl substitutes for the OH-group in many hydrous minerals more easily than the larger Br and I ions (Kendrick 2017).

Iodine is uniquely redox sensitive among the halogens: iodate (IO_3^-) is the dominant form of iodine in seawater, but there can be up to ~5 ppb dissolved organic iodine, and iodide (I^-) is important in surface waters and anoxic basins.

Halogens, Table 1 Physical properties of halogens

	Atomic mass	Phase	Melting point K	Boiling point K	Condensation T 10^{-4} bar K	Electronegativity	Ionization energy kJ mol^{-1}	Atomic radius Å	Ionic radius Å	Common valence states
F	18.998	Gas	53.5	85.0	739	3.98	1681.1	0.7	1.3	**−1**
Cl	35.453	Gas	171.7	239.1	954	3.16	1256.2	1.0	1.8	**−1**, 1, 3, 5, 7
Br	79.904	Liquid	266	332	546?	2.96	1139.9	1.1	2.0	**−1**, 1, 3, 5, 7
I	126.904	Solid	386.9	457.6	535?	2.66	1008.4	1.3	2.2	**−1, 1**, 3, 5, 7

Halogens, Table 2 Halogen abundance data

	Solar	CI chondrite	Primitive mantle	Depleted mantle	Cont. crust	Seawater	Evaporites	Marine sediments
F ppm	0.4	60	15–30	5–15	520–620	1.3		100–1000
Cl ppm	4.8	680	15–30	1–5	140–470	19,300	<600,000	<1000
Br ppb	23	3600	40–80	10–20	1000–2000	66,000	50,000–200,000	500–100,000
I ppb	3	460	5–10	<1	500–1000	58		500–50,000

Seawater iodate is sequestered by algae, and its concentration correlates with other nutrients in seawater, whereas all the other halogens are present as halides and have constant concentrations in seawater (Table 2; Kendrick 2017).

Halogens are beneficial for life: fluoride aids in forming strong teeth and bones in vertebrates; chloride is the dominant anion that enables cellular level electrochemistry; and bromine and iodine are involved in a range of biochemical pathways that probably evolved in fairly primitive prokaryotes. Iodine is essential in the production of thyroid hormones in unicellular and multicellular organisms, and iodine deficiency causes goiter in humans (Kirk 1991; Crockford 2009).

Discovery and Utilization

Chlorine gas was first isolated by Carl Wilhelm Scheele in 1774 and was recognized as an element by Sir Humphry Davy in 1810 (Davy 1811). Iodine was separated from seaweed ash by the French chemist Bernard Courtois in 1811 and independently identified as an element at the end of 1813, by Gay-Lussac and Humphry Davy (Kirk 1991). Bromine was discovered independently in 1825 by Carl Jacob Löwig and in 1826 by Antoine Balard who separated it from seaweed ash. Initial studies on fluorine were dangerous and resulted in the deaths of several nineteenth-century experimenters who were subsequently dubbed the fluorine martyrs. Henri Moissan finally isolated F which was regarded as "a savage beast among the elements" in 1886 and received a nobel prize for this achievement in 1906 (Kirk 1991).

Halogen salts have been in use since ancient times. The name fluorine is derived from the Latin verb fluo meaning flow, because fluorite (CaF_2 or fluorspar) is used as a flux to purge iron of impurities and render slag more liquid at smelting temperatures. Common salt (NaCl – halite) has been used in cooking and food preservation since prehistoric times. Halite is produced commercially by the evaporation of seawater and halogen-salts are mined. Fluorine and chlorine gas are produced by electrolysis of CaF_2 or NaCl, respectively. Today, bromine and iodine are produced by treating naturally occurring Br- and I-rich brines with Cl_2 gas which oxidizes the dissolved halides to produce Br_2 and I_2 gas, and iodine is also produced by mining I-rich caliche.

The halogens have numerous industrial applications that result from their high reactivity, oxidizing properties, and their abilities to bond with C in organic molecules and form strong acids. The largest application of F gas is to make UF_6 which is used for ^{235}U enrichment in the nuclear fuel cycle. Hydrofluoric acid [$HF_{(aq)}$] is used in a variety of laboratory procedures including the digestion of silicate rocks and ArF is used in 193 nm excimer lasers. Prior to being phased out, chlorofluorocarbons (CFCs) which deplete stratospheric ozone, were widely used as refrigerants and aerosol propellants. Chlorine is used as a disinfectant for killing bacteria in drinking water and swimming pools and in the manufacture of paper, paint, textiles, and plastics including PVC (polyvinyl chloride) which is used extensively in the building and automotive industries. Cl compounds are also used in the manufacture of many pharmaceuticals and some insecticides. The largest current use of Br is in flame retardants; however, Br has a variety of uses including in the manufacture of plastics and some insecticides, and AgBr is used in photographic film. Iodide is present in dietary supplements used to ensure the health of livestock and humans (e.g., iodized table salt), and iodine is used in various forms as a disinfectant or antiseptic.

Distribution on Earth and in the Cosmos

The solar system contains 0.4 ppm F, 4.8 ppm Cl, 23 ppb Br, and 3 ppb I, making the halogens the 25th (F), 18th (Cl), 34th (Br), and 50th (I) most abundant elements in the solar system (Table 2; Lodders 2003). The halogens are all moderately volatile and have similar relative abundances in the solar photosphere and CI chondrites (Table 2; Lodders 2003). In contrast, Cl, Br, and I are more depleted in the terrestrial primitive mantle than F (Table 2). This could indicate that the highly incompatible heavy halogens were either partitioned into the Earth's core, or more likely that they were lost during Earth's accretion either with the early oceans and atmosphere or with other incompatible elements and crustal material lost by collisional erosion (Sharp and Draper 2013).

On Earth, the moderately compatible F is concentrated in the mantle and crust and has a low concentration in seawater (Table 2; Kendrick 2017). In comparison, the heavy halogens are concentrated in the surface reservoirs of seawater and sediments (Table 2). A bit less than half the Cl in the surface reservoir is in the oceans which have a salinity of ~3.5 wt% salt (1.9 wt% Cl), and about a quarter is in evaporites which contain up to 60 wt% Cl. Iodine is overwhelmingly concentrated in organic-rich marine sediments which contain 1–50 ppm I. Bromine which has properties intermediate of Cl and I is split between the oceans and organic-rich marine sediments (Table 2). Kelp is a type of seaweed (multicellular macroalgae) that contains an average of 1.0 wt% I and thousands of ppm of Br (Kendrick 2017).

Mid-ocean ridge and oceanic island basalt glasses (MORB and OIB) have typical concentrations of 60–1500 ppm F, 30–1000 ppm Cl, 30–4000 ppb Br, and 1–70 ppb I, with the highest concentrations in enriched OIB and the lowest in depleted MORB. The subduction flux of halogens into the deep mantle is not well known. However, hydrothermal alteration of the oceanic slab is likely to cause greater enrichment of Cl than the other halogens, because F has a low

concentration in seawater and Br and I have low compatibilities in many hydrous minerals (Kendrick 2017). Iodine and bromine can however attain ppm-level concentrations in serpentinized mantle lithosphere (Kendrick 2017).

Significance in Geochemistry and Geochronology

Chloride is the dominant anion in most geofluids, and it acts as an important ligand for the transport of metals in hydrothermal solution (Yardley 2005). As a result, Cl chemistry underpins a wide range of geological processes including chemical mass transfer by hydrothermal fluids in the oceanic crust and in subduction zones and the formation of economically important hydrothermal ore deposits. In addition, the movement of saline formation waters (oil field brines) is sometimes linked to the migration of hydrocarbons. In sedimentary environments with a high water-rock ratio, the concentration of Cl in a geofluid is considered to be "conservative" (i.e., unchanging), and together with halogen abundance ratios (Br/Cl and I/Cl), it is often used to infer a fluid source or migration pathway (Hanor 1994). In higher temperature metamorphic environments with lower fluid-rock ratios, the concentrations of Cl and other halogens are not conservative. Fluid salinity provides important evidence for phase separation of seafloor hydrothermal fluids, and the Cl content of metamorphic minerals are used to track the involvement of saline fluids in metamorphic processes (Kendrick 2017).

Chlorine and F are often described as "volatiles" in the Earth's mantle (along with H_2O, CO_2, and S). However, halogens are generally undersaturated in submarine lavas and behave as lithophile rather than volatile elements in the mantle. Halogens are degassed from subaerial volcanoes as $HF_{(g)}$, $HCl_{(g)}$, $HBr_{(g)}$, and $HI_{(g)}$ and have a significant influence on climate and ozone depletion (Kutterolf et al. 2013).

Bromine and iodine are trace constituents on the Earth but play a critical role in marine biochemistry. In addition, the analysis of halogen abundance ratios provides a critical means for tracing fluid origins and geodynamic processes (Hanor 1994; Kendrick 2017).

The stable isotope compositions of Cl and Br are reported using the delta notation relative to standard mean ocean chloride (SMOC) or bromide (SMOB) where

$$\delta^{37}\mathrm{Cl}\,‰ = \frac{\left(\frac{^{37}\mathrm{Cl}}{^{35}\mathrm{Cl}}\right)_{\mathrm{sample}} - \left(\frac{^{37}\mathrm{Cl}}{^{35}Cl}\right)_{\mathrm{SMOC}}}{\left(\frac{^{37}\mathrm{Cl}}{^{35}\mathrm{Cl}}\right)_{\mathrm{SMOC}}} \times 1000 \quad \text{and}$$

$$\delta^{81}\mathrm{Br}\,‰ = \frac{\left(\frac{^{81}\mathrm{Br}}{^{79}\mathrm{Br}}\right)_{\mathrm{sample}} - \left(\frac{^{81}\mathrm{Br}}{^{79}\mathrm{Br}}\right)_{\mathrm{SMOB}}}{\left(\frac{^{81}\mathrm{Br}}{^{79}\mathrm{Br}}\right)_{\mathrm{SMOB}}} \times 1000$$

(Eggenkamp et al. 2016). Terrestrial δ^{37}Cl varies by about 10 ‰ and has been applied more widely than δ^{81}Br which varies by about 5 ‰ and has been limited to studies of groundwater and atmospheric organo-halogen cycling (Eggenkamp et al. 2016). Recent analyses show the δ^{37}Cl of chondrites and samples from the terrestrial mantle cluster slightly below 0 ‰ suggesting Cl was isotopically uniform in the inner solar nebular (Sharp et al. 2013). However minor variations have been reported for the δ^{37}Cl of Earth's mantle, with δ^{37}Cl values of up to +3 ‰, which are among the highest on Earth, attributed to the subduction of sediments (John et al. 2010). The mechanisms of Cl isotope fractionation on Earth are however not well understood, and the majority of materials from Earth's surface including sediments have δ^{37}Cl of less than zero, with the lowest values of −8 reported for sedimentary pore waters (Barnes and Straub 2010). In contrast to chondrites and the Earth, the Moon exhibits much greater variation in δ^{37}Cl: the minimum value of ~0 ‰ is consistent with a uniform nebular, and maximum values of +25 ‰ have been attributed to fractionation during metal-halide degassing from anhydrous melts at lunar atmospheric pressure (Sharp et al. 2010).

The short-lived ^{36}Cl isotope ($t_{1/2} = 301.3$ ka) can be used to date groundwaters and is one of the most widely used tools for cosmogenic exposure dating. It has been applied to dating a wide variety of processes linked to landforms including young lava flows and glacial retreat aged from thousands of years to about 1 Ma (Ivy-Ochs and Kober 2008). The ^{129}I isotope ($t_{1/2} = 15.7$ Ma) is used in dating much older groundwaters and iodine source rocks from which CH_4 and gas hydrates are derived (Fehn et al. 2000). In addition, the I-Xe system was the first extinct nuclide system to be exploited for dating the early solar system (Hohenberg and Pravdivtseva 2008).

Summary

The halogen group of elements is defined by the ability of each halogen to form a halide ion, but their chemical properties and abundances combine to give each element a unique geochemical cycle. Fluorine is the most reactive halogen and its compatibility in a range of minerals result in a low solubility in aqueous fluids. The heavy halogens are strongly incompatible in the mantle and highly soluble in aqueous fluids. Chlorine is the dominant ligand enabling metal transport in geofluids. Bromine and iodine are trace constituents on Earth, iodine is redox sensitive, and both elements are involved in a number of biochemical pathways. As a result, organic-rich marine sediments are the dominant reservoir of iodine on Earth. Halogen stable and short-lived radiogenic isotopes have been widely applied in groundwater studies, and Cl isotopes, together with halogen abundance ratios, are being employed to investigate geochemical cycling of halogens.

Cross-References

- Bromine
- Chlorine
- Chondrites
- Cosmogenic Nuclides
- Fluorine
- Hydrothermal Solutions
- Iodine
- Mid-Ocean Ridge Basalts (MORB)
- Ocean Biochemical Cycling and Trace Elements
- Oceanic Island Basalts
- Organics: Sources and Depositional Environments
- Stable Isotope Geochemistry

References

Barnes JD, Straub SM (2010) Chorine stable isotope variations in Izu Bonin tephra: implications for serpentinite subduction. Chem Geol 272(1–4):62–74

Chang J (2016) Table of nuclides, KAERI (Korea Atomic Energy Research Institute). Available at: http://atom.kaeri.re.kr/nuchart. Retrieved May 2016

Crockford SJ (2009) Evolutionary roots of iodine and thyroid hormones in cell–cell signaling. Integr Comp Biol 49(2):155–166

Dalou CL, Koga K, Shimizu N, Boulon J, Devidal J-L (2012) Experimental determination of F and Cl partitioning between lherzolite and basaltic melt. Contrib Mineral Petrol 163:591–609

Davy H (1811) On a combination of oxymuriatic gas and oxygene gas. Philos Trans R Soc Lond 101:155–162

Eggenkamp HGM, Bonifacie M, Ader M, Agrinier P (2016) Experimental determination of stable chlorine and bromine isotope fractionation during precipitation of salt from a saturated solution. Chem Geol 433:46–56

Fehn U, Snyder G, Egeberg PK (2000) Dating of pore waters with I-129: relevance for the origin of marine gas hydrates. Science 289 (5488):2332–2335

Hanor JS (1994) Origin of saline fluids in sedimentary basins. In: Parnell J (ed) Geofluids: origin, migration and evolution of fluids in sedimentary basins, Geological Society Special Publication. Geological Society, London, pp 151–174

Hohenberg CM, Pravdivtseva OV (2008) I-Xe dating: from adolescence to maturity. Chem Erde-Geochem 68(4):339–351

Ivy-Ochs S, Kober F (2008) Surface exposure dating with cosmogenic nuclides. Quaternary Science Journal 57(1–2):179–209

John T, Layne GD, Haase KM, Barnes JD (2010) Chlorine isotope evidence for crustal recycling into the Earth's mantle. Earth Planet Sci Lett 298(1–2):175–182

Kendrick MA (2017) Halogens in seawater, marine sediments and the altered oceanic lithosphere. In: Harlov DE, Aranovich LY (eds) The role of halogens in terrestrial and Extraterrestrial processes. Springer, Berlin. In press

Kendrick MA, Arculus RJ, Burnard P, Honda M (2013) Quantifying brine assimilation by submarine magmas: examples from the Galápagos spreading Centre and Lau Basin. Geochim Cosmochim Acta 123:150–165

Kirk KL (1991) The halogens: discovery, occurrence, and biochemistry of the free elements, biochemistry of the elemental halogens and inorganic halides. Springer, New York, pp 1–17

Kutterolf S, Hansteen TH, Appel K, Freundt A, Krüger K, Pérez W, Wehrmann H (2013) Combined bromine and chlorine release from large explosive volcanic eruptions: a threat to stratospheric ozone? Geology 41(6):707–710

Lodders K (2003) Solar system abundances and condensation temperatures of the elements. Astrophys J 591:1220–1247

Sharp ZD, Draper DS (2013) The chlorine abundance of earth: implications for a habitable planet. Earth Planet Sci Lett 369–370:71–77

Sharp ZD, Shearer CK, McKeegan KD, Barnes JD, Wang YQ (2010) The chlorine isotope composition of the moon and implications for an anhydrous mantle. Science 329(5995):1050–1053

Sharp ZD, Mercer JA, Jones RH, Brearley AJ, Selverstone J, Bekker A, Stachel T (2013) The chlorine isotope composition of chondrites and earth. Geochim Cosmochim Acta 107:189–204

Yardley BWD (2005) 100th anniversary special paper: metal concentrations in crustal fluids and their relationship to ore formation. Econ Geol 100(4):613–632

Heat Capacity

Brian F. Woodfield
Department of Chemistry and Biochemistry, Brigham Young University, Provo, UT, USA

Definition

Heat capacity, or sometimes called the specific heat in a physics context, can be defined as

$$C \equiv Q/\Delta T$$

where C is the heat capacity of the material, Q is a known amount of heat put into a system, and ΔT is the resulting temperature rise.

Alternatively, you can think of the heat capacity as the amount of energy, or heat, required to raise the temperature of the material one degree Celsius. From this perspective, heat capacities may appear to be a rather uninteresting physical quantity; however, high-quality heat capacity measurements as a function of temperature play a key role in chemical thermodynamics and provide important insights to the intrinsic physical properties of a wide range of materials. Below we give a brief overview of the role heat capacities can play in chemical thermodynamics, the low temperature physics of materials, and outline how heat capacity measurements are performed.

Chemical Thermodynamics

In order to understand the central role heat capacities play in chemical thermodynamics, a brief review of chemical thermodynamics is necessary. The three foundational laws of thermodynamics can be written mathematically as ("Enthalpy," "Gibbs Energy," and "Entropy")

1. $\Delta U_{universe}=0$
2. $\Delta S_{Universe} \geq 0$
3. $S_{T=o} = 0$ for a perfectly ordered substance.

These laws can be described in words for a chemical or geologic process as (1) the energy content of the universe is constant; (2) for a chemical or geologic reaction to occur, the entropy of the universe must increase; and (3) at absolute zero, the entropy of a perfectly ordered substance is zero. The details and implications of these laws are described elsewhere, but they form the foundation of chemical thermodynamics. A more practical usage of these laws is to introduce the thermodynamic variable ΔG, which can be defined as ("Gibbs Energy" entry)

$$\Delta G = \Delta H - T\Delta S$$

where, for a process to occur, $\Delta G \leq 0$. The important principle to note here is that we can predict stability and the direction of chemical and geological processes by calculating ΔG, which is governed by the balance between enthalpic ("Enthalpy" entry) and entropic ("Entropy" entry) considerations. That is, the driving force for a chemical or geologic process can be described as the interplay between the change in enthalpy and change in entropy for the process. Details on measuring and using enthalpies are described elsewhere ("Enthalpy" entry), but heat capacities play a key role in calculating the entropy changes for reactions.

We show here how to calculate the entropy change for a reaction from the heat capacity. From the second law for a system at equilibrium, the change in entropy can be calculated using

$$\Delta S = \int_{T_1}^{T_2} \frac{q_{rev}}{T}$$

Since the vast majority of processes occur at constant pressure, we can apply the condition that $dH = q_p$ or the enthalpy is equal to the heat of the reaction. Substituting yields,

$$\Delta S = \int_{T_1}^{T_2} \frac{dH}{T}$$

We also note under the same conditions that the definition of the heat capacity can be written in differential form as

$$C_p \equiv q_p/dT = dH/dT$$

which can be rearranged to produce

$$dH = C_p dT$$

Substituting this into our equation for the change in entropy shows us how entropy changes can be calculated from the heat capacity,

$$\Delta S = \int_{T_1}^{T_2} \frac{C_p dT}{T}$$

Thus, the integral of C_P/T as a function of T provides a measure of the change in entropy of a material. However, we can apply the third law of thermodynamics to provide a much more useful relationship. If we change the lower limit of the integration to $T = 0$, we note that

$$\Delta S = \int_{0}^{T_2} \frac{C_p dT}{T} = S(T) - S(0)$$

From the third law, $S(0) = 0$; thus, we are able to calculate an absolute entropy from the heat capacity using

$$S(T) = \int_{0}^{T_2} \frac{C_p dT}{T}$$

This relationship implies that heat capacity measurements must extend from low temperatures near absolute zero up to the temperature of interest, usually 298.15 K or higher. From a practical standpoint, measurements should extend down to 10 K, and preferably even lower in temperature, where the heat capacity can be extrapolated to 0 K using theoretical functions. Thus, measuring the heat capacity of a material from low temperatures and over a wide temperature region allows us to calculate the absolute entropy for that material. These are often called third-law entropies and the measurements are often referred to as third-law calorimetry. Third-law entropies have been tabulated for a wide range of chemically and geologically relevant materials and can be found in various chemically and geologically focused databases.

Having absolute entropies, however, still does not provide us with a measure of the change in entropy for chemical reactions. A generic reaction can be represented by the following

$$a\mathrm{A} + b\mathrm{B} \rightarrow c\mathrm{C} + d\mathrm{D}$$

where A, B, C, and D represent reactants and products for the reaction and a, b, c, and d represent the stoichiometric coefficients. If the absolute entropies for A, B, C, and D have been measured, then the entropy change for the reaction, ΔS_{rxn}, can be calculated using this equation,

$$\Delta S_{rxn} = cS_C + dS_D - aS_A - bS_B$$

Thus, to know the free energy of a process, both the enthalpy and entropy of reaction must be known. In the vast majority of cases, the only route to obtaining the absolute entropies from which the change in entropy of a reaction can be calculated is through the accurate measurement of heat capacities from near absolute zero to above room temperature. While conceptually straightforward, accurate heat capacity measurements over such a wide temperature range are not trivial but play a vital role in understanding the thermodynamic driving forces in chemical geologic reactions. Later, we will give a basic overview of how these measurements are performed. More details on the role of heat capacities in chemical thermodynamics can be found in the excellent reference text, *Chemical Thermodynamics: Principles and Applications* by Ott and Boerio-Goates (2000).

Low Temperature Physics

In addition to chemical thermodynamics, heat capacity data can also play a key role in understanding the intrinsic properties of materials. The total heat capacity is a measure of all the energetic states of a material. Modeling the heat capacity data with theoretical functions provides a means with which to extract valuable information about the magnetic, electronic, and vibrational properties of a sample. Heat capacity data can cover a wide range in temperatures from milliKelvin to thousands of Kelvin, and the temperature dependence of the heat capacity depends on the energy states being thermally accessed. Thus, we often divide the heat capacity data into temperature regions and use different models or fitting expressions to fit the data. Analyzing heat capacity data to extract intrinsic properties comes down to fitting the data to the right function.

In the low temperature regime ($T < 15$ K), lattice vibrations are modeled by a function containing odd powers in temperature, which represents the harmonic oscillators:

$$C_{Lat} = \sum_{n=3,5,7,\ldots} B_n T^n$$

A linear dependence on T (denoted as γT) is traditionally associated with electronic contributions to the heat capacity, but for insulating materials this linear dependence is also due to oxygen vacancies and defects. Magnetic contributions can take on various forms depending on the nature of the magnetism, and for a system of noninteracting energy levels, a Schottky anomaly can occur. A simple two-level system has the form:

$$C_{Sch} = R\left(\frac{\theta}{T}\right)^2 \frac{g_0}{g_1} \frac{e^{\frac{\theta}{T}}}{\left(1 + \frac{g_0}{g_1} e^{\frac{\theta}{T}}\right)^2}$$

where R is the gas constant, θ is the energy separation of the two energy levels in Kelvin, and g_0 and g_1 are the degeneracies for the ground and first excited states, respectively. For interacting magnetic systems such as ferromagnets or antiferromagnets, the magnetic heat capacity has the form:

$$C_{mag} = M_n T^n$$

where M_n is the coefficient and the power n is typically 3/2 for ferromagnets and 3 for antiferromagnets, although more complicated magnetic systems can have different powers of n and there can be gaps in the magnon spectrum.

Data from 10 to 75 K is an intermediate temperature region where there are few theoretical functions that can adequately represent the heat capacity data. Traditionally in this temperature region, the data are fit to a polynomial function to provide sufficient overlap with the low temperature and high temperature fits and to smoothly fit the inflection point around 50 K. Fits are usually of the form:

$$C_{mid\ T} = \sum_{n=0,1,2\ldots6} A_n T^n$$

The high temperature data (T > 35 K) are fit to a sum of Debye and Einstein functions that provide information on the lattice-specific heat

$$C_{high\ T} = m \cdot D(\Theta_D/T) + n_1 \cdot E\left(\Theta_{E,1}/T\right) + n_2 \cdot E\left(\Theta_{E,2}/T\right)$$

where $D(\Theta_D/T)$, $E(\Theta_{E,1}/T)$, and $E(\Theta_{E,2}/T)$ are Debye and Einstein functions; m, n_1, n_2, Θ_D, $\Theta_{E,1}$, and $\Theta_{E,2}$ are all adjustable parameters; and $(m + n_1 + n_2)$ should be approximately equal to the number of atoms in the formula unit. Generally, one Debye and one Einstein function are sufficient to fit high temperature data, but occasionally an extra Einstein function is needed and a $aT + bT^2$ term is often added to account for the differences in C_V, the constant volume heat capacity, and C_p, the constant pressure heat capacity.

Fitting heat capacity data to combinations of these functions in these different temperature regions allows us to extract the intrinsic properties of the materials. Low temperature, where the lattice contribution becomes small, is a particularly useful region to extract the various contributions to the overall behavior of a material. The use of low temperature heat capacity data to understand a wide range of materials is still a useful and important experimental method to understand new and modern materials. An old but still useful reference to learn more about analyzing heat capacity data is

by Gopal (1966), and a few modern examples can be found in these references (Snow et al. 2010; Boerio-Goates et al. 2013; Schliesser et al. 2015; Schliesser and Woodfield 2015a, b).

Heat Capacity Measurements

For decades, high quality heat capacity data, meaning data with accuracies and precisions on the order of 0.1%, were performed using adiabatic or semi-adiabatic techniques. In these methods, large samples were required (10 g to 100 g) and the samples were loaded in calorimeters where an adiabatic environment was created around the samples and known amounts of heat were added followed by measurement of the resulting temperature changes. These methods were highly accurate but also very slow, requiring often one or two months to cover the temperature range from 5 K to 350 K. Few in the world are still using this technique, but details can be found in Gopal (1966).

For the most part, these adiabatic calorimeters have been replaced by commercial relaxation calorimeters such as the Quantum Design Physical Property Measurement System (PPMS) that use a thermal relaxation technique. While these instruments are not as accurate, they are much easier to use and a full set of data can be collected automatically in a matter of days or a week. These instruments are convenient, but a sound knowledge of heat flow and how to properly mount samples is still needed in addition to learning how to properly analyze the data.

The relaxation method is based on adding a pulse of heat to the sample/sample platform and then measuring the temperature relaxation curve as the sample temperature relaxes back to the bath temperature. An analysis of the relaxation curve reveals the time constant, τ_1, from which the heat capacity can be calculated using the following equation:

$$C = \kappa \cdot \tau_1$$

where κ is a measure of the thermal conductivity between the sample and the bath. The standard PPMS instrument, as of this writing, can easily cover 1.9 K to 300 K and various options can extend the range to milliKelvin and to 400 K. Measurements in magnetic fields are also possible. More details on proper measurement techniques for a range of sample types can be found in these references (Shi et al. 2010, 2011).

Conclusion

Heat capacity data provide a fundamental gateway to understanding solid materials. Heat capacity measurements down to near absolute zero can be integrated to provide absolute entropies, and high quality heat capacity measurements over a wide temperature interval can be represented with theoretical models to reveal intrinsic properties.

Cross-References

- ▶ Calorimetry
- ▶ Enthalpy
- ▶ Entropy
- ▶ Equilibrium
- ▶ Free Energy
- ▶ Geochemical Thermodynamics
- ▶ Magnetism
- ▶ Stoichiometry

References

Boerio-Goates J, Smith SJ, Liu S, Lang BE, Li G, Woodfield BF, Navrotsky A (2013) Characterization of surface defect sites on bulk and nanophase anatase and rutile TiO_2 by low-temperature specific heat. J Phys Chem C 117:4544–4550

Gopal ESR (1966) Specific heats at low temperatures. Springer, New York

Ott JB, Boerio-Goates J (2000) Chemical thermodynamics: principles and applications. Academic Press, Cambridge

Schliesser JM, Woodfield BF (2015a) Lattice vacancies responsible for the linear dependence on the low temperature heat capacity of insulating materials. Phys Rev B 91:024109

Schliesser JM, Woodfield BF (2015b) Development of a Debye heat capacity model for vibrational modes with a gap in the density of states. J Phys Condens Matter 27:285402

Schliesser JM, Smith SJ, Li G, Li L, Walker TF, Perry T, Boerio-Goates J, Woodfield BF (2015) Heat capacity and thermodynamic functions of nano-TiO_2 anatase in relation to bulk-TiO_2 anatase. J Chem Thermodyn 81:298–310

Shi Q, Snow CL, Boerio-Goates J, Woodfield BF (2010) Accurate heat capacity measurements on powdered samples using a quantum design physical property measurement system. J Chem Thermodyn 42:1107–1115

Shi Q, Boerio-Goates J, Woodfield BF (2011) An improved technique for accurate heat capacity measurements on powdered samples using a commercial relaxation calorimeter. J Chem Thermodyn 43:1263–1269

Snow CL, Shi Q, Boerio-Goates J, Woodfield BF (2010) Heat capacity, third-law entropy, and low-temperature physical behavior of bulk hematite (α-Fe_2O_3). J Chem Thermodyn 42:1136–1141

Heat-Producing Elements (HPEs)

Hugh StC O'Neill
Research School of Earth Sciences, Australian National University, Acton, Australia

Definition

The heat-producing elements are thorium, uranium, and potassium, which are those elements having radioactive isotopes with abundances and activities that are sufficient to produce geologically significant amounts of radiogenic heat.

Radiogenic Heat Production

In the early solar system, the decay of ^{26}Al, with a half-life of 0.74 Ma, supplied the heat to metamorphose the small planetesimals that accreted from the solar nebula and partially melt larger planetesimals and planetary embryos formed during the initial stages of assembling rocky planets. Another long-extinct radionuclide, ^{60}Fe, with a half-life of 1.5 Ma, was once suggested as an additional heat source, but recent measurements on primitive meteorites indicate that its concentration in the early solar system was too low to matter (e.g., Tang and Dauphas 2012). Today, only four radionuclides (^{40}K, ^{232}Th, ^{235}U, and ^{238}U) have high enough abundances in the solar system combined with sufficient rates of decay to produce significant heat. The radiogenic heat production of a rock or a geochemical reservoir is the sum of the contributions from each of these four isotopes. At time Δt from the present, the radiogenic power (rate of heat production) per unit mass is:

$$Q_R = \Sigma H_{A_M} f_{A_M} [M] \exp\left(\frac{0.693\,\Delta t}{t_{1/2}^{A_M}}\right) \quad (1)$$

where ^{A}M is the isotope A of element M, H_{A_M} is the net energy per unit mass of ^{A}M retained in the Earth (i.e., excluding the energy of beta decays carried off as antineutrinos and neutrinos), f_{A_M} is the isotopic fraction, [M] is the concentration of the element by mass, and $t_{1/2}^{A_M}$ is the half-life of ^{A}M (Table 1).

Serendipitously for geochemists, the three elements involved, namely K, Th, and U, share rather similar chemical properties in the context of global differentiation processes. This is not surprising for Th and U, which are next-nearest neighbors in the actinide series of the periodic table, but the similarity of K with Th and U is more of a felicitous happenstance. As a result of this geochemical coherence, Th/U and K/U in the major geochemical reservoirs of the Earth are thought to be close to their Bulk Silicate Earth (BSE) values. Moreover, to a first approximation, these ratios are also typical of the averages found in many of the common rock types, such as peridotites, basalts, granitoids, and many sediments. Hence, knowing the concentration in a reservoir or even a rock of one of the HPEs is often a good clue to the concentrations of the other two. A more nuanced insight into the distribution of the HPEs in geochemical reservoirs is afforded by the geochemical study of the daughter products of their decay. The stable daughter products of the decay of ^{232}Th, ^{235}U, and ^{238}U are isotopes of Pb plus ^{4}He, while ^{40}K decays in part to another noble gas, ^{40}Ar (Table 2). Other noble-gas isotopes are also produced by nuclear reactions involving U and Th, with particularly ^{21}Ne and the heavy Xe isotopes produced in amounts that are significant to noble-gas geochemistry, although not to heat production. Thus, much may be inferred about the concentrations and distributions of the HPEs in the Earth from Pb isotope geochemistry (e.g., Galer and O'Nions 1985), supplemented by insights from noble gas geochemistry.

Concentrations of Th, U, and K in the Bulk Silicate Earth

The BSE concentrations of Th, U, and K determine the Earth's radiogenic heat production. For Th and U, estimating their BSE concentrations has relied on a cosmochemical argument. Both Th and U are "refractory lithophile elements" (RLEs), a cosmochemically defined group comprising 28 elements, including the major elements Ca and Al, which occur in the same ratios relative to each other in all bulk analyses of chondritic (undifferentiated) meteorites. These ratios are thought to be those of the solar system as a whole, because they appear to be the same within experimental uncertainty as in the solar composition, as derived from modeling spectroscopic measurements of the solar photosphere; but the uncertainty in the solar composition is large for many elements, and for Th and U, spectroscopic measurements are not available. One small group of chondrites, the CI carbonaceous chondrites, appear to match the solar composition in their abundances of nearly all elements except the most volatile and have become the traditional proxy for the solar composition. Chemically, the RLEs are defined by two properties: they are refractory, in that they condense from a gas of solar composition at temperatures higher than the main constituents of rocky planets, the magnesium silicates and iron metal; and they are lithophile, because they do not enter metal or sulfide phases in most chondrites (enstatite chondrites excepted), nor

Heat-Producing Elements (HPEs), Table 1 Heat productivity of the heat-producing elements (*HPEs*) (from Dye (2012), amended)

Isotope A_M	Half life $\tau_{1/2}^{A_M}$ (Ga)	Natural abundance $f^{A}M$ (%)	Heat productivity $H^{A}M$ (μW kg^{-1})	Final decay products
^{40}K	1.25[a]	0.0117	29.1	^{40}Ar (10.72%) and ^{40}Ca (89.28%)
^{232}Th	14.05	100	26.3	^{208}Pb and 6 ^{4}He
^{235}U	0.7038	0.72	568.4	^{207}Pb and 7 ^{4}He
^{238}U	4.468	99.27	95.1	^{206}Pb and 8 ^{4}He

[a]Renne et al. (2010, 2011)

Heat-Producing Elements (HPEs), Table 2 Concentrations of the HPEs in some geochemical reservoirs

Geochemical reservoir	Mass (10^{21} kg)	K	Th	U	Heat production (TW)	Reference
		$cg\ g^{-1}$	$\mu g\ g^{-1}$	$\mu g\ g^{-1}$		
Continental sediments	0.7	1.83	8.1	1.73	0.3	1
Upper crust	6.7	2.32	10.5	2.7	4.2	1
Middle crust	6.9	1.52	4.86	0.97	1.9	1
Lower crust	6.3	0.65	0.96	0.16	0.4	1
Oceanic sediments	0.3	1.83	8.1	1.73	0.1	1
		$\mu g\ g^{-1}$	$ng\ g^{-1}$	$ng\ g^{-1}$		
Parental ocean floor basalt[a] (= Oceanic crust)	6.3	280	52	20	0.03	2
OFB source mantle[b]	–	60	10	4	–	
BSE, chondritic-RLE model	4060	260	85	22	21.4	3
BSE, extreme nonchondritic model	4060	130	43	11	10.8	4
Convecting mantle, chondritic-RLE model[c]	3942	181	55	15	13.9	
Convecting mantle, extreme nonchondritic model[c]	3942	47	11	4	3.2	

References: 1: Huang et al. (2013); 2: O'Neill and Jenner (2012); 3: Palme and O'Neill (2014); 4: O'Neill and Palme (2008)
[a]Ocean floor basalt (*OFB*) is a general term for all the types of basalt making up the oceanic crust, predominantly mid-ocean ridge basalt but also basalt from back-arc basins, seamounts, etc.
[b]From the parental ocean floor basalt, assuming the latter is produced by 20% partial melting
[c]The "convecting mantle" is taken as the bulk silicate earth, less the continental crust and subcontinental lithospheric mantle

partition into the metallic cores formed during planetary differentiation. Iron meteorites are likely samples of some such cores from small planetary bodies. Until recently it has been almost universally assumed that the chondritic (that is, by inference, solar) ratios among the RLEs were preserved during accretion of the Earth. With this assumption, estimating the BSE concentrations of Ca and/or Al relative to Mg, Si, and Fe is all that is required to deduce Th and U abundances in the BSE. An estimate of the ratio of the RLEs to Mg, normalized to the CI-chondrite abundances, denoted $(RLE/Mg)_{CI}$, is 1.21 ± 0.10, implying 85 ng g^{-1} Th and 22 ng g^{-1} U (Palme and O'Neill 2014). Evaluations of Pb isotope systematics in the Earth as a whole (e.g., Galer and Goldstein 1996) are broadly consistent with the BSE having the chondritic Th/U ratio of 3.9 (Blichert-Toft et al. 2010), but the Th/U ratio in the sub-oceanic upper mantle, as sampled by mid-ocean ridge and related basalts, is lower, at ~2.5, compensated for by elevated Th/U in the continental crust (Huang et al. 2013). The differentiation of Th and U between crust and mantle is thought to be related to the oxidation of U^{4+} to water-soluble U^{6+} in the surface environment of the Earth, causing U to be recycled preferentially over Th back into the mantle, a process only possible after the rise in atmospheric oxygen at ~2.4 Ga (Andersen et al. 2015).

Potassium is not a RLE: it is calculated to condense from a gas of solar nebula composition at lower temperatures than the main elements that form rocky planets (Mg, Si, and Fe), defining it as a moderately volatile element. Therefore, its BSE concentration has to be estimated empirically, traditionally by invoking the geochemical similarity with U and averaging observed K/U ratios in oceanic basalts and representative crustal rocks. A more detailed appraisal of element ratios reveals that K is intermediate in its behavior between U and La, another RLE, such that K/(U + 0.03La) makes a better estimator than either K/U or K/La alone. In terrestrial basalts, K/(U + 0.03La) averages about 6000, implying K = 260 μg g^{-1}, and a depletion factor relative to the CI-chondrites and Mg, denoted $(K/Mg)_{CI}$, of 0.20. This depletion factor is similar to those of other elements of comparable cosmochemical volatility, whether these have similar chemical properties like other alkali metals (Na, Rb) or very different properties like boron or fluorine. This argues against there being much K in the Earth's core, a possibility that is sometimes suggested in order to account for the energy powering the core's geodynamo. Likewise, Th-U-Pb isotope systematics may not preclude a small fraction of U in the core (e.g., Wohlers and Wood 2015), but they do suggest it would be almost insignificant. Most elements can be metallized under sufficiently extreme conditions (low oxygen potentials and/or high sulfur potentials and/or high pressures). Finding conditions where K or U partition into Fe-rich metal is necessary to show that they could partition into a planet's core, but it is not sufficient to show that they did partition into the Earth's core. That requires comparing the siderophile tendencies of K or U with those of other elements at equivalent conditions and balancing these tendencies against estimates of their depletion factors in the BSE.

Due to their different accretion histories, other rocky bodies in the solar system may be expected to have different concentrations of the HPEs. The enrichment of RLEs (hence Th and U) relative to Mg and Si is difficult to evaluate, because of the lack of samples from the mantles of any

differentiated planet other than the Earth. By contrast, the depletion of K may be estimated, as on Earth, from basalts. For example, the bulk Moon K/U evaluated from the returned samples from the Moon is approximately five times lower than the average terrestrial ratio (O'Neill 1991), whereas values of K/U in basaltic meteorites from Mars (shergottites) are broadly similar to terrestrial values. K/Th and/or K/U in surface materials are mappable on the planetary scale by orbital gamma-ray spectrometry, but deducing bulk planetary values from such measurements is fraught with difficulty, particularly where surfaces are affected by weathering. Overall, the surfaces of Mars and Mercury have K/Th that are Earth-like rather than Moon-like (Peplowski et al. 2012) and likewise for Venus, from the limited data obtained by the landing missions (Surkov et al. 1987).

The Earth's Heat Budget

The heat production in the BSE from its estimated abundances of K, Th, and U is shown in Fig. 1, for time from the present back to 4.5 Ga, the approximate age of the Earth. Currently, radiogenic heat production from the abundances of Th and U of the "chondritic RLE" model with estimated K as discussed in the previous section is 21.5 ± 3 TW, which is less than half of the global heat flux of 47 TW (Davies and Davies 2010), whose uncertainty is estimated as ± 1 TW, one standard deviation. The difference of 25.5 ± 3 TW principally comes from secular cooling of the mantle and the heat flux out of the core, which, assuming that the concentration of HPEs in the core is negligible, is mediated by the crystallization of the inner core. Because the uncertainties in the values of the various components of the thermal budget of the Earth are highly model-dependent, and have a large covariance, they cannot be quoted satisfactorily as single values; hence, this discussion will omit uncertainties, and focus on average values, given to the nearest 0.5 TW.

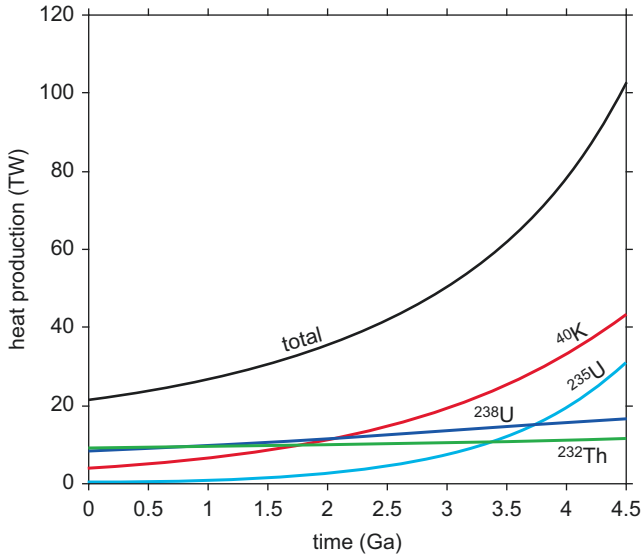

Heat-Producing Elements (HPEs), Fig. 1 Radiogenic heat production in the bulk silicate Earth (*BSE*) with time, with concentrations of the heat-producing elements estimated from the chondritic refractory lithophile element model (260 μg g^{-1} K, 85 ng g^{-1} Th, and 22 ng g^{-1} U)

The heat flux out of the core is not well known; one appraisal suggests anything from 5 to 15 TW may be reasonable (Lay et al. 2008). Recent modeling has tended to favor the higher estimate (Olson et al. 2015), which represents a fundamental change in the understanding of the Earth's heat budget. Previously, the heat flux from the core was thought to be only ~3 to 5 TW, inferred from the global buoyancy flux associated with large mantle plumes at Earth's surface (e.g., Davies 1999). However, it is now argued that the buoyancy flux of plumes is ~3 times larger in the lower mantle (e.g., Bunge 2005), while additional input from the core, as postulated by the more recent models, could be transferred into the mantle by warming of subducted lithosphere that has descended to the base of the mantle or by smaller scale plumes that do not make it to the Earth's surface.

A large fraction of the HPEs in the BSE is in the continental crust, especially the uppermost part of it. In many areas, surface heat flow measurements vary linearly with the local radiogenic heat production in the surface rocks, which is consistent with a broadly exponential decrease of the concentrations of HPEs with depth (Schubert et al. 2001). A detailed inventory of K, Th, and U in crustal rocks has been made by Huang et al. (2013), using an observational approach that is independent of what BSE model is assumed. The average concentrations of crustal reservoirs are summarized in Table 2. Given the chondritic-RLE-ratio model of the BSE, the BSE fractions of the HPEs in the continental crust would be about 30%, with another ~3% in the subcontinental lithospheric mantle (Huang et al. 2013), together producing 7.5 TW of radiogenic heat. Subtracting this value from the total BSE production of 21.5 TW implies 14 TW of radiogenic heat from the rest of the mantle - that is, the convecting mantle plus any isolated mantle reservoirs, should these exist. A dense, negatively buoyant layer above the core-mantle boundary corresponding to the D″ layer of seismology might be an example of the latter. As the total heat flux out of the continental crust is 15 TW (Davies and Davies 2010), the flux from the convecting mantle into the continental lithosphere is 8 TW.

Subtracting the radiogenic heat production of the continental crust (7 TW) from the global heat flux (47 TW) gives the heat flux out of the mantle as 40 TW, while the radiogenic heat production of the total mantle less the subcontinental lithosphere is 14 TW. The ratio of these latter numbers, known as the mantle Urey ratio, is therefore 0.35. While the Urey ratio is often stated to be a key constraint for thermal evolution models, it does not take into account the heat flux

into the mantle from the core. If the input from the core is 15 TW, subtracting this and the internal radiogenic heating of 14 TW from the output of 40 TW gives a deficit of 11 TW, to be supplied by secular cooling. The average specific heat capacity of mantle material, estimated from the heat capacities of mantle minerals (Holland and Powell 2011), is 1300 J K^{-1} kg^{-1}, giving a total heat capacity of the mantle of 5×10^{27} J K^{-1}. As other contributions to the heat budget, like the energy from thermal contraction, are more-or-less irrelevant (Jaupart et al. 2007), present-day secular cooling is therefore 0.07 K per Ma. In the unlikely but conceptually useful scenario in which all factors apart from the increase in the radiogenic heat production (Eq. 1) have not changed over geological time, heat loss would have balanced radiogenic heat production at 2.3 Ga, when the mantle would have been 100 K hotter (calculated by integration of Eq. 1). In actuality, the mantle in the past may have had higher concentrations of the HPEs if the continental crust were smaller or less enriched in its composition, or both, while fluid-dynamic scaling laws suggest that a hotter mantle would have lost heat faster through more vigorous convection.

This discussion of the Earth's thermal budget has rested on the assumption that the BSE has chondritic relative abundances of the RLEs. This assumption has recently come under reexamination (e.g., Campbell and O'Neill 2012), prompted by advances in modeling how the terrestrial planets may have accreted (O'Neill and Palme 2008). Chondritic meteorites may not be a faithful guide to the composition of the Earth. They come from undifferentiated parent bodies, which were too small to have been melted by ^{26}Al heating or other means. Such small bodies are the left-overs from the earliest stages of accretion; by definition, they escaped the subsequent processing by collisions and mergers undergone by the material that formed the terrestrial planets. If, at any stage of the accretion process, crust from previous melting and differentiation events was preferentially eroded from the ensemble of planet-forming bodies and lost, the final composition of the planet would be depleted in the incompatible elements, like the HPEs, that are concentrated into crusts. For the Earth, the Moon-forming impact may have been the last significant collisional erosion event. The upper limit to the extent by which the Earth could have been depleted in K by this process is given by the amount of radiogenic ^{40}Ar in the Earth's atmosphere, which corresponds to 120 ppm K in the BSE; allowing for some undegassed ^{40}Ar in crustal reservoirs, this means that the BSE could be depleted in K by ~ 50%. Given the geochemical coherence of Th and U with K during crust formation, the upper limit to Th and U depletions relative to Ca and Al should be similar. This kind of nonchondritic BSE composition would resolve several paradoxes raised by the chondritic-RLE model (O'Neill and Palme 2008; Campbell and O'Neill 2012). For example, the lower Th and U concentrations might explain why the flux of radiogenic ^{4}He from the mantle is much less than the heat flow expected of the chondritic-RLE model (O'Nions and Oxburgh 1983; Bianchi et al. 2010). The extreme nonchondritic composition (corresponding to a 50% depletion in K, Th, and U over the chondritic-RLE model) requires a mass balance in which the convecting mantle would constitute $>$ 90% of the whole mantle. The proportion of the BSE inventory of the HPEs extracted into the continental crust would be ~60%, and the radiogenic heat production in the mantle would be only 3 TW (Table 2). Such low radiogenic heat production might seem to pose a challenge to thermal evolution models, but one that can be addressed (e.g., Jellinek and Jackson 2015).

Eventually, the concentrations and distributions of the HPEs in the Earth may be constrained observationally from the study of "geoneutrinos" (e.g., Dye 2012; Gando et al. 2013; Huang et al. 2013), which are the detectable antineutrinos produced by the beta decays in the decay chains of ^{232}Th and ^{238}U.

Summary and Conclusions

Ragiogenic heat in the Earth is produced by three elements, K, Th, and U, which share somewhat similar geochemical properties in the context of global differentiation processes. Estimates of the abundances of K, Th, and U in the continental crust imply radiogenic heat production that almost matches heat loss, but models of the composition of the Bulk Silicate Earth based on solar-system abundances and analogies with chondritic meteorites give abundances of K, Th, and U that account for just less than half of the heat currently being lost from the solid Earth. Alternative nonchondritic models suggest lower abundances and even less radiogenic heat. The difference is made up by cooling of the mantle and heat from the Earth's core, evaluating the details of which are central to the understanding of Earth's global geodynamics, both present and past.

Cross-References

- Geochronology and Radiogenic Isotopes
- Potassium
- Thorium
- Uranium

References

Andersen MB, Elliott T, Freymuth H, Sims KW, Niu Y, Kelley KA (2015) The terrestrial uranium isotope cycle. Nature 517:356–359

Bianchi D, Sarmiento JL, Gnanadesikan A, Key RM, Schlosser P, Newton R (2010) Low helium flux from the mantle inferred from

simulations of oceanic helium isotope data. Earth Planet Sci Lett 297:379–386
Blichert-Toft J, Zanda B, Ebel DS, Albarède F (2010) The solar system primordial lead. Earth Planet Sci Lett 300:152–163
Bunge HP (2005) Low plume excess temperature and high core heat flux inferred from non-adiabatic geotherms in internally heated mantle circulation models. Phys Earth Planet Inter 153:3–10
Campbell IH, O'Neill HSC (2012) Evidence against a chondritic earth. Nature 483:553–558
Davies GF (1999) Dynamic earth: plates, plumes and mantle convection. Cambridge University Press, Cambridge
Davies JH, Davies DR (2010) Earth's surface heat flux. Solid Earth 1:5–24
Dye ST (2012) Geoneutrinos and the radioactive power of the earth. Rev Geophys 50. paper number 2012RG000400
Galer SJ, Goldstein SL (1996) Influence of accretion on lead in the earth. In: Basu A, Hart S (eds) Earth processes: reading the isotopic code, AGU geophysical monograph, vol 95. American Geophysical Union, Washington, DC, pp 75–98
Galer SJG, O'Nions RK (1985) Residence time of thorium, uranium and lead in the mantle with implications for mantle convection. Nature 316:778–782
Gando A et al (2013) Reactor on-off antineutrino measurement with Kam-LAND. Phys Rev D 88(033001). https://doi.org/10.1103/PhysRevD.88.033001
Holland TJB, Powell R (2011) An improved and extended internally consistent thermodynamic dataset for phases of petrological interest, involving a new equation of state for solids. J Metamorph Geol 29:333–383
Huang Y, Chubakov V, Mantovani F, Rudnick RL, McDonough WF (2013) A reference earth model for the heat-producing elements and associated geoneutrino flux. Geochem Geophys Geosyst 14:2003–2029
Jaupart C, Labrosse S, Mareschal JC (2007) Temperatures, heat and energy in the mantle of the earth. In: Schubert G (ed) Treatise on geophysics, Mantle dynamics, vol 7. Elsevier, Amsterdam, pp 223–270
Jellinek AM, Jackson MG (2015) Connections between the bulk composition, geodynamics and habitability of earth. Nat Geosci 8:587–593
Lay T, Hernlund J, Buffett BA (2008) Core–mantle boundary heat flow. Nat Geosci 1:25–32
O'Neill HSC (1991) The origin of the moon and the early history of the earth – a chemical model. Part 1: the moon. Geochim Cosmochim Acta 55:1135–1157
O'Neill HSC, Jenner FE (2012) The global pattern of trace-element distributions in ocean floor basalts. Nature 491:698–704
O'Neill HSC, Palme H (2008) Collisional erosion and the non-chondritic composition of the terrestrial planets. Phil Trans R Soc A 366:4205–4238
O'Nions RK, Oxburgh ER (1983) Heat and helium in the earth. Nature 306:429–431
Olson P, Deguen R, Rudolph ML, Zhong S (2015) Core evolution driven by mantle global circulation. Phys Earth Planet Inter 243:44–55
Palme H, O'Neill HSC (2014) Cosmochemical estimates of mantle composition. In: Carlson RW (ed) Treatise on geochemistry, The mantle and Core, vol 3, 2nd edn. Elsevier, Oxford, pp 1–39
Peplowski PN et al (2012) Variations in the abundances of potassium and thorium on the surface of Mercury: results from the MESSENGER Gamma–Ray Spectrometer. J Geophys Res Planet 117:E00L04. https://doi.org/10.1029/2012JE004141
Renne PR, Mundil R, Balco G, Min K, Ludwig KR (2010) Joint determination of ^{40}K decay constants and ^{40}Ar*/^{40}K for the Fish Canyon sanidine standard, and improved accuracy for ^{40}Ar/^{39}Ar geochronology. Geochim Cosmochim Acta 74:5349–5367
Renne PR, Balco G, Ludwig KR, Mundil R, Min K (2011) Response to the comment by WH Schwarz et al. on "Joint determination of ^{40}K decay constants and ^{40}Ar*/^{40}K for the Fish Canyon sanidine standard, and improved accuracy for ^{40}Ar/^{39}Ar geochronology" by PR Renne et al. (2010). Geochim Cosmochim Acta 75:5097–5100
Schubert G, Turcotte DL, Olson P (2001) Mantle convection in the earth and planets. Cambridge University Press, Cambridge
Surkov YA, Kirnozov FF, Glazov VN, Dunchenko AG, Tatsy LP, Sobornov OP (1987) Uranium, thorium, and potassium in the Venusian rocks at the landing sites of Vega 1 and 2. J Geophys Res Solid Earth 92(B4):E537–E540
Tang H, Dauphas N (2012) Abundance, distribution, and origin of ^{60}Fe in the solar protoplanetary disk. Earth Planet Sci Lett 359:248–263
Wohlers A, Wood BJ (2015) A Mercury-like component of early Earth yields uranium in the core and high mantle 142Nd. Nature 520 (7547):337–340

H

Helium

Yuji Sano
Atmosphere and Ocean Research Institute, University of Tokyo, Kashiwa, Japan

Element Data

Atomic Symbol: He
Atomic Number: 2
Atomic Weight: 4.002602
Isotopes and Abundances: ^{3}He, ^{4}He, ^{5}He, ^{6}He, ^{7}He, ^{8}He, ^{9}He, ^{10}He
^{3}He $1 \times 10^{-9} \sim 1 \times 10^{-5}$
^{4}He 0.999999999 ~ 0.99999
^{5}He, ^{6}He, ^{7}He, ^{8}He, ^{9}He, ^{10}He not stable
1 Atm Melting Point: 1.15 K
1 Atm Boiling Point: 4.22 K
Common Valences: 0
Ionic Radii: 140 pm
Pauling Electronegativity: 0
First Ionization Energy: 2370 KJ/mol
Chondritic (CI) Abundance: $2.72 \times 10^{9}/10^{6}$ silicon
Silicate Earth Abundance: $6–7 \times 10^{16}$ mol
Crustal Abundance: 3.4×10^{16} mol
Seawater Abundance: 2.3×10^{12} mol
Core Abundance: not available

Properties

Helium belongs to Group 18 of the periodic table of chemical elements: "noble gas" or "rare gas" element. Its electron shell configuration is $1s^2$, meaning that the s sub-shell is

occupied by two electrons, which produces a chemically closed shell. The first ionization potential is the highest of all elements, with the value of 24.587 eV. Consequently, helium does not combine easily with other elements. No known chemical compound contains helium at standard temperature and pressure. Helium is a considerably mobile element. It even permeates a normal Pyrex glass wall quickly because it is extremely small (1.86×10^{-10} m). Therefore, care should be taken when a natural helium sample is stored in a glass bottle for a long time (Sano and Fischer 2013). Helium has eight isotopes: ^{3}He, ^{4}He, ^{5}He, ^{6}He, ^{7}He, ^{8}He, ^{9}He, and ^{10}He. Among them, the six heavier isotopes (^{5}He, ^{6}He, ^{7}He, ^{8}He, ^{9}He, and ^{10}He) are radioactive, with short half-lives from 7.6×10^{-22} s to 801 ms (Audi et al. 2012). They are not naturally occurring. The two lighter isotopes, ^{3}He and ^{4}He are physically stable, with atomic masses of 3.0160293 and 4.00260325, respectively (Audi et al. 2012). In terrestrial helium samples, the abundance of ^{4}He dominates that of ^{3}He: the isotopic ratio (^{3}He/^{4}He) is 10^{-9}–10^{-5} (Mamyrin and Tolstkhin 1984). Rock and fluid samples from volcanic regions such as hot spot and mid-ocean ridge show higher ^{3}He/^{4}He ratios than air value of 1.38×10^{-6}, while those from continental and oceanic crust indicate lower ratios. There is a clear relationship between geotectonic setting and helium isotopes, because ^{3}He is the only unambiguous mantled derived component (Mamyrin and Tolstkhin 1984). Details of isotopic ratios are given in the section of helium isotopes. The properties of elemental helium mostly derive from ^{4}He. For example, the atomic weight is 4.002602±2, equivalent to the ^{4}He mass. The liquid density and boiling point of helium are, respectively, 120 kg/m^3 and 4.22 K. The gas density is 0.176 kg/m^3 at 101,325 Pa and 273.15 K, the lightest value after molecular hydrogen.

History and Use

Helium is an element of gas at room temperature, colorless, odorless, and non-toxic, and is completely unreactive. Its name derives from "helios" the Greek god of the sun because the element was first detected in solar spectral lines of the suns corona during an eclipse in 1868 by Janssen. On Earth, helium was discovered by Ramsay in 1895 in spectral lines of gases extracted from the mineral cleveite (impure uraninite). Contemporaneously, Cleve and Langer found helium similarly in Sweden and attempted to measure its atomic weight. The existence of terrestrial helium was subsequently confirmed using a spectroscopic method (Crookes 1895). Commercial production of helium gas has been conducted at natural gas wells in Texas, Oklahoma, Kansas, New Mexico, and Montana in the USA. It is used in industry for cryogenic purposes, welding, and space missions in addition to heat transfer in nuclear reactors and as a carrier gas of instruments such as gas chromatographs. Its total production rate was 7.6×10^{9} mol/year in 2006 (US Geological Survey 2009). This value is 10 times greater than the natural crustal degassing rate of 6.1×10^{8} mol/year (Ozima and Podosek 2002), suggesting that there are likely to be anthropogenic sources of helium in the atmosphere.

Geochemical Behavior

Helium is the most abundant element in the universe (approximately 24.0% in weight fraction) after hydrogen (73.9%). Hydrogen and helium are believed to have been produced by nucleosynthesis shortly after the Big Bang. Other elements might be generated by stellar processes and are called "metals" in astronomy. Helium abundance in the solar system is 2.72×10^{9} relative to 10^{6} silicon atoms. Again, it is second largest to hydrogen, 2.79×10^{10} (Anders and Grevesse 1989). Helium is scarce in the terrestrial atmosphere, with abundance of 5.24 ppm (Gluckauf 1946), although it is a member of "atmophile" elements by the Goldschmidt definition because helium is released from the upper atmosphere to interplanetary space by thermal and/or nonthermal escape at the rate of 8.3×10^{8} mol/year (Ozima and Podosek 2002). That figure contrasts markedly to the argon abundance in air, 0.924%. Argon is not rare; it is trapped by Earth's gravity while both helium and argon have radiogenic nuclides as dominant isotopes in the crust and mantle. An approximate balance might prevail between the degassing flux of helium from solid Earth to the air and escape from the atmosphere to space. The typical concentration of helium in surface seawater is 1.7 nmol/kg, which is governed by the solubility equilibrium between air and seawater at 14.4 °C (Sano and Takahata 2006). The total inventory of helium is 2.3×10^{12} mol in oceans, which is two orders of magnitude smaller than that of atmosphere, 9.3×10^{14} mol. The total inventory of helium in the crust is 3.4×10^{16} mol based on the hypothetical contents of 1.3×10^{-6} mol/kg in typical rock (Mamyrin and Tolstikhin 1984). Although the whole mantle inventory is not well documented, it is probably similar to the crust because the average contents of U and Th are two orders of magnitude smaller and its mass is two orders larger. Therefore, the silicate Earth inventory of helium is much greater than that in the atmosphere or oceans.

Biological Utilization and Toxicity

There is no biological utilization of helium. It is totally nontoxic.

Summary

Helium is a member of atmophile elements, enriched in gas phase such as atmosphere, natural gas, and volcanic gas. It is chemically inert, colorless, and odorless. It is rare in the Earth but has become an important geochemical tracer since it is widely considered to be the only unambiguous mantled derived component with high $^3He/^4He$ ratio.

Cross-References

- Argon
- Argon Isotopes
- Atmophile Elements
- Cosmic Elemental Abundances
- Earth's Atmosphere
- Gas Source Mass Spectrometry (GS-MS)
- Geochemistry
- Geochronology and Radiogenic Isotopes
- Helium Isotopes
- Krypton
- Mantle Geochemistry
- Natural Gas
- Neon
- Neon Isotopes
- Noble Gases
- Stable Isotope Geochemistry
- Subduction Zone Geochemistry
- Thorium
- Uranium
- Volcanic Gases
- Xenon
- Xenon Isotopes

References

Anders E, Grevesse N (1989) Abundances of the elements: meteoritic and solar. Geochim Cosmochim Acta 53:197–214

Audi G, Kondev FG, Wang M, Pfeiffer B, Sun X, Blachot J, MacCormick M (2012) The NUBASE2012 evaluation of nuclear properties. CPC 36:1157–1286

Crookes W (1895) The spectrum of the gas from Cleveite. Chem News, August 23

Gluckauf E (1946) A micro-analysis of the helium and neon contents of air. Proc R Soc Lond A Math Phys Sci 185:98–119

Jannsen PJC (1968) Lettre ecrite de Madras le 22 juillet 1868. Compt Rend 67:494

Mamyrin BA, Tolstikhin IN (1984) Helium isotopes in nature. Elsevier, Amsterdam. 273 pp

Ozima M, Podosek FA (2002) Noble gas geochemistry. Cambridge University Press, Cambridge. 286 pp

Ramsey W (1895) Terrestrial helium. Nature 51:512

Sano Y, Fischer TP (2013) The analysis and interpretation of noble gases in modern hydrothermal systems. In: Burnard P (ed) The noble gases as geochemical tracers, advances in isotope geochemistry. Springer, Heidelberg, pp 249–317

Sano Y, Takahata N (2006) Measurement of noble gas solubility in seawater using a quadrupole mass spectrometer. J Oceanogr 61:465–473

US Geological Survey (2009) USGS mineral information: helium. http://minerals.usgs.gov/minerals/pubs/commodity/helium

Helium Isotopes

Yuji Sano
Atmosphere and Ocean Research Institute, Univertsity of Tokyo, Kashiwa, Japan

H

Definition

Stable isotopic ratio of helium ($^3He/^4He$).

Variations in He Isotope Ratios

Helium has two stable isotopes: ^3He and ^4He. Both isotopes were produced by nucleo-synthesis in the very early universe about 100 s after the Big Bang, possibly because of the fusion of deuterium (D) as shown below.

$$D + D \rightarrow {}^3He + n.$$
$$D + D \rightarrow {}^4He + \gamma.$$
$$T + D \rightarrow {}^4He + n.$$
$${}^3He + n \rightarrow {}^4He + \gamma.$$
$${}^3He + D \rightarrow {}^4He + p.$$

In those expressions, n, γ, T, and p, respectively, denote neutron, γ ray, tritium (^3H), and proton. The helium isotopic ratio ($^3He/^4He$) has been calculated approximately 8×10^{-5} (Burles et al. 1999) because the ^4He nucleus is much more stable than that of ^3He. The ratio has evolved through stellar processes. Both ^3He and ^4He are produced by a proton–proton chain reaction occurring deep in stars like the Sun with high pressure and temperature as follows.

$$p + p \rightarrow D + \beta^+ + \nu.$$
$$D + p \rightarrow {}^3He + \gamma.$$
$${}^3He + {}^3He \rightarrow {}^4He + 2\,p.$$

Therein, β^+ and ν, respectively, denote positron and neutrino. The best estimate of the $^3He/^4He$ ratio for the present-day outer convective zone of the Sun is 3.8×10^{-4} based on Apollo experiments and spacecraft observations (Geiss and Gloeckler 1988). However, planetary helium identified in Q phase (acid-resistant residues) of primitive carbonaceous

chondrite showed the $^3He/^4He$ ratio of 1.6×10^{-4} (Wieler et al. 1992), which is markedly lower than the solar value, but appreciably larger than the early universe, even though the origin has not been well understood. Probably planetary helium is more primitive than solar helium because the latter has evolved by a proton–proton chain reaction since the early solar system time: 4.6 Ga. Helium isotopes of different reservoirs are presented in Fig. 1.

Within solid Earth as well as meteorites, ^4He is produced by radioactive decay of U and Th in the samples. The relevant decays are summarized as follows.

$$^{232}Th \rightarrow {}^{208}Pb + 6\,{}^4He + 4\,\beta^-.$$
$$^{238}U \rightarrow {}^{206}Pb + 8\,{}^4He + 6\,\beta^-.$$
$$^{235}U \rightarrow {}^{207}Pb + 7\,{}^4He + 4\,\beta^-.$$

In those expressions, β^- is an electron. Subject to the decay chains of ^{232}Th, ^{238}U, and ^{235}U series isotopes, the growth rate of ^4He in silicate rock is approximated by concentrations of U and Th as shown below.

$$J = 0.2355 \times 10^{-12}\,(U) \times [1 + 0.123(Th/U - 4)].$$

Therein, J, (U), and Th/U denote the ^4He growth rate in units of cm^3/g per year, the concentration of U in parts per million, and the concentration ratio of Th to U in weight. Typical crustal rock of 1 kg mass with U = 3 ppm and Th = 12 ppm produces 3×10^{-14} mol of ^4He per year.

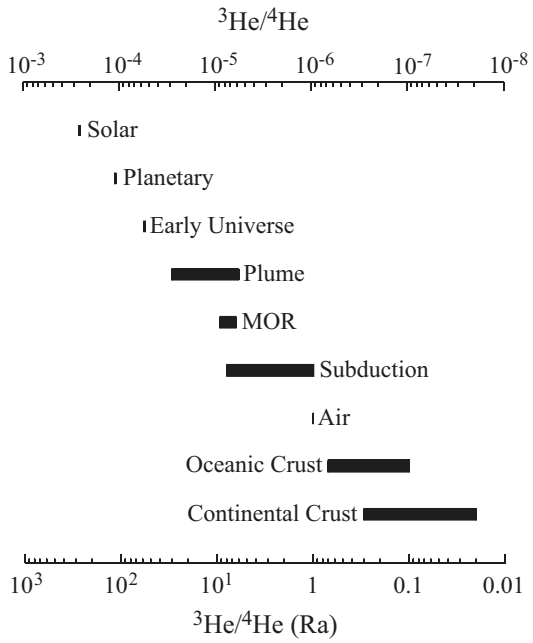

Helium Isotopes, Fig. 1 Helium isotopes of different reservoir in geochemistry and cosmochemistry. There are two ways to express the $^3He/^4He$ ratio, absolute one (*top*) and relative to air value of 1.382×10^{-6} (*bottom*)

Considering the blank level of helium analytical system, it might be possible to date the rock and minerals at several hundred ka by U, Th-^4He dating method if the closed system has been maintained, the initial magmatic and air helium is negligible, and the U and Th contents are measured precisely.

On Earth, helium-3 was first found in natural gas helium by Alvarez and Cornog (1939) using a 60-in cyclotron as a mass spectrograph. Aldrich and Nier (1948) measured the $^3He/^4He$ ratios of the atmosphere, natural gas wells, and several minerals using a helium gas extraction and purification system and a single focusing gas mass spectrometer. They reported that the $^3He/^4He$ ratio of air is about 10 times larger than that of natural gas because of radiogenic helium. Clarke et al. (1969) measured the $^3He/^4He$ ratios of deep Pacific water and found elevated ratios relative to the air. They attributed the excess helium-3 to the terrestrial primordial (planetary) helium derived from the mantle by submarine volcanism. Mamyrin et al. (1969) measured the $^3He/^4He$ ratios of volcanic gases using a magnetic resonance mass spectrometer. They claimed that the high $^3He/^4He$ ratios were derived from the deep Earth, a discovery that was made independently from that by Clarke et al. (1969).

Terrestrial Helium Reservoir

Since the first findings of primordial helium in 1969, many helium isotope data have been reported (Mamyrin and Tolstikhin 1984; Ozima and Podosek 2002). This wealth of data is attributable to the wider use of commercial gas mass spectrometers available since 1980. Based on the helium isotope data, three major reservoirs of terrestrial helium have been inferred: those of the atmosphere, mantle, and crust. Each is described below:

Atmospheric helium: mean residence time of helium in the air is approximately 10^6 years, as estimated from the degassing rate from the solid Earth and the total inventory (Ozima and Podosek 2002). Atmospheric $^3He/^4He$ ratio had been believed to be a constant because the residence time is much longer than the mixing time of air, which is a few years. This idea was inspired by Mamyrin et al. (1970) who measured various air $^3He/^4He$ ratios and reported that the ratio did not vary with latitude, longitude, and altitude (up to 10 km) within error of 2–3%. On this basis, most laboratories engaged in helium isotope measurements have used atmospheric helium as a natural isotopic standard. Sano et al. (1989) measured the $^3He/^4He$ ratios of 20 air samples at several different sampling sites and dates. A change of the atmospheric helium isotope ratio possibly occurred with time: a decrease in $^3He/^4He$ of about 0.74%/year. Although this change might be attributed to the local effects or experimental artifacts, the observations were also consistent with a significant anthropogenic release of crustal He with a low $^3He/^4He$ ratio. Since then, contradictory results have been published in the literature, indicating either a decrease in the $^3He/^4He$ ratio

of the order of 0.1–0.3‰/year during the last few decades or no detectable change since 1973. Very recently, Mabry et al. (2015) reported no significant temporal decrease of the $^3He/^4He$ ratio (0.010 ± 0.033‰/year) during 1978–2011 using a selection of air samples archived in Tasmania. Then atmospheric helium is expected to be homogeneous and a reliable natural standard such as nitrogen. There are four absolute $^3He/^4He$ measurements of atmospheric helium. The average of these measurements, when considering their weighted errors, becomes $(1.382 \pm 0.005) \times 10^{-6}$ (1σ), which is likely to be the best estimate of the atmospheric helium isotopic composition (this value is defined as Ra).

Mantle helium: at first, it was well documented that the $^3He/^4He$ ratio of hundreds mid-ocean ridge basalt (MORB) glass is constant with a value of 6.5–9.5 Ra (where Ra is atmospheric ratio as described above), irrespective of the three different divergent plate boundary systems of the Mid-Atlantic Ridge, East Pacific Rise, and Central Indian Ridge (Graham 2002). The $^3He/^4He$ ratios of submarine hydrothermal fluids do not vary significantly from 7.2 to 9.2 Ra with an average of 8.1 ± 0.5 Ra (1σ) in MOR-volcanism, which is identical to that of the worldwide average of MORB glass (Sano and Fischer 2013). Therefore, the upper mantle above 670 km depth is characterized by a globally constant $^3He/^4He$ ratio of 8.0 ± 1.5 Ra, which suggests that either the $^3He/(U + Th)$ ratio is constant within the upper mantle during the most recent 1 Gyr or the mixing of helium is sufficiently rapid to reduce local heterogeneity (helium isotope anomaly) in the convective mantle. This most important reservoir of primordial helium is defined as MOR-type helium. Another distinctive reservoir results from a large deep component with $^3He/^4He$ ratios significantly higher than 9.5 Ra, probably related to the mantle under 670 km depth. These high ratios were found in active volcanism, occurring within the plate interiors such as Hawaii (ca. 16.6 Ra in Loihi seamount) and Yellowstone (ca. 15.8 Ra in Mud Volcano) in the USA. They are commonly called hot spots, although it is fed anomalously by hot mantle compared with the ambient asthenosphere and possibly originated in the lower mantle. In this context, Iceland is also regarded as a hot spot because of its huge volcanic output, even though it is located on the Mid-Atlantic Ridge. The terrestrial highest $^3He/^4He$ ratio of the fluid sample reached 29 Ra in northwestern Iceland. Seismic tomograms of these three hot spot regions suggest that a continuous low-velocity anomaly has been imaged from the surface to the lower mantle or the core-mantle boundary. The other hot spot regions such as Afar, Azores, Canary Islands, Cape Verde, Galapagos, and Reunion showed the $^3He/^4He$ ratios higher than MOR-type helium. These values higher than 9.5 Ra are defined as plume-type helium (Sano and Fischer 2013). In contrast, some other hot spot regions such as Socorro Island and Cameroon showed values equal to or lower than MOR-type helium. These $^3He/^4He$ ratios might be affected by crustal or radiogenic helium with low $^3He/^4He$ ratios in the source magma or subsurface regions. A third group of helium isotopes higher than the atmosphere was found in hundreds of volcanic rock and fluid samples in subduction zones such as Alaska, the Aleutians, Kamchatka, northeastern Japan, Mariana, the Philippines, Banda, Java, the Solomons, Chile, Ecuador, Colombia, Mexico, and the Cascades in the USA (Hilton et al. 2002). They vary significantly from less than 1Ra to 8Ra, where the lower ratios are probably affected by crustal or radiogenic helium. These geographical variations are related to the tectonic setting of the sampling site, whereas the temporal variations might be attributable to volcanic and seismic activity of the regions (Sano and Fischer 2013). The highest $^3He/^4He$ ratio in a subduction zone is consistent with MOR-type helium, suggesting their origin from the upper mantle. The average of the maximum $^3He/^4He$ ratio of 7.4 ± 1.3 Ra (1σ) is defined as subduction-type helium.

Crustal helium: The $^3He/^4He$ ratio of natural gases in the USA showed approximately 0.1 Ra by early measurements of terrestrial helium isotopes (Aldrich and Nier 1948). To explain the 0.1 Ra value, Morrison and Pine (1955) reported that the crustal production of ^3He in the continental crust is accounted for by successive nuclear reactions: $^6Li\ (n, \alpha)\ ^3H\ (\beta^-)\ ^3He$ where the source of n is reactions between α-particles derived from U and Th decay and light elements such as oxygen and silicon in crustal silicate rocks by $^{18}O(\alpha, n)^{21}Ne$ and $^{29}Si(\alpha, n)^{32}S$. Therefore, the in situ radiogenic $^3He/^4He$ ratio depends on the contents of U, Th, Li, and other light elements such as O, Si, Al, and K. The theoretical $^3He/^4He$ ratio was calculated as shown below

$$\frac{^3He}{^4He} = (n_f + n_a) \times P_t \times \frac{\sigma_{Li} N_{Li}}{\sum_i \sigma_i N_i}$$

In that equation, n_f is the ratio of neutrons produced by the spontaneous fission of ^{238}U and other heavy nuclides to α particles produced by U and Th decay, which is approximately 8×10^{-8}. Also, n_a is the ratio of neutrons to a particles produced by (α, n) reactions with light elements. P_t is the probability that a neutron will reach thermal energy. N_i is the number of atoms of the element (i) in a 1 g sample, and σ_i is the thermal neutron capture cross section of element (i). In fact, n_a is expressed as the following

$$n_a = \frac{\sum_k q_k S_k N_k}{\sum_i S_i N_i}$$

Therein, q_k is the neutron yield produced by a particle in a thick target composed of the element (k); S_k is the relative stopping power of the element (k). The $^3He/^4He$ ratio calculated for typical sedimentary material was approximately 0.015 Ra based on the equations above, which is significantly

lower than the observed natural gases. This extremely low value is defined as radiogenic helium. Crustal rock and fluid samples are principally admixtures of the radiogenic and primordial helium derived from the upper or the lower mantle (Mamyrin and Tolstikhin 1984). A weak positive correlation exists between the $^3He/^4He$ ratios of fluid samples in continental crust and the formation age of the region. This correlation is explained by the *in grow* production of radiogenic helium in addition to initial magmatic helium (mantle derived one either MOR-type or plume-type) in a crustal rock, i.e., the initial $^3He/(U + Th)$ ratios do not vary markedly on a continental scale.

Helium isotopes account for a few minor components of terrestrial samples. They are all related to the nuclear reactions induced by high-energy cosmic rays. First, cosmogenic helium was found in young basaltic lava flows, glacially polished rocks, and moraines. It is produced by the spallation reaction of light elements in silicates by cosmic rays (Kurz 1986). These ^3He abundances are useful to ascertain the erosion rate of uprifting area. Second, tritium (^3H) is generated by spallation of nitrogen and oxygen in the upper atmosphere in addition to past nuclear tests in the 1960s. It is easily assimilated in rainwater and is incorporated in groundwater at recharge areas. Dating of groundwater has been well documented using the ^3H-^3He method (Schlosser et al. 1988). Third, ^3He was produced in cosmic dust by spallation in interplanetary space. The dust is expected to precipitate on the Earth. This component was well identified in deep sea sediments, where the sedimentation rate was extremely low (Amari and Ozima 1985).

Summary

Element "Helium" has two stable isotopes (^3He and ^4He) and six radioactive ones (^5He, ^6He, ^7He, ^8He, ^9He, and ^{10}He). Half lives of the latter ones are significantly short, up to only 0.8 sec. They are not naturally occurring and do not contribute geochemistry and cosmochemistry. There are three helium end members, "solar," "planetary," and "early universe" in cosmochemistry with individual isotopic compositions. Both solar and planetary helium were evolved from hypothetical early universe component with the $^3He/^4He$ ratio increasing. Within the solid Earth, ^4He is produced by radioactive decay of U and Th. On the other hand, major part of ^3He is attributable to planetary (primordial) helium trapped deep in the Earth at the time of accretion. The $^3He/^4He$ ratios of rock and fluid samples from quaternary volcanic regions such as hot spot, mid- ocean ridge, and island arc generally show higher ratios than atmospheric ratio of 1.382×10^{-6}. On the other hand, those collected in nonvolcanic and tectonically stable areas of continental and oceanic crust indicate lower ratios.

Cross-References

- Argon
- Argon Isotopes
- Atmophile Elements
- Cosmic Elemental Abundances
- Earth's Atmosphere
- Gas Source Mass Spectrometry (GS-MS)
- Geochemistry
- Geochronology and Radiogenic Isotopes
- Helium
- Krypton
- Mantle Geochemistry
- Natural Gas
- Neon
- Neon Isotopes
- Noble Gases
- Stable Isotope Geochemistry
- Subduction Zone Geochemistry
- Thorium
- Uranium
- Volcanic Gases
- Xenon
- Xenon Isotopes

References

Aldrich LT, Nier AO (1948) The occurrence of He^3 in natural sources of helium. Phys Rev 74:1590–1594

Alvarez LW, Cornog R (1939) He-3 in helium. Phys Rev 56:379–379

Amari S, Ozima M (1985) Search for the origin of exotic helium in deep-sea sediments. Nature 317:520–522

Burles S, Nollett KM, and Turner MS (1999) Big-Bang nucleosynthesis: linking inner space and outer space. arXiv astro-ph/9903300

Clarke WB, Beg MA, Craig H (1969) Excess ^3He in the sea: evidence for terrestrial primordial helium. Earth Planet Sci Lett 6:213–220

Geiss J, Gloeckler G (1988) Abundances of deuterium and helium-3 in the protosolar cloud. Space Sci Rev 84:239–250

Graham DW (2002) Noble gas isotope geochemistry of mid-ocean ridge and ocean island basalts; characterization of mantle source reservoirs. In: Porcelli D, Ballentine C, Wieler R (eds) MSA special volume: Noble gases in geochemistry and cosmochemistry, vol 47. Mineralogical Society of America, Washington, DC, pp 247–317

Hilton DR, Fischer TP, Marty B (2002) Noble gases in subduction zones and volatile recycling. In: Porcelli D, Ballentine C, Wieler R (eds) MSA Special Volume: Noble Gases in Geochemistry and Cosmochemistry. 47, pp 319–362

Kurz M (1986) Cosmogenic helium in a terrestrial igneous rock. Nature 320:435–439

Mabry JC, Lan T, Boucher C, Burnard PG, Brennwald MS, Langenfelds R, Marty B (2015) No evidence for change of the atmospheric helium isotope composition since 1978 from re-analysis of the Cape Grim Air Archive. Earth Planet Sci Lett 428:134–138

Mamyrin BA, Tolstikhin IN (1984) Helium isotopes in nature. Elsevier. 273 pp

Mamyrin BA, Tolstikhin IN, Anufriyev GS, Kamenskiy IL (1969) Isotopic analysis of terrestrial helium on a magnetic resonance mass spectrometer. Geokhimiya 1969:595–602
Mamyrin BA, Anufriyev GS, Kamenskiy IL, Tolstikhin IN (1970) Determination of the isotopic composition of atmospheric helium. Geochem Int 7:498–505
Morrison P, Pine J (1955) Radiogenic origin of the helium isotopes in rock. Ann N Y Acad Sci 62:71–92
Ozima M, Podosek FA (2002) Noble gas geochemistry. Cambridge University Press, Cambridge/New York. 286 pp
Sano Y, Fischer TP (2013) The analysis and interpretation of Noble gases in modern hydrothermal systems. In: Burnard P (ed) The Noble gases as geochemical tracers, Advances in Isotope Geochemistry. Springer, Heidelberg/New York, pp 249–317
Sano Y, Wakita H, Makide Y, Tominaga T (1989) A 10-year decrease in the atmospheric helium isotope ratio possibly caused by human activity. Geophys Res Lett 16:1371–1374
Schlosser P, Stute M, Dorr H, Sonntag C, Munnich KO (1988) Tritium/^{3}He dating of shallow groundwater. Earth Planet Sci Lett 89:353–362
Wieler R, Anders E, Baur H, Lewis RS, Signer P (1992) Characterization of Q-gases and other noble gas components in the Murchison meteorite. Geochim Cosmochim Acta 56:2907–2921

Henry's Law

William M. White
Department of Earth and Atmospheric Sciences, Cornell University, Ithaca, NY, USA

Synonyms

Gas solubility

Definition

Henry's Law states that the mole fraction of a component in a solution is linearly proportional to its vapor pressure in a gas phase in equilibrium with that solution. Henry's Law also expresses a special case of nonideal behavior where the activity coefficent of a component in a solution is independent of the concentration of that component.

Henry's Law and Gas Solubility

Henry's Law derives its name from nineteenth-century English chemist William Henry (1774–1836) who observed that the concentration of atmospheric gases dissolved in water increased in direct proportion to an increase in pressure. In its modern formulation, Henry's Law expresses the equilibrium solubility of gases in solution, stating:

Henry's Law, Table 1 Henry's Law constants for gases in water at standard temperature and pressure

	mol/m^3 Pa	mol/L atm
O_2	1.30×10^{-05}	1.32×10^{-03}
H_2	2.60×10^{-06}	2.63×10^{-04}
CO_2	3.40×10^{-04}	3.45×10^{-02}
N_2	6.40×10^{-06}	6.48×10^{-04}
He	3.90×10^{-06}	3.95×10^{-04}
Ne	4.50×10^{-06}	4.56×10^{-04}
Ar	1.40×10^{-05}	1.42×10^{-03}
CH_4	1.40×10^{-05}	1.42×10^{-03}

$$X_i = h_i P_i \tag{1}$$

where X_i is the mole fraction of species i in the solution, P_i is the vapor pressure of i in equilibrium with the solution, and h_i is the constant of proportionality known as the Henry's Law Constant, which is unique to each solution and solute and is a function of temperature and total pressure.

Henry's Law may also be written with the concentration of the dissolved species expressed in molality, molarity, parts per million, etc., and the value of Henry's Law constant will depend on the concentration units used. Values for the Henry's Law constants for several atmospheric gases in aqueous solution at standard temperature (298.15 K) and pressure (0.101 MPa) are listed in Table 1 with the dissolved concentration that is expressed in S.I. units, moles/m^3-Pa, and as moles/liter with the vapor pressure expressed in atmospheres. Thus, for example, the concentration of oxygen in pure water in equilibrium with the atmospheric oxygen whose partial pressure is 0.209 atms would be 0.275 mM. A fuller compilation of Henry's Law constants is given in Sander (2015).

Broader Application of Henry's Law

Henry's Law differs from Raoult's Law, which states:

$$X_i = \frac{P_i}{P_i^o} \tag{2}$$

where P_i^o is the pressure of the pure gas phase of i. Raoult's Law expresses the behavior of ideal solutions (or ideal behavior). Such behavior is rare, even in the approximate, and occurs only where interactions between different molecules are the same as between like molecules. In nature, nonideality is the rule. In the general nonideal case, the solubility of a substance will be a function of the concentration of that substance in solution as well as that of other components, temperature, and pressure. Henry's Law predicts that the

solubility of a substance is independent of its concentration in the solution and is thus a special case of nonideal behavior.

In highly dilute solutions, all substances approach Henry's Law behavior. This occurs as interactions between molecules of the solute become so rare compared to solute-solvent interactions that they have a negligible effect on the properties of the solution.

Because all substances in principle exert finite vapor pressures, Henry's Law can be applied to solutions other than gases in liquids, including solid solutions. Henry's Law thus provides a useful definition of a trace component, namely one sufficiently scarce that it does not affect the properties of the substance in which it is dissolved.

Cross-References

- ▶ Earth's Atmosphere
- ▶ Equilibrium
- ▶ Solubility
- ▶ Trace Elements

References

Sander R (2015) Compilation of Henry's law constants (version 4.0) for water as solvent. Atmos Chem Phys 15(8):4399–4981. https://doi.org/10.5194/acp-15-4399-2015

High Field Strength Elements

Vincent J. M. Salters
National High Magnetic Field Laboratory and Department of Earth, Ocean and Atmospheric Sciences, Florida State University, Tallahassee, FL, USA

Definition

This term refers to metals forming cations with a small radius and high charge (valence state), therefore high associated electric field – high field strength. The definition of field strength as charge over ionic radius (Z/r) and importance of field strength in the geochemical behavior of elements was first pointed out by Ahrens (1953). Metal ions with $Z/r > 20$ (with r measured in nanometer) are generally thought to be high field strength elements (Rollinson 1993). Although the high field strength elements (HFSE) consists of all elements whose valence state is three or higher including the rare earth elements, for the platinum group elements, uranium and thorium, in geochemistry the term is mostly reserved for tetravalent Hf, Ti, Zr, pentavalent Nb, Ta, and hexavalent W and Mo.

Geochemical Behavior

The HFSE can be used to geochemically discriminate between tectonic settings of igneous rocks as rocks with HFSE depletion only occur at convergent plate boundaries (Gill 1981). This depletion in calc-alkaline rocks was first noted for Ti (Chayes 1965). The depletion of HFSE is most easily recognized on incompatible element diagrams (Sun et al. 1979) where element concentrations are reported normalized to their chondritic or silicate earth abundance and arranged according to increasing compatibility in a four-phase lherzolite-melt system. On these incompatibility diagrams, igneous rocks from convergent boundaries show a deficiency in Nb, Ta, Ti, Hf, and Zr compared to their neighboring elements. However, not all volcanic rocks in convergent settings have HFSE depletions. Basalts without HFSE depletions are found in the Cascades as well as in the Central Mexico Volcanic Belt.

The deficiencies in the HFSE are attributed to their low solubility in aqueous fluids or their partitioning into accessory phases like rutile (Zack et al. 2002) During subduction, the down-going slab dehydrates and fluxes the overlying mantle. Compared to other elements, the HFSE are less mobile in the slab-derived fluid (Kogiso et al. 1997; Ayers 1998; Johnson and Plank 1999) and mostly remain in the slab. Therefore, the overlying mantle wedge will be enriched in fluid mobile elements resulting in a relative depletion of the HFSE. Subsequent melting of the fluxed mantle wedge transfers the HFSE depletions to the crust. W is potentially the exception and is enriched in arc volcanics compared to elements with similar behavior during melting (U, Th, Ta). With increasing pressure and temperature as the fluid transitions towards a supercritical fluid the solubility of the HFSE into the fluid increases (Kessel et al. 2005a). This transition takes place at pressures in excess of 4 GPa (Kessel et al. 2005b).

HFSE Fractionation

Because of their similar charge and ionic radius, Zr and Hf as well as Nb and Ta are often considered geochemical twins and up till recently their ratios were thought to be chondritic throughout the crust and upper mantle. High precision analyses (Münker et al. 2001) of the Nb/Ta and Zr/Hf ratios have shown this is not the case. Partition studies have shown that both rutile, amphibole, and sphene can significantly fractionate both Nb/Ta and Zr/Hf (Foley et al. 2002; Klemme et al. 2005). A detailed comparison between fluid-dominated and melt-dominated island arc regimes, however, have not shown significant fractionation of Zr/Hf or Nb/Ta, in most cases.

Zr/Hf ratios are relatively similar in arc rocks and MORB (Münker et al. 2004; Kirchenbaur and Münker 2015) although partition studies have shown that Hf is consistently more compatible than Zr in clinopyroxene (Salters and Longhi 1999; Pertermann and Hirschmann 2002; Salters et al. 2002) and melting of four-phase lherzolite can fractionate the Hf/Zr ratio and lead to lower Zr/Hf in the residue. Similarly, Nb partition coefficients are consistently lower than Ta (van Westrenen et al. 2001; McDade et al. 2003) and positive correlations between Nb/Ta and Zr/Hf are expected.

With the high precision HFSE concentration determination it is now known that relative to Ta the accessible silicate earth is depleted in Nb requiring that some of the Earth's Nb reside in a high Nb/Ta reservoir (McDonough 1991; Green 1995; Rudnick et al. 2000; Kamber et al. 2003; Münker et al. 2003). The Nb/Ta ratio is lower than chondritic (Jochum et al. 2000; Münker et al. 2003) in the continental crust (Rudnick and Fountain 1995; Barth et al. 2000), the depleted mantle (Salters and Stracke 2004), and ocean island basalts (Pfänder et al. 2007). Some have argued that the missing Nb may be in the Earth's core (Wade and Wood 2001; Münker et al. 2003) others argue for a hidden reservoir from ancient subducted slabs (Rudnick et al. 2000). The subducted slab is implied as eclogites can have very high Nb/Ta ratios (Barth et al. 2001 2002), although a separate study on slab-derived eclogites do not show Nb enrichment over Ta (Schmidt et al. 2009).

Summary

The difference in behavior of the HFSE in fluid-saturated and fluid absent systems and their affinity for very specific mineral (rutile, amphibole, sphene) makes them very useful fingerprinting magmatic processes.

Cross-References

- ▶ Hafnium
- ▶ Niobium
- ▶ Subduction Zone Geochemistry
- ▶ Tantalum
- ▶ Titanium
- ▶ Trace Elements
- ▶ Zirconium

References

Ahrens LH (1953) The use of ionization potentials. Part 2. Anion affinity and geochemistry. Geochimica et Cosmochimica Acta 3:1–29

Ayers J (1998) Trace element modeling of aqueous fluid – peridotite interaction in the mantle wedge of subduction zones. Contributions to Mineralogy and Petrology 132(4):390–404

Barth MG, McDonough WF, Rudnick RL (2000) Tracking the budget of Nb and Ta in the continental crust. Chemical Geology 165:197–213

Barth MG, Rudnick RL, Horn I, McDonough WF, Spicuzza MJ, Valley JW, Haggerty SE (2001) Geochemistry of xenolithic eclogites from West Africa, Part I: a link between low MgO eclogites and Archean crust formation. Geochimica et Cosmochimica Acta 65:1499–1527

Barth MG, Foley SF, Horn I (2002) Partial melting in Archean subduction zones: constraints from experimentally determined trace element partition coefficients between eclogitic minerals and tonalitic melts under upper mantle conditions. Precambrian Research 113:323–340

Chayes F (1965) Titania and alumina content of oceanic and circumoceanic basalt. Mining Magazine 34:126–131

Foley SF, Tiepolo M, Vannucci R (2002) Growth of early continental crust controlled by melting of amphibolite in subduction zones. Nature 416:837–840

Gill JB (1981) Orogenic Andesites and Plate Tectonics. Springer, Berlin

Green TH (1995) Significance of Nb/Ta as an indicator of geochemical processes in the crust-mantle system. Chemical Geology 120:347–359

Jochum KP, Stolz AJ, Mcorist G (2000) Niobium and tantalum in carbonaceous chondrites: constraints on the solar system and primitive mantle niobium/tantalum, zirconium/niobium, and niobium/uranium ratios. Meteoritics and Planetary Science 35:229–236

Johnson MC, Plank T (1999) Dehydration and melting experiments constrain the fate of subducted sediments. Geochemistry, Geophysics, Geosystems 1:1999GC000014

Kamber BS, Greig A, Schoenberg R, Collerson KD (2003) A refined solution to earth's hidden niobium: implications for evolution of continental crust and mode of core formation. Precambrian Research 126:289–308

Kessel R, Schmidt MW, Ulmer P, Pettke T (2005a) Trace element signature of subduction-zone fluids, melts and supercritical liquids at 120–180 km depth. Nature 437:724–727

Kessel R, Ulmer P, Pettke T, Schmidt MW, Thompson AB (2005b) The water-basalt system at 4 to 6 GPa: phase relations and second critical endpoint in a K-free eclogite at 700 to 1400 degrees C. Earth and Planetary Science Letters 237(3–4):873–892

Kirchenbaur M, Münker C (2015) The behaviour of the extended HFSE group (Nb, Ta, Zr, Hf, W, Mo) during the petrogenesis of mafic K-rich lavas: the Eastern Mediterranean case. Geochimica et Cosmochimica Acta 165:178–199

Klemme S, Prowatke S, Mameter K, Günther D (2005) Partitioning of trace elements between rutile and silicate melts: implications for subduction zones. Geochimica et Cosmochimica Acta 69(9):2361–2371

Kogiso T, Tatsumi Y, Nakano S (1997) Trace element transport during dehydration processes in the subducted oceanic crust: 1. Experiments and implications for the origin of ocean island basalts. Earth and Planetary Science Letters 148:193–205

McDade P, Blundy JD, Wood BJ (2003) Trace element partitioning on the Tinaquillo lherzolite solidus at 1.5 GPa. Physics of the Earth and Planetary Interiors 139(1–2):129–147

McDonough WF (1991) Partial melting of subducted oceanic crust and isolation of its residual eclogitic lithology. Philosophical Transactions Royal Society of London 335:181–192

Münker C, Weyer S, Scherer E, Mezger K (2001) Separation of high field strength elements (Nb, Ta, Zr. Hf) and Lu from rock samples for MC-ICPMS measurements. Geochemistry, Geophysics, Geosystems 2:2001GC000183

Münker C, Pfander JA, Weyer S (2003) Evolution of planetary cores and the Earth-Moon system from Nb/Ta systematics. Science 301:84–87

Münker C, Wörner G, Yogodzinski G, Churikova TG (2004) Behaviour of high field strength elements in subduction zones: constraints from Kamchatka–Aleutian arc lavas. Earth and Planetary Science Letters 224:275–293

Pertermann M, Hirschmann MM (2002) Trace-element partitioning between vacancy-rich eclogitic clinopyroxene and silicate melt. American Mineralogist 87(10):1365–1376
Pfänder JA, Münker C, Stracke A, Mezger K (2007) Nb/Ta and Zr/Hf in ocean island basalts – implications for crust-mantle differentiation and the fate of niobium. Earth and Planetary Science Letters 254:158–172
Rollinson HR (1993) Using Geochemical Data: Evaluation, Presentation and Interpretation. Taylor and Francis, New York
Rudnick RL, Fountain DM (1995) Nature and composition of the continental crust: a lower crustal perspective. Reviews of Geophysics 33:267–309
Rudnick RL, Barth MG, Horn I, McDonough WF (2000) Rutile-bearing refractory eclogites: missing link between continents and depleted mantle. Science 287:278–281
Salters VJM, Longhi JE (1999) Trace element partitioning during the initial stages of melting beneath ocean ridges. Earth and Planetary Science Letters 166:15–30
Salters VJM, Stracke A (2004) The composition of the depleted mantle. Geochemistry, Geophysics, Geosystems 5(5):2003GC000597
Salters VJM, Longhi J, Bizimis M (2002) Near mantle solidus trace element partitioning at pressures up to 3.4 GPa. Geochemistry, Geophysics, Geosystems 3:2001GC000148
Schmidt A, Weyer S, John T, Brey GP (2009) HFSE systematics of rutile-bearing eclogites: new insights into subduction zone processes and implications for the earth's HFSE budget. Geochimica et Cosmochimica Acta 73(2):455–468
Sun S-S, Nesbitt RW, Sharaskin AY (1979) Geochemical characteristics of mid-ocean ridge basalts. Earth and Planetary Science Letters 44:119–138
van Westrenen, W., Blundy, J. D., and Wood, B. J., 2001. High field strength element/rare earth element fractionation during partial melting in the presence of garnet: implications for identification of mantle heterogeneities. Geochemistry, Geophysics, Geosystems, 2(7), 2000GC000133
Wade J, Wood BJ (2001) The Earth's "missing" nobium may be in the core. Nature 409:75–78
Zack T, Kronz A, Foley SF, Rivers T (2002) Trace element abundances in rutiles from eclogites and associated garnet mica schists. Chemical Geology 184(1–2):97–122

High-Resolution Mass Spectrometry

Elizabeth B. Kujawinski
Marine Chemistry and Geochemistry, Woods Hole Oceanographic Institution, Woods Hole, MA, USA

Definition

The use of mass spectrometers with high resolving power (>50,000 at *m/z* 400) and mass accuracy (≤2 ppm).

Overview

All mass spectrometry instruments measure the mass to charge ratio of ions (*m/z*). However, the precision of this measurement depends on the type of mass spectrometer utilized. Quadrupole mass spectrometers generally measure the *m/z* value to the nearest integer, or nominal mass. High-resolution mass spectrometers provide information on the fractional mass, or the digits after the decimal point. Two terms are used to compare these mass spectrometers: mass accuracy and resolving power. Mass accuracy is defined as ((observed mass – true mass)/true mass) and is expressed in parts per million (ppm). Resolving power (R) is defined as the value of the full width at half of the peak's maximum value (FWHM) at a specific *m/z* (often *m/z* 400). The two most common high-resolution mass spectrometers are the time-of-flight (TOF) mass spectrometers (R ~ 1000–10,000) and the Fourier transform (FT)-based mass spectrometers (R ~ 100,000 to 1,000,000). TOF MS is often used for mass analysis of components within fairly simple mixtures and will not be discussed further. The FT-MS, in contrast, is widely used to analyze very complex mixtures, including petroleum and natural organic matter from a variety of environments. For further information on mass analyzers, I refer the reader to a mass spectrometry textbook such as Watson and Sparkman (2007) or Gross (2011).

FT-ICR MS

The focus of this section is the ultrahigh resolution mass spectrometers, or those based on Fourier transform technology. These instruments are comprised of an ionization source, optics to focus and transfer the ion beam, and a magnetic or electric field-based mass analyzer where ion motion is measured in order to determine mass to charge ratio (*m/z*). There are two primary instrument types, the Fourier transform ion cyclotron resonance (FT-ICR) mass spectrometer, which uses a magnetic field to induce ion motion, and the Orbitrap mass spectrometer, which uses electric fields. The two instruments differ in important ways in their ion optics and trapping technologies. Nevertheless, they both rely on the principle that a charged particle will alter its path under the influence of a magnetic or electric field and they both force ions into a circular motion within the magnetic or electric field. Ion packets rotate around a central axis in both instruments, and the frequency of ion motion is inversely related to the ion's mass to charge ratio. To facilitate detection in the FT-ICR MS, ions' orbits are expanded by the application of a radio-frequency (RF) pulse. The movement of each ion group past detection sensors or plates is monitored over time and can be approximated as a decaying sine wave, where the frequency is related to its mass to charge ratio and the amplitude is related to its relative abundance. The detected signal is a superposition of sine waves from ions with unique mass to charge ratios, collectively termed the transient. In each transient, the frequencies and amplitudes of the overlapping sine waves from ions with unique *m/z* are deconvoluted through

Fourier transformation. These frequencies can be converted to *m/z* values through external calibration using standards. In complex mixtures, many hundreds (or thousands) of ions are present in each sample. Because high mass ions have lower frequencies, transients with longer duration are critical to establishing sufficient detection of these ions. In addition, repeat transients can be added together to remove random signals from background noise and to enhance detection of low-abundance ions. Overviews of the design and physics of FT-ICR MS and Orbitrap are available in Marshall et al. (1998) and Zubarev and Makarov (2013), respectively.

The strength of the electric or magnetic field affects the mass accuracy and the dynamic range of ions detected. In Orbitrap technology, the electric field does not have the same resolution as the newest FT-ICR instruments, although this parameter is superior to all non-FT instruments. Recent improvements in the Orbitrap hardware, as well as advances in raw data transformations, have led to Orbitrap mass resolving powers of 500,000 or more at 200 *m/z* (as of May 2017). In FT-ICR MS, the dynamic range and mass accuracy is related to magnetic field strength, because the ICR cell can accommodate more ions and the signal attenuation (or transient) can be measured for a longer period in larger magnets. Thus, more ions are detected, and their *m/z* value is determined with higher resolution. Instruments in common use (as of May 2017) utilize magnetic field strengths of 7-tesla (T), 9.4-T, 15-T, and 21-T, yielding resolving power of 200,000 to >1,000,000 at 400 *m/z*, respectively. These instruments detect thousands of individual ions within each spectrum, often resolved to the baseline (Fig. 1a).

Both the FT-ICR and the Orbitrap mass spectrometer can be interfaced with numerous ionization sources. The most common is electrospray ionization (ESI) which transfers ions in a solution into the MS. For most applications, the ions are dissolved in a solution that contains water and so positive ion mode preferentially ionizes basic functional groups such as amines. Sodiated complexes (i.e., $[M + Na]^+$, where M is the original molecule) are very common for natural mixtures. Indeed, both the protonated and sodiated adducts are often observed in positive ion mode spectra of natural organic matter. By contrast, negative ion mode preferentially ionizes acidic functional groups such as carboxylic acids or phenols. Complexes are also possible but occur less frequently (e.g., chlorine adducts such as $[M + Cl]^-$). Other ionization sources include atmospheric pressure photoionization (APPI), atmospheric pressure chemical ionization (APCI), and matrix-assisted laser desorption ionization (MALDI). These sources use energy to make ions and so some degree of fragmentation is likely. However, the relative benefits and caveats of each source can be effectively managed to address specific science questions. For example, ESI is used for analysis of polar molecules that are dissolved in aqueous solution such as dissolved organic matter. This excludes nonpolar molecules such as hydrocarbons, but these compounds are more appropriately ionized and detected using APCI or APPI. APPI can be used to explore the composition of photoactive molecules, thus allowing the analysis of this specific fraction relative to nonreactive components.

Data

Mass accuracy is high with these instruments because so many periods of ion motion are detected; thus, the frequency and by extension the *m/z* value are known to high precision. With current FT-ICR MS instruments, it is common to achieve mass accuracy below 1 ppm or smaller than the mass of an electron. This enables the determination of an elemental formula based on the mass measurement alone. An elemental formula is the unique combination of elements such as carbon (C), hydrogen (H), oxygen (O), and nitrogen (N) that match the measured *m/z* value within a specified error. Many methods exist to assign elemental formulas to ultrahigh resolution mass spectrometry data (e.g., Koch et al. 2007; Green and Perdue 2015), but they all incorporate the premise that elemental formula assignments for natural mixtures can generally be constrained to C, H, O, and N with minor contributions of sulfur (S) and phosphorus (P). The atoms within an elemental formula can often be arranged in multiple ways yielding structural isomers. The number and complexity of structural isomers increases with mass as the number and variety of atoms increases. Thus, elemental formulas cannot be used for compound identification at the structural level, except for very simple molecules such as carbon dioxide (CO_2) or methane (CH_4) where only one structure is possible. Nevertheless, elemental formulas provide an indication of a compound's class and thus are useful for assessing general mixture composition. For example, lipids are characterized by high hydrogen content relative to carbon (H:C ratio), while aromatic hydrocarbons have many fewer hydrogen atoms for the same carbon number. These differences are often visualized on van Krevelen plots (Fig. 1b), which guide interpretations regarding shifts in composition with experimental parameters.

Although the Fourier transform of ion motion yields an amplitude, the relative abundance of ions should be viewed with caution in FT-MS data. The ionization efficiencies of molecules in ESI are affected dramatically by the sample matrix. Molecules with poor ionization efficiency can be suppressed by less abundant molecules with higher ionization efficiencies. This has been shown nicely in studies where samples are compared before and after chromatographic pre-separation. For natural organic matter, pre-separation significantly enhances the number of ions detected. Ionization efficiency can affect the relative spectral abundances of ions, such that changes in peak height are not necessarily related

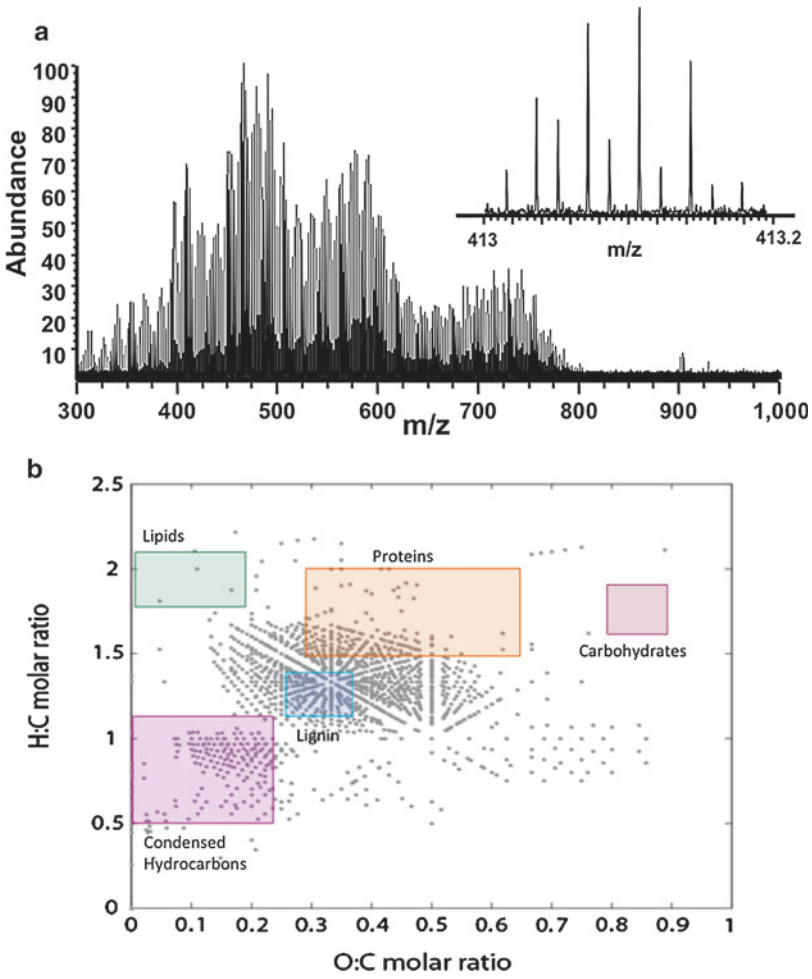

High-Resolution Mass Spectrometry, Fig. 1 (**a**) Representative FT-ICR mass spectrum of Suwannee River dissolved organic matter, collected on a 9.4 T instrument in negative ion mode. The spectrum represents the co-addition of 200 scans (Reprinted from Kujawinski et al. 2004. Copyright (2004), with permission from Elsevier). (**b**) Visualization of FT-MS data using a van Krevelen plot. The data comes from negative ion mode analysis of seawater samples (Reprinted from Kujawinski et al. 2009. Copyright (2009), with permission from Elsevier). Each gray dot corresponds to a unique elemental formula, plotted according to its hydrogen/carbon (H:C) molar ratio and its oxygen/carbon (O:C) molar ratio. Colored boxes indicate regions associated with different compound classes, as compiled in Kujawinski and Behn (2006)

linearly to changes in abundance in the sample. Investigators can mitigate these caveats by injecting samples multiple times to assess peak reproducibility, by focusing their interpretation on molecules with relatively elevated peak heights and by comparing their interpretations based on relative peak height and on presence-absence normalizations (e.g., Kido Soule et al. 2010; Riedel and Dittmar 2014). Many recent studies incorporate one or more of these mitigation strategies and are using multivariate statistics and meta-data to interpret shifts in composition observed in FT-MS data.

Applications

The use of FT-ICR MS in organic geochemistry has exploded since the first papers in the early 2000s. It has been applied to many of the most complex mixtures on Earth, including petroleum (Hughey et al. 2001; Rodgers et al. 2000), soil humic and fulvic acids (Brown and Rice 2000; Kujawinski et al. 2002), and aquatic dissolved organic matter (Koch et al. 2005; Stenson et al. 2003). Over the past decade, studies have moved from descriptive analysis of a few samples (<10) to multivariate statistical analysis of many samples. FT-ICR MS is used effectively to compare compositional changes as a function of different environmental or experimental parameters, yielding molecular-level insights into the fundamental reactions in organic geochemistry (reviewed in Minor et al. 2014). In most cases, these insights are not possible with lower-resolution analyses, thus establishing FT-ICR MS as a uniquely capable mass spectrometer for these efforts. For example, polar components within petroleum are largely invisible to gas chromatography-based instruments due to low volatility. Instead, FT-ICR MS not only detects these molecules but provides a basis for comparing sulfur remediation strategies or for identifying the products of environmental weathering (e.g., Ruddy et al. 2014). Likewise, with its unparalleled ability to resolve thousands of components in complex mixtures, ESI FT-ICR MS has now been used to characterize and compare the polar molecules in dissolved organic matter in all aquatic environments, including (but not limited to) soils (Ohno et al. 2010), rivers (Sleighter and Hatcher 2008), lakes (Minor et al. 2012), seawater (Dittmar

and Koch 2006), glaciers (Bhatia et al. 2010), and hydrothermal vents (Rossel et al. 2015). The Orbitrap has not been applied as extensively as the FT-ICR MS instruments and, in general, does not yield data with similar mass resolving power. However, the faster speed of data acquisition coupled with lower maintenance costs (i.e., the Orbitrap does not require cryogens to cool a superconducting magnet) has made these instruments attractive to organic geochemists studying dissolved organic matter (e.g., Remucal et al. 2012).

Summary

Limitations still exist in the application of FT-MS to organic geochemistry because (1) molecular structure cannot be assigned based on elemental formulas alone and (2) some molecules are not detected due to sample matrix effects. In the first case, structural clues can be gleaned from complementary nuclear magnetic resonance (NMR) spectroscopy measurements (Hertkorn et al. 2008) or from fragmentation (MS/MS) of individual ions (Stenson et al. 2002). These tools are appropriate for the dominant molecules in a mixture but are not practical for low-abundance molecules. Liquid chromatography (LC) can be used to reduce sample complexity by generating subsamples based on physical or chemical properties. Subsamples are then analyzed by ESI FT-ICR MS, and the data is concatenated to yield a more comprehensive view of the original sample (Capley et al. 2010). This approach enhances the detection of lower-abundance ions, particularly those that elute at different times from higher-abundance ions. Alternatively, an LC is coupled directly to the FT-ICR MS to measure full mass spectra along the full chemical gradient. Some hybrid instruments (e.g., the linear ion trap FT-ICR MS) use the low-resolution ion trap MS to collect fragmentation spectra of selected ions, thus enabling structural characterization in tandem with compositional analysis (Kido Soule et al. 2015). Mass spectral databases currently have limited coverage of natural organic molecules, but as they mature, fragmentation spectra will be increasingly useful for identifying compounds within environmental organic mixtures.

Cross-References

- Dissolved Organic Matter (DOM)
- Gas Chromatography–Mass Spectrometry (GC–MS)
- Gas Source Mass Spectrometry (GS-MS)
- Inductively Coupled Plasma Mass Spectrometry (ICP-MS)
- Laser Ablation – Inductively Coupled Plasma Mass Spectrometry
- Organic Geochemistry
- Petroleum
- Thermal Ionization Mass Spectrometry

References

Bhatia MP, Das SB, Charette MA, Longnecker K, Kujawinski EB (2010) Molecular characterization of dissolved organic matter associated with the Greenland ice sheet. Geochim Cosmochim Acta 74:3768–3784

Brown TL, Rice JA (2000) Effect of experimental parameters on the ESI FT-ICR mass spectrum of fulvic acid. Anal Chem 72:384–390

Capley EN, Tipton JD, Marshall AG, Stenson AC (2010) Chromatographic reduction of isobaric and isomeric complexity of fulvic acids to enable multistage tandem mass spectral characterization. Anal Chem 82:8194–8202

Dittmar T, Koch BP (2006) Thermogenic organic matter dissolved in the abyssal ocean. Mar Chem 102:208–217

Green NW, Perdue EM (2015) Fast graphically-inspired algorithm for assignment of molecular formulae in ultrahigh resolution mass spectrometry. Anal Chem 87:5086–5094

Gross JH (2011) Mass spectrometry: a textbook. Springer, Heidelberg. 716 pp

Hertkorn N, Frommberger M, Witt M, Koch BP, Schmitt-Kopplin P, Perdue EM (2008) Natural organic matter and the event horizon of mass spectrometry. Anal Chem 80:8908–8919

Hughey CA, Rodgers RP, Hendrickson CL, Marshall AG (2001) Elemental composition analysis of processed and unprocessed diesel fuel by electrospray ionization Fourier transform ion cyclotron resonance mass spectrometry. Energy Fuel 15:1186–1193

Kido Soule MC, Longnecker K, Giovannoni SJ, Kujawinski EB (2010) Impact of instrument and experiment parameters on reproducibility of ultrahigh resolution ESI FT-ICR mass spectra of natural organic matter. Org Geochem 41:725–733

Kido Soule MC, Longnecker K, Johnson WM, Kujawinski EB (2015) Environmental metabolomics: analytical strategies. Mar Chem 177:374–387

Koch BP, Dittmar T, Witt M, Kattner G (2007) Fundamentals of molecular formula assignment to ultrahigh resolution mass data of natural organic matter. Anal Chem 79:1758–1763

Koch BP, Witt M, Engbrodt R, Dittmar T, Kattner G (2005) Molecular formulae of marine and terrigenous dissolved organic matter detected by electrospray ionization Fourier transform ion cyclotron resonance mass spectrometry. Geochim Cosmochim Acta 69:3299–3308

Kujawinski EB, Behn MD (2006) Automated analysis of electrospray ionization Fourier transform ion cyclotron resonance mass spectra of natural organic matter. Anal Chem 78:4363–4373

Kujawinski EB, Del Vecchio R, Blough NV, Klein GC, Marshall AG (2004) Probing molecular-level transformations of dissolved organic matter: insights from electrospray ionization Fourier-transform ion cyclotron resonance mass spectrometry. Mar Chem 92:23–37

Kujawinski EB, Hatcher PG, Freitas MA (2002) High-resolution Fourier transform ion cyclotron resonance mass spectrometry (FT-ICR-MS) of humic and fulvic acids: improvements and comparisons. Anal Chem 74:413–419

Kujawinski EB, Longnecker K, Blough NV, Del Vecchio R, Finlay L et al (2009) Identification of possible source markers in marine dissolved organic matter using ultrahigh resolution electrospray ionization Fourier-transform ion cyclotron resonance mass spectrometry. Geochim Cosmochim Acta 73:4384–4399

Marshall AG, Hendrickson CL, Jackson GS (1998) Fourier transform ion cyclotron resonance mass spectrometry: a primer. Mass Spectrom Rev 17:1–35

Minor EC, Steinbring CJ, Longnecker K, Kujawinski EB (2012) Characterization of dissolved organic matter in Lake superior and its watershed using ultrahigh resolution mass spectrometry. Org Geochem 43:1–11

Minor EC, Swenson MM, Mattson BM, Oyler AR (2014) Structural characterization of dissolved organic matter: a review of current

techniques for isolation and analysis. Environ Sci: Processes Impacts 16:2064
Ohno T, He Z, Sleighter RL, Honeycutt CW, Hatcher PG (2010) Ultrahigh resolution mass spectrometry and indicator species analysis to identify marker components of soil- and plant biomass-derived organic matter fractions. Environ Sci Technol 44:8594–8600
Remucal CK, Cory RM, Sander M, McNeill K (2012) Low molecular weight components in an aquatic humic substance as characterized by membrane dialysis and Orbitrap mass spectrometry. Environ Sci Technol 46:9350–9359
Riedel T, Dittmar T (2014) A method detection limit for the analysis of natural organic matter via Fourier transform ion cyclotron resonance mass spectrometry. Anal Chem 86:8376–8382
Rodgers RP, Blumer EN, Freitas MA, Marshall AG (2000) Complete compositional monitoring of the weathering of transportation fuels based on elemental compositions from fourier transform ion cyclotron resonance mass spectrometry. Environ Sci Technol 34:1671–1678
Rossel PE, Stubbins A, Hach PF, Dittmar T (2015) Bioavailability and molecular composition of dissolved organic matter from a diffuse hydrothermal system. Mar Chem 177:257–266
Ruddy BM, Huettel M, Kostka JE, Lobodin VV, Bythell BJ, McKenna AM, Aeppli C, Reddy CM, Nelson RK, Marshall AG, Rodgers RP (2014) Targeted petroleomics: Analytical investigation of Macondo Well oil oxidation products from Pensacola Beach. Energy Fuels 28:4043–4050
Sleighter RL, Hatcher PG (2008) Molecular characterization of dissolved organic matter (DOM) along a river to ocean transect of the lower Chesapeake Bay by ultrahigh resolution electrospray ionization Fourier transform ion cyclotron resonance mass spectrometry. Mar Chem 110:140–152
Stenson AC, Landing WM, Marshall AG, Cooper WT (2002) Ionization and fragmentation of humic substances in electrospray ionization Fourier transform-ion cyclotron resonance mass spectrometry. Anal Chem 74:4397–4409
Stenson AC, Marshall AG, Cooper WT (2003) Exact masses and chemical formulas of individual Suwannee River fulvic acids from ultrahigh resolution electrospray ionization Fourier transform ion cyclotron resonance mass spectra. Anal Chem 75:1275–1284
Watson JT, Sparkman OD (2007) Introduction to mass spectrometry. Wiley, London. 819 pp
Zubarev RA, Makarov A (2013) Orbitrap mass spectrometry. Anal Chem 85:5288–5296

History of Geochemistry

William M. White
Department of Earth and Atmospheric Sciences, Cornell University, Ithaca, NY, USA

Definition

Geochemistry grew out of the Renaissance arts of alchemy and metallurgy. Over much of that long past, geochemistry was intimately intertwined with chemistry itself, evolving into a distinct subfield of both chemistry and earth sciences only with the dawn of the twentieth century. It now holds a central role in understanding the Earth, its neighboring planets, and their evolution.

Early Roots in Alchemy and Chemistry

The term "geochemistry" was coined in 1838 by the German-Swiss chemist Christian Friedrich Schönbein, a professor of chemistry and physics at the University of Basel and better known as the discoverer of ozone, who wrote, "*In a word, a comparative geochemistry ought to be launched. . . before the mystery of the genesis of our planets and their inorganic matter may be revealed*" (Krough 2001). Revealing the "mystery of the genesis of our planets and their inorganic matter" remains a remarkably accurate description of what geochemistry has become, with qualification that geochemistry also includes the study of nonliving organic matter.

The roots of geochemistry are, however, much older and intimately intertwined with the roots of chemistry, both nurtured in the fertile soil of alchemy and the practical arts of metallurgists. A principal goal of alchemy was to transform one substance derived from the Earth into another, such as gold. Even as chemists came to recognize that there were certain fundamental substances, elements, that could not be so transformed and sought to identify them, it was in natural substances that they sought them. This continued into the twentieth century when the last two stable elements were identified: hafnium in zirconium ores by Coster and von Hevesy in 1923 and rhenium in platinum ores in 1925 by Noddack, Tacke, and Berg based on the 1869 predictions of Mendeleev.

Georg Agricola's 1556 treatise on mining and metallurgy, *De re metallica*, might be considered the first text on geochemistry, but Gustav Bischof's 4-volume *Lehrbuch der chemischen und physikalischen Geologie* (Bischof 1847) is probably more deserving of that distinction. Among other things, Bischof emphasized the importance of water in what we would call today geochemical cycles and understood that water chemistry reflected weathering reactions with the rocks through which it flowed. At about the same time, Jacques Joseph Ebelman (1845) pointed out the importance of plants in silicate weathering and of marine fauna in precipitating weathering products in the ocean, effectively laying out the carbon cycle as we understand it today (Galvez and Gaillardet 2012). The three-volume *Allgemeine und chemische Geologie* by Justin Roth (1879) replaced Bischof's as the standard text on geochemistry and remained widely cited well into the twentieth century.

Fathers of Geochemistry: Clarke, Goldschmidt, and Vernadsky

Frank W. Clarke (1847–1931) received his B.S. in chemistry from Harvard University in 1868. He went on to serve as an assistant in chemistry at the new Cornell University in 1869, but his interest in geology led him to explore the gorges and

waterfalls bordering the campus and write a guide book on them (Clarke 1869). He went on to subsequent appointments as a chemistry professor in the Boston Dental College, Howard University, and University of Cincinnati. It was during this period that Clarke wrote a remarkable prescient article in the new magazine *Popular Science* entitled *Evolution and the Spectrograph* in which he speculated that the chemistry of the universe had evolved over time (Clarke 1873b), with light elements having been formed earlier than heavier ones. This was based on observations of stellar composition from the newly developed astrospectrograph. His elaboration on that idea years later foreshadows modern nucleosynthetic theory (Clarke 1918, 1925). Other important contributions in those years included a compilation of specific gravities, boiling points, and melting points of chemical compounds for the Smithsonian Institution series *The Constants of Nature* (Clarke 1873a) and a chemistry textbook (Clarke 1884). Clarke served as president of the American Chemical Society in 1901 (Fig. 1).

Clarke became chief chemist of the US Geological Survey in 1883, a position he held until his retirement in 1924. His publication record over this period is remarkable for its abundance (some 136 papers listed by Google Scholar), diversity, and importance. A broad summary of the chemistry of rocks and natural waters, *The Data of Geochemistry* (Clarke 1908), is his most cited work. Clarke nicely summarizes the objective of geochemistry in the fifth edition of this work:

> *To determine what changes are possible, how and when they occur, to observe the phenomena which attend them, and to note their final result are the function of the geochemist.*

Others works include papers on the heat of formation of water from hydrogen and hydroxyl ions, chemical denudation, systematic studies of the chemistry of mineral classes such as micas, silicates, a review of atomic theory and papers on the composition of US rivers and lakes, and, with Henry Washington, works on the composition of igneous rocks (Clarke and Washington 1922) and the Earth's crust (Clarke and Washington 1924), which was based on an average of 5197 analyses selected from a total of over 8000. Many of his papers in his last decade at the Geological Survey are on the inorganic composition of marine invertebrates, summarized in Clarke and Wheeler (1922).

Victor M. Goldschmidt was born to Jewish parents in Zurich in 1888 and moved to Oslo in 1901, received his PhD at the University of Christiania (later Oslo) in 1911, and immediately thereafter became professor and director of the Mineralogical Institute. His work on the metamorphic and magmatic rocks of southern Norway at the time is notable for the first application of the Gibbs Phase Rule to petrology. Using the newly invented x-ray spectrograph, Goldschmidt discovered that the even atomic-numbered rare earth elements (REE) have higher abundances than the odd-numbered ones, a key to nuclear structure. Analyzing mineral structures with the newly invented x-ray diffractometer, he discovered that the REE atomic radii decreased with atomic number, which he called the lanthanide contraction. He and his colleagues went on to determine the ionic radii of 67 elements by 1925 and deduced now well-known relationships between ionic radius, ionic charge, atomic number, and periodic group. This led to his Goldschmidt Rules of substitution (Fig. 2).

His papers on the differentiation of the Earth foreshadowed modern thinking on Earth's formation and evolution (Goldschmidt 1922). By considering their properties and in which phases they occurred in meteorites, Goldschmidt divided the elements into atmophile, lithophile, siderophile, and chalcophile (the Goldschmidt Classification) and argued that the first three groups were concentrated in the atmosphere-hydrosphere, the crust and mantle, and the core, respectively (Goldschmidt 1923), a classification still used today. He recognized that the cosmic abundances of the elements could best be deduced from meteorites and the value of glacial clays as samples of Earth's crust, an approach still used today (see ▶ "Earth's Continental Crust" in this volume), and his own estimate of crustal composition based on analysis of 81 samples compared well with that of Clarke and Washington (1924).

History of Geochemistry, Fig. 1 Frank W. Clarke. U.S. Government photo; NOAA Collection

History of Geochemistry, Fig. 2 Victor M. Goldschmidt in 1908 (From the family collection of Hans Goldschmidt; public domain)

History of Geochemistry, Fig. 3 Vladimir Vernadsky in Paris, 1889 (Photo by Bosch & Co. Public Domain)

In 1929, Goldschmidt accepted a professorship in 1929 at the Mineralogisches Institüt at the University of Göttingen and subsequently published papers on the carbon cycle emphasizing the importance of biochemical reactions. He also pointed out that the amount of CO_2 released through burning of fossil fuels greatly exceeded the volcanic flux and was increasing the CO_2 content of the atmosphere.

In 1935, Goldschmidt resigned his professorship in protest of the Nazi anti-Jewish agitation. Returning to Oslo, he published the ninth volume of his *Geochemische Verteilungsgesetze der Elemente* (the distribution laws of the elements) (Goldschmidt 1937) with data on the abundance of elements in the solar atmosphere, meteorites and terrestrial rocks, and plotted the logarithms of the ratios of atomic species in the solar system relative to the abundance of Si – an approach still used today. His work led directly to the concept of "magic numbers" of nuclei and the shell theory of nuclear structure.

Goldschmidt continued his interest in nuclear physics and was working with Fritz Houtermans on plutonium and the actinide elements (Goldschmidt 1941–1942) at the time of the German invasion in 1940. He was arrested by the Nazis in 1942 and sent to the Berg concentration camp but was released soon afterward, probably because of his work related to phosphate fertilizer. He escaped to Sweden shortly thereafter and then went on to England in 1943, where he worked with officials involved with the war effort. He returned to Norway and his position at Oslo in 1946, but the war had taken a toll on his health and he died in 1947.

Vladimir Vernadsky (1863–1945) was born in St. Petersburg to Ukrainian parents (Fig. 3). He received his PhD in mineralogy from Moscow University in 1897 and was appointed professor there in 1898. Much of his early work was on mineral paragenesis and alumino-silicate minerals. Vernadsky was caught up in the excitement of the newly discovered phenomenon of radioactive decay and was one the first to recognize its significance as a terrestrial energy source, establishing a Radium Commission in 1909. Vernadsky was active in prerevolution Russian politics and served as a member of the Constitutional Democratic Party in parliament. In 1911, he resigned his professorship in Moscow, along with a quarter of the faculty, in protest to a government crackdown on student protests and returned to St. Petersburg where established a geochemical laboratory. After the February Revolution of 1917, Vernadsky was appointed to various government committees and as head of the Dept. of Mineralogy and Geology at Moscow University by the provisional government of Alexander Kerensky, while continuing to hold positions in St. Petersburg (Bailes 1990). However, when the Bolshevik took over in October, he moved to the Ukraine, eventually settling in Kiev. He set about establishing a

Ukrainian Academy of Sciences and, despite the political turmoil and violence of the Russian Civil War, it was during this time that began the work for which he is best known: biogeochemistry, a term he coined, and the elaboration of concept of the biosphere, a term coined earlier by the Austrian geologist Edwin Suess, whom Vernadsky had met in 1912. Vernadsky argued that life was not independent of its surroundings but was itself a geologic force, both affecting and being affected by the inert world, an idea later popularized by J. E. Lovelock (1972) as the Gaia hypothesis.

Vernadsky returned to St. Petersburg in 1921, but in 1922, he accepted an invitation to teach in the Sorbonne in Paris where, among other things, he worked on radioactivity with Marie Curie. He published *La géochimie* (Vernadsky 1924) there in 1924. He returned to Russia in 1926 where another seminal book, *The Biosphere* (Vernadsky 1926), was published. He organized the Biogeochemical Laboratory in St. Petersburg (by then renamed Leningrad), which moved to Moscow in 1934. There he led studies of permafrost, mineral resources, and determining the composition of living organisms and the relationship between health, including human health, and oversupply or deficits of elements such as iodine, calcium, and barium in the local environment. He continued his strong interest in radioactivity and isotopes, leading a program for concentration of heavy water and initiating construction of the first cyclotron in the Soviet Union. Having learned of work on nuclear fusion in Germany and the USA in 1938, Vernadsky began strongly urging the government to initiate a program on the development nuclear energy and to identify uranium deposits within the USSR. His efforts led directly to the establishment of a Uranium Commission and indirectly to the Soviet atomic bomb project, which began in 1943. Although strongly patriotic, Vernadsky was often directly critical of the Stalinist government; these criticisms were tolerated because of his renown and stature. Although he published papers in French, German, and English, Venadsky's work was largely overlooked in the West until the 1980s. His rediscovery has greatly influenced not only geochemistry, but also fields such as ecology and microbiology.

Birth and Development of Isotope Geochemistry

Geochronology

Within the lifetimes of these three scientists, Henri Bacquerel's 1896 discovery of radioactivity revolutionized physics, chemistry, and geochemistry. Rapid progress followed, particularly by Marie Curie in Paris and Ernst Rutherford in Montreal. By 1905, it was understood that uranium and thorium decayed through a chain including radium and polonium; decay constants were approximately known but the ultimate product was not. Yale chemist Bertram Boltwood proposed that is was Pb and recognized the potential to measure geologic time from the buildup of Pb in U-rich minerals, reporting ages up to 2.2 billion years (Boltwood 1907), implying the Earth was vastly older than Lord Kelvin had estimated. Thus was born radiometric geochronology, but not yet isotope geochemistry as isotopes were not known until Fredrick Soddy, a student of Rutherford, proposed them in 1913 and F. W. Aston confirmed them in 1919. By then, it was understood that U decayed to ^{206}Pb and Th to ^{208}Pb. F. W. Clarke (1918), however, questioned Boltwood's U-Pb dating technique because Clarke had found that uranogenic Pb had a variable atomic weight, up to 206.8, seemingly inconsistent with the radiogenic production of ^{206}Pb.

The problem was that no one knew then of ^{235}U, which was discovered in only 1935, or that it decayed to ^{207}Pb. Once Alfred Nier (1939), then at Harvard, had measured the ^{238}U/^{235}U ratio and the decay constants with reasonable accuracy, he was able to produce the first accurate ages and confirm that the age of the Earth was greater than 2.2 billion years. Nier returned to his native Minnesota setting up a laboratory at the University of Minnesota where he continued his work in geochronology, determining the isotopic composition of the elements and natural variations in them, and designing a variety mass spectrometers in the process. In 1940, Nier was able to separate sufficient ^{235}U that its fission properties could be determined. From 1942 to 1945, Nier was part of the Manhattan Project, designing mass spectrometers used to assess U isotope separation. He returned to the University of Minnesota where he continued to work on geochronology, determining the isotopic composition of the elements and their masses, and designing mass spectrometers, including ones for NASA spacecraft, up to his death at age 82 in 1994.

Ultimately, the age of the Earth turned out to be much greater. Russian physicist E. R. Gerling estimated an age of 3.1 billion years in 1942, Authur Holmes estimated it to be 3.3 billion years, and Fritz Houtermans (1953), who had the unenviable distinction of having been a political prisoner of both the Nazis and the Soviets, estimated an age of 4.5 ± 0.3 billion years based on the isotopic composition of Pb ores and the initial solar system Pb isotopic composition measured in iron meteorites.

Rapid progress in geochronology and isotope geochemistry followed directly from the Manhattan Project, not only in Alfred Nier's University of Minnesota lab, but also at the Institute of Nuclear Studies, which Enrico Fermi founded at the University of Chicago in 1945 (and now known as the Enrico Fermi Institute). There, Harrison Brown and some of his fellow Manhattan Project veterans including Harold Urey and Willard Libby decided to establish a new scientific field of "nuclear geochemistry" (Revelle 1994). Brown's former student Claire Patterson (1956), by then at Cal Tech, declared

the issue of the age of the Earth settled when he wrote, "*It seems we should now admit that the age of the Earth is known as accurately and with as much confidence as the concentration of aluminum is known in the Westerly, Rhode Island granite*" (the Westerly granite is the source of the USGS chemical standard W1), concluding from meteorite and terrestrial standards that the Earth was 4.55 ± 0.07 billion years old. Having discovered in the course of his analytical work that Pb contamination was ubiquitous, Patterson spent much of his later career warning of the dangers of anthropogenic Pb in the environment (e.g., Patterson 1965; Settle and Patterson 1982) and is perhaps the scientist most responsible for the removal of Pb from gasoline and paint. Interestingly, while we know from U-Pb dating that solar system formation began 4568.22 ± 0.17 million years ago (Bouvier and Wadhwa 2010), the age of the Earth itself is known no better than Patterson's value.

As the first half of the twentieth century came to a close, W. F. Libby (Libby et al. 1949) had already developed the ^{14}C dating method (for which he won the Nobel Prize in Chemistry in 1960), and a number of other cosmogenic nuclide dating schemes followed in subsequent decades. In 1956, Thomas Aldrich, a former student of Nier, and others (Aldrich et al. 1956) at Carnegie Institution of Washington determined the half-life of ^{87}Rb and showed the Rb-Sr decay system could be used as a geochronometer. About the same time, workers in a number of laboratories, including the same Carnegie group (Wetherill 1957), Jerry Wasserburg, another product of the Institute of Nuclear Studies and student of Harold Urey, and R.D. Russell in Toronto, developed the K-Ar dating method. This method later saw a big advance with the advent of $^{40}Ar/^{29}Ar$ dating, a variation on K-Ar dating technique in which ^{39}Ar is produced from ^{39}K by neutron bombardment (Merrihue and Turner 1966). W. F. Libby had discovered that samarium was radioactive in his doctoral dissertation (Libby 1934), but only 40 years later was Lugmair (1974) able to report the first Sm-Nd ages. The Lu-Hf (Patchett and Tatsumoto 1980) and Re-Os (Allègre and Luck 1980) systems were introduced shortly thereafter, although some previous work had been done on both. The Apollo lunar program also had a big impact on geochronology, not so much with the development of new systems as with a giant step forward in mass spectrometry and analytical precision. Jerry Wasserburg, whom Harrison Brown had recruited after he moved to Cal Tech, was at the forefront of these developments. Across the Atlantic, Claude Allègre at the Institut de Physique du Globe at the University of Paris was also pioneering new approaches and techniques. Wasserburg and Allègre shared the Crawfoord Prize in 1986 for their advancements in isotope geochemistry.

The discovery that primordial ^{3}He was leaking into the oceans through the oceanic crust opened the field of rare gas isotope geochemistry (Clarke et al. 1969), and identification of isotopic variations in other noble gases followed (e.g., Sarda et al. 1988; Staudacher and Allègre 1982) and ultimately revealed primordial heterogeneity in the deep Earth (e.g., Mukhopadhyay 2012). This completed the radiogenic isotope geochemist's toolkit, although developments in analytical techniques have continued to improve them in subsequent decades.

Radiogenic Isotope Geochemistry

Radiogenic isotope ratios proved to have a value beyond measuring geologic time, particularly in understanding crust-mantle evolution. Paul Gast (1960), a former student of Nier, measured Sr isotope ratios in crustal granites and mantle-derived basalts, demonstrating a dramatic difference between them but also concluding that the Earth "*did not contain K, Rb, Cs, U, Ba, and Sr in the proportions found in chondrites.*" Subsequent studies by Gast et al. (1964) demonstrated Pb and Sr isotopic heterogeneity in the mantle, and it soon became clear that "*Oceanic island basalts are derived from a different type of mantle than submarine ridge basalts*" (Hart 1971). The latter, mid-ocean ridge basalts (MORB), as they became known, had compositions consistent with the being partial melts of mantle depleted in incompatible elements, i.e., elements not well accommodated in mantle minerals, by a previous episode of melting. Oceanic island basalts (OIB) lacked that depleted signature. Based in part on this difference, Jason Morgan (1971) proposed that oceanic island volcanoes were produced by convection plumes from the lower mantle, but what were mantle plumes composed of?

The roots of the answer lie in the work of Dick Armstrong (1971), who had been analyzing radiogenic isotope ratios in lavas from island arcs overlying subduction zones. He concluded that sediment was being subducted into the mantle along with oceanic crust and was contributing to the source of these oceanic volcanoes. The greater significance of this was that continental crust could be destroyed and recycled into the mantle as he pointed out. Sediment subduction remained controversial until the remarkable discovery by Tera et al. (1986) of ^{10}Be in arc lavas. Because ^{10}Be is produced only in the atmosphere by cosmic ray spallation and has a half-life of 1.6 million years, this was decisive evidence of sediment being subducted into the mantle.

A couple of years after Lugmair reported the first Sm-Nd age, Don DePaolo and Wasserburg (1976) reported Nd isotopic compositions in a variety of crust and mantle rocks, including MORB and OIB; Claude Allègre's lab in Paris quickly followed with additional data. The Sm-Nd system is particularly useful because the Earth's Sm/Nd ratio is the same, or nearly so, as chondrites, which is not the case for Rb-Sr or U-Th-Pb, as Gast had pointed out. DePaolo and Wasserburg proposed, as Schilling (1973) had earlier, that mantle plumes were derived from primitive mantle, but Pb isotope ratios were not consistent with this idea. And as more

data accumulated, a different explanation seemed required. Hofmann and White (1982) argued that mantle plumes were composed, in part, of subducted oceanic crust and sediment. Subsequent evidence, particularly from stable isotope ratios, has supported that interpretation, which is now widely accepted.

Radiogenic isotope geochemistry has found application far beyond mantle studies. For example, the Sr isotopic composition of ocean water is uniform, but varies with time, reflecting the balance of inputs from ridge crest hydrothermal systems and weathering. Carbonate sediments record this variation providing a geochronological tool for dating marine sediments (Sr isotope chronostratigraphy). Beyond that, this variation in marine Sr isotopic composition provides constraints rates of sea floor spreading and continental weathering through time. In contrast, Nd isotope ratios vary geographically in seawater. Consequently, they can be used as water mass tracers and, through their incorporation in sediments such as Mn nodules, used to deduce past ocean circulation (Albarède et al. 1997). Isotope ratios, particularly Nd and Hf, have also been of enormous value in tracing crustal evolution (e.g., Hawkesworth et al. 2010). Radiogenic isotope ratios have also proved useful in archeology (Bentley 2006); among other notable uses, Müller et al. (2003) used Sr and Pb isotope ratios along with those of oxygen and carbon to determine that Ötsi, the Copper Age alpine mummy discovered in the Alps by German hikers in 1991, was from Italy rather than Austria.

Stable Isotope Geochemistry

In 1947, Harold Urey (Urey 1947) and his University of Chicago colleagues Jacob Bigeleisen and Maria Mayer (1947) demonstrated theoretically that nuclear mass has a temperature-dependent effect on chemical bonding. Urey, who had won the 1934 Noble Prize in chemistry for the discovery of deuterium and had led the U separation efforts for the Manhattan Project, quickly realized that this temperature dependence provided the potential for determining paleotemperatures (Urey et al. 1951). Curiously, his motivation was to test his suspicion that cooling was responsible for the extinction of the dinosaurs (Epstein 1997), which, of course, turned out not to be the case. His students and postdocs demonstrated experimentally that actual fractionations matched the predicted ones (e.g., Epstein et al. 1951). Casare Emiliani was given the task of determining O isotope ratios in the calcite shells of planktonic foraminifera from deep-sea cores. Emiliani (1955) concluded that the climate swings of the Pleistocene were a consequence of small variations in the Earth's orbit and rotation, as Milutin Milanković had theorized half a century earlier. Although not all of Emiliani's conclusions have held up, the idea that Milankovich cycles were the primary driver of climate cycles has become a central paradigm in paleoclimatology (Shackleton and Pisias 1985) and stable isotope ratios have become the premier paleotemperature proxy. Through pioneering work of Danish geochemistry Willi Dansgaard, these studies were augmented by studies of oxygen and later hydrogen isotopes in Greenland and Antarctic ice sheets, providing an extraordinarily detailed history of Pleistocene climate oscillations (e.g., Dansgaard et al. 1969; Jouzel et al. 2007). Dansgaard, along with oceanographer Nickolas Shackleton won the 1995 Crawfoord Prize for their paleoclimate work.

Urey and his academic descendants were responsible for much of the early development of stable isotope geochemistry. Harmon Craig (1953) documented the variation in $\delta^{13}C$ in terrestrial materials demonstrating the systematic depletion of organic carbon in ^{13}C, with the details of the fractionation during photosynthesis worked out by Rodrick Park and Samuel Epstein (Park and Epstein 1960). Craig (1961) also documented the correlation between oxygen and hydrogen isotopes and climate in meteoric water, the so-called meteoritic water line and from that resolved a long-standing question of the origin of hydrothermal water. Other examples include establishing the oxygen and hydrogen fractionation between minerals in water-rock reaction (Taylor and Epstein 1963) and carbon and nitrogen fractionation in the food chain (e.g., DeNiro and Epstein 1978), the latter having value in ecology, archeology, etc., as well as geochemistry.

The carbon cycle has intimately linked the evolution of climate and life on Earth and it is in turn is linked to the oxygen and sulfur cycles through photosynthesis and respiration. When life began is still unclear but the discovery of very negative $\delta^{13}C$ ratios in metasediments from Isua, Greenland (Rosing 1999) and hydrothermal vent deposits in Nuvvuagittuq, Labrador (Dodd et al. 2017) tenuously suggests that life began as early as 3.8 billion years ago. Changes in rates of photosynthesis and burial of organic carbon change the levels of both oxygen and CO_2 in the atmosphere, in turn affecting climate. The work of Robert Berner et al. (Berner et al. 1983), and subsequent papers over the following two decades, using carbon isotopes to deduce the evolution of atmospheric CO_2 was another landmark in stable isotope geochemistry. A more detailed record of atmospheric CO_2 through the Cenozoic was achieved through two other quite different isotopic approaches: compound specific carbon isotopic analysis (e.g., Jasper and Hayes 1994; Pagani et al. 1999) and boron isotopes (e.g., Pearson and Palmer 2000).

Theoretical calculations predicted the fractionation between pairs of isotopes should depend on their mass difference. When Robert Clayton et al. (Clayton et al. 1973) measured both $^{17}O/^{16}O$ and $^{18}O/^{16}O$ ratios in meteorites, they found that this was not the case. Initially thought to be a nucleosynthetic effect, this was subsequently recognized as mass independent fractionation (MIF) resulting from photodissociation and self-shielding (Clayton 2002). Subsequently, MIF has been identified in a variety of terrestrial materials,

particularly stratospheric gases. The most significant such discovery was perhaps that of sulfur isotopes in Archean and early Proterozoic sediments (Farquhar et al. 2000) and their absence in all subsequently deposited sediments. Farquhar and Wing (2003) identified ultraviolet photolysis of SO_2 in the atmosphere as the cause. This discovery provided confirmation that atmosphere first became oxidizing around 2.3 billion years ago, the so-called Great Oxidation Event" (Holland 1984). Remarkably, MIF sulfur has also been found in diamonds and in sulfide inclusions in oceanic island basalts from Mangaia (Cabral et al. 2013) and Pitcairn (Delavault et al. 2016) Islands, both in the central Pacific Ocean, demonstrating that terrestrial geochemical cycles extend from the atmosphere to the base of the mantle.

An important recent advance has been so-called clumped isotope analysis, which involves analysis of the distribution of the isotopes of pairs of elements, for example carbon and oxygen. Wang et al. (2004) demonstrated theoretically that the relative abundance of a specific isotopic species, or isotopologues, $^{18}O^{13}C^{16}O$ in CO_2 gas for example, depends on temperature and Ghosh et al. (2006) demonstrated this experimentally. Consequently, clumped isotopic geothermometry offers an advantage over conventional isotope geothermometry in that equilibration temperature can be determined from an analysis of a single phase as well as the isotopic composition of phase with which it equilibrated (Eiler 2013).

The Evolution of Igneous and Metamorphic Rocks

As F. W. Clarke and his colleagues were analyzing the diverse compositions of igneous rocks in the USGS Laboratory in downtown Washington DC, uptown at Carnegie Institution's new Geophysical Laboratory Norman L. Bowen was experimenting with the melting and crystallization of them to explain this diversity. Bowen (1922), along with Norwegian J.H.L. Vogt, thought of "magmas in the light of the laws of solutions, or, better, of phase equilibrium." Bowen's work demonstrated the importance of fractional crystallization in producing compositional diversity and his book, *The Evolution of Igneous Rocks* (Bowen 1928), laid the groundwork for modern experimental and theoretical petrology. Bowen's colleagues and successors at Carnegie, including O. F. Tuttle, H. S. Yoder, and C. E. Tilley continued this work. Meanwhile in Finland, Pentti Eskola (1920) had developed the facies concept of metamorphic rocks. The development of "hydrothermal bombs" enabled experiments exploring the temperature-pressure-composition relationships of metamorphic rocks and ore-forming fluids by many experimenters, including Helmut Winkler (1957) in Germany. With these data, J. B. Thompson (1955) was able to put Eskola's facies concept into a thermodynamic framework.

These experiments were limited to low pressures, so most of the Earth was out of experimental reach and its seismic structure unexplained. On the other side of the world at the Australian National University (ANU), A. E. (Ted) Ringwood, who made many important contributes to mantle geochemistry, realized that the structure of germinates should mimic those of silicates under high pressure. Based on his experiments with germinate analogs, Ringwood (Ringwood 1966) proposed that the seismic discontinuity at 660 km depth was due to the transformation from tetrahedrally to octahedrally coordinated silicon. With the development of multi-anvil presses (Kawai and Endo 1970) and the diamond anvil cell (Merrill and Bassett 1974), experiments were eventually able to reach pressures corresponding to the Earth's core. This apparatus combined with laser heating enabled Ringwood's ANU colleague Lin-Gun (1976) to confirm the transformation of olivine into octahedrally coordinated $MgSiO_3$, recently named bridgmanite, plus MgO. Subsequently, a post-bridgmanite phase was synthesized at pressures corresponding to the lowermost mantle also using the diamond anvil cell (Murakami et al. 2004).

Experiments of this type led to a more quantitative, and ultimately to a thermodynamic, approach to petrology and to the development of thermobarometry: determination of the temperature and pressure at which a rock equilibrated. One of the first such geothermometers was developed by Buddington and Lindlsey (1964) based on exchange reactions between iron-titanium oxides.

Data acquired in experiments over the decades eventually enabled the development of thermodynamic models, such as THERMOCALC (Powell and Holland 2008), MELTS (Ghiorso et al. 2002), and Perple_X (Connolly 2005), to predict the phase assemblages of igneous and metamorphic rocks as a function of temperature, pressure, and composition. Increasingly, ab initio calculations are used as well (e.g., Lin et al. 2016).

Chemistry of the Earth's Surface

Weathering and the Critical Zone

At the surface of the Earth, in the oceans, and the so-called *Critical Zone*, the region most critical life and human society and defined as Earth's permeable surface from the top of the trees to the bottom of the groundwater zone, water plays predominate role in the rock cycle as Gustav Bischof (1847) had realized. Correns and Von Engelhardt (1939) demonstrated the importance of hydrogen and hydroxyl ions, i.e., pH, in weathering. Krumbein and Garrels (1952) added oxidation state to this, introducing E_H-pH diagrams to geochemistry. If one can identify a single founder of modern low-temperature geochemistry, it is Robert M. Garrels (1916–1988). Over his career, he and his colleagues,

including Hal Helgeson, Fred Mackenzie, and Robert Berner established the thermodynamic approach to water-rock interactions including weathering and chemical sedimentation. His books, including *Solutions, Minerals, and Equilibria* (Garrels and Christ 1965) and *Evolution of Sedimentary Rocks* (Garrels and Mackenzie 1971), are still cited. Helgeson (1968) took this to a new level using a computer program to model the evolution of aqueous solutions reacting with rock. At the low temperatures of the Earth's surface, thermodynamic equilibrium is often not achieved, thus the kinetics of geochemical reactions must also be considered. This same group was among the first to quantitatively investigate the kinetic controls on reaction rates (e.g., Garrels et al. 1949; Helgeson 1971). Much additional progress has been made over the last few decades in understanding the kinetics and thermodynamics of weathering within the critical zone (e.g., Brantley and Lebedeva 2011).

Chemical Oceanography

Robert Boyle made the first systematic determination of the saltiness, i.e., salinity, of seawater in 1674, concluding that it was approximately uniform throughout the oceans. A century later, Antoine Lavoisier (1772) reported the first analysis of seawater, albeit in terms of precipitated salts such as *sel gypseux* ($CaSO_4 \cdot H_2O$), *terre calciane* ($CaCO_3$), *sel d'epsom* ($MgSO_4$), etc., rather than elements. Yet another century later, the 77 samples taken on the HMS Challenger Expedition allowed William Dittmar (1884) to confirm that the major ions are always present in constant proportions to one and other and to total salinity as Georg Forschammer (Forchhammer 1862) had postulated. Svante Arrhenius won the 1903 Noble Prize in chemistry for recognizing that such salts existed in solution as dissociated ions and by the mid-twentieth century, equilibrium constants were well enough known for Garrels and Thompson (1962) to calculate the speciation of these ions.

Antoine Lavoisier realized that seawater was part of a larger geochemical cycle, writing, "*The water of the sea results from a washing of the entire surface of the globe; these are in some ways the rinsing of the grand laboratory of nature*" (Lavoisier 1772). The view that oceans did not merely accumulate salt but were in some sort of steady state with outputs balancing inputs began to emerge in the mid-twentieth century (Conway 1942; Holland 1962; Rubey 1951), culminating with T.F.W. Barth's (1952) introduction of the residence time concept. As data on deep sea sediments accumulated, their importance in the geochemical balance became apparent (Goldberg and Arrhenius 1958). The steady-state concept reached maturity with the work of Mackenzie and Garrels (1966), although it was not until 1979 that ridge crest hydrothermal activity was discovered as the major sink for magnesium and sulfate (Edmond et al. 1979) and research on sources and sinks of elements in the oceans continues. Because the oceans are so vast, much of the effort over the last half century has been large-scale international sampling programs such as GEOSECS and GEOTRACES (e.g., Boyle et al. 2015).

Organic Geochemistry

Much of the research into organic geochemistry has been motivated by the search for hydrocarbon energy reserves. By the late nineteenth and early twentieth century, Canadian T. S. Hunt and American D. White had recognized that the formation of petroleum, natural gas and coal resulted from the progressive transformation of organic matter in the sediments during burial (Durand 2003). Along the same lines, Trask and Wu (1930) concluded that petroleum was derived from *kerogen*, a word introduced by Scottish chemist Alexander Crum Brown. A full understanding of the process of transformation of sedimentary organic matter into petroleum did not come until the second half of the twentieth century, much of that through the work of Louis Tissot and colleagues in France (e.g., Tissot and Welte 1984; Tissot 1967).

Alfred Treib's realization that alkyl metalloporphyrins in petroleum were derived from chlorophyll (Treibs 1934) was an important breakthrough and chemical confirmation of the biological origin of petroleum. Organic compounds such as these whose chemical structure can be related to specific biomolecules are known as *biomarkers.* Biomarkers are used to associate petroleum with the specific sedimentary source rocks, determine migration pathways and in assessing the size, extent, thermal maturity, and potential of deposits and forensically to associate hydrocarbon pollution to specific sources. Biomarkers have also proved useful in unraveling the evolution of life (Briggs and Summons 2014). As noted earlier, carbon isotopic analysis of C_{37} alkadienone, produced by marine algae, has been used to determine atmospheric CO_2 through time (e.g., Pagani et al. 1999). Other organic compounds have proved useful for other paleoclimatology studies, including paleotemperature (Eglinton and Eglinton 2008).

August Pütter (1907) found that the amount dissolved organic carbon (DOC) in seawater exceeded the amount of particulate organic carbon, both living and dead. Indeed, the amount of carbon as DOC is comparable to that of the total living biomass and atmospheric CO_2 (Hedges 1992). Williams and Druffel (1987) showed that deep ocean DOC is surprisingly old, with a radiocarbon age of ~6000 years; most of it appears to be of marine rather than terrestrial origin (Hedges and Mann 1979). Research over the past several decades has shown that organic acids complex a substantial fraction of trace metals dissolved in natural waters (e.g., >99% of Fe^{3+}, ~98% of Zn, ~80% of Cd) (Bruland et al. 2014).

The high molecular weight fraction of DOC was long thought to consist of "geomolecules," i.e., abiologic

condensates of biomolecular fragments (e.g., Burges 1960). New extraction and characterization techniques, such as Fourier transform ion cyclotron resonance mass spectrometry and nuclear magnetic resonance, indicate much of this high molecular weight fraction actually consists of biocondensates and is remarkably uniform in composition throughout the ocean (e.g., Aluwihare et al. 1997).

Organic matter is also an important component of soils. Waksman (1936) wrote that "the chemical composition of humus . . .consists of numerous organic complexes" including lignins, proteins, carbohydrates, fats, organic acids, and alcohols. Here too a paradigm emerged that soil humic substances consist of "geomolecules" formed by condensation of biomolecular fragments and its resistance to microbial attack accounted for its persistence (e.g., Parton et al. 1987). This paradigm is shifting as recent advances suggest that humin consists of molecular aggregates of partially decomposed plant polymers loosely held together by entropic interactions and/or noncovalent bonds and that such aggregates are not inherently stable against decomposition and that environmental and biological factors control the stability of soil organic matter (e.g., Kleber and Johnson 2010).

Biogeochemistry

Organic matter is, of course, an important part of the biogeochemical cycle of carbon. A basic understanding of photosynthesis, respiration, and plant nutrition was achieved by the beginning of the nineteenth century through the work of, among others, Lavoisier, Joseph Priestley, and Nicolas-Théodore de Saussure. By the beginning of the twentieth century, Sergei Winogradsky and Martinus Beijerinck had demonstrated bacterial anaerobic and aerobic nitrogen fixation and bacterial sulfur oxidization and reduction. The role of CO_2 and organic acids in rock weathering was also understood by the mid-nineteenth century; indeed, J. J. Ebelman (Ebelman 1845) had pointed out that CO_2 consumed in weathering reactions was subsequently precipitated in the ocean as Ca- and Mg-carbonates. Jean Baptiste Dumas outlined the biochemical oxygen cycle in the mid-nineteenth century. Nevertheless, it was Vernadsky who integrated biological cycles with geological ones, i.e., biogeochemical cycles.

Alfred Redfield discovered that the dissolved nitrate/phosphate ratio in seawater is nearly the same as that in plankton and furthermore nitrate, phosphate, and carbonate increased in concentration with depth in a ratio of 106C:16N:1P (Redfield 1934): the Redfield Ratio. Since carbon and other key nutrients such as potassium are present in seawater in much great abundance, he concluded that N and P limited biological productivity and essentially laid out the present view of the marine biochemical cycle of these elements (Redfield et al. 1963). In the same period, Aleksandr Vinogradov (1953), a student and successor of Vernadsky, published a more extensive compilation of the elemental composition of marine organisms. By 1983, Bolin et al. (1983) wrote "The main features of the natural cycles of carbon, nitrogen, phosphorus and sulphur (C, N, P, S) have been described," although certainly much more has been learned since then, as described by Wally Broecker, the 2006 Crafoord Prize winner, in his memoir (Broecker 2012).

Much work on biogeochemical cycles has focused on how they have evolved over Earth's history and their interaction with climate. Holland (1962) and Cloud (1968), among others, had argued that the Earth's early atmosphere first became oxidizing around two billion years ago as a result of photosynthesis. Discoveries over the last two decades, including the MIF sulfur isotope work mentioned earlier, now establishes the time of the "Great Oxidation Event" at around 2.3 Ga, although there is evidence of "whiffs" of oxygen in the late Archean (Anbar et al. 2007). Recent studies have also revealed that oxygen levels remained low through most of the Proterozoic only began to rise to levels necessary to support metazoans in the late Proterozoic (e.g., Lyons et al. 2014). It is probably no coincidence that the first metazoan fossils date to this time.

Jean-Baptiste Joseph Fourier (1827) realized that the atmosphere worked like a greenhouse, warming Earth's surface. By the late nineteenth century, the work of Irish physicist John Tyndall and American physicist Samuel Langley, among others, had established the mechanism as adsorption of infrared radiation by CO_2 so that Savante Arrhenius (1896) could predict that burning of fossil fuels would ultimately lead to warming. Urey (1952b) recognized the importance of weathering reactions between CO_2 and silicate rocks in moderating atmospheric CO_2 levels. Subsequent landmarks include the hypothesis of Walker et al. (1981) that silicate weathering and subsequent carbonate precipitation has buffered atmospheric CO_2 over Earth's history in pace with increasing solar luminosity so as to maintain habitable surface temperatures and the previously recited work of Berner et al. (1983) and Berner's subsequent revisions of the "BLAG" model of the carbon, oxygen, and sulfur cycles and climate.

Cosmochemistry

The term "cosmochemistry," coined by Rupert Wildt (1940), can be a bit misleading as its principal focus is the Solar System and its origins. Much of the evidence for that origin comes from meteorites. Like geochemistry itself, its roots predate the term. In 1800, French chemist Charles Barthold made the first chemical analysis of a meteorite, the LL6 chondrite that had famously fallen in Ensisheim, Alsace in 1492. Edward Howard (for whom the howardite achondrites are named), John Williams, and Jacques-Louis Count de Bournon (Howard et al. 1802) analyzed four stones and four irons, and their components, including separated metal and

"small globules" (chondrules, as Gustav Rose would name then 60 years later), and emphasized the similarity of all four stones (all ordinary chondrites). These results moved scientific consensus toward acceptance of an extraterrestrial origin of meteorites advocated by German physicist Ernst Chaladni in his 1794 book, but did not settle the debate. The distinguished Swedish chemist and mineralogist Jöns Jacob Berzelius made the first analysis of a carbonaceous chondrite, *Alais* (CI1), which had fallen in 1806. He reported 12% carbon and noted the similarity of the carbonaceous component to humus, which confused the relatively simple picture of meteorites presented by Howard et al. Things were further confused by the fall of the igneous-textured achondrite *Stannern* in Moravia in 1808, and by *Chassigny*, an SNC achondrite, in France in 1815.

By the mid-nineteenth century, the extraterrestrial origin of meteorites was widely accepted and Robert Greg, Auguste Dabrée, and Adolph Boisse had independently proposed that they were the pieces of a disrupted asteroid or planet. In 1884, Henry Sorby began examining meteorites with the petrographic microscope he had invented, describing chondrules as congealed droplets of fiery rain and proposing that they formed within the solar nebula. Viennese mineralogist Gustav Tschermak's (1883) subsequent microscopic studies became the standard work of this era, and, along with Gustav Rose and Aristides Brezina, were responsible for an early system of meteorite classification.

Both Clarke and Goldschmidt were, as described earlier, interested in the relationship between the compositions of meteorites, the Sun, and the Earth. Oliver Farrington (1901), of Chicago's Field Museum, suggested the bulk Earth has the same composition as meteorites, and indeed chondrites remain the basis of estimating Earth's composition, albeit with some modification. Farrington made a number of other key observations about meteorites, including that iron meteorites had crystallized from liquid slowly and that chondrules had crystallized from liquid rapidly. Subsequent important papers on meteorites and their composition were published over the next few decades by, among others, Harrison Brown and Claire Patterson (1948), at the time both of the University of Chicago, and Harvey Nininger.

Cosmochemistry accelerated in the middle of the twentieth century. Harold Urey wrote a number of influential papers on the origin of the Earth, the cosmic abundances of the elements (e.g., Urey 1951, 1952a), and classification of ordinary chondrites (Urey and Craig 1953). Around this time, radiometric dating had matured enough to establish the age of the meteorites at 4.5 Ga (e.g., Patterson 1956) and more high-quality data was accumulating. Van Schmus and Wood (1967) established the present twofold method of classifying chondrites based on composition/mineralogy and parent body alteration/metamorphism; oxygen isotopes subsequently became an additional criterion of classification. Perhaps the most significant addition to this classification was the recognition that a subset of achondrites, the Shergottites, Nakhlites, and Chassignites (SNC), were from Mars (Smith et al. 1984), confirmed by analyses made by the various NASA and ESA spacecraft, landers, and rovers. Subsequently, NASA's DAWN mission confirmed that another subset of achondrites, the HED meteorites, including *Stannern*, are derived from Vesta.

Harry Lord (1965) calculated the condensation sequence of the solar nebula, an effort subsequently improved upon by many others such as John Larimer and Larry Grossman. These calculations predicted Ca-, Al-, and Ti-rich oxides and silicates should be among the first phases to condense. The discovery of calcium-aluminum inclusions (CAI's) in the newly fallen *Allende* meteorite (Marvin et al. 1970) verified those predictions.

In 1957, Margaret Burbidge along with her husband Geoffrey, William Fowler and Fred Hoyle (Burbidge et al. 1957) laid out the modern polygenetic theory of nucleosynthesis. Shortly thereafter, John Reynolds (1960) discovered isotopic anomalies in xenon from meteorites, some of which were clearly due to the decay of ^{129}I ($t_{1/2}$ = 15.7 Ma), but others that were apparently nucleosynthetic. Isotopic anomalies were subsequently found in other rare gases, the source of which turned out to be presolar grains: star dust from red giants and supernovae (e.g., Ming and Anders 1988), and many other elements.

The discovery of the decay products of very short-lived radionuclides, most notably ^{26}Al (Lee et al. 1976) and ^{53}Mn (Birck and Allègre 1985) in the *Allende* meteorite, demonstrated that newly synthesized nuclides had been added to the solar nebula only shortly before and would eventually result in a detailed quantitative time scale of early solar evolution, surprisingly revealing that the evolved parent bodies of achondrites and irons were older, not younger, that those of more primitive meteorites. It now appears that the inner part of the solar nebula, including the materials from which the Earth formed, was slightly enriched in nuclides produced in red giants and the outer solar system slightly more enriched in nuclides produced in supernovae (e.g., Bouvier and Boyet 2016).

Summary

Geochemistry evolved from same roots in metallurgy and alchemy as chemistry and began to immerge as a distinct subfield of both chemistry and geology in the nineteenth century. The works of F. W. Clarke, V. Goldschmidt, and V. Vernadsky laid the groundwork for the subsequent development and progress of the field in the twentieth and twenty-first centuries. Much of that progress can come from technological developments, as described by Johnson et al. (2013).

Over that period, geochemistry has become an integral part of all aspects of earth and planetary sciences, greatly enriching our knowledge of the nature and evolution of our planet and ourselves and our cosmic neighborhood.

Cross-References

- Anthropogenic CO_2
- Biogeochemistry
- Biomarker: Assessment of Thermal Maturity
- Biomarkers: Petroleum
- Carbon Cycle
- Coal
- Cosmic Elemental Abundances
- Critical Zone
- Geochronology and Radiogenic Isotopes
- Geochemical Classification of Elements
- Geochemical Thermodynamics
- Kinetics of Geochemical Processes
- Low-Temperature Geochemistry
- Magmatic Process Modeling
- Mantle Geochemistry
- Metamorphic Reactions and Processes
- Meteorites
- Nucleosynthesis
- Ocean Biochemical Cycling and Trace Elements
- Ocean Salinity, Major Elements, and Thermohaline Circulation
- Oil-Oil and Oil-Source Rock Correlations
- Organic Geochemistry
- Organic Matter Degradation and Preservation
- Oxidation-Reduction Reactions and Eh-pH (Pourbaix) Diagrams
- Paleoclimatology
- Petroleum
- Soils
- Stable Isotope Geochemistry

References

Albarède F, Goldstein SL, Dautel D (1997) The neodymium isotopic composition of manganese nodules from the southern and Indian oceans, the global oceanic neodymium budget, and their bearing on deep ocean circulation. Geochim Cosmochim Acta 61(6):1277–1291

Aldrich LT, Wetherill GW, Tilton GR, Davis GL (1956) Half-life of Rb^{87}. Phys Rev 103(4):1045–1047

Allègre CJ, Luck JM (1980) Osmium isotopes as petrogenetic and geological tracers. Earth Planet Sci Lett 48(1):148–154

Aluwihare LI, Repeta DJ, Chen RF (1997) A major biopolymeric component to dissolved organic carbon in surface sea water. Nature 387(6629):166–169

Anbar AD et al (2007) A whiff of oxygen before the great oxidation Event? Science 317(5846):1903–1906

Armstrong RL (1971) Isotopic and chemical constraints on models of magma genesis in volcanic arcs. Earth Planet Sci Lett 12(1):137–142

Arrhenius S (1896) Ueber den Einfluss des Atmosphärischen Kohlensäurengehalts auf die Temperatur der Erdoberfläche. Proc R Swed Acad Sci 22(1):1–101

Bailes K (1990) Science and Russian culture in the age of revolutions: V. I. Verndsky and his Scientific School, 1863–1945. Indiana University Press, Bloomington, 238 pp

Barth TW (1952) Theoretical petrology. Wiley, New York

Bentley AR (2006) Strontium isotopes from the earth to the archaeological skeleton: a review. J Archaeol Method Theory 13(3):135–187

Berner RA, Lasaga AC, Garrells RM (1983) The carbonate-silicate geochemical cycle and its efffect on atmopsheric carbon dioxide over the past 100 million years. Am J Sci 283:641–683

Bigeleisen J, Mayer MG (1947) Calculation of equilibrium constants for isotopic exchange reactions. J Chem Phys 15(5):261

Birck J-L, Allègre CJ (1985) Evidence for the presence of ^{53}Mn in the early solar system. Geophys Res Lett 12(11):745–748

Bischof G (1847) Lehrbuch der chemischen und physikalischen Geologie, vol 1. A. Marcus, Bonn

Bolin B et al (1983) Interactions of biogeochemical cycles. In: Bolin B, Cook RB (eds) Major biogeochemical cycles and their interactions. Wiley, New York, pp 1–40

Boltwood BB (1907) Ultimate disintegration products of the radioactive elements; part II, disintegration products of uranium. Am J Sci 23(134):77–88. Series 4

Bouvier A, Boyet M (2016) Primitive solar system materials and earth share a common initial ^{142}Nd abundance. Nature 537(7620):399–402

Bouvier A, Wadhwa M (2010) The age of the solar system redefined by the oldest Pb-Pb age of a meteoritic inclusion. Nat Geosci 3(9):637–641

Bowen N (1922) The reaction principle in petrogenesis. J Geol 30(3):177–198

Bowen NL (1928) The evolution of the igneous rocks. Princeton University Press, Princeton, 332 pp

Boyle EA et al (eds) (2015) GEOTRACES GA-03 - the U.S. GEOTRACES North Atlantic transect, Deep Sea research part II: topical studies in oceanography, vol 116. Elsevier, Amsterdam, 342 pp

Brantley SL, Lebedeva M (2011) Learning to read the chemistry of regolith to understand the critical zone. Annu Rev Earth Planet Sci 39(1):387–416

Briggs DEG, Summons RE (2014) Ancient biomolecules: their origins, fossilization, and role in revealing the history of life. BioEssays 36(5):482–490

Broecker W (2012) The carbon cycle and climate change: memoirs of my 60 years in science. Geochem Perspect 1(2):221–221

Brown H, Patterson C (1948) The composition of meteoritic matter: III. Phase equilibria, genetic relationships and planet structure. J Geol 56(2):85–111

Bruland KW, Middag R, Lohan MC (2014) 8.2 - controls of trace metals in seawater A2 - Holland, Heinrich D. In: Turekian KK (ed) Treatise on geochemistry, 2nd edn. Elsevier, Oxford, pp 19–51

Buddington AF, Lindlsey DH (1964) Iron-Titanium oxide minerals and synthetic equivalents. J Petrol 5:310–357

Burbidge EM, Burbidge GR, Fowler WA, Hoyle F (1957) Synthesis of the elements in stars. Rev Mod Phys 29(4):547–650

Burges A (1960) The nature and distribution of humic acid. Sci Proc R Dublin Soc Ser A 1:770

Cabral RA et al (2013) Anomalous sulphur isotopes in plume lavas reveal deep mantle storage of Archaean crust. Nature 496(7446):490–493

Clarke FW (1869) Views around Ithaca; being a description of the waterfalls and ravines of this remarkable locality. Andrus, McChain & Co., Ithaca, 155 pp

Clarke FW, (1873a) The constants of nature. Smithsonian institution, Washington, DC
Clarke FW (1873b) Evolution and the spectroscope. Pop Sci Mon 2:320–326
Clarke FW (1884) The elements of chemistry. D. Appleton & Company, New York, p 369
Clarke FW (1908) The data of geochemistry. US Geol Surv Bull:770
Clarke FW (1918) Notes on isotopic lead. Proc Natl Acad Sci 4(6):181–188
Clarke FW (1925) The evolution and disintegration of matter. US Geol Surv Prof Pap 132D:51–86
Clarke FW, Washington HS (1922) The average chemical composition of igneous rocks. Proc Natl Acad Sci U S A 8(5):108
Clarke FW, Washington HS (1924) The composition of the earth's crust. US Government Printing Office, Washington, DC
Clarke FW, Wheeler WC (1922) The inorganic constituents of marine invertebrates. US Government Printing Office, Washington, DC
Clarke WB, Beg MA, Craig H (1969) Excess ^{3}He in the sea: evidence for terrestrial primodal helium. Earth Planet Sci Lett 6(3):213–220
Clayton RN (2002) Self-shielding in the solar nebula. Nature 415:860–861
Clayton RN, Grossman L, Mayeda TK (1973) A component of primitive nuclear composition in carbonaceous meteorites. Science 182(4111):485–488
Cloud PE (1968) Atmospheric and hydrospheric evolution on the primitive earth. Both secular accretion and biological and geochemical processes have affected earth's volatile envelope. Science 160(3829):729–736
Connolly JAD (2005) Computation of phase equilibria by linear programming: A tool for geodynamic modeling and its application to subduction zone decarbonation. Earth Planet Sci Lett 236(1–2):524–541
Conway EJ (1942) The chemical evolution of the ocean. Proc R Ir Acad B. JSTOR 48:161–212
Correns CW, Von Engelhardt W (1939) Neue Untersuchungen fiber die Verwitterung des Kalifeldspates. Chem Erde 12:1–22
Craig H (1953) The geochemistry of the stable carbon isotopes. Geochim Cosmochim Acta 3(2):53–92
Craig H (1961) Isotopic variations in meteoric waters. Science 133(3465):1702–1703
Dansgaard W, Johnsen SJ, Møller J, Langway CC (1969) One thousand centuries of climatic record from camp century on the Greenland ice sheet. Science 166(3903):377–380
Delavault H, Chauvel C, Thomassot E, Devey CW, Dazas B (2016) Sulfur and lead isotopic evidence of relic Archean sediments in the Pitcairn mantle plume. Proc Natl Acad Sci 113(46):12952–12956
DeNiro MJ, Epstein S (1978) Influence of diet on the distribution of carbon isotopes in animals. Geochim Cosmochim Acta 42:495–506
DePaolo DJ, Wasserburg GJ (1976) Nd isotopic variations and petrogenetic models. Geophys Res Lett 3:249–252
Dittmar W (1884) Report on researches into the composition of ocean water collected by H. M. S. Challenger during the years 1873–1876. In: Murray J (ed) Challenger Report: Physics and Chemistry, vol 1. H.M. Stationery Office, Neill & Co., Edinburgh, pp 1–211
Dodd MS et al (2017) Evidence for early life in Earth's oldest hydrothermal vent precipitates. Nature 543(7643):60–64
Durand B (2003) Histoire de la géochimie organique. Oil Gas Sci Technol – Rev IFP 58(2):203–231
Ebelman JJ (1845) Sur les produits de la décomposition des espèces minèrales de la famille des silicates. Ann Rev Mines 12:627–654
Edmond JM et al (1979) Ridge crest hydrothermal activity and the balances of the major and minor elements in the ocean: the Galapagous data. Earth Planet Sci Lett 46:1–18
Eglinton TI, Eglinton G (2008) Molecular proxies for paleoclimatology. Earth Planet Sci Lett 275(1–2):1–16
Eiler JM (2013) The isotopic anatomies of molecules and minerals. Annu Rev Earth Planet Sci 41(1):411–441
Emiliani C (1955) Pleistocene temperatures. J Geol 63:538–578
Epstein S (1997) The role of stable isotopes in geochemistries of all kinds. Annu Rev Earth Planet Sci 25(1):1–21
Epstein S, Buchsbaum R, Lowenstam H, Urey HC (1951) Carbonate-water isotopic temperature scale. Geol Soc Am Bull 62(4):417–426
Eskola P (1920) On mineral facies of rocks. Norsk Geol Tidskr 6:143–194
Farquhar J, Wing BA (2003) Multiple sulfur isotopes and the evolution of atmospheric oxygen. Earth Planet Sci Lett 213:1–13
Farquhar J, Bao H, Thiemens M (2000) Atmospheric influence of Earth's earliest sulfur cycle. Science 289(5480):756–758
Farrington OC (1901) The constituents of meteorites. II. J Geol 9(6):522–532
Forchhammer G (1862) On the constitution of sea-water, at different depths, and in different latitudes. J Frankl Inst 74(6):401–403
Fourier J-BJ (1827) Les températures du globe terrestre et des espaces planétaires. Mém Acad R Sci Inst Fr 7:569–604
Galvez ME, Gaillardet J (2012) Historical constraints on the origins of the carbon cycle concept. Compt Rendus Geosci 344(11–12):549–567
Garrels RM, Christ CL (1965) Solutions, minerals and Equilibria. Freeman Cooper, San Francisco, 450 pp
Garrels, R.M., Mackenzie, F.T., 1971. Evolution of sedimentary rocks
Garrels RM, Thompson ME (1962) A chemical model for sea water at 25 degrees C and one atmosphere total pressure. Am J Sci 260(1):57–66
Garrels RM, Dreyer RM, Howland AL (1949) Diffusion of ions through intergranular spaces in water-saturated rocks. Geol Soc Am Bull 60(12):1809–1828
Gast PW (1960) Limitations on the composition of the upper mantle. J Geophys Res 65:1287–1297
Gast PW, Tilton GR, Hedge C (1964) Isotopic composition of lead and strontium from Ascension and Gough Islands. Science 145(3637):1181–1185
Ghiorso MS, Hirschmann MM, Reiners PW, Kress VC (2002) The pMELTS: a revision of MELTS for improved calculation of phase relations and major element partitioning related to partial melting of the mantle to 3 GPa. Geochem Geophys Geosyst 3:1030
Ghosh P et al (2006) 13C-18O bonds in carbonate minerals: a new kind of paleothermometer. Geochim Cosmochim Acta 70(6):1439–1456
Goldberg ED, Arrhenius GOS (1958) Chemistry of Pacific pelagic sediments. Geochim Cosmochim Acta 13(2):153–212
Goldschmidt VM (1922) Über die massenverteilung im erdinneren, vergleicht migt etruktur gewissen meteoriten. Naturwissenschaften 7:105–123
Goldschmidt VM (1923) Geochemische Verteilungsgesetze der Elemente I, Skrifter utgivne af det Norske Videnskapsselskapet Akademii i Oslo I Matematisk-Naturvidenskapelig Klasse, vol 2. Skrifter Norske Videnskaps-Akademi, Oslo, pp 1–17
Goldschmidt VM (1937) Geochemische Verteilungsgesetze der Elemente XI Die Mengenverhältnisse der Elemente und der Atom-Arten. No. 4, 1–148. Skrifter utgivne af det Norske Videnskaps-selskapet Akademii i Oslo I Matematisk-Naturvidenskapelig Klasse
Goldschmidt VM (1941-1942) On super-uraner, grunstoffer med større kjerneladning enn 92. Fra Fysikkens Verden Oslo 3:179–180
Hart SR (1971) Ocean floor basalts, Carnegie inst. Wash, Yearbook, pp 388–394
Hawkesworth CJ et al (2010) The generation and evolution of the continental crust. J Geol Soc 167(2):229–248
Hedges JI (1992) Global biogeochemical cycles: progress and problems. Mar Chem 39(1):67–93
Hedges JI, Mann DC (1979) The lignin geochemistry of marine sediments from the southern Washington coast. Geochim Cosmochim Acta 43(11):1809–1818

Helgeson HC (1968) Evaluation of irreversible reactions in geochemical processes involving minerals and aqueous solutions—I. Thermodynamic relations. Geochim Cosmochim Acta 32(8):853–877
Helgeson HC (1971) Kinetics of mass transfer among silicates and aqueous solutions. Geochim Cosmochim Acta 35(5):421–469
Hofmann AW, White WM (1982) Mantle plumes from ancient oceanic crust. Earth Planet Sci Lett 57:421–436
Holland HD (1962) Model of the evolution of the Earth's atmosphere. In: Engle AEJ, James HL, Leonard BF (eds) Petrologic studies, a volume to honor A E Buddington. Geological Society of America, New York, pp 447–477
Holland HD (1984) The chemical evolution of the atmosphere and oceans. Princeton University Press, Princeton
Houtermans FG (1953) Determination of the age of the earth from the isotopic composition of meteoritic lead. Il Nuovo Cimento (1943–1954) 10(12):1623–1633
Howard E, Williams JL, de Bournon C (1802) Experiments and observations on certain stony and metalline substances, which at different times are said to have fallen on the earth; also on various kinds of native iron. Philos Trans R Soc Lond 92:168–212
Jasper JP, Hayes JM (1994) Reconstruction of paleoceanic P_{CO2} levels from carbon isotopic compositions of sedimentary biogenic components. In: Zahn R, Pedersen TF, Kaminski MA, Labeyrie L (eds) Carbon cycling in the glacial ocean: constraints on the ocean's role in global change. Springer, Berlin, pp 323–341
Johnson CM, McLennan SM, McSween HY, Summons RE (2013) Smaller, better, more: five decades of advances in geochemistry. Geol Soc Am Spec Pap 500:259–302
Jouzel J et al (2007) Orbital and millennial Antarctic climate variability over the past 800,000 years. Science 317(5839):793–796
Kawai N, Endo S (1970) The generation of ultrahigh hydrostatic pressures by a split sphere apparatus. Rev Sci Instrum 41(8):1178–1181
Kleber M, Johnson MG (2010) Chapter 3 – advances in understanding the molecular structure of soil organic matter: implications for interactions in the environment. In: Donald LS (ed) Advances in agronomy. Academic, pp 77–142. Amsterdam
Krough H (2001) From geochemistry to cosmochemistry: the origin of a scientific discipline. In: Reinhardt C (ed) Chemical sciences in the 20th century: bridging boundaries. Wiley-VCH, Weinhiem, pp 160–192
Krumbein WC, Garrels RM (1952) Origin and classification of chemical sediments in terms of pH and oxidation-reduction potentials. J Geol 60(1):1–33
Lavoisier A (1772) Memoire sur l'esprit-de vin dans l'analyse des eaux minerales. Mem Acad R Sci 1772:555–563
Lee T, Papanastassiou DA, Wasserbury GJ (1976) Demonstration of ^{26}Mg excess in Allende and evidence for ^{26}Al. Geophys Res Lett 3:41–44
Libby WF (1934) Radioactivity of neodymium and samarium. Phys Rev 46(3):196–204
Libby WF, Anderson EC, Arnold JR (1949) Age determination by radiocarbon content: world-wide assay of natural radiocarbon. Science 109(2827):227–228
Lin Y, Cohen R, Floris A, Shulenburger L, Driver KP, (2016) Quantum Monte Carlo computations of the $(Mg_{1-X}Fe_X)SiO_3$ Perovskite to post-perovskite phase boundary. In APS Meeting Abstracts, Baltimore
Liu L-G (1976) The post-spinel phase of forsterite. Nature 262(5571):770–772
Lord HC (1965) Molecular equilibria and condensation in a solar nebula and cool stellar atmospheres. Icarus 4(3):279–288
Lovelock JE (1972) Gaia as seen through the atmosphere. Atmos Environ (1967) 6(8):579–580
Lugmair GW (1974) Sm-Nd ages: a new dating method. Meteoritics 9(4):369
Lyons TW, Reinhard CT, Planavsky NJ (2014) The rise of oxygen in earth/'s early ocean and atmosphere. Nature 506(7488):307–315
Mackenzie FT, Garrels RM (1966) Chemical mass balance between rivers and oceans. Am J Sci 264(7):507–525
Marvin UB, Wood JA, Dickey JS (1970) Ca-al rich phases in the allende meteorite. Earth Planet Sci Lett 7(4):346–350
Merrihue C, Turner G (1966) Potassium-argon dating by activation with fast neutrons. J Geophys Res 71(11):2852–2857
Merrill L, Bassett WA (1974) Miniature diamond anvil pressure cell for single crystal x-ray diffraction studies. Rev Sci Instrum 45(2):290–294
Ming T, Anders E (1988) Isotopic anomalies of Ne, Xe, and C in meteorites. II interstellar diamond and SiC: Carriers of exotic noble gases. Geochim Cosmochim Acta 52:1235–1244
Morgan WJ (1971) Convection plumes in the lower mantle. Nature 230:42–43
Mukhopadhyay S (2012) Early differentiation and volatile accretion recorded in deep-mantle neon and xenon. Nature 486(7401):101–104
Müller W, Fricke H, Halliday AN, McCulloch MT, Wartho J-A (2003) Origin and migration of the alpine iceman. Science 302(5646):862–866
Murakami M, Hirose K, Kawamura K, Sata N, Ohishi Y (2004) Post-perovskite phase transition in MgSiO3. Science 304(5672):855–858
Nier AO (1939) The isotopic constitution of radiogenic leads and the measurement of geological time II. Phys Rev 55(2):153–163
Pagani M, Arthur MA, Freeman KH (1999) Miocene evolution of atmospheric carbon dioxide. Paleoceanography 14(3):273–292
Park R, Epstein S (1960) Carbon isotope fractionation during photosynthesis. Geochim Cosmochim Acta 21:110–126
Parton WJ, Schimel DS, Cole CV, Ojima DS (1987) Analysis of factors controlling soil organic matter levels in Great Plains Grasslands1. Soil Sci Soc Am J 51(5):1173–1179
Patchett PJ, Tatsumoto M (1980) Lu-Hf total-rock isochron for the eucrite meteorites. Nature 288:571–574
Patterson C (1956) Age of meteorites and the earth. Geochim Cosmochim Acta 16:230–237
Patterson CC (1965) Contaminated and natural lead environments of man. Arch Environ Health: Int J 11(3):344–360
Pearson PN, Palmer MR (2000) Atmospheric carbon dioxide concentrations over the past 60 milllion years. Nature 406:695–699
Powell R, Holland TJB (2008) On thermobarometry. J Metamorph Geol 26(2):155–179
Pütter A (1907) Der Stoffhaushalt des Meeres. Z Allg Physiol 7:321–368
Redfield AC (1934) On the proportions of organic derivatives in sea water and their relation to the composition of plankton, James Johnstone memorial volume. University Press of Liverpool, Liverpool, pp 176–192
Redfield AC, Ketchum BH, Richards FA (1963) The influence of organisms on the composition of sea-water. In: Hill MN (ed) The sea. Wiley, New York, pp 26–77
Revelle R (1994) Harrison Brown 1917–1986. U.S. National Academy of Sciences, Washinngton, DC
Reynolds JR (1960) Isotopic composition of xenon from enstatite chondrites. Z Naturforsch 15a:1112–1114
Ringwood AE (1966) Mineralogy of the mantle. In: Hurley PM (ed) Advances in earth science. MIT Press, Cambridge, MA, pp 357–399
Rosing M (1999) 13C-depleted carbon microparticles in >3700 Ma seafloor sedimentary rocks from West Greenland. Science 283:674–676
Roth J (1879) Allgemeine und chemische Geologie. Wilhem Hertz, Berlin
Rubey WW (1951) Geologic history of sea water: an attempt to state the problem. Geol Soc Am Bull 62(9):1111–1148
Sarda P, Staudacher T, Allègre CJ (1988) Neon isotopes in submarine basalts. Earth Planet Sci Lett 91:73–88

Schilling J-G (1973) Iceland mantle plume: geochemical study of the Reykjanes ridge. Nature 242:565–571
Settle D, Patterson CC (1982) Magnitudes and sources of precipitation fluxes of industrial and natural leads to the North Pacific at Enewetak. J Geophys Res 87:8857–8869
Shackleton NJ, Pisias NG (1985) Atmospheric carbon dioxide, orbital forcing, and climate. In: Sunquist ET, Broecker WS (eds) The carbon cycle and atmospheric CO2: natural variations Archean to present. AGU, Washington, pp 303–317
Smith MR et al (1984) Petrogenesis of the SNC (shergottites, nakhlites, chassignites) meteorites: implications for their origin from a large dynamic planet, possibly Mars. J Geophys Res Solid Earth 89(S02): B612–B630
Staudacher T, Allègre CJ (1982) Terrestrial xenology. Earth Planet Sci Lett 60(3):389–406
Taylor HP, Epstein S (1963) O^{18}/O^{16} ratios in rocks and coexisting minerals of the Skaergaard intrusion, East Greenland. J Petrol 4(1):51–74
Tera F et al (1986) Sediment incorporation in island-arc magmas: inferences from ^{10}Be. Geochim Cosmochim Acta 50:535–550
Thompson JB (1955) The thermodynamic basis for the mineral facies concept. Am J Sci 253(2):65–103
Tissot CL (1967) Influence de la température et de la pression sur la formation des hydrocarbures dans les argiles à kérogène. In 7th World Petroleum Congress, World Petroleum Congress, Mexico
Tissot BP, Welte DH (1984) Petroleum formation and occurrence. Springer, Berlin, 699 pp
Trask PD, Wu C (1930) Does petroleum form in sediments at time of deposition? AAPG Bull 14(11):1451–1463
Treibs A (1934) Chlorophyll- und Häminderivate in bituminösen Gesteinen, Erdölen, Erdwachsen und Asphalten. Ein Beitrag zur Entstehung des Erdöls. Justus Liebigs Ann Chem 510(1):42–62
Tschermak G (1883) Die mikroskopische Beschaffenheit der Meteoriten erläutert durch photographische Abbildungen. Sweitzerbart, Stuttgart
Urey HC (1947) The thermodynamics of isotopic substances. J Chem Soc 1947:562–581
Urey HC (1951) The origin and development of the earth and other terrestrial planets. Geochim Cosmochim Acta 1(4–6):209–277
Urey HC (1952a) Chemical fractionation in the meteorites and the abundance of the elements. Geochim Cosmochim Acta 2(5):269–282
Urey HC (1952b) On the early chemical history of the earth and the origin of life. Proc Natl Acad Sci 38(4):351–363
Urey HC, Craig H (1953) The composition of the stone meteorites and the origin of the meteorites. Geochim Cosmochim Acta 4(1–2):36–82
Urey HC, Lowenstam HA, Epstein S, McKinney CR (1951) Measurement of paleotemperatures and temperatures of the upper Cretaceous of England, Denmark, and the southeastern United States. Geol Soc Am Bull 62(4):399–416
Van Schmus WR, Wood JA (1967) A chemical-petrologic classification for the chondritic meteorites. Geochim Cosmochim Acta 31(5):747–765
Vernadsky W (1924) La géochimie. Alcan, Paris
Vernadsky V (1926) Biosfera. Scientific Chemico-Technical Publishing, Leningrad
Vinogradov AP (1953) The elementary chemical composition of marine organisms. Yale University, Sears Foundation for Marine Research
Waksman SA (1936) Humus: origin, chemical composition and importance in nature. Williams and Wilkins, Baltimore
Walker JCG, Hays PB, Kasting JF (1981) A negative feedback mechanism for the long-term stabilization of Earth's surface temperature. J Geophys Res Oceans 86(C10):9776–9782
Wang Z, Schauble EA, Eiler JM (2004) Equilibrium thermodynamics of multiply substituted isotopologues of molecular gases. Geochim Cosmochim Acta 68(23):4779–4797
Wetherill GW (1957) Radioactivity of potassium and geologic time. Science 126(3273):545–549
Wildt R (1940) Cosmochemistry. Scientia 67:85–90
Williams PM, Druffel ERM (1987) Radiocarbon in dissolved organic matter in the central North Pacific Ocean. Nature 330:246–248
Winkler HGF (1957) Experimentelle Gesteinsmetamorphose—I Hydrothermale metamorphose karbonatfreier tone. Geochim Cosmochim Acta 13(1):42–69

Holmium

Scott M. McLennan
Department of Geosciences, Stony Brook University, Stony Brook, NY, USA

Element Data
Atomic Symbol: Ho
Atomic Number: 67
Atomic Weight: 164.93033(2)
Isotopes and Abundances: ^{165}Ho, 100%
1 Atm Melting Point: 1474 °C
1 Atm Boiling Point: 2700 °C
Common Valences: +3
Ionic Radii: 90.1 pm (CN6), 101.5 pm (CN8), and 122.1 pm (CN12)
Pauling Electronegativity: 1.23
First Ionization Energy: 580.99 kJ mol^{-1}
Chondritic (CI) Abundance: 0.0567 ppm
Silicate Earth Abundance: 0.126 ppm
Crustal Abundance: 0.78 ppm
Seawater Abundance: 0.33 ppt
Core Abundance: ~0

Properties

Holmium (Ho), named after *Holmia*, the Latin name for Stockholm, is a soft, malleable, dense (8.795 g cm^{-3}), bright silvery-white metal. Its electronic configuration is [Xe] $4f^{11}6s^2$. It is relatively stable at room temperature, readily oxidizes in the presence of water, and readily dissolves in mineral acids. It is a group 3 or IIIB inner transition element, with +3 being its only valence state in geological environments, and is one of the lanthanide rare earth elements (REE). In geochemical terminology, it is grouped with heavy rare earth elements (HREE; Gd-Lu). Holmium has one stable isotope.

More than 270 minerals contain lanthanides as essential structural constituents, but those with Ho as a significant component are restricted to Y and HREE varieties, such as xenotime [$Y(PO_4)$], gadolinite-Y [$Y_2FeBe_2(Si_2O_{10})$], bastnäsite [REE(CO_3)F], allanite [$(REE,Ca,Y)_2(Al,Fe^{2+},Fe^{3+})_3(SiO_4)_3(OH)$], and britholite [$(REE,Ca)_5(SiO_4,PO_4)_3(OH,F)$].

Details of properties, mineralogy, history, and uses of Ho were compiled from Goonan (2011), Chakhmouradian and Wall (2012), Zaimes et al. (2015), Gschneidner (2016), Hammond (2016), and Meija et al. (2016a b).

History and Use

Holmium was first recognized in 1878 by Marc Delafontaine and Jacques-Louis Soret, who termed it "element X," and independently discovered in 1879 by Per Teodor Cleve, who separated the oxide and named it *holmia*; the pure metal was separated in 1911. Holmium has the highest magnetic moment of any natural element and accordingly is used in pole pieces of high-strength magnets. It is also used in a variety of solid-state lasers used for medical, outer space, and military applications. Ho_2O_3 produces red/yellow colorant for glass, cubic zirconia, and jewelry, and the sharp Ho optical absorption peaks make it a good spectrophotometer calibration standard.

Geochemical Behavior

The fundamental importance of Ho in geochemistry is that it is one of the small trivalent rare earth elements, among the most useful trace elements in all areas of geochemistry and cosmochemistry due to their coherent and systematic behavior as a group, largely a consequence of the "lanthanide contraction."

Holmium is typically a trace element in most rocks and minerals. It is classified geochemically and cosmochemically as a highly refractory lithophile element, with a 50% $T_{condensation}$ of 1659 K at 10^{-4} bars (Lodders 2003). In most igneous systems, Ho is incompatible with bulk partition coefficients, $D < 1$. In aqueous systems, Ho normally has very low fluid/rock partition coefficients ($\ll 1$). As a result, Ho contents of clastic sediments typically reflect their average provenance.

In seawater, Ho has very low concentrations (sub-ppt) and residence times (~1820 year) with speciation dominated by Ho^{3+}, $HoCO_3^+$, and $Ho(CO_3)_2^-$. In other aqueous systems (e.g., magmatic, hydrothermal), Ho can reach ppm levels due to elevated temperatures, pH effects, and complexing with various ligands (e.g., F^-, Cl^-, OH^-).

Concentration data are from compilations in Taylor and McLennan (2009) and Nozaki (2001).

Biological Utilization and Toxicity

There are no documented biological uses for Ho. REE (including Ho^{3+}) likely substitute for Ca^{2+} in biological materials and processes. REE concentrations (including Ho) in human tissues and fluids are very low (~ppb to <ppb levels, respectively) due to very low concentrations in natural waters and low uptake rates throughout the food chain (Bulman 2003). At low levels of ingestion, there are no established toxic effects that pose a threat to human health.

Cross-References

- ▶ Incompatible Elements
- ▶ Lanthanide Rare Earths
- ▶ Lithophile Elements
- ▶ Trace Elements
- ▶ Transition Elements

References

Bulman RA (2003) Metabolism and toxicity of the lanthanides. In: Sigel A, Sigel H (eds) Metal ions in biological systems, Vol. 40, The lanthanides and their interrelations and Biosystems. Marcel Dekker, Basel, pp 683–703

Chakhmouradian AR, Wall F (eds) (2012) Rare earth elements. Elements 8:333–376

Goonan TG (2011) Rare earth elements – end use and recyclability. U S Geol Surv Sci Invest Rpt 2011–5094, 15pp

Gschneidner KA Jr (2016) Physical properties of the rare earth metals. In: Haynes WM (ed) CRC handbook of chemistry and physics, 96th edn. CRC Press, Boca Raton, pp 4-115–4-120

Hammond CR (2016) The elements. In: Haynes WM (ed) CRC handbook of chemistry and physics, 96th edn. CRC Press, Boca Raton, pp 4-1–4-42

Lodders K (2003) Solar system abundances and condensation temperatures of the elements. Astrophys J 591:1220–1247

Meija J, Coplen TB, Berglund M, Brand WA, De Bièvre P, Gröning M, Holden NE, Irrgeher J, Loss RD, Walczyk T, Prohaska T (2016a) Atomic weights of the elements 2013. Pure Appl Chem 88:265–291. (IUPAC Technical Report)

Meija J, Coplen TB, Berglund M, Brand WA, De Bièvre P, Gröning M, Holden NE, Irrgeher J, Loss RD, Walczyk T, Prohaska T (2016b) Isotopic compositions of the elements 2013. Pure Appl Chem 88:293–306. (IUPAC Technical Report)

Nozaki Y (2001) Rare earth elements and their isotopes in the ocean. In: Steele JH et al (eds) Encyclopedia of ocean sciences. Academic, London, pp 2354–2366

Taylor SR, McLennan SM (2009) Planetary crusts: their composition, origin and evolution. Cambridge University Press, Cambridge. 378pp

Zaimes GG, Hubler BJ, Wang S, Khanna V (2015) Environmental life cycle perspective on rare earth oxide production. ACS Sustain Chem Eng 3:237–244

Hydrocarbons

John K. Volkman
Oceans and Atmosphere Flagship, CSIRO, Hobart, TAS, Australia

Definition

Hydrocarbons are a class of organic compounds formed solely from carbon and hydrogen. They are broadly classified into two groups: aliphatic and aromatic.

Introduction

The term aliphatic hydrocarbon refers to compounds which may be normal (i.e., straight-chained, designated *n*-), branched, or alicyclic (i.e., containing ring systems, also called naphthenes). Aliphatics may be saturated (i.e., alkanes or "paraffins" having no double or triple bonds with formula C_nH_{2n+2}), or unsaturated (alkenes having one or more double bonds with formulae C_nH_{2n}, C_nH_{2n-2}, etc. or alkynes having one or more triple bonds with formulae C_nH_{2n-2}, C_nH_{2n-4}, etc.). The term olefin is sometimes used to include alkenes, cycloalkenes, and other hydrocarbons containing more than one double bond.

Aliphatic hydrocarbons occur in a wide variety of structural forms each of which can have dramatically different physical properties and chemical reactivities. The simplest naturally occurring hydrocarbon is the gas methane (CH_4; bp −164 °C), which is a saturated alkane and the main constituent of natural gas. The simplest alkene is ethylene ($H_2C{=}CH_2$).

Aromatic hydrocarbons contain ring systems having resonance-stabilized "alternating" double bonds. Aliphatic groups may be attached to the ring (called substituents) or, alternatively, the aromatic ring may be fused to other aromatic or alicyclic rings. Hydrocarbons containing more than two aromatic rings fused together are called polycyclic aromatic hydrocarbons (PAHs). The simplest aromatic hydrocarbon is liquid benzene (C_6H_6; bp 80.1 °C); others include toluene ($CH_3{-}C_6H_5$), naphthalene ($C_{10}H_8$), phenanthrene ($C_{14}H_{10}$), and its structural isomer anthracene ($C_{14}H_{10}$).

Analysis and Identification

Hydrocarbons are extracted from geological materials using organic solvents, such as hexane, chloroform, or dichloromethane, which provide a crude extract containing a variety of organic compounds. The hydrocarbon fraction can be purified using open column chromatography by eluting the hydrocarbons from activated silica and alumina using a nonpolar solvent such as hexane. Elemental sulfur can be removed by treating the extract with activated copper. By judicious choice of solvents and sample:adsorbent ratios, it is usually possible to obtain a clean separation of aliphatic and aromatic hydrocarbons, although some overlap is possible due to the wide range of molecular weights found in the two fractions. The unsaturated hydrocarbon fraction can be further separated according to the number of double bonds present by argentation thin layer chromatography (TLC) or high-performance liquid chromatography (HPLC), where the adsorbent contains adsorbed silver ions which form weak complexes with the double bonds. In these systems, alkanes migrate further than compounds with double bonds. Straight-chain components can be separated from branched-chain ones by adducting straight-chain compounds into urea, thiourea, or molecular sieves, or by using a synthetic zeolite such as silicalite. By judicious choice of the adducting agent, it is also possible to separate simple branched compounds. Gel permeation provides another means of separating hydrocarbons based on molecular size, but this technique is less frequently used.

The amount of aliphatic and aromatic hydrocarbons in an extract can be determined gravimetrically by weighing the fractions after separation, by analysis using Iatroscan thin layer chromatography with flame ionization detection (TLC-FID), or by HPLC with a mass detector. In both cases, considerable care must be exercised to avoid the loss of volatile constituents. An approximate measure of the amount of aromatic hydrocarbons in a sample can be determined using ultraviolet–visible spectroscopy or fluorescence, although this technique typically uses a single calibration to represent a complex mixture.

Each purified fraction is usually analyzed by capillary gas chromatography with flame ionization detection (GC–FID) and by capillary gas chromatography–mass spectrometry (GC–MS) to identify and quantify individual components. The great complexity of hydrocarbon mixtures found in geological samples requires the use of high-resolution capillary columns (often 50 or 60 m in length), but even so the chromatogram of a crude oil often shows a "hump" or baseline rise due to unresolved compounds. This is termed a UCM ("unresolved complex mixture"); for a history of this term, see Farrington and Quinn (2015). Improved resolution of these complex mixtures can be obtained using two-dimensional GC×GC–MS techniques (e.g., Ventura et al. 2008).

The carbon or hydrogen isotope signature of individual hydrocarbons separated by the gas chromatograph can be

determined using GC–irm–MS systems (the so-called CSIA, which is an abbreviation for compound-specific isotope analysis) by passing the effluent from the GC through a combustion furnace and then measuring using an isotope mass spectrometer the isotope composition of the CO_2 or H_2O produced (e.g., Freeman et al. 1990). This ability to ascertain the isotope signature of particular compounds has dramatically improved the ability of organic geochemists to attribute likely sources to different compounds. A further development is the ability to measure the ^{14}C signature of hydrocarbons isolated from geological materials and hence determine their approximate age (e.g., Eglinton et al. 1997).

Occurrence in the Biosphere

Hydrocarbons are ubiquitous in nature where they may occur as solids, liquids, and gases. Hydrocarbons are produced in small quantities by most organisms, and thus small amounts in the range of a few parts per million can be found in all sediments. The distributions in modern sediments can be quite complex due to this variety of natural sources (e.g., Volkman et al. 1986). Some hydrocarbons found in contemporary sediments that have not been contaminated by petroleum products include the C_{30} isoprenoid hydrocarbon squalene, which (as oxidosqualene) is a precursor to the sterols, pristane which is common in zooplankton, phytenes and phytadienes from degradation of phytol, fernenes from certain bacteria, sterenes from sterol degradation, hopenes from bacteria and from degradation of bacterial hopanoids, and C_{25} and C_{30} highly branched isoprenoid (HBI) alkenes from diatoms. Short-chain alkanes, such as *n*-C_{15} and *n*-C_{17}, can be derived from species of microalgae and macroalgae.

Hydrocarbons in Bacteria

The main lipids of bacteria are polar lipids containing straight-chain and methyl-branched (e.g., *iso*- and *anteiso*-odd-chain) fatty acids and polyhydroxylated versions of bacteriohopanepolyols (BHP). Branched alkanes are termed *iso* where the penultimate carbon atom in the chain contains an additional methyl group, or *anteiso* where the carbon atom third from the terminal end contains a methyl substituent. On diagenesis, these lipids can give rise to aliphatic hydrocarbons and hopanoid hydrocarbons respectively. However, a few bacteria and cyanobacteria make significant amounts of a C_{30} hopene called diploptene (hop-22(29)-ene; Bird et al. 1971). Freeman et al. (1994) were able to show using $\delta^{13}C$ values that diploptene in the Cariaco Trench and the Black Sea was likely derived from the lipids of chemoautotrophs living above the oxic/anoxic boundary. Aliphatic hydrocarbons with no odd-even predominance were reported in early studies of the lipids of sulfate-reducing bacteria (Davis 1968), but it is possible that these were contaminants.

Modern sediments deposited under stratified water columns with anoxic bottom waters often contain carotenoid hydrocarbons, such as chlorobactene and isorenieratene derived from the green-colored and brown-colored strains of the green sulfur bacteria (Chlorobiaceae). These lipids are often ^{13}C-enriched (Schouten et al. 2001). On diagenesis, isorenieratene produces a number of compounds including the fully saturated isorenieratane and likely degradation products C_{15}–C_{31} 2,3,6-aryl isoprenoids, which provide biomarkers for photic zone euxinia in ancient seas (Sinninghe Damsté et al. 2001; Slowakiewicz et al. 2015). Chlorobactane can also be used in this way, but it appears to be less common in ancient sediments.

Hydrocarbons in Archaea

In contrast to bacteria, archaea make a diversity of lipids based on isoprenoid chains ether-linked within polar lipids and so are a major source of isoprenoid hydrocarbons in sediments and oils. An example is the C_{20} irregular isoprenoid crocetane (2,6,11,15-tetramethylhexadecane), which is a biomarker for the anaerobic oxidation of methane by archaea (Summons and Lincoln 2012), and a possible marker for photic zone euxinia (Maslen et al. 2009). Methanogens synthesize a variety of isoprenoid hydrocarbons including the C_{25} isoprenoid 2,6,10,15,19-pentamethylicosane (PMI), which can be found in sediments and petroleum (Brassell et al. 1981). Squalane is another methanogen marker, but it can also be formed by reduction of squalene which is widely occurring in aquatic organisms. The C_{40} isoprenoid alkane lycopane is found in a number of organic-rich sediments, but its origins are uncertain and some have attributed it to a phototrophic source rather than from archaea (Wakeham et al. 1993). In the Black Sea and Cariaco Trench, this suggestion is supported by $\delta^{13}C$ evidence (Freeman et al. 1994).

Hydrocarbons in Cyanobacteria

Simple distributions of midchain branched alkanes have been found in some species of cyanobacteria (called blue-green algae in the older literature). These include 7- and 8-methylheptadecane (and traces of the 6-methyl) found in early studies of cyanobacterial lipids by Han and Calvin (1970). Much more complex distributions occur in a few species. For example, Köster et al. (1999) found 21 C_{17}–C_{20} branched alkanes presenting mono-, di-, and trimethyl-branched isomers in cultures of the filamentous cyanobacterium *Calothrix scopulorum*. The major compounds were 4,13-, 5,13-, and 4,5-dimethyl-, and 4,5,13- and 4,5,14-trimethylheptadecane indicating a predominance of substituents at C-4 and C-5 from the end of the chain. Short-chain branched alkanes from cyanobacteria are often found in ancient sediments predating the occurrence of eukaryotes.

Coates et al. (2014) have shown that cyanobacteria produced hydrocarbons from fatty acids by one of two pathways. One involves a two-step conversion of fatty acids first to fatty aldehydes and then alkanes. The second involves a polyketide synthase (PKS) pathway that first elongates the acyl chain followed by decarboxylation to produce a terminal alkene. Their work also revealed new double bond positions (2- and 3-heptadecene) and methyl group positions (3-, 4-, and 5-methylheptadecane).

In addition to diploptene, cyanobacteria synthesize a variety of oxygenated hopanoid derivatives, which on diagenesis can give rise to hopanoid hydrocarbons. 2-Methylbacteriohopanepolyols occur in high proportions in cultured cyanobacteria and in cyanobacterial mats, and thus are a likely source of 2α-methylhopanes and derivatives in organic-rich sediments as old as 2,500 Ma (Summons et al. 1999). In contrast, 3β-methylhopanes are thought to be derived from oxygen-respiring methanotrophs (Eigenbrode et al. 2008).

Hydrocarbons in Microalgae

Hydrocarbons are not usually abundant in microalgae (e.g., Volkman et al. 1986), although many contain the *n*-$C_{21:6}$ alkene (synthesized by decarboxylation of the 22:6 fatty acid) and the pigment β-carotene. An unusual class of highly branched unsaturated C_{25} and C_{30} isoprenoid (HBI) alkenes are abundant in many marine sediments and are now known to be constituents of some diatoms in the genera *Navicula*, *Rhizosolenia*, *Pseudosolenia*, and *Pleurosigma* (e.g., Volkman et al. 1994; Brown and Belt 2016; Kaiser et al. 2016; Belt et al. 2017). HBI alkanes have not been found in oils or sediments older than 92 Ma (Sinninghe Damsté et al. 2004), which implies that this biosynthetic pathway evolved around that time. Certain C_{25} HBIs occur in sea-ice diatoms and the presence of these HBIs in polar sediments has been used as an index of sea-ice extent (Belt et al. 2017).

The green alga *Botryococcus braunii* (from the algal class Trebouxiophyceae) has interested geochemists for many years as it is often associated with organic-rich ancient sediments and today it is being examined as a possible source of biofuels (Largeau et al. 1984; Volkman 2014). Unlike most algae, it contains abundant hydrocarbons and their distribution can be used to define at least four biochemically distinct races A, B, or L (Metzger and Largeau 2005), plus a new race termed S each of which has a distinctive hydrocarbon composition. Race A contains large amounts of long-chain C_{25}–C_{31} alkadienes and alkatrienes derived from the C_{18} monounsaturated fatty acid oleic acid as well as complex mixtures of C_{52}–C_{64} *n*-aldehydes (botryals) formed by aldol condensation of fatty aldehydes and epoxides and complex lipids derived from these lipids. Race B contains C_{30}–C_{37} unusually branched isoprenoid hydrocarbons referred to as botryococcenes as well as squalene and mono- di-, tri-, and tetramethylsqualenes. Race L contains the C_{40} isoprenoid hydrocarbon lycopadiene (2,6R,10R,14,19,23R,27R,31-octamethyldotriaconta-14(E),18(E)-diene). The newly defined S race produces C_{18} and C_{20} *n*-alkanes and epoxy alkanes but lacks botryococcenes and lycopadiene and is thus similar to race A. A related green alga *Choricystis* contains alkanes (*n*-C_{17}, *n*-C_{21} and *n*-C_{23}) and alkenes (*n*-$C_{17:1}$, *n*-$C_{19:1}$, *n*-$C_{21:1}$, *n*-$C_{23:1}$, and *n*-$C_{25:1}$) in different proportions according to the particular strain analyzed.

Hydrocarbons in Vascular Plants

Vascular plants are a major source of organic matter in terrestrial sediments, peats, and coals, and significant inputs can even be recognized in sediments deposited in marine environments far from land. The presence of long-chain (C_{25}–C_{35}) *n*-alkanes showing a strong predominance of odd chain lengths is usually ascribed to plant inputs since such distributions are common in higher plant leaf waxes. Some plant waxes also contain long-chain *iso* and *anteiso*-branched alkanes – tobacco is a good example – but amounts of these hydrocarbons in sediments are usually very minor. Note that long-chain *anteiso*-branched alkanes and the corresponding fatty acids have been found in Antarctic soils containing cryptoendolithic bacteria (Matsumoto et al. 1992).

Various proxies have been proposed based on different carbon-number ranges of *n*-alkanes that purport to distinguish between aquatic submerged vegetation and terrestrial plants. For example, Aichner et al. (2010) showed that emergent aquatic macrophytes contain mainly *n*-C_{27} and *n*-C_{29} alkanes, while C_{21}–C_{23} *n*-alkanes are particularly abundant in floating and submerged aquatic plants (Wang and Liu 2012). Ficken et al. (2000) reported that *n*-alkane distributions from submerged and floating plants ranged from *n*-C_{19} to *n*-C_{33}, maximizing at *n*-C_{25}, with a very low content of C_{29}–C_{31} *n*-alkanes. These authors noted that high relative concentrations of C_{23} and C_{25} *n*-alkanes in cores from Kenyan lakes corresponded to high counts of aquatic pollen taxa, notably Nymphaea (Ficken et al. 2000).

Some plants such as eucalypts also contain abundant volatile sesquiterpene hydrocarbons which can be a major source of atmospheric haze, as typically seen in Australia during summer. However, it is unusual to find significant concentrations of such hydrocarbons in sediments.

Occurrence of Biogenic Hydrocarbons in the Geosphere

The concentration of hydrocarbons in sediments depends on the abundance of the source organism and transfer of its organic matter to sediments, possible formation from other lipids in the sediment and destruction either by biological or abiological processes. Hydrocarbons can be degraded by many

bacteria and such hydrocarbonoclastic bacteria can be found in all modern environments. If this were not so, the globe would be awash with oil from natural seepages alone. Hydrocarbons can be oxidized in air, seawater, and oxic sediments to non-hydrocarbon products or alternatively may be converted to organic sulfur compounds (OSCs) under anoxic conditions by reaction with H_2S, elemental sulfur, or polysulfides.

Many hydrocarbons are also produced by chemical or biological degradation of functionalised lipids, and thus the concentrations of hydrocarbons in sediments generally increase with depth in a core. The complexity of the mixtures can also increase dramatically as the number of structural types and isomeric forms multiplies rapidly. Common examples include the formation of sterenes from dehydration of sterols, phytadienes from phytol, and hopenes from C_{31}–C_{35} polyhydroxyhopanes (bacteriohopanepolyols; BHPs). Alkanes may also be produced by decarboxylation of fatty acids although this is not thought to be significant in recently deposited sediments.

Polycyclic aromatic hydrocarbons (PAHs) are common in many resin-producing plants such as conifers. Retene (1-methyl-7-isopropylphenanthrene) is a major constituent in pine tar and co-occurs with a variety of related compounds. It is not surprising therefore that this general family of compounds is often found in sediments and has been used as a biomarker for conifer contributions to the paleovegetation (e.g., Buggle and Zech 2015). A complicating factor is that retene, dehydroabietin, and 1,2,3,4-tetrahydroretene have been identified in pyrolysates of the green alga *Chlorella protothecoides* and the cyanobacterium *Synechocystis* sp. (Zhou et al. 2000). Wakeham et al. (1980b) recognized five classes of PAH in sediments that have biogenic sources from early stage diagenesis. These were: (1) perylene, the origins of which are still debated but may be from terrestrial fungi (e.g., Zhang et al. 2014); (2) an extended series of phenanthrene homologs; (3) retene and pimanthrene derived from diterpenes; (4) a series of tetra- and pentacyclic PAH derived from pentacyclic triterpenes of the amyrin-type; and (5) tetra- and pentacyclic PAH formed from pentacyclic triterpenes with five-membered E-rings.

Ancient Sediments

Hydrocarbon biomarkers, along with other lipids, have provided considerable information about the depositional environments of ancient sediments and the history of life on Earth (Walters et al. 2010). This information has been instrumental in understanding the factors leading to the deposition of oil shales and petroleum source rocks as well as understanding how the Earth's environment has changed over time. A key proxy has been *n*-alkane distributions which can be ascribed to C-3 or C-4 plants depending on their chain-length distributions and $\delta^{13}C$ values (Garcin et al. 2014). It is becoming common to see a multiproxy approach adopted. For example, Zech et al. (2009) used: (i) the $\delta^{13}C$ of the grass-derived alkanes n-C_{31} and n-C_{33}, (ii) the alkane ratio n-C_{31}/n-C_{27}, and (iii) lacustrine-derived short- and mid-chain alkanes to reconstruct paleoenvironmental changes in the Late Quaternary of NE Argentina.

A great advance has been the ability to measure the δD (δ^2H) content of *n*-alkanes (e.g., Sachse et al. 2012; Guenther et al. 2013), since this can be related to the isotopic composition of the water in which the organism grows and hence its paleoenvironment. δD and $\delta^{13}C$ values of sedimentary biomarkers, such as plant wax alkanes, are being used extensively as paleohydrological proxies, which are able to estimate contributions from C-3, C-4, and CAM plants and changes in climate over a range of geological timescales (e.g., Rose et al. 2016). This has even been exploited in studies of ancient hominids' diet (Uno et al. 2016). However, the isotopic fractionation observed between hydrogen in environmental water and hydrogen in lipids is sensitive to vegetation type and biochemical, physiological, and environmental influences, such as evapotranspiration which are being actively studied (e.g., Guenther et al. 2013).

Other hydrocarbons have been used in paleoenvironmental studies, particularly those associated with vascular plants. In an interesting application, Alexander et al. (1989) were able to use distinctive diterpane and aromatic hydrocarbons produced by trees of the kauri pine group which first became prominent in the Early Jurassic to distinguish Jurassic oils from earlier Permo-Triassic oil in the Eromanga Basin of Australia.

Another category of organic-rich immature ancient sediments that have attracted considerable interest from geochemists is torbanites (also called boghead coals), which contain the fossilized remains of the green alga *Botryococcus braunii* as well as organic matter from bacteria and plants. A variety of hydrocarbons have been described including botryococcenes (markers of the B race of *B. braunii*), *n*-alkanes, isoprenoids, drimanes, macrocyclic alkanes, and various aromatics including alkylnaphthalenes, alkylphenanthrenes, and retene (e.g., Grice et al. 2001).

Hydrocarbons in Coal

Coals contain abundant hydrocarbons ranging from *n*-alkane distributions typical of plant waxes to complex mixtures of PAHs (e.g., Izart et al. 2015). For an overview of the aromatic molecules found in coal, see Radke et al. (1990). Diterpanes are often abundant and have been used in paleoclimate reconstructions. For example, Schulze and Michaelis (1990) studied the hydrocarbons in German coals from the Late Carboniferous Ruhr and Saar Basins. Differences in facies,

maturity, and age were reflected in the distribution of the alkylcyclohexanes. Cyclic diterpenoid hydrocarbons of the phyllocladane type were found in some samples of Carboniferous age. Retene and cadalene have been used as a measure of the relative coniferous input (van Aarssen et al. 2000). PAHs such as benzo[a and e]pyrenes provide markers of combustion of wood during forest fires and peat fires.

While most hydrocarbons in coal are plant-derived, a significant imprint from microbial sources is also common. For example, there is typically a dominance of the C_{30} hopane in the *m*/*z* 191 mass fragmentograms and a high hopanes/steranes ratio (7–46 in Sydney Basin coals; Izart et al. 2015) indicative of the extensive biodegradation of organic matter caused by microbial communities during coal deposition.

Occurrence of Hydrocarbons in Petroleum

With increasing sediment burial, thermal cracking reactions eventually become more important. The high abundance of hydrocarbons in crude oils and thermally mature ancient sediments results from the thermal cracking of macromolecular organic matter (kerogen; Durand 1980) preserved in sediments as well as the release of carbon skeletons that were bound through heteroatoms such as S, N, and O. Kerogen contains diagenetically formed polymeric organic matter plus selectively preserved resistant biopolymers produced by microalgae (algaenans) and higher plants (cutans and suberans; Derenne and Largeau 2001), which survive early diagenesis in sediments. Pyrolysis of these materials yields *n*-alkanes and *n*-alkenes with little odd or even predominance extending in carbon chain length to C_{35} and beyond. Closed-vessel hydrous pyrolysis in which water is added before heating can yield distributions of alkanes remarkably similar to those found in crude oils. Hydropyrolysis (Hy–Py or Hypy; Berwick et al. 2010) at high hydrogen pressures (10 MP) in the presence of a dispersed sulfided molybdenum catalyst also produces mainly hydrocarbon products. Thus, contrary to earlier views that kerogen was formed solely by condensation of lipids, sugars, amino acids, and other biochemicals during early diagenesis, it is now recognized that the kerogen in some sediments can be dominated by resistant biopolymers such as preserved algaenan.

Hydrocarbons are the major constituent of crude oils and natural gas together with smaller amounts of polar compounds and more complex materials such as asphaltenes. As a consequence, hydrocarbons have been the focus of a great number of geochemical studies. Many of these hydrocarbons are termed biomarkers because they retain many of the structural features of their precursor biologically produced lipids. Early studies such as that of Bray and Evans (1961) attempted to use simple *n*-alkanes to identify the source rocks of crude oils, whereas now the great complexity of petroleum hydrocarbon compositions can be exploited. The chain lengths of *n*-alkanes range from C_1 to about C_{40}, although a few oils are known where the *n*-alkanes extend to about C_{100}.

Another common class of branched alkane biomarkers is the isoprenoids which are formed by linking C_5 isoprene (methylbutadiene) units together. Often the most abundant branched alkanes in crude oils are the isoprenoids pristane ($C_{19}H_{40}$) and phytane ($C_{20}H_{42}$). The pristane/phytane ratio in an oil is often used to infer the degree of oxicity of the source rock depositional environment, where values <0.8 in oils are thought to reflect an anoxic depositional environment. A few oils also contain the C_{30} isoprenoid squalane, botryococcanes from green microalgae, and a range of C_{31}–C_{40} isoprenoids from archaea including methanogens (Volkman and Maxwell 1986).

Many polycyclic hydrocarbon biomarkers are used for oil-oil and oil-source rock correlation, as well as to study diagenesis, maturation, and biodegradation of organic matter in sediments and to assess the paleoenvironment prevailing when ancient sediments were deposited (e.g., Peters and Moldowan 1991). Polycyclic hydrocarbons fall into a number of classes depending on the number of carbon atoms in the ring (typically five or six), number of rings, degree of unsaturation, and pattern of alkyl substitution. Cyclic alkanes include the steranes (which have three six-membered rings fused to a five-membered ring plus additional alkyl substituents) which are end-products of sterol diagenesis. The ratio of C_{27}:C_{28}:C_{29} steranes can give an indication of the importance of algal (C_{28}) or plant (C_{29}) contributions to the organic matter. The C_{30} sterane 24-*n*-propylcholestane has been used to infer the presence of algal organic matter (Moldowan et al. 1990), but the related sterane 24-isopropylcholestane is thought to be derived from the sterols of sponges (McCaffrey et al. 1994) and hence can be used to date the first appearance of these organisms. Diasterenes are formed by rearrangement reactions and high levels of diasterenes or diasteranes are often associated with source rocks containing high levels of clay minerals (e.g., Rubinstein et al. 1975), and thus smaller amounts are typically found in coals and carbonate rocks.

Hopanes (which have four six-membered rings fused to a five-membered ring plus various alkyl substituents) are derived from the hopenes and bacteriohopanepolyols (BHPs) synthesized by bacteria and hence are good indicators of bacterial contributions to the organic matter (e.g., Albrecht and Ourisson 1971). Hopane distributions in oils typically range in carbon number from C_{27} to C_{35} with those from C_{31}–C_{35} (sometimes generically termed homohopanes although this strictly refers to the C_{31} components) clearly derived from the corresponding BHPs. A variety of related hopanoids also occur in some oils. These include

25-norhopanes (demethylated hopanes) in which the C-25 methyl group has been removed from its point of attachment at C-10; these demethylated compounds are thought to be produced during late-stage biodegradation of petroleum (e.g., Volkman et al. 1983). If two or three atoms are missing, then the prefix dinor- or trinor-, respectively, is used. Thus, 28,30-dinorhopane (in the older literature 28,30-bisnorhopane) lacks the C-28 and C-30 methyl groups found in hopanes. This unusual hopanoid is found in a variety of settings and it is abundant in some Californian oils (e.g., Schoell et al. 1992). It commonly appears as the free hydrocarbon, rather than in oxygenated forms such as other hopanoids, and its origin is still uncertain. Schoell et al. (1992) suggested an origin from chemoautotrophic bacteria, while Sinninghe Damsté et al. (2014) have suggested an origin from bacteria living at the oxic-anoxic boundary. The 8,14-secohopanes consist of hopanes where the bond between C-8 and C-14 carbon atoms in the C-ring has been broken. Hopane distributions and ratios are used in a number of ways to determine the source, maturity, and extent of biodegradation of an oil (Peters et al. 2005).

Other cyclic hydrocarbons found in crude oils include bicyclic alkanes (sesquiterpanes) which can be derived either from higher plants (e.g., van Aarssen et al. 1990, 2000) or from degradation of hopanes and related compounds (e.g., drimane and homodrimane). Tricyclic terpanes (such as extended cheilanthanes) are found in many oils and are particularly abundant in tasmanite oil shales. Their origins are still the subject of much debate (Dutta et al. 2006). Pentacyclic triterpanes having oleanane, lupane, and ursane skeletons are excellent biomarkers for contributions from vascular plants. Other source markers include cadinanes and bicadinanes common in crude oils from South East Asia, which are derived from a cadinene biopolymer found in fossil and extant dammar resins (van Aarssen et al. 1990). The presence of gammacerane typically indicates a high salinity, stratified depositional environment. A full discussion of these biomarkers can be found in Peters et al. (2005).

Ratios of saturated hydrocarbons, principally various steranes and hopanes, are commonly used as maturity ratios in petroleum studies (e.g., Mackenzie et al. 1988; Peters and Moldowan 1991; Peters et al. 2005). Other proxies have been developed including bicadinanes and related compounds which can be useful maturity indicators for some tertiary oils (Sosrowidjojo et al. 1996). Diamondoids, such as adamantane, are cage-like hydrocarbons with structures resembling those of diamonds, hence their name. They are found in most crude oils, and because of their resistance to thermal and biological destruction, they have proven to be useful biomarkers in petroleum studies. Unlike the biomarkers, they are not produced directly from natural lipids but arise from thermal maturation. They have been used to assess the thermal maturity of highly mature source rocks and crude oils, to assess the extent of oil cracking and as biomarkers for correlating highly biodegraded crude oils (e.g., Fang et al. 2013).

Aromatic hydrocarbons are typically less abundant than aliphatic hydrocarbons in oils have been shown to vary in a systematic way with thermal maturity (e.g., Requejo et al. 1996). This has led to several maturity parameters being proposed. An example is the methyl-phenanthrene index (MPI-1) devised by Radke and Welte (1983), and the trimethylnaphthalene ratio (TNR-2) which proved useful for distinguishing oils from the Java Sea (Radke et al. 1994). Smaller aromatic hydrocarbons can be lost from an oil due to water washing and biodegradation, but PAH and triaromatic steroids are much less affected (e.g., Volkman et al. 1984).

Pollutant Sources of Hydrocarbons

Petroleum-derived hydrocarbons are common in aquatic environments, particularly those near urban centers or where crude oil has been spilled. The techniques of organic geochemistry, such as analysis of biomarkers by GC–MS, are widely used to fingerprint the source of the contamination (e.g., Wakeham et al. 1980a; Volkman et al. 1992; Eganhouse 1997). More advanced analytical methods with a greater resolution, such as two-dimensional GC×GC–MS and ultrahigh resolution Fourier transform ion cyclotron resonance (FT-ICR), are increasingly being used (McKenna et al. 2013). Such techniques were applied to the massive oil spill that followed the explosion on 20 April 2010 of the *Deepwater Horizon* drilling unit, which initiated an uncontrolled release of oil and gas for 87 days from the Macondo seafloor well into the Gulf of Mexico. The Macondo well discharged at least 5 million barrels of oil (~210 million US gallons) and at least 250,000 metric tons of natural gas, largely methane (Joye 2015).

Municipal and sewage outlets are major contributors of hydrocarbons to aquatic environments. Some are petroleum-derived hydrocarbons from industrial sources or road run-off but detergents are also important. Indeed, linear alkyl benzenes (LABs), which are unreacted residues of linear alkylbenzenesulfonate surfactants, have proven to be excellent tracers of urban inputs (Eganhouse 1986).

Complex assemblages of polycyclic aromatic hydrocarbons (PAH) and their alkylated homologs are found in soils and aquatic sediments (Wakeham et al. 1980a). In most cases, these have anthropogenic origins due to increased combustion of fossil fuels (primarily coal) over the last 200 years. In view of the known carcinogenic properties of several PAH, a suite of 16 US EPA priority PAHs are routinely included in analyzes of contaminated sites.

Extraterrestrial Hydrocarbons

Simple organic molecules are continually being delivered to Earth from outer space from meteors and other extraterrestrial bodies. Although most interest has been in compounds such as amino acids that might have been important for questions regarding the origin of life (Pohorille 2002), there has been recent attention to the occurrence of hydrocarbons in space. In 2003 and 2004, telescopes and spacecraft appeared to detect large methane clouds in Mars' atmosphere, but they vanished after a few months. Most recently, NASA's Curiosity rover detected a brief burst of methane in 2013. Methane has now been detected in meteorites from Mars (Blamey et al. 2015). Perhaps more impressive is the occurrence of lakes of liquid methane, ethane, and propane on Saturn's largest moon Titan. These were initially indicated by Data from Voyagers 1 and 2 and later corroborated by the Hubble telescope and the Cassini-Huygens mission Titan.

Summary

Hydrocarbons are ubiquitous in geochemical systems. They can be produced de novo by a variety of organisms, and particular structures, or distributions, can be related to specific sources such as higher plants, microalgae, bacteria, or archaea. They can also be formed in sediments by diagenetic transformations from functionalized lipids by removal of the heteroatom (O, N, P, S, etc.), often accompanied by double bond formation. Hydrocarbons are the major constituents of crude oils due to thermal cracking of the kerogen and algaenans preserved in ancient rocks. The presence of specific biomarkers can be used to indicate the type of depositional environment, and ratios of different isomers can be used as an index of thermal maturity.

Cross-References

- Biogeochemistry
- Biomarker: Assessment of Thermal Maturity
- Biomarkers: Petroleum
- Carbon
- Carbon Isotopes
- Coal
- Gas Chromatography–Mass Spectrometry (GC–MS)
- Hydrogen
- Hydrogen Isotopes
- Kerogen
- Meteorites
- Natural Gas
- Oil-Oil and Oil-Source Rock Correlations
- Organic Geochemistry
- Organics: Sources and Depositional Environments
- Paleoenvironments
- Petroleum

References

Aichner B, Herzschuh U, Wilkes H (2010) Influence of aquatic macrophytes on the stable carbon isotopic signatures of sedimentary organic matter in lakes on the Tibetan Plateau. Org Geochem 41:706–718

Albrecht P, Ourisson G (1971) Biogenic substances in sediments and fossils. Angew Chem Int Ed 10:209–225

Alexander R, Larcher AV, Kagi RI, Price PL (1989) An oil-source correlation study using age-specific plant-derived aromatic biomarkers. In: Moldowan JM, Albrecht P, Philp RP (eds) Biological markers in sediments and petroleum. Prentice Hall, Englewood Cliffs

Belt ST, Brown TA, Smik L, Tatarek A, Wiktor J, Stowasser G, Assmy P, Allen CS, Husum K (2017) Identification of C_{25} highly branched isoprenoid (HBI) alkenes in diatoms of the genus *Rhizosolenia* in polar and sub-polar marine phytoplankton. Org Geochem 110:65–72

Berwick LJ, Greenwood PF, Meredith W, Snape CE, Talbot HM (2010) Comparison of microscale sealed vessel pyrolysis (MSSVpy) and hydropyrolysis (Hypy) for the characterisation of extant and sedimentary organic matter. J Anal Appl Pyrolysis 87:108–116

Bird CW, Lynch JM, Pirt SJ, Reid WW (1971) The identification of hop-22(29)-ene in prokaryotic organisms. Tetrahedron Lett 34:3189–3190

Blamey NJF, Parnell J, McMahon S, Mark DF, Tomkinson T, Lee M, Shivak J, Izawa MRM, Banerjee NR, Flemming RL (2015) Evidence for methane in Martian meteorites. Nat Commun. https://doi.org/10.1038/ncomms8399

Brassell SC, Wardroper AMK, Thomson ID, Maxwell JR, Eglinton G (1981) Specific acyclic isoprenoids as biological markers of methanogenic bacteria in marine sediments. Nature (Lond) 290:693–696

Bray EE, Evans ED (1961) Distributions of *n*-paraffins as a clue to the recognition of source beds. Geochim Cosmochim Acta 22:2–15

Brown TA, Belt ST (2016) Novel tri- and tetra-unsaturated highly branched isoprenoid (HBI) alkenes from the marine diatom *Pleurosigma intermedium*. Org Geochem 91:120–122

Buggle B, Zech M (2015) New frontiers in the molecular based reconstruction of Quaternary paleovegetation from loess and paleosols. Quat Int 372:180–187

Coates RC, Podell S, Korobeynikov A, Lapidus A, Pevzner P, Sherman DH, Allen EE, Gerwick L, Gerwick WH (2014) Characterization of cyanobacterial hydrocarbon composition and distribution of biosynthetic pathways. PLoS One 9(1):e85140. https://doi.org/10.1371/journal.pone.0085140

Davis JB (1968) Paraffinic hydrocarbons in the sulfate-reducing bacterium *Desulfovibrio desulfuricans*. Chem Geol 3:155–160

Derenne S, Largeau C (2001) A review of some important families of refractory macromolecules: composition, origin, and fate in soils and sediments. Soil Sci 166:833–847

Durand B (ed) (1980) Kerogen – insoluble organic matter from sedimentary rocks. Éditions Technip, Paris

Dutta S, Greenwood PF, Brocke R, Schaefer RG, Mann U (2006) New insights into the relationship between Tasmanites and tricyclic terpenoids. Org Geochem 37:117–127

Eganhouse RP (1986) Long-chain alkylbenzenes – their analytical chemistry, environmental occurrence and fate. Int J Environ Anal Chem 26:241–263

Eganhouse RP (ed) (1997) Molecular markers in environmental geochemistry. ACS symposium series, American Chemical Society, Washington, USA

Eglinton TI, Benitez-Nelson BC, Pearson A, McNichol AP, Bauer JE, Druffel ERM (1997) Variability in radiocarbon ages of individual organic compounds from marine sediments. Science 277:796–799

Eigenbrode JL, Freeman KH, Summons RE (2008) Methylhopane biomarker hydrocarbons in Hamersley Province sediments provide evidence for Neoarchean aerobiosis. Earth Planet Sci Lett 273:323–331

Fang CC, Xiong YQ, Li Y, Chen Y, Liu JZ, Zhang HZ, Adedosu TA, Peng P (2013) The origin and evolution of adamantanes and diamantanes in petroleum. Geochim Cosmochim Acta 120:109–120

Farrington JW, Quinn JG (2015) "Unresolved Complex Mixture" (UCM): a brief history of the term and moving beyond it. Mar Pollut Bull 96:29–31

Ficken KJ, Li B, Swain DL, Eglinton G (2000) An *n*-alkane proxy for the sedimentary input of submerged/floating freshwater aquatic macrophytes. Org Geochem 31:745–749

Freeman KH, Hayes JM, Trendel JM, Albrecht P (1990) Evidence from carbon isotope measurements for diverse origins of sedimentary hydrocarbons. Nature (Lond) 343:254–256

Freeman KH, Wakeham SG, Hayes JM (1994) Predictive isotopic biogeochemistry – hydrocarbons from anoxic marine basins. Org Geochem 21:629–644

Garcin Y, Schefuß E, Schwab VF, Garreta V, Gleixner G, Vincens A, Todou G, Séné O, Onana J-M, Achoundong G, Sachse D (2014) Reconstructing C-3 and C-4 vegetation cover using *n*-alkane carbon isotope ratios in recent lake sediments from Cameroon, western Central Africa. Geochim Cosmochim Acta 142:482–500

Grice K, Audino M, Boreham CJ, Alexander R, Kagi RI (2001) Distributions and stable carbon isotopic compositions of biomarkers in Torbanites from different palaeogeographical locations. Org Geochem 32:1195–1210

Guenther F, Aichner B, Siegwolf R, Xu BQ, Yao TD, Gleixner G (2013) A synthesis of hydrogen isotope variability and its hydrological significance at the Qinghai-Tibetan Plateau. Quat Int 313:3–16

Han J, Calvin M (1970) Branched alkanes from blue-green algae. Chem Commun 22:1490–1491

Izart A, Suarez-Ruiz I, Bailey J (2015) Paleoclimate reconstruction from petrography and biomarker geochemistry from Permian humic coals in Sydney Coal Basin (Australia). Int J Coal Geol 138:145–157

Joye SB (2015) *Deepwater Horizon*, 5 years on. Science 349:592–593

Kaiser J, Belt ST, Tomczak M, Brown TA, Wasmund N, Arz HW (2016) C_{25} highly branched isoprenoid alkenes in the Baltic Sea produced by the marine planktonic diatom *Pseudosolenia calcar-avis*. Org Geochem 93:51–58

Köster J, Volkman JK, Rullkötter J, Scholz-Böttcher BM, Rethmeier J, Fischer U (1999) Mono-, di- and trimethyl-branched alkanes in cultures of the filamentous cyanobacterium *Calothrix scopulorum*. Org Geochem 30:1367–1379

Largeau C, Casadevall E, Kadouri A, Metzger P (1984) Formation of *Botryococcus*-derived kerogens – comparative study of immature torbanites and of the extant alga *Botryococcus braunii*. In: Schenck PA, de Leeuw JW, Lijmbach GWM (eds) Advances in organic geochemistry 1983. Pergamon Press, Oxford, pp 327–332

Mackenzie AS, Leythaeuser D, Altebaumer F-J, Disko U, Rullkötter J (1988) Molecular measurements of maturity for Lias delta shales in N.W. Germany. Geochim Cosmochim Acta 52:1145–1154

Maslen E, Grice K, Gale JD, Hallmann C, Horsfield B (2009) Crocetane: a potential marker of photic zone euxinia in thermally mature sediments and crude oils of Devonian age. Org Geochem 40:1–11

Matsumoto GI, Friedmann EI, Watanuki K, Ocampo-Friedmann R (1992) Novel long-chain *anteiso*-alkanes and *anteiso*-alkanoic acids in Antarctic rocks colonized by living and fossil cryptoendolithic microorganisms. J Chromatogr 598:267–276

McCaffrey MA, Moldowan JM, Lipton PA, Summons RE, Peters KE, Jeganathan A, Watt DS (1994) Paleoenvironmental implications of novel C_{30} steranes in Precambrian to Cenozoic age petroleum and bitumen. Geochim Cosmochim Acta 58:529–532

McKenna AM, Nelson RK, Reddy CM, Savory JJ, Kaiser NK, Fitzsimmons JE, Marshall AG, Rodgers RP (2013) Expansion of the analytical window for oil spill characterization by ultrahigh resolution mass spectrometry: beyond gas chromatography. Environ Sci Technol 47:7530–7539

Metzger P, Largeau C (2005) *Botryococcus braunii*: a rich source for hydrocarbons and related ether lipids. Appl Microbiol Biotechnol 66:486–496

Moldowan MJ, Fago FJ, Lee CY, Jacobson SR, Watt DS, Slougui N-E, Jeganathan A, Young DC (1990) Sedimentary 24-*n*-propylcholestanes, molecular fossils diagnostic of marine algae. Science 247:309–312

Peters KE, Moldowan JM (1991) Effects of source, thermal maturity, and biodegradation on the distribution and isomerization of homohopanes in petroleum. Org Geochem 17:47–61

Peters KE, Walters CC, Moldowan JM (2005) The biomarker guide, 2nd edn, vols 1 and 2. Cambridge University Press, Cambridge

Pohorille A (2002) From organic molecules in space to the origins of life and back. Adv Space Res 30:1509–1520

Radke M, Welte DH (1983) The methylphenanthrene index (MPI): a maturity parameter based on aromatic hydrocarbons. In: Bjorøy M et al (eds) Advances in organic geochemistry 1981. Wiley, Chichester, pp 504–512

Radke M, Willsch H, Teichmüller M (1990) Generation and distribution of aromatic hydrocarbons in coals of low rank. Org Geochem 15:539–563

Radke M, Rullkötter J, Vriend SP (1994) Distribution of naphthalenes in crude oils from the Java Sea: source and maturation effects. Geochim Cosmochim Acta 58:3675–3689

Requejo AG, Sassen R, Mcdonald T, Denoux G, Kennicutt MC, Brooks JM (1996) Polynuclear aromatic hydrocarbons (PAH) as indicators of the source and maturity of marine crude oils. Org Geochem 24:1017–1033

Rose C, Polissar PJ, Tierney JE, Filley T, Demenocal PB (2016) Changes in northeast African hydrology and vegetation associated with Pliocene-Pleistocene sapropel cycles. Philos Trans R Soc B Biol Sci 371. https://doi.org/10.1098/rstb.2015.0243

Rubinstein I, Seiskind O, Albrecht P (1975) Rearranged sterenes in a shale: occurrence and simulated formation. J Chem Soc Perkin I:1833–1836

Sachse D, Billault I, Bowen GJ, Chikaraishi Y, Dawson TE, Feakins SJ, Freeman KH, Magill CR, McInerney FA, van der Meer MTJ, Polissar P, Robins RJ, Sachs JP, Schmidt HL, Sessions AL, White JWC, West JB, Kahmen A (2012) Molecular paleohydrology: interpreting the hydrogen-isotopic composition of lipid biomarkers from photosynthesizing organisms. Annu Rev Earth Planet Sci 40:221–249

Schoell M, McCaffrey MA, Fago FJ, Moldowan JM (1992) Carbon isotopic compositions of 28,30-bisnorhopanes and other biological markers in a Monterey crude oil. Geochim Cosmochim Acta 56:1391–1399

Schouten S, Rijpstra WIC, Kok M, Hopmans EC, Summons RE, Volkman JK, Sinninghe Damsté JS (2001) Molecular organic tracers of biogeochemical processes in a saline meromictic lake (Ace Lake). Geochim Cosmochim Acta 65:1629–1640

Schulze T, Michaelis W (1990) Structure and origin of terpenoid hydrocarbons in some German coals. Org Geochem 16:1051–1058

Sinninghe Damsté JS, Schouten S, van Duin ACT (2001) Isorenieratene derivatives in sediments: possible controls on their distribution. Geochim Cosmochim Acta 65:1557–1571

Sinninghe Damsté JS, Muyzer G, Abbas B, Rampen SW, Massé G, Allard WG, Belt ST, Robert JM, Rowland SJ, Moldowan JM,

Barbanti SM, Fago FJ, Denisevich P, Dahl J, Trindade LAF, Schouten S (2004) The rise of the rhizosolenid diatoms. Science 304:584–587
Sinninghe Damsté JS, Schouten S, Volkman JK (2014) C_{27}–C_{30} neohop-13(18)-enes and their saturated and aromatic derivatives in sediments: indicators for diagenesis and water column stratification. Geochim Cosmochim Acta 133:402–421
Slowakiewicz M, Tucker ME, Perri E, Pancost RD (2015) Nearshore euxinia in the photic zone of an ancient sea. Palaeogeogr Palaeoclimatol Palaeoecol 426:242–259
Sosrowidjojo IB, Murray AP, Alexander R, Kagi RI, Summons RE (1996) Bicadinanes and related compounds as maturity indicators for oils and sediments. Org Geochem 24:43–55
Summons RE, Lincoln SA (2012) Biomarkers: informative molecules for studies in geobiology. In: Knoll AH, Canfield DE, Konhauser KO (eds) Fundamentals of geobiology. Blackwell Publishing, Hoboken, New Jersey, pp 269–296
Summons RE, Jahnke LL, Hope JM, Logan GA (1999) 2-Methylhopanoids as biomarkers for cyanobacterial oxygenic photosynthesis. Nature 400:554–557
Uno KT, Polissar PJ, Kahle E, Feibel C, Harmand S, Roche H, Demenocal PB (2016) A Pleistocene palaeovegetation record from plant wax biomarkers from the Nachukui Formation, west Turkana, Kenya. Philos Trans R Soc B Biol Sci 371. https://doi.org/10.1098/rstb.2015.0235
van Aarssen BGK, Cox HC, Hoogendoorn P, de Leeuw JW (1990) A cadinene biopolymer in fossil and extant dammar resins as a source for cadinanes and bicadinanes in crude oils from South East Asia. Geochim Cosmochim Acta 54:3021–3031
van Aarssen BFK, Alexander R, Kagi R (2000) Higher plant biomarkers reflect paleovegetation changes during Jurassic time. Geochim Cosmochim Acta 64:1417–1424
Ventura GT, Kenig F, Reddy CM, Frysinger GS, Nelson RK, Van Mooy B, Gaines RB (2008) Analysis of unresolved complex mixtures of hydrocarbons extracted from late Archean sediments by comprehensive two-dimensional gas chromatography (GC×GC). Org Geochem 39:846–867
Volkman JK (2014) Acyclic isoprenoid biomarkers and evolution of biosynthetic pathways in green microalgae of the genus *Botryococcus*. Org Geochem 75:36–47
Volkman JK, Maxwell JR (1986) Acyclic isoprenoids as biological markers. In: Johns RB (ed) Biological markers in the sedimentary record. Elsevier, Amsterdam, pp 1–46
Volkman JK, Alexander R, Kagi RI, Woodhouse GW (1983) Demethylated hopanes in crude oils and their applications in petroleum geochemistry. Geochim Cosmochim Acta 47:785–794
Volkman JK, Alexander R, Kagi RI, Rowland SJ, Sheppard PN (1984) Biodegradation of aromatic hydrocarbons in crude oils from the Barrow Sub-basin of Western Australia. Org Geochem 6:619–632
Volkman JK, Allen DI, Stevenson PL, Burton HR (1986) Bacterial and algal hydrocarbons in sediments from a saline Antarctic Lake, Ace Lake. Org Geochem 10:671–681
Volkman JK, Holdsworth DG, Neill GP, Bavor HJ Jr (1992) Identification of natural, anthropogenic and petroleum hydrocarbons in aquatic sediments. Sci Total Environ 112:203–219
Volkman JK, Barrett SM, Dunstan GA (1994) C_{25} and C_{30} highly branched isoprenoid alkenes in laboratory cultures of two marine diatoms. Org Geochem 21:407–413
Wakeham SG, Schaffner C, Giger W (1980a) Polycyclic aromatic hydrocarbons in recent lake sediments – I. Compounds having anthropogenic origins. Geochim Cosmochim Acta 44:403–413
Wakeham SG, Schaffner C, Giger W (1980b) Polycyclic aromatic hydrocarbons in recent lake sediments – II. Compounds derived from biogenic precursors during early diagenesis. Geochim Cosmochim Acta 44:415–429
Wakeham SG, Freeman KH, Pease TK, Hayes JM (1993) A photoautotrophic source for lycopane in marine water columns. Geochim Cosmochim Acta 57:159–165
Walters CC, Peters KE, Moldowan JM (2010) History of life from the hydrocarbon fossil record. In: Timmis KN (ed) Handbook of hydrocarbon and lipid microbiology. Springer, Berlin, pp 171–183
Wang Z, Liu WG (2012) Carbon chain length distribution in *n*-alkyl lipids: a process for evaluating source inputs to Lake Qinghai. Org Geochem 50:36–43
Zech M, Zech R, Morras H, Moretti L, Glaser B, Zech W (2009) Late Quaternary environmental changes in Misiones, subtropical NE Argentina, deduced from multi-proxy geochemical analyses in a palaeosol–sediment sequence. Quat Int 196:121–136
Zhang XY, Xu YP, Ruan JP, Ding SU, Huang XY (2014) Origin, distribution and environmental significance of perylene in Okinawa Trough since last glaciation maximum. Org Geochem 76:288–294
Zhou W, Wang RY, Radke M, Wu QY, Sheng GY, Liu ZL (2000) Retene in pyrolysates of algal and bacterial organic matter. Org Geochem 31:757–762

Hydrogen

James G. Brophy and Arndt Schimmelmann
Department of Earth and Atmospheric Sciences, Indiana University, Bloomington, IN, USA

Element Data
Atomic Symbol: H
Atomic Number: 1
Atomic Weight: 1.0079 g/mol
Isotopes and Abundances: $^{1}H \sim 99.97\%$, $^{2}H \sim 0.028\%$. ^{3}H trace
1 Atm Melting Point: −259.14°C
1 Atm Boiling Point: −252.87°C
Common Valences: 1+, −1, 0
Covalent Radius: 37 pm
Pauling Electronegativity: 2.2
First Ionization Energy: 1312 kJ/mol
Chondritic (CI) Abundance: 1.97%
Silicate Earth Abundance: 0.012%
Crustal Abundance: 0.014%
Seawater Abundance: 10.8%
Core Abundance: uncertain

Properties

Hydrogen (H) is the lightest chemical element with only a single proton in the nucleus surrounded by a 1 s electron, therefore placing hydrogen in position 1 of the periodic table.

Natural hydrogen is a mixture of two stable isotopes ^{1}H and ^{2}H (see also ▶ "Hydrogen Isotopes"). Protium, ^{1}H, has no neutrons in its nucleus and is the most common form of hydrogen, with an atomic mass of ~1.0078 Da (dalton) and an isotopic abundance of ~99.972% of all hydrogen on Earth. Deuterium, ^{2}H, contains one proton and one neutron in the nucleus giving it an atomic mass of ~2.014 Da, with an abundance on Earth of ~0.028% complementing that of ^{1}H to yield ~100%. Deuterium has been traditionally abbreviated as D, although ^{2}H is recommended officially. In addition to the two stable isotopes of hydrogen, trace amounts of radioactive tritium, ^{3}H, with a half-life of 12.32 years occurs in the atmosphere and hydrosphere. ^{3}H derives from (1) cosmogenic nucleosynthesis via cosmic ray spallation in the atmosphere, (2) nuclear reactions in the Earth's crust, (3) nuclear testing in the atmosphere during the 1950s and 1960s and nuclear accidents like Chernobyl and Fukushima (Povinec et al. 2013), (4) continuous release of tritium from nuclear power plants, and (5) tritium production facilities in nuclear reactors via neutron activation of mainly lithium. The presence of one proton and two neutrons in the nucleus of tritium yields an atomic mass of ~3.016 Da. ^{3}H has been traditionally abbreviated as T, although ^{3}H is recommended officially. Extremely short-lived, artificial hydrogen nuclides with more than two neutrons in nuclei have been observed. Based on hydrogen's atomic number of 1 and the average abundances of its isotopes on Earth, an average atomic weight of ~1.0079 Da has been assigned by IUPAC (http://ciaaw.org/hydrogen.htm). The relative abundance of deuterium is typically larger in abiotic extraterrestrial organic matter (Martins 2011); hence, the ratio of ^{2}H atoms and ^{1}H atoms in the cosmos is not identical to that on Earth. Common valence states are +1 (e.g., hydrogen chloride, $H^{+}Cl^{-}$), 0 (elemental H_2), and −1 (e.g., in metal hydrides). Elemental hydrogen's boiling point of −252.87° C and its melting point of −259.14°C at 101,325 Pa (i.e., 1 atm) make it difficult to transport and store H_2 in condensed form. The bond length in $^{1}H_2$ is 74.13 pm. Hydrogen's empirical covalent atomic radius is ~37 pm, and its empirical atomic radius is ~25 pm. The relative ~100% mass difference between ^{1}H and ^{2}H is the largest in any stable isotope system, strongly affecting the strength of chemical bonds and promoting large isotope effects. Accordingly, the variation in the ratio of ^{2}H and ^{1}H atoms in natural terrestrial materials is larger than that of any other element (see ▶ "Hydrogen Isotopes").

History and Use

Elemental hydrogen H_2 had been first prepared as a gas in the seventeenth century and was finally recognized to represent an elemental substance in 1766 by English scientist Henry Cavendish who called it "inflammable air." The modern name "hydrogen," i.e., "water former," was coined in 1783 by French scientist Antoine Lavoisier.

Elemental hydrogen is mainly generated industrially via electrolysis of water and by high-temperature chemical reaction of coal or other fossil fuels with water steam. Novel techniques for H_2 generation include biochemical and photoelectrical methods. Elemental hydrogen finds many industrial uses, for example, for the production of clean fuels (e.g., catalytic hydrotreating of diesel for removal of sulfur) and the saturation of carbon-carbon chemical double and triple bonds in oils to make margarine. The vision of a "hydrogen economy" where energy will be stored and distributed in the form of elemental hydrogen faces challenges by the difficulty to store H_2 gas in sufficiently compact form (e.g., compressed or adsorbed H_2 gas for use as vehicular fuel). Iceland's availability of inexpensive geothermal energy enabled it to plan for a hydrogen economy, followed in 2014 by similar ambitions in Japan. Safety concerns focus of the explosive nature of hydrogen/air mixtures. Of all combustible gases, hydrogen gas expresses the widest mixing range with air or oxygen supporting combustion and explosion. Although H_2 is far cheaper and more readily available than helium for use in balloons, the Hindenburg airship disaster of 1937 in Lakehurst, New Jersey, has curbed the acceptance of H_2 in lighter-than-air aviation. Liquid hydrogen is the fuel of choice for large rockets lifting payloads into orbit. Proton nuclear magnetic resonance ^{1}H–NMR spectroscopy and imaging (also termed MRI for medical diagnostic applications) uses the nuclear magnetic spin characteristics of ^{1}H nuclei to investigate chemical environments of hydrogen and the distribution of ^{1}H–containing compound classes. Deuterated "heavy water" $^{2}H_2O$ is used in nuclear reactors to moderate neutrons and as a coolant. Industrially generated tritium $^{3}H_2$ high-pressured gas is employed in nuclear triggers.

Occurrence

Hydrogen is the most abundant form of matter in the universe. As remnants of the Big Bang, hydrogen and helium combined constitute about 99.9% of the mass of the solar system (Lauretta 2011). Hydrogen contributes most to the mass of main sequence stars, where nuclear fusion of hydrogen generates energy. "Nuclear burning" of ^{1}H via proton-proton additive chain reactions occurs in solar-mass stars, whereas larger stars with higher core temperatures "burn" hydrogen with the assistance of carbon, nitrogen, and oxygen nuclei until hydrogen is consumed in the core. After a star has aged to become a white dwarf star, explosive hydrogen "burning" on the star's surface can form a nova (Lauretta 2011) giving rise to nucleosynthesis of heavier elements.

Hydrogen is an atmophile element and is the most abundant element in the solar system making up approximately

74 wt. % by mass. It constitutes approximately 0.0055 wt. % of the atmosphere, 0.014 wt. % of the crust, and 0.012 wt. % of the mantle. On the Earth's surface, hydrogen occurs predominantly as water (H_2O), as methane (CH_4), as various ammonia compounds (NH_4^+), and as organically bound hydrogen. In the uppermost crust, hydrogen is present as OH^- in numerous minerals including clay minerals (e.g., kaolinite), zeolites (e.g., natrolite), hydroxides (e.g., brucite), various sulfates (e.g., gypsum), carbonates (e.g., malachite), phosphates (e.g., apatite), as well as many other minerals (Table 1). Within the deeper parts of the crust, it is primarily present as OH^- in high-temperature silicate minerals such as micas, amphiboles, and serpentine. Within the mantle, a small amount of hydrogen is present as OH^- in hydrous silicates (e.g., phlogopite), but most of it is dissolved as OH^- in nominally anhydrous minerals such as olivine and its high-pressure polymorphs wadsleyite and ringwoodite. Though present in such minerals in extremely small concentrations, the large volume of the mantle translates into volumes of OH^- that rival that found in the Earth's oceans today (Pearson et al. 2014; Schmandt et al. 2014). Water partially dissociates into H^+ and OH^- ($K_W = 10^{-14}$). H^+ plays a critical role in the chemical weathering of silicate minerals wherein H^+ substitutes for structurally bound cations which in turn are released as dissolved ions in solution.

Small fluxes of elemental hydrogen naturally emanate from underground reservoirs to Earth's surface, for example, from ultramafic rocks undergoing serpentinization, from some metal mines, and from some young sediments where microbes generate hydrogen from buried organic matter (Smith et al. 2005). Deep H_2 from serpentinization may react with carbon dioxide to form abiotic (or abiogenic) methane that is not a fossil fuel in terms of being generated from organic sedimentary matter (Etiope and Sherwood-Lollar 2013). Radiation from the decay of radioactive nuclides in the lithosphere results in the radiolytic generation of elemental hydrogen from water (Lefticariu et al. 2010). Elemental hydrogen from radiolysis may power a deep microbial biosphere that is operating independently from sunlight and photosynthesis (Colwell and D'Hondt 2013; Colman et al. 2017).

The vast majority of atoms in the hydrocarbon molecules of natural gas (and to a lesser degree in petroleum) are hydrogen atoms that do not contribute carbon dioxide upon combustion. The use of natural gas therefore exerts a smaller carbon footprint than the combustion of energetically equivalent amounts of coal. The O-H and C-H bonds in atmospheric water and methane absorb infrared wavelengths and thus contribute to greenhouse warming. Much organic hydrogen is stored in methane that is physically trapped in water-bearing clathrates (i.e., methane hydrates) at low temperatures and/or high pressure, for example, on the seafloor and in high-latitude permafrost. Incremental warming may destabilize clathrates at high latitudes resulting in methane emissions into the atmosphere, thereby providing of a positive feedback toward enhanced greenhouse warming.

Hydrogen, Table 1 Some common hydrogen-bearing minerals

Mineral	Mineral group	Formula
Kaolinite	Clay	$Al_2Si_2O_5(OH)_4$
Natrolite	Zeolite	$Na_2Al_2Si_3O_{10}.\ 2H_2O$
Brucite	Hydroxide	$Mg(OH)_2$
Gypsum	Sulfate	$CaSO_4.\ 2H_2O$
Malachite	Carbonate	$Cu_2CO_3(OH)_2$
Apatite	Phosphate	$Ca_5(PO_4)_3(F,cl,OH)$
Muscovite	Mica	$KAl_3Si_3O_{10}(OH)_2$
Hornblende	Amphibole	$(ca,Na)_{2-3}(mg,Fe,al)_5Si_6(Si,al)_2O_{22}(OH)_2$
Serpentine	Serpentine	$Mg_3Si_2O_5(OH)_4$
Phlogopite	Mica	$KMg_3AlSi_3O_{10}(OH)_2$
Olivine	Olivine	Mg_2SiO_4

Biological Utilization and Toxicity

Hydrogen is essential for all life and does not express toxicity. Although life on Earth is typically characterized as being carbon-based, there are about twice as many hydrogen atoms in biomass compared to carbon atoms. For example, carbohydrates and lipids have the approximate stoichiometries of $C(H_2O)_n$ and $(CH_2)_n$, respectively. The hydrogen bonding between biochemicals and surrounding cell water is of paramount importance for tertiary chemical structures of biochemicals (e.g., DNA, enzymes) and their associated biochemical reactivity. Subterranean hydrogen trace gas can energetically support microbial consortia.

Summary and Conclusions

Hydrogen is the lightest and most abundant chemical element in the universe. Life on Earth depends on hydrogen in the form of liquid water and organic hydrogen. It is hard to imagine life on other planets in the universe without the essential participation of hydrogen. The solid surface and much of the outer crust of planet Earth have been chemically altered and physically shaped by the influence of liquid water and ice via weathering and sedimentary transport. A world without substantial quantities of hydrogen in water at and near its surface would look vastly different from Earth (e.g., moon, mars), although hydrogen in lakes of liquid methane occurs on planets like Titan. Hydrogen on Earth further plays important roles as a chemical constituent in fossil fuels, especially in natural gas and oil. Elemental hydrogen may become an important clean fuel for transportation if challenges of fuel

cell development and hydrogen gas storage can be met technologically.

Cross-References

- ▶ Atmophile Elements
- ▶ Chemical Bonds
- ▶ Chemical Weathering
- ▶ Cosmic Elemental Abundances
- ▶ Gas Hydrates
- ▶ Hydrogen Isotopes
- ▶ Natural Gas
- ▶ Nucleosynthesis
- ▶ Ocean Biochemical Cycling and Trace Elements
- ▶ Organic Geochemistry
- ▶ Stable Isotope Geochemistry
- ▶ Water

References

Colman DR, Poudel S, Stamps BW, Boyd ES, Spear JR (2017) The deep, hot biosphere: twenty-five years of retrospection. PNAS 114(27):6895–6903. https://doi.org/10.1073/pnas.1701266114

Colwell FS, D'Hondt S (2013) Nature and extent of the deep biosphere. Rev Mineral Geochem 75:547–574. https://doi.org/10.2138/rmg.2013.75.17

Etiope G, Sherwood Lollar B (2013) Abiotic methane on Earth. Rev Geophys 51:276–299. https://doi.org/10.1002/rog.20011. http://projects.itn.pt/Methasource_2015/Etiope_Sherwood-Lollar2013.pdf

Lauretta DS (2011) A cosmochemical view of the solar system. Elements 7:11–16. https://doi.org/10.2113/gselements.7.1.11

Lefticariu L, Pratt LA, LaVerne JA, Schimmelmann A (2010) Anoxic pyrite oxidation by water radiolysis products – a potential source of biosustaining energy. Earth Planet Sci Lett 292:57–67. https://doi.org/10.1016/j.epsl.2010.01.020

Martins Z (2011) Organic chemistry of carbonaceous meteorites. Elements 7:35–40. https://doi.org/10.2113/gselements.7.1.35

Pearson DG, Brenker FE, Nestola F, McNeill J, Nasdala L, Hutchison MT, Matveev S, Mather K, Silversmit G, Schmitz S, Vekemans B, Vincze L (2014) Hydrous mantle transition zone indicated by ringwoodite included within diamond. Nature 507:221–224. https://doi.org/10.1038/nature13080

Povinec PP, Aoyama M, Biddulph D, Breier R, Buesseler K, Chang CC, Golser R, Hou XL, Ješkovský M, Jull AJT, Kaizer J, Nakano M, Nies H, Palcsu L, Papp L, Pham MK, Steier P, Zhang LY (2013) Cesium, iodine and tritium in NW Pacific waters – a comparison of the Fukushima impact with global fallout. Biogeosciences 10:5481–5496. https://doi.org/10.5194/bg-10-5481-2013

Schmandt B, Jacobsen SD, Becker TW, Liu Z, Dueker KG (2014) Dehydration melting at the top of the lower mantle. Science 344:1265–1268. https://doi.org/10.1126/science.1253358

Smith NJP, Shepherd TJ, Styles MT, Williams GM (2005) Hydrogen exploration: a review of global hydrogen accumulations and implications for prospective areas in NW Europe. In: Doré AG, Vining BA (eds) Petroleum geology: North-West Europe and global perspectives – proceedings of the 6th petroleum geology conference. Petroleum Geology Conferences Ltd., Geological Society, London, p 349

Hydrogen Isotopes

Arndt Schimmelmann and Peter E. Sauer
Department of Earth and Atmospheric Sciences, Indiana University, Bloomington, IN, USA

Definition

Natural hydrogen is a mixture of two stable isotopes ^{1}H and ^{2}H and one radioactive isotope ^{3}H. Protium, ^{1}H, has no neutrons in its nucleus and is the most common form of hydrogen, with an atomic mass of ~1.0078 Da (dalton) and an isotopic abundance of ~99.972% of all hydrogen on Earth. Deuterium, ^{2}H, contains one proton and one neutron in the nucleus giving it an atomic mass of ~2.014 Da, with an abundance on Earth of ~0.028% complementing that of ^{1}H to yield ~100%. Tritium, ^{3}H, bears one proton and two neutrons in its nucleus yielding an atomic mass of ~3.016 Da. Tritium is radioactive with a half-life of 12.32 years. Extremely short-lived, artificial hydrogen nuclides with more than two neutrons in nuclei have been observed.

Introduction and Occurrence

Based on hydrogen's atomic number of 1 and the average abundances of its isotopes on Earth, an average atomic weight of ~1.0079 Da has been assigned by IUPAC (http://ciaaw.org/hydrogen.htm). The relative ~100% mass difference between ^{1}H and ^{2}H is the largest in any stable isotope system, strongly affecting the strength of chemical bonds and promoting large isotope effects. Accordingly, the variation in the ratio of ^{2}H and ^{1}H atoms in nature is larger than that of any other element. The relative abundance of deuterium is typically larger in abiotic extraterrestrial organic matter (Martins 2011); hence, the ratio of ^{2}H atoms and ^{1}H atoms in the cosmos is not identical to that on Earth. Deuterium has been traditionally abbreviated as D, although ^{2}H is recommended officially. Only trace amounts of tritium occur in the atmosphere and hydrosphere. ^{3}H derives from:

1. Cosmogenic nucleosynthesis via cosmic ray spallation in the atmosphere
2. Nuclear reactions in the Earth's crust
3. Nuclear testing in the atmosphere during the 1950s and 1960s and nuclear accidents like Chernobyl and Fukushima (Povinec et al. 2013).
4. Continuous release of tritium from nuclear power plants
5. Tritium production facilities in nuclear reactors via neutron activation of mainly lithium

^{3}H has been traditionally abbreviated as T, although ^{3}H is recommended officially.

Nomenclature of Hydrogen Stable Isotope Ratios and Standardization of δ-Values

The stable isotope ratio of hydrogen $^{2}H/^{1}H$ [correctly: R ($^{2}H/^{1}H$), i.e., $N(^{2}H)/N(^{1}H)$, where N is number of entities; Coplen 2011] is traditionally expressed in terms of $\delta^{2}H$ values (formerly δD) in permil, per mil, or ‰. In compliance with IUPAC guidelines for the International System of Units (SI), Brand and Coplen (2012) introduced the unit mUr (i.e., milliurey) as a replacement of ‰ for expressing $\delta^{2}H$ values. Recommendations by IUPAC give an updated definition of $\delta^{2}H$ values without the previous factor 1000, mandate the use of δ in italics, and deprecate the acronym D for ^{2}H (Coplen 2011):

$$\delta^{2}H = \left[R\left(^{2}H/^{1}H\right)_{sample} - R\left(^{2}H/^{1}H\right)_{standard}\right] \times / R\left(^{2}H/^{1}H\right)_{standard}$$

As of fall 2015, $\delta^{2}H$ values are quantified along an isotope scale that is anchored at its origin (≡ 0 mUr) by Vienna Standard Mean Ocean Water (VSMOW) and additionally constrained by Standard Light Antarctic Precipitation (SLAP) with a defined value ≡ –428 mUr (Brand et al. 2014). Accurate determination of $\delta^{2}H$ values mandates the use of multiple-point calibrations with at least two different hydrogen stable isotope standards to account for instrumental scale compression. A listing of international hydrogen stable isotope standards is available in Brand et al. (2014).

Analytical Methods

The measurement of stable hydrogen isotope ratios has undergone major improvements over the past two decades (Beauchemin and Matthews 2010; Jochmann and Schmidt 2012). Traditional mass spectrometry had required preparation of elemental hydrogen from water and other analytical substrates on vacuum lines prior to admission of gaseous hydrogen samples into the mass spectrometer via manual dual-inlet mode. Many "off-line" chemical methods existed to convert hydrogen from various substrates first to water and subsequently to elemental hydrogen (Schimmelmann and Sauer 2010). The analytical efficiency improved by more than an order of magnitude with the introduction of "on-line" high-temperature conversion methods whereby an analyte is introduced into a peripheral instrument in a stream of helium (e.g., a gas chromatograph or an elemental analyzer), through a reducing high-temperature interface, and into the ion source of a mass spectrometer (Wang and Sessions 2008; Elsner et al. 2012). The introduction of chromium into the high-temperature interface served to scavenge interfering heteroelements like nitrogen and sulfur, optimized the hydrogen yield, and minimized isotopic fractionation (Renpenning et al. 2015). The mass spectrometer determines the hydrogen isotope ratio from the relative ion current intensities of mass-to-charge-3 (i.e., $^{2}H^{1}H^{+}$) and mass-to-charge-2 ($^{1}H_{2}^{+}$) ions. A correction for small amounts of $^{1}H_{3}^{+}$ with mass-to-charge-3 ions is instrument-dependent and is called H_3 factor.

An alternative approach for measuring H isotopes based on differences in the vibrational frequencies of ^{2}H and ^{1}H bonds, cavity ring-down spectroscopy (CRDS), has made major advances toward precise compound-specific measurements of $\delta^{2}H$ values of water and methane (e.g., Affolter et al. 2014). CRDS-based on-line systems are inexpensive, can be field-portable, don't require high vacuum or helium carrier gas, and allow fast sample throughput and now rival traditional mass spectrometry for some applications. However, CRDS is still plagued by matrix effects in complex samples and has larger sample size requirements than traditional isotope ratio mass spectrometer (IRMS) instruments.

Some hydrogen in organic matter is linked to oxygen, nitrogen, and sulfur via relatively weak O—H, N—H, and S—H bonds and can readily exchange with water hydrogen, even at room temperature in the laboratory during sample preparation. Bulk $\delta^{2}H$ values of such organic samples are therefore a composite of C-bound H (typically with a primary isotopic signature) and exchangeable H dependent on the seasonally variable isotopic character of local water and atmospheric moisture. Mitigation of the influence of isotopically exchangeable organic hydrogen is possible (1) via derivatization, where problematic functional groups are replaced by moieties that do not contain exchangeable hydrogen, and (2) via controlled equilibration of exchangeable hydrogen with water vapor or steam with known $\delta^{2}H$ values at standardized conditions (e.g., Sauer et al. 2009).

Radioactive tritium's low environmental concentrations are quantified in terms of radiation intensity in ion chambers, gas-flow-proportional-counter-based tritium monitors, and liquid scintillation spectrometry. The measurement unit is becquerel (Bq), i.e., the number of radioactive decay events per second. The most sensitive approach to quantify ^{3}H is mass spectrometry of the daughter decay product ^{3}He (Wood et al. 1993).

Applications of Hydrogen Stable Isotopes

As the most ubiquitous element, hydrogen is involved in a wide range of geologic, biologic, and astronomical systems, and its isotopes are important for archaeology, biochemistry, (bio)geochemistry, cosmochemistry (Martins 2011), diagnostic medicine, ecology, environmental sciences (Elsner et al.

2012), food authentication and forensics (Ehleringer et al. 2015), fossil fuel exploration (Schimmelmann et al. 2006), glaciology, hydro(geo)logy (Bowen et al. 2011), and paleoclimatology.

Hydrogen Stable Isotope Distribution in Nature

Relative to extraterrestrial materials (McKeegan and Leshin 2001), hydrogen on Earth occupies a relatively narrow isotopic range because almost all organic matter and the hydrogen-rich minerals resulting from weathering of silicates are genetically related to, and isotopically buffered by, the highly active global water cycle and the overwhelmingly large and well-mixed hydrogen pool of the global ocean. The pools of inorganic and organic hydrogen on Earth cover similar, limited δ^2H ranges from about +180 to −530 mUr (Lis and Sauer 2010). In comparison, the δ^2H range of extraterrestrial organic hydrogen from the Murchison meteorite is about four times larger and strongly shifted to ^{2}H-enrichment (Fig. 1), in spite of the fact that mineral hydrogen in meteorites is isotopically comparable to that of terrestrial mineral hydrogen (Yang and Epstein 1983). Based on measurements of Jupiter's atmosphere, the protosolar nebula is thought to have a δ^2H value on the order of −800 mUr (Altwegg et al. 2015). ^{2}H-enrichment increases in the order from interstellar hydrogen to organic molecules in meteorites, to interstellar organic molecules, and has been reported to reach 10,000 mUr (reviewed by Martins 2011). Such a high δ^2H contrast is likely related to isotopic fractionation during the condensation of H-bearing gases in the early stages of solar system evolution and subsequently to the difference in ionic bonding of hydrogen in minerals (primarily as OH^- ions that can equilibrate with H_2O) versus covalent bonding of organic hydrogen to a carbon-based molecular structure (note: the meaning of "organic" is limited to chemical characterization of molecules with a carbon skeleton and does not insinuate any biotic or biogenic origin). Radiation-induced ionization, low temperatures, and high vacuum in space favor very large hydrogen isotopic fractionation during abiogenic syntheses of organics from structurally simple molecules (Yang and Epstein 1983).

Hydrogen Isotopes in the Global Water Cycle

Water vapor evaporating from liquid water is depleted in ^{2}H and leaves behind ^{2}H-enriched water (the same principle applies to oxygen stable isotopes). The isotopic fractionation can be modeled after a Rayleigh distillation. Moist air masses lose ^{2}H-enriched H_2O as rain or snow. The last precipitation from relatively dry air masses in colder climates and at higher elevation is strongly ^{2}H-depleted. As a result, the isotopic pattern of annually averaged precipitation shows ^{2}H-enriched rain in coastal areas near warm oceans and a poleward trend toward ^{2}H-depletion that is enhanced at higher altitude (Fig. 2). The short mixing time of the modern global ocean of ~1500 years results in a narrow range of δ^2H in global ocean water centering around zero mUr or ‰, with a slight ^{2}H-enrichment in areas of enhanced evaporation (e.g., Red Sea) and ^{2}H-depletion where large rivers introduce ^{2}H-depleted freshwater (e.g., Arctic Ocean, Bay of Bengal).

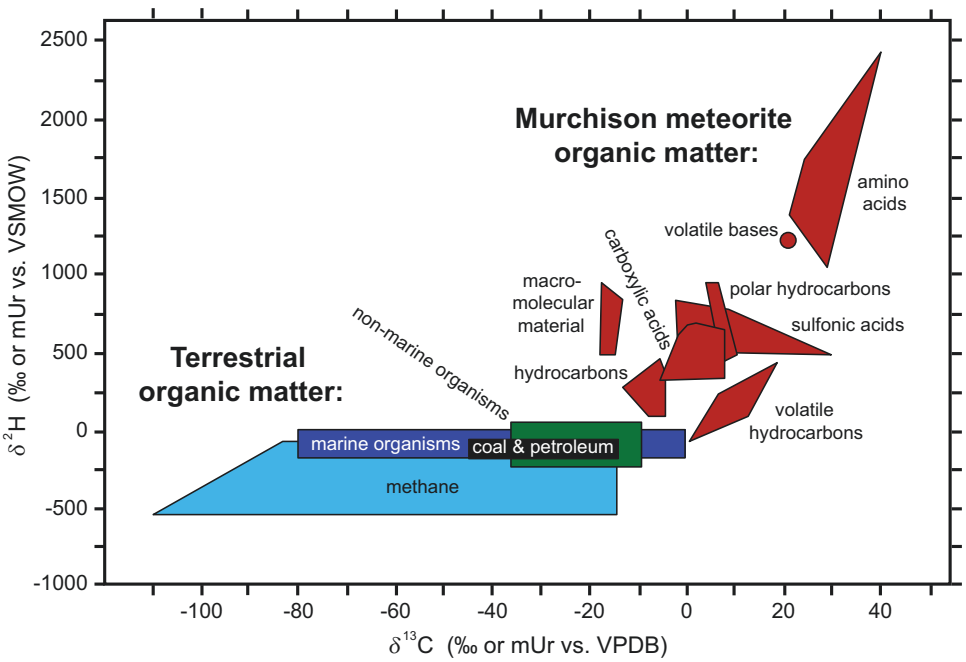

Hydrogen Isotopes, Fig. 1 Hydrogen-carbon stable isotope cross-plot of organic materials and compound classes from the Murchison meteorite (*red fields*) and from terrestrial sources (*blue*, *green*, and *black fields*) expressing a stark difference between extraterrestrial abiogenic and terrestrial biogenic organics (adapted from Sephton and Botta 2005). The stable hydrogen and carbon stable isotope ratios are expressed in traditional δ-units relative to Vienna Standard Mean Ocean Water (VSMOW) and Vienna Pee Dee Belemnite (VPDB) in ‰ or mUr. (Note the much larger isotopic range of more than 2500 mUr for δ^2H values compared to ~150 mUr for δ^{13}C values testifying to much larger isotope fractionation for hydrogen)

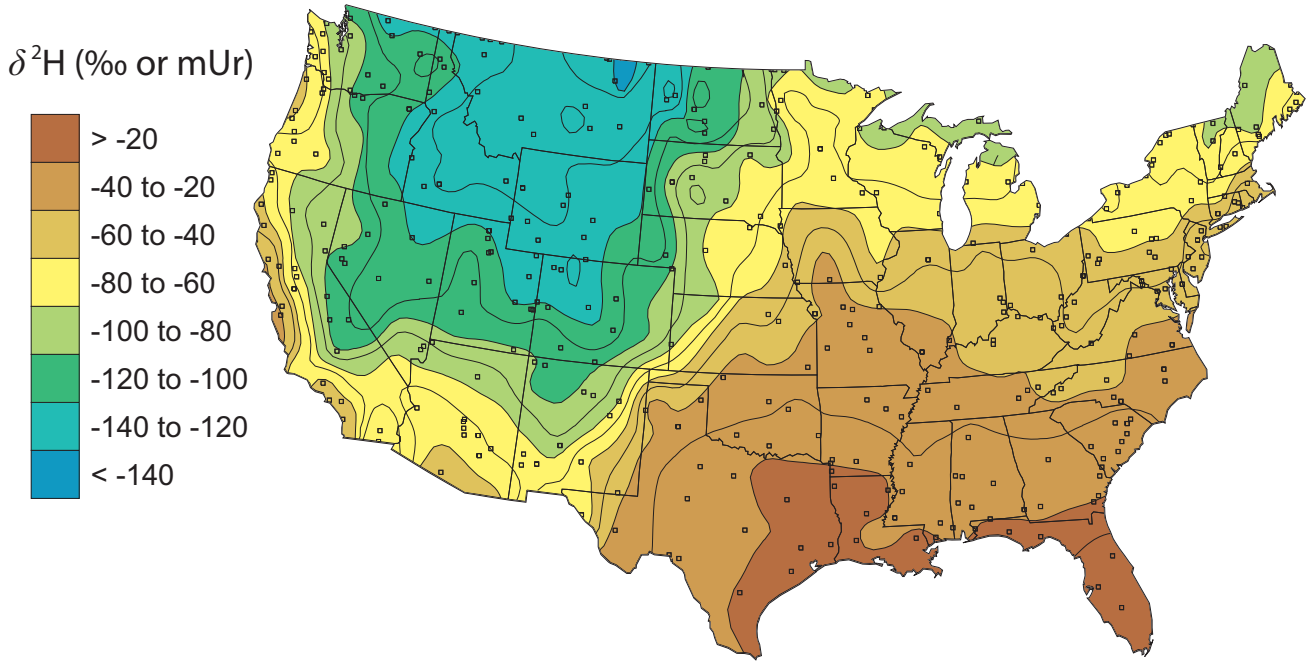

Hydrogen Isotopes, Fig. 2 Mean annual hydrogen isotope distribution in discharge-weighted river waters of the contiguous United States (adapted from Kendall and Coplen 2001). The $^{2}H/^{1}H$ stable isotope ratio is expressed in traditional δ-units along the VSMOW-SLAP isotopic scale in ‰ or mUr

The δ^2H values of brackish waters roughly fall on a mixing line between seawater and freshwater. The storage of large amounts of ^{2}H-depleted ice on polar ice caps and glaciers during ice ages intermittently increased the δ^2H value of the global ocean. Groundwaters on continents are typically "fossil precipitation" that reflects the isotopic character of regional precipitation at the time of groundwater recharge. In most temperate zones where precipitation is sufficient to support perennial rivers, δ^2H values of river water reflect those in local groundwater (Fig. 2).

Hydrogen in Biota

All autotrophic organisms (i.e., mostly photoautotrophic plants utilizing sunlight, but also lithoautotrophic organisms using geochemical energy) receive hydrogen for organic biosynthesis from water, albeit with significant isotopic fractionation depending on the biosynthesized chemical and the biosynthetic pathway (Hayes 2001). Compound-specific δ^2H values of biochemicals from autotrophs are therefore related to, and can serve as proxies for, the isotopic composition of environmental water that had supported biosynthesis. Such an approach requires that isotope variations associated with metabolic effects on the target biomarker are minimal. Paleoenvironmental use of δ^2H values of fossil organic matter needs to avoid the influence of isotopically exchangeable organic hydrogen that is mainly linked to oxygen, nitrogen, and sulfur in the form of O─H, N─H, and S─H because such hydrogen continually exchanges with environmental water and does not reliably carry paleoenvironmental information. Ideal compounds to serve as proxies for the reconstruction of δ^2H values of paleoenvironmental waters only contain carbon-bound hydrogen that does not readily exchange with other hydrogen, for example, *n*-alkanes, long fatty acids that can be esterified, and tree-ring cellulose where O─H is derivatized to form nitric acid esters. Heterotrophic organisms (e.g., animals, fungi) metabolize biomass to form their own biomass, which adds the complication of additional isotopic fractionation and the influence of body water that is isotopically different from water available to autotrophs. Nevertheless, empirical scrutiny of δ^2H values of biochemical biomarkers, compound classes, or tissues of algae, plants, animals, and humans resulted in fruitful applications in archaeology, paleoclimatology, ecology, and forensics (Sachse et al. 2012; Ehleringer et al. 2015). For example, δ^2H values in sedimentary lipids have been used to reconstruct source water variations, and δ^2H values in feather and hair keratin, as well as bone collagen, have been used for tracking migrations and for paleodietary reconstruction. The analytical noise from exchangeable hydrogen in solid analytes can be reduced via controlled equilibration with isotopically characterized water vapor or steam at standardized conditions (Sauer et al. 2009).

Hydrogen in Fossil Fuels, Minerals, and Rocks

A small fraction of the organic matter that is co-deposited with detrital mineral grains in sediments escapes early biodegradation and becomes buried. Microbial methanogenesis liberates ^{2}H-depleted methane as long as the temperature remains low. Compaction, increasing pressure, and slow heating along the geothermal gradient transform biochemicals into geochemicals via chemical reactions that eliminate many of the hydrogen-containing functional groups. With increasing thermal maturity, the hydrogen isotopic character of residual organic matter changes in a predictable pattern (Schimmelmann et al. 2006). At elevated temperatures, carbon-carbon bond cracking within larger organic molecules liberates smaller molecules forming thermogenic gas and oil. Cracking generates short-lived radicals that have an opportunity to engage in limited hydrogen isotopic exchange between relatively ^{2}H-enriched pore water and ^{2}H-depleted organic hydrogen, whereby the resulting organic matter becomes more enriched in ^{2}H. The loss of hydrocarbons from maturing sedimentary organic matter leads to a long-term decrease in the elemental H/C ratio of residual insoluble organic matter called kerogen. Regardless of the complex chemical reactions during maturation, paleoenvironmentally relevant information has been gleaned from δ^{2}H values of chemically complex biogeochemicals, such as kerogen, humic acids, and bulk coal (Schimmelmann et al. 2006). Hydrogen stable isotope ratios of components of natural gas and oil have value for the identification of source rocks and discrimination among genetically different types of natural gas (see entry "Natural Gas"). An exception to the origin of hydrocarbons from fossil sedimentary organic matter is methane derived from purely abiotic sources at depth. At least nine abiotic (or abiogenic) methane production mechanisms have been identified that pertain to either magmatic processes or to gas-water-rock reactions, for example, reactions of carbon dioxide and elemental hydrogen resulting in methane. Abiotic methane tends to be slightly enriched in ^{2}H relative to biogenic methane (Etiope and Sherwood-Lollar 2013).

Weathering of silicates in rocks takes up environmental water to generate hydrogen-rich phyllosilicates. Some hydrogen in phyllosilicates is bonded strongly enough to preserve its hydrogen isotopic character after weathering. Hydrogen isotope fractionation factors have been determined for a variety of clay minerals at different weathering temperatures. The δ^{2}H values of non-exchangeable hydrogen in clay minerals serve as proxy for weathering conditions and the isotopic composition of paleoenvironmental water (Clauer and Chaudhuri 1995). Hydrogen stable isotope ratios have been useful for studying water-rock interaction and the formation of minerals in hydrothermal systems (Shanks 2001).

Summary and Conclusions

The scientific, medical, industrial, and forensic importance of hydrogen isotopes, especially of the stable isotopes protium ^{1}H and deuterium ^{2}H, has increased dramatically since the turn of the millennium, which is in part due to a revolutionary simplification and automation of analytical methods. As the lightest of all elements, hydrogen expresses the largest natural isotope fractionation effects. Hydrogen's enormous natural isotopic range is being exploited by an increasing number of scientific and technical fields. From cosmochemical considerations of life on other planets to ice age paleoenvironmental reconstructions based on hair from extinct mastodons and to medical diagnosis of metabolic disorders, to name a few, hydrogen isotopes express astounding versatility and utility with ever-more exciting applications.

Cross-References

- Analytical Techniques
- Atomic Number, Mass Number, and Isotopes
- Biogenic Methane
- Biogeochemistry
- Compound-Specific Isotope Analysis
- Diagenesis
- Hydrogen
- Hydrologic Cycle
- Low-Temperature Geochemistry
- Meteorites
- Natural Gas
- Organic Geochemistry
- Paleoclimatology
- Stable Isotope Geochemistry

References

Affolter S, Fleitmann D, Leuenberger M (2014) New online method for water isotope analysis of speleothem inclusions using laser absorption spectroscopy (WS-CRDS). Clim Past 10:1291–1304. https://doi.org/10.5194/cp-10-1291-2014

Altwegg K, Balsiger H, Bar-Nun A, Berthelier JJ, Bieler A, Bochsler P, Briois C, Calmonte U, Combi M, De Keyser J, Eberhardt P, Fiethe B, Fuselier S, Gasc S, Gombosi TI, Hansen KC, Hässig M, Jäckel A, Kopp E, Korth A, LeRoy L, Mall U, Marty B, Mousis O, Neefs E, Owen T, Rème H, Rubin M, Sémon T, Tzou CY, Waite H, Wurz P (2015) 67P/Churyumov-Gerasimenko, a Jupiter family comet with a high D/H ratio. Science 347:1261952-1-3. https://doi.org/10.1126/science.1261952

Beauchemin D, Matthews DE (2010) Chapter 10: isotope ratio mass spectrometry (IRMS): light elements (C, H, O, N, S). In: Gross ML, Caprioli RM (eds) The encyclopedia of mass spectrometry, vol 5. Elsevier, Amsterdam/Boston, pp 739–822

Bowen GJ, Kennedy CD, Liu Z, Stalker J (2011) Water balance model for mean annual hydrogen and oxygen isotope distributions in

surface waters of the contiguous United States. J Geophys Res 116: G04011. https://doi.org/10.1029/2010JG001581
Brand WA, Coplen TB (2012) Stable isotope deltas: tiny, yet robust signatures in nature. Isot Environ Health Stud 48:393–409. https://doi.org/10.1080/10256016.2012.666977
Brand WA, Coplen TB, Vogl J, Rosner M, Prohaska T (2014) Assessment of international reference materials for isotope-ratio analysis (IUPAC technical report). Pure Appl Chem 86:425–467. https://doi.org/10.1515/pac-2013-1023
Clauer N, Chaudhuri S (1995) Clays in crustal environments. Isotope dating and tracing. Springer, Berlin. https://doi.org/10.1007/978-3-642-79085-0
Coplen TB (2011) Guidelines and recommended terms for expression of stable-isotope-ratio and gas-ratio measurement results. Rapid Commun Mass Spectrom 25:2538–2560. https://doi.org/10.1002/rcm.5129
Ehleringer JR, Chesson LA, Valenzuela LO, Tipple BJ, Martinelli LA (2015) Stable isotopes trace the truth: from adulterated foods to crime scenes. Elements 11:259–264. https://doi.org/10.2113/gselements.11.4.259
Elsner M, Jochmann MA, Hofstetter TB, Hunkeler D, Bernstein A, Schmidt TC, Schimmelmann A (2012) Current challenges in compound-specific stable isotope analysis of environmental organic contaminants. Anal Bioanal Chem 403:2471–2491. https://doi.org/10.1007/s00216-011-5683-y
Etiope G, Sherwood Lollar B (2013) Abiotic methane on earth. Rev Geophys 51:276–299. https://doi.org/10.1002/rog.20011
Hayes JM (2001) Fractionation of carbon and hydrogen isotopes in biosynthetic processes. Rev Mineral Geochem 43:225–277. https://doi.org/10.2138/gsrmg.43.1.225
Jochmann MA, Schmidt TC (2012) Compound-specific stable isotope analysis. The Royal Society of Chemistry (RCS) Publishing, Cambridge, 376 pp
Kendall C, Coplen TB (2001) Distribution of oxygen-18 and deuterium in river waters across the United States. Hydrol Proc 15:1363–1393. https://doi.org/10.1002/hyp.217
Lis GP, Sauer PE (2010) Variations of abundances of hydrogen isotopes in nature. In: Gross ML, Caprioli RM (eds) The encyclopedia of mass spectrometry, vol 5. Elsevier, Amsterdam/Boston, pp 857–863
Martins Z (2011) Organic chemistry of carbonaceous meteorites. Elements 7:35–40. https://doi.org/10.2113/gselements.7.1.35
McKeegan KD, Leshin LA (2001) Stable isotope variations in extraterrestrial materials. Rev Mineral Geochem 43:279–318. https://doi.org/10.2138/gsrmg.43.1.279
Povinec PP, Aoyama M, Biddulph D, Breier R, Buesseler K, Chang CC, Golser R, Hou XL, Ješkovský M, Jull AJT, Kaizer J, Nakano M, Nies H, Palcsu L, Papp L, Pham MK, Steier P, Zhang LY (2013) Cesium, iodine and tritium in NW Pacific waters – a comparison of the Fukushima impact with global fallout. Biogeosciences 10:5481–5496. https://doi.org/10.5194/bg-10-5481-2013
Renpenning J, Kümmel S, Hitzfeld KL, Schimmelmann A, Gehre M (2015) Compound-specific hydrogen isotope analysis of heteroatom-bearing compounds via gas chromatography – chromium-based high-temperature conversion (Cr/HTC) – isotope ratio mass spectrometry. Anal Chem 87:9443–9450. https://doi.org/10.1021/acs.analchem.5b02475
Sachse D, Billault I, Bowen GJ, Chikaraishi Y, Dawson TE, Feakins SJ, Freeman KH, Magill CR, McInerney FA, van der Meer MTJ, Polissar P, Robins RJ, Sachs JP, Schmidt HL, Sessions AL, White JWC, West JB, Kahmen A (2012) Molecular paleohydrology: interpreting the hydrogen-isotopic composition of lipid biomarkers from photosynthesizing organisms. Annu Rev Earth Planet Sci 40:221–249. https://doi.org/10.1146/annurev-earth-042711-105535
Sauer PE, Schimmelmann A, Sessions AL, Topalov K (2009) Simplified batch equilibration for D/H determination of non-exchangeable hydrogen in solid organic material. Rapid Commun Mass Spectrom 23:949–956. https://doi.org/10.1002/rcm.3954
Schimmelmann A, Sauer PE (2010) Methods to prepare water as H_2 for IRMS measurement of ^{2}H. In: Gross ML, Caprioli RM (eds) Encyclopedia of mass spectrometry, vol 5. Elsevier, Amsterdam/Boston, pp 749–759
Schimmelmann A, Sessions AL, Mastalerz M (2006) Hydrogen isotopic (D/H) composition of organic matter during diagenesis and thermal maturation. Annu Rev Earth Planet Sci 34:501–533. https://doi.org/10.1146/annurev.earth.34.031405.125011
Sephton MA, Botta O (2005) Recognizing life in the solar system: guidance from meteoritic organic matter. Int J Astrobiol 4:269–276. https://doi.org/10.1017/S1473550405002806
Shanks WC III (2001) Stable isotopes in seafloor hydrothermal systems. Rev Mineral Geochem 43:469–525. https://doi.org/10.2138/gsrmg.43.1.469
Wang Y, Sessions AL (2008) Memory effects in compound-specific D/H analysis by gas chromatography/pyrolysis/isotope-ratio mass spectrometry. Anal Chem 80:9162–9170. https://doi.org/10.1021/ac801170v
Wood MJ, McElroy RG, Surette RA, Brown RM (1993) Tritium sampling and measurement. Health Phys 65:610–627. http://journals.lww.com/health-physics/Abstract/1993/12000/Tritium_Sampling_and_Measurement_.2.aspx
Yang J, Epstein S (1983) Interstellar organic matter in meteorites. Geochim Cosmochim Acta 47:2199–2216. https://doi.org/10.1016/0016-7037(83)90043-1

H

Hydrologic Cycle

Giuseppe Mascaro
School of Sustainable Engineering and the Built Environment, Arizona State University, Tempe, AZ, USA

Definition

The *hydrologic cycle* refers to the distribution and circulation of water on Earth's surface and subsurface, oceans, and atmosphere. The cycle is a system of *fluxes* of water among different *reservoirs*, where water is stored according to diverse proportions and phases (liquid and solid in the terrestrial and oceanic components; vapor in the atmosphere). Solar energy, required for evaporation and mixing of water in the atmosphere, and gravity are the drivers of the hydrologic cycle. Given the central role of water in all physical, biological, and chemical processes occurring on Earth, studying and quantifying fluxes and reservoirs of the hydrologic cycle is crucial for understating and managing the environment and our relation to it.

Reservoirs and Fluxes of the Hydrologic Cycle

Figure 1 reports estimates of the global water reserves in the major reservoirs. The total reserves sum up to 1,38 6,000 $\times$ 10^3 km^3, with the oceans making up 96.5% (1,338,000 $\times$ 10^3 km^3) and fresh water 2.5%

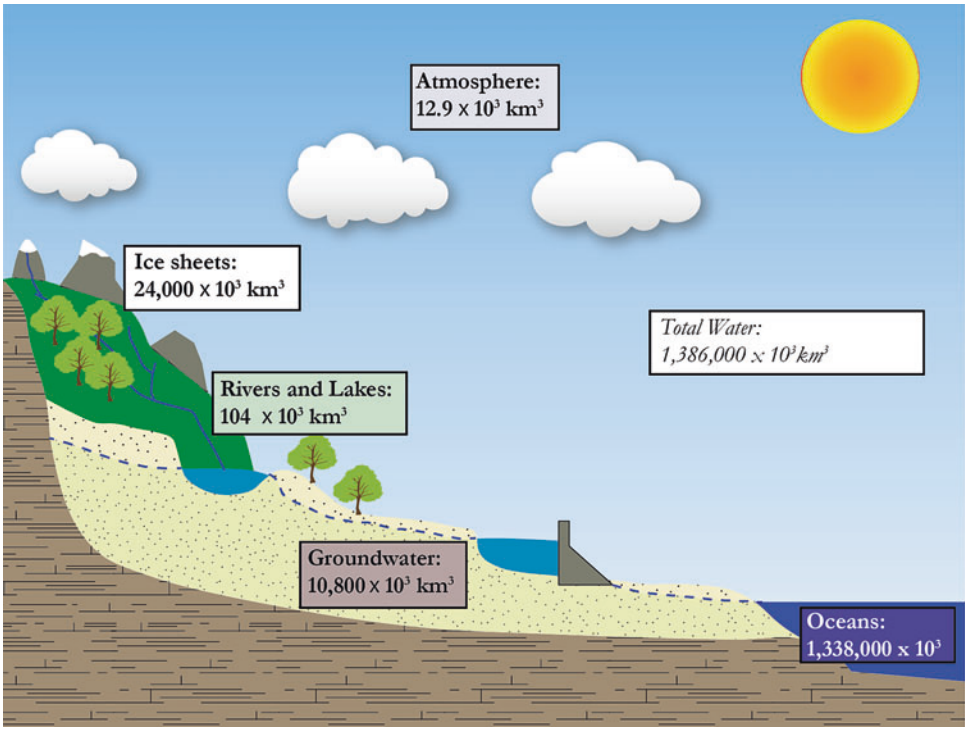

Hydrologic Cycle, Fig. 1 Estimates of the global water reserves in the major reservoirs of the Earth in km^3 (from http://scied.ucar.edu/longcontent/water-cycle)

(35,030 × 10^3 km^3) of the total. The remaining portion is saline water in diverse reservoirs. Ice sheets are the largest storages of fresh water (68.7%), followed by groundwater (30.1%), while surface water (rivers, lakes, and swamps) is a minor portion (about 1%). While the total volume of water remains the same globally, water is in continuous motion among the different reservoirs. Figure 2 shows the main fluxes of the hydrologic cycle. Each major reservoir has input and output fluxes that sum up to zero, based on the principle of mass conservation. For example, the flux of water leaving the oceans through evaporation is 434 × 10^3 km^3/year, which is equal to the water entering this reservoir as precipitation (398 × 10^3 km^3/year), river discharge (35.9 × 10^3 km^3/year), and groundwater flow (0.1 × 10^3 km^3/year). The *residence time* of water in each reservoir can be calculated as the ratio between the volume stored and the total input or output fluxes. The residence times range from more than 3000 years in the oceans to only 9 days in the atmosphere.

Main Processes of the Hydrologic Cycle

The main processes of the hydrologic cycle are depicted in Fig. 2 (red italic font). Water moves from the Earth to the atmosphere via *evaporation* from open water bodies (oceans, lakes, rivers, etc.), soil and vegetation surfaces, and *transpiration* from plants whose roots are capable of extracting water from the soil. A change of phase from liquid to vapor is involved in these processes, which are mainly driven by solar energy, wind, and vapor concentration in the air immediately above the evaporating surface or the canopy. Evaporation and transpiration are often lumped together into the term *evapotranspiration*. Water vapor in the atmosphere is transported over long distances due to pressure and temperature gradients and, if conditions permit, it condensates or freezes leading to *precipitation* occurrence on land and oceans in the forms of rainfall, snow, or hail. Precipitation on land may either be *intercepted* by vegetation and then evaporate, *infiltrate* into the soil, or become *surface runoff*. Water infiltrated in the soil can evapotranspire, flow laterally as *subsurface runoff*, or *percolate* through the vadose zone and recharge the aquifers, thus becoming *groundwater*. Surface runoff converges to rivers and lakes and eventually discharges into the oceans as streamflow. Water in the aquifers flows laterally with velocities that are order of magnitudes lower than streamflow velocities. Depending on the geological, topographic, and climatic settings, groundwater can return to the rivers as baseflow or discharge directly into the oceans (Mays 2012).

Measurements of the Hydrologic Cycle Components

Fluxes and stocks of the hydrologic cycle are measured by ground instruments and remote sensors at various spatial and temporal scales and with different level of accuracy. Ground

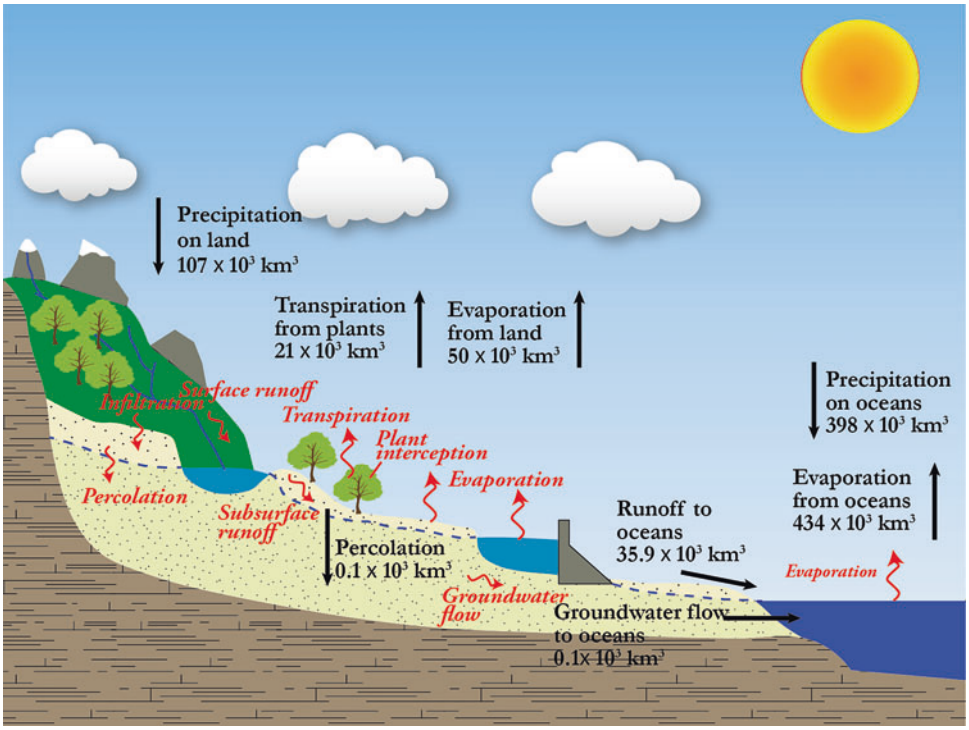

Hydrologic Cycle, Fig. 2 Estimates of the main fluxes of the hydrologic cycle in km^3/year, showed with *black* arrows (from http://scied.ucar.edu/longcontent/water-cycle). The main processes of the hydrologic cycle are indicated with *red* arrows and italic font. They include evaporation from ocean and land (bare soil, lake, reservoirs, and rivers) to the atmosphere; transpiration from plants to the atmosphere; plant interception; infiltration of precipitated water into the vadose zone; percolation of infiltrated water from the vadose zone to the aquifer (delimited by the *dashed blue* line on the top and by the bedrock on the bottom); groundwater flow; and surface runoff, including overland and channel flow

instruments usually provide measurements at a point with relatively high temporal resolution (subdaily). Examples are rain and snow gages, lysimeters for estimation of evapotranspiration, and soil moisture probes. Remote sensors can be ground-based and air- or satellite-borne and are able to provide spatially distributed measurements with various coverage and spatial and temporal resolution. For example, ground weather radars measure rainfall rates at a resolution of few kilometers in space and tens of minutes in time over a circular area with a radius of about 200 km (http://radar.weather.gov/); satellite sensors provide global estimates at relatively coarse spatial (tens of kilometers) and temporal (from one to several days) resolution of several variables, including precipitation (e.g., Global Precipitation Measurement (the website is reported in the References)), soil water content (e.g., Soil Moisture Ocean Salinity Mission (the website is reported in the References) and the Soil Moisture Active and Passive (the website is reported in the References) mission), evapotranspiration (e.g., Moderate Resolution Imaging Spectroradiometer (the website is reported in the References.)), and groundwater variation (Gravity and Recovery Climate Experiment (the website is reported in the References)).

Spatial and Temporal Variability of the Hydrologic Cycle

Due to the complex interaction of dominant weather patterns, latitude, and surface and subsurface characteristics (topography, soil, geology, vegetation, and land cover), the fluxes and stocks of water vary with location, time of the year, and from year to year. Precipitation is characterized by annual totals that mostly depend on latitude (up to 2000 mm/year within the tropics and less than 100 mm/year close to the poles) and elevation, and by marked seasonality in certain regions such as those affected by the monsoons. Evapotranspiration is strongly controlled by latitude (maximum near the equator and almost zero at the poles) and displays diurnal and seasonal cycles, as an effect of the spatial and temporal variability of the solar radiation balance. The spatial distribution of runoff is mostly correlated with that of precipitation, while its time variability is affected by the seasonality of precipitation and evapotranspiration, as well as by the timing of snowmelt (Dingman 2002).

Link Between Hydrologic Cycle, Energy Balance, and Climate Change

The hydrologic cycle is directly linked to the energy balance of the Earth: the evapotranspiration component multiplied by the latent heat of vaporization (~2.45 MJ/Kg at ordinary temperatures and pressures) is the latent heat flux, which is the largest component of the atmospheric energy balance. The term "latent" refers to the fact that, in the phase transition from liquid to vapor, water absorbs energy without changing temperature. This energy is subsequently released during condensation.

The concentration of greenhouse gases in the atmosphere affects the energy balance of the Earth. As a result, an increase in concentration of these gases is expected to impact the hydrologic cycle, possibly causing modifications of spatial patterns and temporal distribution of the main water fluxes and changes in the reservoir storages. For example, recent observations have shown evidence of ongoing changes of parts of the climate system at unprecedented rates that can be associated to higher concentration of greenhouse gases. These include an increase in mean global temperature; melt of mountain glaciers and ice sheets in Antarctic, Greenland, and Arctic regions; and sea level rise. Understanding how global change of climate affects the hydrologic cycle at regional and local scales is crucial for the sustainable management of water resources, as well as for predicting, forecasting, and mitigating water-related hazards. As a result, this represents an active interdisciplinary research area involving hydrologic, climate, social, and political sciences.

Summary

The hydrologic cycle accounts for the movement and storage of water (in its three phases) on Earth. This process is driven by solar energy and is characterized by spatial and temporal variability of both fluxes and storages. The great majority of the Earth's water is contained in the oceans, while only a very small portion is fresh and, thus, useful for human activities. In the land, water moves and is stored in the surface, subsurfaces and biotic components, according to complex processes that are measured with ground and remotely sensed instruments. The hydrologic cycle is intimately tied to the energy balance via the evopotranspiration term. As a consequence, the emission of greenhouse gases in the atmosphere, which is known to impact the energy balance of the Earth, may modify intensity and variability of the hydrologic cycle. Quantifying and predicting the hydrologic cycle at multiple scales through observations and numerical models is crucial for the sustainable management of water resources, mitigation of hydrologic extremes, and preservation of ecosystems.

References

Dingman SL (2002) (re-issued 2008), Physical ydrology, 2nd edn. Waveland Press, 646 pp
Global Precipitation Measurement. http://www.nasa.gov/mission_pages/GPM/main/index.html
Gravity and Recovery Climate Experiment. http://www.csr.utexas.edu/grace/
Mays LW (2012) Ground and surface water hydrology. Wiley, 617 pp
Moderate Resolution Imaging Spectroradiometer. http://www.ntsg.umt.edu/project/mod16
Soil Moisture Ocean Salinity Mission. http://www.esa.int/Our_Activities/Observing_the_Earth/SMOS
Soil Moisture Active and Passive. http://smap.jpl.nasa.gov/

Hydrothermal Alteration

Andri Stefánsson and Barbara I. Kleine
Institute of Earth Sciences, University of Iceland, Reykjavík, Iceland

Definition

Hydrothermal alteration involves the replacement of primary glass and minerals with alteration minerals stable at the conditions of alteration, generally in the temperature range of 50–400 °C. Hydrothermal alteration is sometimes referred to as low-grade metamorphism or metasomatism. The physical and chemical changes leading to the formation of hydrothermal alteration are temperature, pressure, and chemical changes of the system or any combination of these. Hydrothermal alteration is a common feature of geothermal systems. Alteration textures range from weak alteration of only some of the minerals or matrix in the host rocks to complete replacement of the primary minerals by the alteration minerals. Hydrothermal alteration may occur within the crust associated with hot rock or magmatic activity as well as at the Earth's surface.

Alteration Processes

The process of alteration involves the dissolution of primary glasses and minerals by thermal fluids and precipitation of alteration minerals. The primary minerals and glasses are formed at high temperatures and upon cooling become thermodynamically unstable. In contact with thermal fluids, they dissolve forming aqueous and gases species in the fluid. Progressive dissolution results in increased concentrations of the rock-forming elements in the thermal fluids. Eventually, they become saturated with respect to minerals that subsequently may form.

The Source and Chemistry of the Thermal Fluid

The sources of thermal fluids resulting in hydrothermal alteration are mainly three: (1) near surface and groundwater generally meteoric or seawater, (2) magma volatiles exsolved from melt termed juvenile water, and (3) fluids originated from dehydration upon metamorphic reactions. The hydrothermal fluids range in chemical composition from dilute (<100 ppm NaCl) to concentrated brine (up to ~50% NaCl) and have very variable volatile concentrations with the main volatiles often being C-, S-, Cl-, and F-containing compounds (e.g., Arnórsson et al. 2007; Heinrich 2007; Webster and Mandeville 2007).

Formation of Hydrothermal Minerals

Hydrothermal alteration minerals are sometimes referred to as secondary minerals. Many are common, for example, in low-grade metamorphic rocks and hydrothermal ore deposits, whereas others are rare. Common hydrothermal minerals are: quartz and other forms of silica (chalcedony, opal, amorphous silica), illite, sericite, smectites, zeolites, chlorite, serpentine, albite, K-feldspar, epidote, prehnite, actinolite, garnet, sulfides, carbonates, talc, kaolinite, pyrophyllite, sulfates, oxides, and hydroxides (Browne 1978).

The formation of hydrothermal minerals depends on several factors including: (1) temperature, (2) pressure, (3) rock type, (4) permeability, (5) hydrothermal fluid composition, and (6) duration of alteration or extent of reaction.

Hydrothermal mineral stabilities depend on temperature. This is related to changes in the mineral solubilities with temperature. As a result, hydrothermal minerals commonly show temperature-related zonation with typically low-temperature minerals like smectites and zeolites formed at <150 °C and high-temperature geothermal minerals like quartz, albite, chlorite, and epidote formed at 200–300 °C and amphibole, hornblende, and garnet at >300 °C (Kristmannsdóttir 1979).

Fluid pressures in geothermal systems are generally low, rarely exceed ~200 bar, and are not considered to affect the type of hydrothermal alteration. However, changes in pressure can lead to boiling and changes in gas pressure and mineralization. An example is calcite formation associated with depressurization boiling (Simmons and Christenson 1994).

The rock type affects hydrothermal alteration mainly through changes in permeability. In fact, the initial primary mineralogy has limited effects on hydrothermal alteration, particularly at temperatures >200 °C. For example, quartz, albite, K-feldspar, chlorite, epidote, calcite, and pyrite are the dominate alteration minerals associated with rhyolite, andesite, and basalt (Browne 1978).

Permeability is a major factor affecting hydrothermal alteration. The process of hydrothermal alteration involves interaction of fluids with minerals. The availability of fluids and contact between minerals and fluids is therefore of central importance. At low permeability and associated with limited availability and flow of hydrothermal fluids, primary minerals and rocks can withstand alteration to high temperatures. In contrast, along fluid flow paths, e.g., along fractures, the mineralogy is commonly dominated by hydrothermal minerals.

Thermal fluid composition can have a major factor on the nature of hydrothermal alteration. An example of this is the low-temperature alteration of basalts. In fluids of meteoric origin with low CO_2 concentrations and at temperatures of 100–150 °C, fluid-basalt interaction leads to alkaline fluid pH, and formation of smectites, zeolites, chlorite, and quartz (Neuhoff et al. 1999), whereas under similar conditions in CO_2-rich fluids, Ca-Mg-Fe carbonates and quartz predominate the alteration mineralogy (Rogers et al. 2006). At higher temperatures (200–300 °C), the alteration mineralogy can be effected by acidity of the fluids. Strong acids, such as HCl and H_2SO_4, commonly originated from magma gases, can cause the pH of the thermal fluid to be low. This results in formation of argillic alteration consisting of sulfates like alunite and gypsum, kaolinite, illite, smectite, quartz, and oxides, whereas the hydrothermal alteration associated with fluids with low magma gas input is dominated by zeolites, chlorite, epidote, prehnite, quartz, sulfides, and carbonates (e.g., Browne 1978; Lonker et al. 1990, 1993). Argillic alteration can also form at the surface of geothermal systems as a result of magma gases, e.g., when associated with volcanic lakes (e.g., Delmelle and Bernard 1994; Africano and Bernard 2000), and due to oxidations of H_2S to sulfuric acid and formation of low-pH surface fluids (e.g., Markússon and Stefánsson 2011).

The duration of hydrothermal alteration can also play a significant role in both extend of alteration and alteration mineralogy. Increased alteration time can be expected to increase the mass of alteration minerals until all the primary minerals have been replaced. Additionally, progressive fluid-rock interaction may lead to changes in the alteration mineralogy. Such an effect has been demonstrated for low-temperature alterations of basalts, where under closed system conditions alteration mineral assemblages reflect time zonation from clays, to chlorites to zeolites as a function of extent of reaction or reaction time (Neuhoff et al. 1999).

Hydrothermal Alteration and Metal Deposits

Hydrothermal alteration often forms hydrothermal metal deposits. The simplest is a vein that forms where a hydrothermal fluid flows through an open fissure and precipitates minerals along the flow path. At great depth many veins occur close to bodies of intrusive igneous rocks because the igneous rocks serve as heat sources that create convectively driven flows in hydrothermal solutions. Hydrothermal deposits formed at shallower depths are commonly referred to as epithermal. Many of the famous silver and gold deposits are epithermal. Among the most distinctive hydrothermal deposits are porphyry copper deposits, which are invariably associated with igneous intrusions, with some deposits containing many billions of tons of ore. Skarn deposits are formed upon high-temperature alteration of limestone or marble. Most skarns are formed adjacent to igneous intrusions and result in formation of minerals like pyroxene, amphibole, and garnet. Volcanic massive sulfide deposits form alteration of volcanic rocks with seawater beneath the sea. These constitute some of the richest deposits of copper, lead, and zinc known.

Summary

Hydrothermal alteration occurs in geothermal systems and involves the replacement of the primary mineral assemblage by alteration minerals. Changes in temperature, pressure, and chemistry of the system usually induce extensive alteration of the host rock. Hydrothermal alteration processes are of great economic interest as they have an important role in the formation of epithermal mineral deposits such as porphyry copper deposits.

Cross-References

- ▶ Geothermal Systems
- ▶ Hypogene
- ▶ Low-Temperature Geochemistry
- ▶ Supergene

References

Africano F, Bernard A (2000) Acid alteration in the fumarolic environment of Usu volcano, Hokkaido, Japan. J Volcanol Geotherm Res 97:475–495

Arnórsson S, Stefánsson A, Bjarnason JÖ (2007) Fluid-fluid interaction in geothermal systems. Rev Mineral Geochem 65:259–312

Browne PRL (1978) Hydrothermal alteration in active geothermal fields. Annu Rev Earth Planet Sci 6:229–248

Delmelle P, Bernard A (1994) Geochemistry, mineralogy and chemical modeling of the acid crater lake of Kawah-Ijen volcano, Indonesia. Geochim Cosmochim Acta 58:2445–2460

Heinrich W (2007) Fluid immiscibility in metamorphic rocks. Rev Mineral Geochem 65:389–430

Kristmannsdóttir H (1979) Alteration of basaltic rocks by hydrothermal activity at 100–300°C. In: Mortland MM, Farmer VC (eds) International clay conference 1978. Elsevier Scientific Publishing Co., Amsterdam, pp 359–367

Lonker SW, Fitzgerald JD, Hedenquist JW, Walshe JL (1990) Mineral-fluid interactions in the Broadlands-Ohaaki geothermal system, New Zealand. Am J Sci 290:995–1068

Lonker SW, Franzson H, Kristmannsdóttir H (1993) Mineral-fluid interaction in the Reykjanes and Svartsengi geothermal system. Am J Sci 293:605–670

Markússon SH, Stefánsson A (2011) Geothermal surface alteration of basalts, Krýsuvík Iceland – alteration mineralogy, water chemistry and the effects of acid supply in the alteration process. J Volcanol Geotherm Res 206:46–59

Neuhoff PS, Fridriksson T, Arnórsson S, Bird DK (1999) Porosity evolution and mineral paragenesis during low-grade metamorphism of basaltic lavas at Teigarhorn, eastern Iceland. Am J Sci 299:467–501

Rogers KL, Neuhoff PS, Pedersen AK, Bird DK (2006) CO_2 metasomatism in a basalt-hosted petroleum reservoir, Nuussuaq, West Greenland. Lithos 92:55–82

Simmons SF, Christenson BW (1994) Origins of calcite in a boiling geothermal system. Am J Sci 294:361–400

Webster JD, Mandeville CW (2007) Fluid immiscibility in volcanic environments. Rev Mineral Geochem 65:313–362

Hydrothermal Solutions

Jean-François Boily
Department of Chemistry, Umeå University, Umeå, SE, Sweden

Definition

An aqueous solution with temperatures exceeding Earth's surface temperature (*hydro* = water, thermal = hot). Hydrothermal solutions originate in Earth's subsurface and carry dissolved minerals, salts, and gases.

Introduction

In Earth Sciences, hydrothermal solutions are predominantly hot briny aqueous solutions present in Earth's subsurface and surface. They exist in meteoric, seawater, (sedimentary) basinal, metaphormic as well as magmatic systems, and are solvents for mineral-building and carbon-bearing species, as well as gases, and often carry high concentrations of sodium chloride. These solutions are key actors to both mass and heat transport in the subsurface, and have formed vast numbers of hydrothermal mineral deposits throughout geological times. The study of hydrothermal solutions is needed to resolve the conditions under which metals ions migrate in hot briny fluids in Earth's crust to form economically valuable mineral deposits, known as hydrothermal ore deposits (Barnes 1997). Another strong motivation for the study of these solutions lies in the possibility that life may have originated in hydrothermal vents (Wächtershäuser 1990).

Hydrothermal solutions can be produced by a variety processes (Fig. 1) in what (Kesler 2005) describes in unconfined and confined systems. Those in unconfined systems are largely contacted with cool brittle rocks at hydrostatic pressures and are in contact with Earth's surface. Examples of solutions include those of meteoric origin or seawater that have seeped to greater depths via fractions or porous media. Hydrothermal vents represent another source of unconfined hydrothermal solutions, and notably include submarine systems along mid-ocean ridges as well as terrestrial systems (e.g., hot springs, fumaroles, geysers). Those in confined systems are not in contact with the surface. These include connate (or formation) waters trapped in sediments, which are involved in diagenetic processes, as well as those associated with hot and ductile rocks in metamorphic and magmatic settings where water can also be produced as a result of mineral (re)crystallization reactions. Hydrothermal

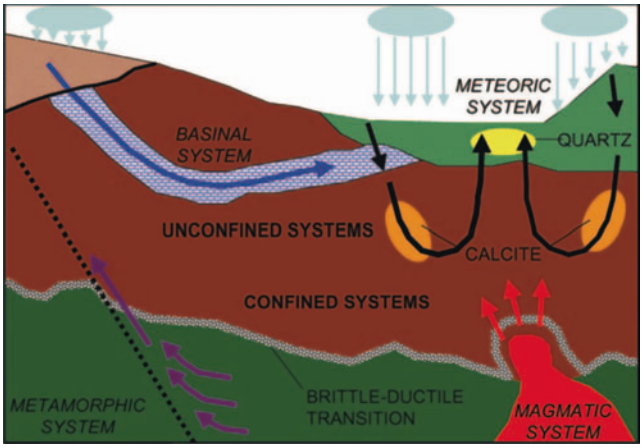

Hydrothermal Solutions, Fig. 1 Schematic representation of hydrothermal systems (Taken from Kessler (2005)

solutions can be directly or indirectly heated by magmas, but also by radioactive decay of host rocks or even frictional heating by faulting of Earth's crust (Stein 2013). Flow of the resulting hot briny aqueous solutions in the subsurface can be driven by gravity, as well as thermal or concentration gradients. As such, hydrothermal solutions can migrate from one geological setting to another, and thus aquire (isotopic) compositions reflecting the rocks and/or external bodies of water with which they have been contacted.

Mineral deposits formed by hydrothermal solutions can be spatially confined in pre-existing pores and fractures or by openings produced by replacement of surrounding rocks. Ore deposition reactions can be triggered by phenomena including, mixing with other fluids, cooling, boiling, loss of pressure, changes in oxygen fugacity, or reactions with host minerals. Deposits can be concentrated as veins in fractured rocks, in pores, disseminated deposits through large volumes of rocks, stratabound deposits in unconsolidated sediments, or even as sorbed on host rock (e.g., invisible gold on sulphide minerals). Deposits of these types as well as fluid inclusions (Roedder 1984) offer a window into the composition of ancient hydrothermal solutions. Modern-day hydrothermal solutions can be studied in hot springs, sedimentary basins, oil fields, and submarine volcanoes. The latter produce chimneys (e.g., black smokers, white smokers) composed of minerals that precipitated as dissolved ions from incoming hydrothermal solutions react with cold seawater.

Comprehensive and historical review-type publications dedicated to hydrothermal solutions in Earth Sciences include those of Palmer et al. (2004), Yardley and Bodnar (2014), and Barnes (2015). In this article, salient physicochemical properties of hydrothermal solutions are presented. This level of knowledge provides the basis upon which geochemical reactions taking place in these fluids can be understood.

Physicochemical Properties of Hydrothermal Solutions

Knowledge of the thermodynamic stability and stoichiometries of aqueous complexes formed in hydrothermal solutions is key to the prediction of the pressure and temperature dependent solubilities of minerals in Earth's subsurface. Most notably, changes in molar volume, polarity, and acidity affect the ability of water at solvating ions and hosting aqueous reactions at various temperatures and pressures. Salient examples of such effects can for example be found in (Palmer et al. 2004) for water (Harvey and Friend 2004; Seward and Driesner 2004), gases (Fernández-Prini et al. 2004), and acids and bases (Tremaine et al. 2004).

The International Association for the Properties of Water and Steam (www.iapws.org) provides, in this regard, pertinent tools for predicting their properties (Wagner and Pruss 2002). The SUPCRT92 code of (Johnson et al. 1992) is a well-known tool in Earth Sciences providing means to estimate the free energies of aqueous species to 1000 °C and 5 kbars using the HKF equations of state (cf. Helgeson and Kirkham 1972, 1974, 1976; Helgeson et al. 1981). At the same time, new experimental and theoretical studies of aqueous speciation and mineral solubility in hydrothermal solutions continuous to advance the field.

The pressure-temperature phase diagram of pure water is characterized by the liquid-vapour curve. This curve denotes the pressure/temperatures pairs at which both liquid and vapour coexist. It ranges from a triple point, where all three phases of water coexist at 273.16 and 611.657 Pa (Bielska et al. 2013; Guildner et al. 1976), to a critical point at 647.096 K and 22.064 MPa. Liquid water is present at pressures above while gaseous water is present at pressures below this curve. Isochores (lines of constant volume) are steeper above the liquid-vapour curve are nearly-vertical because the fluids are nearly imcompressible (Fig. 2). Lines below the curve are, on the other hand, largely horizontal because water vapour is considerably more compressible. Above 373.95 °C solutions become supercritical, such that both liquid and gaseous phases coexist as hydrogen-bonded clusters within a gas-like phase (Wagner and Pruss 1995). These values are however shifted by dissolved salts, such as sodium chloride (Bischoff and Rosenbauer 1988).

Volumetric properties are instrumental to the the study of hydrothermal solutions (Fig. 2). At a thermodynamic level, the total differential of Gibbs free energy (dG)

$$dG = VdP - SdT + \mu dX \quad (1)$$

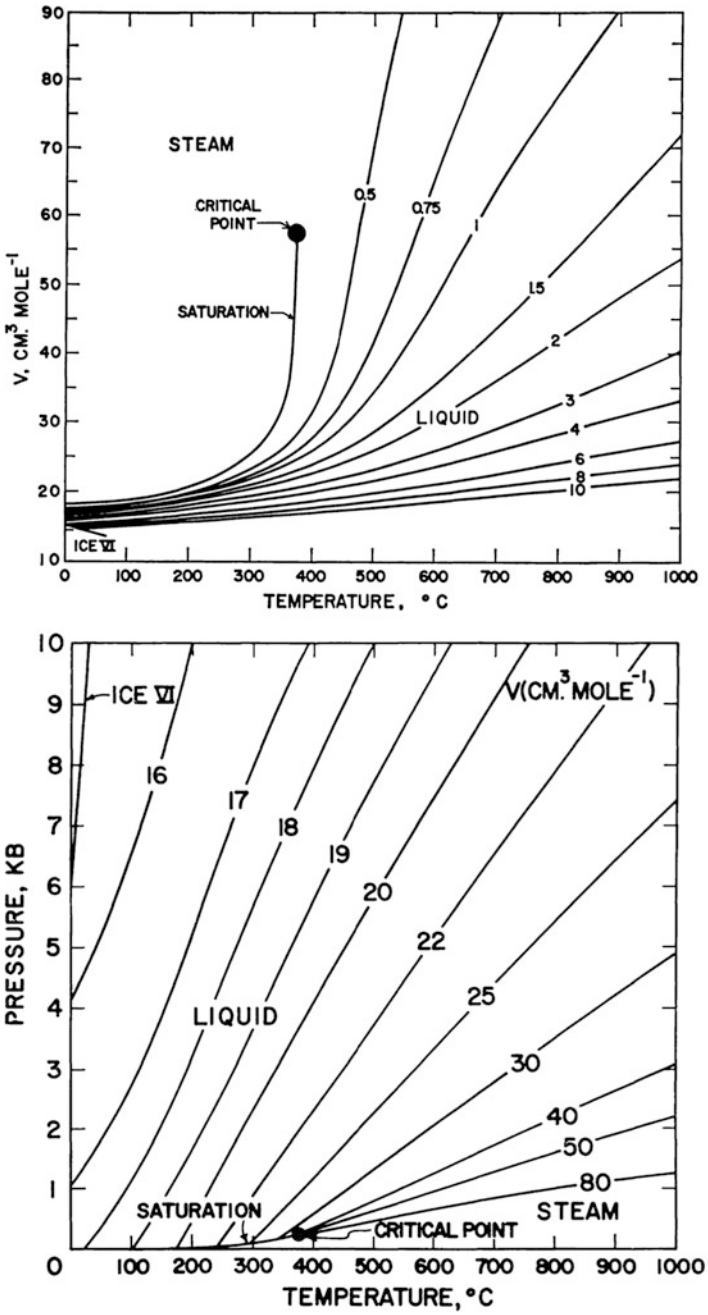

Hydrothermal Solutions, Fig. 2 (**a**) Molal volumes of water as a function of temperature (From Helgeson and Kirkham 1974) (**b**) Molal volumes plotted as isochores. (From Helgeson and Kirkham 1974)

is expressed in terms of the volume (V), entropy (S) and chemical potential of a (μ) system, respectively for gradients in pressure (P), temperature (T) and composition (X). Thus changes in Gibbs free energy as a function of pressure and constant temperature and composition can be derived from volumetric measurements. Yardly and Bodnar (Yardley and Bodnar 2014) provide further details on how enthalpy and entropy have been derived further from such values. Equations are also available for the reliable prediction of density, enthalpy and entropy of water for saturated liquid and vapor (Wagner and Pruss 1993).

The temperature dependence on the dielectric constant (static permittivity) of water (Fig. 3) provides means to understand changes in chemical speciation. For instance, the HKF equation of state expresses solvation contributions to the free energy of the system through Born solvation (ΔG_B):

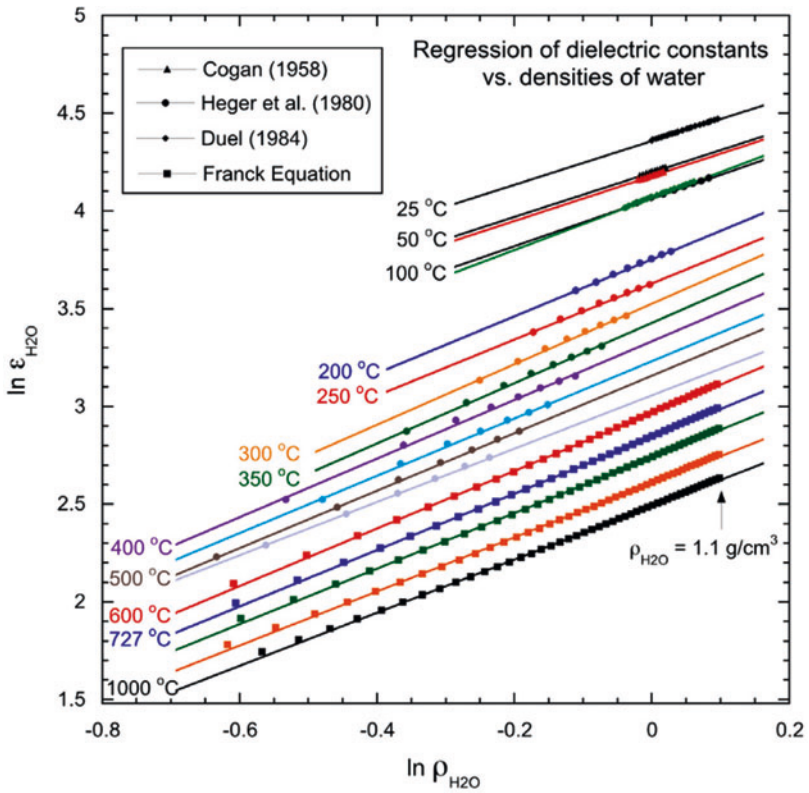

Hydrothermal Solutions, Fig. 3 Relationship between ε and water density (Taken from Sverjensky et al. 2014)

$$\Delta G_B = \omega \frac{1}{\varepsilon} \quad (2)$$

where ω is a species-related parameter. Dielectric constant relates to the dipole moment of the water molecule, and thus to its chemical polarity. The aqueous solutions of high ε consist of polar water molecules with greater abilities to solvate highly charges ions than those of low ε. Because ε is lowered by high temperatures, hydrothermal solutions have the tendency to stabilize species of lower charge than those of at low temperature. This also translates to the stabilization of low-charged aqueous complexes in solutions of low ε (Fig. 3). Recent development in the estimation of ε now allow predictions of speciation to 1200°C and 60 kbars (Pan et al. 2013; Sverjensky et al. 2014). See, for instance, predictions of quartz solubility in *Solubility.*

Finally, temperature- and pressure-induced changes in the self-dissociation of water ($K_w = a_{H^+} \cdot a_{OH^+}$) represent a property of central interest to the study of hydrothermal solutions (Fig. 4), and that is key to the concept of pH. Increasing temperatures facilitate water dissociation, with maximal H^+ and OH^- concentrations achieved at ~249 °C. Above this temperature higher partial molal volumes (lower water densities) work against water self-dissociation by limiting proton transfer reactions via, for instance, Zundel-type clusters ($H_5O_2^+$) (Han et al. 2006). pH neutrality, defined as $-^1/_2 \log K_{w,}$ then becomes strongly temperature- and pressure-dependent.

Summary

Hydrothermal solutions are predominantly hot briny solutions in Earth's subsurface. They can migrate from one geological setting to another as they acquire isotopic and chemical compositions characteristic of the rocks and fluids with which they have been contacted. They are the principle sources of hydrothermal ore deposits that have formed as a result of the precipication of metal ions from hydrothermal solutions, an event that can be triggered by mixing with external bodies of water and/or temperature or pressure changes.

The aqueous speciation of hydrothermal solutions relies upon an understanding of the temperature- and pressure-induced changes in water chemistry. Variations in water partial molal volume, dielectric constant, and ionization constant impact the ability through which water molecules interact with ions and host a range of geochemical reactions.

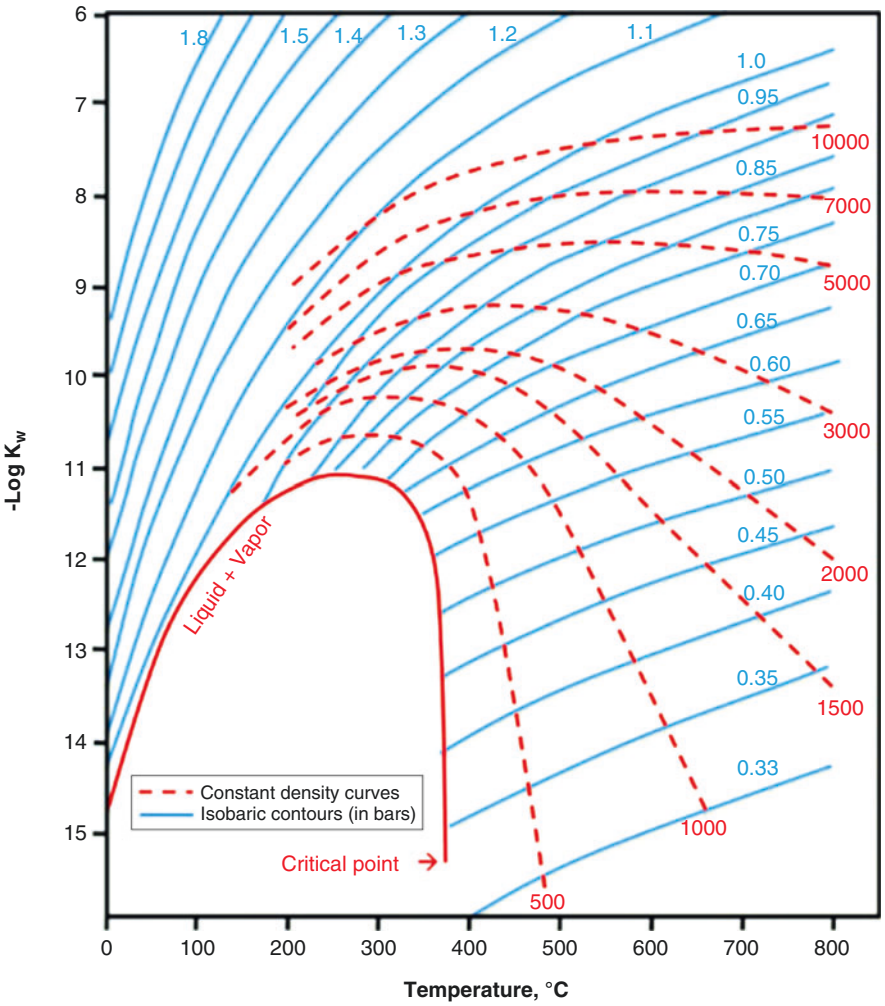

Hydrothermal Solutions, Fig. 4 The pK_w of water with temperature (*absicsa*), pressure (as isochores in *blue*), and density (in *red*) (Taken from Barnes 2015)

Cross-References

- Aqueous Solutions
- Entropy
- Equilibrium
- Fluid–Rock Interaction
- Geochemical Thermodynamics
- Low-Temperature Geochemistry
- Marine Sediment
- Surface Geochemistry
- Volcanic Gases
- Water

References

Barnes HL (1997) Geochemistry of hydrothermal ore deposits. Wiley, New York

Barnes HL (2015) Hydrothermal processes. Geochem Perspect 4:1–92

Bielska K, Havey DK, Scace GE, Lisak D, Harvey AH, Hodges JT (2013) High-accuracy measurements of the vapor pressure if ice references to the triple point. Geophys Res Lett 40:6303–6307

Bischoff JL, Rosenbauer RJ (1988) Liquid-vapor relations in the critical region of the system NaCl-H2O from 380 to 415°C: a refined determination of the critical point and two-phase boundary of seawater. Geochim Cosmochim Acta 52:2121–2126. https://doi.org/10.1016/0016-7037(88)90192-5

Fernández-Prini R, Alvarez JL, Harvey AH (2004) Chapter 3 - aqueous solubility of volatile nonelectrolytes. In: Aqueous systems at elevated temperatures and pressures. Academic Press, London, pp 73–98. https://doi.org/10.1016/B978-012544461-3/50004-1

Guildner LA, Johnson DP, Jones FE (1976) Vapor pressure of water at its triple point. J Res Natl Bur Stand 80A:505–521

Han J, Zhou X, Liu H (2006) Ab initio simulaiton on the mechanism of proton transport in water. J Power Sources 161:1420–1427

Harvey AH, Friend DG (2004) Chapter 1 - physical properties of water. In: Aqueous systems at elevated temperatures and pressures. Academic Press, London, pp 1–27. https://doi.org/10.1016/B978-012544461-3/50002-8

Helgeson HC, Kirkham DH (1972) Theoretical prediction of the thermodynamic behavior of aqueous electrolytes at high pressures and temperatures, I. Summary of the thermodyamic/electrostatic properties of the solvent. Am J Sci 274:1089–1198

Helgeson HC, Kirkham DH (1974) Theoretical prediction of the thermodynamic behavior of aqueous electrolytes at high pressures and temperatures: II. Debye-Hückel parameters for activity coefficients and relative partial molal properties. Am J Sci 274:1199–1261
Helgeson HC, Kirkham DH (1976) Theoretical prediction of the thermodynamic properties of aqueous electrolytes at high pressures and temperatures. III. Equation of state for aqueous species at infinit dilution. Am J Sci 276:97–240
Helgeson HC, Kirkham DH, Flowers GC (1981) Theoretical prediction of the thermodynamic behavior of aqueous-electrolytes at high-pressures and temperatures .4. Calculation of activity-coefficients, osmotic coefficients, and apparent molal and standard and relative partial molal properties to 600-degrees-c and 5 kb. Am J Sci 281:1249–1516
Johnson JW, Oelkers EH, Helgeson HC (1992) SUPCRT92: a software package for calculating the standard molal thermodynamic properties of minerals, gases, aqueous species, and reactions from 1 to 5000 bars and 0 to 1000 °C. Comput Geosci 18:899–947
Kesler SE (2005) Ore-forming fluids. Elements 1:13–18
Palmer DA, Fernández-Prini R, Harvey AH (2004) Aqueous systems at elevated temperatures and pressures. Physical chemistry in water, steam and hydrothermal solutions. Academic Press, London. https://doi.org/10.1016/B978-012544461-3/50000-4
Pan D, Spanu L, Harrison B, Sverjensky DA, Galli G (2013) Dielectric properties of water under extreme conditions and transport of carbonates in the deep earth. Proc Natl Acad Sci U S A 110:6646–6650. https://doi.org/10.1073/pnas.1221581110
Roedder E (1984) Fluid inclusions. Reviews in mineralogy, vol 12. Mineralogical Society of America, Washington, DC
Seward TM, Driesner T (2004) Chapter 5 – hydrothermal solution structure: experiments and computer simulations. In: Palmer DA, Fernández-Prini R, Harvey AH (eds) Aqueous systems at elevated temperatures and pressures. Academic Press, London, pp 149–182. https://doi.org/10.1016/B978-012544461-3/50006-5
Stein CA (2013) Heat flow of the earth. In: Global earth physics. American Geophysical Union, Washington, DC, pp 144–158. https://doi.org/10.1029/RF001p0144
Sverjensky DA, Harrison B, Azzolini D (2014) Water in the deep earth: the dielectric constant and the solubilities of quartz and corundum to 60 kb and 1200 degrees C. Geochim Cosmochim Acta 129:125–145. https://doi.org/10.1016/j.gca.2013.12.019
Tremaine P, Zhang K, Bénézeth P, Xiao C (2004) Chapter 13 - ionization equilibria of acids and bases under hydrothermal conditions. In: Palmer DA, Fernández-Prini R, Harvey AH (eds) Aqueous systems at elevated temperatures and pressures. Academic Press, London, pp 441–492. https://doi.org/10.1016/B978-012544461-3/50014-4
Wächtershäuser G (1990) Evolution of the first metabolic cycles. Proc Natl Acad Sci U S A 87:200–204
Wagner W, Pruss A (1993) International equations for the saturation properties of ordinary water substance – revised according to the international temperature scale of 1990 (vol 16, p 893, 1987). J Phys Chem Ref Data 22:783–787
Wagner W, Pruss A (1995) The IAPWS formulation 1995 for the thermodynamic properties of ordinary water substances for general and scientific use. J Phys Chem Ref Data 31
Wagner W, Pruss A (2002) The IAPWS formulation 1995 for the thermodynamic properties of ordinary water substance for general and scientific use. J Phys Chem Ref Data 31:387–535
Yardley BW, Bodnar RJ (2014) Fluids in the continental crust. Geochem Perspect 3:1–127

Hydrothermal Vents

Wolfgang Bach[1] and Eoghan P. Reeves[2]
[1]Department of Geosciences and MARUM Center for Marine Environmental Research, University of Bremen, Bremen, Germany
[2]Department of Earth Science and Centre for Geobiology, University of Bergen, Bergen, Norway

Definition

Hydrothermal vents are seafloor expressions of seawater circulation within the oceanic crust. Seafloor venting is driven by buoyancy of warm seawater-derived fluids that have mined heat and solutes from the basement rock. Temperatures and compositions of these fluids vary drastically, depending on the proximity of the heat source, basement composition, and local hydrological constraints. The venting of hydrothermal fluids is commonly associated with the deposition of hydrothermal precipitates, including sulfides, sulfates, carbonates, oxides, and hydroxides. In seafloor massive sulfide mounds, accumulation of these precipitates reaches extents that make them potentially economical for mining activities. Hydrothermal vent sites are also oases for life in a deep ocean otherwise mostly barren of macrofauna. Diverse and rich ecosystems can develop around areas of venting, and chemosynthetic microorganisms accomplish the primary production of biomass by converting geochemical energy and hydrothermal inorganic precursor compounds into biomolecules.

Introduction

Submarine venting of fluids occurs abundantly in different seafloor settings (Fig. 1). Along a global system of submarine spreading centers, new oceanic lithosphere continuously forms and exchanges heat and matter with the overlying oceans. Hydrothermal fluids – typified by mineral-rich "black smoker" venting – emanating from the axes of the spreading centers are spectacular manifestations of this interaction. These vent fields are typically tens to hundreds of meters in diameter, often containing multi-spire mounds. They have power outputs between 0.1 and 3.8 GW, and they occur at a frequency of 1–4 fields per 100 km length of spreading ridge (e.g., Baker 2007). Along 55,000 km of mid-ocean ridges (MORs) and 11,000 km of backarc spreading centers – of which only about one third have been explored (many cursorily) for hydrothermal activity – at least 1,300 ± 600 vent fields are predicted to occur

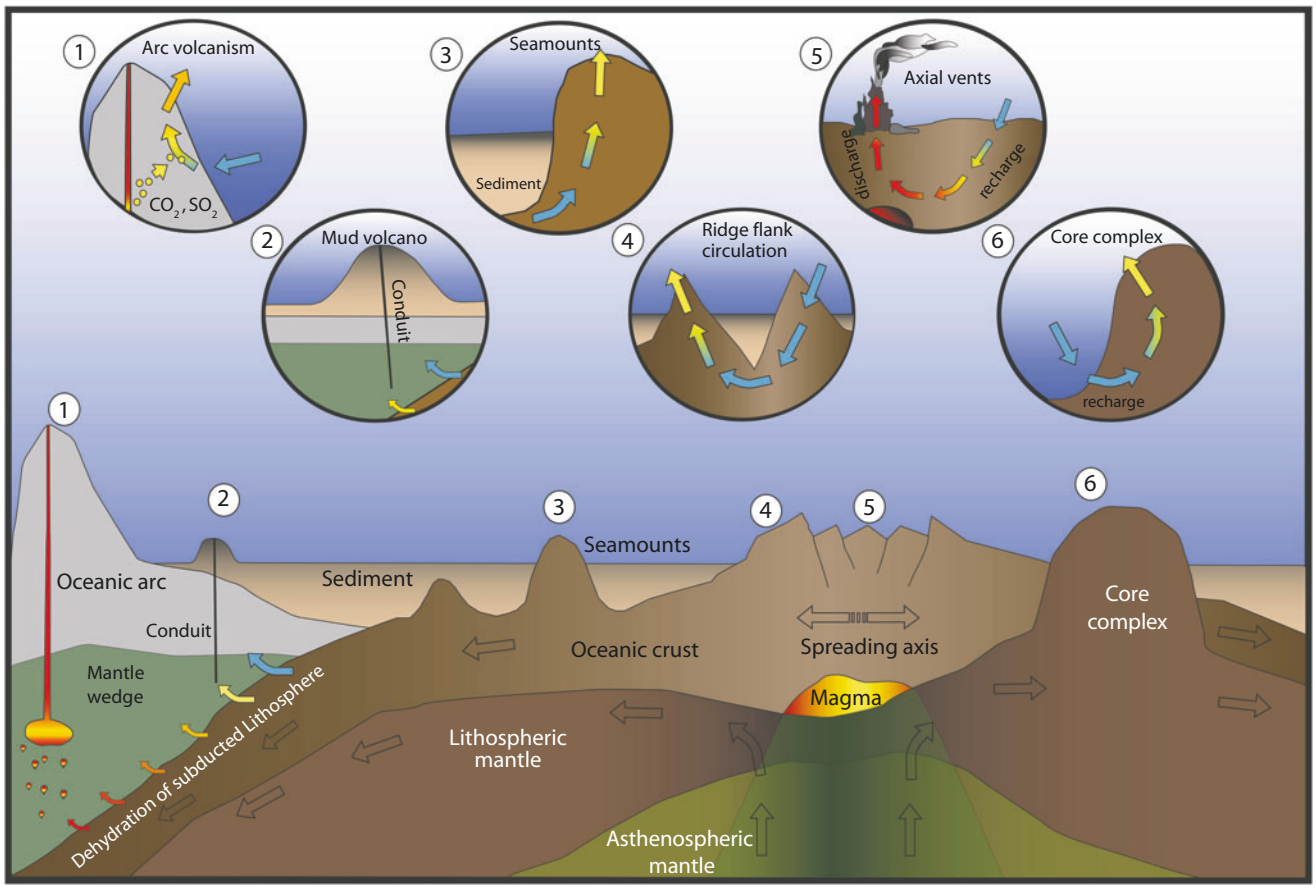

Hydrothermal Vents, Fig. 1 Overview of the different types of hydrothermal venting in the oceans

(Beaulieu et al. 2015). Additional hydrothermal venting can be found along 7,000 km of intraoceanic volcanic arcs (e.g., de Ronde and Stucker 2015). On the order of 1 TW of heat are mined from the oceanic crust by high-temperature (200–400 °C) hydrothermal venting. The size of vent fields, the structure and composition of the vent deposits, and the chemistries of the vent fluids are all highly variable. The type of basement rocks, the distribution of permeability, and the size and longevity of the heat source are just some of the key factors controlling this variability. Slow-spreading MORs (<40 mm/year full rate) tend to host vent fields with higher heat fluxes and larger mineral deposits than their faster-spreading counterparts due to long-lived large-scale tectonic faults (allowing persistent fluid flow) (Wilcock and Delaney 1996; Baker 2007). Fast-spreading MORs (80–160 mm/year full rate) typically tend to host smaller sulfide deposits due to more frequent diking-eruptive events and continuous off-axis migration of deposits.

Seawater descends into the oceanic crust in *recharge zones*, which are spatially not well constrained but can be away from or immediately surrounding the spreading axis. Circulating seawater separates into two fluids with contrasting contents of dissolved gases and ions when it is heated to high temperatures several kilometers beneath the seafloor and encounters the two-phase boundary (critical curve). This leads to a general observation that high-temperature hydrothermal vents show strongly variable salinities. Reaching peak temperatures near ~450 °C or higher in some cases, the seawater-derived fluids leach metals and sulfide from the basement rock in the *root zones* of the hydrothermal vents. They become buoyant and rise up to the seafloor in narrow, pipe-like structures called hydrothermal *upflow zones*. The development of these upflow zones is variably controlled by magmatic diking and tectonic faulting. Cold seawater is typically entrained and heated in the periphery of these zones. Ca-sulfate (anhydrite) precipitates from this heated seawater, however, and can partially isolate the high-temperature upwelling hydrothermal fluids from dilution with this entrained seawater. Entrainment of seawater would cool and oxidize the hydrothermal fluids upon mixing, which would result in metal precipitation in the form of sulfides and oxides. This fluid mixing invariably occurs to some extent, leading to cooler, diffuse fluid seepage at the seafloor on the periphery of the high-temperature vent structures or mounds, which funnel the focused discharge of

hydrothermal fluids. These structures form forests of "chimney" complexes that consist of sulfide, sulfate, and oxide minerals. More than 160 occurrences of seafloor massive sulfide accumulations associated with active hydrothermal vent fields are known, and the abundance of related metal ore has been estimated at 600 million tonnes (Hannington et al. 2011). A sizeable fraction of the metals dissolved in vent fluids are conveyed to hydrothermal plumes in the water column, with important ramifications for the oceanic budget of biogeochemically critical trace metals, such as the nutrient Fe (e.g., Resing et al. 2015).

While the majority of hydrothermal vents are acidic, venting of highly alkaline waters has been documented in the Lost City Hydrothermal Field, 30 km west of the Mid-Atlantic Ridge spreading axis at 30 °N (Kelley et al. 2001). These systems are related to exhumation of mantle rocks in oceanic core complexes. Up to 60-m tall carbonate-hydroxide chimneys vent 40–90 °C solutions that are poor in transition metals and dissolved sulfide and consequently do not precipitate sulfide minerals. Even farther off-axis, in the flanks of MORs, abundant hydrothermal circulation of seawater is evident from heat flow constraints. Few occurrences of low-temperature venting off-axis have been discovered to date (e.g., Wheat and Fisher 2008), however, in part due to their chemical and temperature signals in the water column being much more difficult to detect. These vent fluids likely have compositions similar to seawater but play an important role in global ocean-crust exchange, as the heat and solute flux is much greater than in axial hydrothermal systems.

Water-Rock Interactions

Interactions between rocks that make up the oceanic basement and seawater that circulates within the basement are important in setting the chemical and isotopic composition of the oceans. Along its flow path, the circulating seawater experiences major compositional modifications and isotopic exchange with the crust. These changes include a loss of Mg^{2+} and Na^{+} from the seawater-derived fluid, which then acquires Ca^{2+} and $SiO_{2(aq)}$ from the crust. The release of Ca and silica to the oceans is an important source of these elements, which are used by marine algae (coccolithophores and diatoms) to build calcium carbonate and opal tests. Because these algae fix a large amount of atmospheric CO_2, water-rock interactions within the oceanic crust therefore play a key role in the global carbon cycle. The full details of these interactions are quite complex, but simplified reactions, such as that which occurs when the main mineral constituents of basalt react with seawater to form the secondary minerals chlorite and quartz, exemplify some of the basics of these exchange processes:

$$\underset{\text{Plagioclase}}{CaAl_2Si_2O_8} + \underset{\text{Clinopyroxene}}{CaMgSi_2O_6} + 4Mg^{2+} + 6H_2O \rightarrow \underset{\text{Chlorite}}{Mg_5Al_2Si_3O_{10}(OH)_8} + \underset{\text{Quartz}}{SiO_2} + 2Ca^{2+} + 4H^{+}$$

Many of these reactions, especially those responsible for Mg^{2+} loss and acidity production, are common to many different basement compositions, from ultramafic to felsic rock. Since these reactions create acidity at elevated temperatures, hydrothermal fluids can dissolve large quantities of metals into solution. The composition of the fluids at the deepest part of the hydrothermal circulation cells is controlled (buffered) by secondary minerals that form in the course of fluid-rock interactions in these root zones (e.g., Seyfried et al. 1991). This takes place because silicate, oxide, and sulfide phases in the hydrothermally altered rocks have specific solubilities with respect to metals like Cu, Zn, Fe, and Mn, as well as other components. Specific assemblages of secondary minerals form depending on the pressure-temperature conditions in the root zone, the composition of rocks in that zone, and the mass flux of seawater through the system. It has been shown that ultramafic rock, common at slow-spreading MORs, forms mineral assemblages that are notably distinct from those that form in basaltic rock. Hydrothermal vents hosted in ultramafic rocks hence discharge fluids with systematically higher dissolved H_2 and CH_4, while H_2S and SiO_2 are lower in concentration. In addition, ultramafic rock-hosted systems may be strongly alkaline, if temperatures in the root zone do not exceed about 250 °C. Alkaline fluid venting in the oceans is known from ultramafic settings in MORs and from serpentine mud volcanoes in fore-arc settings. Arc and backarc hydrothermal vents, in contrast, are often more acidic and much less reducing (i.e., have low contents of dissolved H_2). These vents are often affected by very different styles of magma degassing (see below) in addition to common water-rock reactions such as the reaction above. The compositional spectrum of vent fluids in these different settings continues to grow as exploration of deep-sea vents continues. Recent discoveries include vents with liquid sulfur and carbon dioxide, some of which are extremely acidic (summarized in de Ronde and Stucker 2015). Arc and backarc rocks are enriched in elements that are removed from the dewatering subducting oceanic crust. These elements include B, Ba, As, Sb, Ag, Au, etc., which are strongly enriched in arc/backarc hydrothermal vents relative to vents at MORs (e.g., German and Seyfried 2014).

Magma Degassing

Many hydrothermal vent systems on ocean ridges are hosted in mid-ocean ridge basalt (MORB). The mafic magma responsible for MORB typically releases volatile mantle components such as CO_2 and primordial ^3He, plus trace amounts

of N_2 and water, during crustal formation. These species are degassed and entrained in circulating hydrothermal fluids to be vented at the seafloor. They tend to be relatively inert, however, since the only reactive components (CO_2 and N_2) are mostly stable at the acidic pH values and conditions encountered by many hydrothermal fluids. Volatile species are continuously degassed to varying degrees during steady-state hydrothermal circulation around magmatic intrusions, but their abundances in hydrothermal fluids increase drastically during diking-eruptive events. Rapid increases in dissolved CO_2 as well as hydrothermal fluid temperatures, for example, can often indicate some magmatic activity has taken place recently or is currently ongoing.

In contrast to MOR settings, chemical compositions of hydrothermal vents hosted in convergent margin settings (submarine arc/backarc volcanoes) can be profoundly influenced by the different magmatic volatiles degassed there. The presence of extensive slab-derived water (released during partial melting of subducting crust) dramatically changes the melting dynamics in the arc/backarc mantle wedge, leading to more oxidizing, H_2O- and silica-rich melts that degas water- and CO_2-rich fluids containing abundant acidity-generating volatiles (primarily sulfur dioxide (SO_2), HF, and HCl acids). SO_2 reacts with water to create abundant sulfuric acid (H_2SO_4) and often elemental sulfur. These "acid-sulfate" magmatic fluids either vent directly on the seafloor (resembling terrestrial "solfatara" fumaroles) or are entrained into circulating hydrothermal fluids (e.g., Seewald et al. 2015). The strong acidity of these fluids leads to dramatically different styles of crustal alteration than in MOR settings, and has implications for greatly increased metal leaching and transport, and potentially richer ore deposit formation.

Carbon Cycling

Inorganic CO_2 derived from magma degassing is typically the dominant form of carbon in hydrothermal fluids. Although organic carbon is a less abundant dissolved constituent, organic carbon cycling in these settings is complex and an active area of research. As early as the discovery of deep-sea hydrothermal vents in 1977, links were drawn between the physico-chemical conditions of these fluids and their suitability for the formation of organic molecules necessary for early microbial life to emerge (Corliss et al. 1981). Strongly reducing (H_2-rich) fluids, in theory, energetically favor the reduction of CO_2 to organic molecules such as hydrocarbons and other classes of compounds, aided kinetically by mineral catalysts in reactions that mirror the industrial Fischer-Tropsch synthesis. Research in the last decade, however, has discovered only limited evidence for complex organic molecules formed from CO_2 during fluid circulation. Major problems with identifying truly abiotic organic compounds (formed without any biological involvement) include their often trace abundance and the widespread and diverse plethora of organic molecules derived from numerous biological organic materials (McCollom and Seewald 2007). The latter include microbial biomass, vent organisms, or background deep ocean organic carbon sources such as particulate or dissolved organic carbon. The effectiveness of hydrothermal vent fluids in decomposing complex organic matter to a range of organic compounds is best illustrated in the sedimented Guaymas Basin hydrothermal system. There, the ridge axis has been continuously buried with organic-rich pelagic sediment. Magmatic dike and sill intrusions directly into the sediment overburden lead to hydrothermal petroleum formation (both oil and dissolved natural gas) on timescales as short as a few thousand years (Peter et al. 1991), in contrast to the Myr timescales of formation in slowly subsiding sedimentary basins.

The abundance of reduced components (H_2, CH_4, H_2S, Fe^{2+}, Mn^{2+}) in hydrothermal fluids allows diverse chemosynthesis-based ecosystems to develop around hydrothermal vent structures and sites of fluid release, as well as in the hydrothermally heated aquifer within oceanic layer 2A. The base of the food web in this environment is CO_2 fixation by chemosynthetic microorganisms that enzymatically catalyze the oxidation of the reduced solutes (H_2S commonly) in vent fluid and use the energy yields from these redox reactions to produce cellular matter. Microbial carbon fixation is an important component of carbon cycling within hydrothermal vent systems and differs between active and inactive sulfide chimney structures (Reeves et al. 2014). There also appear to be drastic differences in the quantities of available geochemical energy for various metabolic reactions between vents in different ridge and backarc settings, a direct consequence of the diverse types of fluid chemical compositions possible in these environments (Amend et al. 2011).

Summary and Conclusions

Submarine hydrothermal vents occur abundantly along oceanic spreading centers and intraoceanic arcs. They are sites of great geochemical diversity due to varying substrate composition, magma degassing, permeability structure, and subseafloor entrainment of seawater. Metal accumulations in related massive sulfide deposits, as well as rich and diverse chemosynthesis-based ecosystems, continue to make these systems targets for multi- and cross-disciplinary research. Hydrothermal vents directly and vividly illuminate the linkages between plate tectonics and life, and with roughly two thirds of global hydrothermal vents yet to be explored, many exciting discoveries remain to be made.

Cross-References

- Carbon Cycle
- Earth's Oceanic Crust
- Hydrothermal Alteration
- Hydrothermal Solutions
- Mid-Ocean Ridge Basalts (MORB)
- Ocean Biochemical Cycling and Trace Elements
- Ore Deposits
- Organic Geochemistry
- Subduction Zone Geochemistry
- Volcanic Gases

References

Amend JP, McCollom TM, Hentscher M, Bach W (2011) Metabolic energy for chemolithoautotrophs in peridotite-hosted and basalt-hosted hydrothermal systems. Geochim Cosmochim Acta 75:5736–5748

Baker ET (2007) Hydrothermal cooling of mid-ocean ridge axes: do measured and modeled heat fluxes agree? Earth Planet Sci Lett 263:140–150

Beaulieu S, Baker ET, German CR (2015) Where are the undiscovered hydrothermal vents on oceanic spreading ridges? Deep-Sea Res II 121:202–212

Corliss JB, Baros JA, Hoffman SE (1981) An hypothesis concerning the relationship between submarine hot springs and the origin of life on Earth: Proceedings, 26th International Geological Congress, Geology of Oceans Symposium, Paris, July 7–17. Oceanol Acta 4: 59–69

de Ronde CEJ, Stucker VK (2015) Seafloor hydrothermal venting at volcanic arcs and backarcs. In: Sigurdsson H, Houghton B, McNutt S, Rymer H, Stix J (eds) The encyclopedia of volcanoes. Elsevier. https://doi.org/10.1016/B978-0-12-385938-900047-X

German CR, Seyfried WE (2014) Hydrothermal processes. Treatise on geochemistry, vol 8, 2nd edn. Elsevier, pp 191–233. ISBN 9780080983004

Hannington MD, Jamieson J, Monecke T, Petersen S, Beaulieu S (2011) The abundance of seafloor massive sulfide deposits. Geology 39:1155–1158

Kelley DS, Karson JA, Blackman DK, Früh-Green GL, Butterfield DA, Lilley MD, Olson EJ, Schrenk MO, Roe KK, Lebon GT, Rivizzigno P, AT3-60 Shipboard Party (2001) An off-axis hydrothermal vent field near the Mid-Atlantic Ridge at 30°N. Nature 412:145–149

McCollom TM, Seewald JS (2007) Abiotic synthesis of organic compounds in deep-sea hydrothermal environments. Chem Rev 107:382–401

Peter JM, Peltonen P, Scott SD, Simoneit BRT, Kawka OE (1991) ^{14}C ages of hydrothermal petroleum and carbonate in Guaymas Basin, Gulf of California: implications for oil generation, expulsion, and migration. Geology 19:253

Reeves EP, Yoshinaga MY, Pjevac P, Goldenstein NI, Meyerdierks A, Amann R, Bach W, Hinrichs K-U (2014) Microbial lipids reveal carbon assimilation patterns on hydrothermal sulfide chimneys. Environ Microbiol 16:3515–3532. https://doi.org/10.1111/1462-2920.12525

Resing JA, Sedwick PN, German GR, Jenkins WJ, Moffett JW, Sohst BM, Tagliabue A (2015) Basin-scale transport of hydrothermal dissolved metals across the South Pacific Ocean. Nature 523:200–203

Seewald JS, Reeves EP, Bach W, Saccocia PJ, Craddock PR, Shanks WCI, Sylva SP, Pichler P, Rosner M, Walsh E (2015) Submarine venting of magmatic volatiles in the eastern Manus Basin, Papua New Guinea. Geochim Cosmochim Acta 163:187–199

Seyfried WE, Ding K, Berndt ME (1991) Phase equilibria constraints on the chemistry of hot spring fluids at mid-ocean ridges. Geochim Cosmochim Acta 55:3559–3580

Wheat CG, Fisher AT (2008) Massive, low-temperature hydrothermal flow from a basaltic outcrop on 23 ma seafloor of the Cocos plate: chemical constraints and implications. Geochem Geophys Geosyst 9:Q12O14. https://doi.org/10.1029/2008GC002136

Wilcock WSD, Delaney JR (1996) Mid-ocean ridge sulfide deposits: evidence for heat extraction from magma chambers or cracking fronts? Earth Planet Sci Lett 145:49–65

Hypogene

Barbara I. Kleine and Andri Stefánsson
Institute of Earth Sciences, University of Iceland, Reykjavík, Iceland

Definition

The term *hypogene* is mainly used in the field of ore geology. It describes mineralization within and below the Earth's crust that is caused by ascending thermal fluids which derive from a magmatic source. Hypogene also often refers to primary, unaltered ore that formed directly from thermal aqueous solutions that derived from great depths (e.g., Ague and Brimhall 1989; Webb and Rowston 1995; Rakovan 2003). On the contrary the term *supergene* describes mineralization caused by descending fluids close to the Earth's surface and is usually associated with weathering and alteration of the primary mineral assemblage (e.g., Ague and Brimhall 1989; Webb and Rowston 1995; Robb 2013). A variety of the ore-forming minerals formed by hypogene processes are of great economic interest. These are usually associated with porphyry ore and volcanogenic massive sulfide (VMS) deposits (e.g., Galley and Koski 1999; Seedorff et al. 2005).

Origin of the Thermal Fluid

The thermal fluids that lead to the formation of hypogene mineral deposits originate from within a body of magma. For the formation of significant amount of fluids, extensive magmatic volatile exsolution needs to occur within the magma chamber. For the formation of large ore deposits, sufficient amounts of metals need to be washed out from the magmatic sulfides and liquid by the fluids and gathered under the roof of the magma chamber prior the fluid ascends (Candela and

Piccoli 2005). Thereby, the bulk composition and the water content of the magma play an important role on which chemical components will be contained in the resulting thermal fluid. For large mineral deposits of economic value, depth, geometry of magma chamber roof, and homogeneity of the magma chamber, i.e., appearance of convection, are additional crucial criteria for the enrichment of certain metals and other rare elements in the fluid (e.g., Dilles 1987; Cline 1995; Shinohara and Hedenquist 1997). Thermal fluids that derive from a magmatic source commonly carry significant amounts of volatiles such as CO_2. Other chemical components include sulfur and a variety of other major chemical components such as chlorine, sodium, calcium, magnesium, and potassium as well as iron, manganese, copper, zinc, and lead (e.g., Robb 2013). These components may derive from the magmatic source and/or were leached from the surrounding rocks while the fluid was ascending through Earth's crust.

The driving force behind the ascend of the fluids is provided by the heat of the magma at great depth and fluid density. Due to their low density, the fluids can easily transport upward in the crust. Large hypogene mineral deposits commonly form where fluid flow becomes additionally structurally focused, e.g., along shear and fault zones (e.g., Ague 2003).

Formation of Hypogene Mineral Deposits

Minerals that precipitate directly out of the ascending thermal fluid are called primary or hypogene minerals. In contrast to secondary, or supergene minerals, the hypogene minerals have not undergone any alteration caused by descending fluids. The formation of hypogene mineral deposits out of a thermal fluid is dependent on numerous factors such as temperature, pressure, phase separation, fluid-rock reactions, and adsorption (e.g., Robb 2013). Already small changes in one or more of these parameters may lead to mineral precipitation out of the fluid phase. In particular, a decrease in temperature would lead to precipitation of metals from the solution as the solubility of metal-ligand complexes is highly dependent on temperature (Seward and Barnes 1997). The infiltration of magmatic-thermal fluids usually causes significant hydrothermal alteration of the surrounding rock. A characteristic alteration feature of, e.g., hypogene ore deposits within large porphyry ore deposits is distinct potassium alteration of the host rock caused by the infiltration of magmatic-thermal fluids (e.g., Seedorff et al. 2005). The deposition of hypogene minerals usually occurs at several stages throughout the thermal history of the magmatic-thermal fluid. At moderate temperature in the early beginning of magma emplacement and fluid ascending minerals such as quartz and pyrite may precipitate out of the fluid. As the magma chamber grows, eventually more thermal fluids will be released. The temperature above the magma body will increase, and other minerals such as pyrrhotite and chalcopyrite will start to precipitate out of the fluid phase and replace the already existing ones. Further, with the cooling of the magmatic body, minerals will precipitate out of the fluids that are more stable at lower temperatures. Therefore, it is likely that hypogene minerals may be overprinted by several fluid and thermal events throughout the formation of the mineral deposit. The parageneses of hypogene mineral deposits are usually further complicated by recrystallization and replacement during post-hydrothermal metamorphism.

Occurrence of Hypogene Mineral Deposits

Hypogene processes play an important role in the formation of porphyry, orogenic Au deposits and volcanogenic massive sulfide (VMS) deposits. These hypogene minerals (e.g., pyrite, ore-hosting quartz, chalcopyrite, sphalerite, galena) that precipitated out of the ascending thermal fluid commonly occur at the base of the large mineral deposits. Porphyry deposits are nonferrous metallic mineral resources and are characterized by sulfides and oxides within veinlets enveloped by hydrothermally altered rocks. Non-altered, hypogene minerals that can host significant amounts of copper, molybdenum, gold and tungsten occur in the deepest parts of the porphyry deposits just above a commonly intermediate to silicic magma chamber (e.g., Seedorff et al. 2005). The thermal fluids originate directly from the magma, and deposition of hypogene ore is usually associated with potassic alteration of the host rock (e.g. Ulrich et al. 2001). Biotite bearing and sugary quartz veinlets and quartz veins containing molybdenite are the most common vein types that form from the cooling thermal fluid (e.g., Grant et al. 1980; Carten et al. 1988; Proffett 2003). Orogenic Au deposits usually form by the ascending of metamorphic fluids that there released during prograde devolatilization reactions of subducted material (e.g., Goldfarb et al. 2005). However, the source of fluids and metals as part of gold-forming processes in orogenic Au deposits located proximal to magmatic intrusions has been highly debated in the past years (e.g., Goldfarb et al. 1997; Cassidy et al. 1998; Bouchot et al. 2000). There is evidence that many of these gold deposits in metamorphic rocks are products of magmatic exsolution (e.g., Goldfarb et al. 1997; Haeberlin et al. 2004) and ascending magmatic-thermal fluids and the process of mineral precipitation could be classified as hypogene. The ancient VMS deposit at Bald Mountain (Slack et al. 2003) illustrates a complex hypogene mineral deposit pattern. During an initial stage at moderate temperatures, the minerals pyrite, marcasite, sphalerite, and quartz precipitated out of an ascending magmatic-thermal fluid. These hypogene minerals were subsequently replaced by pyrrhotite and

chalcopyrite as temperatures increased. This stage was followed by a phase of mineral precipitation in veins that crosscut the pyrrhotite and chalcopyrite deposit (Slack et al. 2003).

Summary

Hypogene processes are crucial for the formation of large mineral deposits therefore achieve high attention in the research fields of economic ore geology. However, hypogene minerals are usually overprinted by post-hydrothermal metamorphic or fluid events which makes it often difficult to determine the primary mineral assemblage and to unravel the complex fluid history of these mineral deposits.

Cross-References

- ▶ Geothermal Systems
- ▶ Hydrothermal Alteration
- ▶ Supergene

References

Ague JJ (2003) Fluid flow in the deep crust. Treatise Geochem 3, 195–228

Ague JJ, Brimhall, GH (1989) Geochemical modeling of steady state fluid flow and chemical reaction during supergene enrichment of porphyry copper deposits. Econ Geol 84:506–528

Bouchot V, Milési J, Ledru P (2000) Crustal-scale hydrothermal palaeofield and related Variscan Au, Sb, W orogenic deposits at 310–305 Ma (French Massif Central, Variscan belt). SGA News 10:6–12

Candela P, Piccoli P. (2005) Magmatic processes in the development of porphyry-type ore systems. Econ Geol 100:25–37

Carten RB, Geraghty EP, Walker BM, Shannon JR (1988) Cyclic development of igneous features and their relationship to high-temperature hydrothermal features in the Henderson porphyry molybdenum deposit, Colorado. Econ Geol 83:266–296

Cassidy KF, Groves, DI, McNaughton NJ (1998) Late-Archean granitoid-hosted lode-gold deposits, Yilgarn Craton, Western Australia: deposit characteristics, crustal architecture and implications for ore genesis. Ore Geol Rev 13:65–102

Cline J (1995) Genesis of porphyry copper deposits: the behavior of water, chloride, and copper in crystallizing melts. Ariz Geol Soc Dig 20:69–82

Dilles JH (1987) Petrology of the Yerington Batholith, Nevada; evidence for evolution of porphyry copper ore fluids. Econ Geol 82: 1750–1789

Galley AG, Koski R (1999) Setting and characteristics of ophiolite-hosted volcanogenic massive sulfide deposits. Rev Econ Geol 8: 221–246

Goldfarb R, Miller L, Leach D, Snee L (1997) Gold deposits in metamorphic rocks of Alaska. Mineral Deposits Alaska: Econ Geol Monogr 9:151–190

Goldfarb RJ, Baker T, Dube B, Groves DI, Hart CJ, Gosselin P (2005) Distribution, character, and genesis of gold deposits in metamorphic terranes. Econ Geol 100th anniversary 40:407–450

Grant JN, Halls C, Sheppard, SM, Avila W. (1980) Evolution of the porphyry tin deposits of Bolivia. Mining Geol Spec 8:151–173

Haeberlin Y, Moritz R, Fontboté L, Cosca M. (2004) Carboniferous orogenic gold deposits at Pataz, Eastern Andean Cordillera, Peru: geological and structural framework, paragenesis, alteration, and 40Ar/39Ar geochronology. Econ Geol 99:73–112

Proffett JM (2003) Geology of the Bajo de la Alumbrera porphyry copper-gold deposit, Argentina. Econ Geol 98:1535–1574

Rakovan J (2003) A word to the wise: hypogene & supergene. Rocks Miner 78:419–419

Robb L (2013) Introduction to ore-forming processes. Wiley, New York

Seedorff E, Dilles J, Proffett J, Einaudi M, Zurcher L, Stavast W, Johnson D, Barton M (2005) Porphyry deposits: characteristics and origin of hypogene features. Econ Geol 100th anniversary volume 29:251–298

Seward T, Barnes H (1997) Metal transport by hydrothermal ore fluids. Geochem Hydrothermal Ore Deposits 3:435–486

Shinohara H, Hedenquist J (1997) Constraints on magma degassing beneath the Far Southeast porphyry Cu–Au deposit, Philippines. J Petrol 38:1741–1752

Slack J, Foose M, Flohr M, Scully, M, Belkin H (2003) Exhalative and subseafloor replacement processes in the formation of the Bald Mountain massive sulfide deposit, northern Maine. Econ Geol Monogr 11:513–547

Ulrich T, Günther D, Heinrich CA (2001) The evolution of a porphyry Cu-Au deposit, based on LA-ICP-MS analysis of fluid inclusions: Bajo de la Alumbrera, Argentina. Econ Geol 96:1743–1774

Webb M, Rowston P (1995) The geophysics of the Ernest Henry Cu-Au deposit (NW) Qld. Explor Geophys 26:51–59

Incompatible Elements

Catherine Chauvel
ISTerre, University Grenoble Alpes, CNRS, Grenoble, France

Definition

The term "incompatible elements" has been introduced in igneous geochemistry to define trace elements that cannot easily substitute into the major element sites in igneous minerals either because of their large ionic radius or because of their high ionic charge. In contrast, compatible elements are those that enter easily the major element sites.

Use of Incompatible Elements in Geochemistry

When a magma crystallizes, the incompatible elements preferentially remain in the liquid, and when a solid such as mantle peridotite melts, they enter the liquid phase as soon as possible. While this definition is quite broad, the extent to which elements are enriched or depleted into the liquid magmatic phase is easily quantified using the concepts and equations of Gast (1968) and Shaw (1970). The partitioning of elements between a solid and a liquid phase is defined as:

$$K_{elt}^{min/liq} = \frac{C_{elt}^{min}}{C_{elt}^{liq}}$$

where *min* corresponds to mineral, *liq* to liquid, *elt* to element, and *C* to concentration (Fig. 1).

Of course, during partial melting or fractional crystallization, several mineral phases are usually involved, and the overall behavior of the element is governed by the distribution coefficient D that is defined as:

$$D_{elt}^{sol/liq} = \sum_{min} m_{min} K_{elt}^{min/liq}$$

with *sol* the total solid and *m* the mass fraction of the various minerals.

In principle, a trace element can both be incompatible when it does not fit into the mineral assemblage that crystallizes and compatible when the crystallizing assemblage has a different composition. In practice, the term is now used in a looser way, and it only refers to the behavior of a given element during mantle melting.

The enrichment of incompatible elements in the liquid phase is primarily controlled by two parameters, the distribution coefficient *D* and the degree of partial melting *F*. The maximum enrichment is found when both *D* and *F* are small, and it decreases when either *D* or *F* increases following the general relationship that describes the simplest melting equation, the equilibrium batch melting equation:

$$C_{elt}^{liq} = \frac{C_{elt}^{source}}{D^{sol/liq}(1-F)+F}$$

with *C* the concentration of the element of interest. The batch melting equation given above is a simple and easy-to-use model, but it does not necessarily describe the geological reality of melting processes. For further detail, I refer the reader to the original publications of Gast (1968) and Shaw (1970) or to the book written by Bill White (2013).

The first attempt to create an order of incompatibility among trace elements was probably that of Sun and Hanson in 1975 when they compared the behavior of several incompatible elements during mantle melting to produce alkali basalts. In 1988, Hofmann extended the approach and focused on the behavior of a large range of trace elements in both oceanic and continental crust. He suggested an order of incompatibility that is now used by the entire geochemical community and that corresponds to the relative incompatibility of trace elements during formation of oceanic crust. The

W. M. White (ed.), *Encyclopedia of Geochemistry*,
https://doi.org/10.1007/978-3-319-39312-4

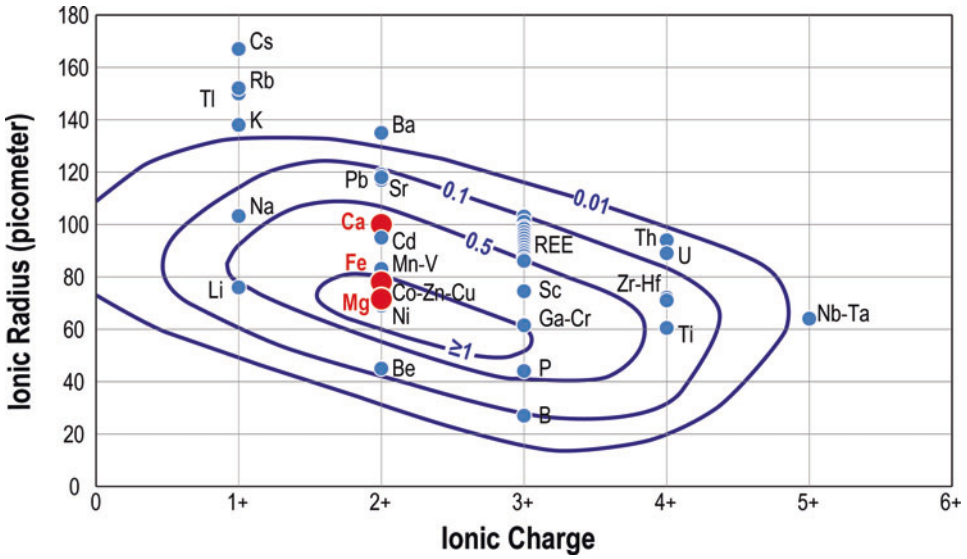

Incompatible Elements, Fig. 1 Ionic radius versus ionic charge for a range of trace elements showing how trace elements can substitute to major elements following Goldschmidt's rules. The *red dots* show the major elements in clinopyroxene and the *blue dots* various trace elements. The *dark blue curves* contour the clinopyroxene/liquid partition coefficients

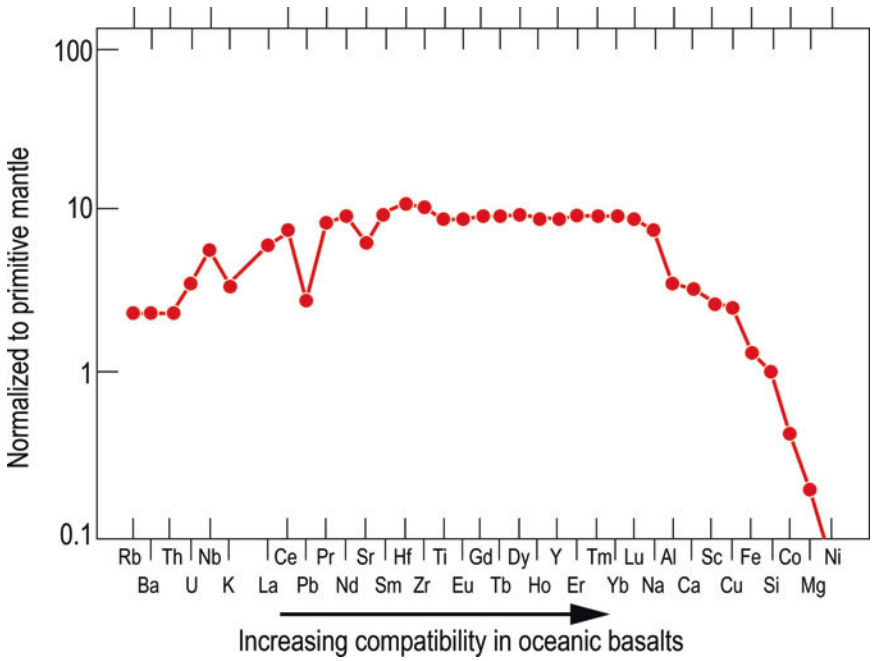

Incompatible Elements, Fig. 2 Major and trace element pattern for average mid-ocean ridge basalt. The concentrations are normalized to primitive mantle concentrations, and the elements are arranged along the X axis as a function of increasing compatibility in oceanic basalts. Adapted from Hofmann (1988). Lead (Pb) shows a very large negative anomaly that is not due to the melting process but comes from the mantle source (see Hofmann et al. 1986 for further details)

most incompatible elements are located on the left side of the figure, and the most compatible elements are on the right end of the list (see Fig. 2).

Typical trace element patterns (also called "spidergrams") are shown in Fig. 3. The continental crust (dark blue symbols) is generally enriched in incompatible elements that have been transferred through magmatic processes from mantle to crust. The mantle has consequently become depleted in these elements, and magmas produced along mid-ocean ridges (MORB, red symbols) show a typical depletion in the most incompatible elements. Ocean island basalts (OIB, green symbols) produced by low degree melting are enriched in the most incompatible elements relative to the more compatible elements. Finally, island arc volcanics (IAV, yellow symbols) have complex patterns due to the combined influence of dehydration/melting of the subducted slab and unusual residual mineralogy during melting in the mantle wedge.

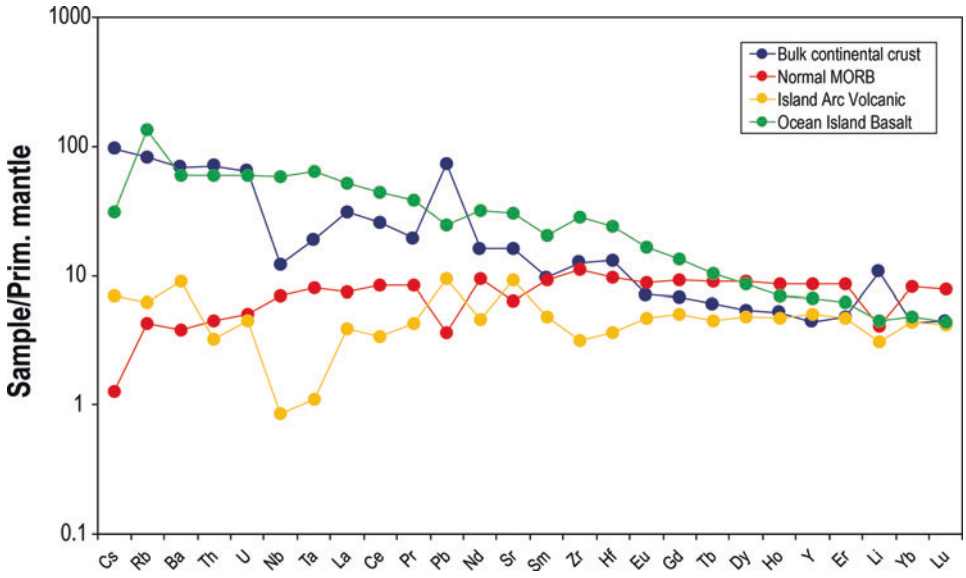

Incompatible Elements, Fig. 3 Trace element patterns normalized to primitive mantle (Sources: bulk continental crust from Rudnick and Gao (2003), normal MORB from Gale et al. (2013), island arc volcanic from Labanieh et al. (2012), ocean island basalt (from Bora Bora, Society Islands) from Chauvel et al. (2011), and primitive mantle from McDonough and Sun (1995))

Conclusion

Incompatible elements are the most useful trace elements to quantify magma formation processes because their enrichment or depletion can be extreme. Applications are numerous and include the modeling of continental crust formation, mantle depletion, and more complex processes such as those occurring in subduction zones.

Cross-References

- ▶ Earth's Continental Crust
- ▶ Large-Ion Lithophile Elements
- ▶ Mantle Geochemistry
- ▶ Mid-Ocean Ridge Basalts (MORB)
- ▶ Oceanic Island Basalts
- ▶ Partial Melting
- ▶ Partitioning and Partition Coefficients
- ▶ Trace Elements

References

Chauvel C, Bureau S, Poggi C (2011) Comprehensive chemical and isotopic analyses of basalt and sediment reference materials. Geostand Geoanal Res 35(1):125–143

Gale A, Dalton CA, Langmuir CH, Su Y, Schilling J-G (2013) The mean composition of ocean ridge basalts. Geochem Geophys Geosyst 14 (3):489–518

Gast PW (1968) Trace element fractionation and the origin of tholeiitic and alkaline magma types. Geochim Cosmochim Acta 32:1057–1086

Hofmann AW (1988) Chemical differentiation of the earth: the relationship between mantle, continental crust and oceanic crust. Earth Planet Sci Lett 90:297–314

Hofmann AW, Jochum KP, Seufert M, White WM (1986) Nb and Pb in oceanic basalts: new constraints on mantle evolution. Earth Planet Sci Lett 79(1):33–45

Labanieh S, Chauvel C, Germa AL, Quidelleur X (2012) Martinique: a clear case for sediment melting and slab dehydration as a function of distance to the trench. J Petrol 53(12):2441–2464

McDonough WF, Sun SS (1995) The composition of the earth. Chem Geol 120:223–253

Rudnick RL, Gao S (2003) 3.01 – Composition of the continental crust. In: Heinrich DH, Karl KT (eds) Treatise on geochemistry, vol 3. Oxford, Pergamon, pp 1–64

Shaw DM (1970) Trace element fractionation during anatexis. Geochim Cosmochim Acta 34:237–243

Sun S-S, Hanson GN (1975) Evolution of the mantle: geochemical evidence from alkali basalt. Geology 3:297–302

White WM (2013) Geochemistry. Wiley, Chichester, p 2. 660p

Indium

Monica Vasiliu and David A. Dixon
Department of Chemistry, University of Alabama, Tuscaloosa, Al, USA

Element Data

Atomic Symbol: In
Atomic Number: 49
Atomic Weight: 114.82
Isotopes and Abundances: ^{111}In 4.3%, ^{115}In 95.7%
1 Atm Melting Point: 429.32 K
1 Atm Boiling Point: 2353 K
Common Valences: 1, 3

(*continued*)

Ionic Radii: (+I) 92, (+III) 132 ppm
Pauling Electronegativity: 1.78
First Ionization Potential: 5.79 eV
Chondritic (CI) Abundance: 0.08 ppm
Silicate Earth Abundance: 0.01 ppm
Crustal Abundance: 0.049 ppm
Seawater Abundance: 10^{-7} ppm
Core Abundance: 0

Properties

Indium is a group 13 element, which is a soft, ductile, and malleable lustrous metallic metal (Emsley 1991, 2001; Anthoni 2006; Anders and Grevesse 1989; McDonough 2005). Indium has a silvery white color, and it is liquid over a wide range of temperatures. It is stable in air and water but dissolves in acids. Similar to gallium, it can wet glass. When heated above its melting point, it ignites and burns with a violet flame.

Out of the two naturally occurring isotopes, the most abundant, ^{115}In, is very weakly radioactive as a β-emitter with a half-life of 6×10^{14} years.

History and Use

Indium was discovered in 1863 by Ferdinand Reich and Hieronymus Theodor Richter at the Freiberg School of Mines in Germany. Reich and Richter were searching for traces of ▶ thallium in samples of ▶ zinc ores and a brilliant violet line in the sample's spectrum revealed the existence of indium. Indium is about as abundant as ▶ silver but is much easier to recover since it typically occurs along with zinc, iron, lead, and copper ores. Indium-rich zinc blends were discovered in 1876 in Colorado and in Bergamo, Italy. Indium was detected in the pumice ejected from in the 1883 eruption of Krakatoa. Some zinc minerals have sufficient indium to give the characteristic strong indigo atomic spectra line without the need of chemical concentration.

Its name comes from the Latin "indium" meaning violet or indigo, which refers to the brightest line in its atomic spectrum.

Indium is used to make indium tin oxide which is an important part of touch screens, flat screen TVs, and solar panels because it conducts electricity, bonds strongly to glass, and is transparent. Indium is used to coat ball bearings of F1 racing cars because, due to its low coefficient friction, additional lubricants are not needed. Indium is used to dope ▶ germanium to make transistors. It is also used in the manufacture of other electrical components such as rectifiers, thermistors, microchips, and photoconductors. When evaporated and allowed to deposit on glass, indium produces a mirror of as good a quality as that of silver. Thus, indium metal is used to form corrosion-resistant mirror surfaces on windows of tall buildings and as a protective film on welder's goggles. Indium foils are used to assess what is going on inside nuclear reactors. Indium is used as a light filter in low pressure sodium vapor lamps. Indium is also used to make low melting alloys (liquid at room temperature), and one of these alloys is used in fire-sprinkler systems in shops and warehouses.

Geochemical Behavior

Indium is one of the least abundant minerals on Earth, and it is very rare to find it uncombined in nature. In Siberia, an indium mineral called indite ($FeIn_2S_4$) has been found. Typically, indium is found associated with zinc minerals and iron, lead, and copper ores. Cultivated soils are reported to be richer in indium (up to 4 ppm) than noncultivated sites. Indium produced by industry comes as the by-product of smelting zinc and lead sulfide ores, some of which can contain 1% indium. World production comes mainly from Canada and is around 75 tons per year; reserves of the metal are estimated to exceed 1500 tons.

Biological Utilization and Toxicity

Indium is not known to have a biological role, although in small doses, its salts may stimulate metabolism. Indium compounds are highly toxic, even though people rarely come in contact with them. If more than a few mg are ingested, they will cause a toxic reaction and affect the liver, heart, and kidneys; indium compounds may be teratogenic.

Environmental effects from indium and indium compounds have not been investigated as indium is not widely dispersed in the environment, but probably it poses no threat to land or marine life at low dose.

Summary

Indium, named after the violet flame observed when it burns and led to its discovery, is not very abundant and is rarely found uncombined in Nature. Indium, which is silvery white in color and a soft, ductile, and malleable lustrous metallic metal, is stable in air and water. Indium, mostly combined with other metals, has a broad range of uses from touch screens, flat screen TVs, and solar panels to the indium foils used in detectors for nuclear radiation. Indium is not known to have a biological role.

References

Anders E, Grevesse, N (1989) Abundances of the elements: meteoritic and solar. Geochim Cosmochim Acta 53:197–214. See http://meteorites.wustl.edu/goodstuff/chondritic_abundances.htm

Anthoni JF (2006) The chemical composition of seawater in http://www.seafriends.org.nz/oceano/seawater.htm

Emsley J (1991) The elements, 2nd edn. Clarendon Press, Oxford

Emsley J (2001) Nature's building blocks an A-Z guide to the elements. Oxford University Press, Oxford

McDonough WF (2005) Compositional model for the Earth's core. In: Carlson RW (ed) The mantle and core. Elsevier, Oxford, pp 547–568. See http://www.knowledgedoor.com/2/elements_handbook/element_abundances_in_the_earth_s_core.html

Inductively Coupled Plasma Mass Spectrometry (ICP-MS)

Maria Schönbächler
Institute of Geochemistry and Petrology, ETH, Zurich, Switzerland

Definition

Inductively coupled plasma mass spectrometry (ICP-MS) represents a major geochemical tool for both elemental and isotope ratio analysis. It allows analyses of elements at concentrations as low as 1 part per trillion (ppt) or even lower depending on instrument and application. This is accomplished by ionizing the sample in an inductively coupled plasma (ICP), followed by ion extraction into a mass spectrometer for separation and quantification of those ions. Different types of mass spectrometers are combined with an ICP source such as quadrupole, sector field mass spectrometry (ICP-SFMS), and multi-collector (MC) ICP-MS instruments. The latter are sector field instruments that feature multiple detectors (normally Faraday cups) for simultaneous detection of ions with different masses. The MC-ICP-MS analyses yield unprecedented precisions for isotope ratio measurements in the parts per million (ppm) range, which are only matched by thermal ionization mass spectrometry (TIMS).

Introduction

Inductively coupled plasma mass spectrometry (ICP-MS) is a versatile technique capable of elemental abundance and isotope ratio analyses. It is widely applied in geochemistry for trace and ultratrace element analysis because of its high sensitivity, the straightforwardness of multielement measurements, and its ability to determine accurate and precise isotope ratios. A broad variety of samples can be analyzed. These range from natural waters to solids, such as rocks, sediments, dust, soil, plants, and other organic matter. Solids must be dissolved prior to introduction into the ICP-MS. Alternatively, a laser ablation system can be used to make in situ isotope and concentration analyses. Gas chromatography-ICP-MS and liquid chromatography-ICP-MS combine chromatographic column systems with ICP-MS. They have important applications in environmental research, e.g., for speciation analyses of organometallic compounds (Bouyssiere et al. 2002).

For ICP-MS analyses, the sample is injected into a plasma in the form of an aerosol and ionized in an inductively coupled plasma (ICP) at temperatures of ~6000–8000 K. After ionization, the ions are extracted into a high-vacuum region (at 10^{-4}–10^{-9} mbar) and further analyzed using specific mass spectrometers. These include (i) quadrupole mass spectrometers that can rapidly measure selected masses over the entire periodic table in sequence and are widespread in geochemical research; (ii) single-collector sector field mass spectrometers (ICP-SFMS, also referred to as high-resolution (HR) ICP-MS), which provide higher sensitivity and/or higher mass resolution than quadrupole ICP-MS; and (iii) multi-collector ICP-MS (MC-ICP-MS) instruments, which are magnetic sector field mass spectrometers fitted with multiple detectors to simultaneously measure different isotopes with the goal to determine isotope ratios at extremely high precision. For solution ICP-MS, where liquid or dissolved solid samples are analyzed, the instrument sensitivity (signal per unit concentration) often reaches the level where the detection limits for many elements are constrained by contamination rather than the instrument sensitivity. These analyses, therefore, need to be carried out in a clean environment.

Basic Principles

The Inductively Coupled Plasma as an Ion Source

The plasma in ICP-MS mass spectrometry consists of a hot, partially ionized gas (typically argon), which contains neutral atoms and molecules, but also ions and electrons (Vanhaecke 2012). The plasma is generated at the end of a quartz torch (Fig. 1), which consists of three concentric tubes. These tubes are used to feed (i) the sample gas (Ar, occasionally combined with N, typically ~1 l/min), (ii) the auxiliary gas (Ar, typically ~1 l/min), and (iii) the coolant gas (Ar, typically at 15–20 l/min) to the plasma. A radiofrequency (RF) induction coil is placed around the tip of the torch (Fig. 1). By sending a RF current through this coil, an oscillating magnetic field is generated. The ions and electrons of the plasma are accelerated and decelerated by the oscillating field, thereby heating the plasma inductively. This leads to high temperatures causing thermal ionization in the hot gas at the center of the plasma

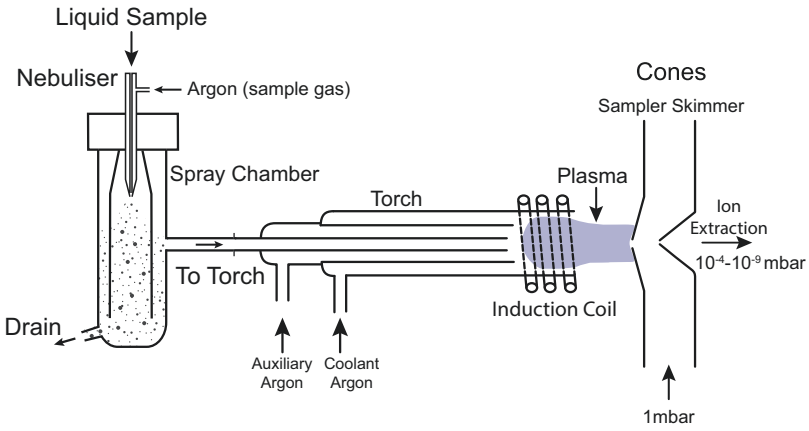

Inductively Coupled Plasma Mass Spectrometry (ICP-MS), Fig. 1 Example of a sample introduction system for ICP-MS adapted for liquid samples. The figure shows nebulizer, spray chamber, torch, plasma, cones, and high-vacuum region. The pressure after the skimmer cone is typically 10^{-3}–10^{-4} mbar with increasingly better vacuum with greater distance from the plasma. A desolvating sample injection system can replace the spray chamber

(Niu and Houk 1996). The plasma is sustained as long as the Ar flow and the RF current through the coil for energy transfer are maintained. For plasma ignition, a high-voltage spark is applied to the Ar flow that strips electrons off the Ar atoms, thereby providing seed electrons for the plasma. At the temperatures of the Ar plasma (~6000–8000 K), elements with first ionization potentials of <10 eV are ionized up to 75% or more and are thus accessible for isotopic analysis with a plasma source (Rehkämper et al. 2001). This includes most elements of the periodic table except, e.g., noble gases.

Sample Introduction into the Plasma

A variety of sample introduction systems have been developed for ICP-MS. The most widely used involves liquid samples, which are converted to an aerosol (fine liquid droplets) using a nebulizer (Fig. 1). This primary aerosol is subsequently introduced into a spray chamber that filters out droplets with diameter >10 µm (Vanhaecke 2012; Olesik 2014). This reduces the sample introduction efficiency 10 to 100-fold depending on the type of nebulizer and spray chamber, but it is required to maintain stable plasma conditions and ascertain efficient atomization and ionization in the ICP. In the plasma, the aerosol droplets evaporate, and individual molecules are released and atomized before ionization takes place (Niu and Houk 1996). Desolvating nebulizer systems are used to reduce the solvent content of the sample aerosol prior to injection into the plasma. They contain a long heated capillary, coated with a semipermeable fluoropolymer membrane to extract the sample solvent (e.g., H_2O). This can enhance the sensitivity of the ICP-MS by a factor 3–10 or more depending on the application, because the balance of the various ionization reactions competing in the plasma is changed. However, desolvating systems are also more prone to retain traces of previously analyzed samples (memory effects), in particular when analyzing solutions at high concentrations, which can require long washout times for cleaning after sample analyses.

Sampler/Skimmer Interface

The extraction of ions from the plasma into the mass spectrometer requires bridging the pressure difference between the ICP source at atmospheric pressure and the mass spectrometer with a mass analyzer region at 10^{-5}–10^{-9} mbar. Such vacuum is necessary, because collisions between sample ions and residual atoms/molecules present in the mass spectrometer severely affect the ability to separate ions of different masses. The ICP region is interfaced to the mass spectrometer via two coaxially placed cones (sampler and skimmer) each with a small, central orifice (~0.6–1.2 mm) through which ions and gas can supersonically expand into the vacuum region (Vanhaecke 2012) (Fig. 1). Most of the extracted plasma gas is removed by the vacuum system. Starting behind the skimmer cone, positive ions are accelerated using static electric fields. A system of ion lenses focus and direct the positive ions to the entrance slit of the analyzer for mass separation and ion detection.

Quadrupole ICP-MS

This type of ICP-MS utilizes a quadrupole filter for mass separation. The filter consists of four parallel rods containing conducting material (Fig. 2). Superimposed DC and AC voltages are applied pairwise to diametrically opposed rods (Vanhaecke 2012) such that the induced fields electrostatically steer ions with *a specific mass-to-charge ratio* (m/z) down the middle of the four rods, where they emerge from the quadruple filter and reach the detector. In ICP-MS, most ions carry a single charge ($z = 1$), such that m/z is reduced to the atomic mass. The quadrupole voltage settings can be selectively changed in quick succession, such that ions with predefined masses pass through the quadrupole filter in a sequence and can be analyzed. Continuous scanning over the whole mass spectrum of the periodic table is possible with a few exceptions (e.g., mass 40 amu is forbidden because $^{40}Ar^{+}$ is abundantly produced in the Ar plasma and would saturate the detector). Continuous scanning yields a mass peak spectrum with peaks (Fig. 2), whose heights are

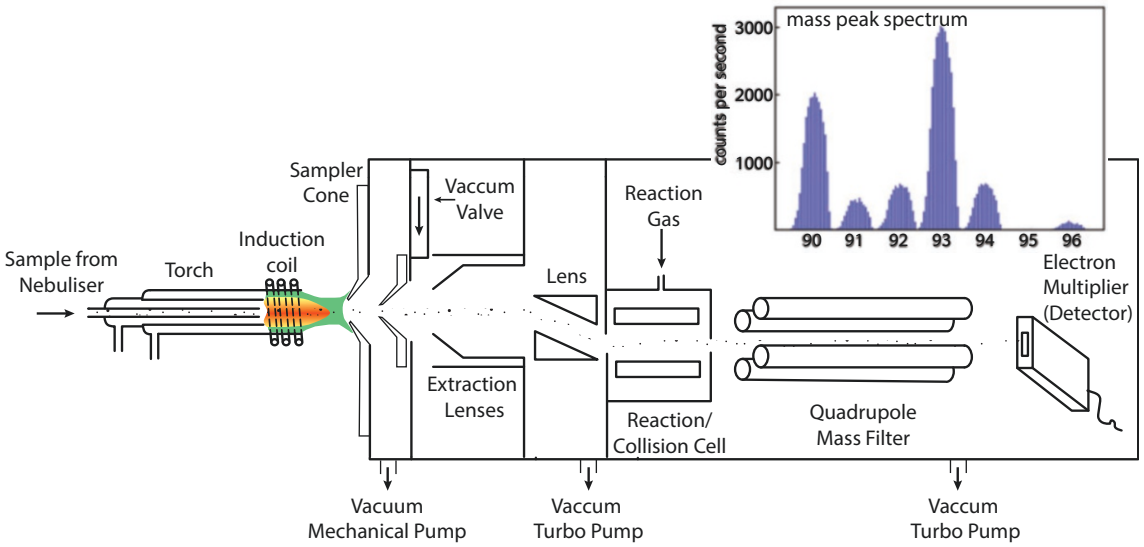

Inductively Coupled Plasma Mass Spectrometry (ICP-MS), Fig. 2 Schematic setup of a quadrupole ICP-MS. Some instruments feature a reaction/collision cell, which allows the user to minimize polyatomic interferences through interaction with a reaction gas. In the *upper right*, a continuous scan over the mass range of Zr and Nb (90–96 amu) is shown

proportional to the number of positive ions transmitted for each specific mass. Rapid jumping from peak to peak (within a few milliseconds) instead of continuous scanning offers the advantage of shorter measurement time. For concentration analyses, it is important that the detector has a large linear dynamic range, i.e., that it is able to detect small to large ion beam intensities and reacts linearly to varying input signals. Present-day detectors can provide a linear dynamic range of nine to ten orders of magnitude. This is typically achieved by employing two detection types (ion counting and analogue mode). In ion counting, each transmitted ion is detected individually (e.g., (Rehkämper et al. 2001; Thomas 2001)). This detection method can be applied up to particle currents of ~10^6 cps (counts per second). At higher count rates, the ion-counting detector is used in analogue mode, operating as a current amplifier. This mode extends the dynamic range of an ion counter by about another three orders of magnitude. Most present-day detectors offer dual mode and automatically switch between ion counting (digital) and analogue mode on the basis of the encountered signal intensities. The integration time of the signal for the ions of a specific mass is normally only milliseconds, which allows for very fast data acquisition of many isotopes.

Important Characteristics of a Mass Spectrometer

Two important characteristics of a mass spectrometer are defined in the following: the abundance sensitivity and the mass resolution. Both provide quantitative information on the instruments' capability to distinguish between ions with small relative mass differences and therefore to resolve neighboring peaks.

The *abundance sensitivity* is a measure for the contribution of a peak to the adjacent peaks because of peak tailing (IUPAC "Gold Book" 1997). It is usually determined as the intensity of the ^{238}U peak tail at mass 237 (Rehkämper et al. 2001). This effect is particularly important when dealing with adjacent isotopes that exhibit a large difference in the isotopic abundance.

The *mass resolution* describes the extent to which an instrument can separate ions with different masses. It is often expressed as the mass difference that the centers of two adjacent peaks of equal height have, such that a valley that corresponds to 10% of the peak height separates them. Or more precisely, the mass resolution is given as M/ΔM, where M is the mass of a peak and ΔM is the mass difference at which a 10% valley between the overlapping peak tails is generated (IUPAC "Gold Book" 1997; Rehkämper et al. 2001). The mass resolution can be determined based on a single peak because ΔM is also equal to the width of a peak at 5% of the peak height, because for two overlapping equal sized peaks, each peak contributes 5% to the observed valley height at 10%.

HR-ICP-MS: Improved Mass Resolution

The mass resolution achievable with quadrupole ICP-MS is ~300. More powerful systems are required for applications, e.g., that suffer from molecular interferences (see below). The double-focusing ICP-SFMS achieves adjustable mass resolutions up to ~10,000. Operated at low mass resolution, it also provides higher sensitivity than quadrupole ICP-MS. The basic principles of ICP-SFMS are as follows. After ionization in the plasma, a set of extraction and focusing lenses (Fig. 3)

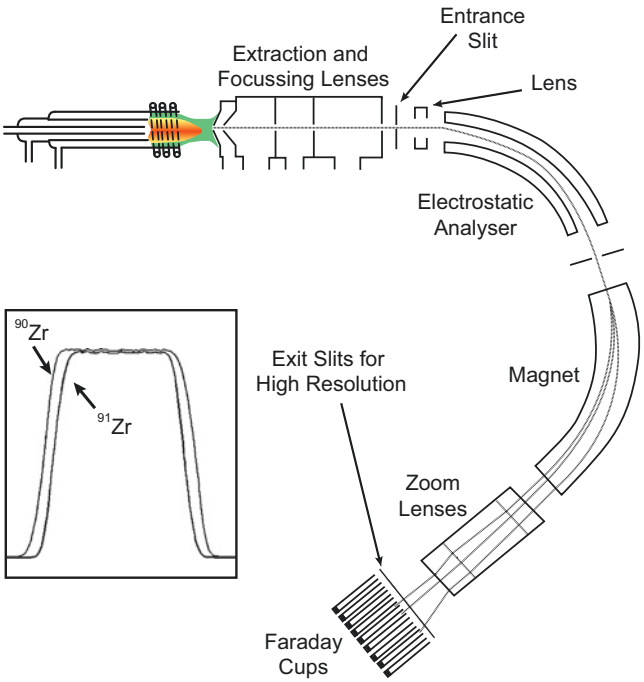

Inductively Coupled Plasma Mass Spectrometry (ICP-MS), Fig. 3 Schematic setup of MC-ICP-MS based on the Nu Plasma II. These instruments are double-focusing magnetic sector ICP-MS with multiple collectors. The term HR-ICP-MS is normally used for single-collector instruments. Commercial MC-ICP-MS are available from Nu Instruments Ltd. (Nu Plasma and Nu Plasma 1700, both with fixed detectors and zoom lenses) and Thermo Fisher Scientific (Neptune *Plus*, with movable detectors). A combination of a narrow entrance slit and individual exit slits in front of the collector(s) is used to achieve high mass resolution, e.g., on the Nu Plasma 1700 or single-collector HR-ICP-MS instruments. Flat-topped overlapping peaks are achieved (see inset for ^{90}Zr and ^{91}Zr peaks scaled to the same signal height)

accelerate the ions and shape the ion beam to fit the entrance slit that is placed before the mass analyzer. The mass analyzer consists of an electrostatic spherical analyzer (ESA) followed by a laminated electromagnet (magnetic sector field) (or the reverse (Vanhaecke 2012; Wieser et al. 2012; Olesik 2014)). The magnet separates ions by both mass (i.e., m/z) and velocity. The plasma, however, produces ions with kinetic energy spreads such that ion separation by a magnet alone would result in broad, fuzzy peaks. The ESA is added to mitigate this effect and filter ions depending on their kinetic energy. In a double-focusing instrument, magnet and ESA are optimally attuned to each other such that ions with identical m/z, but slightly diverging kinetic energies, are focused to one point at the exit slit in front of the detectors, where they can be detected without substantial losses of the ion transmission.

For high mass resolution analyses, the entrance and exit slits are narrowed (Fig. 3). This prevents unwanted ions with marginally different m/z from reaching the detector. Mass resolutions of ~10,000 (M/ΔM) can be realized with present-day instrumentation. However, ion transmission will also be reduced, and the instrument becomes less sensitive.

Normally, HR-ICP-MS instruments are equipped with a *triple-mode detector system* (Vanhaecke 2012). A Faraday cup is installed in addition to the ion-counting detector operated in dual mode. When the signal intensity exceeds the analogue mode capacity of the detector (corresponding to 10^9–10^{12} cps), the ion beam is automatically deflected to the Faraday collector, where the electrical current – carried by the ions – can be measured directly. When ions hit the Faraday collector, they are neutralized by electrons that move from ground to the collector via a high resistance (typically 10^{11} Ω). The potential difference, i.e., voltage created over the resistance, is a measure of the ion signal intensity.

MC-ICP-MS: Achieving High-Precision Isotope Ratio Measurements

The precision of isotope ratio measurements performed with quadrupole ICP-MS instruments is limited to about 2 ‰ mainly by peak shape and the single-collector system (Turner et al. 1998). In MC-ICP-MS, these shortcomings are mitigated by combining an ICP-SFMS with a detector array able to simultaneously detect multiple isotopes. The instrument also offers flat-topped peaks (Fig. 3), which are important to ensure that small fluctuations in the position of the ion beam do not cause spurious results. For example, if the peak maximum is very narrow, tiny variations in the ion beam position will lead to analyses on the peak shoulder, where the signal is lower and thus introduces an error. Additionally, in MC-ICP-MS, several detectors (or more accurately, the exit slits in front of the detectors) are arranged along the focal plane of the mass analyzer to collect the ion currents of different isotopes simultaneously. This way, ion current instabilities are canceled out for isotopic ratio analyses and precise data are achieved.

Since the physical distance between the ion beams of two adjacent isotopes in the focal plane (mass dispersion) depends on their relative mass difference (the heavier the isotopes, the smaller the distance), careful alignment of the detectors to the individual isotope beams needs to be carried out when analyzing different elements. This can be achieved in two ways: (i) the detectors are moved along the focal plane of the mass analyzer and are positioned to collect each isotope beam optimally, or (ii) a zoom lens system is applied to change the mass dispersion, achieving peak alignment even when all detectors are mounted in fixed positions (Fig. 3).

Multi-collector ICP-MS can provide isotope ratio data with precisions of a few ppm. However, such ultrahigh precision can only be obtained after careful purification of the target isotopes from the sample matrix to avoid interferences and matrix effects (see below). The purification procedure generally includes ion exchange chromatography (see "Cross-References").

Additionally, key for high-precision analyses is to control and correct for the instrumental mass fractionation (so-called mass bias). The bias is generally expressed as the deviation of a measured isotope ratio from a reference value, normalized to a mass difference of 1 amu. The mass bias can range from 15% to 40% per amu for B (Boron) to less than 0.5% for Pb and U (Rehkämper et al. 2001). The mass bias originates from heavier ions being transmitted more efficiently through the mass spectrometer, but the cause is not entirely clear (Meija et al. 2012). It could result from the supersonic expansion of ions passing through the sampler cone into the expansion chamber, and space-charge effects in the skimmer cone region, which are generated by mutual repulsion of positively charged ions in the ion beam.

Interferences and Matrix Effects

Interferences and matrix effects are common in ICP-MS and need careful evaluation to obtain accurate and precise data.

Interferences can be (i) isobaric or (ii) polyatomic. (i) Isobaric interferences refer to different elements whose isotopes share a common mass. For example, Ti, V, and Cr possess isotopes at mass 50. Therefore, the signal measured at mass 50 can have contributions from all three elements. Moreover, doubly charged $^{100}Mo^{++}$ or $^{100}Ru^{++}$ can also interfere at mass 50 because the ions are separated by m/z. (ii) Polyatomic interferences arise from ionized molecules that consist of two or more isotopes from different elements present in the plasma adding up to the mass of the isotope of interest. The elements can originate from the sample, the sample solvent, the sample introduction gas, or the Ar of the plasma. The more abundant an element, the more likely it forms molecular interferences. An example for a polyatomic interference is $^{40}Ar^{16}O^{+}$ on $^{56}Fe^{+}$, occurring at mass 56. The ArO^{+} forms from a combination of the plasma Ar and O from the air or the sample solvent. Polyatomic interferences are particularly abundant for isotopes below mass 100.

There are various strategies to deal with interferences. For concentration analyses, interference-free isotopes can be selectively chosen. MC-ICP-MS and HR-ICP-MS often provide sufficient mass resolution (4000–10,000) to resolve overlaps due to molecular ions, because molecules often display slightly different masses than the monoatomic isotopes. In addition, collision/reaction cells are also available to reduce polyatomic molecules through interaction with a reaction gas (Fig. 2) (Olesik 2014).

Matrix effects provoke changes in sensitivity or isotope ratios due to sample components (matrix) other than the target element. They lead to signal suppression or enhancement and affect the instrumental mass bias. If standard and samples are analyzed that are matched with the same matrix and signal intensity, matrix effects can be accounted for. However, very high element concentrations (>2000 ppm) of matrix or target elements can lead to clogging of sample introduction system (e.g., nebulizer) or the cone orifice and should be avoided.

Conclusions

Applications of ICP-MS include the determination of major and trace element concentrations, the measurement of radiogenic and stable isotope ratios, and the possibly of in situ isotope and concentration analyses using a laser ablation system. This versatility underlines the great importance of ICP-MS for present and future geochemical research.

Cross-References

- ▶ Analytical Techniques
- ▶ Ion Exchange Chromatography
- ▶ Laser Ablation – Inductively Coupled Plasma Mass Spectrometry

I

References

Bouyssiere B, Szpunar J, Lobinski R (2002) Gas chromatography with inductively coupled plasma mass spectrometric detection in speciation analysis. Spectrochim Acta B At Spectrosc 57:805–828

IUPAC "Gold Book" (1997) Compendium of chemical terminology, compiled by McNaught AD and Wilkinson A, 2nd edn. Blackwell, Oxford

Meija J, Yang L, Mester Z, Sturgeon RE (2012) Correction of instrumental mass discrimination for isotope ratio determination with multi-collector inductively coupled plasma mass spectrometry. In: Vanhaecke F, Degryse P (eds) Isotopic analysis – fundamentals and applications using ICP-MS. Wiley-VCH, Weinheim, pp 113–137

Niu H, Houk RS (1996) Fundamental aspects of ion extraction in inductively coupled plasma mass spectrometry. Spectrochim Acta B 51:779–815

Olesik JW (2014) Inductively coupled plasma mass spectrometers. In: Turekian KK (ed) Treatise on geochemistry, 2nd edn. Elsevier, Amsterdam, pp 309–336

Rehkämper M, Schönbächler M, Stirling CH (2001) Multiple collector ICP-MS: introduction to instrumentation, measurement techniques and analytical capabilities. Geostand Newslett 25:23–40

Thomas R (2001) A beginner's guide to ICP-MS. Spectroscopy 16 (4):38–42

Turner PJ, Mills DJ, Schröder E, Lapitajas G, Jung G, Iacone LA, Haydar DA, Montaser A (1998) Instrumentation for low- and high-resolution ICP-MS. In: Monaster A (ed) Inductively coupled plasma mass spectrometry. Wiley-VCH, New York, pp 421–501

Vanhaecke F (2012) Single-collector inductively coupled plasma mass spectrometry. In: Vanhaecke F, Degryse P (eds) Isotopic analysis – fundamentals and applications using ICP-MS. Wiley-VCH, Weinheim, pp 31–75

Wieser M, Schwieters J, Douhitt C (2012) Multi-collector inductively coupled plasma mass spectrometry. In: Vanhaecke F, Degryse P (eds) Isotopic analysis – fundamentals and applications using ICP-MS. Wiley-VCH, Weinheim, pp 77–91

Iodine

Hélène Bureau
Institut de Minéralogie, de Physique desMatériaux et de Cosmochimie (IMPMC), Sorbonne Universités – UPMCUniv, Paris, France

Element Data
Atomic Symbol: I
Atomic Number: 53
Atomic Weight[a]: 126.90447
Stable Isotope: ^{127}I
Long-Lived Radioisotope: ^{129}I
1 Atm Melting Point: 113.7
1 Atm Boiling Point: 184.3
1 Atm of Nebular Condensation[b]: 535 K
Common Valences: −I, 0, +I, +III, +V, +VII
Ionic Radius: 206 pm
Pauling Electronegativity: 2.66
First Ionization Potential: 1008.7 kj/mol
Upper Crust Abundance: 1.5 ppm[c]
Bulk Crust Abundance: 0.7 ppm[c]–0.295 ppm[d]
Oceanic Crust Abundance: 777 ppb[d]
Volcanic Rocks: 4–9 ppb[d]
Metamorphic Rocks: 24 ppbI[d]
Sedimentary Rocks: 1.49 ppm[d]
Whole Earth: 40.5 ppb[e]
Silicate Earth Abundance: 10 ppb[fgh]
Chondritic (CI) Abundance: 0.433 ppm[i]
Core Abundance: from 3.3 to 130 ppb[j]
Seawater Abundance: 450.10^{-9} mol/kg[k] (1.8 ppm)
Troposphere: 0.001–0.002 ppbv[l]
From: [a]Meija et al. 2016; [b]Lodders 2003; [c]Rudnick and Gao 2003; [d]Muramatsu and Wedepohl 1998; [e]Allègre et al. 2001; [f]Déruelle et al. 1992; [g]McDonough and Sun 1995; [h]Kargel and Lewis 1993; [i]Palme and Jones 2003; [j]Armytage et al. 2013; [k]Bruland and Lohan 2003; [l]Warneck 2000.

Properties

Iodine is the fourth halogen element located in the group XVII of the periodic table. It has 53 protons and has one stable isotope ^{127}I. Iodine is a minor component on Earth (about 10 ppb for the bulk silicate Earth); it is mostly concentrated in the oceans and crust, where it is strongly associated with life. Iodine is the second heaviest element to be essential in living organisms, the first is tungsten. Iodine has an extinct radiogenic isotope (^{129}I) that is commonly used for geochronology and planetology. Iodine is highly volatile during volcanic eruptions. It contributes to the destruction of the stratospheric ozone.

History and Use

Iodine was discovered in 1811 by Bernard Courtois, a french chemist and saltpeter manufacturer. The name "iode" was given by Joseph Louis Gay-Lussac from the greek "ioeides" meaning violet because of the color of iodine vapor.

It is highly soluble in water; free iodine occurs as I_2. At standard conditions it is a black orthorhombic crystal that can sublimate into a violet gas.

Iodine is commonly used in medicine and pharmaceutical industry. Elemental iodine is used as a disinfectant having a quick antimicrobial action even at low concentrations. It is present in pharmaceuticals and antimicrobial agents. Iodine radioisotopes are used in medical applications. Iodine readily absorbs X-rays and is used as a contrasting agent in medical X-ray imaging. It is a catalyst or reagent in the synthesis of active pharmaceutical ingredients (antibiotics). Calcium iodate, potassium iodate, and potassium iodide are compounds added to animal feeds and to salt for human consumption to prevent medical disorders (e.g., thyroid malfunctioning, mental retardation, abnormal growth in developing fetuses) through lack of iodine in the body. Iodine-based biocides are used in industrial applications such as paints, adhesives, wood treatment, and metalworking fluids. Iodine is also a key ingredient for polarizing films for optics.

Isotopes

Iodine exhibits 37 known isotopes, but only one is stable: ^{127}I. The most common radioisotopes are: ^{129}I (half-life 15.7 million years); ^{125}I (59 days); ^{123}I (13 h); and ^{131}I (8 days). This last is produced by nuclear fission and during nuclear accidents such as Fukushima as illustrated from estimations of release amounts of ^{131}I (Chino et al. 2011).

Today ^{127}I is still produced from cosmic rays, but the original ^{127}I has been transformed in ^{127}Xe. Iodine is an important tracer of the evolution of the solar system's volatile reservoirs, and its presence is inferred from the observation of an excess of its daughter ^{129}Xe:

$$^{129}_{53}\mathrm{I} \rightarrow {}^{129}_{54}\mathrm{Xe} + \beta^-$$

In geochemistry and planetology the pair ^{129}I-^{129}Xe is used to date early stages of the Earth history such as degassing events (Pepin and Porcelli 2006). The isotopic ratios

$^{129}Xe/^{132}Xe$ are used to propose models about the origin and history of volatiles for the Earth and Mars (e.g., Musselwhite et al. 1991; Marty 2012) or to date and characterize chondrites (e.g., Gilmour et al. 2006).

Mineralogy and Geochemistry

All halogen elements are characterized by the s^2p^5 outer shell configuration, with one missing electron in the last electron shell.

Iodine is found in nature in several valence states and in a range of inorganic and organic forms including iodide (I^-), iodate (IO_3^-), elemental iodine (I_2), and organic iodine. Its form depends partly on pH and the redox status of the surrounding environment. The iodide ion is very large making it difficult to fit into the lattice sites of common rock-forming minerals. It is observed in accessory minerals such as amphiboles, apatites, and serpentines. There are rare mineral iodine species, such as iodargyrite (AgI).

Because iodine is highly soluble it is mostly concentrated in seawater, rainfalls, surface waters, pore waters, and fluid inclusions trapped in minerals. Soils contain much more iodine than the rocks from which they are derived. The high affinity of iodine for aqueous fluids makes it a very mobile element.

Geochemistry of Iodine in Terrestrial Reservoirs

Whereas it is classified as a lithophile element (see McDonough and Sun 1995) iodine has also been described by Goldschmidt (1954) as a biophile element.

If the chondritic model applies for the Earth, a strong depletion in iodine in the bulk silicate Earth is observed (McDonough and Sun 1995). This would mean that iodine either has been lost from the Earth or that it is stored and hidden at depth. Because iodine is also chalcophile (Fuge and Johnson 1984), its affinity for sulfur may imply a fractionation of iodine into the core during the Earth's differentiation. The iodine bulk Earth silicate content would range from 7 ppb (O'Neill and Palme 1998) to 10 ppb (Déruelle et al. 1992; Kargel and Lewis 1993; McDonough and Sun 1995). The origin of iodine is still debated. It is proposed that iodine originates either from a solar, or a chondritic or a cometary origin, or from a combination of the latter (see Marty 2012; Palme and O'Neill 2014).

Iodine in Upper Crust, Oceans, and Atmosphere

Iodine is mostly concentrated in the sediments and oceans (about 1.8 ppm). It is present in seawater as water-soluble iodide ion I^-. It is significantly assimilated in organisms such as algae (up to 0.4 wt% I, Lyday 2005). About 70% of the iodine present in the crust is provided by sea water sediments of organic origin and organic matter; it is also present in evaporitic deposits, shales, pelagic clays, limestones, sandstones, and greywackes at levels ranging from 50 to 20,000 ppb, up to 30 ppm in deep-sea carbonates (Muramatsu and Wedepohl 1998).

Rocks contain little iodine and most soil iodine is derived from volatilization of methylated forms from seawater which then enters the soil–plant system via rainfall and dry deposition (Shetaya et al. 2012). It is also shown that iodine is atmophilic, and the areal migration of iodine is an important part of its cycle as it determines the levels of iodine in soils and natural waters.

The atmospheric chemistry of iodine is important (Saiz-Lopez et al. 2012): (1) It helps to understand the iodine cycle. (2) It influences the capacity of the atmosphere to oxidize and remove organic and inorganic species emitted from both natural and anthropogenic sources. This occurs through the catalytic destruction of ozone (e.g., Solomon et al. 1994) and changes to the important radical species such as OH, controlling the oxidizing chemistry. The injection of iodine into the stratosphere may exert a stratospheric ozone depletion equivalent to 30% of the ozone loss through catalytic cycles. Most of iodine injection is marine, but a part is volcanic. (3) Iodine oxides play a role in the formation of ultrafine aerosol particles possibly impacting the climate. (4) In the polar atmosphere, iodine may enhance depletion of gaseous elemental mercury by oxidation to reactive gaseous mercuric compounds that may enter in the food chain after deposition.

Iodine in Igneous Processes and Mantle

Subduction, volcanic activity, and associated processes play a key role in chemical exchanges of iodine between terrestrial repositories. While the external cycle of iodine is starting to be understood, the fluxes and storage of iodine in the planetary interior are still poorly constrained. Iodine is expected to be incompatible during partial melting and differentiation; Br, Cl, and I are not strongly fractionated during partial melting or fractional crystallization, and they are expected to behave similarly in magmas (e.g., Pyle and Mather 2009). The halogen ratios (Br/I, Cl/I) provide information about halogen mantle sources (Kendrick et al. 2012a; Kendrick et al. 2012b), crystallization, and degassing processes in volcanic systems (see Aiuppa et al. 2009).

Magmatic abundances (from a few to a few hundred of ppb I, Déruelle et al. 1992) are determined from the analysis of volcanic glasses. Bulk analysis of whole rocks have also been performed (Shinonaga et al. 1994) showing very low amounts of I. Recent measurements of iodine in volcanic plumes and volcanic fluids (e.g., Snyder and Fehn 2002; Aiuppa et al. 2005; Frische et al. 2006; Witt et al. 2008) show that iodine is degassed from subduction zones volcanism. This is linked to the affinity of iodine for hydrous fluids as confirmed by experiments (Bureau et al. 2000, 2016) showing that iodine is the most hydrophilic halogen element

that totally degas from silicic melts with water. The iodine volcanic contribution to the atmosphere is probably underestimated.

Iodine is very mobile at depth during subduction during dehydration of subducted materials such as serpentinites (e.g., John et al. 2011; Kendrick et al. 2013). Sediments, altered oceanic crust, and serpentinites introduce iodine in the mantle. Fluids fertilize the mantle sources in iodine for arc-related magmatism. Evidences of the shallow recycling of iodine are found in brines and fluids and through their isotopic signatures in ^{129}I (e.g., Snyder and Fehn 2002; Fehn 2012). Iodine is recycled at least in the lithospheric mantle, as evidenced from the study of altered oceanic crust (Chavrit et al. 2016), exhumed mantle wedge peridotites (Sumino et al. 2010), and xenoliths (Broadley et al. 2016). It is difficult today to know if iodine is only recycled at a shallow level or thorough the whole mantle. The deep recycling of I is supported by the presence of iodine in fluid inclusions trapped in upper mantle diamonds (Johnson et al. 2000; Burgess et al. 2002). Experiments show that I storage in the core is possible (Armytage et al. 2013); a deep iodine storage in silicate minerals or in high-pressure melts in the mantle must be experimentally confirmed.

Biological Utilization and Toxicity

Iodine is used by life in biological functions. Organoiodine compounds are produced by marine life forms, such as algae. Iodine is required by animals and humans for the synthesis of hormones in the thyroid gland, and it is essential for growth and development. Because iodine radioisotopes are rapidly taken up by people and organisms, large doses of iodine are given as tablets so as to flood the body with iodine and minimize uptake of iodine radionuclides released in nuclear accidents.

Summary and Conclusions

Iodine is very little abundant in the Earth, and it exhibits different properties: biophilic, hydrophilic, moderately lithophile to volatile during igneous processes, chalcophile, and possibly siderophile at high pressure and temperature. For these reasons, the iodine mass balance calculation and cycles are difficult to assess. Today, there is an apparent depletion with respect to iodine compared to chondrites. However, the overall iodine budget may be subject of examination because the Bulk Silicate Earth iodine content is calculated from MORB values and does not consider the enrichment of ultramafic rocks through hydrothermal alteration and a possible storage in the deep mantle. A part of the iodine may be stored in the core.

Cross-References

- ▶ Bromine
- ▶ Chalcophile Elements
- ▶ Chlorine
- ▶ Fluorine
- ▶ Geochronology and Radiogenic Isotopes
- ▶ Halogens
- ▶ Lithophile Elements
- ▶ Ocean Biochemical Cycling and Trace Elements
- ▶ Ozone and Stratospheric Chemistry
- ▶ Xenon

References

Aiuppa A, Federico C, Franco A, Giudice G, Gurrieri S, Inguaggiato S, Luizzo M, McGonicle AJS, Valenza M (2005) Emission of bromine and iodine from Mount Etna volcano. Geochem Geophys Geosyst 6(8):8

Aiuppa A, Baker DR, Webster JD (2009) Halogens in volcanic systems. Chem Geol 263:1–18

Allègre C, Manhès G, Lewin E (2001) Chemical composition of the earth and the volatility control on planetary genetics. Earth Planet Sci Lett 185:49–69

Armytage RMG, Jephcoat AP, Bouhifd MA, Porcelli D (2013) Metal-silicate partitioning of iodine at high pressures and temperatures: implications for the Earth's core and ^{129}Xe budgets. Earth Planet Sci Lett 373:140–149

Broadley MW, Ballentine CJ, Chavrit D, Dallai L, Burgess R (2016) Sedimentary halogens and noble gases within Western Antarctic xenoliths: implications of extensive volatile recycling to the sub continental lithospheric mantle. Geochim Cosmochim Acta 176:139–156

Bruland KW, Lohan MC (2003) Controls of trace metals in seawater. Pergamon, Oxford, pp 23–47

Bureau H, Keppler H, Métrich N (2000) Volcanic degassing of bromine and iodine: experimental fluid/melt partitioning data and applications to stratospheric chemistry. Earth Planet Sci Lett 183:51–60

Bureau H, Auzende A-L, Marocchi M, Raepsaet C, Munsch P, Testemale D, Mézouar M, Kubsky S, Carrière M, Ricolleau A, Fiquet G (2016) The volcanic degassing of iodine. Geochim Cosmochim Acta 173:114–125

Burgess R, Layzelle E, Turner G, Harris JW (2002) Constraints on the age and halogen composition of mantle fluids in Siberian coated diamonds. Earth Planet Sci Lett 197:193–203

Chavrit D, Burgess R, Sumino H, Teagle DAH, Droop G, Shimizu A, Ballentine CJ (2016) The contribution of hydrothermally altered ocean crust to the mantle halogen and noble gas cycles. Geochim Cosmochim Acta 183:106–124

Chino H, Nakayama H, Nagai H, Terada H, Katata G, Yamazawa H (2011) Preliminary estimation of release amounts of 131I and 137Cs accidentally discharged from the Fukushima Daiichi nuclear power plant into the atmosphere. J Nucl Sci Technol 48(7):1129–1134

Déruelle B, Dreibus G, Jambon A (1992) Iodine abundances in oceanic basalts: implications for Earth's dynamics. Earth Planet Sci Lett 108:217–227

Fehn U (2012) Tracing crustal fluids: applications of natural 129I and 36 cl. Annu Rev Earth Planet Sci 40:45–67

Frische M, Garofalo K, Hansteen TH, Borchers R (2006) Fluxes and origin of halogenated organic trace gases from Momotombo volcano (Nicaragua). Geochem Geophys Geosyst 7(5):1–14

Fuge R, Johnson CC (1984) Evidence for the chalcophile nature of iodine. Chem Geol 43:347–352
Gilmour JD et al (2006) The I-Xe chronometer and the early solar system. Meteorit Planet Sci 41(1):19–31
Goldschmidt VM (1954) Geochemistry. Oxford University Press, London, p 730
John T, Scambelluri M, Frische M, Barnes JD, Bach W (2011) Dehydration of subducting serpentinite: implications for halogen mobility in subduction zones and the deep halogen cycle. Earth Planet Sci Lett 308:65–76
Johnson LH, Burgess R, Turner G, Milledge HJ, Harris JW (2000) Noble gas and halogen geochemistry of mantle fluids: comparison of African and Canadian diamonds. Geochim Cosmochim Acta 64:717–732
Kargel JS, Lewis JS (1993) The compositions and early evolution of earth. Icarus 105:1–25
Kendrick MA, Kamenetsky VS, Phillips D, Honda M (2012a) Halogen systematics (Cl, Br, I) in mid-ocean ridge basalts: a Macquarie Island case study. Geochim Cosmochim Acta 81:82–93
Kendrick MA, Woodhead JD, Kamenetsky VS (2012b) Tracking halogens through the subduction cycle. Geology 40:1075–1078
Kendrick MA, Honda M, Pettke T, Scambelluri M, Phillips D, Giuliani A (2013) Subduction zone fluxes of halogens and noble gases in seafloor and forarc serpentinites. Earth Planet Sci Lett 365:86–96
Lodders K (2003) Solar system abundances and condensation temperatures of the elements. Astrophys J 591:1220–1247
Lyday PA (2005) Iodine and iodine compounds. In: Ullmann's encyclopedia of industrial chemistry, vol A14. Whiley-VCH, Weinheim, pp 282–390
Marty B (2012) The origins and concentrations of water, carbon, nitrogen and noble gases on earth. Earth Planet Sci Lett 313–314:56–66
McDonough WF, Sun SS (1995) The composition of the earth. Chem Geol 120:223–253
Meija J, Coplen TB, Berglund M, Brand WA, De Bièvre P, Gröning M, Holden NE, Irrgeher J, Loss RD, Walczyk T, Prohaska T (2016) Isotopic compositions of the elements 2013 (IUPAC technical report). Pure Appl Chem 88:293–306. http://www.nist.gov/pml/data/comp.cfm
Muramatsu Y, Wedepohl KH (1998) The distribution of iodine in the Earth's crust. Chem Geol 147:201–216
Musselwhite DS, Drake MJ, Swindle TD (1991) Early outgassing of Mars supported by differential water solubility of iodine and xenon. Nature 352:697–699
O'Neill HSC, Palme H (1998) Composition of the silicate earth: implications for accretion and core formation. In: Jackson I (ed) The Earth's mantle: structure composition and evolution – the Ringwood volume. Cambridge University Press, Cambridge, pp 3–126
Palme H, Jones A (2003) Solar system abundances of the elements. In: Treatrise on geochemistry, vol 1. Elsevier Ed, The Netherlands, pp 41–61
Palme H, O'Neill HSC (2014) Cosmochemical estimates of mantle composition. In: Treatrise on geochemistry, 2nd edn. Elsevier Ed, The Netherlands
Pepin RO, Porcelli D (2006) Xenon isotope systematics, giant impacts, and mantle degassing on the early earth. Earth Planet Sci Lett 250:470–485
Pyle DM, Mather TA (2009) Halogens in igneous processes and their fluxes to the atmosphere and oceans from volcanic activity: a review. Chem Geol 263:110–121
Rudnick RL, Gao S (2003) Composition of the continental crust. In: Treatrise on geochemistry, vol 3. Elsevier Ed, The Netherlands, pp 1–64
Saiz-Lopez A, Plane JMC, Baker AR, Carpenter LJ, von Glasow R, Gomez Martin JC, McFiggans G, Saunders RW (2012) Atmospheric chemistry of iodine. Chem Rev 112:1773–1804
Shetaya WH, Young SD, Watts MJ, Ander EL, Bailey EH (2012) Iodine dynamics in soils. Geochim Cosmochim Acta 77:457–473
Shinonaga T, Ebihara M, Nakahara H, Tomura K, Heumann KG (1994) Cl, Br and I in igneous standard rocks. Chem Geol 115:213–225
Snyder GT, Fehn U (2002) Origin of iodine in volcanic fluids: ^{129}I results from the central American volcanic arc. Geochim Cosmochim Acta 66:3827–3838
Solomon S, Burkholder JB, Ravishankara AR, Garcia RR (1994) Ozone depletion and global warming potentials of CF_3I. J Geophys Res 99:20929–20935
Sumino H, Burgess R, Mizukami T, Wallis S, Holland G, Ballentine CJ (2010) Seawater-derived noble gases and halogens preserved in exhumed mantle wedge peridotite. Earth Planet Sci Lett 294:163–172
Warneck P (2000) Chemistry of the natural atmosphere, 2nd edn. Academic Press, London, p 927
Witt MLI, Mather TA, Pyle DM, Aiuppa A, Bagnato E, Tsanev VI (2008) Mercury and halogen emissions from Masaya and Telica volcanoes, Nicaragua. J Geophys Res 113:B06203

Ion Exchange Chromatography

Maria Schönbächler
Institute of Geochemistry and Petrology, ETH, Zurich, Switzerland

Definition

Ion exchange chromatography represents a versatile analytical technique that separates ions and polar molecules in a solution (mobile phase) based on their affinities for an ion exchanger (stationary phase). It is widely used as a preparative technique for Atomic Absorption Spectroscopy (AAS), Multiple Collector Inductively Coupled Plasma Mass Spectrometry (MC-ICP-MS), and Thermal Ionization Mass Spectrometry (TIMS) or techniques using electrical conductivity or UV detectors.

Introduction

Ion exchange chromatography allows for the separation and enrichment of many organic and inorganic compounds and elements from a sample. This widely applied analytical technique is utilized in organic and inorganic geochemistry and also in numerous other fields, such as environmental sciences, economic geology, biochemistry, pharmaceutics, nuclear and food industries, and in water processing/purification processes (Zagorodni 2007). The theory and applications of ion exchange chromatography are described in various books and articles (Harland 1994; Korkisch 1989; Paterson 1970; Peters et al. 1974; Schönbächler and Fehr 2014; Shaw and Haddad 2004; Weston and Brown 1997; Zagorodni 2007). These publications are either of a general nature or focus on specific applications such as high performance liquid chromatography

(HPLC) (Weston and Brown 1997). The latter is often used in low-temperature geochemistry to determine anions and cations in aqueous samples. Schönbächler and Fehr (2014) covered aspects that are important for element separation and enrichment prior to MC-ICP-MS and TIMS. A high degree of element purification is required for these measurements because matrix elements (other elements present than those of interest) can interfere with the analyses of the targeted isotopes. This is particularly important for applications that require accurate high-precision isotope data (precisions < 0.1 permil, Fehr et al. 2004; Rehkämper et al. 2011; Schönbächler et al. 2004). These applications include nontraditional stable isotope studies in geo- and cosmochemistry (Rehkämper et al. 2011; Weiss et al. 2008) and age determinations using radioactive decay systems.

In the following, a brief overview of the basic principles relevant for ion exchange chromatography is given. The focus is on column techniques that employ commercially available ion exchange resins for the separation of inorganic anions and cations prior to MC-ICP-MS and TIMS measurements (Schönbächler and Fehr 2014). The principles, however, are also relevant for other applications, where the eluates are analyzed using other techniques, such as electrical conductivity or UV detectors.

Principles of Ion Chromatography

Ion chromatography generally involves two phases: *a mobile phase*, which moves relative to *a stationary phase*. The sample is initially dissolved in the mobile phase (e.g., a mineral acid), which is then added to the stationary phase, i.e., the ion exchange resin. The dissolved sample components (*the solutes*) in the mobile phase interact with the ion exchange resin (stationary phase) and distribute themselves between mobile and stationary phases according to their relative affinities to each phase. These affinities are specific to each component. Therefore, ion exchange resins retain distinct components to different degrees. This is exploited to separate these components (molecules or elements) from each other.

Structure of Ion Exchange Resins

Stationary phases commonly used are commercially available anion and cation exchange resins. These resins are crossed-linked copolymers composed of styrene and divinylbenzene (DVB) to which functional groups are attached as ion exchange sites (Fig. 1). Based on the functional group, different types of resins can be distinguished:

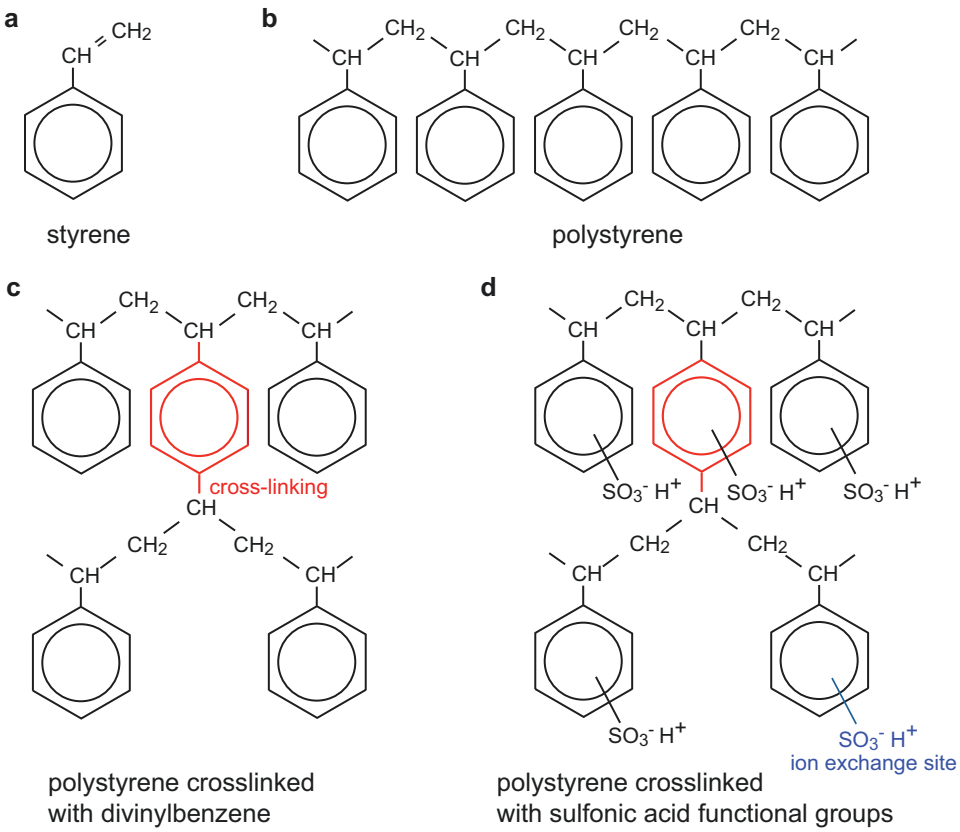

Ion Exchange Chromatography, Fig. 1 The backbone of commercial ion exchange resins is based on (**a**) styrene that forms (**b**) polystyrene chains. The polystyrene chains are cross-linked with divinylbenzene (**c**). To this polymer, functional groups are added. Panel (**d**) illustrates the resin structure of a strong cation exchange resin with sulfonic acid functional groups (After Schönbächler and Fehr 2014)

(i) Strong *cation exchange resins* exchange cations and feature sulfonic ($-SO_3H$) acid functional groups (Korkisch 1989; Smith and Chang 1983). Weak cation exchange resins possess carboxylic acid (–COOH) or phosphonic acid ($–PO_3^{2-}$) functional groups and are chemically less resistant (Smith and Chang 1983). When purchased, the ion exchange sites are occupied by counter ions, such as H^+, Na^+, or NH_3^+. These are replaced during ion chromatography.

(ii) *Anion exchange resins* possess basic functional groups such as quaternary ammonium or ammine groups that facilitate anion exchange. The counter ions of commercial anion resins are often Cl^- but also acetate, formate, or hydroxide anions.

(iii) *Amphoteric exchangers* include both acid and basic ionogenic groups and can thus exchange cations and anions.

(iv) The functional groups of *chelating resins* selectively respond to a specific, small group of ions (Korkisch 1989).

Anion and cation exchange resins are commercially available in the form of small beads. They display a narrow particle size distribution (e.g., 200–400 mesh) and generally contain low levels of contamination from metal ions and organic compounds. The chains produced during the polymerization of styrene are cross-linked to each other through DVB groups (Fig. 1). A higher fraction of DVB increases the degree of cross-linkage between the chains. This improves the mechanical strength and reduces swelling in aqueous solution. Swelling in water is common for these ion exchangers. However, the porosity of the resin also decreases, and the solute less easily reaches the functional groups to exchange ions. Moreover, less functional groups can be attached to higher cross-linked resins. This leads to a less efficient ion exchange process for highly cross-linked resins (Korkisch 1989). Most commercially available resins feature cross-linkages of 4–8% to equalize the different effects.

The Ion Exchange Process

The ion exchange reaction is an equilibrium process. After adding a mobile phase with solute (A) to the stationary phase, the solute will be distributed between the mobile phase and the resin until equilibrium is reached. An ion exchange reaction that involves two ions A and B can be expressed as:

$$a\overline{R}B + bA^a \Leftrightarrow b\overline{R}A + aB^b \quad (1)$$

$\overline{R}$ denotes the ion exchange resin including its functional group that serves as ion exchange site, whereas a and b are the charges of the ions A and B. The ion B is originally attached to the resin. During ion exchange, the counter ions A and B are partially or completely exchanged until equilibrium is established. The reaction is reversible; an increase of solute A in the mobile phase will augment the amount of A sorbed onto the resin. The equilibrium for a distinct solute (also referred to as component or analyte) can be expressed with the *equilibrium distribution coefficient* (K_d):

$$K_d = \frac{\text{amount of solute per gram dry exchanger}}{\text{amount of solute per milliliter of mobile phase}} = \frac{C_{solid}}{C_{liquid}} \quad (2)$$

where C_{solid} is the concentration of the solute in the ion exchange resin (dry form) and C_{liquid} is the concentration of the solute in the liquid that is in equilibrium with the ion exchanger. The distribution coefficient governs the chromatographic separation. Solutes with a high K_d are strongly retained by the resin, whereas a $K_d < 1$ indicates limited interaction with the resin and the solute mainly remains in the mobile phase (Higson 2004).

The Kd values for a specific resin are influenced by various parameters such as the composition of the mobile phase (e.g., acid and solvent media and their concentrations) and resin properties such as functional groups, particle size distributions, and cross-linkage (Korkisch 1989; Schönbächler and Fehr 2014). Distribution coefficients that are experimentally determined for the different ion exchange resins in various types of aqueous media are readily available in literature (Korkisch 1989; Schönbächler and Fehr 2014 and references therein). Overall, the K_d value determined for a solute (in combination with a specific ion exchanger and solvent) remains constant over a wide range of solute concentrations (Korkisch 1989; Letho and Harjula 1995; Schönbächler and Fehr 2014; Zagorodni 2007).

Batch and Column Methods

Two types of ion exchange methods can be considered: (i) the batch and (ii) the column method (Korkisch 1989; Schönbächler and Fehr 2014; Zagorodni 2007).

Batch Method

The sample solution is added to the ion exchange resin in a suitable vessel and equilibrates while stirring or shaking. Subsequently, the ion exchanger is separated from the liquid phase, e.g., by filtration or centrifugation.

Column Method

The resin is filled into a column (Fig. 2) and the sample (mobile phase) passes through the ion exchange resin either driven by gravity (Fig. 2) or pumped at a certain flow rate

(e.g., HPLC). Components of the sample solution that do not interact with the functional groups of the resin ($K_d \ll 1$) pass directly through the column at the speed of the mobile phase. In contrast, components interacting with the resin are delayed. The different sample components therefore move through the column at different speeds and will elute at different times (Fig. 3). The column method can be thought of as a large number of successive batch operations (Letho and Harjula 1995) and can be described using the following model:

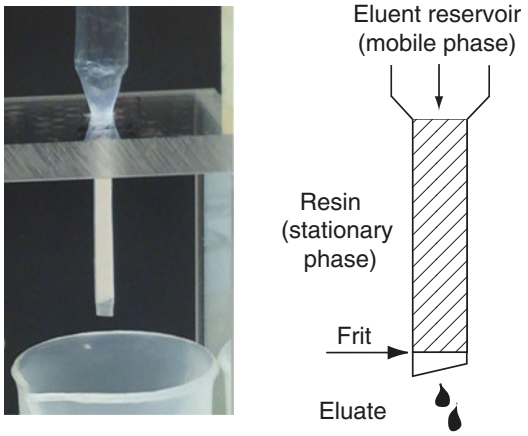

Ion Exchange Chromatography, Fig. 2 Image and schematic of an ion exchange column used in combination with gravitational flow. The frit can be a perforated glass disk, porous Teflon, or other suitable materials that retain the resin but let the mobile phase pass

(1) *Sample loading*: For the purpose of illustration, let us divide the resin reservoir (Figs. 2 and 3) into arbitrary small equal-sized sections. The solute (e.g., A) is loaded onto the resin and equilibrates with the top section of the resin reservoir according to its K_d such that a constant C_{solid}/C_{liquid} ratio is achieved. Subsequently, the sample solution travels to the adjacent section below, with its concentration of solute A reduced by the amount of A sorbed onto the column in the first section. The depleted solution equilibrates with the new resin section and less of solute A will be sorbed onto the column compared to the section above. The same process is repeated when the solution travels to the next section below and so forth. This results in a sorption front, where the concentration of A decreases downward until virtually all the solute A is sorbed onto the column.

(2) *Elution*: After the sample solution, more mobile phase (devoid of solute A) is added onto the column and desorption is initiated. The solution devoid of A equilibrates with the top section of the resin, which contains the solute A. This leads to the removal of A from the resin into the

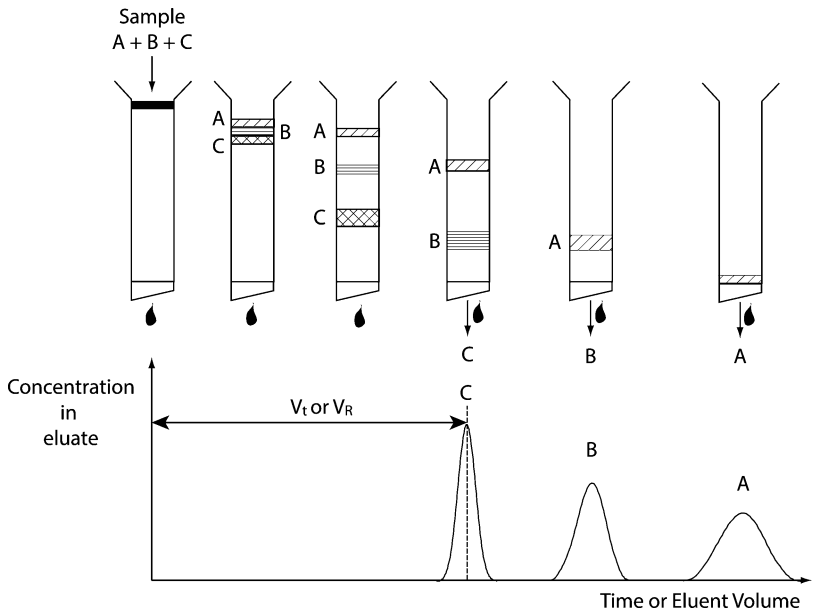

Ion Exchange Chromatography, Fig. 3 Interaction of solutes A, B, and C with the ion exchange resin using the column method. The diagram also shows the elution curve (concentration in the eluate versus time and eluent volume) for the column. Components A, B, and C in a sample solution display distinct K_d (K_d A > K_d B > K_d C) and therefore, move at different speeds. This leads to well-separated elution peaks. Comparison of subsequent elution peaks illustrates that the peak broadens and the peak maximum decreases with increasing time and volume of solution passed through the column (eluent volume). Overall, the longer (and the faster) a solute band travels through the resin, the broader the elution peak becomes (Schönbächler and Fehr 2014 and references therein). The *black arrow* illustrates the retention time or volume for solute C. V_t: retention time – time passed until the peak maximum is reached. V_R: retention volume – volume passed through the column until peak maximum elutes

mobile phase to keep C_{solid}/C_{liquid} constant. The mobile phase, still low in A, moves further down and equilibrates with the section below and so forth. Provided that sufficient new mobile phase is added to the column, a sorption band of solute A moves down the column until it reaches the end of the resin reservoir and elutes (Fig. 3).

Based on Eq. 1, it can be demonstrated that the concentration of the solute recovered in the solution emerging from the column (eluate) approaches a Gaussian curve (Fig. 3). Experimentally obtained elution peaks confirm the theory, although the elution peaks can become asymmetric or show peak tailing, depending on experimental conditions (Schönbächler and Fehr 2014).

The Retention Volume: Mobile Phase Required for Solute Elution

By definition, the *retention volume* (V_R) is the volume of the mobile phase required to pass through the column to reach the maximum of the elution peak for a specific solute (Fig. 3). The following equation applies for V_R (Korkisch 1989):

$$V_R = K_d \times m \tag{3}$$

where m is the mass of the resin (dry) in the column. This equation shows that V_R is a function of K_d. This relationship can be used to estimate the amount of mobile phase required to elute a solute from a specific resin mass. For this estimate, the K_d for the experimental conditions (resin type in combination with the utilized mobile phase) must be available. For example, an experiment with 1 g of dry resin and a solute with a K_d of 1 requires 1 ml mobile phase to elute half of the solute from the column ($=V_R$) and between 1 and 2 ml to elute the entire solute depending on the peak width. The predictions need to be verified by experiments because small changes in the experiment (e.g., resins with different particle size distributions or cross-linkage) affect the K_d values.

The Efficiency of an Ion Exchange Column to Separate Elution Peaks

The goal of ion exchange chromatography is to efficiently separate different sample components. The *selectivity* of a chromatographic system (Weston and Brown 1997; Zagorodni 2007) is a measure of how efficiently two components can be separated from each other (Fig. 3). It is governed by the preference of the ion exchanger for one specific ion over another. The *separation factor* α_A^B for two solutes A and B describes the experimentally determined selectivity of an ion exchanger (Harland 1994):

$$\alpha_A^B = \frac{(C_B)_r \times (C_A)_s}{(C_A)_r \times (C_B)_s} = \frac{(K_d)_B}{(K_d)_A} \tag{4}$$

where C_B and C_A are the concentrations of A and B in the solution (s) and the resin (r), respectively. Large differences between the K_d values of solute A and B yield a separation factor α_A^B significantly different from 1 and indicate a good separation of the elution peaks. Similar K_d values for A and B ($\alpha_A^B < 1$) lead to overlapping elution peaks and full separation of the two components is not possible.

General Considerations

Chromatographic ion exchange procedures can follow different strategies. Many procedures represent mixtures of these strategies:

Strategy (i)

The sample is loaded onto the column in a medium, in which the element(s) of interest are strongly retained by the resin (high K_d), while the majority of the matrix moves almost directly through the column (low K_d). The various matrix elements are then further eluted using one or several types of chemical media, which may vary in concentrations, before the analyte is stripped from the column. An example for this strategy is the cation exchange column used for Ag separation from matrix elements (e.g., Pd and Mo) that interfere during MC-ICP-MS analyses (Schönbächler et al. 2007). In this procedure, the sample is loaded in 0.5 M HNO_3, in which Pd and Mo elute directly, while the Ag sorption band move down the column and elutes after further 16 ml of 0.5 M HNO_3.

Strategy (ii)

The sample is loaded in a medium, where the element of interest directly elutes with the mobile phase, while matrix elements are strongly retained. This procedure requires that enough ion exchange sites are available to accommodate all matrix ions and this limits the sample amount that can be processed in a single column. An example of this strategy is the separation of Li for geological applications (James and Palmer 2000). The sample is loaded onto cation exchange resin in 0.2 M HCl, in which Li only weakly interacts with the resin, while most matrix elements are moderately to strongly retained.

Strategy (iii)

This strategy is referred to as "stick and strip" and represents an end-member of both (i) and (ii). The sample is loaded in a medium, in which the analyte is strongly retained by the resin (extremely high K_d). It remains with the top layer, while matrix elements elute. Thereafter, the analyte is stripped from the resin with a different medium in which the analyte has little or no affinity for the resin (very low K_d). Strategy (iii) does not

depend on analyte bands that move at different speeds through the column (Fig. 3). The analyte is sorbed onto the top layer of the column and then directly stripped. The method can also be inverted, i.e., the matrix elements stick to the top layer of the resin, while the target element directly elutes.

For successful performance of ion exchange chromatography, sufficient ion exchange sites must be available to accommodate and exchange the solute ions. The number of required ion exchanges sites for a given sample amount can be calculated based on the composition of the loaded sample. The result can be compared to the exchange sites available in a certain resin volume estimated from the resin capacity (generally provided by the manufacturer). For strategy (iii), the sample ions can occupy up to 50% of the total ion exchange capacity of the resin (Korkisch 1989), whereas for a true chromatographic separation (strategies i and ii), the sorbed ions should not occupy more than ~3–5% to ensure good separation and narrow elution peaks (Korkisch 1989).

Conclusion

Ion exchange chromatography is key for the separation of many organic and inorganic compounds and elements from a sample matrix and is widely used in geological research. In addition to the ion exchange resins discussed here, more recently designed resins for extraction chromatography (e.g., TRU, Ln, or TODGA resin) are also widely utilized (Pin and Rodriguez 2014). Fast and efficient techniques that yield excellent separation already exist; however, they can be further improved using novel ion exchange materials (Zagorodni 2007) or alternative approaches, such as tandem columns or pressurized column systems with increased flow rates.

Cross-References

- ▶ Analytical Techniques
- ▶ Atomic Absorption, Inductively Coupled Plasma Optical Emission Spectroscopy, and Infrared Spectroscopy
- ▶ Chromium Isotopes
- ▶ Inductively Coupled Plasma Mass Spectrometry (ICP-MS)
- ▶ Lithium Isotopes
- ▶ Organic Geochemistry
- ▶ Thallium Isotopes

References

Fehr MA, Rehkämper M, Halliday AN (2004) Application of MC-ICPMS to the precise determination of tellurium isotope compositions in chondrites, iron meteorites and sulfides. Int J Mass Spectrom 232:83–94
Harland CE (1994) Ion exchange: theory and practice. Royal Society of Chemistry, London
Higson S (2004) Analytical chemistry. Oxford University Press, Oxford
James RH, Palmer MR (2000) The lithium isotope composition of international rock standards. Chem Geol 166:319–326
Korkisch J (1989) Handbook of ion exchange resins: their application to inorganic analytical chemistry. CRC Press, Boca Raton
Letho J, Harjula R (1995) Experimantation in ion exchange studies – the problem of getting reliable and comparable results. React Funct Polym 27:121–146
Paterson R (1970) An introduction to ion exchange. Heyden & Son Ltd, London
Peters DG, Hayes JM, Hieftje GM (1974) Chemical separations and measurements. Theory and practice of analytical chemistry. S. B Saunders Company, Philadelphia
Pin C, Rodriguez J (2014) Separation methods based on liquid–liquid extraction, extraction chromatography, and other miscellaneous solid phase extraction processes. In: Turekian KK (ed) Treatise on geochemistry, 2nd edn. Elsevier, Amsterdam, pp 147–170
Rehkämper M, Schönbächler M, Andreasen R (2011) Application of MC-ICP-MS to isotopic analysis in cosmochemistry. In: Vanhaecke F, Degryse P (eds) Isotopic analysis – fundamentals and applications using ICP-MS. Wiley-VCH, Weinheim, pp 275–315
Schönbächler M, Fehr MA (2014) Basics of ion exchange chromatography for selected geological applications. In: Turekian KK (ed) Treatise on geochemistry, 2nd edn. Elsevier, Amsterdam, pp 123–146
Schönbächler M, Rehkämper M, Lee D-C, Halliday AN (2004) Ion exchange chromatography and high precision isotopic measurements of zirconium by MC-ICP-MS. Analyst 129:32–37
Schönbächler M, Carlson RW, Horan MF, Mock TD, Hauri EH (2007) High precision Ag isotope measurements in geologic materials by multiple-collector ICPMS: an evaluation of dry versus wet plasma. Int J Mass Spectrom 261:183–191
Shaw MJ, Haddad PR (2004) The determination of trace metal pollutants in environmental matrices using ion chromatography. Environ Int 30:403–431
Smith FC, Chang RC (1983) The practice of ion chromatography. Wiley, New York
Weiss DJ, Rehkämper M, Schoenberg R, McLaughlin M, Kirby J, Cambell PGC, Arnold T, Peel K, Gioia S (2008) Application of nontraditional stable-isotope systems to the study of sources and fate of metals in the environment. Environ Sci Technol 42:655–664
Weston A, Brown PR (1997) HPLC and CE: principles and practice. Academic Press, San Diego
Zagorodni AA (2007) Ion exchange materials – properties and applications. Elsevier, Amsterdam

Ion Microprobe

Kazuhide Nagashima
Hawai'i Institute of Geophysics and Planetology, University of Hawai'i at Mānoa, Honolulu, HI, USA

Definition

An ion microprobe is a mass spectrometer that uses the principle of secondary ion mass spectrometry (SIMS) and enables in situ elemental and isotopic analysis of a solid sample.

Operation Principle

Ions accelerated at ~10 kV under high vacuum (i.e., primary ions) are focused onto sample surface. The primary ion bombardment leads to collision cascades in a solid sample. Recoil particles that reach sample surface with an energy exceeding the surface binding energy are ejected from sample surface (i.e., sputtering). The sputtered particles are mostly neutral, while small fraction of them (typically much less than 10%) is ionized (i.e., secondary ions). The secondary ions are extracted into a mass spectrometer and analyzed to determine the elemental and isotopic compositions of sample. While various ions can be used in the primary ion beam, Cs^+, O^-, O_2^-, and O_2^+ are the most common as these ions enhance secondary ionization efficiency. The secondary ions can be positive and negative. The mass spectrometer is usually set to have a polarity opposite to that of the primary ion. Among the mass spectrometers that have been adopted for ion microprobes (magnetic sector, time-of-flight (TOF), quadrupole mass analyzer), the magnetic sector is most common in geochemical applications as it in general has the best quantitative performance. In the magnetic-sector mass spectrometer, secondary ions are spatially separated by the magnet as a function of mass-to-charge ratio. Ions of interest are detected either sequentially by changing strength of magnetic field (i.e., peak jumping) or simultaneously with multiple detectors (i.e., multi-collection).

Advantages of Ion Microprobe Technique

The ion microprobes have several advantages over other analytical techniques used in geochemistry. In situ elemental and isotopic analysis with a high spatial resolution ranging from several tens of microns to submicron is possible. This contrasts with other conventional techniques that require processing of a sample, thereby destroying the textual context. Higher sensitivity is achieved compared to other surface analytical techniques such as electron beam techniques (e.g., EPMA) and laser ablation ICP-MS; quantification of $<$ppb level is possible with ~10 μm spot. All elements from hydrogen to uranium and above can be measured. Since the sputtering process removes materials continuously from surface, analysis as a function of depth can be made (i.e., depth profiling). Two-dimensional analysis (i.e., imaging) is possible either by scanning or direct ion imaging techniques. The scanning ion image is obtained by scanning the primary beam over sample surface and recording secondary ion signals as a function of the primary beam position. Some instruments have stigmatic ion optics and can transmit a mass-filtered, two-dimensional ion image of a sample to an imaging detector. By combining depth-profiling and two-dimensional imaging techniques, three-dimensional analysis is also possible.

There are technical difficulties in geochemical applications using ion microprobes. The ion probe fractionates the elemental and isotopic abundances of a sample during a measurement. This is because the secondary ionization efficiencies depend on not only the properties of the particular element but also chemical composition of the sample (i.e., matrix effect). Physical models to describe the formation of sputtered ions in chemically complex solids are too immature to be accurately correct for the elemental and isotopic fractionation of secondary ions. In addition, the mass spectrometer can also fractionate secondary ions. As a result, quantitative analyses for elemental and isotopic abundances require empirical corrections of the instrumental fractionation using standard materials having similar matrix and well-determined elemental and isotope compositions. The sputtering process produces not only single atom ions but many different molecular ions and multiply charged ions, some of which may overlap to the ion of interest (e.g., $^{16}OH^-$ onto $^{17}O^-$, and $^{178}Hf^{28}Si^+$ onto $^{206}Pb^+$). Because of this, the mass spectrometer in an ion probe is constructed to resolve ion species with small difference in mass-to-charge ratio. Mass resolution is a measure of the instrument ability to resolve peaks with small differences in their mass-to-charge ratios. The large magnetic sector ion probes, such as SHRIMP series (developed at Australian National University) and IMS 1270/1280 series (Cameca, France), have a high mass resolution while keeping relatively high transmission, sufficient for a variety of isotopic analyses in geochemistry. Even with those instruments, atomic isobars are often impossible to be resolved (e.g., ^{87}Rb and ^{87}Sr). It is also possible to suppress molecular interferences using the energy filtering technique, which utilizes a difference in energy distributions of secondary ions between single ions and molecular ions. However, the energy filtering is not sufficient in many applications, especially in isotopic analyses. For more details of ion probes in geochemistry, see a review paper by Ireland (1995).

Successful Applications to Geo-/Cosmo-Chemistry and Recent Advancements

The ion probes have been successfully used in a wide range of geochemical applications, and have led to the important discoveries and contributions. Just a few examples among these include: the Earth's oldest zircons dated with U-Pb isotope systems (e.g., Froude et al. 1983), the carbon isotope signature of the earliest life on Earth (e.g., Mojzis et al. 1996), the

discoveries of silicates formed prior to the solar system formation (e.g., Messenger et al. 2003; Nagashima et al. 2004), the discovery of water in rocks from the mantle of the supposedly bone-dry Moon from OH analyses in lunar glasses and minerals (e.g., Saal et al. 2008).

Since the mid-1990s, many instrumental advances on ion probes have been made. The IMS 1270/1280 instrument is equipped with the multi-collection system that significantly improves analytical precision, and achieves several tenths of a per mil in some isotope systems such as oxygen, magnesium, and sulfur (e.g., Kita et al. 2009). The NanoSIMS instrument (Cameca, France) brought a significant advance in spatial resolution for elemental and isotope analysis. It is capable of focusing the primary ion beam to <100 nm and quantitative analysis with a large sector magnet and multi-collections. In addition to the scanning isotope imaging with NanoSIMS, there has been an advance in isotope imaging using the direct ion imaging; the isotope microscope system has been developed using IMS 1270/1280 and the solid-state two-dimensional detector SCAPS (Nagashima et al. 2004). There have been instrumental advances also in SIMS-related techniques. The MegaSIMS that combines the stigmatic ion microprobe and accelerator mass spectrometer was used for measuring oxygen isotopic composition of the solar wind returned by the Genesis mission (McKeegan et al. 2011). The nanometer resolution isotope analyses are being achieved by instruments built around SIMS and laser photoionization techniques (e.g., Ebata et al. 2012).

Summary

An ion microprobe (SIMS) uses high-energy ion beam to sputter surface materials of a solid sample. Because of this sampling method, the ion microprobe allows in situ elemental and isotopic analysis of a solid sample with μm-scale spatial resolution. Since the sputtering process removes materials continuously from surface, depth profiling is a commonly used technique, and also three-dimensional analysis is possible by combining with two-dimensional imaging analysis. Ion microprobes have been successfully applied to large variety of Geo-/Cosmo-chemical studies and have led to important discoveries.

Cross-References

- ▶ Analytical Techniques
- ▶ Electron Probe Microanalysis (EPMA)
- ▶ Geochemical Reference Materials
- ▶ Geochronology and Radiogenic Isotopes
- ▶ Laser Ablation – Inductively Coupled Plasma Mass Spectrometry
- ▶ Stable Isotope Geochemistry

Bibliography

Ebata S, Ishihara M, Uchino K, Itose S, Matsuya M, Kudo M, Bojo K, Yurimoto H (2012) Development of laser ionization mass nanoscope. Surf Interface Anal 44:635–640

Froude DO, Ireland TR, Kinny PD, Williams IS, Compston W, Williams IR, Myers JS (1983) Ion microprobe identification of 4,100-4,200 Myr-old terrestrial zircons. Nature 304: 616–618

Ireland TR (1995) Ion microprobe mass spectrometry: techniques and applications in cosmochemistry, geochemistry, and geochronology. Adv Anal Geochem 2:1–118

Kita NT, Ushikubo T, Fu B, Valley JW (2009) High precision SIMS oxygen isotope analysis and the effect of sample topography. Chem Geol 264:43–57

McKeegan KD, Kallio APA, Heber VS, Jarzebinski G, Mao PH, Coath CD, Kunihiro T, Wiens RC, Nordholt JE, Moses RW, Reisenfeld DB, Jurewicz AJG, Burnett DS (2011) The oxygen isotopic composition of the Sun inferred from captured solar wind. Science 332:1528–1532

Messenger S, Keller LP, Stadermann FJ, Walker RM, Zinner E (2003) Samples of stars beyond the solar system: silicate grains in interplanetary dust. Science 300:105–108

Mojzis SJ, Arrhenius G, McKeegan KD, Harrison TM, Nutman AP, Friend CRL (1996) Evidence for life on Earth before 3,800 million years ago. Nature 384:55–59

Nagashima K, Krot AN, Yurimoto H (2004) Stardust silicates from primitive meteorites. Nature 428:921–924

Saal AE, Hauri EH, Cascio ML, Van Orman JA, Rutherford MC, Cooper RF (2008) Volatile content of lunar volcanic glasses and the presence of water in the Moon's interior. Nature 454:192–195

Ionic Radii

Hugh Rollinson and Jacob Adetunji
Geoscience, University of Derby, Derby, UK

Definition and Assumptions

An ion is an atom with an electrical charge, achieved either by gaining or losing one or more electrons. *The ionic radius of the ion (r_{ion}) of an atom (either a cation or anion) is a measure of the size of a spherical ion.* The ionic radius is similar to but different from the atomic radius for the ionic size is dependent on the distribution of its outermost electrons and is inversely proportional to the effective nuclear charge experienced by ions. It is calculated from the internuclear distance between a cation and a neighboring anion in a lattice. Ionic radii are typically reported in picometers (pm, 1×10^{-12} m) or in the older literature as Angstroms (Å), where 1 Å = 100 pm.

A typical range of ionic radii is 25–170 pm for four to eightfold coordination (see Table 1).

Methods of Measurement

The wave nature of the electron means that it is difficult to define precisely the size of an atom or of an ion, for the electron cloud density does not stop at some distance from the atomic nucleus, rather it fades away. This means that a somewhat arbitrary decision has to be made about where the boundary of an atom or ion lies. Nevertheless atoms and ions do behave as though they have characteristic sizes. The ionic radius is generally smaller than the atomic radius.

Ionic radii are measured using the methods of X-ray diffraction on solid crystalline materials. This means, of course, that the radii determined are applicable to crystalline solids. X-rays are scattered by electrons and areas of high electron density close to the nucleus can be identified. In detail the internuclear distance can be measured and equates to the sum of the radii of the cation and adjacent anion. Estimating where the boundary between the two lies can be done through the measurement of electron density contour maps and the identification of a minimum in electron density between the cation and anion (Fig. 1). More normally, however, the results are obtained from a large number of measurements which are analyzed in order to produce a self-consistent data set, for it can be assumed that if an ion is in a similar coordination in different crystal structures it will have the same radius each time. In silicate mineralogy ionic radii are most commonly calculated for ions bonded with oxygen.

The Determination of Ionic Radii

Early attempts to measure ionic radii include that of Landé (1920) who measured the ionic radius of iodine in LiI by assuming that the lithium ions are so much smaller than the iodide ions that the lithium fits into holes within the crystal lattice, allowing the iodide ions to touch. On this basis the iodide ion was deduced to be 214 pm. This value was then used to determine the radii of eight other ions. Wasastjerna (1923) estimated ionic radii by considering the relative volumes of ions as determined from electrical polarizability and measurements of refractive index. These results were extended by Goldschmidt (1926). Both Wasastjerna and Goldschmidt used a value of 132 pm for the O^{2-} ion. Pauling (1960) used a semi-empirical method, a combination of theoretical and experimental, to determine the ionic radii based on the concept of electronegativity and effective nuclear charge.

The Shannon (1976) Dataset: "Effective Ionic Radii"

The principal source of ionic radii now used in mineralogy and geochemistry is that of Shannon (1976). This study was built on the earlier work of Shannon and Prewitt (1969) who determined cation radii in oxides and fluorides. The current dataset is based upon the large number of crystal structure refinements that were available by the mid-1970s and is based upon refined oxide and fluoride data from Shannon and Prewitt (1969) augmented with data from "halides, chalcogenides and molecular inorganic compounds." The usefulness of these data was because ionic radii were reported for the different oxidation states of an element taking account of differences of coordination number (the number of anions in contact with a single cation), electronic spin state (d-orbital electron pairing in transition metals) and were calculated to take account of covalency, repulsive forces, and polyhedral distortion. The ionic radii were determined to a first approximation from their internuclear distances and then refined using plots of radii versus unit cell volume (r^3 vs V), whose regular curvilinear form allowed the prediction of radii. Further refinement was made using plots of radii versus coordination number and radii versus oxidation state.

Ionic radii are reported by Shannon (1976) in two forms – *crystal radii* based upon the radius of the oxygen anion (O^{2-}) in sixfold coordination = 126 pm (and F^- in sixfold coordination = 119 pm) and their *effective ionic radii* based upon the oxygen anion (O^{2-}) in sixfold coordination = 140 pm (and F^- in sixfold coordination = 133 pm). The effective ionic radii are the values which have been adopted in mineralogy and geochemistry. They have been calculated from internuclear distances by the subtraction of the relevant cation value and differ from crystal radii by the constant value of 14 pm. The term effective ionic radii is intended to indicate that while these values are useful they are not necessarily "real" and are applicable to bonds which have a significant degree of ionic character. A summary of mineralogically and petrologically useful ionic radii is given in Table 1.

Whittaker and Muntus (1970) proposed a set of values intermediate between the crystal radii and the ionic radii of Shannon and Prewitt (1969) based upon O^{2-} = 126 pm in order to conform with the "radius ratio principles of crystal chemistry." These values have not been widely adopted. Ghosh and Biswas (2003) have provided a more recent theoretical/quantum mechanical approach in the calculation of ionic radii but in their study ignore the importance of the coordination state in governing differences in ionic size. Hence these values have not been adopted in geochemistry.

The ionic radii of Shannon (1976) are most useful for oxides (including silicates). A separate set of values has been determined for sulfides (Shannon 1981) where the

Ionic Radii, Table 1 Ionic radii for petrologically important major and trace elements (Data from Shannon 1976)

				Coordination Number				
ion	charge	spin	Z	4	5	6	7	8
O	-2		*8*	138		140		142
F	-1		*9*	131		133		
Li	1		*3*	59		76		92
Na	1		*11*	99	100	102	112	118
K	1		*19*	137		138	146	151
Rb	1		*37*			152	156	161
Cs	1		*55*			167		174
Mg	2		*12*	57	66	72		89
Ca	2		*20*			100	106	112
Sr	2		*38*			118	121	126
Ba	2		*56*			135	138	142
Al	3		*13*	39	48	53.5		
Si	4		*14*	26		60		
Ti	2		*22*			86		
Ti	3		*22*			67		
Ti	4		*22*	42	51	60.5		74
V	2		*23*			79		
V	3		*23*			64		
V	4		*23*		53	58		72
V	5		*23*	35.5	46	54		
Cr	2	high	*24*			80		
Cr	2	low	*24*			73		
Cr	3		*24*			61.5		
Cr	4		*24*	41		55		
Cr	5		*24*	34.5		49		57
Cr	6		*24*	26		44		
Mn	2	high	*25*	66	75	83	90	
Mn	2	low	*25*			67		
Mn	2		*25*					96
Mn	3		*25*		58			
Mn	3	high	*25*			64.5		
Mn	3	low	*25*			58		
Mn	4		*25*	39		53		
Mn	5		*25*	33				
Mn	6		*25*	25.5				
Mn	7		*25*	25		46		
Fe	2	high	*26*	63		78		92
Fe	2	low	*26*			61		
Fe	3	high	*26*	49		64.5		78
Fe	3	low	*26*			55		
Fe	3		*26*		58			
Fe	4		*26*			58.5		

(*continued*)

Ionic Radii, Table 1 (continued)

				Coordination Number				
ion	charge	spin	Z	4	5	6	7	8
Fe	6		*26*	25				
Fe			*26*					
Co	2	high	*27*	58		74.5		
Co	2	low	*27*			65		
Co	2		*27*		67			90
Co	3	high	*27*			61		
Co	3	low	*27*			54.5		
Co	4	high	*27*			53		
Co	4		*27*	40				
Ni	2		*28*	55	63	69		
Ni	3	high	*28*			60		
Ni	3	low	*28*			56		
Ni	4	low	*28*			48		
Nb	3		*41*			72		
Nb	4		*41*			68		79
Nb	5		*41*	48		64	69	74
Ta	3		*73*			72		
Ta	4		*73*			68	69	
Ta	5		*73*			64		74
Zr	4		*40*	59	66	72	78	84
Hf	4		*72*	58		71	76	83
Th	4		*90*			94		105
U	3		*92*			102.5		
U	4		*92*			89	95	100
U	5		*92*			76	84	
U	6		*92*	52		73	81	86
La	3		*57*			103.2	110	116
Ce	3		*58*			101	107	114.3
Pr	3		*59*			99		112.6
Nd	3		*60*			98.3		110.9
Pm	3		*61*			97		109.3
Sm	3		*62*			95.8	102	107.9
Eu	3		*63*			94.7	101	106.6
Gd	3		*64*			93.8	100	105.3
Tb	3		*65*			92.3	98	104
Dy	3		*66*			91.2	97	102.7
Ho	3		*67*			90.1		101.5
Er	3		*68*			89	94.5	100.4
Tm	3		*69*			88		99.4
Yb	3		*70*			86.8	92.5	98.5
Lu	3		*71*			86.1		97.7

effects of metal-metal and anion-anion bonding also need to be accounted for. Bartelmehs et al. (1989) show that calculated ionic radii for sulfides are 12 pm larger than those for equivalent oxides.

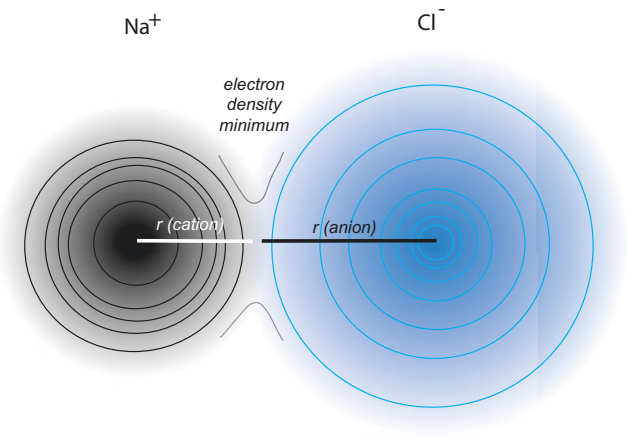

Ionic Radii, Fig. 1 Schematic electron density map for the ionic solid NaCl showing the electron density contours, the electron density minimum between the two ions, and the ionic radii

Patterns in Ionic Radii

As noted above, the ionic radius varies with coordination number, spin state, and other parameters; nevertheless, periodic trends can still be recognized (Fig. 2). It can be seen that ionic radii increase when descending a periodic group (Fig. 2a) and ionic size (for the same ion) increases with increasing coordination number (Fig. 2a, b). Ions in a high-spin state will be larger than the same ion in a low-spin state (see Table 1). Most commonly the ionic radius decreases with increasing positive charge but in anions increases with increasing negative charge.

The Use of Ionic Radii in Mineralogy and Petrology

Classically an accurate knowledge of ionic radii have been used to solve crystal structure types and problems of coordination in mineralogy. With the advent of precise methods of mineral analysis ionic radii have also become useful in solving complex ionic substitutions in minerals. This was formalized by Goldschmidt (1926) who formulated a series of "rules of substitution." These are summarized by White (2013) as follows:

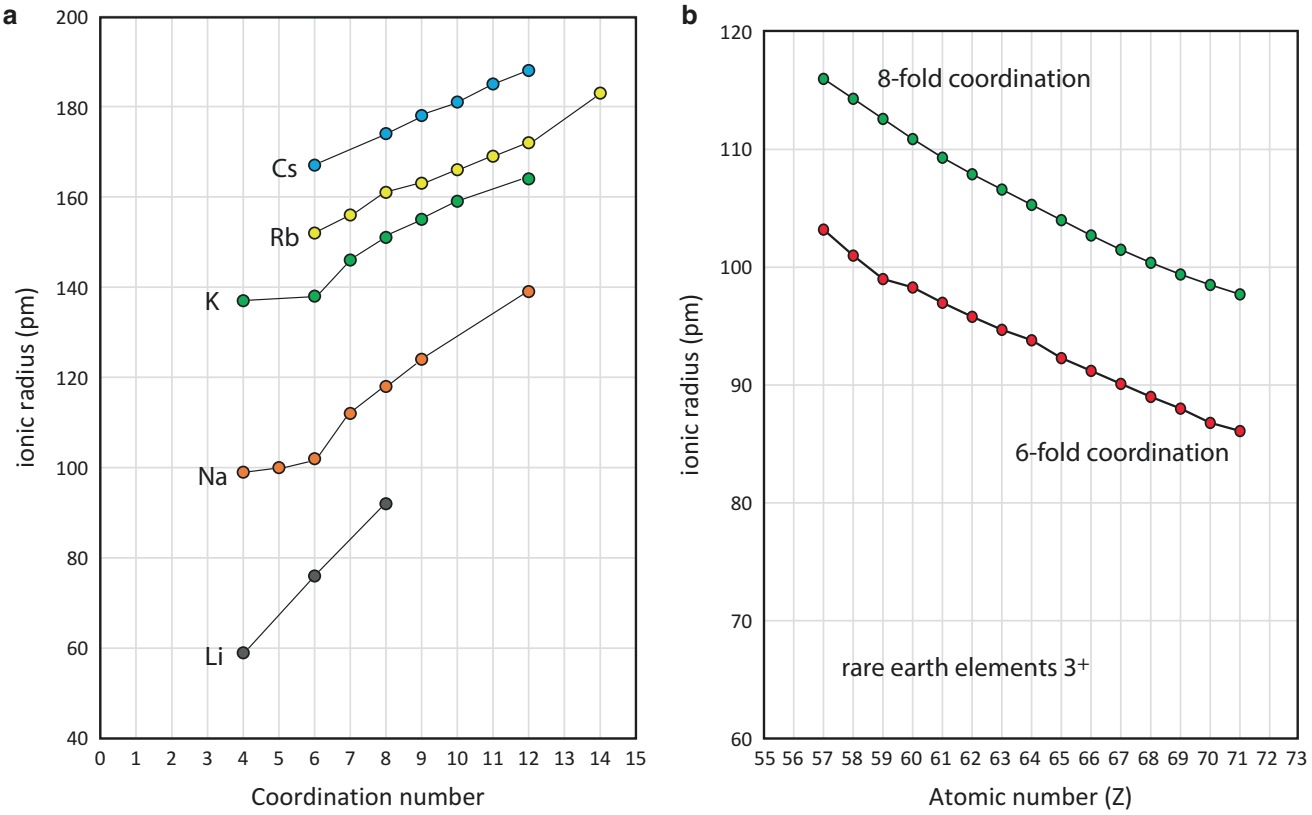

Ionic Radii, Fig. 2 (**a**) Ionic radii for the Group 1 alkali metals showing the increase in ionic radius with increase in atomic number through the group and the increase in ionic radius with coordination number; (**b**) ionic radii for the ions of the rare earth elements with a 3+ charge showing the decrease in ionic radius with increasing atomic number for ions in sixfold and eightfold coordination

1. If two ions have the same radius and the same charge they will enter a given lattice site with equal facility.
2. If two ions have similar radii and the same charge the smaller ion will enter a given site more readily.
3. If two ions have similar radii the ion with the higher charge will enter a given site more readily.
4. Whenever a substitution is possible between two elements with significantly different electronegativities the one with lower electronegativity will be preferentially incorporated.

More recently, however, an accurate knowledge of ionic radii has become important in understanding mineral-melt partition coefficients and in diffusion studies in minerals and melts. For trace elements, Blundy and Wood (2003) show how the lattice strain model of element partitioning predicts a relationship between the log of the mineral-melt partition coefficient and ionic radius, such that for an isovalent series of ions in a particular mineral phase with a specific coordination they define a near-parabolic relationship. These plots are known as Onuma diagrams. Interestingly Tiepolo et al. (Tiepolo et al. 2000) show how subtle differences in partition coefficient as a result of small mineral-chemical differences within amphiboles result in the differential portioning of Nb and Ta requiring a small difference in their ionic radii, differences beyond the limits of resolution of the Shannon (1976) radii.

There is also a relationship between ionic radius and the rate of diffusion in minerals. This is illustrated in the study of Van Orman et al. (2001) who show that in clinopyroxene the diffusion rates of the rare earth elements decrease significantly with increasing ionic radius. They show that the diffusion rate of La is ca 35 times slower than that for the smaller ion of Yb and argue that the relationship between diffusivity and ionic radius is consistent with an elastic strain model for the motion of an ion through a crystal. These results have huge relevance for disequilibrium melting and isotopic equilibrium in the Earth's mantle.

Summary

The ionic radius of the ion of an atom is a measure of the size of a spherical ion. The principal source of ionic radii now used in mineralogy and geochemistry is that of Shannon (1976) and is based upon crystal structure refinements of oxide and fluoride structures. The data set was adopted in geochemistry and mineralogy because ionic radii were reported for the different oxidation states of an element taking account of differences in coordination number, electronic spin state and were calculated to take account of covalency, repulsive forces, and polyhedral distortion. Initially ionic radii were used to solve crystal structure types but increasingly they are used in the understanding of mineral-melt partition coefficients and diffusion studies.

References

Bartelmehs KL, Gibbs GV, Boisen MB Jr (1989) Bond length and bonded-radii variations in sulfide molecules and crystals containing main-group elements: a comparison with oxides. Am Mineral 74:620–626

Blundy J, Wood B (2003) Partitioning of trace elements between crystals and melts. Earth Planet Sci Lett 210(3–4):383–397. https://doi.org/10.1016/S0012-821X(03)00129-8

Ghosh DC, Biswas R (2003) Theoretical calculation of absolute radii of atoms and ions. Part 2. The ionic radii. Int J Mol Sci 4:379–407

Goldschmidt VM (1926) Die gesetze der krystallochemie. Naturwissenschaften 14(21):477–485

Landé CA (1920) Uber die Grösse der Atome. Z Phys 1(3):191–197

Pauling L (1960) The nature of the chemical bond and the structure of molecules and crystals: an introduction to modern structural chemistry, vol 18. Cornell University Press, Ithaca

Shannon RD (1976) Revised ionic radii and systematic studies of interatomic distances in halides and chalcogenides. Acta Crystallogr A32:751–767

Shannon RD (1981) Bond distances in sulphides and a preliminary table of sulfide crystal radii. In: O'Keeffe M, Navrotsky A (eds) Structure and bonding in crystals, vol II. Academic, New York, pp 53–70

Shannon RD, Prewitt CT (1969) Effective ionic radii in oxides and fluorides. Acta Crystallogr B25:925–946. https://doi.org/10.1107/S0567740869003220

Tiepolo M, Vannucci R, Oberti R, Foley SF, Botazzi P, Zanetti A (2000) Nb and Ta incorporation and fractionation in titanian pargasite and kaersutite: crystal-chemical constraints and implications for natural systems. Earth Planet Sci Lett 176:185–201

Van Orman JA, Grove TL, Shimizu N (2001) Rare earth element diffusion in diopside: influence of temperature, pressure and ionic radius, and an elastic model for diffusion in silicates. Contrib Mineral Petrol 141:687–703

Wasastjerna JA (1923) On the radii of ions. Comment Phys-Math Soc Sci Fenn 1(38):1–25

White WM (2013) Geochemistry. Wiley-Blackwell, Oxford, 660 pp

Whittaker EJW, Muntus R (1970) Ionic radii for use in geochemistry. Geochim Cosmochim Acta 34:945–956

Iridium

Thomas C. Meisel
General and Analytical Chemistry, Montanuniversität Leoben, Leoben, Austria

Element Data

Atomic Symbol: Ir
Atomic Number: 77
Atomic Weight: 192.217(3)
Isotopes and Abundances: ^{191}Ir 37.3 ± 2% and ^{193}Ir 62.7 ± 2%
Atm Melting Point: 2447 °C
1 Atm Boiling Point: 4428 °C
Common Valences: +3 and +4

(*continued*)

Ionic Radii: 3+: 68 pm, 4+: 63 pm
Pauling Electronegativity: 2.20
First Ionization Energy: 880 kJ/mol
Chondritic (CI) Abundance: 462 μg/kg (Fischer-Gödde et al. 2010)
Silicate Earth Abundance: 3.5 μg/kg (Becker et al. 2006)
Crustal Abundance: 0.022 μg/kg (Park et al. 2012)
Seawater Abundance: 0.5 to 1 fmol/kg
Core Abundance: ~2.6 mg/kg (McDonough 2014)

Properties

Iridium ($_{77}$Ir) with the electron configuration [Xe] $4f^{14}\ 5d^7\ 6s^2$ is a d-block transition element in the cobalt group (cobalt, rhodium, iridium, and meitnerium) and is one of the six platinum group elements (PGE). The atomic radii of the Os, Ir, Pt subgroup, caused by the lanthanide contraction of the 4*f* group elements, are similar compared to the Ru, Rh, Pd subgroup of the PGE. The almost doubling of the number of nucleons with the same atomic radii leads to elements with the high density and chemical inertness. Iridium possesses a density 22.56 g/cm^3, which is only slightly smaller than that for Os with 22.58 g/cm^3. The valence shell configuration and the high effective nuclear charge are expressed in the high tendency toward complex formation (similar to the horizontal neighbors Os and Pt). Small differences between the valence shells (6*s* and 5*d*) allow iridium to occur in several oxidation states. Possible oxidation states are −1, 0, +1, +2, +3, +4, +5, and +6 with +3 and +4 being the most stable forms. The behavior toward acids on the other hand is similar to its vertical neighbor Rh. Iridium has two stable isotopes ^{191}Ir and ^{193}Ir with mole fractions of 0.373(2) and 0.627(2), respectively. The most stable radioisotope is ^{192}Ir, a strong gamma ray emitter used as a source in industrial radiography.

History and Use

In 1804 iridium ($_{77}$Ir) was discovered by Smithson Tennant in the black residues after aqua regia digestion of crude alluvial platinum ore (Hunt 1987). Iridium forms colorful salts giving this metal the name after an ancient Greek word literally meaning "of rainbows" (ἰριοειδής *irio-eides*).

Specialized applications of Ir are found where high melting point, corrosion resistances, and hardness are of importance. The corrosion and heat resistance, in combination with hardness, allow special applications. Iridium or Pt–Ir alloys have low wear and are used as crucibles, spinnerets, etc. Space and aircraft engine parts are made of iridium alloys to increase the lifetime. Iridium can also be found in corrosion-resistant spark plugs. Iridium is also used in industrial catalysis and also catalytic converters. Enrichments of Ir can be found in the environment of higher traffic density (Fritsche and Meisel 2004).

Geochemical Properties

Iridium is one of the most sensitive and selective elements for neutron activation analysis (NAA). Using this method, a large body of Ir data has been acquired on terrestrial and extraterrestrial samples during the last 50 years. The presence of two stable isotopes (^{191}Ir and ^{193}Ir) also allows the application of isotope dilution mass spectrometry, after preconcentration chemistry, as an accurate measurement procedure, which is now state of the art for Ru, Pd, Re, Os, Ir, and Pt analysis (Meisel and Horan 2016).

Iridium and Mass Extinctions

The marked difference between the meteoritic and crustal Ir abundances and the availability of NAA in the 1970s for the analysis of low abundance sediments lead to the common hypothesis that meteorite impacts are the source for the Ir anomalies observed at Cretaceous–Paleogene (K–Pg also known as Cretaceous–Tertiary or K/T) boundaries observed worldwide (Alvarez et al. 1980). These few mm-thin layers are also associated with shocked quartz, which is clear evidence for high velocity impacts. Iridium anomalies have also been observed in sediment layers associated with other mass extinction events (e.g., Devonian–Carboniferous or Permian–Triassic boundary (Holser et al. 1989; Wang et al. 1993)).

Natural Occurrence

Iridium occurs as native metal mostly associated with common impurities of Pt, Au, Pd, Cu, and Fe or as alloys mostly with Os, Ru, Pt, and Fe. Several Ir sulfides (e.g., cuproiridsite $CuIr_2S_4$) and sulfarsenides (e.g., iridarsenite $[(Ir,Ru)As_2]$) exist in nature (O'Driscoll and González-Jiménez 2016).

The CI concentration for Ir of 462 μg/kg (Fischer-Gödde et al. 2010) is thus well established. Iridium is highly enriched in iron meteorites relative to silicate phases in chondrites. As the results of highly siderophile–chalcophile geochemical behavior, iridium is highly depleted in the Earth's mantle and crust (Day et al. 2016). For upper mantle rocks 3.5 μg/kg (Becker et al. 2006) and for the upper continental crust 0.022 μg/kg (Park et al. 2012) are the estimated abundances, making Ir, along with Rh, Ru, Re, and Os, to be one of the least abundant nonradioactive elements in the Earth's crust.

Biological Utilization and Toxicity

Iridium and iridium compounds have no biological function. Very little is known about the aqueous behavior, the mobility, and toxicity of iridium compounds because of its rareness and very limited industrial use. A possible $Ir(OH)_3^0$ species in the concentration range of 0.5 to 1 fmol/kg has been described for seawater (Bruland and Lohan 2003).

Summary

Iridium is one of the rarest elements in the Earth's crust and is characterized by geochemical behavior similar to that of Os and Ru. As a marker for influx of extraterrestrial material, there has been a significant amount of data collected over the decades. Combined thermal, corrosion, and chemical resistance allows special industrial applications.

Cross-References

- Iron Meteorites
- Native Minerals
- Neutron Activation Analysis
- Osmium
- Palladium
- Platinum
- Platinum Group Elements
- Rhodium
- Ruthenium
- Siderophile Elements

References

Alvarez LW, Alvarez W, Asaro F, Michel HV (1980) Extraterrestrial cause for the cretaceous-tertiary extinction. Science 208: 1095–1108

Becker H, Horan MF, Walker RJ, Gao S, Lorand JP, Rudnick RL (2006) Highly siderophile element composition of the earth's primitive upper mantle: constraints from new data on peridotite massifs and xenoliths. Geochim Cosmochim Acta 70:4528–4550

Bruland KW, Lohan MC (2003) Controls of trace metals in seawater. In: Elderfield H (ed) The oceans and marine geochemistry, vol 6. Elsevier Pergamon, Amsterdam, pp 23–47

Day JMD, Brandon AD, Walker RJ (2016) Highly siderophile elements in earth, mars, the moon, and asteroids. In: Day JMD, Harvey J (eds) Highly Siderophile and strongly Chalcophile elements in high temperature geochemistry and cosmochemistry, vol 81. Mineralogical Society of America, Chantilly/Virgina, pp 161–238

Fischer-Gödde M, Becker H, Wombacher F (2010) Rhodium, gold and other highly siderophile element abundances in chondritic meteorites. Geochim Cosmochim Acta 74:356–379

Fritsche J, Meisel T (2004) Determination of anthropogenic input of Ru, Rh, Pd, Re, Os, Ir and Pt in soils along Austrian motorways by isotope dilution ICP-MS. Sci Total Environ 325:145–154

Holser WT, Schönlaub H-P, Attrep MJ et al (1989) A unique geochemical record at the Permian/Triassic boundary. Nature 337:39–44

Hunt LB (1987) History of iridium. Platin Met Rev 31:32–41

McDonough WF (2014) 3.16 – compositional model for the Earth's core A2. In: Turekian KK, Holland HD (eds) Treatise on Geochemistry, 2nd edn. Elsevier, Oxford, pp 559–577

Meisel T, Horan MF (2016) Analytical methods for the HSE elements. In: Day JMD, Harvey J (eds) Highly Siderophile and strongly Chalcophile elements in high temperature geochemistry and Cosmochemistry, vol 81. Mineralogical Society of America, Chantilly/Virgina, pp 89–106

O'Driscoll B, González-Jiménez JM (2016) An inventory and overview of natural occurrences of the platinum-group minerals (PGM) in extraterrestrial and terrestrial rocks. In: Day JMD, Harvey J (eds) Highly Siderophile and strongly Chalcophile elements in high temperature geochemistry and Cosmochemistry, vol 81. Mineralogical Society of America, Chantilly/Virgina, pp 489–578

Park J-W, Hu Z, Gao S, Campbell IH, Gong H (2012) Platinum group element abundances in the upper continental crust revisited – new constraints from analyses of Chinese loess. Geochim Cosmochim Acta 93:63–76

Wang K, Attrep MJ, Orth CJ (1993) Global iridium anomaly, mass extinction, and redox change at the Devonian-Carboniferous boundary. Geology 21:1071–1074

Iron

Munir Humayun
Department of Earth, Ocean and Atmospheric Science, Florida State University, Tallahassee, FL, USA

Element Data

Atomic Symbol: Fe
Atomic Number: 26
Atomic Weight: 55.847 g/mol
Isotopes and Abundances: ^{54}Fe 5.845%, ^{56}Fe 91.754%, ^{57}Fe 2.119%, ^{58}Fe 0.282%
1 bar Melting Point: 1,538 °C
1 bar Boiling Point: 2,862 °C
Common Valences: 0, +2, +3
Ionic Radii: Fe^{+2} 78 pm (6-fold, high-spin); Fe^{+3} 64.5 pm (6-fold, high-spin)
Pauling Electronegativity: 1.83
First Ionization Potential: 762.5 kJ/mol
Chondritic (CI) Abundance: 18.28 wt. %
Silicate Earth Abundance: 6.26 wt. %
Crustal Abundance: 5.04 wt. %
Seawater Abundance: 30 pg/g
Core Abundance: 78–88 wt. %

Properties

Iron is one of a small group of metals that has been known to humans since antiquity. An entire period of human history, the Iron Age, followed the Bronze Age, as iron alloys replaced Cu alloys for tools and weapons. Since the Industrial Revolution, the production of steel makes iron one of the 2–3 most highly used elements.

Iron is one of the most abundant elements in the terrestrial planets, constituting ~30 wt. % of the Earth, Venus, and Mars. The electronic configuration for neutral Fe is Ar, $3d^6$, $4s^2$; for ferrous ion, Fe^{+2}, is Ar, $3d^6$; and for ferric ion, Fe^{+3}, is: Ar, $3d^5$. As a transition metal, Fe ions have a high-spin state and a low-spin state. The high-spin state of ferrous iron has one orbital (t_{2g}) with paired electrons and 4 orbitals with unpaired electrons contributing its paramagnetic property, while its low-spin state has 3 orbitals (t_{2g}) with fully paired electrons and is diamagnetic. The high-spin state of ferric iron has 5 orbitals each filled with one unpaired electron contributing its paramagnetic property, while its low-spin state has 2 (t_{2g}) orbitals filled with paired electrons and one orbital (t_{2g}) with an unpaired electron and is also paramagnetic. Ferrous and ferric iron both exhibit high-spin states in minerals at low pressure. The unpaired electrons in Fe cause the phenomenon of ferromagnetism. Iron has four stable isotopes. It has one radioactive isotope of interest in cosmochronology and as a planetary heat source: ^{60}Fe (half-life 2.6 Ma).

History and Use

Meteoritic iron has been used in tool making since before civilization (Comelli et al. 2016). The oldest known artifacts include beads found at Gerzeh dating to 3,500 BC and a dagger from Ur, dating to 3,000 BC, both of which contain high nickel contents (7–10 wt. %) indicative of meteoritic iron (Tylecote 1992). The earliest smelting of iron may have been in Anatolia before 2,000 BC. By the start of the Iron Age in 1,200 BC, techniques for smelting iron were widely developed in Africa, Eurasia, and the Indian subcontinent, and steel replaced bronze for weapons and tools.

Smelting of iron ores using coke (carbon) in blast furnaces made iron alloys, especially steels, the most important metals of the Industrial Revolution. Iron alloys are widely used to produce the infrastructure of modern civilization including transportation (e.g., trains, ships, automobiles, aircraft, and spacecraft) and construction (e.g., skyscrapers).

Isotope Cosmochemistry

Iron is the ninth most-abundant element in the cosmos, comparable in abundance to Si and Mg. Given that Fe (A = 56) is approximately twice as heavy as Si (A = 28), the exceptional abundance of Fe stands out from the abundances of other heavy elements that form the iron peak, a group that includes Cr, Mn, Fe, Co, and Ni. The Fe peak nuclei have the highest nuclear binding energy/nucleon, and ^{56}Ni, the progenitor of ^{56}Fe, is a double magic number ($Z = 28$, $N = 28$) nucleus. The synthesis of the isotopes of Fe occurs mainly during nuclear statistical equilibrium burning in the cores of large stars ($M > 15\ M_{solar}$), in the final fusion step preceding a supernova explosion. The most abundant isotope, ^{56}Fe, is produced as ^{56}Ni (half-life 5.9 days), the subsequent decay of which yields ^{56}Co (half-life 77 days) and then ^{56}Fe. Core-collapse (Type II) supernovae produce a massive amount of Fe in their cores, but much of this iron ends up in the subsequent neutron star, so that Type I supernovae (accreting white dwarfs) contribute about half of the Fe in the galaxy (Clayton 2003). The Fe peak nuclei, particularly ^{56}Fe, are the seed nuclei for both the slow neutron capture (s-process) and the rapid neutron capture (r-process) heavy nuclei. Neutron capture modifies the isotope abundances of Fe nuclei, particularly for the neutron-rich ^{58}Fe (s-process). The short-lived ^{60}Fe nuclide (half-life 2.6 Ma; decays to stable ^{60}Ni) is of interest in cosmochemistry both for chronology in the early solar system and as a possible radiogenic heat source in planetary cores (Sahijpal et al. 2007). This isotope has been found to occur globally in deep-sea sediments about 3 Ma old, implying a supernova event close enough to increase the terrestrial ^{60}Fe inventory (Wallner et al. 2016).

Geochemical Behavior

Iron Mineralogy

Telluric iron is metallic iron formed naturally on Earth. It is known from only a handful of locations where the iron contained in basaltic magmas became reduced by carbonaceous sedimentary rocks. The largest telluric iron crystal (22 tons) is found at Uivfaq Disko Island, Greenland, in Tertiary basalts (Bird et al. 1981). Other occurrences have been documented in intrusions in the Permian Siberian Traps (Ryabov and Lapkovsky 2010). Several extraterrestrial minerals, including taenite (γ-Fe, fcc) and kamacite (α-Fe, bcc), consist of native iron alloyed with >5 wt. % Ni. These minerals are the main constituents of iron meteorites, with some of the largest irons weighing as much as 60 tons (Buchwald 1975). In meteorites, Fe also occurs in carbides, oxides, phosphides, and sulfides, e.g., cohenite (Fe_3C), magnetite (Fe_3O_4), schreibersite (Fe-Ni_3P), and troilite (FeS) (Mittlefehldt et al. 1998). The ordinary chondrites, enstatite chondrites, and carbonaceous chondrites of the CB and CR groups contain abundant metallic Fe-Ni alloy. Aqueous alteration in the other carbonaceous chondrites (e.g., CI, CM, CK) resulted in the production of magnetite and Fe-sulfides as the principal Fe hosts.

Ferrous iron is an abundant component of meteoritic and terrestrial minerals and is found in olivines, pyroxenes, spinels, etc., and even as nearly pure fayalite (Brearley and Jones 1998). The fayalite content of olivine is a means of classifying chondrites of low metamorphic grade. Overall, the Fe^{+2} content of olivines and pyroxenes decreases as a function of parent asteroidal redox state with enstatite chondrites having the lowest Fe^{+2} contents (<1 mol. %) in silicate minerals, terrestrial mantle minerals at about 10 mol. %, and lunar and martian minerals at about 20 mol. % (Righter et al. 2006). All terrestrial planets and meteorites (representing the asteroid belt) contain Fe-Mg silicates that are too ferroan to have formed in equilibrium with hot hydrogen gas. The ferrous iron contents of chondritic silicates imply that chondrule formation must have occurred in gases that were enriched in oxygen (by the addition of vaporized ices) implicating asteroidal collisions in their formation (Grossman et al. 2008).

Core Geochemistry

Iron is the dominant constituent of the Earth's core, but it has long been known that pure metallic iron is too dense to explain the observed density of the core. Both the outer and inner core must contain a significant amount of lighter elements (about 10%) in the form of FeO, Fe-Si, or Fe-S, alloyed with liquid or solid metallic iron (Poirier 1994).

The Earth's inner core is solid (ε-Fe, hcp) due to the high confining pressure (330 GPa) at the inner core-outer core boundary. The melting relations of Fe alloys at megabar pressures place a constraint on the temperature of the inner core-outer core boundary (≤6,000 K; Ma et al. 2004) lowered by the addition of Si, O, and S in that relative order (e.g., Fischer et al. 2013).

The high entropy of melting of iron (118 $J.kg^{-1}.K^{-1}$) makes crystallization of the inner core an important heat source for the Earth, powering the magnetic field. If the core has no other source of heat, then the rapid rate of crystallization of the inner core required to supply the inferred heat flux implies a young (<2.5 Ga) inner core (Labrosse et al. 2001).

Mantle Geochemistry

Iron, in the form of ferrous iron (Fe^{+2}), is the most abundant transition metal in the mantle where it is distributed in all the major phases constituting the upper mantle: olivine, orthopyroxene, clinopyroxene, spinel, and garnet. The mole fraction of Fe in mantle olivine is 11 ± 2% (McDonough and Sun 1995). In the lower mantle, iron is partitioned principally into ferropericlase, (Mg, Fe)O, and less in bridgmanite, (Mg, Fe)SiO_3 (Lin et al. 2013).

The low-spin forms of ferrous (62 pm vs. 78 pm) and ferric (55 pm vs. 64.5 pm) iron have smaller ionic radii favored by denser mineral structures at higher pressures. Evidence from mineral physics and geophysics indicates that iron undergoes a high-pressure spin transformation in the Earth's lower mantle from the high-spin to the low-spin state at depths below 1,700 km (Badro et al. 2003; Lin et al. 2013).

The distribution of iron in the upper mantle is considered to be relatively uniform, at 6.26 wt. % (McDonough and Sun 1995). The distribution of Fe (Fe/Mg) plays a principal role in controlling the density of the mantle, with competing influences from Si and temperature. Tomographic evidence indicates that iron is heterogeneously distributed in the mantle, with higher iron contents in the lower mantle beneath the African and Pacific superswells (Trampert et al. 2004). Chemical evidence that there are higher iron contents in the mantle beneath plumes comes from measurements of the Fe/Mn ratio in volcanic lavas erupted at mid-oceanic ridges versus those erupted in plume settings (Fig. 1), particularly Hawaiian lavas (Humayun et al. 2004; Huang et al. 2007). The Fe/Mg ratio is strongly affected by crystal fractionation processes, but the Fe/Mn ratio remains nearly constant during mantle melting (Davis et al. 2013) and subsequent fractionation processes (Fig. 1), unless chemical interactions occur between the core and the mantle. As the largest repository of iron on Earth, the core exerts a subtle influence on the mantle's Fe/Mg ratio by exchanging FeO (say) between solid ferropericlase in the lowermost mantle and the liquid outer core.

The ratio of ferric to ferrous iron in the mantle is controlled by the mantle's mineralogy and oxygen fugacity (Frost and McCammon 2008). The $Fe^{+3}/\Sigma Fe$ of the Earth's mantle has been a subject of much debate since it is several log units higher than expected from iron-wüstite equilibrium. One compelling explanation of the higher $Fe^{+3}/\Sigma Fe$ of the upper mantle involves the coupled substitution, $Fe^{+3}Al^{+3} = Mg^{+2}Si^{+4}$, into bridgmanite in the lower mantle that is thermodynamically favored where the Fe^{+3} is formed by the high-pressure disproportionation of FeO, as $3FeO = Fe_2O_3 + Fe$ (Frost and McCammon 2008). Removal of some of the metal formed in this reaction into the core would have left the lower mantle higher in $Fe^{+3}/\Sigma Fe$. Whole mantle convection then supplied oxidized material to the upper mantle, resulting in an excess $Fe^{+3}/\Sigma Fe$ relative to other planetary mantles (e.g., Mars) that do not reach the stability field of bridgmanite.

Comparative Planetology of Iron

The $Fe^{+3}/\Sigma Fe$ of the Earth's mantle is set near the Quartz-Fayalite-Magnetite (QFM) buffer (Bryndzia and Wood 1990; Bezos and Humler 2005; Cottrell and Kelley 2011), making the Earth's mantle arguably the most oxidized planetary mantle. The mantles of other planets and the Moon have lower redox states (Righter et al. 2006). New techniques, like synchrotron micro-X-ray Absorption Near Edge Structure (micro-XANES), are rapidly advancing our understanding of iron oxidation states in the mantle (Cottrell and Kelley 2011, 2013).

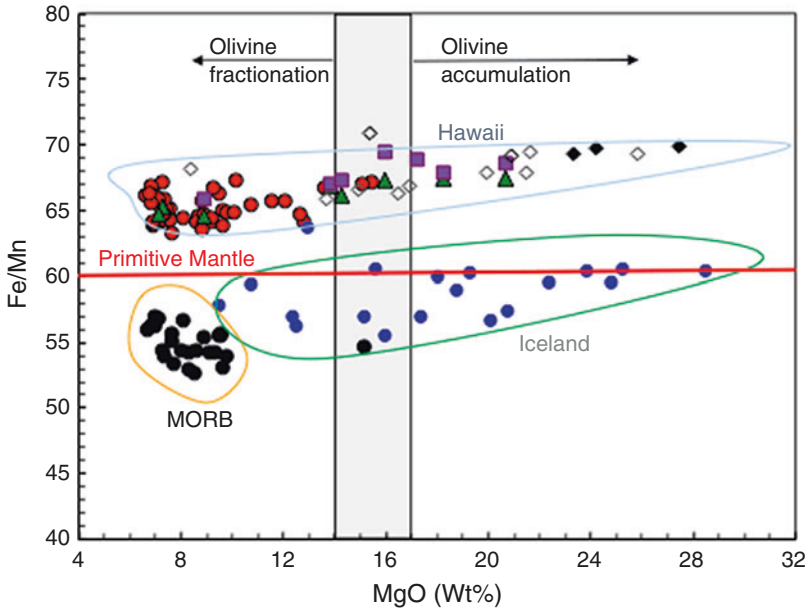

Iron, Fig. 1 Precise Fe/Mn ratios of basaltic rocks determined by solution ICP-MS for mid-oceanic ridge basalts (*MORB*), picrites from Iceland, and picrites and basalts from Hawaiian volcanoes (Humayun et al. 2004; Huang et al. 2007). The Primitive Mantle estimated from peridotites is from McDonough and Sun (1995). The primary melt compositions of Hawaiian lavas are shown as the *gray band*, with the compositional range controlled by olivine accumulation or loss. The Hawaiian volcanoes are individually depicted, Loihi: *filled diamonds*; Kilauea: *green triangles*; Mauna Loa: *open diamonds*; Mauna Kea: *purple squares*; Ko'olau: *red circles*

The surface rocks of Mercury contain the lowest known FeO abundances (~2–4%) of a planetary surface (Weider et al. 2012), while the Moon and Mars have ~15% FeO in their crustal rocks. Terrestrial MORBs have ~6–8% FeO, which may represent high-pressure dissolution of FeO into the Earth's core rather than primary differences in redox state between the Earth, Moon, and Mars (Rubie et al. 2004).

Iron in Earth's Crust

Iron is supplied to the crust mainly as ferrous iron from the mantle ($Fe^{+3}/\Sigma Fe$ ~0.15), but is subsequently oxidized by atmospheric oxygen at the weathering interface between the crust and the atmosphere. Ferrous iron is the most abundant of three natural reducing agents, the others being sulfide (S^{-2}) and organic carbon, $(CH_2O)_n$, in crustal sediments that act as sinks for atmospheric oxygen. Much of the oxidation may be microbially mediated. Modern soils are dominated by ferric iron (e.g., goethite, limonite, maghemite), which act to isolate the atmosphere from reduced crustal rocks.

In the oceanic crust, hydrothermal alteration converts olivine to serpentine, ±brucite, and magnetite, a process that releases significant amounts of H_2, CH_4, H_2S, and other reduced compounds, driving the oxidation of the oceanic crust. The partitioning of iron between serpentine, brucite, and fluid plays a very important role in this hydrothermal chemistry. At $T < 300$ °C, serpentine and brucite take up very little Fe compared to the initial olivine. Since wüstite and ferrous hydroxide are thermodynamically less stable relative to magnetite at these temperatures, the ferrous iron released from the alteration of olivine oxidizes with water to form magnetite and H_2 (McCollom et al. 2016). This is a process of fundamental importance in planetary science requiring olivine, water, CO_2/carbonate, and/or sulfate to create oxidized crust while upward migration of hydrogen (H_2), methane (CH_4), and hydrogen sulfide (H_2S) gases creates local highly reducing environments around serpentinization sites. Serpentinization occurs ubiquitously on Mars, icy asteroids, the Jovian moon Europa, the Saturnian moon Enceladus, Pluto, Kuiper Belt Objects, and extrasolar planets, where it might create important locales for organic synthesis.

Iron on the Martian Surface

The surface of Mars is covered with basaltic rocks exposed to an oxidizing but thin atmosphere. The modern Martian surface is extremely dry, with water frozen as permafrost in the regolith or at the poles or present as traces of water vapor in the atmosphere. In the absence of liquid water or a biosphere, the origin of the oxidized iron that creates the visually striking red hue of the fabled Red planet might be understood in terms of ancient weathering processes on Mars. The ancient Martian meteoritic breccia, NWA 7034/NWA 7533, contains 15% Fe-oxides as magnetite and maghemite, and superparamagnetic goethite, as its principal magnetic minerals of possible Noachian (3.7–4.0 Ga) origin and near IR spectra compatible with much of the Martian highlands (Gattacceca et al. 2014; Beck et al. 2015). In situ investigation by the Mars Exploration Rover (MER) *Opportunity* rover at Meridiani Planum revealed abundant hematite concretions ("blueberries") and ubiquitous jarosite, (K, Na, H_3O, X^+) $Fe_3(SO_4)_2(OH)_6$, a hydrated Fe^{+3}-sulfate, in outcrops around Eagle Crater, evidence for acidic aqueous alteration conditions on early (3.6–3.8 Ga) Mars (Squyres et al. 2004). Detailed in situ studies of iron oxidation state and mineralogy by the MER rover *Spirit* at the Columbia Hills revealed the presence of Fe^{+3}-sulfate soils (Paso Robles) of hydrothermal or fumarolic origin, hematite-rich outcrops, and goethite-

bearing outcrops formed at low water/rock ratios, together with olivine and pyroxene-bearing igneous rocks (Morris et al. 2008). Thus, the Martian iron cycle involved oxidation of basalts during weathering and aqueous alteration creating abundant secondary Fe^{+3} oxides, oxyhydroxides, and sulfates, on the early (3.6–4.0 Ga) Martian surface that have been globally distributed by subsequent aeolian activity as the modern soil (Beck et al. 2015).

Iron in Natural Waters

The solubility product of ferric hydroxide, $Fe(OH)_3$, is $\sim 10^{-36}$ M in contrast to that of ferrous hydroxide, $Fe(OH)_2$, $\sim 10^{-14}$ M (Greenwood and Earnshaw 1984), making ferric iron extremely insoluble in water. Iron is typically found in oxidized surface waters mainly in particles ranging in size from nanoparticles and colloids to larger particles, complexed with organic ligands (Wozniak et al. 2015), bound to dissolved or particulate organic matter or attached to mineral surfaces with only a small fraction as free ions (Dupré et al. 1999; Raiswell and Canfield 2012). In reducing groundwaters or sediment porewaters, microbial respiration converts Fe-oxyhydroxides to ferrous iron which can accumulate significantly until the build-up of hydrogen sulfide (H_2S) regulates the dissolved Fe^{+2} abundance by forming Fe-sulfides, marcasite, and eventually pyrite (Raiswell and Canfield 2012). The presence of pyrite or magnetite framboids in sediments indicates a microbial role for iron deposition from natural waters.

Aqueous iron is extremely low in seawater far from land. Iron exhibits a nutrient-like profile, i.e., low concentrations in surface waters (<500 m depths) increasing to a steady value of 0.4–0.8 nM concentrations in deeper water (Johnson et al. 1997). Its principal supply includes atmospheric aerosol deposition (Wozniak et al. 2015) and hydrothermal plumes in ocean bottom waters (Raiswell and Canfield 2012). The extremely low iron in surface waters results in iron being the limiting nutrient for primary marine biological productivity. This gave rise to the iron fertilization hypothesis that algal blooms stimulated by deliberately adding bioavailable iron (e.g., ferrous acetate) to surface waters of the open oceans could increase burial of organic carbon in the oceans (Raiswell and Canfield 2012). Field tests of iron fertilization have not been promising due to rapid oxidation of the iron and by remineralization of organic carbon in deeper waters (rather than burial in sediment).

Prior to the rise of oxygen in the atmosphere, the Archean ocean may have been green from high levels of dissolved ferrous iron. Annual springtime pulses of oxygen from cyanobacterial photosynthesis resulted in precipitation of insoluble ferric oxyhydroxides or magnetite. The subsequent die-off of marine microbes produced biogenic silica layers. Alternating silica-magnetite sediments were abundant in the Archean and Proterozoic periods and are termed "banded iron formations" (e.g., Hammersley formation, Western Australia). Such rocks are the principal source of iron ore for modern industry. The last episode of banded iron formation occurred during the Neoproterozoic snowball Earth (~700 Ma) due to isolation of the oceans from the atmosphere (Canfield et al. 2008). Hydrothermal sources supply the oceans with abundant iron that, in the absence of oxygen, would result in unusually high water column abundances of dissolved ferrous iron during the Neoproterozoic.

Biological Utilization and Toxicity

Iron plays an important role in biological processes due to the redox chemistry of ferrous and ferric ions, e.g., photosynthesis (iron-sulfur ferredoxins), oxygen transport (heme), metabolism (cytochromes), and nitrogen fixation (MoFe-nitrogenase). Iron is utilized as an essential nutrient by all organisms from archaea and bacteria to plants and animals. In the absence of ligands, ferric iron is extremely insoluble in biological fluids, where Fe^{+3} occurs bound to chelating molecules, like heme, ferritin, and transferrin. In humans, iron deficiency is the most common nutritional deficiency (anemia). Less commonly, iron excess can result in free Fe ions in cells, leading to iron toxicity.

Due to the low solubility of ferric iron, most organisms live in environments where iron availability is limited even when abundant Fe-minerals are present and competition for the biologically available Fe is intense. Microbes and plants secrete siderophores, molecules that complex iron from solution, to help increase biological iron availability. Proteins tightly regulate iron availability in the human body, which poses a challenge for pathogens. Stable isotope tracing of proteins and gene knockouts have helped identify the iron sources for *Staphylococcus* infections (Skaar et al. 2004), providing potential new treatment pathways involving the iron limitation of methicillin-resistant *Staphylococcus aureus* (MRSA).

The chemical cycle of iron near the Earth's surface is likely to be strongly controlled by biological processes. Microbial life plays a vital part in the weathering and dissolution of ferroan minerals by oxidizing ferrous iron to ferric iron resulting in the precipitation of new Fe-minerals. Species like *Acidithiobacillus ferrooxidans* metabolize Fe-sulfides (e.g., pyrite) at low pH releasing ferric iron-bearing sulfuric acid contributing to acid mine waste. Ferric iron-reducing organisms like *Geobacter metallireducens* and *Shewanella putrefaciens* utilize ferric iron as an electron acceptor in anaerobic respiration releasing ferrous iron. Magnetotactic bacteria precipitate magnetite in their magnetosomes. Astrobiologists employ biomineralized magnetites as fossil biomarkers. The difficulties in interpreting the biological origin of magnetite are illustrated by the debate over the origin of

magnetite in carbonate globules of the Martian meteorite, ALH 84001 (Weiss et al. 2004).

Summary

Iron (atomic number 26) is one of the most abundant elements in terrestrial planets, as the dominant constituent of the core and an important constituent of the mantle and crust. Iron naturally occurs in three valence states, as the metal (Fe^0), and as ferrous (Fe^{+2}) and ferric (Fe^{+3}) ions. As the most abundant transition metal in the Earth, it plays a dominant role in controlling oxygen fugacity in the mantle. Since antiquity (the Iron age, 1,200 BC), iron is one of the most widely used industrial raw materials, particularly in the manufacture of steel. In aqueous fluids, iron is extremely insoluble as ferric iron, and the rise of atmospheric oxygen resulted in the formation of thick sedimentary iron ore deposits (banded iron formations) that are the principal source of the metal for modern industry. Iron is an essential nutrient for all organisms, particularly in heme-proteins. Iron-deficiency is a common disease, but in rare instances iron toxicity is known.

Cross-References

- Biogeochemistry
- Chalcophile Elements
- Chondrites
- Cobalt
- Earth's Core
- Earth's Continental Crust
- Hydrothermal Alteration
- Iron Formations
- Iron Isotopes
- Iron Meteorites
- Lithophile Elements
- Mantle Geochemistry
- Magnesium
- Magnetism
- Manganese
- Mercury
- Meteorites
- Mid-Ocean Ridge Basalts (MORB)
- Nickel
- Nucleosynthesis
- Nutrients
- Ocean Biochemical Cycling and Trace Elements
- Oceanic Island Basalts
- Oxide Minerals
- Siderophile Elements
- Transition Elements

References

Badro J, Fiquet G, Guyot F, Rueff J-P, Struzhkin VV, Vanko G, Monaco G (2003) Iron partitioning in Earth's mantle: towards a deep lower mantle discontinuity. Science 300:789–791

Beck P, Pommerol A, Zanda B, Remusat L, Lorand JP, Göpel C, Hewins R, Pont S, Lewin E, Quirico E, Schmitt B, Montes-Hernandez G, Garenne A, Bonal L, Proux O, Hazemann JL, Chevrier VF (2015) A Noachian source region for the "black beauty" meteorite, and a source lithology for Mars surface hydrated dust? Earth Planet Sci Lett 427:104–111

Bezos A, Humler E. (2005) The Fe+3/SFe ratios of MORB glasses and their implications for mantle melting. Geochim Cosmochim Acta 69:711–725

Bird JM, Goodrich CA, Weathers MS (1981) Petrogenesis of Uivfaq iron, Disko Island, Greenland. J Geophys Res B86:11787–11805

Brearley AJ, Jones RH (1998) Chondritic meteorites. Rev Mineral 36:398 pp

Bryndzia LT, Wood BJ (1990) Oxygen thermobarometry of abyssal spinel peridotites: The redox state and C-O-H volatile composition of the Earth's sub-oceanic upper mantle. Am J Sci 290:1093–1116

Buchwald VF (1975) Handbook of iron meteorites. University of California Press, Berkeley, 1418 pp

Canfield DE, Poulton SW, Knoll AH, Narbonne GM, Ross G, Goldberg T, Strauss H (2008) Ferruginous conditions dominated later Neoproterozoic deep-water conditions. Science 321: 949–952

Clayton DD (2003) Handbook of isotopes in the cosmos: hydrogen to gallium. Cambridge University Press, Cambridge, UK, 314 pp

Comelli D, D'Orazio M, Folco L, El-Halwagy M, Frizzi T, Alberti R, Capogrosso V, Elnaggar A, Hassan H, Nevin A, Porcelli F, Rashed MG, Valenti G (2016) The meteoritic origin of Tutankhamun's iron dagger blade. Meteorit Planet Sci 51:1301–1309

Cottrell E, Kelley KA (2011) The oxidation state of Fe in MORB glasses and the oxygen fugacity of the upper mantle. Earth Planet Sci Lett 305:270–282

Cottrell E, Kelley KA (2013) Redox heterogeneity as a function of mantle source. Science 340:1314–1317

Davis FA, Humayun M, Hirschmann MM, Cooper RS (2013) Experimentally determined mineral/melt partitioning of first-row transition elements (FRTE) during partial melting of peridotite at 3 GPa. Geochim Cosmochim Acta 104:232–260

Dupré B, Viers J, Dandurand J-L, Polve M, Benezeth P, Vervier P, Braun J-J (1999) Major and trace elements associated with colloids in organic-rich river waters: ultrafiltration of natural and spiked solutions. Chem Geol 160:63–80

Fischer RA, Campbell AJ, Reaman DM, Miller NA, Heinz DL, Dera P, Prakapenka VB (2013) Phase relations in the Fe-FeSi system at high pressures and temperatures. Earth Planet Sci Lett 373:54–64

Frost DJ, McCammon CA (2008) The redox state of Earth's mantle. Annu Rev Earth Planet Sci 36:389–420

Gattacceca J, Rochette P, Scorzelli RB, Munayco P, Agee C, Quesnel Y, Cournède C, Geissman J (2014) Martian meteorites and Martian magnetic anomalies: a new perspective from NWA 7034. Geophys Res Lett 41:4859–4864

Greenwood NN, Earnshaw A (1984) Chemistry of the elements. Pergamon Press, Oxford, 1542 pp

Grossman L, Beckett JR, Fedkin AV, Simon SB, Ciesla FJ (2008) Redox conditions in the solar nebula: observational, experimental, and theoretical constraints. Rev Mineral Geochem 68:93–140

Huang S, Humayun M, Frey F (2007) Iron/manganese ratio and manganese content in shield lavas from Ko'olau volcano, Hawaii. Geochim Cosmochim Acta 71:4557–4569

Humayun M, Qin LP, Norman MD (2004) Geochemical evidence for excess iron in the mantle beneath Hawaii. Science 306:91–94

Johnson KS, Gordon RM, Coale KH (1997) What controls dissolved iron concentrations in the world ocean? Mar Chem 57:137–161
Labrosse S, Poirier JP, Le Mouël JL (2001) The age of the inner core. Earth Planet Sci Lett 190:111–123
Lin J-F, Speziale S, Mao Z, Marquardt H (2013) Effects of the electronic spin transitions of iron in lower mantle minerals: implications for deep mantle geophysics and geochemistry. Rev Geophys 51:244–275
Ma Y, Somayazulu M, Shen G, Mao H-K, Shu J, Hemley RJ (2004) In situ X-ray diffraction studies of iron to Earth-core conditions. Earth Planet Sci Lett 143-144:455–467
McCollom TM, Klein F, Robbins M, Moskovitz B, Berquó TS, Jöns N, Bach W, Templeton A (2016) Temperature trends for reaction rates, hydrogen generation, and partitioning of iron during experimental serpentinization of olivine. Geochim Cosmochim Acta 181:175–200
McDonough WF, Sun SS (1995) The composition of the Earth. Chem Geol 120:223–253
Mittlefehldt DW, McCoy TJ, Goodrich CA, Kracher A (1998) Non-chondritic meteorites from asteroidal bodies. Rev Mineral 36:195 pp
Morris RV, Klingelhöfer G, Schröder C, Fleisher I, Ming DW, Yen AS, Gellert R, Arvidson RE, Rodionov DS, Crumpler LS, Clark BC, Cohen BA, McCoy TJ, Mittlefehldt DW, Schmidt ME, de Souza PA, Squyres SW (2008) Iron mineralogy and aqueous alteration from Husband Hill through home plate at Gusev crater, Mars: results from the Mössbauer instrument on the Spirit Mars exploration rover. J Geophys Res E113:E12S42. https://doi.org/10.1029/2008JE003201
Poirier J-P (1994) Light elements in the Earth's outer core: a critical review. Phys Earth Planet In 85:319–337
Raiswell R, Canfield DE (2012) The iron biogeochemical cycle past and present. Geochem Perspect 1:220 pp
Righter K, Drake MJ, Scott E (2006) Compositional relationships between meteorites and terrestrial planets. In: Lauretta DS, McSween HY (eds) Meteorites and the early solar system. University of Arizona Press, Tucson, pp 803–828
Rubie DC, Gessmann CK, Frost DJ (2004) Partitioning of oxygen during core formation on the Earth and Mars. Nature 429:58–61
Ryabov VV, Lapkovsky AA (2010) Native iron (-platinum) ores from the Siberian platform trap intrusions. Aust J Earth Sci 57:707–736
Sahijpal S, Soni P, Gupta G (2007) Numerical simulations of the differentiation of accreting planetesimals with ^{26}Al and ^{60}Fe as the heat sources. Meteorit Planet Sci 42:1529–1548
Skaar EP, Humayun M, Bae T, DeBord KL, Schneewind O (2004) Iron-source preference of *Staphylococcus aureus* infections. Science 305:1626–1628
Squyres SW, Grotzinger JP, Arvidson RE, Bell JF, Calvin W, Christensen PR, Clark BC, Crisp JA, Farrand WH, Herkenhoff KE, Johnson JR, Klingelhöfer G, Knoll AH, McLennan SM, McSween HY, Morris RV, Rice JW, Rieder R, Soderblom LA (2004) In situ evidence for an ancient aqueous environment at Meridiani Planum, Mars. Science 306:1709–1714
Trampert J, Deschamps F, Resovsky J, Yuen D (2004) Probabilistic tomography maps chemical heterogeneities throughout the lower mantle. Science 306:853–856
Tylecote RF (1992) A history of metallurgy, 2nd edn. The Institute of Materials, Maney, 205 pp
Wallner A, Feige J, Kinoshita N, Paul M, Fifield LK, Golser R, Honda M, Linnemann U, Matsuzaki H, Merchel S, Rugel G, Tims SG, Steier P, Yamagata T, Winkler SR (2016) Recent near-Earth supernovae probed by global deposition of interstellar radioactive ^{60}Fe. Nature 532:69–72
Weider SZ, Nittler LR, Starr RD, McCoy TJ, Stockstill-Cahill KR, Byrne PK, Devei BW, Head JW, Solomon SC (2012) Chemical heterogeneity on Mercury's surface revealed by the MESSENGER X-ray spectrometer. J Geophys Res E117:E00L05. https://doi.org/10.1029/2012JE004153
Weiss BP, Kim SS, Kirschvink JL, Kopp RE, Sankaran M, Kobayashi A, Komeili A (2004) Magnetic tests for magnetosome chains in Martian meteorite ALH 84001. Proc Natl Acad Sci 101:8281–8284
Wozniak AS, Shelley RU, McElhenie SD, Landing WM, Hatcher PG (2015) Aerosol water soluble organic matter characteristics over the North Atlantic Ocean: implications for iron-binding ligands and iron solubility. Mar Chem 173:162–172

Iron Formations

Clark M. Johnson
Department of Geoscience, University of Wisconsin, Madison, WI, USA

Definition

Iron formations (IFs) are marine chemical precipitates that contain >15 wt.% Fe (James 1954) that were deposited in the Precambrian. Gross (1965) classified IFs into four types, two of which continue in use today: *Algoma,* which are relatively small in total volume and are associated with significant volcanic input including volcanogenic massive sulfide associations, and *Superior,* which are large and laterally extensive, and thought to have formed in passive continental margin settings. IFs have drawn interest from geologists because they represent Fe deposition on a scale not seen in the Phanerozoic and hence record an extensive Fe biogeochemical cycle on the early Earth that does not occur today. The largest IFs supply the vast majority of the world's Fe needs, where the largest mines produce over 200×10^6 tons of Fe per year. Many IFs are characterized by banding at mm to m scales, often defined by alternating silica-rich and silica-poor layers mixed with abundant Fe minerals (Trendall and Blockley 1970), and such IFs are termed "Banded Iron Formations (BIFs)." The laterally extensive layering in BIFs is generally thought to record deposition in relatively deep water, below wave base. Other IFs contain granular or oolitic textures, termed "Granular Iron Formations (GIFs)," and are generally considered to have been deposited in shallow water (Beukes and Klein 1990). Other Fe-rich chemical sediments include jaspers and ironstones, which tend to have more restricted distributions as compared to BIFs. The distribution, origin, and genesis of IFs have been extensively studied over several decades, and a recent comprehensive discussion can be found in Bekker et al. (2014).

Geologic Occurrences

The temporal occurrence of IFs is punctuated, and models for IF genesis have been closely linked to evolution of O_2 levels

(Fig. 1). The oldest occurrences are small, undoubtedly reflecting fragmental preservation of the earliest IF record, and include the 3.7–3.8 Ga Isua and Nuvvaugittuq IFs, the latter of which could be as old as ~4.3 Ga, depending upon interpretation of ^{146}Nd-^{142}Nd ages (O'Neil et al. 2008). The largest IFs are the laterally extensive *Superior*-type IFs that formed in the Neoarchan to Paleoproterozoic, including the famed Hamersley IFs of the Pilbara craton in Western Australia and the Transvaal IFs of the Kaapvaal craton in South Africa that likely reflect deposition in what was once the same continental margin basin (Beukes and Gutzmer 2008). Relative to current models for the evolution of atmospheric O_2 (Lyons et al. 2014), the majority of IFs were deposited prior to the first major rise in atmospheric O_2 ("Great Oxidation Event," or GOE; Fig. 1), although there is evidence for transient increases in atmospheric O_2 prior to the GOE, and increasing evidence that the photic zone of the oceans attained significant free O_2 contents after ~3.2 Ga (Fig. 1). IFs are relatively scarce through the GOE but reappear in the geologic record between ~2.0 and 1.8 Ga. Few IFs have been found in the Mesoproterozoic (Fig. 1), despite excellent preservation of marine basins in the geologic record. This was once thought to record a shift to euxinic ocean conditions, where high sulfide contents would suppress Fe(II) transport (Canfield 1998), but it is now generally accepted that pervasive oceanic anoxia characterized the Mesoproterozoic, but with restricted euxinic environments (Reinhard et al. 2013), and so it is not clear why IF deposition was limited. The last period of major IF deposition is the late Neoproterozoic, broadly correlative with major glaciations and the second major rise in atmospheric O_2 (Fig. 1). The Phanerozoic records scattered occurrences of marine iron stones, interpreted as deposition in shallow, restricted basin conditions on a local scale.

The mineralogy of IFs may include Fe oxides, Fe carbonates, Fe silicates, and quartz but only trace aluminosilicate minerals, reflecting low clastic input (Klein 2005). Pyrite is rare in IFs, except in interbedded siliciclastic units. Simonson (2003) stressed that, contrary to common conception, hematite or goethite are *not* the major Fe-bearing phases in many large IFs that are free from significant weathering, supergene alteration, mineralization, or metamorphism. Klein and Beukes (1992) noted that the average oxidation stage of Fe in IFs is $Fe^{2.4+}$, indicating that, on average, 60% of the Fe in IFs is in ferrous form, equivalent to an assemblage of magnetite (60%) and siderite (40%). The mineralogy of IFs has been used to define various lithofacies, including *oxide* and *carbonate* lithofacies (Beukes et al. 1990), where the *oxide* facies is generally considered to reflect deposition in the most distal environments. The major "primary" Fe oxide in IFs, particularly the large Neoarchean to Paleoproterozoic *Superior*-type IFs, is magnetite. "Primary" hematite is

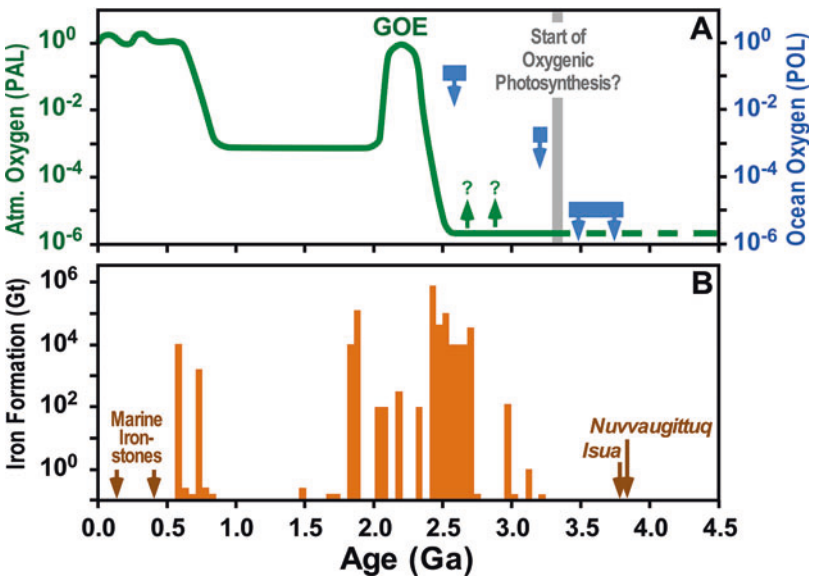

Iron Formations, Fig. 1 Temporal variations in atmospheric O_2 (*green curve* in **a**), shallow ocean O_2 (*blue boxes* in **a**), and iron formation (IF) abundance (**b**). Atmospheric O_2 *curve* relative to Present Atmosphere Level (PAL) (Adapted from Lyons et al. (2014)). GOE marks the "Great Oxidation Event" that may record an "over-shoot" in the first major rise in atmospheric O_2, followed by low periods in most of the Proterozoic. Evidence also exists for transient increases in atmospheric O_2 before the GOE, shown with green arrows. Estimates for maximum O_2 contents in the shallow oceans (photic zone) in *blue boxes* relative to Present Ocean Level (POL) are based on modeling stable Fe isotopes (Czaja et al. 2012, 2013; Li et al. 2013b; Satkoski et al. 2015) and show that the shallow oceans likely had significant free O_2 levels by 3.2 Ga, prior to rise in atmospheric O_2, which is taken to record the latest start of oxygenic photosynthesis. Iron formation abundance (in gigatons) from Bekker et al. (2010). Small volume early IFs also shown, including Isua and Nuvvaugittuq (the latter of which might be as old as ~4.3 Ga). Periods of Phanerozoic marine ironstone deposition also shown

subordinate to magnetite in Paleoproterozoic and older IFs but is much more abundant in Neoproterozoic IFs and Phanerozoic marine ironstones. Iron-bearing carbonates include siderite-magnesite solid solutions (average $Mg_{0.2}Fe_{0.8}CO_3$), ankerite ($Ca_{0.5}Fe_{0.5}CO_3$), and ferroan dolomite. Iron silicates include greenalite, stilpnomelane, and minnesotaite in the *oxide* facies of BIFs (Klein 2005), an order that generally reflects increasing metamorphism. Quartz is almost always present as a major mineral, generally most abundant in *oxide*-facies IFs.

Iron Sources and Relations to Seawater Chemistry

The ultimate source of Fe in IFs has been the subject of extensive debate. Early work suggested a continental source through anoxic weathering and transport of Fe(II) in river systems under anoxic conditions (Cloud 1973). Rare Earth Element (REE) studies documented positive Eu anomalies in IFs, which, based on similar anomalies in modern mid-ocean ridge (MOR) hydrothermal fluids, and the high distribution coefficient for REES on Fe oxides, was taken to indicate a hydrothermal source, where Fe was transported as Fe(II) in relatively anoxic seawater, followed by oxidation to Fe(III) minerals (Klein and Beukes 1989; Derry and Jacobsen 1990; Bau and Möller 1993). This interpretation has largely remained as the accepted origin for Fe in IFs since it was proposed. Broad temporal correlations between IF abundance and seafloor basaltic volcanism have supported the interpretation that Fe in IFs is sourced to MOR hydrothermal fluids (Isley and Abbott 1999). In contrast, Nd isotope data have shown variable contributions from continental Nd, raising the possibility that Fe from continental sources also contributed to IFs (Alexander et al. 2009; Viehmann et al. 2013), potentially bringing us back, at least in part, to Cloud's (1973) original hypothesis.

The high sorption coefficients for a variety of trace elements onto Fe(III) oxides and hydroxides has led to the use of IFs as a repository for long-term records of seawater chemistry. This includes the REEs, as discussed above, as well as redox-sensitive elements and elements cycled by biology. Temporal changes in the abundance of U in IFs, for example, is interpreted to reflect changes in the oxidized (soluble) form of U in seawater, where major peaks in U abundances are seen during the GOE and the late Neoproterozoic rise in atmospheric O_2 (Partin et al. 2013; Fig. 1). Recently, U-Th-Pb geochronology has been used to constrain primary U contents in early Archean jaspers and IFs, and document the oldest known marine redox gradient at 3.2 Ga (Satkoski et al. 2015), which has been interpreted to mark the latest evolution of oxygenic photosynthesis (Fig. 1). Frei et al. (2009) showed small increases in $\delta^{53}Cr$ values in IFs immediately before the GOE, taken to record mobilization of soluble Cr(VI) related to small increases in atmospheric O_2, as well as a very large increase in $\delta^{53}Cr$ values for late Neoproterozoic IFs that coincided with the second rise in atmospheric O_2. Phosphorus is a bio-limiting nutrient, and P abundances in IFs have been used to infer phosphate concentrations in seawater. Bjerrum and Canfield (2002) argued that phosphate drawdown during IF deposition would cause phosphate levels to remain low during peaks in IF deposition, and hence limiting primary productivity, but Konhauser et al. (2007a) argued that competitive sorption of silica would limit phosphate drawdown. Planavsky et al. (2010) documented a large peak in P contents of IF in the late Neoproterozoic immediately after "snowball Earth" events and suggested this recorded a peak in primary productivity and organic carbon burial related to the second rise in atmospheric O_2 (Fig. 1). Some trace elements may be tied to specific microbial processes, such as the key role that Ni plays as a cofactor in enzymes used by methanogens. Konhauser et al. (2009) noted a large decrease in Ni contents in IFs prior to the GOE (Fig. 1), which they interpreted to reflect a "nickel famine" that led to collapse of methane production, which in turn allowed atmospheric O_2 contents to rise.

A key issue in using IFs as a proxy for ancient seawater is the effects of early diagenesis. Although it seems safe to use the overall abundance of IFs to infer an Fe(II)-rich ocean in the Archean and Paleoproterozoic (Holland 1984), more problematic is the use of minerals that may record diagenetic processes, which, if not formed in equilibrium with the oceans, would weaken their use to infer surface environmental conditions. For example, siderite in IFs has $\delta^{13}C$ and $\delta^{18}O$ values that are too low and $^{87}Sr/^{86}Sr$ ratios that are too high to be in equilibrium with the oceans (Becker and Clayton 1972; Beukes et al. 1990; Heimann et al. 2010; Johnson et al. 2013), and therefore inferences of high ambient CO_2 contents based on siderite stability (Ohmoto et al. 2004) may not be correct. In situ analysis of O and Fe isotope compositions of coexisting hematite and magnetite in IFs show that they do not reflect equilibrium with each other or with the oceans (Li et al. 2013a), and such a conclusion extends to magnetite-siderite pairs in IFs (Frierdich et al. 2014). Although there seems little doubt that IFs record biogeochemical processes in marine environments, it is now recognized by many workers that these involve a variety of components, including the source(s) of initial Fe(II), processes of oxidation (commonly envisioned in the shallow oceans), and early diagenetic processes on the seafloor.

The Role of Biology in IF Genesis

Possible relations between IF genesis and biology have been discussed for a century (Harder 1919), despite the fact that

microfossil and organic carbon abundances are very sparse in IFs. Direct morphological evidence for the presence of microbes in the environments of IF deposition includes the first recognized Precambrian microfossils, found in the Gunflint IF (Barghoorn and Tyler 1965), although such associations do not constrain specific biogeochemical roles for microbes. Recent discussions on the potential role for biology in IF genesis have focused on direct and indirect biological pathways for oxidation of hydrothermal Fe(II) to Fe(III)-bearing oxides and hydroxides (Konhauser et al. 2002). Production of Fe(III)-bearing minerals in IFs, relative to the reduced sources of Fe inferred for IFs, requires oxidative pathways, in part under conditions of a reducing atmosphere for the large IFs of the Neoarchean (Fig. 1). Moreover, the large proportion of Fe(II) in IFs (e.g., magnetite and siderite) requires a reductive component (Konhauser et al. 2005). Although the low measured organic carbon contents in IFs has been used to argue against a role for biology in IF genesis (Klein 2005; Planavsky et al. 2012), the low $\delta^{13}C$ values of siderite and high abundance of magnetite in IFs, if converted to the equivalent abundance of organic C, suggests initial organic C contents approaching 5 wt.%, which is two to three orders-of-magnitudes higher than measured values (Li et al. 2013a). The evidence for potential biological roles in IF genesis, therefore, most likely lies in the chemical and isotopic compositions of IFs.

Three pathways have been proposed for oxidation of hydrothermally (or continentally) sourced Fe(II): reaction with free O_2, photoferrotrophy, and UV-photo oxidation. Cloud (1968, 1973) was an early proponent for the first reaction, where free O_2 was supplied by oxygenic photosynthesis:

$$H_2O + CO_2 \rightarrow CH_2O + O_2 \quad (1)$$

followed by oxidation of aqueous Fe(II) to form amorphous ferric hydroxides:

$$4Fe^{2+} + O_2 + 8OH^- + 2H_2O \rightarrow 4Fe(OH)_3 \quad (2)$$

which in turn would convert to hematite via dewatering upon lithification:

$$2Fe(OH)_3 \rightarrow Fe_2O_3 + 3H_2O \quad (3)$$

In this model, the role of biology is indirect in the sense that free O_2 is produced by oxygenic photosynthesis, which then oxidizes Fe(II). Support for this model comes from the recognition that the photic zone of the oceans became oxygenated before the atmosphere (Fig. 1). The second pathway was highlighted by Widdel et al. (1993), where Fe(II) serves as an electron donor and Fe(II) oxidation is coupled to reduction of CO_2 to organic carbon via the reaction:

$$4Fe^{2+} + CO_2 + 4H^+ \rightarrow CH_2O + 4Fe^{3+} + H_2O \quad (4)$$

Kappler et al. (2005) showed that this pathway, using reasonable rates of phototrophic oxidation, could explain the Fe(III) inventories found in IFs. Moreover, it seems reasonable such a pathway was involved in producing Fe(III) contents in early Archean IFs and jaspers when free O_2 contents in the shallow oceans were very low (Fig. 1). The third pathway is an entirely abiological one, where oxidation occurs in the shallow oceans through UV-photo catalyzed reactions (Cairns-Smith 1978):

$$2Fe^{2+} + 2H^+ + h\nu \rightarrow 2Fe^{3+} + H_2 \quad (5)$$

Limitations on this process have been highlighted by Konhauser et al. (2007b), who showed that this process was inhibited in natural seawater compositions as compared to earlier studies that used simple experimental conditions. Constraints on the extent of Fe(II) oxidation, although not the specific pathway, have been supplied by Fe isotope studies, which generally show that partial oxidation occurred at periods of time when atmospheric O_2 contents were relatively low before and after the GOE, but relatively high during the major period of IF deposition in the Neoarchean when photic zone O_2 contents were relatively high (Fig. 1; Dauphas et al. 2004; Planavsky et al. 2012: Czaja et al. 2012; Li et al. 2013a, b).

A biological reduction pathway as the source for Fe(II) in IFs has been proposed based on experimental studies that produce abundant magnetite and siderite from microbial reduction of Fe(III) oxides/hydroxides, and recognition that primary productivity in the photic zone during IF deposition likely produced a "rain" of ferric hydroxides and organic carbon to the seafloor that could support microbial Fe(III) reduction in unlithified, water-rich IF gels (Konhauser et al. 2005). The products of Eqs. 1, 2, and 4 would supply reactants for microbial Fe(III) reduction, and siderite may be produced via:

$$4Fe(OH)_3 + CH_2O + 3HCO_3^- \rightarrow 4FeCO_3 + 3OH^- + 7H_2O \quad (6)$$

This requires additional carbonate beyond that supplied by oxidation of organic carbon, but this fits well with the $\delta^{13}C$ and $\delta^{18}O$ values measured for IF siderite relative to that expected to reflect equilibrium with the oceans (Heimann et al. 2010). Production of magnetite by microbial Fe(III) reduction would occur via:

$$12Fe(OH)_3 + CH_2O \rightarrow 4Fe_3O_4 + CO_2 + 19H_2O \quad (7)$$

A test of this pathway is supplied by O and Fe isotope studies that show "inheritance" of O and Fe isotope compositions in low-temperature magnetite from a common Fe (III) precursor, rather than inter-mineral isotopic equilibrium between magnetite and hematite (Li et al. 2013a). On a basin-wide scale, it has been proposed that microbial Fe(III) reduction may release aqueous Fe(II) from continental margin sediments that is exported to the deep basin (Anderson and Raiswell 2004; Severmann et al. 2008), sometimes referred to as a "benthic iron shuttle", and this has now been recognized in the large Neoarchean IFs based on Fe-Nd isotope relations (Li et al. 2015). The close association of Fe and Si in the Precambrian oceans and Fe precipitates has led to the suggestion that microbial Fe(III) reduction could have also transported, on a basin-wide scale, silica that was released during microbial Fe(III) reduction (Fischer and Knoll 2009), and recent Si isotope studies have shown than such a model can explain the unusually low δ^{28}Si values of quartz in IFs (Reddy et al. 2016; Zheng et al. 2016).

Summary

As chemical precipitates, IFs provide a view of biogeochemical cycling in the Precambrian oceans and demonstrate an "iron world" that was distinct from that of the Phanerozoic. Juxtaposition of redox contrasts is central to all models of IF genesis, reflecting the mixed redox state of Fe in IFs, as well as the large contrast in solubility of dissolved Fe(II) and Fe(III) species at neutral pH. Debate continues as to whether or not the signals recorded in IFs largely reflect seawater compositions or the influence of biology, or, probably most likely, a combination of both. Research on IFs is likely to continue to be strong because the biogeochemical signals recorded in IFs inform us about changes over Earth's history in environmental conditions, including redox, as well as evolution of the biosphere.

Cross-References

- Iron
- Iron Isotopes
- Iron Meteorites
- Ocean Salinity, Major Elements, and Thermohaline Circulation
- Oxidation-Reduction Reactions and Eh-pH (Pourbaix) Diagrams
- Oxygen
- Paleoenvironments
- Water

References

Alexander BW, Bau M, Andersson P (2009) Neodymium isotopes in Archean seawater and implications for the marine Nd cycle in Earth's early oceans. Earth Planet Sci Lett 283:144–155

Anderson TF, Raiswell R (2004) Sources and mechanisms for the enrichment of highly reactive iron in euxinic Black Sea sediments. Am J Sci 304:203–233

Barghoorn ES, Tyler SA (1965) Microorganisms from the Gunflint Chert. Science 147:563–577

Bau M, Möller P (1993) Rare earth element systematics of the chemically precipitated component in early Precambrian iron formations and the evolution of the terrestrial atmosphere-hydrosphere-lithosphere system. Geochim Cosmochim Acta 57:2239–2249

Becker RH, Clayton RN (1972) Carbon isotopic evidence for the origin of a banded iron formation in Western Australia. Geochim Cosmochim Acta 36:577–595

Bekker A, Slack JF, Planavsky N, Krapež B, Hofmann A, Konhauser KO, Rouxel OJ (2010) Iron formation: the sedimentary product of a complex interplay among mantle, tectonic, oceanic and biospheric processes. Econ Geol 105:467–508

Bekker A, Planavsky NJ, Krapež B, Rasmussen B, Hofmann A, Slack JF, Rouxel OJ, Konhauser KO (2014) Iron Formations: their origins and implications for ancient seawater chemistry. In: Treatise on geochemistry, vol 9, 2nd edn. Elsevier, Amsterdam, pp 561–628

Beukes NJ, Gutzmer J (2008) Origin and paleoenvironmental significance of major iron formations at the Archean-Paleoproterozoic boundary. In: Hagemann SG, Rosiere C, Gutzmer J, Beukes N (eds) Banded iron formation-related high-grade iron ore, Reviews in economic geology, vol 15. Society of Economic Geologists, Littleton, pp 5–47

Beukes NJ, Klein C (1990) Geochemistry and sedimentology of a facies transition – from microbanded to granular ironformation – in the early Proterozoic Transvaal Supergroup, South Africa. Precamb Res 47:99–139

Beukes NJ, Klein C, Kaufman AJ, Hayes JM (1990) Carbonate petrography, kerogen distribution, and carbon and oxygen isotope variations in an early Proterozoic transition from limestone to iron-formation deposition, Transvaal Supergroup, South Africa. Econ Geol 85:663–690

Bjerrum CJ, Canfield DE (2002) Ocean productivity before about 1.9 Gy limited by phosphorus adsorption onto iron oxides. Nature 417:159–162

Cairns-Smith AG (1978) Precambrian solution photochemistry, inverse segregation, and banded iron formations. Nature 276:807–808

Canfield DE (1998) A new model for Proterozoic ocean chemistry. Nature 396:450–453

Cloud P (1968) Atmospheric and hydrospheric evolution on the primitive earth. Science 160:729–736

Cloud P (1973) Paleoecological significance of the banded iron-formation. Econ Geol 68:1135–1143

Czaja AD, Johnson CM, Beard BL, Roden EE, Voegelin AR, Nägler TF, Beukes NJ (2012) Evidence for free oxygen in the Neoarchean ocean based on coupled iron-molybdenum isotope fractionation. Geochim Cosmochim Acta 86:118–137

Czaja AD, Johnson CM, Beard BL, Roden EE, Li W (2013) Likely role for limited biological Fe oxidation in the deposition of the 3.7–3.8 Ga Isua banded iron formation determined by multiple scales of Fe isotope analyses. Earth Planet Sci Lett 363:192–203

Dauphas N, van Zuilen M, Wadhwa M, Davis AM, Marty B, Janney PE (2004) Clues from Fe isotope variations on the origin of early Archean BIFs from Greenland. Science 306:2077–2080

Derry LA, Jacobsen SB (1990) The chemical evolution of Precambrian seawater: evidence from REEs in banded iron formations. Geochim Cosmochim Acta 54:2965–2977

Fischer WW, Knoll AH (2009) An iron shuttle for deepwater silica in Late Archean and Early Proterozoic iron formation. Geol Soc Am Bull 121:222–235

I

Frei R, Gaucher C, Poulton SW, Canfield DE (2009) Fluctuations in Precambrian atmospheric oxygenation recorded by chromium isotopes. Nature 461:250–254
Frierdich AJ, Beard BL, Scherer MM, Johnson CM (2014) Determination of the Fe(II)(aq)-magnetite equilibrium iron isotope fractionation factor using the three-isotope method and a multi-direction approach to equilibrium. Earth Planet Sci Lett 391:77–86
Gross GA (1965) Geology of iron deposits in Canada: general geology and evaluation of iron deposits. In: Geological Survey of Canada, Economic geology report, vol 22. Geological Survey of Canada, Ottawa, p 1, 181 p
Harder EC (1919) Iron-depositing bacteria and their geologic relations. US Geol Surv Prof Pap 113:89
Heimann A, Johnson CM, Beard BL, Valley JW, Roden EE, Spicuzza MJ, Beukes NJ (2010) Fe, C, and O isotope compositions of banded iron formation carbonates demonstrate a major role for dissimilatory iron reduction in similar to 2.5 Ga marine environments. Earth Planet Sci Lett 294:8–18
Holland HD (1984) The chemistry of the atmosphere and oceans. Princeton University Press, Princeton, 598 p
Isley AE, Abbott DH (1999) Plume-related mafic volcanism and the deposition of banded iron formation. J Geophys Res 104:15461–15477
James HL (1954) Sedimentary facies of iron-formations. Econ Geol 49:235–284
Johnson CM, Ludois JM, Beard BL, Beukes NJ, Heimann A (2013) Iron formation carbonates: Paleoceanographic proxy or recorder of microbial diagenesis? Geology 41:1147–1150
Kappler A, Pasquero C, Konhauser KO, Newman DK (2005) Deposition of banded iron formations by anoxygenic phototrophic Fe(II)-oxidizing bacteria. Geology 33:865–868
Klein C (2005) Some Precambrian banded iron-formations (BIFs) from around the world: their age, geologic setting, mineralogy, metamorphism, geochemistry, and origins. Am Min 90:1473–1499
Klein C, Beukes NJ (1989) Geochemistry and sedimentology of a facies transition from limestone to iron-formation deposition in the early Proterozoic Transvaal Supergroup, South Africa. Econ Geol 84: 1733–1774
Klein C, Beukes NJ (1992) Time distribution, stratigraphy, sedimentologic setting, and geochemistry of Precambrian iron formations. In: Schopf JW, Klein C (eds) The Proterozoic biosphere: a multidisciplinary study. Cambridge University Press, Cambridge, pp 139–146
Konhauser KO, Hamade T, Raiswell R, Morrice RC, Ferris FG, Southam G, Canfield DE (2002) Could bacteria have formed the Precambrian banded iron formations? Geology 30:1079–1082
Konhauser KO, Newman DK, Kappler A (2005) The potential significance of microbial Fe(III) reduction during deposition of Precambrian banded iron formations. Geobiology 3:167–177
Konhauser KO, Lalonde SV, Amskold L, Holland HD (2007a) Was there really an Archean phosphate crisis? Science 315:1234
Konhauser KO, Amskold L, Lalonde SV, Posth NR, Kappler A, Anbar A (2007b) Decoupling photochemical Fe(II) oxidation from shallow-water BIF deposition. Earth Planet Sci Lett 258:87–100
Konhauser KO, Pecoits E, Lalonde SV, Papineau D, Nisbet EG, Barley ME, Arndt NT, Zahnle K, Kamber BS (2009) Oceanic nickel depletion and a methanogen famine before the Great Oxidation Event. Nature 458:750–754
Li W, Huberty J, Beard B, Valley J, Johnson C (2013a) Contrasting behavior of oxygen and iron isotopes in banded iron formations as determined by in situ isotopic analysis. Earth Planet Sci Lett 384:132–143
Li W, Czaja AD, Van Kranendonk MJ, Beard BL, Roden EE, Johnson CM (2013b) An anoxic, Fe(II)-rich, U-poor ocean 3.46 billion years ago. Geochim Cosmochim Acta 120:65–79
Li W, Beard BL, Johnson CM (2015) Biologically recycled continental iron is a major component in banded iron formations. Proc Natl Acad Sci 112:8193–8198
Lyons TW, Reinhardt CT, Planavsky NJ (2014) The rise of oxygen in Earth's early ocean and atmosphere. Nature 506:307–315
O'Neil J, Carlson RW, Francis D, Stevens RK (2008) Neodymium-142 evidence for Hadean mafic crust. Science 321:1828–1831
Ohmoto H, Watanabe Y, Kumazawa K (2004) Evidence from massive siderite beds for a CO_2-rich atmosphere before approximately 1.8 billion years ago. Nature 429:395–399
Partin CA, Lalonde SV, Planavsky NJ, Bekker A, Rouxel OJ, Lyons TW, Konhauser KO (2013) Uranium in iron formations and the rise of atmospheric oxygen. Chem Geol 362:82–90
Planavsky NJ, Rouxel OJ, Bekker A, Lalonde SV, Konhauser KO, Reinhard CT, Lyons TW (2010) The evolution of the marine phosphate reservoir. Nature 467:1088–1090
Planavsky NJ, Rouxel OR, Bekker A, Hoffman A, Little C, Lyons TW (2012) The iron isotope composition of some banded iron formations. Geochim Cosmochim Acta 80:158–169
Reddy TR, Zheng X-Y, Roden EE, Beard BL, Johnson CM (2016) Silicon isotope fractionation during microbial reduction of Fe(III)-Si gels under Archean seawater conditions and implications for iron formation genesis. Geochim Cosmochim Acta 190:85–99
Reinhard CT, Planavsky NJ, Robbins LR, Partin CA, Gill BC, Lalonde SV, Bekker A, Konhauser KO, Lyons TW (2013) Proterozoic ocean redox and biogeochemical stasis. Proc Natl Acad Sci 110:5357–5362
Satkoski A, Beukes NJ, Li W, Beard BL, Johnson CM (2015) A redox-stratified ocean 3.2 billion years ago. Earth Planet Sci Lett 430:43–53
Severmann S, Lyons TW, Anbar A, McManus J, Gordon G (2008) Modern iron isotope perspective on the benthic iron shuttle and the redox evolution of ancient oceans. Geology 36:487–490
Simonson BM (2003) Origin and evolution of large Precambrian iron formations. Geol Soc Am Spec Pap 370:231–244
Trendall AF, Blockley JG (1970) The iron formations of the Precambrian Hamersley Group, Western Australia. Bull Geol Surv W Aust 119: 1–366
Viehmann S, Hoffmann JE, Münker C, Bau M (2013) Decoupled Hf-Nd isotopes in Neoarchean seawater reveal weathering of emerged continents. Geology 42:115–118
Widdel F, Schnell S, Heising S, Ehrenreich A, Assmus B, Schink B (1993) Ferrous iron oxidation by anoxygenic phototrophic bacteria. Nature 362:834–836
Zheng X-Y, Beard BL, Reddy TR, Roden EE, Johnson CM (2016) Abiologic silicon isotope fractionation between aqueous Si and Fe (III)-Si gel in simulated Archean seawater: implications for Si isotope records in Precambrian sedimentary rocks. Geochim Cosmochim Acta 187:102–122

Iron Isotopes

Noah J. Planavsky[1] and Vincent Busigny[2]
[1]Department of Geology and Geophysics, Yale University, New Haven, CT, USA
[2]Institut de Physique du Globe de Paris, Sorbonne Paris Cité, Université Paris Diderot, Paris, France

Definition

Iron has four naturally occurring isotopes, with ^{56}Fe (91.754%) and ^{54}Fe (5.845%) being the most abundant and ^{57}Fe (2.119%) and ^{58}Fe (0.282%) being relatively rare. Iron isotope variations are reported, using the delta notation (e.g.,

δ^{56}Fe), relative to IRMM-014, a metallic iron standard from the Institute for Reference Materials and Measurements. Iron isotopes have been actively measured since 1999 and have been used to track a wide range of both high- and low-temperature geochemical, as well as cosmochemical processes. Iron isotope work is premised on a strong experimental foundation that is the basis for interpreting both modern environmental and geological iron isotope signals and the system has, arguably, been used most extensively to track the evolution of redox-sensitive iron biogeochemical cycling through Earth's early history and oxygenation.

Introduction

Iron isotopes were originally developed to provide a novel tool for the detection of biosignatures and a means to track environmental iron cycling (e.g., Beard et al. 1999). This work in large part grew from theoretical calculations on the magnitude of equilibrium stable Fe isotope fractionation (e.g., Polyakov 1997; Polyakov and Mineev 2000). Over the past couple decades, there has been a surge of work on the iron isotope system and a large increase in the number of labs actively measuring iron isotopes. There are well over a thousand papers on iron isotopes to date, with bodies of work on modern as well as ancient high- and low-temperature systems. This surge of work has been fueled in large part by the relative ease with which iron isotope measurements can be made using a multicollector inductively coupled plasma mass spectrometer (MC-ICP-MS), although iron isotopes can also be accurately measured by other means (see review in Dauphas and Rouxel 2006). Given the vast scope of iron isotope work we will, below, only scratch the surface of the range of questions and uses to which iron isotopes can and have been applied. We have tried to highlight areas in which iron isotope research has been especially active, and touch upon some of the recent successes of this system.

Methods

Iron isotopes were initially measured with thermal ionization mass spectrometer, TIMS (Völkening and Papanastassiou 1989), while all labs today in which iron isotopes are measured do so via MC-ICP-MS. However, although MC-ICP-MS measurements of iron isotopes are becoming increasingly common, this process remains, by some metrics, challenging. First, iron needs to be separated from all matrix elements by means of column chromatography. Separation of iron is achieved with an anion exchange resin, most typically the AG1-X8 resin (e.g., Beard et al. 1999; Dauphas et al. 2004), although other methods have been presented. The most difficult aspect of MC-ICP-MS measurement is, moreover, overcoming oxygen and nitrogen argide interferences. Several approaches have been used to deal with isobaric interferences, including using a collision cell or a cold plasma to minimize interferences. However, most measurements are now made by resolving the interferences, which entails measurement on the shoulder of interference rather than a flat-topped peak as is typically done with for other isotope systems (Weyer and Schwieters 2003). Lastly, instrument mass bias needs to be corrected by using either sample-standard-bracketing (SSB; Schoenberg and von Blanckenburg 2005), Cu/Ni doping, or a spike on isotopes ^{57}Fe and/or ^{58}Fe (Millet et al. 2012). The ^{56}Fe/^{54}Fe and ^{57}Fe/^{54}Fe ratios are expressed in the usual δ notation in per mil (‰) as:

$$\delta^{5X}\mathrm{Fe}_{\mathrm{sample}} = \left[\left({}^{5X}\mathrm{Fe}/{}^{54}\mathrm{Fe} \right)_{\mathrm{sample}} / \left({}^{5X}\mathrm{Fe}/{}^{54}\mathrm{Fe} \right)_{\mathrm{standard}} - 1 \right] \times 1000$$

where ^{5X}Fe represents either ^{56}Fe or ^{57}Fe, and the standard is generally IRMM-014. However, it should be noted that a few laboratories report Fe isotope composition relative to average igneous rocks, which is shifted by ~0.08‰ relative to IRMM-014 (Beard et al. 2003a). δ^{56}Fe is the most widely used notation in the literature although few labs still use ^{57}Fe because of high precision obtained on the ^{57}Fe measurement.

Biogeochemical Iron Cycling

Iron isotopes have been used extensively to track local and global biogeochemical iron cycling. Microbial processes play an important role in iron redox cycling. Foremost, dissimilatory microbial iron reduction (DIR) leads to extensive iron recycling by readily converting ferric to ferrous iron. Iron isotopes have therefore been proposed to directly track DIR (e.g., Johnson et al. 2008). Dissolved Fe(II) produced by dissimilatory Fe-reducing bacteria can be markedly depleted relative to parent ferric oxides (e.g., Beard et al. 1999). Additionally, Fe(II) from DIR can be nearly 3‰ lower than oxide-associated ferric iron, where fractionations occurring during DIR seem to be linked to isotope exchange between dissolved ferrous iron, sorbed ferrous iron, and reactive ferric iron at the surface of oxide undergoing reduction (Crosby et al. 2005; Crosby et al. 2007). In this light, the bacteria are catalyzing exchange and moving the system toward equilibrium Fe isotope partitioning. This is consistent with the direction of the isotope fractionation, in that ferric iron tends to have a higher coordination number and stronger, stiffer bonds. The equilibrium fractionation between aqueous Fe(II) and Fe(III) is ~3‰ at room temperature, with Fe(III) being enriched in heavy isotope (Welch et al. 2003). Iron oxidation and precipitation thus result in the formation of a light (more negative

δ^{56}Fe value) residual dissolved Fe(II) reservoir and there is not a clear difference between the fractionation that occurs during abiogenic and what occurs during biogenic iron oxidation (Croal et al. 2004; Wu et al. 2011).

Nonredox-dependent processes are typically associated with smaller fractionations than iron oxidation and reduction. For example, precipitation of iron carbonates from Fe(II) results in a fractionation near 0.5‰, enriching the solid in the light isotope (Wiesli et al. 2004). A notable exception to this trend, however, is the potential for large isotope fractionations to occur during pyrite formation in which there is not quantitative Fe scavenging (Guilbaud et al. 2011). As with all isotope systems, iron isotope fractionations will scale with temperature and the temperature dependence of key processes (e.g., iron oxidation) is analytically resolvable (>0.1‰) within the range of Earth's surface temperatures.

A basic understanding of isotope fractionation factors and of the isotope composition of different iron reservoirs paves the way for using iron isotopes to track modern iron cycling. The most intense interest in this application of iron isotopes has been tracking Fe sources into the marine realm. Much of this interest is linked to iron being a key colimiting nutrient in the oceans and to the large uncertainties in the magnitude of different iron input fluxes. Different iron sources to the oceans have in cases isotopically distinct compositions. There are three main seawater Fe sources, dust, hydrothermal fluids, and a sediment flux. Dust has a near uniform δ^{56}Fe values close to 0‰; however, there may be a slight negative fractionation factor associated with leaching Fe from dust particles (Beard et al. 2003a; Revels et al. 2015). Hydrothermal fluids have slightly negative δ^{56}Fe values, between −0.5 and 0‰ (e.g., Sharma et al. 2001; Beard et al. 2003b), but there can be isotope fractionations within the hydrothermal plume – with the direction of the fractionation likely depending on the ratio of iron oxidation to sulfide formation (Bennett et al. 2009). Reducing marine sediments are the most likely to have a distinct iron isotopic composition. Where there is a discrete ferruginous (anoxic and iron rich) zone in the porewaters, there can be large benthic iron flux. Further, this iron flux is strongly isotopically depleted because of DIR or partial oxidation of reduced iron reservoir that has undergone quantitative iron reduction. Sulfidic and oxic sediments will have lower iron fluxes than reducing marine sediments that have less distinct isotopic compositions. Specifically, oxic sediments are likely to have an iron flux near 0‰ (Homoky et al. 2009), while sulfidic sediments have slightly positive δ^{56}Fe values (Severmann et al. 2008). There can be iron isotope fractionation during ligand binding, which will complicate using δ^{56}Fe values as source tracers. In sum, although there is some overlap in isotope values of different iron fluxes, iron isotope can be a useful tool to probe.

Finally, Fe isotopes can also provide valuable insight into the physicochemical processes affecting Fe during soil-water interactions, particles and dissolved load in river systems, and then help to better constrain the fluxes of Fe to the ocean. Riverine particles generally have δ^{56}Fe values in a small range from −0.1 to 0.1‰, similar to igneous rocks and mean continental crust (Beard et al. 2003a; Fantle and DePaolo 2004; Chen et al. 2014). In contrast, dissolved load show a large range of δ^{56}Fe values reflecting various colloidal fractions, mostly Fe-oxyhydroxides and/or Fe bound to organic carbon (Ingri et al. 2006; Ilina et al. 2013). Studies on soil formation and continental weathering demonstrate that the fraction of exchangeable Fe is typically enriched in light isotopes relative to Fe-substrate in rocks (e.g., Brantley et al. 2004). This light isotope signature of the exchangeable Fe in soils is likely the result of complex interplay between ferric iron reduction by microorganisms, adsorption of isotopically heavy ferrous iron on soil minerals, and formation of Fe-rich organic ligands (Brantley et al. 2004; Ingri et al. 2006). An understanding of iron isotopes in these geological systems is still being developed, and has great potential for tracing interactions between the different Fe pools in soil and river systems.

The Sedimentary Iron Isotope Record

There is a >4‰ range in sedimentary iron isotope data from shales, iron oxide-rich rocks, sulfides, and carbonates (Fig. 1). Extreme isotope variability also occurs between mineralogical phases on a micron scale (e.g., as detected by SIMS and laser ablation work), but there is also a several per mil range of Fe isotope variability within bulk samples of sedimentary rocks. This large amount of micron-scale variability is likely linked to a combination of factors, but it is certainly driven in part by fractionations that occur during mineral formation. Significant iron isotope variability in bulk marine sediments is likely a signal for the presence of multiple isotopically distinct dissolved iron reservoirs within aqueous systems although, in specific instances, isotope fractionation during mineral formation may also play a role.

The most obvious temporal trend in the sedimentary iron isotope record is the shift starting during the Archean (ca. ~2.9 to 2.7 Ga) from variable and often highly depleted δ^{56}Fe values to less variable, near-crustal δ^{56}Fe values (Rouxel et al. 2005; Yamaguchi et al. 2005; Johnson et al. 2008) (Fig. 1). This trend is most pronounced in strata from typical continental margin sediments – as hydrothermal systems can be isotopically variable well after the Archean. Although it is clear that this interval of time marks a significant shift in iron cycling, the processes driving this trend in the iron isotope record have been extensively debated. This change in sedimentary iron isotope variability was originally linked to a shift in marine redox conditions and the development and expansion of marine environments where quantitative iron oxidation prevailed (Rouxel et al. 2005). In this case,

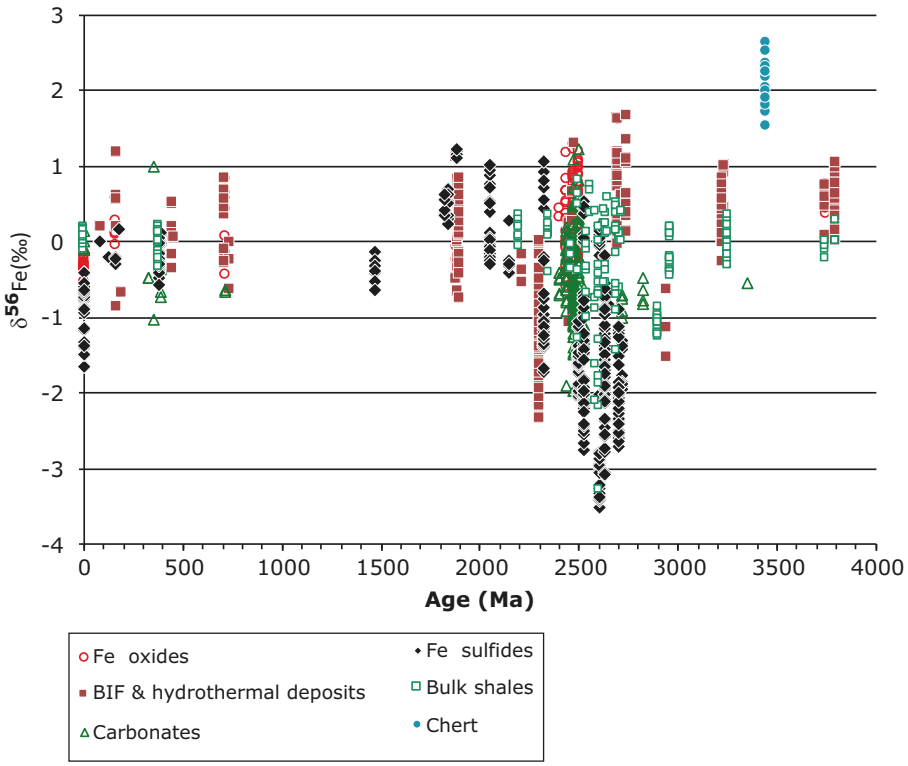

Iron Isotopes, Fig. 1 Iron isotope composition of sedimentary rocks through time (updated from Busigny et al. 2014; Kurzweil et al. 2015; Stevenson et al. (2017); Wawryk and Foden et al. 2015; Delte Raye et al. 2015). There is almost 6‰ variability in the sedimentary record, with the most pronounced variability in the Archean (see text for further information)

negative and positive iron isotope excursions in the early rock record can be linked to partial iron oxidation in a water column without a distinct oxygen chemocline. Partial oxidation would have created isotopically heavy ferric Fe(III) iron and left behind an isotopically depleted dissolved ferrous Fe (II) reservoir, which could be captured and transferred to the sedimentary record (Rouxel et al. 2005; Planavsky et al. 2012; Busigny et al. 2014). In this model, the decline in iron isotope variability observed at ca. 2.4 Ga would be linked to the transition of the upper ocean to a well-oxygenated state.

Alternatively, this iron isotope trend has been interpreted to reflect changes in the extent of DIR (e.g., Yamaguchi et al. 2005; Johnson et al. 2008), where the Fe isotopic shift is attributed to the rise of DIR respiration by bacteria since at least 2.9 Ga (Yamaguchi et al. 2005). As highlighted above, DIR facilitates release of isotopically light ferrous iron. In a low-oxygen and low-sulfate anoxic ocean (i.e., the Archean ocean), extensive light iron from DIR would be released into the water column, where it could be transported to other portions of an ocean basin. Therefore, DIR in the Archean may have led to the development of a very pronounced benthic iron shuttle (Li et al. 2015). Lastly, the very negative Fe isotope values observed in the Archean record may also be linked to the large kinetic fractionation involved in pyrite precipitation in iron-rich oceans (Guilbaud et al. 2011). The disappearance, beginning in the Proterozoic, of markedly negative iron isotope values would then be due to more complete Fe(II) utilization in pyrite precipitation (Guilbaud et al. 2011). However, markedly negative Fe isotope values are also found in euxinic shales, where iron is by definition limiting, and in nonsulfide iron mineral phases (Rouxel et al. 2005; Busigny et al. 2014), indicating that kinetic fractionations associated with pyrite precipitation cannot be the sole explanation for the observed trends in the sedimentary iron isotope record. Indeed, the pyrite precipitation model omits several processes – including biological fractionations and Fe redox – that may contribute to Fe isotope compositions (Czaja et al. 2012).

Although iron isotope variability outside of the Archean has received relatively less attention, several studies have highlighted the utility of iron isotopes as tracers of iron cycling in Proterozoic and Phanerozoic sedimentary successions. Foremost, iron isotopes have been used to track the source of sedimentary iron enrichments. This builds from the principles outlined above – hydrothermal iron is likely to have a near-crustal iron isotope value, relative to iron from a benthic shuttle, which will be strongly isotopically depleted (e.g., Severmann et al. 2006). Further, iron isotopes can be used to detect partial iron oxidation and can thus be used as a local redox proxy.

High Temperature Processes: Terrestrial Mantle and Crustal Rocks

Pioneering work on the iron isotope composition of igneous rocks initially described relative homogeneity and proposed

to use these rocks as geostandard for international normalization (Beard et al. 2003a). Later studies revealed that there are significant variabilities inherited from partial melting and subsequent crystallization processes. During partial melting of mantle peridotite, Fe(III) is more incompatible than Fe(II), thus producing an enrichment in heavy Fe isotope in the melt relative to the source (Williams et al. 2004; Weyer and Ionov 2007; Dauphas et al. 2009, 2014). This process is illustrated by the slightly elevated δ^{56}Fe values of mid-ocean ridge and ocean island basalts, typically around 0.10‰, relative to fertile mantle peridotite, with δ^{56}Fe values of ~0‰ (Beard et al. 2003a; Dauphas et al. 2009). Igneous rocks with the largest range in δ^{56}Fe values are reported from carbonatites, with values from −1.0 to +0.8‰ (Johnson et al. 2010). Mantle metasomatism, as well as subducted Fe, may also generate isotope variability in the mantle (Beard and Johnson 2004; Zhao et al. 2010; Poitrasson et al. 2013). Magma differentiation in crustal level induces Fe isotope fractionation, enriching the residual melt in the heavy Fe isotope relative to crystals, with a $\Delta^{56}Fe_{melt\text{-}crytals}$ value between 0.1 and 0.2‰ (Teng et al. 2008; Schuessler et al. 2009). Granites show relatively large range of δ^{56}Fe variation from 0.1 to 0.4‰, with Si-rich rocks corresponding to the heaviest Fe isotope compositions (Beard et al. 2003a; Poitrasson and Freydier 2005). The δ^{56}Fe-SiO_2 positive correlation may reflect fluid exsolution from siliceous hydrous magmas (e.g., Heimann et al. 2008) or iron structural changes in silicic magma (Dauphas et al. 2014). Despite δ^{56}Fe heterogeneity in granites, the average Fe isotope composition of bulk continental crust is ~0.1‰, and is thus not significantly different from that of oceanic crust (Poitrasson 2006).

Cosmochemistry

Primitive meteorites, including carbonaceous, ordinary, and enstatite chondrites all have δ^{56}Fe values ~0‰, similar to the fertile mantle (Schoenberg and von Blanckenburg 2006; Craddock and Dauphas 2011). Considering that the Earth was made from chondritic material, this similarity suggests that terrestrial core-mantle differentiation did not significantly fractionate Fe isotopes, although ~87% of the total Fe in bulk Earth was included into the core. A limited metal-silicate Fe isotope fractionation is also supported by laboratory experiments (Hin et al. 2012) and negligible $\delta^{56}Fe_{metal\text{-}olivine}$ values (< 0.017‰) predicted by reduced partition function calculation at the temperature of core formation, i.e., T ~ 2000–3000 °C (Polyakov and Mineev 2000). The Fe isotope composition of the Moon has generally been considered as slightly enriched in heavy isotopes (by 0.1‰) relative to bulk silicate Earth, interpreted tentatively as reflecting evaporative Fe loss during the Giant Impact having formed the Moon (e.g., Poitrasson et al. 2004; Weyer et al. 2005; Moynier et al. 2006). However, a recent study determined that lunar dunite samples are enriched in light isotopes and proposed, from a mass-balance approach, that bulk silicate Moon and Earth are in fact identical (Wang et al. 2015). Iron isotope analyses of Shergotty-Nakhla-Chassigny (SNC) meteorites assumed to originate from Mars, and eucrites and diogenites from asteroid Vesta show δ^{56}Fe values ~0‰ (Poitrasson et al. 2004; Schoenberg and von Blanckenburg 2006), similar to fertile mantle iron isotope composition. Taken together, all these data suggest that bulk Fe isotope compositions of rocky planets in the solar system are identical.

Summary and Conclusion

Iron isotopes are now a routinely measured well-established geochemical system with wide range of applications, including tracing modern iron cycling, igneous processes, and the redox evolution of the oceans.

References

Beard BL, Johnson CM, Cox L, Sun H, Nealson KH (1999) Iron Isotope Biosignatures. Science 285:1889–1892

Beard BL, Johnson CM, Skulan JL, Nealson KH, Cox L, Sun H (2003a) Application of Fe isotopes to tracing the geochemical and biological cycling of Fe. Chem Geol 195:87–117

Beard BL, Johnson CM, Von Damm KL, Poulson RL (2003b) Iron isotope constraints on Fe cycling and mass balance in oxygenated Earth oceans. Geology 31:629–632

Beard BL, Johnson CM (2004) Fe isotope variations in the modern and ancient earth and other planetary bodies. Rev Mineral Geochem 55:319–357. https://doi.org/10.2138/gsrmg.55.1.319

Bennett SA, Rouxel O, Schmidt K, Garbe-Schönberg D, Statham PJ, German CR (2009) Iron isotope fractionation in a buoyant hydrothermal plume, 5°S Mid-3353 Atlantic Ridge. Geochim Cosmochim Acta 73:5619–5634

Brantley SL, Liermann LJ, Guynn RL, Anbar A, Icopini GA, Barling J (2004) Fe isotopic fractionation during mineral dissolution with and without bacteria. Geochim Cosmochim Acta 68:3189–3204

Busigny V, Planavsky NJ, Jezequel D, Crowe S, Louvat P, Moureau J, Viollier E, Lyons TW (2014) Iron isotopes in an Archean ocean analogue. Geochim Cosmochim Acta 133:443–462

Chen JB, Busigny V, Gaillardet J, Louvat P (2014) Iron isotopes in the Seine River (France): natural versus anthropogenic sources. Geochim Cosmochim Acta 128:128–143

Craddock PR, Dauphas N (2011) Iron isotopic compositions of geological reference materials and chondrites. Geostand Geoanal Res 35:101–123

Croal LR, Johnson CM, Beard BL, Newman DK (2004) Iron isotope fractionation by anoxygenic Fe(II)-oxidizing phototrophs. Geochimica et Cosmochimica Acta 68:1227–1242. https://doi.org/10.1016/j.gca.2003.09.011

Crosby HA, Johnson CM, Roden EE, Beard BL (2005) Coupled Fe(II)-Fe(III) electron and atom exchange as a mechanism for Fe isotope fractionation during dissimilatory iron oxide reduction. Environ Sci Technol 39:6698–6704

Crosby HA, Roden EE, Johnson CM, Beard BL (2007) The mechanisms of iron isotope fractionation produced during dissimilatory Fe (III)

reduction by Shewanella putrefaciens and Geobacter sulfurreducens. Geobiology 5:169–189
Czaja AD, Johnson CM, Yamaguchi KE, Beard BL (2012) Comment on "abiotic pyrite formation produces a large Fe isotope fractionation". Science 335:538–538
Dauphas N, Rouxel O (2006) Mass spectrometry and natural variations of iron isotopes. Mass Spectrom Rev 25:515–550
Dauphas N, Janney PE, Mendybaev RA, Wadhwa M, Richter FM, Davis AM, Van Zuilen M, Hines R, Foley CN (2004) Chromatographic separation and multicollection-ICPMS analysis of iron. Investigating mass-dependent and-independent isotope effects. Anal Chem 76:5855–5863
Dauphas N, Craddock PR, Asimov PD, Bennett VC, Nutman A, Ohnenstetter D (2009) Iron isotopes may reveal the redox conditions of mantle melting from Archean to present. Earth Planet Sci Lett 288:255–267
Dauphas N, Roskosz M, Alp EE, Neuville DR, Hu MY, Sio CK, Tissot FLH, Zhao J, Tissandier L, Médard E, Cordier C (2014) Magma redox and structural controls on iron isotope variations in Earth's mantle and crust. Earth Planet Sci Lett 398:127–140
Fantle MS, DePaolo DJ (2004) Iron isotopic fractionation during continental weathering. Earth Planet Sci Lett 228:547–562
Foden J, Sossi PA, Wawryk CM (2015) Fe isotopes and the contrasting petrogenesis of A-, I- and S-type granite. Lithos 212–215:32–44. https://doi.org/10.1016/j.lithos.2014.10.015
Guilbaud R, Butler IB, Ellam RM (2011) Abiotic pyrite formation produces a large Fe isotope fractionation. Science 332:1548–1551
Heimann A, Beard BL, Johnson CM (2008) The role of volatile exsolution and sub-solidus fluid/rock interactions in producing high 56 Fe/54 Fe ratios in siliceous igneous rocks. Geochim Cosmochim Acta 72:4379–4396
Hin RC, Schmidt MW, Bourdon B (2012) Experimental evidence for the absence of iron isotope fractionation between metal and silicate liquids at 1GPa and 1250-1300°C and its cosmochemical consequences. Geochim Cosmochim Acta 93:164–181
Homoky WB, Severmann S, Mills RA, Statham PJ, Fones GR (2009) Pore-fluid Fe isotopes reflect the extent of benthic Fe redox recycling: evidence from continental shelf and deep-sea sediments. Geology 37:751–754
Ilina SM, Poitrasson F, Lapitskiy SA, Alekhin YV, Viers J, Pokrovsky OS (2013) Extreme iron isotope fractionation between colloids and particles of boreal and temperate organic-rich waters. Geochim Cosmochim Acta 101:96–111
Ingri J, Malinovsky D, Rodushkin I, Baxter DC, Widerlund A, Andersson P, Gustafsson O, Forsling W, Ohlander B (2006) Iron isotope fractionation in river colloidal matter. Earth Planet Sci Lett 245:792–798
Johnson CM, Beard BL, Roden EE (2008) The iron isotope fingerprints of redox biogeochemical cycling in modern and ancient Earth. Ann Rev Earth Planetary Sci 36:457–493
Johnson CM, Bell K, Beard BL, Shultis AI (2010) Iron isotope compositions of carbonatites record melt generation, crystallization, and late-stage volatile-transport processes. Mineral Petrol 98:91–110
Kurzweil F, Drost K, Wille M, Taubald H, Schöckle D, Schoenberg R (2015) Coupled sulfur, iron and molybdenum isotope data from black shales of the Tepla-Barrandian unit argue against deep ocean oxygenation during the Ediacaran. Geochimica et Cosmochimica Acta 171:121–142. https://doi.org/10.1016/j.gca.2015.08.022
Li W, Beard BL, Johnson CM (2015) Biologically-recycled continental iron: a major component in banded iron formations. Proc Natl Acad Sci 112:8193–8198
Millet MA, Baker JA, Payne CE (2012) Ultra-precise stable Fe isotope measurements by high resolution multiple-collector inductively coupled plasma mass spectrometry with a ^{57}Fe-^{58}Fe double spike. Chem Geol 304:18–25
Moynier F, Albarede F, Herzog G (2006) Isotopic composition of zinc, copper, and iron in lunar samples. Geochim Cosmochim Acta 70:6103–6117
Planavsky N, Rouxel OJ, Bekker A, Hofmann A, Little CTS, Lyons TW (2012) Iron isotope composition of some Archean and Proterozoic iron formations. Geochimica et Cosmochimica Acta 80:158–169. https://doi.org/10.1016/j.gca.2011.12.001
Poitrasson F (2006) On the iron isotope homogeneity level of the continental crust. Chem Geol 235:195–200
Poitrasson F, Freydier R (2005) Heavy iron isotope composition of granites determined by high resolution MC-ICP-MS. Chem Geol 222:132–147
Poitrasson F, Halliday AN, Lee DC, Levasseur S, Teutsch N (2004) Iron isotope differences between Earth, Moon, Mars and Vesta as possible records of contrasted accretion mechanisms. Earth Planet Sci Lett 223:253–266
Poitrasson F, Delpech G, Grégoire M (2013) On the iron isotope heterogeneity of lithospheric mantle xenoliths: implications for mantle metasomatism, the origin of basalts and the iron isotope composition of the Earth. Contrib Mineral Petrol 165:1243–1258
Polyakov VB (1997) Equilibrium fractionation of the iron isotopes: estimation from Mössbauer spectroscopy data. Geochim Cosmochim Acta 6:4213–4217
Polyakov VB, Mineev SD (2000) The use of Mössbauer spectroscopy in stable isotope geochemistry. Geochim Cosmochim Acta 64:849–865
Revels BN, Zhang R, Adkins JF, John SG (2015) Fractionation of iron isotopes during leaching of natural particles by acidic and circumneutral leaches and development of an optimal leach for marine particulate iron isotopes. Geochim Cosmochim Acta 166:92–104
Rouxel OJ, Bekker A, Edwards KJ (2005) Iron isotope constraints on the Archean and Paleoproterozoic ocean redox state. Science 307:1088–1091
Schoenberg R, von Blanckenburg F (2005) An assessment of the accuracy of stable Fe isotope ratio measurements on samples with organic and inorganic matrices by high-resolution multicollector ICP-MS. Int J Mass Spectrom 242:257–272
Schoenberg R, von Blanckenburg F (2006) Modes of planetary-scale Fe isotope fractionation. Earth Planet Sci Lett 252:342–359
Schuessler JA, Schoenberg R, Sigmarsson O (2009) Iron and lithium isotope systematics of the Hekla volcano, Iceland – evidence for Fe isotope fractionation during magma differentiation. Chem Geol 258:78–91
Severmann S, Johnson CM, Beard BL, McManus J (2006) The effect of early diagenesis on the Fe isotope compositions of porewaters and authigenic minerals in continental margin sediments. Geochim Cosmochim Acta 70:2006–2022
Severmann S, Lyons TW, Anbar A, McManus J, Gordon G (2008) Modern iron isotope perspective on the benthic iron shuttle and the redox evolution of ancient oceans. Geology 36:487–490
Sharma M, Polizzotto M, Anbar AD (2001) Iron isotopes in hot springs along the Juan de Fuca Ridge. Earth Planet Sci Lett 194:39–51
Stevenson EI, Fantle MS, Das SB, Williams HM, Aciego SM (2017) The iron isotopic composition of subglacial streams draining the Greenland ice sheet. Geochimica Et Cosmochimica Acta 213:237–254. https://doi.org/10.1016/j.gca.2017.06.002
Teng FZ, Dauphas N, Helz R (2008) Iron isotope fractionation during magmatic differentiation in Kilauea Iki lava lake. Science 320:1620–1622
Völkening J, Papanastassiou DA (1989) Iron isotope anomalies. Astrophys J 347:L43–L46
Wang K, Jacobsen SB, Sedaghatpour F, Chen H, Korotev RL (2015) The earliest Lunar Magma Ocean differentiation recorded in Fe isotopes. Earth Planet Sci Lett 430:202–208
Welch SA, Beard BL, Johnson CM, Braterman PS (2003) Kinetic and equilibrium Fe isotope fractionation between aqueous Fe(II) and Fe (III). Geochim Cosmochim Acta 67:4231–4250

Weyer S, Ionov DA (2007) Partial melting and melt percolation in the mantle: the message from Fe isotopes. Earth Planet Sci Lett 259:119–133
Weyer S, Schwieters J (2003) High precision Fe isotope measurements with high mass resolution MC-ICPMS. Int J Mass Spectrom 226:355–368
Weyer S, Anbar AD, Brey GP, Münker C, Mezger K, Woodland AB (2005) Iron isotope fractionation during planetary differentiation. Earth Planet Sci Lett 240:251–264
Wiesli RA, Beard BL, Johnson CM (2004) Experimental determination of Fe isotope fractionation between aqueous Fe(II), siderite and "green rust" in abiotic systems. Chem Geol 211:343–362
Williams HM, McCammon CA, Peslier AH, Halliday AN, Teutsch N, Levasseur S, Burg JP (2004) Iron isotope fractionation and the oxygen fugacity of the mantle. Science 304:1656–1659
Wu J, Wells ML, Rember R (2011) Dissolved iron anomaly in the deep tropical–subtropical Pacific: evidence for long-range transport of hydrothermal iron. Geochimica et Cosmochimica Acta 75(2):460–468. https://doi.org/10.1016/j.gca.2010.10.024
Yamaguchi KE, Johnson CM, Beard BL, Ohmoto H (2005) Biogeochemical cycling of iron in the Archean–Paleoproterozoic Earth: constraints from iron isotope variations in sedimentary rocks from the Kaapvaal and Pilbara Cratons. Chem Geol 218:135–169
Zhao XM, Zhang HF, Zhu XK, Tang SH, Tang YJ (2010) Iron isotope variations in spinel peridotite xenoliths from North China Craton: implications for mantle metasomatism. Contrib Mineral Petrol 160:1–14

Iron Meteorites

Henning Haack
Maine Mineral and Gem Museum, Bethel, ME, USA

Definition

Iron meteorites are fragments of the metallic cores of asteroids.

Introduction

Iron meteorites are possibly the most foreign geological samples to be found on Earth. Their chemistry, structure, shape, and massive weight make them unlike anything else to be found on the surface of our planet. Due to their unusual properties, iron meteorites are more easily recognized as meteorites than stony meteorites. According to the Meteoritical Bulletin, 1129 out of 62,827 meteorites (as of March, 2016) are iron meteorites. 49 of the known iron meteorites are observed falls (out of a total of 1288 observed meteorite falls); the rest are either prehistoric or have fallen unnoticed. Since iron meteorites will rust when exposed to the humid surface of the Earth, they rarely survive more than a few thousand years. The iron meteorites we find are therefore only those that have fallen in the most recent past.

Origin of Iron Meteorites

Iron meteorites are prime examples of asteroids that underwent an igneous evolution in the early Solar System – i.e., asteroids that melted and subsequently differentiated into a metallic core and a silicate mantle and crust, resulting in a structure broadly similar to the Earth interior. Since iron meteorites are samples of the cores of differentiated asteroids, their presence here on Earth tells us that the parent asteroids must have been destroyed. Estimates of the number of asteroids sampled by our iron meteorites vary, but the number is probably somewhere between 60 and 100. This is a surprising high number. Despite their relative low abundance (4.3%) among observed meteorite falls, iron meteorite sample ~90% of the asteroids were represented in our meteorite collections worldwide.

Studies of iron meteorites can be used to reconstruct their entire evolutionary history: (1) accretion of the parent body from the early protoplanetary disk, (2) heating of the parent body by mainly ^{26}Al inherited from massive stars, (3) melting and differentiation of the parent body, (4) core crystallization, (5) cooling of the core, (6) catastrophic destructing of the asteroid and the core, (7) orbital transfer of the core fragments to Earth-crossing orbit, (8) fall on Earth, and (9) use of iron meteorites by humans.

Accretion of Iron Meteorite Parent Bodies

The iron meteorite parent bodies accreted from dust and particles in the protoplanetary disk. Since the original material subsequently melted, we cannot date phases in the accretion process directly. However, since we know that the parent bodies must have included sufficient amounts of the short-lived radioactive heat source, ^{26}Al, to melt, we can infer that accretion was largely complete within a few hundred thousand years of the birth of the Solar System (Ruzicka et al. 2016; Benedix et al. 2014).

Although the iron meteorites only sample the siderophile (metallic) elements of the original parent body, differences in composition between different types of iron meteorites show that original bulk chemical composition of the parent bodies was variable. In particular, the volatile (low boiling point) siderophiles Ga and Ge show large variations among different groups of iron meteorites. A low concentration of Ga and Ge implies that the parent body accreted at a temperature, which was close to or above the boiling point of these elements, or that volatile elements were able to escape from the parent body after it accreted. The variations in abundance of Ga and Ge between groups of iron meteorites are orders of magnitude larger than the corresponding variation between different types of chondrites. The other major difference between the iron meteorite groups is the oxidation level. Some iron meteorite parent bodies apparently accreted from highly reduced bodies whereas other iron meteorites formed in oxidized bodies. The variation in oxidation state between groups of

iron meteorites is similar to the variation observed among groups of chondrites.

Heating of the Parent Bodies

Heating of differentiated asteroids was due to a short-lived radioactive isotope of Aluminum – ^{26}Al (Ruzicka et al. 2016; Benedix et al. 2014). ^{26}Al has a half-life of 730,000 years and is primarily synthesized in supernova explosions. Decay of ^{26}Al can potentially heat the parent body several thousand degrees centigrade, but due to the short half-life, only early formed bodies were heated. Therefore, although chondrites contain inclusions that formed before the iron meteorites, the iron meteorite parent bodies must have formed earlier than the chondrite parent bodies. In order to melt, the achondrite parent bodies must have accreted within one million years of the birth of the Solar System.

Melting and Differentiation of Iron Meteorite Parent Bodies

Decay of ^{26}Al heated the iron meteorite parent bodies to the point where the metallic elements melted together with a significant fraction of the silicates. When the degree of melting is sufficiently high, the more dense metallic elements will gravitationally separate from the lighter silicates. Whether or not an element goes into the core or stays in the mantle depends on its geochemical properties – not its density. Elements with a preference for the metal phase are called siderophiles, whereas elements with a preference for the silicates are called lithophiles. For example, the heaviest naturally occurring element, uranium, is concentrated in the crust of differentiated asteroids, because it is lithophile. Other elements, like iron, are only moderately siderophile and are therefore fractionated between the metallic core and the silicate mantle and crust. Highly siderophile elements like nickel, iridium, and gold differentiate almost completely into the core. These elements are therefore relatively abundant in iron meteorites but very rare on the surfaces of differentiated bodies like the Earth.

It is possible to date the formation of the core using the decay of the short-lived radioactive isotope ^{182}Hf. ^{182}Hf is lithophile but the decay product, ^{182}W, is siderophile. If a ^{182}Hf atom decays to ^{182}W before core formation, the resulting ^{182}W will differentiate with the rest of the siderophile (metallic) elements and end up in the core. However, if a ^{182}Hf atom decays to ^{182}W after core formation, the resulting ^{182}W will be left behind in the silicate (stony) part of the asteroid. The amount of ^{182}W in the silicate metallic parts of an asteroid are therefore measures of the time where the core formed (Fig. 1).

Core Crystallization

After the heat source, ^{26}Al, had decayed away, cooling of the iron meteorite parent bodies commenced. When the temperature at the base of the mantle had reached the liquidus of the metallic liquid in the core, the first metal began to solidify. This is a very different situation compared to the Earth core, which due to the high pressure at the center crystallizes from the center outward. In the asteroids, the pressure at the center did not exceed a few hundred bar and therefore had an insignificant effect on core crystallization.

During the crystallization process, elements were fractionated between the growing solid and the remaining metallic melt. Some elements, like iridium, are highly compatible with the growing solid phase and were therefore concentrated in the first solid to crystallize. As crystallization proceeded, the remaining liquid was progressively depleted in iridium and

Iron Meteorites, Fig. 1 The 20.1 t iron meteorite Agpalilik and its finder, Vagn Buchwald, in front of the Natural History Museum of Denmark. Vagn Buchwald found Agpalilik in NW Greenland on July 31, 1967. In 1975, Vagn Buchwald published a book with detailed descriptions of all iron meteorites known at that time (Buchwald 1975) (Photo credit: Anne Haastrup Hansen, Natural History Museum of Denmark)

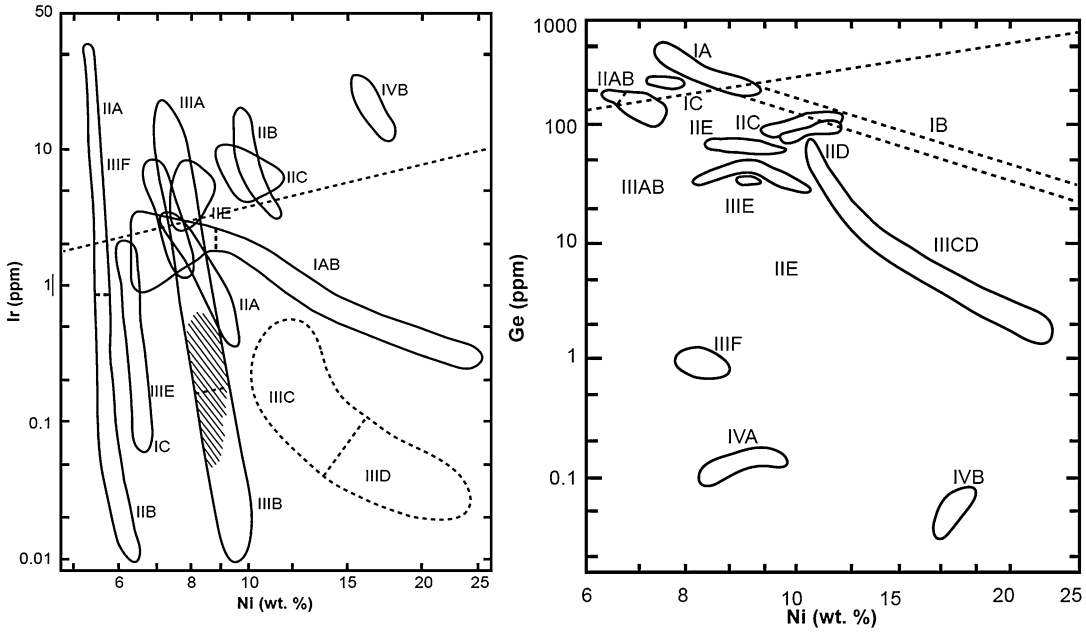

Iron Meteorites, Fig. 2 Iron meteorites can be classified based on their chemical composition. Germanium is a particular useful element to use since different types of iron meteorites in most cases plot in distinct clusters on Ge versus Ni diagrams (**a**). Ge shows minor variation within each group but large variation between groups. Ni versus Ir diagrams show a very different pattern. Iridium is highly variable within each group (**b**). The Iridium variation within each group is smaller than the variation between the groups (Redrawn from Scott and Wasson (1975))

the last metal to solidify was therefore highly depleted in Ir (Fig. 2). Other elements, like S, are highly incompatible with the solid phase and therefore remain in the melt as crystallization proceeds. Since S is a light element, the resulting S-enriched metallic liquid will be buoyant and therefore concentrate below the growing metallic solid, below the base of the mantle. Since S is incompatible, it also lowers the melting point of the metal, and the boyant S-enriched liquid at the top of the core will therefore slow down the crystallization at the uppermost part of the core, in favor of the deeper parts, where the S abundance is lower. The result was probably that the core crystallized in the form of km-sized dendritic structures which grew from the mantle downward (Haack and Scott 1992).

Sulfur also controlled the growth of the solid metal in a different way. As stated above, most siderophile elements are either compatible or incompatible with the crystallizing solid metal. The behavior of each element is a function of the composition of the metallic melt – in particular of the sulfur abundance. Since sulfur itself is highly incompatible, the sulfur concentration of the metallic liquid increases significantly during the crystallization of the core. As a consequence, most elements change their behavior during crystallization. Some elements, like Ga and Ge, even change their behavior from being incompatible to compatible. This can be seen in Fig. 2 where the Ge concentrations in some groups initially increase with Ni concentrations and later revert to a decreasing trend. Ni itself is slightly incompatible and the Ni concentration in the solid therefore increases as the core crystallizes.

Cooling of the Core and Formation of the Widmanstätten Structure

When the core temperature reached ~800 °C, an important phase transition occurred in most of the iron meteorites (exceptions are those relatively rare iron meteorites with Ni concentrations above ~25 wt%). What happened was that a new phase, kamacite, nucleated and grew at the expense of the initial taenite phase. Since kamacite has a lower Ni concentration than the original metal, the growth of kamacite was controlled by the diffusion of Ni through the solid metal. Diffusion of Ni through the original taenite phase is extremely slow, and the resulting intergrowth of kamacite and taenite are therefore never completely equilibrated. The degree of equilibration may therefore be used to measure the cooling rate of the core at the time where kamacite grew. These cooling rates are usually referred to as metallographic cooling rates. Typical metallographic cooling rates are of the order of 1–100°/million years. Since small asteroids cool faster than large asteroids, the cooling rates may be used to constrain the size of the original parent body.

The resulting Widmanstätten structure is the hallmark of iron meteorites. Since the low-Ni kamacite phase is less resistant to etching with nitric acid than the high-Ni taenite phase, the structure may be revealed by etching a polished

Iron Meteorites, Fig. 3 Three different iron meteorites are shown to the same scale, to illustrate the large variation in structure. Gibeon, an IVA iron meteorite with a fine Widmanstätten structure, is shown at the *top*. Carbo, a medium octahedrite, is shown in the *middle*, and Old Woman, a coarsest octahedrite, with low Ni (5.7 wt%) concentration, is shown at the *bottom*. The *white bar* at the *top* is 5 cm long (Photo credit: Jens Astrup, Natural History Museum of Denmark)

surface with weak nitric acid (Fig. 3). The width of the kamacite lamellae in the Widmanstätten structure is mainly controlled by the original Ni concentration. Typical dimensions are in the range between 0.1 and 100 mm, and different types of iron meteorites may therefore often be distinguished on the basis of the appearance of the Widmanstätten structure.

Catastrophic Destruction of the Asteroid and the Core

The fact that iron meteorites from up to ~100 different differentiated asteroids are now present in our meteorite collections shows us that their parent bodies must have been destroyed. Three types of processes appear to have been significant:

Hit and Run Collisions

In the early solar system where planets grew at the expense of smaller bodies, collision rates were many orders of magnitude higher than now. A small number of the impacts were grazing impacts where the projectile was destroyed but escaped accretion with the growing planets. Such so-called hit and run events can potentially strip most of the mantle off a differentiated body and/or remix mantle, core, and crust (Haack and Scott 1992).

Collisional Erosion

Small bodies are much more abundant in the main asteroid belt than large bodies. For any given diameter, D, there are approximately 100 times more bodies with a diameter of 0.1 D. Most impacts experienced by an asteroid are therefore relatively minor cratering events. Over time these may, however, gradually erode the asteroid and eventually expose the core.

Catastrophic Collisions

Larger catastrophic collisions involving "projectiles" that are large enough to destroy and disrupt the asteroid are less common, but several groups of meteorites appear to originate from catastrophically destroyed asteroids (Keil et al. 1994). Although we do not have stony meteorites from the mantle and crust of the iron meteorite parent bodies, some of the cores of iron meteorite parent bodies appear to have been destroyed in single events.

Orbital Transfer of the Core Fragments to Earth Crossing Orbit

Fragments from asteroid collision typically orbit the Sun for millions of years before they collide with a planet or the Sun or become ejected from the Solar System. The travel time can be estimated because meter-sized fragments are exposed to cosmic radiation. It is possible to measure the radiation dose these fragments have received and use that to calculate the cosmic exposure age, which we infer is usually equal to the travel time. Stony meteorites typically have cosmic-ray expose ages up to a few tens of millions of years, whereas iron meteorites have cosmic-ray exposure ages up to two billion years.

Transfer to Earth-crossing orbit is mainly carried out in two steps. After ejection from the parent bodies, the fragments usually end up in semi-stable orbits around the Sun. The so-called Yarkovsky effect causes slow orbital drift in- or outward in the Solar System (depending on whether the object

rotates clockwise or counterclockwise). After millions of years of slow drift, the object will at some point encounter one of the orbital resonances with Jupiter. Gravitational interaction with Jupiter will subsequently rapidly change the orbit (on a time scale less than one million years).

There are probably several reasons that iron meteorites have longer cosmic-ray expose ages. One reason is that they are stronger than stony meteorites and therefore can survive longer in space. Another reason is that the orbits evolve more slowly for iron meteorites. Meter-sized fragments drift in- or outward because of the so-called Yarkovsky effect. The drift is caused by the difference in thermal radiation between the warm dayside and the cold nightside. If the object is rotating, there will be a net force which either accelerates the object or slows it down. However, metallic objects with a high thermal conductivity have a smaller temperature difference between night- and dayside and therefore drift much more slowly.

Since iron meteorites have much longer travel times to Earth-crossing orbit, they also sample the collisional evolution of the asteroid belt on a much longer time scale. This is probably the main reason that iron meteorites appear to sample a much larger number of parent bodies than stony meteorites.

Fall on Earth

Meteorites survive the impact with the Earth because the Earth atmosphere slows them down to subsonic speed, before they hit solid ground. When the object enters the atmosphere at 15–30 km/s, the drag forces are so powerful that even solid metal objects are often torn apart. After each fragmentation event in the atmosphere, the smallest fragments are slowed down more quickly than the large fragments. Since most objects enter the atmosphere at an angle, the resulting fall area is elongated with the biggest fragments concentrated furthest downrange.

Since iron meteorites are heavier and much harder to break apart than stony meteorites, they are also more difficult to slow down. Whereas stony meteorites rarely exceed a few hundred kilograms, iron meteorites commonly have masses of several tons. The most massive iron meteorite known is the 60 ton Hoba from Namibia. Some of the larger fragments of iron meteorites impact the Earth at supersonic speeds. Upon impact, a supersonic iron meteoroid penetrates the surface and vaporizes and creates an explosion crater. Smaller fragments from the same fall usually survive the fall because they are slowed down sufficiently in the atmosphere. These fragments may be found scattered around the explosion crater. Because iron meteorites tend to hit the surface at higher velocities, many of the known explosion craters are caused by iron meteorites. Although only ~4% of meteorite falls are iron meteorites, more than 90% of the smallest and youngest impact craters are caused by iron meteorites.

Use of Iron Meteorites by Humans

Subsequent to their fall on Earth, many iron meteorites have been used to forge tools and weapons, and in some cases, they appear to have had a religious significance (1 – Appendix 6). In North Greenland, the Cape York iron meteorites were the local Inuits' only source of metal (Buchwald 1975). The Inuits have knocked off pieces of some of the Cape York irons since ~700 AD. Tools with Cape York irons can be used to follow trade routes along the west coast of Greenland and more than 1000 km into Canada.

Chemical Classification of Iron Meteorites

The bulk chemical composition of iron meteorites can be used to define clusters of iron meteorites with similar chemistry. Clusters with at least five members are designated iron meteorite groups. Currently 13 such groups of iron meteorites have been defined, where each group is assumed to represent a single parent body. The largest group is IIIAB with almost 300 members. Fifteen percent of the iron meteorites are not included in the main groups (Krot et al. 2014) and are believed to represent another 50–100 parent asteroids.

Historically, iron meteorites were divided into four groups based on their concentration of the highly volatile siderophiles (metallic) elements Ga and Ge (Fig. 2) (Buchwald 1975; Ruzicka et al. 2016; Benedix et al. 2014; Krot et al. 2014; Chabot and Haack 2006). Ga and Ge are very useful for classification purposes, because most iron meteorites fall in tight clusters on Ga and Ge diagrams (Fig. 3). Members of the original group I have the highest abundances of Ga and Ge. Groups II, III, and IV had still lower volatile inventories, with group IV having Ga and Ge abundances 3–4 orders of magnitude below those of group I. Improved analytical techniques allowed the original four groups to be subdivided into smaller groups. The smaller groups had a letter added to the original roman numerals – i.e., IA, IIIA, IIIB, etc. Although the smaller groups were separated in the early studies, later studies added more iron meteorites which closed the gaps between some of the earlier groups. IIIA and IIIB thus became IIIAB, which is the term used today. Also, two silicate-bearing groups IAB and IIICD are now believed to come from the same body and have therefore been merged to a single group (Krot et al. 2014).

Figure 3 shows germanium and iridium plotted nickel for the main groups of iron meteorites. The large differences in Ga abundance between the different groups are probably due to differences in bulk chemical composition between the groups (see section "Accretion of Iron Meteorite Parent Bodies" above). Differences in Ni composition are mainly due to differences in oxidation state of the parent body. In oxidized parent bodies, a larger fraction of the element iron remains in

the mantle. The relative abundance of Ni is therefore larger in oxidized parent bodies. The chemical variation within each group is mainly due to core crystallization (see section "Melting and Differentiation of Iron Meteorite Parent Bodies" above). In groups IIAB and IIIAB, the Ir abundances span more than three orders of magnitude between the early crystallized high-Ir members to the late crystallized low-Ir members.

Structural Types of Iron Meteorites

Etched and polished surfaces of iron meteorite display the characteristic Widmanstätten structure. The structure is composed of alternating lamellae of the low-Ni kamacite phase and the high-Ni taenite phase. Because the Ni content is different in the two phases, iron meteorites with different bulk Ni concentrations also have different ratios of kamacite and taenite. Iron meteorites with very low Ni concentration (~5.5 wt%) have normally transformed to single crystals of kamacite and are referred to as hexahedrites. Likewise, Ni-rich iron meteorites (above ~25 wt% Ni) are usually pure taenite crystals. These irons are called ataxites. Most iron meteorites have intermediate Ni concentrations and can be easily distinguished because of the large variation in width of the kamacite lamellae (Fig. 3). Iron meteorites with Ni concentrations around 5.9 wt% have kamacite bandwidths up to 10 cm, whereas irons with Ni concentration around 14 wt% typically have kamacite bandwidths down to 0.1 mm. Although kamacite bandwidth is mainly controlled by the Ni concentration, the cooling rate of the core, during growth of the kamacite phase, also plays a role.

Connection to Asteroids

Since iron meteorites are believed to originate from the exposed or possible destroyed metallic cores of differentiated asteroids, it follows that there must be asteroids with surfaces that are entirely or partially metallic. Spectral studies of the sunlight reflected from the surfaces of meteorites can be used to constrain the surface mineralogy of asteroids even though their surface features cannot be resolved with even the biggest telescopes. Several silicates, such as pyroxene and olivine, absorb the sunlight at specific wavelength and may therefore be positively identified. Although metal absorbs more of the shorter wavelength than it absorbs long wavelength, it does not have any absorption lines that could have been used to make a positive identification of metal. Several asteroids, like the 150 km diameter, 16 Psyche, do however have spectral characteristics consistent with metal and could therefore be examples of large exposed cores.

Summary

Iron meteorites are core samples of asteroids that melted 4.5 Gy ago and differentiated into a layered structure with a central metallic core, a stony mantle, and a volcanic crust. The more than 1000 known iron meteorites probably represent 50–100 different asteroids. Studies of iron meteorites provide information on the early history of our Solar System and of planetary evolution. The iron meteorites are the best available analogues to the metallic core at the center of the Earth.

References

Benedix GK, Haack H, McCoy TJ (2014) Iron and stony-iron meteorites. In: Davis AM, Turekian K (eds) Treatise on geochemistry, 2nd edn. Elsevier, Amsterdam, pp 267–285

Buchwald VF (1975) Handbook of iron meteorites. University of California Press, Berkeley, 1418 p

Chabot NL, Haack H (2006) Evolution of asteroidal cores. In: Lauretta DS, McSween HY Jr (eds) Meteorites and the early solar system II. University of Arizona Press, Tucson, pp 747–771

Haack H, Scott ERD (1992) Asteroid core crystallization by inward dendritic growth. J Geophys Res 97:14.727–14.374

Keil K, Haack H, Scott ERD (1994) Catastrophic fragmentation of asteroids: evidence from meteorites. Planet Space Sci 42:1109–1122

Krot AN, Scott ERD, Goodrich CA, Weisberg MK (2014) Classification of meteorites and their genetic relationships. In: Davis AM, Turekian K (eds) Treatise on geochemistry, 2nd edn. Elsevier, Amsterdam, pp 1–63

Ruzicka AM, Haack H, Scott ERD, Chabot N (2016) In: Elkins-Tanton LT, Weiss B (eds) Iron and stony-iron meteorites: evidence for the formation, crystallization, and early impact histories of differentiated planetesimals. Submitted to Planetesimals. Cambridge University Press. (should be in press very shortly)

Isotope Dilution

Jon Woodhead
School of Earth Sciences, The University of Melbourne, Melbourne, VIC, Australia

Definition

In its original, and most widely used form, isotope dilution is a method for determining elemental concentrations in samples of minerals, rocks, and fluids. It involves adding a known quantity of an enriched isotope "spike" to the (usually dissolved) sample, followed by isotopic analysis of the resulting spike-sample mixture in an isotope ratio mass spectrometer. One of the main applications of the technique is in radiometric age determinations (geochronology) where the concentrations of parent and daughter isotopes must be measured in order to calculate the geological age of a sample. The

concept has evolved further, with the development of double- and triple-spikes composed of multiple enriched isotopes. These more complex variants are designed to allow the monitoring and correction of instrumental mass bias effects encountered during mass spectrometric isotope ratio measurements of many different elements, allowing the acquisition of isotope ratio data with very high levels of precision and accuracy.

Elemental Concentration Determinations

With the exception of accelerator-based designs, most modern mass spectrometers are not sufficiently sensitive to record the arrival of single atoms in their detectors. Instead, they typically measure only the ratios between different isotopes of an element, based upon ion currents representing many individual atoms. There are, however, situations where it is essential to determine the absolute concentrations of elements – and to a high level of accuracy – here the isotope dilution method is employed. The approach requires the isotopic compositions of both the sample and an isotopically enriched tracer (termed a "spike") to be known. Then, by adding a known quantity of the spike to a known weight of the sample, equilibrating the mixture, and then measuring the resulting isotopic composition, the elemental concentration in the original sample can be readily determined. The term "isotope dilution" stems from the dilution of the isotopic constituents of the sample in the spike-sample mixture.

The method can be applied to all elements for which two or more isotopes are present and also to mono-isotopic elements provided an appropriate long-lived artificially produced isotope exists. Ideally the choice of spike corresponds to an isotope that is present in relatively small abundance in natural samples. Thus, for example, in geochemistry, spikes such as ^{84}Sr, ^{149}Sm, ^{150}Nd, and ^{180}Hf are commonly employed. When available, it can be even more advantageous to use artificially produced isotopes that do not occur in nature such as ^{233}U, ^{229}Th, and ^{205}Pb.

As an example, in Rb-Sr geochronology where we need to know the concentration of the daughter element, Sr, as part of the process of determining an age, an ^{84}Sr-enriched spike is often used. The measured ^{84}Sr/^{86}Sr ratio in a sample-spike mixture is then given by Eq. 1:

$$\left[\frac{84Sr}{86Sr}\right]_{measured} = (Sa84 + Sp84)/(Sa86 + Sp86) \qquad (1)$$

where "Sa86" and "Sa84" are the contributions of ^{86}Sr and ^{84}Sr from the sample and "Sp86" and "Sp84" are the contributions of ^{86}Sr and ^{84}Sr in the ^{84}Sr-enriched spike.

From this simple relationship (Eq. 1) an equation can be derived to allow determination of the element concentration in the sample, expressed in terms of measurable isotope ratios and known quantities (i.e.,weights and isotopic compositions of spike and sample), shown in a generic form below (from Stracke et al. 2014, where the full deviation can be found), Eq. 2:

$$conc_{Sa} = \frac{\frac{A}{B_{mix}} - \frac{A}{B_{Sp}}}{\frac{A}{B_{Sa}} - \frac{A}{B_{mix}}} x \frac{weight_{Sp} conc_{Sp} abundance(B_{Sp}) atwt(element_{Sa})}{weight_{sa} abundance(B_{Sa}) atwt(element_{Sp})} \qquad (2)$$

where subscripts "*Sa*" and "*Sp*" refer to sample and spike, respectively, "*A*" is the enriched isotope (present in both spike and sample, i.e., ^{84}Sr in the case of Sr) and "*B*" is a reference isotope (also present in both; ^{86}Sr in the example shown above), "*atwt*(*element*)" is the atomic weight of the element of interest, and "*abundance*(*B*)" refers to the abundance of the reference isotope. A number of variants of this "isotope dilution equation" can be found in the literature depending on the form of the input parameters and nature of the reference isotopes (natural or artificial) but all essentially perform the same function. In real-world applications the isotope dilution equation is often solved iteratively in concert with a correction for instrumental mass bias effects.

The isotope dilution method was developed in the early twentieth century and is attributed to Hevesy and Hofer (1934) although it did not find mainstream acceptance until the work of Rittenburg and Foster (1940). Since that time, due to the extremely high levels of precision and accuracy obtainable, it quickly became the "gold standard" for trace element determination – a method against which all other analytical techniques may be evaluated.

The optimum mixture ratio of spike to sample is provided by the following, Eq. 3:

$$R^{optimal}_{measured} = \sqrt{(R_{sample} x\, R_{spike})} \qquad (3)$$

When the spike:sample ratio departs from this optimum, notably in strongly over- or under-spiked situations where the isotopic composition of the mixture approaches that of the spike or unknown, respectively, the uncertainty in $R_{measured}$ becomes magnified due to unfavorable error propagation systematics (e.g., Webster 1960). Ideally, therefore, it is useful to have first-order estimate of the likely sample concentration in order to perform optimum spiking and thus obtain the highest quality data.

As a method of concentration determination the technique has many significant advantages. Primarily, as a result of the mass spectrometric measurement, the technique is

characterized by very high analytical precision and accuracy together with high sensitivity and concomitant low limits of detection. In addition, once the spike and sample are equilibrated, any partial loss of the analyte during the chemical separation of the element of interest is inconsequential. Unfortunately, the method can be expensive and time consuming and enriched isotope spikes are often difficult to procure (e.g., ^{229}Th), and in some cases, unavailable (e.g., ^{205}Pb which is no longer manufactured). Recent detailed reviews of the isotope dilution method have been provided by Alonso and Rodriguez-Gonzalez (2013) and Stracke et al. (2014).

Mass Bias Control

The isotope dilution method employing enriched isotope spikes can be used in other ways. For example, in most types of mass spectrometer, the isotope ratios measured at the detectors are not the same as those present in the analyte – they have been modified during their transit through the instrument, primarily through instrument-specific physical processes in the ion source region. In the case of thermal ionization mass spectrometers (TIMS), it is common for lighter isotopes to be measured preferentially since they are mobilized from the metal filament carrying the analyte more readily than heavier isotopes of the same element. In contrast, in Inductively Coupled Plasma Mass Spectrometers (ICPMS), that have an ion source operating at atmospheric pressure, heavier ions tend to be detected preferentially since they more easily navigate space-charge effects occurring in the region of the skimmer cone adjacent to the argon plasma ion source.

A number of methods can be employed to correct for these so-called mass bias effects. If the element in question is characterized by one or more isotopes that are stable (hence invariant) in nature then the ratio of the two can be compared with the measured ratio to estimate the degree of bias, and an appropriate correction then applied to the other isotope ratios. However, for some elements, no stable isotope pair is available to make such a correction, e.g., Pb-isotope analysis. Here the most elegant and effective solution for high precision isotope ratio determination involves simulating the presence of a stable isotope pair by mixing a so-called double spike, comprising two enriched isotopes of known composition, with the sample and measuring the resultant mixture (e.g., Dodson 1963). Double spiking of this type requires two mass spectrometer runs, one with the natural sample and the other with the spike-sample mixture. From these measurements a highly accurate bias-corrected isotope ratio can be determined (e.g., Hamelin et al. 1985). Additional variants involving triple spikes or two double spike runs have been proposed (e.g., see Taylor et al. 2015 for a summary of these techniques for Pb-isotope analysis).

The method is widely applicable and has been used to facilitate high quality isotope ratio determinations in many isotope systems such as Ca, Cr, Fe, Mo, and Cd. Software is also now available to allow the optimum design of double spikes for mass bias correction (Rudge et al. 2009) and to assist in subsequent data deconvolution (Creech and Paul 2014).

Summary

Isotope dilution is an essential technique employed in a wide array of geochemical studies, providing both highly accurate and precise elemental concentration determinations and also a methodology to correct for mass bias effects encountered during isotope ratio mass spectrometry. In both of these applications it allows the acquisition of extremely accurate and precise data that are generally unrivalled by any other technique.

Cross-References

- Analytical Techniques
- Geochronology and Radiogenic Isotopes
- Inductively Coupled Plasma Mass Spectrometry (ICP-MS)
- Lead Isotopes
- Thermal Ionization Mass Spectrometry

References

Alonso JIG, Rodriguez-Gonzalez P (2013) Isotope dilution mass spectrometry. Royal Society of Chemistry, Cambridge

Creech JB, Paul B (2014) IsoSpike: improved double spike inversion software. Geostand Geoanal Res 39:7–15

Dodson MH (1963) A theoretical study of the use of internal standards for precise isotopic analysis by the surface ionization technique: part I – general first-order algebraic solutions. J Sci Instrum 40:289–295

Hamelin B, Manhes G, Albarede F, Allegre CJ (1985) Precise lead isotope measurements by the double spike technique: a reconsideration. Geochim Cosmochim Acta 49:173–182

Hevesy G, Hofer E (1934) Elimination of water from the human body. Nature 134:879

Rittenberg D, Foster GJ (1940) A new procedure for quantitative analysis by isotope dilution with application to the determination of amino acids and fatty acids. J Biol Chem 133:737–744

Rudge JF, Reynolds BC, Bourdon B (2009) The double spike toolbox. Chem Geol 148:95–104

Stracke A, Scherer EE, Reynolds BC (2014) Application of isotope dilution in geochemistry. Treatise Geochem 2nd edition 15:71–86. https://doi.org/10.1016/B978-0-08-095975-7.01404-2

Taylor RN, Ishizuka O, Michalik A, Milton JA, Croudace IW (2015) Evaluating the precision of Pb-isotope measurement by mass spectrometry. J Anal At Spectros 30:198–213

Webster RK (1960) Mass spectrometric isotope dilution analysis. In: Smales AA, Wager LR (eds) Methods in geochemistry. Interscience Publishers, New York, pp 202–246

K

Kerogen

Steven Petsch
Department of Geosciences, University of Massachusetts Amherst, Amherst, MA, USA

Synonyms

Fossil organic matter; Geogenic carbon; Petrogenic carbon; Sedimentary organic matter

Definition

Kerogen is solid-phase, macromolecular organic matter that occurs in sedimentary rocks and is insoluble in common organic solvents.

Occurrence of Kerogen in the Geosphere

As the definition of kerogen is operational, the term "kerogen" does not imply a particular structure, appearance, origin, or composition, beyond being based on chemically reduced organic carbon and not comprising readily identified low-molecular-weight compounds. As such, kerogen encompasses a broad suite of geologic materials that vary in their sources, their chemical and physical properties, and their ultimate fates under geological processes. In typical sedimentary rocks, most organic matter is in the form of kerogen, with 80% or more of the total mass of organic carbon in a given rock coming from Kerogen (Tissot and Welte 1984; Hunt 1996; Hedges and Oades 1997). The remainder of rock organic matter, termed bitumen, comprises solvent-soluble materials that are nominally lower in molecular weight and includes identifiable compounds such as biomarkers. Coarse-grained clastic sedimentary rocks (e.g., sandstones) are typically poor in kerogen, as are biochemical sedimentary rocks (cherts, limestones) and evaporites, but there are exceptions. In contrast, finer-grained clastic sedimentary rocks (mudrocks such as shales and siltstones) commonly contain at least some kerogen, though typically $<1\%$. The "world average shale" contains 1.2% organic carbon (Turekian and Wedepohl 1961), while kerogen-rich mudrocks termed black shales typically contain closer to 5–10% organic carbon. Some particularly kerogen-rich black shales may be upwards of 30% carbon by weight (e.g., the Green River Shale of Wyoming, Utah and Colorado), and coal, which can be considered a special case of kerogen, can be nearly 100% organic matter.

Origin of Kerogen

Much like coal, kerogen represents the remains of biological materials that became incorporated into sediments and ultimately sedimentary rocks. Unlike coal, which mainly derives from the remains of terrestrial plants and occurs as nearly pure organic matter, kerogen in rocks is substantially diluted by inorganic minerals (primarily silicates, carbonates, and sulfides) and derives from a wide array of biological sources. These include materials derived from leaves, wood, spores, and pollen of terrestrial plants, degraded soil organic matter, and for most kerogens, substantial contributions from freshwater and marine algae as well as zooplankton and bacteria. Kerogen also differs from coal in its environments of deposition. While coal formed in low-lying, flooded but essentially terrestrial environments with little to no transport occurring between biological source and sediment deposition, kerogen reflects the transport of organic materials and sediments through soil, fluvial, lacustrine, and/or marine systems. This can result in substantial modification in kerogen composition compared to its original biological sources.

Much effort has been focused on understanding the processes and controls on organic matter preservation in sedimentary rocks, and thus on the formation of kerogen. Early

W. M. White (ed.), *Encyclopedia of Geochemistry*,
https://doi.org/10.1007/978-3-319-39312-4

descriptions of kerogen formation via geopolymerization in which biomolecules underwent random condensation reactions in soils and sediments either abiotically or through the mediation of microorganisms (Tissot and Welte 1984), have been largely replaced, although cross-linking of peptides, sulfurization of carbohydrates, and formation of nitrogen-bearing heterocyclic components may all be important in some settings. Instead, the majority of kerogen formation (which in turn, represents the majority of organic matter burial in sediments and occurrence in sedimentary rocks) results from a combination of (i) the selective preservation of certain biopolymers and other materials (combustion residues, recycled kerogen) that are most resistant to degradation (Hatcher et al. 1983; Tegelaar et al. 1989); (ii) physical protection mechanisms such as association with mineral surfaces (Mayer 1994; Keil et al. 1994) or encapsulation within degradation-resistant biopolymers (Knicker and Hatcher 1997) that prevent or slow the degradation of biological materials; and (iii) limitations on the supply of degradation reactants such as dissolved O_2 (Hartnett et al. 1998; Hedges et al. 1999). Thus, kerogen can be understood as a mixture of components that are selectively preserved, components that have been protected from degradation, and components that experienced only limited time exposed to oxic degradation conditions.

Analysis, Composition, and Kerogen Types

A variety of tools are used in the analysis of kerogen. Organic petrography is the examination of morphological and optical properties of kerogen and coal using transmitted and reflected light microscopy. Morphologically distinct remnants of primarily plant and algal remains are termed macerals and categorized into three maceral groups: liptinite – translucent, yellow-orange materials derived from the lipid-rich remains of ancient leaves, pollen, spores and algae; vitrinite – lustrous, black-brown maceral group derived from woody plant materials; and inertinite – opaque, black-brown brittle materials that represent charred or otherwise heavily degraded woody tissue. Within these groups, various specific macerals are recognized and tied to specifically biological origins. Vitrinite reflectance, in which the percent of incident light reflected off a polished surface containing vitrinite is measured, is an important petrographic technique in evaluating the thermal maturity of coals and vitrinite-bearing kerogens. This, together with subtle changes in the appearance of certain macerals, provides useful information on the burial and thermal history of kerogen- and coal-bearing rocks and their past oil and gas generation.

Kerogen can be classified as Type I, Type II, or Type III on the basis of elemental composition (Tissot and Welte 1984). The three most abundant elements in kerogen are carbon, hydrogen, and oxygen. When expressed as atomic H/C and O/C ratios, kerogen compositions can be displayed on a van Krevelen diagram. Type I kerogens have high H/C ratios (>1) and low O/C ratios (<0.1). Type I is the least common of the three kerogen types. Petrographic analysis reveals that this kerogen comprises mainly liptinite. Type III kerogens are common and most similar to coals in composition with low H/C ratios (<1) and high O/C ratios (>0.1). These kerogens are rich in vitrinite. Type II kerogens are intermediate between Types I and III in H/C and O/C ratios. Type II kerogens are abundant and derived from the degraded remains of marine algae and other plankton, together with degraded remains of terrestrial plants. Kerogens of any type can have anomalously high concentrations of organic sulfur (up to 0.05 atomic S/C ratio) and are termed Type I-S, II-S, or III-S. Many other elements can be found in kerogens, notably redox-sensitive trace metals such as Fe, V, Ni, Mo, U, Cr, Co, Re, and Os.

Rock-Eval pyrolysis is a technique in which programmed heating of kerogen in the absence of O_2 releases CO_2 and hydrocarbon gases (Espitalié et al. 1977). The masses of these gases are measured at different stages of the pyrolysis, as is the residual carbon content following pyrolysis. A variant of a van Krevelen diagram can be constructed from Rock-Eval data, using a hydrogen index (HI) and an oxygen index (OI). A plot of kerogen HI vs. OI values can be used for kerogen typing much like H/C and O/C ratios. Together with T_{max} data (the temperature of maximum hydrocarbon gas generation during Rock-Eval pyrolysis), HI-OI plots can also reveal information about the thermal history of kerogen and its potential for oil and gas generation.

Kerogen's macromolecular nature and varied biological origins have confounded a direct determination of its chemical structure. In addition, many of the analytical techniques applied to kerogen either require demineralization which may alter kerogen composition or are compromised by the presence of minerals (e.g., paramagnetic materials). Spectroscopic techniques such as solid-state ^{13}C nuclear magnetic resonance, Raman, and infrared spectroscopy reveal information about the abundance of different types of chemical bonds and chemical environments in a kerogen (i.e., organic functional groups), but do not specify a three-dimensional structure. The solid-phase nature of kerogen precludes chromatographic analysis, but pyrolysis coupled with gas chromatography and/or mass spectrometry can be used to identify and quantify kerogen fragments and components liberated by pyrolysis and amenable to GC analysis. When pyrolyzed with H_2, H_2O, or methylating agents, further structural information can be obtained. However, only a fraction of the total kerogen, pyrolysis products together with NMR and IR interpretations provide a picture of kerogen structure and composition that is consistent with elemental analysis and organic petrography (Behar and Vandenbroucke 1987). While not defined as a particular structure, kerogen is thus

understood to comprise long polymethylenic moieties (i.e., straight-chain aliphatic groups), polycyclic and partially aromatized components derived from steranes, hopanes and porphyrins, residues from lignin monomers, together with residues and cross-linkages from carbonyl, acid, amine, and thiols, among others.

Fate, Maturation, and Petroleum Generation

Kerogen has long held academic and economic interest as the source from which petroleum reserves derive. As kerogen-bearing sedimentary rocks become deeply buried in sedimentary basins and are exposed to higher temperatures and pressures, kerogen undergoes chemical and physical changes that affect its composition and result in generation of low-molecular-weight hydrocarbons (i.e., crude oil and natural gas). This process is known as thermal maturation. The thermal maturity of a kerogen is a gauge of the time-temperature history of the source rock and can be assessed using vitrinite reflectance and Rock-Eval techniques as well as with spectroscopic techniques and certain lipid biomarkers. Most generally, thermal maturation results in cleavage of low molecular weight fragments from kerogen, namely CH_4, CO_2, H_2O, and *n*-alkanes of various lengths. As such, the pathways of kerogen composition during thermal maturation on a van Krevelen diagram can be understood as the progressive cleavage and loss of these components.

The stages of thermal maturation are separated into diagenesis, catagenesis, and metagenesis (see Killops and Killops 2005). During diagenesis, sediments are still undergoing lithification and are considered thermally immature. The only hydrocarbon generation that occurs is methane produced through biological methanogenesis. As temperatures increase and the rock is now lithified, it enters the stage of catagenesis. Thermal decarboxylation results in loss of CO_2 from organic acids, while *n*-alkyl fragments break off from aliphatic components of kerogen. Initially these result in long *n*-alkanes ($>C_{30}$) but as source rocks progress through the oil window (100–150 °C), low- and medium-length alkanes and other hydrocarbons are produced. With higher temperatures, increasingly shorter alkyl fragments are produced: "wet gas" comprising C_1–C_4 alkanes (methane, ethane, propane, and butane) through the end of catagenesis (approximately 200 °C) followed by "dry gas" made of mainly methane during metagenesis up to temperatures of approximately 250 °C. As hydrocarbons, H_2O and CO_2 are broken off during oil and gas generation, the residual kerogen evolves towards a more condensed structure rich in aromatic and polyaromatic groups. Ultimately, once no further hydrocarbons can be cleaved, kerogen approaches a composition resembling amorphous graphite and with further metamorphism becomes graphite.

The amounts and distribution of petroleum products generated during thermal maturation depends in part on the time-temperature-pressure pathway experienced by the source rock. Geologically slow increases in temperature result in long durations of time spent in the oil window, with commensurate high production of oil. Rapid increases in temperature, in which the source rock rapidly passes the oil window into higher temperatures, results in mainly gas and graphitized kerogen residues. In addition, kerogen composition and type play a role. Type I kerogens and liptinitic components of other kerogens are most capable of yielding oil, while Type III kerogens and vitrinitic components and other kerogens generate limited amounts of oil and instead mostly form natural gas. Severely degraded and precombusted kerogens (i.e., inertinites) generate very little oil or gas upon maturation.

Role of Kerogen in Carbon Cycling

Earth's crust contains some 75 million Gt of carbon, of which approximately 20% is organic carbon. This is orders of magnitude more carbon than the combined mass other surficial carbon reservoirs such as soils, terrestrial and marine biomass, atmospheric gases, and dissolved carbon in the oceans and other aquatic systems. As the majority of crustal organic carbon is kerogen, kerogen thus represents a substantial carbon reservoir in the global carbon cycle. However, the cycling of carbon between geologic carbon reservoirs (namely, kerogen and carbonate minerals) and surficial reservoirs is very slow compared to the cycling among those surficial reservoirs, and residence times for carbon as kerogen or carbonate minerals are hundreds of millions of years.

The global rate of addition of carbon to the kerogen reservoir is not precisely known, but can be constrained. Estimates of global organic carbon delivery to sediments range over an order of magnitude (0.16–2.5 Gt C y^{-1}; Burdige 2007), while the flux of organic carbon that escapes degradation and remineralization during early diagenesis and is thus incorporated into sedimentary rocks as kerogen must necessarily substantially smaller. Mass balance constraints from global carbon cycle models suggest that 0.04–0.1 Gt C y^{-1} is added to the global kerogen reservoir (Petsch 2014a), which sets a rough scale for the magnitude of the flux but does not imply that this rate has been entirely constant through geologic time. Because kerogen derives from biological precursors, kerogen formation ultimately derives from the process of photosynthesis. As such, relatively small changes in the global-scale rate at which kerogen is formed can have substantial impacts on atmospheric reservoirs of CO_2 and O_2 (Holland 1973; Garrels and Lerman 1981, 1984; Berner 1987; Petsch and Berner 1998).

Kerogen also plays a role in the global carbon cycle during rock weathering and erosion. Oxidative weathering of

kerogen during erosion and soil formation consumes O_2 and forms inorganic carbon species such as CO_2. The global rate of oxidative kerogen weathering is approximately equal to the rate of kerogen burial: 0.04–0.1 Gt y^{-1} (Petsch 2014a). Sustained large imbalances between kerogen formation and oxidative kerogen weathering would have caused significant changes in the CO_2 and O_2 concentrations of Earth's atmosphere over geologic timescales, which are not inferred from the rock record. However, small imbalances favoring slightly more weathering or slightly more burial have occurred, driving in part the CO_2 and O_2 concentrations in Earth's atmosphere over geologic time (Kump and Garrels 1986; Berner and Canfield 1989; Petsch and Berner 1998; Berner 2006). One notable example of this is the inferred high atmospheric O_2 content during the Carboniferous, when coal and kerogen burial rates far outpaced oxidative kerogen weathering (Berner 2003; Petsch 2014b).

The role of kerogen in the global carbon cycle remains an active area of research. Kerogen is not necessarily oxidized during weathering. Instead, there is growing recognition that some kerogen may be physically weathered, eroded, transported by fluvial system and ultimately re-buried in sediments without oxidation (Longworth et al. 2007; Galy et al. 2007 2008, 2015; Blair and Aller 2012; Hilton et al. 2008, 2011). Furthermore, some kerogen may be metabolized and incorporated into living biomass during weathering (Petsch et al. 2001; Shillawski and Petsch 2008; Matlakowska et al. 2010, Matlakowska and Sklodowska 2011) and fluvial transport (Caraco et al. 2010).

Summary and Conclusions

Kerogen is a complex, naturally occurring macromolecular form of organic matter found in sedimentary rocks. It derives from biological precursors through selective preservation of materials resistant to chemical and biological degradation, through physical protection mechanisms that impede degradation, and/or in environments where exposure to degradation is limited. While detailed chemical structural information on kerogen cannot be defined due to its structural complexity, randomness, and insolubility, there is broad classification of kerogen into Types I, II, and III based on both chemical and morphological properties. Kerogen is the source material for nearly all petroleum reserves, and understanding of thermal maturation of kerogen and the generation of oil and natural gas holds both academic and economic interest. The global mass of kerogen is estimated at approximately 15 million Gt, orders of magnitude greater than all surficial carbon reservoirs combined. Thus, cycling of carbon into and out of the kerogen reservoir plays a key role in the global carbon cycle and provides a control on the composition of Earth's atmosphere over geologic time.

Cross-References

- ▶ Biogeochemistry
- ▶ Biomarkers: Coal
- ▶ Biomarkers: Petroleum
- ▶ Biopolymers and Macromolecules
- ▶ Black Shales and Sapropels
- ▶ Carbon Cycle
- ▶ Coal
- ▶ Gas Chromatography–Mass Spectrometry (GC–MS)
- ▶ Hydrocarbons
- ▶ Natural Gas
- ▶ Nuclear Magnetic Resonance
- ▶ Oil Shale
- ▶ Organic Geochemistry
- ▶ Organic Matter Degradation and Preservation
- ▶ Petroleum
- ▶ Programmed Temperature Pyrolysis

References

Behar F, Vandenbroucke M (1987) Chemical modelling of kerogen. Org Geochem 11:15–24

Berner RA (1987) Models for carbon and sulfur cycles and atmospheric oxygen: application to Paleozoic geologic history. Am J Sci 287:177–196

Berner RA (2003) The long-term carbon cycle, fossil fuels and atmospheric composition. Nature 426:323–326

Berner RA (2006) GEOCARBSULF: a combined model for Phanerozoic atmospheric O_2 and CO_2. Geochim Cosmochim Acta 70:5653–5664

Berner RA, Canfield DE (1989) A new model of atmospheric oxygen over Phanerozoic time. Am J Sci 289:333–361

Blair NE, Aller RC (2012) The fate of terrestrial organic carbon in the marine environment. Annu Rev Mar Sci 4:401–423

Burdige DJ (2007) Preservation of organic matter in marine sediments: controls, mechanisms and an imbalance in the sediment organic carbon budgets? Chem Rev 107:467–485

Caraco N, Bauer JE, Cole JJ, Petsch S, Raymond P (2010) Millenial-aged organic carbon subsidies to a modern river food web. Ecology 91:2385–2393

Espitalié J, Laporte JL, Madec M, Marquis F, Leplat P, Paulet J, Boutefeu A (1977) Méthode rapide de caractérisation des roches meres, de leur potential pétrolier et de leur degré d'evolution. Rev Inst Fr Pétrol 32:23–42

Galy V, France-Lanord C, Beyssac O, Faure P, Kudrass H, Palhol F (2007) Efficient organic carbon burial in the Bengal Fan sustained by the Himalayan erosional system. Nature 450:407–411

Galy V, Beyssac O, France-Lanord C, Eglinton T (2008) Recyling of graphite during Himalayan erosion: a geological stabilization of carbon in the crust. Science 322:943–945

Galy V, Peucker-Ehrenbrink B, Eglinton T (2015) Global carbon export from the terrestrial biosphere controlled by erosion. Nature 521:204–208

Garrels RM, Lerman A (1981) Phanerozoic cycles of sedimentary carbon and sulfur. Proc Natl Acad Sci USA 78:1318–1327

Garrels RM, Lerman A (1984) Coupling of the sedimentary sulfur and carbon cycles – an improved model. Am J Sci 284:989–1007

Hartnett HE, Keil RA, Hedges JI, Devol AH (1998) Influence of oxygen exposure time on organic carbon preservation in continental margin sediments. Nature 391:572–574
Hatcher PG, Spiker EC, Szeverenyi NM (1983) Selective preservation: the origin of petroleum-forming aquatic kerogen. Nature 305:498–501
Hedges JI, Oades JM (1997) Comparative organic geochemistries of soils and marine sediments. Org Geochem 7(8):319–361
Hedges JI, FS H, Devol AH, Hartnett HE, Tsamakis E, Keil RG (1999) Sedimentary organic matter preservation: a test for selective degradation under oxic conditions. Am J Sci 299:529–555
Hilton RG, Galy A, Hovius N (2008) Riverine particulate organic carbon from an active mountain belt: importance of landslides. Glob Biogeochem Cyc 22:GB2017
Hilton RG, Galy A, Hovius N, Horng, M-J, Chen H (2011) Efficient transport of fossil organic carbon to the ocean by steep mountain rivers: an orogenic carbon sequestration mechanism. Geology 39:71–74
Holland HD (1973) Ocean water, nutrients and atmospheric oxygen. In: Ingerson E (ed) Proceedings of dymposium hydrogeochem biochem. Clarke, Washington, DC, pp 68–81
Hunt JM (1996) Petroleum geochemistry and geology. Freeman, New York
Keil RG, Montluçon DB, Prahl FG, Hedges JI (1994) Sorptive preservation of labile organic matter in marine sediments. Nature 370:549–552
Killops S, Killops V (2005) Introduction to organic geochemistry 2e. Blackwell, Oxford
Knicker H, Hatcher PG (1997) Survival of protein in an organic-rich sediment: possible protection by encapsulation in organic matter. Naturwissenschaften 84:231–234
Kump LR, Garrels RM (1986) Modeling atmospheric O_2 in the global sedimentary redox cycle. Am J Sci 286:337–360
Longworth BE, Petsch ST, Raymond PA, Bauer JE (2007) Linking lithology and land use to sources of dissolved and particulate matter in headwaters of a temperate, passive-margin river system. Geochim Cosmochim Acta 71:4233–4250
Matlakowska R, Sklodowska A (2011) Biodegradation of Kupfershiefer black shale organic matter (Fore-Sudetic Monocline, Poland). Chemosphere 83:1255–1261
Matlakowska R, Narkiewicz W, Sklodowska A (2010) Biotransformations of organic-rich copper-bearing black shale ore by indigenous microorganisms isolated from Lubin copper mine (Poland). Environ Sci Technol 44:2433–2440
Mayer LM (1994) Surface area control of organic carbon accumulation in continental shelf sediments. Geochim Cosmochim Acta 58:1271–1284
Petsch ST (2014a) Weathering of organic carbon. In: Holland HD, Turekian KK (eds) Treatise on geochemistry 2e, 12:217-238. Elsevier, Oxford
Petsch ST (2014b) The global oxygen cycle. In: Holland HD, Turekian KK (eds) Treatise on geochemistry 2e, 10:437-473. Elsevier, Oxford
Petsch ST, Berner RA (1998) Coupling the geochemical cycles of C, P, Fe and S: the effects on atmospheric O_2 and the isotopic records of carbon and sulfur. Am J Sci 298:246–262
Petsch ST, Eglinton TI, Edwards KJ (2001) ^{14}C-dead living biomass: evidence for microbial assimilation of ancient organic carbon during shale weathering. Science 292:1127–1131
Shillawski S, Petsch ST (2008) Release of biodegradable dissolved organic matter from ancient sedimentary rocks. Glob Biogeochem Cycles. https://doi.org/10.1029/2007GB002980
Tegelaar EW, de Leeuw JW, Derenne S, Largeau C (1989) A reappraisal of kerogen formation. Geochim Cosmochim Acta 53:3103–3106
Tissot BP, Welte DH (1984) Petroleum formation and occurrence. Springer, Berlin
Turekian KK, Wedepohl KH (1961) Distribution of the elements in some major units of the earth's crust. Geol Soc Am Bull 72:175–192

Kinetics of Geochemical Processes

Don Sparks
Department of Plant and Soil Sciences, University of Delaware, Newark, DE, USA

Definition

Chemical kinetics. Chemical kinetics is the investigation of rates of chemical reactions and of the molecular processes by which reactions occur where transport is not limiting. **Kinetics** is a generic term referring to time-dependent processes.

Time Scales of Geochemical Processes

An array of reaction time scales occur in geochemical systems and often in combination with one another. They can range from milliseconds for many ion association and some ion exchange, sorption, and redox reactions to years for many mineral solution and mineral crystallization phenomena and for some sorption/release reactions. Ion association reactions include ion pairing, inner and outer-sphere complexation, and chelation in solution. Gas-water reactions involve gaseous exchange across the air-liquid interface. Ion exchange reactions occur when cations and anions are adsorbed (outer-sphere complexation) and desorbed from soil surfaces by electrostatic attractive forces. Ion exchange reactions are reversible and stoichiometric. Sorption reactions can involve adsorption processes including partitioning, outer-sphere and inner-sphere complexation, and multinuclear complexation (e.g., surface precipitation). Mineral-solution reactions include precipitation/dissolution of minerals, and coprecipitation reactions in which small constituents become a part of mineral structures (Amacher 1991; Sparks 1989, 2011).

The type of geosorbent can significantly affect the reaction rate. For example, sorption reactions are often more rapid on clay minerals such as kaolinite and smectites than on vermiculitic and micaceous minerals. This is primarily due to the availability of sites for sorption. Kaolinite has readily available planar external sites, and smectites have primarily internal sites that are also quite available for retention of sorbates. Thus, sorption reactions on these phyllosilciates are often quite rapid, even occurring on time scales of seconds and milliseconds (Sparks 1989, 2005, 2011).

Other phyllosilicates such as vermiculite and micas have multiple sites for retention of sorbates including planar, edge, and interlayer sites, with some of the latter sites partially to totally collapsed. Thus, sorption and desorption reactions on these sites can be slow, tortuous, and mass transfer controlled. Often, an apparent equilibrium may not be reached even after several days or weeks (Sparks 1989, 2011).

Sorption reactions on oxides, hydroxides, and humic substances depend on the type of surface and sorptive being studied but are often very rapid. For example, chemical reaction rates of metals and oxyanions on goethite occurred on millisecond time scales (Grossl et al. 1994, 1997; Zhang and Sparks 1989; Zhang and Sparks 1990a; Zhang and Sparks 1990b). Reaction rates of redox processes can also be very rapid. For example, Parikh et al. (2008) found that 50% of the initial reaction process for As(III) oxidation on Mn-oxides occurred in one minute. Half-times for divalent Pb, Cu, and Zn sorption on peat ranged from 5 to 15 s (Bunzl et al. 1976). A number of studies have shown that heavy metal sorption on oxides (Ainsworth et al. 1994; Bruemmer et al. 1988; Scheidegger et al. 1996a, 1998; Scheidegger and Sparks 1996) and clay minerals (Lövgren et al. 1990) increase with longer residence times. The mechanism for these lower reaction rates is not well understood but has been ascribed to diffusion phenomena, sites of lower reactivity, and surface nucleation/precipitation (Scheidegger et al. 1996b; Sparks 1998, 1999, 2011).

Sorption/desorption of metals and organic chemicals on heterogeneous soils is often very slow which has been attributed to diffusion into micropores of inorganic minerals and into humic substances, retention on sites of varying reactivity, and surface nucleation/precipitation (Borda and Sparks 2008; Matocha et al. 2005; Scheidegger et al. 1996b; Sparks 1989, 1997, 1999, 2002, 2005, 2011).

Application of Chemical Kinetics to Heterogeneous Geomedia

Chemical kinetics can be defined as the investigation of rates of chemical reactions and of the molecular processes by which reactions occur where transport is not limiting (Gardiner 1969). It is extremely difficult, due to mass transfer and diffusion processes to determine the chemical kinetics of geochemical systems that contain multiple components, particle sizes, and porosities. In most cases, both chemical kinetics and multiple transport processes are occurring simultaneously. Transport processes include (Aharoni and Sparks 1991): (1) transport in the solution phase; (2) transport across a liquid film at the particle/liquid interface (film diffusion [FD]); (3) transport in liquid filled macropores (>2 nm), all of which are nonactivated diffusion processes and occur in mobile regions; (4) particle diffusion (PD) processes which include diffusion of sorbate occluded in micropores (<2 nm) (pore diffusion) and along pore wall surfaces (surface diffusion); and (5) diffusion processes in the bulk of the solid, all of which are activated diffusion processes. Pore and surface diffusion within the immediate region can be referred to as interaggregate (interparticle) diffusion while that in the solid is intraaggregate diffusion. In systems where transport is the rate-limiting process, one is studying kinetics, which is a generic term referring to time dependent or nonequilibrium processes.

The actual chemical reaction (CR) at the surface, for example, adsorption, is usually almost instantaneous. The slowest of the CR and transport processes is rate limiting (Sparks 2011).

Rate Laws

There are two important reasons for investigating the rates of soil chemical processes (Sparks 1989, 1995, 1998, 1999, 2002, 2011): (1) to determine how rapidly reactions attain equilibrium and (2) to infer information on reaction mechanisms. One of the most important aspects of chemical kinetics is the establishment of a rate equation or law. By definition, a rate law is a differential equation. For the following reaction (Bunnett 1986; Sparks 1989, 1995, 1998, 1999, 2002, 2011):

$$aA + bB \rightarrow yY + zZ \tag{1}$$

the rate is proportional to some power of the concentrations of reactants A and B and/or other species (C, D, etc.) in the system and a, b, y, and z are stoichiometric coefficients and are assumed to be equal to one in the discussion that follows on rate laws. The power to which the concentration is raised may equal zero (i.e., the rate is independent of that concentration), even for reactant A or B. Rates are expressed as a decrease in reactant concentration or an increase in product concentration per unit time. Thus, the rate of conversion of reactant A above, which has a concentration $[A]$ at any time t, is $(-d[A]/(dt))$ while the rate with regard to product Y having a concentration $[Y]$ at time t is $(d[Y]/(dt))$.

The rate expression for Eq. 1 is therefore,

$$|d[Y]/dt| = |-d[A]/dt| = k[A]^{\alpha}[B]^{\beta} \tag{2}$$

where k is the rate constant and α and β are the orders of the reaction with respect to reactants A and B, respectively, and can be referred to as partial orders for the total reaction. These orders are experimentally determined and not necessarily integral numbers. The sum of all the partial orders (α, β) is the overall order (n) of the total reaction and may be expressed as:

$$n = \alpha + \beta + \ldots \tag{3}$$

Once the values of α, β, etc., are determined experimentally, the rate law is defined. Reaction order provides only information about the manner in which rate depends on concentration. Order does not mean the same as molecularity which concerns the number of reactant particles (atoms, molecules, free radicals, or ions) entering into an elementary reaction. One can define an elementary reaction as one in which no reaction intermediates have been detected or need to be postulated to describe the chemical reaction on a molecular scale. An elementary reaction is assumed to occur in a

single step and to pass through a single transition state (Bunnett 1986).

To demonstrate that a reaction is elementary, one can use experimental conditions that are different from those employed in determining the reaction rate law. For example, if one conducted kinetic studies using a flow technique with set steady-state flow rates, one could see if reaction rate and rate constants changed with flow rate. If they did, one would not be determining mechanistic rate laws (see definition below).

Rate laws serve three purposes: (1) they assist one in predicting the reaction rate; (2) mechanisms can be proposed; and (3) reaction orders can be ascertained. There are four types of rate laws that can be determined for geochemical processes (Skopp 1986): mechanistic, apparent, transport with apparent, and transport with mechanistic. Mechanistic rate laws assume that only chemical kinetics are operational and transport phenomena are not occurring. As mentioned earlier, it is difficult to determine mechanistic rate laws for most geochemical systems. However, as will be discussed later, if initial rates of reactions can be measured and back reactions minimized, one can approximate chemical kinetic measurements with certain geosorbents. Apparent rate laws include both chemical kinetics and transport-controlled processes. Thus, porosity, stirring, mixing, and flow rate all would affect the kinetics. Transport with apparent rate laws emphasize transport limited phenomena. One often assumes first-order or zero-order reactions (see discussion below on reaction order). In determining transport with mechanistic rate laws, one attempts to describe simultaneously transport-controlled and chemical kinetics phenomena. One is thus trying to explain accurately both the chemistry and physics of the system (Skopp 1986; Sparks 2011).

Determination of Reaction Order and Rate Constants/Coefficients

There are three basic ways to determine rate laws and rate constants/coefficients (Bunnett 1986; Skopp 1986; Sparks 1989, 1995, 1998, 1999, 2002, 2011): (1) initial rates, (2) directly using integrated equations and graphing the data, and (3) using nonlinear least square analysis.

Let us assume the following elementary reaction between species A, B, and Y,

$$A + B \underset{k_{-1}}{\overset{k_1}{\rightleftharpoons}} Y \tag{4}$$

A forward reaction rate law can be written as

$$d[A]/dt = -k_1[A][B] \tag{5}$$

where k_1 is the forward rate constant and α and β (see Eq. 2) are each assumed to be 1.

The reverse reaction rate law for Eq. 4 is

$$d[A]/dt = +k_{-1}[Y] \tag{6}$$

where k_{-1} is the reverse rate constant.

Equations 5 and 6 are only applicable far from equilibrium where back or reverse reactions are insignificant. If both forward and reverse reactions are occurring, Eqs. 5 and 6 must be combined such that:

$$d[A]/dt = -k_1[A][B] + k_{-1}[Y] \tag{7}$$

Equation 7 applies the principle that the net reaction rate is the difference between the sum of all reverse reaction rates and the sum of all forward reaction rates.

One way to ensure that back reactions are not important is to measure initial rates. The initial rate is the limit of the reaction rate as time reaches zero. With an initial rate method, one plots the concentration of a reactant or product over a short reaction time period during which the concentrations of the reactants change so little that the instantaneous rate is hardly affected. Thus, by measuring initial rates, one could assume that only the forward reaction in Eq. 4 predominates. This would simplify the rate law to that given in Eq. 5 which as written would be a second-order reaction, first order in reactant A and first order in reactant B. Equation 5, under these conditions, would represent a second-order irreversible elementary reaction. Integrated rate equations can also be used to determine rate constants/coefficients. If one assumes that reactant B in Eq. 5 is in large excess of reactant A, which is an example of the method of isolation to analyze kinetic data, and $Y_o = 0$, where Y_o is the initial concentration of product Y, Eq. 5 can be simplified to:

$$d[A]/dt = -k_1'[A] \tag{8}$$

where $k_1' = k_1[B]$

The first-order dependence of $[A]$ can be evaluated using the integrated form of Eq. 8 using the initial conditions at $t = 0$, $A = A_o$,

$$\log[A]_t = \log[A]_o = -\frac{k_1' t}{2.303} \tag{9}$$

The half-time ($t_{1/2}$) for the above reaction is equal to $0.693/k_1'$ and is the time required for half of reactant A to be consumed.

If a reaction is first order a plot of log $[A]_t$ versus t should result in a straight line with a slope $= k_1'/2.303$ and an intercept of log $[A]_o$. An example of first-order plots for Mn^{2+} sorption on δ-MnO_2 at two initial Mn^{2+} concentrations, $[Mn^{2+}]_o$ (25 and 40 μM), is shown in Fig. 1 where a electron paramagnetic resonance-stopped flow (EPR-SF) spectroscopic method,

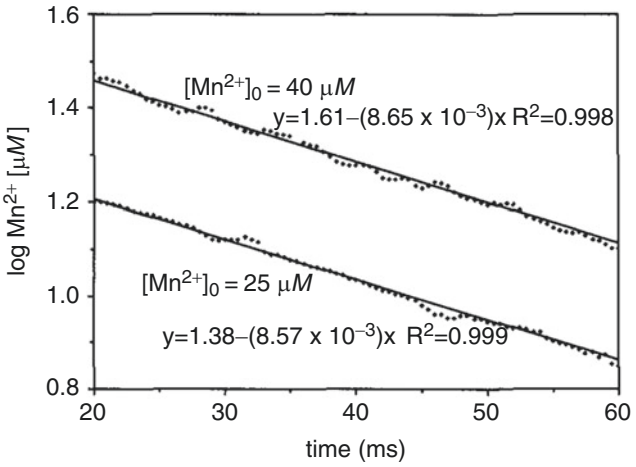

Kinetics of Geochemical Processes, Fig. 1 Initial reaction rates depicting the first-order dependence of Mn^{2+} sorption as a function of time for initial Mn^{2+} concentrations of 25 and 40 μM. (Reprinted by Permission, ASA, CSSA, SSSA.)

which is a form of a chemical relaxation technique, was employed (Fendorf et al. 1993). One sees that the plots are linear at both concentrations which would indicate that the sorption process is first order. The $[Mn^{2+}]_o$ values, obtained from the intercepts in Fig. 1 were 24 and 41 μM, which are in good agreement with the two $[Mn^{2+}]_o$ values and the rate constants were 3.73×10^{-3} and 3.75×10^{-3} s^{-1}, respectively. The fact that the rate constants do not significantly change with concentration is a good indication that the reaction in Eq. 8 is first order under the imposed experimental conditions, that transport/mass transfer are minimized, and that chemical kinetic phenomena are being measured.

It is dangerous to conclude that a particular reaction order is correct, based simply on the conformity of data to an integrated equation. As illustrated above, multiple initial concentrations that vary considerably should be employed to see if the rate is independent of concentration. One should also test multiple integrated equations. It may also be useful to show that reaction rate is not affected by a species whose concentration does not change considerably during an experiment, such as substances not consumed or present in large excess (Bunnett 1986; Sparks 1989, 1991, 1995, 1998, 1999, 2011).

Least squares analysis can also be used to determine rate constants/coefficients. With this method, one fits the best straight line to a set of points that are linearly related as $y = mx + b$ where y is the ordinate and x is the abscissa datum point, respectively. The slope (m) and the intercept (b) can be calculated by least squares analysis.

When kinetic data are plotted, curvature may be observed due to an incorrect assumption of reaction order. If first-order kinetics is assumed and the reaction is really second-order, downward curvature results. If second-order kinetics is assumed but the reaction is first order, upward curvature is observed. Curvature can also be due to fractional, third, higher, or mixed reaction order. Nonattainment of equilibrium often results in downward curvature. Temperature changes during the study can also cause curvature; thus, it is important that temperature be accurately controlled during a kinetic experiment (Sparks 2011).

Methods to Determine Chemical Kinetics in Geochemical Systems

Chemical relaxation techniques such as pressure jump (p-jump) and concentration jump (c-jump e.g., stopped-flow) allow rapid initial rate data collection on time scales of milliseconds where back reactions should be minimized. However, with chemical relaxation techniques, rate "constants" are calculated from linearized rate equations that often include parameters that were determined from equilibrium and modeling studies. Consequently, the rate "constants" are not directly determined (Ginder-Vogel et al. 2009; Ginder-Vogel and Sparks 2010; Sparks 2013, 2014).

Over the past decade or so there have been major advances in the employment of real-time molecular scale kinetic techniques where initial reaction rates can be measured on time scales of milliseconds. This minimizes back reactions and transport, enabling the measurement of chemical kinetics and the determination of reaction mechanisms.

Real-time molecular scale ATR-FTIR and Q-XAS techniques have been employed to elucidate the rapid redox kinetics and mechanisms of As(III) oxidation (Ginder-Vogel et al. 2009; Parikh et al. 2008) and Cr(III) oxidation (Landrot et al. 2010) on Mn-oxides and Ni-Al layered double hydroxide phase precipitate formation on pyrophyllite (Siebecker et al. 2014).

Figure 2 shows Q-XAS and traditional batch data for As (III) oxidation on hydrous Mn-oxide (HMO). An initial concentration of 5 mM of As(III) was used. After one second of reaction the As(V) concentration, indicating oxidation of As(III), reached 0.37 mM and continued to increase rapidly for 45 s to reach a concentration of 1 mM. The As(V) concentration continued to increase for the remainder of the reaction, reaching the initial 1.5 mM concentration after 300 s of reaction time (Ginder-Vogel et al. 2009). A complete XANES spectrum was collected in 980 ms (Fig. 3). In the study of Ginder-Vogel et al. (2009), the oxidation states in both the solution and at the mineral/water interface were probed using Q-XAS. The average oxidation state was then determined by fitting each individual XANES spectra with a linear combination of As(III) and As(V) standard solutions (in this experiment, 5 mM standards were used). The fits provide the molar ratio

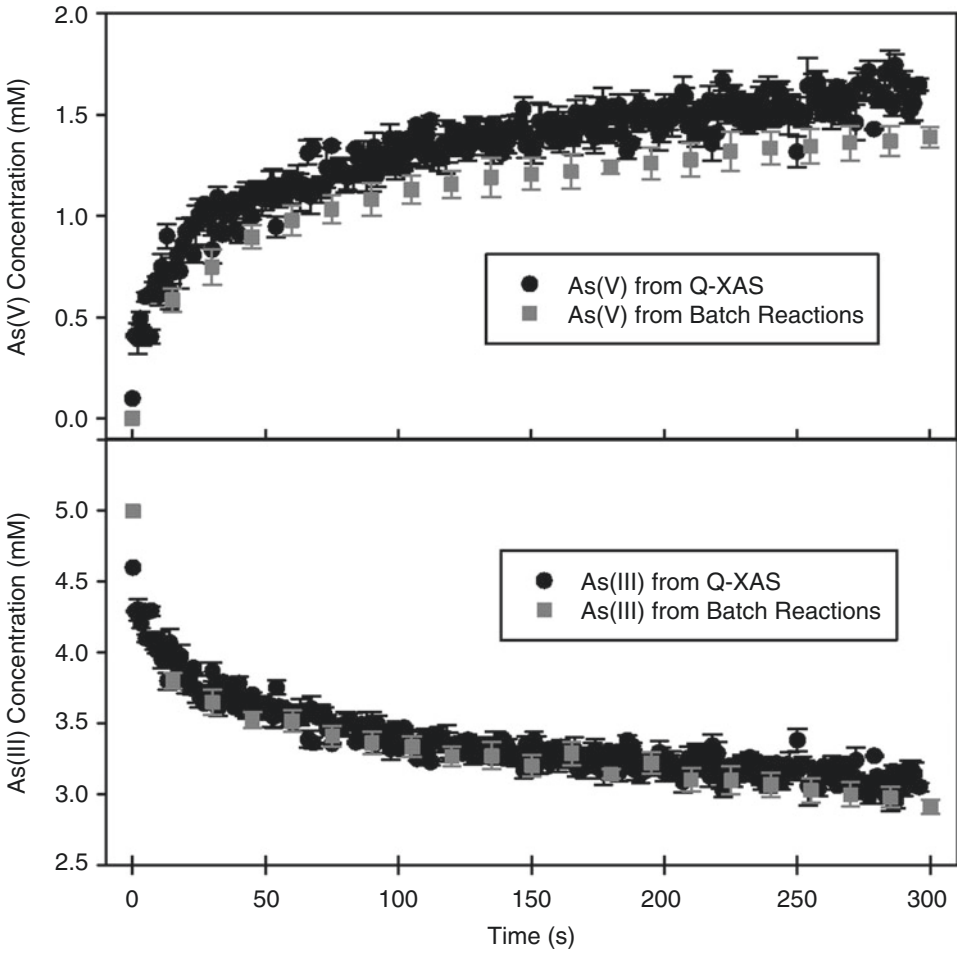

Kinetics of Geochemical Processes, Fig. 2 As(V) and As(III) concentrations determined from traditional batch and Q-XAS reactions. Error bars represent the SD of three measurements made at each time point. XANES spectra and fits used to calculate Q-XAS As concentrations are shown in Fig. 3. (Reprinted from PNAS, Ginder-Vogel M, Landrot G, Fischel JS, Sparks DL, Quantification of rapid environmental redox processes using quick-scanning X-ray absorption spectroscopy (Q-XAS), 106;16124–16128 (2009), with permission from National Academy of Sciences.)

of As in solution, from which the concentrations of As(III) and As(V) in the system can be calculated, using the initial As concentration. In Fig. 3 one sees the XANES spectra for the reaction of As(III) with HMO over time scales ranging from 0.98 to 298.9 s. One sees the rapid transformation of As(III) to As(V) on the HMO surface. Rate constants were determined from first-order plots for both the Q-XAS and batch experiments, based on biphasic kinetics (Table 1) and show, independent of method, that rate constants for As(III) depletion are about an order of magnitude larger during the initial portion of the reaction that in the later segment (Table 1). But, the initial rate constant of As(III) depletion based on Q-XAS was nearly twice as large (4.7×10^{-3}/s) as the rate constant measured with the batch method (2.5×10^{-3}/s, Table 1).

Landrot et al. (2010) employed the same technique as Ginder-Vogel et al. (2009) to measure the rapid, initial kinetics of Cr(III) oxidation on HMO. A complete XANES spectrum was determined in 0.75 s. Data were collected at pHs of 2.5, 3.0, and 3.5 at Cr(III) concentrations of 40–100 mM. Chromium (VI), resulting from the oxidation of Cr(III) on the HMO surface, displays the prominent pre-edge feature in the XAS spectrum, which is related to the proportion of Cr(VI) in the system. Therefore, one only needs to measure the height of the pre-edge feature and compare it to a set of Cr(III)/Cr(VI) mixtures to determine the amount of Cr(VI) present in the system (Landrot et al. 2010; Peterson et al. 1997). One sees in Fig. 4 that the pre-edge feature increases in intensity with time, indicating the oxidation of Cr(III) to Cr(VI). Chromium (III) oxidation is quite rapid during the first 120 s of the reaction, when about 35 mM of chromate was produced. Initial reaction rates were determined by quantifying the Cr(VI) from the pre-edge feature height for each experiment during a time range of 0–1 min of the reaction using the kinetic model below.

With this approach, one of the reactants is fixed at a constant value (but not necessarily in excess) in a set of experiments, while the concentration of the other reactant is successively varied. Therefore, both of the reactants must be considered in the overall rate equation. During the early stage of the reaction, a linear relationship relates [Cr(VI)] and time. The slope of this linear trend is the initial rate i, which is defined as:

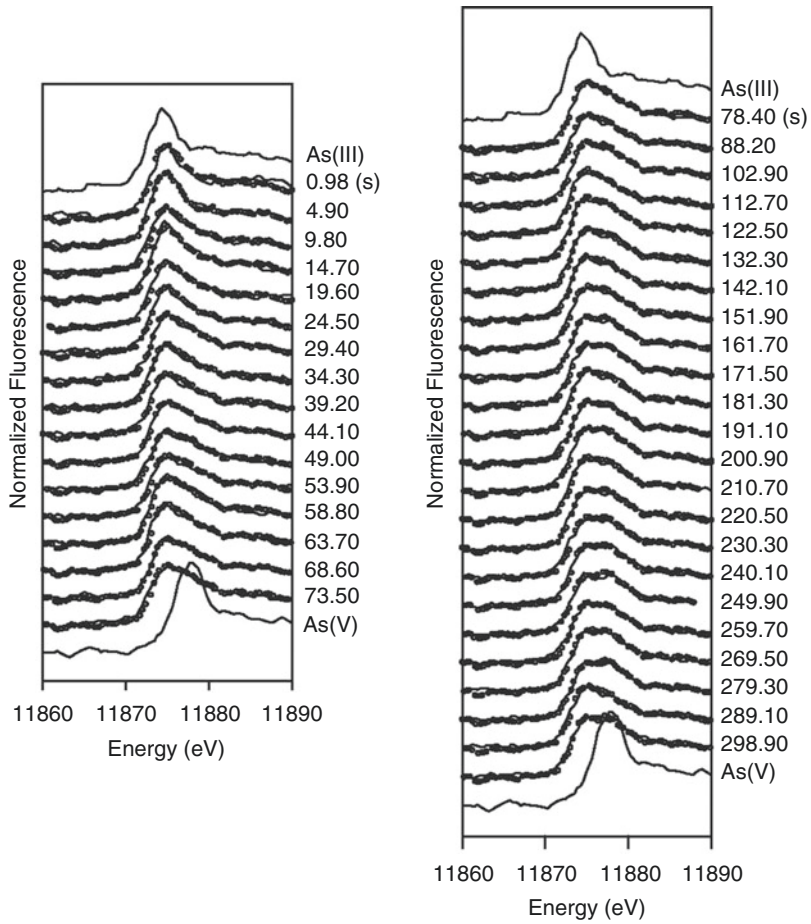

Kinetics of Geochemical Processes, Fig. 3 Data (*solid*) and linear combination fits (*dots*) of individual As K-edge XANES spectra used to determine As(III) and As(V) concentrations during the batch reactions. Each spectrum was collected in approximately 980 ms, with the time (in s) next to each spectrum indicating the time the last data point of each spectrum was collected

Kinetics of Geochemical Processes, Table 1 Apparent, first-order rate constants determined from batch and Q-XAS experiments

Experiment type	Time period (s)	No. of data points	k (s − 1)	$r2$
As (III)–Batch	1–60	4	2.5 (3) × 10 − 3	0.96
As (III)–Batch	135–300	14	6.1 (4) × 10 − 4	0.82
As(III)–Q-XAS	1–30	30	4.7 (4) × 10 − 3	0.91
As(III)–Q-XAS	135–300	168	4.9 (4) × 10 − 4	0.74

The rate constants of As(III) depletion were determined by linear regression analysis of first-order As(III) depletion rate plots
Reprinted from PNAS, Ginder-Vogel M, Landrot G, Fischel JS, Sparks DL, Quantification of rapid environmental redox processes using quick-scanning X-ray absorption spectroscopy (Q-XAS), 106;16124–16128 (2009), with permission from National Academy of Sciences

$$\frac{d[\mathrm{Cr(VI)}]}{dt} = -k[\mathrm{Cr(III)}]_0^{\alpha}[\mathrm{MnO_2}]_0^{\beta} = i \qquad (10)$$

where k, α, and β were defined earlier, 0 represents the initial concentrations, and i is the initial rate of the reaction. To measure the partial rate coefficient of chromium α at a given pH value for the experiments where $[MnO_2]$ was fixed and [Cr(III)] was varied, Eq. 13 was used, which is a simplified expression of Eq. 11 :

$$\frac{i_{\mathrm{exp1}} = -k\left[\mathrm{Cr(III)}_{\mathrm{exp1}}\right]^{\alpha}[\mathrm{MnO_{2fixed}}]^{\beta}}{i_{\mathrm{exp2}} = -k\left[\mathrm{Cr(III)}_{\mathrm{exp2}}\right]^{\alpha}[\mathrm{MnO_{2fixed}}]^{\beta}} \qquad (11)$$

where exp = experiment

Hence:

$$\frac{i_{\mathrm{exp1}}}{i_{\mathrm{exp2}}} = \left(\frac{\left[\mathrm{Cr(III)}_{\mathrm{exp1}}\right]}{\left[\mathrm{Cr(III)}_{\mathrm{exp2}}\right]}\right)^{\alpha} \qquad (12)$$

Therefore:

$$\alpha = \frac{\mathrm{Log}\left(\frac{i_{\mathrm{exp1}}}{i_{\mathrm{exp2}}}\right)}{Log\left(\frac{\left[\mathrm{Cr(III)}_{\mathrm{exp1}}\right]}{\left[\mathrm{Cr(III)}_{\mathrm{exp2}}\right]}\right)} \qquad (13)$$

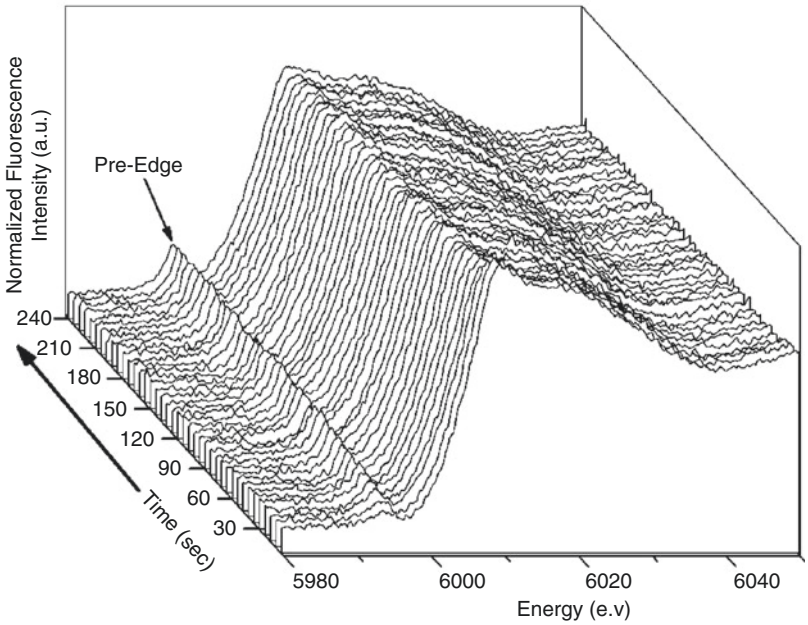

Kinetics of Geochemical Processes, Fig. 4 Cr(III) oxidation kinetics using a Q-XAFS technique, at pH 2.5, [Cr (III)] = 100 mM, [HMO] = 20 g/ L, and 0–240 s. Each XANES spectrum shown represents 3 s of the reaction (average of four 0.75 s spectra). (Reprinted with permission from Landrot G, Ginder-Vogel M, Sparks DL (2010) Kinetics of chromium(III) oxidation by manganese (IV) oxides using quick scanning X-ray absorption fine structure spectroscopy (Q-XAFS) Environ Sci Technol 44:143–149. Copyright (2010) American Chemical Society.)

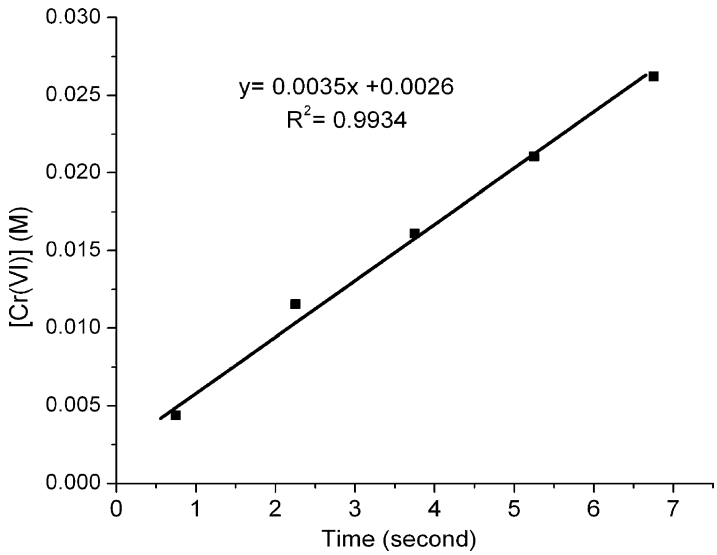

Kinetics of Geochemical Processes, Fig. 5 Initial rate measurement for an experiment at pH 2.5, where [Cr(III)] = 80 mM and [HMO] = 20 g/L. (Reprinted with permission from Landrot G, Ginder-Vogel M, Sparks DL (2010) Kinetics of chromium(III) oxidation by manganese (IV) oxides using quick scanning X-ray absorption fine structure spectroscopy (Q-XAFS) Environ Sci Technol 44:143–149. Copyright (2010) American Chemical Society.)

To measure the partial rate coefficient of manganese β at a given pH value for the experiments where [Cr(III)] was fixed and [MnO_2] was varied, Eq. 16 was used, which is a simplification of Eq. 14:

$$\frac{i_{\text{exp3}} = -k\left[\text{Cr(III)}_{\text{fixed}}\right]^{\alpha}\left[\text{MnO}_{2\ \text{exp3}}\right]^{\beta}}{i_{\text{exp4}} = -k\left[\text{Cr(III)}_{\text{fixed}}\right]^{\alpha}\left[\text{MnO}_{2\ \text{exp}_4}\right]^{\beta}} \tag{14}$$

Thus:

$$\frac{i_{\text{exp3}}}{i_{\text{exp4}}} = \left(\frac{\left[\text{MnO}_{2\ \text{exp3}}\right]}{\left[\text{MnO}_{2\ \text{exp4}}\right]}\right)^{\beta} \tag{15}$$

Therefore:

$$\beta = \frac{\text{Log}\left(\frac{i_{\text{exp3}}}{i_{\text{exp4}}}\right)}{\text{Log}\left(\frac{\left[\text{MnO}_{2\ \text{exp3}}\right]}{\left[\text{MnO}_{2\ \text{exp4}}\right]}\right)} \tag{16}$$

The rate constant k was calculated for each experiment using the i values experimentally measured, and the β and α calculated for each pH values using Eq. 17, which is a rearrangement of Eq. 10:

Kinetics of Geochemical Processes, Table 2 Initial conditions, measured initial rates, and rate parameters[a]

		Initial rates (mol/L/s)			k (s^{-1})		
[Cr(III)] (mM)	[HMO] (g/L)	pH = 2.5	pH = 3	pH = 3.5	pH = 2.5	pH = 3	pH = 3.5
100	20	0.0045/0.0052	0.0045/0.0045	0.0045/0.0047	0.204/0.228	0.277/0.202	0.295/0.364
		(0.00036/0.00071)	*(0.00067/0.00064)*	*(0.0004/0.0006)*			
80	20	0.0035/0.0040	0.0034/0.0035	0.0039/0.0030	0.202/0.220	0.270/0.198	0.353/0.308
		(0.00017/0.00021)	*(0.00031/0.00066)*	*(0.00108/0.00046)*			
60	20	0.0025/0.0029	0.0027/0.0028	0.0022/0.0022	0.197/0.215	0.303/0.208	0.302/0.357
		(0.0002/0.00037)	*(0.0004/0.00017)*	*(0.00043/0.00034)*			
40	20	0.0017/0.0021	0.0015/0.0018	0.0012/0.0012	0.208/0.235	0.266/0.199	0.296/0.363
		(0.00023/0.00003)	*(0.00028/0.00034)*	*(0.00017/0.00017)*			
		Cr partial rate coefficient α					
		1.08/1.01	1.13/1.05	1.43/1.53			
		1.09	**1.09**	**1.48**			
100	20	0.0045/0.0052	0.0045/0.0045	0.0045/0.0047	0.204/0.228	0.277/0.202	0.295/0.364
		(0.00036/0.00071)	*(0.00067/0.00064)*	*(0.0004/0.0006)*			
100	15	0.0035/0.0036	0.0035/0.0036	0.0037/0.0038	0.206/0.207	0.293/0.219	0.291/0.328
		(0.0006/0.0005)	*(0.00046/0.00052)*	*(0.00032/0.00054)*			
100	10	0.002/0.002	0.0023/0.0020	0.0028/0.0029	0.169/0.171	0.287/0.244	0.280/0.311
		(0.00039/0.00039)	*(0.00001/0.00021)*	*(0.0008/0.00059)*			
100	5	0.001/0.0012	0.0010/0.0014	0.0020/0.0022	0.157/0.203	0.257/0.316	0.283/0.346
		(0.00039/0.00001)	*(0.0001/0.0001)*	*(0.00035/0.00031)*			
		Mn partial rate coefficient a					
		0.90/0.98	1.00/1.05	0.58/0.53			
		0.94	**1.02**	**0.55**			
					k (averaged) in s^{-1}		
					pH = 2.5	*pH = 3*	*pH = 3.5*
					0.192/0.211	0.279/0.227	0.300/0.340
					0.201	**0.242**	**0.322**

[a]The partial rate coefficients α, β at pH 2.5, pH 3, and pH 3.5 shown in this table are averaged values from α and β calculated using Eqs. 13 and 16 and by combining the initial rates measured at different experimental conditions. The rate constant for each experiment was measured with Eq. 17. Since all experiments were duplicated, the initial rates and rate parameters are reported with two values separated with "/". The standard error (95% confidence interval) for each initial rate is *italicized*. Averages of duplicate values are highlighted in *bold*

$$k = \frac{i}{[\mathrm{Cr(III)}]^{\alpha}[\mathrm{MnO_2}]^{\beta}} \tag{17}$$

A plot of one initial rate experiment is shown in Fig. 5.

Landrot et al. (2010) found at a given pH and for varying Cr(III) and HMO concentrations that the rate constants were similar (Table 2). This strongly suggests that the k values are chemical rate constants since only temperature should impact the magnitude of the k values. Therefore, the use of a method

like Q-XAS not only provides valuable information on rapid, initial reaction processes but an additional benefit is that one can determine chemical kinetics rate constants.

Together, these provide important insights on reaction mechanisms. Using most other techniques, one cannot significantly reduce or eliminate transport processes. Consequently, the rate parameters that are measured are apparent rate coefficients and not rate constants (Sparks 1989, 2002).

Siebecker et al. (2014) employed a Q-XAS flow technique, for the first time, to measure the rapid (6–15 min) formation of Ni layered double hydroxide (LDH) precipitate phases on pyrophyllite. These results suggest that adsorption and precipitation could occur on similar time scales and perhaps concurrently. Thus, there can be a continuum in sorption processes, which dictates that more robust sorption models need development that capture multiple sorption processes over reaction time.

Summary

This chapter covers the kinetics of geochemical processes and reactions. Time scales of geochemical reactions, rate laws and reaction order, and rate constants/coefficients are discussed. Novel molecular scale real-time methods, with an emphasis on synchrotron-based quick X-ray absorption spectroscopy (Q-XAS), are presented. This method is applied to the investigation of oxidation kinetics of arsenic and chromium on manganese oxides and to rates of layered double hydroxide formation on clay minerals.

Cross-References

- Activation Parameters: Energy, Enthalpy, Entropy, and Volume
- Analytical Techniques
- Arsenic
- Atomic Absorption, Inductively Coupled Plasma Optical Emission Spectroscopy, and Infrared Spectroscopy
- Chromium
- Clay Minerals
- Manganese
- Mass Transfer
- Oxidation-Reduction Reactions and Eh-pH (Pourbaix) Diagrams
- Soils

References

Aharoni C, Sparks DL (1991) Kinetics of soil chemical reactions: a theoretical treatment. In: Sparks DL, Suarez DL (eds) Rates of soil chemical processes, SSSA special publication, vol 27. Soil Science Society of America, Madison, pp 1–18

Ainsworth CC, Pilon JL, Gassman PL, Van Der Sluys WG (1994) Cobalt, cadmium, and lead sorption to hydrous iron oxide: residence time effect. Soil Sci Soc Am J 58:1615–1623

Amacher MC (1991) Methods of obtaining and analyzing kinetic data. In: Sparks DL, Suarez DL (eds) Rates of soil chemical processes, SSSA special publication, vol 27. Soil Science Society of America, Madison, pp 19–59

Borda MJ, Sparks DL (2008) Kinetics and mechanisms of sorption–desorption in soils: a multiscale assessment. In: Violante A, Huang PM, Gadd GM (eds) Biophysico-chemical processes of heavy metals and metalloids in soil environments. Wiley, New York, pp 97–124

Bruemmer GW, Gerth J, Tiller KG (1988) Reaction kinetics of the adsorption and desorption of nickel, zinc and cadmium by goethite: I. Adsorption and diffusion of metals. J Soil Sci 39:37–52

Bunnett JF (1986) Kinetics in solution. In: Bernasconi CF (ed) Investigations of rates and mechanisms of reactions, 4th edn. Wiley, New York, pp 171–250

Bunzl K, Schmidt W, Sansoni B (1976) Kinetics of ion exchange in soil organic matter. IV. Adsorption and desorption of Pb^{2+}, Cu^{2+}, Zn^{2+}, and Ca^{2+} by peat. J Soil Sci 27:32–41

Fendorf SE, Sparks DL, Franz JA, Camaioni DM (1993) Electron paramagnetic resonance stopped-flow kinetic study of manganese (II) sorption–desorption on birnessite. Soil Sci Soc Am J 57:57–62

Gardiner WC Jr (1969) Rates and mechanisms of chemical reactions. Benjamin, New York

Ginder-Vogel M, Sparks DL (2010) The impacts of X-ray absorption spectroscopy on understanding soil processes and reaction mechanisms. In: Balwant S, Markus G (eds) Developments in soil science, vol 34. Elsevier, Burlington, pp 1–26

Ginder-Vogel M, Landrot G, Fischel JS, Sparks DL (2009) Quantification of rapid environmental redox processes using quick-scanning X-ray absorption spectroscopy (Q-XAS). PNAS 106:1612416128

Grossl PR, Eick MJ, Sparks DL, Goldberg S, Ainsworth CC (1977) Arsenate and chromate retention mechanisms on goethite. 2. Kinetic evaluation using a pressure-jump relaxation technique. Environ Sci Technol 31:321–326

Grossl PR, Sparks DL, Ainsworth CC (1994) Rapid kinetics of Cu (II) adsorption/desorption on goethite. Environ Sci Technol 28:1422–1429

Landrot G, Ginder-Vogel M, Sparks DL (2010) Kinetics of chromium (III) oxidation by manganese(IV) oxides using quick scanning X-ray absorption fine structure spectroscopy (Q-XAFS). Environ Sci Technol 44:143–149

Lövgren L, Sjöberg S, Schindler PW (1990) Acid/base reactions and Al (III) complexation at the surface of goethite. Geochim Cosmochim Acta 54:1301–1306

Matocha CJ, Scheckel KG, Sparks DL (2005) Kinetics and mechanisms of soil biogeochemical processes. In: Tabatabai MA, Sparks DL (eds) Chemical processes in soils, vol 8. SSSA, Madison, pp 309–342

Parikh SJ, Lafferty BJ, Sparks DL (2008) An ATR-FTIR spectroscopic approach for measuring rapid kinetics at the mineral/water interface. J Colloid Interface Sci 320:177–185

Peterson ML, Brown GE, Parks GA, Stein CL (1997) Differential redox and sorption of Cr(III/VI) on natural silicate and oxide minerals: EXAFS and XANES results. Geochim Cosmochim Acta 61:3399–3412

Scheidegger AM, Sparks DL (1996) A critical assessment of sorption–-desorption mechanisms at the soil mineral/water interface. Soil Sci 161:813–831

Scheidegger AM, Fendorf M, Sparks DL (1996a) Mechanisms of nickel sorption on pyrophyllite: macroscopic and microscopic approaches. Soil Sci Soc Am J 60:1763–1772

Scheidegger AM, Lamble GM, Sparks DL (1996b) Investigation of Ni sorption on pyrophyllite: an XAFS study. Environ Sci Technol 30:548–554

Scheidegger AM, Strawn DG, Lamble GM, Sparks DL (1998) The kinetics of mixed Ni-Al hydroxide formation on clay and aluminum

oxide minerals: a time-resolved XAFS study. Geochim Cosmochim Acta 62:2233–2245
Siebecker M, Li W, Khalid S, Sparks D (2014) Real-time QEXAFS spectroscopy measures rapid precipitate formation at the mineral-water interface. Nat Commun 5:1–7
Skopp J (1986) Analysis of time dependent chemical processes in soils. J Environ Qual 15:205–213
Sparks DL (1989) Kinetics of soil chemical processes. Academic, San Diego
Sparks DL (1991) Chemical kinetics and mass transfer processes in soils and soil constituents. In: Bear J, Corapcioglu MY (eds) Transport processes in porous media, NATO ASI series E: applied sciences, vol 202. Kluwer Academic Publishers, Dordecht, pp 585–637
Sparks DL (1995) Environmental soil chemistry. Academic, San Diego
Sparks DL (ed) (1997) Soil physical chemistry, 2nd edn. CRC Press, Boca Raton
Sparks DL (1998) Kinetics of soil chemical phenomena: future directions. In: Huang PM, Sparks DL, Boyd SA (eds) Future prospects for soil chemistry, Special publication, vol 55. SSSA, Madison, pp 81–101
Sparks DL (1999) Kinetics and mechanisms of chemical reactions at the soil mineral/water interface. In: Sparks DL (ed) Soil physical chemistry, 2nd edn. CRC Press, Boca Raton
Sparks DL (2002) Environmental soil chemistry, 2nd edn. Academic, San Diego
Sparks DL (2005) Sorption | metals. In: Hillel D, Hatfield JL, Powlson DS, Rosenweig C, Scow KM, Singer MJ, Sparks DL (eds) Encyclopedia of soils in the environment. Elsevier, Oxford, UK, pp 532–537
Sparks DL (2011) Kinetics and mechanisms of soil chemical reactions. In: Handbook of soil sciences. CRC Press, Boca Raton, pp 1–30
Sparks DL (2013) Advances in the use of synchrotron radiation to elucidate environmental interfacial reaction processes and mechanisms in the Earth's critical zone. In: Xu J, Sparks DL (eds) Molecular environmental soil science. Progress in soil science. Springer, Dordrecht, pp 93–114
Sparks DL (2014) Advances in coupling of kinetics and molecular scale tools to shed light on soil biogeochemical processes. Plant Soil 387:1–19
Zhang PC, Sparks DL (1989) Kinetics and mechanisms of molybdate adsorption/desorption at the goethite/water interface using pressure-jump relaxation. Soil Sci Soc Am J 53:1028–1034
Zhang PC, Sparks DL (1990a) Kinetics and mechanisms of sulfate adsorption desorption on goethite using pressure-jump relaxation. Soil Sci Soc Am J 54:1266–1273
Zhang PC, Sparks DL (1990b) Kinetics of selenate and selenite adsorption/desorption at the goethite/water interface. Environ Sci Technol 24:1848–1856

Krypton

Greg Holland
School of Earth and Environmental Sciences,
University of Manchester, Manchester, UK

Element Data
Atomic Symbol: Kr
Atomic Number: 36
Atomic Weight: 83.798 ± 0.002
(*continued*)

Isotopes and Abundances: Percent molar abundances of stable isotopes in the atmosphere are $^{78}Kr = 0.355 \pm 0.003$, $^{80}Kr = 2.286 \pm 0.010$, $^{82}Kr = 11.593 \pm 0.031$, $^{83}Kr = 11.500 \pm 0.019$, $^{84}Kr = 56.987 \pm 0.015$, $^{86}Kr = 17.279 \pm 0.041$
1 Atm Melting Point: 115.78 K
1 Atm Boiling Point: 119.93 K
Common Valences: 0 (rarely 1,2)
Ionic Radii: n/a
Pauling Electronegativity: 3.00
First Ionization Potential: 1350.7 kJ/mol
Chondritic (CI) Abundance: 2.2 ± 0.2 ppb (parts per billion)
Silicate Earth Abundance: 0.1–0.2 ppt (parts per trillion)
Crustal Abundance: ~100 ppt
Seawater Abundance: 0.1–0.2 ppb
Core Abundance: unknown

History and Use

Krypton is one of the three noble gases discovered in 1898 by Sir William Ramsay and Morris William Travers. It is purified by cryogenic cooling with liquid nitrogen followed by passing it over hot titanium metal. Due to the inert nature of noble gases, there are no minerals or ores containing krypton. Solid krypton is white in color and has a cubic crystalline structure. However, unlike the lighter noble gases, it can occasionally form chemical compounds: krypton fluoride (principally KrF_2) is used in some excimer lasers. General uses are limited to the gaseous phase of the element: energy-saving fluorescent lights, flash lamps used for high-speed photography, gas discharge automobile headlights, and fluorescent signage. Monoisotopic ^{83}Kr has found use in MRI imaging (Pavlovskaya et al. 2005).

General Geochemical Behaviour

Krypton is one of the six noble gas elements that are also termed inert or rare gas elements. The term "noble" or "inert" correctly implies that the noble gases, including krypton, hardly ever engage in chemical reactions like most other elements. "Rare gas element" refers to their scarcity within the Earth system. Krypton has six naturally occurring isotopes with additional isotopes from cosmic ray interactions and products from nuclear reactions bringing the total known to 25. Notable unstable Kr isotopes are ^{81}Kr (half-life 229,000 years), produced by spallation reactions in the atmosphere, and ^{85}Kr (half-life = 10.76 years) from ^{238}U decay.

Krypton is colorless, odorless, and nontoxic, and is not used in biological systems. It is a highly volatile element and is extremely atmophile, accounting for 1.14 ± 0.01 ppm (parts per million) of dry tropospheric air. Krypton partitions strongly into the gas phase. Krypton solubility in silicate melt increases with increasing pressure (Paonita 2005) but is independent of temperature (Carroll et al. 1993), whereas solubility decreases with increasing temperature in water (Weiss and Kyser 1978). It is preferentially adsorbed onto organic matter compared to lighter noble gases (Marrocchi et al. 2005).

Uses in Geochemical Studies in Concert with Other Noble Gases

There are many scientific research areas in which Kr plays a critical role in combination with other noble gases. One such example is palaeoclimate studies. Bubbles trapped within polar ice contain gases from the atmosphere that have been trapped undisturbed for up to 10^6 yrs. These trapped gases faithfully reproduce the isotopic and elemental concentrations in the atmosphere. Solubility in water of the heavy noble gases (Kr and Xe), in particular, is strongly temperature dependent; therefore, trapped Kr/Xe ratios are controlled by mean ocean temperature and can be used as a record of ocean temperature variation (Headly and Severinghaus 2007). In addition, thermal diffusion can alter the elemental and isotopic ratio of these trapped noble gases, allowing scientists to reconstruct abrupt warming and cooling periods over the past few hundred thousand years (Severinghaus and Brook 1999). Similarly, basal ice sheet melting and glacial ice melting can be quantified by heavy noble gas/He ratios (Huber et al. 2006). Because the heavier noble gases (Kr and Xe) have solubilities in water that are most sensitive to temperature, reconstruction of palaeotemperatures in both groundwater systems (Aeschbach-Hertig and Solomon 2013) and water trapped within stalagmites/stalactites in caves (Schiedegger et al. 2011) is also possible.

Specific Applications of Krypton Isotope Geochemistry

Groundwater Dating

^{81}Kr is the product of spallation reactions in the atmosphere (proton addition to ^{82}Kr) and has a half-life of 229 kyrs. This potential dating tool for old groundwaters is little used due to very low concentrations of ^{81}Kr (~1000 atoms/liter with ^{81}Kr/Kr 5×10^{-13}). However, groundwaters have been dated using ^{81}Kr measured by AMS (accelerator mass spectrometry) (Collon et al. 2000). With the advent of the high sensitivity ATTA (atom trap trace analysis) mass spectrometer (Aeschbach-Hertig 2014), this environmental tracer and dating tool may be revisited. ^{85}Kr is produced by fission of uranium and plutonium and has a half-life of 10.76 years, making it a relevant tool for understanding shallow groundwater and transport of chemical pollutants. Sources include nuclear-bomb testing and nuclear reactors. ^{85}Kr is more abundant than ^{81}Kr: ~50,000 atoms/liter and ^{85}Kr/Kr 2×10^{-11}. It has a similar half-life to ^{3}H from nuclear bomb testing in 1960s, but, unlike ^{3}H, it is increasing in concentration in the atmosphere. Concentrations of ^{85}Kr in the atmosphere show spatial variability, reflecting primary source locations (Solomon et al. 1998), with concentrations at the North Pole approximately 30% higher than the South Pole (Jacob et al. 1987; Zimmerman et al. 1989).

Cosmic Ray Exposure Dating of Meteorites

Cosmic ray-induced spallation reactions in minerals containing Y, Rb, Sr, and Zr also produce ^{81}Kr. This is the basis of ^{81}Kr exposure dating in rocks that has been utilized for nearly half a century (e.g., Eugster et al. 1967; Marty 1967). The production rate of krypton depends on cosmic ray flux and the concentration of target element. Eventually, ^{81}Kr equilibrium concentration between production and radioactive decay is achieved. ^{81}Kr production rate can be inferred from the well-characterized decay rate, allowing the duration of exposure to cosmic rays to be calculated. Again low concentrations of ^{81}Kr are a challenge, but progress is being made with ultrasensitive RIMS (resonance ionization mass spectrometry) techniques (Strashnov et al. 2011).

Mantle Geochemistry: Source of Earth's Volatiles

Kr measured in igneous rocks, both ocean island basalts (OIBs, e.g., Hawaii) and mid-ocean ridge basalts (MORBs) show isotopic compositions identical to modern atmosphere. For this reason, Kr is often overlooked in noble gas geochemistry of the mantle. However, the subcontinental lithosphere seems to possess Kr isotopic anomalies with interesting implications for origin of volatiles on Earth (Holland et al. 2009). Two principle schools of thought exist for the origin of Earth's volatiles: one is gravitational capture of volatiles directly from the solar nebula (Porcelli et al. 2001); the other is acquisition of volatiles implanted into the accreting dust and planetesimals which subsequently accreted to form the Earth. These two models are not mutually compatible: the gravitational capture theory requires that the solar nebula is still present when the Earth has reached a significant proportion of its present mass, whereas the volatile planetesimal model requires dissipation of the solar nebula to allow implantation of solar wind into dust and fine particles before substantial accretion of material had occurred. The Kr isotopic composition of the subcontinental lithosphere suggests primitive Kr in

the Earth is like that found in carbonaceous chondrites and unlike solar Kr, implying volatiles were accreted into dust and planetesimals.

Mantle Geochemistry: Origin of the Atmosphere

Identification of the starting composition of primordial Kr in the Earth also applies tight constraints on the processes by which the atmosphere is related to the Earth's interior. Kr in the atmosphere is enriched in heavy isotopes relative to solar compositions. These isotopic enrichments are the natural consequence of the loss of noble gas from the atmosphere by processes that caused mass-dependent fractionation. Heavy noble gases, particularly Kr and Xe, are not presently lost from the atmosphere but have been modified by an extant process of atmospheric process of gas loss and mass fractionation (Hunten et al. 1987; Pepin 1991). The model is one of the initial overfractionation followed by buffering back to present-day atmosphere by outgassing of solar Kr from the mantle. Results from the subcontinental lithosphere show that the Earth does not presently contain solar Kr required in the mantle outgassing models (Holland et al. 2009). Therefore, one can therefore conclude that neither early outgassing nor impact-driven degassing of the early mantle is responsible for generating the noble gases in the present-day atmosphere. The relationship between Kr isotopes within the solid Earth and the atmosphere requires, from a noble gas perspective, an external source for the atmosphere. This has been postulated by various workers as a later volatile-rich reservoir which could include comets, asteroids, or Kuiper Belt objects (e.g., Marty and Meibom 2007).

Solar System Studies

Noble gases trapped in meteorites are categorized into solar, planetary, and exotic components and Kr is no exception. The solar Kr component (SW-Kr) is taken to be the average solar system composition as defined by solar wind. The most significant component to planetary noble gases in terms of abundance is Kr-Q. Kr-Q is the component found by etching primitive meteorites (Busemann et al. 2000) and is broadly explained by mass fractionation with respect to SW-Kr. This ubiquitous Q component is best explained by further contributions from exotic components Kr-s (s-process nucleosynthesis) and HL-Kr (another nucleosynthetic component enriched in light and heavy isotopes) (Gilmour 2010). Minor differences between Kr-Q and other planetary components Kr-P1 and Kr-P3 within meteorites suggests minor variation in the proportions the exotic components added to the mixture (Gilmour 2010). In combination with Xe isotopes, which can be used to date early solar system processes, the timing of incorporation of the nucleosynthetic components to the variable planetary components is beginning to yield a consistent story of the variety of supernovae sources that have contributed nucleosynthetic material to our solar system and the timing of processes that have occurred in the first few million years of the solar system to generate the relative abundances of elements and isotopic compositions that we observe in the solar system today.

Summary

In the past, krypton has often been the overlooked member of the noble gas family. In mantle and crustal geochemistry, its isotopic similarity to air has led to a focus on the lighter noble gases, He, Ne, and Ar. In groundwater hydrology, the low concentrations of radioactive krypton isotopes have meant that the focus of research in this area is on other tracers. In solar system science, "xenology" has been taken up by the community to a greater extent than "kryptology." However, with the advent of new ultrasensitive analytical techniques such as ATTA, together with the realization that perhaps krypton has an important future role to play in both terrestrial and solar system geochemistry, future research of krypton looks set to be exciting and fruitful.

Cross-References

- ▶ Atmospheric Evolution
- ▶ Cosmogenic Nuclides
- ▶ Earth's Atmosphere
- ▶ Meteorites
- ▶ Noble gases

References

Aeschbach-Hertig W (2014) Radiokrypton dating finally takes off. Proc Natl Acad Sci USA 111:6856–6857

Aeschbach-Hertig W, Solomon DK (2013) Noble gas thermometry in groundwater hydrology. In: Burnard P (ed) The noble gases as geochemical tracers. Advances in isotope geochemistry. Springer, Berlin, pp 81–122

Anders E, Grevesse N (1989) Abundances of the elements: meteoric and solar. Geochim Cosmochim Acta 53:197–214

Busemann H, Baur H, Wieler R (2000) Primordial noble gases in "phase Q" in carbonaceous and ordinary chondrites studied by closed-system stepped etching. Meteorit Planet Sci 35:949–973

Carroll MR, Sutton SR, Rivers ML, Woolum DS (1993) An experimental study of krypton diffusion and solubility in silicic glasses. Chem Geol 109:9–28

Collon P, Kutchera W, Loosli HH, Purtschert R, Love A (2000) Kr in the Great Artesian Basin, Australia: a new method for dating very old groundwater. Earth Planet Sci Lett 182:103–113

Eugster O, Eberhardt P, Geiss J (1967) Krypton and xenon isotopic composition of three carbonaceous chondrites. Earth Planet Sci Lett 3:249–257

Gilmour J (2010) "Planetary" noble gas components and the nucleosynthetic history of solar system material. Geochim Cosmochim Acta 74:380–393

Headly MA, Severinghaus JP (2007) A method to measure Kr/N_2 ratios in air bubbles trapped in ice cores, and its application in reconstructing past mean ocean temperature. J Geophys Res-Atmos 112:D19105

Heber V, Brooker R, Kelley S, Wood B (2007) Crystal-melt partitioning of noble gases (helium, neon, argon, krypton, xenon) for olivine and clinopyroxene. Geochim Cosmochim Acta 71:1041–1061

Holland G, Cassidy M, Ballentine CJ (2009) Meteorite Kr in earth's mantle suggests a late accretionary source for the atmosphere. Science 326:1522–1525

Huber C, Beyerle U, Leuenberger M, Schwander J, Kipfer R, Spahni R, Severinghaus JP, Weiler K (2006) Evidence for molecular size dependent gas fractionation in firn air derived from noble gases, oxygen, and nitrogen measurements. Earth Planet Sci Lett 243:61–73

Hunten DM, Pepin RO, Walker JCG (1987) Mass fractionation in hydrodynamic escape. Icarus 69:532–549

Jacob DJ, Prather MJ, Wofsy SC, McElroy MB (1987) Atmospheric distribution of ^{85}Kr simulated with a general circulation model. J Geophys Res 92:6614–6626

Marrocchi Y, Razafitianmahravo A, Michot LJ, Marty B (2005) Low-pressure adsorption of Ar, Kr, and Xe on carbonaceous materials (kerogen and carbon blacks), ferrihydrite, and montmorillonite: implications for the trapping of noble gases onto meteoritic matter. Geochim Cosmochim Acta 69:2419–2430

Marty K (1967) Isotopic composition of trapped krypton and xenon in chondrites. Earth Planet Sci Lett 3:243–248

Marty B, Meibom A (2007) Noble gas signature of the late heavy bombardment in the Earth's atmosphere. eEarth 2:43–49

Paonita A (2005) Noble gas solubility in silicate melts: a review of experimentation and theory, and implications regarding magma degassing processes. Ann Geophys 48:647–669

Pavlovskaya GE, Cleveland ZI, Stupic KF, Basaraba RJ (2005) Hyperpolarized krypton-83 as a contrast agent for magnetic resonance imaging. Proc Nat Acad Sci USA 102:18275–18279

Pepin RO (1991) On the origin and early evolution of terrestrial planet atmospheres and meteoritic volatiles. Icarus 92:2–79

Porcelli DR, Woolum D, Cassen P (2001) Deep Earth rare gases: initial inventories, capture from the solar nebula, and losses during Moon formation. Earth Planet Sci Lett 193:237–251

Schiedegger Y, Brennwald MS, Fleitmann D, Jeannin PY, Wieler R, Kipfer R (2011) Determination of Holocene cave temperatures from Kr and Xe concentrations in stalagmite fluid inclusions. Chem Geol 288:61–66

Severinghaus JP, Brook EJ (1999) Abrupt climate change at the end of the last glacial period inferred from trapped air in polar ice. Science 286:930–934

Solomon DK, Cook PG, Sanford WE (1998) Dissolved gases in subsurface hydrology. In: Kendall C, McDonnell JJ (eds) Isotope tracers in catchment hydrology. Elsevier, Amsterdam, pp 291–318

Strashnov I, Blagburn D, Gilmour J (2011) A resonance ionization time of flight mass spectrometer with a cryogenic sample concentrator for isotopic analysis of krypton from extraterrestrial samples. J Anal At Spectrom 26:1763–1772

Weiss RF, Kyser TK (1978) Solubility of krypton in water and seawater. J Chem Thermodyn 23:69–72

Weiss W, Stockburger H, Sartorius H, Rozanski K, Heras C, Ostlund HG (1986) Mesoscale transport of Kr-85 originating from European sources. Nucl Instrum Meth Phys Res Sect B 17:571–574

Zimmerman PH, Feicher J, Rath HK, Crutzer PJ, Weiss W (1989) A global three-dimensional source-receptor model investigation using ^{85}Kr. Atmos Environ 23:25–35

L

Laboratory Simulations of Organic Geochemical Processes at Elevated Temperatures

Jeffrey S. Seewald
Marine Chemistry and Geochemistry Department, Woods Hole Oceanographic Institution, Woods Hole, MA, USA

Definition

Organic matter undergoes a series of chemical transformations when heated in natural environments. The chemical and physical evolution of this material as a function of time and temperature, commonly referred to as thermal maturation, involves numerous organic and inorganic reactions that can be simulated in the laboratory using artificial maturation experiments. A variety of techniques have been developed to provide information regarding the rates of reactions as a function of time and temperature, the amounts of products generated, reaction pathways and mechanisms, and the role of water and other inorganic species.

Introduction

Organic compounds are pervasive in a broad range of geologic environments where they are involved in numerous geochemical processes at elevated temperatures and pressures. The generation and accumulation of petroleum (oil and natural gas) in sedimentary basins is an obvious and economically important example. Others include the transport and deposition of ore-forming metals in hydrothermal systems, sediment diagenesis, and the formation of methane gas-hydrates. Organic compounds formed in many of these environments also represent a source of nutrients and energy that can support microbial communities. Therefore, a major goal for the organic geochemist is to understand geochemical processes that regulate the production and degradation of organic matter. Owing to the complexity and, in many cases, difficulties associated with accessing geologic environments, factors that regulate organic transformations are difficult to determine from field studies alone. Consequently, a variety of approaches involving laboratory experiments have been developed to provide information regarding geochemical processes that regulate the abundance of naturally occurring organic compounds. Many of these efforts are focused on understanding the origin of oil and natural gas in relation to the thermal maturation of organic-rich sediments, while others have examined the generation and stability of organic compounds dissolved in water.

Oil and Natural Gas Formation

The thermal degradation of kerogen to produce liquid oil and natural gas is generally believed to occur at temperatures from 50 °C to 120 °C (Hunt 1996; Tissot and Welte 1984). Continued heating of oil at higher temperatures may result in its subsequent degradation and conversion to natural gas. Because natural maturation processes typically occur on million year time scales, it is common practice to conduct laboratory simulations at temperatures higher than in natural systems to enhance reaction rates and allow observation of organic transformations on laboratory time scales. Results of experiments generating petroleum as a function of time and/or temperature can be used to determine the rate of oil and natural gas formation in sedimentary basins (Behar et al. 1992; Burnham et al. 1987; Espitalié et al. 1977; Lewan 1985; Schenk and Dieckmann 2004). Indeed, such experiments have played an important role in guiding much of the petroleum exploration that has occurred to date in conventional sedimentary systems. A key premise underpinning this practice is the assumption that petroleum generation is primarily a kinetically controlled process in which the effects of time and temperature are interchangeable.

W. M. White (ed.), *Encyclopedia of Geochemistry*,
https://doi.org/10.1007/978-3-319-39312-4

Extrapolation of reaction rates observed at high temperatures in the laboratory to lower temperatures that characterize petroleum producing sedimentary basins is achieved through use of the Arrhenius equation:

$$k = A_0 e^{-(Ea/RT)}$$

where k is the rate constant, A_0 is the pre-exponential constant, E_a is the activation energy, R is the ideal gas constant, and T is temperature. There are important limitations associated with this approach. In particular, because the thermal maturation of sedimentary organic matter to produce oil and natural gas is an inherently complex process involving millions of sequential and parallel reactions, often in complex reaction networks, even the most complex kinetic models based on the Arrhenius equation represent gross simplifications of the natural process (Dominé et al. 1998). Moreover, the substitution of time for temperature during laboratory experiments may introduce significant uncertainty in extrapolated reaction rates since at lower temperatures substantial changes may occur in the relative rates of the reactions involved, the relationship between the rates of molecular diffusion and reaction, thermodynamic drives, and reaction mechanisms. Despite these limitations, laboratory experiments provide one of the few means by which processes associated with natural thermal alteration of sedimentary organic matter can be studied and represent effective tools for predicting the geochemical evolution of sedimentary basins.

Laboratory experiments designed to simulate the maturation of sedimentary organic matter vary widely with respect to complexity, the type of information they provide, and the extent to which they replicate natural systems. Collectively, they involve pyrolysis reactions induced by heating sedimentary organic matter in the absence of molecular oxygen. Major differences are related to whether the experimental system is open or closed, the temperature of the simulation, and the presence or absence of added water. In closed-system experiments, bulk sediments, petroleum source rocks, or isolated kerogen (the fraction of sedimentary organic matter insoluble in common organic solvents) are heated in a confined reaction chamber. A variety of reaction chamber designs and materials have been employed for this purpose, including relatively large volume (~500 ml) stainless steel pressure vessels (Lewan 1997) and smaller volume gold (Behar et al. 1992; Gao et al. 2014; Landais et al. 1989) or quartz tubes (Horsfield and Duppenbecker 1991) that are sealed at both ends. Artificial maturation within sealed gold tubes is typically referred to as confined pyrolysis since confining pressure is applied to the flexible tubes by water within an external pressure vessel to eliminate a vapor headspace above the reactants. During closed-system experiments, reaction products remain in the reaction chamber in intimate contact with the starting materials for prolonged periods of time, thereby promoting secondary reactions. In contrast, during open-system experiments (e.g., see programmed temperature pyrolysis), sediment or kerogen is maintained at or near ambient pressure conditions and is continuously swept by an inert carrier gas (usually helium) to remove volatile products to a detection device for quantitation (Burnham et al. 1987; Espitalié et al. 1977). Rapid removal of reaction products from the reaction chamber minimizes secondary reactions. As a result, there are significant compositional differences between organic products generated during open- and closed-system pyrolysis. In particular, alkenes are a major product during open-system pyrolysis, but are only produced during early heating stages in closed-systems and subsequently disappear during prolonged heating (Tannenbaum and Kaplan 1985). Since alkenes are present at relatively low concentrations in naturally occurring crude petroleum, these observations suggest that closed-system experiments more accurately replicate organic transformations responsible for the generation of oil and natural gas under quasi-closed conditions that prevail in natural sedimentary environments. Temperature conditions and the duration of heating also vary widely during laboratory simulations. Closed-system experiments are typically conducted isothermally at temperatures as high as high 550 °C for periods of time ranging from a few hours to several years (Saxby and Riley 1984). In contrast, open-system pyrolysis experiments typically involve relatively rapid non-isothermal heating (several degrees/min) of samples from ambient conditions to temperatures as high as 1000 °C (Burnham et al. 1987; Espitalié et al. 1977).

Role of Water and Other Inorganic Species

Laboratory experiments have been used extensively to examine the role of water and other inorganic materials such as minerals and sulfur species during organic geochemical processes. During the generation of oil and natural gas, water has been identified as an important variable that influences the composition and amounts of individual organic constituents (Lewan 1997; Price and Wenger 1992). Closed-system laboratory experiments reacting sedimentary organic matter or kerogen with added water (referred to as hydrous or aqueous pyrolysis) can also provide information regarding physical expulsion processes since this approach may produce a free-flowing liquid oil that floats on liquid water within the reaction chamber, allowing expelled products to be distinguished from those retained within the rock matrix (Lewan 1997). Hydrous pyrolysis experiments have demonstrated that in addition to acting as a confining medium, liquid water also participates in many organic reactions and acts as a source of hydrogen and oxygen for the generation of hydrocarbons and oxygen-bearing alteration products such as organic acids and

carbon dioxide (Hoering 1984; Lewan 1997; Seewald 2001; Stalker et al. 1994).

Several experimental studies have focused on investigating chemical reactions involving organic compounds dissolved in water at elevated temperatures and pressures (Reeves et al. 2012; Seewald 2001; Shipp et al. 2014; Siskin and Katritzky 2001). Although relevant to organic-rich petroleum producing sedimentary basins, results of these experiments have widespread application to hydrothermal systems located on land and in the marine environment, where, in most instances, the absence of organic-bearing sediments results in substantially lower organic matter abundance. Hydrothermal systems are characterized by higher temperatures than environments responsible for the generation of petroleum in sedimentary basins, allowing experiments focused on hydrothermal organic geochemistry to be conducted at temperatures comparable to natural systems. Recognizing that organic reactions are influenced by both the organic and inorganic chemical environment in which they occur, and that a significant fraction of organic reactions are redox dependent, many of these experiments have utilized approaches that allow key chemical variables such as the activities of H_2, various sulfur species, and H^+ to be carefully regulated or monitored during an experiment. Experiments containing naturally occurring Fe-bearing mineral assemblages that buffer the activity of aqueous H_2 and H_2S have been used to study the stability of individual aqueous hydrocarbons (McCollom et al. 2001; Seewald 2001). Unlike experiments examining the maturation of sedimentary organic matter or kerogen, these experiments typically contain a single or limited number of model compounds, thereby reducing the number of possible reactions and facilitating the identification of specific reaction pathways that may result in the production or degradation of an individual compound or class of compounds. A major finding of these experiments is that kinetic barriers to the attainment of total thermodynamic equilibrium allow the metastable persistence of many organic compounds such as hydrocarbons, alcohols, and ketones that may react reversibly to attain a partial thermodynamic equilibrium state with respect to other organic compounds, water, and redox-dependent minerals (Seewald 2001; Shipp et al. 2013; Yang et al. 2012). Moreover, these experiments have demonstrated that the presence of liquid water promotes aqueous reactions that utilize reaction pathways and mechanisms not available in dry systems.

Other experiments have been instrumental in demonstrating that minerals and aqueous species may be catalytically active during organic reactions. A variety of sulfur species have been shown to play a catalytic role in both the formation and degradation of diverse reduced carbon compounds. For example, organic sulfur radicals released by the decomposition of sulfur-bearing organic compounds accelerate the cleavage of C–C bonds in kerogen, resulting in the generation of oil at lower temperatures from sulfur-rich source rocks (Lewan 1998), while aqueous organic sulfur compounds such as thiols may play a catalytic role in the high temperature decomposition of oils by a process known as thermochemical sulfate reduction (Amrani et al. 2008). Aqueous inorganic sulfur species have also been implicated as being catalytically active during redox reactions that result in the oxidation of aqueous hydrocarbons (Goldhaber and Orr 1995; Seewald 2001; Toland 1960). The sulfide mineral sphalerite (ZnS) has been shown to act as a heterogeneous catalyst for the making and breaking of C–C bonds during isomerization of dimethylcyclohexanes (Shipp et al. 2014). Other heterogeneous catalysts include clay minerals and transition metals that have been shown to accelerate the degradation of petroleum to natural gas (Mango and Hightower 1997; Tannenbaum and Kaplan 1985).

Summary and Conclusions

Laboratory experiments represent a powerful means to identify and quantify geochemical processes associated with the thermal maturation of organic matter in natural environments. The ability to control physical and chemical conditions and remove many of the complexities associated with natural systems allows an assessment of key variables that regulate organic transformations under geologically relevant conditions. Experiments have demonstrated that organic reactions are strongly influenced by the presence or absence of inorganic chemical species. Liquid water is particularly important in facilitating reaction pathways not available in dry systems, and may facilitate the attainment of metastable thermodynamic equilibrium involving organic compounds, water, and minerals. Water also represents an abundant source of hydrogen and oxygen that can be incorporated into organic alteration products in addition to the limited amounts available in organic matter. Many inorganic and organic species have been shown to catalyze organic reactions in both aqueous and dry systems and participate in redox-dependent organic reactions. Information of this type represents an important foundation for the development of predictive models used to constrain geochemical process that regulate the composition and abundance of organic matter in natural systems.

Cross-References

- ▶ Activation Parameters: Energy, Enthalpy, Entropy, and Volume
- ▶ Carbon
- ▶ Fluid–Rock Interaction
- ▶ Geochemical Thermodynamics
- ▶ Hydrogen

- Kerogen
- Kinetics of Geochemical Processes
- Natural Gas
- Organic Geochemistry
- Oxygen
- Petroleum
- Programmed Temperature Pyrolysis
- Sulfide Minerals
- Sulfur

References

Amrani A, Zhang T, Maa Q, Ellis GS, Tang Y (2008) The role of labile sulfur compounds in thermochemical sulfate reduction. Geochim Cosmochim Acta 72:2960–2972

Behar F, Kressmann S, Rudkiewicz JL, Vandenbroucke M (1992) Experimental simulation in a confined system and kinetic modelling of kerogen and oil cracking. Org Geochem 19:173–189. https://doi.org/10.1016/0146-6380(92)90035-V

Burnham AK, Braun RL, Gregg HR, Samoun AM (1987) Comparison of measuring kerogen pyrolysis rates and fitting kinetic parameters. Energy Fuel 1:452–458

Dominé F, Dessort D, Brévart O (1998) Towards a new method of geochemical kinetic modelling: implications for the stability of crude oils. Org Geochem 12:597–612

Espitalié J, Jl L, Madec M, Marquis F, Leplat P, Paulet J, Boutefeu A (1977) Rapid method for source rocks characterization and for determination of petroleum potential and degree of evolution. Inst Fr Pétr Rev 32:23–42

Gao L, Schimmelmann A, Tang Y, Mastalerz M (2014) Isotope rollover in shale gas observed in laboratory pyrolysis experiments: insight to the role of water in thermogenesis of mature gas. Org Geochem 68:95–106. https://doi.org/10.1016/j.orggeochem.2014.01.010

Goldhaber MB, Orr WL (1995) Kinetic controls on thermochemical sulfate reduction as a source of sedimentary H_2S. In: Vairavamurthy MA, Schoonen MAA (eds) Geochemical transformations of sedimentary sulfur. American Chemical Society, Washington, DC, pp 412–425

Hoering TC (1984) Thermal reaction of kerogen with added water, heavy water, and pure organic substances. Org Geochem 5:267–278

Horsfield B, Dueppenbecker SJ (1991) The decomposition of Posidonia Shale and Green River Shale kerogens using microscale sealed vessel (mssv) pyrolysis. J Anal Appl Pyrolysis 20:107–123

Hunt JM (1996) Petroleum geochemistry and geology, 2nd edn. W.H. Freeman and Co., New York

Landais P, Michels R, Poty B, Monthioux M (1989) Pyrolysis of organic-matter in cold-seal pressure autoclaves – experimental approach and applications. J Anal Appl Pyrolysis 16:103–115

Lewan MD (1985) Evaluation of petroleum generation by hydrous pyrolysis experimentation. Phil Trans R Soc Lond A 315:123–134

Lewan MD (1997) Experiments on the role of water in petroleum formation. Geochim Cosmochim Acta 61:3691–3723

Lewan MD (1998) Sulfur-radical control on rates of natural petroleum formation. Nature 391:164–166

Mango FD, Hightower JW (1997) The catalytic decomposition of petroleum into natural gas. Geochim Cosmochim Acta 61:5347–5350

McCollom TM, Seewald JS, Simoneit BRT (2001) Reactivity of monocyclic aromatic compounds under hydrothermal conditions. Geochim Cosmochim Acta 65:455–468

Price LC, Wenger LM (1992) The influence of pressure on petroleum generation and maturation as suggested by aqueous pyrolysis. Org Geochem 19:141–159. https://doi.org/10.1016/0146-6380(92)90033-T

Reeves EP, Seewald JS, Sylva S (2012) Hydrogen isotope exchange between n-alkanes and water under hydrothermal conditions. Geochim Cosmochim Acta 77:582–599

Saxby JO, Riley KW (1984) Petroleum generation by laboratory-scale pyrolysis over six years simulating conditions in a subsiding basin. Nature 308:177–179

Schenk HJ, Dieckmann V (2004) Prediction of petroleum formation: the influence of laboratory heating rates on kinetic parameters and geological extrapolations. Mar Petrol Geol 21:79–95. https://doi.org/10.1016/j.marpetgeo.2003.11.004

Seewald JS (2001) Aqueous geochemistry of low molecular weight hydrocarbons at elevated temperatures and pressures: constraints from mineral buffered laboratory experiments. Geochim Cosmochim Acta 65:1641–1644

Shipp JA, Gould IR, Herckes P, Shock EL, Williams LB, Hartnett HE (2013) Organic functional group transformations in water at elevated temperature and pressure: reversibility, reactivity, and mechanisms. Geochim Cosmochim Acta 104:194–209

Shipp JA, Gould IR, Shock EL, Williams LB, Hartnett HE (2014) Sphalerite is a geochemical catalyst for carbon−hydrogen bond activation. Proc Nat Acad Sci 111:11642–11645

Siskin M, Katritzky AR (2001) Reactivity of organic compounds in superheated water: general background. Chem Rev 101:825–835

Stalker L, Farrimond P, Larter SR (1994) Water as an oxygen source for the production of oxygenated compounds (including CO_2 precursors) during kerogen maturation. Advances in Organic Geochemistry 1993. Org Geochem 22:477–486

Tannenbaum E, Kaplan IR (1985) Low-M_r hydrocarbons generated during hydrous and dry pyrolysis of kerogen. Nature 317:708–709

Tissot BP, Welte DH (1984) Petroleum formation and occurrence. Springer, New York

Toland WG (1960) Oxidation of organic compounds with aqueous sulfate. J Am Chem Soc 82:1911–1916

Yang Z, Gould IR, Williams L, Hartnett H, Shock EL (2012) The central role of ketones in reversible and irreversible hydrothermal organic functional group transformations. Geochim Cosmochim Acta 98:48–65

Lanthanide Rare Earths

Scott M. McLennan
Department of Geosciences, Stony Brook University, Stony Brook, NY, USA

Definition

Rare earth elements (REE) consist of Group 3 (or Group IIIB) transition elements $_{21}$Sc, $_{39}$Y, $_{57}$La, and f-block (inner transition) elements $_{58}$Ce, $_{59}$Pr, $_{60}$Nd, $_{61}$Pm, $_{62}$Sm, $_{63}$Eu, $_{64}$Gd, $_{65}$Tb, $_{66}$Dy, $_{67}$Ho, $_{68}$Er, $_{69}$Tm, $_{70}$Yb, and $_{71}$Lu. In geochemical usage, the term *rare earth elements* refers only to the lanthanides (La–Lu), and commonly Y due to geochemical behavior similar to Ho. However, Sc typically is excluded in discussions of REE because it is a smaller cation with geochemical behavior closer to the first row (ferromagnesian) transition elements Fe, V, Cr, Co, and Ni, with which it is typically grouped. This well-entrenched geochemical

nomenclature differs from formal chemical nomenclature, thus providing a source of confusion. Geochemists also subdivide REE into light rare earths (LREE: La–Sm) and heavy rare earths (HREE: Gd–Lu) with some further recognizing a group of middle rare earths (MREE; Nd (or Sm)–Tb). The REE promethium (Pm) lacks any stable nuclides or long-lived radionuclides and is not normally considered in geochemical discussions. Although only very rarely used in geochemical literature, the International Union of Pure and Applied Chemistry recommends the term "*lanthanoid*" rather than "*lanthanide*," since in chemistry the word-ending "ide" generally refers to anionic species.

General Geochemistry

The mostly trivalent rare earth elements (REE) are arguably the most significant group of trace elements in geochemistry. The lanthanide series develops by filling 4f orbitals, which do not effectively shield each other from increasing nuclear charge, leading to highly coherent geochemical behavior as a group. Among other things, the trivalent state is especially stable in geological settings (Eu^{2+} and Ce^{4+} being the two notable exceptions) and trivalent ionic radii decrease in a particularly systematic fashion: the "*lanthanide contraction*" (e.g., Douglas 1954; Table 1; Fig. 1). The dominant

Lanthanide Rare Earths, Table 1 Selected rare earth element properties

Symbol	Atomic number (Z)	Ground state[a]	Standard atomic weight[b]	Trivalent (except where noted) Ionic radius (pm)[c]		Pauling electro-negativity[a]	50% Oxide condensation (K at 10^{-4} bar)[d]	Seawater mean residence time (year)[e]	Element
				CN6	CN8				
La	57	[Xe] $5d^16s^2$	138.90547	103.2	116.0	1.10	1578	500	Lanthanum
Ce	58	[Xe] $4f^15d^16s^2$	140.116	101.0	114.3	1.12	1478	50	Cerium
Pr	59	[Xe] $5f^36s^2$	140.90766	99.0	112.6	1.13	1582	240	Praseodymium
Nd	60	[Xe] $5f^46s^2$	144.242	98.3	110.9	1.14	1602	400	Neodymium
Pm	61	[Xe] $5f^56s^2$	(~145)	97	110	~1.2	–	–	Promethium
Sm	62	[Xe] $5f^66s^2$	150.36	95.8	107.9	1.17	1590	400	Samarium
Eu	63	[Xe] $5f^76s^2$	151.964	94.7	106.6	~1.2	1356	410	Europium
Gd	64	[Xe] $4f^75d^16s^2$	157.25	93.8	105.3	1.20	1659	520	Gadolinium
Tb	65	[Xe] $5f^96s^2$	158.92535	92.3	104.0	~1.2	1659	570	Terbium
Dy	66	[Xe] $5f^{10}6s^2$	162.500	91.2	102.7	1.22	1659	740	Dysprosium
Ho	67	[Xe] $5f^{11}6s^2$	164.93033	90.1	101.5	1.23	1659	1820	Holmium
Er	68	[Xe] $5f^{12}6s^2$	167.259	89.0	100.4	1.24	1659	2420	Erbium
Tm	69	[Xe] $5f^{13}6s^2$	168.93422	88.0	99.4	1.25	1659	2430	Thulium
Yb	70	[Xe] $5f^{14}6s^2$	173.054	86.8	98.5	~1.3	1487	2440	Ytterbium
Lu	71	[Xe] $4f^{14}5d^16s^2$	174.9668	86.1	97.7	1.27	1659	2890	Lutetium
Sc	21	[Ar] $3d^14s^2$	44.955908	74.5	87.0	1.36	1659	1000	Scandium
Y	39	[Kr] $4d^15s^2$	88.90584	90.0	101.9	1.22	1659	1670	Ytterbium
Eu^{2+}				117	125				
Ce^{4+}				87.0	97.0				

Sources: [a]Emsley (1998); [b]Meija et al. (2016); [c]Shannon (1976); [d]Lodders (2003); [e]Nozaki (2001), Parker et al. (2016)

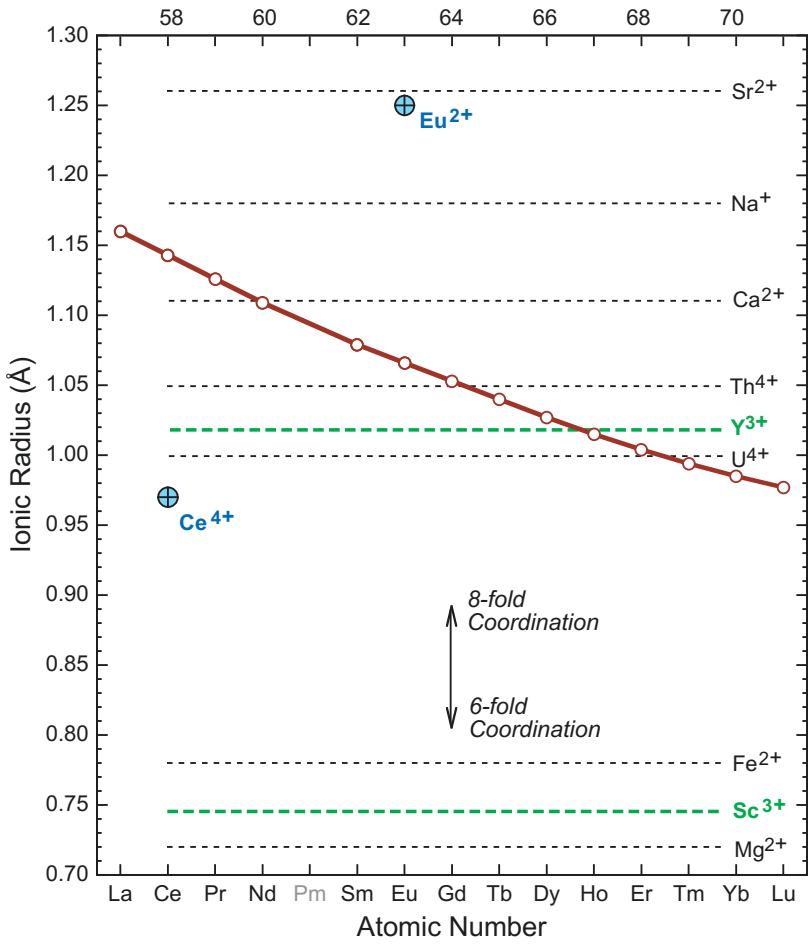

Lanthanide Rare Earths, Fig. 1 Plot of ionic radius versus atomic number for the trivalent lanthanide elements. Also shown for reference are the ionic radii for the other trivalent rare earth elements Y and Sc, for Eu^{2+} and Ce^{4+}, and for other selected cations. The extremely regular decrease in the ionic radii of the trivalent lanthanides is termed the "lanthanide contraction." Note that Sc^{3+} is much smaller than other rare earth elements, more similar in size to Fe^{2+} and Mg^{2+}, which is the reason why it is generally not included with the REE in geochemical literature

controls on the geochemical and cosmochemical behavior of REE are their valence (including redox behavior), size (ionic/crystal radius), volatility (e.g., 50% condensation temperature), and complexing behavior (speciation). Useful reviews of REE geochemistry may be found in Henderson (1984), Taylor and McLennan (1988), Lipin and McKay (1989), Nozaki (2001), Hoatson et al. (2011), Chakhmouradian and Wall (2012), and McLennan and Taylor (2012). Some basic REE properties, of geochemical and cosmochemical interest, are summarized in Table 1.

REE are lithophile and, apart from Sc, in most igneous systems are incompatible (i.e., bulk partition coefficients, $D < 1$) with the degree of incompatibility typically increasing with increasing size (i.e., decreasing atomic number). Accordingly, the trivalent lanthanides (and Y) tend to be concentrated in magmatic liquids and late crystallizing phases. Of the major elements in the crust and mantle, only Na and Ca come close in size (apart from Sc), however substitution for these elements (especially Na) may lead to serious charge imbalances, requiring a coupled substitution (Fig. 1). Traditionally, trivalent lanthanides have also been considered large-ion lithophile elements (LILE) but since their level of incompatibility is more a function of charge than of size, this terminology is now discouraged (Chauvel and Rudnick 2016).

In general, the REE have very low fluid/rock bulk partition coefficients ($D \ll 1$) and thus during most diagenetic, hydrothermal and metamorphic conditions are only significantly redistributed beyond the mineralogical scale at very high fluid/rock ratios. Under aqueous conditions, REE exist mostly as a variety of complexes, with seawater speciation being dominated by metal (REE^{3+}), carbonate ($REECO_3^+$), and bicarbonate ($REE(CO_3)_2^-$), with carbonate complexes being the most abundant. Scandium, on the other hand, is strongly hydrolyzed in seawater (i.e., $Sc(OH)_2^+$, $Sc(OH)_3^0$, $Sc(OH)_4^-$ speciation) (Byrne 2002).

A more controversial influence on REE behavior, notably in aqueous and late-stage magmatic fluids, is the so-called "*tetrad*" or "*double-double*" effect, resulting from 1/4, 1/2, 3/4, and fully filled 4f shells (Masuda et al. 1987). Distinctive M- and W-shaped chondrite-normalized REE patterns have been observed with inflections corresponding to the four tetrads (La-Nd; (Pm)Sm-Gd; Tb-Ho; Er-Lu). McLennan (1994) suggested that many apparent tetrad effects could be artifacts of incomplete analyses, analytical error, inappropriate normalization, or complex mixing processes.

However, claims of tetrad effects continue to appear (e.g., Bau and Koschinsky 2009) and final resolution of the controversy requires systematic interlaboratory comparisons of the same samples by a variety of laboratories and analytical methods.

Eu and Ce Redox Geochemistry

Of great importance to geochemistry is the fact that Eu and Ce commonly exist in other than trivalent states in geological environments ($Eu^{2+/3+}$; $Ce^{3+/4+}$). Reduced Eu^{2+} occurs by reducing, typically magmatic, conditions. The ionic radius of Eu^{2+} is about 17% larger than Eu^{3+} and almost identical to Sr^{2+} (Fig. 1). Accordingly, Eu^{2+} behavior differs considerably, resulting in REE distributions with anomalous Eu abundances (Eu-anomalies; see below). One important example is that Eu becomes highly concentrated in plagioclase feldspar (substituting into the Ca site). Plagioclase is only stable to about 40 km depth on Earth and so anomalous Eu behavior in terrestrial magmatic rocks is commonly taken as a sign of relatively shallow igneous processes (e.g., Taylor and McLennan 1985). Under surficial aqueous conditions, Eu is present in its oxidized form, although under highly reducing and alkaline conditions, Eu reduction could potentially take place (Sverjensky 1984). Evidence for mixed Eu^{2+}/Eu^{3+} under certain hydrothermal conditions has also been documented (e.g., Takahashi et al. 2005).

In contrast, Ce is found in the Ce^{3+} state under magmatic conditions but is readily oxidized under many surficial aqueous conditions, notably in early marine diagenesis to form manganese nodules and under oxidizing weathering conditions. Ce^{4+} is ~15% smaller than Ce^{3+} and tends to form highly insoluble Ce-hydroxide complexes that can thus readily separate from more soluble REE^{3+} complexes, resulting in anomalous REE distribution patterns (Ce-anomalies; see below). The substantial depletion of Ce in seawater (i.e., negative Ce anomalies), resulting ultimately from manganese oxide formation, is a direct manifestation of such redox controls (e.g., Nozaki 2001).

Normalization of Rare Earth Element Abundances

Absolute concentrations of lanthanides are highly variable in rocks, minerals, and natural waters (Table 2), as are relative abundances of adjacent lanthanides in any given sample, due to the Oddo-Harkins (odd-even) effect. Accordingly, it is customary to display lanthanide data as plots of normalized values (on a logarithmic scale) versus atomic number or ionic radius (on a linear scale), termed Coryell-Masuda plots. Yttrium in some cases is also plotted at about the position of the lanthanide Ho, because it typically behaves similarly to this HREE in most geological processes. The two most commonly used datasets for normalization are average chondritic meteorites, reflecting solar and bulk silicate Earth abundances, and average shale, reflecting upper continental crust abundances. Commonly used values are given in Table 2 but for both chondrites and shales, different workers use values that differ by up to ~15% in absolute abundances (but with

Lanthanide Rare Earths, Table 2 Rare earth element abundances in selected geochemical reservoirs (concentrations in ppm except in solar abundances and seawater, as noted)

	Log solar abundance (H = 12.00)[a]	Average volatile-free CI chondrite[b]	Bulk silicate Earth[b]	Oceanic N-MORB basaltic crust[b]	Continental crust[b]			Average Shale[c]	Seawater (ppt)[d]
					Upper	Bulk	Lower		
La	1.10 ± 0.03	0.367	0.546	1.9	30	16	11	38.2	4.17
Ce	1.58 ± 0.04	0.957	1.423	6.0	64	33	23	79.6	0.631
Pr	0.72 ± 0.04	0.137	0.215	0.99	7.1	3.9	2.8	8.83	0.535
Nd	1.42 ± 0.04	0.711	1.057	6.1	26	16	12.7	33.9	2.88
Sm	0.96 ± 0.04	0.231	0.343	2.22	4.5	3.5	3.17	5.55	0.601
Eu	0.52 ± 0.04	0.087	0.129	0.9	0.88	1.1	1.17	1.08	0.152
Gd	1.07 ± 0.04	0.306	0.454	3.5	3.8	3.3	3.13	4.66	0.739
Tb	0.30 ± 0.10	0.058	0.084	0.70	0.64	0.60	0.59	0.774	0.175
Dy	1.10 ± 0.04	0.381	0.566	4.5	3.5	3.7	3.6	4.68	1.06
Ho	0.48 ± 0.11	0.0851	0.126	1.1	0.80	0.78	0.77	0.991	0.330
Er	0.92 ± 0.05	0.249	0.370	2.6	2.3	2.2	2.2	2.85	1.09
Tm	0.10 ± 0.04	0.0356	0.057	0.42	0.33	0.32	0.32	0.405	0.169
Yb	0.84 ± 0.11	0.248	0.368	2.7	2.2	2.2	2.2	2.82	1.12
Lu	0.10 ± 0.09	0.0381	0.057	0.40	0.32	0.30	0.29	0.433	0.227
Sc	3.15 ± 0.04	8.64	13.0	44	13.6	30	35	16	0.98
Y	2.21 ± 0.05	2.25	3.48	25	22	20	19	27	19.6

Sources: [a]Lodders (2003; note that these abundances also equate to assuming $Si=10^{7.51}$); [b]from compilations in Taylor and McLennan (2009); [c]McLennan (1989); [d]Nozaki (2001), Parker et al. (2016)

relative abundances differing by no more than a few percent). In addition to chondrites and shales, other normalization values may be used for specific problems; for example, it is common to normalize data from a related suite of samples to a single sample within the suite to evaluate processes giving rise to variable REE distributions.

Due to variable redox states described above, it is also common that Eu and Ce display anomalous depletion or enrichment on normalized REE plots. These are termed Eu- and Ce-anomalies with negative anomalies denoting relative depletions and positive anomalies denoting relative enrichments. Such anomalies are quantified as follows:

$$Eu/Eu^* = Eu_N/(Sm_N \bullet Gd_N)^{0.5} \text{ and}$$
$$Ce/Ce^* = Ce_N/(La_N \bullet Pr_N)^{0.5}$$

where Eu* and Ce* are the expected values for smooth normalized REE patterns and the subscript "N" denotes the normalized value. Eu/Eu* and Ce/Ce* values of >1 denote positive anomalies whereas values <1 denote negative anomalies and for all but the most precise analyses, anomalies should be greater than ~5% (i.e., $\leq$0.95; $\geq$1.05) to be considered significant.

Isotope Geochemistry Involving Lanthanides

Because the lanthanides have such coherent interelement relationships and are not readily disturbed by later chemical alteration, radiogenic isotope systems involving these elements are especially useful as geochronometers and isotope tracers. The most useful of these is the $^{147}Sm/^{143}Nd$ alpha decay system (^{147}Sm decay constant, $\lambda = 6.54 \bullet 10^{-12}$ year^{-1}) which, for example, is useful for evaluating the timing of extraction of the continental crust from the mantle (DePaolo 1988). The $^{176}Lu/^{176}Hf$ beta decay system ($\lambda = 1.867 \bullet 10^{-11}$ year^{-1}) is well established and useful for examining the fractionation between the least incompatible REE and another refractory element with different geochemical behavior (i.e., high field strength) (Patchett 1983). A final, less used long-lived system involves the branched beta decay of ^{138}La to ^{138}Ce and ^{138}Ba ($T_{1/2} = 3.08 \bullet 10^{11}$ year). In addition to long-lived radiogenic isotope systems, there is one important short-lived system, the alpha decay $^{146}Sm/^{142}Nd$ system. ^{146}Sm has a short half-life ($T_{1/2} = 1.012 \bullet 10^8$ year), considerably less than the age of the Earth, and thus has been "extinct" since early in the history of the solar system. Accordingly, this system can be used to evaluate the fractionation of Sm from Nd very early in planetary histories, prior to the age of the oldest rocks (e.g., early planetary crust formation). A review of isotope geochemistry, including systems involving the lanthanides, can be found in Allègre (2008).

Mineralogy

Most common rock-forming minerals (e.g., olivine, pyroxene, feldspar, micas) do not have cation site conditions (size, charge) that are favorable to substitution of lanthanide REE, which is why they are typically incompatible trace elements for rock-forming minerals under magmatic conditions (i.e., mineral-melt partition coefficients, $K_d < 1$). Nevertheless, both relative and absolute abundances of REE in common rock-forming minerals are highly variable, by orders of magnitude in concentration (Fig. 2). It is this variability, in both abundances and REE pattern shapes (e.g., Eu-anomalies, HREE enrichment), that makes the REE such useful trace elements for evaluating igneous processes because bulk rock REE patterns are sensitive to the mineralogical, and thus the pressure-temperature-compositional, history of the magmatic system (e.g., partial melting, crystal fractionation).

Lanthanides are highly electropositive (i.e., electronegativities in range 1.0–1.3; Table 1) and thus tend to form ionic compounds. REE serve as essential structural constituents in more than 270 different silicate, carbonate, oxide, phosphate, halide, sulfate, arsenate, and vanadate minerals. Among the most abundant REE minerals are bastnäsite [$REE(CO_3)F$], monazite [$(Ce,La,Nd,Th)(PO_4)$], britholite [$(REE,Ca)_5(SiO_4, PO_4)_3(OH,F)$], and xenotime [$YPO_4$]. Some additional REE minerals that are of interest in geochemistry are lanthanite [$(La,Ce,Nd)_2(CO_3)_3 \cdot 8H_2O$], allanite [$(REE,Ca,Y)_2(Al,Fe^{2+}, Fe^{3+})_3(SiO_4)_3(OH)$], the phosphates florencite [$(Ce,La)Al_3(PO_4)_2(OH)_6$], and rhabdophane [$(La,Ce)(PO_4) \cdot H_2O$]. A review of REE mineralogy may be found in Jones et al. (1996).

Sources and Uses of Lanthanides

Based on 2015 United States Geological Survey estimates (Gambogi 2016), China dominates mine production of rare earth elements accounting for 85% of the global production of $1.24 \bullet 10^5$ metric tons of total rare earth oxides, with Australia (8.1%), U.S.A. (3.3%), Russia (2.0%), and Thailand (1.6%) accounting for most of the remaining production. China also possesses the largest fraction (42%) of the global ~$1.3 \bullet 10^8$ metric tons of rare earth oxide reserves. Brazil (17%), Australia (2.5%), India (2.4%), and U.S.A (1.4%) also account for significant reserves, with the remaining ~35% being divided among many countries, including Canada, Greenland, Kyrgyzstan, Malawi, Malaysia, Russia, Sweden, Thailand, Vietnam, Zambia, and others. The past decade has witnessed a considerable increase in REE ore deposit exploration activities due both to a dramatic price increase between 2008 and 2011 (prices subsequently dropped greatly between 2012 and 2016) and growing applications for military and

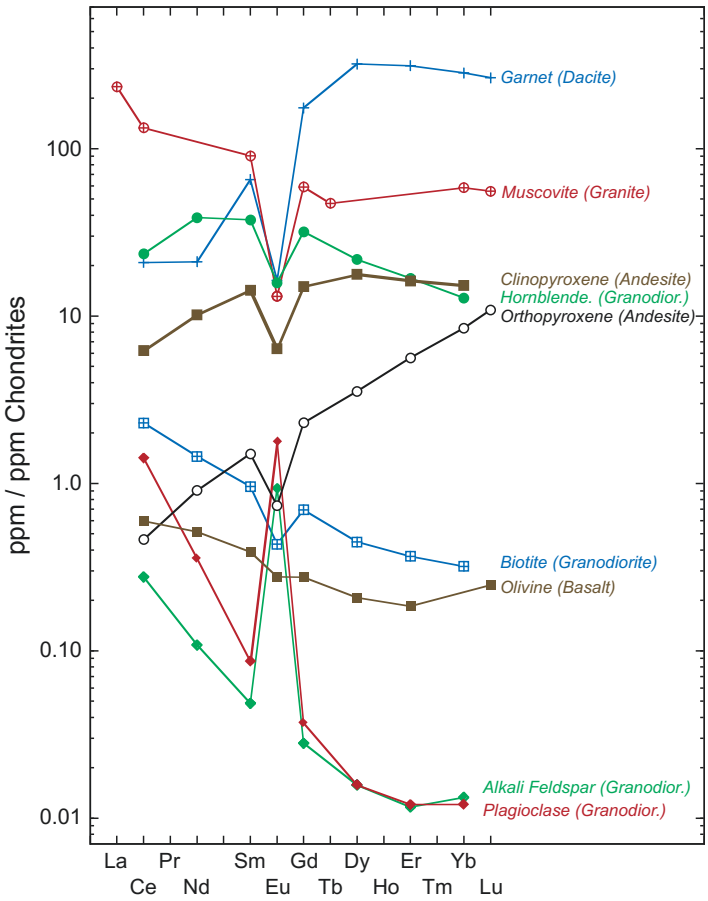

Lanthanide Rare Earths, Fig. 2 Chondrite-normalized REE patterns for selected common igneous rock-forming minerals (with host rocks also shown beside mineral name), illustrating both the overall variation in absolute REE abundances (>10^4) and in the shapes of the REE distributions, including highly variable LREE/HREE ratios and variable Eu-anomalies (Data from the compilation in Taylor and McLennan 1988)

other strategic purposes (e.g., night vision and precision guidance systems, stealth technology).

The major geological settings of REE ore deposits include hydrothermally altered (carbonatite fluid source) Proterozoic dolomitic marbles (Bayan Obo deposit of China, the largest in the world), lateritic ion-adsorption clays (southern China, notable for relative enrichment of scarce HREE), carbonatites (e.g., Mountain Pass, CA, the largest REE deposit in North America), and heavy mineral placer sands. Other REE ores are associated with Precambrian quartz-pebble conglomerate paleoplacers and alkaline magmatism (Castor and Hedrick 2006; Hoatson et al. 2011; Kynicky et al. 2012; Mariano and Mariano 2012).

The industrial applications of rare earth metals and compounds have greatly expanded over the past several decades (Castor and Hedrick 2006; Goonan 2011; Hoatson et al. 2011; Zaimes et al. 2015). Early applications were restricted to polishing agents, incandescent gaslight mantles, and coloring agents in glasses and ceramics. Currently, rare earths have a wide diversity of industrial uses, including (in approximate order of importance by volume) in permanent magnets (e.g., $Nd_2Fe_{14}B$ and $SmCo_5$ magnets); as catalysts in petroleum refining, automobiles, and various other industrial and chemical processes; in various metallurgical applications (e.g., steel and battery alloys); as polishing agents; as coloring agents in glasses and ceramics; and as phosphors in lighting and display screens (e.g., computers, television). Other minor but important uses include as components in lasers (e.g., Nd-YAG and Er-YAG lasers), microwaves (e.g., Y-Fe-garnets or YIG), satellites, chemicals and military systems. In terms of monetary value, applications in magnets, phosphors, and metals account for more than 80% of rare earth oxide markets.

Summary

The lanthanides (La-Lu), along with Y and Sc, comprise the rare earth elements (REE), that are among the most important trace elements for evaluating a wide array of geological processes. In geological settings, they are trivalent (except $Eu^{2+/3+}$ and $Ce^{3+,4+}$), electropositive, and refractory lithophile elements that, apart from Sc, are incompatible in most magmatic settings. In aqueous settings, they have low fluid/rock partition coefficients such that their concentrations in natural waters, along with their oceanic residence times, are very low. Dominant controls on geochemical and cosmochemical distributions are valence (including redox behavior), size and systematic variations in ionic radii (i.e., lanthanide

contraction), volatility, and complexing behavior. Radiogenic isotopes of REE (^{147}Sm-^{143}Nd, ^{176}Lu-^{176}Hf, ^{138}La-^{138}Ce, ^{146}Sm-^{142}Nd) are important geochronometers and isotope tracers. Rare earths are major constituents of >270 (mostly rare) minerals representing most mineral groups (silicates, phosphates, carbonates, etc.) and are mined mainly from hydrothermally altered carbonates, ion-adsorption clays, and carbonatites. Rare earths are strategic metals with wide industrial applications, including many in high technology.

Cross-References

- Cerium
- Complexes
- Cosmic Elemental Abundances
- Dysprosium
- Erbium
- Europium
- Gadolinium
- Geochronology and Radiogenic Isotopes
- Hafnium Isotopes
- Holmium
- Incompatible Elements
- Lanthanum
- Lithophile Elements
- Lutetium
- Neodymium
- Neodymium Isotopes
- Ocean Biochemical Cycling and Trace Elements
- Praseodymium
- Promethium
- Samarium
- Terbium
- Thulium
- Trace Elements
- Transition Elements
- Ytterbium

References

Allègre CJ (2008) Isotope geology. Cambridge University Press, Cambridge, 512pp

Bau M, Koschinsky A (2009) Oxidative scavenging of cerium on hydrous Fe oxide: evidence from the distribution of rare earth elements and yttrium between Fe oxides and Mn oxides in hydrogenetic ferromanganese crusts. Geochem J 43:37–47

Byrne RH (2002) Inorganic speciation of dissolved elements in seawater: the influence of pH on concentration ratios. Geochem Trans 3(2):11–16

Castor SB, Hedrick JB (2006) Rare earth elements. In: Kogel JE et al (eds) Industrial minerals and rocks: commodities, markets, and uses, 7th edn. Society for Mining, Metallurgy, and Exploration, Littleton, CO pp 769–792

Chakhmouradian AR, Wall F (eds) (2012) Rare earth elements. Elements 8:333–376

Chauvel C, Rudnick R (2016) Large-ion lithophile elements. In: White WM (ed) Encyclopedia of geochemistry. Springer, Switzerland. https://doi.org/10.1007/978-3-319-39193-9_232-1

DePaolo DJ (1988) Neodymium isotope geochemistry: an introduction. Springer, Berlin, 187pp

Douglas BE (1954) The lanthanide contraction. J Chem Educ 31:598–599

Emsley J (1998) The elements, 3rd edn. Oxford University Press, Oxford, 292pp

Gambogi J (2016) Rare earths. U S Geol Surv Miner Commod Summ 2016:134–135

Goonan TG (2011) Rare earth elements – end use and recyclability. Scientific investigations report 2011-5094. U. S. Geological Survey, Reston, 15pp

Henderson P (ed) (1984) Rare earth element geochemistry. Elsevier, Amsterdam, 510pp

Hoatson DM, Jaireth S, Miezitis Y (2011) The major rare-earth-element deposits of Australia: geological setting, exploration, and resources. Geoscience Australia, Canberra, 204pp

Jones AP, Wall F, Williams CT (eds) (1996) Rare earth minerals: chemistry, origin and ore deposits.. Chapman & Hall, London, 372pp

Kynicky J, Smith MP, Xu C (2012) Diversity of rare earth deposits: the key example of China. Elements 8:361–367

Lipin BR, McKay GA (eds) (1989) Geochemistry and mineralogy of rare earth elements. Rev Mineral 21:348pp

Lodders K (2003) Solar system abundances and condensation temperatures of the elements. Astrophys J 591:1220–1247

Mariano AN, Mariano A Jr (2012) Rare earth mining and exploration in North America. Elements 8:369–376

Masuda A, Kawakami O, Dohmoto Y, Takenaka T (1987) Lanthanide tetrad effects in nature: two mutually opposite types, W and M. Geochem J 21:119–124

McLennan SM (1989) Rare earth elements in sedimentary rocks: influence of provenance and sedimentary processes. Rev Mineral 21:169–200

McLennan SM (1994) Rare earth element geochemistry and the "tetrad" effect. Geochim Cosmochim Acta 58:2025–2033

McLennan SM, Taylor SR (2012) Geology, geochemistry and natural abundances of the rare earth elements. In: Atwood DA (ed) The rare earth elements: fundamentals and applications. Wiley, Chichester, pp 1–19

Meija J, Coplen TB, Berglund M, Brand WA, De Bièvre P, Gröning M, Holden NE, Irrgeher J, Loss RD, Walczyk T, Prohaska T (2016) Atomic weights of the elements 2013 (IUPAC technical report). Pure Appl Chem 88:265–291

Nozaki Y (2001) Rare earth elements and their isotopes in the ocean. In: Steele JH et al (eds) Encyclopedia of ocean sciences. Academic, London, pp 2354–2366

Parker CE, Brown MT, Bruland KW (2016) Scandium in the open oceans: a comparison with other group 3 trivalent metals. Geophys Res Lett 43:2758–2764

Patchett PJ (1983) Importance of the Lu-Hf isotopic system in studies of planetary chronology and chemical evolution. Geochim Cosmochim Acta 47:81–91

Shannon RD (1976) Revised effective ionic radii and systematic studies of interatomic distances in halides and chalcogenides. Acta Crystallogr A32:751–767

Sverjensky DM (1984) Europium redox equilibrium in aqueous solutions. Earth Planet Sci Lett 67:70–78

Takahashi Y, Kolonin GR, Shironosova GP, Kupriyanova II, Uruga T, Shimizu H (2005) Determination of the Eu(II)/Eu(III) ratios in minerals by X-ray adsorption near-edge structure (XANES) and its application to hydrothermal deposits. Mineral Mag 69:179–190

Taylor SR, McLennan SM (1985) The continental crust: its composition and evolution. Blackwell, Oxford, 312pp
Taylor SR, McLennan SM (1988) Chapter 79, The significance of the rare earths in geochemistry and cosmochemistry. In: Gschneidner KA, Eyring L (eds) Handbook on the physics and chemistry of rare earths, vol 11. North-Holland, Amsterdam, pp 485–578
Taylor SR, McLennan SM (2009) Planetary crusts: their composition, origin and evolution. Cambridge University Press, Cambridge, 378pp
Zaimes GG, Hubler BJ, Wang S, Khanna V (2015) Environmental life cycle perspective on rare earth oxide production. ACS Sustain Chem Eng 3:237–244

Lanthanum

Catherine Chauvel
ISTerre, University Grenoble Alpes, CNRS, Grenoble, France

Element Data
Atomic Symbol: **La**
Atomic Number: **57**
Atomic Weight: 138.9054 g/mol
Isotopes and Abundances: ^{138}La 0.09017%, ^{139}La 99.9098%
1 Atm Melting Point: 920.9 °C
1 Atm Boiling Point: 3456.9 °C
Common Valences: +3
Ionic Radii: 103 pm
Pauling Electronegativity: 1.10
Chondritic (CI) Abundance: 0.2446 microg/g
Silicate Earth Abundance: 0.648 microg/g
Crustal Abundance: 31 microg/g
Seawater Abundance: ≈30 picomole/kg
Core Abundance: unknown

Properties

Lanthanum is a soft and ductile metallic element with a silver-white color that rapidly tarnishes in air. It generally occurs as oxide and hydroxide and in substitution to major elements in minerals.

History and Use

Lanthanum was discovered in Stockholm (Sweden) in 1839 by C.G. Mosander who gave it the name of "latane" [Greek, lanthanein = to lie hidden] because it was "hidden" in cerium carbonate fluoride from the Bastnäs mine (Berzelius 1839). It was isolated only in 1923, almost 100 years later. Lanthanum gave its name to the lanthanide series (also called rare earth elements), a group of 15 similar elements between lanthanum and lutetium in the periodic table.

In the past, lanthanum was not widely used in industry, but the demand increased drastically with the onset of rechargeable batteries for hybrid automobiles.

Geochemical Behavior

Lanthanum, as other rare earth elements, is usually not a constituent of mineral phases on Earth. It is refractory and under most conditions is lithophile and found in the trivalent state. During partial melting and fractional crystallization of magmas, it behaves as an incompatible element and is concentrated in melts. It is therefore enriched in basalts relative to their mantle source and enriched in continental crust relative to Earth mantle. Together with the other rare earth elements, it is widely used in geochemistry to trace geological processes.

Geochronology

Lanthanum has two isotopes, ^{138}La (0.09017%) and ^{139}La (99.9098%). ^{139}La is stable; ^{138}La is radioactive and decays into ^{138}Ce with a half-life of ≈ 292.5 Ga, one of the longest of radioactive decay systems used in isotope geochemistry.

Biological Utilization and Toxicity

Lanthanum has no known biological role and has low to moderate toxicity.

Cross-References

▶ Cerium
▶ Incompatible Elements
▶ Lanthanide Rare Earths
▶ Lithophile Elements
▶ Lanthanide Rare Earths

References

Berzelius (1839) Latanium – a new metal. Philosophical magazine. Ann Phil J Sci XIV:390–391

Large-Ion Lithophile Elements

Catherine Chauvel[1] and Roberta L. Rudnick[2]
[1]ISTerre, University Grenoble Alpes, CNRS, Grenoble, France
[2]Department of Earth Science, University of California, Santa Barbara, CA, USA

Definition

The term large-ion lithophile element (or LILE) is frequently used but poorly defined in the geochemical literature. The word "*lithophile*" comes from the classification of elements suggested by Goldschmidt over a hundred years ago. It describes elements that have an affinity for silicate phases in the Earth. As shown in Fig. 1 from White (2013), the lithophile elements are numerous and generally correspond to elements located at both ends of the periodic table.

The *large-ion* lithophile elements represent only a subset of these lithophile elements and refer to the trace elements characterized by large radius to charge ratio (or low field strength elements; see Fig. 2 below).

Origin of the Term and LILE Geochemistry

The term was first used by Gast (1972) to encompass the cations K, Rb, Sr, Cs, Ba, REE, Th, and U. Gast also included Li as a LILE, since it has a large radius to charge ratio, even though it is small. Because of the confusion in the literature regarding usage of LILE, it is recommended that the term be restricted to lithophile trace elements having large radius to charge ratios and which also have ionic radii greater than those of Ca^{2+} and Na^{1+} (100 and 102 picometers), the largest cations common to rock forming minerals. By this definition, the list of LILE is restricted to K, Rb, Sr, Cs, Ba, and Eu^{2+}.

Because of their large radii, LILE behave incompatibly (see entry ► "Incompatible Elements") during mantle melting and so are highly enriched in mantle melts relative to their source. They are enriched in intraplate basalts (Hofmann 1997) and island arc basalts (Kelemen et al. 2014) relative to more compatible trace elements, but they are depleted in mid-ocean ridge basalts, demonstrating that these lavas derive from a mantle source that experienced prior melt extraction (see entry ► "Mantle Geochemistry"). The LILE are strongly enriched in the upper continental crust (Rudnick and Gao 2014) but occur in lower concentrations in the deep continental crust due to its overall more mafic character and selective loss of some LILE during high-grade metamorphism (see

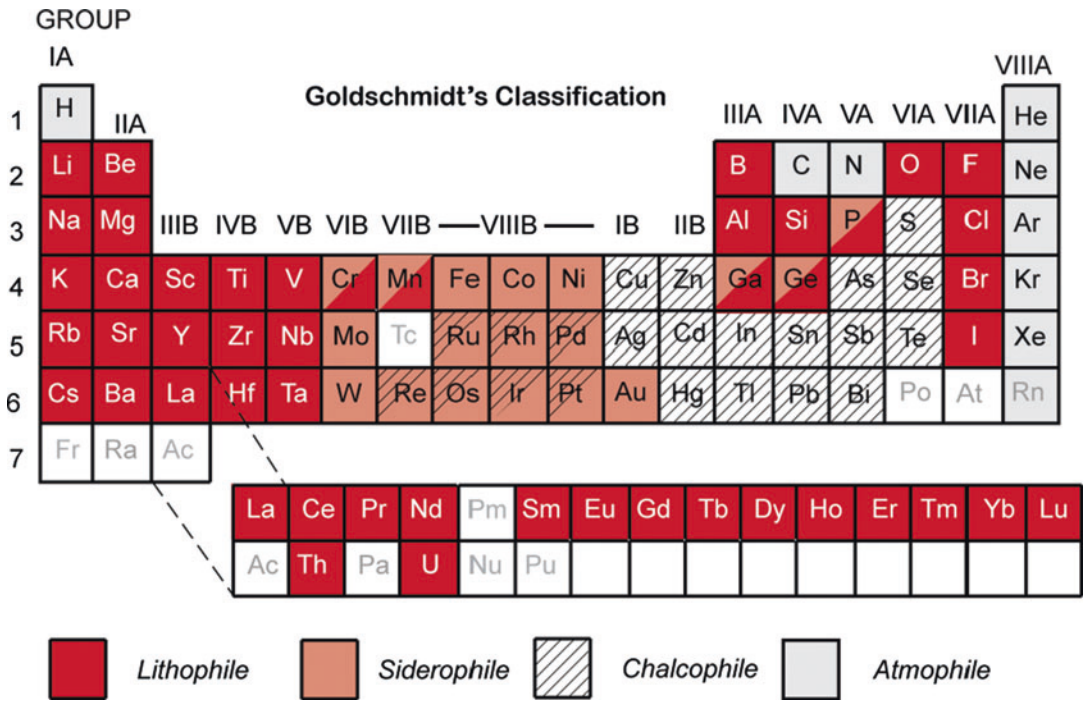

Large-Ion Lithophile Elements, Fig. 1 Goldschmidt's classification of the elements (From White 2013)

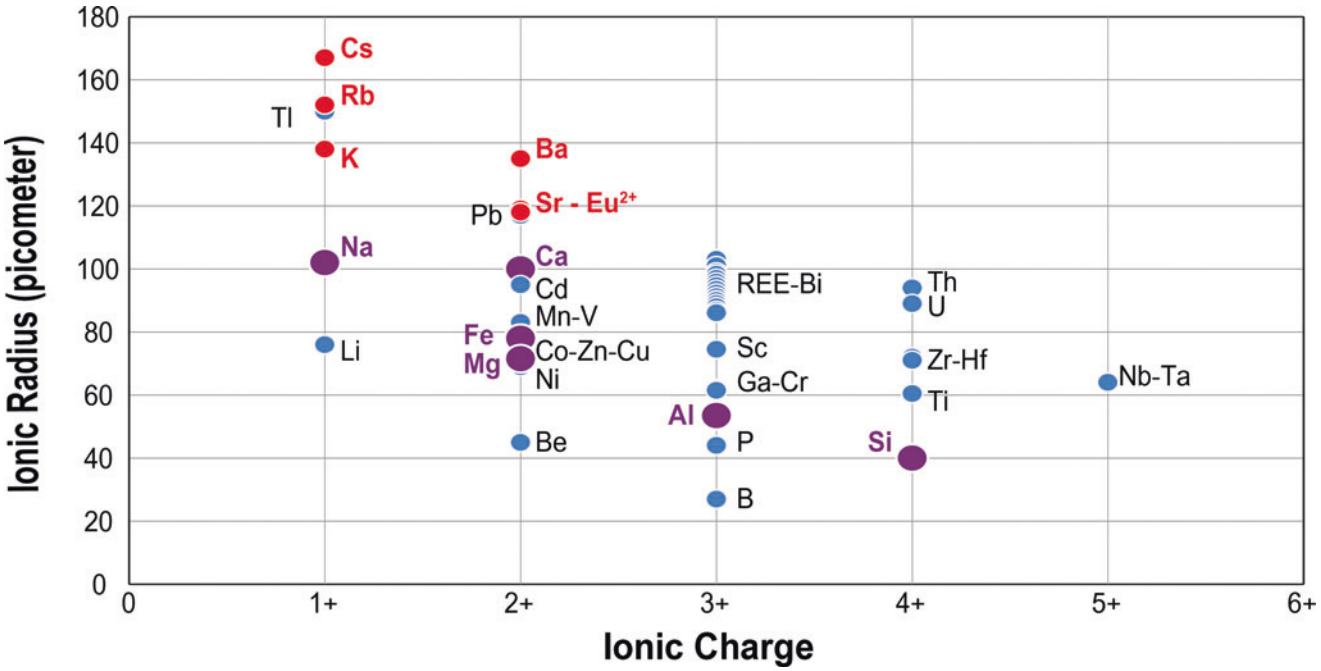

Large-Ion Lithophile Elements, Fig. 2 Ionic radius versus ionic charge diagram showing the LILE in *red*. Major cations are shown in large *purple* symbols and other trace elements are shown as small *blue* symbols

entry ▶ "Earth's Continental Crust"). Between 15–55% of the Earth's LILE budget is found in the continental crust (Rudnick and Fountain 1995).

Summary

The recommended list of large-ion lithophile elements is K, Rb, Sr, Cs, Ba, and Eu^{2+}.

Cross-References

- ▶ Alkali and Alkaline Earth Metals
- ▶ Earth's Continental Crust
- ▶ Incompatible Elements
- ▶ Mantle Geochemistry

References

Gast PW (1972) The chemical composition and structure of the moon. Moon 5:121–148
Hofmann AW (1997) Mantle geochemistry: the message form oceanic volcanism. Nature 385:219–229
Kelemen PB, Hanghøj K, Greene AR (2014) One view of the geochemistry of subduction-related magmatic arcs, with an emphasis on primitive andesite and lower crust. In: Rudnick RL (ed) The crust, Holland HD, Turekian KK (eds) Treatise on geochemistry, 2nd edn. Elsevier, Oxford. pp 749–806
Rudnick RL, Fountain DM (1995) Nature and composition of the continental crust: a lower crustal perspective. Rev Geophys 33:267–309
Rudnick RL, Gao S (2014) Composition of the continental crust. In: Rudnick RL (ed) The crust, Holland HD, Turekian KK (eds) Treatise on geochemistry, 2nd edn. Elsevier, Oxford, pp 1–51
White WM (2013) Geochemistry. Wiley, Chichester. 660p

Laser Ablation – Inductively Coupled Plasma Mass Spectrometry

Takafumi Hirata
Geochemical Research Center, The University of Tokyo, Tokyo, Japan

Definition

Mass spectrometers utilizing atmospheric pressure Ar-ICP as an ion source (ICP-MS) have been widely used for both element and isotopic analyses for geochemical samples such as rocks, minerals, aquatic solutions, as well as gaseous samples. Since the ICP is operating under atmospheric pressure, various sample introduction techniques can be applied for analysis. Among these, the laser ablation sampling technique is likely to become

a method of choice for many geochemists because it is a highly sensitive and versatile method of elemental and isotopic analyses. Laser ablation is the process of removing materials from the surface of solid materials by the irradiation of a laser beam. Laser-induced sample aerosols and vapors will be introduced to the ICP, and the ionized elements are extracted into a high-vacuum and separated by mass. With the LA-ICPMS technique, direct elemental and isotopic analyses can be made without chemical decomposition or dissolution procedures. Moreover, analytical capability for in situ elemental and isotopic analyses can be made in various spatial resolution, ranging from 1 to 1000 μm. The LA-ICPMS technique has opened up new applications for geochemistry, such as in situ stable isotope studies, in situ isotope dating, and simultaneous mappings for major to trace elements (imaging mass spectrometry).

Introduction

The mass spectrometric technique utilizing inductively coupled plasma as an ion source (ICP-MS) has been widely used for both abundance and isotope ratio measurements (e.g., Niu and Houk 1996; Hattendorf et al. 2003; Becker 2007). The basic advantage of the ICP-MS lies in the ion source, which achieves nearly complete ionization efficiency for almost all elements compared to other mass spectrometry techniques, such as thermal ionization mass spectrometry (TIMS) or secondary ion mass spectrometry (SIMS). The ICP high ionization efficiency can be achieved through both the charge-exchange reaction ($Ar^+ + M \rightarrow Ar + M^+$) and electron impact reaction ($M + e^-_{(fast)} \rightarrow M^+ + e^-_{(slow)}$). Moreover, long residence time of the sample in the ICP (i.e., >10 msec) results in smaller contribution of nonmass spectrometric interferences (e.g., matrix effect), providing high quantitative capability for elemental analysis.

The ICP ion source has further analytical advantages as it is possible to analyze dry sample aerosols produced by the laser ablation technique. The laser ablation technique is one of the most versatile solid sampling techniques for the ICP-MS (Durrant 1999; Günther and Hattendolf 2005). The interaction of laser beam with solid materials induce various effects including surface heating and melting to ejection of sample material. The material is released from solid materials as vapor, molten droplets, solid particulates, and its agglomerates. The laser-induced sample particles or vapors are introduced into the ICP, operating at atmospheric pressure, and the produced ions are extracted into the vacuum region through a vacuum interface (Fig. 1). Analytes are separated from major constituents through mass spectrometers, including a magnetic sector (MS), quadrupole (Q), or time-of-flight (TOF)-type mass spectrometers (e.g., Duckworth et al. 1986; Wieser and Schwieters 2005).

Signal intensity for analyses is dependent upon both the concentration and the total amount of sample released. Numerous laser parameters can affect the signal response, and the data quality is influenced by laser types, experimental

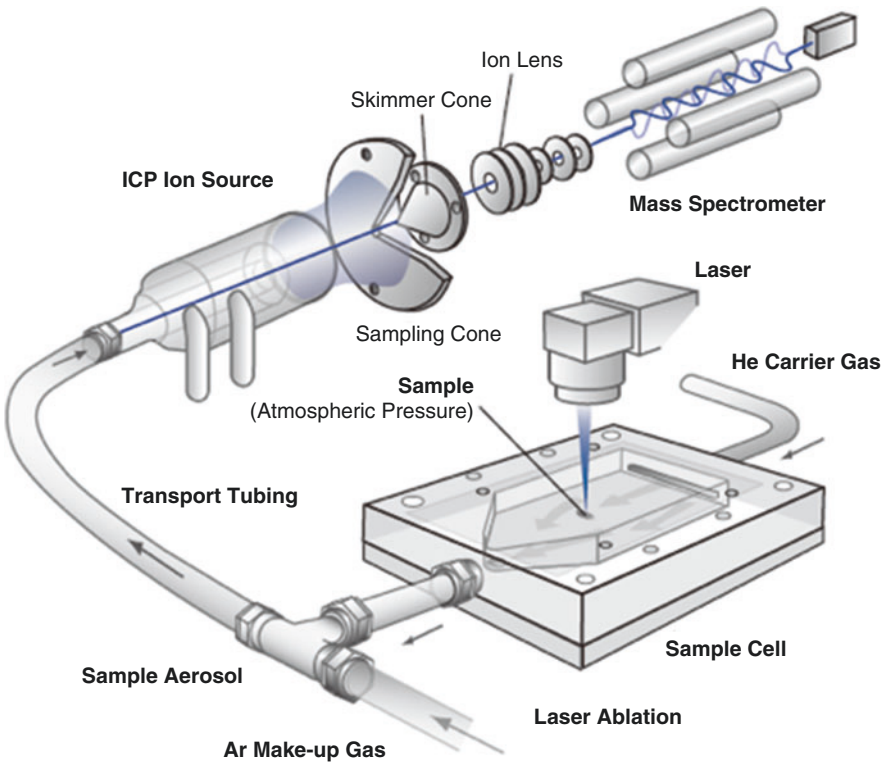

Laser Ablation – Inductively Coupled Plasma Mass Spectrometry,
Fig. 1 Schematic diagram of laser ablation-ICP-mass spectrometer. When focused laser beam with sufficient energy is directed onto the sample, material or constituent elements from surface will be explosively sputtered and evaporated. The laser-induced sample particles or vapors will be transported in mixture of He and Ar gas to the ICP for atomization ionization

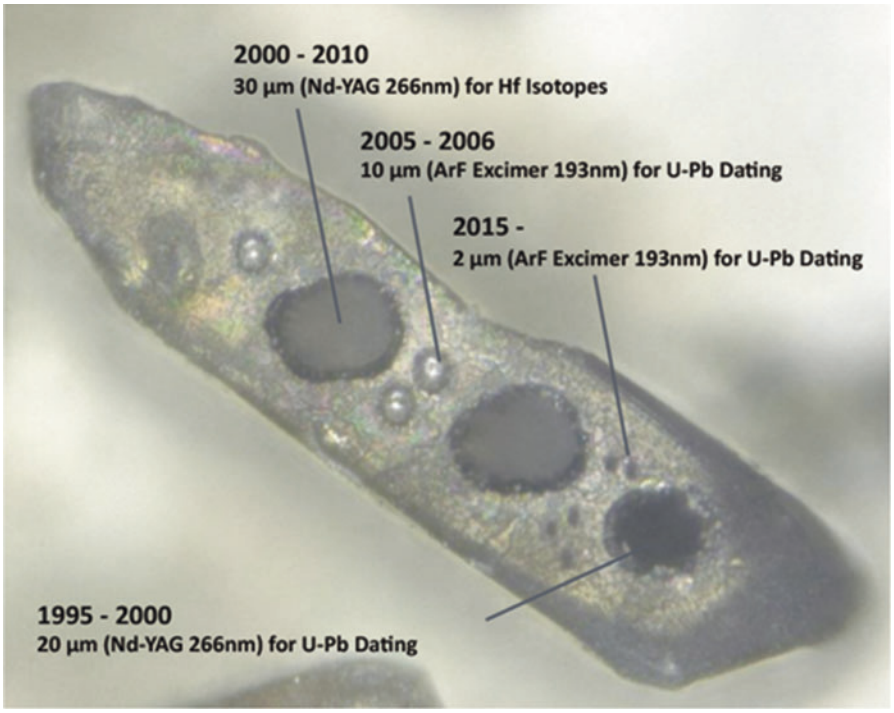

Laser Ablation – Inductively Coupled Plasma Mass Spectrometry,
Fig. 2 Comparison of the ablation pit size for in situ isotope chronology. Progresses in the LA-ICPMS technique can be well demonstrated by the size of ablation pits. With increasing of both the elemental sensitivity of the ICPMS system and better understanding of the mechanism for the laser ablation, smaller ablation pit size can be adopted for in situ elemental and isotopic analyses for geochemical samples (Sample: PMA7, courtesy of Dr. Jean Jacques Peucat, Univ. Rennes, France)

settings, or calibration strategy. Continuous improvements in enhancing the elemental sensitivity of ICP-MS instruments, together with a better understanding of the mechanism of the laser ablation process, have led to successive enhancements in both data quality and spatial resolution for in situ analysis (Fig. 2).

Multi-Element Determinations

The LA-ICPMS technique has been widely used for rapid multielement determinations for major to trace elements in rocks or minerals (e.g., Hattendorf et al. 2003; Jochum et al. 2007; Fricker et al. 2011; YongSheng et al. 2013). Typical size of the laser ablation pit, adopted for the elemental analysis, ranges from approximately 20–60 µm. Despite the slightly poor spatial resolution, the LA-ICPMS technique has major advantages on the elemental sensitivity, compared to the conventional probe techniques, including electron probe microprobe analyzer (EPMA) or micro-X-ray fluorescence (µXRF) techniques (e.g., Weiss et al. 2008).

Limits of detection and the resulting precision of the measurements are significantly influenced by three major parameters: (a) matrix effect, (b) particle size distribution of laser-induced same particles, and (c) mass spectrometric inferences by isobaric ions or polyatomic ions (Longerich et al. 1996; Günther et al. 1997; Kozlov et al. 2003; Koch et al. 2006). Among these, size distribution of the laser-induced sample particles is one of the most important parameters to achieve better precision and accuracy of the measurements (Koch et al. 2004; Kuhn et al. 2004). For geochemical samples, UV wavelength lasers, such as ArF Excimer laser (193 nm) or Nd:YAG 5HG (213 nm), can produce smaller size distribution of the sample particles, which result in higher atomization and ionization efficiency in the ICP. Moreover, with the smaller sample particles, a smoothed signal intensity profile can be obtained, resulting in higher precision in the elemental analysis. With UV laser and with ablation pit of 30–40 µm, typical detection limits of better than 10 ng/g can be achieved by the LA-ICPMS system.

The limits of detection for trace elements in silicates or ceramic materials are generally superior to those for the elements in metallic materials. The lower signal response from metallic materials is mainly due to reduced ablation yield, which is caused by the energy loss through high-thermal conductivity of the metallic materials. Moreover, incomplete heating results in the release of molten particles from solid samples or preferential release of the volatile elements from the samples (i.e., large elemental fractionation during the laser ablation), which can be a major source of analytical error. To minimize the elemental fractionation during the laser ablation, the use of shorter pulse duration could be the best solution as the rate of thermal diffusion for metallic materials (e.g., >10 ps) is significantly longer than the typical pulse duration achieved by femtosecond lasers (10–500 fs) (Koch et al. 2004, 2006; Hirata and Miyazaki 2007). Smaller contribution of the laser-induced heating onto the sample materials can result in minimal size-related elemental fractionation during the laser ablation. With femtosecond lasers, signal responses obtained from metallic Cu improve by a

factor of 20, compared with that obtained with conventional nanosecond lasers (Zeng et al. 2004; Horn and Blanckenburg 2007; Hirata and Kon 2008).

Quantification Protocol

The LA-ICPMS technique has further analytical advantages as it is less sensitive to the matrix effect (non-mass spectrometric interferences) for the analytes. The smaller contribution of the matrix effect is mainly related to two factors. (1) A long-residence time for the ionization process within the ICP with typical time duration for the sample particles exceeding 10 ms, which is significantly longer compared to most other ion sources adopted for the mass spectrometer. (2) Post-ionization system setup in the LA-ICPMS technique as the sampling (laser ablation) and ionization processes are separate steps. This implies that laser operational settings and ionization conditions can be optimized independently. In fact, qualitative or semiquantitative analysis can be made with a nonmatrix matched calibration standard. Nevertheless, it should be noted that the matrix-matched calibration standard is highly desired for elemental and isotopic analysis of solid geochemical materials.

Availability of a calibration standard is a key issue to obtain reliable elemental and isotopic data. For the LA-ICPMS technique, matrix-matched standards have been widely used for the calibration. However, data traceability cannot be maintained based on an inhouse standard, in which the evaluation of heterogeneity would be difficult. To overcome this, calibration using the synthetic glass standards (e.g., USGS BCR-2G, BHVO-2G, BIR-1G etc.), NIST SRM glasses (e.g., NIST SRM610, 612, or 613 etc.) or MPI-DING (MPI-DING glasses KL2-G, ML3B-G, StHs6/80-G, GOR128-G etc.), combined with internal standardization using major-minor elements (e.g., Ca, Si, P, or Sr) is a widely adopted analytical approach (e.g., Myers et al. 1995; Pearce et al. 1997; Jochum et al. 2005; Jochum et al. 2006). Typical precision or accuracy of the abundance measurements ranges from 1% to 20% with a spatial resolution of 30 μm. One of the major sources of the analytical error is the counting statistics, and therefore, great care must be given to control the number of analytes. Although longer ablation can reduce the contribution of counting statistics for the analytes, laser ablation with high aspect-ratio craters (i.e., deep ablation pit) can induce elemental fractionation during analysis (e.g., down-hole fractionation) (Hirata and Nesbitt 1995; Horn et al. 2000). To obtain reliable abundance data, data acquisition must be made with a minimal number of analytes and short-time duration for the laser ablation.

Several additional techniques can be applied for quantitative analysis. Isotope dilution represents an important choice for elemental determinations. For the LA-ICPMS technique, mixing of analytes and enriched-isotopes can be achieved by mixing of laser-induced aerosols released from a sample and standard, which contains the selected enriched isotopes. This can be achieved by applying galvanometric optics (Fig. 3), which is utilizing a pair of two moving mirrors. The position of the laser ablation can be moved by changing the angle of the mirrors. With galvanometric optics, ablation points can be jumped with a time interval of 10 ms or shorter, and therefore, the simultaneous laser ablation for two or more solid materials

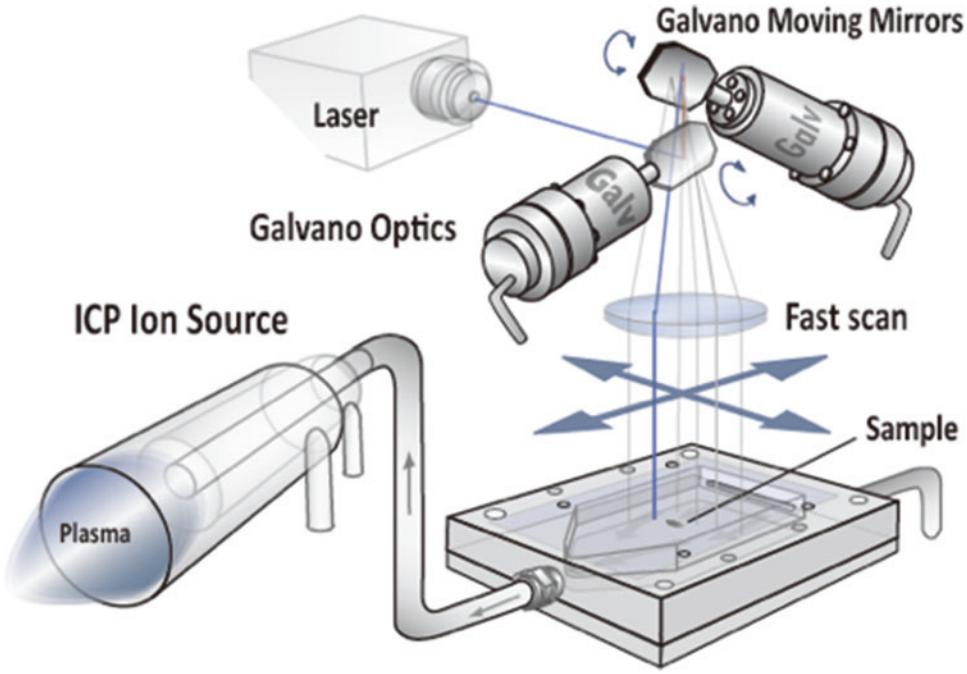

Laser Ablation – Inductively Coupled Plasma Mass Spectrometry,
Fig. 3 Schematic diagram of galvanometric optics for LA-ICPMS. Galvanometric optics consists of two moving mirrors. Ablation points can be moved by adjusting the angle of two mirrors. With the LA system equipped with the galvanometric optics, two or more sample can be ablated nearly at the same time. This suggests that analytes in the different solid materials can be mixed

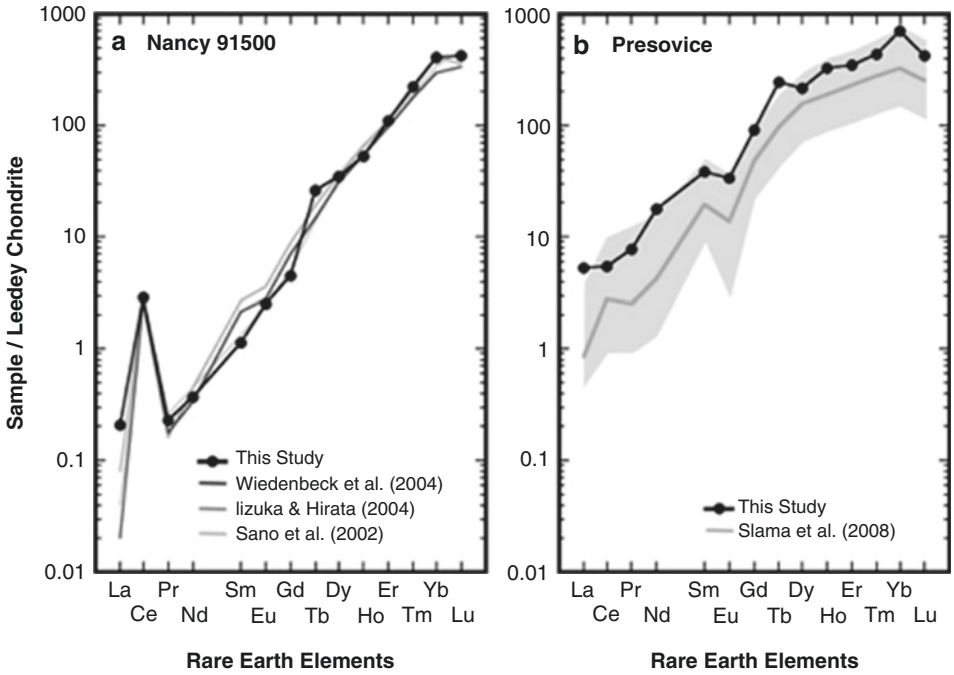

Laser Ablation – Inductively Coupled Plasma Mass Spectrometry,
Fig. 4 Determination of rare earth elements (REE) in zircon samples by means of the standard addition technique. With the galvanometric optics, standard addition technique can be applied for the elemental determinations. The particles released from sample was mixed with the particles released from standard materials, and mixed particles were then introduced into the ICP ion source (Yokoyama et al. 2011)

can be obtained. The sample aerosols released from two or three samples are well mixed in the laser ablation cell, and the mixed aerosols are introduced into the ICP. Based on the signal intensity data for isotopes, the element concentrations can be defined (Fernandez et al. 2008; Heilmann et al. 2009).

With the galvanometric optics, a standard addition method can also be applied by mixing of aerosols released from sample and standard references. The mixing ratio (sample: standard) can be controlled by changing the number of laser shots for each component. Abundances of rare earth elements (REE) in natural zircon samples can be determined by the standard addition technique by mixing of REEs from glass standard material (Fig. 4) (Yokoyama et al. 2011). The galvanometric optics can provide flexible calibration protocols for elemental analysis, where no proper (matrix-matched) calibration standard is available (Fig. 4).

In Situ Isotope Ratio Measurements

Precision and accuracy in isotope ratio measurements can be dramatically improved by the multiple collector system setup adopted in the magnetic sector based ICP-mass spectrometry (MC-ICPMS) (e.g., Albarède et al. 2004; Walczyk 2004). Combination of LA and MC-ICPMS techniques (LA-MC-ICPMS) enables to detect small variations in the isotope ratios of elements in small minerals or inclusions (Iizuka and Hirata 2005; Horn and Blanckenburg 2007; Nishizawa et al. 2010). For in situ isotope ratio measurements, several key parameters, such as size distribution of the aerosols, aspect ratios, aerosol transport efficiencies, ionization efficiencies in the plasma and/or laser-induced isotope fractionation, must be considered to obtain reliable isotope ratio data (Jackson and Günther 2003; Hirata 2012).

Similar to the elemental analysis, advances in laser ablation utilizing shorter wavelength and shorter pulse duration lasers (i.e., femtosecond lasers) provide better analytical results (Guillong et al. 2003; Koch et al. 2006; Russo et al. 2013). With the UV wavelength laser ablation, particle size distribution can be modified toward smaller, and therefore, stable signal intensity profiles. Smoother signal intensity profile is essential for isotope ratio measurements using Faraday collectors caused by slow response of the Faraday amplifier. With unstable or transient signals, the measured isotope ratios can deviate from the accurate ratios (Hirata 2012). To overcome this, analysis of smaller size distribution of the sample particle is important (Guillong and Günther 2002). Introduction of smaller particles results in smaller changes in the plasma conditions, such as kinetic temperature, electron density, or plasma potential. Moreover, with a femtosecond laser ablation, the efficiency of energy transfer from laser photons to electrons in solid samples can be dramatically improved (Hirata and Kon 2008; Poitrasson et al. 2003; Russo et al. 2002). This leads the release of smaller particles from samples. This results in both a stable signal intensity profile and smaller changes in elemental sensitivity and/or mass bias factors for the isotope ratio measurements. With the combination of fs-laser ablation and MC-ICP-MS, a precision of better than 0.1‰ can be achieved for most Fe and Cu-rich materials (e.g., metal, oxide, or sulfide). The resulting precision of the isotope ratio measurements is significantly better than the natural variations in the $^{56}Fe/^{54}Fe$, $^{65}Cu/^{63}Cu$

or $^{98}Mo/^{95}Mo$ ratios (e.g., Horn et al. 2000; Ikehata et al. 2008). The major advantage to use the LA-MC-ICPMS is the reliable and inherent isotopic signature that can be derived from a specific small sample area, avoiding the risk of analysis from secondary growth regions or contaminated areas (e.g., Nishizawa et al. 2010; Yoshiya et al. 2015a, 2015b) (Fig. 5).

In Situ Dating

Applications of several isotope chronometers have been developed by the MC-ICPMS technique comprising the Lu-Hf, Hf-W, and U-Pb isotope chronometers. High ionization efficiency can be achieved by the ICP ion source, and precise and accurate isotopic analyses from small sample size can be obtained by the MC-ICPMS (Thirlwall and Walder 1995; Tiepolo 2003; Iizuka and Hirata 2004, 2005; Snow and Friedrich 2005). Even for more conventional isotope chronometers, such as Rb-Sr, Sm-Nd, and U-Pb dating by TIMS analysis, the MC-ICPMS technique has become a major tool for the measurements as the MC-ICPMS enables a higher sample throughput and simpler chemical separation procedures. In fact, MC-ICPMS has been widely applied for the fast and precise Nd and Hf isotope ratio measurements (e.g., Woodhead 2002; Sims et al. 2008; Be'eri-Shlevin et al. 2010). The ICP-MS technique is now one of the principal methods for isotope analysis for geochronological studies.

For the U-Pb dating method, the isotopic composition of Pb can vary widely due to contribution of radioactive decay of ^{232}Th, ^{235}U, and ^{238}U, by reflecting both the Pb/U and Pb/Th ratios and the age of the samples. Because of small contribution of mass spectrometric interferences onto the Pb, Th, and U isotopes, single collector-based ICP-MS instrument were widely used for the U-Th-Pb age determinations (Hirata and Nesbitt 1995; Crowley et al. 2005; Tiepolo 2003; Simonetti et al. 2005; Cottle et al. 2009; Woodhead et al. 2009; Schaltegger et al. 2015). The resulting precision and accuracy of the U-Th-Pb age determinations can be further improved by a multiple-collector system setup (Jackson et al. 2004). The MC-ICPMS instruments, equipped with a multiple ion counting system setup, can improve the precision of the age determination (Fig. 6), and the data quality achieved by the LA-ICPMS technique is comparable or enhanced compared to those obtained by secondary ion mass spectrometry (SIMS), including SHRIMP-type instruments (Ireland and Williams 2003; Rasmussen et al. 2004; Holden et al. 2009). Moreover, the analysis time for U-Th-Pb age determinations can be significantly reduced by a multiple ion counting system setup to 1–10 sec/spot with shorter analysis time enabling to obtain an age distribution of the zircons collected from a sample (Hattori et al. 2017; O-bayashi et al.

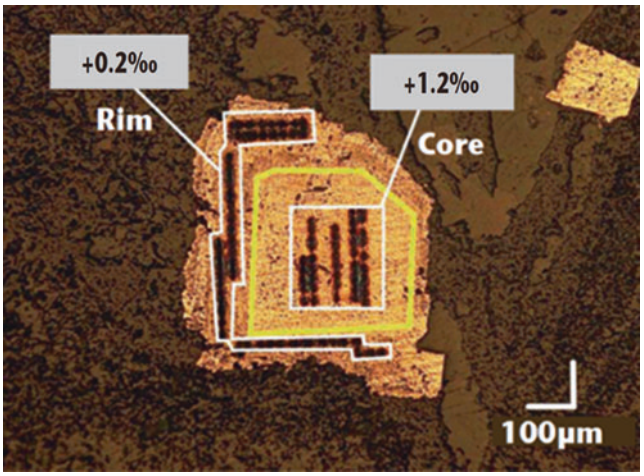

Laser Ablation – Inductively Coupled Plasma Mass Spectrometry, Fig. 5 In situ $^{56}Fe/^{54}Fe$ isotope ratio data obtained from core and rim of the single pyrite grain. Pyrite grain shown here consists of two domains: core and rim. With the LA-MC-ICPMS technique, Fe isotope signature from distinguished can be derived (Nishizawa et al. 2010)

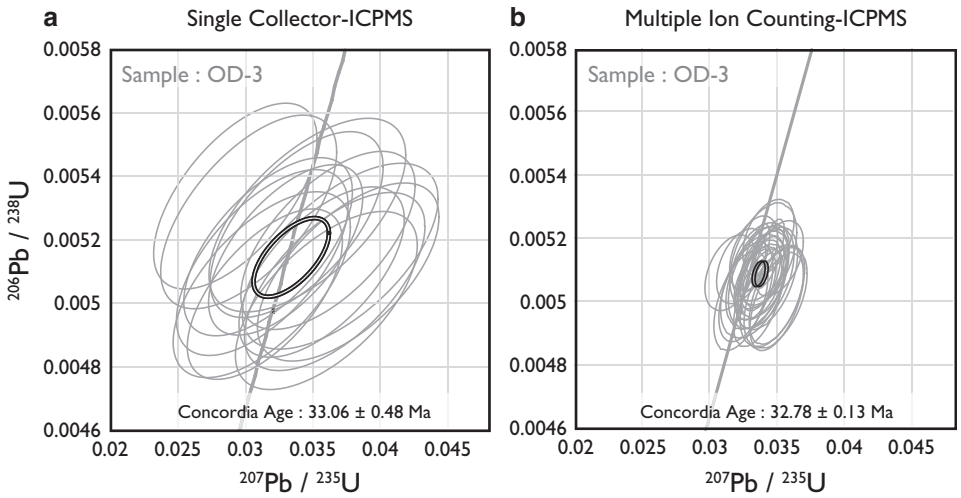

Laser Ablation – Inductively Coupled Plasma Mass Spectrometry, Fig. 6 Comparison in the resulting precision of the Pb/U ratio measurements between single collector-ICPMS and multiple ion counting-ICPMS. With the LA-ICPMS technique combined with multiple ion counting technique, the resulting precision of the U-Pb ages can be dramatically improved. Moreover, total analysis time can be shortened, obviating the laser sampling with high aspect ratio (i.e., deep drilling). Sample is OD-3 standard zircon (Iwano et al. 2013)

2017). This analytical approach allows to decipher the contribution of multiple geological events or multiple sources of the zircons. The "age distribution" is a useful and conventional approach to understand the geological sequence underlying the sample formation. Advantage of the age distribution analysis can be well demonstrated by the growth rate of the continental crust based on the U-Pb ages and Lu-Hf isotope systematics derived from >500 to 20,000 zircon grains (Rino et al. 2004; Iizuka et al. 2006).

With shorter duration time for the laser ablation, the resulting depth of the ablation pit can be smaller than 1 μm, and therefore, age determinations from thin-layer rim of zircon crystal can be made. Schmitt (2011) reported that the U-Th-Pb age derived from the outer rim (<5 μm) of the zircon crystals can reflect the timing of overgrowth through eruption processes (Schmitt 2011). This means that multiple chronological information can be derived from a single zircon grain. With the shorter ablation time achieved by the MC-ICPMS system setup, precise U-Th-Pb ages can be derived from the depth of shallower than 1 μm. This technique can be applied for geochemical evolution processes within magma chambers by determining the difference between crystallization of the zircons and timing of eruption, and thus the U-Th-Pb ages obtained from the rim of zircon crystals can reflect low-temperature geological events (e.g., Rasmussen et al. 2004; Schmitt 2011; Sakata et al. 2017).

Imaging

Images of trace elements or isotopes can provide key information to evaluate the contribution of metamorphic events or movements of elements through secondary heating events. The LA-ICPMS technique is a useful tool to obtain image data of major to trace elements from samples. Elemental and isotope images can be obtained by repeated analysis of line-scanning measurements using the LA-ICPMS technique. Time resolved-signal intensity profile obtained by laser rastering can be converted to a position based-signal intensity profile via the relationship between the rastering rate and the elapsed time. The resulting spatial resolution and the elemental sensitivity is dependent upon several key operational parameters such as size of laser beam, raster rate, and time slice of the data acquisitions (i.e., dwell time for each analytes). Typically laser beam size of 1–100 μm is used for imaging analysis. The LA-ICPMS technique is highly sensitive to determine the abundance of the trace elements (e.g., Ghazi et al. 2002; Durrant 1999; Russo et al. 2013). One of the main advantages to use the LA-ICPMS technique for imaging analysis is that the sample is located under atmospheric pressure, and neither evacuation of the sample housing nor coating with conductive materials is required. Moreover, because of both the minimum sample preparation and the postionization system configurations, the LA-ICPMS technique represents a fast and accurate method for quantitative imaging technique for trace elements from biochemical or geochemical samples (e.g., Jackson et al. 2006; Lobinski et al. 2006; Zoriy et al. 2007; Becker 2007; Becker et al. 2010; Hare et al. 2011; Gordalíza et al. 2011; Konz et al. 2011).

Another important feature of the elemental imaging using the LA-ICPMS technique is the analytical capability for large-sized samples (>10 mm). This is of crucial importance to secure a bridge between the microscopic and macroscopic realm in geochemical studies. The elemental imaging for trace elements is an essential tool to derive inherent information from samples. Figure 7 illustrates an example of the mapping image for ^{57}Fe, ^{60}Ni, ^{103}Rh, ^{178}Hf, ^{182}W, and ^{193}Ir isotopes obtained from calcium and aluminum-rich inclusion (CAIs) in chondrite material, demonstrating a clear difference of the distribution pattern for these isotopes. Difference in the distribution pattern of the isotopes can reflect the cosmochemical features of the elements. Moreover, the images suggest possible contribution of a re-distribution or secondary movement of these elements through heating or weathering. In addition, difference or similarity in the distribution pattern of the elements may provide key information concerning the status of system closure for chronologies.

Several alternative analytical techniques, such as EPMA, SIMS, or μXRF, can be applied for in situ imaging analysis. The SIMS technique allows both high sensitivity and high-spatial resolution (e.g., Chandra and Morrison 1995; McDonnell and Heeren 2007; Becker et al. 2010), whereas the μXRF technique has been recognized as one of the most reliable imaging techniques for the trace elements (Matsuyama et al. 2006; Fukuda et al. 2008; Donner et al. 2011). Despite the unique features of these techniques, they are time-consuming and therefore less suitable for the routine high throughput analysis. More importantly, these techniques are not suitable for imaging analysis for large-sized samples (> 1 mm). The LA-ICPMS technique is likely to become a significant, quantitative, and cost-effective tool for elemental and isotopic imaging, as it is highly user friendly and an efficient method for supplementary in situ imaging.

Summary and Conclusions

The laser ablation-inductively coupled plasma mass spectrometry (LA-ICPMS) technique is widely accepted as one of the most advanced, sensitive, and rapid analytical tools for elemental and isotopic analysis of solid materials. The continuous development of the LA-ICPMS techniques has provided precise elemental and isotopic data. With a better understanding of the mechanism of the laser ablation process, and with a higher elemental sensitivity of the LA-ICPMS technique, the precision of the isotopic ratio

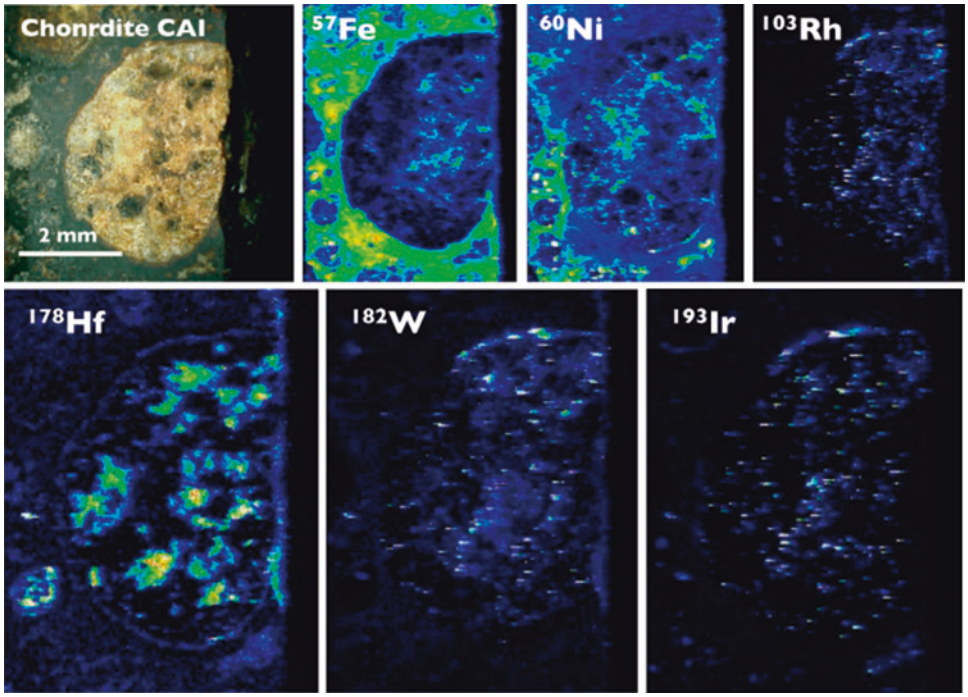

Laser Ablation – Inductively Coupled Plasma Mass Spectrometry, Fig. 7 Isotope imaging for trace elements in CAI. With the LA-ICPMS technique, the elemental and isotopic mapping analyses can be made on various geochemical materials of various sizes (μm scale to mm scale). This is very important to evaluate the contamination, secondary movement of the elements, and/or system closure of the minerals

measurement has successively improved, and new applications were developed in various research fields such as bioscience, material science, and archeological science. Despite its success, it should be noted that there still remain several possible cause for the analytical error such as elemental fractionation occurring during laser ablation, or the limited spatial resolution and elemental sensitivity for the analytes achieved by the LA-ICPMS technique. The complexity in the physical and chemical processes related to the laser ablation of solid samples has prevented a detailed understanding of the elemental and isotopic fractionation induced by laser ablation, and therefore, both the instrumental developments and understanding of further detailed mechanism for the laser ablation would be still a key issue to improve the data quality. Continuous technological developments will enable new analytical methodologies to derive geochemical information from the samples. Based on the rapid growth in analytical capabilities demonstrated in last decade, a realistic prospect is that the LA-ICPMS technique has immediate potential as a reconnaissance method for both the in situ stable isotope geochemistry or isotope chronology. Now the LA-ICPMS technique has evolved into a unique analytical approach, not the alternative choice.

Cross-References

- ▶ Chondrites
- ▶ Geochronology and Radiogenic Isotopes
- ▶ Inductively Coupled Plasma Mass Spectrometry (ICP-MS)
- ▶ Refractory Inclusions in Chondritic Meteorites
- ▶ Stable Isotope Geochemistry
- ▶ Zirconium

References

Albarède F, Telouk P, Blichert-Toft J, Boyet M, Agranier A, Nelson B (2004) Precise and accurate isotopic measurements using multiple-collector ICPMS. Geochim Cosmochim Acta 68:2725–2744

Be'eri-Shlevin Y, Katzir Y, Blichert-Toft J, Kleinhanns IC, Whitehouse MJ (2010) Nd–Sr–Hf–O isotope provinciality in the northernmost Arabian–Nubian shield: implications for crustal evolution. Contrib Mineral Petrol 160:181–201

Becker JS (2007) Inorganic mass spectrometry: principles and applications. Wiley Blackwell and Wiley VCH, New Jersey, United states

Becker JS, Zoriy M, Becker JS, Dobrowolska J, Matusch A (2007) Laser ablation inductively coupled plasma mass spectrometry (LA-ICP-MS) in elemental imaging of biological tissues and in proteomics. J Anal At Spectrom 22:736–744

Becker JS, Breuer U, Hsieh HF, Osterholt T, Kumtabtim U, Wu B, Matusch A, Caruso JA, Qin Z (2010) Bioimaging of metals and biomolecules in mouse heart by laser ablation inductively coupled plasma mass spectrometry and secondary ion mass spectrometry. Anal Chem 82:9528–9533

Chandra S, Morrison GH (1995) Imaging ion and molecular transport at subcellular resolution by secondary ion mass spectrometry. Int J Mass Spectrom 143:161–176

Cottle JM, Hortswood MSA, Parrish RR (2009) A new approach to single shot laser ablation analysis and its application to in situ Pb/U geochronology. J Anal Atom Spectrom 24:1355–1363

Crowley JL, Myers JS, Sylvester PJ, Cox RA (2005) Detrital zircon from the Jack Hills and Mount Narryer, Western Australia: evidence for diverse 14.0 Ga source rocks. J Geol 113:239–263

Donner E, Howard DL, de Jonge MD, Paterson D, Cheah MH, Naidu R, Lombi E (2011) X-ray absorption and micro X-ray fluorescence

spectroscopy investigation of copper and zinc speciation in biosolids. Environ Sci Technol 45:7249–7257
Duckworth HE, Barber RC, Venkatasubramanian LVS (1986) Mass spectroscopy, 2nd edn. Cambridge University Press, Cambridge, MA, 74pp
Durrant JF (1999) Laser ablation inductively coupled mass spectrometry: achievements, problems, prospects. J Anal At Spectrom 12:1385–1403
Fernandez B, Claverie F, Pecheyran C, Alexis J, Donard OFX (2008) Direct determination of trace elements in powdered samples by in-cell isotope dilution femtosecond laser ablation ICPMS. Anal Chem 80:6981–6994
Fricker MB, Kutscher D, Aeschlimann B, Frommer J, Dietiker R, Bettmer J, Günther D (2011) High spatial resolution trace element analysis by LA-ICP-MS using a novel ablation cell for multiple or large samples. Int J Mass Spectrom 307:39–45
Fukuda N, Hokura A, Kitajima N, Terada Y, Saito H, Abe T, Nakai I (2008) Micro X-ray fluorescence imaging and micro X-ray absorption spectroscopy of cadmium hyper-accumulating plant, *Arabidopsis* halleri ssp. gemmifera, using high-energy synchrotron radiation. J Anal At Spectrom 23:1068–1075
Ghazi AM, Wataha CJ, O'Dell NL, Singh BB, Simmons R, Shuttleworth S (2002) Quantitative concentration profiling of nickel in tissues around metal implants: a new biomedical application of laser ablation sector field ICP-MS. J Anal At Spectrom 17:1295–1299
Gordalíza EM, Giesen C, Lázaro A, Fernández DE, Humanes B, Cañas B, Panne U, Tejedor A, Jakubowski A, Gómez-Gómez MM (2011) Elemental bioimaging in kidney by LA-ICP-MS as a tool to study nephrotoxicity and renal protective strategies in cisplatin therapies. Anal Chem 83:7933–7940
Guillong M, Günther D (2002) Effect of particle size distribution on ICP-induced elemental fractionation in laser ablation inductively coupled plasma mass spectrometry. J Anal At Spectrom 17:831–837
Guillong M, Horn I, Günther D (2003) A comparison of 266 nm, 213 nm and 193 nm produced from a single solid state Nd: YAG laser for laser ablation ICP-MS. J Anal At Spectrom 18:1224–1230
Günther D, Hattendolf B (2005) Solid sample analysis using laser ablation inductively coupled plasma mass spectrometry. Trends Anal Chem 24:255–265
Günther D, Frischknecht R, Heinrich C, Kahlert HJ (1997) Capabilities of an argon fluoride 193 nm excimer laser for laser ablation inductively coupled plasma mass spectrometry microanalysis of geological mateirals. J Anal At Spectrom 12:939–944
Hare D, Austin C, Doble P, Arora M (2011) Elemental bio-imaging of trace elements in teeth using laser ablation-inductively coupled plasma-mass spectrometry. J Dent 39:397–403
Hattendorf B, Latkoczy C, Günther D (2003) Laser ablation-ICPMS. Anal Chem 75:341A–347A
Hattori K, Sakata S, Tanaka M, Orihashi Y, Hirata T (2017) U–Pb age determination for zircons using later ablation-ICP-mass spectrometry equipped with six multiple-ion counting detectors. J Anal Atom Spectrom 32:88–95
Heilmann J, Boulyga SF, Heumann KG (2009) Development of an isotope dilution laser ablation ICP-MS method for multi-element determination in crude and fuel oil samples. J Anal At Spectrom 24:385–390
Hirata T (2012) Advances in laser ablation-multi-collector inductively coupled plasma mass spectrometry, Chapter 4. In: Vanhaecke F, Degryse P (eds) Isotopic analysis: fundamentals and applications using ICP-MS. Wiley-VCH Verlag GmbH & Co. KGaA, Somerset, pp 93–112
Hirata T, Kon Y (2008) Evaluation of the analytical capability of NIR femtosecond laser ablation–inductively coupled plasma mass spectrometry. Anal Sci 24:345–353
Hirata T, Miyazaki Z (2007) High-speed camera imaging for laser ablation process: for further reliable elemental analysis using inductively coupled plasma-mass spectrometry. Anal Chem 79:147–152
Hirata T, Nesbitt RW (1995) U–Pb isotope geochronology of zircon: evaluation of the laser probe-inductively coupled plasma mass spectrometry technique. Geochim Cosmochim Acta 59:2491–2500
Holden P, Lanc P, Ireland TR, Harrison TM, Foster JJ, Bruce Z (2009) Mass-spectrometric mining of Hadean zircons by automated SHRIMP multi-collector and single-collector U/Pb zircon age dating: the first 100,000 grains. Int J Mass Spectrom 286:53–63
Horn I, Blanckenburg F (2007) Investigation on elemental and isotopic fractionation during 196 nm femtosecond laser ablation multiple collector inductively coupled plasma mass spectrometry. Spectrochim Acta 62B:410–422
Horn I, Rudnick RL, McDonough WF (2000) Precise elemental and isotope ratio determination by simultaneous solution nebulization and laser ablation-ICP-MS: application to U–Pb geochronology. Chem Geol 164:281–301
Iizuka T, Hirata T (2004) Simultaneous determinations of U-Pb age and REE abundances for zircons using ArF excimer laser ablation-ICPMS. Geochem J 38:229–241
Iizuka T, Hirata T (2005) Improvements of precision and accuracy in in situ Hf isotope microanalysis of zircon using the laser ablation-MC-ICPMS technique. Chem Geol 220:121–137
Iizuka T, Horie K, Komiya T, Maruyama S, Hirata T, Hidaka H, Windley BF (2006) 4.2 Ga zircon xenocryst in an Acasta gneiss from northwestern Canada: evidence for early continental crust. Geology 34:245–248
Ikehata K, Notsu K, Hirata T (2008) In situ determination of Cu isotope ratios in copper-rich materials by NIR femtosecond LA-MC-ICP-MS. J Anal Atom Spectrom 23:1003–1008
Ireland TR, Williams I (2003) Considerations in zircon geochronology by SIMS. In: Hanchar JM, Hoskin PWO (eds) Zircon. Reviews in mineralogy and geochemistry, vol 53. Mineralogical Society of America, Washington, DC, 215–241 pp
Iwano H, Orihashi Y, Hirata T, Ogasawara M, Danhara T, Horie K, Hasebe N, Sueoka S, Tamura A, Hayasaka Y, Katsube A, Ito H, Tani K, Kimura K-J, Chang Q, Kouchi Y, Haruta Y, Yamamoto K (2013) An inter-laboratory evaluation of OD-3 zircon for use as a secondary U–Pb dating standard. Island Arc 22:382–394
Jackson SE, Günther D (2003) The nature and sources of laser-induced isotopic fractionation in laser ablation multicollector inductively coupled plasma mass spectrometry. J Anal At Spectrom 18:205–212
Jackson S, Pearson N, Griffin W, Belousova E (2004) The application of laser ablation-inductively coupled plasma-mass spectrometry to in situ U–Pb zircon geochronology. Chem Geol 211:47–69
Jackson B, Harper S, Smith L, Flinn J (2006) Elemental mapping and quantitative analysis of Cu, Zn, and Fe in rat brain sections by laser ablation ICP-MS. Anal Bioanal Chem 384:951–957
Jochum KP, Nohl U, Herwig K, Lammel E, Stoll B, Hofmann AW (2005) GeoReM: a new geochemical database for reference materials and isotopic standards. Geostand Geoanal Res 29:333–338. https://doi.org/10.1111/j.1751-908X.2005.tb00904.x
Jochum KP, Stoll B, Herwig K, Willbold M, Hofmann AW, Amini M, Aarburg S, Abouchami W, Hellebrand E, Mocek B, Raczek I, Stracke A, Alard O, Bouman C, Becker S, Dücking M, Brätz H, Klemd R, de Bruin D, Canil D, Cornell D, de Hoog CJ, Dalpé C, Danyushevsky L, Eisenhauer A, Gao Y, Snow JE, Groschopf N, Günther D, Latkoczy C, Guillong M, Hauri EH, Höfer HE, Lahaye Y, Horz K, Jacob DE, Kasemann SA, Kent AJR, Ludwig T, Zack T, Mason PRD, Meixner A, Rosner M, Misawa K, Nash BP, Pfänder J, Premo WR, Sun WD, Tiepolo M, Vannucci R, Vennemann T, Wayne D, Woodhead JD (2006) MPI-DING reference glasses for in situ microanalysis: new reference values for element concentrations and isotope ratios. Geochem Geophys Geosyst 7:1–44. https://doi.org/10.1029/2005GC001060

Jochum KP, Stoll B, Herwig K, Willbold M (2007) Validation of LA-ICP-MS trace element analysis of geological glasses using a new solid-state 193 nm Nd: YAG laser and matrix-matched calibration. J Anal At Spectrom 22:112–121

Koch J, Bohlen A, Hergenrer R, Niemax K (2004) Particle size distributions and compositions of aerosols produced by near-IR femto- and nanosecond laser ablation of brass. J Anal At Spectrom 19:267–272

Koch J, Walle M, Pisonero J, Günther D (2006) Performance characteristics of ultra-violet femtosecond laser ablation inductively coupled plasma mass spectrometry at similar to 265 and similar to 200 nm. J Anal At Spectrom 21:932–940

Konz I, Fernandez B, Fernandez ML, Pereiro R, Sanz-Medel A (2011) Absolute quantification of human serum transferrin by species-specific isotope dilution laser ablation ICP-MS. Anal Chem 83:5353–5360

Kozlov B, Saint A, Skroce A (2003) Elemental fractionation in the formation of particulates, as observed by simultaneous isotopes measurement using laser ablation ICP-oa-TOFMS. J Anal At Spectrom 18:1069–1075

Kuhn H, Guillong M, Günther D (2004) Size-related vaporisation and ionisation of laser-induced glass particles in the inductively coupled plasma. Anal Bioanal Chem 378:1069–1074

Lobinski R, Moulin C, Ortega R (2006) Imaging and speciation of trace elements in biological environment. Biochimie 88:1591–1604

Longerich H, Günther D, Jackson S (1996) Elemental fractionation in laser ablation inductively coupled plasma mass spectrometry. Fresenius J Anal Chem 355:538–542

Matsuyama S, Mimura H, Yumoto H, Sano Y, Yamamura K, Yabashi M, Nishino Y, Tamasaku K, Ishikawa T (2006) Development of scanning xray Fuorescence microscope with spatial resolution of 30nm using KirkpatrickBaez mirror optics. Rev Sci Instrum 77:103–102

McDonnell LA, Heeren RMA (2007) Imaging mass spectrometry. Mass Spectrom Rev 26:606–643

Myers AT, Havens RG, Niles WW (1995) Glass reference standards for trace element analysis of geologic materials. Dev Appl Spectrosc 8:132–137pp

Nishizawa M, Yamamoto H, Ueno Y, Tsuruoka S, Shibuya T, Sawaki Y, Yamamoto S, Kon Y, Kitajima K, Komiya T, Maruyama S, Hirata T (2010) Grain-scale iron isotopic distribution of pyrite from Precambrian shallow marine carbonate revealed by femtosecond laser ablation multi-collector ICP-MS technique: potential proxy for the redox state of ancient seawater. Geochim Cosmochim Acta 74:2760–2778

Niu H, Houk RS (1996) Fundamental aspects of ion extraction in inductively coupled plasma mass spectrometry. Spectrochim Acta 51B:779–815

O-bayashi H, Tanaka M, Hattori K, Sakata S, Hirata T (2017) In-situ $^{207}Pb/^{206}Pb$ isotope ratio measurement using dual-daly ion counting ICP-mass spectrometer. J Anal Atom Spectrom 32:686–691

Pearce NJG, Perkins WT, Westgate JA, Gorton MP, Jackson SE, Neal CR, Chenery SP (1997) A compilation of new and published major and trace element data for NIST SRM 610 and NIST SRM 612 glass reference materials. J Geostand Geoanal 21:115–144

Poitrasson F, Mao X, Mao SS, Freydier R, Russo RE (2003) Comparison of ultraviolet femtosecond and nanosecond laser ablation inductively coupled plasma mass spectrometry analysis in glass, monazite, and zircon. Anal Chem 75:6184–6190

Rasmussen B, Fletcher IR, Bengtson S, McNaughton NJ (2004) SHRIMP U–Pb dating of diagenetic xenotime in the Stirling Range Formation, Western Australia: 1.8 billion year minimum age for the Stirling biota. Precambrian Res 133:329–337. https://doi.org/10.1016/j.precamres.2004.05.008

Rino S, Komiya T, Windley BF, Katayama I, Motoki A, Hirata T (2004) Major episodic increases of continental crustal growth determined from zircon ages of river sands: implications for mantle overturns in the early Precambrian. Phys Earth Planet Inter 146:369–394

Russo RE, Mao XL, Gonzalez J, Mao SS (2002) Femtosecond laser ablation. J Anal Atom Spectrom 17:1072–1075

Russo RE, Mao X, Gonzalez JJ, Zorba V, Yoo J (2013) Laser ablation in analytical chemistry. Anal Chem 85:6162–6177

Sakata S, Hirakawa S, Iwano H, Danhara T, Guillong M, Hirata T (2017) A new approach for constraining the magnitude of initial disequilibrium in Quaternary zircons by coupled uranium and thorium decay series dating. Quat Geochronol 38:1–12

Schaltegger U, Schmitt K, Horstwood MSA (2015) U–Th–Pb zircon geochronology by ID-TIMS, SIMS, and laser ablation ICP-MS: recipes, interpretations, and opportunities. Chem Geol 402:89–110

Schmitt AK (2011) Uranium series accessory crystal dating of magmatic processes. Annu Rev Earth Planet Sci 39:321–349

Simonetti A, Heaman LM, Hartlaub RP, Creaser RA, MacHattie TG, Böhm C (2005) U–Pb zircon dating by laser ablation-MC-ICP-MS using a new multiple ion counting Faraday collector array. J Anal Atom Spectrom 20:677–686

Sims KWW, Blichert-Toft J, Kyle PR, Pichat S, Gauthier PJ, Blusztajn J, Kelly P, Ball L, Layne G (2008) A Sr, Nd, Hf, and Pb isotope perspective on the genesis and long-term evolution of alkaline magmas from Erebus Volcano, Antarctica. J Volcanol Geotherm Res 177:606–618

Snow JE, Friedrich JM (2005) Multiple in counting ICPMS double spike method for precise U isotopic analysis at ultra-trace levels. Int J Mass Spectrom 242:211–215

Thirlwall MF, Walder AJ (1995) In situ hafnium isotope ratio analysis of zircon by inductively coupled plasma multiple collector mass spectrometry. Chem Geol 122:241–247

Tiepolo M (2003) In situ Pb geochronology of zircon with laser ablation-inductively coupled plasma-sector field mass spectrometry. Chem Geol 199:159–177

Walczyk T (2004) TIMS versus multicollector-ICP-MS: coexistence or struggle for survival? Anal Bioanal Chem 378:229–231

Weiss Y, Griffin WL, Elhlou S, Navon O (2008) Comparison between LA-ICP-MS and EPMA analysis of trace elements in diamonds. Chem Geol 252:158–168

Wieser ME, Schwieters JB (2005) The development of multiple collector mass spectrometry for isotope ratio measurements. Int J Mass Spec 242:97–115

Woodhead JD (2002) A simple method for obtaining highly accurate, Pb isotope data by MC-ICPMS. J Anal At Spectrom 17:1381–1385

Woodhead J, Hergt J, Meffre S, Large RR, Danyushevsky L, Gilbert S (2009) In situ Pb-isotope analysis of pyrite by laser ablation (multi-collector and quadrupole) ICPMS. Chem Geol 262:344–354

Yokoyama TD, Suzuki T, Kon Y, Hirata T (2011) Determinations of REE abundance and U-Pb age of zircons using multispot laser ablation-ICP-mass spectrometry. Anal Chem 83:8892–8899

YongSheng L, ZhaoChu H, Ming L, Shan G (2013) Applications of LA-ICP-MS in the elemental analyses of geological samples. Chin Sci Bull 58:3863–3878

Yoshiya K, Sawaki Y, Hirata T, Maruyama S, Komiya T (2015a) In-situ iron isotope analyses of pyrites from 3.5 to 3.2 Ga sedimentary rocks of the Barberton Greenstone Belt, Kaapvaal craton. Chem Geol 401:126–139

Yoshiya K, Sawaki Y, Shibuya T, Yamamoto S, Komiya T, Hirata T, Maruyama S (2015b) In-situ iron isotope analyses of pyrites from 3.5 to 3.2 Ga sedimentary rocks of the Barberton Greenstone Belt, Kaapvaal Craton. Chem Geol 403:58–73

Zeng X, Mao XL, Greif R, Russo RE (2004) Experimental investigation of ablation efficiency and plasma expansion during femtosecond and nanosecond laser ablation of silicon. Appl Phys A. https://doi.org/10.1007/s00339-004-2963-9

Zoriy M, Becker JS, Dobrowolska J, Matusch A (2007) Laser ablation inductively coupled plasma mass spectrometry (LA-ICP-MS) in elemental imaging of biological tissues and in proteomics. J Anal At Spectrom 22:736–744

Lead

Dominique Weis
Pacific Centre for Isotopic and Geochemical Research, Earth, Ocean and Atmospheric Sciences, University of British Columbia, Vancouver, BC, Canada

Element Data
Atomic Symbol: Pb
Atomic Number: 82
Atomic Weight: 207.2 g/mol
Isotopes and Abundances: ^{204}Pb 1.4%, ^{206}Pb 24.1%, ^{207}Pb 22.1%, ^{208}Pb 52.10%
^{210}Pb traces, radioactive ($t_{1/2} > 22.3$ yr)
^{205}Pb synthetic
1 Atm Melting Point: 327.5 °C
1 Atm Boiling Point: 1749 °C
Common Valences: 2+, 4+
Ionic Radii: 116 pm and 129, in 6-fold and 8-fold coordination respectively
Pauling Electronegativity: 2.33
First Ionization Potential: 715.6 kj/mol
Chondritic (CI) Abundance: 1–2.4 ppm
Silicate Earth Abundance: ~0.1–0.2 ppm
Crustal Abundance: 14 ppm
Seawater Abundance: 0.03 ppb
Core Abundance: ~0.5 ppm

Properties

Because it has a "magic number" of protons (82), the lead nucleus is particularly stable and is the end product of three separate radioactive decays. The most common valence state of lead is +2, with the +4 valence state being less stable.

Lead belongs to group 14 in the periodic table that together with C, Si, Ge, and Sn shows different chemical properties.

Lead can be sometimes found free in nature, but is mostly mined from the ores galena (PbS), anglesite ($PbSO_4$), cerussite ($PbCO_3$), and minum (Pb_3O_4). Lead is easily mined and refined, and is not considered to be a rare element, even with an abundance of only about 0.0014% in the Earth's crust. Most lead has been obtained by roasting galena in hot air, although more recently, nearly one third of the lead used in the United States is derived through recycling efforts.

History and Use

Together with tin (also a member of group 14), lead has been known since the antiquity. The two letters for the symbol for lead come from the Latin name: plumbum (i.e., waterworks). It is a soft, malleable, and corrosion-resistant material, easily worked into sheets. There is evidence for its use going back almost 6000 years. Hippocrates and Pliny already documented evidence of lead poisoning (Hernberg 2000). The ancient Romans used lead to make water pipes, some of which are still in use today. Because lead is a cumulative poison, the decline of the Roman Empire has been blamed, in part, on lead in the water supply (Nriagu 1983; Delile et al. 2014).

Even if the lead abundance in the Earth's crust is relatively low, lead has been mined for centuries and disseminated throughout the environment; living organisms gradually have incorporated it in their tissues, where it accumulates.

Lead is used to line tanks that store corrosive liquids, such as sulfuric acid (H_2SO_4). Lead's high density makes it useful as a shield against X-ray and gamma-ray radiation, and it is used in X-ray machines and nuclear reactors. Lead is also used as a covering on some wires and cables to protect them from corrosion, as a material to absorb vibrations and sounds and in the manufacture of ammunition. Most of the lead used today is used in the production of lead-acid storage batteries as lead dioxide (PbO_2), such as the batteries found in automobiles.

Lead also forms alloys, several of which are widely used. Conventional solder is an alloy consisting of nearly 50% lead and 50% tin that has a relatively low melting point and is used to join electrical components, pipes, and other metallic items. Type metal is an alloy made of lead, tin, and antimony used to make the type used in printing presses and plates. Babbitt metal, another lead alloy, is used to reduce friction in bearings.

Lead forms many useful compounds that have been used extensively through the years. Litharge is lead monoxide (PbO) and a yellow solid used to make some types of glass, such as lead crystal and flint glass, in the vulcanizing of rubber and as a paint pigment. Lead compounds have been used in various types of paints. The use of lead carbonate in paints has largely been stopped in favor of titanium oxide (TiO_2).

Lead arsenate ($Pb_3(AsO_4)_2$) has been used as an insecticide although other, less harmful, substances have now largely replaced it. Lead nitrate ($Pb(NO_3)_2$) is used to make fireworks and other pyrotechnics. Lead silicate ($PbSiO_3$) is used to make some types of glass and in the production of rubber and paints.

To improve combustion, lead has been used in petrol as an antiknock additive in the form of tetraethyl lead (TEL) and tetramethyl lead (TML). This has represented one of the most

dispersive sources of lead into the environment and into humans because the tiny particle size ensures efficient pulmonary penetration and adsorption. Increased levels of petrol lead can be traced all the way into the Arctic and Antarctica. This source of lead into the environment has been drastically reduced over the years, since the introduction of catalytic converters (1975 in the United States, 1990 in France, 1993 in the United Kingdom) that could not operate with leaded gasoline.

Clair C. Patterson, while working on Pb isotope systematics to establish the absolute age of the Earth in the mid-1960s, discovered the extent of Pb pollution related to its use as an antiknock additive in gasoline (Patterson 1965). He went on a campaign, both in the United States and internationally to quantify the issue, including by coring ice sheets in Greenland and Antarctica and documenting that recent human bones had lead levels much higher (by 1000 times) than the *Homo sapiens sapiens* (Patterson et al. 1991).

Geochemical Behavior

Lead is a relatively volatile element, so it is anticipated that its concentration in the Earth is lower than in chondrites. Lead is a chalcophile element, and it is possible that if the core contains S, it might also contain some Pb. Due to lead's relatively large ionic size, it is an incompatible element, in the range of the incompatibility of the rare Earth elements and not as much as Th or U. Galena is the most common Pb mineral, whereas in silicates, Pb can substitute for K, especially in alkali feldspar.

The element concentration of Pb has been used to constrain the composition and evolution of the Earth's mantle. Most mantle-derived rocks (OIB and MORB) have uniform Ce/Pb ratios ~ 25 that are different from bulk Earth values and also significantly higher than in the continental crust. This indicates that the mantle source of OIB (and MORB) cannot be primitive (Hofmann et al. 1986).

The distribution of Pb in the oceans, together with Al, is distinctive as these two elements are depleted in deep waters relative to surface waters. Studies of the fate of Pb in the open-ocean environments can be used to model ocean metal transport and reactivity (Pb has a high particle reactivity and is scavenged onto particles). In addition, because of Pb high volatility, especially at high temperatures, anthropogenic uses have distributed Pb everywhere on the planet and also in the world oceans (Boyle et al. 2014). With Pb isotope distinctive fingerprinting capability, it is possible to trace the source of contamination and build circulation models and pollutant pathways.

Lead isotopes are extremely useful in geochronology and geochemistry. Three decay systems (^{232}Th,^{238}U, and^{235}U) end in three different Pb isotopes, respectively,^{208}Pb,^{206}Pb, and^{207}Pb. This makes the dating of zircon, a very resistant mineral on Earth, one of the powerful geochronometer available to date geological events in a distant past. With the combination of three isotopic ratios and the recent improvements in analytical techniques allowing to measure isotopic compositions with a better precision, Pb isotopes constitute a powerful tracer in mantle geochemistry, in crustal and planetary evolution.

Biological Utilization and Toxicity

Lead is the only metal, among the six principal pollutants for which the EPA has established NAAQS (National Ambient Air Quality Standards): the limit not to be exceeded is 0.15 μg/m^3. Lead has no known biological role; however, as it can accumulate in the body, it can cause serious health problems.

High lead levels in the human body have been shown to generate many negative health outcomes: (1) effects on the nervous system (decline in cognitive functions, symptoms of depressive disorder, general anxiety disorder), especially for children (low IQ, loss of memory, decrease in academic performance, hyperactivity, inattention); (2) cardiovascular effects such as hypertension and increased blood pressure and subclinical artherosclerosis; (3) effects on the hematologic system with alteration of various blood parameters including heme synthesis; (4) and developmental and reproductive effects, with early birth and associated low birth weight and delayed onset of puberty in males and females.

The major sources of lead in urban environment are: (a) Homes built before 1978 (date when lead-based paints were banned) probably contain lead-based paint. Children are especially susceptible to this source of pollution, as when the paint dries and peels, it cracks and makes lead dust that can be swallowed or inhaled by children. (b) Certain water pipes may contain lead, or are made of lead, especially in houses built before the 1970s. The main risk for contamination here depends on the hardness of the water, as it will form a layer of protective lime deposits in the pipes that will isolate the lead from the water. (c) Lead can be found in some products, such as toys and toy jewelry; recent exposures have occurred with toys produced in countries with less control. (d) Lead has been found in some traditional home remedies or makeup. (e) Certain jobs involve working with lead-based products like smelting, stain glass work, and other activities where lead cannot be replaced by another metal.

The recent crisis of Pb contamination in Flint, Michigan, was related to a change in water supply. Depending on the type of water, Pb can be remobilized from previously contaminated sites or simply from piping if the water stagnates

too long. This also leads to an investigation at the national level by *USA Today* that documented a large number of water systems with significantly too high lead contamination. The EPA stresses that there is no safe level of lead exposure.

Summary

Humans have mined, smelted, and used Pb since ancient times, but its high toxicity very much compromises its value and it is being phased out in many applications. Particularly because of its radiogenic nature and one of the end product of three decay systems, it remains among the most useful of elements in geochemistry.

Cross-References

- ▶ Chalcophile Elements
- ▶ Chondrites
- ▶ Earth's Continental Crust
- ▶ Formation and Evolution of the Earth
- ▶ Geochronology and Radiogenic Isotopes
- ▶ Incompatible Elements
- ▶ Lead Isotopes
- ▶ Mantle Geochemistry
- ▶ Thorium
- ▶ Uranium

References

Boyle EA et al (2014) Anthropogenic lead emissions in the ocean: the evolving global experiment. Oceanography 27(1):69–75. https://doi.org/10.5670/oceanog.2014.10

Delile H, Blichert-Toft J, Goiran JP, Keay S, Albarède F (2014) Lead in ancient Rome's city waters. Proc Natl Acad Sci. https://doi.org/10.1073/pnas.1400097111

EPA. Integrated science assessment for lead (Third external review draft – November 2012). EPA/600/R-10/075C

Hernberg S (2000) Lead poisoning in a historical perspective. Am J Ind Med 38:244–254

Hofmann AW, Jochum K, Seufert M, White WM (1986) Nb and Pb in oceanic basalts – new constraints on mantle evolution. Earth Planet Sci Lett 79:33–45

Nriagu JO (1983) Lead and lead poisoning in antiquity. Wiley, New York

Patterson CC (1965) Contaminated and natural lead environments of man. Arch Environ Health 11(3):344–360

Patterson C, Ericson J, Manea-Krichten M, Shirahata H (1991) Natural skeletal levels of lead in Homo sapiens sapiens uncontaminated by technological lead. Sci Total Environ 107:205–236. https://doi.org/10.1016/0048-9697(91)90260-L

USA Today

http://www.usatoday.com/story/news/2016/03/11/nearly-2000-water-systems-fail-lead-tests/81220466/; http://www.usatoday.com/story/news/nation/2016/03/16/what-lead-levels-in-water-mean/81534336/

Lead Isotopes

Dominique Weis
Pacific Centre for Isotopic and Geochemical Research, Earth, Ocean and Atmospheric Sciences, University of British Columbia, Vancouver, BC, Canada

Introduction

Isotopic ratios of Pb are key geochemical tracers for unraveling the compositional evolution of the solar system, the Earth, and the continental crust, and are an important geochronometer with many different applications.

Lead has of four naturally occurring stable isotopes, ^{204}Pb (1.4%), ^{206}Pb (24.1%), ^{207}Pb (22.1%), and ^{208}Pb (52.10%). ^{204}Pb is non-radiogenic; the latter three are the final decay products of the three decay chains from uranium (^{238}U and ^{235}U) and thorium (^{232}Th), where all the intermediate members of each series have relatively short half-lives and can be ignored on long geological timescales (tens millions of years). Some of the U decay series and ^{230}Th decay present applications for shorter time periods (i.e., volcanic eruption, sedimentation at the bottom of the oceans, coral dating).

^{238}U has a half-life comparable to the age of the Earth, i.e., 4.47 Ga, whereas ^{235}U half-life is much shorter, 0.704 Ga, and as a result, almost all the original ^{235}U present in the Earth at its formation has now decayed into ^{207}Pb. This means that there are minimal relative variations in ^{207}Pb over the last 1.5–2 Ga. ^{232}Th has a half-life (14.01 Ga) comparable to the age of the universe. In addition, ^{210}Pb is a member of the ^{238}U decay chain and has a half-life of 22.2 years.

Lead isotopes were used very early in the development of isotopic analyses to determine the age of the meteorites and the Earth (Patterson 1956). It is also while measuring lead isotopic compositions of various Earth materials that Patterson discovered the extent of Pb contamination the Pb tetraethyl added to gasoline as an antiknock agent (e.g. Patterson 1965). From the human health perspective, this was a very important discovery as Pb accumulates in organisms and has many negative health outcomes, especially on the neurological system. His work eventually led to the removal of Pb from gasoline, paints, and other products.

Pb Isotope Ratio Determinations

Lead is chemically isolated from other elements by cation exchange chromatography, except when it is extracted from galena where it represents 82% of the mineral. Lead isotope ratios have been measured by thermal ionization mass

spectrometry (TIMS) or by multi-collector inductively coupled mass spectrometry (MC-ICPMS). During ionization and transmission through the mass spectrometer, as observed for other isotopic systems, the lead isotope ratios fractionate differentially from the true value as a function of the relative isotope masses. In contrast to other radiogenic systems, such as Sr, Nd, and Hf isotopes, where a stable isotope ratio is available to measure the extent of fractionation, only one isotope is not radiogenic in the case of the Pb system. Lead isotopic compositions have been measured on TIMS instruments for about half a century, and fractionation is monitored by repeated analysis of a Pb standard, such as SRM-981 or SRM-982 (Catazanro et al. 1969) under conditions comparable to those of the samples (especially temperature). This led to precision of about 1.2–1.5 permil for $^{208}Pb/^{204}Pb$, $^{207}Pb/^{204}Pb$, and $^{206}Pb/^{204}Pb$. With time, the addition of double or triple spike allowed for better precision to be achieved (e.g., Galer 1999), but it is only with the development of MC-ICP-MS that precision could be improved by a factor of 10, with doping with a Tl standard allowing for fractionation correction on the basis of $^{205}Tl/^{203}Tl$ (White et al. 2000). Depending on the matrix of the samples, typically two separations through columns are necessary (Nobre Silva et al. 2009). When data from different laboratories are compared, care should be taken that measurements are normalized to the same standard value to avoid interlaboratory bias, and when MC-ICP-MS instruments are used, it is also important to analyze reference materials with comparable matrix (Weis et al. 2006; Fourny et al. 2016).

Geochronology

When discussing Pb isotopic compositions, one usually distinguishes two systems: (a) radiogenic-rich system where the mineral (zircon, titanite, monazite, apatite) has high U and/or Th concentrations and where (b) decay through time generates very radiogenic Pb isotopic compositions (i.e., very high $^{208}Pb/^{204}Pb$, $^{207}Pb/^{204}Pb$, $^{206}Pb/^{204}Pb$) and "common lead" when the Pb isotopic compositions are representative of the source of the rock or mineral, with minimal growth by radioactive decay. These two systems represent two very different applications of Pb isotopic compositions: the radiogenic systems represent a powerful dating tool, providing in many cases the most accurate and precise ages, while common lead has proved extremely useful in tracer geochemistry to model the evolution of Earth's reservoirs.

The ^{238}U-^{206}Pb, ^{235}U-^{207}Pb, and ^{232}Th-^{208}Pb decay systems

For a closed system where the parent and daughter isotopes remain undisturbed from any process other than radioactive decay, the Pb ratios will increase over time due to the decay of ^{238}U, ^{235}U, and ^{232}Th to ^{206}Pb, ^{207}Pb, and ^{208}Pb, respectively, according to the decay equation:

$$\frac{^{206}Pb}{^{204}Pb} = \left(\frac{^{206}Pb}{^{204}Pb}\right)_i + \frac{^{238}U}{^{204}Pb}\left(e^{\lambda_{238U}t} - 1\right), \quad (1)$$

where $^{206}Pb/^{204}Pb$ is the measured isotope ratio of the sample (so-called present-day), $^{238}U/^{204}Pb$ is the measured parent-daughter ratio, $(^{206}Pb/^{204}Pb)_i$ is the initial ratio of the sample at the time where the U-Th-Pb system became closed to elemental and mass exchange, t is the time since system closure, and $\lambda^{238}U$ is the decay constant of ^{238}U.

Comparable equations can be written for both the ^{235}U-^{207}Pb (Eq. 2) and ^{232}Th-^{208}Pb (Eq. 3) decay systems and three isotopic ratios can then be combined.

Uranium- and Thorium-rich ystems

In this case, the initial "common" Pb, if not negligible, is much less abundant than the radiogenic Pb and can be subtracted from the radiogenic Pb. One can then write

$$\frac{^{206}Pb*}{^{238}U} = e^{\lambda_{238U}t} - 1 \quad (4)$$

$$\text{where } \frac{^{206}Pb*}{^{238}U} = \frac{^{206}Pb/^{204}Pb - \left(^{206}Pb/^{204}Pb\right)_0}{^{238}U/^{204}Pb} \quad (5)$$

and the asterisk denotes only the radiogenic Pb produced since time t.

A comparable equation can be written for ^{235}U and ^{207}Pb (Eq. 5).

In the case of U-bearing mineral that behaved as a closed system (for U and all its intermediate decay products) since its crystallization, it will provide a "concordant" age in the two U-Pb systems, which is to say that the ^{238}U-^{206}Pb age equals the ^{235}U-^{207}Pb age. In addition, one can also calculate a 207-206 age by combining the two systems (Eqs. 4 and 5):

$$\frac{^{207}Pb/^{204}Pb - \left(^{207}Pb/^{204}Pb\right)_0}{^{206}Pb/^{204}Pb - \left(^{206}Pb/^{204}Pb\right)_0} = \frac{^{207}Pb*}{^{206}Pb*} = \left(\frac{^{235}U}{^{238}U}\right)\frac{e^{\lambda_{235U}t} - 1}{e^{\lambda_{238U}t} - 1}, \quad (6)$$

The age obtained from this equation will be concordant with those of Eqs. (4 and 5) in the case of a closed system and in a diagram of $^{206}Pb^*/^{238}U$ vs $^{207}Pb^*/^{235}U$, where all concordant ages plot along a curve that Wetherill (1956) called "concordia."

Recently, the potential of in situ U-Pb dating by laser ablation, coupled to either an ICP-MS (HR-ICP-MS or quadrupole) or an MC-ICP-MS, has opened new avenues of research and allowed for a expansion of applications of this robust dating technique, especially on the mineral zircon.

Uranium-poor Systems

When the natural system lacks U and Th, as does the mineral galena (PbS), the Pb isotopic composition of the mineral does not change after crystallization of the mineral and corresponds to the initial composition. In such systems, one can apply the "common lead" method, based on the evolution of Pb in a given system since the origin of the Earth (age T) until the time (t) where Pb is extracted and separated from its radiogenic parents U and Th.

The method was developed by Nier (1938, 1939) who reported systematic variations of Pb isotopic compositions in galena from different geological settings, and Gerling (1942), Holmes (1946), and Houtermans (1946) developed independently models for the evolution of Pb at the scale of the Earth.

$$\begin{aligned}\left(\frac{^{206}Pb}{^{204}Pb}\right)_t &= \left(\frac{^{206}Pb}{^{204}Pb}\right)_0 + \frac{^{238}U}{^{204}Pb}\left(e^{\lambda_{238U}T} - 1\right) \\ &\quad - \frac{^{238}U}{^{204}Pb}\left(e^{\lambda_{238U}t} - 1\right) \\ &= \left(\frac{^{206}Pb}{^{204}Pb}\right)_0 + \frac{^{238}U}{^{204}Pb}\left(e^{\lambda_{238U}T} - e^{\lambda_{238U}t}\right), \qquad (7)\end{aligned}$$

The same equations can be developed for ^{207}Pb and ^{208}Pb. In these equations, T is the age of the Earth, and t corresponds to the time elapsed since removal of a common Pb sample from its source.

Combining these equations leads to very interesting applications, including the first absolute value for the age of the Earth (Patterson 1956) or the common lead dating method: modern single-stage leads in Earth and meteorites (with $t = 0$) define a line, called the geochron, that originates from the Canyon Diablo troilite composition, the primordial Pb isotopic composition of the Earth. Patterson had the brilliant idea to analyze a series of meteorites (three stony meteorites, two iron meteorites with the Canyon Diablo troilite being the least radiogenic compositions measured) and a sample of recent oceanic sediment (representative of the bulk Earth Pb isotopic composition); they all plotted on one Pb-Pb line, giving an age of 4.55 Ga.

All single-stage leads that were removed from their sources at the same time t will lie on a straight line (isochron) in the Pb-Pb diagram.

In nature, there are also intermediary systems, where both U and Th decay into their relative Pb isotopes through time, however in case of a closed system, in a Pb-Pb plot, the equation of the slope will always be proportional to t.

In such a diagram, and because such a diagram and because we are dealing with only one chemical element, mixing between two end-members with different and homogeneous isotopic compositions will also generate a straight line.

Dating of Ancient Rocks

Pb-Pb whole rock dating methods depend only on isotopic compositions and are therefore less sensitive to element mobility compared to other dating methods. Extensive use of Pb-Pb dating was therefore applied to Archean rocks, especially in the North Atlantic Province (Taylor et al. 1980).

Dating of Meteorites

Lead isotope dating systematics have also been applied to extraterrestrial material, such as meteorites (pioneer work of Patterson 1956), and more recently to other planetary bodies such as Mars and the Moon (e.g., Bouvier et al. 2009).

Crust-Mantle Evolution

Typical lower continental crust and upper continental crust are represented by lower crustal xenoliths and modern marine sediments, respectively (these somewhat underestimate the total variance in these reservoirs). MORB and oceanic islands represent the isotopic composition of upper mantle and deep mantle, respectively (Fig. 1).

Lead Isotope Applications

Oceanic Basalts, Implications for Mantle Evolution

In 1964, the analyses of basalts from Gough and Ascension islands provided the first evidence of heterogeneity of the oceanic mantle (Gast et al. 1964). This represented an important milestone in geochemistry as, conventional wisdom was that the mantle was homogeneous. Further work (e.g., Tastumoto 1978), on other oceanic islands, also provided another fundamental observation; most of their Pb isotopic compositions were more radiogenic than the geochron (i.e., had future ages in single-stage history) (Fig. 1). This led to the so-called "Pb paradox" (e.g., Hofmann 2003). Recent volcanic rocks from various areas, including those from subduction zones, define linear trends in Pb isotopic diagrams; these trends have been interpreted as mixing trends between two end-members (among different reservoirs in the Earth's mantle, the mantle and oceanic crust, the mantle and the continental crust), as the age corresponding to the slope of these trends does not have direct age significance. Pb isotopic systematics in mantle-derived rocks also formed the basis, together with Sr and Nd, for the model by Hofmann and

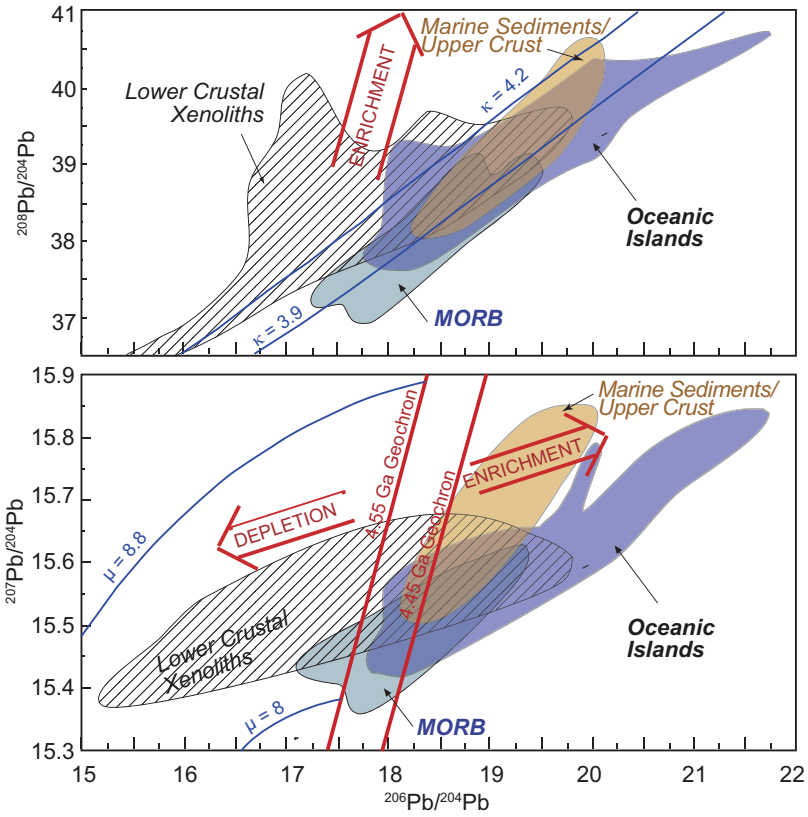

Lead Isotopes, Fig. 1 Pb isotope ratios in major terrestrial reservoirs (Modified from W.M. White 2013). The evolution *blue* curves correspond to the values of κ ($^{232}Th/^{238}U$) and μ ($^{238}U/^{204}Pb$), respectively. All points having evolved in a closed system since the origin of the Earth lie on the geochron

White (1980) suggesting that recycled subducted oceanic crust plays a role in mantle evolution. Recent work on oceanic islands with much improved precision (e.g., Abouchami et al. 2005; Weis et al. 2011) or with in situ techniques (Saal et al. 2005) document much finer scale variations in Pb isotopic compositions that are tentatively attributed to the presence of different reservoirs deep in the Earth mantle, at the core-mantle boundary, with material brought to the surface via a mantle plume.

Continental Crust Growth, Episodic or Recycling

One of the first applications of Pb isotopes was through the analyses of galena, a Pb sulfide where there is no U, and as a result, the Pb isotopic composition is frozen at the time of crystallization of the mineral. This is where Eq. 7 comes into play.

Initially, single-stage models were developed (e.g., Holmes-Houtermans model), however scientists quickly realized that in light of the complexity of the Earth's evolution, it was physically impossible for the host rocks of galena to have been a closed system since the formation of the Earth. More complex systems were developed, with either evolving U/Pb ratios different between the crust and the mantle, or with continental crust evolution in two stages with a major event at 3.7 Ga (Stacey and Kramers 1975). The 1970s and 1980s showed the development of numerous models of crust evolution, with the involvement of various reservoirs with a given U/Pb ratio. There were also strong debates about the role of recycling of Pb between the crust and the mantle (see Armstrong 1968). Doe and Zartman (1979) developed a computer model for the Pb evolution of the Earth with three reservoirs: the upper crust with the highest U/Pb ratio, the lower crust with the lowest U/Pb ratio, and the upper mantle (with an intermediate U/Pb ratio). They argued that crustal accretion began earlier in the Earth evolution and that orogenies mixed mantle and crustal sources, with a U/Pb ratio in between the upper crust and the mantle.

The mineral galena is very common in various rock types. Galena Pb isotopic compositions have been used over the past four or five decades, in models of continental growth, in the sourcing of metals in mineral deposits, and as a geochemical "fingerprint" for distinguishing between different styles of mineralization in a district.

Environmental Applications

Tracing Pb Pollution

Tetraethyl Pb has been used since the early part of the twentieth century as an antiknock additive in gasoline. The amount of Pb that has been released into the atmosphere and then deposited into the environment reached astronomical levels (by 1965, up to 2.6 M tons). Patterson (1980) is the scientist who alerted the world to the widespread distribution of Pb into the environment as well as to the dangers of long-term exposure to Pb. Patterson and colleagues worked for decades

to document the source of anthropogenic Pb via isotopic analyses of soils, seawater, and snow/ice. The fingerprinting was relatively straightforward as the source of the Pb added to gasoline had very distinctive isotopic compositions. In the USA, Pb was extracted from galena-sphalerite depositions of the Mississippi Valley (Heyl et al. 1974); in Europe and Australia, Pb was extracted from the Broken Hill ore deposit characterized by very unradiogenic isotopic compositions.

Anthropogenic contributions of Pb also came from paint, lead smelters, metal manufacturing plants, waste incinerators, and batteries. See element Pb entry.

Seawater

When it became possible to isolate natural Pb from anthropogenic Pb (see review in Boyle et al. 2014), some fundamental applications were developed for Pb isotopes in seawater (i.e., Paul et al. 2015) and other reservoirs where Pb concentrations are very low.

Summary

Lead is present in detectable (i.e., measurable) quantities in many common rocks and minerals. Lead has four isotopes, three of these are radiogenic derived by radioactive decay of uranium and thorium. The isotopic composition of Pb evolves with time in most environments and has been used extensively for dating applications and fingerprinting sources of minerals, lavas, and also pollutants in the environment.

Cross-References

- Chondrites
- Earth's Continental Crust
- Formation and Evolution of the Earth
- Geochronology and Radiogenic Isotopes
- Lead
- Lithophile Elements
- Mantle Geochemistry
- Mid-Ocean Ridge Basalts (MORB)
- Ocean Biochemical Cycling and Trace Elements
- Oceanic Island Basalts
- Thorium
- Uranium
- Uranium Decay Series

References

Abouchami W, Hofmann AW, Galer SJG, Frey FA, Eisele J, Feigenson MD (2005) Lead isotopes reveal bilateral asymmetry and vertical continuity in the Hawaiian mantle plume. Nature 434(7035):851–856

Armstrong RL (1968) A model for Pb and Sr isotope evolution in a dynamic earth. Rev Geophys 6:175–199

Bouvier A, Blichert-Toft J, Albarède F (2009) Martian meteorite chronology and the evolution of the interior of Mars. Earth Planet Sci Lett 280:285–295

Boyle EA et al (2014) Anthropogenic lead emissions in the ocean: the evolving global experiment. Oceanography 27(1):69–75. https://doi.org/10.5670/oceanog.2014.10

Catanzaro EJ, Murphy TJ, Garner EL, Shields WR (1969) Absolute isotopic abundance ratio and atomic weight of terrestrial rubidium. J Res Natl Bur Stand 73A:511–516

Doe BR, Zartman RE (1979) Chapter 2. Plumbotectonics I, the Phanerozoic. In: Barnes HL (ed) Geochemistry of hydrothermal ore deposits, 2nd edn. Wiley-Interscience, New York, pp 22–70

Fourny A, Weis D, Scoates JS (2016) Comprehensive Pb-Sr-Nd-Hf isotopic, trace element, and mineralogical characterization of mafic to ultramafic rock reference materials. Geochem Geophys Geosyst 17(3):739–773. https://doi.org/10.1002/2015GC006181

Galer SJG (1999) Optimal double and triple spiking for high precision lead isotopic measurement. Chem Geol 157(3–4):255–274

Gast PW, Tilton GR, Hedge C (1964) Isotopic composition of lead and strontium from Ascension and Gough Islands. Science 145(3637):1181–1185

Gerling EK (1942) Age of the Earth according to radioactive data. Dokl Acad Sci URSS 24:259–261

Heyl AV, Landis GP, Zartman RE (1974) Isotopic evidence for the origin of Mississippi Valley-type mineral deposits: a review. Econ Geol 69(7):1025–1059

Hofmann AW, White WM (1980) The role of subducted oceanic crust in mantle evolution. Year B Carnegie Inst Wash 79:477–483

Hofmann AW (2003) Sampling mantle heterogeneity through oceanic basalts: isotopes and trace elements. In: Carlson R (ed) Treatise on geochemistry, vol 3, 2nd edn. Elsevier, Amsterdam, pp 67–101

Holmès A (1946) An estimate of the age of the earth. Nature 157:680–684

Houtermans FG (1946) Die Isotopenhäufigkeiten im natürlichen Blei und das Alter des Urans. Naturwissenschaften 33(6):185–186

Nier AO (1938) Variations in the relative abundances of the isotopes of common lead from various sources. J Am Chem Soc 60:1571

Nier AO (1939) The isotopic constitution of radiogenic leads and the measurement of geological times II. Phys Rev 55:153

Nobre Silva IGN, Weis D, Barling J, Scoates JS (2009) Leaching systematics and matrix elimination for the determination of high-precision Pb isotope compositions of ocean island basalts. Geochem Geophys Geosyst 10. https://doi.org/10.1029/2009GC002537

Patterson C (1956) Age of meteorites and the Earth. Geochim Cosmochim Acta 10(4):230–237

Patterson CC (1965) Contaminated and natural lead environments of man. Arch Environ Health 11(3):344–366

Patterson CC (1980) An alternate perspective—lead pollution in the human environment: origin, extent, and significance. In: Lead in the human environment. National Academy of Sciences, Washington, D.C., pp 265–349

Paul M, van de Flierdt T, Rehkämper M, Khondoker R, Weiss D, Lohan MC, Homoky WB (2015) Tracing the Agulhas leakage with lead isotopes. Geophys Res Lett 42(20):8515–8521. https://doi.org/10.1002/2015GL065625

Saal AE, Hart SR, Shimizu N, Hauri EH, Layne GD, Eiler JM (2005) Pb isotopic variability in melt inclusions from the EMI-EMII-HIMU mantle end-members and the role of the oceanic lithosphere. Earth Planet Sci Lett 240(3–4):605–620

Stacey JS, Kramers J (1975) Approximation of terrestrial lead isotope evolution by a two-stage model. Earth Planet Sci Lett 26(2):207–221

Tatsumoto M (1978) Isotopic composition of lead in oceanic basalt and its implication to mantle evolution. Earth Planet Sci Lett 38:63–87

Taylor PN, Moorbath S, Goodwin R, Petrykowski AC (1980) Crustal contamination as an indicator of the extent of early Archaean continental crust: Pb isotopic evidence from the late Archaean gneisses of West Greenland. Geochim Cosmochim Acta 44(10):1437–1453
Weis D, Kieffer B, Maerschalk C, Barling J, de Jong J, Williams GA et al (2006) High-precision isotopic characterization of USGS reference materials by TIMS and MC-ICP-MS. Geochem Geophys Geosyst 7 (8). https://doi.org/10.1029/2006GC001283
Weis D, Garcia MO, Rhodes JM, Jellinek M, Scoates JS (2011) Role of the deep mantle in generating the compositional asymmetry of the Hawaiian mantle plume. Nat Geosci 4(12):831–838
Wetherill GW (1956) Discordant uranium-lead ages, I. EOS Trans Am Geophys Union 37(3):320–326
White WM, Albarède F, Télouk P (2000) High-precision analysis of Pb isotope ratios by multi-collector ICP-MS. Chem Geol 167(3–4):257–270
White WM (2013) Geochemistry. Wiley-Blackwell, Oxford. 660 pp

Lipids (Bacteria and Archaea)

Ann Pearson
Department of Earth and Planetary Sciences, Harvard University, Cambridge, MA, USA

Definition

Lipids are fundamental biochemical constituents of all cells. Membrane lipids form bilayer or monolayer structures and provide physical and energetic barriers between intracellular processes and the external environment. Accessory lipids such as pigments and small-molecule metabolites also are important for cell function. In geosciences, the study of these lipids – known as "biomarkers" – takes advantage of two critical properties: (i) lipids are more resistant to degradation than other molecular classes (e.g., proteins, nucleic acids), allowing long-term preservation in the geologic record; and (ii) lipids have a large variety of chemical structures that can be taxonomically and physiologically diagnostic. Applications of lipid biomarker analysis range widely and tackle questions of recent and ancient Earth history and environmental processes.

Introduction

Geochemical approaches to reconstructing the history of the Earth and its ecosystems rely on a variety of proxies. Lipid biomarkers preserved in sedimentary rocks are an important part of this toolbox, providing records of community composition and the operation of specific metabolic pathways (Brocks and Pearson 2005; Grice and Eiserbeck 2014; Peters et al. 2005). The most valuable biomarkers are taxonomically specific and can be traced to organisms that perform specific functions, e.g., sulfide-oxidizing photosynthesis or anaerobic oxidation of ammonia (Anammox). The biomarker record can reveal information about the redox state of ancient oceans (e.g., Brocks et al. 2005), sources of sediments to continental margins (e.g., Prahl et al. 1992), past thermal histories of the surface ocean (e.g., Sluijs et al. 2006), dynamics of mass extinctions (e.g., Sepúlveda et al. 2009), and the operation of specific biogeochemical cycles (e.g., Rush et al. 2012).

Key to the utility of lipid studies is the fact that these molecules are inherently resistant to degradation. Although most biologically synthesized lipids contain one or more oxygen-, nitrogen-, and/or sulfur-containing groups, diagenesis often removes only these groups, leaving the parent structure largely intact (although with stereochemical and/or other minor structural rearrangements). The resulting molecules are the hydrocarbon skeletons of the original products, and they can persist in low-maturity sedimentary rocks for millions of years (Peters et al. 2005).

Siliciclastic sedimentary rocks (e.g., shales, mudstones) are the major reservoirs of biomarker molecules, although organic-rich marls and carbonate and silicic sediments (oozes) also contain extractible lipids. Records of biomarker lipids date back to at least the Mesoproterozoic ($\geq$1.6 Ga); but lipids previously identified in samples from 2.7 Ga (Brocks et al. 1999) now are known to be contaminants; i.e., at present, there is no confirmed biomarker record of life in the Archean (French et al. 2015a).

Biomarker analyses in recent time or in modern analogue environments often investigate lipids in their original, biological form, called "intact polar lipids" (IPLs; e.g., Schubotz et al. 2009). Ancient sediments typically contain only the hydrocarbon diagenetic products, albeit with some exceptions (Melendez et al. 2013). Analysis of hydrocarbons usually is done by gas chromatography-mass spectrometry (GC/MS), while analysis of biomarkers in IPL form usually is done by liquid chromatography-mass spectrometry (LC/MS). Many advanced technologies exist for both types of analyses (Grice 2014). In all cases, the fundamental goal is to identify diagnostic structures and relate them to their source organisms and environmental processes.

Lipid Structural Classes

The two major structural families of lipids are called ***acetogenic*** and ***isoprenoid*** based on their biosynthetic origins as polymers of acetate (two carbons, C_2) and isoprene (five carbons, C_5), respectively. Bacteria synthesize their major membrane structures from acetogenic lipids, while archaeal membranes are composed of isoprenoid lipids. Most other geochemically useful lipids of both bacterial and archaeal cells (e.g., carotenoid pigments, quinones) are isoprenoids.

Common bacterial and archaeal lipid classes used in geochemical studies are (Fig. 1; parent compound/geologic hydrocarbon):

Fatty acids/n-alkyl lipids – hydrophobic component of bacterial and eukaryotic membrane lipids

Sterols/steranes – polycyclic isoprenoid lipids, generally diagnostic for eukaryotes

Bacteriohopanepolyols (*BHPs*)/*hopanes* – polycyclic isoprenoid lipids, analogues of eukaryotic sterols

Phytol/phytane (*and pristane*) – isoprenoid sidechain of chlorophyll pigments

Carotenoids – isoprenoid accessory pigments for photosynthesis and energy metabolism

Archaeal diethers/phytanes – glycerol dialkyl diether lipids of archaeal bilayer membranes (also called archaeols)

Archaeal tetraethers/biphytanes – glycerol dialkyl glycerol tetraether (GDGT) lipids of archaeal monolayer membranes (also called caldarchaeols)

Bacterial tetraethers – branched, but not isoprenoid, glycerol dialkyl glycerol tetraether (brGDGT) lipids of bacterial monolayer membranes

Ladderanes – cyclobutane chain lipids of Anammox bacteria

Membrane bilayers of bacteria are composed of acetogenic lipids, typically containing a polar (often phospho- or glyco- (***i, ii***)) head group, glycerol backbone, and two esterified alkyl tails (***1***). Hydrolysis of these lipids yields biomarker fatty acids, and subsequent diagenesis ultimately yields alkanes (***2***). Numerous structural variations, including terminal branching (*iso-* or *anteiso-*; Kaneda 1991), unsaturation (always with *cis-* configuration), and mid-chain cyclopropyl versions, all are common and in some cases can provide taxonomic or metabolic information (Bodelier et al. 2009).

Polycyclic isoprenoid lipids such as the eukaryotic compound cholesterol (***3***) are membrane-rigidifying structures. The bacteriohopanepolyols (BHPs) (***4***) are analogous to sterols and share a common biochemical ancestry. Their corresponding hydrocarbons are called hopanes (***5***) and are among the most widely studied lipid biomarkers in geologic investigations (Newman et al. 2016; Ourisson et al. 1987; Summons et al. 1999).

Pigment molecules provide records of photosynthetic life. Lysis of the esterified C_{20} isoprenoid side chains of bacteriochlorophylls and chlorophyll *a* yields phytol (***6***), which during oxic and anoxic diagenesis degrades to pristane (***7***, C_{19}) and phytane (C_{20}), respectively (Didyk et al. 1978). Accessory C_{40} carotenoid pigments, often with terminal aromatic groups (aryl-, e.g., okenone; or diaryl-, e.g., isorenieratene (***8***)), are sufficiently taxonomically specific to reveal different types of photosynthesis in past environments (Brocks et al. 2005; French et al. 2015b; Sinninghe Damsté et al. 1993).

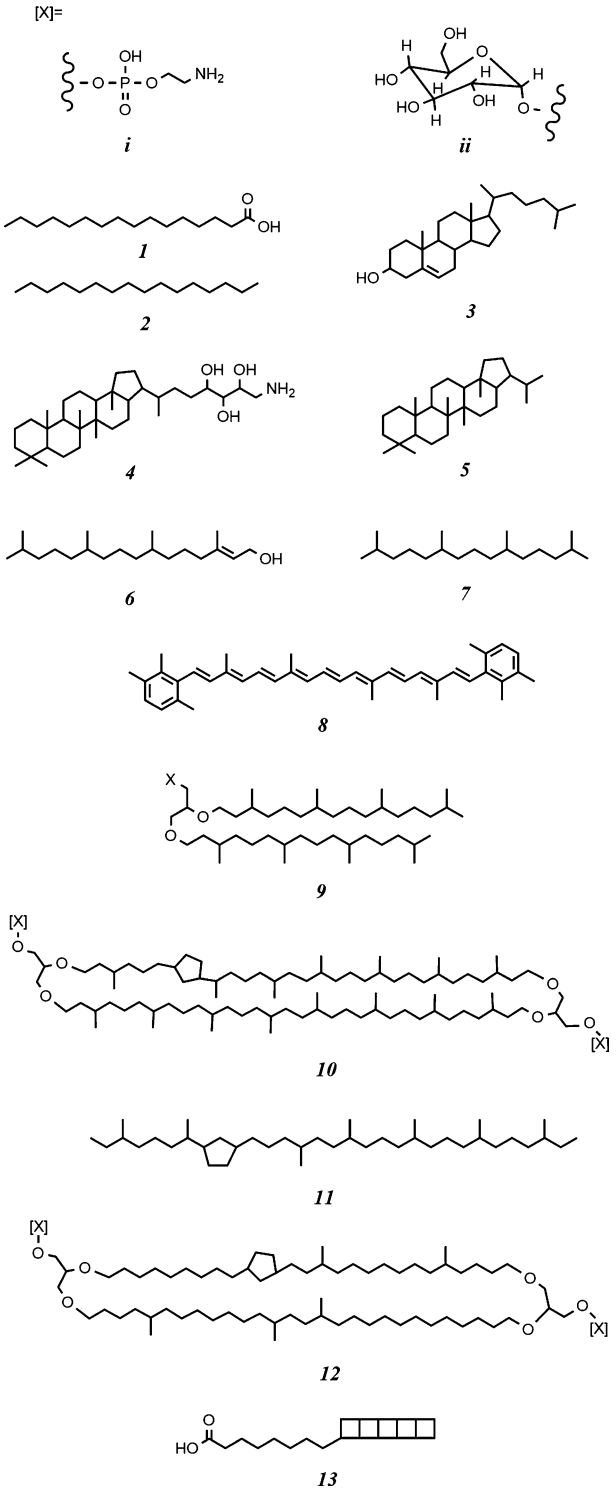

Lipids (Bacteria and Archaea), Fig. 1 Examples of lipid structures commonly used for geochemical studies: (***i, ii***), phospho- and glyco- head groups (many other structures are possible; e.g., Schubotz et al. 2009); (***1***), $C_{16:0}$ fatty acid; (***2***), *n*-C_{16} alkane; (***3***), cholesterol; (***4***), aminobacteriohopanetriol; (***5***), hopane; (***6***), phytol; (***7***), pristane; (***8***), isorenieratene; (***9***), archaeol; (***10***), GDGT-1, containing one cyclopentane ring; (***11***), $C_{40:1}$ biphytane; (***12***), brGDGT IIIb, containing one cyclopentane ring and 5 methyl groups; (***13***), C_{20} [5]-ladderane fatty acid

Lipids of archaea are invariably isoprenoid (Kates 1992). Archaeal membranes are composed of bilayers of diether lipids (***9***) or monolayers of tetraether lipids (***10***; GDGT), also with polar head groups (e.g., ***i, ii***). Due to the ether bonds linking the hydrocarbon side chains to the glycerol moieties, archaeal lipids are highly resistant to degradation. Diagenesis of GDGTs yields biphytanes (***11***), although intact (known as "core," i.e., without polar head groups) tetraether lipids are preserved at least as far back as the Jurassic; Jenkyns et al. 2012). Biphytanes can contain up to four or more internal cyclopentane rings and/or a single cyclohexane ring (Sinninghe Damsté et al. 2002a).

Tetraether lipids also are found in bacteria, although their taxonomic sources remain poorly understood (Weijers et al. 2006, 2009). These lipids resemble archaeal GDGTs, but their hydrocarbon centers are acetogenic (***12***) and contain up to six methyl branches and/or cyclopentane rings in a variety of structural positions (De Jonge et al. 2014). Collectively, they are regarded as "branched" (brGDGTs), even when containing cyclopentane rings; they persist in the geologic record at least since the Eocene (Inglis et al. 2017).

Ladderanes are a class of unusual lipids having concatenated chains of cyclobutane rings (***13***) (Sinninghe Damsté et al. 2002b). They are produced exclusively by the divisions of *Planctomycetes* bacteria that mediate the anaerobic oxidation of ammonia (Strous et al. 1999), where they are thought to provide an impermeable barrier to the toxic intermediate hydrazine. Their resulting diagenetic hydrocarbons are not yet known, although intact ladderanes in ocean waters and sediments provide records of Anammox in the recent past (e.g., Rush et al. 2012).

Selected Applications in Geosciences

Sources of bacteriohopanepolyols (*BHPs*) – Hopanoids are synthesized by a minority of bacteria and are not found in any archaea (Pearson 2014). The high resistance of hopane skeletons (***5***) to biotic and abiotic degradation makes hopanoids excellent tracers for ancient bacterial communities, resulting in several important applications. The ratio of total hopanes to total steranes has been used to interpret changes in the fraction of bacterial versus algal input (Moldowan et al. 1985). Hopane chain length proxies such as the C_{35} homohopane index, defined as $[C_{35}/(\Sigma C_{31}\text{-}C_{35})]$, record the extent of degradation of hopanoids. A higher index, denoting less degradation, is believed to indicate anoxia (Peters et al. 2005).

Some intact BHPs are believed to correspond to specific metabolisms. For example, aminobacteriohopanetriol (***4***) is found in methanotrophs and is observed in environments mediating aerobic methane oxidation (Talbot et al. 2003). The 2-methylhopanoids, previously regarded as markers for Cyanobacteria (Summons et al. 1999), now are regarded also as products of Alphaproteobacteria and perhaps other taxa (Welander et al. 2010). In general, the relatively greater occurrence of hopanoids in terrestrial ecosystems and the physiological association of hopanoids with microbial stress responses indicate they may be important biomarkers for terrestrial and/or benthic microbial activity (Newman et al. 2016).

Carotenoid distributions over time – Carotenoids provide a record of bacterial and algal photosynthesis. The detection of isorenieratane, an early diagenetic product of isorenieratene (***8***), in mid-Holocene sediments of the Black Sea (Sinninghe Damsté et al. 1993), provided evidence that photic-zone euxinia (anoxic, sulfide-containing surface water) predates human influence on the region; isorenieratene is only produced by photosynthetic green sulfur bacteria.

Recent improvements in the detection of a wide variety of carotenoids (French et al. 2015b) allowed their reassessment in geologic sediments dating back to the Proterozoic. This work confirms the extinction of the pigment paleorenieratane at the Permo-Triassic boundary, perhaps associated with the loss of unknown photosynthetic taxa. Conversely, the pigment okenone – found in purple sulfur bacteria (Brocks and Schaeffer 2008) – was shown to be more common than previously believed.

Paleotemperatures from GDGTs and brGDGTs – Accurate reconstruction of past sea surface temperatures (SSTs) and continental mean annual air temperatures (MAATs) is fundamental to a better understanding of paleoclimate. GDGTs of archaea (***10***) are used in the SST proxy known as the TEX_{86} index (Schouten et al. 2002). These compounds are believed to be produced primarily by ammonia-oxidizing, planktonic archaea that are critical and ubiquitous players in the global nitrogen cycle (c.f., Schouten et al. 2013). The distribution of GDGTs in marine surface sediments is calibrated to modern overlying waters (e.g., Tierney and Tingley 2014), and this calibration is subsequently applied to generate paleorecords from sediments. Such records have been fundamental tools for understanding SSTs over Cenozoic and Mesozoic timescales.

The analogous bacterial compounds, brGDGTs, have found utility as MAAT proxies (Weijers et al. 2007). Some of these compounds may be produced by the phylum *Acidobacteria*, although their sources remain generally unknown (Sinninghe Damsté et al. 2014). Calibrations show that brGDGTs are influenced by both temperature and pH and that soils and lakes require separate (region-specific) calibrations (Loomis et al. 2014; Peterse et al. 2012; Tierney et al. 2010). Records generated from brGDGTs have been important for studies of changes in Pleistocene/Quaternary climate patterns, especially over Africa, Asia, and the Caribbean.

Summary

Lipid biomarkers have broad utility in studies of historical geobiology, paleoclimate, and ecosystem reconstruction. Their structural diversity and high potential for preservation make them a critical tool in geochemical investigations of modern and ancient systems.

Cross-References

- ▶ Biogeochemistry
- ▶ Biomarkers: Petroleum
- ▶ Gas Chromatography–Mass Spectrometry (GC–MS)
- ▶ Hydrocarbons
- ▶ Organic Geochemistry
- ▶ Paleoenvironments

Acknowledgments AP is supported by the NASA Astrobiology Institute, the Gordon and Betty Moore Foundation, and the US National Science Foundation.

References

Bodelier PLE, Bär Gillisen MJ, Hordijk K, Sinninghe Damsté JS, Rijpstra WIC, Geenevasen JAJ, Dunfield PF (2009) A reanalysis of phospholipid fatty acids as ecological biomarkers for methanotrophic bacteria. ISME J 3:606–617

Brocks JJ, Pearson A (2005) Building the biomarker tree of life. In: Banfield J (ed) Molecular geomicrobiology. Reviews in mineralogy and geochemistry, vol 59. The Mineralogical Society of America, Chantilly, pp 233–258

Brocks JJ, Schaeffer P (2008) Okenane, a biomarker for purple sulfur bacteria (Chromatiaceae), and other new carotenoid derivatives from the 1640 Ma Barney Creek formation. Geochim Cosmochim Acta 72:1396–1414

Brocks JJ, Logan GA, Buick R, Summons RE (1999) Archean molecular fossils and the early rise of eukaryotes. Science 285:1033–1036

Brocks JJ, Love GD, Summons RE, Knoll AH, Logan GA, Bowden SA (2005) Biomarker evidence for green and purple sulphur bacteria in a stratified Palaeoproterozoic sea. Nature 437:866–870

De Jonge C, Hopmans EC, Zell CI et al (2014) Occurrence and abundance of 6-methyl branched glycerol dialkyl glycerol tetraethers in soils: implications for palaeoclimate reconstruction. Geochim Cosmochim Acta 141:97–112

Didyk BM, Simoneit BRT, Brassell SC, Eglinton G (1978) Organic geochemical indicators of paleoenvironmental conditions of sedimentation. Nature 272:216–222

French KL, Hallmann C, Hope JM, Schoon PL, Zumberge JA, Hoshino Y et al (2015a) Reappraisal of hydrocarbon biomarkers in Archean rocks. Proc Nat Acad Sci USA 112:5915–5920

French KL, Rocher D, Zumberge JE, Summons RE (2015b) Assessing the distribution of sedimentary C_{40} carotenoids through time. Geobiology 13:139–151

Grice K (2014) Principles and practice of analytical techniques in the geosciences. R Soc Chem, UK

Grice K, Eiserbeck C (2014) The analysis and application of biomarkers. In: Holland H, Turekian K (eds) Treatise on geochemistry, vol 12, 2nd edn. Elsevier, Boston, pp 47–78

Inglis GN, Collinson ME, Riegel W, Wilde V, Farnsworth A, Lunt DJ, Valdes P et al (2017) Mid-latitude continental temperatures through the early Eocene in western Europe. Earth Planet Sci Lett 460:86–96

Jenkyns H, Schouten-Huibers L, Schouten S, Sinninghe Damsté JS (2012) Warm middle Jurassic-early cretaceous high-latitude sea surface temperature from the Southern Ocean. Clim Past 8:215–226

Kaneda T (1991) Iso- and anteiso-fatty acids in bacteria: biosynthesis, function, and taxonomic significance. Microbiol Rev 55:288–302

Kates M (1992) Archaebacterial lipids: structure, biosynthesis and function. Biochem Soc Symp 58:51–72

Loomis SE, Russell JM, Eggermont H et al (2014) Effects of temperature, pH and nutrient concentration on branched GDGT distributions in East African lakes: implications for paleoenvironmental reconstruction. Org Geochem 66:25–37

Melendez I, Grice K, Schwark L (2013) Exceptional preservation of Palaeozoic steroids in a diagenetic continuum. Sci Rep 3. https://doi.org/10.1038/srep02768

Moldowan JM, Seifert WK, Gallegos EJ (1985) Relationship between petroleum composition and depositional environment of petroleum source rocks. AAPG Bull 69:1255–1268

Newman DK, Neubauer C, Ricci JN, Wu C-H, Pearson A (2016) Cellular and molecular biological approaches to interpreting ancient biomarkers. Ann Rev Earth Planet Sci 44:493–522

Ourisson G, Rohmer M, Poralla K (1987) Prokaryotic hopanoids and other polyterpenoid sterol surrogates. Annu Rev Microbiol 41:301–333

Pearson A (2014) Lipidomics for geochemistry. In: Holland H, Turekian K (eds) Treatise on geochemistry, vol 12, 2nd edn. Elsevier, Boston, pp 291–336

Peters KE, Walters CC, Moldowan JM (2005) The biomarker guide. Cambridge University Press, Cambridge

Peterse F, van der Meer J, Schouten S, Weijers JWH, Fierer N, Jackson RB, Kim JH, Sinninghe Damsté JS (2012) Revised calibration of the MBT–CBT paleotemperature proxy based on branched tetraether membrane lipids in surface soils. Geochim Cosmochim Acta 96:215–229

Prahl FG, Hayes JM, Xie TM (1992) Diploptene – an indicator of terrigenous organic carbon in Washington coastal sediments. Limnol Oceanogr 37:1290–1300

Rush D, Hopmans EC, Wakeham SG, Villanueva L, Schouten S, Sinninghe Damsté JS (2012) Occurrence and distribution of ladderane oxidation products in different oceanic regimes. Biogeosciences 9:2407–2418

Schouten S, Hopmans EC, Schefuß E, Sinninghe Damsté JS (2002) Distributional variations in marine crenarchaeotal membrane lipids: a new tool for reconstructing ancient sea water temperatures? Earth Planet Sci Lett 204:265–274

Schouten S, Hopmans EC, Sinninghe Damsté JS (2013) The organic geochemistry of glycerol dialkyl glycerol tetraether lipids: a review. Org Geochem 54:19–61

Schubotz F, Wakeham SG, Lipp JS, Fredricks HF, Hinrichs KU (2009) Detection of microbial biomass by intact polar membrane lipid analysis in the water column and surface sediments of the Black Sea. Environ Microbiol 11:2720–2734

Sepúlveda J, Wendler PV, Summons RE, Hinrichs KU (2009) Rapid resurgence of marine productivity after the Cretaceous-Paleogene mass extinction. Science 326:129–132

Sinninghe Damsté JS, Wakeham SG, Kohnen MEL, Hayes JM, de Leeuw JW (1993) A 6,000–year sedimentary molecular record of chemocline excursions in the Black Sea. Nature 362:827–829

Sinninghe Damsté JS, Schouten S, Hopmans EC, van Duin ACT, Geenevasen JAJ (2002a) Crenarchaeol: the characteristic core glycerol dibiphytanyl glycerol tetraether membrane lipid of cosmopolitan pelagic crenarchaeota. J Lipid Res 43:1641–1651

Sinninghe Damsté JS, Strous M, Rijpstra WIC et al (2002b) Linearly concatenated cyclobutane lipids form a dense bacterial membrane. Nature 419:708–712
Sinninghe Damsté JS, Rijpstra WIC, Hopmans EC, Foesel BU, Wüst PK, Overmann J, Tank M, Bryant DA, Dunfield PF, Houghton K, Stotte MB (2014) Ether- and ester-bound iso-diabolic acid and other lipids in members of Acidobacteria subdivision 4. Appl Environ Microbiol 80:5207–5218
Sluijs A, Schouten S, Pagani M, Woltering M, Brinkhuis H, Damsté JSS, Dickens GR, Huber M, Reichart GJ, Stein R, Matthiessen J, Lourens LJ, Pedentchouk N, Backman J, Moran K (2006) Subtropical Arctic Ocean temperatures during the Palaeocene/Eocene thermal maximum. Nature 441:610–613
Strous M, Fuerst JA, Kramer EHM, Logemann S, Muyzer G, van de Pas-Scoonen KT, Webb R, Kuenen JG, Jetten MSM (1999) Missing lithotroph identified as new planctomycete. Nature 400:446–449
Summons RE, Jahnke LL, Hope JM, Logan GA (1999) 2-Methylhopanoids as biomarkers for cyanobacterial oxygenic photosynthesis. Nature 400:554–557
Talbot HM, Watson DF, Pearson EJ, Farrimond P (2003) Diverse biohopanoid compositions of non-marine sediments. Org Geochem 34:1353–1371
Tierney JE, Russell JM, Eggermont H, Hopmans EC, Verschuren D, Sinninghe Damsté JS (2010) Environmental controls on branched tetraether lipid distributions in tropical East African lake sediments. Geochim Cosmochim Acta 74:4902–4918
Tierney JE, Tingley MP (2014) A Bayesian, spatially-varying calibration model for the TEX86 proxy. Geochim Cosmochim Acta 127:83–106
Weijers JWH, Schouten S, Hopmans EC et al (2006) Membrane lipids of mesophilic anaerobic bacteria thriving in peats have typical archaeal traits. Environ Microbiol 8:648–657
Weijers JWH, Schouten S, van den Donker JC, Hopmans EC, Sinninghe Damsté JS (2007) Environmental controls on bacterial tetraether membrane lipid distribution in soils. Geochim Cosmochim Acta 71:703–713
Weijers JWH, Panoto E, van Bleijswijk J et al (2009) Constraints on the biological source(s) of the orphan branched tetraether membrane lipids. Geomicrobiol J 26:402–414
Welander PV, Coleman ML, Sessions AL, Summons RE, Newman DK (2010) Identification of a methylase required for 2-methylhopanoid production and implications for the interpretation of sedimentary hopanes. Proc Nat Acad Sci USA 107:8537–8542

Lithium

Jeffrey G. Ryan
School of Geosciences, University of South Florida, Tampa, FL, USA

Element Data
Atomic Symbol: Li
Atomic Number: 3
Atomic Weight: 6.941
Isotopes and Abundances: ^{6}Li, 7.5%; ^{7}Li, 92.5%
1 Atm Melting Point: 180.5 °C
(*continued*)

1 Atm Boiling Point: 1342 °C
Common Valences: +1
Ionic Radii: 0.76 Å
Pauling Electronegativity: 0.98
First Ionization Energy: 520.2 kJ/mol
Chondritic (CI) Abundance: 1.49 ppm
Silicate Earth Abundance: 1.6 ppm
Crustal Abundance: 17 ppm
Seawater Abundance: 0.18 ppm
Core Abundance: ~0

Properties

Lithium is a low-density (0.5 × H_2O), silvery-white metal, which, while somewhat less reactive in water than sodium or other alkali metals, is nonetheless highly reactive and found in nature only in compounds or as a trace-level constituent in rocks.

History and Use

Johan August Arfvedson isolated lithium from the mineral petalite in 1817 and subsequently identified Li in both lepidolite and spodumene. Today lithium is extracted from brines (from LiCl) and is as well mined from large spodumene-bearing pegmatites. Lithium forms a range of silicate and evaporitic minerals, including Li-variants on micas and sheet silicates (lepidolite, zinnwaldite), inosilicates (spodumene), and tectosilicates (petalite), and a number of lithium-bearing phosphates (amblygdonite, triphilite, lithiophilite). Lithium has a wide range of industrial uses: as the key electrochemical agent in Li-ion batteries, in lubricants, and in medicine (Trujillo et al. 2011). Hiddenite, a green variant of the Li-mineral spodumene, and kunzite, a pink/lavender variant, are sought as gemstones.

Geochemical Behavior

In terms of nucleosynthesis, a portion of available ^{7}Li is thought to have been formed during the Big Bang (Stegman and Walker 1992), but Li is unstable in stellar interiors. Most Li (and nearly all ^{6}Li) forms at low abundances via spallation processes on CNO nuclei in interstellar medium (Stegman and Walker 1992; Vangione-Flam et al. 1999). Cosmochemically lithium is a moderately depleted element that largely follows Mg during nebular condensation (Dreibus et al. 1976). Li abundances in chondritic meteorites range from 1 to 2 ppm (Nichiporuk and Moore 1970, 1974), while

eucrites and lunar basalts range from 2 to 20 ppm Li (Dreibus et al. 1976; Shearer et al. 1994).

The ionic radius of Li^{1+}, at 0.76 Å, is close to that of Mg^{2+} (Shannon 1976), and as such the element substitutes at a $D^{mineral/melt}$ value of 0.1–0.3 into the M1 cation sites in many mafic minerals, in particular olivine, pyroxenes, and amphiboles; into alkali sites in plagioclase; and strongly ($D^{mineral/melt} \approx 0.3 -> 1.0$) into sheet silicate minerals, including micas and (in particular) Mg-bearing sheet silicates like serpentine (e.g., Brenan et al. 1998; Earthref.org 2016; Tomascak et al. 2016). Lithium concentrations are comparatively high in mantle rocks, with abundances in peridotites ranging from 1 to 4 ppm Li (Ryan and Langmuir 1987; Seitz and Woodland 2000). Lithium abundances are consistently low in mafic volcanic rocks, with basalts from all tectonic settings ranging between 2 and 10 ppm Li (Ryan and Langmuir 1987; Ryan and Kyle 2004). Li/Yb ratios are essentially constant in ocean-ridge basalts at ≈1.8, while Li/Dy ratios are constant in ocean island and intraplate lavas (Ryan and Langmuir 1987). This apparent tectonic setting-related difference in Li behavior results from the distinctive pattern of Li mineral-melt partitioning, in that Li, unlike all other commonly studied lithophile elements, substitutes into nearly all mafic silicate mineral phases with $D^{mineral/melt}$ values of similar magnitude.

Differentiated lavas and granitic rocks are higher in Li and can reach values of over 100 ppm, though most are in the range of 10–50 ppm Li, consistent with overall estimates for the continental crust (Teng et al. 2004, 2006; Rudnick and Gao 2014). Li is a conservative species in the oceans at 0.18 ppm, varying with Cl content, while seafloor hydrothermal fluids can have Li contents up to 50 times seawater values (Von Damm et al. 1985). Li is adsorbed by clays during marine alteration, and marine sediments typically contain 30–50 ppm Li (Plank 2014), while altered oceanic basalts can locally reach very high contents but overall are probably around 10 ppm (Donnelly et al. 1980).

During hydrothermal fluid-rock exchanges, Li tends to be mobilized to only a limited degree, even at temperatures as high as 375 °C (Seyfried et al. 1984). During metamorphism, Li concentrations increase slightly with grade (implying Li retention while fluids and other species are lost) until reaching the highest grade (granulite) conditions, where Li shows depletions suggestive of metasomatic removal (Sighinolfi and Gorgoni 1978). Metasediments from greenschist/blueschist to amphibolite facies metamorphic conditions thus largely preserve their original lithium contents, albeit with extensive isotopic re-equilibration (Sighinolfi and Gorgoni 1978; Penniston-Dorland et al. 2012).

With its high charge-to-mass ratio, lithium has the highest chemical diffusivity of any non-gaseous element, with diffusion coefficients several orders of magnitude higher than other alkalies and nearly all other lithophile trace elements (Cunningham et al. 1983; Lundstrom et al. 2005). This unique chemical characteristic of Li can result in comparatively rapid Li isotopic and abundance homogenization of mantle domains, and in the development of marked isotopic heterogeneities across interfaces with strong Li abundance gradients (Richter et al. 2003; Lundstrom et al. 2005).

Biological Utilization and Toxicity

Lithium is not biologically utilized in humans, though it seems to afford some benefit in plant growth. Natural human intake of Li in foods ranges between 0.6 and 3 mg/day, though in areas with high natural Li abundances these values may be >3 times higher without apparent negative effects (Aral and Vecchio-Sadus 2008). Li metal is toxic in high doses, as it can negatively impact neurological function. Li_2CO_3, to a serum level of up to 10 mg/l (close to its toxity level), is a traditional pharmacological treatment for bipolar disorder, though the specifics of how it impacts mood and mental state are still not clearly understood (Aral and Vecchio-Sadus 2008).

Cross-References

- Alkali and Alkaline Earth Metals
- Lithium Isotopes
- Lithophile Elements
- Nucleosynthesis
- Partitioning and Partition Coefficients
- Trace Elements

References

Aral H, Vecchio-Sadus A (2008) Toxicity of lithium to humans and the environment – a literature review. Ecotoxicol Environ Saf 70:349–356

Brenan JM, Neroda E, Lundstrom CC, Shaw HF, Ryerson FJ, Phinney DL (1998) Behavior of boron, beryllium and lithium during melting and crystallization: constraints from mineral-melt partitioning experiments. Geochim Cosmochim Acta 62:2129–2141

Cunningham GJ, Henderson P, Lowry RK, Nolan J, Reed SJB, Long JVP (1983) Lithium diffusion in silicate melts. Earth Planet Sci Lett 65:203–205

Donnelly TW, Thompson G, Salisbury MH (1980) The chemistry of altered basalts at site 417, Deep Sea Drilling Project leg 51. In: Powell R, Laughter F (eds) Initial reports of the Deep Sea Drilling Project, vol 51–53, pp 1319–l330. https://doi.org/10.2973/dsdp.proc.515253.1980

Dreibus G, Spettel B, Wanke H (1976) Lithium as a correlated element, its condensation behaviour, and its use to estimate the bulk composition of the moon and the eucrite parent body. In: Proceedings of the 7th Lunar science conference, pp 3383–3396

Earthref.org (2016) Geochemical Earth Reference Model (GERM). https://earthref.org/GERM/

Lundstrom CC, Chaussidon M, Hsui AT, Kelemen P, Zimmerman M (2005) Observations of Li isotopic variations in the Trinity Ophiolite: evidence for isotopic fractionation by diffusion during mantle melting. Geochim Cosmochim Acta 69:735–751
Nichiporuk W, Moore CB (1970) Lithium in chondritic meteorites. Earth Planet Sci Lett 19:280–286
Nichiporuk W, Moore CB (1974) Lithium, sodium, and potassium abundances in carbonaceous chondrites. Geochim Cosmochim Acta 38:1691–1701
Penniston-Dorland SC, Bebout GE, Pogge von Strandmann PAE, Elliott T, Sorensen SS (2012) Lithium and its isotopes as tracers of subduction zone fluids and metasomatic processes: evidence from the Catalina Schist, California, USA. Geochim Cosmochim Acta 77:530–545
Plank T (2014) The chemical composition of subducting sediments. In: Treatise on geochemistry, 2nd edn. Elsevier. Chap. 4: the crust, pp 607–629
Richter FM, Davis AM, DePaolo DJ, Watson EB (2003) Isotope fractionation by chemical diffusion between molten basalt and rhyolite. Geochim Cosmochim Acta 67:3905–3923
Rudnick RL, Gao S (2014) Composition of the continental crust, Chap. 4.13. In: Holland HD, Turekian KK (eds) Treatise on geochemistry. Elsevier, Amsterdam, pp 1–51
Ryan JG, Kyle PR (2004) Lithium and lithium isotope variations in intraplate mantle sources: insights from McMurdo Group lavas (Mt. Erebus) and other intraplate volcanic rocks. Chem Geol 212:125–142
Ryan JG, Langmuir CH (1987) The systematics of lithium abundances in young volcanic rocks. Geochim Cosmochim Acta 51:1727–1741
Seitz H-M, Woodland AB (2000) The distribution of lithium in peridotitic and pyroxenitic mantle lithologies: and indicator of magmatic and metasomatic processes. Chem Geol 166:47–64
Seyfried WE, Janecky DR, Mottl MJ (1984) Alteration of the oceanic crust: implications for chemical cycles of lithium and boron. Geochim Cosmochim Acta 48:557–569
Shannon RD (1976) Revised effective ionic radii and systematic studies of interatomic distance in halides and chalcogenides. Acta Crystallogr A32:751–767
Shearer CK, Layne GD, Papike JJ (1994) The systematics of light lithophile elements (Li, Be, and B) in lunar picritic glasses: implications for basaltic magmatism on the Moon and the origin of the Moon. Geochim Cosmochim Acta 58:5349–5362
Sighinolfi GP, Gorgoni C (1978) Chemical evolution of high grade metamorphic rocks-anatexis and remotion of material from granulite terranes. Chem Geol 22:157–176
Stegman G, Walker TP (1992) Production of Li, Be, and B in the early galaxy. Astrophys J 385:L13–L16
Teng F-Z, McDonough WF, Rudnick RL, Dalpe C, Tomascak PB, Chappell BW, Gao S (2004) Lithium isotopic composition and concentration of the upper continental crust. Geochim Cosmochim Acta 68:4167–4178
Teng F-Z, McDonough WF, Rudnick RL, Walker RJ, Sirbescu M-LC (2006) Lithium isotopic systematics of granites and pegmatites from the Black Hills, South Dakota. Am Mineral 91:1488–1498
Tomascak PB, Magna T, Dohmen R (2016) Advances in Lithium isotope geochemistry. Springer International Publishing, New York. https://doi.org/10.1007/978-3-319-01430-2
Trujillo M, Hobart D, Smith J (2011) Lithium. In: Periodic table of the elements. Online resource, Los Alamos National Laboratory. http://periodic.lanl.gov/3.shtml
Vangione-Flam E, Casse M, Audouze J (1999) Lithium-beryllium-boron: origin and evolution. Astro-ph/9907171, 1–30
Von Damm KL, Edmond JM, Grant B, Measures CI, Walden B, Weisser F (1985) Chemistry of submarine hydrothermal solutions at 21° N, East Pacific Rise. Geochim Cosmochim Acta 49:2197–2220

Lithium Isotopes

Jeffrey G. Ryan
School of Geosciences, University of South Florida, Tampa, FL, USA

Definition

The large relative mass difference between the lithium isotopes (^{7}Li (~92.5%) and ^{6}Li (~7.5%)) leads to isotopic fractionations of Li during equilibrium and kinetic reactions in Earth systems. Substantial (20–30‰) δ^7Li differences exist between natural waters and rocks. Mafic igneous rocks from all tectonic settings range in δ^7Li from +2‰ to +6‰, suggesting a uniform mantle reservoir, though mantle-derived samples may show variable δ^7Li due to its high chemical diffusivity. Weathering processes lower δ^7Li in surface rocks, with continental δ^7Li at ~0‰. While subduction processes do not usually lead to strong Li isotope shifts, in places where subduction is ceasing, large δ^7Li variations have been observed in lavas.

Introduction

Lithium has two naturally occurring stable isotopes which occur in the Earth at approximately the ^{7}Li/^{6}Li ratio of ~12 encountered in primitive meteorites (Tomascak et al. 2016). The large relative mass difference between its isotopes makes lithium highly susceptible to chemically induced isotopic fractionation. Successful chemical separation of Li and thermal ionization mass spectrometric determinations of Li isotopes on geological samples was first reported by Chan (1987) and Chan and Edmond (1988). Tomascak et al. (1999) presented results using solution multicollector ICP-MS analysis with sample-standard bracketing, and this advance has led to a wealth of new Li isotopic data on a wide range of geological materials and a better understanding of the Li isotopic system overall.

Natural Waters

In aqueous solutions, Li generally exists as an $Li([H_2O]_N)+$ complex coordinated with four oxygens (Jahn and Wunder 2009; Kowalski and Jahn 2011), while in minerals, it can coordinate both octahedrally and tetrahedrally, largely substituting for Mg in silicate phases. ^{7}Li is preferentially concentrated in hydrous fluids, and as such δ^7Li $((({}^7Li/{}^6Li_{sample} - {}^7Li/{}^6Li_{L\text{-}SVEC})/({}^7Li/{}^6Li_{L\text{-}SVEC}))\times 1000$, where L-SVEC is the NIST Li_2CO_3 isotopic reference material) values in the oceans and natural freshwater bodies are 20–30‰ higher than in minerals and rocks. δ^7Li in modern

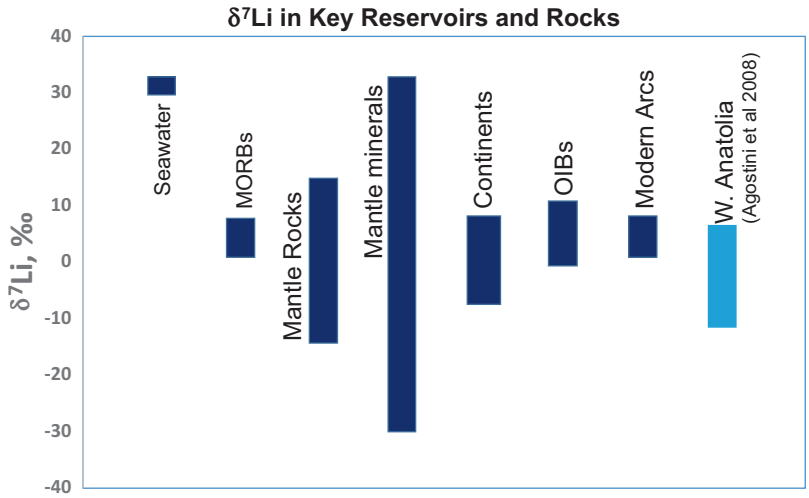

Lithium Isotopes, Fig. 1 δ^7Li variation in key rocks and reservoirs. *Dark bars* based on data compiled in Tomascak et al. (2016); Western Anatolia is from Agostini et al. (2008)

seawater is ~+31‰ (Fig. 1), though evidence from foraminiferal tests suggests a secular variation in the seawater reservoir in the Cenozoic that likely relates to changes in continental Li inputs (Misra and Froelich 2012; Pogge von Strandmann et al. 2013). River water δ^7Li signatures in the dissolved load are elevated, while suspended and bed load signatures verge closer to the value of entrained sediments (Huh et al. 2001). Hydrothermal fluids are typically closer in their δ^7Li to the rocks they interact with, largely ranging between 2‰ and 15‰ in the oceans (Chan et al. 1993, 1994).

Mafic Rocks and the Mantle

Basaltic igneous rocks have largely uniform δ^7Li signatures, with MORBs ranging between +2‰ to +6‰ (Tomascak et al. 2008). Oceanic intraplate basalts show evidence for somewhat greater δ^7Li variability (e.g., higher δ^7Li in HIMU and South Pacific lavas: Ryan and Kyle 2004; Nishio et al. 2005; see also Tomascak et al. 2016). The comparatively limited δ^7Li range in mafic lavas contrasts with the large range in ultramafic samples (−12‰ to +12‰: Brooker et al. 2004; Rudnick and Ionov 2007; Ackerman et al. 2013) and an even larger range in minerals from mantle-derived samples (+30‰ to −28‰: Tomascak et al. 2016). The high overall chemical diffusivity of Li, specifically the substantial relative diffusivity difference between the Li isotopes, is responsible for much of the Li isotopic variability observed in mantle samples, as strong Li isotopic gradients can develop, even in subsolidus conditions, across any boundary where there is a Li abundance gradient (Richter et al. 2003, 2014; Lundstrom et al. 2005). Li diffusivity is likely also responsible for the apparent isotopic homogeneity of mantle sources as sampled by basaltic magmas, as solid-state diffusive homogenization of Li isotopic anomalies in the mantle is possible on a ~10^7–10^8 year scale (Richter et al. 2003). Under low temperature conditions, Li isotopic heterogeneities can develop during the alteration of mafic and ultramafic lithologies by progressive fluid-rock exchanges where Li is taken up in Mg-rich phyllosilicate phases, such as serpentine, in which it is compatible (Decitre et al. 2002; Benton et al. 2004).

Sediments, Metamorphic Rocks and the Continents

Rudnick et al. (2004) and subsequent workers have documented that surficial weathering and alteration processes reduce Li contents and the δ^7Li in soils and sediments. Marine sedimentary sections as well show an overall shift to lower δ^7Li, although both on land and in the oceans, some materials recording very high δ^7Li are preserved. Sediment δ^7Li signatures are reflected in both sedimentary rocks and in metamorphic and granitic igneous rocks formed from sedimentary protoliths (Teng et al. 2004; Chan et al. 2006; Penniston-Dorland et al. 2012; see also Tomascak et al. 2016). Teng et al. (2004) estimated that the δ^7Li of the upper continental crust is 0 ± 2‰, reflecting the influence of weathering-related Li isotopic fractionations. High-pressure metamorphic rocks often record δ^7Li < than 0‰, based on which, some have suggested substantial subduction-related Li isotopic fractionations, though experimental results have argued against this (Zack et al. 2003; Marschall et al. 2007: see below). Current thinking is that fluid-rock diffusive and chemical exchanges associated with the uplift and unroofing of high-P rock suites may be primarily responsible for anomalously low δ^7Li in some samples (Tomascak et al. 2016).

Subduction Cycling of the Li Isotopes

While some early studies of volcanic arc lavas and subduction-related metamorphic rocks have been suggestive of large Li isotopic fractionations during subduction zone processes (e.g., Moriguti and Nakamura 1998; Zack et al. 2003), broader-based studies have not turned up clear evidence for such systematics: Tomascak et al. (2002) and Chan et al. (2002) found that mafic volcanic arc lavas have δ^7Li similar to MORBs, and Marschall et al. (2007) showed both

analytically and experimentally that the potential change in δ^7Li during subduction zone fluid-rock exchanges is likely not more than ±3‰. Benton et al. (2004) found that under forearc P-T conditions, eruptive serpentinites from the Mariana forearc preserve a δ^7Li of only +6‰ to + 7‰, pointing to comparatively modest slab-related increases in δ^7Li, as compared to large increases in δ^{11}B (up to +18‰; Benton et al. 2001). Given that the upper mantle has Li abundances of 1–2 ppm and (thanks to Li diffusivity) a relatively uniform δ^7Li value, slab-derived Li additions may not be sufficient to produce a Li isotopic anomaly in arc source regions, even though Li shows enrichments in arc lavas (Ryan and Langmuir 1987). Interestingly, Agostini et al. (2008), in a time series study of volcanic rocks spanning the transition from subduction to extension in Western Anatolia, found strong, paired Li and B isotopic declines as subduction shut down, followed by a rapid recovery to prevalent mantle values with the onset of extension. They hypothesized that the shutdown of mantle wedge convection and extreme distillation of a slowing downgoing plate permitted the ephemeral development of a highly fractionated δ^7Li reservoir, which quickly became homogenized with the onset of extension.

Conclusions

Thanks in equal parts to high Li solubility in fluids at low temperatures and its high chemical diffusivity at higher temperatures, δ^7Li signatures are relatively uniform at the scales of melting in the mantle and crust but can be highly diverse on a finer scale. Many of the more promising applications of the Li isotopes (deep Earth fluid-rock exchanges, secular variation in the oceans) leverage this finer scale diversity.

Cross-References

- ▶ Boron Stable Isotopes
- ▶ Chemical Weathering
- ▶ Diffusion
- ▶ Lithium
- ▶ Ocean Biochemical Cycling and Trace Elements
- ▶ Stable Isotope Geochemistry
- ▶ Subduction Zone Geochemistry

References

Ackerman L, Špaček P, Magna T, Ulrych J, Svojtka M, Hegner E, Balogh K (2013) Alkaline and carbonate-rich melt metasomatism and melting of subcontinental Lithospheric mantle: evidence from mantle Xenoliths, NE Bavaria, Bohemian Massif. J Petrol 54:2597–2633

Agostini S, Ryan JG, Tonarini S, Innocenti F (2008) Drying and dying of a subducted slab: coupled Li and B isotope variations in Western Anatolia Cenozoic Volcanism. Earth Planet Sci Lett 272:139–147

Benton LD, Ryan JG, Tera F (2001) Boron isotope systematics of slab fluids as inferred from a serpentinite seamount, Mariana forearc. Earth Planet Sci Lett 187:273–282

Benton LD, Ryan JG, Savov IP (2004) Lithium abundance and isotope systematics of forearc serpentinites, Conical Seamount, Mariana forearc: insights into the mechanics of slab-mantle exchange during subduction. Geochem Geophys Geosyst 5:Q08J12. https://doi.org/10.1029/2004GC000708

Brooker RA, James RH, Blundy JD (2004) Trace elements and Li isotope systematics in Zabargad peridotites: evidence of ancient subduction processes in the Red Sea mantle. Chem Geol 212:179–204

Chan LH (1987) Lithium isotope analysis by thermal ionization mass spectrometry of lithium tetraborate. Anal Chem 59:2662–2665

Chan LH, Edmond JM (1988) Variation of lithium isotope composition in the marine environment: a preliminary report. Geochim Cosmochim Acta 52:1711–1717

Chan LH, Edmond JM, Thompson G (1993) A lithium isotope study of hot springs and metabasalts from mid-ocean ridge hydrothermal systems. J Geophys Res 98:9653–9659

Chan LH, Gieskes JM, You CF, Edmond JM (1994) Lithium isotope geochemistry of sediments and hydrothermal fluids of the Guaymas Basin, Gulf of California. Geochim Cosmochim Acta 58:4443–4454

Chan L-H, Leeman WP, You C-F (2002) Lithium isotopic composition of Central American Volcanic Arc lavas: implications for modification of subarc mantle by slab-derived fluids: correction. Chem Geol 182:293–300

Chan L-H, Leeman WP, Plank T (2006) Lithium isotopic composition of marine sediments. Geochem Geophys Geosyst 7:Q06005. https://doi.org/10.1029/2005GC001202

Decitre S, Deloule E, Reisberg L, James RH, Agrinier P, Mével C (2002) Behavior of Li and its isotopes during serpentinization of oceanic peridotites. Geochem Geophys Geosyst 3:1–20. https://doi.org/10.1029/2001GC000178

Huh Y, Chan LH, Edmond JM (2001) Lithium isotopes as a probe of weathering processes: Orinoco River. Earth Planet Sci Lett 194:189–199

Jahn S, Wunder B (2009) Lithium speciation in aqueous fluids at high P and T studied by ab initio molecular dynamics and consequences for Li-isotope fractionation between minerals and fluids. Geochim Cosmochim Acta 73:5428–5434

Kowalski PM, Jahn S (2011) Prediction of equilibrium Li isotope fractionation between minerals and aqueous solutions at high P and T: an efficient ab initio approach. Geochim Cosmochim Acta 75:6112–6123

Lundstrom CC, Chaussidon M, Hsui AT, Kelemen P, Zimmerman M (2005) Observations of Li isotopic variations in the Trinity Ophiolite: evidence for isotopic fractionation by diffusion during mantle melting. Geochim Cosmochim Acta 69:735–751

Marschall HR, Pogge von Strandmann PAE, Seitz H-M, Elliott T, Niu Y (2007) The lithium isotopic composition of orogenic eclogites and deep subducted slabs. Earth Planet Sci Lett 262:563–580

Misra S, Froelich PN (2012) Lithium isotope history of Cenozoic seawater: changes in silicate weathering and reverse weathering. Science 335:818–823

Moriguti T, Nakamura E (1998) Across-arc variation of Li isotopes in lavas and implication for crust/mantle recycling at subduction zones. Earth Planet Sci Lett 163:167–174

Nishio Y, Nakai S, Kogiso T, Barsczus HG (2005) Lithium, strontium, and neodymium isotopic compositions of oceanic island basalts in the Polynesian region: constraints on a Polynesian HIMU origin. Geochem J 39:91–103

Penniston-Dorland SC, Bebout GE, Pogge von Strandmann PA, Elliott T, Sorensen SS (2012) Lithium and its isotopes as tracers of subduction zone fluids and metasomatic processes: evidence from the Catalina Schist, California, USA. Geochim Cosmochim Acta 77:530–545

Pogge von Strandmann PAE, Jenkyns HC, Woodfine RG (2013) Lithium isotope evidence for enhanced weathering during Oceanic Anoxic Event 2. Nat Geosci 6:668–672

Richter FM, Davis AM, DePaolo DJ, Watson EB (2003) Isotope fractionation by chemical diffusion between molten basalt and rhyolite. Geochim Cosmochim Acta 67:3905–3923
Richter F, Watson B, Chaussidon M, Mendybaev R, Ruscitto D (2014) Lithium isotope fractionation by diffusion in minerals. Part 1: pyroxenes. Geochim Cosmochim Acta 126:352–370
Rudnick RL, Ionov DA (2007) Lithium elemental and isotopic disequilibrium in minerals from peridotite xenoliths from far-east Russia: product of recent melt/fluid–rock reaction. Earth Planet Sci Lett 256:278–293
Rudnick RL, Tomascak PB, Njo HB, Gardner LR (2004) Extreme lithium isotopic fractionation during continental weathering revealed in saprolites from South Carolina. Chem Geol 212:45–57
Ryan JG, Kyle PR (2004) Lithium abundance and lithium isotope variations in the mantle sources: insights from intraplate volcanic rocks from Ross Island and Marie Byrd Land (Antarctica) and other oceanic islands. Chem Geol 212:125–142
Ryan JG, Langmuir CH (1987) The systematics of lithium abundances in young volcanic rocks. Geochim Cosmochim Acta 51:1727–1741
Teng F-Z, McDonough WF, Rudnick RL, Dalpé C, Tomascak PB, Chappell BW, Gao S (2004) Lithium isotopic composition and concentration of the upper continental crust. Geochim Cosmochim Acta 68:4167–4178
Tomascak PB, Carlson RW, Shirey SB (1999) Accurate and precise determination of Li isotopic compositions by multi-collector sector ICP-MS. Chem Geol 158:145–154
Tomascak PB, Widom E, Benton LD, Goldstein SL, Ryan JG (2002) The control of lithium budgets in island arcs. Earth Planet Sci Lett 196:227–238
Tomascak PB, Langmuir CH, le Roux PJ, Shirey SB (2008) Lithium isotopes in global mid-ocean ridge basalts. Geochim Cosmochim Acta 72:1626–1637
Tomascak PB, Magna T, Dohmen R (2016) Advances in Lithium Isotope Geochemistry. Springer International Publishing, New York. https://doi.org/10.1007/978-3-319-01430-2
Zack T, Tomascak PB, Rudnick RL, Dalpé C, McDonough WF (2003) Extremely light Li in orogenic eclogites: the role of isotope fractionation during dehydration in subducted oceanic crust. Earth Planet Sci Lett 208:279–290

Lithophile Elements

Frances E. Jenner[1] and Hugh StC O'Neill[2]
[1]Department of Environment, Earth and Ecosystems, The Open University, Milton Keynes, Buckinghamshire, UK
[2]Research School of Earth Sciences, Australian National University, Canberra, Australia

Definition

Lithophile is a term used to refer to elements that are preferentially partitioned into silicate minerals as opposed to sulfides or metals.

The Goldschmidt Classification of the Elements

Goldschmidt (1929; 1937) used various chemical considerations to classify elements as *lithophile* (coined from the Greek for "rock-loving," indicating it is found in silicates), *siderophile* ("iron-loving," therefore partitioning into the Fe-rich metal of planetary cores), *chalcophile* ("copper-loving," meaning it is found in sulfides, like Cu), and *atmophile* (gas-loving). The *Goldschmidt classification* of the elements derived predominantly from the distribution of elements between the various mineral phases that make up *meteorites*, but it can be predicted to a large extent from the standard-state Gibbs free energies of formation of the oxide ($\Delta_f G^\circ_{(Ox)}$) and sulfide ($\Delta_f G^\circ_{(sulf)}$) of the element in its lowest commonly encountered nonzero valence state. These quantities reflect the element's fundamental chemical properties in the chemical environment relevant to most geological processes. For metals (i.e., electropositive elements, meaning elements whose common valence state is positive), a large negative $\Delta_f G^\circ_{(Ox)}$ indicates lithophile tendencies, a positive or small negative difference ($\Delta_f G^\circ_{(Ox)} - \Delta_f G^\circ_{(sulf)}$) indicates chalcophile tendencies, and elements having neither $\Delta_f G^\circ_{(Ox)}$ nor $\Delta_f G^\circ_{(sulf)}$ very negative are likely to be siderophile. The behavior of Fe as summarized in the Gibbs free energies of formation of FeO and FeS can be taken as the benchmark. Electronegative elements are either lithophile or atmophile. The distinction between siderophile and chalcophile elements is not as clear-cut as that between lithophiles on one hand and siderophiles plus chalcophiles on the other, since sulfides are miscible in molten Fe-rich metal. So in the context of core-forming processes in planets, the term "siderophile" is often used to cover both siderophile and chalcophile elements.

The lithophile elements are typically subdivided according to their cosmochemical volatility, a property that is quantified using a theoretical concept, the element's "condensation temperature," Tc, defined as the calculated temperature at which 50% of the element would be condensed out of a cooling gas of solar composition, assuming a constant pressure (traditionally, 10^{-4} bars) and chemical equilibrium (Lodders 2003). With this classification:

Refractory lithophile elements (T_c = 1850–1355 K): a group of 28 elements with Tc greater than the condensation temperatures of the main planet-forming elements Mg, Si, and Fe. The group consists of Be, Al, Ca, Sc, Ti, Sr, Y, Zr, Nb, Ba, the 14 *lanthanide rare earth elements* (REE), Hf, Ta, Th, and U. In the past, V often used to be included, but this element is now usually classified as *siderophile*. Two of these elements, Ca and Al, are major elements in rocky planets and, together with Ti, are essential for forming refractory phases such as hibonite (ideally, $CaAl_{12}O_{19}$) and perovskite ($CaTiO_3$) that host the other refractory lithophile elements in Ca-Al-rich inclusions (CAIs) in unmetamorphosed, hence texturally primitive chondritic meteorites. The relative proportions of the refractory lithophile elements are approximately the same in nearly all groups of *chondrites*, and these proportions match those of the solar composition, as deduced from spectroscopic measurements of the solar photosphere, within uncertainty. Until recently it was widely assumed that the

refractory lithophile elements occur in the bulk silicate Earth in the solar proportions (e.g., Palme and O'Neill 2014), but this assumption is now being questioned (e.g., O'Neill and Palme 2008).

Main group lithophile elements (T_c = 1355–1250 K): Mg and Si. These elements are calculated to condense out of the solar nebular (initially as forsterite, Mg_2SiO_4) at a similar temperature to the most abundant *siderophile* elements, Fe, Ni, and Co. Mg and Si with their associated *oxygen* plus Fe are the main constituents of the rocky planets.

Moderately volatile lithophile elements (T_c = ≥1250 K): *alkali earth metals* (Li, Na, K, Rb, and Cs), *halogens* (F, Cl, Br, and I), and B. These elements are depleted relative to Mg and their solar proportions in all chondritic *meteorites*, except for the CI carbonaceous *chondrites*. They are also depleted in the bulk silicate Earth composition, but with a quite different pattern of depletion compared to any of the depletion patterns recorded in the chondrites (O'Neill and Palme 2008).

Summary and Conclusion

The Goldschmidt classification scheme should be viewed as a guide rather than a definitive classification scheme, because the chemical affiliation of elements is sensitive to differences in temperature, pressure, redox conditions, and sulfur contents. For example, in aubrites (enstatite achondrites), the REEs are almost entirely chalcophile, being held in oldhamite (CaS). Similarly some Si occurs in the metal phase of enstatite chondrites, and it is commonly supposed that the low Si/Mg of the bulk silicate Earth is due to some Si partitioning into **Earth's core** (Palme and O'Neill 2014). There may also be a small deficit of Nb in the bulk silicate Earth, which could be similarly explained (e.g., Wood et al. 2008), as Nb is the refractory lithophile element with the greatest **siderophile** tendency. Hence, whether an element is classified as "lithophile" or not depends on the geochemical process that is being documented.

Cross-References

- ▶ Alkali and Alkaline Earth Metals
- ▶ Chalcophile Elements
- ▶ Chondrites
- ▶ Earth's Core
- ▶ Lanthanide Rare Earths
- ▶ Meteorites
- ▶ Oxygen
- ▶ Periodic Table
- ▶ Refractory Inclusions in Chondritic Meteorites
- ▶ Siderophile Elements

References

Goldschmidt VM (1929) The distribution of the chemical elements. Nature 124:15–17

Goldschmidt VM (1937) The principles of distribution of chemical elements in minerals and rocks. The seventh Hugo Muller Lecture, delivered before the chemical society on 17 Mar 1937. J Chem Soc (Resumed), 655–673

Lodders K (2003) Solar system abundances and condensation temperatures of the elements. Astrophys J 591:1220–1247

O'Neill HSC, Palme H (2008) Collisional erosion and the non-chondritic composition of the terrestrial planets. Phil Trans R Soc A Math Phys Eng Sci 366:4205–4238

Palme H, and St.C O'Neill H (2014) Compositional estimates of mantle composition. In: Carlson RW (ed) Treatise on Geochemistry: The Mantle and Core. Elsevier-Pergamon, Oxford

Wood BJ, Wade J, Kilburn MR (2008) Core formation and the oxidation state of the earth: additional constraints from Nb, V and Cr partitioning. Geochimica et Cosmochimica Acta 72:1415–1426

Low-Temperature Geochemistry

Tori Z. Forbes
Department of Chemistry, University of Iowa, Iowa City, IA, USA

Synonyms

Environmental Geochemistry

Definition

Low-temperature or environmental geochemistry is the study of chemical processes that occur in the earth's surficial environments. While basic aqueous chemistry principles, including acid-base equilibrium, reduction-oxidation reactions, and solubility, are the driving force behind most phenomena, interconnections between geology, hydrology, biology, and atmospheric science require an interdisciplinary approach to investigating these systems. Low-temperature geochemistry is a broad field, but major areas of study include mineral precipitation, chemical weathering, soil chemistry, sedimentary processes and diagenesis, biogeochemical cycles, and contaminant transport.

Introduction to Low-Temperature Geochemistry

In general, geochemistry can be defined as the study of the chemical composition and changes of the earth and other celestial bodies. We further define the subject based upon the overall geologic environment, pressure, or temperature. While the delineations in temperature are somewhat vague, the most

accepted definition for low-temperature geochemistry describes the chemistry of minerals, rocks, solid, water, and atmosphere when the temperature is below 200 °C (Guangzhi 1996). This temperature range typically occurs on the earth's surface or within the first few km of the lithosphere. Surface water, soils, exposed rock formations, groundwater, aquifers, and hydrothermal vents can all be considered systems that are regulated by low-temperature geochemical processes.

Due to the relationship between geochemistry and natural processes that occur within the environment, low-temperature geochemistry is often presented within the context of environmental geochemistry (Ryan 2014). No region on the surface of the earth can be considered a closed system so there are continuous interactions taking place between the various components. Understanding complex environmental systems requires thinking about phenomenon on molecular, regional, and global scales. In addition, it requires using an interdisciplinary approach due to the deep and complex relationship between atmospheric, hydrologic, biotic, and geologic systems (Fig. 1).

Low-temperature geochemistry is also intimately tied to human society because our activities have significant impacts on the processes that are happening on the earth's surface. Sometimes these activities are direct, such as the release of chemical waste form a mine and milling piles. Other times, the connections are less direct, such as the release of small amounts of a compound that undergo chemical transformations that result in a new compound that has much greater detrimental effects on the ecosystem. Thus a major thrust of low-temperature geochemistry is to understand the impact of humans on these processes on the molecular, regional, and global scales.

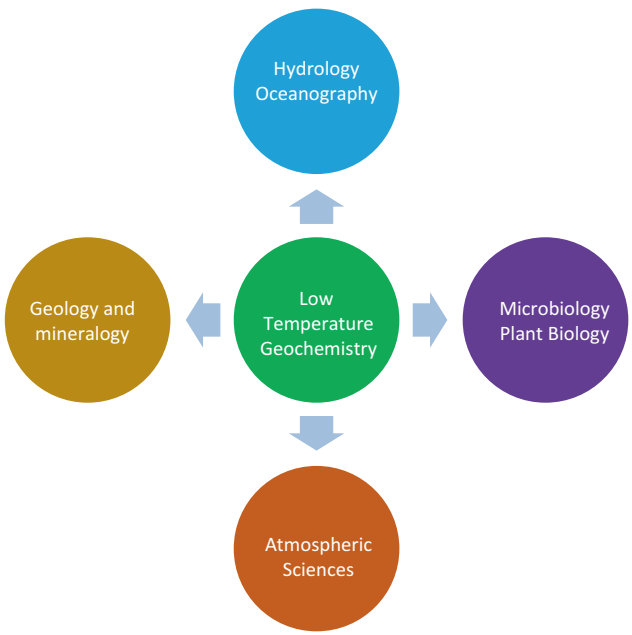

Low-Temperature Geochemistry, Fig. 1 Low-temperature geochemistry requires interdisciplinary thinking due to the interconnections between geology, biology, hydrology, and atmospheric sciences

History and Basic Principles

Low-temperature geochemistry is a relatively new subdiscipline of geology, developing from the molecular scale before encompassing global phenomena. The Norwegian scientist, Victor M. Goldschmidt is often considered to be the founder of geochemistry with his important contributions to mineral reactivity and his guiding principles on elemental substitutions in crystalline phases (Reinhardt 2001). The idea of geochemistry was broadened by the work of Vladimir I. Vernadsky, who determined that chemical reactions resulted in the formation of minerals and more specifically that living organisms could reshape geological systems or even planets (Ryan 2014). Investigations regarding the consequences of anthropogenic activities on environmental and geochemical systems began in the 1960s with concerns regarding contamination of the air, water, and soil. Seminal work during this period found that pesticides were a significant threat to ecosystem health (Carson 1962), acid rain was caused by industrial emissions (Likens and Bormann 1974), and humans were impacting the global climate through emissions of greenhouse gasses (Hansen et al. 1981). Current investigations in low-temperature geochemistry span the range of topics and scale that was laid down by the leaders in this area.

At the most basic level, low-temperature geochemical processes are controlled by fundamental chemical principles that control reactions in aqueous systems (Fig. 2). A major factor in the formation and dissolution of minerals and rocks is acid-base equilibrium and hydrogen ion activity (pH). In water, the hydrogen ion activity (pH) is the driver for many geochemical properties including dissolution, precipitation, crystallization, gas solubilities, and biochemical reactions. The pH of the solution can also be influenced by inorganic constituents, most notably the equilibrium between dissolved carbon dioxide and the carbonate anion (Drever 1997). Reduction and oxidation (redox) reactions are also of importance for elements that can access multiple oxidation states. Hydrogen, nitrogen, oxygen, sulfur, iron, and manganese are abundant and important redox active elements in geochemical systems (Drever 1997). These elements typically control the redox conditions within aqueous solutions, which in turn can determine the speciation, mobility, and toxicity of trace metals and organic compounds. Organisms, such as microbes and fungi, also play an important role in harnessing the chemical energy within geochemical systems to control the redox conditions, molecular speciation, and precipitation of mineral phases. Equilibria between the various inorganic and organic components and their overall energetics and stability (thermodynamics) ultimately determine the overall chemical

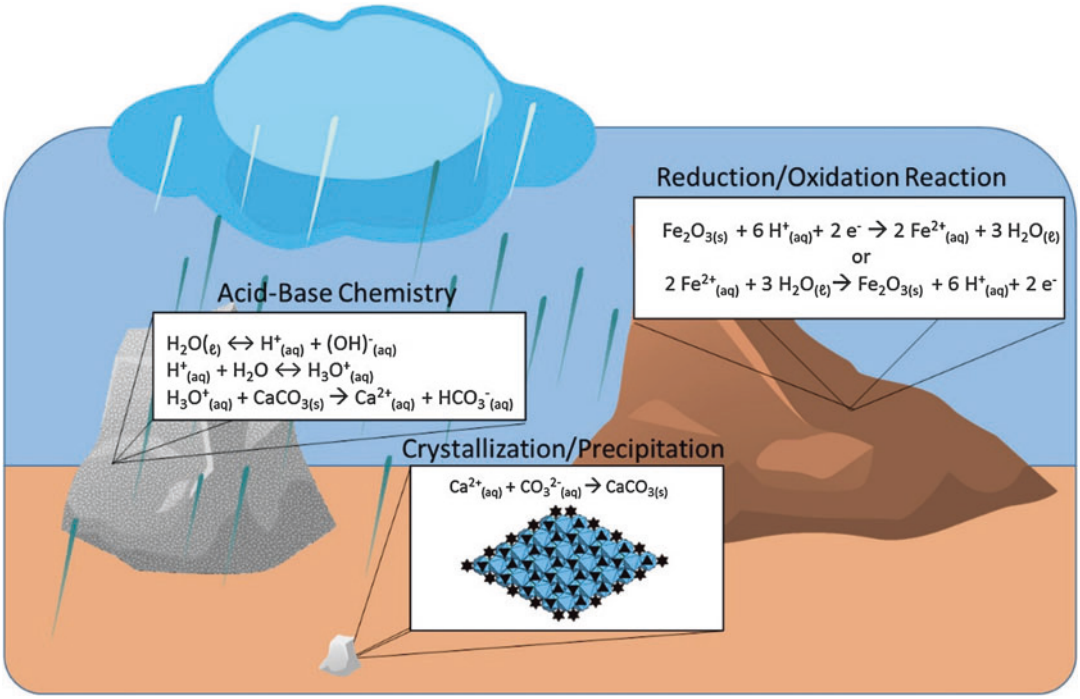

Low-Temperature Geochemistry, Fig. 2 Fundamental chemical reactions, such as acid-base, reduction-oxidation, and crystallization/precipitation, control low-temperature geochemical processes

Low-Temperature Geochemistry, Table 1 Common mineral classes and phases formed from low-temperature geochemistry processes

Hydroxides	**Carbonates**	**Sulfates**
Brucite ($Mg(OH)_2$)	Calcite or aragonite ($CaCO_3$)	Gypsum ($CaSO_4 \cdot 2\,H_2O$)
Manganite MnO(OH)	Magnesite ($MgCO_3$)	Anhydrite ($CaSO_4$)
Goethite (α-FeO(OH)	Siderite ($FeCO_3$)	Cessurite ($SrSO_4$)
Ferrihydrite	Cerussite ($PbCO_3$)	Anglesite ($PbSO_4$)
Bauxite[a]	Malachite $Cu_2CO_3(OH)_2$	
	Dolomite ($MgCa(CO^3)_2$	**Borates**
Clays		Kernite ($Na_2B_4O_6(OH)_2 \cdot 3H_2O$)
Kaolinite ($Al_2Si_2O5(OH)_4$)	**Halides**	Borax ($Na_2B_4O_5(OH)_4 \cdot 8\,H_2O$)
Illite ($K, H_3O)(Al, Mg, Fe)_2(Si, Al)_4O_{10}[(OH)_2, (H_2O)]$	Halite (NaCl)	Ulexite ($NaCaB_5O_6(OH)_6 \cdot 5H_2O$)
	Sylvite (KCl)	Colemanite ($CaB_3O_4(OH)_3 \cdot H_2O$)

[a]Mixture of diaspore, gibbsite, and boehmite

reactions and products within the environment (Drever 1997). These basic chemical principles can be applied to a wide range of geologic media, environments, and processes, and the broad categories of low-temperature geochemistry will be described in the following sections.

Major Topics in Low-Temperature Geochemistry

Mineral Precipitation/Crystallization and Chemical Weathering

A wide range of common mineral phases is formed under low-temperature geochemical conditions by precipitation and crystallization reactions. Precipitation is the direct result of reaching the solubility limit of an aqueous species that leads to the formation of a solid phase (Jarvinen 2009). Crystallization can be considered a precipitation reaction, but more specifically, one that has long-range ordering of the chemical constituents within the crystalline lattice. Amorphous phases may form from precipitation reactions, but minerals must have some degree of crystallinity (Jarvinen 2009). Table 1 provides a summary of common mineral classes and phases that form under low-temperature geochemical environments, although there are a number of less abundant minerals that form under similar conditions. The major mineral types that typically form in surficial or hydrothermal environments include hydroxides, borates, carbonates, halides, sulfides, and clays (Klein 2002).

Changes in chemical equilibria related to pH or redox conditions or through the evaporation of water can result in the precipitation of aqueous species into a solid mineral. Acidic waters can dissolve metal cations, such as Fe(III) and Al(III) and upon mixing with more neutral freshwater, causes the formation of hydrolysis products. These hydrolysis products have low solubility in water and cause the precipitation of hydroxide phases (Stumm and Morgan 1981). In some cases, the metal cation is present in the reduced form, and initial oxidation is required for the precipitation reaction to occur. Such is the case for dissolved Fe (II) oxidizing in the presence of O_2 to form Fe(III), which is then followed by the hydrolysis and precipitation reaction (Stumm and Morgan 1981; Cornell and Schwertmann 2004). Evaporite minerals are formed when saline lakes or restricted sea bodies evaporate, creating extensive deposits in arid regions (Schreiber and Tabakh 2000; Klein 2002). Halides and sulfates are the most common evaporite mineral classes, with gypsum and halite deposits constituting the most common mineral species within the natural deposits (Spencer 2000; Screiber and Tabakh 2000). Carbonates can be marine in origin, and over the history of the earth there has been a shift from low-temperature chemical precipitation to biogenic sources, such as benthic and pelagic organisms (Morse et al. 2007). Calcium carbonate is also a major constituent in freshwater systems and is widely observed in sedimentary rocks and as the building blocks of cave formations (Drever 1997; Klein 2002; Kotz et al. 2006; James and Jones 2015). Borate mineral deposits can be found in marine basins, but the largest known deposits originated as chemical precipitates from thermal springs or hydrothermal solutions associated with volcanic activities (Kistler and Smith 1975; Argust 1998).

Chemical weathering is the change in the composition of the original geologic media, often in the presences of water that occur because of oxidation, hydrolysis, and dissolution of the elements present in the parent rock (Carroll 1962). Some hydroxide phases, like bauxite, form in surficial or low-temperature supergene environments by leaching of silica from aluminum-bearing rocks (Schellmann 1994). The leaching process occurs through initial dissolution of the mineral lattice by the slightly acidic rainwater, followed by hydrolysis and precipitation of the insoluble hydroxide phase upon an increase in the pH of the pore water (Whittington and Muir 2000). Hydrolysis reactions occur when anhydrous mineral absorbs water and water dissociates to H^+ and OH^- ions, which interact with the cations present in the solid and result in structural changes to the solid-state material (Reaction Scheme 1). Overall the reaction causes the formation of a secondary mineral phase from the parent rock, plus soluble species that are removed as the water flows over the surface. Other hydroxide phases, such as goethite and ferrihydrite, can form from an initial oxidation step, such as the oxidation both sulfur and iron in pyrite, followed by hydrolysis and precipitation (Lowson 1982; Nordstrom 1982). Dissolution reactions result in the breakdown of the solid-state mineral into soluble aqueous species. One of the most common mechanisms for dissolution occurs when CO_2 in the atmosphere is dissolved in rainwater to form carbonic acid, which is also referred to as carbonation reactions (Reaction Scheme 3) (Ryan 2014).

Reaction Scheme 1 (Hydrolysis)

$$2\,KAlSi_3O_8(s) + 2\,H^+(aq) + 9\,H_2O_{(\ell)} \rightarrow H_4Al_2Si_2O_{9(s)} + 4\,H_4SiO_{4(aq)} + 2\,K^+{}_{(aq)}$$

Reaction Scheme 2 (Oxidation)

$$FeS_{2(s)} + 15/4\,O_{2(aq)} + 7/2\,H_2O_{(\ell)} \rightarrow Fe(OH)_{3(s)} + 2\,H_2SO_{4(aq)}$$

Reaction Scheme 3 (Dissolution/Carbonation)

$$CO_{2(aq)} + H_2O_{(\ell)} \rightarrow H_2CO_{3(aq)}$$

$$CaCO_{3(s)} + H_2CO_{3(aq)} \rightarrow Ca^{2+}{}_{(aq)} + 2\,H_2CO_{3(aq)}$$

Sedimentary Processes and Diagenesis

Chemical weathering results in the breakdown of rocks and formation of soils, but sedimentation processes utilize geochemical reactions to create new geologic deposits. Sedimentary rocks are formed by the accumulation of sediments (small particles of gravel, sand, silts, and clays) that are held together through lithification (West 1995). Early diagenesis or lithification is the process by which unconsolidated sediments are converted into solid rock and can occur via mechanical (compaction), geochemical (cementing or crystallization), or a combination of both processes. Cementation involves filling the pore space between the individual sediment grains with a binding agent. Under low-temperature regimes, calcium carbonate or iron hydroxides can precipitate from water seeping through the sediments, resulting cementation and lithification to occur (West 1995). Crystallization processes typically focus on the transformation of amorphous or colloidal substances into crystalline mineral phases and generally occur after deposition and even in some cases after lithification of the sedimentary rock.

Changes in the sedimentary rocks at temperatures and pressures lower than the formation of metamorphic rocks is considered late diagenesis (Teodorovich 1961). It is important to point out that late diagenensis is a different process than chemical weathering described above. Recrystallization processes can occur during later diagenesis, most notably in limestones, where aragonite in contact with freshwater can convert into calcite crystals within the solid sedimentary rock. Burial of organic matter within sedimentary rocks results in the chemical transformations of lipids, proteins, carbohydrates, and lignin-humic compounds into hydrocarbons,

which are the major constituents of methane, petroleum, and coal deposits (Singer and Muller 1983).

Chemistry of Soils

Low-temperature geochemical processes are the driving force for the formation and evolution of soils in the surficial environments. Soils are porous media created at the surface by weathering processes and differ from weather rocks because they show a vertical stratification (Sposito 1989). Mechanical weathering processes can result in the breakdown of bulk rock into smaller particles and is combined with chemical weathering processes to form the inorganic components of soils (Sposito 1989). Given the presence of water and dissolved chemical components, soils are excellent environments for microbes and fungi that can control redox reactions and breakdown organic matter (Ehlrich and Newman 2009). This leads to a complex mixture of organic components that are hospitable to plants and larger organisms and a rich and diverse biogeochemical system.

Soils are in continuous flux and exchange both matter and energy with the surrounding air, water, and biome (Sposito 1989). Meteoric water is continually percolating through soils, dissolving soluble chemical species, and transporting it through the soil column. Atmospheric gasses can easily penetrate this porous media, resulting in additional weathering and oxidation reactions (Sposito 1989). Microbial communities can continuously evolve through changes in the chemical and physical conditions of the soil (Ehlrich and Newman 2009). Humans can also influence the soil environment, either directly (intensive agricultural efforts) or indirectly (acid rain), and in turn the soil quality has impacts on overall health of the population (Locke and Zablotowicz 2004; Singh and Agrawal 2008; Brevik and Sauer 2015).

Biogeochemical Cycling

The surficial environment can be considered an open system with continual chemical fluxes between the various components; thus there is continuous movement of elements throughout the global system (Schlesinger 1997). As discussed in the previous sections, meteoric water moves through soils and porous rocks, picking up various chemical components through weathering processes. Some of the chemical constituents in the water can undergo precipitation reactions within the soil or porous rock, resulting in a sink or removal of that particular element from the solution. Interactions with plants and organisms can also cause elements to either remain in the soil or biome or be transported with the hydrologic flux. Other elements can remain dissolved in the water, where it is transferred through the subsurface system and can then be recharged into surface water through seeps and springs. Additional precipitation or redox reactions can occur within the surface water either resulting in precipitation or dissolution of the chemical component, where there can again be interactions with biological systems or dispersion into the atmosphere. Once in the atmosphere, additional chemical reactions can occur that result in addition global dispersion or wet/dry deposition. The impact of human activities must also be accounted for when considering the flux of elements between the biological, geological, hydrological, and atmospheric systems. It is the chemical reactions that occur within these systems combined with the flow and mass balance of elements of interest within these different domains that constitutes the study of biogeochemistry (Schlesinger 1997).

A well-known biogeochemical cycle as illustrated in Fig. 3, which describes the different chemical processes that control the flux of nitrogen throughout the soil, ocean, and atmosphere (Schlesinger 1997). A portion of the nitrogen is

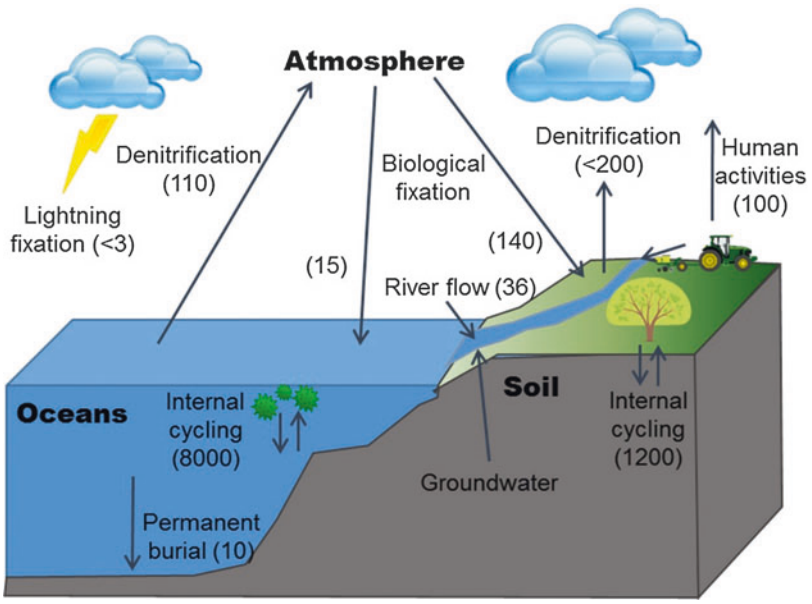

Low-Temperature Geochemistry, Fig. 3 The biogeochemical cycle for nitrogen. Values are provided by Schlesinger (1997) and are in units of 10^{12} g N per year

stored as a reservoir within the organic matter of the soil that can undergo chemical reactions, such as mineralization (Reaction Scheme 4) and nitrification (Reaction Scheme 5). Within the soil column, nitrogen is also involved with an internal cycle of uptake and release within terrestrial plants and additional mass is added to the soil through biological fixation (Reaction Scheme 6). Removal of nitrogen from the soil can occur through denitrification (Reaction Scheme 7) and release to the atmosphere. A second pathway for release is the dissolution of the nitrogen in the form of $NO_3^-{}_{(aq)}$ or $NH_4^+{}_{(aq)}$ that can be transported either by the subsurface groundwater or as run-off into freshwater streams, rivers, and lakes. Eventually the water from the surface and subsurface sources flow into the ocean where there is a large reservoir of dissolved nitrogen species. An internal cycle also occurs in the ocean with the uptake and release of nitrogen by phytoplankton and marine organisms and burial in the ocean sediments. Flux to the ocean can also occur through nitrogenase-catalyzed biological fixation, and removal of nitrogen to the atmosphere occurs through denitrification processes (Kim and Reese 1994). Within the atmosphere, nitrogen can be converted to different forms through fixation by lightning or photocatalyzed redox reactions. Humans can also add to the global nitrogen cycle through release of NO_x gasses or through the overfertilization of agricultural lands (Fields 2004). Changes in the amount of nitrogen in the air or freshwater systems that is the result of human activity can cause significant changes in the nitrogen reservoirs for these systems. This has impacts on the state of these systems as evidenced by the production of acid rain or the eutrophication of the coastal regions, particularly the Gulf of Mexico (Schlesinger 1997; Fields 2004).

Reaction Scheme 4 (mineralization)

$$R - NH_2 + H_2O \rightarrow NH_3 + R - OH$$

Reaction Scheme 5 (nitrification)

$$NH_3 + \frac{1}{2}O_2 + 2e^- \rightarrow NH_2OH + H_2O \rightarrow NO_2^- + 5\,H^+ + 2\,e^-$$

Reaction Scheme 6 (nitrogen fixation)

$$N_2 + 8H^+ + 6e^- \rightarrow 2NH_4^+$$

Reaction Scheme 7 (denitrification)

$$2\,NO_3^- + 12H^+ + 10\,e^- \rightarrow N_2 + 6H_2O$$

Changes that human activity has on global biogeochemical cycles for a wide range of elements are a major area of current scientific investigations. Global warming is the direct result of changes in the carbon cycle, and understanding the details of the chemical reactions that result in fluxes between the different systems is important for more accurate climate models and means for combating climate change (Hansen et al. 1981). As described above, overfertilization of agricultural lands causes an influx of elements that are then washed into freshwater rivers in lakes. While excess nitrogen causes problems in marine environment, the high influx of phosphorus results in the eutrophication of freshwater systems (Correll 1998). Human activity can also influence the global cycling of trace metals due to their use in industrial applications or modern living and then release through improper disposal. Lead (Pb) is an example a trace metal that was impacted by anthropogenic effects when it was added as a fuel additive in the 1970s (Shotyk and Le Roux 2005). During the combustion process, lead was released into the atmosphere through exhaust systems that resulted in dry and wet deposition into surface waters and land. Increased concentrations of lead were observed in soils and the human population until polices were adopted that minimized the use of lead as an additive and in industrial processes (Shotyk and Le Roux 2005).

Contaminant Transport

Low-temperature geochemical processes control the oxidation state and speciation of elements that are harmful to human and ecosystem health, which in turn determines the mobility and fate of contaminants in the environment. Release of contaminants into the environment can be through natural processes or through human activities that catalyze the release of toxic elements and compounds into the environment (McCarthy and Zachara 1989; Brown and Calas 2011). For example, weathering and dissolution of host rocks can occur either through natural ore deposits that are exposed to the atmosphere or groundwater or the leaching from mine and milling tailings. Typically this process is controlled both by the acid-base chemistry of the meteoric water and redox reactions when the rocks are exposed to oxygen present in the atmosphere. Mobility of the contaminant phases in surface or subsurface waters depends on the aqueous speciation and water-rock interactions. Surface interactions typically involve adsorption and binding of the contaminant to mineral phases, which can limit its mobility in the environment (McCarthy and Zachara 1989; Brown and Parks 2001). Contaminant adsorption on mineral surfaces can be reversible and again controlled by the low-temperature geochemical parameters. Interactions with the microbial community can also impact the fate of contaminants in soils and sediments, typically by control of redox parameters and precipitation reactions (McCarthy and Zachara 1989; Ehrilich and Newman 2006). Ultimately the chemical speciation controls the mobility of the contaminant in water, uptake by biological organisms, and the overall public health risk.

Inorganic elements that are of concern for public and ecosystem health include heavy metals, radioactive isotopes, and problematic main group elements. Heavy metals, such as mercury, are naturally occurring elements that become contaminants in the environment due to natural processes (redox, microbial activity) but can also be caused by human activities,

such as mining, release from industrial processes, or accidental dispersion. Speciation of mercury is a major factor in determining health risk, with methylation by bacterial communities resulting in increased uptake and bioaccumulation (Boening 2000). Arsenic is an example of a problematic main group element that occurs naturally and becomes soluble when in the reduce form (arsenite, AsO_3^{3-}) (Bowell et al. 2015). Countries such as Bangladesh, India, China, Mexico, and Argentina have significant arsenic contamination in water sources due to formation of strongly reducing aquifers or closed basins in arid or semiarid climates (Smedley and Kinniburg 2002). Uranium is a naturally occurring radioactive element that has health risks when ingested through drinking water or food sources due to its chemical and radiological toxicity (Brugge et al. 2005). Redox conditions also drive the mobility of uranium in environmental systems, with the oxidize uranyl (UO_2^{2+}) moiety forming soluble complexes over a range of environmentally relevant pH values (Maher et al. 2013).

Organic contaminants are typically the result of human activities and can be controlled by natural geochemical processes that are often utilized by environmental remediation. Volatile organic compounds, plasticizers, pesticides, and chlorinated compounds are the most common organic pollutants in drinking waters (Olson 2003). Due to concerns over the presence of hormones and endocrine disruptors, the USGS comprehensive survey conducted in 2002 also that found steroids (coprostanol, cholesterol), insect repellant (*N*,*N*-diethyltoluamide), caffeine, antimicrobial agents (triclosan), fire retardant (tri(2-chloroehtyl)phosphate), and detergent residues (4-nonylpentol) can be detected in surface waters and are now considered emerging contaminants (Kolpin et al. 2002; Lapworth et al. 2012). Sunlight can cause photochemical reactions that transform natural organic matter into other compounds, such as halogenated species (Mendez-Diaz et al. 2014). Some of these transformations can yield degradation products that are less harmful than the initial material, but some of these reactions were reported to be reversible. An endocrine disruptor, 17α-trembolone has been shown to degrade in the presence of light but then reform in the dark (Qu et al. 2013). Chemical spills of hydrocarbons or chlorinated compounds present in groundwater can be remediated through microbial degradation processes that utilize these compounds as an energy source. For example, tetrachloroethane and trichloroethane are common contaminants in water, but under anerobic conditions microbial communities can be transformed to less chlorinated dichloroethane and vinyl ethane for natural attenuation (Bradley et al. 2005).

Summary

Low-temperature geochemistry is the study of chemical processes that occur in a complex and ever changing environment. It requires understanding fundamental chemical principles applied to geology, hydrology, biology, and atmospheric systems to understand some of the most important processes on the surface of the earth. Mineral precipitation, chemical weathering, sedimentation, diagenesis, soil science, biogeochemical cycling, and contaminant transport impact natural ecosystems and human society. Low-temperature geochemistry also provides a means to understand how interconnected we are with natural processes and our actions can cause significant impacts on global processes.

Beginning with fundamental elemental processes that occur within solid-state minerals and branching out into global topic, low-temperature geochemistry continues to be an important area of scientific study. Continued interest in combating climate change requires advanced understanding of how rocks, soils, natural bodies of water, and the atmosphere are connected through chemical, physical, and biological processes. As we continue to change the landscape and release new chemicals into the environment, there is increased efforts to determine the impact of these emerging contaminants on the ecosystem. Given our relationship and reliance on the natural world, understanding the geochemical processes that occur in low-temperature, surficial environments will continue to be a key research focus for human and global health.

Cross-References

- Biogeochemistry
- Carbon Cycle
- Chemical Weathering
- Diagenesis
- Soils

References

Argust P (1998) Distribution of boron in the environment. Biol Trace Elem Res 66:131–143

Boening DW (2000) Ecological effects, transport, and fate of mercury: a general review. Chemosphere 40:1335–1351

Bowell RJ, Alpers CN, Jamieson HE, Nordstrom DE, Majzlan J (2015) Arsenic: environmental geochemistry, mineralogy, and microbiology, Reviews in mineralogy and geochemistry, vol 79. American Mineralogical Society of America, Washington, DC

Bradley PM, Carr SA, Baird RB, Chapelle FH (2005) Microbial degradation of chloroethenes in groundwater systems. Hydrogeol J 8:104–111

Brevik EC, Sauer TJ (2015) The past, present, and future of soils and human health studies. Soil 1:35–46

Brown GE, Calas G (2011) Environmental mineralogy – understanding element behavior in ecosystems. Compt Rendus Geosci 343:90–112

Brown GE, Parks GA (2001) Sorption of trace elements on mineral surfaces: modern perspectives from spectroscopic studies, and comments on sorption in the marine environment. Int Geol Rev 43:963–1073

Brugge D, deLemos JL, Oldmixon B (2005) Exposure pathways and health effects associated with chemical and radiological toxicity of natural uranium: a review. Rev Environ Health 20:173–199
Carroll D (1962) Rainwater as a chemical agent of geologic processes. A review geological survey water supply paper, vol 1535-G. pp 1–16
Carson R (1962) Silent spring Houghton Mifflin Harcourt, Boston
Cornell RM, Schwertmann U (2004) The Iron oxides: structure, properties, reactions, occurrences, and uses, 2nd edn. Wiley, Berlin
Correll DL (1998) The role of phosphorus in the eutrophication of receiving waters: a review. J Environ Qual 27:263–266
Drever JI (1997) The geochemistry of natural waters: surface and Roundwater environments, 3rd edn. Princeton Hall Publishing, Upper Saddle River
Ehlrich HL, Newman DK (2009) Geomicrobiology, 5th edn. CRC Press, Boca Raton
Ehrilich HL, Newman DK (2006) Geomicrobiology, 5th edn. Taylor and Francis Group, LLC., Boca Raton
Fields S (2004) Global nitrogen: cycling out of control. Environ Health Perspect 112:A556–A563
Guangzhi T (1996) Low temperature geochemistry. Science Press, Beijing
Hansen J, Johnson A, Lacis S, Lebedeff S, Lee P, Rind D, Russell G (1981) Climate impact of increasing atmospheric carbon dioxide. Science 213:957–966
James NP, Jones B (2015) Origins of carbonate sedimentary rocks. Wiley VCH, Berlin
Jarvinen G (2009) Precipitation and crystallization processes. Los Alamos National Laboratory, Los Alamos
Kim J, Reese DC (1994) Nitrogenase and nitrogen fixation. Biochemistry 33:389–397
Kistler RB, Smith W (1975) Boron and borates. In: Lefond SJ (ed) Industrial rocks and minerals. American Institute of Mining, Metallurgical and Petroleum Engineers, Englewood
Klein C (2002) Mineral science. Wiley, New York
Kolpin DW, Furlong ET, Meyer MT, Thurman EM, Zaugg SD, Barber LB, Buxton HT (2002) Pharmaceuticals, hormones, and other organic wastewater contaminants in U.S. streams, 1999–2000: a national reconnaissance. Environ Sci Technol 36:1202–1211
Kotz JC, Treichel PM, Weaver GC (2006) Chemistry and chemical reactivity. Thomson Learning Inc., Belmont
Lapworth DL, Baran N, Stuart ME, Ward RS (2012) Emerging organic contaminants in groundwater: a review of sources, fate and occurrence. Environ Pollut 163:287–303
Likens GE, Bormann FH (1974) Acid rain: a serious regional environmental problem. Science 184:1176–1179
Locke MA, Zablotowicz RM (2004) Pesticides in soil – benefits and limitations to soil health. In: Schjonning P, Elmholt S, Christensen BT (eds) Managing soil quality: challenges in modern agriculture. CABI Publishing, Wallingford
Lowson RT (1982) Aqueous oxidation of pyrite by molecular oxygen. Chem Rev 82:461–497
Maher K, Bargar JL, Brown GE (2013) Environmental speciation of actinides. Inorg Chem 52:3510–3532
McCarthy JF, Zachara JM (1989) Subsurface transport of contaminants. Environ Sci Technol 23:496–502
Mendez-Diaz JD, Shimabuku KK, Ma J, Ennumah ZO, Pignatello JJ, Mitch WA, Dodd MC (2014) Sunlight-driven photochemical halogenation of dissolved organic matter in seawater: a natural abiotic source of organobromine and organoiodine. Environ Sci Technol 48:7418–7427
Morse JW, Arvidson RS, Luttg A (2007) Calcium carbonate formation and dissolution. Chem Rev 107:342–381
Nordstrom DK (1982) Aqueous pyrite oxidation and the consequent formation of secondary iron minerals. In: Kittrick JA, Fanning DS, Hossner LR (eds) Acid sulfate weathering. Soil Science Society of America, Madison
Olson E (2003) What's on tap: grading drinking water in U.S. cities. Natural Resource Defense Council, Washington, DC
Qu S, Kolodziej EP, Long SA, Gloer JB, Patterson EV, Baltrusaitis J, Jones GD, Benchetler PV, Cole EA, Kimbrough KC, Tarnoff MD, Cwiertny DM (2013) Product-to-parent reversion of Trenbolone: unrecognized risks for endocrine disruption. Science 341:1441–1443
Reinhardt C (2001) Chemical sciences in the 21st century: bridging boundaries. Wiley VCH, Berlin
Ryan P (2014) Environmental and low-temperature geochemistry. Wiley, New York
Schellmann W (1994) Geochemical differentiation in laterite and bauxite formation. Can Underwrit 21:131–143
Schlesinger WH (1997) Biogeochemistry: an analysis of global change. Academic, San Diego
Schreiber BC, Tabakh ME (2000) Deposition and early alteration of evaporates. Sedimentology 47:215–238
Shotyk W, Le Roux G (2005) Biogeochemistry and cycling of lead. Met Ions Biol Syst 43:239–275
Singer A, Muller G (1983) Diagenesis in agrillaceous sediments. In: Larsen G, Chilingar GV (eds) Diagenesis in sediments and sedimentary rocks, vol 2. Elsevier Scientific Publishing, Amsterdam
Singh A, Agrawal M (2008) Acid rain and its ecological consequence. J Environ Biol 29:15–24
Smedley PL, Kinniburgh DL (2002) A review of the source, behavior and distribution of arsenic in natural waters. Appl Geochem 17:517–568
Spencer RJ (2000) Sulfate minerals in evaporite deposits. In: Alpers CN, Jambor JL, Nordstron DK (eds) Sulfate minerals: crystallography, geochemistry, and environmental significance, Reviews in mineralogy and geochemistry, vol 40. Mineralogical Society of America, Washington, DC, pp 173–192
Sposito G (1989) The chemistry of soils. Oxford University Press, Oxford, UK
Stumm M, Morgan JJ (1981) Aquatic chemistry. Wiley, New York
Teodorovich GI (1961) Authigenic mineral in sedimentary rocks. Springer Science, New York
West T (1995) Geology applied to engineering. Prentice Hall, Upper Saddle River
Whittington BI, Muir D (2000) Pressure acid leaching of nickel laterites: a review. Miner Process Extr Metall Rev Int J 21:527–599

Luminescence

Tori Z. Forbes
Department of Chemistry, University of Iowa, Iowa City, IA, USA

Definition

Luminescence is the creation of light by chemical or physical processes that does not involve heat. Photoluminescence, which uses light as the excitation source, can be observed in minerals and provides information regarding the presence of trace metals, formation of defect sites, growth conditions, and sample age. Spectroscopic methods can be utilized to determine chemical and physical properties of the mineral specimen, and dating of geologic media can be achieved through thermoluminescence techniques.

Basics of Luminescence

When an electron within a molecule or solid compound is promoted to an excited state through the absorption of energy, there are two possible processes that will return the electron to the ground state. Non-radiative transfer mechanism allows the energy to dissipate through translation, rotational, or vibrational motion of the atoms and occurs on the order of 10^{-11} to 10^{-10} s. Radiation processes release energy through the emission of a photon and are generally classified as luminescence (Ingle and Crouch 1988).

The process of luminescence can be further classified as either fluorescence or phosphorescence depending on the transfer of the electron within the excited state. After energy absorption and promotion, the electron can move between excited singlet states (where the spin of the electrons is still paired) through internal conversion and undergo vibrational relaxation until it reaches the lowest energy excited singlet state. Fluorescence occurs when a radiational transition between the excited singlet state and the ground singlet state results in the release of a photon and occurs on time scales of 10^{-10} to 10^{-6} s. When an electron absorbs energy, it can only be promoted to singlet states, but intersystem crossing can result in the formation of triplet states (where the spin of the electrons is not paired). Additional vibrational relaxation transfers the electron to the lowest energy triplet excited state, followed by radiational deactivation that occurs through the release of a photon. This process is called phosphorescence and takes place on slower time scales (10^{-4} to 10^{4} s) because of the need for intersystem crossing. Different categories of luminescence are distinguished through the excitation energy source (Fig. 1).

Photoluminescence is the most common category of luminescence and describes emission of photons after excitation by electromagnetic radiation. It often occurs through the absorption of ultraviolet or visible light, but some materials may absorb X-rays (X-ray excited luminescence). For both fluorescence and phosphorescence, resulting wavelength of released photon is longer than the absorbed light because the electron is promoted to higher energy excited states (Ingle and Crouch 1988). Energy of the photon released through photoluminescence is typically in the visible range but can also occur in the ultraviolet or infrared regions (Geake and Walker 1975; Rakovan and Waychunas 1996).

Luminescence can also occur when the electron is excited or released by other mechanisms. Cathodoluminescence is caused by promotion of the electron to the excited state with an electron beam (Gotze 2012). If a mechanical action (crushing, tricking, scratching, or rubbing) triggers an electrical excitation, then it can cause phosphorescence and is referred to as triboluminescence, mechanoluminescence, piezoluminescence, or fractoluminescence (Zink 1978; Sweeting 2001). In thermoluminescence, the electron was originally promoted by electromagnetic radiation or some other energy source and then trapped in the excited state (Wintle and Huntley 1982; Forman 1989). The trapping centers are generally defect sites caused by radioactive or stacking faults, but they can also be caused by ion substitution. Upon exposure to heat, the trapped electrons are released and fall back to the ground state, releasing a photon in the process (Wintle and Huntley 1982; Forman 1989).

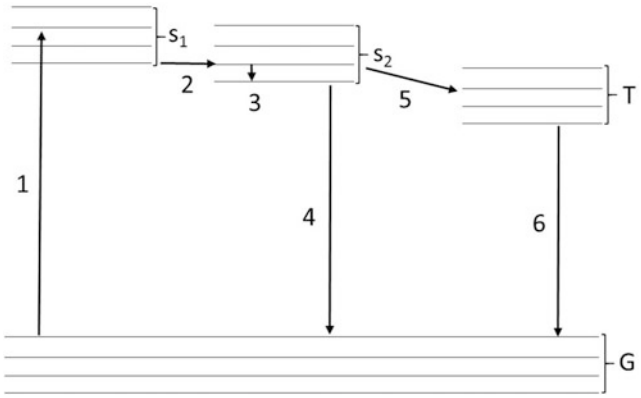

Luminescence, Fig. 1 Diagram of the luminescence process. (*1*) An electron is promoted from the ground state (*G*) to a singlet excited state (S_1) and can (*2*) transfer to a different singlet excited state (S_2). (*3*) Vibrational relaxation lowers the energy until (*4*) the electron moves to the ground state and releases a photon to create fluorescence. Alternatively, intersystem crossing (*5*) results in movement of the electron into an excited triplet state (*T*). (*6*) Phosphorescence occurs with electron transfer from the excited triplet state back to the ground state, which results in the release of a photon

Luminescence in Minerals

In most mineral phases that exhibit photoluminescence, there are atoms present with the correct separation of the energy levels to emit a photon in the visible or ultraviolet region (Rakovan and Waychunas 1996). These atoms are called activators and can be present in either bulk compositions or trace levels. A related process involves absorption of electromagnetic radiation or an electron beam by one atom (the sensitizer) which can then be transferred to the excited state of a second atom (the activator) before the release of a photon (Rakovan and Waychunas 1996). Common activators and sensitizers are manganese (II), chromium (III), tungstates, titanates, molybdates, zirconates, sulfide, uranyl, some hydrocarbons, and rare earth elements (Rakovan and Waychunas 1996; Gaft et al. 2005).

A less common mechanism for photoluminescence occurs through defect centers within the solid-state crystalline lattice. The luminescence mechanisms for defect sites are not

completely understood; however, a well-known type is the Frenkel defect or F-center (Rakovan and Waychunas 1996). This type of defect can occur in halite where the displacement of the Cl^- anion will leave a vacancy and an electron will inhabit the site as a means for overall charge balancing (Rodriguez-Lazcano et al. 2012). Within the vacancy, the electron can be present in an excited state, and photoluminescence occurs when transitions result in the release of a photon in the visible region.

In 1989, Dr. Gerhard Henkel published an exhaustive list of minerals that undergo luminescence and includes 566 mineral species and 59 related substances (Henkel 1989). Only a handful of minerals undergo fluorescence when pure phase, including scheelite ($CaWO_4$) and secondary hexavalent uranium minerals (autinite ($Ca(UO_2)_2(PO_4)_2 \cdot 10–12\ H_2O$)) (Gorobets and Sidorenko 1974; Nikl et al. 2000). Other common minerals such as calcite, fluorite, and apatite will fluoresce when trace amounts of activators (generally Mn^{2+} or UO_2^{2+}) are present in the solid-state materials (Machel et al. 1991; Calderon et al. 1992; Waychunas 2002). The Franklin mine (New Jersey, USA) is home to the largest number of fluorescent mineral specimens observed from one site, including some spectacular specimens that contain bright fluorescence and unusual crystal habits (Wilkerson 1962).

Other types of luminescence are rarer, but can be observed in a handful of mineral species. Thermoluminescence has been observed in apatite, calcite, fluorite, quartz, zircon, lepidolite, and some feldspars (McKeever 1985). In each of these cases, there must be activators present and the luminescence of the specimen is removed after heating. Triboluminescence has been reported in some minerals, but is generally not consistent between specimens. This is the case for calcite, feldspars, sphalerite fluorite, micas, and quartz (Walton 1977; Chapman and Walton 1983). Sphalerite samples are typically the most consistent, and the light associated with the triboluminescence can be observed in the dark.

Luminescence Zoning

Luminescence can be used as a tool for identifying different minerals within a specimen. Intercrystalline luminescence describes the difference in fluorescence for different mineral phases within the same host rock (Rakovan and Waychunas 1996). Typically this will be observed through difference in the color of the resulting fluorescence when the sample is placed underneath ultraviolet radiation. This type of luminescence can be used to distinguish minerals that may look similar in visible light or aid in the isolation of individual crystallites within the matrix. It is important to point out that luminescence may aid in identification, but cannot be used as the only method because certain mineral from the same species may fluoresce different colors from different locations due to difference in the trace element chemistry. Once a mineral has been identified, the specific fluorescent wavelength that it emits can sometimes be helpful to identify its place of origin (Rakovan and Waychunas 1996).

Intracrystalline zoning is defined as variations that occur within individual crystallites. Zoning within minerals occurs when there is a spatial difference in a particular chemical or physical property and provides information regarding the morphological history of the crystal, changes in the deposition environment, growth mechanism, and atomic-level structure. Zoning of the luminescence signal is caused by changes in the activator concentration and is usually the result of the growth process (Rakovan and Waychunas 1996). Zoning can occur as concentric rings or as defects on specific crystal phases (sectoral and intrasectoral zoning) and provides wealth of information regarding the deposition environment and growth of the mineral sample.

Luminescence Spectroscopy

Photoluminescent properties of a mineral specimen can be measured using a spectrometer and can provide information regarding the chemical and physical properties that result in the release of a photon (Waychunas 2014). The energy levels of the ground and excited states are dependent on the identity of the element, oxidation state, coordination geometry, and local site symmetry. Thus, luminescence spectroscopy can determine the presence and identity of the activator, even at trace levels within the sample.

The absorption, excitation, and emission processes can all be probed using this technique. Absorption spectra measure the amount of light absorbed or transmitted by a sample, while the wavelength of the incident radiation is varied to provide information on the energy of the electronic transmission in the ground states to multiple excited states of the activator or luminescence center. Excitation spectroscopy scans the wavelength of the incident beam while monitoring emitted light to impart information regarding the energies that produce luminescence when they are absorbed by the sample. By comparing the absorption and excitation spectra, the exact wavelengths required for luminescence can be determined. The emission spectra are collected by fixing the incident wavelength and scanning through the emitted energy, which shows the transition from that specific excited state that releases the photon (Waychunas 2014). This can provide details regarding the identity of the activator because those specific energy levels can be probed by scanning through the emission spectra. The spectra of both absorption and emission

spectroscopy of unknown activators can be compared to standards to provide identification of the elements in the sample.

Cathodoluminescence spectra can also be collected using an electron-beam instrument like a scanning electron microscopy or an electron microprobe (MacRae et al. 2005; Gotze 2012). The energy from the electron beam can promote electrons from the ground state to the excited state for most activators, so identification of the element responsible for luminescence can be difficult to identify using this technique. However, high-resolution spatial mapping can be obtained for mineral specimens and provide information regarding growth, zoning, impurities, and the crystallization environment (Waychunas 2014).

Luminescence Dating

Soils and sediment may contain thermoluminescence minerals which can be used to determine the geologic age of the sample (Singhvi and Mejdahl 1982; Wintle and Huntley 1982). Minerals, such as calcite, quartz, or zircon, present within the sample matrix, are heated under an inert atmosphere or vacuum, and the emitted light is recorded using a photon sensitive detector (Huntley et al. 1988; Rendell et al. 1993). Electrons are trapped at different depths, and thus, the variation in temperature is related to the irradiation history of the sample, which occurs due to exposure to naturally occurring radioactivity. The spectra of the mineral will change as a result of crystal purity, radiation dose, dose rate, and thermal history. The age is determined by dividing the equivalent dose determined through thermoluminescence by the overall dose rate of the sample (obtained through gamma spectrometry) (Wintle and Huntley 1982; Duller 2004). This technique is particularly useful when dating samples from the quaternary period, but given that the thermal history or impurities may impact the overall emission, thermoluminescence dating is often combined with other methods, such as U-series dating or stratigraphy (Forman 1989; Duller 2004).

Summary

Luminescence in geologic samples can occur through a variety of pathways, but photoluminescence is the most commonly observed form. Luminescence signals can provide information on the presence of trace elements in the sample, crystallite growth, and deposition environment. Spectroscopic techniques can be used to understand the chemical characteristics of the mineral phase, and thermoluminescence is utilized in geochronological studies of soils and sediments.

References

Calderon T, Khanlary M-R, Rendell HM, Townsend PD (1992) Luminescence from natural fluorite crystals. Int J Rad Appl Instrum Part D 20:475–485

Chapman GN, Walton AJ (1983) Triboluminescence of glasses and quartz. J Appl Phys 54:5961–5965

Duller GAT (2004) Luminescence dating of quaternary sediments: recent advances. J Quat Sci 19:183–192

Forman SL (1989) Applications and limitations of thermoluminescence to date quaternary sediments. Quat Int 1:47–59

Gaft M, Reisfeld R, Panczer G (2005) Modern luminescence spectroscopy of minerals and materials. Springer Publishing, Berlin

Geake JE, Walker G (1975) Luminescence of minerals in the near-infrared. In: Karr C Jr (ed) Infrared and Raman spectroscopy of lunar and terrestrial minerals. Academic, New York

Gorobets BS, Sidorenko GA (1974) Luminescence of secondary uranium minerals at low temperatures. Sov At Energy 36:5–12

Gotze J (2012) Application of cathodoluminescence microscopy and spectroscopy in geosciences. Microsc Microanal 18:1270–1284

Henkel G (1989) The Henkel glossary of fluorescence minerals. Fluorescence Mineral Society, Tarzana

Huntley DJ, Godfrey-Smith DI, Thewalt ML, Berger GW (1988) Thermoluminescence spectra of some mineral samples relevant to thermoluminescence dating. J Lumin 39:123–136

Ingle JD Jr, Crouch SR (1988) Spectrochemical analysis. Prentice Hall Publishing, Upper Saddle River

Machel HG, Mason RA, Mariano AN, Mucci A (1991) A causes and emission of luminescence in calcite and dolomite. In: Baker CE, Kopp OE (eds) Luminesce microscopy and spectroscopy: qualitative and quantitative applications. Society for Sedimentary Geology, Tulsa

MacRae CM, Wilson NC, Johnson SA, Phillips PL, Otsuki M (2005) Hyperspectral mapping – combining cathodoluminescence and X-ray collection in an electron microprobe. Microsc Res Tech 67:271–277

McKeever SWS (1985) Thermoluminescence of solids. Cambridge University Press, Cambridge

Nikl M, Bohacek P, Mihokova E, Kobayshi M, Ishii M, Usuki Y, Babin V, Stolovich A, Zazubovich S, Bacci M (2000) Excitonic emission of scheelite tungstates AWO_4(A = Pb, Ca, Ba, Sr). J Lumin 87–89:1136–1139

Rakovan J, Waychunas G (1996) Luminescence in minerals. Mineral Rec 27:7–19

Rendell HM, Khanlary M-R, Townsend PD, Calderon T, Luff BJ (1993) Thermoluminescence spectra of minerals. Mineral Mag 57:217–222

Rodriguez-Lazcano Y, Correcher V, Garcia-Guinea J (2012) Luminescence emission of natural NaCl. Radiat Phys Chem 81:126–130

Singhvi AK, Mejdahl V (1982) Thermoluminescence dating of sediments. Nucl Tracks Radiat Meas 10:137–161

Sweeting L (2001) Triboluminescence with and without air. Chem Mater 13:854–870

Walton AJ (1977) Triboluminescence. Adv Phys 26:887–948

Waychunas G (2002) Apatite. In: Kohn MJ, Rakovan J, Hughes JM (eds) Phosphates: geochemical, Geobiological, and materials importance, Luminescence in reviews in mineralogy and geochemistry, vol 48. Mineralogical Society of America, Washington, DC

Waychunas G (2014) Luminescence spectroscopy. In: Henderson GS, Neuville DR, Downs RT (eds) Spectroscopic methods, Reviews in mineralogy and geochemistry, vol 78. Mineralogical Society of America, Washington, DC

Wilkerson AS (1962) The minerals of Franklin and Sterling Hill, New Jersey, vol 65. The New Jersey Geological Survey, Trenton

Wintle AC, Huntley AG (1982) Thermoluminescence dating of sediments. Quat Sci Rev 1:31–53

Zink JI (1978) Triboluminescence. Acc Chem Res 11:289–295

Lutetium

Scott M. McLennan
Department of Geosciences, Stony Brook University, Stony Brook, NY, USA

Element Data
Atomic Symbol: Lu
Atomic Number: 71
Atomic Weight: 174.9668(1)
Isotopes and Abundances: ^{175}Lu, 97.401(13)% and ^{176}Lu, 2.599(13)%
1 Atm Melting Point: 1663 °C
1 Atm Boiling Point: 3402 °C
Common Valences: +3
Ionic Radii: 86.1 pm (CN6), 97.7 pm (CN8), and 119.4 pm (CN12)
Pauling Electronegativity: 1.27
First Ionization Energy: 523.52 kJ mol^{-1}
Chondritic (CI) Abundance: 0.0254 ppm
Silicate Earth Abundance: 0.057 ppm
Crustal Abundance: 0.30 ppm
Seawater Abundance: 0.227 ppt
Core Abundance: ~0

Properties

Lutetium (Lu), named after *Lutetia*, the Latin name for Paris, is a soft, malleable, ductile, dense (9.841 g cm^{-3}), bright silvery metal. Its electronic configuration is [Xe]4f^{14}5d^{1}6s^{2}. It is relatively stable in air and readily dissolves in mineral acids. It is a group 3 or IIIB inner transition element, with +3 being its only valence state in geological environments, and is one of the lanthanide rare earth elements (REE). In geochemical terminology, it is grouped with heavy rare earth elements (HREE; Gd-Lu). Lutetium has one natural, stable isotope and one long-lived radioisotope (^{176}Lu; $t_{1/2} = 3.713 \times 10^{10}$ year; beta decaying to ^{176}Hf) occurring in nature, listed above with their abundances.

More than 270 minerals contain lanthanides as essential structural constituents, but those with Lu as a significant component are restricted to minerals such as gadolinite-Y [$Y_2FeBe_2(Si_2O_{10})$], xenotime [$Y(PO_4)$], bastnäsite [REE(CO_3)F], allanite [$(REE,Ca,Y)_2(Al,Fe^{2+},Fe^{3+})_3(SiO_4)_3(OH)$], and britholite [$(REE,Ca)_5(SiO_4,PO_4)_3(OH,F)$].

Details of properties, mineralogy, history, and uses of Lu were compiled from Goonan (2011), Chakhmouradian and Wall (2012), Zaimes et al. (2015), Gschneidner (2016), Hammond (2016), and Meija et al. (2016a, b).

History and Use

The early history of Lu was controversial, being identified independently by three workers (Urbain, von Weisbach, James) in 1907, with final attribution of discovery (and naming) going to Georges Urbain in 1909. Lutetium metal was first produced in 1953. Being the rarest of the naturally occurring REE in the Earth, Lu is also the most valuable but has limited commercial use. It has been used as a catalyst in petroleum cracking, and due to its very high density, $LuTaO_4$ has been used in X-ray phosphors. Lu is also used in Tm:LuYAG lasers, PET medical imaging detectors, and LED lights.

Geochemical Behavior

The fundamental importance of Lu in geochemistry is that it is one of the small trivalent rare earth elements, among the most useful trace elements in all areas of geochemistry and cosmochemistry due to their coherent and systematic behavior as a group, largely a consequence of the "lanthanide contraction." The ^{176}Lu/^{176}Hf decay system is an important geochronometer and isotope tracer in a wide variety of geological settings (e.g., Wu et al. 2007).

Lutetium is typically a trace element in most rocks and minerals. It is classified geochemically and cosmochemically as a highly refractory lithophile element, with a 50% $T_{condensation}$ of 1659 K at 10^{-4} bars (Lodders 2003). In most igneous systems, Lu is incompatible with bulk partition coefficients, $D < 1$. In aqueous systems, Lu normally has very low fluid/rock partition coefficients ($\ll 1$). As a result, Lu contents of clastic sediments typically reflect their average provenance.

In seawater, Lu has very low concentrations (sub-ppt) and residence times (~2890 year) with speciation dominated by Lu^{3+}, $LuCO_3^+$, and $Lu(CO_3)_2^-$. In other aqueous systems (e.g., magmatic, hydrothermal), Lu can reach ppm levels due to elevated temperatures, pH effects, and complexing with various ligands (e.g., F^-, Cl^-, OH^-).

Concentration and residence time data are from compilations in Taylor and McLennan (2009) and Nozaki (2001).

Biological Utilization and Toxicity

There are no documented biological uses for Lu. REE (including Lu^{3+}) likely substitute for Ca^{2+} in biological materials and processes. REE concentrations (including Lu) in human tissues and fluids are very low (~ppb to <ppb levels, respectively) due to very low concentrations in natural waters and low uptake rates throughout the food chain (Bulman 2003). At low levels of ingestion, there are no established toxic effects that pose a threat to human health.

Cross-References

- ▶ Incompatible Elements
- ▶ Lanthanide Rare Earths
- ▶ Lithophile Elements
- ▶ Trace Elements
- ▶ Transition Elements

References

Bulman RA (2003) Metabolism and toxicity of the lanthanides. In: Sigel A, Sigel H (eds) Metal ions in biological systems, vol 40, The lanthanides and their interrelations and Biosystems. Marcel Dekker, Basel, pp 683–703

Chakhmouradian AR, Wall F (eds) (2012) Rare earth elements. Elements 8:333–376

Goonan TG (2011) Rare earth elements – end use and recyclability. US Geol Surv Sci Invest Rpt 2011–5094, 15pp

Gschneidner KA Jr (2016) Physical properties of the rare earth metals. In: Haynes WM (ed) CRC handbook of chemistry and physics, 96th edn. CRC Press, Boca Raton, pp 4-115–4-120

Hammond CR (2016) The elements. In: Haynes WM (ed) CRC handbook of chemistry and physics, 96th edn. CRC Press, Boca Raton, pp 4-1–4-42

Lodders K (2003) Solar system abundances and condensation temperatures of the elements. Astrophys J 591:1220–1247

Meija J, Coplen TB, Berglund M, Brand WA, De Bièvre P, Gröning M, Holden NE, Irrgeher J, Loss RD, Walczyk T, Prohaska T (2016a) Atomic weights of the elements 2013. Pure Appl Chem 88:265–291. (IUPAC Technical Report)

Meija J, Coplen TB, Berglund M, Brand WA, De Bièvre P, Gröning M, Holden NE, Irrgeher J, Loss RD, Walczyk T, Prohaska T (2016b) Isotopic compositions of the elements 2013. Pure Appl Chem 88:293–306. (IUPAC Technical Report)

Nozaki Y (2001) Rare earth elements and their isotopes in the ocean. In: Steele JH et al (eds) Encyclopedia of ocean sciences. Academic, London, pp 2354–2366

Taylor SR, McLennan SM (2009) Planetary crusts: their composition, origin and evolution. Cambridge University Press, Cambridge. 378pp

Wu FY, Li XH, Sheng YF, Gao S (2007) Lu-Hf isotope systematics and their applications in petrology. Acta Petrol Sin 23:185–220

Zaimes GG, Hubler BJ, Wang S, Khanna V (2015) Environmental life cycle perspective on rare earth oxide production. ACS Sustain Chem Eng 3:237–244

M

Magmatic Process Modeling

Mark Ghiorso
OFM Research, Seattle, WA, USA

Synonyms

Chemical mass transfer; Computational thermodynamic modeling of magmatic systems; Equilibrium and fractional crystallization, assimilation, recharge of magmas; Magmatic evolution

Definition

Chemical and physical processes that influence the evolution of a magma body from one state to another, including crystal fractionation, equilibrium crystallization, assimilation, recharge, and heat transport, magmatic differentiation, magmatic evolution.

Introduction

Magmatic processes embody the transfer of energy and mass into or out of a body of magma and characterize the irreversible mechanisms driving the magmatic system towards an equilibrium state. They are the coupled, time-dependent, physiochemical phenomena that enable magmatic evolution. Crystallization, volatile degassing, immiscibility, and other aspects of phase change are manifestations of magmatic processes as are preserved rock textures, phase distributions, and chemical zonation. With the spectacular exception of volcanic eruption, magmatic processes are seldom directly observable. We do not witness fractional crystallization, crystal growth, degassing, assimilation, recharge, heat conduction, diffusion, or convection. Their nature is inferred from the cumulative chemical signature and spatial heterogeneity of that signature recorded in the rocks at the reflects nation of the sequence of events that drive magma evolution.

Magmatic geochemists and petrologists justify, by forward modeling, hypotheses concerning process sequences that result in the chemical signatures preserved in the rock record. They have been doing this exercise with greater and greater sophistication for well over a century and a half. But, despite the familiarity and acceptance of this approach, modeling magmatic processes is fraught with both difficulty and uncertainty. Not only is our knowledge of the underlying physiochemical constraints (thermodynamic properties of the phases involved and the kinetics of their interaction) incomplete and derived from sparse, inadequate, and often contradictory experimental data, but computational fluid dynamical tools available to forward model process scenarios are deficit due to deficiencies in theoretical formalism and lack of raw computational power. Accounting explicitly for the physics and chemistry of microscale processes simultaneously with the macrophysics of magma body evolution is not yet computationally feasible. For example, it is beyond our current ability to model crystal growth in a cooling magma body of realistic bulk composition and account for the crystal size distribution of phenocryst phases derived from the process, let alone the texture of the resulting rock, or the chemical signatures preserved in the phenocryst assemblage. Compounding the problem is the nonunique nature of process inversion. Chemical signatures preserved in the igneous rock record may be broadly consistent with a spectrum of process scenarios. In addition, this ambiguity of interpretation is often exacerbated by a myopic focus on a limited number of observables. For example, it is counterproductive to rely exclusively on a particular element or group of elements, a preferred isotopic signature, or a specific favorite mineral phase in trying to unravel the sequence of processes that result in the igneous rock record. An analysis based on this sort of reasoning is typically misleading and usually contradictory to ignored observables or to

W. M. White (ed.), *Encyclopedia of Geochemistry*,
https://doi.org/10.1007/978-3-319-39312-4

unappreciated but plausible physiochemical constraints on system evolution.

Given the complexities and pitfalls inherent to magmatic process modeling, the reader may wonder why it is attempted at all. The answer to this question derives largely from the regularity of the igneous rock record and implications of this regularity in illuminating the nature of the dominant constraints operative during magmatic evolution. If kinetic phenomena driven by far from equilibrium conditions were first-order determinants of source composition and crystallization history of a magma, then we would expect a diversity of magma compositions and crystallization products that were entirely dependent on localized heat flow and eruptive/cooling style; in particular, we would not expect the products of igneous activity to conform to experimentally determined equilibrium phase diagrams. But, of course, igneous rocks do so conform, and this conformation reveals that the first-order characteristic of igneous evolution is that it takes place via a series of states each approximating thermodynamic equilibrium. Approximating, since an equilibrium state cannot naturally progress, unless perturbed and allowed to recover. Modeling an overall irreversible process as a sequence of equilibrium steps is a well-established geochemical technique (Garrels and Mackenzie 1967; Helgeson 1968), but application of this technique demands that rates associated with the formation of reaction products far exceed those that modify magmatic intensive variables or bulk composition. Generally, this assumption is a reasonable one, and thus, magmatic processes are typically modeled as a sequence of equilibrium steps; this is why phase diagrams are applied to the interpretation of equilibrium and fractional crystallization; how trace element modeling is utilized in the analysis of crystallization, assimilation, and recharge events; and why constitutive phase relations are utilized in the context of fluid dynamical simulations.

Techniques Used for Modeling Magmatic Processes

Equilibrium phase diagram calculators are central to magmatic process modeling efforts. These calculators can take a variety of forms. Originally, graphical phase diagrams provided the basis for understanding magmatic evolution (Bowen 1915, 1919, 1922a). The advantage of the graphical phase diagram is that if it is correctly constructed, the diagram embodies thermodynamic principles governing phase relations that extend and interpret the raw experimental data. This filtering of experiments is important and is sometimes underappreciated. The disadvantage of graphical phase diagrams is that they limit the complexity of the chemical system being described due to our inability to visualize in higher dimensional spaces. The use of graphical phase diagrams as a basis for magmatic process modeling faded once computers became generally accessible, and numerical procedures gained acceptance for their novelty and perceived accuracy. The simplest of these numerical calculators are direct and empirical parameterizations of experimental phase relations, and the most complex rely on internally consistent thermochemical models of constituent phases from which reaction boundaries are calculated using the mathematical apparatus of computational thermodynamics. The former class of numerical models generally reproduces the experimental calibrants with higher fidelity. This ability derives from the flexibility of choosing a form for the interpolating functions that is not required to conform to theoretical relationships dictated by an underlying physical theory. By contrast, phase diagram calculators that do conform to the rules of thermodynamics must accommodate experimental constraints with mathematical expressions that guarantee the existence of energy functionals that prescribe specific geometrical relationships at equilibrium between energetic surfaces that characterize the phases. These theoretical constraints impose themselves on the experimental calibration and demand internal consistency between sets of experimental observations that might otherwise appear to be independent. There is nothing in theory that prevents thermodynamically based descriptions of phase relations from achieving the equivalent ability of empirical formulations to reproduce experimental observations, but because thermodynamic models depend on a global analysis of energetic relations in a chemical system, there may in practice be insufficient experimental data to parameterize such a model (or collection of models) in a unique and rigorous manner. The objectives of the two approaches are different: the empirical description is a local interpolation, meant only to be applied locally, whereas the thermodynamic description is a global analysis, capable of extrapolation and meant to reconcile sets of disparate experimental results.

Whether empirical or thermodynamically based phase diagram calculators are used in magmatic process modeling, depends on the objective of the exercise. If recovery of phase relations is all that is desired and if experimental coverage is complete, then empirical calculators are sufficient – such is often the case in fluid dynamical simulations that require estimates of phase proportions. However, if the magmatic process being considered is constrained in such a way that experimental data are inapplicable, then a thermodynamic approach is desirable. A simple example will suffice to illustrate this point.

Why Phase Equilibrium Experiments Are Not Enough

Suppose our modeling objective is to compute closed system equilibrium or fractional crystallization of a basaltic bulk composition magma body (for context, the MORB

Magmatic Process Modeling, Table 1 Bulk compositions used in examples

wt%	MORB	High-silica rhyolite
SiO_2	48.68	77.7
TiO_2	1.01	0.07
Al_2O_3	17.64	12.3
Fe_2O_3	0.89	0.2129
Cr_2O_3	0.0425	
FeO	7.59	0.5084
MnO		
MgO	9.1	0.01
CaO	12.45	0.45
Na_2O	2.65	3.91
K_2O	0.03	4.82
P_2O_5	0.08	
H_2O	0.2	Saturated
CO_2		Saturated

composition listed in Table 1). This is perhaps the simplest magmatic modeling process that can be envisioned and is often illustrated in one form or another in elementary textbooks. By specifying closed system crystallization, the magma is considered chemically isolated, but of course, the body is not thermally isolated from its surroundings, which permits heat to flow out into the surrounding rocks during cooling. If we choose to model this crystallization process empirically, we would need to find experimental data documenting closed system crystallization of this midocean ridge basalt (MORB) in order to parameterize the required functions (or interpolate the provided data). Unfortunately, the experimental data required to empirically parameterize this model are unavailable and are likely to remain unavailable. It is almost impossible to perform a sequence of crystallization experiments on a bulk composition involving elements that have variable oxidation states (e.g., iron), without the system *changing bulk composition* in the process of crystallization due to the loss or absorption of oxygen. In fact, most experimentally determined crystallization sequences on iron-bearing systems are oxygen buffered, meaning that bulk composition evolves with changing temperature to keep constant *the relative oxidation state and not the oxygen content* of the system. As practical as this redox constraint is for experimental configuration, nature, arguably, does not conform to this constraint. In nature, the oxidation state of a magma body is dictated by what phases are crystallizing and by homogeneous equilibria among redox-species in the liquid phase (Osborn 1959 1962; Ghiorso and Carmichael 1985). Consequently, modeling equilibrium or fractional crystallization of magma as a closed system cannot be accomplished by empirical parameterization of experimental data. Those data must be interpreted by deriving from them a thermodynamic model and calculating from that model a true closed system path. Such a path is illustrated for the MORB bulk composition of Table 1 in Fig. 1. Along with the closed system evolution, an equivalent open system crystallization process is illustrated that maintains the same redox state (relative to the Ni-NiO oxygen buffer). The thermodynamic calculator used to generate these results is described in Ghiorso and Sack (1995) and Gualda et al. (2012a). Details of how these calculations were performed are provided in the figure legend and the modeling infrastructure is summarized in an Appendix to this chapter.

The evolution path of the closed system model is calculated by minimization of the Gibbs free energy of the system at each temperature (e.g., Ghiorso 1985). The open system path is calculated by minimizing an alternative thermodynamic potential named after Dmitriĭ Sergeevich Korzhinskiĭ (Ghiorso and Kelemen 1987) who pioneered the field of geochemical analysis of equilibrium phase relations in open systems where the fugacity or chemical potential of a thermodynamic component is fixed by external constraints (e.g., the system is forced to follow an oxygen buffer). The profoundly different redox path followed by the closed system evolution is controlled by the partitioning of ferrous and ferric iron into the crystallizing solid phases. If that partitioning favors ferrous iron into the solid phase(s), then the liquid ferric/ferrous ratio increases and so too does the oxygen fugacity of the magma (Kress and Carmichael 1991). It is fortuitous that for this example, with the exception of the onset of crystallization of spinel, the proportions of phases are not markedly different between the two crystallization scenarios. Compositions of the crystallized ferromagnesian phases differ markedly between the buffered and closed system scenarios (*middle panel*, Fig. 1), and one would expect this difference to carry forward to partitioning of trace elements with variable redox states.

Why Thermodynamic Models of Phase Equilibria Provide Important Constraints on Magmatic Process Modeling

Another example of modeling the magmatic crystallization process is illustrated for a very different bulk composition in Fig. 2, which shows the redox-buffered solidification of a liquid of high-silica rhyolite composition (Table 1). In contrast to the results displayed in Fig. 1, for this bulk composition, crystallization traverses the temperature of the quartz-two-feldspar-fluid "invariant" point (Tuttle and Bowen 1958), and the magma essentially solidifies over a 1 °C interval. This "eutectic-like" behavior is perhaps the closest that nature ever comes to mimicking simple two and three component phase diagrams. The calculations reported were made using rhyolite-MELTS (v. 1.1.0, http://melts.ofm-research.org/) (Gualda et al. 2012).

The crystallization process simulation presented in Fig. 2 provides a convenient reference point to discuss several

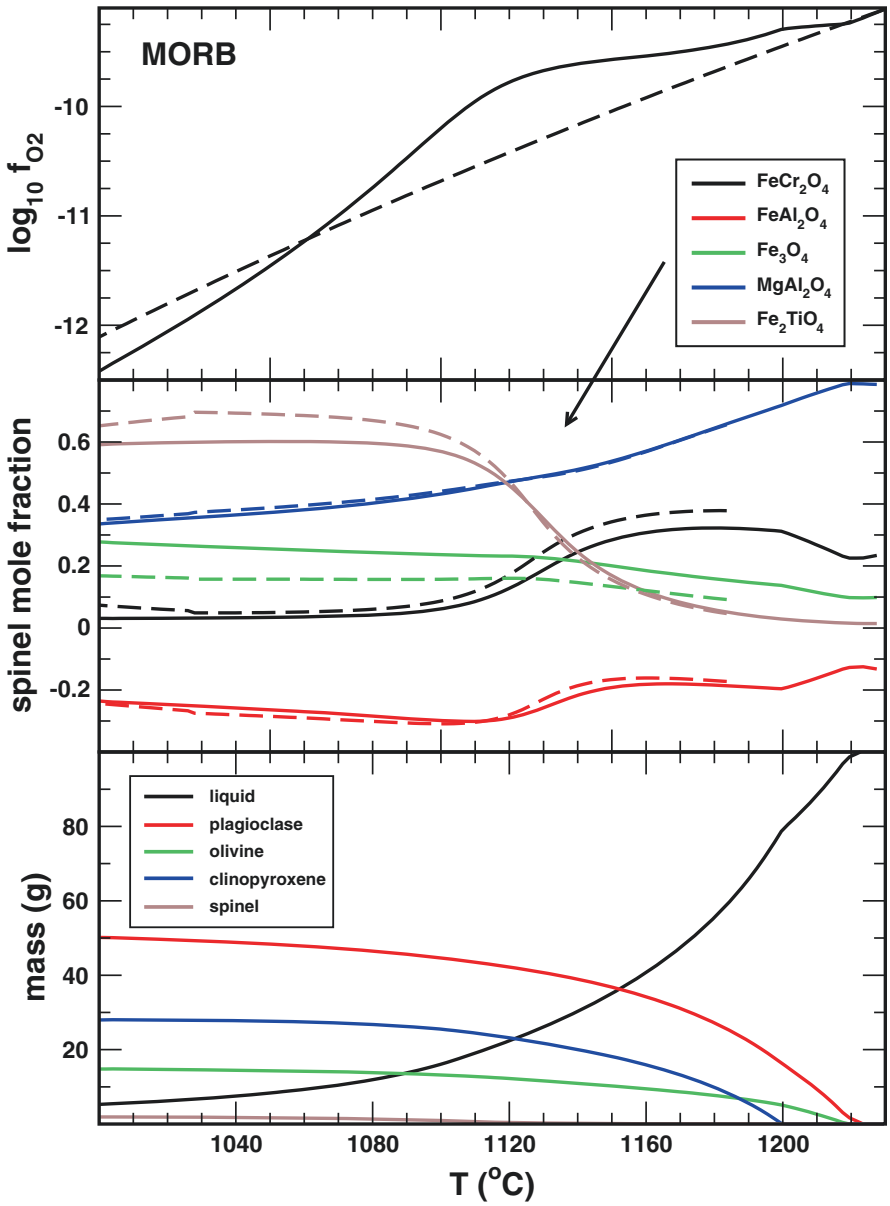

Magmatic Process Modeling, Fig. 1 Equilibrium crystallization of midocean ridge basalt (MORB, Table 1) modeled using the computational thermodynamics package rhyolite-MELTS (Gualda et al. 2012). *Upper panel* shows evolution of the system oxygen fugacity as a function of temperature for the closed system (*solid curve*) and open system (*dashed curve*) case, which parallels the Ni-NiO buffer (O'Neill and Pownceby 1993). The redox state of the closed system model is calculated using the experimental calibration of Kress and Carmichael (1991). *Middle panel* shows the composition of the spinel phase along the magma crystallization path. Note that the buffered path produces a less oxidized spinel that appears about 50 °C below the liquidus temperature of the closed system assemblage. *Lower panel* shows the mass of each phase in the system. Only the closed system path is shown as the open system phase proportions are virtually identical

aspects of modeling magmatic systems. Let us assume that there exists a magma body of high-silica rhyolite bulk composition that is present in the mid to shallow crust. This body may undergo a number of physical processes: crystallization, assimilation of country rocks, recharge of new magma, eruption, to name just a few. How the body arose in the first place is a reflection of additional processes, including perhaps fractional crystallization from a more mafic parent, partial melting, and/or melt extraction. All processes of melt generation require heat; all processes of melt crystallization require the loss of heat. The operative quantity that describes how magmas evolve is the heat content of the body. Heat content is a more natural descriptor than temperature because heat flows from sources to sinks, into and out of the system of interest.

In the upper two panels of Fig. 3, some results from the open system crystallization of the high-silica rhyolite bulk composition reported in Fig. 2 are plotted as a function of the heat content of the system, or the system enthalpy. In a thermodynamic system at fixed pressure, a change in enthalpy is equivalent to a change in total heat content. If the system is in a variable pressure field, a reversible change in heat content is equivalent to a change in system entropy. Passing from more positive to more negative values of enthalpy, therefore represents withdrawal of heat from the magma body, and in the context of knowledge of the thermal regime in which the body resides in the crust, the flux of heat transfer can be related to time. For example, if heat flux out of the magma body is approximately constant, as might be the case if the thermal regime in the country rocks has reached an

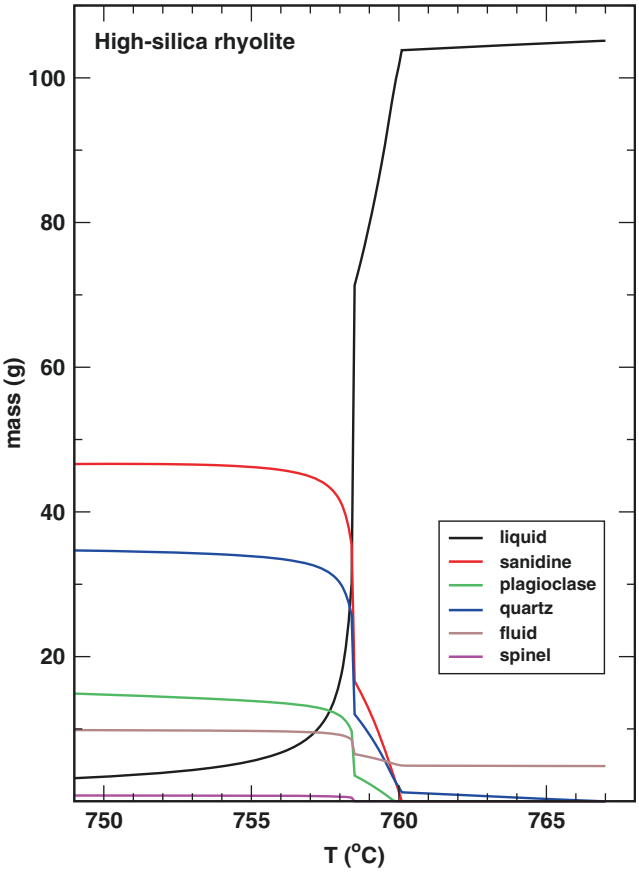

Magmatic Process Modeling, Fig. 2 Equilibrium crystallization of a fluid-saturated high-silica rhyolite (Table 1) modeled using the computational thermodynamics package rhyolite-MELTS (Gualda et al. 2012). The simulation was performed by open system Korzhinski potential minimization (Ghiorso and Kelemen 1987) along the Ni-NiO buffer (O'Neill and Pownceby 1993). The mass of each phase in the system is shown, plotted as a function of temperature

approximate steady state, then the heat content change is linearly proportional to the change in time to withdraw that quantity of heat from the body; the proportionality of course being dependent on, among others things, the size of the reservoir. Consequently, the enthalpy abscissa can be viewed as a measure of the history of the body – a reverse time axis, and it is quite clear that in the case of this high-silica rhyolitic bulk composition, the vast majority of time under which this body crystallizes is spent at a single temperature (± 1 °C). This feature is due to the eutectic nature of crystallization and the fact that latent heat is generated as the liquid crystallizes into the solid assemblage. This heat of crystallization must be removed before the body may be cooled to a lower temperature; for this example, the latent heat completely overwhelms the sensible heat, which is the heat held by the phases themselves. Withdrawal of sensible heat lowers the temperature of the system.

In addition to the heat content of the magma body, which through the phase diagram determines the temperature of the system, it is the volume of the body that dictates the pressure under which crystallization takes place; volume and pressure, just as heat content and temperature, are complimentary thermodynamic descriptors of the equilibrium state of a thermodynamic system. When modeling magmatic processes, it is especially important to keep this in mind. The reason is that the volume of magma is strongly dependent on phase change. Crystallization of mineral phases from the liquid generally leads to a reduction in volume, typically on the order of 3%, while separation of a fluid phase generally involves generation of volume, the magnitude of which is strongly dependent on confining pressure. For the case of the high-silica-rhyolite bulk composition, the third panel of Fig. 3 displays the volume change associated with phase transformation and cooling. Note that the system volume initially decreases as heat is withdrawn, then increases across the interval of major crystallization, reaches a maximum, and subsequently decreases. The slopes of the initial and final segments of the volume curve are negative in these intervals for two reasons: (1) the decrease in volume associated with the crystallization of solids exceeds the increase association with fluid phase separation and (2) a volume decrease is associated with thermal contraction of the system. Just as a distinction is commonly made between sensible and latent heat, so too can volume change be ascribed to either cooling or to phase change. The volume change with cooling is generally negative unless some structural rearrangement of the material intervenes to counteract bond contraction due to diminished thermal motion. Therefore in a cooling magma body, unless a product phase is produced that has substantially higher volume (lower density) than the reactants, the overall trend will be contraction. But, the volume of a magma container cannot assume whatever value is dictated by the internal phase equilibria. The volume of the container is dictated by the physical state of the country rocks that enclose the magma. If those rocks can be deformed at a rate that is comparable to the rate of magma volume change, then the container can accommodate the perturbation. If not, the imposed container volume will result in a change in the internal pressure of magma body and consequently a differential pressure between the magma and surrounding country rocks. The sign of this differential pressure is always the same as that of the volume change and scales as the inverse of the magma compressibility. As an example, the lower most panel of Fig. 3 plots the pressure change that would result if the container holding the high-silica rhyolite was rigid during cooling. A better modeling scenario might be that the container itself contracts with cooling at a rate comparable to the thermal contraction of the magma, which would make the differential pressures plotted in the lower panel of Fig. 3, minimal values. At the onset of crystallization, the pressure differential decreases and then begins to rise, reflecting solid-phase crystallization followed by exsolution of a fluid phase of low density. This

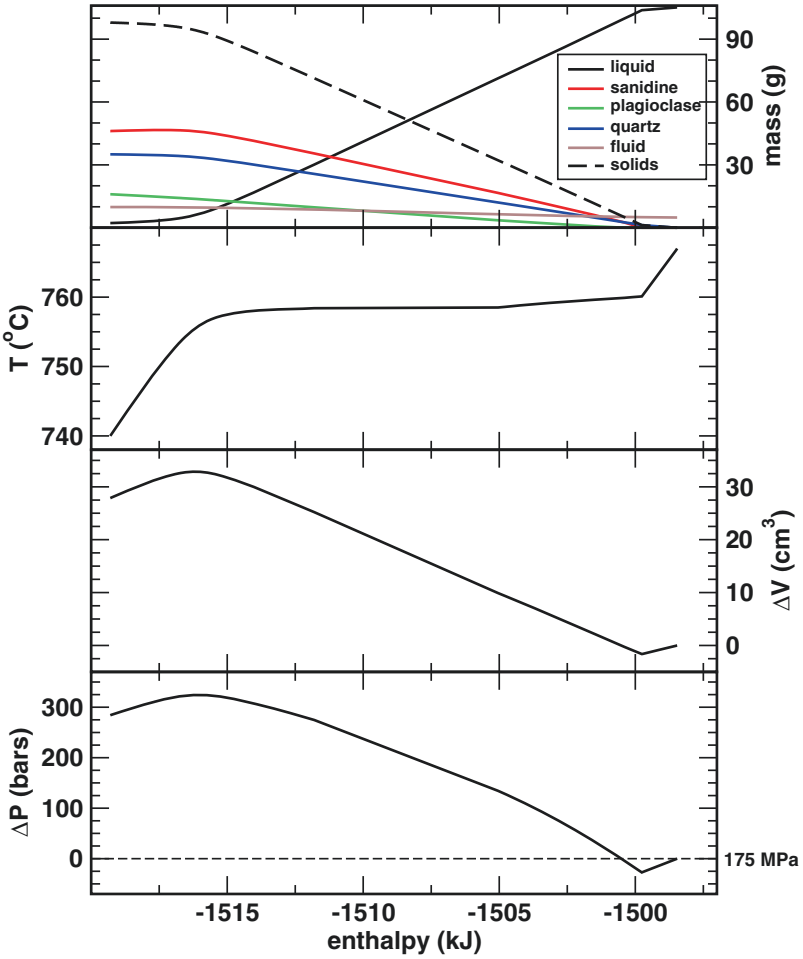

Magmatic Process Modeling, Fig. 3 Equilibrium crystallization of a fluid-saturated high-silica rhyolite (Table 1) modeled as in Fig. 2. *Top panel* shows phase abundances plotted against system enthalpy, which proxies for the total heat content of the magma body. *Second panel from top* shows the temperature of the magma and the *third panel* the volume of the magma. Note that the volume is an extensive quantity computed for the total mass of the system. *The lower 5-fold* ws the pressure relative to 175 MPa calculated on the assumption that the container holding the magma is rigid

partitioning of volatile components from the liquid to the fluid is not a consequence of diminished solubility in the melt, but rather, it is consequence of the change in mass of available liquid and therefore the capacity of the magma to hold these volatile components in solution. Crystallization is therefore driving the pressure increase. In this case, the overpressure developed is on the order of 150 bars when the magma is about 35% crystallized, which may be sufficient to cause fracturing or eruption of the system.

The point of the model developed in Fig. 3 is that a process as simple as crystallization of a magma body, when viewed in the context of a mass and energetically balanced coupled wall rock-magma system, can be profoundly informative. Importantly, the majority of information gleaned from such a model derives directly from the underlying thermodynamic treatment. Is the system chemically open or closed? How is heat transferred in or out of the body? To what extent is the magma container deformable? These questions are dynamic and process oriented. They cannot be answered without an underlying context that couples the chemistry and energetics of the system. In other words, answers to questions involving the evolution of a magma body cannot be provided from phase diagrams or experiments of phase equilibria without the benefit of interpretive theory, and that theory is the underlying thermodynamics of the process. Modeling a magmatic process is an exercise beyond simply understanding the chemical transfers from one phase to another or the physics of transport of material. It is an exercise in understanding how the chemistry and physics are coupled and feedback on one another. Nowhere is this more apparent than when trying to model the process of assimilation or recharge of new magma into an existing magma body. Let us next explore an example of assimilation to understand and illustrate this point further.

Assimilation Processes

Continuing with the high-silica rhyolite magma composition, rhyolite-MELTS (Gualda et al. 2012 as extended by Ghiorso and Gualda (2015) to include mixed H_2O-CO_2 fluid saturation in the liquid phase) can be used to model the chemical reactions accompanying assimilation of calcite ($CaCO_3$) into this magma. Results are displayed in Fig. 4 for the case of the uncontaminated magma starting at a temperature of 759 °C

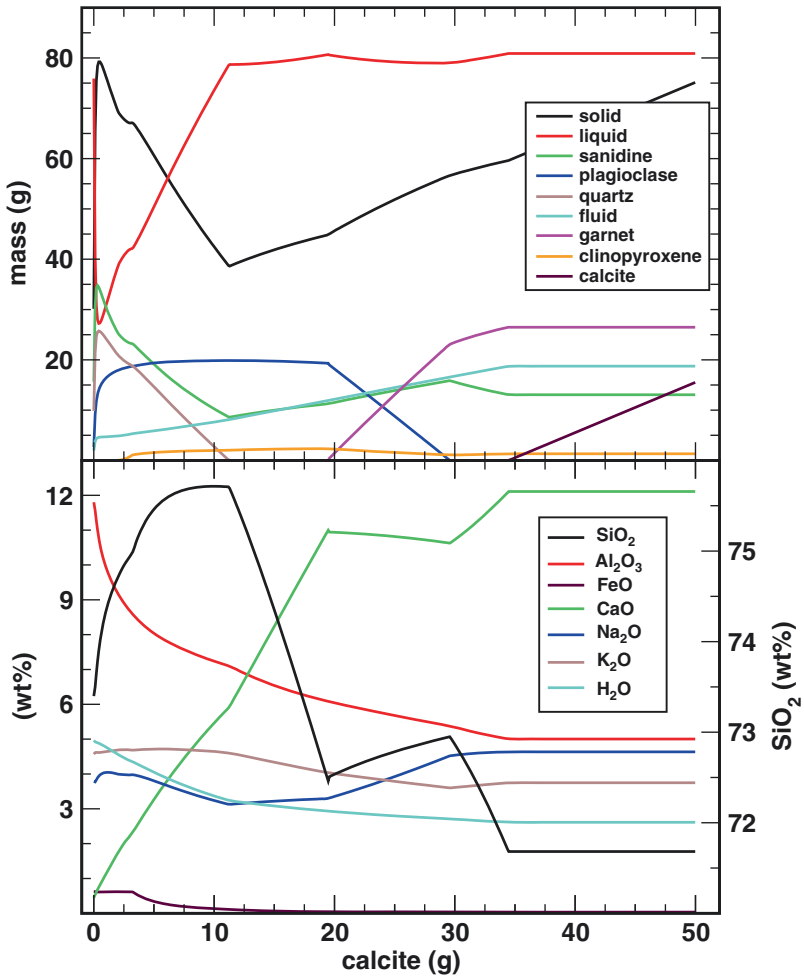

Magmatic Process Modeling, Fig. 4 Assimilation of the mineral calcite into a high-silica rhyolite bulk composition magma. Initial conditions of the magma are 759 °C and 175 MPa, with the assemblage quartz+sanidine +plagioclase stable under fluid saturation. The calcite is titrated into the magma in 0.1 g increments, and the system is maintained at constant temperature. The calculation is performed with rhyolite-MELTS (Gualda et al. 2012) as modified (v. 1.1.0) for the addition of a CO_2-bearing fluid phase (Ghiorso and Gualda 2015). *Upper panel* shows phase abundances plotted as a function of mass of assimilant. *Lower panel* shows composition of the liquid phase; note that the concentration of SiO_2 is read from the right-hand ordinate

and 175 MPa and at saturation with a fluid phase (99 mole% H_2O). These conditions correspond to the calculated onset of the two-feldspar-quartz-fluid saturated "eutectic" for this bulk composition (Fig. 2). Calcite is "titrated" into this system mimicking the physical process of interaction of country rocks with the magma reservoir. Figure 4 displays phase proportions (top panel) and changes in liquid composition (lower panel) accompanying calcite addition. Note that the magma does not saturate with calcite until about 35 g have been added to ~100 g of initial material. Also, note that the stoichiometry of the reaction process is extremely complex. This result is important and quite a general characteristic of the assimilation process in magmatic systems. Assimilation does not necessarily involve melting of the assimilant; the process of assimilation is one of the reactions of material that is out of equilibrium with the magmatic phase assemblage and that reaction may produce or consume solids or may balance product and reactant solid masses to maintain a constant liquid fraction. In the case displayed in Fig. 4, the initial addition (<1 g) of calcite induces solidification, provoking crystallization of sanidine, quartz, and plagioclase, but further addition lifts the bulk composition off of the "eutectic," so that quartz and sanidine are consumed along with the calcite, resulting in the production of plagioclase and liquid. Liquid proportion grows until, after 11 g of calcite have been consumed, the amount of liquid present is comparable to the initial quantity. At this point, all of the quartz in the system is eliminated, and the reaction stoichiometry changes abruptly as further addition of calcite transfers CO_2 to the fluid phase and consumes SiO_2 from the liquid phase to produce silicate mineral products. Eventually, the system saturates with grossular garnet, forming at the expense of plagioclase, and the SiO_2 reduction trend is reversed until the plagioclase is consumed. Ultimately, after ~35 g of calcite are added, the magma saturates in that phase, the coexisting fluid (*not the magmatic liquid*) becomes CO_2 rich, and the solid assemblage garnet, clinopyroxene (a diopside solid solution), sanidine, and calcite are stabilized, producing a skarn-like mineral assemblage. Remarkably, the liquid fraction remains at its initial proportion.

The results plotted in Fig. 4 demonstrate a fascinating record of a complex reaction progress history, but is this record petrologically relevant? More specifically, is the calculation petrologically relevant over and above any

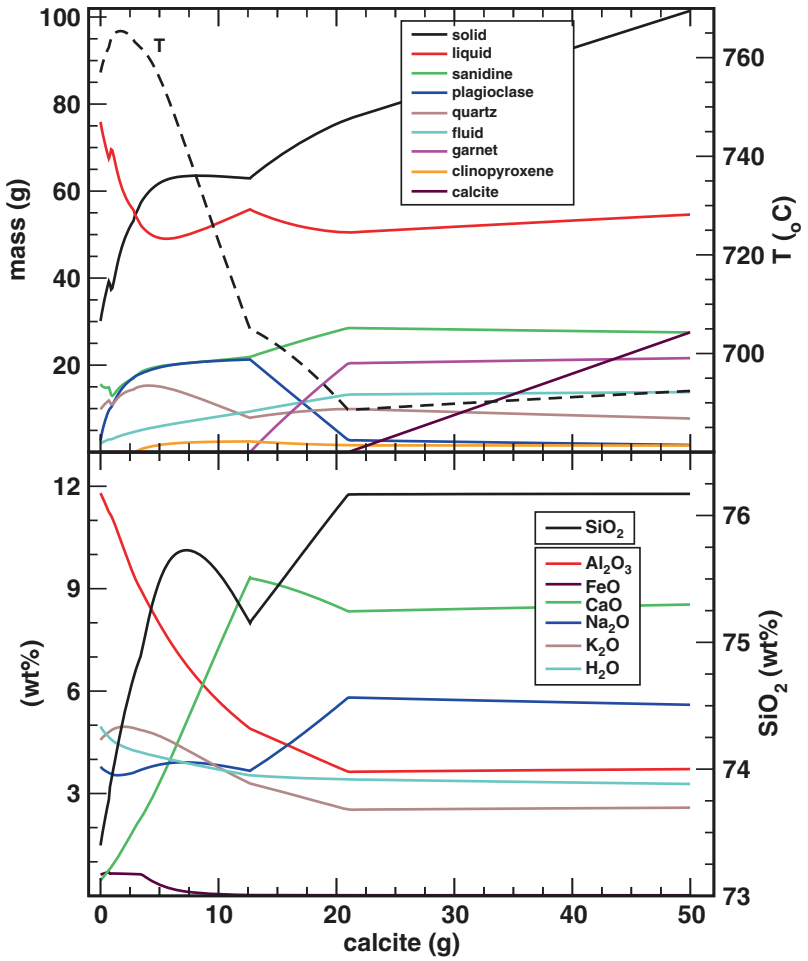

Magmatic Process Modeling, Fig. 5 Assimilation of the mineral calcite into a high-silica rhyolite bulk composition magma. Initial conditions and calculation scheme as in Fig. 4. The calcite +magma system is maintained at constant enthalpy under the assumption that heat flow is negligible compared to reaction rates. It is assumed that the calcite is at the same initial temperature and pressure as the magma. The calculation is performed by maximizing the system entropy at each step, calculating as a consequence the phase proportions, phase compositions, and the temperature of the equilibrium assemblage. *Upper panel* shows phase abundances and temperature plotted as a function of mass of assimilant. Note that the value of temperature is read from the right-hand ordinate. *Lower panel* configured as in Fig. 4

inaccuracies or inadequacies associated with the underlying thermodynamic modeling tools? This is an important question, one that should be asked for every assimilation process modeling undertaken for a magmatic system. Can one simply and arbitrarily titrate any quantity of solid material into magma at some fixed temperature and pressure and expect the result of that calculation to be physically meaningful? Or, in other words, can one independently specify the ratio of the mass assimilated to the mass crystalliz when trying to tease out the chemical or isotopic consequences of an assimilation event? The answer is yes only if the volume and heat content of the magma are allowed to change in a manner consistent with the various heats of reaction associated with consumption of the assimilant and the production of secondary reaction products. But, this change in properties demands specific boundary constraints on the body, *which are generally not satisfied*. Further, the heat content and volume of the assimilant come into consideration in the inventory of sensible heat and sensible volume for the combined system. The proper way to model this process is to explicitly account for both the energy balance and volumetric changes associated with the assimilation process. As in modeling magmatic crystallization, the physics of heat flow through and deformation of the magma container must constrain the permissible reaction path that the system takes during its irreversible evolution. In this light, we examine this assimilation model again under more physical boundary constraints.

In Fig. 5 the evolution of a high-silica rhyolite magma is plotted, starting under the same initial conditions as in Fig. 4, but with the reaction path constrained to maintain energetic balance. Two assumptions are made: (1) that the calcite being assimilated is at the same initial temperature as the magma and (2) that there is no heat loss from the magma+assimilant system during the reaction process. The first assumption is made for convenience and can easily be relaxed. Making this assumption insures that the effects being modeled focus on heats of reaction and do not include the sensible heat contribution required to raise the assimilant to magmatic temperatures. The second assumption may also be relaxed if details are known about the relative rates of heat transfer compared to rates of reaction. As adopted, the rate of heat transfer is assumed to be negligible compared to the rate of the assimilation reaction. Therefore in practical terms, this assumption is equivalent to modeling the process as one where no net heat

transfer occurs, that is the heat content of the magma +assimilant system is assumed to be constant; at constant pressure, for a reversible process, constant heat content is equivalent to constant enthalpy. The calculation is carried out by computing the enthalpy of the added calcite, adding this enthalpy plus the mass of that calcite to the magma, and computing the equilibrium phase assemblage for this new bulk composition at stipulated pressure and at a total enthalpy equal to that of the magma+calcite addition. Technically, this calculation is done by maximizing the total combined system entropy (Ghiorso and Kelemen 1987). While experiments could be configured to evaluate the outcome of the calcite titration scenario modeled in Fig. 4, it would be difficult, if not impossible, to construct an experiment that directly evaluates the energy constrained assimilation scenario modeled in Fig. 5. Yet, the energy-constrained case is more petrologically meaningful (Bohrson and Spera 2001; Spera and Bohrson 2001, 2002; Bohrson et al. 2014), just as the closed system crystallization calculation described above (Fig. 1) embodies the more realistic constraints on the magma crystallization process.

The energy-constrained assimilation scenario plotted in Fig. 5 produces very different results than those shown in Fig. 4. The first feature to note is that the temperature of the system is now a function of the extent of assimilation, which results from the enthalpy balance constraint; temperature is a dependent variable. As calcite is added to the magma, the system responds by reacting the calcite with existing phases to form products. Any heat of reaction must be balanced by a change in temperature in order to zero the total enthalpy change. The perhaps nonintuitive consequence of balancing the heat budget is that the temperature can rise or fall depending on the exact stoichiometry of the reaction. The first person to thoroughly discuss this phenomena from a thermodynamic perspective was Norman L. Bowen (1922b). In the case illustrated in Fig. 5, temperature initially rises, which should have the effect of moving the system away from the quartz-two-feldspar-fluid saturated cotectic. But instead, the rise in calcium content of the melt offsets this temperature increase, maintaining the magma +assimilant system on the eutectic, while crystalizing a higher proportion of plagioclase to sanidine+quartz. Simultaneously, the liquid fraction diminishes as in the isothermal titration case, but unlike that case does not reverse this trend until ~5 g of assimilant are added. The isenthalpic reaction path does not loose either quartz or plagioclase from the product assemblage, and the system saturates in both garnet and calcite at lower levels of added assimilant than under isothermal conditions. Another interesting consequence of the isenthalpic scenario is that the silica content of the residual liquid is much larger at the onset of crystallization of calcite. The final phase assemblage shown in Fig. 5 is liquid+sanidine+plagioclase+quartz+fluid +clinopyroxene+garnet+calcite.

Regardless of the details of these two assimilation scenarios, it is important to appreciate how different the outcomes are and that these differences arise not because of choice of initial magma bulk composition, temperature, and pressure or because of the nature of the assimilant. Modeling the process of assimilation in magmatic systems is entirely dependent on the constraints placed on the physics of the assimilation process, e.g., what is the relative difference in the rate of heat transport compared to the rate of reaction. Each case must be evaluated quantitatively by working out the full reaction-product stoichiometry. Focusing just on trace elements or isotopic signatures and ignoring the phase diagram or heat flow constraints cannot yield either a unique or a meaningful answer. And, importantly, the two illustrative models presented here are still abstract end-members of a continuum of realistic constraints, most of which would require modeling the process with a fully coupled dynamic-thermodynamic approach. To illustrate this point further, let us examine the volumetric consequences of this assimilation scenario and explore whether either the isothermal or isenthalpic end-member cases have verisimilitude.

In Fig. 6, the calcite assimilation scenario is evaluated again, this time under the constraint of fixed volume of the magma+assimilant assemblage; the internal pressure of the magma body is a dependent quantity under these constraints. The physical scenario underlying this case is one of reaction rates exceeding those of deformation of the magma+reactant container. The assumption is made that both the magma and the assimilant maintain a temperature of 759 °C; therefore, these results should be compared to the isobaric-isothermal calculations presented in Fig. 4. The net volume change of the assimilation reaction is positive, so, consequently, the expectation would be that to maintain a constant volume condition the internal pressure of the magma must increase. As discussed above, this is due to the fact that the compressibility of a substance is always positive, so that higher pressure is required to squeeze the product assemblage back down to the volume of the reactant assemblage. Because the solubility of CO_2 in rhyolitic magma is quite low, the assimilation of calcite generates a CO_2-rich fluid, which at these shallow crustal pressures is a low-density or high-volume phase. This fluid phase exsolution drives the pressure increase on assimilation (Fig. 4) to values approaching 500 MPa; the pressure increase trend is only checked once the magma saturates in calcite and fluid production ceases. The phase assemblage formed maintains the preassimilation assemblage quartz+sanidine+plagioclase+fluid, but unlike the isothermal case (Fig. 4), there is no production of garnet, most likely because calcite saturates sooner in the assimilation process, at a CaO concentration in the magma of only 6 wt%.

The pressure increase computed for this assimilation scenario indicates that the constant volume constraint leads to an unrealistically high differential between the magma and surrounding country rocks. Such a large pressure differential will either drive ductile deformation (violating the key assumption

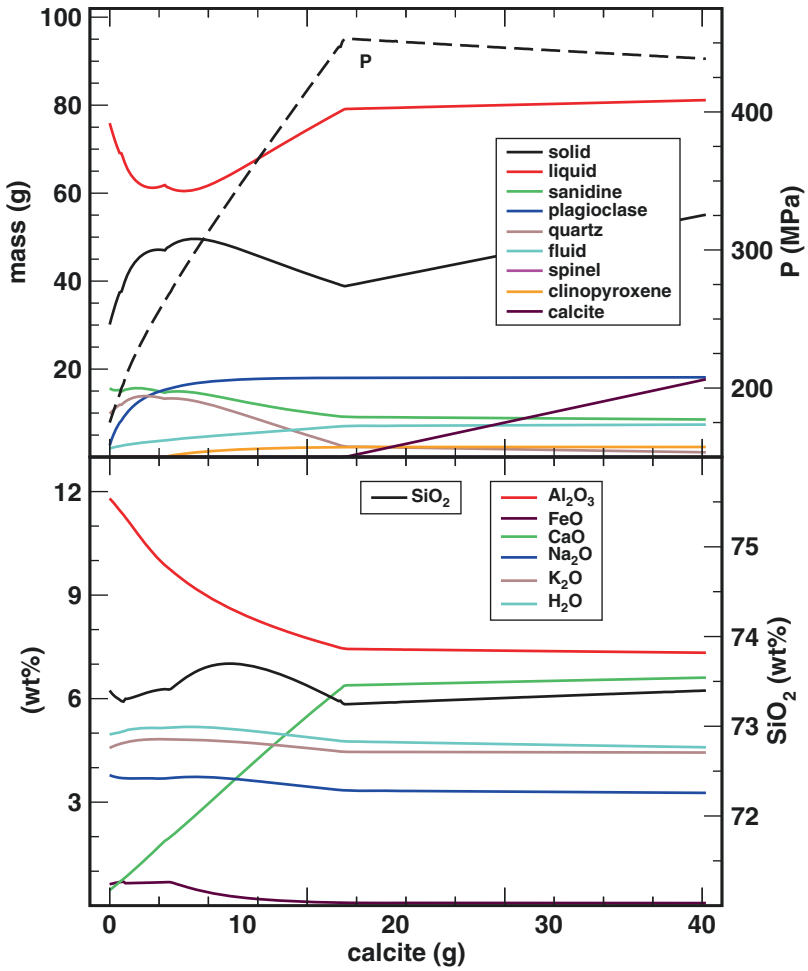

Magmatic Process Modeling, Fig. 6 Assimilation of the mineral calcite into a high-silica rhyolite bulk composition magma. Initial conditions and calculation scheme as in Fig. 4. The calcite +magma system is maintained at constant volume under the assumption that deformation rate is negligible compared to reaction rates; temperature of the magma and the assimilant are held at 759 °C. The calculation is performed by minimizing the Helmholtz free energy at each step, calculating as a consequence the phase proportions, phase compositions, and the pressure of the equilibrium assemblage. *Upper panel* shows phase abundances and pressure plotted as a function of mass of assimilant. Note that the value of pressure is read from the right-hand ordinate. *Lower panel* configured as in Fig. 4

of constant volume) or at least initiate cracking, with expulsion of material to relieve the internal stress; a difference of 200 bars (20 MPa) is generated after addition of *only* ~1 g of assimilant. Perhaps, assimilation alone can initiate a perturbation in the pressure field sufficient to instigate eruption?

Manifesto

Analyzing this calcite assimilation problem within these three different reaction constraint contexts demonstrates something quite fundamental about modeling magmatic processes. The same geochemical scenario, in this case adding calcite to high-silica rhyolitic magma, can yield quite different outcomes, not all of which are easily testable from field observation and certainly not from geochemical data alone. Posing just one scenario, say isothermal-isobaric assimilation, and testing that scenario against observation might broadly reproduce some geochemical trend observed in the rocks, but it may make little physical sense in terms of heat sources or sinks, or the reaction may drive the system into a pressure regime where the assumed underlying phase diagram is no longer applicable. The most robust models of magmatic processes, like the best petrologic insight, are those that account not only for the observations made in the field and the laboratory, but those that also account for the dynamical contexts that constrain the reaction path. We routinely make simplifying assumptions about the state of a magmatic system that we have sampled – we use geothermometers, geobarometers, trace element distribution between phases, we apply phase diagrams, we compare one system to another – all of which are predicated on the implicit assumption that what we are looking at is approximated by an equilibrium state, but how those states are connected to one another in the sequence of events relating the evolution of the system in time and space is often treated as "not our concern." Well, it is our concern. Geochemists and petrologists should not legitimately pose a geochemical scenario that is nonsensical because it violates the physics of transport, nor should geophysicists and geodynamicists posit a physical mechanism of magma generation, transport, or eruption that does not account fully for geochemical observations. Energy (and all of its derivatives, volume, heat capacity, thermal expansion, compressibility, bulk modules, etc.) and composition are not independent

constructs. Acknowledging the interplay between the two is central to magmatic process modeling.

Conclusions and What About Kinetics

Throughout this article, the concept of an irreversible process being modeled as a sequence of local equilibrium states has been exploited. It has been argued that this is a reasonable assumption for understanding magmatic phenomena; indeed, it is an assumption that underlies the majority of the interpretation of igneous and metamorphic rocks and our understanding of water-rock interaction at elevated temperatures. However, this assumption of local reversibility is incorrect in detail. Igneous phenocrysts display chemical and isotopic zonation, and ample evidence exists documenting the existence of xenocrysts and antecrysts in magmatic systems. Crystal growth on syneruptive timescales (Gualda et al. 2012b) create textural features that are demonstrably not in spatial equilibrium. The preserved rock record provides ample evidence of disequilibrium and the importance of interpreting observations in terms of kinetic theory. In fact, one of the most exciting areas of modern petrological research is related to the timescales of magmatic processes (Cooper and Kent 2014; Pamukcu et al. 2015), and much of that information is gleaned from the interpretation of preserved disequilibrium phenomena. Nevertheless, the application of kinetics in magmatic process modeling is in its infancy, and there are many reasons for this. Firstly, disequilibrium phenomena must be modeled in reference to an equilibrium state in order to properly calculate growth rates and reference conditions, requiring either a thermodynamic model or appropriate experiments to characterize that state. Secondly, the length scales of crystal growth or diffusion are small compared to the typical size of a magma body. This scaling issue makes the process of coupling the regime of microphysics kinetics to the regime of large-scale flow of heat and mass computationally intractable. Thirdly, the fundamental data required in order to model kinetic phenomena associated with growth, diffusion, transport, and other disequilibrium features of magmatic systems is sufficiently inadequate that causal predictions of observable phenomena at the hand specimen or thin section scale cannot yet be made. Yet, there is hope that at least on the computational front progress will be forthcoming to produce a fully integrated thermodynamic-kinetic-dynamical modeling tool to explore magmatic processes. Until that time, appropriately constrained thermodynamic models that exploit the simplification of local equilibrium reaction paths still provide a rich and informative window on the geochemical evolution of magmatic systems.

Appendix: From Experiment to Model

Computational thermodynamics simulators (like rhyolite-MELTS (Gualda et al. 2012) and its predecessors) require a complex infrastructure of internally consistent thermodynamic models that work together in order to calculate the equilibrium state of a magmatic system. This complexity is illustrated in Fig. 7. Models are required to calculate properties of stoichiometric end-member minerals, fluids, and melt components and to estimate the thermodynamic properties of

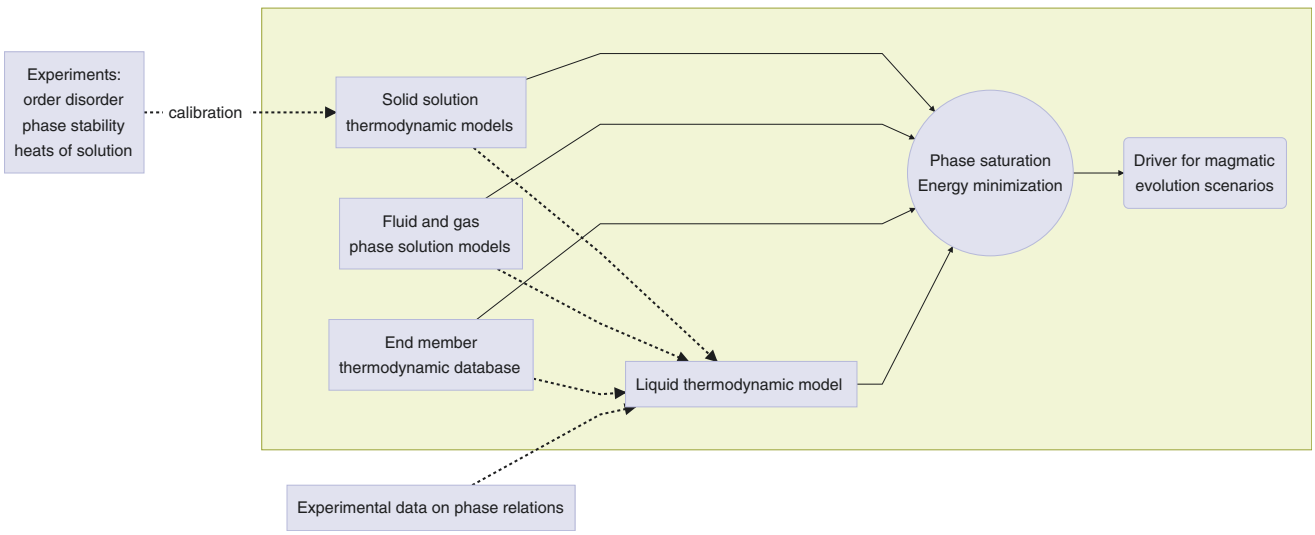

Magmatic Process Modeling, Fig. 7 Illustration of the internal structure and model interdependencies of the MELTS family of magmatic process simulation software. The *yellow box* corresponds to the distributed modeling tool, which incorporates a number of thermodynamic models for mineral, fluid, and melt solutions as well as compact representations of end-member thermodynamic properties. Experimental data required to calibrate the thermodynamic models within MELTS are indicated by *boxes* external to the distributed module. Workflow pathways for calibrating the internal model collection are shown by *dashed lines*. Inputs for performing a model simulation are shown by *solid lines*

mineral, melt, and fluid solutions. What results is a collection of models all providing inputs in order to estimate the thermal and mechanical evolution of a magmatic system. Properties of stoichiometric compounds are often assembled into so-called thermodynamic "databases," although it is important to understand that all quantities contained in these databases are in reality numerical values of fitting parameters to models of heat capacity, third-law entropies, enthalpies of formation, and equation of state formulations. Thermodynamic databases rarely contain primary data; primary data such as heat of solution, heat capacity, or heat content measurements obtained from adiabatic, differential scanning, or drop calorimetry are adjusted in order to make the database predict outcomes that reflect experimentally determined or naturally observed phase relations. This procedure is known as rendering the database internally consistent. In the rhyolite-MELTS modeling hierarchy, the stoichiometric compound end-member "database" is but one component in a collection of models. In this hierarchy, thermodynamic models for minerals and fluids are obtained independently by calibrating against experimental data pertaining exclusively to those phases. Once calibrated and combined with the end-member database, they are utilized in conjunction with experimental data corresponding to heterogeneous phase equilibria determined for magmatic bulk compositions under high-temperature, pressure conditions, to establish an internally consistent collection of models by formulating and calibrating a thermodynamic model for the liquid (melt) state. Thus, the model parameters that describe thermodynamic properties of silicate liquids are *dependent* on (1) the end-member properties database adopted, (2) the solution models adopted for mineral and fluid solutions, and (3) the collection of experimental phase equilibrium data available for model calibration. Once all these calibrations are accomplished, the resulting thermodynamic models are referenced by a computational engine that computes phase saturation and heterogeneous phase equilibrium under specified bulk composition and ancillary thermodynamic constraints (e.g., T and P). Calculation of magmatic evolution scenarios (as described in this chapter) are computed by driving the phase saturation and energy minimization engine in a direction consistent with the petrologic scenario underlying the evolution.

Cross-References

- ▶ Carbonate Minerals and the CO2-Carbonic Acid System
- ▶ Enthalpy
- ▶ Entropy
- ▶ Equilibrium
- ▶ Experimental Mineralogy and Petrology
- ▶ Fractional Crystallization and Assimilation
- ▶ Free Energy
- ▶ Fugacity
- ▶ Geochemical Thermodynamics
- ▶ Gibbs-Duhem Equation
- ▶ Heat Capacity
- ▶ Mass Transfer
- ▶ Oxidation-Reduction Reactions and Eh-pH (Pourbaix) Diagrams
- ▶ Partial Melting
- ▶ Partitioning and Partition Coefficients
- ▶ Phase Equilibria
- ▶ Solid Solution/Exsolution
- ▶ Standard States

Acknowledgments Material support for the preparation of this article from the National Science (EAR-1321924) and Sloan Foundations is greatly acknowledged.

References

Asimow PD, Ghiorso MS (1998) Algorithmic modifications extending MELTS to calculate subsolidus phase relations. Am Mineral 83:1127–1131

Asimow PD, Hirschmann MM, Ghiorso MS, O'Hara MJ, Stolper EM (1995) The effect of pressure-induced solid-solid phase transitions on decompression melting of the mantle. Geochim Cosmochim Acta 59:4489–4506

Bohrson WA, Spera FJ (2001) Energy-constrained open-system magmatic processes. II: application of energy-constrained assimilation-fractional crystallization (EC-AFC) model to magmatic systems. J Petrol 42:1019–1041

Bohrson WA, Spera FJ (2003) Energy-constrained open-system magmatic processes. IV: geochemical, thermal and mass consequences of energy-constrained recharge, assimilation and fractional crystallization (EC-RAFC). Geochem Geophys Geosyst 4. https://doi.org/10.1029/2002GC00316

Bohrson WA, Spera FJ (2007) Energy-constrained recharge, assimilation, and fractional crystallization (EC-RA/E$'$/FC): a visual basic computer code for calculating trace element and isotope variations of open-system magmatic systems. Geochem Geophys Geosyst 8. https://doi.org/10.1029/2007GC001781

Bohrson WA, Spera FJ, Ghiorso MS, Creamer JB (2014) Thermodynamic model for energy-constrained open system evolution of crustal magma bodies undergoing simultaneous assimilation, recharge and crystallization: the magma chamber simulator. J Petrol. https://doi.org/10.1093/petrology/egu036

Bowen NL (1915) Crystallization-differentiation in silicate liquids. Am J Sci, Fourth Ser 39:175–191

Bowen NL (1919) Crystallization-differentiation in igneous magmas. J Geol 27:393–430

Bowen NL (1922a) The reaction principle in petrogenesis. J Geol 30:177–198

Bowen NL (1922b) The behavior of inclusions in igneous magmas. J Geol 30:513–570

Cooper KM, Kent AJR (2014) Rapid remobilization of magmatic crystals kept in cold storage. Nature 506(7849):480–483

Garrels RM, Mackenzie FT (1967) Origin of the chemical compositions of some springs and lakes. In: Equilibrium concepts in natural waters, vol 67, advances in chemistry series. American Chemical Society, Washington, DC, pp 222–242

Ghiorso MS (1985) Chemical mass transfer in magmatic processes. I. Thermodynamic relations and numerical algorithms. Contrib Mineral Petrol 90:107–120

Ghiorso MS (1987) Modeling magmatic systems: thermodynamic relations. In: Carmichael ISE, Eugster HP (eds) Thermodynamic modeling in geologic systems: minerals, fluids and melts. Mineralogical Society of America Reviews in Mineralogy 17(12): pp 443–465
Ghiorso MS (1997a) Thermodynamic models of igneous processes. Annu Rev Earth Planet Sci 25:221–241
Ghiorso MS, Carmichael ISE (1985) Chemical mass transfer in magmatic processes. II. Applications in equilibrium crystallization, fractionation and assimilation. Contrib Mineral Petrol 90:121–141
Ghiorso MS (1997b) Thermodynamic modeling of igneous processes. Annu Rev Earth Planet Sci 25:221–241
Ghiorso MS, Carmichael ISE (1987) Modeling magmatic systems: petrologic applications. In: Carmichael ISE, Eugster HP, (eds) Thermodynamic modeling in geologic systems: minerals, fluids and melts. Mineralogical Society of America Reviews in Mineralogy 17(13): 467–499
Ghiorso MS, Carmichael ISE, Rivers ML, Sack RO (1983) The Gibbs free energy of mixing of natural silicate liquids: an expanded regular solution approximation for the calculation of magmatic intensive variables. Contrib Mineral Petrol 84:107–145
Ghiorso MS, Gualda GAR (2015) An H_2O-CO_2 mixed fluid saturation model compatible with rhyolite-MELTS. Contrib Mineral Petrol. https://doi.org/10.1007/s00410-015-1141-8
Ghiorso MS, Hirschmann MM, Reiners PW, Kress VC III (2002) The pMELTS: a revision of MELTS for improved calculation of phase relations and major element partitioning related to partial melting of the mantle to 3 GPa. Geochem Geophys Geosyst 3(5). https://doi.org/10.1029/2001GC000217
Ghiorso MS, Kelemen PB (1987) Evaluating reaction stoichiometry in magmatic systems evolving under generalized thermodynamic constraints: examples comparing isothermal and isenthalpic assimilation. In: Mysen BO (ed) Magmatic processes: physicochemical principles. Geochemical Society, special publication vol 1, pp 319–336
Ghiorso MS, Sack RO (1995) Chemical mass transfer in magmatic processes. IV. A revised and internally consistent thermodynamic model for the interpolation and extrapolation of solid-liquid equilibria in magmatic systems at elevated temperatures and pressures. Contrib Mineral Petrol 119:197–212
Gualda GAR, Ghiorso MS (2015) MELTS_excel: a Microsoft Excel-based MELTS interface for research and teaching of magma properties and evolution. Geochem Geophys Geosyst 16:315–324
Gualda GAR, Ghiorso MS, Lemons RV, Carley TL (2012a) Rhyolite-MELTS: a modified calibration of MELTS optimized for silica-rich, fluid-bearing magmatic systems. J Petrol 53:875–890
Gualda GAR, Pamukcua AS, Anderson AT Jr, Ghiorso MS, Sutton SR, Rivers ML (2012b) Timescales of quartz crystallization and the longevity of the Bishop giant magma body. PLoS One. https://doi.org/10.1371/journal.pone.0037492
Helgeson HC (1968) Evaluation of irreversible reactions in geochemical processes involving minerals and aqueous solutions. I. Thermodynamic relations. Geochem Cosmochim Acta 32:853–877
Hirschmann MM, Ghiorso MS, Wasylenki LE, Asimow PD, Stolper EM (1998) Calculation of peridotite partial melting from thermodynamic models of minerals and melts. I. Methods and comparison to experiments. J Petrol 39:1091–1115
Hirschmann MM, Ghiorso MS, Stolper EM (1999a) Calculation of peridotite partial melting from thermodynamic models of minerals and melts. II. Isobaric variations in melts near the solidus and owing to variable source composition. J Petrol 40:297–313
Hirschmann MM, Asimow PD, Ghiorso MS, Stolper EM (1999b) Calculation of peridotite partial melting from thermodynamic models of minerals and melts. III. Controls on isobaric melt production and the effect of water on melt production. J Petrol 40:831–851
Kress VC, Carmichael ISE (1991) The compressibility of silicate liquids containing Fe_2O_3 and the effect of composition, temperature, oxygen fugacity and pressure on their redox states. Contrib Mineral Petrol 108:82–92
Kress VC, Ghiorso MS (2004) Thermodynamic modeling of post-entrapment crystallization in igneous phases. J Volcanol Geotherm Res 137:247–260
O'Neill HSTC, Pownceby ML (1993) Thermodynamic data from redox reactions at high temperatures. I. An experimental and theoretical assessment of the electro-chemical method using stabilized zirconia electrolytes, with revised values for the Fe-"FeO", co-CoO, Ni-NiO, and cu-Cu_2O oxygen buffers, and new data for the W-WO_2 buffer. Contrib Mineral Petrol 114:296–314
Osborn EF (1959) Role of oxygen pressure in the crystallization and differentiation of basaltic magma. Am J Sci 257:609–647
Osborn EF (1962) Reaction series for sub-alkaline igneous rocks based on different oxygen pressure conditions. Am Mineral 47:211–226
Pamukcu A, Gualda GAR, Bégué F, Gravley DM (2015) Melt inclusion shapes: timekeepers of short-lived giant magma bodies. Geology. https://doi.org/10.1130/G37021.1
Prigogine I, Defay R (1954) Chemical thermodynamics. Longmans Green and Co., London. 543 pp
Spera FJ, Bohrson WA (2001) Energy-constrained open-system magmatic processes. I: general model and energy-constrained assimilation and fractional crystallization (EC-AFC) formulation. J Petrol 42:999–1018
Spera FJ, Bohrson WA (2002) Energy-constrained open-system magmatic processes. III: energy-constrained recharge, assimilation and fractional crystallization (EC-RAFC). Geochem Geophys Geosyst 3. https://doi.org/10.1029/2002GC00315
Spera FJ, Bohrson WA (2004) Open-system magma chamber evolution: an energy-constrained geochemical model incorporating the effects of concurrent eruption, recharge, variable assimilation and fractional crystallization (EC-E'RAFC). J Petrol 45:2459–2480
Tuttles OF, Bowen NL (1958) Origin of granite in light of experimental studies in the system $NaAlSi_3O_8$-$KAlSi_3O_8$-SiO_2-H_2O. Mem Geol Soc Am 74:1–153

M

Magnesium

Fang-Zhen Teng
Isotope Laboratory, Department of Earth and Space Sciences, University of Washington, Seattle, WA, USA

Element Data

Atomic Symbol: Mg
Atomic Number: 12
Atomic Weight: 24.305 amu
Isotopes and (Abundances):
^{24}Mg (78.99%)
^{25}Mg (10.00%)
^{26}Mg (11.01%)
1 Atm Melting Point: 650 °C (1202 °F)
1 Atm Boiling Point: 1090 °C (1994 °F)

(*continued*)

Common Valences: 2+
Ionic Radii: 72 pm
Pauling Electronegativity: 1.31
First Ionization Energy: 737.2 KJ/mol
Chondritic (CI) Abundance: 9.54 wt.%
Silicate Earth Abundance: 22.8 wt.%
Crustal Abundance: 2.81 wt.%
Seawater Abundance: 0.128 wt.%
Core Abundance: 0

Properties

Magnesium, with symbol Mg and atomic number 12, belongs to the alkaline Earth element (Group II) of the periodic table. The pure Mg is a silvery white metal. It has a melting point of 650 °C and boiling point of 1090 °C at 1 standard atmosphere, i.e., 101.325 kPa (Lide 1993–1994). The electronic configuration of Mg is $[Ne]3s^2$, with the first and second ionization energies of 737.2 and 1450 KJ/mol, respectively. The low ionization energies make Mg ionic in character with a common valance state of 2+ and a typical ionic radius of 0.72 Å or 72 pm for sixfold coordination (Shannon 1976).

Magnesium has three stable isotopes, with mass numbers of 24, 25, and 26, and typical abundances of 78.99%, 10.00%, and 11.01%, respectively (Berglund and Wieser 2011). It has a standard atomic weight of 24.305 (CIAAW 2015). The isotopic abundance varies ~7‰ in $^{26}Mg/^{24}Mg$ ratio in the Earth and can vary much larger in meteoritic materials due to the decay of ^{26}Al to ^{26}Mg, with a half-life of 0.73 Myr (Teng 2017).

History and Use

The name magnesium originates from the Greek word for a district in Thessaly called Magnesia, which itself is derived from the Greek tribal name Magnetes. Magnesium was discovered as an element in 1755 by Joseph Black in the oxide form via heating magnesite. In 1808, Humphry Davy isolated Mg metal through electrolysis of a mixture of magnesium oxide and mercury oxide (Davy 1808). In 1831, Antoine Bussy made a significant amount of Mg metal by reacting magnesium chloride with potassium and later examined its properties (Bussy 1831).

Magnesium metal is mainly obtained by silicothermic Pidgeon process or electrolysis of fused Mg chloride. It is commonly used in metal alloys, especially in Al-Mg alloys, to increase the strength and lower the density. Magnesium metal alloys are widely used in aircraft, automotive, electronics, and other industries. Magnesium compound is also used in fertilizer and medicine as Mg^{2+} ion is important for the synthesis of chlorophyll and photosynthesis in plants and is essential to cells and enzymes in the human body.

Natural Distribution

Magnesium is the seventh most abundant element by atom in the solar system and the fourth most abundant element by weight in the CI chondrites, with a mean solar abundance of 9.54 wt.% (Palme et al. 2014). It is a common element during condensation with a condensation temperature of 1081 °C, which is higher than the moderately volatile elements such as K and Na but lower than the refractory elements such as Al and Ca (Lodders 2003).

Magnesium is the fourth most abundant element by weight in the Earth (below O, Fe, Si) (McDonough and Sun 1995). As Mg is lithophile during core-mantle differentiation, all Mg resides in the silicate Earth. Magnesium is highly compatible during mantle melting and magmatic differentiation as Mg is a major constitute in typical mafic phases such as olivine and pyroxene. Hence, Mg is concentrated in the Earth's mantle than the crust with overall concentration in the silicate Earth increasing with depth (Fig. 1). Magnesium is the fifth most abundant element in the bulk continental crust with an average MgO concentration of 4.66 wt.% and increases from the upper (2.48 wt.%), middle (3.59 wt.%), to the lower continental crust (7.24 wt.%) (Rudnick and Gao 2003). The oceanic crust has an average MgO concentration of 10.3 wt.% (White and Klein 2014), and the mantle has the highest MgO concentration of 37.8 wt.% (McDonough and Sun 1995).

Magnesium is the second most abundant cation in seawater (after Na) with a concentration of 0.128 wt.% or 52.82 mmol/kg (Pilson 2013). It has a residence time of 14 Myr (Li 1982), which is much longer than the mixing time of the ocean. Therefore, Mg is thoroughly mixed in the ocean. Similarly, Mg is also a major cation in riverine water with an average concentration of 4 ppm and ranging from <1 to 50 ppm, mainly depending on the nature of the bedrocks (Holland 1978; Livingstone 1963).

The high abundance of Mg in the silicate Earth makes it a major constituent of many rock-forming minerals (e.g., olivine, garnet, pyroxene, amphibole, mica, spinel, carbonate, sulfate, chlorite, and clay minerals) in igneous, metamorphic, and sedimentary rocks. Of these minerals, Mg is coordinated with six oxygens except in garnet and spinel where Mg is coordinated with eight and four oxygens, respectively.

Geochemical Behaviors

The behavior of Mg during igneous differentiation is well studied and mainly controlled by mafic minerals, as shown

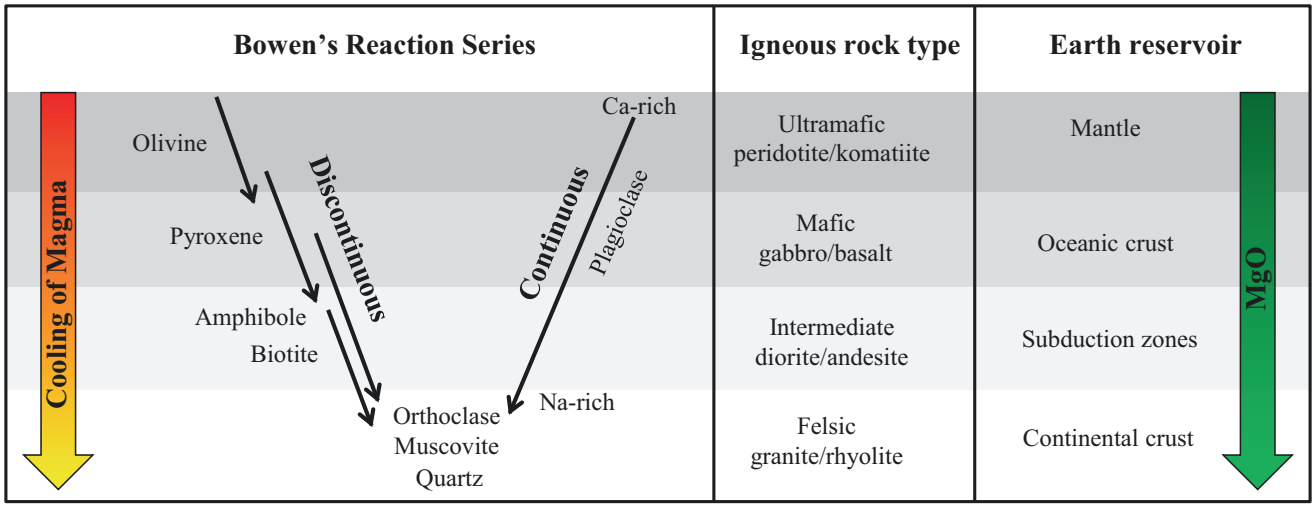

Magnesium, Fig. 1 Magnesium is compatible during mantle melting and magmatic differentiation as Mg is a major constitute in typical mafic phases such as olivine, pyroxene, amphibole, and biotite. Consequently, Mg is widely distributed in all major types of igneous and metamorphic rocks, as illustrated by the Bowen's reaction series, and MgO concentration decreases from the mantle, oceanic crust, lower, middle, to the upper continental crust

in the Bowen reaction series (Bowen 1928). MgO content in magma generally decreases with magmatic differentiation, e.g., from ~8 wt.% in basalt to <1 wt.% in granite due to the early crystallization of mafic minerals.

Though Mg is fluid mobile and expected to be removed from rocks during metamorphic dehydration, it is relatively conservative during prograde metamorphism, because of the continuous stability of Mg-rich minerals in both metapelites and metabasalts during progressive metamorphism. For example, Mg is continuously hosted in chlorite, amphibole, and pyroxene when metamorphic grade increases from blueschist facies to eclogite facies during oceanic crust subduction.

Magnesium is fluid mobile during continental weathering and seafloor alteration when Mg-rich minerals break down and secondary minerals are formed. During these low-temperature water-rock interactions, Mg is redistributed among the hydrosphere, continental crust, and oceanic crust. The most important Mg-rich minerals in igneous and metamorphic rocks that decompose during continental weathering are olivine, pyroxene, amphibole, biotite, and chlorite and in sediments are dolomite, Mg-calcite, and chlorite. During continental weathering, Mg in these minerals is liberated into the solution by hydrolysis reactions with dissolved CO_2 derived from the atmosphere and finally enters the oceans. Continental weathering of Mg-rich minerals thus helps to regulate CO_2 cycling. Magnesium is removed from the seawater to the oceanic crust through formation of Mg-rich silicates during high-temperature hydrothermal reactions at mid-ocean ridges, carbonate precipitation, and adsorption onto clays (Drever 1974; Elderfield and Schultz 1996). Eventually Mg in the oceans is recycled into the mantle by subduction of the oceanic slab.

Summary

Magnesium is a major element and widely distributed in the silicate Earth, hydrosphere and biosphere. Its unique chemical properties make Mg great tracers for high-T magmatic differentiation, low-T chemical weathering, and global elemental cycling, in addition to its wide applications in industry and medicine.

M

Cross-References

- Alkali and Alkaline Earth Metals
- Atomic Number, Mass Number, and Isotopes
- Chondrites
- Earth's Continental Crust
- Earth's Oceanic Crust
- Mantle Geochemistry
- Magnesium Isotopes
- Ocean Salinity, Major Elements, and Thermohaline Circulation
- Periodic Table
- Water

References

Berglund M, Wieser ME (2011) Isotopic compositions of the elements 2009 (IUPAC technical report). Pure Appl Chem 83:397–410

Bowen NL (1928) The evolution of the igneous rocks, 1st edn. Princeton University Press, Princeton

Bussy A (1831) Mémoire sur le Radical métallique de la Magnésie. Annual De Chimie XLVI:434–437

CIAAW (2015) Atomic weights of the elements 2015. www.ciaaw.org/atomic-weights.htm
Davy H (1808) Electro-chemical researches on the decomposition of the earths; with observations on the metals obtained from the alkaline earths, and on the amalgam procured from ammonia. Philos Trans R Soc Lond 98:333–370
Drever JI (1974) The magnesium problem. In: Goldberg ED (ed) Marine chemistry. Wiley, New York, pp 337–357
Elderfield H, Schultz A (1996) Mid-ocean ridge hydrothermal fluxes and the chemical composition of the ocean. Annu Rev Earth Planet Sci 24:191–224
Holland HD (1978) The chemistry of the atmosphere and oceans. Wiley, New York
Li YH (1982) A brief discussion on the mean oceanic residence time of elements. Geochim Cosmochim Acta 46:2671–2675
Lide DR (1993–1994) CRC handbook of chemistry and physics, 74th edn. CRC Press, Boca Raton
Livingstone DA (1963) Chemical composition of rivers and lakes. USGS professional paper
Lodders K (2003) Solar system abundances and condensation temperatures of the elements. Astrophys J 591:1220–1247
McDonough WF, Sun SS (1995) The composition of the Earth. Chem Geol 120:223–253
Palme H, Lodders K, Jones A (2014) Solar system abundances of the elements. In: Davis AM (ed) Planets, asteriods, comets and the solar system, 2nd edn, pp 15–36
Pilson MEQ (2013) An introduction to the chemistry of the sea, 2nd edn. Cambridge University Press, Cambridge
Rudnick RL, Gao S (2003) Composition of the continental crust. In: Rudnick RL (ed) The crust. Elsevier-Pergamon, Oxford, pp 1–64
Shannon RD (1976) Revised effective ionic radii and systematic studies of interatomic distances in halides and chalcogenides. Acta Crystallogr A 32:751–767
Teng F-Z (2017) Magnesium isotope geochemistry. Rev Mineral Geochem 82:219–287
White WM, Klein EM (2014) Composition of the oceanic crust. In: Rudnick RL (ed) The crust, 2nd edn. Elsevier, Oxford, pp 457–496

Magnesium Isotopes

Fang-Zhen Teng
Isotope Laboratory, Department of Earth and Space Sciences, University of Washington, Seattle, WA, USA

Introduction

Magnesium (Mg) is widely distributed in the silicate Earth, hydrosphere, and biosphere and has three stable isotopes, ^{24}Mg, ^{25}Mg, and ^{26}Mg, with the natural abundance of 78.99%, 10.00%, and 11.01%, respectively (Berglund and Wieser 2011). The large mass difference (>8% between ^{24}Mg and ^{26}Mg) has led to large mass-dependent Mg isotope fractionation. To date, >7‰ variation in ^{26}Mg/^{24}Mg has been observed, with carbonates at the light end (δ^{26}Mg = −5.6, Wombacher et al. 2011) and weathered residues at the heavy end (δ^{26}Mg = +1.8, Liu et al. 2014) (Fig. 1). Similar to other isotopes, Mg isotopes are fractionated less at high temperature and fractionated the greatest during low-temperature processes (Teng 2017).

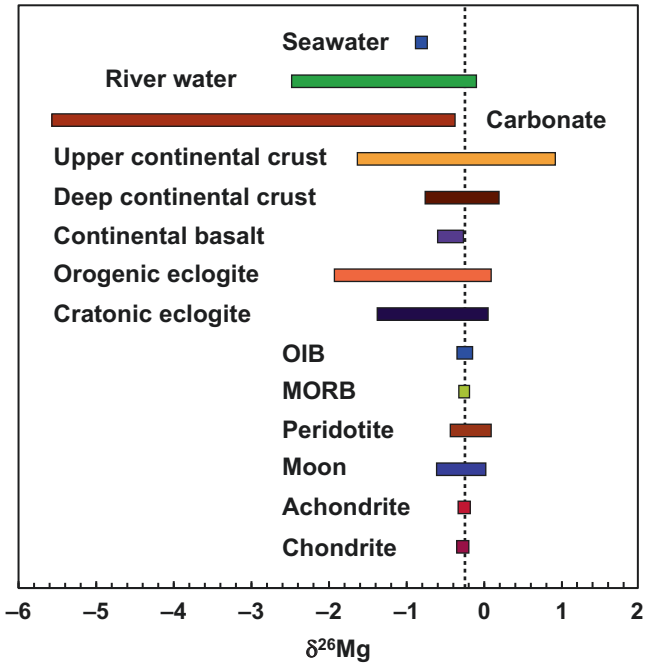

Magnesium Isotopes, Fig. 1 Magnesium isotopic composition of major extraterrestrial and terrestrial reservoirs. The *vertical dotted line* represents the average Mg isotopic composition of the mantle (Teng et al. 2010a)

Magnesium Isotopic Distribution in Major Reservoirs

Chondrite, Achondrite, and the Moon

Magnesium isotopic composition is homogenous among different types of chondrites, with an average δ^{26}Mg = −0.28 ± 0.06 (Teng et al. 2010a). The identical Mg isotopic composition in all major types of chondrites suggests that the primary and secondary processes that affected the chemical and oxygen isotopic compositions of chondrites did not significantly fractionate Mg isotopes.

Magnesium isotopic compositions of most achondrites are similar to chondrites except some angrite and HEDs, which are slightly heavier. Their slightly heavier values likely resulted from impact-induced evaporation or high abundance of isotopically heavy clinopyroxene (Sedaghatpour and Teng 2016).

Magnesium isotopic compositions of lunar samples display a dichotomy between low- and high-Ti samples. Low-Ti basalts, together with lunar highland rocks, breccias, and soils, have similar Mg isotopic composition to chondrites. By contrast, high-Ti basalts have light isotopic composition, which may reflect the source heterogeneity produced

during differentiation of the lunar magma ocean (Sedaghatpour et al. 2013).

The Earth's Mantle

Magnesium isotopic composition of the mantle accounts for that of the bulk Earth as the mantle holds >99.9% of Mg in the Earth. Peridotite xenoliths, MORBs, and OIBs have similar Mg isotopic composition, with an average $\delta^{26}Mg = -0.25 \pm 0.07$ (Teng et al. 2010a; Pogge von Strandmann et al. 2011). This value represents Mg isotopic composition of the Earth, which is similar to that of chondrites and the Moon.

The Continental Crust

The upper continental crust, as represented by granite, shale, and loess, has very heterogeneous $\delta^{26}Mg$ values ranging from −1.64 to +0.92, which likely reflects large Mg isotope fractionation during continental weathering (Li et al. 2010; Huang et al. 2013; Wimpenny et al. 2014). The deep continental crust, as sampled by high-grade metamorphic terranes and granulite xenoliths, also displays a large range in $\delta^{26}Mg$ from −0.76 to +0.19. This large isotopic variation reflects source heterogeneity caused by incorporation of chemically weathered upper crustal materials and by deep-crustal fluid metasomatism (Teng et al. 2013; Wang et al. 2015a; Yang et al. 2016).

The Hydrosphere

The oceans control the Mg isotopic budget of the hydrosphere as it accounts for ~97% of water on the Earth's surface and has the highest Mg concentration in all reservoirs of the hydrosphere (Pilson 2013). Seawaters sampled at various depths and from global location have an identical $\delta^{26}Mg$ value of -0.83 ± 0.09 (2SD), indicating a homogenous Mg isotopic composition of the oceans (Ling et al. 2011, and references therein). By contrast, $\delta^{26}Mg$ values of rivers are highly variable, ranging from −2.5 to −0.1 (Fig. 1), reflecting both Mg isotopic variation in bedrock lithology and Mg isotope fractionation during water-rock interactions (Tipper et al. 2006). Overall, the flux-weighted $\delta^{26}Mg$ of global runoff is estimated to be −1.09 (Tipper et al. 2006), significantly lower than seawater. The isotopic difference between seawater and global runoff indicates the existence of additional heavy inputs or light outputs, which might result from carbonate precipitation, low-T seafloor alteration, and high-temperature hydrothermal alteration.

Behaviors of Magnesium Isotopes During Major Geological Processes

Continental Weathering

Continental weathering produces one of the largest Mg isotope fractionations in nature. Behaviors of Mg isotope fractionation during continental weathering have been extensively investigated, through studies of river waters (Brenot et al. 2008; Pogge von Strandmann et al. 2008; Tipper et al. 2008; Jacobson et al. 2010; Wimpenny et al. 2011); continental weathering profiles of basalt, diabase, and shale (Teng et al. 2010b; Huang et al. 2012; Liu et al. 2014; Ma et al. 2015); as well as laboratory leaching experiments (Wimpenny et al. 2010). These studies found large Mg isotope fractionation during weathering with light Mg isotopes generally preferring fluids to weathered residue, leading to the formation of an isotopically light hydrosphere and a heavy weathered upper continental crust.

Biological Processes

Magnesium isotopes, as an essential element in biosphere, are largely fractionated during biological processes. Large Mg isotope fractionation occurred during incorporation of Mg into chlorophyll (Black et al. 2006). Plants prefer heavy Mg isotopes to nutrient sources during growth, and light isotopes are enriched in leaves relative to roots (Bolou-Bi et al. 2010, 2012). Large Mg isotopic variation was also observed in marine biogenic carbonates, reflecting multiple processes such as kinetic and biogenic vital effect, temperature, precipitation rate, pH, etc. (Saenger and Wang 2014; Teng 2017).

Partial Melting and Magmatic Differentiation

The MgO content in magma generally decreases with magmatic differentiation as Mg is compatible in mafic minerals. Magnesium isotopic composition however does not change during partial melting and differentiation of mafic to felsic magmas (Teng et al. 2007, 2010a; Liu et al. 2010). Studies of coexisting pyroxene and olivine in peridotites and hornblende and biotite in granites found similar Mg isotopic composition. Hence partial melting and fractional crystallization of these minerals do not cause measurable isotopic shifts in the compositions of the melt (Yang et al. 2009; Liu et al. 2010; Xiao et al. 2013).

Metamorphic Dehydration

Magnesium isotope fractionation during metamorphic dehydration is limited as high-grade metamorphic rocks, e.g., granulite and eclogite, have similar Mg isotopic composition to their protoliths (Li et al. 2011; Teng et al. 2013). Studies of genetically related prograde metamorphosed basalts and pelites also show that metamorphic rocks formed at different temperature and pressure have similar Mg isotopic composition, suggesting that metamorphic rocks still preserve isotopic compositions of their protoliths (Li et al. 2014; Wang et al. 2014b, 2015b). The lack of isotope fractionation during prograde metamorphism mainly results from the conservative behavior of Mg as it is always hosted in major rock-forming minerals during metamorphic reactions, and little Mg was lost into fluids.

High-Temperature Equilibrium and Kinetic Isotope Fractionation

Large Mg isotopic variation has been found in Mg-rich minerals in igneous and metamorphic rocks, reflecting both equilibrium and kinetic isotope fractionation. Though Mg isotopes are not significantly fractionated among pyroxene, olivine, biotite, and hornblende (Yang et al. 2009; Liu et al. 2010; Xiao et al. 2013), large Mg isotope fractionation occurs between biotite, pyroxene, olivine, garnet, and spinel in some peridotite, eclogite, and granulite. Garnet is lighter and spinel is heavier than other coexisting minerals (Li et al. 2011; Liu et al. 2011; Xiao et al. 2013; Wang et al. 2012, 2015a, c). The large equilibrium, inter-mineral isotope fractionation reflects the difference in Mg coordination number (CN) as CN is 8 in garnet, 4 in spinel, and 6 in other minerals. In addition, large Mg isotopic variation is also observed in olivine fragments from the Kilauea Iki lava lake, which is negatively correlated with Fe isotopic variation. The coupled Mg and Fe isotope fractionation was produced by interdiffusion of Mg and Fe between olivine and melts (Teng et al. 2011). In situ analysis of zoned olivines by micro-mill, LA-MC-ICPMS, and SIMS confirms this and found remarkable Mg and Fe isotopic zoning, coupled with Mg and Fe elemental zoning in single olivine (Sio et al. 2013). Furthermore, disequilibrium Mg isotope fractionation is also observed among pyroxene, olivine, and spinel in pyroxene-rich peridotite, reflecting kinetic Mg isotope fractionation during mantle metasomatism (Xiao et al. 2013; Hu et al. 2016).

Applications of Magnesium Isotope Geochemistry

Magnesium isotope geochemistry is still in its infancy. Nonetheless, promising applications have emerged. The large equilibrium inter-mineral Mg isotope fractionation associated with garnet and spinel in igneous and metamorphic rocks could be developed as a high-precision geothermometry (e.g., Li et al. 2011; Liu et al. 2011). The large kinetic isotope fractionation induced by diffusion can be used to tell the nature of mineral zoning, i.e., crystal growth or diffusion, which lays the foundation for using mineral zoning as a geospeedometry (e.g., Teng et al. 2011; Sio et al. 2013). The large Mg isotopic variation produced during low-T processes (especially in carbonates) can survive during subduction, leads to form a distinct mantle end member, and is later recorded in mantle/mantle-derived rocks. Thus Mg isotopes can be used as a tracer of subducted carbonates (Yang et al. 2012; Wang et al. 2014a) and origins of cratonic eclogites (Wang et al. 2012, 2015c). The large Mg isotope fractionation in carbonates also has the potential to provide constraints on the evolution of seawater chemistry, paleoclimate environments, and the origin of dolostone (Saenger and Wang 2014). Finally, biological processes significantly fractionate Mg isotopes (Bolou-Bi et al. 2012); hence Mg isotopes may be used to trace biological processes in the deep time.

Summary

The wide distribution of Mg in major reservoirs, coupled with large equilibrium and kinetic isotope fractionation at high- and low-temperature processes, makes Mg isotope geochemistry a promising tool for a high-precision thermometry, a powerful method for telling the nature of mineral zoning and a unique tracer for crust-mantle interactions and biological processes.

Cross-References

- ▶ Magnesium
- ▶ Stable Isotope Geochemistry

References

Berglund M, Wieser ME (2011) Isotopic compositions of the elements 2009 (IUPAC technical report). Pure Appl Chem 83(2):397–410

Black JR, Yin QZ, Casey WH (2006) An experimental study of magnesium-isotope fractionation in chlorophyll-a photosynthesis. Geochim Cosmochim Acta 70:4072–4079

Bolou-Bi EB, Poszwa A, Leyval C, Vigier N (2010) Experimental determination of magnesium isotope fractionation during higher plant growth. Geochim Cosmochim Acta 74(9):2523–2537

Bolou-Bi EB, Vigier N, Poszwa A, Boudot J-P, Dambrine E (2012) Effects of biogeochemical processes on magnesium isotope variations in a forested catchment in the Vosges Mountains (France). Geochim Cosmochim Acta 87:341–355

Brenot A, Cloquet C, Vigier N, Carignan J, France-Lanord C (2008) Magnesium isotope systematics of the lithologically varied Moselle river basin, France. Geochim Cosmochim Acta 72:5070–5089

Hu Y, Teng F-Z, Zhang H-F, Xiao Y, Su B-X (2016) Metasomatism-induced mantle magnesium isotopic heterogeneity: evidence from pyroxenites. Geochim Cosmochim Acta 185:88–111

Huang K-J, Teng F-Z, Wei G-J, Ma J-L, Bao Z-Y (2012) Adsorption- and desorption-controlled magnesium isotope fractionation during extreme weathering of basalt in Hainan Island, China. Earth Planet Sci Lett 359–360:73–83

Huang K-J, Teng F-Z, Elsenouy A, Li W-Y, Bao Z-Y (2013) Magnesium isotopic variations in loess: origins and implications. Earth Planet Sci Lett 374:60–70

Jacobson AD, Zhang Z, Lundstrom C, Huang F (2010) Behavior of Mg isotopes during dedolomitization in the Madison aquifer, South Dakota. Earth Planet Sci Lett 297(3–4):446–452

Li W-Y, Teng F-Z, Ke S, Rudnick RL, Gao S, Wu F-Y, Chappell BW (2010) Heterogeneous magnesium isotopic composition

of the upper continental crust. Geochim Cosmochim Acta 74(23):6867–6884
Li W-Y, Teng F-Z, Xiao Y, Huang J (2011) High-temperature intermineral magnesium isotope fractionation in eclogite from the Dabie orogen, China. Earth Planet Sci Lett 304(1–2):224–230
Li W-Y, Teng F-Z, Wing BA, Xiao Y (2014) Limited magnesium isotope fractionation during metamorphic dehydration in metapelites from the Onawa contact aureole, Maine. Geochem Geophys Geosyst 15(2):408–415
Ling M-X, Sedaghatpour F, Teng F-Z, Hays PD, Strauss J, Sun W (2011) Homogenous magnesium isotopic composition of seawater: an excellent geostandard for Mg isotope analysis. Rapid Commun Mass Spectrom 25:2828–2836
Liu S-A, Teng F-Z, He Y, Ke S, Li S (2010) Investigation of magnesium isotope fractionation during granite differentiation: implication for Mg isotopic composition of the continental crust. Earth Planet Sci Lett 297(3–4):646–654
Liu S-A, Teng F-Z, Yang W, Wu FY (2011) High-temperature intermineral magnesium isotope fractionation in mantle xenoliths from the North China craton. Earth Planet Sci Lett 308:131–140
Liu X-M, Teng F-Z, Rudnick RL, McDonough WF, Cummings M (2014) Massive magnesium depletion and isotopic fractionation in weathered basalts. Geochim Cosmochim Acta 135:336–349
Ma L, Teng F-Z, Jin L, Ke S, Yang W, Gu H-O, Brantley SL (2015) Magnesium isotope fractionation during shale weathering in the Shale Hills critical zone observatory: accumulation of light Mg isotopes in soils by clay mineral transformation. Chem Geol 397:37–50
Pilson MEQ (2013) An introduction to the chemistry of the sea. Cambridge University Press, Cambridge, 529 pp
Pogge von Strandmann PAE, Burton KW, James RH, Van Calstern P, Gislason SR, Sigmarsson O (2008) The influence of weathering processes on riverine magnesium isotopes in a basaltic terrain. Earth Planet Sci Lett 276:187–197
Pogge von Strandmann PAE, Elliott E, Marschall HR, Coath C, Lai Y-J, Jeffcoate AB, Ionov DA (2011) Variations of Li and Mg isotope ratios in bulk chondrites and mantle xenoliths. Geochim Cosmochim Acta 75:5247–5268
Saenger C, Wang Z (2014) Magnesium isotope fractionation in biogenic and abiogenic carbonates: implications for paleoenvironmental proxies. Quat Sci Rev 90:1–21
Sedaghatpour F, Teng F-Z (2016) Magnesium isotopic composition of achondrites. Geochim Cosmochim Acta 174:167–179
Sedaghatpour F, Teng F-Z, Liu Y, Sears DW, Taylor LA (2013) Magnesium isotopic composition of the Moon. Geochim Cosmochim Acta 120:1–16
Sio CK, Dauphas N, Teng F-Z, Chaussidon M, Helz RT, Roskosz M (2013) Discerning crystal growth from diffusion profiles in zoned olivine by in-situ Mg-Fe isotopic analyses. Geochim Cosmochim Acta 123:302–321
Teng F-Z, Wadhwa M, Helz RT (2007) Investigation of magnesium isotope fractionation during basalt differentiation: implications for a chondritic composition of the terrestrial mantle. Earth Planet Sci Lett 261(1–2):84–92
Teng F-Z, Li W-Y, Ke S, Marty B, Dauphas N, Huang S, Wu F-Y, Pourmand A (2010a) Magnesium isotopic composition of the Earth and chondrites. Geochim Cosmochim Acta 74(14):4150–4166
Teng F-Z, Li W-Y, Rudnick RL, Gardner LR (2010b) Contrasting behavior of lithium and magnesium isotope fractionation during continental weathering. Earth Planet Sci Lett 300:63–71
Teng F-Z, Dauphas N, Helz RT, Gao S, Huang S (2011) Diffusion-driven magnesium and iron isotope fractionation in Hawaiian olivine. Earth Planet Sci Lett 308(3–4):317–324
Teng F-Z, Yang W, Rudnick RL, Hu Y (2013) Heterogeneous magnesium isotopic compostion of the lower crust: a xenolith perspective. Geochem Geophys Geosyst 14:3844–3856. https://doi.org/10.1002/ggge.20238
Teng F-Z (2017) Magnesium isotope geochemistry. Rev Mineral Geochem 82:219–287
Tipper ET, Galy A, Gaillardet J, Bickle MJ, Elderfield H, Carder EA (2006) The magnesium isotope budget of the modern ocean: constraints from riverine magnesium isotope ratios. Earth Planet Sci Lett 250:241–253
Tipper ET, Galy A, Bickle MJ (2008) Calcium and magnesium isotope systematics in rivers draining the Himalaya-Tibetan-plateau region: lithological or fractionation control? Geochim Cosmochim Acta 72:1057–1075
Wang S-J, Teng F-Z, Williams HM, Li S (2012) Magnesium isotopic variations in cratonic eclogites: origins and implications. Earth Planet Sci Lett 359–360:219–226
Wang S-J, Teng F-Z, Li S-G (2014a) Tracing carbonate-silicate interaction during subduction using magnesium and oxygen isotopes. Nat Commun 5:5328. https://doi.org/10.1038/ncomms6328
Wang S-J, Teng F-Z, Li S-G, Hong J-A (2014b) Magnesium isotope systematics of mafic rocks during continental subduction. Geochim Cosmochim Acta 143:34–48
Wang S-J, Teng F-Z, Rudnick RL, Li S-G (2015a) The behavior of magnesium isotopes in low-grade metamorphosed mudrocks. Geochim Cosmochim Acta 165:435–448
Wang S-J, Teng F-Z, Bea F (2015b) Magnesium isotopic systematics of metapelite in the deep crust and implications for granite petrogenesis. Geochem Perspect Lett 1:75–83
Wang S-J, Teng F-Z, Rudnick RL, Li S-G (2015c) Magnesium isotope evidence for a recycled origin of cratonic eclogites. Geology 43:1071–1074
Wimpenny J, Gislason SR, James RH, Gannoun A, Pogge Von Strandmann PAE, Burton KW (2010) The behaviour of Li and Mg isotopes during primary phase dissolution and secondary mineral formation in basalt. Geochim Cosmochim Acta 74(18):5259–5279
Wimpenny J, Burton KW, James RH, Gannoun A, Mokadem F, Gislason SR (2011) The behaviour of magnesium and its isotopes during glacial weathering in an ancient shield terrain in West Greenland. Earth Planet Sci Lett 304(1–2):260–269
Wimpenny J, Yin Q-Z, Tollstrup D, Xie L-W, Sun J (2014) Using Mg isotope ratios to trace Cenozoic weathering changes: a case study from the Chinese Loess Plateau. Chem Geol 376:31–43
Wombacher F, Eisenhauer A, Bohm F, Gussone N, Regenberg M, Dullo W-C, Ruggeberg A (2011) Magnesium stable isotope fractionation in marine biogenic calcite and aragonite. Geochim Cosmochim Acta 75:5797–5818
Xiao Y, Teng F-Z, Zhang H-F, Yang W (2013) Large magnesium isotope fractionation in peridotite xenolithis from eastern North China craton: product of melt-rock interaction. Geochim Cosmochim Acta 115:241–261
Yang W, Teng F-Z, Zhang H-F (2009) Chondritic magnesium isotopic composition of the terrestrial mantle: a case study of peridotite xenoliths from the North China craton. Earth Planet Sci Lett 288(3–4):475–482
Yang W, Teng F-Z, Zhang H-F, Li S (2012) Magnesium isotopic systematics of continental basalts from the North China craton: implications for tracing subducted carbonate in the mantle. Chem Geol 328:185–194
Yang W, Teng F-Z, Li W-Y, Liu S-A, Ke S, Liu Y-S, Zhang H-F, Gao S (2016) Magnesium isotopic composition of the deep continental crust. Am Mineral. https://doi.org/10.2138/am-2015-5275. (in press)

Magnetism

H. Tsunakawa[1] and Y. Yamamoto[2]
[1]Department of Earth and Planetary Sciences, Tokyo Institute of Technology, Tokyo, Japan
[2]Center for Advanced Marine Core Research, Kochi University, Kochi, Japan

Definition

All substances can generate the magnetic field more or less, that is, the magnetism. The magnetism is generally categorized as the diamagnetism, paramagnetism, ferromagnetism, antiferromagnetism, and ferrimagnetism. The term "magnetic" is often used as ferromagnetic (including ferrimagnetic), while that of "nonmagnetic" is quoted as non-ferromagnetic.

Introduction

The magnetism basically originates from electrons of a substance. The diamagnetism is caused by the orbital effect of an electron, while the paramagnetism, ferromagnetism, antiferromagnetism, and ferrimagnetism are unique properties due to spin magnetic moments of unpaired electrons in atoms and ions of transition elements (e.g., Fe, Co, Ni). Magnetic properties of a substance and their mechanisms have theoretically and experimentally been studied in physics of the magnetism (e.g., Chikazumi 2009). In the Earth and planetary sciences, mineral magnetic properties and their applications have been investigated to research subjects of the rock magnetism (e.g., Dunlop and Özdemir 1997) and the paleomagnetism (e.g., McElhinny and McFadden 2012).

Diamagnetism

Electrons orbiting an atomic nucleus in an ambient magnetic field generate an opposite field. This magnetism is called the diamagnetism and appears in all substances. The diamagnetism is interpreted as a result of the electromagnetic induction in the classical electromagnetism. The diamagnetism is very weak and is negatively proportional to the strength of the applied magnetic field:

$$M = \chi_d B$$

where M is the diamagnetism intensity, B is the strength of the applied field, and χ_d is the diamagnetic susceptibility. The diamagnetism is antiparallel to the applied field ($\chi_d < 0$). Most values of $|\chi_d|$ are of the order of 10^{-8} [m^3kg^{-1}] with little change with temperature. For example, χ_d is -0.90×10^{-8} m^3kg^{-1} for water (H_2O) and -0.62×10^{-8} m^3kg^{-1} for quartz (SiO_2) at room temperature.

Paramagnetism

Transition elements (e.g., Fe, Co, Ni) and their ions have spin magnetic moments of unpaired electrons. Without an ambient magnetic field, spin magnetic moments have random orientations due to the thermal agitation if there are no effective interactions among the moments. When the magnetic field is applied, orientations of the moments tend to be aligned in parallel to the applied field. This magnetism is the Curie paramagnetism. The Curie paramagnetism of terrestrial rocks is often called the paramagnetism in a simple manner.

A rate of the parallel magnetic moments is proportional to the applied field strength:

$$M = \chi_p B$$

where M is the paramagnetism intensity, B is the strength of the applied field, and χ_p is the paramagnetic susceptibility. The paramagnetic susceptibility is subjected to Curie's law:

$$\chi_p = \frac{C}{T}$$

where C is the Curie constant and T is the absolute temperature in unit of kelvin. If a paramagnetic substance contains n atoms (or cations) with spin magnetic moments per unit volume, then

$$C = \mu_0 \frac{n\mu^2}{3k}$$

where μ is the effective spin magnetic moment per atom, k is the Boltzmann constant ($= 1.3806 \times 10^{-23}$ JK^{-1}), and μ_0 is the permeability of free space ($=4\pi \times 10^{-7}$ Hm^{-1}).

Mafic silicate minerals (e.g., pyroxene, olivine) containing iron elements show the Curie paramagnetism. The paramagnetic susceptibilities of these minerals depend mostly on Fe^{2+} and Fe^{3+} contents. As for olivine, fayalite (Fe_2SiO_4) has $\chi_p = 126 \times 10^{-8}$ m^3kg^{-1} at room temperature while forsterite (Mg_2SiO_4) shows the diamagnetism ($\chi_d = -0.39 \times 10^{-8}$ m^3kg^{-1}).

There is the other type of the paramagnetism, called the Pauli paramagnetism. This mostly appears in some metals due to free electrons (e.g., aluminum). The susceptibility is positive and almost temperature-independent. The Pauli

paramagnetism is comparable to the diamagnetism in strength ($\chi_p \sim 10^{-8}$ m^{3}kg^{-1}).

Ferromagnetism

Strong interaction works among spin magnetic moments in the ferromagnetic substances (e.g., αFe, kamacite of Fe-Ni alloy), that is, the exchange interaction as a quantum mechanical coupling. Adjacent spin magnetic moments are ordered in parallel to each other, resulting in the spontaneous magnetization. The spontaneous magnetization exists even in the absence of the ambient magnetic field, which is quite different from the diamagnetism and the paramagnetism. As the temperature increases, the spontaneous magnetization decreases due to the thermal agitation and then disappears above the Curie temperature (T_C).

According to the Weiss's theory, the exchange interaction is approximated with the magnetic force in the "molecular field" proportional to the spontaneous magnetization intensity. Assuming the Boltzmann distribution, the spontaneous magnetization per unit volume (M_s) is expressed in the following equation.

$$M_s = n\mu L(\alpha)$$

$$\alpha = \mu_0 \frac{\mu w M_s}{kT}$$

where $L(\alpha)$ is the Langevin function and w is a proportional coefficient of the molecular field. Since the above equations give the relationship of M_s with T, T_C is given for $M_s \to 0$. For $T \leq T_c$, $M_s(T)/M_s(0) \approx (1 - T/T_c)^{1/2}$ in a rough approximation, while $M_s(T)/M_s(0) \approx (1 - T/T_c)^{\gamma}$ in the experiment. For iron metal (αFe), $M_s(20\ ^\circ\text{C}) = 1714$ kAm^{-1} (or emu cm^{-3}), $T_c = 770\ ^\circ$C, and $\gamma = 0.34$.

In the quantum mechanical treatment, the Langevin function is replaced by the Brillouin function. For the magnetization of ferromagnetic mineral, size and shape of the mineral should be considered as in subsection of the rock magnetism and the paleomagnetism. Above T_C, ferromagnetic substances show the paramagnetism under the Curie-Weiss law of the following equation.

$$\chi_p = \frac{C}{T - T_C}$$

Antiferromagnetism

In the antiferromagnetic substance, adjacent spin magnetic moments are ordered in antiparallel to each other by the negative exchange interaction. This effect results in null spontaneous magnetization, called the antiferromagnetism. In the case of compounds, strong coupling works through anions of crystal (e.g., oxygens ion in iron oxides) due to another strong interaction, the superexchange interaction. It sometimes orders spin magnetic moments of cations in antiparallel, resulting in null spontaneous magnetization. This magnetism is also categorized as the antiferromagnetism.

An antiferromagneic substance shows smaller positive susceptibility than the paramagnetic susceptibility when the magnetic field is applied, because of the negative (super)exchange interaction. Above the Néel temperature (T_N), the thermal agitation overwhelms the (super)exchange interaction. Thus the antiferromagnetism disappears, and the paramagnetism appears in the similar way to the ferromagnetic substance.

Hematite (αFe_2O_3) is known to be one of the major terrestrial magnetic minerals showing the antiferromagnetism. However it has a weak spontaneous magnetization ($M_s \approx 2.5$ kAm^{-1}) between the Morin transition temperature ($T_M \approx -20\ ^\circ$C) and the Néel temperature ($T_N = 675\ ^\circ$C). This weak magnetization is caused by the spin-canted magnetization: the sublattice magnetizations are mostly in antiparallel direction but are slightly canted in perpendicular to the basal plane of hematite. Such magnetization is called the canted ferromagnetism or the parasitic ferromagnetism, and the Néel temperature is taken as the Curie temperature.

Ferrimagnetism

In some substance with the negative (super)exchange interaction, different magnetic moments of cations in sublattices result in the spontaneous magnetization. This magnetism is called the ferrimagnetism. As the temperature increases, the ferrimagnetism decreases and disappears above the Curie temperature (T_c) in the similar way to the ferromagnetism.

For magnetite (Fe_3O_4: $Fe^{2+}Fe^{3+}{}_2O_4$) of spinel crystal structure, there are two sites in cation sublattices: Fe^{3+} in A sites, and Fe^{2+} and Fe^{3+} in B sites. A magnetic moment of Fe^{2+} is $4\mu_B$ while that of Fe^{3+} is $5\mu_B$, where μ_B is the Bohr magneton (9.27401×10^{-24} J T^{-1}). As the negative superexchange interaction works through O^{2-} between A and B sites, magnetic moments in A and B sites are antiparallel. This results in cancelled magnetic moments of Fe^{3+} in A and B sites, but magnetization due to Fe^{2+} in B sites remains as the spontaneous magnetization with $M_s(20\ ^\circ\text{C}) = 480$ kAm^{-1}.

The ferrimagnetism is inseparably related to the crystal structure as well as the contained cations. M_s of magnetite

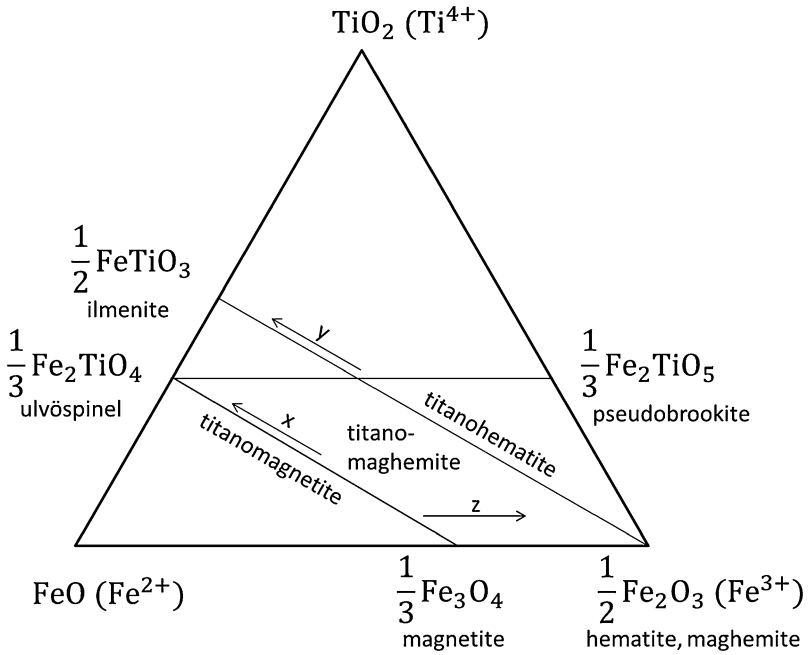

Magnetism, Fig. 1 Major magnetic minerals of terrestrial rocks are shown in the $TiO_2-FeO-Fe_2O_3$ ternary diagram. Parameters of x (titanomagnetite soli-solution line), y (titanohematite soli-solution line), and z (low-temperature oxidation line of titanomagnetite) are explained in the text

with Fe^{2+} and Fe^{3+} monotonously decreases as the temperature increases ($\gamma = 0.43$) with $T_c = 580\ ^\circ C$. Some ferrimagnetic substances behave in quite different manner for the temperature dependence of M_s. For example, Li-Cr ferrite shows negative to positive M_s with increasing temperature. A specific titanohematite with a negative M_s causes the self-reversed thermoremanent magnetization as mentioned in subsection of the rock magnetism.

Magnetic Minerals of Terrestrial and Extraterrestrial Rocks

Rock magnetism is a research field on magnetic minerals in terrestrial and extraterestrial rocks to utilize them. Major magnetic minerals of terrestrial rocks are iron and titanium oxides, in particular, titanomagnetite, titanohematite, and titanomaghemite (Fig. 1).

Titanomagnetite is the ulvöspinel (Fe_2TiO_4) – magnetite (Fe_3O_4) solid solution of cubic spinel crystal structure and expressed as $Fe_{3-x}Ti_xO_4$ or $Fe^{2+}{}_{1+x}Fe^{3+}{}_{2-2x}Ti^{4+}{}_xO^{2-}{}_4$ ($0 \le x \le 1$). As x increases, M_s and T_C gradually decrease: $M_s = 480\ kAm^{-1}$ and $T_C = 580\ ^\circ C$ for ferrimagnetic magnetite (x = 0), while $M_s = 0$ and $T_N = -153\ ^\circ C$ for antiferromagnetic ulvöspinel (x = 1). High-temperature oxidation (or deuteric oxidation) frequently occurs during formation of titanomagnetites of subaerial volcanic rocks, resulting in exsolved ilmenite as thin lamellae. The antiferromagnetic lamellae effectively divide the host ferrimagnetic titanomagnetites into many tiny parts of Ti-poor titanomagnetite which can have stable remanent magnetizations.

Titanohematite, sometimes called hemoilmenite, is the ilmenite ($FeTiO_3$) – hematite (αFe_2O_3) solid solution of rhombohedral crystal structure: $Fe^{2+}{}_yFe^{3+}{}_{2-2y}Ti^{4+}{}_yO^{2-}{}_3$ ($0 \le y \le 1$). Ilmenite (y = 1) is antiferromagnetic ($T_N = -233\ ^\circ C$), while hematite (y = 0) shows the canted ferromagnetism ($T_C = 675\ ^\circ C$) as in subsection of the antiferromagnetism. The titanohematite of intermediate composition ($y \approx 0.5 - 0.7$) exhibits ferrimagnetic behavior to result in the self-reversed thermoremanent magnetization.

Titanomaghemite is the low-temperature oxidation product of titanomagnetite, a degree of which is expressed by the oxidation parameter z ($0 \le z \le 1$). The oxidation changes Fe^{2+} cations into Fe^{3+} with lattice defects. Magnetite, the end-member of titanomagnetite, changes to maghemite (γFe_2O_3, z = 1). It is known that magnetic minerals of the mid-ocean-ridge basalt (MORB) are initially Ti-rich titanomagnetites of $x \approx 0.6$ ($M_s \approx 125\ kAm^{-1}$ and $T_C \approx 150\ ^\circ C$) in most cases. Titanomagnetites of MORB often undergo the low-temperature oxidation, transforming to titanomaghemites.

Iron sulfides are often contained in sedimentary, granitic, and metamorphic rocks. Monoclinic pyrrhotite (Fe_7S_8) is ferrimagnetic ($M_s \approx 80\ kAm^{-1}$, $T_C = 320\ ^\circ C$). Greigite

(Fe_3S_4) is ferrimagnetic ($M_s \approx 125$ kAm^{-1}, $T_C \approx 330$ °C). Pyrite (FeS_2) is paramagnetic while troilite (FeS) is antiferromagnetic ($T_N = 305$ °C). Hydrous iron oxides are found in sediments, soils, and weathered rocks. Goehtite (αFeOOH) is antiferromagnetic ($T_N = 120$ °C) but sometimes ferrimagnetic with very weak magnetization.

The lunar rocks contain kamacite, a ferromagnetic iron-rich Fe-Ni alloy (5–10% Ni) and ilmenite. Magnetic minerals of meteorites are mainly composed of Fe-Ni alloys and magnetites, contents of which depend on the meteorite type. Iron meteorites are composed of Fe-Ni alloys: kamacite, taenite (30–70% Ni), and tetrataenite (~50% Ni), often associated with the Widmanstätten pattern of kamacite and taenite due to very slow cooling at the formation. Magnetic minerals of the Martian rocks have not clearly been identified although some minerals were reported for the Martian soils and meteorites.

Recent progress in the rock magnetism has resulted in significant developments of the environmental magnetism. Magnetic minerals found in sediments (e.g., deep sea sediments, loess) are detrital, aeolian, and authigenic origins which are more or less affected by the climate and by the surrounding environment. Thus variation in magnetic characteristics of sediments is usable as a proxy for past climate and environmental changes.

Remanent Magnetization and the Paleomagnetism

Rocks containing ferro- and/or ferrimagnetic minerals acquire "fossil magnetization" in the ambient magnetic field when they are formed. This is the remanent magnetization, sometimes called the remanence. The natural remanent magnetization (NRM) can give a record of the past magnetic field and has widely been used for restoration of the past geomagnetic field in the paleomagnetism.

Spontaneous magnetization of the magnetic mineral tend to be oriented along the ambient magnetic field, minimizing the magnetic energy against the disturbance such as the thermal agitation. The remanence acquisition is considered as a statistical process, since a rock is regarded as an assemblage of many magnetic minerals. When the ambient field is weak like the geomagnetic field, probability of spontaneous magnetizations parallel to the ambient field is linearly changed with strength of the field. Thus the remanence intensity is proportional to the strength of the ambient field. These parallelism and proportionality are the bases of the paleomagnetism.

Igneous rocks acquire the remanent magnetization during cooling, called thermoremanent magnetization (TRM). As the rocks are cooled from T_C, a parallel component of spontaneous magnetizations becomes larger and is fixed as TRM at the blocking temperature (T_B) where the thermal agitation is enough smaller than the magnetic energy. TRM is considered as the most reliable record of the past geomagnetic field direction (paleodirection) and intensity (paleointentisity), although TRM acquisition is nearly sporadic.

Sediments acquire remanent magnetization at the deposition in the ambient field, since magnetic particles in water (or air) are forced to be parallel to the field. After deposition, orientation of the magnetic particle is locked mainly due to the compaction. This type of the remanent magnetization is called the depositional remanent magnetization (DRM) and/or the post-DRM (pDRM). They have an advantage to give a continuous record of the paleodirection and paleointensity.

Stability of the remanence is sometimes critical in the paleomagnetic study since old rocks have experienced various geological events. If the remanence is stable enough against changes in the ambient field and temperature, a record of the past magnetic field is recovered as a primary component with good reliability. If the remanence is exposed to temperature higher than T_B, the remanence is reset. Reset of the remanence also occurs in the magnetic field larger than the magnetic coercive force of the magnetic grain (often called the coercivity, B_C). Long-time exposure in a weaker field than B_C is possible to reset the remanence by gradual progress of thermal equilibrium. These resets are the process of "remagnetization" yielding a secondary component.

In general the stable remanence is carried by relatively smaller magnetic grains with high T_B and B_C. For terrestrial rocks, carriers of stable remanence are mostly submicron grains of titanomagnetite in which the spontaneous magnetization is uniform due to the single-domain (SD) structure. Larger grains are magnetically divided into multiple domains, that is, the multi-domain (MD) structure. Threshold size between SD and MD is 0.05–0.08 μm for magnetite and ~0.2 μm for Ti-rich titanomagnetite (x = 0.6). If magnetic grains are very small (<~0.03 μm for magnetite), their T_B's become lower than the room temperature resulting in no remanence (the superparamagnetism).

It is not easy to identify submicron magnetic carriers by an optical microscope. In the standard experiment of remanence carriers, magnetic minerals of a bulk sample are identified with measurement of the Curie temperature and with demagnetization by heating and/or applying the alternating field. Applying a strong DC field, measurements of hysteresis curve, and remanence acquisition curve are often used as the nondestructive inspection.

According to paleomagnetic studies, the geomagnetic field has varied on archeological and geological time scales. The largest change is the polarity reversal and the present polarity initiated at ~0.8 Ma. The direction and intensity of the geomagnetic field also change, called the (paleo)secular variation. When averaging the secular variation, the geomagnetic field is almost the geocentric axial dipole field, by which the paleolatitude is estimated in the tectonics. Based on satellite observations, Moon and Mars exhibit crustal magnetic anomalies, suggesting existence of an ancient core dynamo.

Summary

Magnetism is categorized as the diamagnetism, paramagnetism, ferromagnetism, antiferromagnetism, and ferrimagnetism. The diamagnetism and paramagnetism emerge when the magnetic field is applied. The ferromagnetism, antiferromagneism, and ferrimagnetism are originated from the spontaneous magnetization of magnetic minerals, which persists in null ambient field. Terrestrial rock contains ferro- and ferrimagnetic minerals, for example, titanomagnetites. The ferro- and ferrimagnetic minerals allow us to estimate the past magnetic field through remanent magnetizations of those rocks. Advanced studies in the rock magnetism, the paleomagnetism, and the planetary magnetism related to the crustal magnetic fields are referred elsewhere (e.g., Kono 2015; Spohn 2015).

Cross-References

- ▶ Atomic Absorption, Inductively Coupled Plasma Optical Emission Spectroscopy, and Infrared Spectroscopy
- ▶ Earth's Core
- ▶ Iron
- ▶ Meteorites
- ▶ Transition Elements

References

Chikazumi S (2009) Physics of ferromagnetism, 2nd edn. International Series of Monographs on Physics. Oxford University Press, UK, 668 pp

Dunlop DJ, Özdemir Ö (1997) Rock magnetism – fundamentals and frontiers. Cambridge University Press, UK, 573 pp

Kono M (2015) Geomagnetism. In: Schubert G (ed) Treatise on Geophysics, 2nd edn, Elsevier, Netherland, vol 5. 530 pp

McElhinny MW, McFadden PL (2012) Paleomagnetism: continents and oceans, 2nd edn. Academic Press, USA, 386 pp

Spohn T (2015) Physics of terrestrial planets and moons. In: Schubert G (ed) Treatise on Geophysics, 2nd edn, Elsevier, Netherland, vol 10. 651 pp

Manganese

Tammie L. Gerke[1] and Brenda J. Little[2]
[1]Department of Geology and Environmental Earth Science, Miami University Middletown, Middletown, OH, USA
[2]Naval Research Laboratory, Stennis Space Center, Hancock County, MS, USA

Element Data

Atomic Symbol: Mn
Atomic Number: 25
Atomic Weight: 54.9380
Isotopes and Abundances: ^{55}Mn 100%
1 Atm Melting Point: 1246 °C
1 Atm Boiling Point: 2061 °C
Common Valences: $^{+}$2, $^{+}$3, $^{+}$4, $^{+}$6, and $^{+}$7
Ionic Radii: in picometers

Mn(II)	4-coordinate, tetrahedral	80.0
Mn(IV)	4-coordinate, tetrahedral	53.0
Mn(V)	4-coordinate, tetrahedral	47.0
Mn(VI)	4-coordinate, tetrahedral	39.5
Mn(VII)	4-coordinate, tetrahedral	39.0
Mn(II)	6-coordinate, octahedral	81.0
Mn(II)	6-coordinate, octahedral, high spin	97.0
Mn(III)	6-coordinate, octahedral	72.0
Mn(III)	6-coordinate, octahedral, high spin	78.5
Mn(IV)	6-coordinate, octahedral	67.0
Mn(VII)	6-coordinate, octahedral	60.0
Mn(II)	8-coordinate	110.0

Pauling Electronegativity: 1.55
First Ionization Potential: 717.4
Chondritic (CI) Abundance: 1916 ppm (Palme and O'Neill, 2014)
Silicate Earth Abundance: 1050 ppm (Palme and O'Neill, 2014)
Crustal Abundance: 950–1000 ppm
Seawater Abundance:
2×10^{-10}–1.9×10^{-9} kgL^{-1}
Core Abundance: ~300 ppm

Properties

Manganese (Mn) is a transition metal located between chromium and iron in the periodic table of elements. Common oxidation states are $^{+}$2, $^{+}$3, $^{+}$4, $^{+}$6, and $^{+}$7, but possible oxidation states ranging from $^{-}$3 to $^{+}$7 (CCREM 1987) have been

reported. Oxidation states that are unstable in acidic solutions can exist in basic solutions, and conversely (Rayner-Canham and Overton 2003).

History and Use

Use of Mn dates from Stone Age. Mn dioxide was used as a pigment in cave paintings. Ancient Romans and Egyptian added Mn compounds to color glass (Sayre and Smith 1961; Chalmin et al. 2006). Today, Mn is used in steel, battery, and ceramic productions; as a micronutrient in feed for plants and animals; and as an oxidant in organic syntheses (Post 1999). Manganese is also used as an alloying element in US coins (Kuwahara et al. 2001).

The top five producers of Mn with reserves reported in metric tons (MT) are the following: South Africa, 200 MT; Australia, 91 MT; Brazil, 50 MT; China, 44 MT; and Gabon, 22 MT (USGS 2016). Common Mn ore minerals include: braunite ($Mn^{2+}Mn_6^{3+}SiO_{12}$), hausmannite ($Mn^{2+}Mn_2^{3+}O_4$), psilomelane (massive hard manganese oxides), and pyrolusite (Mn^{4+} O_2) (Kirshnaswamy and Sinha 1988). Mn is also present in polymetallic nodules on the sea floor, in fresh water (Rossmann and Callender 1968; Cronan and Thomas 1970) and lacustrine basins (Cornwell and Kipphut 1992).

Geochemical Behavior

Mn in the solar system is used to interpret both early solar chronology and modern observations. ^{53}Mn, with a half-life of 3.7 million years, decays to ^{53}Cr. Variations in Mn and Cr isotope ratios in meteorites provide a mechanism for radiometric dating solar bodies and support theories of nucleosynthetic processes prior to the coalescence of the solar system (Birck and Allegre 1988). Identification of manganese oxides on the surface of Mars suggests the presence of atmospheric oxygen and possible groundwater in the ancient past (Lanza et al. 2016).

Concentration of Mn in carbonaceous Ivuna (CI) chondritic meteorites is 1930 ppm (Lodders 2010). Presently, the total Earth concentration of Mn is approximately 1050 ppm. Wade and Wood (2005) reported a Mn concentration of 1150 ppm for the core during accretion, while the current Mn concentration for the core is estimated to be approximately 300 ppm (McDonough 2014). Earth crustal Mn concentrations range between 950 and 1000 ppm, localized in igneous, metamorphic, and sedimentary rocks (Post 1999). Mn moves through two global crustal cycles that are inter-related by the hydrologic cycle, i.e., the water-terrestrial rock cycle and the lacustrine/marine sediment-water cycle.

Mn geochemistry is complex and controlled primarily by pH-Eh conditions (Kabata-Pendias, 2010). Aqueous Mn^{2+} mainly forms from the weathering of igneous and metamorphic rocks (De Vitre and Davison 1993). Mn^{2+} is mobile under anoxic conditions (Hylander et al. 2000) but becomes insoluble when oxidized to Mn^{3+} and Mn^{4+} and forms insoluble hydrous oxides. The E_h-pH values that determine the solubility and deposition of Mn are illustrated in of Maynard 2014. More oxidized species, e.g., permanganate, are located at positive potentials, while more reduced species (e.g., Mn^0) are found at negative potentials. More basic species are located in the high pH regions and the more acidic species at low pH. A vertical division, e.g., one between Mn^{2+} and Mn $(OH)_2$, indicates an equilibrium that depends on pH and not a redox process. Dissolved Mn^{2+} is stable over the range of pH values found in natural fresh and saline waters (5–8) under mildly reducing conditions. Under oxidizing conditions, Mn^{4+} oxides are highly insoluble. Mn^{2+} carbonates (e.g., rhodocrocite [$MnCO_3$]) are insoluble at high pH in CO_2-rich environments. The predictable E_h-pH relationships for manganese and iron provide a mechanism for separation in slightly reducing sediments (few centimeters below the surface). Because soluble Mn has a larger stability field than soluble iron in that environment, Mn^{2+} is mobilized in pore water while iron is immobilized, either as an oxide or in the presence of sulfur, a sulfide.

Microorganisms are also involved in Mn movement through both global crustal cycles. At circumneutral pH, soluble Mn^{2+} can be oxidized to insoluble Mn^{3+}, Mn^{4+} by Mn-oxidizing microorganisms at rates that are several orders of magnitude faster than abiotic oxidation (Morgan 2005). Microorganisms can also reduce Mn^{4+} to Mn^{2+} (Nealson and Myers 1992).

More than 100 Mn minerals have been identified (Kirshnaswamy and Sinha 1988), formed under a wide range of environmental conditions. The basic structure of most Mn oxides is the MnO_6 octahedron, arranged in either layers or chains/tunnels. Mn oxides have very large surface areas (Dixon and White 2002). In the layered Mn oxide structure (e.g., birnessite [$(Na,Ca,K)_x(Mn^{4+},Mn^{3+})_2O_4 \bullet$ $1.5(H_2O)$]), water and cations can be adsorbed and/or exchanged between the layers. Hollandite [$Ba(Mn^{4+}$, $Mn^{2+})_8O_{16}$], a tunnel-structure, can be partially filled with water molecules, and large uni- or divalent cations (Post 1999). Mn is commonly associated with some transition metals, e.g., Co, Ni, Cu, Zn, Pb, Ba, Tl, W, and Mo, because of the negatively charged $Mn(OH)_4$ and MnO_2 structures (Kabata-Pendias 2010). Highly reactive $Mn^{3+,\ 4+}$ oxides are among the strongest oxidants in natural systems, capable of oxidizing Fe^{2+}, As^{3+}, Ce^{3+}, Pu^{4+}, Co^{2+}, Cr^{3+}, and Au^{1+} (Ta et al. 2015). Because of these properties, Mn oxides control the mobilization and dispersion of metal ions, including heavy metal ions, in soils and sediments (Post 1999).

Pyrolusite (MnO_2) and rhodochrosite are the two most common Mn-containing minerals. Mn oxyhydroxides, e.g., vernadite [$(Mn^{4+},Fe^{3+},Ca,Na)(O,OH)_2 \bullet n(H_2O)$], todorokite [$(Na,Ca,K)_2(Mn^{4+},Mn^{3+})_6O_{12} \bullet 3–4.5(H_2O)$], and birnessite are found in marine Mn nodules (Hein and Petersen 2013). Manganite has been identified as the principal mineral in

shallow water continental-margin nodules (Glasby 1972). Todorokite $[(Na,Ca,K)_2(Mn^{4+},Mn^{3+})_6O_{12}•3–4.5(H_2O)]$, buserite ($Na_4Mn_{14}\ O_{27}•21H_2O$), and birnessite are the most common biogenic Mn oxyhydroxides (Tebo et al. 2005). Biogenetic Mn oxides/oxyhydroxides are cryptocrystalline sheet-like particulates with large surface areas and, like abiotic Mn minerals, are highly reactive (Tebo et al. 2005).

Mn is also present in minerals as an accessory component as it readily substitutes for Fe^{2+} and Mg^{2+} (Ure and Berrow 1982). During magmatic processes, Mn is preferentially incorporated into ferromagnesian silicates, such as olivines, pyroxenes, and clinopyroxenes (Sobolev et al. 2007; Qin and Humayun 2008; Le Roux et al. 2011). In metamorphic rocks, Mn is present in garnets, amphiboles, and calcite (Temmam et al. 2000; Hawthorne et al. 2012).

Biological Utilization and Toxicity

The average human body contains approximately 12 mg Mn (Emsley 2013), stored mainly in the kidneys, liver, thyroid, pituitary, pancreas, and bone (Watts 1990). Manganese is an essential element in humans functioning as an enzyme co-factor and as a constituent of metalloenzymes (Zidenberg-Cherr and Keen 1987; Lucchini et al. 2014). Humans can be exposed to Mn via inhalation, food consumption, and ingestion of water (NAS 1980; US EPA 2004). Exposure to elevated levels of Mn can cause neurological disorders (Gerke et al. 2016), and if humans are exposed to Mn concentrations greater than 500 mg m^{-3} it is considered immediately dangerous to life and health (http://www.cdc.gov/niosh/idlh/7439965.html).

Cross-References

- Chalcophile Elements
- Chondrites
- Chromium Isotopes
- Earth's Core
- Ferromanganese Crusts and Nodules: Rocks That Grow
- Lithophile Elements
- Ore Deposits
- Oxidation-Reduction Reactions and Eh-pH (Pourbaix) Diagrams
- Transition Elements

References

Birck J-L, Allegre CJ (1988) Manganese-chromium isotope systematics and the development of the early solar system. Nature 331:579–584

CCREM Canadian Council of Resource and Environment Ministers (1987) Canadian water quality guidelines. Drinking water. Environ Health Perspect 119(1):138–143

Chalmin E, Vignaud C, Salomon H, Farges F, Susini J, Menu M (2006) Minerals discovered in paleolithic black pigments by transmission electron microscopy and micro-X-ray absorption near-edge structure. Appl Phys A 83(12):213–218

Cornwell JC, Kipphut GW (1992) Biogeochemistry of manganese- and iron-rich sediments in Toolik Lake, Alaska. Hydrobiologia 240:45–59

Cronan DS, Thomas RL (1970) Ferromanganese concretions in Lake Ontario. Can J Earth Sci 7:1346

De Vitre R, Davison W (1993) Manganese particles in freshwater. In: van Leeuwen HP, Buffle J (eds) Environmental particles, vol 2. Lewis, Boca Raton, pp 317–352

Dixon JB, White GN (2002) Manganese oxides. In: Dixon JB, Schulze GG (eds) Soil mineralogy with environmental applications. SSSA, Madison

Emsley J (2013) Manganese the protector. Nat Chem 5:978

Gerke TL, Little BJ, Maynard JB (2016) Manganese deposition in drinking water distribution systems. Sci Total Environ 54:184–193

Glasby GP (1972) The mineralogy of manganese nodules from a range of marine environments. Mar Geol 13(1):57–72

Hawthorne FC, Oberti R, Harlow GE, Maresch WV, Martin RF, Schumacher JC, Welch MD (2012) Nomenclature of the amphibole supergroup. Am Mineral 97:2031–2048

http://www.cdc.gov/niosh/idlh/7439965.html. Retrieved 1 May 2016

Hein JR, Petersen S (2013) The geology of manganese nodules. In: Baker E, Beaudoin Y (eds) Deep Sea minerals: manganese nodules, a physical, biological, environmental, and technical review, 1B. Secretariat of the Pacific Community, pp 7–18

Hylander LD, Meili M, Oliveirac LJ, Castro e Silvad E, Guimaraese J, Araujod DM, Nevesd RP, Stachiwd R, Barrosf AJP, Silvaf GD (2000) Relationship of mercury with aluminum, iron and manganese oxy-hydroxides in sediments from the Alto Pantanal, Brazil. Sci Total Environ 260:97–107

Kabata-Pendias A (2010) Trace elements in soils and plants, 4th edn. CRC Press/Taylor & Francis Group, Boca Raton

Kirshnaswamy S, Sinha RK (1988) Mineral resources, 3rd edn. Oxford/IBH Publishing, New Delhi

Kuwahara RT, Skinner RB III, Skinner RB Jr (2001) Nickel coinage in the United States. West J Med 175(2):112–114. https://doi.org/10.1136/ewjm.175.2.112

Lanza NL et al (2016) Oxidation of manganese in an ancient aquifer, Kimberley formation, Gale crater, Mars. Geophys Res Lett 43:7398–7407

Le Roux V, Dasgupta R, Lee CTA (2011) Mineralogical heterogeneities in the Earth's mantle: constraints from Mn, Co, Ni and Zn partitioning during partial melting. Earth Planet Sci Lett 307:395–408

Lodders K (2010) Solar system abundances of the elements. In: Principles and perspectives in cosmochemsitry. Astrophysics and space science proceedings. Springer, Berlin

Lucchini RG, Guazzetti S, Zoni S, Benedetti C, Fedrighi C, Peli M, Donna F, Bontempi E, Borgese L, Micheletti S, Ferri R, Marchetti S, Smith DR (2014) Neurofunctional dopaminergic impairment in elderly after lifetime exposure to manganese. Neurotoxicology 45:309–317

Maynard JB (2014) Manganiferous sediments, rocks, and ores. In: Holland H, Turekian K (eds) Treatise on geochemistry, 2nd edn. Elsevier 9, 9.11, pp 327–349

McDonough WF (2014) Compositional model for the Earth's core A2. In: Turekian KK, Holland HD (eds) Treatise on geochemistry, 2nd edn. Elsevier, Oxford, pp 559–577

Morgan JJ (2005) Kinetics of reaction between O_2 and Mn(II) species in aqueous solutions. Geochim Cosmochim Acta 69(1):35–48

NAS (1980) Manganese. In: Recommended dietary allowances, 9th revised edn. National Academy of Sciences, Washington, DC, pp 154–157

Nealson KH, Myers CR (1992) Microbial reduction of manganese and iron: new approaches to carbon cycling. Appl Environ Microbiol 58 (2):439–443

Palme H, O'Neill HSC (2014) Cosmochemical estimates of mantle composition. In: Turekian KK, Holland HD (eds) Treatise on geochemistry, 2nd edn. Elsevier, Oxford, pp 1–39
Post JE (1999) Manganese oxide minerals: crystal structures and economic and environmental significance. Proc Natl Acad Sci U S A 96(7):3447–3454
Qin L, Humayun M (2008) The Fe/Mn ratio in MORB and OIB determined by ICP-MS. Geochim Cosmochim Acta 72(6):1660–1677
Rayner-Canham G, Overton T (2003) Descriptive inorganic chemistry, 5th edn. W.H. Freeman, New York
Rossmann R, Callender E (1968) Manganese nodules in Lake Michigan. Science 162:1123–1124
Sayre EV, Smith RW (1961) Compositional categories of ancient glass. Science 133(3467):1824–1826
Sobolev AV et al (2007) The amount of recycled crust in sources of mantle-derived melts. Science 316(5823):412–417
Tebo BM, Johnson HA, McCarthy JK, Templeton AS (2005) Geomicrobiology of manganese (II) oxidation. Trends Microbiol 13(9):421–428
Temmam M, Paquette J, Vali H (2000) Mn and Zn incorporation into calcite as a function of chloride aqueous concentration. Geochim Cosmochim Acta 64(14):2417–2430
U.S. Geological Survey (2016) Mineral commodity summaries 2016. U.S Geological Survey, 202 p. https://doi.org/10.3133/70140094
United States Environmental Protection Agency, Office of Water (2004) Health and ecological criteria division. Washington, DC, Drinking Water Health Advisory for Manganese. EPA-822-R-04-003
Ure AM, Berrow ML (1982) The elemental constituents of soils. In: Environmental chemistry, vol 2. Royal Society of Chemistry, London, pp 94–204
Wade J, Wood BJ (2005) Core formation and the oxidation state of the Earth. Earth Planet Sci Lett 236:78–95
Watts DL (1990) The nutritional relationships of manganese. J Orthomolec Med 5(4):219–222
Zidenberg-Cherr S, Keen CL (1987) Enhanced tissue lipid peroxidation: mechanism underlying pathologies associated with dietary manganese deficiency. In: Kies C (ed) Nutritional bioavailability of manganese. American Chemical Society, Washington, DC

Mantle Geochemistry

Andreas Stracke
Institut für Mineralogie, Westfälische Wilhelms-Universität, Münster, Germany

Definition

Mantle Geochemistry: The study of Earth's mantle by investigating its chemical and isotopic composition.

Basic Facts About Earth's Mantle

Earth's mantle extends from the core-mantle boundary at 2900 km depth, the Gutenberg discontinuity, to the base of Earth's crust, the Mohorovičić discontinuity, at <10 km depth beneath the oceans and ~40–70 km beneath the continents. With about two thirds of Earth's mass, the mantle is the largest silicate reservoir of our planet. Oxygen (O), Mg, Si, Fe, Ca, and Al are its main constituents (Palme and O'Neill 2014). The mantle is mostly peridotitic in composition, with varying mineral assemblage that adapts to the large range of pressure-temperature conditions in the mantle. At upper mantle pressures, a typical mantle peridotite with a density of 3300 kg m^{-3} and a temperature of ca. 1600–1700 K is made up of about 55% olivine, 35% ortho- and clinopyroxene, and up to 10% of an Al-bearing phase, i.e., plagioclase, spinel, or garnet. Adapting to increasing pressure, these minerals transform to progressively denser minerals in the deeper mantle. At ca. 410 and 660 km depth, abrupt increases in mantle density – by about 4 and 9%, respectively – cause sharp discontinuities in seismic velocity. These are caused by structural transformations of the most abundant mineral: from olivine to wadsleyite at ca. 410 km and from spinel to bridgmanite (silicate-perovskite) and magnesiowustite at ca. 660 km depth (Kind and Li 2015). Deeper than 660 km, seismic wave speeds increase continuously until about ca. 200–300 km above the core–mantle boundary (CMB), where a sudden decrease in seismic velocity defines the so-called D″ discontinuity (in short: D″). The observed decrease in seismic velocity and the depth range over which it occurs varies. The most likely cause for occurrence of the D″ is the transition of bridgmanite to post-perovskite (e.g., Cobden et al. 2015; Lay 2015; Garnero et al. 2016). The region between the D″ and the CMB exhibits several complex seismic features (Lay and Garnero 2004; Lay 2015), the most prominent being two large low-shear-wave-velocity provinces (LLSVP), one beneath the central Pacific Ocean and one beneath Africa (Lay et al. 2006). In addition, there are intermittent thin structures with very low seismic wave velocities directly above the CMB, termed ultra-low-velocity zones (ULVZ; Williams and Garnero 1996). The observed seismic heterogeneity of the lowermost mantle above the CMB is likely caused by a complex interplay between phase changes (bridgmanite to post-perovskite), large variations in temperature, mantle composition, or even the presence of partial melt (Garnero et al. 2011; Tackley 2012; Cobden et al. 2015; Deschamps et al. 2015; Lay 2015; Garnero et al. 2016). At the CMB, the mantle has finally reached a density of about 5600 kg m^{-3} and a temperature of ca. 2400–2700 K, which is approximately 1200–1800 K cooler than the outer core. This interface between the solid silicate mantle and the liquid Fe alloy outer core (CMB) thus forms a pronounced thermal boundary layer.

Mantle Convection, Plate Tectonics, and Volcanism

The thermal boundary layers at the CMB and Earth's surface drive solid-state mantle convection: the rise of hot buoyant

material from the interior and the sinking of cold, dense (negatively buoyant) material from the surface. In the present Earth, cold, dense oceanic crust is subducted into the mantle, where it penetrates the 660 km discontinuity and sinks into the lower mantle, in some cases after temporarily stagnating at that depth (Fukao et al. 1992; Grand 1994; van der Hilst et al. 1997; Fukao and Obayashi 2015). Hence a current mode of whole-mantle convection is established, where material is cycled throughout the entire mantle. The vigor of convective motion is described by the Rayleigh number, Ra, a dimensionless parameter that relates thermal buoyancy, which drives mantle convection, and viscosity and thermal diffusivity, which impede mantle convection; the latter by erasing temperature differences that cause thermal buoyancy (Ricard 2015). Hence a greater temperature contrast between a hot basal (the CMB) and cold upper boundary layer (Earth's surface) results in more vigorous convection. Higher viscosity, especially of the lower mantle – which is estimated to be 1 or 2 orders of magnitude more viscous than the upper mantle (e.g., Lithgow-Bertelloni and Richards 1998; van Keken et al. 2014) – decreases convective vigor. The pattern and speed of mantle convection is thus largely determined by its temperature, viscosity, and compositional structure.

The subduction of cold dense oceanic crust is not only a key parameter for mantle convection, it is also the main driving force for plate tectonics (Forsyth and Uyeda 1975), resulting in moving continents, mountain building, and volcanism mostly at plate margins. In response to plate spreading at mid ocean ridges, for example, shallow mantle rises passively and melts partially through adiabatic decompression to form the oceanic crust. This process is responsible for most (about 80%) of Earth's volcanism. The oceanic crust is eventually subducted at convergent plate margins, where new basaltic and andesitic crust is generated by fluid-induced melting of the mantle wedge overlying the subducted slab. Volcanism at convergent plate margins is the second most voluminous type of volcanism on Earth. The eventual subduction of oceanic crust and residual mantle lithosphere into the deeper mantle trigger an upward return flow of hot mantle from the deep interior. An additional source for hot, buoyant material originates from internal thermal boundary layers, most prominently the CMB. Hot, buoyant material may rise from thermal boundary layers in form of focused cylindrical plumes and melt in the shallow mantle away from plate boundaries. Such mantle plumes are thought to source most, but not all, of Earth's "hotspot" volcanism (e.g., Morgan 1971; Steinberger 2000; White 2010, 2015a). On a global scale, this so-called intraplate volcanism is much less voluminous than mid ocean ridge and convergent margin volcanism, but it can nevertheless produce massive volcanic eruptions that form large igneous provinces (LIP), either on continents or the ocean floor. Examples are the Deccan Trap flood basalt province in India and the submarine Ontong Java plateau in the SW Pacific, respectively.

This interplay between mantle convection and plate tectonics on modern Earth has established a global cycle of ocean crust generation by partial mantle melting and its subduction into the mantle. In this way, the mantle has evolved continuously since the onset of plate tectonics.

Initially, however, Earth was much hotter than today owing to (1) the release of gravitational energy during accretion, (2) core formation, and (3) larger radioactive heat production. A hotter and therefore less viscous mantle convects more vigorously. It also starts to melt at greater depth (McKenzie and Bickle 1988), resulting in a greater amount of melt production and the formation of a thick oceanic lithosphere comprising the oceanic crust and underlying residual mantle. The Archean mantle was about 100–300 K hotter than at present (Herzberg et al. 2010). Thus the oceanic lithosphere cooled less effectively and stayed thermally buoyant (e.g., Davies 1992; van Thienen et al. 2004). Whether plate tectonics can occur under such conditions remains enigmatic. In addition, the lower convective stress imposed by a hotter, less viscous mantle may keep the oceanic crust from breaking apart. The Earth may therefore have started out in a stagnant-lid phase, where mantle convection occurred beneath an intact, strong, and immobile lithosphere (Moresi and Solomatov 1995, 1998). However, if the stresses imposed by convection exceed the lithospheric strength, the oceanic lithosphere may break apart and sink back into the mantle (Moresi and Solomatov 1998; O'Neill et al. 2007; van Hunen and van den Berg 2008). Other recently proposed subduction-initiating mechanisms are heat pipe volcanism (Moore and Webb 2013), destabilization of the lithosphere (Rey et al. 2014), or the accumulation of grain damage (Foley et al. 2014). Moreover, if the oceanic crust transforms to eclogite (at $>$40 km depth), the oceanic lithosphere becomes dense enough to subduct (van Hunen and van den Berg 2008). The hotter oceanic lithosphere is also rheologically weak, however, and may become too weak to support its own weight, resulting in slab break-off (van Hunen and van den Berg 2008). The latter causes a temporary loss of slab pull of the dense subducting crust, initiating a period of absent or very slow subduction. In other words, an episodic style of subduction and plate tectonics may occur (Moresi and Solomatov, 1998; O'Neill et al. 2007; Silver and Behn 2008; van Hunen and van den Berg 2008; Moyen and van Hunen 2012; Gerya 2014). These short-term episodes of proto-subduction in the early Earth may have evolved into longer periods of subduction, and hence plate tectonics, as mantle temperature decreased (O'Neill et al. 2007; Sizova et al. 2010; van Hunen and Moyen 2012; Moyen and van Hunen 2012; Moore and Webb 2013).

When exactly a plate tectonic regime similar to modern Earth has been established remains uncertain. The occurrence

of up to 4.4 Gyr old granite-derived zircons implies the existence of thick continental crust, which may have been generated in a subduction zone setting in the Hadean (4.56–4.0 Ga; Harrison 2009; Shirey et al. 2008), although this interpretation remains controversial (e.g., Kemp et al. 2010). Geochemical and petrologic evidence suggests that plate tectonics could have started locally in the early Archean (4.0–3.2 Ga) and progressively became more wide-spread in the late Archean (3.2–2.5 Ga; Condie and Kröner 2008; Shirey and Richardson 2011). Modern-style plate tectonics, operating under similar conditions and producing a similar geologic record as today (e.g., ophiolites, ultrahigh pressure terranes, and paired metamorphic belts), has been firmly established since at least the Neoproterozoic (<1 Ga ago; Stern 2005). The key here, however, is that Earth's mantle may not always have operated in the same way as it does today. Mantle convection and, especially, the interaction between Earth's crust and mantle have probably changed, or simply operated under different conditions in the past.

Mantle Geodynamics

For the present Earth, geodynamics describes the interplay between mantle convection and plate tectonics. The subduction (recycling) of oceanic crust, or more generally the interaction between Earth's crust and mantle, introduces compositionally distinct material into Earth's mantle, where it becomes dispersed by convective stirring. The physicochemical nature of the materials and the convective flow field determine the manner and timescale of their dispersal. Hence the geodynamics of Earth's mantle shapes its compositional structure and evolution and is the framework for interpreting the available geochemical information.

The processes that disperse compositionally distinct material in Earth's convecting mantle are often loosely described as "mixing." It is instructive, however, to use exact terminology in this context. Following Tackley (2015), "mixing requires the homogenization of chemical differences by a combination of stirring and chemical diffusion. Stirring involves stretching, the elongation of material into a thin tendril or lamella by strain caused by the convective flow. This greatly increases the surface area of the material and decreases its width, facilitating chemical diffusion." Solid state chemical diffusion of most elements in Earth's silicate mantle is extremely slow, acting over submeter length scales over geologic time (Hofmann and Hart 1978; Hart 1993). However, the length scale over which the mantle is sampled may differ from the diffusive length scale in the mantle. Materials may therefore not have to be stretched to submeter scales to become "invisible" as compositionally distinct entities. The reason is that "sampling" of the mantle may homogenize compositional heterogeneity over a length (volume) that is greater than the diffusive length scale in the mantle (Olson et al. 1984a; Olson et al. 1984b; Tackley 2015). This sampling scale may simply be the scale (volume) of sampling of mantle rocks (peridotites). It can also refer to partial melting and the subsequent extraction and mixing of melts when using basalts to study mantle heterogeneity (see discussion below).

The "mixing time" is a parameter that determines how long compositional heterogeneity can survive in the mantle. According to Tackley (2015) this is "the time required for heterogeneous materials to get stretched to the length scale of diffusion or sampling, whichever is larger." "Mixing" times remain highly uncertain, because the underlying geodynamic models have made different assumptions about the final length scale of the materials and the speed and nature (turbulent versus laminar) of convective flow (e.g., Olson et al. 1984b; Hoffman and McKenzie 1985; Gurnis and Davies 1986; Christensen 1989; Kellogg and Turcotte 1990). When these models are scaled to similar parameters, a "mixing" time of 3–4 Gyr results for stretching crust to the submeter length scale (Tackley 2015).

Hence the general perception is that mantle convection acts to attenuate compositional heterogeneities, but it may also generate or preserve regions in its convective flow field where material gets isolated for geologically significant timescales (10^6–10^9 years). For example, dispersal across convective cells can be far slower than within a single convective cell (van Keken et al. 2014; Tackley 2015). Some dense materials may also sink to internal boundary layers, especially the CMB region. In this way, the Earth may even have preserved some initial compositional heterogeneity or layering, for example, from magma ocean crystallization (Labrosse et al. 2007) or through potential isolation of early formed reservoirs (e.g., Boyet and Carlson 2005; Tolstikhin and Hofmann 2005). Geodynamic models indeed suggest that layers up to several 100 km thick can survive at the CMB over Earth's entire history (4.56 Gyr), given that they are 2–3% denser than the surrounding mantle. The exact residence time and thickness of the layer, however, strongly depend on its density and viscosity contrast to the surrounding mantle. Dense material at the CMB can not only form during Earth's initial differentiation but also throughout a large part of its history by subduction of oceanic crust (see discussion above). Recent experiments suggest that subducted oceanic crust is denser than the surrounding mantle over its entire depth range (Ricolleau et al. 2010). Thus it will sink to and accumulate at the base of the mantle (CMB). The CMB may therefore be a region that facilitates storage of dense, compositionally distinct materials, consistent with the geophysical evidence for so-called thermochemical piles (Tackley 2012; Deschamps et al. 2015; Lay 2015; Garnero et al. 2016). It may also be the primary source region of mantle plumes (Hofmann and White 1982; French and Romanowicz 2015).

Mantle convection and plate tectonics therefore affect a number of parameters that strongly influence the mantle's chemical evolution. Among the most important are the rate of cycling and the degree of dispersion of different materials in the mantle (e.g., Huang and Davies 2007; van Keken et al. 2014; Tackley 2015). Ultimately, however, at the next passage through a melting zone, the (compositionally distinct) materials partially remelt to form new oceanic crust. Thereby part of the original heterogeneity gets transferred to the crust and, eventually, after some storage time, gets reintroduced back into the mantle in reincarnated form. Another key parameter for understanding the geochemical evolution of the mantle is therefore the processing rate, which is the time it takes for a given volume of mantle to pass through an upper mantle melting region, mostly beneath mid ocean ridges. This parameter is highly uncertain. Current estimates range from ~10 to ~3 Gyr (Tackley 2015; and references therein). On the basis of the present oceanic crust production rate ($A = 2.7–2.9\ km^2\ year^{-1}$), the depth interval of mantle melting (d ~80 km), and mantle density ($\rho = 3000–3300\ kg\ m^{-3}$), a processing rate $P = Ad\rho$ of about $6.5–7.5 \times 10^{14}\ kg\ year^{-1}$ can be calculated (Stracke et al. 2003a; Tackley 2015). At such processing rates, it takes about 5.2–6.2 Gyr to process a mass equivalent to that of the entire mantle (4×10^{24} kg) through a melting regime in the upper mantle. This implies that most of Earth's mantle could have melted at least once during its up to 4.56 Gyr history. Interestingly, the preservation of mantle heterogeneities is mostly determined by the mantle processing rate, and less dependent on other parameters of mantle convection, such as the geometry, viscosity structure, and vigor of convection (Rudge et al. 2005; Huang and Davies 2007).

In summary, geophysical (seismic) studies provide valuable information about the present thermal and compositional structure of Earth's mantle. Numerical geodynamic models of mantle convection and plate tectonics provide valuable information about how the Earth's mantle could have evolved over time. However, the actual composition of the Earth's mantle can only be studied by direct chemical and isotopic investigation of mantle-derived rocks. These provide a picture of its current composition, the extent and scale of mantle heterogeneity, but also a time-integrated perspective about its compositional evolution through geologic history.

Probing Earth's Mantle

Probing the Earth's mantle poses the fundamental problem that most of it is inaccessible. Direct sampling of mantle rocks (mostly peridotites) is only possible at a few localities worldwide where mantle fragments are exposed. These are ophiolite complexes and peridotite massifs on continents, and abyssal peridotites exposed on the ocean floor at transform faults, oceanic core complexes, or slow spreading ridges. Xenoliths in continental or oceanic basalts are small samples of the continental lithospheric or oceanic mantle. Abyssal peridotites are often highly altered through interaction with extracted melt and seawater. Peridotites from ophiolites, peridotite massifs, and mantle xenoliths are also generally affected by melt-rock interaction (metasomatism) and weathering, and are sometimes metamorphosed (Bodinier and Godard 2014).

Owing to the scarcity, small scale, and prevalent modification by secondary processes (metamorphism, metasomatism, alteration) of most available mantle samples, the composition of the Earth's mantle is mostly studied through basalts erupted on the ocean floor. Oceanic basalts are large-scale partial melts from the Earth's mantle that escape contamination by the continental crust and thus indirectly record mantle composition. It has mostly been the numerous isotope and trace element studies of oceanic basalts, therefore, that have shaped our perception of mantle geochemistry over the last five decades (Hofmann 2014; White 2015b).

Chemical Geodynamics

Before the discovery of plate tectonics and the availability of isotope ratio data on mantle-derived rocks, Earth's mantle was thought to be compositionally homogeneous. Only the first isotope data on oceanic basalts (Gast et al. 1964) showed that Earth's mantle is chemically and isotopically heterogeneous and that chemical differences must be able to persist over geologic timescales (several 10^6–10^9 years). Since then, the picture of mantle geochemistry has changed considerably.

A fundamental observation is that mantle-derived melts from different tectonic settings, specifically basalts generated at mid ocean ridges (MORB) and ocean islands (OIB), display systematic isotopic differences. Ocean island basalts (OIB) generally range to higher Sr- and Pb-, but lower Nd- and Hf radiogenic isotope ratios than MORB (Fig. 1), and are isotopically more diverse. These differences were recognized 40–50 years ago (in Sr and Pb isotope ratios at the time; e.g., Hart et al. 1973; Schilling 1973; Sun et al. 1975) and explained in the context of a layered mantle. These early observations were consistent with a lower mantle that was assumed to be "primitive" and an upper mantle that is "depleted." "Primitive" means that it is identical in composition to the bulk silicate earth (BSE), the portion of the Earth that remained after its metal core was extracted. "Depleted" means deprived in those elements that do not easily fit into the crystal lattices of mantle minerals, the so-called incompatible

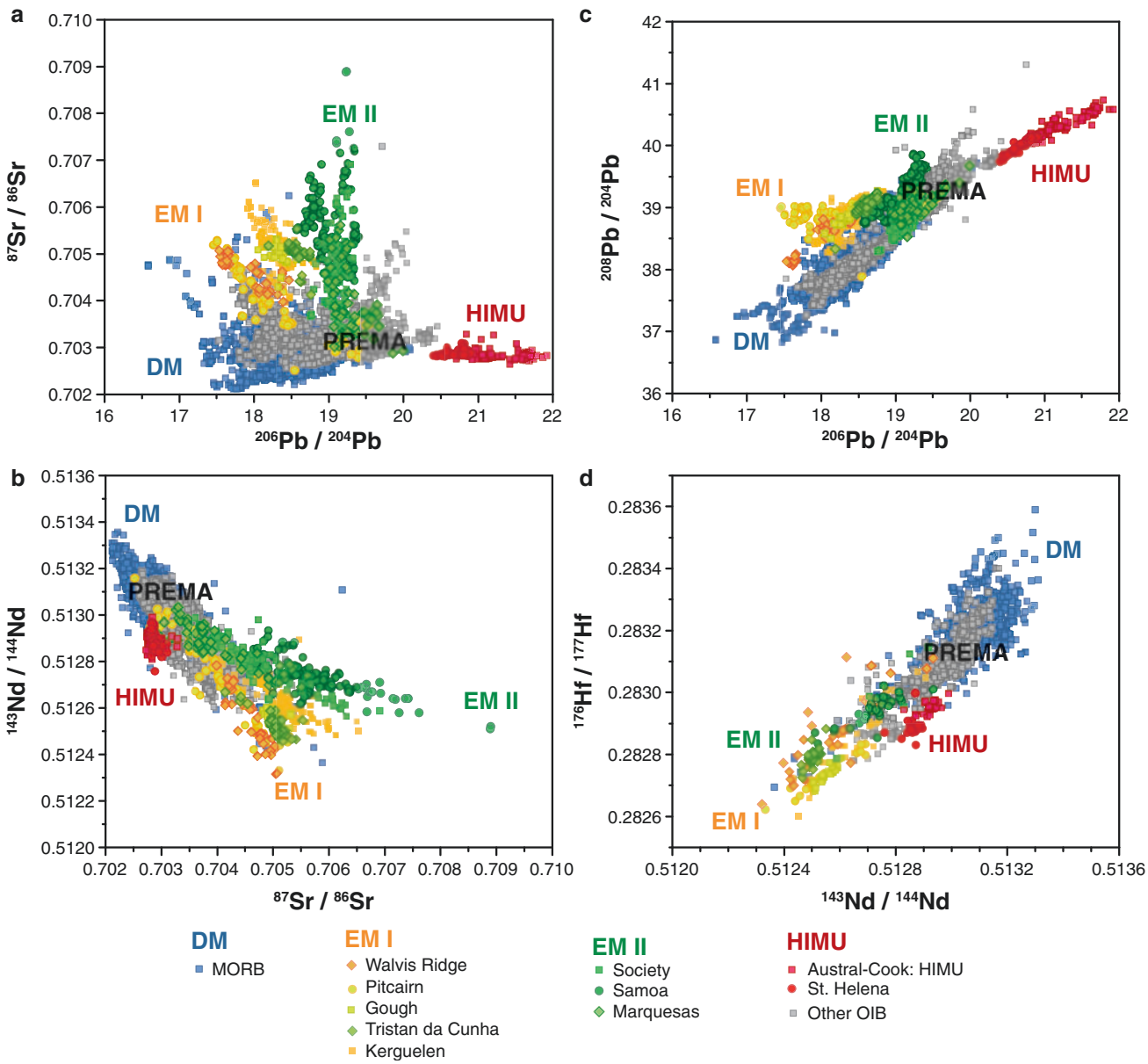

Mantle Geochemistry, Fig. 1 Diagrams of (**a**) $^{206}Pb/^{204}Pb$ versus $^{87}Sr/^{86}Sr$, (**b**) $^{87}Sr/^{86}Sr$ versus $^{143}Nd/^{144}Nd$, (**c**) $^{206}Pb/^{204}Pb$ versus $^{208}Pb/^{204}Pb$, and (**d**) $^{143}Nd/^{144}Nd$ versus $^{176}Hf/^{177}Hf$, in global mid ocean ridge (*MORB*) and ocean island basalts (*OIB*). On a local scale, for example, on the scale of one ocean island or ridge segment, the basalts form linear trends or vectors. On a global scale, the variation is systematic: the local-scale linear trends combine to form arrays that point in 4 or 5 general directions. Formerly, the most extreme isotope ratios at the endpoints of these arrays were interpreted as representing 5 different mantle reservoirs: *1*) the uppermost mantle sampled by MORB, termed Depleted Mantle (*DM*), originally also depleted MORB mantle (*DMM*). The other reservoirs are sampled mostly by OIB and were thought to represent deeper mantle reservoirs. The different varieties are *2*) and *3*) Enriched Mantle 1 and 2 (EM I and EM II), *4*) a compositional range internal to the observed arrays tapped by many OIB and MORB termed PREvalent MAntle (PREMA), and *5*) mantle reservoirs characterized by long-term evolution with high $\mu = {}^{238}U/^{204}Pb$ (HIMU). Compositions intermediate between these 5 end-members were thought to arise from mixing between the large-scale mantle reservoirs (Zindler and Hart 1986; Hart 1988). Since the seminal study by Zindler and Hart (1986), however, the general perception of Earth's mantle has evolved. Today, Earth's mantle is thought to be chemically and isotopically heterogeneous on a range of scales, from the global to the mineral grain scale. This compositional and isotopic heterogeneity likely reflects the continuous depletion by partial melting and the replenishment by recycling different crustal and lithospheric materials back into the mantle over geologic history. Hence the observed systematic variation of isotope ratios in mantle-derived rocks in form of arrays rather reflects a limited number of pathways through which mantle heterogeneity evolves (White 1985; Willbold and Stracke 2010; Stracke 2012; White 2015a; White 2015b). Although the perception of the Earth's mantle has changed, the acronyms DM, EM I, EM II, PREMA, and HIMU remain useful for describing the isotopic variation in mantle-derived melts. The underlying isotope data are taken from the compilation by Stracke (2012)

elements (e.g., Cs, Rb, Ba, Th, U, Nb, Ta, K, Sr, Zr, Pb, Hf, Ti, Na, and the rare earth elements). The process by which incompatible elements become depleted is partial melting, usually at shallow (<100 km) depths in the mantle. Hence formation of the crust by partial melting of the mantle leaves a residual "depleted mantle" (DM). Early geochemical mass balance or "box" models (Allègre et al. 1979; Jacobsen and Wasserburg 1979; O'Nions et al. 1979; DePaolo 1980) inferred that about 30–50% of the mantle must become depleted to account for the incompatible element inventory of Earth's continental crust. This fraction roughly corresponds to the mantle above the 660 km discontinuity which was thought, at the time, to form a boundary between a continuously evolving depleted mantle and an isolated lower mantle which remains "primitive" in composition. Hence MORB were explained by partially melting the depleted upper mantle and OIB by melting materials that consist of a variable mix of depleted upper mantle and primitive lower mantle that rises in the form of mantle plumes (e.g., DePaolo and Wasserburg 1976; Allègre et al. 1979; O'Nions et al. 1979).

With an increasing amount of data it became clear, however, that isotope ratios in OIB range to values that are more extreme than the inferred "primitive" values. As a consequence, five compositionally distinct reservoirs in the mantle were invoked (Zindler and Hart 1986; Fig. 1). These were: (1) the uppermost mantle sampled by MORB, termed Depleted Mantle (DM), originally also termed depleted MORB mantle (DMM). The other reservoirs are sampled mostly by OIB and were thought to represent deeper mantle reservoirs. The different varieties are (2) and (3) Enriched Mantle 1 and 2 (EM I and EM II), (4) a compositional range internal to the observed arrays tapped by many OIB and MORB termed PREvalent MAntle (PREMA), and (5) mantle reservoirs characterized by long-term evolution with high $\mu = {}^{238}U/{}^{204}Pb$ (HIMU). The observed systematic isotope variation in Fig. 1 – in form of arrays that point in 4 or 5 general directions – was explained by mixing these large-scale mantle reservoirs (Zindler and Hart 1986; Hart 1988). Although consistent with the observations, there are several problematic aspects with this interpretation. For example, mixing is observed between some, but not all of these proposed reservoirs (Stracke et al. 2005; White 2015b), and the pattern of the arrays require selective mixing of some components before mixing with others (e.g., Hamelin et al. 1986; Hanan et al. 1986; Douglass and Schilling 2000; Stracke 2012). The latter is especially problematic if "mixing" is thought to occur in the solid state during passage through the mantle (Stracke 2012), a rather unlikely scenario (see discussion above). More importantly, however, it is now known that Earth's mantle is a dynamic, continuously evolving system with mass exchange between the lower and upper mantle. The main driving mechanisms are plate subduction and mantle convection, which also continuously disperse compositionally distinct material within the mantle. In such a dynamic system, it is virtually impossible to maintain a mantle with only five large-scale reservoirs with unique isotope composition (Stracke 2012). The latter would imply that no more than five different geologic events have introduced compositionally different materials into the mantle.

Nevertheless, the observation that isotope arrays point to 4–5 general directions suggests that there is limited number of pathways through which isotopic heterogeneity has developed in the mantle (White 1985; Willbold and Stracke 2010; Stracke 2012; White 2015b). Seemingly, there are a range of processes through geologic time that introduce materials with common geologic heritage and similar composition into the mantle, which then evolve towards broadly similar isotopic compositions.

Processes that Generate Mantle Heterogeneity

Mantle composition has evolved continuously. Because it appears likely that subduction has occurred through most of Earth's history, most of the observed chemical and isotopic variability can be explained within a simple conceptual framework: depletion by partial melting and replenishment by large-scale chemical recycling of the generated oceanic and continental crust back into the mantle (e.g., Willbold and Stracke 2010; Stracke 2012; White 2015a; White 2015b).

On basis of the geodynamic premise that most of the mantle melted at least once in its history (see discussion above), the entire mantle should be variably depleted. However, geochemical mass balance models –based on comparing chemical and isotopic composition of continental crust and mantle – are inconclusive, suggesting that anywhere between 30% and 100% of the mantle could be depleted by melt extraction (e.g., Jacobsen and Wasserburg 1979; O'Nions et al. 1979; DePaolo 1980; Allègre et al. 1983; Zindler and Hart 1986; Hofmann 1988; Boyet and Carlson 2006). The exact fraction of depleted mantle and its overall extent of depletion thus remain unknown. It is clear, however, that partial melting not only extracts incompatible elements from the mantle into the newly formed crust, it also changes the mantle's mineralogical composition by preferentially melting some minerals, particularly clinopyroxene and garnet. Partial melting therefore makes the mantle more refractory, that is, it will produce less melt during its next passage through a melting region in the shallow mantle (for a given temperature; e.g., Salters et al. 2011; Zhou and Dick 2013). Eventually, upon repeated or extensive melting, a given parcel of mantle will become too refractory to produce any further melt, thus effectively limiting the extent of mantle depletion. A large fraction of the total mantle should therefore be mineralogically, compositionally, and isotopically heterogeneous depleted mantle.

This continuous depletion of Earth's mantle through partial melting is counteracted by introducing incompatible element-enriched and isotopically diverse materials back into the mantle. Since the onset of plate tectonics, the primary mechanism for this replenishment has been the subduction of oceanic lithosphere and the overlying sediments, which are the weathering products of the continental crust. Accompanying subduction is the tectonic erosion of the overlying arc crust, which introduces a large amount of (lower) continental crust into the deeper mantle, on the order of the volume of today's continental crust (~2×10^{22} kg) over the course of Earth's history (Clift et al. 2009; Stern 2011; Tatsumi et al. 2014). It is also possible that parts of the subcontinental lithospheric mantle and attached lower crust become denser, thus gravitationally unstable, and sink back into the mantle (e.g., Houseman et al. 1981; McKenzie and O'Nions 1983; Arndt and Goldstein 1989; Kay and Kay 1991; Kay and Kay 1993; Rudnick 1995; Jull and Kelemen 2001). All of these processes transport crust and lithosphere back into the deeper mantle. Once there, the recycled materials become stretched, intermingled, and dispersed by mantle convection. The mantle can thus be envisaged as a collection of recycled materials (presumably from different processes) interspersed in a variably depleted peridotitic mantle "matrix."

All of these mechanisms are thought to contribute to mantle heterogeneity. Isotopic variability along the DM-PREMA array (Fig. 1), for example, is likely caused by continuous production and recycling of oceanic crust (e.g., Christensen and Hofmann 1994; Donnelly et al. 2004; Rudge et al. 2005; Stracke et al. 2005; Rudge 2006; Kellogg et al. 2007). Ancient recycled oceanic crust with different compositions thereby accounts for the enriched, PREMA-type signatures (Fig. 1), whereas partial melting is expected to produce a range of variably depleted residual peridotites (DM). Most of the enriched mantle (EM I and EM II) signatures in MORB and OIB (Fig. 1) can be produced by recycling the compositionally distinct upper and lower continental crust (e.g., Chauvel et al. 1992; Willbold and Stracke 2006; Jackson et al. 2007; Chauvel et al. 2008; Willbold and Stracke 2010; Stracke 2012). Other, more elusive processes create exotic signatures (HIMU, Fig. 1), but overall account for only a small part of the observed mantle heterogeneity. Additional processes that contribute to mantle heterogeneity are metasomatism of the oceanic or continental mantle (e.g., Menzies et al. 1987; McKenzie and O'Nions 1995; Niu and O'Hara 2003; Pilet et al. 2008). These often have a restricted extent and scale, however, and are thus probably of second-order importance for generating global mantle heterogeneity.

Nevertheless, all the processes discussed above transport materials of common heritage that have been processed in a similar, but not identical, manner at different times and locations into the mantle. The various proportions, origins, compositions, and ages of these different materials eventually determine the composition and extent of heterogeneity of a given parcel of mantle rock. Each individual material in a given mantle source may itself be compositionally heterogeneous: the composition of the residual peridotitic mantle may vary because of differing degrees of depletion by melt extraction or refertilization by metasomatism at different times (e.g., Johnson et al. 1990; Bodinier and Godard 2014). Crustal components (oceanic crust, continental crust, and marine sediment) are compositionally and isotopically variable as a result of different conditions of formation (e.g., Plank 2014; Rudnick and Gao 2014; White and Klein 2014), age, varying extents of hydrothermal alteration on the ocean floor (e.g., Staudigel 2014), and modification during subduction (e.g., Bebout 2014; Ryan and Chauvel 2014).

If sampled by partial melting, each mantle source will consequently have a unique, and variable, isotopic composition arising from the various proportions of the different materials it encompasses. The challenge of mantle geochemistry therefore is to identify the number, relative abundance, and nature of these materials – from the local to global scale– with the aim of constraining the importance of the underlying processes and mass fluxes. This is undoubtedly a complex task and hence will be a continuing field of scientific research and debate. It is, however, also of fundamental importance for better understanding the major geochemical cycles and inner workings of our planet.

M

The Scale of Mantle Heterogeneity

Owing to the different composition, size, and distribution of its individual components (e.g., residual peridotitic mantle, various recycled materials), the mantle is heterogeneous on a range of scales, from the 1000 km scale of ocean basins (Dupré and Allègre 1983; Hart 1984), the 1–100 km scale along mid ocean ridges (e.g., Agranier et al. 2005; Graham et al. 2006), down to the cm scale of single hand specimens. The isotopic heterogeneity observed in melt inclusions shows that heterogeneity not only persists down to the kilometer scale of the melting region but perhaps even down to the millimeter scale of individual mineral grains. This shows that heterogeneous components introduced into the mantle become stretched and thinned and are widely distributed throughout the mantle (e.g., Morgan 1999; Meibom and Anderson 2003; Stracke et al. 2003b; Ito and Mahoney 2005; Rudge et al. 2005; Stracke et al. 2005; Kellogg et al. 2007). Large-scale statistical differences caused by differences in the relative abundance of the distinct mantle components may occur, for example, between ocean basins. Whether such potential large-scale "domains" in the Earth's mantle (e.g., DUPAL (Dupré and Allègre 1983; Hart 1984) or SOPITA (Staudigel et al. 1991)) actually represent varying abundances of different materials or are simply an artifact

from different sampling of a statistical distribution of similar materials (e.g., Morgan 1999; Meibom and Anderson 2003; Ito and Mahoney 2005) is a matter of debate. At mid ocean ridges, for example, the observed degree of isotopic variability decreases as the rate of processing of mantle material – as measured by spreading rate – increases (e.g., Allègre et al. 1984; Stracke et al. 2003b; Rubin et al. 2009). These observations confirm that the scale of mantle components is small compared to the maximum dimension over which melts are produced and mixed during melting, melt extraction, and melt evolution. They also show that large-scale tectonic or geodynamic differences of the melting regions (e.g., spreading rate) influence the manner in which heterogeneous mantle components are represented in the erupted melts.

Synthesis

Our perception of the chemical and isotopic composition of Earth's mantle has evolved significantly over the last five decades. It has changed from a homogeneous- to a two-layer mantle (e.g., Hart et al. 1973; Schilling 1973; Sun et al. 1975), to a mantle that comprises a finite number (4 or 5) of large-scale reservoirs (Zindler and Hart 1986), to a mantle that is chemically and isotopically heterogeneous on a range of scales, from the global to the mineral grain scale.

The chemical and isotopic investigation of mantle-derived rocks therefore provides information about the mantle's current state of heterogeneity and its time-integrated chemical evolution on a range of scales. Direct sampling of mantle rocks, for example, allows studying mantle composition down to mineral grain or even smaller length scales. The investigation of mantle composition through studying its melts – basalts – integrates over the sampling volume of partial melting. Depending on the nature of the sampling, therefore, different length scales of compositional heterogeneity in the Earth's mantle may or may not be resolved. Moreover, both the scale and lithological composition of the various mantle materials determine how they are sampled by partial melting. In addition, the subsequent processes of melt extraction, mixing, the reaction of the melts with the mantle through which they pass, and melt differentiation in the crust influence how mantle heterogeneity is preserved in the erupted melts (e.g., Stracke 2012; Rudge et al. 2013). Isolating the information mantle melts convey about mantle composition and evolution thus requires disentangling these various effects, and it should be kept in mind that a bias may persist between source and melt (Stracke 2012).

Investigating different mantle-derived samples grants access to different parts of the mantle. Abyssal peridotites and MORB provide a window into the uppermost mantle that is exposed on the ocean floor, or partially melting in the upper ~100 km of the mantle, respectively. Ocean island basalts (OIB) often, but not always, sample hot, upwelling mantle plumes from thermal boundary layers in the deeper mantle, most prominently the CMB (e.g., Morgan 1971; Hofmann and White 1982; White 2010; White 2015a; White 2015b). Ophiolite complexes and peridotite massifs offer a glimpse of ancient oceanic mantle obducted onto the continents or uplifted subcontinental lithospheric mantle, respectively. Intracontinental basalts sample both the oceanic and subcontinental lithospheric mantle. Although we thus have access to a wide variety of different mantle-derived samples, it should not be forgotten that most of the mantle remains inaccessible. Our perception of global mantle geochemistry is therefore inherently limited and provides only a hint of its actual diversity.

Remaining Questions

How the different pieces of the puzzle of information we collect fit together into a consistent picture of mantle geochemistry is one of the remaining challenges. Different compositional and isotopic parameters often result in different perspectives of mantle geochemistry. One example would be the radiogenic isotope ratios of the noble gases and lithophile elements, which continue to be interpreted within a different framework of mantle geodynamics (e.g., White 2010; Moreira 2013; White 2015a). Novel tools such as the stable isotope ratios of an increasing number of major and trace elements provide a new flux of information that is important for complementing and completing the available information from other tracers. Especially the stable isotope fractionations produced at Earth's surface promise to supply complementary constraints on the mass flux and timing of element cycling between Earth's mantle and crust. These may also contribute to improving our quantitative understanding of how the two opposing processes of mantle depletion and replenishment are coupled to the growth and destruction of continental crust through time.

The exact timescales and related mass fluxes associated with silicate Earth differentiation remain difficult to assess. Nd and Os isotope ratios in abyssal peridotites provide a range of so-called mantle depletion ages (e.g., Harvey et al. 2006; Mallick et al. 2014; Liu et al. 2008) that date back to ca. 2.2 Ga. Signatures of ancient depletion processes can therefore be preserved, but these probably reflect the average timing of a prolonged multistage differentiation and the timescale of mantle stirring or "mixing."

Another unresolved question is whether there is a general compositional dichotomy between the upper and lower mantle as a result of viscosity-related differences in stirring efficiency. In this context it is also important to what extent, if at all, some primordial ("primitive") mantle or early formed reservoirs may have survived. Presently available mantle

samples provide no chemical or isotopic evidence for any remaining truly "primitive" mantle. Storage or isolation of early formed reservoirs over billion-year timescales is only feasible if these are significantly more dense and viscous than the ambient mantle. Moreover, immanent in the very nature of these isolated reservoirs is that any chemical or isotopic evidence for their existence will always be circumstantial, or simply remain elusive. If such reservoirs constitute a significant fraction of Earth's mantle, however, they may bias the composition of the accessible Earth relative to that of the bulk silicate Earth. Whether any isolated (early) or "primitive" reservoirs exist may therefore not only be of conceptual importance for mantle geochemistry. It would also be important for defining the correct reference point for deducing accessible Earth's overall isotopic evolution and for estimating the amount and timing of the mass fluxes among Earth's silicate reservoirs.

Cross-References

- ▶ Chemical Weathering
- ▶ Earth's Continental Crust
- ▶ Earth's Oceanic Crust
- ▶ Formation and Evolution of the Earth
- ▶ Geochemistry
- ▶ Geochronology and Radiogenic Isotopes
- ▶ Hafnium Isotopes
- ▶ History of Geochemistry
- ▶ Hydrothermal Alteration
- ▶ Incompatible Elements
- ▶ Large-Ion Lithophile Elements
- ▶ Lead Isotopes
- ▶ Lithophile Elements
- ▶ Mid-Ocean Ridge Basalts (MORB)
- ▶ Neodymium Isotopes
- ▶ Noble Gases
- ▶ Oceanic Island Basalts
- ▶ Partial Melting
- ▶ Stable Isotope Geochemistry
- ▶ Strontium Isotopes
- ▶ Subduction Zone Geochemistry
- ▶ Trace Elements
- ▶ Volcanism

References

Agranier A, Blichert-Toft J, Graham D, Debaille V, Schiano P, Albarède F (2005) The spectra of isotopic heterogeneities along the Mid-Atlantic ridge. Earth Planet Sci Lett 238:96–109

Allègre CJ, Ben Othman D, Polve M, Richard P (1979) The Nd-Sr isotopic correlation in mantle materials and geodynamic consequences. Phys Earth Planet Inter 19:293–306

Allègre CJ, Hart SR, Minster JF (1983) Chemical structure and evolution of the mantle and the continents determined by inversion of Nd and Sr isotopic data. II. Numerical experiments and discussion. Earth Planet Sci Lett 66:191–213

Allègre CJ, Hamelin B, Dupré B (1984) Statistical analysis of isotopic ratios in MORB: the mantle blob cluster model and the convective regime of the mantle. Earth Planet Sci Lett 71:71–84

Arndt NT, Goldstein SL (1989) An open boundary between lower continental crust and mantle: its role in crust formation and crustal recycling. Tectonophysics 161:201–212

Bebout GE (2014) 4.20 – Chemical and isotopic cycling in subduction zones. In: Turekian HDHK (ed) Treatise on geochemistry, 2nd edn. Elsevier, Oxford, pp 703–747

Bodinier JL, Godard M (2014) 3.4 – Orogenic, ophiolitic, and abyssal peridotites. In: Turekian HDHK (ed) Treatise on geochemistry, 2nd edn. Elsevier, Oxford, pp 103–167

Boyet M, Carlson RW (2005) ^{142}Nd evidence for early (>4.53 Ga) global differentiation of the silicate Earth. Science 309:576–581

Boyet M, Carlson RW (2006) A new geochemical model for the Earth's mantle inferred from ^{146}Sm-^{142}Nd systematics. Earth Planet Sci Lett 262:505–516

Chauvel C, Hofmann AW, Vidal P (1992) HIMU-EM: the French-Polynesian connection. Earth Planet Sci Lett 110:99–119

Chauvel C, Lewin E, Carpentier M, Arndt NT, Marini J-C (2008) Role of recycled oceanic basalt and sediment in generating the Hf-Nd mantle array. Nat Geosci 1:64–67

Christensen U (1989) Mixing by time-dependent convection. Earth Planet Sci Lett 95:382–394

Christensen UR, Hofmann AW (1994) Segregation of subducted ceanic crust in the convecting mantle. J Geophys Res 99:19,867–819,884

Clift PD, Vannucchi P, Morgan JP (2009) Crustal redistribution, crust-mantle recycling and Phanerozoic evolution of the continental crust. Earth Sci Rev 97:80–104

Cobden L, Thomas C, Trampert J (2015) Seismic detection of post-perovskite inside the Earth. In: Khan A, Deschamps F (eds) The Earth's heterogeneous mantle. Springer, pp 391–440

Condie KC, Kröner A (2008) When did plate tectonics begin? Evidence from the geologic record. In: Condie KC, Pease V (eds) When did plate tectonics begin on planet Earth? Geological Society of America Special Papers, vol 440. Geological Society of America, Boulder, pp 281–294

Davies GF (1992) On the emergence of plate-tectonics. Geology 20:963–966

DePaolo DJ (1980) Crustal growth and mantle evolution: inferences from models of element transport and Nd and Sr isotopes. Geochim Cosmochim Acta 44:1185–1196

DePaolo DJ, Wasserburg GJ (1976) Nd isotopic variations and petrogenetic models. Geophys Res Lett 3:249–252

Deschamps F et al (2015) Large-scale thermo-chemical structure of the deep mantle: observations and models. In: Khan A, Deschamps F (eds) The Earth's heterogeneous mantle. Springer, pp 479–515

Donnelly KE, Goldstein SL, Langmuir CH, Spiegelman M (2004) Origin of enriched ocean ridge basalts and implications for mantle dynamics. Earth Planet Sci Lett 226:347–366

Douglass J, Schilling JG (2000) Systematics of three-component, pseudo-binary mixing lines in 2D isotope ratio space representations and implications for mantle plume-ridge interaction. Chem Geol 163:1–23

Dupré B, Allègre CJ (1983) Pb-Sr isotope variation in Indian Ocean basalts and mixing phenomena. Nature 303:142–146

Foley BJ, Bercovici D, Elkins-Tanton LT (2014) Initiation of plate tectonics from post-magma ocean thermochemical convection. J Geophys Res 119:8538–8561

Forsyth D, Uyeda S (1975) On the relative importance of the driving forces of plate motion. Geophys J Int 43:163–200

French SW, Romanowicz B (2015) Broad plumes rooted at the base of the Earth's mantle beneath major hotspots. Nature 525:95–99
Fukao Y, Obayashi M (2015) 1.20 – Deep Earth structure – subduction zone structure in the mantle transition zone. In: Schubert G (ed) Treatise on geophysics, 2nd edn. Elsevier, Oxford, pp 641–654
Fukao Y, Obayashi M, Inoue H, Nenbai M (1992) Subducting slabs stagnant in the mantle transition zone. J Geophys Res 97:4809–4822
Garnero EJ et al (2011) Earth's structure – lower mantle. In: Gupta HK (ed) Encyclopedia of solid earth geophysics, vol 1, 2nd edn. Springer, Dordrecht, pp 154–159
Garnero EJ, McNamara AK, Shim S-H (2016) Continent-sized anomalous zones with low seismic velocity at the base of Earth's mantle. Nat Geosci 9:481–489
Gast PW, Tilton GR, Hedge C (1964) Isotopic composition of lead and strontium from Ascension and Gough Islands. Science 145:1181–1185
Gerya T (2014) Precambrian geodynamics: concepts and models. Gondwana Res 25:442–463
Graham DW, Blichert-Toft J, Russo CJ, Rubin KH, Albarede F (2006) Cryptic striations in the upper mantle revealed by hafnium isotopes in southeast Indian ridge basalts. Nature 440:199–202
Grand SP (1994) Mantle shear structure beneath the Americas and surrounding oceans. J Geophys Res 99:11,591–11,621
Gurnis M, Davies GF (1986) Mixing in numerical models of mantle convection incorporating plate kinematics. J Geophys Res 91:6375–6395
Hamelin B, Dupré B, Allègre CJ (1986) Pb-Sr-Nd isotopic data of Indian Ocean Ridges: new evidence of large scale mapping of mantle heterogeneities. Earth Planet Sci Lett 76:288–298
Hanan BB, Kingsley RH, Schilling J-G (1986) Pb isotope evidence in the South Atlantic for migrating ridge-hotspot interactions. Nature 322:137–144
Harrison TM (2009) The Hadean crust: evidence from > 4 Ga Zircons. Annu Rev Earth Planet Sci 37:479–505
Hart SR (1984) A large-scale isotope anomaly in the southern-hemisphere mantle. Nature 309:753–757
Hart SR (1988) Heterogeneous mantle domains – signatures, genesis and mixing chronologies. Earth Planet Sci Lett 90:273–296
Hart SR (1993) Equilibration during mantle melting – a fractal tree model. Proc Natl Acad Sci 90:11,914–11,918
Hart SR, Schilling JG, Powell JL (1973) Basalts from Iceland and along the Reykjanes Ridge: Sr isotope geochemistry. Nature 246:104–107
Harvey J, Gannoun A, Burton KW, Rogers NW, Alard O, Parkinson IJ (2006) Ancient melt extraction from the oceanic upper mantle revealed by Re-Os isotopes in abyssal peridotites from the Mid-Atlantic ridge. Earth Planet Sci Lett 244:606–621
Herzberg C, Condie K, Korenaga J (2010) Thermal history of the Earth and its petrological expression. Earth Planet Sci Lett 292:79–88
Hoffman NRA, McKenzie DP (1985) The destruction of geochemical heterogeneities by differential fluid motions during mantle convection. Geophys J R Astron Soc 82:163–206
Hofmann AW (1988) Chemical differentiation of the Earth – the relationship between mantle, continental-crust, and oceanic-crust. Earth Planet Sci Lett 90:297–314
Hofmann AW (2014) 3.3 – Sampling mantle heterogeneity through oceanic basalts: isotopes and trace elements. In: Turekian HDHK (ed) Treatise on geochemistry, 2nd edn. Elsevier, Oxford, pp 67–101
Hofmann AW, Hart SR (1978) An assessment of local and regional isotopic equilibrium in the mantle. Earth Planet Sci Lett 38:44–62
Hofmann AW, White WM (1982) Mantle plumes from ancient oceanic crust. Earth Planet Sci Lett 57:421–436
Houseman GA, McKenzie DP, Molnar P (1981) Convective instability of a thickened boundary layer and its relevance for the thermal evolution of continental convergent belts. J Geophys Res 86:6115–6132
Huang J, Davies GF (2007) Geochemical processing in a three-dimensional regional spherical shell model of mantle convection. Geochem Geophys Geosyst 8:Q11006. https://doi.org/11010.11029/12007GC001625
Ito G, Mahoney JJ (2005) Flow and melting of a heterogeneous mantle: 2. Implications for a chemically nonlayered mantle. Earth Planet Sci Lett 230:47
Jackson MG, Hart SR, Koppers AAP, Staudigel H, Konter J, Blusztajn J, Kurz M, Russell JA (2007) The return of subducted continental crust in Samoan lavas. Nature 448:684–687
Jacobsen SB, Wasserburg GJ (1979) Mean age of mantle and crustal reservoirs. J Geophys Res 84:7411–7427
Johnson KTM, Dick HJB, Shimizu N (1990) Melting in the oceanic upper mantle – an ion microprobe study of diopsides in abyssal peridotites. J Geophys Res 95:2661–2678
Jull M, Kelemen PB (2001) On the conditions for lower crustal convective instability. J Geophys Res 106:6,423–6,446
Kay RW, Kay SM (1991) Creation and destruction of lower continental crust. Geol Rundsch 80:259–278
Kay RW, Kay SM (1993) Delamination and delamination magmatism. Tectonophysics 219:177–189
Kellogg L, Turcotte DL (1990) Mixing and the distribution of heterogeneities in a chaotically convecting mantle. J Geophys Res 95:421–432
Kellogg JB, Jacobsen SB, O'Connell RJ (2007) Modeling lead isotopic heterogeneity in mid-ocean ridge basalts. Earth Planet Sci Lett 262:328–342
Kemp AIS, Wilde SA, Hawkesworth CJ, Coath CD, Nemchin A, Pidgeon RT, Vervoort JD, DuFrane SA (2010) Hadean crustal evolution revisited: New constraints from Pb-Hf isotope systematics of the Jack Hills zircons. Earth Planet Sci Lett 296:45–56
Kind R, Li X (2015) 1.21 – Deep earth structure – transition zone and mantle discontinuities. In: Schubert G (ed) Treatise on geophysics, 2nd edn. Elsevier, Oxford, pp 655–682
Labrosse S, Hernlund JW, Coltice N (2007) A crystallizing dense magma ocean at the base of the Earth's mantle. Nature 450:866–869
Lay T (2015) 1.22 – Deep Earth structure: lower mantle and D. In: Schubert G (ed) Treatise on geophysics, 2nd edn. Elsevier, Oxford, pp 683–723
Lay T, Garnero EJ (2004) Core-mantle boundary structures and processes. In: Sparks RSJ, Hawkesworth CJ (eds) The state of the planet: frontiers and challenges in geophysics, vol 150. AGU. Geophysics Monograph, Washington, DC, pp 25–41
Lay T, Hernlund J, Garnero EJ, Thorne MS (2006) A post-perovskite lens and D heat flux beneath the Central Pacific. Science 314:1272–1276
Lithgow-Bertelloni C, Richards MA (1998) The dynamics of cenozoic and mesozoic plate motions. Rev Geophys 36:27–78
Liu CZ, Snow JE, Hellebrand E, Brügmann G, von der Handt A, Büchl A, Hofmann AW (2008) Ancient, highly depleted heterogeneous mantle beneath Gakkel ridge, Arctic ocean. Nature 452:311–316
Mallick S, Dick HJB, Sachi-Kocher A, Salters VJM (2014) Isotope and trace element insights into heterogeneity of subridge mantle. Geochem Geophys Geosyst 15:2438–2453. https://doi.org/2410.1002/2014GC005314
McKenzie D, Bickle MJ (1988) The volume and composition of melt generated by extension of the lithosphere. J Petrol 29:625–679
McKenzie DP, O'Nions RK (1983) Mantle reservoirs and ocean island basalts. Nature 301:229–231
McKenzie D, O'Nions RK (1995) The source regions of ocean island basalts. J Petrol 36:133–159
Meibom A, Anderson DL (2003) The statistical upper mantle assemblage. Earth Planet Sci Lett 217:123–139

Menzies MA, Rogers N, Tindle A, Hawkesworth C (1987) Metasomatic enrichment processes in lithospheric peridotites, an effect of asthenospheric-lithospheric interaction. In: Menzies MA, Hawkesworth C (eds) Mantle metasomatism. Academic, London, pp 313–361
Moore WB, Webb AAG (2013) Heat-pipe Earth. Nature 501:501–505
Moreira M (2013) Noble gas constraints on the origin and evolution of Earth's volatiles. Geochem Perspect 2:229–230
Moresi LN, Solomatov VS (1995) Numerical investigation of 2D convection with extremely large viscosity variations. Phys Fluids 7:2154–2162
Moresi L, Solomatov V (1998) Mantle convection with a brittle lithosphere: thoughts on the global tectonic styles of the Earth and Venus. Geophys J Int 133:669–682
Morgan WJ (1971) Convection plumes in the lower mantle. Nature 230:42–43
Morgan JP (1999) Isotope topology of individual hotspot basalt arrays: mixing curves or melt extraction trajectories. Geochem Geophys Geosyst 1:1003. https://doi.org/10.1029/1999GC000004
Moyen J-F, van Hunen J (2012) Short-term episodicity of Archaean plate tectonics. Geology 40:451–454
Niu YL, O'Hara MJ (2003) Origin of ocean island basalts: a new perspective from petrology, geochemistry, and mineral physics considerations. J Geophys Res 108:2209. https://doi.org/2210.1029/2002JB002048
O'Neill C, Jellinek AM, Lenardic A (2007) Conditions for the onset of plate tectonics on terrestrial planets and moons. Earth Planet Sci Lett 261:20–32
O'Nions RK, Evensen NM, Hamilton PJ (1979) Geochemical modeling of mantle differentiation and crustal growth. J Geophys Res 84:6091–6101
Olson P, Yuen DA, Balsiger D (1984a) Convective mixing and the fine structure of mantle heterogeneity. Phys Earth Planet Inter 36:291–304
Olson P, Yuen DA, Balsiger D (1984b) Mixing of passive heterogeneities by mantle convection. J Geophys Res 89:425–436
Palme H, O'Neill HSC (2014) 3.1 – Cosmochemical estimates of mantle composition. In: Turekian HDHK (ed) Treatise on geochemistry, 2nd edn. Elsevier, Oxford, pp 1–39
Pilet S, Baker MB, Stolper EM (2008) Metasomatized lithosphere and the origin of alkaline lavas. Science 320:916–919
Plank T (2014) 4.17 – The chemical composition of subducting sediments. In: Turekian HDHK (ed) Treatise on geochemistry, 2nd edn. Elsevier, Oxford, pp 607–629
Rey PF, Coltice N, Flament N (2014) Spreading continents kick-started plate tectonics. Nature 513:405–408
Ricard Y (2015) 7.02 – Physics of mantle convection. In: Schubert G (ed) Treatise on geophysics, 2nd edn. Elsevier, Oxford, pp 23–71
Ricolleau A, Perrillat J-P, Fiquet G, Daniel I, Matas J, Addad A, Menguy N, Cardon H, Mezouar M, Guignot N (2010) Phase relations and equation of state of a natural MORB: implications for the density profile of subducted oceanic crust in the Earth's lower mantle. J Geophys Res 115:B08202
Rubin KH, Sinton JM, Maclennan J, Hellebrand E (2009) Magmatic filtering of mantle compositions at mid-ocean-ridge volcanoes. Nat Geosci 2:321–328
Rudge JF (2006) Mantle pseudo-isochrons revisited. Earth Planet Sci Lett 249:494–513
Rudge J, McKenzie D, Haynes PH (2005) A theoretical approach to understanding the isotopic heterogeneity of mid-ocean ridge basalt. Geochim Cosmochim Acta 69:3873–3887
Rudge JF, Maclennan J, Stracke A (2013) The geochemical consequences of mixing melts from a heterogeneous mantle. Geochim Cosmochim Acta 114:112–143
Rudnick RL (1995) Making continental crust. Nature 378:571–578
Rudnick RL, Gao S (2014) 4.1 – Composition of the continental crust. In: Turekian HDHK (ed) Treatise on geochemistry, 2nd edn. Elsevier, Oxford, pp 1–51
Ryan JG, Chauvel C (2014) 3.13 – The subduction zone filter and the impact of recycled materials on the evolution of the mantle. In: Turekian HDHK (ed) Treatise on geochemistry, 2nd edn. Elsevier, Oxford, pp 479–508
Salters VJM, Mallick S, Hart SR, Langmuir CH, Stracke A (2011) Domains of depleted mantle; new evidence from hafnium and neodymium isotopes. Geochem Geophys Geosyst 12:Q10017. https://doi.org/10010.11029/12011GC003874
Schilling JG (1973) Iceland mantle plume: geochemical study of Reykjanes Ridge. Nature 242:565–571
Shirey S, Kamber B, Whitehouse M, Mueller PA, Basu A (2008) When did plate tectonics begin on planet Earth? In: Condie K, Pease V (eds) Geological Society of America, special paper 440, pp 441–429
Shirey SB, Richardson SH (2011) Start of the Wilson Cycle at 3 Ga shown by diamonds from subcontinental mantle. Science 333:434–436
Silver PG, Behn MD (2008) Intermittent plate tectonics? Science 319:85–88
Sizova E, Gerya T, Brown M, Perchuk LL (2010) Subduction styles in the Precambrian: insight from numerical experiments. Lithos 116:209–229
Staudigel H (2014) 4.16 – Chemical fluxes from hydrothermal alteration of the oceanic crust. In: Turekian HDHK (ed) Treatise on geochemistry, 2nd edn. Elsevier, Oxford, pp 583–606
Staudigel H, Park KH, Pringle M, Rubenstone JL, Smith WHF, Zindler A (1991) The longevity of the South-Pacific isotopic and thermal anomaly. Earth Planet Sci Lett 102:24–44
Steinberger B (2000) Plumes in a convecting mantle: models and observations for individual hotspots. J Geophys Res 105:11127–11152
Stern RJ (2005) Evidence from ophiolites, blueschists, and ultrahigh-pressure metamorphic terranes that the modern episode of subduction tectonics began in Neoproterozoic time. Geology 33:557–560
Stern CR (2011) Subduction erosion: rates, mechanisms, and its role in arc magmatism and the evolution of the continental crust and mantle. Gondwana Res 20:284–308
Stracke A (2012) Earth's heterogeneous mantle: a product of convection-driven interaction between crust and mantle. Chem Geol 330–331:274–299
Stracke A, Bizimis M, Salters VJM (2003a) Recycling of oceanic crust: quantitative constraints. Geochem Geophys Geosyst 4:8003. https://doi.org/8010.1029/2001GC000223
Stracke A, Zindler A, Salters VJM, McKenzie D, Blichert-Toft J, Albarède F, Grönvold K (2003b) Theistareykir revisited. Geochem Geophys Geosyst 4:8507. https://doi.org/8510.1029/2001GC000201, pp. 000249
Stracke A, Hofmann AW, Hart SR (2005) FOZO, HIMU and the rest of the mantle zoo. Geochem Geophys Geosyst 6:Q05007. https://doi.org/05010.01029/02004GC000824
Sun SS, Tatsumoto M, Schilling JG (1975) Mantle plume mixing along the Reykjanes Ridge axis: lead isotopic evidence. Science 190:143–147
Tackley PJ (2012) Dynamics and evolution of the deep mantle resulting from thermal, chemical, phase and melting effects. Earth Sci Rev 110:1–25
Tackley PJ (2015) 7.12 – Mantle geochemical geodynamics. In: Schubert G (ed) Treatise on geophysics. Elsevier, Oxford, pp 521–585
Tatsumi Y, Suzuki T, Ozawa H, Hirose K, Hanyu T, Ohishi Y (2014) Accumulation of "anti-continent" at the base of the mantle and its recycling in mantle plumes. Geochim Cosmochim Acta 143:23–33

Tolstikhin IN, Hofmann AW (2005) Early crust on top of the Earth's core. Phys Earth Planet Inter 148:109–130
van der Hilst R, Widiyantoro S, Engdahl ER (1997) Evidence for deep mantle circulation from global tomography. Nature 386: 578–584
van Hunen J, Moyen J-F (2012) Archean subduction: fact or fiction? Annu Rev Earth Planet Sci 40:195–219
van Hunen J, van den Berg AP (2008) Plate tectonics on the early Earth: limitations imposed by strength and buoyancy of subducted lithosphere. Lithos 103:217–235
van Keken PE, Ballentine CJ, Hauri EH (2014) 3.14 – Convective mixing in the Earth's mantle. In: Turekian HDHK (ed) Treatise on geochemistry, 2nd edn. Elsevier, Oxford, pp 509–525
van Thienen P, Vlaar NJ, van den Berg AP (2004) Plate tectonics on the terrestrial planets. Phys Earth Planet Inter 142:61–74
White WM (1985) Sources of oceanic basalts – radiogenic isotopic evidence. Geology 13:115–118
White WM (2010) Oceanic island basalts and mantle plumes: the geochemical perspective. Annu Rev Earth Planet Sci 38:133–160
White WM (2015a) Isotopes, DUPAL, LLSVPs, and Anekantavada. Chem Geol 419:10–28
White WM (2015b) Probing the Earth's deep interior through geochemistry. Geochem Perspect 4:95–251
White WM, Klein EM (2014) 4.13 – Composition of the oceanic crust. In: Turekian HDHK (ed) Treatise on geochemistry, 2nd edn. Elsevier, Oxford, pp 457–496
Willbold M, Stracke A (2006) Trace element composition of mantle end-members: implications for recycling of oceanic and upper and lower continental crust. Geochem Geophys Geosyst 7:Q04004. https://doi.org/04010.01029/02005GC001005
Willbold M, Stracke A (2010) Formation of enriched mantle components by recycling of upper and lower continental crust. Chem Geol 276:188–197
Williams Q, Garnero EJ (1996) Seismic evidence for partial melt at the base of Earth's mantle. Science 273:1528–1530
Zhou H, Dick HJB (2013) Thin crust as evidence for depleted mantle supporting the Marion Rise. Nature 494:195–200
Zindler A, Hart S (1986) Chemical geodynamics. Annu Rev Earth Planet Sci 14:493–571

Marine Sediment

Ann G. Dunlea[1], Rachel P. Scudder[2] and Richard W. Murray[3]
[1]Woods Hole Oceanographic Institution, Woods Hole, MA, USA
[2]Texas A&M University, College Station, TX, USA
[3]Department of Earth and Environment, Boston University, Boston, MA, USA

Definition

Marine sediment is a mixture of material deposited on the seafloor that originated from the erosion of continents, volcanism, biological productivity, hydrothermal vents, and/or cosmic debris. The contributions of these sediment sources to the seafloor are controlled by wind, ocean circulation, and water depth that collectively determine the transport, deposition, and preservation of each sediment type. The alteration of these sediment types ("authigenesis") is also an important process affecting the final composition of marine sediment.

Introduction

The geochemical composition of marine sediment is diverse. Marine sediment is most commonly classified according to the origin of the material(s) composing the bulk sediment, with end-members being referred to as, for example, aluminosilicate, biogenic, or metalliferous (Table 1). Here, we summarize the broad-scale processes and trends in these compositionally defined end-members and further discuss some of the subtleties in their variabilities that lead to the local, regional, and global diversity of deep-sea marine deposits.

The aluminosilicate(s) in marine sediment can be provided by volcanic and terrigenous sources (authigenic aluminosilicates are described separately below). Volcanic ash grains are produced by continental or oceanic eruptions of igneous compositions. Terrigenous sediment results from physical and chemical weathering of upper crustal rocks exposed at the surface of the Earth. Being aluminosilicates, the major element geochemistry of this sediment type exhibits high concentrations of both Al and Ti (along with other commonly associated elements such as K, Na, Rb, etc.) relative to the other sediment types.

Biogenic sediment results from the production, transport, and preservation of minerals initially produced by either plants or animals. The most common biogenic deposits can be divided into calcareous and siliceous, with biogenic apatite contributing a smaller component. Calcareous deposits are enriched in Ca (e.g., calcite, aragonite, dolomite), and siliceous deposits are enriched in Si (e.g., biogenic opal) relative to the other sediment end-members, while biogenic apatite is enriched in P.

Metalliferous sediment most commonly results from hydrothermal processes along mid-ocean ridges. High concentrations of Fe and Mn typically distinguish the bulk geochemistry of metalliferous sediment from the other sediment types, along with concomitant enrichments in Cu, Zn, and other metals near the ridge (Dymond 1981). Farther from the ridge, sinking particulates or sediment on the seafloor may take up additional metals (e.g., Co, Ni, Cu, Zn, rare earth elements) from the water column. Extraterrestrial spherules and micrometeorites are a minor component of sediment and are also metal rich, with elevated concentrations of Fe, Co, and Ni compared to the other sediment types.

Most deep-sea sediment is a mixture of these three main components. Even sediment dominated by one of the above end-members commonly contains significant amounts of the other components. The distributions of each of these sediment types (e.g., Fig. 1) are controlled by wind, ocean

Marine Sediment, Table 1 Average composition of major sediment types

Element	Atomic number	Upper crust (1)	Shale (1)	Pelagic clay (1)	Fe-Mn nodule (1)	Fe-Mn crust (1)	Basal sed. (2)	Ridge sed. (3)
Ag	47	0.06	0.07	0.11	0.09		0.18	6.2 h
Al (%)	13	7.83	8.8	8.4	2.7	0.41	2.73	0.5
As	33	1.6	13	20	140	230		145
Au (ppb)	79	2.3	2.5	2	2	250 w		16 c
B	5	12	100	230	300		123	500
Ba	56	570	580	2,300	2,300	1,000	6,230	6,000 hd
Be	4	3.2	3	2.6	2.5		6.7	
Bi	83	0.054	0.43	0.53	7	29 w	0.17	
Br	35	2.1	20		21		58	
C (%)	6	0.023	1.2	0.45	0.1	0.12		
Ca (%)	20	3.15	1.6	1	2.3	2.2	1.47	
Cd	48	0.1	0.3	0.42	10	3	0.4	4
Ce	58	58	82	101	530	900	34	8.4
Cl	17	150	180					
Co	27	17	19	74	2,700	8,400	82	105
Cr	24	69	90	90	35	9.1	15 d	55
Cs	55	3.7	5	6	1			
Cu	29	39	45	250	4,500	380	790	730
Dy	66	3.5	4.7	7.4	31		20.7	7.3
Er	68	2	3	4.1	18	24	12.9	5.6
Eu	63	1.1	1.2	1.85	9	8.1	5.4	1.5
F	9	700	740	1,300	200		466	
Fe (%)	26	4.17	4.72	6.5	12.5	12.3	20	18
Ga	31	18	19	20	10		6.8	
Gd	64	3.9	5.1	8.3	32	39	22.6	6
Ge	32	1.5	1.6	1.6	0.8		3.3	
Hf	72	4	5	4.1	8		1.6	
Hg	80	0.08	0.18	0.1	0.15			0.4 bf
Ho	67	0.74	1.1	1.5	7	8.2	4.7	
I	53	0.5	19	28	400			
In	49	0.05	0.1	0.08	0.25			
Ir (ppb)	77	0.05	0.05	0.4	7	10 v		0.8 c
K (%)	19	2.56	2.66	2.5	0.7	0.38	1.15	
La	57	30	43	42	157	190	98	29
Li	3	23	66	57	80		125	
Lu	71	0.32	0.42	0.55	1.8	3.9	2.2	0.88
Mg (%)	12	1.64	1.5	2.1	1.6	0.88	2.08	
Mn (%)	25	0.077	0.085	0.67	18.6	20.4	6.1	6
Mo	42	1.6	2.6	27	400	370		30
N	7	20	1,000	600	200			
Na (%)	11	2.54	0.59	2.8	1.7	1.5	2.56	
Nb	41	15	11	14	50		5.1	
Nd	60	26	33	43	158	150	87	23
Ni	28	55	50	230	6,600	3,900	460	430
Os (ppb)	76	0.05	0.05	0.14	2	0.8 v		
P	15	860	700	1,500	2,500	3,900		9,000 b
Pb	82	17	20	80	900	1,400	100	152 h
Pd (ppb)	46	1	(1)	6	6	1.1		21 c
Pr	59	6.6	9.8	10	36	34	19.3	
Pt (ppb)	78	1	(1)	5	200	350		
Rb	37	110	140	110	17		16	
Re (ppb)	75	0.4	0.4	0.3	1			

(*continued*)

Marine Sediment, Table 1 (continued)

Element	Atomic number	Upper crust (1)	Shale (1)	Pelagic clay (1)	Fe-Mn nodule (1)	Fe-Mn crust (1)	Basal sed. (2)	Ridge sed. (3)
Rh (ppb)	45			0.4	13	14		
Ru (ppb)	44			0.2	8			
S	16	530	2,400	2,000	4,700			
Sb	51	0.2	1.5	1	40		17 d	
Sc	21	14	13	19	10			
Se	34	0.14	0.6	0.2	0.6		2.6	
Si (%)	14	30	27.5	25	7.7	2.2	10.8	6.1
Sm	62	4.5	6.2	8.35	35	30	18.6	5
Sn	50	3.3	3	4	2		0.6	
Sr	38	350	170	180	830	1,200	351	
Ta	73	1.5	1.3	1	10		2.1	
Tb	65	0.6	0.84	1.42	5.4	5		
Te	52	0.003	0.07	1	10			
Th	90	11	12	13	30		2.4	
Ti	22	3,300	4,600	4,600	6,700	7,700		240
Tl	81	0.53	0.7	1.8	150		4.8	34 h
Tm	69	0.32	0.44	0.57	2.3	3.6		
U	92	2.8	2.7	2.6	5		4.2	22 f
V	23	140	130	120	500	500		450
W	74	1.3	1.8	4	100			
Y	39	22	26	40	150	190	128	
Yb	70	2	2.8	3.82	20	24	13	5.7
Zn	30	67	95	170	1,200	540	470	380
Zr	40	170	160	150	560		225	

From Li and Schoonmaker (2014). Units are in ppm unless otherwise noted.
Data sources: (1) Li (2000) and references therein; (2) Cronan (1976); (3) Bostrom and Peterson (1969); b = Bostrom (1973); bf = Bostrom and Fisher (1969); c = Crocket et al. (1973); d = Dymond et al. (1973); f = Fisher and Bostrom (1969); h = Horowitz (1970); hd = Heath and Dymond (1977); v = Vonderhaar et al. (2000); w = Wen et al. (1997); REE = Jarvis (1985) for basal sediments, and Bender et al. (1971) for ridge sediments. Pd and Pt values for shale are an educated guess based on the upper crust values

circulation, and water depth that collectively affect the transport, deposition, and preservation of each sediment type. For example, wind will blow dust into the ocean and cause dust to accumulate more rapidly in regions downwind from an arid source of dust. If the dust is deposited in an area of ocean upwelling that has high biological productivity of calcareous plankton, the dust deposition will be mixed into and diluted by the biogenic input. If this sediment is deposited in water deep enough, the biogenic deposit may be dissolved, and the aluminosilicate dust will become the more dominant sediment type again. The dissolution of the biogenic sediment is likely to occur for carbonates if below the carbonate compensation depth (CCD; Millero 2013) or for biogenic opal due to the undersaturation of seawater with respect to biogenic opal (DeMaster 2014). If either dust or biogenic material is deposited close to a hydrothermal vent system, it will be mixed with a metalliferous component. As such, marine sediment is indeed compositionally diverse.

These transport and preservation processes also cause sediment to be thickest along coastlines close to aluminosilicate sources and near equator, where upwelling of nutrient-rich water stimulates biological productivity in the surface water and biogenic sediment has the potential to accumulate rapidly. The slowest accumulating and thinnest sediment occurs in the center of ocean gyres where there is low productivity, low preservation of what little biogenic component is produced, and extremely low supply of wind-blown material that has traversed the vast distance prior to deposition (Fig. 2).

The Prevalence of Authigenic Components in All Sediment

For all sediment, regardless of initial composition, postdepositional processes may produce additional chemical changes to the sediment. Therefore, the chemical composition of each sediment is not static but is continuously changing based on how it geochemically interacts with the surrounding environment in which it is deposited. The postdepositional reactions are referred to as "diagenetic" or "authigenic" processes. Most commonly, "diagenetic processes" refer to changes taking place in sediment after deposition (Berner

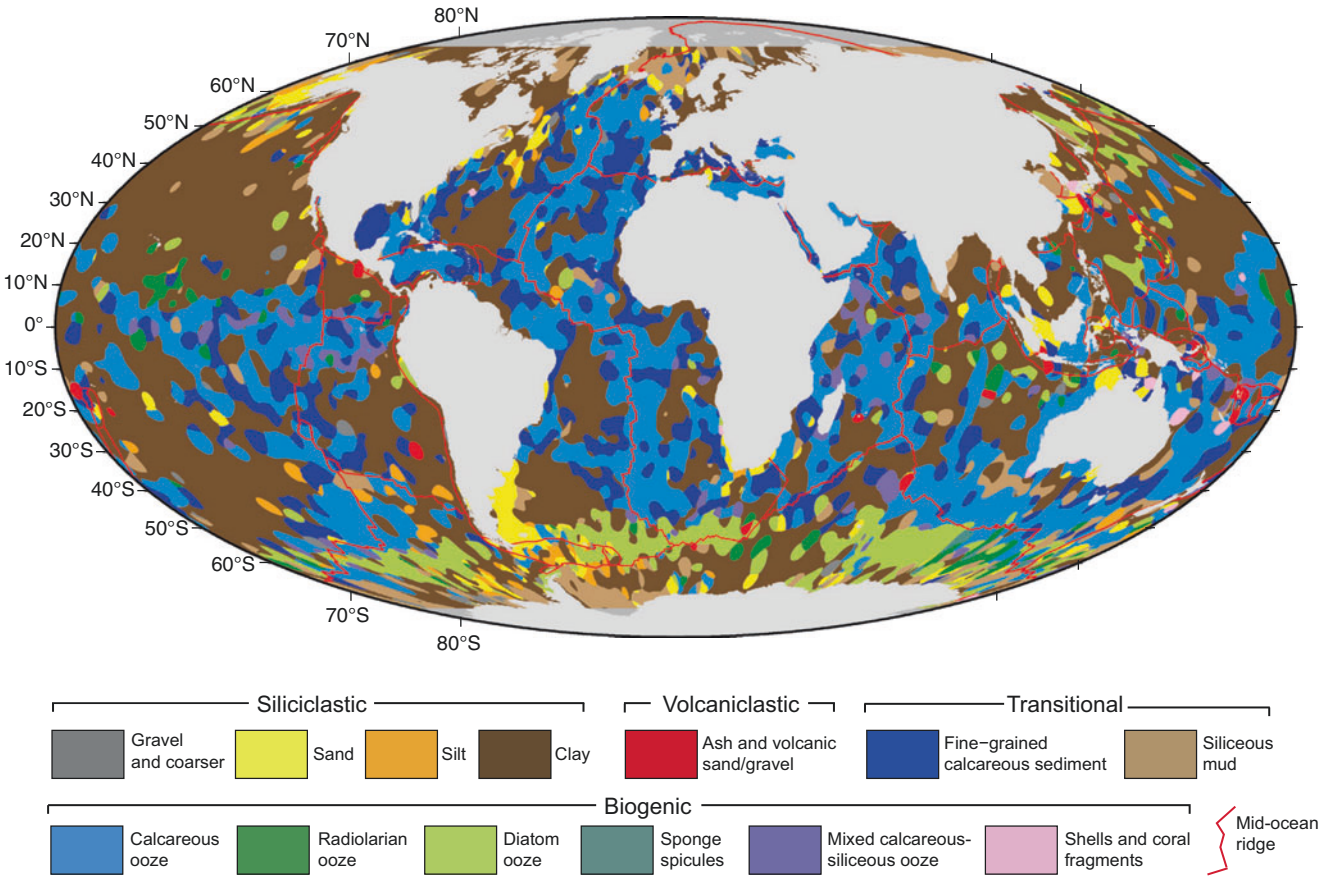

Marine Sediment, Fig. 1 Compilation map of major lithologies of worldwide seafloor sediment (From Dutkiewicz et al. 2015)

1980), while "authigenic processes" refer to the in situ formation of minerals near the seafloor and within the sediment by replacement of a precursor mineral or by direct precipitation from the seawater or surrounding pore fluids (Kastner 1999; Piper and Heath 1989).

The rate at which sediment accumulates (i.e., sedimentation rate), which is inversely related to how long the sediment is in direct contact with ocean bottom water (i.e., the "seawater exposure time"), plays a large role in determining the extent of these reactions (Berner 1980; Ruhlin and Owen 1986). Sediment deposited on the seafloor is initially bathed in ocean bottom water before it is buried and surrounded with porewater. The chemical environment and geochemical reactions that sediment undergoes when exposed to freshly replenished bottom water are very different from the more restricted porewaters. Diagenetic/authigenic reactions in the subseafloor can change individual elemental concentrations, the alkalinity, and/or pH of the porewater. The resulting porewater conditions can subsequently cause additional diagenetic changes. Elements dissolved in porewater can be sensitive indicators of authigenic/diagenetic processes (Schulz 2006) that are dissolving pre-existing minerals or creating new solid phases, commonly referred to as "authigenic minerals."

The use of the term "authigenic minerals" varies between the different research communities studying marine sediment. A number of processes fall under the broad rubric of "authigenesis" including ash alteration, aluminosilicate formation, biogenic deposition, carbonate recrystallization/dolomitization, and biogenic Si diagenesis (including the formation of diagenetic chert), Fe/Mn oxide micronodules or coatings and hydrothermal deposition, geochemical signatures in fish teeth/bones, and/or rare earth and other trace element enrichments. The chemistry of authigenic minerals may be difficult to define as they are usually formed by a combination of a pre-existing minerals and the uptake/release of elements from an aqueous medium (e.g., cation exchange reactions, sorption, or recrystallization). Thus, the composition will include elements from each source. Each of these formation or alteration mechanisms has different implications for the cycling of certain elements involved with each of the sediment types and is discussed in more detail within each section below.

In the context of authigenesis, the concept of "reverse weathering" is a useful construct to consider. Weathering produces ions that are carried by rivers to the ocean where they can reside in a dissolved state over time spans ranging

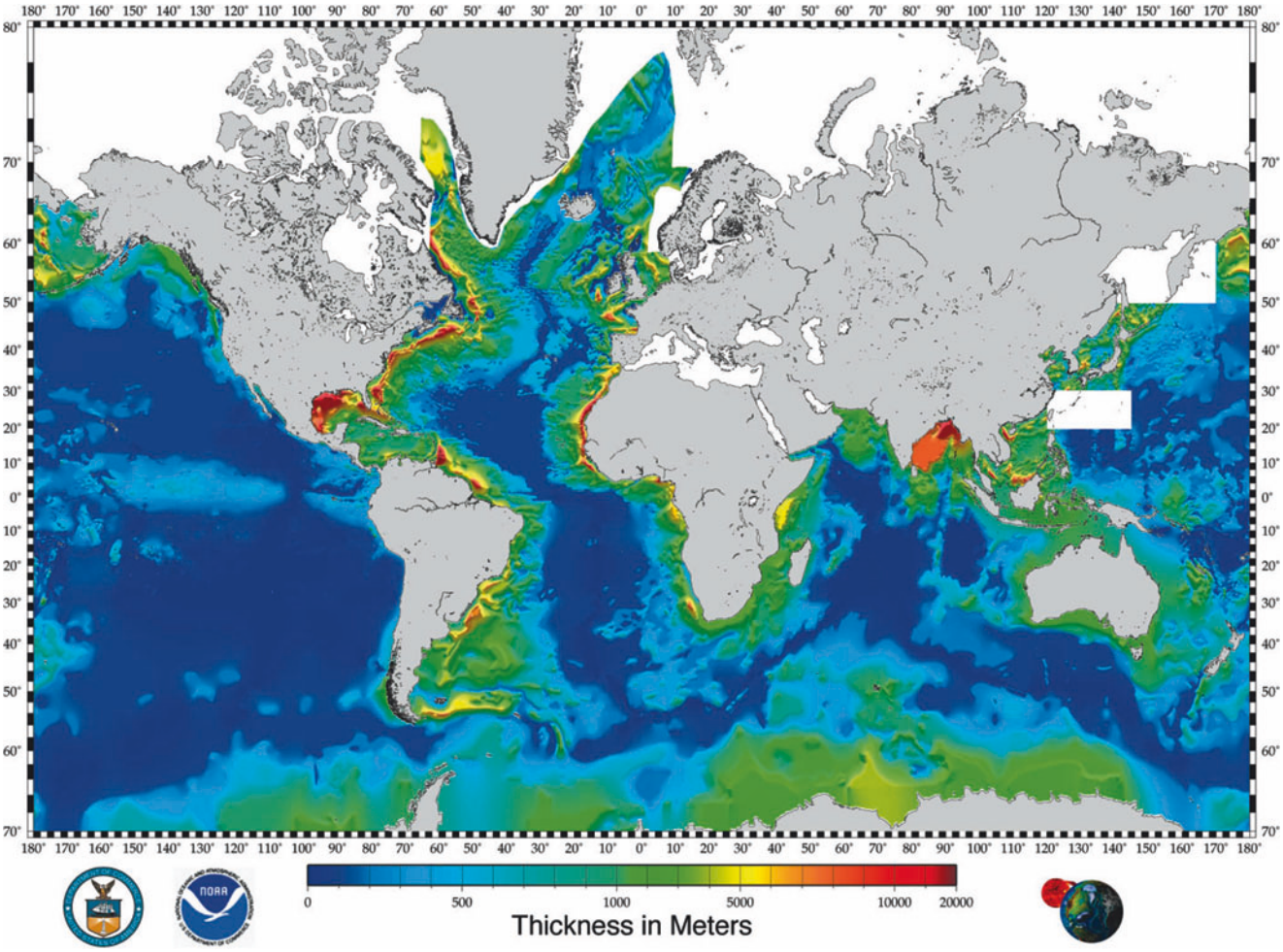

Marine Sediment, Fig. 2 Total sediment thickness of the world's oceans and marginal seas (From Divins 2003)

from several years to hundreds of millions of years (Millero 2013). These ions are eventually removed by biological deposition (e.g., Si or Ca), precipitation with or adsorption onto existing sediment, or incorporation into authigenic aluminosilicates (e.g., Si, Mg, K, Fe). The formation of authigenic aluminosilicates from weathered cations has been referred to as "reverse weathering." The idea of reverse weathering was originally hypothesized by Sillén (1967) and Mackenzie and Garrels (1966) as a removal mechanism to balance the chemical budget of cations (e.g., Mg and K) and HCO_3^- that were transported to the ocean by rivers. Since then, studies have examined the uptake of many of these elements via the existence of authigenic aluminosilicates and basalt alterations associated with hydrothermal fluxes. The presence of authigenic aluminosilicate grains is documented in river delta sediment (e.g., Michalopoulos and Aller 2004), equatorial Pacific biogenic deposits (e.g., Hurd 1973), and pelagic sediment (e.g., Cole 1985). While many of these studies explain their findings with a specific reaction proposed by Mackenzie and Garrels (1966), the specifics and broad suite of reverse weathering reactions that are actively occurring, and their linkages to the carbon cycle, are not yet fully understood.

Aluminosilicates

The Ubiquitous Presence of Volcanic Ash

Volcanic ash has long been recognized in marine sediment, and, given the prevalence of oceanic and continental arc volcanism around the globe, its presence is nearly ubiquitous (Fig. 3a). However, the presence/absence of very fine-grained ash material, and identification of its composition in particular, is challenging given its broad classification as an "aluminosilicate." Volcanic ash can range in composition from mafic to felsic depending on the eruptive source. The major element concentrations of average intermediate ashes (e.g., dacite) are very similar to an average continental crust composition, but the trace and rare earth element concentrations are more variable between the two.

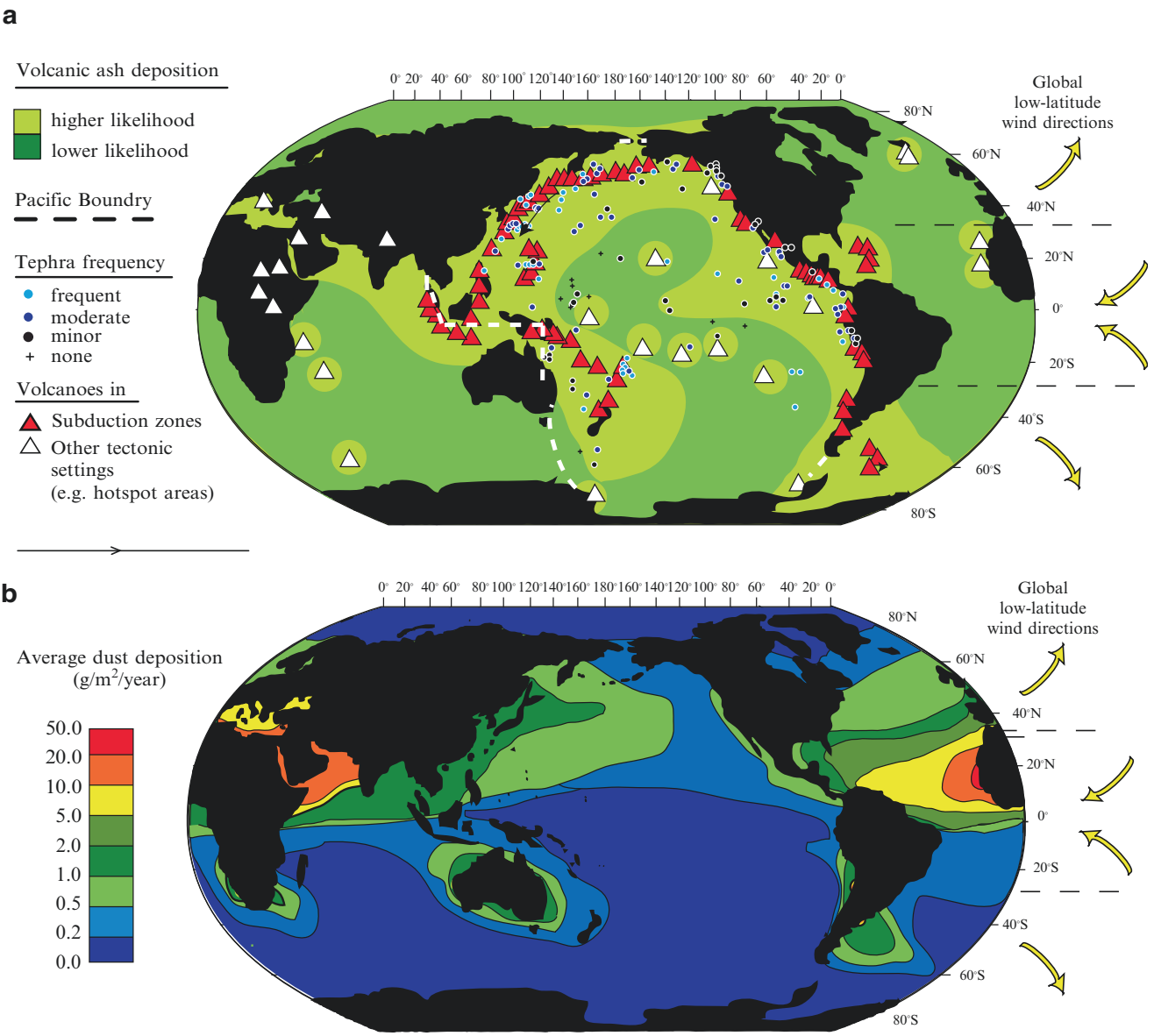

Marine Sediment, Fig. 3 (**a**) Likelihood of volcanic ash deposition in marine sediment. *Lighter green* represents higher likelihood, and *darker green* represents lower likelihood. (**b**) Averaged annual mineral dust fluxes into the world ocean. See figure for color scale (Both images from Olgun et al. 2011)

Deposits of volcanic ash can occur as layers or dispersed in the bulk sediment both on continents and in marine sediment (Ninkovich et al. 1978; Carey and Sigurdsson 1980; Straub and Schmincke 1998; Scudder et al. 2016, and references therein). The term "ash" is generally used in the field of volcanology as a grain size definition (32 μm to 2 mm, e.g., Fisher and Schmincke 1984) for explosive volcanic products (i.e., tephra). Here we use "ash" to indicate a product (mostly volcanic glass) from explosive volcanism no matter which grain size a particle may have. Therefore, we define "discrete ash layers" as a volcanic product that is present as clearly visible beds in the marine sediment that are ash layers of millimeter to centimeter or greater thickness. Less widely recognized than the discrete layers of ash is what has been referred to as "dispersed" ash. "Dispersed ash" is defined as volcanic ash material of various grain sizes (including single μm grains) that is mixed throughout the bulk sediment. This ash occurs in addition to the discrete ash layers (Scudder et al. 2009, 2014, 2016). Dispersed ash is the result of bioturbation of pre-existing discrete ash layers, the settling of airborne or subaqueous ash through the water column, transport by rivers and currents from terrestrially exposed ash deposits, and other processes (e.g., Kutterolf et al. 2014).

The presence of dispersed ash in the marine record has previously been largely overlooked because it is difficult to

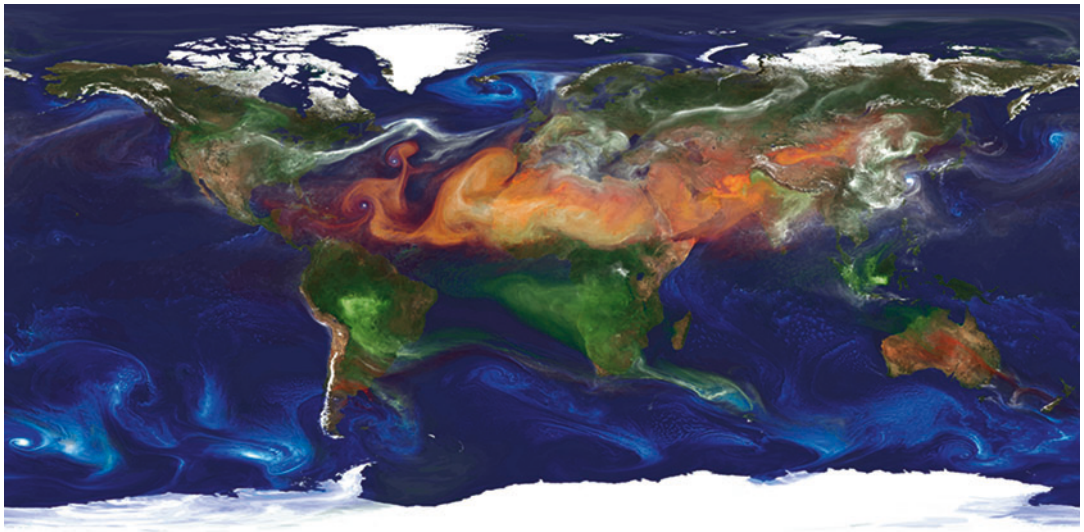

Marine Sediment, Fig. 4 Map of modeled global aerosols. *Red*, dust from the surface; *blue*, sea salt; *green*, smoke from fires; *white*, and sulfate particles from volcanoes and fossil fuel emissions (From NASA Center for Climate Simulation at Goddard Space Flight Center http://gmao.gsfc.nasa.gov/research/aerosol/modeling/)

identify petrographically as a result of its general extremely fine grain size (Rose et al. 2003 and references therein) and/or alteration to authigenic clay (Sigurdsson et al. 1997; Plank et al. 2000). Such alteration (e.g., Schacht et al. 2008) often results in fine-grained material that is unable to be differentiated from detrital terrigenous clay (non-ash, derived from land) on the basis of visual study alone. Recent geochemical studies have found that dispersed ash makes up on average ~30 wt. % of marine bulk sediment (Ziegler et al. 2007; Scudder et al. 2009, 2014; Dunlea et al. 2015a, b), which is consistent with the more qualitative approaches such as the examination of smear slides (Cambray et al. 1993). Ash is commonly altered on and/or below the seafloor by diagenetic reactions. Amorphous volcanic ash shards deposited in marine environments are commonly dissolved, hydrated, and altered on and/or in the seafloor to become zeolite or clay (e.g., smectite) minerals. During the reactions between the grain and seawater or porewater, some elements (e.g., Si, Mg, K) are lost or gained (Gardner et al. 1986; Desprairies et al. 1991; Kastner 1999; Straub et al. 2015), while other elements are immobile, and their concentrations remain relatively unchanged from the parent ash (e.g., Al, Ti, Cr). Weathering of igneous rocks also produces volcanic sediment with a composition reflective of the composition of the eruptive source, although certain element concentrations may be changed during erosion/alteration processes (Pickering et al. 2013).

Eolian Transport and Deposition of Terrigenous Dust

Wind blowing over the continent can entrain dust and transport it long distances from the original site of weathering (e.g., Mahowald et al. 2005). The availability of dust and the direction of the prevailing wind(s) influences where eolian material is deposited on the seafloor (Fig. 3b). The Northern Hemisphere has more continents and thus more dust available to be blown into the ocean. Overall, the dust fluxes in the Northern Hemisphere are an order of magnitude higher than in the Southern Hemisphere, where there are fewer continents and less dust to be transported (Fig. 4). On a regional scale, higher rates of dust deposition occur in regions of the ocean that are closer to and downwind of dust sources (Fig. 3b). The most significant dust sources are arid deserts located below the dry, descending air from Hadley Cell circulation at latitudes of 30°N and 30°S and/or in rain shadows. There is also more dust available for transport in regions that previously experienced rainfall and then became more arid (e.g., the Bodéle Depression in the Sahara Desert) (Schepanski et al. 2009).

During sediment transport, whether in air or water, minerals begin to separate according to size and density. Sedimentary sorting results in an enrichment of heavy minerals (e.g., zircon, monazite, magnetite, rutile) in a relatively coarse size fraction of the sediment. However, these minerals also are present in the finest fractions of eolian-derived sediment as well and can exert a large influence on the resulting sediment composition (Glaccum and Prospero 1980). Thus, repeated reworking (recycling) of sediment tends to strongly enrich deposits associated with heavy minerals (e.g., Zr, Hf, Th, and/or Ti).

Other Transport Mechanisms of Lithogenic Material

There are a few other mechanisms by which aluminosilicates can be transported to the ocean floor. Rivers transport sediment and deposit it near where a river connects to the ocean. Although confined relatively to the coast, riverine deposits

can be extensive and are responsible for some of the thickest deposits of marine sediment (Fig. 2). Sediment and rocks can be frozen into an iceberg that breaks off from glaciers and floats out to sea. The icebergs can travel thousands of kilometers before they melt and release the sediment and rocks frozen inside into the ice to the bottom of the sea. The material deposited by this mechanism is commonly referred to as ice-rafted debris (IRD).

Turbidity currents can also transport or rework sediment on the seafloor. A turbidity current is a quick moving, downslope flow of sediment-laden water. These flows can be triggered when a sediment deposit on a slope becomes too steep, or when a seismic tremor or storm causes the deposit to become unstable and flow downhill.

Identifying Aluminosilicate Sediment Provenance

As discussed earlier, the common aluminosilicate nature of volcanic ash and dust means that they have similar major element composition, and differentiating between the two is challenging. However, there are distinct differences, particularly in the relative proportions of trace elements, that allow volcanic ash and non-ash terrigenous material to be geochemically distinguished from one another. For example, in the Caribbean Sea, average shale and discrete ash layers have similar Al concentrations; however, the Cr concentrations are ~110 ppm and <3 ppm respectively. Therefore, variations in the ratio Cr/Al measured in the sediment reveal the relative proportions of dust vs. ash mixed within the bulk sediment (Peters et al. 2000). Additionally, sample concentrations plotted on ternary diagrams (e.g., La-Sc-Th) and PAAS-normalized rare earth element (REE) patterns can be compared to reference material (Fig. 5b) and aid in determination of the sedimentary components. However, in complex systems, many aluminosilicate sources may be mixed to compose the bulk sediment. In such cases, multivariate statistical analyses can help differentiate and quantify the contributions

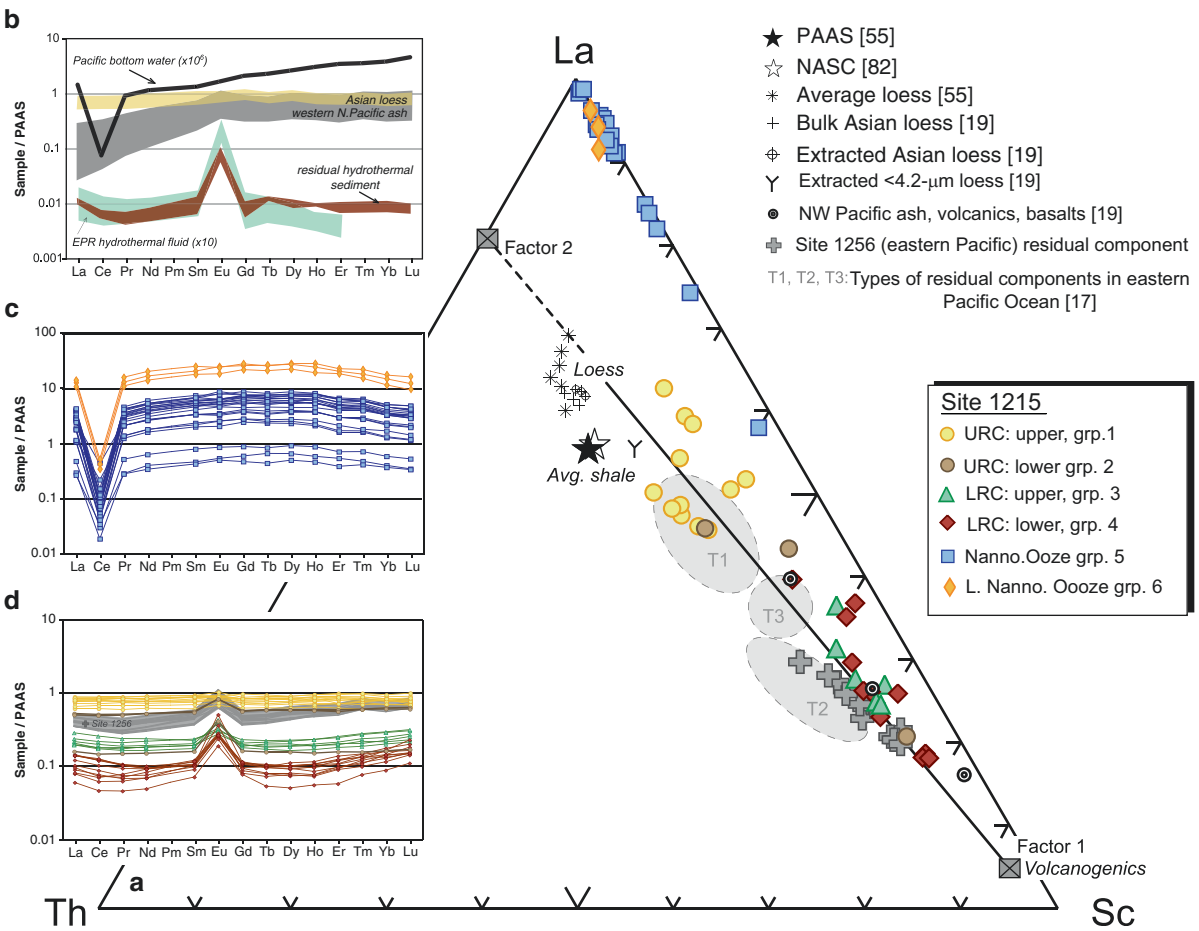

Marine Sediment, Fig. 5 (**a**) La-Sc-Th ternary diagram plotting samples from Site 1215 (central Pacific) and Site 1256 (eastern Pacific) as well as possible end-member compositions for comparison. (**b**) Reference rare earth element (REE) concentrations normalized to an average shale composition (PAAS). (**c**) REE concentrations normalized to PAAS of leached biogenic sediment at Site 1215. The significantly negative Ce anomaly indicates a seawater source for the REEs. (**d**) REE concentrations normalized to PAAS of leached samples from the red clay of Site 1215 and the silty nannofossil ooze from Site 1256. For symbol descriptions, see legend. *URC* upper red clay, *LRC* lower red clay (Figure from Ziegler et al. 2007)

from many different aluminosilicate sources (e.g., Leinen and Pisias 1984; Pisias et al. 2013; Dunlea et al. 2015a; Scudder et al. 2016).

Biogenic Sediment

In the broadest sense, biogenic sediment results from the production, preservation, and diagenetic modification of minerals initially produced by either plants or animals. In addition to organic matter (C_{org}), the vast majority of this sediment is predominated by (i) calcareous shells and oozes precipitated as calcite (hexagonal $CaCO_3$) and/or aragonite (orthorhombic $CaCO_3$), and sometimes authigenically modified to aragonite or dolomite ($CaMg(CO_3)_2$; (ii) siliceous tests/frustrules and oozes (amorphous opal) that can be diagenetically changed into minerals in the opal to quartz series; and (iii) biogenic apatite (e.g., $Ca_{10}(PO_4,CO_3)_6F_2$).

Calcareous Deposits

Some microorganisms that live in seawater, including foraminifera, coccolithophores, pteropods, and others, produce calcareous tests and shells made of calcium carbonate mineral(s) ($CaCO_3$). When the skeletal remains are deposited deeper than a certain depth in the ocean (referred to as the carbonate compensation depth or CCD; Millero 2013), the calcareous shells of the microfossils dissolve (see "carbonate compensation depth" entry in this encyclopedia). If the seafloor is shallower than the CCD, the calcareous shells are more likely to be preserved, although respiration-driven dissolution (Emerson and Bender 1981; Emerson 1985) also plays an important role in carbonate preservation (or lack thereof). Thus, calcareous deposits are found in relatively shallower regions of the seafloor (the flanks of mid-ocean ridges) and below regions of high biogenic carbonate production (e.g., equatorial Pacific upwelling) where the rate of export flux to the seafloor is greater than the dissolution (Goldberg and Arrhenius 1958; Fig. 1). The mineralogy and chemistry of carbonate sediment is reviewed in more detail in Arvidson and Morse (2014).

Planktic and benthic foraminifera incorporate trace amounts of Sr and Mg into the lattice structure of their shells (tests). The incorporation of Mg into calcite is endothermic, and thus more Mg is incorporated into the crystal when the foraminifera are growing at higher temperatures (Lear et al. 2000). Therefore, a high Mg/Ca ratio implies a high temperature of formation, but the geochemical response to temperature can also be influenced by species-specific factors. Some calcareous organisms (e.g., coral aragonite) incorporate Sr into the mineral structure in trace amounts. The precise Sr/Ca ratio in the coral skeleton shows an inverse correlation with the temperature of the seawater at the time of its biomineralization (Rosenthal et al. 2004). Analyses of these Mg/Ca and Sr/Ca ratios in certain calcareous microfossils are used to reconstruct seawater temperatures in the past, but post-depositional recrystallization can affect the record.

Dolomite is a minor component observed in the seafloor sediment as nodules and layers created by diagenetic processes. While the creation of dolomite by substitution of Mg for Ca in calcite ($CaCO_3$) is chemically simple, the dynamics of dolomitization are still being understood. Studies have shown that dolomitization does not require the adjacent aqueous solutions to be supersaturated with respect to calcite or dolomite and that the conversion of dolomite to calcite is not a dissolution-precipitation reaction, but instead a detailed, fine-scale replacement of the pre-existing mineral phase (Merino and Canals 2011).

Siliceous Deposits

Siliceous deposits include sedimentary rocks such as bedded and nodular chert, as well as their diagenetic precursors of deep-sea oozes composed of diatoms, radiolaria, spicules, and silicoflagellates. Although chert accounts for much less than 5% of all sedimentary rocks, siliceous deposits are important components of modern deep-sea sediment in all ocean basins (Fig. 1) and are host to a variety of ore deposits on land (Hein 1987). Important mineralogical associations include barite and phosphorite (associated due to their common formation with siliceous oozes in regions of high biological productivity), as well as petroleum (e.g., Monterey Formation of California, USA; Garrison et al. 1981), uranium, and banded iron formations (e.g., Trendall and Morris 1983). The formation and diagenesis of siliceous deposits is reviewed in further detail in DeMaster (2014).

The mineralogy and preservation of biogenic silica deposits are controlled by diagenetic reactions. Amorphous biogenic silica (opal-A) is secreted by the given plant (e.g., diatom) or animal (e.g., radiolarian) organism. Due to the undersaturation of seawater with respect to opal, the vast majority of the opal-A material dissolves on or within the uppermost centimeters of the seafloor. Preservation of opal-A reaches maximum values of 15–20% in regions of elevated productivity (e.g., McManus et al. 1995), with more typical values being $\leq$10% (e.g., Archer et al. 1993). During burial, continued dissolution of opal-A, and eventual precipitation of disordered cristobalite/tridymite (opal-CT), is both thermodynamically and kinetically regulated (e.g., Williams and Crerar 1985; Meister et al. 2014). Through this process, as well as through the final diagenetic transition from opal-CT to biogenic quartz, the composition of the host sediment plays an important role, with various factors such as the amount of clay or organic material influencing diagenetic rates of formation (e.g., Kastner et al. 1977; Isaacs 1982; Hinman 1990; Bohrmann et al. 1994; Tanner et al. 2013). These diagenetic transformations also profoundly affect the final chemical composition of the resultant chert, primarily due to the

addition of silica as a diluent and associated removal of other elements (e.g., Ca Sr, P, plus others) (Brueckner and Snyder 1985; Murray 1994; Dong et al. 2015). Although there are notable stratigraphic contrasts between bedded and nodular cherts (e.g., Jenkyns and Winterer 1982; Wang et al. 2009), the chemical processes acting during their diagenetic formation are very similar (Tada 1991; Murray et al. 1992).

Biogenic Apatite

Calcium phosphate minerals are a minor component in sediment but if they become concentrated can have a significant effect on the Ca and P concentrations on the bulk sediment in which they are mixed (Ruttenberg 2014). Mineral phosphate is incorporated in marine sediment primarily in the form of authigenic carbonate fluorapatite (CFA) (e.g., $Ca_{10}(PO_4, CO_3)_6F_2$). CFA is a major component of the hard parts of marine fish, such as scales, bones, and teeth, which are deposited in the seafloor. Additionally, diagenesis of P-bearing phases in marine sediment and P exchange with porewater can lead to the authigenic formation of CFA (Ruttenberg and Berner 1993; Filippelli 2011).

Organic matter is generally the primary source of P to marine sediment (Froelich et al. 1982). Of the organic matter, and thus P, in marine sediment, most is deposited in continental margins (Berner 1982). However, in slowly accumulating sediment (such as the center of ocean gyres), the long seawater exposure time allows rare earth elements and other trace elements to be incorporated into the phosphate mineral structure, enriching the average sediment composition in these trace and rare earth elements (Takebe 2005). Therefore, extremely slowly accumulating sediment can concentrate apatite because no other sediment types are diluting the deposition of apatite (e.g., Zhou and Kyte 1992). Even if apatite is still a relatively small component of the pelagic clay (~2–10%), it can strongly influence or even control Ca and P concentrations of the bulk sediment where no calcareous deposits occur (Dunlea et al. 2015a).

Organic Material and Redox-Sensitive Elements

Organic material is often deposited with the biogenic material described above and can affect the geochemical composition of sediment. In the center of ocean gyres, organic material is barely detectable in the sediment. Higher concentrations of elements from organic material (e.g., C, N, P) occur in marine sediment near the coasts and beneath regions of high surface productivity. Oxygen in the bottom water or porewaters will degrade the organic material via oxidation. When organic matter is buried deeper and all of the oxygen is consumed, other inorganic chemical species will begin to degrade the organic material. These reactions and changing redox states cause certain elements to become mobile and will diffuse through the porewaters until they reach a redox state where they return to the solid phase. Redox-sensitive elements (e.g., Fe, Mn, Mo, V, U) can become depleted or concentrated in marine sediment depending on the redox state of the surrounding porewaters.

Metalliferous Sediment

Sediment can become enriched in metals near mid-ocean ridges due to precipitates from a hydrothermal plume but also further from the ridge when sedimentation rates are slow enough to scavenge and concentrate metals from the water column (Boström and Peterson 1969; Gurvich 2006). The hydrothermal fluids of the vent system are greatly enriched in Fe, Mn, Cu, Zn, Ni, and other elements (Von Damm et al. 1985; Elderfield and Schultz 1996). Hydrothermal fluids enriched in metals react with ambient seawater and are primarily deposited on the crest and flank of the ridges (Fig. 6). There, they may undergo additional reactions on or within the sediment to form "hydrothermal" metalliferous sediment, enriched in those elements and others as well (e.g., Dymond 1981).

Further from the ridge, metals in the seawater (from dispersed hydrothermal plumes or weathered from continents) can be deposited with, adsorbed onto, or incorporated into sediment as Fe/Mn-oxyhydroxide micronodules or coatings on existing grains. As accumulation rates decrease, the longer seawater exposure time allows metals to be increasingly scavenged from seawater onto sediment or onto sinking particles that continually form metalliferous sediment (Ruhlin and Owen 1986; Dunlea et al. 2015a). This "hydrogenous" (also referred to as "hydrogenetic" or "diagenetic" by some researchers) metalliferous sediment accumulating further from MORs is enriched in different metals (e.g., Co, Ni, REEs) than "hydrothermal" metalliferous sediment, in addition to Fe and Mn (Marchig and Erzinger 1986; Ruhlin and Owen 1986; Li and Schoonmaker 2014).

Since the dissolved constituents of chemical species derived from hydrothermal plumes can travel thousands of kilometers away from the mid-ocean ridge (e.g., Fitzsimmons et al. 2014; Resing et al. 2015), they are the source of some metals enriched in the "hydrogenous" sediment. Thus, there is no exact distinction between these two types of metalliferous sediment, and it is more informative to recognize the spatial gradient between the two. In general, the maximum influence of hydrothermal input occurs in the axial zone of the source ridge, with a gradual decrease at distances away from the axis (Lyle 1986). Ancient non-lithified and lithified analogues of metalliferous sediment that accumulated in paleoceans and paleoseas occur on the continents and islands within ophiolite belts (e.g., Murray et al. 1990 1991).

In addition to concentrating certain trace elements, authigenic aluminosilicate formation has been documented in high-temperature hydrothermal vent fluids (e.g., Cole and

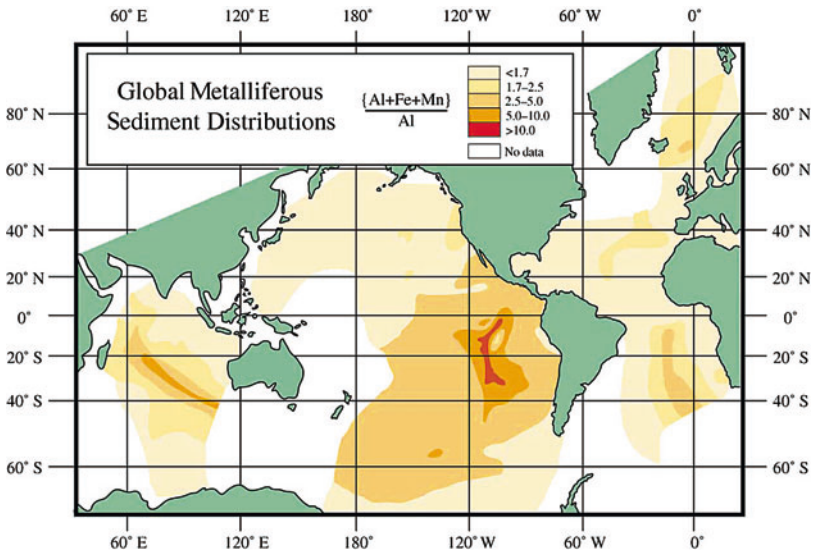

Marine Sediment, Fig. 6 Map of (Al + Fe + Mn)/Al for seafloor marine sediment depicting the global distribution of metalliferous sediment. The highest concentrations of Fe and Mn relative to Al occur near mid-ocean ridge axes (From German and Seyfield 2014)

Shaw 1983), and low-temperature hydrothermal-rich sediment (e.g., Cole 1985; Cuadros et al. 2011). Although Mg is absent in pure hydrothermal fluids (Elderfield and Schultz 1996), reactions with ambient seawater can cause these authigenic aluminosilicates to be enriched in Mg and may be a significant sink for Mg in the ocean (Cuadros et al. 2011). Authigenic aluminosilicates in sediment can also form from the alteration or erosion of basalt (Haymon and Kastner 1986). The sediment formed from basalt alteration will have some refractory element proportions similar to the original basalt, but other elements will be enriched or depleted during the alteration.

Minor Metal Contributions from Cosmic Dust

Between 5 and 270 metric tons of cosmic dust (or micrometeorites) are accreted to Earth everyday (Plane 2012). The main sources of cosmic dust are collisions between asteroids and the sublimation of comets as they approach the sun on their orbits through the solar system. Micrometeorites were first identified in marine sediment during the *HMS Challenger* scientific expedition in 1873–1876 when they isolated extraterrestrial spherules by their magnetic properties (Murray and Renard 1883). The composition of average meteorites and chondrites is enriched in Fe, Ni, Cu, and Co and is discussed in more detail in McDonough and Sun (1995). While the micrometeorites and spherules (e.g., Fig. 7) are more concentrated and easier to identify in slowly accumulating pelagic sediment and crusts (Millard and Finkelman 1970; Murrell et al. 1980; D'Hondt et al. 2011), they still are not significant enough to influence the element concentrations of the bulk sediment relative to other sources (Stuart and Lee 2012; Dunlea et al. 2015b).

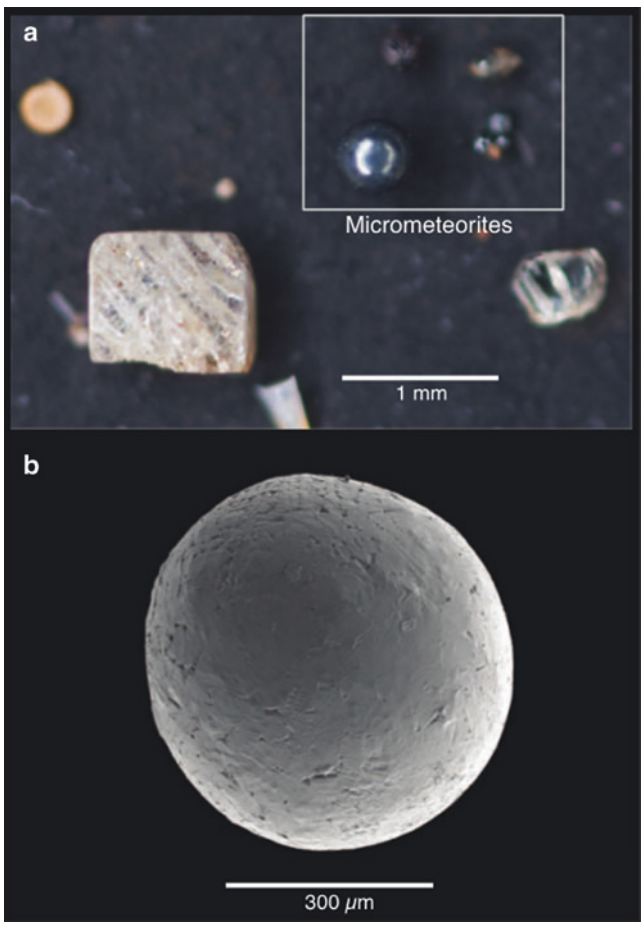

Marine Sediment, Fig. 7 (**a**) Photomicrograph of micrometeorites isolated from South Pacific Gyre pelagic clay sediment, IODP Expedition 329, Site U1365. (**b**) Scanning electron microscope image showing surface details of the larger micrometeorite in (a) (From D'Hondt et al. 2011)

Summary

Marine sediment is compositionally diverse. From the geochemical perspective, sediment is most commonly classified according to the origin of the material(s) composing the bulk sediment, with end-members being referred to as aluminosilicate, biogenic, or metalliferous. Most deep-sea sediment is a mixture of these three main components. The aluminosilicate (s) in marine sediment can be provided by volcanism (eruptions of igneous material) and terrigenous sources (erosion of upper crustal rocks). Biogenic sediment (calcareous, siliceous, apatite) is initially produced by either plants or animals. Metalliferous sediment most commonly results from exhalative processes along mid-ocean ridges and/or uptake of dissolved metals from seawater. Extraterrestrial debris contributes a trace amount of metal-rich material as well. The distributions of each of these sediment types are controlled by wind, ocean circulation, and water depth that collectively affect the transport, deposition, and preservation of each sediment type. For all sediment, regardless of initial composition, postdepositional processes (authigenesis or diagenesis) cause geochemical changes based on how the sediment interacts with the surrounding environment in which it is deposited.

Cross-References

- ▶ Aqueous Solutions
- ▶ Authigenesis
- ▶ Carbonate Compensation Depth
- ▶ Chemical Weathering
- ▶ Clay Minerals
- ▶ Diagenesis
- ▶ Dolomite and Dolomitization
- ▶ Earth's Oceanic Crust
- ▶ Ferromanganese Crusts and Nodules: Rocks That Grow
- ▶ Hydrothermal Alteration
- ▶ Hydrothermal Vents
- ▶ Low-Temperature Geochemistry
- ▶ Meteorites
- ▶ Ocean Biochemical Cycling and Trace Elements
- ▶ Organic Matter Degradation and Preservation
- ▶ Silicate Minerals
- ▶ Volcanism

References

Archer D, Lyle M, Rodgers K, Froelich P (1993) What controls opal preservation in tropical deep-sea sediments? Paleoceanography 8:7–21

Arvidson RS, Morse JW (2014) Formation and diagenesis of carbonate sediments. In: Holland HD, Turekian K (eds) Treatise on geochemistry. Elsevier Ltd., Amsterdam, pp 61–101

Bender M, Broecker W, Gornity V, Middel U, Key R, Sun SS, Biscaye P (1971) Geochemistry of three cores from the East Pacific Rise. Earth Planet Sci Lett 12:425–433

Berner RA (1980) Early diagenesis: a theoretical approach. Princeton University Press, Princeton, p 256

Berner RA (1982) Burial of organic carbon and pyrite sulfur in the modem oceans: its geochemical and environmental significance. Am J Sci 282:451–473

Bohrmann G, Abelmann A, Gersonde R, Hubberten H, Kuhn G (1994) Pure siliceous ooze, a diagenetic environment for early chert formation. Geology 22:207–210

Boström K (1973) The origin and fate of ferromanganese active ridge sediments. Stockh Contrib Geol 27:149–243

Boström K, Fisher DE (1969) Distribution of mercury in East Pacific sediments. Geochim Cosmochim Acta 33:743–745

Boström K, Peterson M (1969) The origin of aluminum-poor ferromanganoan sediments in areas of high heat flow on the East Pacific rise. Mar Geol 7:427–447

Brueckner HK, Snyder WS (1985) Chemical and Sr-isotopic variations during diagenesis of Miocene siliceous sediments of the Monterey formation, California. J Sediment Petrol 55:553–568

Cambray H, Cadet JP, Pouclet A (1993) Ash layers in deep-sea sediments as tracers of arc volcanic activity: Japan and central America as case studies. Island Arc 2:72–86

Carey SN, Sigurdsson H (1980) The Roseau ash: deep-sea tephra deposits from a major eruption on Dominica, lesser antilles arc. J Volcanol Geotherm Res 7:67–86

Cole TG (1985) Composition, oxygen isotope geochemistry and origin of smectite in the metalliferous sediments of the Bauer deep, Southeast Pacific. Geochim Cosmochim Acta 49:221–235

Cole TG, Shaw HF (1983) The nature and origin of authigenic smectites in some recent marine sediments. Clay Miner 18:239–252

Crocket JH, MacDougall JD, Harriss RC (1973) Gold, palladium and iridium in marine sediments. Geochim Cosmochim Acta 37:2547–2556

Cronan DS (1976) Basalt metalliferous sediments from the eastern Pacific. Geol Soc Am Bull 87:928–934

Cuadros J, Dekov VM, Arroyo X, Nieto F (2011) Smectite formation in submarine hydrothermal sediments: samples from the HMS challenger expedition (1872–1876). Clay Clay Miner 59:147–164

DeMaster DJ (2014) The diagenesis of biogenic silica: chemical transformations occurring in the water column, seabed, and crust. In: Holland HD, Turekian K (eds) Treatise on geochemistry. Elsevier Ltd., Amsterdam, pp 103–111

Desprairies A, Riviere M, Pubellier M (1991) Diagenetic evolution of Neogene volcanic ashes (Celebes and Sulu seas). Proc Integr Ocean Drill Program Sci Results 124:489–503

D'Hondt S, Inagaki F, Alvarez Zarikian CA, Expedition 329 Scientists (2011) Expedition 329 reports. In: Proceedings of the integrated ocean drilling program, 329. Tokyo, Integrated Ocean Drilling Program Management International, Inc. https://doi.org/10.2204/iodp.proc.329.2011

Divins DL (2003) Total sediment thickness of the world's oceans & marginal seas. Boulder, NOAA National Geophysical Data Center

Dong L, Shen B, Lee C-TA, Shu X-J, Peng Y, Sun Y, Tang Z, Rong H, Lang X, Ma H, Yang F, Guo W (2015) Germanium/silicon of the Ediacaran-Cambrian Laobao cherts: implications for the bedded chert formation and paleoenvironment interpretations. Geochem Geophys Geosyst 16:751–763

Dunlea AG, Murray RW, Sauvage J, Pockalny RA, Spivack AJ, Harris RN, D'Hondt S (2015a) Cobalt-based age models of pelagic clay in the South Pacific gyre. Geochem Geophys Geosyst 16:2694–2710

Dunlea AG, Murray RW, Sauvage J, Spivack AJ, Harris RN, D'Hondt S (2015b) Dust, volcanic ash, and the evolution of the South Pacific gyre through the Cenozoic. Paleoceanography 30:1078–1099

Dutkiewicz A, Müller RD, O'Callaghan S, Jónasson H (2015) Census of seafloor sediments in the world's ocean. Geology 43:795–798
Dymond J, Corliss JB, Heath GR, Field CW, Dasch EJ, Veeh HH (1973) Origin of metalliferous sediments from the Pacific Ocean. Geol Soc Am Bull 84:3355–3372
Dymond J (1981) Geochemistry of Nazca plate surface sediments: an evaluation of hydrothermal, biogenic, detrital, and hydrogenous sources. Geol Soc Am Mem 154:133–173
Elderfield H, Schultz A (1996) Mid-ocean ridge hydrothermal fluxes and the chemical composition of the ocean. Annu Rev Earth Planet Sci 24:191–224
Emerson S (1985) Organic carbon preservation in marine sediments. In: Sundquist ET, Broecker WS (eds) The carbon cycle and atmospheric CO: natural variations archean to present. American Geophysical Union, Washington, DC. https://doi.org/10.1029/GM032p0078
Emerson S, Bender ML (1981) Carbon fluxes at the sediment-water interface of the deep sea: calcium carbonate preservation. J Mar Res 39:139–162
Filippelli GM (2011) Phosphate rock formation and marine phosphorus geochemistry: the deep time perspective. Chemosphere 84:759–766
Fisher DE, Bostrom K (1969) Uranium rich sediments on the East Pacific Rise. Nature 22:64
Fisher RV, Schmincke HU (1984) Pyroclastic rocks. Springer, Berlin/Heidelberg, p 472
Fitzsimmons JN, Boyle EA, Jenkins WJ (2014) Distal transport of dissolved hydrothermal iron in the deep South Pacific Ocean. Proc Natl Acad Sci 111:16654–16661
Froelich PN, Bender ML, Luedtke NA, Heath GR, DeVries T (1982) The marine phosphorus cycle. Am J Sci 282:474–511
Gardner JV, Nelson CS, Baker PA (1986) Distribution and character of pale green laminae in sediment from Lord Howe rise: a probable late Neogene and quaternary tephrostratigraphic record. Deep Sea Drill Proj Initial Rep 90:1145–1159
Garrison RE, Douglas RG, Pisciotto KE, Isaacs CM, Ingle JC (1981) The Monterey formation and related siliceous rocks of California. Pac Section SEPM 15:327
German CR, Seyfield WE Jr (2014) Hydrothermal processes. In: Holland HD, Turekian KK (eds) Treatise on geochemistry. Elsevier Ltd, Amsterdam, pp 191–233
Glaccum R, Prospero J (1980) Saharan aerosols over the tropical North Atlantic–mineralogy. Mar Geol 37:295–321
Goldberg ED, Arrhenius G (1958) Chemistry of Pacific pelagic sediments. Geochim Cosmochim Acta 13:153–212
Gurvich EG (2006) Metalliferous sediments of the world ocean: fundamental theory of deep-sea hydrothermal sedimentation. Springer, Berlin/Heidelberg, p 416
Haymon RM, Kastner M (1986) The formation of high temperature clay minerals from basalt alteration during hydrothermal discharge on the East Pacific rise axis at 21 N. Geochim Cosmochim Acta 50:1933–1939
Heath GR, Dymond J (1977) Genesis and transformation of metalliferous sediments from the East Pacific Rise, Bauer Deep, and Central Basin, northwest Nazca plate. Geol Soc Am Bull 88:723–733
Hein JR (ed) (1987) Siliceous sedimentary rock-hosted ores and petroleum. Van Nostrand Reinhold, New York, p 304
Hinman N (1990) Chemical factors influencing the rates and sequences of silica phase transitions: effects of organic constituents. Geochim Cosmochim Acta 54:1563–1574
Horowitz A (1970) The distribution of Pb, Ag, Sn, Tl, and Zn in sediments on active oceanic ridge. Mar Geol 9:241–259
Hurd DC (1973) Interactions of biogenic opal, sediment and seawater in the central equatorial Pacific. Geochim Cosmochim Acta 37:2257–2282
Isaacs CM (1982) Influence of rock composition on kinetics of silica phase changes in the Monterey formation, Santa Barbara area, California. Geology 10:304–308
Jarvis I (1985) Geochemistry and origin of Eocene-Oligocene metalliferous sediments from the central equatorial Pacific: Deep Sea Drilling Project Sites 573 and 574. Initial Rep Deep Sea Drill Proj 85:781–804
Jenkyns HC, Winterer EL (1982) Palaeoceanography of Mesozoic ribbon radiolarites. Earth Planet Sci Lett 60:351–375
Kastner M (1999) Oceanic minerals: their origin, nature of their environment and significance. Proc Natl Acad Sci 96:3380–3387
Kastner M, Keene JB, Gieskes JM (1977) Diagenesis of siliceous oozes—I. Chemical controls on the rate of opal-a to opal-CT transformation—an experimental study. Geochim Cosmochim Acta 41:1041–1059
Kutterolf S, Schindlbeck JC, Scudder RP, Murray RW, Pickering KT, Freundt A, Labanieh S, Heydolph K, Saito S, Naruse H, Underwood MB, Wu H (2014) Large volume submarine ignimbrites in the Shikoku Basin: an example for explosive volcanism in the western Pacific during the late Miocene. Geochem Geophys Geosyst 15:1837–1851
Lear C, Elderfield H, Wilson P (2000) Cenozoic deep-sea temperatures and global ice volumes from Mg/Ca in benthic foraminiferal calcite. Science 287:269–272
Leinen M, Pisias N (1984) An objective technique for determining end-member compositions and for partitioning sediments according to their sources. Geochim Cosmochim Acta 48:47–62
Li YH (2000) A compendium of geochemistry: from solar Nebula to the human brain. Princeton University Press, Princeton
Li Y-H, Schoonmaker JE (2014) Chemical composition and mineralogy of marine sediments. In: Holland HD, Turekian K (eds) Treatise on geochemistry. Elsevier Ltd., Amsterdam, pp 1–32
Lyle MW (1986) Major element composition of leg 92 sediments. Deep Sea Drill Proj Initial Rep 92:355–370
Mackenzie FT, Garrels RM (1966) Chemical mass balance between rivers and oceans. Am J Sci 264:507–525
Mahowald NM, Baker AR, Bergametti G, Brooks N, Duce RA, Jickells TD, Kubilay N, Prospero JM, Tegen I (2005) Atmospheric global dust cycle and iron inputs to the ocean. Glob Biogeochem Cycles 19. https://doi.org/10.1029/2004GB002402
Marchig V, Erzinger J (1986) Chemical composition of Pacific sediments near 20 S: changes with increasing distance from the East Pacific rise. Deep Sea Drill Proj Initial Rep 92:371–381
McManus J, Hammond DE, Berelson WM et al (1995) Early diagenesis of biogenic opal: dissolution rates, kinetics, and paleoceanographic implications. Deep-Sea Res 42:871–903
Meister P, Chapligin B, Picard A, Meyer H, Fischer C, Rettenwander D, Amthauer G, Vogt C, Aiello IW (2014) Early diagenetic quartz formation at a deep iron oxidation front in the eastern equatorial Pacific – a modern analogue for banded iron/chert formations? Geochim Cosmochim Acta 137:188–207
Merino E, Canals A (2011) Self-accelerating dolomite-for-calcite replacement: self-organized dynamics of burial dolomitization and associated mineralization. Am J Sci 311:573–607
McDonough WF, Sun S-S (1995) The composition of the earth. Chem Geol 120:223–253
Michalopoulos P, Aller RC (2004) Early diagenesis of biogenic silica in the Amazon delta: alteration, authigenic clay formation, and storage. Geochim Cosmochim Acta 68:1061–1085
Millard HT, Finkelman RB (1970) Chemical and mineralogical compositions of cosmic and terrestrial spherules from a marine sediment. J Geophys Res 75:2125–2134
Millero FJ (2013) Chemical oceanography, 4th edn. CRC Press/LLC Taylor & Francis Group, Boca Raton, p 469

Murray RW (1994) Chemical-criteria to identify the depositional environment of chert – general-principles and applications. Sediment Geol 90:213–232
Murray J, Renard AF (1883) On the microscopic characters of volcanic ashes and cosmic dust, and their distribution in deep-sea deposits. Proc Roy Soc Edinb 12:474–495
Murray RW, Buchholtz ten Brink MR, Jones DL, Gerlach DC, Russ GP III (1990) Rare earth elements as indicators of different marine depositional environments in chert and shale. Geology 18:268–271
Murray RW, Brink ten M, Gerlach DC (1991) Rare earth, major, and trace elements in chert from the Franciscan complex and Monterey group, California: assessing REE sources to fine-grained marine sediments. Geochim Cosmochim Acta 55:1875–1895
Murray RW, Jones DL, Buchholtz ten Brink MR (1992) Diagenetic formation of bedded chert: evidence from chemistry of the chert-shale couplet. Geology 20:271–274
Murrell MT, Davis PA, Nishiizumi K, Millard HT (1980) Deep-sea spherules from Pacific clay: mass distribution and influx rate. Geochim Cosmochim Acta 44:2067–2074
Ninkovich D, Sparks R, Ledbetter M (1978) The exceptional magnitude and intensity of the Toba eruption, Sumatra: an example of the use of deep-sea tephra layers as a geological tool. Bull Volcanol 41:286
Olgun N, Duggen S, Croot PL, Delmelle P, Dietze H, Schacht U, Óskarsson N, Siebe C, Auer A, Garbe-Schönberg D (2011) Surface Ocean iron fertilization: the role of airborne volcanic ash from subduction zone and hot spot volcanoes and related iron fluxes into the Pacific Ocean. Glob Biogeochem Cycles 25:GB4001. https://doi.org/10.1029/2009GB003761
Peters JL, Murray RW, Sparks JW, Coleman DS (2000) Terrigenous matter and dispersed ash in sediment from the Caribbean Sea: results from leg 165. Proc Ocean Drill Program Sci Results 165:115–124
Pickering KT, Underwood MB, Saito S, Naruse H, Kutterolf S, Scudder RP, Park J-O, Moore GF, Slagle A (2013) Depositional architecture, provenance, and tectonic/eustatic modulation of Miocene submarine fans in the Shikoku Basin: results from Nankai trough Seismogenic zone experiment. Geochem Geophys Geosyst 14:1722–1739. https://doi.org/10.1002/ggge.20107
Piper DZ, Heath GR (1989) Hydrogenous sediment. Geol North Am N:337–345
Pisias NG, Murray RW, Scudder RP (2013) Multivariate statistical analysis and partitioning of sedimentary geochemical data sets: general principles and specific MATLAB scripts. Geochem Geophys Geosyst 5:4015–4020
Plane JMC (2012) Cosmic dust in the earth's atmosphere. Chem Soc Rev 41:6507–6518
Plank T, Ludden JN, Escutia C, Shipboard SP (2000) Leg 185 summary: inputs to the Izu–Mariana subduction system. Proc Integr Ocean Drill Program Initial Rep 185:1–63. https://doi.org/10.2973/odp.proc.ir.185.101.2000
Rose WI, Gu Y, Watson IM, Yu T (2003) The February–March 2000 eruption of Hekla, Iceland from a satellite perspective. In: Robock A, Oppenheimer C (eds) Volcanism and the Earth's atmosphere. American Geophysical Union, Washington, DC
Rosenthal Y et al (2004) Laboratory inter-comparison study of Mg/Ca and Sr/Ca measurements in planktonic foraminifera for paleoceanographic research. Geophys Geochem Geosyst 5. https://doi.org/10.1029/2003GC000650
Resing JA, Sedwick PN, German CR, Jenkins WJ, Moffett JW, Sohst BM, Tagliabue A (2015) Basin-scale transport of hydrothermal dissolved metals across the South Pacific Ocean. Nature 523:200–203
Ruhlin D, Owen R (1986) Factors influencing the rare earth element composition of hydrothermal precipitates, East Pacific rise. Initial Rep Deep Sea Drill Proj 92:383–389
Ruttenberg KC (2014) The global phosphorus cycle. In: Holland HD, Turekian K (eds) Treatise on geochemistry. Elsevier Ltd., Amsterdam, pp 499–558
Ruttenberg KC, Berner RA (1993) Authigenic apatite formation and burial in sediments from non-upwelling, continental marine environments. Limnol Oceanogr 37:1460–1482
Schacht U, Wallmann K, Kutterolf S, Schmidt M (2008) Volcanogenic sediment–seawater interactions and the geochemistry of pore waters. Chem Geol 249:321–338
Schepanski K, Tegen I, Macke A (2009) Saharan dust transport and deposition towards the tropical northern Atlantic. Atmos Chem Phys 9:1173–1189. https://doi.org/10.5194/acp-9-1173-2009
Schulz HD (2006) Quantification of early diagenesis: dissolved constituents marine pore water. In: Schulz HD, Zabel M (eds) Marine geochemistry, 2nd edn. Springer, Heidelberg, p 574
Scudder RP, Murray RW, Plank T (2009) Dispersed ash in deeply buried sediment from the Northwest Pacific Ocean: an example from the Izu–Bonin arc (ODP site 1149). Earth Planet Sci Lett 284:639–648
Scudder RP, Murray RW, Schindlbeck JC, Kutterolf S, Hauff F, McKinley CC (2014) Regional-scale input of dispersed and discrete volcanic ash to the Izu-Bonin and Mariana subduction zones. Geochem Geophys Geosyst 15:4369–4379
Scudder RP, Murray RW, Schindlbeck JC, Kutterolf K, Hauff F, Underwood MB, Gwizd S, Lauzon R, McKinley CC (2016) Geochemical approaches to the quantification of dispersed volcanic ash in marine sediment. Prog Earth Planet Sci:3. https://doi.org/10.1186/s40645-015-0077-y
Sigurdsson H, Leckie RM, Acton GD, Shipboard SP (1997) Caribbean volcanism, cretaceous/tertiary impact, and ocean climate history: synthesis of leg 165. Proc Integr Ocean Drill Program Initial Rep 165:862
Sillén LG (1967) The ocean as a chemical system. Science 156:1189–1197
Straub SM, Schmincke HU (1998) Evaluating the tephra input into Pacific Ocean sediments: distribution in space and time. Geol Rundsch 87:461–476
Straub SM, Woodhead JD, Arculus RJ (2015) Temporal evolution of the Mariana arc: mantle wedge and subducted slab controls revealed with a tephra perspective. J Petrol 56:409–439
Stuart F. M., Lee M. R. (2012) Micrometeorites and extraterrestrial He in a ferromanganese crust from the Pacific Ocean. Chem Geol 322–323, 209–214. https://doi.org/10.1093/petrology/egv005
Tada R (1991) Compaction and cementation in siliceous rocks and their possible effect on bedding enhancement. In: Einsele G, Ricken W, Seilacher A (eds) Cycles and events in stratigraphy. Springer, New York, pp 480–491
Takebe M (2005) Carriers of rare earth elements in Pacific deep-sea sediments. J Geol 113:201–215
Tanner PWG, Armstrong HA, Owen AW (2013) Rare earth element and La-Th-Sc analysis of cherts from the highland border complex, Scotland: geochemical determination of the sedimentary environment in greenschist facies rocks. Scott J Geol 49:15–31
Trendall AF, Morris RC (eds) (1983) Iron formations: facts and problems. Elsevier, Amsterdam, p 558
Von Damm KL, Edmond JM, Grant B, Walden B, Weiss RF (1985) Chemistry of submarine hydrothermal solutions at 21 N, East Pacific rise. Geochim Cosmochim Acta 49:2197–2220
Vonderhaar DL, McMurtry GM, Garge-Schoenberg D, Stueben D, Esser BK (2000) Platinum and other related element enrichments in Pacific ferromanganese crust deposits. In: Glenn CR, Prevot-Lucas L, Lucas J (eds) Marine authigenesis: from global to microbial, vol 66, Special Publication. Society for Sedimentary Geology, Tulsa, pp 287–309
Wang Y, Xu H, Merino E, Konishi H (2009) Generation of banded iron formations by internal dynamics and leaching of oceanic crust. Nat Geosci 2:781–784

Wen X, DeCarlo EH, Li YH (1997) Inter-element relationships in ferromanganese crusts from the central Pacific Ocean: their implications for crust genesis. Mar Geol 136:277–297
Williams LA, Crerar DA (1985) Silica diagenesis, II. General mechanisms. J Sediment Res 55:312–321
Zhou L, Kyte FT (1992) Sedimentation history of the South Pacific pelagic clay province over the last 85 million years inferred from the geochemistry of Deep Sea drilling project hole 596. Paleoceanography 7:441–465
Ziegler CL, Murray RW, Hovan SA, Rea DK (2007) Resolving eolian, volcanogenic, and authigenic components in pelagic sediment from the Pacific Ocean. Earth Planet Sci Lett 254:416–432

Mass Transfer

Peter C. Lichtner
OFM Research—Southwest, Santa Fe, NM, USA

Definition

Mass transfer involves the movement of matter from one location to another or from one phase to another, through the processes of advection, diffusion, dispersion, and chemical reaction (Lichtner 1996). For many applications in geochemistry, a porous medium must be considered which consists of voids filled with liquid and gas and a solid framework made up of aggregates of mineral grains. To describe such systems mathematically, the concept of a continuum is used in which the properties of the system are assumed to vary continuously over space, with the possible exception of material discontinuities at boundaries. The existence of a representative elemental volume, or REV, which characterizes the system locally is assumed. The REV is large compared to grain and pore sizes so that it is possible to define meaningful average quantities but small compared to variations in the fundamental variables describing the system, such as temperature, pressure, and solute concentration. It should be noted that the continuum formulation does not account for the distribution of solids and pore geometry within a REV.

Diffusive Flux

Diffusive mass transfer takes place in response to a gradient in concentration, or more generally chemical potential, according to Fick's law which in a pure phase has the form

$$\vec{J}_i = -D\vec{\nabla}C_i, \tag{1}$$

for the ith chemical constituent with concentration C_i, where D is the diffusion coefficient and where the gradient operator $\vec{\nabla}$ is defined as $\vec{\nabla} = (\partial/\partial x, \partial/\partial y, \partial/\partial z)$. Thus, for example, the x-component of the flux describes diffusion along the x-axis according to

$$(J_i)_x = -D\frac{\partial C_i}{\partial x}. \tag{2}$$

The diffusion coefficient is actually species dependent; however, this leads to a rather complicated description with the introduction of an electric field to enforce charge balance in the case of diffusion of cations and anions (Haase 1969; Lichtner 1985; Lichtner 1996).

In a porous medium, the diffusive flux within a pore volume is related to the bulk flux by

$$A_{\text{pore}}J_{\text{pore}} = AJ, \tag{3}$$

where J denotes the bulk diffusive flux and J_{pore} the diffusive flux through the pore space. It follows that

$$J = \frac{A_{\text{pore}}}{A}J_{\text{pore}}. \tag{4}$$

It is generally assumed that the areal porosity is equal to the volumetric porosity

$$\varphi = \frac{A_{\text{pore}}}{A} = \frac{V_{\text{pore}}}{V}, \tag{5}$$

where A_{pore} and V_{pore} denote the cross-sectional pore area and pore volume, respectively, with bulk area A and volume V. In addition, the diffusive flux in a porous medium is modified by the tortuosity τ representing the length of a fluid pathway between two points compared to a straight line. The diffusive flux in a porous medium then becomes

$$\vec{J}_i = -\varphi\tau D\,\vec{\nabla}C_i. \tag{6}$$

The tortuosity is also considered to be a function of porosity through various empirical constitutive relations.

Another mass transfer process occurring in porous media is dispersion typically described as a Fickian-like process but requiring a dispersion tensor (Bear and Cheng 2010). The tensorial property accounts for dispersive mass transfer along and perpendicular to the direction of flow as opposed to the coordinate axes. However, there is evidence that the process is not Fickian (see Bear and Cheng (2010) for more details).

Advective Flux

Advective transport describes the movement of some quantity via the bulk fluid flow, for example, flow through a pipe, column filled with sand, or a river. For flow in a porous

medium, Darcy's law is used in which the volumetric flow rate q, a vector, is given by in the absence of gravity

$$\vec{q} = -\frac{k}{\mu}\vec{\nabla} p, \tag{7}$$

proportional to the rock permeability k and pressure gradient $\vec{\nabla} p$ and inversely proportional to the fluid viscosity μ. The advective flux of the ith constituent has the form

$$\vec{F}_i = \vec{q}\, C_i. \tag{8}$$

The Darcy velocity is related to the average pore velocity $\vec{v}$ through the porosity φ

$$\vec{v} = \frac{\vec{q}}{\varphi}. \tag{9}$$

Chemical Reactions

Chemical reactions describe mass transfer within a single phase (homogeneous reactions) or between two or more phases (heterogeneous reactions). This form of mass transfer may be formulated in various representations. For homogeneous reactions mass transfer is described through a reaction rate Γ_r of the rth reaction that can be written in the general form

$$\varnothing \rightleftharpoons \sum_i \nu_{ir} A_i, \tag{10}$$

with stoichiometric coefficients ν_{ir}, dimensionless constants giving the number of moles of the ith chemical constituent in the rth reaction and assigned as positive for products, negative for reactants as the reaction proceeds from left to right, and zero if the species does not occur in the reaction. The reaction rate is defined by

$$\frac{1}{\nu_{ir}}\frac{dC_i}{dt} = \Gamma_r, \quad \nu_{ir} \neq 0, \tag{11}$$

and is the same for all species involved in the reaction.

For heterogeneous reactions, however, involving more than one phase the situation is much more complicated (Lichtner 2016). One approach is to treat heterogeneous reactions in the same manner as a homogeneous reaction through the use of the mineral-specific surface area—area per unit volume—and this is the approach taken in what follows. The rate is then averaged over a REV. An alternative, but more complex approach, is to impose boundary conditions at the liquid–solid interface which equates the reaction rate at the surface to the solute flux. Such an approach is used in pore-scale models.

Reaction rates may be calculated either by specifying a kinetic rate law or assuming conditions of local equilibrium and imposing law of mass action constraints to calculate the rate. In the case of mineral reactions, the latter assumption leads to the formation of chemical shock fronts.

The reaction rate for local chemical equilibrium Γ_r^{leq} is obtained in the limit as the kinetic rate constant approaches infinity. A typical rate expression corresponding to Eq. 10 has the form

$$\Gamma_r = k_r\left(1 - \frac{Qr}{K_r}\right), \tag{12}$$

with activity product

$$Q_r = \prod a_i^{\nu_{ir}}. \tag{13}$$

For a finite rate constant k_r, equilibrium is achieved when

$$K_r = Q_r, \tag{14}$$

which implies the reaction rate is zero. However, direct calculation in the limit $k_r \to \infty$ gives the indeterminate result

$$\Gamma_r^{\text{leq}} = \lim_{k_r \to \infty} \Gamma_r \to \infty \times 0 \tag{15}$$

To obtain the actual value for the local equilibrium rate, it is necessary to solve the reactive transport equations constrained by the corresponding algebraic mass action relations given by Eq. 14.

Mass Conservation

From the constituent fluxes for diffusion, advection, and reaction, mass conservation equations can be derived. Given a finite bulk volume V of a porous medium with porosity φ, the change in the number of constituents inside the volume can be related to the constituents entering and leaving the volume and their internal generation and consumption by the conservation equation

$$\frac{d}{dt}\int_V \varphi C_i dV = -\int_S \left(\vec{F}_i + \vec{J}_i\right).\, \vec{n}\, dS + \int_V \Gamma_{id} V, \tag{16}$$

where S denotes the surface of the volume V, $\vec{n}$ denotes the unit normal to the surface, and Γ_i represents the reaction rate or source/sink term, which, for example, could be associated with the presence of a well. The minus sign multiplying the surface integral occurs because the flux of matter flowing out of the volume is taken to be positive.

The finite volume conservation equation can be converted into a local conservation equation (meaning at a point $\vec{r}$ in

space) by making use of Gauss' equation. This equation states that the integral of the divergence of a vector field over a finite volume is equal to the integral over its surface according to the equation

$$\int_S \vec{U} \cdot \vec{n}\, dS = \int_V \vec{\nabla} \cdot \vec{U}\, dV \tag{17}$$

Applying Gauss' equation to the finite volume conservation equation enables the surface integral to be converted to a volume integral

$$\int_S \left(\vec{F}_i + \vec{J}_i\right) \cdot \vec{n}\, dS = \int_V \vec{\nabla} \cdot \left(\vec{F}_i + \vec{J}_i\right) dV \tag{18}$$

Substituting this relation back into Eq. 16 and collecting all terms inside the volume integral then yields

$$\int_V \left\{ \frac{\partial}{\partial t} \varphi C_i + \vec{\nabla} \cdot \left(\vec{F}_i + \vec{J}_i\right) - \Gamma_i \right\} dV = 0. \tag{19}$$

Since the volume is completely arbitrary, in order for the integral to vanish identically, it is necessary that the integrand vanishes leading to the local conservation equation

$$\frac{\partial}{\partial t} \varphi C_i + \vec{\nabla} \cdot \left(\vec{F}_i + \vec{J}_i\right) = \Gamma_i. \tag{20}$$

This is a partial differential equation representation of the finite volume conservation equation for the *i*th constituent. The equation relates the change in concentration at a point in space based on a continuum representation of a porous medium to the divergence of the flux and generation rate at that point. For immobile species such as minerals, the flux terms are zero.

To fully describe the coupling between the various properties caused by changes in material properties such as porosity, tortuosity, permeability, and others due to chemical reactions, additional constitutive relations are required that have not been discussed here. These constitutive equations can result in reaction instabilities, for example, producing such effects as wormhole dissolution patterns. However, they are empirical relations that are not well understood. Mineral surface and its change with reaction is one such relation that is very difficult to quantify.

Applications

There are numerous applications of the reactive transport equations to various problems both at laboratory and field scales. These include nuclear waste disposal, geothermal energy, biogeochemical processes, and issues related to climate change such as permafrost degradation.

Geochemical processes such as contaminant migration including colloid-facilitated transport and colloid filtration, karst formation, interaction between soil and atmosphere in climate modeling, geochemical weathering (Moore et al. 2012), and many others have been described with the aid of reactive transport equations (Appelo and Postma 1993; Steefel et al. 2005).

Recently, reactive transport equations have been applied to a wide spectrum of diverse processes including colloid-facilitated transport of sulfonamides in groundwater arising from dissolved organic matter (Zhou et al. 2016).

Finally, the single continuum formulation can be extended to multiple interacting continua to account for fractured porous media characterized by a bimodal distribution in material properties corresponding to fractures and the rock matrix (Lichtner and Karra 2014).

Because of a large number of equations that are necessary to solve simultaneously for large-scale multicomponent problems, complex computer codes have been developed to solve the reactive transport equations using massively parallel computing machines with hundreds of thousands of processor cores (Hammond and Lichtner 2010).

Summary

Mass transfer consists of contributions from advection, diffusion, and chemical reactions. These processes are coupled through mass conservation equations resulting in a system of generally nonlinear partial differential equations that must be solved numerically. The theory has been applied to a wide set of diverse problems in geochemical systems.

References

Appelo CAJ, Postma D (1993) Geochemistry, groundwater and pollution. Balkema, Rotterdam. 536 p

Bear J, Cheng AH-D (2010) Modeling groundwater flow and contaminant transport, Theory and applications of transport in porous media, vol 23. Springer, New York. 834 p

Haase R (1969) Thermodynamics of irreversible processes. Addison-Wesley, Boston. 509 p

Hammond GE, Lichtner PC (2010) Field-scale model for the natural attenuation of uranium at the Hanford 300 area using high performance computing. Water Resour Res 46:1–31. https://doi.org/10.1029/2009WR008819

Lichtner PC (1985) Continuum model for simultaneous chemical reactions and mass transport in hydrothermal systems. Geochim Cosmochim Acta 49:779–800

Lichtner PC (1996) Continuum formulation of multicomponent-multiphase reactive transport. In: Lichtner PC, Steefel CI, Oelkers EH (eds) Reactive transport in porous media, reviews in mineralogy, vol 34. The Mineralogical Society of America, Washington, DC, pp 1–81

Lichtner PC (2016) Kinetic rate laws invariant to scaling the mineral formula unit. Am J Sci 316:437–469

Lichtner PC, Karra S (2014) Modeling multiscale-multiphase-multicomponent reactive flows in porous media: application to CO_2 sequestration and enhanced geothermal energy using PFLOTRAN. In: Al-Khoury R, Bundschuh J (eds) Computational models for CO_2 geo-sequestration & compressed air energy storage. CRC Press, Boca Raton, pp 81–136

Moore J, Lichtner PC, White AF, Brantley SL (2012) Using a reactive transport model to elucidate differences between laboratory and field dissolution rates in regolith. Geochim Cosmochim Acta 93:235–261

Steefel CI, DePaolo DJ, Lichtner PC (2005) Reactive transport modeling: an essential tool and a new research approach for the Earth sciences. Earth Planet Sci Lett 240:539–558

Zhou D, Thiele-Bruhn S, Arenz-Leufen MG, Jacques D, Lichtner P, Engelhardt I (2016) Impact of manure-related DOM on sulfonamide transport in arable soils. J Contam Hydrol 192:118–128

Mercury

Charles N. Alpers
U.S. Geological Survey, California Water Science Center, Sacramento, CA, USA

Element Data
Atomic Symbol: **Hg**
Atomic Number: **80**
Atomic Weight: 200.592 g/mol
Isotopes and abundances: ^{196}Hg 0.15%, ^{198}Hg 9.97%, ^{199}Hg 16.87%, ^{200}Hg 23.1%, ^{201}Hg 13.18%, ^{202}Hg 29.86%, ^{204}Hg 6.87%
1 Atm Melting Point: −38.85 °C
1 Atm Boiling Point: 356.66 °C
Common Valences: 0, 1+, 2+
Ionic Radii: 97 pm (3-fold, 1+), 119 pm (4-fold, 1+), 69 pm (2-fold, 2+), 96 pm (4-fold, 2+), 102 pm (6-fold, 2+), 114 pm (8-fold, 2+)
Pauling Electronegativity: 2.0
First Ionization Potential: 1007.1 kJ/mol
Chondritic (CI) Abundance: 13.6 mg/kg
Silicate Earth Abundance: 0.006 mg/kg
Crustal Abundance: 0.05 mg/kg
Seawater Abundance: 0.05×10^{-9} kg/L
Core Abundance: 0.05 mg/kg

Properties

Mercury is a metallic element that is liquid at room temperature, silver in color, and very dense. The metal occurs primarily as a sulfide (cinnabar) in the Earth's crust, a vapor in the Earth's atmosphere, and an aqueous complex with dissolved organic matter (DOM) in natural waters. Mercury forms amalgams with many other metals, including copper, lead, gold, and silver. Monomethylmercury (CH_3Hg^+ or MeHg), produced primarily by conversion of Hg^{2+} by anaerobic microbes, is toxic to human and ecological receptors.

History and Use

Mercury is one of the seven metals known since antiquity, along with copper, gold, iron, lead, silver, and tin. Its name derives from the Roman god Mercurius, known for speed and mobility. The atomic symbol Hg is derived from the Greek *hydrargyrum* meaning water silver, in reference to its liquid nature and color at standard temperature and pressure. A common name for liquid, elemental mercury is quicksilver. The ancient, alchemical symbol for the element mercury (Fig. 1) is the same symbol used for the planet Mercury, the only such pairing.

Ancient civilizations used mercury for ceremonial and symbolic purposes; large quantities of the pure liquid have been found in tombs in China, Egypt, and Central America. Alchemists tried for centuries to make precious metals from mercury and various forms of sulfur. The failure of these efforts helped lead to modern chemistry.

Large mercury mines at Almadén, Spain; Idrija, Slovenia; and Huancavelica, Peru accounted for most of global mercury production prior to 1850 CE. Between 1850 and 2000 CE, significant mercury production continued in Spain and Slovenia and also took place in the United States (primarily California), Italy, China, Mexico, and the former USSR (Hylander and Meili 2003).

Historically, mercury was used for recovery of gold and silver by amalgamation, since at least 500 BCE. Large-scale precious-metal mining operations phased out amalgamation in favor of cyanide extraction in the early 1900s; however, artisanal miners in many countries continue to use mercury (Telmer and Veiga 2009). Mining and mineral processing have contributed millions of kg of mercury to the environment, and mercury-contaminated landscapes continue to pose environmental challenges.

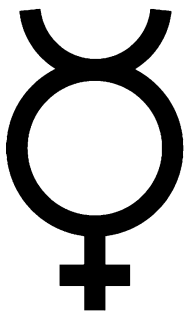

Mercury, Fig. 1 Alchemical symbol for mercury

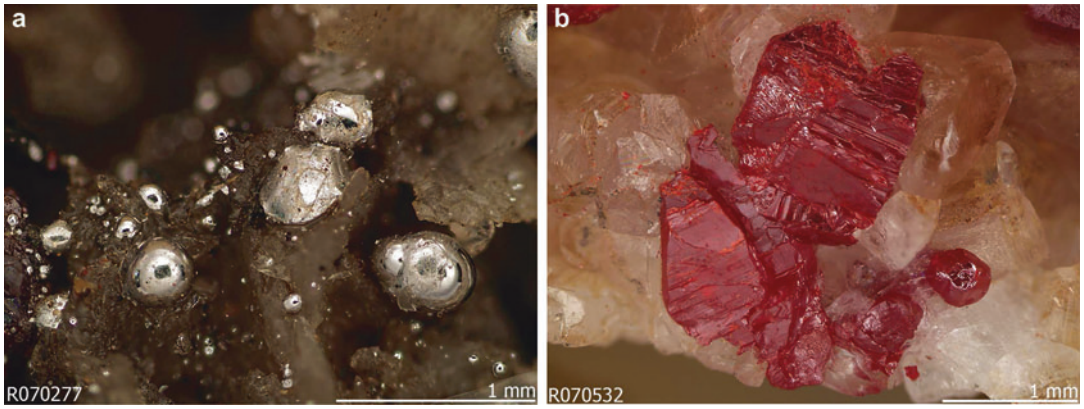

Mercury, Fig. 2 Photographs of mercury minerals. (**a**) native mercury (Hg), RRUFF 070277, in massive and drusy quartz from the Socrates mine, Sonoma County, California, USA; (**b**) cinnabar (HgS), RRUFF 070532, on calcite from Caracas, San Luis Potosi, Mexico; from Hazen et al. (2012); used by permission from the Mineralogical Society of America and from RRUFF (Lafuente et al. 2015)

Other industrial uses of mercury have included pigment (vermillion), explosives (fulminate), medical, dental, agricultural (fungicide), electrical devices, measuring instruments, lighting, batteries, catalysts, paint, and chlor-alkali processing (Hylander and Meili 2005). Most of these industrial uses have been phased out, especially after information regarding mercury toxicity became widely known in the late 1960s.

Isotopes and Cosmochemistry

There are seven stable isotopes of mercury: ^{196}Hg, ^{198}Hg, ^{199}Hg, ^{200}Hg, ^{201}Hg, ^{202}Hg, and ^{204}Hg. Of 33 known radioisotopes, the two longest living are ^{194}Hg, with a half-life ($t_{½}$) of 444 yr, and ^{203}Hg ($t_{½} = 0.128$ yr).

Stable isotopes of mercury are increasingly being used to trace mercury sources and biogeochemical processes in the environment (see *Mercury Isotopes*).

Mineralogy and Geochemistry

Based on Goldschmidt's classification, mercury is a chalcophile element. In minerals, mercury cations bond to oxygen, other chalcogenides (As, S, Sb, Se, and Te), and halides (Br, Cl, and I), as well as with arsenate, carbonate, phosphate, silicate, sulfate, and other anions (Hazen et al. 2012). The most common mercury minerals in the Earth's crust are cinnabar (α-HgS, rhombic) (Fig. 2), metacinnabar (β-HgS, cubic), and livingstonite ($HgSb_4S_8$, monoclinic); mercury also occurs in solid solution in sulfides (e.g., sphalerite, ZnS, cubic) and sulfosalts (e.g., tetrahedrite-tennantite, $(Cu,Fe)_{10}(Fe,Zn)_2(Sb,As)_4S_{13}$, cubic). As of 2012, there were 90 known minerals with mercury as an essential or important constituent (Hazen et al. 2012).

Because of its high volatility, mercury has low abundance in the solar photosphere and is greatly depleted in most meteorites (e.g., Allende CV chondrite) relative to CI chondrites, the most primitive meteorite class. Grains of HgS found in CM chondrites (Devouard et al. 1998) may have formed by aqueous alteration rather than directly from the solar nebula. Mercury may have been incorporated in meteorite parent bodies as a trace element in metal alloys, Fe-Ni sulfides, or as a chemisorbed species (Lauretta et al. 1999).

On Earth, the global mercury cycle features fluxes to the atmosphere and hydrosphere from natural sources including volcanoes, geothermal areas, forest fires, erosion, evasion from saline and fresh waterbodies, and soil degasification and also from anthropogenic sources including fossil-fuel combustion, chlor-alkali plants, mining, and other industrial pollution (Fig. 3). In the atmosphere, Hg^0 has an average residence time of about 6 months and is converted to Hg^{2+}, a more soluble form that is incorporated in precipitation and dry deposition (Fitzgerald and Lamborg 2014). Model results accounting for pre-1850 anthropogenic emissions (Amos et al. 2013) indicate that 57–60% of present-day deposition represents legacy anthropogenic mercury previously deposited and subsequently reemitted, ~26% is from primary anthropogenic emissions, and 13–17% is natural (Fig. 3). The largest anthropogenic Hg emissions in 2010 were from artisanal and small-scale gold mining (37%), coal burning (24%), nonferrous metal production (10%), and cement production (9%) (UNEP 2013). Releases of Hg to water are dominated by point sources from nonferrous metal production and consumer product waste, with smaller contributions from chlor-alkali plants and oil refining; nonpoint sources of Hg from contaminated sites are primarily from Hg and precious-metal mining sites (UNEP 2013).

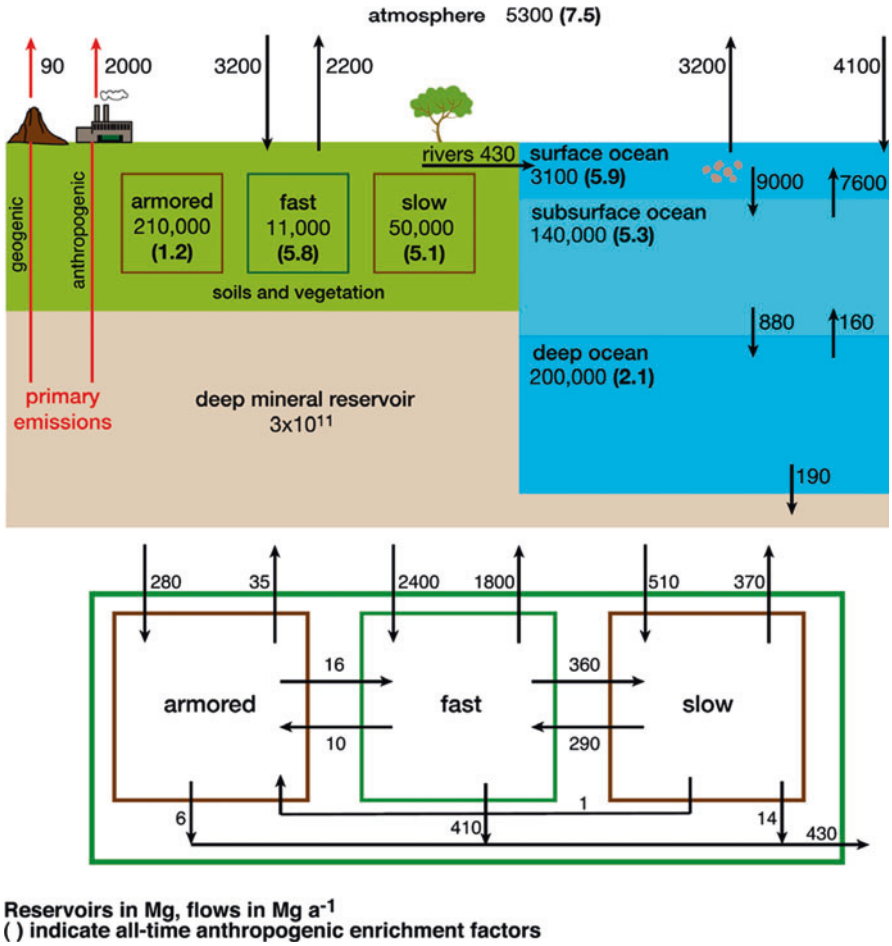

Mercury, Fig. 3 Simulated present-day global Hg budget and all-time anthropogenic enrichments factors. Terrestrial-atmosphere exchange is given in the *top panel* for the sum of terrestrial reservoirs. The *bottom panel* shows the breakdown and cycling between the different terrestrial reservoirs. All terrestrial reservoirs receive inputs from Hg^{2+} deposition (fast = 800, slow = 510, and armored = 280 Mg yr^{-1}). The fast reservoir also receives inputs from Hg^0 deposition (1600 Mg yr^{-1}). All terrestrial reservoirs lose Hg through respiration (fast = 520, slow = 360, and armored = 30 Mg yr^{-1}) and biomass burning (fast = 320, slow = 9, and armored = 5 Mg yr^{-1}). Photoreduction from the fast terrestrial reservoir is 950 Mg yr^{-1} (From Amos et al. (2013); used by permission from John Wiley and Sons and the American Geophysical Union)

Aqueous Behavior

According to hard and soft acids and bases theory, Hg^{2+} is a soft cation, which has stronger binding affinity with soft anions relative to hard anions ($SeH^- > SH^- > OH^- > Br^- > Cl^- > F^-$, Riccardi et al. 2013). In natural waters, dissolved Hg^{2+} has a strong affinity for DOM. Laboratory experiments (Haitzer et al. 2002, 2003) and spectroscopic studies using extended X-ray absorption fine structure (Xia et al. 1999) have demonstrated that aqueous Hg^{2+} binds strongly to thiol/sulfhydryl (SH^-) groups on DOM. In surface waters carrying suspended sediment, inorganic mercury transport is dominated by particulates, which reach highest concentration during high-flow conditions.

Some microbes convert Hg^{2+} to MeHg, typically at anoxic to sub-oxic conditions in the water column or in shallow sediments of lakes, reservoirs, stream channels, floodplains, estuaries, and the oceans. Sulfate-reducing bacteria and iron-reducing bacteria are considered the primary agents in microbial methylation of Hg^{2+} (Gilmour et al. 1992; Ullrich et al. 2001; Fleming et al. 2006; Kerin et al. 2006).

The genetic basis for microbial methylation of Hg^{2+} was discovered by Parks et al. (2013); a corrinoid acts as a methyl carrier, and Fe-S proteins are electron donors for corrinoid cofactor reduction. Abiotic methylation of Hg^{2+} also occurs by reaction with humic matter (Weber 1993) or acetic acid (Gårdfeldt et al. 2003), and by sunlight-mediated Hg^{2+}-DOM interactions (Siciliano et al. 2005), but is considered to be minor compared with net microbial methylation in most environments (Ullrich et al. 2001). Nanoparticles of HgS may be bioavailable to Hg-methylating bacteria (Zhang et al. 2014) and may be stabilized against aggregation by DOM (Graham et al. 2012).

The net rate of Hg^{2+} methylation is the difference between rates of Hg^{2+} methylation and MeHg degradation (demethylation), which also takes place by both biotic and abiotic pathways. Microbial pathways of demethylation include reductive demethylation (producing CH_4) and oxidative demethylation (producing CO_2). The reductive demethylation pathway typically results in reduction of Hg^{2+} to Hg^0, whereas the oxidative pathway liberates Hg^{2+} that is available for re-methylation. Abiotic degradation of MeHg occurs by exposure to UV radiation.

The chemical speciation of Hg^{2+} influences its availability for methylation. Speciation of Hg^{2+} has been determined by pyrolysis (Biester and Nehrke 1997), selective extraction

(Bloom et al. 2003), and EXAFS (Kim et al. 2003). Experiments with mercury stable isotope tracers (Jonsson et al. 2012) have determined the following order of availability for methylation: aqueous Hg^{2+} > Hg^{2+}-NOM (natural organic matter) > Hg^{2+}-FeS (mackinawite) > α-HgS (cinnabar) > β-HgS (metacinnabar). Methylation of Hg^{2+} and exposure of aquatic organisms to MeHg may be disconnected spatially or temporally because of transport controls (Jonsson et al. 2014; Eagles-Smith et al. 2016).

Biological Utilization and Toxicity

Most research has indicated that mercury has no beneficial function and is toxic to all forms of life to varying degrees, depending on its chemical form. Recent findings suggest a possible physiological role for Hg^{2+} in bacteria, whose phototropic growth rate increased with increasing Hg^{2+} concentration (Grégoire and Poulain 2016).

In humans, MeHg is a neurotoxin that crosses the blood-brain barrier. At highest risk for health problems related to MeHg exposure are children under 18 and developing fetuses. Symptoms from severe exposure to MeHg (Minamata disease) include ataxia (loss of muscle control), numbness in extremities, sensory loss, speech impairment, and tremors; in infants with fetal exposure, symptoms include growth and developmental problems, mental retardation, microcephaly, and seizures (Harada 1995; Harada et al. 2005). Chronic exposure to lower levels of methylmercury (the "lesser Minamata" profile) is associated with dizziness; dysesthesia; fatigue; hair loss; hand and leg tremor; gastrointestinal upset; headache; insomnia; memory loss; metallic taste; nausea; pain in joints, back, or chest; staggering; and trouble thinking or preforming complex tasks (Fukuda et al. 1999; Hightower 2009). The principal pathway to human exposure is consumption of high-trophic-level fish with elevated methylmercury concentrations. Mercury fish consumption advisories in 49 of 50 states in the USA recommend limited or no consumption of Hg-contaminated fish, with more restrictive recommendations for more sensitive groups.

Dimethylmercury ($(CH_3)_2Hg$), which exists in pure form as a liquid with high vapor pressure, is even more neurotoxic to humans than monomethylmercury. The death of a researcher from a single exposure to "one to several drops" of dimethylmercury that permeated through a latex glove (Nierenberg et al. 1998) led to improved guidelines for safe handling (OSHA 1998).

Inhalation of mercury vapor can produce harmful effects on the human kidneys, lungs, and digestive, immune, and nervous systems and can be fatal. In the late 1800s, hatmakers who used mercury to create felt from animal hairs were exposed to mercury vapors leading to "mad hatter's" syndrome, also known as "the Danbury shakes" (Bigham et al. 2005). In addition to being neurotoxic, inorganic Hg^{2+} is nephrotoxic (kidneys), hematotoxic (blood), and genotoxic (DNA).

Ecological effects of MeHg have been documented in birds, fish, and mammals (Scheuhammer et al. 2007). Chronic effects include reproductive impairment. The primary pathway to ecological MeHg exposure is diet. MeHg biomagnifies by three- to fivefold per step in aquatic food webs, concentrating in proteins as cysteine complexes. Bioaccumulation factors (ratio of MeHg in organism to water) range from ~10^3 in phytoplankton to ~10^7 in predatory fish.

Summary

Mercury is a trace element that is concentrated in hydrothermal mineral deposits and active geothermal systems. It has a strong affinity for reduced sulfur, occurring primarily in sulfide minerals and as aqueous complexes with thiol functional groups on natural organic matter. Mercury has no known beneficial function in higher organisms and is differentially toxic depending on its speciation. Monomethylmercury, a potent neurotoxin, is readily bioaccumulated and biomagnifies with increasing trophic level in food webs. Mercury had many industrial uses historically, but most have been phased out because of toxicity concerns. Legacy sources of mercury from historical mining and other anthropogenic activity persist in many areas, and global mercury pollution continues from fossil-fuel combustion, affecting human health and ecosystems.

Cross-References

- ▶ Biogeochemistry
- ▶ Complexes
- ▶ Dissolved Organic Matter (DOM)
- ▶ Geothermal Systems
- ▶ Gold
- ▶ History of Geochemistry
- ▶ Iron
- ▶ Mercury Isotopes
- ▶ Mineralogy
- ▶ Native Minerals
- ▶ Natural Gas
- ▶ Ore Deposits
- ▶ Organic Geochemistry
- ▶ Oxidation-Reduction Reactions and Eh-pH (Pourbaix) Diagrams
- ▶ Periodic Table
- ▶ Silver
- ▶ Sulfide Minerals
- ▶ Sulfur

- ▶ Sulfur Cycle
- ▶ Trace Elements
- ▶ Volcanism
- ▶ Water

Bibliography

Amos HM, Jacob DJ, Streets DG, Sunderland EM (2013) Legacy impacts of all-time anthropogenic emissions on the global mercury cycle. Global Biogeochem Cycles 27:410–421. https://doi.org/10.1002/gbc.20040

Biester H, Nehrke G (1997) Quantification of mercury in soils and sediment – acid digestion versus pyrolysis. Fresenius J Anal Chem 358:446–452

Bigham G, Henry B, Bessinger B (2005) Mercury – a tale of two toxins. Nat Resour Environ 19:26–30

Bloom NS, Preus E, Katon J, Hiltner M (2003) Selective extraction to assess the biogeochemically relevant fraction of inorganic mercury in sediments and soils. Anal Chim Acta 479:233–248

Bloss FD (1994) Crystallography and crystal chemistry. Mineralogical Society of America, Washington DC. 293p

Devouard B, Lauretta DS, Buseck PR (1998) Chemical history of P and Hg in the early solar system: nebular vs. parent body processing. Paul Pellas symposium, Muséum National d'Histoire Naturelle, Paris, p 41, 23–24 July 1998

Eagles-Smith CA, Wiener JG, Eckley CS, Willacker JJ, Evers DC, Marvin-DiPasquale M, Obrist D, Fleck JA, Aiken GR, Lepak JM, Jackson AK, Webster JP, Stewart AR, Davis JA, Alpers CN, Ackerman JA (2016) Mercury in western North America: a synthesis of environmental contamination, fluxes, bioaccumulation, and risk to fish and wildlife. Sci Total Environ 568:1213–1226

Fitzgerald WF, Lamborg CH (2014) Geochemistry of mercury in the environment, Ch. 11.4. Treatise on geochemistry, 2nd edn. Elsevier BV. https://doi.org/10.1016/B978-0-08-095975-7.00904-9

Fleming EJ, Mack EE, Green PG, Nelson DC (2006) Mercury methylation from unexpected sources: molybdate-inhibited freshwater sediments and an iron-reducing bacterium. Appl Environ Microbiol 72:457–464

Fukuda Y, Ushijima K, Kitano T, Sakamoto M, Futatsuka M (1999) An analysis of subjective complaints in a population living a methylmercury-polluted area. Environ Res A 81:100–107

Gårdfeldt K, Munthe J, Stromberg D, Lindqvist O (2003) A kinetic study on the abiotic methylation of divalent mercury in the aqueous phase. Sci Total Environ 304:127–136

Gilmour CC, Henry EA, Mitchell R (1992) Sulfate stimulation of mercury methylation in freshwater sediments. Environ Sci Technol 26:2281–2287

Graham AH, Aiken GR, Gilmour CC (2012) Dissolved organic matter enhances microbial mercury methylation under sulfidic conditions. Environ Sci Technol 46:2715–2723

Grégoire DS, Poulain AJ (2016) A physiological role for Hg^{II} during phototrophic growth. Nat Geosci 9:121–125. https://doi.org/10.1038/ngeo2629

Haitzer M, Aiken GR, Ryan JN (2002) Binding of Hg(II) to dissolved organic matter: the role of the mercury-to-DOM concentration ratio. Environ Sci Technol 36:3564–3570

Haitzer M, Aiken GR, Ryan JN (2003) Binding of Hg(II) to dissolved organic matter: influence of pH and source of humic substances. Environ Sci Technol 37:2436–2441

Harada M (1995) Minimata disease: methylmercury poisoning in Japan caused by environmental pollution. Crit Rev Toxicol 25:1–24

Harada M, Fujino T, Oorui T, Nakachi S, Nou T, Kizaki T, Hitomi Y, Nakano N, Ohno H (2005) Follow-up study of mercury pollution in indigenous tribe reservations in the province of Ontario, Canada, 1975–2002. Bull Environ Contam Toxicol 74:689–697

Hazen RM, Golden J, Downs RT, Hystad G, Grew ES, Azzolini D, Sverjensky DA (2012) Mercury (Hg) mineral evolution: a mineralogical record of supercontinent assembly, changing ocean geochemistry, and the emerging terrestrial biosphere. Am Mineral 97:1013–1042

Hepler LG, Olofsson G (1975) Mercury: thermodynamic properties, chemical equilibria, and standard potentials. Chem Rev 75:585–602

Hightower JM (2009) Diagnosis: mercury – money, politics & poison. Island Press/Shearwater Books, Washington DC. 307 p

Hylander LD, Meili M (2003) 500 years of mercury production: global annual inventory by region until 2000 and associated emissions. Sci Total Environ 304:13–27. https://doi.org/10.1016/S0048-9697(02)00553-3

Hylander LD, Meili M (2005) The rise and fall of mercury: converting a resource to refuse after 500 years of mining and pollution. Crit Rev Environ Sci Technol 35:1–36. https://doi.org/10.1080/10643380490492485

Jonsson S, Skyllberg U, Nilsson MB, Westlund P-O, Shchukarev A, Lundberg E, Björn E (2012) Mercury methylation rates for geochemically relevant Hg^{II} species in sediments. Envron Sci Technol 46:11653–11659. https://doi.org/10.1021/es3015327

Jonsson S, Skyllberg U, Nilsson MB, Lundberg E, Andersson A, Björn E (2014) Differentiated availability of geochemical mercury pools controls methylmercury levels in estuarine sediment and biota. Nat Commun 5:4624. https://doi.org/10.1038/ncomms5624

Kerin E, Gilmour CC, Roden E, Suzuki MT, Coates JD, Mason RP (2006) Mercury methylation among the dissimilatory iron-reducing bacteria. Appl Environ Microbiol 72:7919–7921

Kim CS, Bloom NS, Rytuba JJ, Brown GE Jr (2003) Mercury speciation by X-ray absorption fine structure spectroscopy and sequential chemical extractions: a comparison of speciation methods. Environ Sci Technol 37:5102–5108

Lafuente B, Downs RT, Yang H, Stone N (2015) The power of databases: the RRUFF project. In: Armbruster T, Danisi RM (eds) Highlights in mineralogical crystallography. De Gruyter, Berlin, pp 1–30. https://doi.org/10.1515/9783110417104-003

Lauretta DS, Devouard B, Buseck PR (1999) The cosmochemical behavior of mercury. Earth Planet Sci Lett 171:35–47

Lide DR (ed) (2008) CRC handbook of chemistry and physics, 88th edn. Taylor & Francis Group, Boca Raton

McDonough WF (2005) Compositional model for the earth's core. In: Carlson RW (ed) The mantle and core. Elsevier Ltd, Oxford, pp 547–568

Nierenberg DW, Nordstren RE, Chang MB, Seigler RW, Blayney MB, Hochberg F, Toribara TY, Cernichiari E, Clarkson T (1998) Delayed cerebellar disease and death after accidental exposure to dimethylmercury. N Engl J Med 338:1672–1676

OSHA (Occupational Safety and Health Administration) (1998) Dimethylmercury. OSHA Hazard Information Bulletins. U.S. Department of Labor. https://www.osha.gov/dts/hib/hib_data/hib19980309.html. Accessed 15 Oct 2016

Palme H, O'Neill HSC (2014) Cosmochemical estimates of mantle composition. In: Turekian K, Holland HDH (eds) Treatise on geochemistry, vol 3.1, 2nd edn. Elsevier, Oxford, pp 1–39

Parks JM, Johs A, Podar M, Bridou R, Hurt RA Jr, Smith SD et al (2013) The genetic basis for bacterial mercury methylation. Science 339:1332–1335. https://doi.org/10.1126/science.1230667

Riccardi D, Guo H-B, Parks JM, Gu B, Summers AO, Miller SM, Liang L, Smith JC (2013) Why mercury prefers soft ligands. J Phys Chem Lett 4:2317–2322. https://doi.org/10.1021/jz401075b

Scheuhammer AM, Meyer MW, Sandheinrich MB, Murray MW (2007) Effects of environmental methylmercury on the health of wild birds, mammals, and fish. Ambio 36:12–18. https://doi.org/10.1579/0044-7447(2007)36[12:EOEMOT]2.0.CO;2

Siciliano SD, O'Driscoll N, Tordon R, Hill J, Beauchamp S, Lean DRS (2005) Abiotic production of methylmercury by solar radiation. Environ Sci Technol 39:1071–1077

Telmer KH, Veiga MM (2009) World emissions of mercury from artisanal and small scale gold mining. In: Pirrone N, Mason R (eds) Mercury fate and transport in the global atmosphere. Springer, Berlin, pp 131–172. https://doi.org/10.1007/978-0-387-93958-2_6

Ullrich SM, Tanton TW, Abdrashitova SA (2001) Mercury in the aquatic environment: a review of factors affecting methylation. Crit Rev Environ Sci Technol 31:241–293

UNEP (United Nations Environment Programme) (2013) Global mercury assessment 2013: sources, emissions, releases and environmental transport. UNEP Chemicals Branch, Geneva

Weber JH (1993) Review of possible paths for abiotic methylation of mercury(II) in the aquatic environment. Chemosphere 26:2063–2077

Xia K, Skyllberg UL, Bleam WF, Bloom PR, Nater EA, Helmke PA (1999) X-ray absorption spectroscopic evidence for the complexation of Hg(II) by reduced sulfur in soil humic substances. Environ Sci Technol 33:257–261

Zhang T, Kucharzyk KH, Kim B, Deshusses MA, Hsu-Kim H (2014) Net methylation of mercury in estuarine sediment microcosms amended with dissolved, nanoparticulate, and microparticulate mercuric sulfides. Environ Sci Technol 48:9133–9141. https://doi.org/10.1021/es500336j

Mercury Isotopes

Bridget A. Bergquist
Department of Earth Sciences, University of Toronto, Toronto, ON, Canada

Introduction

Mercury is a globally distributed pollutant that bioaccumulates in aquatic food webs, leading to dangerous exposure in humans and wildlife (Driscoll et al. 2013; Fitzgerald and Lamborg 2014). Despite decades of research, there are still knowledge gaps that hinder the understanding of both the modern and past Hg cycle and make it challenging to predict how changes in emissions and climate will affect the Hg cycle (Amos et al. 2013; Fitzgerald and Lamborg 2014; Amos et al. 2015). A rapidly growing tool to study Hg is Hg stable isotope geochemistry, which was largely driven by the discovery of large mass independent fractionation (MIF) of Hg isotopes both experimentally and in nature (Buchachenko et al. 2004; Bergquist and Blum 2007; Buchachenko et al. 2007). Hg is unique in that it exhibits several types of stable isotopic fractionation including conventional mass-dependent fractionation (MDF) and at least three types of MIF. Although Hg isotope geochemistry is a young field, both MDF and MIF signatures are already being used to successfully trace sources, quantify certain transformations of Hg, and understand bioaccumulation of Hg in the environment (see reviews: Bergquist and Blum 2009; Hintelmann 2012; Blum et al. 2014). Hg isotopes are also being developed as proxies of large volcanic inputs and other environmental changes in the geologic record (Grasby et al. 2016; Thibodeau and Bergquist 2016; Thibodeau et al. 2016).

Methods and Nomenclature

There are seven stable isotopes of Hg that undergo isotopic fractionation in nature: ^{196}Hg (0.15%), ^{198}Hg (9.97%), ^{199}Hg (16.87%), ^{200}Hg (23.1%), ^{201}Hg (13.18%), ^{202}Hg (29.86%), and ^{204}Hg (6.87%). All are measured simultaneously with high precision by cold vapor multicollector inductively coupled plasma mass spectrometry (CV-MC-ICPMS). Most methods introduce Hg to the mass spectrometer as Hg^0 vapor after reduction of Hg^{2+} in a solution, with the Hg^0vapor being stripped from the solution on a gas-liquid separator (Lauretta et al. 2001). One of the largest challenges with making accurate and high precision measurements by MC-ICPMS is that the instrument itself induces large instrumental mass fractionation, which is sensitive to sample matrix that needs to be corrected in order to obtain the natural isotopic composition of a sample. Blum and Johnson (2017) recently reviewed the state-of-the-art techniques and difficulties associated with Hg isotope measurements. In brief, the highest quality measurements quantitatively separate and purify Hg from complex matrices and use both strict sample-standard bracketing and a thallium internal monitor to correct for instrumental mass bias.

Hg isotopic values are reported using conventional delta notation (δ) as per mil (‰) deviations from the NIST 3133 reference material (Eq. 1) (Blum and Bergquist 2007).

$$\delta^{xxx}\mathrm{Hg} = \left[\left(^{xxx}\mathrm{Hg}/^{198}\mathrm{Hg}\right)_{\mathrm{sample}} / \left(^{xxx}\mathrm{Hg}/^{198}\mathrm{Hg}\right)_{\mathrm{NIST3133}} - 1\right] \times 1000 \quad (1)$$

where xxx is the mass of the Hg isotope (^{199}Hg, ^{200}Hg, ^{201}Hg, ^{202}Hg, ^{204}Hg). Most groups use the ^{202}Hg/^{198}Hg ratio (i.e., δ^{202}Hg) to report MDF.

MIF values of Hg are reported using capital delta notation (Δ) also in units of per mil (‰), which is the deviation in the measured isotope ratios from the theoretically predicted isotope ratios by MDF (Eqs. 2, 3, 4, and 5). Typically, kinetic MDF laws (Young et al. 2002) are used to estimate MIF unless authors are confident that equilibrium conditions existed in their study.

$$\Delta^{199}\mathrm{Hg} = \delta^{199}\mathrm{Hg} - \left(0.2520 \times \delta^{202}\mathrm{Hg}\right) \quad (2)$$

$$\Delta^{200}\mathrm{Hg} = \delta^{200}\mathrm{Hg} - \left(0.5024 \times \delta^{202}\mathrm{Hg}\right) \quad (3)$$

$$\Delta^{201}\mathrm{Hg} = \delta^{201}\mathrm{Hg} - \left(0.7520 \times \delta^{202}\mathrm{Hg}\right) \quad (4)$$

$$\Delta^{204}\mathrm{Hg} = \delta^{204}\mathrm{Hg} - \left(1.4930 \times \delta^{202}\mathrm{Hg}\right) \quad (5)$$

Mechanisms of Hg Isotope Fractionation

Much like the traditional stable isotope systems (i.e., C, O, S, H, N), Hg MDF is ubiquitous in nature and occurs during abiotic and biological redox, speciation, and phase changes. MDF occurs because atoms with different masses affect the vibrational energies and activation energies of molecules and their bonds as well as molecular and atomic velocities and diffusivity (Bigeleisen and Mayer 1947; Urey 1947; Bigeleisen 1949; Schauble 2004). Kinetic and equilibrium reactions follow MDF laws, and the relationships between the different isotopic ratios can be predicted using atomic masses.

In addition to MDF, Hg isotopes also exhibit a 10‰ range in MIF in natural samples (Blum et al. 2014). Unlike Hg MDF, large Hg MIF is thought only to occur in photochemical reactions, with different photochemical reactions displaying unique patterns of MIF for different isotopes of Hg. Because MIF signatures are only affected by a limited number of reactions, the extent and ratio of MIF from different isotopes is often preserved and can be used as a reliable tracer of different sources when the sources have different MIF signatures. At present, three different types of MIF are observed for Hg isotopes including (1) large odd-mass Hg MIF (odd-MIF) caused by magnetic isotope effect (MIE) during aqueous and heterogeneous surface photochemistry, (2) small odd-MIF caused by nuclear volume effect (NVE), and (3) even-mass Hg MIF (even-MIF) that is thought to occur during atmospheric photochemical gas phase reactions.

The largest Hg MIF is produced by the MIE, which occurs during kinetic reactions containing radical pair intermediates (Turro 1983; Buchachenko 2001). In particular during photochemical reactions, the MIE can change the rate of reactions for the odd Hg isotopes relative to the even isotopes because of their nonzero nuclear spin and nuclear magnetic moments, which interact with the magnetic moments of unpaired electrons. In addition, the radical pair intermediate must be long lived enough for the MIE to be expressed. Thus, the MIE is observed in aqueous or heterogeneous photochemical reactions, and not gas phase photochemical reactions, because the MIE requires a solvent cage (e.g., water) to extend the lifetime of the radical pair so that MIE can compete with dissociation into free radicals.

The other odd-MIF mechanism for Hg is the NVE, which is also referred to as the nuclear field shift effect, and results in smaller MIF for Hg (less than 0.5‰) (Estrade et al. 2009; Zheng and Hintelmann 2010; Ghosh et al. 2013). The NVE is only observed for heavier elements and arises due to nuclear volumes and charge radii not scaling linearly with mass when isotopes get bigger (Bigeleisen 1996; Schauble 2007). Even-odd differences arise because odd isotopes have nuclear charge radii that are smaller than what would be predicted by mass. Differences in nuclear charge radii affect bond strengths, which can result in isotope fractionation that does not correlate with the differences in isotope mass.

MIF Hg anomalies that are not odd isotope only are also observed in atmospheric samples and samples that have a high proportion of atmospherically derived Hg (Gratz et al. 2010; Chen et al. 2012; Demers et al. 2013; Rolison et al. 2013; Demers et al. 2015; Strok et al. 2015). These MIF anomalies are referred to as even-MIF, and currently the mechanism of even-MIF is not known and the isotope effect may affect both even and odd isotopes. It is proposed to occur during gas phase atmospheric photochemical oxidation of Hg^0 (Chen et al. 2012; Sun et al. 2016).

Hg MIF Cycles

Together both MDF and MIF are used to understand Hg cycling in the environment, but MDF is not as simple to summarize because MDF occurs during many processes including those that impart MIF. Thus, the simpler MIF cycles will be summarized here.

Hg exists in the atmosphere mostly in its reduced form, gaseous elemental Hg^0, which has a long residence time (~0.5 to 1 year) allowing it to be distributed globally (Fitzgerald and Lamborg 2014). Hg in the atmosphere is emitted from both primary and secondary sources with primary sources accounting for less than half of the total Hg emissions to the atmosphere (UNEP 2013; Fitzgerald and Lamborg 2014; Amos et al. 2015). Primary sources are dominantly anthropogenic today (e.g., coal combustion, gold mining). Most emissions are secondary sources with Hg being re-emitted back to the atmosphere after deposition from waters, soils, and biomass burning.

Hg that cycles through atmospheric, marine, and terrestrial reservoirs will likely acquire MIF through some sort of photochemistry (see Fig. 1). Gaseous Hg^0 in the atmosphere has slight negative odd-MIF, resulting from photochemical reduction in surface waters and cloud droplets. In contrast, atmospheric Hg^{2+} species have positive odd-MIF due to photochemical reduction in cloud droplets. When Hg deposits to surfaces, it deposits as either Hg^0 or Hg^{2+}. Soils tend to have negative odd-MIF because most of their Hg comes from Hg^0 that was taken up by plants, which uptake Hg^0 through their stomata and transfer it to soils by litterfall. Sediments far from runoff sources (e.g., open ocean sediments) that transport negative odd-MIF Hg from soils and surfaces tend to have positive odd-MIF Hg since their main source of Hg is through wet and dry deposition of Hg^{2+}. Many sediments

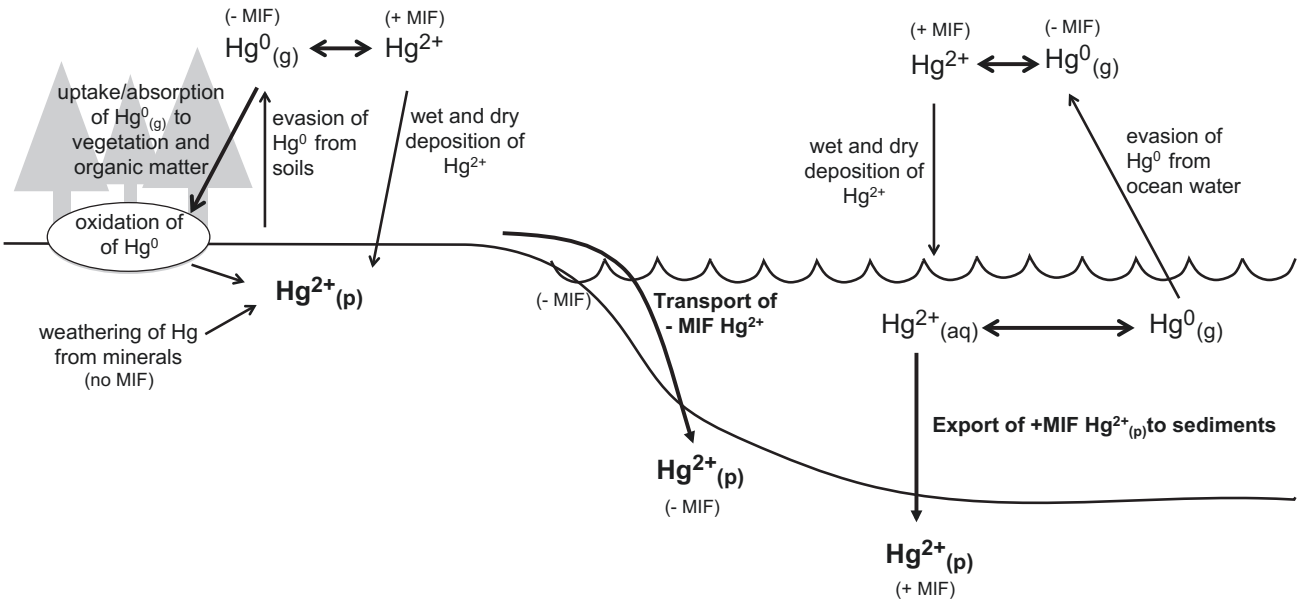

Mercury Isotopes, Fig. 1 A simplified schematic of the odd-MIF cycle of Hg isotopes. The +MIF and –MIF are the signature of the odd-MIF associated with the pool of Hg

receive Hg from both runoff and direct Hg^{2+} deposition and thus have isotopic compositions that are a mixture of Hg^0 and Hg^{2+} isotopic signatures.

Even-MIF is produced in the atmosphere and is thought to occur during photochemical gas phase oxidation of Hg^0. It is observed in atmospheric Hg^{2+} species, which have positive $\Delta^{200}Hg$ and negative $\Delta^{204}Hg$ (Gratz et al. 2010; Chen et al. 2012; Demers et al. 2013; Enrico et al. 2016). Because oxidized Hg^{2+} species are less than 10% of total atmospheric Hg, the oxidization of Hg^0 to Hg^{2+} imparts a bigger isotopic signature on the Hg^{2+} than the large Hg^0 pool. Thus, very little even-MIF is observed in Hg^0. Because of this, even-MIF is a good tracer of atmospheric inputs of Hg^{2+} species.

Select Applications

Tracing Isotopically Distinct Pools of Hg in Sediments and Surface Waters

One of the more practical applications of Hg isotopes, both MDF and MIF signatures, is source identification and tracing of Hg from anthropogenic sources in surface waters and ecosystems (e.g., Foucher et al. 2009; Feng et al. 2010; Perrot et al. 2010; Sonke et al. 2010; Gehrke et al. 2011a; Bartov et al. 2013; Foucher et al. 2013; Wiederhold et al. 2015; Donovan et al. 2016; Jimenez-Moreno et al. 2016). The success of this application is largely due to the particle-reactive behavior of Hg. Many studies show that the majority of Hg (>90%) in a diverse range of aquatic systems is transported in association with particles, dominantly particulate organic carbon and clays minerals (Benoit et al. 1998; Mason and Sullivan 1998; Roulet et al. 1998; Appleton et al. 2001; Lawson et al. 2001; Choe et al. 2003; Conaway et al. 2003). Because Hg released into aquatic systems quickly absorbs to particles and does not significantly participate in transformations that would lead to Hg isotopic fractionation, anthropogenic Hg released from point sources into aquatic systems often maintains its source signature. In addition, Hg from anthropogenic sources such as gold mining and industrial sources is typically isotopically distinct from background runoff from soils and land (see review: Blum et al. 2014).

An example of tracing multiple sources of Hg into a complex aquatic ecosystem was in San Francisco Bay. By analyzing Hg isotopes in the sediments, two distinct sources were observed entering the bay (Gehrke et al. 2011a). A clear pattern was observed with isotopically heavier Hg entering the southern parts of the bay from historic Hg mine waste and isotopically lighter sources impacting the more northern part of the bay, which were from historic gold mining and modern industrial Hg. In addition to sediments, the Hg contamination was traced into the food web (Gehrke et al. 2011b). Even though isotopic fractionation occurs during methylation, incorporation into the food web, and trophic transfer, the isotopic differences in the distinct sources of Hg entering the bay were maintained within fish.

Source Tracing in Atmospheric Samples

Because of the difficulties in collecting enough atmospheric Hg for isotopic analyses, the application of source tracing in the atmosphere is not as developed as aquatic source tracing. However, methods are improving and initial studies show that isotopic differences exist that will be useful for source

apportionment for both gaseous Hg^0 (Gratz et al. 2010; Rolison et al. 2013; Demers et al. 2015; Fu et al. 2016) and oxidized Hg^{2+} species in the atmosphere (Estrade et al. 2010; Gratz et al. 2010; Chen et al. 2012; Rolison et al. 2013; Sherman et al. 2015; Das et al. 2016; Huang et al. 2016; Xu et al. 2017). In particular, the many sources of Hg^0 to the atmosphere have large differences in the isotopic composition. This coupled with the relative stability of Hg^0 should allow for local sources to be distinguished from regional and global background signatures.

Tracing What Pools of Hg Are Bioaccumulated in the Food Web

Once in aquatic systems, Hg can be transformed into methylmercury (MeHg), the form of Hg that bioaccumulates in aquatic food webs and poses a health risk for humans and wildlife via fish consumption (Mason et al. 1995; Driscoll et al. 2013; Fitzgerald and Lamborg 2014). Methylation in the environment can happen in many environments, and the links between Hg sources, methylation, and MeHg in biota are not easy to trace. Because different pools of MeHg can have different isotopic signatures, Hg isotopes can be useful in understanding how Hg is getting into the food web. There are many studies of Hg isotopes in freshwater biota (e.g., Bergquist and Blum 2007; Gantner et al. 2009; Laffont et al. 2009; Perrot et al. 2010; Gehrke et al. 2011b; Kwon et al. 2012; Sherman and Blum 2013; Tsui et al. 2014; Kwon et al. 2015; Lepak et al. 2015; Xu et al. 2016) and marine biota (e.g., Senn et al. 2010; Blum et al. 2013; Zheng et al. 2015). Hg isotopes in fish and biota reflect many factors including where Hg is methylated, species of Hg accumulated, trophic level, what depth MeHg is foraged from, the residence time of MeHg, and the source of Hg for methylation.

Understanding Depositional Patterns of Hg to Soils

An exciting application of Hg isotopes is as a tool to quantify sources of Hg to soils (Demers et al. 2013; Jiskra et al. 2015; Enrico et al. 2016; Zheng et al. 2016; Obrist et al. 2017). Soils are one of the largest reservoirs of Hg, and they are important sinks of anthropogenic Hg as well as potential sources of Hg to downstream ecosystems and the atmosphere. Hg can be deposited to soils via Hg^0 uptake and adsorption by plants and soils or via dry and wet deposition of oxidized Hg^{2+} species, or Hg can weather from parent rock material. These three different sources of Hg have very different Hg isotopic signatures (both MDF and MIF), and isotopic mixing models can estimate the contribution of the different sources. All sites studied thus far are dominated by Hg^0 deposition, with deposition of Hg^{2+} species being mostly less than 30% and contributions from parent rock Hg even less. Furthermore, in a study of 10 sites across North America, Zheng et al. (2016) found that Hg isotopes in forest soils showed strong correlation to precipitation. The correlation is driven by a higher proportion of Hg^0 deposition at wetter sites, which is likely driven by their higher forest productivity (thus higher plant-derived Hg inputs) and more developed organic horizons that may enhance direct Hg^0 uptake.

Past Proxy of Volcanic Hg

In addition to understanding the modern cycle of Hg, Hg chemostratigraphy is being developed as a tool to investigate the connection between changes in volcanism and mass extinctions (see review: Bergquist 2017). Most of the largest extinctions on Earth are associated with large igneous province volcanism (LIPS), but whether these LIPS triggered the mass extinctions is disputed largely due to the difficulty in correlating evidence for LIPS with mass extinction records (Bond and Wignall 2014; Bond and Grasby 2017). Because large amounts of Hg are emitted from volcanism, it is argued that increases in Hg preserved in the sedimentary records with the fossils can be used as a proxy for increased volcanic inputs. However, this interpretation has been challenged (Font et al. 2016; Smit et al. 2016) and this has led to arguments over whether elevated Hg in marine sediments is actually due to increased volcanism versus other sources, increased preservation of Hg, or postdepositional enrichments of Hg.

Since different sources of Hg and mechanisms for enriching Hg in sediments may have different isotopic signatures, Hg isotopes can help resolve the source of elevated Hg during extinction events (Grasby et al. 2016; Thibodeau et al. 2016). Although there is not much data on volcanic Hg, it appears that volcanic Hg and Hg from biomass and organic rich rocks have very different isotopic signatures (Zambardi et al. 2009; Blum et al. 2014). Thibodeau et al. (2016) measured Hg and Hg isotopes across the end-Triassic mass extinction. Elevated Hg was observed throughout the extinction intervals, and biotic recovery did not occur until after Hg levels returned to background levels. The Hg isotopic signatures associated with the elevated Hg were consistent with volcanic Hg. Grasby et al. (2016) also observed elevated Hg through the end-Permian extinction, but the Hg isotopic signatures were more consistent with biomass and organic rich rocks. Thus, the Hg anomalies were interpreted to be from massive wildfires and increased soil erosion. There is a lot of potential for exploring the links between major biotic and environmental changes and volcanism in the past using Hg concentrations and Hg isotopes (Thibodeau and Bergquist 2016).

Summary

The field of Hg stable isotope geochemistry is a rapidly expanding field that has proven extremely useful in understanding and quantifying many aspects of the Hg

biogeochemical cycle. Furthermore, the application of Hg isotopes is now expanding beyond the Hg cycle. As more laboratories become capable of producing high quality data, it will be exciting to see what new discoveries Hg isotopes will help yield.

Cross-References

- Analytical Techniques
- Mercury
- Sulfur Isotopes
- Trace Elements
- Volcanic Gases

References

Amos HM, Jacob DJ, Streets DG, Sunderland EM (2013) Legacy impacts of all-time anthropogenic emissions on the global mercury cycle. Glob Biogeochem Cycles 27(2):410–421. https://doi.org/10.1002/gbc.20040

Amos HM et al (2015) Observational and modeling constraints on global anthropogenic enrichment of mercury. Environ Sci Technol 49(7):4036–4047. https://doi.org/10.1021/es5058665

Appleton JD, Williams TM, Orbea H, Carrasco M (2001) Fluvial contamination associatied with artisanal gold mining in the Ponce Enríquez, Portovelo-Zaruma and Nambija areas, Ecuador. Water Air Soil Pollut 131(1–4):19–39. https://doi.org/10.1023/A:1011965430757

Bartov G et al (2013) Environmental impacts of the Tennessee Valley Authority Kingston coal ash Spill. 1. Source apportionment using mercury stable isotopes. Environ Sci Technol 47(4):2092–2099. https://doi.org/10.1021/es303111p

Benoit J, Gilmour CC, Mason R, Riedel G, Riedel G (1998) Behavior of mercury in the Patuxent River estuary. Biogeochemistry 40(2–3):249–265. https://doi.org/10.1023/A:1005905700864

Bergquist BA (2017) Mercury, volcanism, and mass extinctions. Proc Natl Acad Sci 114(33):8675–8677. https://doi.org/10.1073/pnas.1709070114

Bergquist BA, Blum JD (2007) Mass-dependent and -independent fractionation of Hg isotopes by photoreduction in aquatic systems. Science 318(5849):417–420. https://doi.org/10.1126/science.1148050

Bergquist BA, Blum JD (2009) The odds and evens of mercury isotopes: applications of mass-dependent and mass-independent isotope fractionation. Elem 5(6):353–357. https://doi.org/10.2113/gselements.5.6.353

Bigeleisen J (1949) The relative velocities of isotopic molecules. J Chem Phys 17:675–678

Bigeleisen J (1996) Nuclear size and shape effects in chemical reactions. Isotope chemistry of the heavy elements. J Am Chem Soc 118(13):3676–3680

Bigeleisen J, Mayer MG (1947) Calculation of equilibrium constants for isotopic exchange reactions. J Chem Phys 15:261–267

Blum JD, Bergquist BA (2007) Reporting of variations in the natural isotopic composition of mercury. Anal Bioanal Chem 388(2):353–359. https://doi.org/10.1007/s00216-007-1236-9

Blum JD, Johnson MW (2017) Recent developments in mercury isotopic analysis, Reviews in Mineralogy and Geochemistry, Vol. 82 Non-Traditional Stable Isotopes, Chapter 17, 733–758

Blum JD, Popp BN, Drazen JC, Choy CA, Johnson MW (2013) Methylmercury production below the mixed layer in the North Pacific Ocean. Nat Geosci 6(10):879–884. https://doi.org/10.1038/ngeo1918

Blum JD, Sherman LS, Johnson MW (2014) Mercury isotopes in earth and environmental sciences. Annu Rev Earth Planet Sci 42:249–269. https://doi.org/10.1146/annurev-earth-050212-124107

Bond DPG, Grasby SE (2017) On the causes of mass extinctions. Palaeogeogr Palaeoclimatol Palaeoecol 478:3–29

Bond DPG, Wignall PB (2014) Large igneous provinces and mass extinctions: an update. Geol Soc Am Spec Pap 505:29–55

Buchachenko AL (2001) Magnetic isotope effect: nuclear spin control of chemical reactions. J Phys Chem A 105(44):9995–10011. https://doi.org/10.1021/jp011261d

Buchachenko AL, Kouznetsov DA, Shishkov AV (2004) Spin biochemistry: magnetic isotope effect in the reaction of creatine kinase with CH3HgCl. J Phys Chem 108(5):707–710

Buchachenko AL et al (2007) Magnetic isotope effect for mercury nuclei in photolysis of bis(p-trifluoromethylbenzyl)mercury. Dokl Phys Chem 413:39–41

Chen J, Hintelmann H, Feng X, Dimock B (2012) Unusual fractionation of both odd and even mercury isotopes in precipitation from Peterborough, ON, Canada. Geochim Cosmochim Acta 90:33–46. https://doi.org/10.1016/j.gca.2012.05.005

Choe K-Y, Gill GA, Lehman R (2003) Distribution of particulate, colloidal, and dissolved mercury in San Francisco Bay estuary. 1. Total mercury. Limnol Oceanogr 48(4):1535–1546. https://doi.org/10.4319/lo.2003.48.4.1535

Conaway CH, Squire S, Mason RP, Flegal AR (2003) Mercury speciation in the San Francisco Bay estuary. Mar Chem 80(2–3):199–225. https://doi.org/10.1016/S0304-4203(02)00135-4

Das R et al (2016) Mercury isotopes of atmospheric particle bound mercury for source apportionment study in urban Kolkata, India. Elementa-Sci Anthropocene 4: 1–12. https://doi.org/10.12952/journal.elementa.000098

Demers JD, Blum JD, Zak DR (2013) Mercury isotopes in a forested ecosystem: implications for air-surface exchange dynamics and the global mercury cycle. Glob Biogeochem Cycles 27(1):222–238. https://doi.org/10.1002/gbc.20021

Demers JD, Sherman LS, Blum JD, Marsik FJ, Dvonch JT (2015) Coupling atmospheric mercury isotope ratios and meteorology to identify sources of mercury impacting a coastal urban-industrial region near Pensacola, Florida, USA. Glob Biogeochem Cycles 29(10):1689–1705. https://doi.org/10.1002/2015GB005146

Donovan PM, Blum JD, Singer MB, Marvin-DiPasquale M, Tsui MTK (2016) Isotopic composition of inorganic mercury and methylmercury downstream of a historical gold mining region. Environ Sci Technol 50(4):1691–1702. https://doi.org/10.1021/acs.est.5b04413

Driscoll CT, Mason RP, Chan HM, Jacob DJ, Pirrone N (2013) Mercury as a global pollutant: sources, pathways, and effects. Environ Sci Technol 47(10):4967–4983. https://doi.org/10.1021/es305071v

Enrico M et al (2016) Atmospheric mercury transfer to peat bogs dominated by gaseous elemental mercury dry deposition. Environ Sci Technol 50(5):2405–2412. https://doi.org/10.1021/acs.est.5b06058

Estrade N, Carignan J, Sonke JE, Donard OFX (2009) Mercury isotope fractionation during liquid-vapor evaporation experiments. Geochim Cosmochim Acta 73(10):2693–2711. https://doi.org/10.1016/j.gca.2009.01.024

Estrade N, Carignan J, Donard OFX (2010) Isotope tracing of atmospheric mercury sources in an urban area of Northeastern France. Environ Sci Technol 44(16):6062–6067. https://doi.org/10.1021/es100674a

Feng X et al (2010) Tracing mercury contamination sources in sediments using mercury isotope compositions. Environ Sci Technol 44(9):3363–3368. https://doi.org/10.1021/es9039488

Fitzgerald WF, Lamborg CH (2014) Geochemistry of mercury in the environment. In: Treatise of geochemistry, vol 11, 2nd edn. Elseveir, Amesterdam, pp 91–129

Font E et al (2016) Mercury anomaly, Deccan volcanism and the end-Cretaceous mass extinction, REPLY. Geol Forum 44(3):e382. https://doi.org/10.1130/G37717Y.1

Foucher D, Ogrinc N, Hintelmann H (2009) Tracing mercury contamination from the Idrija mining region (Slovenia) to the Gulf of Trieste using Hg isotope ratio measurements. Environ Sci Technol 43(1):33–39. https://doi.org/10.1021/es801772b

Foucher D, Hintelmann H, Al TA, MacQuarrie KT (2013) Mercury isotope fractionation in waters and sediments of the Murray Brook mine watershed (New Brunswick, Canada): tracing mercury contamination and transformation. Chem Geol 336:87–95. https://doi.org/10.1016/j.chemgeo.2012.04.014

Fu XW, Marusczak N, Wang X, Gheusi F, Sonke JE (2016) Isotopic composition of gaseous elemental mercury in the free troposphere of the Pic du Midi Observatory, France. Environ Sci Technol 50(11):5641–5650. https://doi.org/10.1021/acs.est.6b00033

Gantner N, Hintelmann H, Zheng W, Muir DC (2009) Variations in stable isotope fractionation of Hg in food webs of Arctic Lakes. Environ Sci Technol 43(24):9148–9154. https://doi.org/10.1021/es901771r

Gehrke GE, Blum JD, Marvin-DiPasquale M (2011a) Sources of mercury to San Francisco Bay surface sediment as revealed by mercury stable isotopes. Geochim Cosmochim Acta 75(3):691–705. https://doi.org/10.1016/j.gca.2010.11.012

Gehrke GE, Blum JD, Slotton DG, Greenfield BK (2011b) Mercury isotopes link mercury in San Francisco Bay forage fish to surface sediments. Environ Sci Technol 45(4):1264–1270. https://doi.org/10.1021/es103053y

Ghosh S, Schauble EA, Couloume GL, Blum JD, Bergquist BA (2013) Estimation of nuclear volume dependent fractionation of mercury isotopes in equilibrium liquid-vapor evaporation experiments. Chem Geol 336:5–12. https://doi.org/10.1016/j.chemgeo.2012.01.008

Grasby SE et al (2016) Isotopic signatures of mercury contamination in latest Permian oceans. Geology 45:55–58. https://doi.org/10.1130/G38487.1

Gratz LE, Keeler GJ, Blum JD, Sherman LS (2010) Isotopic composition and fractionation of mercury in Great Lakes precipitation and ambient air. Environ Sci Technol 44(20):7764–7770. https://doi.org/10.1021/es100383w

Hintelmann H (2012) Use of stable isotopes in mercury research. In: Mercury in the environment: pattern and process. University of California Press, Berkeley, pp 55–71

Huang Q et al (2016) Isotopic composition for source identification of mercury in atmospheric fine particles. Atmos Chem Phys 16(18):11773–11786. https://doi.org/10.5194/acp-16-11773-2016

Jimenez-Moreno M et al (2016) Sources and fate of mercury pollution in Almaden mining district (Spain): evidences from mercury isotopic compositions in sediments and lichens. Chemosphere 147:430–438. https://doi.org/10.1016/j.chemosphere.2015.12.094

Jiskra M et al (2015) Mercury deposition and re-emission pathways in boreal forest soils investigated with Hg isotope signatures. Environ Sci Technol 49(12):7188–7196. https://doi.org/10.1021/acs.est.5b00742

Kwon SY et al (2012) Absence of fractionation of mercury isotopes during trophic transfer of methylmercury to freshwater fish in captivity. Environ Sci Technol 46(14):7527–7534. https://doi.org/10.1021/es300794q

Kwon SY, Bluma JD, Nadelhoffer KJ, Dvonch JT, Tsui MTK (2015) Isotopic study of mercury sources and transfer between a freshwater lake and adjacent forest food web. Sci Total Environ 532:220–229. https://doi.org/10.1016/j.scitotenv.2015.06.012

Laffont L et al (2009) Anomalous mercury isotopic compositions of fish and human hair in the Bolivian Amazon. Environ Sci Technol 43(23):8985–8990. https://doi.org/10.1021/es9019518

Lauretta DS, Klaue B, Blum JD, Buseck PR (2001) Mercury abundances and isotopic compositions in the Murchison (CM) and Allende (CV) carbonaceous chondrites. Geochim Cosmochim Acta 65(16):2807–2818. https://doi.org/10.1016/s0016-7037(01)00630-5

Lawson NM, Mason RP, Laporte J-M (2001) The fate and transport of mercury, methylmercury, and other trace metals in chesapeake bay tributaries. Water Res 35(2):501–515. https://doi.org/10.1016/s0043-1354(00)00267-0

Lepak RF et al (2015) Use of stable isotope signatures to determine mercury sources in the Great Lakes. Environ Sci Technol Lett 2(12):335–341. https://doi.org/10.1021/acs.estlett.5b00277

Mason RP, Sullivan KA (1998) Mercury and methylmercury transport through an urban watershed. Water Res 32(2):321–330. https://doi.org/10.1016/s0043-1354(97)00285-6

Mason RP, Reinfelder JR, Morel FMM (1995) Bioaccumulation of mercury and methylmercury. Water Air Soil Pollut 80(1–4):915–921. https://doi.org/10.1007/bf01189744

Obrist D et al (2017) Tundra uptake of atmospheric elemental mercury drives Arctic mercury pollution. Nature 547:201–204. https://doi.org/10.1038/nature22997

Perrot V et al (2010) Tracing sources and bioaccumulation of mercury in fish of Lake Baikal- Angara River using Hg isotopic composition. Environ Sci Technol 44(21):8030–8037. https://doi.org/10.1021/es101898e

Rolison JM, Landing WM, Luke W, Cohen M, Salters VJM (2013) Isotopic composition of species-specific atmospheric Hg in a coastal environment. Chem Geol 336:37–49. https://doi.org/10.1016/j.chemgeo.2012.10.007

Roulet M et al (1998) Distribution and partition of total mercury in waters of the Tapajós River Basin, Brazilian Amazon. Sci Total Environ 213(1–3):203–211. https://doi.org/10.1016/S0048-9697(98)00093-X

Schauble EA (2004) Applying stable isotope fractionation theory to new systems. Non-traditional stable isotopes. Rev Mineral Geochem 55:65–111

Schauble EA (2007) Role of nuclear volume in driving equilibrium stable isotope fractionation of mercury, thallium, and other very heavy elements. Geochim Cosmochim Acta 71(9):2170–2189. https://doi.org/10.1016/j.gca.2007.02.004

Senn DB et al (2010) Stable isotope (N, C, Hg) study of methylmercury sources and trophic transfer in the Northern Gulf of Mexico. Environ Sci Technol 44(5):1630–1637. https://doi.org/10.1021/es902361j

Sherman LS, Blum JD (2013) Mercury stable isotopes in sediments and largemouth bass from Florida lakes, USA. Sci Total Environ 448:163–175. https://doi.org/10.1016/j.scitotenv.2012.09.038

Sherman LS, Blum JD, Dvonch JT, Gratz LE, Landis MS (2015) The use of Pb, Sr, and Hg isotopes in Great Lakes precipitation as a tool for pollution source attribution. Sci Total Environ 502:362–374. https://doi.org/10.1016/j.scitotenv.2014.09.034

Smit J, Koeberl C, Claeys P, Montanari A (2016) Mercury anomaly, Deccan volcanism, and the end-Cretaceous mass extinction. Geol Forum 44(2):171–174. https://doi.org/10.1130/G37683C.1

Sonke JE et al (2010) Sedimentary mercury stable isotope records of atmospheric and riverine pollution from two major European heavy metal refineries. Chem Geol 279(3–4):90–100. https://doi.org/10.1016/j.chemgeo.2010.09.017

Strok M, Baya PA, Hintelmann H (2015) The mercury isotope composition of Arctic coastal seawater. Compt Rendus Geosci 347(7–8):368–376. https://doi.org/10.1016/j.crte.2015.04.001

Sun G et al (2016) Mass-dependent and -independent fractionation of mercury isotopes during gas-phase oxidation of elemental mercury vapor by atomic Cl and Br. Environ Sci Technol 50(17):9232–9241. https://doi.org/10.1021/acs.est.6b01668

Thibodeau AM, Bergquist BA (2016) Do mercury isotopes record the signature of massive volcanism in marine sedimentary records? Geology 45:95–96
Thibodeau AM et al (2016) Mercury anomalies and the timing of biotic recovery following the end-Triassic mass extinction. Nat Commun 7:11147. https://doi.org/10.1038/ncomms11147
Tsui MT et al (2014) Variation in terrestrial and aquatic sources of methylmercury in stream predators as revealed by stable mercury isotopes. Environ Sci Technol 48(17):10128–10135. https://doi.org/10.1021/es500517s
Turro NJ (1983) Influence of nuclear spin on chemical reactions: magnetic isotope and magnetic field effects (a review). Proc Natl Acad Sci 80(2):609–621. https://doi.org/10.1073/pnas.80.2.609
UNEP (2013) Global mercury assessment 2013: sources, emissions, releases, and environmental transport. UNEP Chemicals Branch, Geneva
Urey HC (1947) The thermodynamic properties of isotopic substances. J Chem Soc (London) 85:562–581
Wiederhold JG et al (2015) Mercury isotope signatures in contaminated sediments as a tracer for local industrial pollution sources. Environ Sci Technol 49(1):177–185. https://doi.org/10.1021/es5044358
Xu XY, Zhang QG, Wang WX (2016) Linking mercury, carbon, and nitrogen stable isotopes in Tibetan biota: implications for using mercury stable isotopes as source tracers. Sci Rep 6. https://doi.org/10.1038/srep25394
Xu H et al (2017) Seasonal and annual variations in atmospheric Hg and Pb isotopes in Xi'an, China. Environ Sci Technol 51(7):3759–3766. https://doi.org/10.1021/acs.est.6b06145
Young ED, Galy A, Nagahara H (2002) Kinetic and equilibrium mass-dependent isotope fractionation laws in nature and their geochemical and cosmochemical significance. Geochim Cosmochim Acta 66(6):1095–1104. https://doi.org/10.1016/s0016-7037(01)00832-8
Zambardi T, Sonke JE, Toutain JP, Sortino F, Shinohara H (2009) Mercury emissions and stable isotopic compositions at Vulcano Island (Italy). Earth Planet Sci Lett 277(1–2):236–243. https://doi.org/10.1016/j.epsl.2008.10.023
Zheng W, Hintelmann H (2010) Nuclear field shift effect in isotope fractionation of mercury during abiotic reduction in the absence of light. J Phys Chem A 114(12):4238–4245. https://doi.org/10.1021/jp910353y
Zheng W, Xie ZQ, Bergquist BA (2015) Mercury stable isotopes in ornithogenic deposits as tracers of historical cycling of mercury in Ross Sea, Antarctica. Environ Sci Technol 49(13):7623–7632. https://doi.org/10.1021/acs.est.5b00523
Zheng W, Obrist D, Weis D, Bergquist BA (2016) Mercury isotope compositions across North American forests. Glob Biogeochem Cycles 30(10):1475–1492. https://doi.org/10.1002/2015GB005323

Metamorphic Reactions and Processes

Eleanor C. R. Green
Institute of Geochemistry and Petrology, ETH Zürich, Zürich, Switzerland

Definition

A metamorphic reaction is a **chemical reaction** that produces, or changes, an assemblage of metamorphic mineral and fluid phases in a rock. The changes affect the compositions of the phases and may also include changes in the phases that are present. Metamorphic processes are those processes that drive metamorphic reactions, by causing a change in the chemical conditions of the rock, such as the pressure or temperature. Metamorphic processes also commonly drive **deformation**.

Introduction

A metamorphic rock is a rock that has undergone mineralogical changes due to changing thermodynamic conditions since its formation. Prior to any metamorphism, the original rock, or protolith, may have been formed by solidification of a melt (an igneous protolith) or the lithification of discrete grains derived from weathering (a sedimentary protolith). Mineralogical changes are driven by metamorphic processes, which give rise to a great diversity of metamorphic minerals and mineral assemblages. Mineralogical change can be viewed as a change in the lattice structures – that is, the minerals – present in the system. The lattice structures differ in their capacity to accommodate a given element. Thus, a change in the available lattice structures is accompanied by redistribution of elements among the lattices. Both the change of available lattice structures and the redistribution of elements can be described as "metamorphic reaction."

The mineral assemblage present in a rock is the source of the rock's physical properties. It is well known that the conversion of basalts and gabbros to eclogite in a subducting slab entails a ~10% increase in density, which contributes significantly to **slab pull** and thus the **subduction** process itself (Aoki and Takahashi 2004; Arrial and Billen 2013; Chen et al. 2013; Hacker et al. 2003; Peacock 1993). Rock rheological properties, and tensorial properties such as seismic wave velocities and thermal conductivity, are functions not only of the mineral assemblage but also of its **microstructure**. Metamorphic processes influence the broader evolution of the Earth.

Metamorphic geology attempts to interpret metamorphic rocks in terms of the processes that generated them. One of its great assets is the mathematical framework of thermodynamic **phase equilibrium**. The **phase equilibrium** framework can be used to model metamorphic processes quantitatively, as long as these processes operated close to equilibrium. This entry assumes that preserved metamorphic mineral assemblages were generally in thermodynamic equilibrium, to a good approximation, when they ceased to evolve. The assumption is broadly justified by the sequences of assemblages observed in the eroded remains of mountain belts, repeated through space and time, which inspired a qualitative thermodynamic interpretation many decades before quantitative modeling was possible (e.g., Eskola 1920; Turner 1948).

In recent years, much effort within metamorphic geology has been expended on the development and application of quantitative thermodynamic modeling. To enable such

modeling, equations of state must be calibrated to represent the thermodynamic properties of the phases involved. The ultimate goal is to predict the stable mineral assemblage, including the distribution of elements among the minerals, under a given set of conditions. An applied metamorphic study commonly starts with fieldwork accompanied by petrographic interpretation and mineral analysis of rock samples. Using quantitative modeling, it aims to reconstruct the pressure–temperature–time path along which the rock traveled during its mineralogical development. The history of the rock in pressure–temperature space is a history of the metamorphic processes that acted on it and a window into the tectonic or magmatic processes that drove metamorphism.

A wide range of metamorphic processes can be described within the framework of equilibrium thermodynamics. Thermodynamic analysis is not, however, sufficient to link metamorphic processes with the tectonic or magmatic processes in which they originate. Most obviously, the thermodynamic approach does not include time as a variable, so thermal models must be developed that can be compared with geochronological data. The last section of this entry addresses the integration of various geophysical, geochemical, and thermodynamic methods into full geodynamic models.

Metamorphic Environments

Metamorphic processes take place in a number of terrestrial environments. Necessarily, these are environments in which the thermodynamic stability fields of new mineral assemblages are accessed and in which kinetic barriers to thermodynamic equilibration are overcome on a significant length scale. High temperatures and the presence of fluid facilitate the **diffusion** of ions down **chemical potential** gradients, forming more thermodynamically favorable chemical structures. For example, metamorphic processes take place where a system of **hydrothermal fluid** transfer or circulation can be maintained, where rock is heated through burial in compressional regimes, and where heat is advected via intruding magmas and conducted into the host rock. Hydrothermal metamorphism plays an important role in the concentration of ores ("mineralization") and is thus a focus of economic geology (Pirajno 1992). It is pervasive at mid-ocean ridges and is also associated with magmatic intrusions into continental crust. When such intrusions cause local mineralogical changes due to conduction of heat into country rock, the process is known as contact metamorphism and the affected area is described as a contact aureole. In contrast, metamorphism affecting a large area is known as regional metamorphism. It is generally tectonic in origin and accompanied by **deformation**. The study of regional metamorphism has been a primary driver for the development of metamorphic geology as a discipline and tool.

A Conceptual Model for Regional Metamorphism

Long before a detailed thermodynamic interpretation of metamorphism had been established, it was known that particular sequences of metamorphic rocks are repeated around the globe. A well-known example is that of Barrow zones, in which a series of index minerals (chlorite, biotite, garnet, staurolite, kyanite, and sillimanite) are developed in metapelites with increasing degree of metamorphism (increase of metamorphic grade). The consistency of such patterns across both space and time could be explained if rocks of similar bulk composition were to crystallize the same sequence of mineral assemblages while traversing the same region of pressure–temperature (P–T) space. This is the basis of the **metamorphic facies** concept, attributed to Eskola (1920). A **metamorphic facies** comprises rocks from the same compositional group (metabasites, metapelites, or calcareous rocks) that formed within a particular region of P–T space and therefore contain a predictable set of key minerals. Most of the facies proposed by Eskola (1920), and later Fyfe and Turner (1966), were defined in terms of the mineral assemblages seen in metabasic rocks. For example, the amphibolite facies occupies a P–T interval of approximately 2–10 kbar and 550–700 °C (Fig. 1). In this facies, a metabasic rock will contain a mineral assemblage characterized by hornblende + plagioclase. A metapelite, on the other hand, does not have a single set of index minerals that directly corresponds to the amphibolite facies. Instead, index minerals such as garnet, staurolite, kyanite, and sillimanite occupy various P–T intervals that overlap with amphibolite facies conditions. The names of the metabasite facies are often used to refer to regions of P–T space, even if the rock under discussion is metapelitic or calcareous.

Maps locating metamorphic mineral facies quantitatively in P–T space were presented by, for example, Fyfe and Turner (1966) and have been extensively investigated through experiment and thermodynamic modeling (Miyashiro 1961; Moody et al. 1983). The wide boundaries separating facies in Fig. 1 reflect variation in bulk composition within the metabasite compositional group, especially with respect to the fluid components.

Two ideas must now be established so that the facies concept can be understood in detail. The first of these is the idea of local or mosaic equilibrium, summarized in Korzhinskii (1959) and Thompson (1959). This describes what, in practical terms, is meant by a rock being "at equilibrium" at an instant in time. Starting from any given spatial origin, chemical equilibration with neighboring grains takes place out to a radius defined by the **diffusion** length scale of the rock at that time. From a thermodynamic perspective, the rock "system" extends only as far as this kinetically controlled limit.

The second core insight extends beyond the purview of instantaneous thermodynamic equilibrium, introducing the

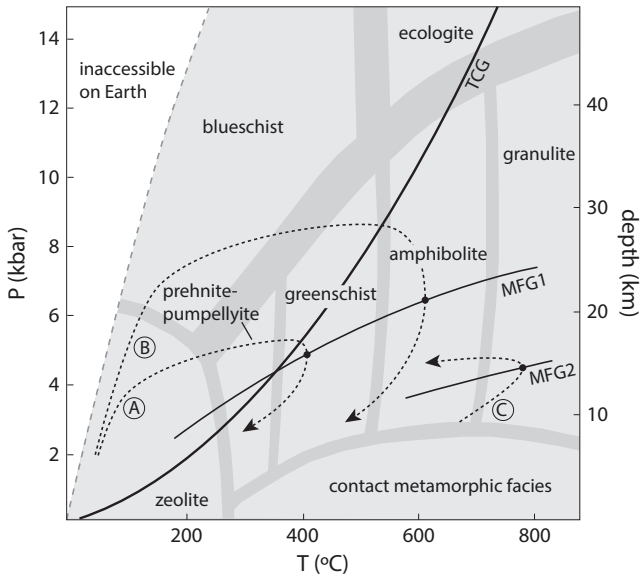

Metamorphic Reactions and Processes, Fig. 1 A diagram in pressure–temperature (*P–T*) space, with depths also marked, showing the location of metamorphic facies and a selection of thermal gradients and rock *P–T* paths. **Metamorphic facies** are shown in *gray*. Since the occurrence of their characteristic mineral assemblages is also a function of bulk composition, they occupy loosely defined regions of *P–T* space, as suggested by the broad borders shown. A typical continental geotherm (*TCG*) is represented. Rock packages *A* and *B* come from different depths in the same column of rock, undergoing metamorphism during burial and exhumation. They follow the clockwise *P–T* paths shown as dotted curves. These paths indicate a phase of rapid burial, followed by a phase of heating that continues after exhumation has begun. The shallower rock A reaches its maximum temperature, marked by a *black dot*, before the deeper rock *B* does. The mineral assemblages preserved in *A*, *B*, and other rocks in the column record a locus of *P–T* points, the metamorphic field gradient. This is assumed to represent the locus of maximum temperature points, as shown in the figure (*MFG1*). However, MFG1 does not resemble the path taken by any one rock package. Rock *C* is from an unrelated location. It experiences heating of magmatic origin, to well above the TCG, while undergoing shallow burial. After the episode of heating is over, it cools near isobarically. Its mineral assemblage records a point on metamorphic field gradient *MFG2*

dimension of time. Consider first the path taken by a small package of rock through *P–T* space, during a regional metamorphic event comprised of burial followed by exhumation. The rock experiences prograde metamorphism through an up-temperature sequence of facies, until it reaches a maximum temperature, loosely defined as the "metamorphic peak." As it begins to cool, it undergoes further retrograde metamorphic evolution, until the length scale of local equilibrium becomes negligible due to cooling and loss of fluid availability. Petrographic and thermodynamic analysis may constrain multiple points on this rock's pressure–temperature–time (*P–T–t*) path (Vernon and Clarke 2008, Chap. 3). For a typical burial and exhumation process, such as that responsible for Barrow zones, the *P–T–t* path will be clockwise as shown in Fig. 1, with peak pressure reached before peak temperature. This is because the rock heats up only slowly in response to burial, by conduction from the warmer surroundings, with temperatures continuing to rise for some time after exhumation begins.

In such a typical burial and exhumation process, correlated *P–T–t* paths are taken by different small packages of rock at different depths within the same overall column of rock. Packages at shallower depths in the column experience lower maximum temperatures than packages deeper in the column (Fig. 1). Furthermore, shallower packages reach their peak temperature earlier than deeper packages, reflecting the evolution of the metamorphic geotherm by conductive relaxation over the course of exhumation. Thus, sequences of metamorphic assemblages record the thermal evolution of a tectonic unit with respect to the time and depth coordinates, throughout much of the causal event. The various tectonic and magmatic drivers of metamorphism are associated with characteristic styles of *P–T–t* path. In contrast to the clockwise path described above, for example, magmatic heating at low pressure typically generates a rather flat, anticlockwise *P–T–t* path. Heating is accompanied by a small increase in pressure as the crust deforms and thickens and is followed by near-isobaric cooling (Fig. 1).

The concept of **metamorphic facies** was understood from the beginning as a manifestation of thermodynamic control on mineralogical development, led by the work of Eskola (1920) and Goldschmidt (1915) on metabasite facies and the application of the **Gibbs phase rule**. Nevertheless, a period of decades elapsed between these pioneering studies and the development of a broad consensus that thermodynamic equilibrium operates throughout the prograde path of a rock. A decisive contribution was made by Carmichael (1969), who described how metamorphic reaction could take place continuously along the prograde path, even when reacting grains were spatially separated within the equilibrium length scale (see following section). Arguably, the conceptual model for metamorphism that is outlined above was completed by England and Richardson (1977). These authors modeled the thermal evolution of tectonically thickened continental crust, eliciting the asynchronous nature of *P–T–t* paths in a column of rock. An excellent summary of metamorphic processes in orogeny, including a much more detailed scientific history, is given by Johnson and Harley (2012), Chap. 7.

A Model System for Metamorphic Phase Equilibria

The **metamorphic facies** concept invokes a thermodynamic system in which pressure and temperature are externally imposed, with their conjugate variables, volume, and entropy, assuming values in response. Likewise, the system is implied to have a fixed bulk chemical composition, with the conjugate variables of **chemical potential** being dependent. Applying

the local equilibrium paradigm, it is evident that the system comprises a volume contained within the **diffusion**-determined length scale of equilibration. To first order, the bulk composition of the system refers to the bulk composition within this volume, although this definition is qualified below. Control by bulk composition in rocks can be contrasted with the buffering of the **chemical potential** of O_2, μ_{O_2}, in a petrological experiment. The experiment is buffered in order to modulate the gain or loss of the mobile H_2 component through the walls of the capsule, which must then take place such as to maintain μ_{O_2}.

Pressure P, temperature T, and **chemical potential** μ_i of component i are intensive variables, subject to contact equilibrium, meaning that they spontaneously evolve to be constant in all parts of a system. A preliminary condition for defining **phase equilibrium** within the system is then that $\nabla P = 0, \nabla T = 0$, and $\nabla \mu_i = 0$, where ∇ is the gradient operator, such that $\nabla x = 0$ implies spatial uniformity. It is usually assumed that there are no significant barriers to the spatial equilibration of temperature and pressure, since these can be transmitted directly through mineral lattices in the form of vibrational phenomena. The process of attaining $\nabla \mu_i = 0$ is slower, since this involves redistribution of matter within the system by **diffusion**. It is the spatial extent of contact equilibrium of the μ_i that limits the system volume. In recent work, however, Tajčmanová et al. (2014) proposed that gradients might be maintained in pressure over a length scale for which $\nabla \mu_i = 0$, in some scenarios.

In a system with pressure, temperature, and bulk composition held constant, the appropriate formulation of equilibrium is that of **Gibbs–Duhem**:

$$S\,dT - V\,dP + \sum_i n_i\,d\mu_i = 0, \tag{1}$$

where S is the system entropy, V the volume, and n_i the amount of component i in the system. The **Gibbs–Duhem** relation states that the temperature, pressure, and chemical potentials in the system cannot vary independently of each other while at equilibrium. As a rock proceeds along its P–T–t path, maintaining equilibrium and a constant bulk composition, the chemical potentials of components continuously adjust in response to changing pressure and temperature. As this takes place, material is spatially redistributed, countering the tendency for chemical potential gradients to develop in space. Since the driving force of any nonuniform **chemical potential** is felt across the equilibration length scale, any two grains within the equilibrated volume are in chemical contact, whether or not they are in physical contact. Thus, the spatial distribution of phases is irrelevant from the perspective of **phase equilibrium**; rather, the thermodynamic changes to the equilibrium assemblage are quantified as changes to mineral compositions and mineral modal proportions. These principles encapsulate and generalize the arguments made by Carmichael (1969), in explaining why, during Barrovian metamorphism, the replacement of kyanite by sillimanite in Barrovian metamorphism usually involves **nucleation** of sillimanite at a distance from the kyanite. As the system is chemically unified, sillimanite is not obliged to grow directly from kyanite, but instead grows where the energy barriers to **nucleation** are smaller.

It is not necessarily the whole of each grain that participates in the equilibrium among minerals. More precisely, equilibrium is maintained along grain edges, with cation exchange taking place at the grain interfaces, and grain-boundary **diffusion** mediated by metamorphic fluid. Within-grain **diffusion** may be orders of magnitude slower than fluid-mediated **diffusion** along grain boundaries, and thus equilibration within grains may not keep pace with the evolving composition at grain boundaries. This may give rise to compositional zoning in individual grains. In reality, **diffusion** rates vary among chemical components i, and in different minerals, and so therefore do length scales over which equilibration occurs. Aluminum, for example, is rather immobile, as discussed by Carmichael (1969). Both of these factors would, in theory, be taken into account in establishing the true bulk composition of the system.

Quantitative Thermodynamic Modeling: Equations of State

The previous section established a standard thermodynamic system that can be used for modeling **phase equilibrium** in many metamorphic contexts. Subsequent sections will discuss quantitative thermodynamic modeling in practical terms. It is first necessary to outline how the thermodynamic properties of individual mineral phases are captured in mathematical form and how quantitative multiphase equilibria are calculated based on these properties.

The focus of this entry is a category of thermodynamic models of mineral phases that will be described as "comprehensive" models. "Comprehensive" models contain sufficient chemical components to be used in forward calculations approximating natural metamorphic mineral assemblages. They are built on internally consistent datasets of end-member properties and comprise multidimensional **activity–composition** relations, involving mixing-on-sites and sometimes order–disorder. Examples are the models of White et al. (2007, 2014a) and Green et al. (2016). In concentrating exclusively on the use of comprehensive models, this entry passes apologetically over a long history of qualitative and quantitative thermodynamic modeling within metamorphic petrology. This history begins with the first application of Gibbs phase rule to metamorphic mineral assemblages by Goldschmidt (1915). It includes fundamental insight into metapelite phase relations acquired by projection

(Thompson 1957) and encompasses a major literature on single-reaction geothermometry and geobarometry.

The ultimate goal of a thermodynamic modeler is to take each metamorphic mineral and construct a realistic equation of state for it. The equation of state is a function that represents the response of the mineral's state variables to changing conditions imposed upon it. For a pure end-member of a mineral in metamorphic geology, it is generally sufficient to construct the state variable volume, enthalpy, and entropy as a function of temperature and pressure (though in fact, if a mineral lattice behaves elastically as required at equilibrium, it undergoes tensorial strain and is strictly governed by the stress tensor rather than the pressure). These properties are then assembled in order to derive the **Gibbs energy**. For minerals that undergo **solid solution**, these same properties are also functions of the mineral's composition.

Among the common rock-forming minerals, there is often good experimental data constraining the equation of state for the main end-members of **solid solution**s. Such data comprise detailed measurements of isobaric heat capacity, isothermal compressibility, and thermal expansivity (e.g., Angel et al. 1988; Robie and Hemingway 1995; Winter and Ghose 1979). An internally consistent dataset of end-members, such as that of Holland and Powell (2011), collates all such measurements and subjects them to some form of optimization procedure. The use of an internally consistent dataset helps to fill gaps in experimentally measured end-member data and to overcome inconsistencies in the experiments. The latter might arise if, for example, a crystal grown in an experiment were to undergo a symmetry change during quenching, such that the measured phase was not the same as the equilibrium one, or if its equilibrium properties were significantly affected by chemical impurities or structural defects.

At an arbitrary intermediate composition in a phase showing **solid solution**, there is unlikely to be much direct information. As a result it is commonplace to treat **solid solution**s as a mixture of end-members, taking end-member thermodynamic properties from an internally consistent dataset and describing the properties due to mixing separately, via an **activity–composition** (a–x) model. The a–x model is calibrated semiempirically; the calibration makes use of available data, which usually lie along binary compositional joins, but also relies on heuristic inferences about the likely magnitudes of parameters (Powell et al. 2014). The simplest type of a–x relation to demonstrate a thermodynamic form is the ideal mixing-on-sites model. Here, the enthalpy is that of a mechanical mixture of end-members, while the entropy is purely configurational and summed over each of the sites in the mineral where cation mixing takes place. In recent years the ideal mixing-on-sites model has been largely replaced by more complex forms of a–x relation, in which ideal mixing-on-sites is augmented by, for example, strongly nonideal enthalpies of mixing and representations of cation order–disorder. The ultimate requirement for such models is that the forward calculations should compare well with observations (see, e.g., Diener and Powell 2012; Green et al. 2016).

Quantitative Thermodynamic Modeling: Calculating Multiphase Equilibria

Once a thermodynamic model is available to represent each of the required phases, the stable mineral assemblage can be calculated. A common approach is the **Gibbs energy** minimization method. Each thermodynamic model is written in the form of a **Gibbs energy** surface in P–T–X_i space. At a given bulk composition, the lowest-energy common tangent is sought among the **Gibbs energy** surfaces for all the phases (Fig. 2). The tangent will usually involve a subset of the phases under consideration. The equilibrium composition of each phase in the subset is given by the intersection of its **Gibbs energy** surface in X_i space with the tangent, and the modal proportion of the phase can be found by mass balance.

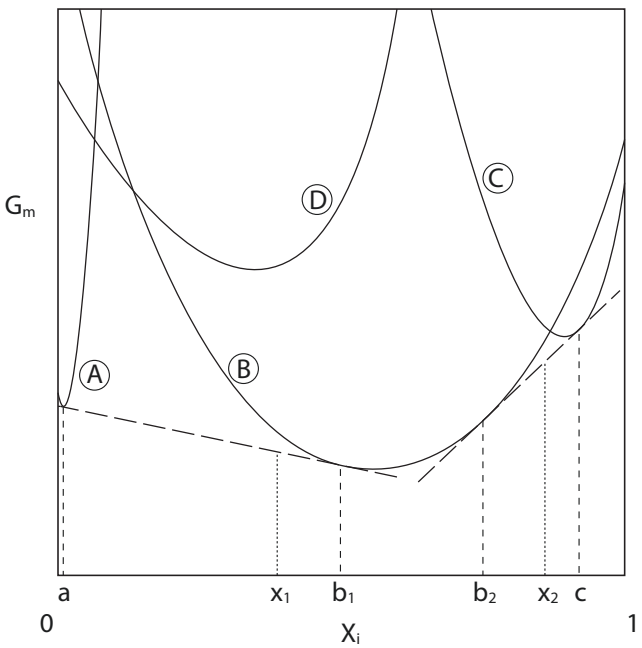

Metamorphic Reactions and Processes, Fig. 2 The common tangent construction for identifying stable assemblages. The chemical system is binary, i.e., it has two components, i and j, and composition can be expressed by the proportion of i, X_i. Gm is the **Gibbs energy** of phases A–D, which are mixtures (they might be **solid solution**s or fluids). For each phase, the **Gibbs energy** is plotted as a function of composition, at a fixed pressure and temperature. At bulk composition x_1, the stable assemblage is $A + B$, where A has composition a and B has composition b_1. The molar proportion of B in the assemblage is given by the fractional distance of x_1 along the path $X_i = a$ to $X_i = b_1$. For bulk composition x_2, the stable assemblage is $B + C$, where B has composition b_2 and C has composition c. Between compositions b_1 and b_2, the stable assemblage would simply be phase B, with a composition equal to the bulk composition. Phase D is nowhere part of the stable assemblage

Alternatively, the problem can be formulated by breaking down the **Gibbs energy** for phase p into expressions for the chemical potentials of the end-members in the model, writing $G = \sum_m c_m \mu_m$. Here, at (P, T), c_m is the proportion of the end-member m in phase p, and μ_m is its **chemical potential**. The chemical potential is given by

$$\mu_m = \left(\frac{\partial G}{\partial n_m}\right)_{P,T,n_{l\neq m}} = \mu_m^0 + \mathrm{R}T\ln\left(a_m^p\right), \qquad (2)$$

where G is the **Gibbs energy** of the phase, μ_m^0 is the **chemical potential** of the pure end-member at (P, T), R is the gas constant, and a_m^p is the activity of m in phase p. This form highlights the relationship between μ_m and a_m^p, with a_m^p related to the composition of the phase via the a–x model. Next, an independent set of balanced reactions among the end-members of co-existing phases is written. For each reaction in the independent set, a statement of chemical equilibrium can be written in the form

$$\sum_m \nu_{m,r}\,\mu_m = 0, \qquad (3)$$

where $\nu_{m,r}$ is the reaction coefficient of end-member m in reaction r and μ_m is its **chemical potential**. Smith and Missen (1982) show that this set of equilibria equates to fixing constant chemical potentials throughout the system, where the chemical potentials might alternatively be defined in terms of oxides, for example. Equilibrium phase compositions and modal proportions are then found by solving a set of simultaneous nonlinear equations, consisting of the independent set of statements of chemical equilibrium (Eq. 3), combined with mass balance constraints. This latter method is in some ways more mathematically tractable than the **Gibbs energy** minimization method, though it does not directly show which assemblage is the most stable one possible.

Quantitative **phase equilibrium** calculations are easily carried out using specialized software. Programs currently used for metamorphic problems include Perple_X (Connolly 2009), THERIAK-DOMINO (de Capitani and Petrakakis 2010), and THERMOCALC (Powell and Holland 1988). The practicalities of calculation via an independent set of reactions are discussed in Powell et al. (1998) and the **Gibbs energy** minimization method by Connolly (2009). Readers should be aware, however, that automated methods have no built-in metamorphic insight and not necessarily any understanding of thermodynamic requirements that should constrain, for example, the topology of a calculated phase diagram. They do not replace more traditional approaches to interpreting and characterizing stable phase relations. Such methods are discussed by, for example, Vernon and Clarke (2008).

Forward Modeling of Metamorphic Phase Equilibria: Grids and Pseudosections

Forward modeling of phase equilibria consists of calculations made to predict the thermodynamically stable assemblage in an idealized model system, under conditions chosen by the user. The specification of the thermodynamically stable assemblage includes the phase compositions and modal proportions. Calculations are usually used to build up a phase diagram that summarizes the predictions in a form pertinent to the motivating problem.

Figure 3 shows two related phase diagrams, calculated in the relatively simple system K_2O–FeO–MgO–Al_2O_3–SiO_2–H_2O (KFMASH), with muscovite, quartz, and a pure H_2O fluid "in excess," i.e., present in all assemblages. Panel (a) of the figure is a **petrogenetic grid** or P–T projection. A **petrogenetic grid** shows the relationship in P–T space between stable portions of univariant equilibria, summarizing the changes in stable assemblage (a univariant equilibrium has a single degree of freedom with respect to thermodynamic variables and so appears as a curve in P–T space, with T and all mineral compositions being fully specified if a value for P is given). **Petrogenetic grid**s have a long history in metamorphic geology. Semiquantitative grids were constructed based on inferences from field and experimental observations (e.g. Harte and Hudson 1979), combined with Schreinemakers stability analysis derived from the **Gibbs phase rule**. Using such diagrams, the expanding dataset on metamorphic mineral assemblages in rocks could be logically assembled. Quantitative **petrogenetic grid**s began to be calculated once internally consistent thermodynamic datasets became available (e.g. Spear and Cheney 1989). Sets of grids, in various informative chemical systems, are still routinely published with new families of thermodynamic models (e.g. White et al. 2014a).

In applied forward modeling studies, it is rare to need to calculate a new **petrogenetic grid**. The most commonly calculated type of phase diagram is a **pseudosection**, as shown in Fig. 3b. A **pseudosection** is a map of the stable phase assemblages present at a given bulk composition, most often in P–T space. Individual **pseudosection**s must be calculated for multiple samples in a study. **Pseudosection**s were first envisaged by Hensen (1971).

The P–T **pseudosection** in Fig. 3b will now be considered in detail. The backbone of the figure is made up of the segments of univariant reaction that can be "seen" by the bulk rock composition, highlighted as heavy lines that correspond to segments of the reactions in Fig. 3a. In a **pseudosection** calculated for more components, fewer and shorter segments of univariant reaction would likely be "seen" by the bulk composition. Either side of a univariant reaction lie at divariant fields (white), labeled with three non-excess phases. The divariant fields give way to trivariant fields (pale gray, two non-excess phases), which give way likewise to a

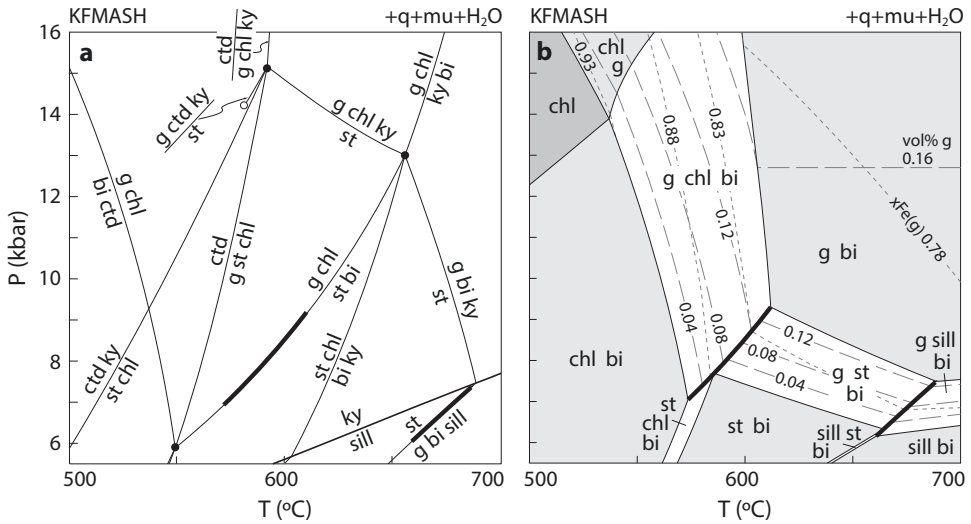

Metamorphic Reactions and Processes, Fig. 3 Comparison of calculated phase diagrams in the system K_2O–FeO–MgO–Al_2O_3–SiO_2–H_2O (KFMASH), with quartz, muscovite, and a pure H_2O fluid in excess, that is, everywhere present. The diagrams were calculated with the thermodynamic models of White et al. (2014a), using the software THERMOCALC. Mineral phases are biotite (*bi*), chlorite (*chl*), chloritoid (*ctd*), garnet (*g*), kyanite (*ky*), muscovite (*mu*), quartz (*q*), sillimanite (*sill*), and staurolite (*st*). (**a**) A **petrogenetic grid** showing stable univariant reactions. Invariant points in the KFMASH system, where five non-excess phases are stable, are shown as *black dots*. An *open dot* indicates where the g + ctd + ky = st reaction runs into its KFASH subsystem and terminates. *Heavy lines* indicate segments of reaction that also appear in (**b**). The **petrogenetic grid** for these thermodynamic models was first presented by White et al. (2014a), Fig. 1a. (**b**) A *P–T* **pseudosection** showing the stable phases present in a rock of bulk composition (mole %) K_2O: 3.38; FeO; 8.18; MgO: 4.29; Al_2O_3: 10.56; SiO_2: 73.59. Univariant reactions "seen" by the bulk composition are shown as heavy *black curves* and correspond to the heavy curves in (**a**). *White* fields are divariant, *pale gray* fields trivariant, and *darker gray* fields quadrivariant. Contours of vol% garnet are shown as *gray long–dashed curves*, with discontinuities across univariant reactions. Contours of $x_{Fe} = \frac{Fe^{2+}}{Fe^{2+}+Mg}$ in garnet are shown as *short-dashed curves* and are continuous across univariant reactions. A **pseudosection** for the same rock composition, covering a larger *P–T* window, can be seen in White et al. (2014a), Fig. 4a

quadrivariant field (dark gray, labeled with "chl," top-left quadrant). Along univariant reactions and in divariant fields, the compositions of phases are independent of the bulk composition. This ceases to be true for fields of higher **variance**, as mass balance requirements become necessary to specify the equilibria fully. Geometric constraints are imposed on the **pseudosection** topology by the **Gibbs phase rule**. Counting the univariant reactions as infinitely thin fields containing four phases (plus the three phases in excess), assemblages change by exactly one phase when crossing a boundary. Intersections occur between two boundaries, along each of which one phase enters or leaves the assemblage. Thus, intersections involve a meeting of four fields, in which two fields on opposite sides of the intersection contain n phases, while the two remaining fields contain $n - 1$ and $n + 1$ phases.

Across fields, mineral compositions and modal proportions change continuously. Modal and compositional contours show discontinuities in slope where they cross field boundaries. Across univariant reactions, modal proportions show absolute discontinuities in values, since mass balance must be achieved while exchanging one phase for another in the assemblage. In the metamorphic literature, the term "metamorphic reaction" is often used to describe the compositional changes, growth, and consumption of minerals that take place while traversing fields. Alternatively the term "metamorphic reaction" may be reserved for univariant reactions. In most cases, new phases do not enter or leave the assemblage via a univariant reaction. Instead they simply leave the assemblage when their mass-balanced modal proportions reach zero; or, conversely, they enter the assemblage once mass balance is consistent with positive proportions of the mineral. For example, on a down-temperature trajectory at 10 kbar across Fig. 3b, garnet leaves the assemblage on falling below 575 °C at the boundary of a divariant field.

For a given rock sample of interest, establishing a suitable bulk composition to use in a **pseudosection** calculation is nontrivial. Building on the discussion in a previous section, an appropriate bulk composition would represent a volume with dimensions equal to the length scale of equilibration, including only the rims of **zoned minerals**. This idealized volume is sometimes described as the "(effective) equilibration volume," although this idea is notional, given that the equilibration length scale varies by chemical component. In principle a representative equilibrium length scale may be estimated via careful petrographic analysis in thin section, and point counting may be used to eliminate grain cores. More often, however, the bulk composition used for modeling is simply an XRF analysis of a whole-rock sample. The bulk

composition used for a **pseudosection** may contribute to the uncertainties in the modeling by a magnitude comparable to the uncertainties in the thermodynamic models themselves (Green et al. 2016; Palin et al. 2016a). Certain components of the bulk composition are notoriously difficult to assess: the bulk ferrous to ferric iron ratio is rarely analyzed, while volatile components present at the time of equilibrium will not normally be preserved in the rock. There is no reliable way to compensate for this missing information, so instead it is important to test the sensitivity of the **pseudosection** calculations to the unknown components. This can be done by calculating **pseudosection**s of T at fixed P or P at fixed T, versus the component of interest, keeping other components of the bulk composition constant. The latter figures are known as T–X or P–X **pseudosection**s.

Like all modeling that generates compelling diagrams as output, there is a danger of taking the results of **phase equilibrium** modeling too literally. A first-order requirement is to test the output against natural and experimental observations. **Pseudosection**s can be used to explain Barrow zone metamorphic sequences, as well as the lower pressure Buchan zone series, with key minerals appearing and disappearing at plausible temperatures (Johnson et al. 2015; White et al. 2014b). They reproduce experimental data on partially molten amphibolites and granulites (Green et al. 2016). Considering that the thermodynamic models are calibrated largely on measurements of individual mineral end-member properties, this represents a remarkable success for current thermodynamic model development and indeed for the thermodynamic view of metamorphism as a whole. Nevertheless, the results of individual calculations should be treated with appropriate skepticism.

Forward Modeling of Metamorphic Phase Equilibria: Thermobarometry

Perhaps the most common use of **pseudosection**-based forward modeling is in **thermobarometry** – that is, estimating the P–T conditions of the peak metamorphic mineral assemblage. The **pseudosection** approach to **thermobarometry** is a case of forward modeling to solve the inverse problem. The calculation of a **pseudosection** is clearly a forward approach, since it involves applying a range of driving thermodynamic variables and calculating the resulting mineral assemblages. However, the ultimate aim is to establish the thermodynamic conditions that gave rise to a mineral assemblage. **Pseudosection thermobarometry** should be contrasted with the approach of "classical **thermobarometry**," a straightforwardly inverse method in which a geothermometer/geobarometer reaction pair is used to solve for pressure and temperature given the observed mineral compositions (e.g., Bhattacharya et al. 1992; Johnson and Brown 2004; Kohn and Spear 1989; Powell and Holland 2008). In this comparison, a major strength of the **pseudosection** approach is that it incorporates the observed bulk rock composition as a constraint. This helps in assessing realistic uncertainties on the estimated pressure and temperature. It also acts as a check that there are no serious flaws in the relationship between pressure, temperature, and mineral composition that is encoded in the thermodynamic models.

In applying **pseudosection** modeling to **thermobarometry**, the aim is to associate the peak metamorphic assemblage observed in thin section with a matching field on the **pseudosection**. The position of this field in P–T space indicates a window in which the peak metamorphic conditions may be found. The size of the window suggests the magnitude of the uncertainty in this P–T estimate. It should be interpreted with some care, however. The 2 σ uncertainty in the position of field boundaries might be up to ±100 °C and ±2 kbar, derived from uncertainties in both the thermodynamic model calibration and the bulk composition (Green et al. 2016; Palin et al. 2016a; Powell and Holland 2008). The calculation of T–X or P–X **pseudosection**s will indicate whether the uncertainties are much increased by the estimate of volatile and oxidized components in the thermobarometric study. If the field in which the observed assemblage is found is much smaller than the uncertainty in the field boundaries, then the uncertainty in the field boundaries is more indicative than the size of the field – after all, within the model uncertainties, the field might not exist at all. Conversely, the observed assemblage might not appear on the **pseudosection**, but might differ from a calculated assemblage only by a mineral that appears in a small proportion. This might arise from uncertainties in the modeling, rather than a major failure thereof. Alternatively, a discrepancy between rock and **pseudosection** may indicate that one of the observed phases does not belong to the equilibrium assemblage.

The uncertainties suggested above are much larger than are quoted for many single-reaction barometers and, especially, thermometers. Single-reaction thermobarometers are often carefully calibrated based on a wide range of observations of coexisting minerals. The stated uncertainty reflects how well the calibration can be made to fit this selection of data, given the assumptions made in data processing. However, it is not truly a measure of the uncertainty on the estimated pressure or temperature when the single-reaction barometer or thermometer is applied to a rock. The uncertainty will not allow for the significant bias that might arise from, for example, the assumed ferric to ferrous iron ratio in the calibration of a Fe–Mg exchange thermometer. Nor will it take account of experimental bias, if the dataset is calibrated against experimental data, or bias in prior estimates of rock equilibration pressures or temperatures, if calibrated against a natural dataset. By contrast, the calibration of the comprehensive models described above includes data from a range of

complementary sources that tend to expose bias. The larger values of uncertainties assigned to **pseudosection thermobarometry** may represent the limits of the pressure and temperature constraints that can be obtained from a general rock, given current knowledge of mineral thermodynamics. Powell and Holland (2008) present a detailed discussion of uncertainties in single-reaction and **pseudosection thermobarometry**.

Alternative Thermodynamic Systems

So far this entry has only discussed one conceptual framework, in which thermodynamic equilibrium is controlled by pressure, temperature, and bulk composition. This framework appears to be a powerful model for understanding rocks on a prograde *P–T–t* path, as the coherence of the facies concept testifies. Metamorphic processes are, however, diverse. The categories of process described in this section entail a different view of the thermodynamic system. In most of these categories, it is the bulk composition that can no longer be treated as a constant property of the system. Such processes can still be treated quantitatively with the "comprehensive" thermodynamic models discussed above, although, in some cases, the process of calculation is laborious using existing software.

Many metamorphic processes are open-system processes involving fractionation, with material systematically added to or excluded from the system over time. A well-known example is the progressive sequestration of material into the cores of porphyroblasts such as garnet. As the porphyroblast grows, its center becomes isolated from the equilibrated system due to low **diffusion** rates within grains, and this changes the effective bulk composition of the system. Another example is the progressive loss of melt from a system, although this may occur episodically rather than continuously, as pressure builds in the pore space. Fractionating systems can be approximated in forward modeling by iteratively modifying the bulk composition to remove the newly excluded phase (e.g., Marmo et al. 2002; Palin et al. 2016b).

A different category of open-system process is one involving metasomatism, in which net mass transfer causes a change in local bulk composition that is not related to, but instead controls, changes in local phase equilibria. This category would include a scenario of "external buffering," whereby fluid of a given composition enters a rock over a long time period, preventing the evolution of fluid composition by reaction with solid phases that would occur in the absence of incoming fluid.

While rocks seem to undergo prograde metamorphism at constant bulk composition, a much larger range of processes may operate along the retrograde *P–T–t* path, particularly in rocks of high metamorphic grade. White et al. (2008) discuss the formation of coronae around porphyroblasts on the retrograde path. They successfully model the observed coronae as a case of stranded equilibrium, in which **chemical potential** gradients were unable to flatten over the width of the reaction rim owing to a diminishing length scale of **diffusion**. The controlling variables of the system in this instance are pressure, temperature, and **chemical potential**. Because such reaction-driven **microstructure**s indicate kinetic barriers to complete equilibration, they are sometimes interpreted as disequilibrium features that lie outside the paradigm of thermodynamic equilibrium. However, in the coronae, **chemical potential** gradients are quite well defined and behave systematically and predictably from core to rim. Consequently, at each point along a radial path from the porphyroblast through the corona to the matrix, a local equilibrium can be considered to apply, with a full set of thermodynamic variables operating, though the values of key **chemical potentials** vary along the radial path.

It can easily be imagined that volume may replace pressure as the constant variable in some processes, if only transiently. Melt loss is often modeled as a constant-pressure process, under the assumption that melt is expelled when it reaches a threshold volume fraction of the assemblage. However, the system might sometimes resemble a rigid, constant-volume pore space, in which melt accumulates until it reaches a threshold pressure. Powell et al. (2005) consider this possibility and, more generally, discuss the appropriate choice of independent variables in a range of contexts.

Phase Equilibrium and Deformation

Thermodynamic equilibrium modeling is a well-validated approach for interpreting metamorphic processes. It predicts the stable mineral assemblage present in a rock, including mineral compositions, under given thermodynamic conditions. The simplest metamorphic processes involve local equilibrium at fixed pressure, temperature, and bulk composition, requiring no spatial or time dimensions to be considered in the problem.

The thermodynamic framework is not, of course, enough to explain everything seen in a metamorphic thin section. High-grade metamorphic rocks show distinctive **microstructure**s, which, except in cases such as the reaction coronae described above, are deformation-induced phenomena. As these rocks approach peak metamorphic temperature, ductile **deformation** can be expected to occur continuously and pervasively. **Deformation** transports matter in response to differential stress, dependent on bulk rheological properties, while contact equilibration of **chemical potential** entails movement of cations to achieve a lowest-energy distribution among mineral lattices. Hypothetically these conflicting forces could inhibit equilibrium; certainly there is likely to

be intense interplay between them on the thin section scale. It is through **deformation** that the volume of an assemblage can change with pressure. Meanwhile, metamorphic reactions influence rheological properties, causing the growth of strong grains such as garnet, and weakening other parts of the system when **aqueous fluid** is generated as a reaction product. The success of prograde-path thermodynamic modeling suggests that **deformation** can be neglected at peak metamorphic conditions, implying that **diffusion** down **chemical potential** gradients keeps pace with the stress-driven movement of material. The retrograde path is more complicated (e.g., Hobbs et al. 1984; Vernon and Ransom 1971), and the outcome of interactions between **deformation** and equilibration becomes difficult to predict. For example, **deformation** gives rise to channelized fluid movement, and late-stage metamorphic reactions occur along and adjacent to these channels after reaction has ceased in the dry parts of the rock due to the greatly limited **diffusion** rates. The fluid promotes reaction by enhancing **diffusion** and is also a reactant in the formation of hydrous retrograde mineral assemblages.

Metamorphic Processes in the Wider Geological Context

The thin section to outcrop scales is of ongoing interest to metamorphic petrologists as a means of gaining insight into metamorphic processes. Over such scales, equilibrium thermodynamics predicts the stable mineral assemblage present in a rock, while fabrics and **microstructure**s record the rock's response to differential stress. However, metamorphic histories of individual rocks are key to understanding Earth processes on much greater scales – processes that leave metamorphism as their imprint on the geological record. Geodynamic modeling addresses the evolution of the planet on a regional or whole-Earth scale, being concerned with the distribution of materials and heat. In an early example, the tectonothermal models of England and Richardson (1977) described the evolution of isotherms by conductive relaxation during orogeny and in a subducted sediment wedge. Thanks to increasing computational power, considerable physico-chemical complexity can now be incorporated into geodynamic models. In a detailed model on an appropriate length scale, the crust is represented as a series of layers with different **rheology** corresponding to different rock types (e.g., Beaumont et al. 2009). Future geodynamic modeling will be directly integrated with **phase equilibrium** calculations.

Phase equilibrium studies model the chemistry of **major** and **minor elements** that significantly affect equilibria. However, an array of geochemical methods provide key information linking metamorphism with **geodynamics**. **Radiometric dating** allows ages to be assigned to metamorphic events. Since thermal conduction and tectonic movements are both associated with characteristic timescales, the age data obtained in a given metamorphic terrane can help distinguish between possible scenarios driving the metamorphic event (Agard et al. 2009). **Trace element** analysis is used to infer paleotectonic environments and to track processes such as partial melting. While they are not considered to have a meaningful influence on the equilibrium assemblage, they partition variably into different phases, producing distinctive patterns which are then treated as markers of processes that have otherwise been erased from the metamorphic record. Ideally, all three geochemical approaches would be approached in an integrated way. Konrad-Schmolke et al. (2008) and Palin et al. (2016c) make an attempt at this, discussing the relationship between **phase equilibrium** and trace element modeling. However, to combine these complementary methods fully, a vastly more detailed knowledge of partition coefficients will be needed, characterizing their dependence on the mineral composition.

Summary

Metamorphic processes involve changes of mineral assemblage and hence material properties of rocks, in response to Earth processes that redistribute heat and rocky material. Feedbacks between the two oblige Earth scientists to pay metamorphic geology close attention. The study of metamorphic processes requires an understanding of rocks as chemical systems, containing crystalline lattice phases (minerals) and fluids. Quantitative thermodynamic modeling provides an invaluable framework through which to explore such chemical systems and their response to the controlling variables of pressure and temperature.

Cross-References

- ▶ Activity and Activity Coefficients
- ▶ Equilibrium
- ▶ Fluid–Rock Interaction
- ▶ Free Energy
- ▶ Geochemical Thermodynamics
- ▶ Kinetics of Geochemical Processes

References

Agard P, Yamato P, Jolivet L, Burov E (2009) Exhumation of oceanic blueschists and eclogites in subduction zones: timing and mechanisms. Earth-Sci Rev 92:53–79

Angel RJ, Hazen RM, McCormick TC, Prewitt CT, Smyth JR (1988) Comparative compressibility of end-member feldspars. Phys Chem Miner 15:313–318

Aoki I, Takahashi E (2004) Density of MORB eclogite in the upper mantle. Phys Earth Planet In 143–144:129–143

Arrial P-A, Billen MI (2013) Influence of geometry and eclogitization on oceanic plateau subduction. Earth Planet Sci Lett 363:34–43

Beaumont C, Jamieson RA, Butler JP, Warren CJ (2009) Crustal structure: a key constraint on the mechanism of ultra-high-pressure rock exhumation. Earth Planet Sci Lett 287:116–129

Bhattacharya A, Mohanty L, Maji A, Sen SK, Raith M (1992) Non-ideal mixing in the phlogopite–annite binary: constraints from experimental data on Mg–Fe partitioning and a reformulation of the biotite–garnet geothermometer. Contrib Mineral Petrol 111:87–93

Carmichael DM (1969) On the mechanism of prograde metamorphic reactions in quartz-bearing pelitic rocks. Contrib Mineral Petrol 20:244–267

Chen Y, Ye K, TF W, Guo S (2013) Exhumation of oceanic eclogites: thermodynamic constraints on pressure, temperature, bulk composition and density. J Metamorph Geol 31:549–570

Connolly JAD (2009) The geodynamic equation of state: what and how. Geochem Geophys Geosyst 10:Q10014

de Capitani C, Petrakakis K (2010) The computation of equilibrium assemblage diagrams with Theriak/Domino software. Am Mineral 95:1006–1016

Diener JFA, Powell R (2012) Revised activity–composition models for clinopyroxene and amphibole. J Metamorph Geol 30:131–142

England PC, Richardson SW (1977) The influence of erosion upon the mineral facies of rocks from different metamorphic environments. J Geol Soc Lond 134:201–213

Eskola PE (1920) The mineral facies of rocks. Nor Geol Tidsskr 6:143–194

Fyfe WS, Turner FJ (1966) Reappraisal of the metamorphic facies concept. Contrib Mineral Petrol 12:354–364

Goldschmidt WM (1915) Geologisch-petrographische Studien im Hochgebirge des stidlichen Norwegens. III. Die Kalksilikatgneise und Kalksilikatglimmerschiefer im Trondhjem-Gebiete. Norsk Videnskapelig Selskap i Oslo Skrifter, Matematisk-Naturvidenskapelig Klasse 10

Green ECR, White RW, Diener JFA, Powell R, Holland TJB, Palin RM (2016) Activity–composition relations for the calculation of partial melting equilibria in metabasic rocks. J Metamorph Geol 34:845–869

Hacker BR, Abers GA, Peacock SM (2003) Subduction factory 1. Theoretical mineralogy, densities, seismic wave speeds, and H_2O contents. J Geophys Res Solid Earth 108:2156–2202

Harte B, Hudson NFC (1979) Pelite facies series and the temperatures and pressures of Dalradian metamorphism in E Scotland. In: Harris AL, Holland CH, Leake BE (eds) The Caledonides of the British Isles – reviewed. Geological Society special publications. Geological Society, London, pp 323–337

Hensen BJ (1971) Theoretical phase relations involving cordierite and garnet in the system FeO–MgO–Al_2O_3–SiO_2. Contrib Mineral Petrol 33:191–214

Hobbs BE, Archibald NJ, Etheridge MA, Wall VJ (1984) Tectonic history of the Broken Hill block, Australia. In: Kröner A, Greiling R (eds) Precambrian tectonics illustrated. Schweizerbart Science Publishers, Stuttgart, pp 353–368

Holland TJB, Powell R (2011) An improved and extended internally consistent thermodynamic dataset for phases of petrological interest, involving a new equation of state for solids. J Metamorph Geol 29:333–383

Johnson TE, Brown M (2004) Quantitative constraints on metamorphism in the Variscides of Southern Brittany – a complementary pseudosection approach. J Petrol 45:1237–1259

Johnson MRW, Harley SL (2012) Orogenesis: the making of mountains. Cambridge University Press, Cambridge

Johnson TE, Kirkland CL, Reddy SM, Fischer S (2015) Grampian migmatites in the Buchan Block, NE Scotland. J Metamorph Geol 33:695–709

Kohn MJ, Spear FS (1989) Empirical calibration of geobarometers for the assemblage garnet + plagioclase + quartz. Am Mineral 74:77–84

Konrad-Schmolke M, Zack T, O'Brien PJ, Jacob DE (2008) Combined thermodynamic and rare earth element modelling of garnet growth during subduction: examples from ultrahigh-pressure eclogite of the Western Gneiss Region, Norway. Earth Planet Sci Lett 272:488–498

Korzhinskii DS (1959) Physicochemical basis of the analysis of the paragenesis of minerals. Consultants Bureau, New York

Marmo BA, Clarke GL, Powell R (2002) Fractionation of bulk rock composition due to porphyroblast growth: effects of eclogite facies mineral equilibria, Pam Peninsula, New Caledonia. J Metamorph Geol 20:151–165

Miyashiro A (1961) Evolution of metamorphic belts. J Petrol 2:277–311

Moody JB, Meyer D, Jenkins JE (1983) Experimental characterization of the greenschist/amphibolite boundary in mafic systems. Am J Sci 283:48–92

Palin RM, Weller OM, Waters DJ, Dyck B (2016a) Quantifying geological uncertainty in metamorphic phase equilibria modelling; a Monte Carlo assessment and implications for tectonic interpretations. Geosci Front 7:591–607

Palin RM, White RW, Green ECR, Diener JFA, Powell R, Holland TJB (2016b) High-grade metamorphism and partial melting of basic and intermediate rocks. J Metamorph Geol 34:871–892

Palin RM, White RW, Green ECR (2016c) Partial melting of metabasic rocks and the generation of tonalitic–trondhjemitic–granodioritic (TTG) crust in the Archaean: constraints from phase equilibrium modelling. Precambrian Res 287:73–90

Peacock SM (1993) The importance of blueschist → eclogite dehydration reactions in subducting oceanic crust. Geol Soc Am Bull 105:684–694

Pirjino F (1992) Hydrothermal mineral deposits: principles and fundamental concepts for the exploration geologist. Springer, Berlin/Heidelberg

Powell R, Holland TJB (1988) An internally consistent dataset with uncertainties and correlations: 3. Applications to geobarometry, worked examples and a computer program. J Metamorph Geol 6:173–204

Powell R, Holland TJB (2008) On thermobarometry. J Metamorph Geol 26:155–179

Powell R, Holland TJB, Worley B (1998) Calculating phase diagrams involving solid solutions via non-linear equations, with examples using THERMOCALC. J Metamorph Geol 16:577–588

Powell R, Guiraud M, White RW (2005) Truth and beauty in metamorphic phase-equilibria: conjugate variables and phase diagrams. Can Mineral 43:21–33

Powell R, White RW, Green ECR, Holland TJB, Diener JFA (2014) On parameterizing thermodynamic descriptions of minerals for petrological calculations. J Metamorph Geol 32:245–260

Robie RA, Hemingway BS (1995) Thermodynamic properties of minerals and related substances at 298.15 K and 1 bar (10^5 Pascals) pressure and at higher temperatures. US Geol Surv Bull 2131:461–461

Smith WR, Missen RW (1982) Chemical reaction equilibrium analysis: theory and algorithms. Wiley InterScience, New York

Spear FS, Cheney JT (1989) A petrogenetic grid for pelitic schists in the system SiO_2–Al_2O_3–FeO–MgO–K_2O–H_2O. Contrib Mineral Petrol 101:149–164

Tajčmanová L, Podladchikov Y, Powell R, Moulas E, Vrijmoed JC, Connolly JA (2014) Grain-scale pressure variations and chemical equilibrium in high-grade metamorphic rocks. J Metamorph Geol 32:195–207

Thompson JB Jr (1957) The graphical analysis of mineral assemblages in pelitic schists. Am Mineral 42:842–858

Thompson JB (1959) Local equilibrium in metasomatic processes. In: Abelson PH (ed) Researches in geochemistry. Wiley, New York, pp 427–457

Turner FJ (1948) Mineralogical and structural evolution of the metamorphic rocks. Geological Society of America Memoir, vol 30. The Geological Society of America, New York
Vernon RH, Clarke GL (2008) Principles of metamorphic petrology. Cambridge University Press, New York
Vernon RH, Ransom DM (1971) Retrograde schists of the amphibolite facies at Broken Hill, new South Wales. J Geol Soc Aust 18:267–277
White RW, Powell R, Holland TJB (2007) Progress relating to calculation of partial melting equilibria for metapelites. J Metamorph Geol 25:511–527
White RW, Powell R, Baldwin JA (2008) Calculated phase equilibria involving chemical potentials to investigate the textural evolution of metamorphic rocks. J Metamorph Geol 26:181–198
White RW, Powell R, Holland TJB, Johnson TE, Green ECR (2014a) New mineral activity–composition relations for thermodynamic calculations in metapelitic systems. J Metamorph Geol 32:261–286
White RW, Powell R, Johnson TE (2014b) The effect of Mn on mineral stability in metapelites revisited: new *a–x* relations for manganese-bearing minerals. J Metamorph Geol 32:809–828
Winter JK, Ghose S (1979) Thermal expansion and high-temperature crystal chemistry of the Al_2SiO_5 polymorphs. Am Mineral 64:573–586

Meteorites

Michael K. Weisberg
Department of Physical Sciences, Earth and Planetary Sciences, Kingsborough Community College and Graduate Center, City University of New York, New York, USA

Definition

Meteorites are rock fragments dislodged from a celestial body, launched into interplanetary space, which pass through the Earth's atmosphere and land on the surface. However, rocks that similarly fell to the surface of the Moon and Mars (or any other planetary body) are also meteorites. Additionally, a rock launched from a planetary body and falls back to that same body is also considered a meteorite. A comprehensive definition (from Rubin and Grossman 2014) is a meteorite is a natural, solid object larger than 10 μm in size, derived from a celestial body, that was transported by natural means from the body on which it formed to a region outside the dominant gravitational influence of that body and that later collided with a natural or artificial body larger than itself (even if it is the same body from which it was launched). Weathering and other secondary processes do not affect an object's status as a meteorite as long as something recognizable remains of its original minerals or structure. A meteorite that is between 10 μm and 2 mm in size is called a micrometeorite. A meteoroid is a 10-μm- to 1-m-size natural solid object moving in interplanetary space. A micrometeoroid is a meteoroid 10 μm to 2 mm in size.

Meteorites represent a remarkable range of Solar System materials and record an extensive range of conditions and processes from the early history of the Solar System to geological processes on asteroids and planets to the evolution of stars and life. Most meteorites are thought to have originated from the asteroid belt, some, such as CI chondrites, may be from comets, and some are from the Moon and Mars. Spectral reflectance and space missions provide the data for linking meteorites to specific asteroids. For example, ordinary chondrites have spectral features similar to S-type asteroids. This relationship was confirmed when samples from the S-type asteroid called 25143 Itokawa, returned by the Hayabusa mission, were shown to have mineral compositions and oxygen isotope ratios identical to the L group of ordinary chondrites.

Types of Meteorites

Meteorites are considered falls or finds. The former indicates that it was observed to fall and then recovered, whereas finds are collected but no witnessed account of it falling. Based on the ratio of metal to silicate, meteorites are divided into stones, stony irons, and irons with stones dominated by silicate minerals; irons are mostly Fe,Ni metal and stony irons are intermediate mixtures of silicates and Fe,Ni. The major silicate minerals in most meteorites are olivine [$(Fe,Mg)_2SiO_4$] and/or pyroxene [$(Fe,Mg,Ca)SiO_3$] and feldspar group [$KAlSi_3O_8 – NaAlSi_3O_8 – CaAl_2Si_2O_8$] minerals. The major metallic (Fe,Ni) minerals are kamacite and taenite, and a common sulfide is troilite (FeS). Stony meteorites from asteroids are divided into chondrites and achondrites. Chondrites are so named due to the presence of small (~ millimeter-sized) spherical inclusions called chondrules and are essentially sedimentary rocks composed of mixtures that may include chondrules, lithic and mineral fragments, metal and sulfides, calcium-aluminum-rich inclusions, amoeboid olivine aggregates, organic materials, presolar grains, and a fine-grained matrix (Fig. 1). They are meteorites that have unfractionated elemental abundances relative to the sun, except for volatility-related depletions (Figs. 2 and 3). They are over 4.5 billion years old and are generally interpreted to be from primitive (undifferentiated) Solar System bodies (asteroids and/or comets). However, paleomagnetic study of the Allende CV chondrite shows that it records a parent body magnetic field suggesting it resided on a body that may have had a differentiated interior with a metallic core (Weiss et al. 2010).

Materials from asteroids that have been modified (melted) through planetary-scale differentiation are called achondrites. These meteorites are generally igneous rocks (e.g., basalts) or breccias of igneous rock fragments (Fig. 1). The term primitive achondrite is applied to recrystallized rocks that may retain textural or chemical memory of their chondrite

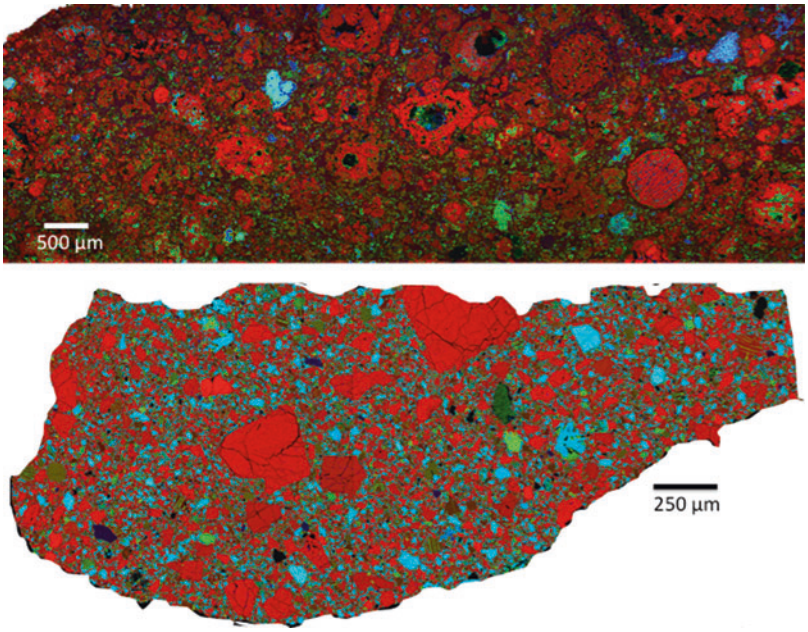

Meteorites, Fig. 1 Mg-Ca-Al (red-green-blue) composite element map of the Vigarano CV3 chondrite (*top*) and the Zmenj howardite (*bottom*). The image of Vigarano shows chondrules of different textures and compositions. Most chondrules are red, due to the magnesian composition of their olivine and pyroxene that dominate the chondrules with minor blue to green (Al,Ca-rich) mesostasis interstitial to the mafic silicates. Calcium-aluminum-rich inclusions are blue due to the high abundance of Al-rich minerals such as anorthite, melilite, and/or fassaite. (Image courtesy of Denton Ebel, American Museum of Natural History.) The Zmenj howardite is an achondrite breccia of olivine (*bright red*), pyroxene (*darker red*), plagioclase (*blue*), and Ca-pyroxene (*green*) (Image courtesy of Joseph S. Boesenberg, Brown University)

precursors. Some primitive achondrites may represent melts, partial melts, or melt residues from local heating events on planetary bodies during the earliest stages of planetary differentiation or possibly from local impact events (e.g., McCoy et al. 1996).

Chondrites

The chondrites are classified into groups based on a combination of their petrologic features (e.g., chondrule abundance, chondrule size, mineral assemblages, and mineral compositions), whole rock chemistry (Fig. 3), and oxygen (and other stable) isotope ratios (Fig. 4). The chondrites are classified as O (ordinary), C (carbonaceous), and E (enstatite) with numerous others that do not easily fit into these three categories. These "classes" are further subdivided into groups. Eight carbonaceous chondrite groups are currently recognized. These include CI, (Ivuna-like), CM (Mighei-like), CO (Ornans-like), CV (Vigarano-like), CK (Karoonda-like), CR (Renazzo-like), CB (Bencubbin-like), and CH (high iron – ALH 85085-like). The ordinary chondrite groups are named H, L, and LL, based on the abundance of iron and the ratio of metallic iron (Fe^0) to oxidized iron

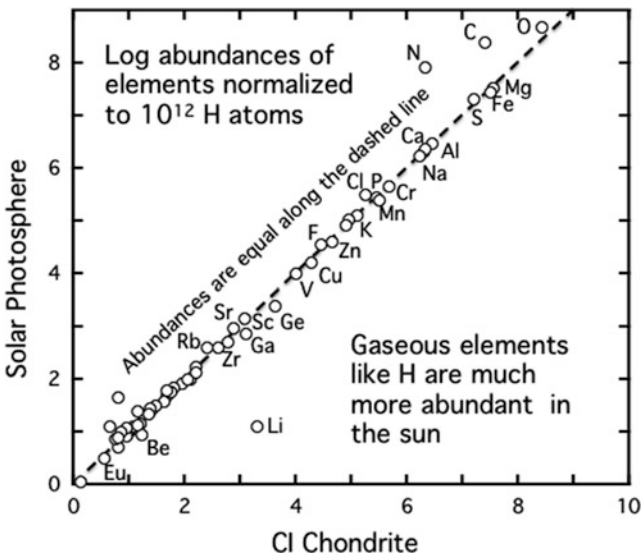

Meteorites, Fig. 2 Abundances of elements (normalized to 10^{12} H atoms) in the solar photosphere plotted against the abundances of elements in CI chondrite showing that CI chondrites have essentially solar composition except for the highly volatile elements. The composition of the Solar photosphere was measured by spectroscopy and the chondrites were analyzed in the laboratory (Data are from Grevesse and Suaval (1998), as reported by Palme and Jones (2003))

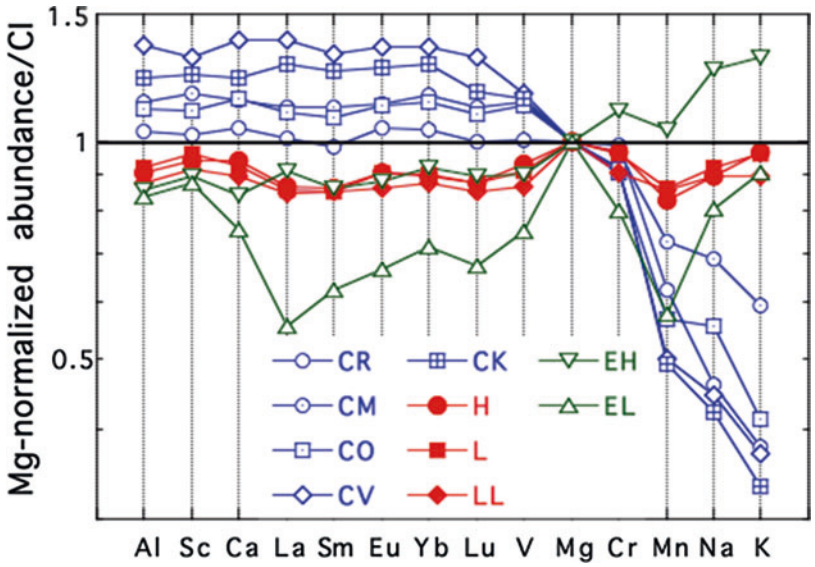

Meteorites, Fig. 3 Average Mg- and CI-normalized abundances of elements in the different chondrite groups. Elements are according to volatility. Most chondrites are unfractionated from CI (solar) with respect to the refractory lithophile elements and show increasing depletions related to volatility (Data from Kallemeyn and Wasson (1981, 1982, 1985), Kallemeyn et al. (1978, 1989, 1991, 1994, 1996), Sears et al. (1982), and Wasson and Kallemeyen (1988))

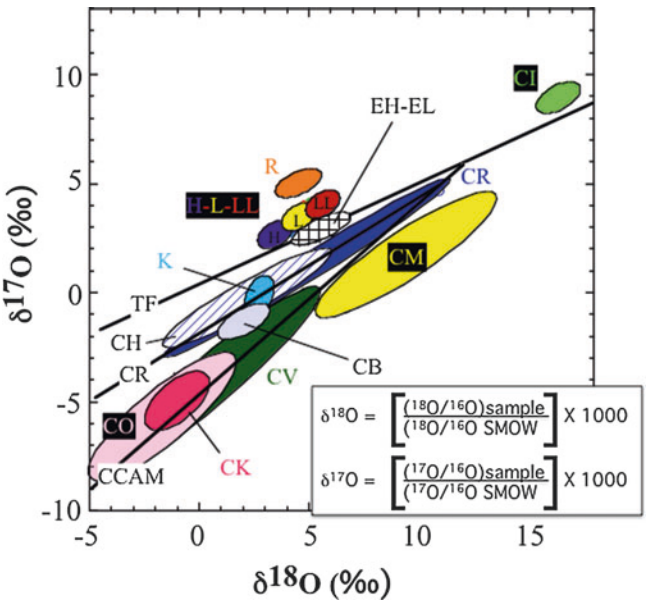

Meteorites, Fig. 4 Oxygen three-isotope diagram showing the fields occupied by the different chondrite groups. TF refers to the terrestrial fractionation line; CCAM is the carbonaceous chondrite anhydrous mixing line. Also shown is a line defined by the CR (and related CB and CH) chondrites (Modified from Weisberg et al. (2006), data from Clayton and Mayeda (1984) and Clayton and Mayeda (1996, 1999))

(FeO): H chondrites have the highest iron content and highest Fe^0/FeO ratios (H, 0.58; L, 0.29; LL, 0.11) among ordinary chondrites and LL chondrites the lowest. In the equilibrated ordinary chondrites (petrologic types 4–6), this is also reflected in their olivine [(in mol% Fa) (H, 16–20; L, 23–26; LL, 27–32) and low-Ca pyroxene endmember compositions. Based on mineralogy and bulk chemistry, the enstatite chondrites are divided into EH (high iron) and EL (low iron) groups (Keil 1969). The R (Rumuruti-like) chondrites have whole chondrite and oxygen isotopic characteristics that preclude their affiliation to either the C, O, or E chondrite classes, as do the K chondrites.

There are a number of chondrites that do not fit into any of the existing groups. These meteorites are referred to as anomalous or ungrouped. They may be anomalous members of chondrite groups or the first representatives of new groups. For example, two metal-rich chondrites (Northwest Africa 5492 and Grosvenor Mountains 95551) were recognized to be similar materials distinct from any other chondrite group and have been interpreted to be the first samples of a new "G" chondrite group (Weisberg et al. 2015).

Chondrites record a range of aqueous and thermal alteration and are assigned values (on a scale of 1–7, referred to as petrologic types) depending on the degrees to which they have been altered. The most primitive, least altered chondrites, considered to be essentially pristine, are labeled type 3.00. Few chondrites are considered to be type 3.00. One example is Acfer 094, an ungrouped C chondrite that shows a minimal amount of secondary alteration. Chondrites that have been altered by pre-terrestrial water-rock interactions have values less than 3.0 with type 1.0 indicating the highest degree of aqueous alteration. Type 1.0 chondrites are dominated by serpentine and clay minerals and lack any anhydrous silicates. Chondrites that have been thermally altered and show some degree of recrystallization and/or chemical equilibration have values greater than 3.00 with type 7 indicating the highest degree of thermal alteration and recrystallization.

Components of Chondrites

Chondrules are the most common components of many chondrite groups, particularly the ones designated type 2 and 3. Chondrules are igneous spheres formed by flash heating at temperatures of ~1720 to 2120 K followed by rapid cooling. In types 4–7, chondrule boundaries become progressively indistinct due to recrystallization. In most type 1 chondrites, such as the CI group, chondrules are not present, and it is unclear whether they were present in the protolith prior to extensive aqueous alteration or if they were never present in these chondrites at all. The heat source for chondrule formation remains a major unresolved question in meteorite studies. Lightening, shock waves, and current sheets in the early Solar Nebula as well as collisions between early-formed planetesimals have been proposed.

Calcium-aluminum-rich inclusions (CAIs), sometimes called refractory inclusions, are materials that are noteworthy for being rich in refractory element-bearing minerals. Some are interpreted to be fluffy, unmelted aggregates of minerals that condensed from the Solar Nebula. They are generally dated (based on ^{26}Al-^{26} Mg, ^{207}Pb-^{206}Pb and I-Xe isotope systems) to be older than chondrules by about 2–3 million years and generally considered the first solids formed from the Solar Nebula gas. Based on the ^{207}Pb-^{206}Pb isotope system, some CAIs are as old as 4568 Ma (Bouvier and Wadhwa 2010). Their mineral assemblages and compositions bear resemblance to predictions of minerals expected to condense from gas of solar composition as it cools under equilibrium conditions.

Interstitial to the chondrules and CAIs is a fine-grained (micrometer-submicrometer-sized) component of chondrites referred to as matrix. Matrix is a mixture of materials that range from being highly primitive in some chondrites to highly altered in others (e.g., CM chondrites). It is a component of chondrites dominated by silicates but also harbors primitive amorphous materials, organic matter, and interstellar (presolar) grains. Interestingly, although all chondrites are mixtures of many components, their whole rock chemistries average out to near solar. This has led to the hypothesis of complementarity and that the components of each chondrite group formed locally within the early Solar System.

Achondrites

The achondrites are derived from parent bodies that experienced large-scale partial melting, isotopic homogenization, and subsequent differentiation. Achondrite groups include the genetically related eucrites, diogenites, and howardites, the angrites, and the aubrites. Mesosiderites and pallasites are stony irons from differentiated bodies and thus can be considered as related to achondrites. Primitive achondrite groups include ureilites, acapulcoites and lodranites, brachinites, and winonaites.

Eucrites and diogenites are basalts and orthopyroxene cumulates, respectively, thought to have originated in near-surface lava flows or intrusives on a common asteroidal parent body. However, most eucrites and diogenites are brecciated. Howardites are polymict breccias containing eucrite and diogenite components (Delaney et al. 1984). Howardites, eucrites, and diogenites have similar whole-rock oxygen isotopic compositions and similar Fe/Mn ratios in their pyroxenes, suggesting a close genetic relationship, and are sometimes referred to as HED meteorites. Similarities in the mineralogical compositions of the HEDs and the surface mineralogy of asteroid 4 Vesta, as determined by ground-based visible and near-infrared reflectance spectroscopy, suggests that the HEDs are derived from this asteroid (Binzel and Xu 1993; McCord et al. 1970). This link is supported by data from the Dawn space mission, which orbited Vesta between 2011 and 2012.

Angrites are medium- to coarse-grained (up to 2–3 mm) igneous rocks of generally basaltic composition but with mineralogies consisting of Ca-Al-Ti-rich pyroxene, Ca-rich olivine, and anorthitic plagioclase with accessory spinel, troilite, kirschsteinite, whitlockite, titanomagnetite, and Fe,Ni metal (Mittlefehldt et al. 1998; Mittlefehldt and Lindstrom 1990; Yanai 1994). Oxygen isotope compositions of the angrites are similar to those of the HED meteorites, brachinites, and mesosiderites (Fig. 5). However, the mineralogies and compositions of the angrites suggest that they are not related to any of these other meteorite groups.

The aubrites are highly reduced achondrites with mineral assemblages, mineral compositions, and stable isotope ratios similar to the enstatite chondrites and are often referred to as enstatite achondrites (Watters and Prinz 1979). All of the aubrites are breccias with the exception of the Shallowater aubrite, which has an igneous texture. They consist mostly (~75–95 vol%) of nearly FeO-free enstatite, with minor albitic plagioclase and nearly FeO-free diopside and forsterite. Other phases include accessory Si-bearing Fe,Ni metal and a variety of sulfides similar to those in the enstatite chondrites (Wheelock et al. 1994). The highly reduced-state, oxygen isotope composition and the presence of ferroan alabandite [(Fe,Mn)S] in the aubrites link them to the EL chondrites. However, they are probably derived from different asteroidal parent bodies (Keil 1989).

Mesosiderites are breccias composed of roughly equal proportions of silicates and Fe,Ni metal plus troilite (Floran et al. 1978; Hewins 1983). Their silicate fraction consists of mineral and lithic clasts in a fine-grained fragmental or igneous matrix. The lithic clasts are largely basalts, gabbros, and pyroxenites with minor amounts of dunite and rare anorthosite. Mineral clasts consist of coarse-grained orthopyroxene, olivine, plagioclase, and Fe,Ni-metal.

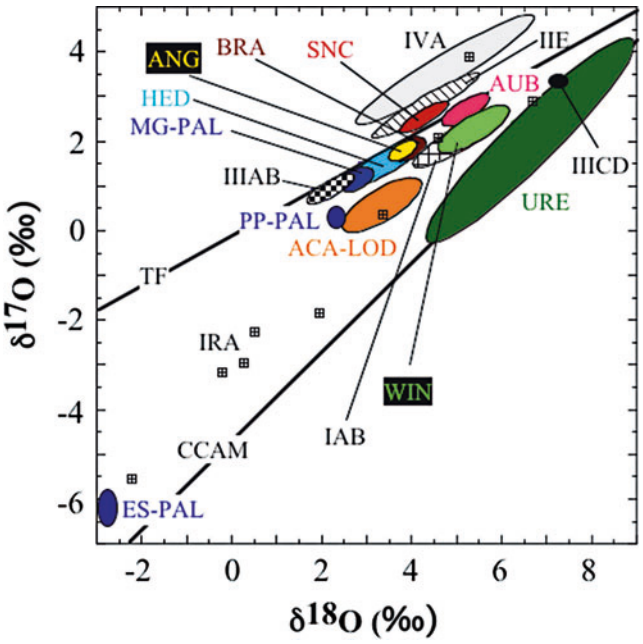

Meteorites, Fig. 5 Oxygen three-isotope diagram showing the fields for the achondrite groups. *ACA-LOD* acapulcoites and lodranites; *ANG* angrites; *AUB* aubrites; *BRA* brachinites, *HED* howardites, eucrites, diogenites; *IRA* ungrouped irons; *SNC* shergottites, nakhlites, chassignites; *WIN* winonaites; *MG-PAL* main group pallasites; *PP-PAL* pyroxene pallasites; *ES-PAL* Eagle Station Pallasites. IVA, IIAB, IICD, and IIE are iron meteorite groups (From Weisberg et al. (2006))

The pallasites are essentially olivine (35–85 vol%)-metal (and troilite) assemblages. There are three different types of pallasites that are distinguished by differences in their silicate mineralogy and composition, metal composition, and oxygen isotope composition. These include the main group pallasites, the Eagle Station pallasites, and the pyroxene-pallasites (Boesenberg et al. 2000; Mittlefehldt et al. 1998). The differences among the pallasite groups suggest that they originated on separate asteroidal bodies.

The ureilites are an example of a primitive achondrite. They are a major meteorite group with over 400 known specimens. Most are monomict and more than 25 are polymict breccias. They have textures, mineralogies, and lithophile element chemistries that suggest they are highly fractionated rocks from an achondrite parent body, yet their oxygen isotope compositions do not follow a mass-dependent fractionation trend characteristic of planetary differentiation. Instead, they plot along the CCAM line, overlapping the CV chondrites (Fig. 5) (Clayton and Mayeda 1988). The ureilites are olivine-pyroxene rocks with interstitial carbon (graphite and micro-diamonds) mixed with metal, sulfides, and minor silicates. Most are essentially devoid of feldspar with the exception of the polymict ureilites and some rare exceptions. Ureilites can be subdivided into three major types (olivine-pigeonite, olivine-orthopyroxene, and polymict ureilites).

The acapulcoites and lodranites are closely related primitive achondrites. The acapulcoites are fine-grained (150–230 μm), equigranular rocks composed of olivine, pyroxene, plagioclase, metal, and troilite, while lodranites are coarse-grained (540–700 μm) olivine, pyroxene rocks depleted in troilite and plagioclase (McCoy et al. 1996; Mittlefehldt et al. 1998; Nagahara 1992). The whole-rock oxygen isotope compositions of acapulcoites and lodranites overlap on the three-isotope diagram (Fig. 5). Rare relict chondrules have been reported in several acapulcoites suggesting that they are close to their chondrite precursor. Brachinites are olivine-rich primitive achondrites that are close to chondritic and unfractionated in composition. Winonaites are primitive achondrites that have roughly chondritic mineralogy and chemical composition, but achondritic, recrystallized textures (Benedix et al. 1998; Kimura et al. 1992).

Irons

The iron meteorites consist mostly of Fe,Ni and are known for their characteristic Widmanstätten structure, an intergrowth of the Fe,Ni phases kamacite and taenite. These meteorites are windows in to the interior (cores) of differentiated bodies. Currently, there are 13 recognized groups of iron meteorites based on their Ni and trace siderophile element (Ga, Ge, Ir) abundances (Fig. 6) (Choi et al. 1995). Letters combined with Roman numerals are used to name the groups (e.g., IA, IVB). Ga and Ge are the most volatile siderophile elements and tend to be strongly fractionated between the iron groups. Geochemical differences between the groups are due to pre-accretion processes, but the geochemical trends within some of these groups are consistent with fractional crystallization, with each group forming in the core of a separate asteroid (Scott 1972). A large number (as much as 40%) of iron meteorites do not fit into the well-described groups. These ungrouped irons may represent extreme fractional crystallization products of the known groups, others could be impact melt products, as opposed to forming as cores. Some may represent the only sample of their parent asteroid.

Some irons contain silicate inclusions (e.g., IAB, IIICD, and IIE). They contain variable amounts of low-Ca pyroxene, high-Ca pyroxene, olivine, plagioclase, troilite, graphite, phosphates, and Fe,Ni-metal and minor amounts of daubreelite and chromite. These irons do not show large fractionations in siderophile elements as in the other irons, and their origin has been debated; suggested origins include crystallization of an S-rich core, partial asteroidal differentiation followed by impact mixing, and formation in isolated impact melt pools (Kracher 1982; McCoy et al. 1993). The IAB and IIICD irons have mineralogy and oxygen isotope

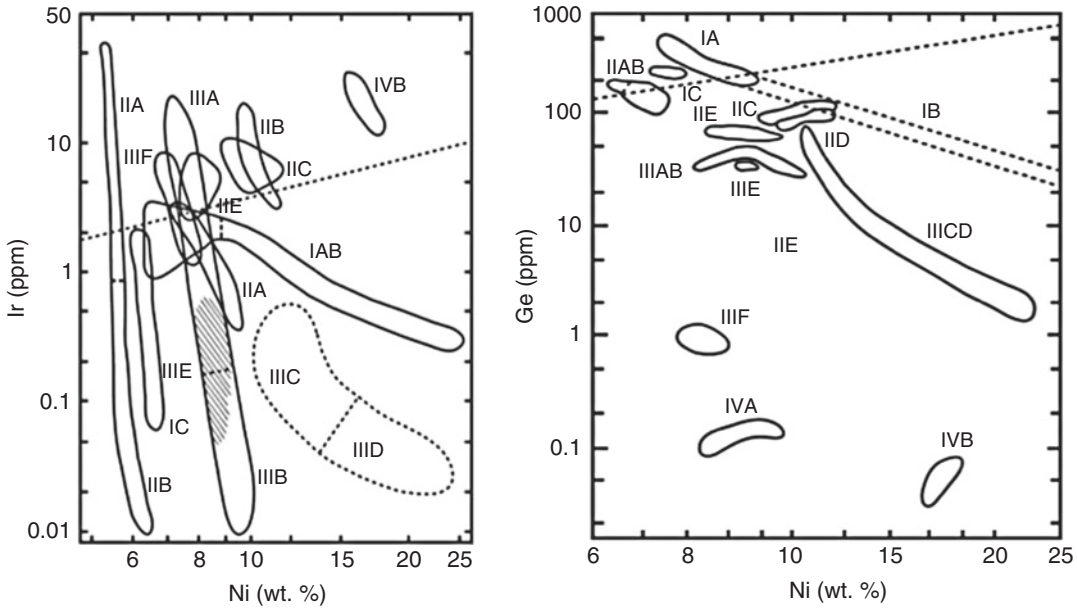

Meteorites, Fig. 6 Classification of iron meteorites based on siderophile element (Ni, Ir, Ga) abundances (Modified from Scott and Wason (1975))

compositions (Fig. 5) similar to winonaites, and it has been suggested that the silicate inclusions in IAB and winonaites formed on the same or similar parent body (Benedix et al. 2000).

Martian Meteorites

The Martian meteorites are rocks from the crust of Mars. They are volcanic (e.g., basaltic shergottites and nakhlites) and plutonic (lherzolitic and olivine-phyric shergottites, Chassigny, ALH 84001) rocks (McSween 2002; McSween and Treiman 1998; Mittlefehldt 1994). Their oxygen isotope compositions define a unique slope-0.52 mass fractionation line in three-isotope space (Fig. 5) suggesting their origin from the same, differentiated parent body. The relatively young crystallization age of some of these meteorites (<1.3 Ga) suggests derivation from a planet-sized body. Most importantly, gases trapped in impact-produced glass inclusions and veins in some Martian meteorites are compositionally similar to the Martian atmosphere, as determined by the Viking Landers, indicating that these meteorites are from the planet Mars (Bogard and Johnson 1983; Nyquist et al. 2001).

While all other Martian meteorites have relatively young crystallization ages, the age of ALH 84001 is ~4.5 Ga and, thus, is a fragment of the ancient Martian crust. It consists mainly of coarse, up to 6-mm long, orthopyroxene crystals (96%), with minor chromite, plagioclase (maskelynite), phosphate, and accessory phases such as olivine, augite, pyrite, and carbonates. One of the most historically intriguing aspects of this Martian meteorite is that it had been interpreted to contain fossils of nano-bacteria, as well as other evidence of life, of Martian origin (McKay et al. 1996).

Lunar Meteorites

Lunar meteorites include a wide range of rock types including brecciated and unbrecciated mare basalts, mixed mare/highland breccias, highland regolith breccias, and highland impact-melt breccias (e.g., Papike et al. 1998). The lunar meteorites have mineral chemistries (e.g., Fe/Mn ratios in pyroxenes) and bulk chemical and oxygen isotope compositions similar to samples collected by the Apollo and Luna missions. However, some lunar meteorites come from areas not sampled by these missions and some (e.g., Northwest Africa 773) sample lithologies unknown from and thus complement the mission samples. NWA 773 consists of two lithologies, a fragmental regolith breccia and an olivine gabbro.

Deciphering the Meteorite Record

Stable isotopes, particularly the three isotopes of oxygen (^{16}O, ^{17}O, and ^{18}O), have played a major role in classifying meteorites as well as identifying genetic relationships between meteorite groups and tracing primary and secondary processes (Clayton 2003). Plotted on a three-isotope diagram ($\delta^{17}O$ vs. $\delta^{18}O$, Figs. 4 and 5), various meteorite groups occupy specific regions, supporting their classification by

other techniques. The line labeled TF on Figs. 4 and 5 is the terrestrial fractionation line. The 0.52 slope indicates that all materials plotting along this line may be related by mass-dependent fractionation. Note that all rocks from both the Earth and Moon plot along this line. Primitive meteorites plot on lines defined by mixing of ^{16}O–rich and ^{16}O–poor oxygen reservoirs, as opposed to mass-dependent fractionation. For example, many of the C chondrites plot along a slope ~ 1 line, often referred to as the carbonaceous chondrite anhydrous mixing (CCAM) line. Most C chondrites occupy regions below, whereas O and R chondrites generally plot above, the TF line. Interestingly, E chondrites and their achondrite equivalents (the aubrites) plot on the TF line overlapping the Earth and Moon. This has led to the inference that the E chondrites are genetically related to the Earth-Moon system. This relationship is further supported by stable isotopes of Cr, Ti, Ni, and Zn (Javoy 1995; Paniello et al. 2012; Warren 2011). The only exception is Si isotopes, which are different (Fitoussi and Bourdon 2012; Savage and Moyier 2013).

Summary

As of 2017, there are more than 60,000 known meteorites (as reported in the Meteoritical Bulletin Database of the Meteoritical Society). Most of these are derived from asteroids, some may be from comets, 190 are Martian meteorites and 293 are from the Moon. They are a valuable, wide-ranging resource of Solar System materials available for geochemical analysis, providing objects from the earliest history of our Solar System. They include materials from both primitive (undifferentiated) and differentiated asteroids; they reveal the age of the Solar System and give us the only samples we currently have from the crust of Mars.

References

Benedix GK, McCoy TJ, Keil K, Boggard DD, Garrison DH (1998) A petrologic and isotopic study of winonaites: evidence for early partial melting, brecciation, and metamorphism. Geochim Cosmochim Acta 62:2535–2553

Benedix GK, McCoy TJ, Keil K, Love SG (2000) A petrologic study of the IAB iron meteorites: constraints on the formation of the IAB-winonaite parent body. Meteorit Planet Sci 35:1127–1141

Binzel RP, Xu S (1993) Chips off of asteroid 4 Vesta: evidence for the parent body of basaltic achondrite meteorites. Science 260:186–191

Boesenberg JS, Davis AM, Prinz M, Weisberg MK, Clayton RN, Mayeda TK (2000) The pyroxene pallasites, vermillion and Yamato 8451: not quite a couple. Meteorit Planet Sci 35:757–769

Bogard DD, Johnson P (1983) Martian gases in an Antarctic meteorite. Science 221:651–654

Bouvier A, Wadhwa M (2010) The age of the solar system redefined by the oldest Pb–Pb age of a meteoritic inclusion. Nat Geosci 3:637–641

Choi BG, Ouyang X, Wasson JT (1995) Classification and origin of IAB and IICD iron meteorites. Geochim Cosmochim Acta 59:593–612

Clayton RN (2003) Oxygen isotopes in meteorites. In: Davis AM (ed) Treatise on Geochemistry 1, Meteorites, Comets, and Planets. Elsevier-Pergamon, Oxford, pp 129–142

Clayton RN, Mayeda TK (1984) Oxygen isotope compositions of enstatite chondrites and aubrites. J Geophys Res 89:C245–C249. Proceeding of the fifteenth Lunar and Planetary Science Conference

Clayton RN, Mayeda TK (1988) Formation of ureilites by nebular processes. Geochim Cosmochim Acta 52:1313–1318

Clayton RN, Mayeda TK (1996) Oxygen-isotope studies of achondrites. Geochim Cosmochim Acta 60:1999–2018

Clayton RN, Mayeda TK (1999) Oxygen isotope studies of carbonaceous chondrites. Geochim Cosmochim Acta 63:2089–2104

Delaney JS, Prinz M, Takeda H (1984) The polymict eucrites. J Geophys Res Supplement, 89:C251–C288. Proceedings of the 15th Lunar and Planetary Science Conference

Fitoussi C, Bourdon B (2012) Silicon isotope evidence against an enstatite chondrite earth. Science 335:1477–1480

Floran RJ, Caulfield JBD, Harlow GE, Prinz M (1978) Impact origin for the Simondium, Pinnaroo, and Hainholz mesosiderites: implications for impact processes beyond the earth-moon system. Proc Lunar Planet Sci Conf 9:1083–1114

Grevesse N, Sauval AJ (1998) Standard solar composition. Space Sci Rev 85:161–174

Hewins RH (1983) Impact versus internal origins for mesosiderites. J Geophys Res 88:B257–B266

Javoy M (1995) The integral enstatite chondrite model of the earth. Geophys Res Lett 22:2219–2222

Kallemeyn GW, Wasson JT (1981) The compositional classification of chondrites: I the carbonaceous chondrite groups. Geochim Cosmochim Acta 45:1217–1230

Kallemeyn GW, Wasson JT (1982) The compositional classification of chondrites: III Ungrouped carbonaceous chondrites. Geochim Cosmochim Acta 46:2217–2228

Kallemeyn GW, Boynton WV, Willis J, Wasson JT (1978) Formation of the Bencubbin polymict meteoritic breccia. Geochim Cosmochim Acta 42:507–515

Kallemeyn GW, Rubin AE, Wang D, Wasson JT (1989) Ordinary chondrites: bulk compositions, classification, lithophile-element fractionations, and composition-petrographic type relationships. Geochim Cosmochim Acta 53:2747–2767

Kallemeyn GW, Rubin AE, Wasson JT (1991) The compositional classification of chondrites: V. The Karoonda (CK) group of carbonaceous chondrites. Geochim Cosmochim Acta 55:881–892

Kallemeyn GW, Rubin AE, Wasson JT (1994) The compositional classification of chondrites: VI The CR carbonaceous chondrite group. Geochim Cosmochim Acta 58:2873–2888

Kallemeyn GW, Rubin AE, Wasson JT (1996) The compositional classification of chondrites: VII the R chondrite group. Geochim Cosmochim Acta 60:2243–2256

Keil K (1969) Mineralogical and chemical relationships among enstatite chondrites. J Geophys Res 73:6945–6976

Keil K (1989) Enstatite meteorites and their parent bodies. Meteoritics 24:195–208

Kimura M, Tsuchiayama A, Fukuoka T, Iimura Y (1992) Antarctic primitive achondrites, Yamato-74025, −75300, and −75305: their mineralogy, thermal history, and the relevance to winonaites. Proc NIPR Symp Antarct Meteorites 5:165–190

Kracher A (1982) Crystallization of a S-saturated -melt, and the origin of the iron meteorite groups IAB and IIICD. Geophys Res Lett 9:412–415

McCord TB, Adams JB, Johnson TV (1970) Asteroid Vesta: spectral reflectivity and compositional implications. Science 168: 1445–1447

McCoy TJ, Scott ERD, Haack H (1993) Genesis of the IIICD iron meteorites: evidence from silicate-bearing inclusions. Meteoritics 28:552–560

McCoy TJ, Keil K, Clayton RN, Mayeda TK, Bogard DD, Garrison DH, Huss GR, Hutcheon ID, Wieler R (1996) A petrologic, chemical and isotopic study of monument draw and comparison with other acapulcoites: evidence for formation by incipient partial melting. Geochim Cosmochim Acta 60:2681–2708
McKay DS, Gibson EK, Thomas-Keprta VH, Romanek CS, Clement SJ, Chillier XDF, Maechling CR, Zare RN (1996) Search for past life on Mars: possible relic biogenic activity in martian meteorite ALH84001. Science 273:924–930
McSween HY Jr (2002) The rocks of Mars, from far and near. Meteorit Planet Sci 37:7–25
McSween HY Jr, Treiman AH (1998) Martian meteorites. In Planetary Materials (J.J. Papike ed.) Rev Mineral 36:6-1–6-53
Mittlefehldt DW (1994) ALH84001, a cumulate orthopyroxenite member of the martian meteorite clan. Meteoritics 29:214–221
Mittlefehldt DW, Lindstrom MM (1990) Geochemistry and genesis of the Angrites. Geochim Cosmochim Acta 54:3209–3218
Mittlefehldt DW, McCoy TJ, Goodrich CA, Kracher A (1998) Non-chondritic meteorites from asteroidal bodies in planetary materials (J.J. Papike, ed.) Rev Mineral 36:4.1–4.495
Nagahara H (1992) Yamato-8002: partial melting residue on the "unique" chondrite parent body. Proc NIPR Symp Antarct Meteorit 5:191–223
Nyquist LE, Bogard DD, Shih C-Y, Greshake A, Stöffler D, Eugster O (2001) Ages and geologic histories of martian meteorites. Space Sci Rev 96:105–164
Palme H, Jones A (2003) Solar abundances of the elements. In: Davis AM (ed) Treatise on geochemistry 1, meteorites, comets, and planets. Elsevier-Pergamon, Oxford, pp 41–61
Paniello R, Day JMD, Moynier F (2012) Zn isotopic evidence for the origin of the moon. Nature 490:376–379
Papike JJ, Ryder G, Shearer CK (1998) Lunar samples. In planetary materials (J.J. Papike. Ed.) Rev Mineral 36:5.1–5.234
Rubin AE, Grossman JN (2014) Meteorite and meteoroid: a new comprehensive definition. Meteorit Planet Sci 45:114–122
Savage PS, Moynier F (2013) Silicon isotopic variation in enstatite meteorites: clues to their origin and earth-forming material. Earth Planet Sci Lett 361:487–496
Scott ERD (1972) Chemical fractionation in iron meteorites and its interpretation. Geochim. Cosmochim. Acta 36:1205–1236
Scott ERD, Wasson JT (1975) Classification and properties of iron meteorites. Rev Geophys Space Phys 13:527–546
Scott ERD, Haack H, Love SG (2001) Formation of mesosiderites by fragmentation and reaccretion of a large differentiated asteroid. Meteorit Planet Sci 36:869–881
Sears DWG, Kallemeyn GW, Wasson JT (1982) The compositional classification of chondrites: II The enstatite chondrite groups. Geochim Cosmochim Acta 46:597–608
Warren PH (2011) Stable-isotopic anomalies and the accretionary assemblage of the earth and Mars: a subordinate role for carbonaceous chondrites. Earth Planet Sci Lett 311:93–100
Wasson JT, Kallemeyn GW (1988) Composition of chondrites. Philos Trans R Soc Lond A325:535–544
Watters TR, Prinz M (1979) Aubrites: their origin and relationship to enstatite chondrites. Proc Lunar Planet Sci Conf 10:1073–1093
Weisberg MK, McCoy TJ, Krot AE (2006) Systematics and evaluation of meteorite classification. In: Lauretta D, McSween HY Jr (eds) Meteorites and the early solar system II. University of Arizona Press, Tucson, pp 19–52
Weisberg MK, Ebel DS, Nagashima D, Kita N, Humayun M (2015) Petrology and geochemistry of chondrules and metal in NWA 5492 and GRO 95551: a new type of metal-rich chondrite. Geochim Cosmochim Acta 167:269–285
Weiss BP, Gattacceca J, Sabine S, Rochette P, Christensen UR (2010) Paleomagnetic record of meteorites and early planetesimal differentiation. Space Sci Rev 152:341–390
Wheelock MM, Keil K, Floss C, Taylor GJ, Crozaz G (1994) REE geochemistry of oldhamite-dominated clasts from the Norton County aubrite: igneous origin of oldhamite. Geochim Cosmochim Acta 58:449–458
Yanai K (1994) Angrite Asuka-881371: preliminary examination of a unique meteorite in the Japanese collection of Antarctic meteorites. Proc NIPR Symp Antarct Meteorites 7:30–41

Mid-Ocean Ridge Basalts (MORB)

Charles H. Langmuir
Department of Earth and Planetary Sciences, Harvard University, Cambridge, MA, USA

Definition

Mid-ocean ridge basalts are the volcanic rocks erupted at the global system of ocean ridges. They are the most common volcanic rock type on Earth. They provide insights into the mantle from which they are derived by partial melting and the processes in ocean ridge volcanic systems through which they pass on their way to the surface.

Introduction

The global system of ocean ridges is a continuous line of volcanism that wraps around the globe reaching a total length of more than 60,000 km. Ridges are the sites of formation of new oceanic crust, and over time have created the entire ocean floor, with the exception of some additions through intraplate volcanism and sediments that gradually accumulate as the crust ages. The rocks created at ocean ridges are the most common rocks on Earth, covering two-thirds of the Earth's surface, i.e., oceanic crust. Ocean ridge volcanism is about 75% of all volcanic activity on Earth (Crisp 1984), but is largely hidden from view since most of it occurs several thousand meters below sea level. The ocean ridge volcanoes erupt basaltic magmas called "ocean ridge basalt." While not all ocean ridges are in the middle of their hosting oceans, this basalt has become known as "mid-ocean ridge basalt," or MORB. MORB is the most common volcanic rock type in the world.

MORB began to be investigated only in the 1960s, just after the discovery of the mid-ocean ridge and the development of plate tectonics. Steady sampling over the last 50 years has gradually provided data on more than 30,000 samples that can be used to define the average composition and variability on all scales. With the advent of a global public database, PETDB (www.petdb.org) (Lehnert et al. 2000), all published location and geochemical data for these ocean ridge samples

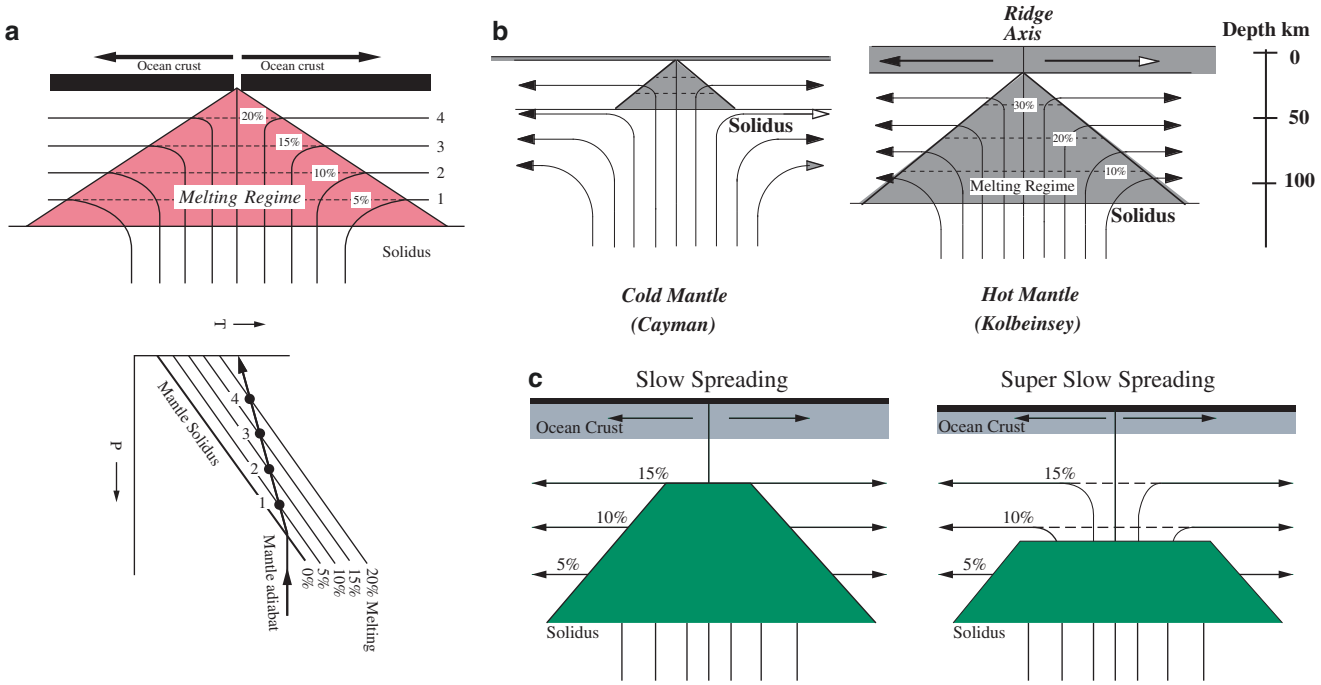

Mid-Ocean Ridge Basalts (MORB), Fig. 1 Illustration of the means by which parental magmas for MORB are generated in the mantle. A: Demonstration of how decompression of the mantle beneath the ridge leads to a melting and a "melting regime" where melt forms and is extracted to form the oceanic crust. B: Illustration of the effect of mantle temperature on the melting regime; colder mantle intersects the solidus at shallower depths, hence melts less and creates thinner crust. C: Illustration of the effect of spreading rate on the melting regime at constant temperature. As spreading rate decreases, cooling from the surface is able to penetrate more deeply into the mantle, stopping melting at greater depth

M

are available. Even unpublished data from US cruises are also available. There are many additional unpublished locations and data from European, Russian, Japanese, and Chinese cruises that are not in the public domain. All samples in PETDB can be readily visualized in a geographical reference frame using GEOMAPAPP (www.geomapapp.org) (Carbotte et al. 2004). The last few decades have thus revealed and defined the most abundant rock on Earth.

MORB as a Product of Pressure Release Melting

Because the ridges are constantly spreading apart, there is little impediment to the magmas reaching the surface, and for that reason, MORB are the most direct products of Earth's interior and the least modified during ascent. The mean composition of MORB then defines the composition of Earth's most extensive crustal reservoir, and is as well the best available constraint from which the composition of the upper mantle can be inferred.

MORB compositions are influenced by the primary melt that is formed by partial melting of the mantle, and the processes of chemical exchange and removal of crystals (called "differentiation") that take place during cooling before eruption. The primary melt is influenced by the temperature, pressure, and composition of the mantle. In general, MORB are generated by "pressure release melting" (Fig. 1a). The temperature at which the mantle begins to melt, called the solidus, increases substantially with pressure. Therefore, at high pressures, the mantle is solid, but as it rises beneath the ridge, the pressure decreases, and melting begins as the solidus is crossed. The amount of melting is then controlled by the depth at which the crossing of the solidus occurs, and the distance over which the mantle rises as it melts. Mantle at higher temperatures will begin melting deeper, and hence rise further, melting more than mantle that is cooler (Fig. 1b). At very slow spreading rates, surface cooling penetrates into the mantle, causing slightly lower extents of melting in these settings (Fig. 1c). The amount of melt may also be influenced by the chemical composition of the mantle.

Once the melts exit the melting regime, they may interact with the cold mantle lid overlying the melting regime, and then cool and crystallize in the crust, forming the lower oceanic crust, before the lavas are erupted on the sea floor. The erupted melts then have been influenced by multiple processes – melting of the mantle, transport of the melts through the uppermost mantle, and cooling and crystallization within the crust. Constraints on the importance and consequences of these various processes come from experiments, theory, and the compositions of MORB themselves, and how these compositions vary in different settings around the ocean ridge system.

Average MORB Compositions

Information about the chemical compositions of MORB comes from three distinct types of measurements, all of which are available through PetDB. The first are the major elements, generally referring to those oxides that are present at levels higher than about 0.05 wt.%. The major elements are conveniently measured on MORB glasses by electron microprobe, leading to a very large data set of tens of thousands of analyses. Major elements provide information about extents of cooling in the crust, as well as the composition and extent of melting of the mantle from which they are derived. Trace elements have been more difficult to determine but now are routinely measured by inductively-coupled plasma mass spectrometry, from which thousands of analyses are available. Trace elements provide more information about the variations in the composition of the mantle source that melted. The most difficult measurements are those of the radiogenic isotopes, but for the commonly measured isotopes of Sr, Nd, and Pb, there is also a substantial data set of many thousands of measurements, with progressively less data for Hf, Os, and the noble gases. The isotopic compositions are the most direct indication of the mantle source, and because their evolution is time dependent, they also provide constraints on the long-term history of the mantle sources of MORB.

The mean composition of MORB has been best determined by Gale et al. (2013), who used all the available data from PETDB and added several thousand additional analyses. MORB volcanism occurs along long cracks in the ocean crust that are periodically offset by transform faults or other smaller offsets. These offsets demark the boundaries between ridge segments. There are about 750 ridge segments along the entire ocean ridge. To avoid the problem of uneven sampling along the ridge system, Gale et al. first constructed averages for each ridge segment, and then ridge segment averages were averaged. Earlier efforts defining mean compositions, based on simple averages of smaller numbers of samples (Sun and McDonough 1989; Hofmann 1988; Arevalo and McDonough 2010), nonetheless came up with rather similar values, suggesting the mean composition is now well determined (Table 1).

A distinctive type of ocean ridge basalt is erupted at spreading centers behind active convergent margins, called back-arc basins. These back-arc spreading centers erupt back-arc basin basalts (BABB) (Sinton and Fryer 1987) that are distinguished from MORB from open ocean spreading centers by their inclusion of an "arc component" in their chemical composition, which varies in composition with distance to the arc (Langmuir et al. 2006; Kelley et al. 2006). When the back-arc spreading center is close to the arc, the BABB have high K_2O and H_2O, reflecting contributions from the downgoing slab.

Mid-Ocean Ridge Basalts (MORB), Table 1 The composition of ALL MORB

	n	ALL MORBMean	±(95% conf)
MgO	430	**7.58**	0.12
SiO_2	430	**50.47**	0.08
FeO	430	**10.43**	0.21
CaO	430	**11.39**	0.09
Na_2O	430	**2.79**	0.03
Al_2O_3	430	**14.70**	0.12
TiO_2	430	**1.68**	0.05
K_2O	430	**0.160**	0.014
P_2O_3	409	**0.184**	0.012
MnO	379	**0.184**	0.005
Ba	392	**29.2**	3.8
Be	139	**0.76**	0.05
Ce	410	**14.86**	1.26
Co	350	**43.0**	0.7
Cr	369	**249**	12
Cs	272	**0.034**	0.006
Cu	357	**74**	2
Dy	411	**6.08**	0.30
Er	410	**3.79**	0.17
Eu	411	**1.36**	0.05
Ga	300	**17.5**	0.2
Gd	386	**4.99**	0.23
Hf	398	**2.79**	0.15
Ho	404	**1.28**	0.05
La	412	**5.21**	0.53
Li	255	**6.5**	0.3
Lu	410	**0.53**	0.02
Mo	185	**0.46**	0.05
Nb	402	**5.24**	0.59
Nd	418	**12.03**	0.78
Ni	365	**92**	5
Pb	370	**0.57**	0.03
Pr	390	**2.24**	0.12
Rb	380	**2.88**	0.44
Sc	338	**39.8**	0.8
Sm	417	**3.82**	0.15
Sn	200	**0.92**	0.06
Sr	413	**129**	4
Ta	352	**0.34**	0.04
Tb	397	**0.90**	0.04
Th	395	**0.404**	0.081
Tl	200	**0.020**	0.001
U	374	**0.119**	0.013
V	337	**309**	13
W	209	**0.12**	0.02
Y	410	**36.8**	1.9
Yb	411	**3.63**	0.18
Zn	338	**91.3**	3.1
Zr	412	**116.9**	8.4
$^{87}Sr/^{88}Sr$	272	**0.702819**	0.000067
$^{143}Nd/^{144}Nd$	272	**0.513074**	0.000017
$^{206}Pb/^{204}Pb$	245	**18.412**	0.090

(*continued*)

Mid-Ocean Ridge Basalts (MORB), Table 1 (continued)

$^{207}Pb/^{204}Pb$	245	**15.515**	0.010
$^{208}Pb/^{204}Pb$	245	**38.100**	0.091
$^{176}Hf/^{177}Hf$	138	**0.283**	0.000
Sm/Nd	416	**0.325**	0.005
Zr/Hf	398	**40.64**	0.95
Ba/Th	376	**71.93**	8.32
Nb/U	366	**44.37**	1.99

In addition to BABB, other diverse components make up the global average, and the regional diversity of compositions reveals much about the composition and history of the mantle. Major elements, trace elements, and isotopes each provide different sets of information.

Major Elements and Mineralogy

The mineralogy of MORB is straightforward. Olivine is the first phase to crystallize, followed by plagioclase and then clinopyroxene. At much lower temperatures, Fe-Ti oxides and low Ca pyroxene can appear, although these phases virtually never appear as phenocrysts in MORB. In almost all sampled MORB olivine and plagioclase are the most abundant phenocrysts. Clinopyroxene is less common. Fe-Ti oxides occur largely in the groundmass. Removal of these phases during cooling in the crust and uppermost mantle leads to the "liquid line of descent," the path of compositions created by cooling and removal of crystals. Calculations based on experimental data can be used to model the liquid lines of descent very accurately. What is remarkable about many MORB suites is how well samples from a particular region lie along liquid lines of descent calculated from the highest temperature basalts from the same region. Examples of MORB suites and liquid lines of descent from different regions are shown in Fig. 2. The oxide MgO is used as the horizontal axis because it is a very effective proxy for the temperatures of erupted magmas. The mean erupted temperature appears to vary slightly with spreading rate for MORB far from hot spots (Rubin and Sinton 2007), with slightly lower eruptive temperatures at faster spreading ridges, probably because of shallower magma systems that are more efficiently cooled by the surface.

The simplicity of MORB major element variations on a segment scale, illustrated for two segments in Fig. 2, is surprising given the great complexity that has emerged from the study of the plutonic rocks of the lower portions of ocean ridges (see e.g., Lissenberg et al. 2013). Very complex processes are apparent in the plutonic rocks, leading many in that community to argue that the liquid lines of descent of MORB should be very complicated and difficult to unravel (Coogan and O'Hara 2015). Given the plutonic complexity, it is remarkable how well individual MORB suites plot along simple liquid lines of descent. Whatever the origin of this fact, this observation makes it possible to back-project lower temperature MORB to the higher temperature (higher MgO) compositions that are more closely related to melts coming out of the mantle. These corrected compositions can then best

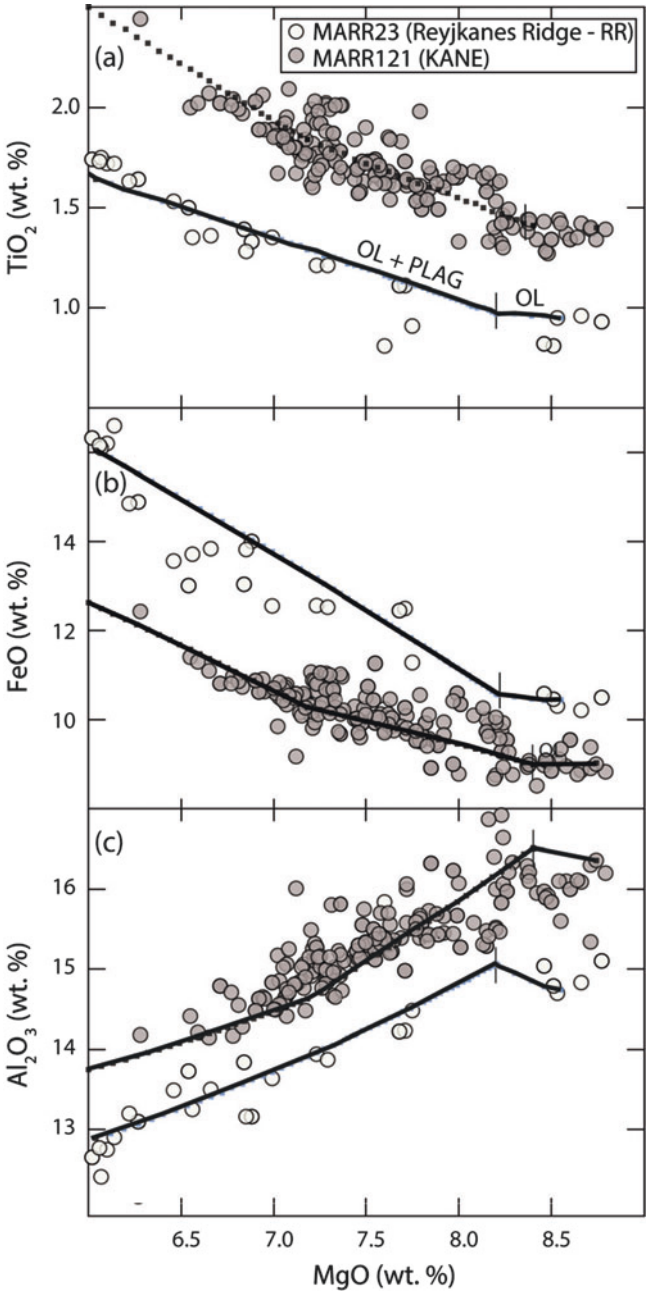

Mid-Ocean Ridge Basalts (MORB), Fig. 2 Data from a shallow (Reykjanes) and a deep (Kane) ridge segment with liquid lines of descent showing the smooth trends exhibited by lavas from individual ridge segments, and the large contrasts between mean compositions from different ridge segments. Note that the deeper ridge segment has lower Fe and Ti, and higher Al (and Na, not shown) than the shallower ridge segment (Modified from Gale et al. 2014)

be used to understand how MORB form, and what controls the variations exhibited by liquid lines of descent from different regions.

One method to correct, or normalize, compositions is to move them back along a liquid line of descent to a constant MgO content, normally 8 wt.%, which has the advantage of providing normalized compositions within the range of MORB observations (Klein and Langmuir 1987). Alternatively, compositions can be back-tracked to a composition in equilibrium with the mantle, which has an olivine composition of Fo_{90} or 90% of the MgO end-member (Stolper and Newman 1994). Gale et al. (2013) showed that the two methods produce similar results. $Na_{8.0}$ or Na_{90} refers to Na_2O contents normalized to a particular value. Normalizing in this way then allows comparisons of parental compositions around the global system of ocean ridges. These comparisons then show the systematics of MORB major element compositions, and allow a demonstration of how these systematics relate to tectonic variables such as spreading rate, proximity to hot spots, and the overall depth of the ridge axis.

Figure 3a, b shows the relationships among MORB major elements for individual ridge segments normalized to Fo_{90}, for ridge segments that have more than three samples available (Gale et al. 2014). The data are systematic and show clear relationships. Fe_{90} is negatively correlated with Si_{90}, Al_{90}, and Na_{90}, while Na_{90} and Al_{90} are positively correlated. The slowest spreading ridges, with spreading rates less than 20 mm/year, indicated by the open symbols in Fig. 3a, b, are slightly offset from the data from faster spreading ridges. There are also correlations between these chemical parameters and the depth of the segment from which the samples were recovered. Samples from shallow ridges have lower

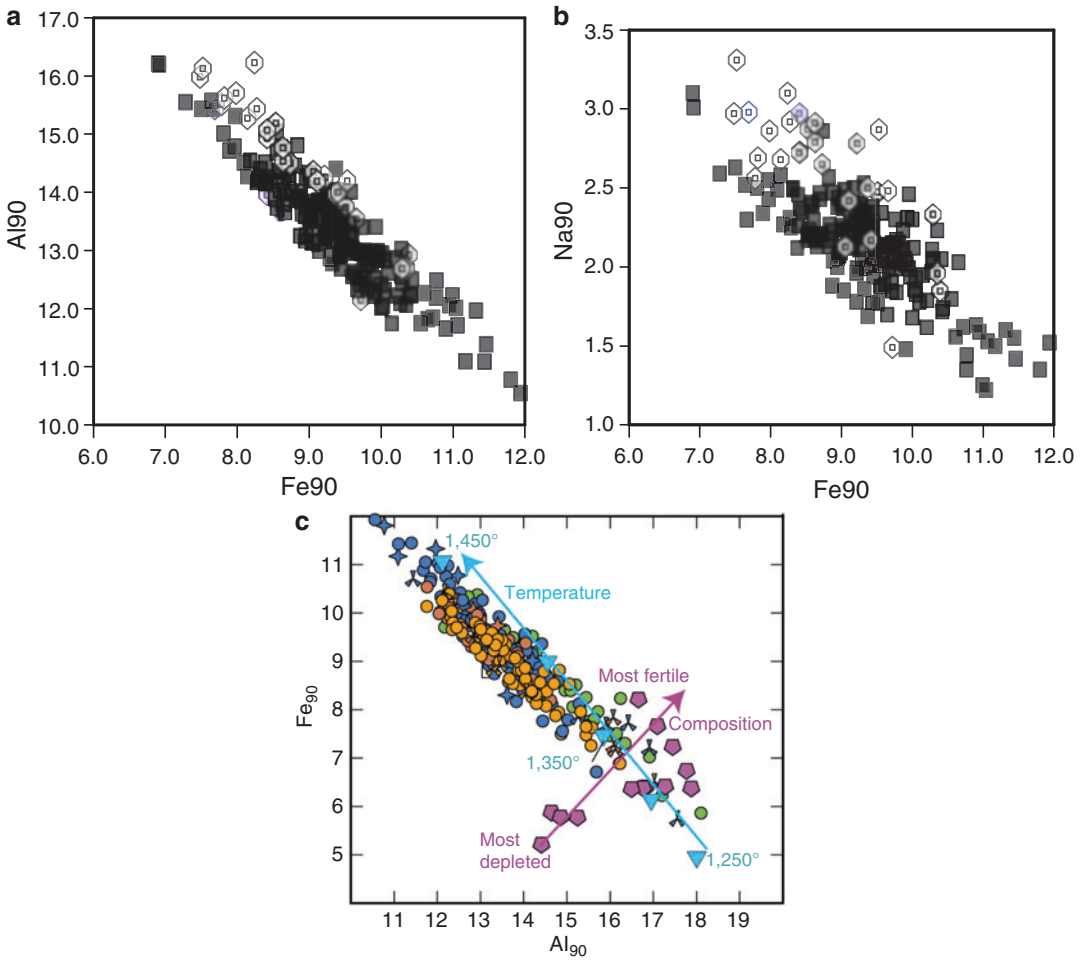

Mid-Ocean Ridge Basalts (MORB), Fig. 3 Variation of segment average major element compositions corrected to a composition in equilibrium with mantle olivine. A,B, Data for all segments except back-arc basins and hot spot centers with Th90 > 0.5. Super-slow spreading ridge segments are indicated by the open symbol. They are offset to higher Na90 and Al90 owing to a thick lithospheric lid at super-slow spreading rates. C,D Comparison of the data to trends for variable mantle temperature and variable mantle composition. *Pentagons* are experiments on mantle of different compositions. *Arrows* are calculated variations for temperature and composition. Note the principal component of the variation is well explained by mantle temperature, and not by mantle composition (Segment averages are from Gale et al. 2014)

$Na_{8.0}$, $Al_{8.0}$, and $Si_{8.0}$, and higher $Fe_{8.0}$ than samples from the deepest ridges. This contrast is also apparent by examining the liquid lines of descent in Fig. 2.

Klein and Langmuir (1987) originally proposed that these systematic variations in ocean ridge compositions were primarily the result of variations in mantle temperature, an inference that had been partially suggested on the basis of abyssal peridotite data by Dick et al. (1984). The reasoning behind this model is straightforward, and illustrated in Fig. 1b. Where the mantle is hotter, it begins melting at greater depth, and melts more as the mantle upwells toward the surface. This creates a large melting region with high extents of melting at ridges that overlie hotter mantle as compared to ridges that overlie colder mantle. The larger extents of melting dilute the Na and Al contents of the melts, while the elements Si and Fe are primarily responsive to the mean pressure of melting. The deeper average melting regime where the mantle is hot leads to higher pressures of melting and hence lower Si and higher Fe contents. The ocean crust is buoyant relative to the mantle. The large and deep melting regimes where the mantle is hotter lead to greater extents of melting and hence greater thicknesses of ocean crust, which rise to higher elevations as they equilibrate gravitationally with the underlying mantle. These early inferences remain consistent with all the new observational and experimental data.

Two alternative hypotheses have been proposed to account for the variations in ridge compositions seen in Fig. 3. Shen and Forsyth (1995) proposed that the dominant control was spreading rate. A thicker lithospheric lid at slower spreading rates (see Fig. 1c) would create smaller extents of melting, and the highest values of $Na_{8.0}$ do indeed occur primarily at the slowest spreading ridges. Niu and O'Hara (2008) proposed that the dominant control was mantle composition. They suggested that deeper ridges were underlain by sources with higher Na and lower Fe contents, which would lead to a mantle of higher density. The high density of the mantle would cause the ridge to be deep, and the high Na contents of the mantle source would lead to the high Na contents observed in basalts at the slowest spreading rates.

Both these arguments have elements of truth. As is apparent in Fig. 3a, b, the slowest spreading ridges do tend to have higher Na contents. This offset occurs across the entire range of mantle temperatures, however, and is a second-order effect. There must also be a range of mantle compositions at ocean ridges. This is very apparent in the trace element and isotope compositions, which are distinctive at and near ocean islands. Model curves for the effects of mantle composition, however, shown in Fig. 3c, d, show that the compositional variations produced by such inevitable variations are orthogonal to the main trend of the data, so this must also be a second-order effect. These conclusions are reinforced by the recent seismic data that show slower seismic velocities, and hence higher mantle temperatures, beneath ocean ridges with thicker crust (Dalton et al. 2014).

Back-arc basins also occupy a large range of mantle temperatures (Klein and Langmuir 1987; Taylor and Martinez 2003; Langmuir et al. 2006; Kelley et al. 2006), encompassing almost the entire range observed at open ocean ridges. The melting mechanisms in this environment, however, must greatly differ from the open ocean ridges, because very low $Ti_{8.0}$ and $Na_{8.0}$ at back-arc basins coincide with very low Fe contents. In general, back-arc basins are derived by higher extents of melting for the same depth as other ridges, owing to the water present in their source regions that causes higher average extents of melting in those environments.

Trace Elements

Trace elements show much larger variations than the major elements – up to a factor of 100 for the most highly incompatible elements such as Ba, Rb, and Th (Fig. 4a). These large trace element variations lead to the terms "enriched" and "depleted" when referring to MORB. The boundary between "enriched" and "depleted" generally refers to rare earth element (REE) patterns that are enriched or depleted in the lighter REE relative to chondritic meteorites, which reflect the bulk Earth composition (Sun et al. 1979) Fig. 4b). The ratio $(La/Sm)_N$, where the "N" refers to normalization to chondritic meteorites, reflects this enrichment or depletion. Since there are many more measurements of major elements than REE, the major element ratio K_2O/TiO_2 is often used as a proxy for $(La/Sm)_N$. Enriched MORB (E-MORB) have $(La/Sm)_N > 1.5$, which corresponds to $K_2O/TiO_2 \sim 0.2–0.25$, depending on the region. E-MORB are in part associated with ridges near ocean islands, as documented extensively by Schilling and coworkers (Schilling 1975; Schilling et al. 1982), but also occur sporadically along sections of ridges far from any known islands or hot spots. D-MORB are strongly depleted in the lighter REE, and have $(La/Sm)_N \sim 0.6$. The most commonly erupted MORB, N-MORB, has $(La/Sm)_N$ of ~0.8. There has also been a term for MORB in between N-MORB and E-MORB, called T-MORB (T for transitional). A boundary between N-MORB and T-MORB would occur at $(La/Sm)_N = 0.8$, or $K_2O/TiO_2 = 0.12$. In fact, there is a continuous range from highly depleted to very strongly enriched, and the boundaries between the different classes are quite arbitrary. But generally speaking, T-MORB have flat REE patterns, E-MORB have enriched patters, and N- and D- MORB have depleted patterns. The overall trace element patters from one ocean basin to another are remarkably similar – there is a progressive continuum from "enriched" to "depleted" that is widespread.

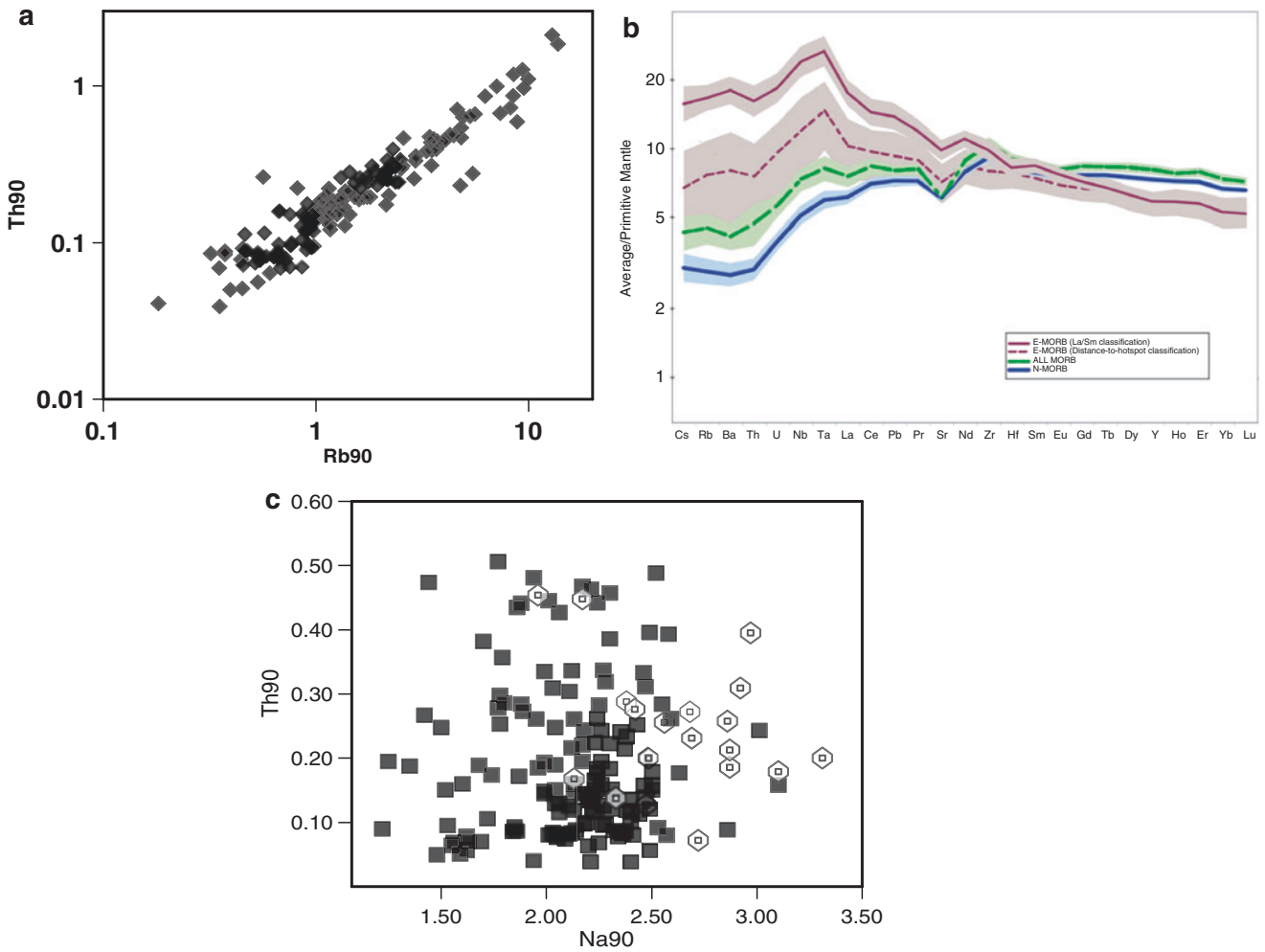

Mid-Ocean Ridge Basalts (MORB), Fig. 4 (**a**) Plot of Ba versus Th for segment averages corrected for fractionation to equilibrium with mantle olivine showing almost two orders of magnitude variations. Variations are greater than two orders of magnitude in individual samples. Note that the factor of variation far exceeds those shown for the major elements in Fig. 3 (Data from Gale et al. 2013). (**b**) Examples of normalized trace element abundances for average MORB, normal MORB far from hot spots, and enriched MORB. Normal MORB are depleted in the lighter rare earth elements (La, Ce), while enriched MORB are enriched in these and other elements. (**c**) Demonstration of the complete lack of correlation between highly incompatible elements and major elements. Segments from hot spot centers with Th90>0.5 have been excluded for clarity. They would simply extend the vertical axis to higher values

The trace element data along with the isotopes discussed below provide convincing evidence for mantle heterogeneity. The major elements suggest extents of melting vary by a factor of three – far less than would be able to account for the trace element variations. Furthermore, there is no correlation between highly incompatible elements and the major elements (Fig. 4c). In addition, enriched MORB often occur in the vicinity of ocean islands, and these regions are high temperature, leading to low abundances of elements such as Na.

Clearly, there are processes that greatly modify the highly incompatible trace element composition of the mantle without having significant effects on its major element composition. A common hypothesis for trace element-enriched MORB is the presence of recycled crust in the mantle, more enriched than the mantle itself, which melts out to produce enriched compositions (Hofmann and White 1982). A difficulty with this model is that recycled crust should also modify the major element composition of the mantle, making it difficult to explain the lack of correlation between major and trace elements. An alternative model is that the heterogeneity is created by the ubiquitous movement of low degree melts (Langmuir et al. 1992; Niu et al. 2002; Donnelly et al. 2004), which are small in mass but extremely high in trace element concentrations. Adding a percent or two of such a melt can change source abundances by orders of magnitude, while having negligible effect on the major elements. The origin of the trace element heterogeneity in MORB is far from settled.

Radiogenic Isotopes

Radiogenic isotopes show substantial variations in MORB, though much smaller in magnitude than the variations that are observed on ocean islands. The hallmark of virtually all isotopic values is that they reflect a long-term depletion of the mantle source relative to bulk Earth compositions. This depletion is consistent in general with the trace element depletion relative to chondritic meteorites. The depleted upper mantle reservoir indicated by the isotopes is widely considered to be the complement of the overall enriched compositions that characterize the continental crust.

In detail, the isotopic variations are complex (see review by White and Klein 2014). There are subtle differences between the Atlantic, Pacific, and Indian Ocean basins which are not yet clearly explained, but seem to require two distinct processes that have given rise to the diverse heterogeneity (Iwamori et al. 2010). The south Atlantic and Indian oceans are marked by variations that have been called the "Dupal anomaly" (Hart 1984), which tends to have higher values of $^{87}Sr/^{86}Sr$ at lower values of the Pb isotope ratios such as $^{206}Pb/^{204}Pb$. Within any one region, there are rough correlations between the parent/daughter ratios and the radiogenic isotopes, but this relationship is not global. This is not surprising, since trace elements can be strongly influenced by very recent processes, while the radiogenic isotopes are integrating a multibillion year history.

Outstanding Problems

The current knowledge of MORB is based almost entirely on abundant sampling along active ocean ridges where the youngest volcanic rocks are exposed. Older rocks become rapidly covered in sediment, and even when recovered they cannot be dated easily because of their alteration and very low potassium contents. It is often thought that ridges go through cycles of more and less abundant volcanism, which should be expressed in MORB compositions, and there is also the possibility of longer term variations with time. This temporal domain is virtually unexplored.

There is another large remaining conundrum, which is the relationship between the plutonic rocks that make up two-thirds of the ocean crust, and the lavas that are easily sampled at the surface. Work on the small numbers of plutonic rocks that have been recovered show a diverse set of complex processes operated on them. How this complexity can be reconciled with the very straightforward liquid lines of descent and global systematics that are evident in the erupted lavas will be an unfolding future story. How this story unfolds may also have consequences for the current interpretations of MORB compositions.

Summary

MORB are the most common rock type on Earth, and have become well characterized by five decades of study leading to tens of thousands of chemical analyses.Variations in the temperatures of eruption are largely controlled by crustal processes, which lead to liquid lines of descent at various pressures.Variations in parental magma compositions are controlled largely by mantle temperature.Hot mantle leads to higher extents of melting, thicker crust, and shallower ocean ridges.Variations in spreading rate and mantle composition are important second-order effects for the major elements and total melt production.Highly incompatible trace elements and isotopes are controlled largely by mantle heterogeneity.The relationship between the erupted volcanics and the thick plutonic sequences that make up most of the ocean crust poses puzzling problems that remain to be fully elucidated.

Cross-References

- ▶ Earth's Oceanic Crust
- ▶ Fractional Crystallization and Assimilation
- ▶ Geochronology and Radiogenic Isotopes
- ▶ Inductively Coupled Plasma Mass Spectrometry (ICP-MS)
- ▶ Incompatible Elements
- ▶ Lanthanide Rare Earths
- ▶ Magmatic Process Modeling
- ▶ Mantle Geochemistry
- ▶ Oceanic Island Basalts
- ▶ Subduction Zone Geochemistry
- ▶ Trace Elements

M

References

Arevalo R, McDonough WF (2010) Chemical variations and regional diversity observed in MORB. Chem Geol 271(1):70–85

Carbotte SM, Arko R, Chayes DN, Haxby W, Lehnert K, O'hara S et al (2004) New integrated data management system for Ridge 2000 and MARGINS research. EOS Trans Am Geophys Union 85(51):553–559

Coogan LA, O'Hara MJ (2015) MORB differentiation: in situ crystallization in replenished-tapped magma chambers. Geochim Cosmochim Acta 158:147–161

Crisp JA (1984) Rates of magma emplacement and volcanic output. J Volcanol Geotherm Res 20(3-4):177–211

Dalton CA, Langmuir CH, Gale A (2014) Geophysical and geochemical evidence for deep temperature variations beneath mid-ocean ridges. Science 344(6179):80–83

Dick HJB, Fisher RL, Bryan WB (1984) Mineralogical variations of the uppermost mantle along ocean ridges. Earth Planet Sci Lett 7:7–106

Donnelly KE, Goldstein SL, Langmuir CH, Spiegelman M (2004) Origin of enriched ocean ridge basalts and implications for mantle dynamics. Earth Planet Sci Lett 226:347–366

Gale A, Dalton CA, Langmuir CH, Su Y, Schilling J-G (2013) The mean composition of ocean ridge basalts. Geochem Geophys Geosyst 14:489–518

Gale A, Langmuir CH, Dalton CA (2014) The global systematics of ocean ridge basalts and their origin. J Petrol 55(6):1051–1082. https://doi.org/10.1093/petrology/egu017
Hart SR (1984) A large-scale isotope anomaly in the Southern Hemisphere mantle. Nature 309:753–757
Hofmann AW (1988) Chemical differentiation of the Earth: the relationship between mantle, continental crust, and oceanic crust. Earth Planet Sci Lett 90(3):297–314
Hofmann AW, White WM (1982) Mantle plumes from ancient oceanic crust. Earth Planet Sci Lett 57(2):421–436
Iwamori H, Albaréde F, Nakamura H (2010) Global structure of mantle isotopic heterogeneity and its implications for mantle differentiation and convection. Earth Planet Sci Lett 299(3):339–351
Kelley KA, Plank T, Grove TL, Stolper EM, Newman S, Hauri E (2006) Mantle melting as a function of water content beneath back-arc basins. J Geophys Res Solid Earth 111(B9)
Klein EM, Langmuir CH (1987) Global correlations of ocean ridge basalt chemistry with axial depth and crustal thickness. J Geophys Res Solid Earth Planets 92:8089–8115
Langmuir CH, Klein EM, Plank T (1992) Petrological systematics of mid-ocean ridge basalts: constraints on melt generation beneath ocean ridges. In: Phipps Morgan J, Blackman DK, Sinton JM (eds) Mantle flow and melt generation at mid-ocean ridges, Monograph 71, American geophysical union. AGU, Washington, DC, pp 183–280
Langmuir, C.H., A. Bézos, S. Escrig, S.W. Parman, Chemical systematics and hydrous melting of the mantle in back-arc basins, in: Fisher CR, Christie DM, Lee SM, and Givens S, (Ed), Back-arc spreading systems: geological, biological, chemical, and physical interactions 166, AGU, Washington, DC, 2006, pp. 87-146
Lehnert K, Su Y, Langmuir CH, Sarbas B, Nohl U (2000) A global geochemical database structure for rocks. Geochem Geophys Geosyst 1(5)
Lissenberg CJ, MacLeod CJ, Howard KA, Godard M (2013) Pervasive reactive melt migration through fast-spreading lower oceanic crust (Hess Deep, equatorial Pacific Ocean). Earth Planet Sci Lett 361:436–447
Niu Y, O'Hara MJ (2008) Global correlations of ocean ridge basalt chemistry with axial depth: a new perspective. J Petrol 49:633–664
Niu Y, Regelous M, Wendt IJ, Batiza R, O'Hara MJ (2002) Geochemistry of near-EPR seamounts: importance of source vs. process and the origin of enriched mantle component. Earth Planet Sci Lett 199(3):327–345
Rubin KH, Sinton JM (2007) Inferences on mid-ocean ridge thermal and magmatic structure from MORB compositions. Earth Planet Sci Lett 260:257–276
Schilling J-G (1975) Azores mantle blob: rare earth evidence. Earth Planet Sci Lett 25:103–115
Schilling JG, Kingsley R, Devine J (1982) Galapagos hot spot-spreading center system. 1, Spatial petrological and geochemical variations (83°W-101°W). J Geophys Res 87:5593–5610
Shen Y, Forsyth D (1995) Geochemical constraints on initial and final depths of melting at ocean ridges. J Geophys Res 100:2211–2237
Sinton JM, Fryer P (1987) Mariana trough lavas from 18°N: implications for the origin of back-arc basin basalts. J Geophys Res 92(B12):12782–12802
Stolper E, Newman S (1994) The role of water in the petrogenesis of Mariana trough magmas. Earth Planet. Sci Lett. 121:293–325
Sun SS, McDonough WS (1989) Chemical and isotopic systematics of oceanic basalts: implications for mantle composition and processes. Geol Soc Lond, Spec Publ 42(1):313–345
Sun SS, Nesbitt RW, Sharaskin AY (1979) Geochemical characteristics of mid-ocean ridge basalts. Earth Planet Sci Lett 44(1):119–138
Taylor B, Martinez F (2003) Back-arc basin basalt systematics. Earth Planet Sci Lett 210(3):481–497
White WM, Klein EM (2014) 4.13 – Composition of the oceanic crust. In: Holland HD, Turekian KK (eds) Treatise on geochemistry, 2nd edn. Elsevier, Oxford, pp 457–496

Mineral Defects

Kurt Schwartz[1] and Maik Lang[2]
[1]GSI Helmholtz Center for Heavy Ion Research, Darmstadt, Germany
[2]Department of Nuclear Engineering, University of Tennessee, Knoxville, TN, USA

Definition

Crystal defects can be most simply defined as distortions of the periodic arrangement of atoms in a "perfect" crystalline lattice. Above absolute zero temperature, defects are present in all crystals at certain concentrations. An increase in temperature increases the number of defects significantly. Depending on their dimensions, defects can be classified into point defects, line defects, planar defects, and bulk defects. Defects can be introduced in minerals through various means, such as self-radiation. Radiation-induced defects in minerals have been observed long before the discovery of radioactivity. Berzelius observed thermo-luminescence in gadolinite ($(Y,Ce)_2Fe^{2+}Be_2O_2(SiO_4)_2$) caused by α-decay of uranium and thorium trace elements (Berzelius 1815). Unaware of the underlying processes, Baumhauer etched fission-fragment tracks in apatite as early as the nineteenth century (Baumhauer 1894).

Classification of Defects

1. *Point (zero-dimensional) defects*

Point defects are distortions at a single lattice position, such as vacant atomic sites, which are called vacancies (Itoh and Stoneham 2001; Kittel 2004). Due to electrical charge neutrality, an equal number of anion and cation vacancies must be present at any time in ionic crystals (*Schotky defects*). *Frenkel defects* are a type of vacancy – interstitial pairs in the lattice, which can form if an atom is moved from its lattice site into an interstitial position. In ionic crystals both anion and cation Frenkel defects exist. Point defects can also be impurity elements substituting regular atoms (anions or cations in ionic crystals). Such defects can be introduced by contamination of minerals with foreign species. If the equilibrium charge of the impurity atom is different from the host crystal, vacancies can compensate the charge difference, e.g., Mg^{2+} impurity in NaCl (rock salt) has the microstructure of $Mg^{2+}v_c^-$ (v_c^- is a cation vacancy having a negative charge). The large variety of point defects that can be present in a mineral are illustrated in Fig. 1 for NaCl. Point defects are also color centers in dielectric materials which give rise to color in some minerals.

The point-defect concentration depends on temperature. The equilibrium concentration of vacancies (n) is equal to $n/N = \exp(-E_v/k_BT)$, where E_v is the energy to create a vacancy, N is the concentration of lattice atoms (ions), and k_B is the Boltzmann constant. For example, vacancies in NaCl have an E_v of about 2 eV, which corresponds to an anion vacancy concentration of $n_{va} \sim 5 \times 10^{11}\text{cm}^{-3}$ at T = 1000 K (close to the melting point).

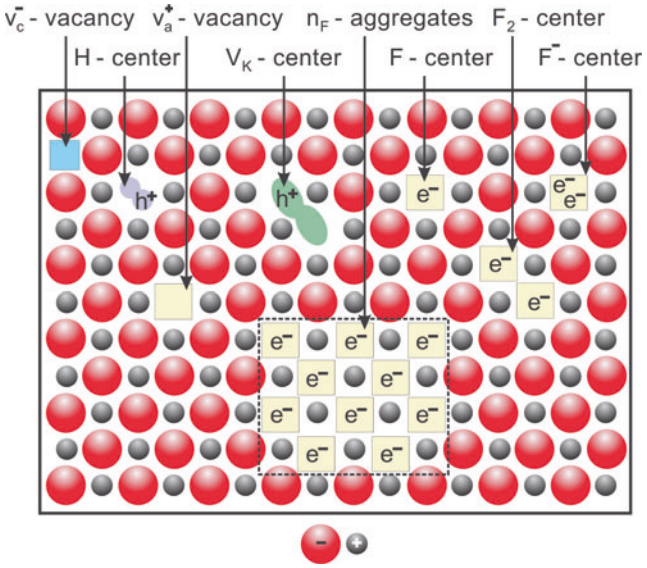

Mineral Defects, Fig. 1 Color centers in NaC1 crystals: v_c^- – cation vacancy; H – anion molecule X_2^- replacing an regular anion; v_a^+ – anion vacancy; V_K – anion molecule X_2^- replacing two regular anions (self trsapprd hole); nF – F-center aggregate (quasi Li colloid); F – center ($v_a^+e^-$), F_2 – ($2v_a^+2e^-$); F^- – ($v_a^+2e^-$)

At elevated temperatures, point defects are mobile and can interact with other defects forming complex defects or defect aggregates (see Fig. 1). The defect diffusion coefficient is equal to $D(T) = D_0\exp(-Q/k_BT)$, where D_0 is the pre-exponential coefficient and Q the activation energy. Usually the magnitude of Q is larger for vacancies than for interstitials. In NaCl, Q is for both anion and cation vacancies about 2 eV, whereas for neutral chlorine interstitial atoms Q = 0.1 eV.

2. *Line (one-dimensional) defects*

The main line defects within an atomic structure are dislocations. There are two types of dislocations – edge and screw (Fig. 2). Edge dislocations are an additional half- plane of atoms introduced into the lattice. Screw dislocations are usually produced by an atomic-step spiral during crystal growth. Mixed edge and screw dislocations are present in many minerals. The main characteristic for dislocations is the Burgers vector (***b***), which is determined by the so-called Burgers-circuit – the missing link is the vector ***b*** (Fig. 2). For edge dislocations, ***b*** is normal to the dislocation line, and for screw dislocations, ***b*** is parallel. The Burgers vector determines the dislocation formation energy (E_{disl}) and is approximately $E_{disl} \sim Gb^2$, where G is the shear modulus (the magnitude for G in various solids is in the range of 10–150 GPa).

Edge and screw dislocations are created by deviations during growth processes, internal mechanical stresses, and plastic deformations. Dislocations are also mobile at elevated temperatures and can interact with other defects to annihilate or form more complex defect structures. Line defects can be also created by aggregation of point defects (vacancies or

Mineral Defects, Fig. 2 Edge and screw dislocations

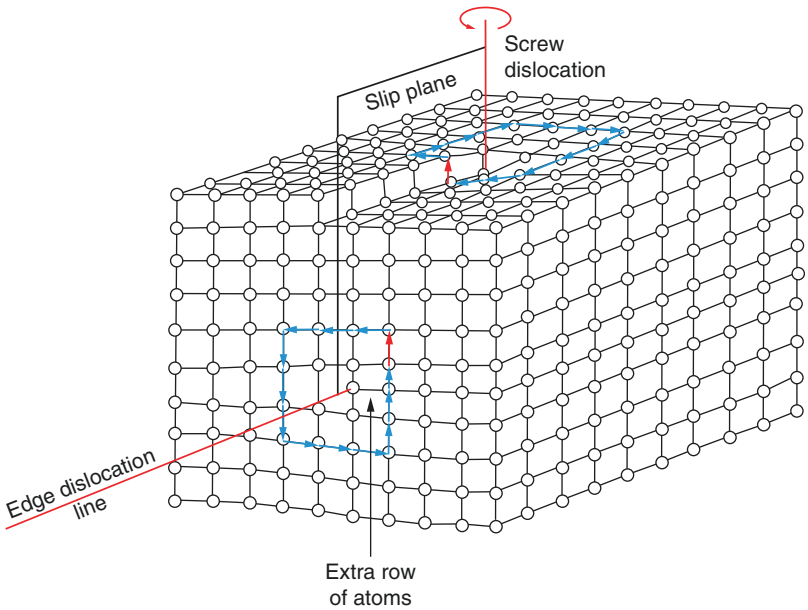

interstitials), which occurs, for example, in ionic crystals as a result of particle irradiation (Hobbs et al. 1973; Hirth and Kubin 2009).

3. *Planar (two-dimensional) defects*

The main planar defects are stacking faults, which are defined as local discontinuities in the stacking sequence of the periodic atomic arrangement in the lattice, e.g., ABC in cubic crystals. Details on the structure of stacking faults depend on the crystal symmetry of the host material. Planar defects can be introduced into a material during crystal growth, by interaction of point defects/dislocations, and by plastic deformation. Stacking faults are more commonly observed in layered minerals.

4. *Bulk (three-dimensional) defects*

Three dimensional or bulk defects are voids, cracks and impurity clusters. Bulk defects occur on a much larger scale than all other aforementioned crystal defects. Voids are lattice regions with a large number of missing atoms from regular lattice sites, i.e., vacancy aggregates. Voids can form during mineral growth, under irradiation, and plastic deformation.

Finally, impurity atoms of large concentrations can form impurity clusters that lead to local material regions with different phases than the host mineral, the so-called precipitates.

Radiation Damage in Minerals From Self-irradiation

Radiation effects in solids were first observed in colored rock salt (NaCl) and fluorite (CaF_2) minerals (Dyar and Guntar 2008). Various minerals can emit a thermo-luminescence signal as a consequence of the presence of radiation-induced defects (Berzelius 1815). Radiation damage in minerals is created through the decay of unstable, natural-occurring radioactive isotopes (^{226}Ra, ^{238}U, ^{232}Th, etc.) that are incorporated in minerals during or after formation. These heavy isotopes were produced by supernova explosions long before the birth of our solar system. The overall level of radiation from these radioisotopes on Earth is currently low. Nevertheless, over geological time intervals, significant amount of radiation damage can accumulate that can lead in extreme cases to the loss of crystallinity of an entire mineral sample (Ewing et al. 2000).

Radiation-damage studies in solids were mainly stimulated by the need of materials for nuclear applications in the 50s of the twentieth century. There are two general mechanisms for damage creation in solids: atomic displacements (Seitz and Koehler 1956) and electronic excitations (Itoh and Stoneham 2001). Atomic displacements lead to the formation of vacancies and interstitials in all materials from metals to insulators, while electronic excitation creates radiation damage only in the latter. Primary atomic displacements induce secondary collisions, and at high absorbed doses, defect aggregates, dislocations and bulk defects are created.

In the 60s of the last century, a new electronic mechanism of Frenkel-defect creation was proposed for ionic crystals. It was observed that different types of radiation (X- or γ-rays, electrons, α-particles, etc.) produce electron–hole pairs and excitons in insulators, which eventually form Frenkel pairs (vacancies and interstitials, see (Itoh and Stoneham 2001) and references within). This electronic or exciton mechanism is active in some dielectric materials if the energy of the electronic excitations, E_{exc}, is higher than the energy required to create a Frenkel pair E_{FD}. The exciton mechanism can explain the formation of structural defects in some materials from initial electronic excitations. Once the Frenkel pairs are created, they can move and produce color centers and, at higher radiation dose, defect aggregates and dislocations. In insulators, the exciton mechanism is much more efficient in producing defects than atomic displacements. Alkali halides and alkaline earth halides have an active exciton mechanism, whereas it is absent in many oxides (MgO, Al_2O_3, Y_2O_3 etc.). Radiation damage can only be created in these oxides through atomic collisions.

Of special interest is damage in minerals that is induced by nuclear fission of uranium ($^{238}U^{92}$) which is as trace element present in many minerals. The spontaneous fission is a radioactive decay event, in which a uranium nucleus splits in two daughter products $^{238}U^{92} \rightarrow {}^{140}Xe^{54} + {}^{96}Sr^{38} + 2^{1}n^{0}$ (one example of many possible daughter-product pairs) that carry a high kinetic energy (about 200 MeV in total). The fast fission products slow-down in the mineral lattice and produce a trail of damage, the so-called ion tracks (Itoh and Stoneham 2001; Itoh et al. 2009). An ion track is in general a small, cylindrical damage region around the ion path with the length between 10 and 100 μm and a diameter of only a few nanometers.

Radiometric Dating

Radiometric dating is a technique used for mineral or rock samples containing radioactive isotopes. The method is based on a chain of radioactive decays which lead to a stable daughter element, e.g., $^{238}U^{92} \rightarrow {}^{206}Pb^{82}$ or $^{235}U^{92} \rightarrow {}^{207}Pb^{82}$. The radioactive decay has a different rate for various elements and the main parameter for the decay is the half-life time $\tau_{1/2}$. During this time, half of the initial radioactive parent atoms decay. The decay process can be described by the following age equation: $t = \lambda^{-1}\ln(1 + N_f/N_0)$, where t is the age of the mineral, N_f is the number of final isotopes (daughters), N_0 is the number of initial radioactive atoms

(parents), and $\lambda = \ln 2/\tau_{1/2}$ is the decay constant of the radioactive isotope. The decay constant λ is known for all radioactive isotopes, while the concentration of initial and final isotopes N_0 and N_f must be determined by modern analytical techniques with a high accuracy (Wagner and Van der Haute 1992). It should be noted that the time t only represents the age of the host mineral if the radionuclides were incorporated during mineral formation. Otherwise, this parameter refers to the elapsed time since radionuclide incorporation. If the mineral is exposed to elevated temperatures during some time of the decay of radionuclides, they become mobile and diffuse through the mineral. Above a critical temperature, which depends on the chemical composition of the mineral, the unstable radioactive elements or the stable daughter products will diffuse out of the host mineral, which puts the limit to this type of dating. It was shown that the presence of defects will affect the diffusion process (Shuster and Farley 2009).

For the decay process $^{238}U^{92} \rightarrow {}^{206}Pb^{82}$ the half-life is $\tau_{1/2} \approx 4.5 \times 10^9$ years and for $^{235}U^{92} \rightarrow {}^{207}Pb^{82}$ $\tau_{1/2} \approx 700 \times 10^6$ years. Thus, these uranium isotopes can be used to determine the age of extremely old minerals and rocks. The oldest mineral dated is zircon, $ZrSiO_4$ (found in Australia), having an age of $(4.404 \pm 0.008) \times 10^9$ years. This has led to the conclusion that the oldest minerals formed shortly after the birth of Earth.

To determine ages of much younger geological samples, other isotopes are needed with a significantly shorter half-life, such as those used in the Rb-Sr method with $\tau_{1/2} \approx 50 \times 10^6$ years or ^{14}C with $\tau_{1/2} \approx 5700$ years (more details in Wagner and Van der Haute 1992).

Fission Tracks in Minerals

The principle of fission-track dating is similar to that of other radioactive dating techniques. Unstable $^{238}U^{92}$ nuclei ($\tau_{1/2} \approx 8.4 \times 10^{15}$ years) undergo spontaneous fission and produce two medium-sized daughter products of high kinetic energy (e.g., 80-MeV ^{132}Xe). These fission fragments induce tracks in the host mineral that exhibit a high sensitivity for chemical etching. Chemical etching is used to enlarge fission tracks to micrometer scale (in the form of hollow features) until they are detectable by optical microscopy. This yields the concentration of fission tracks, which is equal to the concentration of daughter products. The estimation of the present concentration of $^{238}U^{92}$ is more complicated and requires modern analytical methods, such as neutron-activation analysis. For this technique, the mineral is bombarded with thermal neutrons that induce nuclear fission of $^{235}U^{92}$, which is easily measured via the detection of fission products. The ratio of $^{238}U^{92}/^{235}U^{92}$ is known and the age of the geological or archeological sample can be determined using the previously described age equation. Fission-track dating is used to date some of the oldest minerals. Since defects anneal at high temperature, tracks recover and shrink in size. Thus, the track-size distribution also contains information about the thermal history of a mineral. If the temperature is high enough to anneal all fission tracks, the clock is reset to "zero." The critical temperatures for zircon, $ZrSiO_4$, and titanate, $CaTiSiO_5$, are about 240 °C and 300 °C, respectively. Fission track formation and annealing under conditions relevant to Earth's interior has been simulated by combining simultaneously irradiation, high temperature and high pressure and applying state-of-the-art materials characterization techniques (Lang et al. 2009; Kluth et al. 2012; Li et al. 2012).

Summary

There exists a wide range of defects in minerals from individual point defects to large, three-dimensional defect structures. Defects are induced in minerals through different processes, such as during crystal growth and self-irradiation. Defects diffuse at elevated temperatures and oftentimes form more complex defects or anneal with each other. Defects can dramatically change the physio-chemical properties of a material (Itoh and Stoneham 2001; Kittel 2004). One of the most prominent examples is the color of minerals, which can be induced by the underlying defect structure. Finally, defects are of great importance in geochronology, and fission-tracks are, for example, used to obtain the thermal history of archeological and geological samples.

Cross-References

- ▶ Equilibrium
- ▶ Luminescence
- ▶ Raman Microspectroscopy
- ▶ Stoichiometry
- ▶ Synchrotron X-Ray Fluorescence Analysis
- ▶ X-Ray Diffraction

References

Baumhauer H (1894) Die Resultate der Ätzmethode in der kristallographischen Forschung, an einer Reihe von kristallisierten Koerpern dargestellt. W. Engelmann, Leipzig

Berzelius J (1815) Afhandl Fys Kem Min, 4, 217

Dyar MD, Guntar ME (2008) Mineralogy and optical mineralogy. Mineralogical Society of America, Chantilly

Ewing RC, Meldrum A, Wang LM, Wang S (2000) Radiation-induced Amorphization. Rev Mineral Geochem 39:317–361

Hirth JP, Kubin L (2009) Dislocations in solids. North-Holland, Amsterdam

Hobbs LW, Hughes AE, Pooley D (1973) A study of interstitials clusters in irradiated alkali halides using direct electron microscopy. Proc R Soc Lon A 332:167–185
Itoh N, Stoneham M (2001) Materials modification by electronic excitation. Academic, Cambridge
Itoh N, Duffy DM, Khaksohouri S, Stoneham AM (2009) Making tracks: electronic excitation roles in forming swift heavy ion tracks. J Phys Condens Matter 21:474205
Kittel C (2004) Introduction to solid state physics. Willey, New York
Kluth P, Afra B, Rodriguez MD, Lang M, Trautmann C, Ewing RC (2012) Morphology and annealing kinetics of ion tracks in minerals. EPJ web of conferences, 35, p 03003
Lang M, Lian J, Zhang FX, Hendriks BWH, Trautmann C, Neumann R, Ewing RC (2009) Fission tracks simulated by swift heavy ions at crustal pressures and temperatures. Earth Planet Sci Lett 274:355–358
Li WX, Lang M, Gleadow AJW, Zdorovets MV, Ewing CR (2012) Thermal annealing of unetched fission tracks in apatite. Earth Planet Sci Lett 321–322:121–127
Seitz F, Koehler JS (1956) In: Seitz F, Turnbull D (eds) Solid state physics, vol 2. Academic, New York, pp 307–442
Shuster DL, Farley KA (2009) The influence of artificial radiation damage and thermal annealing on helium diffusion kinetics in apatite. Geochim Cosmochim Acta 73:183–196
Wagner GA, Van der Haute P (1992) Fission track dating. Ferdinand Elke, Stuttgart

Mineral Genesis

Alain J. Baronnet
Aix-Marseille Université, CNRS, CINAM, Campus Luminy, Marseille, France

Definition

Mineral genesis addresses the questions of where, why, and how minerals form and disappear, on and in the Earth (see also ► Crystal Chemistry).

The Crystalline Earth and Its Dynamics

Minerals, essentially as natural crystals, are the major constituents of the core, the mantle, and the crust of our planet. In the mantle, they form the viscous solid matter involved in slow convective movements which act as the force-transmitting medium for plate tectonics. As such, minerals undergo phase transitions, polymorphic transitions, and more generally nucleation, growth as well as resorption. This occurs in response to local and/or temporal changes in pressure/stress, temperature, and chemical composition. Internal heat production of the Earth is ultimately the cause of mineral dynamics. Most active and diverse kinetic phenomena of these kinds are expected to take place where temperature gradients and chemical gradients are prominent, i.e., in and on the crust.

Mineral growth in the continental crust is mainly located at:

1. Cooling magmas, either intrusive or effusive
2. Metamorphic regions connected to orogens
3. Continental hydrothermal aureoles developed in country rocks in relation to cooling intrusive bodies
4. Weathering and bio-materials located at the relatively sharp interface between the geosphere and atmosphere or ocean floor

Mineral growth is promoted in the oceanic crust mainly at:

1. Magma reservoirs/newly born tectonic plate interfaces and at hydrothermal vents, close to mid-oceanic ridges
2. The seafloor-seawater interface where freshly deposited sediments start to lithify in depth
3. Sinking tectonic plates, where the moving material cross-cuts isotherms and therefore recrystallize to adapt to more severe pressure-temperature conditions

Mineral resorption, as melting or dissolution, roughly balances mineral production in volume, at the million-years timescale. Mineral sinks are mainly at the solid tips of diving plates and below the mid-ocean ridges where ascending mantle material undergoes partial melting due to depressurization and ocean water income. On the other hand, aqueous solutions of various salts insure dissolution, transport, and crystallization of many mineral species, especially those involved in ore deposits. This takes place when solutions flow through porous and/or fractured rocks. Convective flow is activated by locally contrasted water densities. These density contrasts are sensitive to abrupt geological events like a magma intrusion in the crust that disturbs the normal geothermal gradient. Accordingly, hydrothermal convecting systems develop in country rocks around hot intrusive magmas, as well as inside the cooling oceanic crust mostly cooled down from the top by seawater.

Departure from Equilibrium for Mineral Birth and Growth

Like any crystal, a mineral has to nucleate and grow up to a microscopic or macroscopic size before be considered a solid phase. Crystalline nucleation (birth) and growth (size increase) stages follow each other necessarily, whereas resorption (size decrease) may occur on occasion. They all need some departure from equilibrium in the geologic host system. Nucleation and growth need a positive departure from equilibrium, while resorption needs a negative one. Such departures are expressed in a condensed way by:

$$\Delta\mu = \mu_l - \mu_c$$

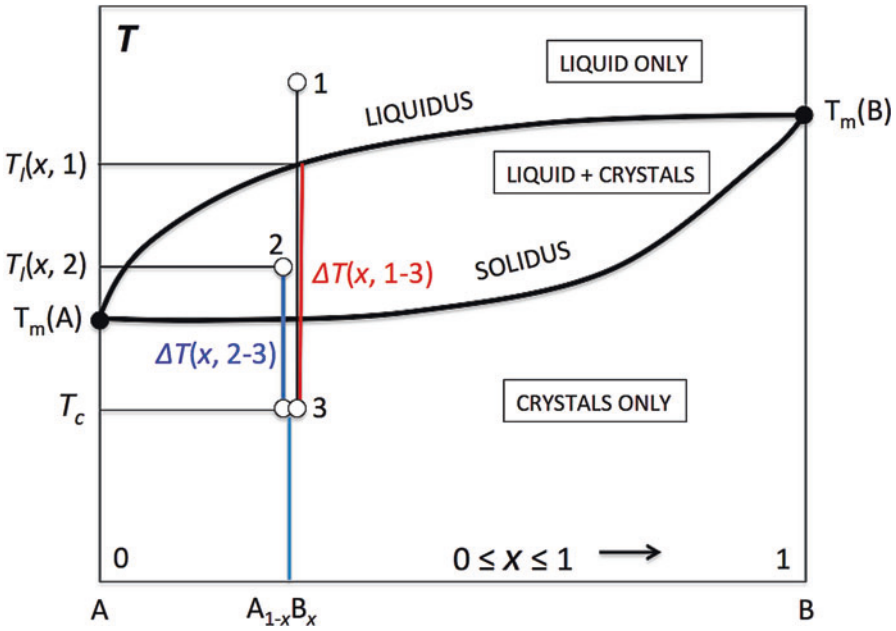

Mineral Genesis, Fig. 1 Definition of supercooling ΔT in a binary mineral system. A and B are the two pure mineral end-members of the $A_{1-x}B_x$ solid solution compositions. T_m(A) and T_m(B) are melting points of A and B, respectively. Cooling from above the liquidus temperature (*1*) down to a subsolidus crystallization temperature (*3*) corresponds to the efficient supercooling $\Delta T = T_l(x, 1) - T_c$. Cooling now from the subliquidus region (*2*) down to (*3*) gives $\Delta T = T_l(x, 2) - T_c$

with $\Delta\mu$ as the difference of the chemical potential of the minimum mineral unit in the surrounding medium μ_l and its chemical potential once in the crystal μ_c. The lowest μ represents the preferred (equilibrium) state for the crystal unit. Thus, $\Delta\mu$ is the driving force for crystallization ($\Delta\mu > 0$) or resorption ($\Delta\mu < 0$).

For growth or resorption from the melt, undercooling $\Delta T = T_l - T_c$ refers to the driving force for crystallization (Fig. 1). For small departures from equilibrium, $\Delta\mu$ is linearly related to ΔT by:

$$\Delta\mu = \Delta H_l \cdot \Delta T / N \cdot T_l$$

where ΔH_l is the fusion latent heat of the crystal, N the Avogadro number, and T_l the liquidus temperature.

Note that ΔT is always related to T_c, the actual crystallization temperature. The direct use of ΔT would require natural conditions under which the abrupt cooling step of the melt is followed by a T_c plateau (isothermal drop) instead of the more realistic, almost linear, cooling rate of a magma. However, a positive and continuous correlation exists between the cooling rate (dT/dt) and ΔT regarding nucleation and growth features.

For growth or dissolution from aqueous solutions, where at least a binary mixture (solute and solvent) is present, the departure from equilibrium writes:

$$\Delta\mu = \mathrm{k}T_c \ln\left(a/a_{eq}\right)$$

where k is the Boltzmann's constant, and a and a_{eq} are the actual and the equilibrium activities of the minimal mineral unit, respectively. More precisely, (a/a_{eq}) relies on the product of the actual activities of all chemical species in solution divided by the equilibrium constant at T_c. For the most general case of sparingly soluble minerals (e.g., silicates), activities are well approximated by concentrations, X, expressed in mole fractions. Introducing the relative supersaturation σ of the solution regarding the solute:

$$\sigma = \left(a - a_{eq}\right)/a_{eq} \approx \left(X - X_{eq}\right)/X_{eq}$$

so that:

$$\Delta\mu = \mathrm{k}T_c \ln(1 + \sigma)$$

that is $\Delta\mu \approx \mathrm{k}T_c\sigma$ for small supersaturations. In solution growth, the driving force of crystallization is thus directly proportional to the relative supersaturation. This force can now be varied at constant crystallization temperature.

Solid-state growth as a "crystals-to-crystals" transformation prevails during crystallization of medium-grade to high-grade metamorphic rocks. In this case, departure from equilibrium is accounted for by the concept of "overstepping" which measures the amount of penetration inside the stability field of the mineral phase(s) of interest drawn in the suitable phase diagram. Mineral transformations in low-grade metamorphic rocks and surficial environments take place mostly by a dissolution-crystallization process. In these cases, the higher solubility of the unstable parent mineral maintains a suitable supersaturation with respect to the less soluble, stable, daughter mineral.

Nucleation of Minerals

Primary Nucleation and Secondary Nucleation

Primary nucleation corresponds to the early first appearance of crystals of a new-born phase. This phenomenon is quantified by the nucleation rate N as the number of crystal nuclei

which appear in a unit volume per unit time (see also ▶ Crystal Chemistry). Homogeneous primary nucleation (HoN) is a concept in which nuclei appear at random in the system. Although HoN rates may be reasonably predicted, Nature proceeds by heterogeneous primary nucleation (HeN) instead, i.e., nuclei appear on singular places of the system (dirt particles; boundaries of the system: walls of a magma chamber, solution–air interface; preexisting crystals acting as substrates, grain boundaries between neighboring minerals in metamorphic rocks, etc.).

Nucleation is the most energy-consuming event in crystals life. Compared with other crystal growth processes, it usually needs a large $\Delta\mu$ to start being significant (Fig. 2). Difficulty of nucleation comes from the high energy cost for creating the new surface of nuclei against their always positive surface energy/tension. The smaller the crystal embryo, the higher its surface/volume ratio and therefore the higher this surface energy relative contribution. This originates a nucleation barrier to be overcome thanks to a minimum applied $\Delta\mu$ for nucleation to start. Below this critical $\Delta\mu$, there is a dead zone or metastable zone in which no spontaneous nucleation would take place. Beyond the metastable zone, N increases steeply to become explosive (crystalline precipitation). However, from the melt, from a devitrifying glass and for highly soluble minerals in aqueous solutions (e.g., halite NaCl, chalcantite $CuSO_4$—$5H_2O$), the metastable zone is narrow so that small N may be maintained. On the other hand, sparingly soluble minerals (layer silicates in general and clays in particular, calcite $CaCO_3$, apatite $Ca_5(PO_4)_3(OH,F,Cl)$, etc.) may have huge metastable zones and explosive nucleation becomes the rule in free aqueous solutions. At near ambient temperatures, it is common that such minerals nucleate in fact from precursor phases that may or may not (e.g., hydrogels) be poorly crystalline themselves and may precipitate first. The benefit of this process is the lowered interface energy between the precursor phase and the final phase. This process is adopted in mostly abiotic contexts like in poor soils as well as in a purely organic context like during carbonate biomineralization of mollusk shells.

Magmatic crystallization along a cooling path may disturb the predicted order of phase nucleation. For instance, in basic silicate melts with diopside composition, CaO—MgO—$2SiO_2$ olivine $(Mg,Fe)_2SiO_4$ may crystallize prior to the stable clinopyroxene $CaMg(SiO_3)_2$, thus violating attempts from the equilibrium phase diagram (Kirkpatrick et al. 1981). Silica monomers are common in the melt and in the olivine structure, whereas they contrast with the silica chain structure of diopside. Accordingly, the interface energy of olivine against the melt will be lower than that of diopside, therefore favoring easy nucleation (Kirkpatrick 1983). It is a general rule that metastable and unstable phases nucleate more easily than stable phases at moderate temperatures!

Nucleation phenomena are dramatically different at high departure from equilibrium, when taking place in aqueous solutions compared to those in magmas. In solutions, the nucleation rate increases monotonously to infinity for large values of σ with the size of critical nuclei, those having been able to overshoot the nucleation barrier, decreasing to the size of the "structural formula volume." It is not so in melts, where ΔT increase means a decrease of T_c and therefore increased viscosity of the liquid. High viscosity involves difficult rearrangement of potential crystal-building units to form nuclei, thereby slowing down nucleation (Fig. 2). Under extreme departure from equilibrium, amorphous or crystalline precipitates form from solutions, and glass from the melt. These extreme conditions are fulfilled at hydrothermal submarine trenches where solutions are quenched (300–400 °C to 4 °C in a few seconds), at the crust of fluid acidic lava flow (obsidian), and during submarine basic lava eruptions on the seafloor (pillow lavas).

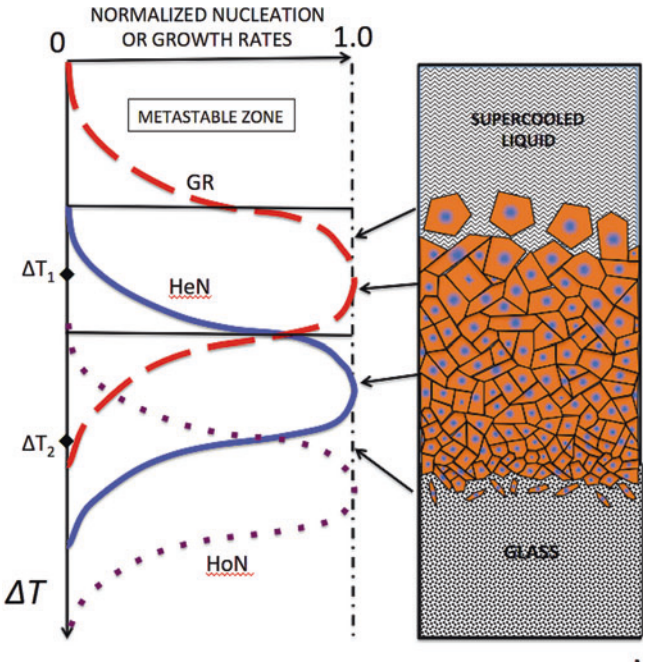

Mineral Genesis, Fig. 2 Normalized homogenous (HoN), heterogeneous (HeN) nucleation, and growth (GR) rates as a function of melt supercooling ΔT- Left hand side. Resulting amorphous and crystalline material facing these crystallization regimes in case of a unique ΔT applied- Right-hand side. Under increasing ΔT's we observe successively: (1) a metastable zone as a liquid (no nuclei available for possible crystal growth); (2) assemblage of coarse crystals (sluggish nucleation with high growth rates) with or without a residual liquid; (3) "dry" assemblage of medium-sized crystals (both significant nucleation and crystal growth rates); (4) "dry" assemblage of fine-grained crystals (abundant nucleation but small growth rates); (5) crystallites embedded in glass (explosive nucleation and small crystal growth rates shortly applied); (6) liquid frozen as a glass (zero values for both heterogeneous nucleation and growth rates). Basalt crystallization may be envisaged as following a two-step process: small ΔT_1 applied in the magma chamber giving large phenocrysts in a liquid followed by a high ΔT_2 in the lava during the eruption, giving then tiny microlites in a residual glass issued from the former liquid

Secondary nucleation is a mechanism of production of new crystals of an otherwise already existing phase by mutual shocks and/or scratches. It is not uncommon during tectonic shear of brittle metamorphic rocks and water/ice transport of detrital rocks, but virtually absent in hydrothermal and igneous rocks. In hydrothermal systems, minerals are not allowed to "fly around" to collide since they nucleate heterogeneously on opening walls of veins, caves, druses, or other substrates. In viscous melts, they can hardly impinge each other while they move as following viscous flow lines (Jambon 1980).

Crystal Growth of Unique Mineral Grains

The growth stage follows nucleation and leads to a crystal of microscopic or macroscopic size. The critical nucleus size is the size of the crystal above which it enters crystal growth strictly speaking. At fixed temperature, this size is an inverse function of the departure from equilibrium. It may theoretically vary from infinite size at equilibrium (no growth) to the size of a single formula unit at very large departures (no nucleation).

A freely growing crystal usually looks like a polyhedron limited by flat faces. It is the feeding of the outer surface of this polyhedron by "growth units (= chemical formula units)" that make faces advance outward parallel to themselves, and therefore the crystal to grow as a whole. The mineral habit (Kostov 1965; Kostov and Kostov 1999; Sunagawa 1987), as the observed crystal shape, is determined by the ratio of the mean growth rates of adjacent faces. This shape is bounded by the slowest growing faces among all those dense in their surface atomic structure and may be modeled by the Bravais-Donnay-Harker law (Bravais 1866; Donnay and Harker 1937). "Well-developed" faces are in fact those with the slowest growth rate!

Both the growth rates and the growth mechanisms of a single face depend on:

1. Its surface crystal structure
2. The presence of adsorbed impurities (including the solvent) on it
3. The presence of outcropping dislocations with dominant screw type (see ▶ Mineral Defects)
4. The amount of positive disequilibrium in the system
5. The relative flux (amplitude and direction) of the growth medium with respect to it
6. Temperature T_c, although moderately

Pressure has little effect.

Growth Mechanisms of Individual Faces

The crystal structure of a face is primarily a planar cut of the 3-D crystal structure parallel to it. In complex mineral structures, this cut exposes the surface which offers the lowest density of broken bonds with the weakest bond strengths, or an appropriate combination thereof. For example, the (001) face of potash mica growing from solution will expose the alkali-bearing interlayer where K─O bonds are the weakest. The actual surface rearranges itself to compensate for the rupture of symmetry of bonding and for the disturbed electric charges. All faces belonging to the same crystallographic form, that is, they are crystallographically equivalent, have the same surface structure, e.g., (100), (010), (001), $(\bar{1}00)$, $(0\bar{1}0)$, and $(00\bar{1})$ of the {100} cubic form of galena. Potential faces of a mineral can be classified into three structural types based on the arrangement of atomic, ionic, or molecular bonding running parallel to the face (Hartman and Perdok 1955): (1) F faces (F for flat) as smooth faces for which at least two interconnected and uninterrupted chains of strong bonds are present, i.e., inside the (001) face of mica in which three distinct . . .O─Si─O─Si─O─Si. . . of such periodic bond chains (PBC's) are present; (2) S faces (S for stepped) as striated faces with a single set of PBC's; (3) K faces (K for kinked) looking like rough faces and containing no PBC.

In minerals with a complex composition and structure, the classification of a face may be ambiguous because bond chains are commonly of different strengths so that there is a gradual continuity between those three types.

Almost only F faces are present on the habit of minerals. Relative growth rates of S and K faces are too fast for those faces to be able to truncate the polyhedron made by F faces.

Under moderate $\Delta\mu$, F faces grow layer-by-layer. There are two possible layer-by-layer growth mechanisms (Fig. 3a, b): the two-dimensional nucleation mechanism (TDNM; Stranski 1928) and the spiral growth mechanism (SGM; Burton et al. 1951; Dekeyser and Amelinckx 1955). The TDNM is the most energy-consuming process since it implies the repeated birth (nucleation) of new growth islands in which most of the growth units are poorly linked to the substrate. On the other hand, the layer spreading is rather easy. Therefore, TDNM requires a large $\Delta\mu$ and is identified by the presence of single or piled-up growth islands on the face (Fig. 3a).

The SGM is constrained by the outcrop of one screw dislocation (see ▶ Mineral Defects) or more, on the face. A spiral step (Fig. 3b) starts from each dislocation outcrop and winds up permanently around it. Growth units stack here tightly at the border of the step. The latter is permanently present during growth while insuring extension of the helical lattice plane. Here the growth normal to the face is achieved by lateral spread of spiral steps. SGM requires small $\Delta\mu$'s only since the birth of a new layer becomes unnecessary. This is the usual growth mechanism of an F face on macroscopic minerals (Sunagawa 1977, 1984). Well-localized and sharp-tipped growth pyramids (growth hillocks) on a face reveal

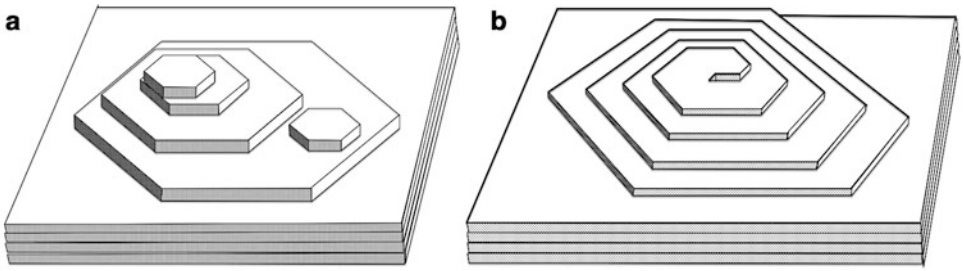

Mineral Genesis, Fig. 3 Layer-by-layer growth mechanisms of a flat face: (**a**) two-dimensional nucleation mechanism evidenced by scattered and piled-up growth islands, (**b**) spiral growth mechanism: the growth pyramid is centered by the step source, i.e., where the screw dislocation line outcrops. The successive turns of the unique polygonal growth step form pyramid facets made by regular "trains of steps."

outcropping screw dislocations. For both TDNM and SGM, the feeding of the face by growth units is mainly controlled by surface diffusion of growth units. At intermediate $\Delta\mu$'s, volume diffusion of growth units becomes rate-limiting so that growth on crystal corners and edges prevail, thus giving an hollow-faced habit (hollow crystals to skeletal crystals, ultimately dendrites).

Under high to very high $\Delta\mu$'s, F faces may lose their planar form and become rough (kinetic roughening).

Growth Events and Mineral Habit Changes

Following the supersaturation/undercooling decay, which follows nucleation of a mineral phase, the sequence of growth events for a single crystal may be (Sunagawa 1977; Baronnet 1984):

1. Heterogeneous 3-D nucleation
2. Face development by 2-D nucleation
3. Generation of screw defects
4. Final spiral growth stage. The crystal may stop growing at stage (2) if screw dislocation(s) did not form

When considering the set of faces as a whole, the crystal habit changes with time as follows. Soon after nucleation, it may possibly adopt a dendritic/hollow/skeletal habit (e.g., Welsch et al. 2013) for which surface energy is far from minimized in case of very high $\Delta\mu$'s: spinifex texture of olivine and/or pyroxenes in pillow lava, snow crystals are examples. This habit then re-organizes into a rather anisotropic shape, where re-entrant pits disappear and elongation occurs along the strongest PBC directions, e.g., [001] for acicular to prismatic pyroxenes and amphiboles, and [100], [110], $[1\bar{1}0]$ together for micas and clay minerals giving a {001} flattened habit. This emphasizes the relatively high growth rates of faces on which strong dangling bonds occur. With further decay of $\Delta\mu$, such habit anisotropy decreases to give a more compact (isometric) shape. If true equilibrium of the crystal with its medium could be reached, then the crystal would adopt its equilibrium shape on which any (*hkl*) face is at a distance from the crystal center proportional to its crystal–medium interface free energy. This ideal situation is rarely met in Nature, except for some daughter minerals in fluid inclusions (e.g., NaCl and KCl as perfect cubes) and with the negative shape of cavities in alpha-quartz containing primary fluid inclusions.

Specific impurity or inhibitor atoms, ions, or molecules may slow down or even stop the growth of specific faces and/or make new faces appear. Trace amount of Mg, Mn, and Sr, or Ca/CO_3 imbalance, deeply modifies the synthetic habit of calcite (Paquette and Reeder 1995). They act even in trace amounts as they may poison the few growth unit incorporation sites (kinks) present on an F face. Subsequent incorporation in the crystal bulk structure may or may not happen. Accordingly, chemical characterization of the past growth medium from habit observations is hazardous.

Unequal partition of screw dislocations among symmetrically equivalent faces may "distort" the growth habit, altering its apparent symmetry, this being due to central distances of symmetry-equivalent faces no longer equal. Certain "whisker" or needle-like habits are striking examples where the tip face grows fast by a unique/axial spiral while other lateral faces are stopped as defect-free faces, i.e., not able to grow anymore by the TDNM mechanism under insufficient $\Delta\mu$ (halite NaCl, sphalerite ZnS).

The flux of the growth medium with respect to the faces may also lead to face development dissymmetry, provided growth is at least partly volume-diffusion controlled. Faces upstream grow quicker than faces downstream, and laminar flow results in a better face quality in the former case. Fluid inclusions form preferentially behind downstream faces because of a turbulent flowtail: anisotropy and polarity of the quality of alpha-quartz crystals have been used to identify solution flow directions in hydrothermal veins.

Resorption of Unique Mineral Grains

Dissolution or melting of minerals also starts from their surfaces. Preferential sites for resorption are corners and edges where detachment of dissolution units is the easiest.

Etch pits with the shape of inverted pyramids, often centered on defects, also form on flat faces. Rounded shapes result, but they are transient. Starting from a sufficiently large crystal or from a crystal polished as a sphere would lead to a polyhedral, now stationary, habit. The latter would be limited by the fastest resorbing faces, i.e., those which were growing formerly the fastest, and therefore which were not present on the growth habit. Consequently, neither euhedral nor rounded habits are fully confident indicators of growth or resorption, respectively.

Growth and Sector Zonings

Irregularities in growth rates of individual faces, volume diffusion-growth rate feedback, temperature, and/or changes in the mother medium chemistry are major sources of growth zoning. Such growth zoning consists of "ghost-in-ghost" marks that trace successive growth habits of single crystals during their life time (Fig. 4a, b). Unconformities similar to those known in structural geology may develop if one or more resorption stages occurred during the growth history.

Sector zoning refers to isochronous and different chemical compositions left in the crystal volume behind distinct faces which are not crystallographically equivalent: sand-glass marks in Ti-rich augite, Ag-rich {111} versus Ag-poor {100} forms of argentiferous galena (Fig. 4a), etc. Individual crystal sectors are often inward-pointing pyramids that are the part of the crystal bulk swept across by a growing face. Both growth and sector zonings are indications of global disequilibrium of the crystal with respect to its surrounding. This is far from detrimental since the growth history of a mineral can be read in this case (Baronnet 1984; Sunagawa 1984).

Collective Behavior of Growing Minerals

Explosive nucleation on foreign dots or spherical substrate followed by anisotropic growth results in fibroradiating textures where individual crystals radiate out because of geometrical selection (fibrous zeolites, malachite $Cu_2(OH)_2CO_3$, etc.). Another example is crystal branching, a common process by which spherulites form, for which crystals nucleate continuously on already formed crystals while keeping a repeatable, usually small, disorientation. This disorientation may, or more commonly may not, be a twin operation. For example, branching originates the macroscopically "curved faces" of dolomite $CaMg(CO_3)_2$ or azurite $Cu_3(OH)_2(CO_3)_2$, sheaves of stilbite $NaCa_2Al_5Si_{13}O_{36}$—14 H_2O, twisted fibers of chalcedony SiO_2, and more generally split crystals and spherulites (Grigor'ev 1965). These crystals of less crystallographic quality are now called mesocrystals (Cölfen and Antonietti 2008). The latter are also quite common among biominerals which are no more pure minerals but organo-mineral composites at different scales. They are envisaged to form mostly by particle attachment or

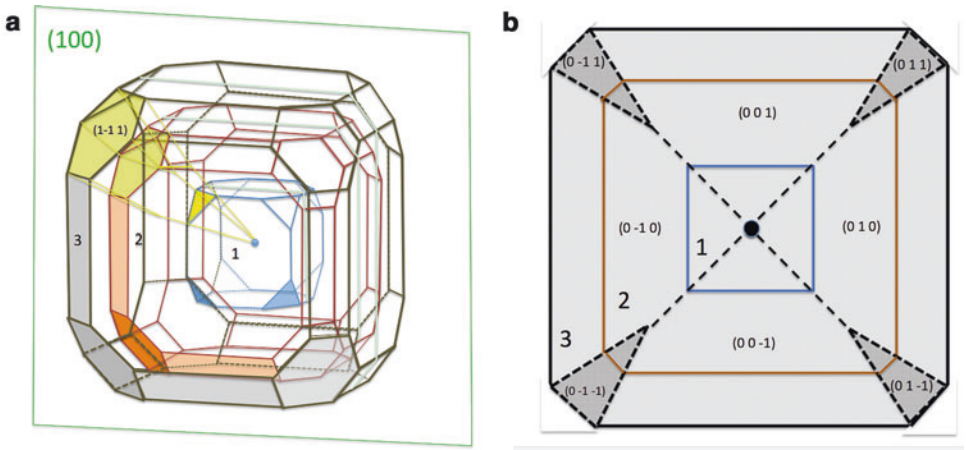

Mineral Genesis, Fig. 4 Galena morphology as a euhedral crystal with cubic symmetry that may combine the {1 0 0}, {1 1 0}, and {1 1 1} forms. (**a**) Three stages of growth (1–3) of the same single crystal illustrating varying mean growth rate ratios between the different forms. The early morphology {1 0 0} + {1 1 1} (a cube truncated at each corner; stage 1, blue) evolves to {1 0 0} + {1 1 1} + {1 1 0} (the same but in addition truncation of all edges of the cube; stages 2, brown and 3, grey). The trajectory of the (1 −1 1) face is highlighted as yellow lines as the edges of the (1 −1 1) growth sector pyramid. Note that any morphology feature wins one dimension once buried inside the growing crystal: corners become lines, edges become surfaces, and surfaces become volumes. All faces of the same form assumed to grow at the same rate. (**b**) (1 0 0) cross-section of the same crystal passing through its center (pale green traces in (**a**)); here the ratio of overgrowth widths along <1 1 0> and <1 0 0> is equal to the ratio of the mean growth rates of {1 1 0} and {1 0 0} in the same time interval

self-organization (discontinuous growth) in the growth medium (De Yoreo et al. 2015). Even purely mineral-mineral crystalline composites are able to mimic life-evocating shapes of "fossils" of primitive organisms, thus rendering extra-planetary recognition of life from recovered "fossil" morphologies somewhat hazardous (Garcia-Ruiz et al. 2009, 2017).

When growth conditions tend to equilibrium from positive departures, a set of crystals of the same mineral will evolve toward reducing its excess surface free energy by changing its grain size. Smallest crystals will resorb, while the biggest will grow at their expense so that their number will decrease and their mean grain size as a whole will increase. This is the so-called Ostwald ripening process (Ostwald 1897), which originates from increased solubility or decreased melting point for crystal sizes mainly in the micrometer range and below. Mineral ripening (Baronnet 1982) operates frequently in monomineralic rocks exposed a long time to metamorphic and hydrothermal conditions (calcite in marbles, alpha-quartz in quartzites, illite in diagenetic rocks, and hydrothermal veins, etc.), and in case of highly soluble minerals near ambient conditions. A unique crystal with its equilibrium shape per mineral phase would be the very end of ripening in a closed system.

Conclusions

Appearance and development of minerals on and in Earth are strongly linked to positive departures from thermodynamic equilibrium caused by the moving matter of our planet. Destabilized mineral systems try their best to walk a while along the pathway toward a new equilibrium. Mineral crystallization participates to this trip. Despite the huge timescales of the Earth history, true equilibrium is rarely reached in rocks. This is the reason why we are able to learn a lot on mineral genesis from reading the mineral structures, microstructures, habits, textures, and chemistry (e.g., Cordier and Leroux 2008), because most of such kinetic fingerprints were not rubbed out by equilibrium attainment.

Cross-References

- Crystal Chemistry
- Experimental mineralogy and petrology
- Fluid–Rock Interaction
- Hydrothermal solutions
- Magmatic Process Modeling
- Mineral defects
- Mineralogy
- Ore deposits
- Paragenesis
- Solid Solution/Exsolution
- Solubility
- Stoichiometry

References

Baronnet A (1982) Ostwald ripening in solution. The case of calcite and mica. Estud Geol 38:185–198

Baronnet A (1984) Growth kinetics of the silicates. A review of basic concepts. Fortschr Mineral 62:187–232

Bravais A (1866) Etudes Cristallographiques. Gauthier-Villars, Paris

Burton WK, Cabrera N, Frank FC (1951) The growth of crystals and the equilibrium structure of their surfaces. Philos Trans R Soc Lond 243:299–358

Cölfen H, Antonietti M (2008) Mesocrystals and nonclassical crystallization. Wiley, Chichester, p 288

Cordier P, Leroux H (2008) Ce que disent les minéraux. Belin-Pour la science, Paris

De Yoreo et al (2015) Crystallization by particle attachment in synthetic, biogenic, and geologic environment. Science 349(6247):aaa6760

Dekeyser W, Amelinckx S (1955) Les dislocations et la croissance des cristaux. Masson, Paris

Donnay JDH, Harker D (1937) A new law of crystal morphology extending the law of Bravais. Am Mineral 22:446–467

Garcia-Ruiz JM, Melero-Garcia E, Hyde ST (2009) Morphogenesis of self-assembled nanocrystalline materials of barium carbonate and silica. Science 323:362–365

Garcia-Ruiz JM, Nakouzi E, Kotopoulou E, Tamborino L, Steinbock O (2017) Biomimetic mineral self-organization from silica-rich spring waters. Sci Adv 3:e1602285

Grigor'ev DP (1965) Ontogeny of minerals. Israel Program for Scientific Translations, Jerusalem

Hartman P, Perdok WG (1955) On the relations between structure and morphology of crystals. Acta Crystallogr 8:49–52

Jambon A (1980) Isotopic fractionation: a kinetic model for crystals growing from silicate melts. Geochim Cosmochim Acta 44:1373–1380

Kirkpatrick RJ (1983) Theory of nucleation in silicate melts. Am Mineral 68:66–77

Kirkpatrick RJ, Kuo LC, Melchior J (1981) Crystal growth in incongruently-melting compositions: programmed cooling experiments with diopside. Am Mineral 66:223–241

Kostov I (1965) Crystal habit and mineral genesis. Bull Strasimir Dimitrov Inst Geol 14:33–49

Kostov I, Kostov RI (1999) Crystal habit of minerals, Bulgarian academic monographs 1. Prof. Marin Drinov Academic Publishing House and Pensoft, Sofia, p 415

Ostwald W (1897) Studien über die Bildung und Umwandlung fester Körper. Z Phys Chem 22:289–330

Paquette J, Reeder RJ (1995) Relationship between surface structure, growth mechanism, and trace element incorporation in calcite. Geochim Cosmochim Acta 59:735–749

Stranski IN (1928) Zur Theorie der Kristallswachstums. Z Phys Chem A 136:259–278

Sunagawa I (1977) Natural crystallization. J Cryst Growth 42:214–223

Sunagawa I (1984) Growth of crystals in Nature. In: Sunagawa I (ed) Materials science of the Earth's interior. Terra Scientific Publication Company, Tokyo, pp 61–103

Sunagawa I (1987) Morphology of Minerals. In: Sunagawa I (ed) Morphology of crystals: part B. Terra Scientific Publication Company, Tokyo, pp 509–587

Welsch B, Faure F, Famin V, Baronnet A, Bachélery P (2013) Dendritic crystallization; a single process for all the textures of olivine in basalts? J Petrol 54(3):539–574

Mineralogy

Michael F. Hochella Jr.
Department of Geosciences, Virginia Tech, Blacksburg, VA, USA
Geosciences Group, Pacific Northwest National Laboratory, Richland, WA, USA

Definition

Mineralogy is the scientific study of minerals. The issue at hand is the definition of the term "mineral," which was first used in Medieval Latin in the late fourteenth century as *minerale*, or "something mined." The term survives today in common use forms, for example, "mineral water" and "vitamins and minerals" that have nothing to do with the science of mineralogy. The minerals of mineralogy are most traditionally defined in the past decade or two as naturally occurring inorganic substances, produced by geochemical processes, with an ordered, repeating atomic arrangement (a crystalline substance) whose composition can be described by a chemical formula resulting in a definite, but not necessarily fixed, composition. Samples of the same mineral vary in terms of minor and/or trace element composition, and in the case of solid solution, major element composition as long as these substitutions do not change the average crystalline atomic structure. If a change does occur, a new mineral name, not just a varietal name, would be warranted. However, the formal definition of mineral, and therefore mineralogy, is changing (see last section of this article below).

Introduction

The scientific definition of "mineral" has changed with time precisely because the term goes back centuries. As our understanding of these substances advance (Skinner 2005; Dyar et al. 2008; Klein and Dutrow 2008; Klein and Philpotts 2012; Nesse 2012; Haldar 2013; Vaughan 2014), and as we better understand Earth systems science (the extraordinary connectedness of all scientific fields), so does our organization of how we perceive and organize concepts. The general trends have been to modernize the definition to remove what may be historically arbitrary, or even unnecessary, and to also change the definition from more exclusive to one that is more inclusive. For example, natural philosophers centuries ago separated the planet into categories of air, water, and earth and earth into animal, vegetable, and mineral. From this, most definitions well into the twentieth century (and even a few today) exclude inorganic, crystalline compounds produced directly by living organisms (e.g., carbonate minerals that later form a limestone) or indirectly (sulfides that form extracellularly, but as a result of biochemical processes that later become an ore deposit) as not being minerals due to their biologically related origins. This exclusion serves no purpose, and several more recent definitions of minerals have not carried on this exclusionary practice. Equivalently, the part of most mineral definitions that necessitate traditional views of highly ordered crystallinity is also beginning to fall away. The great majority of mineral definitions still state that minerals must be crystalline, which have precisely ordered arrangements of atoms, and are periodic, that is, repeating the same structural units (unit cells), over and over again as described by conventional translational symmetry. However, common and exceptionally important environmental minerals, for example, ferrihydrite and schwertmannite, are accepted by the International Mineralogical Association (IMA) as minerals, but the structure of ferrihydrite is highly disordered, and schwertmannite is poorly ordered within nanoregions that are separated by amorphous material. The IMA also accepts the naturally occurring quasicrystal, icosahedrite, as a mineral. Icosahedrite possesses highly ordered atomic arrangements, but, as a quasicrystal, it is not periodic, lacking conventional translational symmetry. Some now consider naturally occurring organic crystals, and even liquid crystals, as minerals, but, in all of these cases, there is much debate.

In 2009, the IMA set up various commissions and working groups to try to drive forward new mineral classification schemes, and how each will be defined based on all the new findings and evolving thought in the mineralogical sciences.

History

Mineralogy is thought to be one of the earliest fields of science. Like plants, animals, and water, minerals (and rocks which are most typically solid aggregates of one or more minerals) have always been resources readily available to hominids (any of the ancient family of erect bipedal primate mammals, of which only *Homo sapiens* exist today). As cognitive ability led to recognition of mineral properties and eventually experimentation, minerals clearly became one of the core ingredients of the development of the first technologies. Witness the Stone Age, which would last for over 3 million years, defined by fashioning minerals and rocks ideal for cutting, grinding, and pounding, as well as for producing very sharp edged and highly pointed objects. The Stone Age was followed by the Bronze Age which began in approximately the sixth millennium BCE. This time was near the beginning of the extraction of specific metals (copper and tin to make bronze, but also gold – traceable to at least the fifteenth millennium BCE – and many other metals) from rocks and minerals. This was followed by the Iron Age near

the beginning of the first millennium BCE using iron-based minerals that provided even a much wider range of technological advantage. These rock/mineral extraction and production technologies, along with the earlier stone tools developed during the Stone Age, radically changed the world under which the first civilizations began due to the beginnings of agriculture and domestication of animals as far back as the ninth millennium BCE.

Using a different line of reasoning which is just as transformative to human development, imagine the technological advantage of being able to make fire "on demand." This was done, in part, by the discovery that forcefully impacting or striking certain minerals or rocks, such as pyrite, marcasite, or pentlandite, against a hard surface like flint or quartzite can produce sparks suitable for starting fires. Anthropologists are not certain of the first users of mineral-based strikers, but it is clear that *Homo erectus*, some 400,000 years ago, were using fire. Much more recently in the Paleolithic period, some 40,000–50,000 years ago, *Homo sapiens* made fire routinely, and fire strikers in some (or perhaps many) cases may have been used. Very effective iron strikers are well known from near the beginning of the Iron Age forward, probably starting nearly 3 millennia ago.

Fast-forward to today, to the present beginnings of the third millennia AD, we find that mobile phones (i.e., pocket computers, very powerful ones) would not work without elements extracted from minerals containing rare earth elements. The latest jet engine technology would not stand a chance without exotic metal technologies that depend on many other common and rare elements across the periodic table which are only made available by finding economically viable concentrations of certain minerals (not easy to do, to say the least) and discovering economically viable and hopefully environmentally safe ways to extract target elements from those minerals (also a great scientific and technical challenge). Just as importantly, and ultimately much more central to our very existence, key proteins (e.g., enzymes) in our bodies cannot function without metallic cofactors (reactive components in proteins) held within amino acid chains, elements that even in us were sourced via the (bio) geochemical weathering of minerals. Simply put, biology does not work without minerals. And as far as the origin of life itself, scientists that study this typically include minerals, or mineral components, as substrates and/or catalysts in reactions critical to processes that are central to the core of their constructs, experiments, and hypotheses.

Because of the central role that minerals have always played in human history, mineralogy was one of the first sciences to be developed, even, perhaps surprisingly, before the science of geology (Laudan 1987). James Hutton, the eighteenth century Scottish naturalist and founder of modern geology, considered Georgius Agricola, the sixteenth century German physician – natural historian who classified about 600 minerals – as the founder of what we know today as the science of mineralogy. Agricola's most famous work, *De re metallica* (Latin, for *On the Nature of Minerals*) was written entirely in Latin and published in 1556, the year after his death. It was a brilliant and complete treatise (for its time) on minerals, mining, and processing/smelting for metal recovery. This work was also key in the history in the development in the science of chemistry and curiously was first translated to English by Herbert Hoover, who would later become President of the United States in 1929, and his wife, a geologist. This late sixteenth-century work completely replaced the work of Pliny the Elder in this general field of knowledge. Pliny was the first century Roman naturalist who was also the author of the very first encyclopedia. In the centuries after Agricola, and now every single decade, mineralogy continues to advance as an ultramodern and vibrant science.

Mineral Types, Numbers, and Classification

Minerals exist in every part of the Earth system, from high in the atmosphere to deep in the oceans and everywhere in between, and are by far the major constituent of our rocky planet. They also make up meteors and are in fact found throughout the universe, surely making up or contributing to countless other planets (perhaps 100 billion in this galaxy alone, and there are more than 100 billion galaxies altogether). Within galaxies, nebulae are solar system incubators which are made up of high concentrations of gas and dust; the dust consisting of a wide assortment of mineral nanoparticles which represent groups of minerals that we would readily recognize such as oxides, silicates, sulfides, and carbonates. These are the mineral components of future planets. As on this planet, elements from the entire periodic table are available. Temperature and pressure conditions vary dramatically during planetary formation and aging, and in the presence of reactants and catalysts in solid, liquid, and gaseous forms, mineral formation of every conceivable species will be created.

To date, from everywhere on and in Earth that is accessible to us, as well as from our moon, meteorites, and interplanetary dust particles, just over 5,000 minerals have been identified, characterized, and accepted, with a few hundred more awaiting IMA approval, and a few to several tens of new minerals still newly discovered every year.

On this planet, with the makeup of Earth's crust being mostly the elements silicon and oxygen (about 75% by mass), a little over 90% of the crust is made up of silicate minerals (any mineral that has at least silicon and oxygen as major components), of which there are well over 1,000 known varieties. Other elements most commonly found in silicates are the rest of the most common elements represented in the crust, namely (in decreasing order of abundance), aluminum,

iron, calcium, sodium, potassium, and magnesium. Quartz (SiO_2) is the "simplest" and most common single mineral in the crust, but the feldspar group primary minerals (nominally albite $NaAlSi_3O_8$, orthoclase $KAlSi_3O_8$, and anorthite $CaAl_2Si_2O_8$) are by far the most common collectively. Silicates stable at high pressures make up even a higher percentage of the Earth's mantle, which is 84% of the entire Earth by volume.

The basic building block of silicate minerals is the silica tetrahedron $[SiO_4]^{4-}$. Note that aluminum, the next most abundant element in the crust after oxygen and silicon, also forms tetrahedra $[AlO_4]^{5-}$, and silica, or silica and alumina tetrahedra, polymerize (link together) to various extents to form the different types of silicate minerals. The other most common elements chemically bond the various polymerized units together, giving us the vast variety of known silicates. Complete, three-dimensional polymerization generates the tectosilicates (also known as framework silicates); two-dimensional polymerization generates the phyllosilicates (also known as sheet or layer silicates – micas and clays are members of this type); one-dimensional polymerization generates the inosilicates (also known as chain silicates, with amphiboles representing double chains species and pyroxenes representing single chains); ring polymerization generates cyclosilicates; individual silica tetrahedron generate the orthosilicates (also known as island silicates, with olivine as the prime example).

With the dominance of oxygen and silicon in our crust and mantle, one might think that the rest of the mineral kingdom on Earth (nearly 4,000 more minerals) would be relegated to corners of the planet, and with little importance. Nothing could be further from the truth. These minerals provide most of the absolutely necessary elements needed by living organisms (from phosphorus that is key to building the backbone of DNA and RNA to the cellular energy molecule, ATP, to all necessary micronutrients), and most synthetic material components besides carbon for plastics, that is, all that goes into metallic materials (from steel to wiring to airplane wings), semiconducting metals (all electronics and computers), and ceramics and glass (from dinner plates and bricks to windows). Modern civilization would not be possible without all these minerals. Nonsilicate minerals also include the minerals made from single elements (e.g., gold, copper, sulfur, carbon – graphite and diamond). The thousands of other nonsilicate minerals are classified according to the mineral formula's anionic element or groups, with the rest of the periodic table involved. These mineral classes (with the anionic element or group in parentheses along with a type example – name and mineral formula – for each) include the sulfides ($S^{1-,2-}$, pyrite FeS_2); oxides (O^{2-}, hematite Fe_2O_3); hydroxides (OH^-, goethite FeOOH); carbonates (CO_3^{2-}, calcite $CaCO_3$); sulfates (SO_4^{2-}, gypsum $CaSO_4 . H_2O$); phosphates (PO_4^{2-}, apatite $Ca_5(PO_4)_3(OH)$); and halides (Cl^- and F^-, halite NaCl and fluorite CaF_2).

Present and Future Challenges in the Mineralogical Sciences

Harrison et al. (2013) oversaw a 2-year project in which mineralogists (and Earth, planetary, and environmental scientists in related fields) from around the world were asked to consider the greatest present and future questions facing the mineralogical sciences, such that if they would be answered, they would make the biggest difference from the most fundamental to the most applied applications. All of the results from the open survey were condensed down to 100 questions (this list can be downloaded at www.elementsmagazine.org/under the Supplements tab). The very nature of the survey itself speaks clearly to the relevance and staying power of this ancient, now modern science, which is the simple fact that minerals are related, either directly or indirectly, to every subfield of all the Earth, planetary, and environmental sciences. Whether one is a paleontologist or an atmospheric scientist, a geomorphologist, or an aqueous biogeochemist, studying the early solar system or the evolution of Earth's crust, minerals are important, or perhaps entirely central, to your field of study.

Of all mineral sciences-related subjects, the science of Earth sustainability deserves a special mention. In the face of continuing human population pressures and the fact that atmospheric, soil, groundwater, and biosystem resources are approaching or have already begun to cross decline thresholds, mineralogy holds a central position in understanding how to achieve a sustainable state for Earth. It is well known that most physical, chemical, and biological processes on Earth are either influenced to some degree or fully driven by the properties of minerals. But with only approximately 5,000 mineral species presently described – not many relative to millions of prokaryotic and eukaryotic species combined – their diversity and range of influence may seem, by comparison, relatively modest. Yet minerals exert their influence by constituting (as they always will) the bulk of this Earth system and having a wide range of compositions and structures that are expressed in a remarkable (even dramatic) diversity of physical and chemical properties. Further, minerals are more complex than previously thought because of the discovery that their chemical and physical properties vary as a function of particle size when smaller than a few to perhaps as much as several tens of nanometers in at least one dimension. These variations are most likely due, at least in part, to differences in surface and near-surface atomic structure, as well as crystal shape and surface topography as a function of size in this smallest of size regimes. It has now been established that these variations make a difference in important geochemical and biogeochemical reactions and kinetics, forming the "new" science of nanomineralogy. This recognition is broadening and enriching our view of how minerals influence the hydrosphere, pedosphere, biosphere, and atmosphere (Hochella et al. 2008).

Mineralogy is as important to Earth sustainability issues as most other branches of science. But as has become apparent, it

is the combination of mineralogy with other sciences, such as hydrology and aqueous geochemistry, biogeochemistry, microbiology, atmospheric science, nanoscience, and the medical sciences that makes it so powerful. Starting with the advent of Stone Age tools to fire strikers, minerals have made vital contributions to the human endeavor for literally hundreds of thousands of years. Direct contributions, in terms of the extraction of mineral resources, will continue indefinitely. However for the future, it is the interaction of minerals with the human-impacted hydrosphere, atmosphere, and biosphere that will play a big role in dictating the sustainability, or, if not, the failed sustainability, of planet Earth.

Conclusion

As we have seen above, humans have recognized and utilized minerals with extraordinary creativity for many millennia. Clearly, this utilization has literally changed the world. A modern view of the science of minerals, through which we can easily recognize today as a very careful observational and systematic study, was brought to us over 450 years ago by Georgius Agricola. The centuries in between did not disappoint, with thousands of major developments in our understanding of this planetary construction material. Whether using minerals to understand plate tectonics, the origin of life, global climate change, or catalytic chemistry on a grand scale, they have unlocked more secrets than most observers can imagine. Now, by using powerful computers backed by ingenious software and models, transmission electron microscopes that have subatomic-resolution analytic capabilities, and synchrotrons that cost hundreds of millions of dollars producing light with unimaginable peak brilliances for science, and the very serious connection with other sciences, in particular physics and biology, it is not surprising that our view of minerals has changed, certainly including in ways that we could not have anticipated. This should indicate that a new look at the mineral kingdom is in order. One way to do that is shown in Fig. 1. The figure (from Caraballo et al. 2015) uses the concept of short-, medium-, and long-range atomic order, or just order for short (SRO less than a nanometer, MRO 2–3 nm, and LRO more than 3 nm, respectively, with "order" referring to the perfection/reproducibility/periodicity of the atomic arrangement of the material; the more perfectness over many atomic

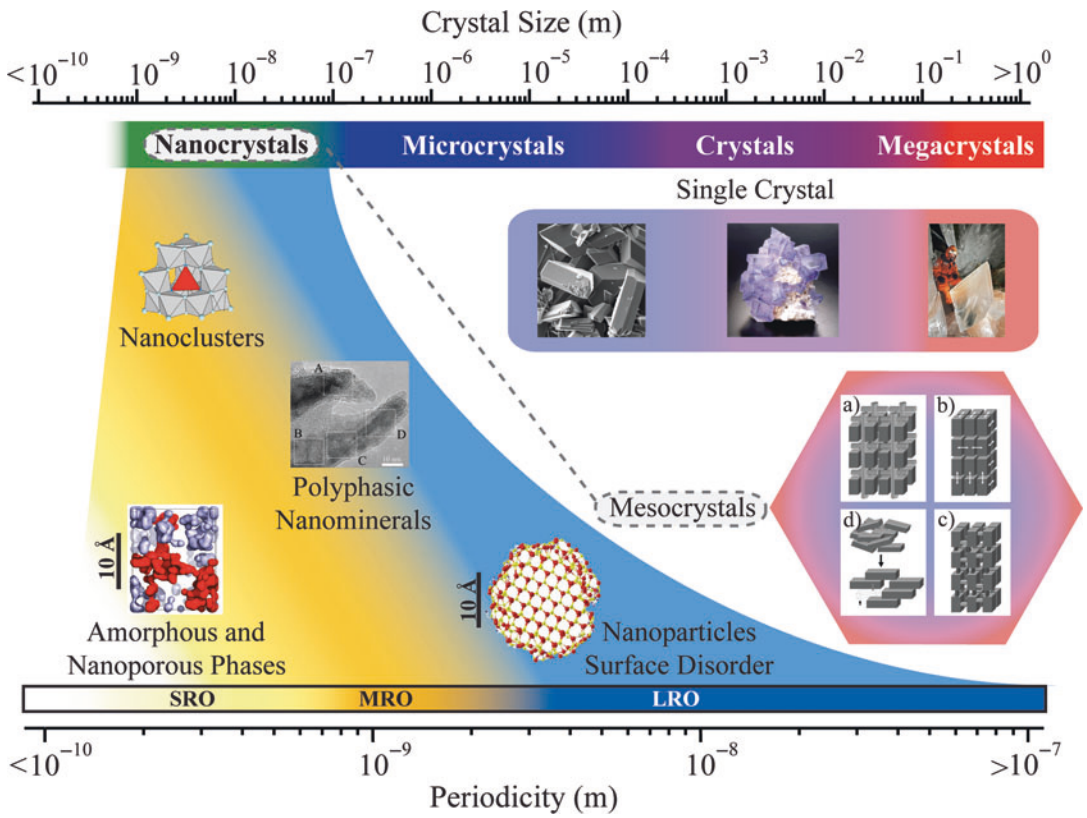

Mineralogy, Fig. 1 Schematic organization of naturally occurring materials using periodicity (short, medium, and long-range order) as the key parameter, and secondarily crystal size. Glasses only exhibit SRO, with the mineral kingdom exhibiting MRO and LRO, and a remarkable range of crystal sizes (see text for further discussion). Four types of mesocrystals are shown within the inset based on the materials/forces that hold/align the crystalline units together: (**a**) organic matrices, (**b**) physical fields and interparticle forces, (**c**) mineral bridges, and (**d**) space constrains (From Caraballo et al. (2015). See this reference for details)

dimensions, the higher the order). A glassy/amorphous material has only SRO, moving only weakly into MRO. Crystalline materials possess MRO (the smallest nanominerals) to LRO.

In Fig. 1, the lower Y-axis shows periodicity on an absolute distance scale (showing the ranges of SRO, MRO, and LRO using shades of white, yellow, and blue), as well as crystal size that becomes particularly important in the nanoscale, a new definition of the term "mineral" (entirely what the term "mineralogy" is based upon) emerges. Because amorphous materials, those showing only SRO, have unique chemical and mechanical characteristics, they deserve a major – and separate – materials category (naturally occurring glass is not a mineral). This is nothing new and has been supported by vast amounts of science for more than a century. However, as soon as a naturally occurring material shows atomic order even in the MRO range (e.g., the smaller nanocrystals, and polyphasic nanominerals like schwertmannite), it can now be defined as a mineral. Further, due to the inextricable link between the biotic and abiotic worlds around Earth's near surface, biominerals are minerals, as much so as a mineral in a rock or a meteorite, or a naturally occurring organic crystal. There are no other requirements that are needed to define a mineral. The definition becomes simple and inclusive, stripping away unnecessary requirements:

Definition: Mineralogy is the science of minerals. Minerals are naturally occurring materials that show at least medium-range atomic order.

Compare that with the unimaginably complex world of proteins, whose types number in the millions. Definition: Proteins are large macromolecules consisting of one or more long chains of amino acid residues.

Cross-References

- ▶ Carbonate Minerals and the CO2-Carbonic Acid System
- ▶ Clay Minerals
- ▶ Crystal Chemistry
- ▶ Halide Minerals
- ▶ Mineralogy
- ▶ Mineral Defects
- ▶ Native Minerals
- ▶ Oxide Minerals
- ▶ Silicate Minerals
- ▶ Sulfate Minerals
- ▶ Sulfide Minerals

References

Caraballo MA, Michel FM, Hochella MF Jr (2015) The rapid expansion of environmental mineralogy in unconventional ways: beyond the accepted definition of a mineral, the latest technology, and using nature as our guide. Am Mineral 100:14–25

Dyar MD, Gunter M, Tasa D (2008) Mineralogy and optical mineralogy. Mineralogical Society of America, Chantilly, 708 pp

Haldar S (2013) Introduction to mineralogy and petrology. Elsevier, Waltham, 356 pp

Harrison RJ, Hochella MF Jr, Murphy K, Vaughan DJ (2013) One hundred mineralogical questions impacting the future of Earth, planetary, and environmental sciences. Elements 8:168–170

Hochella MF Jr, Lower SK, Maurice PA, Penn RL, Sahai N, Sparks DL, Twining BS (2008) Nanominerals, mineral nanoparticles, and earth systems. Science 319:1631–1635

Klein C, Dutrow B (2008) Manual of mineral science, 23rd edn. New York: Wiley

Klein C, Philpotts A (2012) Earth materials: introduction to mineralogy and petrology. Cambridge University Press, New York, 533 pp

Laudan R (1987) From mineralogy to geology: the foundations of a science 1650–1830. University of Chicago Press, Chicago, 285 pp

Nesse W (2012) Introduction to mineralogy. Oxford University Press, New York, 496 pp

Skinner HCW (2005) Biominerals. Mineral Mag 69:621–641

Vaughan DJ (2014) Minerals: a very short introduction. Oxford University Press, Oxford, 137 pp

Molybdenum

Anthony Chappaz[1], Jennifer B. Glass[2] and Timothy W. Lyons[3]
[1]Department of Earth and Atmospheric Sciences, Central Michigan University, Mount Pleasant, MI, USA
[2]School of Earth and Atmospheric Sciences, Georgia Institute of Technology, Atlanta, GA, USA
[3]Department of Earth Sciences, University of California – Riverside, Riverside, CA, USA

M

Element Data

Atomic Symbol: **Mo**
Atomic Number: **42**
Atomic Weight: 95.94 g/mol
Isotopes and Abundances: Seven stable isotopes ^{92}Mo (14.84%), ^{94}Mo (9.25%), ^{95}Mo (15.92%), ^{96}Mo (16.68%), ^{97}Mo (9.55%), ^{98}Mo (24.13%), and ^{100}Mo (9.63%)
1 Atm Melting Point: 2,623 °C
1 atm Boiling Point: 4,639 °C
Common valences: +VI, +V, +IV, +III, +II, +I, 0, and-II
Ionic Radii: 210 pm
Pauling Electronegativity: 2.16
First Ionization Energy: 684.32 kJ mol^{-1}
Chondritic (CI) Abundance: 1–2 ppm
Silicate Earth Abundance: 25–66 ppb
Crustal Abundance: 1–2 ppm
Seawater Abundance: 9.8 ppb
Core Abundance: 5 ppm

Properties

From a geochemical perspective, molybdenum (Mo) is fascinating because it has seven stable isotopes and seven oxidation states that can be accessed at low reduction potentials. Molybdenum's wide range of geochemical variability makes it particularly relevant in studies of Earth processes. Its versatility in redox behavior also makes Mo a vital metal center in the active site of numerous enzymes (Leimkühler and Iobbi-Nivol 2015).

History and Use

Molybdenum is a transition metal discovered in 1778 by Carl Scheele. The name derives from *molybdos*, ancient Greek for lead, because molybdenite (a Mo-rich ore) was often confused with lead. Molybdenum has important applications in metallurgy, while also serving as an essential micronutrient for life. In recent years, its elemental and isotopic distributions through history have emerged as effective geochemical proxies for tracking the oxygenation history of Earth's early oceans and atmosphere.

Molybdenum's average concentration in Earth's crust is 1–2 ppm (McLennan 2001). The main economic source of Mo is molybdenite ($Mo^{IV}S_2$), although molybdate minerals such as wulfenite ($PbMo^{VI}O_4$) and powellite ($CaMo^{VI}O_4$) are also extracted. Most of the Mo produced worldwide is for metallurgical applications, mainly in alloys (Braithwaite and Haber 2013). Minor Mo applications include use as a fertilizer, a lubricant (MoS_2), and for medical imagery (radioisotope ^{99}Mo).

Molybdenum Geochemistry

Chemical weathering of molybdenite ores and other Mo-containing sulfide phases, such as pyrite, releases Mo in the environment where it is transported via association with organic matter and iron (Fe)/manganese (Mn) oxyhydroxides into aquatic systems (Wichard et al. 2009; Glass et al. 2013). In the modern oxic ocean, Mo exhibits a conservative behavior, a very long residence time (~440 kyr), and has the highest concentration among the transition metals (~105 nM; Miller et al. 2011). In most freshwaters, dissolved Mo concentrations are in the low nanomolar (nM) range (Chappaz et al. 2008; Glass et al. 2013).

Thermodynamic models predict Mo speciation in oxygenated waters is dominated by the oxyanion molybdate ($Mo^{VI}O_4^{2-}$), although recent studies are investigating the possible importance of Mo(V) and (VI) species in seawater (Wang et al. 2009, 2011). Molybdenum burial in sediment under oxic conditions is controlled by adsorption reactions involving molybdate and Fe/Mn oxyhydroxides (Chappaz et al. 2008; Scholz et al. 2013).

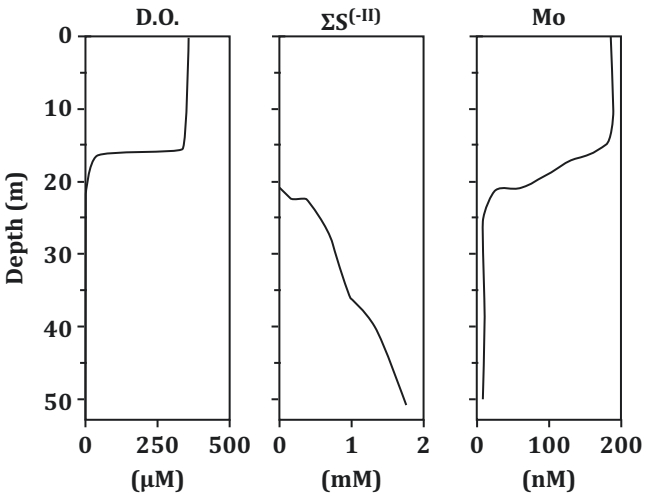

Molybdenum, Fig. 1 Dissolved oxygen (*DO*), sulfide (ΣS-II), and Mo concentrations in water column from a meromictic lake (Modified from Geochimica et Cosmochimica Acta, Vol. 165, Havig, J. R., McCormick, M. L., Hamilton, T. L., and Kump, L. R. (2015), The behavior of biologically important trace elements across the oxic/euxinic transition of meromictic Fayetteville Green Lake, New York, USA, 389–406, Copyright (2016), with permission from Elsevier). Note the high solubility under oxic water-column conditions and the rapid decline in Mo levels in the presence of dissolved sulfide

In sulfidic waters, oxygen atoms in molybdate (MoO_4^{2-}) are progressively replaced by sulfur atoms to form thiomolybdate species ($MoO_{4-x}S_x^{2-}$;Helz et al. 1996; Erickson and Helz 2000; Vorlicek et al. 2015). This substitution reaction is usually coupled with a steep decline in total Mo concentrations at the interface between oxygenated and sulfidic waters (Fig. 1) (Emerson and Huested 1991; Havig et al. 2015).

Two main pathways can lead to Mo burial in sediments under sulfidic conditions: (1) reaction with Fe–S mineral phases and (2) interaction with organic matter (Helz et al. 2011; Dahl et al. 2013; Chappaz et al. 2014; Ardakani et al. 2016; Dahl et al. 2016). The net result is non-conservative behavior under sulfidic conditions and sediment enrichments that can exceed crustal levels by two orders of magnitude when appreciable levels of dissolved sulfide extend into the water column.

Biological Utilization and Toxicity

Almost all life forms utilize Mo-containing enzymes, although many more types of Mo enzymes are present in prokaryotes than eukaryotes (Zhang and Gladyshev 2008). Molecular phylogenies suggest the great antiquity of Mo-containing enzymes and their likely existence in the

last universal common ancestor (Schoepp-Cothenet et al. 2012). The oxyanion molybdate ($Mo^{VI}O_4^{2-}$) may have been involved in prebiotic synthesis of RNA (Benner and Kim 2015).

Over 50 enzymes involved in the global cycles of carbon, nitrogen, and sulfur, as well as four that are essential to human health, require Mo as a metal cofactor (Schwarz et al. 2009). Molybdenum is most commonly incorporated into enzymes bound to heterocyclic pterin molecules ("molybdopterins"), with the important exception of the molybdenum-iron cofactor in nitrogenase, the microbial enzyme that catalyzes the reduction of dinitrogen (N_2) gas to ammonia (Fig. 1). Recent isotopic evidence suggests that biological fixation by Mo nitrogenase dates back to at least 3.2 billion years ago (Stüeken et al. 2015), although molecular clock dating suggests a later origin (Boyd and Peters 2013).

Due to the importance of Mo in the nitrogen cycle, low levels of this metal may limit key steps in microbial nitrogen fixation and nitrate assimilation by plants and phytoplankton (Glass et al. 2012). Microbial nitrate respiration may also be limited by low nM Mo concentrations in anoxic groundwaters (Thorgersen et al. 2015). It is also possible that scarce Mo in the ancient oceans stalled aspects of the early evolution of life (Anbar and Knoll 2002; Glass et al. 2009; Lyons et al. 2014 2015).

A Powerful Paleo-Redox Proxy

Molybdenum's unique redox properties and its high number of natural isotopes have attracted the attention of geoscientists studying Earth's early oxygenation history, including relationships to the early prokaryotic and eukaryotic life. For example, patterns of Mo enrichment in organic-rich marine rocks deposited beneath euxinic (anoxic and sulfidic) waters can track the earliest onset of oxidative weathering (Anbar et al. 2007), the presence of local euxinia (Scott and Lyons 2012), the strength of the connection between a given basin and the open ocean (Algeo and Lyons 2006), and the areal extent of euxinia in the ancient ocean on a global scale (Scott et al. 2008; Reinhard et al. 2013; reviewed in Lyons et al. 2014). The isotopic composition of Mo in euxinic deposits can similarly fingerprint the global extent of euxinic marine deposition (Arnold et al. 2004; Poulson et al. 2006; Dickson et al. 2012; Kendall et al. 2015).

Summary

Molybdenum's economic importance remains intact despite the many uncertainties about Mo geochemistry (Braithwaite and Haber 2013). Among those gaps, two stand as major opportunities for future research: (1) the specific mechanisms controlling Mo burial in anoxic sedimentary records and (2) a refined understanding of how varying levels of Mo bioavailability in ancient oceans may have contributed to (or limited) the evolution of life on Earth. Nevertheless, enough is known already about the relationships to marine redox conditions and the presence of sulfide in particular to place molybdenum among the most useful trace metals in studies of coevolution of the environment and life on ancient Earth.

Cross-References

- ▶ Atmospheric Evolution
- ▶ Ferromanganese Crusts and Nodules: Rocks That Grow
- ▶ Molybdenum Isotopes
- ▶ Nitrogen Cycle
- ▶ Nutrients
- ▶ Ocean Biochemical Cycling and Trace Elements
- ▶ Ore Deposits
- ▶ Oxidation-Reduction Reactions and Eh-pH (Pourbaix) Diagrams
- ▶ Oxygen
- ▶ Paleoenvironments
- ▶ Sulfur
- ▶ Transition Elements

References

Algeo TJ, Lyons TW (2006) Mo-total organic carbon covariation in modern anoxic marine environments: implications for analysis of paleoredox and paleohydrographic conditions. Paleoceanogr 21. https://doi.org/10.1029/2004PA001112

Anbar AD, Knoll AH (2002) Proterozoic Ocean chemistry and evolution: a bioinorganic bridge? Science 297:1137–1142

Anbar AD, Duan Y, Lyons TW, Arnold GL, Kendall B, Creaser RA, Kaufman AJ, Gordon GW, Scott C, Garvin J, Buick R (2007) A whiff of oxygen before the great oxidation event? Science 317:1903–1906

Ardakani OH, Chappaz A, Sanei H, Mayer B (2016) Effect of thermal maturity on remobilization of molybdenum in black shales. Earth Planet Sci Lett 449:311–320

Arnold GL, Anbar AD, Barling J, Lyons TW (2004) Molybdenum isotope evidence for widespread anoxia in mid-proterozoic oceans. Science 304:87–90

Benner SA, Kim HJ (2015) The case for a martian origin for Earth life. In: Hoover RB, Levin GV, Rozanov AYu, Wickramasinghe NC (eds) Instruments, methods, and missions for astrobiology XVII, proceedings of SPIE, vol 9606, 96060C

Boyd ES, Peter JW (2013) New insights into the evolutionary history of biological nitrogen fixation. Front Microbiol. https://doi.org/10.3389/fmicb.2013.00201

Braithwaite ER, Haber J (2013) Molybdenum: an outline of its chemistry and uses, Studies in inorganic chemistry, vol 19. Elsevier, Amsterdam

Chappaz A, Gobeil C, Tessier A (2008) Geochemical and anthropogenic enrichments of Mo in sediments from perennially oxic and seasonally anoxic lakes in eastern Canada. Geochim Cosmochim Acta 72:170–184

Chappaz A, Lyons TW, Gregory DD, Reinhard CT, Gill BC, Li C, Large RR (2014) Does pyrite act as an important host for molybdenum in modern and ancient euxinic sediments? Geochim Cosmochim Acta 126:112–122
Dahl TW, Chappaz A, Fitts JP, Lyons TW (2013) Molybdenum reduction in a sulfidic lake: evidence from X-ray absorption fine-structure spectroscopy and implications for the Mo paleoproxy. Geochim Cosmochim Acta 103:213–231
Dahl TW, Chappaz A, Hoek J, McKenzie CJ, Svane S, Canfield DE (2016) Evidence of molybdenum association with particulate organic matter under sulfidic conditions. Geobiology. https://doi.org/10.1111/gbi.12220
Dickson AJ, Cohen AS, Coe AL (2012) Seawater oxygenation during the Paleocene-Eocene thermal maximum. Geology 40:639–642
Emerson SR, Huested SS (1991) Ocean anoxia and the concentrations of molybdenum and vavadium in seawater. Mar Chem 34:177–196
Erickson BE, Helz GR (2000) Molybdenum(VI) speciation in sulfidic waters: stability and lability of thiomolybdates. Geochim Cosmochim Acta 64:1149–1158
Glass JB, Wolfe-Simon F, Anbar AD (2009) Coevolution of metal availability and nitrogen assimilation in cyanobacteria and algae. Geobiology 7:100–123
Glass JB, Axler RP, Chandra S, Goldman CR (2012) Molybdenum limitation of microbial nitrogen assimilation in aquatic ecosystems and pure cultures. Front Microbiol. https://doi.org/10.3389/fmicb.2012.00331
Glass JB, Chappaz A, Eustis B, Heyvaert AC, Waetjen DP, Hartnett HE, Anbar AD (2013) Molybdenum geochemistry in a seasonally dysoxic Mo-limited lacustrine ecosystem. Geochim Cosmochim Acta 114:204–219
Havig JR, McCormick ML, Hamilton TL, Kump LR (2015) The behavior of biologically important trace elements across the oxic/euxinic transition of meromictic Fayetteville Green Lake, New York, USA. Geochim Cosmochim Acta 165:389–406
Helz GR, Miller CV, Charnock JM, Mosselmans JFW, Pattrick RAD, Garner CD, Vaughan DJ (1996) Mechanism of molybdenum removal from the sea and its concentration in black shales: EXAFS evidence. Geochim Cosmochim Acta 60:3631–3642
Helz GR, Bura-Nakic E, Mikac N, Ciglenecki I (2011) New model for molybdenum behavior in euxinic waters. Chem Geol 284:323–332
Kendall B, Komiya T, Lyons TW, Bates SM, Gordon GW, Romaniello SJ, Jiang GQ, Creaser RA, Xiao SH, McFadden K, Sawaki Y, Tahata M, Shu DG, Han J, Li Y, Chu XL, Anbar AD (2015) Uranium and molybdenum isotope evidence for an episode of widespread ocean oxygenation during the late Ediacaran period. Geochim Cosmochim Acta 156:173–193
Leimkühler S, Iobbi-Nivol C (2015) Bacterial molybdoenzymes: old enzymes for new purposes. FEMS Microbiol. https://doi.org/10.1093/femsre/fuv043
Lyons TW, Reinhard CT, Planavsky NJ (2014) The rise of oxygen in Earth's early ocean and atmosphere. Nature 506:307–315
Lyons TW, Fike DA, Zerkle A (2015) Geomicrobiology and microbial geochemistry: emerging biogeochemical views of Earth's ancient microbial worlds. Elements 11:415–421
McLennan SM (2001) Relationships between the trace element composition of sedimentary rocks and upper continental crust. Geochem Geophys Geosyst, 2, Art. no. 2000GC000109
Miller CA, Peucker-Ehrenbrink B, Walker BD, Marcantonio F (2011) Re-assessing the surface cycling of molybdenum and rhenium. Geochim Cosmochim Acta 75:7146–7179
Poulson RL, Siebert C, McManus J, Berelson WM (2006) Authigenic molybdenum isotope signatures in marine sediments. Geology 34:617–620
Reinhard CT, Planavsky NJ, Robbins LJ, Partin CA, Gill BC, Lalonde SV, Bekker A, Konhauser KO, Lyons TW (2013) Proterozoic Ocean redox and biogeochemical stasis. PNAS 110:5357–5362
Schoepp-Cothenet B, van Lis R, Philippot P, Magalon A, Russell MJ, Nitschke W (2012) The ineluctable requirement for the trans-iron elements molybdenum and/or tungsten in the origin of life. Sci Rep 2:263
Scholz F, McManus J, Sommer S (2013) The manganese and iron shuttle in a modern euxinic basin and implications for molybdenum cycling at euxinic ocean margins. Chem Geol 355:56–68
Schwarz G, Mendel RR, Ribbe MW (2009) Molybdenum cofactors, enzymes and pathways. Nature 460:839–847
Scott C, Lyons TW (2012) Contrasting molybdenum cycling and isotopic properties in euxinic versus non-euxinic sediments and sedimentary rocks: refining the paleoproxies. Chem Geol 324:19–27
Scott C, Lyons TW, Bekker A, Shen Y, Poulton SW, Chu X, Anbar AD (2008) Tracing the stepwise oxygenation of the Proterozoic Ocean. Nature 452:456–U455
Stüeken EE, Buick R, Guy BM, Koehler MC (2015) Isotopic evidence for biological nitrogen fixation by molybdenum-nitrogenase from 3.2 Gyr. Nature 520:666–669
Thorgersen MP, Lancaster WA, Vaccaro BJ, Poole FL, Rocha AM, Mehlhorn T (2015) Molybdenum availability is key to nitrate removal in contaminated froundwater environments. Appl Environ Microbiol 81:4976–4983
Vorlicek TP, Chappaz A, Groskreutz LM, Young N, Lyons TW (2015) A new analytical approach to determining Mo and re speciation in sulfidic waters. Chem Geol 403:52–57
Wang DL, Aller RC, Sanudo-Wilhelmy SA (2009) A new method for the quantification of different redox-species of molybdenum (V and VI) in seawater. Mar Chem 113:250–256
Wang DL, Aller RC, Sanudo-Wilhelmy SA (2011) Redox speciation and early diagenetic behavior of dissolved molybdenum in sulfidic muds. Mar Chem 125:101–107
Wichard T, Mishra B, Myneni SCB, Bellenger JP, Kraepiel AML (2009) Storage and bioavailability of molybdenum in soils increased by organic matter complexation. Nat Geosci 2:625–629
Zhang Y, Gladyshev VN (2008) Molybdoproteomes and evolution of molybdenum utilization. J Mol Biol 379:881–899

Molybdenum Isotopes

Jane Barling[1], Jie Yang[2] and Yu-Hsuan Crystal Liang[3]
[1]Department of Earth Sciences, University of Oxford, Oxford, UK
[2]School of Earth and Environmental Sciences, University of St Andrews, Fife, UK
[3]Institute of Earth Sciences, Academia Sinica, Nangang, Taipei, TAIWAN

Introduction

Molybdenum isotopes are produced by three nucleosynthetic processes: the p- (proton process), r- (rapid neutron capture), and s- (slow neutron capture) processes. The seven naturally occurring isotopes (^{92}Mo, ^{94}Mo, ^{95}Mo, ^{96}Mo, ^{97}Mo, ^{98}Mo, and ^{100}Mo) are all stable or extremely long-lived: ^{100}Mo decays to ^{100}Ru with a half-life of ~10^{19} years (NNDC Chart of Nuclides). These isotopes extend over a mass range of ~8% and their natural abundances are rather uniform (~9%

to 25%). These characteristics, in conjunction with improvements in mass spectrometry since the mid-1990s, have resulted in the detection of small fractionations of Mo isotope ratios in meteoritic and terrestrial samples. It is now known that Mo isotopes are heterogeneously distributed in the solar system, resulting in mass-independent variations of Mo isotope ratios in meteoritic samples (Burkhardt et al. 2011). Compared to meteorites, Earth is enriched in s-process Mo isotopes implying, in conjunction with oxygen isotope data, that meteorites might not be representative of the Mo isotopic composition of the bulk Earth (Burkhardt et al. 2011). The improvements in mass spectrometry have also resulted in the recent revision of the absolute isotopic composition and atomic weight of terrestrial Mo (Berglund and Wieser 2011).

Isotope fractionations may vary with the masses of the isotopes: mass-dependent fractionation or be mass-independent (MIF), e.g., as a result of nucleosynethic processes. The only known natural terrestrial MIF of Mo is in samples from the Oklo natural reactor in Gabon (Bros et al. 2003; Wieser et al. 2012). In contrast, investigations since the late 1990s have shown that mass-dependent fractionation of Mo isotopes in natural samples ranges over 2.4‰/amu and may result from a wide range of physical, chemical, and biological processes (Fig. 1 and references therein).

Analytical Methods

Molybdenum isotope ratios are measured by thermal ionization mass spectrometers (TIMS) and multicollector inductively coupled-plasma mass spectrometers (MC-ICP-MS). Analysis of Mo isotopes by TIMS has a long history dating back to the 1960s (see: Wieser and De Laeter 2007) and continues to be used and improved. However, it was the advent of MC-ICP-MS in the 1990s with its improved analytical precision and smaller sample size requirements, compared to TIMS (Lee and Halliday 1995; Anbar et al. 2001; Siebert et al. 2001), that provided the impetus for the development of Mo isotope geochemistry. Most Mo isotope ratios today are measured by MC-ICP-MS.

Molybdenum isotopic compositions are typically reported in delta-notation, as per mil (‰) deviations in the $^{98}Mo/^{95}Mo$ ratio relative to a reference standard:

$$\delta^{98}Mo/^{95}Mo_{sample}(‰) = \left(\left({}^{98}Mo/^{95}Mo_{sample}/{}^{98}Mo/^{95}Mo_{standard}\right) - 1\right) \times 1000$$

In the absence of a certified standard reference material (SRM) for Mo isotope ratios, initial choices of reference standard were arbitrary. Recently, however, the NIST SRM 3134 has been proposed as the international reference standard for Mo isotopes and a number of interlaboratory calibrations have been made (e.g., Goldberg et al. 2013).

Natural Mass Dependent Fractionation

The important biogeochemistry of Mo, which involves varied redox chemistry and covalent bonding, both known drivers of isotope fractionation, made this element an early target for investigation of stable mass-dependent isotope fractionation in a heavy metal (Anbar 2004). Initial studies focused on samples from low temperature environments and were quick to notice the similarity in the isotopic composition of Mo in seawater and in sediments deposited under euxinic conditions (i.e., anoxic and sulfidic) and the large isotope fractionation between Mo in seawater and in manganese crusts, which form in oxic seawater conditions (Fig. 1). This led to the proposal that the $\delta^{98}Mo/^{95}Mo$ of seawater might covary with the relative proportions of anoxic (sic) and oxic sedimentation and thus be utilized as a paleoredox proxy (Barling et al. 2001; Siebert et al. 2003).

The hypothesis that Mo isotope fractionation between seawater and Mn crusts resulted from inefficient scavenging of Mo by Mn oxides under oxic conditions was confirmed experimentally (Barling and Anbar 2004), while the lack of isotope fractionation between seawater and euxinic sediments was attributed to the quantitative removal of Mo from the water column under euxinic conditions (Helz et al. 1996). Theoretical and sample based studies determined that Mo isotopes are fractionated during the step-wise conversion of molybdate (MoO_4^{2-}) to tetrathiomolybdate (MoS_4^{2-}), but that this is only expressed under conditions where removal of Mo from the water column is nonquantitative (Tossell 2005; Nägler et al. 2011).

Application of Mo isotopes as a paleoproxy requires a sound understanding of the modern marine Mo cycle and characterization of the sources and sinks of Mo (Anbar and Rouxel 2007). Recent data (Fig. 1) have confirmed the isotopic homogeneity of seawater and characterized sources (rivers and hydrothermal fluids) and sinks (oxic, suboxic, anoxic and euxinic, marine sediments, and carbonates) for Mo in the modern ocean. These have been used to revise the original simple box model on which the paleoproxy was based (e.g., Cheng et al. 2015). Since the first application of Mo isotopes as a paleoredox proxy by Arnold et al. (2004) it has become clear that Mo isotopes are not a stand-alone paleoredox proxy, but rather a useful tool in a multiproxy approach to understanding paleoredox (Lyons et al. 2009).

Application of Mo isotopes as a paleoproxy has largely been focused in the Archean and Proterozoic where they have contributed, in conjunction with other paleoredox proxies, to understanding the rise of oxygen in Earth's early ocean (Lyons et al. 2014). The evolution of oxygenic photosynthesis is generally accepted to be the cause of the rise of oxygen in the atmosphere and oceans, but when this happened is still intensely debated (Farquhar et al. 2011). Planavsky et al. (2014) have used $\delta^{98}Mo/^{95}Mo$ values consistent with Mn oxide interaction to infer oxygenic photosynthesis in

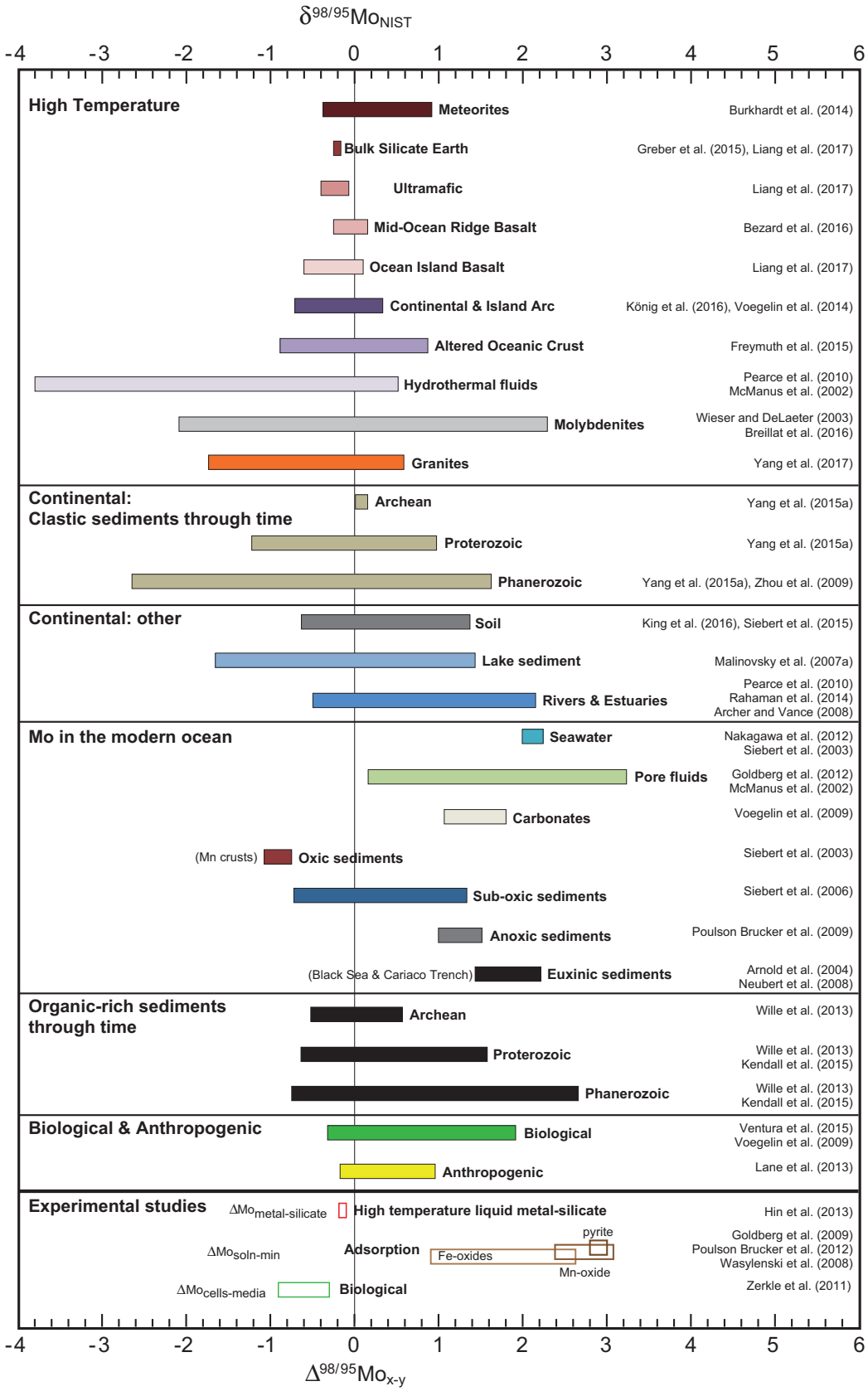

Molybdenum Isotopes, Fig. 1 (continued)

Archean (2.95 Ga) shallow marine settings. However, it is the Mo isotope record in organic-rich sediments that has received the most attention, providing evidence for a reducing atmosphere in the Archean prior to 2.7 Ga and early "whiffs" of oxygen prior to the Great Oxidation Event (Wille et al. 2013 and references therein). This record exhibits a ~2‰ range in $\delta^{98}Mo/^{95}Mo$ through most of the Proterozoic, intermediate between the narrow range of Archean $\delta^{98}Mo/^{95}Mo$ (<1‰) and the Phanerozoic/present day range (>3‰), reflecting the increasing proportion of oxic ocean floor (Fig. 1). The Phanerozoic is however punctuated by Ocean Anoxic Events and more local fluctuations in ocean redox that have been investigated using Mo isotopes (e.g., Dickson et al. 2016). Molybdenum isotopes have also been used to investigate the connection between ocean redox and radiations and extinctions of the fossil record since the Ediacaran (ca. 635–542 Ma; e.g., Chen et al. 2015).

Most paleoredox studies have been on the marine record but more recently attention has turned to continentally derived clastic sediments. These provide a record of contemporaneous atmospheric oxygen levels and like the marine record of organic-rich sediments, testify to the rise of oxygen through Earth's history (Fig. 1). The average Mo isotopes of clastic sediments show that the continental crust has become lighter over time suggesting that supracrustal processes have resulted in the preferential loss of heavy Mo to the hydrosphere (Yang et al. 2015a). Samples from other continental settings such as estuaries, lakes, and in soils have received less attention, as has Mo isotope fractionation related to biological and human activity (Fig. 1).

Even though it has been clear from Mo isotope measurements of molybdenites (Breillat et al. 2016 and references therein) that hydrothermal processes (200–1200 °C) are associated with significant Mo isotope fractionation (Fig. 1), the potential for Mo isotope fractionation in other high temperature environments has been largely overlooked until recently. It is now known that magmatic systems, particularly those involving a fluid phase (subduction zone volcanics and granites), exhibit Mo isotope fractionations spanning nearly 2.5‰. In contrast, Mo isotope fractionation is absent during crystal fractionation in anhydrous magmatic systems (Yang et al. 2015b). Mo isotope variations in the mantle, MORB, and OIB are small and may reflect the presence of residual sulfide melts during small degrees of partial melting of the mantle (Liang et al. 2017). The Mo concentrations and isotopic compositions of basalts, komatiites, and peridotites have also been used to constrain the Mo concentration and isotopic composition of the BSE (Fig. 1). Average Mo isotope ratios for magmatic iron meteorites and enstatite-, ordinary- and carbonaceous chondrites typically overlap the BSE estimate, while Mo isotopes derived from the silicate portion of differentiated planetary bodies trend to values heavier than terrestrial magmatic samples (Burkhardt et al. 2014). Lunar basalts have Mo isotopes similar to MORB (Burkhardt et al. 2014).

Interpretation of Mo isotope fractionation in natural samples is aided by theoretical and experimental investigations of processes with the potential to fractionate isotopes. The relatively few such studies have investigated biological activity, adsorption, aqueous speciation (Malinovsky et al. 2007b), leaching of mine waste (Skierszkan et al. 2016), and partitioning between metal and silicate liquids (Fig. 1).

Summary and Conclusions

The seven naturally occurring isotopes of Mo have rather uniform abundances and extend over a mass range of ~8%. These characteristics, in conjunction with the interesting biogeochemistry of Mo, made Mo an early target for investigation of stable mass-dependent isotope fractionation in a heavy metal. To date, fractionation of Mo isotope ratios in natural samples range over 2.4‰/amu. Investigations have focused predominantly on marine samples leading to a better understanding of the modern marine Mo cycle. Initial observations of the contrasting Mo isotopic compositions of modern oxic and euxinic sediments led to the proposal that the $\delta^{98}Mo/^{95}Mo$ could be developed as a paleoredox proxy. Since then Mo isotopes have become a useful tool in multiproxy investigations of paleoredox, contributing in particular, to understanding of the rise of oxygen through Earth's history.

Mo isotope fractionation is less well documented in samples from continental environments, for biological and human activity and for samples from high temperature settings. There have also been comparatively few theoretical and experimental investigations of Mo isotope fractionation. Given the wide range in $\delta^{98}Mo/^{95}Mo$ in samples associated with high and low temperature fluids, analysis and theoretical and experimental investigations of samples and processes involving a fluid phase seem likely to be promising areas of future research.

Cross-References

- ▶ Ab Initio Calculations
- ▶ Analytical Techniques
- ▶ Atmospheric Evolution

Molybdenum Isotopes, Fig. 1 Mass-dependent fractionation of Mo isotopes in natural and experimental samples. *Bars* represent the range of values for each category; the references are for the maximum and minimum values reported. Molybdenum isotopic compositions have been renormalized to NIST SRM 3134 where necessary. For additional data sources see "References."

- ▶ Atomic Number, Mass Number, and Isotopes
- ▶ Black Shales and Sapropels
- ▶ Ferromanganese Crusts and Nodules: Rocks That Grow
- ▶ Inductively Coupled Plasma Mass Spectrometry (ICP-MS)
- ▶ Meteorites
- ▶ Molybdenum
- ▶ Nucleosynthesis
- ▶ Oklo Natural Nuclear Reactors
- ▶ Stable Isotope Geochemistry
- ▶ Subduction Zone Geochemistry
- ▶ Thermal Ionization Mass Spectrometry

References

Anbar AD (2004) Molybdenum stable isotopes: observations, interpretations and directions. Rev Mineral Geochem 55:428–454

Anbar AD, Rouxel O (2007) Metal stable isotopes in paleoceanography. Annu Rev Earth Planet Sci 35:717–746

Anbar AD, Knab KA, Barling J (2001) Precise determination of mass-dependent variations in the isotopic composition of molybdenum using MC-ICPMS. Anal Chem 73(7):1425–1431

Archer C, Vance D (2008) The isotopic signature of the global riverine molybdenum flux and anoxia in the ancient oceans. Nat Geosci 1(9):597–600

Arnold GL, Anbar AD, Barling J, Lyons TW (2004) Molybdenum isotope evidence for widespread anoxia in mid-Proterozoic oceans. Science 304(5667):87–90

Barling J, Anbar AD (2004) Molybdenum isotope fractionation during adsorption by manganese oxides. Earth Planet Sci Lett 217(3–4):315–329

Barling J, Arnold GL, Anbar AD (2001) Natural mass-dependent variations in the isotopic composition of molybdenum. Earth Planet Sci Lett 193(3–4):447–457

Berglund M, Wieser ME (2011) Isotopic compositions of the elements 2009 (IUPAC technical report). Pure Appl Chem 83(2):397–410

Bezard R, Fischer-Gödde M, Hamelin C, Brennecka GA, Kleine T (2016) The effects of magmatic processes and crustal recycling on the molybdenum stable isotopic composition of Mid-Ocean Ridge Basalts. Earth Planet Sci Lett 453:171–181

Breillat N, Guerrot C, Marcoux E, Négrel P (2016) A new global database of δ^{98}Mo in molybdenites: a literature review and new data. J Geochem Explor 161:1–15

Bros R, Hidaka H, Kamei G, Ohnuki T (2003) Mobilization and mechanisms of retardation in the Oklo natural reactor zone 2 (Gabon) – inferences from U, REE, Zr, Mo and Se isotopes. Appl Geochem 18(12):1807–1824

Burkhardt C, Kleine T, Oberli F, Pack A, Bourdon B, Wieler R (2011) Molybdenum isotope anomalies in meteorites: constraints on solar nebula evolution and origin of the Earth. Earth Planet Sci Lett 312:390–400

Burkhardt C, Hin RC, Kleine T, Bourdon B (2014) Evidence for Mo isotope fractionation in the solar nebula and during planetary differentiation. Earth Planet Sci Lett 391:201–211

Chen X, Ling H-F, Vance D, Shields-Zhou A, Zhu M, Poulton SW, Och LM, Jiang S-Y, Li D, Cremonese C, Archer C (2015) Rise to modern levels of ocean oxygenation coincided with the Cambrian radiation of animals. Nat Commun 6:7142

Cheng M, Li C, Zhou L, Xie S-C (2015) Mo marine geochemistry and reconstruction of ancient ocean redox states. Sci China Earth Sci 58(12):2123–2133

Dickson AJ, Jenkyns HC, Porcelli D, van den Boorn S, Idiz E (2016) Basin-scale controls on the molybdenum-isotope composition of seawater during Ocean Anoxic Event 2 (Late Cretaceous). Geochim Cosmochim Acta 178:291–306

Farquhar J, Zerkle AL, Bekker A (2011) Geological constraints on the origin of oxygenic photosynthesis. Photosynth Res 107:11–36

Freymuth H, Vils F, Willbold M, Taylor RN, Elliott T (2015) Molybdenum mobility and isotopic fractionation during subduction at the Mariana arc. Earth Planet Sci Lett 432:176–186

Goldberg T, Archer C, Vance D, Poulton SW (2009) Mo isotope fractionation during adsorption to Fe (oxyhydr)oxides. Geochim Cosmochim Acta 73(21):6502–6516

Goldberg T, Archer C, Vance D, Thamdrup B, McAnena A, Poulton SW (2012) Controls on Mo isotope fractionations in a Mn-rich anoxic marine sediment, Gullmar Fjord, Sweden. Chem Geol 296–297:73–82

Goldberg T, Gordon G, Izon G, Archer C, Pearce CR, McManus J, Anbar AD, Rehkämper M (2013) Resolution of inter-laboratory discrepancies in Mo isotope data: an intercalibration. J Anal At Spectrom 28(5):724–735

Greber ND, Puchtel IS, Nägler TF, Mezger K (2015) Komatiites constrain molybdenum isotope composition of the Earth's mantle. Earth Planet Sci Lett 421:129–138

Helz GR, Miller CV, Charnock JM, Mosselmans JFW, Pattrick RAD, Garner CD, Vaughan DJ (1996) Mechanism of molybdenum removal from the sea and its concentration in black shales: EXAFS evidence. Geochim Cosmochim Acta 60(19):3631–3642

Hin RC, Burkhardt C, Schmidt MW, Bourdon B, Kleine T (2013) Experimental evidence for Mo isotope fractionation between metal and silicate liquids. Earth Planet Sci Lett 379:38–48. https://doi.org/10.1016/j.epsl.2013.08.003

Kendall B, Komiya T, Lyons TW, Bates SM, Gordon GW, Romaniello SJ, Jiang G, Creaser RA, Xiao S, McFadden K, Sawaki Y, Tahata M, Shu D, Han J, Li Y, Chu X, Anbar AD (2015) Uranium and molybdenum isotope evidence for an episode of widespread ocean oxygenation during the late Ediacaran Period. Geochim Cosmochim Acta 156:173–193

King EK, Thompson A, Chadwick OA, Pett-Ridge JC (2016) Molybdenum sources and isotopic composition during early stages of pedogenesis along a basaltic climate transect. Chem Geol 445:54–67

König S, Wille M, Voegelin A, Schoenberg R (2016) Molybdenum isotope systematics in subduction zones. Earth Planet Sci Lett 447:95–102

Lane S, Proemse BC, Tennant A, Wieser ME (2013) Concentration measurements and isotopic composition of airborne molybdenum collected in an urban environment. Anal Bioanal Chem 405(9):2957–2963

Lee DC, Halliday AN (1995) Precise determinations of the isotopic compositions and atomic weights of molybdenum, tellurium, tin and tungsten using ICP magnetic sector multiple collector mass spectrometry. Int J Mass Spectrom Ion Process 146/147:35–46

Liang Y-H, Halliday AN, Siebert C, Fitton JG, Burton KW, Wang K-L, Harvey J (2017) Molybdenum isotope fractionation in the mantle. Geochim Cosmochim Acta 199:91–111

Lyons TW, Anbar AD, Severmann S, Scott C, Gill BC (2009) Tracking euxinia in the ancient ocean: a multiproxy perspective and Proterozoic case study. Annu Rev Earth Planet Sci 37:507–534

Lyons TW, Reinhard CT, Planavsky NJ (2014) The rise of oxygen in Earth's early ocean and atmosphere. Nature 506:307–315

Malinovsky D, Hammarlund D, Ilyashuk B, Martinsson O, Gelting J (2007a) Variations in the isotopic composition of molybdenum in freshwater lake systems. Chem Geol 236(3–4):181–198

Malinovsky D, Baxter DC, Rodushkin I (2007b) Ion-specific isotopic fractionation of molybdenum during diffusion in aqueous solutions. Environ Sci Technol 41(5):1596–1600

McManus J, Nägler TF, Siebert C, Wheat CG, Hammond DE (2002) Oceanic molybdenum isotope fractionation: diagenesis and hydrothermal ridge-flank alteration. Geochem Geophys Geosyst 3(12):1–9
Nägler TF, Neubert N, Boettcher ME, Dellwig O, Schnetger B (2011) Molybdenum isotope fractionation in pelagic euxinia: evidence from the modern Black and Baltic Seas. Chem Geol 289(1–2):1–11
Nakagawa Y, Takano S, Firdaus ML, Norisuye K, Hirata T, Vance D, Sohrin Y (2012) The molybdenum isotopic composition of the modern ocean. Geochem J 46(2):131–141
Neubert N, Nägler TF, Böttcher ME (2008) Sulfidity controls molybdenum isotope fractionation into euxinic sediments: evidence from the modern Black Sea. Geology 36:775–778
NNDC – Chart of Nuclides. National Nuclear Data Center, Brookhaven National Laboratory. http://www.nndc.bnl.gov/chart/
Pearce CR, Burton KW, Pogge von Strandmann PAE, James RH, Gislason SR (2010) Molybdenum isotope behaviour accompanying weathering and riverine transport in a basaltic terrain. Earth Planet Sci Lett 295(1–2):104–114
Planavsky NJ, Asael D, Hofmann A, Reinhard CT, Lalonde SV, Knudson A, Wang X, Ossa FO, Pecoits E, Smith AJB, Beukes NJ, Bekker A, Johnson TM, Konhauser KO, Lyons TW, Rouxel OJ (2014) Evidence for oxygenic photosynthesis half a billion years before the Great Oxidation Event. Nat Geosci 7:283–286
Poulson Brucker RL, McManus J, Severmann S, Berelson W (2009) Molybdenum behavior during early diagenesis: insights from Mo isotopes. Geochem Geophys Geosyst 10(6) https://doi.org/10.1029/2008GC002180
Poulson Brucker RL, McManus J, Poulton SW (2012) Molybdenum isotope fractionations observed under anoxic experimental conditions. Geochem J 46(3):201–209
Rahaman W, Goswami V, Singh SK, Rai VK (2014) Molybdenum isotopes in two Indian estuaries: mixing characteristics and input to oceans. Geochim Cosmochim Acta 141:407–422
Siebert C, Nägler TF, Kramers JD (2001) Determination of molybdenum isotope fractionation by double-spike multicollector inductively coupled plasma mass spectrometry. Geochem Geophys Geosyst. https://doi.org/10.1029/2000GC000124
Siebert C, Nägler TF, von Blanckenburg F, Kramers JD (2003) Molybdenum isotope records as a potential new proxy for paleoceanography. Earth Planet Sci Lett 211(1–2):159–171
Siebert C, McManus J, Bice A, Poulson R, Berelson WM (2006) Molybdenum isotope signatures in continental margin marine sediments. Earth Planet Sci Lett 241:723–733
Siebert C, Pett-Ridge JC, Opfergelt S, Guicharnaud RA, Halliday AN, Burton KW (2015) Molybdenum isotope fractionation in soils: influence of redox conditions, organic matter, and atmospheric inputs. Geochim Cosmochim Acta 162:1–24
Skierszkan EK, Mayer KU, Weis D, Beckie RD (2016) Molybdenum and zinc stable isotope variation in mining waste rock drainage and waste rock at the Antamina mine, Peru. Sci Total Environ 550:103–113
Tossell JA (2005) Calculating the partitioning of the isotopes of Mo between oxidic and sulfidic species in aqueous solution. Geochim Cosmochim Acta 69(12):2981–2993
Ventura GT, Gall L, Siebert C, Prytulak J, Szatmari P, Hurlimann M, Halliday AN (2015) The stable isotope composition of vanadium, nickel, and molybdenum in crude oils. Appl Geochem 59:104–117
Voegelin AR, Nägler TF, Samankassou E, Villa IM (2009) Molybdenum isotopic composition of modern and Carboniferous carbonates. Chem Geol 265(3–4):488–498
Voegelin AR, Pettke T, Greber ND, von Niederhausern B, Nägler TF (2014) Magma differentiation fractionates Mo isotope ratios: evidence from the Kos Plateau Tuff (Aegean Arc). Lithos 190–191:440–448
Wasylenki LE, Rolfe BA, Weeks CL, Spiro TG, Anbar AD (2008) Experimental investigation of the effects of temperature and ionic strength on Mo isotope fractionation during adsorption to manganese oxides. Geochim Cosmochim Acta 72:5997–6005
Wieser ME, De Laeter JR (2003) A preliminary study of isotope fractionation in molybdenites. Int J Mass Spectrom 225:177–183
Wieser ME, De Laeter JR (2007) Absolute isotopic composition of molybdenum and the solar abundances of the p-process nuclides 92,94Mo. Phys Rev C: Nucl Phys 75(5):055802/1–055802/8
Wieser ME, Barry S, De Laeter JR (2012) Fission yields of molybdenum in the Oklo natural reactor. J Radioanal Nucl Chem 293(3):949–954
Wille M, Nebel O, Van Kranendonk MJ, Schoenberg R, Kleinhanns IC, Ellwood MJ (2013) Mo-Cr isotope evidence for a reducing Archean atmosphere in 3.46-2.76 Ga black shales from the Pilbara, Western Australia. Chem Geol 340:68–76
Yang J, Barling J, Halliday AN (2015a) Molybdenum isotope fractionation in clastic sediments. Goldschmidt abstracts 3502
Yang J, Siebert C, Barling J, Savage P, Liang Y-H, Halliday AN (2015b) Absence of molybdenum isotope fractionation during magmatic differentiation at Hekla volcano, Iceland. Geochim Cosmochim Acta 162:126–136
Yang J, Barling J, Siebert C, Stephens E, Halliday AN (2017) The molybdenum isotopic composition of I-, S- and A- type granitic suites. Geochimic Cosmochim Acta in press. Doi.org/10.1016/j.gca.2017.01.027
Zerkle AL, Scheiderich K, Maresca JA, Liermann LJ, Brantley SL (2011) Molybdenum isotope fractionation by cyanobacterial assimilation during nitrate utilization and N_2 fixation. Geobiology 9(1):94–106
Zhou L, Gao S, Hawkesworth C, Archer C, Xie S-C (2009) Preliminary Mo isotope data of Phanerozoic clastic sediments from the northern margin of the Yangtze block and its implication for paleoenvironmental conditions. Chin Sci Bull 54(5):822–829

N

Native Minerals

Satoshi Matsubara
Department of Geology and Paleontology, National Museum of Nature and Science, Tokyo, Japan

Synonyms

Native elements

Definition

Native minerals are basically the natural substances that occur in the state of chemical elements or their alloys.

Classification

The term "native minerals" is not used but "native elements" or simply "elements" in the field of mineralogy, and some minerals that occur as carbides, nitrides, silicides, and phosphides as well as chemical elements or their alloys are traditionally classified into the class of "native elements and alloys" (Gaines et al. 1997) or simply "elements" (Strunz and Nickel 2001). As of 2014, the mineral names including native minerals are summarized in Fleischer's glossary of mineral species (Back 2014).

Native minerals are divided to the following three groups.

1. Metals and intermetallic alloys

A few native metals have nearly pure composition, but almost all of them are under the state of solid solution, e.g., between Au and Ag (Fig. 1) (referred as electrum), which are isostructural, and among Os, Ir, and Ru (referred as iridosmine) in case of different structure in pure metals, respectively, or intermetallic alloys, e.g., between Hg and other metals (referred as amalgam). In this group, 33 minerals are recognized as native elements composed of 25 elements such as Al, Ti, V, Cr, Fe, Ni, Cu, Zn, Mo, Ru, Rh, Pd, Ag, Cd, In, Sn, Sb, W, Os, Ir, Pt, Au, Hg, Pb, and Bi. Intermetallic alloys are recognized as 50 species. Among them, $Al_{63}Cu_{24}Fe_{13}$ and $Al_{71}Ni_{24}Fe_5$ discovered from meteorites have unusual quasicrystalline structure with quasiperiodic fivefold or tenfold rotation symmetry and were approved as new minerals under the name of icosahedrite in 2012 and of decagonite in 2015, respectively, by the Commission on New Minerals, Nomenclature and Classification, IMA.

2. Nonmetals

In this group, five native elements are recognized such as C, Si, S, As, and Te. Carbon and sulphur minerals have nearly pure composition, and four polymorphs (diamond, graphite, chaoite, and lonsdaleite) and three polymorphs (sulphur, sulphur-β, and rosickýite) exist, respectively. Arsenic minerals generally have solid solution between Sb, e.g., stibarsen ($Sb_{0.5}As_{0.5}$); in addition, three polymorphs (arsenic, arsenolamprite, and pararsenolamprite) exist.

3. Metallic and nonmetallic carbides, nitrides, silicides, and phosphides

In the field of mineralogy, these compounds traditionally are classified as native elements. Many minerals of this group have been discovered from extraterrestrial materials and two species are known as carbides (e.g., cohenite, $(Fe,Ni,Co)_3C$), four species as nitrides (e.g., osbornite, TiN), six species as silicides (e.g., hapkeite, Fe_2Si), and eight species as phosphides (e.g., barringerite, $(Fe,Ni)_2P$).

The occurrences of the native elements are divided into nine types: (1) in terrestrial rocks, (2) in ultramafic rocks (including kimberlite and lamproite) (account for about 38%), (3) in mafic rocks, (4) in felsic rocks, (5) in

W. M. White (ed.), *Encyclopedia of Geochemistry*,
https://doi.org/10.1007/978-3-319-39312-4

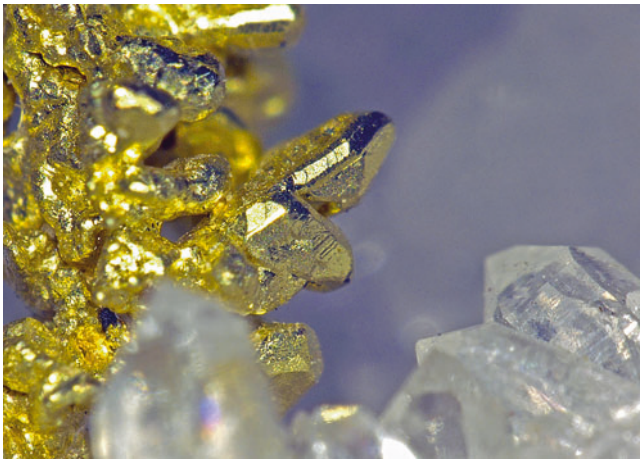

Native Minerals, Fig. 1 Photomicrograph of native gold crystals in hydrothermal quartz vein from the Nakase mine, Hyogo Prefecture, Japan. Field view: approximately 3.5 × 4.0 mm

metamorphic or metasomatic rocks, (6) in hydrothermal veins (account for about 18%), (7) in others (oxidation products, volcanic sublimate, etc.) and (8) in placer deposits (unknown original rocks), and (9) in extraterrestrial materials (meteorites, cosmic dusts, lunar rocks, etc.) (account for about 21%).

The mineral names of the native elements, chemical compositions, crystal system, and main occurrences are demonstrated in Table 1.

Summary

136 mineral species are classified into groups of native minerals (native elements) such as chemical elements or their alloys, carbides, nitrides, silicides, and phosphides (CNMNC 2016).

Native Minerals, Table 1 Mineral names of native elements. Mineral names are arranged alphabetically in every group. Abbreviations are as follows: (1) UL, (2) MF, (3) FL, (4) MT, (5) HY, (6) OT, (7) PL, and (8) ET. Also crystal systems are as follows: cubic, cub; tetragonal, tet; hexagonal, hex; trigonal (rhombohedral), trig; orthorhombic, orth; monoclinic, mon; triclinic, tric

Mineral name	Composition	Crystal system	Main occurrence
(Native metals)			
Aluminum	Al	Cub	MF, HY, OT
Antimony	Sb	Trig	HY
Awaruite	$Ni_2Fe \sim Ni_3Fe$	Cub	UL
Bismuth	Bi	Trig	HY
Cadmium	Cd	Hex	MF
Chromium	Cr	Cub	PL (inclusions in diamond)
Copper	Cu	Cub	OT, MT
Gold	Au	Cub	HY, PL
Garutite	(Ni,Fe,Ir)	Hex	UL
Hexaferrum	(Fe,Os,Ru,Ir)	Hex	UL
Hexamolybdenum	(Mo,Ru,Fe)	Hex	ET
Indium	In	Tet	FL
Iridium	Ir	Cub	UL, PL
Iron (kamacite = Ni-bearing iron)	Fe	Cub	MF, ET
Lead	Pb	Cub	MT, HY
Mercury	Hg	Trig (<−38.9 °C)	HY
Nickel	Ni	Cub	UL, MT
Osmium	Os	Hex	UL, PL
Palladium	Pd	Cub	UL, OT
Platinum	Pt	Cub	UL, MF, HY, PL
Rhodium	Rh	Cub	UL
Rutheniridosmine	(Ir,Os,Ru)	Hex	UL
Ruthenium	Ru	Hex	UL, PL
Silver	Ag	Cub	HY, OT
Stibarsen	$Sb_{0.5}As_{0.5}$	Trig	HY
Taenite	(Fe,Ni)	Cub	ET
Tetrataenite	FeNi	Tet	ET
Tin	Sn	Tet	FL
Titanium	Ti	Hex	UL
Tungsten	W	Cub	PL (inclusions in yttriaite-(Y))

(*continued*)

Native Minerals, Table 1 (continued)

Mineral name	Composition	Crystal system	Main occurrence
Vanadium	V	Cub	OT
Wairauite	CoFe	Cub	UL
Zinc	Zn	Hex	OT
(Intermetallic alloys)			
Anyuiite	$Au(Pb,Sb)_2$	Tet	UL, PL
Atokite	$(Pd,Pt)_3Sn$	Cub	UL
Auricupride	Cu_3Au	Cub	UL
Belendorffite	Cu_7Hg_6	Trig	HY
Bogdanovite	$(Au,Te,Pb)_3(CuFe)$	Cub	OT
Bortnikovite	Pd_4Cu_3Zn	Tet	UL
Cabriite	Pd_2CuSn	Orth	UL
Chengdeite	Ir_3Fe	Cub	UL, PL
Chromferide	$Fe_{1.5}Cr_{0.2}$	Cub	HY
Cupalite	(Cu,Zn)Al	Orth	UL
Damiaoite	$PtIn_2$	Cub	HY
Danbaite	$CuZn_2$	Cub	UL
Decagonite	$Al_{71}Ni_{24}Fe_5$	Decagonal	ET
Eugenite	$Ag_{11}Hg_2$	Cub	HY
Ferchromide	$Cr_{1.5}Fe_{0.2}$	Cub	HY
Ferronickelplatinum	Pt_2FeNi	Tet	UL
Hongshiite	(Pt,Fe)Cu	Trig	UL
Hunchunite	Au_2Pb	Cub	PL
Icosahedrite	$Al_{63}Cu_{24}Fe_{13}$	Icosahedral	ET
Jedwabite	$Fe_7(Ta,Nb)_3$	Hex	PL
Khatyrkite	$(Cu,Zn)Al_2$	Tet	UL
Kitagohaite	Pt_7Cu	Cub	PL
Kolymite	Cu_7Hg_6	Cub	HY
Leadamalgam	$Pb_{0.7}Hg_{0.3}$	Tet	HY
Luanheite	Ag_3Hg	Hex	PL
Maldonite	Au_2Bi	Cub	HY
Moschellandsbergite	Ag_2Hg_3	Cub	HY
Nielsenite	$PdCu_3$	Tet	UL
Niggliite	PtSn	Hex	UL, MF
Nisnite	Ni_3Sn	Cub	UL
Norilskite	$(Pd,Ag)_{2-x}Pb$ ($x = 0.08–0.11$)	Trig	MF
Novodneprite	$AuPb_3$	Tet	HY
Paolovite	Pd_2Sn	Orth	UL, MF
Paraschachnerite	$Ag_{1.2}Hg_{0.8}$	Orth	HY
Plumbopalladinite	Pd_3Pb_2	Hex	UL, MF
Potarite	PdHg	Tet	UL, PL
Rustenburgite	$(Pt,Pd)_3Sn$	Cub	UL, MF
Schachnerite	$Ag_{1.1}Hg_{0.9}$	Hex	HY
Skaergaardite	CuPd	Cub	UL, MF
Sorosite	$Cu_{1-x}(Sn,Sb)$ ($x = 0.1–0.2$)	Hex	PL
Stannopalladinite	Pd_3Sn_2	Orth	UL MF
Taimyrite-I	$(Pd,Cu,Pt)_3Sn$	Orth	UL
Tatyanaite	$(Pt,Pd,Cu)_9Cu_3Sn_4$	Orth	UL
Tetra-auricupride	CuAu	Tet	UL
Tulameenite	Pt_2FeCu	Tet	UL
Weishanite	$(Au,Ag)_{1.2}Hg_{0.8}$	Hex	HY
Yixunite	Pt_3In	Cub	MT
Yuanjiangite	AuSn	Hex	PL
Zhanghengite	CuZn	Cub	ET

(*continued*)

Native Minerals, Table 1 (continued)

Mineral name	Composition	Crystal system	Main occurrence
Zvyagintsevite	$(Pd,Pt,Au)_3(Pb,Sn)$	Cub	UL, MF
(Native nonmetals)			
Arsenic	As	Trig	HY, MT
Arsenolamprite	As	Orth	HY
Chaoite	C	Hex	MT
Diamond	C	Cub	UL, MT,PL
Graphite	C	Hex, trig	MT, MF
Lonsdalite	C	Hex	ET
Pararsenolamprite	As	Orth	HY
Rosickýite	S	Mon	OT
Silicon	Si	Cub	UL (inclusions in gold), MT
Sulfur	S	Orth	OT
Sulfur-β	S	Mon	OT
Tellurium	Te	Trig	HY
(Metallic and nonmetallic carbides)			
Cohenite	$(Fe,Ni,Co)_3C$	Orth	ET, MF
Haxonite	$(Fe,Ni)_{23}C_6$	Cub	ET
Isovite	$(Cr,Fe)_{23}C_6$	Cub	PL
Khamrabaevite	(Ti,V,Fe)C	Cub	MF
Moissanite	SiC	Hex, trig	UL, ET
Niobocarbide	(Nb,Ta)C	Cub	PL
Qusongite	WC	Hex	UL
Tantalcarbide	TaC	Cub	PL
Tongbaite	Cr_3C_2	Orth	UL
Yarlongite	$Cr_4Fe_4NiC_4$	Hex	UL
(Metallic and nonmetallic nitrides)			
Carlsbergite	CrN	Cub	ET
Nierite	Si_3N_4	Trig	ET
Osbornite	TiN	Cub	ET
Qingsongite	BN	Cub	UL
Roaldite	$(Fe,Ni)_4N$	Cub	ET
Siderazot	Fe_5N_2	Hex	OT
(Metallic silicides)			
Brownleeite	MnSi	Cub	ET
Gupeiite	Fe_3Si	Cub	ET
Hapkeite	Fe_2Si	Cub	ET
Linzhiite	$FeSi_2$	Tet	UL
Luobusaite	$Fe_{0.83}Si_2$	Orth	UL
Mavlyanovite	Mn_5Si_3	Hex	UL
Naquite	FeSi	Cub	UL
Palladosilicide	Pd_2Si	Hex	UL
Perryite	$(Ni,Fe)_8(Si,P)_3$	Trig	ET
Suessite	Fe_3Si	Cub	ET
Xifengite	Fe_5Si_3	Hex	ET
Zangboite	$TiFeSi_2$	Orth	UL
(Metallic phosphides)			
Allabogdanite	$(Fe,Ni)_2P$	Orth	ET
Andreyivanovite	FeCrP	Orth	ET
Barringerite	$(Fe,Ni)_2P$	Hex	ET
Florenskyite	FeTiP	Orth	ET
Halamishite	Ni_5P_4	Hex	MT
Melliniite	$(Ni,Fe)_4P$	Cub	ET
Monipite	MoNiP	Hex	ET

(*continued*)

Native Minerals, Table 1 (continued)

Mineral name	Composition	Crystal system	Main occurrence
Murashkoite	FeP	Orth	MT
Negevite	NiP_2	Cub	MT
Nickelphosphide	$(Ni,Fe)_3P$	Tet	ET
Schreibersite	$(Fe,Ni)_3P$	Tet	ET, MF
Transjordanite	Ni_2P	Hex	MT
Zuktamrurite	FeP_2	Orth	MT

Cross-References

- ▶ Aluminum
- ▶ Antimony
- ▶ Arsenic
- ▶ Bismuth
- ▶ Cadmium
- ▶ Chromium
- ▶ Cobalt
- ▶ Copper
- ▶ Elements: Metalloids
- ▶ Gold
- ▶ Indium
- ▶ Iridium
- ▶ Iron
- ▶ Lead
- ▶ Mercury
- ▶ Meteorites
- ▶ Mineralogy
- ▶ Molybdenum
- ▶ Nickel
- ▶ Osmium
- ▶ Palladium
- ▶ Platinum
- ▶ Platinum Group Elements
- ▶ Rhenium
- ▶ Rhodium
- ▶ Ruthenium
- ▶ Selenium
- ▶ Silicon
- ▶ Silver
- ▶ Sulfur
- ▶ Tellurium
- ▶ Tin
- ▶ Titanium
- ▶ Zinc

References

Back ME (2014) Fleischer's glossary of mineral species 2014. The Mineralogical Record Inc., Tucson

Commission on New Minerals, Nomenclature and Classification, International Mineralogical Association (2016) Available via IMA CNMNC. http://nrmima.nrm.se//. Accessed 18 Feb 2016

Gaines RV, Skinner HCW, Foord EE, Mason B, Rosenzweig A (1997) Dana's new mineralogy, 8th edn. Wiley, New York, pp 1–36

Strunz H, Nickel EH (2001) Strunz mineralogical tables, 9th edn. E. Schweizerbart'sche Verlagsbuchhandlung (Nägele u. Obermiller), Stuttgart, pp 33–55

Natural Gas

Giuseppe Etiope
Sezione Roma 2, Istituto Nazionale di Geofisica e Vulcanologia, Rome, Italy

Definitions

Natural gas is a mixture of gaseous hydrocarbons and nonhydrocarbon gases typically produced in subsurface sedimentary rocks, frequently associated with crude oil or coal beds. Hydrocarbon gases are almost exclusively alkanes, dominantly methane (CH_4, generally from 70 to 90 vol.%), and, subordinately, ethane (C_2H_6, 1 to 10 vol.%), propane (C_3H_8, generally <5 vol.%), and butane (C_4H_{10} < 1–2 vol.%). Nonhydrocarbon gases, such as CO_2, N_2, He, H_2, and H_2S, are generally present as minor constituents. Natural gas is formed through microbial or thermal degradation of organic matter in sedimentary rocks, typically shale or limestone (source rocks), in coal-beds, and through oil cracking and biodegradation. The gas can move inside the porous source rocks (primary migration), migrate to external rocks and accumulate in trapped permeable "reservoir" rocks (secondary migration), and move from a reservoir to another, or seep to the Earth's surface (tertiary migration and seepage; Fig. 1) (Hunt 1996; Etiope 2015).

In the petroleum geology literature, the term "natural gas" does not refer to geothermal or volcanic H_2O- or CO_2-rich gas where hydrocarbons are a minor component. The term can however include hydrocarbon-rich gas originated abiotically, in considerable concentrations (up 90 vol.%), in some igneous rocks (see "Origin").

The methane produced in subsurface source rocks is typically "fossil," i.e., radiocarbon (^{14}C) free (carbon older than 50,000 years BP) and can be termed "geological methane." Modern microbial methane is instead produced and dispersed

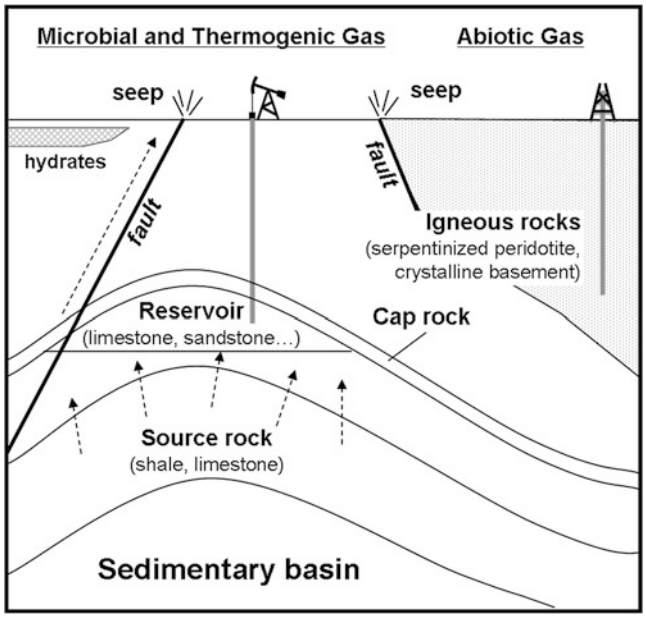

Natural Gas, Fig. 1 Scheme of the main natural gas occurrences

within shallow sediments and bottom waters in estuaries, deltas, bays, lakes, marshes, wetlands, and shallow permafrost. Although this modern gas could also be broadly called "natural gas," it does not represent a fossil-fuel source for petroleum industry and literature.

Origin

The natural gas currently exploited as energy source originates through the microbial or thermal degradation of organic matter, coal, or oil in sedimentary rocks, typically shale and limestone. Microbial and thermogenic gases are cumulatively termed *biotic* because of the derivation from biologic compounds, mainly lipids and carbohydrates, in marine (sapropelic) and terrestrial (humic) organic matter.

Microbial (or biogenic) gas is mainly produced during diagenesis of sediments (Hunt 1996) by specialized microorganisms that decompose organic matter and form CH_4 at relatively low temperatures (typically up to 60–80 °C; or above 100 °C by extremophiles in special hydrothermal systems). Although the term "bacterial methane" is also used in the literature, it should be remembered that Bacteria do not produce methane, only Archaea do it. After organic matter is decomposed, methane is formed through two main biochemical pathways: CO_2 or carbonate reduction ($CO_2 + 8H^+ + 8e^- \rightarrow CH_4 + 2H_2O$), and acetate fermentation ($CH_3COOH \rightarrow CH_4 + CO_2$), depending on burial depth and organic matter (e.g., Whiticar et al. 1986). In special conditions, trace amounts of ethane and propane can be formed (Formolo 2010). Microbial methane is also produced in coal-beds, in early and late stages of coalification (Rice 1993) and by oil biodegradation (secondary microbial methanogenesis), via carbonate reduction. This secondary microbial gas may constitute large gas resources (Milkov 2011). Microbial gas is very dry, i.e., it consists almost entirely of methane. Generally (but not always), it indicates relatively shallow gas source rocks and reservoirs.

Thermogenic gas is produced in deeper sedimentary rocks by the thermal degradation (catagenesis) of organic matter, kerogen, coal (primary cracking), or oil (secondary cracking) at higher temperatures, typically up to 250 °C. Organic matter maturation includes a series of intermediate products, such as geopolymers (kerogen), bitumen, then converted into hydrocarbons, as described in classic petroleum geochemistry literature (e.g., Tissot and Welte 1984; Hunt 1996). Vitrinite reflectance is the main parameter to define thermal maturity (Hunt 1996). Thermogenic gas can be independent from or associated with oil reservoirs and can have variable amounts of ethane, propane, butane, and heavier (C_{5+}) hydrocarbons. It also frequently contains measurable quantities of non-hydrocarbon gases.

Abiotic hydrocarbon-rich gas can be produced in special geological conditions by chemical reactions that do not require the presence of organic matter. These reactions include gas-water-rock reactions (for example, Fischer-Tropsch type reactions, like the Sabatier reaction between carbon dioxide and hydrogen) occurring at relatively low temperatures, often below 150 °C, in mafic and ultramafic rocks (Etiope and Sherwood Lollar 2013). Abiotic methane is also produced, in low concentrations (typically parts per billion to parts per million), by magmatic and high temperature (>250 °C) reactions in geothermal systems (Etiope and Sherwood Lollar 2013) but, as anticipated above, it is not typically termed "natural gas."

Nonhydrocarbon gases (mainly CO_2, N_2, H_2S, H_2, and He) are often associated with hydrocarbons as they can originate through organic or inorganic processes that can occur within, beneath, or in proximity to the petroliferous sedimentary rocks (Hunt 1996). The organic processes are mainly thermogenic, e.g., kerogen decarboxylation (producing CO_2 during catagenesis), thermochemical sulfate reduction (producing mainly H_2S), thermal degradation of organic N-containing compounds (producing N_2), and oil biodegradation (producing mainly CO_2 after hydrocarbon production). Bacterial sulfate reduction can also produce H_2S and CO_2. Inorganic reactions include kaolinite-carbonate reactions (producing CO_2), metamorphism of ammonium-rich clays (producing N_2), thermo-methamorphism of limestone (CO_2), radioactive decay of U and Th (producing He), and magma degassing (mainly CO_2 and He).

The identification of natural gas origin may start observing the relative abundance of methane (C_1), ethane (C_2), and propane (C_3) (i.e., the Bernard ratio $C_1/(C_2 + C_3)$, or the gas

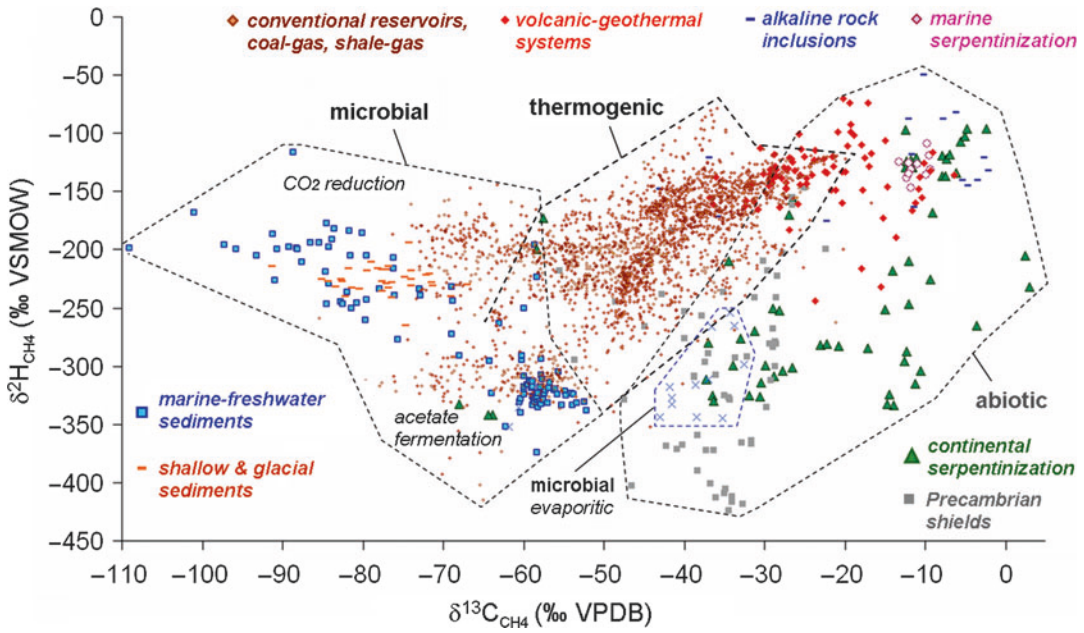

Natural Gas, Fig. 2 Stable C and H isotope values of methane (CH_4) in different geological systems and related genetic mechanisms (biotic and abiotic). Biotic (microbial and thermogenic) gas data are from a global inventory of natural gas in conventional (reservoir) and unconventional (shale-gas, coal-gas) petroleum systems (Sherwood et al. 2017), and from Coleman et al. (1988), Whiticar et al. (1986) and Tazaz et al. (2013). Abiotic gas data are from Etiope and Sherwood Lollar (2013), Etiope et al. (2016), and Etiope (2017a, b). Abiotic gas must be considered as "dominantly abiotic," as it may be mixed with variable amounts of biotic gas

wetness, expressed as $\Sigma C_{2-5}/\Sigma C_{1-5}$). Microbial gas generally has a Bernard ratio > 1000. But this diagnostic tool may be misleading as it fails to detect post-genetic alterations of the molecular composition of the gas (molecular fractionation of thermogenic gas leading to high Bernard ratios) and secondary genetic processes (secondary microbial methane). The critical step for identifying the origin of natural gas is the analysis of the stable isotope composition of carbon ($^{13}C/^{12}C$) and hydrogen ($^{2}H/^{1}H$) in methane (expressed as $\delta^{13}C$ and $\delta^{2}H$ in ‰ (per mil) relative to Vienna Pee Dee Belemnite, VPDB, and Vienna Standard Mean Ocean Water, VSMOW, standards; e.g., Schoell (1980)). The isotopic data are typically plotted in a $\delta^{13}C$ vs. $\delta^{2}H$ diagram, an empirical diagram that differentiates the genetic fields of microbial, thermogenic, and abiotic methane (Fig. 2). Worldwide occurrences of thermogenic and microbial gases have a well-defined distribution in regards to carbon and hydrogen isotopes. Microbial methane is generally characterized by $\delta^{13}C$ values lower than −50‰. Thermogenic methane is typically in the range between −50 and −30‰; but highly mature source rocks can provide methane with $\delta^{13}C$ values up to −20‰, and low maturity rocks (early thermogenesis) can lead to values as low as −70‰. Abiotic CH_4 has a wide range of $\delta^{13}C$ and $\delta^{2}H$ values and, although overlapping with part of the thermogenic field, is characterized by an overall shift towards more ^{13}C–enriched and more ^{2}H–depleted values (Fig. 2).

Use of $\delta^{13}C$ in relation to the Bernard ratio is beneficial for determining the mixing between microbial and thermogenic gas and the source rock maturity. The changes in the molecular and stable isotopic composition of natural gas with increasing thermal maturity are a direct result of the kinetics of the formation mechanisms. During the first stages of catagenesis, at relatively low temperatures (low maturity), gas is "wet" (i.e., rich in alkanes heavier than methane). Wetness (defined above) can range between 10 and 100. With increasing maturity (time and temperature) gas becomes "dry," less rich in C_2–C_5 due to the thermal cracking of heavy alkanes. Wetness can drop to values below one. If the carbon isotopic composition is not evaluated, this type of dry thermogenic gas can be confused with microbial gas, which generally has wetness <0.1. Additional interpretative tools use the isotopic composition of nonhydrocarbon gases (especially CO_2 and N_2).

Occurrences

Natural gas occurs in porous, sedimentary, organic-rich source rocks (shales, marls, and limestones), and coal-beds, where it is initially generated, and in more permeable sedimentary rocks (sandstones, fractured limestones) and, not rarely, even in igneous and metamorphic rocks (fractured volcanic or crystalline basement rocks; e.g., Farooqui 2009),

where it accumulated. Permeable reservoir rocks represent "conventional" gas resources. Scarcely permeable reservoirs (e.g., tight-gas sandstones) and source rocks (shale-gas) represent "unconventional" resources, as they require stimulation methods to improve economic recovery rates. Gas hydrates and coal-beds (coal-bed methane, CBM; or coal seam gas, CSG) are also unconventional gas resources.

More than 50% of conventional reservoired oil and gas was generated by source rocks formed within two relatively short geological time periods, between 144 and 169 Myrs ago (Upper Jurassic) and between 88 and 119 Myrs ago (Aptian-Turonian) (Klemme and Ulmishek 1991). From the reservoir rocks, natural gas can migrate through faults to the Earth's surface (seepage), entering shallow aquifers, soil, and the atmosphere via diffuse exhalation (microseepage), springs and seeps (macroseeps), such as mud volcanoes, and oil or gas seeps, including natural "eternal" fires (Etiope 2015). Natural gas source rocks, reservoirs, and seeps are distributed throughout the petroliferous sedimentary basins of all continents. The largest gas reservoirs are located in Russia, Iran, Qatar, and Algeria.

In ocean bottom sediments, microbial or thermogenic natural gas can occur as gas hydrates or clathrates, ice-like crystalline solids stable under specific pressure and temperature conditions, composed of rigid cages of water molecules that enclose guest gas molecules. Methane hydrates generally occur in deep-sea sediments or shallow seabed in Arctic regions, and likely contain one order of magnitude more methane than the 220 Gt of carbon estimated to occur in all conventional gas reservoirs (Milkov 2004). Permafrost on land, in subpolar regions, may also host significant amounts of methane clathrates, either microbial or thermogenic.

Abiotic natural gas has been widely reported, in concentrations reaching orders of 80–90 vol.%, in deep boreholes in crystalline shields in Canada, South Africa, and Finland (Sherwood Lollar et al. 1993), and in surface seeps and springs in serpentinized ultramafic rocks (peridotites) of continental ophiolites, peridotite massifs, and igneous intrusions, in at least 17 countries in North America, Europe, Asia, and Oceania (Etiope and Sherwood Lollar 2013; Etiope and Schoell 2014; Etiope 2017b). Volumes of this gas in the rocks are not known but the high gas flux, observed at the surface in some cases, suggests the presence of pressurized pools.

Energy Resource

Natural gas in conventional and unconventional petroleum systems is a nonrenewable resource. Thermogenic gas accumulations account for approximately 80% of the world's natural gas resources (Rice 1993). Shale-gas represents an increasingly important source of gas in the United States, Canada, and China. Commercial accumulations of abiotic methane have not been identified by the petroleum industry, so far; less than 1% of the CH_4 in most oil and gas fields was estimated to be abiotic (Jenden et al. 1993). The recent discoveries of abiotic gas in continental ultramafic rocks and Precambrian crystalline shields could, however, represent new resource prospects for the future.

In total, natural gas accounts for about 24% of the world's energy consumption. Global natural gas production, consumption, and reserves have been estimated (end of 2015) at approximately 3539, 3469, and 186,900 billion cubic meters, respectively (BP 2016).

Summary

Natural gas is a mixture of hydrocarbons (methane, ethane, propane, butane) and nonhydrocarbon gases (CO_2, N_2, H_2S, H_2, and trace amounts of noble gases) originated in sedimentary source rocks (shales, marls, and limestones) and stored in reservoir rocks (sandstones, limestones, and subordinately igneous/metamorphic rocks). The gas is produced biotically by microbial or thermal degradation of marine (sapropelic) or terrestrial (humic) organic matter in marine sediments and coal formations (coal-bed gas), and by oil cracking and biodegradation. Abiotic natural gas, generated by gas-water-rock chemical interactions (e.g., Fischer-Tropsch type reactions), has been increasingly discovered in recent years in Precambrian shields and serpentinized ultramafic rocks in ophiolites and peridotite massifs. Microbial and thermogenic gas can also be stored as hydrates in marine sediments and onshore permafrost. From source rocks and reservoirs, the gas can migrate along faults to the Earth's surface, where it exhales to the atmosphere through gas seeps and mud volcanoes. Reservoired natural gas presently accounts for one fourth of the world's energy consumption.

Cross-References

- ▶ Biogenic Methane
- ▶ Black Shales and Sapropels
- ▶ Carbon
- ▶ Carbon Isotopes
- ▶ Coal
- ▶ Gas Hydrates
- ▶ Geochemical Exploration
- ▶ Hydrocarbons
- ▶ Kerogen
- ▶ Organic Geochemistry
- ▶ Petroleum
- ▶ Surface Geochemistry

References

BP (2016) BP statistical review of world energy. 65th edition, bp.com/statisticalreview#BPstats

Coleman D, Liu CL, Riley KM (1988) Microbial methane in the shallow Paleozoic sediments and glacial deposits of Illinois, U.S.A. Chem Geol 71:23–40

Etiope G (2015) Natural gas seepage. The Earth's hydrocarbon degassing. Springer, Switzerland, 199 pp

Etiope G (2017a) Methane origin in the Samail ophiolite. Comment on "modern water/rock reactions in Oman hyperalkaline peridotite aquifers and implications for microbial habitability" by Miller et al. 2016. Geoch Cosm Acta 197:467–470

Etiope G (2017b) Abiotic methane in continental serpentinization sites: an overview. Procedia Earth Plan Sci 17:9–12

Etiope G, Schoell M (2014) Abiotic gas: atypical but not rare. Elements 10:291–296

Etiope G, Sherwood Lollar B (2013) Abiotic methane on Earth. Rev Geophys 51:276–299

Etiope G, Vadillo I, Whiticar MJ, Marques JM, Carreira PM, Tiago I, Benavente J, Jiménez P, Urresti B (2016) Abiotic methane seepage in the Ronda peridotite massif, southern Spain. Appl Geochem 66:101–113

Farooqui MY and 11 coauthors (2009) Evaluating volcanic reservoirs. Oil field Review 21: 36–47

Formolo M (2010) The microbial production of methane and other volatile hydrocarbons. In: Kenneth N (ed) Timmis handbook of hydrocarbon and lipid microbiology. Springer, New York, pp 113–126

Hunt JM (1996) Petroleum geochemistry and geology. W.H. Freeman and Co, New York, 743 pp

Jenden PD, Hilton DR, Kaplan IR, Craig H (1993) Abiogenic hydrocarbons and mantle helium in oil and gas fields. In: Howell D (ed) Future of energy gases, USGS professional paper, vol 1570, pp 31–35

Klemme HD, Ulmishek GF (1991) Effective petroleum source rocks of the world: stratigraphic distribution and controlling depositional factors. AAPG Bull 75:1809–1851

Milkov AV (2004) Global estimates of hydrate-bound gas in marine sediments: how much is really out there? Earth Sci Rev 66:183–197

Milkov AV (2011) Worldwide distribution and significance of secondary microbial methane formed during petroleum biodegradation in conventional reservoirs. Org Geochem 42:184–207

Rice DD (1993) Biogenic gas: controls, habitats, and resource potential. In: Howell DG (ed) The future of energy gases – U.S, Geological survey professional paper, vol 1570. United States Government Printing Office, Washington, pp 583–606

Schoell M (1980) The hydrogen and carbon isotopic composition of methane from natural gases of various origins. Geochim Cosmochim Acta 44:649–661

Sherwood OA, Schwietzke S, Arling VA, Etiope G (2017) Global inventory of gas geochemistry data from fossil fuel, microbial and biomass burning sources, version 2017. Earth Syst Sci Data Discuss. https://doi.org/10.5194/essd-2017-20

Sherwood Lollar B, Frape SK, Weise SM, Fritz P, Macko SA, Welhan JA (1993) Abiogenic methanogenesis in crystalline rocks. Geochim Cosmochim Acta 57:5087–5509

Tazaz AM, Bebout BM, Kelley CA, Poole J, Chanton JP (2013) Redefining the isotopic boundaries of biogenic methane: methane from endoevaporites. Icarus 224:268–275

Tissot BP, Welte DH (1984) Petroleum formation and occurrence. Springer, New York

Whiticar MJ, Faber E, Schoell M (1986) Biogenic methane formation in marine and freshwater environments: CO_2 reduction versus acetate fermentation – isotope evidence. Geochim Cosmochim Acta 50:693–709

Neodymium

Michael Bizimis and Howie D. Scher
Earth and Ocean Sciences, University of South Carolina, Columbia, SC, USA

Element Data
Atomic Symbol: **Nd**
Atomic Number: **60**
Atomic Weight: 144.242 g/mole
Isotopes and Abundances:
^{142}Nd: 27.153%
^{143}Nd: 12.173%
^{144}Nd: 23.798%
^{145}Nd: 8.293%
^{146}Nd: 17.189%
^{148}Nd: 5.756%
^{150}Nd: 5.638%
1 Atm Melting Point: 1294 K
1 Atm Boiling Point: 3347 K
Common Valences: 3+
Ionic Radii: 112 pm (eightfold coordination)
Pauling Electronegativity: 1.14
First Ionization Potential: 5.5250 eV
Chondritic (CI) Abundance: 0.475 ppm
Silicate Earth Abundance: 1.25 ppm
Crustal Abundance: 20 ppm
Seawater Abundance: 2–60 pmol/kg
Core Abundance: ~0

Properties

Neodymium (Nd) is a silvery-white-yellow metal with an atomic number (Z) of 60, electronic configuration of [Xe] $4f^4 6s^2$, and atomic weight of 144.242(3) (Meija et al. 2016a, b). It is a group IIIB inner transition element and one of the lanthanide and rare-earth elements. Neodymium is a refractory element, with a melting point of 1294 K, boiling point of 3347 K, and density of 7.01 g/cm^3. It is a lithophile element under the Goldschmidt classification, and it is dominantly found in the trivalent state, with Nd^{3+} ionic radius of ~1.12×10^{-10} m at eightfold coordination.

History and Use

Nd was discovered in 1885 by Austrian chemist Carl F. Auer von Welsbach and is named from the Greek word *neos*

didymos (new twin) (Holden 2001). The usage of neodymium has increased significantly in the last three decades after the discovery of neodymium-boron-iron alloys that make very strong permanent magnets. These magnets have found its use in a wide variety of electronics and electric motors. Nd is also used in the manufacturing of crystals for lasers and didymium glass used for glass blowing and welder's goggles. As Nd is incompatible in all major rock-forming minerals, it concentrates in late-stage highly differentiated melts and accessory minerals, like phosphates. The main commercial sources of Nd are currently rare-earth element-rich carbonatite deposits, where the key mineral is bastnaesite $(REE)CO_3F$, monazite $(REE)PO_4$, and some carbonate-bearing iron oxide deposits (Kiruna type, Sweden, Bayan Obo, Mongolia). In all cases, Nd is found together with other light rare earths (La, Ce, Pr, Sm).

Geochemical Behavior

The major importance of Nd is that it is one of the larger trivalent rare-earth elements, among the most useful trace elements in all areas of geochemistry and cosmochemistry due to their coherent and systematic behavior as a group. ^{143}Nd is also the decay product of ^{147}Sm, and ^{142}Nd is the decay product of ^{146}Sm. Nd has two radioactive isotopes, ^{144}Nd with a half-life ($T_{1/2}$) of 2.4×10^{15} years (McSween and Huss 2010) and ^{150}Nd with a half-life of 9.11×10^{18} years (Argyriades et al. 2009), both too long to have any practical applications in geochronology and are thus considered effectively stable.

As a lithophile element, Nd is thought to wholly partition in the silicate portion of the Earth with effectively no Nd in the Earth's core. Primitive CI-chondrite meteorites, thought to represent the initial composition of the solar nebular for refractory elements, have an estimated 0.457–0.474 ppm Nd concentration (McDonough and Sun 1995; Palme and O'Neill 2003). The Nd concentration of the primitive mantle (or bulk silicate earth) is estimated at 1.25–1.37 ppm (McDonough and Sun 1995; Palme and O'Neill 2003). Due to its relatively large ionic radius and 3+ charge, Nd is moderately to highly incompatible in upper mantle mineralogy (olivine, pyroxene, spinel, and garnet). Of these minerals, clinopyroxene has the highest Nd concentrations (typically in the order of several ppm or less), where Nd substitutes for Ca in the M2 crystallographic site that is of similar size ($\sim 1 \times 10^{-10}$m) as the Nd ionic radius in eightfold coordination, likely through a coupled substitution of Al^{3+} for Si^{4+} or Na^{1+} for Ca^{2+} (Wood and Blundy 2001). As an incompatible element, Nd is preferentially concentrated in melts from the mantle, and its concentration in the continental crust is near 20 times than of the primitive mantle, between 16 and 27 ppm, with an average of 20 ppm (Rudnick and Gao 2003), the range being largely due to the uncertainty of the proportions of upper, middle, and lower crust in reconstructing the bulk continental crust composition. In turn, the upper mantle source of mid-oceanic ridge volcanism and the presumed residue of continental crust extraction is depleted in Nd relative to the primitive mantle with Nd concentration estimated between 0.71 and 0.58 ppm (Salters and Stracke 2004; Workman and Hart 2005). The mean Nd concentration of mid-oceanic ridge basalts, the most voluminous volcanism on Earth sourced from this depleted mantle, is 12 ± 0.78 ppm (Gale et al. 2013).

Due to the different compatibility of Sm and Nd in most petrogenetically important minerals, melting and crystallization processes create variable Sm/Nd ratios in minerals and melts that over time generate variable amounts of radiogenic ^{143}Nd over the stable ^{144}Nd, denoted by the $^{143}Nd/^{144}Nd$ ratio, making the $^{147}Sm/^{143}Nd$ decay system, one of the most important geochronological and isotope tracer systems. ^{142}Nd, the decay product of now extinct ^{146}Sm with a somewhat uncertain half-life of 68 Ma (Kinoshita et al. 2012) to 103 Ma (Marks et al. 2014), is an increasingly important tracer in evaluating the evolution of the terrestrial mantle during the first 300 hundred million years of Earth's history (Rizo et al. 2012), and the terrestrial $^{142}Nd/^{144}Nd$ isotope systematics are central in the discussion of whether Earth evolved with a chondritic composition or not (Carlson and Boyet 2009).

In typical seawater composition and pH = 8.2, Nd exists primarily as a carbonate ion species $Nd(CO_3)_2^-$ and $NdCO_3^+$. In the absence of strong organic complexing ligands, like humic acids (Sonke and Salters 2006), Nd is highly particle reactive and readily adsorbed in hydrated Fe and Mn oxide phases and particulate surfaces (Schijf et al. 2015), resulting in very low concentrations in seawater on the order of 2–60 pmol/kg (Goldstein and Hemming 2003). In the pelagic ocean setting, Nd concentration increases with depth, which appears to be controlled by processes involving sinking particles. Despite the nutrient-like behavior of Nd concentrations, Nd isotopes vary with salinity (e.g., von Blanckenberg 1999) suggesting a residence time shorter than ocean mixing (~1500 years, Broecker and Peng 1982). The residence time of Nd in seawater ranges from 200 to 1000 years (Tachikawa et al. 1999; Arsouze et al. 2009; Rempfer et al. 2011).

Biological Utilization and Toxicity

Nd does not appear to have a specific biological function, likely due to its extremely low concentration in natural waters that prevented organisms for developing a use for it. Yet, some evidence suggests that under acidic conditions where Nd becomes increasingly soluble, methanotrophic microbes can utilize Nd and other light rare earths to stimulate growth

(Pol et al. 2014). Neodymium is thought as moderately toxic in humans, although specific data is scarce. Neodymium dusts and salts are considered as irritating to the eyes and mucus membranes and moderately irritating to the skin (Rim et al. 2013). However, as Nd concentrations are low in the environment, any health effects are mostly anecdotal and appear isolated to those with occupational exposure either closely related to mining or processing of the ore (Pagano et al. 2015).

Cross-References

- ▶ Chondrites
- ▶ Earth's Continental Crust
- ▶ Lanthanide Rare Earths
- ▶ Lithophile Elements
- ▶ Mantle Geochemistry
- ▶ Mid-Ocean Ridge Basalts (MORB)
- ▶ Neodymium Isotopes
- ▶ Ore Deposits
- ▶ Samarium

References

Argyriades J, the NEMO Collaboration et al (2009) Measurement of the double-beta decay half-life of ^{150}Nd and search for neutrinoless decay modes with the NEMO-3 detector. Phys Rev C 80(3):032501

Arsouze T, Dutay J-C, Lacan F, Jeandel C (2009) Reconstructing the Nd oceanic cycle using a coupled dynamical – biogeochemical model. Biogeosciences 6:2829–2846

Broecker WS, Peng T-H (1982) Tracers in sea. Eldigio Press, Palisades, Lamont – Doherty Geological Observatory, 690 pp

Carlson RW, Boyet M (2009) Short-lived radionuclides as monitors of early crust–mantle differentiation on the terrestrial planets. Earth Planet Sci Lett 279(3–4):147–156

Gale A, Dalton CA, Langmuir CH, Su Y, Schilling J-G (2013) The mean composition of ocean ridge basalts. Geochem Geophys Geosyst 14(3):489–518

Goldstein SL, Hemming SR (2003) Long-lived isotopic tracers in oceanography, paleoceanography, and ice-sheet dynamics. Treatise Geochem 6:453–489

Holden NE (2001) History of the origin of the chemical elements and their discoverers. BNL-NCS-63859-01/10-REV, Brookhaven National Laboratory. http://www.nndc.bnl.gov/publications/preprints/origindc.pdf

Kinoshita N et al (2012) A shorter ^{146}Sm half-life measured and implications for ^{146}Sm-^{142}Nd chronology in the solar system. Science 335(6076):1614–1617. https://doi.org/10.1126/science.1215510

Marks NE, Borg LE, Hutcheon ID, Jacobsen B, Clayton RN (2014) Samarium–neodymium chronology and rubidium–strontium systematics of an Allende calcium–aluminum-rich inclusion with implications for ^{146}Sm half-life. Earth Planet Sci Lett 405:15–24

McDonough WF, Sun S-S (1995) The composition of the earth. Chem Geol 120:223–253

McSween HY, Huss GR (2010) Cosmochemistry. Cambridge University Press, Cambridge. 549 p

Meija J, Coplen Tyler B, Berglund M, Brand Willi A, De Bièvre P, Gröning M, Holden Norman E, Irrgeher J, Loss Robert D, Walczyk T, Prohaska T (2016a) Atomic weights of the elements 2013 (IUPAC technical report). Pure Appl Chem 88:265

Meija J, Coplen Tyler B, Berglund M, Brand Willi A, De Bièvre P, Gröning M, Holden Norman E, Irrgeher J, Loss Robert D, Walczyk T, Prohaska T (2016b) Isotopic compositions of the elements 2013 (IUPAC technical report). Pure Appl Chem 88:293

Pagano G, Guida M, Tommasi F, Oral R (2015) Health effects and toxicity mechanisms of rare earth elements – knowledge gaps and research prospects. Ecotoxicol Environ Saf 115:40–48

Palme H, O'Neill HSC (2003) Cosmochemical estimates of mantle composition. Treatise Geochem 2:1–38

Pol A, Barends TRM, Dietl A, Khadem AF, Eygensteyn J, Jetten MSM, Op den Camp HJM (2014) Rare earth metals are essential for methanotrophic life in volcanic mudpots. Environ Microbiol 16(1):255–264. https://doi.org/10.1111/1462-2920.12249

Rempfer J, Stocker TF, Joos F, Dutay J-C, Siddall M (2011) Modelling Nd-isotopes with a coarse resolution ocean circulation model: sensitivities to model parameters and source/sink distributions. Geochim Cosmochim Acta 75(20):5927–5950

Rim KT, Koo KH, Park JS (2013) Toxicological evaluations of rare earths and their health impacts to workers: a literature review. Saf Health Work 4(1):12–26

Rizo H, Boyet M, Blichert-Toft J, O'Neil J, Rosing MT, Paquette J-L (2012) The elusive Hadean enriched reservoir revealed by ^{142}Nd deficits in Isua Archaean rocks. Nature 491(7422):96–100

Rudnick RL, Gao S (2003) The composition of the continental crust. In: Gao S (ed) Treatise on geochemistry, vol 3. Elsevier, Amsterdam, pp 1–64

Salters VJM, Stracke A (2004) Composition of the depleted mantle. Geochem Geophys Geosyst 5:Q05004. https://doi.org/10.1029/2003GC000597

Schijf J, Christenson EA, Byrne RH (2015) YREE scavenging in seawater: a new look at an old model. Mar Chem 177(Part 3):460–471

Sonke JE, Salters VJM (2006) Lanthanide–humic substances complexation. I. Experimental evidence for a lanthanide contraction effect. Geochim Cosmochim Acta 70(6):1495–1506

Tachikawa K, Jeandel C, Roy-Barman M (1999) A new approach to the Nd residence time in the ocean: the role of atmospheric inputs. Earth Planet Sci Lett 170(4):433–446

von Blanckenburg F (1999) Tracing past ocean circulation? Science 286(5446):1862–1863

Wood BJ, Blundy JD (2001) The effect of cation charge on crystal-melt partitioning of trace elements. Earth Planet Sci Lett 188:59–71

Workman RK, Hart SR (2005) Major and trace element composition of the depleted MORB mantle(DMM). Earth Planet Sci Lett 231:53–72

N

Neodymium Isotopes

Michael Bizimis and Howie D. Scher
Earth and Ocean Sciences, University of South Carolina, Columbia, SC, USA

Introduction

Isotope ratios of Nd are key geochemical tracers for unraveling the compositional evolution of terrestrial planets, as well as an important geochronometer. Neodymium has seven natural isotopes: ^{142}Nd (27.153%), ^{143}Nd (12.173%),

^{144}Nd (23.798%), ^{145}Nd (8.293%), ^{146}Nd (17.189%), ^{148}Nd (5.756%), and ^{150}Nd (5.638%) (Meija et al. 2016). ^{147}Sm decays to ^{143}Nd through α-decay with a half-life of 1.06×10^{11} year that corresponds to a decay constant ($\lambda_{Sm}{}^{147}$) of 6.54×10^{-12} year^{-1}. ^{146}Sm decays to ^{142}Nd through α-decay and a half-life estimated between 68×10^6 year (Kinoshita et al. 2012) and 103×10^6 year (Meissner et al. 1987; Marks et al. 2014). Due to its slightly lower ionic radius, Sm is generally more compatible than Nd in the Earth's mantle. The fractionation of Sm from Nd during melting and crystallization processes changes the Sm/Nd ratios in minerals, which, over time, will change the relative abundance of ^{143}Nd and ^{142}Nd. These changes in Nd isotopes are important for understanding the evolution of different terrestrial reservoirs and the processes that influence their chemical evolution.

Nd Isotope Ratio Determinations

Neodymium is chemically isolated from other elements by cation-exchange chromatography (Richard et al. 1976; Pin and Zalduegui 1997). Neodymium isotope ratios are determined by thermal ionization mass spectrometry (TIMS) or by multicollector inductively coupled mass spectrometry (MC-ICPMS). During ionization and/or transmission through the mass spectrometer, the Nd isotope ratios fractionate relative to their true value as a function of their mass. This instrument-induced mass fractionation is typically described by an exponential mass law and can thus be corrected for if one (stable) ratio is known a priori. The ratio ^{146}Nd/^{144}Nd = 0.7219 is conventionally used for this fractionation correction (Hamilton et al. 1983). Additional instrument bias can be corrected by measuring a widely available pure Nd standard, typically the "La Jolla" standard with accepted ^{143}Nd/^{144}Nd = 0.511858 (Lugmair and Carlson 1978) or the JNdi-1 with accepted ^{143}Nd/^{144}Nd = 0.512115 (Tanaka et al. 2000). When data from different laboratories is compared, care should be taken that measurements are normalized to the same standard value to avoid interlaboratory bias. Table 1 shows typical high-precision Nd isotope ratio determinations by TIMS for the La Jolla and JNdi-1 standards (Carlson et al. 2007).

The ^{147}Sm-^{143}Nd Decay System

For a closed system where the parent and daughter isotopes remain undisturbed from any process other than radioactive decay, ^{143}Nd/^{144}Nd will increase over time due to the decay of ^{147}Sm to ^{143}Nd according to the decay equation:

$$\frac{^{143}\mathrm{Nd}}{^{144}\mathrm{Nd}} = \left(\frac{^{143}\mathrm{Nd}}{^{144}\mathrm{Nd}}\right)_i + \frac{^{147}\mathrm{Sm}}{^{144}\mathrm{Nd}}\left(e^{\lambda_{\mathrm{Sm}}t} - 1\right), \quad (1)$$

where ^{143}Nd/^{144}Nd is the measured (i.e., present day) isotope ratio of the sample, ^{147}Sm/^{144}Nd is the measured parent-daughter ratio, ^{143}Nd/^{144}Nd$_i$ is the initial ratio of the sample at the time that the Sm-Nd system became closed to mass exchange, and t is the time since system closure.

The ^{147}Sm/^{144}Nd parent-daughter atom ratio is calculated from the Sm and Nd concentrations as

$$\frac{^{147}\mathrm{Sm}}{^{144}\mathrm{Nd}} = \left(\frac{[\mathrm{Sm}]/\mathrm{Sm}_{\mathrm{AtW}} * \mathrm{N_A} * {}^{147}\mathrm{Sm}_{\mathrm{AtAb}}}{[\mathrm{Nd}]/\mathrm{Nd}_{\mathrm{AtW}} * \mathrm{N_A} * {}^{144}\mathrm{Nd}_{\mathrm{AtAb}}}\right), \quad (2)$$

where [Sm] and [Nd] are concentrations, $\mathrm{Sm_{AtW}}$ and $\mathrm{Nd_{AtW}}$ are element atomic weights, $^{147}\mathrm{Sm_{AtAb}}$ and $^{144}\mathrm{Nd_{AtAb}}$ are the abundance of the two isotopes, and $\mathrm{N_A}$ is Avogadro's number.

For a set of cogenetic samples with identical ^{143}Nd/^{144}Nd$_i$ and variable ^{147}Sm/^{144}Nd, for example, rocks from a common source or minerals from within a single rock, their ^{143}Nd/^{144}Nd ratios will increase over time proportionally to their ^{147}Sm/^{144}Nd and will fall along a straight line on a ^{143}Nd/^{144}Nd vs. ^{147}Sm/^{144}Nd plot, called the isochron. The slope of this line ($e^{\lambda t} - 1$) allows calculation of the age of the samples, i.e., the time since the Sm-Nd system closed. As Sm and Nd are generally immobile in fluids and low-temperature alteration, the Sm-Nd isotope system is well suited to date ancient rocks. This is especially useful for mafic rocks that generally have a greater range in Sm/Nd ratios than felsic rocks. An example of dating of Archean mafic rocks is shown in Fig. 1 for a series of ancient lavas with island arc affinities (rhyolites, basalts, boninites) from the Gadwal greenstone terrane, Dharwar craton, India, where ^{143}Nd/^{144}Nd versus ^{147}Sm/^{144}Nd values form a well-defined isochron of 2.7 Ga (Khanna et al. 2014).

Of the common petrogenetic minerals, garnet most strongly fractionates the Sm/Nd ratio. Sm is significantly

Neodymium Isotopes, Table 1 Example of measured Nd isotope ratios

	^{142}Nd/^{144}Nd	^{143}Nd/^{144}Nd	^{145}Nd/^{144}Nd	^{146}Nd/^{144}Nd$_{(m)}$	^{148}Nd/^{144}Nd	^{150}Nd/^{144}Nd
La Jolla	1.1418444	0.511871	0.348413	0.7221844	0.2415826	0.2364560
JNdi-1	1.1418444	0.512126	0.348414	0.7225158	0.2415803	0.2364489

The ^{146}Nd/^{144}Nd ratio is the measured ratio. The other ratios are corrected for fractionation relative to ^{146}Nd/^{144}Nd = 0.7219. After Carlson et al. (2007)

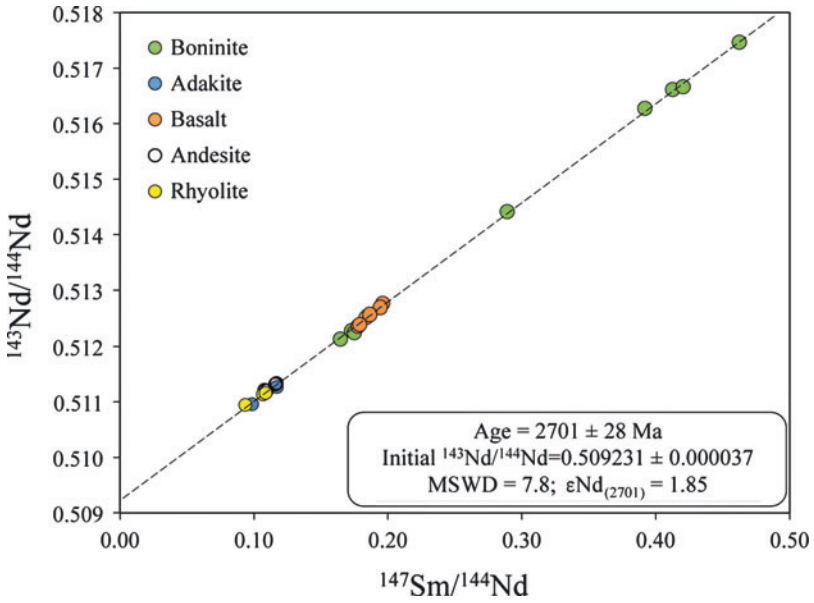

Neodymium Isotopes, Fig. 1 An example of a Sm-Nd isochron constructed by island arc-related metavolcanics from Gadwal greenstone terrane, Dharwar, India. After (Khanna et al. 2014). The best-fit line defined by these rocks has an age of 2.701 ± 0.028 Ga. The intercept defines the initial $^{143}Nd/^{144}Nd_i$ of the source of the volcanics with a calculated $\varepsilon_{Nd(2,701)} = 1.85$. This positive value suggests that the source of these volcanics is a depleted mantle that evolved over time with a time-integrated Sm/Nd ratio greater than CHUR. Isochron age was calculated with the program ISOPLOT (Ludwig 2003)

more compatible than Nd in garnet, leading to high Sm/Nd ratios and significant ingrowth of ^{143}Nd over time, making garnet geochronology an important tool for dating metamorphic processes (Baxter and Scherer 2013). Recent advances in sample manipulation and mass spectrometry allow age determinations of separate domains within single garnet crystals by the Sm/Nd isochron method, providing high spatial and temporal resolution of growth rates and metamorphic reaction rates (Ducea et al. 2003; Pollington and Baxter 2011).

The Nd Isotopic Evolution of the Earth and the CHUR Reservoir

The Nd isotopic evolution of the Earth is thought to be described by the "chondritic uniform reservoir" or CHUR (DePaolo and Wasserburg 1976). This assumes that the material from which Earth was accreted had Sm/Nd and $^{143}Nd/^{144}Nd_i$ similar to chondritic meteorites. This assumption is justified, as both Sm and Nd are refractory elements with similar condensation temperatures. Sm and Nd are also lithophile, hence exclusively incorporated in silicate minerals and Earth's silicate reservoirs (crust and mantle). The CHUR composition is $^{143}Nd/^{144}Nd_{CHUR} = 0.512630$ and $^{147}Sm/^{144}Nd_{CHUR} = 0.1960$ leading to a solar system initial composition of $^{143}Nd/^{144}Nd_{SSI} = 0.506686 \pm 0.000070$ at 4.5685×10^9 year (Bouvier et al. 2008). The bulk silicate Earth is generally thought to have the same $^{143}Nd/^{144}Nd$ evolution as CHUR (but see below for the ^{142}Nd), thereby making the CHUR values a useful reference point for evaluating the time-integrated Sm/Nd evolution of different terrestrial reservoirs.

ε_{Nd} Notation

The comparison between different reservoirs and CHUR is facilitated best with the ε_{Nd} notation, which is the normalized difference of the sample's $^{143}Nd/^{144}Nd$ ratio relative to $^{143}Nd/^{144}Nd_{CHUR}$ in parts per 10,000:

$$\varepsilon_{\mathrm{Nd}} = \left(\frac{\frac{^{143}\mathrm{Nd}}{^{144}\mathrm{Nd}}rock}{\frac{^{143}\mathrm{Nd}}{^{144}\mathrm{Nd}}CHUR} - 1 \right) \times 10000 \qquad (3)$$

Rocks with $^{143}Nd/^{144}Nd$ higher than $^{143}Nd/^{144}Nd_{CHUR}$ have positive ε_{Nd} and those with lower $^{143}Nd/^{144}Nd$ than $^{143}Nd/^{144}Nd_{CHUR}$, negative ε_{Nd}. For example, mid-oceanic ridge basalts have a mean $^{143}Nd/^{144}Nd = 0.513074$ (Gale et al. 2013) and $\varepsilon_{Nd} = 8.5$ (typical range of ε_{Nd} 5 to 12), consistent with a derivation from the depleted mantle with greater time-integrated Sm/Nd ratio than CHUR. Crustal rocks have negative (and also highly variable) ε_{Nd} consistent with an origin from a reservoir with low time-integrated Sm/Nd ratio compared to CHUR (Fig. 2). Rocks with ε_{Nd} between that of the depleted mantle and the crust, for example, some ocean island basalts or arc lavas, are often thought to originate from a source that contains crustal material that was recycled back into the mantle (Hofmann 1997). The positive ε_{Nd} of mid-oceanic ridge magmas and negative ε_{Nd} of crustal rocks have led to the generally accepted paradigm that extraction of continental crust left behind a melt-depleted mantle that is now the source of mid-oceanic ridge volcanism.

From the decay Eq. 1, the initial $^{143}Nd/^{144}Nd_i$ ratio of a rock at the time of its formation can be calculated from its measured $^{143}Nd/^{144}Nd$ and $^{147}Sm/^{144}Nd$, provided that its age

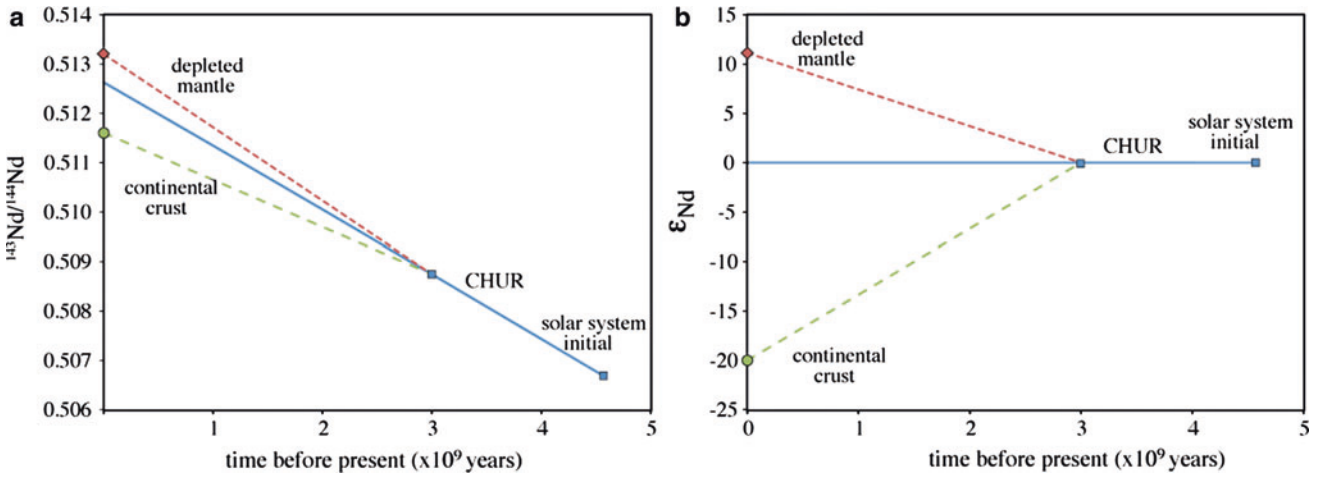

Neodymium Isotopes, Fig. 2 (**a**) Schematic evolution of the $^{143}Nd/^{144}Nd$ ratio of the depleted mantle and continental crust relative to the chondritic uniform reservoir (*CHUR*), here taken as equivalent to the primitive mantle. This example assumes a depleted mantle and continental crust reservoirs with present-day $^{143}Nd/^{144}Nd$ of 0.5132 and 0.5116, respectively, and single-stage evolution from CHUR 3×10^9 ago. The depicted depleted mantle has higher $^{147}Sm/^{144}Nd = 0.225$ and the crust lower $^{147}Sm/^{144}Nd = 0.144$ ratios than CHUR and evolve to more radiogenic and unradiogenic $^{143}Nd/^{144}Nd$ ratios, respectively, than CHUR over time. (**b**) Same data as in (**a**) but the $^{143}Nd/^{144}Nd$ isotope compositions of these reservoirs are compared using the ε_{Nd} notation. CHUR, by definition, has $\varepsilon_{Nd} = 0$. The depleted mantle with higher $^{147}Sm/^{144}Nd$ ratio than CHUR has increasingly positive ε_{Nd} over time, and the continental crust with lower $^{147}Sm/^{144}Nd$ ratio than CHUR has increasingly negative ε_{Nd}

is known. The ε_{Nd} notation can be used to compare the initial $^{143}Nd/^{144}Nd_i$ of a rock at some time t in the past, to that of CHUR at the same time t, ($CHUR_t$), by calculating $^{143}Nd/^{144}Nd_{CHUR(t)}$ at time t using the present-day CHUR values above and substituting in Eq. 3.

Time-Integrated Sm/Nd Ratios of Terrestrial Reservoirs and Model Ages

The $^{143}Nd/^{144}Nd$ of a rock, or any reservoir, effectively records the time-integrated fractionation of the Sm/Nd ratio in that rock. As Sm is more compatible than Nd in the Earth's mantle, melting creates residual rocks with relatively high Sm/Nd that generate over time higher, i.e., more radiogenic, $^{143}Nd/^{144}Nd$ than the bulk silicate Earth (primitive mantle) with CHUR composition. In turn, melts generated from the mantle, for example, melts giving rise to the continental crust, have lower Sm/Nd and evolve over time toward relatively lower, or less radiogenic, $^{143}Nd/^{144}Nd$ than CHUR. This concept is shown schematically in Fig. 2, where the $^{143}Nd/^{144}Nd$ evolution of three reservoirs, namely, CHUR, depleted mantle, and continental crust, is plotted as a function of time. $^{147}Sm/^{144}Nd$ (and therefore Sm/Nd) of the depleted mantle reservoir is calculated assuming it was extracted from CHUR at a single event some time t in the past. If a younger age of extraction from CHUR is chosen, the $^{147}Sm/^{144}Nd$ of that reservoir will be higher, and the $^{143}Nd/^{144}Nd$ versus time evolution curve will be steeper to reach the present-day $^{143}Nd/^{144}Nd$ of the reservoir, demonstrating the concept of time-integrated fractionation.

Conversely, if the parent-daughter ratio of the rock or reservoir is known, and it has not changed over time due to secondary processes like alteration, then the time of extraction of that rock from bulk silicate Earth (or any other reservoir) can be calculated. In other words, this "model age" is effectively the time when the rock had the same isotopic composition as its parental reservoir. The concept of model age has been proven useful for estimating the age and rate of extraction of continental crust from bulk silicate Earth or the depleted mantle (Allègre and Rousseau 1984; Arndt and Goldstein 1987; Hawkesworth and Kemp 2006).

This initial Nd isotope composition, or $\varepsilon_{Nd(i)}$, allows tracking the Nd isotopic evolution of mantle reservoirs and the crust-mantle system over time. The generally robust behavior of the Sm/Nd system during alteration allows precise dating of Archean rocks and has been central in the investigation of the Earth's early silicate differentiation history. Mafic Archean rocks as old as about 3.7–3.8 Ga have positive $\varepsilon_{Nd(i)}$ (Bennett et al. 1993; Frei et al. 2004; Blichert-Toft and Puchtel 2010; Hoffmann et al. 2011). This requires that by 3.7 Ga, there already existed a mantle reservoir with higher Sm/Nd ratio than CHUR, suggesting an early differentiation of the Earth. This further requires the formation of a complementary enriched reservoir with lower Sm/Nd than CHUR.

The ^{146}Sm-^{142}Nd System

Excess ^{142}Nd (i.e., high $^{142}Nd/^{144}Nd$) in some ~3.8 Ga old rocks from Isua, Greenland, compared to modern terrestrial samples, requires that a depleted reservoir with high Sm/Nd

ratio had already formed while ^{146}Sm was still extant, between 4.53 and 4.42 Ga (Caro et al. 2006; Bennett et al. 2007; O'Neil et al. 2008; Rizo et al. 2011). This early, depleted reservoir must have survived convective mixing in the early Archean-Hadean time for about 700 Ma after formation of the Earth, in order to become the source of these Isua rocks at 3.8 Ga. The lack of ^{142}Nd excesses in terrestrial samples after 2.7 Ga (Debaille et al. 2013) requires subsequent destruction of that early depleted reservoir, possibly due to convective stirring and mixing in the mantle (Caro 2011).

A puzzling aspect of the ^{142}Nd isotope systematics is that chondrite meteorites have a variable ^{142}Nd deficit (average 20 ppm) compared to terrestrial samples (Boyet and Carlson 2005; Carlson and Boyet 2009; Gannoun et al. 2011). To explain this discrepancy, it was originally proposed that the Earth begun with a chondritic composition, followed by early differentiation and isolation of an incompatible element-enriched, low Sm/Nd reservoir from the rest of the convecting planet (a so-called "hidden" reservoir) within the first 30 My of the Earth's history (Bourdon et al. 2008; Carlson and Boyet 2009). An alternative is that the Earth formed from material with higher Sm/Nd ratio than CHUR, i.e., the Earth is non-chondritic (Caro and Bourdon 2010). Yet, the observation that meteorite ^{142}Nd anomalies also correlate with ^{145,148,150}Nd anomalies points to nucleosynthetic Nd heterogeneity in the early solar nebula (Gannoun et al. 2011; Burkhardt et al. 2016; Fukai and Yokoyama 2016), which would eliminate the need for a hidden reservoir or a significantly non-chondritic Earth.

Seawater

The distribution of Nd in seawater is closely correlated with salinity (von Blanckenburg 1999) leading to its use as a conservative tracer of ocean circulation (Goldstein and Hemming 2003). As the Sm-Nd isotope system is not appreciably disturbed during weathering and transport, the Nd isotope signature of the weathering flux into the oceans reflects the age and lithology of crustal sources (Roy et al. 2007). Due to the short residence time of Nd in seawater and the fortuitous distribution of ancient and juvenile crustal material over the Earth's surface, major water masses can be traced using Nd isotopes as they mix in the thermohaline circulation with deep waters. Pioneering work in this field first illustrated ocean basin scale Nd isotope variations (Piepgras and Wasserburg 1980; Piepgras and Wasserburg 1982; Shaw and Wasserburg 1985; Piepgras and Wasserburg 1987) and highlighted the use of seawater Nd as a water mass tracer in the modern and ancient oceans. In general, the North Atlantic waters have low ^{143}Nd/^{144}Nd and highly negative ε_{Nd} (<-13), while Pacific waters have more radiogenic ^{143}Nd/^{144}Nd and less negative ε_{Nd} (<-3), and Indian and Southern Ocean waters fall in between. The low ε_{Nd} of North Atlantic waters is explained by the North Atlantic basin being surrounded by old, highly unradiogenic crustal rocks (e.g., the Canadian shield), while the Pacific basin is surrounded by younger volcanic systems with contributions from the depleted mantle. Critically, the conservative behavior of Nd isotopes is not compatible with observations of nutrient-like behavior of Nd concentrations, which has been termed as the "Nd paradox" (Goldstein and Hemming 2003) and points to a missing flux of Nd into the oceans. Detailed depth profiles of seawater Nd isotopes also revealed significant deviations from conservative behavior along continental margins (Jeandel et al. 2007), pointing to some possible sources of Nd to the oceans. Recent work to resolve this paradox has focused on submarine groundwater discharge (Johannesson and Burdige 2007) pore fluid flux at the margins (Abbott et al. 2015) and eolian inputs (Greaves et al. 1999). During planning for the international GEOTRACES (www.geotraces.org) program, Nd isotopes were identified as a key parameter that will be measured at every GEOTRACES station. Nd isotope results from international GEOTRACES cruises in the Atlantic Ocean, Ross Sea, Pacific Southern Ocean, and Bay of Bengal highlight the importance of advection of water masses in the Nd isotope systematics of seawater (Stichel et al. 2012; Amakawa et al. 2013; Basak et al. 2015; Stichel et al. 2015; Lambelet et al. 2016).

Summary

The radioactive decay of ^{147}Sm into ^{143}Nd and ^{146}Sm into ^{142}Nd through time has produced variations in Nd isotope ratios in terrestrial and extraterrestrial materials. As Sm is more compatible than Nd during melt extraction from the mantle and during crystallization of mafic minerals, there are significant differences in the Sm/Nd ratio and Nd isotopic composition of rocks and minerals on and within the Earth. As a result, variations in Nd isotopes have proved to be extraordinarily useful in geochronology, igneous and metamorphic petrology, and terrestrial and marine provenance studies.

Cross-References

- Chondrites
- Earth's Continental Crust
- Formation and Evolution of the Earth
- Geochronology and Radiogenic Isotopes
- Lanthanide Rare Earths
- Lithophile Elements
- Mantle Geochemistry
- Mid-Ocean Ridge Basalts (MORB)

▶ Neodymium
▶ Ocean Biochemical Cycling and Trace Elements
▶ Samarium

References

Abbott AN, Haley BA, McManus J, Reimers CE (2015) The sedimentary flux of dissolved rare earth elements to the ocean. Geochim Cosmochim Acta 154:186–200

Allègre CJ, Rousseau D (1984) The growth of the continents through geological time studied by Nd isotope analysis of shales. Earth Planet Sci Lett 67:19–34

Amakawa H et al (2013) Neodymium isotopic composition and concentration in the Southwest Pacific Ocean. Geochem J 47:409–422

Arndt NT, Goldstein SL (1987) Use and abuse of crust-formation ages. Geology 15:893–895

Basak C et al (2015) Neodymium isotopic characterization of Ross Sea Bottom Water and its advection through the southern South Pacific. Earth Planet Sci Lett 419:211–221

Baxter E, Scherer E (2013) Garnet: timekeeper of tectonometamorphic processes. Elements 9:433–438

Bennett VC, Nutmna AP, McCulloch TM (1993) Nd isotopic evidence for transient, highly depleted mantle reservoirs in the early history of the Earth. Earth Planet Sci Lett 119:299–317

Bennett VC, Brandon AD, Nutman AP (2007) Coupled 142Nd-143Nd isotopic evidence for Hadean mantle dynamics. Science 318(5858): 1907–1910

Blichert-Toft J, Puchtel IS (2010) Depleted mantle sources through time: evidence from Lu–Hf and Sm–Nd isotope systematics of Archean komatiites. Earth Planet Sci Lett 297(3–4):598–606

Bourdon B, Touboul M, Caro G, Kleine T (2008) Early differentiation of the Earth and the Moon. Phil Trans R Soc A 366(1883):4105–4128

Bouvier A, Vervoort JD, Patchett PJ (2008) The Lu–Hf and Sm–Nd isotopic composition of CHUR: constraints from unequilibrated chondrites and implications for the bulk composition of terrestrial planets. Earth Planet Sci Lett 273(1–2):48–57

Boyet M, Carlson RW (2005) 142Nd evidence for early (>4.53 Ga) global differentiation of the silicate earth. Science 309:576–581

Burkhardt C et al (2016) Meteoritic Nd isotope constraints on the origin and composition of the Earth. Lunar and planetary science conference, 47, p 1908

Carlson RW, Boyet M (2009) Short-lived radionuclides as monitors of early crust–mantle differentiation on the terrestrial planets. Earth Planet Sci Lett 279(3–4):147–156

Carlson RW, Boyet M, Horan M (2007) Chondrite barium, neodymium, and samarium isotopic heterogeneity and early Earth differentiation. Science 316(5828):1175–1178

Caro G (2011) Early silicate Earth differentiation. Annu Rev Earth Planet Sci 39(1):31–58

Caro G, Bourdon B (2010) Non-chondritic Sm/Nd ratio in the terrestrial planets: consequences for the geochemical evolution of the mantle–crust system. Geochim Cosmochim Acta 74(11):3333–3349

Caro G, Bourdon B, Birck J-L, Moorbath S (2006) High-precision 142Nd/144Nd measurements in terrestrial rocks: constraints on the early differentiation of the Earth's mantle. Geochim Cosmochim Acta 70(1):164–191

Debaille V et al (2013) Stagnant-lid tectonics in early Earth revealed by 142Nd variations in late Archean rocks. Earth Planet Sci Lett 373:83–92

DePaolo DJ, Wasserburg GJ (1976) Nd isotopic variations and petrogenetic models. Geophys Res Lett 3:249–252

Ducea MN et al (2003) Sm–Nd dating of spatially controlled domains of garnet single crystals: a new method of high-temperature thermochronology. Earth Planet Sci Lett 213(1–2):31–42

Frei R, Polat A, Meibom A (2004) The Hadean upper mantle conundrum: evidence for source depletion and enrichment from Sm-Nd, Re-Os, and Pb isotopic compositions in 3.71 Gy boninite-like metabasalts from the Isua Supracrustal Belt, Greenland. Geochim Cosmochim Acta 68(7):1645–1660

Fukai R, Yokoyama T (2016) Nucleosynthetic neodymium isotope anomalies in carbonaceous and ordinary chondrites. Lunar and planetary science conference, 47, p 1298

Gale A et al (2013) The mean composition of ocean ridge basalts. Geochem Geophys Geosyst 14(3):489–518

Gannoun A, Boyet M, Rizo H, El Goresy A (2011) 146Sm–142Nd systematics measured in enstatite chondrites reveals a heterogeneous distribution of 142Nd in the solar nebula. Proc Natl Acad Sci 108(19):7693–7697

Goldstein SL, Hemming SR (2003) Long-lived isotopic tracers in oceanography, paleoceanography, and ice-sheet dynamics. Treatise Geochem 6:453–489

Greaves MJ, Elderfield H, Sholkovitz ER (1999) Aeolian sources of rare earth elements to the Western Pacific Ocean. Mar Chem 68:31–38

Hamilton PJ, O'Nions RK, Bridgwater D, Nutman A (1983) Sm-Nd studies of Archaean metasediments and metavolcanics from West Greenland and their implications for the Earth's early history. Earth Planet Sci Lett 62:263–272

Hawkesworth CJ, Kemp AIS (2006) Evolution of the continental crust. Nature 443:811–817

Hoffmann JE et al (2011) The origin of decoupled Hf–Nd isotope compositions in Eoarchean rocks from southern West Greenland. Geochim Cosmochim Acta 75(21):6610–6628

Hofmann AW (1997) Mantle geochemistry: the message from oceanic volcanism. Nature 385:219–229

Jeandel C et al (2007) Isotopic Nd compositions and concentrations of the lithogenic inputs into the ocean: a compilation, with an emphasis on the margins. Chem Geol 239(1–2):156–164

Johannesson KH, Burdige DJ (2007) Balancing the global oceanic neodymium budget: evaluating the role of groundwater. Earth Planet Sci Lett 253:129–142

Khanna T, Bizimis M, Yogodzinski G, Mallick S (2014) Hafnium–neodymium isotope systematics of the 2.7 Ga Gadwal greenstone terrane, Eastern Dharwar craton, India: implications for the evolution of the Archean depleted mantle. Geochim Cosmochim Acta 127:10–24

Kinoshita N et al (2012) A shorter 146Sm half-life measured and implications for 146Sm-142Nd chronology in the Solar System. Science 335(6076):1614–1617

Lambelet M et al (2016) Neodymium isotopic composition and concentration in the western North Atlantic Ocean: results from the GEOTRACES GA02 section. Geochim Cosmochim Acta 177:1–29

Ludwig K (2003) Isoplot version 3.00, A geochronological toolkit for Microsoft Excel. Berkeley Geochronology Center. Special publication. no 4

Lugmair GW, Carlson RW (1978) The Sm–Nd history of KREEP. In: Proceedings of the 9th lunar planetary science conference. Houston, pp 689–704

Marks NE et al (2014) Samarium–neodymium chronology and rubidium–strontium systematics of an Allende calcium–aluminum-rich inclusion with implications for ^{146}Sm half-life. Earth Planet Sci Lett 405:15–24

Meija J et al (2016) Isotopic compositions of the elements 2013 (IUPAC technical report). Pure Appl Chem 88:293

Meissner F, Schmidt-Ott W-D, Ziegeler L (1987) Half-life and α-ray energy of146Sm. Z Phys A At Nucl 327(2):171–174

O'Neil J, Carlson RW, Francis D, Stevenson RK (2008) Neodymium-142 evidence for Hadean mafic crust. Science 321(5897): 1828–1831

Piepgras DJ, Wasserburg GJ (1980) Neodymiun isotopic variations in seawater. Earth Planet Sci Lett 50:128–138

Piepgras DJ, Wasserburg GJ (1982) Isotopic composition of neodymium in waters from the Drake Passage. Science 217:207–214
Piepgras DJ, Wasserburg GJ (1987) Rare earth element transport in the western North Atlantic inferred from Nd isotopic observations. Geochim Cosmochim Acta 51:1257–1271
Pin C, Zalduegui JFS (1997) Sequential separation of light rare-earth elements, thorium and uranium by miniaturized extraction chromatography: application to isotopic analyses of silicate rocks. Anal Chim Acta 339:79–89
Pollington AD, Baxter EF (2011) High precision microsampling and preparation of zoned garnet porphyroblasts for Sm–Nd geochronology. Chem Geol 281(3–4):270–282
Richard PN, Shimizu N, Allègre CJ (1976) $^{143}Nd/^{144}Nd$, a natural tracer: an application to oceanic basalts. Earth Planet Sci Lett 31:269–278
Rizo H, Boyet M, Blichert-Toft J, Rosing M (2011) Combined Nd and Hf isotope evidence for deep-seated source of Isua lavas. Earth Planet Sci Lett 312(3–4):267–279
Roy M, van de Flierdt T, Hemming SR, Goldstein SL (2007) 40Ar/39Ar ages of hornblende grains and bulk Sm/Nd isotopes of circum-Antarctic glacio-marine sediments: implications for sediment provenance in the southern ocean. Chem Geol 244(3–4):507–519
Shaw HF, Wasserburg GJ (1985) Sm-Nd in marine carbonates and phosphates: implications for Nd isotopes in seawater and crustal ages. Geochim Cosmochim Acta 49:503–518
Stichel T, Frank M, Rickli J, Haley BA (2012) The hafnium and neodymium isotope composition of seawater in the Atlantic sector of the Southern Ocean. Earth Planet Sci Lett 317–318:282–294
Stichel T et al (2015) Separating biogeochemical cycling of neodymium from water mass mixing in the Eastern North Atlantic. Earth Planet Sci Lett 412:245–260
Tanaka T et al (2000) JNdi-1: a neodymium isotopic reference in consistency with LaJolla neodymium. Chem Geol 168(3–4):279–281
von Blanckenburg F (1999) Tracing past ocean circulation? Science 286(5446):1862–1863

Neon

Manuel Moreira
Institut de Physique du Globe de Paris, Sorbonne Paris Cité, UMR CNRS 7154, Université Paris Diderot, Paris, France

Element Data
Atomic Symbol: Ne
Atomic Number: 10
Atomic Weight: 20.179 g/mole
Isotopes and Abundances:
^{20}Ne: 90.48%
^{21}Ne: 0.27%
^{22}Ne: 9.25%
Common Valence: 1 s2 2 s2 2p6
Atomic Radius: 0.51 A
1 atm Melting Point: 24.56 K
1 atm Boiling Point: 27.07 K
First Ionization Energy: 21.565 eV

(*continued*)

Sun Abundance (Solar photosphere) [Calculated]: Ne/H = 6.9 10^{-5} (Alecian et al. 2005)
Bulk Solar Wind Abundance [Measured]: Ne/H = 6.6 10^{-5} (Heber et al. 2012)
Chondrites CI Abundance: 360 ± 160 ppt (Mazor et al. 1970)
Phase Q Abundance: 30–1400 ppt (Busemann et al. 2000)
Atmosphere Abundance: 18.18 ppm (volume)
Depleted Mantle Abundance: 0.1–0.5 ppt (weight) (Moreira and Kurz 2013)
Core Abundance: Unknown
Seawater (Pacific) Abundance: ~18 10^{-8} cm^3 g^{-1} at STP (e.g., (Bieri et al. 1966).

Properties

Neon is the second noble gas, the family of elements of the last column of the periodic table. It is chemically inert.

History and Use

Neon was discovered a few years after argon, in 1898, by Ramsay and Travers (1898). Its atomic number is 10 and it has three stable isotopes 20Ne, 21Ne, and 22Ne. Its atomic mass is 20.179, which reflects the relative proportion of the three isotopes (90.48, 0.27, and 9.25%, respectively (Eberhardt et al. 1965)). The neon isotopes ^{20}Ne and ^{22}Ne were discovered by Thomson (1913), whereas the existence of the less abundant neon isotope 21Ne was suggested by Aston (1920) and later proved by Hogness and Kvalnes (1928). Neon is a gas at normal pressure and temperature conditions. It has a low solubility in silicates ($k \sim 2.5 \times 10^{-4}$ cm^3 STP/g/bar at 1400 °C) and in water ($k \sim 10^{-2}$ cm^3 STP/g/bar at 7.5 °C) (Jambon et al. 1986; Lux 1987; Potter and Clynne 1978; Sano and Takahata 2005). Neon is atmophile and one of the most volatile elements in the solar nebula (half-temperature of condensation of 9.1 K (Lodders 2003)). The main budget of terrestrial neon is the atmosphere where it represents ~18.18 ppm in volume, the second most abundant noble gas on Earth, after argon.

Industrial neon can be extracted from air by distillation. Air is compressed and cooled to remove water, CO_2, and other impurities. The purified air is then cooled again until the gases turn into liquids. Then, in distillation towers, neon is separated from other gases. There are not many industrial uses of neon. Neon is mainly employed as filler in lamps and signs (with argon) and in lasers. Neon is a noble gas, rare, so no

mineral is formed by neon. It is not toxic and not used in biological utilization.

Neon is extracted from geological samples in different ways depending of the sample type. For mantle-derived samples, crushing under vacuum is common to release neon contained in fluid or melt inclusions such as minerals or silicate glasses. Heating and melting under vacuum is also used for all solids in order to fully degas the samples. UV laser allows in situ analyzes with ablation spots with a diameter of ~50 μm. Small samples (~0.1 mg) can be degassed using lasers of appropriate power (e.g., Yb-doped laser). All these extraction techniques have in common that they are performed under vacuum to avoid air contamination in the samples.

The neon dissolved in water can be extracted by vaporizing water under vacuum, which allows the noble gases to leave the liquid phase because of their low solubility. After the extraction phase from the samples, the gas purification consists generally in the exposure to hot titanium sponge and/or to nonevaporable getters (made of Zr, Al, V, Fe) at high temperatures (>600 °C) in order to crack all the reactive molecules and to trap all the atoms except those of noble gases. Hydrogen is trapped at room temperature on these getters. Once the gas has been purified, noble gases are generally separated on activated charcoal at different temperatures. He is separated from other noble gases at ~20 K whereas neon will be introduced from heavy noble gases at ~70 K. Neon is then expended into the mass spectrometer for analysis. Due to its low abundance in mantle-derived samples (e.g., less than a ppt in mid-ocean ridge basalts), neon is difficult to analyze and the analytical blanks are often a major issue. This is less critical for more gas rich samples such as meteorites or water samples. The very low abundances also require the measurement of neon by mass spectrometry in static mode (no pumping) and most often, detection on electron multipliers instead of faraday cups.

Although one of the most abundant elements in the Solar System (the 5th) (Alecian et al. 2005), neon is very rare in chondrites and in terrestrial planets (less than 1 ppb in CI (Mazor et al. 1970), and 11 ppt in Earth in g/g of planet). This reflects its highly volatile behavior during condensation in the solar nebula. Its origin on Earth is debated as it is for other volatiles, and it can be threefold: chondritic (late veneer or during late accretion) (Marty 2012; O'Brien et al. 2014), solar (dissolution of solar gases of a primary solar atmosphere into a molten primitive Earth followed by its degassing after the loss of this primary atmosphere (Sasaki 1999)), and cometary (Bar-Nun and Owen 1998). The neon isotopic composition in the Earth's mantle suggests a contribution of solar neon during accretion (solar wind implantation or dissolved solar gases) (Honda et al. 1991; Sarda et al. 1988), but the neon isotopic composition of the atmosphere requires either a neon loss from the atmosphere with isotopic fractionation (Hunten et al. 1987) or a chondritic addition (Marty 2012).

Summary

Neon, the second noble gas, was discovered in 1898 by Ramsay and Travers. On Earth, it is the second noble gas in abundance due to its very high volatility. Its origin on Earth is still debated, but it is generally proposed that it involves a mixture of chondrites, comets, and solar gases either by a dissolution of a primordial atmosphere into a magma ocean or by solar wind implantation in planetary precursors formed closed to the Sun.

Cross-References

- Argon
- Earth's Atmosphere
- Helium
- Krypton
- Neon Isotopes
- Noble Gases
- Xenon

References

Alecian G, Richard O, Vauclair S, Grevesse N, Asplund M, Sauval A (2005) The new solar chemical composition. Eur Astron Soc Publ Ser 17:21–30. https://doi.org/10.1051/eas:2005095

Aston FW (1920) The constitution of atmospheric neon. Philos Mag Ser 6 39:449–455

Bar-Nun A, Owen T (1998) Trapping of gases in water ice and consequences to comets and the atmospheres of the inner planets. In: Schmitt BB, de Bergh C, Festou M (eds) Solar system ices. Kluwer Academic, Dordrecht, pp 353–366

Bieri R, Koide M, Goldberg E (1966) The noble gas contents of pacific seawaters. J Geophys Res 71:5243–5264

Busemann H, Baur H, Wieler R (2000) Primordial noble gases in "phase Q" in carboncaceous and ordinary chondrites studied by closed-system stepped etching. Meteorit Planet Sci 35:949–973

Eberhardt P, Eugster E, Marti K (1965) A redetermination of the isotopic composition of atmospheric neon. Z Naturforsch 20a:623–624

Heber VS, Baur H, McKeegan K, Neugebauer M, Reisenfeld D, Wieler R, Wiens R (2012) Isotopic fractionation of solar wind: evidence from fast and slow solar wind collected by the Genesis Mission. Astrophys J 759:121–133

Hogness RR, Kvalnes HM (1928) The ionization processes in methane interpreted by the mass spectrograph. Phys Rev 32:942–945

Honda M, McDougall I, Patterson DB, Doulgeris A, Clague D (1991) Possible solar noble-gas component in Hawaiian basalts. Nature 349:149–151

Hunten DM, Pepin RO, Walker JCB (1987) Mass fractionation in hydrodynamic escape. Icarus 43:22–28

Jambon A, Weber H, Braun O (1986) Solubility of He, Ne, Ar, Kr and Xe in a basalt melting in the range 1250–1600°C. Geochemical implications. Geochim Cosmochim Acta 50:401–408

Lodders K (2003) Solar system abundances and condensation temperatures of the elements. Astrophys J 591:1220–1247

Lux G (1987) The behavior of noble gases in silicate liquids: solution, diffusion, bubbles and surface effects, with application to natural samples. Geochim Cosmochim Acta 51:1549–1560

Marty B (2012) The origins and concentrations of water, carbon, nitrogen and noble gases on Earth. Earth Planet Sci Lett 313-314:56–66
Mazor E, Heymann D, Anders E (1970) Noble gases in carbonaceous chondrites. Geochim Cosmochim Acta 34:781–824
Moreira M, Kurz MD (2013) Noble gases as tracers of mantle processes and magmatic degassing. In: Burnard P (ed) The noble gases as geochemical tracers. Springer, Berlin, pp 371–391
O'Brien DP, Walsh KJ, Morbidelli A, Raymond SN, Mandell AM (2014) Water delivery and giant impacts in the 'Grand Tack' scenario. Icarus 239:74–84
Potter RW II, Clynne MA (1978) The solubility of the noble gases He, Ne, Ar, Kr, and Xe in water up to the critical point. J Solut Chem 7:837–844
Ramsay W, Travers MW (1898) On the companions of argon. Proc R Soc Lond 63:437–440
Sano Y, Takahata N (2005) Measurement of noble gas solubility in seawater using a quadrupole mass spectrometer. J Oceanogr 61:465–473
Sarda P, Staudacher T, Allègre CJ (1988) Neon isotopes in submarine basalts. Earth Planet Sci Lett 91:73–88
Sasaki S (1999) Presence of a primary solar-type atmosphere around the earth: evidence of dissolved noble gas. Planet Space Sci 47:1423–1431
Thomson JJ (1913) Bakerian lecture: rays of positive electricity. Proc R Soc Ser A 89:1–20

Neon Isotopes

Moreira Manuel
Institut de Physique du Globe de Paris, Sorbonne Paris Cité, UMR CNRS 7154, Université Paris Diderot, Paris, France

Definition

Neon, the second element of the noble gas family, has three stable isotopes: ^{20}Ne, ^{21}Ne, and ^{22}Ne.

Introduction

The two most abundant isotopes (^{20}Ne and ^{22}Ne) were discovered in 1913 by Thomson using the first "mass spectrometer" ever built (Thomson 1913). They are the first stable isotopes of the same element that have been discovered. In 1920, Aston suggested the existence of the ^{21}Ne (Aston 1920), which was later confirmed in 1928 by Hogness and Kvalnes (1928). The relative abundance in the atmosphere of the three neon isotopes has been estimated by several authors (Dibeler et al. 1947; Nier 1950; Vaughan et al. 1934), and the commonly adopted values are those of Eberhardt et al. (1965), who determined the following abundances: 90.50 ± 0.07% ^{20}Ne, 0.268 ± 0.002% ^{21}Ne, and 9.23 ± 0.07% ^{22}Ne. This corresponds to isotopic ratios of 9.80 ± 0.08 and 0.0290 ± 0.0003 for ^{20}Ne/^{22}Ne and ^{21}Ne/^{22}Ne, respectively, for the Earth's atmosphere.

The Primordial Composition: The Solar Neon

The determination of the neon isotopic ratio of the Sun has been the subject of many works on meteorites and lunar samples returned by the Apollo and the Luna missions. Early in the 1960s, noble gas measurements on primitive meteorites have suggested that the solar ^{20}Ne/^{22}Ne ratio is 30% higher than the atmospheric one (Zähringer 1962). A ^{20}Ne/^{22}Ne ratio above 13 for the solar wind, higher than the Earth's atmosphere ratio of 9.80, was confirmed by the analyzes of lunar soil grains (Eberhardt et al. 1970) and of metal foils exposed to the solar wind for a few hours during the Apollo 11 and 12 landings (Geiss et al. 1970). The solar wind isotopic ratios have been precisely estimated on the Genesis targets exposed to the solar wind for 850 days after their return (e.g., Grimberg et al. 2006; Heber et al. 2009; Pepin et al. 2012). The solar wind is isotopically fractionated compared to the photosphere and therefore does not provide the composition of the Sun. Heber et al. (2009) have corrected for this isotopic fractionation and proposed that the ^{20}Ne/^{22}Ne ratio of the Sun is 13.36 ± 0.09 (Heber et al. 2012), whereas the solar wind ratio is above 13.7 (Grimberg et al. 2006; Heber et al. 2009; Pepin et al. 2012).

Reactions Producing Neon Isotopes in Solids

Although the three neon isotopes mostly have a primordial origin, two processes can alter the neon isotopic compositions in crustal and mantle rocks, as well as in extraterrestrial materials. Neon isotopes are produced by cosmogenic and nucleogenic reactions. Cosmogenic isotopes are produced during spallation reactions on major elements induced by either high-energy protons in space or by secondary neutrons and muons produced in the atmosphere reaching the surface (the first meters) on Earth. The production ratios in meteorites are ~0.8 and ~0.9 for ^{20}Ne/^{22}Ne and ^{21}Ne/^{22}Ne, respectively (from the stony meteorites compilation of Schultz and Franke 2000) and ~1 and ~0.8 in terrestrial quartz (Niedermann et al. 1993). The cosmogenic isotopes are used in geomorphology and in cosmochemistry to determine exposure ages. In addition to spallation processes, nucleogenic reactions can also alter the trapped neon isotopic compositions. The major nucleogenic reactions producing neon isotopes are ^{17}O(α, n)^{20}Ne, ^{18}O(α,n)^{21}Ne, and ^{25}Mg(n,α)^{22}Ne with production ratios of ~0.3 and ~3.5 for ^{20}Ne/^{22}Ne and ^{21}Ne/^{22}Ne, respectively (Leya and Wieler 1999; Yatsevich and Honda 1997). This process is significant in U and Th rich materials, which is the case of crustal minerals and rocks. Nucleogenic neon is also observed in the mantle-derived rocks and allows explanation of the variation of the ^{21}Ne/^{22}Ne ratio in oceanic basalts sources (Honda et al. 1991; Sarda et al. 1988). These

secondary reactions producing neon isotopes tend to decrease the $^{20}Ne/^{22}Ne$ and increase the $^{21}Ne/^{22}Ne$.

Neon in Chondrites: The Neon Alphabet

Neon isotopes show the existence of mainly four components in variable proportions in chondrites. These components are the implanted solar wind, presolar grains (diamonds, SiC, graphites), the cosmogenic end-member discussed above and the phase Q, and a carbonaceous phase mainly carrying the heavy noble gases (Fig. 1). These components can be found in the literature with various names, leading to the concept of the "neon alphabet" (Q, P1, Ne-A1; e.g., Ott 2014). Neon-B refers to implanted solar wind. This component has a $^{20}Ne/^{22}Ne$ of ~12.5–13.0 and is observed in gas-rich meteorites and lunar soil grains (Black 1972; Black and Pepin 1969). Before 2007, Neon-B was proposed to represent a mixture between the "normal" implanted solar wind and implanted neon from solar flares (Solar Energetic Particles, SEP). However, this has been challenged after the analyzes of Genesis probe targets (Wieler et al. 2007). Neon-B rather characterizes the implanted solar wind at steady state coupled with sputtering since it has been shown that neon isotopes are fractionated during solar wind implantation (Grimberg et al. 2006). A scenario able to explain the neon isotopic composition of neon B proposes that the heavy isotopes are implanted deeper than the light ones, leading to a surface of the grains enriched in light isotopes. When sputtering occurs, it produces an isotopic composition heavier than that of the solar wind itself (Raquin and Moreira 2009). Presolar grains have neon isotopic compositions different from those of the Sun. They show $^{20}Ne/^{22}Ne$ ratios of 8.5–8.9 for presolar diamonds, with values down to 0.01 for presolar SiC and graphite, the later suggesting a pure ^{22}Ne component either deriving from the radioactive decay of ^{22}Na or from the direct nucleosynthetic production of pure 22Ne. This later component has however little influence of the global budget of neon in chondrites, which is mainly dominated by Neon-B, presolar diamonds, and cosmogenic neon.

Solar-Like Neon in the Earth's Mantle

Since the pioneering works of Craig and Lupton (1976), Kyser and Rison (1982), Poreda and Radicati di Brozolo (1984), and Sarda et al. (1988), it is clearly established that the mantle shows a solar-like composition, different from the atmospheric composition and from carbonaceous chondrites. Neon in Midocean-Ridge Basalts (MORB) and Oceanic Island basalts (OIB) show a mixture between the atmospheric component and a component having a $^{20}Ne/^{22}Ne$ ratio higher than 12.5, which can only reflect a solar origin (Honda et al. 1991 1993; Moreira et al. 1995 2001; Sarda et al. 2000; (Porcelli et al. 2001; Sasaki 1999; Yokochi and Marty 2004; Mukhopadhyay 2012). The exact origin of the solar component in the mantle is still matter of debates because three origins are possible. The subduction of cosmic dust

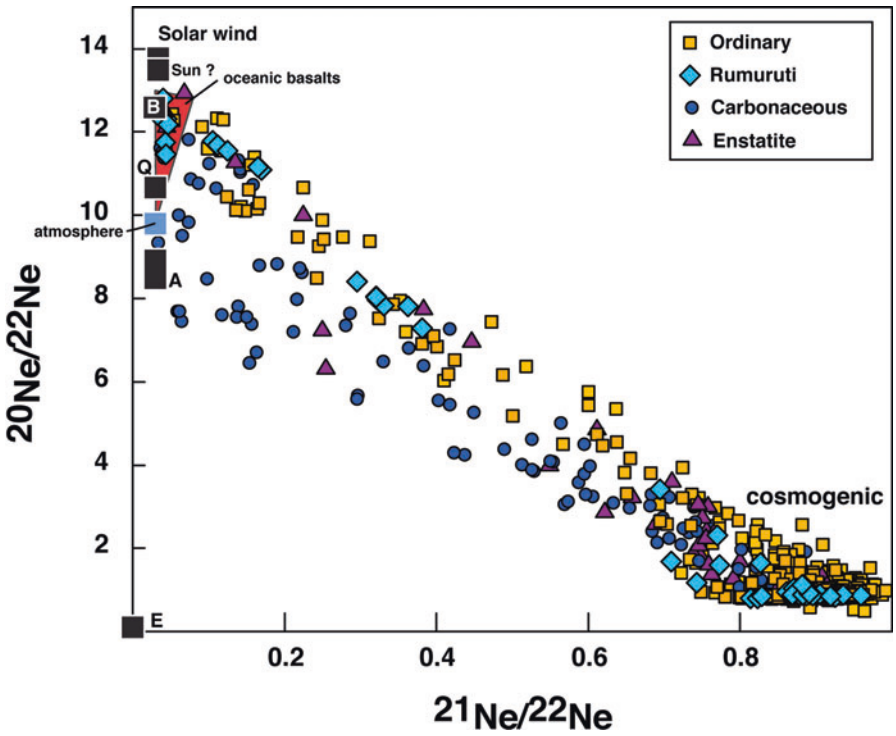

Neon Isotopes, Fig. 1 Neon isotopes in chondrites, in the solar wind and of the probable Sun neon isotopic ratios. The red triangle shows the isotopic compositions of oceanic basalts (MORB and OIB). Neon end-member (A, Q, E, and cosmogenic) are also represented. The figure is modified from Moreira (2013)

(interplanetary dust, or IDP) having implanted solar wind into the OIB and MORB sources has been proposed as a possible origin for the solar-like neon in the mantle (Allègre et al. 1993; Anderson 1993). However, only the smallest IDPs (<10 μm) contribute to the He and Ne budget in sediments because they do not suffer significant heating during the entry into the atmosphere (Farley et al. 1997). The largest ones reach temperatures high enough to degas them. Therefore only a very small fraction (~0.5%) of the extraterrestrial material falling onto Earth contributes to solar helium and neon in sediments that could be subducted, which is not enough to explain the neon budget of the Earth's mantle. Moreover, it appears difficult for the implanted solar neon to survive subduction due to its relatively high diffusivity (Hiyagon 1994; Schwarz et al. 2005). Therefore, it seems unlikely that the solar-like neon observed in the mantle is derived from the subduction of cosmic dust. A primordial origin deriving either from the dissolution of solar gases captured by the planet (Porcelli et al. 2001; Sasaki 1999; Yokochi and Marty 2004; Mukhopadhyay 2012) or from the solar wind irradiation of planetary precursors is therefore proposed and still matter of discussion (Raquin and Moreira 2009; Tolstikhin and Hofmann 2005; Trieloff et al. 2000).

Atmospheric Neon: Late Veneer or Atmospheric Loss?

The difference between the atmospheric and solar $^{20}Ne/^{22}Ne$ observed in the mantle has been explained in two ways. The neon in the mantle has a solar-like isotopic composition (Honda et al. 1991; Sarda et al. 1988). Therefore, if the atmosphere was degassed from the mantle, its Ne composition should have been solar, different from the present-day composition of the atmosphere. Neon loss from the atmosphere with a preferential loss of ^{20}Ne compared to ^{22}Ne can explain the atmospheric $^{20}Ne/^{22}Ne$ (Hunten et al. 1987). On the other hand, late addition of chondrites with a Neon-A signature can also explain the atmospheric composition by mixing between solar neon degassed from the mantle and chondritic neon, corresponding to ~1% of late veneer material (Marty 2012).

Summary

Neon has three stable isotopes. In geochemistry and cosmochemistry, neon isotopes are mainly used either to date exposure ages using the cosmogenic production or as a tracer of the origin of volatiles on Earth. They provide significant constraints on the origin and evolution of the Earth's atmosphere.

Cross-References

- ▶ Argon Isotopes
- ▶ Helium Isotopes
- ▶ Krypton
- ▶ Neon
- ▶ Noble Gases
- ▶ Xenon Isotopes

References

Allègre CJ, Sarda P, Staudacher T (1993) Speculations about the cosmic origin of He and Ne in the interior of the Earth. Earth Planet Sci Lett 117:229–233

Anderson DL (1993) Helium-3 from the mantle: primordial signal or cosmic dust ? Science 261:170–176

Aston MA (1920) The constitution of atmospheric neon. Philos Mag Ser 6 39:449–457

Black DC (1972) On the origins of trapped helium, neon and argon isotopic variations in meteorites – I. Gas-rich meteorites, lunar soil and breccia. Geochim Cosmochim Acta 36:347–375

Black DC, Pepin RO (1969) Trapped neon in meteorites-II. Earth Planet Sci Lett 6:395–405

Craig H, Lupton J (1976) Primordial neon, helium, and hydrogen in oceanic basalts. Earth Planet Sci Lett 31:369–385

Dibeler V, Mohler F, Reese R (1947) Mass-spectromter study of rare gases. U.S. Department of Commerce National Bureau of Standards, Research Paper RP1799 38, pp 617–620

Eberhardt P, Eugster E, Marti K (1965) A redetermination of the isotopic composition of atmospheric neon. Z Naturforsch 20a:623–624

Eberhardt P, Geiss J, Graf H, Grögler N, Krähenbühl U, Schwaller H, Schwarzmüller J, Stettler A, (1970) Trapped solar wind noble gases, exposure age and K/Ar age in Apollo 11 lunar fine material. Apollo 11 lunar science conference 2. Pergammon Press, Houston, pp 1037–1070

Farley KA, Love SG, Patterson DB (1997) Atmospheric entry heating and helium retentivity of interplanetary dust particles. Geochim Cosmochim Acta 61:2309–2316

Geiss J, Eberhardt P, Buhler F, Meister J, Signer P (1970) Apollo 11 and 12 solar wind composition experiments: fluxes of He and Ne isotopes. J Geophys Res 75:5972–5979

Grimberg A, Baur H, Bochsler P, Buhler F, Burnett DS, Hays CC, Heber VS, Jurewicz AJG, Wieler R (2006) Solar wind neon from genesis: implications for the Lunar noble gas record. Science 314:1133–1135

Heber VS, Wieler R, Baur H, Olinger C, Friedmann A, Burnett DS (2009) Noble gas composition of the solar wind as collected by the Genesis Mission. Geochim Cosmochim Acta 73:7414–7432

Heber VS, Baur H, McKeegan K, Neugebauer M, Reisenfeld D, Wieler R, Wiens R (2012) Isotopic fractionation of solar wind: evidence from fast and slow solar wind collected by the Genesis Mission. Astrophys J 759:121–133

Hiyagon H (1994) Retention of solar helium and neon in IDPs in deep sea sediment. Science 263:1257–1259

Hogness RR, Kvalnes HM (1928) The ionization processes in methane interpreted by the mass spectrograph. Phys Rev 32:942–945

Honda M, McDougall I, Patterson DB, Doulgeris A, Clague D (1991) Possible solar noble-gas component in Hawaiian basalts. Nature 349:149–151

Honda M, McDougall I, Patterson DB, Doulgeris A, Clague D (1993) Noble gases in submarine pillow basalt glasses from Loihi and Kilauea, Hawaii: a solar component in the Earth. Geochim Cosmochim Acta 57:859–874

Hunten DM, Pepin RO, Walker JCB (1987) Mass fractionation in hydrodynamic escape. Icarus 43:22–28
Kyser TK, Rison W (1982) Systematics of rare gas isotopes in basic lavas and ultramafic xenoliths. J Geophys Res 87:5611–5630
Leya I, Wieler R (1999) Nucleogenic production of neon isotopes in Earth's crust and upper mantle induced by alpha particles from the decay of U and Th. J Geophys Res 104:15439–15450
Marty B (2012) The origins and concentrations of water, carbon, nitrogen and noble gases on Earth. Earth Planet Sci Lett 313–314: 56–66
Moreira M (2013) Noble gas constraints on the origin and evolution of Earth's volatiles. Geochem Perspect 2:229–403
Moreira M, Staudacher T, Sarda P, Schilling J-G, Allègre CJ (1995) A primitive plume neon component in MORB: the Shona ridge-anomaly, South Atlantic (51–52°S). Earth Planet Sci Lett 133:367–377
Moreira M, Breddam K, Curtice J, Kurz M (2001) Solar neon in the Icelandic mantle: evidence for an undegassed lower mantle. Earth Planet Sci Lett 185:15–23
Mukhopadhyay S (2012) Early differentiation and volatile accretion recorded in deep-mantle neon and xenon. Nature 486: 101–104
Niedermann S, Graf T, Marti K (1993) Mass spectrometric identification of cosmic rays produced non in terrestrial rocks with multiple neon components. Earth Planet Sci Lett 118:65–73
Nier AO (1950) A redetermination of the relative abundances of the isotopes of neon, krypton, rubidium, xenon and mercury. Phys Rev 79:450–454
Ott U (2014) Planetary and pre-solar noble gases in meteorites. Chemie der Herde 74:519–544
Pepin RO, Schlutter DJ, Becker RH, Reisenfeld DB (2012) Helium, neon, and argon composition of the solar wind as recorded in gold and other Genesis collector materials. Geochim Cosmochim Acta 89:62–80
Porcelli D, Woolum D, Cassen P (2001) Deep Earth rare gases: initial inventories, capture from the solar nebula, and losses during Moon formation. Earth Planet Sci Lett 193:237–251
Poreda R, Radicati di Brozolo F (1984) Neon isotope variations in Mid-Atlantic Ridge basalts. Earth Planet Sci Lett 69:277–289
Raquin A, Moreira M (2009) Air 38Ar/36Ar in the mantle: implication on the nature of the parent bodies of the Earth. Earth Planet Sci Lett 287:551–558
Sarda P, Staudacher T, Allègre CJ (1988) Neon isotopes in submarine basalts. Earth Planet Sci Lett 91:73–88
Sarda P, Moreira M, Staudacher T, Schilling J-G, Allègre CJ (2000) Rare gas systematics on the southernmost mid-Atlantic Ridge: constraints on the lower mantle and the dupal source. J Geophys Res 105:5973–5996
Sasaki S (1999) Presence of a primary solar-type atmosphere around the earth: evidence of dissolved noble gas. Planet Space Sci 47:1423–1431
Schultz L, Franke L (2000) Helium, neon and argon in meteorites, a data compilation. Max-Planck-Institute for Chemistry, Mainz
Schwarz WH, Trieloff M, Altherr R (2005) Subduction of solar-type noble gases from extraterrestrial dust: constraints from high-pressure low-temperature metamorphic deep-sea sediments. Contrib Mineral Petrol 149:675–684
Thomson JJ (1913) Bakerian lecture: rays of positive electricity. Proc R Soc Ser A 89:1–20
Tolstikhin I, Hofmann AW (2005) Early crust on top of the Earth's core. Phys Earth Planet Inter 148:109–130
Trieloff M, Kunz J, Clague DA, Harrison D, Allègre CJ (2000) The Nature of pristine noble gases in mantle plumes. Science 288:1036–1038
Vaughan AL, William JH, Tate JT (1934) Isotopic abundance ratios of C, N,A,Ne and He. Phys Rev 46:327
Wieler R, Grimberg A, Heber VS (2007) Consequences of the non-existence of the "SEP" component for noble gas geo-and cosmochemistry. Chem Geol 244:382–390
Yatsevich I, Honda M (1997) Production of nucleogenic neon in the Earth from natural radioactive decay. J Geophys Res 102:10291–10298
Yokochi R, Marty B (2004) A determination of the neon isotopic composition of the deep mantle. Earth Planet Sci Lett 225:77–88
Zähringer J (1962) Ueber die Uredelgase in den Achondriten Kapoeta und Staroe Pesjanoe. Geochim Cosmochim Acta 26:665–680

Neutron Activation Analysis

James R. Budahn
U.S.Geological Survey, Denver, CO, USA

Definition

Neutron activation analysis (NAA), discovered in 1936, is an analytical technique that relies on the measurement of gamma rays emitted from a sample that was irradiated by neutrons. The rate at which gamma rays are emitted from an element in a sample is directly proportional to the concentration of that element. The major advantages of NAA are that (1) it is a multielement technique capable of simultaneously determining up to about 50 elements in many materials; (2) it is nondestructive and therefore does not suffer from the errors associated with sample preparation, the most important source of error in most analytical techniques; (3) it has very high sensitivities for most of the elements that can be determined by NAA, most detection limits range from 0.05 to 50 ppm; (4) it is highly precise and accurate, overall errors of less than 2% relative standard deviation can be achieved for many elements; and (5) samples as small as a few micrograms can be analyzed by NAA.

Principle

The process for analyzing samples by NAA involves irradiating them at or near a neutron source. Neutrons are captured by naturally occurring elements in the sample to produce unstable radioactive isotopes (radionuclides). Beta particles, and in some cases gamma rays, are emitted from the radionuclides to produce stable nuclei. The energies of these gamma rays are, in general, distinct for a specific nuclide, and the rate at which these photons are emitted with a particular energy can be measured using high-resolution semiconductor detectors. Because the production and decay rate of gamma-ray radiation are dependent on the half-life of the nuclide, elemental measurements can be optimized by varying the irradiation and the decay times (i.e., how long the sample is near a neutron source and when the sample is counted).

Procedure

The most common procedure for NAA involves encapsulating the samples and suitable standards in heat-sealed polyethylene or quartz vials and simultaneously irradiating them in a research nuclear reactor. Typical research nuclear reactors have neutron fluxes ranging between 10^{10} and 10^{15} n/cm^2/s. Ideally, the samples are irradiated in a "lazy susan" facility that revolves around the core of the reactor, thereby ensuring that the samples and standards experience the same neutron fluence (i.e., flux multiplied by time). Alternatively, samples can be irradiated by neutron point sources, such as californium-252, that have neutron fluxes ranging between 10^5 and 10^{10} n/cm^2/s. Following sequential decay periods, each standard and sample is counted utilizing high-resolution germanium detectors coupled to a multichannel analyzer system. Counting of samples over sequential decay periods optimizes the determination of 35–50 elements in various types of samples. The analyzer system converts the signals that result from gamma-ray photons impinging the detector into digital electronic pulses and stores this information into a few energy-related channels (i.e., an energy region). Gamma-ray counts accumulated in an energy region above the background counts produce photopeaks. After the counting is complete, these data are processed using sophisticated computer programs that smooth the spectral data and determine the net areas of the gamma-ray photopeaks and translate the area data into count rates (e.g., cpm). These programs are capable of resolving overlapping and complex photopeak energy regions. Final data reduction procedures involve correcting the count rate data for decay time differences, electronic deadtime losses, and unresolved interferences and comparing the sample data (e.g., cpm/weight) to the standard data (e.g., cpm/μg) to calculate elemental abundances in the sample. In some cases, especially when it is not practical to irradiate multiple standards, elemental abundances can be determined using the k_0 method which is based on activities (i.e., cpm/ug) calculated from activation equations.

Errors In Analysis

The principal error in the analysis of materials by NAA is the counting statistic error, which is based on the signal-to-background ratio at the gamma-ray energy region of interest. A one-sigma error for a photopeak area determination is approximately equal to the square root of the total counts (i.e., background plus net counts) divided by the net counts. For example, a peak area determination with 2000 total counts and a net area of 1000 counts produces a counting error of about 4.5%. An additional error for some elemental determinations is due to unresolved interferences. The most serious interferences are those that result when identical radionuclides are produced from different nuclear reactions: for example, high concentrations of U fission products can significantly interfere with the accurate determination of La, Ce, Nd, Mo, and Zr abundances. In addition, the determinations of some elements can suffer because the photopeaks produced by gamma rays emitted by two or more radionuclides are not readily resolved. In these cases, empirical corrections are integrated into the data reduction procedure.

Self-shielding is a phenomenon that occurs when the neutron flux experienced by a sample is attenuated, thereby reducing the neutron activation of the nuclides in self-shielded samples. This effect occurs when a sample contains extremely high concentrations of elements with very high probabilities that a neutron will be captured, which is measured in terms of a neutron capture cross section.

Other errors can result from inhomogeneous neutron fluxes and not maintaining the identical distance between the samples and the detector.

Detection Limits

Elemental detection limits for NAA are variable because of variations in nuclear parameters. Specifically, the production of a radionuclide depends on the neutron capture cross section of the target isotope of the specific element. In general, elements that have cross sections less than 2 barns (a barn being equal to 10^{-24} cm^2) have detection limits greater than 2 ppm, whereas elements with cross sections greater than 5 barns have detection limits less than 1 ppm. Also important is the number of gamma rays emitted by a radionuclide (i.e., the branching intensity). In some cases, only a small fraction of the total emissions from a specific nuclide is in the form of gamma rays. Another important nuclear parameter affecting detection limits is the isotopic abundance of the target nuclide. Detection limits are also matrix dependent. Samples with high concentrations of readily activated elements and that emit a considerable number of high-energy gamma rays, such as Na and Sc, can generate high background count rates, which raise the detection limits. Some of these emissions can blocked from detection by electronic anticoincidence techniques, thereby reducing the background rates.

Summary

Neutron activation analyses remain at the forefront of techniques for the quantitative multielement analyses of major, minor, and trace elements in hundreds of different types of materials. NAA is especially important in the analyses of geochemical reference materials because of the nondestructive nature of the technique. The following list includes some materials that have been readily analyzed by NAA: fish, teeth, bones, chemicals, bird feathers, wheat, metal, alloys, rocks,

animal shells, wood, tree needles, soil, rocks, lunar samples, meteorites, minerals, water, hair, fingernails, fossils, bullets, paint, silica glass, and biomass fuel oils.

Cross-References

- ▶ Analytical Techniques
- ▶ Geochemical Reference Materials
- ▶ Trace Elements

References

Amiel S (1981) Non-destructive activation analysis. Stud Anal Chem 3:385
De Soete D, Gijbels R, Hoste J (1972) Neutron activation analysis. Wiley, New York, p 836
Friedlander G, Kennedy JW, Macias ES, Miller JM (1981) Nuclear and radiochemistry. Wiley, New York, p 684
Glascock MD (1998) Activation analysis. In: Alfassi ZB (ed) Instrumental multielement chemical analysis. Kluwer, Dordrecht, pp 93–150
Hoffman EL (1992) Instrumental neutron activation analysis. J Geochem Explor Spec Issue Geoanalysis 44:297–320
Reeves RD, Brooks RR (1978) Trace element analysis of geologic materials. Wiley, New York, p 421
Simonits A, De Corte F, Hoste J (1975) Single-comparator methods in reactor neutron-activation analysis. J Radioanal Chem 24:31–46

Nickel

William L. Griffin[1] and Mathieu Chassé[2]
[1]Earth and Planetary Sciences, Macquarie University, North Ryde, NSW, Australia
[2]Institut de minéralogie, de physique des matériaux, et de cosmochimie (IMPMC), Sorbonne universités – UPMC, Paris, France

Element Data
Atomic Symbol: **Ni**
Atomic Number: **28**
Atomic Weight: 58.69
Isotopes and Abundances: ^{58}Ni 68.0769%, ^{60}Ni 26.2231%, ^{61}Ni 1.1399%, ^{62}Ni 3.6345%, ^{64}Ni 0.9256%
1 Atm Melting Point: 1455 °C
1 Atm Boiling Point: 2913 °C
Common Valences: 2+
Ionic Radii: fourfold, 55 pm; fourfold square, 49 pm; fivefold, 0.63 pm; sixfold, 9 pm
(*continued*)

Pauling Electronegativity: 1.91
First Ionization Energy: 737.1 kJ/mol
Chondritic (CI) Abundance: 1.091%
Silicate Earth Abundance: 0.186%
Crustal Abundance: 47 ppm
Seawater Abundance: ~2–10 nM/kg
Core Abundance: ~5.2%

Properties

Nickel has an atomic number of 28, an atomic weight of 58.69, and a density of 8.9 g/cm^3. It is a silvery metal that melts at 1455 °C and boils at 2913 °C; it is magnetic, malleable, and ductile and conducts electricity (www.rsc.org/periodic-table).

Ni has five naturally occurring stable isotopes and up to 18 radioactive isotopes, all long extinct. Up to 0.4 permil difference in Ni-isotope composition is observed between coexisting kamacite and taenite in iron meteorites and is ascribed to diffusion during exsolution and cooling (Lazar et al. 2012). However, the isotopic composition of Ni in chondritic meteorites and Earth is probably identical within current analytical capabilities (Lazar et al. 2012). Significant fractionation of Ni isotopes can occur in low-temperature processes such as lateritic weathering of ultramafic rocks; progressive weathering leads to isotopically lighter soils ($\Delta^{60}Ni_{Soil\text{-}Bedrock} = -0.47$ ‰) (Ratié et al. 2015).

Ni is a transition element, with the electronic configuration [Ar]3d^{8}4s^2; consequently it shows both siderophile (iron-loving) and lithophile (silicate-loving) behavior. In the crust and upper mantle, it normally occurs as Ni^{2+}, whereas in the Earth's core, it is alloyed with iron.

History and Use

Nickel (Ni) was first isolated from NiAs (niccolite) and named by A. F. Cronstedt in 1751. The name derives from the Saxon "nickel," a malicious sprite ("Kupfernickel") who prevented them from extracting copper from niccolite, which they had mistaken for chalcopyrite ($CuFeS_2$). Its properties were determined by J.B. Richter in 1804.

The main use of Ni (*ca* 65%) is for the production of stainless steel, with demand increasing by ca 5%/annum (International Nickel Study Group; www.insg.org). It is also used in the production of nonferrous alloys or so-called "superalloys" which show better resistance to corrosion and are widely used in jet engines and turbines. Smaller proportions are used in various surface treatments such as electroplating and as hydrogenation catalysts.

Ores and Production

World usage of Ni amounts to between 1.8 and 2 million tonnes/year (2014–2015).

Nickel is mined almost entirely from two types of deposit, magmatic sulfides and lateritic horizons, developed through the weathering of ultramafic rocks, usually in tropical areas (e.g., New Caledonia, Venezuela, the Dominican Republic, Brazil, Madagascar, and eastern Australia). Magmatic sulfides occur in ultramafic lava flows (komatiites; Fig. 1) in Archean cratons, in large intrusions of layered gabbros, and in the Sudbury giant impact crater. In all of these, the major ore mineral is pentlandite $(Ni,Fe)_9S_8$, but Ni also forms a range of other sulfides, arsenides, and antimonides. While magmatic sulfide ores are important resources, >70% of the world's supply of Ni is mined from lateritic deposits. During weathering, Ni concentrates in Ni-bearing limonite (Fe oxyhydroxide) and garnierite (referring to a group of green Ni-bearing magnesium phyllosilicates including serpentine, talc, sepiolite, smectite, and chlorite) in the middle-upper parts of the weathering profile, providing a resource that is easily mined and processed.

Geochemistry

The cosmic abundance of Ni estimated from carbonaceous chondrites is 10,910 ppm (Palme et al. 2014); estimates for its abundance in Earth lie between 17,000 and 19,000 ppm. Most of this is concentrated in the Earth's core; analyses of iron meteorites suggest the core contains *ca* 5 wt% Ni (McDonough 2014), leaving *ca* 1860 ppm in the mantle (Palme and O'Neill 2014) and 47 ppm in the continental crust (Rudnick and Gao 2014). Ni substitutes readily into the Mg-rich minerals of the mantle and is largely retained in the residue during partial melting. Ni concentrations in the crust are correspondingly quite low. The worldwide distribution of Ni in different rock types is shown in Fig. 1; Fig. 2 provides more detail on its distribution in mantle rocks. The variability shown in Fig. 2 is easily understood in terms of the relative abundance of Ni in the important minerals of mantle rocks (Fig. 3). This behavior is related to the charge and ionic radii of Ni. Under crustal and upper mantle conditions, the most common oxidation state of nickel is Ni(II). The effective ionic radius of Ni(II) depends on its coordination number ($^{[4]}$Ni, 0.55 Å; $^{[4]}$Ni square, 0.49 Å; $^{[5]}$Ni, 0.63 Å; and $^{[6]}$Ni, 0.69 Å). The identical charge and similarity in ionic radii between $^{[6]}$Ni and $^{[6]}$Mg allow significant substitution of Mg by Ni in olivine, the main Ni bearer among mantle-related minerals (Fig. 3). In addition, these distributions reflect mineral-mineral partitioning. Ni can substitute for Mg but not for Ca, which explains the higher Ni concentration in orthopyroxene compared to clinopyroxene (Fig. 3). Ni substitution may also be favored in the Mg site of spinel, which is smaller than the Mg site of garnet.

The solubility of Ni in pure water is low (<2 μg/L), but in the presence of dissolved organic compounds, it can form complexes that are soluble. In anoxic conditions, it precipitates in sulfide phases (NiS, pyrite). Atmospheric concentrations of Ni are dominated by anthropogenic pollution, principally from the burning of oil, and have increased by

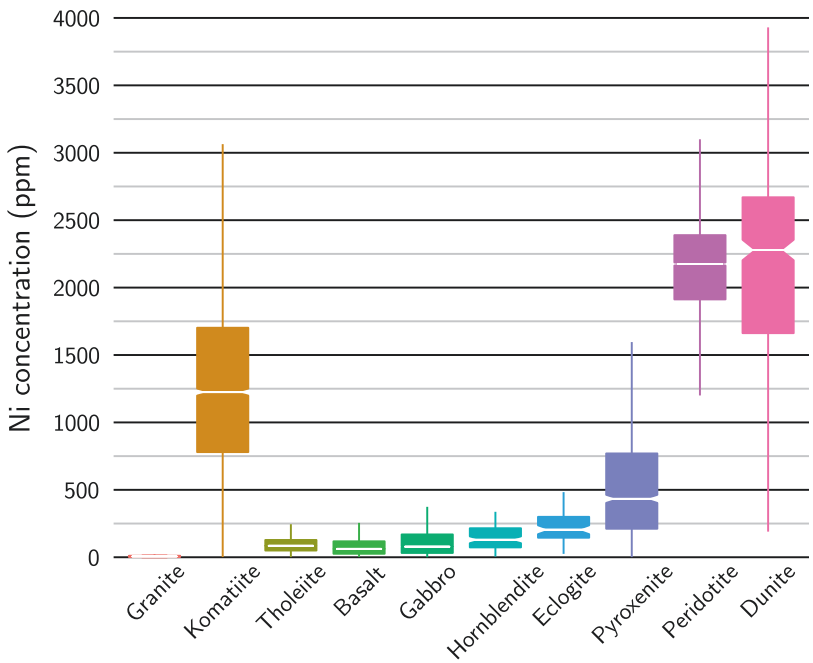

Nickel, Fig. 1 Distribution of Ni concentration in various lithotypes (Data from GEOROC, Sarbas and Nohl (2008); 18,359 analyses). The boxes represent the first and third quartiles of the data distribution. The horizontal line represents the median, and the width of the adjacent notches shows the 95% confidence interval about the median. The "whiskers" represent 1.5 x midrange (arithmetic mean of maximum and minimum values) beyond the first or third quartile

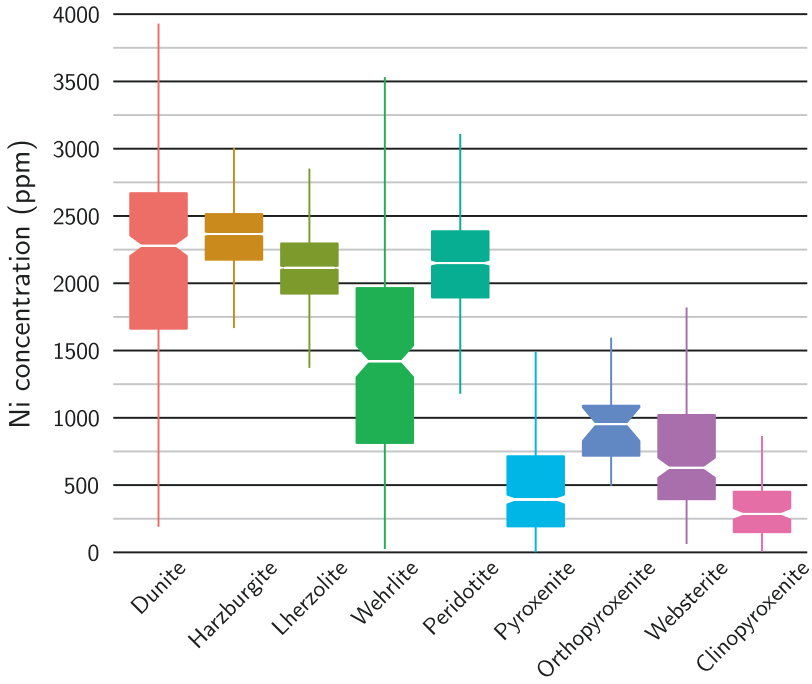

Nickel, Fig. 2 Distribution of Ni concentration in various mantle-related lithotypes. (Data from GEOROC, Sarbas and Nohl (2008); 5,403 analyses.)

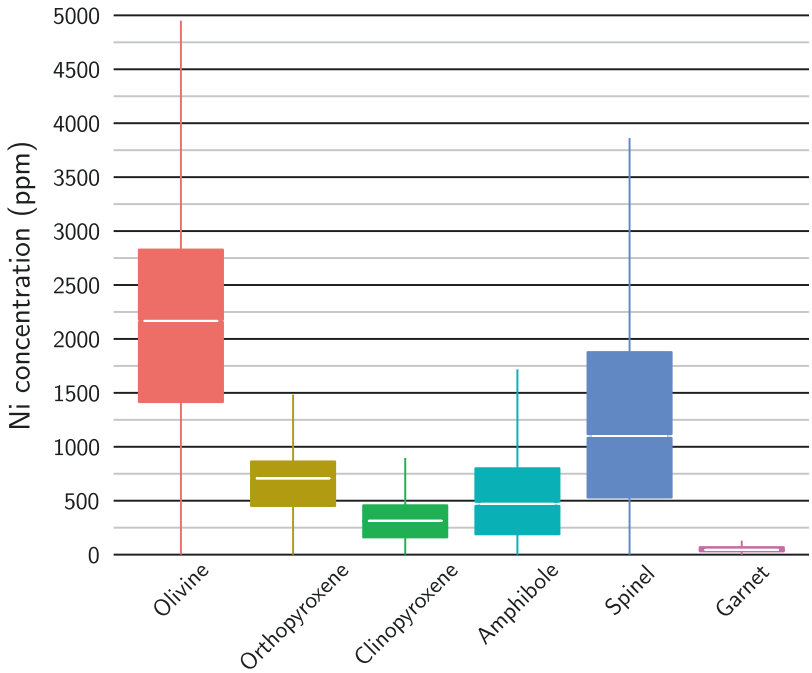

Nickel, Fig. 3 Distribution of Ni concentration in various mantle-related minerals. (Data from GEOROC, Sarbas and Nohl (2008) and authors' unpublished data; 105,630 analyses.)

a factor of >500 since the beginning of the Industrial Revolution (Pacyna and Pacyna 2001). Contributions to atmospheric Ni from smelting operations account for *ca* 10% of the total; they have declined in recent years due to better emission controls, but previously devastated large areas in the vicinity of smelters at, e.g., Sudbury in Canada and the Kola Peninsula in arctic Russia.

Biological Utilization and Toxicity

Ni is known to be toxic in high doses, but they are reached only in special situations. However, Ni contamination of groundwater can represent a hazard, especially in acidic conditions where it can be leached from soils (Nieminen et al. 2007).

Nickel is an important micronutrient in the oceans, and dissolved Ni is variably enriched (ca 10 nM/kg) in deeper waters and depleted (ca 2 nM/kg) in surface waters, following the pattern of other micronutrients such as Fe and Zn, as well as P and Si. This distribution suggests that diatoms actively control the distribution of Ni in ocean waters (Twining et al. 2012). The methanogenic bacteria that dominated Archean life appear to have been addicted to Ni. It has been proposed that a decline in the Ni contents of banded iron formations late in the Archean reflects a decrease in the availability of Ni in ocean water. This "nickel famine" may have led to the rise of the cyanobacteria, and their production of oxygen led in turn to the Great Oxidation Event at the end of the Archean (Saito 2009; Konhauser et al. 2009), allowing the evolution of multicellular life.

Summary

Nickel shows a very diverse range of geochemical behavior, being both a siderophile and a lithophile element. It has been important to mankind since the Bronze Age and is a mainstay of modern industrial society. It also is an essential element in the biogeochemistry of the oceans.

Cross-References

- ▶ Iron Meteorites
- ▶ Lithophile Elements
- ▶ Mantle Geochemistry
- ▶ Ore Deposits
- ▶ Periodic Table
- ▶ Siderophile Elements
- ▶ Sulfide Minerals
- ▶ Transition Elements

References

Konhauser KO et al (2009) Oceanic nickel depletion and a methanogen famine before the Great Oxidation Event. Nature 458:750–753
Lazar C, Young ED, Manning CE (2012) Experimental determination of equilibrium nickel isotope fractionation between metal and silicate from 500 °C to 950 °C. Geochim Cosmochim Acta 86:276–295
McDonough WF (2014) 3.16 – compositional model for the Earth's core A2. In: Turekian KK, Holland HD (eds) Treatise on geochemistry, 2nd edn. Elsevier, Oxford, pp 559–577
Nieminen TM, Ukonmaanaho L, Rausch N, Shotyk W (2007) Biogeochemistry of nickel and its release into the environment. Met Ions Life Sci 2:1–30
Pacyna EC, Pacyna JM (2001) An assessment of global and regional emissions of trace metals to the atmosphere from anthropogenic sources worldwide. Environ Rev 9:269–298
Palme H, O'Neill HSC (2014) 3.1 – cosmochemical estimates of mantle composition. In: Turekian KK, Holland HD (eds) Treatise on geochemistry, 2nd edn. Elsevier, Oxford, pp 1–39
Palme H, Lodders K, Jones A (2014) 2.2 – solar system abundances of the elements A2. In: Holland HD, Turekian KK (eds) Treatise on geochemistry, 2nd edn. Elsevier, Oxford, pp 15–36
Ratié G, Jouvin D, Garnier J, Rouxel O, Miska S, Guimaraes E, Cruz VL, Sivry Y, Zelano I, Montarges Pelletier E, Thil F, Quantin C (2015) Nickel isotope fractionation during tropical weathering of ultramafic rocks. Chem Geol 402:68–76
Rudnick RL, Gao S (2014) 4.1 – composition of the continental crust. In: Holland HD, Turekian KK (eds) Treatise on geochemistry, 2nd edn. Elsevier, Oxford, pp 1–51
Saito M (2009) Less nickel for more oxygen. Nature 458:714–715
Sarbas M, Nohl U (2008) The GEOROC database as part of a growing geoinformatics network. In: Geoinformatics conference, Postdam
Twining BS, Baines SB, Vogt S, Nelson D (2012) Role of diatoms in nickel biogeochemistry in the ocean. Glob Biogeochem Cycles 26. https://doi.org/10.1029/2011GB004233

Niobium

Carsten Münker
Institut für Geologie und Mineralogie, Universität zu Köln, Köln, Germany

Element Data
Atomic Symbol: **Nb**
Atomic Number: **41**
Atomic Weight: 92.90637
Isotopes and Abundances: ^{93}Nb, 100%
1 Atm Melting Point: 2477 °C
1 Atm Boiling Point: 4744 °C
Common Valences: 5+
Ionic Radii: 6-fold: 64 pm
Pauling Electronegativity: 1.6
First Ionization Potential: 652 kJ/mol
Chondritic (CI) Abundance: 283 ppb
Silicate Earth Abundance: 595 ppb
Crustal Abundance: 8 ppm
Seawater Abundance: 1–4 pmol/kg
Core Abundance: 450–500 ppb

Properties

Niobium is a transition metal of low toxicity with the atomic number of 41. Niobium has one stable isotope (93) with an atomic mass of 92.90637(2) (CIAAW 2015) The now extinct isotope ^{92}Nb with a half-life of 34.7 Ma is currently being investigated as a potential chronometer in cosmochemistry

(e.g., Münker et al. 2000, Schönbächler et al. 2000), decaying to ^{92}Zr by electron capture. In nature, Nb occurs in +5 valence state, although lower valence states are known from synthetic systems. Its atomic radius is 146 pm and its ionic radius in +5 valence state and sixfold coordination is 64 pm (Shannon 1976). Due to its high ratio of charge to ionic radius, Nb is classified in geochemistry as *high field strength element*.

History and Use

Niobium was first discovered in 1801 by the English chemist C. Hatchett (1802), which he named *columbium.* In 1845, the German chemist Heinrich Rose (1845) discovered that Ta-rich minerals contained a second element he named *niobium*, after Niobe, the daughter of Greek mythological figure Tantalus, reflecting the extreme geochemical similarity between Nb and Ta. It was subsequently discovered that *columbium* and *niobium* are identical. Not until 1949 was the name *niobium* adopted as official name for the element, but since then *columbium* had been used frequently in the North American literature, in particular in metallurgy.

Economically important Nb deposits are hosted by carbonatites or pegmatitic granites that in most cases exhibit a paired enrichment of both Nb and Ta to ore grade level. Important economical grade minerals include pyrochlore and columbite/tantalite, the latter mineralization is often referred to as COLTAN. Countries with the world's largest Nb deposits include Brazil, Canada, Australia, and some African countries, with Brazil presently supplying most of the industrially used Nb (USGS 2015). Technically, Nb is mainly used as steel alloy, for instance, in gas pipelines, jet and rocket engines, heat-resisting equipment, and superconducting alloys.

Geochemical Behavior

Niobium is a highly refractory element with a 50% condensation temperature of 1559K (Lodders 2003) and has traditionally been regarded as behaving lithophile during Earth's differentiation. Ratios of Nb and similarly refractory elements like Ta or Zr are nearly constant in most groups of chondrites, and only CV chondrites rich in refractory components deviate from this general pattern (Münker et al. 2003). The solar system abundance of Nb as estimated from CI chondrites is 283 ppb; the estimated abundance in the bulk silicate Earth is 595 ppb (Münker et al. 2003 in Palme and O'Neill 2014). The estimate for the bulk silicate Earth takes into account recent findings that, in contrast to its entirely lithophile geochemical twin Ta, Nb behaved moderately siderophile at the low oxygen fugacities prevailing during early core formation on Earth (Wade and Wood 2001). This provides a viable explanation why silicate Earth's Nb/Ta is significantly lower (14.0 ± 0.3) than the chondritic Nb/Ta of 19.9 ± 0.6 (Münker et al. 2003). The corresponding concentration of Nb in the core is between 450 and 500 ppb, assuming that all of the missing Nb in the silicate Earth has indeed been sequestered into the core (Wade and Wood 2001). There are suggestions that some of the missing Nb is stored via subduction zone processes in silicate reservoirs in the deep Earth and not in the core (e.g., Rudnick et al. 2000; Kamber and Collerson 2000). However, the observation that Nb/Ta in early Archean mafic rocks is indistinguishable from values in Phanerozoic rocks (Münker et al. 2003) argues against this view.

During silicate melting on Earth, Nb behaves highly incompatible in mantle minerals and is therefore depleted in the mantle and enriched in the crust. In the continental crust, the Nb content is estimated to 8 ppm with a content of 12 ppm and an Nb/Ta between 12 and 13 in the upper crust (Barth et al. 2000; Rudnick and Gao 2014). Relative to similarly incompatible elements like La or U-Th, however, Nb is markedly depleted in the continental crust, mirroring its selective depletion in subduction zone magmas that contributed to the bulk of the continental crust. The selective depletion of Nb in subduction-related lavas and the continental crust is caused by its lower solubility in subduction zone fluids and by its retention in Ti-rich phases like rutile in subducting oceanic crust and possibly in subducting sediments (e.g., Zack et al. 2002; Hermann and Rubatto 2009). Together with its geochemical twin Ta, Nb is therefore a viable tracer for elemental mass balances in subduction zone systems, and it is now known that Nb can be soluble in subduction zones to some extent at high pressures and in Cl^-- and F^--rich environments, leading to distinct Nb/Ta fractionation patterns (e.g., Münker et al. 2004; König et al. 2010; Kirchenbaur and Münker 2015). Hence, employing Nb/Ta ratios in igneous and metamorphic rocks has now become an important tool to better understand the role of residual phases such as rutile, titanite, or amphibole during silicate melting.

Due to its high valence state, Nb tends to hydrolize easily and is not very soluble in seawater, with an estimated concentration between 1 and 4 pmol/kg (Firdaus et al. 2011; Bruland et al. 2014). Notably, elevated Nb/Ta in seawater as high as 85 (Firdaus et al 2011) indicate that Nb can be highly fractionated from its geochemical twin Ta in aqueous systems, likely due to their different complexing behaviors. Once more data will become available for aqueous systems, combined Nb and Ta studies may have great potential to better understand weathering processes and ocean circulation.

Biological Utilization and Toxicity

Niobium has no known biological role. Niobium salts have been shown to be toxic, but only at very high doses (Haley et al 1962).

Summary

Niobium is a highly refractory incompatible element and one of the high field strength elements. Although generally considered lithophile, it has some siderophile tendency, and up to 500 ppb, Nb may be in the core. It has low solubility and is generally considered immobile. Compared to elements of similar incompatibility, it is depleted in the Earth's crust and in subduction zone magmas.

Cross-References

- ▶ High Field Strength Elements
- ▶ Incompatible Elements
- ▶ Ore Deposits
- ▶ Periodic Table
- ▶ Subduction Zone Geochemistry
- ▶ Tantalum
- ▶ Transition Elements

References

Barth MG, McDonough WF, Rudnick RL (2000) Tracking the budget of Nb and Ta in the continental crust. Chem Geol 165:197–213

Bruland KW, Middag R, Lohan MC (2014) Controls of trace metals in seawater. In: Mottl MJ, Elderfield H (eds) The oceans and marine geochemistry, Treatise on geochemistry, vol 8. Elsevier, Amsterdam, pp 19–51

CIAAW (2015) Commission on isotopic abundances and atomic weights. http://ciaaw.org/atomic-weights.htm

Firdaus ML, Minami T, Norisuye K, Sohrin Y (2011) Strong elemental fractionation of Zr-Hf and Nb-Ta across the Pacific Ocean. Nat Geosci 4:227–230

Haley TJ, Komesu N, Raymond K (1962) Pharmacology and toxicology of niobium chloride. Toxicol Appl Pharmacol 4(3):385–392

Hatchett C (1802) An analysis of a mineral substance from North America, containing a metal hitherto unknown. Philos Trans R Soc Lond 92:49–66

Hermann J, Rubatto D (2009) Accessory phase control on the trace element signature of sediment melts in subduction zones. Chem Geol 265:512–526

Kamber BS, Collerson KD (2000) Role of 'hidden' deeply subducted slabs in mantle depletion. Chem Geol 166:241–254

Kirchenbaur M, Münker C (2015) The behaviour of the extended HFSE group (Nb, Ta, Zr, Hf, W, Mo) during the petrogenesis of mafic K-rich lavas: the Eastern Mediterranean case. Geochim Cosmochim Acta 165:178–199

König S, Münker C, Schuth S, Luguet A, Hoffmann JE, Kuduon J (2010) Boninites as windows into variable trace element mobility in subduction zones. Geochim Cosmochim Acta 74(2):684–704

Lodders K (2003) Solar system abundances and condensation temperatures of the elements. Astrophys J 591:1220–1247

Münker C, Weyer S, Mezger K, Rehkämper M, Wombacher F, Bischoff A (2000) ^{92}Nb-^{92}Zr and the early differentiation history of planetary bodies. Science 289:1538–1542

Münker C, Pfänder JA, Weyer S, Büchl A, Kleine T, Mezger K (2003) Evolution of planetary cores and the earth – moon system from Nb/Ta systematics. Science 301:84–87

Münker C, Wörner G, Yogodzisnki G, Churikova T (2004) Behaviour of high field strength elements in subduction zones: constraints from Kamchatka-Aleutian arc lavas. Earth Planet Sci Lett 224(3–4):275–293

Palme H, O'Neill HSC (2014) Cosmochemical estimates of mantle composition. In: Carlson RW (ed) The mantle and core, Treatise on geochemistry, vol 3. Elsevier, Amsterdam, pp 1–39

Rose H (1845) On two new metals, pelopium and niobium, discovered in the bavarian tantalites. Philos Mag Ser 3 26(171):179–181

Rudnick RL, Barth M, Horn I, McDonugh MF (2000) Rutile-bearing refractory eclogites: missing link between continents and depleted mantle. Science 287:278–281

Rudnick RL, Gao S (2014) Composition of the continental crust. In: Rudnick RL (ed) The crust, Treatise on geochemistry, vol 4. Elsevier, Amsterdam, pp 1–51

Schönbächler M, Rehkämper M, Halliday AN, Lee DC, Bourot-Denise M, Zanda B, Hattendorf B, Günther D (2000) Niobium-zirconium chronometry and early solar system development. Science 295:1705–1708

Shannon RD (1976) Revised effective ionic radii and systematic studies of interatomic distances in halides and chalcogenides. Acta Crystallogr A32:751–767

Wade J, Wood BJ (2001) The Earth's 'missing' Nb may be in the core. Nature 409:75–78

Zack T, Kronz A, Foley SF, Rivers T (2002) Trace element abundances in rutiles from eclogites and associated garnet mica schists. Chem Geol 184:97–122

Nitrogen

Pierre Cartigny
Institut de Physique du Globe de Paris, Sorbonne Paris Cité, Université Paris Diderot, Paris, France

N

Element Data

Atomic Symbol: **N**
Atomic Number: **13**
Atomic Weight: 14.0067 g/mol
Isotopes and Abundances: ^{15}N (0.36%), ^{14}N (both stable)
Dinitrogen (78 molar percent of atmosphere) is gaseous at standard Pressure and Conditions.
Common Valences: primarily −3 (nitride, ammoniac), 0 (dinitrogen) and +5 (nitric acid)
Chondritic (CI) Abundance: ~2500 ppm
Silicate Earth Abundance: 2–20 ppm
Crustal Abundance: 83 ppm
Core Abundance: –

Properties

Nitrogen is the 5th element of the periodic table. With an electronic structure [He] $2s^2$ $2p^3$, nitrogen can either lose or gain up to five and three electrons, respectively, and can

therefore occur under a wide range of redox states from −3 to +5. The main reduced to oxidized species include nitride (N^{3-} in diamond, ammonium, and ammoniac), atmospheric dinitrogen gas (N^0 in N_2) to oceanic dissolved nitrate (N^{5+} in NO_3^-).

Nitrogen has 16 isotopes, two are stable (^{14}N ~ 99.64%, ^{15}N ~ 0.36%), the 14 others being radioactive with too short half-lives (<10 min) to have any potential geochemical application. Resulting atomic mass of nitrogen of 14.0067 (Coplen 2001) and variations in its stable isotope ratio is a central tool in stable isotope geochemistry.

Nitrogen is the fifth most abundant element in the solar system (~1105 ppm N, Lodders 2003) and is comparatively depleted on Earth with estimated Bulk Earth of ~3 to ~28 ppm N (Cartigny and Marty 2013). On Earth, nitrogen is unevenly distributed. The atmosphere is a nitrogen-rich reservoir where N_2 gas represents 78.084% mole fraction (~3.9×10^{21} g N) together with minor but significant greenhouse gases such as nitrous oxide (N_2O), other nitrogen oxides (NO_x, 100 ppt–1 ppm), ammonia (NH_3, 10 ppt–1 ppb), and particulate nitrate and ammonium (1 ppt–10 ppb) occurring in aerosols (Brasseur et al. 1999). The crust and sediments typically contain 100–1000 ppm levels (Busigny and Bebout 2013), the Earth's mantle is N-poor with estimated N-contents of 0.26–36 ppm. The nitrogen content of the Earth's core remains unknown with contradicting experimental evidence.

The main source of nitrogen to the hydrosphere is atmospheric in origin being massively cycled by biological activity (at a rate of ~2×10^{14} g N/y; Galloway 2003), particularly by primary producers (e.g., phytoplankton and cyanobacteria). Without a strong return flux (denitrification and anaerobic ammonium oxidation), present-day atmospheric nitrogen (~4×10^{21} gN) would be entirely sequestered within less than 100 million years (My).

Unlike other elements, crustal nitrogen is originally sourced from the atmosphere by biological activity (i.e., mantle nitrogen contribution and abiotic atmospheric reduction are negligible). Nitrogen enters the rock cycle as organic matter matures releasing nitrogen as ammonium ion (NH_4^+). Having similar charge and ionic radius to potassium, ammonium then substitutes for – and follows the fate of – potassium in potassic minerals (e.g., clays, feldspars, and micas; Busigny and Bebout 2013). The occurrence of ammonium in crustal rocks is therefore primarily of atmospheric origin.

Very few N-forming minerals exist in nature; they occur in very specific environments such as volcanic fumerolles, evaporitic systems, atmospheric deposits (Atacama desert), or meteorites (see Table 1 in Holloway and Dahlgren 2002). Ammonium is generally only a substitutional impurity, buddingtonite the ammonium feldspar ($NH_4AlSi_3O_8$) being a noticeable case. Nitrate-forming minerals are rare as well (nitrate is a very soluble species), but it is worth mentioning that nitre (KNO_3, the word *nitrogen* coming actually from *nitre-forming*) and saltpetre were important sources of nitrogen entering the composition of gun-powder and fertilizers.

Nowadays, since the advent (1909–1913) of industrial abiotic dinitrogen reduction into ammoniac through the so-called Haber-Bosch process where $N_2 + 3H_2 \rightarrow NH_3$ (Bosch 1966), the main source of nitrogen entering fertilizers is actually atmospheric with over 1.4×10^{14} gNH_3 produced every year, i.e., close to the flux of biological nitrogen fixation. Present-day nitrogen cycle is thus a good example of a heavily anthropized cycle. Nearly 100% of world production of synthetic ammonia relies on the Haber-Bosch process and the resulting massive production (and use) of fertilizers is generally described as the *detonator of the population explosion* (Smil 1999). With only half of fertilizers being fixed by plants, nitrate pollution of groundwaters, rivers, and estuaries leads to biological blooming which results in anoxic waters during their subsequent degradation.

Cross-References

- ▶ Biogeochemistry
- ▶ Nitrogen Cycle
- ▶ Nitrogen Isotopes

References

Bosch C (1966) The development of the chemical high pressure method during the establishment of the new ammonia industry (1931 Nobel Lecture). In: Nobel lectures, chemistry 1922–1941. Elsevier, Amsterdam. Available at http://www.nobelprize.org/nobel_prizes/chemistry/laureates/1931/bosch-lecture.html

Brasseur GP, Orlando JJ, Tyndall GS (1999) Atmospheric chemistry and global change. Oxford University Press, Oxford

Busigny V, Bebout GE (2013) Nitrogen in the silicate earth: speciation and isotopic behavior during mineral-fluid interactions. Elements 9:353–358

Cartigny P, Marty B (2013) Nitrogen isotopes and mantle geodynamics: the emergence of life and the atmosphere-crust-mantle connection. Elements 9:359–366

Coplen TB (2001) Atomic weights of the elements 1999. Pure Appl Chem 73:667–683

Galloway JN (2003) The global nitrogen cycle. In: Holland HD, Turekian KK (eds) Treatise on geochemistry. Pergamon, Oxford, pp 557–583

Holloway JM, Dahlgren RA (2002) Nitrogen in rock: occurrences and biogeochemical implications. Global Biogeochem Cycles 16:1118

Lodders K (2003) Solar system abundances and condensation temperatures of the elements. Astrophys J 591:1220–1247

Smil V (1999) Detonator of the population explosion. Nature 400:415

Nitrogen Cycle

Monica M. Palta[1] and Hilairy Ellen Hartnett[2]
[1]Department of Environmental Studies and Science, Pace University, New York, NY, USA
[2]School of Earth and Space Exploration and School of Molecular Sciences, Arizona State University, Tempe, AZ, USA

Definition

The nitrogen cycle describes the biogeochemical transformation of the element nitrogen into a variety of chemical species within ecosystems the transfer of those nitrogen-containing species among atmospheric, terrestrial, and aquatic ecosystems.

Pools in the Nitrogen Cycle

The vast majority of global nitrogen (N) is in a form or setting that makes it unavailable to organisms for their uptake and metabolism. Atmospheric nitrogen (in the form of N_2) makes up roughly 50% of the total nitrogen on Earth; the remaining nitrogen is primarily in rocks of Earth's mantle and crust and is highly unavailable biologically (Canfield et al. 2010). Nitrogen in rocks is generally in the form of NH_4 in silicates (clays), although a few NO_3- bearing minerals are known. In igneous rocks, N content is usually <0.1 wt%. Nitrogen in sedimentary rocks can be much higher (up to ~2 wt%). Due to the low reactivity of rock-derived nitrogen, nitrogen in the mantle and crust of the Earth is typically excluded from consideration in the nitrogen cycle. Atmospheric nitrogen thus holds roughly 90% of the nitrogen relevant to the global nitrogen cycle, with nearly all of that nitrogen in the form of N_2 (Chapin et al. 2011). The ocean holds the second largest pool of nitrogen (roughly 9%), but a sizeable portion of this nitrogen (99.98%) is located in ocean sediments and deep water (Chapin et al. 2011) and thus has a very low turnover time relative to other terrestrial and aquatic pools. In the terrestrial pool of the nitrogen cycle, soils hold roughly 23 times the total nitrogen found in terrestrial biomass (Chapin et al. 2011). Most soil nitrogen is in organic form, due to the rapid uptake of nitrogen by organisms; the pool of inorganic nitrogen in soil at any given time is very small (Schlesinger and Bernhardt 2013).

Overview of Nitrogen Cycle

The nitrogen cycle involves incorporation of nitrogen into biological molecules and the breakdown of those molecules into inorganic forms of nitrogen that have varying biological availability and reactivity. The largest pool of nitrogen on Earth is the atmosphere, where the dominant form of nitrogen is N_2 gas. The formidable energy required to break the triple bond in N_2 gas means this large pool of nitrogen is predominantly unavailable biologically. However, two to three billion years ago, both photosynthesis and the microbial process of N_2 fixation, which converts one mole of N_2 to two moles of ammonia (NH_3) using nitrogenase, evolved. Photosynthesis and N_2 fixation created larger pools of organic carbon and bioavailable nitrogen in terrestrial and aquatic systems; these molecules were now available for processing and recycling by other organisms. Of the 203 Tg of reactive (biologically available) nitrogen generated annually from natural sources, one-third is terrestrially derived and two-thirds are marine-derived (Table 1; e.g., Fowler et al. 2013). Most organisms cannot fix nitrogen, but rather obtain nitrogen as NH_4^+, NO_3^- (which is then converted to NH_4^+ through assimilatory NO_3^- reduction), or as organic nitrogen (Fig. 1). The latter is the form in which many heterotrophs (including animals and fungi) obtain nitrogen, while plants and some heterotrophs (including bacteria) are able to use inorganic forms of nitrogen. Bioavailable forms of inorganic nitrogen range from fully reduced to fully oxidized forms and include NH_3, NH_4^+, NO, NH_2OH, N_2O, NO_2^-, and NO_3^- (Fig. 1, Table 2).

A number of different reactions govern fluxes of nitrogen between different types of bioavailable forms and between terrestrial, aquatic, and atmospheric pools of

Nitrogen Cycle, Table 1 Global nitrogen fluxes (Table modified from Fowler et al. 2013)

Nitrogen fluxes	Tg N $year^{-1}$
Sources of fixed nitrogen	
Anthropogenic	
Fertilizer production	100
Chemical production	20
N_2 fixation, agricultural	60
Combustion to NO_x	40
Natural	
Lightning	5
N_2 fixation, marine	140
N_2 fixation, terrestrial	58
Sinks for fixed nitrogen	
Denitrification, marine	100–280
N burial, marine	20
Nitrogen fluxes between pools	
Wet and dry atmospheric deposition	100
NH_3 emissions, terrestrial	60
NH_3 emissions, marine	9
N_2O emissions, marine	5.5
NO emissions from soil	5
N_2O emissions from soil	13

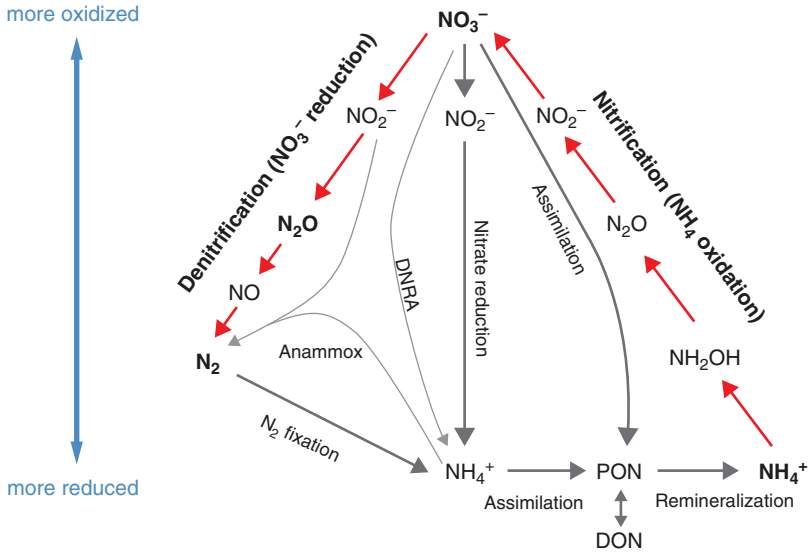

Nitrogen Cycle, Fig. 1 The major biological nitrogen transformation pathways and the relative oxidation state at which they occur

Nitrogen Cycle, Table 2 Redox state of common environmentally relevant nitrogen species

Species	Valence state
NH_3, NH_4^+	−III
NH_2OH	−I
N_2	0
N_2O	+1
NO	+II
NO_2^-	+III
NO_3^-	+V

nitrogen (Figs. 1 and 2). Nitrogen is cycled internally in terrestrial and aquatic systems primarily via the metabolic processes of microbes and plants (assimilation, mineralization, nitrification, and dissimilatory nitrate reduction to ammonium (DNRA)). These processes are especially sensitive to oxygen and pH and are typically highly coupled with one another. A subset of microbial processes in terrestrial and aquatic systems (i.e., denitrification, anammox, and, to a lesser extent, nitrification) returns nitrogen to the atmosphere in the form of nitrogen gas (NO, N_2O, N_2).

Humans have radically altered the global nitrogen cycle. The invention of the Haber-Bosch process (a synthetic nitrogen fixation reaction) in the early 1900s allowed the industrial production of NH_4^+ for fertilizer. This process has radically altered the nitrogen cycle by more than doubling the amount of bioavailable nitrogen in terrestrial systems (Table 1). The dramatic increase of bioavailable nitrogen in both aquatic and terrestrial systems has had large impacts on ecosystems, altering both internal fluxes of nitrogen and feedbacks between the atmosphere and biosphere. Human activities, including combustion of fossil fuels, changes in land use, and inputs of inorganic nitrogen to terrestrial and aquatic systems in the form of fertilizer, have greatly increased fluxes of nitrogen (NO_2, NO, N_2O) to the atmosphere.

Fluxes in the Nitrogen Cycle

Major fluxes in the nitrogen cycle are either internal to terrestrial, aquatic, or atmospheric pools or move nitrogen between these pools (Fig. 2). Fluxes are mediated primarily by biological transformations (i.e., microbial respiration and plant production); less common are a few abiotic phenomena that convert nitrogen from one molecular form to another. The key flux in the nitrogen cycle, nitrogen fixation, is a microbial process that moves atmospheric nitrogen (N_2) into a form useable by plants and other microbes (NH_4^+). Although not typically considered a major component of the nitrogen cycle, abiotic chemical reactions can convert some forms of nitrogen gas into forms that enter terrestrial and aquatic pools. For example, lightning strikes are responsible for a small amount of nitrogen fixation (~2% of annual nitrogen fixation; Galloway et al. 2008), and various forms of nitrogen gas are miscible (NH_3) or reactive (NO_x) with water, which moves nitrogen from the atmosphere to aquatic and/or terrestrial systems. Current models suggest that in the early Earth's atmosphere, long prior to the evolution of nitrogen fixation, lightning and high-energy meteorite impacts were primarily responsible for producing NO that would be converted to NO_3^- and NO_2^- through photochemical and aqueous phase reactions (Canfield et al. 2010).

Internal cycling of nitrogen within terrestrial and aquatic systems largely involves conversion of nitrogen between various inorganic, biologically reactive forms and between inorganic and organic forms of nitrogen. Figure 2 shows an example of internal cycling within a coastal marine ecosystem (labeled "Ecosystem N cycle"), where nitrogen moves between different inorganic and organic forms, as well as gaseous (g) and aqueous (aq) forms. Ecosystem cycling includes the following major fluxes: **nitrification** (microbial oxidation, over several intermediary steps, of NH_4^+ to NO_3^-),

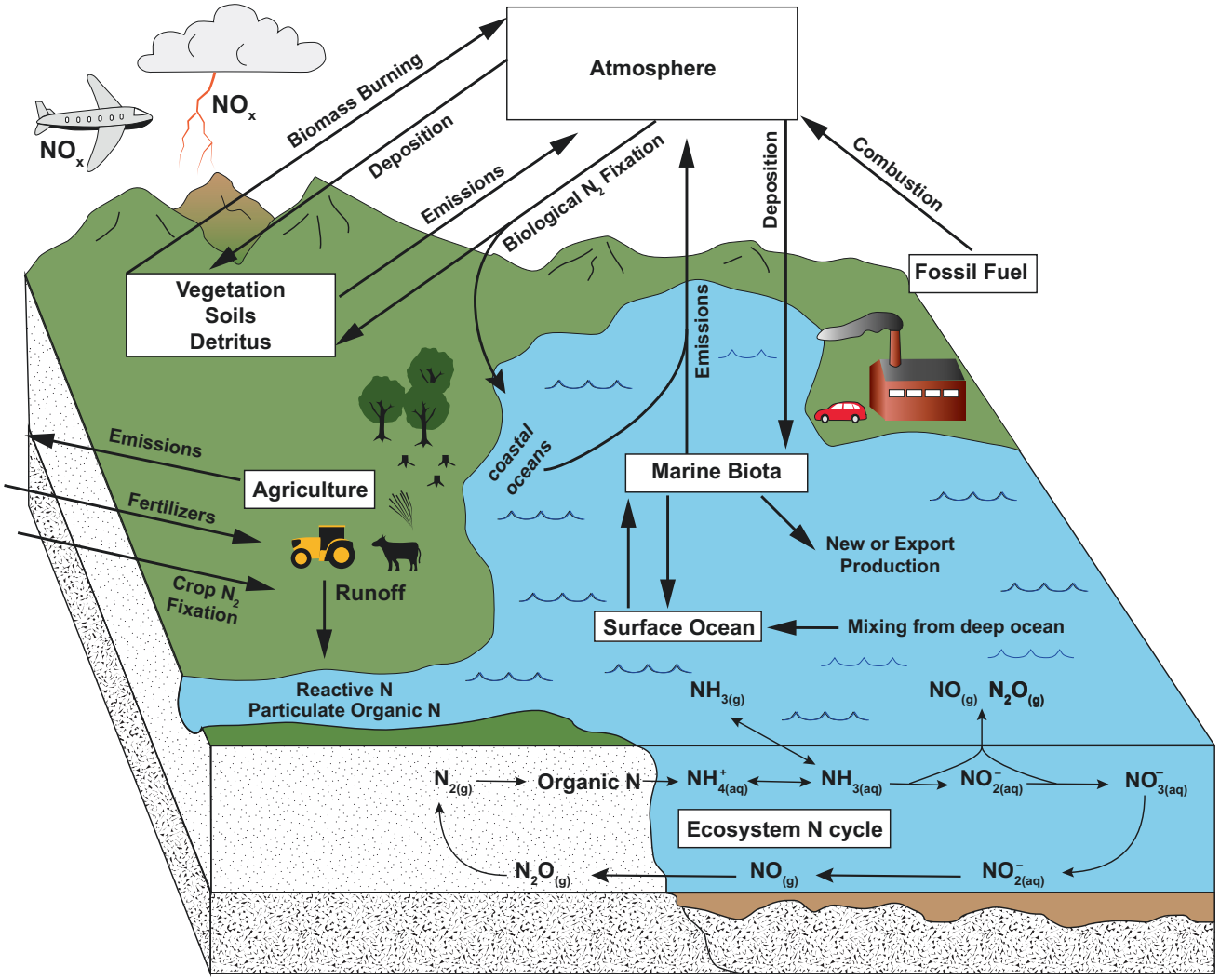

Nitrogen Cycle, Fig. 2 The nitrogen cycle. Fluxes occur between major global pools (atmospheric, terrestrial, and aquatic ecosystems) and between pools within these ecosystems. An example of internal ecosystem cycling is shown for a coastal marine ecosystem (labeled "Ecosystem N cycle"), where nitrogen moves between different types of molecules, including inorganic and organic, and gaseous (g) and aqueous (aq) forms. Human activities, including agricultural practices, fossil fuel combustion, and biomass burning, have heavily influenced the nitrogen cycle. Anthropogenic influence includes increased inorganic (reactive) flux from the terrestrial to aquatic pool through runoff, and increased nitrogen flux (of nitrogen gases) from the terrestrial to atmospheric pool. Atmospheric deposition of reactive nitrogen onto terrestrial ecosystems has also increased due to human activities

NO_3^- reduction (to NO_2^-), **dissimilatory nitrate reduction to ammonium (DNRA)** (microbial reduction of NO_2^- to NH_4^+), **assimilation** (NH_4^+ to organic nitrogen), and **mineralization** or **ammonification** (organic nitrogen to NH_4^+) (Fig. 1). **Denitrification** and **ammonia oxidation (anammox)** by microbes convert NO_3^- and NH_4^+, over a few intermediary steps, to nitrogen gas, returning nitrogen to the atmosphere (Fig. 1). The terminal form of nitrogen in both these processes is N_2. Microbial nitrification and abiotic NH_4^+ volatilization can also result in the production of N_2O and NH_3^+ gas, respectively (Fig. 1).

The concentration of oxygen (redox status) in water, soil, and sediments strongly influences which processes related to nitrogen cycling can occur in a given system at a given point in time (Fig. 1, Table 2). Nitrogen loses and gains electrons during abiotic and biotic chemical transformation, with the oxidation state of nitrogen ranging from −3 to +5 (an eight electron difference). Nitrification is an oxidizing reaction that requires the largest transfer of electrons (oxidation state change of −3 to +5) in the nitrogen cycle and thus requires high oxygen availability. This process is carried out in several steps that transfer oxygen to the nitrogen molecule: first, bacteria (primarily *Nitrosomonas* species) convert NH_4^+ to NH_2OH using the enzyme ammonium monooxygenase and NH_2OH to NO_2^- using hydroxylamine oxidoreductase. *Nitrobacter* species are then primarily responsible for

converting NO_2^- to NO_3^- using the enzyme nitrite oxidoreductase. Most other fluxes in the nitrogen cycle (denitrification, nitrogen fixation, DNRA, and anammox) are reduction reactions that occur under anaerobic conditions. Anammox does involve an increase in oxidation state for its final step (i.e., N_2H_4 to N_2, catalyzed by hydroxylamine oxidoreductase), but this reaction is anaerobic nonetheless.

Coupling of Fluxes and Flux Balances

Because the products of one process involving nitrogen are often the inputs for another, fluxes in the nitrogen cycle are coupled with and balance one another. For example, denitrification relies on nitrification in the absence of external NO_3^- inputs, which leads to a predominance of coupled nitrification-denitrification in many ecosystems. Nitrogen assimilation is tightly coupled to mineralization and is controlled by nutrient limitations. If organisms in an ecosystem are limited in their metabolic processes by nitrogen relative to other needed nutrients (e.g., carbon and phosphorus), nitrogen assimilation will constitute a larger flux than nitrogen mineralization, and organic nitrogen will constitute a larger pool within that system than those of biologically available (inorganic) nitrogen species. The nitrogen cycle is thus tightly coupled with that of phosphorus and carbon, globally and within ecosystems. Finally, the balance between N_2 fixation and denitrification in terrestrial and aquatic ecosystems determines total global terrestrial and marine pool sizes (see Table 1).

Fluxes of nitrogen between different pools is also tightly linked with fluxes of water, both because the presence of water in a terrestrial system can influence redox status of soils, and therefore internal cycling, and because water can transport nitrogen in the form of dissolved gas and ions. Because NO_3^- is highly soluble in water compared to NH_4^+, for example, and less readily adsorbed to charged surfaces in soil, NO_3^- tends to be the dominant form of inorganic nitrogen that is transported between terrestrial and aquatic systems.

Anthropogenic Alterations to the Nitrogen Cycle

Human activities have had both direct and indirect effects on pools and fluxes in the nitrogen cycle, but never so much as in the last century. One of the most seminal changes by humans in the nitrogen cycle has been perpetuated by the invention of the Haber-Bosch process, or industrial-scale N fixation. The invention of this process was a tremendous boon for global food supply and resulted in increased population growth worldwide. However, it has also doubled the production of reactive N in terrestrial ecosystems (Fowler et al. 2013). Inadvertent N fixation also occurs through other anthropogenic activities, i.e., fossil fuel combustion and industrial processes (e.g., electricity production). Nitrogen-fixing agricultural crops cultivated by humans also contribute significant amounts of reactive N to terrestrial ecosystems (Fowler et al. 2013) (Table 1). The result of these large anthropogenic sources of reactive N has been doubling in global N cycling over the last century (Fowler et al. 2013). Further, reactive N is accumulating in the environment, because although roughly 20%, by some estimates, of N fertilizer is lost to the atmosphere as N_2 in croplands, gaseous nitrogen emissions cannot keep pace with N fertilizer applications (Wang et al. 2017).

Hydrologic and atmospheric transport processes disperse reactive N widely outside of where it is formed, and this dispersal can have large-scale, cascading environmental consequences (Galloway et al. 2003). For example, urban and agricultural runoff transports inorganic nitrogen (especially NO_3^-) deposited as fertilizer in terrestrial systems to freshwater aquatic systems; this reactive nitrogen eventually makes its way to estuaries. Although a great deal of reactive N is denitrified when it reaches marine systems (Table 1), excess reactive nitrogen in surface water causes eutrophication, hypoxia, loss of biodiversity, and habitat degradation in aquatic systems in general and coastal ecosystems in particular on a global scale (Galloway et al. 2003; McCrackin et al. 2017). NO_3^- is also a ubiquitous contaminant in aquifers worldwide due to fertilizer use; NO_3^- in drinking water can cause a number of human health problems (Spalding and Exner 1993). The emissions of nitrogenous trace gases (NH_3, NO_x, N_2O) have increased exponentially from preindustrial emissions, with the source being primarily terrestrial soils (Table 1); this is largely due to conversion of nitrogen fertilizer by microbes into gaseous forms of nitrogen (Galloway et al. 2003). Fossil fuel combustion is the primary source of NO_x gases to the atmosphere, however (Table 1). Reactive nitrogen in the atmosphere in the form of NO_x is linked to the oxidizing capacity of the atmosphere, and plays a key role in the photochemical production of ozone, which in turn increases pollution (smog) in and the greenhouse potential of the troposphere (Galloway et al. 2003; Fowler et al. 2013). N_2O is a potent greenhouse gas with 298 times the atmospheric heat-trapping ability of carbon dioxide (CO_2) over a 100-year period, on a per-molecule basis. It is relatively inert in the troposphere, but plays a role in stratospheric ozone destruction (Portmann et al. 2012). Finally, NH_x, NO_y (all oxidized forms of nitrogen other than N_2O), and organic nitrogen can fall from the atmosphere onto terrestrial and aquatic systems as dry or wet deposition, resulting in ecosystem acidification, fertilization, and eutrophication (Galloway et al. 2003). Atmospheric transport and subsequent deposition of reactive nitrogen was estimated to be 34 Tg N $year^{-1}$

during the preindustrial area, but had increased to 100 Tg N $year^{-1}$ in 1995; in 2050, this process is estimated to increase to 200 N $year^{-1}$ (Galloway et al. 2008).

Summary

Nitrogen is an essential element for all life, yet the vast majority of nitrogen on the Earth exists as N_2 gas – a form that is unavailable to most organisms. Nitrogen has a wide range of redox states, and life has evolved many complex nitrogen cycling metabolisms to obtain and retain this most valuable element. Reactions that convert nitrogen among different species, including (but not limited to) N_2, NH_4^+, NO_3^-, and organic nitrogen, are present in all domains of life. These reactions are generally coupled to energy-yielding metabolisms; however, nitrogen fixation ($N_2 + 6H^+ \rightarrow 2NH_3$) requires significant energy input, and 16 ATP are needed for this reaction. Because nitrogen is often the limiting nutrient in both aquatic and terrestrial ecosystems, the nitrogen cycle is necessarily tightly coupled to the global cycles of phosphorus and carbon. The pre-anthropogenic global nitrogen budget was essentially in balance between N_2 fixation (predominantly by microbes) and microbial denitrification. In the twentieth century, however, human activity has had a profound impact on the nitrogen cycle, second only to the human impact on the carbon cycle. Anthropogenic nitrogen fixation, primarily through the Haber-Bosch process, which produces NH_3 from atmospheric N_2, has disrupted the balance between nitrogen sources and nitrogen sinks. Nitrogen sources now exceed nitrogen sinks by more than 40% and perhaps as much as a factor of three (see Table 1). This excess reactive nitrogen from anthropogenic inputs has caused eutrophication, hypoxia, increases in greenhouse gases (e.g., N_2O), loss of biodiversity, and habitat degradation in aquatic coastal ecosystems.

Cross-References

- Acid Deposition
- Atmospheric Evolution
- Biogeochemistry
- Carbon Cycle
- Earth's Atmosphere
- Nitrogen
- Nutrients
- Oxidation-Reduction Reactions and Eh-pH (Pourbaix) Diagrams
- Oxygen
- Ozone and Stratospheric Chemistry
- Phosphorus

References

Canfield DE, Glazer AN, Falkowski PG (2010) The evolution and future of earth's nitrogen cycle. Science 330(6001):192–196. https://doi.org/10.1126/science.1186120

Chapin FS III, Matson PA, Vitousek PM (2011) Principles of terrestrial ecosystem ecology. Springer, New York

Fowler D et al (2013) The global nitrogen cycle in the twenty-first century. Philos Trans R Soc B-Biol Sci 368(1621). https://doi.org/10.1098/rstb.2013.0164

Galloway JN, Aber JD, Erisman JW, Seitzinger SP, Howarth RW, Cowling EB, Cosby BJ (2003) The nitrogen cascade. Bioscience 53(4):341–356

Galloway JN, Townsend AR, Erisman JW, Bekunda M, Cai ZC, Freney JR, Martinelli LA, Seitzinger SP, Sutton MA (2008) Transformation of the nitrogen cycle: Recent trends, questions, and potential solutions. Science 320(5878):889–892. https://doi.org/10.1126/science.1136674

McCrackin ML, Jones HP, Jones PC, Moreno-Mateos D (2017) Recovery of lakes and coastal marine ecosystems from eutrophication: a global meta-analysis. Limnol Oceanogr 62(2):507–518. https://doi.org/10.1002/lno.10441

Portmann RW, Daniel JS, Ravishankara AR (2012) Stratospheric ozone depletion due to nitrous oxide: influences of other gases. Philos Trans R Soc B-Biol Sci 367(1593):1256–1264. https://doi.org/10.1098/rstb.2011.0377

Schlesinger WH, Bernhardt ES (2013) Biochemistry: an analysis of global change, 3rd edn. Academic, Boston

Spalding RF, Exner ME (1993) Occurrence of nitrate in groundwater – a review. J Environ Qual 22(3):392–402

Wang C, Houlton BZ, Dai W, Bai E (2017) Growth in the global N-2 sink attributed to N fertilizer inputs over 1860 to 2000. Sci Total Environ 574:1044–1053. https://doi.org/10.1016/j.scitotenv.2016.09.160

N

Nitrogen Isotopes

Pierre Cartigny and Vincent Busigny
Institut de Physique du Globe de Paris, Sorbonne Paris Cité, Université Paris Diderot, Paris, France

Introduction

Together with those of carbon, nitrogen stable isotopes (^{14}N and ^{15}N) represent one of the most widely applied tracers in isotope geochemistry, with over 120 articles published every year having "nitrogen isotopes" in their title. Nitrogen is cycled between the different envelopes of the Earth – hydrosphere, atmosphere, crust, and mantle – and can occur as various species depending on pressure, temperature, and redox conditions. The origin and fate of nitrogen between these pools can be constrained using its isotope composition.

Nitrogen isotopes are primarily used in the fields of environment and paleoenvironment studies, sediment diagenesis, soil formation and evolution, and archeological and paleodiet studies. There are comparatively less applications in the

field of cosmochemistry and high-temperature geochemistry (i.e., mantle and crustal environments), and this reflects the need to use more complex analytical techniques compared with the former.

This entry provides a brief overview of questions that have been addressed using natural variations of N stable isotopes. It will omit studies that used either artificially ^{15}N–enriched compounds; these are commonly used in plant physiology and agriculture to establish detailed biogeochemical mechanisms (e.g., identify and quantify the biological and chemical pathways between these N pools). It is however worth mentioning that the semiconservative DNA replication – rejecting the conservative and dispersive hypotheses – was demonstrated using ^{15}N–enriched (Meselson and Stahl 1958).

Nitrogen Stable and Unstable Isotopes

Nitrogen has two stable isotopes, ^{14}N (~99.632%) and ^{15}N (~0.368%), leading to an atomic mass of 14.0067. Fourteen radioactive isotopes have been identified but have too short half-lives to be useful in geochemistry. Note however that ^{13}N (half-life ~9.92 min) is used in medical studies for positron emission tomography (PET). It requires ^{13}N to be made on-site in a cyclotron, $^{13}NH_3$ being synthesized and injected to the patient for PET imaging to deduce a large number of cardiac parameters (blood flux, volume of the ventricles) and, if any, cardiac abnormalities. In the following, the term "N isotopes" will refer only to N stable isotopes (^{14}N and ^{15}N).

The two stable isotopes of nitrogen are neither radioactive nor radiogenic. Therefore, on a bulk Earth scale, their abundance did not change through time. The relative abundance of N isotopes on Earth is grossly speaking that of our solar system, and they were produced in stars as part of the so-called C-N-O cycle (see Furi and Marty 2015 for a more subtle assessment). Atmospheric ^{14}N is the main source of ^{14}C($^{14}N + n \rightarrow {}^{14}C + {}^{1}p$), which decays back to ^{14}N with a half-life of 5730 ± 40 years. This reaction in particular ($^{14}N \rightarrow {}^{14}N$) and other reactions (e.g., ^{14}C production from ^{17}O) are not significant enough to change the abundance of terrestrial ^{14}N through time. The same applies to ^{15}N; its abundance did not change through time.

Stable isotope variations of terrestrial nitrogen originate from vibrational effects and are therefore quite limited. Terrestrial $^{15}N/^{14}N$ ratios range mostly between 3.356 and 3.750×10^{-3}, and these variations are expressed using the conventional delta notation where $\delta^{15}N_{sample} = [(^{15}N/^{14}N_{sample})/(^{15}N/^{14}N_{atmospheric\ nitrogen}) - 1] \times 1000$ with $^{15}N/^{14}N_{atmospheric\ nitrogen} = 0.0036764 \pm 0.0000041$ (Junk and Svec 1958; Mariotti 1983). In cosmochemical studies, the variations are much larger ($^{15}N/^{14}N$ from 1.838 to 22.059×10^{-3}), and these result from stable isotope fractionation processes, nuclear reactions, and nucleosynthetic anomalies. In the literature, these large variations are expressed using either $^{15}N/^{14}N$ or $^{14}N/^{15}N$ ratios and/or $\delta^{15}N$ notation.

Analytical Techniques

Nitrogen isotopes are almost exclusively measured using N_2 as an analyte and electron-impact gas-source ion-ratio mass spectrometers (IRMS) operating in dynamic pumping mode (i.e., the sample is either ionized, accelerated, and detected or immediately pumped away). Historically, nitrogen was extracted from its matrix, quantitatively converted to N_2 gas, purified using *offline* vacuum extraction techniques before being analyzed by dual-inlet mass spectrometry. Sample size is typically >5 micromoles and precision on $\delta^{15}N$ better than 0.1‰ (1σ). The historical method for solid sample analysis (e.g., rocks, minerals, soils) – generally referred to as Dumas combustion – consists in oxidizing the sample in a sealed tube at ~900 °C, nitrogen oxides (if any) being reduced by copper at ~600 °C and CO_2, SO_2, and H_2O being separated from N_2 using either liquid nitrogen or calcium oxide (e.g., Kendall and Grim 1990). Presently, nitrogen can be extracted using various methods, including crushing, laser ablation, and laser or furnace heating (either in oxidized, inert, or reducing conditions), and purified using gas chromatography and/or chemical and cryogenic techniques. It is also worth mentioning that N and O isotopes of nitrate are commonly analyzed using cultured denitrifying bacteria releasing N_2O.

The coupling of elemental analyzers to IRMS (EA-IRMS) in the early 1980s opened the path to online, nearly fully automated, analyses of N content and isotope composition (Preston and Owens 1983). The sample loaded in tin capsule is combusted (flash combustion) in a stream of helium. This releases C, N, S, and H, which are converted to CO_2, N_2, SO_2, and H_2O using various chemical compounds (including Cu at ~600 °C) and are subsequently separated using gas chromatography. This method does not require prior vacuum N extraction and purification, is slightly more sensitive than the abovementioned method, and can produce several dozen of analyses per day, still with very good precisions on $\delta^{15}N$ better than 0.15‰ (1σ).

These two techniques account for the majority of applications of $\delta^{15}N$ in geochemistry. Both of them require submicromole N amount, and, in most cases, data are obtained together with C isotope composition. Yet for smaller samples size (sub-nano to even picomole of N), these techniques are not sensitive enough and require other types of instrumentation such as static vacuum mass spectrometers (as used in noble gas geochemistry). In this case, the sample gas is entirely introduced, expanded, and analyzed in the mass spectrometer, leading to an increase of sensitivity by several orders of magnitude but a decrease of precision to

typically ±1‰ (Wright et al. 1988; see *analytical boxes* in Cartigny and Marty 2013; Furi and Marty 2015). Offline extraction and purification methods are the same as above, nitrogen being also analyzed as N_2, but special care is required to monitor atmospheric contamination. To date, this type of technique has been limited to less than ten laboratories in the world.

Secondary ion mass spectrometry (SIMS) provides alternative to determine N isotope composition on small samples. This method is almost nondestructive and can operate at high spatial resolution (typically ~ 20 μm), the isotope analysis being determined from secondary CN^- ions. This method is precise but requires standards having the same composition than the investigated samples, so that precision and accuracy vary as a function of both matrix and N concentration (~1‰ for $\delta^{15}N$ in diamonds, to 20‰ for the analysis of solar wind nitrogen, Marty et al. 2011). High-resolution SIMS are quite expensive instruments and therefore restricted to few laboratories (and even less are involved in the analysis of $\delta^{15}N$). Remote analysis of comets or molecular clouds can be determined using high-resolution spectroscopy for molecules/ions such as HCN, NH_2, and NH_3 but not N_2. The precision is typically of several tens of per mil. Similar methods (high-resolution IR spectroscopy) are presently being developed for the analysis of non-symmetric terrestrial gaseous N-bearing molecules such as N_2O. Finally, the development of site-specific N isotope composition is emerging with applications in forensic (Aranda et al. 2011, a field outside the scope of this overview) and atmospheric (Toyoda and Yoshida 1999; Heil et al. 2014) sciences.

Cosmochemistry

Nitrogen isotope composition varies greatly among extraterrestrial materials (sometimes even within a single object), and, for many years, no clear understanding of the mechanisms driving N isotope variability was achieved. A long-standing hypothesis was that N isotope variability of meteorites reflects isotopic heterogeneity of the solar nebula. Indeed, N isotopes are synthesized by two distinct astrophysical processes (^{14}N during hydrostatic hydrogen burning and ^{15}N during explosive hydrogen and helium burning), and the isotope variability could thus reflect variable influx from different stars to the solar system. At present, the role of chemical, likely photochemically induced, reactions is emerging (Furi and Marty 2015), i.e., with a view rather similar to that deduced from O isotope cosmochemistry.

The key observation is that the Sun (and therefore the primitive solar nebula) is enriched in light N isotope ($\delta^{15}N \sim -400$‰, Marty et al. 2011, Fig. 1) with respect to meteorites and planets, a result strikingly similar to what is observed for O isotopes. Such ^{15}N–depleted compositions are also found only in rare refractory nitride minerals (TiN) and the atmosphere of giant planets, including Jupiter and Saturn (Fig. 1). The former are described as representing

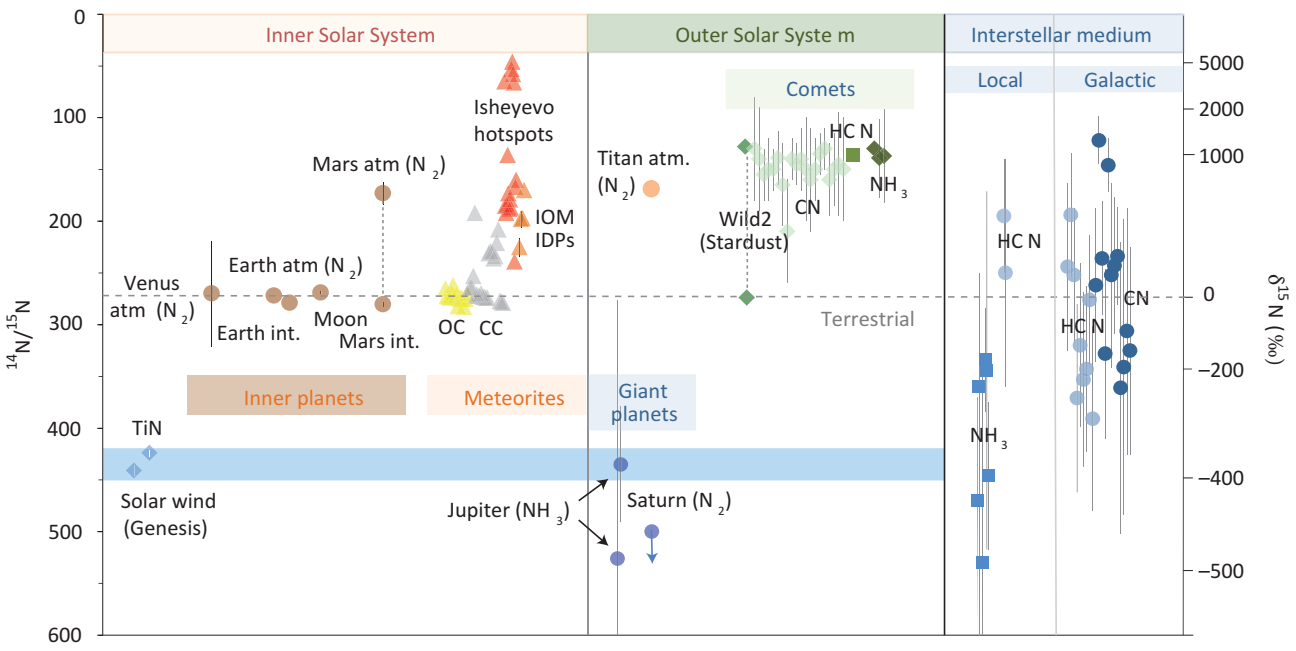

Nitrogen Isotopes, Fig. 1 Nitrogen isotope variations in solar system objects and reservoirs. The value of the protosolar nebula (blue shading) is defined by the measurement of solar wind nitrogen, TiN, and the atmospheres of the giant planets: all other solar system objects are comparatively significantly enriched in ^{15}N (From Furi and Marty 2015, reproduced with permission)

high-temperature solar nebula condensate, whereas the latter acquired their N isotope composition by accretion of the gas left from the Sun accretion and/or trapped nitrogen flushed from the inner disk by the protosun.

All other objects including primitive and differentiated meteorites are comparatively enriched in ^{15}N (Fig. 1), typically by 400 ± 50‰ ($\delta^{15}N \sim 0 \pm 50$‰). Significant differences exist among primitive meteorites classes and within a group of meteorites. The most reduced (enstatite chondrites) are more depleted in ^{15}N ($\delta^{15}N$ from −50 to 0‰, average ~ −25‰; Grady et al. 1986) than the more oxidized carbonaceous CI and CM chondrites ($\delta^{15}N \sim +40$‰; Kerridge 1985). Other carbonaceous chondrites display a large range, with CV and CO being characterized by the more negative $\delta^{15}N$ values of this group ($\delta^{15}N \sim -20$ and −10‰, respectively). Ordinary chondrites show average $\delta^{15}N$ values close to that of the Earth's atmosphere (~0‰; Hashizume and Sugiura 1995).

Various reservoirs of telluric planets including Earth, Mars interior, Venus atmosphere, and the Moon have mostly similar N isotope compositions, consistent with their formation within the inner part of the accretion disk. Interestingly, both Mars and Earth show atmospheric ^{15}N enrichment compared to their mantle of ~600 and ~5‰, respectively, and this originates from two different processes. For Mars, atmospheric ^{15}N enrichment reflects hydrodynamic escape or pickup charge exchange with solar wind ions and subsequent nonthermal escape with preferential loss of ^{14}N to space. Given that there is neither evidence for recent tectonic activity nor biological fixation, N exchange and re-equilibration between Mars inner and outer reservoirs appear unlikely. In contrast, owing to its larger size, the occurrence of life, and plate tectonics, the case for Earth is fundamentally distinct from Mars and discussed hereafter. Finally, it is worth noting that Earth is comparatively depleted in ^{15}N compared with most primitive meteorites, including carbonaceous chondrites. The only class of meteorites with $\delta^{15}N$ values matching those of bulk silicate Earth is enstatite chondrites. Together with O isotopes, nitrogen was one of the first recognized elements to share similarities with this class of meteorites. Since then, such similarity has been extended to many elements such as Zn, Mo, Ru, Cr, Sr, Ti, and Ca (Javoy et al. 2010).

In detail, a single meteorite can display strong N isotope heterogeneity, reflecting a multitude of processes and origins. For example, the Isheyevo carbonaceous chondrite shows a range > 5000‰ (Fig. 1). Presolar grains carry tremendous isotope anomalies ($^{15}N/^{14}N$ from ~$0.2 - 100 \times 10^{-3}$, Zinner et al. 2007), but the low concentration of this component in meteorites induces limited isotope variability on bulk samples. Spallation reactions can produce significant amount of light elements, including nitrogen. They are most recognizable on the rare isotopes (i.e., ^{15}N enrichment) and can be easily targeted using exposure proxies (e.g., $^{38}Ar/^{36}Ar$). More importantly for this overview, $\delta^{15}N$ variability also reflects photochemically induced isotope fractionation effects, and the large isotope fractionation between N-bearing molecules (HCN and NH_3, Fig. 1) is a likely illustration (next section also reports a case for photochemical effects on Earth). By analogy with the so-called mass-independent fractionation of O isotopes, N isotope variations could result from photochemistry during interactions with UV light originating from the forming Sun and/or other stars. For instance, N_2 could react and form molecules such as ammonia or cyanide that would then be transferred/condensed to ice and dust and subsequently to meteorites and planets. As for O isotopes, the exact mechanism remains unclear and UV photochemical effects could result from isotope selective reactions or reflect self-shielding effects. Accordingly, compared with heavy elements that are commonly used to trace solar nebula heterogeneity, light elements such as N bear the potential to highlight chemical processes that occurred in the solar nebula.

Atmospheric Nitrogen Species and Deposits

The main (i.e., 78% molar fraction) gaseous species of Earth atmosphere is diatomic nitrogen (N_2). The isotope composition of atmospheric N_2 is homogeneous and used as the international reference for $\delta^{15}N$ notation, i.e., $\delta^{15}N_{atmosphere} \equiv 0$‰ (Mariotti 1983). Several other N-bearing gas and/or aerosols occur in the atmosphere such as NH_4, N_2O, NO_X, or HNO_3, and their origin and fate can be studied from their N isotope composition.

A good example of photochemically induced isotope fractionation is illustrated by nitrate recorded in Antarctic snow/ice, which shows large range of $\delta^{15}N$ values from 0 to +300‰ (Savarino and Morin 2011, Fig. 2). This range results from the photolysis of nitrate in snow, leading to the release of ^{15}N–depleted NO_x and the accumulation of residual ^{15}N–enriched nitrate. This process can be modeled using a Rayleigh distillation (with a fractionation factor $\alpha \sim 0.94$, i.e., −60‰) and seems to be only expressed where snow accumulation rates are low. For other locations such as Greenland, where accumulation rates are higher and for which photochemical processing of nitrate is accordingly less important, the N isotope composition of nitrate is consistently less variable, although very negative $\delta^{15}N$ values can be reached (down to −60‰). In contexts where accumulation rates are the largest (e.g., Greenland Summit), the secular evolution of $\delta^{15}N$ values from ~ +10 down to ~ 0‰ in preindustrial times to present (Fig. 3) was suggested to reflect the anthropogenic influence on the N cycle (Hastings et al. 2009). Along with the development of industrial N fixation at the beginning of the twentieth century, the N cycle became massively anthropogenized, with present-day industrial nitrogen fixation close to biological flux (~2×10^{14} gN.yr.$^{-1}$, Galloway

2003, with $\delta^{15}N$ ~0‰, Michalski et al. 2015), consistent with the trend of decreasing $\delta^{15}N$ through time (Fig. 3). However, the observed trend is challenged by the lack of known values at ~ + 10‰ for preindustrial sources and could instead relate to an increase in anthropogenic atmospheric acidity, the isotope variation reflecting the resulting change in nitrate partitioning between gas and particles (Geng et al. 2014).

Another application of N isotopes consists in quantifying abrupt temperature changes from gas bubbles trapped in ice. The variability does not reflect changes in atmosphere composition because N_2 and Ar have long residence times. Two combined effects contribute to $\delta^{15}N$ variability. The first effect corresponds to gravitational fractionation in the first ~100 m of the ice sheet, which behaves as a porous media, and the second effect is thermal fractionation resulting from abrupt temperature warming (Severinghaus et al. 1998). After an abrupt increase in air temperature – as illustrated by the so-called Dansgaard-Oeschger events in Greenland ice cores – the resulting temperature gradient leads to heavier gas species ($^{15}N^{14}N$, ^{40}Ar, $^{18}O^{16}O$) in the colder, i.e., deeper part of the firn. When used together with Ar isotopes, it allows deducing both the magnitude of temperature increase (typically >10 °C with precision of ~2.5 °C) and duration (typically <100 years) for most of the Dansgaard-Oeschger events (Landais 2011).

Among atmospheric compounds, nitrous oxide (N_2O, half-life of 120 years) receives peculiar attention because it is a powerful atmospheric greenhouse gas (~ 300 times more efficient than CO_2) and is a cause of ozone layer depletion. The concentrations of N_2O in the atmosphere have increased from 270 to 330 ppm since preindustrial times. The average $\delta^{15}N_{bulk}$ of tropospheric N_2O is 6.5‰, yet varying with location and time and decreasing by 0.040‰/yr (Rockmann and Levin 2005). Emissions are biotic, with the majority (~2/3) being produced in soils from bacterial and fungal anaerobic denitrification and aerobic nitrification processes (see next section). The other part is produced in the ocean, but N_2O origins, fluxes, and fate are still poorly constrained in this environment. In soils, N_2O emissions depend upon a large number of parameters including agricultural practices (N application rate, crop type, fertilizer type) and soil conditions (soil moisture, soil organic C content, soil pH, and texture) resulting in a large variability on both spatial and temporal scales (Thomson et al. 2012). To better address

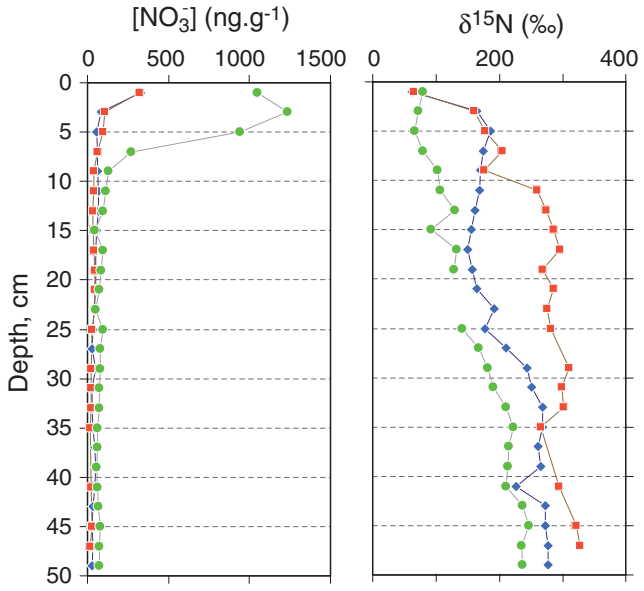

Nitrogen Isotopes, Fig. 2 Typical snow pit profiles in central Antarctica (Dome C) showing the strong denitrification of the snow in a very short depth accompanied by a strong ^{15}N enrichment of nitrate (Modified from Savarino and Morin 2011)

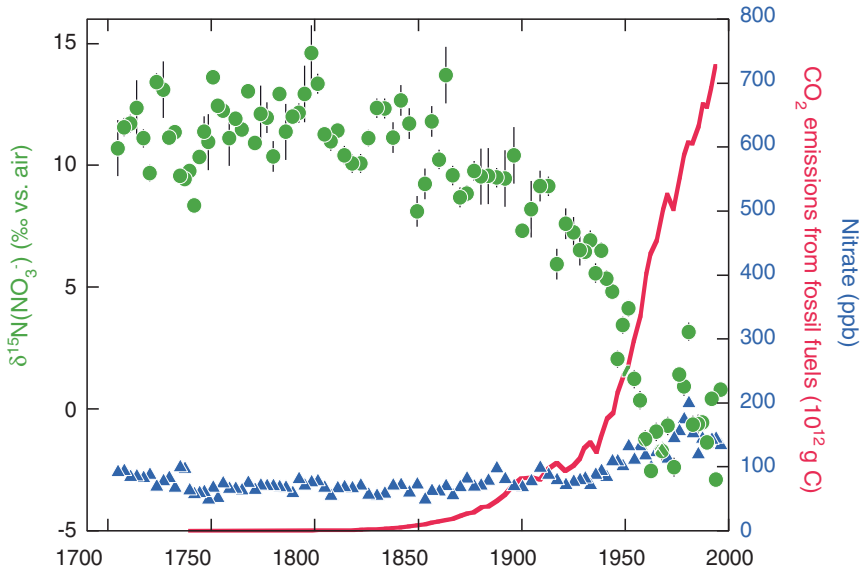

Nitrogen Isotopes, Fig. 3 Secular evolution of $\delta^{15}N$ of nitrate (solid circles) and nitrate concentration (open triangles) in a 100 m ice core from Summit, Greenland, spanning ~1718 to 2006 together with global CO_2 emissions from fossil fuels. The trend was originally suggested to reflect a change in $\delta^{15}N$ emissions (Hastings et al. 2009) but was recently suggested to reflect a change in atmospheric acidity (Geng et al. 2014) (Modified from Hastings et al. 2009)

this issue, studies now commonly include site-specific analysis of nitrogen (the isotope composition of internal and external nitrogen atoms within N_2O). Notably, there is a strong site preference of ~18.7‰ for the central N atom (Yoshida and Toyoda 2000) with temporal trends being ~−0.064 and −0.014‰/yr. for terminal and central N atom, respectively (Rockman and Levin 2005). Clearly, N isotope geochemistry is central for understanding the global N_2O cycle.

Finally, the analysis of N isotope composition of urban and rural aerosols is developing, but its interpretation is generally simplified to isotope fingerprinting, i.e., N isotope composition reflecting the characteristics of their source, neglecting therefore secondary processes that can be significant (Widory 2007 and see above). Much remained to be done in this field.

Paleoenvironment and Paleo-Ecosystem Reconstruction

Nitrogen in sedimentary rocks initially derives from the atmosphere, and in the absence of life, there would be no nitrogen in sediments. Moreover, without a strong return flux, atmospheric nitrogen would be fixed by biological activity within 100 My (1.4 10^{14}gN/yr., Galloway 2003). In sediments, nitrogen is mostly carried by organic matter and detrital K-bearing minerals such as clays or feldspars, in which ammonium (NH_4^+) enters by substitution with potassium (K^+) due to similar charge and ionic radius. The nitrogen isotope signature of bulk sedimentary rocks reflects mostly primary organic matter composition and is often used as a proxy of marine paleoenvironments and paleo-ecosystems. There are two main reasons for studying N in sedimentary rocks. First, N is a major nutrient, essential to all kinds of biological activity/organisms on Earth. It constitutes the basis of molecules such as amino acids, DNA, RNA, and proteins, and therefore the N isotope signature can provide constrains on specific metabolic activity, probing traces of life in the sedimentary record (Honma 1996). Second, N is a redox-sensitive element, with diverse chemical species (e.g., N_2, NO_3^-, NH_4^+) controlled by local redox conditions. The nitrogen isotope composition will depend on the fate and recycling of nitrogen compounds in the ocean and can shed light on the redox structure of the ocean, which is of particular interest for Precambrian environment reconstruction but also for understanding changes in the Phanerozoic such as those related to Cretaceous oceanic anoxic events (OAE). The modifications of sedimentary N isotope composition through time can thus be used as a proxy of biological evolution and varying environmental conditions (see reviews by Ader et al. 2016; Stueken et al. 2016).

Nitrogen enters the oceanic biogeochemical cycle through N_2 fixation by aerobic or anaerobic autotrophs (such as phytoplankton and cyanobacteria) in which N_2 is reduced to NH_4^+ and assimilated with minimal isotope fractionation (−2 to +1‰; e.g., Wada et al. 1975, Fig. 4). This reaction is based on nitrogenase enzyme, which requires molybdenum as a cofactor. Recent experimental study demonstrated that

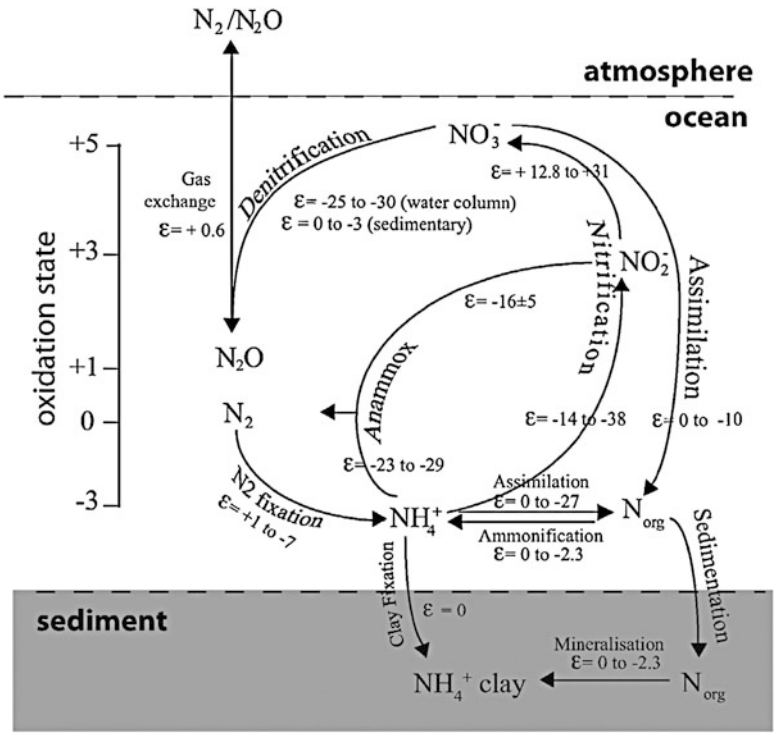

Nitrogen Isotopes, Fig. 4 Schematic diagram of the principal biogeochemical processes driving the modern N cycle. Nitrogen isotope fractionations are expressed using the ε-notation where $\varepsilon_{reactant\text{-}product} \sim {}^{TM}_{reactant} - \delta_{product}$ (Reproduced from Ader et al. (2016) with permission)

alternative cofactors such as Fe and V can also be used and produce larger isotope fractionation with organic matter depleted in ^{15}N down to −8‰ relative to N_2 (Zhang et al. 2014). After their death, organic matter mineralization releases N as ammonium (NH_4^+), with very little isotopic fractionation. In the presence of free O_2, NH_4^+ is oxidized to nitrate (NO_3^-) during a two-step process called nitrification, which is associated with significant N isotope fractionation >20‰ (Sigman et al. 2009, Fig. 4). This fractionation is rarely expressed in modern marine environments since the transformation of NH_4^+ to NO_3^- is generally complete. In O_2-depleted environments such as oxygen minimum zones or anoxic sediments, nitrates are partially reduced by denitrification or anammox (i.e., anaerobic ammonium oxidation) into gaseous N_2 or N_2O (for N_2O see atmospheric section). During denitrification, ^{14}N is preferentially released relative to ^{15}N, leaving residual marine NO_3^- enriched in heavy isotope (average marine $\delta^{15}N_{NO3-}$ ~ +5‰, Fig. 4). The heavy isotope signature of NO_3^- is transferred by assimilation to organisms living in the water column and then recorded in sedimentary organic matter. Accordingly, assuming a steady-state system, the N isotope composition of organic matter in modern marine environment reflects mainly the relative proportion of N denitrification and fixation. In O_2-free environments such as the Archean oceans, nitrification and thus subsequent denitrification are unlikely, and dissolved N species are probably dominated by NH_4^+ (Beaumont and Robert 1999). Ammonium can be assimilated by living organisms with an isotope fractionation up to −27‰, favoring ^{14}N in organic matter (Pennock et al. 1996). In the case of quantitative NH_4^+ consumption, this fractionation is, again, not expressed, and the $\delta^{15}N$ of dissolved NH_4^+ is readily recorded in sedimentary organic matter. For instance, ammonium assimilation has been invoked from negative $\delta^{15}N$ down to −5‰ recorded in sediments from the ~2.2Ga Aravalli Supergroup, India (Papineau et al. 2009, Fig. 5).

Postdepositional Modifications of Sedimentary N Isotope Composition

An important aspect of ancient sedimentary rock studies is the evaluation of possible $\delta^{15}N$ modifications related to diagenesis and metamorphism (Ader et al. 2016, Fig. 4). Organic matter degradation occurs in water column and near sediment-water interface during early diagenesis and during thermal maturation associated with burial diagenesis and metamorphism. In oxic environments, early diagenesis can impart a shift in $\delta^{15}N$ values toward more positive values, up to ~3‰ (Lehmann et al. 2002). In contrast, organic matter degradation under anoxic and suboxic conditions either preserves original nitrogen isotope values or slightly lowers $\delta^{15}N$ values down to −1‰ (Lehmann et al. 2002). Metamorphism

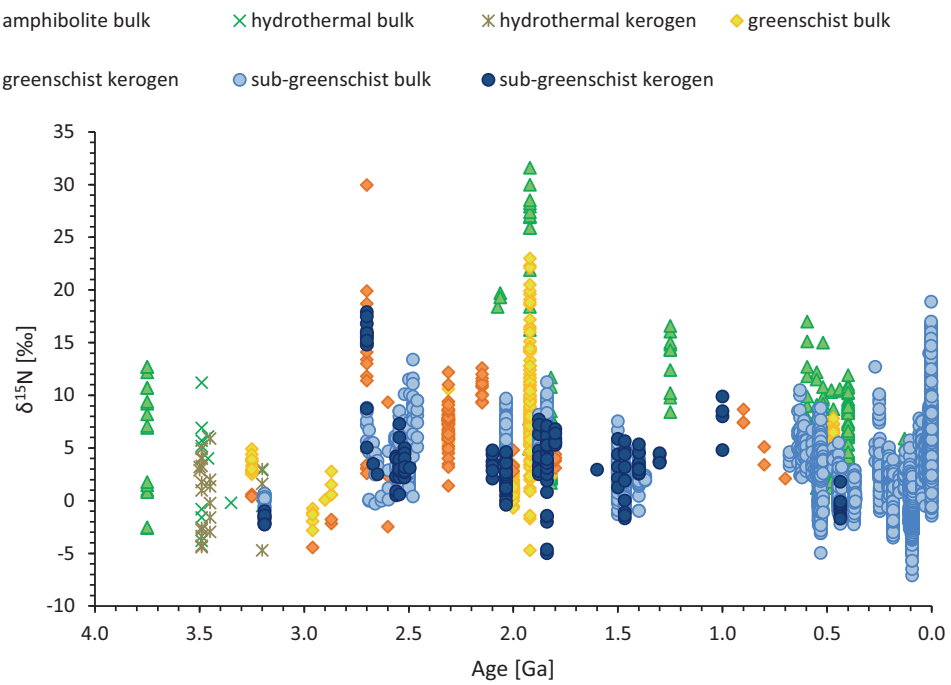

Nitrogen Isotopes, Fig. 5 Secular trends in nitrogen isotope of marine samples, separated by metamorphic grade. Note that sub-greenschist and green schist facies kerogens (evolved organic matter) and bulk rock samples typically overlap, suggesting limited metamorphic alteration. However, amphibolite facies rocks tend to be characterized by ^{15}N–enriched compositions compared with samples of lower metamorphic grade. The large variations of $\delta^{15}N$-values through time emphasized from low metamorphic grade samples therefore highlight profound changes in the nitrogen cycle (Modified from Stueken et al. (2016) with the very kind help of the first author)

associated with sediment burial induces only minor modifications (< 1‰) for metamorphic grade lower than greenschist facies (see review in Ader et al. 2016; higher metamorphic grade is discussed below).

Selected Applications of N Isotopes to the Sedimentary Record

One of the most important changes in the Earth history is the oxygenation of the ocean and atmosphere. The oxygenation of the atmosphere occurred about 2.4 Gy as recorded by mass-independent fractionations of S isotopes; for the ocean the situation is not so clear, and, over the last 20 years, N isotopes have been used to discuss this issue (Beaumont and Robert 1999; Zerkle et al. 2017 and ref. therein). The rationale is that N forms NO_3^- in the presence of dissolved O_2, and due to subsequent partial denitrification, the residual NO_3^- becomes increasingly enriched in heavy isotopes, thus imparting positive $\delta^{15}N$ values in organic matter deposited in sediments. The compilation of all data available places the onset of marine dissolved NO_3^- in the Neoarchean and Paleoproterozoic (Stueken et al. 2016). Extremely positive $\delta^{15}N$ values, up to +50‰ (Thomazo et al. 2011; Stueken et al. 2015a, Fig. 5), were observed in sedimentary rocks from the 2.7 Ga Tumbiana Formation and could correspond to the first oxidative distillation of the NH_4^+ reservoir (Thomazo et al. 2011). An alternative interpretation suggested that volatilization of NH_3 in an alkaline lake could leave residual NH_4^+ enriched in heavy isotope (Stueken et al. 2015a) but such high values have not yet been found even in the most alkaline modern lakes.

In parallel to the reconstruction of ocean redox structure, N isotopes of the sedimentary record have been used as tracers of metabolic activity. For instance, $\delta^{15}N$ values near 0‰ measured in 3.2–2.75 Ga sedimentary rocks of low metamorphic grade (Fig. 5) indicate that the biomass was dominated by N_2-fixing autotrophic organisms (Stueken et al. 2015b). This finding places a minimum age constraint of 3.2 Ga on the origin of biological N_2 fixation. If we consider that the occurrence of nitrogen in sedimentary rocks attests for the occurrence of life, then the minimum age constraint becomes 3.8 Gy (Honma 1996).

In the Phanerozoic, low $\delta^{15}N$ values (−7 to 0‰, Fig. 5) are systematically observed in sediments deposited during Cretaceous OAE and are associated with high concentration of total organic carbon (up to 20%). These low $\delta^{15}N$ values are interpreted as evidence for N_2-fixing organisms thriving in a water column highly depleted in oxygen, which would be related to warm and wet greenhouse climate periods and associated thermohaline stratification of the ocean (e.g., Rau et al. 1987; Zhang et al. 2014). Intense denitrification would in this case limit any contribution of residual nitrate to the bulk $\delta^{15}N$ signature of the biomass. A compilation through the entire Phanerozoic shows that low and high $\delta^{15}N$ values correspond to greenhouse and icehouse climate periods, respectively, thus suggesting that long-term $\delta^{15}N$ variations are controlled by climate rather than redox variations (Algeo et al. 2014). Sedimentary denitrification would dominate during greenhouse periods owing to higher eustatic (global sea-level) elevations and greater on-shelf burial of organic matter, whereas water-column denitrification would dominate during icehouse modes owing to lower eustatic elevations.

Nitrogen Chemical Geodynamics

Biological activity does not only mediate transfers from the atmosphere to sediments (see above) but also to the crust and the mantle. Nitrogen is a unique element because it originally requires living organisms to enter the rock record (abiotic reactions exist but are negligible, see below). It thus represents a unique tracer of chemical geodynamics. In this context too, N isotopes have been successfully applied. For instance, they have been used to constrain and quantify the loss of nitrogen and other fluid-mobile elements during subduction. Nitrogen isotopes were also used to trace the presence of subducted surface material in the Earth's mantle because a significant difference exists between mantle and surface N isotope signatures, being, respectively, ^{15}N–depleted and ^{15}N–enriched relative to the atmosphere (see Cartigny and Marty 2013).

As mentioned above, the introduction of N into the rock record arises from maturation of organic matter, which releases ammonium ions. Ammonium is then substituted for potassium, thus following the fate of potassic minerals: mainly clays at low P-T conditions and micas under higher metamorphic grade (Busigny and Bebout 2013 for review). As temperature increases, metamorphic reactions can induce fluid devolatilization. The release of ^{15}N–depleted fluids (N_2 and/or NH_3) produces an increase of $\delta^{15}N$ value in the residual rock, typically from $\delta^{15}N \sim +5$ up to +15‰ (Bebout and Fogel 1992). The nitrogen budget can be derived from Rayleigh model, based on theoretical fractionation factors, ammonium content, and correlations with large ion lithophile elements (K, Rb, and Cs). An important result is that N in subduction zones can either be preserved or released during metamorphism, depending on geothermal gradient. In *cold* (e.g., 8 °C/km) subduction zones, N is stable and preserved in potassic minerals (e.g., phengitic micas), and $\delta^{15}N$ remains constant. Nitrogen is thus massively subducted to depths in excess of 90 kilometers. In contrast, significant amounts of N are devolatilized in *warm* subduction zones (> 15 °C/km). At present, the average fluxes of N input in subducted slab and output from volcanic arcs by degassing are 9.6×10^{11} and 0.7×10^{11} gN/yr., respectively (Busigny et al. 2011). Therefore about 80% of N buried in subduction zones is recycled to the deep mantle and is characterized by a majority of positive $\delta^{15}N$ values (Fig. 6).

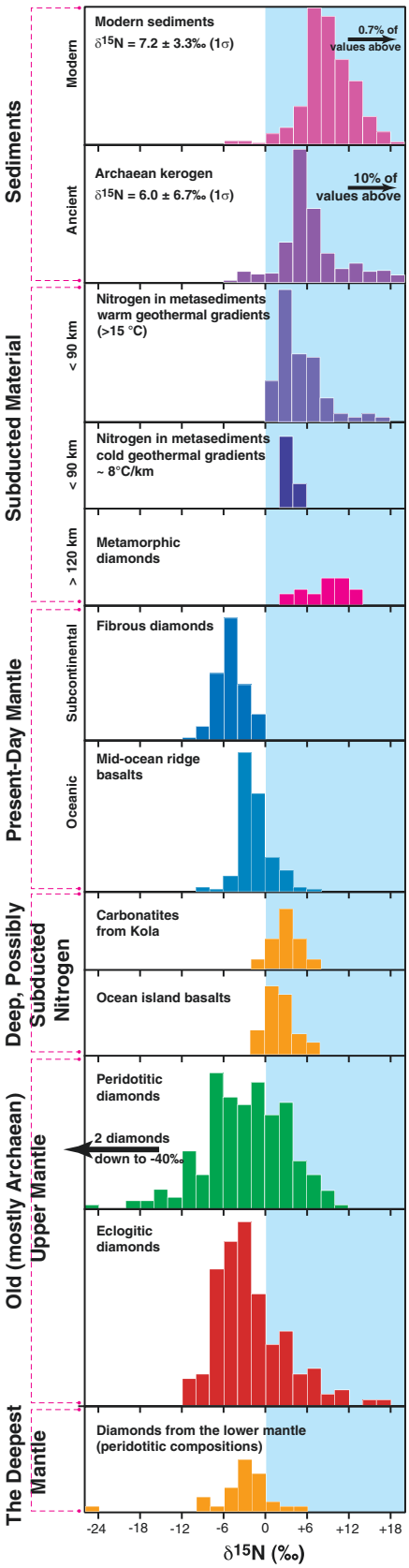

Nitrogen Isotopes, Fig. 6 Comparative histograms of $\delta^{15}N$ values for modern and ancient sediments, subducted nitrogen (warm and cold environments), present-day convective mantle, ancient mantle and lower mantle, and magmas possibly sampling nitrogen recycled to mantle depths. Note that modern and ancient sediments do not reveal any obvious secular isotopic trends (but see Fig. 5) (From Cartigny and Marty 2013)

The Earth mantle contains little nitrogen (likely between 0.26 and 36 ppmN), and its study remains limited to few samples such as diamonds, basaltic glasses (and their gas vesicles), and volcanic fumaroles. Nitrogen isotopes remain difficult to investigate primarily owing to atmospheric contamination (although this can be quantified using Ar isotopes) and assimilation. The exception is diamond since N is the main diamond impurity (with an average concentration of 150 ppmN) but for which genesis ages and depth of formation remain often under-constrained. The $\delta^{15}N$ values of samples from the Earth mantle are scattered but are primarily negative. Importantly, both the so-called diamond coats and fibrous diamonds and mid-ocean ridge basalts (all <500 My) distinctively point to a present-day mantle $\delta^{15}N \sim -5‰$ (Fig. 6). Older diamonds (possibly Archean) with silicate inclusions pointing to peridotitic composition display more scattered $\delta^{15}N$ values with two third being negative. This makes N isotope a powerful tracer of recycled material and was used to discuss the origin of eclogitic (i.e., basaltic) composition, their ^{13}C–depleted isotope composition being often attributed to recycling of organic matter in the mantle. Yet their $\delta^{15}N$ are strikingly similar to peridotitic diamonds and do not emphasize a recycled origin for most of them (Cartigny and Marty 2013 for review). However consistent evidence for deep recycling of nitrogen was found from the study of metamorphic diamonds formed in crustal rocks subducted to ultrahigh pressures (> 3.5 GPa), some lamproïtes, ocean island basalts, and some deep diamonds (Cartigny and Marty 2013 for review).

The average flux of N in modern subduction zones, subtracted from N loss in volcanic arcs, is seven times larger than mantle degassing flux (Busigny et al. 2011). This implies that crustal N is preferentially recycled to the mantle, likely inducing secular evolutions of atmospheric, crustal, and mantle N contents. Given their isotope characteristics, the exchanges between ^{15}N–enriched surface materials and ^{15}N–depleted mantle also predict secular evolutions of their N isotope compositions which have been searched in crustal and mantle records. Although there is no consensus yet, addressing this question is fundamental. If the Archean atmosphere had ~2 to 3 present nitrogen atmospheric levels (NAL), it would result in N_2 radiative forcing (i.e., N_2 as a greenhouse gas), resulting from pressure broadening and Rayleigh scattering. It could explain why the Earth remained warm despite the faint young sun, i.e., without requiring high amounts of greenhouse gases such as CO_2 or methane (Goldblatt et al. 2009; Wordsworth and Pierrehumbert 2013). Considering an average N content of the continental crust of 83 ppmN (Rudnick and Gao 2003)

with a $\delta^{15}N$ value of +6‰ and that crustal N is of atmospheric origin, without biological activity, present nitrogen atmospheric level (NAL) would be 20% higher with a $\delta^{15}N > 1.2‰$. These are minimum values as some nitrogen was recycled in the Earth's mantle. Yet, the study of fluid inclusions and crustal/sedimentary (Archean and Proterozoic) rocks led, so far, to contradicting conclusions. Studies of several Archean crustal rocks (giant quartz veins) and 2.7 Gy kerogens suggest significant $\delta^{15}N$ evolution of atmospheric nitrogen from $>$ + 40‰ to present value of 0‰ (Jia and Kerrich 2004) when others evidenced rather constant $\delta^{15}N$ values (Marty et al. 2013). Similarly, NAL may have decreased (from 3 NAL, Goldblatt et al. 2009) or increased (from 0.5 NAL, Marty et al. 2013) through time. Mantle $\delta^{15}N$ values could have evolved from more negative values (e.g., from $< -40‰$), but the evidence presently relies on a few samples, and if any, this evolution happened early in the Earth history, Archean samples pointing to $\delta^{15}N$ values $\sim -5‰$ (Cartigny and Marty 2013). Here, further studies are needed for reaching a consensus.

The Neglected Role of Abiotic Reactions

In the modern oxic world, atmospheric nitrogen fixation is primarily driven by biological activity, but in the ancient anoxic world, the role of abiotic atmospheric nitrogen reduction might have been significant. This is a fundamental issue as it raises the question of abiotic amino acids genesis (see discussion in Stueken et al. 2016). By analogy with the Miller's experiments (Miller 1953), we need to understand whether present and ancient deep hydrothermal systems could represent favorable environments where significant abiotic nitrogen reduction might occur. In this case, high concentration of ammonium in clays or micas would not necessarily represent an indirect evidence for life. At present, abiotic nitrogen reduction remains little investigated (see the experimental work by Brandes et al. 1998). Such reactions have been suggested in hydrothermal systems and were characterized by very negative $\delta^{15}N$ values down to $\sim -16‰$ (Li et al. 2014). Much work remains to be done in this field, and N isotopes of future studies may provide fingerprints of biotic vs. abiotic processes.

"You Are What You Eat": Paleo-Diet and Archeological Investigations

The application of N isotopes to paleo-diet and archeological investigations (this section) and in forensics science (next section) is primarily a *fingerprinting* approach. This kind of approach involved generally multi-isotope systems (C, H, O, B, Sr, Pb, etc.) but is restricted here to N isotopes.

Application of N isotopes to determine paleo-diets relies on two observations. First, as N is cycled through the body of animals/humans, ^{14}N is preferentially lost, leading to ^{15}N enrichment of tissues (DeNiro and Epstein 1981). This is also illustrated by ^{15}N depletion of urine relative to the diet. Throughout the trophic chain, the predators gain the N isotope composition of their preys, which is then further ^{15}N–enriched, typically by 3‰ (Minagawa and Wada 1984; Fig. 7). Therefore N isotope composition indicates the trophic level position of both marine and continental organisms (Fig. 7). Second there is a difference between continental (grass, wheat, fruits) and marine (seashells, fish, algae) diets, the former being ^{15}N–depleted relative to the latter. This difference also exists for carbon and can be jointly used with N isotopes. Therefore, although there are some overlaps, a vegetarian will be more ^{15}N–depleted than someone being omnivore or eating only meat.

These applications extend beyond the field of geochemistry but provide a good example of interdisciplinary interactions with the field of human sciences. Typically undertaken with the analysis of C isotopes (e.g., to constrain the proportion of C3 and C4 plant species in the diet of herbivores), N isotopes revealed when agriculture was introduced in the diet and more generally when a group changed their subsistence strategy. Nitrogen isotopes demonstrated that Neanderthals had large herbivores on their diet, therefore implying that they were top-level predators and accomplished hunters (Richards and Trinkausc 2009). Similarly, the zonation of tooth can help archeologists determine when animals or humans weaned their babies and, again, what kind of food they had.

Forensics Science with a Focus on Nitrate Pollution

Nitrogen isotopes remain less used than carbon and hydrogen isotopes in forensics science, which are collectively used as a

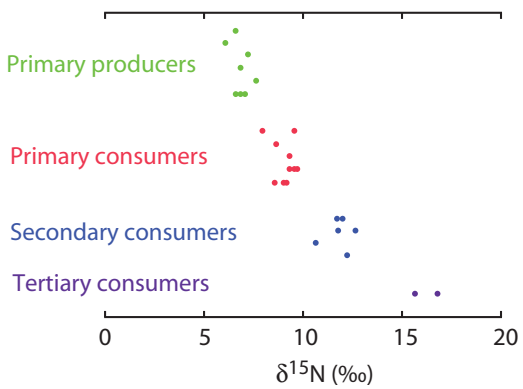

Nitrogen Isotopes, Fig. 7 Illustration of the stepwise enrichment of $\delta^{15}N$ along food chains (Modified from Minagawa and Wada 1984)

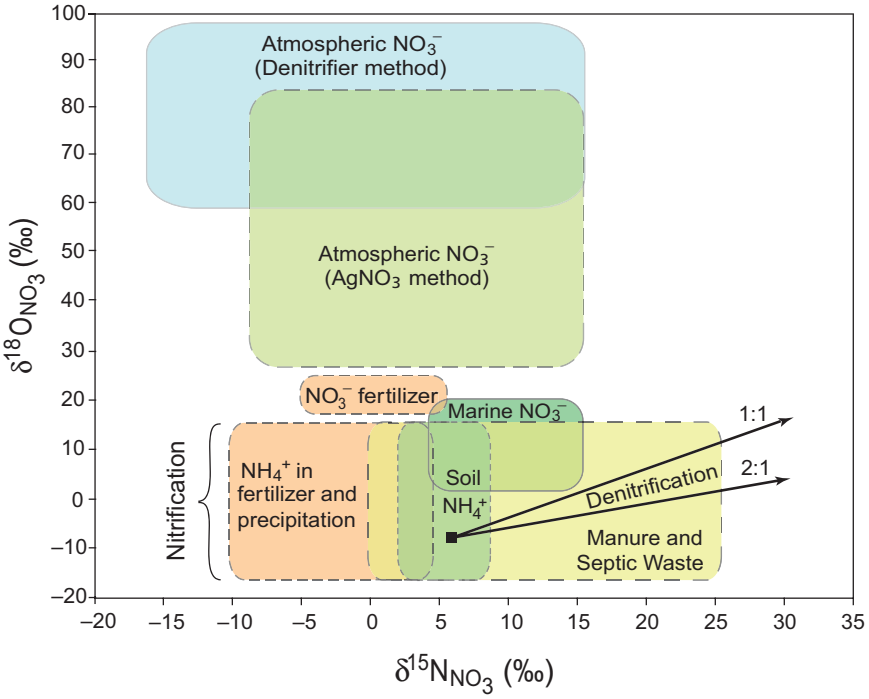

Nitrogen Isotopes, Fig. 8 Typical values of $\delta^{15}N$ and $\delta^{18}O$ of nitrate derived or nitrified from various N sources. Atmospheric. The two arrows indicate typical expected slopes for data resulting from denitrification of nitrate with initial $\delta^{15}N = +6‰$ and $\delta^{18}O = -9‰$. The typical ranges of $^{TM18}O_{NO3}$ values produced by nitrification of ammonium and organic matter are denoted by "nitrification" (Modified from Kendall et al. 2007)

fingerprint to distinguish genuine products from counterfeits. In this section, we will specifically focus on a very important application that arises from the anthropization of the N cycle. With only half of fertilizers being fixed by crop plants and owing to nitrate (NO_3^-) release from intensive agriculture, *nitrate concentrations in drinking water supplies have risen above acceptable levels in many areas of the world* (Kendall et al. 2007). Increase in nitrate levels of groundwaters, rivers, and estuaries induces biological blooming which leads, due to the subsequent degradation of organic matter, to eutrophic waters in many locations. Monitoring nitrate levels and determining their sources and fate and the role and rate of (bio-) remediation are key data to understand and subsequently change common practices (although sometimes the *good* practice could consist in stopping pumping water of a contaminated aquifer !). Understanding the origin and fate of nitrate can be complex because various sources exist (Fig. 8): fertilizers which contain both ammonium ($\delta^{15}N$ from −10 to +5‰ that will get oxidized to nitrate) and nitrate ($\delta^{15}N$ from −10 to +5‰), animal and septic manure ($\delta^{15}N$ from 0 to +25‰), and atmosphere deposits (but also organic nitrogen) and owing to isotope effects that occur through biotic denitrification mechanisms (see paleoenvironments and paleo-ecosystems section). However, in most cases, the sources are known (Fig. 8) and studied, and mixing processes can be modeled and distinguished from isotope variations related to other physico-chemical reactions. Denitrification isotope effects can be recognized from the slope ~1 to ~2 between $\delta^{15}N$ and $\delta^{18}O$ evolving toward ^{15}N- and ^{18}O–enriched isotope

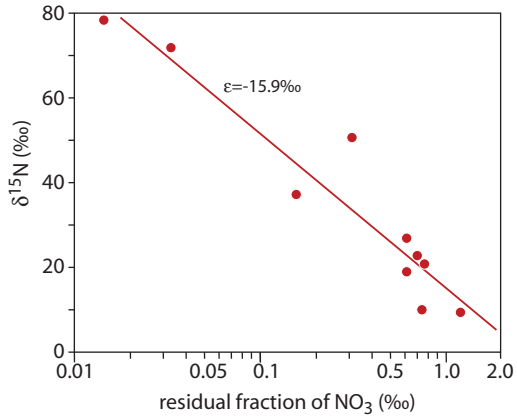

Nitrogen Isotopes, Fig. 9 Dependence between nitrogen isotope ratio and the fraction of residual nitrate in a sandy aquifer. Note the linear trend between the two parameters when the nitrate concentration is displayed in logarithmic scale: this is typical of open-system process (Rayleigh distillation) here typified for nitrate reduction (Modified from Böttcher et al. 1990)

compositions (see Fig. 8). This relationship allows both a quantitative modeling and forecasting the evolution of nitrate concentration (Böttcher et al. 1990; Fig. 9). Extrapolation of $\delta^{15}N$ and $\delta^{18}O$ values to their likely origin allows to recognize the source of nitrate pollution. It is worth noting that N isotopes can only develop their full potential in conjunction with other geochemical parameters, including boron, strontium, and oxygen (both $\delta^{18}O$ and $\delta^{17}O$) isotopes (Kendall et al. 2007; Widory et al. 2004). Finally, because

residual nitrate evolves toward ^{15}N–enriched compositions (modulo the isotope fractionation during assimilation and processes through the animal body), inputs of nitrate into estuaries or coastal ecosystems can easily be recognized by increasing $\delta^{15}N$ through time.

Conclusion

Despite being unevenly distributed on Earth and in extraterrestrial samples, several methods have been developed to analyze accurately N content and isotope composition. In modern and primitive Earth, the cycling of atmospheric nitrogen to the silicate Earth requires biological activity, and this makes nitrogen a unique tracer of life in the rock record. In every overviewed contexts, N isotopes have brought unique constraints that could hardly be deduced from other geochemical systems. It is however worth mentioning that N isotopes can only reach their full potential when considered together with other systematics.

Cross-References

- ▶ Archeological Geochemistry
- ▶ Biogeochemistry
- ▶ Nitrogen
- ▶ Nitrogen Cycle

References

Ader M, Thomazo C, Sansjofre P, Busigny V, Papineau D, Laffont R, Cartigny P, Halverson GP (2016) Interpretation of the nitrogen isotopic composition of Precambrian sedimentary rocks: assumptions and perspectives. Chem Geol 429:93–110

Algeo TJ, Meyers PA, Robinson RS, Rowe H, Jiang GQ (2014) Icehouse-greenhouse variations in marine denitrification. Biogeosciences 11:1273–1295

Aranda R, Stern LA, Dietz ME, McCormick MC, Barrow JA, Mothershead RF (2011) Forensic utility of isotope ratio analysis of the explosive urea nitrate and its precursors. Forensic Sci Int 206:143–149

Beaumont V, Robert F (1999) Nitrogen isotope ratios of kerogens in Precambrian cherts: a record of the evolution of atmosphere chemistry? Precambrian Res 96:63–82

Bebout GE, Fogel ML (1992) Nitrogen-isotope compositions of metasedimentary rocks in the Catalina schist, California: implications for metamorphic devolatilization history. Geochim Cosmochim Acta 56:2839–2849

Böttcher J, Strebel O, Voerkelius S, Schmidt HL (1990) Using stable isotope fractionation of nitrate–nitrogen and nitrate–oxygen for evaluation of microbial denitrification in a sandy aquifer. J Hydrol 114:413–424

Brandes JA, Boctor NZ, Cody GD, Cooper BA, Hazen RM, Yoder HS (1998) Abiotic nitrogen reduction on the early earth. Nature 395:365–367

Busigny V, Bebout GE (2013) Nitrogen in the silicate earth: speciation and isotopic behavior during mineral-fluid interactions. Elements 9:353–358

Busigny V, Cartigny P, Philippot P (2011) Nitrogen isotopes in ophiolitic metagabbros: a re-evaluation of modern nitrogen fluxes in subduction zones and implication for the early earth atmosphere. Geochim Cosmochim Acta 75:7502–7521

Cartigny P, Marty B (2013) Nitrogen isotopes and mantle geodynamics: the emergence of life and the atmosphere-crust-mantle connection. Elements 9:359–366

Deniro MJ, Epstein S (1981) Influence of diet on the distribution of nitrogen isotopes in animals. Geochim Cosmochim Acta 45:341–351

Furi E, Marty B (2015) Nitrogen isotope variations in the solar system. Nat Geosci 8:515–522

Galloway JN (2003) The global nitrogen cycle. In: Holland HD, Turekian KK (eds) Treatise on geochemistry. Pergamon, Oxford, pp 557–583

Geng L, Alexander B, Cole-Daib J, Steig EJ, Savarino J, Sofen ED, Schauer AJ (2014) Nitrogen isotopes in ice core nitrate linked to anthropogenic atmospheric acidity change. PNAS 111: 5808–5812

Goldblatt C, Claire MW, Lenton TM, Matthews AJ, Watson AJ, Zahnle KJ (2009) Nitrogen-enhanced greenhouse warming on early earth. Nat Geosci 2:891–896

Grady MM, Wright IP, Carr LP, Pillinger CT (1986) Compositional differences in enstatite chondrites based on carbon and nitrogen stable isotope measurements. Geochim Cosmochim Acta 50:2799–2813

Hashizume K, Sugiura N (1995) Nitrogen isotopes in bulk ordinary chondrites. Geochim Cosmochim Acta 59:4057–4069

Hastings MG, Jarvis JC, Steig EJ (2009) Anthropogenic impacts on nitrogen isotopes of ice-core nitrate. Science 324:1288–1288

Heil J, Wolf B, Brüggemann N, Emmenegger L, Tuzson B, Vereecken H, Mohn J (2014) Site-specific ^{15}N isotopic signatures of abiotically produced N_2O. Geochim Cosmochim Acta 139:72–82

Honma H (1996) High ammonium contents in the 3800 ma Isua supracrustal rocks, central West Greenland. Geochim Cosmochim Acta 60:2173–2178

Javoy M, Kaminski E, Guyot F, Andrault D, Sanloup C, Moreira M, Labrosse S, Jambon A, Agrinier P, Davaille A, Jaupart C (2010) The chemical composition of the earth: Enstatite chondrite models. Earth Planet Sci Lett 293:259–268

Jia YF, Kerrich R (2004) ^{15}N-enriched Precambrian kerogen and hydrothermal systems. Geochem Geophys Geosys 5. https://doi.org/10.1029/2004GC000716

Junk G, Svec HJ (1958) The absolute abundance of the nitrogen isotopes in the atmosphere and compressed gas from various sources. Geochim Cosmochim Acta 14:234–243

Kendall C, Elliott EM, Wankel SD (2007) Tracing anthropogenic inputs of nitrogen to ecosystems, chapter 12. In: Michener RH, Lajtha K (eds) Stable isotopes in ecology and environmental science, 2nd edn. Blackwell Publishing, Oxford, pp 375–449

Kendall C, Grim E (1990) Combustion tube method for measurement of nitrogen isotope ratios using calcium-oxide for total removal of carbon-dioxide and water. Anal Chem 62:526–529

Kerridge JF (1985) Carbon, hydrogen and nitrogen in carbonaceous chondrites – abundances and isotopic compositions in bulk samples. Geochim Cosmochim Acta 49:1707–1714

Landais A (2011) Utility of stable isotopes of N and Ar as tracers to retrieve past air temperature from air trapped in ice cores. In: Baskaran M (ed) Handbook of environmental isotope geochemistry. Springer-Verlag, Berlin/Heidelberg, pp 865–886

Lehmann MF, Bernasconi SM, Barbieri A, McKenzie JA (2002) Preservation of organic matter and alteration of its carbon and nitrogen isotope composition during simulated and in situ early sedimentary diagenesis. Geochim Cosmochim Acta 66:3573–3584

Li L, Zheng YF, Cartigny P, Li JHY (2014) Anomalous nitrogen isotopes in ultrahigh-pressure metamorphic rocks from the Sulu orogenic belt: effect of abiotic nitrogen reduction during fluid-rock interaction. Earth Planet Sci Lett 403:67–78
Mariotti A (1983) Atmospheric nitrogen is a reliable standard for natural ^{15}N abundance measurements. Nature 303:685–687
Marty B, Chaussidon M, Wiens RC, Jurewicz AJG, Burnett DS (2011) A ^{15}N poor isotopic composition for the solar system as shown by genesis solar wind samples. Science 332:1533–1536
Marty B, Zimmermann L, Pujol M, Burgess R, Philippot P (2013) Nitrogen isotopic composition and density of the Archean atmosphere. Science 342:101–104
Meselson M, Stahl FW (1958) The replication of DNA in Escherichia Coli. PNAS 44:671–682
Michalski G, Kolanowski M, Riha KM (2015) Oxygen and nitrogen isotopic composition of nitrate in commercial fertilizers, nitric acid, and reagent salts. Isot Environ Health Stud 51:382–391
Miller SL (1953) A production of amino acids under possible primitive earth conditions. Science 117:528–529
Minagawa M, Wada E (1984) Stepwise enrichment of ^{15}N along food-chains - further evidence and the relation between $\delta^{15}N$ and animal age. Geochim Cosmochim Acta 48:1135–1140
Papineau D, Purohit R, Goldberg T, Pi DH, Shields GA, Bhu H, Steele A, Fogel ML (2009) High primary productivity and nitrogen cycling after the Paleoproterozoic phosphogenic event in the Aravalli Supergroup, India. Precambrian Res 171:37–56
Pennock JR, Velinsky DJ, Ludlam JM, Sharp JH, Fogel ML (1996) Isotopic fractionation of ammonium and nitrate during uptake by Skeletonema Costatum: implications for $\delta^{15}N$ dynamics under bloom conditions. Limnol Oceanogr 41:451–459
Preston T, Owens NJP (1983) Interfacing an automatic elemental analyzer with an isotope ratio mass-spectrometer – the potential for fully automated total nitrogen and ^{15}N analysis. Analyst 108:971–977
Rau GH, Arthur MA, Dean WE (1987) $^{15}N/^{14}N$ variations in cretaceous Atlantic sedimentary sequences: implication for past changes in marine nitrogen biogeochemistry. Earth Planet Sci Lett 82:269–279
Richards MP, Trinkausc E (2009) Isotopic evidence for the diets of European Neanderthals and early modern humans. PNAS 106:16034–16039
Rockmann T, Levin I (2005) High-precision determination of the changing isotopic composition of atmospheric N_2O from 1990 to 2002. J Geophys Res 110:D21304
Rudnick RL, Gao S (2003) The composition of the continental crust. In: Rudnick RL (Volume ed) *The crust*, vol. 3. Holland HD, Turekian KK (Series eds) Treatise on Geochemistry. Elsevier-Pergamon, Oxford, pp 1–64
Savarino J, Morin S (2011) The N, O, S isotopes of oxy-anions in ice cores and polar environments. In: Baskaran M (ed) Handbook of environmental isotope geochemistry. Springer-Verlag, Berlin/Heidelberg, pp 835–864
Severinghaus JP, Sowers T, Brook EJ, Alley RB, Bender ML (1998) Timing of abrupt climate change at the end of the Younger Dryas interval from thermally fractionated gases in polar ice. Nature 391:141–146
Sigman DM, DiFiore PJ, Hain MP, Deutsch C, Wang Y, Karl DM, Knapp AN, Lehmann MF, Pantoja S (2009) The dual isotopes of deep nitrate as a constraint on the cycle and budget of oceanic fixed nitrogen. Deep-Sea Res I 56:1419–1439
Stueken EE, Buick R, Schauer AJ (2015a) Nitrogen isotope evidence for alkaline lakes on late Archean continents. Earth Planet Sci Lett 411:1–10
Stueken EE, Buick R, Guy BM, Koehler MC (2015b) Isotopic evidence for biological nitrogen fixation by Mo-nitrogenase at 3.2 Gyr. Nature 520:666–669
Stueken EE, Kipp MA, Koehler MC, Buick R (2016) The evolution of Earth's biogeochemical nitrogen cycle. Earth-Sci Rev 160:220–239
Thomazo C, Ader M, Philippot P (2011) Extreme ^{15}N-enrichments in 2.72-Gyr-old sediments: evidence for a turning point in the nitrogen cycle. Geobiology 9:107–120
Thomson AJ, Giannopoulos G, Pretty J, Baggs EM, Richardson DJ (2012) Biological sources and sinks of nitrous oxide and strategies to mitigate émissions. Phil Trans Roy Soc B 367:1157–1168
Toyoda S, Yoshida N (1999) Determination of nitrogen isotopomers of nitrous oxide on a modified isotope ratio mass spectrometer. Anal Chem 71:4711–4718
Wada E, Kadonaga T, Natsuo S (1975) ^{15}N abundance in naturally occurring substances and global assessment of denitrification from isotopic viewpoint. Geochem J 9:139–148
Widory D (2007) Nitrogen isotopes: tracers of origin and processes affecting PM10 in the atmosphere of Paris. Atmos Environ 41:2382–2390
Widory D, Kloppmann W, Chery L, Bonnin J, Rochdi H, Guinamant J-L (2004) Nitrate in groundwater: an isotopic multi-tracer approach. J Contam Hydrol 72:165–188
Wordsworth R, Pierrehumbert R (2013) Hydrogen-nitrogen greenhouse warming in Earth's early atmosphere. Science 339:64–67
Wright IP, Boyd SR, Franchi IA, Pillinger CT (1988) High-precision determination of nitrogen stable isotope ratios at the sub-nanomole level. J Phys E 21:865–875
Yoshida N, Toyoda S (2000) Constraining the atmospheric N_2O budget from intramolecular site preference in N_2O isotopomers. Nature 405:330–334
Zerkle AL, Poulton SW, Newton RJ, Mettam C, Claire MW, Bekker A, Junium CK (2017) Onset of the aerobic nitrogen cycle during the great oxidation event. Nature 542:465–467
Zhang XN, Sigman DM, Morel FMM, Kraepiel AML (2014) Nitrogen isotope fractionation by alternative nitrogenases and past ocean anoxia. PNAS 111:4782–4787
Zinner E, Amari S, Guinness R, Jennings C, Mertz AF, Nguyen AN, Gallino R, Hoppe P, Lugaro M, Nittler LR, Lewis RS (2007) NanoSIMS isotopic analysis of small presolar grains: search for Si(3)N (4) grains from AGB stars and al and Ti isotopic compositions of rare presolar SiC grains. Geochim Cosmochim Acta 71:4786–4813

Noble Gases

Chris J. Ballentine and Peter H. Barry
Department of Earth Sciences, University of Oxford, Oxford, UK

Definition

The noble gases occupy Group 0 (column 18) of the periodic table, comprised of the following elements: helium, neon, argon, krypton, xenon, and radon (not discussed here). They are colorless, odorless, monatomic, and unreactive gases at standard temperature and pressure.

Introduction: History and Uses

***Helium*:** The spectral signature of helium was first observed from the Sun by Janssen and Lockyer in 1868, with Lockyer

credited for proposing this as a new element. Helium was first isolated and identified in clevite, a uranium-rich mineral, by both Cleve and Langlet and independently by Ramsay in 1895.^{4}He is formed by alpha particles during the decay of natural uranium and thorium in the crust, with commercial sources provided in rare natural gas fields containing helium at concentrations between ~0.1 and 0.3%.

Helium is used in many cryogenic applications, most notably as a liquid in the cooling of superconducting magnets used in medical MRI scanners, but is also used for pressurizing and gas purging in many industrial applications, controlled atmospheres, specialist welding, leak detection, and breathing mixtures. In 2006, total global proven reserves and probable resources were estimated to be 51.9 billion standard cubic meters. In 2014, global helium production/use was estimated to be 180 million standard cubic meters (USGS 2015).

***Neon*:** Discovered in air by Ramsay and Travers in 1898, the main source of commercial neon today is through cryogenic fractional distillation of liquid air. Best known for its use as a lighting source in neon discharge tubes, it is also a vital component in excimer laser gas mixes used by semiconductor manufacturers. Semiconductor lithography applications using excimer lasers account for 70% of neon demand with global production in 2014 at ~400 million liters liquid neon (Corbett et al. 2015).

***Argon*:** Cavendish first observed argon in 1785 as a residual gas after removing all chemically active species from air. It was later confirmed as a component of air and subsequently named by Ramsey and Rayleigh in 1894. Like neon, the main source of commercial argon today is obtained through cryogenic fractional distillation of liquid air. This process produces ~700,000 tonnes of argon globally each year (2001). Argon is used as an inert blanket gas in the microchip and food industries and in cryogenics when the less expensive but more reactive nitrogen is not an appropriate coolant. Additional uses of argon include laser applications, to generate high energy plasma and – in liquid phase – as a scintillation target for neutrino and dark matter detectors (Acosta-Kane et al. 2008).

***Krypton*:** Discovered in 1898 by Ramsay and Travers in air, commercial krypton is also produced by cryogenic fractional distillation of air. Krypton gas finds use in lasers, as a filling for double glazing, incandescent lights, and specialist cryogenic uses as a liquid.

***Xenon*:** Also discovered in 1898 by Ramsay and Travers. Commercial xenon is produced by cryogenic fractional distillation of air. Global production is about 10,000 m^3 at standard pressure and temperature (6 tonnes) of which 15% is used in medical applications as an anesthetic. In addition, xenon gas is used in modern flash bulbs; in the liquid form, it is used as a supercritical solvent, as a scintillation target for dark matter detectors, and as fuel for ion propulsion engines used in satellite positioning (Royal Society of Chemistry 2016).

Cosmochemistry

The isotopic compositions and abundances of the noble gases in the Sun are referred to as the solar composition. This provides the reference point for chemically differentiating between meteoritic, cometary, and planetary materials. The best analog for the solar composition is solar wind, and its noble gas composition has been successfully determined by the recent NASA Genesis return mission, which trapped solar wind implanted into a variety of target materials (Wiens et al. 2007; Meshik et al. 2014; Crowther and Gilmour 2013) and returned them to Earth for analysis.

The observed differences between solar and terrestrial compositions are used to identify the various origins and processes that trap volatile elements during meteorite and planetary formation (Marty 2012; Halliday 2013). Some noble gases are produced by radioactive decay and cosmogenic reactions; excess abundances in these isotopes are used to provide temporal constraints on these trapping and formation processes.

Similar to other highly volatile elements such as nitrogen and carbon, the noble gas composition of the most primitive meteorites and carbonaceous chondrites are depleted by several orders of magnitude relative to the solar abundance of silicon; solar volatiles are not efficiently captured in rock-forming bodies. Superimposed upon this general depletion, light noble gases are more depleted than heavy gases (He < Ne < Ar < Kr < Xe). Furthermore, lighter isotopes of the same element are more depleted than heavier isotopes relative to the solar reference (Huss et al. 1996; Busemann et al. 2000; Ott 2014).

Noble gases in meteorites are trapped in different solid phases. For example, most of the Ar, Kr, and Xe found in meteorites are found in a carbonaceous residue that remains after Hf/HCl acid treatment (i.e., "Q-phase"). In addition to Q-phase gases, noble gases are found in silicon, carbon, graphite, and nano-diamonds formed before the collapse of the solar nebula. The latter "pre-solar grains" provide isotopic compositions of Kr and Xe that are formed by s-, r-, and p-nucleosynthetic processes occurring in stars and supernovae (Ott 2014).

In addition to Q-phase and pre-solar noble gases, significant sources of noble gas, particularly He and Ne, include ion implantation of solar wind and noble gases produced by the high energy impact of cosmogenic rays. The latter provide a crucial temporal history of meteorite breakup exposing fresh surfaces (Wieler et al. 2016) and the travel time of Martian meteorites between ejection from Mars and impact on Earth (Nyquist et al. 2001).

Cometary activity and meteorite breakup deliver ^{3}He-rich material to Earth in the form of interplanetary dust particles (IDPs). These provide a significant cosmogenic flux to Earth, as IDPs retain solar wind implanted ^{3}He, which can be resolved in ocean floor sediments. Over periods of known IDP deposition, ^{3}He concentrations provide a measure of sedimentation rate. In areas of known sediment accumulation, variance in IDP flux can be attributed to, for example, high levels of cometary activity (McGee and Mukhopadhyay 2013).

Mantle Geochemistry

Three dominant sources of noble gases exist in the Earth's mantle: (i) those trapped during the accretionary process, (ii) noble gases recycled from the planetary surface into the mantle, and (iii) those produced by the decay of extinct (^{244}Pu and ^{129}I) and extant radionuclides (U, Th, and K) within the mantle. The first work on mantle materials soon identified a dichotomy; all samples from mid-ocean ridges exhibit a very narrow range in ^{3}He/^{4}He (7–9 R_A) (where R_A = the ^{3}He/^{4}He of air = 1.4×10^{-6}), whereas most plume-influenced samples from intraplate volcanics have ^{3}He/^{4}He values significantly higher (>9 R_A) and some lower than those from the mid-ocean ridges. Due to the fact that ^{3}He is dominantly sourced during accretion and ^{4}He through the radioactive decay of U and Th, this ratio provides a proxy for ^{3}He/U ratios in different mantle domains. The resulting layered mantle model dominated the community understanding of mantle structure and evolution for a quarter of a century, a mantle in which a well-mixed upper mantle, above the 660 km seismic discontinuity, was lithophile depleted (see lithophiles) and degassed compared to a less depleted, heterogeneous, and more volatile rich lower mantle (Kurz et al. 1982; Allègre et al. 1983; O'Nions and Oxburgh 1983; Moreira 2013). Later improvements in seismic observation of the mantle and numerical simulation of mantle convection found significant mass transfer between upper and lower mantle and a far more complex picture than the two layered mantle model (Van Der Hilst et al. 1997; Van Keken et al. 2002).

The Ne isotopic composition of mid-ocean ridge source mantle is indistinguishable from the solar-wind-irradiated trapped component found in meteorites (Trieloff et al. 2002; Ballentine et al. 2005; Ballentine and Holland 2008). In contrast, there is some evidence in plume-derived Ne isotopes of a solar nebular signature (Yokochi and Marty 2004; Mukhopadhyay 2012), although this interpretation remains contested (Moreira 2013). Similarly, the primordial MORB-source mantles Kr and Xe are also consistent with delivery of a trapped component within accreting material (Holland et al. 2009; Caracausi et al. 2016). This result precludes models in which the dominant sources of volatiles in Earth's mantle are derived from equilibration of an early magma ocean with a massive early (solar) atmosphere.

Xe isotopic values approaching solar values have nevertheless been found in some plume-derived samples, and this may suggest an early accretionary role for solar nebula gases (Yokochi and Marty 2004; Mukhopadhyay 2012). Because ^{129}I decays to ^{129}Xe ($t_{1/2}$ = 15.7 Ma), ^{129}Xe/^{130}Xe isotopic compositions can be used to infer source I/Xe compositions in the earliest Earth history. Results from the Iceland plume show that volatiles from this source have lower I/Xe than mid-ocean ridge samples, and that this signature has been preserved since ^{129}I became extinct in the first ~100 Ma of Earth history. This data is also used to argue that mixing of noble gases from the Iceland plume mantle source with mid-ocean ridge sourced volatiles does not occur at any significant level (Mukhopadhyay 2012).

The primordial heavy noble gases in the mid-ocean ridge basalt source mantle are accompanied by atmosphere noble gases with an elemental composition consistent with subduction of an ocean/pore-fluid signature into the mantle (Holland and Ballentine 2006). This oceanic pore-fluid signature is observed in both halogens and noble gases in fluids subducted to ~100 km depth (Sumino et al. 2010), demonstrating preservation of the pore-fluid signal to depths at which transfer into the deeper mantle can be envisaged. Linking subduction flux of the noble gases to volatile species such as carbon and nitrogen (Marty and Jambon 1987; Barry and Hilton 2016) has provided a powerful tool to trace major volatile subduction into the mantle (Hilton et al. 2002).

The location and processes, recorded by the noble gases, that enable preservation of different accretionary volatile components in the mantle since the formation of Earth and the superposition of radiogenic and recycled noble gases remain at the frontier of the current research effort.

Earth's Atmosphere

The noble gas composition of Earth's atmosphere is well mixed and provides the reference abundance and isotopic composition for most noble gas terrestrial studies (e.g., Sano et al. 2013). With the exception of ^{40}Ar and He, the atmosphere contains >98–99% of all terrestrial noble gases. The pattern of the non-radiogenic noble gas isotopes is, similar to chondrites, strongly depleted in both light elements and light isotopes relative to solar. Xe abundances are, however, depleted by an order of magnitude more than would be expected using the chondritic pattern as a reference, and very strongly isotopically fractionated. This is often referred to as the "missing xenon" paradox (Marty 2012).

Xe isotopes derived from the extinct radioisotopes ^{129}I and ^{244}Pu can be resolved in the atmosphere. These are highly depleted relative to predicted amounts and are used to argue

that the earliest atmosphere was not retained until "closure" at ~40–100 Ma after the Earth formed (Pepin and Porcelli 2006; Avice and Marty 2014). The proportion of radiogenic noble gas isotopes from extant radionuclides has increased in the atmosphere over geological time due to Earth degassing. This is most notably seen in ^{40}Ar relative to ^{36}Ar and is a key measure of mantle outgassing efficiency and continental crustal growth (Allègre et al. 1996; Pujol et al. 2013). Analysis of fluids trapped in ancient minerals and free fracture fluids shows a light isotope enrichment in shielded Xe isotopes (^{124,126,128}Xe) (Pujol et al. 2011; Holland et al. 2013). It is argued that this is evidence of xenon loss from Earth's atmosphere that provides one explanation for the missing xenon (Pujol et al. 2011; Marty 2012).

Over the last 1Ga, changes in the isotopic composition and partial pressure of the noble gases in the terrestrial atmosphere have been small and implicitly assumed negligible in work using the modern atmosphere as a reference.

Ice, Oceans, and Crustal Fluids

The physical processes of diffusion and solubility which fix atmosphere-derived noble gases into ice and water are well understood. Small differences in environmental conditions such as temperature and salinity provide measurable changes in the noble gas content of ice and water, preserving temporal records of environmental change.

Transient temperature gradients fractionate air trapped within firn through thermal diffusion which is then preserved in air bubbles in ice. Ice cores therefore provide a temporal record of both temperature change and rate of change (Severinghaus and Brook 1999; Winckler and Severinghaus 2013).

Similarly, when water equilibrates with the atmosphere, the concentration of noble gases in the water phase is determined by the temperature and salinity of the water as well as the partial pressure of the noble gases. Dynamical features of air dissolving into water can introduce nonequilibrium air concentrations into the water, but these are reasonably well understood.

In ocean environments, noble gas concentrations that deviate from equilibrium are used to diagnose and quantify ice formation, melting, and/or bubble injection through increased wave activity. Argon can be used to provide a baseline for N_2 and O_2 activity, allowing differentiation between physical and biogeochemical activity and thus identification of the processes controlling biologic production and denitrification.

Non-atmosphere input occurs in the form of ^{3}He from mid-ocean ridges and atmosphere tritium decay ($t½ = 12.3$ years). The former provides a tool for deriving basin-scale mixing, global model verification, and trace element addition to different ocean bodies through hydrothermal activity. The latter provides information about the age and extent of recent surface water incursion (Schlosser and Winckler 2002; Stanley and Jenkins 2013).

On the continents for a known location (altitude) and freshwater recharging an aquifer (near zero salinity), local temperatures at recharge can typically be determined from the noble gas concentrations in water to better than ±0.3–0.5 °C (Ballentine and Hall 1999). With knowledge of the mean residence time of the water in a given aquifer, changes in the local paleoclimate can be reconstructed (Kipfer et al. 2002; Aeschbach-Hertig and Solomon 2013).

Like ocean water, tritium-^{3}He can be used to provide a mean residence time (MRT) for young (<50 years) groundwaters. ^{85}Kr ($t½ = 10.76$ years) released into the atmosphere by anthropogenic nuclear activity has similar potential but requires large sample volumes and specialized atom trap trace analysis (ATTA) techniques. Cosmogenically produced ^{39}Ar ($t½ = 269$ years) is formed in the atmosphere and has the potential to significantly extend the capability to trace young groundwater. It also requires ATTA technology for analytical determination; however, recent advances in the technique has allowed for smaller sample quantities to be accurately measured (Yang et al. 2013; Ritterbusch et al. 2014).

With the development of ATTA, cosmogenic ^{81}Kr can now also be determined in groundwater and ice. With a half-life of 229,000 years., ^{81}Kr extends the ability to date water MRTs and ice core ages beyond the limit of ^{14}C dating to over ~1 Ma (Aggarwal et al. 2015). For fluids with MRTs >1 Ma, the radiogenic noble gases (^{4}He, ^{21,22}Ne, ^{40}Ar, ^{131,132,134,136}Xe) can be used if the accumulation rate is known (Ballentine and Burnard 2002). For a closed system which releases all noble gases into the fluid phase, this is given by the concentration of radioelements and has been used to identify fluids in the crust >1 Ga (Holland et al. 2013). When an aquifer is open to flux into the system, the external flux rate needs to be determined; this may be from local proximal formations with high radioelement concentrations (Tolstikhin et al. 2011) or by using flux estimates based on the steady-state release of radiogenic noble gases from the whole crust (Torgersen 2010).

When a second fluid phase such as natural gas, oil, or carbon dioxide passes through the groundwater system, the noble gases equilibrate between phases as a function of local conditions (temperature, pressure, and salinity) and fluid volume ratio, and/or whether the process is open or closed system (Zhou et al. 2005; Barry et al. 2016). In well-behaved systems, the resulting noble gas content of either phase preserves a quantitative record of this phase interaction. This has been used to identify the role of groundwater in oil and gas migration to trap and identify sources and sinks of non-hydrocarbon gases such as CO_2, N_2, and commercial helium accumulation (Ballentine et al. 2002; Gilfillan et al. 2009; Prinzhofer 2013, Byrne et al. 2016). Similar principles apply in hydrothermal systems where boiling or other phase

separation processes can be traced (Sano and Fischer 2013) and their role in mineral deposition investigated (Kendrick et al. 2001).

Geochronology

Noble gas accumulation rates within minerals provide a wealth of information for geochronological applications throughout cosmochemistry and the Earth sciences. Arguably the largest impact has been the exploitation of K decay to ^{40}Ar ($t½ = 1250$ Ma). Early development of K-Ar was very rapidly superseded by reactor neutron conversion of K to ^{39}Ar, with simultaneous measurement of ^{40}Ar-^{39}Ar providing accuracy and a temporal range applicable "from archaeology to planetary sciences" (Kelley 2002; Jourdan et al. 2016).

A related offshoot to ^{40}Ar-^{39}Ar chronology is the conversion of halogens (F, Cl, Br, I) by neutron reaction to noble gas isotopes, providing a powerful analytical tool for halogen determination in samples where other techniques (particularly for Br and I) do not provide the necessary sensitivity (e.g., Ruzié-Hamilton 2016).

Cosmogenic nuclides provide surface exposure ages on meteorites and terrestrial surfaces alike (Niedermann 2002; Dunai et al. 2007; Wieler et al. 2016), while (U-Th)/He takes advantage of the low closure temperature in minerals (e.g., apatite) and provides a thermochronological history that can delineate the cooling history of rocks in a temperature range unobtainable by other techniques (Farley 2002, Reiners et al. 2004).

Summary and Conclusions

Noble gases have a wide array of terrestrial geochemical applications in addition to great utility in cosmochemistry. Due to the unique sources of different isotope species, the noble gases can be readily exploited to differentiate between atmospheric, mantle, crustal, and extraterrestrial volatile sources. Furthermore, radiogenic noble gas species can be used to provide temporal constraints on the timing of geologic closure events. Together, noble gases form a unique and extremely diverse set of geochemical tracers that have far-reaching applications in Earth and planetary sciences.

Cross-References

- ▶ Cosmogenic Nuclides
- ▶ Earth's Continental Crust
- ▶ Fluid–Rock Interaction
- ▶ Geothermal Systems
- ▶ Geochronology and Radiogenic Isotopes
- ▶ Mantle Geochemistry
- ▶ Periodic Table
- ▶ Radon
- ▶ Water

References

Acosta-Kane D, Acciarri R, Amaize O et al (2008) Discovery of underground argon with low level of radioactive Ar-39 and possible applications to WIMP dark matter detectors. Nucl Instrum Methods Phy Res Sect A 587:46–51

Aggarwal PK, Matsumoto T, Sturchio NC, Chang HK, Gastmans D, Araguas-Araguas LJ, Jiang W, Lu Z-T, Mueller P, Yokochi R, Purtschert R, Torgersen T (2015) Continental degassing of ^{4}He by surficial discharge of deep groundwater. Nat Geosci 8:35–39

Allègre CJ, Staudacher T, Sarda P, Kurz M (1983) Constraints on evolution of Earth's mantle from rare gas systematics. Nature 303:762–766

Allègre CJ, Hofmann AW, O'Nions RK (1996) The argon constraints on mantle structure. Geophys Res Lett 23:3555–3557

Aschbach-Hertig W, Solomon DK (2013) Noble gas thermometry in groundwater. In: Burnard P (ed) The noble gases as geochemical tracers. Springer, Berlin/Heidelberg, pp 81–122

Avice G, Marty B (2014) The iodine-plutonium-xenon age of the moon-earth system revisited. Phil Trans R Soc A 372:20130260

Ballentine CJ, Burnard P (2002) Production and release of noble gases in the continental crust. Rev Mineral Geochem 47:481–538

Ballentine CJ, Hall CM (1999) Determining paleotemperature and other variables by using an error weighted, nonlinear inversion of noble gas concentrations in water. Geochim Cosmochim Acta 63:2315–2336

Ballentine CJ, Holland G (2008) What CO_2 well gases tell us about the origin of noble gases in the mantle and their relationship to the atmosphere. Phil Trans R Soc London 360:4183–4203

Ballentine CJ, Marty B, Burgess R (2002) Tracing fluid origin, transport and interaction in the crust. Rev Mineral Geochem 47:539–614

Ballentine CJ, Marty B, Sherwood Lollar B, Cassidy M (2005) Neon isotopes constrain convection and volatile origin in the Earth's mantle. Nature 433:33–38

Barry PH, Hilton DR (2016) Release of subducted sedimentary nitrogen throughout Earth's mantle. Geochem Persp Lett 2:148–159

Barry PH, Lawson M, Meurer WP, Warr O, Mabry JC, Byrne DJ, Ballentine CJ (2016) Noble gases solubility models of hydrocarbon charge mechanisms in the Sleipner vest methane field. Geochim Cosmochim Acta 194:291–309

Busemann H, Baur H, Wieler R (2000) Primordial noble gases in "phase Q" in carbonaceous and ordinary chondrites studied by closed system etching. Meteorit Planet Sci 35:949–973

Byrne DJ, Barry PH, Lawson M, Ballentine CJ (2016) Noble gases in conventional and unconventional hydrocarbon systems, Special publication. Geological Society, London

Caracausi A, Avice G, Burnard PG, Füri E, Marty B (2016) Chondritic xenon in the Earth's mantle. Nature 533:82–85

Corbett M, Thirsk M, Tuane A (2015) http://www.semi.org/en/node/57646

Crowther SA, Gilmour JD (2013) The genesis solar xenon composition and its relationship to planetary xenon signatures. Geochim Cosmochim Acta 123:17–34

Dunai TJ, Stuart FM, Pik R et al (2007) Production of He-3 in crustal rocks by cosmogenic thermal neutrons. Earth Planet Sci Lett 258:228–236

Farley KA (2002) (U-Th)/He dating: techniques, calibrations, and applications. Rev Mineral Geochem 47:819–844

Gilfillan SM, Sherwood Lollar B, Holland G, Blagburn D, Stevens S, Schoell M, Cassidy M, Ding Z, Zhou Z, Lacrampe-Couloume G,

N

Ballentine CJ (2009) Solubility trapping in formation water as dominant CO_2 sink in natural gas fields. Nature 458:614–618
Halliday AN (2013) The origins of volatiles in the terrestrial planets. Geochim Cosmochim Acta 105:146–171
Hilton DR, Fischer TP, Marty B (2002) Noble gases and volatile recycling at subduction zones. Rev Mineral Geochem 47:319–370
Holland G, Ballentine CJ (2006) Seawater subduction controls the heavy noble gas composition of the mantle. Nature 441:186–191
Holland G, Cassidy M, Ballentine CJ (2009) Meteorite Kr in Earth's mantle suggests a late accretionary source for the atmosphere. Science 326:1522–1525
Holland G, Sherwood Lollar B, Li L, Lacrampe-Couloume G, Slater GF, Ballentine CJ (2013) Deep fracture fluids isolated in the crust since the Precambrian era. Nature 497:357–360
Huss GR et al (1996) The "normal planetary" noble gas component in primitive chondrites: compositions, carrier, and metamorphic history. Geochim Cosmochim Acta 60:3311–3340
Jourdan F, Mark D, Veratis C (2016) Advances in $^{40}Ar/^{39}Ar$ dating: from archaeology to planetary sciences. Geological Society, London, 378pp
van Keken PE, Hauri EH, Ballentine CJ (2002) The generation, preservation, and destruction of chemical heterogeneity. Annu Rev Earth Planet Sci 30:493–525
Kelley S (2002) K-Ar and Ar-Ar dating. Rev Mineral Geochem 47:481–538
Kendrick MA, Burgess R, Pattrick RAD, Turner G (2001) Fluid inclusion noble gas and halogen evidence on the origin of Cu-Porphyry mineralizing fluids. Geochim Cosmochim Acta 65:2651–2668
Kipfer R, Aschbach-Hertig W, Peeters F, Stute M (2002) Noble gases in lakes and groundwaters. Rev Mineral Geochem 47:615–700
Kurz MD, Jenkins WJ, Hart SR (1982) Helium isotopic systematics of oceanic islands and mantle heterogeneity. Nature 297:43–47
Marty B (2012) The origins and concentrations of water, carbon, nitrogen and noble gases on earth. Earth Planet Sci Lett 313:56–66
Marty B, Jambon A (1987) C/3He in volatile fluxes from the solid earth: implications for carbon geodynamics. Earth Planet Sci Lett 83:16–26
McGee D, Mukhopadhyay S (2013) Extraterrestrial He in sediments: from recorder of asteroid collisions to timekeeper of global environmental changes. In: Burnard P (ed) The noble gases as geochemical tracers. Springer, Berlin/Heidelberg, pp 155–176
Meshik A, Hohenberg C, Pravdivtseva O, Burnett D (2014) Heavy noble gases in solar wind delivered by genesis mission. Geochim Cosmochim Acta 127:326–347
Moreira M (2013) Noble gas constraints on the origin and evolution of Earth's volatiles. Geochem Perspect 2:229–403
Mukhopadhyay S (2012) Early differentiation and volatile accretion recorded in deep-mantle neon and xenon. Nature 486:101–124
Niedermann S (2002) Cosmic-ray-produced noble gases in terrestrial rocks: dating tools for surface processes. Rev Mineral Geochem 47:731–784
Nyquist LE, Bogard DD, Shih CY et al (2001) Ages and geologic histories of Martian meteorites. Space Sci Rev 96:105–164
O'Nions RK, Oxburgh ER (1983) Heat and helium in the earth. Nature 306:429–431
Ott U (2014) Planetary and pre-solar noble gases in meteorites. Chem Erde-Geochem 74:519–544
Pepin RD, Porcelli D (2006) Xenon istope systematics, giant impacts, and mantle degassing on the early Earth. Earth Planet Sci Lett 250:470–485
Prinzhofer A (2013) Noble gases in oil and gas accumulations. In: Burnard P (ed) The noble gases as geochemical tracers. Springer, Berlin/Heidelberg, pp 55–79
Pujol M, Marty B, Burgess R (2011) Chondritic-like xenon trapped in Archean rocks: a possible signature of the ancient atmosphere. Earth Planet Sci Lett 308:298–306
Pujol M, Marty B, Burgess R et al (2013) Argon isotopic composition of Archaean atmosphere probes early earth geodynamics. Nature 498:87–90
Reiners PW, Spell TL, Nicolescu S, Zanetti K (2004) Zircon (U-Th)/He thermochronometry: he diffusion and comparisons with $^{40}Ar/^{39}Ar$ dating. Geochim Cosmochim Acta 68:1857–1887
Ritterbusch F, Ebser S, Welte J, Reichel T, Kersting A, Purtschert R, Aeschbach-Hertig W, Oberthaler MK (2014) Groundwater dating with atom trap trace analysis of ^{39}Ar. Geophys Res Lett. https://doi.org/10.1002/2014GL061120
Royal Society of Chemistry (2016) http://www.rsc.org/Education/EiC/issues/2009Jan/xenon-noble-gas-inert.asp
Ruzié-Hamilton L, Clay PL, Bugess R, Joachim B, Ballentine CJ, Turner G (2016) Chemical Geology 437:77–87
Sano Y, Fischer TP (2013) The analysis and interpretation of noble gases in modern hydrothermal systems. In: Burnard P (ed) The noble gases as geochemical tracers. Springer, Berlin/Heidelberg, pp 249–317
Sano Y, Marty B, Burnard P (2013) Noble gases in the atmosphere. In: Burnard P (ed) The noble gases as geochemical tracers. Springer, Berlin/Heidelberg, pp 17–31
Schlosser P, Winckler G (2002) Noble gases in lakes and groundwaters. Rev Mineral Geochem 47:701–730
Severinghaus JP, Brook EJ (1999) Abrupt climate change at the end of the last glacial period inferred from trapped air in polar ice. Science 286:930–934
Stanley RH, Jenkins WJ (2013) Noble gases in seawater as tracers for physical and biogeochemical processes. In: Burnard P (ed) The noble gases as geochemical tracers. Springer, Berlin/Heidelberg, pp 55–79
Sumino H, Burgess R, Holland G, Mizukami T, Wallis SR, Ballentine CJ (2010) Seawater-derived noble gases and halogens preserved in exhumed mantle wedge peridotite. Earth Planet Sci Lett 294:163–172
Tolstikhin I, Waber HN, Kamensky I et al (2011) Production, redistribution and loss of helium and argon isotopes in a thick sedimentary aquitard-aquifer system (Molasse Basin, Switzerland). Chem Geol 286:48–58
Torgersen T (2010) Continental degassing flux of He-4 and its variability. Geochem Geophys Geosyst 11:Q06002
Trieloff M, Kunz J, Allègre CJ (2002) Noble gas systematics of the Rèunion mantle plume source and the origin of primordial noble gases in Earth's mantle. Earth Planet Sci Lett 200:297–313
USGS (2015) http://minerals.usgs.gov/minerals/pubs/commodity/helium/mcs-2015-heliu.pdf
Van de Hilst RD, Widiyantoro S, Engdahl ER (1997) Evidence for deep mantle circulation from global tomography. Nature 386:578–584
Wieler R, Huber L, Busemann H et al (2016) Noble gases in 18 Martian meteorites and angrite northwest Africa7812 exposure ages, trapped gases, and a re-evaluation of the evidence for solar cosmic ray-produced neon in shergottites and other achondrites. Meteorit Planet Sci 51:407–428
Wiens RC, Burnett DS, Hohenberg CM, Meshik A, Heber V, Grimberg A, Wieler R, Reisenfeld DB (2007) Solar and solar-wind composition results from the genesis mission. Space Sci Rev 130:161–171
Winckler G, Severnghaus JP (2013) Noble gases in ice cores: indicators of the Earth's climate history. In: Burnard P (ed) The noble gases as geochemical tracers. Springer, Berlin/Heidelberg, pp 33–53
Yang GM, Cheng CF, Jiang W, Lu ZT, Purtschert R, Sun YR, Tu LY, Hu SM (2013) Analysis of ^{85}Kr: a comparison at the 10^{-14} level using microliter samples. Sci Rep 3:1596. https://doi.org/10.1038/srep01596
Yokochi R, Marty B (2004) A determination of the neon isotopic composition of the deep mantle. Earth Planet Sci Lett 225:77–88
Zhou Z, Ballentine CJ, Kipfer R, Schoell S, Thibodeaux S (2005) Noble gas tracing of groundwater/coalbed methane interaction in the San Juan Basin, USA. Geochim Cosmochim Acta 69:5413–5428

Nuclear Magnetic Resonance

Corey D. Pilgrim
Department of Chemistry, University of California, Davis, Davis, CA, USA

Synonyms

Continuous wave NMR (CW-NMR); Fourier transform NMR (FT-NMR); Magnetic resonance; NMR; Solid-state NMR (SSNMR)

Definition

Nuclear magnetic resonance (NMR) is a powerful analytical tool to both elucidate structure and measure dynamics of chemical systems. Using a powerful magnet and radio-frequency (RF) pulses, the spins of nuclei are perturbed and allowed to relax, generating signals specific to the chemical environment the nuclei are contained within. A broad range of nuclei are NMR active (most notably ^{1}H, ^{13}C, and ^{29}Si). Chemical analysis can be performed on both liquid and solid samples, with sample volumes ranging from microliters to milliliters. Analysis can also be performed at variable temperatures and pressures using specialized probe designs.

Governing Physics

NMR relies principally on the idea that every nucleus has an inherent spin, which is a type of angular momentum that is not defined in the classical sense. Classical spin deals with the rotation of a particle around a central axis – with this rotation comes an angular momentum vector that points orthogonally to the direction of the rotation. Nuclear spin has no basis in rotational motion, yet it still acts as an angular momentum vector – it is an intrinsic property of the nucleus. Wolfgang Pauli theorized that electrons have spin of one-half, and it has since been shown that neutrons and protons also have spin of one-half (Levitt 2008). Here it can be noted that particles with half-integer spin (like the electron, proton, and neutron) are known as "fermions" and particles with integer spin (such as the photon) are known as "bosons."

Nuclear spin (also referred to as I) manifests itself in different isotopes depending on the amount of neutrons and protons in the nucleus. The two main isotopes of hydrogen, ^{1}H and ^{2}H, are chemically identical because they share the same number of protons and electrons (one each), but they differ by one neutron – this causes the nuclear spin to be different ($I = ½$ and 1, respectively). As NMR is the measurement of species with nuclear spin, I must be greater than 0 for the nuclei to be considered "NMR active." I is equal to 0 when the number of protons and the number of neutrons in the nucleus are even numbered, such as the case with ^{32}S (16 protons and 16 neutrons). In all other instances (odd/odd, odd/even, and even/odd pairings of protons and neutrons), the nuclei are NMR active (Hore 1995). Nuclei with spin one-half (^{1}H, ^{13}C, ^{31}P, ^{29}Si, etc.) are the simplest to understand, but quadrupolar nuclei ($I > ½$, such as ^{2}H, ^{17}O, ^{27}Al, etc.) exist and are of great importance in the field of NMR spectroscopy. There are $2I + 1$ degenerate spin states associated with I, as in the case of classical angular momentum. Thus, for a spin $I = ½$ nuclei, there are $2(½) + 1 = 2$ degenerate spin states.

NMR spectroscopy probes what is known as the Zeeman effect. The Zeeman effect occurs when identical spin states are placed in a magnetic field and split into distinct energy levels. Particles with angular momentum have a magnetic moment such that $M = \gamma\hbar I$, and these magnetic moments will align with the strong static field. Here, γ is the gyromagnetic ratio. For a spin one-half system, this causes the spins to align either parallel or antiparallel to the external magnetic field, with enough thermal energy in the system (via a Boltzmann distribution of spins) to cause an almost even population in each energy level, though there are slightly more spins in the parallel state – this is why NMR is known as an insensitive measurement. The slight excess of spin in the parallel state leads to a magnetic moment, which does not align perfectly with the external magnetic field (due to the quantization of the energy levels from the Zeeman effect). There is thus some magnetization in the xy-plane, but this averages to zero due to the precession of the magnetic moment. The skewed nuclear magnetic moment in the static field experiences a torque, which will change the direction of the angular momentum of the nucleus. This torque causes the spin to move and is known as Larmor precession. This precession occurs at what is known as the Larmor frequency (with γ the gyromagnetic ratio and B_0 the strength of the external magnetic field):

$$\omega_L = \gamma B_0 \tag{1}$$

The magnetic moment can be interpreted as a stationary vector by using the rotating frame approximation, where the frame of reference for the moment is rotating with the same frequency and direction as the Larmor frequency in the xy-plane. This approximation allows the z-magnetization to be seen as a stationary, vertical vector.

The Larmor frequency equates the strength of the static magnetic field to the frequency of precession. This frequency is also the frequency of light that is needed to excite the spins in the lower energy state to the higher energy spin state, following Planck's equation. This excitation is the central phenomenon in NMR, probing the different energy levels of

the spin states. In large external magnetic fields, the Larmor frequency of the proton (^{1}H) lies in the range of radio-frequency (RF) along the electromagnetic spectrum. Thus, RF waves are used to excite the nuclear spins to probe the chemical environments of the analytes at hand.

The NMR Experiment

A typical NMR experiment follows this formula:

1. An ensemble of spins is placed inside a static magnetic field.
2. The sample is irradiated with an RF pulse to focus the spins.
3. The spins are allowed to relax back to the original orientation, and the induced current is measured.
4. The irradiation is repeated many times to enhance the net signal.
5. The data is analyzed after the "free induction decay" is transformed from the time domain to a frequency domain via a Fourier transform.

Starting off with the first step in the sequence, it is necessary to place the sample into a strong static field such that the spins split by the Zeeman effect, leading to a net magnetization parallel the external field, and the magnetic moments of the spins precess as previously described.

An RF pulse is sent through a resonant circuit (with the coil centered on the sample) to start the second step. This pulse effectively applies a magnetic field (generally called B_1) to the z-directional magnetization vector, M_z, to focus it into the xy-plane. The pulse is tuned in both duration and power such that M_z is shifted 90° onto either the x- or y-axis, which yields the following equation for the magnetization under the rotating frame approximation:

$$M_x(t) = M_{z,0} \tag{2}$$

With the magnetization tipped into the x-direction (in the case above), the pulse is turned off, and the spectrometer is turned to the receive mode and thus begins the third step. The magnetic moments start to relax back to their original directions in the static magnetic field, B_0. The magnetization in the x-direction is given by

$$M_x(t) = M_{z,0}\cos(\omega_L t)e^{-t/T_2} \tag{3}$$

Without the magnetic field B1, the magnetic moments oscillate around the z-axis with the Larmor frequency. The cosine wave is at a maximum at t = 0, and the exponential is added as a damping factor to account for the relaxation (in this case, the damping factor is spin-spin relaxation which accounts for the T_2 constant) back to where the magnetization is in the z-direction. As the magnetic moments oscillate, they induce a current in the coil (as a moving magnetic field will always induce an electric current). This current is then measured by the coil that surrounds the sample and leads to the "free induction decay" or FID, mentioned above.

Steps 1–3 are repeated multiple times to increase the signal, as each successive FID builds upon the last to create one superimposed FID. The signal-to-noise ratio scales with the square root of the number of scans. Once the desired signal-to-noise ratio (and signal amplitude) has been achieved, data collection is finished, and a Fourier transform of the FID from the time domain (t) into the frequency domain (Ω) is implemented:

$$S(\Omega) = \int_0^\infty s(t)e^{-i\Omega t}dt \tag{4}$$

The Fourier transform is a complex function, as it consists of real and imaginary parts. The real portion of the spectrum is known as the absorption spectrum, while the imaginary portion is known as the dispersive spectrum. The absorption spectrum is the spectrum associated with FT-NMR analysis, and it is a plot of the different Larmor frequencies of the nuclei in the ensemble (and the molecule overall), measured along the x-axis as a difference from the carrier frequency that was pulsed through the sample. The Larmor frequency of each nucleus depends on the chemical environment it experiences – thus, separate signals that show up on the spectrum indicate separate magnetic environments. This fact helps to elucidate the structure of the chemicals under consideration since the structural settings give rise to differences in the magnetic environments. Functional groups can be identified; bond distances, bonding, conformations, and rates of interconversion can all be measured.

Instrument Design

The NMR instrument can be separated into two main components, the magnet and the spectrometer.

The magnet is generally a high-field superconducting coil that takes liquid helium and liquid nitrogen to maintain the currents necessary to produce the large magnetic field. Permanent magnets do exist, but are lower field and do not provide as high a resolution as superconducting magnets. The field strengths of superconducting magnets range from 7 to 23.5 T. The large cylindrical magnet also houses the sample probe. The probe is usually a tunable LC-type circuit

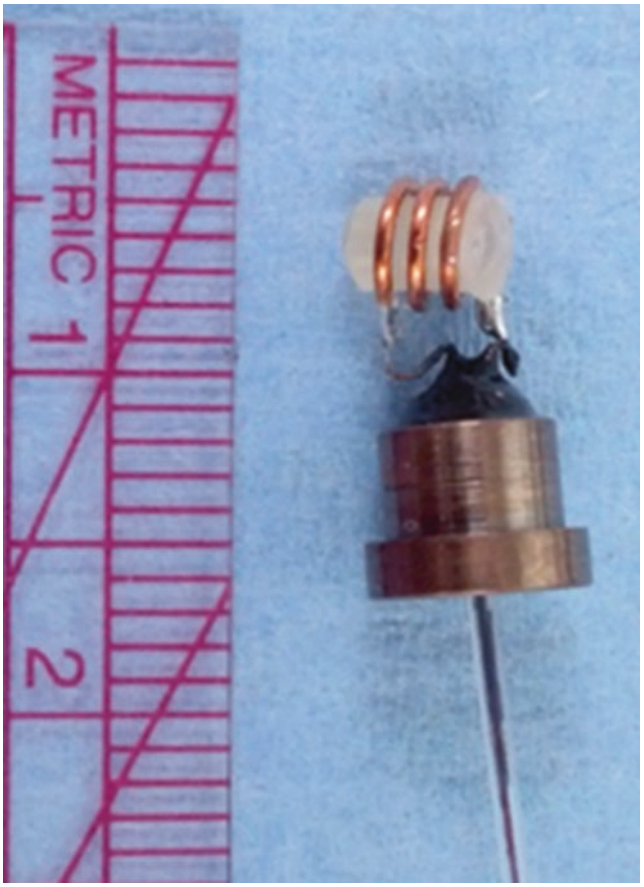

Nuclear Magnetic Resonance, Fig. 1 A simple solenoid sample coil

that provides the irradiation to the sample nuclei. This coil is also sensitive enough to measure the induced current of the nuclei once they start to relax after being perturbed (Fig. 1). To achieve the best resolution, the magnetic field must be homogeneous around the sample. Electromagnets, called "shimming coils," are used to homogenize the magnetic field around the actual sample. Magnetic fields are generated by the application of current to these electromagnets, which constructively or destructively alter the local magnetic field around the sample. The homogenization of the local field leads to sharper linewidths and more symmetric peaks.

The second half of the instrument, the spectrometer, is where the RF synthesizers, duplexers, receivers, and controllers reside. A high-power electrical pulse is sent from the spectrometer to the coil to perturb the nuclei and then is turned off quickly. One of the most important parts to an NMR spectrometer is the high-speed duplexer, which is a very fast switch that protects the sensitive receiving electronics from high-power pulses. The electronics must be able to function in rapid succession, as experiments can occur within microseconds of one another. The modern receiver relies on digital quadrature detection to process the data. The receiver splits the signal from the probe into real and imaginary phases, converts the analog signal to a digital signal, and compares the signal to a reference frequency. This data is then manipulated, and the spectrum is analyzed.

The Bloch Equations

The Bloch equations are a description of how the magnetic moment of the nuclear spins (M) interacts with a static magnetic field (B) after the influence of a strong RF pulse, following the torque equation (Bloch 1946) and using the vector cross product:

$$\boldsymbol{\tau} = \boldsymbol{M}\, x\, \boldsymbol{B} \tag{5}$$

The equation is modified to show how the magnetic moments are changed in the magnetic field, knowing that $\boldsymbol{M} = \gamma\hbar\boldsymbol{I}$ (γ is once again the gyromagnetic ratio of the nuclei):

$$\boldsymbol{\tau} = \hbar\frac{d\boldsymbol{I}}{dt} = \frac{\hbar}{\hbar\gamma}\frac{d\boldsymbol{M}}{dt} = \frac{1}{\gamma}\frac{d\boldsymbol{M}}{dt} \rightarrow \frac{d\boldsymbol{M}}{dt} = \gamma\boldsymbol{\mu}\, x\, \boldsymbol{B} \tag{6}$$

Describing the torque in the laboratory frame of reference, the vectors are defined in three dimensions such that

$$\frac{d}{dt}\begin{pmatrix} M_x \\ M_y \\ M_z \end{pmatrix} = \gamma \begin{pmatrix} M_x \\ M_y \\ M_z \end{pmatrix} x \begin{pmatrix} B_x \\ B_y \\ B_z \end{pmatrix} \tag{7}$$

The overall magnetic field **B** is given by a combination of magnetic fields during the NMR experiment. At the initial point in the experiment, there is a strong static magnetic field $\mathbf{B_0}$ in the z-direction and a smaller R-induced magnetic field $\mathbf{B_1}$ in the xy-plane. If the $\mathbf{B_1}$ pulse is directed in the x-direction, the **B** vector becomes

$$\begin{pmatrix} B_x \\ B_y \\ B_z \end{pmatrix} = \begin{pmatrix} B_1 \cos\omega_{rf}t \\ B_1 \sin\omega_{rf}t \\ B_0 \end{pmatrix} \tag{8}$$

Substituting Eq. (8) into the torque equation, Eq. (7), yields

$$\frac{d}{dt}\begin{pmatrix} M_x \\ M_y \\ M_z \end{pmatrix} = \gamma \begin{pmatrix} M_x \\ M_y \\ M_z \end{pmatrix} x \begin{pmatrix} B_1 \cos\omega_{rf}t \\ -B_1 \sin\omega_{rf}t \\ B_0 \end{pmatrix} \tag{9}$$

The γ is a scalar, and the Larmor and Rabi frequencies are defined as $\omega_{L=}\gamma B_0$ and $\omega_{R=}\gamma B_1$. Substituting these definitions into Eq. (9) yields

$$\begin{pmatrix} \frac{dM_x}{dt} \\ \frac{dM_y}{dt} \\ \frac{dM_z}{dt} \end{pmatrix} = \begin{pmatrix} M_x \\ M_y \\ M_z \end{pmatrix} x \begin{pmatrix} \gamma B_1 \cos \omega_{rf} t \\ -\gamma B_1 \sin \omega_{rf} t \\ \gamma B_0 \end{pmatrix}$$

$$= \begin{pmatrix} M_x \\ M_y \\ M_z \end{pmatrix} x \begin{pmatrix} \omega_R \cos \omega_{rf} t \\ -\omega_R \sin \omega_{rf} t \\ \omega_L \end{pmatrix} \quad (10)$$

which simplifies to

$$\begin{pmatrix} \frac{dM_x}{dt} \\ \frac{dM_y}{dt} \\ \frac{dM_z}{dt} \end{pmatrix} = \begin{pmatrix} \omega_L M_y + M_z \omega_R \sin \omega_{rf} t \\ M_z \omega_R \cos \omega_{rf} t - \omega_L M_x \\ -M_x \omega_R \sin \omega_{rf} t - M_y \omega_R \cos \omega_{rf} t \end{pmatrix} \quad (11)$$

Equation (11) is the set of coupled differential equations known as the Bloch equations in the lab frame. This set is conveniently transformed into the rotating frame of reference, where the z-magnetization is stationary, and the frame of reference rotates with the Larmor frequency, by applying a rotation matrix:

$$\boldsymbol{T}^{rot} = \begin{pmatrix} \cos \omega_{rf} t & \sin \omega_{rf} t & 0 \\ -\sin \omega_{rf} t & \cos \omega_{rf} t & 0 \\ 0 & 0 & 1 \end{pmatrix} \quad (12)$$

Redefining new magnetization vectors (u, v, and M_z), Bloch derived

$$\begin{pmatrix} u \\ v \\ M_z \end{pmatrix} = \boldsymbol{T}^{rot} \begin{pmatrix} M_x \\ M_y \\ M_z \end{pmatrix}$$

$$= \begin{pmatrix} M_x \cos \omega_{rf} t + M_y \sin \omega_{rf} t \\ -M_x \sin \omega_{rf} t + M_y \cos \omega_{rf} t \\ M_z \end{pmatrix} \quad (13)$$

After substituting in u, v, and M_z to the torque equation and solving for the derivatives of these new functions, the end result is

$$\begin{pmatrix} \frac{du}{dt} \\ \frac{dv}{dt} \\ \frac{dM_z}{dt} \end{pmatrix} = \begin{pmatrix} v(\omega_{rf} - \omega_L) \\ -u(\omega_{rf} - \omega_L) - M_z \omega_R \\ v\omega_R \end{pmatrix} \quad (14)$$

This set of coupled differential equations is known as the Bloch equations for a rotating frame of reference and accounts for the perceived oscillation of three directions of magnetization if one were sitting on a packet rotating at the Larmor frequency in the xy-plane.

Bloch noticed the phenomenon of relaxation when deriving these equations (signals decaying along a first-order path versus time) and coined the terms longitudinal (T_1 or spin-lattice) and transverse (T_2 or spin-spin) relaxation times. The longitudinal relaxation time T_1 is the time that it takes for the M_z signal to relax back to its original state after being perturbed by the RF pulse. The mechanism for this relaxation, for the I = 1/2 case, is due to the interaction of the nuclei with its surrounding rotational and vibrational environments. The energy contained in the excited state is dissipated to neighboring electric and magnetic fields. Quadrupolar nuclei as well as paramagnetic ions also allow for fast dissipation of this energy. The transverse relaxation time, T_2, is the time that it takes for the spins to dephase and lose coherence in the xy-plane. This dephasing is an adiabatic process where the energy is dissipated between spins, and information is lost. As the net magnetization is regained in the z-direction but lost in the xy-plane, T_1 is always greater than, or equal to, T_2.

The relaxation pathway that yields T_1 is a first-order process that affects only M_z:

$$M_z(t) = M_{z,eq} - \left(M_{z,eq} - M_z(0)\right) e^{-\frac{t}{T_1}} \quad (15)$$

T_2 is also a first-order process for M_x and M_y, so the two magnetizations are defined as

$$M_x(t) = M_x(0) e^{-\frac{t}{T_2}} \text{ and } M_y(t) = M_y(0) e^{-\frac{t}{T_2}} \quad (16)$$

Substituting these into Eq. (14), the rotating Bloch equations, with relaxation effects:

$$\begin{pmatrix} \frac{du}{dt} \\ \frac{dv}{dt} \\ \frac{dM_z}{dt} \end{pmatrix} = \begin{pmatrix} v(\omega_{rf} - \omega_L) - \frac{u}{T_2} \\ -u(\omega_{rf} - \omega_L) - M_z \omega_R - \frac{v}{T_2} \\ v\omega_R - \frac{M_z - M_0}{T_1} \end{pmatrix} \quad (17)$$

These equations have since been modified to deal with the kinetics of chemical reactions (McConnell 1958). This McConnell formalism has been widely used to determine the rates of exchange reactions in solution, typically in the case where a complexed ligand around a solvated metal ion replaces itself with a free ligand in solution. The rate of exchange for bound water molecules in solution has also been studied for a myriad of metal centers (Helm and Merbach 1999). McConnell postulated that on the NMR timescale, magnetization would not only transfer due to relaxation mechanisms but that nuclei would exchange between sites and affect magnetization transfer as well. For this to

occur, he made a series of assumptions. The first was that the rate of exchange of magnetization was directly proportional to the rate of chemical exchange. The second was that the process could either be described as a set of elementary (one-step) reactions. Thus, for a two-site exchange reaction between sites A and B (depicting first-order or pseudo-first-order reaction conditions), it was formulated that the following equations can be used to depict chemical exchange, with the rates of the forward and reverse reaction given by k_A and k_B, respectively, and from the law of detailed balance, $\frac{k_A}{k_B} = \frac{X_B}{X_A} = P_B$ where "X_i" is the mole fraction of site "i" and P_B is the ratio of mole fractions.

Now the system of equations is split into two, one set for each of the exchanging sites:

$$\begin{pmatrix} \frac{du_A}{dt} \\ \frac{dv_A}{dt} \\ \frac{dM_{z,A}}{dt} \end{pmatrix} = \begin{pmatrix} v_A(\omega_{rf} - \omega_L) - \frac{u_A}{T_{2,A}} - k_A u_A + k_A P_A u_B \\ -u_A(\omega_{rf} - \omega_L) - M_{z,A}\omega_R - \frac{v_A}{T_{2,A}} - k_A v_A + k_A P_A v_B \\ v_A \omega_R - \frac{M_{z,A} - M_{0,A}}{T_{1,A}} - k_A M_{z,A} + k_A P_A M_{z,B} \end{pmatrix} \quad (18)$$

$$\begin{pmatrix} \frac{du_B}{dt} \\ \frac{dv_B}{dt} \\ \frac{dM_{z,B}}{dt} \end{pmatrix} = \begin{pmatrix} v_B(\omega_{rf} - \omega_L) - \frac{u_B}{T_{2,B}} - k_B u_B + k_B P_B u_A \\ -u_B(\omega_{rf} - \omega_L) - M_{z,B}\omega_R - \frac{v_B}{T_{2,B}} - k_B v_B + k_B P_B v_A \\ v_B \omega_R - \frac{M_{z,B} - M_{0,B}}{T_{1,B}} - k_B M_{z,B} + k_B P_B M_{z,A} \end{pmatrix} \quad (19)$$

These equations look daunting but can be easily solved using desktop mathematical software to yield spectra, or even to fit experimental spectra and extract rate parameters.

Application to Geochemistry

NMR has been used to determine chemical speciation and elucidate the phase and characteristics of minerals (specifically using solid-state NMR as a complementary technique to X-ray crystallography) and has been used to measure reactions that occur in the geosphere. The probes have also been engineered to measure systems under extreme environments. Specifically, high-pressure NMR measurements are now used to understand the chemistry of the deep Earth. Diamond-anvil cells are most widely used with solid-state NMR measurements and can reach

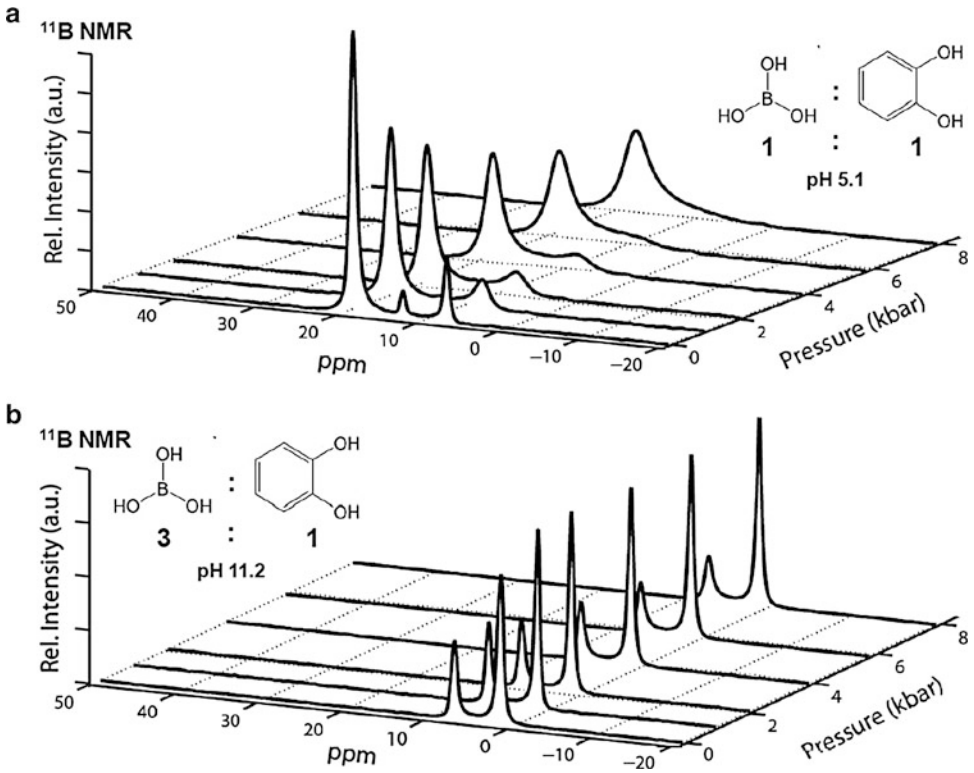

Nuclear Magnetic Resonance, Fig. 2 The complexation of boric acid by catechol as a function of pressure, leading to coalescence at pressures of 0.8 GPa

up to 20 GPa in pressure (Meier et al. 2014). Piston cylinder cells are typically used for solution-state NMR and can reach up to 2.0 GPa in pressure. Solution chemistry at higher pressure is dominated by solvent effects, although the kinetics of reaction can sometimes be measured due to coalescence of signals (Pautler et al. 2014) (Fig. 2).

Conclusion

Nuclear magnetic resonance is an analytical method with profound potential for geochemistry, both in solid and solution state. It is sensitive to molecular structure and chemical dynamics and samples those dynamics at the most important timescales (microseconds to seconds). It is a relatively insensitive, yet nondestructive, technique that is widely pervasive in academia and industry. Although solid-state NMR is relatively common in the geochemical and mineralogical literature, less common is the solution state at geochemical conditions of high temperatures and pressures, though constant advances are being made in this field.

Cross-References

► Analytical Techniques

References

Bloch F (1946) Nuclear induction. Phys Rev 70:460–474
Meier T, Herzig T, Haase J (2014) Moissanite anvil cell design for giga-pascal nuclear magnetic resonance. Rev Sci Instrum 85:043903
Helm L, Merbach AE (1999) Water exchange on metal ions: experiments and simulations. Coord Chem Rev 187:151–181
Hore PJ (1995) Nuclear magnetic resonance. Oxford University Press, Oxford
Levitt MH (2008) Spin dynamics, 2nd edn. Wiley, Chichester
McConnell HM (1958) Reaction rates by nuclear magnetic resonance. J Chem Phys 28:430–431
Pautler BG, Colla CA, Johnson RL, Klavins P, Harley SJ, Ohlin CA, Sverjensky DA, Walton JH, Casey WH (2014) A high-pressure NMR probe for aqueous geochemistry. Angew Chem Int Ed 53:9788–9791

Nucleosynthesis

Jitendra Nath Goswami
Physical Research Laboratory, Ahmedabad, India

Definition

Nucleosynthesis is the creation of all the atomic nuclides known to us through a variety of processes that started with an explosive event, the so-called "Big-Bang" and followed by nuclear processes that include fusion, neutron capture, proton capture, energetic particle interactions, and spallation. Fusion of protons and neutrons led to formation of deuterium, helium, and very little of lithium. It continues today with fusion, neutron, and proton capture in large stars, supernova explosions as well as spallation resulting from collisions between preexisting nuclei and cosmic rays.

Origin and Abundances of the Elements

The elements and their isotopes, present in our solar system, and in other stellar systems, are products of nuclear and energetic processes taking place in various astrophysical environments, starting with the "Big-Bang," that marks the beginning of our universe. The term "Nucleosynthesis" broadly refers to the various energetic astrophysical processes involved in the formation of the nuclides known to us.

There are 81 naturally occurring stable elements, starting with Hydrogen ($Z = 1$) to Bismuth ($Z = 83$), along with two unstable elements, Technetium ($Z = 43$) and Promethium ($Z = 61$). In addition, there are nine other unstable elements that include Thorium ($Z = 90$) and Uranium ($Z = 92$). The total number of nuclides, both stable and long-lived, is more than 300.

Studies of early solar system solids, present in meteorites, revealed fossil records of nearly a dozen short-lived, now-extinct nuclides (e.g., ^{41}Ca, ^{26}Al, ^{60}Fe, ^{129}I, ^{244}Pu) that are now identified as products of stellar nucleosynthesis. Injection of these nuclides from an exploding stellar source into the proto-solar cloud is generally considered as the trigger for the collapse of the cloud leading to formation of the proto-Sun and some of the first solar system solids (Goswami and Vanhala 2000). Fossil records (decay products) of these now-extinct radionuclides are preserved in early solar system solids.

Formation of the First Nuclides

Synthesis of the nuclides, in particular, H and He, dates back to the beginning of our universe, following the so-called "Big-Bang" event. The extremely high energy density during the very early stages of our universe provided a high temperature ($>10^{10}$ K) radiation environment dominated by energetic gamma ray photons. The equivalence of energy and matter ($E = mc^2$) led to formation of a rapidly changing populations of subatomic particles, in particular, protons and neutrons, as well as mu-meson, electron, and their antiparticles in such an environment. Although formation and destruction reactions are in equilibrium at this stage, protons will be more abundant because of their lower mass. The formation of deuterons (^{2}H) took place after temperature dropped significantly and followed by formation of ^{3}H, ^{3}He, and ^{4}He. This led to a

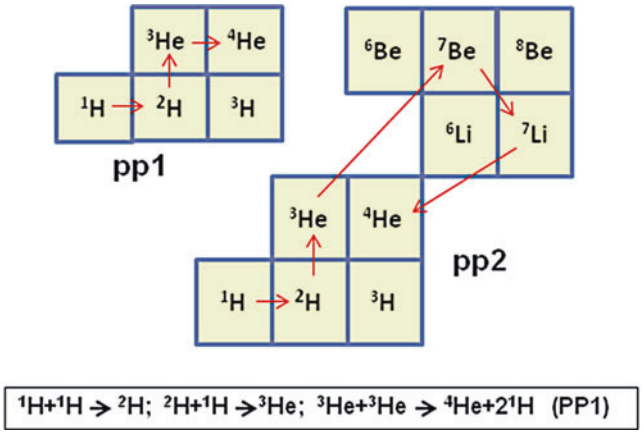

Nucleosynthesis, Fig. 1 Hydrogen Burning (PP1 & PP2 Chains)

decrease in abundance of neutrons resulting in lower abundances of ^{7}Li and ^{7}Be. Formation of the first nuclides in the early universe followed two dominant pathways, designated PP1 and PP2 chains and, a minor one, the PP3 chain.

A proposal made by George Gamow and his colleagues in late 1940s (Alpher et al. 1948) suggested that neutrons will constitute a significant fraction of matter following the big-bang event and facilitate production of elements, starting with deuteron, through successive neutron capture. The absence of stable nuclides with mass 5 and 8 made the suggestion untenable.

It was also realized at that time that the energy radiated by the Sun, attributed to its gravitational collapse, cannot sustain solar luminosity for more than tens of millions years, an extremely small duration compared to the age of the Sun, inferred to be in excess of 4 billion years, based on geological evidences. The suggestion that nuclear reactions in stellar interior can replenish energy radiated by the star was based on studies on nuclear transmutation by Hans Bethe (1939), who also proposed the reactions responsible for energy generation in stars and for the Sun in particular (Fig. 1).

Synthesis of Nuclides in Stellar Interior

Two seminal papers in the field of nucleosynthesis, published in 1957 by Burbidge, E. M. et al. and A. G. W. Cameron, provided a broad outline of the nuclear processes taking place in stellar interior and also during explosive stellar events (e.g., supernova) leading to formation of the nuclides. This was preceded by the suggestion that nuclear reactions in stars can lead to formation of chemical elements heavier than helium (Hoyle 1946 1954). It was also established that a few of the low mass nuclides (lithium, beryllium, and boron) are products of energetic particle interactions in space environment (Reeves 1994). These early studies of nucleosynthesis were followed by a large volume of work taking into account the finer details of various stellar sites and nucleosynthesis processes. Explaining the abundances of the elements as well as their isotopes in our Solar System was the main focus and these are now known with very high accuracy (see e.g., Anders and Grevesse 1989; Lodders 2010). The Nobel lectures by Penzias (1979) and Fowler (1984) provide a very engrossing description of the development in the field of nucleosynthesis.

Even though a variety of stellar sources have contributed towards the formation of the Solar System, the very uniform elemental and isotopic composition of solar system matter suggest an *extremely well-mixed proto-solar cloud* whose collapse led to formation of our Solar System. An explosive stellar event, a supernova, is the most probable trigger for this collapse (Goswami and Vanhala 2000).

A new dimension was added to the field of stellar nucleosynthesis following the identification of "stardust" (microscopic interstellar grains), refractory in nature, in primitive meteorites (Anders and Zinner 1993). These grains, nano- to micrometer in size, reveal large isotopic anomalies, relative to average solar system composition and host records of stellar environments in their formation sites (Asymptotic Giant Branch (AGB) star, Novae, Supernovae). This provides a gateway for studies of nucleosynthesis processes in specific stellar environment, beyond the realm of the Solar System (see also, Meyer and Zinner 2006).

Synthesis of the naturally occurring elements and their isotopes present in the Solar System solids may be divided into three broad segments: primordial nucleosynthesis (H, He), energetic particle (cosmic ray) interactions (Li, Be, B), and stellar nucleosynthesis (C and heavier elements). A concise description of these processes is presented in the following.

Primordial Nucleosynthesis

Our ideas of primordial nucleosynthesis are based on the standard Big-Bang model of our universe that suggests formation of hydrogen and nearly all of helium within the first few minutes following this explosive event. The agreement between the predicted relative abundances of the first nuclides (^{1}H, ^{2}H, ^{3}He, ^{4}He) that formed in the early universe, with their observed abundances at present, in regions of our universe, which have not experienced much of chemical evolution, supports this view (Peebles 1971). A very refreshing discussion is also provided by S. Weinberg (1977).

Cosmic Ray Spallation

The next group of elements, Li, Be, and B, are not primary product of stellar nucleosynthesis. These elements are destroyed easily in energetic nuclear processes taking place in stellar interiors. They are produced by interaction of

energetic particles present in interstellar space (Galactic Cosmic Rays) with ambient interstellar matter. Collisions of energetic carbon and oxygen ions in cosmic rays with hydrogen atoms in interstellar medium lead to production of these three elements (see, e.g., Reeves 1994). The source of energetic cosmic rays could be an exploding star (a supernova) or interstellar matter accelerated by supernova shocks. A small fraction of Li is also contributed from primordial nucleosynthesis, while stellar nucleosynthesis adds to the inventory of both ^{7}Li and ^{11}Be.

Stellar Nucleosynthesis

Energy generation in the interior of a star is driven by "nuclear fusion," starting with fusion of hydrogen to form helium (^{4}He), the dominant mode of energy production in stars (Bethe 1939). The fusion chain of exothermic reactions continues with successive burning of He, C, O, and Si in stellar interior, leading to formation of iron (^{56}Fe), beyond which fusion become an endothermic reaction.

Formation of elements beyond the iron group takes place through capture of neutrons by preexisting nuclides and follows two distinct paths, the "s" (slow) or "r" (rapid) process. The proton-rich nuclides that are away from the line of beta-stability are produced by photo-nuclear reactions, the "p" process. An outline of the various nucleosynthesis processes, involving burning of seed nuclides, starting with Hydrogen, is presented in the following.

Hydrogen Burning

There are several pathways for fusion of hydrogen to form helium when the internal temperature of the star exceeds 10^{7} K, sufficient to overcome the coulomb barrier. In solar mass stars, it proceeds via the proton-proton (PP-I) chain:

$$^{1}\mathrm{H}+{}^{1}\mathrm{H}\rightarrow {}^{2}\mathrm{H}+\gamma;{}^{2}\mathrm{H}+{}^{1}\mathrm{H}\rightarrow {}^{3}\mathrm{He}+\gamma;{}^{3}\mathrm{He}+{}^{3}\mathrm{He}\rightarrow {}^{4}\mathrm{He}+2{}^{1}\mathrm{H}$$

Even though produced in small amount, ^{3}He can react through different channels (PP-II and PP-III), yielding ^{7}Be, ^{7}Li, and ^{8}B as intermediate products that finally end up as ^{4}He. In massive star with higher core temperature, conversion of H to He can proceed via C─N─O cycle with ^{12}C, present initially in the star acting as a catalyst. ^{14}N is a major product of the CNO cycle along with minor amounts of ^{13}C,^{15}N and ^{17}O.

Helium Burning

Gradual exhaustion of hydrogen in the core of the star will make hydrogen burning weaker, leading to contraction of the core, and make it dense enough to raise the temperature of the Helium-rich core to ~10^{8} K that can initiate Helium burning. The most important reaction at this stage is the "triple-alpha" reaction that converts ^{4}He to ^{12}C. Several other important nuclides, ^{16}O, ^{18}O, ^{22}Ne, ^{25}Mg, are also produced during this stage via successive exothermic alpha capture by ^{14}N, an end product of hydrogen burning through C─N─O cycle:

$$\begin{aligned}
{}^{4}\mathrm{He}+4\,\mathrm{He}+4\mathrm{He} &\rightarrow {}^{12}\mathrm{C}+\gamma;\\
{}^{12}\mathrm{C}+{}^{4}\mathrm{He} &\rightarrow {}^{16}\mathrm{O}+{}^{4}\mathrm{He};\\
{}^{14}\mathrm{N}+{}^{4}\mathrm{He} &\rightarrow {}^{18}\mathrm{F}+\gamma;\\
{}^{18}\mathrm{F} &\rightarrow {}^{18}\mathrm{O}+\mathrm{e}^{+}+\nu;\\
{}^{18}\mathrm{O}+{}^{4}\mathrm{He} &\rightarrow {}^{22}\mathrm{Ne}+\gamma;\\
{}^{22}\mathrm{Ne}+{}^{4}\mathrm{He} &\rightarrow {}^{25}\mathrm{Mg}+\mathrm{n}
\end{aligned}$$

Successive capture of alpha particles by ^{14}N, end product of hydrogen burning through the CNO cycle, also leads to production of ^{18}O and ^{22}Ne. For stars with mass less than 8 solar mass, He burning marks the last stage of energy generation process that leads to a stellar core enriched in carbon and oxygen.

Carbon and Oxygen Burning

Nuclear burning in stars with mass less than 8 solar mass cannot raise the core temperature needed for nuclear burning beyond helium. They end their life as a cool and dense white dwarf. However, in more massive stars, the core temperature is high enough (10^{9} K) to initiate He burning, followed by successive burning of carbon and oxygen. This leads to production of ^{20}Ne, ^{23}Na, and ^{24}Mg via carbon burning, while ^{28}Si, ^{31}P, and ^{32}Si are products of oxygen burning. Synthesis of elements at this stage can also follow production via capture of alpha (^{4}He) particle and proton by carbon and oxygen that can lead to synthesis of nearly all the elements between Ne and Ar.

Silicon Burning and the "e" (Equilibrium) Process

Silicon burning, the last stage of nuclear fusion in stellar interior, takes place when the core temperature reaches ~3×10^{9} K. The high temperature environment leads to endothermic photo-disintegration of preexisting nuclei around silicon via (γ, α) reaction, prior to initiation of the fusion process. This provides a copious source of alpha particles that are captured by nuclides having intermediate masses leading to formation of precursors of the iron group nuclides. Interactions among the nuclides – alpha particles,

proton, and neutrons – lead to formation of the iron group nuclides with equilibrium abundances; the nuclides having higher binding energy being more abundant. The relative abundances of the iron group nuclides during the "e" (equilibrium) process depend on the nature of both strong and weak nuclear interactions, in particular, electron capture and neutrino emission.

Explosive Nucleosynthesis

The end of silicon burning will leave a massive star with a core composed primarily of Fe-group elements that will be surrounded by layers enriched with elements (H, He, C, O, Ne, Si) that are products of earlier evolutionary stages of the star. Exhaustion of nuclear energy source in the interior of the star will lead to collapse of the stellar core that will trigger an explosion (a supernova event) resulting in expulsion of the outer layers of the star as well as further processing of material in the inner layers of the star. This transient phase of nuclide processing is termed as "explosive nucleosynthesis." The nonequilibrium nature of this phase leads to synthesis of nuclides with very different abundance pattern than those produced in the slow hydrostatic burning inside a stellar object, even though the seed nuclides are the same. The abundance of a sizable number of intermediate mass nuclides in the solar system can be explained as products of "explosive nucleosynthesis."

A low mass star, which generally ends its life as a white dwarf, may also suffer a catastrophic end. This happens if the white dwarf has a companion from which it accretes matter and its mass exceeds a critical mass and become unstable and explodes. Such an explosion is termed as a Type-I supernova to distinguish it from the explosion of high mass massive stars, termed as Type-II supernova. White dwarfs are primarily left over carbon- and oxygen-rich cores of low mass stars, and their explosive end primarily leads to synthesis of iron group of nuclides (Fe, Co, Ni).

Elements Beyond the Iron Group

Synthesis beyond the iron group of elements follows two processes that are termed as *r-process,* involving rapid neutron capture, and the *s-process,* characterized by slow neutron capture.

r-Process

The r-process is effective when the neutron densities are high enough to facilitate build-up of heavier elements beyond iron via successive neutron capture by the Fe group as well as other heavy elements. Even though these elements will be far removed from the line of β-stability, as long as neutron capture rate exceed the beta decay rates, they will eventually suffer successive beta decay and end up as stable high mass nuclide (Fig. 2).

s-Process

Unlike the relatively fast r-process, the slow neutron capture takes place in stellar environments that provide relatively low flux of neutrons over a significant period of time. In such a setting, the neutron capture timescales could be longer than or comparable to beta decay timescales and bypassing unstable neutron-rich nuclide is not possible as in the r-process. The main sources of neutrons for the s-process are the two reactions: $^{13}C\ (\alpha, n)\ ^{16}O$ and $^{22}Ne\ (\alpha, n)\ ^{25}Mg$; ^{22}Ne is a product of successive alpha capture by ^{14}N. Thus, both the seed nuclides (^{13}C and ^{14}N) are products of hydrogen burning via C─N─O cycle. These reactions take place in low mass stars during the red-giant phase of their evolution, following H and He burning, when nuclear burning takes place in a thin He shell between the carbon- and oxygen-rich core and the H-rich outer envelope. He-burning in massive stars is another plausible site for s-process synthesis. Spectroscopic evidence for the presence of the unstable element Technetium in low mass stars (red giant; Merrill 1952) also makes them a plausible site for s-process synthesis providing an important link in the s-process path around mass 100.

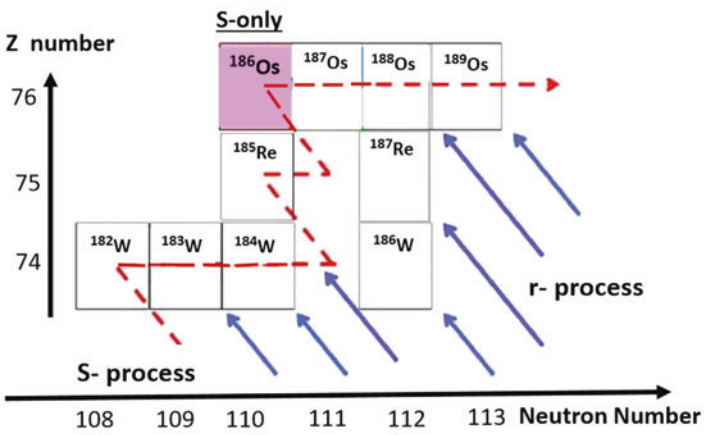

Nucleosynthesis, Fig. 2 Pathways for S (slow: red) and R (rapid: blue) processes for synthesis of elements (isotopes) beyond the iron group

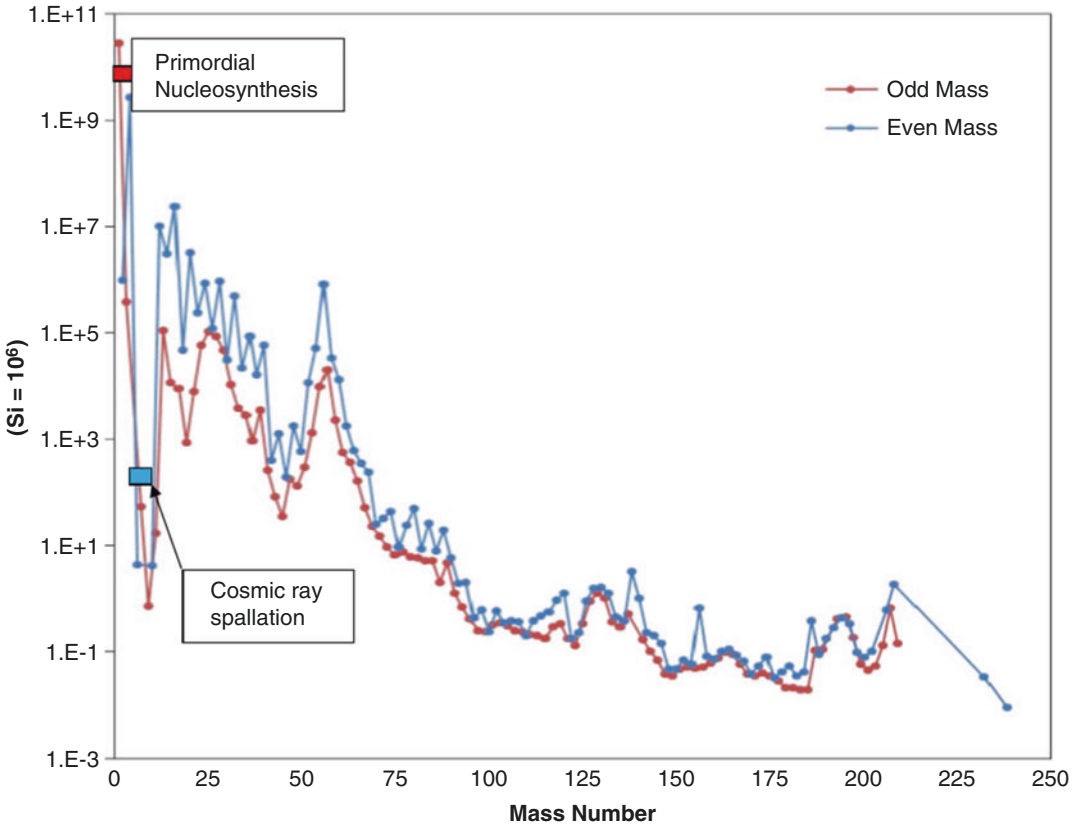

Nucleosynthesis, Fig. 3 Abundances of nuclides

p-Process

A group of *proton-rich* stable nuclides having very low abundances cannot be produced by the nucleosynthesis processes outlined above. These are stable neutron-deficient nuclides, heavier than iron, which are observed only in solar system matter and grouped as product of p-process, as they were initially thought to be product of proton capture. However, there is no suitable astrophysical site where proton capture (p, γ) may dominate over photonuclear reaction like (γ, n) or (γ, p). These nuclides are generally considered to be products of photonuclear reaction involving s- and r-process nuclides that lead to formation of proton-rich isotopes which finally end up as proton-rich stable nuclides via (γ, p) and (γ, α) reactions (Arnould and Goriely 2003) (Fig. 3).

Summary

Our understanding of stellar nucleosynthesis processes, since the time of the early work by Burbidge et al. (1957) and Cameron (1957), that attempted to explain the solar system abundances of nuclides compiled by Suess and Urey (1956), based on studies of meteorites as well as spectroscopic observation of the Sun, has improved significantly. It is now possible to identify specific nucleosynthesis processes responsible for synthesis of nuclides present in the solar system and also understand the lower abundances of the odd mass nuclides.

Advances in studies of nucleosynthesis allow one to predict abundance pattern of the Fe-group nuclei and beyond, with a fair degree of accuracy, by considering contributions from both Type-I and type II supernova (Timmes et al. 1995). The s-process systematics can lead to the abundance peaks beyond the iron group, at mass numbers around 84, 138, and 208, with magic neutron numbers 50, 82, and 126, respectively. Another group of heavy nuclides, at mass numbers, 80, 130, and 195, preceding the s-process peaks, can be explained by considering r-process systematics (Fowler 1984). A general discussion of various nucleosynthesis processes and their connection to solar system abundances of nuclides is provided by Cox (1989). Several other areas related to field of nucleosynthesis include chemical evolution of our galaxy that deals with star formation rates, stellar evolution models and stellar nucleosynthesis (see, e.g., Clayton 1988) and cosmo-chronology (Symbalisty and Schramm 1981), timescales of nucleosynthesis of the radioactive nuclides present in the early solar system and, also present day solar system.

A major impetus for studies in Stellar nucleosynthesis came following the discovery of microscopic grains of silicon carbide, graphite, and diamonds in primitive meteorites with

large isotopic anomalies, relative to solar system solids (see e.g., Meyer and Zinner 2006). The stellar origin of these grains can be inferred from the very different abundance pattern of H and C isotopes, relative to solar system matter, thus hosting nucleosynthesis records that are not homogenized as in the case of our solar system.

Cross-References

- ▶ Atomic Number, Mass Number, and Isotopes
- ▶ Carbon Isotopes
- ▶ Cosmic Elemental Abundances
- ▶ Cosmogenic Nuclides
- ▶ Hydrogen Isotopes
- ▶ Meteorites
- ▶ Presolar Grains
- ▶ Stable Isotope Geochemistry

References

Alpher RA, Bethe HA, Gamow G (1948) The origin of chemical elements. Phys Rev 73:803

Anders E, Grevesse N (1989) Abundances of the elements: meteoritic and solar. Geochim Cosmochim Acta 53:197–214

Anders E, Zinner E (1993) Interstellar grains in primitive meteorites. Meteoritics 28:490–514

Arnould M, Goriely S (2003) The p-process of stellar nucleosynthesis: astrophysics and nuclear physics status. Phys Rep 384:1–84

Bethe HA (1939) Energy production in stars. Phys Rev 55:103

Burbidge EM, Burbidge GR, Fowler WA, Hoyle F (1957) Synthesis of the elements in stars. Rev Mod Phys 29:547–650

Cameron AGW (1957) Stellar evolution, nuclear astrophysics and nucleogenesis. Chalk River Report, Atomic Energy of Canada Ltd., CRL-41; see also Publ Astron Soc Pacific 69:201–222

Clayton DD (1988) Stellar nucleosynthesis and chemical evolution of the solar neighbourhood. In: Kerridge JF, Matthews MS (eds) Meteorites and the early solar system. Arizona University Press, Tucson, pp 1021–1062

Cox PA (1989) The elements: their origin, abundances and distributions. Oxford University Press, Oxford, 207 pp

Fowler WA (1984) The quest for the origin of the elements. Science 226:922–935

Goswami JN, Vanhala HAT (2000) Extinct nuclides and the formation of the solar system. In: Mannings V, Boss A, Russell S (eds) Protostar & planets IV. Arizona University Press, pp 965–996

Hoyle F (1946) The synthesis of the elements from hydrogen. Mon Not R Astron Soc 106:343–383

Hoyle F (1954) On nuclear reactions occurring in very hot STARS. I. The synthesis of elements from carbon to nickel. Astrophys J Suppl 1:121–146

Lodders K (2010) Solar system abundances of the elements. In: Goswami A, Reddy BE (eds) Principles and perspective in cosmochemistry. Springer, Berlin, pp 379–417

Merrill PW (1952) Spectroscopic observations of stars of class S. Astrophys J 116:21–26

Meyer BS, Zinner E (2006) In: Lauretta DS, McSween HY Jr (eds) Meteorites and the early solar system II. University of Arizona Press, Tucson, pp 69–108

Peebles PJ (1971) Physical cosmology. Princeton University Press, Princeton

Penzias AA (1979) The origin of the elements. Science 205:549–554

Reeves H (1994) On the origin of the light elements (Z < 6). Rev Mod Phys 66:193–216

Suess HE, Urey HC (1956) Abundances of the elements. Rev Mod Phys 28:53–74

Symbalisty EMD, Schramm DN (1981) Nucleocosmochronology. Rep Prog Phys 44:293–328

Timmes FX, Wooseley SE, Weaver TA (1995) Galactic chemical evolution: helium through Zinc. Astrophys J 98(Suppl):617–658

Weinberg S (1977) The first three minutes, 1993rd edn. Basic Books, New York, 203 pp

Nutrients

J. A. Brandes
Skidaway Institute of Oceanography and Department of Marine Science, University of Georgia, Savannah, GA, USA

Synonyms

Bioessential compounds; Essential elements

Definition

Nutrients are elements or compounds used by organisms in the production of biomass, cellular function, or related structural material.

Introduction

Nutrients are elements or compounds used by organisms in the production of biomass, cellular function, or related structural material (Odum 1959). Nutrients that are required for proper cellular functioning are described as *essential nutrients*. Traditionally, major essential nutrients (utilized by organisms in approximate percentage or greater abundances in biomass) have been considered to be N, P, and S. However, essential trace nutrients are also required for growth and proper cellular function; these include Fe, Co, Zn, Ni, V, and many others (see Fig. 1). Part of what defines an element as a nutrient is its potential for limitation, which is the reason that O and H are not typically defined as nutrients, even though they are required for the production of biomass, and water is a requirement for all known life. In addition to elements used in biomass, inorganic ions such as Cl^-, Mg^{2+}, Na^+, and K^+ are also required for cellular function and may be considered essential nutrients. Finally, some

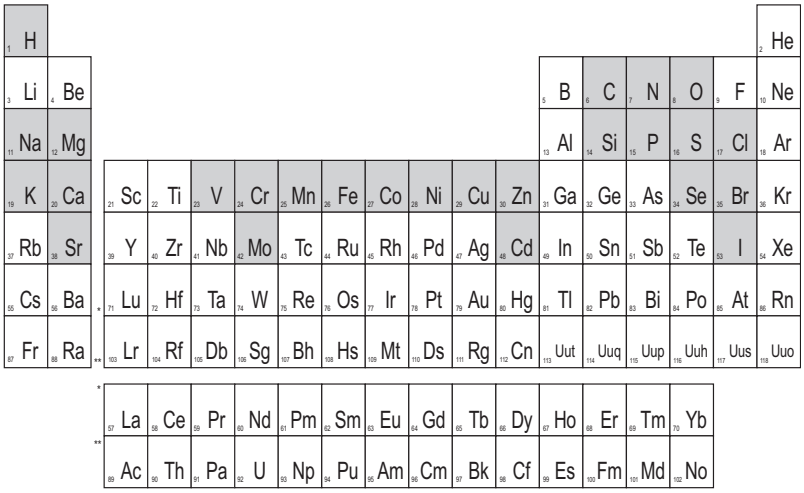

Nutrients, Fig. 1 Shaded elements are those identified as nutrients or involved in cellular function

organisms require Si to form inorganic shells and will be growth limited in silicate-depleted environments.

Another important aspect of a nutrient is its chemical form and consequent bioavailability. Different species may have very different abilities to access the nutrients in their environment and may require that a nutrient be in a specific form. For example, ocean waters contain over half a millimole per liter of nitrogen, far in excess of need if all were available for marine organisms. However, most of this N is in the form of dissolved N_2 gas, which, with a very strong triple bond, is not accessible by most organisms for their growth needs. Only organisms with specialized enzymatic systems that can reduce N_2 and form organic nitrogen forms can access this pool (Sohm et al. 2011). Furthermore, not all primary producers can access N in its oxidized forms (e.g., NO_3^- or NO_2^-). Similarly, much of the supply of Fe to the ocean away from continental margins is in the form of insoluble iron oxides that are considered unavailable to primary producers without chemical reduction to more soluble compounds (Norman et al. 2014). Several significant taxa of marine primary producers require Co in the organically bound form of cobalamin (vitamin B-12) in order to use it (Moore et al. 2013).

Nutrient Limitation

The concept of nutrient limitation dates back to the "law of the minimum" developed by Justus von Liebig and expanded upon by FF Blackman (von Liebig 1840; Blackman 1905; Odum 1959). Von Liebig postulated that growth of plants was limited by the scarcest resource and not by total resources. This has been refined to indicate that scarcity is in relation to the relative availability of other nutrients. The most famous of such relationships is the "Redfield ratio" developed by Alfred Redfield (1934). Redfield found that the proportions of carbon to nitrogen to phosphorus used by marine primary producers were 106C:16N:1P. As there is typically less than a 16:1 stoichiometry in bioavailable N vs bioavailable P, N is thought to be the primary limiting major nutrient over long time scales in the ocean. However, there are major regions of the surface ocean (where primary productivity takes place) that contain significant amounts of both bioavailable N and P. These are described as "high-nutrient low-chlorophyll" (HNLC) waters and are limited by the trace nutrient Fe (Moore et al. 2013). In freshwater environments, P is generally thought of as the primary limiting nutrient, especially since the implementation of P-limiting policies to combat eutrophication (Schindler et al. 2016).

There is also considerable evidence for nutrient co-limitation in the environment, where two or more nutrients are found in limiting concentrations. Several regions of the global surface ocean are nearly as depleted in P as N. Addition of only N to these environments results in only a small increase in biomass as compare to addition of both N and P. Other co-limiting nutrient pairs found in the environment have been N, P and Fe, N and Co, Fe and Si, and Fe and Zn (Moore et al. 2013).

Nutrient availability can differ greatly between environments. While Ca and S are plentiful in marine ecosystems, they can be limiting in terrestrial forests and croplands. Such limitation can be exacerbated by enhanced leaching caused by acid rain (St. Clair et al. 2008) and also by the release of toxic elements such as Al during leaching events that may prevent the uptake of Ca (Schaberg et al. 2001).

Organisms can in some cases ameliorate nutrient limitation in their environment. Although the Redfield ratio appears remarkably robust over most of the ocean (Anderson and Sarmiento 1994), individual organisms have shown a wide range of nutrient uptake ratios under simulated limiting conditions (Bertilsson et al. 2003), either by proportional reduction in the cellular production of high N content proteins or P-rich phospholipids or by the substitution of metals in

enzymatic systems (e.g., Co for Zn) (Moore et al. 2013). Over longer time scales, some organisms can evolve to reduce their relative requirements for certain elements (e.g., substituting S for P in membrane lipids) (van Mooy et al. 2009). In addition, organisms employ a wide range of strategies for collecting, storing, and concentrating scarce nutrient resources. These include storage as insoluble intracellular pools (polyphosphates) (Diaz et al. 2016), production of extracellular organic compounds to chelate and solubilize metals (Hopkinson and Morel 2009), and physical movement to gather nutrients from subsurface regions.

Nutrient Proxies

Patterns of nutrient availability in the surface ocean have been investigated using proxies as indicators of past biological productivity and CO_2 uptake (Deutch and Weber 2012). Commonly used proxies include Cd:Ca ratios in foraminifera shells (for P) (Boyle 1988) and the ^{15}N of organic N in sediments, biomarkers, and encased in diatom frustules (for bioavailable N and N-cycling processes) (Ren et al. 2012). Such studies have indicated significant shifts in global nutrient patterns during glacial maxima (Straub et al. 2013). The present-day environment is experiencing a large (2–3× pre-industrial levels) anthropogenic input of N and P from agricultural and industrial sources (Codispoti 2007). This is subsequently exported through runoff and riverine transport to coastal oceanic environments, resulting in the shift of several from oligotrophic (primary producer growth rates and biomass limited by nutrient availability) to eutrophic (containing high primary producer growth rates and biomass limited by light availability or other factors) states (Fulweiler et al. 2012).

Summary

Nutrients comprise a subset of elements and compounds required for life. Environments typically have one or more nutrients that may be considered as limiting or potentially limiting to organism growth. However many organisms can mitigate such limitations by adjustment of required nutrient ratios or substitution of a more abundant nutrient for a more limiting one.

Cross-References

- ▶ Biogeochemistry
- ▶ Biological Pump
- ▶ Carbon
- ▶ Iron
- ▶ Nitrogen
- ▶ Paleoproductivity
- ▶ Phosphorus

References

Anderson LA, Sarmiento JL (1994) Redfield ratios of remineralization determined by nutrient data analysis. Glob Biogeochem Cycles 8(1):65–80

Bertilsson S et al (2003) Elemental composition of marine Prochlorococcus and Synechococcus: implications for the ecological stoichiometry of the sea. Limnol Oceanogr 22(2):185–198

Blackman FF (1905) Optima and limiting factors. Ann Bot 19:281–295

Boyle EA (1988) Cadmium: chemical tracer of deepwater paleoceanography. Paleoceanography 3(4):471–489

Codispoti LA (2007) An oceanic fixed nitrogen sink exceeding 400 Tg Na-1 vs the concept of homeostasis in the fixed-nitrogen inventory. Biogeosciences 4(2):233–253

Deutsch C, Weber T (2012) Nutrient ratios as a tracer and driver of ocean biogeochemistry. Annu Rev Mar Sci 4:113–141

Diaz JM et al (2016) Polyphosphate dynamics at station ALOHA, North Pacific subtropical gyre. Limnol Oceanogr 61(1):227–239

Fulweiler RW, Rabalais NN, Heiskanen AS (2012) The eutrophication commandments. Mar Pollut Bull 64(2):319–324

Hopkinson BM, Morel FMM (2009) The role of siderophores in iron acquisition by photosynthetic marine microorganisms. Biometals 22(4):659–669

Moore CM et al (2013) Processes and patterns of oceanic nutrient limitation. Nat Geosci. https://doi.org/10.1038/NGEO1765

Norman L et al (2014) Iron biogeochemistry in aquatic systems: from source to bioavailability. Chimia 68(11):764–771

Odum EP (1959) Fundamentals of ecology, 2nd edn. Saunders, Philadelphia

Redfield AC (1934) On the proportions of organic derivatives in sea water and their relation to the composition of plankton, James Johnstone memorial volume. University Press of Liverpool, pp 176–192

Ren H, Sigman DM, Thunell RC, Prokopenko MG (2012) Nitrogen isotopic composition of planktonic foraminifera from the modern ocean and recent sediments. Limnol Oceanogr 57(4):1011–1024

Schaberg PG, DeHayes DH, Hawley GJ (2001) Anthropogenic calcium depletion: a unique threat to forest ecosystem health? Ecosyst Health 7(4):214–228

Schindler DW et al (2016) Reducing phosphorus to curb Lake eutrophication is a success. Environ Sci Technol 50(17):8923–8929

Sohm JA, Webb EA, Capone DG (2011) Emerging patterns of marine nitrogen fixation. Nat Rev Microbiol 9(7):499–508

St. Clair SB, Sharpe WE, Lynch JP (2008) Key interactions between nutrient limitation and climatic factors in temperate forests: a synthesis of the sugar maple literature can. J For Res 38:401–414

Straub M et al (2013) Changes in North Atlantic nitrogen fixation controlled by ocean circulation. Nature 501:200–203

Van Mooy BAS et al (2009) Phytoplankton in the ocean use non-phosphorus lipids in response to phosphorus scarcity. Nature 458:69–72

Von Liebig (1840) In: Playfair L (ed) Organic chemistry in its applications to agriculture and physiology. Taylor and Walton, London, 418 pp

O

Ocean Biochemical Cycling and Trace Elements

Hein J. W. de Baar, Steven M. A. C. van Heuven and Rob Middag
NIOZ Royal Netherlands Institute for Sea Research, Department of Ocean Systems (OCS), and Utrecht University, Den Burg, The Netherlands

Definition

Ocean biochemical cycling refers to the distribution of nutrients and bio-essential elements at low concentration that is controlled by their uptake by phytoplankton in surface waters, sinking and remineralization of organic remains in deeper waters, and subsequent redistribution by thermohaline circulation.

Introduction

Dissolved inorganic carbon (C as DIC) varies around ~2 millimoles [mM = 10^{-3} M] in seawater and is pivotal for life in the sea. Much less abundant are the nutrients nitrate and phosphate that occur in the micromole [μM = 10^{-6} M] range and are essential for each living organism. Also essential for life are several trace nutrient elements, notably Fe and Zn, that occur in the nanomolar [nM = 10^{-9} M] range or even lower such as Co in the picomolar [pM = 10^{-12} M] range. Several other trace elements also occur in the nanomolar [nM] to picomolar [pM] range. Finally a few ultratrace elements occur in the femtomolar [fM = 10^{-15} M] range in seawater.

The distribution of many of the chemical elements in seawater is strongly controlled by biological processes, not only in the modern ocean but also due to the major role of biological evolution in the chemical evolution of the oceans (Vernadsky 1926; Redfield 1958; Lovelock 1979; Holland 1984).

Ocean Biological Cycle Requires Bio-essential Elements

The primordial atmosphere and ocean did not comprise free O_2 (see ▶ Precambrian Geochemistry). In the mildly reducing Archean ocean (~3.8–2.5 Gy before present), the transition metals manganese (Mn), iron (Fe), cobalt (Co), nickel (Ni), copper (Cu), and zinc (Zn) would have been readily soluble as Mn^{2+}, Fe^{2+}, Co^{2+}, Ni^{2+}, $CuCl^{2-}$, and Zn^{2+}, respectively (De Baar and La Roche 2003; Saager et al. 1989; Lewis and Landing 1991), and would no doubt have been present at relatively high concentrations in this primordial ocean where reduced sulfide was also present (Turner et al. 2001). As the first life evolved, these transition metals were incorporated in many biochemical functions. As a result, *all* modern cellular organisms living today, prokaryotes and eukaryotes, comprise and hence require the following chemical elements in order of their typical abundance in the living cell:

$$C > N > P >>> Fe > Zn > Mn > Cu > Ni >> Co \quad (1)$$

The major biochemical functions are listed in Table 1.

The initially reducing ocean environment eventually became oxidizing as more and more free O_2 was generated by photosynthesis (Crowe et al. 2013) and the bio-essential trace elements, notably Fe and Mn, precipitated by oxidation. Notably Fe, which once was present abundantly in seawater and therefore incorporated in many biochemical functions during evolution, nowadays is in very low concentrations in seawater and often the limiting bio-essential element for growth of phytoplankton. Thus by producing O_2, the algae eventually themselves caused their own Fe limitation.

Within the marine ecosystem of today, the unicellular phytoplankton or algae and the zooplankton and bacterioplankton are the most abundant in terms of biomass. The net growth or net decomposition of the overall plankton pool corresponds to net loss or gain, respectively, of significant amounts of these nine bio-essential elements in the ambient

W. M. White (ed.), *Encyclopedia of Geochemistry*,
https://doi.org/10.1007/978-3-319-39312-4

Ocean Biochemical Cycling and Trace Elements, Table 1 The nine chemical elements that are essential for life and their major biochemical functions, their symbols, and their names in bold print. Essential also relates to the concept that each one of these can occasionally be a limiting element for growth in conditions that may occur of very low availability, i.e., low abundance as per the concepts of limitation after Von Liebig (De Baar 1994). Please be informed that there exist several different types of superoxide dismutases, all with the same function but with quite different metal elements as cofactor. Not listed are hydrogen (H) that occurs in every biological molecule and oxygen (O) that also is very common notably in various organic functional groups; both are so very abundant in the water molecule (H_2O), i.e., never potentially limiting, that they are not being treated as essential elements. Sulfur is listed here, but is abundant as major sulfate ion in seawater and never bio-limiting. The uptake of Mg for chlorophyll is trivial compared to the very high background concentration at ~0.48 mol.L^{-1} of Mg in ambient seawater (Reynolds 2006). Next to the nine elements essential for all life (bold print) and S and Mg, also listed are six more elements that play a role in specific taxonomic groups, among which Si and Ca are most important for formation of hard parts (e.g., shells, frustules, corals) and Mo for N_2 fixation by diazotrophs. Compilation after Twining and Baines (2013) also based on Sunda (1989), Michibata and Sakurai (1990), Frausto da Silva and Williams (1994, 2001), De Baar and La Roche (2003), Wolfe-Simon et al. (2005, 2006), Bruland and Lohan (2003), Bruland et al. (2014)

Atomic number	Mass	Symbol	Name	Major biochemical function
6	12.011	**C**	**Carbon**	Carbohydrates and in every biochemical molecule
7	14.007	**N**	**Nitrogen**	Amino acids in proteins and many other molecules and functions
12	24.305	Mg	Magnesium	Central atom in chlorin ring of chlorophyll molecule, active site of RuBisCO
14	28.086	Si	Silicon	Opaline (SiO_2) external frustules of diatoms, skeletons of radiolaria
15	30.974	**P**	**Phosphorus**	Phospholipids, ATP
16	32.065	S	Sulfur	Methionine, cysteine, ferredoxin
20	40.078	Ca	Calcium	Calcite and aragonite skeletons and shells, coral reefs
23	50.942	V	Vanadium	Unique high concentration in blood cells of Ascidiacea (sea squirts) (Michibata and Sakurai 1990)
25	54.938	**Mn**	**Manganese**	O_2-evolving enzyme, superoxide dismutase, arginase, phosphotransferases
26	55.854	**Fe**	**Iron**	Electron transport in photosynthesis and respiration, nitrate and nitrite reductases, N_2 fixation: conversion of hydrogen peroxide to water, peroxidase reduction of reactive oxygen species, superoxide dismutase
27	58.933	**Co**	**Cobalt**	Vitamin B12 in C and H transfer reactions
28	58.693	**Ni**	**Nickel**	Urease hydrolysis of urea, superoxide dismutase
29	63.546	**Cu**	**Copper**	Photosynthesis electron transport, mitochondrial electron transport, ascorbic acid redox, superoxide dismutase
30	65.39	**Zn**	**Zinc**	Carbonic anhydrase, alkaline phosphatase, RNA polymerase, tRAN synthetase, reverse transcriptase, carboxypeptidase, superoxide dismutase
42	95.94	Mo	Molybdenum	N_2 fixation, nitrate reductase
48	112.41	Cd	Cadmium	Carbonic anhydrase

seawater. The more the biology has an impact on the oceanic presence of an element, the more the distribution of such element deviates from salinity. Therefore the ocean distributions of these nine bio-essential elements are non-conservative, i.e., deviating from the constant proportions of the major elements that constitute the overall salinity (see entry ▶ Ocean Salinity, Major Elements, and Thermohaline Circulation).

Other Chemical Elements with a Biological Role

In addition several taxa of marine organisms also incorporate other chemical elements for biological functions (Table 1), and this may, more or less, affect the ocean distribution of such element.

Sulfur (S) is utilized by most organisms, but the background concentration of sulfate in seawater is very high and not really affected. Similarly the uptake of Mg for plant chlorophyll hardly affects the very high background concentration of Mg in seawater.

Bio-calcification is by organisms that secrete hard shells and skeletons of $CaCO_3$ in either crystalline forms of either calcite or aragonite. By removal of both Ca^{2+} and HCO_3^- from seawater, both are also somewhat nonconservative, somewhat because this biological role is small relative to the high abundance of Ca^{2+} and to a lesser extent HCO_3^- in seawater. The major calcite producers in the open ocean are the group of coccolithophorid phytoplankton and the foraminifera zooplankton. The most abundant pelagic aragonite producers are the pteropods, and aragonite also forms naturally in corals and in almost all mollusk shells.

The other major type of hard parts is the opaline silicon oxide (SiO_2) that is produced by the important group of the diatoms among the phytoplankton, which are deemed to represent in the order of ~40% of all primary production in the oceans, and the radiolaria among the zooplankton. The concentration of dissolved silicate in seawater is relatively

modest in the micromole [$\mu M = 10^{-6}$ M] range and non-conservative due to this role in biology. Therefore silicate is commonly classified with the other major nutrients nitrate and phosphate.

There are three more trace elements that have a known biological function in some organisms. Vanadium (V) has very rare biological functions in ascidians (sea squirts) and a few other organisms (Michibata and Sakurai 1990). Molybdenum (Mo) is essential for nitrogen fixation that is one of the important biochemical pathways that play a role in controlling the oceanic nitrogen inventory (La Roche and Breitbarth 2005). Cadmium (Cd) has been found to serve as the pivotal atom in the enzyme carbonic anhydrase of a few diatom species investigated thus far (Xu et al. 2008).

Brief Outline of Marine Ecosystem Cycling of Elements

The basis of the marine ecosystem is photosynthesis, i.e., the primary production in the oceans. This is by either (i) single-cell phytoplankton or (ii) multicellular macroalgae or (iii) the symbiontic zooxanthellae within coral structures. The single-cell phytoplankton can be either prokaryotes, that is, cells without a nucleus, or eukaryote cells that do have a nucleus. Multicellular macroalgae and single-cell zooxanthellae both are eukaryotes. Marine photosynthesis in the oceans tends to follow the overall reaction

$$\begin{aligned} &106\mathrm{DIC} + 122\mathrm{H_2O} + 16\mathrm{NO_3}^- + 1\mathrm{HPO_4}^{2-} \\ &\quad + (\mathrm{Mn, Fe, Co, Ni, Cu, Zn}) + \text{energy} \rightleftarrows \\ &\quad \left[(\mathrm{CH_2O})_{106}(\mathrm{NH_3})_{16}(\mathrm{HPO_4})_1(\mathrm{Mn, Fe, Co, Ni, Cu, Zn})\right]_{\text{organic biomass}} \\ &\quad + 138\mathrm{O_2} \end{aligned} \tag{2}$$

adapted after Redfield, Ketchum, and Richards (1963) but here also including the six bio-essential trace elements (Mn, Fe, Co, Ni, Cu, Zn) for which their very low relative amount is subject of research nowadays (see below section Trace Nutrient Elements). The resulting organic biomass is energetically rich and hence serves as a food and energy source for bacteria and animals in the reverse reaction (2), i.e., remineralization or respiration.

In a real phytoplankton bloom in surface waters or in the ensuing export of biogenic debris into the deeper waters, the element ratio values may deviate considerably from the values given in above Eq. 2. However due to deep ocean mixing, such deviations tend to "average" such that at any given station, the proportions are more close to those in Eq. 2, but still significant variations exist.

The above stoichiometric constants (i.e.,106, 16, 1, −138), known as the Redfield ratios, were at the time largely based on concentrations measured mostly in the North Atlantic region. Since then variations in ocean distributions of, for example, nitrate and phosphate, and the causes thereof have been discussed on the basis of then available larger more worldwide datasets (Fanning 1992; De Baar et al. 1997), and significant adjusted values of the stoichiometric constants have been derived and advocated (e.g., Anderson and Sarmiento 1994), as reviewed by Sarmiento and Gruber (2006) and others.

Photosynthesis occurs only within the upper euphotic zone of the oceans where it produces major amounts of dissolved oxygen O_2, which can become a few percent oversaturated in daytime during an intense phytoplankton bloom. The euphotic zone is defined as the depth the zone where sunlight is available to the 1% light depth as its lower boundary. In very clear waters, the depth of the euphotic zone can be as deep as 70–80 m. However due to the abundance of algae and other plankton, this is often much less due to "self-shading," while in nearshore waters, the presence of mineral particles (sand, silt) restricts light penetration to just a few meters or less.

The reverse reaction is respiration by either bacteria (here including the Archaea) or zooplankton and higher animals up the food chain to fish, octopus, sharks, and whales. This takes place throughout the water column. Most respiration takes place within the upper water column (<100 m depth) and remineralizes in the order of ~90% of all photosynthetic produced biomass. This respiration consumes dissolved O_2, but this is rapidly replenished from the overlying atmosphere. Also C, N, and P and Fe, Zn, Cu, Mn, Ni, and Co are returned to the seawater and can be used once again for photosynthesis. Overall this is a quite efficient ~90% recycling of resources.

However some ~10% of biomass settles, as mostly dead debris, into the intermediate waters (100–1000 m depth range) and here is remineralized almost completely. Of this remaining 10%, around ~9% of total primary production is remineralized, dissolved O_2 is consumed, and the concentration of O_2 decreases significantly. On the other hand, DIC, nitrate, phosphate, Fe, Zn, Cu, Mn, Ni, and Co are replenished again. Finally the ~1% of primary production that escapes remineralization within the upper 1000 m settles into the deep ocean and is the food supply for all life in the deep waters and in the sediments. Life in deep waters consumes some 0.9% and leaves merely ~0.1% for the benthic biota at the seafloor that consumes ~0.09% such that merely the leftover ~0.01% is buried more or less forever within the sediments.

When now combining (Fig. 1) this biological cycling of elements with the thermohaline circulation of the deep ocean, it is realized that throughout the long journey (lasting 1000–2000 years) of the deep water from the northern North Atlantic, around Antarctica, and eventually ending up in the North Pacific, there is a steady raindown of biogenic debris settling from the surface ocean into the intermediate and deep waters.

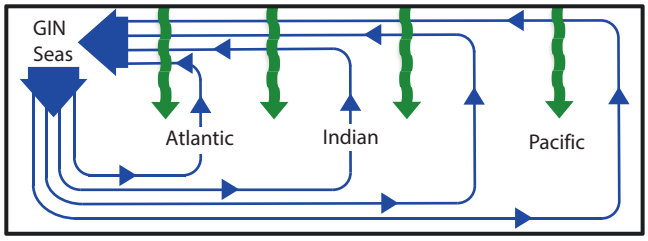

Ocean Biochemical Cycling and Trace Elements, Fig. 1 Combination of ocean circulation (*blue arrows*) with vertical settling of biogenic debris (*green arrows*) to explain the concept of accumulation of remineralized DIC and nutrients when deep water becomes older. This figure is redrafted in color after original of Broecker and Peng (1982). Formation of deep water in the Greenland-Iceland-Norwegian (GIN) Seas, see entry on ▶ Ocean Salinity, Major Elements, and Thermohaline Circulation. Notice that for simplicity of the graph, the deep water formation in the Antarctic Ocean is not shown

Within the intermediate and deep waters, the debris is remineralized to dissolved DIC and nutrients, and O_2 is consumed (Eq. 2 in reverse direction). The net result is a steady accumulation of DIC and nutrients, and steady decrease of dissolved O_2, from the relatively "young" northern North Atlantic Deep Water to eventually the quite "old" North Pacific Deep Water (Fig. 2).

Major Nutrient Elements: Nitrate, Phosphate, and Silicate

Due to net photosynthesis (Eq. 2) in surface waters, the dissolved **nitrate** (NO_3^-) and **phosphate** (HPO_4^{2-}) are removed, and very low, often bio-limiting, concentrations remain in surface waters of the temperate and tropical oceans (Fig. 2). In contrast these major nutrients are not fully depleted in surface waters of firstly the Antarctic Ocean and also the equatorial Pacific and the Subarctic North Pacific. These ocean regions represent some 30–40% of the world oceans and are known as the high-nutrient low-chlorophyll (HNLC) waters. For these HNLC waters, we now know that the combination of iron limitation and light limitation prevents the regional phytoplankton to develop blooms to full depletion of the major nutrients. For this HNLC condition, see the below section on "Trace Nutrient Iron (Fe)."

As noted earlier, silicate is an important nutrient for diatoms, which undergo seasonal blooms. At the end of winter, there are ample N, P, and Si in surface waters, and once more sunlight appears in early spring, massive diatom blooms take place. Rapidly within 3–4 weeks, all dissolved Si is removed from surface waters, and the spring diatom blooms collapse due to Si limitation.

Another aspect is that the opaline frustule remains intact in seawater with a low dissolved silicate concentration that actually is strongly undersaturated versus opal. This is because the living diatoms have an organic coating on the frustules, preventing direct contact with the undersaturated seawater and hence preventing dissolution. Yet upon senescence the diatom debris will settle downward and hence export into deeper waters. Meanwhile the organic coating also disappears, e.g., due to bacterial consumption, and the frustules tend to dissolve. The rate of dissolution depends strongly on the surface/volume ratio such that the smaller frustules of small diatoms rapidly disappear due to dissolution, but very large diatom frustules may rapidly (~100 m/day or more) sink all the way down the ~4 km deep water column to the seafloor. Thus overall the dissolution of settling diatom frustules is a balancing act between dissolution and settling, where size plays a key role. As a result the apparent typical depth of opal dissolution is deeper than for respiration input of nitrate and phosphate, and overall the concentration of dissolved silicate increases more steadily with depth (Fig. 2). Again in combination (Fig. 1) with deep circulation, the dissolved silicate in the deep North Pacific is about threefold higher than in the deep North Atlantic (Fig. 2).

At locations where intense blooms of large-size diatoms occur in surface waters, the rain rate of settling opal dominates the sedimentation at the seafloor. Here thick layers of opaline sediments accumulate. Even bottom waters with the highest dissolved silicate at ~150 μM still are undersaturated versus opal, such that the deposit tends to dissolve. This leads to even higher concentrations in the pore waters within the sediments, and the pore water reaches equilibrium such that from there on, the opal remains preserved.

Within the Antarctic Ocean, there is major upwelling of deep waters, bringing ample supply of major nutrients N, P, and Si to the euphotic zone in the surface waters. The circumpolar Antarctic polar Front is the major region where large diatoms utilize this ample supply and grow intensely (Smetacek et al. 1997), and as a result, the underlying sediments comprise thick layers of opal, representing the major (~70%) ocean sink of dissolved Si. When comparing the river input of dissolved Si with the overall dissolved Si budget of seawater, one derives an oceanic residence time of ~10,000 years for Si (Tréguer and Rocha 2013), as compared to the ~1000 years' time of ocean mixing. This implies that, on average, once a Si atom has entered the oceans via rivers, it will be at the surface once every ~1000 years and from there on take part in the cycle of diatom growth and dissolution. This cycle will occur some nine to ten times before the SiO_2 is buried "forever" in the thick layers of opaline diatom ooze.

It has been estimated that worldwide, the cycles of N and Si are of comparable magnitude, i.e., their average ocean cycling is in a Si:N = 1:1 ratio or thereabout (Sarmiento and Gruber 2006). However it is less well realized that large variations exist; most notably the Antarctic diatoms tend to be very heavily silicified such that a ratio Si:N in the 2–3 range is more valid here. Given the key role of large Antarctic diatoms in the global Si cycle (Tréguer and Rocha 2013), and

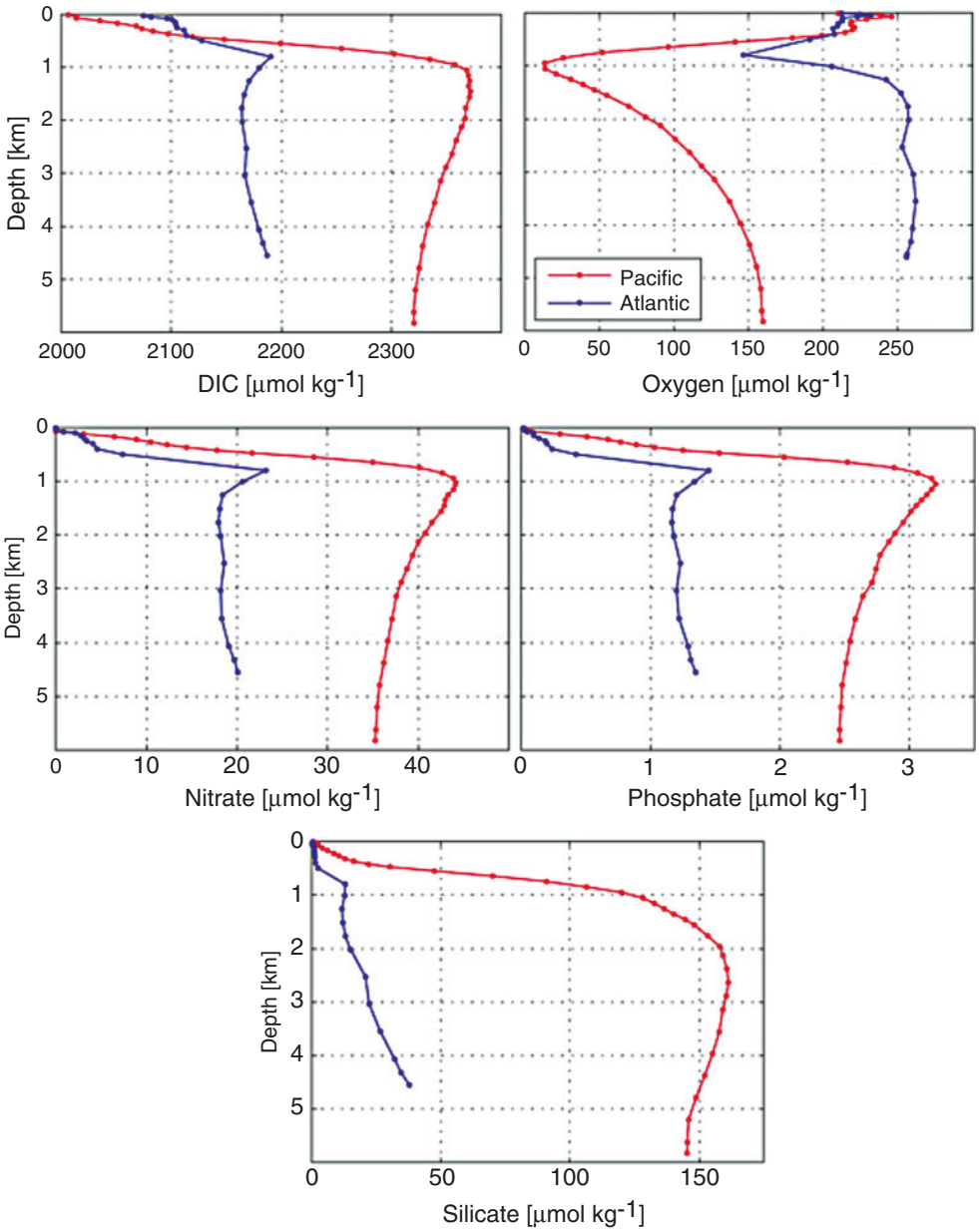

Ocean Biochemical Cycling and Trace Elements,

Fig. 2 Vertical distributions of the DIC, dissolved oxygen, and the major nutrients nitrate, phosphate, and silicate in the Northwest Atlantic Ocean (*blue*) versus the Northeast Pacific Ocean (*red*). Higher DIC in deep Pacific versus deep Atlantic is due to (i) respiration of organic matter plus (ii) dissolution of $CaCO_3$. Higher nitrate and phosphate in deep Pacific versus Atlantic due to respiration, also explaining the opposite lower dissolved oxygen. Data for Bermuda Atlantic Time-Series Station (BATS) of GEOTRACES cruise GA02-64PE321 aboard RV Pelagia, station 21 (31°45.92′N, 64°04.95′W at 13 June 2010), after Rijkenberg et al. (2015), is available at (www.geotraces.org). Data for North Pacific is from RV Melville cruise 318M2004 along WOCE line PO2, station 119 (30.00°N,159.70°W at 4 August 2004), is available in GLODAP-2 via CCHDO. (https://cchdo.ucsd.edu/cruise/318M200406). Circulation age (Matsumoto 2007) of the deep waters (>1500 m) at the North Atlantic station is ~200 years; the ^{14}C age is ~800 years. Circulation age of the deep waters (>1500 m) at the North Pacific station is ~1100 years; the ^{14}C age is ~2100 years

the key role of the Antarctic Ocean in world circulation, this should not be, but often is, overlooked in simulation modeling of the world ocean biogeochemical cycles.

Trace Nutrient Elements

Each of the trace elements in the oceans does have one or more sources and one or more sinks, respectively, briefly summarized in Panel A (also see entry ▶ Ocean Salinity, Major Elements, and Thermohaline Circulation, its Fig. 1).

The importance in biology of the six bio-essential trace metal elements (Table 1) is in the order Fe > Zn > Mn > Cu > Ni >> Co (as per Eq. 1). However here Fe and Mn are together discussed first, given the great significance of redox chemistry and hydrothermal supply for both elements. Next Zn, Cu, Ni, and Co are discussed and finally the three minor "biological" trace metal elements V, Mo, and Cd that play a special role for some, but by no means all, organisms.

Iron (Fe) is by far the most important trace metal transition element in biology, with many biochemical functions. Here the relative ease of redox between Fe(II) and Fe(III) is pivotal in, for example, electron transfer within the living cell (Table 1).

In the modern O_2-rich ocean waters, the dissolved Fe in 0.2 µm filtered seawater is in the Fe(III) oxidation state and is predominantly (~99%) bound to organic ligands forming Fe (III)-organic complexes. The remaining ~1% is dominated by

the 0.92% inorganic species $Fe(OH)_{3(dissolved)}$ and further 0.045% $Fe(OH)_4^-$, 0.037% $Fe(OH)_2^+$, and merely 3×10^{-11}% free Fe^{3+} ion. In the same O_2-rich seawater conditions, the thermodynamics of the redox half reaction

$$Fe^{2+} \rightleftarrows Fe^{3+} + e \quad (3)$$

predicts the ratio Fe^{2+}/Fe^{3+} of these free ions is $10^{0.42}$ or 2.63 (De Baar and De Jong 2001). Taking this ratio and given the above speciation of Fe(III) states and the speciation of Fe (II) states (Panel B), the overall ratio Fe(II)/Fe(III) is in the order of 10^{-12} in O_2-rich seawater. When now taking a mildly anoxic environment without O_2 and with a sulfide concentration of 10 μM such as in pore waters of reduced marine sediments, Eq. 3 now yields the free ion ratio Fe^{2+}/Fe^{3+} of $10^{17.4}$. Taking into account the speciation, the overall ratio Fe(II)/Fe(III) is in the order of 10^7 in mildly reducing anoxic pore waters. Thus from open ocean waters to mildly anoxic pore waters, the ratio is shifted by a dramatic factor of 10^{19}. This major shift is the key to understanding the driving redox forces for the cycling of Fe in the oceans. Finally, deeper in the sediments at higher S^{2-} concentrations, there occurs precipitation of various iron sulfide deposits, thus removing Fe from solution in pore waters. Thus there is an optimal depth within the sediment where O_2 is absent and S^{2-} is still quite low where mobilization of Fe is optimal for Fe diffusing upward into overlying waters.

Panel A. External sources and sinks of dissolved trace metals in ocean waters

The external sources and sinks, and the several processes within the ocean waters (Panel B), all may affect the distribution of any given trace element in ocean waters.

River inflow is modified by estuarine mixing of the fresh river water with saline seawater. As a result there is massive flocculation of colloids (defined in Panel B) from the original river water. Most of the river inflow of many trace metals, notably Fe, is removed and deposited in estuarine sediments, such that only a small percentage truly enters the oceans but still can be traced over long distances (Klunder et al. 2012b).

Aeolian deposition into surface waters of dust coming from the continents may be either as wet deposition with rainwater or as dry deposition. Rainwater has a wide range of pH values with final deposition in the pH range 4–7, i.e., acidic and more favorable for partial dissolution of metals from dust than surface seawater at pH ~8 (Jickells and Spokes 2001).

Oxidation and reduction (redox) affects those metals that have two or more oxidation states within the overall redox range of the oceans, sediments, and hydrothermal vents. In the modern O_2-rich ocean, the major dissolved states Mn^{2+} and Fe^{3+} are thermodynamically unstable and tend to deposit solid oxyhydroxides such as MnO_2 and $Fe(OH)_3$ but more often some poorly defined amorphous Fe-Mn oxyhydroxide phases. Within marine sediments the respiration of organic matter (reverse Eq. 2) by bacteria consumes the available O_2 in pore waters, and supply from overlying waters is slow due to restricted vertical diffusion. Once the dissolved O_2 is almost all removed, other specialized bacteria take over and use other oxidants (electron acceptors) that are more favorable under the conditions. These are in sequence first the dissolved nitrate NO_3^- being reduced to ammonia (NH_4OH) with nitrite (NO_2^-), nitrous oxide (N_2O), and N_2 as intermediates or also end products. Once nitrate is depleted, there secondly follows the reduction of solid MnO_2 to high concentrations of dissolved Mn^{2+} and thirdly reduction of solid $Fe(OH)_3$ to high Fe^{2+} concentrations. These very high concentrations of Mn^{2+} and Fe^{2+} in the pore waters diffuse upward in bottom waters from where they are by ocean lateral mixing transported to the open ocean, with steady loss due to the very slow or slow oxidation of Mn^{2+} and Fe^{2+}, respectively. Similar redox chemistry is known to take place for dissolved cerium Ce^{3+} versus solid oxidized CeO_2. Deeper in the sediment, there is reduction of the abundant sulfate SO_4^{2-} to the reduced sulfite S^{2-} state. Latter sulfide leads to precipitation of generally very insoluble FeS, CuS, ZnS, and CdS.

Hydrothermal vent effluents at mid-ocean ridges have a high temperature in the 300–400 °C range and are very strongly reducing. This is accompanied by very high concentrations of reduced Mn^{2+} and Fe^{2+} as well as elevated concentrations of dissolved Co, Cu, Zn, Ag, Cd, and Pb (Von Damm et al. 1985). Once in contact with ambient, cold (2 °C), O_2-rich seawater, most of the Fe and Mn precipitate again as oxyhydroxides, also including the other metals, this leading to metalliferous sediments on the crest of mid-ocean ridges.

(*continued*)

For example, near Elephant Island, Antarctica, there is a distinct plume of dissolved Fe coming off the extensive shelf sediments, clearly discernible and accompanied by higher levels of Mn and Al versus the low background concentrations (Fig. 3).

When the bottom waters overlying anoxic sediments also have a low O_2 content, such as in the 100–1000 m depth range of the Northwest Indian Ocean or in the subsurface waters at the East Equatorial Pacific, this dissolved Fe can be

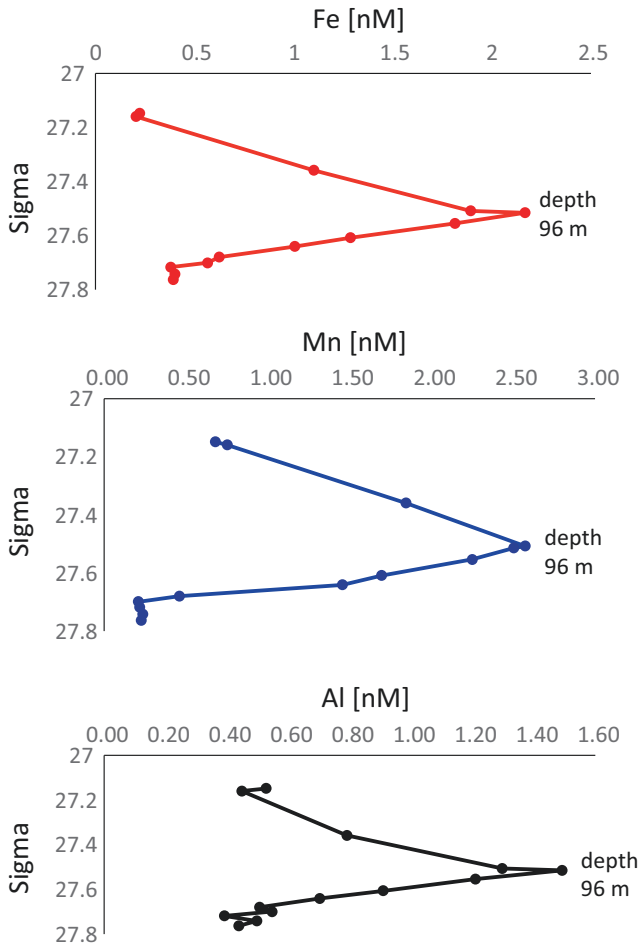

Ocean Biochemical Cycling and Trace Elements, Fig. 3 Distinct plumes of coinciding elevated dissolved Fe, Mn, and Al coming off the shelf near Elephant Island, Antarctica. Concentrations in nanomolar per liter [nM = 10^{-9} Mol.L^{-1}]. Vertical axis is sigma for density (e.g., sigma = 27.6 for density = 1027.6 kg.m^{-3}) increasing steadily with increasing depth. The maximum concentrations are at ~96 m depth (After Klunder et al. (2014). Data in Geotraces IDP 2014 (www.geotraces.org))

maintained at elevated concentrations in the order of 1–6 nM (Landing and Bruland 1987; Saager et al. 1989; Vu and Sohrin 2013).

In the high temperatures (300–400 °C) of extremely reducing hydrothermal effluents, the concentration of dissolved Fe may be as high as 1–2.5 millimolar (e.g., Von Damm et al. 1985, 1998), i.e., some three to eight million times higher than ambient deep ocean water. However due to mixing with ambient cold and oxidizing seawater, this is rapidly removed by oxidation and sedimentation on the ridge crest forming metalliferous sediments. Nevertheless the hydrothermal Fe source is so highly enriched that, despite the major loss at the ridge crest sediments, the plume can be traced at million-fold lower 1–3 nM Fe concentrations over hundreds of kilometers versus the low background concentration of Fe at ~0.3–0.4 nM in deep waters. For example, at the Antarctic Zero Meridian, there is an extensive ~1200 km wide plume of hydrothermal Fe near the Bouvet triple junction where three mid-ocean ridges meet (Fig. 4) and where undoubtedly intense hydrothermal effluents must exist. This plume is accompanied with high Mn also from hydrothermal input. Similarly at the Arctic Gakkel Ridge, an extensive hydrothermal plume of both Fe and Mn was found (not shown; Klunder et al. 2012a, Middag et al. 2011a), extending more than 500 km. Similarly extended plumes have been recently reported for the Pacific Ocean (Resing et al. 2015). Over that extent the concentrations of dissolved Fe and Mn steadily diminish due to combination of continued oxidation as well as dilution by mixing with ambient waters low in Fe and Mn. The decrease of dissolved Fe continues until a threshold concentration is reached that equals the concentration of Fe-binding organic ligands that from there on maintain the remaining dissolved Fe in solution. For assessing the net hydrothermal supply of Fe to the world oceans at large, this far-field extent of the relatively low-level (1–3 nM) plumes (Klunder et al. 2011, 2012a, 2014) with their slow chemical changes is most relevant.

The longest ocean trace element section thus far is in the West Atlantic Ocean and nicely shows all the processes contributing to the distribution of dissolved Fe (Fig. 5). There is a hydrothermal plume at ~2500 m depth just south of the equator that despite the long westward distance away from the Mid-Atlantic Ridge still is discernible versus the low 0.4–0.6 nM background deep dissolved Fe. Just north of the equator (~10 °N), the subsurface Fe maximum at 200–1000 m depth coincides with a strong O_2 minimum suggesting a reductive source of the elevated Fe. These O_2 minimum waters flow westward ("into the paper"), then turn around clockwise, and more northerly (~40 °N) become an eastward return flow that still carries the elevated Fe signal.

Sahara dust input causes elevated dissolved Fe in surface waters in the 20–30 °N region, accompanied by higher Mn and Al as well, where Al is the classical tracer of dust supply (Fig. 6). This high Fe in otherwise oligotrophic (nutrient-depleted) surface waters does support N_2 fixation by *Trichodesmium* phytoplankton in the Sargasso Sea near Bermuda.

Iron Limitation of High-Nutrient Low-Chlorophyll (HNLC) Regions

There are three regions where major nutrients N, P, and Si are in ample supply in surface waters, but still phytoplankton blooms are not able to utilize this resource. These are the Southern Ocean and the equatorial Pacific and Subarctic North Pacific, together representing ~30% of ocean surface waters. The hypothesis of Fe limitation of these HNLC regions was first tested in Fe addition experiments in bottle

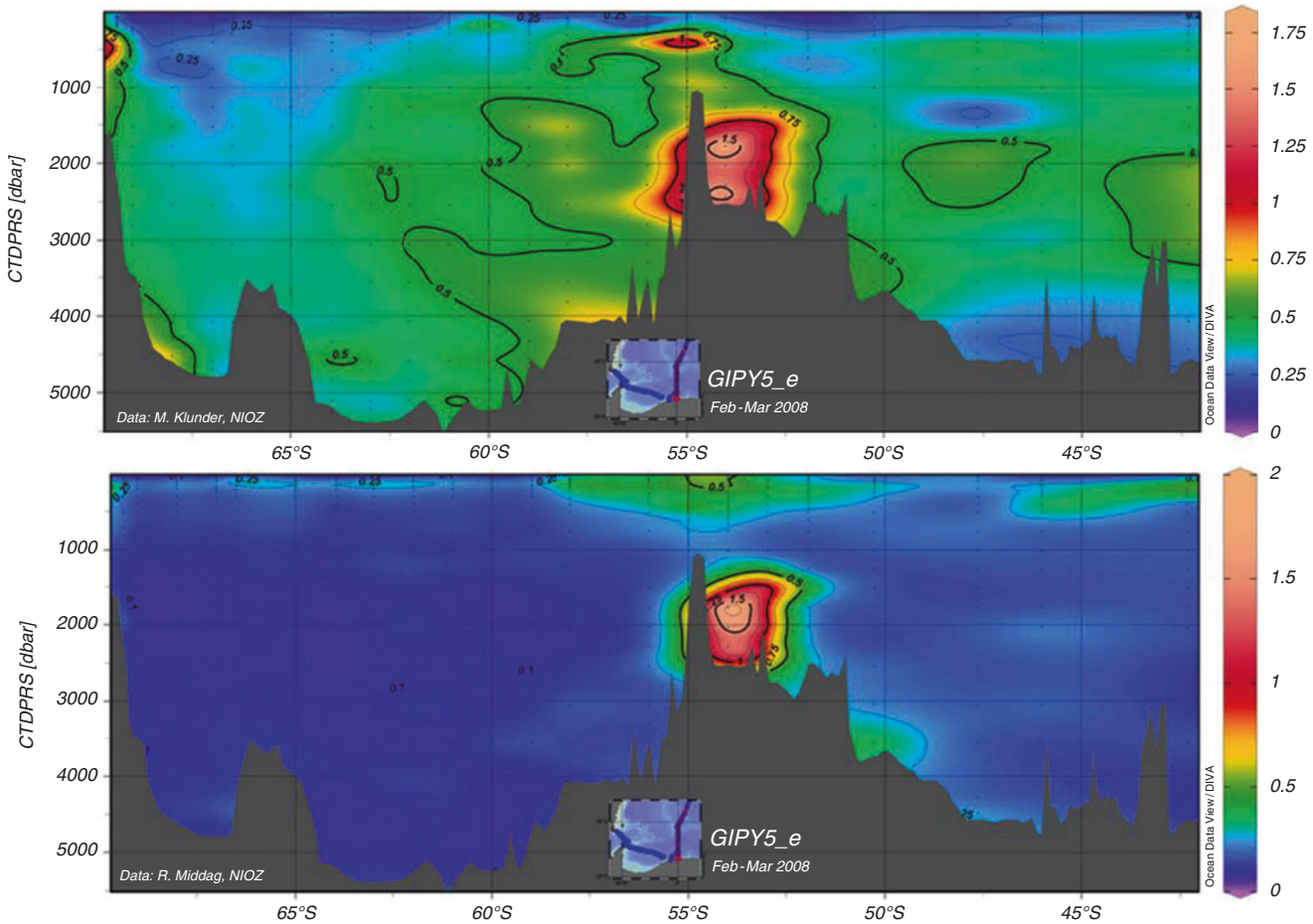

Ocean Biochemical Cycling and Trace Elements, Fig. 4 *Upper* graph: dissolved Fe at a 3000 km long section at the Antarctic Zero Meridian after Klunder et al. (2011). Vertical axis is pressure [decibar] that is virtually identical to depth [meter]. Notice very low Fe in surface waters notably near the Antarctic continent, vertically separated from the enriched hydrothermal plume at great depth >1000 m. *Lower* graph: dissolved Mn along the same section after Middag et al. (2011b). Notice very low Mn in surface waters notably near the Antarctic continent, vertically separated from the enriched hydrothermal plume at great depth >1000 m. The elevated Mn at the surface at 54 °S is due to a recent aeolian dust event, also found for Fe at the surface (less distinct in the above contour plot) and dissolved Al at the surface (not shown) (Data in Geotraces IDP 2014 (www.geotraces.org). Graphics www.eGeotraces.org using Ocean Data View (R. Schlitzer))

incubations in the Subarctic North Pacific (Martin and Fitzwater 1988) and in the Southern Ocean (De Baar et al. 1990; Buma et al. 1991). Next at the Polar Front, it was found that local naturally elevated Fe concentrations made the difference in stimulating three distinct blooms of phytoplankton accompanied by uptake of CO_2 (de Baar et al. 1995; Smetacek et al. 1997).

These and other findings led to a suite of large-scale *in situ* Fe fertilization experiments where an area of 50 km^2 or even 200 km^2 ocean surface water was fertilized with dissolved Fe. The major finding was that indeed, Fe addition did always stimulate phytoplankton blooms, but light limitation due to deep mixing in storms did also play a key role (de Baar et al. 2005). Therefore we now know that the phytoplankton in the HNLC regions is limited by a combination of light and iron limitation. The surface water values of Fe in the Antarctic (Fig. 4) are very low, notably ~0.1 nM near the Antarctic continent. There may be several reasons for this. Here the very deep (~1500 m) shelf under the continental ice sheet extending far over the sea is exceptional as it is not a source of Fe to overlying waters. The ice sheet acts as a cap largely preventing any biochemistry in the water column, and hence the underlying sediment is not a source of reduced Fe. In addition, the low dissolved Fe around Antarctica is due to very low dust input.

Panel B. Processes within ocean waters affecting the distribution of dissolved trace metals

Colloids. Throughout natural waters, both freshwater and seawater, there exists a continuum of physical/chemical state from truly dissolved to a wide range of colloidal sizes to truly particles. In the open

(*continued*)

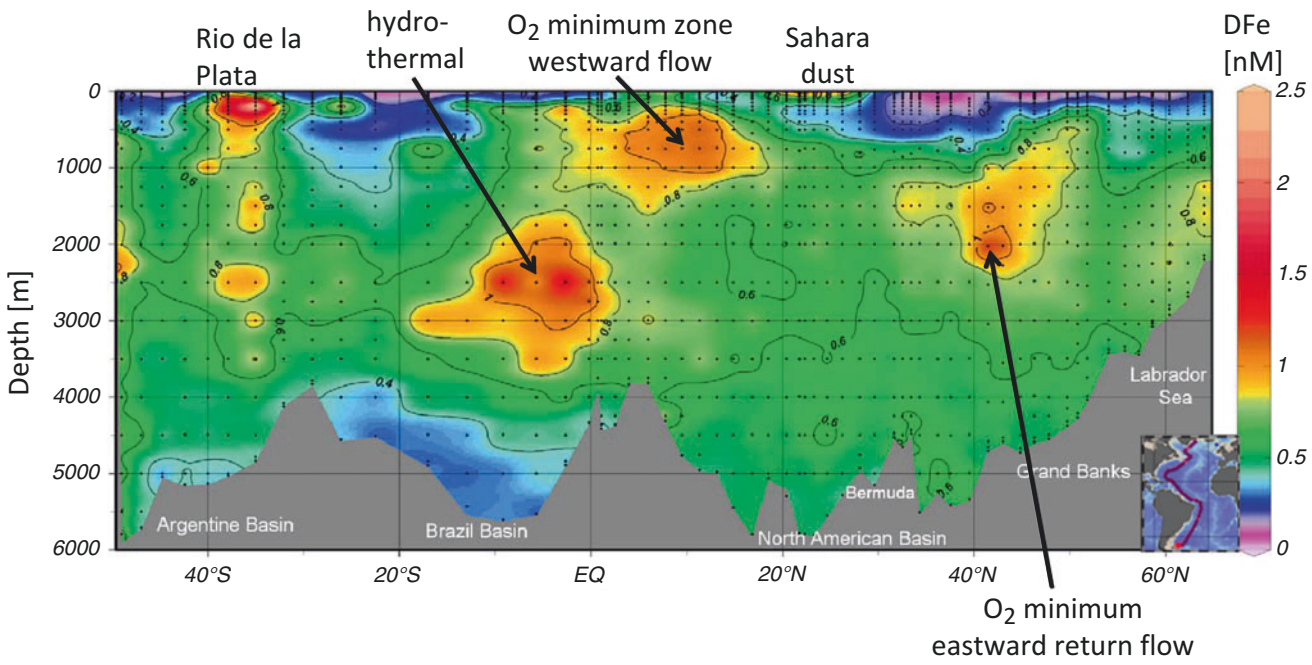

Ocean Biochemical Cycling and Trace Elements, Fig. 5 Section of dissolved Fe in the West Atlantic Ocean, Geotraces section GA02 (After Rijkenberg et al. 2014. Graphics using Ocean Data View (R. Schlitzer). All data as shown above by Rijkenberg and coworkers is in Geotraces IDP 2014 (www.geotraces.org))

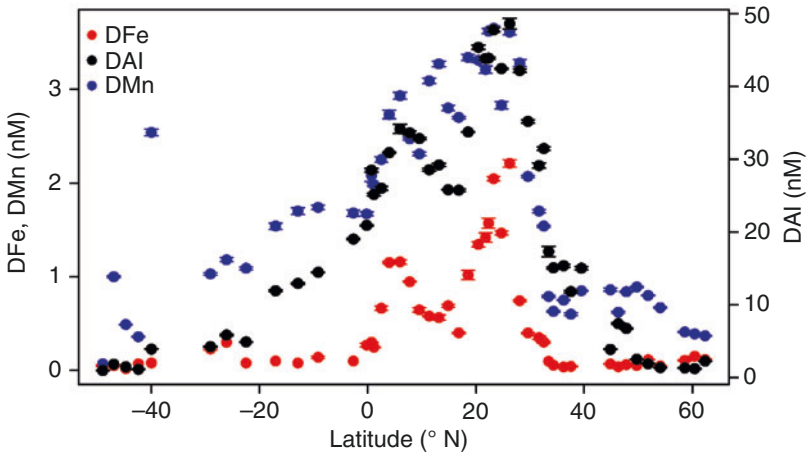

Ocean Biochemical Cycling and Trace Elements, Fig. 6 Surface water distributions of dissolved Fe, Al, and Mn along the West Atlantic section Geotraces GA02 (After Rijkenberg et al. 2014. Data is in Geotraces IDP 2014 (www.geotraces.org))

ocean, colloids can be defined by ultrafiltration methods to be in the ~0.02–0.2 μm (micron) size classes (Nishioka et al. 2001, 2005), the pool <0.02 μm then is defined as the soluble fraction, and all sizes above 0.2 μm are defined as particles. Colloids can play a significant role, for example, formation of Fe colloids in hydrothermal plumes. However due to space restrictions, here we must largely ignore the colloids and operationally define the dissolved trace metals by the size cutoff of 0.2 μm pore size filtration devices.

(*continued*)

Chemical speciation of dissolved trace metals results from the interaction of the free metal ion, for example, Fe^{3+} interacts with those ions of seawater to which it has great chemical affinity. For example, taking into account only the inorganic ions in seawater, the total dissolved Fe comprises 92% $Fe(OH)_{3(dissolved)}$, 4.5% $Fe(OH)_4^-$, 3.7% $Fe(OH)_2^+$, and merely 3×10^{-9}% free Fe^{3+} ion (Millero et al. 1995). Thus the concentration of free Fe^{3+} ion is a factor 3×10^{-11} less abundant than the total dissolved Fe(III). For the reduced Fe(II) state that can occur due to

(*continued*)

photoreduction (see below), there are 76% free Fe^{2+} ion, 23% $FeCO_{3(dissolved)}$, and minor concentrations of $FeHCO_3^+$, $Fe(CO_3)_2^{2-}$, and $Fe(OH)^+$ ions. Similar inorganic speciations have been calculated for all trace metal elements in seawater (Turner et al. 1981; Byrne et al. 1988). These calculations also include other divalent metals like Co(II), Ni(II), Cu(II), and Zn(II), trivalent metals like Al(III), and the REE(III), as well as for those metals existing as oxyanions such as V existing predominantly as vanadate HVO_4^{2-} ion, Cr existing mostly as chromate CrO_4^{2-} ion, and Mo existing mostly as molybdate MoO_4^{2-} ion.

Organic complexation of the free ion by dissolved organic ligands (largely unknown functional groups) has been found to be very significant for several trace metals, most notably Fe, Zn, Cu, and Co, that also happen to be bio-essential trace elements, as well as Cd that shows a strong relationship with the biological cycle. Using voltametric techniques it has been found that ~99% of dissolved Fe is organically bound (Gledhill and Van den Berg 1994; Gledhill and Buck 2012). The above inorganic speciation thus represents merely ~1% of the total dissolved Fe. Similarly 98% of dissolved Zn is bound by organic complexes. Notably for Fe this organic complexation is favorable for maintaining dissolved Fe in solution; without the stabilization by organic complexation, most of the dissolved Fe would tend to be removed by oxidative precipitation.

Photoreduction within the upper euphotic zone of the oceans is known to cause a (diurnal) shift from the Fe(III) to the Fe(II) oxidation state, with implications for overall distribution of Fe in different pools, and hence the availability of Fe for uptake by biota (Rijkenberg et al. 2004, 2005, 2006). Similarly photoreduction of particulate MnO_2 may lead to Mn dissolution such that the dissolved Mn^{2+} in surface seawater increases (Sunda et al. 1983; Sunda and Huntsman 1988, 1990, 1994) in favor of uptake by biota.

Uptake by phytoplankton (and also by bacteria and viruses) of bio-essential elements Mn, Fe, Co, Ni, Cu, and Zn is a major pathway in the ocean cycling of these trace metals, as per Eq. 2. Net result is the removal of dissolved metals from the euphotic zone (the upper water down to 1% penetration of incoming sunlight, typically 40–80 m depth in open oceans) in surface waters (all waters shallower than 100 m depth). The true internal metal content of phytoplankton has been difficult to distinguish from metals adsorbed at the outside of the cell; see below adsorptive scavenging. However novel irradiance techniques using a

(*continued*)

synchrotron have been a breakthrough in being able to clearly discern internal "true biological" metal atoms from those adsorbed external on the outside of the cell wall (Twining 2003; Twining and Baines 2013). Upon senescence by nutrient limitation and/or grazing or viral lysis, some "dead" biogenic debris settles down into intermediate waters (100–1000 m depth) where most is remineralized and the metals return to the dissolved state. Particles settling below 1000 m further mineralize and further return the metals to the dissolved state.

Adsorptive scavenging is the removal of dissolved trace metals from seawater by adsorption onto the outer surfaces of settling biogenic particles. This is very effective for adsorption of positive ions; the negatively charged oxyanions are not affected. Some redox metals, notably Mn and Fe, will next oxidize further at this surface, and such freshly formed Fe-Mn oxyhydroxides are known to be very effective adsorbing agents for a suite of other trace metals. Otherwise organic functional groups of the particles also are deemed to be effective scavengers (Balistrieri et al. 1981). Upon settling into intermediate (100–1000 m depth) and deep (>1000 m depth) waters, the biogenic debris is respired, and the trace metals are remineralized back again as dissolved metals into the seawater. Some trace metals immediately adsorb again onto other deep particles and are once again removed from solution. From concentrations of dissolved trace metals that remain in surface waters, it is impossible to derive how much has been removed by true internal biological uptake and how much removed by external adsorptive scavenging. However in the deep waters, one may discern deep water scavenging simply when the concentration of a bio-essential trace metal is less than expected from the concentration of a major nutrient phosphate or silicate. From such approach we know that there is significant deep water scavenging of Fe, Mn, Cu, and Ni, but apparently not of Zn and Cd.

Manganese (Mn) is essential in several metalloproteins within marine phytoplankton (Table 1). In seawater it exists in the reduced [Mn^{2+}] state that in the well-oxygenated open ocean is prone to slow oxidation to the insoluble MnO_2. However in reducing sediments of the continental shelf, the MnO_2 dissolves again to high levels of [Mn^{2+}] in pore waters, and the [Mn^{2+}] diffuses into overlying waters, where it can be traced over long distances (Wu et al. 2014). In an oxygen minimum zone, this higher [Mn^{2+}] can be mixed over even longer lateral distances, e.g., in the East Equatorial Pacific (Martin and Knauer 1985) and the Northwest Indian Ocean (Saager et al. 1989).

In the open ocean, the surface water concentrations of dissolved Mn can range up to ~2–4 nM due to partial dissolution of aeolian dust supply from land. Photoreduction of Mn in the euphotic zone is known to enhance such dissolution (Sunda et al. 1983; Sunda and Huntsman 1988, 1990, 1994). The ~2–4 nM concentrations are deemed to be in ample supply for the needs of phytoplankton. In surface waters of the remote Southern Ocean with low dust input, the dissolved Mn is considerably lower in the 0.1–0.9 nM range (Fig. 4; Middag et al. 2011b, 2012, 2013). The lowest values in the 0.04–0.12 nM range are near the Antarctic continent, where the very deep (~1500 m) shelf under the extended continental ice sheet is exceptional as it is not a source of Mn (Middag et al. 2011b), as opposed to the extensive shelves around the Antarctic Peninsula acting as a source of Mn (Fig. 3) due to reductive dissolution in the anoxic pore waters (Middag et al. 2012, 2013).

In Antarctic surface waters, the net removal of dissolved Mn covaries with net removal of part of the dissolved phosphate, with an apparent Mn:P uptake ratio by plankton in the 0.36–0.39 $\times$ 10^{-3} mol.mol^{-1} range (Middag et al. 2011b, 2013). In the deep waters of Atlantic and Antarctic Oceans, the dissolved Mn is remarkably uniform at very low 0.1–0.15 nM concentrations (Van Hulten et al. 2017). However, Mn plumes with much higher concentrations up to 3 nM or even 10 nM (Arctic Gakkel Ridge) exist over mid-ocean ridges due to hydrothermal input, the plumes extending several hundred kilometers horizontally and almost 1000 m above the ridge crest (Middag et al. 2011a, b; Resing et al. 2015, Wu et al. 2014). Sampling with submersibles of the emitting high temperature strongly reducing vent fluid gives very high Mn concentrations up to ~1 millimolar concentration, i.e., up to ten million times the low background dissolved concentration of ~0.1 nM (Von Damm et al. 1985, 1998 versus Middag et al. 2011b, 2013; Van Hulten et al. 2017). Just like for Fe (see above), most of the hydrothermal Mn deposits rapidly in metalliferous sediments at the ridge crest, yet the million times lower 1–10 nM concentration remaining in the plume can be seen over more than 1000 km away from the ridge crest, versus the low 0.1 nM background concentration in deep waters (Fig. 4).

Zinc (Zn) is the second most important trace metal element in biology. Its most important function is in the enzyme carbonic anhydrase that enhances the reaction rate some ten million times for the conversion of bicarbonate HCO_3^- ion to CO_2. For phytoplankton this is most helpful as it allows to take up not only CO_2 but also HCO_3^-, which is far more abundant, and convert the latter to CO_2, which is necessary as only CO_2 is utilized in photosynthesis. Thus at conditions of relatively low ambient $[CO_2]_{aqueous}$, the algae can also assimilate HCO_3^-.

The divalent Zn(II) state in seawater is ~98% bound by organic complexation with dissolved organic molecules; the remaining is ~1.5% free [Zn^{2+}] ion and ~0.5% inorganic species [$ZnCO_{3(aqueous)}$] and [$ZnSO_{4(aqueous)}$]. Presumably the 98% organic complexation helps to maintain the Zn in solution because the free [Zn^{2+}] ion is prone to loss due to adsorptive scavenging on marine particles.

The ocean distribution of dissolved Zn very closely follows that of major nutrient silicate (Fig. 5). This is consistent with its biochemical functions (Table 1), and perhaps the close relation with silicate hints at a key biological relationship with diatoms. Surface water concentrations are low in the order of 0.1 nM but higher at 2–3 nM in the Antarctic Ocean, such that this is not only a HNLC region for major nutrients but also for trace nutrient Zn. Deep water concentrations increase from 2 nM in the deep North Atlantic to 6–8 nM in the deep Antarctic to 10 nM in the deep North Pacific.

Copper (Cu) has several functions in biology (Table 1). In seawater the divalent Cu(II) state is virtually 100% bound by strong organic complexation. There is ample total dissolved Cu at ~0.5–1.5 nM in surface waters of the North Atlantic, and therefore Cu is deemed not to be limiting for phytoplankton growth, unless the very strong organic complexation would hinder plankton uptake. The concentration increases steadily with depth to 2.0–2.5 nM at around 4000 m depth. This steady increase resembles that of major nutrient silicate. Nevertheless when comparing the deep North Atlantic with the deep North Pacific, the steady increase of dissolved silicate with increasing age of deep water is hardly followed by an increase of dissolved Cu in older deep waters of the Pacific. Therefore it is generally assumed that there is net scavenging removal of Cu from deep waters that prevents Cu from accumulating a high dissolved concentration in old deep waters.

Nickel (Ni) has perhaps the least biochemical functions of the bio-essential trace elements (Table 1). In seawater Ni dominantly exists as the free hydrated Ni(II) state. The vertical distribution of Ni is perhaps best described by a correlation with both phosphate and silicate. There is ample Ni at ~2 nM in surface waters; therefore Ni is deemed not to be a limiting element for phytoplankton growth.

Cobalt (Co) has a key functionality as the metallocenter of vitamin B12 and can also substitute for Zn in carbonic anhydrase. Cobalt exists in the Co(II) state in seawater and is for ~90% bound as Co-organic complexes. Cobalt also has similar redox chemistry to that of iron and manganese. The oxidized Co(III) state is highly insoluble due to precipitation of Co(III) oxyhydroxides. Conversely, at low ambient O_2, this may be reduced again, and Co(II) is remobilized into the dissolved state. Indeed concentrations of Co, Fe, and Mn are considerably higher in O_2 minimum zones, such as off West Africa (Noble et al. 2012).

Vanadium (V) exists in seawater primarily as the vanadate oxyanion [HVO_4^{2-}] (Butler 1990) at a concentration between 30 and 36 nmol.kg^{-1} (Collier 1984). The role of

V in proteins found in blood cells of ascidians (sea squirts) is very special (Michibata and Sakurai 1990) and most intriguing but so unique that it does not affect the concentration of V in ocean waters.

Molybdenum (Mo) is together with Fe required for the process of N_2 fixation by the so-called diazotrophs (N_2 fixers) among which *Trichodesmium* is the "model" organism (La Roche and Breitbarth 2005). Molybdenum exists in seawater as Mo(IV) in the molybdate oxyanion state [MoO_4^{2-}] and as such not prone to adsorptive scavenging loss. The high concentration in seawater at ~104 nM renders Mo the most abundant trace metal element in the oceans, where it is deemed a conservative element varying only slightly as function of salinity (Collier 1985). Given this high abundance, Mo is by no means limiting for growth and functioning of the diazotrophs; however, the other trace element Fe as required for N_2 fixation is often very low and limiting in surface waters. The process of N_2 fixation also requires high seawater temperatures above ~20 °C. In the warm waters of the Sargasso Sea, directly under the influence of major deposition of Fe-rich aeolian dust derived from the Sahara, there exists an important niche for *Trichodesmium* to form major blooms. Recently the requirement of temperatures above ~20 °C has been challenged (Rivero-Calle et al. 2016).

Cadmium (Cd) was long considered to have no biological function, at most toxic, as it may as a look-alike of Zn occupy, and hence disable, places in the cell where Zn ought to be and function. However the discovery of the very close relationship of dissolved Cd with major nutrient phosphate in the oceans (Boyle et al. 1976; Bruland 1980) led to more investigations of interactions between Cd and phytoplankton. Now we know that in fact Cd can substitute for Zn in phytoplankton, in conditions where there is not enough Zn available. Moreover there exist intrinsic Cd-cofactored carbonic anhydrases, for certain diatoms thus far studied, i.e., sometime during biological evolution, this true Cd-based enzyme has developed (Lane and Morel 2000; Lane et al. 2005; Xu et al. 2008). In seawater the Cd(II) exists for some 64% as an organic complex, the remaining Cd(II) exists for some 30% as chlorine inorganic species, and merely 3% free [Cd^{2+}] ion.

In general surface water concentrations of Cd are very low indicating uptake and/or scavenging removal by plankton. However surface waters of the Southern Ocean have high dissolved Cd, thus here also mimicking the HNLC condition of phosphate. The North Atlantic Deep Water (NADW) originates from Atlantic surface waters and has relatively low concentrations of both Cd and phosphate, as opposed to the high concentrations in the Antarctic Intermediate Water (AAIW) and Antarctic Bottom Water (AABW) coming from the south and flowing northward.

An Update on the Extended Redfield Stoichiometry

The stoichiometry of the nine bio-essential major and trace elements most likely varies considerably between phytoplankton species, as well as due to some degree of adjustment that the algae can make vis-à-vis availability of each of these nine essential elements in the ambient seawater. Conversely depending on the essential elements being more or less available, the composition of the plankton will vary, albeit within certain limits below which the cell cannot function anymore.

During more than 25 years, it has been, and still very much is, a challenge to resolve the stoichiometric "constants" of the six bio-essential trace metals (e.g., Bruland et al. 1991; De Baar et al. 2008). In an excellent recent review by Twining and Baines (2013), the various approaches have been synthesized. From this the order of magnitude values are listed in Table 3, by no means as the final truth but merely as an indication of the current state-of-the-art.

In general the mixing of ocean waters tends to some extent to "average" the wide variability in living plankton and settling biogenic debris. Nevertheless the distributions of each of the nine bio-essential elements in the oceans have more variability than most people realize, this also for the "classical" major elements. Therefore upon further investigations, it remains to be seen whether or not the ranges as listed in Table 3 (e.g., 117 ± 14 for carbon or $(10 \pm 9) \times 10^{-3}$ for iron) will in due course become either narrower or wider.

Recently completed and ongoing world ocean research programs such as WOCE, CLIVAR, and GEOTRACES (www.geotraces.org) are providing newer, larger, and more accurate datasets of the dissolved major and trace elements, which undoubtedly will lead to future adjustments and refinements in the numbers presented in Table 3. For example, the apparent biological uptake ratio Mn/P derived from water column profiles of GEOTRACES in 2008 in the Southern Ocean is in the $0.3–0.4 \times 10^{-3}$ range (Middag et al. 2013), that is, in the lower part of the range in Table 3.

Other Trace Elements

Recently Bruland et al. (2014) produced an excellent overview of the trace metals in seawater that comprises all trace elements, those with key biological functions as above discussed and virtually all of those, more than 40 elements, that are not bio-limiting, their abundance not controlled by biology, or without a biological function at all. They also provide an extensive table comprising almost all trace elements and their abundance in seawater. Below only 3 of the 55 nonbiological trace elements are discussed, but Table 4 comprises all 55 largely abiotic trace elements, complementary to Tables 1 and 2 for "biological" elements.

Ocean Biochemical Cycling and Trace Elements, Table 2 Concentrations in seawater of the nine chemical elements that are **essential for all life in bold print** as well as four chemical elements that play a role in specific taxonomic groups. Each element symbol is preceded by its atomic number #. Major dissolved inorganic species, i.e., not taking into account here the strong organic complexation for several trace elements as discussed in main text for such element. Given concentrations are typical values; real concentrations vary around these as function of depth and geographic location. Not listed are Mg and Ca that also play a role in specific taxonomic groups but are listed among the major ions of sea salt (see entry ▶ Ocean Salinity, Major Elements, and Thermohaline Circulation), as is S in abundant dissolved sulfate, and hence Mg, Ca, and S never are bio-limiting

#		Major inorganic species	Concentration	North Atlantic Ocean		Antarctic Ocean		North Pacific Ocean	
			Unit	Surface	Deep	Surface	Deep	Surface	Deep
6	**C**	HCO_3^-	[μmol.kg^{-1}]	2050	2200	2210–2220	2240–2260	2000	~2350
7	**N**	NO_3^-	[μmol.kg^{-1}]	<1	25	25–30	30–38	<1	45
14	Si	H_4SiO_4	[μmol.kg^{-1}]	<1	40	35–63	83–129	<1	170
15	**P**	HPO_4^-	[μmol.kg^{-1}]	<0.1	1.2–1.5	1.6–1.9	2.26–2.35	<0.1	2.5–3.3
23	V	HVO_4^{2-}	[nmol.kg^{-1}]	Quite uniform at ~30–37 [μmol.kg^{-1} in all ocean waters, mostly conservative					
25	**Mn**	Mn^{2+}	[nmol.kg^{-1}]	0.2–3.0	0.1–0.15	0.04–0.5	~0.1	~1–2	~0.2
26	**Fe**	$Fe(OH)^{2+}$	[nmol.kg^{-1}]	0.2–2.0	0.6	0.02–0.1	0.4	0.05	0.6
27	**Co**	Co^{2+}	[pmol.kg^{-1}]	30	60	20–85	~60	10–50	50–250
28	**Ni**	Ni^{2+}	[nmol.kg^{-1}]	2	4	5.5–6.5	5.5–7.0	2.1	11
29	**Cu**	$CuCO_3^0$	[nmol.kg^{-1}]	1 ± 0.5	1.3–2.2	1–2	2–4	<0.5	5
30	**Zn**	Zn^{2+}	[nmol.kg^{-1}]	0.1	2	2.5–3.1	6.2–7.8	0.07	9
42	Mo	MoO_4^{2-}	[nmol.kg^{-1}]	Quite uniform at ~104 μmol.kg^{-1} in oceans, conservative varying slightly with salinity					
48	Cd	$CdCl_2^0$	[pmol.kg^{-1}]	10	300	400–600	770–860	1.4	1100

DIC Atlantic: see Fig. 4; DIC Antarctic: van Heuven et al. 2011; DIC Pacific: see Fig. 4
P Atlantic: see Fig. 4; P Antarctic: Baars et al. (2014); P Pacific: see Fig. 4
N in Atlantic: see Fig. 4; N in Antarctic: de Baar et al. 1997; N in Pacific: see Fig. 4
Si Atlantic: see Fig. 4; Si Antarctic: Zhao et al. 2014; Si Pacific: see Fig. 4
V worldwide: Collier (1984)
Mn Atlantic: Van Hulten et al. 2017; Mn Antarctic: Middag et al. 2011b, 2012, 2013; Mn Pacific: Resing et al. 2015
Fe Atlantic: Rijkenberg et al. 2014; Fe Antarctic: Klunder et al. 2011, 2014 and Gerringa et al. 2015; Fe Pacific: Martin et al. 1989
Co Atlantic: Middag et al. 2015b, Noble et al. 2012. Co Antarctic: Saito et al. 2010; Co Pacific: Hawco et al. 2016, values >50 pM in O_2 minimum zone
Ni Atlantic: Middag et al. 2015b; Ni Antarctic: Cameron and Vance 2014; Ni Pacific: Bruland 1980
Cu Atlantic: Middag et al. 2015b; Cu Antarctic; Bown et al. 2016; Cu Pacific: Bruland 1980
Zn Atlantic: Middag et al. 2015b; Zn Antarctic: Zhao et al. (2014); Zn Pacific: Martin et al. 1989
Mo worldwide: Collier (1985); see also Singh et al. (2011)
Cd Atlantic: Middag et al. (2015b); Cd Antarctic: Baars et al. (2014); Cd Pacific: Bruland 1980
Data tables in Bruland (1980), Martin et al. (1989), Baars et al. (2014), and Zhao et al. (2014) and in online supplement of Gerringa et al. (2015). The other datasets available at www.geotraces.org and in the datasets cited in captions of Figs. 2, 3, 4, 5, 6, 7, and 8

Ocean Biochemical Cycling and Trace Elements, Table 3 An illustration of the current (2017) state-of-the-art for the order of magnitude of stoichiometric "constants" for the extended Redfield Eq. 2. As per the latter Eq. 2, the data are normalized to value 1 for P (phosphorus). Values for major elements C, N, P, and O_2 after Anderson and Sarmiento (1994). Instead for the trace elements Fe, Zn, Mn, Cu, Ni, and Co, typical ranges are given after Twining and Baines (2013; their Fig. 4)

Major elements	C	(117 ± 14)
	N	(16 ± 1)
	P	1
	O_2	(−170 ± 10)
Trace elements	Fe	(0.2–20) × 10^{-3}
	Zn	(0.1–0.6) × 10^{-3}
	Mn	(0.2–4.0) × 10^{-3}
	Cu	(0.2–2.0) × 10^{-3}
	Ni	(0.1–1.8) × 10^{-3}
	Co	(0.005–2.0) × 10^{-3}

Aluminum (Al) has a high abundance in rocks and soils of the planet but has very low concentrations in the oceans. Dissolved trivalent Al is highly prone to adsorption on particles and perhaps the ultimate scavenging-type trace element in the oceans. The major external source for Al is deposition of aeolian dust coming from the continents. Consequently, an elevated concentration of dissolved Al in surface seawater is strong evidence for dust input, notably Sahara dust that is blown by prevailing winds all across the North Atlantic in the 10–20 °N region (Fig. 6). However due to the intensive scavenging loss, Al rapidly disappears from seawater. This is nicely shown in Fig. 7 where at first glance the distribution of Al looks like that of major nutrient silicate, yet in fact it is the opposite. Where silicate is low, Al is high; where Si is high, Al is low. This amazing mirror image of Al versus Si is partly due to North Atlantic surface water being depleted in nutrient Si but receiving massive supply of Al in aeolian dust from the Sahara.

Ocean Biochemical Cycling and Trace Elements, Table 4 Concentrations in seawater of the 55 trace elements that are not bio-limiting, and/or their abundance not controlled by biology, or without a biological function at all. For elements with key biological functions, see Tables 1 and 2. Not listed are noble gases and elements of which no stable isotopes exist in seawater, although radioisotopes ^{232}Th and ^{238}U with very long half-life are listed; the long half-life is such that these are treated as virtually stable isotopes in the oceans. This Table 4 is based on the informative Table in Bruland et al. (2014), plus a few extra chemical elements not listed by Bruland et al. (2014)

Atomic number	Symbol	Name	Major species	Concentration range	Concentration typical
3	Li	Lithium	Li^+	(Conservative)	25.9 μmol.kg^1
4	Be	Beryllium	$Be(OH)^+$, $Be(OH)_2{}^0$	4–30 pmol.kg^{-1}	~23 pmol.kg^{-1}
5	B	Boron	H_3BO_3	(Conservative)	416 μmol.kg^{-1}
13	Al	Aluminum	$Al(OH)_4{}^-$, $Al(OH)_3{}^0$	0.3–40 nmol.kg^{-1}	~2 nmol.kg^{-1}
21	Sc	Scandium	$Sc(OH)_3{}^0$	8–20 pmol.kg^{-1}	~16 pmol.kg^{-1}
22	Ti	Titanium	$Ti(OH)_4{}^0$, $TiO(OH)_2{}^0$	6–250 pmol.kg^{-1}	~150 pmol.kg^1
24	Cr	Chromium	$CrO_4{}^-$	3–5 nmol.kg^{-1}	~4 nmol.kg^{-1}
31	Ga	Gallium	$Ga(OH)_4{}^-$	5–60 pmol.kg^{-1}	~20 pmol.kg^{-1}
32	Ge	Germanium	H_4GeO_4	1–100 pmol.kg^{-1}	~70 pmol.kg^{-1}
32	Ge	MethylGe	$CH_3Ge(OH)_3{}^0$, $(CH_3)_2$, $Ge(OH)^0$	(Two conservative species)	400 pmol.kg^{-1}
33	As	Arsenic	$HAsO_4{}^{2-}$	17–25 nmol.kg^{-1}	23 nmol.kg^{-1}
34	Se	Selenium	$SeO_4{}^{2-}$	0.5–2.3 nmol.kg^{-1}	1.8 nmol.kg^{-1}
37	Rb	Rubidium	Rb^+	(Conservative)	~1.4 μmol.kg^{-1}
39	Y	Yttrium	$Y(CO_3)^+$, $Y(oh)_2{}^+$	60–300 pmol.kg^{-1}	200 pmol.kg^{-1}
40	Zr	Zirconium	$Zr(OH)_5{}^-$, $Zr(OH)_4{}^0$	9–300 pmol.kg^{-1}	~160 pmol.kg^{-1}
41	Nb	Niobium	$Nb(OH)_6{}^-$, $Nb(OH)_5{}^0$	1–4 pmol.kg^{-1}	~ 3 pmol.kg^{-1}
43	(Tc)	(Technetium)	(Does not occur in nature, except extinct Oklo natural nuclear fission reactor in Gabon)		
44	Ru	Ruthenium	$Ru(OH)_n{}^{4-n}$		<50 fmol.kg^{-1}?
45	Rh	Rhenium	$Rh(OH)_n{}^{3-n}$, $Rh(cl)_n{}^{3-n}$	0.4–1 pmol.kg^{-1}	0.8 pmol.kg^{-1}
46	Pd	Palladium	$PdCl_4{}^-$	0.2–1 pmol.kg^{-1}	~0.7 pmol.kg^{-1}
47	Ag	Silver	$AgCl_2{}^-$, $AgCl_3{}^{2-}$	1–35 pmol.kg^{-1}	20 pmol.kg^{-1}
49	In	Indium	$In(OH)_3{}^0$	0.04–2 pmol.kg^{-1}	~0.1 pmol.kg^{-1}
50	Sn	Tin	$SnO(OH)_3{}^-$, $Sn(OH)_4{}^0$	1–20 pmol.kg^{-1}	4 pmol.kg^{-1}?
51	Sb	Antimony	$Sb(OH)_6{}^-$	(~Conservative)	1.6 nmol.kg^{-1}
52	Te	Tellurium	$Te(OH)_6{}^0$	0.5–1.5 pmol.kg^{-1}	~0.6 pmol.kg^{-1}
53	I	Iodine	$IO_3{}^-$	350–460 nmol.kg^{-1}	450 nmol.kg^{-1}
55	Cs	Cesium	Cs^+	(Conservative)	2.2 nmol.kg^{-1}
56	Ba	Barium	Ba^{2+}	30–150 nmol.kg^{-1}	110 nmol.kg^{-1}
57	La	Lanthanum	$LaCO_3{}^+$	8–40 pmol.kg^{-1}	~35 pmol.kg^{-1}
58	Ce	Cerium	$CeCO_3{}^+$	1.5–10 pmol.kg^{-1}	5 pmol.kg^{-1}
59	Pr	Praseodymium	$PrCO_3{}^+$	1–8 pmol.kg^{-1}	4 pmol.kg^{-1}
60	Nd	Neodymium	$NdCO_3{}^+$	4–50 pmol.kg^{-1}	30 pmol.kg^{-1}
61	(Pm)	(Promethium)	Does not occur in nature (unstable radioisotopes can form in nuclear reactor)		
62	Sm	Samarium	$SmCO_3{}^+$	1–10 pmol.kg^{-1}	5 pmol.kg^{-1}
63	Eu	Europium	$EuCO_3{}^+$	0.2–2.5 pmol.kg^{-1}	0.8 pmol.kg^{-1}
64	Gd	Gadolinium	$Gd(CO_3)^{2-}$	1.5–12 pmol.kg^{-1}	9 pmol.kg^{-1}
65	Tb	Terbium	$Tb(CO_3)^{2-}$	0.5–2 pmol.kg^{-1}	~1 pmol.kg^{-1}
66	Dy	Dysprosium	$Dy(CO_3)^{2-}$	2–14 pmol.kg^{-1}	9 pmol.kg^{-1}
67	Ho	Holmium	$Ho(CO_3)^{2-}$	0.8–2.2 pmol.kg^{-1}	1.6 pmol.kg^{-1}
68	Er	Erbium	$Er(CO_3)^{2-}$	1.5–12 pmol.kg^{-1}	10 pmol.kg^{-1}
69	Tm	Thulium	$Tm(CO_3)^{2-}$	0.3–2 pmol.kg^{-1}	1 pmol.kg^{-1}
70	Yb	Ytterbium	$Yb(CO_3)^{2-}$	1–12 pmol.kg^{-1}	6 pmol.kg^{-1}
71	Lu	Lutetium	$Lu(CO_3)^{2-}$	0.2–2 pmol.kg^{-1}	~1 pmol.kg^{-1}
72	Hf	Hafnium	$Hf(OH)_4{}^0$, $Hf(OH)_5{}^-$	0.06–1 pmol.kg^{-1}	~0.3 pmol.kg^{-1}
73	Ta	Tantalum	$Ta(OH)_5{}^0$	0.01–0.3 pmol.kg^{-1}	~0.1 pmol.kg^{-1}
74	W	Tungsten	$WO_4{}^{2-}$	(Conservative)	55 pmol.kg^{-1}
75	Re	Rhenium	$ReO_4{}^-$	(Conservative)	40 pmol.kg^{-1}
76	Os	Osmium	$H_3OsO_6{}^-$	3–8 fmol.kg^{-1}	~ 6 fmol.kg^{-1}

(*continued*)

Ocean Biochemical Cycling and Trace Elements, Table 4 (continued)

Atomic number	Symbol	Name	Major species	Concentration range	Concentration typical
77	Ir	Iridium	$Ir(OH)_3^0$ (?)	0.5–1 fmol.kg^{-1}	
78	Pt	Platinum	$PtCl_4^{2-}$?	0.2–1.5 pmol.kg^{-1}	~0.8 pmol.kg^{-1}?
79	Au	Gold	$AuCl_2^-$?, $Au(OH)_3^0$?	10–100 fmol.kg^{-1}	~50 fmol.kg^{-1}
80	Hg	Mercury	$HgCl_4^{2-}$	0.2–10 pmol.kg^{-1}	~1 pmol.kg^{-1}?
81	Tl	Thallium	Tl^+, $TlCl^0$	60–75 pmol.kg^{-1}	70 pmol.kg^{-1}
82	Pb	Lead	$PbCO_3^0$	4–150 pmol.kg^{-1}	~10 pmol.kg^{-1}
83	Bi	Bismuth	$Bi(OH)^{2+}$, BiO^+	0.04–0.5 pmol.kg^{-1}	~0.1 pmol.kg^{-1}
90	^{232}Th	Thorium	$Th(OH)_3(CO_3)^-$?	0.3–0.6 pmol.kg^{-1}	~0.3 pmol.kg^{-1}
92	^{238}U	Uranium	$UO_2(CO_3)_3^{4-}$	(Conservative)	~13.5 nmol.kg^{-1}

In contrast, in the Antarctic Ocean, the surface silicate is high (HNCL region), but with the Antarctic being so remote from land, there is no significant dust input of Al. As a result the Antarctic waters are high in Si and very low in Al (Middag et al. 2011c, 2012, 2013). When these Antarctic waters flow northward as AAIW and AABW into the Atlantic basin, they bring along the high Si but low Al signal. This in combination with intensive scavenging may explain the opposite distributions. Indeed by ocean biogeochemical simulation modeling of these processes, it is possible to reproduce the distributions of both Si and Al along this section (Van Hulten et al. 2014).

Iridium (Ir) has the record of lowest concentration of trace elements in the oceans. Iridium is extremely rare in the Earth's crust. This in fact is the reason why an anomalous Ir-enriched layer in sedimentary rocks was identified as clear evidence of asteroid impact, asteroids having a higher Ir concentration than crustal rocks of planet Earth (Smit and Hertogen 1980; Alvarez et al. 1980). This asteroid impact is deemed to have caused the demise of the dinosaurs. Iridium is trivalent in seawater and akin to above trivalent Al likely to be also rapidly scavenged. Thus any input from land that in the first place already comprises very little Ir would next also be removed quickly from the ocean water column. Indeed dissolved Ir is extremely low in the 0.5–1.0 femtomolar range (1 femtomol. L^{-1} = fM = 10^{-15} mol.L^{-1}) (Anbar et al. 1996).

Lead has a very low natural background dissolved concentration (Pb<10 pmol), and this is consistent with the fact that it is very susceptible to adsorptive scavenging. However due to the use from ~1930 onward of gasoline with tetraethyl-Pb additive (as an antiknock agent), massive amounts of Pb have been emitted in the atmosphere over North America and Europe. This large-scale pollution was noticed by Claire Patterson through his efforts to date the age of our planet using Pb isotopic abundances in rocks, which occasionally led to spurious results. Patterson realized this was due to inadvertent contamination in his laboratory and was one of the first geochemists to construct a clean room laboratory and to develop and apply rigorously ultraclean methods. This was successful, and eventually in 1956, the date of the Earth was estimated at 4.55 billion years, a value repeatedly confirmed.

Meanwhile Patterson initiated pioneering work to detect traces of Pb in the environment. Using the best ultraclean sampling methods of the time, samples were collected and analyzed for dissolved Pb in the Pacific Ocean and in year 1979 in the Sargasso Sea near Bermuda in the North Atlantic Ocean (Flegal and Patterson 1983; Schaule and Patterson 1981, 1983). Due to prevailing wind directions, the North Atlantic is downwind of North America and major recipient of the anthropogenic Pb signal.

Moreover, Patterson almost singlehandedly crusaded to abandon Pb in gasoline and eventually succeeded, such that the emissions of Pb into the atmosphere have greatly diminished from the late 1970s onward (Bryson 2003). The Bermuda Atlantic Time-Series Station (BATS) showed that concentrations of dissolved Pb steadily decreased from maximum ~160–170 pM in the upper 500 m in 1979 (Schaule and Patterson 1983) to ~20 pM in the same 500 m depth range in year 2011(Boyle et al. 2014).

Using the most advanced state-of-the-art clean PRISTINE sampling equipment (Rijkenberg et al. 2015) along the complete West Atlantic section (including the BATS site), the dissolved Pb was measured (Fig. 8).

The upper waters of the North Atlantic nowadays have lower dissolved Pb than in the 1979–2008 era, but the subsurface waters in the ~500 to ~2500 m depth range still carry part of the pollutant signal of past high Pb emissions. Given the scavenging-type nature of dissolved Pb, luckily this pollutant signal will eventually disappear from the ocean water column. In the southernmost part of the section, it is noticed that the subsurface waters of Antarctic origin (AAIW at ~1000 m and AABW over the seafloor) are virtually free of Pb, apparently truly "pristine," due to the fact that the dust supply to the Antarctic Ocean is very low.

Combination of this long section (Fig. 8) with two meridional sections in the North and South Atlantic, by the USA and the UK, respectively, has been shown and discussed by Malakoff (2014).

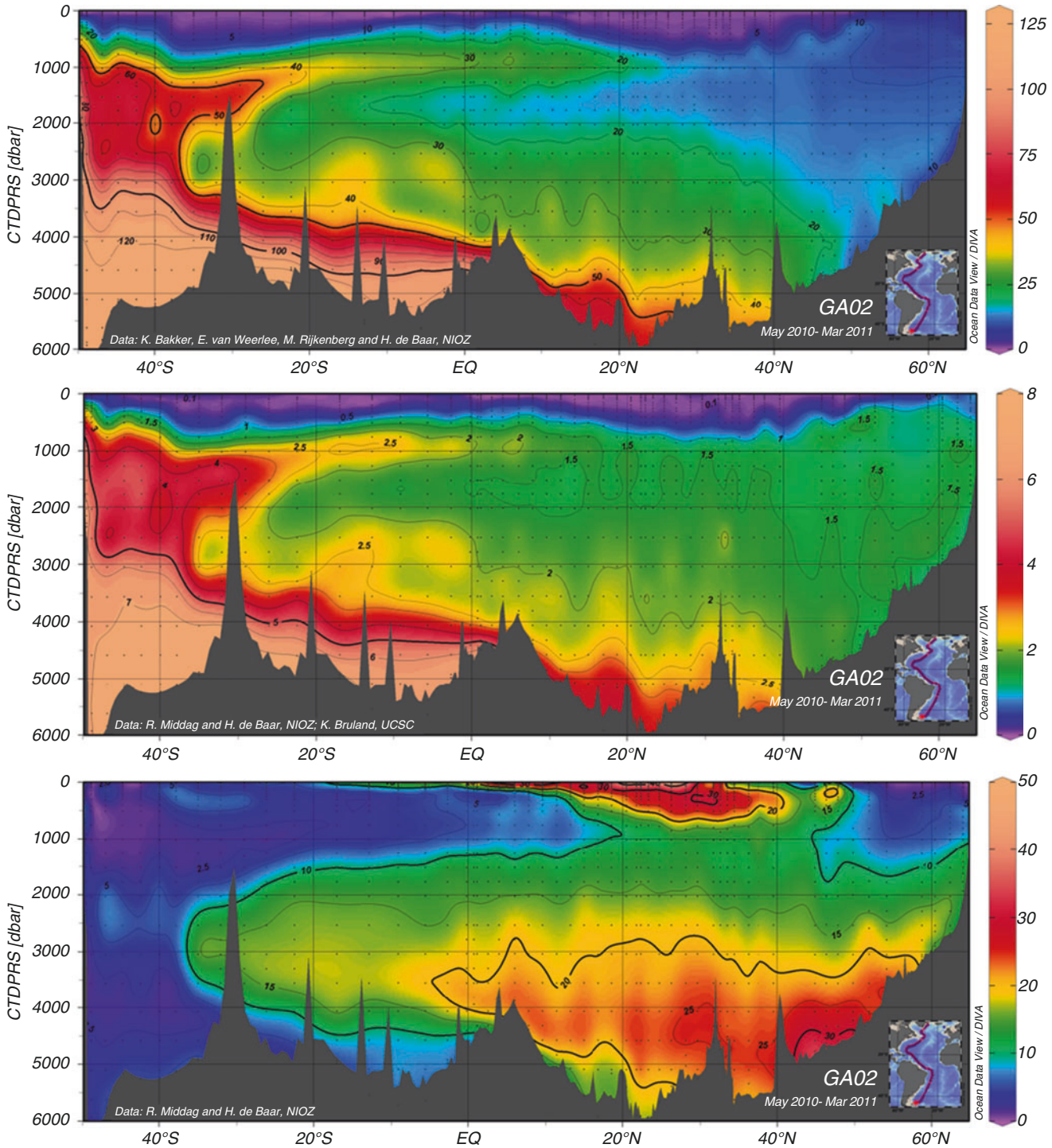

Ocean Biochemical Cycling and Trace Elements, Fig. 7 Section West Atlantic, Geotraces GA02. *Upper* graph: silicate [µmol/kg], after Middag et al. (2015a). *Middle* graph: Zn [nM], after Middag et al. (2015b). *Lower* graph: Al [nM] after Middag et al. (2015a). Vertical axis is pressure [decibar] that is virtually identical to depth [meter] (All data as shown here by Middag and coworkers is in Geotraces IDP 2014 (www.geotraces.org). Graphics www.eGeotraces.org using Ocean Data View (R. Schlitzer))

Summary

The natural chemical elements exist in seawater in concentrations ranging over 15 orders of magnitude from Cl at ~0.56 mol.kg^{-1} seawater down to Ir at ~0.5 × 10^{-15} mol.kg^{-1} seawater. The most abundant ions exist in constant proportions. Together these major ions constitute the dissolved salt content or salinity of seawater.

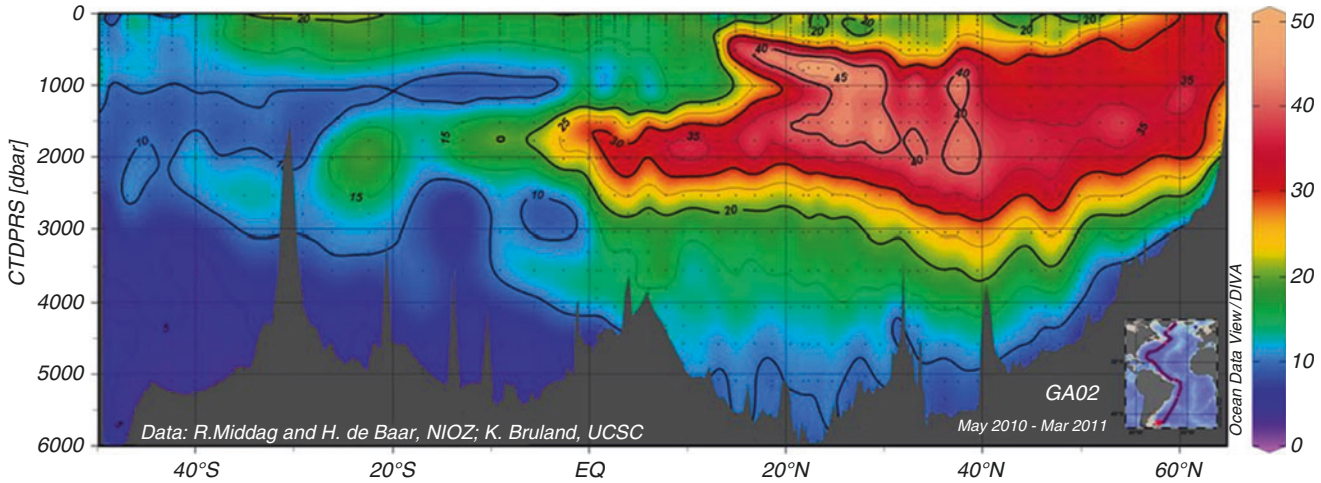

Ocean Biochemical Cycling and Trace Elements, Fig. 8 Section of dissolved Pb in the West Atlantic Ocean, Geotraces. Vertical axis is pressure [decibar] that is virtually identical to depth [meter]. The still contaminated North Atlantic waters and overall surface waters are in contrast with the subsurface waters of Antarctic origin (AAIW at ~1000 m and AABW over the seafloor) that are virtually free of Pb. The vertical profile of this dataset at the BATS near Bermuda is reported by Middag et al. (2015) (See also Malakoff 2014). All data as shown here by Middag and coworkers is in Geotraces IDP 2014 (www.geotraces.org). Graphics www.eGeotraces.org using Ocean Data View (R. Schlitzer)

Life in the oceans requires not only C, N, and P but also six trace nutrient elements Mn, Fe, Co, Ni, Cu, and Zn. Photosynthesis by marine algae utilizes these overall nine nutrient elements from seawater in fairly uniform proportions or stoichiometry. The reverse remineralization or respiration by marine bacteria and animals recycles these nutrient elements back into the seawater. Moreover important taxonomic groups also use other chemical elements, most notably Ca for producing $CaCO_3$ shells and coral reefs and Si for producing opaline SiO_2 external frustules of diatom algae. In the temperate and tropical oceans, the major nutrients N, P, and Si are depleted from surface waters. In contrast in the Antarctic Ocean and some other high-nutrient low-chlorophyll (HNLC) regions, there are plenty of major nutrients N, P, and Si, but the ecosystem is limited due to a lack of Fe in combination with light limitation. Due to deep remineralization, there are higher concentrations of nutrients N, P, Si, Co, Ni, Cu, and Zn in deep waters. The trace nutrients Mn and Fe have multiple oxidation states. Both Mn and Fe are involved in the biological cycle but also are affected by aeolian dust supply, oxidative scavenging removal from seawater, and opposed reductive dissolution within anoxic marine sediments and supply from hydrothermal vents.

The remaining 55 chemical elements and their low concentrations in seawater are listed. Yet only three are discussed: Al is the key tracer for aeolian dust input into the oceans, Ir has the record of lowest concentration in seawater, and Pb has elevated abundance due to past use of leaded gasoline.

Cross-References

- Aluminum
- Biogeochemistry
- Cadmium
- Calcium
- Carbonate Minerals and the CO2-Carbonic Acid System
- Cobalt
- Colloids
- Copper
- Geochemistry
- Hydrothermal Solutions
- Iridium
- Iron
- Lead
- Magnesium
- Manganese
- Molybdenum
- Nickel
- Nitrogen
- Nutrients
- Ocean Biochemical Cycling and Trace Elements
- Ocean Salinity, Major Elements, and Thermohaline Circulation
- Oxidation-Reduction Reactions and Eh-pH (Pourbaix) Diagrams
- Phosphorus
- Precambrian Geochemistry
- Silicon

- Stoichiometry
- Trace Elements
- Vanadium
- Zinc

References

Alvarez LW, Alvarez W, Asaro F, Michel HV (1980) Extraterrestrial cause for the cretaceous–tertiary extinction. Science 208(4448):1095–1108

Anbar AD, Wasserburg GJ, Papanastassiou DA, Anderson PS (1996) Iridium in natural waters. Science 273:1524–1528

Anderson LA, Sarmiento JL (1994) Redfield ratios of remineralization determined by nutrient data analysis. Global Biogeochem Cycles 8:65–80

Baars O, Abouchami W, Galer SJ, Boye M, Croot PL (2014) Dissolved cadmium in the Southern Ocean: distribution, speciation and relation to phosphate. Limnol Oceanogr 58:385–399

Balistrieri L, Brewer PG, Murray JW (1981) Scavenging residence times of trace metals and surface chemistry of sinking particles in the deep ocean. Deep-Sea Res 28A:101–121

Bown J, Laan P, Ossebaar S, Bakker K, Rozema P, De Baar HJW (2016) Bioactive trace metal timeseries during Austral summer in Ryder Bay, Western Antarctic Peninsula. Deep-Sea Res II. https://doi.org/10.1016/j.dsr2.2016.07.004i

Boyle EA, Sclater FR, Edmond JM (1976) On the marine geochemistry of cadmium. Nature 263:42–44

Boyle EA, Lee J-M, Echegoyen Y, Noble A, Moos S, Carrasco G, Zhao N, Kayser R, Zhang J, Gamo T, Obata H, Norisuye K (2014) Anthropogenic lead emissions in the ocean: the evolving global experiment. Oceanography 27(1):69–75. https://doi.org/10.5670/oceanog.2014.10

Broecker WS, Peng T-H (1982) Tracers in the sea. Eldigio Press, New York. 690p

Bruland KW (1980) Oceanographic distributions of Cd, Zn, Cu, and Ni in the North Pacific. Earth Planet Sci Lett 47:176–198

Bruland KW, Lohan MC (2003) Controls of trace metals in seawater. In: Elderfield H (ed) The oceans and marine geochemistry. Treatise on geochemistry, vol 6. Elsevier, Amsterdam. pp 23–47. ISBN: 0-08-044341-9

Bruland KW, Donat JR, Hutchins DT (1991) Interactive influences of bioactive trace metals on biological production in oceanic waters. Limnol Oceanogr 36:1555–1577

Bruland KW, Middag R, Lohan MC (2014) Controls of trace metals in seawater. Chapter 8.2. In: Holland HD, Turekian KK (eds) Treatise on geochemistry, 2nd edn. Elsevier, Oxford, pp 19–51

Bryson B (2003) Getting the lead out. Chapter 10. In: A short history of nearly everything. Doubleday (Publishing), Doubleday, London. pp 193–205

Buma AGJ, de Baar HJW, Nolting RF, Van Bennekom AJ (1991) Metal enrichment experiments in the Weddell-Scotia Seas: effects of Fe and Mn on various plankton communities. Limnol Oceanogr 36(8):1865–1871

Butler A (1990) The coordination and redox chemistry of vanadium in aqueous solution. In: Chasteen ND (ed) Vanadium in biological systems: physiology and biochemistry. Springer, The Netherlands. pp 25–49

Byrne RH, Kump LR, Cantrell KJ (1988) The influence of temperature and pH on trace metal speciation in seawater. Mar Chem 25:163–181

Cameron V, Vance D (2014) Heavy nickel isotope compositions in rivers and the oceans. Geochim Cosmochim Acta 128:195–211

Collier RW (1984) Particulate and dissolved vanadium in the North Pacific Ocean. Nature 309:441–444

Collier RW (1985) Molybdenum in the northeast Pacific Ocean. Limnol Oceanogr 30:1351–1354

Crowe SA, Døssing LN, Beukes NJ, Bau M, Kruger SJ, Frei R (2013) Atmospheric oxygenation three billion years ago. Nature 501(7468):535–538

De Baar HJW (1994) Von Liebig's law of the minimum and plankton ecology (1899–1991). Prog Oceanogr 33:347–386

De Baar HJW, De Jong JTM (2001) Distributions, sources and sinks of iron in seawater. Review chapter 5. In: Turner D, Hunter KA (eds) Biogeochemistry of iron in seawater. IUPAC book series on analytical and physical chemistry of environmental systems, vol 7. John Wiley & Sons, Chichester. pp 123–253

De Baar HJW, La Roche J (2003) Metals in the oceans; evolution, biology and global change. In: Lamy F, Wefer G (eds) Marine scientific frontiers for Europe. Springer, Berlin, pp 79–105

De Baar HJW, Buma AGJ, Nolting RF, Cadée GC, Jacques G, Tréguer PJ (1990) On iron limitation of the Southern Ocean: experimental observations in the Weddell and Scotia Seas. Mar Ecol Prog Ser 65:105–122

De Baar HJW, de Jong JTM, Bakker DCE, Löscher BM, Veth C, Bathmann U, Smetacek V (1995) Importance of iron for phytoplankton spring blooms and CO_2 drawdown in the Southern Ocean. Nature 373:412–415

De Baar HJW, Van Leeuwe MA, Scharek R, Goeyens L, Bakker KMJ, Fritsch P (1997) Nutrient anomalies in Fragilariopsis kerguelensis blooms, iron deficiency and the nitrate/phosphate ratio (A.C. Redfield) of the Antarctic Ocean. Deep-Sea Res II 44(1/2):229–260

De Baar HJW, Boyd PW, Coale KH, Landry MR, Tsuda A, Assmy P, Bakker DCE, Bozec Y, Barber RT, Brzezinski MA, Buesseler KO, Boyé M, Croot PL, Gervais F, Gorbunov MY, Harrison PJ, Hiscock WT, Laan P, Lancelot C, Law C, Levasseur M, Marchetti A, Millero FJ, Nishioka J, Nojiri Y, Van Oijen T, Riebesell U, Rijkenberg MJA, Saito H, Takeda S, Timmermans KR, Veldhuis MJW, Waite A, Wong CS (2005) Synthesis of iron fertilization experiments: from the iron age in the age of enlightenment. In: Orr JC, Pantoja S, Pörtner H-O (eds) The ocean in a high CO_2 world. Special Issue of J Geophys Res (Oceans) 110:C09S16. https://doi.org/10.1029/2004JC002601. pp 1–24

De Baar HJW, Gerringa LJA, Laan P, Timmermans KR (2008) Efficiency of carbon removal per added Fe in ocean fertilization. Mar Ecol Prog Ser 364:269–282

Fanning KA (1992) Nutrient provinces in the sea: concentration ratios, reaction ratios and ideal covariation. J Geophys Res 97:5693–5712

Flegal AR, Patterson CC (1983) Vertical concentration profiles of lead in the central Pacific at 15 °N and 20 °S. Earth Planet Sci Lett 64:19–32

Frausto da Silva JJR, Williams RJP (1994) The biological chemistry of the elements. Clarendon Press, Oxford

Frausto da Silva JJR, Williams RJP (2001) The biological chemistry of the elements, 2nd edn. Clarendon Press, Oxford

Gerringa LJA, Laan P, Van Dijken GL, Van Haren H, De Baar HJW, Arrigo KR, Alderkamp AC (2015) Sources of iron in the Ross Sea Polynya in early summer. Mar Chem 177(Part 3):447–459. https://doi.org/10.1016/j.marchem.2015.06.002

Gledhill M, Buck KN (2012). The organic complexation of iron in the marine environment, a review. Front Microbio 3: article 69. https://doi.org/10.3389/fmicb.2012.00069

Gledhill M, Van den Berg CMG (1994) Determination of complexation of iron(III) with natural organic complexing ligands in seawater using cathodic stripping voltammetry. Mar Chem 47:41–54

Hawco NJ, Ohnemus DC, Resing JA, Twining BS, Saito MA (2016) A dissolved cobalt plume in the oxygen minimum zone of the eastern tropical South Pacific. Biogeosciences 13:5697–5717. https://doi.org/10.5194/bg-13-5697-2016. www.biogeosciences.net/13/5697/2016/

Holland HD (1984) The chemical evolution of the atmosphere and oceans. Princeton University Press, Princeton. 582p

Jickells TD and Spokes LJ (2001) Atmospheric iron inputs to the oceans. Review chapter 5. In: Turner D, Hunter KA (eds) Biogeochemistry of Iron in Seawater. IUPAC book series on analytical and physical chemistry of environmental systems, vol 7. pp 85–121

Klunder MB, Laan P, Middag R, De Baar HJW, Van Ooijen JC (2011) Dissolved iron in the Southern Ocean (Atlantic sector). Deep-Sea Res II Top Stud Oceanogr 58(25):2678–2694
Klunder MB, Laan P, Middag R, De Baar HJW, Bakker K (2012a) Dissolved iron in the Arctic Ocean: important role of hydrothermal sources, shelf input and scavenging removal. J Geophys Res 117: C04014, https://doi.org/10.1029/2011JC007135
Klunder MB, Bauch D, Laan P, De Baar HJW, Van Heuven SMAC, Ober S (2012b) Dissolved Fe in the Arctic shelf seas and surface waters of the central Arctic Ocean: impact of Arctic river water and ice-melt. J Geophys Res 117:C01027
Klunder MB, Laan P, De Baar HJW, Middag R, Neven I, Van Ooijen JC (2014) Dissolved Fe across the Weddell Sea and Drake Passage: impact of DFe on nutrient uptake. Biogeosciences 11(3):651–669
La Roche J, Breitbarth E (2005) Importance of the diazotrophs as a source of new nitrogen in the ocean. J Sea Res 53:67–91
Landing WM, Bruland KW (1987) The contrasting biogeochemistry of iron and manganese in the Pacific Ocean. Geochim Cosmochim Acta 51:29–43
Lane TW, Morel FM (2000) A biological function for cadmium in marine diatoms. Proc Natl Acad Sci 97:4627–4631
Lane TW, Saito MA, George GN, Pickering IJ, Prince RC, Morel FM (2005) Biochemistry: a cadmium enzyme from a marine diatom. Nature 435:42–42
Lewis BL, Landing WM (1991) The biogeochemistry of manganese and iron in the Black Sea. Deep-Sea Res II 38:773–803
Lovelock J (1979) Gaia: a new look at life on earth. Oxford University Press, Oxford, New York. ISBN 0-19-286218-9
Malakoff D (2014) Chemical atlas shows where seas are tainted—and where they can bloom. Science 343:1070
Martin JH, Fitzwater SE (1988) Iron deficiency limits phytoplankton growth in the northeast Pacific subarctic. Nature 331:341–343
Martin JH, Knauer GA (1985) VERTEX: manganese transport through oxygen minima. Earth Planet Sci Lett 67:35–47
Martin JH, Gordon RM, Fitzwater S, Broenkow WW (1989) VERTEX: phytoplankton/iron studies in the Gulf of Alaska. Deep-Sea Res A Oceanograph Res Pap 36:649–680
Matsumoto K (2007) Radiocarbon-based circulation age of the world oceans. J Geophys Res 112:C09004. https://doi.org/10.1029/2007JC004095. 2007
Michibata H, Sakurai H (1990) Vanadium in ascidians. In: Chasteen ND (ed) Vanadium in biological systems: physiology and biochemistry. Springer, Netherlands, pp 153–171
Middag R, De Baar HJW, Laan P, Klunder MB (2011a) Fluvial and hydrothermal input of manganese into the Arctic Ocean. Geochim Cosmochim Acta 75(9):2393–2408
Middag R, De Baar HJW, Laan P, Cai PH, Van Ooijen JC (2011b) Dissolved manganese in the Atlantic sector of the Southern Ocean. Deep-Sea Res II 58:2661–2677
Middag R, Van Slooten C, De Baar HJW, Laan P (2011c) Dissolved aluminium in the Southern Ocean. Deep-Sea Res II 58:2647–2660
Middag R, De Baar HJW, Laan P, Huhn O (2012) The effects of continental margins and water mass circulation on the distribution of dissolved aluminium and manganese in Drake Passage. J Geophys Res Oceans 117:C01019
Middag R, De Baar HJW, Klunder MB, Laan P (2013) Fluxes of dissolved aluminum and manganese to the Weddell Sea and indications for manganese co-limitation. Limnol Oceanogr 58(1):287–300. https://doi.org/10.4319/lo.2013.58.1.0287
Middag R, Van Hulten MMP, Van Aken HM, Rijkenberg MJA, Gerringa LJA, Laan P, De Baar HJW (2015a) Dissolved aluminium in the ocean conveyor of the West Atlantic Ocean: effects of the biological cycle, scavenging, sediment resuspension and hydrography. Mar Chem 177(Part 1):69–86. https://doi.org/10.1016/j.marchem.2015.02.015
Middag R, Seferian R, Conway TM, John SG, Bruland KW, De Baar HJW (2015b) Intercomparison of dissolved trace elements at the Bermuda Atlantic time series station. Mar Chem 177(Part 3):476–489. 10.1016/j.marchem.2015.06.014
Millero FJ, Yao W, Aicher J (1995) The speciation of Fe(II) and Fe(III) in natural waters. Mar Chem 50:21–39
Nishioka J, Takeda S, Wong CS, Johnson WK (2001) Size-fractionated iron concentrations in the northeast Pacific Ocean: distribution of soluble and small colloidal iron. Mar Chem 74 (2001) 157–179
Nishioka J, Takeda S, de Baar HJW, Laan P, Croot PL, Boye M, Timmermans KR (2005) Change in the concentrations of iron in different size fractions during an iron fertilization experiment in the Southern Ocean. EisenEx Mar Chem 95:51–63
Noble AE, Lamborg CH, Ohnemus DC, Lam PJ, Goepfert TJ, Measures CI, Frame CH, Casciotti KL, DiTullio GR, Jennings J, Saito MA (2012) Basin-scale inputs of cobalt, iron, and manganese from the Benguela-Angola front to the South Atlantic Ocean. Limnol Oceanogr 57:989–1010
Redfield AC (1958) The biological control of chemical factors in the environment. Am Sci 46:205–222
Redfield AC, Ketchum BH, Richards FA (1963) The influence of organisms on the composition of sea water. 26–77. M. N. Hill, others, The sea, v. 2. Interscience: New York
Resing JA, Sedwick PN, German CR, Jenkins WJ, Moffett JW, Sohst BM, Tagliabue A (2015) Basin-scale transport of hydrothermal dissolved metals across the South Pacific Ocean. Nature 523:200–203. https://doi.org/10.1038/nature14577
Reynolds, CS (2006) The ecology of phytoplankton. Cambridge University Press, p 172. (book series ECB Ecology Biodiversity and Conservation)
Rijkenberg MJA, Gerringa LJA, Neale PJ, Timmermans KR, Buma AGJ, De Baar HJW (2004) UVA variability overrules UVB ozone depletion effects on the photoreduction of iron in the Southern Ocean. Geophys Res Lett 31:L24310. https://doi.org/10.1029/2004GL020829
Rijkenberg MJA, Fischer AC, Kroon JJ, Gerringa LJA, Timmermans KR, Wolterbeek HT, De Baar HJW (2005) The influence of UV irradiation on the photoreduction of iron in the Southern Ocean. Mar Chem 93(2–4):119–129
Rijkenberg MJA, Gerringa LJA, Carolus VE, Velzeboer I, De Baar HJW (2006) Enhancement and inhibition of iron photoreduction by individual ligands in open ocean seawater Geochim. Cosmochim Acta 70:2790–2805
Rijkenberg MJA, Middag R, Laan P, Gerringa LJA, van Aken HM, Schoemann V, De Jong JTM, De Baar HJW (2014) The distribution of dissolved iron in the West Atlantic Ocean. PLoS One 9(6): e101323. https://doi.org/10.1371/journal.pone.0101323
Rijkenberg MJA, de Baar HJW, Bakker K, Gerringa LJA, Keijzer E, Laan M, Laan P, Middag R, Ober S, Van Ooijen JC, Ossebaar S, Van Weerlee EM, Smit MG (2015) "PRISTINE", a new high volume sampler for ultraclean sampling of trace metals and isotopes. Mar Chem 177:501–509. https://doi.org/10.1016/j.marchem.2015.07.001
Rivero-Calle S, Del Castillo CE, Gnanadesikan A, Dezfuli A, Zaitchik B, Johns DG (2016) Interdecadal Trichodesmium variability in cold North Atlantic waters, global biogeochem. Cycle 30:1620–1638. https://doi.org/10.1002/2015GB005361
Saager PM, De Baar HJW, Burkill PH (1989) Manganese and iron in Indian Ocean waters. Geochim Cosmochim Acta 53:2259–2267
Saito MA, Goepfert TJ, Noble AE, Sedwick PN, DiTullio GR (2010) A seasonal study of dissolved cobalt in the Ross Sea of Antarctica: micronutrient control, absence of observed scavenging, and relationships with Zn, cd, and P. Biogeosciences 7:4059–4082
Sarmiento JL, Gruber N (2006) Ocean biogeochemical dynamics. Princeton University Press, Princeton. xii + 503p
Schaule BK, Patterson CC (1981) Lead concentrations in the northeast Pacific: evidence for global anthropogenic perturbations. Earth Planet Sci Lett 54:97–116
Schaule BK, Patterson CC (1983) Perturbations of the natural lead depth profile in the Sargasso Sea by industrial lead. In: Wong CS, Boyle E,

O

Bruland KW, Burton JD, Goldberg ED (eds) Trace metals in seawater. Plenum, New York, pp 487–503
Singh SP, Singh SK, Bhushan R (2011) Behavior of dissolved redox sensitive elements (U, Mo and Re) in the water column of the Bay of Bengal. Mar Chem 126:76–88
Smetacek V, HJW DB, Bathmann UV, Lochte K, van der Loeff MM R (eds) (1997) Ecology and biogeochemistry of the Antarctic circumpolar current during austral spring: Southern Ocean JGOFS cruise ANT X/6 of RV polarstern. Deep-Sea Res Part II, Top Stud Oceanogr 44(1&2):1–519
Smit J, Hertogen J (1980) An extraterrestrial event at the cretaceous-tertiary boundary. Nature 285:198–200
Sunda WG (1989) Trace metal interactions with marine phytoplankton. Biol Oceanogr 6(5–6):411–442
Sunda WG, Huntsman SA (1988) Effect of sunlight on redox cycles of manganese in the south western Sargasso Sea. Deep-Sea Res 35:1297–1317
Sunda WG, Huntsman SA (1990) Diel cycles in microbial manganese oxidation and manganese redox speciation in coastal waters of the Bahama Islands. Limnol Oceanogr 35:325–338
Sunda WG, Huntsman SA (1994) Photoreduction of manganese oxides in seawater. Mar Chem 46:133–152
Sunda WG, Huntsman SA, Harvey GR (1983) Photoreduction of manganese oxides in seawater and its geochemical and biological implications. Nature 301:234–236
Tréguer PJ, Rocha CLDL (2013) The world ocean silica cycle. Annu Rev Mar Sci 5:477–501
Turner DR, Whitfield M, Dickson AG (1981) The equilibrium speciation of dissolved components in freshwater and seawater at 25 °C and 1 atm pressure. Geochim Cosmochim Acta 45:855–881
Turner D, Hunter KA, De Baar HJW (2001) Introduction, chapter 1. In: Biogeochemistry of iron in seawater, IUPAC Book Series on Analytical and Physical Chemistry of Environmental Systems, Vol. 7, John Wiley & Sons, Chichester. pp 1–8
Twining BS (2003) The accumulation and trophic transfer of trace metals by protozoa. PhD thesis. Stony Brook University, Stony Brook
Twining BS, Baines SB (2013) The trace metal composition of marine phytoplankton. Annu Rev Mar Sci. 2013 5:191–215. https://doi.org/10.1146/annurev-marine-121211-172322
Van Heuven SMAC, Hoppema M, Huhn O, Slagter H, De Baar HJW (2011) Direct observations of increasing CO_2 in the Weddell Gyre along the Prime Meridian during 1973–2008. Deep-Sea Res II 58:2613–2635
Van Hulten MMP, Sterl A, Middag R, De Baar HJW, Gehlen M, Dutay JC, Tagliabue A (2014) On the effects of circulation, sediment resuspension and biological incorporation by diatoms in an ocean model of aluminium. Biogeosciences 11:3757–3779. https://doi.org/10.5194/bg-11-3757-2014
Van Hulten M, Middag R, Dutay JC, De Baar H, Roy-Barman M, Gehlen M, Tagliabue A, Sterl A (2017) Manganese in the west Atlantic Ocean in the context of the first global ocean circulation model of manganese. Biogeosciences 14:1123–1152. https://doi.org/10.5194/bg-14-1123-2017
Vernadsky V (1926) The biosphere. English translation by David B. Langmuir, New York, Copernicus, 1998. ISBN 0-387-98268-X, 192 pp
Von Damm KL, Edmond JM, Grant B, Measures CI, Walden B, Weiss RF (1985) Chemistry of submarine hydrothermal solutions at 21N, East Pacific Rise. Geochim Cosmochim Acta 49:2197–2220
Von Damm KL, Bray AM, Buttermore LG, Oosting SE (1998) The geochemical controls on vent fluids from the lucky strike vent field, mid-Atlantic ridge, earth planet. Sci Lett 160:521–536
Vu HTD, Sohrin Y (2013) Diverse stoichiometry of dissolved trace metals in the Indian Ocean. Sci Rep 3:1745. https://doi.org/10.1038/srep01745
Wolfe-Simon FD, Grzebyk D, Schofield O, Falkowski PG (2005) The role and evolution of superoxide dismutase in algae. J Phycol 41:453–465
Wolfe-Simon F, Starovoytov V, Reinfelder JR, Schofield O, Falkowski PG (2006) Localization and role of manganese superoxide dismutase in a marine diatom. Plant Physiol 142:1701–1709
Wu J, Roshan S, Chen G (2014) The distribution of dissolved manganese in the tropical–subtropical North Atlantic during US GEOTRACES 2010 and 2011. Mar Chem 166:9–24
Xu Y, Feng L, Jeffrey PD, Shi Y, Morel FMM (2008) Structure and metal exchange in the cadmium carbonic anhydrase of marine diatoms. Nature 452:56–61
Zhao Y, Vance D, Abouchami W, De Baar HJW (2014) Biogeochemical cycling of zinc and its isotopes in the Southern Ocean. Geochim Cosmochim Acta 125:653–672

Ocean Salinity, Major Elements, and Thermohaline Circulation

Hein J. W. de Baar, Steven M. A. C. van Heuven and Rob Middag
NIOZ Royal Netherlands Institute for Sea Research, Department of Ocean Systems (OCS), and Utrecht University, Den Burg, The Netherlands

Definition

Salinity is the total amount of dissolved salts in seawater, generally reported in grams/kg (parts per thousand). Salinity is in turn dominated by only a few major elements in ionic form: Na^+, Mg^{2+}, Ca^{2+}, K^+, Sr^{2+}, Cl^-, SO_4^{2-}, Br^-, F^-, and HCO_3^-. Temperature together with salinity determines the density of seawater, which governs the vertical circulation of the oceans, known as the thermohaline circulation.

Introduction

Ocean geochemistry is the discipline focusing mostly on the inorganic constituents of seawater in the world oceans. Interactions with biology and organic chemistry, and external sources and sinks, such as rivers, atmosphere, hydrothermal vents, and sediments, do play a role. Marine geochemistry comprises a far wider range including other aspects of inorganic geochemistry and organic geochemistry, and secondly not only the seawater but also investigations focusing on the underlying marine sediments and their inorganic and organic contents.

Seawater comprises above all the water molecule (H_2O) and in addition all of the existing 91 chemical elements in their dissolved state in water, in concentrations ranging many orders of magnitude. Most abundant at ~0.5–0.6 moles per liter (M for molar) are the major constituents of dissolved

Ocean Salinity, Major Elements, and Thermohaline Circulation, Table 1 The major ion composition of seawater at salinity S = 35.

Ion	Atomic weight (or molecular for SO_4^{2-})	Ocean concentration [gram.kg^{-1}] at S = 35	Ocean concentration Molar [mol. L^{-1} = mol.dm^{-3}]	Rivers average concentration (Molar [mol.dm^{-3}])	Ocean residence time versus rivers input [Year]
Cl^-	35.453	19.354	0.55952	0.00023	83,900,000 (83.9 million)
SO_4^{2-}	64.063	2.712	0.0282		
Br^-	79.904	0.0673	0.00086		
F^-	18.998	0.0013	0.0000068		
B	10.811	0.0045	0.000416	0.0000017	8,500,000 (8.5 million)
HCO_3^-			~0.0018 (variable)		
Na^+	22.990	10.76	0.48067	0.000315	52,600,000 (52.6 million)
Mg^{2+}	24.305	1.29	0.054	0.000000016	11,600,000 (11.6 million)
Ca^{2+}	40.078	0.4121	0.00106	0.00364	1,000,000 (1 million)
K^+	39.098	0.399	0.0105	0.0000345	10,500,000 (10.5 million)
Sr^{2+}	87.62	0.0079	0.000081	0.0000007	4,000,000 (4 million)

Latter value is close to the world average salinity 34.7 of the modern ocean. Compilation after Dittmar (1884), Wilson (1975), Quinby-Hunt and Turekian (1983), Murray (1992), and Sarmiento and Gruber (2006). Riley (1965) described the historical development of salinity and its measurement. The molar concentrations in seawater at S = 35 have been calculated from the original [gram.kg^{-1}] divided by the atomic weight and adjusted for a "typical" density of seawater of 1027 [gram.dm^{-3} = kg.m^{-3}] or 1.027 kg/Liter. This chosen density is merely an example value, in this choice for water with temperature of ~10 °C at the sea surface (density) or collected from the deep and brought up to the surface (potential density). Calcium (Ca) varies somewhat (~1%) between surface waters and deep waters. Mg and Sr are in the same group in the periodic table as Ca and also show some variations, that however are too small deviations from being "conservative" to affect salinity at its current accuracy. Boron (B) exists as both neutral $B(OH)_3$ and negatively charged $B(OH)_4^-$ ion in seawater, their relative proportion being a function of pH (Dickson 1990). At "typical" pH = ~8 for modern surface waters the concentration of $B(OH)_4^-$ is insignificant for the current accuracy of measured conductivity from which salinity is calculated. Similarly, the HCO_3^- ion is barely significant for overall conductivity, i.e., derived salinity. For the overall world ocean, a "typical" salinity of 35 is commonly used. Similarly in laboratory experiments, and in all sorts of calculations, one commonly uses a salinity of 35

seasalt, the ions Na^+ and Cl^- (Table 1). These and other major elements are the topic of this chapter.

Three orders of magnitude less abundant is Dissolved Inorganic Carbon (C as DIC) varying around ~2 millimoles [mM = 10^{-3} M], and pivotal for life in the sea; this is treated in the chapter on "▶ Carbonate Minerals and the CO_2-Carbonic Acid System" (Lerman and Mackenzie, this volume).

Much less abundant are the nutrients nitrate and phosphate that occur in the micromole [μM = 10^{-6} M] range and are essential for each living organism. Also essential for life are several trace nutrient elements. The nutrients, trace nutrients, and other trace elements are treated in the chapter on "▶ Ocean Biochemical Cycling and Trace Elements" (De Baar et al. this volume).

Most of the chemical elements have several isotopes, which can be either radioactive isotopes or stable isotopes, that provide useful insights into ocean processes and are described in other chapters.

Major Ions in Seawater and Salinity

Upon accurate analyses of 77 seawater samples, Dittmar (1884) confirmed previous findings of Marcet and of Forchhammer that, regardless of the absolute concentration of the total solids, the ratios between the more abundant major chemical elements are virtually constant (Table 1). Since then, these major constituents of seawater are classified as being "conservative." Variation is ascribed exclusively to there being more or less pure water in anyone given sample of seawater due to net precipitation or net evaporation at the sea surface, respectively, or due to mixing of two water masses with different total salt content. These findings lead to the concept of salinity (after Forchhammer), that is the total amount of dissolved salts in seawater. Salinity is expressed as gram per kg seawater [absolute salinity; gram.kg^{-1}] that is dimensionless and hence can also be expressed as per mille unit $^0/_{00}$ or nowadays as practical salinity without any unit at all (IOC 2010).

The salinity in the world oceans varies in a narrow range between ~33 and ~38, such that 35 is taken as the "typical" value (Table 1). The nice thing of the uniform proportions is that when you measure just one, you know them all, and also their summation, the salinity. This was done for 65 years until the ~1960s by measuring the chlorine concentration and from this calculate salinity. Nowadays, the salinity is measured by the electrical conductivity of seawater that depends on the total amount of ionic charges, the more charged ions, the better the conductivity, and the higher the derived salinity. The combined and very accurate measurements by electronic sensors throughout the ~4000 m deep water column of the oceans of conductivity (for salinity); in situ temperature; and pressure (for depth) yield the three key variables Salinity,

O

Temperature, and Pressure (S, T, p) that together determine the density [kg.dm^{-3}] of seawater at the given location and depth. The density is calculated very accurately with the thermodynamic equation of state of seawater (IOC 2010). For the two other parameters, the temperature in the oceans varies from around −1.85 °C (the freezing point of seawater) to ~25 °C or in some tropical seas even 30 °C or higher; nevertheless, the temperature of deep ocean waters is quite uniform around ~2 °C. The pressure increases with depth to 380 atmosphere at the average ~ 3800 m depth of the oceans, or at most ~1000 atm in the deepest ~10 km deep oceanic trenches.

The variations of density are small, but extremely important as these small differences in density of different water masses are the drivers of the "thermohaline" circulation of the oceans. The density of ocean waters ranges from ~1020 to ~1030 gram.dm^{-3} (or kg.m^{-3}), i.e., seawater is 2–3% more dense (heavier) than pure water. The very small range of about 1% (i.e., from 102% to 103%) of the overall density represents the complete window that drives the circulation. Therefore physical oceanographers are keen to obtain very accurate estimates of salinity, currently at around the third decimal point, e.g., 35.456 with an accuracy of ±0.001.

One must be aware of minor deviations of some chemical elements from the constant proportions, i.e., from being conservative. For example, Dittmar (1884) already noticed that the Ca^{2+} in deep water samples was slightly higher than in the upper waters. This is due to the net uptake from upper water by biocalcification, that is the production by organisms of solid $CaCO_3$ for biogenic shells and corals.

$$Ca^{2+} + 2\,HCO_3^- \rightleftarrows CaCO_{3(crystalline)} + CO_2 + H_2O \quad (1)$$

Upon senescence of the shell-forming organism, the heavy (density ~ 2700 kg.m^{-3}) $CaCO_3$ shells settle into deep waters and beyond a given depth horizon enter waters that are undersaturated versus solid $CaCO_3$, such that the shells slowly dissolve. The overall result is that the deep waters comprise, on average, about 1% more dissolved Ca^{2+} ions than the surface waters.

The relative composition of the dissolved salts in seawater appears to have been fairly very uniform over the past 541 million years to present, the Phanaerozoic Eon. Evidence for this comes from marine evaporite deposits (e.g., Ryan 2008). Occasionally a semi-enclosed sea has become completely enclosed, and during evaporation of the water, the seasalt has deposited in a well-known sequence in the reverse order of the solubilities of the minerals. Therefore the order of precipitation from sea water is:

1. Calcite ($CaCO_3$) and dolomite ($CaMg(CO_3)_2$)
2. Gypsum ($CaSO_4$-$2H_2O$) and anhydrite ($CaSO_4$).
3. Halite (i.e., common salt, NaCl)
4. Potassium and magnesium salts

Given the dominance of Na^+ and Cl^- in seawater, the thickness of the halite layer (NaCl) amounts to some 90% of the overall deposit. When adding up the contents of all the layers, one finds the ratio of elements to be the same as in modern seawater. Given the age of the studied evaporite deposit one knows that, at that time in the past, the dissolved seasalt was the same composition as today.

For example, the Messinian Salinity Crisis (MSC) that occurred from 5.96 to 5.33 million years in the past is deemed to be caused by the closing and opening again, perhaps several times, of the Strait of Gibraltar, thus cutting off the Mediterranean Sea from the Atlantic Ocean (Hsu 1983; Roveri et al. 2014). This caused complete dessication of the Mediterranean Sea, perhaps several times, and as a result thick packages of evaporites were laid down and nowadays can be found and sampled in the sediments throughout the Mediterranean Sea. The water from the Mediterranean would have been redistributed in the world ocean, but not the salt that remained in the deposits. As a result there must have been a global decrease in salinity. The total element composition of the MSC evaporites closely confirms that of modern seawater. From worldwide estimates of all such evaporite deposits and their ages, it is concluded the seawater composition has been fairly stable during at least the past 541 million years, although some deviations are known (e.g. Blättler and Higgins 2014).

Residence Times and Mass Balance

In the hydrological cycle, the oceans lose water by evaporation and rivers return the water to the ocean. The river water contains very little dissolved salts (Table 1), and also in very different proportions than seawater. Notably in Table 1 for the positive ions in river water the predominance is

$$Ca^{2+} > Mg^{2+} > K^+ > Na^+ > Sr^{2+} \quad (2)$$

whereas in seawater the predominance is

$$Na^+ > Mg^{2+} > Ca^{2+} > K^+ > Sr^{2+} \quad (3)$$

For the ocean one may assume that the inflow of water does on average equal the net loss by evaporation, a stable situation and that is called a steady state. When now dividing the large ocean volume of 1330×10^6 km^3 by the annual ~36×10^3 km^3.year^{-1} freshwater inflow one obtains the ~37,000 years residence time of water in the oceans, this relative to river inflow (plus groundwater discharge).

Next one can for the major chemical elements (Table 1) multiply this water residence time with the ratio of concentrations [mol.dm^{-3}] in seawater and in river water

$$Residence\ time = (volume_{ocean}/inflow_{rivers}) \times (concentration_{ocean}/concentration_{rivers}) \quad (4)$$

and obtain the residence time [year] of major elements in the oceans (Table 1). These residence times are very long, from 52.6 million to 83.9 million years for major elements Na and Cl, respectively, to ~10 million years for Mg and K, but "only" 1 million year for Ca. For the latter, this results from biocalcification. While, as already mentioned, some of these shells dissolve again in the deep sea, a portion remains intact and becomes buried within marine sediments as lime deposits.

If their concentrations do not change through time, then a steady state must exist, by and large, for each of the dissolved major elements of the seasalt. Somehow the loss term from seawater must be found in marine deposits. An obvious removal term of dissolved major ions is the occasional formation of marine evaporites at various locations of the globe, such as those underlying the Mediterranean Sea. Another sink are the vast and often also quite thick calcareous minerals, the buried fossil shells of $CaCO_3$, that also comprise some trace amounts of akin elements Mg and Sr. Also, because the crystal $CaMg(CO_3)_2$ or dolomite is thermodynamically more stable than $CaCO_3$ (limestone), very slow post-depositional transformation, i.e., dolomitization, occurs within the sediments.

$$2\ CaCO_{3\ (limestone)} + Mg^{2+} \rightleftarrows CaMg(CO_3)_{2\ (dolomite)} + Ca^{2+} \quad (5)$$

As a result, the concentration of Mg^{2+} in pore waters of such sediments is lower than in the overlying seawater, and extra Mg^{2+} diffuses from the sea into the sediment pore waters. This is an extra loss term for Mg^{2+} from seawater.

Another sink term for Mg, and K, is their reaction with degraded clays coming from land and suspended in the river outflow, to various marine type clay minerals that in the process have taken up extra Mg and K. This "reverse weathering" hypothesis (Mackenzie and Garrels 1966) was at first difficult to test in the laboratory due to the very slow reactions. However, this was eventually demonstrated in long-term experiments on the formation of authigenic aluminosilicates in the sediments of the Amazon delta (Michalopoulos and Aller 1995). Meanwhile the discovery in 1977 and beyond of hydrothermal circulation of seawater at Mid Ocean Ridges did provide an answer at least for Mg (Corliss et al. 1979). The cold (~2 °C) deep seawater entering the rocks through cracks heats up enormously and reacts with the rocks, and the hot seawater plumes coming out at ~380 °C have lost all dissolved Mg. Hence, hydrothermalism is a major sink for removal of Mg from ocean waters.

The top 10 rivers in terms of water discharge supply the majority of all fresh water and its dissolved ions into the oceans (Martin and Meybeck 1979). For example, the Amazon, Zaire, and Mississippi rivers draining into the Atlantic Ocean, together represent almost 50% of all river inflow into the world oceans. Almost all large rivers are regularly monitored for volume flow and dissolved major ions, such that, despite interannual variability, a quite reliable worldwide estimate can be obtained, at least for our era.

Overall, the above simple approach merely comparing river supply with ocean content and loss to evaporites, limestone deposits, reverse weathering, and hydrothermalism is quite satisfactory as a steady state model for the, mostly conservative, major elements of seawater (Table 1). However, many minor and trace elements (see chapter "▶ Ocean Biochemical Cycling and Trace Elements") require a more complete concept of ocean mass balance (Fig. 1) including consideration of several other sources and sinks:

- River input source
- Aeolian supply source of terrestrial dust as either dry deposition or wet deposition
- Gas exchange with the atmosphere notably for CO_2 and O_2, as source or as sink
- Hydrothermal supply or loss, for example, an iron source (Fe), or sink of magnesium (Mg)
- Radioactive production source or radioactive decay loss within the oceans
- Sedimentation loss
- Diffusive fluxes into or out of sediment pore waters

This also implies that for deriving a steady state mass balance for any one chemical element of interest, one has to add up all the sources, as well as add up all the sinks. Next one somehow hopes these are equal, or adjusts these, such that the sum of sources more or less equals the sum of sinks. Finally one can compare these sums [moles.year^{-1}] with the total ocean inventory [moles] to derive a residence time [year] for the given chemical element.

During the Last Glacial Maximum (LGM), large ice caps covered large parts of North America and Europe. The volume of these ice caps corresponded with an ~120 m lower sea level than today. As a result of the corresponding lower overall volume of the seawater in the oceans, the salinity was higher in the LGM (Adkins et al. 2002), with a different salinity distribution in the major oceans than today, but the relative proportions of dissolved salts remained the same. Modern day salinities are all within 0.5 of the global average salinity of 34.7, whereas salinities during the last glacial

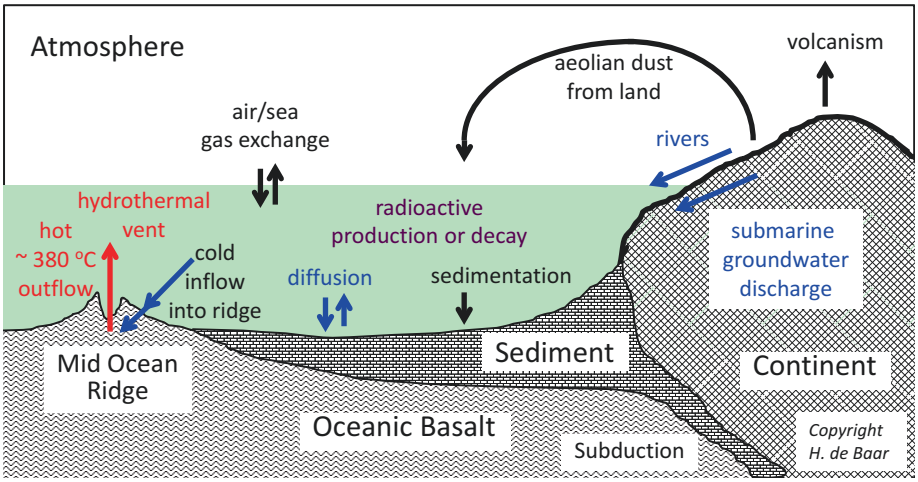

Ocean Salinity, Major Elements, and Thermohaline Circulation, Fig. 1 Box cartoon of ocean inventory box (azure color) with all sources and sinks, and in steady state ideally: $\Sigma_{sources} = \Sigma_{sinks}$, where $\Sigma_{sources}$ = Rivers + dust + air to sea gas inflow + hydrothermal input + radioactive production + diffusion from sediment and Σ_{sinks} = Air to sea gas outflow + hydrothermal output + radioactive decay + sedimentation + diffusion into sediment

maximum (LGM) ranged from 35.8 in the North Atlantic to as high as 37.1 in the Southern Ocean.

Circulation of Deep Ocean Waters

The world ocean distributions of chemical elements are more strongly controlled by the circulation of deep ocean waters, that is all waters below ~500 m depth, than by the circulation of the upper ocean (all waters shallower than ~500 m). Thus in order to understand the cycling and distribution of the chemical elements, one at least also needs to have some understanding of the deep Thermohaline Circulation (Van Aken 2007).

The ultimate driver of this deep circulation is the formation of deep waters. This sinking is primarily caused by a seasonal increase of density in the winter in polar regions. Firstly by winter cooling; secondly by seasonal formation of sea-ice resulting in the remaining seawater having a higher salinity, the water overall gets a higher density.

In the Arctic region, this winter process is most intense in February in the Greenland-Iceland-Norwegian Seas (GIN-Seas; Hopkins 1991; Van Aken 2007; Seidov et al. 2013, 2014) north of Iceland. This deep basin fills up with this denser water and overflows at the relatively shallow Denmark Strait between Iceland and Greenland, and the straits between Iceland, the Faeroes, and Scotland. These overflows sink again to near the bottom of the northern North Atlantic Ocean and flow southwards, along the Western Atlantic Ocean basin due to Coriolis acceleration. This North Atlantic Deep Water (NADW) also picks up some waters that were formed in winter in the Labrador Sea (between Canada and Greenland) that are less dense and therefore sink only to ~1200 m depth. Moreover within the Mediterranean Sea there is heating and net evaporation of seawater. This warmer but more saline (S ~ 38) water sinks and eventually overflows at Gibraltar Strait into the Atlantic Ocean, where this Mediterranean Overflow Water (MOW) spreads out at ~1200 m depth as far as the West Atlantic. By vertical mixing, the MOW causes the underlying NADW to become more saline.

After some 400–500 years, the NADW enters the Antarctic Circumpolar Current. In the Antarctic Weddell Sea, there is similar formation of cold Weddell Sea Deep Water (WSDW) during the Antarctic winter (July–August). This eventually outflows into all three major ocean basins as Antarctic Bottom Water (AABW). At the Antarctic Polar Front, there is also sinking of waters but only to ~1000 m depth, this Antarctic Intermediate Water (AAIW) also outflows into all three major ocean basins. As a result of these outflows of Antarctic origin waters, the deep Indian Ocean is filled up until its boundary with Asia at 20–30 °N. The oldest deep waters of the northern Indian Ocean have an "age" of ~1000 years; in other words, it has been ~1000 years ago that this water last was at the surface. Similarly, the deep Pacific Ocean fills from south to north and in the deep North Pacific Ocean exists the oldest deep waters with ages in the 1500–1800 or even 2200 years range.

The abovementioned ages are based on the distribution of ^{14}C in the deep oceans. More recently, Matsumoto (2007) has revised these conventional ages (his Fig. 1) by accounting for two key mechanisms and has arrived at somewhat younger ages (his Fig. 4), notably ~200 years for the Northwest Atlantic location, and ~1200 years respectively for the Northeast Pacific region. The age difference of ~1000 years between these two positions would then be a bit less, but still very long. Other age estimations have been made (Khatiwala et al. 2012;

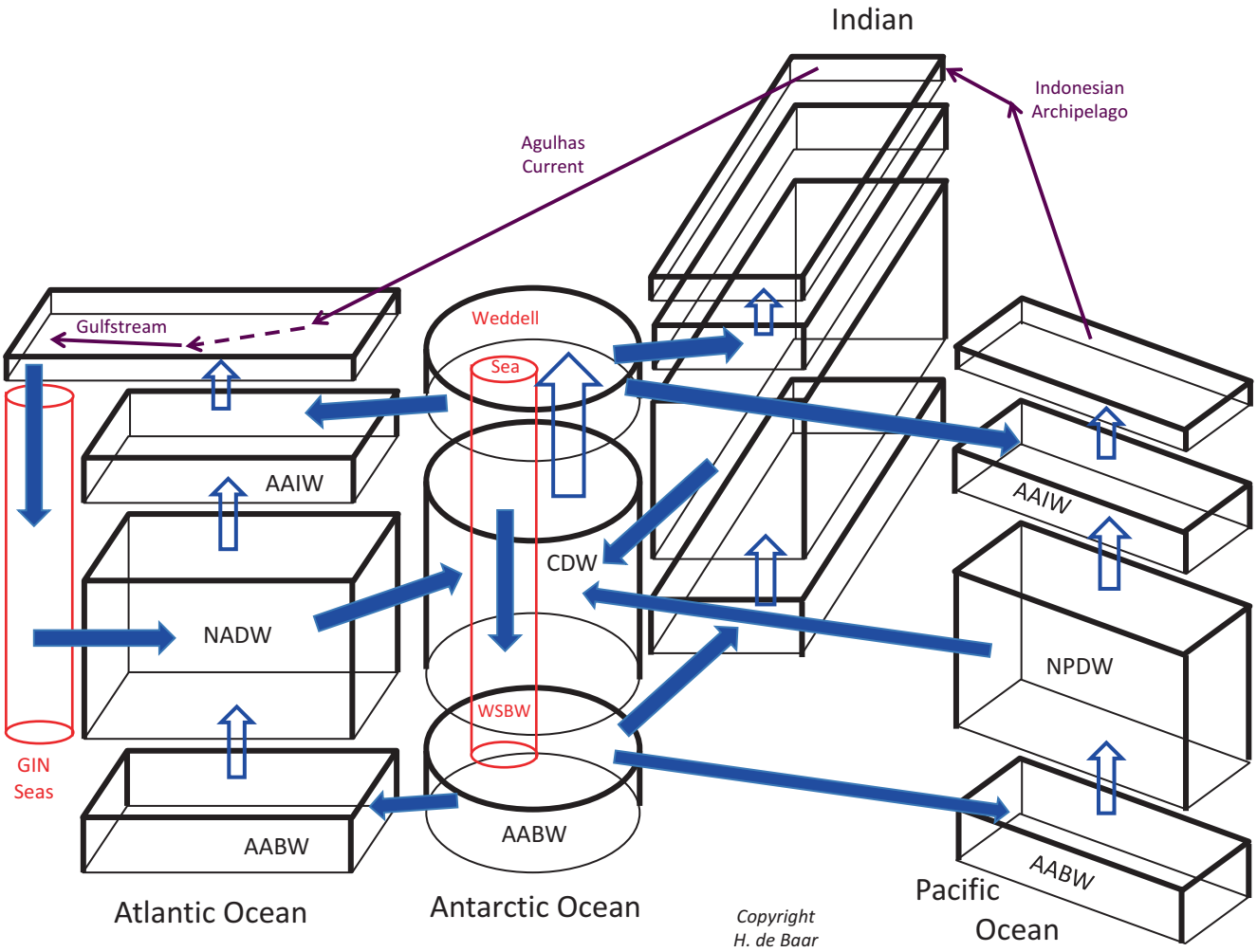

Ocean Salinity, Major Elements, and Thermohaline Circulation, Fig. 2 Simplified scheme of circulation in the deep ocean basins. Filled blue arrows are (vertical) deep water formation and (horizontal) flow. Formation of deep waters shown in red. Not shown are several other (smaller) sources, in the Labrador Sea, the Mediterranean Overflow Water (MOW), in the Ross Sea and along some other sectors around Antarctica. The open blue arrows are for general upwelling that closes the water budget by returning water to the uppermost boxes in all oceans. From the Pacific Ocean, there is a return flow (shown in purple) via the Indonesian Archipelago, Agulhas Current, Gulf Stream resuppplying the GIN-Seas. Antarctic Ocean is all waters south of the Antarctic Polar Front (APF) at ~50 °S, the APF is defined by the surface expression of the 2 °C isotherm (Deacon 1984). Drafted after similar schemes that exist in the literature (e.g. Schmitz 1996; his Fig. I-91 at page 106) and at the internet (e.g. http://ccsr.aori.u-tokyo.ac.jp/old/ehtml/eocean.html)

Gebbie and Huybers 2012) yet all agree that the age difference between deep North Atlantic and deep North Pacific Oceans is in the order of ~1000 years or more (Fig. 2).

Summary

Salinity of seawater in the oceans comprises the small number of chemical elements that occur in very high concentration in seawater. These major elements in seawater have very long residence times in the oceans, for example, 52.6 million and 83.9 million years for major elements Na and Cl, respectively, and ~10 million years for Mg and K, but "only" 1 million year for Ca. This in comparison to the relatively very brief mixing time of seawater between the ocean basins in the order of "merely" ~1000 years yields a very constant ratio of these major elements in seawater. One exception is again Ca that due to its involvement in the biogeochemical cycle of $CaCO_3$ shells and corals has a slightly lower concentration in surface waters relatively to deep waters. From quantitative studies of worldwide evaporite deposits, it has been estimated that the seawater composition has been fairly stable during at least the past 541 million years. In the modern ocean, the "thermohaline" circulation of deep waters is driven by small differences of seawater density due to differences in temperature and salinity.

Winter cooling and sea-ice formation in polar winters cause surface waters to become more dense and sink into

the deep polar seas, from where these waters outflow into all other oceans.

Cross-References

- Alkali and Alkaline Earth Metals
- Carbonate Minerals and the CO2-Carbonic Acid System
- Chlorine
- Evaporites
- Geochemistry
- Hydrothermal vents
- Magnesium
- Ocean Biochemical Cycling and Trace Elements
- Sodium

References

Adkins JF, McIntyre K, Schrag DP (2002) The salinity, temperature, and delta 18O of the glacial deep ocean. Science 298(5599):1769–1773

Blättler CL, Higgins JA (2014) Calcium isotopes in evaporites record variations in Phanerozoic seawater SO_4 and Ca. Geology 42:711–714

Corliss JB, Dymond J, Gordon LI, Edmond JM, Von Herzen RP, Ballard RD, Green K, Williams D, Bainbridge A, Crane K, Van Andel TH (1979) Submarine thermal springs on the Galapagos Rift. Science 203:1073–1083

Deacon GER (1984) The Antarctic circumpolar ocean. Cambridge University Press, Cambridge, 180p

Dickson AG (1990) Thermodynamics of the dissociation of boric acid in synthetic seawater from 273.15 to 318.5 K. Deep-Sea Res 37:755–766

Dittmar W (1884) Report on researches into the composition of ocean water, collected by H.M.S. Challenger. Chall Rep Phys Chem 1:1–251

Gebbie G, Huybers P (2012) The mean age of ocean waters inferred from radiocarbon observations: sensitivity to surface sources and accounting for mixing histories. J Phys Oceanogr 42:291–305

Hopkins TS (1991) The GIN sea – a synthesis of its physical oceanography and literature review 1972–1985. Earth Sci Rev 30(3–4): 175–318

Hsu KJ (1983) "A voyage of the Glomar challenger". The Mediterranean was a desert. Princeton University Press, Princeton

IOC (2010) The international thermodynamic equation of seawater – 2010: calculation and use of thermodynamic properties. Intergovernmental oceanographic commission, manuals and guides no. 56, UNESCO (English), 196 p. Free download at: http://www.teos-10.org/pubs/TEOS-10_Manual.pdf

Khatiwala S, Primeau F, Holzer M (2012) Ventilation of the deep ocean constrained with tracer observations and implications for radiocarbon estimates of ideal mean age. Earth Planet Sci Lett 325–326:116–125

Mackenzie FT, Garrels RM (1966) Chemical mass balance between rivers and oceans. Am J Sci 264:507–525

Martin JM, Meybeck M (1979) Elemental mass-balance of material carried by major world rivers. Mar Chem 7:173–206

Matsumoto K (2007) Radiocarbon-based circulation age of the world oceans. J Geophys Res 112:C09004. https://doi.org/10.1029/2007JC004095

Michalopoulos M, Aller RC (1995) Rapid clay mineral formation in Amazon delta sediments: reverse weathering and oceanic elemental cycles. Science 270:614–617

Murray JW (1992) The oceans. In: Butcher SS, Charlson RJ, Orians GH, Wolfe GU (eds) Global biogeochemical cycles. Academic, London, pp 175–211

Quinby-Hunt MS, Turekian KK (1983) Distribution of elements in sea water. Eos Trans AGU 64:130–131

Riley JP (1965) Historical Introduction. Chapter 1 in: Riley JP, Skirrow G (ed) Chemical Oceanography, Academic Press, London and New York, vol. 1st edn. pp 1–41

Roveri M, Flecker R, Krijgsman W, Lofi J, Lugli S, Manzi V, Sierro FJ, Bertini A, Camerlenghi A, De Lange G, Govers R, Hilgen FJ, Hübscher C, Meijer PT, Stoica M (2014) The Messinian salinity crisis: past and future of a great challenge for marine sciences. Mar Geol 352:25–58

Ryan WBF (2008) Modeling the magnitude and timing of evaporative drawdown during the Messinian salinity crisis. Stratigraphy 5(3–4):227–243

Sarmiento JL, Gruber N (2006) Ocean biogeochemical dynamics. Princeton University Press, Princeton, xii + 503p

Schmitz, WJ Jr (1996) On the world ocean circulation, vol. I. Technical Report WHOI-96-03; page 106 of 148p

Seidov D, Baranova OK, Biddle M, Boyer TP, Johnson DR, Mishonov AV, Paver C, Zweng MM (2013) Greenland-Iceland-Norwegian seas regional climatology. Regional Climatology Team, NOAA/NODC. https://doi.org/10.7289/V5GT5K30. See also: https://www.nodc.noaa.gov/OC5/regional_climate/gin-seas-climate/

Seidov D, Antonov JI, Arzayus KM, Baranova OK, Biddle M, Boyer TP, Johnson DR, Mishonov AV, Paver C, Zweng MM (2014) Oceanography north of 60^0N from world ocean database. Prog Oceanogr. https://doi.org/10.1016/j.pocean.2014.02.003

Van Aken H (2007) The oceanic thermohaline circulation: an introduction. Springer, New York, XVIII + 326p

Wilson TRS (1975) Salinity and the major elements of seawater. Chapter 6 In: Riley JP, Skirrow G (ed) Chemical oceanography, Academic Press, London, New York, San Francisco, vol. 1, 2nd edn. pp 365–413

Oceanic Island Basalts

Matthew Gerard Jackson
Department of Earth Science, University of California Santa Barbara, Santa Barbara, CA, USA

Definitions

Ocean island basalts (generally referred to as OIBs) are a type of basalt erupted within the oceans, mainly in intraplate settings. Thus, OIB volcanism contrasts with the other principal types of volcanism in the ocean basins that occur along plate boundaries: mid-ocean ridge basalt (MORB) volcanism, where basalt is erupted at divergent plate boundaries, and subduction zone (or arc) volcanism, where lavas are formed in association with subduction at convergent plate boundaries. OIBs are erupted at volcanic hotspots, which correspond to the surface location of upwelling mantle plumes. Mantle plumes are buoyantly upwelling regions of the mantle that are thought to have unusually high mantle temperatures.

OIB, Hotspots, and Mantle Plumes

Many hotspots are located in intraplate settings in the oceans. However, some hotspots are colocated with mid-ocean ridges (e.g., Iceland hotspot), and at least one hotspot is located near a subduction zone, and complicated plume-trench interactions are suggested (e.g., Samoa hotspot). In the latter case, the subducting Pacific plate may interact with the upwelling Samoan plume, drawing the plume toward the downgoing slab (Druken et al. 2014).

While the term "ocean island basalt" corresponds to rock formed by intraplate volcanism that occurs in the ocean basins, OIBs are not always basaltic. OIBs encompass a broad range of compositions and span both tholeiite and alkali basalt compositions. While primitive OIBs are basaltic, highly evolved equivalents also exist, and intraplate hotspot lavas with phonolitic, trachytic, or dacitic compositions also occur. In fact, rhyolitic eruptions are common at the large central volcanoes of Iceland, and these provide an important example of the extreme variation in lava compositions identified at oceanic hotspot localities. Carbonatites, which are mantle melts composed of primary mantle carbonates, offer an additional example of the extreme compositional variability present in oceanic hotspot lavas.

Ocean island basalts do not erupt strictly on islands. In fact, most of the volume of intraplate hotspot volcanism is erupted underwater. Many intraplate hotspot volcanoes never breach the water surface to erupt lavas subaerially, and these hotspot volcanoes exist as submarine seamounts for their entire lifespan. Oceanic hotspot volcanoes that do breach the water surface to become islands ultimately subside thermally after volcanism ceases. Thus, the processes of thermal subsidence and subaerial erosion, which effectively reduce the mass of the volcano above water, act to turn ocean islands into seamounts. Indeed, most OIBs are actually found as seamounts (Staudigel and Koppers 2015).

OIBs erupted at the Hawaiian (Weis et al. 2011) and Louisville (Koppers et al. 2012) hotspots can be explained by upwelling of a deep-seated, thermally buoyant mantle plume that partially melts beneath the oceanic plate, and the resulting melts upwell to feed an active hotspot volcano that resides above the hotspot. Because mantle plumes generally drift slowly with respect to plate velocities at the surface, a chain of age-progressive hotspot volcanoes forms over the upwelling mantle plume as the plate moves laterally over the hotspot: younger, active volcanoes are found near the hotspot, and volcanoes further downstream (in the direction of plate motion) are older and volcanically inactive. Most major hotspot-related island chains appear to be plume related (French and Romanowicz 2015), and some hotspot chains are long lived: the Hawaii and Louisville chains have produced volcanism for just over 80 million years, and it is proposed that hotspots currently active in the Cook Islands have been active for over 100 million years (Koppers et al. 2003). In the Indian Ocean, the volcanism associated with the Kerguelen mantle plume spans an age range of ~120 million years (Frey et al. 2000).

However, there does not appear to be a single mechanism responsible for generating hotspot volcanism in the ocean basins. Not all OIB localities are associated with age-progressive chains of volcanoes. Instead, some OIBs are erupted as isolated seamounts that are not part of a chain (e.g., Bermuda), and these isolated seamounts do not clearly relate to a deep-seated or long-lived plume. OIBs are also erupted along chains that do not exhibit age progressions (e.g., the Pukapuka ridge; Janney et al. 2000) and are thus not easily explained by volcanism that results from an upwelling mantle plume. The mechanisms responsible for hotspot volcanism and OIB generation at these localities are not well understood, but could relate to melting of fertile blobs in the upper mantle or shallow melting that results from tectonic stresses in the lithosphere (e.g., Sandwell et al. 1995). These alternative mechanisms for generating hotspot volcanism are not unimportant: there are >45,000 seamounts that extend >1 km above the ocean floor (Staudigel and Koppers 2015), and most of these seamounts are not clearly related to plume-fed hotspot chains.

Geochemistry and Crustal Recycling

The trace element characteristics of OIB vary considerably. Tholeiitic OIB erupted at localities like Hawaii is less enriched in incompatible elements (e.g., Rb, Ba, Th, U) – which prefer to be in the melt relative to the solid mantle that partially melted to generate the melt – than alkalic OIB (Fig. 1). While this may reflect enrichment of incompatible elements in the mantle source of alkalic OIB compared to the mantle source of tholeiitic lavas, a more likely explanation is that alkalic OIBs are the result of lower degree melting of the mantle than tholeiitic OIBs. Indeed, low degrees of mantle melting concentrate the incompatible elements in the melt relative to high degree melting (Schilling and Winchester 1967; Hofmann 2003). The degree of melting depends on both the mantle temperature and the depth to which upwelling mantle can rise. Evidence suggests that mantle plumes are hotter than the ambient depleted upper mantle that sources MORB melts (Putirka et al. 2007; Herzberg et al. 2007), yet hotspot lavas at many localities appear to be the result of low degrees of melting. The paradox of low degree melting at many hotspot localities might be explained by the role of oceanic lithosphere, which is thick in regions where the oceanic plate is old. A thick oceanic lithosphere serves to stop plume upwelling and effectively halts further adiabatic melting, thereby reducing the degree of melting (Dasgupta et al. 2010).

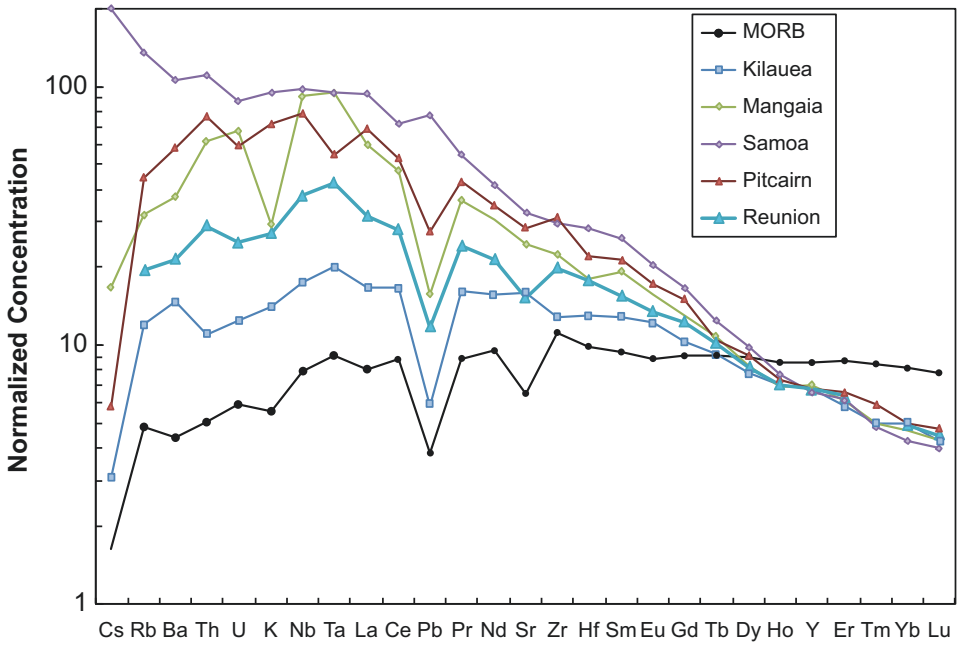

Oceanic Island Basalts, Fig. 1 Primitive mantle normalized trace element patterns for OIB from different localities. Alkalic OIB from Pitcairn, Samoa, and Mangaia is more enriched in incompatible elements than tholeiitic lavas from Hawaii and MORB tholeiites. (Figure modified after White (2013), except for Mangaia (Woodhead 1996) and MORB (Gale et al. 2013).)

The composition of the mantle that melts to generate OIBs provides important insights into the evolution and dynamics of the mantle over geologic time. Unlike major and trace elements, radiogenic isotopic ratios, like $^{87}Sr/^{86}Sr$, $^{143}Nd/^{144}Nd$, and $^{206}Pb/^{204}Pb$, are not fractionated between the mantle and melts that are extracted from the mantle and as such are "fingerprints" of the mantle source of the melts. These isotopic systems provide a window into the composition of the inaccessibly deep Earth that is sampled by OIB. For over five decades, it has been known that basalts from different oceanic islands exhibit heterogeneous radiogenic isotopic compositions (Gast et al. 1964), and the global radiogenic isotopic variability observed in OIBs is described by at least four different isotopic end-members that are often referred to as HIMU (high μ, = $^{238}U/^{204}Pb$), EM1 (enriched mantle I), EM2 (enriched mantle II), and DM (depleted mantle). However, the origin of this isotopic variability is still the source of debate. A long-standing hypothesis is that subducted oceanic crust (Hofmann and White 1982) and continental crust (White and Hofmann 1982) that are isotopically heterogeneous can explain much of the radiogenic isotopic diversity observed in OIB globally. Large amounts of oceanic crust (20 km^3/year) and sediment derived primarily from the continents (0.5–0.7 km^3/year) are subducted into the mantle. If subduction has been operating for three billion years, and if subduction of oceanic crust has been constant over that time period, then ~4% of the mantle's mass is comprised of subduction oceanic crust. Similarly, ~0.1% of the mass of the mantle is subducted sediment. This subducted material enters the convecting mantle where it can reside for billion-year time scales, before being recycled into the mantle source of OIB. OIB from different localities has distinct radiogenic isotopic compositions that have been linked to a diversity of crustal protoliths of different ages that were subducted into the mantle. Stable isotopic measurements of OIB, including oxygen isotopes and mass independently fractionated sulfur isotopes (Eiler et al. 1997; Cabral et al. 2013), support the hypothesis that OIB sample melts of crustal protoliths that were once at the Earth's surface. Additionally, OIB exhibits incompatible element-enriched radiogenic isotopic signatures (higher $^{87}Sr/^{86}Sr$ and $^{206}Pb/^{204}Pb$ and lower $^{143}Nd/^{144}Nd$) that provide powerful evidence that the mantle sources of these hotspots have been enriched by recycling of ancient subducted crustal material into the shallow upper mantle. In comparison, MORB derived from the upper mantle by higher degrees of partial melting tend to exhibit more incompatible element-depleted (lower $^{87}Sr/^{86}Sr$ and $^{206}Pb/^{204}Pb$ and higher $^{143}Nd/^{144}Nd$) radiogenic isotopic compositions. Thus, plate-tectonic processes operating at the surface, including subduction, ultimately control the composition of the mantle sources that melt to generate OIB (Fig. 2).

Primordial Signature from the Deep Mantle

While OIB samples material that was subducted into the mantle, some OIB thought to be sourced by deep-seated mantle plumes exhibits primitive noble gas characteristics (Courtillot et al. 2003). For example, compared to MORB sampling the upper mantle, OIB can have elevated $^3He/^4He$ ratios that are associated with the primitive materials that constitute the building blocks of the terrestrial planets. The preservation of high $^3He/^4He$ in the mantle sources of these lavas suggests that

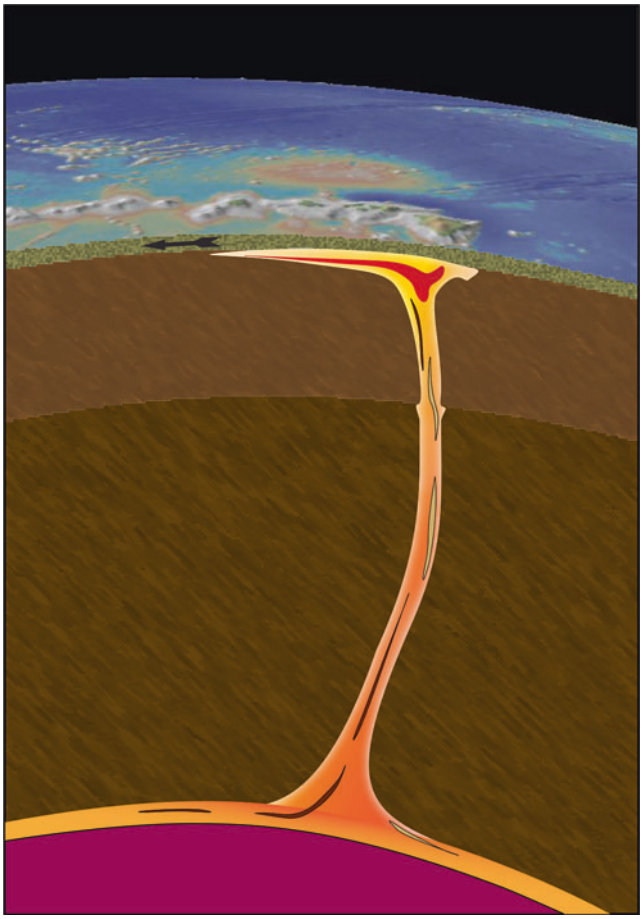

Oceanic Island Basalts, Fig. 2 The Hawaiian hotspots are thought to be fed by a buoyantly upwelling mantle plume that rises from the core-mantle boundary. (From White, 2014.)

ancient, primitive domains have survived in the mantle in spite of convective mixing processes that have operated in the mantle since Earth's accretion at >4.5 Ga. Supporting the hypothesis that high $^{3}He/^{4}He$ domains sample ancient domains preserved in the mantle, Mukhopadhyay (2012) found that high $^{3}He/^{4}He$ OIB exhibits different $^{129}Xe/^{130}Xe$ than MORB and the Earth's atmosphere. Because all $^{129}Xe/^{130}Xe$ isotopic heterogeneity in the Earth was generated during the lifetime of ^{129}I (half-life of 15.7 million years), the discovery of low $^{129}Xe/^{130}Xe$ in hotspot lavas indicates that the high $^{3}He/^{4}He$ reservoir formed within ~100 million years of Earth's accretion.

Some OIBs are melts of mantle domains that host ancient, primordial signatures and other OIB sample mantle domains that have a component of subducted crust that has been incorporated (recycled) into the mantle that melts to form OIB. In fact, many OIBs exhibit a mixture of primitive and recycled signatures. Regions of anomalously slow seismic velocity in the deepest mantle, referred to as large low shear wave velocity provinces (LLSVPs), are suggested to host both primitive and subducted crustal material that may be intimately associated within the LLSVPs (Li et al. 2014). The bases of deep-seated mantle plumes may extend to the LLSVPs. If mantle plumes are sourced by the LLSVPs, these plumes may convey primitive and subducted material to the shallow mantle where they are melted to generate OIB melts.

Summary

Ocean island basalts result from melting hot, buoyantly upwelling mantle beneath the world's ocean basins. Ocean island basalts sample ancient subducted crust that has been recycled through the mantle. These basalts also provide evidence that ancient, primordial reservoirs have survived in the deep Earth since accretion.

Cross-References

- ▶ Formation and Evolution of the Earth
- ▶ Geochronology and Radiogenic Isotopes
- ▶ Incompatible Elements
- ▶ Mantle Geochemistry
- ▶ Mid-Ocean Ridge Basalts (MORB)
- ▶ Partial Melting

References

Cabral RA, Jackson MG, Rose-Koga EF, Koga KT, Whitehouse MJ, Antonelli MA, Farquhar J, Day JMD, Hauri EH (2013) Anomalous sulphur isotopes in plume lavas reveal deep mantle storage of Archaean crust. Nature 496:490–493

Courtillot V, Davaille A, Besse J, Stock J (2003) Three distinct types of hotspots in the Earth's mantle. Earth Planet Sci Lett 205:295–308

Dasgupta R, Jackson MG, Lee C-TA (2010) Major element chemistry of ocean island basalts – conditions of mantle melting and heterogeneity of mantle source. Earth Planet Sci Lett 289:377–392

Druken KA, Kincaid C, Griffiths RW, Stegman DR, Hart SR (2014) Plume–slab interaction: the Samoa–Tonga system. Phys Earth Planet Inter 232:1–14

Eiler JM, Farley KA, Valley JW, Hauri E, Craig H, Hart SR, Stolper EM (1997) Oxygen isotope variations in ocean island basalt phenocrysts. Geochim Cosmochim Acta 61:2281–2293

French SW, Romanowicz B (2015) Broad plumes rooted at the base of the Earth's mantle beneath major hotspots. Nature 525:95–99

Frey FA, Coffin M, Wallace P, Weis D, Zhao X, Wise S, Wähnert V, Teagle DAH, Saccocia PJ, Reusch DN, Pringle MS, Nicolaysen KE, Neal CR, Müller RD, Moore CL, Mahoney JJ, Keszthelyi L, Inokuchi H, Duncan RA, Delius H, Damuth JE, Damasceno D, Coxall HK, Borre MK, Boehm F, Barling J, Arndt NT, Antretter M (2000) Origin and evolution of a submarine large igneous province: the Kerguelen Plateau and Broken Ridge, southern Indian Ocean. Earth Planet Sci Lett 176:73–89

Gale A, Dalton CA, Langmuir CH, Su Y, Shilling J-G (2013) The mean composition of ocean ridge basalts. Geochem Geophys Geosyst 14. https://doi.org/10.1029/2012GC004334
Gast PW, Tilton GR, Hedge C (1964) Isotopic composition of lead and strontium from Ascension and Gough Islands. Science 145:1181–1185
Herzberg C, Asimow PD, Arndt N, Niu Y, Lesher CM, Fitton JG, Cheadle MJ, Saunders AD (2007) Temperatures in ambient mantle and plumes: constraints from basalts, picrites, and komatiites. Geochem Geophys Geosyst 8. https://doi.org/10.1029/2006gc001390
Hofmann AW (2003) Sampling mantle heterogeneity through oceanic basalts: isotopes and trace elements. In: Carlson RW (ed) Executive Editors: Holland HD, Turekian KK, p 568. Treatise on geochemistry, vol 2. Elsevier, pp 61–101. https://doi.org/10.1016/B0-08-043751-6/02123-X. ISBN 0-08-043751-6
Hofmann AW, White WM (1982) Mantle plumes from ancient oceanic crust. Earth Planet Sci Lett 57:421–436
Janney PE, Macdougall JD, Natland JH, Lynch MA (2000) Geochemical evidence from the Pukapuka volcanic ridge system for a shallow enriched mantle domain beneath the South Pacific Superswell. Earth Planet Sci Lett 181:47–60
Koppers AAP, Staudigel H, Pringle MS, Wijbrans JR (2003) Short-lived and discontinuous intraplate volcanism in the South Pacific: hot spots or extensional volcanism? Geochem Geophys Geosyst 4. https://doi.org/10.1029/2003GC000533
Koppers AAP, Yamazaki T, Geldmacher J, Gee JS, Pressling N, Hoshi H, Anderson L, Beier C, Buchs DM, Chen L-H, Cohen BE, Deschamps F, Dorais MJ, Ebuna D, Ehmann S, Fitton JG, Fulton PM, Ganbat E, Hamelin C, Hanyu T, Kalnins L, Kell J, Machida S, Mahoney JJ, Moriya K, Nichols ARL, Rausch S, Sano S-I, Sylvan JB, Williams R (2012) Limited latitudinal mantle plume motion for the Louisville hotspot. Nat Geosci 5:911–917
Li M, McNamara AK, Garnero EJ (2014) Chemical complexity of hotspots caused by cycling oceanic crust through mantle reservoirs. Nat Geosci 7:366–370
Mukhopadhyay S (2012) Early differentiation and volatile accretion recorded in deep-mantle neon and xenon. Nature 486:101–104
Putirka KD, Perfit M, Ryerson FJ, Jackson MG (2007) Ambient and excess mantle temperatures, olivine thermometry, and active vs. passive upwelling. Chem Geol 241:177–206
Sandwell DT, Winterer EL, Mammerickx J, Duncan RA, Lynch MA, Levitt DA, Johnson CL (1995) Evidence for diffuse extension of the Pacific plate from Pukapuka ridges and cross-grain gravity lineations. J Geophys Res 100:15087–15099
Schilling J-G, Winchester JW (1967) Rare-earth fractionation and magmatic processes. In: Runcorn SK (ed) Mantles of the Earth and terrestrial planets. Wiley, New York, pp 267–283
Staudigel H, Koppers AAP (2015) Seamounts and island building. In: Sigurdsson H, Houghton B, Rymer H, Stix J, McNutt S (eds) The encyclopedia of volcanoes. Academic Press, pp 405–421. https://doi.org/10.1016/B978-0-12-385938-9.00022-5. ISBN: 9780123859389
Weis D, Garcia MO, Rhodes JM, Jellinek AM, Scoates JS (2011) Role of the deep mantle in generating the compositional asymmetry of the Hawaiian mantle plume. Nat Geosci 4:831–838
White WM (2013) Geochemistry. Wiley-Blackwell, Oxford
White WM (2014) Hot spots and mantle plumes. In: Harff J, Meschede M, Petersen S, Thiede J (eds) Encyclopedia of marine geosciences. Springer, The Netherlands, pp 1–20
White WM, Hofmann AW (1982) Sr and Nd isotope geochemistry of oceanic basalts and mantle evolution. Nature 296:821–825
Woodhead JD (1996) Extreme HIMU in an oceanic setting: the geochemistry of Mangaia Island (Polynesia), and temporal evolution of the Cool-Austral hotspot. J Volcanol Geotherm Res 72:1–19

Oil Seeps and Coastal Bitumen

David McKirdy[1], Andrew Ross[2] and Asrarur Talukder[2]
[1]Department of Earth Sciences, School of Physical Sciences, The University of Adelaide, Adelaide, SA, Australia
[2]CSIRO Earth Science and Resource Engineering (CESRE), Kensington, NSW, Australia

Definitions

An **oil seep** is a place where liquid or semi-solid petroleum, commonly in association with gaseous hydrocarbons, escapes at a low rate to the Earth's surface. Those located on the sea floor produce tar or asphalt that may eventually be transported to the shore where it strands as **coastal bitumen**.

Introduction

Each year an estimated 600,000 metric tons of oil enters the global marine environment from natural seepage (NRC 2003), accounting for 47% of the total annual input and making it the single most important contributor of oil to the world's oceans (Kvenvolden and Cooper 2003). In the wake of major accidental releases of crude oil, such as the *Exxon Valdez* tanker spill in Prince William Sound, Alaska (Kvenvolden et al. 1995), and the *Deepwater Horizon* blowout in the Gulf of Mexico (Boufadel et al. 2014), it becomes necessary to distinguish the resulting marine tar residues from coastal bitumen (natural or anthropogenic) already present on the adjacent shorelines. This is achieved using various isotopic and molecular fingerprinting techniques (Peters et al. 2005).

Seep Locations

One of the first studies of global marine oil seepage, dating from a time when reports of marine seeps were scarce, concluded that there is a strong correlation between areas of high seepage potential and tectonic activity, best exemplified by the tectonically unstable circum-Pacific region (Wilson et al. 1974). Hydrocarbon seeps are now known to be widespread along both active and passive continental margins, and the mechanisms of their formation are varied. Numerous examples are described by Abrams (1996) and Judd and Hovland (2007). Typically, petroleum fluids are released to the seabed from over-pressured subsurface reservoirs where the cap rock has been breached by diapir intrusion, faulting, or other fractures. The resulting seeps are manifest on the seabed as

mud volcanoes, pock marks, and authigenic carbonate deposits (Talukder 2012).

Among the most extensive and best documented oil and asphalt seeps are those in the Gulf of Mexico (Brüning et al. 2010; Sahling et al. 2016), Angola (Jones et al. 2014) and off the coast of southern California (Lorenson et al. 2009). The seeps at Coal Oil Point, Santa Barbara, California (Del Sontro et al. 2007; Farwell et al. 2009; Hostettler et al. 2004) are especially prolific, releasing up to 27,000 liters of oil per day (Hornafius et al. 1999).

Methods of Detection and Sampling

Such seepage may be accompanied by flares of methane and other hydrocarbons rising through the water column that are detectable by sonar techniques (Talukder et al. 2013). Seafloor sampling of seeps typically employs the use of piston and gravity cores, grabs, or remotely operated vehicles which permit more precise sampling of discrete areas of seepage. Where oil films reach the surface, the presence of submarine seeps has been inferred by direct observation from vessels or by using various remote sensing techniques. These include airborne laser fluorescence (Thompson et al. 1991); satellite synthetic aperture radar (De Beukelaer et al. 2003); ship based x-band radar (Crooke et al. 2015); and visual (Hu et al. 2009) and spectral methods (Wettle et al. 2009).

While dispersed in near-surface sediments, exposed on the seafloor, rising through the water column and at the sea surface, the oil undergoes various alteration processes that include evaporative fractionation, water washing, biodegradation, and photo-oxidation. The net result of these processes is to increase the overall viscosity and density of the seeped oil. The progress of this alteration can be monitored by appropriate sampling techniques and organic geochemical analyses (Abrams and Dahdah 2011; Peters et al. 2005).

Upon evaporation and further weathering, surficial oil slicks may produce tar balls or mats (Warnock et al. 2015), some of which are then carried by currents and waves to the shore where they strand as coastal bitumen on ocean beaches.

Origin of Australian Coastal Bitumens

Natural seeps discharging oil into the ocean are common within the Indonesian Archipelago (Noble et al. 2009) where they are the likely sources of the waxy bitumens that strand along the northern, western, and southern coastlines of Australia (Edwards et al. 2016). The evidence for such long-distance transport of tar balls from their as yet unspecified points of origin into Australian waters by a combination of the Indonesian Throughflow (Gordon 2005) and the Leeuwin Current (McGowran et al. 1997) is based on their content of a distinctive suite of biomarker hydrocarbons that are also found in oils from Indonesia (Currie et al. 1992; McKirdy et al. 1986, 1994). These include botryococcane, bicadinanes, oleanane, and 4-methylsteranes. Reports of such bitumen stranding date back to the mid-1800s, although tanker cleaning operations in the Java and Banda seas may augment the current influx of tar balls to the beaches of southern Australia. A study of six beaches in 1991–1992 revealed a maximum waxy bitumen loading of 2 kg per 100 m. Asphaltite, a heavier variety of local coastal bitumen, is less common, arguably less traveled and considered by Hall et al. (2014) to be a manifestation of low-intensity seepage from tar mats exposed by submarine canyons on Australia's southern continental slope. It is carried ashore by a combination of seasonal upwelling currents and winter storms.

Impact on Local Ecosystems

Submarine oil seepage is typically episodic. Its rate is variable in space and time, and yet in places sufficient to impact adversely on local wildlife (Henkel et al. 2014) and the amenity of adjacent beaches. On the other hand, deposits of asphalt emanating from seafloor seeps provide a substrate for extensive and diverse chemosynthetic communities (Cordes et al. 2010; MacDonald et al. 2003; Sahling et al. 2016; Schubotz et al. 2011). In the same manner, both pelagic tar balls and benthic asphaltite may be colonized by a variety of marine biota including goose barnacles, bryozoa, and serpulid worms (Edwards et al. 2016). Thus, it is now recognized that oil seeps are important natural laboratories for understanding not only the fate of crude oil in the marine environment, but also how marine ecosystems adapt to the influx of petroleum.

Conclusions

Oil seeps are the major source of crude oil entering the marine environment. The escape of petroleum hydrocarbons to the seafloor is a natural worldwide phenomenon that has both resource and environmental implications. The presence of a seep is evidence of an active petroleum system in the underlying offshore sedimentary basin and therefore may lead to the discovery of new fossil fuel resources. The composition of the resulting tar or asphalt deposit, at the site of the seep or subsequently washed ashore as coastal bitumen, provides important clues to the age and depositional environment of the parent oil's source rock. Finally, the geographic distribution of tar balls stranded along the adjacent shoreline provides a predictive template for the ultimate destination of any crude oil accidentally released during offshore drilling or production.

Cross-References

- Biomarkers: Petroleum
- Carbon Isotopes
- Gas Chromatography–Mass Spectrometry (GC–MS)
- Hydrocarbons
- Natural Gas
- Oil-Oil and Oil-Source Rock Correlations
- Organic Geochemistry
- Petroleum

References

Abrams MA (1996) Distribution of subsurface hydrocarbon seepage in near surface marine sediments. In: Schumacher D, Abrams MA (eds) Hydrocarbon migration and its near-surface expression. American Association of Petroleum Geologists Memoirs 66. American Association of Petroleum Geologists, Tulsa, pp 1–14

Abrams M, Dahdah NF (2011) Surface sediment hydrocarbons as indicators of subsurface hydrocarbons: Field calibration of existing and new surface geochemistry methods in the Marco Polo area, Gulf of Mexico. Am Assoc Petrol Geol Bull 95:1907–1935

Boufadel MC, Abdollahi-Nasab A, Geng X, Galt J, Torlapati J (2014) Simulation of the landfall of the Deepwater Horizon oil on the shorelines of the Gulf of Mexico. Environ Sci Technol 48:9496–9505

Brüning M, Sahling H, MacDonald I, Ding F, Bohrmann G (2010) Origin, distribution, and alteration of asphalts at the Chapopote Knoll, southern Gulf of Mexico. Mar Pet Geol 27:1093–1106

Cordes EE, Cunha MR, Galeron J, Mora C, Olu-Le Roy K, Sibuet M, Van Gaever S, Vanreusel A, Levin LA (2010) The influence of geological, geochemical, and biogenic habitat heterogeneity on seep biodiversity. Mar Ecol 31:51–65

Crooke E, Talukder A, Ross A, Trefry C, Caruso M, Carragher P, Stalvies C, Armand S (2015) Determination of sea-floor seepage locations in the Mississippi Canyon. Mar Pet Geol 59: 129–135

Currie TJ, Alexander R, Kagi RI (1992) Coastal bitumens from Western Australia – long distance transport by ocean currents. Org Geochem 18:595–601

De Beukelaer SM, MacDonald IR, Guinnasso NL Jr, Murray JA (2003) Distinct side-scan sonar, RADARSAT SAR, and acoustic profiler signatures of gas and oil seeps on the Gulf of Mexico slope. Geo-Mar Lett 23:177–186

Del Sontro TS, Leifer I, Luyendyk BP, Broitman BR (2007) Beach tar accumulation, transport mechanisms, and sources of variability at Coal Oil Point, California. Mar Poll Bull 54:1461–1471

Edwards DS, Vinall DR, Corrick AJ, McKirdy DM (2016) Natural bitumen stranding on the ocean beaches of Southern Australia: a historical and geospatial review. Trans Roy Soc S Aust 140:152–185

Farwell C, Reddy CM, Peacock E, Nelson RK, Washburn L, Valentine DL (2009) Weathering and the fallout plume of heavy oil from strong petroleum seeps near Coal Oil Point, CA. Env Sci Technol 43:3542–3548

Gordon AE (2005) Oceanography of the Indonesian seas and their Throughflow. Oceanography 18:14–27

Hall PA, McKirdy DM, Grice K, Edwards DS (2014) Australasian asphaltite strandings: their origin reviewed in light of the effects of weathering and biodegradation on their biomarker and isotopic profiles. Mar Pet Geol 57:572–593

Henkel LA, Nevins H, Martin M, Sugarman S, Harvey JT, Ziccardi MH (2014) Chronic oiling of marine birds in California by natural petroleum seeps, shipwrecks, and other sources. Mar Poll Bull 79:155–163

Hornafius JS, Quigley D, Luyendyk BP (1999) The world's most spectacular marine hydrocarbon seeps (Coal Oil Point, Santa Barbara Channel, California): quantification of emissions. J Geophys Res 104:20703–20711

Hostettler FD, Rosenbauer RJ, Lorenson TD, Dougherty J (2004) Geochemical characterization of tarballs on beaches along the California coast. Part I - Shallow seepage impacting the Santa Barbara Channel Islands, Santa Cruz, Santa Rosa and San Miguel. Org Geochem 35:725–746

Hu C, Li X, Pichel WG, Muller-Karger FE (2009) Detection of natural oil slicks in the NW Gulf of Mexico using MODIS imagery. Geophys Res Lett 36:L01604

Jones DOB, Walls A, Clare M, Fiske MS, Weiland RJ, O'Brien R, Touzel DF (2014) Asphalt mounds and associated biota on the Angolan margin. Deep Sea Res Part I: Oceanogr Res Pap 94:124–136

Judd AG, Hovland M (2007) Seabed fluid flow: the impact on geology, biology and marine environment. Cambridge University Press, New York, 475 p

Kvenvolden KA, Cooper CK (2003) Natural seepage of crude oil into the marine environment. Geo-Mar Lett 23:140–146

Kvenvolden KA, Hostettler FD, Carlson PR, Rapp JB, Threkeld CN, Warden A (1995) Ubiquitous tar balls with a California-source signature on the shorelines of Prince William Sound, Alaska. Env Sci Technol 29:2684–2269

Lorenson TD, Hostettler FD, Rosenbauer RJ, Peters KE, Kvenvolden KA, Dougherty JA, Gutmacher CE, Wong FL, Normark WR (2009) Natural offshore seepage and related tarball accumulation on the California coastline; Santa Barbara Channel and the southern Santa Maria Basin; source identification and inventory. U.S. Geological Survey Open-File Report 2009–1225 and MMS Report 2009–030, 116 p and spreadsheets

MacDonald IR, Sager WW, Peccini MB (2003) Gas hydrate and chemosynthetic biota in mounded bathymetry at mid-slope hydrocarbon seeps: northern Gulf of Mexico. Mar Geol 198(1–2), 133–158

McGowran B, Li Q, Cann J, Padley D, McKirdy DM, Shafik S (1997) Biogeographic impact of the Leeuwin Current in southern Australia since the late middle Eocene. Palaeogeogr Palaeoclimatol Palaeoecol 136:19–40

McKirdy DM, Cox RE, Volkman JK, Howell VJ (1986) Botryococcane in a new class of Australian non-marine crude oils. Nature 320:57–59

McKirdy DM, Summons RE, Padley D, Serafini KM, Boreham CJ, Struckmeyer HIM (1994) Molecular fossils in coastal bitumens from southern Australia: signatures of precursor biota and source rock environments. Org Geochem 21:265–286

Noble R, Orange D, Decker J, Teas P, Baillie P (2009) Oil and gas seeps in deep marine sea floor cores as indicators of active petroleum systems in Indonesia. In: Proceedings of 33rd annual convention, Indonesian Petroleum Association, IPA09-G-044, pp 385–394

NRC (2003) Oil in the sea III: inputs, fates, and effects. National Academies Press, Washington, DC, 280 p

Peters KE, Walters CC, Moldowan JM (2005) The biomarker guide. vol 2: Biomarkers and isotopes in petroleum systems and Earth history, 2nd edn. Cambridge University Press, Cambridge, pp 475–1155

Sahling H, Borowski C, Escobar-Briones E, Gaytán-Caballero A, Hsu C-W, Loher M, MacDonald IR, Marcon Y, Pape T, Römer M, Rubin-Blum M, Schubotz F, Smrzka D, Wegener D, Bohrmann G (2016) Massive asphalt deposits, oil seepage, and gas venting support abundant chemosynthetic communities at the Campeche Knolls, southern Gulf of Mexico. Biogeosciences 13:4491–4512

Schubotz F, Lipp JS, Elvert M, Kasten S, Mollar PX, Zabel M, Bohrmann G, Hinrichs K (2011) Petroleum degradation and

associated microbial signatures at the Chapopote asphalt volcano, southern Gulf of Mexico. Geochim Cosmochim Acta 75:4377–4398
Talukder AR (2012) Review of submarine cold seep plumbing systems: leakage to seepage and venting. Terra Nova 24:255–272
Talukder AR, Ross A, Crooke E, Stalvies C, Trefry C, Qi X, Fuentes D, Arman S, Revill A (2013) Natural hydrocarbon seepage on the continental slope to the east of Mississippi Canyon in the northern Gulf of Mexico. Geochem Geophys Geosys 14:1940–1956
Thompson M, Reminton C, Purnomo J, MacGregor D (1991) Detection of liquid hydrocarbon seepage in Indonesian offshore frontier basins using airborne laser fluorosensor (ALF). The results of a Pertamina/BP Joint study. In: Proceedings of the 20th annual convention, Indonesian Petroleum Association, IPA 91-11.15, pp 663–689
Warnock AM, Hagen SC, Passeri DL (2015) Marine tar residues: a review Water Air Soil Poll 226(3):68
Wettle M, Daniel PJ, Logan GA, Thankapppan M (2009) Assessing the effect of hydrocarbon oil type and thickness on a remote sensing signal: a sensitivity study based on the optical properties of two different oil types and the HYMAP and Quickbird sensors. Remote Sens Environ 113:2000–2010
Wilson RD, Monaghan PH, Osanik A, Price LC, Rogers MA (1974) Natural marine oil seepage. Science 184:857–865

Oil Shale

Justin E. Birdwell
Central Energy Resources Science Center, U.S. Geological Survey, Denver, CO, USA

Synonyms

Cannel coal; Immature source rock; Kukersite; Lamosite; Marinite; Tasmanite; Torbanite

Definition

Oil shales are fine-grained sedimentary rocks formed in many different depositional environments (terrestrial, lacustrine, marine) containing large quantities of thermally immature organic matter in the forms of kerogen and bitumen. If defined from an economic standpoint, a rock containing a sufficient concentration of oil-prone kerogen to generate economic quantities of synthetic crude oil upon heating to high temperatures (350–600 °C) in the absence of oxygen (pyrolysis) can be considered an oil shale.

Introduction

The term oil shale is often described as a misnomer, in that the organic component is primarily kerogen, not oil and the mineral matrix is not necessarily clay mineral-rich, but can include a variety of different phases (Miknis and McKay 1983). Oil shales are essentially a type of petroleum source rock, the key differences being that: (1) oil shales have not been buried to sufficient depths or exposed to high enough temperatures for long enough to have generated petroleum; and (2) have organic matter contents that are higher than what is typically considered necessary for a "good" source rock (total organic carbon, TOC > 10 wt%; Cook and Sherwood 1991). Deposits of oil shale are found around the world and range in geologic age from Precambrian to Tertiary. The term has a long history of use, predating the "shale oil" and "shale gas" revolution of the early twenty-first century in the United States. Oil shale is sometimes applied to "shale-hosted oil" or "tight oil" formations, like the Eagle Ford Shale and Bakken Formation, respectively, causing much confusion. Unlike humic coals, oil shales are more prone to generate liquid petroleum products upon heating and contain a higher concentration of mineral matter (>33 wt%; Yen and Chilingar 1976). It should be noted that in addition to being used as a source of synthetic oil, in some cases, oil shales are also burned to generate electricity similar to coal, as is done in Estonia.

Properties

The critical property for determining oil shale resource potential is its grade, defined as the yield of synthetic crude oil generated under pyrolysis conditions normalized to the mass of rock processed. Oil shale grade can be determined by well-established, laboratory pyrolysis methods. Two of the most commonly used pyrolysis tools for characterizing oil shale and other source rocks are the Fischer assay method (ASTM 1990; Johnson et al. 2010) and programmed pyrolysis, more commonly known as Rock-Eval analysis (Peters 1986). Both methods involve rapidly heating a sample (~100 g for Fischer assay; ~100 mg for Rock-Eval) to high temperatures (500–550 °C) and either collecting the synthetic oil product for quantification and possibly subsequent characterization (Fischer assay) or measuring the evolved hydrocarbons and other products with a variety of detectors (Rock-Eval). Results are commonly reported as wt% oil, gallons of oil per short-ton of rock (GPT), or milligrams of hydrocarbons per gram of rock (mg-HC/g). The grade cutoff for determining oil shale commercial viability will depend on a number of factors, but rocks that can generate at least 25 GPT (~10 wt% oil or ~100 mg-HC/g) are generally considered to be commercial grade in the United States (Birdwell et al. 2013). It should be noted that the economic viability of oil shale in most countries is also dependent on high oil prices. For example, development of oil shale resources has not been commercially viable in the United States without subsidies since the 1920s despite the enormous resource potential determined for the principal basins of the Green River Formation (Eocene) in Colorado, Utah, and Wyoming (Johnson et al. 2010; Birdwell et al. 2013).

Categorization schemes for typing oil shales have been developed based on depositional environment and dominant maceral types (Hutton 1987, 1995; Cook and Sherwood 1991). The six types described by Hutton (1987) include terrestrial cannel coal, lacustrine lamosite and torbanite, and marine kukersite, tasmanite, and marinite. Some of these oil shale types contain organic matter derived from petrographically identifiable organisms, such as the planktonic green microalgae *Botryococcus braunii* in some torbanites and green algae *Tasmanites* in tasmanites-type oil shales. Cannel coals are found in New Zealand, Australia, and the United States and contain abundant spores, resins, and organic matter from vascular plants, like vitrinite. The Green River Formation (United States) and Rundle (Australia) Tertiary oil shales are typical examples of lamosites and contain amorphous organic matter derived primarily from lacustrine algae. Devonian-Mississippian oil shales like the New Albany Shale in the eastern United States are often described as marinites and contain organic matter derived primarily from marine phytoplankton.

Oil shales have a wide range of organic matter content (from around 10 up to over 60 wt% TOC) and variable mineralogy across the spectrum of mudrocks. Bitumen (fraction soluble in organic solvents) typically represents around 20wt% of the organic matter present in oil shale (Yen and Chilingar 1976), with the remainder consisting of kerogen (insoluble fraction). The kerogen is generally hydrogen-rich (oil-prone type I or type II kerogens; atomic hydrogen-to-carbon ratios from ~1.0 up to 1.6) with a range of heteroatom (nitrogen, oxygen, sulfur; NSO) contents. For example, the kukersite (Ordovician) found in Estonia is known to be particularly high in oxygen, Ghareb oil shale (Cretaceous) from Israel and Jordan has a very high organic sulfur content, and the kerogen present in Glen Davis torbanite (Permian) from Australia has an unusually low concentration of NSO heteroatoms. Oil shale can contain a range of different mineral phases, including quartz, feldspars, carbonates, various clays, and pyrite. Phosphate minerals are common in some formations, like the Phosphoria Formation (Permian) in the western United States, and calcareous (calcite content >50 wt% on an organic-free basis) marine oil shales are found in several important oil shale deposits. Lacustrine oil shales are often mineralogically very diverse, as demonstrated by the different mineralogical units within the Green River Formation in the Piceance Basin of Colorado (Boak and Poole 2015).

History and Use

The most common use of oil shale historically has been as a source of synthetic liquid crude oil generated by "retorting" or "destructive distillation" (e.g., pyrolysis). Industrial applications of oil shales date back to the nineteenth century in Scotland and other places in Europe, where it was often used as a source of kerosene. This fuel production from oil shale led to the term "kerogen" being defined as the organic precursor of the kerosene product (Jenson 1922). While many oil shale industries ceased operating in the twentieth century, others continue to exist in a number of countries (Dyni 2006), including Estonia, Brazil, China, and Russia using a variety of retorting technologies (Baughman 1978; Speight 2012). Development of oil shale resources are under consideration or in various preliminary stages in the United States, Jordan, Australia, Mongolia, and several other places around the world.

Prospects for utilization of oil shale resources have been inevitably tied to the fortunes of the petroleum industry. During periods of high crude oil prices or concerns over reliable supplies, the development of oil shale has been pursued, particularly in countries with significant resources like the United States (Ogunsola et al. 2013). However, the higher costs associated with the production of synthetic crude oil from oil shale relative to other liquid fuel resources has prevented the widespread development of oil shale in the absence of government subsidies except in a few countries.

Summary

Oil shale deposits around the world represent a substantial but largely untapped petroleum resource. The viability of oil shale as a feedstock for the large-scale production of liquid hydrocarbon fuels continues to be dependent on the cost of producing from conventional crude oil resources and, increasingly, unconventional petroleum sources. The geochemical characteristics of oil shales are similar to those of traditional petroleum source rocks making them useful materials in the study of geochemical processes like petroleum generation through catagenesis and properties of organic-rich sedimentary rocks.

Cross-References

- Black Shales and Sapropels
- Kerogen
- Organic Facies
- Organic Geochemistry
- Organics: Sources and Depositional Environments
- Petroleum
- Programmed Temperature Pyrolysis

References

ASTM D3904-90 (1990) Test method for oil from oil shale (Resource evaluation by the Fischer assay procedure) [withdrawn 1996]. ASTM International, West Conshohocken. https://doi.org/10.1520/D3904-90

Baughman GL (1978) Synthetic fuels data handbook, 2nd edn. Cameron Engineers, Inc., Denver, CO, 438 p
Birdwell JE, Mercier TJ, Johnson RC, Brownfield ME (2013) In-place oil shale resources examined by grade in the major basins of the Green River Formation, Colorado, Utah, and Wyoming. U.S. Geological Survey fact sheet 2012–3145, Reston, VA, 4 p
Boak J, Poole S (2015) Mineralogy of the Green River Formation in the Piceance Creek Basin, Colorado. In: Smith ME, Carroll AR (eds) Stratigraphy and paleolimnology of the Green River Formation, Western USA. Springer, Netherlands, pp 183–209
Cook AC, Sherwood NR (1991) Classification of oil shales, coals and other organic-rich rocks. Org Geochem 17:211–222
Dyni JR (2006) Geology and resources of some world oil-shale deposits. U.S. Geological Survey scientific investigations report 2005–5294, Reston, VA, 42 p
Hutton AC (1987) Petrographic classification of oil shales. Int J Coal Geol 8:203–231
Hutton AC (1995) Organic petrography of oil shales. In: Snape C (ed) Composition, geochemistry and conversion of oil shales. NATO ASI series, vol 455. Kluwer, Boston, pp 17–33
Jenson JB (1922) Shaloilogy and oil-shale nomenclature. Chem Metall Eng 22:509–512
Johnson RC, Mercier TJ, Brownfield ME, Pantea MP, Self JG (2010) An assessment of in-place oil shale resources of the Green River Formation, Piceance Basin, Colorado: Oil Shale and Nahcolite Resources of the Piceance Basin, Colorado. U.S. Geological Survey digital data series DDS-69-Y, Chapter 1, Reston, VA, 187 p
Miknis FP, McKay JF (1983) Preface. In: Miknis FP, McKay JF (eds) Geochemistry and chemistry of oil shales. ACS symposium series, vol 230. American Chemical Society, Washington, DC, pp ix–x
Ogunsola OI, Hartstein AM, Ogunsola O (2013) Oil shale: a solution to the liquid fuel dilemma. ACS symposium series, vol 1032. American Chemical Society, Washington, DC, 325 p
Peters KE (1986) Guidelines for evaluating petroleum source rock using programmed pyrolysis. Am Assoc Pet Geol Bull 70: 318–329
Speight JG (2012) Shale oil production processes. Gulf Professional Publishing, Oxford. 200 p
Yen TF, Chilingar GV (1976) Introduction to oil shales. In: Yen TF, Chilingar GV (eds) Oil shale. Elsevier, Amsterdam, pp 1–12

Oil-Oil and Oil-Source Rock Correlations

Norelis D. Rodriguez
Chevron Energy Technology Company, Houston, TX, USA

Definition

Oil-oil and oil-source rock correlations are studies whose primarily objective is to unravel the relationships among oils and source rocks, independent of maturity and/or alteration effects. Oil-oil correlations aim to establish a genetic relationship among multiple oil samples or classifying them into oil families, while oil-source rock correlations aim to establish a genetic relationship between oils and potential source rock intervals (Peters et al. 2005).

Oil-Source Rock Correlation

Oil-source rock correlation studies are primarily carried out during oil and gas exploration in order to identify the main source rock intervals within a basin. Defining source rock presence, quality, distribution, and maturity is at the foundation of establishing a working petroleum system (Magoon and Dow 1994). Exploration applications of correlation studies include (1) assessing the number and character of effective source rocks, (2) identifying migration pathways, (3) providing input data for volumetric assessments, and (4) supporting data for oil field development (Waples and Curiale 1999). At a higher resolution, correlation studies can also be used to address reservoir continuity problems in producing reservoirs (Curiale 2008) and to map source rock facies variations within a basin (Peters et al. 1986; Rodriguez and Philp 2015).

Preserved lipid components that can be unmistakably linked to biological precursors in the original organic matter are known as biomarkers (Seifert and Moldowan 1981) and are one of the main data types used in petroleum geochemistry and correlation studies, specifically. Distributions of alkanes, isoprenoids, terpanes, hopanes, and steranes are routinely used in correlation studies. Biomarkers, in combination with bulk compositional data, and isotopic compositions (C, H, S, N) represent the main toolbox used in oil-oil and oil-source rock correlations. Although these organic components are typically used, successful results have also been obtained using trace metals (e.g., Lopez and Lo Monaco 2017) and aromatic hydrocarbons, porphyrins, and NSOs (e.g., Curiale 1994).

Oil-Oil Correlation

Oil-oil correlations are used in lieu of oil-source rock correlations particularly when there is limited access to potential and/or effective source rock samples for analyses. In these instances, correlations among oils from multiple locations allow extrapolations regarding type and potential extension of effective source rocks (Trinidade et al. 1995). Figure 1 provides an example in which oil-oil correlations were used to establish oil families and source rock facies variations in the rift grabens of the Central Sumatra Basin. Close to identical m/z 191 terpane distributions in all three samples indicate they were generated by similar source rock intervals. However, differences in *n*-alkane distributions, as well as in the presence/absence of the biomarkers botryococcane and β-carotane, indicate variations in the depositional environment for these source rock intervals.

Oil-oil and oil-source rock correlations can be difficult in cases where there are (1) multiple source rock units at multiple maturity levels contributing to charge, (2) facies variations within source rock units, and (3) organic variability caused by carrier beds and reservoir rocks (Curiale 2008). Moreover,

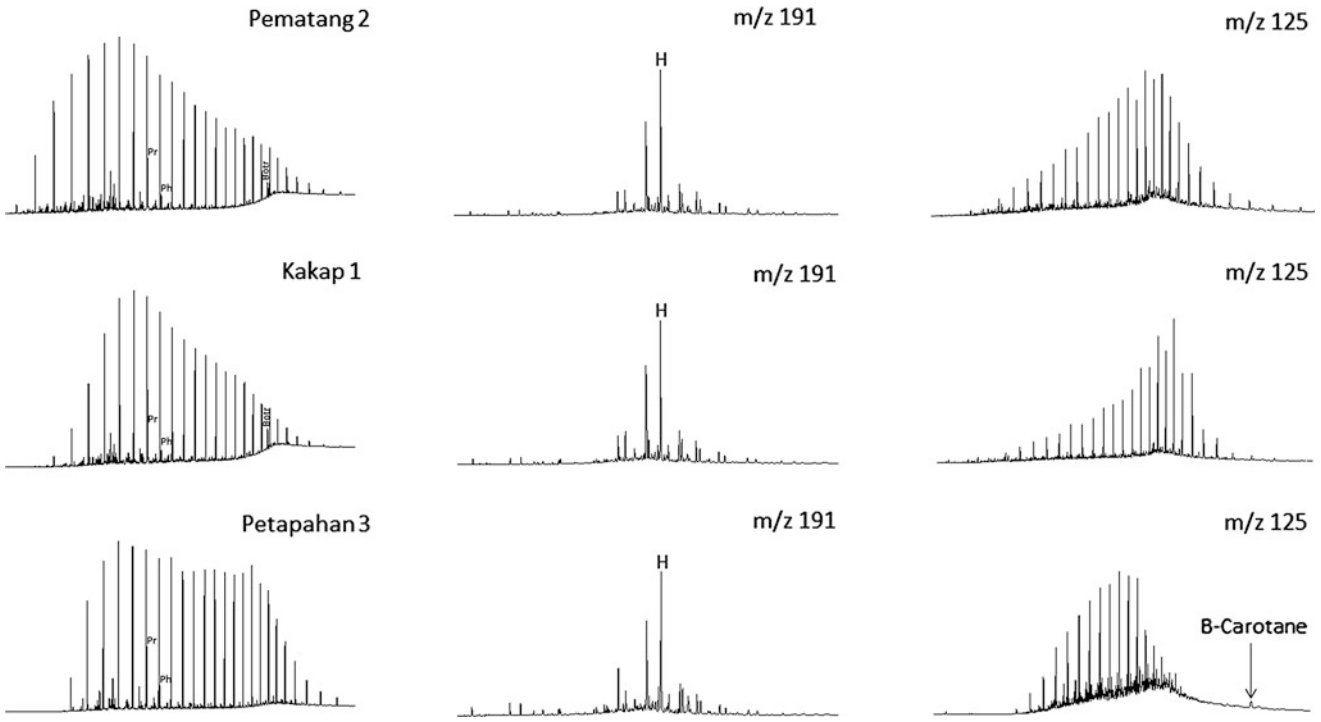

Oil-Oil and Oil-Source Rock Correlations, Fig. 1 Example of oil-oil correlation of oils from three grabens in the Central Sumatra Basin. All three samples show almost identical m/z 191 terpane distributions. The Biomarker Botryococcane is present in the Pematang 2 and Kakap 1 sample and absent in the Petapahan 3 sample. Conversely, β-carotane is present in the Petapahan 3 sample and absent in the other two. The Pematang 2 and Kakap 1 samples represent deep lacustrine facies of the Brown Shale Fm., while the Petapahan 3 sample was generated by saline lacustrine facies of the same source rock formation (Rodriguez and Philp 2015)

in-reservoir processes such as biodegradation, thermochemical sulfate reduction, and phase segregation can alter the original oil chemistry. Molecular signatures can be further complicated by processes like migration fractionation and migration contamination (Curiale 2002). Meaningful correlations studies must consider the potential effect of secondary processes, rely on a representative sampling base (Katz, personal communication), and fully integrate the geochemical interpretation with the stratigraphic and structural evolution of the basin.

Cross-References

- ▶ Biomarkers: Petroleum
- ▶ Lipids (Bacteria and Archaea)
- ▶ Organic Facies
- ▶ Organic Geochemistry
- ▶ Petroleum

References

Curiale JA (1994) Correlation of oils and source rocks – a conceptual and historical perspective. In: Magoon LB, Dow WG (eds) The petroleum system – from source to trap: AAPG Memoir 60. pp 251–260

Curiale JA (2002) A review of the occurrences and causes of migration contamination in crude oil. Org Geochem 33:1839–1400

Curiale JA (2008) Oil-source rock correlations – limitations and recommendations. Org Geochem 39:1150–1161

Lopez L, Lo Monaco S (2017) Vanadium, nickel and sulfur in crude oils and source rocks and their relationship with biomarkers: implications for the origin of crude oils in Venezuelan basins. Org Geochem 104:53–68

Magoon LB, Dow WG (1994) The petroleum system. In: Magoon LB, Dow WG (eds) The petroleum system—from source to trap: AAPG Memoir 60. pp 3–24

Peters KE, Moldowan JM, Schoell M, Hempkins WB (1986) Petroleum isotopic and biomarker composition related to source rock organic matter and depositional environment. Org Geochem 10:17–27

Peters KE, Walters CC, Moldowan JM (2005) The biomarker guide, Biomarkers and isotopes in petroleum exploration and earth history, vol 2. Cambridge University Press, New York, 1155 p

Rodriguez ND, Philp RP (2015) Source rock facies distribution predicted from oil geochemistry in the Central Sumatra Basin, Indonesia. AAPG Bull 99:2005–2022

Seifert WK, Moldowan M (1981) Paleoreconstruction by biological markers. Geochim Cosmochim Acta 45:783–794

Trinidade LAF, Dias JL, Mello MR (1995) Sedimentological and geochemical characterization of the Lagoa Feia Formation, rift phase of the Campos Basin, Brazil. In: Katz BJ (ed) Petroleum source rocks. Springer-Verlag, pp 149–165

Waples DW, Curiale JA (1999) Oil-oil and oil-source rock correlations. In: Beaumont EA, Foster NH (eds) Chapter 8 of Exploring for oil and gas traps. American Association of Petroleum Geology, Tulsa, pp 8-1–8-71

Oklo Natural Nuclear Reactors

Mark J. Rigali
Sandia National Laboratories, Albuquerque, NM, USA

Synonyms

Fissiogenic isotopes; Fission products

Definition

Natural nuclear reactors have been discovered in the Oklo and the associated Okelobondo and Bangombe uranium ore deposits in the Republic of Gabon on the coast of Equatorial West Africa. The reactors occur as small lenticular bodies of high-grade uranium ore (20–60% by weight) in the uranium ore deposits. The natural reactors reached criticality and began fission reactions 1.95 billion years ago. They operated for as long as 140,000 years. The primary fuel for the natural reactors was a fissionable isotope of uranium, ^{235}U. The reactors were discovered in 1972 when it was realized that ^{235}U was consumed and fission products were produced within seventeen high-grade uranium ore bodies, the Oklo and the associated Okelobondo and Bangombe uranium ore deposits. Today, these natural nuclear reactors serve as useful analogs for on-going research in the development of nuclear waste containment strategies.

Discovery of the Natural Nuclear Reactors

Although the possibility of natural nuclear reactors was considered in the 1950s (Koroda 1956), this prediction was not confirmed until 1972 when a routine analysis of a uranium ore standard at the nuclear-fuel processing plant in Pierrelatte, France, revealed a slight depletion in ^{235}U (Cowan 1976). Uranium has three naturally occurring isotopes in following proportions: 99.27% for ^{238}U, 0.72% for ^{235}U, and 0.0056% for ^{234}U. The measurement indicated that ^{235}U made up 0.7171% of the standard, only slightly lower than 0.72%. However, this value was considered unusually low, and an investigation was started to determine its origin. As scientists considered the cause of the depletion, they initially assumed that the uranium standard had been contaminated with ^{235}U-depleted uranium tailings, a waste product left over from the process used to produce enriched ^{235}U uranium for use as fuel in man-made nuclear reactors (Cowan 1976). When this turned out not to be the case, the investigation led to the Oklo uranium mine in the Republic of Gabon, on the coast of Equatorial West Africa. Analyses on samples obtained directly from the Oklo ore body revealed even greater depletions in ^{235}U. These strongly depleted samples were associated with specific regions of the ore deposit where the ore occurred in concentrations as high as 20–60% uranium by weight. Because there was no known natural process that could fractionate ^{235}U from uranium's more abundant isotope ^{238}U, scientists were initially baffled by the ^{235}U depletions observed in some of the Oklo ore samples. As the investigation continued, an amazing discovery was made. The relative abundances of a number of isotopes unique to nuclear fission reactions were observed in the ^{235}U-depleted ores. The missing ^{235}U had been consumed by fission in the high-grade uranium ore bodies. The conclusion was that nature created the first nuclear reactors to operate on Earth nearly two billion years before Enrico Fermi's nuclear reactor was constructed at Staggs Field in Chicago (Cowan 1976).

Conditions for the Formation of Natural Reactors

What fortuitous circumstances led to the formation of natural fission reactors? Natural nuclear reactors, like their man-made counterparts, require a number of special conditions in order to operate. First, spontaneous fission of ^{238}U takes place, causing its nucleus to split. This produces two or more fragment atoms usually of unequal mass (fission products) γ-rays, and several neutrons. If fissile ^{235}U nuclei are nearby, they can absorb these neutrons and split, releasing more neutrons. The reactions can be sustained if enough ^{235}U nuclei are present to absorb the neutrons produced by previous fissions. Nuclear reactors require significant amounts of fissionable material in order to start and maintain fission reactions. At Oklo, the natural reactor fuel was primarily ^{235}U. Two billion years ago, the rise in atmospheric oxygen mobilized uranium and enabled the dissolution and subsequent reprecipitation of uranium to form the high-grade uranium ore zones where nuclear fission reactions were initiated and sustained (Gauthier-Lafaye 2002). These zones contain 20–60% uranium, mainly in the form of uraninite, UO_2 (Gauthier-Lafaye et al. 1989). In addition to the high concentration of uranium, two billion years ago the relative abundance of ^{235}U was 3.68% of total U and is five times greater than today (0.72%) because ^{235}U decays faster than ^{238}U. A relative abundance of 3.68% is similar to the relative abundance of ^{235}U in the fuel of modern man-made pressure water nuclear reactors (Gauthier-Lafaye 2002). This high relative abundance of ^{235}U together with the high concentrations of uranium ore minerals enabled sustainable fission reactions in the high-grade zones that became the natural nuclear reactors. Yet another requirement for natural nuclear reactor operation is the presence of a neutron moderator. Moderators slow down the neutrons emitted from the fission of ^{235}U so that they are more readily absorbed by other ^{235}U nuclei, sustaining

fission reactions. At Oklo, the neutron moderator was primarily water present in the porous and fractured rocks which host the reactors. However, it has been suggested that carbon associated with organic matter (described below) may have also played a role as a neutron moderator/reflector in some reactors (Naudet 1991; Bentridi et al. 2013). A final requirement is that there is a minimum of neutron poisons in the reactor zones. Elements such as boron, vanadium, and rare earth elements (REEs) can readily absorb neutrons inhibiting or preventing the fission of ^{235}U (Gauthier-Lafaye 2002). These elements were not present in sufficient quantities in the natural reactors to inhibit reactor operation.

Chemical, Physical, and Geologic Properties of the Natural Reactors

To date, 17 natural nuclear reactors have been discovered in the Oklo and the associated Okelobondo and Bangombe uranium ore deposits in the Republic of Gabon (Bentridi et al. 2013). The reactors occur as small bodies in the uranium ores. They vary in size considerably. The largest (reactor 2) is a 12-m by 20-m lens-shaped body that is 50-cm thick, while the smallest, known as the Bangombe reactor, is a 5-m by 1-m lens-shaped body that is a few cm thick (Gauthier-Lafaye 2002). The natural reactors are located in hydrothermally altered and fractured clastic sedimentary rocks. They are found in the 7–10-m thick Cl layer of the basal FA Formation of the 2.1-Ga-old Paleoproterozoic Francevillian Series. The Cl layer consists of beach sands and tidal deposits of fine-grained sandstones, mudstones, and shales. In addition to the high uranium content, occurring mainly as uraninite, authigenic clay minerals, metallic inclusions, small quantities of galena, other sulfides, and hematite are also present in the natural reactors. Many of them also contain variable amounts of solid, graphitic organic matter. This carbon-rich material, also called solid graphitic bitumen, consists mainly of a highly condensed polycyclic aromatic hydrocarbon matrix thoroughly intermixed with poorly crystalline, fine-grained graphite (Nagy et al. 1993; Nagy and Rigali 1993). The solid graphitic bitumen apparently originated as liquid petroleum (Gauthier-Lafaye and Weber 1989) through the reaction of hydrothermal solutions with older organic solids, a process known as hydrous pyrolysis. The petroleum migrated into the reactors enclosing uraninite grains which had participated in the fission reactions and their incorporated fission products. Heat and radiation rapidly turned the viscous petroleum into the graphitic solid. Natural reactors 1–6 at Oklo contain only trace amounts of this carbonaceous substance. Here, the uraninite is associated mainly with clay minerals. The other reactors are organic matter rich with parts of these reactors containing as much as 66% organic carbon by weight. The uraninite occurs with both carbonaceous matter and clay minerals in heterogeneous distributions within these reactors. Some parts of the organic-rich reactors are uraninite in virtually pure clays, and other parts are mainly uraninite enclosed in the solid, graphitic organic substance.

Conditions During Natural Reactor Operation

The natural reactors reached criticality 1.95 billion years ago and operated for ~10^6 years (Gauthier-Lafaye 2002). During this time, ^{239}Pu was produced from the abundant isotope of uranium, ^{238}U, by neutron capture and two subsequent β decay reactions:

$$^{238}\mathrm{U} + \mathrm{n} \rightarrow {}^{239}\mathrm{Np} + \beta-$$

$$^{239}\mathrm{Np} \rightarrow {}^{239}\mathrm{Pu} + \beta-$$

^{239}Pu is also a fissionable material, and small amounts of the ^{239}Pu produced participated in fission reactions at Oklo. However, the majority of the ^{239}Pu created by neutron capture did not fission. It decayed, becoming ^{235}U through the following reaction:

$$^{239}\mathrm{Pu} \rightarrow {}^{235}\mathrm{U} + {}^{4}\mathrm{He}$$

In this manner, the Oklo natural nuclear reactors produced additional ^{235}U to sustain fission reactions. In fact, as much as 45% of the total amount of ^{235}U consumed in fission reactions was produced by the decay of ^{239}Pu (Holliger and Devillers 1981). Taking into account the additional ^{235}U produced by the decay of ^{239}Pu, it is estimated that a total of 6 tons of ^{235}U were consumed by fission reactions in the natural reactors (Naudet 1991). During natural reactor operation at Oklo, temperatures in the reactors reached as high as 400 °C (Gauthier-Lafaye 2002). As a result of heat and circulating fluids, the reactors experienced the progressive dissolution of the quartz sandstone host rock and the concomitant formation of a clay envelope around the reactor cores that was impervious to fluid flow (Bentridi et al. 2013). The cores finally collapsed with the progressive loss of quartz in and around the reactors leading to a significant reduction of porosity and water in the core. Their eventual collapse together with the consumption of significant quantities of the ^{235}U fuel led to the reactor cores becoming subcritical and finally shutting down. In the organic matter-rich reactors where this material appears to have also contributed to neutron moderation, the reactor shutdown may have been due in part to the redistribution and migration of the organic matter as viscous bitumen away from the reactor cores (Bentridi et al. 2013).

Scientific Relevance of the Oklo Natural Fission Reactors

The Oklo natural reactors are complex geologic and geochemical occurrences and are a natural laboratory in which to study the conditions of reactor formation and operation. They present a unique opportunity for scientists to study the long-term geochemical behavior of uranium together with fissiogenic isotopes in geologic environments. Fission products have been retained in the natural reactors and adjacent rocks to varying degrees. U, Th, Pu, and several fission products, including isotopes of Ag, Mo, Sn, Nb, Zr, Bi, Pd, Ru, Rh, Te, La, Nd, Pr, Sm, Ce, and Gd, have been found within the reactors and in the rocks in their vicinity (Curtis et al. 1989; Holliger 1992; Gauthier-Lafaye 2002). While Pu was retained primarily with uranium in the uraninite of the reactors, there is evidence for its migration together with rare earth elements has been found because of their presence in clays and apatites within and near the reactor cores (Bros et al. 1993; Bros et al. 1996). Other fission products such as Tc, Ru, Rh, Pd, and Bi are retained in metallic inclusions found in close proximity to the uraninite. Still others, such as the noble gases, I, Rb Ba, Sr, and Cs, have been lost in large quantities from the uraninite of the reactors and are largely absent in the adjacent host rocks of the reactors (Gauthier-Lafaye 2002). However, evidence for the retention of small amounts of fissiogenic Sr, Ba, and Cs isotopes in one of the reactors, carbonaceous matter-rich natural reactor 10, has been reported (Hidaka et al. 1994; Hidaka and Gauthier-Lafaye 2008). Isotopes of these three elements are of particular interest because they are produced in high yields during nuclear fission, and they are also soluble and readily transported by aqueous solutions in geologic environments.

Because a number of fission and decay products were retained in the natural reactors while still others were lost, the reactors have modern anthropogenic relevance. This relevance can be stated as follows. Since the components and the geochemical and hydrologic environments in and around the natural reactors were able to contain a number of radionuclides, the Oklo natural reactors may be useful analogs for modern nuclear waste containment considerations and strategies (Nagy and Rigali 1993; Gauthier-Lafaye 2002). To date, several decades of studies have revealed that a number of physical and chemical factors have influenced the degree of retention of fission products in the natural fission reactors. Retention of fission products is controlled in part by the mineral assemblages in the natural reactors and their response to microscale variations in pressure and temperature together with the composition of the uraninite fuel (Curtis et al. 1989). Other factors, such as chemical alteration, exsolution, and diffusion, were important mechanisms affecting the loss of Pb and the fission products Mo, Ru, Rh, and Pd from uraninites in the Oklo natural reactors (Janeczek and Ewing 1995). However, many of these fission products were precipitated in galena (PbS) and metallic inclusions or in the immediate vicinity of the reactor zones. In addition, where it is present in the natural nuclear reactors, solid graphitic carbonaceous matter appears to inhibit the migration of U, Pb, and a number of fission products from these reactors (Nagy et al. 1993; Nagy and Rigali 1993). These studies all indicate that Oklo natural reactors have value as analogs for the storage of man-made radioactive waste.

Summary

The Oklo, Okelobondo, and Bangombe uranium ore deposits in the Republic of Gabon are unique as they host the world's only known natural fission reactors. A number of fortuitous circumstances including high concentrations of fissionable ^{235}U, the presence of significant quantities of water, and the absence of neutron poisons contributed to their formation and operation nearly 2 Ga ago. The natural reactors represent complex geochemical and hydrologic milieus. It is important to consider the heterogeneous textural patterns of their components as well as their interaction with the surrounding geochemical environments during 2 Ga of geologic time to properly evaluate their origin as well as their potential utility to modern nuclear waste containment strategies.

Cross-References

- Barium
- Caesium
- Geochronology and Radiogenic Isotopes
- Geologic Time Scale
- Hydrothermal Alteration
- Hydrothermal Solutions
- Lanthanide Rare Earths
- Lead
- Lead Isotopes
- Noble Gases
- Nucleosynthesis
- Petroleum
- Radioactivity
- Strontium
- Uranium
- Uranium Decay Series

References

Bentridi S-E, Gall B, Gauthier-Lafaye F, Seghour A, Pape A, Medjadi D-E (2013) Criticality of Oklo natural reactors: realistic model of reactor zone 9. IEEE Trans Nucl Sci 60:278–283

Bros R, Turpin L, Gauthier-Lafaye F, Holliger P, Stille P (1993) Occurrence of naturally enriched 235 uranium: the implications for Pu behavior in a natural environment. Geochim Cosmochim Acta 57:1351–1358
Bros R, Carpena J, Sere V, Beltritti A (1996) Occurrence of Pu and fissiogenic REE in hydrothermal apatites from the fossil nuclear reactor 16 at Oklo. Radiochim Acta 74:277–282
Cowan GA (1976) A natural fission reactor. Sci Am 235:36–47
Curtis D, Benjamin T, Gancarz A, Loss R, Rosman K, DeLaeter J (1989) Fission product retention in the Oklo natural fission reactors. Appl Geochem 4:49–62
Gauthier-Lafaye F (2002) 2 billion year old natural analogs for nuclear waste disposal: the natural nuclear fission reactors in Gabon (Africa). C R Phys 3:839–849
Gauthier-Lafaye F, Weber F (1989) The Francevillian (Lower Proterozoic) uranium ore deposits of Gabon. Econ Geol 84:2267–2285
Gauthier-Lafaye F, Weber F, Ohmoto H (1989) Natural fission reactors of Oklo. Econ Geol 84:2286–2295
Hidaka H, Gauthier-Lafaye F (2008) Ba isotopic signature for early differentiation between Cs and Ba in natural fission reactors. Geochim Cosmochim Acta 72:4123–4135
Hidaka H, Sugiyama T, Ebihara M, Holliger P (1994) Isotopic evidence for the retention of 90Sr from excess Zr in the Oklo natural fission reactors: implication for geochemical behavior of fissiogenic Rb, Sr, Cs and Ba. Earth Planet Sci Lett 122:173–182
Holliger P (1992) Geochemical and isotopic characterization of the reaction zones (uranium, transuranium, lead and fission products). In: Proceedings of the Joint Commission European Communities-Commissariat a l'Energie Atomique, 2nd meeting, Brussels, EUR, pp 27–38
Holliger P, Devillers C (1981) Contribution a l'etude de la temperature dans Jes reacteurs fossiles d'Oklo par la mesure du rapport isotopique du lutetium. Earth Planet Sci Lett 52:76–84
Janeczek J, Ewing R (1995) Mechanisms of lead release in the natural fission reactors in Gabon. Geochim Cosmochim Acta 59:1917–1931
Koroda PF (1956) On the nuclear physical stability of the uranium minerals. J Chem Phys 25:781–782
Nagy B, Rigali MJ (1993) Newly discovered, organic matterrich natural fission reactors at Oklo and Bangombe: are they useful analogs for long-term anthropogenic nuclear waste containment? In: Waste management '93 conference proceedings, pp 897–900
Nagy B, Gauthier-Lafaye F, Holliger P, Mossman DJ, Leventhal JS, Rigali MJ (1993) Role of organic matter in the Proterozoic Oklo natural fission reactors, Gabon, Africa. Geology 21:655–658
Naudet R (1991) Oklo: Des Reacteurs Nucleaires. Commissariat a l'Energie Atomique, Paris, p 695

Onuma Diagrams

Chenguang Sun
Department of Earth, Environmental and Planetary Sciences, Rice University, Houston, TX, USA

Definition

Onuma diagrams are a type of graphs used in geochemistry to illustrate the systematic variations between **partition coefficients** (see ▶ Partitioning and Partition Coefficients) and ionic radii of major or trace element ions with various valence states. This type of graphs was named after a Japanese geochemist, Naoki Onuma. Together with Hideo Higuchi, Hiroshi Wakita, and Hiroshi Nagasawa, Onuma published the first study using these diagrams (Onuma et al. 1968). In Onuma diagrams, the partition coefficients are plotted on a logarithmic scale, while the ionic radii are shown on a linear scale. Figure 1 is an example showing the partition coefficients of trace elements between plagioclase and clinopyroxene from Sun et al. (2017). As shown in Fig. 1, the partition coefficients of isovalent cations in the large cation site of plagioclase display a parabolic relationship with the ionic radii, whereas the parabolic patterns change tightness with the cation charges. According to the parabola defined by isovalent cations in a specific lattice site, these diagrams can be used to predict partition coefficients of trace element cations with the same charges and to further constrain their site occupancies in a mineral of interest.

History

Previously, Goldschmidt (1937) outlined the effects of cation size and charge on element partitioning through three general rules: (1) ions with the same charge and similar ionic radii have the same partition coefficients; (2) smaller cations have larger partition coefficients than larger cations with identical charges; (3) for cations with similar sizes, those with higher valence states have larger partition coefficients. These general rules remain true under many conditions; however, as demonstrated in Nagasawa (1966), the influences of cation size have to be considered with reference to the major cations in the lattice site. Based on the strain energy change in the crystal lattice, Nagasawa (1966) developed the first quantitative model for partitioning of isovalent cations in ionic crystals. Following Nagasawa (1966), Onuma et al. (1968) measured phenocryst-melt trace element partition coefficients and confirmed that the relative size differences between the trace element cations and the major cations in the lattice site determine the partition coefficients of isovalent cations, which gives rise to the parabolic patterns in Onuma diagrams.

A later study of Brice (1975) developed a similar but simpler model taking account of this effect of size differences, which has been widely since the experimental study of Blundy and Wood (1994). According to the Brice equation, the parabolic pattern in Onuma diagrams is determined by three parameters, the strain-free partition coefficients corresponding to the peak of the parabola, the Young's modulus governing the width of the parabola, and the strain-free cation size controlling the peak position. These lattice strain parameters also vary with the cation charges, which gives rise to the change of parabolic patterns with the cation valence state (see Fig. 1). For a specific lattice site, cations with higher charges have tighter parabolas in Onuma diagrams; however,

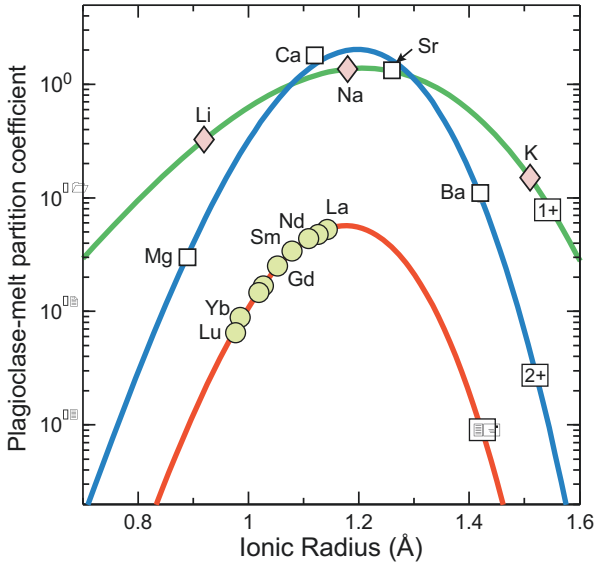

Onuma Diagrams, Fig. 1 Onuma diagram showing the partition coefficients of trace elements between plagioclase and a lunar basaltic melt from Run An-Red-2 in Sun et al. (2017). The thick curves indicate the parabola fits to the equation of Brice (1975) for individual groups of isovalent cations

the peak of the parabolas for isovalent cations also vary parabolically with the cation charges and reaches the maximum values when trace element cations have charges similar to the major cations in the lattice site (Wood and Blundy 2003).

Cross-References

► Partitioning and Partition Coefficients

References

Blundy J, Wood B (1994) Prediction of crystal–melt partition coefficients from elastic moduli. Nature 372(6505):452–454

Brice JC (1975) Some thermodynamic aspects of the growth of strained crystals. J Cryst Growth 28(2):249–253

Goldschmidt VM (1937) The principles of distribution of chemical elements in minerals and rocks. The seventh Hugo Müller Lecture, delivered before the Chemical Society on March 17th, 1937. J Chem Soc:655–673

Nagasawa H (1966) Trace element partition coefficient in ionic crystals. Science 152(3723):767–769

Onuma N, Higuchi H, Wakita H, Nagasawa H (1968) Trace element partition between two pyroxenes and the host lava. Earth Planet Sci Lett 5:47–51

Sun C, Graff M, Liang Y (2017) Trace element partitioning between plagioclase and silicate melt: the importance of temperature and plagioclase composition, with implications for terrestrial and lunar magmatism. Geochim Cosmochim Acta 206:273–295

Wood BJ, Blundy JD (2003) Trace element partitioning under crustal and uppermost mantle conditions: the influences of ionic radius, cation charge, pressure, and temperature. Treatise Geochem 2:568

Ore Deposits

Michel Cuney
GeoRessources, University of Lorraine, CNRS, CREGU, Vandoeuvre les Nancy, France

Synonyms

Mineral deposits; Mineral resources

Definition

Strictly speaking, an ore ("mine" in Latin) is a natural rock containing one or more useful substances that can possibly be extracted (mined) and processed to meet the demand of the society. Even if an economic connotation is generally associated with this term, there are many examples of ore mining driven by the imperative need of the substance without economic considerations. A typical example is uranium production during the 1950s which was dictated by the military programs. Moreover, the profitability of a given ore deposit may vary largely through time according to economic conditions and improvements in extractive metallurgy. Concentrations that are of too small volume or too low grade to be mined are called mineral occurrences or showings. The term ore deposit is most commonly applied to rocks containing metallic ore minerals in the native state (e.g., Au, Ag, Cu) or combined with other elements to form more complex minerals oxides (e.g., Fe, Al, Mn), sulfides (e.g., Pb, Zn), silicates (e.g., Ni, V), carbonates (e.g., Ca), phosphates (e.g., rare earth elements: REE), and others. The chemical elements in the Earth's crust are in concentrations (known as the Clarke) from percent level (Si, Al, Na, K, Fe, Mg, Ca) to ppb (milligram/ton of rock), but most of them, in the order of ppm (gram/ton). Metals occur in all types of rocks but usually in concentrations that are too low to be mined. In an ore deposit, the chemical elements are concentrated by factors ranging from 8 for iron deposits to several thousand for gold, uranium, and mercury when compared to the average concentrations in the Earth's crust.

Ore deposits are formed by the same processes that produce ordinary rocks but with a combination of conditions permitting to reach stronger enrichments of the elements or compounds in very small volumes of the Earth's crust, making up what is called a metallogenic system. The processes leading to the concentration of elements and minerals are extremely various. They are driven at depth by dynamic interactions between the Earth's core, mantle, and crust and at the surface by interactions between the hydrosphere, biosphere, and atmosphere. Even meteoritic impacts may play a

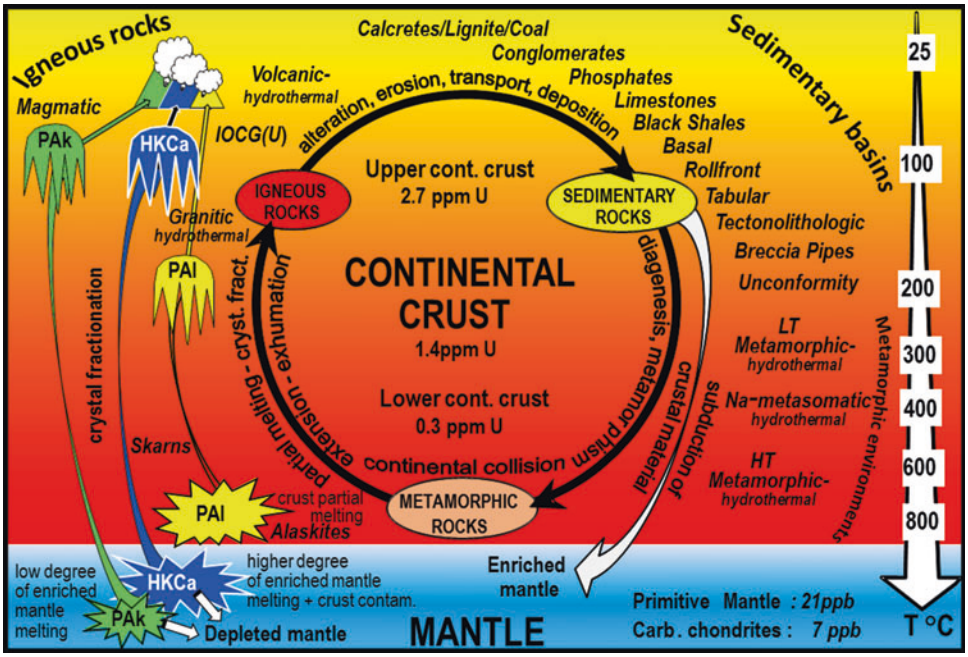

Ore Deposits, Fig. 1 Position of the major types of uranium deposit types (in *italic*) through the geological cycle with the major fractionation mechanisms (Modified from Cuney (2011))

role in the genesis of some deposits. For example, uranium deposits formed at nearly all steps of the geological cycle, from high-grade metamorphic conditions to plutonic, metasomatic, hydrothermal, basinal diagenetic, metamorphic, volcanic, sedimentary, and superficial environments (Cuney 2011) (Fig. 1). Even if the volume of an ore deposit is generally small compared to other common geological units, its genesis commonly involves mass transfer through large sections of the mantle and/or of the Earth's crust. An ore body contains ore minerals intermixed with other minerals, called gangue minerals, from which they must be separated. Mineral processing begins with the crushing of the ore to optimum grind size. The ore minerals are then physically separated from the gangue minerals, taking advantage of differences in their physical properties, such as density, particle size and shape, and electrical, magnetic, and surface properties. The resulting concentrate is then used for metal extraction through a more or less complex extractive metallurgy flow sheet which has to be designed for each type of ore deposits.

By extension, the term ore deposit or mineral deposit is applied to any substance extracted from the continental crust by humans and includes elements that are not metals such as building materials; biogenic substances accumulated and transformed by geological processes, such as sedimentary phosphates, fossil organic materials (coal, oil, and gas), and even fresh water resources; or those extracted from the evaporation of seawater either by natural processes (rock salt, potash, salars) or by human intervention (salt marshes). Mineral resources can be classified into three main groups (Fig. 2):

- The energy deposits or resources (peat, lignite, coal, oil, natural gas, oil and gas shale, oil sands, uranium, thorium), whose major use is to produce much of the primary energy, but fossil fuels are also used for organic synthesis products; they represent more than 90% of the mineral resources produced in the world.
- The metallic deposits or resources that fall into three categories:
- Ferrous metals: with iron and the metals used in alloys with him (Co, Cr, Mn, Mo, Nb, Ni, Ta, Ti, V, W. . .)
- Nonferrous metals: Al, As, Bi, Cd, Cu, Ga, Ge, Hg, Li, Pb, Sb, REE's, Te, Zn. . .
- Precious metals: (Au, Ag, and platinoids) produced in very low volume but, with a very high market value, predominantly used for jewelry or for hoarding and more subordinately for specific industrial applications
- The nonmetallic resources are available in three categories:
- Construction materials representing the most important volume; they are used either in their raw form (sand and other natural stones: granite, limestone, marble...), or grounded (aggregates), or after more or less extensive transformations (clays to produce bricks, limestone and clay to make cement. . .).
- Industrial minerals: e.g., asbestos, barite, clays, industrial diamonds, diatomite, feldspars, fluorite, graphite, gypsum, anhydrite, magnesite, phosphates, potash, salt (rock, brine, and sea salts), sulfur, talc, pyrophyllite, vermiculite, zircon, phosphates, and potash are used for fertilizers, feldspar, and kaolin for ceramics.

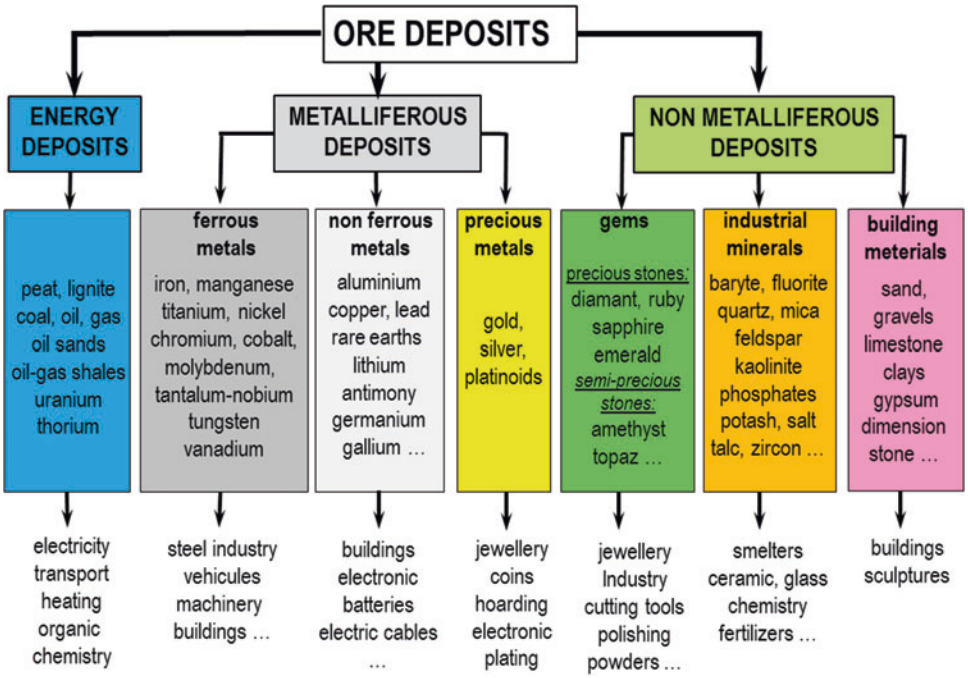

Ore Deposits, Fig. 2 The different categories of ore deposits or mineral resources and their main use by the different segments of the society

- Gems including precious stones (diamond, ruby, sapphire, and emerald) and semiprecious stones (tourmaline, amethyst, peridot. . .).

In addition, not all mined ores are strictly natural; more and more frequently tailings from former mines become a profitable ore. For example, in 2013, de Beers recovered 815,036 carats of diamonds from 6,133,799 tons of old tailings surrounding the Kimberley mines in South Africa. Such developments could enable minimizing the footprint of the mineral industry on the environment and also contribute to the sustainable use of the mineral resources.

Classifications

Many geological parameters have been used for ore deposit classification, such as the presence of certain metals or minerals (e.g., gold, magnetite), shape of the ore body (dissemination, vein, layer, etc.), geological environment (continental or marine basins), local tectonic regime (shear zone, breccia), geotectonic setting (collisional, island arc, continental margin), formation temperatures, and chemical composition of the fluids. Individual deposits present an extreme variability due to their formation involving frequently a combination of different processes and factors. Therefore, a classification of ore deposits does not appear straightforward. It is why some authors prefer to classify deposits into associations and types, which are related by common geological setting and paragenesis, but not necessarily by similar genetic processes (Laznicka 1993). Exploration and mining geologists tend to prefer pragmatic and empirical classifications rather than genetically based models. Also, many scientists use the type of rock to which the deposits are spatially associated, such as volcanic- or granite-related, turbidite-hosted gold deposits (Laznicka 1985, 1993; Jebrak and Marcoux 2015). Others use more taxonomic terminologies such as "deposit types" (Cox and Singer 1986; e.g., porphyry copper, orogenic gold, lateritic nickel) or deposit styles (Carlin style Au, Bushveld style PGE (platinum group elements), Witwatersrand style Au, Olympic Dam style IOCG: iron oxide copper gold). Nongenetic classifications are considered to minimize errors and controversy. However, although a stringent genetic classification of ore deposits is very difficult, it should represent an ultimate objective using the progress of scientific research which continuously modifies and improves ore-forming models and mineral system models.

Guilbert and Park (1986) have shown that the evolution of the classifications reflect the development of the knowledge of ore deposit formation increasing with the development of new techniques, experimental work, and modeling. The classification of Guilbert and Park (1986), which derives from the one of Lindgren (1933), is one of the most detailed and comprehensive. In contrast, Robb (2005) selected a classification simply based on the association between ore deposits and the three main categories of host rock, namely, igneous, sedimentary, and metamorphic, which are considered to reflect the fundamental processes active in the Earth's crust. He considers that ores are rocks and can generally be attributed to an igneous or sedimentary/surficial origin. However, such a relation works perfectly for syngenetic deposits

because they are formed at the same time as the host rock itself, but for epigenetic mineralization, such as those deposited by hydrothermal fluids in veins, the ore may occur in virtually any rock type without having any genetic link with the enclosing rock. Moreover, the same ore-forming process can be developed on more than one rock categories within the same deposit, and the formation of many deposits lies in intermediate position between genetic end members. For example, the Kuroko massive sulfide deposits result from combined interplay of volcanic, intrusive, sedimentary, and diagenetic processes. In addition, supergene processes may represent the crucial step to reach economic grade for a mineralization with a primary igneous or sedimentary origin. For example, the genesis of high-grade hematite-banded iron formation includes iron concentration during sedimentation, then during percolation of basinal brines, and finally by tropical weathering.

Compared to ore deposit models, which intend to understand how deposits form, the mineral system approach (Wyborn et al. 1994) focuses on answering the question of "where?" ore deposits form and integrates all geological scales from deposit to continental scales. Four critical elements are considered in the mineral system: (i) the fluid source region; (ii) the metal/other critical solute source regions, both considered at the regional scale; (iii) the fluid fractionation site at the ore district scale; and (iv) the metal depositional site. All these elements are reported on a series of maps in Global Information Systems (GIS; Bonham-Carter, 1994). Then, using the relevant mineral system model for a particular type of deposit, statistical approaches such as "Weights of Evidence" modeling allow the development of predictive maps for targeting the exploration of new deposits (Partington and Sale 2004). Such approaches become essential in finding more and more deeply buried deposits and evaluating economic risks in their exploration.

In the present contribution, we have used and slightly modified the classification of Pohln (2011) which is based primarily on the five main petrogenetic process systems occurring on Earth, which are magmatism, sedimentation, diagenesis, metamorphism, and surficial weathering. We have excluded metamorphosed deposits which just present a modification from pre-existing deposits formed by other processes. The five main types are: (i) magmatogenic, (ii) supergene, (iii) sedimentary, (iv) diagenetic-hydrothermal, and (v) metamorphogenic-hydrothermal ore deposits. Only some of the major deposit types have been selected for more detailed descriptions.

Magmatogenic Ore Deposits

Magmatogenic ore deposits are further subdivided into four subtypes: (i) orthomagmatic base metal deposits, (ii) orthomagmatic deposits related to peralkaline magmas, (iii) pegmatites, and (iv) hydrothermal deposits.

Orthomagmatic base metal deposits mainly include metal oxide (magnetite, ilmenite, chromite), Ni-Cu-sulfide sulfides, and precious metal (Pt, Pd, Au) mineralization. They result from magmatic fractionation with segregation of minerals or sulfide-rich immiscible melt droplets within large silicate basic to ultrabasic magma intrusions. Gravitational settling due to the large density contrast between the residual melt and the minerals and the melt droplets is the fundamental concentrating mechanism. However, the implication of hydrous or carbonic fluids is more and more evidenced in the recent studies. For example, in magmatic Ni-Cu deposits, most sulfide zones carrying appreciable PGE contents are characterized by pegmatitic textures and the presence of hydrous minerals, pointing to a high fluid activity during the magmatic segregation. Orthomagmatic ore bodies generally form layers in stratified magmatic rocks but also lenses or crosscutting dykes and veins. Such deposits occur in a large variety of intrusion styles: Fe-Ni-Cu-sulfide and PGE ores hosted by Archaean komatiite lavas such as those of the Yilgarn Craton in Western Australia; Alpine-type chromium-PGE mineralization settled within ophiolites, and as seams in layered mafic intrusions; Cu-Ni-PGE "reefs" found within layered mafic intrusions; conduit-hosted Cu-Ni-PGE in complex mafic-ultramafic intrusions; Ni-Cu-PGE in magma bodies resulting from meteoritic impact; Cr-PGE in Ural-Alaska-type ultramafic ring intrusions; Ti-Fe in Mesoproterozoic anorthosite-ferrodiorite complexes; Kiruna-type orthomagmatic iron oxide and apatite deposits in intermediate to felsic igneous rocks; apatite-Fe-Nb-Zr, or REE-U-F in carbonatite plugs and nephelinite intrusions. Only three major types of these deposits will be described: chromite deposits, Ni-Cu deposits, and PGE deposits.

Chromite deposits result from fractional crystallization of ultramafic and mafic magmas and gravity settling of Cr-rich spinels which form a cumulate layer at the base of the intrusive. There are two main types of chromite deposits: stratiform and podiform. Stratiform deposits consist of extensive chromite-rich layers (a few millimeters to several meters thick) alternating with silicate layers including dunite, peridotite, pyroxenite, and less commonly gabbroic rocks. They occur within basal portions of Archaean mafic-ultramafic layered intrusions such as the Bushveld Complex in South Africa. These deposits contain large resources of low-grade chromite (average 10.7% Cr_2O_3). Podiform chromite deposits consist of irregularly shaped massive chromite pods. They generally occur in the olivine-rich portions (dunites) of ophiolitic complexes, referred as "Alpine-type," and are located along major faults.

Ni-Cu deposits result from the separation from a parental magma of a sulfur-rich immiscible liquid concentrating Fe-Ni-Cu, from which pyrrhotite (FeS), pentlandite $(Fe, Ni)_9S_8$, and chalcopyrite ($CuFeS_2$) crystallize during cooling. The Ni-Cu ore bodies tend to occur in embayments at or near

the base of intrusions because sulfide liquids are heavier than silicate liquids and therefore sink to the bottom of the magma chamber. The host magmatic bodies consist of layered intrusions, stocks, ultramafic sills, and flows. The largest deposits are of Archaean and Proterozoic age. Typical Ni-Cu deposits include those hosted by the Sudbury layered intrusion (Ontario, Canada), the Kambalda ultramafic flow in Australia, and the Thompson District ultramafic sill in Manitoba (Canada).

Platinum group elements (platinum, Pt; palladium, Pd; iridium, Ir; rhodium, Rh; osmium, Os; and ruthenium, Ru) may occur both with Ni-Cu-sulfide and chromite mineralization. However, the fundamental mechanisms involved in PGE concentration and deposition result from a not so well-understood multistage process. PGE can concentrate during high-temperature deposition of chromites, but they can also be incorporated into immiscible liquids and remobilized and reconcentrated during metasomatic and hydrothermal activity. The PGE production comes dominantly from the Merensky Reef in the Bushveld Complex in South Africa and the Ni-Cu deposits of the Noril'sk-Talnakh District in Russia. The mineralized Merensky Reef forms less than 1 m thick but laterally persistent, disseminated, sulfide-poor horizons within polycyclic mafic-ultramafic cumulate sequences. The principal ore minerals are pyrrhotite, chalcopyrite, pentlandite, PGE, sulfides, arsenides, and tellurides. The Noril'sk-Talnakh deposit is essentially a magmatic Ni-Cu deposit containing high PGE concentrations (6 g/t). The ore bodies occur at or near the base of 50–350 m thick complexly differentiated gabbro-dolerite intrusions emplaced during the late Permian to Triassic time along rifts of the Siberian platform.

Orthomagmatic deposits related to peralkaline magmas are a source of a different set of metals. Peralkaline fractionated magmas are commonly considered to derive from very low degrees of partial melting of the mantle that generates alkali basalts, followed by several stages of magmatic fractionation. Their geodynamic setting is typically anorogenic. They form small to large, commonly concentrically zoned, circular to ovoid plutonic to volcano-plutonic complexes associated with ring dikes. These complexes may comprise a wide range of intrusions, from gabbros to highly fractionated granites or syenites, always emplaced at a very high structural level. Associated ore deposits essentially result from extreme crystal fractionation. The high temperature and peralkalinity of these melts permit a high solubility of incompatible elements such as Zr, REE, U, Th, and Nb and cause their continuous enrichment until the most extreme stages of magmatic fractionation. These ore deposits are always hosted by the last and most fractionated magma batches at the roof or at the margin of the peralkaline plutonic complex. When these melts crystallize, complex Zr-REE-Nb-Th-U silicates, phosphates, and/or oxides are formed. One of the best examples of the REE-U-Zn-Th mineralization is the Kvanefjeld deposit in the Ilimaussaq plutonic complex in southern Greenland which is hosted by layered lujavrites, a highly fractionated peralkaline syenite.

Pegmatites can host a variety of ore minerals containing Be, Li, Rb, Cs, Ta-Nb, U, Th, REE, Mo, Bi, Sn, and W, generally belonging to the group of the so-called rare metals, industrial minerals (feldspars, kaolin, quartz), as well as numerous types of gemstones. Pegmatites are also orthomagmatic deposits but originate either from the extreme fractionation of a parental pluton, generally of granitic composition, which becomes highly enriched in volatiles (water, B, F, Cl) and rare metals or directly from the partial melting of the continental crust (Černý et al. 2005). Equivalents of these types of mineralization also occur in granitic and volcanic rocks. Three main types of mineralized pegmatites/granites are recognized: (i) LCT pegmatites (LCT for Li and columbo-tantalite), equivalent of the peraluminous high phosphorus rare metal granites (PHP-RMG) (e.g., Beauvoir granite in France), spatially associated with large peraluminous leucogranite complexes, with Li-Ta>Nb-Be-Sn mineralization; (ii) NYF pegmatites (NYF for Nb, Y, and F) equivalent of the peralkaline rare metal granites (PAK-RMG), associated with peralkaline granite complexes (A1 type) with Nb>Ta-Zr-REE-U-Th mineralization; and (iii) mixed pegmatites intermediate between the two proceedings probably corresponding to the peraluminous low phosphorous rare metal granites (PLP-RMG) and deriving from extreme fractionation of high-K calc-alkaline granites (A2 type) with Nb≈Ta-Sn mineralization.

Pegmatites typically derived from partial melting in the continental crust are represented by the low-grade disseminated uraninite mineralization concentrated in granitic pegmatoids occurring in migmatitic domains. The type example is the Rössing deposit in Namibia (246,500 t U at 300 ppm U) whose mineralization is hosted by granitic pegmatite sheets called alaskites. They are intrusive into epicontinental sediments metamorphosed to a high grade with partial melting. The large accumulation of mineralized alaskite dikes at Rössing results from the combination of six parameters:

(i) A U-rich source represented by intracontinental platform sediments, probably with synchronous felsic volcanism
(ii) Low degree of partial melting
(iii) Structural control of alaskite emplacement
(iv) A chemical barrier represented by the Rössing Formation marbles, stopping the rise of the alaskitic melts, because of skarn formation reactions with production of carbon dioxide, shifting melt solidus to higher temperatures
(v) A redox barrier represented by graphite and sulfides in the Rössing Formation, creating low fO_2 conditions that prevented U fractionation in magmatic fluids

(vi) Favorable climatic conditions that oxidized uraninite in the weathering zone and precipitate uranophane in fractures that have enriched the upper part of the deposit

Hydrothermal deposits occur within an extreme variety of geological settings. The relative importance of magmatic and external fluids involved in their genesis cannot be always clearly estimated. They are classically considered as formed from metal-enriched magmatic fluids exsolved from crystallizing magma bodies, frequently highly fractionated. However, as an example, the fluids observed in most tungsten deposits from China and Europe correspond dominantly to metamorphic fluids. Also, vein-type uranium deposits occurring within the granites or in enclosing rocks were formed $40–50 \times 10^6$ year after granite emplacement with the involvement of diagenetic and meteoric fluids. In fact, in hydrothermal ore deposits, the origin of the fluids ranges from magmatic to metamorphic, diagenetic, meteoric, and seawater. Indications on the origin of the fluids are provided by isotopic characterization of hydrothermally altered minerals associated with the deposits. Hydrothermal deposits comprise magnetite-Cu-Co-Au, W, Zn-Pb-Ag, Mo-Bi-Au, and Sn-As-Pb-Zn-W-Mo skarns; contact-metasomatic Pb-Ag-Zn ore; iron-oxide-copper-gold (U-REE) deposits (IOCG); Cu-Mo-Au and Sn-W porphyries; Kuroko-type submarine volcanogenic deposits; volcanic-hosted massive sulfides (VMS); Sn-W-Cu veins; epithermal Ag-base metal; and Au-Ag deposits. Many of these deposits are related to plutonic and subvolcanic magma bodies generally of granitoidic composition and occur in the roof of the intrusions or in enclosing metamorphic rocks; VMS and epithermal Au-Ag deposits are developed near the surface in association with volcanic centers on land or submarine.

Porphyry deposits produce mainly Cu-Mo or Cu-Au-Ag, sometimes W. The term porphyry copper refers to very large, low-grade, epigenetic mineralization disseminated within granitic intrusions. There are several episodes of intrusive activity, with several stocks, dike swarms, and intrusive breccias. Porphyritic textures result from their high-level emplacement in the crust. Ore extraction typically requires mass mining techniques with open pit mines that extend over several square kilometers. Porphyry copper provinces coincide, worldwide, with orogenic belts predominantly of Cenozoic and, to a lesser extent, Mesozoic age. The most remarkable one is the series of Circum-Pacific deposits related to oceanic crust subduction settings where they occur in island arcs and at continental margins. Porphyry-type deposits are uncommon during the Paleozoic and are rare during the Proterozoic. Porphyries in island arc settings have primitive initial Sr isotopic ratios ($0.702 < {}^{87}Sr/{}^{86}Sr < 0.705$) reflecting a derivation either from upper mantle material or recycled oceanic crust, whereas the intrusions occurring in continental settings have higher initial Sr isotopic ratios due to interaction with the crust. Mineralization may occur entirely within the stock, or within the country rock, or in both, or in associated volcanics. Sulfide minerals (pyrite, chalcopyrite, bornite, and molybdenite) mostly occur on fractures or disseminated in the potassic alteration zone. Strong alteration zones develop in and around mineralized granitic rocks and may reach 10–20 times the size of the deposit. Ideally, mineralized porphyries will have a central area associated with secondary biotite or K-feldspar and surrounding shells of quartz and sericite (cream to slightly greenish phyllic zone) and then a greenish chlorite, epidote, sodic plagioclase, and carbonate (propylitic zone) alteration. In some cases, a white argillic zone occurs. The deposits have commonly a central very low-grade zone enclosed by shells dominated by bornite, then chalcopyrite, and finally pyrite. Molybdenite distribution is variable. Radial fracture zones outside the pyrite halo may contain Pb-Zn veins with Au-Ag values. Where sulfide mineralization occurs, surface weathering often produces rusty-stained bleached zones from which the metals are leached and redeposited near the water table to form an enriched zone of secondary mineralization. In the potassic alteration zone, mineralization is associated with vapor-rich fluid inclusions (with SO_2, H_2S, CO_2, HCl, HF, and most Cu and Au) and highly saline fluid inclusions (35 to >70 wt.% of K, Na, Ca, Fe, Mo, and Cu chlorides) which result from the boiling of a magmatic fluid. Numerous features, such as magma compositions; their metal and volatile contents; their state of oxidation; the number, size, relative timing, and depth of emplacement; and variations in the type of country rock, lead to a wide variety of porphyry copper styles. Porphyry systems are dominated by magmatic fluids mixed with variable quantities of meteoric fluids. The average porphyry copper deposit represent about 10^9 t ore at 0.5–1.5% Cu, 0.01–0.04% Mo, and <1.5 g/t Au. Giant deposits contain more than 2×10^6 t Cu, the Chuquicamata supergiant deposit reaches 24×10^6 t Cu, and the largest one, El Teniente in central Chile, contains more than 94×10^6 t Cu. Apart from copper, by-product metals include significant tonnages of Ag, Au, Mo, Re, Pb, Zn, and Mn and minor amounts of As, Bi, Sn, W, U, and Pt.

Epithermal gold deposits occur within 1–2 km of the surface and are deposited in veins or stockworks from hydrothermal fluids at temperatures ranging from less than 100 to about 300 °C. The deposits are often formed at active continental margins in areas of active volcanism. Two types of fluids are distinguished: the so-called low-sulfidation (LS) fluids, which are reduced with a near-neutral pH, and high-sulfidation (HS) fluids, which are more oxidized and acidic. LS fluids are considered to be a mixture of meteoric and magmatic water and gold deposition occurs when boiling occurs, whereas HS fluids are mainly of magmatic origin and gold is deposited when the solution cools and/or mixes with meteoric water. LS deposits may also produce economic

quantities of Ag and minor amounts of Pb, Zn, and Cu, whereas HS systems more often produce Cu and Ag. Similarly to porphyry copper deposits, one of the largest epithermal gold deposit provinces is distributed around the Pacific volcanic "Rim of Fire." Epithermal gold deposits contribute significantly to the world's gold supply. Gold grades are highly variable in epithermal deposits ranging from 1 to more than 150 g/t.

Supergene Ore Deposits

Supergene ore deposits result from weathering. Earth materials interact with water, air, the biosphere, and the energy provided by the sun. During fragmentation and alteration of rocks, metals are concentrated either in situ as an insoluble residuum (e.g., bauxite) or by precipitation after limited movement in soil and ground water (e.g., lateritic nickel deposits). For infiltration deposits, such as those of Cu and U, lateral transport distances may reach 1 to several hundred kilometers. Three subcategories are identified:

(i) Residual deposits which include bauxite and lateritic Au, Fe, and Mn ore deposits
(ii) Supergene enrichment deposits generally developed on primary sulfide ore (Cu, Au, Ag), as lateritic Ni as in New Caledonia and Nb in the Araxa carbonatite in Brazil
(iii) Infiltration deposits that are typically represented by roll-front-type uranium deposits (e.g., Wyoming Province in the USA and the huge province of the Chu-Saryssu and Syr Darya Basins in southern Kazakhstan) occurring in continental to marginal marine sandstone

Roll-front deposits represent the best example of epigenetic U deposition resulting from meteoric water infiltration in sandstone. Host rocks were deposited in fluvial and lacustrine environments, in marine marginal plains, or in channel, lagoonal, and beach-bar settings. The source of U may be U-rich granites or volcanics external to the sediments and/or synsedimentary U trapped in reducing conditions or interlayered U-rich volcanic ashes. The reduced sandstone contains disseminated organic matter and pyrite and occurs down the hydrologic gradient relatively to the oxidized sandstone. The reductants are either of synsedimentary origin, resulting from the maturation of detrital organic matter (plant debris) during diagenesis, or epigenetic, deriving from the infiltration of reduced fluids migrated from deep oil reservoirs along faults (e.g., South Texas). In most models, U is transported by oxidized low temperature meteoric waters infiltrated through permeable sandstones confined between two aquitards corresponding to mudstone or shale. The reduced sandstone is oxidized and takes a pink red color due to hematite, or a yellow-orange color due to limonite, or even may become white gray when iron has been totally leached out. Uranium distribution is controlled by the interplay of the permeability of the sediments and the distribution of reducing components. Bacterial sulfate reduction is increasingly evidenced in the genesis of roll-front deposits and indicated by the presence of framboidal pyrite and strongly negative $\delta^{34}S$ values of secondary pyrite intimately intergrown with coffinite or nyngyoite. The resulting ore bodies exhibit C shapes in cross section and are sinuous along the roll-front interface. In south Kazakhstan, the rolls may extend laterally over more than 100 km. Resources range from a few 10^2t to several 10^4t U, at grades averaging 0.05–0.25% U.

Synsedimentary Ore Deposits

Ore deposits of this type result from exogenous process systems involving physical or chemical transport in water and deposition simultaneously with the sediments. Two subtypes are distinguish according to distance of transport of the metals from their source: (i) allochthonous: colluvial, alluvial, or coastal placers and (ii) autochtonous mainly occurring in marine sediments such as sulfide-rich black shales; sedex-type Cu-Sb-Zn-Pb-Ag (Au); Palaeoproterozoic banded iron formation (BIF) of Algoma- and superior-type and banded Mn ore; oolitic Fe and Mn ore; and deep-sea manganese nodules and crusts (Mn-Cu-Ni-Co-PGE).

Allochthonous synsedimentary ore deposits result from mechanical sorting by density of heavy minerals and their concentration in colluvial to alluvial (Au, U, W, Pt, columbite, cassiterite, diamonds) to coastal (rutile, ilmenite, zircon, monazite) placers.

Autochthonous synsedimentary ore deposits result from metal transport in aqueous solution from land or from seafloor hydrothermal sources for black shales and sedex deposits. The world's largest metal concentrations formed in the Paleoproterozoic when photosynthetic cyanobacteria expanded rapidly, oxidizing the atmosphere and seawater and precipitating iron dissolved in the oceans with the huge banded iron formations. Many giant base metal deposits (sedimentary-exhalative, "sedex" Cu, Pb, Zn) are the product of hot metalliferous fluids venting on the seafloor. In contrast to mid-ocean black-smoker activity, sedex deposits occur along rifts in shallow epicontinental seas.

Diagenetic-hydrothermal Ore Deposits

Three subtypes are recognized: (i) stratabound and/or stratiform sediment-hosted Cu deposits, (ii) Mississippi Valley type (MVT), and (iii) unconformity-related uranium deposits. These deposits result from physical and chemical changes affecting thick sedimentary basins. During basinal subsidence, the salinity of pore fluids increases with temperature and pressure rise to become diagenetic fluids. Such hot chloride-rich fluids are strongly enriched in a large variety of metals (Pb, Zn, Cu, U…) (Fig. 3). They can migrate according to pressure variations, either toward basin margins,

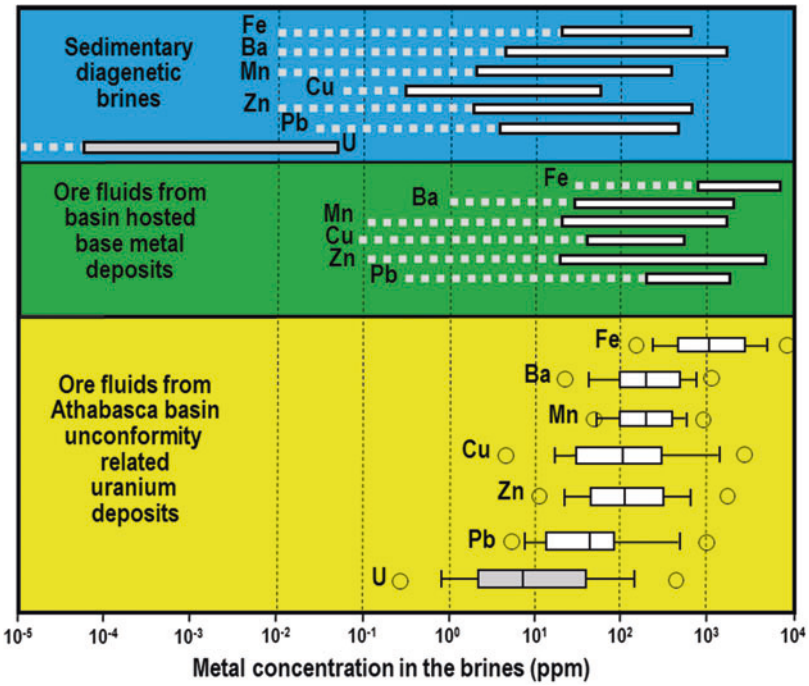

Ore Deposits, Fig. 3 Ranges of metal concentrations in diagenetic brines from sedimentary basins, in ore fluids from basin-hosted base metal (Pb, Zn, Ba) deposits and fluid inclusions associated with the Athabasca unconformity-related deposits (Modified from Richard et al. (2015)). Boxplots show 5th and 95th percentiles (*symbols*), 10th and 90th percentiles (*whiskers*), 25th and 75th percentiles (*box edges*), and the median (*inner bar*). The *boxes* represent the ranges of metal concentrations in each of the selected studies. *Gray* dotted lines represent the lower ranges of metal concentrations

or may infiltrate into the crystalline basement. The deposition of the metals often occurs at low-permeability barriers in copper shales or when redox conditions are reached for unconformity-related deposits.

Stratabound and/or stratiform sediment-hosted Cu deposits are best exemplified by the European copper shale (also known as the Kupferschiefer). It forms a thin strata extending over more than 600,000 km^2 in the Central European Permian rift basin. Economic metal grades are only known to southern basin margins (Silesia in Poland and the Harz District with Mansfeld and Sangerhausen in Germany). The mineralized shale is a euxinic sediment deposited in a shallow sea with a well aerated upper water column. Detrital import was very small with quiet deposition conditions as shown by the preservation of the fine lamination of the sediments. A controversy exists between syn- and epigenetic models. Recent data tend to support an epigenetic diagenetic origin. The ore bodies are perfectly stratiform, but they present crosscutting relations with the copper shale stratum. The metals are considered to be transported by oxidized, sulfate-bearing, Ca-Mg-K-Cl diagenetic fluids flowing up toward basin margins from deeper parts of the basin, leaching the metals from Permian molasse red bed sediments and volcanics. Deposition mechanisms include decreasing T and P; mixing with cool, alkaline, meteoric water; and reduction by reaction with organic matter and sulfides of the shale. Most ore minerals replace rock-forming minerals with microscopic veinlets of different spatial orientation. Copper shale deposits in Poland have grades of 1.2–2.8% Cu and 30–80 g/t Ag. The thickness of the ore bodies varies from 1.2 to more than 20 m. Mining occurs at depths between 600 and 1,200 m. Besides copper, Pb, Ag, Ni, Au, Pd, Pt, Re, Se, and sulfuric acid are produced. Reserves of 2.4×10^9 t of ore are reported. In Germany, the Mansfeld District has produced about 1.5×10^6 t Cu until 1970.

Mississippi Valley type (MVT) Pb-Zn-(F-Ba) deposits correspond to epigenetic ore deposits typically hosted in marine dolostone. Most occur in Cambrian to Triassic rocks. The largest MVT deposits are in North America with the Viburnum Trend and the Old Lead Belt (Southeast Missouri Lead district), Tri-State, Upper Mississippi Valley, Central and East Tennessee, and Pine Point. MVT deposits typically are in districts covering hundreds or even thousands square kilometer. Ore controls are district specific, such as depositional margins of shale units, limestone-dolostone transitions, reef complexes, solution collapse breccias, faults, and basement topography. Most MVT ore districts are the product of regional to subcontinental scale migration of diagenetic brines (10–30 wt% salts) at temperatures comprised between 50 and 200 °C. Typically, the mineralization is epigenetic and stratabound in platform carbonate sequences or in foreland thrust belts, and they occur at shallow depths at the margins of basins, unrelated to any igneous activity. The ore mineralogy is simple: sphalerite, galena, pyrite, marcasite with dolomite, calcite, and quartz as gangue minerals. Carbonate host-rock dissolution leads to slumping, collapse, and brecciation. Individual MVT deposits are generally small, generally less than 10×10^6 t ore. In the Upper Mississippi Valley district, the average deposit size is between 0.1 and 0.5×10^6 t, and a few contained up to 3×10^6 t ore. Deposit grades rarely exceed 10% Pb+Zn. An exception is the Polaris deposit, in the Canadian Arctic Archipelago with 22×10^6 t ore at 18% Pb+Zn. Most deposits have Zn/(Zn+Pb) values between 0.5 and 1.0.

Unconformity-related uranium deposits mainly occur in the Athabasca Basin (Saskatchewan, Canada) and in the vicinity of the Kombolgie Basin in the Northern Territory, Australia. The deposits associated with the Athabasca Basin represent the world largest high-grade U ore bodies (up to 19.5% U for about 260,000 t U for the McArthur deposit). They are located in the vicinity of an unconformity between an Archaean to Paleoproterozoic basement and a Paleo- to Mesoproterozoic intracontinental siliciclastic basin. Their exceptional grade and size results from the combined efficiency of a series of U-fractionation mechanisms. U enrichment of the basement is exceptional with considerable amounts of uranium trapped in the Paleoproterozoic epicontinental platform sediments, comprising U-rich graphitic schist, meta-arkose, and calc-silicate, in uraninite-bearing leucogranites and pegmatoids derived by partial melting of these metasediments during the Hudsonian orogenesis, followed by the emplacement of Paleoproterozoic Th-U-rich high-K calc-alkaline granitoids, and finally the formation of late Hudsonian vein-type U deposits (e.g., Beaverlodge, Gunnar). High efficiency of U extraction from source rocks is shown by the alteration of highly refractory minerals such as monazite and zircon in the sandstone, the regolith, and the basement by acidic, hot (160–220 °C, about 1 kbar), oxidized, and Na-Ca-Mg-rich (up to 6 molar Cl) basinal diagenetic brines generated within continental, oxidized, organic-free, siliciclastic formations. The brines are very similar to MVT brines with high contents of Fe, Cu, Zn, and Pb but differ by their high U content (Fig. 3). Exceptional trapping conditions resulted from (i) the strong redox gradient developed between the oxidized basal Athabasca sandstone and the epicontinental Paleoproterozoic carbon-rich metasediments of the basement and (ii) the creation of large openings by reverse faulting and intensive quartz dissolution.

Metamorphogenic-hydrothermal Ore Deposits

Prograde and retrograde metamorphogenic-hydrothermal ore deposits comprise orogenic Au deposits in accretion-subduction collision complexes, a large part of the Cu-Co ore deposits of the Copperbelt in Zambia and the Democratic Republic of Congo, and the Mt Isa copper deposit in Australia. During prograde metamorphic, dehydration reaction occurring within large volumes of rocks liberates a huge mass of fluids with variable salt, CO_2, CH_4, and N_2 contents. These fluids can transport metals which will precipitate where chemical and physical traps are present. Orogenic gold deposits are commonly related to such processes.

Mine Life Cycle

Mining activities start with the exploration and evaluation of an area of interest. If the evaluation is positive, a mine can be developed, and commercial mining production can start. However, the phases before production take a long time and require large capital investments. There are five main phases in the development of a mine.

Phase 1 – Exploration means the search for mineral resources suitable for a profitable exploitation. It includes researching and analyzing all the geological information and historic exploration data already available on the area in libraries; geological surveys; Ministry of Mines; reports from former exploration companies, conducting topographical, geological, geochemical, and geophysical studies to delineate the most prospective areas; and exploratory drilling, trenching, and sampling for ranking the prospectivity of the discovered anomalies and showings. GIS softwares are now commonly used to compile all available information and to build prospective maps allowing to choose the best targets for their detailed evaluation. Contacts and diffusion of the information about the work which is being done with the country and local authorities and with the local population has to start since the beginning of the operations and has to be repeated regularly. Also, a baseline assesses the state of the land before mining, including measurement of geochemical background concentration of metals in waters, soil, plants, and fauna. The biologic diversity and the existence of potentially endangered species have to be surveyed.

Phase 2 – Evaluation means determining the technical feasibility and commercial viability of a discovered mineral resource. It includes determining volume and grade of deposits by systematic grid drilling, evaluating and testing ore extraction methods and metallurgical ore treatment processes, surveying transportation and infrastructure requirements, and conducting prospective market and finance studies. This stage leads to the production of a feasibility study that provides estimations of the proved and probable mineral reserves which is used for taking the decision to develop a mine.

Phase 3 – Development involves establishing access to and commissioning facilities to extract, treat, and transport the ore from the deposit and associated preparations for commercial production. Depending on the selected type of mining, it may include constructing roads and tunnels and removal of overburden and waste rock for the development of open pits, excavations, sinking shafts, and underground drifts.

Phase 4 – Production corresponds to the activities of obtaining a saleable product from the ore deposit on a commercial scale. It includes the geometallurgic extraction of the product and any processing before sale.

Phase 5 – Closure occurs after mining operations have ceased and includes restoration and rehabilitation of the site using the budgets which have been provisioned since the phase 2.

The budget of exploration and mine development increases dramatically at each phase, because of increasing costs of the technologies which are used. After each phase, the

manager has to decide whether it is worth to continue the development of the exploration/mining project or to stop it.

The Environment and Public Acceptance

In the middle of the sixteenth century, Agricola, in his book "*De Re Metallica*," already reports that mining was criticized for its harmful effects on the environment and more surprisingly also on moral aspects, accusing mining to have only an objective of personal enrichment. Five centuries later, such critics remain the main grounds of the opposition to the mining industry. One of the most visible effects of mining is the creation of large to extremely large excavations and the storage of mine tailings which may represent a long-term source of pollution of the surrounding biosphere and waters, when not adequately managed. However, during most mining, only a very limited amount of land is disturbed compared to total landmass, and the disturbance is generally only locally visible. For example, Natural Resources Canada has estimated that less than 0.01% of Canada's total landmass was used in metal and mineral mining in over 100 years. But the image of mining activity is strongly tarnished by a series of catastrophic events such as the failure of the Bento Rodrigues dam in Brazil in November 2015, liberating huge amounts of iron ore tailings and causing the death of at least 17 persons. Even technologies, such as geothermal power plants considered as having low footprint, generate environmental problems with the production of salty waters enriched in heavy metals. Therefore, steady improvements of the environmental impacts of mining and continuous information of the populations since the first stages of exploration to gain a better societal acceptance of the mining projects are a necessity. Compromises have to be found, because the location of mineral deposits is dictated by nature and every citizen consumes minerals and mineral-derived products for building and heating homes, transport, electronic equipments, medicinal use, and numerous articles of daily life. It should be also taken into consideration that mining activity is creating some the highest amounts of value per unit area of land used. Also, mining should not be only developed in remote countries, where the mining law may be less constraining for preserving the quality of the local environment and the welfare of the local population. In many countries, especially in Canada and Australia, the mining laws are extremely strict. The law dictates that miners should pay to remediate the damage they cause and requires applicants of prospecting or mining rights to make financial provisions for the rehabilitation or management of negative impacts on the environment before the opening of the mine. The provisions are meant to ensure that the state will not be burdened with rehabilitation costs.

Taking a different view angle, mines can also be considered as potential disposal sites for the safe storage of society's unavoidable production of toxic or nontoxic waste. But for the most hazardous substances such as high-level nuclear wastes, underground waste disposal are specifically built. The technologies developed for the selection of such waste disposal sites and the ways of storing the waste benefit greatly from the lessons learned from the scientific study of ore deposits and underground mining. These operations have revealed how Mother Nature has preserved hazardous solid and gaseous substances in the form of mineral deposits such as huge reservoirs of natural gas during hundreds of 10^6 year, very high-grade uranium deposits as in the Athabasca Basin in Canada since 1.5×10^9 year, and even natural nuclear reactors at Oklo in Gabon, since 2×10^9 year.

Sustainable Mining

Mineral resources are considered as nonrenewable resources, except for the sodium, potassium, and magnesium salts harvested from seawater evaporation and some sands and gravel deposits which can be renewed by the continuous erosion of the reliefs. A sustainable management of the ore resources should ideally respect the following rules: (i) comprehensive extraction of valuable substances from the ore, (ii) the lowest possible consumption in their use, (iii) improvement of their recycling rate, and (iv) increase in the efficiency of using natural resources, especially energy. In fact, comprehensive extraction of the valuable substances from a given ore is limited by rapidly increasing costs and energy consumption when mining lower-grade ores, increasing the rate of recovery, and/or extracting additional substances occurring in the same ore body. For example, in the huge Olympic Dam IOCG deposit in Australia, Cu-Au-Ag-U are simultaneously recovered. However, the deposit also contains large resources of other elements such as iron (10–90% hematite), rare earths (45×10^6 at ~0.5% REE), and other elements which are not recovered because the processing costs would be too high in the present economic conditions. Despite the improvements made in the recent years in the use of natural resources in developed countries, a moderation in the growth of ore mineral extraction is not foreseeable in the near future because of the increasing demand of developing countries and the rapid growth of the world population.

Metals are high-value resources and can in principle be easily reused and recycled to turn waste into resources. The expected benefits of recycling are reduced environmental impacts by minimizing primary metal production and increased security of metal availability, but metal recycling still replaces only a small part of the primary production for most of them. Recycling is limited by the barrier of the cost of recovery. Today up to 90% of the steel reaching its end of life is recycled, but some of the elements from the alloys cannot be recycled. While in some cases they may contribute to the

quality of the recycled steel (e.g., silicon, Mo, Nb, Mn, and W), other elements such as copper or platinum group elements are lost and may decrease the performance of the recycled products. A UNNEP (2013) report provides a comprehensive review of the possibilities and limits of metal recycling.

An ever-going debate is the question about the existence of a sufficient mass of ore minerals for an ever-increasing consumption of our society and the preservation of the resources for the future generations. Theoretically, as our planet has a limited size, the mineral resources are in principle finite. One of the first alarms was given by the Club of Rome in 1972 which predicted a shortage of mineral resources for the years 1990–2000. The imminent scarcity of many minerals is regularly announced in the media but has not yet arrived. Peak production has been predicted for many metals but has been always shifted through time. The "life index" calculated from the ratio between the total known reserves of a given substance and its yearly world consumption (R/C) is totally misleading, because reserves given by the mineral industry correspond to the amount of ore minerals which has been carefully estimated by regular drilling. The capital investment for reserve estimations being very large, mining companies limit their evaluations typically for the next 5–30 years. Consequently, a division of total known reserves by the yearly consumption (R/C) will systematically predict that in 5–30 years' time, our economy will run out of the respective minerals. The confusion mainly results from the misunderstanding of the terms reserve and resource. As stated above, a reserve is an estimation made by mining companies of a natural material of intrinsic economic interest in such form, quality, and quantity that it can be mined in the present of foreseeable future legal, economic, and technological conditions. The reserves are defined according to rigorous reporting procedure such as the JORC code in Australia, CIM (Canada), SME (USA), SAMEREC (South Africa), PERC (Europe), and now CRIRSCO which intend to provide a generic international standard stripped of legal or regulatory components that apply only within individual countries, for international reporting of exploration results, mineral resources, and mineral reserve evaluations.

Comparatively to the mineral resources, the reserves are less well defined because of a lower level of geological knowledge. With increasing capital investments, additional geological investigations are performed to increase the confidence in the evaluation of the resources from inferred to indicated and measured (Fig. 4). Then, after taking into consideration the mining techniques and the feasibility of metallurgical processing of the ore, economic, marketing, legal, environmental, social, security, and governmental factors, the resources can be upgraded as reserves. The reserve is probable or proven according to the degree of the knowledge of the geology of the deposits, mainly constrained by the density of drilling.

Besides, it should be taken into consideration that the search for most mineral commodities has generally not gone much deeper than a few hundred meters below the surface and mostly land has been explored for mineral deposits. The deepest mines are known for gold deposits which may reach a depth of 4,000 m. Metal mining on the continental platforms and seafloor has a large future potential. Science and technology will continue to improve to enable the exploration of deeper and less accessible part of the Earth, to mine lower-grade deposits, and to process more refractory ore, to provide the mineral resources needed for the development of the world community.

Additionally, many mineral substances are increasingly replaced by synthetic products. For example, steel in cars is replaced by plastic, carbon fibers, and ceramics. The availability of some critical raw materials may become temporally limited, especially when their production is dominantly controlled by one country, which makes possible political decisions distorting the markets. But recent events have shown that mining companies are able to react rapidly to temporary mineral commodity shortage through the discovery of new

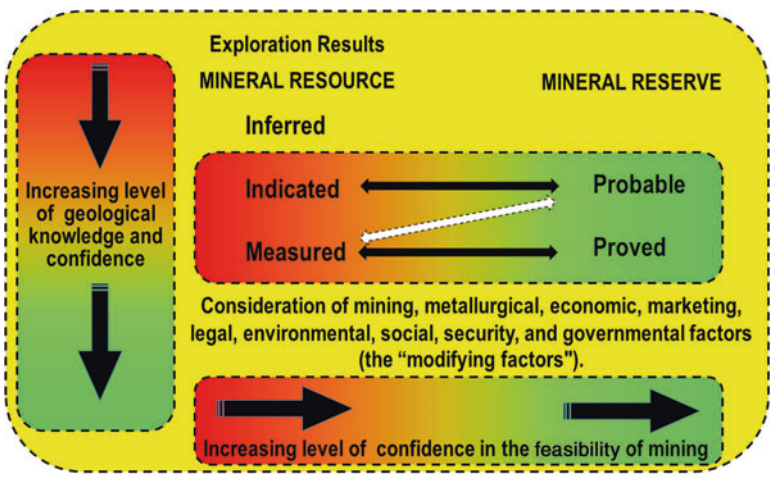

Ore Deposits, Fig. 4 CRIRSCO-type general classification scheme for ore deposit resources and reserves

deposits and the industrial research is also capable to rapidly find substitutes. But, finally the most important constraint in the future, for increasing ore mineral production, will be the cost of energy. The mining and mineral industries worldwide use large amounts of energy, in the order of 4–7% of the present global energy use. The cost of mineral resource extraction and processing and the amount of energy required to produce are mainly driven by three physical parameters:

(i) The average grade of the metal being mined, which is proportional to the amount of rock to be moved and processed, to which the importance of the overburden to be removed has to be added
(ii) The average grain size of the ore mineral which constrains the amount of energy required for comminution and beneficiation
(iii) The Gibbs free energy of the metal in its typical host mineral which is proportional to the energy requirement of smelting

Therefore, decreasing the grade of the mined substance, increasing the degree of recovery by finer grinding, and processing more refractory minerals increase the cost of production and the quantity of necessary energy. Nevertheless, new ore processing technologies, such as in situ recovery of metals by injecting fluids able to dissolve the ore minerals directly in the ore bodies, already used extensively since the 1960s for uranium in roll-front deposits, application of pulsed fields of high intensity (electromagnetic, microwaves, or mechanical) that induce the formation of micro-fractures that weaken the rock and facilitate the access of the chemical reaction for the dissolution of the ore minerals, and bio-heap leaching, represent much less energy-demanding technologies. Bio-heap leaching requires lower capital and operating costs; no milling step can be used to process low-grade ores, wastes, and small deposits; and the metal tenor may be built up by recycling solution over heaps.

Summary and Conclusions

Ore deposit study and the development of guides for their exploration is the objective of metallogeny. Besides the series of synthetic books on the geology of ore deposits referred in the present paper, Hedenquist et al. (2005) offer a recent synthesis of the metallogenic concepts for most deposit types. In the future, the consumption of mineral resources is expected to continue to increase worldwide, both because of the strong demographic growth and the improvement of living conditions in emerging countries. Despite the progress of recycling, new supply of raw materials based on the discovery of new deposits will remain a necessity. Exploration is therefore the first step in a quest for mineral and energy resources which will continue to increase strongly in the twenty-first century. Such a development will be fundamentally based on innovation, conceptual innovation in ore deposit scientific research, and technological innovation for the development of new mining and ore processing techniques. Metallogeny in the twenty-first century will tend to go toward the understanding of increasingly larger systems with the development of techniques such as multispectral satellite imagery, of GIS systems 3D modeling, and of investigations at an ever more detailed scale of the deposits, their minerals, and the ore-forming fluids with increasingly powerful analytical tools. The metallogenic scientific research will increasingly be shifted from a dominantly descriptive understanding of the system to a process-based approach of the mineral systems at all scales. Deposits will be searched in less accessible parts of the globe, at greater depths, and under the oceans, and sustainability of mining will be improved by using more efficient metallurgical processing and extracting useful commodities from rocks that traditionally have not been thought to be viable ores. Societal acceptance will be the major challenge.

Cross-References

- Fluid–Rock Interaction
- Fractional Crystallization and Assimilation
- Geochemical Exploration
- Geothermal Systems
- Hydrothermal Alteration
- Hydrothermal Solutions
- Hypogene
- Magmatic Process Modeling
- Supergene
- Volcanism

References

Bonham-Carter GF (1994) Geographic information systems for geoscientists – modelling with GIS. Elsevier Science, New York, 398pp

Černý P, Blevin PL, Cuney M, London D (2005) Granite-related ore deposits. Econ Geol 100th Anniversary Volume:337–370

Cox DP, Singer DA (eds) (1986) Mineral deposit models, USGS bulletin, vol 1693, 379pp

Cuney M (2011) Uranium and thorium: The extreme diversity of the resources of the world's energy minerals. In: Sinding-Larsen R, Wellmer F-W (eds) Non-renewable resource issues: geoscientific and societal challenges, International year of planet Earth. Springer, New York, pp 91–129

Guilbert JM, Park CF Jr (1986) The geology of ore deposits. W.H. Freeman and Co., San Francisco, 985pp

Hedenquist JW, Thompson JFH, Goldfarb RJ, Richards JP (eds) (2005) Economic geology 100th anniversary volume. Society of Economic Geologists, Littleton, 1146pp

Jebrak M, Marcoux E (2015) Geology of mineral resources. Geological Association of Canada, Canada, 668pp

Laznicka P (1985) Empirical metallogeny: Phanerozoic environments, associations and deposits, vol 1. Elsevier, New York, 1002pp
Laznicka P (1993) Precambrian empirical metallogeny: Precambrian lithologic associations and ore deposits, vol 2. Elsevier, Amsterdam. 1622pp
Lindgren WA (1933) Mineral deposits, 4th edn. McGraw-Hill, New York, 930pp
Partington GA, Sale MJ (2004) Prospectivity mapping using GIS with publicly available earth science data – a new targeting tool being successfully used for exploration in New Zealand. In: Pacrim 2004 congress. Australasian Institute of Mining and Metallurgy, Adelaide, pp 239–250
Pohln WI (2013) Economic geology principles and practice: metals, minerals, coal and hydrocarbons - introduction to formation and sustainable exploitation of mineral deposits. Wiley, 663 pp
Richard A, Cathelineau M, Boiron MC, Mercadier J, Banks D, Cuney M (2015) Metal-rich fluid inclusions provide new insights into unconformity-related U deposits (Athabasca Basin and Basement, Canada). Mineral Deposita 51(2):249–270
Robb LJ (2005) Introduction to ore-forming processes. Blackwell, Malden, 373p
UNNEP (2013) http://www.unep.org/resourcepanel-old/Portals/24102/PDFs/UNEP_summarybooklet_2b_130911_web.pdf
Wyborn LAI, Heinrich CA, Jaques AL (1994) Australian Proterozoic mineral systems: essential ingredients and mappable criteria. In: Proceedings of the Australian Institute of Mining and Metallurgy annual conference, Melbourne, pp 109–115

Organic Facies

R. Paul Philp
ConocoPhillips School of Geology and Geophysics, University of Oklahoma, Norman, OK, USA

Definition

An organic facies is a mappable subdivision of a designated stratigraphic unit, distinguished from the adjacent subdivisions on the basis of both the chemical and petrographic characteristics of its insoluble organic constituents (palynofacies or macerals), without regard to the inorganic aspects of the sediments, which in turn permits the prediction of the likely occurrence, and lateral variability, of hydrocarbon source potential as a function of depositional environment.

Introduction

The concept of organic facies has evolved over the past 40 years following early publications by Rogers (1980), Jones and Demaison (1982), and Jones (1987). In the past two decades, knowledge and understanding of organic facies has become even more important with the enormous changes in exploration strategies resulting from, first, the shale gas boom and, second, the shale oil boom which followed a few years later. In both of these cases, the initial successes evolved as a result of breakthroughs in horizontal drilling technology in the mid-1990s which were subsequently combined with hydraulic fracturing leading to production of gas and oil from shales previously thought of only as source rocks but which were subsequently realized to be both source and reservoir rocks. Properties of the shales, particularly permeability, prevented the efficient expulsion of the oil, and if the maturity levels were high enough, the trapped oil was converted to gas and if not it remained there as oil. In both cases, the hydraulic fracturing releases the tightly trapped oil or gas such that it can be produced. Evaluation of the shales to find the most potentially productive organic facies is now a key part of any successful exploration strategy. A similar approach has been developed characterizing and mapping the most productive lithofacies, and clearly future work should focus on integrating data used to characterize lithofacies and organic facies.

Prior to discussing the evolution of organic facies, a broad definition of the concept will be provided. The characterization of organic facies integrates petrographic and geochemical techniques to study the insoluble organic matter, or kerogen, in source rocks. The microscopy or petrography provides information on the palynofacies, or macerals, and characterizes all aspects of the kerogen assemblage: in other words identification of individual insoluble particulate components (macerals) and assessment of their absolute and relative proportions and preservation states. (It can be argued that there are differences between palynofacies and macerals. In my opinion, there are more similarities than differences, and to a large extent, it depends upon the method of identifying the insoluble organic constituents which are ultimately collectively referred to as kerogen. It should also be noted that the concept of palynofacies was first introduced by Combaz (1964). He defined palynofacies to mean the relative proportions of microscopic organic constituents remaining after treatment of the rock with HCl and HF plus a concentration step, which is basically the same process used to isolate kerogen.) A useful and comprehensive review article on the evolution of the concept of palynofacies and organic facies was published in 2012 by Filho et al. (2012). When combined with the geochemical data, such as total organic carbon (TOC) or richness of the source rock HI-hydrogen index from Rock Eval data), the organic facies model describes the conditions of the depositional environment and the hydrocarbon source rock potential. In recent years, there has been a concerted effort to integrate bulk geochemical parameters as well as the more specific molecular geochemical parameters based on molecular biomarkers when defining organic facies. These compounds (biomarkers) in many cases are associated with a specific type of organic matter and therefore provide another parameter to identify the organic matter or facies and add another layer of confidence when attempting to delineate the distribution of a specific organic facies within a petroleum

system. In other words, it brings together the petrographic characterization and geochemical characteristics based on the organic (preliminary insoluble) matter in the source rock. Taken together data from these two disciplines can be used to define mappable source rock units within a basin and provide a far better assessment of the petroleum potential of various facies within a particular petroleum system. In addition the development of the organic facies concept allows the prediction of the likely occurrence (and lateral variability) of hydrocarbon source potential as a function of the depositional environment. Variability may be observed at the slide scale (cms) or basin scale (kms) depending on the objectives of the study being undertaken at any time. Characterization of organic facies can be used to identify both small and large cycles related to transgressive-regressive events based on paleoecological and paleoclimate conditions.

Kerogen

A more detailed discussion on kerogen can be found elsewhere in the volume, but it is important when trying to understand how the organic facies concept evolved to include a brief review on our understanding of kerogen and how these views have changed over time. It is important since as our understanding of kerogen changed that in turn led to the development of the organic facies concept. Today it is commonly accepted that kerogen, the insoluble organic fraction in sedimentary rocks, is the key intermediate in oil and gas production. The understanding of kerogen has changed over time but really started to receive attention following the publication of a paper by Forsman and Hunt (1958) and then the paper by McIver (1967) at the World Petroleum Congress that formalized the role of kerogen in oil and gas production. (The word kerogen itself is from two Greek words, *keros* and *gen*, meaning oil or gas forming.) Kerogen by definition is the fraction of organic matter that is totally insoluble in all organic solvents and remains after all the minerals, including carbonates, silicates, and pyrites, have been removed. Kerogen generally represents the bulk of organic carbon present in a source rock, and it comprises the various macerals that can be related to the organic facies. So while the general concept of kerogen has been with us for many years and has not really changed, our understanding of the structure of kerogen has changed dramatically over time.

Following the recognition of kerogen and its role in the generation of oil and gas, there were many publications in the 1960s and 1970s that were related to developing a molecular structure for kerogen and suggesting that it was polymer, although no monomers were ever identified (Durand 1980), and it was finally realized there are no unique molecular structures for kerogen. It soon became apparent that a far more useful characteristic related to kerogen structure was based on the elemental composition of kerogen, in the same manner coal chemists had been characterizing coals based on the elemental composition (van Krevelen 1961). It should also be noted that coal petrographers had also been characterizing coals based on their petrographic composition for many years as documented in the classic book by Stach and the Teichmullers (1982), originally published in the 1960s. Tissot and Welte (1984) saw the similarities between coal characterization and kerogen characterization and introduced a kerogen classification scheme based on the H/C and O/C ratios in the same manner as the coal classification scheme developed years earlier by van Krevelen. Tissot and Welte (1984) proposed that kerogens could be divided in four basic types, namely, types I, II, III, and IV. Kerogens of type I, II, and III, respectively, were proposed to be derived from lacustrine, marine, and higher plant source materials and with the type IV kerogens being an inert form of kerogen, often dominated by inertinite. This was a rather simplistic way of characterizing the kerogens since rarely would you find a pure lacustrine or pure marine, for example. Following the development and commercial availability of the Rock Eval pyrolysis system, kerogens were characterized using the hydrogen index (HI) and oxygen index (OI) rather than the H/C and O/C ratios (Espitalie et al. 1977) as described in the "▶ Kerogen" entry in this volume.

Another significant and landmark breakthrough came when organic petrographers started to look at kerogens under the microscope and recognize that kerogens, just like coals, were made up of many different macerals or palynofacies and not one homogeneous type of organic material with a polymeric structure. Kerogen was actually a conglomerate of remnants of organic materials derived from a variety of sources including marine, lacustrine, and terrestrial sources, and again this combination of macerals gives rise to the different organic facies. The relative proportions of these macerals in the kerogen and their associated H/C and O/C ratios, or HI and OI values, would ultimately determine whether the kerogen was oil prone or gas prone.

At this point in the early 1980s, it was starting to be recognized that kerogens did not simply exist as the four well-defined types but in reality had a continuum of compositions ranging all the way from lacustrine to the inert form of kerogen, determined largely by source material and the depositional environment. For example, a lacustrine source rock may initially be thought of as a source rock dominated by algal source material. However, within a lacustrine environment, samples collected far offshore in the deeper part of the lake would indeed be predominantly algal, but closer inshore, the facies may also contain a significant input of higher plant material that may have been washed in from the shore or brought in by river transport. Although the near shore sample would be classified as lacustrine, it would have a significant

higher plant component and produce a different product than the sample collected from deeper in the center of the lake.

Organic Facies

The reason for this preceding introduction is to point out that with the significant effort that has been applied to developing these shale gas and shale oil deposits, it has become very clear that shales that were once thought of as homogeneous black shales are in most cases extremely heterogeneous with significant variations in organic matter type and content. This has led to an increased awareness of the concept of organic facies, a term formally introduced by Jones and Demaison in 1982, which did not see extensive use in the early years but has now evolved into a far more widely used concept. The classic definition of organic facies provided by them was: "An organic facies is a mappable subdivision of a designated stratigraphic unit, distinguished from the adjacent subdivisions on the basis of the character of its organic constituents, without regard to the inorganic aspects of the sediments." In the early reports, the geochemical data being utilized was limited to the bulk parameters, such as the Rock Eval data, but more recently, the biomarker data has become an important tool in characterizing the organic facies. Within a shale gas or shale oil prospect, there will be many distinguishable organic facies that will not be equally productive. Hence distinguishing and characterizing the various organic facies will be one very important piece of information that will be used to determine the target depth for any horizontal well that will be drilled to try and optimize production.

Variations in kerogen type within a shale reflect variation in the organic facies, and this is clearly illustrated in Fig. 1a, b which shows a set of samples of similar maturity, close to the onset of oil generation, from the Woodford shale from the Anadarko Basin, Oklahoma. The variations observed in this

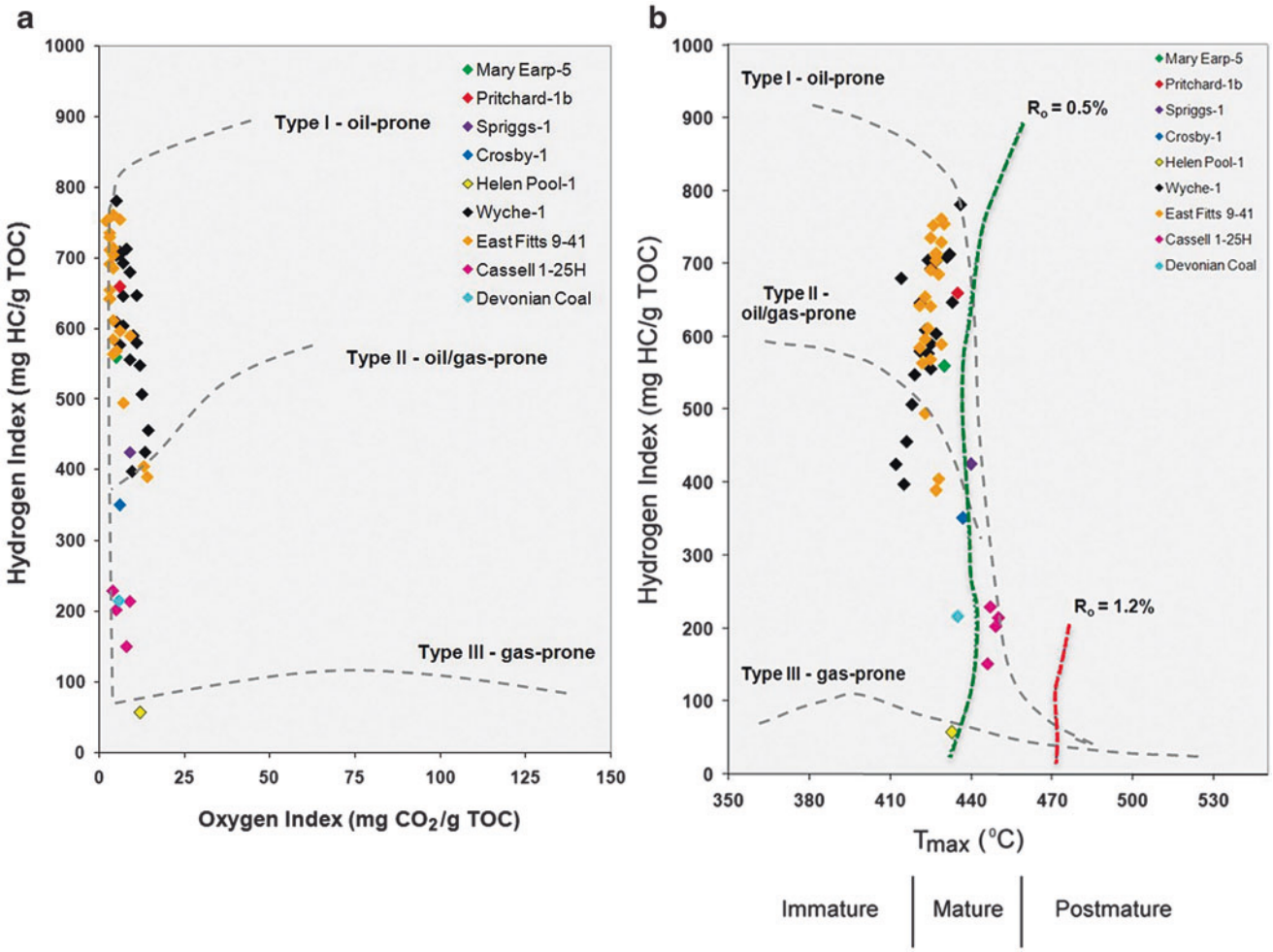

Organic Facies, Fig. 1 (**a**, **b**) Rock Eval data showing the variability in samples of the Woodford shale from a number of wells in the Anadarko Basin, Oklahoma. All the samples are just below the onset of oil generation, and hence the differences shown in these diagrams are a result of variations in the organic facies

diagram are not maturity related but reflect variations in the organic facies. This of course leads to the next question: why do we see such variations in the organic matter content and resulting organic facies?

The answer is relatively simple in general terms and can be related to the way in which organic-rich source rocks are formed. Source rocks contain a variety of organic matter derived from many different sources (i.e., plants, algae, fungi, bacteria, etc.) being deposited in a variety of depositional environments. Some of the organic matter gets preserved, some degraded. However as a result of a complex series of reactions related to changes in the depositional environment, changes in salinity of water, temperature, oxicity, and other factors, one particular depositional environment may see a significant variation in the nature of the mixture of organic matter that ultimately gets buried and preserved and generates oil or gas. Furthermore depending on the location of the sample within a specific depositional environment, there may be significant variations in the organic matter content of the source rock. Hence it became clear that kerogens should not be simply divided into these four major types since rarely would you find a "pure" lacustrine or "marine" kerogen. This leads Jones and Demaison to develop the organic facies concept so that rather than having four distinct types of kerogen, there is a continuum of kerogen types with the "pure" lacustrine and "pure" higher plant kerogens being the extremes with all the possible intermediate values in between.

The reason that such a concept is valid and important is that it is widely accepted that different types of source material will generate different types of hydrocarbon products. Thus in very simplistic terms, it can be expected that marine phytoplankton will generate primarily oil, whereas higher plant material will generate gas. Therefore if one automatically assumes your source rock kerogen is a marine kerogen based on the region where it plots on the pseudo-van Krevelen diagram, you would assume it will always primarily produce oil. However a source that is comprised of a mixture of lacustrine and higher plant material can still plot in that same region and would produce a mixture of oil and gas. An understanding of the concept of organic facies would have prevented such an error in the interpretation.

In addition modeling studies designed to predict the quantities of oil and gas that may be generated from a particular source rock type require activation energies and frequency factors as two of the important input factors to the model. These parameters will vary depending on the type of organic matter in the source rock. So again as with the example above, simply assuming that your kerogen is a marine kerogen based on where it plots on the modified van Krevelen plot and ignoring the fact that it could be a mixture of higher plant and lacustrine material will lead to erroneous parameters being used in the model and hence incorrect output from the model. This is discussed in more detail below. Ideally for any model, the most reliable set of parameters will be custom derived for the specific facies under investigation rather than a set of generic parameters available in the literature.

In 1987, Jones published his paper entitled "Organic Facies," and this was probably the first detailed description of the concept in which he defined seven organic facies ranging from type A dominated by algal material with very high HI values (>850 mgs HC/g TOC) to type D reflecting a highly oxidized, reworked kerogen with little hydrocarbon potential. A summary of these types of organic facies is given in Table 1. Tyson (1995) subsequently suggested that these facies could be associated into three groups based on the paleo-oxygenation and redox conditions in the basin in the following manner: types A, AB, B, and BC were deposited under anoxic-dysoxic conditions; types C and CD were deposited under proximal fluvio-deltaic to prodeltaic-oxic shelf conditions, and then type D was deposited under oxic distal conditions. Tyson (1995) also proposed that in addition to the paleo-oxygenation and redox conditions in the basin, other major paleoenvironmental controls included the relative proximity of the depositional site to active siliciclastic sediment and terrestrial OM sources and climatic controls on the preservation, production, and export of terrestrial OM. Table 2 shows a more comprehensive version of the description of organic facies incorporating both the descriptions of Jones (1987) and then the additional information from Tyson (1995).

Organic Facies, Table 1 A summary of the organic facies as defined by Jones (1987)

Organic facies	H/C at 0.5% R_0	Pyrolysis yield		Dominant organic matter
		HI	OI	
A	>1.45	>850	10–30	Algal; amorphous
AB	1.35–1.45	650–850	20–50	Amorphous; minor terrestrial
B	1.15–1.35	400–600	30–80	Amorphous; common terrestrial
BC	0.95–1.15	250–400	40–80	Mixed; some oxidation
C	0.75–0.95	125–250	50–150	Terrestrial; some oxidation
CD	0.60–0.75	50–125	40–150+	Oxidized; reworked
D	<0.6	<50	20–200+	Highly oxidized; reworked

Organic Facies, Table 2 A combination of geochemical data and palynofacies characteristics that can be used to characteristic organic facies. While this table does not indicate nature of products that could be expected from different facies under appropriate maturity conditions, the general trend would be from oil prone to gas prone moving from type A to types CD and D, although type D would probably be nonproductive (Data from Jones (1987), Tyson (1995, 1996). Table reproduced from Filho et al. 2012)

Organic facies	A	AB	B	BC	C	CD	D
Palynofacies characteristics							
% "AOM" of kerogen	Dominant			Mod	Usually low/absent		
"AOM" matrix fluorescence	Highest		Mod-weak		Weak	Usually absent	
% prasinophytes of plankton	Highest	Mod	Rare	Usually very rare			
% phytoclasts of kerogen	Low (dilution)			Mod	Usually dominant		
Opaque: translucent phytoclasts	Often high			Usually low		Increases	
Geochemical characteristics (for immature sediments)							
Hydrogen index	≥850	≥650	≥400	≥250	≥125	50–125	≤50
Kerogen type	I	I/II	II	II/III	III	III/IV	IV
TOC%	5–20+	3–10+		3–3+	≤3	<0.5	
Environmental factors							
Proximal-distal trend	Distal			Proximal		Distal	
Oxygen regime	Anoxic	Anoxic-dysoxic			Oxic		V. Oxic
Sediment accumulation rate	Low	Varies		High		Mod	Low
Organic facies	**A**	**AB**	**B**	**BC**	**C**	**CD**	**D**

Following the work of Jones (1987) and Tyson (1995), Pepper and Corvi (1995) discussed problems associated with accurately defining the kinetic parameters necessary to model the thermal degradation of kerogen resulting from the widespread variability in the composition of the kerogen. In order to simplify their approach, they adopted a relatively simple kerogen kinetic classification scheme based on the organic facies concept and a classification scheme developed by Barwise in the early 1980s but gave no reference for his scheme citing proprietary reasons. Unlike the Jones scheme, they only defined six types of organic facies A–F with some slight differences in their definitions compared to those defined by Jones. Organic facies A–C are dominated by aquatic algal and bacterial derived lipids, with early diagenetic processes determining the ultimate chemistry of marine algal/bacterial soluble organic matter (SOM) in siliciclastic-poor (A) and siliciclastic-rich (B) sediments. Organic facies C lipids are derived from freshwater algae that experienced sulfate – free diagenesis in nonmarine lacustrine basins. Organic facies D–F are all from nonmarine environments with an input of terrigenous organic matter and bacteria. Relative to organic facies F, organic facies D/E has a higher proportion of higher plant/bacterially derived material relative to lignin. However it is still important to recognize that although there are differences in the different schemes for defining the different facies, there are many similarities between them, with the most oil prone being algal rich, and then with increasing terrigenous input and possible oxidation, the facies become oil and gas prone and then gas prone and then inert.

Organic Facies and Sequence Stratigraphy

The concept of sequence stratigraphy is well suited for identifying the environments of deposition and temporal/spatial stratigraphic occurrence of organic facies. The papers by Jones (1987) and Pepper and Cervi (1995) did not make any significant attempts to integrate the organic facies concept with sequence stratigraphic models that have been developed for many years and are now an integral part of interpreting the sedimentary record and predicting organic-rich potential source rocks. It is well established over geologic time that the oceans have risen and fallen in a cyclical manner. A relative sea level cycle consists of (i) a falling and turnaround stage in which lowstand systems tract (LST) strata are deposited, (ii) a relatively rapid rise in sea level in which transgressive tract systems strata are deposited, and (iii) highstand or regressive systems tract strata deposited when sea level rise slows down relative to that responsible for the transgressive systems tract strata. So during LST with falling sea level, the shelf is exposed and eroded leading to a sequence boundary. However at the same time this is transporting land plant material from onshore during the erosion process leading to a facies that will contain both marine and terrestrial higher plant material. But as the sea level turns around and starts to rise, the input of both terrestrial source organic material and also eroded sedimentary material will decrease relative to the LST. The condensed section forms during the TST formation, and this is generally the most organic-rich section and has the greatest potential for source rock formation. During the HST formation, sea level is still

rising, but there is enough sediment being transported to fill any accommodation space on the shelf resulting in the shoreline moving seaward. So when considering that organic facies are differentiated on the basis of their organic matter content and nature of depositional environment, both of which are driven by sea level change, the importance of integrating organic facies with changes in the sequence stratigraphic strata, also driven by sea level changes, should be obvious. Taken together organic facies and sequence stratigraphy can greatly improve the ability to recognize productive source rock units and map these on a basin-wide scale. It has been well documented that there are repetitive lithofacies variations that can be recognized within a sequence stratigraphic framework resulting from the sea level changes and accompanying erosion of sediments and associated deposition in the marine environment. Further integration of organic facies with lithofacies variations into a sequence stratigraphic framework should provide an even better understanding of the temporal and lateral variations of organic-rich shales and ultimately their source potential.

Pepper and Cervi (1995) did provide a limited integration of their organic facies into a sequence stratigraphic framework by indicating that one of the major advantages of using organic facies lies in its potential to link global kinetic parameters to broad sedimentary facies. From a regional seismic survey, a simple paleographical map can be constructed and a rudimentary understanding of the gross depositional environment established with the systems tract strata from which the potential source rock facies could be forecast in the following manner:

Organic facies A – deposited in a transgressive to maximum flooding system on a carbonate platform, lagoon, and intra-shelf topographic depression

Organic facies B – transgressive to maximum flooding system on clastic depositional margin

Organic facies C – relative lake high stands with major lacustrine depositional system

Organic facies D/E – developed either behind shoreline of transgressive systems tractor during aggradation of the top sets in response to the highstand system

Organic facies F – essentially belonging to same systems tract as organic facies D/E but generally distinguished on basis of interpreted age, climate/paleoaltitude, or position relative to seismically defined shoreline

Organic Facies Variations in the Woodford Shale, Anadarko Basin, Oklahoma

In Fig. 1 the heterogeneity of the Woodford shale resulting from variations in the organic facies in different wells was illustrated. In order to further illustrate that variability, Fig. 2 shows data from a single core taken through the Woodford

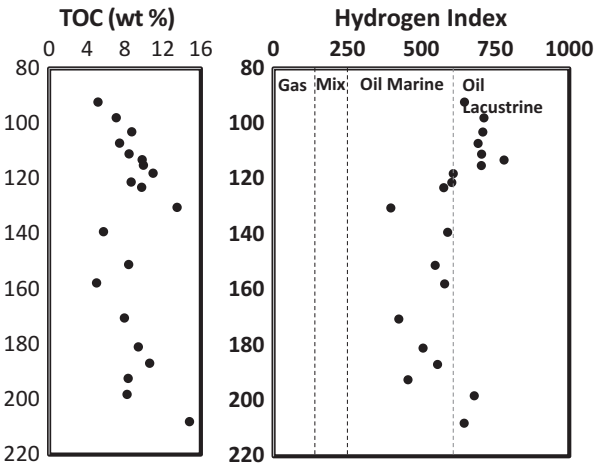

Organic Facies, Fig. 2 Variability in the Woodford shale from a single well as illustrated by variations in the TOC and HI values reflecting variations in the organic facies

shale and illustrates variations observed in two bulk parameters (TOC and HI values). For many years ago, the Woodford shale was thought of as a marine shale of Devonian age. Subsequently it was divided into three distinct facies, the Upper, Middle, and Lower Woodford on the basis of fossil evidence, but under the classic kerogen definition, all of these samples would have been classified as type II kerogens. More recent work has shown organic facies variations within each of the Upper, Middle, and Lower formations due to variations in conditions of the depositional environment, which in turn influenced the type of organisms growing in the water column and input of higher plant material with the changing conditions. It has been shown that over time changing sea level had a significant impact on circulation patterns within the Anadarko Basin leading to restricted circulation during the deposition of the Middle Woodford and development of euxinic conditions. Moving from the Middle Woodford into the Upper Woodford, the basin became less restricted, euxinic conditions were less apparent, and different organisms thrived. This leads to variations in the TOC values within the overall formation and influenced the petroleum potential of different facies within the shale. The important issue here is to illustrate how misleading it is to simply characterize the Woodford as a marine shale and not take into consideration changes in sea level and environmental conditions leading to variability in organic matter content and therefore variations in the potential to produce hydrocarbons for the different facies.

Summary

With the evolution of shale oil and shale gas prospects along with the associated horizontal drilling and hydraulic

fracturing, characterization of organic facies and their association with lithofacies have become an extremely important exploration and production tool. Identification and characterization of organic facies provides valuable information on richness and potential of the source rock. Furthermore when integrated into a sequence stratigraphic framework, along with information on the lithofacies, a comprehensive evaluation on the distribution and production potential of a specific organic facies within a petroleum system can be determined. This is turn provides a more realistic evaluation of potential production from a petroleum system compared to that obtained by simply evaluating a source rock as a kerogen type.

Cross-References

- ▶ Coal
- ▶ Hydrocarbons
- ▶ Kerogen
- ▶ Natural Gas
- ▶ Oil Shale
- ▶ Organic Geochemistry
- ▶ Organic Matter Degradation and Preservation
- ▶ Organics: Sources and Depositional Environments
- ▶ Petroleum
- ▶ Programmed Temperature Pyrolysis

References

Combaz A (1964) Les palynofacies. Rev Micropaleontol 7:205–218

Durand B (1980) Sedimentary organic matter and kerogen. Definition and quantitative importance of kerogen. In: Durand B (ed) Kerogen, insoluble organic matter from sedimentary rocks. Editions Technip, Paris, pp 13–34

Espitalie J, La Porte J, Madec M, Marquis F, Le Plat P, Boutefeu A (1977) Methode rapide de caracterisation des roches meres de leur potential petrolier et de leur degre d'evolution. Rev l'Inst Francais Petrole 32:23–42

Filho JGM, Menezes TR, Mendonca J de Oliverira AD da Silva TF, Rondon NF, da Silva FS (2012) Organic facies: Palynofacies and organic geochemistry approaches. In: Panagiotaras D (ed) Geochemistry-earth's system processes. ISBN:978–953–51-0586-2. http://www.intechopen.com/books/geochemistry-earth-s-system-processes/organic-facies-palynofacies-and-organic-geochemistry-approaches

Forsman JP, Hunt JM (1958) Insoluble organic matter (kerogen) in sedimentary rocks. Geochim Cosmochim Acta 15:170–182

Jones RW (1987) Organic facies. In: Brooks J, Welte D (eds) Advances in petroleum geochemistry, vol 2. Academic, London, pp 1–90

Jones RW, Demaison GJ (1982) Organic Facies-stratigraphic concepts and exploration tool. In: Saldivar-Sali A (ed) Proceedings of the second ASCOPE conference and exhibition. ASEAN Council on Petroleum, Manilla, pp 51–68

McIver RD (1967) Composition of kerogen-Clue to its role in the origin of petroleum. In: Proceedings of the 7th world petroleum congress, Mexico City, vol 2, pp 26–36

Pepper AS, Corvi PJ (1995) Simple kinetic models of petroleum formation. Part I. Oil and gas generation from kerogen. Mar Pet Geol 12(3):291–319

Rogers MA (1980) Application of organic facies concepts to hydrocarbon source rocks evaluation. In: Proceedings of the 10th world petroleum congress, Houston, vol 2, pp 31–42

Stach E, Mackowsky M-T, Teichmuller M, Taylor GH, Chandra D, Teichmuller R (1982) Stach's textbook of coal petrology, 3rd edn. Bebruder Borntraeger, Berlin

Tissot B, Welte DH (1984) Petroleum formation and occurrence, 2nd edn. Springer-Verlag, Heidelberg

Tyson RV (1995) Sedimentary organic matter. Organic facies and palynofacies. Chapman and Hall, London, 615pp

Tyson RV (1996) Sequence-stratigraphical interpretation of organic facies variations in marine siliciclastic systems: General principles and application to the onshore Kimmeridge Clay Formation, UK. In: Hesselbo SP, Parkinson DN (eds.) Sequence Stratigraphy in British Geology. Geol Soc Spec Publ 103:75–96

van Krevelen DW (1961) Coal-typology-chemistry-physics-constitution. Elsevier Science, Amsterdam

Organic Geochemistry

John K. Volkman
Oceans and Atmosphere Flagship, CSIRO,
Hobart, TAS, Australia

Definition

Organic geochemistry is the study of the origins and fates of organic matter and its constituents in the geosphere (including sediments, soils, rocks, coal, and petroleum), aquatic environments, and atmosphere. It is particularly focused on the interactions of the C cycle with those of other major elements such as major nutrients (N and P), other elements, and trace metals and how these have changed over geological time.

Introduction

Organic geochemistry encompasses studies of the origins and fates of organic matter in sediments, soils, coals, oils, gases, atmosphere, and marine and lacustrine water bodies (Johns 1986; Fleet et al. 1988; Engel and Macko 1993; Killops and Killops 1993; Rullkötter 2003; Volkman 2006). It is a relatively new field of endeavor which traces its origins to the identification by Treibs in 1934 of alkyl metalloporphyrins in crude oils that could be related to the structure of chlorophyll. This landmark research provided the first convincing evidence for the biological origin of some of the constituents of petroleum. Since then the field has expanded greatly and has become considerably more interdisciplinary as it seeks answers to how organic matter is produced, transported, recycled, transformed, and preserved in modern and ancient environments.

Organic geochemistry can be classified into a number of general themes such as: production and fate of organic matter in aquatic ecosystems; chemical and isotopic composition of biologically produced organic matter; transfer of lipids and other biochemicals in aquatic food webs; the effect of environmental conditions on the preservation and degradation of organic matter in modern sediments; processes and reactions leading to the formation of humic and fulvic material, coals, and kerogen; environmental chemistry tracing the source, transport, and fate of organic pollutants; isotope geochemistry; chemical oceanography; organic matter in meteorites and moon rocks; molecular archaeology; assessment of changes to paleoenvironments and climate over geological periods; generation and composition of petroleum and natural gas; catagenesis and destruction of organic matter at high maturities. The field is not limited to studies of lipids and hydrocarbons, but it encompasses studies of amino acids, porphyrins, chlorophylls, carotenoids, sugars, proteins, carbohydrates, and anthropogenic compounds. Scientists in the field also freely borrow knowledge and techniques from the disciplines of chemistry, geology, microbiology, biology, paleontology, ecology, physics, statistics, limnology, and oceanography. This wide knowledge base contributes greatly to the fascination of the subject and its many applications.

Analytical Techniques

Modern organic geochemistry often requires access to highly sophisticated analytical equipment to study the low abundances and complex mixtures of compounds present in geological materials. Capillary gas chromatography (GC) linked to a flame ionization detector (FID) or other detectors is widely used for the analysis of C_1–C_{60} compounds. The most common combination is capillary GC linked to a mass spectrometer (GC–MS) which enables compounds to be identified from their characteristic mass spectra (Philp 1985; Peters et al. 2005). Mass spectrometers include quadrupole, ion trap, magnetic sector, and time of flight. High sensitivity is combined with the requirement to separate small amounts of a compound present in complex mixtures. Recent advances in instrumentation such as the development of a capillary gas chromatograph linked via a combustion tube to an isotope ratio mass spectrometer (GC–irm–MS or CSIA which stands for compound-specific isotope analysis) now permits the $^{13}C/^{12}C$ ratio ($\delta^{13}C$ value) and $^{2}H/^{1}H$ ($\delta^{2}H$ or δD) ratio of individual compounds to be determined. For δD measurements, compounds separated by GC are converted to H_2 through a pyrolysis furnace (typically 0.5 mm i.d. × 34 cm long and operated at ca. 1450 °C). δD values are compared with a reference gas with a known δD value injected via the interface to the MS. CSIA of nitrogenous compounds using GC–irm-MS traditionally includes two separate conversion processes: the oxidation of nitrogenous compounds to N_2 and NOX and the reduction of the NOX to N_2. Recently, Kamata and Chikaraishi (2014) reported an improved system that combines these two processes into one unit by introducing a high-temperature combustion reactor and demonstrated its utility for measuring $\delta^{15}N$ in amino acids.

High performance liquid chromatography (HPLC) is the method of choice for separating and identifying more polar compounds such as carotenoids and chlorophylls, polar lipids including phospholipids, glycolipids and triacylglycerols, glycerol dialkyl glycerol tetraethers (GDGTs) and branched GDGTs (Schouten et al. 2013), bacteriohopanepolyols (BHPs; Talbot et al. 2003), or for high molecular weight compounds.

Pyrolysis, either on-line or off-line, open or closed, is often used to break down the organic matter into smaller components which can then be analyzed by GC–MS and HPLC. Pyrolysis can provide information about the amount, type, and thermal maturity of the organic matter. Off-line (batch) pyrolysis in sealed vessels (e.g., MSSVpy) at specific temperatures, often carried out in gold tubes, has the advantage that products can be isolated for further separation and identification of components. Curie-point or flash pyrolysis at high temperatures (typically 610 °C or 650 °C) produces complex distributions of alkenes and alkanes as well as more polar lipids. In the case of ancient organic-rich sediments, these are often dominated by *n*-alkene/*n*-alkane pairs from breakdown of algal biopolymers (algaenans – see later).

Hydropyrolysis (Hy-Py or Hypy; Berwick et al. 2010) involves the pyrolysis of kerogen, shales, sediments, or biological material at high hydrogen pressures (10 MP) in the presence of a dispersed sulfided molybdenum catalyst. This can convert a high percentage of the kerogen (ca. 30%) into GC-amenable components that were previously covalently bound to the kerogen. Stepwise pyrolysis involves pyrolysis of a kerogen sample initially at a low temperature (typically ca. 300 °C) and the residue is then pyrolyzed again at an increased temperature and the process repeated until further products are no longer obtained. The products are typically swept directly into the GC injector and analyzed by GC–MS. This has the advantage that compounds are released according to their bond strength and so each pyrogram is different and may be enriched in diagnostic biomarkers that might be minor components of a single total flash pyrolysis (e.g., Zhang et al. 2016; Zhang and Volkman 2017).

^{1}H and ^{13}C nuclear magnetic resonance (NMR) and Fourier transform infrared (FT-IR) spectrometers are also used to provide structural information on the organic matter in kerogen, coals, or sediments. NMR is particularly useful for the identification of novel organic compounds, although this usually requires isolation of the compound from complex mixtures. FT-IR has been used in a diversity of applications ranging from identifying the geometry of double bonds in

alkenones to studying the structure of coal and investigating clay-mineral interactions. Electron paramagnetic resonance (EPR) of semiquinone radicals has been used to characterize the humification stages of organic matter and to define different soil fingerprints in speleothems.

Compound-specific radiocarbon (^{14}C) analysis (CSRA) provides information on the $\Delta^{14}C$ values of individual compounds that can be used to identify multiple sources of carbon within an individual sample. Initially, preparative capillary GC or HPLC was used to isolate individual compounds by fraction collection prior to graphitization and CSRA. This procedure is time consuming and careful attention is needed to minimize the introduction of extraneous carbon. Precise ^{14}C measurements are possible on samples of individual compounds provided that they contain at least 20 μg of carbon. More recently, gas ion sources developed for ^{14}C accelerator mass spectrometry (AMS) have been modified and improved to accept CO_2 directly from a GC with pyrolysis interface allowing analytical instrumentation to be directly interfaced to an AMS (Roberts et al. 2013).

The Biomarker Concept

A central concept common to many studies in organic geochemistry is the use of biomarkers (also termed biological markers, chemical fossils (Eglinton and Calvin 1967), and signature lipids) to infer likely sources of organic matter (e.g., Johns 1986; Bianchi and Canuel 2011; Volkman and Smittenberg 2016; Derrien et al. 2017). These organic compounds have a distinct chemical structure which can either exist as such in a particular organism or be related by known microbial or chemical transformation pathways to compounds synthesized by specific groups of organisms. Biomarkers are available for most of the groups of organisms that contribute organic matter to sediments. Many new lipids have been discovered in plants, algae, and bacteria by organic geochemists during the course of organic geochemistry studies. In some cases, the compounds were first identified in sediments and only later was it possible to identify a source organism and even today the sources of some compounds are still unknown (so-called orphan lipids).

The role of genetic changes is crucial to our understanding of how different life forms have evolved over time. DNA sequencing studies can show which organisms possess specific biochemical pathways and are providing a better conceptual basis for understanding why particular biomarkers occur in different organisms. This new information will help establish timelines for the first appearance of a variety of age-diagnostic biomarkers (e.g., Sinninghe Damsté et al. 2004; Briggs and Summons 2014; Volkman 2014 and references therein). In the same way that physical fossils have underpinned our understanding of the evolution of life, organic geochemists use biomarkers to understand the evolution of life's biosynthetic pathways over geological time and thus fulfill the promise inherent in the use of the term "chemical fossil." For example, sterol biosynthesis is an oxygen-intensive process so the presence of complex steranes derived from sterols deposited in ancient rocks not only signals the presence of eukaryotes but also aerobic metabolic processes (Gold et al. 2017). Advances in molecular biology are increasingly being applied to organic geochemical studies of recent sediments to allow identification of organisms present in the depositional environment and to study the processes involved in cycling of major elements such as C and N in different environmental settings (e.g., Coolen et al. 2004, 2008).

Biomarkers for Vascular Plants

Many biomarkers have been described for higher plants, and thus the identification of terrestrial organic matter in sediments is relatively straightforward even when the organic material is transported far from land. Plant wax lipids and lignin phenols are the two most common classes of molecular markers used in these studies, often supplemented with compound-specific isotope data. General markers include long-chain (C_{20}–C_{30}) *n*-alkanes showing strong odd/even predominance and long-chain alcohols and fatty acids showing strong even/odd predominance. Such compounds in atmospheric particles and sediments have been used to estimate the relative contributions of C3 vs. C4 type plants in the source area (e.g., Diefendorf et al. 2011). The major sterol in most plants is 24-ethylcholesterol (sitosterol), with lesser amounts of another C_{29} sterol 24-ethylcholesta-5,22E-dien-3β-ol (stigmasterol) and the C_{28} sterol 24-methylcholest-5-en-3β-ol (campesterol). C_{29} sterols often dominate the sterol distributions in lacustrine sediments, and the predominance of C_{29} steranes in a crude oil is often taken to indicate a high level of plant lipid contribution to the original source rocks (e.g., Peters et al. 2005). Vascular plants contain a variety of diterpenoid and triterpenoid lipids, the latter dominated by oleanane, ursane, and lupane skeletons (e.g., Koch et al. 2011). Other more-specific biomarkers include betulin for birch plants and resin acids for conifers. The latter give rise to a variety of degradation products including the aromatic hydrocarbon retene, which has been used to map changes in plant communities in the ancient past (e.g., Saito et al. 2013).

Biomarkers for Microalgae

Microalgae are major contributors of organic matter to sediments and fortunately they have a variety of distinctive biochemical pathways that give rise to distinctive biomarkers. For example, the polycyclic hydrocarbon dinosterane which occurs in some crude oils is derived from the C_{30} sterol dinosterol, which is common in a class of marine phytoplankton called dinoflagellates. The presence of dinosterane in oils

provides good evidence that some of the organic matter in the oil's source rock was derived from dinoflagellates. Other distinctive algal lipids include very long-chain (C_{37}–C_{40}) alkenones and alkenoates synthesized by certain haptophytes such as *Emiliania huxleyi*, *Gephyrocapsa* spp., *Isochrysis* spp., and *Chrysotila* spp. These compounds are now used routinely to reconstruct past surface ocean temperatures from the ratio of di- and tri-unsaturated alkenones in sediment cores (see later).

Chlorophyll *a* concentrations provide an indirect measure of total phytoplankton biomass in seawater, while the abundance of specific carotenoids can be used to characterize the community composition of marine phytoplankton in oceanic waters. For example, prasinoxanthin is found in certain green microalgae, 19′-hexanoyloxyfucoxanthin in haptophytes, and peridinin in dinoflagellates. Such studies have revealed the important role played by eukaryotic nanoplankton and picoplankton and the prokaryotic cyanobacteria and prochlorophytes in oligotrophic oceanic waters (Wright and Jeffrey 2005).

Microalgae contain abundant fatty acids, and these can show features specific to different algal groups. For example, green algae typically show a dominance of C_{18} polyunsaturated fatty acids (PUFA) whereas dinoflagellates can have high quantities of 22:6n-3, and diatoms contain abundant 20:4n-6 and 20:5n-3. Some dinoflagellates contain unique C_{28} PUFA (Volkman et al. 1998). The nomenclature used here is number of carbon atoms:number of double bonds where (n-x) specifies the position of the double bond closest to the end methyl group. Since PUFA are rapidly degraded in seawater and sediments, their presence can often be used as an indication of organic matter associated with living cells.

Certain sterols can also provide evidence for contributions to the organic matter in recent sediments or seawater from microalgae. C_{28} sterols such as 24-methylcholesta-5,22E-dien-3β-ol and 24-methylenecholesterol are common in diatoms but are not unique to these microalgae. Other interesting sterols in diatoms include those with C-23 side-chain methylation, 4-methyl sterols more usually associated with dinoflagellates, the C_{30} sterol gorgosterol more commonly associated with corals, but now known to be produced by some diatoms, and sterols with Δ^7-unsaturation found in some green algae (e.g., Giner and Wikfors 2011 and references therein). Indeed, as more data have been acquired, it is clear that a great variety of sterol distributions can be found in microalgae including sterols more often associated with other organisms (Volkman et al. 1998). For example, marine eustigmatophytes contain abundant cholesterol more usually associated with animals, while freshwater eustigmatophytes contain 24-ethylcholesterol usually associated with plants.

Another class of unusual biomarkers are C_{25} and C_{30} highly branched isoprenoid (HBI) alkenes which occur in many recent and ancient sediments. A diatom origin was established by the identification of C_{25} HBIs in cultures of *Haslea osteraria* and C_{30} HBIs in *Rhizosolenia setigera* by Volkman et al. (1994). Since then other diatom sources have been identified and a number of applications have emerged including the use of HBI alkenes as indicators of sea-ice extent (Massé et al. 2011; Pieńkowski et al. 2017) and as food-web tracers (Goutte et al. 2013). HBI alkene distributions have also been instrumental in establishing the concept of age diagnostic biomarkers which recognizes that some compounds appear in the sediment record at a defined point in time (e.g., Moldowan 2000). HBI alkanes have not been found in oils or sediments older than 92 Ma (Sinninghe Damsté et al. 2004) which implies that this biosynthetic pathway for HBI alkenes evolved around that time. This concept has proven to be a powerful tool in assessing the age of petroleum samples and for examining the correspondence between the fossil and biomarker record (e.g., Taylor et al. 2006; Briggs and Summons 2014).

Another interesting class of algal lipid is the C_{30} and C_{32} *n*-alkyl diols synthesized by eustigmatophytes (Volkman et al. 1992) and some diatoms (Rampen et al. 2014 and references therein). These compounds have the interesting feature that the dominant isomers in eustigmatophytes are the alkyl-1,15-diols, but in diatoms the alkyl-1,14-diols predominate. These compounds are now used to infer paleotemperatures and upwelling conditions (see later).

Biomarkers for Bacteria

Specific branched and/or unsaturated fatty acids can be used to determine the biomass of different bacterial groups in sediments and seawater. *Iso*- and *anteiso*-branched C_{15} and C_{17} fatty acids and *cis*-vaccenic acid (18:1n-7) are found in many bacteria, whereas 10-methylhexadecanoic acid and *iso*-17:1 are more commonly associated with sulfate-reducing bacteria. The abundance of these acids in the phospholipid fraction isolated from sediments can be used as a measure of the microbial biomass present.

The most common triterpenoid class in sediments are the hopanoids, where they can be found with a variety of functional groups including alkenes, ketones, acids, and alcohols. In most cases these are diagenetic products of C_{35} bacteriohopanepolyols (BHPs; Talbot et al. 2003), although direct inputs of C_{30} hopanoids such as diplopterol and diploptene from bacteria and cyanobacteria are also possible. Intact BHPs can also be found in recent sediments and have shown to be useful tracers for terrestrial soil-derived organic matter in estuaries and coastal environments.

Derivatives of 2-methylhopanoids are prominent biomarkers in modern and ancient sediments and have been used as proxies for cyanobacteria and, by extension, for dating the first appearance of oxygenic photosynthesis. However, substantial evidence from cultures and genomic studies now indicates that some organisms other than cyanobacteria

can make 2-methylhopanoids. Studies have shown that hpnP, the gene encoding the C-2 hopanoid methylase, is found in diverse modern environments but cyanobacterial hpnP genes are rarer and tend to be localized to specific habitats. Ricci et al. (2014) found that hpnP occurrence is significantly correlated with environments known to support plant–microbe interactions and in microbial communities including stromatolites, hot springs, and hypersaline microbial mats. 2-Methylhopanoids are enriched in sessile microbial communities inhabiting environments low in oxygen and fixed nitrogen with high osmolarity.

Biomarkers for Archaea

The domain Archaea includes a variety of fascinating microorganisms including the so-called extremophiles such as methanogens, thermophiles, and halophiles. The discovery of mesophilic archaea showed that not all species within the Archaea are extremophiles and we now know that archaea are widely distributed in nature including the open ocean. Two major clades (named initially simply Group I and Group II) are known and these were classified as members of the Crenarchaeota and Euryarchaeota, respectively. Group I archaea have been reclassified as a separate phylum called Thaumarchaeota and are geochemically interesting since they may be the most ancient archaea and are among the most abundant organisms in the ocean (see Pearson and Ingalls 2013).

Archaea predominantly contain lipids based on isoprenoid biochemistry (Volkman and Maxwell 1986). Methanogens contain a number of distinctive biomarker hydrocarbons including the C_{25} isoprenoid alkane 2,6,10,15,19-pentamethylicosane which is found in modern to Cretaceous marine sediments (Brassell et al. 1981). Other archaeal lipids include 3,7,11,15,18,22,26,30-octamethyldotriacontane found in petroleum and as a degradation product from Messel oil shale kerogen, squalane which is found in some crude oils and 2,6,10,14,18-pentamethylicosane which occurs in halophilic bacteria.

Biphytanyl (C_{40}) isoprenoid hydrocarbon chains from archaeal lipids were first discovered in sedimentary systems more than 30 years ago and since then it has become clear that their source must be environmentally widespread. These chains occur in compounds known as glycerol dialkyl glycerol tetraethers (GDGTs), which is short for *sn*-2,3-di-*O*-biphytanyldiglycerol tetraethers. The core structures are most often abbreviated as GDGT-0, GDGT-1, GDGT-2, GDGT-3, and GDGT-4, with the numerals 0–4 denoting the number of internal cyclopentane rings. The GDGT containing a cyclohexane group is called crenarchaeol and is abbreviated as "cren" or GDGT-5. A related compound that has a longer chromatographic retention time is referred to as the crenarchaeol regioisomer. GDGTs occur as part of intact polar lipids (IPLs) such as phospholipids and glycolipids. These compounds are quite stable in sediments and have been developed into a number of paleoproxies (see later).

Organic Geochemistry of Modern Environments

Biomarker and isotope studies can be used to classify the sources of the organic matter in seawater or sediments into general classes such as vascular plants, microalgae, bacteria, archaea, and secondary consumers (Meyers and Ishiwatari 1993; Volkman 2006; Bianchi and Canuel 2011) as described above. In a few cases, specific biomarkers can even be related to particular species. Since some organisms are restricted to particular environments, the presence of diagnostic biomarkers can be used to infer the environmental conditions which prevailed when the sediment was deposited.

Just as paleontologists use morphological fossils as stratigraphic tools, organic geochemists use "chemical fossils" to define an analogous "molecular stratigraphy." The concept that "the present is the key to the past" has been a driving force for numerous studies of organic compounds in modern aquatic environments. These have provided insights into the sources of organic matter and how it is degraded and transported within each type of ecosystem. For example, the presence of an oxic–anoxic boundary in the water column of bodies such as the Black Sea is recorded in the sediments by the preservation of biomarkers derived from the bacteriochlorophylls and carotenoids of obligate phototrophic green sulfur bacteria present in the water column. Regions of high productivity such as the Black Sea as well as the upwelling areas off Peru and Namibia have been a major focus of organic geochemical studies since these provide recent models for the formation of ancient organic-rich black shales (oil shales and sapropels) which can be excellent petroleum source rocks.

Bulk radiocarbon (^{14}C) measurements have been widely used to constrain the sources, sinks, and processing of sedimentary organic carbon (e.g., Smittenberg et al. 2004). Griffith et al. (2010) constructed a box model that predicts $^{14}C_{TOC}$ in the sediment mixed layer. Their model allows three distinct organic carbon pools to be defined ("degradable," "semi-labile," and "refractory"). This approach has demonstrated the presence of pre-aged organic carbon in surface sediments including soil-derived terrestrial organic carbon, reworked marine organic carbon, and/or anthropogenic carbon. Through the use of compound-specific $\Delta^{14}C$ measurements, Eglinton et al. (1997) were able to show that in the Black Sea there was considerable isotopic heterogeneity in the *n*-alkanes indicating both fossil and contemporary sources. Compounds reflecting different source inputs to the Arabian Sea exhibit a range of 10,000 years in conventional ^{14}C ages. The great advantage of radiocarbon measurements of biomarkers is that sediment chronologies can be constructed independent of detrital organic carbon influences.

Early Stage Diagenesis

Although only a small quantity of the organic matter produced in the water column reaches the sediment due to a range of degradation reactions, the amount of organic carbon in the lithosphere (estimated at 2×10^{16} tonnes) is vastly greatly than that found in the oceans (1×10^{12} tonnes). Once the organic matter is deposited, it is further transformed by bacterial and chemical processes leading to breakdown and transformation of the organic compounds present. Despite decades of research, our understanding of the mechanisms by which organic matter is stabilized and sequestered in aquatic sediments remains far from complete. It is now thought that the intrinsic reactivity of the organic matter supplied to soils and sediments is less important than its distribution in the sedimentary matrix and association with mineral matter such as iron (Eglinton 2012). This controls its accessibility to the organisms that degrade it into simple organic compounds, and ultimately to CO_2.

A difficulty in the use of biomarkers for paleoenvironmental reconstructions is the effect of degradation, both in the water column and sediment, on the distribution of compounds. Nierop et al. (2017) have shown that early diagenetic alteration of organic matter depends largely on the degree of bottom water oxygenation rather than subsequent anaerobic degradation within the sediments, even at longer timescales. Lipids show a wide range of susceptibilities to degradation, but some compounds such as sterols and alkenones are sufficiently resistant that they can be used for reconstructions of depositional conditions that prevailed millions of years ago. Chlorophylls are degraded in marine and lacustrine sediments, mostly to colorless products although some macrocycles survive as porphyrin derivatives. Photodegradative processes can play a significant role in the degradation of lipids and chlorophylls in the water column and even in surface sediments in the case of shallow waters (e.g., Rontani et al. 2012). Cuny et al. (2002) have proposed a "Chlorophyll Phytyl side chain Photodegradation Index," which is the molar ratio of phytyldiol (3-methylidene-3,7,11-trimethylhexadecan-1,2-diol) to phytol, as a measure of the mean amount of chlorophyll photodegraded within the marine euphotic zone.

Carotenoids degrade very rapidly and thus are rarely useful as source indicators in older sediments unless deposited under anoxic conditions. Their degradation rates vary widely and are not simply a function of their high degree of unsaturation. Fucoxanthin and related pigments break down to loliolide, isololiolide, and dihydroactinioliolide (via unstable bicyclic furanoxides) which, however, can be detected in sediments (Repeta 1989).

Polyunsaturated acids (PUFA) are rapidly removed so that their presence in a sediment is usually indicative of living biomass. Similarly, fatty acids present in phospholipids can be used as a measure of microbial biomass. Sterols are more resistant to biodegradation, but they too can be transformed to saturated sterols (stanols), steroidal ketones (including ster-4-en-3-ones), and stanones and unsaturated hydrocarbons (sterenes). Although early research suggested that alkenones might be very resistant to biodegradation, it is now clear that they can be degraded to some extent by bacterial and chemical processes (Rontani et al. 2013). Long-chain *n*-alkanols appear to be relatively stable in soils whereas fatty acids are rapidly turned over.

Lignin from terrestrial plants is considered to be less reactive in soils and oxic sediments than other plant biochemicals such as cellulose, cutin, and free lipids, although substantial degradation can still occur (e.g., Opsahl and Benner 1995). In aerobic soils, white- and brown-rot fungi play a major role in lignin degradation. Once lignin reaches the marine environment, degradation by bacteria or photooxidation becomes important. Lignin is thought to be generally refractory under anaerobic conditions.

Under anoxic conditions, especially when Fe contents are low, sulfur can be naturally incorporated into organic matter leading to the formation of organic sulfur compounds (OSC). This usually proceeds with sulfur attachment to the carbon atom originally substituted with a functional group such as double bond or carbonyl group. The inorganic sulfur species may be either hydrogen sulfide, polysulfides, or elemental sulfur as shown by compound-specific S-isotope studies (Werne et al. 2008). This reaction is geochemically important since it leads to selective preservation of lipid skeletons which otherwise would be quite labile and readily degraded in sediments. It also provides a link between the carbon and sulfur cycles in sedimentary environments.

A recurring theme has been the importance of photic zone euxinia (PZE) in the preservation of organic carbon leading to organic-rich oil shales and exceptional fossil preservation (e.g., Melendez et al. 2013). PZE has been associated with oceanic anoxic events and mass extinction. Under these conditions, the bottom water anoxic layer extends into the photic zone giving rise to layers of anoxygenic phototrophic sulfur bacteria having distinctive biomarkers based on chlorobactane, isorenieratane, and their likely degradation products (C_{15} to C_{31} 2,3,6-aryl isoprenoids) (e.g., Slowakiewicz et al. 2015).

Geosynthesis of organic material can also occur during early diagenesis. For example, macromolecules (also referred to as geopolymers or protokerogen) can be formed by condensation and polymerization reactions involving humic acids, fulvic acids, and humins. With continuing burial, the organic matter is further transformed to become the insoluble organic matter called kerogen. This occurs at relatively low temperatures less than 50 °C and was initially thought to be the main process explaining high contents of organic matter in ancient sediments (e.g., Tissot and Welte 1984). However, it

is now well established that preservation of resistant biopolymers produced by some plants and algae is also a major factor in explaining high contents of organic matter in ancient sediments such as oil shales (Tegelaar et al. 1989; Zhang et al. 2016). These biopolymers are called cutan and suberan in plants and algaenans in microalgae. Note that not all algae produce these polymers (they occur in green algae, eustigmatophytes, and dinoflagellates; Gelin et al. 1999) and a variety of structures, mostly ether-linked, have been described. When subjected to high temperature, these preserved biopolymers can produce abundant aliphatic hydrocarbons having a wide carbon number range typical of that found in petroleum. Isolation of algaenans from microalgae for structural elucidation involves a complex and tedious chemical purification, but a quick indication for the presence of algaenan can be provided by pyrolysis which yields a series of *n*-alkene/*n*-alkane pairs (e.g., Zhang et al. 2016; Zhang and Volkman 2017).

Stable Isotope Geochemistry

Stable isotope ratios are used to deduce origins of organic matter. Much of this work has focused on $^{13}C/^{12}C$ ratios, although this approach is now being extended to nitrogen, sulfur, oxygen, and hydrogen isotopes. The $^{13}C/^{12}C$ ratio in organic compounds reflects the isotopic composition of the original CO_2 or bicarbonate ions plus the combination of thermodynamic and kinetic isotope fractionations occurring during assimilation and metabolism. The range of isotope ratios found varies from one group of organisms to another. Thus, plants which use the C3 pathway have $\delta^{13}C$ values of −23‰ to −34‰, whereas those using the C4 pathway are isotopically enriched and typically range from −6‰ to −23‰.

The isotope ratio of the bulk organic matter in sediments is an average of all the sources present and can be used as a signature of autotrophic carbon fixation. An example of this style of work is that of Vonk et al. (2010) who combined elemental, molecular, and isotopic ($\delta^{13}C$ and $\Delta^{14}C$) analyses to study the sources, degradation, and transport of permafrost-derived soil organic matter from the Kolyma River to the East Siberian Sea. Using a three end-member dual-carbon isotopic mixing model, these authors were able to demonstrate a strong contribution of organic matter from coastal erosion (51 ± 11% to 60 ± 12%) to waters up to 500 km seawards from the coast.

The development of CSIA has revealed remarkable differences in isotope values and confirmed the diversity of sources giving rise to the distributions of hydrocarbons in ancient sediments and crude oils. Measurements of the $^{13}C/^{12}C$ ratio in alkenones in ancient sediments have also enabled calculations to be made of $pCO_2(aq)$ of the oceanic waters present when the sediments were deposited (e.g., Jasper et al. 1994; Benthien et al. 2005).

Another area where $\delta^{13}C$ measurements of individual compounds is providing insights into carbon cycles is the identification of isotopically depleted bacterial lipids typical of methane-oxidizing bacteria (methanotrophs). Such values are often associated with organic-rich oil shales and sediments in which there are oxygen-deficient bottom waters and an active methane cycle. For example, Volkman et al. (2015) found depleted carbon isotope values (−43.7‰ to −50.8‰) in bacterially derived C_{29} and C_{30} neohop-13(18)-enes and hop-17(21)-enes in the Eocene Huadian oil shale in China.

Larsen et al. (2015) have shown that the $\delta^{13}C$ patterns of amino acids accurately record biological sources across widely varying oceanographic conditions. Based on the four most informative amino acids for distinguishing between diatom and bacterial sources (i.e., isoleucine, lysine, leucine, and tyrosine), these authors determined that in sediments from the Peru upwelling, bacterially derived amino acids ranged from 10% to 15% in the sediment layers from the last 5000 years, and up to 35% during the last glacial period. The $\delta^{15}N$ values of amino acids have also proven to be good tracers of food-web relationships and trophic level (Steffan et al. 2013).

Measurements of δD in individual compounds is now becoming more routine although suitable instrumentation is only found in specialist geochemical laboratories. Most attention has focused on *n*-alkanes as recorders of the aqueous environment in which the plant grew. δD ratios of sedimentary biomarkers are now used as paleohydrological proxies over a range of geological timescales although a number of caveats that affect the isotopic fractionation observed between hydrogen in environmental water and hydrogen in lipids need to be considered (e.g., Guenther et al. 2013). The δD of alkenones has also been used as a paleosalinity indicator (see later).

Atmospheric Chemistry

The techniques of organic geochemistry have been widely applied to study the source and fate of atmospheric aerosols and particulate matter (Simoneit 1999). Much of this work has focused on specific volatile pollutants such as polycyclic aromatic hydrocarbons (PAHs), petroleum-derived hydrocarbons, and halogenated compounds such as polychlorinated biphenyls (PCBs). For example, retene and dehydroabietic acid have been utilized as tracers for conifer smoke in urban aerosols. Degradation products from biopolymers (e.g., levoglucosan from cellulose) are also excellent tracers. Geochemists have also studied the transport of plant wax components such as *n*-alkanes, *n*-alkanols, and alkyl esters thousands of kilometers out to sea (e.g., Saliot 2009).

Molecular Archaeology

Another growing application of organic geochemistry is to the field of archaeology, particularly in the characterization of preserved organic materials in pottery. Some applications have included the confirmation that asphalt from the Dead Sea was used in the mummification process from at least 2600 BCE. This finding relied on showing that sterane distributions in modern asphalts and the black material in mummies were identical, and distinct from local oil seeps. Food remains in pottery vessels have been identified from characteristic distributions of fatty acids, sterols, and wax esters thus provide important data on food preferences in ancient civilizations. Wood tar pitches are also amenable to detailed chemical examination and it has been shown that they were in widespread use from the Mesolithic period up to the Middle Ages. Quantities of archaeological material as small as 10–100 mg can be characterized using these GC–MS techniques when combined with new extraction techniques (Correa-Ascencio and Evershed 2014). Genetic fingerprinting techniques are also widely being used although contamination with modern materials still presents considerable analytical problems.

Paleoenvironmental Assessment

Organic geochemistry continues to provide important information about how environments have changed on Earth over time from the biomarker and isotope signatures preserved in ancient sediments. A major focus has been on identifying the biotic and environmental changes associated with major extinction events (e.g., Saito et al. 2014) and for reconstructing paleorecords of past temperature and CO_2 levels.

Proxies for Paleotemperature Changes

Organic geochemists have played a major role in devising a number of lipid proxies to study changes in Earth's climate over geological time (see Wakeham 1993; Eglinton and Eglinton 2008 for reviews). Alkenones provided the first biomarker proxy for climate change and these are now widely used to estimate paleotemperatures (e.g., Volkman 2000; Eglinton and Eglinton 2008) for sea surface temperature (SST) following the discovery that the ratio of di- to tri-unsaturated compounds in haptophytes changes systematically with temperature. The proposal for a new paleotemperature index, $\boldsymbol{U^K_{37}}$, by Brassell et al. (1986), opened up a new field of research in which the concentrations of biomarker compounds could be used for quantitative estimation of the SST prevailing when the sediments were deposited. The $\boldsymbol{U^K_{37}}$ index was later simplified to $U^{K'}_{37}$ by Prahl and Wakeham (1987), since the 37:4 methyl alkenone is only abundant in sediments from colder regions and in some lakes.

$$\boldsymbol{U^K_{37}} = ([37:2] - [37:4])/([37:2] + [37:3] + [37:4])$$
$$U^{K'}_{37} = [37:2]/([37:2] + [37:3]).$$

where the alkenones are designated by (number of carbon atoms):(number of double bonds).

Organic-based proxies have inherent uncertainties due to ecological biases, and indeed studies have shown that $U^{K'}_{37}$ values can be affected to a small extent by biological and abiological processes (e.g., Volkman 2000; Rontani et al. 2013). Nonetheless, $U^{K'}_{37}$ has now been used in numerous paleotemperature studies resulting in hundreds of publications. Various calibrations with temperature have been proposed and there is some evidence for a regional bias (Sikes and Volkman 1993), but the calibration of Müller et al. (1998) is widely applicable.

$$U^{K'}_{37} = 0.033\ \mathrm{T} + 0.069.$$

Note that the alkenone distributions in lacustrine and coastal haptophytes are very different from those found in open marine species and so very different temperature calibrations apply in such cases and these appear to be less robust.

Another paleotemperature proxy is the TEX_{86} proxy which is based on the polar, relatively high molecular weight GDGT tetraether lipids from pelagic archaea (Schouten et al. 2003; Kim et al. 2008).

$TEX_{86} = [III + IV + V'] / [II + III + IV + V']$ where the roman numerals refer to specific GDGT isomers.

There are now many studies using TEX_{86}. For example, Jenkyns et al. (2004) used TEX_{86} to infer an average sea surface temperature of ca 15 °C for the Arctic Ocean about 70 million years ago. This implied an equator-to-pole gradient in SST of ca. 15 °C during this interval and, by extrapolation, suggested that polar waters were generally warmer than 20 °C during the middle Cretaceous (ca. 90 Ma).

The MBT-CBT proxy for the reconstruction of paleotemperatures and past soil pH is based on the distribution of branched glycerol dialkyl glycerol tetraether (brGDGT) membrane lipids. MBT stands for "Methylation of Branched Tetraethers" and CBT stands for "Cyclization of Branched Tetraethers."

$$\mathrm{CBT} = -\log((\mathrm{Ia} + \mathrm{IIb}) / (\mathrm{Ia} + \mathrm{IIa}))$$

$$\mathrm{MBT} = (\mathrm{Ia} + \mathrm{Ib} + \mathrm{Ic}) / (\mathrm{Ia} + \mathrm{Ib} + \mathrm{Ic} + \mathrm{IIa} + \mathrm{IIb} + \mathrm{IIc} + \mathrm{IIIa} + \mathrm{IIIb} + \mathrm{IIIc})$$

Where the compounds listed are specific branched GDGTs.

Peterse et al. (2012) extended the soil dataset on which these proxies were based to 278 globally distributed surface soils of which 26% contained all nine brGDGTs. They presented new transfer functions for the reconstruction of pH based on the CBT index:

$\mathrm{pH} = 7.90 - 1.97 \times \mathrm{CBT}$ ($r^2 = 0.70$; RMSE = 0.8; n = 176), as well as for mean annual temperature (MAT) based on the CBT index and methylation index using the seven most abundant GDGTs (defined as MBT′):

MAT = 0.81 − 5.67 × CBT + 31.0 × MBT′ (r^2 = 0.59; RMSE = 5.0 °C; n = 176). An example is the work of Schoon et al. (2015) who used TEX_{86} to infer SSTs across the Palaeocene-Eocene Thermal Maximum (PETM; ca. 56 Ma) were relatively low before the event, but increased by ca. 7 °C afterwards. At another section (Fur), a remarkably similar temperature record was obtained for MAT using the MBT′-CBT proxy.

LDI (long chain diol index) is a new index based on C_{28} and C_{30} long chain 1,13- and 1,15-alkyl diols synthesized by marine phytoplankton presumed to be eustigmatophytes (Rampen et al. 2012). It is defined as:

$LDI = FC_{30–1,15} / (FC_{28–1,13} + FC_{30–1,13} + FC_{30–1,15})$ where F is the fractional abundance. From a large dataset, Rampen et al. (2012) established a relationship between LDI and sea surface temperature (SST):

LDI = 0.033 × SST + 0.095; R^2 = 0.969, n = 162) over a temperature range of −3 to 27 °C. It is now apparent that extensive oxic degradation can affect the LDI values and thus affect the inferred temperature (Rodrigo-Gamiz et al. 2016). Another complication is the possibility that in nearshore areas there may be large inputs of riverine-derived C_{32} diols (Lattaud et al. 2017).

Studies of cultures of the diatoms of the genus *Proboscia* have shown a strong effect of temperature on the degree of saturation and the chain length distribution of long chain 1,14-alkyl diols quantified as the diol saturation index (DSI) and diol chain length index (DCI), respectively (Rampen et al. 2014). Based on the global spread of alkyl diol abundances, Rampen et al. (2014) have proposed the use of 1,14-diols versus 1,13-diols [C_{28} + C_{30} 1,14-diols]/[(C_{28} + C_{30} 1,13-diols) + (C_{28} + C_{30} 1,14-diols)] as an indicator for high nutrient or upwelling conditions, although this may not be true in all regions.

Some studies have used all three paleotemperature proxies to assess changes in environmental conditions. For example, Plancq et al. (2015) compared three proxies ($U^{K'}_{37}$, TEX_{86}, and LDI) and were able to show that sapropels deposited between 3.1 and 2.8 Ma in the Mediterranean likely reflected better preservation of organic matter, induced by the development of a strong thermohaline stratification of the water column and to oxygen-depleted bottom waters. The second series of sapropels, deposited between 2.7 and 2.6 Ma, was more likely the result of enhanced primary productivity in a weakly stratified water column. Becker et al. (2015) not only compared results from these same three proxies but developed a method for determining all three in a single normal phase high performance LC–atmospheric pressure chemical ionization mass spectrometry (NP-HPLC–APCI-MS) analysis. Reconstructed SST values differed considerably between the proxies for the Last Glacial Maximum (LGM) and the period of sapropel S1 formation at ca. 10 kyr BP, but trends during the late Holocene were similar. Part of the discrepancy was attributed to changes in the composition of alkenone-producing microalgae and partly to habitat change due to changes in nutrient availability.

An important goal in paleoceanography is to reconstruct past ocean salinity. This is usually done using oxygen isotope values of planktonic foraminifera combined with SST reconstructions. However, this approach relies on multiple proxies resulting in potentially large uncertainty. Schouten et al. (2006) showed that salinity and growth rate, but not temperature, affected the δD values of alkenones in *E. huxleyi* and *G. oceanica* in culture. Kasper et al. (2015) therefore tested whether the hydrogen isotope composition of C_{37} alkenones might be used to assess salinity changes in the eastern South African continental shelf in the Mozambique Channel. No clear changes were observed in the δD-alkenone record throughout the 39,000 years of the core record despite known changes in global seawater δD related to glacial–interglacial ice volume effects. This was attributed to a high soil OM input during the glacial period and low input during the Holocene as deduced from BIT index values. The authors suggested that a more pronounced influence of freshwater at the core location during the glacial period resulted in alkenones depleted in D during that time. The correlation between the BIT index and δD of alkenones during the glacial period suggests that increased continental runoff potentially changed the growth conditions of the alkenone-producing haptophytes, promoting coastal haptophyte species with generally more enriched δD-alkenone values.

Petroleum Geochemistry

One of the main commercial applications of organic geochemistry has been to the field of petroleum exploration (Hunt 1979; Tissot and Welte 1984; Brooks and Fleet 1987; Orr and White 1990; Moldowan et al. 1992). These techniques have also proven valuable for studying the origins of gases, coals, oil shales, peats, and lignites. Crude oils are produced when organic-rich rocks are heated to temperatures sufficiently high to crack C–C bonds (so-called oil window). The hydrocarbons produced then migrate to a suitable reservoir rock and will accumulate there provided that a good seal is present. Shale oil occurs when the hydrocarbons are still locked into the rock and can only be produced commercially by fracturing the rock (so-called fracking).

Characteristic distributions of biomarkers (Peters and Moldowan 1993; Peters et al. 2005) have been used to correlate crude oils in reservoirs with their source rocks (e.g., Volkman 1988; see ▶ Hydrocarbons entry). Such information enables the petroleum scientist to identify petroleum migration paths, estimate the oil prospectivity of a field, and suggest

further sites for drilling. Changes in biomarker isomer ratios can be used to infer the extent of thermal maturation and hence whether a potential source rock lies within the "oil window." The presence of specific biomarkers can often be used to deduce the type of environmental setting when the source rock sediments were deposited. Many oils are the result of multiple accumulations, some of which may be biodegraded and water washed.

The formation of petroleum depends on a number of factors including the type and amount of organic matter in the source rocks, the thermal maturity of the organic matter, and the presence of suitable migration pathways, traps, and seals. The type of organic matter, which is usually expressed in terms of maceral composition, can be determined by optical or physicochemical means. Hydrogen-rich macerals such as alginite are considered to be a much better source of petroleum (i.e., they are oil-prone), than inertinite or vitrinite. The reflectance of vitrinite macerals (measured as vitrinite reflectance in units of %Ro) is often used as a measure of thermal maturity; the main phase of oil generation usually occurs in the range 0.65–1.3%Ro.

A commercial instrument called the Rock-Eval is now widely used to characterize source rock samples. In this system, the finely ground source rock is heated in an inert atmosphere under various temperature conditions to yield free hydrocarbons (the S_1 peak) plus hydrocarbons liberated by pyrolysis of the kerogen (the S_2 peak). The amounts of hydrocarbons that can be liberated from the rock (the genetic potential) is simply S_1 plus S_2 expressed as a proportion of the mass of rock. Thermal maturity can be estimated from the temperature at which the maximum in the S_2 response occurs (T_{max}), although this does show some variations between kerogen types.

Basin modeling is now widely used to reconstruct the history of oil and gas generation in a particular region (Welte et al. 1997). In this process, geochemical information about the factors that affect petroleum formation such as source rock quality and migration is integrated with geological information on depositional history, subsidence rates, erosion and tectonic events, and geothermal gradients to provide a conceptual framework showing how the basin evolved. Numerical simulations are then carried out to investigate whether all the factors necessary for oil generation and accumulation can be found in the basin, and at what geological time, thus substantially minimizing the exploration risk.

Many oils are biodegraded in the reservoir, causing characteristic changes in hydrocarbon composition. The first hydrocarbons to be removed are those with simple structures such as the *n*-alkanes and methyl-branched compounds. Isoprenoids and bicyclic alkanes are more resistant and so they are degraded at lower rates. Steranes and diasteranes are remarkably resistant to biodegradation and so they are often used to correlate oils even those with compositions that have been greatly modified by microbial action. Eventually, even steranes can be biodegraded and the first isomers to be removed are those still possessing the original "biological" 20R stereochemistry. Similar techniques are often applied in environmental studies to identify sources of spilled crude oil or to study the pathways by which the oil is degraded in the environment. A notable example was the use of the abundance of the C_{30} hopane as an internal marker for assessing the rate at which oil derived from the *Exxon Valdez* oil spill in Alaska was degraded in sediments (Bence et al. 1996).

The zone of maximum hydrocarbon production is usually referred to as the catagenic zone. At later stages, gaseous hydrocarbons such as methane tend to dominate the hydrocarbons produced and at even higher burial temperatures exceeding 150 °C, the metagenesis stage is reached where the kerogen is converted to a carbon residue.

Organic Matter in Space

Organic geochemical techniques have not been restricted to samples from Earth but have also been used to characterize organic matter in meteorites (Clemett et al. 1993; McKay et al. 1996) and to look for chemical evidence of past life on the moon and Mars. A plethora of papers have appeared since the 1970s on the amino acids found in meteorites (e.g., Shock and Schulte 1990), and a number of hypotheses have been advanced to explain their extraterrestrial formation. These have included Miller-Urey synthesis, Fischer-Tropsch synthesis, photochemical ion-molecule reactions, and aqueous alteration of preexisting condensed phases. More recent work has identified other compound classes such as hydroxy fatty acids, dicarboxylic acids, and polycyclic aromatic hydrocarbons. Complex aromatic molecules have also been identified in interplanetary dust particles. In 1996, NASA scientists put forward evidence that life may have been detected on Mars based on analysis of a Martian meteorite found in Antarctica (McKay et al. 1996), although this was later disputed. This evidence included the presence of polycyclic aromatic hydrocarbons and the occurrence of putative bacteria-like fossils in carbonate globules containing magnetite and Fe-sulfide mineral phases which the scientists conjectured could be explained by biogenic processes.

Summary and Future Prospects

Modern organic geochemistry is a multifaceted, multidisciplinary science which has found applications in a diversity of topics in Earth science and environmental science. In petroleum research, biomarkers have become standard tools for the petroleum industry and new parameters continue to be developed particularly to characterize high maturity or mixed

and biodegraded oils. The area of paleoenvironment assessment has driven many new developments including new biomarker proxies thus greatly increasing our understanding about how Earth's environment has changed over geological time. Organic geochemists have been at the forefront of technological analytical developments and this will undoubtedly continue with an increasing emphasis on measurement technologies that are more sensitive and have better resolution (e.g., 2D gas chromatography: GC × GC) and by extension to a variety of isotopes not just those of carbon and hydrogen.

Cross-References

- ▶ Analytical Techniques
- ▶ Archeological Geochemistry
- ▶ Biomarker: Assessment of Thermal Maturity
- ▶ Biomarkers: Coal
- ▶ Biomarkers: Petroleum
- ▶ Biopolymers and Macromolecules
- ▶ Carbon Cycle
- ▶ Carbon Isotopes
- ▶ Coal
- ▶ Compound-Specific Isotope Analysis
- ▶ Diagenesis
- ▶ Earth's Atmosphere
- ▶ Gas Chromatography–Mass Spectrometry (GC–MS)
- ▶ Hydrocarbons
- ▶ Kerogen
- ▶ Lipids (Bacteria and Archaea)
- ▶ Nitrogen Cycle
- ▶ Nuclear Magnetic Resonance
- ▶ Oil Shale
- ▶ Paleoenvironments
- ▶ Petroleum
- ▶ Phosphorus
- ▶ Porphyrins
- ▶ Programmed Temperature Pyrolysis
- ▶ Soils

References

Becker KW, Lipp JS, Versteegh GJM, Woermer L, Hinrichs K-U (2015) Rapid and simultaneous analysis of three molecular sea surface temperature proxies and application to sediments from the sea of Marmara. Org Geochem 85:42–53

Bence AE, Kvenvolden KA, Kennicutt MCI (1996) Organic geochemistry applied to environmental assessments of Prince William sound, Alaska, after the Exxon Valdez oil spill–a review. Org Geochem 24:7–42

Benthien A, Andersen N, Schulte S, Müller PJ, Schneider RR, Wefer G (2005) The carbon isotopic record of the $C_{37:2}$ alkenone in the South Atlantic: last glacial maximum (LGM) vs. holocene. Palaeogeog Palaeoclimat Palaeoecol 221:123–140

Berwick LJ, Greenwood PF, Meredith W, Snape CE, Talbot HM (2010) Comparison of microscale sealed vessel pyrolysis (MSSVpy) and hydropyrolysis (Hypy) for the characterisation of extant and sedimentary organic matter. J Anal Appl Pyrol 87:108–116

Bianchi TS, Canuel EA (2011) Chemical biomarkers in aquatic ecosystems. Princeton University Press, Princeton

Brassell SC, Wardroper AMK, Thomson ID, Maxwell JR, Eglinton G (1981) Specific acyclic isoprenoids as biological markers of methanogenic bacteria in marine sediments. Nature 290:693–696

Brassell SC, Eglinton G, Marlowe IT, Pflaumann U, Sarnthein M (1986) Molecular stratigraphy: a new tool for climatic assessment. Nature 320:129–133

Briggs DEG, Summons RE (2014) Ancient biomolecules: their origins, fossilization, and role in revealing the history of life. BioEssays 36:482–490

Brooks J, Fleet AJ (eds) (1987) Marine petroleum source rocks. Blackwell Scientific, London

Clemett SJ, Maechling CR, Zare RN, Swan PD, Walker RM (1993) Identification of complex aromatic molecules in individual interplanetary dust particles. Science 262:721–725

Coolen MJL, Muyzer G, Rijpstra WIC, Schouten S, Volkman JK, Sinninghe Damsté JS (2004) Combined DNA and lipid analyses of sediments reveal changes in Holocene haptophyte and diatom populations in an Antarctic lake. Earth Planet Sci Letts 223:225–239

Coolen MJL, Talbot HM, Abbas B, Ward C, Schouten S, Volkman JK, Sinninghe Damsté JS (2008) Sources for sedimentary bacteriohopanepolyols as revealed by 16S rDNA stratigraphy. Environ Microbiol 10:1783–1803

Correa-Ascencio M, Evershed RP (2014) High throughput screening of organic residues in archaeological potsherds using direct acidified methanol extraction. Anal Methods 6:1330–1340

Cuny P, Marty JC, Chiaverini J, Vescovali I, Raphel D, Rontani J-F (2002) One-year seasonal survey of the chlorophyll photodegradation process in the northwestern Mediterranean Sea. Deep-Sea Res Part II–Top Stud Oceanog 49:1987–2005

Derrien M, Yang LY, Hur J (2017) Lipid biomarkers and spectroscopic indices for identifying organic matter sources in aquatic environments: a review. Water Res 112:58–71

Diefendorf AF, Freeman KH, Wing SL, Graham HV (2011) Production of *n*-alkyl lipids in living plants and implications for the geologic past. Geochim Cosmochim Acta 75:7472–7485

Eglinton TI (2012) Geochemistry – a rusty carbon sink. Nature 483:165–166

Eglinton G, Calvin M (1967) Chemical fossils. Sci Am 216:32–43

Eglinton TI, Eglinton G (2008) Molecular proxies for paleoclimatology. Earth Planet Sci Lett 275:1–16

Eglinton TI, Benitez-Nelson BC, Pearson A, McNichol AP, Bauer JE, Druffel ERM (1997) Variability in radiocarbon ages of individual organic compounds from marine sediments. Science 277:796–799

Engel MH, Macko SA (eds) (1993) Organic geochemistry: principles and applications. Plenum Press, New York

Fleet AJ, Kelts K, Talbot MR (eds) (1988) Lacustrine petroleum source rocks. Blackwell Scientific, Oxford

Gelin F, Volkman JK, Largeau C, Derenne S, Sinninghe Damsté JS, de Leeuw JW (1999) Distribution of aliphatic, nonhydrolyzable biopolymers in marine microalgae. Org Geochem 30:147–159

Giner J-L, Wikfors GH (2011) "Dinoflagellate sterols" in marine diatoms. Phytochemistry 72:1896–1901

Gold DA, Caron A, Fournier GP, Summons RE (2017) Paleoproterozoic sterol biosynthesis and the rise of oxygen. Nature 543:420–423

Goutte A, Cherel Y, Houssais M-N, Klein V, Ozouf-Costaz C, Raccurt M, Robineau C, Massé G (2013) Diatom-specific highly branched isoprenoids as biomarkers in Antarctic consumers. PLoS One 8(2):e56504

Griffith DR, Martin WR, Eglinton TI (2010) The radiocarbon age of organic carbon in marine surface sediments. Geochim Cosmochim Acta 74:6788–6800

Guenther F, Aichner B, Siegwolf R, BQ X, Yao TD, Gleixner G (2013) A synthesis of hydrogen isotope variability and its hydrological significance at the Qinghai-Tibetan Plateau. Quat Int 313:3–16

Hunt JM (1979) Petroleum geochemistry and geology. WH Freeman, San Francisco

Jasper JP, Hayes JM, Mix AC, Prahl FG (1994) Photosynthetic fractionation of ^{13}C and concentrations of dissolved CO_2 in the central equatorial Pacific during the last 255,000 years. Paleoceanography 9:781–798

Jenkyns HC, Forster A, Schouten S, Sinninghe Damsté JS (2004) High temperatures in the Late Cretaceous arctic ocean. Nature 432:888–892

Johns RB (ed) (1986) Biological markers in the sedimentary record. Elsevier, Amsterdam

Kamata K, Chikaraishi Y (2014) Stable nitrogen isotope analysis of amino acids by using gas chromatography/isotope ratio mass spectrometry (GC/IRMS) system with high-temperature combustion interface. Bunseki Kagaku 63:279–282

Kasper S, Van Der Meer MTJ, Castaneda IS, Tjallingii R, Brummer G-JA, Sinninghe Damsté JS, Schouten S (2015) Testing the alkenone D/H ratio as a paleo indicator of sea surface salinity in a coastal ocean margin (Mozambique Channel). Org Geochem 78:62–68

Killops SD, Killops VJ (1993) An introduction to organic geochemistry. Longman Scientific and Technical, New York

Kim J-H, Schouten S, Hopmans EC, Donner B, Sinninghe Damsté JS (2008) Global sediment core-top calibration of the TEX_{86} paleothermometer in the ocean. Geochim Cosmochim Acta 72:1154–1173

Koch BP, Souza Filho PWM, Behling H, Cohen MCL, Kattner G, Rullkötter J, Scholz-Böttcher B, Lara RJ (2011) Triterpenols in mangrove sediments as a proxy for organic matter derived from the red mangrove (*Rhizophora mangle*). Org Geochem 42:62–73

Larsen T, Bach LT, Salvatteci R, Wang YV, Andersen N, Ventura M, McCarthy MD (2015) Assessing the potential of amino acid ^{13}C patterns as a carbon source tracer in marine sediments: effects of algal growth conditions and sedimentary diagenesis. Biogeosciences 12:4979–4992

Lattaud J, Kim JH, De Jonge C, Zell C, Sinninghe Damsté JS, Schouten S (2017) The C_{32} alkane-1,15-diol as a tracer for riverine input in coastal seas. Geochim Cosmochim Acta 202:146–158

Massé G, Belt ST, Crosta X, Schmidt S, Snape I, Thomas DN, Rowland SJ (2011) Highly branched isoprenoids as proxies for variable sea ice conditions in the Southern Ocean. Antarctic Sci 23:487–498

McKay DS, Gibson EK Jr, Thomas-Keprta KL, Vali H, Romanek CS, Clemett SJ, Chillier XDF, Maechling CR, Zare RN (1996) Search for past life on mars: possible relic biogenic activity in Martian meteorite ALH84001. Science 273:924–930

Melendez I, Grice K, Trinajstic K, Ladjavardi M, Greenwood P, Thompson K (2013) Biomarkers reveal the role of photic zone euxinia in exceptional fossil preservation: an organic geochemical perspective. Geology 41:123–126

Meyers PA, Ishiwatari R (1993) Lacustrine organic geochemistry – an overview of indicators of organic matter sources and diagenesis in lake sediments. Org Geochem 20:867–900

Moldowan JM (2000) Trails of life. Chem Br 36(8):34–37

Moldowan JM, Albrecht P, Philp RP (eds) (1992) Biological markers in sediments and petroleum. Prentice Hall, Englewood Cliffs

Müller PJ, Kirst G, Ruhland G, von Storch I, Rosell-Melé A (1998) Calibration of the alkenone paleotemperature index $U^{K'}_{37}$ based on core-tops from the eastern South Atlantic and global ocean (60ºN–60ºS). Geochim Cosmochim Acta 62:1757–1772

Nierop KGJ, Reichart GJ, Veld H, Sinninghe Damsté JS (2017) The influence of oxygen exposure time on the composition of macromolecular organic matter as revealed by surface sediments on the Murray Ridge (Arabian Sea). Geochim Cosmochim Acta 206:40–56

Opsahl S, Benner R (1995) Early diagenesis of vascular plant tissues: lignin and cutin decomposition and biogeochemical implications. Geochim Cosmochim Acta 59:4889–4909

Orr WL, White CM (1990) Geochemistry of sulfur in fossil fuels, American Chemical society symposium series, 429. American Chemical Society, Washington

Pearson A, Ingalls AE (2013) Assessing the use of Archaeal lipids as marine environmental proxies. Ann Rev Earth Planet Sci 41:359–384

Peters KE, Moldowan JM (1993) The biomarker guide. Interpreting molecular fossils in petroleum and ancient sediments. Prentice Hall, Englewood Cliffs

Peters KE, Walters CC, Moldowan JM (2005) The biomarker guide, vols 1 and 2, 2nd edn. Cambridge University Press, Cambridge

Peterse F, Van Der Meer J, Schouten S, Weijers JWH, Fierer N, Jackson RB, Kim J-H, Sinninghe Damsté JS (2012) Revised calibration of the MBT-CBT paleotemperature proxy based on branched tetraether membrane lipids in surface soils. Geochim Cosmochim Acta 96:215–229

Philp RP (1985) Fossil fuel biomarkers. Elsevier, New York

Pieńkowski AJ, Gill NK, Furze MFA, Mugo SM, Marret F, Perreaux A (2017) Arctic sea-ice proxies: comparisons between biogeochemical and micropalaeontological reconstructions in a sediment archive from Arctic Canada. Holocene 27:665–682

Plancq J, Grossi V, Pittet B, Huguet C, Rosell-Melé A, Mattioli E (2015) Multi-proxy constraints on sapropel formation during the late Pliocene of central Mediterranean (southwest Sicily). Earth Planet Sci Letts 420:30–44

Prahl FG, Wakeham SG (1987) Calibration of unsaturation patterns in long-chain ketone compositions for palaeotemperature assessment. Nature 330:367–369

Rampen SW, Willmott V, Kim J-H, Uliana E, Mollenhauer G, Schefuss E, Sinninghe Damsté JS, Schouten S (2012) Long chain 1,13-and 1,15-diols as a potential proxy for palaeotemperature reconstruction. Geochim Cosmochim Acta 84:204–216

Rampen SW, Willmott V, Kim J-H, Rodrigo-Gamiz M, Uliana E, Mollenhauer G, Schefuss E, Sinninghe Damsté JS, Schouten S (2014) Evaluation of long chain 1,14-alkyl diols in marine sediments as indicators for upwelling and temperature. Org Geochem 76:39–47

Repeta DJ (1989) Carotenoid diagenesis in recent marine sediments: III. Degradation of fucoxanthin to loliolide. Geochim Cosmochim Acta 53:699–707

Ricci JN, Coleman ML, Welander PV, Sessions AL, Summons RE, Spear JR, Newman DK (2014) Diverse capacity for 2-methylhopanoid production correlates with a specific ecological niche. ISME J 8:675–684

Roberts ML, Von Reden KF, Burton JR, McIntyre CP, Beaupre SR (2013) A gas-accepting ion source for accelerator mass spectrometry: progress and applications. Nucl Inst Methods Phys Res Sect B 294:296–299

Rodrigo-Gamiz M, Rampen SW, Schouten S, Sinninghe Damsté JS (2016) The impact of oxic degradation on long chain alkyl diol distributions in Arabian Sea surface sediments. Org Geochem 100:1–9

Rontani J-F, Charriere B, Forest A, Heussner S, Vaultier F, Petit M, Delsaut N, Fortier L, Sempéré R (2012) Intense photooxidative degradation of planktonic and bacterial lipids in sinking particles collected with sediment traps across the Canadian Beaufort Shelf (Arctic Ocean). Biogeosciences 9:4787–4802

Rontani J-F, Volkman JK, Prahl FG, Wakeham SG (2013) Biotic and abiotic degradation of alkenones and implications for $U^{K'}_{37}$ paleoproxy applications: a review. Org Geochem 59:95–113

Rullkötter J (2003) Geochemistry, organic. In: Meyers RA (ed) Encyclopedia of physical science and technology, 3rd edn. Academic, London, pp 549–574

Saito R, Kaiho K, Oba M, Takahashi S, Chen Z-Q, Tong J (2013) A terrestrial vegetation turnover in the middle of the Early Triassic. Global Planet Change 105:152–159

Saito R, Oba M, Kaiho K, Schaeffer P, Adam P, Takahashi S, Nara FW, Chen Z-Q, Tong J, Tsuchiya N (2014) Extreme euxinia just prior to the Middle Triassic biotic recovery from the latest Permian mass extinction. Org Geochem 73:113–122

Saliot A (2009) Sources markers in aerosols, oceanic particles and sediments. In: Erca: from the human dimensions of global environmental change to the observation of the Earth from Space, vol 8, pp 189–197

Schoon PL, Heilmann-Clausen C, Schultz BOP, Sinninghe Damsté JS, Schouten S (2015) Warming and environmental changes in the eastern North Sea Basin during the Palaeocene-Eocene Thermal Maximum as revealed by biomarker lipids. Org Geochem 78:79–88

Schouten S, Hopmans EC, Forster A, van Breugel Y, Kuypers MMM, Sinninghe Damsté JS (2003) Extremely high sea-surface temperatures at low latitudes during the middle Cretaceous as revealed by archaeal membrane lipids. Geology 31:1069–1072

Schouten S, Ossebaar J, Schreiber K, Kienhuis MVM, Langer G, Benthien A, Bijma J (2006) The effect of temperature, salinity and growth rate on the stable hydrogen isotopic composition of long chain alkenones produced by *Emiliania huxleyi* and *Gephyrocapsa oceanica*. Biogeosciences 3:113–119

Schouten S, Hopmans EC, Sinninghe Damsté JS (2013) The organic geochemistry of glycerol dialkyl glycerol tetraether lipids: a review. Org Geochem 54:19–61

Shock EL, Schulte MD (1990) Summary and implications of reported amino acid concentrations in the Murchison meteorite. Geochim Cosmochim Acta 54:3159–3173

Sikes EL, Volkman JK (1993) Calibration of alkenone unsaturation ratios ($U^{K'}_{37}$) for paleotemperature estimation in cold polar waters. Geochim Cosmochim Acta 57:1883–1889

Simoneit BRT (1999) A review of biomarker compounds as source indicators and tracers for air pollution. Environ Sci Poll Res 6:159–169

Sinninghe Damsté JS, Muyzer G, Abbas B, Rampen SW, Massé G, Allard WG, Belt ST, Robert JM, Rowland SJ, Moldowan JM, Barbanti SM, Fago FJ, Denisevich P, Dahl J, Trindade LAF, Schouten S (2004) The rise of the rhizosolenid diatoms. Science 304:584–587

Slowakiewicz M, Tucker ME, Perri E, Pancost RD (2015) Nearshore euxinia in the photic zone of an ancient sea. Palaeogeog Palaeoclim Palaeoecol 426:242–259

Smittenberg RH, Hopmans EC, Schouten S, Hayes JM, Eglinton TI, Sinninghe Damsté JS (2004) Compound-specific radiocarbon dating of the varved Holocene sedimentary record of Saanich Inlet, Canada. Paleoceanography 19:1–16

Steffan SA, Chikaraishi Y, Horton DR, Ohkouchi N, Singleton ME, Miliczky E, Hogg DB, Jones VP (2013) Trophic hierarchies illuminated via amino acid isotopic analysis. Plos One 8. https://doi.org/10.1371/journal.pone.0076152

Talbot HM, Squier AH, Keely BJ, Farrimond P (2003) Atmospheric pressure chemical ionisation reversed-phase liquid chromatography/ion trap mass spectrometry of intact bacteriohopanepolyols. Rapid Comm Mass Spectrom 17:728–737

Taylor DW, Li HQ, Dahl J, Fago FJ, Zinniker D, Moldowan JM (2006) Biogeochemical evidence for the presence of the angiosperm molecular fossil oleanane in Paleozoic and Mesozoic non-angiospermous fossils. Paleobiology 32:179–190

Tegelaar EW, de Leeuw JW, Derenne S, Largeau C (1989) A reappraisal of kerogen formation. Geochim Cosmochim Acta 53:3103–3106

Tissot BP, Welte DH (1984) Petroleum formation and occurrence. Springer, Berlin

Volkman JK (1988) Biological marker compounds as indicators of the depositional environments of petroleum source rocks. In: Fleet AJ, Kelts K, Talbot MR (eds) Lacustrine petroleum source rocks, Geological Society special publication no. 40. Geological Society, London, pp 103–122

Volkman JK (2000) Ecological and environmental factors affecting alkenone distributions in seawater and sediments. Geochem Geophys Geosyst 1, Paper number 2000GC000061

Volkman JK (ed) (2006) Marine organic matter: biomarkers, isotopes and DNA, The handbook of environmental chemistry, volume 2, part N. Springer, Berlin/Heidelberg

Volkman JK (2014) Acyclic isoprenoid biomarkers and evolution of biosynthetic pathways in green algae of the genus *Botryococcus*. Org Geochem 75:36–47

Volkman JK, Maxwell JR (1986) Acyclic isoprenoids as biological markers. In: Johns RB (ed) Biological markers in the sedimentary record. Elsevier, Amsterdam, pp 1–42

Volkman JK, Smittenberg RH (2016) Lipid biomarker proxies for paleoenvironmental reconstruction of estuarine environments. In: Weckström K, Gell P, Saunders K, Skilbeck G (eds) Applications of paleoenvironmental techniques to estuarine systems, Developments in paleoenvironmental research, vol. 20. Springer, Berlin/Heidelberg/New York, pp 173–212

Volkman JK, Barrett SM, Dunstan GA, Jeffrey SW (1992) C_{30}–C_{32} alkyl diols and unsaturated alcohols in microalgae of the class Eustigmatophyceae. Org Geochem 18:131–138

Volkman JK, Barrett SM, Dunstan GA (1994) C_{25} and C_{30} highly branched isoprenoid alkenes in laboratory cultures of two marine diatoms. Org Geochem 21:407–413

Volkman JK, Barrett SM, Blackburn SI, Mansour MP, Sikes EL, Gelin F (1998) Microalgal biomarkers: a review of recent research developments. Org Geochem 29:1163–1179

Volkman JK, Zhang ZR, Xie XM, Qin JZ, Borjigin T (2015) Biomarker evidence for *Botryococcus* and a methane cycle in the Eocene Huadian oil shale, NE China. Org Geochem 78:121–134

Vonk JE, Sanchez-Garcia L, Semiletov I, Dudarev O, Eglinton T, Andersson A, Gustafsson Ö (2010) Molecular and radiocarbon constraints on sources and degradation of terrestrial organic carbon along the Kolyma paleoriver transect, east Siberian Sea. Biogeosciences 7:3153–3166

Wakeham SG (1993) Reconstructing past oceanic temperatures from marine organic biogeochemistry, chemical fossils and molecular stratigraphy. Environ Sci Technol 27:29–33

Welte DH, Horsfield B, Baker DH (eds) (1997) Petroleum and basin evolution. Springer, Heidelberg

Werne JP, Lyons TW, Hollander DJ, Schouten S, Hopmans EC, Sinninghe Damsté JS (2008) Investigating pathways of diagenetic organic matter sulfurization using compound-specific sulfur isotope analysis. Geochim Cosmochim Acta 72:3489–3502

Wright SW, Jeffrey SW (2005) Pigment markers for phytoplankton production. In: Volkman JK (ed) Marine organic matter: biomarkers, isotopes and DNA, The handbook of environmental chemistry. volume 2 Reactions and processes. Part N. Springer, Berlin, pp 71–104

Zhang ZR, Volkman JK (2017) Algaenan structure in the microalga *Nannochloropsis oculata* characterized from stepwise pyrolysis. Org Geochem 104:1–7

Zhang ZR, Volkman JK, Xie XM, Snowdon LR (2016) Algaenan-derived mid-chain ketones from step-wise pyrolysis of the Huadian oil shale, NE China. Org Geochem 91:89–99

Organic Matter Degradation and Preservation

Sandra Arndt[1] and Douglas Edward LaRowe[2]
[1]BGeosys, Department Geoscience, Environment and Society (DGES), Université Libre de Bruxelles, Bruxelles, Belgium
[2]Department of Earth Sciences, University of Southern California, Los Angeles, CA, USA

Definition

Organic matter degradation is the disintegration of mainly photosynthetically produced organic matter by microorganisms. It proceeds via multiple enzymatic reactions involving different microorganisms and oxidants as well as a number of intermediate compounds. Depending on the degradation pathway, organic matter is directly oxidized to carbon dioxide, partly oxidized to intermediate compounds or reduced to methane. In the simplest of terms, preservation can be simply defined as the incompleteness of degradation.

Global Importance

Life depends on the continuous recycling of bioactive elements. The resulting global biogeochemical cycles are intimately connected through the biological process of photosynthesis, which fixes energy in carbon bonds and respiration, which breaks the organic bonds and thereby releases energy. On long time scales, organic matter, OM, production generally exceeds respiration and a small fraction of the photosynthetically produced organic carbon escapes degradation to be preserved and buried in sediments (Berner 2003). This small imbalance between photosynthesis and respiration connects the short- and long-term carbon cycles, controls the long-term evolution of atmospheric CO_2, and has enabled the accumulation of oxygen in the atmosphere (Berner 2003). However, compilations of field data reveal that OM production, degradation, and preservation rates vary significantly in space (Burdige 2007; Arndt et al. 2013) and time (Berner 2003). Understanding the processes that control the degradation and preservation of OM during transport and burial is important for predicting the impact and feedbacks of past, present, and future global change on global biogeochemical cycles and climate.

OM Degradation and Preservation in the Earth System

Organic matter represents the largest reactive reservoir of reduced carbon in the Earth system, divided between an estimated 1760 Pg C of soil OM, 1000 Pg C in recent surface sediments (excluding deep sediments), and 688 Pg C dissolved in the ocean (Eglinton and Repeta 2004). Almost all of the organic matter that is degraded or preserved in the Earth System originates from photosynthetic activity in the terrestrial (global net primary productivity, NPP = ~59 Pg C $year^{-1}$) or marine biosphere (global NPP = ~49 Pg C $year^{-1}$). In addition, weathering of old OM in rocks, remobilization of organic matter from thawing permafrost, chemoautotrophy, as well as secondary production by microbes and animals contribute to the global organic matter pool (Eglinton and Repeta 2004; Middelburg 2011). Approximately two-thirds of the terrestrially produced OM is rapidly degraded within soils or glacial environments. The remainder escapes immediate degradation and is either degraded slowly or temporarily stored before being transported downstream with old, weathered OM into lakes, streams, rivers, coastal transition zones and, ultimately, the ocean (Regnier et al. 2013). An estimated 1.9 Pg C $year^{-1} \pm 1.0$ Pg C $year^{-1}$ of total soil C (mostly particulate OM and dissolved OM, but also dissolved inorganic carbon) is exported to inland waters. Only 0.45 Pg C $year^{-1}$ of the terrestrial derived OM reaches the coastal ocean and 0.1–0.35 Pg C $year^{-1}$ makes it to the open ocean (Regnier et al. 2013; Bauer et al. 2013). Thus, the intermittent storage and transport of OM along the land-ocean continuum modulates the degradation of terrestrial OM on short and long timescales. However, the exact amounts of OM that are degraded and temporarily or permanently preserved during its transit from land to ocean remain unknown (Regnier et al. 2013). Like terrestrially derived OM, a large fraction of the OM produced in the surface ocean is rapidly degraded with only approximately 10–20% of the primarily produced OM (of which ca. 27% is dissolved OM) escaping degradation in the surface ocean (Dunne et al. 2007; Hansell and Carlson 2015). Dissolved organic matter, DOM, is transported to the deep ocean by convection and mixing. While a large fraction of the exported DOM is degraded at mid-depths, an estimated 0.1 Pg C $year^{-1}$ is transfered to the large, apparently refractory, deep ocean DOM reservoir (~680 Pg) that persists through multiple ocean mixing cycles (Hansell and Carlson 2015). Particulate OM, POM, sinks to the ocean floor and can also be laterally transported by ocean currents (Eglinton and Repeta 2004). It is further degraded during its transport, resulting in an attenuation of the export flux. Between 0.28% and 30% (5.7% average) of the export flux reaches depths greater than 1.5 km and <1–5% of the export flux is deposited on the seafloor. Degradation during burial further reduces this flux such that <0.3% of the original exported flux is ultimately sequestered in deep sediment layers (Honjo et al. 2008; Dunne et al. 2007; Eglinton and Repeta 2004).

The Process of OM Degradation and Preservation

OM degradation and preservation are often thought of as two sides of the same coin. However, this view is somewhat simplistic. It is important to realize that OM preservation is not solely defined by the absence of degradation but can also be directly controlled by other factors, such as the addition of so-called necromass derived from remnants of bacterial cell walls, cell exudates, or cell lysis products to the sinking or buried OM pool. Nevertheless, OM degradation still exerts the dominant control on OM preservation, and many of the additional controls on preservation are indirectly linked to the process of OM degradation.

The degradation of OM generally proceeds via multiple enzymatic reactions involving millions of different organisms and organic compounds, as well as a number of different oxidants and intermediate compounds (Arndt et al. 2013). Note that although microbes dominate organic matter consumption, fungi, as well as animals, such as corals, sea sponges, and suspension feeders also consume detrital organic matter (Bianchi 2011; Middelburg 2017). A fraction of the consumed carbon is excreted as faeces or pseudofaeces, further contributing to the sedimentary pool.

OM Composition

The composition of OM, from freshly produced to heavily degraded, ranges in size and composition from simple, small monomers to large polymers and humic substances (de Leeuw and Largeau 1993). In the terrestrial biosphere, primary production is mainly carried out by multicellular plants, with litter, roots, and root-zone exudates that often contain rigid polymers such as cellulose and lignin, complex carbohydrates, or phenolic polymers for structural support (de Leeuw and Largeau 1993). In contrast, marine primary production is dominated by single celled organisms and, therefore, rich in lipids and nitrogenous compounds (Burdige 2007; Arndt et al. 2013). All these compounds are present in the environment at various stages of degradation from unprocessed and reactive to highly processed and less reactive OM. In addition, it has also been suggested that, despite its low contribution compared to primary production, secondary production by microbes and animals might exert an important control on the composition of sedimentary organic matter that is eventually buried (Lomstein et al. 2012; Middelburg 2017).

Microbes and Terminal Electron Acceptors

This heterogeneous mix of organic compounds is mainly degraded by millions of individual microorganisms with highly diverse metabolic potentials and requirements in synergetic or competitive interactions (Jørgensen and Marshall 2016; Jørgensen and Boetius 2007; Jørgensen 2006). They can use different oxidants (i.e., terminal electron acceptors, TEAs, O_2, NO_3^-, Mn(VI), Fe(III), and SO_4^{2-}) to degrade OM and produce a number of intermediate organic compounds. Although some microorganisms can take up OM directly, most rely on the production of extracellular hydrolytic enzymes in order to make large organic compounds accessible to the entire community. Fermenters, in turn, are then often required to convert these smaller organic compounds into substrates that can be used by other heterotrophs. Consequently, an interconnected group of microorganisms is often required to break down organic matter into terminal products such as CO_2, H_2, and CH_4. Depending on the degradation pathway, OM is thus directly oxidized to CO_2, partly oxidized to intermediate compounds or reduced to CH_4. The main sequence of these different degradation pathways roughly follows the decreasing amount of energy available from them.

Controls on OM Degradation and Preservation

Although OM degradation and preservation are intimately linked, the relative significance of different mechanisms in controlling OM degradation versus preservation may vary (Burdige 2007). The reason for this difference is the low preservation efficiency of OM in the Earth system. Ultimately, only a tiny fraction of the photosynthetically produced OM is preserved in the sediment and small changes in degradation rates translate into pronounced changes in preservation rates. It is therefore important to keep in mind that a mechanism that exerts only a subtle control on OM degradation may play an import role for OM preservation.

In general, OM degradation and preservation rates are controlled by a dynamic and complex interplay of different environmental factors that can be broadly divided into quantity and quality controls (Fig. 1).

Quantity Control

OM degradation and preservation are first and foremost determined by the quantity of available carbon. In this respect, one can distinguish consumer- and donor-controlled systems (Arndt et al. 2013; Middelburg 2017). Consumer-controlled systems, such as the surface soil layer and the photic layers of aquatic systems and sediments have a control over carbon delivery by enhancing OM production or transport, while donor-controlled systems, such as deep soil layers, the deep ocean, and marine sediments outside of the photic zone, have little or no control over C input. In those systems, organic matter degradation is closely linked to organic matter export efficiencies. For instance, a higher vertical transport rate increases the deposition flux of OM to marine sediments and reduces the degree of alteration and thus the aging of organic matter in the water column.

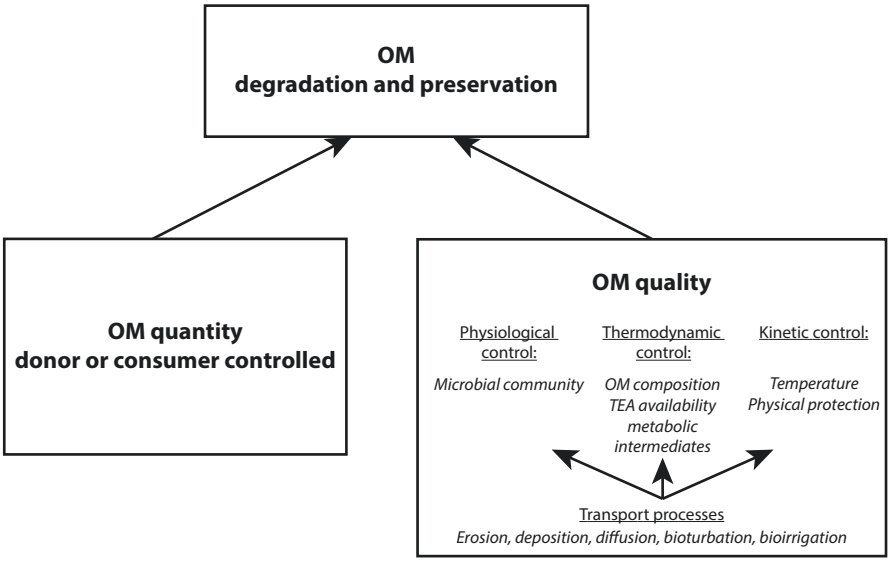

Organic Matter Degradation and Preservation, Fig. 1 The degradation and preservation of organic matter (*OM*) is controlled by the quantity and quality of organic matter (Adapted from Arndt et al. 2013). The organic matter supply to an environment can be donor or consumer controlled and its degradation and preservation in this environment is thermodynamically and/or kinetically controlled through the different physiological abilities of the resident microbial community that compete for common substrates. In addition, transport processes exert an indirect control through their influence on organic matter alteration (and thus composition), terminal electron acceptor (TEA), metabolic intermediate concentrations, and microbial community structure

Quality Control

Organic matter quality (i.e., its susceptibility to microbial transformation or reactivity) exerts an important influence on rates of OM degradation and preservation. The historic view is that OM quality is primarily determined by its chemical structure. However, it has become increasingly clear that OM quality is "not an inherent, or absolute, property of the organic matter itself, but results from the interaction between the organic matter and its environment" (Mayer 1995). Recent observations and laboratory experiments indicate that OM quality is controlled by a complex and dynamic interplay between OM structure and numerous environmental factors (e.g., Schmidt et al. 2011; Burd et al. 2016). The source and transit path of OM, its composition, the nature of the resident microbial community, temperature, physical protection, macrofaunal activity, deposition rate, and thermodynamic constraints all are thought to influence rates of OM degradation (Arndt et al. 2013; Burd et al. 2016), which vary by at least 10 orders of magnitude (Middelburg 1989).

OM Composition

One of the most important guideposts to understanding the link between OM composition and OM quality is the recognition that terrestrial OM is generally less reactive than marine OM (Burdige 2007). This quality difference has been explained with differences in the chemical structures between terrestrial OM, which is made up of moderately or highly resistant biopolymers, and marine OM, dominated by comparably labile biopolymers (de Leeuw and Largeau 1993). In addition to its original chemical composition, the continuous alteration of OM during transport and burial influences the quality of the residual OM. Observations show a pronounced decrease of OM quality with time (Middelburg 1989). This observation has been explained with preferential degradation of more reactive OM compounds during OM degradation. A continuous degradation of OM during transport and burial will thus result in the selective preservation of unreactive compounds and an overall decrease in OM quality (Tegelaar et al. 1989). In addition, the formation of geopolymers through humification or condensation–polymerization during transport and, especially, burial also contributes to the overall decrease of OM quality with time (Tissot and Welte 1984; Burdige 2007).

Microbial Community Structure

Because a vast array of microorganisms consumes, produces, and transforms organic compounds, the microbial community structure exerts an important control on apparent OM quality. Unlike macrofauna, microorganisms can be dispersed over vast distances in short time spans, have the ability to use different electron donors and acceptors (within one organism), can achieve dormancy, can respond rapidly to shifting environmental variables, and can evolve and exchange genetic material with distantly related organisms much faster than their macroscopic counterparts (Nemergut et al. 2013). The rate at which these organisms are active depends on their access to energy and nutrients, their inherent metabolic capabilities, and the presence and/or absence of other microorganisms and viruses that carry out ecological functions such as

predation and vitamin, antibiotic and extracellular enzyme production (Lever et al. 2015; Jørgensen and Marshall 2016). For instance, it has long been thought that most bacteria cannot ingest organic compounds larger than ~600 g/mol (Decad and Nikaido 1976), but many of the organic compounds that reach sediments are larger than this (e.g., proteins, nucleic acids, lipids). Aerobic organisms have the ability to oxidize organic matter compounds directly to CO_2 but are confined to the usually thin oxic zone (few mm to a cm deep, although it can extend to 100s of meters in the organic lean ocean gyres). In contrast, the anaerobic food chain usually requires an initial hydrolytic step to break down high molecular weight compounds through extracellular and membrane-bound enzymes into smaller organic molecules such as monomeric sugars and amino acids. These hydrolytic products can then be oxidized by microorganisms to CO_2 or transformed by fermenting and acetogenic bacteria to hydrogen and organics such as volatile organic acids. The terminal step in this anaerobic food chain involves the utilization of these latter compounds by microorganisms that reduce manganese/iron oxides, sulfate, or produce methane. In addition, newly discovered physiologies, such as extracellular electron transfer for remote oxidation of OM by cable bacteria (Nielsen et al. 2010), may require revision of the traditional view of OM degradation pathways.

Thermodynamics

Most of the organic matter that is consumed by microorganisms is used to gain energy. Although there are many factors that govern the rates at which organisms will consume energy, there is a growing consensus that the rates at which catabolic reactions proceed in relatively low-energy settings are related to the amount of energy that is available from them (Jin and Bethke 2003; LaRowe et al. 2012). In other words, the rate of OM degradation slows down as the amount of Gibbs energy available from it decreases. The Gibbs energy yield of organic matter degradation is determined by the nature of the available terminal electron acceptor, the organic compounds being processed, and the end products of the decomposition reaction, as well as temperature, pressure, and the chemical composition of the environment (LaRowe and Van Cappellen 2011). For instance, OM degradation rates in anaerobic sediments in which the dominant electron acceptor is sulfate tend to be slower than in oxic settings. When only organic carbon compounds with a low energetic potential remain, reaction rates can slow even further.

Physical Protection

The observed correlation between the content of organic matter in soils and sediments and mineral surface area indicates that physical protection of organic matter by interactions with the mineral matrix exerts an important control on OM degradation and, in particular, preservation (Mayer 1994; Hedges and Keil 1995; Blair and Aller 2012). Sorption of organic matter to mineral surfaces or its inclusion in aggregates provides means of protecting reactive organic matter from degradation during transport and burial and, thus, favors preservation. Multiple mechanisms, such as the protection from or steric limitations of hydrolytic enzyme attack and condensation reactions (Mayer 1994; Hedges and Keil 1995; Eglinton and Repeat 2004) have been proposed to explain the observed physical protection of organic matter by minerals, although this remains the subject of much debate.

Temperature

Like all other biogeochemical processes, temperature is a master variable that generally speeds up reaction rate as it rises. However, organic matter degradation is not a simple chemical reaction, but a complex, multi-step process involving a number of different OM compounds, enzymes, oxidants, and intermediate products. As a consequence, the control of temperature on organic matter degradation rates also depends on physiological adaption, selection pressure, and the reaction path (Arnosti et al. 1998; Finke and Jørgensen 2008; Robador et al. 2010). For instance, organic matter degradation rates in temperate environments strongly increase during the warm season and fall during cooler months. In contrast, organic matter degradation rates in permanently cold Arctic sediments are not necessarily slower than those in temperate or tropical environments (Jørgensen 2006). This seemingly contradictory observation is the direct result of the physiological adaption of the in-situ bacterial community to the prevailing environmental conditions.

Transport Processes

Transport processes, such as bioturbation, bioirrigation, and deposition rates may exert an important direct and/or indirect control on organic matter degradation and preservation (Middelburg 2017). In soils and oxic sediments, invertebrates such as polychaetes rework the upper centimeters and influence degradation rates through feeding and burrowing activities, the ventilation of these burrows, or mixing of fresher organic material to deeper layers. This activity may enhance or inhibit organic matter degradation. For instance, within the bioturbated zone of oxic sediments, short-term redox oscillations, the mixing of fresh and labile with old and degraded OM (so-called priming), bioturbation-mediated particle manipulation, grazing, and excretion/secretion may enhance degradation rates, while the production of tube linings, halophenols, or body structural products and the direct feeding on depositing organic matter could inhibit organic matter degradation (Arndt et al. 2013; Middelburg 2017). In addition, the interaction between different macrobenthic animals may enhance the supply of organic matter to the sediment.

Finally, in marine sediments, organic matter degradation and preservation often correlate with sediment deposition rates. However, deposition rate only exerts a control on organic matter degradation/preservation if deposition rates are high enough and/or the organic matter is unreactive enough to escape degradation in the upper, mixed layer (Emerson et al. 1985). One can broadly distinguish different high deposition settings (Blair and Aller 2012). High-energy, mobile muds generally reveal high organic matter degradation and low preservation due to enhanced oxygen exposure and efficient metabolite exchange. Low-energy facies show low organic matter degradation rates and enhanced organic matter preservation as a result of extreme accumulation rates and, often, high loads of fossil organic carbon. Small, mountainous river systems exhibit the highest organic matter preservation favored by the delivery of large amounts of fossil organic matter and average, but periodically high, accumulation rates.

Summary

Organic matter degradation and preservation play a key role in global biogeochemical cycles and climate. The degradation of OM generally proceeds via multiple enzymatic reactions involving millions of different organisms, billions of organic compounds, and a number of different oxidants, as well as intermediate compounds. As a result, OM degradation and preservation is controlled by a dynamic and complex interplay of different environmental factors. Attempts to isolate the impact of a single variable on the rate of OM degradation have often led to contradictory results. It is therefore becoming increasingly clear that OM degradability is not an intrinsic property of the organic matter itself but an ecosystem property. Correspondingly, the likelihood that a given organic compound will be degraded by a microbial community or be preserved will depend on the chemical formula and structure of that compound, in addition to the metabolic capabilities of the resident microorganisms in response to environmental factors such as electron acceptor and intermediate metabolite concentrations, temperature, and physical associations with minerals or other organic compounds.

Cross-References

- Biological Pump
- Carbon Cycle
- Diagenesis
- Dissolved Organic Matter (DOM)
- Marine Sediment
- Organic Geochemistry
- Organics: Sources and Depositional Environments

References

Arndt S, Jørgensen BB, LaRowe DE, Middelburg JJ, Regnier P (2013) Quantification of organic matter degradation in marine sediments: a synthesis and model review. Earth Sci Rev 123:53–86

Arnosti C, Jørgensen BB, Sageman J, Thamdrup B (1998) Temperature dependence of microbial degradation of organic matter in marine sediments: polysaccharide hydrolysis, oxygen consumption, and sulfate reduction. Mar Ecol Prog Ser 165:59–70

Bauer JE, Cai W-J, Raymond PA, Bianchi TS, Hokinson CS, Regnier PAG (2013) The changing carbon cycle of the coastal ocean. Nature 504:61–70

Berner RA (2003) The long-term carbon cycle, fossil fuels and atmospheric composition. Nature 426:323–326

Bianchi TS (2011) The role of terrestrially derived organic carbon in the coastal ocean: a changing paradigm and the priming effect. Proc Natl Acad Sci U S A 108:19473–19481

Blair NE, Aller RC (2012) The fate of terrestrial organic carbon in the marine environment. Ann Rev Mar Sci 4:401–423

Burd AB, Frey S, Cabre A, Ito T, Levine NM, Lønborg C, Long M, Mauritz M et al (2016) Terrestrial and marine perspectives on modeling organic matter degradation pathways. Glob Chang Biol 22:121–136

Burdige DJ (2007) Preservation of organic matter in marine sediments: controls, mechanisms, and imbalance in sediment organic carbon budgets? Chem Rev 107:467–485

de Leeuw JW, Largeau C (1993) A review of macromolecular organic compounds that comprise living organisms and their role in kerogen, coal and petroleum formation. In: Engel MH, Macko SA (eds) Organic geochemistry: principles and applications. Plenum Press, New York, pp 23–62

Decad GM, Nikaido H (1976) Outer membrane of gram-negative bacteria. XII. Molecular-sieving function of cell wall. J Bacteriol 128:325–336

Dunne JP, Sarmiento JL, Gnanadesikan A (2007) A synthesis of global particle export from the surface ocean and cycling through the ocean interior and on the seafloor. Glob Biogeochem Cycles 21:1–16

Eglinton TI, Repeta DJ (2004) Organic matter in the contemporary ocean. In: Holland HD, Turekian KK (eds) Treatise on geochemistry, vol 6. Elsevier, Amsterdam, pp 145–180

Emerson S, Fisher K, Reimers C, Heggie D (1985) Organic carbon dynamics and preservation in deep-sea sediments. Deep Sea Res 32:1–21

Finke N, Jørgensen BB (2008) Response of fermentation and sulfate reduction to experimental temperature changes in temperate and Arctic marine sediments. ISME J 2:815–829

Hansell DA, Carlson CA (2015) Biogeochemistry of marine dissolved organic matter, 2nd edn. Academic, San Diego

Hedges JJ, Keil RG (1995) Sedimentary organic matter preservation: an assessment and speculative synthesis. Mar Chem 49:81–115

Honjo S, Manganini S, Krishfield RA, Francois R (2008) Particulate organic carbon fluxes to the ocean interior and factors controlling the biological pump: a synthesis of global sediment trap programs since 1983. Prog Oceanogr 76:217–285

Jin Q, Bethke CM (2003) A new rate law describing microbial respiration. Appl Environ Microbiol 69:2340–2348

Jørgensen BB (2006) Bacteria and marine biogeochemistry. In: Schulz HD, Zabel M (eds) Marine geochemistry. Springer, Berlin, pp 169–206

Jørgensen BB, Boetius A (2007) Feast and famine – microbial life in the deep-sea bed. Nat Rev Microbiol 5:770–781

Jørgensen BB, Marshall IPG (2016) Slow microbial life in the seabed. Ann Rev Mar Sci 8:311–332

LaRowe D, Van Cappellen P (2011) Degradation of natural organic matter: a thermodynamic analysis. Geochim Cosmochim Acta 75:2030–2042

LaRowe DE, Dale AW, Amend JP, Van Cappellen P (2012) Thermodynamic limitations on microbially catalyzed reaction rates. Geochim Cosmochim Acta 90:96–109

Lever MA, Rogers K, Lloyd KG, Overmann J, Schink B, Thauer R, Hoehler TM, Jørgensen BB (2015) Life under extreme energy limitation: a synthesis of laboratory- and field-based investigations. FEMS Microbiol Rev 39:688–728
Lomstein BA, Langerhuus AT, D'Hondt S, Jørgensen BB, Spivack AJ (2012) Endospore abundance, microbial growth and necromass turnover in deep subseafloor sediments. Nature 484:101–104. Lomstein
Mayer LM (1994) Surface area control of organic carbon accumulation in continental shelf sediments. Geochim Cosmochim Acta 58:1271–1284
Mayer LM (1995) Sedimentary organic matter preservation: an assessment and speculative synthesis – a comment. Mar Chem 49:123–126
Middelburg JJ (1989) A simple rate model for organic-matter decomposition in marine-sediments. Geochim Cosmochim Acta 53:1577–1581
Middelburg JJ (2011) Chemoautotrophy in the ocean. Geophys Res Lett. https://doi.org/10.1029/2011GL049725
Middelburg JJ (2017) Reviews and synthesis: to the bottom of carbon processing at the seafloor. Biogeosci Discuss. https://doi.org/10.5194/bg-2017-362
Nemergut DR, Schmidt SK, Fukami T, O'Neill SP, Bilinski TM, Stanish LF, Knelman JE, Darcy JL, Lynch RC, Wickey P, Ferrenberg S (2013) Patterns and processes of microbial community assembly. Microbiol Mol Biol Rev 77:342–356. https://doi.org/10.1128/MMBR.00051-12
Nielsen LP, Risgaard-Petersen N, Fossing H (2010) Electric currents couple spatially separated biogeochemical processes in marine sediment. Nature 463:1071–1074
Regnier PAG et al (2013) Anthropogenic perturbation of the carbon fluxes from land to ocean. Nat Geosci 6:597–607
Robador A, Brüchert V, Steen AW, Arnosti C (2010) Temperature induced decoupling of enzymatic hydrolysis and carbon remineralization in long-term incubations of Arctic and temperate sediments. Geochim Cosmochim Acta 74:2316–2326
Schmidt MWI, Torn MS, Abiven S, Dittmar T, Guggenberger G, Janssens IA, Kleber M, Kogel-Knabner I, Lehmann J, Manning DAC, Nannipieri P, Rasse DP, Weiner S, Trumbore SE (2011) Persistence of soil organic matter as an ecosystem property. Nature 478:49–56
Tegelaar EW, de Leeuw JW, Derenne S, Largeau C (1989) A reappraisal of kerogen formation. Geochim Cosmochim Acta 53:3103–3106
Tissot BP, Welte DH (1984) Petroleum formation and occurrence. Springer, Heidelberg

Organic Matter in Fossils

A. D. Muscente[1], Andrew D. Czaja[2], Leigh Anne Riedman[1] and Caitlin Colleary[3]
[1]Department of Earth and Planetary Sciences, Harvard University, Cambridge, MA, USA
[2]Department of Geology, University of Cincinnati, Cincinnati, OH, USA
[3]Department of Geosciences, Virginia Tech, Blacksburg, VA, USA

Definition

Because all organisms on Earth consist of complex organic biomolecules, any fossil may contain organic matter. Indeed, organic matter represents one of the most common fossil materials, occurring within skeletal elements (shells and bones) and making up organically preserved microorganisms, plants, and exceptionally preserved eukaryotes (i.e., animals and algae with remains of non-biomineralized tissues).

Introduction

Remains of organisms in the geologic record occur in a variety of preservational styles, which vary with regard to fossil composition, scale, and dimensionality, in addition to anatomy and morphology. All fossils have the potential for preservation of organic matter, making such material an active area of paleontological and geobiological research. Overall, fossils vary widely in terms of organic matter quantity, composition, and form. The major types of fossils containing organic matter (Fig. 1) include organically preserved microfossils, skeletal fossils, carbonaceous compressions, fossils of secondarily mineralized soft tissues, and small carbonaceous fossils (thin carbon films freed from rock matrixes via hydrofluoric acid maceration). Skeletons (bones, shells, sclerites, spicules, tests, and teeth) produced by biomineralizing organisms make up the bulk of the fossil record, and observations of organic material within small shelly fossils (Martí Mus 2014), brachiopods (Forchielli et al. 2012), and vertebrate bones (Asara et al. 2007; Surmik et al. 2016) affirm that they sometimes retain organic matter. That said, the preservation of organics within skeletal fossils has historically received little attention. Instead, most research on fossils containing organic matter has focused on organically preserved microfossils, plants, animals, and macroalgae. These fossils occur less commonly than skeletal remains because microbial processes rapidly destroy non-biomineralized tissues in typical sedimentary environments (Muscente et al. 2017). Preservation of such fossils requires circumstances conducive to preservation of organics, specifically, conditions that limit scavenging and microbial decomposition of tissues and ensure organic matter survival over geologic time (Muscente et al. 2017). Regardless of the circumstances responsible for its preservation, the presence of organic matter ultimately allows for integrated studies of fossil morphology, ultrastructure, biochemistry, and physiology.

Sources and Post Burial Processes

Organisms contain various types of organic biomolecules. Proteins, carbohydrates, lipids, and nucleic acids represent the major groups, which in turn, make up an assortment of biopolymers (macromolecules with repeated subunits). Microbial and diagenetic (e.g., thermal maturation) processes result in the degradation and alteration of these biomolecules over time. Prior to burial and throughout diagenesis, microbes drive the chemical decay and decomposition of tissues, a process involving hydrolysis of large molecules into smaller

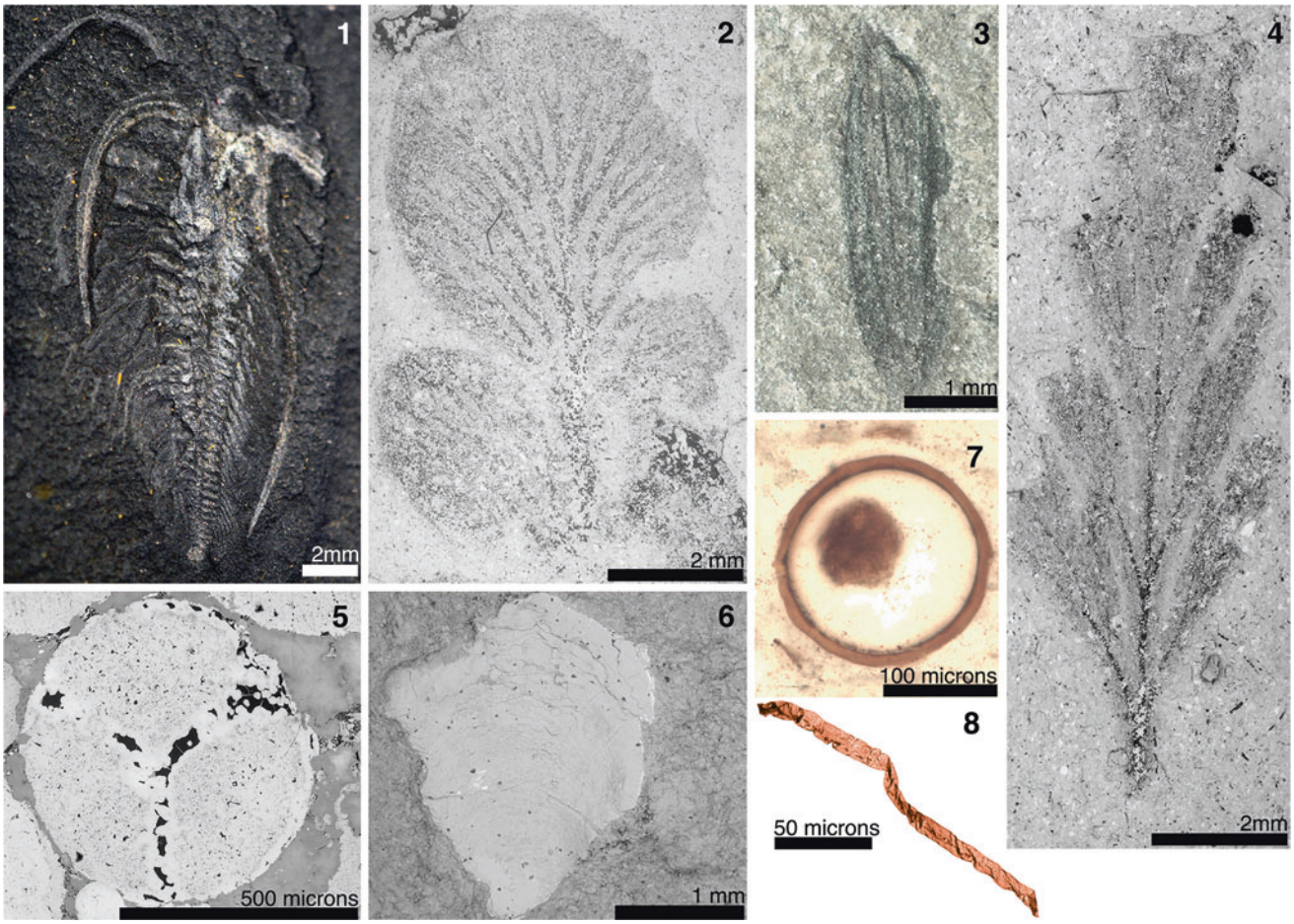

Organic Matter in Fossils, Fig. 1 Fossils containing organic matter. (*1*) Carbonaceous compression of *Marrella* from Burgess Shale, Canada (Muscente et al. 2017). (*2*, *4*) Carbonaceous compressions of plants, Solite Quarry, Triassic Cow Branch Formation, USA (Muscente and Xiao 2015b). (*3*) *Wiwaxia* sclerite, Cambrian Kaili Formation, Guizhou Province, China. (*5*) phosphatized embryo from the Weng'an phosphorite, Ediacaran Doushantuo Formation, Guizhou Province, China. Organic matter within embryo is *black* in the image. (*6*) Linguiform brachiopod shell containing organic matter, lower Cambrian Shuijingtuo Formation, Hubei Province, South China. (*7*) Organic-walled microfossil in thin section, Svanbergfjellet Formation, Svalbard. (*8*) Filamentous small carbonaceous fossil, Alinya Formation, Australia

ones. Although microbial decay always begins prior to thermal maturation, the two processes proceed concurrently late in diagenesis. Thermal alteration causes further degradation, leading to polymerization of biomolecules into long-chain aliphatic compounds (Stankiewicz et al. 2000). This process is sometimes called "kerogenization" (Cai et al. 2012) because it leads to formation of insoluble ("kerogen") components, which are characteristic of organic matter mixtures in the geologic record. Nonetheless, this term is misleading, as polymerization generates an array of compounds, and the mixtures themselves often retain soluble components, like remnants of proteins (Stankiewicz et al. 2000; Schweitzer et al. 2008). Other aspects of diagenesis also alter organic matter from its starting state. Microbial production of sulfide, for example, drives sulfurization and the formation of organosulfur compounds within fossil organic matter (Muscente et al. 2015; McNamara et al. 2016). In any case, the major groups of biomolecules vary considerably in their recalcitrance to microbial processes and thermal maturation, and therefore, in their potential for survival over geologic time. In terms of preservation potential and resistance to decay, biomolecules typically take the following order: nucleic acids < proteins < carbohydrates < lipids < biopolymers (Tegelaar et al. 1989; Briggs 2003).

Organic matter within a fossil may represent indigenous biomolecules of the organism, exogenous organics derived from hydrocarbon migration within a rock, or a mixture of sources. These possibilities can be explored through the application of advanced analytical methods (see below) along with taphonomic analysis. In carbonaceous compressions and small carbonaceous fossils, organic matter occurs as thin films on bedding surfaces. Such layers form through the collapse and coalescence of multiple tissues (Rex and Chaloner 1983) by way of diagenetic polymerization (Stankiewicz et al. 2000). The preservation of fine anatomical details suggests that each thin film derives from a single

organism (Martí Mus 2014), and geochemical analyses of macroalgae compressions generally corroborate this interpretation, showing that within specific geologic deposits, different taxa contain organics with distinct isotopic signatures (Loduca and Pratt 2002). Similarly, geochemical analyses of carbonaceous microfossils, which are typically preserved as hollow, three-dimensional structures with walls and sheaths composed of organic matter, demonstrate that their organics derive from various pathways of carbon fixation (House et al. 2000) and do not record significant averaging of carbon isotope values due to hydrocarbon migration. Even so, diagenetic emplacement of carbonaceous material remains a concern for all types of organically preserved fossils, particularly secondarily mineralized fossils (Muscente et al. 2015).

In skeletal fossils, organics generally represent indigenous materials. These materials derive from the organic matrixes on which the biominerals originally formed and grew (Glover and Kidwell 1993). Fossils of organophosphatic brachiopods sometimes consist of alternating layers of organic-rich and organic-poor phosphatic material, and therefore, closely resemble recent specimens in terms of shell ultrastructure (Zabini et al. 2012). Taphonomically demineralized skeletal fossils also provide evidence of indigenous organic matter. Biomineral dissolution leaves behind carbonaceous residue. If weathering or lab preparation leads to demineralization, the carbonaceous fossil may retain its three-dimensionality, as exemplified in weathered organophosphatic brachiopods (Zabini et al. 2012) and tubular shelly fossils (Muscente and Xiao 2015a). Alternatively, if demineralization occurs early in diagenesis, concomitant with burial compaction, this residue coalesces into a compressed but cohesive fossil (Muscente and Xiao 2015a). This process provides a reasonable explanation for the preservation of skeletal elements as carbonaceous compressions (Martí Mus 2014) and small carbonaceous fossils (Butterfield and Harvey 2012).

Analytical Methods

Geochemical study of organic-walled microfossils has accelerated in recent years with the advent of a number of microanalytical techniques that allow for the analysis of individual fossils. A technique is chosen based on both the questions to be answered and the preservational conditions of the fossils. Some fossils can be extracted from their host matrixes via hydrofluoric or hydrochloric acid maceration, whereas others must be studied in situ in thin (~30 μm) and thick (~150 μm) sections. Applicable analytical techniques include energy dispersive spectroscopy (EDS), confocal laser scanning microscopy (CLSM), secondary ion mass spectrometry (SIMS, Nano-SIMS and time-of-flight SIMS), X-ray near edge absorption spectroscopy (XANES), Raman spectroscopy, and Fourier transform infrared spectroscopy (FTIR).

Scanning electron microscopy (SEM) is typically used to study fossil morphology and ultrastructure and, when combined with energy dispersive spectroscopy (EDS), allows for characterization of organic components and associated minerals (Muscente and Xiao 2015b). Confocal laser scanning microscopy (CLSM) is used to make two- and three-dimensional images of organic fossils based on their fluorescence (Schopf et al. 2006). Kerogen fluoresces weakly with laser excitation, and the strength of the emission is inversely related to the degree of thermal alteration so that more thermally mature fossils are more difficult to image (Czaja et al. 2016).

Mass spectrometry is a common technique to study the carbon isotope compositions of fossil organic matter, which can help constrain the physiology of ancient organisms. Secondary ion mass spectrometry (SIMS) provides the capability of collecting in situ measurements of carbon isotopic values from individual microfossils (House et al. 2000, 2013; Williford et al. 2013). This method and its relatives (Nano-SIMS and time-of-flight SIMS) can be used to produce 2-D elemental or molecular maps of small areas (up to 100 × 100 μm). These can be used to show the relationship of various elements within fossil structures. Such work can illuminate elemental relationships within fossil material and provide data for assessing the biogenicity of objects of uncertain origin (Oehler et al. 2009).

Several techniques are used to determine the composition of organic matter in fossils and to provide evidence of biological origin. XANES is used to characterize molecular components of organic matter (Boyce et al. 2001; De Gregorio and Sharp 2006). This technique typically has a high spatial resolution and can be used to study individual fossil microorganisms and produce 2-D maps (Muscente et al. 2015). Raman spectroscopy and FTIR spectroscopy are in situ techniques that measure the molecular structure of organic and inorganic materials based on vibrations of molecular bonds and larger molecular structures using lasers for excitation. These techniques are typically used to determine the carbonaceous nature and molecular structure of possible fossil organic material (Arouri et al. 2000; Kudryavtsev et al. 2001; Olcott Marshall and Marshall 2014; Schopf and Kudryavtsev 2005). Raman spectroscopy is also used to measure the degree of thermal alteration of fossil organic matter and reconstruct the metamorphic histories of geologic units containing organically preserved fossils (Beyssac et al. 2002; Schopf et al. 2005; Kouketsu et al. 2014).

Complex Organic Biomolecules

As mentioned above, complex biomolecules vary in their rates of degradation. Nucleic acids, for example, contain the most biological information but are also the quickest to degrade. The oldest sequenced genome is from a ~700,000 year old horse preserved in permafrost (Orlando et al. 2013) and extremely degraded DNA has been reported

on the scale of millions of years. It is possible that with advancements in analytical techniques, this ancient DNA can become a rich source of information.

Proteins can provide details of an organism's physiology and evolutionary relationships and can preserve on significantly longer time scales than DNA. In vertebrates, proteins like collagen, which break down into bonded amino acids called peptides, have been reported from a ~68 million-year-old *Tyrannosaurus rex* bone (Asara et al. 2007) and amino acids fragments have been reported from ~235 Ma reptiles (Surmik et al. 2016). Such bold claims, however, require strong support and just as mentioned above, exogenous organic matter and contaminants from the field and lab are a major concern. Indeed, follow-up studies have called into question the provenance of the *T. rex* biomolecules (Buckley et al. 2008) and this story continues to develop. The oldest complete protein so far detected comes from an ostrich eggshell (~3 Ma; Demarchi et al. 2016); the structure of the shell and the protein's affinity for calcite are hypothesized to have enabled this long-term preservation.

Chitin is a long-chain polymer and major constituent in the exoskeletons of arthropods. A modified chitin-protein complex containing up to 59% of the chitin concentrations seen in modern animals has been found in fossil arthropods (310 and 417 million years old; Cody et al. 2010). The decay of this complex is prevented by condensation of fatty acids onto a structurally modified chitin-protein molecular scaffold.

Melanin is a common pigment, which occurs within organelles (melanosomes) in numerous clades of animals. Different types of melanin produce different colors, and the melanosomes that contain them vary in shape and size. Notably, the discovery of fossilized melanosomes ushered in a novel field of paleobiology: the study of color patterns in ancient animals. By studying melanosomes in feathers, for example, paleontologists determined that the well-known feathered dinosaur *Sinosauropteryx* possessed a red and white striped tail (Zhang et al. 2015). Even so, fossilized melanosomes have been a subject of debate (Vinther 2016), as some authors have proposed that the structures are actually fossils of microbes. Recently, various studies have presented evidence that fossilized melanosomes of various ages contain chemical traces of melanin (Lindgren et al. 2012; Colleary et al. 2015; Clements et al. 2016). Such traces represent maturation products of melanin rather than the original biomolecules (Colleary et al. 2015). Nonetheless, such data support the use of fossilized melanosomes for analyses of coloration in ancient life and affirm that work on biomolecule preservation in fossils should remain a top priority.

Summary

Regardless of preservational style, any fossil may contain organic matter, as evidenced by observations of carbonaceous material within skeletal elements, small carbonaceous fossils, carbonaceous compressions, and secondarily mineralized tissues. The organic matter within a specific fossil may represent biomolecules indigenous to the organism, organics introduced via hydrocarbon migration, or compounds derived from both sources. In all cases, organically preserved fossils constitute important windows to the evolutionary history of life on Earth, particularly the rise of microbial life and the radiation of animals. Fossils with indigenous organic matter merit particular attention. Such fossils may contain biomolecules (e.g., chitin and melanin) of paleobiologic and geobiologic significance in diagenetically altered but recognizable forms. Thus, analyses of the organic matter in such fossils may illuminate the original biochemical makeups and affinities of those ancient organisms.

Cross-References

- Biopolymers and Macromolecules
- Carbon
- Carbon Isotopes
- Diagenesis
- Geochemistry
- Kerogen
- Organic Geochemistry
- Organic Matter Degradation and Preservation
- Organics: Sources and Depositional Environments
- Precambrian Geochemistry
- Precambrian Organic Matter
- Raman Microspectroscopy

References

Arouri KR, Greenwood PF, Walter MR (2000) Biological affinities of Neoproterozoic acritarchs from Australia: microscopic and chemical characterisation. Org Geochem 31:75–89

Asara JM, Schweitzer MH, Freimark LM, Phillips M, Cantley LC (2007) Protein sequences from mastodon and *Tyrannosaurus rex* revealed by mass spectrometry. Science 316:280–285

Beyssac O, Goffé B, Chopin C, Rouzaud JN (2002) Raman spectra of carbonaceous material in metasediments: a new geothermometer. J Metamorph Geol 20:859–871

Boyce CK, Hazen RM, Knoll AH (2001) Nondestructive, in situ, cellular-scale mapping of elemental abundances including organic carbon in permineralized fossils. Proc Natl Acad Sci U S A 98:5970–5974

Briggs DEG (2003) The role of decay and mineralization in the preservation of soft-bodied fossils. Annu Rev Earth Planet Sci 31:275–301

Buckley M et al (2008) Comment on "Protein sequences from mastodon and *Tyrannosaurus rex* revealed by mass spectrometry.". Science 319:33

Butterfield NJ, Harvey THP (2012) Small carbonaceous fossils (SCFs): a new measure of early Paleozoic paleobiology. Geology 40:71–74

Cai Y, Schiffbauer JD, Hua H, Xiao S (2012) Preservational modes in the Ediacaran Gaojiashan Lagerstätte: Pyritization, aluminosilicification,

and carbonaceous compression. Palaeogeogr Palaeoclimatol Palaeoecol 326–328:109–117
Clements T, Dolocan A, Martin P, Purnell MA, Vinther J, Gabbott SE (2016) The eyes of Tullimonstrum reveal a vertebrate affinity. Nature 532:500–503
Cody GD, Gupta NS, Briggs DEG, Kilcoyne ALD, Summons RE, Kenig F, Plotnick RE, Scott AC (2010) Molecular signature of chitin-protein complex in Paleozoic arthropods. Geology 39:255–258
Colleary C, Dolocan A, Gardner J, Singh S, Wuttke M, Rabenstein R, Habersetzer J, Schaal S, Feseha M, Clemens M, Jacobs BF, Currano ED, Jacobs LL, Sylvestersen RL, Gabbott SE, Vinther J (2015) Chemical, experimental, and morphological evidence for diagenetically altered melanin in exceptionally preserved fossils. Proc Natl Acad Sci U S A 112:12592–12597
Czaja AD, Beukes NJ, Osterhout JT (2016) Sulfur-oxidizing bacteria prior to the great oxidation event from the 2.52 Ga Gamohaan formation of South Africa. Geology 44:983–986
De Gregorio BT, Sharp TG (2006) The structure and distribution of carbon in 3.5 Ga apex chert: implications for the biogenicity of Earth's oldest putative microfossils. Am Mineral 91:784–789
Demarchi B et al (2016) Protein sequences bound to mineral surfaces persist into deep time. eLife 5:17092
Forchielli A, Steiner M, Hu S, Lüter C, Keupp H (2012) Taphonomy of the earliest Cambrian linguliform brachiopods. Acta Palaeontol Pol 59:185–207
Glover CP, Kidwell SM (1993) Influence of organic matrix on the postmortem destruction of molluscan shells. J Geol 101:729–747
House CH, Oehler DZ, Sugitani K, Mimura K (2013) Carbon isotopic analyses of ca. 3.0 Ga microstructures imply planktonic autotrophs inhabited Earth's early oceans. Geology 41:651–654
House CH, Schopf JW, McKeegan KD, Coath CD, Harrison TM, Stetter KO (2000) Carbon isotopic composition of individual Precambrian microfossils. Geology 28:707–710
Kouketsu Y, Mizukami T, Mori H, Endo S, Aoya M, Hara H, Nakamura D, Wallis S (2014) A new approach to develop the Raman carbonaceous material geothermometer for low-grade metamorphism using peak width. Island Arc 23:33–50
Kudryavtsev AB, Schopf JW, Agresti DG, Wdowiak TJ (2001) In situ laser-Raman imagery of Precambrian microscopic fossils. Proc Natl Acad Sci U S A 98:823–826
Lindgren J, Uvdal P, Sjövall P, Nilsson DE, Engdahl A, Schultz BP, Thiel V (2012) Molecular preservation of the pigment melanin in fossil melanosomes. Nat Commun 3:1–7
LoDuca ST, Pratt LM (2002) Stable carbon-isotope compositions of compression fossils from lower Paleozoic Konservat-Lagerstätten. PALAIOS 17:287–291
Martí Mus M (2014) Interpreting 'shelly' fossils preserved as organic films: the case of hyolithids. Lethaia 47:397–404
McNamara ME, van Dongen BE, Lockyer NP, Bull ID, Orr PJ (2016) Fossilization of melanosomes via sulfurization. Palaeontology 59:337–350
Muscente AD, Michel FM, Dale JG, Xiao S (2015) Assessing the veracity of Precambrian 'sponge' fossils using in situ nanoscale analytical techniques. Precambrian Res 263:142–156
Muscente AD, Schiffbauer JD, Broce J, Laflamme M, O'Donnell K, Boag TH, Meyer M, Hawkins AD, Huntley JW, McNamara M, MacKenzie LA, Stanley GD Jr, Hinman NW, Hofmann MH, Xiao S (2017) Exceptionally preserved fossil assemblages through geologic time and space. Gondwana Res 48:164–188
Muscente AD, Xiao S (2015a) New occurrences of *Sphenothallus* in the lower Cambrian of South China: implications for its affinities and taphonomic demineralization of shelly fossils. Palaeogeogr Palaeoclimatol Palaeoecol 437:141–146
Muscente AD, Xiao S (2015b) Resolving three-dimensional and subsurficial features of carbonaceous compressions and shelly fossils using backscattered electron scanning electron microscopy (BSE-SEM). PALAIOS 30:462–481
Oehler DZ, Robert F, Walter MR, Sugitani K, Allwood A, Meibom A, Mostefaoui S, Selo M, Thomen A, Gibson EK (2009) NanoSIMS: insights to biogenicity and syngeneity of Archaean carbonaceous structures. Precambrian Res 173:70–78
Olcott Marshall A, Marshall CP (2014) Vibrational spectroscopy of fossils. Palaeontology 58:201–211
Orlando L et al (2013) Recalibrating *Equus* evolution using the genome sequence of an early middle Pleistocene horse. Nature 499:74–78
Rex GM, Chaloner WG (1983) The experimental formation of plant compression fossils. Palaeontology 26:231–252
Schopf JW, Kudryavtsev AB (2005) Three-dimensional Raman imagery of Precambrian microscopic organisms. Geobiology 3:1–12
Schopf JW, Kudryavtsev AB, Agresti DG, Czaja AD, Wdowiak TJ (2005) Raman imagery: a new approach to assess the geochemical maturity and biogenicity of permineralized Precambrian fossils. Astrobiology 5:333–371
Schopf JW, Tripathi AB, Kudryavtsev AB (2006) Three-dimensional confocal optical imagery of Precambrian microscopic organisms. Astrobiology 6:1–16
Schweitzer MH, Avci R, Collier T, Goodwin MB (2008) Microscopic, chemical and molecular methods for examining fossil preservation. Comptes Rendus Palevol 7:159–184
Stankiewicz BA, Briggs DEG, Michels R, Collinson ME, Flannery MB, Evershed RP (2000) Alternative origin of aliphatic polymer in kerogen. Geology 28:559–562
Surmik D, Boczarowski A, Balin K, Dulski M, Szade J, Kremer B, Pawlicki R (2016) Spectroscopic studies on organic matter from Triassic reptile bones, upper Silesia, Poland. PLoS One 11: e0151143
Tegelaar EW, De Leeuw JW, Derenne S, Largeau C (1989) A reappraisal of kerogen formation. Geochim Cosmochim Acta 53:3103–3106
Vinther J (2016) Fossil melanosoems or bacteria? A wealth of findings favours melanosomes. BioEssays 38:220–225
Williford KH, Ushikubo T, Schopf JW, Lepot K, Kitajima K, Valley JW (2013) Preservation and detection of microstructural and taxonomic correlations in the carbon isotopic compositions of individual Precambrian microfossils. Geochim Cosmochim Acta 104:165–182
Zabini C, Schiffbauer JD, Xiao S, Kowalewski M (2012) Biomineralization, taphonomy, and diagenesis of Paleozoic lingulid brachiopod shells preserved in silicified mudstone concretions. Palaeogeogr Palaeoclimatol Palaeoecol 326–328:118–127
Zhang F, Kearns SL, Orr PJ, Benton MJ, Zhou Z, Johnson D, Xu X, Wang X (2015) Fossilized melanosomes and the colour of cretaceous dinosaurs and birds. Nature 463:1075–1078

Organics: Sources and Depositional Environments

Elisabeth Sikes
Department of Marine and Coastal Sciences, Rutgers the State University of New Jersey, New Brunswick, NJ, USA

Synonyms

Detrital organic matter; Nonliving organic matter; Organic carbon; Organic matter

Definition

"Organics" is the short form used for detrital organic matter. It is the nonliving remains of organisms found in sediments, soils, and water. It is comprised of organic molecules often in macromolecular form.

Introduction

The sequestration of organic matter (OM) in depositional environments controls the levels of CO_2 in the atmosphere, the global carbon cycle, and hence, climate. The fate of organic matter that is transported from the land to the sea remains one of the fundamental questions in global carbon cycling (Hedges et al. 1997) even after decades of research (Bianchi et al. 2017). There is general agreement that continental shelves represent the largest sink of both terrestrial and marine organic carbon globally, with estimates suggesting that as much as much as a quarter of the total carbon buried in marine sediments is of terrestrial origin (Berner 1982; Hedges and Keil 1995; Raymo 1997). Two important controls on the preservation of organic matter are the composition of the organic matter and the depositional environment.

Detrital organic matter is the nonliving remains of organisms found in sediments, soils, and water. It is comprised of organic molecules often in complex, macromolecular form. The initial source of all complex organic matter is photosynthesis whereby inorganic carbon is fixed by autotrophs. Higher plants, marine or lacustrine algae, or microbes are the dominant primary producers. Once carbon is fixed, that is, reduced to organic molecules by autotrophs, it is a valuable energy source. Heterotrophs consume this organic matter whether living or dead and derive energy from oxidizing it while converting a portion of it to their own biomass. In this process, the composition of the portion of that carbon that is utilized for biosynthesis is modified. Consequently, the composition of the organic matter changes between its initial fixation by autotrophs, through secondary biosynthesis by heterotrophs. Multiple transformations often occur before and during deposition in sediment and soil. Multicellular organisms consume living or nonliving particulate organic matter (POM) and excrete waste, but in aquatic and marine settings, microbes such as bacteria (and others such as Achaea) also utilize dissolved organic matter (DOM) excreted by phytoplankton or released by cell rupture and feeding of heterotrophs. Dissolved organic matter also enters these systems through leaching of soil organic matter. Dissolved organic matter in particular is also subject to nonbiologically mediated reactions such as photodegradation (Blough and Del Vecchio 2002; Del Vecchio and Blough 2002). Despite all the alterations of organic matter along the pathway from production to preservation, many organic compounds still reflect their origins.

Composition of Detrital Organic Matter

Understanding the chemical composition of the sources of organic matter is useful because these can be related to the organic matter preserved in depositional environments and ultimately the sediment record. Collectively, nonliving organic matter in the environment, also referred to as detrital organic matter, is made up of the major biochemicals, protein, carbohydrates, and lipids. Proteins, composed of amino acids, contain most of the organic nitrogen in detrital matter. Carbohydrates are aliphatic compounds composed from simple sugar units and are used as storage molecules and structural materials. Cellulose is the main structural polysaccharide in higher plants. Lipids are composed of a wide range of compounds ranging from fats and waxes to alcohols and oils, and they also include steroids and hydrocarbons. Lignins are structural lipid molecules found in vascular plants that are used in cellular walls and these make up a significant proportion of the biomass particularly in woody plants. Cellulose and lignin are broken down by fungi and other microbes into their constituent units that are found in detrital matter. What distinguishes lipids in detrital organic matter from amino acids and carbohydrates is that amino acids and carbohydrates have structures that are largely ubiquitous among organisms. In contrast lipids, because of their range of distinct structures and the fact that they are preserved, means that even the modified and monomeric units serve as biomarkers for organic matter. This makes them useful for determining sources.

Determining Sources of Organic Matter

Lipids have widely varying reactivities as well as sources and structures. Lipid biomarkers, although a small portion of the total organic pool, have been successfully used to estimate the sources and reactivity of organic carbon in riverine and coastal systems (e.g., Alin et al. 2008; Drenzek et al. 2009; Goñi et al. 2008; Jaffé et al. 2006; Pearson et al. 2001; Sikes et al. 2009). Recalcitrant compounds, such as *n*-alkanes and *n*-alcohols, are widely distributed and well preserved in sediments, and their distribution of chain lengths have proven useful for source determination (Hermes and Sikes 2016; Meyers 1997; Oros and Simoneit 2001; Prahl and Muehlhausen 1989). For example, the longer chain (C_{25}–C_{33}) *n*-alkanes are indicative of epicuticularleaf waxes (Eglinton and Hamilton 1967; Kolattukudy 1976) and shorter chain lengths (C_{15}–C_{25}) come from aquatic and marine plants (e.g., Ficken et al. 2000; Jaffé et al. 2001).

The carbon isotopic composition of organic matter ($\delta^{13}C$) is a useful tool for distinguishing algal- from land-derived sources of organic matter in coastal environments because algal and vascular plants have distinct isotopic signatures

(Jaffé et al. 2001; Kennicutt et al. 1987). Geochemical signatures of $\delta^{13}C$ in organic matter have been used to indicate that there is dilution of land-derived POM by algal sources along estuaries (e.g., Benner 2004). Whereas combining biomarker with bulk $\delta^{13}C$ analyses on particulate organic matter has improved the ability to differentiate sources in these complex environments (e.g., Canuel and Hardison 2016; Sikes et al. 2009). Combining biomarkers with compound specific isotopes and/or multiple isotopes analyses exploits the chemical and isotopic differences among terrestrial vegetation, marine algae, and bacteria. The $\delta^{13}C$ of a biomarker can help constrain its origin. This has proven extremely effective for determining organic carbon sources and uptake in complex coastal systems (e.g., Canuel and Hardison 2016; Canuel and Martens 1996; Goñi et al. 2008; Sikes et al. 2009).

Optical properties (absorbance and fluorescence) have proven to be extremely useful tools for interrogating the composition of dissolved organic carbon in freshwater and marine systems (Cory and McKnight 2005; Jaffe et al. 2008; Komada et al. 2002; Stedmon et al. 2007). Advanced 3D excitation-emission matrix fluorescence spectroscopy (EEMs) is a nondestructive technique that distinguishes terrestrial and marine components, as well as aromatic and protein-like components in dissolved organic carbon (e.g., Coble 2007; Fellman et al. 2010).

Transformation of Organic Matter Across the Terrestrial-Ocean Transition

Export of organic carbon by rivers is positively related to the yield of suspended sediment, meaning that POM export is mostly controlled by physical erosion (Galy et al. 2015; Lyons et al. 2002). Globally ½ to ¾ of the terrestrial organic matter delivered to the ocean is remineralized along continental margins (Burdige 2005). Of the terrestrial organic matter that survives and makes it to the marine environment, ~90% of is buried in slope and shelf sediments with about 50%, focused into deltaic depocenters (Berner 1982; Blair and Aller 2012; Burdige 2005; Hedges and Keil 1995). The storage of organic carbon in terrestrial environments before delivery to the coastal ocean results in the common occurrence of pre-aged organic carbon in continental margin surface sediments (Bao et al. 2016). The mineral matrices are typically invoked as the primary mode of stabilization and sequestration of organic matter in sediments (Keil et al. 1994; Kennedy and Wagner 2011). This organic matter can be subject to further resuspension-deposition during which it is modified (Sun et al. 2002) and ages further (Bao et al. 2016).

The land-ocean interface and the coastal ocean are tremendously variable and dynamic. The rates of organic carbon burial and oxidation are influenced by terrigenous inputs, sediment transport processes, depositional conditions, oxygen levels, and marine productivity with these processes occuring over broad spatial and temporal scales (Bauer et al. 2013; Bianchi et al. 2016) Fig. 1. Anthropogenic impacts that affect watersheds also impact the coastal ocean and these influences can cause coastal eutrophication and changes in the supply of terrestrial sediment. Eutrophication drives bottom-water hypoxia, the areas of which have expanded during the twentieth century (Altieri and Gedan 2015). The change to greater anoxia has largely increased the preservation of organic carbon in estuaries and continental shelves (Bauer et al. 2013; Bianchi et al. 2016).

An important conduit for terrestrial organic carbon to the coastal ocean is through estuaries. Estuaries are recognized as a complex component of the global carbon cycle that regulate the delivery of land-derived sediment and transform the amount and composition of organic carbon from rivers

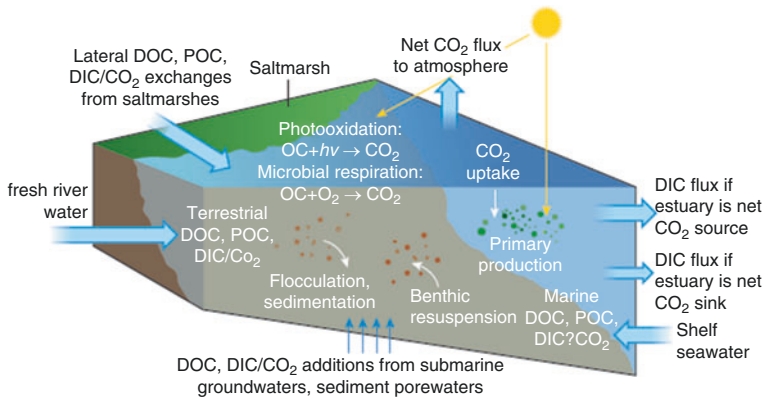

Organics: Sources and Depositional Environments, Fig. 1 Major processes affecting carbon sources and fluxes in estuaries. Estuaries contain a mixture of organic carbon sources derived from terrestrial materials carried by rivers, local inputs from marshes and primary production and marine inputs. Organic carbon is lost owing to salinity-induced flocculation, sedimentation, microbial respiration and photooxidation. These processes cause estuaries to be important zones of transformation in the export of organic carbon to the ocean (Bianchi et al. 2011)

O

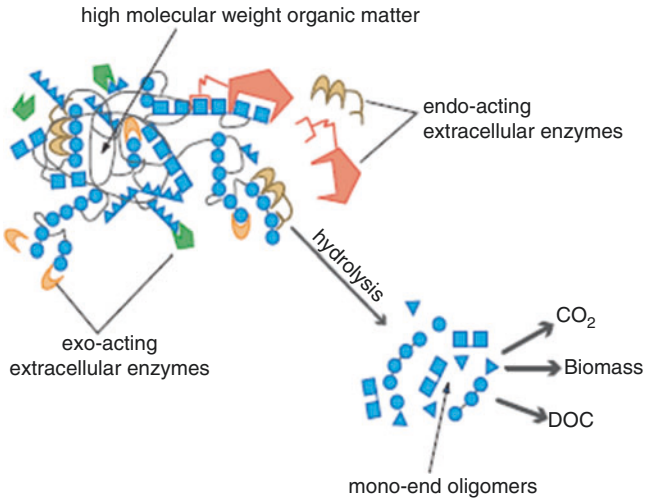

Organics: Sources and Depositional Environments, Fig. 2 Microbes can hydrolize high moleculare weight OM using extracellular enzymes. This produces smaller monomers. The structures of the initial and resulting molecules are not known. Overall many of the factors in the early steps of carbon transformations in aquatic and marine systems remain unknown (Arnosti 2011; Bianchi 2011)

through a wide array of degradation processes (Fig. 1). By being productive in their own right, estuaries add a complex mix of marine and marsh derived organic matter to the system (Abril et al. 2002; Bruesewitz et al. 2013; Canuel and Zimmerman 2006; Cole et al. 2007; Hermes and Sikes 2016; Mannino and Harvey 2000; Medeiros et al. 2012). The biogeochemical fate of organic matter in estuaries remains poorly quantified leading to continuing uncertainty with respect to the role of estuaries and coastal oceans in regulating atmospheric CO_2 (Bauer et al. 2013).

The transformation of organic matter can be biologically mediated or abiotic. For example, photooxidation alters and removes DOM from surface waters (Fig. 2) (Amon and Benner 1996; Benner and Opsahl 2001; Gonsior et al. 2009; Helms et al. 2013) and studies show that terrestrial and plankton-derived organic carbon exhibit different degrees of photochemical lability (Hernes and Benner 2003; Obernosterer and Benner 2004; Rontani et al. 2012). Microbial degradation consumes both dissolved and particulate organic matter and this process is also a source of modified organic matter (Figure 2) (Arnosti 2011; Komada et al. 2002; McCallister et al. 2004; Sun et al. 2002; Tremblay et al. 2007; Ziervogel and Arnosti 2009; Zimmerman and Canuel 2001). Notably, the interaction of biotic and abiotic transformations can affect organic carbon reactivity. The concept of priming – that fresh, labile carbon may enhance the reactivity of semi-labile and recalcitrant carbon – has long existed in the soils literature (Bingeman et al. 1953; Hamer et al. 2004; Kuzyakov et al. 2000) and has recently been advocated as an important factor in the degradation of terrestrial organic carbon in aquatic and marine systems (Aller and Blair 2006; Bianchi 2011; Blair and Aller 2012).

Overall, the biogeochemical transformation of organic matter as it moves from terrestrial source to marine sink remains only roughly characterized. Characterization requires multiproxy approaches that combine multi-isotopic and biomarker techniques (Blair et al. 2004; Goñi et al. 1997, 1998, 2006, 2008; Gordon and Goñi 2003; McCallister and del Giorgio 2008; Onstad et al. 2000; Sikes et al. 2009). Riverine multitracer studies have demonstrated that preaged terrestrial and recycled fossil organic matter is a significant component of the carbon mobilized and delivered to marine sediments (e.g., Drenzek et al. 2007, 2009; Goñi et al. 1997, 2006, 2008; Leithold et al. 2006; Pearson and Eglinton 2000; Pearson et al. 2001). Bulk organic carbon stable isotope and radiocarbon compositions reveal the diversity and complexity characteristic of organic carbon buried in marginal seas. This primarily relates to differences in marine and terrestrial inputs, the composition of the terrestrial component (e.g., vascular plant OM, soil, and petrogenic OM inputs), and processes modulating the fate of organic carbon within the marine environment (e.g., priming). This widely contrasting behavior of OM among these systems illustrates that the reactivity of organic carbon is a product of its chemical composition and regional conditions (Bianchi et al. 2017).

Fate of Organic Matter: The Ocean

The source and make-up of organic matter influences the fate of organic carbon in soils as well as marine sediments. Several mechanisms suggested to be responsible for the preservation are based upon the assumption that preservation, i.e., persistence, is related to chemical structure and or physical environment. (1) Recalcitrant organic matter may occur as biologically produced resistant macromolecules such as lignin, peptidoglycan, algenans, or pyrogenic carbon (Dickens et al. 2004) which may be selectively preserved within soils and sediments. (2) Rapid burial spatially protects organic matter from decomposition via reduced access to microorganisms, and their hydrolyzing enzymes, and restricts diffusion of oxygen reducing aerobic decomposition. (3) The redox state of the environment is a fundamental control with preservation in anoxic environments substantially higher than in oxic environments.

In the open ocean, about 90% of the organic matter produced by phytoplankton in the surface photic zone is consumed by zooplankton and microbial heterotrophs leaving only a few percent to sink out as particulate matter which in turn is further altered and consumed as it falls through the water column affecting the quality and reducing the quantity that finally reaches the depositional environment of the deep sea floor (Lee and Wakeham 1988). As particulate matter sinks, heterotrophic activity preferentially removes the more

labile compounds such as proteins and carbohydrates and the remaining fraction becomes more refractory and enriched in lipids such as sterols and long chain alkanes and alkenones (Wakeham and Lee 1993). Overall the fraction organic carbon that can be identified as the major biochemicals diminishes with time in favor of macromolecular composites such as humic substances and kerogen which comprise most of sedimentary organic matter (Hatcher et al. 1983; Hedges et al. 2000).

In general, there is a correspondence between the amount of organic matter in the sediments, the overlying productivity, and the rate of sedimentation (Emerson 1985). Reactivity of organic matter is conditional. Organic material may be reactive in one environment, such as aerobic soils, but relatively stable in another such as in anoxic sediments. The role of oxygen in controlling both the amount and type of preservation the sediments is fundamental with the length of oxygen–exposure time being an important controlling variable (Hartnett et al. 1998). In all likelihood, there is a continuum of reactivities defined by source materials and ecosystem properties (Bianchi et al. 2017; Blair and Aller 2012).

Summary

The fixation of organic matter converts CO_2 to reduced carbon removing it from the atmosphere and marine environment. The breakdown, and eventual remineralization back to CO_2 of this OM are important processes in the global carbon and oxygen cycles. Natural organic matter is the largest reactive reservoir of reduced carbon on Earth. If we consider autotrophy the initial source of all organics, then the ocean and its sedimentary environments are the ultimate sink. Knowledge of the diverse sources of organics outstrips our understanding of the complex interactions of detrital organics within the global carbon cycle. In particular, the carbon cycle of the coastal ocean is a dynamic component of the global carbon budget that remains poorly understood. Understanding the alteration of organic material flowing from rivers to the ocean and carbon fluxes within and between coastal subsystems is becoming an increasing area of research over the past few decades because the alteration by climate and anthropogenic changes within these systems are substantial. Understanding and accurately accounting for the factors regulating the organic and inorganic carbon fluxes between and within terrestrial and marine systems is important for achieving closure of the global carbon budget (Fig. 1).

Cross-References

- Biogeochemistry
- Biomarkers: Coal
- Biomarkers: Petroleum
- Carbon Cycle
- Carbon Isotopes
- Dissolved Organic Matter (DOM)
- Kerogen
- Organic Facies
- Organic Geochemistry
- Organic Matter Degradation and Preservation

References

Abril G, Nogueira M, Etcheber H, Cabeçadas G, Lemaire E, Brogueira MJ (2002) Behaviour of organic carbon in nine contrasting European estuaries. Estuar Coast Shelf Sci 54:241–262

Alin SR, Aalto R, Goñi MA, Richey JE, Dietrich WE (2008) Biogeochemical characterization of carbon sources in the Strickland and fly rivers, Papua New Guinea. J Geophys Res 113. https://doi.org/10.1029/2006JF000625

Aller RC, Blair NE (2006) Carbon remineralization in the Amazon-Guianas tropical mobile mudbelt: a sedimentary incinerator. Cont Shelf Res 26:2241–2259

Altieri AH, Gedan KB (2015) Climate change and dead zones. Glob Chang Biol 21:1395–1406

Amon RMW, Benner R (1996) Photochemical and microbial consumption of dissolved organic carbon and dissolved oxygen in the Amazon River system. Geochim Cosmochim Acta 60:1783–1792

Arnosti C (2011) Microbial extracellular enzymes and the marine carbon cycle. Ann Rev Mar Sci 3:401–425

Bao R, McIntyre C, Zhao M, Zhu C, Kao S-J, Eglinton TI (2016) Widespread dispersal and aging of organic carbon in shallow marginal seas. Geology 44:791–794

Bauer JE, Cai W-J, Raymond PA, Bianchi TS, Hopkinson CS, Regnier PAG (2013) The changing carbon cycle of the coastal ocean. Nature 504:61–70

Benner R (2004) What happens to terrestrial matter in the ocean? Mar Chem 92:307–310

Benner R, Opsahl S (2001) Molecular indicators of the sources and transformations of dissolved organic matter in the Mississippi River plume. Org Geochem 32:597–611

Berner RA (1982) Burial of organic-carbon and pyrite sulfur in the modern ocean – its geochemical and environmental significance. Am J Sci 282:451–473

Bianchi TS (2011) The role of terrestrially derived organic carbon in the coastal ocean: a changing paradigm and the priming effect. Proc Natl Acad Sci USA 108:19473–19481

Bianchi TS, Schreiner KM, Smith RW, Burdige DJ, Woodard S, Conley DJ (2016) Redox effects on organic matter storage in coastal sediments during the Holocene: a biomarker/proxy perspective. Ann Rev Earth Planet Sci 44:295–319

Bianchi TS, Cui X, Blair NE, Burdige DJ, Eglinton TI, Galy V (2017) Centers of organic carbon burial and oxidation at the land-ocean interface. Org Geochem (in press)

Bingeman CW, Varner JE, Martin WP (1953) The effect of the addition of organic materials on the decomposition of an organic soil. Soil Sci Soc Am Proc 17:34–38

Blair NE, Aller RC (2012) The fate of terrestrial organic carbon in the marine environment. Ann Rev Mar Sci 4:401–423

Blair NE, Leithold EL, Aller RC (2004) From bedrock to burial: the evolution of particulate organic carbon across coupled watershed-continental margin systems. Mar Chem 92:141–156

Blough NV, Del Vecchio R (2002) Chromophoric DOM in the coastal environment. In: Carlson CA, Hansell DA (eds) Biogeochemistry of dissolved organic matter. Academic, London, pp 509–547

Bruesewitz DA, Gardner WS, Mooney RF, Pollard L, Buskey EJ (2013) Estuarine ecosystem function response to flood and drought in a shallow, semiarid estuary: nitrogen cycling and ecosystem metabolism. Limnol Oceanogr 58:2293–2309

Burdige DJ (2005) Burial of terrestrial organic matter in marine sediments: a re-assessment. Glob Biogeochem Cycles 19. https://doi.org/10.1029/2004GB002368

Canuel EA, Hardison AK (2016) Sources, ages, and alteration of organic matter in estuaries. Ann Rev Mar Sci 8:409–434

Canuel EA, Martens CS (1996) Reactivity of recently deposited organic matter: degradation of lipid compounds near the sediment-water interface. Geochim Cosmochim Acta 60:1793–1806

Canuel EA, Zimmerman AR (2006) Composition of particulate organic matter in the southern Chesapeake Bay: sources and reactivity. Estuaries 22:980–944

Coble PG (2007) Marine optical biogeochemistry: the chemistry of ocean color. Chem Rev 107:402–418

Cole JJ, Prairie YT, Caraco NF, McDowell WH, Tranvik LJ, Striegl RG, Melack J (2007) Plumbing the global carbon cycle: integrating inland waters into the terrestrial carbon budget. Ecosystems 10:171–184

Cory RM, McKnight DM (2005) Fluorescence spectroscopy reveals ubiquitous presence of oxidized and reduced quinones in dissolved organic matter. Environ Sci Technol 39:8142–8149

Del Vecchio R, Blough NV (2002) Photobleaching of chromophoric dissolved organic matter in natural waters: kinetics and modeling. Mar Chem 78:231–253

Dickens AF, Gelinas Y, Masiello CA, Wakeham SG, Hedges J (2004) Reburial of fossil organic carbon in marine sediments. Nature 427:336–339

Drenzek NJ, Montluçon DB, Yunker MB, Macdonald RW, Eglinton TI (2007) Constraints on the origin of sedimentary organic carbon in the Beaufort Sea from coupled molecular ^{13}C and ^{14}C measurements. Mar Chem 103:146–162

Drenzek NJ, Hughen KA, Montluçon DB, Southon JR, dosSantos GM, Druffel ERM, Giosan L, Eglinton TI (2009) A new look at old carbon in active margin sediments. Geology 37:239–242

Eglinton G, Hamilton RJ (1967) Leaf epicuticular waxes. Science 156:1322–1335

Emerson S (1985) Organic carbon preservation in marine sediments. In: Sundquist ET, Broecker WS (eds) The carbon cycle and CO_2: natural variations Archean to present. American Geophysical Union, Washington, DC, pp 78–87

Fellman JB, Hood E, Spencer RGM (2010) Fluorescence spectroscopy opens new windows into dissolved organic matter dynamics in freshwater ecosystems: a review. Limnol Oceanogr 55:2452–2462

Ficken KJ, Li B, Swain DL, Eglinton G (2000) An n-alkane proxy for the sedimentary input of submerged/floating freshwater aquatic macrophytes. Org Geochem 31:745–749

Galy V, Peucker-Ehrenbrink B, Eglinton T (2015) Global carbon export from the terrestrial biosphere controlled by erosion. Nature 521: 204–207

Goñi MA, Ruttenberg KC, Eglinton TI (1997) Sources and contribution of terrigenous organic carbon to surface sediments in the Gulf of Mexico. Nature 389:275–278

Goñi MG, Ruttenberg KC, Eglinton TI (1998) A reassessment of the sources and importance of land-derived organic matter in surface sediments from the Gulf of Mexico. Geochim Cosmochim Acta 62:3055–3075

Goñi MA, Monacci N, Gisewhite R, Ogston A, Crockett J, Nittrouer CA (2006) Distribution and sources of particulate organic matter in the water column and sediments of the fly River Delta, Gulf of Papua (Papua New Guinea). Estuar Coast Shelf Sci 69:225–245

Goñi MA, Monacci N, Gisewhite R, Crockett J, Nittrouer CA, Ogston A, Alin SR, Aalto R (2008) Terrigenous organic matter in sediments from the fly river delta-clinoform system (Papua New Guinea). J Geophys Res 113. https://doi.org/10.1029/2006JF000653. 000627 pp

Gonsior M, Peake BM, Cooper WT, Podgorski D, D'Andrilli J, Cooper WJ (2009) Photochemically induced changes in dissolved organic matter identified by ultrahigh resolution Fourier transform ion cyclotron resonance mass spectrometry. Environ Sci Technol 43:698–703

Gordon ES, Goñi MA (2003) Sources and distribution of terrigenous organic matter delivered by the Atchafalaya River to sediments in the northern Gulf of Mexico. Geochim Cosmochim Acta 43:2359–2375

Hamer U, Marschner B, Brodowski S, Amelung W (2004) Interactive priming of black carbon and glucose mineralisation. Org Geochem 35:823–830

Hartnett HE, Keil RG, Hedges JI, Devol AH (1998) Influence of oxygen exposure time on organic carbon preservation in continental margin sediments. Nature 391:572–574

Hatcher PG, Spiker EC, Szevereny NM, Maciel GE (1983) Selective preservation and origin of petroleum-forming aquatic kerogen. Nature 305:498–501

Hedges JI, Keil RG (1995) Sedimentary organic matter preservation: an assessment and speculative synthesis. Mar Chem 49:81–115

Hedges JI, Keil RG, Benner R (1997) What happens to terrestrial organic matter in the ocean? Org Geochem 27:195–212

Hedges J, Eglinton G, Hatcher P, Kirchman D, Arnosti C, Derenne S et al (2000) The molecularly-uncharacterized component of nonliving organic matter in natural environments. Org Geochem 31:945–958

Helms JR, Stubbins A, Perdue EM, Green NW, Chen H, Mopper K (2013) Photochemical bleaching of oceanic dissolved organic matter and its effect on absorption spectral slope and fluorescence. Mar Chem 155:81–91

Hermes AL, Sikes EL (2016) Particulate organic matter higher concentrations, terrestrial sources and losses in bottom waters of the turbidity maximum, Delaware estuary, U.S.A. Estuar Coast Shelf Sci 180:179–189

Hernes PJ, Benner R (2003) Photochemical and microbial degradation of dissolved lignin phenols: implications for the fate of terrigenous dissolved organic matter in marine environments. J Geophys Res 108:3291. https://doi.org/10.1029/2002JC001421

Jaffé R, Mead R, Hernandez ME, Peralba M, DiGuida OA (2001) Origin and transport of sedimentary organic matter in two subtropical estuaries: a comparative, biomarker-based study. Org Geochem 32:507–526

Jaffé R, Rushdi AI, Medeiros PM, Simoneit BRT (2006) Natural product biomarkers as indicators of sources and transport of sedimentary lipids in a subtropical river. Chemosphere 64:1870–1884

Jaffe R, McKnight DM, Maie N, Cory RM, McDowell WH, Campbell JL (2008) Spatial and temporal variations in DOM composition in ecosystems: the importance of long-term monitoring of optical properties. J Geophys Res 113:G04032. https://doi.org/10.1029/2008JG000683

Keil RG, Montluçon DB, Prahl FG, Hedges JI (1994) Sorptive preservation of labile organic matter in marine sediments. Nature 370:549–552

Kennedy MJ, Wagner T (2011) Clay mineral continental amplifier for marine carbon sequestration in a greenhouse ocean. Proc Natl Acad Sci USA 108:9776–9781. https://doi.org/10.1073/pnas.1018670108

Kennicutt MC II, Barker C, Brooks JM, DeFreitas DA, Zhu GH (1987) Selected organic matter source indicators in the Orinoco, Nile and Changjing deltas. Org Geochem 15:41–51

Kolattukudy PE (1976) Chemistry and biochemistry of natural waxes. Elsevier, Amsterdam

Komada T, Schofield OME, Reimers CE (2002) Fluorescence characteristics of organic matter released from coastal sediments during resuspension. Mar Chem 79:81–97

Kuzyakov Y, Friedel JK, Stahr K (2000) Review of mechanisms and quantification of priming effects. Soil Biol Biochem 32:1485–1498

Lee C, Wakeham SG (1988) Organic matter in seawater: biogeochemical processes. In: Riley JP (ed) Chemical oceanogrpahy. Academic, New York, pp 1–57

Leithold EL, Blair N, Perkey DW (2006) Geomorphologic controls on the age of particulate organic carbon from small mountainous and

upland rivers. Glob Biogeochem Cycles 20. https://doi.org/10.1029/2005GB002677
Lyons WB, Nezat CA, Carey AE, Hicks AM (2002) Organic carbon fluxes to the ocean from high standing islands. Geology 30:443–446
Mannino A, Harvey HR (2000) Terrigenous dissolved organic matter along an estuarine gradient and its flux to the coastal ocean. Org Geochem 31:1611–1625
McCallister SL, del Giorgio PA (2008) Direct measurement of the $\delta^{13}C$ signature of C respired by bacteria in lakes: linkages to potential carbon sources ecosystem baseline metabolism and CO_2 fluxes. Limnol Oceanogr 53:1204–1216
McCallister SL, Bauer JE, Cherrier JE, Ducklow HW (2004) Assessing sources and ages of organic matter supporting river and estuarine bacterial production: a multiple-isotope (Delta C-14, delta C-13, and delta N-15) approach. Limnol Oceanogr 49:1687–1702
Medeiros PM, Sikes EL, Thomas B, Freeman KH (2012) Flow discharge influences on input and transport of particulate and sedimentary organic carbon along a small temperate river. Geochim Cosmochim Acta 77:317–334
Meyers PA (1997) Organic geochemical proxies of paleoceanographic, paleolimnologic, and paleoclimatic processes. Org Geochem 27: 213–250
Obernosterer I, Benner R (2004) Competition between biological and photochemical processes in the mineralization of dissolved organic carbon. Limnol Oceanogr 49:117–124
Onstad GD, Canfield DE, Quay PD, Hedges JI (2000) Sources of particulate organic matter in rivers from the continental USA: lignin phenol and stable carbon isotope compositions. Geochim Cosmochim Acta 64:3539–3546
Oros DR, Simoneit BRT (2001) Identification and emission factors of molecular tracers in organic aerosols from biomass burning. Part 1. Temperate climate conifers. Appl Geochem 16:1513–1544
Pearson A, Eglinton TI (2000) The origin of *n*-alkanes in Santa Monica Basin surface sediment: a model based on compound specific $\Delta^{14}C$ and $\delta^{13}C$ data. Org Geochem 31:1103–1116
Pearson A, McNichol AP, Benitez-Nelson BC, Hayes JM, Eglinton TI (2001) Origins of lipid biomarkers in Santa Monica Basin surface sediment: a case study using compound -specific $\Delta^{14}C$ analysis. Geochim Cosmochim Acta 65:3123–3137
Prahl FG, Muehlhausen LA (1989) Lipid biomarkers as geochemical tools for paleoceanographic study. In: Berger WH, Smetacek VS, Wefer G (eds) Productivity in the oceans: present and past. Wiley, Chichester, pp 271–289
Raymo ME (1997) Carbon cycle models: how strong are the constraints? In: Ruddiman WF (ed) Tectonic uplift and climate change. Plenum Press, New York, pp 367–381
Rontani JF, Charriere B, Petit M, Vaultier F, Heipieper HJ, Link H, Chaillou G, Sempere R (2012) Degradation state of organic matter in surface sediments from the southern Beaufort Sea: a lipid approach. Biogeosciences 9:3513–3530
Sikes EL, Uhle ME, Nodder SD, Howard ME (2009) Sources of organic matter in a coastal marine environment: evidence from n-alkanes and their d13C distributions in the Hauraki gulf, New Zealand. Mar Chem 113:149–163
Stedmon CA, Thomas DN, Granskog M, Kaartokallio H, Papadimitriou S, Kuosa H (2007) Characteristics of dissolved organic matter in Baltic coastal sea ice: Allochthonous or autochthonous origins? Environ Sci Technol 41:7273–7279
Sun M-Y, Aller RC, Lee C, Wakeham SG (2002) Effects of oxygen and redox oscillation on degradation of cell-associated lipids in surficial marine sediments. Geochim Cosmochim Acta 66: 2003–2012
Tremblay LB, Dittmar T, Marshall AG, Cooper WJ, Cooper WT (2007) Molecular characterization of dissolved organic matter in a north Brazilian mangrove porewater and mangrove-fringed estuaries by ultrahigh resolution Fourier transform-ion cyclotron resonance mass spectrometry and excitation/emission spectroscopy. Mar Chem 105:15–29
Wakeham S, Lee C (1993) Production, transport, and alteration of particulate organic matter in the marine water column. In: Engel MH, Macko SA (eds) Organic geochemistry. Plenum Press, New York, pp 145–169
Ziervogel K, Arnosti C (2009) Enzyme activities in the Delaware estuary affected by elevated suspended sediment load. Estuar Coast Shelf Sci 84:253–258
Zimmerman AR, Canuel EA (2001) Bulk organic matter and lipid biomarker composition of Chesapeake Bay surficial sediments as indicators of environmental processes. Estuar Coast Shelf Sci 53:319–341

Osmium

Richard J. Walker
Department of Geology, University of Maryland, College Park, MD, USA

Element Data
Atomic Symbol: **Os**
Atomic Number: **76**
Atomic Weight: 190.2
Isotopes and Abundances:
184: 0.0174%
186: 1.5935%
187: 1.5129%
188: 13.296%
189: 16.217%
190: 26.376%
192: 40.988%
1 Atm Melting Point: 3030 °C
1 Atm Boiling Point: 5010 °C
Common Valences: 0, +3, +4, +8
Ionic Radii: 53–77 pm
Pauling Electronegativity: 2.2
First Ionization Potential: 8.44 eV
Chondritic (CI) Abundance: 490 ppb
Silicate Earth Abundance: 3.9 ppb
Crustal Abundance: 0.031 ppb (continental), 0.055 (oceanic)
Seawater Abundance: 10 pg/L
Core Abundance: 2800 ppb

Properties

Osmium is a highly refractory, bluish-white metal (hexagonal close packed). It is hard and brittle and has a density of 22,600 kg/m^3, the highest of any element. Osmium is not a

structural constituent of any mineral, but it alloys with iridium and ruthenium and is also found in high abundance in some sulfide minerals, such as laurite (RuS_2). Osmium has oxidation states ranging from 0 to +8, but in nature 0, +3, +4, and +8 probably predominate.

History and Use

Osmium was discovered by Smithson Tennant in 1804. The element has two major commercial uses. Because of its hardness, it has been used in fountain pen nibs, and it remains commonly used for staining biological tissues for microscopy.

Geochemical Behavior

Osmium is one of the six platinum-group elements (PGE; Os, Ir, Ru, Pt, Rh, Pd). It is geochemically termed "siderophile" because it has a strong propensity to partition into metallic iron, rather than silicates (Goldschmidt 1937). As such, most of Earth's Os is contained in the core. Osmium also has a tendency to partition into sulfide melts and some sulfide minerals, so it is also referred to as a "chalcophile" element.

Osmium isotopic abundances vary in nature due to the radioactive decay of other elements: ^{187}Re decays to ^{187}Os by β^- emission (2.3 keV maximum β^- energy, half-life 4.16×10^{10} years) and is the basis for the Re-Os method of geochronology; ^{190}Pt forms ^{186}Os by α decay (α energy 3.19 MeV, half-life $\sim 4.50 \times 10^{11}$ years), which forms the basis of the Pt-Os system. Variations in the abundance of ^{186}Os are measurable only in Pt-rich materials because of the long half-life and very low isotopic abundance of ^{190}Pt (0.0129%).

Cosmochemistry

The solar abundance is 0.675 atoms Os per 10^6 atoms Si, corresponding to an average concentration of Os in CI chondrities of ~490 ppb (Anders and Grevesse 1989). Osmium, along with the other PGE, is concentrated in planetary cores. It is typically enriched, relative to chondritic meteorites, in most iron meteorites that sample asteroidal cores. By contrast, Os abundances in unbrecciated basaltic achondrites, such as angrites and eucrites, can be very low (<0.01 ppb) (Dale et al. 2012).

The chondritic relative abundances of the PGE in Earth's mantle has led to the conclusion that core formation in the early Earth strongly depleted the silicate mantle of these elements, and their present abundances are likely the result of a late influx of meteoritic material (Chou 1978).

Igneous and Metamorphic Rocks

The bulk silicate Earth concentration of Os is ~3.9 ppb Os, as estimated from variably melt-depleted mantle peridotites (Fischer-Gödde et al. 2011). During basalt formation by partial melting of the mantle, Os behaves as a strongly compatible element and remains predominantly in the residual peridotite. As a consequence of its compatibility, its abundance in the oceanic crust is very low, ~0.055 ppb (Peucker-Ehrenbrink et al. 2012). The concentration of Os in the continental crust is similar, averaging ~0.031 ppb Os (Rudnick and Gao 2003). Ocean island basalts tend to have higher abundances, ranging up to 0.5 ppb (Day 2013), and high MgO volcanic rocks, such as komatiites, can have abundances >3 ppb (Puchtel et al. 2009). The concentration of Os in metamorphic rocks has been little explored. Limited data suggest concentrations broadly follow those of igneous or sedimentary precursors (Penniston-Dorland et al. 2012).

Sedimentary Rocks

Because Os^{4+} is probably hydrolyzed and scavenged from seawater as $OsO_2 \cdot xH_2O$, the residence time of Os in the ocean is short ($<10^3$ years) and the abundance very low (~10 pg/L) (Chen and Sharma 2009). In oxidized sediments, cosmic influx may have slightly enhanced the observed abundances of Os: shales 0.05–0.45 ppb and quartz-rich sandstones 0.06–0.08 ppb (Koeberl et al. 1994). Osmium concentrations are typically higher in sedimentary rocks formed under reducing conditions, e.g., 0.2–0.7 ppb in Black Sea sediments (Ravizza et al. 1991), 0.9–4 ppb in black shales (Kendall et al. 2009), and >200 ppb in some mineralized black shales (Horan et al. 1994). In black shales and hydrocarbon deposits, much of the Os is radiogenic ^{187}Os from the decay of ^{187}Re. The Re-Os isotope system can therefore be used for dating these materials (Selby and Creaser 2005; Kendall et al. 2009).

Biological Utilization and Toxicity

Osmium has no known biological role. While Os metal is not toxic, osmium tetraoxide (OsO_4) is volatile and highly toxic, causing lung, skin, and eye damage and has a US NIOSH exposure limit of 0.2 ppb or 0.0016 $mg.m^3$. Given its low natural abundance, however, exposures at these levels are extremely rare.

Cross-References

- ▶ Chalcophile Elements
- ▶ Earth's Core
- ▶ Meteorites
- ▶ Osmium Isotopes
- ▶ Platinum Group Elements
- ▶ Rhenium
- ▶ Siderophile Elements

References

Anders E, Grevesse N (1989) Abundances of the elements: meteoritic and solar. Geochim Cosmochim Acta 53:197–214

Chen C, Sharma M (2009) High precision and high sensitivity measurements of osmium in seawater. Anal Chem 81:5400–5406

Chou C-L (1978) Fractionation of siderophile elements in the earth's upper mantle. In: Proceedings of the lunar and planetary science conference 9th, pp 219–230

Dale CW, Burton KW, Greenwood RC, Gannoun A, Wade J, Wood BJ, Pearson DG (2012) Late accretion on the earliest planetesimals revealed by the highly siderophile elements. Science 336:72–75

Day JMD (2013) Hotspot volcanism and highly siderophile elements. Chem Geol 341:50–74

Fischer-Gödde M, Becker H, Wombacher F (2011) Rhodium, gold and other highly siderophile element abundances in orogenic peridotites and peridotite xenoliths. Chem Geol 280:365–383

Goldschmidt VM (1937) The principles of distribution of chemical elements in minerals and rocks. J Chem Soc:655–673

Horan MF, Morgan JW, Grauch RI, Coveney RM, Murowchick JB, Hulbert LJ (1994) Rhenium and osmium isotopes in black shales and Ni-Mo-PGE-rich sulfide layers, Yukon territory, Canada, and Hunan and Guizhou provinces, China. Geochim Cosmochim Acta 58:257–265

Kendall B, Creaser RA, Selby D (2009) ^{187}Re-^{187}Os geochronology of Precambrian organic-rich sedimentary rocks. Geol Soc Lond Spec Publ 326:85–107

Koeberl C, Reimold WU, Shirey SB, LeRoux FG (1994) Kalkkop Crater, Cape Province, South Africa: confirmation of impact origin using osmium isotope systematics. Geochim Cosmochim Acta 58:1229–1234

Penniston-Dorland SC, Walker RJ, Pitcher L, Sorensen SS (2012) Mantle-crust interactions in a paleosubduction zone: evidence from highly-siderophile element systematics of eclogite and related rocks. Earth Planet Sci Lett 319–320:295–306

Peucker-Ehrenbrink B, Hanghøj K, Atwood T, Kelemen PB (2012) Rhenium-osmium isotope systematics and platinum group element concentrations in oceanic crust. Geology 40:199–202

Puchtel IS, Walker RJ, Brandon AD, Nisbet EG (2009) Pt-Re-Os and Sm-Nd isotope and HSE and REE systematics of the 2.7 Ga Belingwe and Abitibi komatiites. Geochim Cosmochim Acta 73:6367–6389

Ravizza G, Turekian KK, Hay BJ (1991) The geochemistry of rhenium and osmium in recent sediment from the Black Sea. Geochim Cosmochim Acta 55:3741–3752

Rudnick RL, Gao S (2003) Composition of the continental crust. In: Rudnick RL (ed) The crust, Treatise on geochemistry, vol 3. Elsevier B.V, Amsterdam, pp 1–64

Selby D, Creaser RA (2005) Direct radiometric dating of hydrocarbon deposits using rhenium-osmium isotopes. Science 308:1293–1295

Osmium Isotopes

Richard J. Walker
Department of Geology, University of Maryland, College Park, MD, USA

Definition

The Re-Os system is a long-lived radiogenic isotope system system based on two siderophile (iron-loving) elements. With a ^{187}Re half-life of ~42 Ga, the system can potentially be used for dating rocks and minerals ranging from the age of the solar system to high Re/Os minerals <1 Ma. Because of the highly variable Re/Os ratios in different types of rocks, the system is also valuable for tracing crustal recycling into the mantle, and anthropogenic contributions of heavy metals to waterways, among numerous other applications.

Introduction

The ^{187}Re-^{187}Os system has relevance to a wide range of cosmochemical and geochemical applications. The isotope ^{187}Re decays by β^- emission to ^{187}Os with a decay constant of 1.67×10^{-11}year^{-1} ($t_{½} = 41.6 \times 10^9$ years), with an approximately ±1% uncertainty (Smoliar et al. 1996). Both Re and Os are highly siderophile and under some conditions also chalcophile. The system has been used as a tracer to study the effects of planetary core formation (Righter and Drake 1997), as well as subsequent accretion of planetesimals to planetary mantles after cessation of core formation (Morgan 1985). The system has also been commonly applied to the study of the timing of mantle melting, particularly in the subcontinental lithospheric mantle (SCLM) (Pearson et al. 1995), as well as diverse chronologic applications ranging from dating iron meteorites (Luck et al. 1980) to constraining the timing of petroleum emplacement in oil sand deposits (Selby and Creaser 2005). When applied as a tracer, Os isotopes have been used to assess crustal recycling into the mantle sources of ocean island basalts (Day 2013), for determining the changing contributions of Os from mantle, continental crustal, and organic-rich sedimentary sources to the oceans (Peucker-Ehrenbrink and Ravizza 2000) and for tracking anthropogenic heavy metal contributions to freshwater and marine sediments (Turekian et al. 2007).

Overview of the Geochemistry of Re and Os

In nature, Re is comprised of two isotopes, ^{185}Re (37.40 at.%) and ^{187}Re (62.60 at.%), and has an atomic weight of 186.207 (Gramlich et al. 1973). Osmium is made up of seven stable isotopes: ^{184}Os, ^{186}Os, ^{187}Os, ^{188}Os, ^{189}Os, ^{190}Os, and ^{192}Os. In addition to the production of ^{187}Os from the decay of ^{187}Re, ^{186}Os is produced from ^{190}Pt by α emission, with a decay constant of $\sim 1.5 \times 10^{-12}$year^{-1} (Walker et al. 1997). Therefore, the absolute abundances of Os isotopes and the atomic weight of Os vary in nature because both ^{186}Os and ^{187}Os are radioactive decay products. Isotopic ratios and atomic percentages for the University of Maryland interlaboratory reference material are provided in Table 1.

Osmium Isotopes, Table 1 Isotopic composition of the University of Maryland *Johnson-Matthey* interlaboratory reference material

Isotopic ratio	Measured ratio	2a uncertainty	Isotope	Percentage composition	Atomic weight
$^{184}Os/^{188}Os$	0.0013037	4	^{184}Os	0.0173%	190.240
$^{186}Os/^{188}Os$	0.119850	4	^{186}Os	1.5935%	
$^{187}Os/^{188}Os$	0.113787	9	^{187}Os	1.5129%	
$^{189}Os/^{188}Os$	1.00000		^{188}Os	13.296%	
$^{190}Os/^{188}Os$	1.983736	30	^{189}Os	16.217%	
$^{192}Os/^{188}Os$	*3.08271*		^{190}Os	26.376%	
			^{192}Os	40.988%	

Measurement of the System

Early studies of the Re-Os isotope system were hindered by the lack of sensitive and precise mass spectrometric methods. Techniques such as secondary ionization mass spectrometry and resonance ionization mass spectrometry were initially employed to measure Os isotopes, but these techniques yielded relatively imprecise results (Luck et al. 1980). In the early 1990s, it was recognized that Os and Re were amenable to negative thermal ionization mass spectrometry (NTIMS), as negatively charged tri- and tetra-oxide species, respectively (Creaser et al. 1991). This discovery led to a revolution in the sensitivity and precision of measurements of these elements, as well as ushering in a much broader range of applications. Inductively coupled plasma mass spectrometry (ICP-MS) is now also commonly used to measure the isotopic compositions of Re and Os (Nowell et al. 2008).

Both acid and fusion digestions are used to dissolve phases and equilibrate enriched isotopes (spikes) with sample. The latter aspect is especially critical because of the numerous oxidation states and species possible for each element. At present, there is no one technique that is equally applicable to all matrices. Low-temperature (<150 °C) acid-based digestion techniques under reducing conditions (Birck et al. 1997) typically have low blanks but can have limitations in the dissolution of acid-resistant phases. High-temperature (>200 °C) oxidizing digestions achieved with, for example, *aqua regia* can lead to the production of volatile species of each element, so oxidizing digestions are normally done in closed vessels (Shirey and Walker 1995). Unlike lower-temperature digestions, high-temperature oxidative digestions can dissolve acid-resistant phases, such as chromite and noble metal alloys, but they leave most silicates partially or completely undigested. This may not be problematic for most rocks, because Re and Os are primarily concentrated in sulfides, alloys, and oxides, and excluded from for the structures of silicates, although there are some exceptions (Ishikawa et al. 2014). Fusion techniques include nickel sulfide fire-assay (Hoffman et al. 1978) and sodium-peroxide digestion (Morgan and Walker 1989). Fusions result in the complete digestion of all phases but are normally characterized by higher blanks.

Once sample digestion and equilibration is achieved, Os can be separated from a rock matrix by distillation (b.p. for OsO_4 is 105 °C) (Walker 1988) or solvent extraction (Cohen and Waters 1996; Birck et al. 1997). Rhenium is separated using anion exchange chromatography (Morgan and Walker 1989).

Geochronologic Applications

Dating rocks or minerals using the Re-Os system is either done by conventional isochron methods, or by model age calculations, usually assuming derivation of the material to be dated from a reservoir that had previously evolved with chondritic Re/Os. Rhenium-Os isochron dating has most commonly been applied to iron meteorites and some terrestrial igneous and sedimentary systems. For the system to be useful, geochemical processes must lead to sufficient variation in Re/Os. For example, organic-rich sedimentary rocks, such as black shales, are one type of rock commonly dated by Re-Os isochrons (Ravizza and Turekian 1989). They are usually characterized by high and variable Re/Os, but for precise age determination, it may be necessary to selectively analyze only the hydrogenous component of the rock (Selby and Creaser 2003).

The system can also be used to date single minerals. For example, molybdenite (MoS_2) has been shown to be a particularly robust mineral for achieving high precision Re-Os geochronology of some rocks (Stein et al. 2001). The system has also been used to date single sulfide grains incorporated in diamond (Pearson et al. 1998).

Cosmochemical Applications

Rhenium and Os are among the most refractory elements and were therefore among the first elements to condense from the solar nebula. As highly siderophile elements (HSE), they were primarily incorporated into metal during subsequent accretion and melting events, so the system is useful in the study of metals present in chondrites, stony irons, and iron meteorites. To date, the system primarily has been used to determine the ages of iron meteorites (Smoliar et al. 1996) and for characterizing the origins of materials added to the terrestrial planets through late accretion (Morgan 1985; Meisel et al. 2001). Some iron meteorites, as well as bulk chondrites, do not plot within analytical uncertainties of a primordial reference isochron, and the deviations have been interpreted to reflect open-system behavior long after the parent bodies formed.

The Re-Os System in the Earth's Mantle

Because of the limited removal of Re and especially Os from the mantle by partial melting processes, the vast proportion of Re and Os in the silicate Earth are retained in the mantle. Attempts to determine the bulk silicate Earth (BSE) concentrations of Re and Os and $^{187}Os/^{188}Os$ have largely been conducted by projecting data for variably melt-depleted mantle peridotites to fertile Lu, Al_2O_3, or MgO compositions (e.g., Meisel et al. 2001). The $^{187}Os/^{188}Os$ of the BSE averages ~0.129 (Meisel et al. 2001). This ratio is within the range of bulk chondrites and provides strong evidence that the HSE were added to the mantle after cessation of core formation by a process termed late accretion, or late veneer (Morgan 1985). The ratio is also noteworthy in that it is substantially higher than ratios observed in bulk samples of carbonaceous chondrites, but overlaps with ratios common for bulk enstatite and ordinary chondrites (Fig. 1). This indicates that late-accreted materials were more like ordinary or enstatite chondrites, rather than volatile-rich carbonaceous chondrites (Walker 2009).

Determination of the Os isotopic composition of the oceanic mantle has been difficult. In particular, the study of the system in mid-ocean ridge basalts (MORB), which are commonly used to provide averaged chemical and isotopic snapshots of different portions of the oceanic mantle, has been challenging due to the very low concentration of Os in MORB (Gannoun et al. 2007). Low Os concentrations make the Os isotopic compositions of basalts subject to modification as a result of contamination with oceanic crust and seawater. Most studies of the Os isotopic composition of MORB (e.g., Gannoun et al. 2007) have reported generally similar $^{187}Os/^{188}Os$ ratios ranging from chondritic (~0.126) to considerably suprachondritic (>0.15).

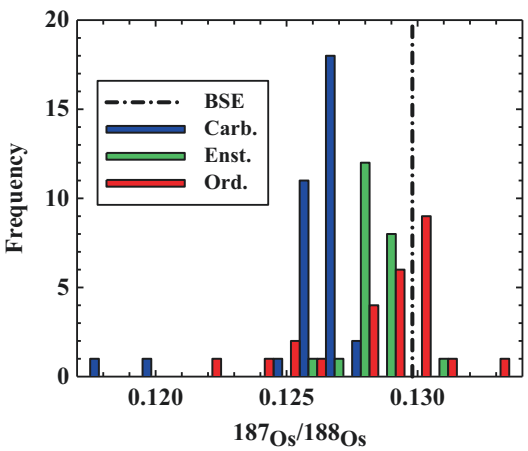

Osmium Isotopes, Fig. 1 Histogram plot showing estimate of the $^{187}Os/^{188}Os$ of the bulk silicate Earth (BSE) versus data for bulk samples of carbonaceous, enstatite, and ordinary chondrites (Figure modified from Walker 2009)

Other sources of information about the Os isotopic composition of the oceanic mantle are oceanic peridotites, also known as abyssal peridotites. The $^{187}Os/^{188}Os$ ratios for abyssal peridotites are much more restricted in range than for MORB and average approximately 0.125 (e.g., Lassiter et al. 2014). Limited isotopic overlap between MORB and abyssal peridotites may reflect lithospheric contamination of MORB, isotopic overprinting of abyssal peridotites resulting from mantle metasomatism, or the sampling of different materials in the oceanic mantle.

Osmium isotopes are useful for determining the timing of SCLM formation because mantle melting leads to the removal of some or all Re from the residues of melting that become SCLM (Pearson et al. 1995). Osmium model ages for peridotites with chemical evidence for strong melt depletion are calculated by comparing the measured isotopic composition with a reference growth model (chondritic) for the ambient mantle. A major contribution of Os isotopes to solid Earth geochemistry was the discovery that most ancient cratons are underlain by SCLM of approximately the same age as the overlying craton, suggesting that the creation of craton and underlying lithospheric mantle is intimately related (Pearson et al. 1995). By contrast, in some locations, such as the North China Craton, Os isotopes have provided chronological evidence that ancient SCLM underlying Archean craton has been removed, perhaps through lithospheric delamination (Gao et al. 2002).

Ocean island basalts (OIB) and related rocks are the surface manifestations of intraplate volcanism. Osmium isotopic data for OIB are commonly filtered for samples with very low Os abundances (e.g., < 50 pg/g), as these samples are susceptible to contamination through interactions with crustal or seawater Os. The $^{187}Os/^{188}Os$ ratios of OIB lavas with comparatively high Os concentrations generally range from that of the average oceanic mantle (0.125) to 20–30% percent higher (Day 2013). Osmium isotopic heterogeneity observed in OIB is mainly attributed to the incorporation of diverse recycled crustal components in their mantle sources (Day 2013).

The Re-Os System in the Earth's Crust and Hydrosphere

All of Earth's crust was extracted from the mantle at some point in Earth history. The tendency of Os to be strongly compatible and Re to be mildly incompatible during mantle melting means that both oceanic and continental crust are characterized by Re concentrations that are only slightly higher, and Os concentrations that are much lower, than mantle concentrations. Both oceanic and continental crusts are, therefore, characterized by high Re/Os, and even oceanic or continental crust of moderate age can have a very high $^{187}Os/^{188}Os$.

The Re-Os systematics of oceanic crust in the form of MORB is well studied. Less is currently known about the system in the continental crust and the arc lavas that are an important building block of it. The study of the Re-Os isotopic systematics of arc lavas has faced many of the same problems as studies of MORB and OIB. Low initial concentrations of Os leave them susceptible to contamination with radiogenic Os from crustal rocks or fluids. Arc lavas have $^{187}Os/^{188}Os$ ratios ranging from chondritic to >1, although most are within the chondritic range (Alves et al. 2002). This suggests that at least some continental crust originated with mantle-like $^{187}Os/^{188}Os$.

The average $^{187}Os/^{188}Os$ ratio of the upper continental crust has been estimated through studies of loess (Peucker-Ehrenbrink and Jahn 2001) and river waters and sediments (Sharma et al. 1999). The $^{187}Os/^{188}Os$ of these materials is typically >1. The high average $^{187}Os/^{188}Os$ ratio of the continental crust that is currently being eroded is also indicated by the $^{187}Os/^{188}Os$ of modern seawater to be approximately 1.05 (Chen and Sharma 2009). This ratio, however, has greatly varied over the past 100 Ma as a result of variable input of Os to the oceans from crustal versus mantle sources, as well as a result of substantial contributions of non-radiogenic Os to the oceans at 65 Ma, from the Chicxulub impactor, the Deccan Traps, or a combination (Peucker-Ehrenbrink and Ravizza 2000).

Most Os that is produced for industrial use, such as for biological tissue staining, or is produced as an ancillary product in the extraction and purification of other heavy metals, comes from platinum-group element-rich deposits, such as the Bushveld Complex, in South Africa, and is characterized by low, generally mantle-like $^{187}Os/^{188}Os$ ratios. Because of the isotopic contrast between such materials and crustal Os, Os isotopes have also been used in the tracing of anthropogenic contaminants to surface waters (Turekian et al. 2007; Chen et al. 2009).

Summary

The Re-Os isotopic system is widely used for dating a variety of cosmo- and geochemical systems including iron meteorites, organic-rich sedimentary rocks, molybdenites, and sulfide inclusions in diamonds. The system also serves as an important tracer of late-accreted materials to the Earth, recycled crustal components in the mantle, and crustal contributions to the oceans.

Cross-References

► Geochronology and Radiogenic Isotopes
► Osmium

References

Alves S, Schiano P, Capmas F, Allègre CJ (2002) Osmium isotope binary mixing arrays in arc volcanism. Earth Planet Sci Lett 198:355–369
Birck JL, Roy Barman M, Capmas F (1997) Re-Os isotopic measurements at the femtomole level in natural samples. Geostand Newslett 20:19–27
Chen C, Sharma M (2009) High precision and high sensitivity measurements of osmium in seawater. Anal Chem 81:5400–5406
Chen C, Sedwick PN, Sharma M (2009) Anthropogenic osmium in rain and snow reveals global-scale atmospheric contamination. Proc Natl Acad Sci 106:7724–7728
Cohen AS, Waters FG (1996) Separation of osmium from geological materials by solvent extraction for analysis by thermal ionization mass spectrometry. Anal Chim Acta 332:269–275
Creaser RA, Papanastassiou DA, Wasserburg GJ (1991) Negative thermal ion mass spectrometry of osmium, rhenium, and iridium. Geochim Cosmochim Acta 55:397–401
Day JMD (2013) Hotspot volcanism and highly siderophile elements. Chem Geol 341:50–74
Gannoun A, Burton KW, Parkinson IJ, Alard O, Schiano P, Thomas LE (2007) The scale and origin of the osmium isotope variations in mid-ocean ridge basalts. Earth Planet Sci Lett 259:541–556
Gao S, Rudnick RL, Carlson RW, McDonough WF, Liu Y-S (2002) Re-Os evidence for replacement of ancient mantle lithosphere beneath the North China craton. Earth Planet Sci Lett 198:307–322
Gramlich JW, Murphy TJ, Garner EL, Shields WR (1973) The atomic weight of rhenium. J Res Natl Bur Stand A 77:691–698
Hoffman EL, Naldrett AJ, Van Loon JC (1978) The determination of all the platinum group elements and gold in rocks and ore by neutron activation analysis after preconcentration by a nickel sulphide fire-assay technique on large samples. Anal Chim Acta 102:157–166
Ishikawa A, Senda R, Suzuki K, Dale CW, Meisel T (2014) Re-evaluating digestion methods for highly siderophile element and ^{187}Os isotope analysis: evidence from geological reference materials. Chem Geol 384:27–46
Lassiter JC, Byerly BL, Snow JE, Hellebrand E (2014) Constraints from Os-isotope variations on the origin of Lena Trough abyssal peridotites and implications for the composition and evolution of the depleted upper mantle. Earth Planet Sci Lett 403:178–187
Luck J-M, Birck J-L, Allègre CJ (1980) ^{187}Re-^{187}Os systematics in meteorites: early chronology of the solar system and age of the galaxy. Nature 283:256–259
Meisel T, Walker RJ, Irving AJ, Lorand J-P (2001) Osmium isotopic compositions of mantle xenoliths: a global perspective. Geochim Cosmochim Acta 65:1311–1323
Morgan JW (1985) Osmium isotope constraints on Earth's late accretionary history. Nature 317:703–705
Morgan JW, Walker RJ (1989) Isotopic determinations of rhenium and osmium using fusion, distillation and ion exchange separations, as applied to meteorites. Anal Chim Acta 222:291–300
Nowell GM, Luguet A, Pearson DG, Horstwood MA (2008) Precise and accurate $^{186}Os/^{188}Os$ and $^{187}Os/^{188}Os$ measurements by Multi-Collector Plasma Ionisation Mass Spectrometry (MC- ICP-MS) part I: solution analyses. Special Issue on Highly Siderophile Element Geochemistry. Chem Geol 248:363–393
Pearson DG, Carlson RW, Shirey SB, Boyd FR, Nixon PH (1995) Stabilisation of Archean lithospheric mantle: a Re–Os isotope study of xenoliths from the Kaapvaal craton. Earth Planet Sci Lett 134:341–357
Pearson DG, Shirey SB, Harris JW, Carlson RW (1998) Sulphide inclusions in diamonds from the Koffiefontein kimberlite, S Africa: constrains on diamond ages and mantle Re-Os systematics. Earth Planet Sci Lett 160:311–326

Peucker Ehrenbrink B, Jahn B-M (2001) Rhenium-osmium isotope systematics and platinum group element concentrations: loess and the upper continental crust. Geochem Geophys Geosyst 2:1–24, 2001GC000172
Peucker-Ehrenbrink B, Ravizza GE (2000) The marine osmium isotope record. Terra Nova 12:205–219
Ravizza GE, Turekian KK (1989) Application of the ^{187}Re-^{187}Os system to black shale geochronometry. Geochim Cosmochim Acta 53:3257–3262
Righter K, Drake MJ (1997) Metal-silicate equilibrium in a homogeneously accreting earth: new results for Re. Earth Planet Sci Lett 146:541–553
Selby D, Creaser RA (2003) Re–Os geochronology of organic rich sediments: an evaluation of organic matter analysis methods. Chem Geol 200:225–240
Selby D, Creaser RA (2005) Direct radiometric dating of hydrocarbon deposits using rhenium-osmium isotopes. Science 308:1293–1295
Sharma M, Wasserburg GJ, Hofmann AW, Chakrapani GJ (1999) Himalayan uplift and osmium isotopes in oceans and rivers. Geochim Cosmochim Acta 63:4005–5012
Shirey SB, Walker RJ (1995) Carius tube digestion for low-blank rhenium-osmium analysis. Anal Chem 34:2136–2141
Smoliar MI, Walker RJ, Morgan JW (1996) Re-Os ages of group IIA, IIIA, IVA and IVB iron meteorites. Science 271:1099–1102
Stein HJ, Markey RJ, Morgan JW, Hannah JL, Scherstén A (2001) The remarkable Re ± Os chronometer in molybdenite: how and why it works. Terra Nova 13:479–486
Turekian KK, Sharma M, Williams GG (2007) The behavior of natural and anthropogenic osmium in the Hudson River-Long Island Sound estuarine system. Geochim Cosmochim Acta 71:4135–4140
Walker RJ (1988) Low-blank chemical separation of osmium and rhenium from gram quantities of silicate rock for measurement by resonance ionization mass spectrometry. Anal Chem 60:1231–1234
Walker RJ (2009) Highly siderophile elements in the Earth, Moon and Mars: update and implications for planetary accretion and differentiation. Chem Erde 69:101–125
Walker RJ, Morgan JW, Beary E, Smoliar MI, Czamanske GK, Horan MF (1997) Applications of the ^{190}Pt-^{186}Os isotope system to geochemistry and cosmochemistry. Geochim Cosmochim Acta 61:4799–4808

Oxidation-Reduction Reactions and E_h-pH (Pourbaix) Diagrams

William H. Casey
Department of Chemistry and Department of Earth and Planetary Sciences, University of California, Davis, CA, USA

Synonyms

Eh-pH diagrams; Redox; pε-pH Diagrams

Definition

Oxidation-reduction (redox) reactions are those in which electrons are transferred between atoms resulting in a consequent change in the valence state of those atoms. Atoms losing electrons are said to be oxidized, and those gaining electrons are said to be reduced in such reactions. E_h, the hydrogen-electrode-scale electric potential, is a measure of the oxidation state of a system at equilibrium relative to a hydrogen electrode and can be combined with pH to produce diagrams that show which species will predominate among a chosen set in aqueous solution for a given oxidation state and acidity. The variable pε, which is the negative log of the chemical activity of electrons in solution, is directly related to, and sometimes used in place of, E_h.

The Hydrogen Electrode and the Table of Thermodynamic Values

The modern thermodynamic framework of the geochemistry of oxidation and reduction can be traced back to experiments in G. N. Lewis's era in the early twentieth century and perhaps even further to Humphrey Davy in the early nineteenth century, whereby electrochemical cells were constructed to transform matter and isolate new elements. In these cells, the potential for transferring electrons between two materials was measured. The simplest and most relevant example is the conversion of iron species ($FeCl_2$ and $FeCl_3$ electrolytes) coupled to a hydrogen electrode, whereby $H_2(g)$ is oxidized to two hydrogen ions (H^+):

$$H_2(g) + 2\,FeCl_3(aq) = 2\,HCl(aq) + 2\,FeCl_2(aq) \quad (1)$$

If the components are in their standard states, that is, $pH_2(g) = 1$ atm, $[HCl(aq)] = [FeCl_2] = [FeCl_3] = 1$ m, 0.77 V is the electric potential, or voltage (E°) measured by this constructed cell. At this point, a decision was made to pin the thermodynamic table of energies (Table 1) to the hydrogen electrode, that is, one half of the above cell:

$$2\,e^- + 2\,H^+(aq) = H_2(g) \quad (2)$$

defined to have $E^\circ = 0.0$ V if the constituents are in their standard states. This arbitrary decision means that the entire measured voltage, 0.77 V, is assigned to only one half of the reaction:

$$Fe^{3+}(aq) + e^- = Fe^{2+}(aq); E^\circ = 0.77\ V \quad (3)$$

It is for this reason that the Gibbs energy for $H^+(aq)$, the electron (e^-), and $H_2(g) = 0.0$ kJ mol^{-1} – they are *defined* to be so. There is, of course, no such thing as a pure half reaction, like Eqs. (2) or (3). They are all equations like (1) but referenced to a choice that Eq. (2) is set to zero volts, which means that there exists an offset for the energy scales for the standard hydrogen electrode (SHE) and the absolute vacuum

O

Oxidation-Reduction Reactions and E_h-pH (Pourbaix) Diagrams, Table 1 Some standard reduction potentials in water at 25° (Adapted from Rock 1983)

Half-reaction	E°/Volts
$Ca^{2+}(aq) + 2\ e^- = Ca^\circ(s)$	−2.866
$Mg^{2+}(aq) + 2\ e^- = Mg^\circ(s)$	−2.363
$Pu^{3+}(aq) + 3\ e^- = Pu^\circ(s)$	−2.031
$Fe^{2+}(aq) + 2\ e^- = Fe^\circ(s)$	−0.440
$Sn^{2+}(aq) + 2\ e^- = Sn^\circ(s)$	−0.14
$Pb^{2+}(aq) + 2\ e^- = Pb^\circ(s)$	−0.126
$2H^+(aq) + 2\ e^- = H_2^\circ(g)$	0.0
$Ag^+(aq) + e^- = Ag^\circ(s)$	+0.799
$O_2(g) + 2H^+(aq) + 2\ e^- = H_2O_2(aq)$	+0.682
$MnO_2(s) + 4\ H^+ + 2\ e^- = Mn^{2+}(aq) + 2\ H_2O(l)$	+1.23
$PbO_2(s) + 4\ H^+ + 2\ e^- = Pb^{2+}(aq) + 4\ H_2O(l)$	+1.455
$Co^{3+}(aq) + e^- = Co^{2+}(aq)$	+1.808

scale (AVS), where the energy corresponds to that required to separate the electron and the proton in a vacuum to infinite distance (see Xu and Schoonen 2000).

The Nernst Expression

The Nernst relation relates the voltages measured in a glass cell to the standard-state Gibbs energies, G°, that are tabulated:

$$-nFE^\circ = G^\circ \tag{4}$$

and this version requires that the electron be written on the left-hand side of the reaction, such as Eq. (3). F is the Faraday constant, whose value is 96,485 Coulombs per mole, and n is the number of transferred electrons in the reaction.

For reactions that are not at standard-state conditions, the Nernst expression is expanded, and here we express it using individual ions rather than electrolytes, which is not essential. Complete electrolytes are often used (e.g., Rock et al. 1994; Casey et al. 1996) because the activity coefficients are measured and thus without extra thermodynamic assumptions.

$$\begin{aligned} E_h &= E^\circ - \frac{2.303RT}{nF}\log\left(\frac{a_{Fe^{2+}}}{a_{Fe^{3+}}}\right) \\ &= 0.77V - \frac{2.303RT}{nF}\log\left(\frac{a_{Fe^{2+}}}{a_{Fe^{3+}}}\right) \end{aligned} \tag{5}$$

E_h is known as the redox or hydrogen scale potential; R is the gas constant and T is thermodynamic, or absolute, temperature; and a is the chemical activity of the species. There are several more points worth mentioning about this form of the Nernst expression or "Eh" equation. First, the subscript to the measured voltage, E_h, arises because this refers always to the standard hydrogen electrode (Eq. 2), which is implicit. Secondly, this expression requires that the electron appear on the left side of the half reaction (e.g., Eq. 3) and "n" electrons are transferred. Thirdly, one can view the activity of the electron in Eq. (3) as being converted to the voltage, E_h. Finally, the factor of 2.303 arises because the conventional equilibrium expression is in terms of Napierian logarithms, ($RT \ln K = -\Delta G_{rxn}^\circ$), but Eq. (5) relates the logarithm of activities in base-ten logarithms to voltages, $2.303 \log(x) = \ln(x)$. The parameters K and ΔG_{rxn}° are the equilibrium constant for the reaction and the standard-state Gibbs energy of reaction, respectively. The assembly of constants before the logarithm $\frac{2.303RT}{F}$ comes out to 0.05941 V/log unit at ambient conditions, which is why a typical glass electrode changes its voltage by 59.4 mV for every unit change in pH at room temperature.

The Pe Scale

One could formally define an equilibrium half reaction for iron reduction, remembering that the hydrogen half reaction is always implied:

$$K = \left(\frac{a_{Fe^{2+}}}{a_{Fe^{3+}}a_{e^-}}\right) \text{ and } pe = pe^o - \log\left(\frac{a_{Fe^{2+}}}{a_{Fe^{3+}}}\right) \tag{6}$$

which establishes the activity of the electron in solution, a fictitious quantity, but one that emphasizes the similarity to pH. The E_h scale arose from electrochemistry where voltages are independently controlled, but the pe scale is often more intuitive for geochemists in thermodynamic calculations. Both E_h and pe can be interconverted easily, and both are intensive state functions of the system:

$$\begin{aligned} pe^\circ &= \frac{-\Delta G_{rxn}^\circ}{2.303 \cdot nRT} = \frac{FE_h^\circ}{2.303RT} = 16.9E_h^\circ; \\ pe &= \frac{-\Delta G_{rxn}}{2.303 \cdot nRT} = \frac{FE}{2.303RT} = 16.9E; \end{aligned} \tag{7}$$

Electron-Exchange Reactions that Also Involve Proton Exchanges

At the most fundamental level, there are two classes of chemical reactions in aqueous solutions: (i) ligand-exchange reactions and (ii) electron-exchange reactions. Reaction (3) is a purely electron-exchange reactions. If, however, the electron was transferred to a partly hydrolyzed ion, electron exchange is associated with a simultaneous proton transfer, as in Reaction (2). For example, Fe(III) in solution hydrolyzes more extensively than Fe(II). So a reaction to reduce ferric iron to ferrous iron could affect a partly hydrolyzed species:

$$\mathrm{FeOH^{2+}(aq) + H^+ + e^- = Fe^{2+}(aq) + H_2O;} \quad E^o = 0.91\ \mathrm{V} \tag{8}$$

$$\text{with a } \Delta G_{rxn}{}^{\circ} = -87.7\ \mathrm{kJ\ mol^{-1}} \quad \text{and } E^{\circ} = \frac{87.7\ \mathrm{kJ \cdot mol^{-1}}}{1 \cdot 96.4\mathrm{kJ \cdot mol^{-1} \cdot V^{-1}}} = 0.91\ \mathrm{V} \tag{9}$$

or:

$$E_h = 0.91\ \mathrm{V} - \frac{2.303RT}{F}\log\frac{a_{\mathrm{Fe^{2+}}}a_{\mathrm{H_2O}}}{a_{\mathrm{FeOH^{2+}}}a_{\mathrm{H^+}}} \tag{10}$$

By convention, the activity of water is taken as unity because it is on the Raoult's law scale and virtually all aqueous solutions have a mole fraction of water near unity. Evaluating the constants at 298 K, remembering that $\mathrm{pH} = -\log(a_{\mathrm{H^+}})$and separating the terms leads to an expression that varies both with E_h and pH:

$$E_h = 0.91\ \mathrm{V} - 0.0592\log\frac{a_{\mathrm{Fe^{2+}}}}{a_{\mathrm{FeOH^{2+}}}} - 0.0592\mathrm{pH} \tag{11}$$

The equation relating measured redox potential (E_h) to solute activities at nonstandard-state conditions now includes pH as an essential variable.

Pourbaix (eh-pH) Diagrams

Garrels and Christ (1962) made popular an approach to organizing redox reactions in mineral reactions that developed in the early twentieth century by other workers. In particular, Pourbaix (1976) compiled an atlas of diagrams that show the predominant aqueous species that exists at various conditions of redox potential (E_h) and pH, with a goal to understanding metal corrosion (see Bunker and Casey 2016). These diagrams have proven to be enormously useful in interpreting corrosion reactions and for understanding the phase transformations in rocks and soil. Other compilations have been made (Brookins 1988; Schweitzer and Pesterfield 2010), and web utilities now exist to make diagrams (see, e.g., Inorganic Chemistry Royal Institute of Technology, KTH, SE-100 44, Stockholm, Sweden; https://www.kth.se/en/che/medusa/downloads-1.386254). The central assumption is that redox potential and hydrogen-ion activity can serve as master variables to control the valence states of elements (E_h) and the acid-base chemistry (pH).

The idea is that a line can be assigned to the boundary between the species in aqueous solution. For Eq. (5), a horizontal line can be assigned as the boundary where the activities of the two species are equal, i.e., $a_{\mathrm{Fe^{2+}}} = a_{\mathrm{Fe^{3+}}}$ and $E_h = 0.77V$. Unlike a phase diagram, species persist on both sides of the line, but the labeled species is the predominant one. Hence, these diagrams are *predominance* diagrams. The line is horizontal because Eq. (5) is purely an electron-exchange reaction. Similarly, a vertical line can be assigned to purely proton-exchange or acid-base reactions. Thus the reaction $\mathrm{Fe^{3+}(aq) + H_2O = FeOH^{2+}(aq) + H^+(aq)}$ does not depend upon E_h because iron does not change valence state. The equilibrium constant $K_1 = 10^{-2.19} = \frac{a_{\mathrm{FeOH^{2+}}}a_{\mathrm{H^+}}}{a_{\mathrm{Fe^{3+}}}a_{\mathrm{H_2O}}}$ fixes that vertical line at pH = 2.19 when $a_{\mathrm{Fe^{3+}}} = a_{\mathrm{FeOH^{2+}}}$and, as usual, $a_{\mathrm{H_2O}} = 1$. So, vertical lines correspond to acid-base reactions, like hydrolysis, and horizontal lines correspond to purely electron-exchange reactions.

Reactions like Eq. (8) that involve both proton and electron exchanges are slopes in both E_h and pH. Again, setting equal the activities of the two species in the reaction, $a_{\mathrm{Fe^{2+}}} = a_{\mathrm{FeOH^{2+}}}$, the Nernst equation yields a line in the predominance diagram with an appreciable slope: $E_h = 0.91\ \mathrm{V} - 0.0592\mathrm{pH}$. Similarly, one can choose to include solids in the Pourbaix diagram, although now one must also choose a total dissolved concentration of the metal. For example, an acid-base reaction can be written to include hematite (α-Fe_2O_3(s)):

$$\mathrm{Fe_2O_3}(s) + 6\ \mathrm{H^+}(aq) = 2\ \mathrm{Fe^{3+}}(aq) + 3\ \mathrm{H_2O}(l), \quad \Delta G_{rxn}{}^{o} = +8.2\ \mathrm{kJ\ mol^{-1}} \tag{12}$$

yielding an equilibrium constant that depends only on pH, as expected, but one must specify a value for $a_{\mathrm{Fe^{3+}}}$ in order to make the diagram:

$$K = 10^{-1.45} = \frac{a^2_{\mathrm{Fe^{3+}}}a^3_{\mathrm{H_2O}}}{a^6_{\mathrm{H^+}}a_{\mathrm{Fe_2O_3}}} \approx \frac{a^2_{\mathrm{Fe^{3+}}}}{a^6_{\mathrm{H^+}}} \tag{13}$$

Similar lines must be drawn to make the various hydrolysis products of Fe(III) (e.g., $\mathrm{FeOH^{2+}}$(aq)), giving rise to sets of vertical lines.

Or, the reaction could be written to involve an electron-exchange step as well, describing the reductive dissolution of hematite so that one achieves a line with both pH and E_h as key variables:

$$\mathrm{Fe_2O_3}(s) + 6\ \mathrm{H^+}(aq) + 2\ e^- = 2\ \mathrm{Fe^{2+}}(aq) + 3\ \mathrm{H_2O}(l), \quad \Delta G_{rxn}{}^{o} = -153.6\ \mathrm{kJ\ mol^{-1}} \tag{14}$$

$$E_h = 0.80\ \mathrm{V} - \frac{0.0592}{2}\log\frac{a^2_{\mathrm{Fe^{2+}}}}{a^6_{\mathrm{H^+}}} \tag{15}$$

that simplifies to a line on the Pourbaix diagram with both pH and E_h as key variables, once a value for $a_{\mathrm{Fe^{3+}}}$ is chosen:

$$E_h = 0.80\ \mathrm{V} - 0.0592 \cdot \log(a_{\mathrm{Fe^{2+}}}) - 0.177\mathrm{pH} \tag{16}$$

The boundaries of the Pourbaix diagram for most geochemists is given by the stability field of water. The upper

O

stability field is given by the oxidation of water to O_2 to exceed the confining pressure (1 atm) and so that O_2 comes boiling out solution:

$$E_h = 1.23\ \text{V} - 0.0592 \cdot pH \tag{17}$$

and the lower boundary is the corresponding potential where water (or actually protons) are reduced to make H_2(g) boil out of solution at pressures of 1 atm:

$$E_h = 0.0\ \text{V} - 0.0592 \cdot pH \tag{18}$$

All of these features are illustrated in Fig. 1, which shows a particularly simple Pourbaix diagram for iron in water in the topmost figure. Here the dashed lines give the stability fields of water, the vertical lines denote the acid-base reactions, the horizontal lines denote purely redox reactions, and the sloped lines indicate reactions that require both electron and proton transfers. In the bottom figure, the corresponding partial pressures of O_2 and H_2 are given, as the redox equilibrium could be equivalently expressed as the partial pressures (or actually fugacities) of these gases. These are redox-active gases because of the equilibrium, 2 H_2(g) + O_2(g) = 2 H_2O(l), which can be interconverted to a voltage (E_h) via the hydrogen electrode (Eq. 2).

The Perils of E_h as a Master Variable

Many of the problems in environmental geochemistry depended very sensitively on the redox state of the metal, so the promise of a master variable to control the valence states was profound. The solubilities of minerals formed by precipitation of metals vary by many, many orders of magnitude depending upon the valence state. For the iron system, at pH = 7, the solubility of $Fe(OH)_2$(s) is $\sim 10^{12}$ greater than

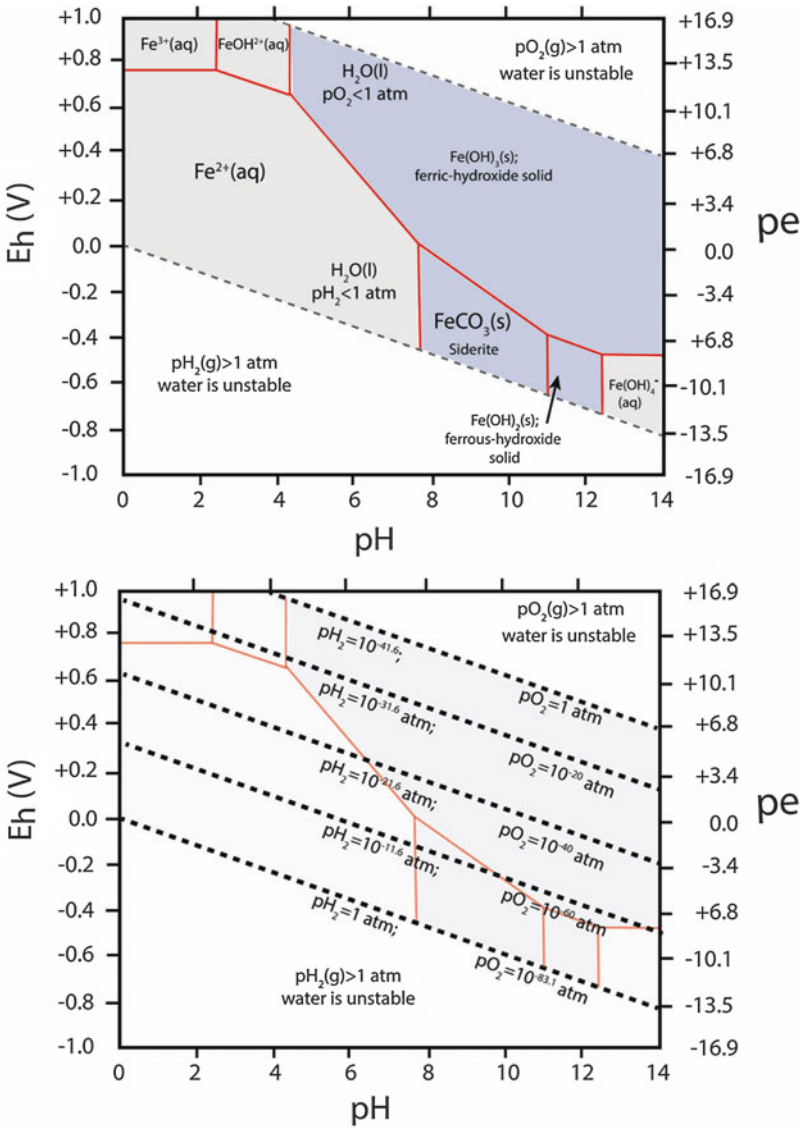

Oxidation-Reduction Reactions and E_h-pH (Pourbaix) Diagrams, Fig. 1 (*top*) The Eh-pH (Pourbaix) diagram for 10^{-4} m total dissolved iron and 10^{-2} m total dissolved carbonate species, with the stability fields of water under electrolysis shown as dashed lines and the stability fields between solutes and solids shown as *red lines* (Adapted from Garrels and Christ 1962; Bunker and Casey 2016). Conditions where solutes predominate are colored *gray*. Conditions where a solid predominates are shown in *blue*. (*bottom*) The calculated partial pressures of the redox-active gases O_2(g) and H_2(g) superimposed on the Pourbaix diagram at various values of E_h and pH

α-FeOOH(s) (Baes and Mesmer 1976). An active and urgent area of research is the redox state of radioactive transuranic elements. Considering plutonium as one example, it can exist in valence states of Pu(III), Pu(IV), Pu(V), and Pu(VI) in water and in the existence of strongly ligated complexes (see Neck et al. 2007). The solubilities vary by many orders of magnitude, and these, of course, determine the rate of migration through geological media as ions and to the biosphere.It made sense when Baas-Becking and colleagues (1960) showed that different environments at the Earth's surface had characteristic voltages relative to a hydrogen electrode, that is, E_h values, and electrochemists can define a system potential using electrodes. Thus, common codes for predicting chemical speciation in water require both pH and E_h to make predictions of mineral solubilities, aqueous complexation, gas fugacities, etc. What was promised by E_h is another master variable that could accurately predict the redox state of all metals dissolved in solution, just as pH could be used as a master variable to predict the protonation states of various molecules. One could either measure E_h and calculate the ratio of activities valence states for metals or alternatively assess a ratio of activities (e.g., $\frac{a_{Fe^{2+}}}{a_{Fe^{3+}}}$ in Eq. (5)) and get the "master variable," E_h, directly.

The approach failed, and for several reasons, that were not the fault of Baas-Becking. When the E_h values measured from redox couples in deep, old aquifers were compared with the results of direct voltage measurements, there was profound disagreement. Groundwaters that were inferred to have been stable since the last Ice Age had redox couples in profound disequilibrium (see Lindberg and Runnells 1984). One reason is that rates of many electron exchanges among solutes, particularly for multiple electrons, are slow unless catalyzed by biota and enzymes. Sulfate reduction to sulfide, for example, is an eight-electron step. It proceeds rapidly at the Earth surface when heterotrophic bacteria couple the reaction to enzymatic oxidation of organic matter, but without the catalysts, it is very slow. Similarly, measured methane concentrations are in disequilibrium with dissolved carbonate concentrations because it is a slow multiple-electron reaction and doesn't respond to the measured E_h value. Single-electron reactions are sometimes fast, such as Eq. (3), but this is a thin filament upon which to hang all thermodynamic equilibrium calculations.

These diagrams, of course, assume equilibrium. It also should be remembered that one chooses the species to be included in the diagram, including whether to include metastable species. The diagrams emphasize the presence of the dominant species, meaning the one that accounts for most of the concentration, but all other species are copresent. Depending upon the stoichiometry of the reaction, a small error in E_h leads to a large error in the ratio of stable species activities in solution, since voltages are linear but the activities are logarithmic.

There are experimental problems – the E_h measurement in the field is via a platinum electrode that doesn't respond reversibly at all conditions and can be easily poisoned so that it responds unequally to some reactions. Some reactions are fast in one direction but slow in reverse. Thus, the field E_h measurement cannot be trusted. Finally, there is a problem with the very meaning of E_h as a master variable. When one measures a solution pH, there is a real meaning – it is the negative logarithm of the concentration of protons, and this is an appreciable number. At pH = 7, the hydrogen-ion concentration, or equivalently the hydronium-ion concentration, is about 10^{-7} m. Water molecules provide a "bank" for protons. An oxygen that needed a proton can find one in the solvent. Similarly a hyperprotonated functional group can transfer the proton to the "bank" that is the bulk solvent. Because it is a solvent property, pH has meaning.

Not so for dissolved electrons. Save for highly radiolyzed solutions, the concentration of solvated electrons in water is negligible. There is no "bank" of electrons unless one has a reactive electrode, like a charged mercury drop, placed in the solution and interacting with the solutes. This means that E_h is a property of the *solutes* not the *solvent*. Whether an electron-exchange reaction proceeds depends upon an electron donor (e.g., Co^{2+}(aq)) actually colliding with an electron acceptor (e.g., SO_4^{2-}) and both having an appropriate molecular-orbital configuration to allow the reaction to proceed. There is no master variable for redox reactions in natural waters, or, stated differently, in the absence of an electrode driving processes, the E_h is a property of the solutes not the solvent.

O

The Practical use of Redox Potential

The field has instead characterized sets of redox reactions that are characteristic of general environments, which can be categorized by the presence of oxidants such as O_2(aq) (see McMahon and Chappelle 2008). Thus, for example, an *oxic* environment has no measurable dissolved iron because the metal is in the oxidized ferric state and insoluble minerals form. Dissolved iron can be detected in *suboxic* environments but is usually absent in anoxic environments because of equilibrium with insoluble sulfide minerals that form as sulfate is reduced to sulfide.

The array of possible reactions is treated in most water-chemistry textbooks (e.g., Morel and Hering 1993), but these cascade in a predictable way largely because of the influence of bacteria and enzymes. Oxidation of reduced organic matter provides the electrons, and the hierarchy of electron acceptors varies according to the available energy, as different microbial communities organize themselves both spatially and temporally. Thus, O_2(aq) is removed from solution first, followed by NO_3^-, chlorinated hydrocarbons, Mn(IV), Fe(III), SO_4^{2-}, and finally CO_2, making water, N_2, chloride ion, Mn(II), Fe

(II), H_2S, and CH_4, respectively. The cascade corresponds to energy available for the microbial community.

Summary

Redox potential, or Eh, is one master variable that is used to calculate the valence states of solutes in aqueous solutions. It refers to the voltage of the solution relative to the standard hydrogen electrode and derives from electrochemistry, where the potential is controlled by a working electrode. It is enormously useful as a means of estimating the speciation of aqueous solutions and is one variable, along with pH, in the Eh-pH diagrams known as Pourbaix diagrams. These diagrams identify the predominant aqueous complex, gas, or solid at given conditions. Problems arise when applying it to natural waters where there is no working electrode because of slow electron-exchange rates, unequal electrode responses, and the nature of Eh as reflecting the properties of solutes.

Cross-References

- ▶ Acid–Base Reactions
- ▶ Activity and Activity Coefficients
- ▶ Enthalpy
- ▶ Entropy
- ▶ Equilibrium
- ▶ Free Energy
- ▶ Geochemical Thermodynamics
- ▶ Iron
- ▶ Kinetics of Geochemical Processes
- ▶ Oxygen

References

Baas Becking LGM, Kaplan IR, Moore D (1960) Limits of the natural environment in terms of pH and oxidation-reduction potentials. J Geol 68:243–284

Brookins DG (1988) Eh-pH diagrams for geochemistry. Springer. ISBN: 0-387-18485-6

Bunker BC, Casey WH (2016) The aqueous chemistry of oxides. Oxford University Press, Oxford, England, 620 pp

Baes CF, Mesmer RE (1976) The hydrolysis of Cations. Krieger Publishing, Malabar

Casey WH, Rock PA, Chung J-B, Walling EM, McBeath MK (1996) Gibbs energies of formation of metal-carbonate solid solutions 2: the $Ca_xSr_{1-x}CO_3(s)$ system at 298 K and 1 bar. Am J Sci 296:1–22

Garrels RM, Christ CL (1962) Solutions, minerals, and equilibria. Freeman, Cooper and Company, San Francisco

Lindberg RD, Runnells DD (1984) Ground water redox reactions: an analysis of equilibrium state applied to eh measurements in geochemical modeling. Science 225:925–927

McMahon PB, Chapelle FH (2008) Redox processes and water quality of selected principal aquifer systems. Ground Water 46:259–271

Morel FMM, Hering JG (1993) Principles and applications of aquatic chemistry. Wiley-Interscience, New York, NY, USA

Neck V, Altmaiera M, Fanghänela T (2007) Solubility of plutonium hydroxides/hydrous oxides under reducing conditions and in the presence of oxygen. C R Chim 10:959–977

Pourbaix M (1976) Atlas of electrochemical equilibria. National Association of Corrosion Engineers, Houston

Rock PA, Casey WH, McBeath MK, Walling EM (1994) A new method for determining Gibbs energies of formation of metal-carbonate solid solutions: 1. The $Ca_xCd_{1-x}CO_3(s)$ system at 298 K and 1 bar. Geochim Cosmochim Acta 58:4231–4291

Rock PA (1983) Chemical thermodynamics. University Science Books, Mill Valley

Schweitzer GK, Pesterfield LL (2010) The aqueous chemistry of the elements. Oxford University Press, Oxford, England

Xu Y, Schoonen MAA (2000) The absolute energy positions of the conduction and valence bands of selected semiconducting minerals. Am Mineral 85:543–556

Oxide Minerals

Patrick Nadoll
GeoZentrum Nordbayern, Geochemistry – Economic Geology, Friedrich-Alexander-University Erlangen-Nuremberg, Erlangen, Germany

Synonyms

Oxide minerals; Oxides

Definition

Oxide minerals are inorganic compounds in which positively charged ions of metals or transition elements bond to negatively charged oxygen, O^{2-}. Oxide minerals are classified into simple and complex oxides and are commonly distinguished from other oxygen-bearing minerals such as silicates, sulfates, borates, phosphates, and carbonates. Hydroxide minerals, which contain a hydroxyl group (OH^{1-}) instead of O^{2-}, and oxyhydroxides, which comprise both hydroxyl group and oxygen, are often included in the group of oxide minerals (Deer et al. 2013, 2011; Dyar et al. 2008; Gaines et al. 1997; Klein and Dutrow 2007; Wenk and Bulakh 2004). Oxides are generally harder and denser than hydroxides. The latter predominantly occur as secondary alteration and weathering products (Klein and Dutrow 2007). Ice (H_2O) is considered a simple oxide in which hydrogen is the cation. The International Mineralogy Association (IMA) lists over 1000 approved oxide and hydroxide minerals (http://rruff.info/ima/; Back 2014).

Mineralogy

More than 40 elements are found to form oxides and more than 25 elements are known to form hydroxides in nature (Back 2014; Deer et al. 2013; Klein and Dutrow 2007; Wenk and Bulakh 2004). Table 1 lists 23 common and other important oxides and hydroxides.

Oxide minerals can be divided into classes and groups based on their crystal structure and cation site distribution. Several classification schemes exist: Nickel-Strunz (Strunz and Nickel 2001), IMA (Mills et al. 2009), and Dana (Gaines et al. 1997; Klein and Dutrow 2007). The main classes are simple oxides (XO, X_2O, XO_2, and X_2O_3), complex or multiple oxides (XY_2O_4), and hydroxides (OH^{1-}) (Deer et al. 2013; Dyar et al. 2008; Wenk and Bulakh 2004). These classes can be further subdivided into six groups: (1) periclase group, (2) zincite group, (3) hematite group, (4) rutile group, (5) spinel group, and (6) goethite group (Table 1) (Deer et al. 2013; Dyar et al. 2008; Gaines et al. 1997; Klein and Dutrow 2007; Wenk and Bulakh 2004).

Oxide Minerals, Table 1 List of common and other important oxides and hydroxides and their diagnostic properties. Crystal family—Iso: isometric (cubic), Hexag.: hexagonal, Tetrag.: tetragonal, Ortho.: orthorhombic, Monocl.: monoclinic, Tricl.: triclinic. H: Mohs hardness. Compiled using the following references: (Back 2014; Deer et al. 2011; Dyar et al. 2008; Klein and Dutrow 2007; Mills et al. 2009; Smyth and McCormick 1995; Wenk and Bulakh 2004)

Oxide class	Oxide group	Mineral, Formula	Crystal family	Occurrence	Color	H
XO	Periclase group	Periclase, MgO	Iso.	Metamorphosed limestones and dolomites	Various colors or colorless	$5^{1/2}$
	Zincite group	Zincite, (Zn, Mn)O	Hexag.	Weathering product, metamorphic rocks	Yellow to red	4–5
X_2O		Cuprite, Cu_2O	Iso.	Alteration product, secondary	Red	$3^{1/2}$–4
		Ice, H_2O	Hexag.	Snow, ice	White or colorless	$2^{1/2}$
XO_2	Rutile group	Rutile, TiO_2	Tetrag.	Granites, pegmatites, metamorphic rocks, detrital	Red-brown-black	$6–6^{1/2}$
		Pyrolusite, MnO_2		Sedimentary, hydrothermal, secondary	Grey	$6–6^{1/2}$
		Cassiterite, SnO_2		Granites, pegmatites and greisen; mainly hydrothermal	Reddish brown to black	6–7
		Uraninite, UO_2	Iso.	Granites, syenite pegmatites, high-T hydrothermal	Brown-black, grey	5–6
X_2O_3	Hematite group	Hematite, Fe_2O_3	Hexag.	Sedimentary and metamorphic rocks, BIFs, rarely magmatic	Reddish brown	$5–6^{1/2}$
		Corundum, Al_2O_3		Aluminous igneous and metamorphic rocks	Various colors or colorless	9
		Ilmenite, $FeTiO_3$		Igneous and metamorphic rocks, beach sands	Black	5–6
XY_2O_4	Spinel group	Spinel, $MgAl_2O_4$	Iso.	Igneous and metamorphic rocks, sediments	Various	$7^{1/2}$–8
		Magnetite, Fe_3O_4		Igneous and metamorphic rocks, sediments, BIFs	Black	$5–6^{1/2}$
		Chromite, $FeCr_2O_4$		Ultrabasic rocks, serpentinites	Black	$5^{1/2}$
		Franklinite, (Zn, Fe, Mn) $(Fe,Mn)_2O_4$		Metamorphic rocks, hydrothermal	Red, black	6
		Gahnite, $ZnAl_2O_4$		Granitic pegmatites, metamorphic rocks, hydrothermal	Dark green	$7^{1/2}$–8
		Chrysoberyl, $BeAl_2O_4$	Ortho.	Rare, granitic rocks, pegmatites, mica-schists, sediments	Yellow-green	$8^{1/2}$
		Fe-Columbite, (Fe, Mn) Nb_2O_6		Granitic rocks and pegmatites	Black	6
Hydroxides		Brucite, $mg(OH)_2$	Hexag.	Alteration mineral	Various colors	$2^{1/2}$
		Manganite, MnO(OH)	Monocl.	Low-T hydrothermal, hot springs	Brown-black	4
		Gibbsite, $al(OH)_3$		Weathering product, bauxite	Various colors	$2^{1/2}$–$3^{1/2}$
	Goethite group	Diaspore, α-AlO(OH)	Ortho.	Weathering product, bauxite	White or colorless	$6^{1/2}$–7
		Goethite, α-FeO(OH)		Alteration mineral, hot springs	Yellowish brown to red	$5–5^{1/2}$

Physical and Chemical Properties

Metal and transition element cations occupy interstices in the crystal structure. Ionic bonding is most common among oxide minerals; therefore, the ionic radii of the respective cations govern the structure and complexity of the corresponding oxide (e.g., Dyar et al. 2008; Wenk and Bulakh 2004). The ionic radii of the cations bonding with oxygen are always smaller than oxygen itself (<1.4 Å (Shannon 1976; Shannon and Prewitt 1969)). Oxides are often opaque or translucent but can exhibit various colors due to intrinsic crystallographic controls or minor and trace element substitution. As Table 1 illustrates, oxides generally have a high hardness due to the high coordination number of the ions in their crystal structure (Jaffe 1996). The presence of a hydroxyl group results in a lower hardness in hydroxides (Jaffe 1996; Nikischer 2011).

Oxygen fugacity is one of the main governing factors when considering the stability of oxide minerals in nature. A comprehensive account of the importance of oxygen fugacity can be found in the Reviews in Mineralogy volume 25 (Lindsley 1991). Oxides are inherently dependent on the oxygen fugacity conditions that prevail; however, they may exist as metastable phases even if conditions are unfavorable (Lindsley 1991). Oxygen fugacity also controls element partitioning between oxides, and between oxides and other minerals, particularly for elements with variable valency such as Fe, V, and Cr (e.g., Frost 1991; Ryabchikov and Kogarko 2006).

Several oxide minerals exhibit magnetic properties. Magnetite is a ferrimagnetic mineral, whereas a number of other Fe-oxides (e.g., hematite and goethite) have ferromagnetic properties (Banerjee 1991; Cornell and Schwertmann 2003). Chromite, franklinite, and ilmenite are also magnetic but belong to the group of paramagnetic minerals (Klein and Dutrow 2007; Lindsley 1991; Wenk and Bulakh 2004). Many oxide minerals also act as semi-conductors (Cornell and Schwertmann 2003; Wenk and Bulakh 2004).

Occurrence

Oxides are common minerals that occur as minor or accessory phases in the Earth's crust and Upper Mantle. Spinel group members, baddeleyite, rutile, and ilmenite are common minerals in the Upper Mantle (Deer et al. 2011; Dyar et al. 2008; Haggerty 1976, 1995; Klein and Dutrow 2007). In banded iron formations or chromite layers, oxides are the principal rock-forming compounds. Hydroxides are the main compounds in areas where alteration and weathering (i.e., oxidation and hydration) are pervasive such as in supergene oxidation zones, soils, and laterites (Delvigne 1998).

Oxide minerals can occur as primary (magmatic-hydrothermal) and secondary (products of mineral alteration) minerals in magmatic, volcanic, and metamorphic rocks and as resistant detrital grains in sediments (Klein and Dutrow 2007; Lindsley 1991). Biogenic oxides such as Mn (IV)-oxides, −hydroxides, and -oxyhydroxides occur where microbial activity produces mineral compounds through oxidation of bioavailable transition metals (Tebo et al. 2004).

Before the Great Oxidation Event at approximately 2.4 Ga (Holland 2006), oxides were restricted to species with a low oxidation state of the respective cation as the partial pressure of oxygen was low. The increased availability of oxygen led to an unprecedented rise in the formation of new minerals (Sverjensky and Lee 2010).

Applications and Economic Significance

Several oxide minerals are of economic significance and important sources of metals: Fe (hematite, magnetite), Cr (chromite), Mn (pyrolusite, manganite, psilomelane), Zn (zincite), Sn (cassiterite), Ti (ilmenite, rutile), and Al (bauxite) (Deer et al. 2011; Gaines et al. 1997; Ramdohr 1980). Some varieties of oxides, such as corundum (Al_2O_3), spinel ($MgAl_2O_4$), chrysoberyl ($BeAl_2O_4$), or baddeleyite (ZrO_2, cubic zirconia), are used as precious stones or gems. For example, rubies form when Cr and V substitute Al in corundum, causing an intense red color. When Fe and Ti substitute Al, a blue color is apparent and the corresponding gem is called sapphire (Deer et al. 2011).

Among the most ubiquitous oxide minerals are magnetite and hematite, which are primary iron ore minerals. Both occur in a range of host rocks and are often associated with mineral deposits such as banded iron formations, mineralized skarns, porphyry Cu-Mo-Ag-Au, and iron ore copper-gold deposits. Chromite is the primary constituent in chromite ore deposits such as the Bushveld igneous complex in South Africa. The widespread occurrence of common oxides such as Fe-Ti oxides and chromite, and their ability to incorporate a variety of foreign cations into their structure, has qualified them as petrogenetic indicators and useful tools for geochemical exploration (e.g., Dare et al. 2014; Dupuis and Beaudoin 2011; Knipping et al. 2015; Nadoll et al. 2014; Razjigaeva and Naumova 1992; Sack and Ghiorso 1991; Zack et al. 2004). Furthermore, magnetic oxides can help to target deposits or prospective areas with geomagnetic surveys (Cornell and Schwertmann 2003; Sandrin et al. 2007) and record the geomagnetic field for paleomagnetic investigations (Dyar et al. 2008).

Strategic elements such as the rare earth elements (REE) Ce, Y, and La can often be found in Ca-, Ti-, U-, Th-, or Ta-Nb-bearing oxides such as perovskite (CaTiO3) or aeschynite-(Ce) ((Ce,Ca,Fe,Th)(Ti,Nb)2(O,OH)6)), which

can be found as accessory mineral phases in granites, nepheline syenites, carbonatites, or pegmatites (Möller et al. 1989). Due to its ferroelectric and high-temperature superconducting properties, perovskite is also an important mineral for the electronic industry (Wenk and Bulakh 2004).

Due to their high affinity to heavy metals and other toxic elements, Mn- and Fe-oxides, −hydroxides, and -oxyhydroxides can directly or indirectly deactivate pollutants through surface adsorption and therefore play an important role for environmental applications (Cornell and Schwertmann 2003; Kumpiene et al. 2008; Tebo et al. 2004). On the other hand, U-oxides can pose a significant environmental hazard due to the radioactive radiation they emit.

Summary

Many fundamental aspects of mineralogy have been revealed through the detailed study of oxide minerals (e.g., Smyth et al. 2000). Their relatively simple structure and ability to incorporate a variety of foreign cations makes them primary targets for petrological and geochemical studies. Their economic and environmental significance is indisputable, and recent years have seen an increased interest in them for a variety of geological and technical applications.

Cross-References

- ▶ Ore Deposits
- ▶ Mineralogy

References

2017, IMA Database of mineral properties. http://rruff.info/ima/, 2017, RRUFF Project in partnership with the IMA

Back ME (2014) Fleischer's Glossary of Mineral Species. Mineralogical Record 11:434

Banerjee SK (1991) Magnetic Properties of Fe-Ti Oxides. In: Lindsley DH (ed) Oxide minerals: petrologic and magnetic significance, vol 25. Mineralogical Society of America, Chelsea, pp 107–128

Cornell RM, Schwertmann U (2003) The iron oxides: structure, properties, reactions, occurrences, and uses. Wiley-VCH, Weinheim

Dare SAS, Barnes S-J, Beaudoin G, Méric J, Boutroy E, Potvin-Doucet C (2014) Trace elements in magnetite as petrogenetic indicators. Mineral Deposita 49:785–796

Deer WA, Howie RA, Zussman J (2013) An introduction to the rock-forming minerals. Pearson, Harlow. 495 p

Deer WA, Howie RA, Zussman J, Bowles JFW, Vaughan DJ (2011) Rock-forming minerals vol 5A: non-silicates: oxides, hydroxides and sulphides. Geological Society, London

Delvigne JE (1998) Atlas of micromorphology of mineral alteration and weathering. Mineralogical Association of Canada, Ottawa. 509 p

Dupuis C, Beaudoin G (2011) Discriminant diagrams for iron oxide trace element fingerprinting of mineral deposit types. Mineral Deposita 46:319–335

Dyar MD, Gunter ME, Tasa D (2008) Mineralogy and optical mineralogy. Mineralogical Society of America, Chantilly, p 708

Frost BR (1991) Stability of oxide minerals in metamorphic rocks. In: Lindsley DH (ed) Oxide minerals: petrologic and magnetic significance, Reviews in Minerology, vol 25. Mineralogical Society of America, Chelsea, pp 469–487

Gaines RV, Skinner HCW, Foord EE, Mason B, Rosenzweig A (1997) Dana's new mineralogy. American Chemical Society, Wiley/VCH, New York. 1819 p

Haggerty SE (1976) Opaque mineral oxides in terrestrial igneous rocks. In: Rumble D III (ed) Oxide minerals, Short course notes, vol 3. Mineralogical Society of America, Chelsea, pp Hg-101–Hg-135

Haggerty SE (1995) Upper mantle mineralogy. J Geodyn 20:331–364

Holland HD (2006) The oxygenation of the atmosphere and oceans. Philos Trans R Soc 361:903–915

Jaffe HW (1996) Chrystal chemistry and refractivity. Cambridge University Press, Cambridge, UK. 352 p

Klein C, Dutrow B (2007) Manual of mineral science. Wiley, New York. 716 p

Knipping JL, Bilenker LD, Simon AC, Reich M, Barra F, Deditius AP, Wälle M, Heinrich CA, Holtz F, Munizaga R (2015) Trace elements in magnetite from massive iron oxide-apatite deposits indicate a combined formation by igneous and magmatic-hydrothermal processes. Geochim Cosmochim Acta 171:15–38

Kumpiene J, Lagerkvist A, Maurice C (2008) Stabilization of As, Cr, Cu, Pb and Zn in soil using amendments – a review. Waste Manag 28:215–225

Lindsley DH (1991) Oxide minerals: petrologic and magnetic significance. Mineralogical Society of America, Chelsea. 509 p

Mills SJ, Hatert F, Nickel EH, Ferraris G (2009) The standardisation of mineral group hierarchies: application to recent nomenclature proposals. Eur J Mineral 21:1073–1080

Möller P, Cerny P, Saupe F (1989) Lanthanides, Tantalum and Niobium: Mineralogy, Geochemistry, Characteristics of Primary Ore Deposits, Prospecting, Processing and Applications. Proceedings of a workshop in Berlin, November 1986. Springer, Berlin/Heidelberg. 380 p

Nadoll P, Angerer T, Mauk JL, French D, Walshe J (2014) The chemistry of hydrothermal magnetite: a review. Ore Geol Rev 61:1–32

Nikischer T (2011) Atlas of non-silicate minerals in thin section. Can Mineral 49:1338–1338

Ramdohr P (1980) *The ore minerals and their intergrowths* (English translation of the 4th edition). Pergamon Press, Oxfod/New York. 1205 p

Razjigaeva NG, Naumova VV (1992) Trace element composition of detrital magnetite from coastal sediments of northwestern Japan Sea for provenance study. J Sediment Petrol 62:802–809

Ryabchikov ID, Kogarko LN (2006) Magnetite compositions and oxygen fugacities of the Khibina magmatic system. Lithos 91:35–45

Sack RO, Ghiorso MS (1991) Chromian spinels as petrogenetic indicators; thermodynamics and petrological applications. Am Mineral 76:827–847

Sandrin A, Berggren R, Elming S-A (2007) Geophysical targeting of Fe-oxide Cu-(Au) deposits west of Kiruna, Sweden. J Appl Geophy 61:92–101

Shannon R (1976) Revised effective ionic radii and systematic studies of interatomic distances in halides and chalcogenides. Acta Crystallogr A 32:751–767

Shannon RD, Prewitt CT (1969) Effective ionic radii in oxides and fluorides. Acta Crystallogr B 25:925–946

Smyth JR, Jacobsen SD, Hazen RM (2000) Comparative crystal chemistry of dense oxide minerals. Rev Mineral Geochem 41:157–186

Smyth JR, McCormick TC (1995) Crystallographic data for minerals. In: Ahrens TJ (ed) Mineral physics & crystallography: a handbook of physical constants. American Geophysical Union, Washington, DC, pp 1–17
Strunz H, Nickel EH (2001) Strunz mineralogical tables. Schweizerbart, Stuttgart. 869 p
Sverjensky DA, Lee N (2010) The great oxidation event and mineral diversification. Elements 6:31–36
Tebo BM, Bargar JR, Clement BG, Dick GJ, Murray KJ, Parker D, Verity R, Webb SM (2004) Biogenic manganese oxides: properties and mechanisms of formation. Annu Rev Earth Planet Sci 32:287–328
Wenk HR, Bulakh A (2004) Minerals: their constitution and origin. Cambridge University Press, Cambridge
Zack T, von Eynatten H, Kronz A (2004) Rutile geochemistry and its potential use in quantitative provenance studies. Sediment Geol 171:37–58

Oxygen

Edward D. Young
Department of Earth, Planetary, and Space Sciences, UCLA, Los Angeles, CA, USA

Element Data
Atomic Symbol: O
Atomic Number: 8
Atomic Weight: 15.999
Isotopes and Abundances: ^{16}O, 99.763%; ^{17}O, 0.037%; ^{18}O, 0.200%
1 Atm Melting Point: −218.79 °C
1 Atm Boiling Point: −182.96 °C
Common Valences: 2, 1, −1, −2
Ionic Radii: 136 pm (threefold coordination), 138 pm (fourfold coordination), 140 pm (sixfold coordination)
Pauling Electronegativity: 3.44
First Ionization Energy: 1313.9 kJ/mol
Chondritic (CI) Abundance: 0.46 mass fraction
Silicate Earth Abundance: 0.44 mass fraction
Crustal Abundance: 0.47 mass fraction
Seawater Abundance: 0.89 mass fraction
Core Abundance: 0.005–0.05 mass fraction

Properties

Oxygen is distinguished from virtually all other elements by its extraordinary electronegativity. It is surpassed in its affinity for electrons only by fluorine. For this reason, concentrations of oxygen play a critical role in many geochemical cycles and in the basic structures of rocky planets. The multiple valence states of numerous geochemically relevant elements are linked to the availability of oxygen.

Oxygen is also distinctive in being a major component of not only rock, but also of volatile components in planetary bodies. The oxygen-bearing volatiles include H_2O, CO_2, and SO_2.

The electronic configuration $1s^2\ 2s^2\ 2p^4$ lends itself to forming covalent bonds with other oxygen atoms. The dioxygen molecule, O_2, is a colorless and odorless gas comprising 21% of Earth's atmosphere. Oxygen is classified as a lithophile element and occurs mainly in the crust and mantle of rocky planets. Bonding between Si and O is approximately 50% covalent and 50% ionic (Pauling 1980). Silicon is coordinated by four oxygen atoms forming the $[SiO_4]^{4-}$ group that polymerizes to varying degrees to form the basis for the crystal structures of silicates, the most common rock-forming minerals.

Because oxygen has ionic radii of several times those of the cations it bonds to (Shannon 1976), the crystal structures of rock-forming oxide and silicate minerals can be described as tightly packed oxygen atoms with cations occupying the interstices of the oxygen atoms. Oxygen therefore constitutes about 90% of the volume and about half the mass of typical rocks.

There are three stable isotopes of oxygen: ^{16}O, ^{17}O, and ^{18}O. These isotopes are especially useful as tracers in geochemical reactions because the mass differences are relatively large compared with the average atomic mass of oxygen, resulting in readily measurable partitioning of isotopes between phases, and because oxygen occurs in great abundance in rock, water, and air.

History

Three people are variously credited with the discovery of dioxygen gas in the eighteenth century. Swedish apothecary Karl Wilhelm Scheele in 1771 discovered the gas as a product of heating mercuric oxide, magnesium nitrate, potassium nitrate, and silver carbonate. He referred to this emitted gas as "fire air," a reference to the fact that the gas ignited charcoal dust. He published the result in 1777 (Scheele 1777). His discovery predates those of Antoine Laurent de Lavoisier and Joseph Priestly, but his publication postdated these works.

Lavoisier, a French chemist, explored the properties of air as a reagent for combustion beginning in 1772 (Guerlac 1961). He gave oxygen its name in 1779 and recognized that reactions with oxygen were responsible for combustion. Prior to Lavoisier's insight, combustion was thought to release the fictive, ethereal substance referred to as "phlogiston." Lavoisier discovered that phosphorous and sulfur gained weight when combined with air rather than losing weight as predicted by the phlogiston theory. He also showed that air is ~20% oxygen (on a molecular basis).

During this same period, British clergyman and natural philosopher Joseph Priestley conducted experiments in 1771 and 1772 showing that plants emit a gaseous component found in air that is in turn consumed by animals, foreshadowing the discoveries of photosynthesis and respiration, processes that produce and consume oxygen in air, respectively. He further recognized the liberation of oxygen from heated mercuric oxide in 1774 (West 2014) and published his result in 1775 (Priestley 1775). Priestly mistakenly believed that the gas that would be named oxygen by Lavoisier was a "dephlogisticated air." Because Priestly published first, his discovery of oxygen is often given priority.

Stellar Origins

Oxygen is the third most abundant element in the Galaxy, superseded only by H and He (Lodders 2003). The lightest and most abundant isotope of oxygen, ^{16}O, is produced by helium fusion (He burning) mainly in large stars that are at least ten times the mass of the Sun. It is the most abundant nuclide synthesized in stars (Clayton 2003). ^{16}O created in stars is ejected into the interstellar medium by the explosion of Type II supernovae where it is then available for incorporation into the next generation of stars. Because it is a product of He burning, the synthesis of ^{16}O is not dependent on the existence of other "metals" (metals is the term used for elements heavier than H and He in astronomy). It is therefore a primary nuclide.

The stellar nucleosynthesis of the two heavier isotopes of oxygen, ^{17}O and ^{18}O, relies on the prior existence of ^{16}O, ^{12}C, and ^{14}N; stars with no "metals" cannot produce these isotopes of oxygen. ^{17}O and ^{18}O are therefore secondary nuclides and are rare compared with ^{16}O. ^{17}O is produced in lower mass stars in their red giant phase or from novae (Clayton 2003). It is made from H and ^{16}O during hydrogen fusion (H burning) in the CNO cycle. ^{18}O is synthesized during He burning in massive stars using ^{14}N as a reactant (Clayton 2003). Novae and ejecta from red giant stars disperse ^{17}O to the interstellar medium while ^{18}O is scattered by Type II supernovae.

As stars produce more "metals," the secondary ^{17}O and ^{18}O nuclides grow in abundance with the square of time while the amount of ^{16}O grows linearly with time. The overall $^{17}O/^{16}O$ and $^{18}O/^{16}O$ isotopic ratios are therefore expected to have grown approximately linearly with time in the Milky Way Galaxy in a process known as Galactic chemical evolution (Tinsley and Cameron 1974; Young et al. 2011).

Cosmochemical Significance

The nonideal partial pressure of oxygen, oxygen fugacity, is a thermodynamic quantity that characterizes the level of oxidation for a system. The fugacity, f_{O_2}, is meant to correct the pressure of O_2 in a system from a standard state of one bar and from a mole fraction in the gas of unity. The f_{O_2} symbol is therefore usually an abbreviated way of writing f_{O_2}/P_{O_2} where the denominator pressure P_{O_2} is understood to be unity (pure O_2 at one bar); oxygen fugacity is a measure of the activity, or nonideal concentration, of O_2. It can always be defined thermodynamically to measure the degree of oxidation even in circumstances where the quantity of free dioxygen is for all practical purposes indistinguishable from zero. The parameter $\Delta IW = \log(f_{O_2}) - \log(f_{O_2})_{IW}$, quantifies the difference in oxygen fugacity at a given temperature from that defined by the equilibrium reaction Fe (Iron) + ½O_2 = FeO (Wüstite), the IW reaction. The oxygen fugacity of a planet or planetesimal can be calculated relative to the IW reference using corrections for the concentrations of FeO in the bulk silicate portion and Fe in the metal core:

$$\Delta IW = 2\log\left(\frac{x_{FeO}^{silicate}}{x_{Fe}^{metal}}\right) + 2\log\left(\frac{\gamma_{FeO}^{silicate}}{\gamma_{Fe}^{metal}}\right),$$

where x are mole fractions of the species indicated and γ are activity coefficients that correct for nonideal mixing. The intrinsic oxygen fugacity of the Earth is constrained by the 8 weight percent FeO in the mantle and its Fe-rich core to a ΔIW value of -1 using nonideal mixing or -2 based on the assumption of ideal mixing. Estimates of the amount of oxygen in Earth's core vary from approximately 0.5% by mass to as much as 5% by mass (Huang et al. 2011; Badro et al. 2015; Rubie et al. 2015).

Studies of meteorites reveal that, like the Earth, most rocky bodies in the solar system formed with oxygen fugacities approximately five orders of magnitude higher than that defined by a hydrogen-rich gas of solar composition (Fig. 1). The presence of significant amounts of iron bonded to oxygen in silicates in chondrite meteorites testifies to this relatively high oxygen fugacity during rock formation in the early solar system (Grossman et al. 2012).

The fugacity of oxygen in the protoplanetary gas was controlled by the reaction H_2 + ½O_2 = H_2O (Krot et al. 2000). In order to form rocks like those comprising the Earth, the ratio of H_2O/H_2 must have increased by a factor of nearly 400 relative to the solar value. The relative abundances of water ice and H_2 gas were, therefore, the first-order controls on the fugacity of oxygen and the oxidation state of the elements comprising rocky planets.

The distribution of the three isotopes of oxygen among planets and asteroids constitutes one of the most distinctive and mysterious chemical features of the solar system (Clayton et al. 1973). In general, for the great majority of physicochemical processes, kinetic and equilibrium variations in $^{18}O/^{16}O$ ratios should be approximately twice those for

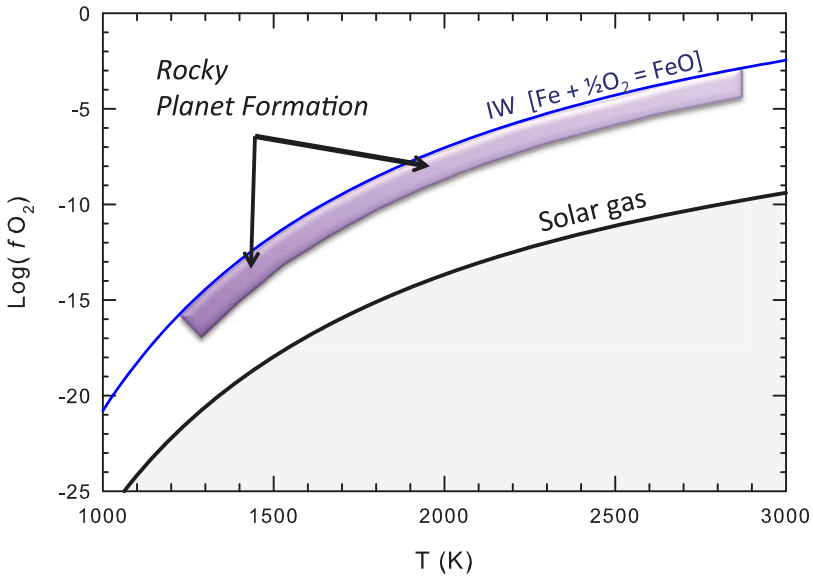

Oxygen, Fig. 1 Plot of the logarithm of oxygen fugacity versus temperature (K) for a gas of solar composition and for the equilibrium Fe (Iron) + ½O_2 = FeO (Wüstite) (IW). The conditions corresponding to rock formation in the early solar system are indicated

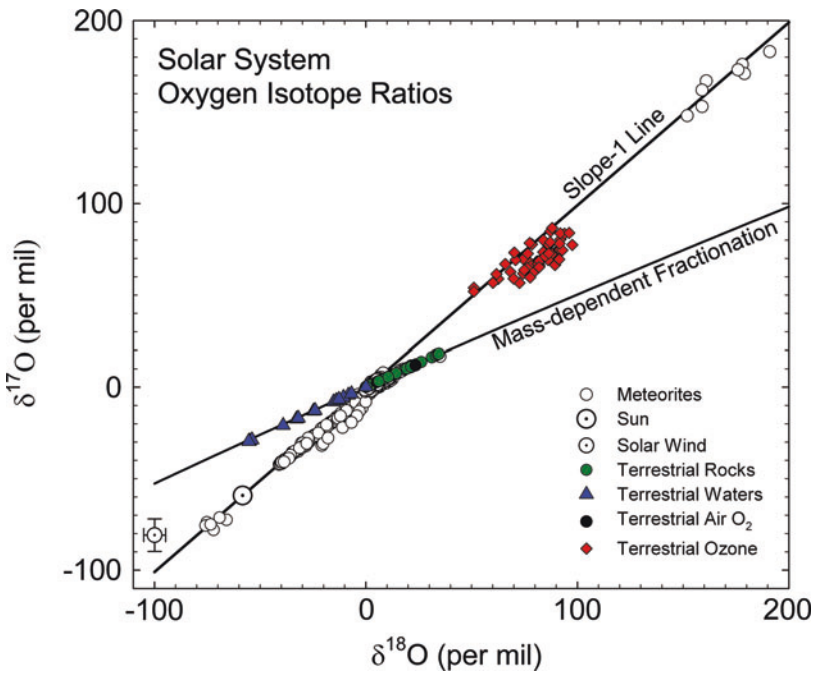

Oxygen, Fig. 2 Plot of oxygen isotope ratios for solar system materials. The ratios $^{17}O/^{16}O$ and $^{18}O/^{16}O$ are represented as per mil deviations from Vienna Standard Mean Ocean Water (VSMOW) such that for reservoir i $\delta^{17}O = 1000[(^{17}O/^{16}O)_i/(^{17}O/^{16}O)_{VSMOW} - 1]$ (and similar for $\delta^{18}O$). The slope-1 line that characterizes the solar system is shown for reference. The mass-dependent fractionation line represents fractionation of oxygen relative to Earth's mantle

$^{17}O/^{16}O$ ratios because of the 2:1 ratio in the mass differences involved (18 − 16 = 2 vs. 17 − 16 = 1). In other words, the fractionations are mass dependent. However, the dominant trend exhibited by minerals in meteorites that come from a variety of asteroid types is one in which $^{18}O/^{16}O$ ratios vary by about the same magnitude as $^{17}O/^{16}O$ ratios. This mass-independent ~1:1 relationship between oxygen isotope ratios includes the terrestrial planets and the Sun (McKeegan et al. 2011). The ^{16}O-rich and ^{16}O-poor ends of the array of solar system oxygen isotope ratios are evidently anchored by the Sun and pristine waters, respectively (Young 2007) (Fig. 2).

Explanations for this enigmatic trend include the residual effects of Galactic chemical evolution, intramolecular disequilibrium during oxidation reactions, and CO photochemistry (Young et al. 2008). In the case of CO photochemistry, the 1:1 relationship between the two oxygen isotope ratios arises because of the effect of CO self shielding whereby abundant $C^{16}O$ shields ultraviolet (UV) light that would otherwise liberate oxygen by the reaction $C^{16}O + UV \rightarrow C + {}^{16}O$, depriving the ensuing reservoir of liberated oxygen of ^{16}O. Atomic oxygen reacts with hydrogen to produce water, thus a paucity of atomic ^{16}O causes a paucity of ^{16}O in water, simultaneously increasing $^{18}O/^{16}O$ and $^{17}O/^{16}O$ in the water

(Yurimoto and Kuramoto 2004; Lyons and Young 2005). Any explanation for the oxygen isotope distributions in the solar system must account for the fact that all evidence points toward water having high $^{18}O/^{16}O$ and $^{17}O/^{16}O$ compared with rocks in the early solar system.

The apparent excess of $^{17}O/^{16}O$ relative to $^{18}O/^{16}O$ compared with expectations from normal "mass-dependent" isotope partitioning is expressed as the $\Delta^{17}O$ value (usually in per mil). This iconic parameter appears to be a fingerprint-like characteristic for each body formed in the solar system. Two important exceptions are the Earth and Moon, which stand out in having identical $\Delta^{17}O$ values that signify extensive intermingling of the proto-Earth and proto-lunar reservoirs (Wiechert et al. 2001; Young et al. 2016). The intermingling is most often attributed to the giant impact that evidently formed the Moon.

Applications of Oxygen Isotopes in Geochemistry

Shifts in the oxygen isotopic compositions of waters and rocks are used as records of water-rock interactions. Under hydrothermal conditions, exchange of oxygen between water and rock at temperatures greater than ~300 °C decreases $^{18}O/^{16}O$ in the rock. These signatures can be used for identifying regions that are likely to host mineralization (Taylor 1974).

Differences in oxygen isotope ratios between minerals formed at thermodynamic equilibrium can be used as geothermometers, providing estimates of equilibration temperatures in igneous and metamorphic rocks. Minerals with different structures, and therefore different bond strengths involving oxygen, make the best thermometers (e.g., quartz formed in equilibrium with magnetite).

Isotopes of oxygen are also used to trace reactions between water and rock on a global scale. An important example is the oxygen isotopic composition of ocean water over geological timescales. New oceanic crust formed at midocean ridges experiences ingress of seawater that reacts with rock at high temperatures near 300 °C. Far from the ridges, older ocean crust is infiltrated by cool water resulting in submarine weathering. At high temperatures, reactions with basalt increase the $^{18}O/^{16}O$ of the water. At low temperatures, reactions with basalt decrease the $^{18}O/^{16}O$ of the water. The relative rates of these two opposing reactions serves as a buffer for the oxygen isotopic composition of Earth's oceans (Muehlenbachs and Clayton 1976).

Harold Urey first pointed out that the temperature-dependent $^{18}O/^{16}O$ partitioning between calcite and water in the oceans could be used to reconstruct the temperatures of the oceans with time (Urey 1948). Since that original suggestion, the calcite-water oxygen isotopic paleothermometer has been a mainstay of paleoclimate reconstruction. The pattern of glacial-interglacial cycles over the last 600,000 years was enabled by this method, for example. Subsequent refinements dealt with the effect of sequestration of light oxygen isotopes in ices on ocean water $^{18}O/^{16}O$ (Shackleton and Opdyke 1973), confounding the temperature isotopic signals in the carbonate grown in the water. More recently, the uncertainties associated with the convolution of the isotopic effects of temperature and ice volume have been circumvented by the use of the relative abundances of $^{13}C{-}^{18}O$ bonds in carbonate. The concentrations of these heavy isotope bond pairs provide an intramineral isotope thermometer that is independent of the isotopic composition of the water and thus of ice volume (Gosh et al. 2004).

Oxygen in the Atmosphere

Twenty one percent of the molecules in Earth's air are O_2 (more precisely, the molecular mixing ratio of O_2 in air is 21%). The concentration of dioxygen in air is the result of two cycles operating on disparate timescales. On shorter timescales of about a 1,000 years (Bender et al. 1994), the concentration of O_2 in air is a balance between the global rate of O_2 production by photosynthesis and the global rate of O_2 uptake by aerobic respiration. Oxygen generated by photosynthesis comes ultimately from the oxygen comprising water. On longer geological timescales, O_2 uptake by weathering and the effective oxygen production by carbon burial (or rather, the absence of a long-term sink in the form of carbon oxidation) control the amount of O_2 in air over hundreds of thousands to millions of years (Lasaga and Ohmoto 2002). Short-term variations in O_2 abundance in air arise from variations in the rates of photosynthesis and respiration, while the long-term cycle of weathering and carbon burial governs the permissible amount of oxygen in Earth's atmosphere over geological time. The first appearance of significant levels of atmospheric dioxygen appeared during the Great Oxygenation Event (GOE) about 2.4 billion years before present in the Paleoproterozoic Era (Holland 2006). The possibility that there were multiple "whiffs" of O_2 prior to the GOE and marked decreases in O_2 after the GOE is debated (Lyons and Reinhard 2009). Regardless, atmospheric O_2 levels rose from maximal values of just 1–3% after the GOE to nearer to present-day levels of more than 5–18% in the Neoproterozoic. Widespread carbon deposition in the Carboniferous Period led to still higher concentrations of atmospheric O_2 (Catling and Claire 2005).

Molecular oxygen in Earth's atmosphere is not in oxygen isotopic equilibrium with the oceans. The $^{18}O/^{16}O$ ratio of atmospheric O_2 is greater than that of ocean water by about 2.3–2.4%, a value that is several times greater than that dictated by thermodynamic equilibrium. The high $^{18}O/^{16}O$ in air is referred to as the Dole effect (Dole 1935) and reflects the kinetic isotope effect of respiration and the lack of a significant isotope effect associated with photosynthesis.

In the stratosphere, O_2 photolysis by ultraviolet light (wavelengths $\leq$ 240 nm) liberates atomic oxygen that reacts to form ozone that in turn reacts with atomic oxygen or is photolyzed ($\lambda < 340$ nm) to form dioxygen. This Chapman cycle, named for its discoverer (Chapman 1930), can be described by the reactions

$$\begin{aligned}
&O_2 + h\nu \rightarrow O + O \\
&O + O_2 \xrightarrow{M} O_3 \\
&O_3 + h\nu \rightarrow O_2 + O \\
&O_3 + h\nu_{(\lambda<306\text{nm})} \rightarrow O_2 + O(^1D), \\
&O(^1D) \xrightarrow{M} O \\
&O_3 + O \rightarrow O_2 + O_2
\end{aligned}$$

where M signifies a collision partner (mainly N_2), $O(^1D)$ is the excited singlet state of oxygen, and $h\nu$ refers to the energy of the UV light. The actinic flux of UV light (i.e., the integrated flux from the top of the atmosphere) and the number density of oxygen molecules conspire to produce a peak in the rate of ozone production at an altitude of approximately 25 km. The reaction that produces ozone (O_3) causes a large mass-independent oxygen isotope effect of several per cent (tens of per mil) (Thiemens and Heidenreich 1983).

Dioxygen in air is anomalously low in ^{17}O relative to Earth's rocks and waters by 0.4 per mil ($\Delta^{17}O = 0.04\%$). Approximately 60% of this deficit is another manifestation of the Dole effect, 30% balances an excess in ^{17}O carried by $O(^1D)$ in the stratosphere caused by the mass independent fractionation associated with ozone formation, and 10% is due to evaporation and transpiration (evapotranspiration) of the water that provides the oxygen produced by photosynthesis (Young et al. 2014).

The ^{17}O deficit in dioxygen in air depends on the rate of O_2 turnover by photosynthesis, the concentration of O_2 determined by the balance between photosynthesis and respiration, and the concentration of CO_2. Carbon dioxide enters the budget because $O(^1D)$ transfers excess ^{17}O imparted by ozone photolysis to CO_2. Carbon dioxide mixes from the stratosphere to the troposphere where it exchanges oxygen isotopes with water at ground level. Water is in effect an infinite reservoir of oxygen so that exchange between CO_2 and H_2O creates a sink for ^{17}O. The greater the concentration of CO_2, the more ^{17}O is lost from the atmosphere.

Because biological processing of oxygen removes the stratospheric-induced ^{17}O deficit caused by the flux of CO_2 from the stratosphere to ground level, differences in $\Delta^{17}O$ in atmospheric O_2 have been used as a monitor of gross primary productivity (Luz et al. 1999; Blunier et al. 2002). Disambiguating the effects of changing CO_2 concentration and biological productivity is a challenge (Young et al. 2014). $\Delta^{17}O$ values in Neoproterozoic sulfates in the so-called cap carbonates have been used as evidence for high CO_2 concentrations in the waning stages of the Neoproterozoic global glaciation (snowball Earth) (Bao et al. 2008).

The concentration of the doubly substituted dioxygen isotopologue $^{18}O^{18}O$ in the atmosphere can be used as another measure of biological productivity. This is because the abundance of $^{18}O^{18}O$ is driven toward thermodynamic equilibrium by isotope exchange reactions with atomic oxygen in air, causing an excess of $^{18}O^{18}O$ relative to the purely random distribution, but this isotopic species is depleted by photosynthesis (Yeung et al. 2015).

Biological Utilization and Toxicity

Free dioxygen in Earth's atmosphere is a consequence of photosynthesis and thus is an important biosignature in the search for extraterrestrial life. Consumption of oxygen by aerobic respiration provides the energy for all higher organisms.

Summary

Oxygen is the third most abundant element in the solar system and the most abundant element synthesized in stars. The electronegativity of oxygen influences the size of a planet's metallic core and is a key ingredient for the diversity of life. The three stable isotopes of oxygen are powerful tracers of cosmochemical, geochemical, and biogeochemical processes.

Cross-References

- Activity and Activity Coefficients
- Atmospheric Evolution
- Biogeochemistry
- Carbon Cycle
- Chondrites
- Earth's Atmosphere
- Earth's Core
- Formation and Evolution of the Earth
- Geochemical Thermodynamics
- Iron
- Meteorites
- Nucleosynthesis
- Oxygen Isotopes

References

Badro J, Brodholt JP, Piet H, Siebert J, Ryerson FJ (2015) Core formation and core composition from coupled geochemical and geophysical constraints. Proc Natl Acad Sci U S A 112:12310–12314

Bao H, Lyons JR, Zhou C (2008) Triple oxygen isotope evidence for elevated CO_2 levels after a Neoproterozoic glaciation. Nature 453:504–506

Bender ML, Sowers T, Labeyrie L (1994) The Dole effect and its variations during the last 130,000 years as measured in the Vostok ice core. Glob Biogeochem Cycles 8:363–376
Blunier T, Barnett B, Bender ML, Hendricks MB (2002) Biological oxygen productivity during the last 60,000 years from triple oxygen isotope measurements. Glob Biogeochem Cycles 16(3):3-1. https://doi.org/10.1029/2001GB001460
Catling DC, Claire MW (2005) How Earth's atmosphere evolved to an oxic state: a status report. Earth Planet Sci Lett 237:1–20
Chapman S (1930) A theory of upper-atmosheric ozone. Mem R Meteorol Soc III(26):103–125
Clayton DD (2003) Handbook of isotopes in the cosmos: hydrogen to gallium. Cambridge University Press, Cambridge
Clayton RN, Grossman L, Mayeda TK (1973) A component of primitive nuclear composition in carbonaceous meteorites. Science 182:458–488
Dole M (1935) The relative atomic weight of oxygen in water and in air. J Am Chem Soc 57:2731
Gosh P, Eiler J, Adkins JF, Balta B, Schauble E, Wanamaker AD, Introne C, Kreutz K (2004) Ratio of multi-substituted isotopologues in natural carbonates, a novel tool to study palaeo temperature. EOS Trans. AGU, Fall Meeting Suppl., San Francisco, Abstract P11A-0554l
Grossman L, Fedkin AV, Simon SB (2012) Formation of the first oxidized iron in the solar system. Meteorit Planet Sci 47:2160–2169
Guerlac H (1961) Lavoisier. The crucial year. Cornell University Press, Ithaca
Holland HD (2006) The oxygenation of the atmosphere and oceans. Philos Trans R Soc B 361:903–915
Huang H, Fei Y, Cai L, Jing F, Hu X, Xie H, Zhang L, Gong Z (2011) Evidence for an oxygen-depleted liquid outer core of the Earth. Nature 479:513–516
Krot AN, Fegley B, Lodders K (2000) Meteoritical and astrophysical constraints on the oxidation state of the solar nebula. In: Mannings V, Boss AP, Russell SS (eds) Protostars and planets IV. University of Arizona Press, Tucson, pp 1019–1054
Lasaga AC, Ohmoto H (2002) The oxygen geochemical cycle: dynamics and stability. Geochim Cosmochim Acta 66:361–381
Lodders K (2003) Solar system abundances and condensation temperatures of the elements. Astrophys J 591:1220–1247
Luz B, Barkan E, Bender ML, Thiemens MH, Boering KA (1999) Triple-isotope composition of atmospheric oxygen as a tracer of biosphere productivity. Science 400:547–550
Lyons TW, Reinhard CT (2009) Oxygen for heavy-metal fans (News & Views). Nature 461:179–181
Lyons JR, Young ED (2005) CO self-shielding as the origin of oxygen isotope anomalies in the early solar nebula. Nature 435(7040):317–320
McKeegan KD, Kallio APA, Heber VS, Jarzebinski G, Mao PH, Coath CD, Kunihiro T, Wiens RC, Nordholt JE, Moser RWJ, Reisenfeld DB, Jurewicz AJG, Burnett DS (2011) The oxygen isotopic composition of the Sun inferred from captured solar wind. Science 332:1528–1532
Muehlenbachs K, Clayton RN (1976) Oxygen isotope composition of the oceanic crust and its bearing on seawater. J Geophyhs Res 81:4365–4369
Pauling L (1980) The nature of silicon-oxygen bonds. Am Mineral 65:321–323
Priestley J (1775) Experiments and observations on different kinds of air. J Johnson, St. Paul's Church, London
Rubie DC, Jacobson SA, Morbidelli A, O'Brien DP, Young ED, de Vries J, Nimmo F, Palme H, Frost DJ (2015) Accretion and differentiation of the terrestrial planets with implications for the compositions of early-formed solar system bodies and accretion of water. Icarus 248:89–108
Scheele KW (1777) Chemische Abhandlung von der Luft und dem Feuer: nebst einem Vorbericht von Torbern Bergman (Chemical treatise on air and fire with a preface by Torbern Bergman). Magn. Swederus (Swedish Academy), Uppsala/Leipzig
Shackleton NJ, Opdyke ND (1973) Oxygen isotope and paleomagnetic stratigraphy of equatorial Pacific Core V28-238: oxygen isotope temperatures and ice volume on a 105 year and 106 year scale. Quat Res 3:39–55
Shannon RD (1976) Revised effective ionic radii and systematic studies of interatomic distances in halides and chalcogenides. Acta Crystallogr A 32(5):751–767
Taylor HP (1974) The application of oxygen and hydrogen isotope studies to problems of hydrothermal alteration and ore deposits. Econ Geol 69:843
Thiemens MH, Heidenreich HE (1983) The mass-independent fractionation of oxygen: a novel effect and its possible cosmochemical implications. Science 219:1073–1075
Tinsley BM, Cameron AGW (1974) Possible influence of comets on the chemical evolution of the Galaxy. Astrophysics and Space Science 31:31–35
Urey HC (1948) Oxygen isotopes in nature and in the laboratory. Science 108:489–495
West JB (2014) Joseph Priestley, oxygen, and the enlightenment. Am J Physiol Lung Cell Mol Physiol 306:L111–L119
Wiechert UH, Halliday AN, Lee D-C, Snyder GA, Taylor LA, Rumble D (2001) Oxygen isotopes and the Moon-forming giant impact. Science 294:345–348
Yeung LY, Ash JL, Young ED (2015) Biological signatures in clumped isotopes of O_2. Science 348(6233):431–434
Young ED (2007) Strange water in the solar system. Science 317:211–212
Young ED, Kuramoto K, Marcus RA, Yurimoto H, Jacobsen SB (2008) Mass-independent oxygen isotope variation in the solar nebula. In: MacPherson GJ, Mittlefehldt DW, Jones JH, Simon SB (eds) Reviews in mineralogy & geochemistry, oxygen in the solar system, vol 68. Mineralogical Society of America, Geochemical Society, Chantilly, pp 187–218
Young ED, Gounelle M, Smith RL, Morris MR, Pontoppidan KM (2011) Astronomical oxygen isotopic evidence for supernova enrichment of the solar system birth environment by propagating star formation. Astrophys J 729(1):43–56
Young ED, Yeung LY, Kohl I (2014) On the $\Delta^{17}O$ budget of atmospheric O_2. Geochem Cosmochim Acta 135:102–125
Young ED, Kohl IE, Warren PH, Rubie DC, Jacobson SA, Morbidelli A (2016) Oxygen isotopic evidence for vigorous mixing during the Moon-forming giant impact. Science 351:493–496
Yurimoto H, Kuramoto K (2004) Molecular cloud origin for the oxygen isotope heterogeneity in the solar system. Science 305:1763–1766

Oxygen Isotopes

Hisayoshi Yurimoto
Natural History Sciences, Hokkaido University, Sapporo, Japan

Definition

Natural oxygen is a mixture of three stable isotopes ^{16}O (99.762%), ^{17}O (0.038%), and ^{18}O (0.200%). Isotope ratios of $^{17}O/^{16}O$ and $^{18}O/^{16}O$ normally vary in natural

materials by up to 5% and 10%, respectively, which are mass-dependent isotope fractionation. Mass-independent isotope fractionations also occur in oxygen for extraterrestrial materials and atmospheric molecules. These isotope fractionations are useful as tracers in geochemical and cosmochemical reactions and are applied to diverse geochemical topics as the origin of the solar system and the evolution of the atmosphere, hydrosphere, and lithosphere and paleoclimate.

Introduction

Oxygen is the third most abundant element in the universe and the most abundant element of the terrestrial planets. The presence of oxygen in both gaseous and solid phases makes oxygen isotopes (terrestrial relative abundances: $^{16}O = 99.762\%$, $^{17}O = 0.038\%$, and $^{18}O = 0.200\%$) important tracers of various fractionation processes in the solar nebula, which are essential for understanding the evolution of gaseous, liquid, and solid phases in geochemistry and cosmochemistry.

The ^{16}O is produced by helium burning mainly in massive stars (Clayton 2003). The synthesis of ^{16}O is not dependent on the existence of other elements heavier than He. ^{16}O is a primary nuclide.

On the other hand, stellar nuclide synthesis of ^{17}O and ^{18}O need the prior existence of ^{16}O, ^{12}C, and ^{14}N. Therefore, these isotopes are secondary nuclides. ^{17}O is produced from H and ^{16}O by hydrogen burning in the CNO cycle of lower mass stars in their red giant phase or from novae (Clayton 2003). ^{17}O is produced from ^{14}N as a reactant by He burning in massive stars (Clayton 2003).

Nomenclature of Oxygen Isotope Ratios and Standardization of δ-Values

Oxygen isotope ratios are normally expressed in δ units, which are deviations in part per thousand (permil, ‰) in the $^{17}O/^{16}O$ and $^{18}O/^{16}O$ ratios from Standard Mean Ocean Water (SMOW; also referred to as VSMOW; Gröning et al. 2007) with $^{17}O/^{16}O = 0.0003829$ and $^{18}O/^{16}O = 0.0020052$ (McKeegan and Leshin 2001):

$$\delta^{17,18}O_{SMOW} = \left[\left(^{17,18}O/^{16}O\right)_{sample} / \left(^{17,18}O/^{16}O\right)_{SMOW} - 1\right] \times 1000.$$

On a three-isotope diagram of $\delta^{18}O$ versus $\delta^{17}O$, compositions of nearly all terrestrial samples plot along a single line of slope 0.52 called the terrestrial fractionation (TF) line. This line reflects mass-dependent fractionation from a single homogeneous source during chemical and physical processes that results from differences in the masses of the oxygen isotopes (Fig. 1). The slope 0.52 results from changes in $^{17}O/^{16}O$ that are nearly half those in $^{18}O/^{16}O$ because of isotopic mass differences; the precise value of the slope depends on the nature of the isotopic species or isotopologues (e.g., Thiemens 2006). This is a mass fractionation line. In contrast, O-isotopic compositions of the vast majority of extraterrestrial samples, including primitive (chondrites) and differentiated (achondrites) meteorites, deviate from the terrestrial fractionation line, reflecting mass-independent fractionation processes. The deviation from the terrestrial fractionation line is commonly expressed as:

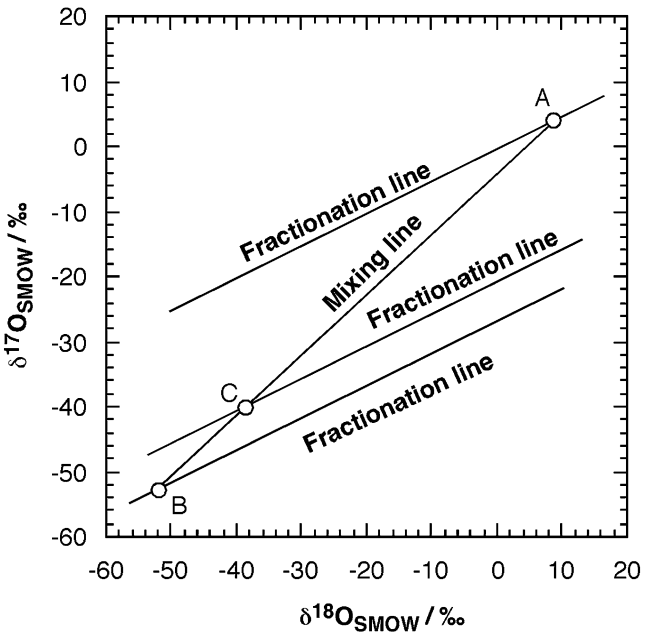

Oxygen Isotopes, Fig. 1 Relationship between mass-dependent isotope fractionation lines and mixing lines on the three-oxygen isotope diagram. Point C is a result of mixing between points A and B

$$\Delta^{17}O_{SMOW} = \delta^{17}O_{SMOW} - 0.52\,\delta^{18}O_{SMOW}.$$

For carbonate minerals, the reporting standard may be PDB (belemnite from the Peedee formation, South Carolina) or VPDB. The relation between scales of PDB and SMOW is (Coplen et al. 1983):

$$\delta^{18}O_{SMOW} = 1.03091\,\delta^{18}O_{PDB} + 30.91.$$

Analytical Methods

Conventionally, oxygen isotope ratios are measured on CO_2 or O_2 gas by isotope ratio mass spectrometry (IRMS; Nier 1940). A dual inlet system is used for precise determination of

isotope ratios. Recently a continuous flow inlet system coupled with gas chromatograph (CF-IRMS) was developed for rapid and small sample analyses (Komatsu et al. 2008). For in situ small quantity sampling from minerals, a laser ablation method with fluorination technique is useful to measure O isotopes (Young et al. 1998).

An alternative approach for measuring O isotopes of gas molecules is by laser absorption spectroscopy. Cavity ring-down spectroscopy and off-axis spectroscopy have made major advances toward precise compound-specific measurements of three O isotopes (Johnson et al. 2011; Steig et al. 2014). The precision of oxygen isotope ratios measured by this method becomes competitive with conventional IRMS methods.

Secondary ion mass spectroscopy (SIMS) has been applied to in situ microanalysis of three oxygen isotopes of minerals (Yurimoto et al. 1994). The spatial resolution becomes down to 1 μm with precision of several permil (Yurimoto et al. 1998) and 8 μm with precision of smaller than one permil (Yurimoto et al. 2011). Oxygen isotope ratio imaging is available by SIMS with micrometer resolution and several permil in precision (Yurimoto et al. 2003).

Mass-Dependent Fractionation Relations and Geothermometers

Isotope fractionation between phases depends on differences in the thermodynamic free energies of the isotopically substituted compounds. Equilibrium fractionation factor, α, of oxygen isotopes between two phases (X and Y) is expressed as:

$$\alpha_{X-Y} = \left({}^{18}\mathrm{O}/{}^{16}\mathrm{O}\right)_X / \left({}^{18}\mathrm{O}/{}^{16}\mathrm{O}\right)_Y = \left[1 + \left(\delta^{18}\mathrm{O}_{\mathrm{SMOW}}\right)_X/1000\right] / \left[1 + \left(\delta^{18}\mathrm{O}_{\mathrm{SMOW}}\right)_Y/1000\right].$$

Fractionation factors often are reported as:

$$1000 \ln \alpha_{X-Y} \approx 1000\,(\alpha_{X-Y} - 1) \approx \left(\delta^{18}\mathrm{O}_{\mathrm{SMOW}}\right)_X - \left(\delta^{18}\mathrm{O}_{\mathrm{SMOW}}\right)_Y$$

when the isotope ratios of samples are similar to that of the reference.

The isotopic fractionation between phases generally decreases with increasing temperature, with 1000 ln α_{X-Y} approaching 0 at high temperature. This relation is typically expressed as:

$$1000 \ln \alpha_{X-Y} = A\left(10^6 T^{-2}\right) - B$$

where A and B are constants, and T is temperature in K. Temperature dependences of mineral–water and mineral–mineral ^{18}O fractionation factors serve as geothermometers virtually independent of pressure (Fig. 2).

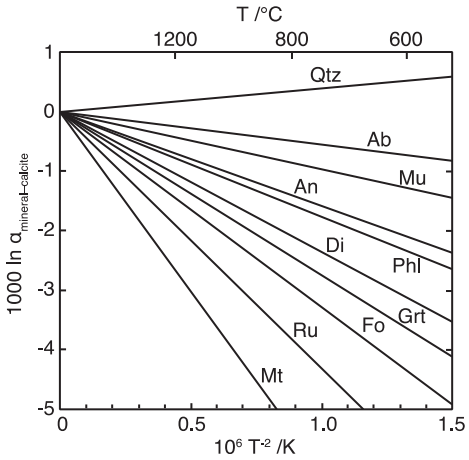

Oxygen Isotopes, Fig. 2 Oxygen isotope fractionation between mineral and calcite as a function of temperature (Data from Chacko et al. 2001). *Ab* albite, *An* anorthite, *Di* diopside, *Fo* forsterite, *Grt* garnet, *Mt* magnetite, *Mu* muscovite, *Phl* phlogopite, *Qtz* quartz, *Ru* rutile

Global climate results from heat transfer between the equator and the polar areas induced by the unequal solar energy flux to the Earth. This heat transfer drives global circulation of water, i.e., evaporation of ocean water, convection, and condensation/precipitation of water vapor. As a result, oxygen isotope fractionations record thermodynamic processes in the atmosphere–ice sheet–ocean system. Therefore, oxygen isotope measurements of ice sheet and marine sediments yield global climate records (Fig. 3). Chronological variations of oxygen isotope ratios correlate between ice sheets, atmosphere, and seawater over the past 360,000 years, supporting the Milankovitch theory for glacial–interglacial cycles (Hays et al. 1976).

Oxygen Isotope Distribution of the Galaxy and the Solar System

Oxygen isotope composition of universe changes with time by stellar nucleosynthesis known as galactic chemical evolution (Tinsley and Cameron 1974; Clayton 2003). Part of this oxygen isotope evolution of the galaxy is observed in presolar grains surviving in extraterrestrial materials, e.g., a comet, interplanetary dust particles, and chondrites (Zinner 2014). The oxygen isotope ratios distribute from 2×10^{-5} to 5×10^{-2} for $^{17}O/^{16}O$ (−950 to 130000 ‰ for $\delta^{17}O_{SMOW}$) and from 2×10^{-5} to 2×10^{-2} for $^{18}O/^{16}O$ (−990 to 9000‰ for $\delta^{18}O_{SMOW}$). The distribution is far larger than those observed among materials formed in the solar system

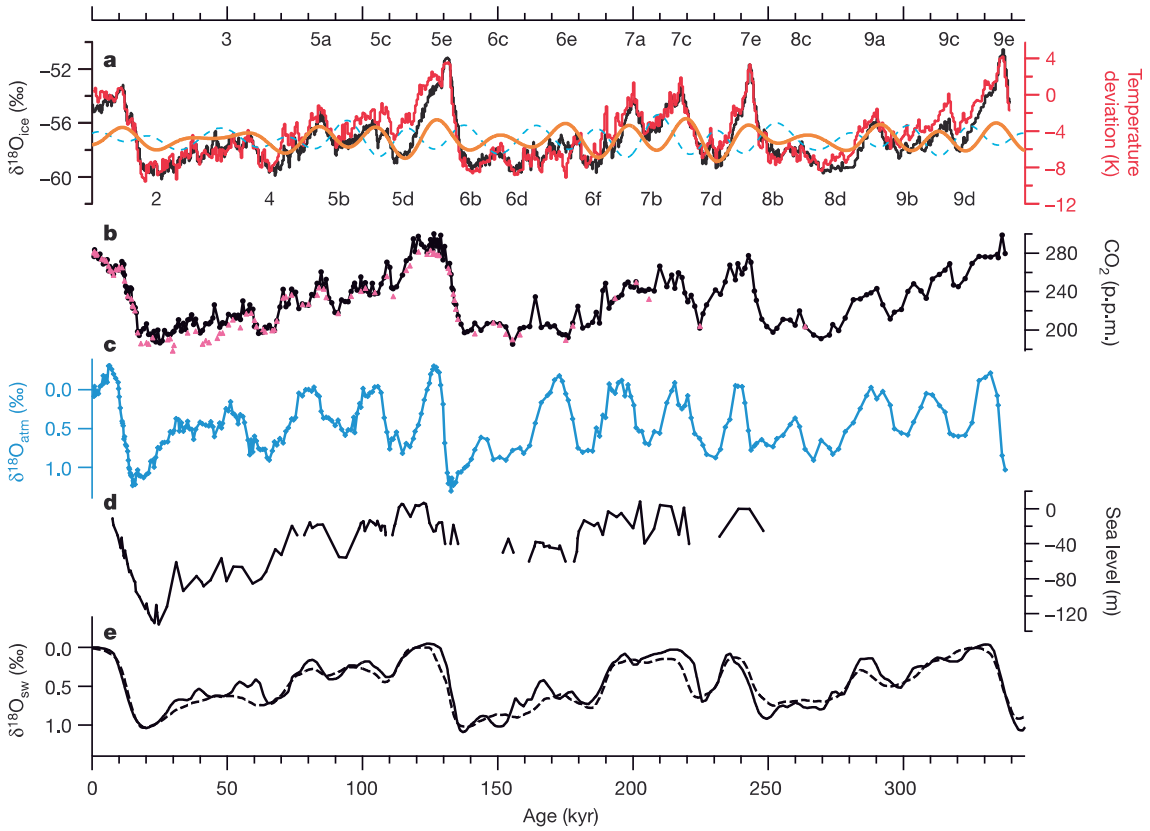

Oxygen Isotopes, Fig. 3 Chronological variation of oxygen isotopes recording global climate change (from Kawamura et al. 2007). (**a**) $\delta^{18}O$ of ice core of Dome Fuji, Antarctica (black), and temperature deviation (red), (**b**) atmospheric CO_2 concentration from the Dome Fuji core, (**c**) $\delta^{18}O$ of atmospheric O_2 from the Dome Fuji core, (**d**) sea level change, and (**e**) $\delta^{18}O$ of seawater

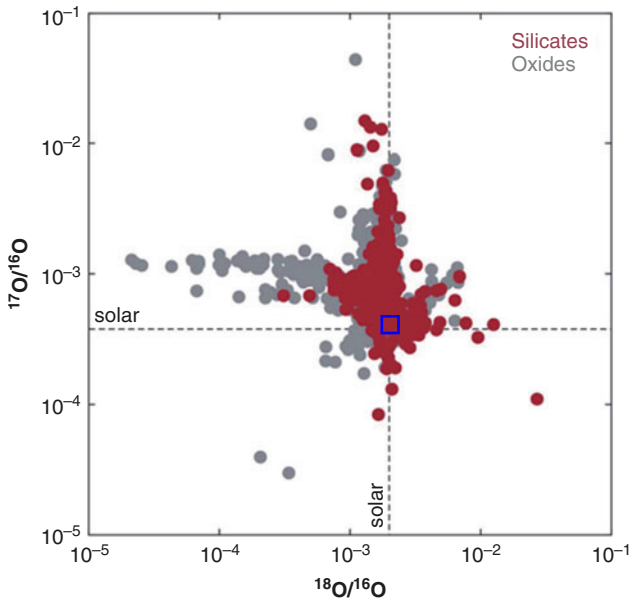

Oxygen Isotopes, Fig. 4 Oxygen isotope distribution in the galaxy. Red circle, presolar silicate grains; gray circle, presolar oxide grains (from Floss and Haenecour 2016). Oxygen isotope ratios reported from materials formed in the solar system are plotted in the blue square around the solar value, corresponding to Fig. 5

(Fig. 4). The diverse nucleosynthetic production of isotopes of elements including oxygen was mixed during formation of the solar system, but small isotopic heterogenic distribution between carbonaceous and noncarbonaceous meteorites has remained for oxygen with other elements due to incomplete mixing of their presolar feedstock (Warren 2011).

Mass-independent distribution of oxygen isotope in the solar system was found in 1973 in meteorites (Clayton et al. 1973). After the discovery, our meteorite collection has been largely developed mainly by new finds from Antarctica and African desert areas and new analytical techniques, mainly SIMS, applied to measure oxygen isotopes of the classic and new meteorite collections (Clayton 1993; Yurimoto et al. 2008). The oxygen isotope compositions in the solar system distribute essentially along slope-1 line on the three-oxygen isotope diagram (Fig. 5). The end members represent ~−100‰ for the ^{16}O-rich end and ~ + 200‰ for the ^{16}O-poor end. The oxygen isotope distribution in the solar system is quite different systematics from those in the galaxy, indicating that the oxygen isotope distribution in the solar system did not originate by nucleosynthesis but plausibly by photochemical processes (Yurimoto et al. 2007).

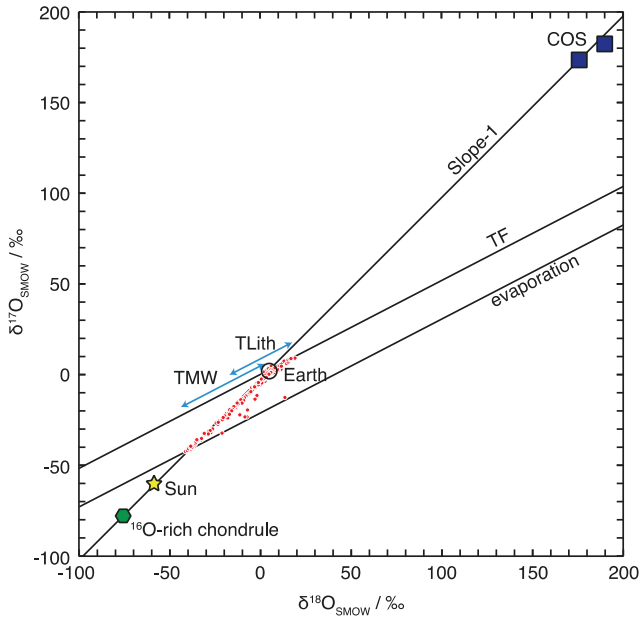

Oxygen Isotopes, Fig. 5 Oxygen isotope distribution in the solar system. Red circle, meteorites (from frontispiece of Rev. Mineral Geochem. 68, 2008); Earth, bulk silicate earth; Sun, solar value (McKeegan et al. 2011); COS, cosmic symplectite (Sakamoto et al. 2007); ^{16}O-rich chondrule, an extreme ^{16}O-rich chondrule (Kobayashi et al. 2003); TLith, terrestrial lithosphere which distributes on the TF line (Farquhar and Johnston 2008); TMW, terrestrial metric water which distributes on the TF line (Farquhar and Johnston 2008); TF, terrestrial fractionation line; Slope-1, slope one line; evaporation, fractionation line by evaporation and condensation

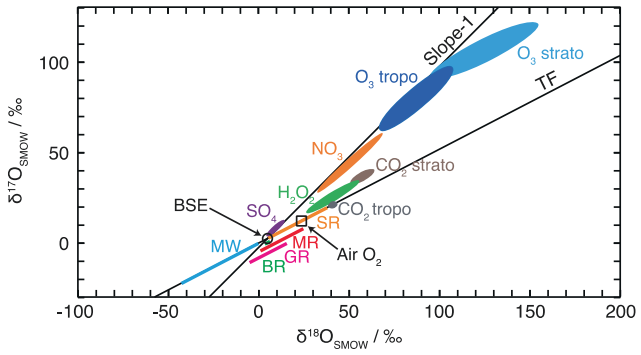

Oxygen Isotopes, Fig. 6 Oxygen isotope distribution on the Earth (Data from Hoefs 2004; Thiemens 2006). Circle, bulk silicate earth (BSE); square, atmospheric oxygen (Air O_2); BR, basaltic rock which distributes on the TF (terrestrial fractionation) line; GR, granitic rock which distributes on the TF line; MR, metamorphic rock which distributes on the TF line; SR, sedimentary rock; MW, meteoric water; CO_2 tropo, tropospheric CO_2; CO_2 strato, stratospheric CO_2; O_3 tropo, tropospheric O_3; O_3 strato, stratospheric O_3. Other symbols correspond to atmospheric molecules indicated. Note that plots of BR, GR, and MR are shifted downward in order to avoid overlap their lines

Oxygen Isotope Distribution of the Earth

Oxygen isotopes on the Earth basically distribute under control of thermodynamic processes along mass-dependent fractionation line, i.e., terrestrial mass fractionation line, on the three-oxygen isotope diagram (Fig. 6). Some atmospheric compounds exhibit a mass independently distribution as a result of photochemical processes.

Ocean water is the oxygen isotope standard (SMOW) and hence by definition has $\delta^{17,18}O_{SMOW} = 0‰$, but small variations in seawater of $\delta^{18}O_{SMOW}$ (±1‰) occur and correlate with salinity variations associated with evaporation or precipitation and mixing with meteoritic water. Meteoritic water is ultimately derived from the evaporation of seawater and hence has negative $\delta^{18}O_{SMOW}$ values as a consequence of Rayleigh distillation processes which deplete meteoritic water in ^{18}O (Gat and Gonfiantini 1981). The oxygen isotope changes correlate with mean annual temperature and with hydrogen isotopes, which correlation is termed the meteoric water line (MWL).

The average composition of the Earth is inferred $\delta^{18}O_{SMOW} = 5.7 \pm 0.5‰$ by a narrow ^{18}O range of mid-ocean ridge basalts (MORB) and fresh ultramafic rocks from upper mantle, but small variations in oxygen isotopes in mantle rocks are observed resulting of subduction and recycling surface materials to the mantle. Fresh igneous rocks have similar $\delta^{18}O$ values to mid-ocean ridge basalts (MORB) (Eiler 2001). Compared to basalts, granitic rocks show large $\delta^{18}O$ variation because of enhanced potential for hydrothermal alterations and crustal contaminations.

Original oxygen isotopic compositions of authigenic minerals in sedimentary rocks reflect the isotope fractionation between the mineral and the water which the mineral formed. Therefore, they are valuable paleoenvironmental indicators, recording temperature and water $\delta^{18}O$ (Urey 1948). This is particularly useful for carbonate sediments. $\delta^{18}O$ values are generally between −3 and +1‰ for aragonite and calcite, equivalent to paleothermometers of roughly 10–25 °C (Hudson and Anderson 1989).

The conventional $\delta^{18}O$ paleothermometers often need to assume the ^{18}O ratio in water to calculate paleotemperatures. This assumption is not necessary if clumped isotopes are used for paleothermometers. The clumped isotopes are heavy isotopes that are bonded to other heavy isotopes. The clumped-isotope thermometer of carbonate is defined as ^{13}C–^{18}O order/disorder of the crystal lattice, i.e., an intra-mineral isotope thermometer basing on the temperature dependence of the clumping of ^{13}C and ^{18}O into bonds within the carbonate mineral lattice that is independent of the isotopic composition of the water (Ghosh et al. 2006; Eiler 2007).

Oxygen isotopic compositions of metamorphic rocks reflect fluid–rock interaction during metamorphism. Thus the $\delta^{18}O$ of metamorphic rocks distribute widely over those of granitic rock and sedimentary rock.

In the atmosphere, mass-dependent fractionation behavior for oxygen isotopes is observed between meteoric

water molecular oxygen and tropospheric carbon dioxide. On the other hand, mass-independent fractionation effects are observed in atmospheric ozone, nitrate, sulfate, carbon monoxide, hydrogen peroxide, nitrogen dioxide, and, to lesser extent, molecular oxide and carbon dioxide (Thiemens 2006; Farquhar and Johnston 2008).

Summary

Natural oxygen is a mixture of three stable isotopes ^{16}O, ^{17}O, and ^{18}O. Mass-dependent and mass-independent isotope fractionations are observed in nature. Oxygen isotopes are useful tracers to determine the origin of natural materials and molecule, and cosmochemical and geochemical processes.

Cross-References

- Achondrites
- Chondrites
- Chondrules
- Earth's Atmosphere
- Earth's Oceanic Crust
- Geothermometry and Geobarometry
- Hydrothermal Alteration
- Metamorphic Reactions and Processes
- Meteorites
- Mid-Ocean Ridge Basalts (MORB)
- Ocean Biochemical Cycling and Trace Elements
- Ocean Salinity, Major Elements, and Thermohaline Circulation
- Oxygen
- Paleoclimatology
- Paleoenvironments
- Presolar Grains
- Refractory Inclusions in Chondritic Meteorites
- Stable Isotope Geochemistry
- Thermal Ionization Mass Spectrometry

References

Chacko T, Cole DR, Horita J (2001) Equilibrium oxygen, hydrogen and carbon fractionation factors applicable to geologic systems. Rev Mineral Geochem 43:1–81

Clayton RN (1993) Oxygen isotopes in meteorites. Annu Rev Earth Planet Sci 21:115–149

Clayton DD (2003) Handbook of isotopes in the cosmos: hydrogen to gallium. Cambridge University Press, Cambridge

Clayton RN, Grossman L, Mayeda TK (1973) A component of primitive nuclear composition in carbonaceous meteorites. Science 182:485–488

Coplen TB, Kendall C, Hopple J (1983) Comparison of stable isotope reference samples. Nature 302:236–238

Eiler JM (2001) Oxygen isotope variations of basaltic lavas and upper mantle rocks. Rev Mineral Geochem 43:319–364

Eiler JM (2007) 'Clumped-isotope' geochemistry – the study of naturally-occurring, multiply-substituted isotopologues. Earth Planet Sci Lett 262:309–327

Farquhar J, Johnston DT (2008) The oxygen cycle of the terrestrial planets: insights into the processing and history of oxygen in surface environments. Rev Mineral Geochem 68:463–492

Floss C, Haenecour P (2016) Presolar silicate grains: abundances, isotopic and elemental compositions, and the effects of secondary processing. Geochem J 50:3–25

Gat JR, Gonfiantini R (1981) Stable isotope hydrology: deuterium and oxygen-18 in the water cycle. Technical report series no. 210, International Atomic Energy Agency, Vienna, 337 pp

Ghosh P, Adkins J, Affek H, Balta B, Guo W, Schauble EA, Schrag D, Eiler JM (2006) ^{13}C -^{18}O bonds in carbonate minerals: a new kind of paleothermometer. Geochim Cosmochim Acta 70:1439–1456

Gröning M, Van Duren M, Andreescu L (2007) Metrological characteristics of the conventional measurement scales for hydrogen and oxygen stable isotope amount ratios: the δ-scales. In: Fajgelj A, Belli M, Sansone U (eds) Combining and reporting analytical results. Proceedings of an international workshop on "combining and reporting analytical results: the role of traceability and uncertainty for comparing analytical results", Royal Society of Chemistry, Rome, 6–8 Mar 2006, pp 62–72

Hays JD, Imbrie J, Shackleton NJ (1976) Variations in the Earth's orbit: pacemaker of ice ages. Science 194:1121–1132

Hoefs J (2004) Stable isotope geochemistry. Springer, Berlin/Heidelberg, p 244

Hudson JD, Anderson TF (1989) Ocean temperatures and isotopic compositions through time. Trans R Soc Edinb Earth Sci 80:183–192

Johnson LR, Sharp ZD, Galewsky J, Strong M, Van Pelt AD, Dong F, Noone D (2011) Isotope correction for laser instrument measurement bias at low water vapor concentration using flasks: application to measurements from Mauna Loa Observatory, Hawaii. Rapid Commun Mass Spectrom 25:608–616

Kawamura K, Parrenin F, Lisiecki L, Uemura R, Vimeux F, Severinghaus JP, Hutterli MA, Nakazawa T, Aoki S, Jouzel J, Raymo ME, Matsumoto K, Nakata H, Motoyama H, Fujita S, Goto-Azuma K, Fujii Y, Watanabe O (2007) Northern Hemisphere forcing of climatic cycles in Antarctica over the past 360,000 years. Nature 448:912–916

Kobayashi S, Imai H, Yurimoto H (2003) New extreme ^{16}O-rich reservoir in the early solar system. Geochem J 37:663–669

Komatsu DD, Ishimura T, Nakagawa F, Tsunogai U (2008) Determination of the $^{15}N/^{14}N$, $^{17}O/^{16}O$, and $^{18}O/^{16}O$ ratios of nitrous oxide by using continuous-flow isotope-ratio mass spectrometry. Rapid Commun Mass Spectrom 22:1587–1596

McKeegan KD, Leshin LA (2001) Stable isotope variations in extraterrestrial materials. In: Valley JW, Cole DR (eds) Stable isotope geochemistry, vol 43. Mineralogical Society of America, Washington, DC, pp 279–318

McKeegan KD, Kallio APA, Heber VS, Jarzebinski G, Mao PH, Coath CD, Kunihiro T, Wiens RC, Nordholt JE, Moses RW Jr, Reisenfeld DB, Jurewicz AJG, Burnett DS (2011) The oxygen isotopic composition of the Sun inferred from captured solar wind. Science 332:1528–1532

Nier AO (1940) A mass spectrometer for routine isotope abundance measurements. Rev Sci Instrum 11:212–216

Sakamoto N, Seto Y, Itoh S, Kuramoto K, Fujino K, Nagashima K, Krot AN, Yurimoto H (2007) Remnants of the early solar system water enriched in heavy oxygen isotopes. Science 317:231–233

Steig EJ, Gkinis V, Schauer AJ, Schoenemann SW, Samek K, Hoffnagle J, Dennis KJ, Tan SM (2014) Calibrated high-precision ^{17}O-excess measurements using cavity ring-down spectroscopy with laser-current-tuned cavity resonance. Atmos Meas Tech 7:2421–2435

Thiemens MH (2006) History and applications of mass-independent isotope effects. Annu Rev Earth Planet Sci 34:217–262
Tinsley BM, Cameron AGW (1974) Possible influence of comets on the chemical evolution of the Galaxy. Astrophys Space Sci 31:31–35
Urey HC (1948) Oxygen isotopes in nature and in the laboratory. Science 108:489–495
Warren PH (2011) Stable isotopes and the noncarbonaceous derivation of ureilites, in common with nearly all differentiated planetary materials. Geochim Cosmochim Acta 75:6912–6926
Young ED, Coutts DW, Kapitan D (1998) UV laser ablation and IRM-GCMS microanalysis of $^{18}O/^{16}O$ and $^{17}O/^{16}O$ with application to a calcium–aluminium-rich inclusion from the Allende meteorite. Geochim Cosmochim Acta 62:3161–3168
Yurimoto H, Nagasawa H, Mori Y, Matsubaya O (1994) Micro-distribution of oxygen isotopes in a refractory inclusion from the Allende meteorite. Earth Planet Sci Lett 128:47–53
Yurimoto H, Ito M, Nagasawa H (1998) Oxygen isotope exchange between refractory inclusion in Allende and solar nebula gas. Science 282:1874–1877
Yurimoto H, Nagashima K, Kunihiro T (2003) High precision isotope micro-imaging of materials. Appl Surf Sci 203–204:793–797
Yurimoto H, Kuramoto K, Krot AN, Scott ERD, Cuzzi JN, Thiemens MH, Lyons JR (2007) Origin and evolution of oxygen isotopic compositions of the solar system. In: Reipurth B, Jewitt D, Keil K (eds) Protostars and planets V. University of Arizona Press, Tucson, pp 849–862
Yurimoto H, Krot AN, Choi B-G, Aleon J, Kunihiro T, Brearley AJ (2008) Oxygen isotopes of chondritic components. Rev Mineral Geochem 68:141–186
Yurimoto H, Abe K, Abe M, Ebihara M, Fujimura A, Hashiguchi M, Hashizume K, Ireland TR, Itoh S, Katayama J, Kato C, Kawaguchi J, Kawasaki N, Kitajima F, Kobayashi S, Meike T, Mukai T, Nagao K, Nakamura T, Naraoka H, Noguchi T, Okazaki R, Park C, Sakamoto N, Seto Y, Takei M, Tsuchiyama A, Uesugi M, Wakaki S, Yada T, Yamamoto K, Yoshikawa M, Zolensky ME (2011) Oxygen isotopic compositions of asteroidal materials returned from Itokawa by the Hayabusa mission. Science 333:1116–1119
Zinner E (2014) Presolar grains. In: Treatise on geochemistry, vol 1, 2nd edn. Elsevier, Amsterdam, pp 181–213

Ozone and Stratospheric Chemistry

Slimane Bekki[1] and Joël Savarino[2]
[1]LATMOS-IPSL (Laboratoire Atmosphères, Milieux, Observations Spatiales), Sorbonne Universités-UPMC, Paris Saclay-UVSQ, CNRS, Paris, France
[2]Laboratoire de Glaciologie et Géophysique de l'Environnement, Université Grenoble-Alpes, UMRCNTS/UGA, Grenoble, France

Definition

The stratosphere is the atmospheric layer comprised between 8–18 km for at its lowest altitudes and 40–60 km at its highest altitudes, which correspond more or less to the stratospheric ozone layer thickness. In this part of the atmosphere, intense UV radiation from the Sun fuels an active and energetic photochemical reactor leading to the formation of two important by-products: the ozone molecule (O_3), an oxygen allotrope, and heat that mostly originates from absorption of UV radiation by ozone. While heat causes a strong vertical stability of the air mass in the stratosphere (stratified atmosphere), large concentrations of ozone form a UV-protective shield allowing the development of life on the Earth's surface. The intense UV radiations combined with the ozone concentration generate a distinct stratospheric chemistry where nitrogen, oxygen, and halogen compounds are highly coupled in cycles that maintain the chemical stability of this UV-protective atmospheric layer (UVs break down atmospheric molecular oxygen, leading to the formation of ozone that better absorb UV radiations than the parent molecules). In the industrialized era, emissions of halogenated compounds have destabilized this fragile chemical stability by creating "ozone-killer" molecules, reducing the thickness of the ozone layer and allowing harmful UV radiations to reach the ground. The stratosphere is also a key atmospheric compartment for the stability of the radiative budget of the Earth and thus its climate. The presence of tiny droplets of sulfuric acid in the stratosphere acts as an aerosol layer that reflects incoming solar radiation, thus cooling the Earth's ground temperature; it also plays a significant role in the ozone budget by providing surfaces where heterogeneous chemistry can generate ozone-destroying radical species. This acid cloud layer is exacerbated during powerful volcanic eruptions where megatons of sulfur are directly injected into the stratosphere.

Ozone Stratospheric Chemistry

Ozone

This chapter introduces the main concepts about the stratospheric ozone chemistry and budget. We start by recalling briefly the history of ozone research. Then, we describe the main features of ozone distribution. The next section reviews the basic chemistry of stratospheric ozone. An analysis of the phenomenon of the so-called "ozone hole" is presented in the fourth section. The last section is devoted to the overall perturbation of stratospheric ozone by the emissions of ozone-destroying substances and the interactions with climate change.

Historical Perspectives and Background

Ozone (trioxygen O_3) was first identified at Basel in 1840 by German chemist C.F. Schöenbein from its pronounced smell following electrical discharges in the air (Schöenbein 1840). The same particular smell, characteristic of ozone, can be found near photocopy machines when it has been used intensively. Schöenbein named this gas "ozone" from the Greek word "ozein" meaning "to smell." The chemical nature of ozone was determined from extensive laboratory studies

initiated by M. De la Rive and C. Marignac in Geneva in 1845. A. Houzeau then detected ozone in the atmosphere in 1858 after performing the first atmospheric measurements at Rouen, France. French chemist Albert Levy conducted systematic measurements of atmospheric ozone in Paris during 30 years in the late nineteenth century. A range of scientists investigated the absorption radiative properties of ozone. The important finding was that the quasi-absence of solar UV radiation (below about 300 nm) at the surface must have been due to absorption of UV by atmospheric ozone, notably the Hartley band (Cornu 1879; Hartley 1881). Using ozone absorption properties, French physicists H. Buisson and C. Fabry then designed a spectrograph and made the first measurements of the thickness of the ozone layer (i.e., ozone column corresponding to the vertically integrated ozone concentration) in 1913. Based on Buisson and Fabry spectrograph, the British scientist G.M.B. Dobson developed in Oxford, UK, in 1920 a spectrophotometer, which is still used nowadays to measure the ozone column (Dobson and Harrison 1926). The first successful attempt to measure the vertical profile of ozone was led by Swiss scientist F.W.P. Götz at the start of the 1930s (Götz et al. 1934). Later, German physicists V. H. Regener started making measurements from balloons (Regener 1964). These height-resolved ozone observations showed that the ozone concentration was peaking in the lower stratosphere, at 20–25 km. Since the late 1970s, the global distribution of atmospheric ozone has been extensively monitored with instruments on board satellites.

Although in relatively low concentration of a few molecules per million air molecules, atmospheric ozone is essential to sustaining life on the Earth's surface. Indeed, by absorbing solar radiation between 240 and 320 nm, it shields living organisms including humans from the very harmful ultraviolet radiation UV-B. About 90% of the ozone resides in the stratosphere, the region that extends from the tropopause, whose altitude ranges from 8 km at the poles to 18 km in the tropics, to the stratopause located at about 50 km altitude (Brasseur and Solomon 2005). Stratospheric ozone is communally referred as the "ozone layer." The remaining 10% of the ozone is found in the troposphere, the region that extends from the surface to the tropopause. Tropospheric ozone is a major pollutant near the surface. Ozone also reacts with a number of other gases and is the main source of the hydroxyl radical, OH, that is responsible for the oxidation and removal of most trace gases including pollutants in the atmosphere. Finally, ozone absorbs not only solar radiation but also outgoing infrared radiation and so plays a significant and complex role in the Earth's energy budget. For all these reasons, ozone is considered as one of the key species for the chemistry and radiative balance of the atmosphere (Jacob 1999; Brasseur and Solomon 2005).

Unlike the major atmospheric constituents, such as nitrogen, molecular oxygen, carbon dioxide, or methane, the ozone vertical profile does not exhibit a maximum at the Earth's surface and then a uniform decrease with height. The ozone concentration is low in the troposphere except near the surface where it is formed in air polluted by human activities. Then its concentration increases sharply from the tropopause to reach a maximum in the lower stratosphere, between 15 and 20 km at high latitude winter and between 25 and 30 km in the tropics (Fig. 1). Above 30 km, the ozone concentration decreases rapidly with height. Its particular vertical distribution results from the existence of a strong source of ozone in the stratosphere and not at ground level.

The absorption efficiency of solar ultraviolet radiation (240–320 nm) during its passage through the atmosphere depends on the total number of ozone molecules along the path of the sunrays. This represents the total amount of ozone in a column of air extending from the surface to the top of the atmosphere. It is calculated by integrating vertically the altitude-dependent local concentration and is commonly referred to as the thickness of the ozone layer or ozone column, often expressed in Dobson unit (Schwartz and Warneck 1995). The bulk of the ozone column is found in the lower stratosphere, between 15 and 30 km (see Fig. 1). The ozone column varies from region to region and season

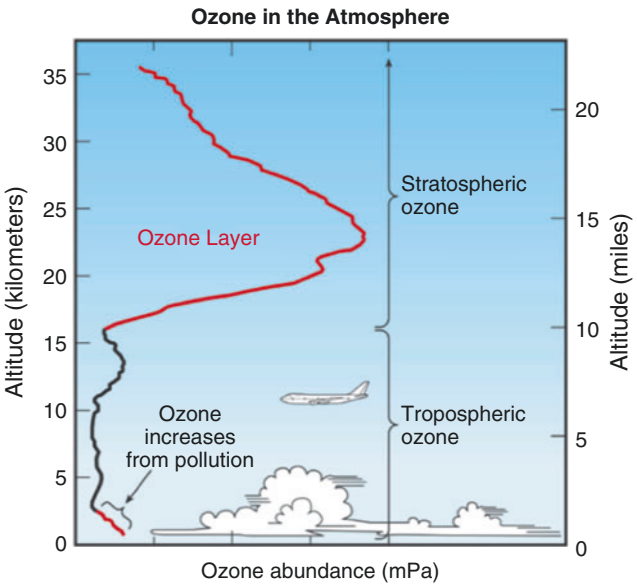

Ozone and Stratospheric Chemistry, Fig. 1 Typical vertical profile of ozone concentration (in ozone partial pressure in mPa). About 90% of ozone resides in the stratosphere and is commonly referred as the stratospheric ozone layer. The vertical extent or thickness of the layer varies from region to region and with season. Note that in the troposphere, notably near the surface, ozone is also produced by the oxidation of hydrocarbons in the presence of high levels of nitrogen oxides; this so-called "smog" photochemistry is typical of polluted air and explained the enhanced levels of ozone found near the ground in some areas (Hegglin et al. 2014)

over the globe. On average, the total column ozone is about 300 DU, which is equivalent to a 3 mm ozone-pure thick layer if all the ozone molecules were brought down to Earth's surface and uniformly distributed over the globe (Brasseur and Solomon 2005).

Chapman Cycle: Ozone Chemistry in a Pure Oxygen Atmosphere

In 1930, the physicist Sydney Chapman proposed a theory that considers the balance between the formation and destruction of ozone from oxygen radicals only (Chapman 1930). It lays the foundation of stratospheric ozone photochemistry. The sequence of selected reactions constitutes a cycle that allows developing a simple theory of stratospheric ozone in a pure oxygen atmosphere (Bekki and Lefevre 2009).

The formation of stratospheric ozone occurs naturally by chemical reactions involving solar ultraviolet radiation (sunlight) and oxygen molecules, which make up about 21% of the atmosphere. The production of ozone is a two-step mechanism:

$$O_2 + h\nu \rightarrow O + O;\ \lambda < 242\ \text{nm} \quad J_1 \qquad \text{(R1)}$$

$$O + O_2 \rightarrow O_3^* + M \rightarrow O_3 + M^* \quad k_2 \qquad \text{(R2)}$$

The photolysis of molecular oxygen (R1) occurs only for photons at wavelengths below 242 nm, which explains why this source is mostly present in the middle and upper atmosphere. Ozone is then produced by the recombination of oxygen atoms with molecular oxygen following the three-body reaction (R2) where M, a third body (nitrogen (N_2) or oxygen (O_2)), acts as a stabilizing partner, absorbing the excess of energy produced during the formation of the metastable ozone, O_3^* (Lin and Leu 1982). This reaction is very fast and requires only a fraction of second in the stratosphere. It also causes a release of 24 kcal of heat per mole of ozone formed. This exothermic reaction explains the positive gradient temperature observed in the stratosphere.

Like molecular oxygen, ozone is a strong absorber of solar radiation and can dissociate:

$$O_3 + h\nu \rightarrow O_2 + O \quad J_3 \qquad \text{(R3)}$$

At wavelengths above 310 nm, the photolysis of ozone leads to the direct production of $O(^3P)$, referred as O to simplify the notations. At wavelengths below about 310 nm, the photolysis of ozone produces oxygen atom in the excited state $O(^1D)$, a very reactive form of oxygen atom that decays to $O(^3P)$, the ground state of oxygen atom. The oxygen atoms excited $O(^1D)$ produced by R3 is almost instantly deactivated back to its fundamental level $O(^3P)$ by collision. Although this channel is not treated explicitly here, J_3 corresponds to the total photolysis rate of ozone including the excited state channel.

Finally, ozone and atomic oxygen are destroyed simultaneously by the reaction:

$$O + O_3 \rightarrow 2\ O_2 \quad k_4 \qquad \text{(R4)}$$

It is possible to establish the balance of ozone and atomic oxygen in the stratosphere from the four reactions above, considering only the oxygen species. Ignoring transport processes, the continuity equations (i.e., the time-dependent concentration change due to the sum of production and destruction terms for the species considered) describing the evolution of the O and O_3 concentration are expressed by:

$$\frac{d[O]}{dt} = 2J_1[O_2] + J_3[O_3] - k_2[O_2][O][M] - k_4[O_3][O] \qquad (1)$$

$$\frac{d[O_3]}{dt} = k_2[O][O_2][M] - k_4[O][O_3] - J_3[O_3] \qquad (2)$$

It is worth pointing out that the photolysis of ozone (R3) does not lead to a net loss of it. Indeed, the produced oxygen atom reacts immediately with O_2 to reform ozone via reaction R2.

The rapid exchange between O_3 and O operates via R2 and R3 throughout the troposphere and the stratosphere. Because of its short lifetime, the oxygen atom O is always in photochemical equilibrium with ozone and molecular oxygen. The assumption of steady-state for O (i.e., $d[O]/dt = 0$ meaning production rate = destruction rate) allows us to derive the abundance ratio between O and O_3 using Eq. 1,

$$\frac{[O]}{[O_3]} = \frac{\left(2J_1\frac{[O_2]}{[O_3]} + J_3\right)}{k_2[O_2][M] + k_4[O_3]} \simeq \frac{J_3}{k_2[O_2][M]} \qquad (3)$$

The abundance ratio between O and O_3 can be simplified because the photolysis of O_3 (J_3) is so much faster than photolysis of O_2 (i.e., $J_3 >> 2J_1[O_2]/[O_3]$) and the rate of (R4) is several orders of magnitude slower than the rate of (R2).

The relative abundance of O compared to O_3 increases rapidly with altitude. It is, however, only above about 60 km that the ratio $[O]/[O_3]$ becomes greater than 1. Below 60 km, the concentration of O_3 is greater than that of O by several orders of magnitude. In these circumstances, it is useful to combine O and O_3 to define a hypothetical species O_x, called the odd oxygen family, with $O_x = O + O_3$.

Since $[O] << [O_3]$ in the troposphere and stratosphere, $[O_x] \sim [O_3]$ and the evolution equation of O_3 can simply be derived by summing Eqs. 1 and 2 in conjunction with Eq. 3:

$$\frac{d[O_3]}{dt} + \frac{d[O]}{dt} \approx \frac{d[O_3]}{dt} = 2J_1[O_2] - 2k_4[O][O_3] = 2\left(J_1[O_2] - \frac{k_4 J_3 [O_3]^2}{k_2[O_2][M]}\right) \quad (4)$$

The steady-state ozone concentration ($\frac{d[O_3]}{dt} = 0$) can then be derived from Eq. 4,

$$[O_3] = [O_2]\left(\frac{k_2[M]J_1}{k_4 J_3}\right)^{\frac{1}{2}} = x_{O_2}[M]\left(\frac{k_2 J_1[M]}{k_4 J_3}\right)^{\frac{1}{2}} \text{ with } x_{O_2} = \frac{[O_2]}{[M]} \quad (5)$$

The rate of molecular oxygen photolysis (i.e., J_1) increases with altitude, while $[M]$ decreases at the same time. As a result, the ozone concentration profile calculated from Eq. 5 shows a maximum in the stratosphere, which is consistent with observations.

Global Stratospheric Ozone Chemistry

Although, the Chapman Theory gives approximately the correct altitude distribution, Eq. 5 overestimates observed ozone concentrations by a factor of 2. Note that transport only redistribute the ozone spatially, it is neither a sink nor a source of ozone. Indeed, global mass balance budgets of ozone have shown that loss processes do not balance the production rate, so there should be missing loss processes not taken into account in the chapman model (Johnston 1975). This discrepancy is the most compelling argument to expend the chapman reaction scheme, involving other trace constituents that act as ozone destroyer, notably hydrogen radicals (Bates and Nicolet 1950; Hampson 1964), nitrogen oxides (Crutzen 1970; Johnston 1971), and chlorine radicals (Stolarski and Cicerone 1974; Molina and Rowland 1987). Note that P.J. Crutzen, M. Molina, and F.S. Rowland were awarded the Nobel Prize in 1995 "*for their work in atmospheric chemistry, particularly concerning the formation and decomposition of ozone.*"

These radicals destroy ozone via chemical catalytic cycles. The simplest catalytic cycles are of the form:

Cycle X

$$X + O_3 \rightarrow XO + O_2 \quad k_5 \quad (R5)$$

$$XO + O \rightarrow X + O_2 \quad k_6 \quad (R6)$$

$$\text{net} : O + O_3 \rightarrow 2\,O_2$$

where X is the minor constituent that is the catalyst of the cycle of reactions.

The net overall reaction, reflecting the simultaneous disappearance of odd oxygen pairs, is equivalent to the reaction R4. However, the reactions involved in the cycle above are faster and are initiated by a catalyst, which, by definition, is not consumed in the process. One can then understand how a radical X with a concentration much lower than that of ozone (in practice, up to a million times less) can destroy a large number of O_3 molecules until the radical is converted into less reactive molecules. The rate of destruction of O_3 by the cycle X is determined by the rate of reaction XO + O. Indeed, it is much slower that the reaction X + O_3, which reform XO very quickly. The destruction rate of ozone by the cycle above can be written as:

$$\frac{d[O_x]}{dt} = -2k_6[XO][O] \quad (6)$$

where k_6 is the rate of the reaction between XO and O.

The factor 2 stems from the fact that two molecules of O_3 are destroyed at each pass through the cycle. In the stratosphere, X corresponds to H, OH, NO, Cl, or Br. The relative importance of these species depends on their concentrations and the reaction rates of their specific catalytic cycles. Whatever the catalyst X involved, it can be noted that the general cycle above requires the presence of atomic oxygen O. Therefore, this type of process is very effective above 30 km altitude, when the concentration of O becomes sufficient. At lower altitudes, the destruction of odd oxygen also occurs through other types of catalytic cycles, which do not require atomic oxygen. For example, one of the most effective catalytic cycles in the lower stratosphere involves a coupling bromine and chlorine radicals.

The ozone-destroying radicals mainly originate from the stratospheric oxidation of source gases emitted at the Earth's surface. Most trace gases are quickly destroyed in the troposphere by oxidation and/or dissolution in clouds. However, certain gases have sufficiently long lifetimes in the troposphere (i.e., removed very slowly in the troposphere) for them to be transported in significant quantities into the stratosphere through air motions. The sources of stratospheric ozone-destroying hydrogen radicals (OH, HO_2) are water vapor and methane emitted at the surface. The source of stratospheric nitrogen oxides radicals (NO, NO_2) is the oxidation of nitrous oxide (N_2O) emitted at ground level by biological processes or linked to human activities. The only significant natural source of stratospheric chlorine is the oxidation of a chlorinated organic compound, methyl chloride CH_3Cl, which is emitted by the oceans. On the top of this natural source, there have been industrial sources of chlorinated organic compounds, typically chlorofluorocarbons (CFCs), for over 50 years. Almost all of these industrial compounds emitted at the surface enter the stratosphere because their lack of chemical reactivity results in very long

lifetimes in the troposphere, up to 100 years (Brasseur and Solomon 2005).

Polar Ozone

The total column ozone has been regularly measured for over half a century in the polar regions. In Antarctica, the observations until the late 1970s show an austral spring maximum, with an average over the month of October of about 350 Dobson Units (DU). From the early 1980s, a rapid and continuous decline in total column ozone is observed every spring above Antarctica. The Antarctic monthly mean thickness of the ozone layer in October is currently close to 200 DU. Local minima below even 100 DU have sometimes been seen since the late 1990s, which represents a decrease of nearly 70% of the total ozone column compared with measurements taken twenty years earlier. The analysis of individual vertical ozone profiles (Fig. 1) shows a destruction even more pronounced with often an almost complete disappearance of ozone in the lower polar stratosphere, between around 15 and 20 km (Brasseur and Solomon 2005).

Satellite measurements have revealed the geographical extension of this phenomenon, known as the "ozone hole," with the reduction in ozone taking place over a wide circular area centered on the South Pole (Fig. 2). This area indicates the polar vortex, an enormous ring of circling fast-moving air. Although of large magnitude, it is important to note that this now recurring feature of the southern Antarctic spring remains a seasonal phenomenon. The ozone destruction indeed starts at the end of August, when sunlight comes back on the edge of the polar vortex after the winter polar night. The rate of ozone decrease peaks in September and minimum values for total column are usually reached in October. Antarctic ozone columns remain low in November. Then, they quickly recover values close to 1970s climatology at the end of December.

When the ozone hole was discovered by a team from the British Antarctic Survey in 1987 (Farman et al. 1985), a rise in atmospheric chlorine content was proposed in an attempt to explain a phenomenon that, at that time, was totally unexpected. Indeed, as a result of human activities, the atmospheric concentration of chlorine has grown almost exponentially since the mid-twentieth century, resulting in 5-fold increase compared to preindustrial values. However, the large spring polar ozone depletion cannot be accounted for by the catalytic cycles of destruction discussed previously because they are not effective enough in the lower stratosphere due to the lack of atomic oxygen. An unusual chemistry operates in the polar regions, during winter and spring, that makes ozone very sensitive to the atmospheric chlorine content. This particular chemistry is linked to the existence of chemical reactions occurring on the surface of clouds that form during winter and beginning of spring in the Antarctic lower stratosphere. This heterogeneous chemistry on polar

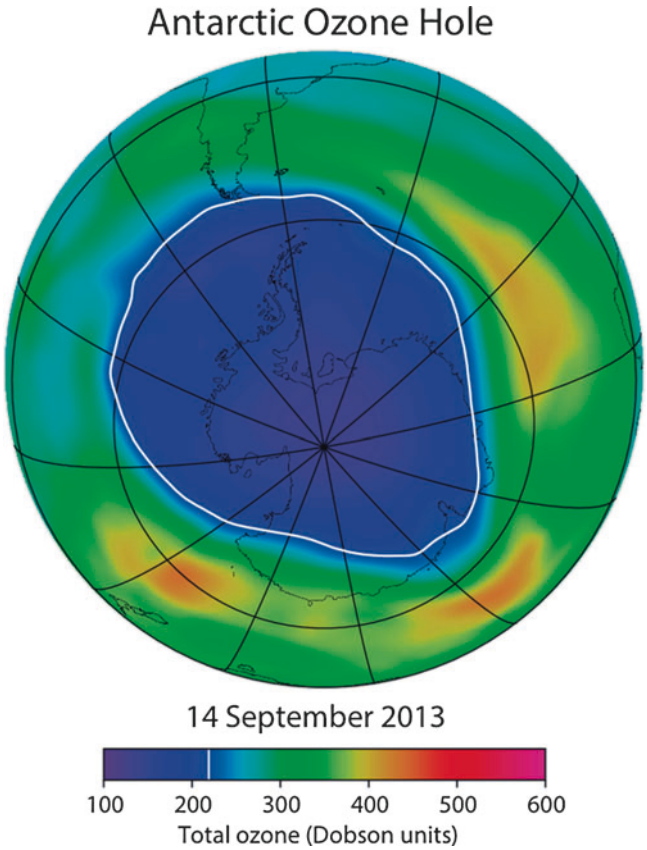

Ozone and Stratospheric Chemistry, Fig. 2 Total ozone values are for high southern latitudes on 14 September 2013 as measured by a satellite instrument. The *dark blue* and *purple* regions over the Antarctic continent show the severe ozone depletion or "ozone hole" now found during every austral spring. The ozone hole area is usually defined as the geographical area within the 220-DU contour (see *white line*) on total ozone maps (Hegglin et al., 2014)

stratospheric clouds converts chlorine compounds, communally called reservoir species (HCl, $ClONO_2$), into ozone-destroying chlorine radicals such as the chlorine monoxide (ClO) (McElroy et al. 1986; Solomon et al. 1986). The resulting high levels of chlorine radicals greatly increase the probability that ClO reacts with itself to form a complex, the dimer Cl_2O_2 (Molina and Molina 1987). This three body reaction initiates a powerful ozone-destroying catalytic cycle in the winter polar regions that is responsible for 50–70% of the observed ozone destruction:

Cycle dimer ClO

$$\mathrm{ClO} + \mathrm{ClO} + M \rightarrow \mathrm{Cl_2O_2} + M \quad k_7 \qquad \text{(R7)}$$

$$\mathrm{Cl_2O_2} + h\nu \rightarrow \mathrm{Cl} + \mathrm{ClO_2} \quad J_8 \qquad \text{(R8)}$$

$$\mathrm{ClO_2} + M \rightarrow \mathrm{Cl} + \mathrm{O_2} + M \quad k_9 \qquad \text{(R9)}$$

$$2(\mathrm{Cl} + \mathrm{O_3} \rightarrow \mathrm{ClO} + \mathrm{O_2}) \quad k_{10} \qquad \text{(R10)}$$

O

$$\text{net}: \ 2O_3 \rightarrow 3O_2$$

No atomic oxygen is involved in this cycle, and it needs little sunlight to operate effectively because the photolysis of the chlorine dimer (Cl_2O_2), its rate-limiting step, is fast. The chlorine dimer may also be thermally decomposed to give back ClO. However, at the low temperatures encountered in the polar vortex, the thermal decomposition of Cl_2O_2 can usually be neglected against its photolysis. Assuming quasi-steady state for Cl_2O_2 (destruction = production), the rate of ozone destruction can be expressed:

$$\frac{d[O_3]}{dt} = -2J_8[Cl_2O_2] = -2k_7[ClO][ClO][M] \qquad (7)$$

where the factor 2 is explained by the number of ozone molecules destroyed for each molecule of Cl_2O_2 photolyzed.

This expression shows that the rate of ozone destruction is proportional to the square of the concentration of chlorine. It is estimated that the levels of chlorine in the stratosphere have tripled since the 1960s, resulting in a factor 9 increase in polar ozone destruction rate by the ClO dimer cycle. This quadratic dependence largely explains the relatively sudden appearance of the phenomenon of the ozone hole. Due to the large increase in ClO levels, the cycle that couples ClO and BrO becomes important in the polar regions. This cycle is responsible for 30–50% of the overall seasonal polar ozone destruction (Bekki and Lefevre 2009). Along with the increase in atmospheric chlorine content, its role has also risen rapidly in recent decades as a result of increasing emissions of long-lived anthropogenic bromine-carrying compounds into the atmosphere. The destruction of polar ozone described above continues until the warming of the polar vortex during spring which leads to the evaporation of polar stratospheric clouds and hence disappearance of heterogeneous chemistry. Without it, chlorine radicals are converted back into reservoirs species during spring.

Past and Future Evolution of Ozone at Global Scale

The balance of stratospheric ozone is controlled by hydrogen, nitrogen, chlorine, and bromine radicals, whose levels in the stratosphere are themselves determined by the levels of gas sources emitted at ground level. The main gas sources are water vapor and methane (CH_4) for hydrogen compounds, nitrous oxide (N_2O) for nitrogen compounds, chlorofluorocarbons (CFCs) for chlorinated compounds, and methyl bromide (CH_3Br) and halons for brominated compounds. The most significant factor for the evolution of the ozone layer during the last century has been the considerable increase in industrial emissions of long-lived chlorine and bromine compounds. These gases are decomposed in the stratosphere under the influence of intense ultraviolet radiation, releasing the atoms of chlorine and bromine that destroys ozone through catalytic cycles. Because of the widespread use of chlorofluorocarbons in the industry, the stratospheric chlorine content has risen almost exponentially since the 1960s. As a result of growing emissions of halons, the stratospheric bromine content has also increased during the recent decades, although to a lesser extent than the chlorine content (Brasseur and Solomon 2005; WMO 2014).

The measurements unambiguously show that the change in atmospheric composition since the 1980s has led to a reduction in global stratospheric ozone. The decline in total column averaged over the year has reached about 3–4%, a value far greater than the 1% natural variations of ozone. The amplitude of long-term changes in the ozone layer varies with latitude and season. The greatest reduction in the total ozone column occurs at high latitudes in the southern hemisphere (−15 to −25% on annual averages) as a result of the Antarctic ozone hole that forms each austral spring. In the northern hemisphere, the decrease is also the most pronounced at high latitudes (−4% to −6% on annual averages) and again mostly by some ozone depletion inside the arctic polar vortex during winter and spring. The ozone decrease observed at mid-latitudes largely results from transport of ozone-depleted air from polar regions, as well as direct destruction of ozone by global catalytic cycles that do not require heterogeneous chemistry on polar stratospheric clouds, Finally, ozone has not changed significantly in tropical regions.

Concerns arising from the discovery of the Antarctic ozone hole in 1985 and from a possible alteration of the stratospheric ozone layer by human activities have led to a process of regulating the production and emission of long-lived compounds that are sources of chlorine and bromine in the stratosphere. The Montreal Protocol (1987) was negotiated and ratified by producing countries to conduct a concerted reduction in emissions that would ultimately lead to elimination of these products in the industry. The protocol has been amended several times since 1987 by adopting increasingly stringent measures and extending its scope to a larger number of chlorine and bromine-carrying gases. Developed countries have halted production of halons in 1994 and of the most dangerous chlorinated compounds (CFCs, methyl chloroform CH_3CCl_3, and carbon tetrachloride CCl_4) in 1996. In most applications, CFCs are now replaced by hydrochlorofluorocarbons (HCFCs) that have much shorter lifetimes in the lower atmosphere or hydrofluorocarbons (HFCs) that contain no more chlorine atoms. Implementation of the Montreal Protocol has led to a stabilization of total chlorine content since mid-1990s. The effectiveness of the Montreal Protocol is now well established with the atmospheric burden of CFC-11 (lifetime of about 45 years) declining since 1996, while that the burden of CFC-12 (lifetime of 100 years) has stabilized. Given these findings and the most probable scenarios of production, the most likely return to the atmospheric chlorine contents to levels comparable to those that preceded

the appearance of the ozone hole is not expected to occur before the middle of this century (WMO 2014).

The slow decay of stratospheric halogen levels should lead to a gradual reduction of the large polar ozone losses and an overall increase in the thickness of the ozone layer. It is worth pointing out that although the chlorine content by the end of the century is expected to be comparable to that of 1960s, before the appearance of the ozone hole, the atmospheric composition will nevertheless be very different from that of 1960s. Indeed, human activities since 1960s have led to an important increase in the concentrations of greenhouse gases such as CO_2, CH_4, and N_2O, which will carry on during this century. Although the magnitude of this future increase is now difficult to quantify, it is already well established that the growing emissions of greenhouse gases has led to a warming of the Earth's surface and the lower atmosphere, accompanied by a cooling of the stratosphere. In the upper stratosphere, this cooling should result in increase in ozone levels because the efficiency of the catalytic ozone destruction decreases when the temperature decreases. In the lower stratosphere, on the contrary, lower temperatures will promote more frequent formation of stratospheric clouds and therefore will tend to counteract the effects of the chlorine reduction on the destruction of polar ozone in winter and spring. Our ability to predict the long-term evolution of temperature in the stratosphere has therefore become a key factor in determining the future of the ozone layer. In a sense, the issue of stratospheric ozone will be increasingly linked in the coming years with the issue of greenhouse gases emissions and climate change (Brasseur and Solomon 2005; Bekki and Lefevre 2009; WMO 2014).

Stratospheric Sulfur Chemistry

This section is devoted to the sulfur cycle and budget in the stratosphere, notably focusing on stratospheric aerosol particles because they play a very significant role in stratospheric ozone chemistry and in the radiative balance of the atmosphere, especially after large volcanic eruptions (Hamill et al. 1997; Brasseur and Solomon 2005; SPARC 2006). The first section introduces the life cycle of stratospheric sulfur. We then review stratospheric sulfur oxidation chemistry and key aerosol microphysical processes. The next section presents the perturbations of the stratospheric aerosol layer by large volcanic eruptions and the effects on ozone and climate. The last section is devoted to the possibility of cooling the climate intentionally through deliberate sulfur injections in the stratosphere in order to counteract the climate warming from increasing concentrations of GHGs (the so-called sulfur geo-engineering).

Sulfur Life Cycle

Elevated concentrations of aerosol particles are found all over the globe in the lower stratosphere, between about 10 and 35 km. It was first discovered in 1961 by Junge et al. (1961) who noted that, as balloon-borne instruments rose into the stratosphere, they registered an increase in the concentration of large particles (Hamill et al. 1997). Further measurements have shown that stratospheric aerosols consisted primarily of submicron liquid (super-cooled) sulfate aerosols.

Figure 3 illustrates the processes that govern the stratospheric aerosol life cycle and global distribution. Most of the sulfur enters the stratosphere under the form of gases through the tropical tropopause (around 17 km in the tropics and 8 km in the polar regions). The source gases originate from

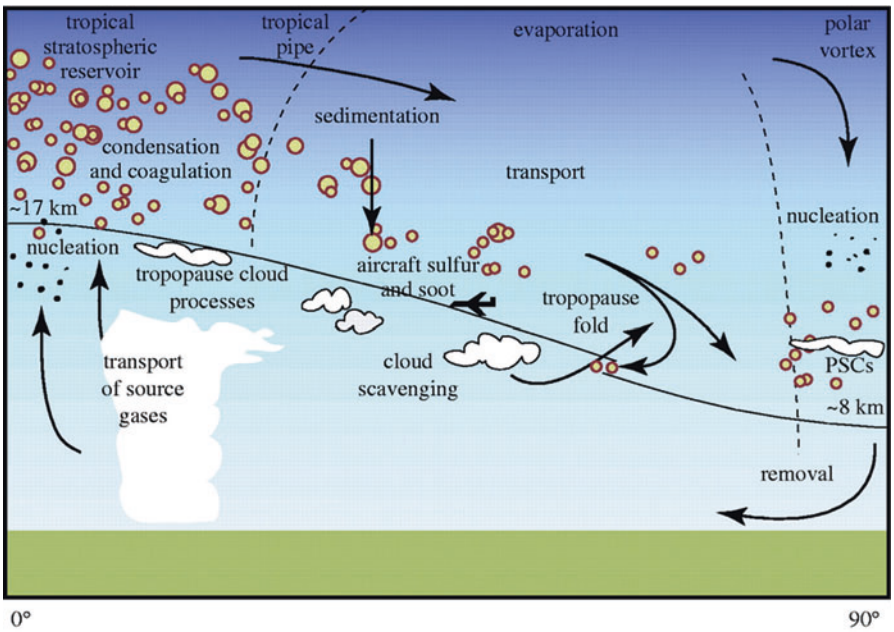

Ozone and Stratospheric Chemistry, Fig. 3 Schematic of the stratospheric aerosol life cycle (SPARC 2006 adapted from Hamill et al. 1997)

emissions at the Earth's surface or even direct injections by large volcanic eruptions. Once in the tropical stratosphere, they are transported throughout the stratosphere by the Brewer-Dobson circulation (ascending in the tropics and descending in the subtropics). During their stratospheric transit, they are oxidized and converted into sulfuric acid (H_2SO_4). Gaseous H_2SO_4 either combines with water vapor to nucleate and form new very small sulfate aerosols or condenses on pre-existing aerosol particles. Once formed, sulfate particles evolve under the action of several microphysical processes (condensation/evaporation, coagulation, sedimentation (Seinfeld and Pandis 1998)). Particles grow by coagulation and by co-condensation of H_2O and H_2SO_4, which is produced by the oxidation of sulfur gases. Sulfate aerosol particles evaporate completely above 35 km because of the increase of the temperatures in this region of the atmosphere. In the end, aerosols are removed from the stratosohere by their gravitational sedimentation. Once in the troposphere, they are then removed by wet (i.e., precipitating clouds) and dry (i.e., sticking to the earth's surface) deposition.

Conversion of Reduced Sulfur Gases into Sulfate

During nonvolcanic (also called background) conditions, the main precursor of stratospheric aerosol particles is thought to be carbonyl sulfide (OCS), the only long-lived sulfur species (Crutzen 1976). Apart OCS, all the reduced sulfur compounds are rapidly oxidized in the troposphere and thus, once emitted at the surface, they have little time to reach the stratosphere before being removed. In contrast, the vast majority of OCS emitted at the surface, predominantly from natural sources, reaches the stratosphere. It is worth pointing out that other nonvolcanic sulfur dioxide (SO_2) sources and tropospheric sulfate particles might also be important (Brock et al. 1995; Sheng et al. 2015), especially in the tropics where the vertical transport of air from the surface to the tropical tropopause can be rapid. Once it is in the stratosphere, OCS is photolyzed to give SO_2:

$$OCS + h\nu \rightarrow S + CO \quad J_{11} \qquad \text{(R11)}$$

$$S + O_2 \rightarrow SO_2 \quad k_{12} \qquad \text{(R12)}$$

Then the oxidation of SO_2 is initiated by the hydroxyl radical OH

$$SO_2 + OH + M \rightarrow HSO_3 + M \quad k_{13} \qquad \text{(R13)}$$

with M being an air molecule.

R15 is very rapidly followed by the following reactions:

$$HSO_3 + O_2 \rightarrow SO_3 + HO_2 \quad k_{14} \qquad \text{(R14)}$$

$$SO_3 + H_2O \rightarrow H_2SO_4 \quad k_{15} \qquad \text{(R15)}$$

The limiting step in the SO_2 oxidation sequence R13–R14–R15 is the reaction with OH (R13). The e-folding lifetime of SO_2 in the stratosphere is about 1 or 2 months. The net effect of the sequence can be summarized by Bekki (1995),

$$\text{Net}: SO_2 + OH + O_2 + H_2O \rightarrow H_2SO_4 + HO_2$$

The sequence converts OH into HO_2 and consumes one molecule of H_2O. When SO_2 levels are high, for instance following an injection of SO_2 by a volcanic eruption, SO_2 conversion to sulfate particles is expected to reduce levels of OH, the main atmospheric oxidant.

As gaseous H_2SO_4, the end oxidation product, has a very low saturation vapor pressure at the temperatures prevailing in the lower stratosphere, it quickly combines with H_2O to form new very small sulfate particles via binary homogeneous nucleation, typically at the tropical tropopause or in the polar regions. However, in most of the lower stratosphere, where there are quite a few particles available, gaseous H_2SO_4 tends to co-condense with H_2O on pre-existing particles and make them grow. The average composition of stratospheric sulfate aerosols is about 75% by weight of H_2SO_4, which is roughly equivalent to a molecular composition of one molecule of H_2SO_4 for two molecules of H_2O. As the result, the H_2SO_4 conversion into sulfate can be expressed by,

$$H_2SO_4 + 2H_2O \rightarrow \text{Sulphate}$$

Aerosols also grow via coagulation. Coagulation is the process of two aerosols of various sizes colliding with each other and combining into a single larger particle (Kremser et al. 2016). Finally, sulfate particles are mostly removed from the stratosphere by gravitational sedimentation. The sedimentation velocity of a particle is very strongly dependent on its size. When the sedimentation of a population of particles is considered, the critical characteristic is the particle size distribution, i.e., concentration of particles as a function of size. Size distribution is also critical for a range of properties such as the amount of surface area available for heterogeneous chemical reactions or for their scattering efficiency of sunlight (a key property for their cooling effect on climate; (Seinfeld and Pandis 1998; Jacob 1999; SPARC 2006)).

At the top of the stratospheric aerosol layer (~30-35 km), sulfate aerosols also evaporate and release H_2SO_4 in the gas-phase. There are indications that H_2SO_4 can then be photolyzed by visible sunlight to give SO_3, which in turn is also subject to photolysis and give back SO_2 (Kremser et al. 2016).

$$H_2SO_4 + h\nu \rightarrow SO_3 + H_2O \quad J_{16} \qquad \text{(R16)}$$

$$SO_3 + h\nu \rightarrow SO_2 + O \quad J_{17} \qquad \text{(R17)}$$

As the result, the dominant sulfur species above the stratospheric aerosol layer is SO_2.

Impacts of Volcanic Eruptions

Although rare, major volcanic eruptions have an important impact on the stratospheric aerosol levels and loading, as illustrated by satellite data for the last 30 years (Fig. 4). They inject massive amount of sulfur, mostly under the form of SO_2, directly into the stratosphere, resulting in very large enhancements in sulfate aerosol levels lasting up to several years. For example, the largest volcanic eruption of the last 50 years is the eruption of Mount Pinatubo, Philippines, in June 1991. It injected about 15–20 Mega-tons of sulfur into the stratosphere, which is more than an order of magnitude greater than the annual stratospheric sulfur mass flux into the stratosphere from tropospheric surface sources during a nonvolcanic period.

The drastic increases in stratospheric aerosol loading impact stratospheric ozone and climate. They influence ozone because large volcanic sulfate aerosol particles act as sites for heterogeneous reactions that lead to ozone destruction when the atmospheric levels of halogens (chlorine, bromine) are high (see ozone section). They also impact climate because sulfate aerosols scatter the incoming sunlight back to space and hence cool the surface. To illustrate these effects, let us consider the Mount Pinatubo eruption. The injection of SO_2 and conversion into sulfate led to stratospheric sulfate aerosol loadings and surface area densities (aerosol surface available for heterogeneous chemical reactions) enhanced by up two orders of magnitude, resulting in enhanced heterogeneous chemistry that converts chlorine- and bromine-containing reservoir species such $ClONO_2$ and $BrONO_2$ into ozone-destroying radicals. Global stratospheric ozone dropped by several percentages after the Mt. Pinatubo eruption (WMO 2010). Stratospheric aerosol optical depth increased by almost two orders of magnitude (Fig. 4, bottom), enhancing the planetary albedo and hence cooling the Earth's surface by about half degree (Kremser et al. 2016). The volcanic forcing of climate represents one of the two major natural external climate forcers; the other one is the solar variability.

Geo-Engineering

Actual mitigation efforts to reduce global warming are already falling far short of what many analysts think is needed to avoid dangerous changes in climate. These failings arise from a political logic that will soon be difficult to rectify. Deep cuts may be too costly and thus politically difficult to

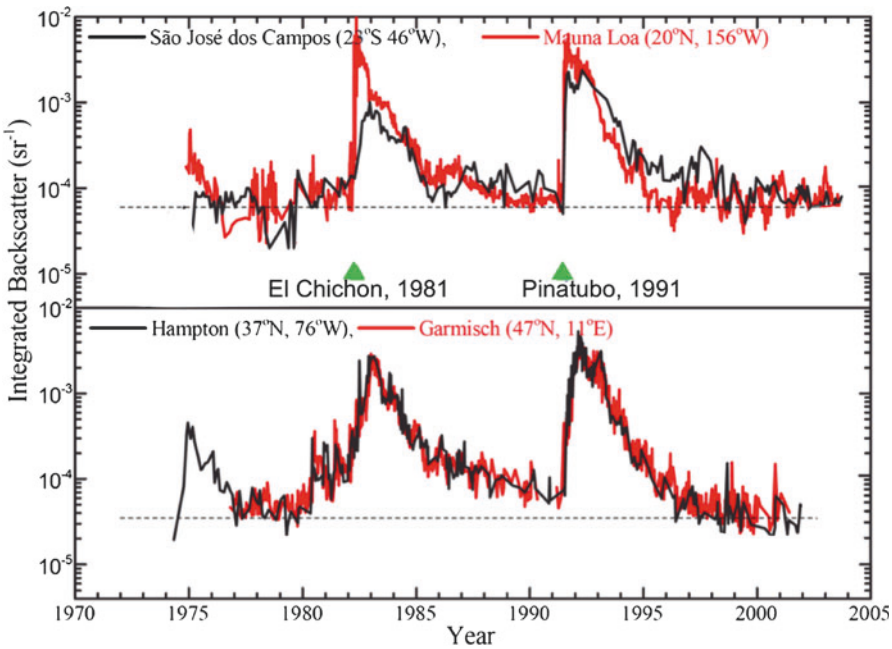

Ozone and Stratospheric Chemistry, Fig. 4 History of integrated backscatter from two tropical sites (São José dos Campos and Mauna Loa) and two mid-latitude sites (Hampton and Garmisch). Integrated backscattering indicates the aerosol load of the stratosphere. The *dashed horizontal lines* are meant only to aid the reader. The times of the most significant volcanic eruptions during the period are indicated in the *top panel* with the *green triangles* (El Chichon 1981, Mexico and Pinatubo 1991, Philippines). It can clearly be seen that these two major stratospheric eruptions are responsible for the large increase of the optical opacity of the stratosphere at the global scale, induced by the formation of sulfuric acid aerosols (Adapted from SPARC, 2006)

O

implement, organize, and sustain; they imply radical change in energy systems that will be difficult to implement and manage effectively in many countries even if they could gain the needed political support. More importantly, it has been proven extremely difficult to design competent international institutions for coordinating and enforcing worldwide efforts to mitigate emissions (e.g., the Kyoto protocol, COP21). As a result, the possibility of modifying the climate intentionally through large-scale technical schemes (also called geo-engineering) in order to counteract the warming effect of greenhouse gases (GHGs) has started to be considered more seriously, even by prominent scientists (Crutzen 2006; Wigley 2006; Lenton and Vaughan 2009).

Climate geo-engineering is a large-scale engineering of our environment in order to counteract the effect of changes in atmospheric composition due to human activities, in particular the increase of GHGs. Most of the proposed schemes are based on the decrease of solar flux reaching the surface to balance the increase in thermal infrared radiation reaching the surface from increasing GHG concentrations. They are based on injection of gases or particles to increase the albedo (i.e., the reflectivity) of the Earth atmosphere and clouds. By analogy with the global cooling observed after volcanic emissions of sulfur in the stratosphere, it has been proposed to inject sulfur in the stratosphere in order to enhance the stratospheric aerosol loading and hence the scattering back to space of the incoming solar radiation. According to the literature review, at least mega-tons of sulfur appears to be necessary for counteracting significantly the climate warming driven by increasing GHGs with highly uncertain costs, results, and consequences, notably on stratospheric ozone (e.g., Robock et al. 2009). Geo-engineering can certainly not be considered as a long-term solution to the climate change problem and any induced perturbation in the Earth's climate system may have unwanted consequences that should be carefully evaluated before any implementation.

Conclusions

While making only ≈10% of the mass of the atmosphere, the stratosphere plays a crucial role for the stability of the chemical and radiative balance of the Earth. The presence of a rich layer of ozone protects the Earth's ground from harmful UV radiations that otherwise would prevent the development of life on the Earth's surface. In return, by absorbing UV radiations this ozone layer generates a temperature inversion that makes the stratosphere particularly stable dynamically in comparison of the troposphere. In some way, the ozone stratospheric layer creates its own living conditions. However, the stability of the ozone layer has been drastically challenged by emissions of human manufactured halogenated species, which can cross the tropopause barrier and result in catalytic destruction of ozone. Equally, during powerful volcanic eruptions, the formation of a highly enhanced sulfate aerosol layer in the stratosphere strongly disturbs the energy and chemical balance of the stratosphere, leading to significant decreases in stratospheric ozone concentrations. In this regard, given the importance of stratospheric ozone for climate, chemistry, and life on Earth, any geo-engineering actions that would lead to change the radiative properties of the stratosphere in order to balance global warming should be viewed with a lot of caution, at minimum with distrust and critical analysis.

Cross-References

- Bromine
- Chlorine
- Earth's Atmosphere
- Nitrogen Cycle
- Oxygen
- Sulfur
- Sulfur Cycle
- Volcanic Gases
- Volcanism

References

Bates DR, Nicolet M (1950) The photochemistry of atmospheric water vapor. J Geophys Res 55(3):301–327. https://doi.org/10.1029/JZ055i003p00301

Bekki S (1995) Oxidation of volcanic SO_2: a sink for stratospheric OH and H_2O. Geophys Res Lett 22(8):913–916. https://doi.org/10.1029/95GL00534

Bekki S, Lefevre F (2009) Stratospheric ozone: History and concepts and interactions with climate. Eur Phys J Conf 1:113–136

Brasseur G, Solomon S (2005) Aeronomy of the middle atmosphere – chemistry and physics of the stratosphere and mesosphere, 3rd edn. Springer, Dordrecht

Brock CA, Hamill P, Wilson JC, Jonsson HH, Chan KR (1995) Particle formation in the upper tropical troposphere: a source of nuclei for the stratospheric aerosol. Science 270(5242):1650–1653. https://doi.org/10.1126/science.270.5242.1650

Chapman S (1930) A theory of upper atmospheric ozone. Q J R Meteorol Soc 3:103–125

Cornu A (1879) Sur la limite ultra-violette du spectre solaire a diverses altitudes. Proc R Soc Lond 29:47–55

Crutzen PJ (1970) The influence of nitrogen oxides on atmospheric ozone content. Q J R Meteorol Soc 96(30):320–325. https://doi.org/10.1029/JC076i030p07311

Crutzen PJ (1976) The possible importance of CSO for the sulfate layer of the stratosphere. Geophys Res Lett 3(2):73–76. https://doi.org/10.1029/GL003i002p00073

Crutzen PJ (2006) Albedo enhancement by stratospheric sulfur injections: a contribution to resolve a policy dilemma? Clim Chang 77:211. https://doi.org/10.1007/s10584-006-9101-y

Dobson GMB, Harrison DN (1926) Measurements of the amount of ozone in the Earth's atmosphere and its relation to other geophysical conditions. Proc R Soc Lond A Containing Papers of a Mathematical and Physical Character 110(756):660–693

Farman JC, Gardiner BG, Shanklin JD (1985) Large losses of total ozone in Antarctica reveal seasonal ClO_x/NO_x interaction. Nature 315:207–210

Götz FWP, Meetham AR, Dobson GMB (1934) The vertical distribution of ozone in the atmosphere. Proc R Soc Lond 145(855):416–446

Hamill P, Jensen EJ, Russell PB, Bauman JJ (1997) The life cycle of stratospheric aerosol particles. Bull Am Meteorol Soc 78(7):1395–1410. https://doi.org/10.1175/1520-0477(1997)078<1395:TLCOSA>2.0.CO;2

Hampson J (1964) Chemical instability of the stratosphere. Paper presented at the International Association of Meteorology and Atmospheric Physics (IUGG) symposium on atmospheric radiation, Leningrad

Hartley WN (1881) On the absorption of solar rays by atmospheric ozone. J Chem Soc Trans 39:111–128. https://doi.org/10.1039/CT8813900111

Hegglin MI, Fahey DW, McFarland M, Montzka SA, Nash ER (2014) Twenty questions and answers about the ozone layer: 2014 update. Scientific assessment of ozone depletion: 2014. World Meteorological Organization, Geneva

Jacob DJ (1999) Introduction to atmospheric chemistry. Princeton University Press, Princeton

Johnston HS (1971) Reduction of stratospheric ozone by nitrogen oxide catalysts from supersonic transport exhaust. Science 173:517–522

Johnston HS (1975) Global ozone balance in the natural stratosphere. Rev Geophys 13(5):637–649. https://doi.org/10.1029/RG013i005p00637

Junge CE, Chagnon CW, Manson JE (1961) Stratospheric aerosols. J Meteorol 18(1):81–108. https://doi.org/10.1175/1520-0469(1961)018<0081:SA>2.0.CO;2

Kremser S, Thomason LW, von Hobe M, Hermann M, Deshler T, Timmreck C, Toohey M, Stenke A, Schwarz JP, Weigel R, Fueglistaler S, Prata FJ, Vernier J-P, Schlager H, Barnes JE, Antuña-Marrero J-C, Fairlie D, Palm M, Mahieu E, Notholt J, Rex M, Bingen C, Vanhellemont F, Bourassa A, Plane JMC, Klocke D, Carn SA, Clarisse L, Trickl T, Neely R, James AD, Rieger L, Wilson JC, Meland B (2016) Stratospheric aerosol – observations, processes, and impact on climate. Rev Geophys 54:278–335. https://doi.org/10.1002/2015RG000511

Lenton TM, Vaughan NE (2009) The radiative forcing potential of different climate geoengineering options. Atmos Chem Phys 9(15):5539–5561

Lin CL, Leu MT (1982) Temperature and third-body dependence of the rate constant for the reaction $O + O_2 + M \rightarrow O_3 + M$. Int J Chem Kinet 14(4):417–434. https://doi.org/10.1002/kin.550140408

McElroy MB, Salawitch RJ, Wofsy SC, Logan JA (1986) Reductions of Antarctic ozone to synergistic interactions of chlorine and bromine. Nature 321:759–762

Molina LT, Molina MJ (1987) Production of Cl_2O_2 from the self-reaction of the CIO radical. J Phys Chem 91:433–436

Molina LT, Rowland FS (1987) Stratospheric sink for chlorofluoromethanes: chlorine atom catalyzed destruction of ozone. Nature 249:810–814

Regener VH (1964) Measurement of atmospheric ozone with the chemiluminescent method. J Geophys Res 69(18):3795–3800. https://doi.org/10.1029/JZ069i018p03795

Robock A, Marquardt A, Kravitz B, Stenchikov G (2009) Benefits, risks, and costs of stratospheric geoengineering. Geophys Res Lett 36:L19703. https://doi.org/10.1029/2009gl039209

Schöenbein C (1840) Recherche sur la nature de l'odeur qui se manifeste dans certaines actions chimiques. C R Acad Sci 10:706–710

Schwartz SE, Warneck P (1995) Units for use in atmospheric chemistry (IUPAC Recommendations 1995). Pure Appl Chem:67. https://doi.org/10.1351/pac199567081377

Seinfeld JH, Pandis SN (1998) Atmospheric chemistry and physics, vol 1. Wiley, New York

Sheng J-X, Weisenstein DK, Luo B-P, Rozanov E, Stenke A, Anet J, Bingemer H, Peter T (2015) Global atmospheric sulfur budget under volcanically quiescent conditions: aerosol-chemistry-climate model predictions and validation. J Geophys Res 120(1):256–276. https://doi.org/10.1002/2014jd021985

Solomon S, Garcia R, Rowland FS, Wuebbles DJ (1986) On the depletion of Antarctic ozone. Nature 321:755–758

SPARC (2006) SPARC Assessment of stratospheric aerosol properties (ASAP). SPARC report no. 4. World Climate Research Programme

Stolarski RS, Cicerone RJ (1974) Stratospheric chlorine: a possible sink for ozone. Can J Chem 52(8):1610–1615. https://doi.org/10.1139/v74-233

Wigley TML (2006) A combined mitigation/geoengineering approach to climate stabilization. Science 314(5798):452–454. https://doi.org/10.1126/science.1131728

WMO (2010) Scientific assessment of ozone depletion: 2010. Global ozone research and monitoring project – report no. 52. World Meteorological Organization, Geneva

WMO (2014) Scientific assessment of ozone depletion: 2014. Global ozone research and monitoring project – report no. 55. World Meteorological Organization, Geneva

P

Paleoclimatology

Larry C. Peterson
Rosenstiel School of Marine and Atmospheric Science, University of Miami, Miami, FL, USA

Definition

Paleoclimatology is the study of past climates and their causes and effects on the timescale of Earth history. A key motivation for the study of past climates comes from the fact that modern instrumental records are limited in duration and fail to capture the full range of natural variability in the climate system. As paleoclimatology has matured as a discipline, it has contributed critical insights into the nature of past climate change over a broad range of timescales. Furthermore, paleoclimate reconstructions provide critical validation for numerical climate models that are usually tuned to reproduce the state of present-day climates. The ability of models to reproduce past climates as they are depicted in the paleoclimate record lends greater confidence in their capacity to forecast future climate developments.

A vast wealth of information about past changes in the Earth's climate is recorded in archives as diverse as tree rings, ice, cave deposits, and rocks and sediments that have formed in both marine and terrestrial settings. To use these resources, one must be able to extract information on past climate conditions from the physical, chemical, and biological components preserved in the geologic record. Such information comes almost entirely from indirect measures, known as *proxies*, that can be calibrated in some way to key climate variables. Fortunately, a diverse array of proxy types is available to choose from, many of them geochemical in nature.

Paleoclimatology had its beginnings in the mid-nineteenth century when observations of the wide distribution of glacial deposits led to realization that Earth had experienced a series of ice ages in the recent past that involved the growth and disappearance of massive ice sheets in the Northern Hemisphere. A key limitation of glacial deposits on land, however, is that the stratigraphic record is often incomplete, with more recent ice advances obliterating evidence of earlier advances. The accurate dating of glacial deposits is also an issue and generally limited to the age range (<40 Kyr) dateable using radiocarbon methods. Indeed, as late as the early 1960s, it was believed by many that the most recent series of ice ages totaled only four in number.

Paleoclimatology took a major step forward with work on deep-sea sediments that began in earnest in the 1950s with the introduction of coring methods that allowed recovery of a few tens of meters of sediment. This led to concerted study of glacial-interglacial cycles in the Quaternary and spurred the development of many of the climate proxies we use today. With the advent of the Deep Sea Drilling Project (DSDP) in the late 1960s, and the refinement of drilling technology by DSDP and successor programs that continue today, new opportunities arose to extend paleoclimate studies back well in excess of 100 Myrs. Much older rock sequences on the continents provide climate records that extend back to early Earth history. Excellent general introductions to the broad field of paleoclimatology can be found in the books by Cronin (2010) and Ruddiman (2013).

Climate Proxies

The development of proxies and refinement of analytical techniques applied to geologic archives have exploded in recent decades and have greatly enhanced our abilities to reconstruct a wide spectrum of climate and ocean parameters from the geologic record. Proxies can be divided into several categories based on the type of measurement. A review of some of the most widely used proxies is given here, together with brief descriptions of the main variables of interest associated with each. More comprehensive reviews of climate proxies are given by Henderson (2002), Katz et al. (2010),

W. M. White (ed.), *Encyclopedia of Geochemistry*,
https://doi.org/10.1007/978-3-319-39312-4

and Lea (2014). Additional information can be found in cross-referenced articles cited at the end.

Fossil assemblages: The relative abundance of skeletal-producing microorganisms in marine sediments can be used to estimate past ocean temperatures, productivity, and sea ice distribution, among other properties. Foraminifera, an extremely diverse group of unicellular protists, have proven the most useful microfossil group for paleoclimate studies. They produce a calcium carbonate shell, or "test," a few hundred microns in size, and live in surface waters and the upper water column as an important group of zooplankton, as well as on the seafloor itself. The distribution of planktic species in the modern ocean correlates strongly with sea surface temperature (SST, e.g., Rutherford et al. 1999) and can be used to estimate SSTs using the transfer function technique of Imbrie and Kipp (1971). Transfer functions are a category of regression models and can be derived for any fossil group for which modern relationships to variables like SST or salinity are known. The technique is not without limitations because of the potential for secondary controls on the assemblage makeup, such as productivity changes, or no-analog situations where faunas/floras in the sediments have no modern counterpart in the calibration dataset. Transfer functions also have temporal limitations because many of the species that comprise older assemblages are extinct.

On land, pollen grains and spores that accumulate in lakes and bogs provide a record of past vegetation in an area. Studies of modern pollen rain and vegetation patterns indicate a good spatial correspondence between them. Pollen data are typically corrected for differences in pollen and spore production rate, as well as for differing rates of preservation and dispersal, but generally yield reliable estimates of the composition of the surrounding vegetation (Overpeck et al. 1985). While vegetation reconstructions are relatively straightforward, the climatic inferences that can be drawn are often qualitative, with changes interpreted in terms of wetter/drier or warmer/colder conditions.

Tree rings have long been recognized as a major source of both chronologic and climatic information (Cook and Kairiukstis 1990). The mean width of a ring in any one tree is a function of many variables, including the tree species and age, the availability of stored nutrients in the tree and soil, and a host of other climate variables, including temperature, precipitation, and sunlight. Tree ring studies have become very sophisticated and involve careful cross-dating (dendrochronology), standardization, and analysis techniques. Although climate information has most often been gleaned from tree ring width, variations in tree ring density and in the isotopic composition of the wood itself have proven useful as well.

Stable isotopes: Measurement of the stable isotope ratios of oxygen ($^{18}O/^{16}O$) and carbon ($^{13}C/^{12}C$) in the calcium carbonate ($CaCO_3$) skeletons of fossil foraminifera from marine sediments is one of the most powerful and widely used tool sets in the arsenal of the paleoclimatologist. Oxygen isotope records can be used to estimate past water temperatures, the size of ice sheets, and local salinity variations, while carbon isotope records can be used to infer deep-ocean circulation patterns and provide estimates of past oceanic nutrient levels and carbon cycling. Isotope ratios for each system are expressed in delta (δ) notation, which relates the isotopic composition of a sample to the known isotopic ratio of a standard. For oxygen isotopes,

$$\delta^{18}O = \left[\frac{\left(\frac{^{18}O}{^{16}O}\right)_{sample} - \left(\frac{^{18}O}{^{16}O}\right)_{std}}{\left(\frac{^{18}O}{^{16}O}\right)_{std}} \right] \times 1000 \qquad (1)$$

with units of parts per thousand (‰). Carbon isotope values, $\delta^{13}C$, are calculated and reported in the same form.

The use of $\delta^{18}O$ ratios as a proxy for paleotemperature began in the late 1940s with Harold Urey's observation (Urey 1947) that the $^{18}O/^{16}O$ composition of calcite should vary as a function of the temperature at which the mineral precipitated. Experimental studies confirmed this prediction and led to the development of the first paleotemperature equation (Epstein et al. 1953) with the form

$$T = 16.5 - 4.3 \times \left(\delta^{18}O_{calcite} - \delta^{18}O_{water}\right) + 0.14 \times \left(\delta^{18}O_{calcite} - \delta^{18}O_{water}\right)^2 \qquad (2)$$

where T and $\delta^{18}O_{water}$ are the temperature (°C) and oxygen isotope value of the water in which the organism lived and $\delta^{18}O_{calcite}$ is the measured oxygen isotope value of the calcite. Analysis of this calcite yielded a paleotemperature equation with a sensitivity of approximately −0.24‰ change in $\delta^{18}O$ per 1 °C increase in temperature. Cesare Emiliani, a doctoral student working with Urey, exploited the new $\delta^{18}O$ paleothermometer by measuring planktic foraminifera in sediment cores from the Caribbean and equatorial Atlantic and documented regular cyclic variations in their isotopic composition that he interpreted as glacial-interglacial cycles (Emiliani 1955). Though Emiliani acknowledged that small variations in the isotopic composition of seawater were likely, he interpreted the bulk of the $\delta^{18}O$ signal as evidence that tropical surface waters cooled by as much as 6–8 °C during the recurring ice ages.

A significant paradigm shift came with the first $\delta^{18}O$ measurements of benthic (seafloor dwelling) foraminifera from downcore samples for which planktic $\delta^{18}O$ data were also available (Shackleton 1967). Nicholas Shackleton found that the magnitude of observed benthic variations was nearly the same as those of the planktic's and argued that benthic foraminifera could not be recording a temperature signal since the bottom waters they inhabited were already close to

freezing. Hence, the dominant component of the isotopic signal recorded by both planktic and benthic foraminifera must reflect variations in the oxygen isotopic composition of the ocean due to what is now called the "ice volume effect." A common feature of stable isotope behavior in nature is that of Rayleigh fractionation which occurs as isotopes move between gaseous and liquid reservoirs. As water evaporates, molecules containing the heavier ^{18}O isotope evaporate less readily than those containing the lighter ^{16}O isotope. Conversely, fractionation during condensation concentrates the heavier isotope in the precipitation (rain or snow), further enriching the clouds (water vapor) in the lighter $H_2{}^{16}O$ molecules. In the modern hydrologic cycle, water evaporated from the ocean returns there relatively quickly through precipitation, summer melting of snow/ice, and continental runoff. During glacial periods, however, when extensive ice sheets grow on land, the oceans become enriched in the heavier $H_2{}^{18}O$ molecules at the expense of $H_2{}^{16}O$ molecules, which are preferentially stored in the ice sheets. An important consequence of this observation is that the growth and melting of continental ice sheets create a whole-ocean $\delta^{18}O$ signal that provides a chronostratigraphic framework for making global correlations based on $\delta^{18}O$ variations in the sediment record. A standard oxygen isotope stratigraphy for the late Pliocene-Pleistocene is now well established as represented by the composite $\delta^{18}O$ record of Fig. 1 (Lisiecki and Raymo 2005).

As with oxygen isotopes, variations in $\delta^{13}C$ result from fractionation of ^{13}C and ^{12}C by physical or chemical processes. In the ocean, the $\delta^{13}C$ of the dissolved inorganic carbon reservoir ($\delta^{13}C_{DIC}$) largely reflects the utilization and remineralization of the carbon in organic matter. Phytoplankton in the surface ocean preferentially utilize the isotopically light ^{12}C to build soft tissue during photosynthesis. The breakdown or remineralization of this soft tissue as the organic remains settle through the water column after death puts nutrients and CO_2 with more negative $\delta^{13}C$ values (~ −25‰ today) back into the ocean at depth. In the deep ocean, waters longer isolated from the surface typically exhibit higher concentrations of nutrients and more negative $\delta^{13}C_{DIC}$ values because of their steady accumulation over time. Consequently, a deepwater mass close to its source region is likely to have more positive $\delta^{13}C_{DIC}$ values and low nutrient levels, whereas an "older" water mass more distant from its formation area will have more negative $\delta^{13}C_{DIC}$ values and higher nutrient levels. The distinct $\delta^{13}C$ characteristics of different deepwater masses can therefore be exploited to reconstruct circulation patterns (e.g., Lynch-Stieglitz and Fairbanks 1994). On timescales longer than the residence time of carbon in the oceans, the average $\delta^{13}C$ of the ocean's DIC reservoir is controlled by the $\delta^{13}C$ signatures and fluxes of carbon sources and sinks. Carbon is supplied to the ocean from the chemical weathering of continental rocks and by hydrothermal/volcanic outgassing, while carbon is removed from the ocean through deposition of carbonate and organic carbon in marine sediments. Changes in carbon isotopes of marine carbonates and organic matter through time hence serve as archives of changes in carbon sources and sinks (Kump and Arthur 1999).

Two other isotope systems finding increased application in marine sediments involve the stable isotopes of nitrogen and boron. Sedimentary nitrogen isotopes are one of the primary tools for studying past changes in the nitrogen cycle (Sigman et al. 2009). In the ocean, relatively little isotopic fractionation

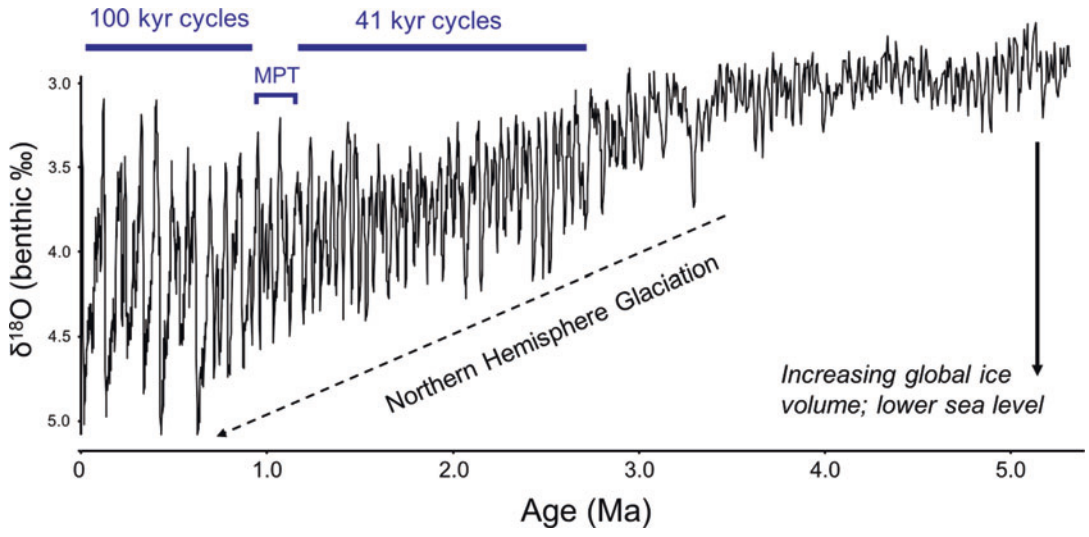

Paleoclimatology, Fig. 1 Averaged record of globally distributed oxygen isotope ratios ($\delta^{18}O$) from benthic foraminifera showing the pattern of climate variability over the past 5 Myr (Data from Lisiecki and Raymo 2005). More positive values indicate more ice and colder temperatures though the ice effect dominates over this timescale. Increasing $\delta^{18}O$ after 3 Ma records the onset and evolution of Northern Hemisphere glaciation. Label "MPT" marks the Mid-Pleistocene Transition

occurs during N_2 fixation by cyanobacteria, resulting in newly fixed nitrogen with a signature like that of air (0‰). In contrast, there is a large fractionation (ε = 20–30‰) associated with water column denitrification as well as fractionation associated with biological uptake (ε = 2.5–6‰). The $\delta^{15}N$ of sinking organic matter thus has the potential to record changes in inputs, outputs, and utilization of biologically available nitrogen (NO_3^-).

Ocean pH is an important component of the ocean carbonate system and is controlled by the ratio of alkalinity to dissolved inorganic carbon (DIC). The reconstruction of past ocean pH is possible because boron occurs as two species in seawater whose relative concentrations are pH-dependent (Foster and Rae 2016). Boron is present in seawater primarily as the trigonal $B(OH)_3$ species (boric acid) and the tetrahedral $B(OH)_4^-$ species (borate), the latter of which has an isotopic composition approximately 20‰ more negative than B $(OH)_3$. Since only $B(OH)_4^-$ is incorporated into marine carbonate, the $\delta^{11}B$ of carbonates changes with B speciation and therefore with pH. Knowledge of ocean pH, in turn, gained from fossil marine carbonates is valuable as it can be used to investigate past changes in atmospheric pCO_2. Paleo-pH values do not uniquely constrain pCO_2 but can be used to calculate it if assumptions about past ocean alkalinity and DIC are made. Using this methodology, atmospheric pCO_2 values up to ten times present levels have been measured for the earliest Cenozoic (~60 Ma).

Elements: The oceanic distribution of certain trace elements reflects processes of climatic interest, and many of these elements substitute for calcium in carbonate shell material. One of the most valuable proxies for seawater temperature is based on the substitution of magnesium into biogenic calcite. It has long been known that calcitic shells of marine organisms in the tropics contain more magnesium than subpolar shells, but it wasn't until the 1990s that species-specific calibrations of Mg/Ca to temperature were developed for foraminifera. Since then, the application of the technique has proceeded rapidly (Lea et al. 1999; Allen et al. 2016). Mg/Ca thermometry has some distinct advantages over other temperature proxies. First, the oceanic residence times for Ca and Mg are relatively long (10^6 and 10^7 years, respectively) which means that the Mg/Ca ratio of seawater may be assumed constant over glacial/interglacial timescales, in contrast to oceanic $\delta^{18}O$ which is influenced by changes in global ice volume. Second, because Mg/Ca and $\delta^{18}O$ can be measured in the same foraminiferal calcite, the temperatures obtained from Mg/Ca can be used in combination with $\delta^{18}O$ to reconstruct variations in the isotopic composition of seawater ($\delta^{18}O_{water}$), which provides an indirect measure of salinity (Schmidt et al. 2006). The biggest limitation to Mg/Ca paleothermometry is that dissolution can preferentially remove the more soluble Mg-enriched portions of the calcitic shells (Brown and Elderfield 1996).

In corals, the ratio of strontium to calcium (Sr/Ca) is temperature dependent (Beck et al. 1992), though non-environmental factors can have an influence as well. Measurements of Sr/Ca in corals capture the annual temperature cycle and allow for collection of high-resolution temperature time series in the tropical ocean. Studies of coral Sr/Ca have proven particularly useful for studying the past behavior of the El Niño-Southern Oscillation (ENSO) system in the tropical Pacific (Gagan et al. 1998).

Variations in the ratio of cadmium to calcium (Cd/Ca) in benthic foraminifera have provided important evidence for reorganization of deepwater circulation patterns during Pleistocene glacial-interglacial cycles. In the present ocean, Cd concentrations closely resemble those of the nutrient phosphorus (Boyle 1988), which increases with water mass age because of the steady rain of organic matter from the surface ocean to the deep sea and its subsequent remineralization. Changes in Cd/Ca concentration in benthic foraminiferal shells thus reflect changes in the age of a water mass, in a manner generally consistent with $\delta^{13}C$. Foraminiferal Cd/Ca and $\delta^{13}C$ measured together in sediment cores from the Atlantic were among the first data to suggest that production rates of North Atlantic Deep Water (NADW) were greatly reduced during the last glacial (Boyle and Keigwin 1982).

Biomarkers: Biomarkers are organic molecules unique to a specific organism or group of organisms. They are typically resistant to degradation and preserved in sediments and rocks after all other traces of the organism have disappeared. Some of the most useful biomarkers can be used to reconstruct physical parameters such as temperature. Alkenones are a group of long-chained organic molecules ($C_{37–39}$) produced by only a few predominantly marine phytoplankton, including the widespread coccolithophore *Emiliania huxleyi* and related species. The alkenones produced can have two or three double bonds in their structure with the degree of unsaturation responding linearly to water temperature (Prahl and Wakeham 1987). For temperature estimation, this is written as the $U^{K'}_{37}$ ratio, the amount of di-unsaturated to the total of the di- and tri-unsaturated C_{37} alkenones ((37:2)/(37:2 + 37:3)). The $U^{K'}_{37}$ index has been calibrated to sea surface temperature using a global set of modern surface sediments (e.g., Conte et al. 2006). One limitation of the $U^{K'}_{37}$ proxy is that there is an upper temperature limit (~29 °C) that can be reconstructed. A second is that the relevant coccolithophorids don't grow in polar waters, which also precludes their use at the coldest temperatures. Nonetheless, advantages include that alkenone temperatures obtained reflect near-surface temperatures since the alkenone producers are phytoplankton and therefore live in the uppermost photic zone.

A newer biomarker proxy for measuring sea surface temperature is TEX_{86} (Schouten et al. 2002), a method based on compounds known as C_{86} glycerol tetraethers (GDGTs). These are membrane lipids synthesized in the water column by another

group of microorganisms, the Thaumarchaeota, and come with variable numbers of cyclopentane structures. The proportions of these different GDGTs produced by the Thaumarchaeota vary with temperature, according to the formula:

$$T = 56.2 \times TEX_{86} - 10.78 \quad (3)$$

where T is the temperature in °C and TEX_{86} is defined as the ratio of the sum of the quantities of GDGTs 2, 3, and 4′ to the sum of the quantities of GDGTs 1, 2, 3, and 4′. Below about 5 °C, the variation in TEX_{86} becomes negligible, so this proxy also has limitations in the coldest waters. Like alkenones, GDGTs are resistant to postdepositional processes that destroy most organic compounds and can be found in marine sediments up to Jurassic in age. The TEX_{86} method for temperature can also be applied in lacustrine settings.

An important group of terrestrial biomarkers come from the waxes that coat the leaves of vascular plants. These are long-chain n-alkyl compounds associated with cuticle, a multilayered waxy structure on the exterior of leaves and fruits. Cuticle has multiple functions, but one of its primary roles is to protect against moisture loss. Leaf wax compounds and their stable carbon ($\delta^{13}C$) and deuterium/hydrogen (δD) isotopic composition can provide valuable information about changes in vegetation and water availability (e.g., Hughen et al. 2004; Schefuß et al. 2005). The stable $\delta^{13}C$ from these compounds varies among vegetation types that utilize either the C3 (woody trees) or C4 (grasses, shrubs) photosynthetic pathways and can be used as an indicator of the relative contributions of these two types of vegetation. The hydrogen isotopic composition (δD) encoded in plant wax compounds can be used to infer the isotopic composition of the source water, usually precipitation, and is commonly used to reconstruct past hydrologic conditions (Tierney et al. 2013). Leaf waxes can be found in both terrestrial and marine sediment sequences, the latter where input occurs by rivers or wind.

Other isotope systems: Two other isotopic proxies have found increasing use in tracing past ocean circulation. One of the more promising is the isotopic composition of dissolved neodymium (Nd), specifically the $^{143}Nd/^{144}Nd$ isotope ratio, expressed as ε_{Nd} (Rutberg et al. 2000). Seawater Nd isotopes are dominated by continental inputs that enter the oceans through rivers and atmospheric deposition. ε_{Nd} values of different water masses thus reflect the geology of surrounding terranes relative to the location where deepwater masses form. They can be used to track changes in ocean circulation because Nd has a short residence time (~500–1000 years) relative to the timescale of ocean mixing (~1500 years) (Goldstein and Hemming 2003) and because fossil fish teeth and Fe-Mn coatings on sediment grains preserve a record of seawater ε_{Nd} (Palmer and Elderfield 1986). The most extreme end-members in the modern ocean are the deep North Atlantic (where NADW is formed with low ε_{Nd} values derived from old continental crust) and the deep North Pacific (where older deep waters are found with high ε_{Nd} values acquired from young volcanic arcs). In theory, changes in ε_{Nd} can be used as a water mass tracer so long as the assumption of constant end-member compositions is valid.

Another proxy that can provide information about the strength of the ocean's large-scale overturning circulation is based on protactinium (Pa) and thorium (Th). ^{231}Pa and ^{230}Th are both insoluble products formed by the natural decay of dissolved uranium (U) in the water column (Marchal et al. 2000). As U has a constant concentration in seawater, these nuclides are created uniformly at a known rate, but they are scavenged by sinking particles at unequal rates, with ^{230}Th remaining in the water for only a few tens of years before being incorporated into the underlying sediments, while ^{231}Pa is supported in the water column for ~100–200 years. In today's Atlantic Ocean, with its overturning circulation driven by formation of NADW, ^{230}Th transport to the Southern Ocean is minimal due to its short residence time and ^{231}Pa transport is high. This results in relatively low $^{231}Pa/^{230}Th$ ratios in the underlying sediment. However, as found by McManus et al. (2004), when the Atlantic's overturning circulation slows or shuts down (as hypothesized) during glacial periods, the $^{231}Pa/^{230}Th$ ratio in sediments becomes elevated as there is less removal of ^{231}Pa to the Southern Ocean. Subsequent work has shown that the use of $^{231}Pa/^{230}Th$ as a physical circulation proxy must be applied with caution since ^{231}Pa and ^{230}Th removal from seawater can be influenced by the composition of sinking particles, with ^{231}Pa having an affinity for biogenic silica (Lippold et al. 2009).

As this review suggests, there is no one perfect proxy for past climates. But as new proxies have developed, the increasing availability of overlapping proxies based on completely different chemical or physical systems provides for multiple validations of primary climate signals. For example, past sea surface temperatures can now be determined by faunal transfer functions, oxygen isotopes, foraminiferal Mg/Ca, and alkenone undersaturation in the same deep-sea sediment core and often the same samples. Similarly, inferences about past ocean circulation patterns can come from $\delta^{13}C$ and Cd/Ca in benthic foraminifers, as well as from Nd isotopes in diagenetic coatings and $^{231}Pa/^{230}Th$ in bulk sediment.

The Climate System and Timescales of Change

Earth's climate system can be divided into five major components: the lithosphere, the hydrosphere (oceans, lakes and rivers, groundwater), the cryosphere (ice sheets, glaciers, and sea ice), the atmosphere, and the biosphere. Climate involves a myriad of interactions among these components over timescales ranging from seconds to millions of years. At the most basic level, paleoclimatology involves trying to

understand the causes (forcing) and effects (the response) of climate change. Paleoclimate records provide the direct evidence of how climate has responded as deciphered from our toolbox of proxies, while the nature of the forcing and the various interactions between components must be inferred and understood from modern observations, first principles, and modeling.

Three fundamental kinds of climate forcing have been identified that impact Earth's climate system. These can be summarized as:

Tectonic forcing: The slow reshaping of the Earth's surface by plate tectonics is driven by the internal heat generated deep in the Earth by radioactive decay. As tectonic plates move, so do the continents, and this redistribution has an important effect on the spatial heterogeneity of the Earth's energy balance via differences in the albedos (reflectivity) and thermal properties of land versus ocean. The collision of continents, the uplift of mountains and their subsequent erosion, and the volcanism associated with mid-ocean ridges and trenches where ocean lithosphere is created and recycled impact climate over very long timescales (10–100 Myrs). Similarly, the opening and closing of ocean basins and critical gateways drive changes in ocean circulation, which can modify the distribution of heat and salt and influence marine primary productivity, as well as conditions on the adjacent continents. Tectonic processes have important geochemical impacts on climate because on long timescales, the global carbon cycle is characterized by the involvement of rocks, which contain more CO_2 than all other reservoirs on Earth combined. Atmospheric CO_2 levels reflect the balance between inputs and outputs, and CO_2 on tectonic timescales is added via volcanic outgassing, metamorphism, and diagenesis and removed via silicate weathering and storage in rock and sediment as carbonate and organic carbon (Berner et al. 1983; Kump et al. 2000). Recycling of oceanic crust at subduction zones returns the CO_2, stored in carbonates and organic carbon, back to the mantle, where the cycle is completed. Variability in the relative rates of these processes on tectonic timescales is what controls the long-term oscillations between what have come to be called greenhouse and icehouse worlds.

Astronomical forcing: On timescales of 10^4–10^5 years, climate variability is largely driven by changes in the Earth's orbit with respect to the Sun. These changes affect climate by altering the amount of solar insolation received by season and latitude. For any position on the Earth's surface, the insolation received at the top of the atmosphere is a function of the solar constant and the effects of three distinct orbital elements: obliquity, eccentricity, and precession (Berger 1988). Each operates with a characteristic periodicity and impacts climate in a different way. Changes in obliquity, or the degree to which the Earth's axis is tilted with respect to the plane of solar orbit, affect the intensity of seasons and the amount of sunlight each hemisphere receives during the year. The present angle of tilt is 23.5°, but over a period of 41 Kyr, it varies between about 21.5° and 24.5°. The shape of Earth's orbit around the Sun also varies through time, ranging from nearly circular to slightly (~5%) elliptical or eccentric. Changes in the eccentricity of Earth's orbit alter the Earth-Sun distance, subsequently reducing or increasing the amount of radiation received at the Earth's surface in different seasons. There are both 100 and 413 Kyr cycles associated with eccentricity. Finally, precession refers to the slow turning of the Earth's axis of rotation through a circular path, like the motion of a wobbling top, completing a full 360° rotation in a cycle that takes about 23 Kyr. Because the direction of the Earth's axis of rotation determines at which point in the Earth's orbit the seasons will occur, precession also plays a role in the timing and intensity of seasons.

In the early twentieth century, the Serbian mathematician Milutin Milankovitch proposed that recent ice ages affecting the Northern Hemisphere began when the three orbital cycles align to favor an extended period of more solar radiation in the winter and less in the summer at high northern latitudes (~65°N). These conditions would favor higher winter temperatures, but also more water vapor in the air, leading to greater snowfall. More importantly, reduced summer insolation would lead to cooler summers that favor less melting of winter snow and gradual glacier formation. Milankovitch developed the mathematical basis for calculating the insolation values for a given latitude and season (Milankovitch 1941), and his insolation curves, meticulously calculated by hand, formed the basis for early attempts to compare the timing of insolation minima to the ages of glacial deposits on land. Milankovitch's "orbital theory" fell into disfavor in the late 1946s as radiocarbon dating of glacial deposits on the continents revealed their incompleteness and internal complexity. However, as noted already, a fundamental shift in the study of paleoclimates occurred with the advent of coring methods that made possible the collection of more continuous deep-sea records, and the work of pioneers like Emiliani and Shackleton led to development of the $\delta^{18}O$ proxy that initiated the field of paleoceanography. Hays et al. (1976) later provided the first clear evidence that the orbital changes postulated by Milankovitch played a key role in driving the late Quaternary ice age cycles, serving as a "pacemaker" that determines their timing. Since then, the Milankovitch periodicities have been found in varying significance in most climate records of sufficient length and resolution. Climate variability on orbital timescales is largely superimposed on longer-term, tectonic-scale climate variability and is most characteristic of "icehouse" worlds where large ice sheets and their highly reflective nature provide feedbacks that amplify the relatively weak insolation changes. Evidence for the orbital forcing of climate has been found as far back as 1.4 billion years ago, in the Proterozoic Eon.

Radiative/atmospheric forcing: Forcing that arises from changes in the concentration of radiatively active trace gases in the atmosphere is a critical component of the climate system. Changes in concentration of the so-called greenhouse gases (e.g., carbon dioxide, methane, nitrous oxide) come about when the atmosphere is no longer in equilibrium with the sources and sinks of the gas. Though water vapor is the single most important greenhouse gas, changes in its tropospheric concentration are largely a natural consequence of temperature change (i.e., warm air holds more moisture) and therefore are usually treated as a feedback in climate models. Atmospheric CO_2 is the greenhouse gas with the most impact on climate, and there is abundant evidence from the geologic past for this connection on timescales ranging from orbital to tectonic.

Variations in past atmospheric CO_2 levels on orbital timescales are best documented in ice cores drilled from the modern ice caps in Greenland and the Antarctic, from which gases extracted from bubbles in the ice have provided time series of changes in atmospheric composition. The oldest continuous ice core records recovered to date extend back 800 Kyrs in Antarctica. Over the last 800 Kyrs (Fig. 2), atmospheric CO_2 levels have fluctuated between about 180 and 300 parts per million by volume (ppmv), corresponding closely with glacial and interglacial climates. The complex reasons for these CO_2 changes have yet to be fully worked out. Glacial cooling of ocean surface waters can explain some small portion of the CO_2 decrease by its effect on gas solubility (cold water holds more dissolved gas);

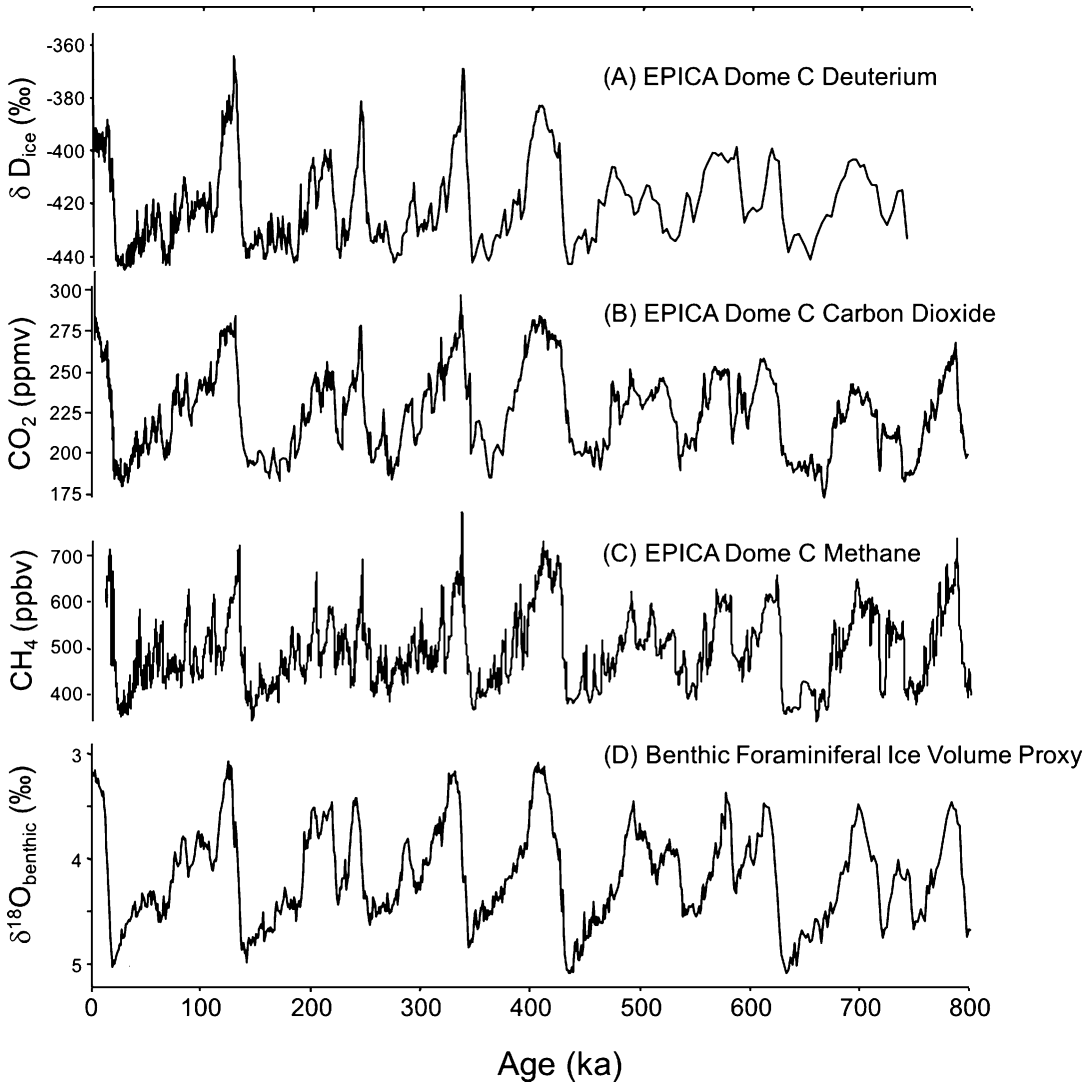

Paleoclimatology, Fig. 2 Comparison of ice core records of temperature and atmospheric greenhouse gases to global ice volume for the last 800 Kyr. (**a**) Deuterium isotopes, a proxy for air temperature, from the EPICA Dome C ice core, Antarctica (Jouzel et al. 2007); (**b**) atmospheric CO_2 (ppmv) from ice core air bubbles, EPICA Dome C, Antarctica (Luthi et al. 2008); (**c**) atmospheric methane (CH_4; ppbv), EPICA Dome C, Antarctica (Loulergue et al. 2008); (**d**) deep-sea benthic foraminiferal $\delta^{18}O$, a proxy for global ice volume (Lisiecki and Raymo 2005)

however, most of the explanation for lowered glacial CO_2 appears tied to the transfer and storage of carbon into the deep ocean (Sigman et al. 2010). This may have come about through higher rates of photosynthesis and biologic productivity, leading to more carbon export into the deep ocean, or by changing patterns of deep-ocean overturning that allowed CO_2 to accumulate in bottom waters. Regardless of mechanism, it is evident that carbon cycling is intrinsically related to climate change over glacial-interglacial cycles and that the ocean is involved since it contains the largest source of readily exchangeable carbon. Methane concentrations also track the glacial-interglacial changes (Fig. 2), probably because there were fewer wetlands in the colder, drier glacial periods.

Reconstructed atmospheric CO_2 concentrations for the Phanerozoic are shown in Fig. 3 and include measurements based on multiple paleo-CO_2 proxies and estimates derived independently from geochemical modeling (e.g., Berner and Kothavala 2001). Though measurements and models show considerable uncertainty and variation over these long timescales, both point to atmospheric CO_2 levels in the past at times much higher than present and corresponding to periods of well-documented global warmth. A strong first-order correlation also exists between periods of low CO_2 and the presence of long-lived, aerially extensive continental glaciations. This comparison builds confidence in the validity of the simulated and reconstructed CO_2 history as well as the long-term relationship between CO_2 and climate, though keeping in mind that the link between CO_2 and global temperature cannot, on its own, explain all past climate variations.

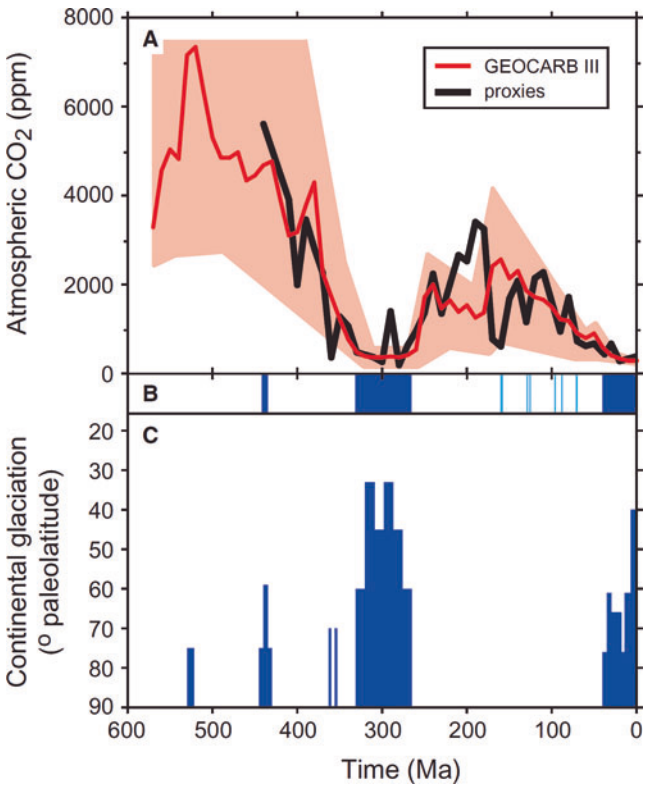

Paleoclimatology, Fig. 3 Comparison of atmospheric CO_2 and climate from Royer et al. (2004) for the Phanerozoic, the time interval since the first appearance of multicellular life with skeletal hard parts at the base of the Cambrian Period. (**a**): Comparison of model predictions (GEOCARB III; shaded area shows error range) with estimated CO_2 levels based on multiple proxy lines of evidence. Both curves use 10 Myr time steps. (**b**): Intervals of well-known glacial (*dark blue*) or cool climates (*light blue*). (**c**): Summary of latitudinal distribution of direct physical-glacial evidence (e.g., tillites, striated bedrock) after accounting for continental paleo-position (Reprinted by permission from the Geological Society of America)

Other factors can alter the radiative balance of the planet besides the concentrations of greenhouse gases. The luminosity, or brightness, of the Sun provides the energy to drive atmospheric circulation and constitutes the input for Earth's surface heat budget. Radiative energy from the Sun is variable at very small timescales, owing to solar storms and other disturbances, but variations in solar activity, particularly the frequency of sunspots, are also documented at decadal to millennial timescales. When viewed over the entire span of Earth history, the output from the Sun has increased steadily since its formation. Low solar luminosity during Precambrian time underlies the "Faint Young Sun Paradox" (Güdel 2011), the paradox being that a Sun only 70% as strong as today would yield a frozen world with no possibility of liquid water or the emergence of life, and yet both were present. The solution to this mystery is generally attributed to an early atmosphere loaded with high levels of CO_2 and perhaps methane because of increased volcanic activity.

Another critical factor is albedo, the extent to which the atmosphere and Earth's surface reflect the incoming solar radiation back to space. The albedo of the Earth's surface can be affected by land surface changes, such as desertification, but the largest changes are related to the presence of snow and the waxing and waning of ice sheets and sea ice. Fresh snow has an albedo of 0.8–0.9 which means that 80–90% of the incoming solar radiation is reflected. As ice sheets grow, the area of high albedo increases, further reducing the solar energy absorbed and leading to more cooling. Conversely, warming decreases ice cover and hence the albedo, increasing the amount of solar energy absorbed, leading to more warming. The planetary albedo can also be altered by the amount of aerosol particles in the atmosphere. In the stratosphere, the dominant aerosol source is from volcanic eruptions, while in the lower troposphere, the source can be either natural or man-made (e.g., pollutants).

Cenozoic Climate History

Paleoclimate studies over the last half century have yielded an increasingly detailed view of how climate has changed over Earth history, ranging from climate states much warmer to

much colder than present. A review of climate for the Cenozoic (the last 66 Myrs) highlights some of the changes that have occurred and insights that have been gained. The Cenozoic, though it represents only a small fraction of Earth's existence, is the time interval best known because of the availability of well-preserved paleoclimate archives, such as deep-sea benthic foraminiferal oxygen isotope ($\delta^{18}O$) records (e.g., Zachos et al. 2001, 2008).

The asteroid impact associated with the mass extinction marking the end of the Cretaceous Period (66 Ma) came at a time of extreme greenhouse climates, which continued into the early Cenozoic (Fig. 4). This high-CO_2 world (~2000–4000 ppmv) is thought to have been driven by faster rates of seafloor spreading and volcanic emissions and by subduction and recycling of the carbonate-rich tropical Tethyan Seaway in the early Cenozoic. Tropical and subtropical floras and faunas occurred at high latitudes until at least 40 Ma, and geochemical proxies from marine sediments indicate the presence of warm oceans at all depths.

The highest known global temperatures of the Cenozoic occurred during a geologically brief interval spanning the Paleocene-Eocene boundary (Fig. 4). This "hyperthermal" event, the Paleocene-Eocene Thermal Maximum (PETM), began rapidly about 55.5 Ma and lasted approximately

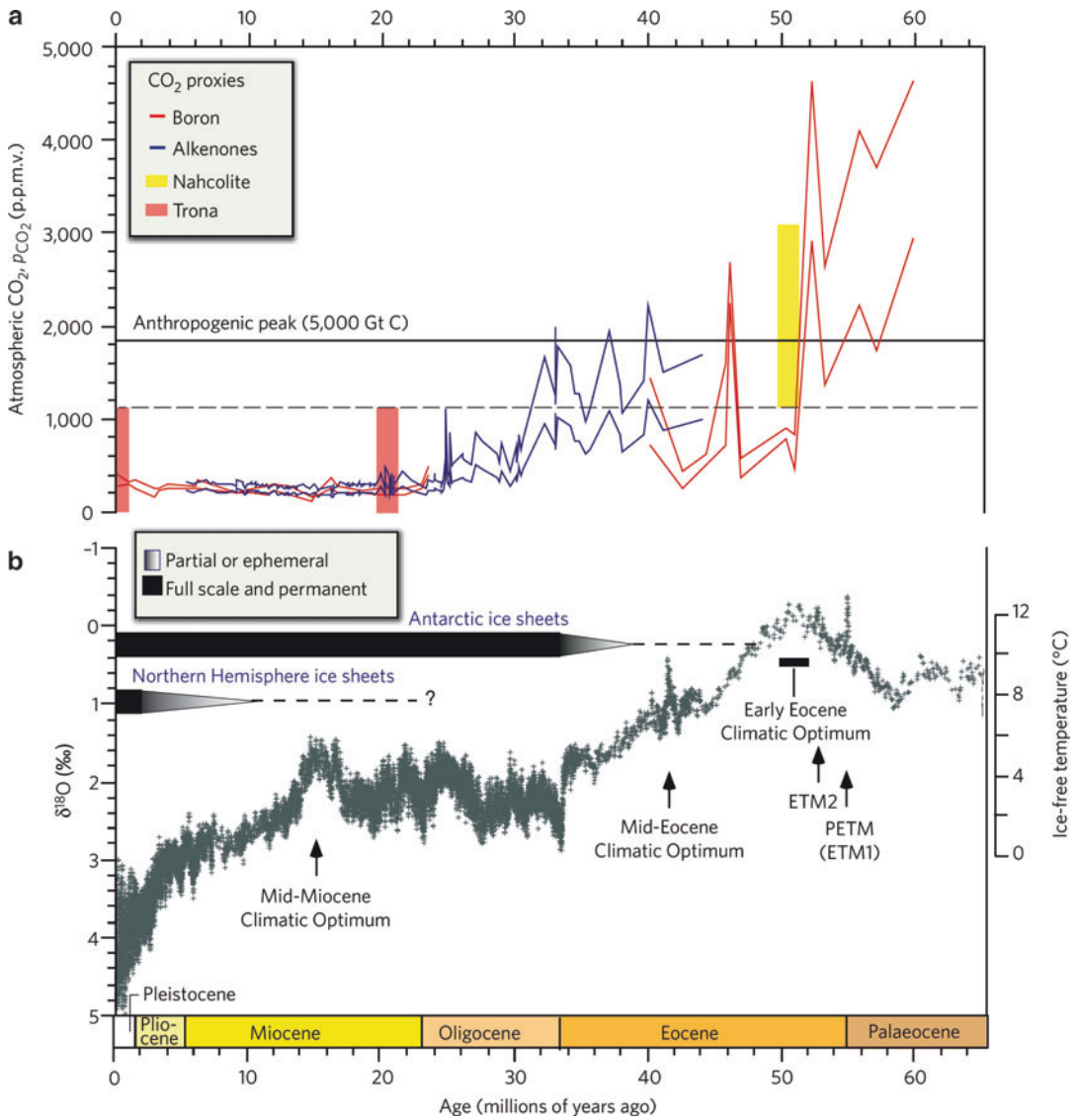

Paleoclimatology, Fig. 4 Evolution of atmospheric CO_2 levels and global climate over the course of the Cenozoic. (**a**) Atmospheric CO_2 from a compilation of marine and lacustrine proxy records. The vertical distance between the upper and lower colored lines shows the range of uncertainty for the alkenone and boron pCO_2 proxies. (**b**) Cenozoic climate as recorded by deep-sea benthic foraminiferal $\delta^{18}O$ time series from Deep Sea Drilling Project and Ocean Drilling Program sites. The $\delta^{18}O$ temperature scale on the right axis is computed on the assumption of an ice-free world; it therefore applies only to the time preceding the onset of large-scale glaciation on Antarctica (about 34 Ma) (Reprinted by permission from Macmillan Publishers Ltd.: Nature; Zachos et al. (2008))

170 Kyr. Its onset was marked by repeated, rapid, and massive releases of isotopically light fossil carbon, as indicated by carbon isotopes in such diverse materials as marine foraminifera, organic carbon, and soil carbonates on land. Sea surface and continental air temperatures increased by more than 5 °C (9 °F) during the transition into the PETM, while SSTs in the high-latitude Arctic may have been as warm as 23 °C (73 °F), comparable to modern subtropical and warm-temperate seas. The extreme warming was accompanied by widespread extinctions in both marine and terrestrial ecosystems, deep-ocean acidification, and expanded low-oxygen conditions in the water column.

The enormous source of fossil carbon that led to the PETM is still unclear (Thomas et al. 2002; Dickens 2003). The most widely cited candidate is carbon sourced from frozen methane hydrates that may have dissociated (melted) as their stability field crossed a threshold triggered by the warming of the late Paleocene. Other suggested sources include the large-scale combustion of terrestrial peat sequences, the desiccation and oxidation of organic matter in large epicontinental seaways, the impact of a volatile-rich comet, and the intrusion of igneous bodies into organic-rich sediments during the opening of the North Atlantic that released thermogenic methane and CO_2 through contact metamorphism. Problems exist with each of these hypotheses, however, and to date, no single explanation fully satisfies the evidence. Multiple sources of carbon release may well be required to explain this event.

Following the PETM, global temperatures declined but then gradually increased again to near-PETM levels during a period known as the Early Eocene Climatic Optimum (Fig. 4). This temperature maximum was followed by a steady decline in global temperatures toward the Eocene-Oligocene boundary. The global cooling is reflected in marine sediments and paleontological records from the continents by gradual shifts in faunal and floral assemblages toward the equator. Uplift of the Himalayas and Tibetan Plateau caused by the collision of the Indian subcontinent with Asia beginning about 40 Ma likely contributed to late Cenozoic cooling through erosion and the drawdown of CO_2 via enhanced weathering of silicate minerals (Archer 2009). As this uplift has continued until the present day, it has influenced and strengthened the monsoon circulation in these regions.

The cooling trend of the late Eocene was punctuated about 34 Ma by a rapid positive shift of more than 1.5‰ in deep-sea benthic $\delta^{18}O$ values that occurred over just a few hundred thousand years. Though some of this $\delta^{18}O$ change near the Eocene-Oligocene boundary can be attributed to deep-ocean cooling, the bulk of the signal reflects the initial growth of a permanent continent-sized ice sheet in Antarctica (Lear et al. 2008). Physical evidence for an ice sheet close to present size comes from ice-rafted materials in Southern Ocean sediments that date to this time, indicating the calving of icebergs from ice that reached the ocean's edge. The climatic stresses triggered by this pronounced transition from the early Cenozoic greenhouse world to the glaciated icehouse world of today drove significant extinction of animals and plants, both on the continents and in the ocean (Prothero 1994).

Conditions allowing rapid ice growth on Antarctica at the Eocene-Oligocene transition are thought to have been reached through a combination of declining CO_2 levels and orbitally driven changes in summer insolation (DeConto and Pollard 2003). However, it is likely that tectonics also played an important role. This period saw the gradual opening of the ocean passage between Tasmania and Antarctica, followed by the opening of the Drake Passage between South America and Antarctica. The latter, which left Antarctica thermally isolated within a cold polar sea, produced global effects on atmospheric and oceanic circulation (Barker et al. 2007).

An ice sheet in Antarctica persisted during the Oligocene, and global climate was cooler and drier, with a major expansion of grasslands and a retreat of tropical forests toward the equator. The late Oligocene and early to middle Miocene were warmer, though not nearly as warm as the Eocene, and the Antarctic ice sheet was diminished in size but still present. After a period of global warmth known as the Mid-Miocene Climatic Optimum (Fig. 4), cooling resumed about 14 Ma, and the Antarctic ice sheet expanded again to cover much of the continent. This cooling continued through the late Miocene and accelerated into the early Pliocene. During this period, the Northern Hemisphere remained ice-free, and studies of fossil pollen show cool-temperate Pliocene floras at high latitudes on Greenland and the Arctic Archipelago.

One of the most important analogs for a future high CO_2 world is the time interval between about 3.3 and 3.0 Ma in the late Pliocene. This relatively recent interval had continent-ocean configurations, ecosystems, and bipolar ice sheet extents similar to today. More importantly, the orbital configuration was nearly identical, while proxy CO_2 estimates from sediment cores in a range of ocean basins indicate peak Pliocene CO_2 values comparable to present-day values of ~400 ppmv. This Pliocene analog thus allows the study of the effects of higher CO_2 levels, while other large-scale boundary conditions were close to modern. Although the high latitudes were significantly warmer, tropical sea surface and air temperatures were comparable to today. Both drill core data and ice sheet simulations show complete deglaciation of the Greenland and West Antarctic ice sheets with global sea levels up to 20 m higher than present (Raymo et al. 2011).

The record of benthic foraminiferal $\delta^{18}O$ shows that Northern Hemisphere glaciation began about 3 Ma (Fig. 1). Several mechanisms have been proposed to explain the conditions that led to Northern Hemisphere ice growth including tectonic closure of the Panamanian seaway and its effect on ocean circulation, mountain uplift that altered the path of

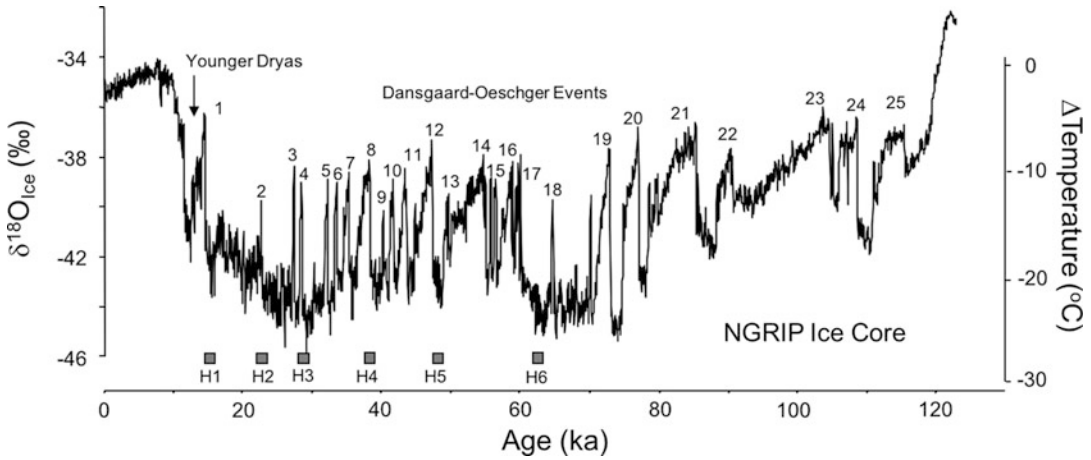

Paleoclimatology, Fig. 5 High-resolution $\delta^{18}O$ measurements of ice from the NGRIP ice core in Greenland (North Greenland Ice Core Project Members 2004). The $\delta^{18}O$ of ice records air temperature (expressed in terms of temperature anomaly on the right axis) and reveals pervasive century- to millennial-scale variability. The abrupt cooling of the Younger Dryas and the rapid warmings that characterize Dansgaard-Oeschger interstadial events are numbered. Heinrich events (labeled H1–H6) are discrete layers of ice-rafted debris found in sediment cores from a wide swath of the subpolar North Atlantic

the jet stream, and decreasing atmospheric CO_2 levels (Ruddiman 2013). The gradual cooling at high latitudes that followed, and the increasing ice sheet extent recorded by $\delta^{18}O$ and other proxies, led to a period of low-amplitude climate oscillations characterized by the 41 Kyr period of Earth's obliquity, consistent with the orbital pacing predicted by Milankovitch theory. Then, in one of the most puzzling climate events of the late Cenozoic, known as the Mid-Pleistocene Transition (MPT, ~1250–700 Ka), the dominant periodicity of Earth's climate cycles inexplicably changed from 41 Kyr to 100 Kyr (Fig. 1), resulting in cold glacial intervals of increased severity and duration. This reorganization took place in the absence of any change in the underlying orbital forcing, suggesting a fundamental shift internal to the climate system (e.g., Elderfield et al. 2012). Furthermore, of the three orbital parameters that affect climate, the 100 Kyr eccentricity cycle has the least impact on insolation, so the sudden dominance of this periodicity in climate records after the MPT implies increasing nonlinearity in the climate response. This is referred to as the 100,000-year problem and serves as a reminder that our understanding of long-term climatic change is far from complete.

During the Last Glacial Maximum (LGM), from ~26.5 to 20 Kyr, the ice sheets in the Northern Hemisphere reached their maximum size with twice the volume of ice currently found in Antarctica. The massive ice sheets locked away water and lowered sea level by about 120 m (~400 ft.), which exposed the continental shelves, joining land masses together in some places and creating such features as the Bering Land Bridge and more extensive coastal plains. Much of the world was colder, drier, and dustier, the latter indicated by dust levels in ice cores that were as much as 25 times greater than now (Lambert et al. 2008).

One of the most surprising discoveries to come from the paleoclimate record is the rapidity with which large magnitude changes can occur. The most dramatic insights into this behavior first came from ice core studies in Greenland in the 1980s which showed that significant changes in regional temperature occurred in the past over timescales of a few years to decades at most. The best studied of these events is the Younger Dryas, an abrupt return to near-glacial temperatures in the high-latitude North Atlantic lasting roughly a millennium during the last deglaciation (Fig. 5). Rapid temperature excursions were subsequently found to be a characteristic feature of Greenland climate during the last glacial period. These excursions, known as Dansgaard-Oeschger or D-O events, recurred roughly every 1500 years and show up as abrupt warmings over Greenland of as much as 10–12 °C followed by a more gradual return to cold glacial conditions. Later studies showed that D-O events in Greenland are closely matched by SST changes recorded in high-accumulation-rate sediments in the North Atlantic (Bond et al. 1993). In addition, discrete layers of ice-rafted debris found in subpolar North Atlantic sediments, called Heinrich events, were deposited periodically during the coldest phases of the D-O cycles (Fig. 5) and are thought to have originated from icebergs that came out of the Hudson Strait, dropping their detrital load as they melted while being carried by currents across the North Atlantic (Hemming 2004). Though these abrupt climate events are best defined in Greenland ice for the last glacial period, many records from around the world, and from earlier glacials as well, have now been found that show evidence of large and rapid climate events with similar temporal behavior (see review in Clement and Peterson 2008). These events are of considerable interest and concern because they involve sudden shifts of Earth's climate

system from one stable equilibrium state to another, implying "tipping points" where small, gradual changes in one component of the system can lead to a large change in the entire system through feedbacks.

At present, the favored explanation for the abrupt climate events seen in ice cores and elsewhere centers on freshwater input to the high-latitude North Atlantic and its effect on heat transport into the region via disruption of the Atlantic's meridional overturning circulation (MOC). It is argued that freshwater discharges into the North Atlantic Ocean from the surrounding landmasses abruptly weaken the MOC in the Atlantic by reducing salinity and increasing stratification in the areas of modern deepwater formation. The reduction in sinking disrupts the delivery of heat from the tropics via surface currents, causing cold events in Greenland and related events around the globe, such as a southward shift in the tropical rain belts. Periodic releases of meltwater from the surrounding ice sheets seem a likely culprit, an observation consistent with the primary association of these events with glacial times. Though it is now reasonably well established that variations in the MOC accompanied the Younger Dryas and most of the abrupt D-O events recorded in Greenland (Henry et al. 2016), many questions remain, and the ultimate climate driver for these rapid excursions is not fully understood.

Summary

In 1895, the Swedish scientist Svante Arrhenius proposed that the cooling that led to the ice ages could have been produced by a drop in the concentration of atmospheric CO_2 relative to then-current levels. He further proposed that industrial emissions could potentially raise Earth's temperature in the coming centuries. As we ponder a climate future now undeniably impacted by human activities, the need to understand Earth's climate history and the full range of natural mechanisms and past variability has taken on greater importance. Paleoclimatology provides that retrospective view and has evolved into a mature and exciting discipline. The discussion in this entry barely scratches the surface of our growing knowledge of Earth's climate past, and the reader is encouraged to consult cited sources and cross-references for additional information.

Cross-References

- Biological Pump
- Boron Stable Isotopes
- Carbon Isotopes
- Carbonate Compensation Depth
- Chemical Weathering
- Geologic Time Scale
- Marine Sediment
- Neodymium Isotopes
- Nitrogen Isotopes
- Ocean Biochemical Cycling and Trace Elements
- Ocean Salinity, Major Elements, and Thermohaline Circulation
- Oxygen Isotopes
- Paleoenvironments
- Paleoproductivity
- Paleotemperatures
- Stable Isotope Geochemistry
- Uranium Decay Series

References

Allen KA, Hönisch B, Eggins SM, Haynes LL, Rosenthal Y, Yu J (2016) Trace element proxies for surface ocean conditions: a synthesis of culture calibrations with planktic foraminifera. Geochim Cosmochim Acta 193:197–221

Archer D (2009) The long thaw: how humans are changing the next 100,000 years of Earth's climate. Princeton University Press, Princeton

Barker PF, Filippelli GM, Florindo F, Martin EE, Scher HD (2007) Onset and role of the Antarctic circumpolar current. Deep-Sea Res II Top Stud Oceanogr 54(21):2388–2398

Beck JW, Edwards RL, Ito E, Taylor FW, Recy J, Rougerie F, Joannot P, Henin C (1992) Sea-surface temperature from coral skeletal strontium/calcium ratios. Science 257(5070):644–647

Berger A (1988) Milankovitch theory and climate. Rev Geophys 26(4):624–657

Berner RA, Kothavala Z (2001) GEOCARB III: a revised model of atmospheric CO2 over Phanerozoic time. Am J Sci 301: 182–204

Berner R, Lasaga A, Garrels R (1983) The carbonate-silicate geochemical cycle and its effect on atmospheric carbon dioxide over the past 100 million years. Am J Sci 283:641–683

Bond G, Broecker W, Johnsen S, McManus J, Labeyrie L, Jouzel J, Bonani G (1993) Correlations between climate records from North Atlantic sediments and Greenland ice. Nature 365(6442):143–147

Boyle EA (1988) Cadmium: chemical tracer of deepwater paleoceanography. Paleoceanography 3(4):471–489

Boyle EA, Keigwin LD (1982) Deep circulation of the North Atlantic over the last 200,000 years: geochemical evidence. Science 218(4574):784–787

Brown S, Elderfield H (1996) Variations in Mg/Ca and Sr/Ca ratios of planktonic foraminifera caused by postdepositional dissolution – evidence of shallow Mg-dependent dissolution. Paleoceanography 11(5):543–551

Clement AC, Peterson LC (2008) Mechanisms of abrupt climate change of the last glacial period. Rev Geophys 46:RG4002. https://doi.org/10.1029/2006RG000204

Conte MH, Sicre MA, Rühlemann C, Weber JC, Schulte S, Schulz-Bull D, Blanz T (2006) Global temperature calibration of the alkenone unsaturation index (U^k_{37}) in surface waters and comparison with surface sediments. Geochem Geophys Geosyst 7:Q02005. https://doi.org/10.1029/2005GC001054

Cook ER, Kairiukstis LA (eds) (1990) Methods of dendrochronology: applications in the environmental sciences. Springer Science & Business Media, Springer Dordrecht (Netherlands)

Cronin TM (2010) Paleoclimates: understanding climate change past and present. Columbia University Press, New York

DeConto RM, Pollard D (2003) Rapid Cenozoic glaciation of Antarctica induced by declining atmospheric CO_2. Nature 421(6920):245–249
Dickens GR (2003) Rethinking the global carbon cycle with a large, dynamic and microbially mediated gas hydrate capacitor. Earth Planet Sci Lett 213:169–183
Elderfield H, Ferretti P, Greaves M, Crowhurst S, McCave IN, Hodell D, Piotrowski AM (2012) Evolution of ocean temperature and ice volume through the mid-Pleistocene climate transition. Science 337(6095):704–709
Emiliani C (1955) Pleistocene temperatures. J Geol 63:538–578
Epstein S, Buchsbaum R, Lowenstam HA, Urey HC (1953) Revised carbonate-water isotopic temperature scale. Geol Soc Am Bull 64:1315–1325
Foster GL, Rae JW (2016) Reconstructing ocean pH with boron isotopes in foraminifera. Annu Rev Earth Planet Sci 44:207–237
Gagan MK, Ayliffe LK, Hopley D, Cali JA, Mortimer GE, Chappell J, McCulloch MT, Head MJ (1998) Temperature and surface-ocean water balance of the mid-Holocene tropical western Pacific. Science 279:1014–1018
Goldstein SL, Hemming SR (2003) Long-lived isotopic tracers in oceanography, paleoceanography, and ice-sheet dynamics. In: Elderfield H (ed) The oceans and marine geochemistry, vol 6, pp 453–489
Güdel M (2011) Faint young sun paradox. In: Encyclopedia of astrobiology. Springer, Berlin/Heidelberg, pp 577–580
Hays JD, Imbrie J, Shackleton NJ (1976) Variations in the Earth's orbit: pacemaker of the ice ages. Science 194:1121–1132
Hemming S (2004) Heinrich events: massive late Pleistocene detritus layers of the North Atlantic and their global climate imprint. Rev Geophys 42:RG1005. https://doi.org/10.1029/2003RG000128
Henderson GM (2002) New oceanic proxies for paleoclimate. Earth Planet Sci Lett 203(1):1–13
Henry LG, McManus JF, Curry WB, Roberts NL, Piotrowski AM, Keigwin LD (2016) North Atlantic ocean circulation and abrupt climate change during the last glaciation. Science 353(6298):470–474
Hughen KA, Eglinton TI, Xu L, Makou M (2004) Abrupt tropical vegetation response to rapid climate changes. Science 304:1955–1959
Imbrie J, Kipp NG (1971) A new micropaleontological method for quantitative paleoclimatology: application to a late Pleistocene Caribbean core. In: Turekian K (ed) The late Cenozoic ice ages. Yale University Press, New Haven/London, pp 71–181
Jouzel J, Masson-Delmotte V, Cattani O, Dreyfus G, Falourd S, Hoffmann G, Minster B, Nouet J, Barnola JM, Chappellaz J, Fischer H (2007) Orbital and millennial Antarctic climate variability over the past 800,000 years. Science 317:793–796
Katz ME, Cramer BS, Franzese A, Hönisch B, Miller KG, Rosenthal Y, Wright JD (2010) Traditional and emerging geochemical proxies in foraminifera. J Foraminifer Res 40(2):165–192
Kump LR, Arthur MA (1999) Interpreting carbon-isotope excursions: carbonates and organic matter. Chem Geol 161:181–198
Kump LR, Brantley SL, Arthur MA (2000) Chemical weathering, atmospheric CO_2, and climate. Annu Rev Earth Planet Sci 28:611–667
Lambert F, Delmonte B, Petit JR, Bigler M, Kaufmann PR, Hutterli MA, Stocker TF, Ruth U, Steffensen JP, Maggi V (2008) Dust-climate couplings over the past 800,000 years from the EPICA Dome C ice core. Nature 452(7187):616–619
Lea DW (2014) Elemental and isotopic proxies of past ocean temperatures. In: Holland HD, Turekian KK (eds) Treatise on geochemistry, vol 8, 2nd edn. Elsevier, Oxford, pp 373–397
Lea DW, Mashiotta TA, Spero HJ (1999) Controls on magnesium and strontium uptake in planktonic foraminifera determined by live culturing. Geochim Cosmochim Acta 63(16):2369–2379
Lear CH, Bailey TR, Pearson PN, Coxall HK, Rosenthal Y (2008) Cooling and ice growth across the Eocene-Oligocene transition. Geology 36(3):251–254
Lippold J, Grützner J, Winter D, Lahaye Y, Mangini A, Christl M (2009) Does sedimentary $^{231}Pa/^{230}Th$ from the Bermuda Rise monitor past Atlantic meridional overturning circulation? Geophys Res Lett 36: L12601. https://doi.org/10.1029/2009GL038068
Lisiecki LE, Raymo ME (2005) A Pliocene–Pleistocene stack of 57 globally distributed benthic $\delta^{18}O$ records. Paleoceanography 20:PA1003. https://doi.org/10.1029/2004PA001071
Loulergue L, Schilt A, Spahni R, Masson-Delmotte V, Blunier T, Lemieux B, Barnola JM, Raynaud D, Stocker TF, Chappellaz J (2008) Orbital and millennial-scale features of atmospheric CH_4 over the past 800,000 years. Nature 453:383–386
Lüthi D, Le Floch M, Bereiter B, Blunier T, Barnola JM, Siegenthaler U, Raynaud D, Jouzel J, Fischer H, Kawamura K, Stocker TF (2008) High-resolution carbon dioxide concentration record 650,000–800,000 years before present. Nature 453(7193):379–382
Lynch-Stieglitz J, Fairbanks RG (1994) A conservative tracer for glacial ocean circulation from carbon isotope and paleonutrient measurements in benthic foraminifera. Nature 369:308–310
Marchal O, Francois R, Stocker TF, Joos F (2000) Ocean thermohaline circulation and sedimentary $^{231}Pa/^{230}Th$ ratio. Paleoceanography 15:625–641
McManus JF, Francois R, Gherardi J-M, Keigwin LD, Brown-Leger S (2004) Collapse and rapid resumption of Atlantic meridional circulation linked to deglacial climate changes. Nature 428:834–837. https://doi.org/10.1038/nature02494
Milankovitch M (1941) Canon of insolation of the earth and its application to the ice ages. Royal Serbian Academy Press, Spec Pub 132, pp 1–626
North Greenland Ice Core Project Members (2004) High-resolution record of Northern Hemisphere climate extending into the last interglacial period. Nature 431:147–151
Overpeck JT, Webb T, Prentice IC (1985) Quantitative interpretation of fossil pollen spectra: dissimilarity coefficients and the method of modern analogs. Quat Res 23(1):87–108
Palmer MR, Elderfield H (1986) Rare earth elements and neodymium isotopes in ferromanganese oxide coatings of Cenozoic foraminifera from the Atlantic Ocean. Geochim Cosmochim Acta 50(3):409–417
Prahl FG, Wakeham SG (1987) Calibration of unsaturation patterns in long-chain ketone compositions for palaeotemperature assessment. Nature 330(6146):367–369
Prothero DR (1994) The Eocene-Oligocene transition: paradise lost. Columbia University Press, New York
Raymo ME, Mitrovica JX, O'Leary MJ, DeConto RM, Hearty PJ (2011) Departures from eustasy in Pliocene sea-level records. Nat Geosci 4(5):328–332
Royer DL, Berner RA, Montañez IP, Tabor NJ, Beerling DJ (2004) CO_2 as a primary driver of Phanerozoic climate. GSA Today 14(3):4–10
Ruddiman WF (2013) Earth's climate past and future, 3rd edn. WH Freeman and Company, New York
Rutberg RL, Hemming SR, Goldstein SL (2000) Reduced North Atlantic deep water flux to the glacial Southern Ocean inferred from neodymium isotope ratios. Nature 405:935–938
Rutherford S, D'Hondt S, Prell WL (1999) Environmental controls on the geographic distribution of zooplankton diversity. Nature 400:749–753
Schefuß E, Schouten S, Schneider R (2005) Climatic controls on central African hydrology during the last 20,000 years. Nature 437:1003–1006
Schmidt MW, Vautravers MJ, Spero HJ (2006) Rapid subtropical North Atlantic salinity oscillations across Dansgaard-Oeschger cycles. Nature 443(7111):561–564
Schouten S, Hopmans EC, Schefuß E, Damste JSS (2002) Distributional variations in marine crenarchaeotal membrane lipids: a new tool for reconstructing ancient sea water temperatures? Earth Planet Sci Lett 204(1):265–274

Shackleton NJ (1967) Oxygen isotope analyses and Pleistocene temperatures re-assessed. Nature 215:15–17
Sigman DM, Karsh KL, Casciotti KL (2009) Nitrogen isotopes in the ocean. In: Steele JH (ed) Encyclopedia of ocean sciences, 2nd edn. Academic, London, pp 40–54
Sigman DM, Hain MP, Haug GH (2010) The polar ocean and glacial cycles in atmospheric CO_2 concentration. Nature 466(7302):47–55
Thomas DJ, Zachos JC, Bralower TJ, Thomas E, Bohaty S (2002) Warming the fuel for the fire: evidence for the thermal dissociation of methane hydrate during the Paleocene–Eocene thermal maximum. Geology 30:1067–1070
Tierney JE, Smerdon JE, Anchukaitis KJ, Seager R (2013) Multidecadal variability in East African hydroclimate controlled by the Indian Ocean. Nature 493(7432):389–392
Urey HC (1947) The thermodynamic properties of isotopic substances. J Chem Soc 1947:562–581
Zachos J, Pagani M, Sloan L, Thomas E, Billups K (2001) Trends, rhythms, and aberrations in global climate 65 Ma to present. Science 292:686–693
Zachos JC, Dickens GR, Zeebe RE (2008) An early Cenozoic perspective on greenhouse warming and carbon-cycle dynamics. Nature 451(7176):279–283

Paleoenvironments

B. D. A Naafs and R. D. Pancost
Organic Geochemistry Unit, School of Chemistry, University of Bristol and Cabot Institute, Bristol, UK

Definition

A paleoenvironment is an environment that has been preserved in a natural archive, such as marine sediments and rocks, at some time in the past. However, most paleoenvironments are not preserved, and therefore, a major question is how to decipher these ancient environments using the limited archives that remain. Using a range of (geochemical but also sedimentological and biological) techniques, we can use natural archives to reconstruct not just climatological parameters such as the temperature or precipitation but also a wide variety of environmental parameters such as oxygen content of the atmosphere or pH of seawater. Over the last 40 years, scientists have been able to provide detailed reconstructions of the paleoenvironment on earth ranging from the more recent Pleistocene ice ages to the early Paleozoic and even Precambrian.

Introduction

Paleoenvironments that are commonly studied from a geochemical perspective include a wide variety of marine, lacustrine, and freshwater systems. Material can be obtained from fieldwork and using rock outcrops, which provide valuable information of ancient paleoenvironments throughout the Phanerozoic (e.g., Song et al. 2013) and Proterozoic (e.g., Arnold et al. 2004). For continuous high-resolution records from the late Cretaceous and Cenozoic, material obtained by the Integrated Ocean Discovery Project (IODP) is often used to provide a detailed insight into ancient marine environments (e.g., Zachos et al. 2001) but also terrestrial environments via geochemical signals delivered to these marine archives (e.g., de Menocal 1995; Peterson et al. 2000). Although often more challenging to exploit due to the difficulty in developing age models, terrestrial archives are also incredibly useful and include sabkhas (McKenzie 1981), paleosols (Quade et al. 2013), peat (Barber et al. 2003), and loess deposits (Zhisheng et al. 2005).

Geochemists evaluate the distributions and isotopic compositions of bulk samples as well as that of major, minor, and trace elements (e.g., S, B, Li, Cu, Ca) in these samples. More recently the distribution and especially the carbon and increasingly hydrogen isotopic compositions of organic lipids are determined in natural archives. These distributions are then compared with those observed in modern systems to reconstruct key environmental parameters. Examples are the various organic and inorganic proxies used to reconstruct atmospheric CO_2 levels (Freeman and Hayes 1992; Jasper et al. 1994; Foster 2008; Bolton et al. 2016), sea surface temperatures (Brassell et al. 1986; Elderfield and Ganssen 2000; Ghosh et al. 2006), hydrological cycle (Kohn and Law 2006; Sachse et al. 2012), global ice volume (Hays et al. 1976; Elderfield et al. 2012), dominant vegetation type (Cerling et al. 1997), and oceanic anoxia (Summons and Powell 1986; Emerson and Huested 1991; Wilkin et al. 1996).

For many parameters, a range of complimentary proxies exist. For example, the state of oceanic anoxia can be inferred by studying sulfur speciation, trace metal abundance, and isotope ratios, as well as through the presence of diagnostic biomarkers such as lycopene and isorenieratane. Together these allow geochemist to carefully reconstruct changes in the state of oxygenation of the ocean during the geological past.

Over the last 40 years, geochemists have generated a wide range of paleoenvironmental reconstructions, providing insight into specific ancient depositional environments, better understanding of the causes and consequences of biotic events in Earth history, and a better understanding about the interactions and feedbacks in the Earth system. In addition, a thorough understanding of the paleoenvironment enhances our ability to recover valuable resources. In particular, paleoenvironmental reconstructions have been an essential component in our exploration for fossil fuels and understanding of conditions leading to fossil fuel formation (Bechtel et al. 2012; Fustic et al. 2012). The conditions under which the source organic matter was deposited and the fuels were generated are largely defined by geochemical parameters. Similarly, some types of ore deposits arise from post-depositional alteration of material deposited in a particular

depositional environment or under particular environmental conditions such as an anoxic water column (Southam and Beveridge 1994; Spirakis 1996).

Complicating Factors

Fully characterizing a particular paleoenvironment, however, from the data available in the sediments is not a simple task. Geochemical parameters can be altered by secondary (postdepositional) processes during diagenesis, such as selective preservation (Zonneveld et al. 2010) in the case of lipid biomarkers or recrystallization of calcite (Fantle and DePaolo 2007), that biases the information preserved in the geological record. For example, the lipid distribution and its isotopic composition in sediments and rocks can be altered upon burial due diagenesis and thermal maturation (Seifert and Moldowan 1980; Schimmelmann et al. 2006). In addition, unique and complex conditions during deposition that have no obvious modern analogue can also contribute to the difficulty of deciphering the significance and meaning of the geochemical signatures in the rock record. For example, sea surface and terrestrial temperatures during greenhouse periods in the geological past were likely higher than any were on earth at present, and tropical temperatures persisted far into the high latitudes (e.g., Bijl et al. 2009; Pross et al. 2012; Naafs and Pancost 2016). These paleoenvironments lack a modern analogue.

In addition, the chemical composition of seawater has a strong influence on many inorganic (calcite-based) proxies such as $\delta^{18}O$, Mg/Ca, and B isotopes. However the seawater composition has changed over (geological) time (Ridgwell 2005; Coggon et al. 2010). As the exact chemistry of past seawater at a particular point in the geological past is poorly constrained beyond the Neogene (~20 Myr), it becomes difficult to interpret these proxy estimates in deep time, and assumptions have to be made regarding the composition of past seawater.

Another problem is the complexity of the geochemical signature in the rock record. The mixing of sediments and source materials in any environment produces a complex geochemical signature, making it difficult to tease apart individual parameters.

Recent Developments

Recent developments include new geochemical approaches to reconstruct marine and terrestrial temperatures using both organic and inorganic proxies. The organic TEX_{86} and MBT/CBT paleothermometers are based on the distribution of archaeal and bacterial membrane lipids and can provide information about past sea surface temperatures, past mineral soil and peat pH, and overlying mean annual temperature during the last ~200 million years (Weijers et al. 2007; Schouten et al. 2013; Naafs et al. 2017; Robinson et al. 2017). In addition, the clumped isotope composition (Δ_{47}) of biogenic calcite and soil carbonates (Quade et al. 2013) is increasingly used to reconstruct both ocean and soil temperature in the geological past. Together these proxies demonstrate that during the early Eocene, a period characterized by high pCO_2, the mid- and high latitudes were characterized by a subtropical climate with temperatures and vegetation currently only found at the low latitudes (Keating-Bitonti et al. 2011; Pross et al. 2012).

The ongoing development of the boron isotope-pH proxy (Foster and Rae 2015), which can be used to reconstruct pCO_2 if other variables can be constrained, led to detailed reconstructions of atmospheric CO_2 during key periods of the Cenozoic such as the late Pliocene/early Pleistocene (Martinez-Boti et al. 2015).

Over the last few years, a number of studies used a range of geochemical proxies such as calcium, lithium, and osmium stable isotopes to reconstruct terrestrial weathering rates during key events of the Mesozoic and Cenozoic such as the Cretaceous oceanic anoxic events (Blättler et al. 2011; Pogge von Strandmann et al. 2013) or Paleocene/Eocene thermal maximum (Dickson et al. 2015).

In addition, integration of geochemical analyses and results from climate and/or biogeochemical modeling experiments has greatly advanced our understanding of the paleoenvironment. The proxy record has often poor spatial coverage but can provide crucial constrains for global or regional high-resolution climate and biogeochemical computer models. Examples are the Cretaceous oceanic anoxic events where geochemical proxy data of oceanic anoxia was used to constrain biogeochemical model results and provided novel insights into the extent of bottom water anoxia during these events (Monteiro et al. 2012) or the early Eocene where geochemical temperature proxy data was used to constrain general circulation models (Lunt et al. 2012).

Summary

Using a wide range of inorganic and organic geochemical techniques, scientists have been able to reconstruct the paleoenvironment of a large part of the Phanerozoic. These geochemical studies in a wide variety of paleoenvironments provide important information about the processes and mechanisms that operate in Earth's climate system, which is vital for the petroleum and mining industries.

References

Arnold GL, Anbar AD, Barling J, Lyons TW (2004) Molybdenum isotope evidence for widespread anoxia in mid-proterozoic oceans. Science 304:87–90. https://doi.org/10.1126/science.1091785

Barber KE, Chambers FM, Maddy D (2003) Holocene palaeoclimates from peat stratigraphy: macrofossil proxy climate records from three oceanic raised bogs in England and Ireland. Quat Sci Rev 22:521–539. https://doi.org/10.1016/S0277-3791(02)00185-3

Bechtel A, Jia J, Strobl SAI, Sachsenhofer RF, Liu Z, Gratzer R, Püttmann W (2012) Palaeoenvironmental conditions during deposition of the Upper Cretaceous oil shale sequences in the Songliao Basin (NE China): implications from geochemical analysis. Org Geochem 46:76–95. https://doi.org/10.1016/j.orggeochem.2012.02.003

Bijl PK, Schouten S, Sluijs A, Reichart G-J, Zachos JC, Brinkhuis H (2009) Early Palaeogene temperature evolution of the southwest Pacific Ocean. Nature 461:776–779. https://doi.org/10.1038/nature08399

Blättler CL, Jenkyns HC, Reynard LM, Henderson GM (2011) Significant increases in global weathering during Oceanic Anoxic Events 1a and 2 indicated by calcium isotopes. Earth Planet Sci Lett 309:77–88. https://doi.org/10.1016/j.epsl.2011.06.029

Bolton CT, Hernandez-Sanchez MT, Fuertes M-A, Gonzalez-Lemos S, Abrevaya L, Mendez-Vicente A, Flores J-A et al (2016) Decrease in coccolithophore calcification and CO_2 since the middle Miocene. Nat Commun 7. https://doi.org/10.1038/ncomms10284

Brassell SC, Eglinton G, Marlowe IT, Pflaumann U, Sarnthein M (1986) Molecular stratigraphy: a new tool for climatic assessment. Nature 320:129–133. https://doi.org/10.1038/320129a0

Cerling TE, Harris JM, MacFadden BJ, Leakey MG, Quade J, Eisenmann V, Ehleringer JR (1997) Global vegetation change through the Miocene/Pliocene boundary. Nature 389:153–158. https://doi.org/10.1038/38229

Coggon RM, Teagle DAH, Smith-Duque CE, Alt JC, Cooper MJ (2010) Reconstructing past seawater Mg/Ca and Sr/Ca from mid-ocean ridge flank calcium carbonate veins. Science 327:1114–1117. https://doi.org/10.1126/science.1182252

de Menocal PB (1995) Plio-Pleistocene African climate. Science 270:53–59. https://doi.org/10.1126/science.270.5233.53

Dickson AJ, Cohen AS, Coe AL, Davies M, Shcherbinina EA, Gavrilov YO (2015) Evidence for weathering and volcanism during the PETM from Arctic Ocean and Peri-Tethys osmium isotope records. Palaeogeogr Palaeoclimatol Palaeoecol 438:300–307. https://doi.org/10.1016/j.palaeo.2015.08.019

Elderfield H, Ganssen G (2000) Past temperature and $\delta^{18}O$ of surface ocean waters inferred from foraminiferal Mg/Ca ratios. Nature 405:442–445. https://doi.org/10.1038/35013033

Elderfield H, Ferretti P, Greaves M, Crowhurst S, McCave IN, Hodell D, Piotrowski AM (2012) Evolution of ocean temperature and ice volume through the mid-Pleistocene climate transition. Science 337:704–709. https://doi.org/10.1126/science.1221294

Emerson SR, Huested SS (1991) Ocean anoxia and the concentrations of molybdenum and vanadium in seawater. Mar Chem 34:177–196. https://doi.org/10.1016/0304-4203(91)90002-E

Fantle MS, DePaolo DJ (2007) Ca isotopes in carbonate sediment and pore fluid from ODP Site 807A: the Ca^{2+}(aq)–calcite equilibrium fractionation factor and calcite recrystallization rates in Pleistocene sediments. Geochim Cosmochim Acta 71:2524–2546. https://doi.org/10.1016/j.gca.2007.03.006

Foster GL (2008) Seawater pH, pCO_2 and [CO_3^{2-}] variations in the Caribbean Sea over the last 130 kyr: a boron isotope and B/Ca study of planktic foraminifera. Earth Planet Sci Lett 271:254–266. https://doi.org/10.1016/j.epsl.2008.04.015

Foster GL, Rae JWD (2015) Reconstructing ocean pH with boron isotopes in foraminifera. Annu Rev Earth Planet Sci. https://doi.org/10.1146/annurev-earth-060115-012226

Freeman KH, Hayes JM (1992) Fractionation of carbon isotopes by phytoplankton and estimates of ancient CO_2 levels. Glob Biogeochem Cycles 6:185–198. https://doi.org/10.1029/92gb00190

Fustic M, Hubbard SM, Spencer R, Smith DG, Leckie DA, Bennett B, Larter S (2012) Recognition of down-valley translation in tidally influenced meandering fluvial deposits, Athabasca Oil Sands (Cretaceous), Alberta, Canada. Mar Pet Geol 29:219–232. https://doi.org/10.1016/j.marpetgeo.2011.08.004

Ghosh P, Adkins J, Affek H, Balta B, Guo W, Schauble EA, Schrag D et al (2006) ^{13}C–^{18}O bonds in carbonate minerals: a new kind of paleothermometer. Geochim Cosmochim Acta 70:1439–1456. https://doi.org/10.1016/j.gca.2005.11.014

Hays JD, Imbrie J, Shackleton NJ (1976) Variations in the Earth's orbit: pacemaker of the ice ages. Science 194:1121–1132. https://doi.org/10.1126/science.194.4270.1121

Jasper JP, Hayes JM, Mix AC, Prahl FG (1994) Photosynthetic fractionation of ^{13}C and concentrations of dissolved CO_2 in the central equatorial Pacific during the last 255,000 years. Paleoceanography 9:781–798. https://doi.org/10.1029/94PA02116

Keating-Bitonti CR, Ivany LC, Affek HP, Douglas P, Samson SD (2011) Warm, not super-hot, temperatures in the early Eocene subtropics. Geology 39:771–774. https://doi.org/10.1130/G32054.1

Kohn MJ, Law JM (2006) Stable isotope chemistry of fossil bone as a new paleoclimate indicator. Geochim Cosmochim Acta 70:931–946. https://doi.org/10.1016/j.gca.2005.10.023

Lunt DJ, Dunkley Jones T, Heinemann M, Huber M, LeGrande A, Winguth A, Loptson C et al (2012) A model–data comparison for a multi-model ensemble of early Eocene atmosphere–ocean simulations: EoMIP. Clim Past 8:1717–1736. https://doi.org/10.5194/cp-8-1717-2012

Martinez-Boti MA, Foster GL, Chalk TB, Rohling EJ, Sexton PF, Lunt DJ, Pancost RD et al (2015) Plio-Pleistocene climate sensitivity evaluated using high-resolution CO_2 records. Nature 518:49–54. https://doi.org/10.1038/nature14145

McKenzie JA (1981) Holocene dolomitization of calcium carbonate sediments from the coastal sabkhas of Abu Dhabi, U.A.E.: a stable isotope study. J Geol 89:185–198

Monteiro FM, Pancost RD, Ridgwell A, Donnadieu Y (2012) Nutrients as the dominant control on the spread of anoxia and euxinia across the Cenomanian-Turonian oceanic anoxic event (OAE2): model-data comparison. Paleoceanography 27:PA4209. https://doi.org/10.1029/2012pa002351

Naafs BDA, Pancost RD (2016) Sea-surface temperature evolution across Aptian Oceanic Anoxic Event 1a. Geology 44:959–962. https://doi.org/10.1130/G38575.1

Naafs BDA, Inglis GN, Zheng Y, Amesbury MJ, Biester H, Bindler R, Blewett J et al (2017) Introducing global peat-specific temperature and pH calibrations based on brGDGT bacterial lipids. Geochim Cosmochim Acta 208:285–301. https://doi.org/10.1016/j.gca.2017.01.038

Peterson LC, Haug GH, Hughen KA, Röhl U (2000) Rapid changes in the hydrologic cycle of the tropical Atlantic during the last glacial. Science 290:1947–1951. https://doi.org/10.1126/science.290.5498.1947

Pogge von Strandmann PAE, Jenkyns HC, Woodfine RG (2013) Lithium isotope evidence for enhanced weathering during Oceanic Anoxic Event 2. Nat Geosci 6:668–672. https://doi.org/10.1038/ngeo1875

Pross J, Contreras L, Bijl PK, Greenwood DR, Bohaty SM, Schouten S, Bendle JA et al (2012) Persistent near-tropical warmth on the Antarctic continent during the early Eocene epoch. Nature 488:73–77. https://doi.org/10.1038/nature11300

Quade J, Eiler J, Daëron M, Achyuthan H (2013) The clumped isotope geothermometer in soil and paleosol carbonate. Geochim Cosmochim Acta 105:92–107. https://doi.org/10.1016/j.gca.2012.11.031

Ridgwell A (2005) A mid Mesozoic revolution in the regulation of ocean chemistry. Mar Geol 217:339–357. https://doi.org/10.1016/j.margeo.2004.10.036

Robinson SA, Ruhl M, Astley DL, Naafs BDA, Farnsworth AJ, Bown PR, Jenkyns HC et al (2017) Early Jurassic North Atlantic sea-surface temperatures from TEX_{86} palaeothermometry. Sedimentology 64:215–230. https://doi.org/10.1111/sed.12321

Sachse D, Billault I, Bowen GJ, Chikaraishi Y, Dawson TE, Feakins SJ, Freeman KH et al (2012) Molecular paleohydrology: interpreting the hydrogen-isotopic composition of lipid biomarkers from photosynthesizing organisms. Annu Rev Earth Planet Sci 40:221–249. https://doi.org/10.1146/annurev-earth-042711-105535

Schimmelmann A, Sessions AL, Mastalerz M (2006) Hydrogen isotopic (D/H) composition of organic matter during diagenesis and thermal maturation. Annu Rev Earth Planet Sci 34:501–533. https://doi.org/10.1146/annurev.earth.34.031405.125011

Schouten S, Hopmans EC, Sinninghe Damsté JS (2013) The organic geochemistry of glycerol dialkyl glycerol tetraether lipids: a review. Org Geochem 54:19–61. https://doi.org/10.1016/j.orggeochem.2012.09.006

Seifert WK, Moldowan JM (1980) The effect of thermal stress on source-rock quality as measured by hopane stereochemistry. Phys Chem Earth 12:229–237. https://doi.org/10.1016/0079-1946(79)90107-1

Song H, Wignall PB, Tong J, Yin H (2013) Two pulses of extinction during the Permian-Triassic crisis. Nat Geosci 6:52–56. https://doi.org/10.1038/ngeo1649.

Southam G, Beveridge TJ (1994) The in vitro formation of placer gold by bacteria. Geochim Cosmochim Acta 58:4527–4530. https://doi.org/10.1016/0016-7037(94)90355-7

Spirakis CS (1996) The roles of organic matter in the formation of uranium deposits in sedimentary rocks. Ore Geol Rev 11:53–69. https://doi.org/10.1016/0169-1368(95)00015-1

Summons RE, Powell TG (1986) Chlorobiaceae in Palaeozoic seas revealed by biological markers, isotopes and geology. Nature 319:763–765. https://doi.org/10.1038/319763a0

Weijers JWH, Schouten S, van den Donker JC, Hopmans EC, Sinninghe Damsté JS (2007) Environmental controls on bacterial tetraether membrane lipid distribution in soils. Geochim Cosmochim Acta 71:703–713. https://doi.org/10.1016/j.gca.2006.10.003

Wilkin RT, Barnes HL, Brantley SL (1996) The size distribution of framboidal pyrite in modern sediments: an indicator of redox conditions. Geochim Cosmochim Acta 60:3897–3912. https://doi.org/10.1016/0016-7037(96)00209-8

Zachos J, Pagani M, Sloan L, Thomas E, Billups K (2001) Trends, rhythms, and aberrations in global climate 65 Ma to present. Science 292:686–693. https://doi.org/10.1126/science.1059412

Zhisheng A, Yongsong H, Weiguo L, Zhengtang G, Clemens S, Li L, Prell W et al (2005) Multiple expansions of C4 plant biomass in East Asia since 7 Ma coupled with strengthened monsoon circulation. Geology 33:705–708. https://doi.org/10.1130/g21423.1

Zonneveld KAF, Versteegh GJM, Kasten S, Eglinton TI, Emeis KC, Huguet C, Koch BP et al (2010) Selective preservation of organic matter in marine environments; processes and impact on the sedimentary record. Biogeosciences 7:483–511. https://doi.org/10.5194/bg-7-483-2010

Paleoproductivity

Gerold Wefer
MARUM – Center for Marine Environmental Sciences, University of Bremen, Bremen, Germany

Definition

Two factors are important in the reconstruction of past productivity:

1. The biogenic flux (organic and inorganic biogenic material formed at the surface that sinks to the deep ocean)
2. The availability of nutrients, especially phosphate and nitrogen

Various methods are employed for reconstructing past productivity in the ocean. Paleoproductivity is not directly measureable so it has to be derived from "surrogate data" that are closely related to the environmental parameters. These are thus referred to as proxy variables or, for short, proxies (see Wefer et al. 1999 for a review). A proxy is a measureable parameter for variables that were observable in the past (but no longer are today). As a general rule, paleoproductivity proxies record conditions in the sunlit surface waters. There is, however, another approach for estimating productivity in surface waters from material produced on the seafloor. Herguera and Berger (1994) used the abundance of benthic foraminifera in sediments as a measure of productivity because their abundance is related to food supply, which is the amount of organic substance on the seafloor.

The first paleoproductivity reconstructions were made using the accumulation rates of organic substances in sediments (Müller and Suess 1979). Since other fluxes have also been applied, including opal, carbonate, and particulate barite, assemblages of planktonic and benthic organisms are also useful for reconstructing productivity conditions because some species occur preferentially in high-productivity conditions. Various isotope and element ratios are used for reconstructions of past primary productivity or for the availability of nutrients. These include the stable carbon isotopic composition of dissolved inorganic carbon in the water column (13C/12C, expressed as δ13C). In the present-day ocean, the δ13C values of inorganic carbon are negatively correlated with nitrate and phosphate. The ratio of cadmium to calcium is used as a tracer for the phosphate content of surface waters. The nitrogen isotopes, 15 N/14 N, are also employed. These document the utilization of nitrate relative to its availability.

High-productivity regions in today's ocean are mainly located in the temperate to high-latitude regions. Wind-driven mixing, and thus the supply of nutrients from deeper waters into the surface layer, is greatest in these regions. Other high-productivity areas include the equatorial and coastal upwelling regions, where divergence also leads to the injection of deeper, more nutrient-rich waters. The upper continental margins record the highest deposition of organic carbon. Conditions there are favorable for incorporating organic material quickly into the sediment, and these regions often have low oxygen content.

Proxies

Deposition of organic material and other biogenic sediment components.

The accumulation of any sedimentary component of biogenic origin reflects a balance between production in surface waters, dilution by other sedimentary components, and dissolution/degradation both during export through the water column and in shallow sediments. There is a general relationship between productivity in the surface waters and the deposition and accumulation of organic carbon in the underlying sediments. This relationship, however, is influenced by a number of other factors and thus is not a quantitative measure. For example, organic materials can also be introduced from the land through dust or rivers. The distinction between marine and terrestrial material can be determined using carbon isotope ratios or biomarkers. The accumulation of organic material is influenced by differing decomposition rates of organic material on the way from the surface down to the sediments. Substantial changes also occur at the sediment surface. Accumulation is also affected by oxygen content and horizontal transport. As an order of magnitude, it can be assumed that only 10% of the surface production reaches the sediments, and of that amount only 10% is preserved. Because of its long residence time at the sediment surface, a large proportion of the organic carbon is broken down by bacteria. This is initially accomplished using free oxygen, and later by the reduction of nitrate, manganese and iron oxides, and dissolved sulfate.

Organism Assemblages

A number of different organism assemblages (i.e., the relative abundances of certain species within a population of one type of organism) are employed to reconstruct past productivity. Sediment traps may be used to establish correlations between the flux of organic carbon and assemblages of particular groups of organisms (e.g., phytoplankton or zooplankton). Isotope tracers such as 230Th and 210Pb are used to normalize the particle flux. Opaline siliceous fossil assemblages are often used, as they occur predominantly in high-productivity regions. These include the skeletons of diatoms, radiolarians, and silicoflagellates. The most bountiful depositional region for oceanic opal is in the Southern Ocean. When using opaline shells, we must keep in mind that they are individual proxies for the productivity of diatoms, radiolarians, or silicoflagellates and not necessarily for the total paleoproductivity. A number of transfer functions have been applied to the reconstruction of paleoproductivity using calcareous microfossil assemblages, and these are particular applicable in tropical and subtropical areas.

Stable Isotopes

The ratios of stable carbon and nitrogen isotopes are proxies for nutrients. Nutrient content is deduced from the difference in δ13C between shallow-living versus deep-living planktonic foraminifera in the surface waters and between planktonic and benthic foraminifera. Reconstructions based on δ13C values from foraminifera require additional information, for example, the calcification depths of planktonic foraminifera or the depth of living benthic foraminifera within the sediments or on the sediment surface. For the nitrogen isotopes, fractionation occurs during the uptake of nitrogen by phytoplankton, whereby 14 N is preferentially incorporated. The methodology is being constantly improved. For the study of nitrogen isotopes, not only is the total organic material analyzed, but also individual products of organisms, for example, of diatoms (Studer et al. 2015).

Trace Elements

Selected trace elements, including uranium, vanadium, and molybdenum, as well as cadmium and barium, are also used as paleoproductivity proxies. In order to apply these, their properties must be very well understood, for example, their dissolution properties under oxidizing and reducing conditions.

Reconstructions

It is difficult to make general statements about productivity in the past. The system is extremely complex, and different parts of the oceans react differently to climate and circulation changes. This is also because there is no single proxy that can be used to directly determine paleoproductivity. It is always necessary to use a number of different proxies together, which are sometimes not in agreement with each other, in order to make a statement. For example, during the glacials, high amounts of organic material are also deposited off Angola and Namibia, but with less opal than in warmer periods. This is explained by a nutrient change in upwelled waters, between glacial and interglacial periods. Changes in the (sub)antarctic silica distribution system seem to be involved (Berger et al. 2010).

Throughout Earth's history, there have been many high-productivity events that have been viewed in connection with the development of CO_2 in the atmosphere. A conspicuous example is seen in the oceanic anoxic events (OAE) of the Cretaceous, documented by alternating organic-rich and carbonate-rich facies (Arthur et al. 1985). These have a connection to orbital cycles. The high rates of deposition for organic material during the OAEs, however, are also related to low oxygen conditions in the deep water. A possible relationship to increased volcanic activity is also being debated.

There is also presently an intensive debate over the possibility of a connection between the low CO_2 content of the atmosphere and increased productivity during more recent Pleistocene glacial periods. In some regions, higher productivity observed during glacial periods has been explained by stronger trade winds. Other factors, however, have to be

considered for these productivity changes, including increased nutrient input from remote regions via ocean circulation (Jakob et al. 2016). The Antarctic, one of the most productive areas in the ocean, is viewed as a key region. Not all of the available macronutrients are being used there today. It has been suggested that this may be due to a lack of trace element micronutrients essential for phytoplankton growth (iron hypothesis, Martin 1990). This hypothesis has been resurrected by Abelmann et al. (2015) who, based on sediment-core data from the Atlantic sector of the Southern Ocean, inferred a seasonal sea-ice zone with a highly productive system for the glacials, characterized by diatoms and a high proportion of organic substance sinking into deeper water. In this hypothesis, iron is enriched by dust input on the ice surface during periods of ice cover and is released when it melts into the stratified surface waters.

A further question is how the productivity of the ocean reacts to global warming. Based on observation data, Bakun (1990) suggests that global upwelling intensifies with warming, resulting in fertility increases. This has been confirmed off northwest Africa, for example (McGregor et al. 2007). But when different regions are compared, there is often no recognizable common pattern. Narayan et al. (2010), for example, identified linear trends of upwelling intensity occurring from 1960 to 2012 in the four important regions off the coasts of NW Africa, Namibia, California, and Peru. Their results support the hypothesis of Bakun (1990) that coastal upwelling intensity has strengthened since 1960 in line with increasing atmospheric CO_2 values. They also indicate, however, that different datasets produce different results. More recent modeling studies provide evidence that by the end of this century, coastal upwelling will begin earlier and be more intense in the high but not in low latitudes (Wang et al. 2015).

Summary

Paleoproductivity describes fluctuations in biological productivity in the geological past, which can be qualitatively and semiquantitatively reconstructed using information gleaned from marine sediment archives. Knowledge of past biological productivity in the oceans is of great interest because it exhibits (proxy variables, short proxy) close ties to modern productivity (ecosystems in the ocean), to oceanic circulation with respect to the availability of nutrients, and to the carbon cycle vis-a-vis the removal of CO_2 from surface waters (and therefore from the atmosphere). Furthermore, organic matter deposited in the sediments is the origin of hydrocarbons. This entry gives an overview on proxies used for reconstructions and examples of paleoproductivity patterns in the past.

Cross-References

- ▶ Biomarker: Assessment of Thermal Maturity
- ▶ Biomarkers: Coal
- ▶ Biomarkers: Petroleum
- ▶ Carbon Isotopes
- ▶ Iron
- ▶ Marine Sediment
- ▶ Molybdenum
- ▶ Nitrogen
- ▶ Nitrogen Isotopes
- ▶ Organic Geochemistry
- ▶ Paleoclimatology
- ▶ Phosphorus
- ▶ Vanadium

References

Abelmann A, Gersonde R, Knorr G, Zhang X, Chapligin B, Maier E, Esper O, Friedrichsen H, Lohmann G, Meyer H, Tiedemann R (2015) The seasonal sea-ice zone in the glacial Southern Ocean as a carbon sink. Nat Commun 6(8136):1–12

Arthur MA, Dean WE, Schlanger SO (1985) Variations in the global carbon cycle during the Cretaceous related to climate, volcanism, and changes in atmospheric CO2. In: Broecker WS, Sunquist ET (eds) The carbon cycle and atmospheric CO: natural variations Archean to present. American Geophysical Union, Washington, DC, pp 504–530

Bakun A (1990) Global climate change and intensification of coastal upwelling. Science 247(4939):198–201

Berger WH, Schulz M, Wefer G (2010) Quaternary oceans and climate change: lessons for the future? Int J Earth Sci 99:171–189

Herguera JC, Berger WH (1994) Glacial to postglacial drop in productivity in the western equatorial Pacific: Mixing rate vs. nutrient concentrations. Geology 22(7):629–632

Jakob KA, Wilson PA, Bahr A, Bolton CT, Pross J, Fiebig J, Friedrich O (2016) Plio-Pleistocene glacial-interglacial productivity changes in the eastern equatorial Pacific upwelling system. Paleoceanography 31(3):453–470

Martin JH (1990) Glacial-interglacial CO_2 change: the iron hypothesis. Paleoceanography 5(1):1–13

McGregor HV, Dima M, Fischer HW, Mulitza S (2007) Rapid 20th century increase in coastal upwelling off northwest Africa. Science 315:637–639

Müller PJ, Suess E (1979) Productivity, sedimentation rate, and sedimentary organic matter in the oceans – I. Organic carbon preservation. Deep-Sea Res 26:1347–1362

Narayan N, Paul A, Mulitza S, Schulz M (2010) Trends in coastal upwelling intensity during the late 20th century. Ocean Sci 6:815–823

Studer AS, Sigman DM, Martinez-Garcia A, Benz V, Winckler G, Kuhn G, Esper O, Lamy F, Jaccard SL, Wacker L, Oleynik S, Gersonde R, Haug GH (2015) Antarctic Zone nutrient conditions during the last two glacial cycles. Paleoceanography 30(7):845–862

Wang D, Gouhier TC, Menge BA, Ganguly AR (2015) Intensification and spatial homogenization of coastal upwelling under climate change. Nature 518:390–394

Wefer G, Berger WH, Fischer G, Bijma J (1999) Clues to ocean history – a brief overview of proxies. In: Fischer G, Wefer G (eds) Use of proxis in paleoceanography: examples from the South Atlantic. Springer, Berlin/Heidelberg, pp 1–68

Paleotemperatures

Jennifer E. Hertzberg[1] and Matthew W. Schmidt[2]
[1]Department of Marine Sciences, University of Connecticut, Groton, CT, USA
[2]Department of Ocean, Earth and Atmospheric Sciences, Old Dominion University, Norfolk, VA, USA

Definition

A paleotemperature is the temperature of a location, either on land or in the ocean, at a specific time in the geologic past. Scientists use paleothermometers to reconstruct past temperature records from archives – natural features of the Earth that preserve clues about past climate and environmental change. Examples of archives include marine and lacustrine sediment, glacial ice, and corals. Paleothermometers are often referred to as temperature proxies, which are measurable physical, geological, geochemical, or biological characteristics that get preserved in archives, standing in for instrumental measurements. Each proxy is associated with a calibration that transforms the proxy measurements into the parameter of interest, which in this case is temperature.

Scientists rely on proxy measurements from archives because direct observations of temperature extend back only as far as the middle of the nineteenth century (Smith et al. 2008). Direct temperature measurements of the ocean extend back even less. These limits to the length of instrumental records make it difficult to constrain the range of natural climate variability, the degree of twentieth century warming, and climate sensitivity to greenhouse gas forcing. Accurate paleotemperature reconstructions are the only way to extend the short observational period farther into the past.

This entry describes paleotemperature proxies from marine and terrestrial archives. The paleotemperature proxies presented here are by no means an exhaustive list, but instead highlight the geochemical proxies that are used most frequently for paleotemperature reconstructions.

Assemblages of Planktonic Foraminifera

Foraminifera are marine protozoa (unicellular zooplankton) that can either be found free-floating in the open, upper layers of the ocean (planktonic), or living on or in seafloor sediment (benthic). They secrete characteristic tests, or shells, often composed of calcium carbonate (calcite, $CaCO_3$), that accumulate on the seafloor after death. There are ~50 living species of planktonic foraminifera in the modern oceans, and they are found in diverse oceanic regions from the warm tropics to cold polar waters (Kucera 2007). The greatest planktonic species diversity can be found in the tropics, with diversity generally decreasing with increasing latitude. Differences in the species composition, or assemblage, of planktonic foraminifera contain information about the temperature of the waters they inhabit (Murray 1897). Statistical techniques can be used to determine sea surface temperature (SST) from assemblages, including transfer functions (Imbrie and Kipp 1971) and the modern analog technique (Hutson 1980; Howard and Prell 1992). Studies comparing both methods find little difference between them (Ortiz and Mix 1997), but there are limitations to the overall approach. Both methods are based on the assumption that temperature is the main control on the assemblages; other factors, such as food availability, light requirements, and ocean circulation changes can also alter species distributions (Wefer et al. 1999). Finally, there is uncertainty in relating habitat (depth and seasonal) to SST at a certain time of the year.

Mg/Ca Ratios

Mg/Ca ratios in benthic and planktonic foraminifera have become widely used proxies for reconstructing bottom and upper water column paleotemperatures, respectively. The underlying basis for Mg/Ca paleothermometry is that the substitution of Mg^{2+} for Ca^{2+} in calcite is endothermic and therefore favored at higher temperatures. As a result, the Mg/Ca ratio of foraminiferal calcite increases with increasing temperature.

The temperature dependence on Mg uptake into planktonic foraminiferal tests has been determined using culture-based, sediment trap, and core-top calibrations. Culture-based calibrations rely on growing planktonic foraminifera under controlled laboratory conditions in which the temperature is fixed independently of other environmental parameters (e.g., Nürnberg et al. 1996; Lea et al. 1999; Russell et al. 2004; Allen et al. 2016). Sediment trap calibrations measure planktonic foraminifera collected in sediment trap time series from regions with high seasonal temperature variability (e.g., Anand et al. 2003). Core-top calibrations measure Mg/Ca ratios of modern or recently deposited planktonic foraminifera from the seafloor and then calibrate the ratios against the water column temperature overlying the sediment core site based on the foraminifera's preferred depth habitat (e.g., Lea et al. 2000; Dekens et al. 2002). Core-top calibrations are used most often to determine the relationship between Mg/Ca ratios in benthic foraminifera and bottom water temperature (Rosenthal et al. 1997; Lear et al. 2002; Bryan and Marchitto 2008).

Despite differences between calibration methods, studies show that most species of planktonic foraminifera have a temperature sensitivity of a ~9–10% exponential increase in Mg/Ca per degree Celsius (Lea et al. 1999; Elderfield and

Ganssen 2000; Dekens et al. 2002; Anand et al. 2003). Culturing studies find that salinity also influences the uptake of Mg into planktonic foraminiferal tests, with Mg/Ca ratios increasing by 3–8% per salinity unit increase (Nürnberg et al. 1996; Lea et al. 1999; Hertzberg and Schmidt 2013; Hönisch et al. 2013; Allen et al. 2016). In contrast, the sensitivity of Mg/Ca to temperature in benthic foraminifera is more variable between species and may be influenced by other factors, including bottom water carbonate ion concentration (Lear et al. 2002; Elderfield et al. 2006; Bryan and Marchitto 2008). As benthic foraminifera dwell on the bottom of the ocean, where temperatures are lower than at the sea surface, their Mg/Ca ratios tend to fall on the lower end of the exponential relationship with temperature. Thus, the Mg/Ca paleothermometer for benthic foraminifera is less sensitive than for planktonic foraminifera, often making bottom water Mg/Ca-temperature estimates more difficult.

Postdepositional processes can alter Mg/Ca ratios in planktonic foraminifera because saturation with respect to calcite decreases in the ocean with increasing depth. Depth transect studies show that, in general, Mg/Ca ratios decrease with increasing water depth, especially below the regional lysocline (Brown and Elderfield 1996; Lea et al. 2000; Dekens et al. 2002; Regenberg et al. 2014). Partial dissolution of foraminifera tests can bias Mg/Ca ratios due to the heterogeneous distribution of Mg within the test and the higher solubility of Mg-rich calcite (Brown and Elderfield 1996; Dekens et al. 2002). However, methods have been developed to account for this effect (Rosenthal and Lohmann 2002; Dekens et al. 2002; Regenberg et al. 2014).

Recent advances in Mg/Ca paleothermometry include the analysis of multiple planktonic species that live at a range of depths and the analysis of individual foraminiferal tests from the same stratigraphic interval. By analyzing species with a range of depth habitats, scientists can reconstruct past changes in the vertical temperature profile of the ocean (Schmidt et al. 2012; Parker et al. 2015). To gain insight into short-term variability at times in the past, scientists are now using individual planktonic foraminifera Mg/Ca analyses from a single depth horizon in a sediment core (Ford et al. 2015). This approach allows scientist to reconstruct past changes in overall temperature variability and has provided insight into past changes in seasonality and El Niño Southern Oscillation variability.

Mg/Ca ratios in ostracods can be also used to reconstruct bottom water temperatures (e.g., Cronin et al. 2000). Ostracods are benthic bivalved Crustacea that secrete calcite shells during molting. Similar to foraminifera, the amount of magnesium in the calcite shells is largely controlled by the water temperature in which the organism secreted the shell (Dwyer et al. 2002). A positive correlation between water temperature and Mg/Ca in ostracods has been observed, although postdepositional processes such as dissolution also impact Mg/Ca ratios (Cronin et al. 2000). The main difference between foraminifera and ostracod Mg/Ca paleothermometry is that the calibration between temperature and Mg/Ca in ostracods is linear, as opposed to exponential for foraminifera.

Oxygen Isotopic Composition of Foraminifera

The oxygen isotopic composition of both planktonic and benthic foraminiferal calcite has been used for decades as a proxy for reconstructing past SSTs (Emiliani 1955). It is expressed as $\delta^{18}O_{Calcite}$ ($\delta^{18}O_C$), the deviation of the $^{18}O/^{16}O$ ratio relative to the VPDB standard in per mil (‰). Based on laboratory and natural experiments, a number of general and species-specific foraminiferal relationships between SST and $\delta^{18}O_C$ have been published (Epstein et al. 1953; Shackleton 1974; Erez and Luz 1983; Kim and O'Neil 1997; Bemis et al. 1998; Marchitto et al. 2014). In general, $\delta^{18}O_C$ decreases by ~0.21–0.23 ‰ for a 1 °C increase in temperature (Ravelo and Hillaire-Marcel 2007). However, foraminiferal $\delta^{18}O_C$ values are a function of both temperature and the oxygen isotopic composition of the seawater ($\delta^{18}O_{SW}$) in which they grow. Furthermore, $\delta^{18}O_{SW}$ varies with changes in salinity, as evaporation and precipitation cause local $\delta^{18}O_{SW}$ to increase and decrease, respectively. On longer timescales, changes in continental ice volume cause $\delta^{18}O_{SW}$ to decrease globally with melting of ice and increase globally with ice sheet growth. Mixing of water masses with different $\delta^{18}O_{SW}$ values can also influence local $\delta^{18}O_{SW}$. Thus, only if $\delta^{18}O_{SW}$ is known (or at least constrained) can $\delta^{18}O_C$ provide unique paleotemperatures. Other limitations to the $\delta^{18}O_C$ temperature proxy are vital effects such as photosynthetic activity of algal symbionts (Duplessy et al. 1970; Bemis et al. 1998), changing depth habitats of planktonic foraminifera, and the carbonate ion concentration of seawater (Spero et al. 1997).

Because $\delta^{18}O_C$ is a function of both temperature and $\delta^{18}O_{SW}$, researchers developed a method using paired Mg/Ca temperatures and $\delta^{18}O_C$ measurements on foraminifera to reconstruct past $\delta^{18}O_{SW}$ variability. When applied to surface-dwelling planktonic foraminifera, this method has been shown to be a robust proxy for reconstructing sea surface salinity variability once changes in continental ice volume are taken into account (Schmidt et al. 2006; Schmidt and Lynch-Stieglitz 2011). Researchers have also used this method with benthic foraminifera to reconstruct bottom water $\delta^{18}O_{SW}$ change as a proxy for continental ice volume variability over the past 1.5 Ma (Elderfield et al. 2012). The most significant advantage of this approach to calculate $\delta^{18}O_{SW}$ variability is that Mg/Ca can be measured on the same shells that carry $\delta^{18}O_C$ information, so there is no ambiguity in timing between the signals.

Clumped Isotopes in Carbonates

Recently, a considerable amount of interest has been invested in the development of a paleothermometer based on clumped stable isotope analyses of $CaCO_3$. Although the multiply substituted isotopologue ($^{13}C^{16}O^{18}O$) is rare and difficult to measure, the approach is based on the thermodynamic prediction that the abundance of multiple isotope substitutions in $CaCO_3$ increases as temperature decreases (Schauble et al. 2006; Passey et al. 2010). Therefore, unlike for temperature reconstructions based on $\delta^{18}O$ values, temperature reconstructions based on this method are not influenced by changes in the $^{18}O/^{16}O$ ratio of the water from which the mineral was precipitated. Initially, synthetically grown carbonates were used to identify the relationship between temperature and Δ_{47} values (Ghosh et al. 2006). Since then, calibration efforts have extended to shallow and deepwater corals, mollusks, and fish otoliths (Ghosh et al. 2006, 2007; Came et al. 2007; Thiagarajan et al. 2011). In addition, recent work has included the initial development of clumped isotopes in foraminifera and coccolithophores (Tripati et al. 2010, 2014). The resulting relationship for both inorganic and organic calcite shows a sensitivity of ~0.004–0.005 ‰ per °C.

Although clumped isotopes are becoming a more widely applied tool for geosciences, its application to the field of paleoceanography has been somewhat limited because of several factors. First, large sample sizes are required for a single analysis (in the range of 3–8 mg $CaCO_3$). Second, because the measurement of Δ_{47} is analytically challenging, it is necessary to replicate each measurement three to five times in order to reduce the standard error to less than ±2 °C. Third, only limited calibration data is available, especially for temperatures below 15 °C.

The abundance of ^{13}C–^{18}O bonds in a $CaCO_3$ sample is measured on the CO_2 liberated from the sample in phosphoric acid using gas source mass spectrometry (Ghosh et al. 2006; Guo et al. 2009). This allows for both Δ_{47} and $\delta^{18}O$ analysis on the same sample, resulting in the determination of both calcification temperature and the $\delta^{18}O$ value of the water from which the mineral precipitated. Therefore, as analytical methods continue to improve, this technique has considerable potential for becoming an important paleothermometer for future paleoceangraphic studies.

Biomarker Proxies: Alkenones and TEX_{86}

Although the Mg/Ca paleothermometer has advantages compared with the $\delta^{18}O_C$ proxy, it also has limitations including the influences of dissolution, calibrations based only on modern species, geographic limitations to regions inhabited by foraminifera, and temporal variability in seawater Mg/Ca ratios over millions of years. Biomarker-based SST proxies, such as the alkenone $U^{k'}_{37}$ (Brassell et al. 1986; Prahl and Wakeham 1987) and TEX_{86} (Schouten et al. 2002) indices, can overcome some of these limitations due to the ubiquitous appearance of the associated biomarkers in marine sediments temporally and spatially, especially during times and in regions where foraminifera do not exist. Similar to foraminifera-based proxies, the carriers of biomarkers accumulate and get preserved on the seafloor and can be sampled and extracted from sediment cores.

Alkenones are long-chain organic compounds produced by marine haptophyte algae (phytoplankton) known as coccolithophores. Because algae require sunlight to perform photosynthesis, they reside at or near the sea surface, making them a useful tool for reconstructing SST. The $U^{k'}_{37}$ index is based on the proportions of di- and tri-unsaturated ketones within the alkenones and varies positively with growth temperature. A decrease in temperature leads to an increase in the degree of unsaturation. Prahl and Wakeham (1987) and Prahl et al. (1988) developed the first quantitative calibration of alkenone unsaturation to growth temperature based on coccolithophores grown in the laboratory at known temperatures, and it appeared to reliably estimate SST based on samples collected from the ocean. Since then, large datasets of core-top $U^{k'}_{37}$ SST calibrations have been developed and show strong convergence with the original laboratory based calibration (Conte et al. 2006). Unfortunately, one of the main drawbacks to the $U^{k'}_{37}$ paleotemperature proxy is that it has an upper temperature limit of ~28 °C and a lower limit of ~1 °C (Herbert 2014). This precludes SST reconstructions based on the $U^{k'}_{37}$ index from the coldest and warmest regions of the ocean and from exceptionally warm periods in Earth's history.

Other ambiguities related to the alkenone paleotemperature proxy are depth and seasonal variations of alkenone-producing species in the ocean (Herbert 2014) and the potential for postdepositional transport of fine-grained alkenone carriers (Ohkouchi et al. 2002). Sunlight can penetrate to depths below the sea surface; thus, alkenones can be produced at a range of depths as long as light is sufficient for photosynthesis. Another drawback to this proxy is that phytoplankton production is seasonal in most ocean locations, so the $U^{k'}_{37}$ temperatures can be biased to the season of maximum production.

The TEX_{86} paleothermometer is another biomarker-based proxy developed more recently and holds promise for overcoming the temperature limitations of the alkenone temperature proxy. The TEX_{86} (TetraEther indeX of 86 carbons) index is based on the number of cyclopentane rings in membrane lipids, known as glycerol dialkyl glycerol tetraethers (GDGTs), which are produced by marine Thaumarchaeota (Schouten et al. 2002). The TEX_{86} paleothermometer is based on observations from culturing and mesocosm experiments that the number of cyclopentane rings in GDGTs

increases with increasing growth temperature (Wuchter et al. 2004). Schouten et al. (2002) noted a relationship between the number of rings in the GDGTS in marine surface samples and overlying SST and developed the first TEX_{86} temperature calibration based on 40-sediment core-top samples from 15 locations. Subsequent calibrations involving the addition of hundreds of core-top samples all note the highest correlation between the TEX_{86} index and SST (Kim et al. 2010). However, other studies have noted a bias in TEX_{86} temperatures where they are representative of subsurface rather than sea surface temperatures (Hertzberg et al. 2016). Unlike coccolithophorids that live near the sea surface, archaea live throughout the water column, which may help explain the subsurface signal (Schouten et al. 2002). While the exact cause of the subsurface bias is still unknown, a new calibration to subsurface temperature has been developed (Tierney and Tingley 2015). Despite this uncertainty, the TEX_{86} temperature proxy, which can reconstruct warmer temperatures than the alkenone SST proxy, has been used to reconstruct SSTs from the early Eocene when atmospheric pCO_2 levels may have reached ~2000 ppmv (Bijl et al. 2009).

The TEX_{86} paleothermometer can also be applied to lacustrine sediments for reconstructions of terrestrial temperatures, as GDGT-producing Thaumarchaeota also exist in lakes (Powers et al. 2004). The mechanistic basis of the proxy is the same in these systems, although separate calibrations are necessary (Tierney et al. 2010). In addition, soil GDGTs and methanogenic archaea can potentially complicate TEX_{86} in lakes, but these effects do not appear to be systematic (Tierney 2014). Nevertheless, the lacustrine TEX_{86} paleothermometer has been applied to a number of lakes, in, for example, Africa (Tierney et al. 2008).

Sr/Ca Ratios in Corals

Corals associated with reefs (as opposed to deep-sea corals) grow in regions of warm SST making them a useful archive for tropical SST reconstructions. These corals secrete aragonite in annual bands, so high-resolution paleotemperature reconstructions are possible. Sr^{2+} substitution in corals has inverse temperature dependence due to the exothermic nature of the reaction in which Sr^{2+} substitutes for Ca^{2+} in aragonite. Typically, Sr/Ca ratios are first calibrated with modern instrumental SST records to establish a coral-specific Sr/Ca-temperature relationship, which is then applied to the older skeleton of the same coral, or to fossil corals for reconstructions past SST (e.g., Felis et al. 2009; Hereid et al. 2013).

Coral Sr/Ca ratios appear to also be strongly influenced by vital effects (Alpert et al. 2016). Growth rate and symbiotic activity have a marked influence on coral Sr/Ca, and culture studies have shown that coral Sr/Ca responds to changes in seawater pH and light. Researchers have also noted offsets in temperature sensitivity and mean Sr/Ca ratios in neighboring colonies collected from the same reef (Goodkin et al. 2005; Alpert et al. 2016). A potential explanation for these vital effects is that corals accrete their skeleton within an isolated calcifying fluid that is continuously depleted in Sr/Ca as aragonite precipitation proceeds (Cohen et al. 2006). Changes in the carbonate ion concentration of the calcifying fluid can drive variations in the amount of aragonite precipitation and cause variations in the magnitude of calcifying fluid Sr/Ca depletion. DeCarlo et al. (2016) developed a method to account for these vital effects by combining Sr/Ca with U/Ca ratios, which decrease as carbonate ion concentrations increase. This new method, termed coral Sr-U thermometry, has the potential to offer significantly improved reliability for reconstructing past ocean temperatures from corals.

Terrestrial Temperature Proxies

Terrestrial temperature proxies provide information on Earth's surface air temperature. Geochemical proxies such as oxygen ($\delta^{18}O$) and deuterium (δD) isotopic values of glacial ice, and nitrogen and argon isotopic ratios of air bubbles trapped in ice, can be used to estimate past atmospheric temperatures.

Ice cores are a valuable paleoclimate archive because of the large number of variables that can be derived from both the ice and the air that is trapped within the ice as it forms. In addition to temperature, ice cores are used for reconstructions of atmospheric CO_2 and CH_4 concentrations, dust, and concentrations of salts, to name a few. Ice cores can be drilled from the polar regions of Greenland and Antarctica and from high-altitude tropical and subtropical locations. Oxygen and deuterium isotopes measured in ice can be used as a temperature proxy because isotopic fractions of the heavier ^{18}O and ^{2}H in snowfall are temperature dependent, and there is a strong spatial correlation between mean annual temperature and the mean isotopic fraction of ^{18}O or ^{2}H in precipitation (Dansgaard et al. 1993; Grootes et al. 1993). Evaporation fractionation, which depends on surface conditions (e.g., SST, wind speed, relative humidity), controls the isotopic composition of atmospheric water vapor. Fractionation occurs as an air mass moves poleward, cooling and condensing, which leads to fractionation as the air mass progressively loses heavy isotopes from the water vapor. As a result of this process, known as Rayleigh distillation, the predominant control on the polar isotopic composition of water vapor is the temperature difference between the evaporative source and the final region of deposition (Masson-Delmotte, et al. 2006). Thus, past changes in evaporation conditions or

atmospheric transport can induce biases in temperature reconstructions based on $\delta^{18}O$ or δD. A parameter known as deuterium excess ($d = \delta D - 8(\delta^{18}O)$) takes advantage of the combined measurements of $\delta^{18}O$ and δD to correct past temperature reconstructions from changes in evaporation conditions (Cuffey and Vimeux 2001). Prominent ice core temperature records from Greenland include GRIP (Greenland Ice-core Project Members 1993; Dansgaard et al. 1993), GISP2 (Grootes et al. 1993), and NGRIP (North Greenland Ice Core Project members 2004) and from Antarctica include Vostok (Petit et al. 1999), EPICA Dome C (EPICA community members 2004), and WAIS Divide (WAIS Divide Project Members 2013). Note that this is not a complete list of all available ice core records.

Measurements of the $\delta^{15}N$ and $\delta^{40}Ar$ of air bubbles trapped in ice cores can be used for temperature reconstructions during periods of abrupt temperature change. When rapid temperature change occurs, a transient temperature gradient is established in the firn (the region of partially compacted snow) until a stable depth temperature gradient in the upper part of the ice is restored. Under a vertical temperature gradient, the gases in the firn undergo a thermal fractionation, with the heaviest species being concentrated at the coldest end (Masson-Delmotte et al. 2006). Analyses of $\delta^{15}N$ and $\delta^{40}Ar$ in ice core air bubbles, which are constant in the atmosphere over long timescales, can be combined with firn modeling to provide estimates of past abrupt temperature changes (Severinghaus et al. 1998). This method has proven especially useful for reconstructing temperature changes from Greenland ice cores across abrupt climate change intervals such as Dansgaard-Oeschger events of the last glacial period and the millennial-scale events of the last deglaciation (Severinghaus and Brook 1999; Landais et al. 2004).

Conclusions

Each paleotemperature proxy has a unique set of advantages and disadvantages. Depending on the location and time period of interest, scientists will use the proxies that best suit their needs. Often, reconstructing temperature using two or more proxies can help to make climate records more robust. If the paleotemperatures measured using multiple proxies disagree, it may indicate an environmental control on the proxy unrelated to temperature. Finally, robust and reliable age models are key to any paleotemperature reconstruction. Temperature proxies also continue to undergo refinement as new discoveries are made and better technologies and methods are made available for measurements. The geochemical paleotemperature proxies discussed in this entry are by no means an exhaustive list, and the reader is encouraged to consult the references for more details.

Cross-References

- ▶ Carbonate Compensation Depth
- ▶ Oxygen Isotopes
- ▶ Paleoclimatology
- ▶ Paleoenvironments
- ▶ Paleoproductivity
- ▶ Stable Isotope Geochemistry

References

Allen KA, Hönisch B, Eggins M, Haynes LL, Rosenthal Y, Yu J (2016) Trace element proxies for surface ocean conditions: a synthesis of culture calibrations with planktonic foraminifera. Geochim Cosmochim Acta 193:197–221

Alpert AE, Cohen AL, Oppo D, DeCarlo TM, Gove J, Young C (2016) Comparison of equatorial Pacific sea surface temperature variability and trends with Sr/Ca records from multiple corals. Paleoceanography 31:252–265

Anand P, Elderfield H, Conte MH (2003) Calibration of Mg/Ca thermometry in planktonic foraminifera from a sediment trap time series. Paleoceanography 18:1050

Bemis BE, Spero HJ, Bijma J, Lea DW (1998) Reevaluation of the oxygen isotopic composition of planktonic foraminifera: experimental results and revised paleotemperature equations. Paleoceanography 13:150–160

Bijl PK, Schouten S, Sluijs A, Reichart G, Zachos JC, Brinkhuis H (2009) Early Palaeogene temperature evolution of the southwest Pacific Ocean. Nature 461:776–779

Brassell SC, Eglinton G, Marlowe IT, Pflaumann U, Sarnthein M (1986) Molecular stratigraphy: a new tool for climatic assessment. Nature 320:129–133

Brown SJ, Elderfield H (1996) Variations in Mg/Ca and Sr/Ca ratios of planktonic foraminifera caused by postdepositional dissolution: evidence of shallow Mg-dependent dissolution. Paleoceanography 11:543–551

Bryan SP, Marchitto TM (2008) Mg/Ca–temperature proxy in benthic foraminifera: new calibrations from the Florida Straits and a hypothesis regarding Mg/Li. Paleoceanography 23:PA2220

Came R, Eiler J, Veizer J, Azmy K, Brand U, Weidman C (2007) Coupling of surface temperatures and atmospheric CO_2 concentrations during the Palaeozoic era. Nature 449:198–201

Cohen AL, Gaetani GA, Lundalv T, Corliss BH, George RY (2006) Compositional variability in a cold-water scleractinian, *Lophelia pertusa*: new insights into "vital effects". Geochem Geophys Geosyst 7: Q12004

Conte MH, Sicre M, Rühlemann C, Weber JC, Schulte S, Schulz-Bull D, Blanz T (2006) Global temperature calibration of the alkenone unsaturation index ($U^{K'}_{37}$) in surface waters and comparison with surface sediments. Geochem Geophys Geosyst 7:Q02005

Cronin TM, Dwyer GS, Baker PA, Rodriguez-Lazaro J, DeMartino DM (2000) Orbital and suborbital variability in deep North Atlantic bottom water temperature obtained from Mg/Ca ratios in the ostracode Krithe. Palaeogeogr Palaeoclimatol Palaeoecol 162:45–57

Cuffey KM, Vimeux F (2001) Covariation of carbon dioxide and temperature from the Vostok ice core after deuterium-excess correction. Nature 412:523–527

Dansgaard W, Johnsen SJ, Clausen HB, Dahl-Jensen D, Gundestrup NS, Hammer CU, Hvidberg CS, Steffensen JP, Sveinbjoornsdottie AE, Jouzel J, Bond G (1993) Evidence for general instability of past climate from a 250-kyr ice-core record. Nature 364:218–220

DeCarlo TM, Gaetani GA, Cohen AL, Foster GL, Alpert AE, Stewart JA (2016) Coral Sr-U thermometry. Paleoceanography 31:626–638

Dekens PS, Lea DW, Pak DK, Spero HJ (2002) Core top calibration of Mg/Ca in tropical foraminifera: refining paleotemperature estimation. Geochem Geophys Geosyst 3:1–29

Duplessy JC, Lalou C, Vinot AC (1970) Differential isotopic fractionation in benthic foraminifera and paleotemperatures reassessed. Science 168:250–251

Dwyer GS, Cronin TM, Baker PA (2002) Trace elements in ostracodes. In: Holmes JA, Chivas AR (eds) Applications of the Ostracoda to Quaternary research. American Geophysical Union, Washington, DC, pp 205–225

Elderfield H, Ganssen G (2000) Past temperature and $\delta^{18}O$ of surface ocean waters inferred from foraminiferal Mg/Ca ratios. Nature 405:442–445

Elderfield H, Yu J, Anand P, Kiefer T, Nyland B (2006) Calibrations for benthic foraminiferal Mg/Ca paleothermometry and the carbonate ion hypothesis. Earth Planet Sci Lett 250:633–649

Elderfield H, Ferretti P, Greaves M, Crowhurst S, McCave IN, Hodell D, Piotrowski AM (2012) Evolution of ocean temperature and ice volume through the Mid-Pleistocene climate transition. Science 337:704–709

Emiliani C (1955) Pleistocene temperatures. J Geol 63:538–578

EPICA community members (2004) Eight glacial cycles from an Antarctic ice core. Nature 429:623–628

Epstein S, Buchsbaum R, Lowenstam HA, Urey HC (1953) Revised carbonate-water isotopic temperature scale. Geol Soc Am Bull 64:1315–1325

Erez J, Luz B (1983) Experimental paleotemperature equation for planktonic foraminifera. Geochim Cosmochim Acta 47:1025–1031

Felis T, Suzuki A, Kuhnert H, Dima M, Lohmann G, Kawahata H (2009) Subtropical coral reveals abrupt early-twentieth-century freshening in the western North Pacific Ocean. Geology 37:527–530

Ford HL, Ravelo AC, Polissar PJ (2015) Reduced El Niño-Southern Oscillation during the Last Glacial Maximum. Science 347:255–258

Ghosh P, Adkins J, Affek H, Balta B, Guo W, Schauble E, Schrag D, Eiler J (2006) ^{13}C-^{18}O bonds in carbonate minerals: a new kind of paleothermometer. Geochim Cosmochim Acta 70:1439–1456

Ghosh P, Eiler J, Campana S, Feeney R (2007) Calibration of the carbonate 'clumped isotope' paleothermometer for otoliths. Geochim Cosmochim Acta 71:2736–2744

Goodkin NF, Hughen KA, Cohen AL, Smith SR (2005) Record of Little Ice Age sea surface temperatures at Bermuda using a growth-dependent calibration of coral Sr/Ca. Paleoceanography 20:PA4016

Greenland Ice-core Project (GRIP) Members (1993) Climate instability during the last interglacial period recorded in the GRIP ice core. Nature 364:203–207

Grootes PM, Stuiver M, White JWC, Johnsen S, Jouzel J (1993) Comparison of oxygen isotope records from the GISP2 and GRIP Greenland ice cores. Nature 366:552–554

Guo W, Mosenfelder JL, Goddard WA, Eiler J (2009) Isotope fractionations associated with phosphoric acid digestion of carbonate minerals: insights from first principles theoretical modeling and clumped isotope measurements. Geochim Cosmochim Acta 73: 7203–7225

Herbert TD (2014) 8.15: alkenone paleotemperature determinations. In: Holland HD, Turekian KK (eds) Treatise on geochemistry, 2nd edn. Elsevier, Oxford, pp 399–433

Hereid KA, Quinn TM, Taylor FW, Shen CC, Edwards RL, Cheng H (2013) Coral record of reduced El Nino activity in the early 15th to middle 17th centuries. Geology 41:51–54

Hertzberg JE, Schmidt MW, Bianchi TS, Smith RW, Shields MR, Marcantonio F (2016) Comparison of eastern tropical Pacific TEX_{86} and *Globigerinoides ruber* Mg/Ca derived sea surface temperatures: insights from the Holocene and Last Glacial Maximum. Earth Planet Sci Lett 434:320–332

Hertzberg JE, Schmidt MW (2013) Refining *Globigerinoides ruber* Mg/Ca paleothermometry in the Atlantic Ocean. Earth Planet Sci Lett 383:123–133

Hönisch B, Allen KA, Lea DW, Spero HJ, Eggins SM, Arbuszewski J, deMenocal P, Rosenthal Y, Russell AD, Elderfield H (2013) The influence of salinity on Mg/Ca in planktic foraminifers – evidence from cultures, core-top sediments and complimentary $\delta^{18}O$. Geochim Cosmochim Acta 121:196–213

Howard WR, Prell WL (1992) Late quaternary surface circulation of the southern Indian Ocean and its relationship to orbital variations. Paleoceanography 7:79–117

Hutson WH (1980) The Agulhas current during the late Pleistocene: analysis of modern faunal analogs. Science 207:64–66

Imbrie J, Kipp NG (1971) A new micropaleontological method for quantitative paleoclimatology: application to a late Pleistocene Caribbean core. In: Turekian KK (ed) The Late Cenozoic glacial ages. Yale University Press, Connecticut, pp 71–181

Kim JH, van der Meer J, Schouten S, Helmke P, Willmott V, Sangiorgi F, Koc N, Hopmans E, Sinninghe Damsté JS (2010) New indices and calibrations derived from the distribution of crenarchaeal isoprenoid tetraether lipids: implications for past sea surface temperature reconstructions. Geochim Cosmochim Acta 74:4639–4654

Kim ST, O'Neil JR (1997) Equilibrium and nonequilibrium oxygen isotope effects in synthetic carbonates. Geochim Cosmochim Acta 61:3461–3475

Kucera M (2007) Planktonic foraminifera as tracers of past oceanic environments, Chapter 6. In: Hillaire-Marcel C, de Vernal A (eds) Developments in marine geology. Elsevier, Oxford, pp 213–262

Landais A, Caillon N, Grachev A, Barnola JM, Chapellaz J, Jouzel J, Masson-Delmotte V, Leuenberger M (2004) Quantification of rapid temperature change during DO event 12 and phasing with methane inferred from air isotopic measurements. Earth Planet Sci Lett 225:221–232

Lea DW, Mashiotta TA, Spero HJ (1999) Controls on magnesium and strontium uptake in planktonic foraminifera determined by live culturing. Geochim Cosmochim Acta 63:2369–2379

Lea DW, Pak DK, Spero HJ (2000) Climate impact of Late Quaternary Equatorial Pacific sea surface temperature variations. Science 289:1719–1724

Lear CH, Rosenthal Y, Slowey N (2002) Benthic foraminiferal Mg/Ca-paleothermometry: a revised core-top calibration. Geochim Cosmochim Acta 66:3375–3387

Marchitto TM, Curry WB, Lynch-Stieglitz J, Bryan SP, Cobb KM, Lund DC (2014) Improved oxygen isotope temperature calibrations for cosmopolitan benthic foraminifera. Geochim Cosmochim Acta 130:1–11

Masson-Delmotte V, Dreyfus G, Braconnot P, Johnsen S, Jouzel J, Kageyama M, Landais A, Loutre M-F, Nouet J, Parrenin F, Raynaud D, Stenni B, Tuenter E (2006) Past temperature reconstructions from deep ice cores: relevance for future climate change. Clim Past 2:145–165

Murray J (1897) On the distribution of the pelagic foraminifera at the surface and on the floor of the ocean. Nat Sci (Ecology) 11:17–27

North Greenland Ice Core Project members (2004) High-resolution record of Northern Hemisphere climate extending into the last interglacial period. Nature 431:147–151

Nürnberg D, Bijma J, Hemleben C (1996) Assessing the reliability of magnesium in foraminiferal calcite as a proxy for water mass temperatures. Geochim Cosmochim Acta 60:803–814

Ohkouchi N, Eglinton TI, Keigwin LD, Hayes JM (2002) Spatial and temporal offsets between proxy records in a sediment drift. Science 298:1224–1227

Ortiz JD, Mix AC (1997) Comparison of Imbrie-Kipp transfer function and modern analog temperature estimates using sediment trap and core top foraminiferal faunas. Paleoceanography 5:43–54

Parker AO, Schmidt MW, Chang P (2015) Tropical North Atlantic subsurface warming events as a fingerprint for AMOC variability during Marine Isotope Stage 3. Paleoceanography 30:1425–1436
Passey BH, Levin NE, Cerling TE, Brown FH, Eiler JM (2010) High-temperature environments of human evolution in East Africa based on bond ordering in paleosol carbonates. Proc Natl Acad Sci 107:11245–11249
Petit JR, Jouzel J, Raynaud D, Barkov NI, Barnola J-M, Basile I, Bender M, Chappellaz J, David M, Delaygue G, Delmotte M, Kotlyakov VM, Legrand M, Lipenkov VY, Lorius C, Pepin L, Ritz C, Saltzman E, Stievenard M (1999) Climate and atmospheric history of the past 420,000 years from the Vostok ice core, Antarctica. Nature 399:429–436
Powers LA, Werne JP, Johnson TC, Hopmans EC, Sinninghe Damste JS, Schouten S (2004) Crenarchaeotal membrane lipids in lake sediments: a new paleotemperature proxy for continental paleoclimate reconstruction? Geology 32:613–616
Prahl FG, Muehlhausen LA, Zahnle DL (1988) Further evaluation of long-chain alkenones as indicators of paleoceanographic conditions. Geochim Cosmochim Acta 52:2303–2310
Prahl FG, Wakeham SG (1987) Calibration of unsaturation patterns in long-chain ketone compositions for paleotemperature assessment. Nature 330:367–369
Ravelo AC, Hillaire-Marcel C (2007) The use of oxygen and carbon isotopes of foraminifera in paleoceanography, Chapter 18. In: Hillaire-Marcel C, de Vernal A (eds) Developments in marine geology. Elsevier, Oxford, pp 735–764
Regenberg M, Regenberg A, Garbe-Schönberg D, Lea DW (2014) Global dissolution effects on planktonic foraminiferal Mg/Ca ratios controlled by the calcite-saturation state of bottom waters. Paleoceanography 29:127–142
Rosenthal Y, Boyle EA, Slowey N (1997) Temperature control on the incorporation of magnesium, strontium, fluorine, and cadmium into benthic foraminiferal shells from Little Bahama Bank: prospects for thermocline paleoceanography. Geochim Cosmochim Acta 61:3633–3643
Rosenthal Y, Lohmann GP (2002) Accurate estimation of sea-surface temperatures using dissolution corrected calibrations for Mg/Ca paleothermometry. Paleoceanography 17:1044
Russell AD, Hönisch B, Spero HJ, Lea DW (2004) Effects of seawater carbonate ion concentration and temperature on shell U, Mg, and Sr in cultured planktonic foraminifera. Geochim Cosmochim Acta 68:4347–4361
Schauble E, Ghosh P, Eiler J (2006) Preferential formation of ^{13}C-^{18}O bonds in carbonate minerals, estimated using first-principles lattice dynamics. Geochim Cosmochim Acta 70:1439–1456
Schmidt MW, Vautravers MJ, Spero HJ (2006) Rapid subtropical North Atlantic salinity oscillations across Dansgaard-Oeschger cycles. Nature 443:561–564
Schmidt MW, Lynch-Stieglitz J (2011) Florida Straits deglacial temperature and salinity change: implications for tropical hydrologic cycle variability during the Younger Dryas. Paleoceanography 26:PA4205
Schmidt MW, Chang P, Hertzberg JE, Them TR, Ji L, Otto-Bliesner BL (2012) Impact of abrupt deglacial climate change on tropical Atlantic subsurface temperatures. Proc Natl Acad Sci 109:14348–14352
Schouten S, Hopmans EC, Schefuß E, Sinninghe Damsté JS (2002) Distributional variations in marine crenarchaeotal membrane lipids: a new tool for reconstructing ancient sea water temperatures? Earth Planet Sci Lett 204:265–274
Severinghaus JP, Sowers T, Brook EJ, Alley RB, Bender ML (1998) Timing of abrupt climate change at the end of the Younger Dryas interval from thermally fractionated gases in polar ice. Nature 391:141–146
Severinghaus JP, Brook E (1999) Simultaneous tropical-Arctic abrupt climate change at the end of the last glacial period inferred from trapped air in polar ice. Science 286:930–934
Shackleton NJ (1974) Attainment of isotopic equilibrium between ocean water and the benthonic foraminifera genus *Uvigerina*: isotopic changes in the ocean during the last glacial. In: Labeyrie J (ed) Les méthodes quantitatives d'étude des variations du climat au cours du Pléistocene. Colloques Int. duc. N. R. S, Paris, pp 203–209
Smith TM, Reynolds RW, Peterson TC, Lawrimore J (2008) Improvements to NOAA's historical merged land-ocean surface temperature analysis. J Climate 21:2283–2296
Spero HJ, Bijma J, Lea DW, Bemis BE (1997) Effect of seawater carbonate concentration on foraminiferal carbon and oxygen isotopes. Nature 390:497–500
Thiagarajan N, Adkins J, Eiler J (2011) Carbonate clumped isotope thermometry of deep-sea corals and implications for vital effects. Geochim Cosmochim Acta 75:4416–4425
Tierney JE, Russell JM, Huang Y, Sinninghe Damste JS, Hopmans EC, Cohen AC (2008) Northern Hemisphere controls on tropical southeast African climate during the past 60,000 years. Science 322:252–255
Tierney JE, Russell JM, Eggermont H, Hopmans EC, Verschuren D, Sinninghe Damste JS (2010) Environmental controls on branched tetraether lipid distributions in tropical East African lake sediments. Geochim Cosmochim Acta 74:4902–4918
Tierney JE (2014) Biomarker-based inferences of past climate: the TEX_{86} paleotemperature proxy. In: Turekian KK, Holland HD (eds) Treatise on geochemistry, Organic geochemistry, vol 12, 2nd edn. Elsevier, Oxford, pp 379–393
Tierney JE, Tingley MP (2015) A TEX_{86} surface sediment database and extended Bayesian calibration. Sci Data 2:150029
Tripati A, Eagle R, Thiagarajan N, Gagnon A, Bauch H, Halloran P, Eiler J (2010) ^{13}C-^{18}O isotope signatures and 'clumped isotope' thermometry in foraminifera and coccoliths. Geochim Cosmochim Acta 74:5697–5717
Tripati A, Sahany S, Pittman D, Eagle RA, Neelin JD, Mitchell JL, Beaufort L (2014) Modern and glacial tropical snowlines controlled by sea surface temperature and atmospheric mixing. Nat Geosci 7:205–209
WAIS Divide Project Members (2013) Onset of deglacial warming in West Antarctica driven by local orbital forcing. Nature 500:440–444
Wefer G, Berger WH, Bijma J, Fischer G (1999) Clues to ocean history: a brief overview of proxies. In: Fischer G, Wefer G (eds) Use of proxies in paleoceanography: examples from the South Atlantic. Springer, Berlin, pp 1–68
Wuchter C, Shouten S, Coolen MJL, Sinninghe Damsté JS (2004) Temperature-dependent variation in the distribution of tetraether membrane lipids of marine Crenarchaeota: implications for TEX_{86} paleothermometry. Paleoceanography 19:PA4028

Palladium

James M. Brenan
Department of Earth Sciences, Dalhousie University, Halifax, NS, Canada

Element Data
Atomic Symbol: **Pd**
Atomic Number: **46**
Atomic Weight: 106.42

(*continued*)

Isotopes and Abundances: ^{102}Pd 1.02%, ^{104}Pd 11.14%, ^{105}Pd 22.33%, ^{106}Pd 27.33%, ^{108}Pd 26.46%, ^{110}Pd 11.72%
0.1 MPa Melting Point: 1554.9 °C
0.1 MPa Boiling Point: 2990 °C
Common Valences: +2, +4
Ionic Radii: 4-fold: 64 pm (+2); 6-fold: 86 pm (+2), 61.5 pm (+4)
Pauling Electronegativity: 2.2
First Ionization Energy: 804.39 kJ/mol
Chondritic (CI) Abundance: 574 ng/g
Silicate Earth Abundance: 7.1 ng/g
Crustal Abundance: 1.5 ng/g
Seawater Abundance: 0.2–0.7 pmol/kg
Core Abundance: 3100 ng/g

Definition

Atomic number 46 is a dense, moderately refractory, precious metal with a bright silvery-white luster. Discovered in 1804, and named for the Pallas asteroid detected 2 years earlier, it is widely used for automobile catalysts as well as electrical components, jewelry, dental restoration, and hydrogen purification.

History and Uses

William Wollaston reported the discovery of palladium in 1804 (Wollaston 1804), which was purified from the aqua regia solution he used to dissolve naturally occurring platinum alloy (at the time known as platina; see entry for ▶ "Platinum"). This was the material likely derived from placer deposits of the Choco District of Columbia, which had been exploited by the pre-Hispanic aboriginals to produce jewelry and useful objects (fishing hooks, sewing needles, awls, tweezers). In his report to the Royal Society of London, Wollaston proposed the name palladium ". . .from the planet that had been discovered nearly at the same time by Dr. Olbers," referring to the discovery of the Pallas asteroid (originally considered to be a planet) by the German astronomer Heinrich Olbers on March 28, 1802. Palladium is principally used in automobile catalytic converters for engine emission control but is also employed in the industrial sector for electrical components, is alloyed with gold for use in dental restorations, and also to produce "white gold" for jewelry. Palladium has a significant solubility and selective permeability for hydrogen, at the exclusion of other gases, the latter enhanced by alloying with silver, or certain rare-earth elements. These unique characteristics are exploited for the commercial production of high purity hydrogen. A detailed account of the history of palladium, including important discoveries and scientific work, can be found in the book "*History of Platinum and its Allied Metals*" by McDonald and Hunt (1982).

Elemental and Physical Properties

Palladium has an atomic weight of 106.42[1], ground state electron configuration of [Kr]4d^{10}, with melting and boiling points at 0.1 MPa of 1554.9 °C and 2990 °C, respectively (Arblaster 2007). Palladium is a relatively dense metal (12,023 kg/m^3), similar to lead (11,340 kg/m^3). Palladium is considered to be moderately volatile, with a 50% condensation temperature of 1051 °C (Lodders 2003). Palladium has six stable isotopes: 102 (1.02[1]%), 104 (11.14[8]%), 105 (22.33[8]%), 106 (27.33[3]%), 108 (26.46[9]%), 110 (11.72[9]), as well as the now-extinct radioactive ^{107}Pd, which undergoes beta-decay to ^{107}Ag, with a half-life of 6.5×10^6 years. In addition to the neutral metal, the common oxidation states are 2+ and 4+. The radius of the neutral atom is 169 pm (Clementi et al. 1967), and Pd crystallizes in the cubic close-packed structure (space group Fm-3 m) with a metallic radius of 135.7 pm (Rao and Rao 1964). The size of the cation varies as follows (from Shannon 1976): 59 pm (+1, II-fold), 64 pm (+2, IV-fold, square planar), 86 pm (+2, VI-fold), 76 pm (+3, VI-fold), and 61.5 pm (+4, VI-fold). Useful texts that provide synopses of the chemical properties of Pd can be found in Cotton (1997) and in a compendium of papers edited by Hartley (1991).

Geochemical Behavior and Reservoir Abundance

Palladium is both highly siderophile and strongly chalcophile and is grouped with other 5th and 6th row transition metals having similar chemical properties: Pt, Rh, Ru, Os, and Ir; see entries for ▶ "Platinum Group Elements" (PGE) and ▶ "Siderophile Elements". Owing to its large ionic radius, Pd does not readily dissolve into rock-forming minerals, such as olivine and chromite (Brenan et al. 2016), but instead concentrates in base metal sulfides or forms accessory minerals. In terms of the latter, merenskyite ($PdTe_2$), stibiopalladinite (Pd_5Sb_2), arsenopalladinite ($Pd_8(As_{2.5},Sb_{0.5})_3$), atokite ($Pd_3Sn$), sobolevskite (PdBi), and Pd-bearing isoferroplatinum ($(Pt,Pd)_3(Fe,Cu)$) are some of the more common varieties found at world-class Pd deposits, such as Noril'sk, in Russia (see below; Kozyrev et al. 2002). An extensive compilation of palladium-bearing minerals is provided in Cabri (2002).

The abundance of Pd in the carbonaceous chondrite Orgueil is 574 ng/g (Horan et al. 2003), taken as similar to

the bulk earth concentration, which has now been highly fractionated between the core (3100 ng/g; McDonough 2003), upper mantle (7.1[1.3] ng/g; Becker et al. 2006), and crust (continental: 1.5 ng/g; Rudnick and Gao 2003; oceanic: 2.122 ng/g; Peucker-Ehrenbrink et al. 2012). The relative proportions of the PGE are close to chondritic in the upper mantle, although Pd is in slight excess to the others (Becker et al. 2006), with a relative fractionation similar to impact breccias on the lunar surface (Puchtel et al. 2008). The abundance of Pd in the upper mantle is also much higher and relatively unfractionated than expected for equilibrium between metal and silicate (Mann et al. 2012). Many believe this is the result of late accretion of chondritic material following core formation. The palladium content of seawater (0.2–0.7 pmol/kg) is similar to the heavy rare-earth elements (Bruland and Lohan 2003), although the crustal abundance of Pd is >100x lower. Calculations indicate that the dominant Pd species in seawater is $[PdCl_4]^{2-}$ at 25 °C, pH 8.2, 0.1 MPa (Byrne et al. 1988).

The existence of live ^{107}Pd in the early solar system was first documented by Kelly and Wasserburg (1978) by detection of excess ^{107}Ag in the Santa Clara iron meteorite. Since then, several studies have used this isotopic system to date the crystallization of iron meteorites, as large differences in Pd/Ag occur by metal-sulfide fractionation (e.g., Carlson and Hauri 2001; Chen and Wasserburg 1990). Whereas Ag is more volatile than Pd, differences in Pd/Ag can also arise due to evaporation and condensation processes acting in the early solar nebula. This has given rise to variation in the ^{107}Ag/^{109}Ag in chondritic meteorites, which has been used to establish the source and timing of addition of volatile-bearing materials to the Earth-Moon system (Schönbächler et al. 2010). Carlson et al. (2008) provided an overview of the applications of PGE isotopic systems, including Pd/Ag, in geo- and cosmochemistry.

Economic concentrations of Pd require >10,000-fold enrichment relative to crustal background values. This can occur when mantle-derived magmas reach saturation in immiscible sulfide liquid. The largest Pd deposits are found at Noril'sk (Russia), concentrated in massive sulfides formed within the magmatic conduit system of the 250 Ma Siberian Traps. Other significant deposits are associated with the Bushveld Igneous Complex of South Africa, as well as Sudbury (Canada) and Stillwater (USA). Global production in 2015 was ~180,000 kg, at an average market price of ~ $26,000/kg. The reader is referred to *Platinum Metals Review*, which provides a range of technical and historical information on the allied platinum group metals.

Summary

Palladium is a bright, silvery-white precious metal characterized by high density and moderately high melting temperature and unique surface catalytic properties. The principal uses of palladium are for automobile catalytic converters as well as electrical components, jewelry, dental restoration, and hydrogen purification. Palladium is highly siderophile, as well as chalcophile, and is therefore concentrated in Earth's core, with complementary depletions in the silicate mantle, crust, and surface reservoirs. Palladium has one extinct isotope ($t_{1/2}$ = 6.5 Ma), that was present in the early solar system, decaying to the more volatile ^{107}Ag. This isotopic system has been used to establish early solar system chronology and to establish the source and timing of addition of volatile-bearing materials to the Earth-Moon system. Extreme concentration of Pd relative to crustal background values is needed to produce minable terrestrial deposits, requiring the massive extraction capacity of immiscible sulfide melts that form in silicate magmas.

Cross-References

- Chalcophile Elements
- Chondrites
- Formation and Evolution of the Earth
- Geochemical Classification of Elements
- Natural Gas
- Ore Deposits
- Osmium
- Platinum
- Platinum Group Elements
- Rhenium
- Rhodium
- Ruthenium
- Siderophile Elements
- Sulfide Minerals
- Transition Elements

References

Arblaster JW (2007) Vapour pressure equations for the platinum group elements. Platin Met Rev 51:130–135

Becker H, Horan MF, Walker RJ, Gao S, Lorand J-P, Rudnick RL (2006) Highly siderophile element composition of the Earth's primitive upper mantle: constraints from new data on peridotite massifs and xenoliths. Geochim Cosmochim Acta 70:4528–4550

Brenan JM, Bennett N, Zajacz Z (2016) Experimental results on fractionation of the highly siderophile elements (HSE) at variable pressures and temperatures during planetary and magmatic differentiation. Rev Mineral Geochem 81:1–88

Bruland KW, Lohan MC (2003) Controls of trace metals in seawater. In: Elderfield H (ed) The oceans and marine geochemistry. Holland HD, Turekian KK (eds in Chief) Treatise on geochemistry, vol 6, Elsevier, Amsterdam

Byrne RH, Kump LR, Cantrell KJ (1988) The influence of temperature and pH on trace metal speciation in seawater. Mar Chem 25:163–181

Cabri LJ (2002) The platinum group minerals. In: Cabri L (ed) The geology, geochemisty, mineralogy and mineral beneficiation of platinum-group elements. C.I.M. special, vol 54. Elsevier, Amsterdam, pp 13–130
Carlson RW, Hauri EH (2001) Extending the ^{107}Pd-^{107}Ag chronometer to low Pd/Ag meteorites with multicollector plasma-ionization mass spectrometry. Geochim Cosmochim Acta 65:1839–1848
Carlson RW, Shirey SB, Schönbächler M (2008) Applications of PGE radioisotope systems in geo- and cosmochemistry. Elements 4:239–245
Chen JH, Wasserburg GJ (1990) The isotopic composition of Ag in meteorites and the presence of ^{107}Pd in protoplanets. Geochim Cosmochim Acta 54:1729–1743
Clementi E, Raimondi DL, Reinhardt WP (1967) Atomic screening constants from SCF functions. II. Atoms with 37–86 electrons. J Chem Phys 47:1300–1307
Cotton SA (1997) Chemistry of precious metals. Chapman and Hall, London. 374 pp
Hartley FR (ed) (1991) Chemistry of the platinum group metals. Recent developments, Studies in inorganic chemistry, vol 11. Elsevier, Amsterdam. 642 pp
Horan MF, Walker RJ, Morgan JW, Grossman JN, Rubin AE (2003) Highly siderophile elements in chondrites. Chem Geol 196:5–20
Kelly WR, Wasserburg GJ (1978) Evidence for the existence of ^{107}Pd in the early solar system. Geophys Res Lett 5:1079–1082
Kozyrev SM, Komarova MZ, Emelina LN, Oleshkevich OI, Yakovleva OA, Lyalinov DV, Maximov VI (2002) The mineralogy and behaviour of PGM during processing of the Noril'sk-Talnakh PGE-Cu-Ni ores. In: Cabri L (ed) The geology, geochemisty, mineralogy and mineral beneficiation of platinum-group elements. C.I.M. special, vol 54. Elsevier, Amsterdam, pp 13–130
Lodders K (2003) Solar system abundances and condensation temperatures of the elements. Astrophys J 591:1220–1247
Mann U, Frost D, Rubie D (2012) Partitioning of Ru, Rh, Pd, Re, Ir and Pt between liquid metal and silicate at high pressures and high temperatures: implications for the origin of highly siderophile element concentrations in the Earth's mantle. Geochim Cosmochim Acta 84:593–613
McDonald D, Hunt LB (1982) A history of platinum and its allied metals. Johnson-Matthey, London. 450 pp
McDonough WF (2003) Compositional model for the earth's core. In: Carlson RW (ed) The mantle and core. Holland HD, Turekian KK (eds in Chief) Treatise on geochemistry, vol 2, Elsevier, Amsterdam
Peucker-Ehrenbrink B, Hanghoj K, Atwood T, Keleman PB (2012) Rhenium-osmium isotope systematics and platinum group element concentrations in oceanic crust. Geology 40:199–202
Puchtel IS, Walker RJ, Odette JB, Kring DA (2008) Osmium isotope and highly siderophile element systematics of lunar impact melt breccias: implications for the late accretion history of the Moon and Earth. Geochim Cosmochim Acta 72:3022–3042
Rao CN, Rao KK (1964) Effect of temperature on lattice parameters of some silver-palladium alloys. Can J Phys 42:1336–1342
Rudnick RL, Gao S (2003) Composition of the continental crust. In: Rudnick RL (ed) The crust. Holland HD, Turekian KK (eds in Chief) Treatise on geochemistry, vol 3, Elsevier, Amsterdam
Schönbächler M, Carlson RW, Horan MF, Mock TD, Hauri EH (2010) Heterogeneous accretion and the moderately volatile element budget of Earth. Science 328:884–887
Shannon RD (1976) Revised effective ionic radii and systematic studies of interatomic distances in halides and chalcogenides. Acta Crystallogr A32:751–767
Wollaston WH (1804) On a new metal, found in crude platina. Philos Trans R Soc 94:419–430

Paragenesis

Denton S. Ebel[1] and Robert J. Kamilli[2]
[1]Department of Earth and Environmental Sciences, Columbia University, New York, NY, USA
[2]Tucson Office – Geology, Minerals, Energy and Geophysics Science Center, U.S. Geological Survey, Tucson, Arizona, USA

Definition

Paragenesis is the sequence of formation of associated minerals in rocks and rock suites (Craig and Vaughan 1994, p. 164). The concept of mineral paragenesis, *sensu stricto*, applies to the characteristics of mineral associations that connote contemporaneous formation, presumably in chemical equilibrium. The word paragenesis comes from the Greek, meaning "born beside."

The classical usage of paragenesis is to describe the temporal order of mineral deposition in an ore deposit, or paragenetic sequence, for example, in the Stassfurt salt deposits (Clarke 1911; Warren 2006). Mineral paragenesis is closely related to the concept of mineral zoning, where the variation occurs in space, rather than time. In its broadest sense, the term can be applied to any sequence or assemblage of minerals related by common formation conditions. Recent conceptual developments in mineralogy frame paragenesis from stellar atmospheres, to protoplanetary disks, to planets, to plate tectonics, and to the evolution of life (Hazen et al. 2008).

History

The concept of paragenesis was introduced by the Russian Academician V. M. Severgin (1816) and developed by distinguished German mineralogist and crystallographer Johann Friedrich August Breithaupt (1849). The study of mineral paragenesis was developed in the late nineteenth century following the development of the petrographic microscope. Efforts to understand the distribution of the elements using paragenetic concepts began in the twentieth century (Vernadsky 1910; Goldschmidt 1937), and experimental petrology and theoretical geochemistry were applied to quantitative petrogenetic studies (Clarke 1911; Korzhinskii 1959; Thompson 1970; Winkler 1979). The second half of the twentieth century saw an emphasis on geologic context, with detailed mapping and attention to cross-cutting features, especially of mineral deposits. This became essential to the understanding of the time and space relationships of geological entities. The recent revolution in our understanding of meteorites, stellar environments, and the rocky planets and

moons has allowed extension of paragenetic concepts beyond the Earth.

Paragenesis of Stellar and Nebular Rocks

The very first minerals formed in the atmospheres of giant stars. A suite of ~15 minerals in micron to submicron grains is present in the "presolar" fraction isolated from primitive chondritic meteorites of age 4.5678 Ga (Davis 2011). These minerals, and micron-scale rocks, are associated by occurrence and formation history. They record their source star type, and galactic chemical evolution in their isotopes. Thus they constitute the most primitive paragenetic mineral sequences: oxides (hibonite, spinel) formed in O-rich stellar environments and carbides formed in C-rich ones (diamond, SiC, TiC).

The high-temperature minerals formed in our own Solar Nebula, prior to planetary differentiation, include three paragenetic groups with distinct chemical affinities. Refractory Ca- and Al-rich inclusions (CAIs) form distinct objects with ~10 primary minerals, often in distinct layers. Glassy Mg-silicate-rich chondrules, partially or fully melted in space, constitute the volumetric majority of chondrites. Metal-sulfide nodules or metal grains are a distinct component of most chondrites. These three paragenetic mineral groups characterize the primary variability among primitive meteorites (Grossman 1996; Weisberg et al. 2006). While they differ in terms of volatility, as a condensation sequence (Ebel 2006), great controversy surrounds the timing and formation mechanism, the parageneses, of these mostly submillimeter, high-temperature planetary precursors.

The aqueous and thermal alteration of primitive chondrite parent bodies forms paragenetic groups including nepheline, grossularite, and sodalite (from CAIs); clays and other phyllosilicates (in chondrules); and phosphates (from P-bearing metal). Accretion by impacts forms high-pressure, shock-formed minerals (e.g., maskelynite, majorite), which with their parent minerals constitute unique paragenetic sequences (Sharp and DeCarli 2006). Alteration and shock expand the suite of mineral species that occur in chondrites to about 250 (Rubin 1997). Incorporated ices were the source of water for aqueous alteration, although ices are not preserved in the meteoritic record. The associations and formation sequences of ices (cryominerals), for example, their parageneses on Titan and Pluto, are active fields of planetary science research.

Paragenesis of Planetary Bodies

Accretion into larger bodies induces melting and core-mantle differentiation, recorded by the achondrite meteorites (primarily basalts, irons, and stony irons). Sulfide nodules in iron meteorites contain a distinct paragenetic suite including carbides, nitrides, and sulfides derived from trace constituents originally dissolved in molten iron, and immiscible in slowly cooled subsolidus iron in early planetesimal cores. The basaltic achondrite meteorites record paragenetic sequences of early mantle formation on dry (e.g., Vesta) and wet (e.g., Mars) planetary bodies, the latter likely similar to Earth's Hadean Eon (> 4.03 Ga). Hazen (2013) lists about 420 mineral species likely formed during this period of mineral evolution.

Post-Hadean terrestrial processes such as plate tectonics, subduction-related volcanism and high-pressure metamorphism, continent formation, fluid-rock interactions, differentiation of high-silica magmas, and massive sulfide formation are all recorded in paragenetic sequences. Advanced geological processes and the evolution of life and an oxidizing atmosphere are responsible for much of the vast terrestrial mineral kingdom, with about 5100 species (NRMIMA 2016). Detailed study of the paragenetic associations among mineral species offers important clues to each of many terrestrial geological processes.

Paragenetic Models

Studies of the genesis of all kinds of rocks have consistently yielded similar sequences of mineral formation in similar environments, leading to generalized models of mineral formation. Paragenetic models often involve graphical representations of time, space, parent or bulk composition, introduction or loss of chemical constituents, physicochemical environment, and kinetics. Any single-rock body will generally show only a small part of any generalized model.

Bowen's Reaction Series

The most famous paragenetic model is known as Bowen's reaction series (Bowen 1928; Fig. 1), developed to describe the evolution or differentiation of igneous rocks by the process of fractionation. Bowen realized that since minerals that crystallize from a magma have a different composition from the magma, if reaction of the early formed minerals with the magma were somehow impeded and/or the magma and crystals were separated, rocks could be produced of different compositions from that of the parent magma.

Bowen described two separate reaction series. In the continuous series, plagioclase feldspar crystallizing from a magma is more calcium rich than the magma itself, but it reacts continuously with the magma to become more sodium rich. If the early, calcium-rich plagioclase is removed from the magma, the magma becomes richer in sodium, thereby crystallizing more sodium-rich plagioclase. Mafic minerals rich in magnesium and iron form the discontinuous series. Early

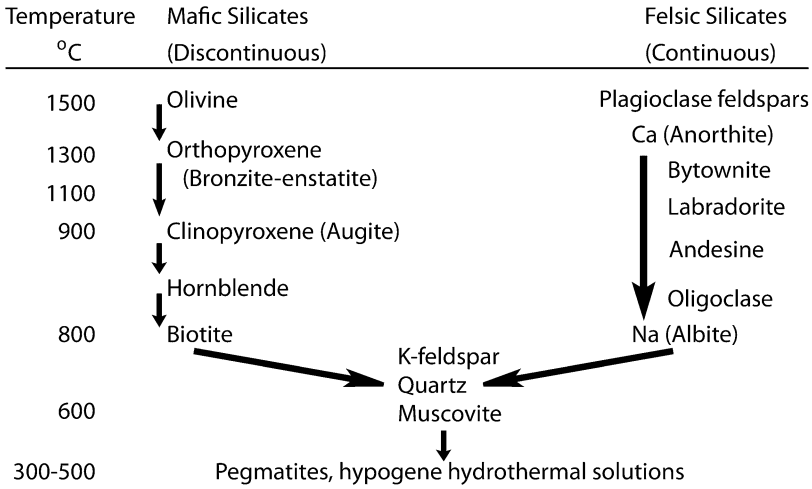

Paragenesis, Fig. 1 Bowen's reaction series describing the mineral and genetic interrelationships of plutonic rocks

formed olivine in a magma is converted to pyroxene by reaction with the magma. Similarly, pyroxene is converted to amphibole and amphibole to biotite. The separation of crystals from magma will produce a crystal fraction that is more mafic than the remaining magma. Through these two parallel series, a basaltic magma can differentiate by fractional crystallization. On Earth, differentiation can proceed to low-temperature granitic compositions of potassium feldspar, muscovite mica, and quartz. Examples of complete igneous sequences from basalt to granite are rare, and we now know that other mechanisms produce differentiation sequences. Nevertheless, Bowen's reaction series remains a useful, simple model for observed parageneses of igneous rocks on all the terrestrial planets.

Emmons' Zoning Model

As a magma differentiates, the concentration of constituents incompatible with mineral structures, such as water, carbon dioxide, fluorine, copper, lead, and zinc, will commonly increase in the residual magma. At some point late in magma crystallization, a water-rich phase may physically separate from the magma. This process leads to the formation of many types of hydrothermal mineral deposit, resulting in a typical paragenetic sequence often systematically distributed in space, time, or both. An empirical paragenetic sequence can be thought of as varying from high temperature to low, deep to shallow, or early to late. No single mineral deposit contains all these assemblages, but many show several intervals in the order given. Generalized zoning and paragenetic sequences for mineral deposits (modified from Guilbert and Park 1986, after Emmons 1936) are:

1. *Barren or low grade*: Quartz, potassium feldspar, biotite, chalcopyrite, molybdenite, trace pyrite, carbonates, and anhydrite. Potassic alteration
2. *Molybdenum-tungsten*: Quartz, wolframite, scheelite, molybdenite, and cassiterite. Potassic or no alteration
3. *Copper*: Chalcopyrite, quartz, pyrite or pyrrhotite, tennantite, bornite, chalcocite, and enargite. Quartz-sericite-pyrite alteration
4. *Copper*: Tennantite, tetrahedrite, chalcopyrite, quartz, and pyrite. Sericitic, argillic, and propylitic alteration
5. *Zinc*: Quartz, sphalerite, galena, chalcopyrite, tennantite-tetrahedrite, Ca-Fe-Mn carbonates, and sparse pyrite
6. *Lead*: Quartz, argentiferous galena, sphalerite, rhodochrosite, rhodonite, and sparse pyrite
7. *Silver-manganese*: Quartz, calcite, siderite, rhodochrosite, silver sulfosalts, and sparse pyrite. Sericitic-argillic-propylitic alteration
8. S. *Barren interval*: Most commonly occurring barren zone. Quartz, carbonates, and small amounts of pyrite, chalcopyrite, sphalerite, and galena
9. *Gold-silver*: Bonanza gold and silver, quartz, chalcedony, amethyst, adularia, alunite, silver sulfosalts, tellurides and selenides, rhodochrosite, and other carbonates. Some potassic, some sericitic, and some propylitic alteration
10. *Antimony*: Stibnite, quartz, lead-antimony sulfosalts, and galena
11. *Mercury*: Cinnabar, chalcedony, quartz, barite, fluorite, and carbonates
12. *Barren*: Chalcedony, quartz, barite, fluorite, carbonates, small amounts of mercury, antimony, or arsenic minerals

Determination of Paragenetic Sequences in Ore Deposits

Paragenetic sequences must be determined by documentation and interpretation of geochemical, spatial, and textural relationships among mineral phases (Ramdohr 1980). Criteria used are mutual growth relationships, layering, vertical and

horizontal separation, cross-cutting and offsetting relationships, and alteration and replacement textures (e.g., Foley et al. 1993). A common challenge is to decipher whether minerals in contact with or close to each other actually formed at the same time and in chemical equilibrium. Time relationships are based on individual crystal growth habits and growth textures between minerals that result from contemporaneous crystallization. It is generally easier to show that minerals did not form in equilibrium rather than the reverse. Alteration and replacement textures indicate the preserved process of one mineral changing to another.

The most common criterion for determining relative ages is contact relationships between minerals or veins that contain them. Usually the younger mineral is molded around the other. Early formed minerals tend to be euhedral, whereas later minerals will conform to the remaining spaces between the euhedral minerals and be either subhedral or anhedral. However, it is possible for a euhedral mineral to be younger than surrounding minerals if it was formed by replacement: this can be recognized by the presence of inclusions of the replaced mineral. Sometimes the replacing mineral will inherit a texture or morphology that is a characteristic of the replaced mineral. This phenomenon is called pseudomorphism.

Cross-cutting veins, especially where the older vein is offset by the younger, offer indisputable proof of relative ages of the minerals in ore deposits that contain multiple veins of differing ages and mineral assemblages. It is possible, however, that a mineral in an early vein might be replaced by a mineral formed by a younger event. This could yield an incorrect relative age if macroscopic relationships are not complemented by microscopic interpretation of replacement textures.

A common complication in studying an ore deposit is that the paragenetic sequence apparently violates itself due to cyclic processes. For example, if a deposit contains early veins and late veins, but "early" veins are observed to cut "late" veins, it can be inferred that more than one cycle of mineralization must have occurred. The identification of the paragenetic sequence requires an identification of distinguishing mineralogical or textural characteristics of each vein generation. One can then sequentially "strip out" each generation of veins, starting with the latest until the earliest vein is identified. Similar difficulties occur in metamorphic rocks, where prograde metamorphic minerals formed at extreme temperature and pressure may be replaced by retrograde minerals during cooling and decompression.

A paragenetic sequence may also vary in different parts of a large ore body, due to isolation of fluids, varying chemical parameters within the ore body and other factors. For example, particularly in epithermal ore deposits, some minerals, once deposited, will dissolve when the hydrothermal fluid becomes undersaturated with respect to that mineral. This is especially common with barite and calcite. The former existence of minerals can sometimes be identified by the presence of euhedral holes (casts) that have the crystal form of the missing mineral.

The interpretation of a paragenetic sequence requires careful, time-consuming study on both macroscopic and microscopic scales. Without a thorough understanding of the time-space relationships of a rock or geologic body, the interpretation of geochemical and other data is often ambiguous and misleading.

Example Paragenetic Diagram

Figure 2 is an example of a paragenetic diagram that is complex due to repeated episodes or cycles of faulting, hydrothermal brecciation, and mineralization. From oldest to youngest, the stages occurred as follows:

1. Hydrothermal brecciation and deposition of minerals that form the breccia matrix.
2. Main ore-depositing stage.
3. Deposition of coarse quartz and white, lamellar calcite intergrowths.

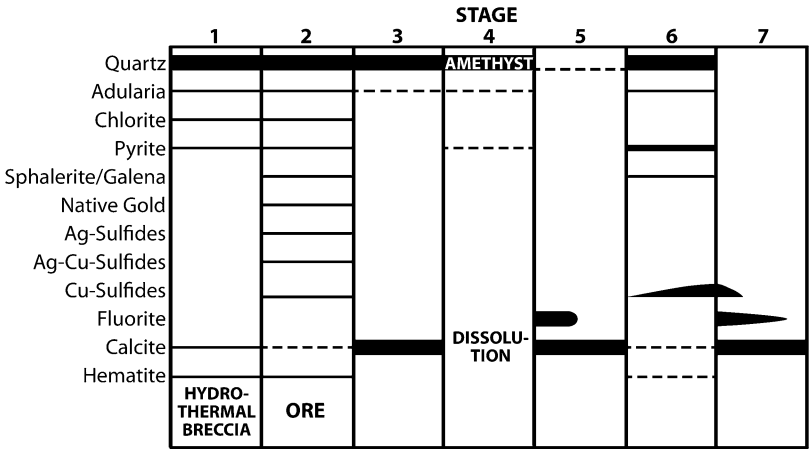

Paragenesis, Fig. 2 Paragenetic diagram illustrating mineralization in the Mogollon District, New Mexico (after Kamilli and Ratté 1995). Line width gives qualitative expression of mineral abundance. *Dashed lines* show minerals that are sporadic in occurrence

4. Partial-to-complete dissolution of calcite and concomitant replacement by quartz.
5. Deposition of fluorite and calcite.
6. A stage possibly contemporaneous with stage 2, but distinguished by the abundance of copper-bearing minerals.
7. Deposition primarily of black calcite.

The most important inference about the mineralization shown in the diagram is that it involved a repetition of all or parts of stages 1–5 at least twice and probably many times in different parts of the hydrothermal system. Compare this interpretation to intervals 8, 9, and 12 above.

Paragenetic Research Using Fluid Inclusions

Fluid inclusions are small quantities of fluid, generally water-rich, trapped within minerals. They are extremely valuable in interpreting the physicochemical history of the enclosing mineral (Roedder 1984; Goldstein and Reynolds 1994). Fluid inclusions may be primary (formed with the enclosing mineral) or secondary (formed after the enclosing mineral crystallized). Primary inclusions are identified by their relationship to the crystal habit of the enclosing mineral. Secondary inclusions form when a mineral grain fractures, allowing fluid to flow in and subsequently recrystallize the walls of the fracture to form an undulating plane of inclusions. Secondary inclusions record the history of fluids that a mineral experienced after it formed. These secondary fluid inclusion planes are analogous to cross-cutting veins in a mineral deposit. Careful study and identification of fluid inclusion paragenesis and recognition of the paragenetic sequence of secondary inclusions are essential to any study using fluid inclusions to interpret the geologic history of the enclosing rock.

Summary

Mineral paragenesis describes sequences or assemblages of minerals related by common formation conditions. Although most fully developed for ore deposits, the concept of paragenesis can be applied to all rock-forming environments including stellar atmospheres, disks around young stars, and planetary bodies. The most evolved planetary bodies, such as the Earth, host the most complex paragenetic mineral associations.

Cross-References

- Chondrites
- Epigenesis
- Equilibrium
- Fluid–Rock Interaction
- Geochemical Exploration
- Geothermal Systems
- Hydrothermal Alteration
- Hydrothermal Solutions
- Hypogene
- Magmatic Process Modeling
- Metamorphic Reactions and Processes
- Meteorites
- Mineral Genesis
- Mineralogy
- Natural Gas
- Nucleosynthesis
- Phase Equilibria
- Presolar Grains
- Supergene
- Volcanism

References

Bowen NL (1928) The evolution of the igneous rocks. Dover Publications, 1956, New York, 334 pp
Breithaupt JFA (1849) die Paragenesis der Mineralien. Mineralogisch, geognostich und chemisch beleuchte, mit besonderer Rücksicht auf Bergbau. Freiberg [Breithaupt JFA (1849) The paragenesis of the minerals. Mineralogical, geognostic and chemically illuminated, with special regard to mining]
Clarke FW (1911) Data of geochemistry. USGS Bulletin 491
Craig JR, Vaughan DJ (1994) Ore microscopy and ore petrography. Wiley, New York, 434pp
Davis AM (2011) Stardust in meteorites. Proc Natl Acad Sci 108:19142–19146
Ebel DS (2006) Condensation of rocky material in astrophysical environments. In: Lauretta D, McSween HY Jr (eds) Meteorites and the early solar system II. University of Arizona, Tucson, pp 253–277
Emmons WH (1936) Hypogene zoning in metalliferous lodes. 16th Int Geol Congr Rep, Part 1, pp 417–432
Foley NK, Caddey SW, Byington CB, Vardiman DM (1993) Mineralogy, mineral chemistry, and paragenesis of gold, silver, and base-metal ores of the north amethyst vein system, San Juan Mountains, Mineral County, Colorado. USGS Professional Paper 1537
Goldschmidt VM (1937) The principles of distribution of chemical elements in minerals and rocks. J Chem Soc 1937:655–673
Goldstein RH, Reynolds TJ (1994) Systematics of fluid inclusions in diagenetic minerals. Society for Sedimentary Geology, Tulsa, 198 pp
Grossman JN (1996) Chemical fractionations of chondrites: signatures of events before chondrule formation. In: Hewins R, Jones RH, Scott ERD (eds) Chondrules and the protoplanetary disk. University of Cambridge, Cambridge, pp 243–253
Guilbert JM, Park EF (1986) The geology of ore deposits. W.H. Freeman and Co., New York, 985 pp
Hazen RM (2013) Paleomineralogy of the Hadean Eon: a preliminary species list. Am J Sci 313:807–843
Hazen RM, Papineau D, Bleeker W, Downs RT, Ferry JM, McCoy TJ, Sverjensky DA, Yang H (2008) Mineral evolution. Am Mineral 93:1693–1720
Kamilli RJ, Ratté JC (1995) Geologic studies of the Mogollon mining district; does a porphyry system lie below? In: Pierce FW, Bolm JG

(eds) Porphyry copper deposits of the American Cordillera. Arizona Geological Society Digest 20, Tucson, pp 455–463
Korzhinskii DS (1959) Physicochemical basis of the analysis of the paragenesis of minerals. Consultants Bureau, New York
NRMIMA (2016) http://nrmima.nrm.se//imalist.htm
Ramdohr P (1980) The ore minerals and their intergrowths, International series in earth science, vol 35, 2nd edn. Pergamon Press, London, 1205 pp
Roedder E (1984) Fluid inclusions. Rev Mineral 12:644 pp
Rubin AE (1997) Mineralogy of meteorite groups. Meteorit Planet Sci 32:231–247
Severgin VM (1816) A new system of minerals based on external characteristics. The Imperial Academy of Sciences Publishing House, St. Petersburg. (in Russian)
Sharp TG, DeCarli PS (2006) Shock effects in meteorites. In: Lauretta D, McSween HY Jr (eds) Meteorites and the early solar system II. University of Arizona, Tucson, pp 653–677
Thompson JB (1970) Geochemical reactions and open systems. Geochim Cosmochim Acta 34:529–551
Vernadsky VI (1910) Paragenesis of chemical elements in the earth's crust. Jour 12th Conf Russ, Naturalists and Physicians, 73–91
Warren JK (2006) Evaporites: sediments, resources and hydrocarbons. Springer, Berlin, 1035 pp
Weisberg MK, McCoy TJ, Krot AN (2006) Systematics and evaluation of meteorite classification. In: Lauretta D, McSween HY Jr (eds) Meteorites and the early solar system II. University of Arizona, Tucson, pp 19–52
Winkler HGF (1979) Petrogenesis of metamorphic rocks, 5th edn. Springer, Berlin, 348 pp

Partial Melting

Paul D. Asimow
Division of Geological and Planetary Sciences, California Institute of Technology, Pasadena, CA, USA

Synonyms

Fusion; Magma genesis

Definition

Partial melting is the transformation of some fraction of the mass of a solid rock into a liquid as a result of decompression, heat input, or addition of a flux. The resulting liquid is called magma and becomes lava if it erupts from a volcano. The understanding that partial, rather than complete, melting is the norm in natural systems is essential to appreciating the geochemical importance of melting in the Earth and planets. During partial melting, the liquid differs from the source rock and from coexisting residual minerals in composition and in physical properties such as density and viscosity. The low viscosity, low density (usually), and interconnected texture of the liquid during partial melting allow the melt to migrate from the source and thereby trigger physical phenomena like volcanism as well as chemical segregation of the Earth, Moon, and meteorite parent bodies into distinctive layers such as crust, mantle, and core. The elements that concentrate into the crust, for example, are not the lightest elements but rather those with the strongest chemical preference to dissolve in magma, which carries them upwards. At the present day, most of the Earth's crust is too cold and the mantle at too high a pressure for partial melting to occur. Therefore, regions of volcanic activity are not simply areas where magma is tapped, but rather they overlie areas where magma is being created by partial melting of previously solid rocks and then migrating to the surface.

Mechanisms of Partial Melting

Melting, as taught in basic physical science classes, occurs when the temperature of a solid material is increased to its melting point, followed by the addition of latent heat to transform the solid into a liquid. It is usually discussed only in the case of a pure material that melts completely at a single temperature. This leads to the intuitions that melting of rocks should be associated with increasing the temperature of the source rocks and that complete melting should be common. The phase relations of rocks, however, are more complicated than those of a pure substance at constant ambient pressure in ways that combine to mean melting can occur without temperature increase and to make partial melting much more common than complete melting.

Natural rocks are typically mechanical mixtures of several minerals, and many of those minerals are solid solutions of more than one chemical component. Both of these features cause melting to begin at a temperature called the solidus and end at a temperature called the liquidus, with an interval of coexisting solids and liquid or partial melting, in between. Only for a pure substance are the solidus and liquidus the same. Both the solidus and liquidus temperatures are functions of pressure; for most substances, the melting temperatures increase with pressure.

Furthermore, in the solid Earth, change of the temperature of large rock masses due to conduction of heat is a slow and inefficient process. This means that there is rarely an external heat source to provide the latent heat to drive complete melting. Instead, the main melting processes in the solid Earth are decompression melting, in which rocks are transported to lower pressure and this brings them into the partial melting interval, and flux melting, in which fluid components that lower the solidus temperature migrate into a source region and bring about partial melting. In the absence of an external heat source, melting is generally accompanied, surprisingly, by decreasing rather than increasing temperature. An important limiting case of decompression melting is adiabatic

melting, which is the behavior that results when there is no conduction of heat at all.

Decompression Melting

Decompression melting is the main mechanism for formation of basaltic magma on Earth in settings such as mid-ocean ridges, hotspots, continental rifts, and back-arc basins. It is also probably important on other terrestrial planets, but the rate of decompression depends on the acceleration due to gravity, which can lead to distinctive processes on different worlds. The importance of this mechanism is a natural result of plate tectonics and mantle convection, which produce upwelling flow fast enough to transport hot rock towards the surface and reduce the pressure on it nearly adiabatically, i.e., without significant loss of heat by conduction. Adiabatic decompression causes cooling of only about 10 K GPa^{-1}, whereas the solidus temperature of mantle rocks decreases with decreasing pressure by about 130 K GPa^{-1}. Hence, if solid mantle is drawn upwards by plate tectonic flow or its own convective buoyancy, it may intersect its solidus and begin melting (McKenzie and Bickle 1988).

With continued upwelling and pressure decrease, the extent of partial melting and the volume of melt generated increases. This is what happens at mid-ocean ridges, where steady plate separation causes hot mantle rock to continuously rise to low pressure and undergo decompression melting. This is inherently a partial melting process due to the limited availability of latent heat. This partial melting causes an ultramafic peridotite source to be separated into a mafic, basaltic magma (a liquid) and a solid residue, accompanied by fractionation of each major and trace element into the liquid or the solid residue according to its geochemical behavior. The liquid segregates and ascends to form the oceanic crust. In turn, this explains the compositional, mineralogical, and seismological differences between, for example, oceanic crust and mantle.

Away from mid-ocean ridges, however, the crust and the uppermost mantle are too cold and therefore rigid to flow upwards or melt by this decompression mechanism. This cold layer is called the lithosphere. Beneath the lithosphere lies the asthenosphere, which is hot enough to flow in response to motions of the overlying lithosphere and is hot enough to undergo partial melting if it flows upwards to low enough pressure. Therefore, partial melting and generation of basaltic magma can begin in response to horizontal extension that thins the lithosphere and allows the asthenosphere to move upward, such as in well-developed continental rifts. Beneath thick old lithosphere that is not thinned by extension, intersection of the solidus by decompression requires either unusually hot mantle temperatures or unusually low solidus temperatures due to volatile components or recycled crust, which explains the attention to these factors in explaining intra-plate hotspot volcanoes and continental flood basalts (Maclennan et al. 2001; Pertermann and Hirschmann 2003; Asimow et al. 2004; Herzberg et al. 2007).

As decompression continues beyond the initial intersection with the solidus, the system reaches higher extents of melting. The further it can ascend, a function of the depth where it crosses the solidus and the thickness of the lithosphere above, the more melt will be generated (Langmuir et al. 1992). Figure 1 introduces a series of phase diagrams for a two-component model chemical system that illustrate the progress of such decompression melting. We consider, as is usually done for convecting systems, that the process is slow enough to be approximated as reversible, because mantle flow is a creeping flow without turbulence. On the other hand, we consider that the flow is fast enough that heat transport is dominated by advection, with a negligible role for conduction, which means it is approximately adiabatic ($Q = 0$, where Q is conductive heat flow into a mantle parcel). The second law of thermodynamics ($dS = Q/T + \sigma$, where dS is the change in entropy, T is absolute temperature, and σ is irreversible entropy production) then indicates that we can approximate such decompression as a constant entropy process, $dS = 0$ (Asimow et al. 1997). Note that some authors consider conservation of enthalpy to be a better approximation (Ganguly 2005).

Flux Melting

Many of Earth's most dramatic and hazardous volcanoes and most of the addition of juvenile magmatic material to the continents occur above subduction zones. This is surprising from the decompression perspective discussed above because subduction is a downwards flow of cold material – the opposite of the upwards flow of hot material that promotes decompression melting. There must be a different mechanism of partial melting at work.

Partial melting in the subduction zone environment results from the introduction of water, which can be derived from the oceanic sediments, altered oceanic crust, and perhaps serpentinized mantle of the subducting slab (Grove et al. 2006). At high pressures, where water can readily dissolve in magma, it acts as a flux (a chemical agent that promotes melting at lower temperature); Fig. 2 demonstrates the origin of such solidus depression in a model two-component rock-water system. The diagrams illustrate that, depending on how much water is added, melting may begin at temperatures intermediate between the dry solidus and the water-saturated solidus. The addition of water and other chemical components to a rock at conditions where it was solid to begin with, but partially molten as a result of the change in composition, is flux melting. This is the second most efficient source of magmatism, by volume, on Earth.

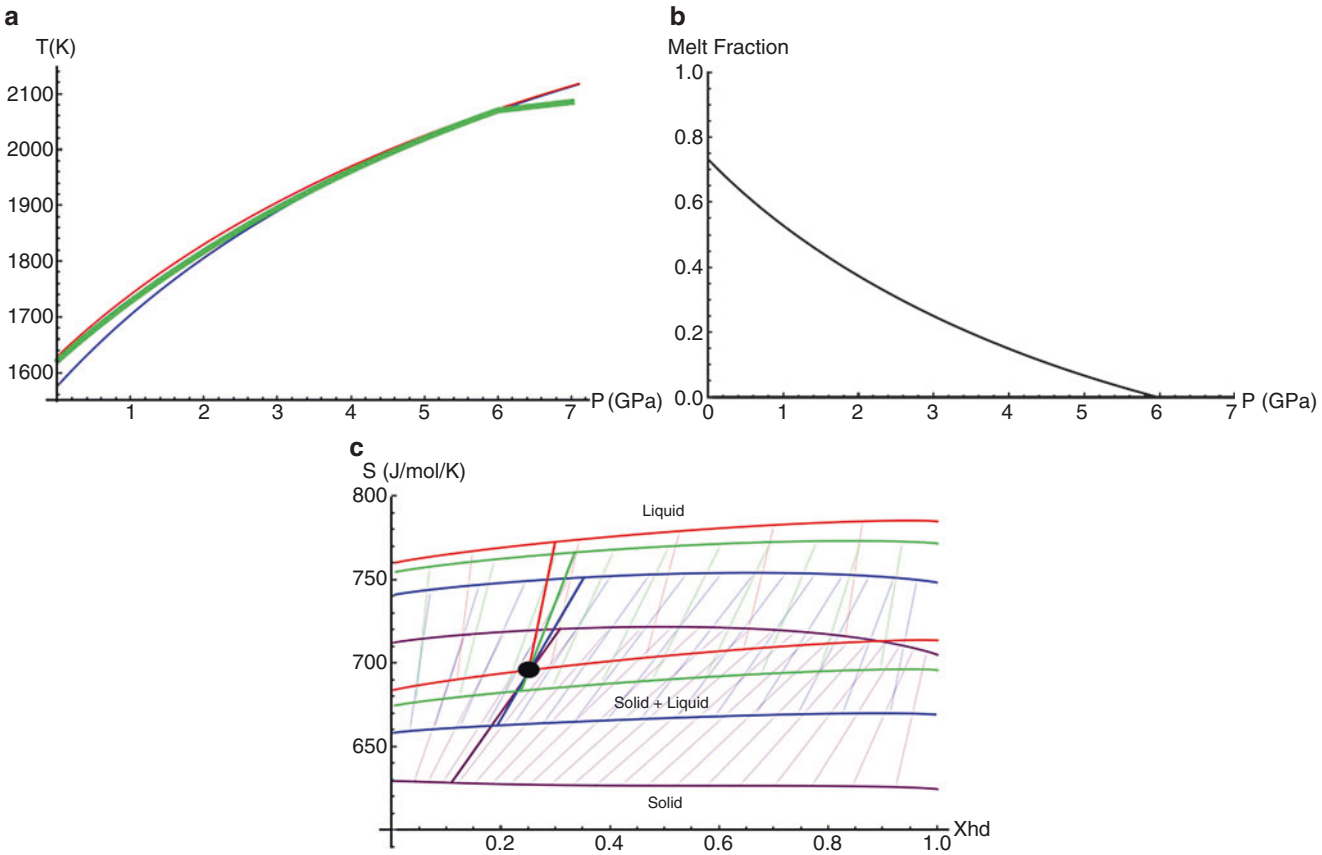

Partial Melting, Fig. 1 The use of phase diagrams and thermodynamics to analyze the progress of decompression melting in a simplified two-component chemical system. The system is $CaMgSi_2O_6$ (diopside) – $CaFeSi_2O_6$ (hedenbergite) and composition is expressed by mole fraction of the hedenbergite component, X_{hd}. (**a**) A pressure-temperature plot showing the solidus (*blue*) and liquidus (*red*) of the composition $X_{hd} = 0.25$ as well as a constant entropy decompression path (heavy *green*) that intersects the solidus at 6 GPa pressure and continues partial melting all the way to zero pressure. It is not possible to predict just by inspection of this diagram how rapidly melting will proceed or what the P-T path will be. (**b**) The extent of melting, or mass fraction of liquid, at equilibrium along the selected constant entropy decompression path; melting begins at 6 GPa and gradually increases as pressure drops, reaching 73% melting at zero pressure. (**c**) The results shown in (**a**) and (**b**) can actually be calculated directly by inspection of this diagram, which shows four constant pressure snapshots of the Entropy (S) – Composition (X_{hd}) phase diagram, at 6 GPa (*red*), 4 GPa (*green*), 2 GPa (*blue*), and zero pressure (*purple*). At each pressure, the solidus is the lower heavy curve, the liquidus is the upper heavy *curve*, and *light lines* are representative *tie-lines* connecting coexisting solids and liquids. The large *black circle* indicates the fixed total entropy and bulk composition of the system. At each pressure, the composition and entropy of the coexisting solid and liquid and the mass fraction of liquid can be found by examining the endpoints of the *tie-line* that passes through the *center* of the *black circle* and applying the lever rule. Since entropy and composition are the conserved quantities in isentropic decompression batch melting, this is the best set of variables to plot in order to visualize the partial melting process directly

The details of flux melting at subduction zones are complex and a matter of active debate in the scientific literature (Grove et al. 2009). The importance of sediment melting, basalt dehydration, basalt melting, and serpentinite dehydration in various layers of the slab are probably variable among subduction zones and through time. One view holds that only under special circumstances in the modern world and perhaps more commonly in the Archean, the hydrated, basaltic part of the subducting oceanic crust heats up enough by conduction to reach its solidus and melt directly. In this view, it is much more common for the hydrated basalt to cross dehydration boundaries and lose its water, which greatly increases its solidus temperature, before melting (Hacker et al. 2003). In this case, the partial melting that drives subduction-related volcanoes occurs instead above the subducting slab but beneath the overriding lithosphere, in the area known as the mantle wedge. The contrary view emphasizes the role of direct slab melting (Drummond et al. 1996; Kogiso et al. 2009) as the most efficient way to transfer water and other components from the subducting slab to the overlying volcanic arc (Turner and Langmuir 2015). Also, the physical pathways for flux components from their source in the slab to the melting regions in

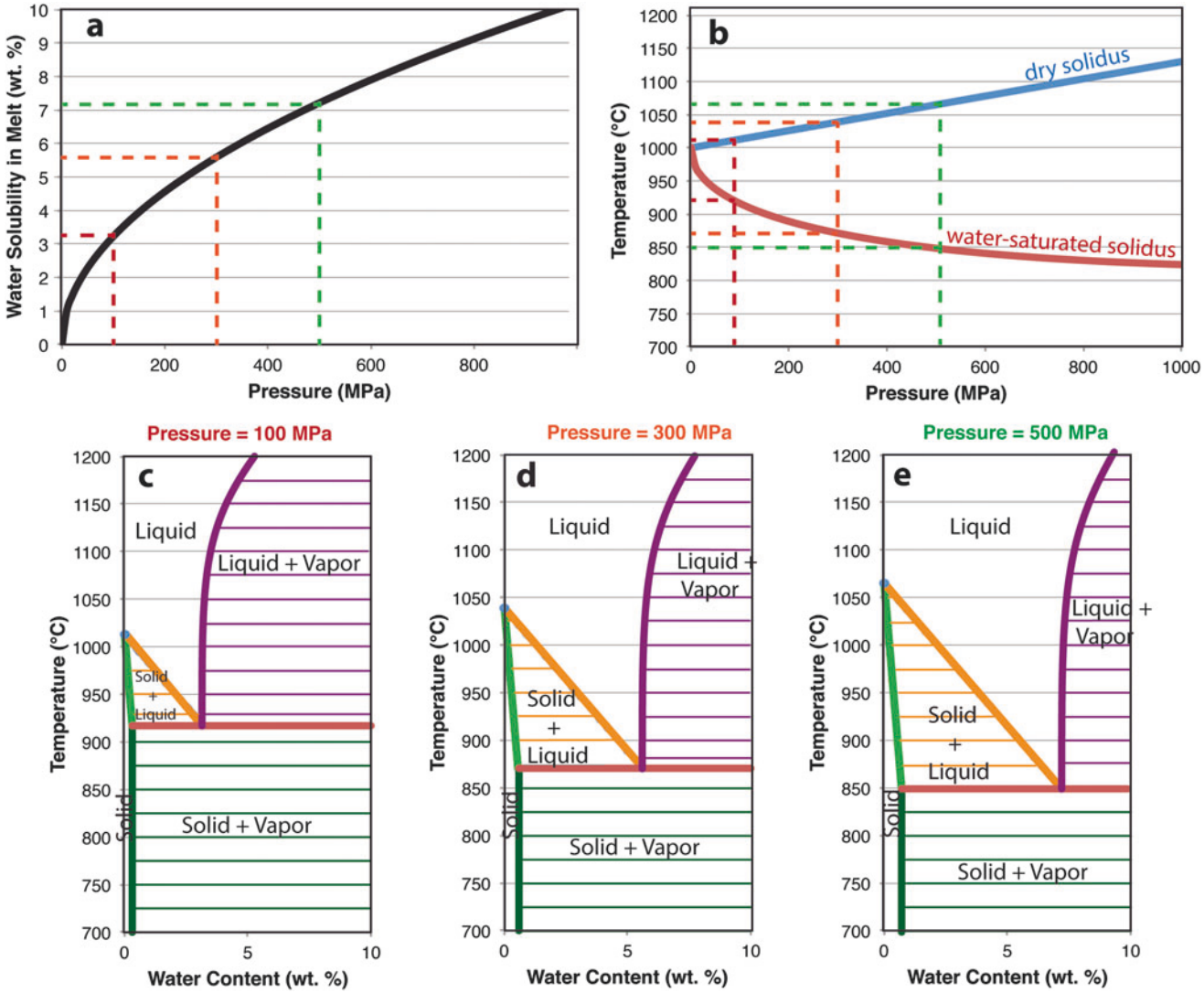

Partial Melting, Fig. 2 An interconnected series of diagrams that demonstrate the mechanism of flux melting of rock by addition of water, at pressure-temperature conditions where the rock would otherwise be solid. (**a**) The solubility of water in basaltic liquid, i.e., the maximum amount of water that can be dissolved before saturation with a separate vapor phase occurs, increases approximately as the square root of total pressure. The solubilities at three pressures (100 MPa, 300 MPa, and 500 MPa) are illustrated by the *dashed, colored lines*. (**b**) The solidus (lowest temperature where melt occurs) of most rocks, in the absence of water, increases with increasing pressure (*blue line* labeled "dry solidus"). However, the water-saturated solidus temperature (*red curve*), along which the rock coexists with vapor and the water concentration in the liquid equals the solubility, decreases with increasing pressure. With intermediate water contents, melting might begin anywhere between these two limits. The reason for this "solidus depression" effect is seen in the lower three panels. Each of these is a temperature vs. water content phase diagram drawn at constant total pressure of (**c**) 100 MPa, (**d**) 300 MPa, and (**e**) 500 MPa. The space is divided into fields where one phase (*solid* or *liquid*) exists alone (the vapor field is off-scale to the *right*) and fields where two phases coexist and their compositions are fixed to the boundaries of the field, at either end of the light *horizontal tie-lines*. The form of these diagrams results from three physical assumptions: (1) water is incompatible in the solid and partitions strongly into the liquid; the ratio of water content along the *light green line* to that along the *orange line* shows the partition coefficient; (2) the amount of freezing point depression is proportional to the concentration of water in the liquid, as expected for addition of a small amount of any incompatible solute to a solution, so that the *orange lines* beginning from the *blue dots* indicating dry solidus temperatures are *straight* and have about the same negative slope on each diagram; and (3) the lowering of the melting point is limited by the solubility of water in the liquid, which determines the locations of the red lines indicating water saturated solidus temperatures

shallower layers of the slab or in the mantle wedge are an area of active research. Hydrous components may be immobile in peridotite close to the cold slab and may initially freeze and generate an enriched, hydrated mantle source. Either by transport to high pressure where hydrous minerals decompose or by migration horizontally or vertically into the hot interior of the mantle wedge, the flux may reach sources at conditions that are above their

P

hydrated solidus and there drive partial melting and generation of magma to feed the overlying volcanic arc.

Heating by Conduction

Although decompression and flux addition are the fastest ways to generate partial melting, there are volcanoes that cannot be explained by either of these mechanisms. These include large rhyolitic caldera-forming systems in continental interiors, such as Yellowstone (Huang et al. 2015) and Long Valley (Simon et al. 2014), in North America. The continental crust and lithosphere, along a typical conductive geotherm, are colder everywhere than even the water-saturated solidus of the most easily melting rocks. The lithosphere being too rigid to flow and undergo decompression melting, upwards transport of heat by emplacement of melts from below or by heat conduction is needed. Both of these are likely to be concentrated above areas of melt generation in the underlying mantle. Hence, although the main source of mass in a large rhyolite volcano may be within the crust, one expects to find a mantle component (Wotzlaw et al. 2013). When rising basalt magma encounters the base of the continental crust, their relative buoyancy and contrast in temperatures promote magma ponding and crystallization. The latent heat release and perturbation of the geotherm provide the relatively focused heat source needed to promote hydrous melting of overlying crustal rocks (Annen et al. 2006). The granitic magmas that dominate the upper crust may then be derived from various combinations of material derived from differentiation of the basaltic underplate and from partial melting of the overlying crust; different authors have emphasized the relative roles of these contributions at various places and times in the evolution of the continental crust (Bonin 2004). Crustal partial melting is not necessarily related to such mantle-derived heat sources, though. Overthickened crust in a collisional orogen may gradually heat up to its solidus from radiogenic heat (Clark et al. 2011).

Summary

Magma, under almost all natural circumstances on terrestrial planets and meteorite parent bodies, is generated by a process of partial melting. Hence volcanism and magmatic activity are inevitably coupled to chemical and physical segregation of molten components from residual solid components, which explains much about the typical compositions of igneous rocks as well as the differentiation of planets into layers at various scales. Partial melting processes can be understood and classified into those associated with lowering of pressure, addition of low-melting point components, and conduction of heat into the source area.

Cross-References

- ▶ Entropy
- ▶ Experimental Mineralogy and Petrology
- ▶ Fractional Crystallization and Assimilation
- ▶ Geochemical Thermodynamics
- ▶ Incompatible Elements
- ▶ Magmatic Process Modeling
- ▶ Mantle Geochemistry
- ▶ Mid-Ocean Ridge Basalts (MORB)
- ▶ Oceanic Island Basalts
- ▶ Oxidation-Reduction Reactions and Eh-pH (Pourbaix) Diagrams
- ▶ Partitioning and Partition Coefficients
- ▶ Phase Equilibria
- ▶ Silicate Melts
- ▶ Solid Solution/Exsolution
- ▶ Subduction Zone Geochemistry
- ▶ Volcanism

References

Annen C, Blundy J, Sparks R (2006) The genesis of intermediate and silicic magmas in deep crustal hot zones. J Petrol 47 (3):505–539

Asimow PD, Hirschmann MM, Stolper EM (1997) An analysis of variations in isentropic melt productivity. Philos Trans R Soc Lond A 355:255–281

Asimow PD, Dixon JE, Langmuir CH (2004) A hydrous melting and fractionation model for mid-ocean ridge basalts: application to the Mid-Atlantic Ridge near the Azores. Geochem Geophys Geosyst 5 (1):Q01E16. https://doi.org/10.1029/2003GC000568

Bonin B (2004) Do coeval mafic and felsic magmas in post-collisional to within-plate regimes necessarily imply two contrasting, mantle and crustal, sources? A review. Lithos 78(1):1–24

Clark C, Fitzsimons IC, Healy D, Harley SL (2011) How does the continental crust get really hot? Elements 7(4):235–240

Drummond MS, Defant MJ, Kepezhinskas PK (1996) Petrogenesis of slab-derived trondhjemite-tonalite-dacite/adakite magmas. Trans Roy Soc Edinb Earth Sci 87:205–215

Ganguly J (2005) Adiabatic decompression and melting of mantle rocks: an irreversible thermodynamic analysis. Geophys Res Lett 32(6): LO6312

Grove TL, Chatterjee N, Parman SW, Medard E (2006) The influence of H_2O on mantle wedge melting. Earth Planet Sci Lett 249(1-2):74–89. https://doi.org/10.1016/J.Epsl.2006.06.043

Grove TL, Till CB, Lev E, Chatterjee N, Medard E (2009) Kinematic variables and water transport control the formation and location of arc volcanoes. Nature 459(7247):694–697. https://doi.org/10.1038/Nature08044

Hacker BR, Abers GA, Peacock SM (2003) Subduction factory – 1. Theoretical mineralogy, densities, seismic wave speeds, and H_2O contents. J Geophys Res Solid Earth 108(B1):2029. https://doi.org/10.1029/2001JB001127

Herzberg C, Asimow PD, Arndt N, Niu YL, Lesher CM, Fitton JG, Cheadle MJ, Saunders AD (2007) Temperatures in ambient mantle and plumes: constraints from basalts, picrites, and komatiites. Geochem Geophys Geosyst 8(2):Q02006. https://doi.org/10.1029/2006gc001390

Huang H-H, Lin F-C, Schmandt B, Farrell J, Smith RB, Tsai VC (2015) The Yellowstone magmatic system from the mantle plume to the upper crust. Science 348(6236):773–776
Kogiso T, Omori S, Maruyama S (2009) Magma genesis beneath Northeast Japan arc: a new perspective on subduction zone magmatism. Gondwana Res 16(3-4):446–457. https://doi.org/10.1016/J.Gr.2009.05.006
Langmuir CH, Klein EM, Plank T (1992) Petrological systematics of mid-ocean ridge basalts: constraints on melt generation beneath ocean ridges. In: Phipps Morgan J, Blackman DK, Sinton JM (eds) Geophysical monograph series, vol 71. American Geophysical Union, Washington, DC, pp 183–280
Maclennan J, McKenzie D, Gronvold K (2001) Plume-driven upwelling under central Iceland. Earth Planet Sci Lett 194(1-2):67–82
McKenzie D, Bickle MJ (1988) The volume and composition of melt generated by extension of the lithosphere. J Petrol 29:625–679
Pertermann M, Hirschmann MM (2003) Anhydrous partial melting experiments on MORB-like eclogite: phase relations, phase compositions and mineral-melt partitioning of major elements at 2-3 GPa. J Petrol 44(12):2173–2201. https://doi.org/10.1093/Petrology/Egg074
Simon JI, Weis D, DePaolo DJ, Renne PR, Mundil R, Schmitt AK (2014) Assimilation of preexisting Pleistocene intrusions at Long Valley by periodic magma recharge accelerates rhyolite generation: rethinking the remelting model. Contrib Mineral Petrol 167(1):1–34
Turner SJ, Langmuir CH (2015) What processes control the chemical compositions of arc front stratovolcanoes? Geochem Geophys Geosyst 16(6):1865–1893
Wotzlaw J-F, Schaltegger U, Frick DA, Dungan MA, Gerdes A, Günther D (2013) Tracking the evolution of large-volume silicic magma reservoirs from assembly to supereruption. Geology 41(8):867–870

Particle-Induced X-Ray Emission (PIXE)

Masanori Kurosawa
Faculty of Life and Environmental Sciences, University of Tsukuba, Tsukuba, Ibaraki, Japan

Definition

Particle-induced X-ray emission (PIXE) is a nondestructive method for analyzing many elements simultaneously by measuring the characteristic X-rays induced by a high-energy ion beam directed onto specimens. For high-sensitivity trace-element analyses, a proton beam accelerated with 2–3 MeV of energy by a small accelerator is normally used as the ion beam. For this reason, the method is sometimes called proton-induced X-ray emission. The proton beam used for measurements is typically focused onto a spot ranging in size from 0.1 μm to several tens of micrometers, so the analytical instrument is also referred to as a proton (or nuclear) microprobe, by analogy with the electron microprobe.

Analytical Features

The use of an energy-dispersive spectrometer (EDS) such as a Li- or Si-drifted silicon detector to measure the characteristic X-rays makes simultaneous multi-elemental analysis possible. Usually, elements heavier than sodium can be analyzed. Micro-PIXE, that is, PIXE measurements made with a microbeam, uses the same X-ray detection method as a scanning electron microscope equipped with an EDS, but the background of micro-PIXE measurements is greatly reduced; consequently, elements present at levels of just a few ppm can be detected (Ryan et al. 1990; Czamanske et al. 1993). Micro-PIXE scanning with a submicrometer-sized beam is often used for trace-element mapping of various types of samples (Watt and Grime 1995; Fraser 1995). A 2–3-MeV proton beam can penetrate silicate samples to a depth of several tens of micrometers, which exceeds the penetration depth of an electron beam. The horizontal spread of the X-ray generating region induced by the proton beam, however, is much smaller than that induced by an electron beam. The deep penetration of the proton beam and its ability to generate X-rays from deep within a sample make the PIXE method suitable for elemental analyses of single fluid inclusions inside a host mineral (Kurosawa et al. 2003).

PIXE has a great analytical advantage in that it can be used to detect trace amounts of heavy elements in matrices composed of light elements because of the low X-ray background. Therefore, it is commonly used for trace-element analyses of silicate and carbonate minerals, glasses, aerosols, dried biological materials, and semiconductors. Rock thin sections, thin films, and powder-form samples supported by organic thin films are usually analyzed in a vacuum sample chamber, but it is also possible to analyze samples in ambient air (external-PIXE). Although the flight distance (range) of a 2–3-MeV ion beam in air is short (several centimeters), the beam can be extracted from a vacuum beam line to the air near the sample through a thin foil. Thus, it is also possible to analyze liquid or gaseous specimens and biological bodies, as well as large archeological objects and precious art or craft items, that cannot be inserted into a vacuum chamber. External-PIXE is used mainly for qualitative analyses of major and minor elements in such samples.

Quantitative Analysis

The calculations for quantification of PIXE analysis results use experimentally determined and fundamental physical parameters such as the X-ray generation conditions, detector solid angle and sensitivity, ion beam energy loss in the samples, X-ray self-absorption, and beam irradiation magnitudes (Reuter et al. 1975; Campbell 1995). The calculations to correct for energy loss, X-ray absorption, and secondary fluorescence effects are very similar to the ZAF correction of electron probe microanalysis. Software packages have also been developed for quantification of PIXE results (e.g., Campbell et al. 2010). The analytical error is usually better

than 10–15% for ppm concentration ranges (Czamanske et al. 1993). Detection limits of PIXE analyses depend on the atomic numbers of the elements being measured, the energy and total irradiation of the ion beam, and the bulk composition of the sample, all of which affect the generation of X-rays by the ion beam and the degree of self-absorption of the X-rays (Johansson and Johansson 1976; Sie et al. 1991; Campbell 1995). For optimal detection limits, K X-ray peaks are generally measured for elements with atomic numbers smaller than about 45, and L X-ray peaks are measured for heavy elements with atomic numbers greater than 45. The absolute detection limits are on the order of 10^{-13} g for microbeam analyses of transition-metal elements in fluid inclusions (Kurosawa et al. 2003). With micro-PIXE, it is theoretically possible to detect trace elements at levels of 10^{-15} to 10^{-16} g in thin organic films (Johansson 1995).

Future Work

Most PIXE analyses are performed at accelerator facilities, but a portable PIXE system that uses an alpha emission source (^{210}Po) is available for outdoor measurements of major and trace element compositions and for identification of minerals and pigments (Pappalardo et al. 2004). Since the portable PIXE demonstrates a strength of the higher sensitive analyses under a vacuum condition, it is suitable for in situ elemental analysis of samples on lunar and planetary surfaces. Thus, the instrument combined with an X-ray fluorescence analytical system has also been developed for the Mars exploration rover (Gellert et al. 2015).

Cross-References

- ▶ Electron Probe Microanalysis (EPMA)
- ▶ Synchrotron X-Ray Fluorescence Analysis

References

Campbell JL (1995) Instrumentation, fundamentals, and quantification. In: Johansson SAE, Campbell JL, Malmqvist KG (eds) Particle-induced X-ray emission spectrometry (PIXE). Wiley, New York, pp 19–100

Campbell JL, Boyd NI, Grassi N, Bonnick P, Maxwell JA (2010) The Guelph PIXE software package IV. Nucl Instrum Methods Phys Res B268:3356–3363

Czamanske GK, Sisson TW, Campbell JL, Teesdale WJ (1993) Micro-PIXE analysis of silicate reference standards. Am Mineral 78:893–903

Fraser DG (1995) The nuclear microprobe – PIXE, PIGE, RBS, NRA and ERDA. In: Potts PJ, Bowles JFW, Reed SJB, Cave MR (eds) Microprobe techniques in the earth sciences. Chapman and Hall, London, pp 141–162

Gellert R, Clark BC III, the MSL and MER Science Teams (2015) In situ compositional measurements of rocks and soils with the alpha particle X-ray spectrometer on NASA's Mars rovers. Elements 11:39–44

Johansson SAE (1995) Introduction to PIXE. In: Johansson SAE, Campbell JL, Malmqvist KG (eds) Particle-induced X-ray emission spectrometry (PIXE). Wiley, New York, pp 1–17

Johansson SAE, Johansson TB (1976) Analytical application of particle induced X-ray emission. Nucl Instrum Methods 137:473–516

Kurosawa M, Shimano S, Ishii S, Shima K, Kato T (2003) Quantitative trace element analysis of single fluid inclusions by proton-induced X-ray emission (PIXE): application to fluid inclusions in hydrothermal quartz. Geochim Cosmochim Acta 67:4337–4352

Pappalardo G, Costa E, Marchetta C, Pappalardo L, Romano FP, Zucchiatti A, Prati P, Mando PA, Migliori A, Palombo L, Vaccari MG (2004) Non-destructive characterization of Della Robbia sculptures at the Bargello museum in Florence by the combined use of PIXE and XRF portable systems. J Cult Herit 5:183–188

Reuter W, Lurio A, Cardone F, Ziegler JF (1975) Quantitative analysis of complex targets by proton-induced x rays. J Appl Phys 46:3194–3202

Ryan CG, Cousens DR, Sie SH, Griffin WL, Suter GF (1990) Quantitative PIXE microanalysis of geological material using the CSIRO proton microprobe. Nucl Instrum Methods Phys Res B47:55–71

Sie SH, Ryan CG, Suter GF (1991) Micro-PIXE (particle-induced X-ray emission analysis) applications in mineral research. Scanning Microsc 5:977–987

Watt F, Grime GW (1995) The high-energy ion microprobe. In: Johansson SAE, Campbell JL, Malmqvist KG (eds) Particle-induced X-ray emission spectrometry (PIXE). Wiley, New York, pp 101–165

Partitioning and Partition Coefficients

Chenguang Sun
Department of Earth, Environmental and Planetary Sciences, Rice University, Houston, TX, USA

Definition

Partitioning is used in geochemistry to describe the equilibrium distribution of a chemical species between two coexisting phases. The concentration ratio of this species between the two phases (α and β) is defined as the **partition coefficient** (D) to quantitatively measure the equilibrium fractionation,

$$D_i^{\alpha/\beta} = C_i^{\alpha}/C_i^{\beta}, \quad (1)$$

where C denotes the concentration of species i in each phase. The species could be a cation, anion, or chemical compound, while the coexisting phases may be present as solids, liquids, or vapors. According to different forms of concentration, the partition coefficient can be defined by weight fractions, molar contents, and volume percentages of the species.

Different species may behave in distinct manners with a wide spectrum of partition coefficients. Depending on its

relative affinity with the reference phase α, a species is classified as compatible when $D^{\alpha/\beta} > 1$ or incompatible when $D^{\alpha/\beta} < 1$. When the species is a fundamental constitution of phase β, the partition coefficient is then named as the solubility of this species in phase α. The partitioning concept is also applicable to measure the fractionation of two similar species between equilibrium phases. The corresponding "partition coefficient" is usually called the exchange coefficient.

History and Use

Earth's interior has two major compositional layers: a metallic core overlaid by a silicate mantle and crust. In the silicate Earth, magmatic processes along with plate tectonics play a major role in modulating chemical differentiation. An initial interest of partitioning studies in geochemistry is to understand magmatic processes using fractionation of trace element (<0.1 wt%) between crystals and melts. Relative partition coefficients of trace elements were qualitatively estimated using **Goldschmidt's rules** i.e., the size and charge of an ion determines its partitioning behaviors in various minerals (Goldschmidt 1937). Since the Apollo missions, planetary differentiation became one of the main themes in geochemistry, which also demands knowledge of element partitioning in systems relevant to core formation, such as metal-silicate and sulfide-silicate melts.

Prior to the advancement of experimental partitioning studies, bulk chemical analyses of mineral separates and matrices from quenched volcanic lavas have been used to quantitatively determine crystal-melt partition coefficients for trace elements by assuming chemical equilibrium. Using this phenocryst-matrix approach, Onuma et al. (1968) made a fundamental observation that isovalent trace element partition coefficients vary parabolically with their ionic radii in a semi-log graph. This type of graphs was later named as Onuma diagrams (see ▶ "Onuma Diagrams"), which have been widely used to investigate partitioning behaviors of trace elements in a specific mineral. The main challenges of this phenocryst-matrix approach include (1) distinguishing phenocrysts from xenocrysts that are not in equilibrium with glass matrices and (2) identifying phenocrysts without mineral or melt inclusions. The former may be prevented by careful petrographic studies or using well-constrained laboratory experiments, while the latter can be overcome by recently developed in situ analytical methods. For these reasons, the methods used in partitioning studies gradually changed to a combination of high temperature experiments and in situ chemical analyses, while the phenocryst-matrix approach is still actively used in recent literature (e.g., Mollo et al. 2017).

Due to the lack of partitioning data, trace element partition coefficients were previously considered as constant. However, later experimental partitioning studies demonstrated that trace element partition coefficients could vary by orders of magnitude, depending on temperature, pressure, composition, and/or redox condition. The variable partitioning data further motivated geochemists to develop quantitative understanding of trace element partitioning behaviors in various systems using new thermodynamic theories and experimental measurements.

Thermodynamic Basis

The theoretical basis of partitioning is the exchange reaction of a chemical species between two equilibrium phases. The exchange reaction varies with the valence states of this species and the major compositions of the phases. Following is a brief overview of thermodynamic principles (see ▶ "Geochemical Thermodynamics") for three major systems (i.e., mineral-melt, metal-silicate melts, and sulfide-silicate melts) relevant to high-temperature planetary processes.

Mineral-Melt Systems

The equilibrium exchange of a chemical species [i] between a crystal and a silicate melt can be described using the following reaction (e.g., Wood and Blundy 2003)

$$[i^{n+}]_{\text{melt}} = [i^{n+}]_{\text{crystal}}, \tag{2}$$

where n denotes the valence state of the species. The equilibrium constant (K) (see ▶ "Equilibrium Constant") can be expressed as

$$\begin{aligned} \ln K_i &= \ln\left(\frac{a_i^{\text{crystal}}}{a_i^{\text{melt}}}\right) = \ln\left(\frac{C_i^{\text{crystal}}\gamma_i^{\text{crystal}}}{C_i^{\text{melt}}\gamma_i^{\text{melt}}}\right) = -\frac{\Delta G}{RT} \\ &= -\frac{\Delta H}{RT} + \frac{\Delta S}{R} - \frac{P\Delta V}{RT}, \end{aligned} \tag{3}$$

where a, and γ are thermodynamic activity, and activity coefficient of species [i] (see ▶ "Activity and Activity Coefficients"), respectively; ΔG, ΔH, ΔS, and ΔV are the changes of Gibbs free energy, enthalpy, entropy, and volume for the exchange reaction, respectively; and R is the gas constant. Simply combining Eq. 3 with Eq. 1 gives rise to the generic thermodynamic expression for the partition coefficient of species [i] between a crystal and a melt,

$$\begin{aligned} \ln D &= \ln K_i - \ln\left(\frac{\gamma_i^{\text{crystal}}}{\gamma_i^{\text{melt}}}\right) \\ &= -\frac{\Delta H}{RT} + \frac{\Delta S}{R} - \frac{P\Delta V}{RT} - \ln\left(\frac{\gamma_i^{\text{crystal}}}{\gamma_i^{\text{melt}}}\right). \end{aligned} \tag{4}$$

In general, the activity coefficient of the chemical species varies with its concentration at a given temperature but

approaches a constant at a low concentration level according to Henry's law (see ▶ "Henry's Law").

The Lattice Strain Model

In ionic crystals, substitution of a cation into the lattice site has to overcome the strain energy change (ΔG_{strain}), which depends on the elastic property (i.e., Young's modulus, E) of the specific lattice site and the relative size differences between the cation (r_i) and the strain-free lattice site (r_0) (Brice 1975; see Fig. 1a–c). The Gibbs free energy change can be written as,

$$\Delta G = \Delta G_0 - \Delta G_{strain}^{crystal} + \Delta G_{strain}^{melt}, \tag{5a}$$

$$\Delta G_{strain}^{crystal} = 4\pi E N_A \left[\frac{r_0}{2}(r_0 - r_i)^2 - \frac{1}{3}(r_0 - r_i)^3\right], \tag{5b}$$

where ΔG_0 is the change of Gibbs free energy for strain-free exchange of an ideal cation with the same charge between the crystal and melt, and N_A is Avogadro's number. In the liquid phase, the Young's modulus and hence the strain energy change are negligible. Accordingly, the partition coefficient of a trace element has the following expression,

$$D_i = D_0 \exp\left\{-\frac{4\pi E N_A}{RT}\left[\frac{r_0}{2}(r_0 - r_i)^2 - \frac{1}{3}(r_0 - r_i)^3\right]\right\}, \tag{6a}$$

$$\ln D_0 = -\frac{\Delta H_0}{RT} + \frac{\Delta S_0}{R} - \frac{P\Delta V_0}{RT} - \ln\left(\frac{\gamma_0^{crystal}}{\gamma_0^{melt}}\right), \tag{6b}$$

where D_0 is the strain-free partition coefficient of the ideal cation, determining the maximum partition coefficients of the parabola in Onuma diagrams (see Fig. 1c).

Initially presented in Brice (1975), Eq. 6a has been well known as the **Brice equation** or the **lattice strain model**. Interestingly, prior to Brice (1975), Nagasawa (1966) had already developed a similar equation, which was used by Onuma et al. (1968) and Beattie (1994) to demonstrate the parabolic relationship between partition coefficients and ionic radii. Because Brice's equation is more straightforward and easier to use, since the first experimental test by Blundy and Wood (1994), it became popularized in geochemistry and widely used for modeling the partitioning of isovalent trace element cations between minerals and melts. The most successful application of the lattice strain model in crystal-melt systems is on rare earth elements (REE; see ▶ "Lanthanide Rare Earths") that are typically present as trivalent cations with similar ionic radii. The challenges for other isovalent cations include multiple site occupancies (e.g., Zr and Hf in garnet; van Westrenen et al. 2001a), multiple valence states (e.g., V, Cr, and Co), and crystal field effects (e.g., V, Cr, Mn, Fe, Co, and Ni).

The Electrostatic Model

Inverted from the experimentally determined partitioning data, the lattice strain parameters (D_0, E, and r_0) of heterovalent cations in the same lattice site vary systematically with the cation charge. The strain-free partition coefficients (D_0) and the cation charge follow a parabolic relationship (Fig. 2a), which could be well explained by the **electrostatic model** of Wood and Blundy (2003),

$$D_0^{Z+} = D_{00} \exp\left[\frac{-\Phi}{RT}(Z - Z_0)^2\right], \tag{7}$$

where Φ is a constant factor for the electrostatic work, controlling the opening of the parabola; Z is the charge of the ideal cation; Z_0 is the charge of major cations in the lattice site; and D_{00} is the strain-free partition coefficients for cations of charge Z_0.

The strain-free lattice size (r_0) displays a week correlation with the cation charge; however, the Young's modulus (E) shows a strong positive correlation with the cation charge, which agrees well with the Hazen–Finger equation (Hazen and Finger 1979) parameterized for homogeneous isotropic materials (Fig. 2b). A striking feature of the electrostatic model (Eq. 7) is that it allows estimation of the poorly constrained **noble gas** (see ▶ "Noble Gases") partition coefficients. Because the Young's modulus of noble gases (0+) in the lattice site is negligible according to the Hazen–Finger

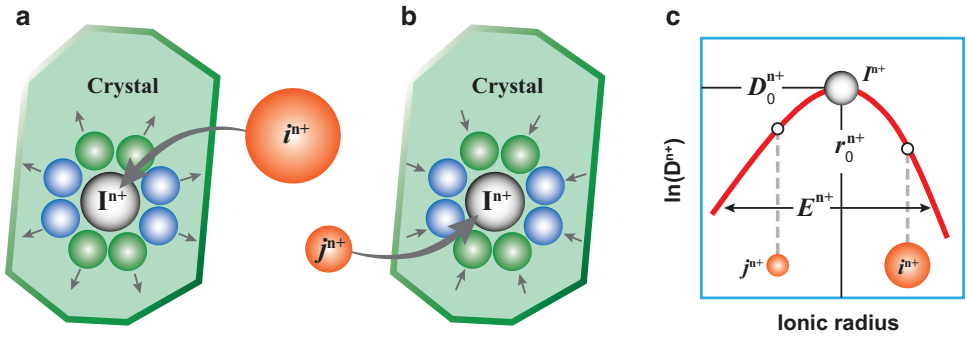

Partitioning and Partition Coefficients, Fig. 1 Cartoon drawings showing cation substitution into the crystal lattice site (**a** and **b**), and a schematic Onuma diagram showing their crystal-melt partitions (**c**). i^{n+} indicates a lager cation, j^{n+} denotes a smaller one, and I^{n+} represents the strain-free cation in the lattice site

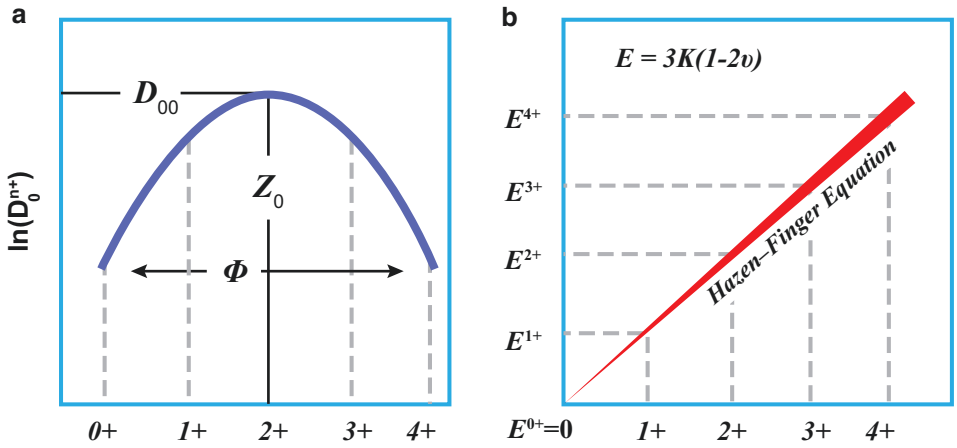

Partitioning and Partition Coefficients, Fig. 2 Illustrations of the parabolic relationship between the strain-free partition coefficients (D_0) with cation charges (**a**) and the positive relationship between the Young's moduli (E) and cation charges (**b**). Z_0 in (**a**) indicates the major cation charge in the lattice site. Equation inset in (**b**) shows the relation between Young's modulus (E) and bulk modulus (K), in which υ is the Poisson's ratio of the material (Wood and Blundy 2003)

equation, the noble gas partition coefficients can be directly calculated using Eq. 7, when the strain-free partition coefficients are available for monovalent, divalent, and trivalent cations in the same lattice site.

Metal-Silicate Systems

The equilibrium exchange of a chemical species [i] between a liquid metal alloy and a silicate melt can take place through the following reaction (e.g., Righter and Drake 2003),

$$[i^{n+}]_{\text{silicate}} + \frac{n}{2}[O^{2-}]_{\text{silicate}} = [i]_{\text{metal}} + \frac{n}{4}[O_2]_{\text{gas}}, \quad (8)$$

The equilibrium constant (K) can be expressed as

$$\begin{aligned} \ln K_i &= \ln\left(\frac{a_i^{\text{metal}}(fO_2)^{n/4}}{a_i^{\text{silicate}}\left(a_{O^{2-}}^{\text{silicate}}\right)^{n/2}}\right) \\ &= \ln\left(\frac{C_i^{\text{metal}}\gamma_i^{\text{metal}}}{C_i^{\text{silicate}}\gamma_i^{\text{silicate}}}\right) - \frac{n}{2}\ln a_{O^{2-}}^{\text{silicate}} + \frac{n}{4}\ln fO_2 \\ &= -\frac{\Delta G}{RT}. \end{aligned} \quad (9)$$

Note that this equilibrium constant is distinct from that in a mineral-melt system (Eq. 3) because this metal-silicate exchange reaction requires the change of oxidation states (fO_2). Accordingly, the metal-silicate partition coefficient has the following thermodynamic expression,

$$\begin{aligned} \ln D_i^{\text{metal/silicate}} = &-\frac{\Delta H}{RT} + \frac{\Delta S}{R} - \frac{P\Delta V}{RT} - \ln\left(\frac{\gamma_i^{\text{metal}}}{\gamma_i^{\text{silicate}}}\right) \\ &+ \frac{n}{2}\ln a_{O^{2-}}^{\text{silicate}} - \frac{n}{4}\ln fO_2. \end{aligned} \quad (10)$$

Although trace elements in a silicate melt may obey Henry's law and have constant activity coefficients, the activity of O^{2-} in the silicate melt strongly depends on the melt compositions. As well known in material science, trace elements in liquid metal alloys also have composition-dependent activity coefficients due to their strong interactions with the major constitutions (e.g., Fe, C, S, and Si) in the alloy (e.g., Ma 2001).

The metal-silicate partitioning of a chemical species could also be described through an alternative reaction by coupling Fe exchange with the species of interest (e.g., Wade and Wood 2005),

$$[i\,O_{n/2}]_{\text{silicate}} + \frac{n}{2}[Fe]_{\text{metal}} = [i]_{\text{metal}} + \frac{n}{2}[FeO]_{\text{silicate}}. \quad (11)$$

This reaction has a different thermodynamic expression for the partition coefficient,

$$\begin{aligned} \ln D_i = &-\frac{\Delta H}{RT} + \frac{\Delta S}{R} - \frac{P\Delta V}{RT} - \ln\left(\frac{\gamma_i^{\text{metal}}}{\gamma_i^{\text{silicate}}}\right) \\ &- \frac{n}{2}\ln a_{FeO}^{\text{silicate}} + \frac{n}{2}\ln a_{Fe}^{\text{metal}}. \end{aligned} \quad (12)$$

An advantage of this treatment is that it could avoid the use of oxygen fugacity, which may not be straightforward to constrain in high-pressure experiments or during planetary processes. However, this does not imply a negligible effect of oxygen fugacity on metal-silicate partitioning, as the oxygen fugacity controls FeO activity in a metal-saturated silicate melt.

The metal-silicate partitioning for anion species may follow different reactions. For instance, Tsuno et al. (2013) considered oxygen as free atoms in liquid metal alloys ($[FeO]_{\text{silicate}} = [Fe]_{\text{metal}} + [O]_{\text{metal}}$), while Boujibar et al. (2014) regarded sulfur as S^{2-} both in liquid metal alloys and silicate melts ($[Fe^{2+}]_{\text{silicate}}+[S^{2-}]_{\text{silicate}}=[FeS]_{\text{metal}}$; from the combination of their Eqs. 4 and 7). However, the thermodynamic expressions of the anion partition coefficients are similar to Eq. 12, supporting the effects of temperature, pressure, composition, and/or redox condition.

Sulfide-Silicate Systems

The equilibrium exchange of a chemical species between a sulfide melt and a silicate liquid does not require the valence change of the chemical species. Simply, the exchange reaction could be written as the same form of Eq. 2, rendering a thermodynamic expression of sulfide-silicate partition coefficients similar to Eq. 4. However, the stabilization of sulfide liquids in a silicate melt is determined by the reaction (e.g., Fincham and Richardson 1954),

$$\left[O^{2-}\right]_{\text{silicate}} + \frac{1}{2}[S_2]_{\text{gas}} = \left[S^{2-}\right]_{\text{sulfide}} + \frac{1}{2}[O_2]_{\text{gas}}, \quad (13)$$

where ½S_2 may be replaced by SO_2 with one additional O_2 on the right hand side. Taking account of sulfide saturation in the silicate melt, the sulfide-silicate chemical exchange could be described as (e.g., Gaetani and Grove 1997)

$$\left[i\ O_{n/2}\right]_{\text{silicate}} + \frac{n}{4}[S_2]_{\text{gas}} = \left[i\ S_{n/2}\right]_{\text{sulfide}} + \frac{n}{4}[O_2]_{\text{gas}}. \quad (14a)$$

This exchange reaction can be well characterized under controlled low-pressure laboratory conditions but introduces an extra term fS_2, a poorly constrained intensive parameter in planetary interiors.

At the saturation of FeS, a dominant component in sulfide melts, the exchange of a minor or trace element cation between sulfide and silicate melts could also be considered through a reaction coupled with Fe^{2+} exchange (e.g., Kiseeva and Wood 2013),

$$\left[i\ O_{n/2}\right]_{\text{silicate}} + \frac{n}{2}[FeS]_{\text{sulfide}} = \left[i\ S_{n/2}\right]_{\text{sulfide}} + \frac{n}{2}[FeO]_{\text{silicate}}. \quad (14b)$$

Accordingly, the sulfide-silicate partition coefficient has the following thermodynamic expression,

$$\ln D_i = -\frac{\Delta H}{RT} + \frac{\Delta S}{R} - \frac{P\Delta V}{RT} - \ln\left(\frac{\gamma_i^{\text{sulfide}}}{\gamma_i^{\text{silicate}}}\right) - \frac{n}{2}\ln a_{\text{FeO}}^{\text{silicate}} + \frac{n}{2}\ln a_{\text{FeS}}^{\text{sulfide}}. \quad (15)$$

Similar to those for mineral-melt (Eqs. 6a, b) and metal-silicate (Eq. 12) systems, sulfide-silicate partition coefficients, as shown in Eq. 15, are also a function of temperature, pressure, composition, and/or redox condition.

Mineral-Melt Partition Coefficients

Mineral-melt partition coefficients are widely used to track high-temperature magmatic processes through igneous rocks. Specific applications include, but not limited to, (1) modeling chemical differentiation during mantle melting or magma crystallization (e.g., Shaw 2000; Liang 2008; Dasgupta et al. 2009a; see ▶ "Magmatic Process Modeling"), (2) constraints on the composition and redox conditions of parental melts and/or mantle sources (e.g., Papike 1996; Lee et al. 2010; Le Roux et al. 2011; Trail et al. 2011), and (3) development of geothermometers and geobarometers (e.g., Watson et al. 2006; Liang et al. 2013; Sun and Liang 2015, 2017). As major rock-forming minerals in the upper mantle and lower crust, olivine, pyroxene, garnet, plagioclase, and amphibole have been systematically investigated for partitioning behaviors of trace elements through high-temperature experiments.

Olivine

The general formula for olivine crystals is M_2TO_4, in which M indicates the octahedral site and T denotes the tetrahedral site. The M site mainly contains Mg^{2+} and Fe^{2+} in VI-fold coordination with ionic radii (see ▶ "Ionic Radii") of 0.72 and 0.78 Å, respectively (Shannon 1976), while the T site is primarily composed of Si^{4+} in IV-fold coordination ($^{IV}Si^{4+}$: 0.26 Å). Impurities of minor or trace elements, if any, are mainly incorporated into the larger M site. Because small divalent cations, e.g., Ni^{2+} (0.69 Å; VI-fold), Co^{2+} (0.745 Å), and Mn^{2+} (0.83 Å), have ionic radii similar to Mg^{2+} and Fe^{2+}, they are generally compatible in olivine ($D \geq 1$; Fig. 3a). Large divalent cations, e.g., Sr^{2+} (1.18 Å) and Ba^{2+} (1.35 Å), however, are difficult to fit into the M site due to the lattice strain energy (cf. Eq. 6a) and thus are incompatible in olivine ($D < 1$; Fig. 3a).

For cations with 1+, 3+, 4+, and 5+ charges, the substitution involves the replacement of Mg^{2+}, Fe^{2+}, or Si^{4+} by other cations (e.g., Al^{3+} or Fe^{3+}) (i.e., **coupled substitution**) for charge balance, which leads to strong compositional dependence of trace element partitioning. Substitution of these cations into the divalent M site has to overcome the electrostatic work (Eq. 7) in addition to the lattice strain energy. For instance, although the ionic radii of pentavalent cations, e.g., Nb^{5+} and Ta^{5+} (0.64 Å), are close to major cations in the M site, the excess electrostatic work prevents the partitioning of these cations in olivine. This is also the case for the partitioning of tetravalent cations, e.g., Ti^{4+} (0.605 Å), Hf^{4+} (0.71 Å), and Zr^{4+} (0.72 Å), in olivine. Due to the larger deviation of their valence from that (2+) of major cations in the M site, pentavalent cations appear to be more incompatible than tetravalent cations and monovalent cations (e.g., Na^{+}).

Small trivalent cations, e.g., Sc^{3+} (0.745 Å), V^{3+} (0.64 Å), and Cr^{3+} (0.615 Å), have ionic radii close to major cations in the M site and in turn are moderately compatible in olivine ($D = \sim 0.05–5$). Given their variable valence states in response to redox conditions, V and Cr have a wide range of partition coefficients. As REE have significantly larger ionic radii

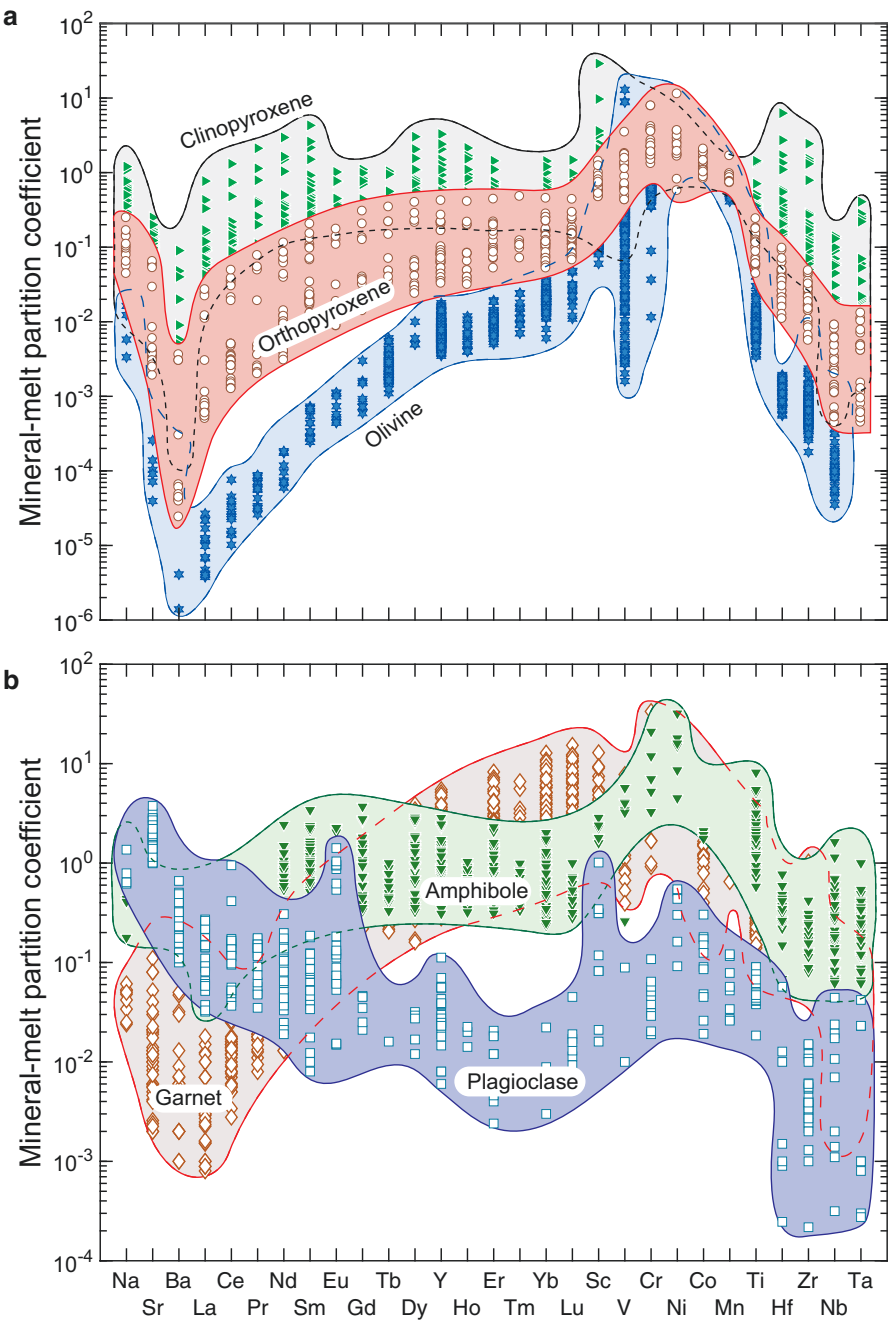

Partitioning and Partition Coefficients, Fig. 3 Spider diagrams showing the experimentally determined partition coefficients of trace elements in olivine-melt, clinopyroxene-melt, orthopyroxene-melt, garnet-melt, plagioclase-melt, and amphibole-melt systems. Data sources can be found in Sun and Liang (2012, 2013a), Yao et al. (2012), Sun et al. (2017), and Shimizu et al. (2017). Note the different scales along Y-axes in (**a**) and (**b**)

(i.e., 0.861–1.032 Å), their partition coefficients are overall smaller than those of Sc^{3+}. With the increase of ionic radii from Lu to La, REE become highly incompatible in olivine.

Notably, for a given trace element, the experimentally determined olivine-melt partition coefficient also varies by one to four orders of magnitude due to the effects of temperature, pressure, and composition (and fO_2 for multivalent cations; e.g., V), which complicate the direct use of partition coefficients. Several predictive models have been developed using experimental partitioning data for calculating olivine-melt partition coefficients of individual trace elements (e.g., Beattie et al. 1991; Evans et al. 2008; Mallmann and O'Neill 2013; Matzen et al. 2017). In particular for REE, a generalized lattice strain model is available in Sun and Liang (2013a). However, the accuracy of these models is not uniform, which demands special attention for geological applications.

Pyroxene

The general formula for pyroxene crystals is XYT_2O_6. The *T* site could accommodate tetrahedrally coordinated Si^{4+} and Al^{3+} ($^{IV}Al^{3+}$: 0.39 Å), whereas *X* and *Y* denote two octahedral sites, a larger *M2* site and a smaller *M1* site. The *M1* site is

occupied by small cations in VI-fold coordination, including Mg^{2+}, Fe^{2+}, and Al^{3+} ($^{VI}Al^{3+}$: 0.535 Å); in addition to Mg^{2+} and Fe^{2+}, the *M2* site could also hold larger cations, Ca^{2+}, Na^{+}, and K^{+}. The *M2* coordination number increases from VI-fold to VIII-fold with the enrichment of large cations (e.g., Ca^{2+}) on the site (Cameron and Papike 1981). Practically, VI-fold and VIII-fold are applied to cations in the *M2* sites of orthopyroxene and clinopyroxene, respectively. Because ionic radii of cations become larger for greater coordination numbers, the same cations in clinopyroxene *M2* site are effectively bigger than those in orthopyroxene *M2* site (e.g., $^{VIII}Ca^{2+}$–1.12 Å vs. $^{VI}Ca^{2+}$–1.0 Å, $^{VIII}Mg^{2+}$–0.89 Å vs. $^{VI}Mg^{2+}$–0.72 Å, and $^{VIII}Fe^{2+}$–0.92 Å vs. $^{VI}Fe^{2+}$–0.78 Å). Overall, with higher Ca contents, the *M2* site in clinopyroxene is larger than that in orthopyroxene. This enables clinopyroxene to accommodate trace element cations with large ionic radii (e.g., REE^{3+}, Sr^{2+}, Ba^{2+}, Na^{+}) and in turn results in greater partition coefficients of these cations in clinopyroxene (Fig. 3a).

Small divalent cations (e.g., Ni^{2+} and Co^{2+}) with ionic radii similar to $^{VI}Mg^{2+}$ and $^{VI}Fe^{2+}$ preferentially enter the *M1* site in pyroxenes. The slightly larger divalent cation, Mn^{2+}, could freely go to both *M2* and *M1* sites. All three are generally compatible in pyroxenes and have partition coefficients comparable to those in olivine. Similar to Ni^{2+} and Co^{2+}, small tetravalent and pentavalent cations (e.g., Ti^{4+}, Hf^{4+}, Zr^{4+}, Nb^{5+}, and Ta^{5+}) also go to the *M1* site, but their partition coefficients are about one to three orders of magnitude greater that those in olivine. This can be attributed to their different crystal structures. As partitioning of 3+, 4+, and 5+ cations into divalent cation sites requires coupled substitution with trivalent cations (e.g., Al^{3+}) for charge balance (e.g., Gaetani and Grove 1995; Lundstrom et al. 1998), Al-enriched pyroxenes tend to have higher affinity with these high-valent cations. An extreme example can be found in Blundy et al. (1998), in which heavy REE becomes compatible in high-Al clinopyroxenes.

The effects of temperature, pressure, and composition result in one to three orders of magnitude variations in experimentally determined pyroxene-melt trace element partition coefficients (Fig. 3a). However, selection of partition coefficients for relevant geological settings could be readily achieved using thermodynamic-based predictive models calibrated against experimental data (e.g., Gaetani and Grove 1995; Salters et al. 2002). Particularly, generalized lattice strain models are also available for the partitioning of REE (Wood and Blundy 1997; Sun and Liang 2012; Yao et al. 2012) and Ti, Hf and Zr (Hill et al. 2011; Sun and Liang 2013b).

Garnet

The general formula for garnet is $X_3Y_2T_3O_{12}$, in which *X*, *Y*, and *T* indicate the dodecahedral, octahedral, and tetrahedral sites, respectively. The *X* site is controlled by VIII-fold coordinated divalent cations, Ca^{2+}, Fe^{2+}, Mg^{2+}, and Mn^{2+}, while the *Y* site is governed by VI-fold coordinated small trivalent cations, Al^{3+}, Cr^{3+}, and Fe^{3+}. Tetrahedrally coordinated Si^{4+} dominates the *T* site. With increasing pressure, the garnet structure favors the replacement of small trivalent cations in the *Y* site by Si^{4+} and Mg^{2+}, leading to the Mg- and Si-rich end-member garnet, majorite. In general, the *X* and *Y* sites are the major locations in the garnet lattice to incorporate trace element cations. Large cations, e.g., REE^{2+}, Sr^{2+}, Ba^{2+}, Na^{+}, favor the *X* site, small cations, e.g., Cr^{3+}, V^{3+}, and Ti^{5+} (and perhaps Nb^{5+} and Ta^{5+}), preferentially enter the less spacious *Y* site, whereas intermediate cations, e.g., Ni^{2+}, Co^{2+}, Sc^{3+}, Zr^{4+}, and Hf^{4+}, may occupy both *X* and *Y* sites. With increasing Ca content, the *X* site in garnet becomes bigger, which enhances the substitution of larger cations.

The partition coefficients of trace elements in garnet are overall comparable to those in pyroxenes, except for REE. Similar to those in olivine and pyroxene, heavy REE have ionic radii closer to the major cations in garnet *X* site and thus are easier to substitute into the lattice site than the larger light REE. The relatively more rigid structure of garnet, however, determines a tighter parabola for REE in Onuma diagrams. This gives rise to an important characteristic of REE partitioning in garnet, i.e., heavy REE are generally compatible in garnet while light REE are incompatible (Fig. 3b). The relative differences between light- and heavy-REE partition coefficients in garnet are comparable to those in olivine despite that all REE are incompatible in olivine (Fig. 3a). In high-temperature geochemistry, this special feature of REE partitioning in garnet has been widely used as a geochemical indicator for assessing the presence of garnet in magma sources.

As a minor cation in garnet *Y* site, Cr^{3+} appears to be more compatible than other trace element cations in garnet (Fig. 3b). With a slightly larger ionic radius, V^{3+} has to overcome the lattice strain energy for substitution into the *Y* site, determining its smaller partition coefficients. Because of its excess electrostatic energy and smaller ionic radii, Ti^{5+} is less compatible in garnet than V^{3+}. Due to the multiple-site occupancies, the intermediate cations are difficult to understand solely based on the charge and site. As shown in van Westrenen et al. (2001a), the relative compatibilities of Zr and Hf may overturn, depending upon the major element composition of garnet.

Several models have been constructed to explain the large variation of experimentally determined trace element partition coefficients between garnet and silicate melts (e.g., van Westrenen et al. 2001b; Salters et al. 2002; van Westrenen and Draper 2007; Sun and Liang 2013a). Salters et al.'s models were calibrated for individual trace elements based on the thermodynamic expression of Eq. 4, whereas others are generalized lattice strain models but only for REE.

Plagioclase

The plagioclase structure follows a general formula MT_4O_8. The *T* site is occupied by tetrahedrally coordinated smaller cations, Si^{4+} and Al^{3+}, whereas the *M* site holds larger cations, Ca^{2+}, Na^{+}, and K^{+} in VII- to IX-fold coordination, and thus is the major place to incorporate trace element cations. Monovalent and divalent cations can enter the *M* site by replacing Na^{+} and Ca^{2+}, respectively. Large high-valent cations (e.g., REE^{3+}, U^{5+}, and Th^{5+}) require coupled substitution mechanisms for charge balance. For instance, the substitution of REE^{3+} for Ca^{2+} is coupled with Na^{+} replacing Ca^{2+}. However, it remains unclear which site (*M* or *T*) smaller high-valent cations (e.g., Ti^{4+}, Hf^{4+}, and Zr^{4+}) may occupy (e.g., Peters et al. 1995; de Vries et al. 2012).

Given the large ionic radii of Ca^{2+} ($^{VIII}Ca^{2+}$: 1.12 Å) and Na^{+} ($^{VIII}Na^{+}$: 1.18 Å), the *M* site is significantly more spacious than the cation sites in olivine (*M* site), pyroxenes (*M1* and *M2* sites), and garnet (*X* and *Y* sites). This effectively makes plagioclase favor larger cations (e.g., Sr^{2+}, Ba^{2+}, and light REE^{3+}) in the *M* site than smaller ones (e.g., Ni^{2+}, Co^{2+}, and heavy REE^{3+}). As shown in Fig. 3b, the larger cations are relatively more compatible in plagioclase than the smaller ones. Because the ionic radii of Sr^{2+} (1.26 Å) and Eu^{2+} (1.25 Å) are very similar to that of Ca^{2+}, they are the most compatible trace elements in plagioclase. Due to the presence of highly incompatible Eu^{3+} at relatively oxidized conditions, Eu partition coefficients appear to have a large variation bounded by the partition coefficients of Eu^{2+} and Eu^{3+} (Fig. 3b).

A notable feature of plagioclase-melt trace element partition coefficients is their strong dependence upon plagioclase anorthite contents in addition to temperature. Using a simple linear relation between $RT\ln(D)$ and plagioclase anorthite contents, several models have been developed to describe the partition coefficients of individual trace elements (e.g., Blundy and Wood 1991; Bindeman et al. 1998; Tepley et al. 2010). Generalized lattice strain models are also available in Wood and Blundy (2003) and Dohmen and Blundy (2014). A most recent calibration of the lattice strain model can be found in Sun et al. (2017) for plagioclase-melt partition coefficients of monovalent, divalent, and trivalent cations.

Amphibole

The chemical formula of amphibole crystals is more complex than those of olivine, pyroxene, garnet, and plagioclase. Conventionally, the amphibole formula is written as $AB_2C_5T_8O_{22}(OH)_2$. According to the nomenclature of amphibole subgroups (Hawthorne et al. 2012), here *A* denotes a large vacancy site partially filled by Li^{+} and large cations, Na^{+}, K^{+}, Ca^{2+}, and Pb^{2+}; *B* indicates the *M4* site holding Li^{+} and large cations, Ca^{2+}, Na^{+}, Fe^{2+}, Mg^{2+}, and Mn^{2+}; *C* includes the medium (*M1* and *M3*) and small (*M2*) octahedral sites occupied by Fe^{2+}, Mg^{2+}, Mn^{2+}, Al^{3+}, Cr^{3+}, Fe^{3+}, Ti^{4+}, and Li^{+}; *T* is the tetrahedral site dominated by Si^{4+} and Al^{3+} (and very rarely Ti^{4+}); and OH shows the anion site for OH^{-}, F^{-}, Cl^{-}, and O^{2-}.

The large number of cation sites in amphibole results in flexible substitution of trace elements, with variable charges and sizes, for the major cations. The large divalent cations, Sr^{2+} and Ba^{2+}, may substitute Ca^{2+} in both *A* and *B* sites. Small cations, e.g., Ni^{2+}, Co^{2+}, Sc^{3+}, V^{3+}, Zr^{4+}, and Hf^{4+}, likely behave similar as Cr^{3+} entering the *C* sites. With ionic radii nearly identical to that of Ti^{4+} (IV–0.42 Å and VI–0.605 Å), small pentavalent cations, Nb^{5+} and Ta^{5+} (IV–0.48 Å, VI–0.64 Å), may also enter the *C* site. Large trivalent cations, REE^{3+}, are believed to occupy the *B* sites, which may be split into two distinct M4 sites (e.g., Tiepolo et al. 2007). In addition, the spacious *A* site may also hold some REE, especially light REE, as those in plagioclase *M* site.

The partition coefficients of trace elements between amphibole and silicate melts vary by about one order of magnitude as a function of temperature, pressure, and composition (Fig. 3b). The absolute values and overall variations are similar to those for clinopyroxene. Exceptions are the large divalent cations (Sr^{2+} and Ba^{2+}) and the small high-valent cations (Ti^{4+}, Nb^{5+}, and Ta^{5+}), which appear to be relatively more compatible in amphibole. Their partition coefficients in amphibole are about one order of magnitude greater than those in clinopyroxene. Predictive models have been calibrated against experimentally determined amphibole-melt partition coefficients for a comprehensive list of trace elements (Tiepolo et al. 2007). A generalized lattice strain model is also available in Shimizu et al. (2017) for REE.

Metal-Silicate Partition Coefficients

Metal-silicate partition coefficients are used to constrain the composition and formation of metallic cores of terrestrial planets (see ▶ "Earth's Core"), which have great implications for planetary formation and differentiation (e.g., Wood et al. 2006). Two fundamental observations that motivate metal-silicate partitioning studies are (1) density deficit of the Earth core with respect to pure iron (e.g., Birch 1952) and (2) apparent anomalies of certain trace elements in Earth's mantle (e.g., Ringwood 1966). The elements of interest for the former are mainly centered on light elements such as Si, O, S, and C, while those for the latter mainly include excess siderophile elements (e.g., Ni and Co; see ▶ "Siderophile Elements") and missing lithophile (e.g., Nb; see ▶ "Lithophile Elements") and volatile elements (e.g., N).

Existing experimental partitioning studies have shown that metal-silicate partition coefficients of these elements also vary over orders of magnitude as a function of temperature, pressure, composition, and oxidation state (Fig. 4a). The moderately siderophile elements Ni and Co become less siderophile at elevated pressures, and therefore, the apparent excess of Ni

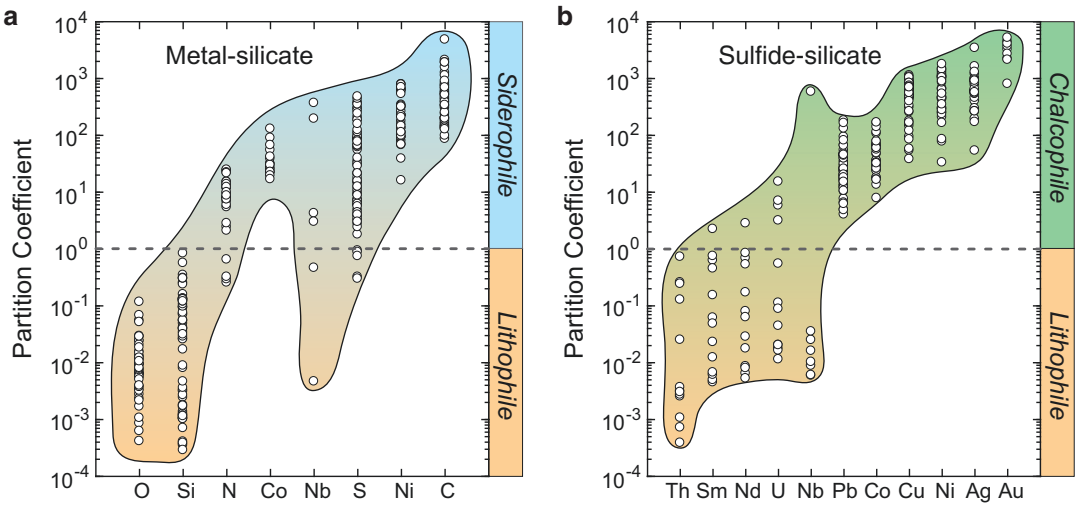

Partitioning and Partition Coefficients, Fig. 4 Spider diagram showing the experimentally determined partition coefficients of trace elements between liquid metal alloys and silicate melts (**a**) and between sulfide liquids and silicate melts (**b**). The metal-silicate partitioning data are from Li and Agee (2001), Wade and Wood (2001), Tsuno et al. (2013), Boujibar et al. (2014), Li et al. (2016) and Dalou et al. (2017). The sulfide-silicate partitioning data are from Gaetani and Grove (1997), Ripley et al. (2002), Li and Audétat (2012), Kiseeva and Wood (2013), Wood and Kiseeva (2015), Wohlers and Wood (2015), and Hart and Gaetani (2016)

and Co in Earth's mantle is likely artificial due to the applications of low-P partitioning data. In particular, the Ni and Co partitioning data indicate a core-mantle equilibrium pressure in the Earth upper mantle (~50 GPa), likely the magma ocean depth during planetary accretion (Li and Agee 2001). At high pressures and temperatures (e.g., P > 25 GPa, and T > 2700 °C), conventional lithophile elements, Si and O, behave close to siderophile, supporting the incorporation of a substantial amount of Si and O in the core for explaining the density deficit (Tsuno et al. 2013). Another lithophile element Nb may become highly siderophile at low oxidation states and high pressures (>23 GPa), making the core a potential "reservoir" for the Earth's missing Nb (Wade and Wood 2001).

The volatile elements C, S, and N appear to have distinct metal-silicate partition coefficients (e.g., Boujibar et al. 2014; Chi et al. 2014; Li et al. 2016; Dalou et al. 2017). C remains highly siderophile for a wide range of experimental conditions, while S and N behave generally as moderately siderophile elements but becomes more lithophile under relatively more reduced conditions. However, their differential partitioning behaviors pose a challenge for the single-stage core formation model that should have produced a more C-depleted primitive Earth's mantle.

Predictive models have also been experimentally calibrated for individual trace elements based on the thermodynamic expressions of metal-silicate partitioning (Eqs. 10 or 12). Interested readers are referred to the aforementioned studies for representative models. With the expanding experimental measurements, these models are continuously updated for additional elements or a broader range of pressures, temperatures, compositions, and/or redox conditions.

Sulfide-Silicate Partition Coefficients

Sulfide is present as immiscible droplets during magmatic processes at various geological settings (e.g., Lee et al. 2012) and is also considered significant for core formation and planetary accretion (e.g., Gaetani and Grove 1997; Dasgupta et al. 2009b; Wohlers and Wood 2015; Li et al. 2016). The elements of interest for sulfide-silicate partitioning studies mostly include chalcophile (sulfide-loving) elements (see ▶ "Chalcophile Elements"), siderophile elements, and more recently lithophile elements (e.g., REE, Nb, U, and Th). Similar to those in mineral-melt and metal-silicate systems, experimentally determined sulfide-silicate partition coefficients of trace elements also display considerable variations in response to changes in temperature, pressure, composition, and redox condition (Fig. 4b).

Chalcophile (e.g., Cu, Ag, and Pb) and siderophile elements (e.g., Au, Ni, Co) are highly compatible in sulfide, indicating the importance of sulfide for modulating the compositions of these elements in planetary interiors. Among those, Au appears to be the most sulfide-loving element with partition coefficients in the range of 800–5000. Cu, Ni, and Ag show similar compatibilities in sulfide (D = ~30–1800), but both are slightly less chalcophile than Au. Pb and Co are moderately chalcophile with similar affinities for sulfide (D = ~4–180). As a major host of precious metals such as Au and Ag, sulfide also bears economic implications for metal ores (see ▶ "Ore Deposits"). Generalized thermodynamic models are available in Kiseeva and Wood (2013) for chalcophile and siderophile element partitioning between sulfide and silicate melts.

The partition coefficients of lithophile elements such as REE, Nb, U, and Th vary by about three to five orders of magnitude, much greater than those of chalcophile and siderophile elements. When the silicate melts are depleted in FeO, these conventional lithophile elements become weakly chalcophile in sulfide-silicate systems (e.g., Wohlers and Wood 2015). As an extreme example, Nb highly favors the sulfide liquid with a partition coefficient of >600 when FeO becomes a minor or trace component in the coexisting silicate melt (<1 wt%; Wood and Kiseeva 2015). In addition, U and Nd appear to be relatively more compatible than Th and Sm in sulfide, respectively, underscoring the potential role of sulfide in fractionating lithophile elements during magmatic processes and planetary accretion. However, due to the lack of experimental data, generalized predictive models have not been developed for lithophile elements.

Summary

Element partitioning determines the chemical fractionation between coexisting equilibrium phases during various planetary processes. As a quantitative measure of partitioning, the partition coefficient enables geochemists to track ancient or ongoing geological processes through the chemical compositions of minerals and rocks from the planetary interior. However, the partition coefficient of a given element exhibits considerable variations with changes in temperature, pressure, redox condition, and phase compositions, which may even alter the conventional geochemical classification of elements (see ▶ "Geochemical Classification of Elements") to various extents. Thus, constant partition coefficients must be used with caution. The large variations of partition coefficients can be generally understood through thermodynamic models, but for quantitative understanding of specific geological processes, these models have to be calibrated using experimental measurements under relevant conditions.

Cross-References

- ▶ Activity and Activity Coefficients
- ▶ Chalcophile Elements
- ▶ Earth's Core
- ▶ Equilibrium Constant
- ▶ Geochemical Classification of Elements
- ▶ Geochemical Thermodynamics
- ▶ Henry's Law
- ▶ Ionic Radii
- ▶ Lithophile Elements
- ▶ Magmatic Process Modeling
- ▶ Noble Gases
- ▶ Onuma Diagrams
- ▶ Ore Deposits
- ▶ Siderophile Elements

References

Beattie P (1994) Systematics and energetics of trace–element partitioning between olivine and silicate melts: implications for the nature of mineral/melt partitioning. Chem Geol 117:57–71

Beattie P, Ford C, Russell D (1991) Partition coefficients for olivine-melt and orthopyroxene-melt systems. Contrib Mineral Petrol 109:212–224

Bindeman IN, Davis AM, Drake MJ (1998) Ion microprobe study of plagioclase-basalt partition experiments at natural concentration levels of trace elements. Geochim Cosmochim Acta 62:1175–1193

Birch F (1952) Elasticity and constitution of the Earth's interior. J Geophys Res 57:227–286

Blundy JD, Wood BJ (1991) Crystal-chemical controls on the partitioning of Sr and Ba between plagioclase feldspar silicate melts and hydrothermal solutions. Geochim Cosmochim Acta 55:193–209

Blundy J, Wood B (1994) Prediction of crystal-melt partition coefficients from elastic moduli. Nature 372:452–454

Blundy JD, Robinson JAC, Wood BJ (1998) Heavy REE are compatible in clinopyroxene on the spinel lherzolite solidus. Earth Planet Sci Lett 160:493–504

Boujibar A, Andrault D, Bouhifd MA, Bolfan-Casanova N, Devidal JL, Trcera N (2014) Metal-silicate partitioning of sulphur new experimental and thermodynamic constraints on planetary accretion. Earth Planet Sci Lett 391:42–54

Brice JC (1975) Some thermodynamic aspects of the growth of strained crystals. J Cryst Growth 28:249–253

Cameron M, Papike JJ (1981) Structural and chemical variations in pyroxenes. Am Mineral 66:1–50

Chi H, Dasgupta R, Duncan MS, Shimizu N (2014) Partitioning of carbon between Fe–rich alloy melt and silicate melt in a magma ocean–implications for the abundance and origin of volatiles in Earth Mars and the Moon. Geochim Cosmochim Acta 139:447–471

Dalou C, Hirschmann MM, von der Handt A, Mosenfelder J, Armstrong LS (2017) Nitrogen and carbon fractionation during core–mantle differentiation at shallow depth. Earth Planet Sci Lett 458:141–151

Dasgupta R, Hirschmann MM, McDonough WF, Spiegelman M, Withers AC (2009a) Trace element partitioning between garnet lherzolite and carbonatite at 6.6 and 8.6 GPa with applications to the geochemistry of the mantle and of mantle-derived melts. Chemical Geology 262:57–77

Dasgupta R, Buono A, Whelan G, Walker D (2009b) High-pressure melting relations in Fe-C-S systems: implications for formation evolution and structure of metallic cores in planetary bodies. Geochim Cosmochim Acta 73:6678–6691

de Vries J, van Westrenen W, van den Berg A (2012) Radiogenic heat production in the Moon: constraints from plagioclase-melt trace element partitioning experiments. In: Lunar and Planetary Sci Conference, Houston, TX, USA vol 43, pp 1737

Dohmen R, Blundy J (2014) A predictive thermodynamic model for element partitioning between plagioclase and melt as a function of pressure temperature and composition. Am J Sci 314:1319–1372

Evans TM, O'Neill HSC, Tuff J (2008) The influence of melt composition on the partitioning of REEs Y Sc Zr and Al between forsterite and melt in the system CMAS. Geochim Cosmochim Acta 72:5708–5721

Fincham CJB, Richardson FD (1954) The behaviour of sulphur in silicate and aluminate melts. Proc Roy Soc Lond Ser A Math Phys Sci, 223:40–62

Gaetani GA, Grove TL (1995) Partitioning of rare earth elements between clinopyroxene and silicate melt Crystal–chemical controls. Geochim Cosmochim Acta 59:1951–1962
Gaetani GA, Grove TL (1997) Partitioning of moderately siderophile elements among olivine silicate melt and sulfide melt: constraints on core formation in the Earth and Mars. Geochim Cosmochim Acta 61:1829–1846
Goldschmidt VM (1937) The principles of the distribution of chemical elements in minerals and rocks. J Chem Soc Lond 140:655–673
Hart SR, Gaetani GA (2016) Experimental determination of Pb partitioning between sulfide melt and basalt melt as a function of P, T and X. Geochim Cosmochim Acta 185:9–20
Hawthorne FC, Oberti R, Harlow GE, Maresch WV, Martin RF, Schumacher JC, Welch MD (2012) Nomenclature of the amphibole supergroup. Am Mineral 97:2031–2048
Hazen RM, Finger LW (1979) Bulk modulus-volume relationship for cation-anion polyhedra. J Geophys Res Solid Earth 84:6723–6728
Hill E, Blundy JD, Wood BJ (2011) Clinopyroxene-melt trace element partitioning and the development of a predictive model for HFSE and Sc. Contrib Mineral Petrol 161:423–438
Kiseeva ES, Wood BJ (2013) A simple model for chalcophile element partitioning between sulphide and silicate liquids with geochemical applications. Earth Planet Sci Lett 383:68–81
Lee CTA, Luffi P, Chin EJ, Bouchet R, Dasgupta R, Morton DM, Le Roux V, Yin QZ, Jin D (2012) Copper systematics in arc magmas and implications for crust–mantle differentiation. Science 336:64–68
Lee CTA, Luffi P, Le Roux V, Dasgupta R, Albaréde F, Leeman WP (2010) The redox state of arc mantle using Zn/Fe systematics. Nature 468:681–685
Le Roux V, Dasgupta R, Lee CTA (2011) Mineralogical heterogeneities in the Earth's mantle: constraints from Mn, Co, Ni and Zn partitioning during partial melting. Earth and Planetary Science Letters 307:395–408
Li J, Agee CB (2001) The effect of pressure temperature oxygen fugacity and composition on partitioning of nickel and cobalt between liquid Fe-Ni-S alloy and liquid silicate: implications for the Earth's core formation. Geochim Cosmochim Acta 65:1821–1832
Li Y, Audétat A (2012) Partitioning of V Mn Co Ni Cu Zn As Mo Ag Sn Sb W Au Pb and Bi between sulfide phases and hydrous basanite melt at upper mantle conditions. Earth Planet Sci Lett 355:327–340
Li Y, Dasgupta R, Tsuno K, Monteleone B, Shimizu N (2016) Carbon and sulfur budget of the silicate Earth explained by accretion of differentiated planetary embryos. Nat Geosci 9:781–785
Liang Y (2008) Simple models for dynamic melting in an upwelling heterogeneous mantle column: analytical solutions. Geochim Cosmochim Acta 72:3804–3821
Liang Y, Sun C, Yao L (2013) A REE-in-two-pyroxene thermometer for mafic and ultramafic rocks. Geochim Cosmochim Acta 102:246–260
Lundstrom CC, Shaw HF, Ryerson FJ, Williams Q, Gill J (1998) Crystal chemical control of clinopyroxene–melt partitioning in the Di-Ab-An system: implications for elemental fractionations in the depleted mantle. Geochim Cosmochim Acta 62:2849–2862
Ma Z (2001) Thermodynamic description for concentrated metallic solutions using interaction parameters. Metall Mater Trans B 32:87–103
Mallmann G, O'Neill HSC (2013) Calibration of an empirical thermometer and oxybarometer based on the partitioning of Sc Y and V between olivine and silicate melt. J Petrol 54:933–949
Matzen AK, Wood BJ, Baker MB, Stolper EM (2017) The roles of pyroxenite and peridotite in the mantle sources of oceanic basalts. Nat Geosci. https://doi.org/10.1038/NGEO2968
Mollo S, Blundy JD, Giacomoni P, Nazzari M, Scarlato P, Coltorti M, Langone A, Andronico D (2017) Clinopyroxene-melt element partitioning during interaction between trachybasaltic magma and siliceous crust: Clues from quartzite enclaves at Mt. Etna volcano. Lithos 284:447–461
Nagasawa H (1966) Trace element partition coefficient in ionic crystals. Science 152:767–769
Onuma N, Higuchi H, Wakita H, Nagasawa H (1968) Trace element partition between two pyroxenes and the host lava. Earth Planet Sci Lett 5:47–51
Papike JJ (1996) Pyroxene as a recorder of cumulate formational processes in asteroids Moon Mars Earth: reading the record with the ion microprobe. Am Mineral 81:525–544
Peters MT, Shaffer EE, Burnett DS, Kim SS (1995) Magnesium and titanium partitioning between anorthite and Type B CAI liquid: dependence on oxygen fugacity and liquid composition. Geochim Cosmochim Acta 59:2785–2796
Righter K, Drake MJ (2003) Partition coefficients at high pressure and temperature. Treatise Geochem 2:425–449
Ringwood AE (1966) Chemical evolution of the terrestrial planets. Geochim Cosmochim Acta 30:41–104
Ripley EM, Brophy JG, Li C (2002) Copper solubility in a basaltic melt and sulfide liquid/silicate melt partition coefficients of Cu and Fe. Geochim Cosmochim Acta 66:2791–2800
Salters VJ, Longhi JE, Bizimis M (2002) Near mantle solidus trace element partitioning at pressures up to 3.4 GPa. Geochem Geophys Geosyst 3:1–23
Shannon RD (1976) Revised effective ionic radii and systematic studies of interatomic distances in halides and chalcogenides. Acta Crystallographica Section A 32:751–767
Shaw DM (2000) Continuous (dynamic) melting theory revisited. Can Mineral 38:1041–1063
Shimizu K, Liang Y, Sun C, Jackson CR, Saal AE (2017) Parameterized lattice strain models for REE partitioning between amphibole and silicate melt. Am Mineral (in press). https://doi.org/10.2138/am-2017-6110
Sun C, Liang Y (2012) Distribution of REE between clinopyroxene and basaltic melt along a mantle adiabat: effects of major element composition water and temperature. Contrib Mineral Petrol 163:807–823
Sun C, Liang Y (2013a) The importance of crystal chemistry on REE partitioning between mantle minerals (garnet clinopyroxene orthopyroxene and olivine) and basaltic melts. Chem Geol 358:23–36
Sun C, Liang Y (2013b) Distribution of REE and HFSE between low-Ca pyroxene and lunar picritic melts around multiple saturation points. Geochim Cosmochim Acta 119:340–358
Sun C, Liang Y (2015) A REE-in-garnet-clinopyroxene thermobarometer for eclogites granulites and garnet peridotites. Chem Geol 393:79–92
Sun C, Liang Y (2017) A REE-in-plagioclase-clinopyroxene thermometer for crustal rocks. Contrib Mineral Petrol 172(4):1–20
Sun C, Graff M, Liang Y (2017) Trace element partitioning between plagioclase and silicate melt: the importance of temperature and plagioclase composition with implications for terrestrial and lunar magmatism. Geochim Cosmochim Acta 206:273–295
Tepley FJ, Lundstrom CC, McDonough WF, Thompson A (2010) Trace element partitioning between high-An plagioclase and basaltic to basaltic andesite melt at 1 atmosphere pressure. Lithos 118:82–94
Tiepolo M, Oberti R, Zanetti A, Vannucci R, Foley SF (2007) Trace-element partitioning between amphibole and silicate melt. Rev Mineral Geochem 67:417–452
Trail D, Watson EB, Tailby ND (2011) The oxidation state of Hadean magmas and implications for early Earth's atmosphere. Nature 480:79–82
Tsuno K, Frost DJ, Rubie DC (2013) Simultaneous partitioning of silicon and oxygen into the Earth's core during early Earth differentiation. Geophys Res Lett 40:66–71
van Westrenen W, Draper DS (2007) Quantifying garnet-melt trace element partitioning using lattice–strain theory: new crystal-chemical and thermodynamic constraints. Contrib Mineral Petrol 154:717–730

van Westrenen W, Blundy JD, Wood BJ (2001a) High field strength element/rare earth element fractionation during partial melting in the presence of garnet: implications for identification of mantle heterogeneities. Geochem Geophys Geosyst 2(7), https://doi.org/10.1029/2000GC000133
van Westrenen W, Wood BJ, Blundy JD (2001b) A predictive thermodynamic model of garnet-melt trace element partitioning. Contrib Mineral Petrol 142:219–234
Wade J, Wood BJ (2001) The Earth's 'missing' niobium may be in the core. Nature 409:75–78
Wade J, Wood BJ (2005) Core formation and the oxidation state of the Earth. Earth Planet Sci Lett 236:78–95
Watson EB, Wark DA, Thomas JB (2006) Crystallization thermometers for zircon and rutile. Contrib Mineral Petrol 151:413–433
Wohlers A, Wood BJ (2015) A Mercury-like component of early Earth yields uranium in the core and high mantle ^{142}Nd. Nature 520:337–340
Wood BJ, Blundy JD (1997) A predictive model for rare earth element partitioning between clinopyroxene and anhydrous silicate melt. Contrib Mineral Petrol 129:166–181
Wood BJ, Blundy JD (2003) Trace element partitioning under crustal and uppermost mantle conditions: the influences of ionic radius cation charge pressure and temperature. Treatise Geochem 2:568
Wood BJ, Kiseeva ES (2015) Trace element partitioning into sulfide: how lithophile elements become chalcophile and vice versa. Am Mineral 100:2371–2379
Wood BJ, Walter MJ, Wade J (2006) Accretion of the Earth and segregation of its core. Nature 441:825–833
Yao L, Sun C, Liang Y (2012) A parameterized model for REE distribution between low-Ca pyroxene and basaltic melts with applications to REE partitioning in low-Ca pyroxene along a mantle adiabat and during pyroxenite-derived melt and peridotite interaction. Contrib Mineral Petrol 164:261–280

Peat

Thomas J. Kelly[1], Ian T. Lawson[2] and Lydia E. S. Cole[3]
[1]School of Geography, University of Leeds, Leeds, UK
[2]Department of Geography and Sustainable Development, University of St Andrews, Edinburg, Scotland, UK
[3]Department of Zoology, Biodiversity Institute, University of Oxford, Oxford, UK

Definition

Peat is an organic soil composed of partially decomposed plant and, to a lesser extent, animal remains. Precise definitions of "peat" vary but are mostly based on a combination of thickness (typically >30 cm) and organic matter content (typically >50–65%; e.g., Wüst et al. 2003; Page et al. 2011; Dargie et al. 2017). Their high organic matter content means that peats have a high carbon concentration, up to 48–60 wt% in very pure peats (Shimada et al. 2001; Loisel et al. 2014; Lawson et al. 2015). The term "histosol," used in the FAO and USDA soil taxonomies, includes peats.

Peat Formation, Peatlands, and Peatland Classification

Peat has a long geological history dating back to the Late Devonian (Greb et al. 2006). Burial and heating slowly transform ancient peat deposits into extensive coal and lignite deposits, which are economically important; some modern peat accumulating environments can therefore be used as analogues to understand coal formation (Phillips and Bustin 1998). Peat accumulations are found on every continent, from Antarctica, the lowland and montane tropical peatlands of Africa, South America, and Southeast Asia, to the vast peatlands of the temperate, boreal, and arctic regions of North America and Eurasia (e.g., Fenton 1980; Gorham 1991; Page et al. 2011). Most modern peatlands are Holocene in age (Yu 2012). Although older sites are known – for example, the exceptional 1.35 million year peat sequence at Tenaghi Phillipon in Greece (Tzedakis et al. 2006) – peat formation appears to have been relatively limited during the globally cold/dry glacial intervals of the Quaternary.

Peat accumulation is relatively slow; long-term accumulation rates vary between different peatland environments but are typically less than 1 mm/yr. (e.g., Barber et al. 1994; Arlen-Pouliot and Bhiry 2005), with some higher accumulation rates recorded in the tropics (e.g., Lähteenoja et al. 2012). In general, peat accumulates when the rate of production of plant litter – including roots, stems, wood, and leaves – exceeds the rate of decomposition and other losses (e.g., fire). In most terrestrial environments, litter decomposition by microbes and invertebrates can easily keep pace with litter supply. In saturated conditions, waterlogging slows the rate of oxygen diffusion from the surface into the litter and soil. Year-round waterlogging can result in permanently anoxic conditions, which exclude most invertebrates and many microbes, severely reducing the rate of litter decay. Other factors such as low pH and low nutrient status may also play a role in inhibiting litter decomposition (Clymo 1984).

Peat can therefore accumulate in a wide variety of situations, typically wherever the substrate is wet for most of the year. Peatland settings include moss banks (Fenton 1980), palsa mires in permafrost areas (Christensen et al. 2012), floating islands or rafts on lakes and rivers (Zaccone et al. 2017), blanket peat in wet upland areas (Tipping 2008), coastal mangroves or marshes (Orson et al. 1987; Ezcurra et al. 2016), depressions in formerly glaciated areas (Ireland and Booth 2011), and abandoned river channels (Lähteenoja et al. 2009) (Fig. 1). Modern-day peatlands are usually classified on the basis of their vegetation and/or geochemistry (Wheeler and Proctor 2000). Vegetation and geochemistry are likely to share a causal connection: environmental gradients described by pH and basic cations (e.g., Ca^{2+}) appear to be important in determining vegetation composition in northern

Peat, Fig. 1 Geographically and geochemically diverse types of peatland: (**a**) Quistococha peatland palm swamp in the Peruvian Amazon; (**b**) intact blanket peatland with hummock and hollow microtopography at Slieveanora, Northern Ireland, UK; (**c**) palsa peatland in Stordalen, within the Swedish subarctic; and (**d**) degraded upland blanket bog in Northern Ireland, UK (Credit to T.J.K. (**a**–**c**) and L.E.S.C. (**d**))

peatlands (Wells 1996; Wheeler and Proctor 2000). Peatlands may be classified as ombrotrophic (purely rain-fed) or minerotrophic (largely groundwater-fed), but this classification can be problematic if only because many nutrient-poor groundwater-fed fens have similar vegetation communities to ombrotrophic peatlands (Wheeler and Proctor 2000). Northern peatlands can perhaps be more securely divided into "bogs," with pH $<$ 5.5 and low Ca^{2+} concentrations, and "fens" which have pH $>$ 5.5 and higher Ca^{2+} concentrations (Wheeler and Proctor 2000). There are cases where this classification may prove inadequate such as in the "iron fens" of Colorado, some of which have both low pH ($<$4.5) and high Ca^{2+} concentration (e.g., Cooper et al. 2002; Chimner et al. 2010), and within the broad division between bog and fen, there is substantial variation in peatland vegetation associations (Hájek et al. 2006). Nevertheless, this division is generally found to be a useful one in northern peatlands, and a strong contrast between "bog" and "fen" vegetation also appears to hold in some parts of the tropics (e.g., Lähteenoja et al. 2009).

Other environmental gradients are also important in peatlands, in particular water table depth and the availability of nutrients other than calcium (Wheeler and Proctor 2000). For example, in some tropical and subtropical systems, nitrogen (N) and phosphorus (P) may be more critical in controlling plant communities than pH and the quantity of basic cations such as Ca^{2+} (e.g., Bridgham and Richardson 1993; Sjögersten et al. 2011).

Significance

Although they cover only c. 3% of the Earth's surface, peatlands play a disproportionately large role in the global carbon cycle due to their high carbon density per area and their ability to act as long-term stores of atmospheric CO2 (Gorham 1991; Rydin and Jeglum 2006). In some parts of the world, such as Finland and the Congo Basin, the soil carbon stored in peatlands either equals or exceeds that in the aboveground biomass of vegetation across the region as a whole

(Turunen et al. 2002; Dargie et al. 2017). There is some uncertainty as to the total amount of carbon stored in peatlands, but a review of the available data places the value at c. 600 GtC (Page et al. 2011), approaching that held in the atmospheric pool (c. 850 GtC; IPCC 2013). Most peat carbon is stored in temperate and boreal peatlands (517–526 GtC; Page et al. 2011), with a smaller amount in the tropics (70–130 GtC; Dargie et al. 2017).

Carbon losses from peatlands are a particular concern due to their contribution to atmospheric greenhouse gas emissions, and hence to climate change. Some of the main pathways include gaseous losses resulting from decomposition (CO_2 and CH_4), water-borne losses (e.g., dissolved organic carbon), and losses due to burning (CO_2, CO, and CH_4). Gaseous losses have been a particular focus for research, as the anaerobic conditions found in peatlands result in the production of methane, which is a more potent greenhouse gas than carbon dioxide (Christensen et al. 2012; Bridgham et al. 2013). Annual methane emissions from northern peatlands alone have been estimated at around 0.046 Gt CH_4-C (Gorham 1991).

Water-borne losses of carbon from peatlands occur in the form of dissolved organic carbon (DOC) and particulate organic carbon (POC). DOC forms as peat decomposes and builds up in the pore waters within the peat matrix until it is flushed out by water passing through (Holden 2005; Limpens et al. 2008). POC usually results from peatland erosion, which can occur at the margins of peatlands (e.g., in proximity to a river channel), or below the surface (Holden 2005). In temperate peatlands, DOC may account for around 10% of peatland carbon losses, with a similar loss occurring as POC (Holden 2005), although there is substantial variation (Yu 2012). DOC and POC losses are often greater in degraded areas, such as deforested peatlands in the tropics (Moore et al. 2013).

Under natural conditions, peatlands are generally too wet to burn, but peat surface layers can ignite during dry weather. When artificially drained, unnaturally dry conditions are created, making peatlands very vulnerable to fire (Turetsky et al. 2014). Recent losses of carbon from fires in disturbed tropical peatlands have been particularly significant. Peatland fires in SE Asia in 1997, a particularly severe episode, are thought to have released 2.97–9.42 Gt CO_2, equivalent to 13–40% of the global anthropogenic greenhouse gas emissions for that year (Page et al. 2002).

Peatlands therefore require careful management in order to avoid unintentional carbon emissions, and considerable effort has been invested in restoring degraded peatland areas (Chimner et al. 2017). Peat is economically important, as a fuel and as a horticultural substrate and soil improver (Schilstra 2001; Chimner et al. 2017). Peatlands and their distinctive landscapes can be culturally important, not least for the whisky industry, and they are important habitats for often highly specialized plants and animals. They are scientifically important, particularly for paleoecological research: the botanical composition of the peat and other less obvious characteristics, such as its microfossil assemblages, make it possible to reconstruct the development of a peatland in great detail over thousands of years (Chambers and Charman 2004). Peatlands, and their globally significant carbon stocks, are also highly vulnerable to mismanagement and, in some instances, to future climate change. More research is needed to fully understand the processes that lead to peat formation around the world and to predict the impact of future changes in climate and land use on peatland carbon storage.

Summary

Peat accumulates in a wide range of different waterlogged environments, and its high carbon concentration means that although peatland areas cover only a small fraction of the earth's surface, they play a large role in the global carbon cycle. Greenhouse gas emissions from some disturbed peatlands have been particularly large in recent years. Peatlands are also culturally important, home to a range of unique plants and animals, and act as archives of paleoenvironmental information which has enabled an increased understanding of past environmental and climatic changes.

Cross-References

- ▶ Anthropogenic CO_2
- ▶ Carbon Cycle
- ▶ Coal
- ▶ Dissolved Organic Matter (DOM)
- ▶ Hydrologic Cycle
- ▶ Organic Matter Degradation and Preservation
- ▶ Paleoenvironments
- ▶ Soils

References

Arlen-Pouliot Y, Bhiry N (2005) Palaeoecology of a palsa and a filled thermokarst pond in a permafrost peatland, subarctic Quebec, Canada. The Holocene 15:408–419

Barber KE, Chambers FM, Maddy D, Stoneman R, Brew JS (1994) A sensitive high-resolution record of late Holocene climatic change from a raised bog in northern England. The Holocene 4:198–205

Bridgham SD, Richardson CJW (1993) Hydrology and nutrient gradients in North Carolina peatlands. Wetlands 13:207–218

Bridgham SD, Cadillo-Quiroz H, Keller JK, Zhuang Q (2013) Methane emissions from wetlands: biogeochemical, microbial, and modeling perspectives from local to global scales. Glob Chang Biol 19:1325–1346

Chambers FM, Charman DJ (2004) Holocene environmental change: contributions from the peatland archive. The Holocene 14:1–6

Chimner RA, Lemly JM, Cooper DJ (2010) Mountain fen distribution, types and restoration priorities, San Juan Mountains, Colorado, USA. Wetlands 30:763

Chimner RA, Cooper DJ, Wurster FC, Rochefort L (2017) An overview of peatland restoration in North America: where are we after 25 years? Restor Ecol 25:283–292

Christensen TR, Jackowicz-Korczyński M, Aurela M, Crill P, Heliasz M, Mastepanov M, Friborg T (2012) Monitoring the multi-year carbon balance of a Subarctic Palsa Mire with Micrometeorological Techniques. Ambio 41(Supplement 3):207–217

Clymo RS (1984) The limits to peat bog growth. Philos Trans R Soc Lond B 303:605–654

Cooper DJ, Andrus RA, Arp CD (2002) *Sphagnum balticum* in a Southern Rocky Mountains iron fen. Madrono 49:186–188

Dargie GC, Lewis SL, Lawson IT, Mitchard ETA, Page SE, Bocko YE, Ifo SA (2017) Age, extent and carbon storage of the central Congo Basin peatland complex. Nature 542:86–90

Ezcurra P, Ezcurra E, Garcillán PP, Costa MT, Aburto-Oropeza O (2016) Coastal landforms and accumulation of mangrove peat increase carbon sequestration and storage. PNAS 19:4404–4409

Fenton JHC (1980) The rate of peat accumulation in Antarctic Moss Banks. J Ecol 68:211–228

Gorham E (1991) Northern peatlands: role in the carbon cycle and probable responses to climatic warming. Ecol Appl 1:182–195

Greb SF, DiMichele WA, Gastaldo RA (2006) Evolution and importance of wetlands in earth history. Geol Soc Am Spec Pap 399:1–40

Hájek M, Horsák M, Hájková P, Dítě D (2006) Habitat diversity of central European fens in relation to environmental gradients and an effort to standardise fen terminology in ecological studies. Perspect Plant Ecol Evol Syst 8:97–114

Holden J (2005) Peatland hydrology and carbon release: why small-scale process matters. Phil Trans R Soc A 363:2891–2913

Huijnen V, Wooster MJ, Kaiser JW, Gaveau DLA, Flemming J, Parrington M, Inness A, Murdiyarso D, Main B, van Weele M (2016) Fire carbon emissions over maritime southeast Asia in 2015 largest since 1997. Sci Rep 6:26886

IPCC (2013) In: Stocker TF et al (eds) Climate change 2013: the physical science basis. Cambridge University Press, Cambridge

Ireland AW, Booth RK (2011) Hydroclimatic variability drives episodic expansion of a floating peat mat in a North American kettlehole basin. Ecology 92:11–18

Lähteenoja O, Ruokolainen K, Schulman L, Alvarez J (2009) Amazonian floodplains harbour minerotrophic and ombrotrophic peatlands. Catena 79:140–145

Lähteenoja O, Reátegui YR, Räsänen M, Torres DD, Oinonen M, Page S (2012) The large Amazonian peatland carbon sink in the subsiding Pastaza-Marañón foreland basin, Peru. Glob Chang Biol 18:164–178

Lawson IT, Kelly TJ, Aplin P, Boom A, Dargie G, Draper FCH, Hassan PNZBP, Hoyos-Santillan J, Kaduk J, Large D, Murphy W, Page SE, Roucoux KH, Sjögersten S, Tansey K, Waldram M, Wedeux BMM, Wheeler J (2015) Improving estimates of tropical peatland area, carbon storage, and greenhouse gas fluxes. Wetl Ecol Manag 23:327–346

Limpens J, Berendse F, Blodau C, Canadell JG, Freeman C, Holden J, Roulet N, Rydin H, Schaepman-Strub G (2008) Peatlands and the carbon cycle: from local processes to global implications – a synthesis. Biogeosci Discuss 5:1379–1419

Loisel J, Yu Z, Beilman DW, Camill P, Alm J, Amesbury MJ, Anderson D, Andersson S, Bochicchio C, Barber KE, Belyea LR, Bunbury J, Chambers FM, Charman DJ, De Vleeschouwer F, Fiałkiewicz-Kozieł B, Finkelstein SA, Gałka M, Garneau M, Hammarlund D, Hinchcliffe W, Holmquist J, Hughes PDM, Jones MC, Klein ES, Kokfelt U, Korhola A, Kuhry P, Lamarre A, Lamentowicz M, Large D, Lavoie M, MacDonald G, Magnan G, Makila M, Mallon G, Mathijssen P, Mauquoy D, McCarroll J, Moore TR, Nichols J, O'Reilly B, Oksanen P, Packalen M, Peteet D, Richard PJH, Robinson S, Ronkainen T, Rundgren M, Sannel ABK, Tarnocai C, Thom T, Tuittila ES, Turetsky M, Valiranta M, van der Linden M, van Geel B, van Bellen S, Vitt D, Zhao Y, Zhou W (2014) A database and synthesis of northern peatland soil properties and Holocene carbon and nitrogen accumulation. The Holocene 24:1028–1042

Moore R, Evans CD, Page SE, Garnett MH, Jones TG, Freeman C, Hooijer A, Wiltshire AJ, Limin SH, Gauci V (2013) Deep instability of deforested tropical peatlands revealed by fluvial organic carbon fluxes. Nature 493:660–663

Orson RA, Warren RS, Niering WA (1987) Development of a tidal marsh in a New England river valley. Estuaries 10:20–27

Page SE, Siegert F, Rieley JO, Boehm H-DV, Jaya A, Limin S (2002) The amount of carbon released from peat and forest fires in Indonesia during 1997. Nature 420:61–65

Page SE, Rieley JO, Banks CJ (2011) Global and regional importance of the tropical peatland carbon pool. Glob Chang Biol 17:798–818

Phillips, S., and Bustin, R.M. (1998) Accumulation of organic rich sediments in a dendritic fluvial/lacustrine mire system at Tasik Bera, Malaysia: implications for coal formation. International Journal of Coal Geology, 36: 31–61

Rydin H, Jeglum J (2006) The biology of Peatlands. Oxford University Press, Oxford

Schilstra, A.J. (2001) How sustainable is the use of peat for commercial energy production? Ecological Economics, 39: 285–293

Shimada S, Takahashi H, Haraguchi A, Kaneko M (2001) The carbon content characteristics of tropical peats in Central Kalimantan, Indonesia: estimating their spatial variability in density. Biogeochemistry 53:249–267

Sjögersten S, Cheesman AW, Lopez O, Turner BL (2011) Biogeochemical processes along a nutrient gradient in a tropical ombrotrophic peatland. Biogeochemistry 104:147–163

Tipping R (2008) Blanket peat in the Scottish Highlands: timing, cause, spread and the myth of environmental determinism. Biodivers Conserv 17:2097–2113

Turetsky MR, Benscoter B, Page SE, Rein G, van der Werf GR, Watts A (2014) Global vulnerability of peatlands to fire and carbon loss. Nat Geosci 8:11–14

Turunen J, Tomppo E, Tolonen K, Reinikainen A (2002) Estimating carbon accumulation rates of undrained mires in Finland – application to boreal and subarctic regions. The Holocene 12:69–80

Tzedakis PC, Hooghiemstra H, Pälike H (2006) The last 1.35 million years at Tenaghi Philippon: revised chronostratigraphy and long-term vegetation trends. Quat Sci Rev 25:3416–3430

Wells ED (1996) Classification of peatland vegetation in Atlantic Canada. J Veg Sci 7:847–878

Wheeler BD, Proctor MCF (2000) Ecological gradients, subdivisions and terminology of north-west European mires. J Ecol 88:187–203

Wüst RA, Bustin RM, Lavkulich LM (2003) New classification systems for tropical organic-rich deposits based on studies of the Tasek Bera Basin, Malaysia. Catena 53:133–163

Yu ZC (2012) Northern peatland carbon stocks and dynamics: a review. Biogeosciences 9:4071–4085

Zaccone C, Lobianco D, Shotyk W, Ciavatta C, Appleby PG, Brugiapaglia E, Casella L, Miano TM, D'Orazio V (2017) Highly anomalous accumulation rates of C and N recorded by a relic, free-floating peatland in Central Italy. Sci Rep 7:43040

Periodic Table

Karen Harpp
Department of Geology, Colgate University, Hamilton, NY, USA

Synonyms

Periodic chart

Introduction and Definition

The modern periodic table is a schematic arrangement of all known elements, in order of increasing atomic number (i.e., number of protons in an element, its defining characteristic; Fig. 1) and hence their mass. The elegance of the periodic table is that the two-dimensional layout conveys far more than just atomic number and mass. Incorporated into the design is information about how electrons are arranged around the nucleus, the reactivities of elements, and patterns in the elements' chemical properties. If one understands these aspects of the periodic table, it can also provide insight into how elements behave in Earth's geochemical systems.

History

Even by the mid-1800s, it was common knowledge among scientists that many of the approximately 50 elements that had been identified at the time could be grouped into subsets sharing similar chemical behavior. Alexandre-Emile Béguyer de Chancourtois (France; 1820–1886), John Newlands (U.K.; 1837–1898), Lothar Meyer (Germany; 1830–1895), and Dmitri Mendeleev (Russia; 1834–1907) were among researchers who independently came to the critical conclusion that the periodicity of chemical behavior was a function of elements' atomic numbers and masses.

Not all proposals for what ultimately became the periodic table met with immediate acceptance in the scientific community. For instance, De Chancourtois (the only geologist of the group) designed a cylindrical chart, arranging the elements in a spiral so that similar elements were aligned in a column (the Telluric Helix). Unfortunately, because his publisher did not include the complex graphic in the original paper, de Chancourtois only received delayed credit for his ideas (Scerri 2006). Shortly thereafter, Newlands proposed the Law of Octaves, noting that the atomic numbers of elements with similar chemical behavior "generally differ either by 7 or by some multiple of seven; in other words, members of the same group stand to each other in the same relation as the extremities of one or more octaves in music" (Newlands 1865). It appears as though the Chemical Society of London did not take to his musical analogy, however, and they rejected his paper (Kean 2010).

Meyer and Mendeleev published their periodic tables of the elements at nearly the same time, ultimately sharing the Davy Medal for their discoveries in 1882 (Newlands subsequently received a Davy Medal 5 years later). Both scientists left gaps in the table where no elements existed at the time, but Mendeleev actually predicted that new ones would be found (Fig. 2). His estimates of their densities and atomic weights proved quite accurate, cementing his position as the father of the modern periodic table.

Guide to the Periodic Table

Most periodic tables include every element's symbols, name, atomic number, and atomic mass. The *atomic number* of an element is the same as the number of protons and electrons in a neutral atom. *Atomic mass* is an average of the masses of all the element's isotopes, weighted according to their abundance on Earth. Elements are organized in order of increasing atomic number. Hydrogen, the lightest element, has one proton and sits in the uppermost corner of the periodic table; uranium, the heaviest naturally occurring element, has 92 protons and is found near the very bottom of the table.

As one moves left to right across the periodic table, the number of protons in the elements' nuclei and the number of electrons around a neutral atom increase systematically, one by one. As atomic number increases, the accompanying electrons are arranged in a sequence of structured shells around the nucleus. Each shell is able to accommodate a limited quantity of electrons, a number that increases as the atoms get larger. Specifically, the first shell can only hold 2, the second can manage 8, the third can accommodate 18, and the fourth houses up to 32 electrons. Elements in the same period, or row, have their electrons stored in the same number and type of shells.

Within each shell, electrons occupy subshells, which in turn host atomic orbitals. There are several types of subshells, each with a limited capacity for electrons: s subshells host a maximum of 2 electrons, p subshells hold up to 6, d can accommodate 10 electrons, and f subshells hold up to 18 electrons. Elements in the first row in the periodic table only have a 1s subshell, with a capacity of 2 electrons. Consequently, the first row of the table consists of only 2 elements, hydrogen and helium (Fig. 1). The second and third row elements have an outer electron shell with an s and a p subshell, giving them the capacity for 8 electrons, thus there are 8 elements in the second and third rows of the periodic table. The fourth and fifth period elements also have d subshells, allowing an additional 10 elements into each row. The sixth and seventh

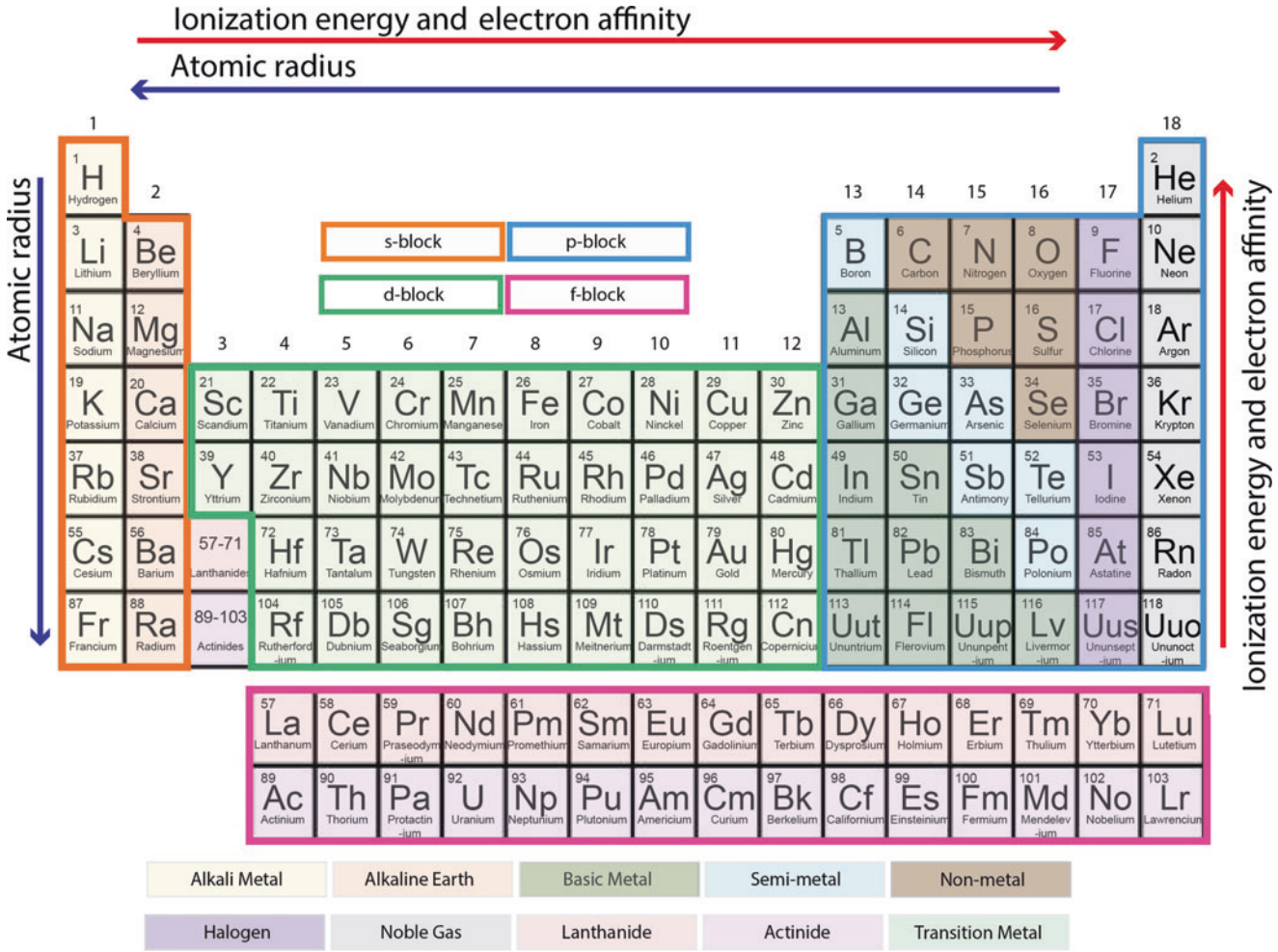

Periodic Table, Fig. 1 Periodic table of the elements. Atomic numbers are in the *upper left* corner of each element's box; atomic weights are not shown. Group numbers are located *above* each column of elements. Non-metallic character increases from the *bottom left* of the table to the *upper right*; metallic character increases in the opposite direction, from lowest in the *upper right* corner to highest in the *lower left* corner. Blue and red arrows indicate directions of increasing ionization energy, electron affinity, and atomic energy. Electron affinity is the amount of energy released when an electron is added to the neutral atom; electronegativity is a measure of an atom's ability to attract electrons

periods include f subshells and therefore 14 additional elements.

Another way to look at the periodic table is to categorize elements according to the subshells being filled, in blocks (Fig. 1). For instance, because s-orbitals can only manage 2 electrons, the s-block elements are in the first two columns on the left side of the periodic table (Groups 1 and 2; Fig. 1). Elements in which the new electrons are filling p subshells are in the p-block; because p-orbitals have the capacity for 6 electrons, there are six columns in the p-block (Groups 13 through 18). The d-block, with its 10-electron capacity, consists of Groups 3 through 12, and includes the transition metals. The f-block's 14 spaces are usually displayed at the bottom of the periodic table and are made up of the lanthanide and actinide elements (the f-block really belongs in the sixth row, but they have been shifted to the lower part of most periodic tables to keep the tables more compact).

For the most part, this process works in a straightforward way: the larger the atomic number, the larger the atom. A subtlety arises, however, involving the d- and f-orbitals. Instead of housing their electrons around the periphery of the atom, as with the s- and p-orbitals, the d- and f-orbitals are embedded deep within the electron cloud. As most beginning chemistry students will attest, this phenomenon poses a challenge when learning how to arrange electrons around atoms properly. Several alternative versions of the periodic table have been designed to mitigate this problem inherent in the electron configuration system. In 1929, Charles Janet published an extended version of the periodic table (the left-step periodic table; Fig. 3), which laid the atoms out in a step-wise pattern; one simply starts at hydrogen and moves along from left to right

Reihen	Gruppo I. — R^1O	Gruppo II. — RO	Gruppo III. — R^2O^3	Gruppo IV. RH^4 RO^2	Gruppo V. RH^3 R^2O^5	Gruppo VI. RH^2 RO^3	Gruppo VII. RH R^2O^7	Gruppo VIII. — RO^4
1	H=1							
2	Li=7	Be=9,4	B=11	C=12	N=14	O=16	F=19	
3	Na=23	Mg=24	Al=27,3	Si=28	P=31	S=32	Cl=35,5	
4	K=39	Ca=40	—=44	Ti=48	V=51	Cr=52	Mn=55	Fe=56, Co=59, Ni=59, Cu=63.
5	(Cu=63)	Zn=65	—=68	—=72	As=75	Se=78	Br=80	
6	Rb=85	Sr=87	?Yt=88	Zr=90	Nb=94	Mo=96	—=100	Ru=104, Rh=104, Pd=106, Ag=108.
7	(Ag=108)	Cd=112	In=113	Sn=118	Sb=122	Te=125	J=127	
8	Cs=133	Ba=137	?Di=138	?Ce=140	—	—	—	— — — —
9	(—)	—	—	—	—	—	—	
10	—	—	?Er=178	?La=180	Ta=182	W=184	—	Os=195, Ir=197, Pt=198, Au=199.
11	(Au=199)	Hg=200	Tl=204	Pb=207	Bi=208	—	—	
12	—	—	—	Th=231	—	U=240	—	— — — —

Periodic Table, Fig. 2 One of Mendeleev's first periodic tables (1871). The *dashes* indicate positions where Mendeleev predicted new elements would be discovered (From https://en.wikipedia.org/wiki/File:Mendeleev%27s_1871_periodic_table.jpg)

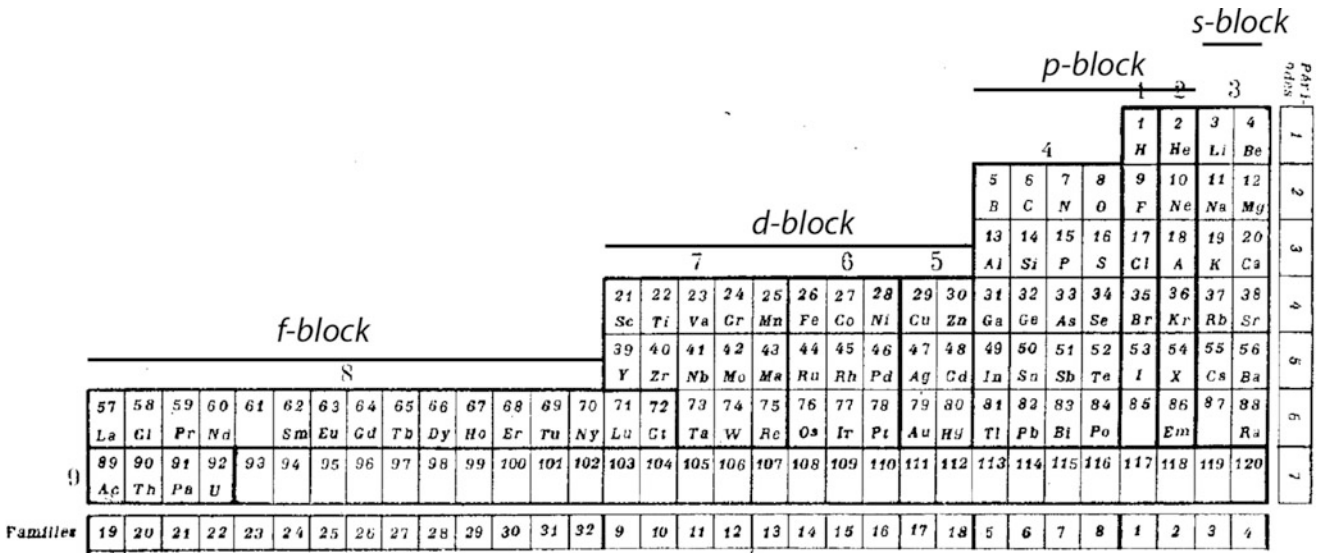

Periodic Table, Fig. 3 A version of the Janet left-step periodic table (1929). Atomic numbers and element symbols are displayed in each box for elements that existed at the time of the table's design. The indications for the orbital blocks are an addition to his table, and were not part of the original annotations. Note that H and He should sit in the s-block according to our current understanding of electron configurations (Modified from Janet (1929))

adding electrons in the appropriate blocks. Theodor Benfey designed a spiral periodic table (Seaborg 1964; Fig. 4), in which the smallest atom, hydrogen, is at the center, and the progressively larger atoms are built by following the serpent-like spiral. The d-block is the transition metal peninsula, and the f-block is the lanthanide and actinide peninsula in the table.

Periodicity

The notion of chemical periodicity is where the elegance of the periodic table begins to emerge. The arrangement of the table conveys important information about the structure, and therefore the reactivity, of atoms.

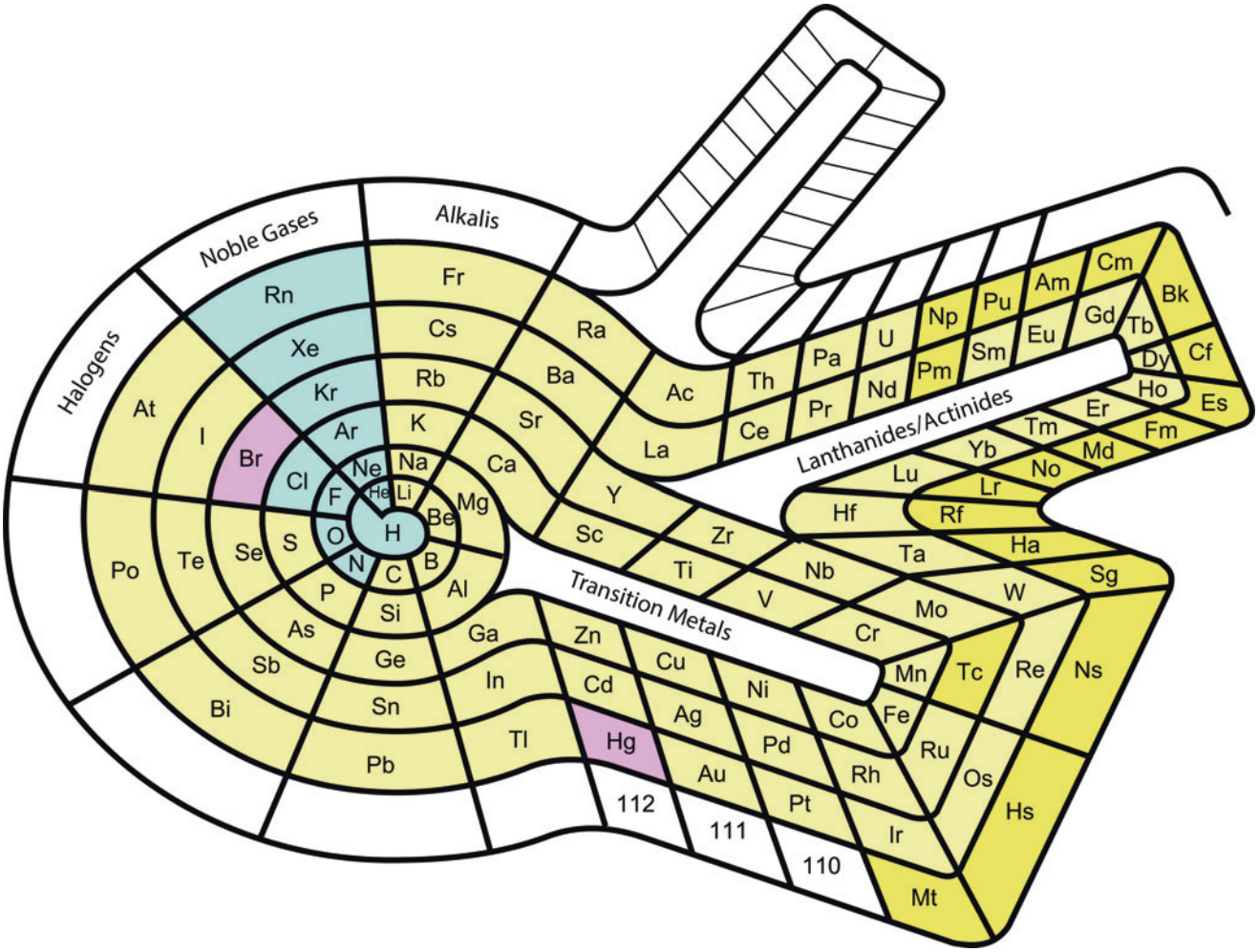

Periodic Table, Fig. 4 Version of the Benfey spiral periodic table (1964). Note that the blank "peninsula" is intended to be predictive for heavier elements that may be discovered in the future (the "super-actinides"). *Blue*: Gases (at room temperature); *Pink*: Liquids at room temperature; *Pale yellow*: Solids; *Dark yellow*: Experimentally produced elements (Modified from https://commons.wikimedia.org/wiki/File:Periodic_system_Benfey_format.svg)

An atom is at its most stable when it has a filled outer electron shell, or valence shell. The chemical behavior of an element is dictated by a fundamental objective: to fill its outer electron shell, or valence shell, completely. Because elements within a vertical group have the same outer electron configurations, they will share physicochemical characteristics as well.

Elements with nearly full electron shells are on a mission to obtain those last few electrons necessary to reach full orbital occupancy. The most extreme set of elements in this category are the halogens, the second-to-last column on the right, Group 17 (Fig. 1). These elements reside in the p-block and have 7 electrons in their valence shell, in desperate need of only one additional electron. Consequently, they have high electronegativity (the tendency to take an electron from other atoms; fluorine has the highest electronegativity of any element, at 4.0) and high-ionization energies (the energy required to remove an electron from an atom). The halogens therefore tend to form anions with −1 charges.

In contrast, elements in Group 1, the alkalis, are generally found in a +1 valence state and have a habit of reacting energetically to achieve that condition (e.g., the reaction of sodium metal, Na, with water to make Na^+ is strongly exothermic, often dangerously so). All the alkalis have one extra electron that they strive to lose.

Elements with completely filled electron shells are in the last group to the far right on the table, the noble gases. These elements have electron shells that are filled to capacity. This is where they get their other common name, the inert gases; they are unlikely to either donate or acquire electrons in chemical reactions and are fundamentally unreactive.

Within a group, several additional patterns emerge. From top to bottom, atomic radii increase, and the outermost electrons are found progressively farther from the nucleus

(Fig. 1). This in turn makes it easier to remove electrons from an atom, resulting in decreasing ionization energy and electronegativity from top to bottom in a group, with only a few exceptions.

In the other dimension, horizontal rows are referred to as *periods*. Moving from left to right along a period, atomic radius generally decreases, as the electron cloud is drawn closer to the more positively charged nucleus. Consequently, electrons are held tighter within the atom, causing ionization energy and electronegativity to increase from left to right along a row. This phenomenon is particularly apparent in the lanthanide and actinide elements (known collectively as the rare earth elements; Fig. 1), which make up the f-block relegated to the bottom of the periodic table. Electrons in these nuclei are housed as much as two energy levels below the outer electron shell, which causes two phenomena unique to the rare earth elements. First, the addition of more electrons and protons to each element in the rows increases the electrostatic forces holding the atoms together, resulting in a larger than expected decrease in ionic radii from left to right across the periodic table. This phenomenon was named the "lanthanide contraction" by Goldschmidt in 1925. Second, because the outer electron shells of the rare earth elements are identical, all of the elements in the suite behave the same way chemically (with a few exceptions), making them quite useful in geochemical applications (see ▶ "Lanthanide Rare Earths") but particularly troublesome to purify. According to Sam Kean (2010), a chemist determined to isolate thulium from the other lanthanides began with hundreds of kilograms of ore, from which he removed tiny amounts of thulium. He had to perform the process over 15,000 times to extract a few grams of the element (and even then, the thulium was still a bit contaminated by other lanthanides, because, as Kean writes, "there just wasn't enough of a chemical handle to grasp them and pull them out").

Elemental Abundances

The abundance of elements in nature is not included in the traditional periodic table. Nevertheless, it is possible to extract some insight from information that is available on every periodic table: the atomic numbers.

Early investigations into elemental abundances revealed important perspectives on the formation of elements in stars (see ▶ "Nucleosynthesis"). Two scientists, Giuseppe Oddo in 1914 and William Harkins in 1917, noted that elements with even atomic numbers were more abundant than their odd-numbered neighbors on the periodic table. What is now known as the Oddo-Harkins Rule postulates that during nucleosynthesis, nuclei with odd numbers of protons are more likely to capture other odd-numbered nuclei, fusing to form a new atom with an even number of protons (see ▶ "Atomic Number, Mass Number, and Isotopes"). In contrast, elements with even atomic numbers are more stable, making it less likely that they will undergo fusion to form larger elements. Nuclei with an even number of protons and an even number of neutrons have higher binding energies and are therefore more stable than ones with odd numbers of either protons or neutrons. The abundances of the lanthanides in the solar system exhibit the Oddo-Harkins effect clearly (see ▶ "Lanthanide Rare Earths").

Geochemical Affinity and Periodicity

The abundances of elements in Earth's major reservoirs (its core, silicate mantle, atmosphere, hydrosphere, and crust), however, do not mirror the composition of the solar system. When the major Earth reservoirs formed, elements were rearranged ("differentiated") according to their behavior under varying physiochemical conditions, much of which can be explained in the context of elemental abundance in the major Earth reservoirs.

Victor Goldschmidt, one of the most important pioneers of modern geochemistry, was a Swiss-born mineralogist who moved to Norway, where he published a series of works entitled *Geochemische Verteilungsgesetze der Elemente* in 1926. In this work (and subsequent; Goldschmidt 1937), he classified the known chemical elements according to where they were found in nature, primarily (see ▶ "Geochemical Classification of Elements"). He defined four main categories for elemental behavior: (a) Lithophile (rock-loving); (b) Atmophile (gas-loving); (c) Chalcophile (ore- or chalcogen-loving, i.e., elements from the oxygen family, mostly sulfur, and oxygen excepted); and (d) Siderophile (iron-loving).

The group (or groups) to which an element belongs is dictated by its chemical properties. Lithophile elements are cations predominantly from the s- and f-blocks (Fig. 1) that combine readily with oxygen, and thus are strongly enriched in Earth's crust, mostly in silicate phases. They tend to form stable ions (e.g., the alkali and alkali earth elements, Groups 1 and 2) or strong covalent bonds (e.g., silicon, phosphorus) and have extreme electronegativities (high or low). Atmophile elements are volatile, meaning they evaporate easily and exist on Earth mostly in either liquid or gas phases. Consequently, the Earth is strongly depleted in atmophile elements compared to the solar system, which were lost during the early stages of Earth's formation. Atmophiles are noble gases, atoms that form strong, covalently bonded molecules (e.g., N_2, O_2), or ones that form stable molecules with oxygen (e.g., H as H_2O and C as CO_2).

Chalcophile elements form strong bonds primarily with sulfur, often as sulfides. They range from transition metals to heavy nonmetals, primarily from Groups 11, 12, and the

heavier elements from Groups 13 through 16, and tend to form covalent or metallic bonds owing to their intermediate electronegativities (Fig. 1). These elements are depleted in the Earth's crust and presumably concentrated in the core, and their ores are sources of many commercially important metals. The chalcophiles share some common characteristics with siderophile elements. Siderophiles are transition metals from the d-block that tend to be soluble in iron in solid or molten states. Because they do not form strong bonds with oxygen, they are predominantly concentrated in Earth's core and are relatively rare in the crust, making them precious metals from an economic perspective.

The periodic table provides further insight into the geochemical behavior of elements concentrated in Earth's silicate reservoir, the mantle and crust. The primary upper mantle minerals (olivine, pyroxene, plagioclase, garnet, and spinel) are made of a small number of elements, primarily Si, Mg, Fe, Al, and Ca; these are also the major elements in the Earth, owing to their abundance and prevalence in common minerals. If the crust is also considered, Ti, K, P, and Mn are also major elements for the same reason. Elements that do not constitute a stoichiometric or lattice-building component of these minerals are referred to as trace elements.

If a trace element has a similar ionic radius and charge to the lattice-building elements in a mineral, it is able to fit into the mineral's crystal structure and is therefore deemed a "compatible" element. Those with either ionic radii or charges that are inconsistent with the lattice builders will not be incorporated easily into the structures and are "incompatible" elements. When a mineral melts, the incompatible elements move preferentially into the liquid phase, owing to their less-stable configurations within the solid minerals; in contrast, compatible elements remain in the residual solid during melting. Whether an element behaves compatibly or incompatibly in the mantle or crust can be determined by examining periodic table trends. Most compatible elements reside in the same column on the periodic table as the major element it is replacing, or for the transition metals in the same row.

Elements with ionic radii too large to fit into most silicate minerals are classified as Large Ion Lithophiles (LIL) and are primarily the heavier elements from the first two columns in the periodic table (Groups 1 and 2, the alkalis and alkali earths; Fig. 1). Because their large volume distorts the lattices of common mantle minerals, these elements are highly incompatible and strongly enriched in the Earth's crust.

A second set of trace elements is incompatible in mantle minerals not because of their ionic size but owing to their high ionic charges (>3+). Substitution of an ion with a mismatched charge in a lattice site necessitates that charge balance be maintained by a coupled substitution, an energetically unfavorable event (i.e., if Ta^{5+} substitutes into a site that normally takes a trivalent cation, another +3 site must be occupied by an ion with only a +1 charge). Elements with the highest ionic charges are in the left columns of the d-block, among the transition metals, and are known as the High-Field-Strength elements. Even though ions such as Zr^{+4}, Hf^{+4}, Ta^{+5}, and Nb^{+5} have ionic radii that fit comfortably into most mantle and crust mineral, their excessive charges cause them to be highly incompatible and concentrated strongly in Earth's crust.

Conclusions

Despite its deceptively simple appearance, the periodic table encapsulates a remarkable wealth of information about the fundamental building blocks of matter.

Its systematic organization makes it possible to predict an element's chemical behavior, physical properties, and geochemical affinities, making it one of the most important reference tools for earth scientists.

Additional Resources

There are many useful and creative versions of the periodic table available online. Just a few of them are listed below:

1. The Royal Society of Chemistry has an interactive periodic table, with historical perspectives, videos, and a set of original artistic representations of the elements: http://www.rsc.org/periodic-table
2. A periodic table incorporating photographs of all the elements can be found here: http://periodictable.com/
3. The University of Nottingham hosts a website that includes videos about most of the elements: http://www.periodicvideos.com/
4. WebElements includes geochemically relevant information in a periodic table, such as elemental abundances in different environments: http://www.webelements.com/geology.html
5. In 1959, Green produced a version of the periodic table for geochemists, which included elemental abundances in different rock types, seawater, meteorites, and the universe, as well as their abundances in common minerals. More recently, Railsback (2003) compiled a complex but comprehensive periodic table for earth scientists, organized by ionic charge, and intended to convey interrelationships among elements in different geochemical settings (Railsback 2003): http://www.gly.uga.edu/railsback/PT.html
6. In the category of not particularly useful but fun, a periodic table anagram won the Special Category Prize in 1999 at Anagrammy.com (http://www.anagrammy.com/winners/Mike%20Keith). Exactly the same letters are on each side of the equation, arranged differently. The most

intriguing part is that if you replace the element names with their atomic numbers, those add up as well (Michael Keith)
7. Finally, no overview of the periodic table is complete without the Elements Song, written in 1959 by Tom Lehrer, who also performs it in the video: https://www.youtube.com/watch?v=DYW50F42ss8

Cross-References

- ▶ Alkali and Alkaline Earth Metals
- ▶ Atmophile Elements
- ▶ Atomic Number, Mass Number, and Isotopes
- ▶ Chalcophile Elements
- ▶ Earth's Continental crust
- ▶ Earth's Core
- ▶ Earth's Oceanic Crust
- ▶ Electronegativity
- ▶ Elements: Metalloids
- ▶ Formation and Evolution of the Earth
- ▶ Geochemical Classification of Elements
- ▶ High Field Strength Elements
- ▶ Ionic Radii
- ▶ Lanthanide Rare Earths
- ▶ Large-Ion Lithophile Elements
- ▶ Lithophile Elements
- ▶ Mantle Geochemistry
- ▶ Nucleosynthesis
- ▶ Platinum Group Elements
- ▶ Quantum Numbers
- ▶ Siderophile Elements
- ▶ Trace Elements
- ▶ Transition Elements
- ▶ Unified Atomic Mass Unit, Avogadro Constant, and Mole

References

De Chancourtois A-EB (1862) Mémoire sur un classement naturel des corps simples ou radicaux appelé *vis tellurique*. Comptes Rendus 54:757–761

Emsley J (2011) Nature's building blocks: everything you need to know about the elements. Oxford University Press, Oxford

Goldschmidt VM (1925) Geochemische verteilungsgesetze der element, Part V. Isomorphie und polymorphie der sesquioxyde. Die lanthaniden kontraktion und ihre konsequenzen. Oslo

Goldschmidt VM (1926) Geochemische verteilungsgesetze der elemente. Skrifter Norske Videnskaps. Akad, Oslo

Goldschmidt VM (1937) The principles of distribution of chemical elements in minerals and rocks. The seventh Hugo Müller Lecture, delivered before the chemical society. J Chem Soc:655–673

Gray HB, Simon JD, Trogler WC (1995) Braving the elements. University Science, Sausalito

Green J (1959) Geochemical table of the elements for 1959. Geol Soc Am Bull 70:1127–1184

Harkins WD (1917) The evolution of the elements and the stability of complex atoms. J Am Chem Soc 39(5):856–879

Janet C (1929) The helicoidal classification of the elements. Chemical News 138:372–374

Kean S (2010) The disappearing spoon and other true tales of madness, love, and the history of the world from the periodic table of the elements. Back Bay Books, New York

Lodders K (2010) Solar system abundances of the elements. Astrophys J 591:1220–1247

McDonough WF, Sun S-S (1995) The composition of the Earth. Chem Geol 120:223–253

Mendeleev D (1869) Ueber die beziehungen der eigenschaften zu den atomgewichten der elemente [On the relationship of the properties of the elements to their atomic weights]. Zeitschrift für Chemie 12:405–406

Mendeleev D (1871) Die periodische gesetzmässigkeit der chemischen elemente. Zhurnal Russkoe Fiziko-Khimicheskoe Obshchestvo 3:25. Annalen der Chemie und Pharmacie Supplement 8:133–229. [German version, 1872]

Newlands JAR (1865) On the law of octaves. Chemical News 12:83

Oddo G (1914) Die molekularstruktur der radioaktiven atome. Z Anorg Chem 87:253–268

Railsback LB (2003) An earth scientist's periodic table of the elements and their ions. Geology 31:737–740. http://geology.gsapubs.org/content/31/9/737.short; http://www.gly.uga.edu/railsback/PTPopups2.html

Scerri E (2006) The periodic table. Oxford University Press, Oxford

Seaborg G (1964) Plutonium: the ornery element. Chemistry 37(6):12–17

Petroleum

Philippe Ungerer
Materials Design S.A.R.L., Montrouge, France

P

Definition

Petroleum, from greek *petra* (rock) and latin *oleum* (oil), is a mixture of natural origin, made of numerous organic molecules, mostly hydrocarbons, from 1 to 80 carbon atoms. Petroleum is found as a liquid phase (oil), a gaseous phase (▶ *Natural Gas*), or a solid-like phase (bitumen) in the porosity and cracks of reservoir rocks where it has accumulated. These different forms result from a common origin, as petroleum is the product of the thermal or bacterial degradation of sedimentary organic matter in deep strata of sedimentary basins. The range of conditions produces a continuum of compositions between natural gas, oil, and bitumen.

History

Natural ▶ *Oil-seeps* have been used as sealing agent, adhesive, cosmetics, and fuel in oil lamps, from three millennia before BC in Ancient Egypt and the Middle East. *Biomarker*

analysis has allowed to trace back the origin of these bitumen (Connan 1999). In Asia, hand-dug wells were used to produce petroleum from 900 BC (Hunt 1995; Thornton 2015). In Europe, petroleum was also mined locally (e.g., in Pechelbronn, France) in the seventeenth century. The industrial production of oil by drilling wells – instead of mining – and processing oil in refineries appeared in 1857 in Ploiesti (Romania) and in 1859 in Titusville (Pennsylvania, USA). The increase of oil and gas production during the twentieth century was made possible by the discovery of new accumulations, particularly in the Middle East where the largest fields of oil (Ghawar, Saudi Arabia) and of natural gas (North Dome – South Pars, Qatar, and Iran) of the world were discovered in the 1948 and 1971, respectively. In the second half of the twentieth century, exploration was also successful in offshore continental margins (North Sea, Gulf of Mexico, Alaska, among others). Since 2000, exploration has extended to offshore areas with water depths of 1–3 km (e.g., S. Atlantic, W. Mediterranean sea) and arctic regions. According to Campbell and Laherrère (1998), the rate of new discoveries should not compensate for the production from conventional reservoirs (i.e., allowing economic production rates with the original reservoir permeability). The oil and gas industry is indeed producing an increasing volume of unconventional resources which need specific technologies to increase production rates. These are mainly extraheavy oils and bitumen (e.g., W. Canada), shale gas (e.g., Barnett formation, USA), and shale oil (e.g., Bakken formation, USA).

Distribution of Petroleum Reserves

A summary of oil and gas reserves and distribution is given in Table 1. Estimates of reserves are subject to significant uncertainties (10–20%) and their precise definition may change according to the data source. The percentage of oil in place that can be produced economically with current technology (i.e., the recovery factor) is approximately 35% (world average) for conventional oil reservoirs and approach 80% for natural gas (IFPEN 2017). There are important variations depending on reservoir characteristics. The resources of extraheavy oils and bitumen have been shown separately in Table 1 because they involve important volumes of oil in place (747 Gt) and low recovery factors (<10%) in current estimates. The possible resources of shale oil (US DOE-EIA 2013) are not shown in Table 1, as it is uncertain whether their production will be economic on a significant basis. Until 2016, the cumulated amount of oil and natural gas liquids produced worldwide is estimated to 200 Gt (IFPEN 2017). This is larger than the remaining reserves of conventional oil (178 Gt in Table 1).

Petroleum Composition

Petroleum composition is highly variable, as it results from a series of complex transformations involving chemical reactions and basin-scale migration (see below section on "Origin" and "Petroleum Migration"). In addition to its variability, petroleum composition is delicate to understand because it cannot be preserved in its original phase state when brought in surface conditions. For instance, the low molecular weight components e.g., (methane, C_2–C_4 alkanes, CO_2, H_2S) are gaseous in surface conditions and they may be dissolved in a liquid phase due to the high pressure prevailing in reservoir conditions. As another example, a methane-rich natural gas often contains significant concentrations of gasoline-range and gas-oil range hydrocarbons, which are dissolved in the gas phase in reservoir conditions, and liquid in surface conditions (Pedersen et al. 2014).

Finally, petroleum contains dissolved organic compounds of high molecular weight (asphaltenes, waxes). The abundance of these compounds in bitumen or in high wax oils explains their solid-like behavior, and their presence in

Petroleum, Table 1 Distribution of proven reserves, original oil in place (OOIP), and natural gas reserves on a global basis. Conventional oil reserves include natural gas liquids, i.e., hydrocarbons of natural gas collected in a liquid state by processing in surface conditions. Extraheavy oils reserves (including "bitumen" and "tar sands") are taken from the same source as a conventional oil (BP 2017) and the corresponding OOIP are taken from Total (2006). Oil reserves are expressed in billion tons (Gt) assuming average densities of 1000 kg/m^3 for extraheavy oils for volume/mass conversions. Natural gas reserves (source: BP 2017) are expressed in Tm^3 (10^{12}) in standard surface conditions

	Conventional (crude oil and Natural gas liquids)	Extraheavy oils		Natural gas (Tm^3)
Region	Proven reserves (2016), Gt	Estimated reserves (2016), Gt	Estimated OOIP, Gt	Proven reserves (2016)
North America	7.6	26.9	318	11.1
South America	15.1	35.7	207	7.6
Europe-Eurasia	21.8	–	222	56.7
Middle-east	110.1	–		79.4
Africa	16.9	–		14.3
Asia-Pacific	6.4	–		17.5
Total world	178	62.6	747	186.6

Petroleum, Table 2 Main petroleum fractions ranked by normal boiling temperature (Tb) and economic use. Direct use refers to fractions or compounds obtained by distillation or more specific separations, and conversion refers to chemical transformations by specific processes (thermal or catalytic) in refineries

Fraction	Tb, °C	Standard state at 25 °C, 1 atm	Carbon number range	Main direct use (products obtained by distillation or separations)	Main conversion products (obtained by chemical transformation)
Methane	−162	Gas	1	Distribution gas	Methanol, H_2
Other gases (C_2-C_4 alkanes, CO_2, H_2S)	−89 to 0	Gas	0–4	LPG fuel	Light olefins (ethylene, propylene), ethers
Gasoline (alkanes, cycloalkanes, aromatics)	0–204	Liquid	4–11	Fuel, chemicals	Light aromatics and olefins (e.g., paraxylene, ethylene)
Gas oil	204–315	Liquid	11–18	Diesel fuel, jet fuel	
Atmospheric and vacuum gas oil (AGO- VGO)	315–538	Liquid	14–40	Fuel oil, lubricant bases, waxes	Gasoline and diesel fuel
Vacuum residue (mostly polyaromatics)	>538	Amorphous solid	22–100[a]	Road asphalt, roof sealing	Gasoline and diesel fuel, coke

[a]Indicative maximum number of carbons of crude oil asphaltenes.

reservoir oils may also cause solid deposits when brought to surface conditions.

Whether petroleum is a natural gas, a reservoir oil, or a bitumen, its composition is first described by its main boiling point fractions (Table 2). It is worth noting that some families are systematically absent from natural petroleum: this is particularly the case of alkenes (also named olefins) of linear, branched, or cyclic structure. Similarly, three- and four-membered saturated cycles are marginal building units in petroleum hydrocarbons, their absence being explained by the lower stability of these small cycles compared with five-and six-membered cycles. A common characteristic of all petroleum fractions is the absence of the radioactive ^{14}C isotope of carbon, as a consequence of residence time of organic matter and petroleum $>10^6$ years in the subsurface. Petroleum fractions are also displaying a lighter ^{13}C composition than standard ($\delta^{13}C = -25$ to -100‰ for methane, usually -25‰ to -35‰ for other fractions) which is caused by the isotopically lighter carbon of living organisms and hence of sedimentary organic matter. Deuterium is also displaying lighter than average concentrations (Schoell 1980).

Light hydrocarbons (1–4 carbon atoms) are the major compounds of natural gas, and they are also found dissolved in reservoir oils. Methane represents generally 60–95% of natural gas and 0–50% of reservoir oil on a molar basis.

Nonhydrocarbon compounds of low molecular weight (CO_2, H_2S, N_2) show variable concentrations: 70% of natural gas reserves are reported to contain molar fractions of CO_2 lower than 2% vol and H_2S contents lower than 1% vol (Rojey et al. 1997). Occasional CO_2 contents of 10% and higher have been reported, possibly linked with magmatic contribution (e.g., 8–18% in Lula field offshore Brazil). H_2S concentrations in excess of 10% are also found in some deep reservoirs (e.g., 15.3% H_2S in Lacq field, France). Nitrogen content is generally low in natural gas and associated gas (0–3%) but may be higher in deep gas reservoirs (e.g., 14% in Groningen field, Netherlands).

The gasoline fraction usually contains linear and branched alkanes, monocyclic alkanes (alkylcyclopentanes, alkylcyclohexanes), and light aromatics (benzene, toluene, xylene isomers, and other alkylbenzenes). Among cyclic hydrocarbons, the unsubstituted end-members (cyclopentane, cyclohexane, benzene) are generally less abundant than the methyl-, dimethyl-, or ethyl- bearing compounds of the same families. Compared with heavier fractions, the composition of gasoline-range hydrocarbons is more delicate to sample because of possible evaporation of volatile compounds. It is also less specific of petroleum origin. It provides, however, useful indications of possible compositional variations revealing different blocks in a given reservoir.

The gasoil and intermediate distillate fractions contain linear and branched alkanes, naphthenes (i.e., cyclic alkanes), and aromatic hydrocarbons (Fig. 1). On average, these fractions display comparable mass fractions. The distribution of linear alkanes generally displays a broad distribution providing some insight in petroleum origin: a distribution showing a clear maximum above C_{20} and significant odd/even preference is an indication of a low degree of secondary reactions and an exponentially decreasing tail is an indication of more transformations. The absence of n-alkanes is an indication of oil biodegradation.

With the exception of isoprenoids, branched alkanes (alkanes bearing a branched methyl group every fourth carbon) are more difficult to identify because of the very large number of isomers. Among isoprenoids, pristane and phytane display comparable abundance to linear alkanes of similar molecular weight (Fig. 2).

Cyclic hydrocarbons in the gasoil fraction and vacuum gasoil fraction are either fully saturated (naphthenes with

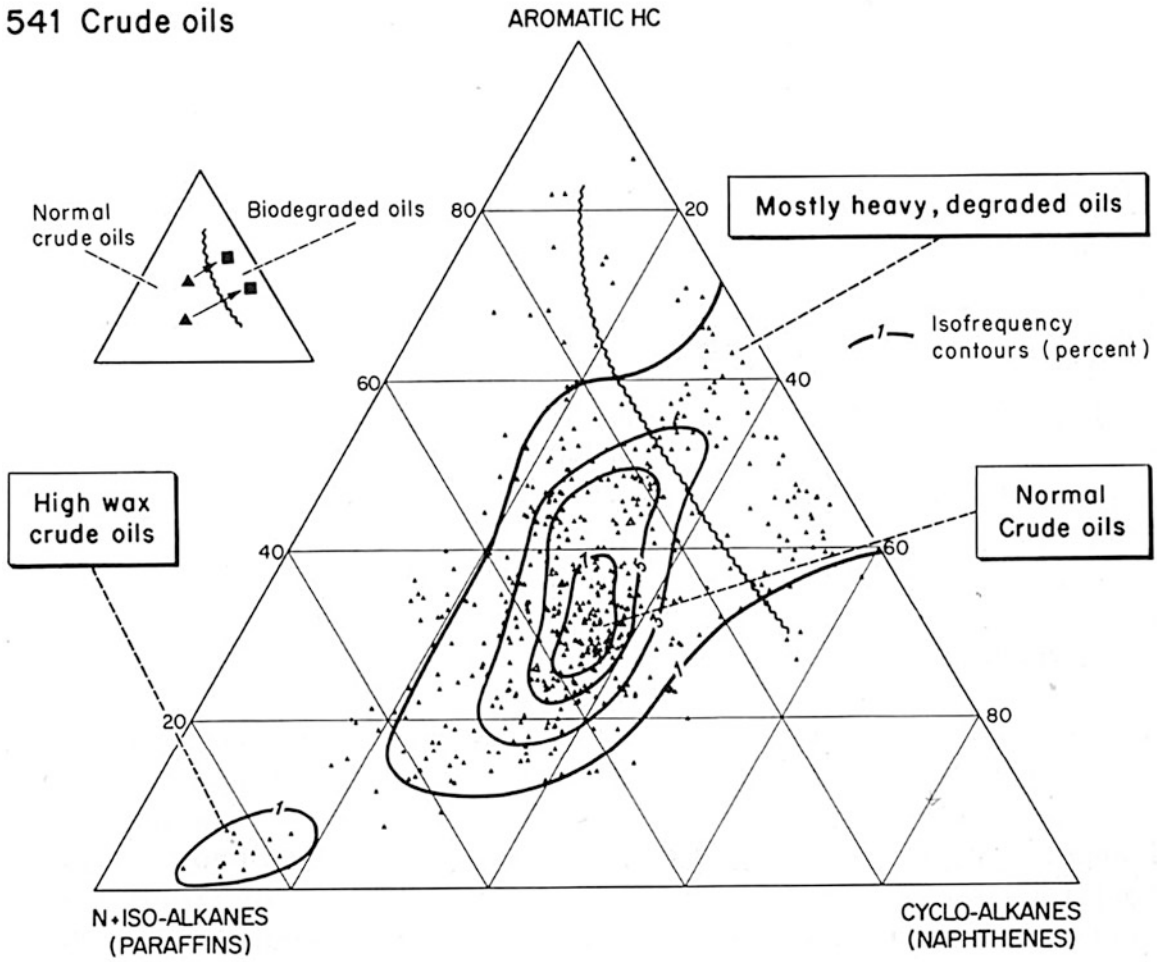

Petroleum, Fig. 1 Distribution of the oil fraction boiling above 210 °C in a ternary diagram (n + iso alkanes, naphthenes, aromatics) (After Tissot and Welte 1984)

1–5 condensed cycles), aromatic (1–5 cycles), or mixed (naphthenoaromatics). In these fractions, polycyclic naphthenes comprise several families of biomarkers analyzed by ▶ GC-MS to trace oil origin: steranes (four condensed cycles), hopanes, gammacerane, and oleananes (five condensed cycles), among others. Among polycyclic hydrocarbons, alkyl-substituted molecules (e.g., methylnaphthalenes, dimethylnaphthalenes) are more abundant than the condensed molecule (e.g., naphthalene). In gasoil and vacuum gasoil fractions, the structure of polyaromatic molecules and the decrease of alkyl substituents are often linked with the aromatization of polycyclic naphthenes at advanced stages of thermal degradation.

The heavy molecular weight compounds of crude oils present in vacuum residue are defined as solubility classes: resins are soluble in light alkanes, and asphaltenes are not. The presence of polyaromatic nuclei in asphaltenes (Fig. 3) explains why they can aggregate by stacking and segregate if aggregates are large enough (Mullins et al. 2012). Their elemental analysis (atomic H/C = 0.9–1.25 according to Rogel et al. 2012, 2013) and their investigation by Atomic force microscopy (Schuler et al. 2015) reveal important variations in structure and molecular weight. Resins and asphaltenes commonly display significant contents in sulfur, nitrogen, and oxygen.

Although dominated by hydrocarbons, petroleum contains also organic compounds including sulfur, oxygen, or nitrogen in functional groups or embedded in chains and cycles. These are mostly sulfur-bearing (thiols R-SH, alkylsulfides, thiophene derivatives), nitrogen-bearing (e.g., amines, pyrole derivatives), oxygen-containing compounds (e.g., alkanols, carboxylic acids), and organometallic compounds (Filby and Branthaver 1987). Ni- and VO-▶ *Porphyrins* are typical examples. As a general rule, the percentage of non-hydrocarbon compounds is small for light fractions and increases with molecular weight. Crude oils may contain up to 7% wt sulfur (average < 1%), up to 200 ppm of Nickel and up to 1500 ppm of Vanadium.

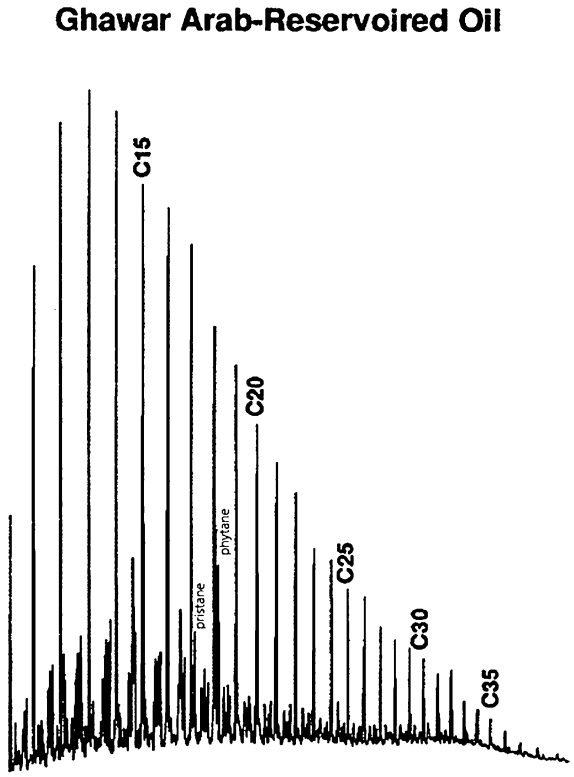

Petroleum, Fig. 2 C15+ chromatogram of a representative sample of Ghawar reservoired oil (After Carrigan et al. 1995)

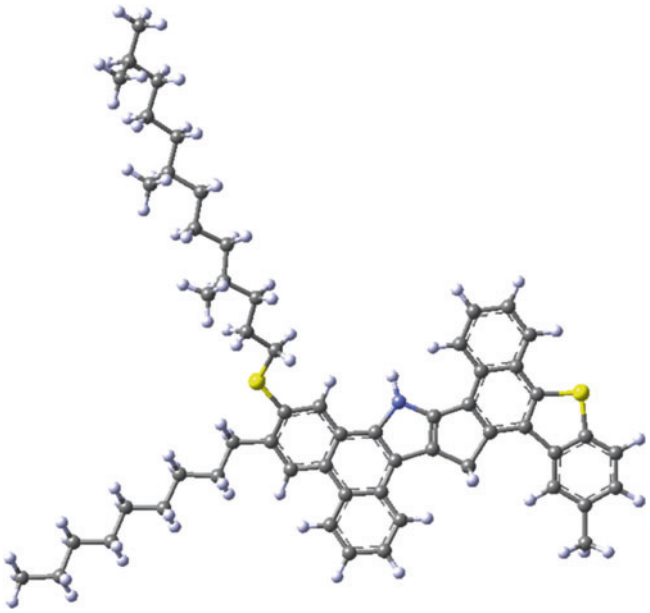

Petroleum, Fig. 3 Example of molecular structure of asphaltene ($C_{59}H_{71}NS_2$) in which the polyaromatic nucleus is derived from Atomic force microscopy data (Schuler 2015). Alkyl chains and functional groups containing nitrogen (blue) and sulfur (yellow) are included to approach the average composition of asphaltenes from heavy oils. This is just one out of many possible structures of asphaltenes

Among the average properties that serve to characterize the composition of petroleum, gas-oil ratio, and oil density are of particular importance. Both properties are measured after liquid-vapor separation in standard surface conditions. The gas-oil ratio (or GOR) is the volume ratio of vapor to liquid, expressed in std. m^3 of gas per m^3 of oil. Oil density defines the main categories of reported petroleum resources: light oils (less than 870 kg/m^3), medium and heavy oils (870–1000 kg/m^3), and extraheavy oils (>1000 kg/m^3). High density is generally associated with a high content of high boiling point fractions, as illustrated in Fig. 4.

Origin

Petroleum is the byproduct of the thermal evolution of ▶ *Kerogen*, the organic matter contained in fine-grained sediments, called source rocks. In 1934, Treibs attributed the origin of petroleum ▶ *Porphyrins* (Treibs 1934) to parent molecules of living organisms like chlorophyll (Fig. 5). Now there is no doubt that petroleum is dominantly issued from the transformation of biogenic material. The investigation of petroleum *biomarkers* and their origin in living microbial, vegetal, or animal organisms has become an important branch of ▶ *Organic Geochemistry*, based on ▶ *Gas Chromatography-mass Spectrometry (GC-MS)* among other techniques. The biogenic origin of petroleum is also supported by its negative $\delta^{13}C$, because carbon produced by photosynthesis is isotopically lighter than the atmospheric CO_2 source (see ▶ "Carbon Isotopes").

The deposition of organic-rich source rocks occurs in specific sedimentary environments in which a fair organic productivity and good preservation conditions prevail (see ▶ "Organic Matter Degradation and Preservation"). Preservation requires anoxic conditions (i.e., a very low ▶ *Fugacity* of oxygen). The Black Sea and Great African lakes are contemporary examples. Analyzing preservation

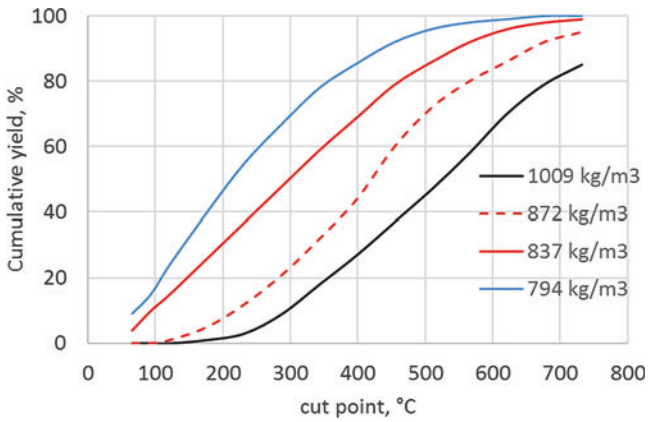

Petroleum, Fig. 4 Boiling point distribution of two light oils (std density 794 and 837 kg/m^3), an intermediate oil (872 kg/m^3), and an extraheavy oil (1009 kg/m^3) (Redrawn from Boduszynski et al. 1998)

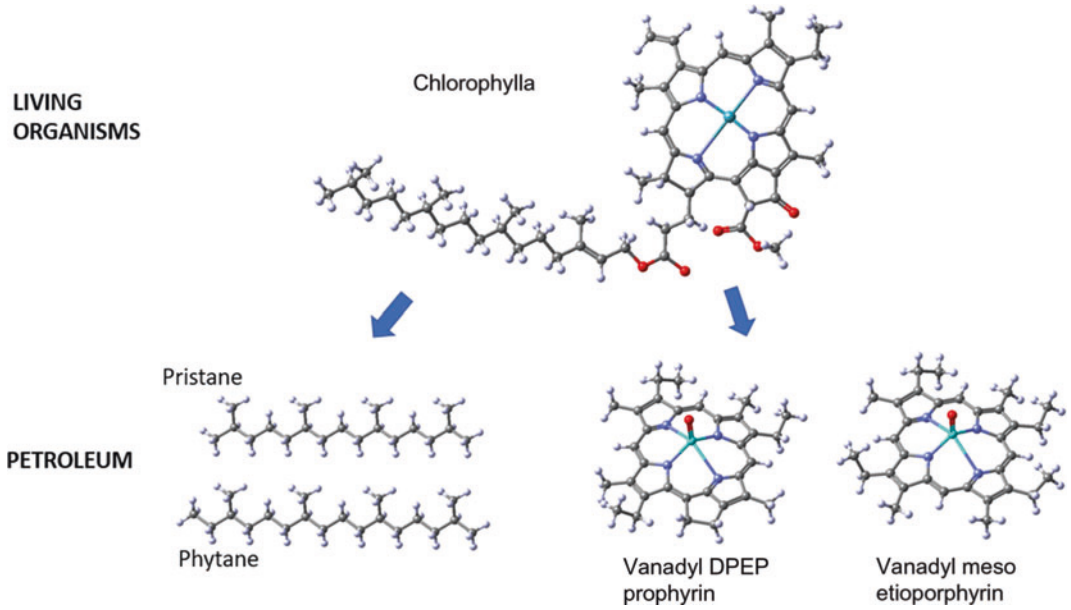

Petroleum, Fig. 5 Example of common petroleum *biomarkers* (vanadyl ▶ *Porphyrins*, pristane, phytane) and typical precursor (chlorophyll *a*). Chlorophyll *a* is a universal Mg-porphyrin involved in photosynthesis in living plants (color code as Fig. 3 for C, H, N, and oxygen in red). Arrows summarize a multistage diagenetic process involving the rupture of the alkyl chain and the exchange (▶ *Chelation*) of Mg^{2+} ion (emerald blue) by the vanadyl group $(VO)^{2+}$

conditions in the context of plate tectonics, as initiated by Tissot and Welte (1984), helps understanding the occurrence of organic-rich sediments. For instance, good source rocks deposited in the early phases of opening of the Atlantic ocean during Lower Cretaceous: the Bucomazi formation, Congo coastal basin (Burwood et al. 1995), the La Luna and Querequal formations in Venezuela (Talwani 2002), and the Lagoa Feia formation in Campos basin, offshore Brazil (Trindade et al. 1995). This helped exploration to find large accumulations in the Southern Atlantic presalt units.

Building upon the findings of ▶ *Coal* science (van Krevelen 1993), it has been recognized in the 1970s that different types of kerogen could be identified and that their composition followed systematic paths with increasing depth in a given basin (Tissot et al. 1974). The van Krevelen diagram (H/C vs O/C) allows to identify three main types, corresponding to different types of sedimentary environment (Fig. 6): type I kerogen, deposited in confined anoxic lakes such as the Green River Shales (Uinta basin, USA) is characterized by high H/C (1.35–1.55) at low depths of burial; type II kerogen, deposited in anoxic marine environments such as the Lower Torcian shales (Paris Basin, France) or the Upper Jurassic Kimmeridge Clay (North Sea) is displaying slightly lower H/C (1.2–1.3) at low depth; it is the most common form of organic matter in prolific source rocks; type III kerogen, originated from higher plants, is found in organic-rich shales or coals in deltaic environments like the Mahakam Delta (Indonesia). It displays a higher initial oxygen content (O/C = 0.1–0.3) and lower hydrogen content (H/C = 0.8–1.0).

In a given area with continuous sedimentation, three successive stages are observed with increasing depth (Fig. 6).

During the immature stage (organic diagenesis), petroleum formation has not significantly started and only small quantities of biomarkers are present. This stage is characterized by the degradation of labile functional groups of kerogen, such as amines, carboxylic acid, carbonyl, and hydroxyl. It results in the loss of CO_2 and H_2O.

The mature stage (also called "catagenesis" or "oil window"), starting below depths of 2–3 km, is characterized by the maximum amount of petroleum amount in organic-rich rocks. High molecular weight compounds are generated first, then augmented with larger amounts of gasoil- and gasoline-range hydrocarbons; these fractions decrease in their turn while light C_1–C_4 hydrocarbons increase, so that the content of liquid-behaving compounds shows a maximum (peak oil generation).

The overmature stage (metagenesis), below 3.5–5 km, is characterized by the final stages of the thermal degradation responsible for the decrease of gasoline-range and heavier fractions. Most C_2+ alkanes are then degraded into methane and polyaromatic solids (pyrobitumen).

The thermal degradation process described above is named *maturation*. There is, however, no universal maturity indicator to quantify maturation. In addition to the position in the van Krevelen diagram (Fig. 6b), the main maturity indicators measured on organic matter samples are the vitrinite

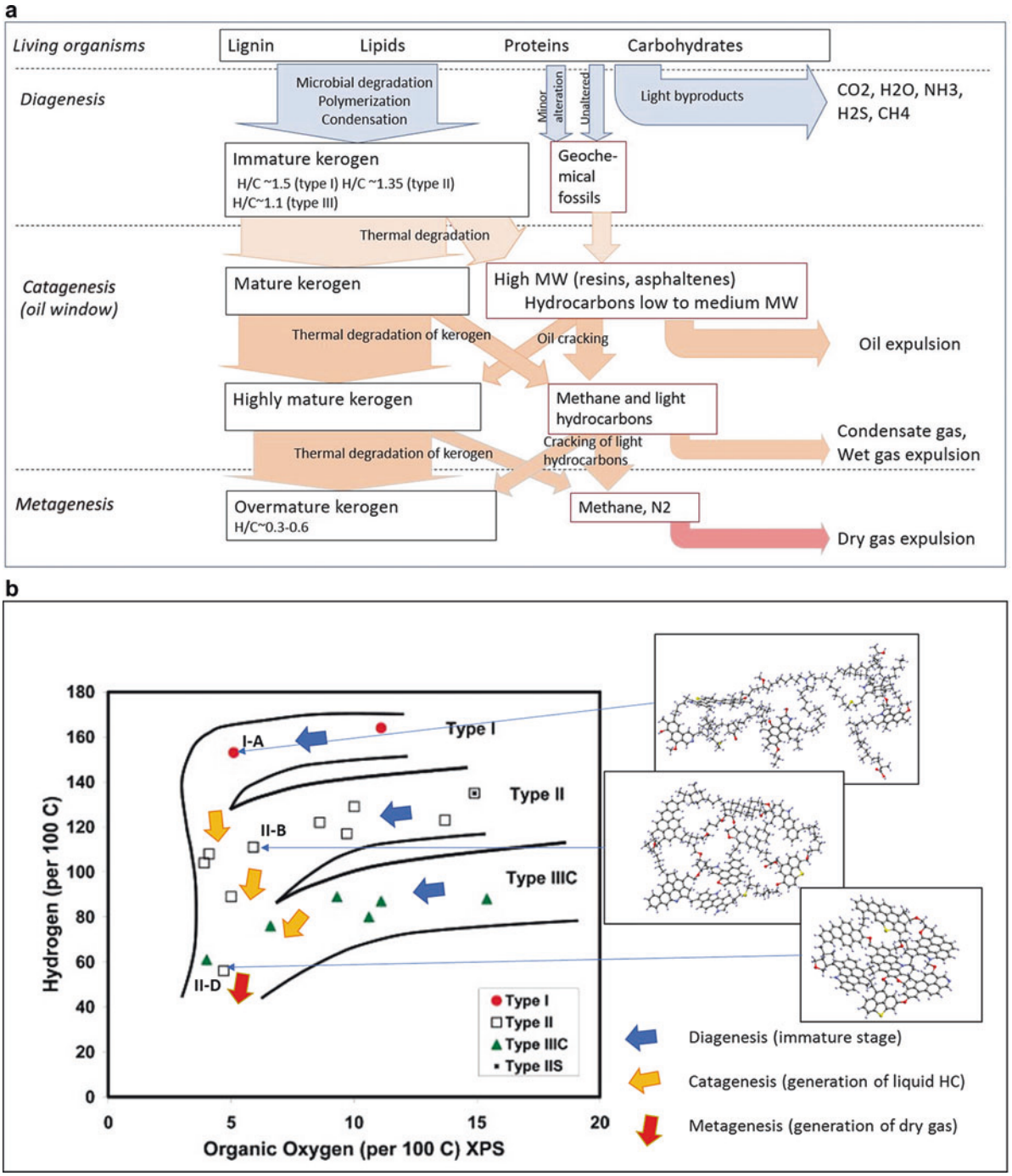

Petroleum, Fig. 6 (a) Schematic diagram indicating the successive stages of petroleum formation in a basin with continuous sedimentation, adapted from a diagram of Tissot and Welte (1984). (b) van Krevelen diagram illustrating the change of atomic composition and schematic molecular structure of kerogen with organic type and maturity (Adapted from Kelemen et al. 2007 and Ungerer et al. 2015)

reflectance, obtained from optical reflectivity measurements of specific components of kerogen, and the peak temperature Tmax measured in programmed temperature pyrolysis. Maturity indicators are also defined to estimate the thermal degradation of oils from their composition (Radke and Welte 1981; Mackenzie and McKenzie 1983). These are based on the dilution or degradation of biomarkers (e.g., pristane/n-alkane, sterane isomerization) or on the dealkylation of polyaromatic structures (e.g., methylphenanthrene index), among other examples.

The isotopic composition carbon is providing indications of petroleum origin: thermogenic gas displays ^{13}C content similar to oil (usually $\delta^{13}C = -30$ to $-40‰$), and biogenic methane generated at temperatures lower than 80 °C displays

lighter isotopic composition ($\delta^{13}C = -50$ to -100‰). The presence of C_2+ hydrocarbons in gas is another marker of thermogenic origin, as opposed to biogenic gas in which C_2+ hydrocarbons are absent.

When source rocks are buried under a column of sediments, temperature increases due to the local geothermal gradient (generally 20–30 °C/km, with important variations and extreme values reaching 80 or 90 °C/km). This is the main factor of organic matter thermal degradation and petroleum formation. When maturation progresses, the remaining kerogen is more aromatic and its hydrogen content decreases as a result of the release of hydrocarbons (Tissot et al. 1974).

Thermal degradation is controlled by chemical *kinetics* at moderate temperatures in sedimentary basins (typically 70–150 °C) where source rocks are submitted to long heating times (1–100 Myr, i.e., 3×10^{13} to 3×10^{15} s). Petroleum formation can be simulated by pyrolysis in the laboratory, where higher temperatures (300–500 °C) compensate for shorter heating time (1–10^7 s). This has provided the basis of *Rock-Eval pyrolysis*, a standard thermal analysis under inert gas flow specifically designed to characterize the petroleum generation potential and kerogen maturity of large series of source rock samples (Espitalié et al. 1985/1986). Alternative methods of pyrolysis in high pressure vessels allow investigation of secondary reactions (Lewan 1985; Behar et al. 1997). Being kinetically controlled, thermal degradation explores lower free energy conformations of the kerogen + petroleum system, and it is thus essentially irreversible. The role of liquid water and natural catalysts (clay minerals) does not appear necessary to explain the main aspects of petroleum formation. The main influence of minerals is more likely to adsorb preferentially the polar and aromatic compounds, compared with the alkanes. Reservoir oils are indeed richer in alkanes than source rock extracts (Vandenbroucke 1993).

The *kinetics* of petroleum formation and cracking are generally modelled by first order reactions:

$$dx/dt = Kx$$

where x is the initial petroleum and generation potential and K is the rate constant (1/s) that changes with temperature according to Arrhenius law:

$$K = A \exp(-E/RT)$$

where A a prefactor, E an apparent activation energy, R universal gas constant (8.3145 J/mol/K), and T absolute temperature (K). In order to address a large range of conditions and kerogen types, several parallel and successive reactions are included, with activation energies in the range 190–250 kJ/mol (Tissot et al. 1987; Burnham et al. 1987; Ungerer 1990; Behar et al. 1997). Based on ▶ Paleotemperature reconstructions, these models allow to understand the timing and spatial distribution of petroleum formation in a given basin. These models account for the differences in petroleum potential between major ▶ *Kerogen* types: type I kerogen, generates 600–800 mg of *hydrocarbons and NSO compounds* per g of initial total organic carbon (TOC); type II kerogen, generates 400–600 mg/g TOC; and type III kerogen issued from higher plants generates 100–300 mg/g TOC. Type III kerogen generates mostly methane and C_2–C_4 hydrocarbons, but hydrogen-rich type III containing long alkyl chains are also considered to generate significant gasoline-range hydrocarbons and heavier fractions.

The role of pressure in petroleum formation *kinetics* is modest compared to temperature. Detailed kinetic models, based on free radical mechanisms, explain why natural petroleum does not contain linear alkenes, which are important products in low pressure pyrolysis (Enguehard et al. 1990). Detailed kinetic models are also useful in understanding the role of high pressure conditions (20–120 MPa) and hydrocarbon structure on the rates of thermal degradation (Dominé et al. 1991, 2002; Burklé-Vitzthum et al. 2011).

Petroleum Migration

Petroleum migration is an essential step of petroleum formation and accumulation, involving important changes of composition. The understanding of migration is primarily based on the possible phase state and properties of petroleum in the conditions prevailing in sedimentary basins. The water solubility of hydrocarbons is lower than a few ppm in diesel-range fractions and above (McAuliffe 1966). As a result, petroleum forms a separate phase from pore water. At very high pressure ($P > 35$ MPa), petroleum is most often forming a single phase even when it contains a high percentage of methane (Fig. 7).

Another important property for petroleum migration is its viscosity (μ_i), which controls flow rates in porous media through the two-phase Darcy's law:

$$u_i = -\frac{K}{\mu_i} k_{r\,i}(\nabla P_i - \rho_i g)$$

Viscosity changes by several orders of magnitude with petroleum composition and local conditions: it is lower than 0.1 mPa.s for natural gas, 1–100 mPa.s for most oils. It reaches 100 Pa.s for bitumen at low temperature (Fig. 8). This is why bitumen appears solid at human timescale although it is a complex fluid.

Petroleum migration is generally described with the main steps illustrated in Fig. 9.

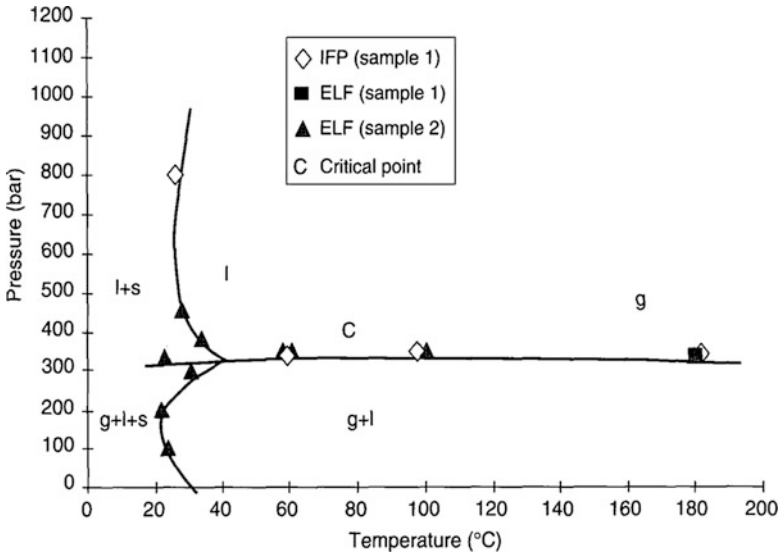

Petroleum, Fig. 7 P, T phase diagram of a methane-rich petroleum fluid (Ungerer et al. 1995) showing gas + liquid (g + l) phase split below 310 bar, and a monophasic region for higher pressure, either vapor (g) above 80 °C or liquid (l) below 80 °C. Wax crystallization below 20–30 °C results in three phases (g + l + s) below 310 bar and two phases (l + s) above 310 bar

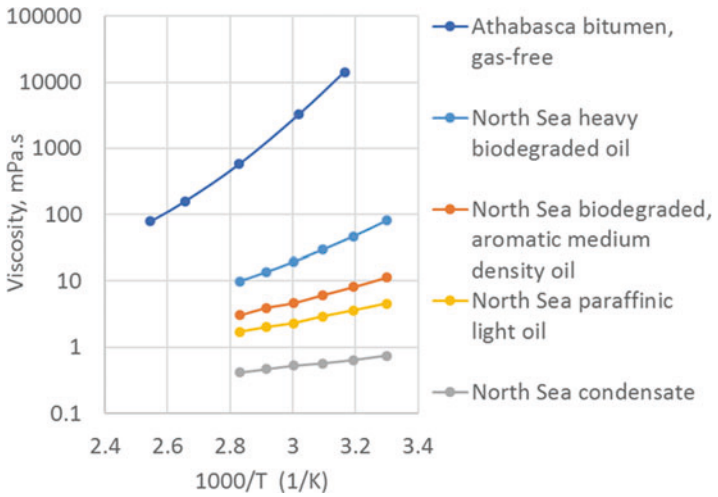

Petroleum, Fig. 8 Viscosity of Athabasca bitumen (Data from Mehrotra and Svrcek 1986) and of selected oils from North Sea Viking graben (Data from Roenningsen et al. 1991) as a function of inverse temperature at ambient pressure (P = 1 atm)

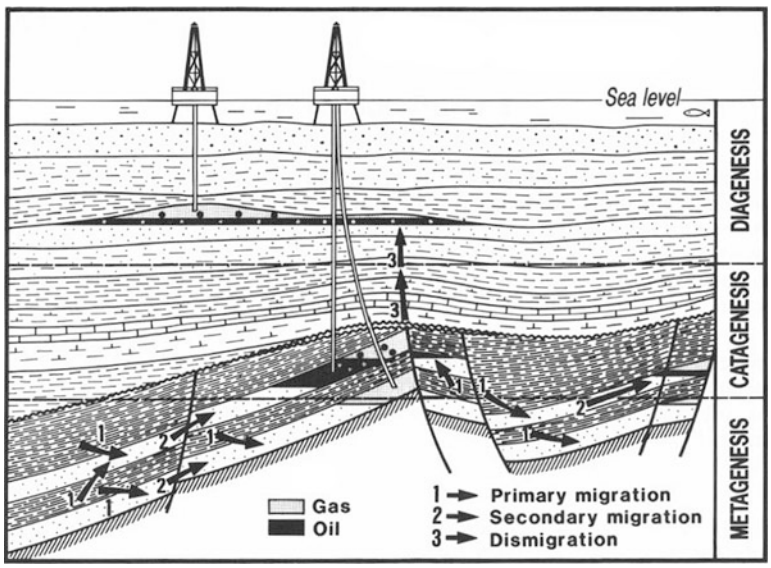

Petroleum, Fig. 9 Schematic cross-section illustrating primary migration and secondary migration, inspired by the case studies of the North sea Viking graben (reprinted from Durand 1988, with permission)

P

Primary migration refers to the expulsion of petroleum from source rocks, i.e., from low porosity shales with permeability (K in Darcy's law) as low as 1 nanodarcy (10^{-21} m^2), toward surrounding carrier beds. This process is considered to be controlled mostly by fluid pressure build-up, molecular scale transport (Collell et al. 2014) and compaction. Expulsion occurs when a sufficient amount of petroleum has been generated, creating a continuous path of saturated pores or microfractures (Vandenbroucke 1993). It is considered to require a total organic carbon content (TOC) of 0.5%wt at least for type II organic matter.

Secondary migration, in which petroleum flows inside more permeable units or faults, is a process dominated by gravity, capillary forces, and phase behavior. In this process, low permeability strata (called caprocks) plays an essential role in favoring horizontal migration. Caprocks may be ▶ *Evaporites* (halite, anhydrite) or shales. Migration follows the top of permeable units until it faces other obstacles (anticline, fault, pinch-out) where petroleum may eventually get trapped. Secondary migration is often associated with a liquid-gas phase split in the reservoir, as a result of pressure decrease along migration path. The consequences of phase split with decreasing reservoir pressure are the following: accelerated migration of the gas phase due to its lower viscosity and lower density; decreasing GOR of reservoir oil; decreasing condensate content of the gas and molecular fractionation (Carpentier et al. 1996). When a deep gas migrates into a shallower reservoir, the liquid dropout may generate light oil accumulations (oil rim) below the gas accumulation.

The distances covered during secondary migration are commonly a few hundred meters to a few km vertically, a few km to several hundreds of km horizontally. Together with prolific source rock deposition and maturation conditions, favorable structure to long-distance migration explains the size of the Middle East accumulations, as illustrated in Fig. 10.

The composition of the oil in a given trap results from the mixing of areas with different maturity, the less mature providing more heavy compounds (resins, asphaltenes) and the more mature providing lighter ▶ *Hydrocarbons* and gas. It is generally considered that diffusivity and thermally driven natural convection in the reservoir are sufficient to equilibrate petroleum composition vertically. Significant differences in composition persist horizontally when permeability barriers or large horizontal distances prevent petroleum from homogenizing. The mixing of light oil or gas with a heavy oil may cause the segregation of highly viscous oil (tar mats) near the oil-water contact.

A third stage of migration may be defined to address the leakage of accumulations (Fig. 9). On a geological timescale, an accumulation of petroleum may lose ▶ *Hydrocarbons* in various ways: erosion of caprock; differential subsidence reducing trap volume; growth of gas cap causing spill-over of oil; leakage through fractures; aerobic and anaerobic

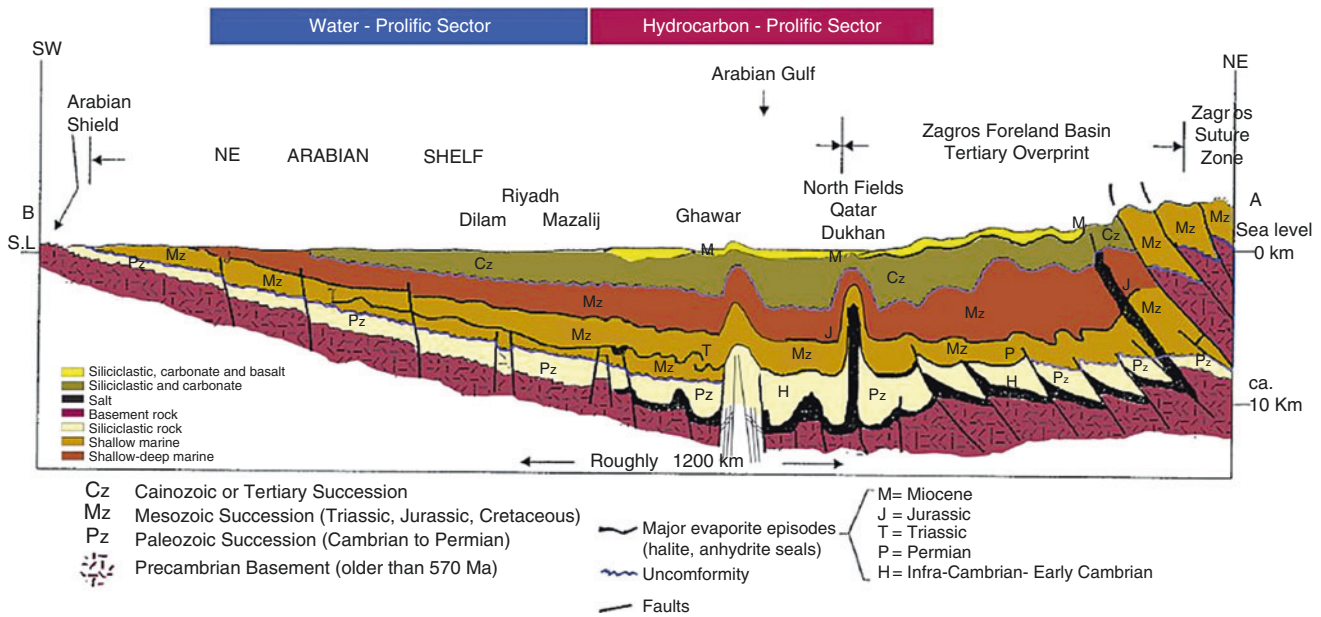

Petroleum, Fig. 10 SW-NE cross-section across Saudi Arabia, Qatar, and Iran showing the geological context of major Middle East petroleum accumulations (reprinted from Jagu et al. 2016, with permission). Prolific source rocks are Upper Jurassic Tuwaiq mountain and Hanifa formations (Carrigan et al. 1995), which have sourced the Jurassic reservoirs; paleozoic Silurian intervals that have sourced Permian and Ordovician accumulations (Konert et al. 2001). Several basin-wide evaporitic episodes have provided efficient caprocks allowing long-distance horizontal migration and preservation of major oil fields (e.g., Ghawar) and *natural gas* fields (South Pars, North Dome) on the Arabian platform as well as large accumulations in the Zagros thrustbelt and its foreland

biodegradation of petroleum, which may occur up to 80 °C (Connan et al. 1997; Aitken et al. 2004); and thermal cracking of gasoline-range and heavier fractions of oil into lighter alkanes (mostly methane) and pyrobitumen in high temperature reservoirs. Thermal cracking of oil into gas occurs mainly at temperatures above 150 °C, and some deep reservoir fluids are still containing significant concentrations of gasoline-range and gasoil-range hydrocarbons although the reservoir temperature is 190 °C (Ungerer et al. 1995). Biodegradation is specific as light linear alkanes and saturated ▶ *Hydrocarbons* are preferentially degraded. It results in a significant increase in density and viscosity, and also higher concentrations in sulfur and metals (Huc 2010). Biodegradation in shallow reservoirs explains the origin of extraheavy oils and bitumen in Western Canada (Fig. 11) and Venezuela (Eschard and Huc 2008; Talwani 2002).

Interactions with Mineral Diagenesis

In an oil-saturated reservoir rock, mineral ▶ *Diagenesis* is considerably slowed down as it requires a continuous ▶ *Water* phase. Pore filling with oil or gas interrupts the growth of diagenetic minerals (e.g., clay minerals) and also the porosity reduction by pressure solution, which is the dominant mode of compaction (Gratier et al. 2013). In the example of the Ekofisk field (Norwegian North Sea), a high porosity (up to 35%) is preserved in the oil-saturated zone while porosity is reduced to a few % in the water-saturated zone of the same chalk reservoir (Van den Bark and Thomas 1981). The unconsolidated nature of oil sands in W. Canada and in Venezuela is probably also caused by an early migration of oil in the reservoir. This may have important effects on oil production such as producing loose sand together with extraheavy oils (Tremblay et al. 1997). It may also cause significant surface subsidence when petroleum is replaced by injected water (Doornhof et al. 2006).

In evaporitic series, thermal sulfate reduction (TSR) of calcium sulfate (e.g., anhydrite) by *hydrocarbons* may generate important amounts of H_2S and other reduced form of sulfur, together with CO_2, at temperatures in the range 100–140 °C mainly (Machel 2001). These reactions are responsible for high H_2S contents in ▶ *Natural Gas* and associated gases in SW France, Western Canada, and the Middle East, among other regions (see ▶ "Sulfur Cycle").

Petroleum in the Global Carbon Cycle

According to BP statistical review (2017), the global production of oil was 4.6 Gt/yr. (i.e., ~4 Gt of carbon) and the production of natural gas was 3.55 Tm3/yr. (i.e., ~2 Gt of carbon) in 2016. The total flux (6 Gt of carbon/yr) represents 10% and 5% of the yearly fluxes of carbon between ocean/atmosphere and atmosphere/continent, which are estimated to ~60 GtC per year and 120 GtC/yr., respectively (IPCC 2013).

Based on reserve estimates of Table 1, average recovery factors, and other sources (e.g., shale oil estimates from US DOE-EIA 2013), the overall amount of petroleum in the subsurface may be roughly estimated to 2720 Gt (~900 Gt in conventional reservoirs, 750 Gt in extraheavy oil and bitumen reservoirs, 900 Gt of shale oil, and 175 Gt in natural

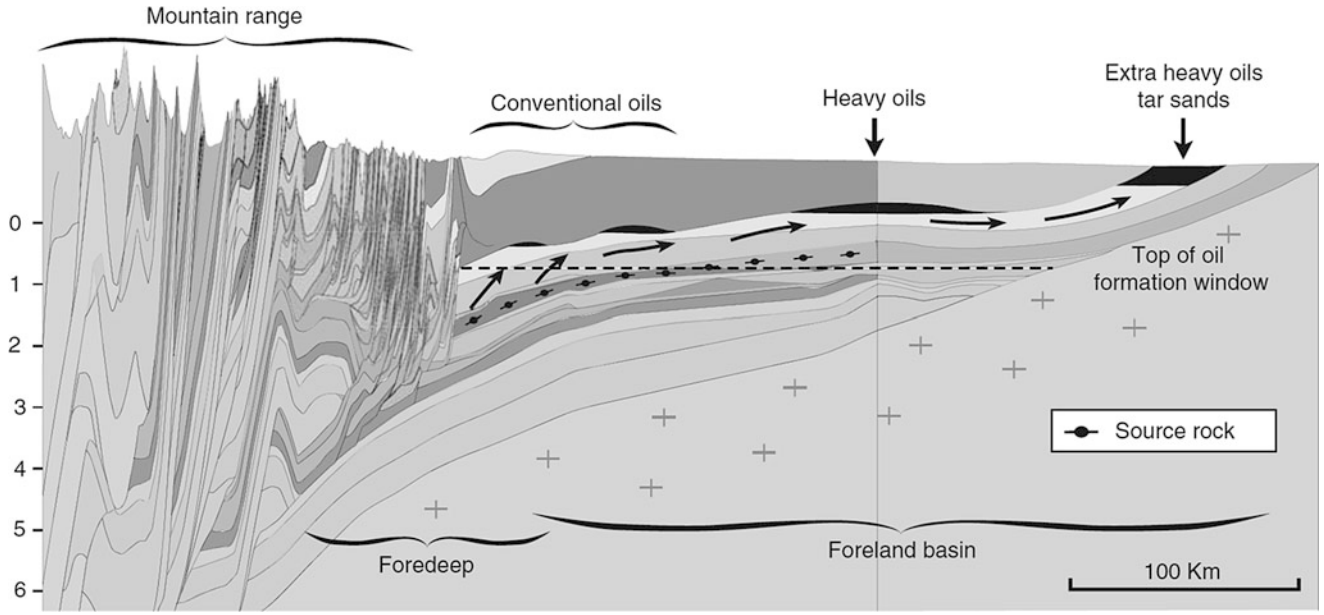

Petroleum, Fig. 11 Schematic geological cross-section of foreland basin showing the location of conventional oils, heavy oils, and extra-heavy oils as a result of petroleum generation in deep source rocks, migration along carrier beds, and biodegradation in shallow reservoirs (reprinted from Eschard and Huc 2008 with permission)

gas accumulations, excluding natural gas hydrates). A small fraction of this amount (<10%) appears as technically recoverable.

Summary

Petroleum composition is highly variable and complex, as a consequence of the large range of conditions during its formation and accumulation along geologic time. The origin of petroleum by thermal degradation of the sedimentary organic matter is the dominant process, bacterial degradation playing a significant role in methane generation and oil biodegradation. The influence of phase equilibria and petroleum migration on the distribution and composition of petroleum accumulations is also reasonably understood.

This knowledge has contributed to the success of oil and gas exploration. However, the rate of new significant discoveries slows down because fewer regions are still unexplored. Conventional petroleum accumulations appear as a finite resource from which more than 50% has been produced. In the long range, petroleum production will rely increasingly on the production of unconventional resources (particularly extraheavy oils and bitumen).

Cross-References

- Biomarkers: Petroleum
- Biomarker: Assessment of Thermal Maturity
- Carbon Cycle
- Carbon Isotopes
- Coal
- Diagenesis
- Evaporites
- Gas Chromatography–Mass Spectrometry (GC–MS)
- Gas Hydrates
- Hydrocarbons
- Hydrogen
- Kerogen
- Kinetics of Geochemical Processes
- Natural Gas
- Oil Seeps and Coastal Bitumen
- Oil Shale
- Oil-Oil and Oil-Source Rock Correlations
- Organic Geochemistry
- Organic Matter Degradation and Preservation
- Paleotemperatures
- Phase Equilibria
- Porphyrins
- Programmed Temperature Pyrolysis
- Sulfur Cycle
- Water

Acknowledgments The author thanks Guy Maisonnier, Roland Vially, Bernard Durand, and François Roure for their help and advice in preparing this manuscript.

References

Aitken CM, Jones DM, Larter SR (2004) Anaerobic degradation in deep subsurface oil reservoirs. Nature 431(7006):291–294

Behar F, Vandenbroucke M, Tang Y, Marquis F, Espitalie J (1997) Thermal cracking of kerogen in open and closed systems: determination of kinetic parameters and stoichiometric coefficients for oil and gas generation. Org Geochem 26(5):321–339

Boduszynski MM, Rechsteiner CE, Shafizadeh ASG, Carlson MSK (1998) Composition and properties of heavy crudes. Unitar centre, report 1998.202

BP Statistical Review of World Energy, 66th edition, June 2017. BP p.l.c. 1 St James's Square, London SW1Y 4PD , UK

Burklé-Vitzthum V, Bunaceur R, Marquaire P-M, Montel F, Fusetti L (2011) Thermal evolution of n- and iso-alkanes in oils. Part 1: pyrolysis model for a mixture of 78 alkanes (C1-C32) including 13,206 free radical reactions. Org Geochem 42(5):439–450

Burnham AK, Braun RL, Gregg HR (1987) Comparison of methods for measuring kerogen pyrolysis rates and fitting kinetic parameters. Energy Fuel 1:452–458

Burwood R, de Witte SM, Mycke B, Paulet J (1995) Petroleum geochemical characterization of the lower Congo coastal basin Bucomazi formation. In: Katz BJ (ed) Petroleum source rocks. Springer, Berlin, pp 235–263

Campbell CJ, Laherrère JH (1998) The end of cheap oil. Sci Am 1998:78–83

Carpentier B, Ungerer P, Kowalewski I, Magnier C, Courcy JP, Huc AY (1996) Molecular and isotopic fractionation of light hydrocarbons between oil and gas phases. Org Geochem 24(12):1115–1139

Carrigan WJ, Cole GA, Colling EL, Jones PJ (1995) Geochemistry of the upper Jurassic Tuwaiq mountain and Hanifa formation petroleum source rocks of Eastern Saudi Arabia. In: Katz BJ (ed) Petroleum source rocks. Springer, Berlin, pp 67–87

Collell J, Ungerer P, Galliero G, Yiannourakou M, Montel F, Pujol M (2014) Molecular simulation of bulk organic matter in type II shales in the middle of the oil formation window. Energy Fuel 28(12):7457–7466

Connan J (1999) Use and trade of bitumen in antiquity and prehistory: molecular archaeology reveals secrets of past civilizations. Philos Trans R Soc B 354(1379):33–50. https://doi.org/10.1098/rstb.1999.0358

Connan J, Lacrampe-Couloume G, Magot M, (1997) Anaerobic biodegradation of petroleum in reservoirs: a widespread phenomenon in nature. In: 18th international meeting on organic geochemistry, Maastricht, Book of Abstracts, Part 1, pp 5–6

Dominé F (1991) High pressure pyrolysis of n-hexane, 2,4-dimethylpentane and 1-phenylbutane. Is pressure an important geochemical parameter? Org Geochem 17(5):619–634

Dominé F, Bounaceur R, Scacchi G, Marquaire P-M, Dessort D, Pradier B, Brevart O (2002) Up to what temperature is petroleum stable? New insights from a 5200 free radical reactions model. Org Geochem 33(12):1487–1499

Doornhof D, Kristiansen TG, Nagel NB, Pattillo PD, Sayers C (2006) Compaction and subsidence. Schlumberger Oilfield Rev 18(3): 50–68

Durand B (1988) Understanding of HC migration in sedimentary basins – present state of knowledge. Org Geochem 13:445–459

Eschard R, Huc AY (2008) Habitat of biodegraded heavy oils: industrial implications. Oil Gas Sci Technol – Rev IFP 63(5):587–607

Espitalié J, Deroo G, Marquis F (1985/1986) La pyrolyse Rock Eval et ses applications. Revue de l'Institut Français du Pétrole, Part 1: 40: 563–579. Part 2: 40:755–784; Part 3: 41:73–89

Enguehard F, Kressmann S, Dominé F (1990) Kinetics of dibutylether pyrolysis at high pressure- experimental study. Org Geochem 16:155–160

Filby RH, Branthaver JF (1987) Metal complexes in fossil fuels – geochemistry, characterization, and processing, ACS symposium series, vol 344. American Chemical Society, Washington, DC, 485 pp

Gratier JP, Dysthe D, Renard F (2013) The role of pressure solution creep in the ductility of the earth's upper crust. Adv Geophys, Elsevier 54:47–179

Huc AY (2010) Heavy crude oils: from geology to upgrading: an overview. Editions Technip, Paris, 442 p

Hunt JM (1995) Petroleum geochemistry and geology, 2nd edn. Freeman, New York, 743 p

IFPEN (2017) Personal communications from G. Maisonnier and R. Vially. July 2017

IPCC (2013) Climate change 2013: the physical science basis, Chapter 6. In: Ciais Ph, Sabine Ch (eds) Carbon and other geochemical cycles. Downloaded from https://www.ipcc.ch/report/ar5/wg1/

Jagu MM, Nader FH, Roure F, Matenco L (2016) Optimal reservoirs for CCS and EOR in the kingdom of Saudi Arabia: an overview. Arab J Geosci 9:604, pp 1–15

Kelemen SR, Afeworki M, Gorbaty ML, Sansone M, Kwiatek PJ, Walters CC, Freund H, Siskin M, Bence AE, Curry DJ, Solum M, Pugmire RJ, Vandenbroucke M, Leblond M, Behar F (2007) Direct characterization of Kerogen by X-ray and solid-state 13C nuclear magnetic resonance methods. Energy Fuel 21(3):1548–1561

Konert G, Afifi AM, Al-Hajri SA (2001) Paleozoic stratigraphy and hydrocarbon habitat of the Arabian plate. GeoArabia 6(3):407–442

Lewan MD, Illich H, Raiswell R, Mackenzie AS, Durand B, Manning DAC, Comet PA, Berner A, de Leeuw JW (1985) Evaluation of petroleum generation by hydrous pyrolysis experimentation [and discussion]. Philos Trans R Soc Lond A 315:123–134

Machel HG (2001) Bacterial and thermochemical sulfate reduction in diagenetic settings – old and new insights. Sediment Geol 140: 143–175

Mackenzie A, McKenzie D (1983) Isomerization and aromatization of hydrocarbons in sedimentary basins formed by extension. Geol Mag 120(5):417–470

McAuliffe C (1966) Solubility in water of paraffin, cycloparaffin, olefin, acetylene, cycloolefin, and aromatic hydrocarbons. J Phys Chem 70(4):1267–1275

Mehrotra AK, Svrcek WY (1986) Viscosity of compressed Athabasca bituem. Can J Chem Eng 64:844–847.14

Mullins OC, Sabbah H, Eyssautier J, Pomerantz AE, Barré L, Andrews AB, Ruiz-Morales Y, Mostowfi F, McFarlane R, Goual L, Lepkowicz R, Cooper T, Orbulescu J, Leblanc RM, Edwards J, Zare RM (2012) Advances in asphaltene science and the Yen-Mullins model. Energy Fuel 26:3986–4003

Pedersen KS, Christensen PL, Shaikh JA (2014) Phase behavior of petroleum reservoir fluids. CRC press, London, 465 p

Radke M, Welte DH (1981) The Methylphenanthrene Index (MPI-1) a maturity parameter based on aromatic hydrocarbons. In: Advances in organic geochemistry 1981. Wiley, Chichester, pp 504–512, 1983

Roenningsen HP, Björndal B, Hansen AB, Pedersen WB (1991) Wax precipitation from North Sea crude oils. 1. Crystallization and dissolution temperatures, and Newtonian and non-Newtonian flow properties. Energy Fuel 5:895–908

Rogel E, Ovalles C, Moir M (2012) Asphaltene chemical characterization as a function of solubility: effects on stability and aggregation. Energy Fuels 26:2655–2662

Rogel E, Ovalles C, Pradhan A, Leung P, Chen N (2013) Sediment formation in residue hydroconversion processes and its correlation to asphaltene behavior. Energy Fuel 27(11): 6587–6593

Rojey A, Jaffret C, Cornot-Gandolphe S, Durand B, Jullian S, Valais M (1997) Natural gas: production, processing, transport. Technip Editions, Paris, 401 p

Schoell M (1980) The hydrogen and carbon isotopic composition of methane from natural gases of various origins. Geochim Cosmochim Acta 44(5):649–661

Schuler BM, Meyer G, Pena D, Mullins OC, Gross L (2015) Unraveling the molecular structures of asphaltenes by Atomic force microscopy. J Am Chem Soc 137:9870–9876

Talwani M (2002) Energy study- Latin America: the Orinoco oil belt in Venezuela (or Heavy oil to the rescue?). James A Baker III institute for public policy, Rice University, Houston, Sept 2002

Thornton SE (2015) The history of oil exploration in the Union of Myanmar. In: AAPG/SEG international conference & exhibition, Melbourne, 13–16 Sept 2015

Tissot BP, Welte DH (1984) Petroleum formation and occurrence, 2nd edn. Springer, Berlin, 700 p

Tissot B, Durand B, Espitalié J, Combaz A (1974) Influence of the nature and diagenesis of organic matter in formation of petroleum. Am Ass Petr Geol Bull 58:499–506

Tissot BP, Pelet R, Ungerer P (1987) Thermal history of sedimentary basins, maturation indices, and kinetics of oil and gas generation. AAPG Bull 71(12):1445–1466

Total Exploration and production (2006) Extraheavy oils and bitumen – reserves for the future. *Know how series*, Total SA, Paris, 2 place de la Coupole, La Défense 6, 92400 Courbevoie, France. www.total.com

Treibs A (1934) Chlorophyll– und Häminderivate in bituminösen Gesteinen, Erdölen, Erdwachsen, und Asphalten. Ein Beitrag zur Entstehung des Erdöls. Justus Liebig Ann Chemie 510: 42–62

Tremblay B, Sedgwick G, Forshner K (1997) Simulation of cold production in heavy-oil reservoirs: wormhole dynamics. Soc Petrol Eng 12(2):100. https://doi.org/10.2118/35387-PA

Trindade LAF, Dias JL, Mello MR (1995) Sedimentological and geochemical characterization of the Lagoa Feia formation, rift phase of the Campos basin, Brazil. In: Katz BJ (ed) Petroleum source rocks. Springer, Heidelberg, pp 149–165

Ungerer P (1990) State of the art of research in kinetic modeling of oil formation and expulsion. Org Geochem 16(1–3):1–25

Ungerer P, Faissat B, Leibovici C, Zhou H, Behar E, Moracchini G, Courcy JP (1995) High pressure – high temperature reservoir fluids: investigation of synthetic condensate gases containing a solid hydrocarbon. Fluid Phase Equilib 111: 287–311

Ungerer P, Collell J, Yiannourakou M (2015) Molecular modeling of the volumetric and thermodynamic properties of Kerogen: influence of organic type and maturity. Energy Fuel 29(1):91–105

US DOE-EIA (Department of Energy – Energy Information Administration) (2013) Technically recoverable shale oil and shale gas resources: an assessment of 137 shale formations in 41 countries outside the United States. Public report, 730 p, Jun 2013. Washington DC 20585 (USA). Downloaded from www.eia.gov

Van den Bark E, Thomas O (1981) Ekofisk: first of the giant oil fields in Western Europe. AAPG Bull 65:2341–2363

van Krevelen DW (1993) Coal – typology – physics – chemistry – constitution, 1st edn. Elsevier, Amsterdam

Vandenbroucke M (1993) Migration of hydrocarbons. In: Bordenave ML (ed) Applied petroleum geochemistry. Editions Technip, Paris, pp 123–148

Phase Equilibria

Robert W. Luth
Department of Earth and Atmospheric Sciences, University of Alberta, Edmonton, AB, Canada

Definition

Phase equilibria is the application of the principles of thermodynamics to the study of equilibrium relationships within or between phases, corresponding to homogeneous and heterogeneous phase equilibria, respectively. These phases may be minerals within a rock, a fluid percolating through the pore space of a sediment, a gas, or a combination of these. The study of phase equilibria is used to constrain the stability of individual minerals and assemblages of minerals in pressure-temperature-composition space, to obtain estimates of pressure or temperature of equilibration of metamorphic and igneous rocks and to evaluate conditions of origin of various magmas.

Introduction

The study of phase equilibria is firmly rooted in thermodynamics as formulated by J.W. Gibbs in the late nineteenth century (Gibbs 1961). In phase equilibria, the problem is to determine the conditions at which a given portion of the universe – a system – is at equilibrium, with minimum energy. If the thermodynamic properties of the system, including the Gibbs free energy, enthalpy, entropy, molar volume, heat capacity, isothermal compressibility, thermal expansivity, and the activity-composition relationships for all multicomponent phases in the system, are all known, then the phase equilibria may be calculated. In practice, however, some of this information is usually lacking, and so techniques for the graphical analysis of phase equilibria have been developed to allow evaluation of heterogeneous equilibria based on limited experimental data. Here, we shall first define some terms to provide a common terminology. Second, we shall look at the fundamental constraints on phase equilibria provided by thermodynamics by applying the phase rule and by looking at the inter-relationship of free energy, pressure, temperature, and composition that gives rise to phase diagrams. Finally, we will examine graphical analysis of phase equilibria, concentrating on Schreinemakers' analysis of the arrangement of univariant curves about an invariant point (Schreinemakers 1965).

Originally published in: Marshall CP, Fairbridge RW (eds) Encyclopedia of Geochemistry, Springer Netherlands, 1999.

Definitions

System

The portion of the universe under consideration. The choice of how the system is defined is the observer's choice. Several types of systems are commonly defined. An isolated system is one in which no energy or matter is transferred into or out of the system. A closed system is one in which energy but no matter may be transferred into or out of the system. An open system is one in which both energy and matter may be transferred into or out of the system.

Component (c)

Components make up the minimum set of chemical constituents necessary to describe the chemical variation in the system. These constituents need not correspond to physical entities such as mineral endmembers. The selection of components must allow for all possible chemical variations in phases in the system. For example, if the system is a crystal of potassium feldspar, $KAlSi_3O_8$, at atmospheric pressure, then one component ($c = 1$) will suffice if temperatures are less than ~ll50°C. At ~l150 °C, the crystal will melt incongruently to a SiO_2-enriched liquid and crystalline leucite ($KAlSi_2O_6$). At this point, two components (c = 2) are necessary to describe the chemical variation in the system. These two components could be $KAlSi_2O_6$ and SiO_2; $KAlO_2$ and SiO_2; $KAlO_2$ and $Si(KAl)_{-1;}$ or $KAlSi_3O_8$ and either $KAlO_2$ or SiO_2, or any other combination that encompasses the chemical variability present in the system.

Phase (p)

A chemically homogeneous, uniform portion of the system that is mechanically separable from the rest of the system, at least in principle. Each phase is bounded by physical interfaces. Each phase may occur in different places in a system. For example, if the system is a rock containing quartz and feldspar crystals, all of the quartz crystals constitute a single phase. If all the feldspar crystals have the same composition, they too would be a single phase. Another example is a mixture of oil and water at room temperature, two liquids that do not intermix but rather remain immiscible, although the scale of physical domains may be small. All the droplets of oil are the same phase, as is all of the surrounding water phase.

State Variable

A property of a system that has a fixed value at equilibrium. Extensive state variables are those that depend on the amount of matter in the system, such as volume and total internal

energy. Intensive state variables are those that are independent of the amount of matter and include density, temperature, pressure, and concentration, among others. Extensive state variables may be converted to intensive state variables by dividing by the number of moles (or grams) of material, to calculate molar (or specific) volume from total volume, for example.

Variance or Degrees of Freedom (f)

The number of independent intensive variables that must be fixed to define uniquely the equilibrium state. If a system has no degrees of freedom ($f = 0$), it is invariant; if it has one degree of freedom ($f = 1$), it is univariant; and if it has two degrees of freedom ($f = 2$), it is divariant or bivariant.

Gibbs Phase Rule

The phase rule is an elegant, simple equation that results from the conditions of equilibrium between phases in a system. The phase rule may be expressed as:

$$f + p = c + 2. \quad \text{(l)}$$

Clear derivations of the phase rule are given in Ricci (1951), Prigogine and Defay (1954), Morse (1980), Spear (1993), and Anderson and Crerar (1993).

Homogeneous Phase Equilibria

Equilibria within single phases involves the thermodynamic requirements for equilibrium, which are that the pressure and temperature must be uniform throughout the phase, and the free energy of the phase must be at a minimum. To formulate the free energy for the phase as a function of composition, pressure, and temperature, a model for the activities of the components of the phase must be formulated. Different aspects of homogeneous phase equilibria are considered in the entries under ▶ "Activity and Activity Coefficients," ▶ "Aqueous Solutions," and ▶ "Equilibrium."

Heterogeneous Phase Equilibria

Equilibria between phases is the realm of heterogeneous phase equilibria, and phase relationships in systems of increasing complexity will be considered in turn.

One-Component Systems

From the phase rule, a one-component system may contain one, two, or three coexisting phases, with variances of two, one, and zero, respectively. As an example, consider the system with the single component SiO_2 (Fig. 1). The *P-T* diagram consists of three fields, labeled coesite, low quartz, and high quartz, respectively, which represent the stability fields of these three polymorphs of SiO_2. Application of the phase rule to these fields, with c = 1 and p = I, yields a variance of two, which requires that both the intensive variables such as pressure and temperature be specified to determine the state of the system. Graphically, this may be visualized by looking at point A (Fig. 1), which is located in the divariant low quartz field. From A, both pressure and temperature may be varied independently (as shown by the arrows) and the system would remain single phase, with only low quartz present. In order to know exactly where A is requires both pressure and temperature to be specified.

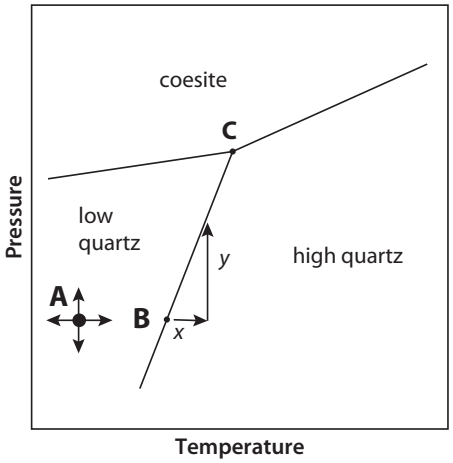

Phase Equilibria, Fig. 1 Schematic pressure-temperature projection of phase relations in the system SiO_2. Points A, B, and C are discussed in the text

In contrast, along the curve separating the fields of low quartz and high quartz, these two phases coexist. Therefore, this curve represents the conditions of pressure and temperature at which these two phases are in equilibrium. Application of the phase rule with $c = 1$ and $p = 2$ yields a variance of one, which means that only one intensive variable needs to be specified to define the system of coexisting low quartz and high quartz completely. This situation may be illustrated graphically by considering the point B on the univariant curve (Fig. 1). A change in T of x requires a corresponding change in P of y to remain on the equilibrium boundary as required to preserve the coexistence of low quartz and high quartz. Therefore, only one of the intensive variables is independent, with the other being a dependent variable.

For the system to be invariant ($f = 0$) requires three phases coexisting in equilibrium. Such a situation exists at point C (Fig. 1), where low quartz, high quartz, and coesite all coexist. In this situation, neither pressure nor temperature may be specified independently; they are dictated by the pressure and temperature of the unique point on the *P-T* diagram where the system of three phases can exist.

Free Energy Diagrams in One-Component Systems

A one-component system such as that shown in Fig. 1 may be used to illustrate the inter-relationship between the state variables P, T, $\overline{G}$ (molar Gibbs free energy), $\overline{S}$ (molar entropy), and $\overline{V}$ (molar volume). For clarity, consider only the phases low quartz and high quartz. The functional relationships of $\overline{G}_{low\ quartz}$ and $\overline{G}_{high\ quartz}$ to T at constant pressure are illustrated in Fig. 2. Because $(\partial G/\partial T)_P = -\overline{S}$, and because entropy is positive, the slopes of the curves in G-T space are negative. Similarly, the relationship $\partial G/\partial P)_T = \overline{V}$, and the requirement of positive molar volumes (nonnegative densities) leads to positive slopes in isothermal (constant T) G-P diagrams (Fig. 3).

The temperature T_1 (Fig. 2), where $\overline{G}_{low\ quartz} = \overline{G}_{\text{high quartz}}$, represents the temperature at which low quartz and high quartz coexist, corresponding to the temperature of the univariant curve at this pressure. The pressure P_1 (Fig. 3), where the $\overline{G}$ curves for low quartz and high quartz intersect, represents the pressure at which these two phases coexist at this temperature, which would correspond to a point on the univariant curve (Fig. 1) in P-T space.

From Figs. 2 and 3, information regarding the relative stability of the two phases at differing P, T conditions may be inferred. The stable phase is that with the lowest $\overline{G}$, which is low quartz at low T (Fig. 2) and high P (Fig. 3). The P-T phase diagram (Fig. 1) shows the same information in a different format. Starting at point B, low quartz is stable at lower T and at higher P relative to high quartz.

All of these diagrams may be related in a three-dimensional $\overline{G}$-T-P diagram (Fig. 4). The bottom face of this diagram corresponds to Fig. 2, where a slice at constant P has been taken through the diagram. The left-hand face of the diagram corresponds to Fig. 3, where T has been held constant. On a P-T diagram (Fig. 1), the univariant curve where low quartz and high quartz coexist corresponds to a projection of the line of intersection (I in Fig. 4) of the $\overline{G}_{\text{low quartz}}$ and $\overline{G}_{\text{high quartz}}$ planes onto the P-T face. Unlike the $\overline{G}$-T and $\overline{G}$-P sections, where one intensive variable is held fixed (P and T, respectively, in Figs. 2 and 3), the P-T projection does not hold $\overline{G}$ fixed, but rather represents the locus of points at which $\overline{G}_{\text{low quartz}} = \overline{G}_{\text{high quartz}}$.

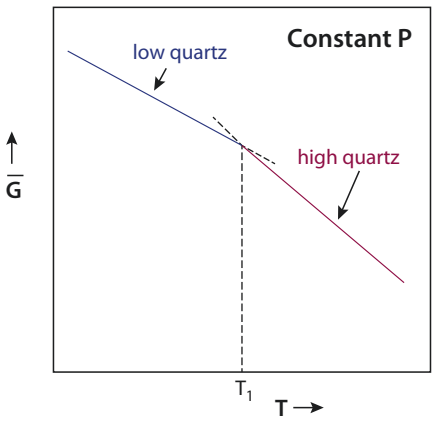

Phase Equilibria, Fig. 2 Schematic molar Gibbs free energy ($\overline{G}$)-temperature (T) section at constant pressure for a portion of the system SiO_2

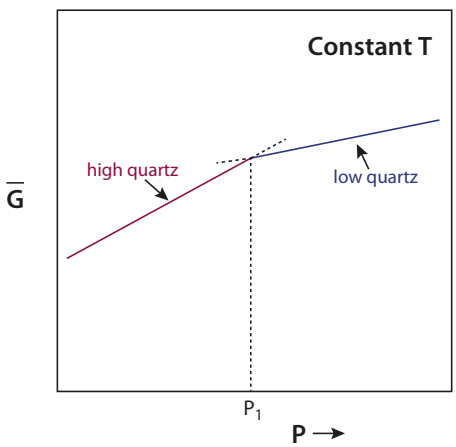

Phase Equilibria, Fig. 3 Schematic molar Gibbs free energy ($\overline{G}$)-pressure (P) section at constant T for phases in the system SiO_2

Two-Component (Binary) Systems

Systems with two components introduce composition as a variable, with the compositions of all phases constrained to be colinear in composition space. Phases may either have fixed composition (e.g., quartz SiO_2) or variable composition (e.g., plagioclase, with composition between $NaAlSi_3O_8$ and $CaAl_2Si_2O_8$). Three dimensions are required to illustrate the phase relationships in terms of P, T, and X (composition).

Application of the phase rule leads to four possible situations:

- $f = 0$ (invariant), with four phases coexisting
- $f = 1$ (univariant), with three phases coexisting
- $f = 2$ (divariant), with two phases coexisting
- $f = 3$, with one phase present

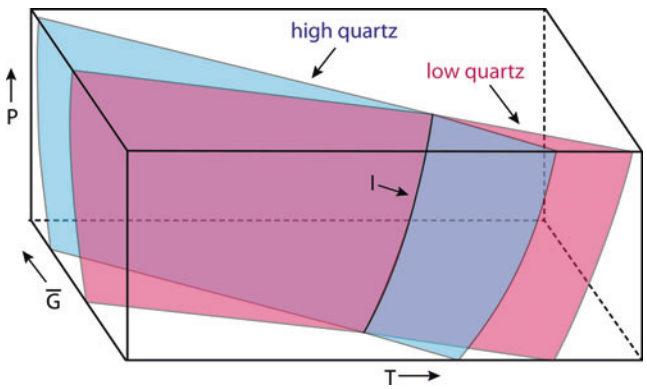

Phase Equilibria, Fig. 4 Schematic $\overline{G}$-T-P diagram illustrating the relationship between the $\overline{G}$ surfaces for low quartz and high quartz

Analogous to the one-component case, invariant situations plot as points on *P-T* projections, univariant situations as lines, and $f \geq 2$ as fields.

Free Energy Diagrams in Two-Component Systems

Graphical depictions of possible relationships between the compositions of the phases and *P, T,* and *G* are shown in Figs. 5 and 6. These *G-X* diagrams illustrate graphically the principles of equilibrium between phases (see ▶ "Equilibrium"). Considering first phases with fixed compositions, the free energies of three phases (A, B, and C) in a binary system are illustrated in Fig. 5a and b. In the first diagram, the equilibrium assemblages (those with the lowest free energies) are A + B and B + C. Any mixture of A + C would plot along the short-dashed line in Fig. 5a, and could reduce its energy by reacting to form either A + B or B + C, depending on the bulk composition. Bulk compositions to the left of the composition of the B phase (Fig. 5a) would break down to A + B, and those to the right would react to form B + C. At different conditions of *P* and *T* (Fig. 5b), the assemblage A + C (represented by any point on the long-dashed line connecting A to C) is stable relative to assemblages of A + B or B + C.

Relating these two diagrams (Figs. 5a, b) to a *P-T* projection (Fig. 5c), the field labeled B represents the situation in Fig. 5a, and the field labeled A + C represents the situation in Fig. Pl6b. Even though the high-*T*, low-*P* field in Fig. 5c is labeled B, comparison with Fig. 5a illustrates that the divariant assemblages A + B and B + C are stable in this field as well as the trivariant assemblage of B alone. At a *P* and *T* along the univariant reaction curve separating these two fields, the free energies of the three phases would be colinear in a $\overline{G}$-X diagram.

If one (or more) of the phases in the system has a variable composition, the situation is more complex (Fig. 6). The free energy for the phase of variable composition is a curve in $\overline{G}$-X space. At conditions of *P* and *T* where the assemblage A + C is

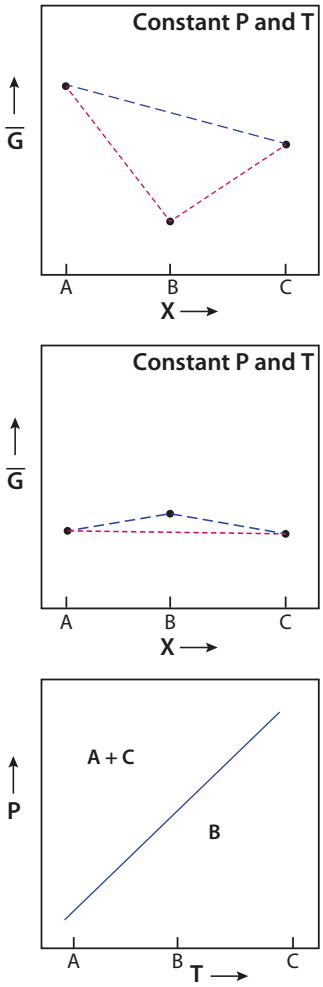

Phase Equilibria, Fig. 5 (**a**) Schematic $\overline{G}$-composition *(X)* section at constant *P* and *T* for three phases of fixed composition in a binary system at conditions where phase B is stable. See text for discussion. (**b**) Schematic $\overline{G}$-*X* section at constant *P* and *T* for three phases of fixed composition in a binary system at conditions where phase B is metastable relative to A + C. (c) Schematic *P-T* projection of the binary system illustrated in (**a**) and (**b**). Field labeled B corresponds to section in (**a**). Field labeled A+ C corresponds to section in (**b**)

Phase Equilibria, Fig. 6 Schematic $\overline{G}$-*X* sections at different conditions of *P* and *T* for a binary system wherein one phase (B) has variable composition. (**a**) Phase B is metastable relative to A+ C at the *P, T* conditions of this section. (**b**) Phase B is in equilibrium with A + C at the *P, T* conditions of this section. (**c**) The assemblage A + C is metastable relative to B-containing assemblages at the *P, T* conditions of this section

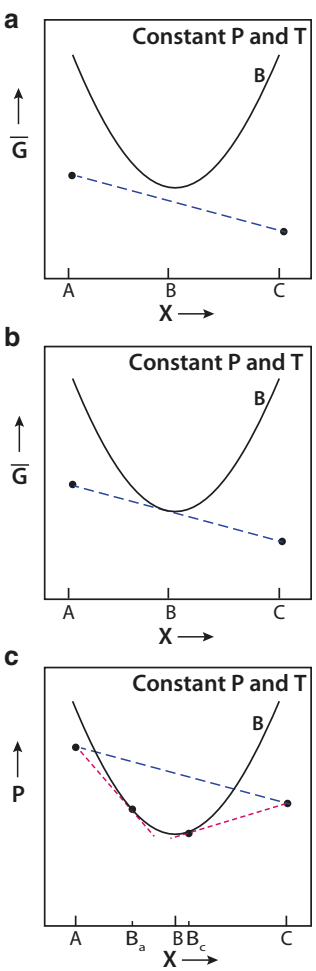

stable relative to B-containing assemblages, the relative free energies are as illustrated in Fig. 6a. At conditions along the univariant reaction, the line connecting A and C in $\overline{G}$-X space is tangential to the curve representing the free energy of solution B (Fig. 6b). At conditions in the B stability field, the situation is as shown in Fig. 6c. Note that the compositions of the solution B that coexist with phase A and with phase C are different (denoted B_a and B_c, respectively, in Fig. 6c). At the P and T illustrated in Fig. 6c, the assemblage present depends on bulk composition: the divariant assemblage A + B_a for bulk compositions between those two compositions; the trivariant assemblage B (with varying composition) for bulk compositions between B_a and B_c; and the divariant assemblage B_c + C for bulk compositions between Be and C. The P-T projection of these phase relationships would be similar to that in Fig. 5c, with the univariant curve representing the locus of P, T points for which the schematic $\overline{G}$-X relationships in Fig. 6b hold.

Three-Component (Ternary) Systems

Systems with three components introduce another compositional variable. The compositions of all phases, either fixed or variable in composition, must be coplanar in a three-component composition space. It is customary to illustrate these compositional relationships in an equilateral triangle, with each component occupying an apex (Fig. 7a). Because of the added compositional variable, four dimensions are required to illustrate the phase relationships in terms of *P*, *T*, and composition. Projections and sections of the phase relationships into three or two dimensions are therefore customary.

Application of the phase rule leads to five possible situations:

- $f = 0$ (invariant), with five phases coexisting
- $f = 1$ (univariant), with four phases coexisting
- $f = 2$ (divariant), with three phases coexisting
- $f = 3$, with two phases present
- $f = 4$, with one phase present

In *P-T* projection, invariant situations plot as points on P-T projections, univariant reactions as lines, and $f \geq 2$ as fields. The possible univariant reactions are of two types, depending on the compositions of the phases involved. The first type is a eutectic-like reaction (also called a terminal stability reaction) such as: A + C + E = B (Fig. 7b). In this type of reaction, the composition of the terminal phase (B) lies in the interior of the triangle defined by the compositions of the other three phases. The other type of reaction is a join-crossing reaction such as: A+ D = C + E (Fig. 7c). In this reaction, the composition of the fourth phase lies exterior to the triangle formed by the other three phases.

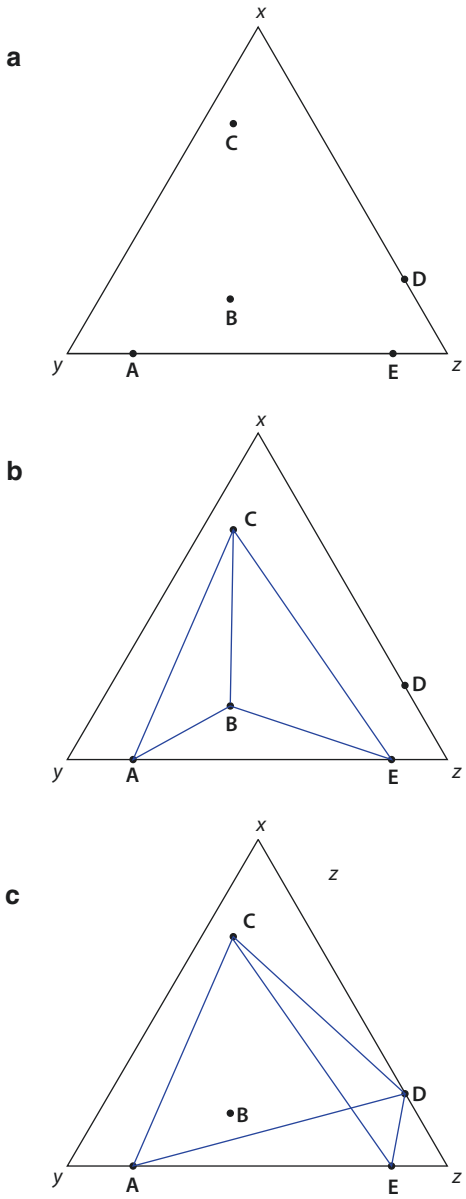

Phase Equilibria, Fig. 7 (**a**) Ternary composition space represented with an equilateral triangle. Components of the system are *x, y,* and *z*. Phases present are A, B, C, D, and E. (**b**) Tie-lines for the eutectic-like ternary reaction A + C + E = B in the system *x, y, z*. (**c**) Tie-lines for the join-crossing ternary reaction A+ D = C + E in the system *x, y, z*

Free Energy Diagrams in Three-Component Systems

Three dimensions are required to illustrate the $\overline{G}$-X relationships for ternary systems. By analogy with the binary case, equilibrium between phases is achieved in ternary systems when the free energies of the phases are coplanar in $\overline{G}$-*X* space. If one or more phases have variable compositions (solid or liquid solutions), the equilibrium case occurs when the planes defined by the free energies of the phases of fixed composition are tangential to the curved surfaces representing the free energies of the variable composition phases.

Systems with Four or More Components

Four components require three dimensions (and considerable artistic talent) to portray the compositional relationships alone. It is customary to represent the composition space with a tetrahedron, with each component represented at an apex. Often, the compositions will be projected from one component apex onto an equilateral triangle to facilitate representation in two dimensions. From the phase rule, six phases coexist at an invariant point, and five phases are involved in univariant reactions.

The two types of univariant reactions discussed above for ternary systems have analogs in quaternary systems. The eutectic-like reaction has the composition of the fifth phase interior to the polyhedron whose apices are the compositions of the other four phases. Algebraically, this type of reaction would be expressed: A + B + C + D = E. The join-crossing reaction would have the composition of the fifth phase exterior to the polyhedron whose apices are the compositions of the other four phases. Algebraically, the reaction stoichiometry would be A+ B + C = D + E. Because one join that is being crossed is a three-phase join (A+ B + C in the example above; geometrically a plane) this type of reaction is referred to as a plane-piercing reaction.

The principles outlined in the previous sections hold equally well for systems with more components, with the added complexity in illustrating or conceptualizing the relationships between phases. For these reasons, algebraic or analytical techniques, rather than graphical, are used for these systems.

The Arrangement of Univariant Curves About an Invariant Point

For a system of c components, $c + 2$ phases coexist at an invariant point. From this point, $c + 2$ univariant curves radiate outward in variable space. F.A. Schreinemakers, in a series of articles from 1915 to 1925, developed a method for determining systematically the arrangement of these univariant curves requiring only the compositions of the $c + 2$ phases coexisting at the invariant point (Schreinemakers 1965).

Terminology

Each univariant reaction is denoted by the phase not participating in the reaction, surrounded by parentheses. In a similar fashion, divariant fields are denoted by the phases not present. For example, in the binary system illustrated in Fig. 8, the reaction A + C = B would be denoted (D), and the divariant assemblage A + C would be denoted by (B, D).

The number of assemblages of a given variance may be determined by application of the combinatorial formula (Zen 1966):

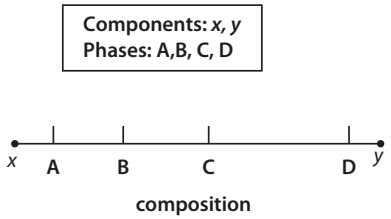

Phase Equilibria, Fig. 8 The binary system x, y with the compositions of phases A, B, C, and D plotted. See text for discussion

$$M(c+2,p) = \frac{(c+2)!}{p!(c+2-p)!} \tag{1}$$

where $M(c + 2, p)$ is the number of combinations of $c + 2$ possible phases (the number of phases that coexist at the invariant point, where c is the number of components in the system) and p is the number of phases in the assemblage of interest. For the binary example (Fig. 8), application of this formula yields four univariant curves [4!/((3!)(1!))] and six divariant assemblages [4!/((2!)(2!))].

These univariant curves would represent the reactions:

$$\mathrm{B} + \mathrm{D} = \mathrm{C} \qquad (\mathrm{A})$$

$$\mathrm{A} + \mathrm{D} = \mathrm{C} \qquad (\mathrm{B})$$

$$\mathrm{A} + \mathrm{D} = \mathrm{B} \qquad (\mathrm{C})$$

$$\mathrm{A} + \mathrm{C} = \mathrm{B} \qquad (\mathrm{D})$$

and the divariant assemblages would be:

$$\mathrm{A} + \mathrm{B} \qquad (\mathrm{A}, \mathrm{D})$$

$$\mathrm{A} + \mathrm{C} \qquad (\mathrm{B}, \mathrm{D})$$

$$\mathrm{A} + \mathrm{D} \qquad (\mathrm{B}, \mathrm{C})$$

$$\mathrm{B} + \mathrm{C} \qquad (\mathrm{A}, \mathrm{D})$$

$$\mathrm{B} + \mathrm{D} \qquad (\mathrm{A}, \mathrm{C})$$

$$\mathrm{C} + \mathrm{D} \qquad (\mathrm{A}, \mathrm{B})$$

Several rules summarize Schreinemakers' method.

Rule 1 (The Fundamental Postulate)

A univariant curve, either stable or metastable, separates two divariant assemblages. On one side of this curve, one of the two divariant assemblages is more stable than the other assemblage. On the other side of the curve, the relative stabilities of the two assemblages are reversed.

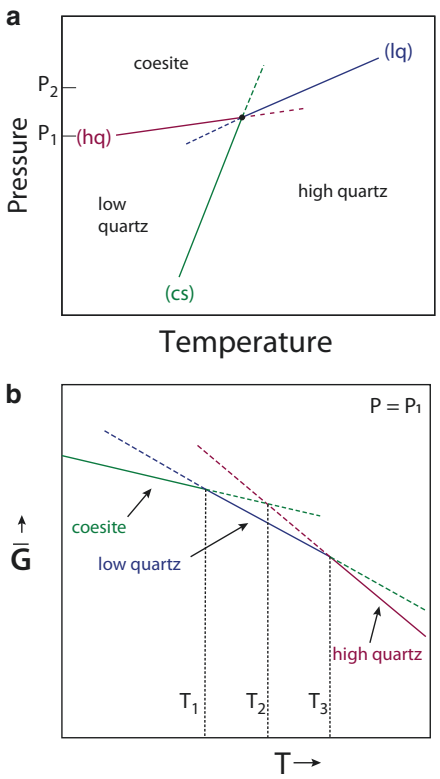

Phase Equilibria, Fig. 9 (**a**) Schematic *P-T* projection for the system SiO_2. The univariant reactions have been labeled with the "missing-phase" notation. (**b**) Schematic $\overline{G}$-*T* diagram corresponding to pressure P_1 of (**a**)

This rule may be understood readily by considering the free energy surfaces (or curves) for the divariant assemblages. Returning to the simple one-component case of SiO_2 (Fig. 9a), three univariant reactions are labeled (cs), (lq), and (hq), which represent coesite, low quartz, and high quartz, respectively. The reaction (hq) separates the divariant assemblages of coesite and low quartz. In the missing-phase notation, these divariant assemblages are (lq, hq) and (hq, cs), respectively. At P_1 (Fig. 9b), coesite is more stable (i.e., has a lower free energy) than is low quartz at $T < T_1$. At $T > T_1$, the relative stabilities are reversed.

The logic applies equally well to metastable reactions. Consider the reaction (lq), coesite = high quartz, which is metastable at P_1. Coesite is more stable (less metastable) than is high quartz at $T < T_2$, and high quartz is more stable (less metastable) than is coesite at $T > T_2$. In both situations, both coesite and high quartz are metastable relative to low quartz.

Rule 2

A divariant assemblage **(**A, B**)** occurs in a region of $<180°$ about the invariant point between the univariant curves **(**A**)** and **(**B**).** The consequence of this rule is that the angle between neighboring stable univariant curves is $<180°$. This rule is used extensively to determine the stable fields of divariant assemblages.

Rule 3

Any divariant assemblage that extends across the univariant curve (X) contains the phase X. This rule holds for both stable curve (X) contains the phase X. This rule holds for both stable and metastable curves.

Use of Schreinemakers' Analysis in Arranging Univariant Curves

An extremely powerful method for quickly and accurately deriving the arrangement of univariant curves about an invariant point uses Schreinemakers' system of notation that capitalizes on the correspondence between the stoichiometry of the univariant reactions and the arrangement of the corresponding univariant curves. This point is best illustrated by example. In the binary system *x-y* (Fig. 8a), the reaction (D) may be written A + C = B. According to Schreinemakers' univariant scheme (Zen 1966) there is a corresponding arrangement of univariant curves, such that univariant curves (A) and (C) are on one side of (D) and univariant curve (B) is on the other. This topology may be written concisely in a form that parallels the reaction:

$$(\mathrm{A})(\mathrm{C}) \mid (\mathrm{D}) \mid (\mathrm{B})$$

where the univariant curve (D) is set off by vertical lines to illustrate that this is the curve about which (A), (C), and (B) are arrayed.

Once any reaction is written with positive stoichiometric coefficients, the corresponding arrangement of the other univariant curves may be determined immediately. This procedure works independent of the complexity of the system, including for multicomponent systems that are difficult or impossible to illustrate in two or three dimensions.

The steps of the procedure for determining the arrangement of univariant reactions about an invariant point may be illustrated for a binary system. The same procedure applies to systems with more components.

1. Write the reactions and the corresponding univariant schemes. From Fig. 8, we see that the reactions are:

$$\mathrm{B} + \mathrm{D} = \mathrm{C}$$

$$\mathrm{A} + \mathrm{D} = \mathrm{C}$$

$$\mathrm{A} + \mathrm{D} = \mathrm{B}$$

$$\mathrm{A} + \mathrm{C} = \mathrm{B}$$

and the corresponding univariant schemes are:

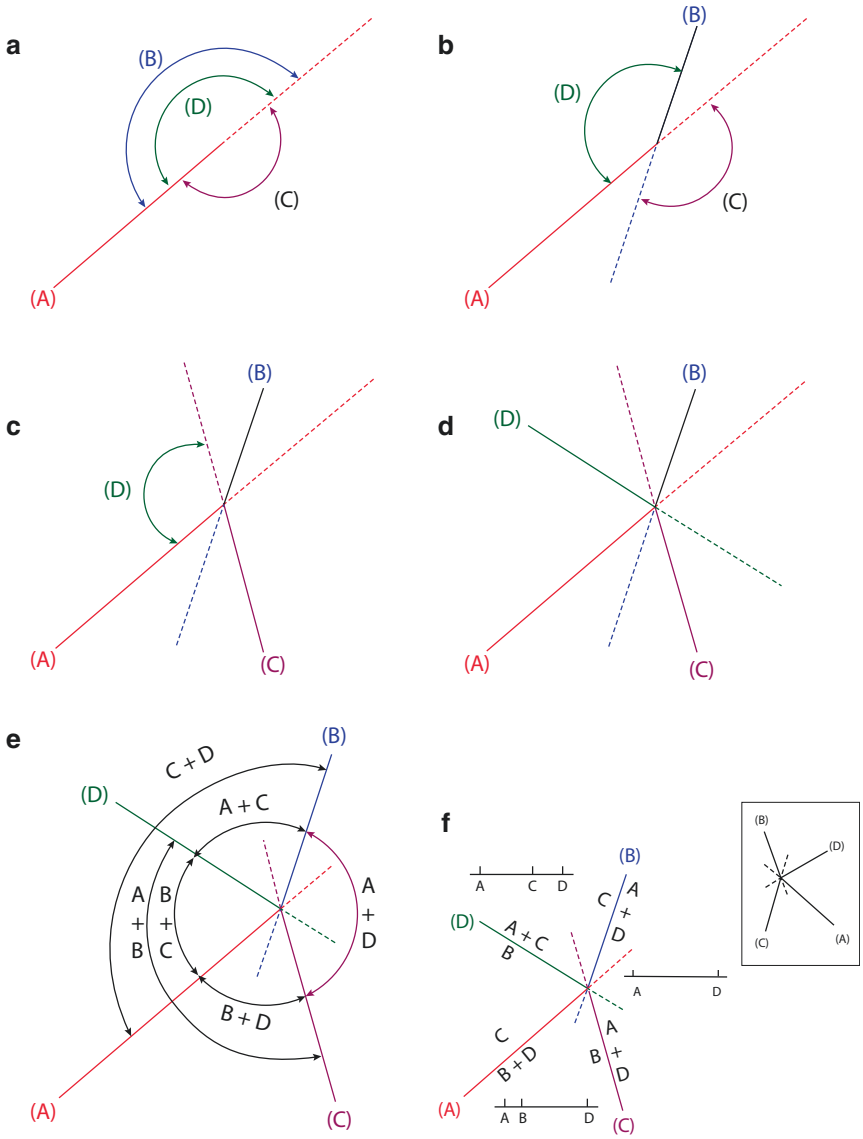

Phase Equilibria, Fig. 10 Construction of univariant curves about an invariant point for a binary system. See text for discussion

(B)(D)|(A)|(C)

(A)(D)|(B)|(C)

(A)(D)|(C)|(B)

(A)(C)|(D)|(B)

2. Begin by drawing (A), and indicate allowable locations for (B), (D), and (C) as shown by the arcs in Fig. 10a.
3. Draw **(B)** in its permissible sector (Fig. 10b). Using the univariant scheme for **(B),** narrow down the allowable locations for (C) and (D).
4. Draw (C) in its permissible sector (Fig. 10c), between the metastable extensions of (A) and (B). Using the univariant scheme for (C), narrow down the allowable sector for to between the stable part of (A) and the metastable extension of (C).
5. Draw (D) (Fig. 10d).
6. Indicate the fields of stability for the six divariant assemblages:

Assemblage	Missing-phase notation	Stable between univariant curves
A + B	(C, D)	(C), (D)
A + C	(B, D)	(B), (D)
A + D	(B, C)	(B), (C)
B + C	(A, D)	(A), (D)
B + D	(A, C)	(A), (C)
C + D	(A, B)	(A), (B)

as shown in Fig. 10e.

Labeling the univariant curves with the appropriate reactions is now straightforward, because the divariant (two-phase) assemblage involved in each reaction is stable only on one side of the reaction. This labeling, and the use of the compositional join rather than arrows to represent permissible divariant assemblages, cleans up the diagram and yields the finished product (Fig. 10f). Note that two mirror image (enantiomorphic) possibilities exist (Fig. 10f and inset), and selection of the correct one, as well as the correct orientation in *P-T* space, requires additional information.

Application of Schreinemakers' Analysis to One-Component Systems

Returning again to the SiO_2 system (Fig. 9a), the three reactions may be written:

$$l_q = h_q \qquad (cs)$$

$$c_s = l_q \qquad (hq)$$

$$c_s = h_q \qquad (lq)$$

where lq = low quartz, hq = high quartz, and cs = coesite. There are three divariant assemblages:

$$l_q \qquad (hq, cs)$$

$$h_q \qquad (lq, cs)$$

$$c_s \qquad (lq, hq)$$

Application of rule 2 generates two possible enantiomorphic versions of the *P-T* projection (Fig. 11). As discussed above, additional information (e.g., relative densities or experimental constraints on phase equilibria) is required to decide between these two enantiomorphs and to orient the phase diagram properly with respect to the pressure and temperature axes.

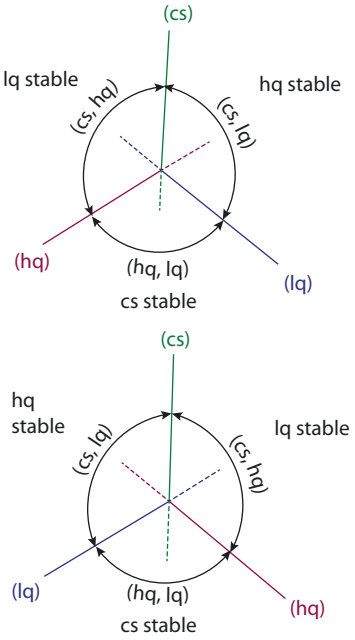

Phase Equilibria, Fig. 11 Enantiomorphic pair of possible arrangements of univariant curves about the invariant point where coesite + high quartz + low quartz coexist. *Arrows* indicate stability fields for divariant assemblages labeled with "missing-phase" notation. See text for discussion

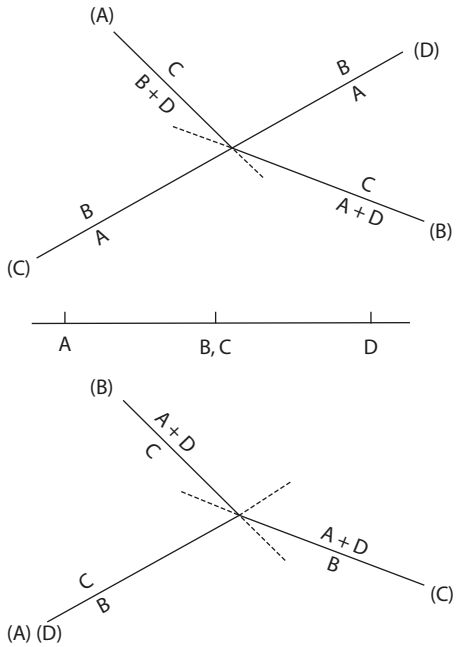

Phase Equilibria, Fig. 12 Two possible configurations of univariant curves about invariant points in binary systems, illustrating the effect of compositional degeneracy (polymorphism)

Application of Schreinemakers' Analysis to Binary Systems

The example worked above illustrates the principles of the application of this method to binary systems. A complication is introduced by degeneracy, where the compositions of two of the phases are the same. The logic outlined above still applies, but two of the univariant reactions overlap in either their stable portions, or such that the stable portion of one overlaps with the metastable extension of the other. Two examples of such degenerate situations are illustrated in Fig. 12.

Applications of Schreinemakers' Analysis to Ternary Systems

In a ternary system, the five phases that coexist at the invariant point are coplanar in composition space (Fig. 7a). In the general case, the system is defined by three components *x, y,* and *z* and contains phases A, B, C, D, and E, all with differing *x/y* or *x/z*. From the invariant point at which A + B + C + D + E coexist, five univariant reactions, each involving four phases, will radiate.

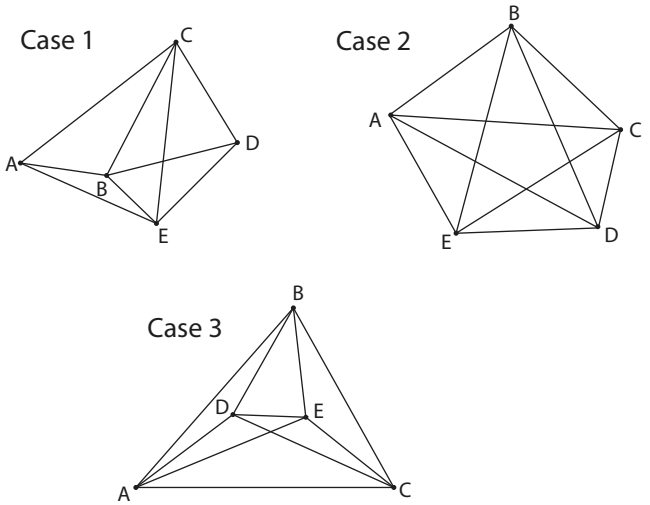

Phase Equilibria, Fig. 13 Ternary composition space, illustrating the three possible (nondegenerate) arrangements of *five* phases that coexist at an invariant point

In general, there are three possible (nondegenerate) compositional arrays of five phases (Fig. 13). Each of these arrays generates a different arrangement of univariant reactions about the invariant point (Fig. 14). In each case, only one of the enantiomorphic pairs is illustrated.

Degeneracy of two types is possible in ternary (and higher-order) systems. One type, polymorphism, is analogous to the case considered for the binary system (Fig. 12). The other type is generated when the compositions of three (or more) of the phases involved in the invariant point are colinear. This colinearity means that these three phases are a binary subsystem within the ternary. Degeneracy of either type leads to coincidence of two, or more, of the univariant reactions, which then coincide, superimposing either stable portions (analogous to the binary case illustrated in Fig. 12b), or the stable portion of one overlapping the metastable portion of the other (Fig. 12a). The "cookbook" approach outlined above works equally well for degenerate situations as for nondegenerate ones, as long as the coincidence of some of the univariant curves is borne in mind. This coincidence is obvious immediately upon writing the reactions. For the example shown in (Fig. 15), the reactions are:

$$\mathrm{B} + \mathrm{D} = \mathrm{C} + \mathrm{E}$$

$$\mathrm{A} + \mathrm{C} + \mathrm{D} = \mathrm{E}$$

$$\mathrm{A} + \mathrm{B} + \mathrm{D} = \mathrm{E}$$

$$\mathrm{A} + \mathrm{C} = \mathrm{B}$$

$$\mathrm{A} + \mathrm{C} = \mathrm{B}$$

This list illustrates two points: (D) and (E) are the same, and they are binary univariant reactions involving three phases; they are univariant by restriction in the ternary case, where the restriction is the compositional colinearity.

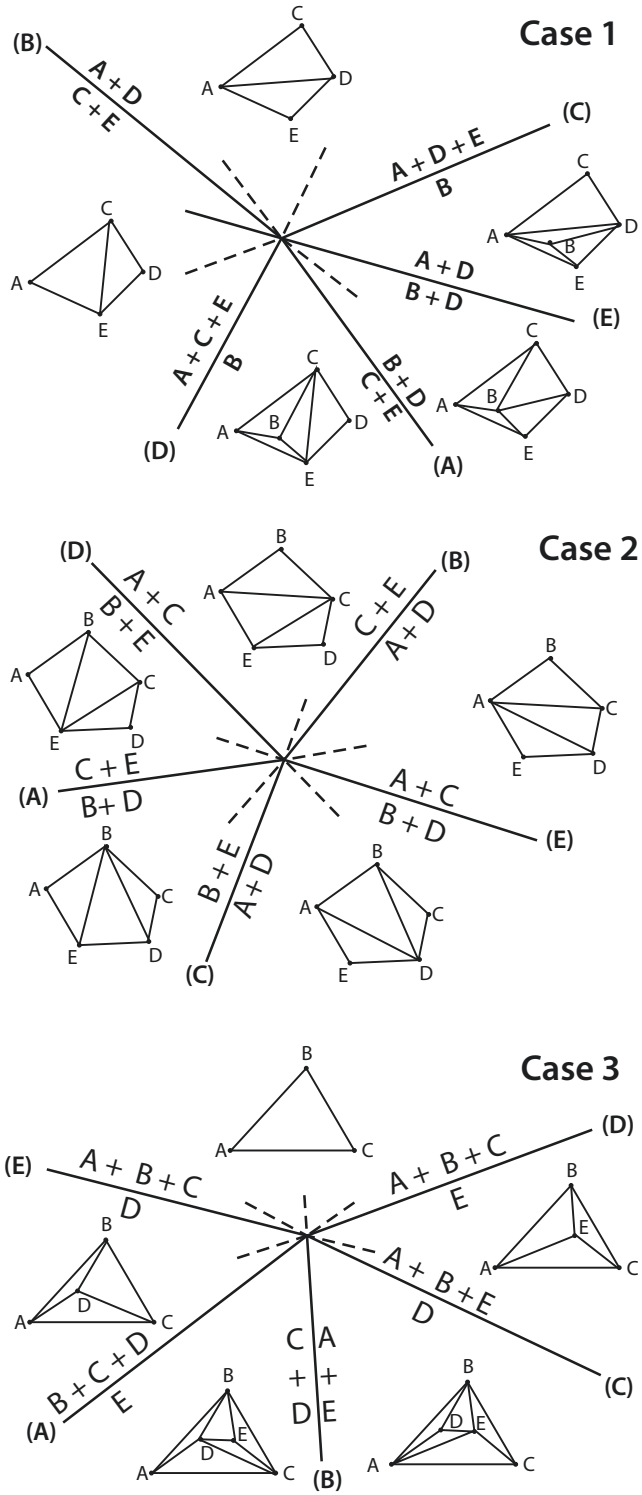

Phase Equilibria, Fig. 14 Arrangements of univariant curves about invariant points corresponding to the three different compositional situations in nnn 13. Only one of each enantiomorphic pair is illustrated for each case

P

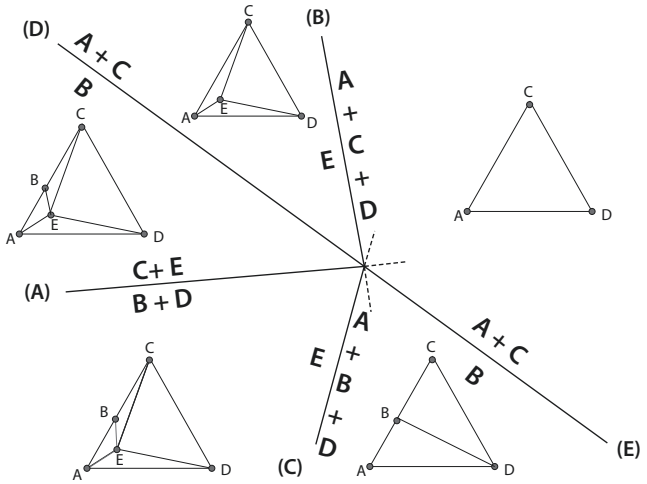

Phase Equilibria, Fig. 15 Example of the arrangement of univariant curves about an invariant point in a ternary system with a degeneracy wherein three phases are colinear in composition space

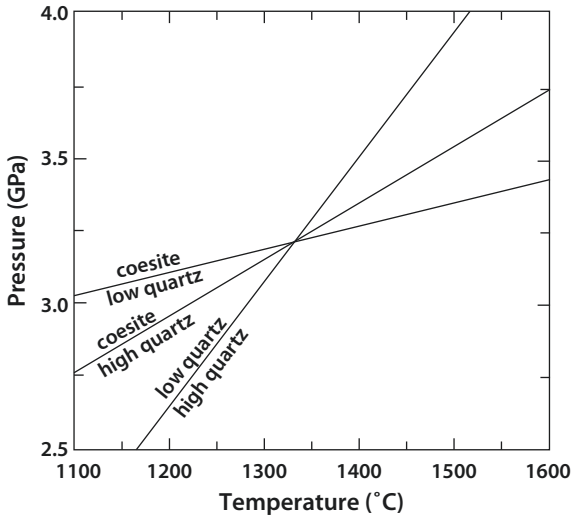

Phase Equilibria, Fig. 16 Phase relationships calculated with TWQ program of Berman, using database of Berman (1988)

Calculation of Phase Equilibria

With the recent progress in establishing internally consistent thermodynamic databases (Helgeson et al. 1978; Berman 1988; Holland and Powell 1990), it has become feasible to calculate phase equilibria with (often) good precision. There are two approaches to this problem. The first is to minimize the free energy of the entire system, exploring all possible phases. The second, more relevant to calculation of phase equilibria specifically, is to calculate $\overline{G}$ as a function of P and T for each phase or the ΔG for the reaction of interest. For example, for the reaction):

$$\mathrm{SiO_2(low\ quartz)} = \mathrm{SiO_2(high\ quartz)}$$

the ΔG for the reaction is the difference between the free energies of the product and reactant. The derivative form of the relevant equation for a single component system is:

$$d\Delta G = \left(\frac{\delta \Delta G}{\delta T}\right)_P dT + \left(\frac{\delta \Delta G}{\delta P}\right)_T dP \qquad (2)$$

Substitution of -ΔS and ΔV for the two derivatives in eq (2) and integrating yields:

$$\Delta G(P,T) - \Delta G\left(P_{ref}, T_{ref}\right) = \int_{T_{ref}}^{T} -\Delta S dT + \int_{P_{ref}}^{P} \Delta V dP \qquad (3)$$

The first integral may be expressed in terms of heat capacities because of the relationship between heat capacity and entropy:

$$\frac{\Delta C_p}{T} = \left(\frac{\delta(\Delta S)}{\delta T}\right)_P \qquad (4)$$

Substitution of the integral form of eq (4) into eq (3) yields:

$$\Delta G(P,T) - \Delta G\left(P_{ref}, T_{ref}\right) = -\int_{T_{ref}}^{T} \left(\Delta S + \int_{T_{ref}}^{T} \frac{\Delta C_p}{T} dT\right) dT + \int_{P_{ref}}^{P} \Delta V dP \qquad (5)$$

These data are provided by the internally consistent thermodynamic databases now available. As an example, application of Berman's (1988) database to phase relationships in the SiO_2 system yields the results in Fig. 16. The point of intersection of the three curves corresponds to point C in Fig. 11, but all three curves proceed straight through this point, rather than terminating at it, because both stable and metastable equilibria have been calculated in Fig. 16. In order to determine the correct array of curves around the invariant point, we need to apply Schreinemakers' analysis to these calculated curves. Doing so, by the analysis outlined previously, yields the arrangement of curves illustrated schematically in Fig. 11.

Summary

The study of phase equilibria is essential to much of petrology and geochemistry. The ability to analyze phase stabilities graphically provides a powerful tool in constraining natural systems. The recent progress in formulating internally consistent thermodynamic databases has not eliminated the need

for the ability to analyze a phase diagram, differentiate between stable and metastable equilibria, and ensure that the phase diagram is thermodynamically valid.

References

Anderson GM, Crerar DA (1993) Thermodynamics in geochemistry: the equilibrium model. Oxford University Press, New York, 588 pp

Berman RG (1988) Internally-consistent thermodynamic data for minerals in the system Na_2O–K_2O–CaO–MgO–FeO–$Fe_2O_3AlO_3$ SiO_2-TiO_2-H_2O-CO_2. J Petrol 29:445–522

Gibbs JW (1961) The Scientific Papers of J Willard Gibbs, Thermodynamics, vol 1. Dover Publications, New York, 434 pp

Helgeson HC, Delany JM, Nesbitt HW, Bird DK (1978) Summary and critique of the thermodynamic properties of rock forming minerals. Am J Sci 278-A:1–229

Holland TJB, Powell R (1990) An enlarged and updated internally consistent thermodynamic dataset with uncertainties and correlations: the system K_2O- Na_2O- CaO- MgO- MnO- FeO Fe_2O_3-Al_2O_3-TiO_2-SiO_2,-C-H_2-O_2. J Metamorph Geol 8:89–124

Morse SA (1980) Basalts and phase diagrams. An introduction to the quantitative use of phase diagrams in igneous petrology. Springer, New York, 493 pp

Prigogine I, Defay R (1954) Chemical thermodynamics (trans: Everett DH). Wiley, New York, 543 pp

Ricci JE (1951) The phase rule and heterogeneous equilibrium. Van Nostrand, New York, 505 pp

Schreinemakers FAH (1965) Papers by FAH Schreinemakers, Volumes 1 and 2. Collected by the Pennsylvania State University. Originally published in Proceedings of Koninklijke Akademie van Wetenschappen Te Amsterdam

Spear FS (1993) Metamorphic phase Equilibria and pressure temperature-time paths. Mineralogical Society of America, Washington, DC, 799 pp

Zen E-A (1966) Construction of pressure-temperature diagrams for multicomponent systems after the method of Schreinemakers – a geometric approach. US Geol Surv Bull 1225:56 pp

Phosphorus

Karl B. Föllmi
Institute of Earth Sciences, University of Lausanne, Lausanne, Switzerland

Element Data
Atomic Symbol: P
Atomic Number: 15
Atomic Weight: 30.97 g/mol
Isotopes and Abundances: ^{31}P (stable, 100%), radioactive isotopes from ^{24}P to ^{46}P, with ^{32}P (short-lived; half-life = 14.3 days) and ^{33}P (short-lived; half-life = 25.4 days) being the longest-lived ones

(*continued*)

1 Atm Melting Point: 44.1 °C
1 Atm Boiling Point: 280 °C
Common Valences: +5, +3, +2, +1, −2, −3
Ionic Radii: 2.12 Å (−3) and 0.29 Å (+5)
Pauling Electronegativity: 2.19
First Ionization Energy: 1012 kJ/mol
Chondritic (CI) Abundance: 926 ppm
Silicate Earth Abundance: 90 ppm
Crustal Abundance: 1120 ppm
Seawater Abundance: 0.06 ppm
Core Abundance: 2000 ppm

Properties, Origin, and Behavior

Elemental phosphorus is known in four allotropic varieties – white or yellow, red, violet, and black P, with different specific densities (1.82 g/cm^3, 2.34 g/cm^3, 2.36 g/cm^3, and 2.69 g/cm^3, respectively). Elemental phosphorus is highly reactive in the presence of oxygen, ignites and starts to luminescence ("phosphorescence": white phosphorus), hence its name, which literally means "carrier of light." Phosphorus does not occur in elemental form under natural conditions and is always present in oxidized form as phosphate. Its cosmic origin is related to neutron capture on silicon in neon-burning shells within massive stars (>8 solar mass) and also in carbon- and neon-burning layers during supernova explosions (Koo et al. 2013). Within the solar nebula phosphorus represents a relatively volatile element and chondritic meteorites display different degrees of phosphorus depletion (Wolf and Palme 2001). As a lithophile element, phosphorus behaves in an incompatible way during the early crystallization of basaltic magmas, due to its high solubility in melts, the partition coefficient between phosphorus and melt being smaller than 1 (Toplis et al. 1994). Once apatite and other phosphate minerals have formed, phosphorus behaves in a compatible way. On the Earth's surface, under natural conditions, the weathering of phosphate-containing minerals and rocks is the prime source of phosphorus to the biosphere.

History and Use

In 1669, H. Brandt (Hamburg) extracted phosphorus from a mixture of sand and urine, in his search of the philosopher's stone. In 1777, A. Lavoisier classified phosphorus as an element. In 1838 or 1839, W. Buckland showed the sedimentary phosphate-rich deposits of southern England to J. Liebig, who advertised their use as a source of fertilizers. In 1842, J. Lawes dissolved sedimentary phosphate in H_2SO_4 in order to produce a soluble fertilizer (Föllmi 1996). In the following, igneous and

sedimentary phosphate-rich occurrences and guano deposits were and are still increasingly used as a source of phosphate in the production of fertilizers. Besides that, phosphorus is used in the production of food additives, detergents, pesticides, and steel alloys. ^{32}P is applied as a radionuclide tracer.

Geochemistry and Occurrence

Phosphorus occurs in the form of phosphate-bearing minerals in igneous, metamorphic, and sedimentary rocks, and sediments (Fig. 1). It is also part of organic complexes, which may be preserved in the sedimentary reservoirs. Phosphate minerals principally belong to the apatite group $Ca_5(PO_4)_3(OH, F, Cl, CO_3)$ (Filippelli 2008). Non-apatite phosphate-containing minerals such as Whitlockite are comparably rare. In igneous rocks, fluorapatite is concentrated in carbonatites and silica-poor alkali intrusions, which are actually exploited in Russia, Finland, Brazil, and South Africa (Pufahl and Groat 2017). The igneous deposits can be as old as Palaeoproterozoic but mainly date from the Phanerozoic. In sedimentary deposits, the principal phosphate-bearing mineral is francolite – a carbonate fluorapatite (Jarvis et al. 1994). The most important regions in which sedimentary phosphate deposits are presently mined are located in China, Morocco, the United States, Jordan, Egypt, Peru, Tunisia, and Israel, in decreasing order of importance. The sedimentary reservoirs were preferentially formed during the late Neoproterozoic and Early Cambrian, Ordovician, Permian, Jurassic and Late Cretaceous, Paleocene, Late Oligocene, and Miocene (Cook and McElhinny 1979). Ninety-five percent of all exploitable reserves are sedimentary in origin, whereas the igneous occurrences represent the remaining 5% (Pufahl and Groat 2017). World reserves are estimated at more than 300 Gt and world phosphate rock production is projected to increase from 223 Mt/year (2015) to 255 Mt/year (2019) (U.S. Geol. Survey 2016).

Phosphorus, Fig. 1 Example of a sedimentary phosphatic deposit: a nodular phosphatic layer is preserved in an open-marine, deeper-water micritic carbonate. The dark phosphatic particles and nodules partly consist of broken and transported remains of fossils, such as ammonites; Albian (Cretaceous), Helvetic thrust-and-fold zone, Interlaken, Switzerland

Biological Utilization and Toxicity

In the form of phosphate, phosphorus represents an element essential for life, which is considered to determine primary productivity rates on geological time scales (Tyrrell 1999: Filippelli 2008). As such, its cycle is directly linked to the cycles of other biophile elements, notably those of carbon and oxygen. This implies that one molecule of phosphate may drive the transformation of over 100 CO_2 molecules into organic matter in marine planktonic ecosystems (Redfield 1958). In terrestrial ecosystems, the C:P transformation ratio may exceed 500 (Berner et al. 1993). It is mainly in this capacity that phosphorus is exploited, and its use as constituent of fertilizers is an important factor in feeding the ever increasing human population (Childers et al. 2011). The obvious side effect is the human-induced increase in phosphorus flux rates and notably the transfer of phosphorus to the oceans has been more than doubled in the last 75 years (Harrison et al. 2005). Eutrophication related to phosphorus overloading affects terrestrial, lacustrine and marginal marine ecosystems (Föllmi 2011). This has also a considerable impact on the oxygen households of lacustrine and marginal marine waters, leading to their depletion and the installation of so-called dead zones (Diaz and Rosenberg 2008).

Summary

Phosphorus is an element with unique characteristics, which does not only allow to trace important processes during the formation of the solar nebula and within our Earth but also to link phosphorus to important processes in the biosphere. Through its capacity as an essential element for life, it interfaces directly with the cycles of other biophile elements, such as carbon and oxygen. This to a degree that primary productivity rates and the oxygenation of the atmosphere and hydrosphere are often held to be directly dependent on the amount of phosphorus available. The use of phosphorus in fertilizers is one of the building blocks behind the "green revolution," allowing to feed an ever increasing population, but has also induced eutrophication in terrestrial and marine environments, with a negative impact on life's diversity and aquatic oxygen households. Global phosphorus resources are limited and as a nonrenewable element, mitigation pathways are presently more and more investigated in order to promote the sustainable use of this element.

Cross-References

- Biogeochemistry
- Carbon
- Chondrites
- Lithophile Elements
- Nucleosynthesis
- Nutrients
- Ocean Biochemical Cycling and Trace Elements
- Partitioning and Partition Coefficients

References

Berner RA, Ruttenberg KC, Ingall ED, Rao JL (1993) The nature of phosphorus burial in modern marine sediments. In: Wollast R, Mackenzie FT, Chou L (eds) Interactions of C, N, P and S biochemical cycles and global change, NATO ASI series, vol 14. Springer, Berlin, pp 365–378

Childers DL, Corman J, Edwards M, Elser JJ (2011) Sustainability challenges of phosphorus and food: solutions from closing the human phosphorus cycle. Bioscience 61:117–124

Cook PJ, McElhinny MW (1979) A re-evaluation of the spatial and temporal distribution of sedimentary phosphate deposits in the light of plate tectonics. Econ Geol 74:315–330

Diaz RJ, Rosenberg R (2008) Spreading dead zones and consequences for marine ecosystems. Science 321:926–928

Filippelli GM (2008) The global phosphorus cycle: past, present, and future. Elements 4:89–95

Föllmi KB (1996) The phosphorus cycle, phosphogenesis and marine phosphate-rich deposits. Earth-Sci Rev 40:55–124

Föllmi KB (2011) Phosphorus, phosphorites. In: Reitner J, Thiel V (eds) Encyclopedia of geobiology, Encyclopedia of earth sciences series, vol 15. Springer, Berlin, pp 732–736

Harrison JA, Seitzinger SP, Bouwman AF, Caraco NF, Beusen AHW, Vörösmarty CJ (2005) Dissolved inorganic phosphorus export to the coastal zone: results from a spatially explicit, global model. Glob Biogeochem Cycles 19, GB4S03

Jarvis I, Burnett WC, Nathan Y et al (1994) Phosphorite geochemistry- state-of-the-arts and environmental concerns. In: Föllmi KB (ed) Concepts and controversies in phosphogenesis, Eclogae geologicae Helvetiae, vol 87. Birkhäuser Verlag, Basel, pp 643–700

Koo BC, Lee YH, Moon DS, Yoon SC, Raymond JC (2013) Phosphorus in the young supernova remnant Cassiopeia a. Science 342:1346–1348

Pufahl PK, Groat LA (2017) Sedimentary and igneous phosphate deposits: formation and exploration: an invited paper. Econ Geol 112:483–516

Redfield AC (1958) The biological control of chemical factors in the environment. Am Scient 46:205–221

Toplis MJ, Libourel G, Carroll MR (1994) The role of phosphorus in crystallization processes of basalt: an experimental study. Geochim Cosmochim Acta 58:797–810

Tyrrell T (1999) The relative influences of nitrogen and phosphorus on oceanic primary productivity. Nature 400:525–531

USGS (2016) USGS mineral commodity summaries: phosphate rock. https://minerals.usgs.gov/minerals/pubs/commodity/phosphate_rock/mcs-2016-phosp.pdf

Wolf D, Palme H (2001) The solar system abundances of phosphorus and the nebular volatility of phosphorus. Meteor Planet Sci 36:559–571

Platinum

James M. Brenan
Department of Earth Sciences, Dalhousie University, Halifax, NS, Canada

Element Data
Atomic Symbol: **Pt**
Atomic Number: **78**
Atomic Weight: 195.084
Isotopes and Abundances: ^{190}Pt 0.012%, ^{192}Pt 0.782%, ^{194}Pt 32.864%, ^{195}Pt 33.775%, ^{196}Pt 25.211%, ^{198}Pt 7.356%
0.1 MPa Melting Point: 1768.2 °C
0.1 MPa Boiling Point: 3876 °C
Common Valences: +2, +4
Ionic Radii: 4-fold: 60 pm (+2); 6-fold: 80 pm (+2), 62.5 pm (+4)
Pauling Electronegativity: 2.28
First Ionization Energy: 864.39 kJ/mol
Chondritic (CI) Abundance: 866.8 ng/g
Silicate Earth Abundance: 7.6 ng/g
Crustal Abundance: 1.5 ng/g
Seawater Abundance: 0.2–1.5 pmol/kg
Core Abundance: 5700 ng/g

Definition

Atomic number 78 is a dense, refractory, precious metal with a bright silvery-white luster and high resistance to oxidation. First isolated in 1757, it is widely used in jewelry production and catalytic converters in automobiles.

History and Uses

The material referred to as "platina," derived from the Spanish for "little silver," was first described to the Royal Society of London by William Watson in 1750. These were samples likely derived from placer deposits of the Choco District of Columbia, which had been exploited by the pre-Hispanic natives to produce jewelry and useful objects (fishing hooks, sewing needles, awls, tweezers). Subsequent analysis by William Lewis determined this to be a new-found material and that ". . ..it follows, that platina is not, as some believe, gold naturally debased by the admixture of some other metallic body, but a metal of the peculiar kind, essentially different

from all others" (Lewis 1757). Platinum is a highly-valued metal due to its high melting point, resistance to oxidation, and catalytic properties. Most Pt is used to catalyze key reactions involved in hydrocarbon fuel production (reforming and isomerization to enhance octane rating) and in automobile catalytic converters for engine emission control. A nearly equivalent amount of Pt is also used for jewelry. High thermal stability and resistance to corrosion makes Pt an ideal material for laboratory ware (i.e., crucibles), thermocouples, and electrical contacts. Other important applications are in health care, owing to the biocompatibility of Pt, including applications in angioplasty and implanted medical devices. Cisplatin (cis-Diamminedichloroplatinum[II]; cis-[Pt(NH3)2Cl2]) and its derivatives are drugs used in the treatment of ovarian and testicular cancer. A detailed account of the history of platinum, including important discoveries and scientific work, can be found in the book "*History of Platinum and its Allied Metals*" by McDonald and Hunt (1982).

Elemental and Physical Properties

Platinum has an atomic weight of 195.084[9], ground state electronic configuration of $[Xe]4f^{14}5d^{9}6s$, with melting and boiling points at 0.1 MPa of 1768.2 °C and 3876 °C, respectively (Arblaster 2007). Platinum is amongst the most dense of the elements (21,090 kg/m^3), similar to gold (19,300 kg/m^3) and about twice that of lead (11,340 kg/m^3). Platinum is considered to be a refractory element with a 50% condensation temperature of 1135 °C (Lodders 2003). Platinum has five stable isotopes: 192 (0.782[24]%), 194 (32.864[410]%), 195 (33.775[240]%), 196 (25.211[340]%), 198 (7.356[130]%), as well as the radioactive ^{190}Pt (0.012[2]%), which undergoes alpha-decay to ^{186}Os, with a half-life of 1.4×10^{11} years (see entry for ▶ "Osmium Isotopes"). In addition to the neutral metal, the common oxidation states are 2+ and 4+. The radius of the neutral atom is 177 pm (Clementi et al. 1967), and Pt crystallizes in the cubic close-packed structure (space group Fm-3 m) with a metallic radius of 139 pm (Waseda et al. 1975). The size of the cation varies as follows (from Shannon 1976): 60 pm (+2, IV-fold, square planar), 80 pm (+2, VI-fold), 62.5 pm (+4, VI-fold), and 57 pm (+5, IV-fold). Useful texts that provide synopses of the chemical properties of Pt and allied elements can be found in Cotton (1997) and in a compendium of papers edited by Hartley (1991).

Geochemical Behavior and Reservoir Abundance

Platinum is both highly siderophile and strongly chalcophile and is grouped with other 5th and 6th row transition metals having similar chemical properties: Pd, Rh, Ru, Os, and Ir; see entries for ▶ "Platinum Group Elements" (PGE) and ▶ "Siderophile Elements". Experiments have shown that Pt does not readily dissolve into rock-forming minerals, such as olivine and chromite (Brenan et al. 2016), but instead concentrates in base metal sulfides or forms accessory platinum group minerals, such as platinum-bearing telluride ($PtTe_2$; moncheite) or arsenide ($PtAs_2$; sperrylite), native metal, or alloyed with iron (Pt_3Fe, PtFe; isoferro- and tetraferroplatinum, respectively) and other platinum group elements (PGE). An extensive compilation of platinum-bearing minerals is provided in Cabri (2002).

The abundance of Pt in the carbonaceous chondrite Orgueil is 866.8 ng/g (Horan et al. 2003), taken as similar to the bulk earth concentration, which has now been highly fractionated into the core (5700 ng/g; McDonough 2003), upper mantle (7.6[1.3] ng/g; Becker et al. 2006), and crust (continental: 1.5 ng/g; Rudnick and Gao 2003; oceanic: 2.072 ng/g; Peucker-Ehrenbrink et al. 2012). The relative proportions of the PGEs are close to chondritic in the upper mantle (Becker et al. 2006) as well as higher and relatively unfractionated than expected for equilibrium between metal and silicate (Mann et al. 2012). Many believe this is the result of late accretion of chondritic materials following core formation. The platinum content of seawater (0.2–1.5 pmol/kg) is similar to that of the heavy rare-earth elements (Bruland and Lohan 2003), although the crustal abundance of Pt is >100x lower. Calculations indicate that the dominant Pt species in seawater is $[PtCl_4]^{2-}$ at 25 °C, pH 8.2, 0.1 MPa (Byrne et al. 1988).

Coupled enrichments in ^{186}Os/^{188}Os (due to ^{190}Pt decay) and ^{187}Os/^{188}Os (due to ^{187}Re decay) are observed in lavas formed in mantle plumes, such as Hawaii. The origin of this variation is debated and variously interpreted as recording outer core "reflux" into the mantle (Brandon et al. 1998), contamination of the magma source by certain rare sediment types (Scherstén et al. 2004) or eclogite (Luguet et al. 2008), or the presence of residual accessory minerals with elevated Pt/Os and Re/Os (Luguet et al. 2008). Carlson (2005) provides a comprehensive review of the use of the Pt-Re-Os isotopic system in geochemistry and geochronology.

Economic concentrations of Pt require >10,000-fold enrichment relative to crustal background values. This can occur when mantle-derived magmas reach saturation in immiscible sulfide liquid, or by accumulation of Pt-rich accessory minerals, or through the action of hydrothermal fluids. The largest Pt deposits are found in the Bushveld Igneous Complex of South Africa, occurring in chromitite (UG2 and Platreef) and pegmatoidal norite (Merensky Reef) horizons. Other important resources include the Norilsk (Russia), Sudbury (Canada), and Stillwater (USA) deposits. Global production in 2015 was ~160,000 kg, at an average market price of ~ $40,000/kg. The reader is referred to Platinum Metals Review, which

provides a range of technical and historical information on the allied platinum group metals.

Summary

Platinum is a bright, silvery-white precious metal characterized by high density and melting temperature, resistance to oxidation, and unique surface catalytic properties. The principal uses for this metal are for jewelry, catalysis of industrial processes, such as hydrocarbon refining, as well as automobile engine emission control. Platinum is highly siderophile, as well as chalcophile, and is therefore concentrated in Earth's core, with complementary depletions in the silicate mantle, crust, and surface reservoirs. Anomalously elevated abundances of ^{186}Os, a product of ^{190}Pt decay, in hot-spot related magmas may reflect a contribution of core material to Earth's mantle, although more recent interpretations underscore the possible role of accessory phases with elevated Pt/Os, or contribution from unusual surface inputs to mantle reservoirs. Extreme concentration of Pt relative to crustal background values is needed to produce minable deposits, requiring the massive extraction capacity of immiscible sulfide melts that form in silicate magmas.

Cross-References

- Chalcophile Elements
- Chondrites
- Formation and Evolution of the Earth
- Geochemical Classification of Elements
- Natural Gas
- Ore Deposits
- Osmium
- Osmium Isotopes
- Palladium
- Platinum Group Elements
- Rhenium
- Rhodium
- Ruthenium
- Siderophile Elements
- Sulfide Minerals
- Transition Elements

References

Arblaster JW (2007) Vapour pressure equations for the platinum group elements. Platin Met Rev 51:130–135

Becker H, Horan MF, Walker RJ, Gao S, Lorand J-P, Rudnick RL (2006) Highly siderophile element composition of the Earth's primitive upper mantle: constraints from new data on peridotite massifs and xenoliths. Geochim Cosmochim Acta 70:4528–4550

Brandon AD, Walker RJ, Morgan JW, Norman MD, Prichard HM (1998) Coupled Os-186 and Os-187 evidence for core-mantle interaction. Science 280:1570–1573

Brenan JM, Bennett N, Zajacz Z (2016) Experimental results on fractionation of the highly siderophile elements (HSE) at variable pressures and temperatures during planetary and magmatic differentiation. Rev Mineral Geochem 81:1–88

Bruland KW, Lohan MC (2003) Controls of trace metals in seawater. In: Elderfield H (ed) The oceans and marine geochemistry. Holland HD, Turekian KK (eds in Chief) Treatise on geochemistry, vol 6. Elsevier, Amsterdam

Byrne RH, Kump LR, Cantrell KJ (1988) The influence of temperature and pH on trace metal speciation in seawater. Mar Chem 25:163–181

Cabri LJ (2002) The platinum group minerals. In: Cabri L (ed) The geology, geochemisty, mineralogy and mineral beneficiation of platinum-group Elements. C.I.M. Special, vol 54. Canadian Institute of Mining, Metallurgy and Petroleum, Montreal, pp 13–130

Carlson RW (2005) Application of the Pt-Re-Os isotopic systems to mantle geochemistry and geochronology. Lithos 82:249–272

Clementi E, Raimondi DL, Reinhardt WP (1967) Atomic screening constants from SCF functions. II. Atoms with 37–86 electrons. J Chem Phys 47:1300–1307

Cotton SA (1997) Chemistry of precious metals. Chapman and Hall, London. 374 pp

Hartley FR (ed) (1991) Chemistry of the platinum group metals. Recent developments, Studies in inorganic chemistry, vol 11. Elsevier, Amsterdam. 642 pp

Horan MF, Walker RJ, Morgan JW, Grossman JN, Rubin AE (2003) Highly siderophile elements in chondrites. Chem Geol 196:5–20

Lewis W (1757) Experimental examination of platina. Philos Trans R Soc 50:156–166

Lodders K (2003) Solar system abundances and condensation temperatures of the elements. Astrophys J 591:1220–1247

Luguet A, Pearson DG, Nowell GM, Dreher ST, Coggon JA, Spetsius ZV, Parman SW (2008) Enriched Pt-Re-Os isotope systematics in plume lavas explained by metasomatic sulfides. Science 319:453–456

Mann U, Frost D, Rubie D (2012) Partitioning of Ru, Rh, Pd, Re, Ir and Pt between liquid metal and silicate at high pressures and high temperatures: implications for the origin of highly siderophile element concentrations in the Earth's mantle. Geochim Cosmochim Acta 84:593–613

McDonald D, Hunt LB (1982) A history of platinum and its allied metals. Johnson-Matthey, London. 450 pp

McDonough WF (2003) Compositional model for the Earth's core. In: Carlson RW (ed) The mantle and core. Holland HD, Turekian KK (eds in Chief) Treatise on geochemistry, vol 2. Elsevier, Amsterdam

Peucker-Ehrenbrink B, Hanghoj K, Atwood T, Keleman PB (2012) Rhenium-osmium isotope systematics and platinum group element concentrations in oceanic crust. Geology 40:199–202

Rudnick RL, Gao S (2003) Composition of the continental crust. In: Rudnick RL (ed) The crust. Holland HD, Turekian KK (eds in Chief) Treatise on geochemistry, vol 3. Elsevier, Amsterdam

Scherstén A, Elliott T, Hawkesworth C, Norman M (2004) Tungsten isotope evidence that mantle plumes contain no contribution from the Earth's core. Nature 427:234–237

Shannon RD (1976) Revised effective ionic radii and systematic studies of interatomic distances in halides and chalcogenides. Acta Crystallogr A32:751–767

Waseda Y, Hirata K, Ohtani M (1975) High-temperature thermal expansion of platinum, tantalum, molybdenum, and tungsten measured by x-ray diffraction. High Temp High Pressures 7:221–222

Platinum Group Elements

Igor S. Puchtel
Department of Geology, University of Maryland, College Park, MD, USA

Definition

The Platinum Group Elements (PGE: Osmium, Iridium, Ruthenium, Rhodium, Platinum, and Palladium), also known as *platinum group metals and platinoids*, are transition metals located in the d-block of the Periodic Table of Elements (Groups VIII, IX, and X, Periods 5 and 6). The atomic radii of the Os, Ir, and Pt subgroup, caused by the lanthanide contraction of the 4*f* group elements, are similar to those of the Ru, Rh, Pd subgroup of the PGE. The almost doubling of the number of nucleons with the same atomic radii makes Os, Ir, and Pt the densest elements on Earth. Based on their behavior in magmatic systems, the PGE are subdivided into the iridium-group PGE (Ir-PGE: Os, Ir, Ru, Rh) and the palladium-group PGE (Pd-PGE: Pt, Pd) (Barnes et al. 1985; Barnes 1999).

Introduction

The PGE were discovered in the eighteenth through early nineteenth centuries by Lewis (1753, 1757), Tennant (1804), and Wollaston (1805); a detailed account of the history of the PGE can be found in McDonald and Hunt (1982). Studies of PGE abundances, combined with three radiogenic isotope systems that contain the PGE, in terrestrial and extraterrestrial materials, afford a unique view of early Solar System evolution and planet formation and differentiation. Unique chronological applications include dating of formation of sulfides, gold, organic-rich sediments, ultramafic lava flows, and meteorites. Although analytical techniques for precise analysis of PGE have only recently become available, these elements are now an important part of the geochemical toolbox.

PGE Abundances in the Bulk Silicate Earth

PGE have strong affinity for liquid metal and sulfide relative to silicate melt, which determines their both highly siderophile and chalcophile nature (i.e., $D^{\text{metal, sulfide/silicate}} >> 10^4$: Borisov et al. 1994; Borisov and Palme 1995; Fleet et al. 1999; Brenan et al. 2016). The PGE provide unique insights into processes of planetary accretion, core formation, and mantle differentiation. During the initial planetary differentiation and core formation, ~99.8% of the terrestrial PGE budget was sequestered into the core, stripping the mantle almost entirely of PGE. However, the relative abundances of individual PGE in the Bulk Silicate Earth (BSE) are too close to those in chondritic meteorites, and the absolute abundances are two to three orders of magnitude too high, to be the result of the core segregation event. The PGE abundances in the BSE are best explained by addition of 0.3–0.8% of chondritic materials to Earth after the core formation was complete (Morgan 1986; Walker 2009), based on the concept of late accretion (Chou et al. 1983; Morgan 1985). Issues related to the late accretion hypothesis are highly debated, including the time frame within which the late accreted materials were delivered to Earth and homogenized within the mantle, as well as the compositions of late accreted materials (Walker et al. 2015). Other hypotheses that were proposed to account for PGE present in the BSE include inefficient core formation (Arculus and Delano 1981; Jones and Drake 1986) and lowered metal-silicate partition coefficients resulting from metal segregation at elevated temperatures and pressures, as may have occurred at the base of a deep magma ocean (Li and Agee 1996; Righter and Drake 1997). Hybrid models that include aspects of all three hypotheses may ultimately be necessary to account for all of the observed PGE characteristics of the BSE (Walker 2009).

The PGE abundances in the BSE have been determined via analysis of mantle xenoliths and orogenic peridotite samples worldwide (Becker et al. 2006; Fischer-Gödde et al. 2011) to be (ng/g): 3.9 ± 0.5 (Os), 3.5 ± 0.4 (Ir), 7.0 ± 0.9 (Ru), 1.2 ± 0.2 (Rh), 7.6 ± 1.3 (Pt), and 7.1 ± 1.3 (Pd). While Os, Ir, Rh, and Pt occur in broadly chondritic relative abundances in the BSE, the Ru/Ir and Pd/Ir ratios are 20 to 30% higher. The PGE pattern of the BSE is, thus, not exactly matched by any chondrite group. However, it compares well with the PGE compositions of some lunar impact melt rocks formed during the Late Heavy Bombardment event at 4.0 – 3.8 Ga. This may indicate that the composition of late accreted materials is somewhat different from that of the chondritic meteorites residing in our collections (Puchtel et al. 2008; Fischer-Gödde et al. 2011; Sharp et al. 2014; Walker et al. 2015). Great promise for providing genetic fingerprints of late-stage accretionary additions to Earth and Moon is shown by Ru isotopes (Walker et al. 2015). Mass-independent nucleosynthetic isotopic anomalies have been observed in Ru present in whole-rock meteorites and their components (Fujii et al. 2006; Chen et al. 2010; Fischer-Gödde et al. 2015); the nature and magnitude of these Ru anomalies can be used to investigate the stellar origins of matter in the Solar System, as well as nebular mixing processes.

More than 90% of the PGE budget of the BSE resides in two types of sulfides (Alard et al. 2000; Lorand and Alard

2001; Luguet et al. 2007). The high-temperature Os-Ir-Ru-Rh-rich Fe-Ni monosulfide solid solution (*mss*) forms rounded inclusions in olivine, whereas low-temperature irregular-shaped Cu-Ni sulfides occupy intergranular space. During partial melting of mantle peridotite, Cu-Ni sulfides enter the melt, whereas the *mss* remains trapped in the melting residue until the degree of melting reaches *ca.* 25% (Keays 1995), at which point all the sulfide in the residue gets consumed and, as the degree of melting continues to increase, the magma becomes sulfide-undersaturated. As a result, at low degrees of partial melting, the resulting basalts are generally PGE-poor and are strongly enriched in Pd-PGE relative to Ir-PGE. At higher degrees of partial melting, the resulting picrites and komatiites have higher PGE contents and are only slightly to moderately enriched in Pd-PGE relative to Ir-PGE. Therefore, during partial melting of the mantle, Ir-PGE are compatible with the melting residue, although to a different degree, and Pt and Pd are incompatible (e.g., Barnes et al. 1985; Rehkämper et al. 1999; Puchtel and Humayun 2000).

Olivine and chromite are two major liquidus phases controlling composition of mafic and ultramafic magmas during differentiation. At the mantle oxygen fugacities of the FMQ buffer, all PGE are incompatible, although to a different degree, in olivine, and Pt and Pd are also incompatible in chromite, whereas Os, Ir, Rh, and Ru are compatible (Puchtel and Humayun 2001; Brenan et al. 2003, 2012; Puchtel et al. 2004).

PGE-Based Chronometry

Three radiogenic isotope decay systems include the PGE as a parent element ($^{107}Pd \rightarrow {}^{107}Ag$), daughter element ($^{187}Re \rightarrow {}^{187}Os$), or both ($^{190}Pt \rightarrow {}^{186}Os$). A key feature of these systems is that they track the unique behavior of the PGE during planet formation and differentiation and thus, afford information on processes to which other isotope systems, such as lithophile-element based, are not sensitive. Unique chronological applications include dating the formation of mafic-ultramafic lavas and layered intrusions, ore deposits, organic-rich sediments, meteorites, and even inclusions in diamonds. These systems also serve as isotopic tracers for such processes, as crust-mantle differentiation, recycling of oceanic crust into the mantle, core-mantle exchange, deposition of extraterrestrial materials on Earth's surface, and volatile-element depletion of planetary bodies (Walker et al. 1997; Shirey and Walker 1998; Carlson 2005; Walker 2009). Because of the low content in the Earth's crust, PGE are sensitive indicators of presence of extraterrestrial materials in rocks derived from terrestrial impact craters, such as the Chicxulub crater buried underneath the Yucatán Peninsula in Mexico (Gelinas et al. 2004) or Chesapeake Bay impact structure in Virginia, USA (Lee et al. 2006).

PGE Measurements

Due to their high ionization potential, PGE are difficult to ionize. Currently, Os and Ru isotopic compositions and Os concentrations in a variety of terrestrial and extraterrestrial materials are most efficiently measured via negative thermal ionization mass-spectrometry (N-TIMS: Creaser et al. 1991; Völkening et al. 1991), whereas Ir, Ru, Rh, Pt, and Pd concentrations are commonly determined via the inductively coupled plasma mass-spectrometry (ICP-MS) technique (Greenfield 1994). For high-precision measurements of Os and Ru isotopic compositions, the latest generation of thermal ionization mass-spectrometers, *ThermoFisher Triton®*, is being utilized, which allows to attain external precision of analysis of 10–15 ppm for Os and 6–7 ppm for Ru (2SD), based on the long-term reproducibility of the laboratory standards (e.g., Brandon et al. 2006; Puchtel et al. 2009, 2014; Bermingham et al. 2016). High-precision measurements of Ru isotopic compositions are also currently performed by multi-collector ICP-MS with an external precision of ca. 13 ppm (Fischer-Gödde et al. 2015).

PGE Mineral Deposits

The Earth's mantle is the principal reservoir, from which PGE deposits in the crust are derived. PGE mineralization has been identified in various rock types and at various stratigraphic levels in layered intrusions of any age, size, and magmatic lineage, but the most important deposits occur as relatively narrow stratiform reefs in the lower to central ultramafic-mafic portions of large tholeiitic intrusions of late Archean to early Proterozoic age (Maier 2005). In order to form a PGE ore deposit, PGE concentrations need to be raised by more than four orders of magnitude relative to the typical crustal abundances. This level of enrichment can be reached as a result of sulfide saturation and relies principally on the high-extraction capacity of sulfide liquid that sequesters PGE from silicate magmas. The majority of the world's PGE reserves are held in a small number of large deposits, most of which occur within the unique 2.05 billion-year-old Bushveld Complex of South Africa; the latter hosts 75% of the world's resources of Pt, 54% of Pd resources, and 82% of Rh resources (Mungall and Naldrett 2008; Naldrett et al. 2008).

Health Aspects of the PGE

The PGE are used in a number of therapies to enhance public health and well-being. Platinum alloys are essential components of prosthetic teeth and heart implant devices. Anticancer drugs cis-platin, carboplatin, and oxaliplatin are used to treat certain types of malignant tumors.

Environmental Aspects of the PGE

A detailed review of the environmental aspects of PGE is provided by Rauch and Morrison (2008). The PGE are increasingly used in a growing number of applications and ever-increasing emissions result in elevated concentrations of these elements in the environment. Automobile catalytic converters, which use Pt, Pd, and Rh, are the main source of PGE that are emitted into urban and roadside environment. Transport of PGE by stormwater may results in contamination of aquatic environments, where PGE can be present in a bioavailable form. However, currently available data are insufficient for an accurate assessment of associated potential risks.

Summary

The Platinum Group Elements (PGE: Os, Ir, Ru, Rh, Pt, and Pd) are transition metals located in the d-block of the Periodic Table of Elements (Groups VIII, IX, and X, Periods 5 and 6). The PGE have strong affinity for liquid metal and sulfide relative to silicate melt, which determines their both highly siderophile and chalcophile nature; they provide unique insights into processes of planetary accretion, core formation, and mantle differentiation. The PGE abundances in the BSE have been determined via analysis of mantle xenoliths and orogenic peridotite samples worldwide. These abundances are best explained by addition of 0.3–0.8% of chondritic materials to Earth after the core formation was complete (the late accretion hypothesis). Based on their behavior in magmatic systems, the PGE are subdivided into the iridium-group PGE (Ir-PGE: Os, Ir, Ru, Rh) and the palladium-group PGE (Pd-PGE: Pt, Pd). During mantle melting, Ir-PGE are moderately to strongly compatible, whereas Pd-PGE are moderately to strongly incompatible with the melting residue. Three PGE-based radiogenic isotope decay systems track the unique behavior of the PGE during planet formation and differentiation. Unique chronological applications include dating the formation of mafic-ultramafic lavas and layered intrusions, ore deposits, organic-rich sediments, meteorites, and even inclusions in diamonds. These systems also serve as isotopic tracers for such processes as crust-mantle differentiation, recycling of oceanic crust into the mantle, core-mantle exchange, deposition of extraterrestrial materials on Earth's surface, and volatile-element depletion of planetary bodies. The majority of the world's PGE reserves are held in a small number of large deposits, most of which occur within the unique 2.05 billion-year-old Bushveld Complex of South Africa. The PGE are increasingly used in a growing number of applications and emissions result in elevated concentrations of these elements in the environment. However, currently available data are insufficient for an accurate assessment of associated potential risks.

Cross-References

- ▶ Chalcophile Elements
- ▶ Geochronology and Radiogenic Isotopes
- ▶ Inductively Coupled Plasma Mass Spectrometry (ICP-MS)
- ▶ Iridium
- ▶ Ore Deposits
- ▶ Osmium
- ▶ Palladium
- ▶ Platinum
- ▶ Rhodium
- ▶ Ruthenium
- ▶ Siderophile Elements
- ▶ Thermal Ionization Mass Spectrometry

References

Alard O, Griffin WL, Lorand J-P, Jackson SE, O'Reilly SY (2000) Non-chondritic distribution of the highly siderophile elements in mantle sulfides. Nature 407(6806):891–894

Arculus RJ, Delano JW (1981) Siderophile element abundances in the upper mantle – evidence for a sulfide signature and equilibrium with the core. Geochim Cosmochim Acta 45(8):1331–1343

Barnes S-J (1999) Elements: platinum group. In: Marshall CP, Fairbringe RW (eds) Encyclopedia of geochemistry. Kluwer Academic Publishers, Dordrecht/Boston/London, p 219

Barnes S-J, Naldrett AJ, Gorton MP (1985) The origin of the fractionation of platinum-group elements in terrestrial magmas. Chem Geol 53(3–4):303–323

Becker H, Horan MF, Walker RJ, Gao S, Lorand J-P, Rudnick RL (2006) Highly siderophile element composition of the Earth's primitive upper mantle: constraints from new data on peridotite massifs and xenoliths. Geochim Cosmochim Acta 70(17): 4528–4550

Bermingham KR, Walker RJ, Worsham EA (2016) Refinement of high precision Ru isotope analysis using negative thermal ionization mass spectrometry. Int J Mass Spectrom 403:15–26

Borisov A, Palme H (1995) The solubility of iridium in silicate melts: new data from experiments with $Ir_{10}Pt_{90}$ alloys. Geochim Cosmochim Acta 59(3):481–485

Borisov A, Palme H, Spettel B (1994) Solubility of palladium in silicate melts: implications for core formation in the Earth. Geochim Cosmochim Acta 58(2):705–716

Brandon AD, Walker RJ, Puchtel IS (2006) Platinum-osmium isotope evolution of the Earth's mantle: constraints from chondrites and Os-rich alloys. Geochim Cosmochim Acta 70(8):2093–2103

Brenan JM, McDonough WF, Dalpé C (2003) Experimental constraints on the partitioning of rhenium and some platinum-group elements between olivine and silicate melt. Earth Planet Sci Lett 212 (1–2):135–150

Brenan JM, Finnigan CF, McDonough WF, Homolova V (2012) Experimental constraints on the partitioning of Ru, Rh, Ir, Pt and Pd

between chromite and silicate melt: the importance of ferric iron. Chem Geol 302–303:16–32
Brenan JM, Bennett NR, Zajacz Z (2016) Experimental results on fractionation of the Highly Siderophile Elements (HSE) at variable pressures and temperatures during planetary and magmatic differentiation. Rev Mineral Geochem 81(1):1–87
Carlson RW (2005) Application of the Pt-Re-Os isotopic systems to mantle geochemistry and geochronology. Lithos 82(3–4): 249–272
Chen JH, Papanastassiou DA, Wasserburg GJ (2010) Ruthenium endemic isotope effects in chondrites and differentiated meteorites. Geochim Cosmochim Acta 74(13):3851–3862
Chou C-L, Shaw DM, Crocket JH (1983) Siderophile trace elements in the Earth's oceanic crust and upper mantle. J Geophys Res 88(S2): A507–A518
Creaser RA, Papanastassiou DA, Wasserburg GJ (1991) Negative thermal ion mass-spectrometry of osmium, rhenium, and iridium. Geochim Cosmochim Acta 55(1):397–401
Fischer-Gödde M, Becker H, Wombacher F (2011) Rhodium, gold and other highly siderophile elements in orogenic peridotites and peridotite xenoliths. Chem Geol 280(3–4):365–383
Fischer-Gödde M, Burkhardt C, Kruijer TS, Kleine T (2015) Ru isotope heterogeneity in the solar protoplanetary disk. Geochim Cosmochim Acta 168:151–171
Fleet ME, Crocket JH, Liu M, Stone WE (1999) Laboratory partitioning of platinum-group elements (PGE) and gold with application to magmatic sulfide-PGE deposits. Lithos 47(1–2):127–142
Fujii T, Moynier F, Telouk P, Albarède F (2006) Mass-independent isotope fractionation of molybdenum and ruthenium and the origin of isotopic anomalies in Murchison. Astrophys J 647 (2):1506
Gelinas A, Kring DA, Zurcher L, Urrutia-Fucugauchi J, Morton O, Walker RJ (2004) Osmium isotope constraints on the proportion of bolide component in Chicxulub impact melt rocks. Meteorit Planet Sci 39(6):1003–1008
Greenfield S (1994) Inductively coupled plasmas in atomic fluorescence spectrometry. A review. J Anal At Spectrom 9(5):565–592
Jones JH, Drake MJ (1986) Geochemical constraints on core formation in the Earth. Nature 322(6076):221–228
Keays RR (1995) The role of komatiitic and picritic magmatism and S-saturation in the formation of ore deposits. Lithos 34 (1–3):1–18
Lee SR, Horton JW, Walker RJ (2006) Confirmation of a meteoritic component in impact-melt rocks of the Chesapeake Bay impact structure, Virginia, USA – evidence from osmium isotopic and PGE systematics. Meteorit Planet Sci 41(6):819–833
Lewis W (1753) Experimental examination of a white metallic substance said to be found in the gold mines of the Spanish West Indies, and is there known by the appellations of platina, platina di Pinto, Juan Blanca. Philos Trans R Soc 48:638–689
Lewis W (1757) Experimental examination of platina. Philos Trans R Soc 50:156–166
Li J, Agee CB (1996) Geochemistry of mantle-core differentiation at high pressure. Nature 381(6584):686–689
Lorand J-P, Alard O (2001) Platinum-group element abundances in the upper mantle: new constraints from in situ and whole-rock analyses of Massif Central xenoliths (France). Geochim Cosmochim Acta 65 (16):2789–2806
Luguet A, Shirey SB, Lorand J-P, Horan MF, Carlson RW (2007) Residual platinum-group minerals from highly depleted harzburgites of the Lherz massif (France) and their role in HSE fractionation of the mantle. Geochim Cosmochim Acta 71 (12):3082–3097
Maier WD (2005) Platinum-group element (PGE) deposits and occurrences: mineralization styles, genetic concepts, and exploration criteria. J Afr Earth Sci 41(3):165–191
McDonald D, Hunt LB (1982) A history of platinum and its allied metals. Johnson-Matthey, London
Morgan JW (1985) Osmium isotope constraints on Earth's late accretionary history. Nature 317(6039):703–705
Morgan JW (1986) Ultramafic xenoliths: clues to Earth's late accretionary history. J Geophys Res 91(B12):12375–12387
Mungall JE, Naldrett AJ (2008) Ore deposits of the platinum-group elements. Elements 4(4):253–258
Naldrett T, Kinnaird J, Wilson A, Chunnett G (2008) Concentration of PGE in the Earth's crust with special reference to the Bushveld complex. Earth Science Frontiers 15(5):264–297
Puchtel IS, Humayun M (2000) Platinum group elements in Kostomuksha komatiites and basalts: implications for oceanic crust recycling and core-mantle interaction. Geochim Cosmochim Acta 64(24):4227–4242
Puchtel IS, Humayun M (2001) Platinum group element fractionation in a komatiitic basalt lava lake. Geochim Cosmochim Acta 17(65):2979–2993
Puchtel IS, Humayun M, Campbell A, Sproule R, Lesher CM (2004) Platinum group element geochemistry of komatiites from the Alexo and Pyke Hill areas, Ontario, Canada. Geochim Cosmochim Acta 68(6):1361–1383
Puchtel IS, Walker RJ, James OB, Kring DA (2008) Osmium isotope and highly siderophile element systematics of lunar impact melt breccias: implications for the late accretion history of the Moon and Earth. Geochim Cosmochim Acta 72(12):3022–3042
Puchtel IS, Walker RJ, Brandon AD, Nisbet EG (2009) Pt-Re-Os and Sm-Nd isotope and HSE and REE systematics of the 2.7 Ga Belingwe and Abitibi komatiites. Geochim Cosmochim Acta 73 (20):6367–6389
Puchtel IS, Walker RJ, Touboul M, Nisbet EG, Byerly GR (2014) Insights into early Earth from the Pt-Re-Os isotope and highly siderophile element abundance systematics of Barberton komatiites. Geochim Cosmochim Acta 125:394–413
Rauch S, Morrison GM (2008) Environmental relevance of the platinum-group elements. Elements 4(4):259–263
Rehkämper M, Halliday AN, Fitton JG, Lee D-C, Wieneke M, Arndt NT (1999) Ir, Ru, Pt and Pd in basalts and komatiites: new constraints for the geochemical behavior of the platinum group elements in the mantle. Geochim Cosmochim Acta 63(22):3915–3934
Righter K, Drake MJ (1997) Metal-silicate equilibrium in a homogeneously accreting earth: new results for Re. Earth Planet Sci Lett 146 (3–4):541–553
Sharp M, Gerasimenko I, Loudin LC, Liu J, James OB, Puchtel IS, Walker RJ (2014) Characterization of the dominant impactor signature for Apollo 17 impact melt rocks. Geochim Cosmochim Acta 131:62–80
Shirey SB, Walker RJ (1998) The Re-Os isotope system in cosmochemistry and high-temperature geochemistry. Annu Rev Earth Planet Sci 26:423–500
Tennant S (1804) On two metals, found in the black powder remaining after the solution of platina. Philos Trans R Soc Lond 94:411–418
Völkening J, Walczyk T, Heumann KG (1991) Osmium isotope ratio determinations by negative thermal ionization mass spectrometry. Int J Mass Spectrom Ion Process 105(2):147–159
Walker RJ (2009) Highly siderophile elements in the Earth, Moon and Mars: update and implications for planetary accretion and differentiation. Chem Erde-Geochem 69(2):101–125
Walker RJ, Morgan JW, Beary ES, Smoliar MI, Czamanske GK, Horan MF (1997) Applications of the ^{190}Pt-^{186}Os isotope system to geochemistry and cosmochemistry. Geochim Cosmochim Acta 61(22):4799–4807
Walker RJ, Bermingham K, Liu J, Puchtel IS, Touboul M, Worsham EA (2015) In search of late-stage planetary building blocks. Chem Geol 411:125–142
Wollaston WH (1805) On the discovery of palladium; with observations on other substances found with platina. Philos Trans R Soc Lond 95:316–330

Poisson-Boltzmann Equation

Joan E. Curry
Department of Soil, Water and Environmental Science, University of Arizona, Tucson, AZ, USA

Definition

The Poisson-Boltzmann equation relates the electrostatic potential to the charge density as a function of spatial position in a system of charges. It has broad applicability and is particularly important for understanding the distribution of ions in geochemical systems.

Essential Concepts

The Poisson-Boltzmann equation forms the basis for a continuum understanding of strong electrolyte solutions, electrical double layers at charged surfaces, clay swelling, and colloidal stability, all of which are important topics in geochemistry. Practically it links the charge density and the electrostatic potential (and electric field through the derivative of the electrostatic potential) in a system of charged particles and may include solid surfaces. It is based on the well-known work by Gouy and Chapman, is further developed by Debye and Hückel, and is the electrostatic component of the DLVO (Debye, Landau, Verwey, and Overbeek) theory of colloidal stability, all being foundational work in colloid chemistry in the early twentieth century (see Verwey and Overbeek 1948). Poisson's equation, one of Maxwell's equations, relates the electrostatic potential as a function of position, ψ, to the charge density, ρ, as

$$\nabla^2\psi = -\frac{\rho}{\varepsilon\varepsilon_0}$$

In one dimension:

$$\frac{d^2\psi(x)}{dx^2} = -\frac{\rho(x)}{\varepsilon\varepsilon_o}$$

where the charge density is a sum of the contributions of all ionic species, $\rho(x) = \sum_i z_i e n_i(x)$, and n_i(x) is the concentration of ionic species i. Together with the Boltzmann expression, for each ionic species, $n_i(x) = n_{i\infty}e^{-z_i e\psi(x)/kT}$, we have the Poisson-Boltzmann equation

$$\frac{d^2\psi(x)}{dx^2} = -\frac{\sum_i z_i e n_{i\infty} e^{-z_i e\psi(x)/kT}}{\varepsilon\varepsilon_o}$$

where z_i is the valence of species i, e is the charge on an electron, k is the usual Boltzmann constant, and T is the absolute temperature in degrees Kelvin. $n_{i\infty}$ is the bulk concentration of ions of species i, ε is the dielectric constant of the medium, and ε_o is the usual permittivity of a vacuum.

The Poisson-Boltzmann equation is used in geoscience applications to describe the electrostatic potential and charge distribution around a charged particle in aqueous solution.

For a symmetrical 1:1 electrolyte such as NaCl,

$$\frac{d^2\psi(x)}{dx^2} = -\left[\frac{en_\infty e^{-e\psi(x)/kT} - en_\infty e^{e\psi(x)/kT}}{\varepsilon\varepsilon_o}\right]$$

And with $\varphi(x) = \frac{e\psi(x)}{kT}$, the equation can be rearranged as

$$\frac{d^2\varphi(x)}{dx^2} = \frac{2e^2 n_\infty}{\varepsilon\varepsilon_o kT}\sinh\varphi(x) = \kappa^2\sinh\varphi(x)$$

where κ^{-1} is the characteristic decay length of the charge distribution and is known as the Debye length where κ is given by

$$\kappa = \left(\frac{2n_\infty e^2}{\varepsilon\varepsilon_o kT}\right)^{1/2} \quad (\mathrm{m}^{-1})$$

This equation requires numerical solution, but in the limit of low potentials (<25 mV), truncation of the linearized exponential terms yields

$$\frac{d^2\varphi(x)}{dx^2} = \kappa^2\varphi(x)$$

which has an analytical solution and is the starting point for the Debye-Hückel solution theory (see entry ▶ "Debye-Hückel Equation" in this encyclopedia).

Applications

Considering a charged mineral surface in an aqueous solution, the concept of the electrical double layer has found great usefulness in describing the distribution of ions in solution around the charged particle. A diffuse cloud of ions enriched in the ionic species with the opposite charge from the surface charge forms around the surface. The cloud forms in response to the competing forces on the ions due to surface charge and the entropic tendency to dilute the high concentration of ions near the surface. The result is a diffuse cloud of ions and a nonzero electrostatic potential relative to the bulk solution in the region of the cloud. Overlap of the clouds on two like

charged particles in solution gives rise to a repulsive interaction and nonzero electrostatic potential at the midpoint between the surfaces which is related to the force opposing the approach of the surfaces. This has been measured experimentally for smooth mica surfaces in aqueous salt solutions (Israelachvili and Adams 1978).

The distance dependence of the force is related to the extent to which the double-layer cloud extends from the surface and depends on the ionic strength through the inverse Debye length (κ^{-1}). When two surfaces approach, solution of the Poisson-Boltzmann equation with appropriate boundary conditions predicts the magnitude of the repulsive force. Together with the van der Waals attraction, these two additive energies comprise the original DLVO theory of colloidal stability (see Israelachvili (2011) 3rd edition for further info). As can be seen by an examination of the expression for the inverse Debye length (κ^{-1}), low ionic strength expands the diffuse counterion cloud, and for the case of two clay sheets in aqueous solution in KNO_3 at 10^{-4}M, the repulsive force is measurable at 10s of nanometers. The ionic strength can be increased by increasing the salt concentration or by replacing monovalent with divalent ions. The repulsive force between clay particles in 10^{-4} M $CaCl_2$ solution appears at a shorter range allowing closer approach of the particles. This can be the difference between a swelling clay and a collapsed clay. In fact, ion exchange of a sodic-based soil with calcium can decrease swelling in clay materials. If the particles approach close enough for the van der Waals force to compete with the electrostatic repulsion, due to the overlap of the diffuse ionic clouds, it is possible that the overall force between the particles will be attractive and the particles will reversibly or irreversibly adhere (see Israelachvili (2011) 3rd edition for further info).

Summary

In summary, the Poisson-Boltzmann equation forms the starting point for understanding the behavior of charged particles in natural and engineered aqueous solutions. It is a cornerstone for the DLVO theory of colloidal stability which remains a central concept in geochemistry.

Cross-References

- ▶ Activity and Activity Coefficients
- ▶ Clay Minerals
- ▶ Colloids
- ▶ Debye-Hückel Equation
- ▶ Surface Geochemistry

References

Israelachvili JN (2011) Intermolecular and surface forces, 3rd edn. Academic, Burlington

Israelachvili JN, Adams GE (1978) Measurement of forces between two mica surfaces in aqueous electrolyte solutions in the range 0–100 nm. J Chem Soc Faraday Trans 1(74):975–1001

Verwey EJW, Overbeek JTHG (1948) Theory of the stability of lyophobic colloids. Elsevier, New York

Polonium

Monica Vasiliu and David A. Dixon
Department of Chemistry, University of Alabama, Tuscaloosa, AL, USA

Element Data
Atomic Symbol: Po.
Atomic Number: 84.
Atomic Weight: (209).
Isotopes and Abundances: traces of ^{210}Po, ^{211}Po, ^{216}Po, ^{218}Po.
1 Atm Melting Point: 527 K.
1 Atm Boiling Point: 1235 K.
Common Valences: +6, +4, +2, −2.
Ionic Radii: (+IV) 65, (−II) 230 ppm.
Pauling Electronegativity: 2.0.
First Ionization Potential: 8.41 eV.
Chondritic (CI) Abundance:
Silicate Earth Abundance:
Crustal Abundance: traces in uranium ores.
Seawater Abundance:
Core Abundance:

Properties

Polonium is a reactive, silvery-gray, extremely rare radioactive semimetal (Emsley 1991, 2001). It dissolves in dilute acids but is only slightly soluble in alkaline solutions. The solution formed by dissolving polonium in acids has a pink color, the color of the Po^{2+} ion, and it rapidly turns yellow as α-radiation forms oxidizing species in aqueous solution that convert Po^{2+} to Po^{4+}. Polonium has a relatively high vapor pressure for a solid element as about half of a sample of polonium will evaporate within 3 days. Polonium has chemical properties similar to selenium and tellurium. Most of the interest in Po is due to its radioactivity. The half-life of ^{209}Po, which does not occur naturally, is 105 y. The half-lives of

^{210}Po, ^{211}Po, ^{216}Po, and ^{218}Po are 138.4 d, 0.52 s, 0.15 s, and 3.11 m, respectively. Thus, the common isotope ^{210}Po is only found in trace amounts in uranium ore as it is a daughter product from the decay of ^{238}U.

History and Use

After Becquerel's discovery in 1898 of radiation from the uranium ore pitchblende (uranium oxide, U_3O_8), Marie and Pierre Curie studied pitchblende to determine the source of the radiation. They knew that uranium was one source of the radiation, but the amount of radiation could not come only from the uranium. After months of work of purifying tons of pitchblende, they isolated a new element, and Marie Curie named it polonium in honor of her homeland, Poland. Polonium is hundreds of times more radioactive than uranium. The existence of polonium had been predicted by Mendeleev in 1891 on the basis of his periodic table. He realized that there should be an element following bismuth that would resemble tellurium and predicted that it would have an atomic weight of 212.

Polonium is an α-emitter and is usually used as a thin film on a stainless steel for antistatic devices. Polonium was used in textile mills to eliminate static charges and in brushes to remove the accumulated dust in the manufacture of photographic plates. One gram of polonium reaches a temperature of 500 °C as a result of α-radiation emission and is used as a source of heat for space equipment. Polonium can be mixed or alloyed with beryllium to provide a source of neutrons which normally only access to a nuclear reactor can provide.

Geochemical Behavior

Polonium occurs rarely in nature in uranium ores and has so few uses that it is extracted from natural ores only for research purposes. All of the commercially produced polonium in the world is from Russia. About 100 g/year of polonium is produced by bombarding bismuth with neutrons in a nuclear reactor.

The radioactive disequilibrium between ^{210}Po and ^{210}Pb has been used as a chronometer to date glassy eruption flows in mid-ocean ridges, which are difficult to access (Rubin et al. 1994). The short half-life of ^{210}Po of 138.4 d means that it can only be used to determine if an event has occurred very recently. The use of this chronometer is based on the volatilization of Po in volcanic emissions above 400 °C likely as halides and its return to its equilibrium values. This method was used to determine when and for how long the ridge at 9° 50′ N on the East Pacific Rise erupted in the early 1990s.

Biological Utilization and Toxicity

Polonium has no biological role and is extremely dangerous because of its intense radioactivity (α-emitter) which overrides the toxicity concerns of tellurium, the noxious element just above polonium in the periodic table. Polonium is considered to be more than 10^{11} times more dangerous than hydrogen cyanide. ^{210}Po was used to assassinate Alexander Litvinenko, a Russian dissident residing in London in 2006.

^{210}Po has recently been found in the tobacco used in cigarettes and other products. ^{210}Po is soluble and circulates through the body to every tissue and cell and has been detected in the blood and urine of smokers. The circulating ^{210}Po causes genetic damage and early death from liver and bladder cancers, stomach ulcers, leukemia, cirrhosis of liver, and cardiovascular diseases.

Cross-References

- ▶ Elements: Metalloids
- ▶ Radioactivity
- ▶ Selenium
- ▶ Tellurium
- ▶ Uranium Decay Series

References

Emsley J (1991) The elements, 2nd edn. Clarendon Press, Oxford

Emsley J (2001) Nature's building blocks an A-Z guide to the elements. Oxford University Press, Oxford

Rubin KH, Macdougall JD, Perfit MR (1994) ^{210}Po-^{210}Pb dating of recent volcanic eruptions on the sea floor. Nature 368:841–844

Polyoxometalates and Other Metal-Oxo Clusters in Nature

May Nyman

Department of Chemistry, Oregon State University, Corvallis, OR, USA

Definition

Metal-oxo clusters are broadly defined as polynuclear species (meaning containing two or more metal cations) with ligands of H_2O, OH^-, and O^{2-} and are molecular. Molecular means they have a distinct chemical formula. In the laboratory, they are ideally synthesized in water in a discrete form (meaning all clusters present in the aqueous synthesis solution have the exact same formula and geometry). Solubility of these

clusters in water necessitates a negative or positive charge; and the metal-oxo clusters are isolated by crystallization with counterions of the opposite charge. *Polyoxometalates*, commonly known as POMs, are one subset of metal-oxo clusters. These are discrete polynuclear metal-oxo clusters specifically composed of the early d^0 transition metals in their highest oxidation state with no valence electrons. These POM-forming metal cations include V^{5+}, Nb^{5+}, Ta^{5+}, Mo^{6+}, and W^{6+}. POMs are negatively charged and possess predominantly O^{2-} ligands. All metal-oxo clusters represent an important intermediate form between monomers and infinite solid lattices or surfaces in both the laboratory and in nature: they can be considered as soluble pieces of metal oxide. However, there are few metals that can form and be isolated as discrete metal-oxo clusters as defined here, with only the simple ligands derived from water (H_2O, OH^-, and O^{2-}). This is why POMs are uniquely important – this is readily accomplished with POMs.

Synthesis and Structure of POMs in the Laboratory

The synthesis of POMs of tungsten, molybdenum, and vanadium has been known for a long time. The first crystallographic solid-state structure obtained of a POM was that of silicotungstic acid, $H_3[SiW_{12}O_{40}]$ by J. F. Keggin (1933), and this common structural motif has since been dubbed the Keggin ion (more below). V^{5+}, Mo^{6+}, and W^{6+} exist in water, respectively, as oxoanions, VO_4^{3-}, MoO_4^{2-}, and WO_4^{2-}; and when salts of these are dissolved in water, the self-buffering pH is highly alkaline. Acidification of these solutions results in POM self-assembly, and predominance diagrams (Baes and Mesmer 1976) inform us the stability fields in water are in the acidic range (generally below 4); and the most common structural/compositional types include decavanadate $[V_{10}O_{28}]^{6-}$, heptamolybdate $[Mo_7O_{24}]^{6-}$, and dodecatungstate $[W_{12}O_{42}]^{12-}$ (Fig. 1a–c). On the other hand, POMs of Nb^{5+} and Ta^{5+} are formed by dissolution of the metal oxide in a highly alkaline solution, and the hexametalate, $[M_6O_{19}]^{8-}$ (M = Nb, Ta), dominates these solutions (Fig. 1d). These POMs are called isopolyanions, when only the aforementioned metals compose the cluster. Also note, these clusters dominate in the simplest of aqueous solutions. Many other cluster types can be obtained by varying the supporting electrolytes, performing synthesis in alternative media (i.e., organic solvents) or conditions (i.e., hydrothermal), or adding a "heterometal" to form a heteropolyanion. Heteropolyanions are known for all of the POM-forming metals except Ta, and the Keggin ion and derivatives thereof are the most common structural motif. The Keggin ion has five different polymorphs known as rotational isomers (α, β, γ, δ, ε), and α, δ, and ε (Fig. 2) are the most stable and common across the metal-oxo clusters described here. All the Keggin ions consist of four sets of three mutually edge-sharing MO_6 octahedra (M = metal), for a total of 12 octahedra. The linkage of the trimers define the rotational isomers: in the α-isomer, the trimers are all corner linked, and in the ε-isomer, they are all edge-sharing. In the δ-isomer, three are edge-linked and the fourth is corner linked. For the POMs, the

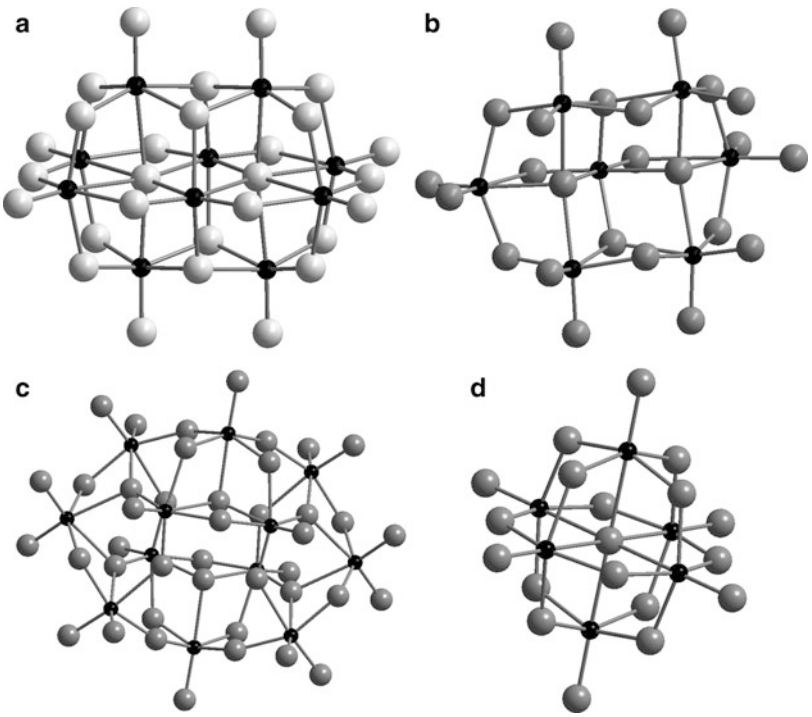

Polyoxometalates and Other Metal-Oxo Clusters in Nature, Fig. 1 Common isopolyanions of polyoxometalates that dominate speciation diagrams (Baes and Mesmer, 1976) (**a**) Vanadium: decavanadate, $[V_{10}O_{28}]^{6-}$. (**b**) Molybdenum: heptamolybdate, $[Mo_7O_{24}]^{6-}$. (**c**) Tungsten: dodecatungstate, $[W_{12}O_{42}]^{12-}$. (**d**) Hexametalate, $[M_6O_{19}]^{8-}$, M = Nb^{5+}, and Ta^{5+}. *Black spheres* are metals; *gray spheres* are oxygens

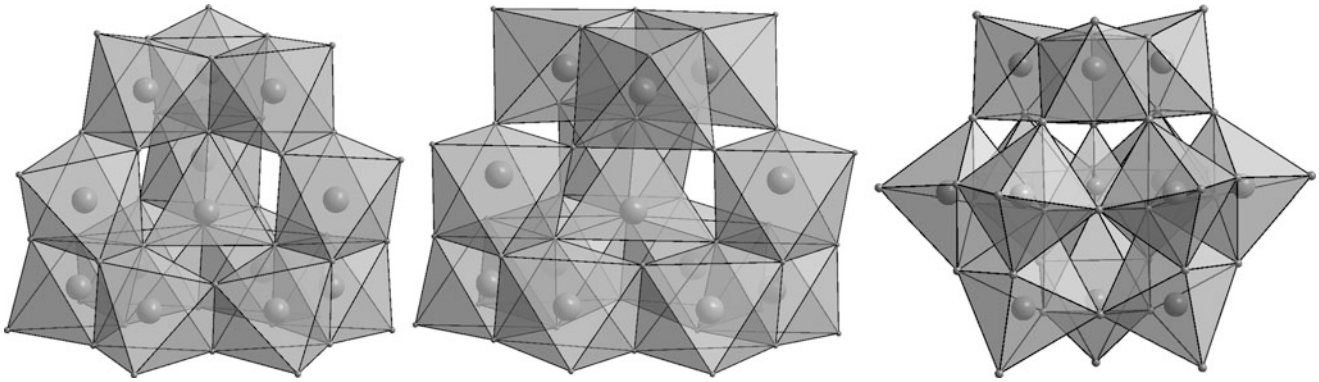

Polyoxometalates and Other Metal-Oxo Clusters in Nature, Fig. 2 The three most commonly observed Keggin ion polymorphs: ε *left*, δ *middle*, and α *right. Gray* polyhedra are MO_4 tetrahedra (one per Keggin ion in the center) and MO_6 octahedra (12 per Keggin ion); M = the various metal cations discussed in this article

α-isomer is by far the most readily obtained. However, electrochemical reduction can result in conversion to the other isomers that are stabilized by localization of a pair of electrons at the metals that bridge the shared edge of two trimers, forming a metal-metal bond.

The reason the POM-forming metals can be easily isolated without ligation is their position on the periodic table, inside the "metal-oxo wall" (Winkler and Gray 2012). These metals in their highest oxidation state in water always exist as an "*yl*" species, meaning they have a doubly bonded oxo ligand that is relatively inert to hydrolysis and condensation reactions that would ultimately result in precipitation of an infinite metal oxide lattice. The strong double bond is achieved by overlap of the empty d_{xz} and d_{yz} orbitals of the metal with the filled p_x and p_y orbitals of the oxo; and this tendency is lessened in metals with partially filled d-orbitals, such as the later transition metals (Fe, Co, etc.). This inert *yl*-oxo acts as a ligand on the surface of the cluster, protecting it from further reactivity that leads to precipitation of a metal oxide. Uranyl POMS have been discovered more recently (Burns et al. 2005; Nyman and Burns 2012; Qiu and Burns 2013), and these self-assemble from the (UO_2^{2+}) species, also due to the inert *yl*-oxos. However, these POMs always exhibit capsule geometries because there are two oxos in a transconfiguration: the oxo is a protective shell on both the outside and inside of the capsule.

Importance of Metal-Oxo Clusters in Metal Oxide Dissolution and Precipitation in Nature

The POM-forming metals are not abundant in nature; however, POMs are found in rare mineral forms, which are discussed below. Nonetheless, the discrete molecular nature that POMs can be isolated in the solid-state and redissolved makes them valuable experimental and theoretical models for understanding reactivity at a metal oxide surface. Important reactions in the hydrosphere and geosphere include dissolution and precipitation of mineral phases (including weathering and biomineralization), adsorption of ions onto metal oxide surfaces, and contaminant transport in the environment. Dissolution and precipitation of clusters is intimately tied to the $O^{2-}/OH^{-}/H_2O$ ligand exchange and interconversion between these ligands via protonation/deprotonation as a function of pH and total solution composition. Recent experimental and theoretical studies showed that ligand exchange reactivity of clusters has amphoteric behavior, similar to solubility of minerals (Rustad and Casey 2012). This means the exchange of the $O^{2-}/OH^{-}/H_2O$ ligand can take place by initial association of a hydronium or a hydroxide. These studies are only possible experimentally and computationally with well-defined molecular species such as POMs.

Metal-oxo clusters have been considered as important pre-nucleation clusters to common minerals including calcium carbonate and ferrihydrite. More broadly, precipitation of metal oxides has been proposed recently to proceed via aggregation of pre-nucleation clusters, rather than atom-by-atom growth (Banfield et al. 2000; Gebauer et al. 2008; Baumgartner et al. 2013; Gebauer et al. 2014). Calcium carbonate grows by first formation of very uniformly sized particles, which when observed by small-angle X-ray scattering can be considered nearly molecular (Bolze et al. 2002); and this is true even at very low concentrations.

Iron Oxides

Arrangements of polyhedra within metal oxide lattices that closely resemble POMs and other molecular clusters have provoked hypotheses that these clusters may serve as pre-nucleation clusters to metal oxide phases, and therefore attempted synthesis and isolation of these clusters have taken some priority among chemists and geochemists. For example, the long-known structure of magnetite features the

ε-polymorph of the Keggin ion, with Fe^{3+} occupying the tetrahedral lattice site and Fe^{2+} and Fe^{3+} occupying the octahedral lattice sites. More recently, a structural model for ferrihydrite was proposed from X-ray scattering data, revealing a δ-Keggin ion building block (Michel et al. 2007). This provoked more intense efforts to isolate a discrete iron-oxo Keggin ion cluster from water and was accomplished in 2015 (Sadeghi et al. 2015). In this very recent study, the authors showed that via removal of protecting ligands and counterions in water, ferrihydrite rapidly formed. While these studies suggested the possible importance of the Keggin ion molecular cluster in iron oxide mineral formation, there is still much to be understood. For instance, the ratio of octahedra to tetrahedra in the cluster is 12:1, while in the structural model of ferrihydrite, it is 4:1. Thus, rearrangement must occur for the conversion of the Keggin ion to ferrihydrite. Finally, in an even more recent study, it was suggested that no polynuclear species bigger than a dimer form prior to precipitation of ferrihydrite (Zhu et al. 2016). In summary the role of discrete molecular clusters in formation of ferrihydrite is not yet fully comprehended.

Aluminum Oxides

While iron is the third most abundant metal in the earth's crust, aluminum is the second most abundant. Unlike iron, discrete, molecular metal-oxo clusters of aluminum *can* be readily isolated; in particular the Keggin ion, ε-$[AlO_4Al_{12}(OH)_{24}(H_2O)_{12}]^{7+}$ (also referred to as Al_{13}), which is the same polymorph as the Keggin ion of magnetite. The ease of synthesizing and isolating Al_{13} lends to another reason geochemists have sought a synthetic analogue of the iron Keggin ion: Fe and Al are both trivalent with similar coordination geometries in minerals. On the other hand, Fe^{3+} is a much stronger Lewis and Bronsted acid than Al^{3+}, so hydrolysis reactions are difficult to control (pKa for Fe^{3+} and Al^{3+}, respectively, 2.19 and 4.97). Likewise, exchange of a water molecule bound to Fe^{3+} in a ligated cluster (Panasci et al. 2012) is ~3–5 orders of magnitude faster than that bound to Al^{3+} in a Keggin ion (Casey 2006). The mineral akdalaite (ICSD-28379), also the structural model for ferrihydrite, possesses the Al Keggin ion core. On the other hand, there has been considerable recent interest in another aluminum polycation that has been compared to the layered mineral brucite (Casey 2006). It is also a tridecamer and has 13 aluminum octahedra arranged in a plane, $[Al_{13}(OH)_{24}(H_2O)_6]^{15+}$, and is referred to as "flat Al_{13}" (Wang et al. 2011; Mensinger et al. 2012). Determining the relevance of this cluster as a pre-nucleation species in nature remains a challenge for the future. The Al_{13} Keggin cluster, however, has been identified in acidic mine drainage (Furrer et al. 2002), consistent with predominance diagrams showing the Al_{13} species dominate at pH 3–4 (Casey 2006).

Polyoxometalates and Other Clusters Found in Nature

Some metal-oxo clusters that can be synthesized in the lab are found in minerals formed in geological hydrothermal conditions. Numerous minerals containing decavanadate have been found and structurally characterized from the Uravan (uranium, vanadium) deposits in Colorado and Utah (Kampf et al. 2014a). This includes fully oxidized V^{5+} and mixed V^{4+}/V^{5+}. Countercations are predominantly common alkalis and alkaline earths, including magnesium, calcium, sodium, and potassium and also aluminum. Minerals featuring a dodecaniobate POM, $[Nb_{12}O_{42}]^{24-}$, have been found in São Paulo, Brazil, and Norway, respectively, named menezesite and aspedamite (Atencio et al. 2008; Cooper et al. 2012). Also found in Norway is the mineral peterandresenite that contains the common hexaniobate, $[Nb_6O_{19}]^{8-}$ (Friis et al. 2014). The dodecaniobate $[Nb_{12}O_{42}]^{24-}$ has never been synthesized in the laboratory, but the analogous $[M_{12}O_{42}]^{12-}$ (M = Mo, W) is readily made by oxidative dissolution of first-row transition metals in tungstic acid solution (Gunter et al. 1990). This structure type (Fig. 3) features unusual face-sharing octahedra of W or Nb. The cluster features six dimers of face-sharing octahedra, and the dimers are corner linked and create a central cavity with twelve oxo-binding sites. This cavity is occupied by Ba^{2+} in menezesite and Th^{4+} in aspedamite. Aspedamite has six additional Nb octahedra decorating the cluster by corner-sharing, and its 12 octahedral sites are occupied by nine Nb^{5+}, one Ti^{4+}, and two Fe^{3+}. Counterions are mainly

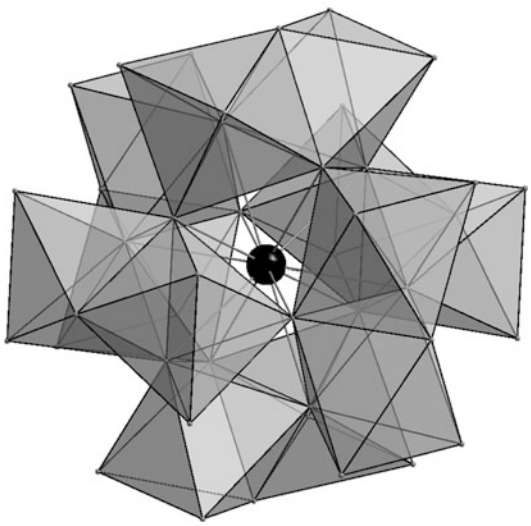

Polyoxometalates and Other Metal-Oxo Clusters in Nature, Fig. 3 Structure of $A[M_{12}O_{42}]$; synthesized in the laboratory with M = W, found in the mineral menezesite and aspedamite with M = Nb or Nb/Fe, respectively. *Gray* octahedra are the W/Nb/Fe MO_6; *black sphere* is a metal cation (i.e., Ba, Th, Mg, etc.) in the 12-coordinate cavity site

iron in aspedamite and mixed alkaline earth and Ti/Zr in menezesite. In the mineral ophirite(Kampf et al. 2014b), lacunary trivacant B-α-$[FeW_9O_{34}]^{9-}$ clusters sandwich a tetrad of Zn/Mn octahedra, a structural motif readily synthesized in the laboratory (Fe^{3+} occupies the central tetrahedral site) (Limanski et al. 2002). Lacunary POMs are defined as POMs with missing octahedra: from the tungstate Keggin ion, one, two, or three octahedra can be removed (via pH increase) to form these species, and they are commonly stabilized by binding other metals in the vacancies. In this sense, lacunary clusters behave as inorganic ligands to metal cations or small metal-oxo clusters.

Other metal-oxo clusters are represented in mineralogy, outside of POMs. In the rare mineral zunyite (Barclay-Kamb 1960), the Al_{13} Keggin ion is found, but it is the α-isomer with O^{2-} ligands instead of the common ε or δ isomers that are synthesized in the lab with H_2O and OH^- ligands, and the high negative charge $[Al_{13}O_{40}]^{41-}$ is counterbalanced by Si^{4+} cations that link the clusters into a three-dimensional network. Notably, the Al_{13} α-isomer has never been formed in the laboratory. Another cluster not prior observed in the laboratory is bouazzerite from Morocco, an Fe-Bi-arsenate polyanion (Brugger et al. 2007). Given that many of these cluster-containing minerals have been discovered and structurally characterized very recently, we anticipate additional discoveries in the future.

Conditions under which these minerals form in geological settings are vastly different than that in the laboratory. As an example, aspedamite forms in a granitic pegmatite, meaning saline, 400–700 °C, 3–4 kilobars of pressure, and a time scale up to millions of years (Cooper et al. 2012). pH of the geochemical fluids is most likely slightly alkaline. In comparison, in the laboratory, temperatures rarely exceed 200 °C, and pressure ranges from atmospheric pressure to the autogenous pressure of water (a few bars). Synthesis/crystallization times range from a few hours to several months, and the pH can be varied from highly acidic to highly basic. The instances in which clusters that grow in geological settings cannot be obtained under standard laboratory conditions (i.e., the α-Al_{13} Keggin ion) point toward these synthons as a challenge for the future for synthetic chemists.

Summary

Discrete, molecular metal-oxo cluster that can be synthesized in the lab or exist in nature have commonalities and differences. Both clusters in geochemistry and in synthesis are active fields of research. Therefore, the commonalities are becoming more abundant as new minerals, synthons, or reaction pathways are discovered. Rare minerals containing V, Nb, Ta, Mo, or W contain building block forms that resemble the polyoxometalates (POMs), which are readily synthesized and isolated in the laboratory. However, some differences are noted, due to the vast differences in geological time and settings compared to typical laboratory conditions. For example, the face-sharing Nb-polyhedron is a structural motif found in mineral forms but has not yet been synthesized in the lab. More common to geochemistry is clusters of earth-abundant aluminum and iron. Iron clusters that are recognized as building blocks in ferrihydrite have only been synthesized recently from water. However, unlike the POMs, these cannot exist with supporting ligands. Aluminum clusters are easily made in the laboratory in aqueous conditions and do not require supporting ligands. They generally do not exist in nature, as the acidic aqueous conditions in which they form are not common in the natural environment.

References

Atencio D, Coutinho JMV, Doriguetto AC, Mascarenhas YP, Ellena J, Ferrari VC (2008) Menezesite, the first natural heteropolyniobate, from Cajati, Sao Paulo, Brazil: description and crystal structure. Am Mineral 93:81–87

Baes CF, Mesmer RE (1976) The hydrolysis of cations. Wiley, New York

Banfield JF, Welch SA, Zhang HZ, Ebert TT, Penn RL (2000) Aggregation-based crystal growth and microstructure development in natural iron oxyhydroxide biomineralization products. Science 289:751–754

Barclay-Kamb W (1960) The crystal structure of zunyite. Acta Crystallogr 13:15–24

Baumgartner J, Dey A, Bomans PHH, Le Coadou C, Fratzl P, Sommerdijk NAJM, Faivre D (2013) Nucleation and growth of magnetite from solution. Nat Mater 12:310–314

Bolze J, Peng B, Dingenouts N, Panine P, Narayanan T, Ballauff M (2002) Formation and growth of amorphous colloidal $CaCO_3$ precursor particles as detected by time-resolved SAXS. Langmuir 18:8364–8369

Brugger J, Meisser N, Krivovichev S, Armbruster T, Favreau G (2007) Mineralogy and crystal structure of bouazzerite from Bou Azzer, Anti-Atlas, Morocco: Bi-As-Fe nanoclusters containing Fe^{3+} in trigonal prismatic coordination. Am Mineral 92:1630–1639

Burns PC, Kubatko KA, Sigmon G, Fryer BJ, Gagnon JE, Antonio MR, Soderholm L (2005) Actinyl peroxide nanospheres. Angew Chem Int Ed 44:2135–2139

Casey WH (2006) Large aqueous aluminum hydroxide molecules. Chem Rev 106:1–16

Cooper MA, Abdu YA, Ball NA, Cerny P, Hawthorne FC, Kristiansen R (2012) Aspedamite, ideally (12)(Fe^{3+}, Fe^{2+})(3)Nb4[Th(Nb, Fe^{3+}) 12O42]{(H_2O),(OH)}12, A new heteropolyniobate mineral species from the Herrebokasa Quarry, Aspedammen, Ostfold, Southern Norway: description and crystal structure. Can Mineral 50:793–804

Friis H, Larsen AO, Kampf AR, Evans RJ, Selbekk RS, Sanchez AA, Kihle J (2014) Peterandresenite, $Mn_4Nb_6O_{19}$•$14H_2O$, a new mineral containing the Lindqvist ion from a syenite pegmatite of the Larvik Plutonic Complex, southern Norway. Eur J Mineral 26:567–576

Furrer G, Phillips BL, Ulrich KU, Pothig R, Casey WH (2002) The origin of aluminum flocs in polluted streams. Science 297:2245–2247

Gebauer D, Volkel A, Colfen H (2008) Stable prenucleation calcium carbonate clusters. Science 322:1819–1822

Gebauer D, Kellermeier M, Gale JD, Bergstrom L, Colfen H (2014) Pre-nucleation clusters as solute precursors in crystallisation. Chem Soc Rev 43:2348–2371

Gunter JR, Schmalle HW, Dubler E (1990) Crystal-structure and properties of a new magnesium heteropoly-tungstate, $Mg_7(Mgw_{12}O_{42})$

$(OH)_4(H_2O)_8$, and the isostructural compounds of manganese, iron, cobalt and nickel. Solid State Ionics 43:85–92
Kampf AR, Hughes JM, Marty J, Nash BP, Chen YS, Steele IM (2014a) Bluestreakite, $K_4Mg_2(V^{4+}{}_2V^{5+}{}_8O_{28}) \cdot 14H_2O$, A new mixed-valence decavanadate mineral from the Blue Streak Mine, Montrose County, CO: crystal structure and descriptive mineralogy. Can Mineral 52:1007–1018
Kampf AR, Hughes JM, Nash BP, Wright SE, Rossman GR, Marty J (2014b) Ophirite, $Ca_2Mg_4[Zn_2Mn_2{}^{3+}(H_2O)_2(Fe^{3+}W_9O_{34})_2]\bullet 46H_2O$, a new mineral with a heteropolytungstate tri-lacunary Keggin anion. Am Mineral 99:1045–1051
Keggin JF (1933) Structure of the molecule of 12-phosphotungstic acid. Nature 131:908–909
Limanski EM, Piepenbrink M, Droste E, Burgemeister K, Krebs B (2002) Syntheses and X-ray characterization of novel $[M_4(H_2O)_2(XW_9O_{34})_2]^{n-}$ (M = Cu^{II}, X = Cu^{II}; and M = Fe^{III}, X = Fe^{III}) polyoxotungstates. J Clust Sci 13:369–379
Mensinger ZL, Wang W, Keszler DA, Johnson DW (2012) Oligomeric group 13 hydroxide compounds-a rare but varied class of molecules. Chem Soc Rev 41:1019–1030
Michel FM, Ehm L, Antao SM, Lee PL, Chupas PJ, Liu G, Strongin DR, Schoonen MAA, Phillips BL, Parise JB (2007) The structure of ferrihydrite, a nanocrystalline material. Science 316:1726–1729
Nyman M, Burns PC (2012) A comprehensive comparison of transition-metal and actinyl polyoxometalates. Chem Soc Rev 41:7354–7367
Panasci AF, Ohlin CA, Harley SJ, Casey WH (2012) Rates of water exchange on the $[Fe\text{-}_4(OH)_2(hpdta)_2(H_2O)_4]$ molecule and its implications for geochemistry. Inorg Chem 51:6731–6738
Qiu J, Burns PC (2013) Clusters of actinides with oxide, peroxide, or hydroxide bridges. Chem Rev 113:1097–1120
Rustad JR, Casey WH (2012) Metastable structures and isotope exchange reactions in polyoxometalate ions provide a molecular view of oxide dissolution. Nat Mater 11:223–226
Sadeghi O, Zakharov LN, Nyman M (2015) Aqueous formation and manipulation of the iron-oxo Keggin ion. Science 347:1359–1362
Wang W, Wentz KM, Hayes SE, Johnson DW, Keszler DA (2011) Synthesis of the hydroxide cluster $[Al_{13}(\mu_3\text{-}OH_6)(\mu\text{-}OH)_{18}(H_2O)_{24}]^{15+}$ from an aqueous solution. Inorg Chem 50:4683–4685
Winkler JR, Gray HB (2012) Electronic structures of oxo-metal ions. Struct Bond 142:17–28
Zhu M, Frandsen C, Wallace AF, Legg B, Khalid S, Zhang H, Morup S, Banfield JF, Waychunas GA (2016) Precipitation pathways for ferrihydrite formation in acidic solutions. Geochim Cosmochim Acta 172:247–264

Porphyrins

J. William Louda
Department of Chemistry and Biochemistry and the Environmental Sciences Program, Florida Atlantic University, Boca Raton, FL, USA

Definition

Porphyrins are heterocyclic macrocycle organic molecules. These tetrapyrroles occur with (chlorophylls and bacteriochlorophylls) or without (hemes, cytochromes) the fifth so-called isocyclic (aka exocyclic or 13, 14-cycloethano) ring.

Introduction

Porphyrins are ubiquitous in all life forms. Figure 1 has the structures of the chlorophylls and protoheme as examples of these two main macrocyclic tetrapyrrole nuclei. While performing their function in cells, the vast majority of porphyrins contain a central chelated metal, magnesium or iron in the cases of the chlorophylls and the hemes, respectively. It is these biological dihydroporphyrins and porphyrins that form the precursors to a huge variety of geoporphyrins, also called "petroporphyrins" (Corwin 1960), for their occurrence in rocks, shales, and sediments.

Geoporphyrin Precursors: Biological Pigments

There is a large number of chlorophylls, bacteriochlorophylls, and hemes (Fig. 1) that can serve as precursors to the geoporphyrins. A chapter by Hugo Scheer (2006) has a complete listing of these biotic pigments and several variations not depicted here.

Chlorophyll-a (CHLa Fig. 1) is distributed throughout all eukaryotic oxygenic photosynthetic organisms as well as the prokaryotic cyanobacteria. Chlorophyll-b (CHL-b) accompanies CHLa in green algae (chlorophytes) and higher plants. The chlorophylls-c (CHL-c: $\text{-}c_1/\text{-}c_2/\text{-}c_3$) accompanying CHLa are characteristic pigments in diatoms, dinoflagellates and a few other taxa (see Jeffrey et al. 2011; Scheer 2006). The bacteriochlorophylls (BCHLs) are present in the anoxygenic photosynthetic bacteria. BCHL-a and -b are characteristic of purple sulfur bacteria are tetrahydro (7,8 and 17,18) porphyrins and differ only by substitution on carbon #8, having an ethyl or vinyl respectively (Fig. 1). The BCHLs-c, -d, -e, and -g are in the green sulfur bacteria. One can easily imagine a wide C-number range of geoporphyrins arising from the BCHLs-c through -e, even without invoking alkylation reactions during diagenesis.

Geoporphyrins

The concept of "biological markers" or "chemical fossils" in the field of organic geochemistry is a direct outgrowth of Professor Alfred Treibs linkage of the structure of deoxophylloerythroetioporphyrin (DPEP), which was isolated from bitumen in shales and sediments, as well as a broad spectrum of petroleum samples, to the nucleus of CHL-a (Treibs 1936). Numerous references are covered elsewhere (Baker and Louda 1986, 2002; Callot 1991; Keely et al. 1990). The present treatise follows the contribution "Porphyrins" by Chris Boreham in the previous edition (Boreham 1999) of the Encyclopedia of Geochemistry. Space limitation here precludes large reference citations.

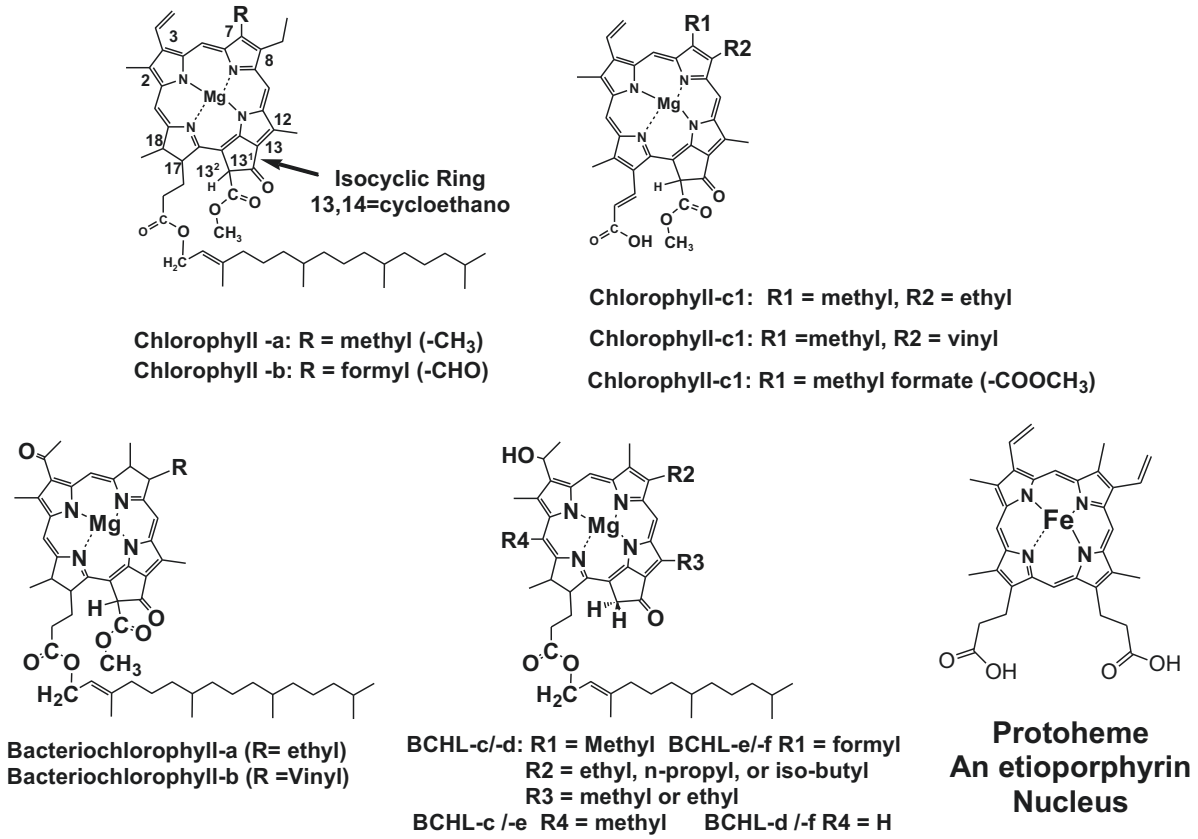

Porphyrins, Fig. 1 Structures of chlorophylls, bacteriochlorophylls, and protoheme

The most widely known types or nuclei of geoporphyrins are the DPEP and etioporphyrin (ETIO) series which differ by the presence or absence of the isocyclic ring (ring-V: Fig. 1) inherited from the chlorophylls. Carbon numbering of any peripheral substituents is shown in Fig. 1. The ETIO series is 2 amu (m/z) heavier than the corresponding DPEP series at each carbon number due to the lack of isocyclic ring. DPEP is a 32 carbon compound (C32-DPEP, 476 m/z). "Routine" analysis of geoporphyrins often involves determination of the molecular weight (carbon number) of each series present (Baker et al. 1967). As opposed to regular high voltage electron impact (70 eV) mass spectrometry (EI-MS), which gives small molecular ions and a plethora of overlapping methyl (M-15) and other fragmentation peaks. Low-voltage (e.g., 12–14 eV) EI-MS (Baker and Louda 1986) and many newer techniques have yielded a preponderance of molecular ions. For example, electrospray ionization (ESI-MS: Ramos et al. 2016), positive-ion electrospray ionization Fourier Transform Ion-Cyclotron Resonance MS (ESI-FT-ICR-MS: Liu et al. 2015), and HPLC-Orbitrap high resolution MS (Woltering et al. 2016) are just a few of the more advanced techniques used these days.

Geoporphyrin/Petroporphyrin Varieties

Geologic porphyrins and metalloporphyrins are known to exist with a wide variety of nuclei and exocyclic modifications (Fig. 2), derived from the interplay of specific biological precursors and postdepositional diagenetic/catagenetic modifications. Each series can be related to the ETIO-series (C32-E = 476 m/z) by hydrogen deficiencies due to exocyclic cyclizations, hydrogenations, and/or dehydrogenations. Thus, the DPEP series (C32 DPEP = 478 m/z) is E-2, resulting from the cycloethano group (aka isocyclic ring). The DPEP type porphyrins also fall into a larger group called the cycloalkanoporphyrins or CAPs. As true DPEP has a five membered exocyclic ring, consisting of a 13^2–15 cycloethano moiety, it becomes a CAP5. Beyond mass spectral typing of geoporphyrin distributions, the HPLC separation of individual porphyrins and their structural identification (e.g., NMR) then takes geoporphyrin analysis to be taken to the next level, allowing for a better understanding of the pigments present and an improvement on the estimation of their putative precursors (chlorophylls, bacteriochlorophylls, hemes, etc.).

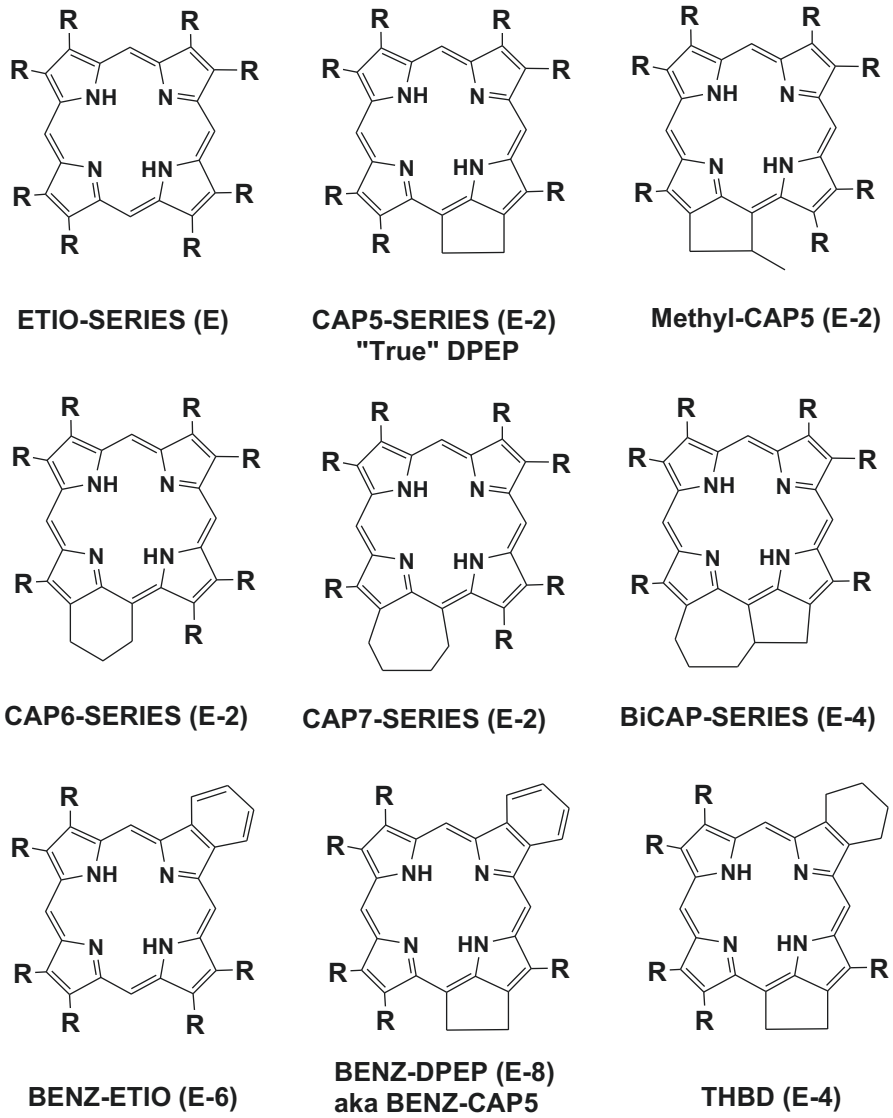

Porphyrins, Fig. 2 *ETIO* etioporphyrin, *CAP* CycloAlkanoPorphyrin, *DPEP* deoxophyllo-erythroetioporphyrin, *Bi-CAP* Bi-CycloAlkanoPorphyrin, *Benz* benzene-like, *THBD* TetraHydroBenz-DPEP. Numbers modifying a CAP series refer to the numbers of carbon atoms forming the exocyclic ring structures. Parentheses refer to mass spectral differences, in nominal amu (m/z), relative to the ETIO-series

Only the DPEP (CAP-5) and certain ETIO-series geoporphyrins are believed to derive directly from their putative precursors, namely chlorophylls or hemes, respectively. ETIO-series porphyrins "may" also arise from the opening of the isocyclic ring (ring-V) of the DPEP series. The remaining geoporphyrin nuclei arise through diagenetic alterations including cyclizations, aromatizations and alkylation/dealkylation reactions. For example, the CAP-6 series having a cyclopropane (6-membered) ring can easily derive from reactions similar or identical to the mesorhodin reaction of mesoporphyrin-IX (see Fischer and Orth 1937 as detailed in Baker and Louda 2002). The benzoporphyrins (BENZ-ETIO and BENZ-DPEP; aka BENZ-CAP5) have been suggested as arising by a variety of possible reactions (see summary in Baker and Louda 2002). The CAP7 and BiCAP series likely derive from the cyclopheophorbide reactions detailed later herein.

Metallo-Geoporphyrins

Biological precursors to the geoporphyrins are mainly the Mg^{2+} and Fe^{2+}/Fe^{3+} chelates, the chlorophylls, and hemes, respectively. Fe^{3+} hemes also have an axial ligand such as Cl^{-}.

Sedimentary and petroleum geoporphyrins contain V^{4+}, as vanadyl (VO^{2+}), Ni^{2+} and to a lesser extent Cu^{2+} (Baker and Louda 1986, 2002; Callot 1991; Keely 2006). Coal (ETIO) porphyrins contain Fe^{3+}, Ga^{3+}, and Mn^{3+} (Bonnett and Czechowski 1981; Filby and Branthaver 1987). In general, Ni-PHs arise in the bitumen (solvent extractable portion) and VO-PHs within kerogen/sulfur complexes of the bulk organic matter (aka kerogen). The analyses of marine sediments provided by the Deep Sea Drilling Project (DSDP: Baker and Louda 1986, 2002) detailed the defunctionalization of phorbides, their aromatization to free base porphyrins and

the chelation of Ni^{2+}, as well as the "release" of VO-PHs with increasing thermal stress over time. Copper, highly dealkylated etioporphyrins porphyrins (Cu-PHs) have been reported in deep sea sediments (Baker and Palmer 1978; Baker and Louda 1984, 1986; Premovic et al. 2000) and are surmised to be redeposited terrestrial (coal) porphyrins, which underwent metal replacement by copper in acidic oxygenated river water.

Precursor-Product Considerations: Diagenesis and the ETIO Dilemma

The premier precursor-product alteration (diagenesis) scheme is the Treibs' hypothesis (Treibs 1936) wherein CHLa is processed into DPEP through a series of defunctionalizations (demetallation, ester hydrolysis, decarbomethoxylation, vinyl reduction, aromatization, and ketone loss).

Figure 3 is a representation of some of the known pathways of CHLa senescence/death alteration and organic diagenesis. The main (Treibs' Scheme) route flows down the center of this figure and involves the sequential defunctionalization and aromatization to yield C32 DPEP. The alteration of CHLa to pyropheophorbide-a (pPBIDa) occurs both during cellular senescence/death (Louda et al. 1998, 2002, 2011) and heterotrophic (e.g., zooplankton) grazing (Bianchi et al. 1998). Cyclization of pPBIDa yields cyclopheophorbide-a (CYCLO) which, through a series of oxidations (giving hydroxychlorophyllone, chlorophyllone) and ring-V opening (chlorophyllonic acid, chlorophyllactone: see Watanabe et al. 1993 and Baker and Louda 2002), yields a C33 BiCAP or CAP7 (see Fig. 3), respectively. CYCLO has been identified from deep sea sediments Baker and Louda 1986, 2002) and contemporaneous anoxic marls (Louda et al. 2000). Oxidative scission of the isocyclic ring (Ring-V) yields a few purpurins (-7, -18) and chlorins (-e4, -e6, -p6) (Baker and Louda 1986, 2002; Louda et al. 2011). As shown in Fig. 3, the transformation of CHLa to purpurin-18 and then chlorin-p6, via decarboxylation and aromatization, yields a C30 open-β etioporphyrin. All steps shown have been observed in the natural sediments and the microalgal incubation studies given above, except for the identification of C33BiCAP and C30 ETIO as those sequences were not "mature" enough.

All alternate Chlorophylls (CHLb, CHLs-c1/-c2/-c3, CHLd, and the BCHLs) can easily be envisioned and potentially shown to follow these or closely related routes, especially the route to DPEP (CAP5), with but a few minor adjustments. For example, reduction or removal of the 8-formyl moiety in CHLb, no need for aromatization step with the CHLs-c, and various hydroxyl, ketone and/or acetyl losses in the BCHLs. The BCHLs–c/–d would give a DPEP series with a C32 to C36 distribution due to their extended alkylation patterns.

Hendry et al. (1987) described the biological alterations of chlorophylls as being of two types. Type-I involves reactions that retain the pigment nature with a macrocyclic tetrapyrrole nucleus. Type-II reactions are those that destroy the pigment character and lead to open tetrapyrroles (bilins) and/or smaller remnants. Type-II reactions include those described by Matile et al. 1996) yielding the 19-formyl-1-oxo-bilanes and more fully degraded products. Type-I reactions have been divided (Baker and Louda 2002) into Types-IA and -IB for those that either (IA) retain the nucleus of the biological precursor (DPEP from chlorophyll and ETIO from hemes or (IB) have the isocyclic ring of the chlorophyll nucleus cleaved to ETIO precursor pigments (e.g., Puruprin-18) and/or novel exocyclic rings added, such as with the CAP6, CAP7, and, through cyclopheophorbide-a, BiCAP series (see Fig. 3).

Geoporphyrins as Diagenetic/Catagenetic (Organic Maturation) Indicators

Except for coals, which contain a vast predominance of ETIO-series porphyrins, petroleum and their source rocks are found to contain both Ni and VO porphyrins as a mixture of DPEP and ETIO series, with DPEP dominating in "immature" (Baker and Louda 1986, 2002; Callot 1991; Keely et al. 1990; Ocampo et al. 1992 and others) samples.

The ETIO Dilemma: Is D Converted to E, is D Destroyed faster than E, or do both Occur?

The potential of a DPEP-to-ETIO crossover during organic maturation was popularized by the work of Didyk and others (Didyk et al. 1975). The DPEP-to-ETIO ratio has been used for decades as an indicator of thermal maturity, as modified by source input in certain cases (e.g., In Baker and Louda 1986, 2002; Callot 1991). A study of the con-familial petroleum crudes from the Big Horn Basin revealed a remarkable linear relationship ($r^2 = 0.9997$) between percent DPEP and vanadyl porphyrin (VO-PH) yields (Baker et al. 1987). This relationship argues strongly for a faster destruction of DPEP than the ETIO series porphyrins without a need for a D-to-E crossover by the thermocatalytic opening of the isocyclic ring. As maturity increases, higher carbon number porphyrins, mainly of the DPEP series, were observed to be released until dealkylation of the bitumen containing VO-PHs occurred with a concurrent lowering of the D-to-E ratio (aka %D).

Certain ETIO series precursors deriving from the chlorophylls were discussed above (Fig. 3 and text). As mentioned earlier, the putative or accepted ETIO series precursors are the hemes (see Fig. 1). However, many potential ETIO series porphyrins can indeed be derived from chlorophyll nuclei during senescence/death and early diagenetic processes. For

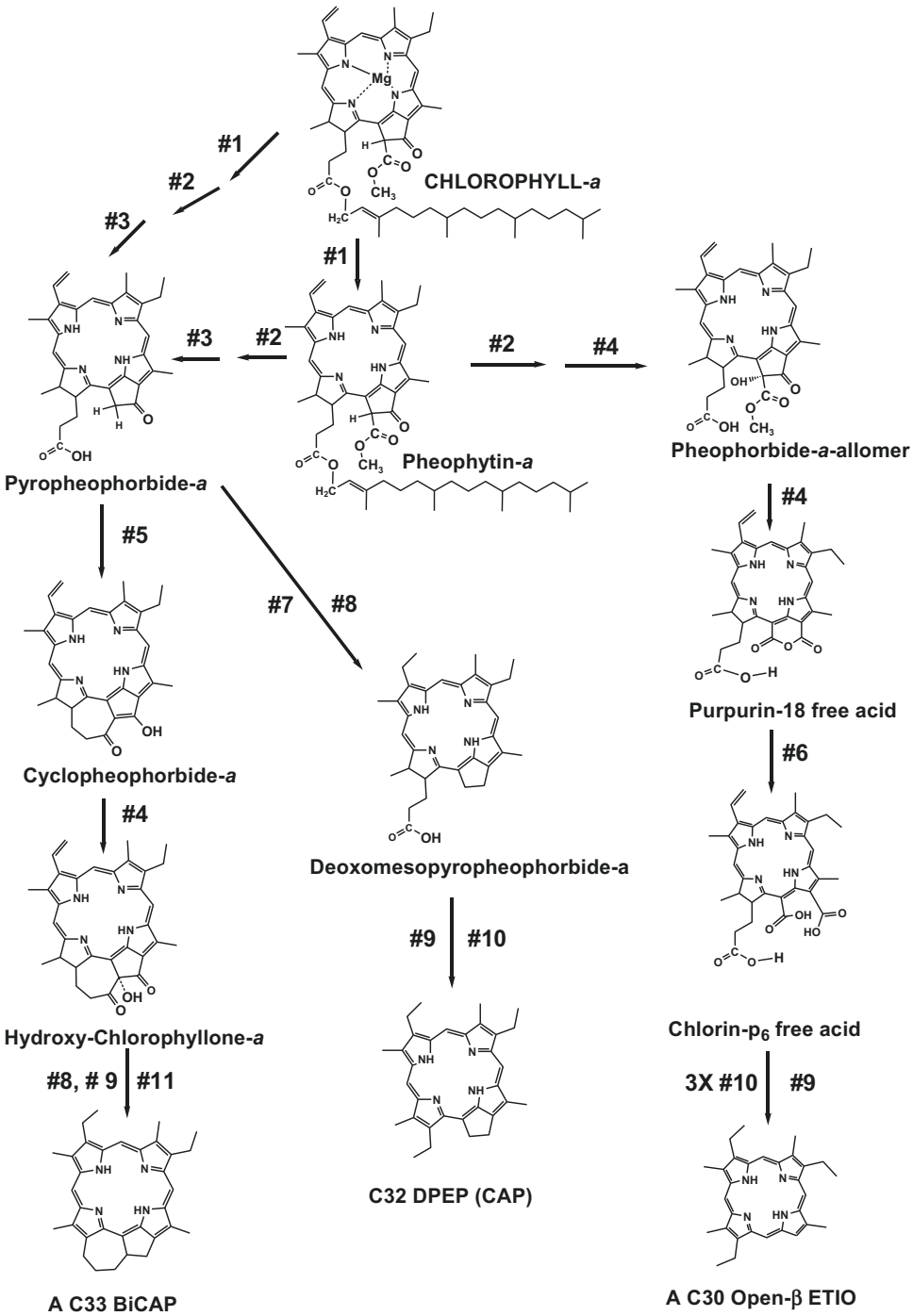

Porphyrins, Fig. 3 Biological-geological alteration of Chlorophyll-a. *Reactions involved* are: #1 (magnesium loss: -Mg^{2+}, +2 H^{+}), #2 (phytol loss: hydrolysis), #3 (decarbomethoxylation; hydrolysis of methyl formate moiety), #4 (oxidation), #5 (cyclization via dehydration), #6 (hydrolytic ring opening), #7 (reduction of vinyl to ethyl), #8 (ketone loss: reduction to alcohol→ dehydration→ reduction of 13^1–13^2 double bond {speculative?}), #9 (aromatization: 17,18-didehydrogenation), #10 (decarboxylation: -CO_2), #11 ("dehydration-reduction": loss of –OH)

example, following a 5.5 year incubation of the diatom *Navicula* sp., kept under dark, and anoxic and room temperature (25 °C) conditions, it was found that purpurin-18 aromatized to purpuroporphyin, in addition to the generation of chlorin-p_6 (Louda et al. 2011). Both of these pigments are theoretical direct precursors to a C30 beta-free etioporphyrin. Other oxidative ring opening reactions lead to many different chlorins, such as chlorin-e6 which is a potential precursor to a C31 etioporphyrin.

Still the question of whether or not geologic DPEP series porphyrins are converted to ETIO series by the thermal/thermocatalytic scission of the isocyclic ring remains for the future to answer.

Dealkylation of the geologic metalloporphyrins occurs during late diagenesis/catagenesis. In vitro dealkylation of ETIO-I at 450 °C was shown by Yen et al. (1969). Hydrous pyrolysis experiments at 350 °C for 48 h performed on an upper Miocene olive-gray claystone revealed both the release

of VO-PHs and the dealkylation of Ni- and VO-PHs (Baker and Louda 2002).

The change in dominance of DPEP to ETIO series and the lowering of the mean carbon number and range preceding the total demise of geoporphyrin in highly thermally mature sediments, shales, and bitumen (oil) signals the final stage of geoporphyrin maturation.

Summary

Porphyrins, in a geochemical context, are the products of the diagenesis and catagenesis of structures derived from their biological precursors, the chlorophylls, and hemes. These precursor compounds can and do undergo much alteration during the senescence/death of and predation on source biota. Geochemical maturation of the metallo-geoporphyrins (aka Ni and VO petroporophyrins) leads to both a DPEP (CAP)- to ETIO-series dominance change plus dealkylation reactions which lowers the average molecular weight and carbon number range. Geoporphyrins are useful in assessing the thermal maturity of samples and, in certain cases, source biota. When considering the history and origins of organic geochemistry, the porphyrins are clearly the premier biomarkers.

Cross-References

- ▶ Biogeochemistry
- ▶ Biomarker: Assessment of Thermal Maturity
- ▶ Biomarkers: Coal
- ▶ Biomarkers: Petroleum
- ▶ Chelation
- ▶ Copper
- ▶ Diagenesis
- ▶ High-Resolution Mass Spectrometry
- ▶ Kerogen
- ▶ Marine Sediment
- ▶ Nickel
- ▶ Oil Seeps and Coastal Bitumen
- ▶ Oil Shale
- ▶ Petroleum
- ▶ Vanadium

References

Baker EW, Louda JW (1984) Highly dealkylated copper- and nickel-etioporphyrins in marine sediments. Org Geochem 6:183–192

Baker EW, Louda JW (1986) Porphyrins in the geologic record. In: Johns RB (eds) Biological markers in the sedimentary record. Methods in geochemistry and geophysics, vol. 24. Elsevier, Amsterdam, pp 125–225

Baker EW, Louda JW (2002) The legacy of the Treibs' samples. In: Prashnowsky A (ed) Alfred Treibs memorial volume. Halbig-Druck, Wurzburg, pp 3–128

Baker EW, Palmer SE (1978) Geochemistry of porphyrins. In: Dolphin D (ed) The porphyrins, vol I. Academic, New York, pp 486–552

Baker EW, Yen TF, Dickie JP, Rhode RE, Clark LF (1967) Mass spectrometry of porphyrins-II. Characterization of petroporphyrins. J Am Chem Soc 89:3631–3639

Baker EW, Louda JW, Orr WH (1987) Application of metalloporphyrin biomarkers as petroleum maturity indicators; the importance of quantitation. Org Geochem 11:303–309

Bianchi TS, Bauer JE, Druffel ERM, Lambert CD (1998) Pyropheophorbide-*a* as a tracer of suspended particulate organic matter from the NE Pacific continental margin. Deep-Sea Res-II 45:715–731

Bonnett R, Czechowski F (1981) Metals and metal complexes in coal. Philos Trans Roy Soc Lond A300:51–63

Boreham C (1999) Porphyrins. In: Marshall CP, Fairbridge RW (eds) Encyclopedia of geochemistry. Kluwer, Dordrecht, pp 519–522

Callot HJ (1991) Geochemistry of chlorophylls. In: Scheer H (ed) Chlorophylls. CRC Press, Boca Raton, pp 339–364

Corwin AH (1960) Petroporphyrins. In: Proceedings of fifth world petroleum congress, pp 119–129

Didyk B, Alturki YIA, Pillinger CT, Eglinton G (1975) The petroporphyrins of a cretaceous oil. Chem Geol 15:193–208

Filby RH, Branthaver JF (1987) Metal complexes in fossil fuels: geochemistry, characterization and processing. American Chemical Society, Washington DC, 436pp

Fischer H, Orth H (1937) Die Chemie des Pyrrols, Halfte 1. Akad. Verlagsgesellschaft M. B. H., Leipzig, 764 pp

Hendry GAF, Houghton JD, Brown SB (1987) The degradation of chlorophyll – a biological enigma. (Tansley review no. 11). New Phytol 107:255–302

Jeffrey SW, Wright SW, Zapata M (2011) Microalgal classes and their signature pigments. In: Roy S, Llewellyn C, Egeland ES, Johnsen G (eds) Phytoplankton pigments: characterization, chemotaxonomy and applications in oceanography. Cambridge University Press, Cambridge, pp 3–77

Keely BJ (2006) Geochemistry of Chlorophylls. In: Biochemistry, Biophysics and Biological Functions of Chlorophylls. (Edited by B. Grimm, R. Porra, W. Rudiger W. and H. Scheer) Advances in Photosynthesis and Respiration-2006:535–561

Keely BJ, Prowse WG, Maxwell JR (1990) The Treibs hypothesis: an evaluation based on structural studies. Energy Fuels 4:628–634

Liu H, Wang Z, Ji S, Shi Q, Guo A, Lu J (2015) Characterization of vanadyl and nickel porphyrins enriched from heavy residues by positive-ion electrospray ionization FT-ICR mass spectrometry. Energy Fuels 29:4803–4813

Louda JW, Li J, Liu L, Winfree MN, Baker EW (1998) Chlorophyll degradation during senescence and death. Org Geochem. 29:1233–1251

Louda JW, Loitz JW, Rudnick DT, Baker EW (2000) Early diagenetic alteration of chlorophyll-*a* and bacteriochlorophyll-*a* in a contemporaneous marl ecosystem. Org Geochem 31:1561–1580

Louda JW, Liu L, Baker EW (2002) Senescence- and death-related alteration of chlorophylls and carotenoids in marine phytoplankton. Org Geochem 33:1635–1653

Louda JW, Mongkhonsri P, Baker EW (2011) Chlorophyll degradation during senescence and death-III: three to ten year experiments, implications for ETIO-series generation. Org Geochem 42:688–699

Matile P, Hortensteiner S, Thomas H, Krautler B (1996) Chlorophyll breakdown in senescent leaves. Plant Physiol 112:1403–1409

Ocampo R, Bauder C, Callot HJ, Albrecht P (1992) Porphyrins from Messel oil shale (Eocene, Germany): structure elucidation, geochemical and biological significance, and distribution as a function of depth. Geochim Cosmochim Acta 56:745–761

Premovic PI, Nikolic ND, Tonsa IR, Pavlovic MS, Premovic MP, Dulanovic DT (2000) Copper and copper(II) porphyrins of the cretaceous-tertiary boundary at Stevns Klint (Denmark). Earth Planet Sci Lett 177:105–118
Ramos CI, Figueira F, Poleto MD, Amando FM, Verli H, Tome JP, Neves MGP (2016) ESI-MS/MS of expanded porphyrins: a look into their structure and aromaticity. J Mass Spectrom 51:342–349
Scheer H (2006) An overview of chlorophylls and bacteriochlorophylls: biochemistry, biophysics, functions and applications. In: Grimm B, Porra RJ, Rudiger W, Scheer H (eds) Chlorophylls and bacteriochlorophylls. Biochemistry, functions and applications. Vol. 25 of advances in photosynthesis and respiration. Springer, Dordrecht, pp 1–26
Treibs A (1936) Chlorophyll- und Haminderivate in organischen Mineralstoffen. Angew Chem 49:682–686
Watanabe N, Yamamoto K, Ihshikawa H, Yagi A, Sakata K, Brinen LS, Clardy J (1993) New chlorophyll-a-related compounds isolated as antioxidants from marine bivalves. J Nat Prod 56:305–317
Woltering M, Tulipani S, Boreham CJ, Walshe J, Schwark L, Grice K (2016) Simultaneous quantitative analysis of Ni, VO, Cu, Zn and Mn geoporphyrins by liquid chromatography-high resolution multi-stage mass spectrometry: method development and validation. Chem Geol 441:81–91
Yen TF, Boucher LJ, Dickie JP, Tynan EC, Vaughan GB (1969) Vanadium complexes and porphyrins in asphaltenes. J Inst Petrol 55:87–99

Potassium

Ricardo Arevalo Jr.
Planetary Environments Lab, NASA Goddard Space Flight Center, Greenbelt, MD, USA

Element Data
Atomic Symbol: K
Atomic Number: 19
Atomic Weight: 39.098 amu
Isotopes and (Abundances): ^{39}K (93.258%), ^{40}K (0.012%), ^{41}K (6.730%)
1 Atm Melting Point: 63.5 °C (146.3 °F)
1 Atm Boiling Point: 759 °C (1398 °F)
Common Valences: 1+
Ionic Radii: fourfold: 151 pm, sixfold: 152 pm, eightfold: 165 pm, Pauling: 133 pm
Pauling Electronegativity: 0.82
First Ionization Potential: 418.8 kJ/mol
Chondritic (CI) Abundance[a]: 530 μg/g
Silicate Earth Abundance[b]: 240 μg/g
Crustal Abundance[c]: 1.49 wt%
Seawater Abundance[d]: 380 mg/L
Core Abundance: generally < 10 μg/g (estimates vary; see text for details)
[a](Lodders 2003)
(*continued*)
[b](McDonough and Sun 1995)
[c](Rudnick and Gao 2003)
[d](CRC 2001)

Properties

Potassium (K) is a member of Group IA of the periodic table and thus considered an alkali element. Native K manifests as a soft, silvery, and low-density (0.89 g/cm^3) metal that is malleable, ductile, and thermally and electrically conductive. Like other alkali metals, K is highly reactive under ambient atmospheric conditions. Elemental K tarnishes rapidly in the presence of oxygen gas (O_2), and in the presence of liquid water (H_2O), K reacts aggressively to form potassium hydroxide (KOH) and flammable hydrogen gas (H_2); this exothermic chemical reaction releases significant heat in the form of a characteristic lilac flame (www.rsc.org/periodic-table).

Along with the other elements located in Group IA, K belongs to the *s*-block of the periodic table. The specific electron configuration of K is often written as [*Ar*] *4 s*^{1}, comparable to that of the inert noble gas argon (Ar) but with the addition of a single, unpaired outer shell electron held in the *4 s* (*spherical*) orbital. Because *s* orbital electrons are only loosely bound (relative to electrons occupying *p*, *d*, and/or *f* orbitals), K and the other members of Group IA are easily ionized to form single-charged cations (i.e., 1+ valence state) (CRC 2001).

Of the three naturally occurring isotopes of K, ^{39}K (93.258%) and ^{41}K (6.730%) are stable, whereas ^{40}K (0.012%) is radioactive with a half-life ($t_{½}$) of 1.25 Gyr. As a radioisotope, ^{40}K decays through two pathways: 89.3% of ^{40}K decays to stable ^{40}Ca via beta decay, and the remaining 10.7% decays to stable ^{40}Ar via electron capture or positron emission. Because the average human body contains between 100 and 150 g of K, thousands of atoms of ^{40}K decay within our bodies each second, leading some communities to consider K as a "natural" cause of genetic mutation in humans and other animals and plants (Emsley 2001).

History and Use

The name *potassium* is derived from the English word "potash," meaning pot ashes (referring to plant ashes soaked in a pot of water). The origin of the symbol K comes from the Neo-Latin word "kalium," meaning alkali. On October 6th, 1807, a Cornish chemist/inventor named Humphry Davy became the first person to isolate native K. This feat was accomplished by splitting KOH into elemental K and molecular OH (which would further react into water and oxygen

gas) via electrolysis. In 1808, French chemists Louis-Josef Gay-Lussac and Louis Jacques Thenard built upon this discovery by isolating native K via heating of KOH and iron filings up to high temperatures (Emsley 2001).

In the realm of geology, K is the ninth most common element found in the continental crust (Rudnick and Gao 2003). Economically viable concentrations of K are found in variety of mined and manufactured salts (commonly referred to as "potash"), such as alkali-rich sylvite (KCl), langbeinite ($K_2Mg_2(SO_4)_3$), carnallite ($KMgCl_3$•$6(H_2O)$), and polyhalite ($K_2Ca_2Mg(SO_4)_4$•$2H_2O$). Estimated domestic potash resources total about seven billion metric tons; the USA extracted 850,000 marketable tons of K_2O equivalent alone in crop year 2014 (Jasinski 2016). Consumption of K in the commercial industry is controlled primarily by agricultural fertilizers (approximately 85% of US potash sales), with significantly smaller quantities used to manufacture potassium hydroxide (KOH), potassium chloride (KCl), and potassium carbonate (KCO_3), which are used in: industrial water treatments; soap manufacturing; metal treatment and recycling; fire extinguishers; textiles; and food products among other commercial applications (Searls 2001).

Chemistry/Geochemical Behavior

The homologous behavior of the elements in Group IA, resulting from the similar electronic structures of the constituent members, allows for reciprocal substitution for one another in geological materials. For example, because Na^+ and K^+ share identical valence states and similar ionic radii, they can substitute freely for one another in pyroxenes and feldspars with no charge balancing and only minimal strain imposed on the mineral lattice (Wood and Blundy 2003). In contrast, fitting a multivalent transition metal (such as manganese, Mn^{2+}) or high-field strength element (such as hafnium, Hf^{4+}) into the same site would require a coupled substitution to achieve electroneutrality, plus significantly more work to accommodate higher lattice strain energies.

Similar to the other alkali metals, K is categorized as a Large Ion Lithophile Element (LILE) due to its large atomic and ionic radii and its affinity for oxygen-rich geological phases (e.g., silicate rocks and minerals). Although a minimal amount of K (i.e., <10 μg/g) has been inferred to reside within the Earth's core (Oversby and Ringwood 1972; Chabot and Drake 1999; McDonough 2003; Corgne et al. 2007), some studies have challenged these conclusions (Lewis 1971; Lee and Jeanloz 2003; Murthy et al. 2003). Regardless, during silicate differentiation of the Earth and other planetary bodies, K behaves as an incompatible element, concentrating in melt phases rather than remaining behind during melting, or being forced into solidifying minerals during crystallization. Like the other LILE, K is also a fluid mobile element (Taylor and McLennan 1985) and thus commonly associated with metasomatism, hydrothermal alteration, and slab dehydration processes. As a result, the continental crust contains ten times more K than the modern mantle (Hofmann 1988; Sun and McDonough 1989; Arevalo et al. 2009), and significant quantities of K can be found in seafloor sediment (Plank and Langmuir 1998) and the dissolved loads of rivers (Meybeck 1987) due to continental weathering.

Geological Importance

Along with thorium (Th) and uranium (U), K is one of "the big three" long-lived radioactive elements driving the internal heat production within the Earth. The decay of ^{40}K through time also serves as a primary control on the abundance of ^{40}Ar in the atmosphere, as well as the foundation for K-Ar and ^{40}Ar-^{39}Ar radiometric dating techniques. As such, constraining the abundance of K in the Earth (and other rocky planets) has major ramifications for understanding the chemical evolution and dynamics of planetary interiors. However, K is moderately volatile during planetary accretion (Lodders 2003), challenging quantitative models of the composition of the Earth that hinge on chemical relationships between our planet and chondritic meteorites (McDonough and Sun 1995; Javoy 1999; Lyubetskaya and Korenaga 2007). Independent estimates of the abundance of K in the silicate portion of the Earth are disparate and range from as low as 130 μg/g up to 550 μg/g (Arevalo et al. 2009 and references therein). In order to account for the planet's volatile element depletion as well as the potential for nonzero K sequestration in the core, K/U and/or K/Th ratios are invoked frequently as proxies of the absolute abundance and spatial distribution of K in the Earth, other terrestrial planets, and meteorite parent bodies. Because K, Th, and U behave similarly during partial melting and fractional crystallization processes, K/U and K/Th ratios observed in mantle-derived materials may be inferred to represent the compositions of their respective sources.

Although variability in K/U ratios measured in localized suites of oceanic basalts has been observed, studies that have focused on characterizing the composition of a globally representative collection of mantle-derived materials agree on the representative K/U ratio of the modern mantle within the uncertainties of their respective models (Arevalo et al. 2009; Jenner and O'Neill 2012; Gale et al. 2013). Convergence on the quantity of K in the mantle (as extrapolated through the relationship between K and U), in conjunction with established models of K in the continental crust (Rudnick and Gao 2003), suggests that the silicate Earth contains on the order of 280 μg/g K (Arevalo et al. 2009). Because the quantity of Th (~80 ng/g) and U (~20 ng/g) in the silicate Earth are relatively well established due to their more

refractory behavior in the solar nebula and exclusion from the planet's core, approximately 20 TW (or 10^{12} W) of radiogenic heat must be produced from K, Th, and U alone (Arevalo et al. 2009), equating to some 43% of the planet's total surface heat flow of 46 TW (Jaupart et al. 2007). Due to the shorter half-life of ^{40}K relative to the absolute age of the Earth (approx. 4.5 Gyr), 12 times more ^{40}K was extant during the earliest stages of the planet's formation versus today. Interestingly, the shorter half-life of ^{40}K compared to those of ^{232}Th ($t_{½}$ ~ 14 Gyr) and ^{238}U ($t_{½}$ ~ 4.5 Gyr), and the higher absolute abundance of K relative to U in the silicate Earth (K/U ~ 10^4), implicates that K was the primary source of radiogenic heat (other than short-lived radionuclides) during differentiation of the early Earth (Fig. 1). Together, K, Th, and U generated five times more radiogenic heat in the geological past compared to today.

Despite varying proximities to the sun, neither Mercury (Peplowski et al. 2011) nor Venus (Vinogradov et al. 1973) nor Mars (Taylor et al. 2006) appear significantly depleted in K/Th relative to the Earth, as measured from orbit (Fig. 2); this is a surprising discovery due to the volatile behavior of K relative to the more refractory nature of Th. The moon (Prettyman et al. 2006) and the asteroid Vesta (Prettyman et al. 2015), on the other hand, are significantly depleted in volatile elements relative to the Earth based on their respective K/Th ratios.

Biological Utilization and Toxicity

Along with ionic sodium (Na^+), chloride (Cl^-), magnesium (Mg^{2+}), and calcium (Ca^{2+}), K ions serve as electrolytes or substances that conduct electricity in the body. However, unlike other electrolytes K^+ ions are concentrated within cellular structures; in fact, 98% of the K in the human body is located within cells, with the remaining 2% found in extracellular fluids including blood. Cell membranes offer channels through which K^+ and Na^+ may be exchanged against a concentration gradient, termed "sodium-potassium pumps"; there are an estimated 10^{13} of these pumps in each square centimeter of the human body, supporting cellular health and operations (Emsley 2001).

Biologically speaking, K is critical to the proper function of cells, tissues, and organs in the human body. Specifically, K plays a key role in: skeletal and smooth muscle contraction, regulating intracellular fluids, solubilizing proteins, operating nerve impulses, maintaining healthy blood pH levels, and bone support. Dietary sources suggest that the average person should consume some 4.7 mg of K daily to support healthy bodily function, and over-the-counter supplements can be found in many forms, such as tablets, capsules, and liquids, to augment K intake as needed (http://umm.edu/health).

Potassium homeostasis is maintained by balancing consumption of K-containing foods/supplements along with the elimination of excess K through urine and to a lesser extent sweat. Kidney malfunction; laxatives; and diuretics, such as alcohol, coffee, and other caffeinated drinks, can contribute to excessive losses and lead to a deficiency of K in the body, a condition known as hypokalemia. Although mild hypokalemia may not generate any noticeable symptoms, more severe conditions may manifest as muscle weakness, fatigue, and/or cramps, as well as potentially dangerous heart arrhythmias (http://umm.edu/health). Hyperkalemia, or excess K in the body, can result in: gastrointestinal distress including stomach

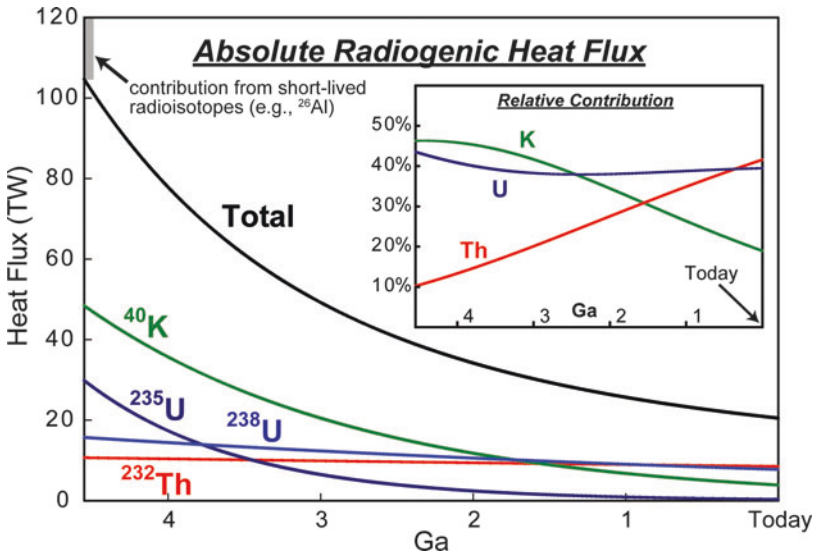

Potassium, Fig. 1 Earth's radiogenic heat production from the decay of long-lived radionuclides, namely ^{40}K, ^{232}Th, ^{235}U, and ^{238}U, through geological time. For the first 2 Gyr following accretion, K acted as the planet's primary source of radiogenic heat (Figure modified from Arevalo et al., 2009)

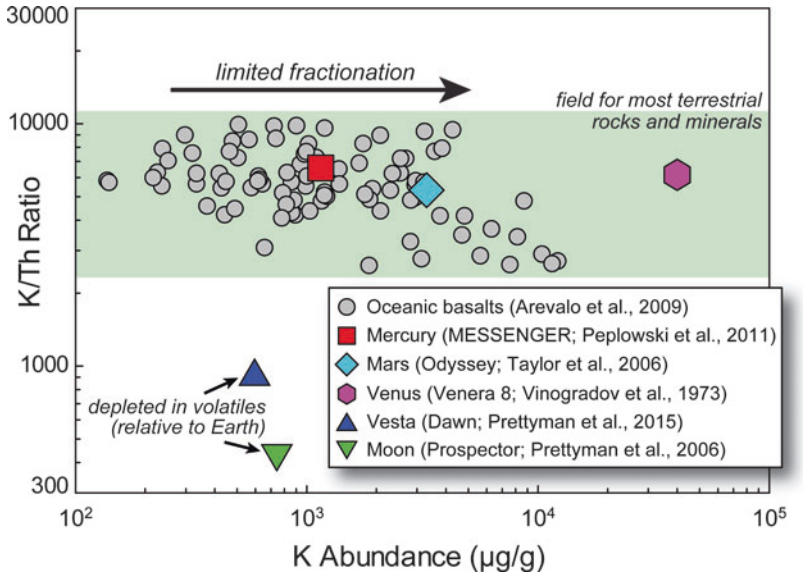

Potassium, Fig. 2 Ratios of K/Th measured in terrestrial oceanic basalts compared to average values determined for the surfaces of other planetary bodies (based on remote observations from orbiting spacecraft); K/Th ratios provide a gauge of volatile element depletion. Surprisingly, K is not depleted in Mercury, Venus, nor Mars relative to the Earth, suggesting a decoupling between proximity to the sun and the loss of volatiles during planetary accretion. The moon and the asteroid Vesta, in contrast, are significantly depleted in K/Th

cramps, diarrhea, and vomiting; muscular weakness and ascending paralysis; and cardiovascular arrhythmia (Saxena 1989). The most common cause of hyperkalemia is kidney failure, though fatal injections of concentrated KCl have been applied as a means to murder, capital punishment, and euthanasia (Emsley 2001).

Summary

Potassium (K) is an alkali metal and member of Group IA; as a native element, K is unstable under atmospheric conditions. Like other members of Group IA, K is easily ionized (to K^+) and behaves as a fluid mobile and highly incompatible LILE. Commercially, K is used primarily as an agricultural fertilizer. In the human body, K serves as a vital electrolyte. In the realm of geology, K is concentrated in the continental crust relative to the modern mantle, with only a small fraction (if any) sequestered in the core (though estimates vary).

The decay of ^{40}K produces radiogenic heat, contributes to atmospheric levels of ^{40}Ar, and serves as the foundation for K-Ar and ^{40}Ar-^{39}Ar radiometric dating techniques. The silicate portion of the Earth contains approximately 280 µg/g K. Surprisingly, none of the other terrestrial planets (i.e., Mercury, Venus, and Mars) appear significantly depleted in K/Th relative to the Earth, as measured from orbit; in contrast, the moon and Vesta are measurably depleted in K/Th.

Cross-References

- Alkali and Alkaline Earth Metals
- Argon Isotopes
- Calcium Isotopes
- Geochronology and Radiogenic Isotopes
- Large-Ion Lithophile Elements
- Mantle Geochemistry
- Ore Deposits
- Periodic Table
- Radioactivity
- Thorium
- Uranium

References

Arevalo R Jr et al (2009) The K/U ratio of the silicate Earth: insights into mantle composition, structure and thermal evolution. Earth Planet Sci Lett 278:361–369

Chabot NL, Drake MJ (1999) Potassium solubility in metal: the effects of composition at 15 kbar and 1900°C on partitioning between iron alloys and silicate melts. Earth Planet Sci Lett 172:323–335

Corgne A et al (2007) How much potassium is in the Earth's core? New insights from partitioning experiments. Earth Planet Sci Lett 256:567–576

CRC (2001) Handbook of chemistry and physics, 82nd edn. CRC Press LLC, Boca Raton

Emsley J (2001) Nature's building blocks: an A–Z guide to the elements. Oxford University Press, Oxford

Gale A et al (2013) The mean composition of ocean ridge basalts. Geochem Geophys Geosyst 14:489–518

Hofmann AW (1988) Chemical differentiation of the Earth: the relationship between mantle, continental crust, and oceanic crust. Earth Planet Sci Lett 90:297–314
http://umm.edu/health
http://www.rsc.org/periodic-table
Jasinski SM (2016) Potash. In Survey USG (ed) Mineral commodities summaries. pp 128–129
Jaupart C et al (2007) Temperatures, heat and energy in the mantle of the Earth. In Schubert G (ed) Treatise of geophysics. Elsevier B.V, Mantle dynamics, vol. 7, pp 253–303
Javoy M (1999) Chemical Earth models. C R Academy of Sciences Ii A 329:537–555
Jenner FE, O'Neill HS (2012) Analysis of 60 elements in 616 ocean floor basaltic glasses. Geochem Geophys Geosyst 13:Q02005
Lee KKM, Jeanloz R (2003) High-pressure alloying of potassium and iron: radioactivity in the Earth's core? Geophys Res Lett 30:2312
Lewis JS (1971) Consequences of the presence of sulfur in the core of the earth. Earth Planet Sci Lett 11:130–134
Lodders K (2003) Solar system abundances and condensation temperatures of the elements. Astrophys J 591:1220–1247
Lyubetskaya T, Korenaga J (2007) Chemical composition of Earth's primitive mantle and its variance: 1. Method and results. J Geophys Res Solid Earth 112:B03212. https://doi.org/10.1029/2005JB004223
McDonough WF (2003) Compositional model for the Earth's core. In: Carlson RW (ed) The mantle and core. Elsevier-Pergamon, Oxford, pp 547–568
McDonough WF, Sun SS (1995) The composition of the Earth. Chem Geol 120:223–253
Meybeck M (1987) Global chemical weathering of surficial rocks estimated from river dissolved loads. Am J Sci 287:401–428
Murthy VR et al (2003) Experimental evidence that potassium is a substantial radioactive heat source in planetary cores. Nature 423:163–165
Oversby VM, Ringwood AE (1972) Potassium distribution between metal and silicate and its bearing on the occurrence of potassium in the earth's core. Earth Planet Sci Lett 14:345–347
Peplowski PN et al (2011) Radioactive elements on Mercury's surface from MESSENGER: implications for the planet's formation and evolution. Science 333:1850–1852
Plank T, Langmuir CH (1998) The chemical composition of subducting sediment and its consequences for the crust and mantle. Chem Geol 145:325–394
Prettyman TH et al (2006) Elemental composition of the lunar surface: analysis of gamma ray spectroscopy data from Lunar Prospector. J Geophys Res Planets 111:E12007
Prettyman TH et al (2015) Concentrations of potassium and thorium within Vesta's regolith. Icarus 259:39–52
Rudnick RL, Gao S (2003) Composition of the continental crust. In: Rudnick RL (ed) The crust. Elsevier-Pergamon, Oxford, pp 1–64
Saxena K (1989) Clinical features and management of poisoning due to potassium chloride. Med Toxicol Adverse Drug Exp 4:429–443
Searls JP (2001) Potash. In Survey USG (ed) pp 59.51–59.10
Sun S-S, McDonough WF (1989) Chemical and isotopic systematics of oceanic basalts: implications for mantle composition and processes. In: Saunders AD, Norry MJ (eds) Magmatism in the ocean basins, vol 42. Geological Society Special Publication, Boston, pp 313–345. https://doi.org/10.1144/GSL.SP.1989.042.01.19
Taylor SR, McLennan SM (1985) The continental crust: its composition and evolution. Blackwell Scientific Publications, Oxford
Taylor GJ et al (2006) Bulk composition and early differentiation of Mars. J Geophys Res Planets 111:E03510
Vinogradov AP et al (1973) The content of uranium, thorium, and potassium in the rocks of Venus as measured by Venera 8. Icarus 20:253–259
Wood BJ, Blundy JD (2003) Trace element partitioning under crustal and uppermost mantle conditions: the influences of ionic radius, cation charge, pressure, and temperature. In: Carlson RW (ed) The mantle and core. Elsevier-Pergamon, Oxford, pp 395–424

Praseodymium

Scott M. McLennan
Department of Geosciences, Stony Brook University, Stony Brook, NY, USA

Element Data
Atomic Symbol: Pr
Atomic Number: 59
Atomic Weight: 140.90766(2)
Isotopes and Abundances: ^{141}Pr, 100%
1 Atm Melting Point: 931°C
1 Atm Boiling Point: 3520 °C
Common Valences: +3
Ionic Radii: 99.0pm (CN6), 112.6 pm (CN8), and 128.6 pm (CN12)
Pauling Electronegativity: 1.13
First Ionization Energy: 528.1kJ mol^{-1}
Chondritic (CI) Abundance: 0.0964 ppm
Silicate Earth Abundance: 0.215 ppm
Crustal Abundance: 3.9 ppm
Seawater Abundance: 0.535 ppt
Core Abundance: ~0

Properties

Praseodymium (Pr), from the Greek *prasios* (green) and *didymos* (twin), is a soft, ductile, malleable, moderately dense (6.773 g cm^{-3}), silvery metal. Its electronic configuration is [Xe]4f^{3}6s^2. It is moderately stable at room temperature and readily dissolves in mineral acids. It is a group 3 or IIIB inner transition element, with +3 being its only valence state in geological environments, and is one of the lanthanide rare earth elements (REE). In geochemical terminology, it is grouped with light rare earth elements (LREE; La – Sm). Praseodymium has only one natural, stable isotope.

More than 270 minerals contain lanthanides as essential structural constituents, but those with Pr as a major component are restricted to LREE varieties, including monazite [(Ce,La,Nd,Th)(PO$_4$)], bastnäsite [REE(CO$_3$)F], allanite [(REE,Ca,Y)$_2$(Al,Fe^{2+},Fe^{3+})$_3$(SiO$_4$)$_3$(OH)], and britholite [(REE,Ca)$_5$(SiO$_4$,PO$_4$)$_3$(OH,F)]. In addition, Pr may be enriched in ion adsorption lateritic kaolinite-halloysite clay deposits that are mined for REE.

Details of properties, mineralogy, history, and uses of Pr were compiled from Goonan (2011), Chakhmouradian and Wall (2012), Zaimes et al. (2015), Gschneidner (2016), Hammond (2016), and Meija et al. (2016a, b).

History and Use

Praseodymium was discovered in 1885 by Carl Auer von Welsbach, who separated the compound didymia (previously thought to be the oxide of a single element) into the salts of two rare earth elements, neodymia and praseodymia. Praseodymium metal was isolated in 1931. By far, the most important use of praseodymium is as an additive to neodymium magnets. It is also used to provide yellow coloration to ceramics, enamels, and glass. Additional uses include additives to various metals, batteries, lasers, and catalytic converters.

Geochemical Behavior

The fundamental importance of Pr in geochemistry is that it is one of the large trivalent rare earth elements, among the most useful trace elements in all areas of geochemistry and cosmochemistry due to their coherent and systematic behavior as a group, largely a consequence of the "lanthanide contraction."

Praseodymium is typically a trace element in most rocks and minerals. It is classified geochemically and cosmochemically as a highly refractory lithophile element with a 50% $T_{condensation}$ of 1582 K at 10^{-4} bars (Lodders 2003). In most igneous systems, Pr is incompatible with bulk partition coefficients, $D < 1$. In aqueous systems, Pr normally has very low fluid/rock partition coefficients ($\ll 1$). As a result, Pr contents of clastic sediments typically reflect their average provenance abundances.

In seawater, Pr has very low concentrations (sub-ppt) and residence times (~240 year) with speciation dominated by Pr^{3+}, $PrCO_3^+$, and $Pr(CO_3)_2^-$. In other aqueous systems (e.g., magmatic, hydrothermal), Pr can reach ppm levels due to elevated temperatures, pH effects, and complexing with various ligands (e.g., F^-, Cl^-, OH^-).

Concentration and residence time data are from compilations in Taylor and McLennan (2009) and Nozaki (2001).

Biological Utilization and Toxicity

There are no documented biological uses for Pr, but in China REE have been added to fertilizers and to stock feed to promote growth. REE (including Pr^{3+}) likely substitute for Ca^{2+} in biological materials and processes. REE concentrations (including Pr) in human tissues and fluids are very low (tens of ppb to <ppb levels, respectively) due to very low concentrations in natural waters and low uptake rates throughout the food chain (Bulman 2003). At low levels of ingestion, there are no established toxic effects that pose a threat to human health.

Cross-References

- ▶ Incompatible Elements
- ▶ Lanthanide Rare Earths
- ▶ Lithophile Elements
- ▶ Trace Elements
- ▶ Transition Elements

References

Bulman RA (2003) Metabolism and toxicity of the lanthanides. In: Sigel A, Sigel H (eds) Metal ions in biological systems, vol. 40, the lanthanides and their interrelations and biosystems. Marcel Dekker, Basel, pp 683–703

Chakhmouradian AR, Wall F (eds) (2012) Rare earth elements. Elements 8:333–376

Goonan TG (2011) Rare earth elements – end use and recyclability. U. S. Geological Survey Scientific Investigation Report 2011–5094, 15pp

Gschneidner KA Jr (2016) Physical properties of the rare earth metals. In: Haynes WM (ed) CRC handbook of chemistry and physics, 96th edn. CRC Press, Boca Raton, pp 4–115–4–120

Hammond CR (2016) The elements. In: Haynes WM (ed) CRC handbook of chemistry and physics, 96th edn. CRC Press, Boca Raton, pp 4–1–4–42

Lodders K (2003) Solar system abundances and condensation temperatures of the elements. Astrophys J 591:1220–1247

Meija J, Coplen TB, Berglund M, Brand WA, De Bièvre P, Gröning M, Holden NE, Irrgeher J, Loss RD, Walczyk T, Prohaska T (2016a) Atomic weights of the elements 2013. Pure Appl Chem 88:265–291. (IUPAC Technical Report)

Meija J, Coplen TB, Berglund M, Brand WA, De Bièvre P, Gröning M, Holden NE, Irrgeher J, Loss RD, Walczyk T, Prohaska T (2016b) Isotopic compositions of the elements 2013. Pure Appl Chem 88:293–306. (IUPAC Technical Report)

Nozaki Y (2001) Rare earth elements and their isotopes in the ocean. In: Steele JH (ed) Encyclopedia of ocean sciences. Academic, London, pp 2354–2366

Taylor SR, McLennan SM (2009) Planetary crusts: their composition, origin and evolution. Cambridge University Press, Cambridge. 378pp

Zaimes GG, Hubler BJ, Wang S, Khanna V (2015) Environmental life cycle perspective on rare earth oxide production. ACS Sustain Chem Eng 3:237–244

Precambrian Geochemistry

Tsuyoshi Komiya
Department of Earth Science and Astronomy,
The University of Tokyo, Tokyo, Japan

Definition

The Precambrian is divided into the Hadean (4567–4030 Ma), Archean (4030–2500 Ma), Proterozoic (2500–542 Ma) Eons. The Archean and Proterozoic are further subdivided into the Eoarchean (4030–3490 Ma), Paleoarchean

(3490–3240), Mesoarchean (3240–2780 Ma) and Neoarchean (2780–2430 Ma), and into the Eoproterozoic (2430–2060 Ma), Paleoproterozoic (2060–1600 Ma), Mesoproterozoic (1600–1000 Ma) and Neoproterozoic Eras (1000–542 Ma), respectively (Ogg et al. 2008).

The boundary between the Hadean and Archean is defined by the oldest rock on the earth, the 4.03 Ga Acasta Gneiss Complex, which comprises orthogneisses of various ages and lithologies, and mafic to intermediate enclaves within the gneisses (Fig. 1, loc. A). On the other hand, the boundary between the Archean and Proterozoic is not defined by a specific event because of apparent diachronous and transitional changes of tectonics and sedimentation, and thermal, crustal, surface environmental, and biological evolutions during over 500 m.y. The so-called Proterozoic-style geology, characterized by platform and passive margin sedimentation of thick and coherent volcanosedimentary rocks on continental basements and rifts, started in the Mesoarchean in South Africa and Pilbara but became common in the Proterozoic. Atmospheric oxygen contents drastically increased from 2.5 to 2.2 Ga, known as the Great Oxidation Event.

The Hadean

No Hadean rocks or geologic bodies are preserved on the Earth, but the Hadean minerals are found from not only the Archean clastic sedimentary rocks and granitoids but also younger sedimentary rocks. The Paleoarchean conglomerate in Narryer Complex of the Yilgarn craton (Fig. 1, loc. B) contains many Hadean (up to *ca.* 4.4 Ga) zircons, whose geochemistry of rare earth element (REE) patterns, Ti contents and mineral inclusions indicate they crystallized from granitoid magmas. Moreover, their higher oxygen isotope values, Ce anomalies and large variation of Hf isotope ratios suggest that liquid water, oxidized mantle, and early mantle evolution with/without continental formation goes back to

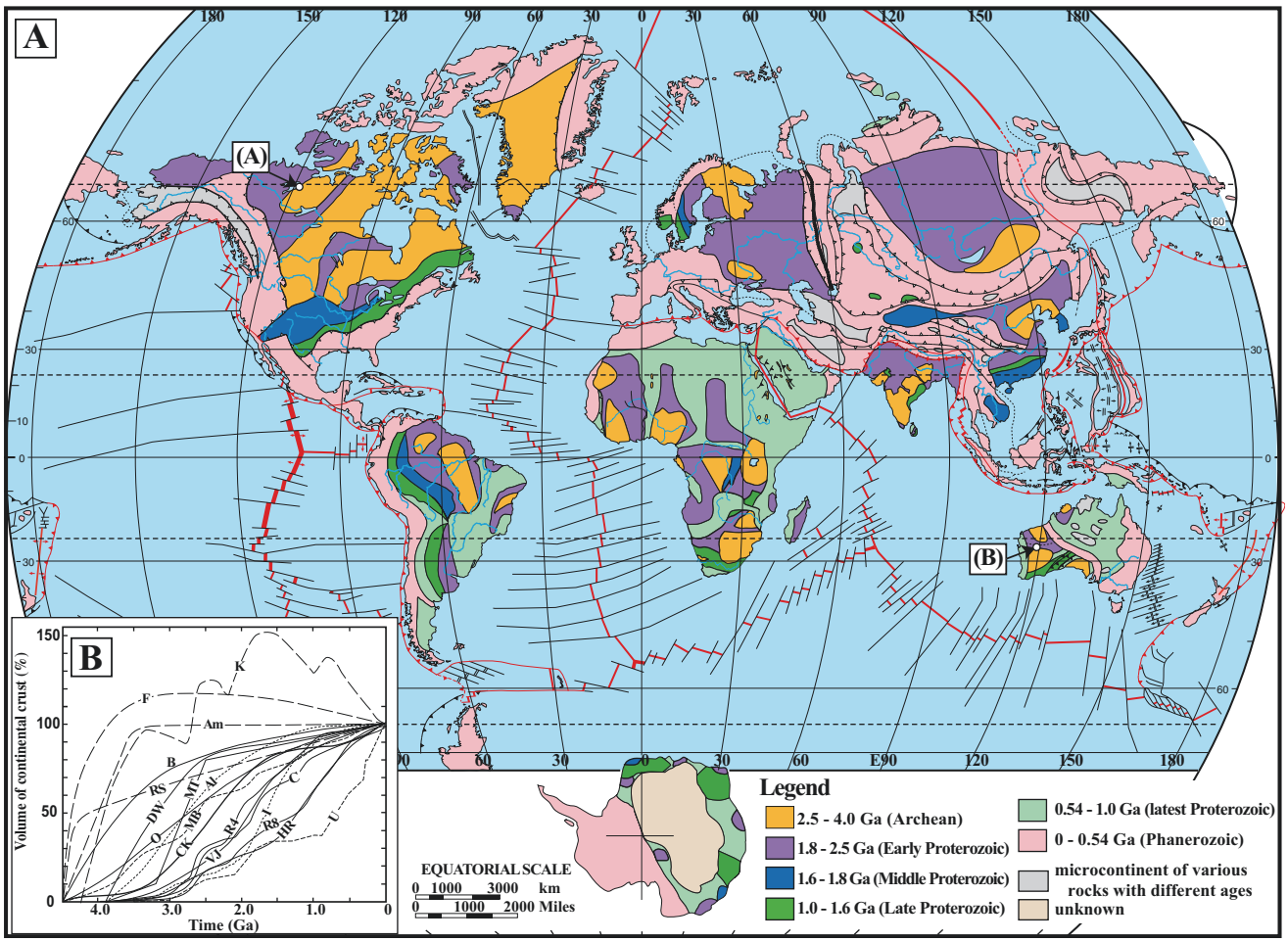

Precambrian Geochemistry, Fig. 1 (**a**) Compilation map of orogenic belts worldwide (Modified after Utsunomiya et al. 2007). The alphabets mean localities, described in the text. (**b**) Summary of estimated continental growth curves, whose differences are mainly due to difference in estimate of recycling of continental materials and methods (Modified after from Komiya 2011)

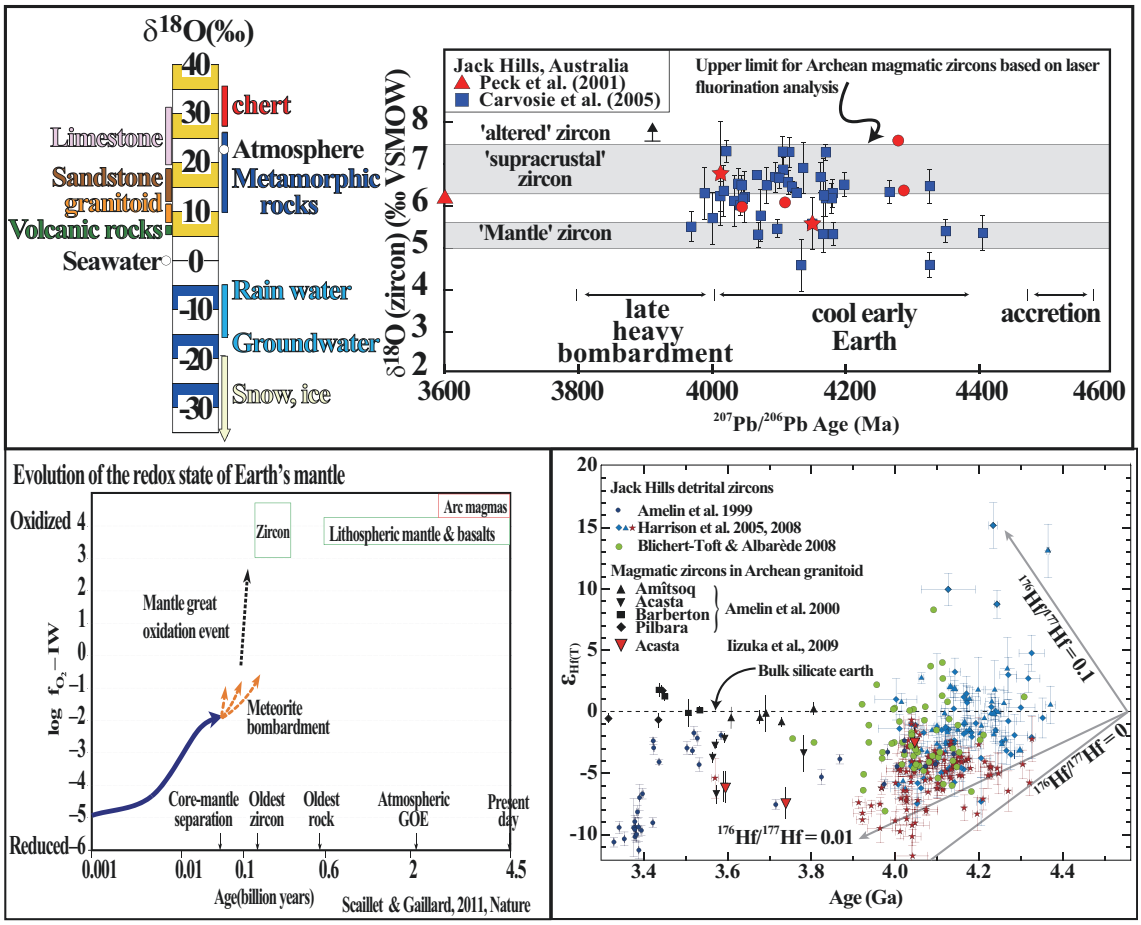

Precambrian Geochemistry, Fig. 2 (**a**) Oxygen isotope values of the Hadean zircons from the Jack Hills, Western Australia (Cavosie et al. 2005). (**b**) Evolution of the redox state of Earth's mantle (Scaillet and Gaillard 2011). (**c**) Hafnium isotope values of the Hadean and Archean zircons (Harrison 2009)

early earth (Fig. 2). All modern terrestrial rocks have excess of ^{142}Nd, which is a daughter isotope from an extinct isotope of ^{146}Sm ($\tau_{1/2} = 68$ myr), relative to chondrites (Fig. 3). The ^{142}Nd anomaly indicates early differentiation and/or crustal formation before *ca.* 4.2 Ga, and also suggests a hidden reservoir with a low ε^{142}Nd value within a deep mantle, escape of ^{146}Sm-poor early crusts during planetesimal accretion or accretion of nonchondritic materials. On the other hand, some of Archean materials have positive and negative anomalies of the ε^{142}Nd values relative to modern terrestrial materials, suggesting homogenization of the mantle after the early differentiation. All modern terrestrial rocks also have excess of ^{182}W, which is a daughter isotope from an extinct isotope of ^{182}Hf ($\tau_{1/2} = 8.9$ myr), relative to chondrites, and some of the Archean rocks are more enriched in ^{182}W than modern terrestrial rocks (Fig. 4). The anomaly indicates early core formation with/without early mantle differentiation. Ages of impact melt rocks on the Moon and lunar meteorites suggest the Late Heavy Bombardment event from *ca.* 4.1 to 3.8 Ga, when many asteroids collided with terrestrial planets.

Solid Earth Evolution in the Precambrian

Estimates of continental growth are highly varied (Fig. 1) but can be divided into two major groups: (1) early crustal growth and subsequent recycling and (2) continuous or episodic crustal growth (see Komiya 2011). The estimates from the Earth's thermal history implied rapid growth of continental crusts (F, K in Fig. 1), whereas the estimates from their present distribution display slow growth (HR, U). The estimates from mantle and crustal compositions suggest moderate increase in the Proterozoic to Phanerozoic (CK, O, Al, MB, MT). Age distribution and Hf isotopes of detrital zircons showed significant continental recycling including intracontinental recycling, crustal reworking and crust–mantle recycling, and supported the early growth of continental crusts (C, I, R4, R8, Am, K, VJ).

The Archean continental crusts account for *ca.* 20% of present continental volumes (Fig. 1), and mainly comprise supracrustal rocks and intrusive granitoid batholiths, the so-called granite-greenstone belt terrains. The greenstone

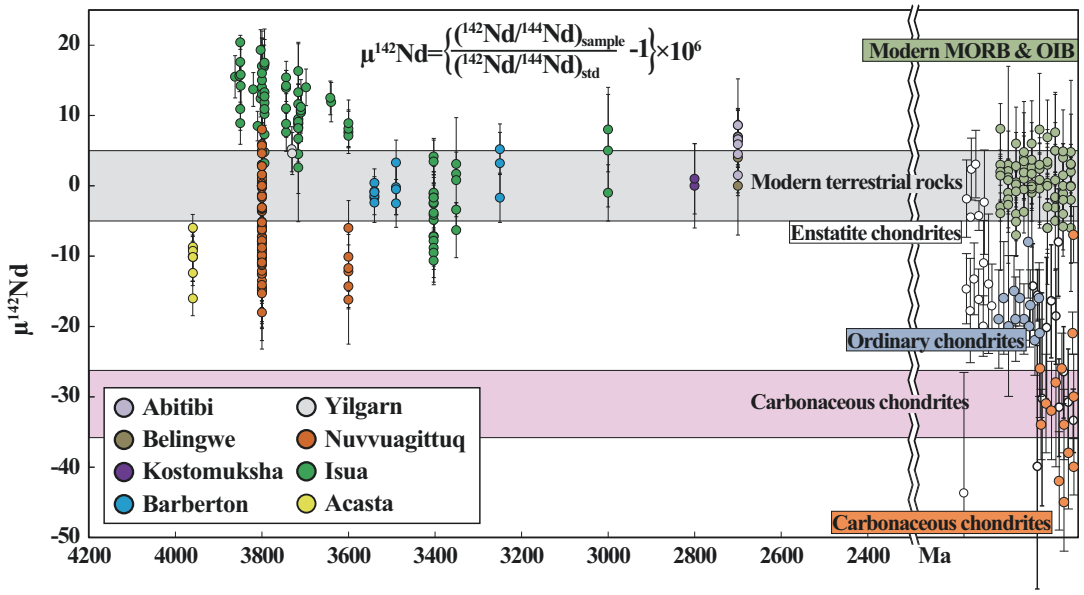

Precambrian Geochemistry, Fig. 3 Summary of $\mu^{142}Nd$ values of Precambrian rocks along with terrestrial modern rocks and carbonaceous, ordinary, and enstatite chondrites. The terrestrial rocks have excess of the $\mu^{142}Nd$ values compared with the carbonaceous chondrites, suggesting early differentiation before 4.2 Ga and hidden reservoirs or accretion of nonchondritic materials

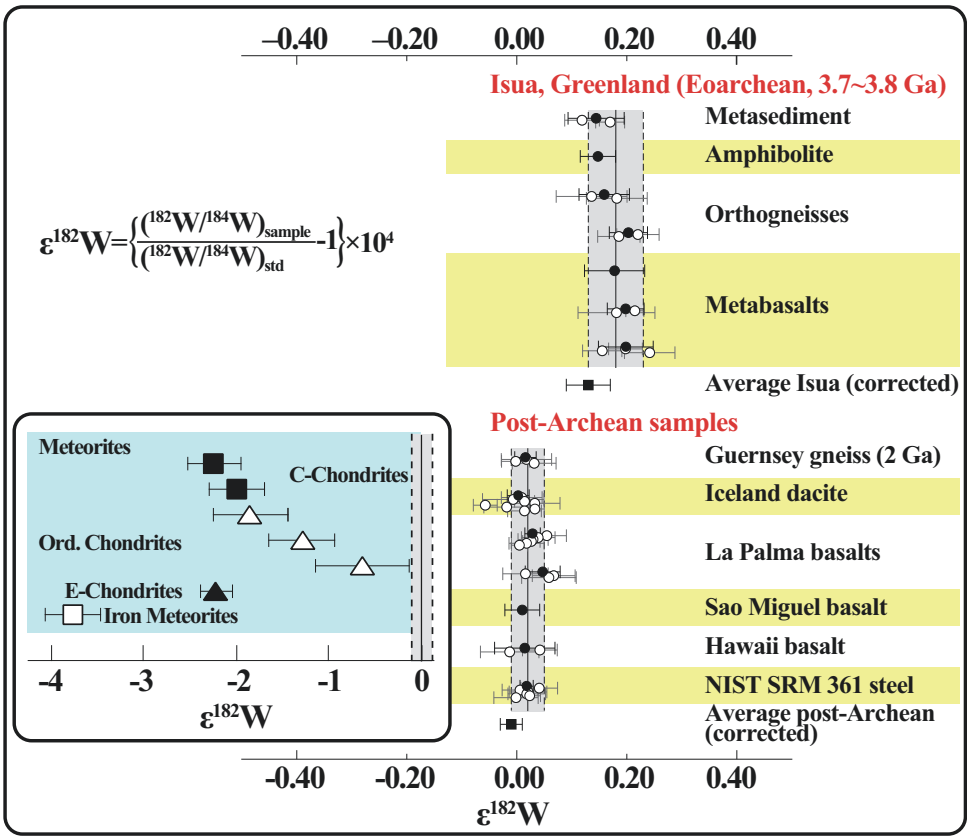

Precambrian Geochemistry, Fig. 4 Summary of $\varepsilon^{182}W$ values of the Eoarchean rocks along with terrestrial post-Archean rocks and meteorites. The terrestrial rocks have positive anomaly of the $\varepsilon^{182}W$ values, indicating the early core formation with/without early mantle differentiation

belts comprise a possible ophiolitic ultramafic body, ultramafic (komatiitic) and mafic volcanic rocks, chemical and minor clastic sedimentary rocks. Potential mantle temperatures of the Archean upper and plume-source mantles were estimated to be hotter by 150–200 °C than the modern equivalents from MgO, FeO, and SiO_2 contents of the mafic and komatiitic rocks, respectively (Fig. 5a). The higher mantle temperature results in thick oceanic crusts and thin, small, and

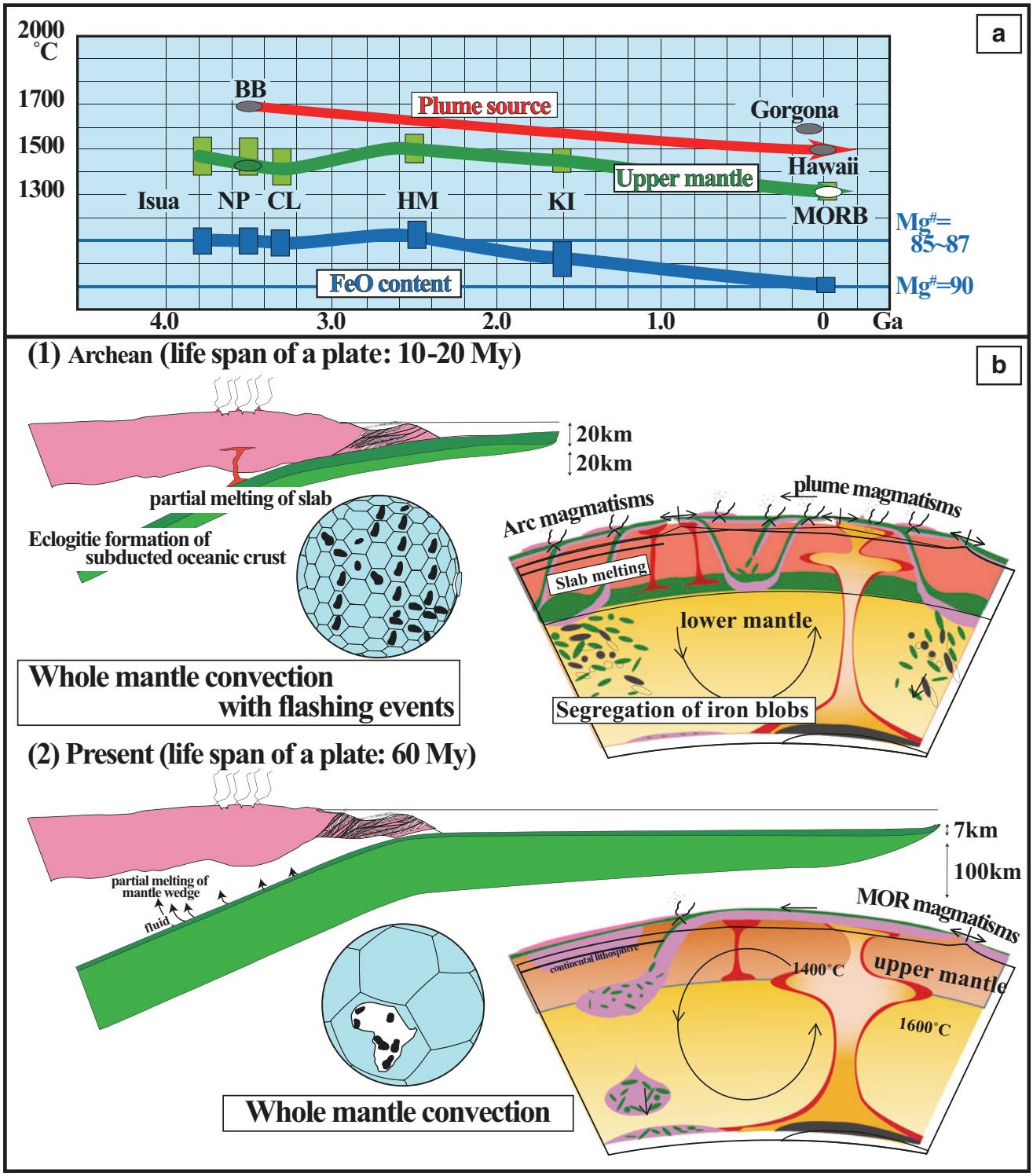

Precambrian Geochemistry, Fig. 5 (**a**) Secular variations of potential mantle temperatures of the upper and plume-source mantles and iron content of the upper mantle through the time. (**b**) Cartoons of modes of oceanic lithospheres and material circulation in whole mantles in Archean and Phanerozoic

young oceanic lithospheres (Fig. 5b). The Eoarchean mafic rocks are commonly depleted in Nb contents relative to modern MORB and OIB (Fig. 6a). The depletion is mainly due to crustal contamination with/without secondary alteration, but even if the secondary influence were corrected, they have lower Nb/Yb ratios (Fig. 6a). Their low Nb/Yb ratios suggest

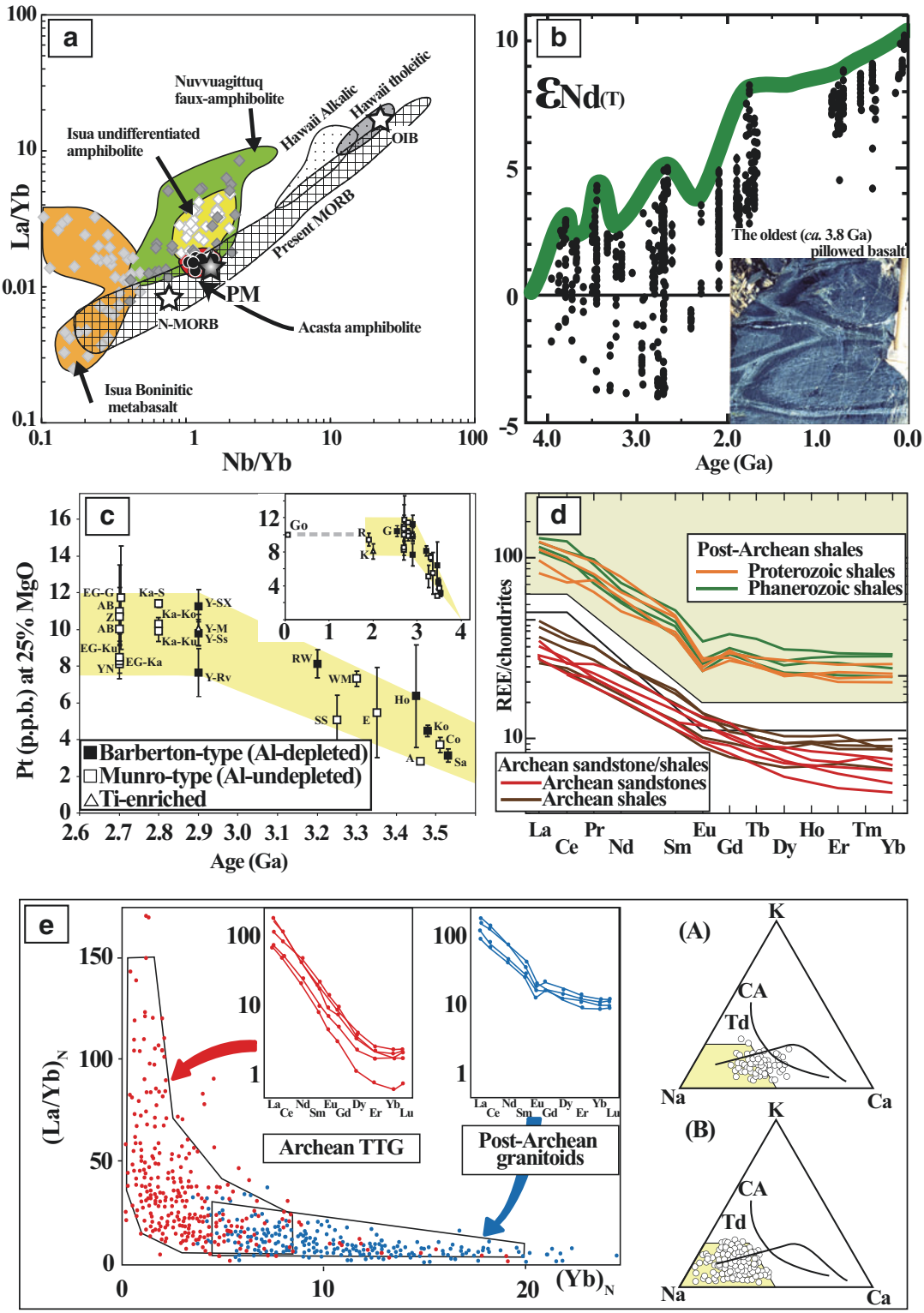

Precambrian Geochemistry, Fig. 6 (**a**) A Nb/Yb vs. La/Yb diagram of the Eoarchean mafic rocks along with modern MORBs and OIBs. The mafic rocks are depleted in Nb contents relative to the modern basalts, suggesting the suprasubduction zone magmatism or deep mantle differentiation in the early earth. (**b**) Secular change of εNd values of mafic volcanic rocks through the time, showing the Nd isotopic evolution of the residual depleted mantle. (**c**) Secular change of platinum contents of komatiites at 25% in MgO contents, which shows that the Pt contents increased in the Archean possibly due to late meteorite impacts (Maier et al. 2009). (**d**) Comparison of REE patterns of the Archean and post-Archean shales. (**e**) Geochemical and petrological characteristics of the Archean and post-Archean granitoids (Martin 1999). The Archean granitoid has TTG compositions and is characterized by depletion of HREE and lack of Eu anomaly, evident for slab-melting

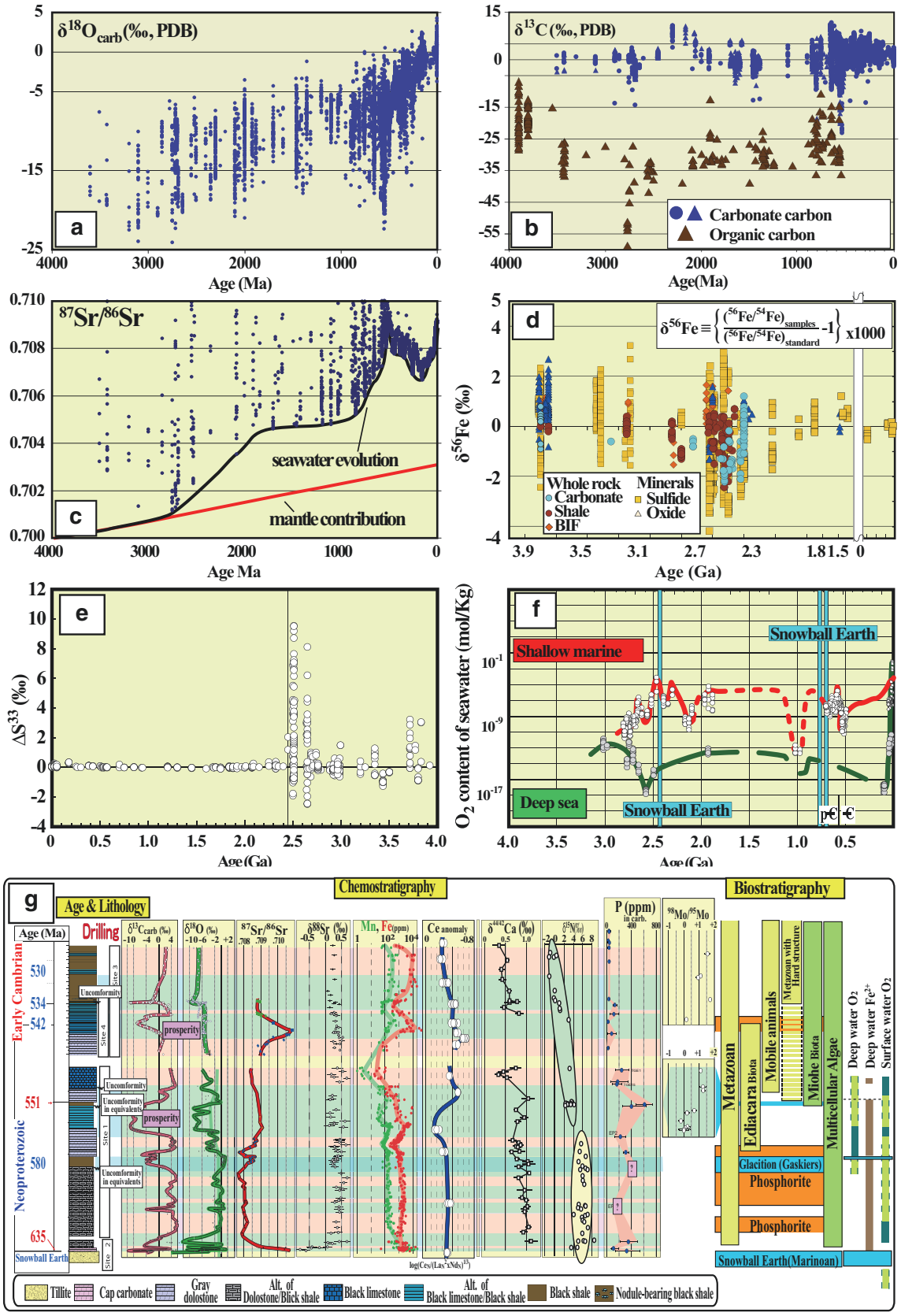

Precambrian Geochemistry, Fig. 7 (continued)

that they were formed in suprasubduction zones or from a Nb-poor source mantle, which underwent deep mantle differentiation in the early Earth. Figure 6b displays an Nd isotope evolution curve of a depleted (upper) mantle based on Nd isotope values of mafic rocks through the time and shows its progressive depletion with intermittent rejuvenation during the rapid continental growth. Figure 6c shows increase of platinum contents of komatiites at 25 wt% MgO contents, suggesting PGE contents, namely highly siderophile elements, increased through the time possibly due to late meteorite accretion. Figure 6d shows compositions of the Archean and post-Archean shales, and the post-Archean shales have distinct negative Eu anomalies. Figure 6e shows REE patterns of the Archean and post-Archean granitoids, and suggests that there has been no change in the composition of the upper crust after the Archean. Most Archean granitoid have tonalite-trondhjemite-granodiorite compositions and are characterized by depletion of the HREE and lack of Eu anomalies, suggesting that they were formed through partial melting of subducted oceanic crust (slab melting) in the garnet stability field.

Surface Environmental Evolution in the Precambrian

Oxygen isotope values of carbonate rocks and fossil carbonates increased through the time (Fig. 7a). Assuming that the $\delta^{18}O$ value of seawater was constant through the time and the primary $\delta^{18}O$ values are preserved, temperature of seawater is estimated to be *ca.* 70 °C in the Archean. But, the low $\delta^{18}O$ values are probably due to secondary alteration because the $\delta^{18}O$ values are susceptible to secondary alteration or due to secular change of $\delta^{18}O$ value of seawater. Figure 7b displays secular changes of carbonate and organic carbon isotope ratios through the time. The $\delta^{13}C_{carb}$ values show positive excursions in the Paleoproterozoic and Neoproterozoic, possibly due to increase of organic burial and atmospheric oxygen contents, and the large and frequent fluctuations since the Ediacaran. The low (<−25‰) $\delta^{13}C_{org}$ values in the Eoarchean suggest presence of early life, and quite low (<−40‰) $\delta^{13}C_{org}$ values in the Mesoarchean indicate aerobic or anaerobic methanotrophs. Sr isotope ratios of carbonate are a proxy of ratio of continental to hydrothermal influxes into seawater and the sudden increase in the Mesoarchean and Neoproterozoic suggest rapid growth of continental crusts (Fig. 7c). The presence of low (<−2‰) $\delta^{56}Fe$ values suggests bacterial-dissimilatory iron reduction since the Eoarchean whereas the high $\delta^{56}Fe$ values are indicate ferruginous ocean before the Paleoproterozoic and in the Ediacaran (Fig. 7d). The presence of mass-independent fractionation in sulfur isotopes indicates low atmospheric oxygen contents before the Paleoarchean (Fig. 7e). Figure 7f displays secular change of oxygen contents of shallow marine and deep seawater through the time based on REE contents of carbonate minerals and suggests oxygen contents of the shallow marine increased in the Neoarchean whereas deep-sea in the Phanerozoic. The drastic increase of atmospheric oxygen in the Neoarchean to Paleoproterozoic is named the Great Oxidation Event. After the Event, banded iron formations disappeared because the ocean changed from the ferruginous to sulfidic ocean.

The Ediacaran to Early Cambrian transition is a key period of the evolution of the earth: drastic changes of surface environments such as Snowball Earth and emergence of Metazoa (Fig. 7g). Chemostratigraphies of C, O, Sr, and Ca isotopes and Fe, Mn, REE, and P contents of carbonates, Mo isotopes of black shales and C and N of organic matter are proxies to estimate primary productivity, continental weathering influx, temperature, nutrient contents (P, N), and redox condition of seawater. The positive excursions of Sr isotopes indicate high continental influxes at *ca.* 580, 570–550, and 540 Ma, corresponding to timings of biological evolution. Phosphorus contents of carbonate rock were very high until *ca.* 550 Ma, and then decreased, suggesting the seawater was enriched in phosphate until then. High N and Ca isotope values indicate that seawater was depleted in nitrate and Ca contents until *ca.* 550 Ma, and then increased. Molybdenum isotopes of black shale, and Fe and Mn contents and REE patterns of carbonate rocks indicate that seawater became more oxic since *ca.* 550 Ma. The geochemical evidence suggests that the emergence of Metazoan in the Early Ediacaran was caused under a relatively less oxic and phosphate-rich condition, whereas their diversification occurred under an oxic, nitrate, and Ca-rich condition. Especially, the transition from phosphate to nitrate- and Ca-rich seawater possibly resulted in diversification of motile and Ca-biomineralizing animals.

Precambrian Geochemistry, Fig. 7 (**a**) Oxygen isotopic evolution of carbonate rocks and Phanerozoic calcitic fossils (Shields and Veizer 2002). (**b**) Isotope variations of carbonate and organic carbons through the time (Modified after Shields and Veizer 2002). (**c**) Sr isotope evolution of carbonate rocks (Shields and Veizer 2002). (**d**) Iron isotope variations of whole rocks and minerals through the time. (**e**) Mass-independent fractionation in sulfur isotopes through the time (Farquhar et al. 2007). (**f**) Secular changes of oxygen contents of shallow marine and deep seawater. (**g**) A summary of the chemostratigraphies of C, O, radiogenic and stable Sr, and Ca isotopes and Fe, Mn, REE, and P contents of carbonates or carbonate rocks, Mo isotope values of black shales, and nitrogen isotopes of organic matter from the Ediacaran to the early Cambrian (Han et al. 2016)

Summary and Conclusions

It is widely considered that the Earth underwent some significant events such as planetesimal accretion, giant impact, magma ocean, core formation, early mantle differentiation, and Late Heavy Bombardment in the Hadean. But, the direct evidence is not preserved in the present Earth, and extinct radiogenic nuclides of ^{146}Sm-^{142}Nd and ^{182}Hf-^{182}W systems provide valuable insight into the early Earth. From the Archean to Proterozoic, thermal evolution and increase of atmospheric oxygen are important factors controlling the Earth's evolution. The decrease of mantle temperature resulted in the beginning of plate tectonics, continental formation, and mantle dynamics. The emergence of oxygen-producing organisms and the consequent expansion of oxidized surface environments led to the Great Oxidation Event, secular change of atmosphere and seawater compositions, and emergence of eukaryotes and metazoans. Many geochemical proxies to record the changes have been developed, especially after the recent establishment of stable isotope measurements of heavy transition metals so that the detailed pictures of secular changes of solid earth and surface environments through geologic time are being obtained.

References

Cavosie AJ, Valley JW, Wilde SA, E.I.M.F (2005) Magmatic δ^{18}O in 4400–3900 Ma detrital zircons: a record of the alteration and recycling of crust in the Early Archean. Earth Planet Sci Lett 235:663–681

Han J, Zhang X, Komiya T (2016) Integrated evolution of cnidarians and oceanic geochemistry before and during the Cambrian explosion. In: Goffredo S, Dubinsky Z (eds) The cnidaria, past, present and future: the world of Medusa and her sisters. Springer International Publishing, Cham, pp 15–29

Harrison TM (2009) The Hadean crust: evidence from >4 Ga zircons. Annu Rev Earth Planet Sci 37:479–505

Komiya T (2011) Continental recycling and true continental growth. Russ Geol Geophys 52:1516–1529

Maier WD, Barnes SJ, Campbell IH, Fiorentini ML, Peltonen P, Barnes S-J, Smithies RH (2009) Progressive mixing of meteoritic veneer into the early Earth/'s deep mantle. Nature 460:620–623

Martin H (1999) Adakitic magmas: modern analogues of *Archaean granitoids*. Lithos 46:411–429

Ogg JG, Ogg G, Gradstein FM (2008) The concise geologic time scale. (177 pp. Cambridge University Press, Cambridge

Scaillet B, Gaillard F (2011) Redox state of early magmas. Nature 480:48–49

Shields G, Veizer J (2002) Precambrian marine carbonate isotope database: version 1.1. Geochem Geophys Geosyst 3. https://doi.org/10.1029/2001GC000266

Utsunomiya A, Ota T, Windley BF, Suzuki N, Uchio Y, Munekata K, Maruyama S (2007) History of the Pacific superplume: implications for Pacific paleogeography since the late proterozoic. In: Yuen DA, Maruyama S, Karato S, Windley BF (eds) Superplumes: beyond plate tectonics. Springer, New York, pp 363–408

Precambrian Organic Matter

Roger Summons
Earth, Atmospheric, and Planetary Sciences Department, Massachusetts Institute of Technology, Cambridge, MA, USA

Definition

Precambrian organic matter comprises all carbonaceous materials preserved in, and indigenous to, sedimentary rocks deposited during the Proterozoic and Archean Eons. These carbonaceous materials range in mass from small individual organic molecules such as simple hydrocarbons, through macromolecules and microscopic fossils, and extending all the way to massive accumulations of petroleum.

Historical Perspective

Organic matter, preserved in Precambrian sedimentary rocks, is an important repository for chemical data pertinent to the quest to understand the origins, evolution, and history of life on Earth (Eglinton 1969; Gaines et al. 2009; McKirdy 1974). As for the Phanerozoic, organic carbon and organic carbon compounds complement other sources of historical biogeochemical information derived from physical fossils, sedimentary fabrics, mineral deposits, sedimentary inorganic chemistry, and a numerous and growing collection of stable isotopic systems. A necessary underlying assumption is that any significant accumulation of sedimentary organic matter is the result of biological carbon assimilation, and this assumption is supported by the large carbon isotopic separation between the inorganic and organic carbon indicative of a biogeochemical carbon cycle operating since at least 3.45 billion years ago (Ga) (Schidlowski 2001). Sedimentary rocks older than this exist, but they are sparse and difficult to characterize, whereas after 3.45 Ga they become increasingly common, better understood in the sense of depositional settings, and afford evidence of both the antiquity of life and its influence on the development of the terrestrial environment through time.

Prevalence and Preservation

The prevalence of organic matter in Proterozoic sedimentary rocks is evidently not significantly different from that in Phanerozoic equivalents. However, the loss of sedimentary record through tectonic movements leading to erosion or to deep burial means that the chances of finding minimally

altered material decrease with increasing age. Archean sediments are particularly depleted for this reason. Systematic surveys of organic matter in Archean and Proterozoic rocks (Hayes et al. 1983; McKirdy 1974) used atomic hydrogen to carbon *(H/C)* ratios, X-ray patterns, visual analysis, and mineral assemblages to evaluate thermal alteration. It was found that despite the recognition of occasional Archean rocks with high organic carbon contents, they were invariably metamorphosed to the extent that remaining organic matter approached the composition of graphite with *HIC* ratios 0.0–0.5 (Hayes et al. 1983). Those Archean samples with higher than average *HIC* ratios were characterized by the presence of uranium or thorium bearing minerals (see below). Rocks of Proterozoic age also show evidence of significant thermal alteration, although they have a higher proportion of examples with moderate to good preservation (Hayes et al. 1983; McKirdy 1974). Subsequent detailed studies of some of those units (Brocks and Summons 2003; Crick et al. 1988; Hayes et al. 1992) have confirmed that for the Proterozoic, at least, there are numerous examples of abundant and very well-preserved organic matter as old as 1.64 Ga.

Kerogen

Kerogen is, by definition, insoluble, macromolecular, and immobile sedimentary organic matter. A specific example would be organic walled microfossils bearing strong morphological resemblances to their precursor organisms and which are composed of organic biopolymers. More often than not, however, kerogen is amorphous. Because it is immobile, kerogen is generally accepted as a form of organic matter that must be native to the host rock and formed by organisms living at the time of sedimentation. An exception to this generalization would be organic matter that encapsulates radioactive mineral grains. These are thucholites and are thought to have formed when migrating hydrocarbons became trapped and polymerized by the associated ionizing radiation (Rasmussen et al. 1993). A related process, possibly combined with natural biodegradation and thermal metamorphism, could have resulted in some more massive accumulations of poorly crystalline carbon such as the ~2 Ga Karelian shungite (Melezhik et al. 1999) which has the characteristics of migrated hydrocarbon and is the apparent remains of ancient, petrified oil fields (Melezhik et al. 2004). In the case of this material, spectroscopic studies show nanomolecular layers with similarities to natural and synthetic cokes. High-resolution transmission electron microscopy (HRTEM) images and nanodiffraction patterns of shungites suggest a material with partial shells of disordered carbon resembling bent stacks of graphene layers (Kovalevski et al. 2001). Thus, carbon in thucholites and shungites has experienced the combined and extreme effects of time, temperature, and/or radiolysis, and this has destroyed virtually all original and diagnostic chemical structure (Dahl et al. 1988; Kovalevski et al. 2001).

Carbon Cycle Reconstruction

Arguably, it has been the isotopic analyses of Precambrian kerogens and co-eval carbonates that has yielded most paleobiological knowledge including evidence for both the antiquity of life and the uniformity of fundamental biogeochemical processes through time (Des Marais 2001; Hayes and Waldbauer 2006; Schidlowski 1988; Schidlowski et al. 1983). Severe thermal alteration can disrupt or destroy the original C-isotopic signals of organic matter; screening for these effects is essential and has been useful for identifying and correcting for corrupted isotopic signals (Des Marais 2001). More recently, microRaman spectroscopy has been used to evaluate the H/C ratio of Precambrian kerogens and, if needed, make adjustments to C-isotopic data (Ferralis et al. 2016). Moreover, the isotopic composition of inorganic carbon, which is also used to evaluate secular change in the C-cycle, is complementary to that of organic carbon provided it has not been affected by diagenesis (Knoll et al. 1986). Studies, which have taken all these issues into account, now abound and indicate that sedimentary record of carbon isotopes is rich in informative detail. Thus, the C-isotopic data record a history of global secular change and offer the means to follow the evolution of the global carbon cycle (Des Marais 1997, 2001; Des Marais et al. 1992; Hayes and Waldbauer 2006; Rothman 2015; Rothman et al. 2003; Hayes et al. 1999) and concomitant change in the surface environment (Eigenbrode and Freeman 2006) and to conduct chemostratigraphic correlations in the Proterozoic (Derry et al. 1992; Halverson et al. 2005).

Precambrian organic matter also encodes other isotopic signals, organic nitrogen being a prime example. Nitrogen cycle reconstructions have been the primary target with considerable success despite the fact that most N in ancient sediments is preserved as ammonium with lower amounts of organic-N (Beaumont and Robert 1999; Godfrey and Falkowski 2009; Godfrey et al. 2013; Stüeken et al. 2015a, b; Thomazo et al. 2011). Data gathered so far indicate that a predominantly anaerobic N-cycle existed prior to the Great Oxidation Event (GOE) (Stüeken et al. 2016) after which emerged a pervasive aerobic marine nitrogen cycle (Zerkle et al. 2017). Although rarely reported, the isotope data for sulfur bound into organic matter can complement isotope data from pyrites in its capacity to reveal signals imparted by the Precambrian S-cycle (Bontognali et al. 2012). When coupled with ^{34}S data for co-eval sulfate and sulfide, the isotopic composition of organic sulfur compounds can be

informative about microbial sulfate reduction, sedimentary diagenesis (Amrani 2014; Meshoulam et al. 2016), as well as photochemical processes involving atmospheric sulfur species.

Morphologically Complex Organic Matter

In the Precambrian, there has long been a strong recognition of the ubiquity and distinctive appearance of organic-walled microscopic fossils and that they are informative about the progress of microbial evolution (Awramik and Barghoorn 1977; Barghoorn 1971; Barghoorn and Schopf 1965; Schopf and Walter 1983). Preservation in silica was generally seen offering the most favorable taphonomic window allowing a three-dimensional perspective on fossil morphologies (Schopf and Kudryavtsev 2009; Schopf et al. 2007; Wacey et al. 2011). This field is not without risk (Brasier et al. 2002), however, since it has been shown that abiogenic self-assembly of microscopic silica-carbonate structures can sometimes mimic microscopic fossils (García Ruiz et al. 2002, 2003; Hofmann 2004) requiring the application of multiple and complementary microscopic and microchemical approaches to distinguish genuine biotic remains (Brasier et al. 2006, 2015; Schopf and Kudryavtsev 2009; Wacey et al. 2012).

Shales have also been productive targets in the search for Precambrian organic-walled microscopic fossils. Objects with multiple eukaryote characteristics predominate (Javaux et al. 2001, 2003; Knoll 1992, 2014), especially in the Neoproterozoic, and are demonstrably providing a sharper picture of eukaryotic evolution (Agić et al. 2017; Butterfield 2000, 2015; Javaux and Knoll 2017; Knoll 2014) as well as being useful for biostratigraphy (Cohen and Macdonald 2015; Grey 2005; Grey and Willman 2009; Strauss et al. 2014). Some phosphorites have also been productive as a taphonomic medium (Xiao et al. 1998).

Techniques for microchemical analysis of amorphous Precambrian organic matter and individual organic microfossils have advanced significantly with secondary ion mass spectrometry (SIMS) methods able to precisely measure individual C-isotopic compositions (House et al. 2000, 2013; Williford et al. 2015), while scanning transmission X-ray microscopy (STXM) techniques and microRaman mapping can shed light on aspects of molecular preservation (Alleon et al. 2015, 2016, 2017) and chemical differences at the micron scale (Ferralis et al. 2016). Numerous additional-spectroscopy techniques including micro-Fourier transform infrared (micro-FTIR), X-ray photoelectron (XPS), electron probe microanalysis (EPMA), and fluorescence extend the array of ways to probe the chemistry and thermal histories of microscopic fossils (Hackley et al. 2017; Muirhead et al. 2017). Accordingly, and applying principles established through the chemical study of Phanerozoic organic matter, there clearly exists additional valuable isotopic and chemical signals encoded in optically recognizable microfossils and, logically, in the associated amorphous substances.

Bitumen: Solvent-Soluble Organic Matter

Early attempts to detect diagnostic organic molecules (biomarkers) in extractable organic matter (bitumen) offered considerable promise for learning more about early life on the Earth (e.g., Eglinton et al. 1964). However, some subsequent studies correctly pointed to inconsistencies between the chemical stabilities of some putative Precambrian molecular fossils (e.g., optically active amino acids) and the severe thermal histories to which the host rocks had been subjected (e.g., Hayes et al. 1983). This problem, and some apparently incongruous carbon isotopic relationships between Precambrian bitumens (Hoering 1965, 1966; Logan et al. 1995), which are mobile, and co-existing kerogens, which are not, led to a general cautionary approach to the potential of volatile or mobile organic compounds to yield credible information (e.g., Hoering 1965). However, given the nature, prevalence, and distribution of petroleum in sediments worldwide, it seemed that no method existed that could completely dispel concerns about migration of these mobile materials into the Precambrian from more recent strata.

Biomarkers are widely and confidently used in petroleum exploration and in studies of sedimentary geochemical processes. There is now a rich compendium of compounds for which chemical structure, biological origin, and diagenetic alteration pathways have been rigorously documented (Peters et al. 2005). Hydrocarbons, which are derived from and are diagnostic for bacteria, algae, and plants, have been described, and their occurrences determined with sufficient certainty that they are now routinely used to assign the thermal history, the lithology, and depositional settings of the sediments in which they were deposited. For example, heat-driven chemical reactions are known to convert molecules with original biological structures into thermodynamically more stable forms or "geo-isomers." The extent of conversion can be correlated with independent indices of temperature history such as kerogen elemental *H/C* ratio, reflectance, and fluorescence measurements or Rock-Eval pyrolysis parameters (Peters et al. 2005).

Studies of Precambrian hydrocarbons have been most informative and convincing when addressing the contents, compositions, and biological significance of biomarkers in the Neoproterozoic where deposits of petroleum and an abundance of low maturity petroleum source rocks were recognized in Oman (Grantham 1986; Grantham et al. 1988),

Eastern Siberia (Fowler and Douglas 1987), and Australia (Crick et al. 1988; Jackson et al. 1986; Summons et al. 1988). Detailed studies of these deposits confirmed the presence of eukaryotic steranes, bacterial triterpanes, carotenoids, porphyrins, acyclic isoprenoids, and mid-chain branched alkanes with unusual carbon number predominances that marked them as distinct from Phanerozoic counterparts (Bhattacharya et al. 2017; French et al. 2015b; Grosjean et al. 2009, 2012; Kelly et al. 2011; Klomp 1986). Hydropyrolysis experiments were able to show that many of these hydrocarbons were generated from co-eval kerogens (Love et al. 2008). The most abundant fossil steroids in these rocks, in particular, can be attributed to the Neoproterozoic rise to prominence of eukaryotic phytoplankton (Knoll et al. 2007). However, other steranes that are rare in, or absent from, younger sedimentary sequences were also detected (Bender et al. 2013, 2015; McCaffrey et al. 1994), some of which have been attributed to an origin from sponges (Brocks et al. 2016; Love et al. 2009).

In situ bitumens from older rock sequences have also been studied for their potential to reveal clues to the antiquity of particular microbial taxa and their biochemical pathways. Archean rocks from Australia and South Africa did yield assemblages of hydrocarbons of paleobiological interest (Brocks et al. 1999; Summons et al. 1999; Waldbauer et al. 2009), but these results subsequently became clouded in doubt. Manifold problems included the fact that the studied rocks, mostly from cores drilled for mineral exploration, had not been collected or archived with a view to conducting trace level organic analyses. The prevalence of potential sources of contamination (Brocks et al. 2008) as well as anomalous isotopic data and spatial distributions (Brocks 2011; Rasmussen et al. 2008) contributed further uncertainty. The inability to demonstrate that the reported Archean hydrocarbons, beyond all doubt, were indigenous and syngenetic to the host then led to an experiment where new cores were drilled into Archean sequences of the Pilbara Craton of Western Australia. Two sedimentary sequences that had previously yielded putative Archean biomarkers in drill core samples obtained for mineral exploration were re-drilled along with a third core through sequence of highly metamorphosed shales that served as a control. The cores were drilled, archived, sampled, and analyzed under stringently clean conditions and the results were unambiguous. Although non-diagnostic diamondoid and polyaromatic hydrocarbons were present, sterane, triterpane, and acyclic isoprenoid were undetectable in the fresh cores (French et al. 2015a). Further, the results showed that there were limits to the stability of saturated hydrocarbons and the degree of thermal metamorphism and age beyond which ancient sediments will not yield biologically recognizable biomarkers.

At the present time, the 1.64 Ga Barney Creek Formation, of the McArthur Basin in northeastern Australia, where present in wells that are at or below the maturity threshold for oil generation, is the oldest package of sediment that records the presence of a wide range of biomarker hydrocarbons including acyclic isoprenoids, tricyclic terpanes, pentacyclic hopanoid and gammacerane triterpanes, and C_{40} carotenoid-derived saturated and aromatic hydrocarbons (Brocks et al. 2005; Brocks and Schaeffer 2008). The only steroids identified comprise 4-methyl and desmethyl triaromatic steroids at ppm levels. These steroids lack the side-chain methylation that is characteristic of steroids produced by many eukaryotes and could be of bacterial origin. The most recent biomarker studies of Archean, Paleoproterozoic, and Mesoproterozoic sedimentary rocks, conducted in the era of heightened contamination awareness, reveal a similar picture of nondetection of eukaryote-specific 24-alkylated steranes (Blumenberg et al. 2012; Flannery and George 2014; Luo et al. 2015). In the Neoproterozoic, however, new data on secular trends in the distributions of steroidal biomarkers together with information derived from molecular clock analyses are revealing a surprisingly detailed and consistent picture about the emergence of algae and animals during the Cryogenian Period (Brocks et al. 2017; Erwin 2015; Gold et al. 2016; Hoshino et al. 2017; Love et al. 2005).

Future Potential

Precambrian organic matter, where sufficiently well preserved to reveal molecular detail, offers considerable further potential for detailed and productive study (Briggs and Summons 2014). Mistakes from the past have led to a deeper appreciation for the prevalence of contamination (Illing et al. 2014), and how to detect and avoid it (Jarrett et al. 2013) in rock sequences that have been altered through thermal metamorphism and radiolysis (Bruisten et al. 2013). Further discoveries of taxonomically informative organic-walled microscopic and macroscopic fossils (Cohen and Macdonald 2015; Cohen et al. 2015) and of indigenous and diagnostic molecular fossils (Schinteie and Brocks 2017) can be used to improve phylogenies derived from the DNA of contemporary organisms (Dacks et al. 2016), to calibrate and test molecular clocks (Gold et al. 2017), and overall, to provide further insight into the emergence and diversification of complex life on the Earth (Knoll and Nowak 2017). Last, but not least, the ability to measure the isotopic compositions of multiple elements in the same sample of organic matter, or even the same microscopic fossil, opens new windows into the microbial physiologies and the evolution of Precambrian biogeochemical cycles (Ader et al. 2016; Grotheer et al. 2017; House et al. 2000; Sessions 2016; Stüeken et al. 2016; Williford et al. 2015).

Cross-References

- Atmospheric Evolution
- Biogeochemistry
- Biomarkers: Petroleum
- Carbon
- Carbon Cycle
- Carbon Isotopes
- Ion Microprobe
- Kerogen
- Nitrogen Cycle
- Organic Geochemistry
- Organic Matter in Fossils
- Programmed Temperature Pyrolysis
- Raman Microspectroscopy

References

Ader M, Thomazo C, Sansjofre P, Busigny V, Papineau D, Laffont R, Cartigny P, Halverson GP (2016) Interpretation of the nitrogen isotopic composition of Precambrian sedimentary rocks: assumptions and perspectives. Chem Geol 429:93–110. https://doi.org/10.1016/j.chemgeo.2016.02.010

Agić H, Moczydłowska M, Yin L (2017) Diversity of organic-walled microfossils from the early Mesoproterozoic Ruyang Group, North China Craton-a window into the early eukaryote evolution. Precambrian Res 297:101–130

Alleon J, Bernard S, Remusat L, Robert F (2015) Estimation of nitrogen-to-carbon ratios of organics and carbon materials at the submicrometer scale. Carbon 84:290–298. https://doi.org/10.1016/j.carbon.2014.11.044

Alleon J, Bernard S, Le Guillou C, Marin-Carbonne J, Pont S, Beyssac O, McKeegan KD, Robert F (2016) Molecular preservation of 1.88 Ga gunflint organic microfossils as a function of temperature and mineralogy. Nat Commun 7:11977. https://doi.org/10.1038/ncomms11977

Alleon J, Bernard S, Le Guillou C, Daval D, Skouri-Panet F, Kuga M, Robert F (2017) Organic molecular heterogeneities can withstand diagenesis. Sci Rep 7:1508. https://doi.org/10.1038/s41598-017-01612-8

Amrani A (2014) Organosulfur compounds: molecular and isotopic evolution from biota to oil and gas. Annu Rev Earth Planet Sci 42:733–768. https://doi.org/10.1146/annurev-earth-050212-124126

Awramik SM, Barghoorn ES (1977) The gunflint microbiota. Precambrian Res 5:121–142

Barghoorn ES (1971) The oldest fossils. Sci Am 224:30–43

Barghoorn ES, Schopf JW (1965) Microorganisms from the late Precambrian of Central Australia. Science 150:337

Beaumont V, Robert F (1999) Nitrogen isotope ratios of kerogens in Precambrian cherts: a record of the evolution of atmosphere chemistry? Precambrian Res 96:63–82

Bender M, Schmidtmann M, Rullkötter J, Summons RE, Christoffers J (2013) Identification of a fossil Sterane biomarker in crude oil – an Androstane with a modified carbon skeleton. Eur J Org Chem 2013:5934–5945. https://doi.org/10.1002/ejoc.201300788

Bender M, Schmidtmann M, Summons RE, Rullkötter J, Christoffers J (2015) A geomimetic approach to the formation and identification of fossil Sterane biomarkers in crude oil: 18-nor-D-homo-Androstane and 5α, 14β-Androstane. Chem Eur J 21:12501–12508

Bhattacharya S, Dutta S, Summons RE (2017) A distinctive biomarker assemblage in an Infracambrian oil and source rock from western India: molecular signatures of eukaryotic sterols and prokaryotic carotenoids. Precambrian Res 290:101–112

Blumenberg M, Thiel V, Riegel W, Kah LC, Reitner J (2012) Biomarkers of black shales formed by microbial mats, late Mesoproterozoic (1.1 Ga) Taoudeni Basin, Mauritania. Precambrian Res 196–197:113–127. https://doi.org/10.1016/j.precamres.2011.11.010

Bontognali TRR, Sessions AL, Allwood AC, Fischer WW, Grotzinger JP, Summons RE, Eiler JM (2012) Sulfur isotopes of organic matter preserved in 3.45-billion-year-old stromatolites reveal microbial metabolism. Proc Natl Acad Sci 109:15146–15151

Brasier MD, Green OR, Jephcoat AP, Kleppe AK, Van Kranendonk MJ, Lindsay JF, Steele A, Grassineau NV (2002) Questioning the evidence for Earth's oldest fossils. Nature 416:76–81

Brasier M, McLoughlin N, Green O, Wacey D (2006) A fresh look at the fossil evidence for early Archaean cellular life. Philos Trans R Soc B-Biol Sci 361:887–902. https://doi.org/10.1098/Rstb.2006.1835

Brasier MD, Antcliffe J, Saunders M, Wacey D (2015) Changing the picture of Earth's earliest fossils (3.5–1.9 Ga) with new approaches and new discoveries. Proc Natl Acad Sci 112:4859–4864

Briggs DEG, Summons RE (2014) Ancient biomolecules: their origins, fossilization, and role in revealing the history of life. BioEssays 36:482–490. https://doi.org/10.1002/bies.201400010

Brocks JJ (2011) Millimeter-scale concentration gradients of hydrocarbons in Archean shales: live-oil escape or fingerprint of contamination? Geochim Cosmochim Acta 75:3196–3213. https://doi.org/10.1016/j.gca.2011.03.014

Brocks JJ, Schaeffer P (2008) Okenane, a biomarker for purple sulfur bacteria (*Chromatiaceae*), and other new carotenoid derivatives from the 1640†ma Barney Creek formation. Geochim Cosmochim Acta 72:1396–1414

Brocks JJ, Summons RE (2003) Sedimentary hydrocarbons, biomarkers for early life. In: Schlesinger WH (ed) Biogeochemistry. Elsevier, Amsterdam

Brocks JJ, Logan GA, Buick R, Summons RE (1999) Archean molecular fossils and the early rise of eukaryotes. Science 285:1033–1036. https://doi.org/10.1126/science.1096806

Brocks JJ, Love GD, Summons RE, Knoll AH, Logan GA, Bowden SA (2005) Biomarker evidence for green and purple sulphur bacteria in a stratified Palaeoproterozoic sea. Nature 437:866

Brocks JJ, Grosjean E, Logan GA (2008) Assessing biomarker syngeneity using branched alkanes with quaternary carbon (BAQCs) and other plastic contaminants? Geochim Cosmochim Acta 72:871–888

Brocks JJ, Jarrett AJM, Sirantoine E, Kenig F, Moczydłowska M, Porter S, Hope J (2016) Early sponges and toxic protists: possible sources of cryostane, an age diagnostic biomarker antedating Sturtian snowball earth. Geobiology 14:129–149. https://doi.org/10.1111/gbi.12165

Brocks JJ, Jarrett AJM, Sirantoine E, Hallmann C, Hoshino Y, Liyanage T (2017) The rise of algae in Cryogenian oceans and the emergence of animals. Nature 548:578–581. https://doi.org/10.1038/nature23457. http://www.nature.com/nature/journal/v548/n7669/abs/nature23457.html – supplementary-information

Bruisten BJ, Jarret AJM, Schinteie R, Colangelo-Lillis J, Reuning L, Littke R, Brocks JJ (2013) Pockets of Proterozoic hydrocarbons and implications for the Archaean. Mineral Mag 77:781

Butterfield NJ (2000) *Bangiomorpha pubescens* n. gen., n. sp.: implications for the evolution of sex, multicellularity, and the Mesoproterozoic/Neoproterozoic radiation of eukaryotes. Paleobiology 26:386–404. https://doi.org/10.1666/0094-8373(2000)026<0386:BPNGNS>2.0.CO;2

Butterfield NJ (2015) Early evolution of the Eukaryota. Palaeontology 58:5–17. https://doi.org/10.1111/pala.12139

Cohen PA, Macdonald FA (2015) The Proterozoic record of eukaryotes. Paleobiology 41:610–632. https://doi.org/10.1017/pab.2015.25

Cohen PA, Macdonald FA, Pruss S, Matys E, Bosak T (2015) Fossils of putative marine algae from the cryogenian glacial interlude of Mongolia. PALAIOS 30:238–247
Crick IH, Boreham CJ, Cook AC, Powell TG (1988) Petroleum geology and geochemistry of middle Proterozoic McArthur Basin, Northern Australia II: assessment of source rock potential. AAPG Bull 72:1495–1514
Dacks JB, Field MC, Buick R, Eme L, Gribaldo S, Roger AJ, Brochier-Armanet C, Devos DP (2016) The changing view of eukaryogenesis–fossils, cells, lineages and how they all come together. J Cell Sci 129:3695–3703
Dahl J, Hallberg R, Kaplan IR (1988) Effects of irradiation from uranium decay on extractable organic matter in the Alum Shales of Sweden. Org Geochem 12:559–571. https://doi.org/10.1016/0146-6380(88)90147-7
Derry LA, Kaufman AJ, Jacobsen SB (1992) Sedimentary cycling and environmental change in the late Proterozoic: evidence from stable and radiogenic isotopes. Geochim Cosmochim Acta 56:1317–1329
Des Marais DJ (1997) Isotopic evolution of the biogeochemical carbon cycle during the Proterozoic Eon. Org Geochem 27:185–193
Des Marais DJ (2001) Isotopic evolution of the biogeochemical carbon cycle during the Precambrian. Rev Mineral Geochem 43:555–578
Des Marais DJ, Strauss H, Summons RE, Hayes JM (1992) Carbon isotope evidence for the stepwise oxidation of the Proterozoic environment. Nature 359:605–609
Eglinton G (1969) Organic geochemistry the organic chemist's approach. In: Organic geochemistry. Springer, New York, pp 20–73
Eglinton G, Scott PM, Besky T, Burlingame AL, Calvin M (1964) Hydrocarbons from a one-billion-year-old sediment. Science 145:263–264
Eigenbrode JL, Freeman KH (2006) Late Archean rise of aerobic microbial ecosystems. Proc Natl Acad Sci 103:15759–15764. https://doi.org/10.1073/pnas.0607540103
Erwin DH (2015) Early metazoan life: divergence, environment and ecology. Philos Trans R Soc B 370:20150036
Ferralis N, Matys ED, Knoll AH, Hallmann C, Summons RE (2016) Rapid, direct and non-destructive assessment of fossil organic matter via microRaman spectroscopy. Carbon 108:440–449
Flannery EN, George SC (2014) Assessing the syngeneity and indigeneity of hydrocarbons in the ~1.4 Ga Velkerri formation, McArthur Basin, using slice experiments. Org Geochem 77:115–125. https://doi.org/10.1016/j.orggeochem.2014.10.008
Fowler MG, Douglas AG (1987) Saturated hydrocarbon biomarkers in oils of late Precambrian age from Eastern Siberia. Org Geochem 11:201–213
French KL, Hallmann C, Hope JM, Schoon PL, Zumberge JA, Hoshino Y, Peters CA, George SC, Love GD, Brocks JJ, Buick R, Summons RE (2015a) Reappraisal of hydrocarbon biomarkers in Archean rocks. Proc Natl Acad Sci 112:5915–5920
French KL, Rocher D, Zumberge JE, Summons RE (2015b) Assessing the distribution of sedimentary C40 carotenoids through time. Geobiology 13:139–151. https://doi.org/10.1111/gbi.12126
Gaines SM, Eglinton G, Rullkötter J (2009) Echoes of life: what fossil molecules reveal about earth history. Oxford University Press, New York
García Ruiz JM, Carnerup A, Christy AG, Welham NJ, Hyde ST (2002) Morphology: an ambiguous indicator of biogenicity. Astrobiology 2:353–369. https://doi.org/10.1089/153110702762027925
Garcia-Ruiz JM, Hyde ST, Carnerup AM, Christy AG, Van Kranendonk MJ, Welham NJ (2003) Self-assembled silica-carbonate structures and detection of ancient microfossils. Science 302:1194–1197
Godfrey LV, Falkowski PG (2009) The cycling and redox state of nitrogen in the Archaean ocean. Nat Geosci 2:725
Godfrey LV, Poulton SW, Bebout GE, Fralick PW (2013) Stability of the nitrogen cycle during development of sulfidic water in the redox-stratified late Paleoproterozoic Ocean. Geology 41:655–658
Gold DA, Grabenstatter J, de Mendoza A, Riesgo A, Ruiz-Trillo I, Summons RE (2016) Sterol and genomic analyses validate the sponge biomarker hypothesis. Proc Natl Acad Sci 113:2684–2689
Gold DA, Caron A, Fournier GP, Summons RE (2017) Paleoproterozoic sterol biosynthesis and the rise of oxygen. Nature 543:420–423
Grantham PJ (1986) The occurence of unusual C_{27} and C_{29} sterane predominances in two types of Oman crude oil. Org Geochem 9:1–10
Grantham PJ, Lijmbach J, Posthuma J, Hughes Clarke MW, Willink RJ (1988) Origin of crude oils in Oman. J Pet Geol 11:61–88
Grey K (2005) Ediacaran palynology of Australia. Association of Australasian Palaeontologists, Canberra
Grey K, Willman S (2009) Taphonomy of Ediacaran acritarchs from Australia: significance for taxonomy and biostratigraphy. PALAIOS 24:239–256
Grosjean E, Love GD, Stalvies C, Fike DA, Summons RE (2009) Origin of petroleum in the Neoproterozoic-Cambrian South Oman Salt Basin. Org Geochem 40:87–110
Grosjean E, Love GD, Kelly AE, Taylor PN, Summons RE (2012) Geochemical evidence for an Early Cambrian origin of the 'Q'oils and some condensates from north Oman. Org Geochem 45:77–90
Grotheer H, Greenwood PF, McCulloch MT, Böttcher ME, Grice K (2017) $\delta^{34}S$ character of organosulfur compounds in kerogen and bitumen fractions of sedimentary rocks. Org Geochem 110:60–64. https://doi.org/10.1016/j.orggeochem.2017.04.005
Hackley PC, Walters CC, Kelemen SR, Mastalerz M, Lowers HA (2017) Organic petrology and micro-spectroscopy of Tasmanites microfossils: applications to kerogen transformations in the early oil window. Org Geochem 114:23. https://doi.org/10.1016/j.orggeochem.2017.09.002
Halverson GP, Hoffman PF, Schrag DP, Maloof AC, Rice AHN (2005) Toward a Neoproterozoic composite carbon-isotope record. Geol Soc Am Bull 117:1181–1207
Hayes JM, Waldbauer JR (2006) The carbon cycle and associated redox processes through time. Philos Trans R Soc B 361:931–950
Hayes JM, Kaplan IR, Wedeking KW (1983) Precambrian organic geochemistry: preservation of the record. In: Schopf JW (ed) Earth's earliest biosphere: its origin and evolution. Princeton University Press, Princeton, pp 93–135
Hayes JM, Summons RE, Strauss H, Des Marais DJ, Lambert IB (1992) Proterozoic biogeochemistry. In: Schopf JW, Klein C (eds) The proterozoic biosphere: a multidisciplinary study. Cambridge University Press, Cambridge, pp 81–133
Hayes JM, Strauss H, Kaufman AJ (1999) The abundance of ^{13}C in marine organic matter and isotopic fractionation in the global biogeochemical cycle of carbon during the past 800 Ma. Chem Geol 161:103–125
Hoering TC (1965) The extractable organic matter in Precambrian rocks and the problem of contamination. Carnegie Inst Wash Yearb 64:215–218
Hoering TC (1966) Criteria for suitable rocks in Precambrian organic geochemistry. Year B Carnegie Inst Wash 65:365–372
Hofmann HJ (2004) Archean microfossils and abiomorphs. Astrobiology 4:135–136
Hoshino Y, Poshibaeva A, Meredith W, Snape C, Poshibaev V, Versteegh GJM, Kuznetsov N, Leider A, van Maldegem L, Neumann M, Naeher S, Moczydłowska M, Brocks JJ, Jarrett AJM, Tang Q, Xiao S, McKirdy D, Das SK, Alvaro JJ, Sansjofre P, Hallmann C (2017) Cryogenian evolution of stigmasteroid biosynthesis. Sci Adv 3:e1700887
House CH, Schopf JW, McKeegan KD, Coath CD, Harrison TM, Stetter KO (2000) Carbon isotopic composition of individual Precambrian microfossils. Geology 28:707–710

House CH, Oehler DZ, Sugitani K, Mimura K (2013) Carbon isotopic analyses of ca. 3.0 Ga microstructures imply planktonic autotrophs inhabited Earth's early oceans. Geology 41:651–654

Illing CJ, Hallmann C, Miller KE, Summons RE, Strauss H (2014) Airborne hydrocarbon contamination from laboratory atmospheres. Org Geochem 76:26–38. https://doi.org/10.1016/j.orggeochem.2014.07.006

Jackson MJ, Powell TG, Summons RE, Sweet IP (1986) Hydrocarbon shows and petroleum source rocks in sediments as old as 1.7×10^9 years. Nature 322:727–729

Jarrett AJM, Schinteie R, Hope JM, Brocks JJ (2013) Micro-ablation, a new technique to remove drilling fluids and other contaminants from fragmented and fissile rock material. Org Geochem 61:57–65. https://doi.org/10.1016/j.orggeochem.2013.06.005

Javaux EJ, Knoll AH (2017) Micropaleontology of the lower Mesoproterozoic roper group, Australia, and implications for early eukaryotic evolution. J Paleontol 91:199–229

Javaux EJ, Knoll AH, Walter MR (2001) Morphological and ecological complexity in early eukaryotic ecosystems. Nature 412:66–69

Javaux EJ, Knoll AH, Walter M (2003) Recognizing and interpreting the fossils of early eukaryotes. Orig Life Evol Biosph 33:75–94

Kelly AE, Love GD, Zumberge JE, Summons RE (2011) Hydrocarbon biomarkers of Neoproterozoic to lower Cambrian oils from eastern Siberia. Org Geochem 42:640–654. https://doi.org/10.1016/j.orggeochem.2011.03.028

Klomp UC (1986) The chemical structure of a pronounced series of isoalkanes in South Oman crudes. Org Geochem 10:807–814

Knoll AH (1992) The early evolution of eukaryotes: a geological perspective. Science 256:622–627

Knoll AH (2014) Paleobiological perspectives on early eukaryotic evolution. Cold Spring Harb Perspect Biol 6:a016121

Knoll AH, Nowak MA (2017) The timetable of evolution. Sci Adv 3:e1603076

Knoll AH, Hayes JM, Kaufman AJ, Swett K, Lambert IB (1986) Secular variation in carbon isotope ratios from upper Proterozoic successions of Svalbard and East Greenland. Nature 321:832–838

Knoll AH, Summons RE, Waldbauer JR, Zumberge J (2007) The geological succession of primary producers in the oceans. In: Falkwoski P, Knoll AH (eds) The evolution of primary producers in the sea. Elsevier, Boston, pp 133–163

Kovalevski VV, Buseck PR, Cowley JM (2001) Comparison of carbon in shungite rocks to other natural carbons: an X-ray and TEM study. Carbon 39:243–256

Logan GA, Hayes JM, Hieshima GB, Summons RE (1995) Terminal Proterozoic reorganization of biogeochemical cycles. Nature 376:53–56

Love GD, Grosjean E, Fike DA, Grotzinger JP, Bowring SA, Condon DJ, Lewis AN, Stalvies C, Snape CE, Summons RE (2005) A >90 million year molecular record of Neoproterozoic sponges (*Porifera*) in the south Oman salt basin. In: 22nd international meeting on organic geochemistry, Seville

Love GD, Stalvies C, Grosjean E, Meredith W, Snape CE (2008) Analysis of molecular biomarkers covalently bound within Neoproterozoic sedimentary kerogen. In: Kelley PH, Bambach RK (eds) Paleontological Society Papers. The Paleontological Society, pp 67–83

Love GD, Grosjean E, Stalvies C, Fike DA, Grotzinger JP, Bradley AS, Kelly AE, Bhatia M, Meredith W, Snape CE, Bowring SA, Condon DJ, Summons RE (2009) Fossil steroids record the appearance of Demospongiae during the Cryogenian period. Nature 457:718–721. https://doi.org/10.1038/nature07673. http://www.nature.com/nature/journal/v457/n7230/suppinfo/nature07673_S1.html

Luo G, Hallmann C, Xie S, Ruan X, Summons RE (2015) Comparative microbial diversity and redox environments of black shale and stromatolite facies in the Mesoproterozoic Xiamaling formation. Geochim Cosmochim Acta 151:150–167. https://doi.org/10.1016/j.gca.2014.12.022

McCaffrey MA, Moldowan MJ, Lipton PA, Summons RE, Peters KE, Jeganathan A, Watt DS (1994) Paleoenvironmental implications of novel C_{30} steranes in Precambrian to Cenozoic Age petroleum and bitumen. Geochim Cosmochim Acta 58:529–532

McKirdy DM (1974) Organic geochemistry in Precambrian research. Precambrian Res 1:75–137

Melezhik VA, Fallick AE, Filippov MM, Larsen O (1999) Karelian shungite – an indication of 2.0-Ga-old metamorphosed oil-shale and generation of petroleum: geology, lithology and geochemistry. Earth Sci Rev 47:1–40

Melezhik VA, Filippov MM, Romashkin AE (2004) A giant Palaeoproterozoic deposit of shungite in NW Russia: genesis and practical applications. Ore Geol Rev 24:135–154. https://doi.org/10.1016/j.oregeorev.2003.08.003

Meshoulam A, Ellis GS, Said Ahmad W, Deev A, Sessions AL, Tang Y, Adkins JF, Liu J, Gilhooly WP, Aizenshtat Z, Amrani A (2016) Study of thermochemical sulfate reduction mechanism using compound specific sulfur isotope analysis. Geochim Cosmochim Acta 188:73–92. https://doi.org/10.1016/j.gca.2016.05.026

Muirhead DK, Parnell J, Spinks S, Bowden SA (2017) Characterization of organic matter in the Torridonian using Raman spectroscopy. Geol Soc Lond Spec Publ 448:71

Peters KE, Walters CC, Moldowan JM (2005) The biomarker guide, 2nd edn. Cambridge University Press, Cambridge

Rasmussen B, Glover JE, Foster CB (1993) Polymerisation of hydrocarbons by radioactive minerals in sedimentary rocks: diagenetic and economic significance. In: Bitumens in ore deposits. Springer, Berlin, pp 490–509

Rasmussen B, Fletcher IR, Brocks JJ, Kilburn MR (2008) Reassessing the first appearance of eukaryotes and cyanobacteria. Nature 455:1101–1104

Rothman D (2015) Earth's carbon cycle: a mathematical perspective. Bull Am Math Soc 52:47–64

Rothman DH, Hayes JM, Summons RE (2003) Dynamics of the Neoproterozoic carbon cycle. Proc Natl Acad Sci USA 100:8124–8129

Schidlowski M (1988) A 3,800-million-year isotopic record of life from carbon in sedimentary rocks. Nature 333:313–318

Schidlowski M (2001) Carbon isotopes as biogeochemical recorders of life over 3.8 Ga of Earth history: evolution of a concept. Precambrian Res 106:117–134

Schidlowski M, Hayes JM, Kaplan IR (1983) Isotopic inferences of ancient biochemistries – carbon, sulfur, hydrogen, and nitrogen. In: Schopf JW (ed) Earth's earliest biosphere: its origin and evolution. Princeton University Press, Princeton, pp 149–186

Schinteie R, Brocks JJ (2017) Paleoecology of Neoproterozoic hypersaline environments: biomarker evidence for haloarchaea, methanogens, and cyanobacteria. Geobiology 15:641. https://doi.org/10.1111/gbi.12245

Schopf JW, Kudryavtsev AB (2009) Confocal laser scanning microscopy and Raman imagery of ancient microscopic fossils. Precambrian Res 173:39–49. https://doi.org/10.1016/j.precamres.2009.02.007

Schopf JW, Walter MR (1983) Archean microfossils- new evidence of ancient microbes. In: Earth's earliest biosphere: its origin and evolution (A 84-43051 21-51). Princeton University Press, Princeton, pp 214–239

Schopf JW, Kudryavtsev AB, Czaja AD, Tripathi AB (2007) Evidence of Archean life: stromatolites and microfossils. Precambrian Res 158:141–155

Sessions AL (2016) Factors controlling the deuterium contents of sedimentary hydrocarbons. Org Geochem 96:43–64. https://doi.org/10.1016/j.orggeochem.2016.02.012

Strauss JV, Rooney AD, Macdonald FA, Brandon AD, Knoll AH (2014) 740 Ma vase-shaped microfossils from Yukon, Canada: implications for Neoproterozoic chronology and biostratigraphy. Geology 42:659–662

Stüeken EE, Buick R, Guy BM, Koehler MC (2015a) Isotopic evidence for biological nitrogen fixation by molybdenum-nitrogenase from 3.2 Gyr. Nature 520:666–669
Stüeken EE, Buick R, Schauer AJ (2015b) Nitrogen isotope evidence for alkaline lakes on late Archean continents. Earth Planet Sci Lett 411:1–10
Stüeken EE, Kipp MA, Koehler MC, Buick R (2016) The evolution of Earth's biogeochemical nitrogen cycle. Earth Sci Rev 160:220–239. https://doi.org/10.1016/j.earscirev.2016.07.007
Summons RE, Powell TG, Boreham CJ (1988) Petroleum geology and geochemistry of the middle Proterozoic McArthur Basin, Northern Australia: III. Composition of extractable hydrocarbons. Geochim Cosmochim Acta 52:1747–1763
Summons RE, Jahnke LL, Hope JM, Logan GA (1999) 2-methylhopanoids as biomarkers for cyanobacterial oxygenic photosynthesis. Nature 400:554–556
Thomazo C, Ader M, Philippot P (2011) Extreme 15N-enrichments in 2.72-Gyr-old sediments: evidence for a turning point in the nitrogen cycle. Geobiology 9:107–120. https://doi.org/10.1111/j.1472-4669.2011.00271.x
Wacey D, Kilburn MR, Saunders M, Cliff J, Brasier MD (2011) Microfossils of sulphur-metabolizing cells in 3.4-billion-year-old rocks of Western Australia. Nat Geosci 4:698–702
Wacey D, Menon S, Green L, Gerstmann D, Kong C, McLoughlin N, Saunders M, Brasier M (2012) Taphonomy of very ancient microfossils from the ~3400Ma Strelley pool formation and ~1900Ma gunflint formation: new insights using a focused ion beam. Precambrian Res 220:234–250
Waldbauer JR, Sherman LS, Sumner DY, Summons RE (2009) Late Archean molecular fossils from the Transvaal Supergroup record the antiquity of microbial diversity and aerobiosis. Precambrian Res 169:28–47
Williford KH, Ushikubo T, Lepot K, Kitajima K, Hallmann C, Spicuzza MJ, Kozdon R, Eigenbrode JL, Summons RE, Valley JW (2015) Carbon and sulfur isotopic signatures of ancient life and environment at the microbial scale: Neoarchean shales and carbonates. Geobiology 14:105. https://doi.org/10.1111/gbi.12163
Xiao S, Zhang Y, Knoll AH (1998) Three-dimensional preservation of algae and animal embryos in a Neoproterozoic phosphorite. Nature 391:553–558
Zerkle AL, Poulton SW, Newton RJ, Mettam C, Claire MW, Bekker A, Junium CK (2017) Onset of the aerobic nitrogen cycle during the Great Oxidation Event. Nature 542:465–467

Presolar Grains

Peter Hoppe
Particle Chemistry Department, Max Planck Institute for Chemistry, Mainz, Germany

Definition

Presolar grains are nanometer- to micrometer-sized dust grains that are found in small quantities in primitive meteorites, interplanetary dust particles (IDPs), and in cometary matter. They are older than our Solar System and formed in the winds of evolved stars and in the ejecta of stellar explosions, as evidenced by large isotopic abundance anomalies.

Introduction

Our Solar System formed from the collapse of an interstellar gas and dust cloud some 4.57 billion years ago. Originally it was thought that all the matter that went into the making of our Solar System was completely mixed and isotopically homogenized. First hints about the presence of isotopically anomalous minerals in meteorites were found in the 1960s (Reynolds and Turner 1964; Black and Pepin 1969). It took another 20 years before Ed Anders and co-workers were able to isolate the first presolar minerals, silicon carbide (SiC), nanodiamonds, and (graphitic) carbon (in the following referred to as "graphite"), as carrier of isotopically anomalous noble gases from carbonaceous chondrites at the University of Chicago (Bernatowicz et al. 1987; Lewis et al. 1987; Amari et al. 1990). After their isolation it was found that SiC and graphite carry large isotopic anomalies also in their major elements and in many other minor/trace elements. It became quickly clear that these grains must have a presolar origin, i.e., they are older than our Solar System, and that they represent a sample of stardust that can be analyzed in the laboratory. In contrast, the origin of nanodiamonds is still a matter of debate today. The reason for this is their small size of only 2–3 nm, two to three orders of magnitude smaller than those of presolar SiC and graphite grains, which currently does not allow to measure isotopic compositions of individual nanodiamonds but only of ensembles of millions of grains. The major element carbon of these grain ensembles has approximately solar isotopic composition, which makes it difficult to decide which fraction of nanodiamonds is true stardust.

Following the discovery of carbonaceous presolar grains other types of presolar grains were identified in acid-resistant residues of meteorites in the 1990s, namely, silicon nitride (Si_3N_4) (Nittler et al. 1995) and refractory oxides (Hutcheon et al. 1994; Nittler et al. 1994). The most abundant presolar grain type, the silicates, remained undetected for a long time and was identified only at the beginning of this millennium (Messenger et al. 2003). The reason for this is that presolar silicates, other than carbonaceous presolar grains or refractory presolar oxides, cannot be separated by chemical treatments from meteorites. Only the development of new isotope measurement techniques (ion imaging) based on secondary ion mass spectrometry (SIMS) made the in situ discovery of presolar silicates possible.

Especially presolar graphite grains, but also SiC, contain small subgrains, e.g., titanium carbide (TiC) and other refractory carbides (Bernatowicz et al. 1991).

Measurements of isotopic compositions, physical properties, and mineralogies of individual presolar grains can give detailed information on the parent stars and on all stages in the life cycle of presolar grains, from the formation in circumstellar environments to the incorporation into planetary bodies (asteroids, comets) in the Solar System. In the last three

decades laboratory studies of presolar grains have provided a wealth of astrophysical information, namely, on stellar nucleosynthesis and evolution, galactic chemical evolution (GCE), dust formation around stars, dust processing in the interstellar medium (ISM), the types of stars that contributed dust to the Solar System, and the early Solar System history. The following two sections describe the isotopic compositions, physical properties, and stellar sources of carbonaceous and oxygen-rich presolar grains. Detailed references can be found in recent review papers by Lodders and Amari (2005), Hoppe (2008), Meyer et al. (2008), and Zinner (2014).

Carbonaceous Presolar Grains

Silicon carbide is the best studied presolar mineral. Reasons for this are that (i) it is relatively abundant in primitive meteorites (up to 100 ppm), (ii) it can be separated by physical and chemical treatments in almost pure form from meteorites, (iii) many grains are larger than 1 μm, and (iv) it has high abundances of minor/trace elements. Based on the isotopic compositions of C, N (the most abundant minor element), and Si, presolar SiC is divided into distinct populations: mainstream (MS), and the minor grain types AB, C, X, Y, Z, and nova. The vast majority of presolar SiC (~90%) belongs to the MS group. These grains have $^{12}C/^{13}C$ ratios between 10 and 100 (Solar System: 89) and mostly higher than solar $^{14}N/^{15}N$ ratios (Fig. 1). Silicon isotopic abundance anomalies are smaller than those in C and N with typical enrichments in the heavy Si isotopes ^{29}Si and ^{30}Si of several percent. Other important characteristics of MS grains are enrichments in elements that are produced by the s-process (slow-neutron capture reactions) and isotopic patterns expected for the s-process. Based on a comparison with stellar models and astronomical observations, it is generally accepted that MS grains formed in the winds of low-mass (1–3 $M_\odot$) red giant stars of about solar metallicity (metallicity is the mass fraction of all elements heavier than He) on the asymptotic giant branch (AGB) of evolution. Also the Type Y and Z grains are likely from low-mass AGB stars, but from those with lower than solar metallicity, as indicated by specific Si-isotopic signatures. The origin of the Type AB grains is still a matter of debate. The most promising stellar sources are born-again AGB stars (AGB stars that experience a very late thermal pulse) and J-type carbon stars that can account for the very low $^{12}C/^{13}C$ ratios (<10) observed in AB grains (Fig. 1). Grains from supernova explosions (the final stage of stars heavier than about 8 $M_\odot$) are the Type X and C grains. X grains account for about 1% of all presolar SiC grains, and C grains for less than 0.1%. X and C grains have mostly higher than solar $^{12}C/^{13}C$ ratios and all have lower than solar $^{14}N/^{15}N$ ratios (Fig. 1). X grains often have very high N abundances (at the percent level), and they may be related to the very rare presolar

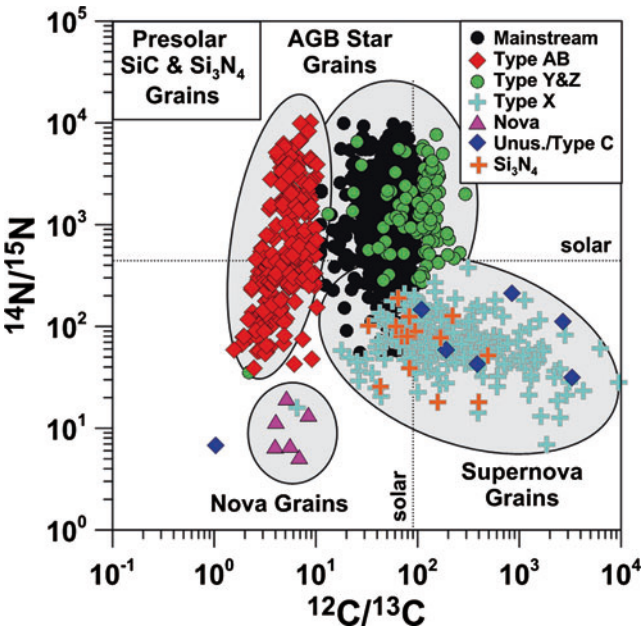

Presolar Grains, Fig. 1 Carbon- and N-isotopic systematics of presolar SiC and Si_3N_4. The solar isotopic ratios are shown by *dashed lines* for comparison. Data are taken from the Washington University Presolar Grain Data Base (http://presolar.wustl.edu/PGD/Presolar_Grain_Database.html; (Hynes and Gyngard 2009). Figure adapted from Hoppe (2011)

Si_3N_4 grains (found only at the ppb level) which share the isotopic characteristics of X grains (Fig. 1). Silicon-isotopic anomalies are much larger than those of grains from AGB stars; while X grains show strong depletions in the heavy Si isotopes (up to a factor of 5 relative to solar isotopic abundances), C grains are strongly enriched in these isotopes (up to a factor of 4). Other important signatures of supernova SiC grains are high abundances of ^{26}Mg from the decay of radioactive ^{26}Al (half-life 720,000 years) and evidence for incorporation of other radioactive nuclides, namely, ^{32}Si (half-life 153 years), ^{44}Ti (half-life 60 years), and ^{49}V (half-life 330 days) when the grains condensed. As the name implies the nova grains (<0.1% of SiC) are believed to come from nova explosions (triggered by mass-transfer from a companion star to a white dwarf) which are predicted to produce grains with very low $^{12}C/^{13}C$ and $^{14}N/^{15}N$ ratios (Fig. 1).

Presolar graphite grains are round and mostly larger than 1 μm. They are found at abundance levels up to ~10 ppm in primitive meteorites. Basically, two populations can be distinguished: low-denisty (LD) grains, which account for about 25% of all graphite grains, and high-density (HD) grains. Although the range of $^{12}C/^{13}C$ ratios (2–7000) is similar to that observed in presolar SiC (Fig. 1), the distribution of $^{12}C/^{13}C$ is different. Most HD grains show higher than solar $^{12}C/^{13}C$, with a peak in the distribution near $^{12}C/^{13}C = 500$. In contrast, most LD grains show lower than solar $^{12}C/^{13}C$ ratios. Based on inferred high ^{26}Al abundances, large

excesses in ^{15}N and ^{18}O, large excesses or deficits in the heavy Si isotopes, and evidence for the presence of radioactive ^{44}Ti and ^{41}Ca (half-life 105,000 years) at the time of grain formation, it is believed that the majority of LD grains formed in the ejecta of supernova explosions. The high $^{12}C/^{13}C$ ratios together with the chemical composition of subgrains and isotopic compositions of Si and heavy elements, on the other hand, suggest an origin from low-metallicity AGB stars for most HD grains. Extremely large isotope anomalies in Ca and Ti along with low $^{12}C/^{13}C$ ratios in some HD grains indicate small contributions from born-again AGB stars. Evidence for ^{22}Na decay (half-life 2.6 years) as source of so-called Ne-E(L) in presolar graphite together with low $^{12}C/^{13}C$ ratios suggests an origin of a small fraction (~1%) of presolar graphite grains from nova explosions.

Oxygen-Rich Presolar Grains

Abundances of presolar O-rich grains vary strongly among meteorites, apparently reflecting parent body processing. Presolar oxide abundances range up to ~50 ppm; presolar silicate abundances are higher, up to ~200 ppm in meteorites, ~375 ppm on average in so-called primitive IDPs, and up to the percent level in individual IDPs. Estimates for the abundance of O-rich presolar dust in matter from comet 81P/Wild 2 returned by NASA's STARDUST mission bear large uncertainties but are compatible with inferred abundances for IDPs. Presolar silicates have typical sizes of 200–300 nm. The same holds for presolar oxides identified in situ; chemically separated oxides, on the other hand, have sizes up to several μm. Most oxide grains are corundum and other forms of Al_2O_3, spinel, and hibonite; a few chromite, titanium oxide, and iron oxide grains were found as well. Presolar silicates show a range of chemical compositions. Most grains have nonstoichiometric compositions with (Mg + Fe)/Si ratios between 1 (pyroxene-like) and 2 (olivine-like). Multicomponent grains, consisting of oxide-silicates assemblages, were found as well. Information on the mineralogy is still limited because sample preparation (production of electron-transparent sections by focused ion beam lift-out) is very time-consuming. Crystalline grains (~25%), mostly olivine, amorphous to weakly nanocrystalline grains (~50%), and so-called GEMS (~25%), glass with embedded metal and sulfide, were identified.

Based on the O-isotopic compositions, O-rich presolar grains are divided into four distinct populations (Fig. 2). Most abundant (~70%) are Group 1 grains. These grains have higher than solar $^{17}O/^{16}O$ and close to solar $^{18}O/^{16}O$ ratios and silicates show Si-isotopic compositions similar to those observed in SiC MS grains. A comparison with stellar models and astronomical observations suggests that Group 1 grains originate from 1.2–2.2 $M_\odot$ red giant and AGB stars

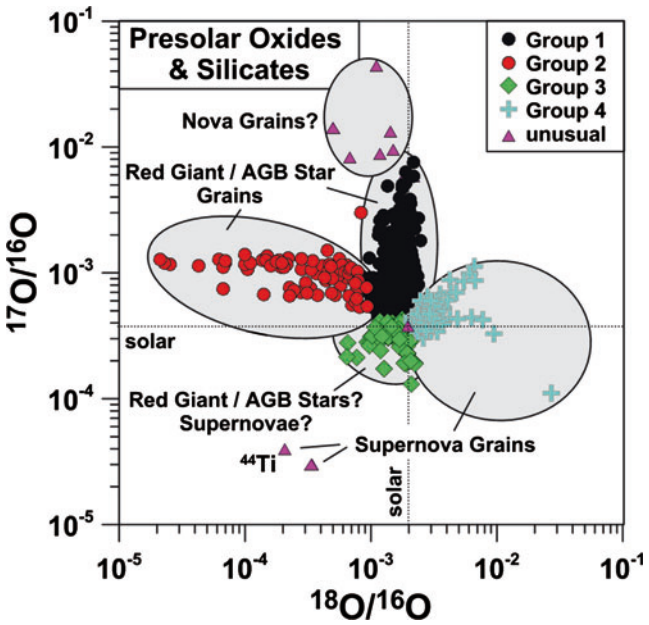

Presolar Grains, Fig. 2 Oxygen-isotopic systematics of presolar oxides and silicates. The solar isotopic ratios are shown by *dashed lines* for comparison. Data are taken from the Washington University Presolar Grain Data Base (http://presolar.wustl.edu/PGD/Presolar_Grain_Database.html; (Hynes and Gyngard 2009). Figure adapted from Hoppe (2011)

of about solar metallicity. Group 2 grains have enhanced ^{17}O and large depletions in ^{18}O (Fig. 2). The proposed stellar sources are low-mass (<1.5 $M_\odot$) red giant and AGB stars that underwent so-called cool bottom processing. The origin of Group 3 grains, most of which show slight depletions in ^{17}O and ^{18}O (Fig. 2), is still not fully understood. Most Group 3 grains appear to originate from low-mass (<1.2 $M_\odot$) red giant and AGB stars of lower than solar metallicity and those with subsolar $^{17}O/^{18}O$ ratios might have a supernova origin. Group 4 grains exhibit enrichments in ^{18}O and a range of $^{17}O/^{16}O$ ratios (Fig. 2). Supernovae are considered the most likely stellar sources. Only two grains show strong enrichments in ^{16}O, the expected predominant signature of supernova grains. One of them carries now extinct ^{44}Ti, as observed in carbonaceous supernova grains. Recent studies indicate that supernova grains are more abundant among small (<150 nm) grains. Some grains have very high $^{17}O/^{16}O$ ratios (Fig. 2), higher than predicted for red giant and AGB stars, and these grains are possibly from nova explosions.

Summary

Primitive meteorites, IDPs, and cometary matter contain small quantities of nanometer- to micrometer-sized dust grains that carry large isotopic abundance anomalies. These

grains, called presolar grains, are older than our Solar System and formed in the winds of evolved stars and in the ejecta of stellar explosions. Laboratory studies have provided a wealth of astrophysical information, namely, on stellar nucleosynthesis and evolution, GCE, dust formation around stars, dust processing in the ISM, the types of stars that contributed dust to the Solar System, and the early Solar System history.

Cross-References

- ▶ Chondrites
- ▶ Ion Microprobe
- ▶ Meteorites
- ▶ Nucleosynthesis

References

Amari S, Anders E, Virag A, Zinner E (1990) Interstellar graphite in meteorites. Nature 345:238–240

Bernatowicz T, Fraundorf G, Ming T, Anders E, Wopenka B, Zinner E, Fraundorf P (1987) Evidence for interstellar SiC in the Murray carbonaceous meteorite. Nature 330:728–730

Bernatowicz T, Amari S, Zinner E, Lewis RS (1991) Interstellar grains within interstellar grains. Astrophys J 373:L73–L76

Black DC, Pepin RO (1969) Trapped neon in meteorites. II Earth Planet Sci Lett 6:395–405

Hoppe P (2008) Reservoir for comet material: circumstellar grains. Space Sci Rev 138:43–57

Hoppe P (2011) Measurements of presolar grains. In: Proceedings of the 11th symposium on Nuclei in the Cosmos (NIC XI), 19 –23 July 2010, Heidelberg. Available online at http://pos.sissa.it/cgi-bin/reader/conf.cgi?confid=100#session-21

Hutcheon ID, Huss GR, Fahey AJ, Wasserburg GJ (1994) Extreme ^{26}Mg and ^{17}O enrichments in an Orgueil corundum: identification of a presolar oxide grain. Astrophys J 425:L97–L100

Hynes KM, Gyngard F (2009) The presolar grain data base: http://presolar.wustl.edu/~pgd. Lunar Planet Sci. 40:abstract #1398

Lewis RS, Tang M, Wacker JF, Anders E, Steel E (1987) Interstellar diamonds in meteorites. Nature 326:160–162

Lodders K, Amari S (2005) Presolar grains from meteorites: remnants from the early times of the solar system. Chem Erde 65:93–166

Messenger S, Keller LP, Stadermann F, Walker RM, Zinner E (2003) Samples of stars beyond the solar system: silicate grains in interplanetary dust. Science 300:105–108

Meyer BS, Nittler LR, Nguyen AN, Messenger S (2008) Nucleosynthesis and chemical evolution of oxygen. Rev Mineral Geochem 68:31–53

Nittler LR, Alexander CMOD, Gao X, Walker RM, Zinner EK (1994) Interstellar oxide grains from the Tieschitz ordinary chondrite. Nature 370:443–446

Nittler LR, Hoppe P, Alexander CMOD, Amari S, Eberhardt P, Gao X, Lewis RS, Strebel R, Walker RM, Zinner E (1995) Silicon nitride from supernovae. Astrophys J 453:L25–L28

Reynolds JH, Turner G (1964) Rare gases in the chondrite Renazzo. J Geophys Res 69:3263–3281

Zinner E (2014) Presolar Grains. In: Davis AM (ed) Meteorites and cosmochemical processes. Elsevier, Amsterdam, pp 181–213

Programmed Temperature Pyrolysis

Kenneth E. Peters[1,2] and Leonardo Briceño Rodriguez[3]
[1]Schlumberger, Mill Valley, CA, USA
[2]Department of Geological Sciences, Stanford University, Stanford, CA, USA
[3]Schlumberger, Mexico City, Mexico

Definition

Programmed pyrolysis is a laboratory method commonly used to characterize organic matter in sedimentary rocks; it involves heating of a rock sample at progressively higher temperatures in the absence of oxygen in order to evaluate it as a petroleum source or reservoir rock or to determine kinetic parameters that describe the thermal decomposition of the organic matter to petroleum.

Introduction

This article focuses on the application of pyrolysis to petroleum resources. Pyrolysis at a programmed rate of increasing temperature is used to volatilize and crack organic matter from petroleum source-rock samples for characterization by various detectors. For example, programmed pyrolysis coupled with flame ionization and thermal conductivity detection monitors evolved hydrocarbons and other products and is suitable for screening large numbers of rock samples (Espitalié et al. 1977; Peters 1986). More detailed fingerprinting of these products can be obtained using other detectors, as in pyrolysis-gas chromatography or pyrolysis-mass spectrometry (Larter 1984). Other pyrolysis studies focus on polymers, biomass, and biology (e.g., Voorhees 1984). Many environmental studies include pyrolysis of air particulates and other pollutants, wastewater, soils, and sediments (Munson 2006). Pyrolysis has been used to study meteorites and search for evidence of life on Mars and other planets (Sephton 2017).

Open-system programmed temperature pyrolysis is used in exploration for conventional and unconventional petroleum resources to (1) rapidly and inexpensively measure properties of organic matter that can be used to evaluate the quantity, quality, and thermal maturity of large numbers of candidate source-rock samples from wellbores, (2) identify petroleum reservoir intervals and thermal maturity gradients with depth, and (3) provide kinetic parameters for source

Modified version from "Programmed Temperature Pyrolysis" published in Peters KE and Rodriguez LB (2017).

rocks that can be used in computerized basin and petroleum system modeling (BPSM) to simulate the transformation of organic matter to petroleum during burial in sedimentary basins. Commercial programmed pyrolysis instruments that address items 1 and 2, such as Rock-Eval® or SR Analyzer™, heat ~100 mg samples of drill cuttings or core from wells under an inert atmosphere using a single programmed ramp of increasing temperature, typically 25 °C/min (Espitalié et al. 1977; Peters 1986; Peters and Cassa 1994).

Specialized programmed pyrolysis instrumentation is used for item 3 to obtain accurate temperatures for the thermal decomposition of organic matter used in kinetic determinations. Early work summarized by Tissot and Espitalié (1975) showed that the laboratory maturation of organic matter in source-rock samples can be described by parallel series of independent first-order reactions. The recommended method for kinetic analysis of pyrolysis results generates a discrete activation energy distribution and corresponding frequency factor for thermally immature equivalents of the source rock and requires at least three pyrolysis temperature ramps on aliquots of each sample (~3–10 mg) that span a 20-fold variation of comparatively low rates, such as 1, 5, and 25 °C/min (Peters et al. 2015b). Instrument design, thermocouple orientation and size, and sample weight are key factors that influence the quality of the resulting kinetic parameters. Several commercial instruments that can be used to measure kinetic parameters include Pyromat II™, Hawk™, SR Analyzer™, and Rock-Eval 6®.

Although this paper focuses on pyrolysis and discrete sampling as described above, these data can be complemented by direct and indirect wireline measurements of total organic carbon (TOC; Peters et al. 2016a) and by downhole fluid analysis (DFA). For example, neutron-induced capture and inelastic gamma ray spectroscopy using a high-resolution scintillator differentiates complex lithologies and provides quantitative TOC values at typical well logging speeds (Gonzalez et al. 2013). DFA employs near-infrared, visible, and fluorescence spectroscopy for continuous measurements of fluid properties that are especially useful to evaluate reservoir fluid gradients and connectivity (Mullins et al. 2014, 2015).

Quality, Quantity, and Thermal Maturity of Rock Samples

Most petroleum industry or service laboratories use Rock-Eval pyroanalyzers, so the following discussion will emphasize the development and use of these systems. However, the methods and results obtained by other systems, such as the SR Analyzer, are similar. Various generations of Rock-Eval pyroanalyzers are currently used (Espitalié et al. 1977; Lafargue et al. 1998). Rock-Eval pyrograms and calculated parameters for large numbers of closely spaced samples in wells can be used to identify petroleum source rocks as well as petroleum reservoir rocks (Peters 1986; Peters and Cassa 1994). The method can be used as a screening tool to identify few key samples for further, more sophisticated geochemical analyses, such as gas chromatography-mass spectrometry (GCMS) of candidate petroleum source-rock extracts for biomarker (molecular fossil) composition (Peters et al. 2005).

Conventional and unconventional petroleum resources are fundamentally different and require different vertical sample spacing within wells for useful pyrolysis interpretations (Peters et al. 2015a, 2016a). As discussed below, conventional and unconventional exploration commonly require 10-m and 1-m or less sample spacing, respectively. Exploration for conventional resources aims to find petroleum that migrated from organic-rich, thermally mature source rock to reservoirs and traps. Unconventional rock or sediment units require stimulation, such as hydraulic fracturing, to produce the retained petroleum based on the balance between petroleum viscosity and rock matrix permeability. According to this definition, gas shales and gas hydrates are unconventional targets because very low permeability impedes the escape of hydrocarbon gases, such as methane, without stimulation. Shale oil in "tight" mudstones is an unconventional resource because the oil cannot readily pass through narrow pore throats in the rock. Oil sands are also unconventional resources because viscous biodegraded oil cannot readily escape from otherwise high-permeability sandstone without stimulation.

Petroleum Generation Kinetics for Rock Samples

Kinetic parameters for the transformation of organic matter to petroleum are required to compute petroleum yields and generation rates in basin and petroleum system modeling. Artificial maturation based on programmed pyrolysis of organic matter in source-rock samples can be used to generate independent first-order reactions that are constrained by a distribution of activation energies and a corresponding pre-exponential factor (Tissot and Espitalié 1975). These kinetic parameters were used in many early BPSM simulations (e.g., Sweeney et al. 1987; Espitalié et al. 1988; Ungerer 1990; Issler and Snowdon 1990). The method assumes that thermal alteration of organic matter can be described by independent, parallel first-order reactions that conform to the Arrhenius equation (e.g., Ungerer and Pelet 1987). This assumption may be oversimplified because petroleum generation comprises multiple cracking reactions, including initiation, propagation, and termination steps (Stainforth 2009) that involve free radicals, acid thermolysis, and carbonium ion reactions

with α-olefins (Kissin 1987). In addition, Stainforth (2009) infers that primary migration of petroleum through the source-rock network rather than kerogen cracking is the rate-limiting step in petroleum expulsion. Kerogen consists of particulate organic matter in sedimentary rocks that is insoluble in organic solvents. Despite these issues, most workers obtain source-rock kinetic parameters using programmed pyrolysis, partly because measured and predicted petroleum generation rate curves from open-system pyrolysis are similar to those observed in natural maturation series. These observations suggest that programmed pyrolysis experiments can be used to reliably predict maturation over geologic time (e.g., Schenk and Horsfield 1998). Predictions from BPSM that are based on laboratory kinetics agree with field data from exploration wells (e.g., Fig. 9 in Kuhn et al. 2012).

Some publications recommend open-system pyrolysis using a single temperature ramp and fixed frequency factor (e.g., Waples 2016 and references therein), but this is not recommended because one-ramp kinetics result in the potential for significant error (Peters et al. 2015b, 2016b). Several publications describe how to optimize kinetic parameters based on open-system programmed pyrolysis. Braun and Burnham (1987) showed that fitting to a single heating rate yields unreliable kinetic results for source rocks when both the activation energy (E_a, kcal/mol) distribution and pre-exponential factor (A, s^{-1}) are optimized. Model fitting based on single-ramp kinetics is deemed unacceptable by Vyazovkin and Wight (1999), and it is not recommended by the Kinetics Committee of the International Confederation for Thermal Analysis and Calorimetry (Vyazovkin et al. 2014). Sundararaman et al. (1992) and Dieckmann (2005) also showed that a single pyrolysis heating rate experiment gives unreliable discrete E_a distributions. Both authors concluded that reliable kinetic results require multiple pyrolysis experiments on aliquots of the source-rock sample at widely differing heating rates.

Other methods that differ from open-system programmed pyrolysis have been proposed to obtain kinetic parameters for the thermal decomposition of organic matter. These include closed-system isothermal pyrolysis, such as hydrous pyrolysis (e.g., Lewan et al. 1979; Lewan and Ruble 2002), microscale sealed vessel pyrolysis (MSSV, e.g., Horsfield et al. 1989), or gold tube reactors (e.g., Behar et al. 1992). Some papers discuss the reliability of kinetics determined using open- versus closed-system pyrolysis (e.g., Schenk and Horsfield 1993; Ritter et al. 1995; Barth et al. 1996; Lewan and Ruble 2002). In this paper, we focus on open-system programmed pyrolysis because it is the most commonly used and likely the most reliable method to obtain source-rock kinetic parameters.

Methods

Rock-Eval Pyrolysis

For Rock-Eval pyrolysis, samples of drill cuttings, sidewall core, or conventional core are first screened by binocular microscope and then crushed to fine sand particle size (0.125–0.25 mm), and ~100 mg of each dried (<50 °C) sample is loaded into pyrolysis crucibles. The samples are pyrolyzed under flowing helium at 100–300 °C for several min, followed by heating at 25 °C/min to 550–600 °C or 850 °C, depending on the pyroanalyzer model. Pyrolysis products from each sample, such as hydrocarbons (compounds that contain carbon and hydrogen) and generated by the pyrolysis, are measured in ~20–30 min. Programmed temperature pyrolysis also produces large quantities of nonhydrocarbons (compounds that contain nitrogen, sulfur, and oxygen, in addition to carbon and hydrogen). Both hydrocarbons and nonhydrocarbons are measured by a flame ionization detector (FID).

Programmed temperature pyrolysis and TOC data from wells are best interpreted using large numbers of samples taken at closely spaced intervals from each well. For conventional exploration, 10-m spacing is recommended, regardless of lithology (Peters and Cassa 1994). For unconventional exploration, increased resolution of 1-m spacing or less may be needed to optimize the best zone to position horizontal wells within source-rock units prior to hydraulic fracturing. Wireline tools offer the advantage of continuous rather than discrete measurements of TOC but cannot be used to interpret kerogen quality or thermal maturity (e.g., compare Figs. 3.3 and 3.7 in Peters et al. 2016a).

A "sweet spot" is that portion of unconventional source rock having more favorable porosity, permeability, water saturation, fluid properties, and/or rock stress that is likely to produce more petroleum than adjacent rock (Peters et al. 2016a). Identification of sweet spots requires properly scaled geochemical measurements. Multiple geochemical logs (see below) can be used to create maps to identify the lateral and vertical distributions of sweet spots. For critical samples that define source rock, reservoir rock, or potential productive zones for horizontal wells, interpretations from the pyrolysis results should be verified by other analyses, such as organic petrography, vitrinite reflectance, gas chromatography of extracts, and petrophysical measurements. This paper does not describe geomechanical properties of the rock, such as Young's modulus, Poisson's ratio, or preexisting fracture orientation, which must also be considered for positioning of horizontal wells within source-rock intervals (Peters et al. 2016a).

Kinetic Measurements

For kinetic measurements, the ideal sample consists ~3–10 mg of organic-rich, unweathered source rock that has

undergone diagenesis but has not yet generated appreciable petroleum (vitrinite reflectance equivalent $\leq$0.5%). Whole rock samples typically yield kinetic parameters similar to isolated kerogen (Tegelaar and Noble 1994; Reynolds and Burnham 1995). The organofacies in the sample must be representative of that within the effective source rock in the study area because the rate of thermal decomposition of organic matter to petroleum can differ for different source rocks (Tegelaar and Noble 1994) and even vertically or laterally within the same source rock (Peters et al. 2006).

Continuous temperatures are measured during each programmed pyrolysis experiment using a calibrated thermocouple in close contact with the sample. Performance and accuracy of temperature measurements for each pyrolysis system need to be evaluated independently. Products volatilized during decomposition of the kerogen are transferred to a flame ionization detector, typically by helium flow at 50 ml/min. Pyrolyzate peaks for kerogen decomposition can be processed by using various types of software, such as Kinetics05 or Kinetics2015, using methods originally described by Burnham and Braun (1999). Kinetic parameters are determined by iterative linear–nonlinear regression, where energy weighting factors are determined by constrained linear regression for a given frequency factor and the logarithm of the frequency factor is varied under Levenberg–Marquardt nonlinear regression (Levenberg 1944) until the root mean square deviation between measured and calculated generation rates of pyrolyzate yields a minimum.

Samples of thermally immature source rock that are age equivalent with the effective source rock in a basin are commonly unavailable. In such cases, a common but flawed practice in BPSM is to use default kinetic parameters available in the software for other source rocks that are assumed to contain organic matter similar to that in the study area based on kerogen type (e.g., Waples et al. 1992) or depositional environment and stratigraphic age (e.g., Pepper and Corvi 1995). We do not recommend this assumption because kerogen type as defined by Rock-Eval pyrolysis hydrogen index (HI, mg hydrocarbon/g TOC) is not systematically linked to kinetic response and it is risky to infer kerogen type or kinetics based on source-rock depositional environment (Peters et al. 2006). Thus, default kinetics for source rock from one basin may not apply to that in other basins, even when the HI for immature equivalents of each source rock is identical.

Interpreting Rock-Eval Pyrograms

An example of a programmed temperature pyrogram shows products generated from low-maturity source rock that has not yet reached the oil-generative window (Fig. 1, upper left). The thick red line shows oven temperature through time. The shaded peaks represent S1 (volatile hydrocarbon yield at 300 °C), S2 (hydrocarbons cracked from kerogen in the range 300–550 °C), and S3 (carbon dioxide generated up to 390 °C). S1 generally increases at the expense of S2 during thermal maturation of source rocks (Fig. 1, right column), although loss of some S1 due to expulsion can occur. S1 is high in active source rocks and reservoir rocks that contain petroleum. S2 is a better indicator of generative potential (quality) than TOC (quantity), which does not differentiate between oil-prone, gas-prone, or inert carbon. S2 is high in potential and active source rocks but low in postmature (spent) source rocks, non-source rocks, and many reservoir rocks. Ideally, S3 indicates carbon dioxide cracked from the kerogen. However, some carbonate-rich rocks that contain clays generate carbon dioxide below the 390 °C trap temperature (Peters 1986). Oxidation of organic matter in weathered outcrop samples and over-grinding during sample preparation can also elevate S3. S1 and S2 are measured by FID, while S3 is measured by thermal conductivity detection (TCD). FID measures hydrocarbons and nonhydrocarbons (e.g., sulfur-, nitrogen-, or oxygen-containing compounds) provided that the latter contain carbon atoms.

Rock-Eval T_{max} is a measure of thermal maturity based on programmed pyrolysis oven temperature that should not be confused with geologic temperature. In the absence of fluid or particulate contamination (discussed below), T_{max} commonly correlates with other thermal maturity parameters, such as vitrinite reflectance (R_o). For example, Jarvie et al. (2001) recommend the following formula to convert Rock-Eval pyrolysis T_{max} to R_o:

$$R_o(\text{calculated}) = (0.0180)(T_{max}) - 7.16 \quad (1)$$

The formula was derived from a collection of shale samples containing low-sulfur type II and type III kerogen (Jarvie et al. 2001) but can be inaccurate for type I kerogens. Kerogen type is defined by Rock-Eval HI in Table 1. Use of the formula is not recommended for very low- or high-maturity samples (where T_{max} is <420 °C or >500 °C) or when S2 is less than 0.5 mg HC/g rock. However, these correlations are best determined on a case-by-case basis (Wüst et al. 2013). T_{max} determined on very small S2 peaks (<0.2 mg HC/g rock) can be inaccurate. HI can be low, while T_{max} is high compared to isolated kerogen from organic-lean (<1 wt.% TOC) clay-rich rocks due to adsorption of pyrolyzate on clays (Peters 1986).

The production index [PI = S1/(S1 + S2)] increases with depth in fine-grained rocks because thermally reactive components in the kerogen (S2) are gradually converted to volatile hydrocarbons (S1). Coarse-grained conventional reservoir rocks stained with oil show anomalously high S1 and PI values that deviate from the depth trend in the adjacent fine-grained rocks. In some cases, T_{max} may be suppressed due to carry-over of heavy ends in the oil from S1 to S2 (Fig. 1, lower left). Oil-based drilling mud additives can

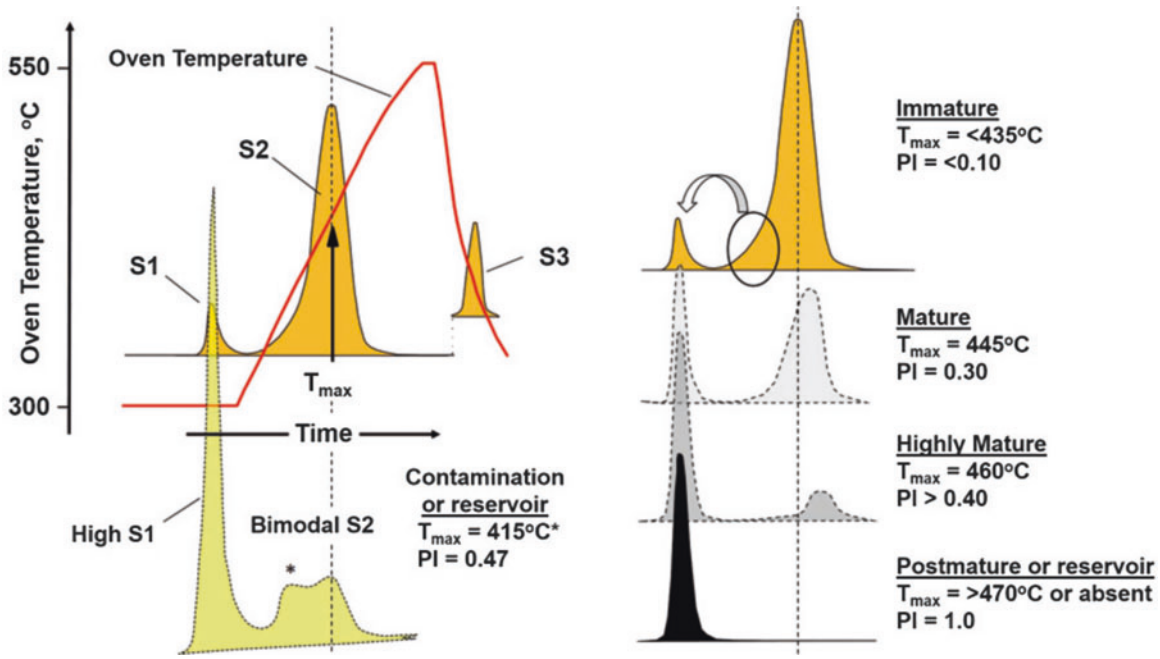

Programmed Temperature Pyrolysis, Fig. 1 Schematic programmed temperature pyrogram *(upper left)* shows S1 (volatile petroleum) and S2 (kerogen pyrolyzate, mg hydrocarbons (HC)/g rock), S3 (organic carbon dioxide, mg CO_2/g rock), and T_{max} (oven temperature in °C at the maximum of the S2 peak). Calculated parameters include hydrogen index (HI = 100 × S2/TOC, mg HC/g TOC), oxygen index (OI = 100 × S3/TOC, mg CO2/g TOC), and production index [PI = S1/(S1 + S2)]. Crude oil or contamination by oil-based drilling mud can yield anomalously high S1, high PI, and low T_{max} (*asterisk* at lower left, S3 not shown). Column at *right* shows typical evolution of S1, S2, T_{max}, and PI due to increasing thermal maturation of source rock. Pyrograms that show high S1 and PI with a very low or no S2 peak could represent postmature source rock or petroleum reservoir rock

Programmed Temperature Pyrolysis, Table 1 Programmed pyrolysis and vitrinite reflectance (R_o) parameters used to determine quantity, quality, and thermal maturity of rock samples. The three segments of the table must be interpreted separately. Thickness of the rock unit is also important for volumetric considerations

Quantity[a]			Quality[b]				Thermal maturity[c]		
Amount	TOC_o, wt. %	TOC_m, wt. %	Type	HI_o, mg HC/g TOC	Product	Stage	Ro, wt.%	Tmax (°C)	PI, [S1/(S1 + S2)]
Poor	<1	<1	I	>600	Oil	Immature	0.20–0.60	<435	<0.10
Fair	1–2	1.0–1.5	II	300–600	Oil	Early mature	0.60–0.65	435–445	0.10–0.15
Good	2–3	1.5–2.0	II–III	200–300	Oil/ gas	Peak mature	0.65–0.90	445–450	0.25–0.40
Very good	3–4	2.0–2.5	III	50–200	Gas	Late mature	0.90–1.35	450–470	>0.40
Excellent	>4	>2.5	IV	<50	None	Postmature	>1.35	>470	–

[a]TOC_o = original total organic carbon content for thermally immature source rock, TOC_m = measured total organic carbon for thermally mature or postmature source rock (unconventional target). Approximate values determined using data for nine top shale gas plays (Data from Jarvie 2012a)
[b]Type = kerogen type based on pyrolysis hydrogen index, HI_o (= 100 × S2/TOC for thermally immature source rock)
[c]R_o = oil-immersion vitrinite reflectance, T_{max} = pyrolysis oven temperature at maximum of S2 peak; for onset of oil generation: type I ~445 °C, type II ~435 °C, type III ~440 °C; PI = production index, where S1 = petroleum volatilized at 300 °C and S2 = petroleum cracked from the kerogen in the range 300–550 °C during pyrolysis at 25 °C/min

also interfere with pyrolysis measurements, especially S1 and PI. Oil-based contamination of cutting samples commonly yields a large S1 peak, a low-temperature shoulder that interferes with the S2 peak and represents heavy ends of the oil rather than kerogen, and a corresponding anomalously low T_{max} value (Fig. 1, lower left). S1 values >1 mg HC/g rock and anomalously high PI may indicate contamination of cutting samples by migrated oil or oil-based contamination. Such samples are routinely extracted with organic solvent (e.g., *n*-heptane) and reanalyzed in order to derive more accurate

measures of HI and T_{max} (Peters 1986; Peters and Cassa 1994). Provided that their presence is recognized, particulate additives, such as walnut hulls or polyethylene, can be removed under a binocular microscope.

Hydrogen index [HI = 100(S2)/TOC] and oxygen index [OI = 100(S3)/TOC) are based on combined pyrolysis and TOC parameters. Modified Van Krevelen plots of OI versus HI or plots of T_{max} versus HI must be used with caution to infer kerogen type and approximate level of thermal maturity (Espitalié et al. 1977; Peters 1986). Because kerogen consists of mixtures of macerals, plot locations on the modified Van Krevelen diagram can be deceptive (Dembicki 2009). Macerals are microscopically recognizable particles of kerogen that show distinct physicochemical properties. The three main maceral groups include liptinite, vitrinite, and inertinite. For example, a mixture of oil-prone type II (liptinite macerals) and inert type IV (inertinite macerals) might plot near the type III pathway on the Van Krevelen diagram, which could be incorrectly interpreted to indicate kerogen dominated by vitrinite macerals with the potential to generate only hydrocarbon gases. Pyrolysis-gas chromatography of such a sample could be used to reveal significant oil-generative potential (e.g., Peters et al. 1983; Pepper and Corvi 1995).

Jarvie (2012a) derived original hydrogen indices (HI_o) for thermally immature samples of the ten top North American shale gas plays: Barnett, Bossier, Eagle Ford, Fayetteville, Haynesville, Marcellus, Montney, Muskwa, Utica, and Woodford formations. He determined the average present-day TOC (TOC_m) on collections of samples from those plays showing mostly gas window thermal maturity. The equation below excludes data from the Haynesville Shale, which began with an unusually high HI_o, (722 mg HC/g TOC), resulting in a point far off the correlation line. The remaining nine data points show a linear correlation between TOC_o and TOC_m with a high correlation coefficient (>0.98):

$$TOC_m = 0.5468(TOC_o) + 0.3261 \quad (2)$$

This relationship was used to calculate the approximate cutoff values for poor, fair, good, very good, and excellent TOC_m for unconventional targets in Table 1. These TOC values represent quantity (not quality), and they are based on an average HI_o of ~438 ± 62 mg HC/g TOC. Peters et al. (2005, pp. 97–100) provide mass balance calculations to determine TOC_o from TOC_m.

Historical Development of Rock-Eval Pyroanalyzers

Since the 1970s, various Rock-Eval pyroanalyzers were developed to characterize rock samples from wellbores and outcrops, and these have become the most popular programmed pyrolysis instruments used by the petroleum industry. Many commercial laboratories still use Rock-Eval 2 instruments (Espitalié et al. 1977), which include automatic sampling and microprocessor control not available in Rock-Eval 1. In Rock-Eval 2, the S1 peak includes all hydrocarbons volatilized at 300 °C over a 3-min isothermal heating. TOC is determined separately on splits of the same sample by combustion. Rock-Eval 3 (oil show analyzer) effectively separates the volatile components into two peaks, S0 and S1. S0 includes light gas or condensate hydrocarbons in the range C_1–C_8 that are volatilized during a 90 °C isothermal heating for 1–5 min, while S1 includes hydrocarbons volatilized at 300 °C during a 3-min isothermal heating. Contamination of samples during drilling or evaporative loss during sample handling can seriously affect S0 values. Rock-Eval 3 combusts the residue from the pyrolysis, which allows determination of TOC without the need to split rock samples for separate pyrolysis and TOC analyses. Since the combustion in Rock-Eval 3 occurs at the same maximum temperature as the original pyrolysis (550–600 °C), TOC values for highly mature rock samples are commonly lower than conventional combustion results (>1,000 °C) because they may contain organic matter that is not readily oxidized.

The Rock-Eval 6 pyroanalyzer improves on earlier versions by providing S1, S2, S3, as well as carbonate carbon and TOC. Similar results can be obtained using the SR Analyzer TPH/TOC™. Combustion in the Rock-Eval 6 oven occurs at 850 °C, resulting in more efficient oxidation for TOC determination.

Data Interpretation Using Geochemical Logs

Geochemical logs simplify data interpretation by showing large amounts of pyrolysis, TOC, and other data, such as vitrinite reflectance, versus depth in wells (Fig. 2). Multiple geochemical logs can be used to create maps (Demaison 1984; Dahl and Yukler 1991) to identify the lateral and vertical distributions of sweet spots. Trends and anomalous data are readily apparent on geochemical logs and can be validated by examination of pyrograms, inquiries about well conditions or sampling methods, and, if necessary, repeat or additional analyses.

Geochemical logs that include carbonate content and the oil saturation index (OSI = 100 × S1/TOC) provide information on both geomechanics and geochemistry that is useful to evaluate unconventional resources. OSI can be used to indicate zones within unconventional strata that are likely to be productive, provided that significant amounts of brittle carbonate or silicate minerals are present to effectively receive proppant upon hydraulic fracturing. The injected proppant keeps fractures open, thereby increasing surface area in the target rock and increasing fluid flow into the well. Proppant

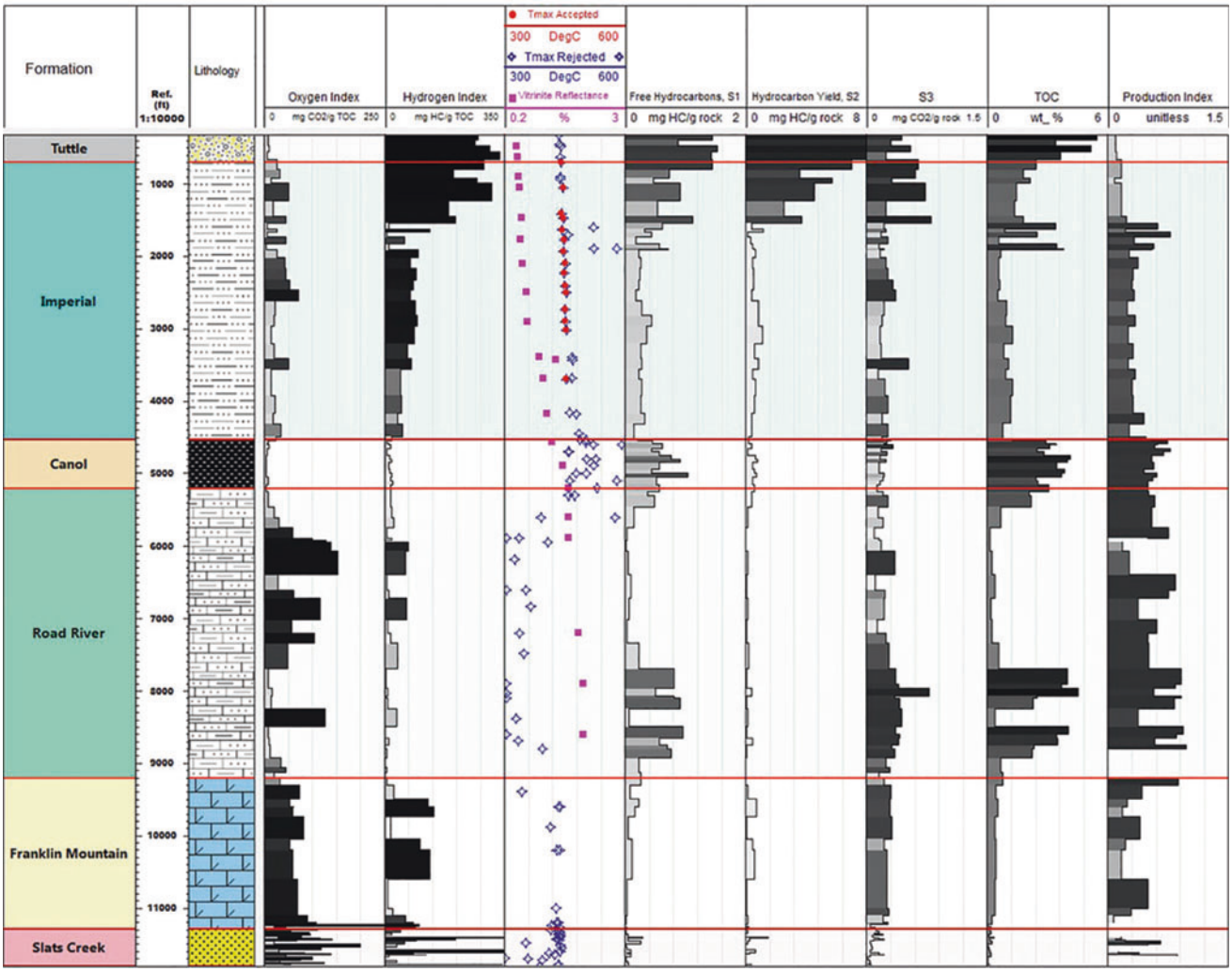

Programmed Temperature Pyrolysis, Fig. 2 Typical geochemical log of programmed pyrolysis, TOC, and vitrinite reflectance data for the Caribou N-25 well, Mackenzie Corridor, Canada. Accepted and rejected T_{max} data are indicated using *solid* and *open* symbols, respectively (Raw data are from Allen et al. 2008)

consists of sand or man-made ceramic particles injected during hydraulic fracturing in order to increase exposed surface area in the rock and enhance gas and oil production. Zones that readily fracture and have OSI values >100 mg oil/g TOC are favorable for unconventional oil recovery (Jarvie 2012b).

Interpretation of geochemical logs can be facilitated using automated software. For example, AGEL (automated geochemical log interpretation) is proprietary Schlumberger software that interprets large amounts of pyrolysis, TOC, and vitrinite reflectance data using a set of interactive and heuristic rules. Figure 2 shows an AGEL geochemical log with accepted and rejected data for the Caribou N-25 well from the Mackenzie Corridor, Canada. Interpretation of raw data and the log would have been difficult without the use of heuristic rules to screen anomalous results. Note that the correlation between R_o and T_{max} differs from that in Eq. 1 as follows ($R = 0.96$):

$$R_o(\text{measured}) = (0.0132)(T_{max}) - 5.25 \quad (3)$$

Although programmed pyrolysis and TOC data represent a valuable screening tool to evaluate hundreds or thousands of measurements, some pitfalls must be acknowledged (for more details, see Peters 1986; Peters and Cassa 1994; Dembicki 2009):

1. Pyrolysis sample size should be uniformly near 100 mg.
2. There is no simple relation between TOC and S1 or S2 (quantity versus quality).
3. Bitumen, migrated oil, and oil-based drilling additives can interfere with parameters, particularly S1, S2, PI, HI, and T_{max}. Extraction to remove these fluids results in loss of S1 during evaporation of the solvent and may not improve measurements of S2, HI, and T_{max}.

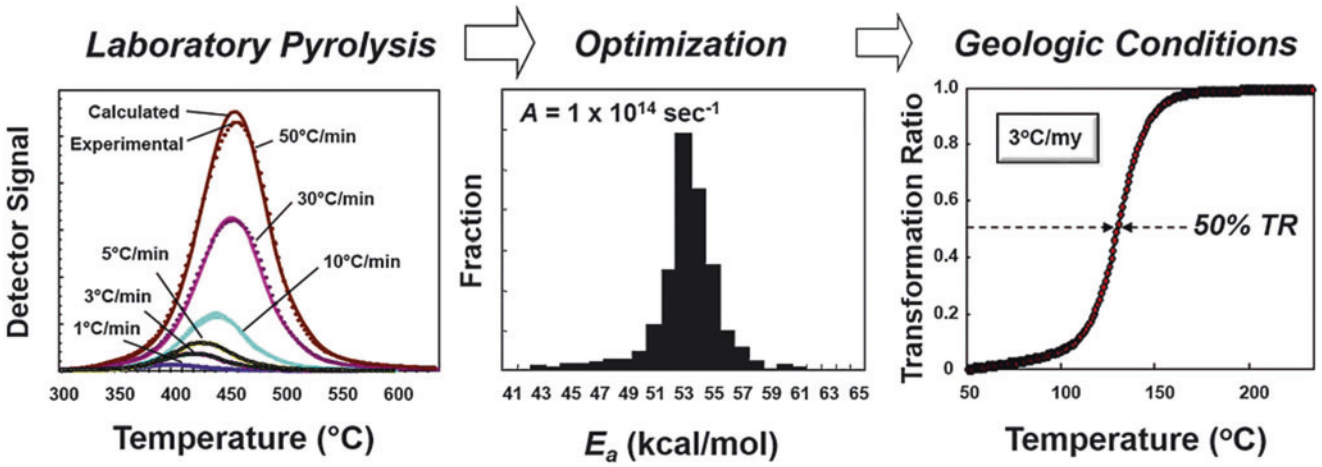

Programmed Temperature Pyrolysis, Fig. 3 *Left:* pyrograms for six programmed pyrolysis experiments on aliquots of the same thermally immature source-rock sample *(dotted curves)* fit using Kinetics05 software *(solid curves).* Extremely slow (<1 °C/min) or fast (>30 °C/min) heating rates are not recommended due to volatilization or thermal lag effects (Peters et al. 2016b). *Center:* calculated E_a distribution versus fraction (i.e., transformation ratio) and A value. *Right:* Extrapolation to geologic conditions assuming a constant heating rate of 3 °C/my. Fraction = transformation ratio or extent of conversion of kerogen to petroleum. This plot is useful to compare the response of different source-rock kerogens. In BPSM, the burial history and paleo-heat flow would be used to calculate extent of conversion

Lithology and mineral/organic matter ratio can influence response (Espitalie et al. 1980; Katz 1983; Dahl et al. 2004).

4. T_{max} is inaccurate for small peaks (<0.2 mg HC/g rock).
5. Some carbonate-rich rocks can contribute to S3 and OI.
6. Some coals (>50 wt.% TOC) show anomalously high HI values.
7. Pyrograms should be examined, especially when contamination or migrated oil is suspected.
8. Geochemical logs simplify interpretation and should be constructed using data that have been evaluated using heuristic rules to control data quality.

Extrapolation of Kinetic Measurements to Geologic Time

Discrete activation energy (DAE) modeling requires optimization of both E_a and A to determine the rate of kerogen decomposition at any laboratory temperature. The "compensation law" shows that a wide range of E_a and A combinations can satisfy the Arrhenius equation for the laboratory rate constant, but extrapolation of incorrect E_a and A to geologic time can result in incorrect temperature predictions (Peters et al. 2016b). DAE uses a single frequency factor for all possible activation energies associated with the discrete distribution. The value of A can be optimized by the software (e.g., Kinetics05, Kinetics2015; http://geoisochem.com/software/kinetics2015/index.html) or it can be an assumed, universal value (not recommended). Use of a universal value for A (e.g., 1×10^{14} s^{-1}; Waples 2016 and references therein) can lead to erroneous results (Peters et al. 2016b). For robust solutions, the pyrolysis experiments must include three or more widely differing heating rates using an energy spacing of 1 kcal/mol or less (Fig. 3).

Summary

Programmed temperature pyrolysis, TOC, and vitrinite reflectance are rapid and inexpensive tools that are commonly combined in geochemical logs to evaluate the quantity, quality, and thermal maturity of source-rock organic matter and the presence of petroleum in conventional or unconventional rock units. Pyrolysis and TOC measurements are most effective when based on large numbers of closely spaced samples in wellbores: typically 10-m or <1-m spacing in conventional or unconventional resources, respectively.

Good, very good, and excellent quantities of organic carbon are in the ranges 2–3, 3–4, and >4 wt.% TOC for thermally immature equivalents of conventional source rocks and 1.5–2.0, 2.0–2.5, and >2.5% for thermally mature unconventional source rocks. Four measured and three calculated parameters from Rock-Eval programmed temperature pyrolysis are as follows:

1. S1 represents free hydrocarbons (gas and oil) in the sample (mg HC/g rock). S1 > 1 mg/g rock may indicate an oil show. Crude oil and oil-based drilling mud can interfere with S1 and other pyrolysis parameters.
2. S2 represents hydrocarbons cracked from the kerogen (mg HC/g rock), which indicates the remaining

potential of the rock to generate oil and gas if buried further. Particulate additives, such as walnut hulls or polyethylene, can interfere with HI, T_{max}, and other pyrolysis parameters.

3. S3 is the amount of carbon dioxide generated from the kerogen (mg CO_2/g rock). Some carbonate minerals decompose below 390 °C and can interfere with S3. Oxidation due to weathering of outcrop samples or overgrinding during sample preparation can also contribute to S3.
4. T_{max} is the oven temperature at the maximum yield of S2, which gives an indication of the level of thermal maturity of the kerogen. T_{max} is sensitive to the type of organic matter, e.g., the onset of oil generation can occur at slightly different T_{max} values.
5. Calculated parameters include hydrogen index (HI = 100 × S2/TOC), oxygen index (OI = 100 × S3/TOC), and production index [S1/(S1 + S2)]. HI in thermally immature rock identifies oil-prone type I (>600 mg HC/g TOC) and type II (300–600 mg HC/g TOC) kerogen, whereas type III (50–200 mg HC/g TOC) yields mostly hydrocarbon gas. The relative thermal maturity of organic matter in samples can be estimated by (1) location on the modified Van Krevelen diagram of OI versus HI and (2) approximate T_{max}, where immature <435 °C, mature = 435–470 °C, and postmature >470 °C.

Open-system programmed pyrolysis of source-rock samples can be used to generate kinetic parameters for petroleum generation assuming independent first-order reactions that are constrained by a distribution of activation energies and a corresponding frequency factor. The method assumes that thermal alteration of organic matter can be described by first-order reactions that conform to the Arrhenius law. Most workers obtain source-rock kinetic parameters using programmed pyrolysis rather than other methods, such as hydrous pyrolysis, because measured and predicted petroleum generation rate curves from open-system pyrolysis are similar to those of natural maturation series. Predictions from BPSM that are based on laboratory kinetics agree with field data from exploration wells.

Cross-References

- ▶ Carbon
- ▶ Geochemical Reference Materials
- ▶ Kerogen
- ▶ Kinetics of Geochemical Processes
- ▶ Petroleum

References

Allen TL, Fraser TA, Osadetz KG (2008) Rock-Eval/TOC data for 18 wells, Peel Plateau and Plain, Yukon Territory (65o 50′ to 67o 00′ N; 133o 45′ to 135o 15′ W). Yukon Geological Survey, Open File 2008–1, 14 p. plus spreadsheet(s). www.geology.gov.yk.ca/pdf/of2008_1(2).xls

Barth T, Smith BJ, Nielsen SB (1996) Do kinetic parameters from open pyrolysis describe petroleum generation by simulated maturation? Bull Can Petrol Geol 44:446–457

Behar F, Kressman S, Rudkiewicz JL, Vandenbroucke M (1992) Experimental simulation in a confined system and kinetic modeling of kerogen and oil cracking. Org Geochem 19:173–189. https://doi.org/10.1016/ 0146-6380(92)90035-V

Braun RL, Burnham AK (1987) Analysis of chemical reaction kinetics using a distribution of activation energies and simpler models. Energy Fuel 1:153–161. https://doi.org/10.1021/ef00002a003

Burnham AK, Braun RL (1999) Global kinetic analysis of complex materials. Energy Fuel 13:1–22. https://doi.org/10.1021/ef9800765

Dahl B, Yukler MA (1991) The role of petroleum geochemistry in basin modelling of the Oseberg Area, North Sea. In: Merrill RK (ed) AAPG treatise of petroleum geology handbook. Source and migration processes and evaluation techniques. Am Assoc Petrol Geol, Tulsa, pp 65–85

Dahl B, Bojesen-Koefoed J, Holm A, Justwan H, Rasmussen E, Thomsen E (2004) A new approach to interpreting Rock-Eval S2 and TOC data from kerogen quality assessment. Org Geochem 35:1461–1477

Demaison G (1984) The generative basin concept. In: Demaison G, Murris RJ (eds) Petroleum geochemistry and basin evaluation. Am Assoc Petrol Geol Mem 35. American Association of Petroleum Geologists, Tulsa, pp 1–14

Dembicki H (2009) Three common source rock evaluation errors made by geologists during prospect or play appraisals. Am Assoc Petrol Geol 93:341–356

Dieckmann V (2005) Modelling petroleum formation from heterogeneous source rocks: the influence of frequency factors on activation energy distribution and geological prediction. Mar Pet Geol 22:375–390. https://doi.org/10.1016/j.marpetgeo.2004.11.002

Espitalié J, Madec M, Tissot B, Menning, JJ, Leplat P (1977) Source rock characterization methods for petroleum exploration. Proceedings of the 1977 offshore technology conference, Houston, TX, vol 3, pp 439–444

Espitalie J, Madec M, Tissot B (1980) Role of mineral matrix in kerogen pyrolysis: influence on petroleum generation and migration. Am Assoc Petrol Geol Bull 4:59–66

Espitalié J, Ungerer P, Irwin I, Marquis F (1988) Primary cracking of kerogens. Experimenting and modeling C_1, C_2-C_5, C_6-C15 and C_{15+}classes of hydrocarbons formed. Org Geochem 13:893–899

Gonzalez J, Lewis R, Hemingway J, Grau J, Rylander E, Schmitt R (2013) Determination of formation organic carbon content using a new neutron-induced gamma ray spectroscopy service that directly measures carbon. SPWLA 54th annual logging symposium, 22–23 June, pp 1–15

Horsfield B, Disko U, Leistner F (1989) The micro-scale simulation of maturation: outline of a new technique and its potential applications. Geol Rundsch 78:361–373. https://doi.org/10.1007/BF01988370

Issler DR, Snowdon LR (1990) Hydrocarbon generation kinetics and thermal modeling, Beaufort-Mackenzie Basin. Bull Can Petrol Geol 38:1–16

Jarvie DM (2012a) Shale resource systems for oil and gas: part 1 – shale-gas resource systems. In: Breyer JA (eds) Shale reservoirs – giant resources for the 21st century. Am Assoc Petrol Geol

Mem 97. American Association of Petroleum Geologists, Tulsa, pp 69–87
Jarvie DM (2012b) Shale resource systems for oil and gas: part 2 – shale-oil resource systems. Am Assoc Petrol Geol Mem 97:89–119
Jarvie DM, Claxton BL, Henk F, Breyer JT (2001) Oil and shale gas from the Barnett Shale, Fort Worth Basin, Texas. Abstract Am Assoc Petrol Geol Bull 85:A100
Katz BJ (1983) Limitations of Rock-Eval pyrolysis for typing organic matter. Org Geochem 4:195–199
Kissin YV (1987) Catagenesis and composition of petroleum: origin of n-alkanes and isoalkanes in petroleum crudes. Geochim Cosmochim Acta 51:2445–2457. https://doi.org/10.1016/0016-7037(87)90296-1
Kuhn PP, di Primio R, Hill R, Lawrence JR, Horsfield B (2012) Three-dimensional modeling study of the low-permeability petroleum system of the Bakken formation. Am Assoc Petrol Geol Bull 96:1867–1897. https://doi.org/10.1306/03261211063
Lafargue E, Espitalié J, Marquis F, Pillot D (1998) Rock-Eval 6 applications in hydrocarbon exploration, production and in soil contamination studies. Rev Inst Fr Pétrol 53:421–437
Larter SR (1984) Application of analytical pyrolysis techniques to kerogen characterization and fossil fuel exploration/exploitation. In: Voorhees KJ (ed) Analytical pyrolysis: techniques and applications. Butterworths, London, UK, pp 212–275
Levenberg K (1944) A method for the solution of certain nonlinear problems in least squares. Q Appl Math 2:164–168
Lewan MD, Ruble TE (2002) Comparison of petroleum generation kinetics by isothermal hydrous and nonisothermal open-system pyrolysis. Org Geochem 33:1457–1475. https://doi.org/10.1016/S0146-6380(02)00182-1
Lewan MD, Winters JC, McDonald JH (1979) Generation of oil-like pyrolyzates from organic-rich shales. Science 203:897–899. https://doi.org/10.1126/science.203.4383.897
Mullins O, Pomerantz AE, Zuo JY, Dong C (2014) Downhole fluid analysis and asphaltene science for petroleum reservoir evaluation. Ann Rev Chem Biomol Eng 5:325–345
Mullins O, Wang K, Kauerauf A, Zuo JY, Chen Y, Dong C, Elshahawi H (2015) Evaluation of coexisting reservoir fluid gradients of GOR, asphaltene and biomakers as determined by charge history and reservoir fluid dynamics. Society of Petrophysicists and Well Log Analysts (SPWLA) 56th SPWLA logging symposium, Long Beach, 18–22 July, pp 1–14
Munson TO (2006) Chapter 7: Environmental applications of pyrolysis. In: Applied pyrolysis handbook. CRC Press, Boca Raton, FL, pp 133–173
Pepper AS, Corvi PJ (1995) Simple kinetic models of petroleum formation: part I—oil and gas generation from kerogen. Mar Pet Geol 12:291–319. https://doi.org/10.1016/0264-8172(95)98381-E
Peters KE (1986) Guidelines for evaluating petroleum source rocks using programmed pyrolysis. Am Assoc Petrol Geol Mem 70:318–329
Peters KE, Cassa MR (1994) Applied source-rock geochemistry. Am Assoc Petrol Geol Mem 60:93–120
Peters KE, Rodriguez LB (2017) Programmed Temperature Pyrolysis. In: Sorkhabi R (ed) Encyclopedia of petroleum geoscience, Springer Cham. https://doi.org/10.1007/978-3-319-02330-4_7-1
Peters KE, Whelan JK, Hunt JM, Tarafa ME (1983) Programmed pyrolysis of organic matter from thermally altered cretaceous black shales. Am Assoc Petrol Geol Bull 67:2137–2146
Peters KE, Walters CC, Moldowan JM (2005) The biomaker guide, 2nd edn. Cambridge University Press, Cambridge, 1155 p
Peters KE, Walters CC, Mankiewicz PJ (2006) Evaluation of kinetic uncertainty in numerical models of petroleum generation. Am Assoc Petrol Geol Bull 90:1–20. https://doi.org/10.1306/08090504134
Peters KE, Burnham AK, Walters CC (2015a) Petroleum generation kinetics: single- versus multiple heating-ramp open-system pyrolysis. Am Assoc Petrol Geol Bull 99:591–616
Peters KE, Schenk O, Hosford Scheirer A, Wygrala B, Hantschel T (2015b, in press) Basin and petroleum system modeling of conventional and unconventional petroleum resources. In: Hsu C, Robinson P (eds) Practical advances in petroleum production and processing. Springer, New York
Peters KE, Burnham AK, Walters CC (2016a) Petroleum generation kinetics: single versus multiple heating-ramp open-system pyrolysis: reply. Am Assoc Petrol Geol Bull 100:690–694
Peters KE, Xia X, Pomerantz D, Mullins O (2016b) Chapter 3: Geochemistry applied to evaluation of unconventional resources. In: Ma Z, Holditch S (eds) Unconventional oil and gas resources handbook. Elsevier, Waltham, pp 71–126
Reynolds JG, Burnham AK (1995) Comparison of kinetic analysis of source rocks and kerogen concentrates. Org Geochem 23:11–19. https://doi.org/10.1016/0146-6380(94)00114-G
Ritter U, Myhr MB, Vinge T, Aareskjold K (1995) Experimental heating and kinetic models of source rocks: comparison of different methods. Org Geochem 23:1–9. https://doi.org/10.1016/0146-6380(94)00108-D
Schenk HJ, Horsfield B (1993) Kinetics of petroleum generation by programmed-temperature closed- versus open system pyrolysis. Geochim Cosmochim Acta 57:623–630. https://doi.org/10.1016/0016- 7037(93)90373-5
Schenk HJ, Horsfield B (1998) Using natural maturation series to evaluate the utility of parallel reaction kinetics models: an investigation of Toarcian shales and carboniferous coals, Germany. Org Geochem 29:137–154. https://doi.org/10.1016/S0146-6380(98)00139-9
Sephton MA (2017) Thermal extraction for organic-matter containing materials to answer questions both on earth and in space. First Break 35:113–117
Stainforth JG (2009) Practical kinetic modeling of petroleum generation and expulsion. Mar Pet Geol 26:552–572. https://doi.org/10.1016/j.marpetgeo.2009.01.006
Sundararaman P, Merz PH, Mann RG (1992) Determination of kerogen activation energy distribution. Energy Fuel 6:793–803. https://doi.org/10.1021/ef00036a015
Sweeney JJ, Burnham AK, Braun RL (1987) A model of hydrocarbon generation from type I kerogen: application to Uinta Basin, Utah. Am Assoc Petrol Geol Bull 71:967–985
Tegelaar EW, Noble RA (1994) Kinetics of hydrocarbon generation as a function of the molecular structure of kerogen as revealed by pyrolysis-gas chromatography. Org Geochem 22:543–574. https://doi.org/10.1016/0146-6380(94)90125-2
Tissot BP, Espitalié J (1975) L'evolution thermique de la matiere organique des sediments: applications d'une simulation mathematizue. Rev Inst Fr Petrol 30:743–777
Ungerer P (1990) State of the art of research in kinetic modeling of oil formation and expulsion. Org Geochem 16:1–25
Ungerer P, Pelet R (1987) Extrapolation of the kinetics of oil and gas formation from laboratory experiments to sedimentary basins. Nature 327:52–54. https://doi.org/10.1038/327052a0
Voorhees KJ (1984) Analytical pyrolysis: techniques and applications. Butterworths, London, UK, 486 p
Vyazovkin S, Wight CA (1999) Model-free and model fitting approaches to kinetic analysis of isothermal and nonisothermal data. Thermochim Acta 340–341:53–68. https://doi.org/10.1016/S0040-6031(99)00253-1
Vyazovkin S, Chrissafis K, Di Lorenzo ML, Koga N, Pijolet N, Roduit B, Sbirrazzouli N, Sunol JJ (2014) ICTAC Kinetics Committee recommendations for collecting experimental thermal analysis data for kinetic computations. Thermochim Acta 590:1–23. https://doi.org/10.1016/j.tca.2014.05.036
Waples D (2016) Petroleum generation kinetics: single versus multiple heating-ramp open-system pyrolysis: discussion. Am Assoc Petrol Geol Bull 100:683–689
Waples DW, Suizu M, Kamata H (1992) The art of maturity modeling: part 2—alternative models and sensitivity analysis. Am Assoc Petrol Geol Bull 76:47–66

Wüst RAJ, Nassiuchuk BR, Brezovski R, Hackley PC, Willment N (2013) Vitrinite reflectance versus pyrolysis Tmax data: assessing thermal maturity in shale plays with special reference to the Duvernay shale play of the Western Canadian Sedimentary Basin, Canada: Society of Petroleum Engineers Unconventional Resources Conference and Exhibition-Asia Pacific, 11–13 November, Brisbane, SPE-167031-MS, 11 p. https://doi.org/10.2118/167031-MS

Promethium

Scott M. McLennan
Department of Geosciences, Stony Brook University, Stony Brook, NY, USA

Element Data
Atomic Symbol: Pm
Atomic Number: 61
Atomic Weight: ~145
Isotopes and Abundances: -
1 Atm Melting Point: 1042 °C
1 Atm Boiling Point: ~3000 °C
Common Valences: +3
Ionic Radii: 97 pm (CN6), 110 pm (CN8), and 127 pm (CN12)
Pauling Electronegativity: —~1.2
First Ionization Energy: 538.6 kJ mol^{-1}
Chondritic (CI) Abundance: 0 ppm
Silicate Earth Abundance 0 ppm
Crustal Abundance: 0 ppm
Seawater Abundance: 0 ppt
Core Abundance: 0 ppm

Properties

Promethium (Pm), originally called prometheum and named after *Prometheus*, one of the Titans of classical mythology, is a moderately dense (7.264 g cm^{-3}) silvery-white metal with an electronic configuration of $[Xe]4f^5 6s^2$. It is a group 3 or IIIB inner transition element and is one of the lanthanide rare earth elements (REE). Promethium does not exist in nature apart from negligible abundances of short-lived isotopes that form as decay products. Promethium has no natural stable or long-lived radioactive isotopes but does possess at least 38 short-lived isotopes with half-lives ranging from <1 μs to 17.7 years (^{145}Pm). Since Pm essentially does not occur in nature, there are no minerals that contain it as a significant component. Details of properties, history, and uses of Pm were compiled from Zaimes et al. (2015), Gschneidner (2016), and Hammond (2016).

History and Use

The existence of promethium was predicted in 1902 by Bohuslav Brauner and, after several mistaken and inconclusive identifications, was first produced in 1945 by Marinsky, Glendenin, and Coryell at Oak Ridge National Laboratory by separating it from the fission products of irradiated uranium. Although not found in nature, ^{147}Pm ($t_{1/2}$ = 2.62 years) is relatively easy to produce and used as a radioactive source in nuclear batteries, phosphor-based light sources, fluorescent light starters, and thickness gauges.

Geochemical Behavior

Promethium has been identified in the emission spectra of rare Ap stars (Cowley et al. 2004), an observation that provides supportive evidence for the theory of stellar nucleosynthesis of heavy elements.

Biological Utilization and Toxicity

There are no known biological uses for Pm. ^{147}Pm emits X-rays during decay and as such is theoretically dangerous if exposed in sufficient concentration. Under most circumstances, however, Pm is in such low concentrations that it is not hazardous, but concentrated Pm requires the same precautions as any low- to medium-level radioactive material.

Cross-References

▶ Lanthanide Rare Earths
▶ Nucleosynthesis

References

Cowley CR, Bidelman WP, Hubrig S, Mathys G, Bord DJ (2004) On the possible presence of promethium in the spectra of HD 101065 (Przybylski's star) and HD 965. Astron Astrophys 419:1087–1093
Gschneidner KA Jr (2016) Physical properties of the rare earth metals. In: Haynes WM (ed) CRC handbook of chemistry and physics, 96th edn. CRC Press, Boca Raton, pp 4-115–4-120
Hammond CR (2016) The elements. In: Haynes WM (ed) CRC handbook of chemistry and physics, 96th edn. CRC Press, Boca Raton, pp 4-1–4-42
Zaimes GG, Hubler BJ, Wang S, Khanna V (2015) Environmental life cycle perspective on rare earth oxide production. ACS Sustain Chem Eng 3:237–244

Protactinium

Julie Prytulak
Department of Earth Science and Engineering, Imperial College London, London, UK

Element Data
Atomic Symbol: **Pa**
Atomic Number: **91**
Atomic Weight: 231.0359 g mol^{-1}
Isotopes and Abundances: ^{231}Pa ($t_{1/2}$ 32,760 year) ~100% ^{234}Pa ($t_{1/2}$ 70 s)
1 Atm Melting Point: 1569 °C
1 Atm Boiling Point: 4000 °C
Common Valences: 5+, 4+, 6+
Ionic Radii: Pa^{5+} VI-fold: 78 pm, VIII-fold 91 pm
Pauling Electronegativity: 1.5
First Ionization Energy: 568 kJ mol^{-1}
Chondritic (CI) Abundance: 2.7 fg/g
Silicate Earth Abundance: 7.5 fg/g
Crustal Abundance: 880 fg/g
Seawater Abundance: 1 fg/g
Core Abundance: ~0

Properties

The element protactinium (Pa) is a short-lived nuclide belonging to the decay chain of 235-Uranium and the third element in the actinide series (Z = 91) with an atomic mass of 231.0359. At room temperature it is a tetragonal solid gray metal, with a calculated density of 15.37 g/cm^3 and an atomic radius of 1.63 pm when XII-fold coordinated in its metallic state (Elson 1954). The electron configuration of Pa is [Rn] $5f^2$ $6d^1$ 7 s^2. It has been suggested that Pa most closely resembles Nb and Ta in terms of its chemical behavior, and theoretical considerations of its mineral-melt partitioning have used Nb and Ta as proxy elements (e.g., Blundy and Wood 2003).

History and Use

The name "protactinium" was officially adopted in 1949 by the IUPAC and derives its meaning from the Greek "*protos*" (first) and actinium, since it is parental or "before" ^{227}Ac. Protactinium was little known outside its nuclear applications during its rather fascinating history through the scientific prediction of its existence, the trial and error of its isolation, and the debate over its official designation. All of which largely took place under the backdrop of WWI and II and rising government interest in nuclear research. Today, although its combined toxicity and rarity limits commercial application, it has been successfully employed to geochemically investigate strikingly disparate topics such as high-temperature investigations of mantle melting and low-temperature investigation of water masses through time.

Protactinium has a rather riveting history of discovery as it was actively sought by competing research groups. The search for Pa can be traced back to Mendeleev's 1871 periodic table, where a vacancy between Th and U in Group V was postulated to contain a hypothetical element "eka-tantalum." In 1900, William Crookes isolated protactinium, but did not recognize it as a new element, instead calling it uranium-X. It transpired that uranium-X was in fact the minor ^{234}Pa isotope, which was named "brevium" by Fajans and Gohring (1913) due to its 1.17 min half-life. The discovery of the more abundant ^{231}Pa in 1917 is generally credited to independent work in 1917 of both Lise Meitner and Otto Hahn in Germany (Hahn and Meitner 1918) and Frederick Soddy and John Cranston (Soddy and Cranston 1918) in Glasgow, UK.

Soddy and others devised the displacement rule for decay series in 1913. The radioactive displacement principle has two simple tenents: (1) if a radioelement emits an alpha particle, its position in the table shifts two places to the left, (2) if it emits a beta particle, it shifts once place to the right. Uranium-X was an obvious discrepancy: a beta emitter with the chemistry of Th and in Group IV. The existence of such an element was required to complete uranium decay chains. Thus the search for the "mother of actinium" began in earnest. It was a painstaking process, as months of decay were required to accumulate enough material to be measured and demonstrate the existence of a new element. Given the position of the unknown element on the periodic table, its chemistry was thought to be similar to Ta. Thus the approach adopted by Meitner and Hahn was to separate large amounts of Ta from pitchblende and wait to see if it produced measurable actinium.

There are many reviews on the historical discovery of protactinium including factual accounts (e.g., Myasoedov et al. 2006) and recent synopses (Wilson 2012). Sime (1986) presents a particularly engrossing account, which incorporates WWI correspondence during the discovery of Pa, translated from German, between Meitner and Hahn.

Natural Occurrence

Protactinium is extremely rare. The global stock of the element is 125 g of 99.9% pure Pa which was extracted from

60 tonnes of spent uranium fuel by the UK Atomic Energy Authority in 1961 (Emsley 2001). In natural settings, as part of a U-series decay chain, the abundance of ^{231}Pa is dictated by its half-life and the concentration of ^{235}U with which it attains secular equilibrium. The decay constant of ^{231}Pa is 2.116×10^{-5} (Robert et al. 1969). Thus the abundance of ^{231}Pa can be calculated from U for terrestrial reservoirs of interest including the continental crust (U = 2.7 ug/g; Rudnick and Gao 2012), the mantle (U = 0.0229 ug/g; Palme and O'Neill 2012), CI chondrites (U = 0.0081 ug/g; Palme and O'Neill 2012), and seawater (U = 0.003 ug/g; Emsley 2001).

It is very difficult to directly determine mineral-melt partition coefficients for Pa, and it is assumed to be highly incompatible in most phases (see discussion in Blundy and Wood 2003). The exception is zircon, where directly determined partition coefficients (D) are available ($D_{Pa}^{zircon} = 0.9$ to 2.2 (Schmitt 2007)). Irrespective of some compatibility in zircon, Pa concentrations increase with magmatic evolution in magmatic products. Mid-ocean ridge basalts with MgO abundances >6 wt% generally contain on the order of 10s up to a few hundred fg/g (e.g., Goldstein et al. 1993; Elkins et al. 2014) while ocean island basalts and arc lavas with MgO >6 wt% generally display greater concentrations on the order of several hundred fg/g (e.g., Bourdon et al. 2006; Avanzinelli et al. 2012), reflecting the higher abundance of U in these rock types. The highest concentrations of Pa are found in materials such as uranium ores, which can contain on the order of 0.3 ug/g (Elson 1954).

Measurement and Applications

The minute abundances of naturally occurring Pa, combined with its high radioactivity (and thus toxicity), currently restrict applications to scientific research.

Isolation and Measurement

A key issue with the measurement of Pa by radiometric techniques such as alpha counting is the interference of vastly more abundant radioactive elements in the sample (e.g., Th, Ra). To avoid these complications, much effort was made to chemically isolate Pa from matrix elements. Many initial separation protocols were prompted by the nuclear industry in the 1930s to 1960s. A useful compilation of research conducted during the Manhattan project forms much of the background for present-day separation protocols (Hyde 1954). Perhaps the most vexing problem with protactinium isolation is its refusal to stay in solution. Protactinium has extremely low solubility even in concentrated percholoric, hydrochloric, and nitric acids. This is due to polymerization processes, the particle reactivity of Pa, and the extreme ease with which it undergoes hydrolysis. Current analytical protocols typically use hydrofluoric acid to achieve Pa solubility. Thus chemical separation of Pa is not for the faint hearted, as extremely dangerous acids must be employed to separate this highly toxic, radioactive element (e.g., Pickett et al. 1994; Regelous et al. 2004).

Once a purified Pa fraction is obtained, alpha counting requires weeks for a single measurement with precisions on the order of 5–10%. A significant step forward was the first thermal ionization mass spectrometry (TIMS) measurements of protactinium (Pickett et al. 1994). The technique does not have the complications of interfering radioactivity, as it is a mass measurement, but does require the addition of an artificial spike isotope (^{233}Pa) for precise and accurate measurement. The half life of ^{233}Pa is 26.967 days (Usman and MacMahon 2000), thus spike preparation, isolation of Pa from sample matrix, and measurement must all take place in the space of a few months to ensure that enough ^{233}Pa remains to be measured.

Preparation of ^{233}Pa is generally undertaken by "milking" a solution of ^{237}Np, with which ^{233}Pa will be in secular equilibrium (e.g., Pickett et al. 1994; Regelous et al. 2004). The process is time consuming and the spike must be continually and carefully recalibrated (e.g., Prytulak et al. 2008). An alternative procedure involves neutron activation of ^{232}Th in a nuclear reactor (e.g., Bourdon et al. 1999). The procedure has the advantages of rapid production of ^{233}Pa and removal of the need to recalibrate the spike with time. The requirement of frequent access to a nuclear reactor, however, can curtail the number of researchers able to employ this approach.

Although TIMS measurements were a significant improvement on the days to weeks that alpha counting methods require for Pa analysis, the ionization efficiency of Pa is low (<0.7%) and a single measurement requires 50–100 fg of Pa and several hours (Pickett et al. 1994). More recent protocols using multicollector inductively coupled plasma mass spectrometry (MC-ICPMS) with improved ionization efficiency (~0.9%) drastically reduce collection time to minutes and sample requirements to as low as 20 fg/g (e.g., Regelous et al. 2004). Thus MC-ICPMS protocols are currently the method of choice for analyzing Pa abundances in natural samples. Finally, Christl et al. (2007) have explored the measurement of Pa by accelerator mass spectrometry (AMS). This technique may have the advantage of even faster sample throughput, which is attractive for research requiring high sample density such as paleoceanography (see below).

Applications

A comprehensive review of both high- and low-temperature U-series decay applications are given in Bourdon et al. (2003). Below some common examples are highlighted with inclusion of more recent literature.

High-Temperature Igneous Processes

Uranium, Pa, and Th have different valences, partition coefficients, and chemical affinities. Thus, they are easily fractionated from one another and the return to secular equilibrium of the disturbed decay chain yields time information. An analytical rule of thumb is that the precision with which Pa and Th can be measured in silicate materials means that useful time information can be obtained for up to five times the half-life of the daughter in question. Therefore ^{231}Pa can be used to resolve magmatic processes on the order of 160kyr and ^{230}Th on the order of 350kyr. Employing both systems is more robust than one alone and can provide useful tests for concordance and secondary disturbances (e.g., Cheng et al. 1998; Condomines et al. 2003; Sims et al. 2008).

Measurement of combined ^{235}U-^{231}Pa and ^{238}U-^{230}Th disequilibria in volcanic materials have been used, for example, to model rates of mantle upwelling and magma transport beneath ocean islands and mid-ocean ridges (e.g., Bourdon et al. 2006; Elkins et al. 2014), magma generation in arcs (e.g., Turner et al. 2006; Avanzinelli et al. 2012), and the melt productivity of the mantle (e.g., Prytulak and Elliott 2009). In all of these approaches the greatest sources of ambiguity lie not in the precision of measurement, but in the range of range of mantle porosity values and for the mineral-melt partition coefficients of each nuclide.

Low-Temperature Paleoceanography

The contrasting half-lives of the U-series decay chain nuclides have been exploited in paleoceanography. Specific to protactinium, the ^{231}Pa/^{230}Th ratio of water masses and deep marine sediments has been investigated as a tool for past ocean circulation, with the greatest focus on the rate of Atlantic Meridional Overturning Circulation, and its causal link to abrupt climate change (e.g., McManus et al. 2004; Lippold et al. 2009; Bradtmiller et al. 2014).

The Earth's oceans are in steady state with respect to uranium, which has a residence time of 450,000 years. The production rate of Pa and Th from U-decay yields a constant oceanic ^{231}Pa/^{230}Th activity ratio of 0.093. However, due to their high particle reactivity and low solubility, both Pa and Th are scavenged from the water column by suspended particles (e.g., Anderson et al. 1983). The scavenging of ^{231}Pa and ^{230}Th results in excesses in marine sediments. Thorium and Pa excesses in this context are defined as the unsupported ^{230}Th and ^{231}Pa resulting from the decay of U in the water column and must be calculated taking into account ^{230}Th and ^{231}Pa produced from detrital U. Thorium is more easily adhered to sinking particles than Pa and thus has a very short residence time of tens of years compared to Pa, which is on the order of a couple hundred years (e.g., Henderson and Anderson 2003). The residence time of Pa is similar to the timescale of deep water transport in the Atlantic Ocean. Thus, all else being equal, approximately half of the Pa budget may be transported from the Atlantic without corresponding transport of Th. The resulting variation in ^{231}Pa/^{230}Th of marine sediments can be modeled to infer changes in water mass circulation (e.g., Burke et al. 2011). There are, however, important caveats to the application of ^{231}Pa/^{230}Th as an ocean circulation tracer, which complicate its interpretation. These include changes in scavenging rates and documented preferential scavenging of Pa by opal and the observation that Pa contents vary greatly vertically in a single water column (e.g., Thomas et al. 2006).

Biological Utilization and Toxicity

Protactinium plays no known biological role. The rarity of the element minimizes its risk to the general population. The dominant toxicological risk is from radioactive decay as part of the ^{238}U and ^{235}U decay chains.

Summary

Analytical advances in the measurement of the vanishingly small natural abundances of protactinium have heralded a surprising breadth of scientific applications in the past 15 years. Although the ^{235}U-^{231}Pa decay system is not as established as the related ^{238}U-^{230}Th decay system, the measurement of Pa provides an invaluable cross check on both geochronological applications and "tracer" studies employing the better studied ^{238}U decay chain. Other model parameters in paleoceanography or uncertainties in partition coefficients are now the limiting factor in geochemical interpretation of ^{235}U-^{231}Pa disequilibria, rather than any analytical hindrance.

Cross-References

- ▶ Geochronology and Radiogenic Isotopes
- ▶ Inductively Coupled Plasma Mass Spectrometry (ICP-MS)
- ▶ Mid-Ocean Ridge Basalts (MORB)
- ▶ Oceanic Island Basalts
- ▶ Paleoclimatology
- ▶ Thermal Ionization Mass Spectrometry
- ▶ Uranium
- ▶ Uranium Decay Series

References

Anderson RF, Bacon MP, Brewer PG (1983) Removal of ^{230}Th and ^{231}Pa from the open ocean. Earth Planet Sci Lett **62**:7–23

Avanzinelli R, Prytulak J, Skora S, Heumann A, Koetsier G, Elliott T (2012) Combined ^{238}U-^{230}Th and ^{235}U-^{231}Pa constraints on the transport of slab-derived material beneath the Mariana Islands. Geochim Cosmochim Acta 92:308–328

Blundy J, Wood B (2003) Mineral-melt partitioning of uranium, thorium and their daughters In: Bourdon B, Henderson GM, Lundstrom CC, Turner SP (eds) Uranium-series geochemistry. Reviews in mineralogy and geochemistry, vol 52. pp 59–123

Bourdon B, Joron J-L, Allegre CJ (1999) A method for ^{231}Pa analysis by thermal ionization mass spectrometry in silicate rocks. Chem Geol 157:147–151

Bourdon B, Henderson GM, Lundstrom CC, Turner SP (2003) Uranium-series geochemistry. Rev Mineral Geochm 52. 656pp

Bourdon B, Ribe NM, Stracke A, Saal AE, Turner SP (2006) Insights into the dynamics of mantle plumes from uranium-series geochemistry. Nature 444:713–717

Bradtmiller LI, McManus JF, Robinson LF (2014) ^{231}Pa/^{230}Th evidence for a weakened but persistent Atlantic meridional overturning circulation during Heinrich Stadial 1. Nat Commun 5:5817. https://doi.org/10.1038/ncomms6817

Burke A, Marchal O, Bradtmiller LI, McManus JF, Francois R (2011) Application of an inverse method to interpret ^{231}Pa/^{230}Th observations from marine sediments. Paleoceanography 26. https://doi.org/10.1029/2010PA002022

Cheng H, Edwards RL, Murrell MT, Benjamin TM (1998) Uranium-thorium-protactinium dating systematics. Geochim Cosmochim Acta 62(21–22)

Christl M, Wacker L, Lippold J, Synal H-A, Suter M (2007) Protactinium-231: a new radionuclide for AMS. Nucl Instrum Methods Phys Res 262:379–384

Condomines M, Gauthier P-J, Sigmarsson O (2003) Timescales of magma chamber processes and dating of young volcanic rocks. In: Bourdon B, Henderson GM, Lundstrom CC, Turner SP (eds) Uranium-series geochemistry. Reviews in mineralogy and geochemistry, vol 52. pp 125–174

Elkins LJ, Sims KWW, Prytulak J, Blichert-Toft J, Elliott T, Blusztajn J, Fretzdorff S, Reagan M, Haase K, Humphris S, Schilling J-G (2014) Melt generation beneath Arctic Ridges: implications from measurements of U decay series disequilibria in the Mohns, Knipovich and Gakkel ridges. Geochim Cosmochim Acta 127:140–170

Elson RE (1954) The chemistry of protactinium. In: Seaborg GT, Katz JJ (eds) The actinide elements. McGraw-Hill Book, New York, pp 103–129

Emsley J (2001) Nature's building blocks: an A-Z guide to the elements. Oxford University Press, Oxford. 538 p

Fajan K, Gohring OH (1913) Ueber das Uran X2-das neue Element der Uranreihe. Phys Z 14:877

Goldstein SJ, Murrell MT, Williams RW (1993) ^{231}Pa and ^{230}Th chronology of mid-ocean ridge basalts. Earth Planet Sci Lett 115:151–159

Hahn O, Meitner L (1918) Die muttersubstanz des Actiniums, ein neues radioactives Element von langer Lebensdauer. Phys Z 19:208

Henderson GM, Anderson RF (2003) The U-series toolbox for paleoceanography. In: Bourdon B, Henderson GM, Lundstrom CC, Turner SP (eds) Uranium-series geochemistry. Reviews in mineralogy and geochemistry, vol 52. pp 493–531

Hyde EK (1954) Radiochemical separations of the actinide elements. In: Seaborg GT, Katz JJ (eds) The actinide elements. McGraw-Hill Book, New York, pp 542–595

Lippold J, Grutzner J, Winter D, Lahaye A, Mangini A, Christl M (2009) Does sedimentary ^{231}Pa/^{230}Th from the Bermuda Rise monitor past Atlantic Meridional Overturning Circulation? Geophys Res Lett 36. https://doi.org/10.1029/2009GL038068

McManus JF, Francois R, Gherardi J-M, Keigwin LD, Brown-Leger S (2004) Collapse and rapid resumption of Atlantic meridional circulation linked to deglacial climate changes. Nature 428:834–837

Myasoedov BF, Kirby HW, Tananaev IG (2006) Protactinium. In: Morss LR, Edelstein NM, Fuger J (eds) The chemistry of the actinide and transactinide elements. Springer, Dordrecht, pp 161–252

Palme H, O'Neill HSC (2012) Cosmochemical estimates of mantle composition. In: Holland H, Turekian K (eds) Treatise on geochemistry, vol 3, 2nd edn. Elsevier, Amsterdam, pp 1–39

Pickett DA, Murrell MT, Williams RW (1994) Determination of femtogram quantities of protactinium in geologic samples by thermal ionization mass spectrometry. Anal Chem 66:1044–1049

Prytulak J, Elliott T (2009) Determining melt productivity of mantle sources from ^{238}U-^{230}Th and ^{235}U-^{231}Pa disequilibria: an example from Pico Island, Azores. Geochim Cosmochim Acta 73:2103–2122

Prytulak J, Elliott T, Hoffmann DL, Coath CD (2008) Assessment of USGS BCR-2 as a reference material for silicate rock U-Pa disequilibrium measurements. Geostand Geoanal Res 32:55–63

Regelous M, Turner SP, Elliott TR, Rostami K, Hawkesworth CJ (2004) Measurement of femtogram quantities of protactinium in silicate rock samples by multicollector inductively coupled plasma mass spectrometry. Anal Chem 76:3584–3589

Robert J, Miranda CF, Muxart R (1969) Mesure de la periode du protactinium-231 par microcalorimetrie. Radiochim Acta 11:104–108

Rudnick RL, Gao S (2012) Composition of the continental crust. In: Holland H, Turekian K (eds) Treatise on geochemistry, vol 4, 2nd edn. Elsevier, Amsterdam, pp 1–51

Schmitt AK (2007) Ion microprobe analysis of (^{231}Pa)/(^{235}U) and an appraisal of protactinium partitioning in igneous zircon. Am Mineral 92:691–694

Sime RL (1986) The discovery of protactinium. J Chem Educ **63**:653–657

Sims KWW, Hart SR, Reagan MK, Blusztajn J, Staudigel H, Sohn RA, Layne GD, Ball LA, Andrews J (2008) ^{238}U-^{230}Th-^{226}Ra-^{210}Pb-^{210}Po, ^{232}Th-^{228}Ra, and ^{235}U-^{231}Pa constraints on the ages and petrogenesis of Vailulu'u and Malumalu lavas, Samoa. Geochem Geophys Geosyst 9. https://doi.org/10.1029/2007GC001651

Soddy F, Cranston JA (1918) The parent of actinium. Proc R Soc Lond A Math Phys 94:384–404

Thomas AL, Henderson GM, Robinson LF (2006) Interpretation of the ^{231}Pa/^{230}Th paleocirculation proxy: new water-column measurements from the southwest Indian Ocean. Earth Planet Sci Lett 241:493–504

Turner S, Regelous M, Hawkesworth C, Rostami K (2006) Partial melting processes above subducting plates: constraints from ^{231}Pa-^{235}U disequilibria. Geochim Cosmochim Acta 70:480–503

Usman K, MacMahon TD (2000) Determination of the half-life of ^{233}Pa. Appl Radiat Isot 52:585–589

Wilson R (2012) Peculiar protactinium. Nat Chem 4:586

Q

Quantum Numbers

David A. Dixon
Department of Chemistry, University of Alabama, Tuscaloosa, AL, USA

Definition

One of the results of quantum mechanics is that at the atomic level, energy is discrete. This was first observed experimentally in atomic spectra. The solution of the Schrödinger equation gives eigenfunctions and eigenvalues. The numerical solutions of this equation have constants in them which turn out to be integers or half-integers, the latter in the case of spin. These integer or half-integer constants are generally referred to as quantum numbers.

Overview

The Schrödinger wave equation was developed to provide a mathematical description of DeBroglie's matter waves. DeBroglie showed that every particle has a wavelength λ related to its momentum p by the equation $p\lambda = h$ where h is Planck's constant. The kinetic energy operator in the Schrödinger equation is a second derivative (gradient), and the form of the equation means that sines and cosines (e^{ix}) or exponentials are possible solutions. A general set of references for quantum mechanics with a focus on quantum chemistry is provided (Karplus and Porter 1970; Pauling and Wilson 1985; Szabo and Ostlund 1996; Messiah 1999; Pilar 2001; Schatz and Ratner 2002; Lowe and Peterson 2006; McQuarrie 2008; Atkins and Friedman 2011; Engel and Reid 2013; Levine 2014).

Particle in a Box

A simple problem is the particle in a box with infinite walls. The solution of the Schrödinger equation for the motion in this simple box is subject to the conditions that the wave function be everywhere continuous and the first derivative be continuous. The boundary conditions for the particle in the box with infinite walls mean that the wave function has to go to zero at the boundaries so that one can only fit a discrete integer or half-integer number of waves for any energy level. The energy solution for a mass m and box length a is

$$E_n = h^2n^2/8ma^2 \quad (1)$$

where n is the integer quantum number and h is Planck's constant. Clearly the energy is discrete. The particle in a box solution is not just a simple example but can be used to explain the results of the UV-visible spectra of conjugated polyenes as an example. If one has a three-dimensional box, then there are three quantum numbers, one for each dimension. Classically, there are six constants of the motion in three dimensions, the momentum in each direction (p_x, p_y, p_z) and the particles position (x, y, z). However, in quantum mechanics, there are only three quantum numbers (one per dimension) because of the Heisenberg uncertainty principle. This principle relates canonical conjugate variables as $\Delta px \Delta x \geq h/4\pi$. In one dimension, if one precisely knows the energy ($KE = p^2/2\ m$), then one cannot precisely know the position x so x is now represented by a wave. An example of this is the zero-point energy of a system. A second example is the 1 s orbital for the electron in the H atom with a precise energy of 13.6 eV, the ionization potential. The 1 s orbital is a probability distribution where one is expected to have a certain probability of finding the electron in a region of space, but one cannot define precisely where it is due to the energy and hence the momentum being known exactly.

W. M. White (ed.), *Encyclopedia of Geochemistry*,
https://doi.org/10.1007/978-3-319-39312-4

Harmonic Oscillator

As another example, consider the quantum mechanical solution for the harmonic oscillator in one dimension. The solution of this equation yields a single quantum number of the vibrational motion in one dimension. The energy is

$$E = \tfrac{1}{2}(h/2\pi)\omega(n + \tfrac{1}{2}) \quad (2)$$

where h is Planck's constant, ω is the frequency given by $\sqrt{}(k/m)$ where k is the force constant and m is the appropriate reduced mass, and the quantum number n is an integer. The corresponding eigenfunctions are the Hermite polynomials. The quantum number arises because the wave function is everywhere finite, and the series solution of the differential equation does not converge unless it is truncated giving an integer quantum number. Notice that the lowest energy is not zero. There is always a zero-point energy for the harmonic oscillator.

Rigid Rotor

The next set of quantum numbers to consider is that for the solution of the rigid rotor in two dimensions. Here we transform from Cartesian x, y, and z coordinates to spherical polar coordinates. If the distance between the two atoms in a simple diatomic molecule, as an example, is fixed, then there are two degrees of freedom so there are two quantum numbers. The quantum number of the projection onto the x,y plane is the φ quantum number m_l and is an integer ranging from $-l$ to $+ l$. This is the quantum number of the L_z angular momentum operator and arises from φ being single valued over the range 0 to 2π. The other quantum number is l which arises from the solution of the equation for θ and is again due to truncation of a power series to keep the wave function finite. The differential equation for l does depend on m_l. The l quantum number is a positive integer and is $l = 0, 1, 2, \ldots$. This is the quantum number of the L^2 angular momentum operator. The complete solution to the rigid rotor are spherical harmonics with the associated Legendre polynomials for θ and the $e^{im\varphi}$ for φ. The energy is

$$E = l(l+1)(h/2\pi)^2/2I$$

where I is the moment if inertia. In this case, the energy of the lowest state is zero. The two good quantum numbers are l and m_l arising from the L_z and L^2 operators which commute.

Atoms

For atoms and molecules, one makes the Born-Oppenheimer approximation to separate the nuclear and electronic motion. The solution for the one-electron H atom is essentially that for the rigid rotor plus the inclusion of the distance of the electron from the proton. The solutions are products of the associated Legendre polynomials for the angular component and the associated Laguerre polynomials for r. The resulting quantum numbers are

$$m_l = -l, -(l-1), \ldots 0, 1, 2, \ldots l$$
$$l = 0, 1, 2\ldots$$
$$n = 1, 2, \ldots.$$

The angular parts have been discussed above. The radial equation solution depends on the value of l, and the quantum number n again arises because of the need to keep the power series finite. In the one-electron atom, the energy depends only on the value of n

$$E = 2.18 \times 10^{-18}\mathrm{J}\left(Z^2/n^2\right)$$

where Z is the atomic number and 2.18×10^{-18} J is a constant known as the Rydberg energy.

The final quantum number needed to describe an atom is $m_s = \pm \tfrac{1}{2}$, the spin, which arises from the solution of the relativistic Schrödinger equation for the electron.

The quantum numbers for the H atom give rise to the normal orbital labels as follows:

Orbital	n	l	m_l
1s	1	0	0
2s	2	0	0
2p	2	1	−1,0,1
3s	3	0	0
3p	3	1	−1,0,1
3d	3	2	−2,−1,0,1,2
4s	4	0	0
4p	4	1	−1,0,1
4d	4	2	−2,−1,0,1,2
4f	4	3	−3,−2,−1,0,1,2,3

For a polyelectronic atom, the energy is far more complex than for H, and there is a splitting of the orbital energies such that the degeneracy of n is split and one obtains:

$$1s < 2s < 2p < 3s < 3p < 4s < 3d < 4p < 5s < 4d < 5p < 6s < 4f < 5d < 6p\ldots.$$

The periodic table is generated by using the Pauli exclusion principle that no two electrons can have the same quantum numbers as they are fermions and the Aufbau principle (two electrons per orbital and filling the orbitals from the lowest energy ones). We then use the approximation for atoms that L (total orbital angular momentum quantum number) and S (total spin angular momentum quantum number)

are good quantum numbers as is their sum J = L + S. This is good for values of Z < 40 for a qualitative approach. For larger Z, the effects of relativity need to be considered, and this leads to a spin-orbit LS terms in the Hamiltonian so that L and S are no longer good quantum numbers, and only J = L + S is a good quantum number. This gives rise to the term symbols for the atom, $^{2S+1}L_J$. The values for L and S are obtained by vector sums of the individual angular momentum components. The values of L are labeled as S(L = 0), P(L = 1), D(L = 2), F(L = 3), G(L = 4), H(L = 5)... . The values of 2S + 1 are labeled as follows: singlet(S = 0), doublet (S = ½), triplet (S =1), quartet (S = 3/2), quintet (S = 2).... The ordering of the states is given by Hund's rules:

1. The lowest energy term has the greatest spin multiplicity.
2. For the same spin multiplicity, the term with the greatest orbital angular momentum has the lowest energy.
3. If the unfilled subshell is exactly or more than half full, the level with the maximum value of J has the lowest energy. If the unfilled subshell is less than half full, the level with the lowest J value has the lowest energy.

Conclusions

Quantum numbers arise in the solution of the Schrödinger equation due to the presence of boundary conditions and the properties of a well-behaved wave function solution. The quantum numbers are used to describe the discrete energy levels of a system at small scales. The periodic Table of the elements can be readily explained with the use of four quantum numbers, the Pauli exclusion principle, and the Aufbau principle. Three of these four quantum numbers arise from the solution of the equation describing the solution of the electron in the hydrogen atom, and the fourth is due to the ±½ spin of the electron. Quantum numbers are also important in rotational spectroscopy as well as in vibrational spectroscopy, with the latter quantum numbers being important for isotope fractionation factors.

Cross-References

- ▶ Ab Initio Calculations
- ▶ Atomic Number, Mass Number, and Isotopes
- ▶ Periodic Table

References

Atkins P, Friedman R (2011) Molecular quantum mechanics, 5th edn. Oxford, Oxford

Engel T, Reid P (2013) Physical chemistry, 3rd edn. Pearson, New York

Karplus M, Porter RN (1970) Atoms and molecules: an introduction for students of physical chemistry. W. A. Benjamin, Menlo Park

Levine I (2014) Quantum chemistry, 7th edn. Pearson, New York

Lowe JP, Peterson KA (2006) Quantum chemistry, 3rd edn. Elsevier/Academic Press, Amsterdam

McQuarrie DA (2008) Quantum chemistry, 2nd edn. University Science, Mill Valley

Messiah A (1999) Quantum mechanics. Dover, Mineola. (Original pub date, 1958)

Pauling L, Wilson EB Jr (1985) Introduction to quantum mechanics with applications to chemistry. Dover, Mineola. (Original pub date, 1935)

Pilar FL (2001) Elementary quantum chemistry, 2nd edn. Dover, Mineola. (Original pub date, 1990)

Schatz GC, Ratner MA (2002) Quantum mechanics in chemistry. Dover, Mineola. (Original pub date, 1993)

Szabo A, Ostlund NS (1996) Modern quantum chemistry: introduction to advanced electronic structure theory. Dover, Mineola. (Original pub date, 1989)

R

Radioactivity

Don Porcelli
Department of Earth Sciences, Oxford University, Oxford, UK

Definition

Radioactivity is the process of spontaneous decay of atomic nuclei, releasing energy and atomic particles. The main types of radioactive decay involve nuclear transmutations from a radioactive parent isotope to a stable daughter isotope either directly or through a series of decays of progressively smaller unstable nuclei. A radioactive isotope is an atomic species that has insufficient nuclear binding energy to overcome instability due to an excess of either protons or neutrons. There are many naturally occurring radioactive isotopes of a wide range of elements that are present in the environment, although many more, highly unstable isotopes also have been created in the laboratory.

There are three main effects of radiation to the natural environment: decay produces the emission of high energy radiation that can interact with the environment and can lead to radiation exposure; the release of decay energy results in the production of heat within the Earth; and the generation of daughter nuclides can be used for geochronology.

The Radioactive Decay Law

Radioactive decay is a statistical process that depends upon the instability of the isotope and is completely unpredictable for any individual nucleus. The rate of radioactive decay of an isotope N follows the well-known radioactive decay law, where the fraction of atoms, λ (the decay constant), that decay over a period of time is fixed and is an intrinsic characteristic of the isotope:

$$dN/dt = -\lambda N \quad (1)$$

This can be integrated to describe the resulting isotope abundance with time;

$$N = N_0 e^{-\lambda t} \quad (2)$$

and the amount of daughter isotope atoms produced is equal to $D = N_o - N$. The half-life of N ($t_{1/2}$) is the time required for half of the atoms of N to decay. It is related to the decay constant by

$$t_{1/2} = \ln 2/\lambda \quad (3)$$

Therefore, the greater the decay constant, the faster the decay and the shorter the half-life. The infrequently used mean lifetime of an atom is $\tau = 1/\lambda$.

The rate of decay is reported in the SI unit the Becquerel (Bq), equal to one decay per second. The Curie (Ci) is equal to 3.7×10^{10} decays per second, the approximate radioactivity of 1 g of ^{226}Ra. The abundance of a short-lived nuclide can be reported as an activity (N), which is equal to the decay rate (dN/dt).

Radiometric geochronology methods are based on the constant decay rate of isotopes in the environment and involve either determining how much of a radioactive element has decayed away from a known abundance or how much of a radiogenic daughter has accumulated compared to the amount of radioactive parent remains.

Modes of Decay

There are three main types of decay in the natural environment.

Beta Decay

Beta decay releases a beta particle (a high energy electron or positron), resulting in no change in the total number of

W. M. White (ed.), *Encyclopedia of Geochemistry*,
https://doi.org/10.1007/978-3-319-39312-4

nucleons (A, the number of neutrons plus protons), but there is a change in atomic number (Z, the number of protons), resulting in a daughter nucleus of a different element than that of the parent. In β-decay, within the nucleus of a neutron-rich (relative to stable isotopes of the element) isotope, a neutron is converted into a proton, which releases a high energy electron (β^-) along with a neutrino, e.g., $^{14}C \rightarrow {}^{14}N + \beta^- + \nu + Q$, where Q is the energy released as kinetic energy of the decay products and as electromagnetic, very high-frequency gamma (γ) radiation. In β^+ decay, within the nucleus of a proton-rich isotope, a proton is converted into a neutron, a positron (β^+), and a neutrino, e.g., $^{26}Al \rightarrow {}^{26}Mg + \beta^+ + \nu + Q$. A less common decay mechanism is electron capture, where the nucleus of a proton-rich isotope incorporates one of the orbiting electrons and emits a neutrino, while a proton is converted into a neutron, e.g., $^{40}K + e \rightarrow {}^{40}Ar + \nu + Q$.

Beta radiation is moderately ionizing and can be blocked with a few millimeters of aluminum. Electromagnetic energy is highly ionizing and requires considerable shielding (e.g., 1 cm of lead will absorb 50% of a γ flux).

Alpha Decay

During alpha decay, there is emission from the parent nuclide of an alpha (α) particle composed of two protons and two neutrons (i.e., a ^{4}He nucleus). The result is a change in both A and Z. An example is $^{238}U \rightarrow {}^{234}Th + \alpha + Q$, where energy Q is released both as kinetic energy of the α-particle and the daughter nuclide and as gamma radiation. The charged α-particles do not travel far (a few cm in air, 10^{-3} times that in water, and readily blocked) due to interactions between the charged particle and bound electrons, and so is the type of radiation with the least penetrating power. Where α-particles are retained within a solid as ^{4}He atoms, their accumulation can be used like other stable daughter isotopes for geochronology.

Fission Decay

Spontaneous fission involves the decay of the nucleus into larger fragments, typically two subequal atoms, releasing substantial energy along with neutrons and gamma radiation. This occurs as an alternative decay mode, e.g., ^{238}U spontaneously fissons 5×10^{-7} times the rate of alpha decay, with a fixed spectrum of isotopes of Xe, Mo, and other elements. The fragments are ejected into the surrounding medium and in minerals leave a track of damage. The accumulation of these tracks is equivalent to the accumulation of stable daughter isotopes and is the basis of fission track dating.

Induced fission occurs when a nucleus interacts with a neutron and becomes unstable. This requires a neutron flux and generally occurs in nuclear reactors. There has been one reported natural occurrence, in Oklo, Gabon 2Ga ago when there was a higher proportion of ^{235}U in U, where sufficient ^{238}U was concentrated to provide a high neutron source by spontaneous fission and where there was water to moderate neutron energies to optimize reaction with ^{235}U. This left production of telltale isotopes, e.g., U, Nd, Xe, and Ru (de Laeter and Hidaka 2007) in the deposit.

Some isotopes are subject to more than one mode of decay, e.g., ^{238}U decays by both α-decay (to ^{234}Th) and spontaneous fission, and ^{40}K decays by both electron capture (to ^{40}Ar) and β^-decay (to ^{40}Ca) according to well-defined branching ratios.

Determination of Decay Constants

The decay constant for each separate isotope is determined by direct measurement of either decay radiation or the accumulation of daughter isotopes from a measured abundance of the radioisotope. For very long-lived isotopes, a comparison can be made between the age determined using a decay scheme involving a radioactive parent with a well-constrained decay constant (generally ^{238}U) and decay schemes of other radioactive elements (Blum 1995).

There is consistent evidence that the value for λ for each isotope is a constant, especially on the scale needed for geochronology and environmental studies, through comparison between different schemes over a range of time scales, direct measurements, and limitations on the variation in the underlying controlling fundamental constants that affect nucleus decay (Uzan 2003).

An exception to this is for decay by electron capture, which by involving an electron orbiting in an inner shell, may be subtly affected by environmental conditions. The only major isotope of environmental relevance subject to electron capture is ^{40}K; the value for λ has been calculated to only increase by 0.025% at a pressure of 25GPa (equivalent to a depth of 700 km) (Lee and Steinle-Neumann 2008) and experimentally found to not be significantly affected (to within 1%) in the chemical environment (Norman et al. 2001).

Sources of Radioactive Isotopes

There are various reasons why naturally unstable isotopes with a wide range of half-lives (shown in parentheses below) are found in the environment.

Long-lived isotopes were produced during nucleosynthesis in stars or supernovae along with stable isotopes and were then incorporated into the Earth during formation. These isotopes have not fully decayed away and form the basis for the various decay schemes used for geochronology over Earth history. The primary sources of natural radioactivity, as well as of heat production within the Earth, are the long-lived isotopes ^{238}U (4.47×10^9a), ^{235}U (7.04×10^8a), ^{232}Th

(1.41×10^{10}a), and ^{40}K (1.40×10^{9}a). Other long-lived isotopes include ^{147}Sm (1.06×10^{11}a), ^{87}Rb (4.88×10^{10}a), ^{187}Re (4.6×10^{10}a), and ^{176}Lu (3.71×10^{10}a).

Short-lived isotope daughters are continually produced as intermediate isotopes within the ^{238}U, ^{235}U, and ^{232}Th decay series that ultimately produce stable Pb isotopes. These include isotopes of a range of different elements that can become separated in the environment due to chemical or physical processes, for example, ^{222}Rn escapes from rocks and soils to the atmosphere, where it decays and produces other radioactive daughters.

Short-lived isotopes in the early solar system were also produced in stellar environments and have half-lives long enough to be incorporated into the early Earth but not to survive to the present day. Their earlier presence in some meteorite minerals formed early in solar system history is inferred from enrichments in the stable daughter isotopes. This includes ^{53}Mn (3.7 Ma) ^{107}Pd (6.5 Ma), ^{182}Hf (9 Ma), ^{129}I (16 Ma), ^{244}Pu (82 Ma), and ^{146}Sm (103 Ma), as well as ^{26}Al (0.7×10^{6}a), which was also an important heat source in the early solar system and may have caused melting of very early-formed small bodies (Lee et al. 1977).

Cosmogenic nuclides. The Earth is continuously bombarded by cosmic rays largely from beyond the solar system and composed of high energy particles, primarily protons, that interact with the nuclei of atoms in the atmosphere and exposed surfaces, producing various radioactive isotopes through a series of nuclear reactions. The concentrations are generated in very low but detectable concentrations and can be used to quantify processes occurring over very short time scales [using, e.g., ^{7}Be (53 days), ^{32}P (14.3 days), and ^{35}S (87.5 days)] or to date environmental processes over longer periods [using, e.g., ^{3}H (12.3a), ^{10}Be (1.4 Ma), ^{14}C (5730a), ^{36}Cl (0.3 Ma), ^{39}Ar (269 a), and ^{129}I (80 Ma)].

Anthropogenic isotopes are produced within nuclear reactors and by reactions related to nuclear explosions. While there are many very short-lived isotopes, there are some that are sufficiently long-lived to disperse in the environment. This includes ^{3}H, ^{14}C, ^{90}Sr (29a), ^{99}Tc (0.21 Ma), ^{129}I, ^{137}Cs (30a), ^{237}Np (2.1 Ma), ^{241}Am (430a), and several U and Pu isotopes (Hu et al. 2010).

Measurement Methods for Radiation and Radioactive Isotope Concentrations

Various detectors can be used to quantify the emission rates of different types of radiation, and the abundances of the radioactive isotopes can be measured by quantifying the radiation resulting from decay (L'Annunziata 2012). In some circumstances, an isotope will decay to another short-lived isotope that can be more readily measured and can then be related to the abundance of the parent.

Alpha spectrometry can be used to detect and count emitted alpha particles, where the contributions from the decay of different isotopes can be distinguished by their distinctive α-particle energies. Since α-particles can readily interact with surrounding atoms, and so escape detection, good chemical separation, and purification from other elements are critical.

Beta spectrometry, for counting emitted beta particles, uses the ionizing or excitation effects of the charged β-particles for detection and is commonly done with a Geiger-Müller counter, which employs a gas-filled tube where ions are ionized by each intercepted β-particle, and this is converted into an electrical pulse. These counters do not distinguish between beta particles by energy and so require chemical separation to quantify the contributions from different isotopes rather than total radiation. The isotopes ^{3}H and ^{14}C emit low-energy electrons and require an alternative method such as liquid scintillation counting, in which a sample is dissolved in a solvent solution containing compounds that convert energy received from each β-particle into light, and the resulting pulses are counted.

In gamma spectrometry, emitted gamma rays are detected when they ionize target atoms, and the resulting charge is measured. Gamma rays can penetrate a considerable distance in solid material, so that isotopes of interest do not need to be separated from sample material before counting. Gamma energy spectra can be used to measure various radioactive isotopes simultaneously. The detection limit is typically several orders of magnitude higher than for beta and alpha counting.

As an alternative to determining radioactive isotope abundances by radiation measurements, the atoms present can be measured directly by mass spectrometry. In general, short-lived nuclides, with high radiation fluxes due to high values of λ and despite low atomic abundances, can be more readily measured by counting. The abundances of long-lived nuclides are more precisely measured by mass spectrometry. However, the optimal method for each isotope depends upon the available amount and nature of the sample, the element involved, and specific analytical considerations.

Radioactivity Exposure and Hazards

The natural terrestrial background of radioactivity is largely due to the decay the radioactive isotopes in the ^{238}U, ^{235}U, and ^{232}Th decay chains, along with ^{40}K, and so is controlled by the distribution of K, U, and Th in rocks and soils. Bioaccumulation of these elements can enrich radioactive isotopes and increase exposure. For example, there is ^{40}K (as well as ^{14}C) in food and in the body, ^{210}Po in tobacco, and ^{210}Pb in aquatic biota. The use of natural materials for construction, such as granites and shales that are enriched in

U and Th, can increase radiation within buildings. However, the greatest exposure is from ^{222}Rn in the ^{238}U decay series, which is mobile as an inert gas and can escape from rocks and soils and accumulate within buildings. It has a short half-life (3.8 days) and then decays to a series of other short-lived isotopes that together can account for a substantial fraction of natural exposure.

The radioactivity of naturally occurring radioactive materials (NORM) can be concentrated through industrial activities (IAEA 2003). Combustion of coal concentrates U and Th in fly ash and processing of phosphate rocks for fertilizer leaves similarly enriched residual waste. Similarly, U and Th can be found in waste from metal mining and tailings and in mineral sands that are processed for Zr, Ti, and REE. During oil and gas production, formation wastewaters can accompany extraction and are enriched in Ra isotopes that are then concentrated in sulfate precipitates within pipelines.

Artificially produced radionuclides produced from nuclear explosions or released from waste discharges or nuclear accidents are widely distributed due to dispersion by atmospheric transport or ocean circulation. This includes isotopes of a wide range of elements and with very different half-lives. A clear of example of the global impact of nuclear explosions is ^{14}C, which is naturally produced in the atmosphere due to neutrons from cosmic ray reactions; the atmospheric concentration of ^{14}C almost doubled by the early 1960s due to additional neutron fluxes from aboveground nuclear testing and subsequently dropped only after such testing was banned. Similar peaks occurred for ^{3}H and ^{36}Cl as well. Exposure hazards due to nuclear accidents and discharges depend upon the transport properties and exposure pathways involved for each isotope. The radioactive isotopes most responsible for radiation exposure by the general population after the Fukushima (2011) and Chernobyl (1986) reactor incidents were ^{131}I, ^{134}Cs, and ^{137}Cs, which were dispersed through the atmosphere (Steinhauser et al. 2014). The impact of intentional and accidental discharges can be seen even in remote areas. Discharges into the ocean from the Sellafield nuclear reprocessing plant in the UK have led to a plume of low-level ^{137}Cs and ^{129}I and ^{236}U that can be traced into the Arctic Ocean. Similarly, low levels of ^{238}Pu (88 a),^{239}Pu (24 ka), ^{240}Pu (6.6 ka), ^{137}Cs, and ^{241}Am are found in soils even in remote Arctic regions (AMAP 2016).

Cross-References

- ▶ Analytical Techniques
- ▶ Atomic Number, Mass Number, and Isotopes
- ▶ Cosmogenic Nuclides
- ▶ Fission Track Analysis
- ▶ Geochronology and Radiogenic Isotopes
- ▶ High-Resolution Mass Spectrometry
- ▶ Nucleosynthesis
- ▶ Radon
- ▶ Uranium Decay Series

References

Arctic Monitoring and Assessment Programme (2016) AMAP Assessment 2015: radioactivity in the Arctic. Oslo

Blum JD (1995) Isotope decay data. In: Ahrens TJ (ed) Global Earth physics, a handbook of physical constants. American Geophysical Union, Washington, DC, pp 271–282

de Laeter JR, Hidaka H (2007) The role of mass spectrometry to study the Oclo-Bangombé natural reactors. Mass Specrom Rev 26:683–712

Hu Q-H, Wang J-Q, Wang J-S (2010) Sources of anthropogenic radionuclides in the environment: a review. J Environ Radioact 101:426–437

IAEA (2003) Extent of environmental contamination by naturally occurring radioactive material (NORM) and technological options for mitigation. Technical Report Series 419. Vienna

L'Annunziata ML (2012) Handbook of radioactivity analysis, 3rd edn. Elsevier, Oxford

Lee K, Steinle-Neumann G (2008) Ab-initio study of the effects of pressure and chemistry on the electron-capture radioactive decay constants of ^{7}Be, ^{22}Na, and ^{40}K. Earth Planet Sci Lett 267:628–636

Lee T, Papanastassiou DA, Wasserburg GJ (1977) Aluminium-26 in the early solar system: fossil or fuel. Astrophys J 211:L107–L110

Norman EB et al (2001) Influence of physical and chemical environments on the decay rates of ^{7}Be and ^{40}K. Phys Lett B519:15–22

Steinhauser G, Brandl A, Johnson TE (2014) Comparison of the Chernobyl and Fukushima nuclear accidents: review of the environmental impacts. Sci Total Env 470–471:800–817

Uzan J-P (2003) The fundamental constants and their variation: observational and theoretical status. Rev Mod Phys 75:403–455

Radium

William M. White
Department of Earth and Atmospheric Sciences, Cornell University, Ithaca, NY, USA

Element Data

Atomic Symbol: Ra
Atomic Number: 88
Atomic Weight: 226.03
Isotopes and Abundances: ^{226}Ra ($t_{1/2}$ = 1599 y) ~100%, ^{228}Ra ($t_{1/2}$ = 5.76 y), ^{223}Ra ($t_{1/2}$ = 11.4 d), ^{224}Ra ($t_{1/2}$ = 3.6 d)
1 Atm Melting Point: 696 °C
1 Atm Boiling Point: 1500 °C
Common Valences: 2+
Ionic Radii: 148 pm

(*continued*)

Pauling Electronegativity: 0.9
First Ionization Energy: 509.29 kJ/mol
Chondritic (CI) Abundance: 4.6×10^{-3} ppt (0.17 Bq/kg; Girault et al. 2017)
Silicate Earth Abundance: 7.9×10^{-3} ppt
Crustal Abundance: 0.47 ppt
Seawater Abundance: 0.14–0.83 fmol/L
Core Abundance: ~0

Properties

Radium has no stable or long-lived isotopes and exists in nature only because it is continually produced by radioactive decay, ultimately of U and Th. Its longest-lived and consequently most abundance isotope, ^{226}Ra, is part of the ^{238}U decay series chain and the daughter of ^{230}Th. Concentrations in the silicate Earth and crust listed here assume ^{226}Ra is in secular radioactive equilibrium with ^{238}U; other isotopes are orders of magnitude less abundant. ^{228}Ra and ^{224}Ra are part of the ^{232}Th decay chain; ^{223}Ra is part of the ^{235}U decay chain. Pure Ra is a soft silvery-white metal with a density of 5500 kg/m^3, but rapidly reacts with air to form radium nitride. Radium is highly radioactive; the Curie (Ci) unit of radioactivity was defined as the activity of 1 g of Ra and is equal to 3.7×10^{10} decays per second or becquerels (Bq), which is the SI unit of radioactive decay. ^{223}Ra, ^{224}Ra, and ^{226}Ra decay by emission of α particles; ^{228}Ra decays by emission of a β^- particle.

As the heaviest alkaline earth element, Ra behaves as an lithophile element and most Ra salts are soluble in water ($RaSO_4$ being the most notable exception), although less so than salts of the lighter alkaline earths. In many respects, its chemistry is similar to that of the next heaviest alkaline earth, barium.

History and Use

Radium was first isolated and identified as a new element spectroscopically by Marie and Pierre Curie in 1898; the pure metal was isolated 10 years later (Emsley 2001). In the early twentieth century, Ra was used to produce luminous paints for watch dials, etc., by mixing radium bromide with zinc sulfide, with the α-particles stimulating fluorescence of ZnS. It was also used in health treatments, generally very much to the detriment of the patients involved, before the hazards of radioactivity were fully realized.

Today, use of Ra is limited to treatment of some metastasized cancers and as a radiation source for some types of industrial radiography.

Radium Geochemistry

Radium's large ionic radius makes it incompatible in most common minerals and it behaves similarly to other large ion lithophile elements in magmatic systems. Owing to the short half-lives of Ra isotopes, the distribution of Ra in crystalline rocks will closely follow that of its parents, U and Th. However, as a consequence of alpha-recoil during its production by one (in the case of ^{228}Ra) or more α-decays, some Ra atoms will be ejected from crystals and the remainder will occupy damaged crystal sites, making it susceptible to leaching during weathering. Nevertheless, Michel (1984) found that ^{226}Ra was present in excess over ^{238}U in weathered granite and was concentrated in the leachable fraction, suggesting Ra lost from primary minerals is quickly incorporated into secondary ones. At low temperature, Ra is most compatible in sulfates such as anhydrite and barite and, to a lesser extent, carbonates such as aragonite (Langmuir and Riese 1985).

In soils, ^{226}Ra/^{238}U activity ratios averaged over entire soil profiles are close to radioactive equilibrium, but Ra is generally enriched in surface soil and in the exchangeable and organic fractions. Conversely, soil minerals are typically Ra-depleted relative to U. This likely reflects the effects of vegetation, in which Ra is strongly concentrated over U. The result of this vegetative uptake is to move Ra upward in the soil and concentrate it in the organic fraction (Greeman et al. 1999).

In low ionic strength stream and groundwaters, Ra is mainly present as uncomplexed Ra^{2+} ion. Its behavior, however, is dominated by its rapid absorption onto solid surfaces in low ionic strength solution (Krishnaswami et al. 1982). Its transport in groundwater is consequently strongly retarded. The very different half-lives of the four Ra isotopes can be used to distinguish processes occurring at different rates and time scales, making them particularly useful in groundwater migration studies (Porcelli and Swarzenski 2003). The discovery of high concentrations of ^{226}Ra in coastal waters of South Carolina led to the recognition of the importance of submarine groundwater discharge (Moore 1996), and subsequent Ra studies have helped to quantify submarine groundwater discharge elsewhere (Moore 2010).

Decay of Th in sediments rather than riverine input is the principal source of Ra in seawater. Within the ocean, Ra distribution closely follows that of Ba, with a nearly constant Ba/Ra ratio of about 4.5×10^{-9} mol/mol (Ku and Luo 1994; Foster et al. 2004). Both elements are depleted in surface waters due to particle scavenging but are mostly regenerated within the upper 250–1000 m. Both elements have seawater residence times of the order of 10^4 years and behave quasi-conservatively in the deep ocean. As its residence time is longer than its half-life, Ra largely decays within the ocean

rather than being removed. Because of its conservative behavior and the differing half-lives of its four isotopes, Ra is used as a tracer of ocean circulation and mixing (e.g., Ku and Luo 1994; Charette et al. 2015).

Based on the extent of radioactive disequilibrium between parent and daughter nuclides, Ra isotopes, like other nuclides in the U-series decay chain, can be useful geochronological tools. The short half-life of ^{226}Ra makes it useful mainly on times scales of thousands of years, making it particularly useful in studies of magmatic processes (e.g., Hawkesworth et al. 2004). For example, excesses of the activity of ^{226}Ra over its parent ^{230}Th have revealed surprisingly short time scales between melt segregation in the mantle and eruption at the surface in island arc volcanoes (e.g., Gill and Williams 1990; Turner et al. 2001). Radium isotopes have also been used to date travertine deposits (e.g., Sturchio 1990; Soligo and Tuccimei 2008) and the residence times of water hydrothermal systems at mid-ocean ridges (e.g., Kadko and Butterfield 1998). Radium can be present at concentrations orders of magnitude above levels considered safe for drinking in saline formation waters pumped to the surface in petroleum production and in barite precipitated on equipment. ^{228}Ra/^{226}Ra ratios can be used to establish the age of these precipitates and distinguish between sources of contaminated soils (Zielinski et al. 2001).

Biological Utilization and Toxicity

Radium has no biological function; its toxicity derives from its radioactivity. As an alpha-emitter, it is particularly damaging to tissue when inhaled or ingested. The U.S. Environmental Protection Agency considers levels in drinking water above 5 pCi/L (0.185 Bq/L) to be unsafe. An additional hazard associated with Ra is its decay to radon (Rn), which as a noble gas is particularly mobile and easily inhaled.

Summary

Radium is present in the Earth only as a consequence of its continued production through decay of U and Th; because of the short half-lives of its isotopes, its concentration is extremely low. Despite this, and despite its very limited practical use, Ra has proved valuable to geochemists in a wide variety of ways, ranging from studying groundwater to magma migration and ocean mixing. In addition, studies of naturally occurring Ra inform understanding of the behavior of Ra in radioactive nuclear waste.

Cross-References

- ▶ Alkali and Alkaline Earth Metals
- ▶ Barium
- ▶ Geochronology and Radiogenic Isotopes
- ▶ Hydrothermal Vents
- ▶ Incompatible Elements
- ▶ Large-Ion Lithophile Elements
- ▶ Lithophile Elements
- ▶ Ocean Salinity, Major Elements, and Thermohaline Circulation
- ▶ Radioactivity
- ▶ Radon
- ▶ Soils
- ▶ Subduction Zone Geochemistry
- ▶ Sulfate Minerals
- ▶ Uranium Decay Series

References

Charette MA, Morris PJ, Henderson PB, Moore WS (2015) Radium isotope distributions during the US GEOTRACES North Atlantic cruises. Mar Chem 177:184–195

Emsley J (2001) Nature's building blocks: A-Z guide to the elements. Oxford University Press, Oxford

Foster DA, Staubwasser M, Henderson GM (2004) ^{226}Ra and Ba concentrations in the Ross Sea measured with multicollector ICP mass spectrometry. Mar Chem 87:59–71

Gill JB, Williams RW (1990) Th isotope and U-series studies of subduction-related volcanic rocks. Geochim Cosmochim Acta 54:1427–1442

Girault F, Perrier F, Moreira M, Zanda B, Rochette P, Teitler Y (2017) Effective radium-226 concentration in meteorites. Geochim Cosmochim Acta 208:198–219

Greeman DJ, Rose AW, Washington JW, Dobos RR, Ciolkosz EJ (1999) Geochemistry of radium in soils of the eastern United States. Appl Geochem 14:365–385

Hawkesworth C, George R, Turner S, Zellmer G (2004) Time scales of magmatic processes. Earth Planet Sci Lett 218:1–16

Kadko D, Butterfield DA (1998) The relationship of hydrothermal fluid composition and crustal residence time to maturity of vent fields on the Juan de Fuca ridge. Geochim Cosmochim Acta 62:1521–1533

Krishnaswami S, Graustein WC, Turekian KK, Dowd JF (1982) Radium, thorium and radioactive lead isotopes in groundwaters: Application to the in situ determination of adsorption-desorption rate constants and retardation factors. Water Resources Research 18:1663–1675. https://doi.org/10.1029/WR018i006p01663

Ku T-L, Luo S (1994) New appraisal of radium-226 as a large-scale oceanic mixing tracer. J Geophys Res Oceans 99:10255–10273

Langmuir D, Riese AC (1985) The thermodynamic properties of radium. Geochim Cosmochim Acta 49:1593–1601

Michel J (1984) Redistribution of uranium and thorium series isotopes during isovolumetric weathering of granite. Geochim Cosmochim Acta 48:1249–1255

Moore WS (1996) Large groundwater inputs to coastal waters revealed by ^{226}Ra enrichments. Nature 380:612–614

Moore WS (2010) The effect of submarine groundwater discharge on the ocean. Annu Rev Mar Sci 2:59–88

Porcelli D, Swarzenski PW (2003) The behavior of U- and Th-series nuclides in groundwater. Rev Mineral Geochem 52:317–361
Soligo M, Tuccimei P (2008) Radium-226 chronology of Holocene travertine from Esanatoglia (Central Italy). Quat Geochronol 3:89–98
Sturchio N (1990) Radium isotopes, alkaline earth diagenesis, and age determination of travertine from mammoth Hot Springs, Wyoming, U.S.A. Appl Geochem 5:631–640
Turner S, Evans P, Hawkesworth C (2001) Ultrafast source-to-surface movement of melt at island arcs from ^{226}Ra-^{230}Th systematics. Science 292:1363–1366
Zielinski RA, Otton JK, Budahn JR (2001) Use of radium isotopes to determine the age and origin of radioactive barite at oil-field production sites. Environ Pollut 113:299–309

Radon

Don Porcelli
Department of Earth Sciences, Oxford University, Oxford, UK

Element Data
Atomic Symbol: **Rn**
Atomic Number: **86**
Atomic Weight: 222.018
1 Atm Melting Point: −71 °C
1 Atm Boiling Point: −62 °C
Common Valences: 0
Atomic Radius: 220 pm
Pauling Electronegativity: 2.0
First Ionization Potential: 10.747 eV
Crustal Abundance: ~35 mBq g^{-1}
Seawater Abundance: ~0.6–6 Bq m^{-3}

Properties

Radon is a noble gas (with a filled outer electron shell), with three naturally occurring isotopes, all of them radioactive. Each is produced by decay of a radium isotope parent within one of the ^{238}U, ^{235}U, and ^{232}Th decay series. Rn is colorless, odorless, and generally unreactive in the natural environment. The longest-lived isotope, ^{222}Rn, is the most abundant, although ^{220}Rn contributes a significant fraction of the total Rn radioactivity very close to where it is being continuously produced by parent ^{224}Ra decay. Rn does not readily form chemical compounds or interact with most natural materials but has been found to adsorb onto activated charcoal, zeolites, and silica gel in the laboratory. The solubility of Rn in water, at 1 atmosphere pressure and 20 °C, is 230 cm^3/kg.

Radon, Table 1 Data for Naturally-Occurring Radon Isotopes

	^{222}Rn	^{220}Rn	^{219}Rn
Half-life $t_{1/2}$	3.83 days	55.6 s	3.96 s
Decay constant λ	2.09×10^{-6} s^{-1}	0.0127 s^{-1}	0.175 s^{-1}
Decay series	^{238}U	^{232}Th	^{235}U
Immediate parent	^{226}Ra	^{224}Ra	^{223}Ra
Immediate daughter	^{218}Po	^{216}Po	^{215}Po
Relative abundance[a]	99.98%	0.02%	0.00006%
Relative activity[a]	1	1.2	0.05
Conversion: 1 Bq=	4.8×10^5atoms	80 atoms	5.7 atoms

[a]Assuming the average crustal values of (Th/U)wt = 3.8 and (^{238}U/^{235}U) molar = 138

Since Rn is present in very low concentrations and decays rapidly, it is measured through decay counting, usually either by alpha counting of Rn decay or gamma counting of the decay of its daughter products. The abundance of each isotope (atoms, N) is typically reported as the activity, or rate at which the atoms decay (in Bq, decays per second), where the activity $dN/dt = \lambda N$ for each isotope with decay constant λ (Table 1).

History and Use

Radon was discovered through a series of experiments, starting in 1899, investigating the properties of radioactive substances by the Curies, Rutherford, and Dorn. Radioactive gaseous emanations from thorium (^{220}Rn) and radium (^{222}Rn) were finally identified as constituting a new element by Rutherford (Marshall and Marshall 2003) and used to determine the short half-lives, atomic masses, and chemical properties.

There are no significant direct uses of Rn. Although there are some claims that exposure to natural environments enriched in ^{222}Rn has therapeutic effects, these are not accepted by health organizations.

Geochemical Behavior

The distribution of Rn in rocks reflects the distribution of U and Th. In closed systems within minerals and rocks where decay series nuclides cannot readily escape, a state of secular equilibrium is maintained where the decay rate of each Rn isotope is equal to the production rate through decay by the corresponding parent Ra isotope, which in turn is equal to the decay rate of the U or Th isotope at the top of the decay series. Radon concentrations are highest in rocks with U mineralization, and high in granites and organic-rich shales, but are low in sandstones. The average concentration of

^{226}Ra in soils is ~25 Bq/kg (and so ~1.2 × 10^7 atoms ^{222}Rn/kg) (UNSCEAR 1982).

Radon can escape from minerals through alpha recoil, when the decay of the parent Ra atom imparts sufficient energy on the resulting Rn atom to propel it ~10 nm through mineral structures in a random direction. The Rn atom may cross the mineral surface and come to rest in water-filled pore space or fracture, or be implanted into an adjacent mineral from which it can migrate out through the damaged mineral lattice of the recoil track. The proportion of Rn produced that is released this way depends upon the size and shape of U- and Th-bearing minerals as well as the distribution of Ra in secondary phases and adsorption sites. This can be up to ~10% in groundwaters and may be substantially greater in soils. Subsequent migration of Rn in unsaturated soil profiles upwards depends upon the diffusive path in vapor-filled pores and fractures, advective vapor migration, and partitioning with any pore water present. In aquifers, Rn transport is dominated by groundwater advection.

The diffusive and advective fluxes of Rn can be used to quantify various short-term transport processes (Baskaran 2016). In the hydrosphere, the recoil flux of ^{222}Rn out of solids provides a measure of the recoil fluxes of the short-lived isotopes of U, Th, Pa, Ra, and Po and can be used to calculate transport rates of these elements in groundwaters (Porcelli 2008). The concentrations of ^{222}Rn in groundwaters is high due to the high ratio of U-bearing rock to water in aquifers, and so groundwater discharge into surface waters, which have low ^{222}Rn due to a lower supply and loss to the atmosphere, can be identified in rivers, lakes, and oceanic shelves. In the deep oceans, ^{222}Rn is in secular equilibrium with dissolved ^{226}Ra except in the upper ~100 m, where ^{222}Rn is partially lost to the atmosphere, and near the seafloor, where ^{222}Rn is enriched due to a diffusive flux from the underlying sediments. The variations near the sediment-water and water-air interfaces have been used to study vertical transport processes in these zones and mixing between water masses (Smith et al. 2011).

There have been reports of increased ^{222}Rn fluxes preceding or accompanying tectonic activity and so providing an indicator of an upcoming earthquake. However, such occurrences have not been uniform between sites or even spatially and temporally at a single site. Moreover, the mechanisms for release and transport of ^{222}Rn, and the conditions under which there is unambiguous association with tectonic activity, have not been clearly established (Woith 2015).

High fluxes of radon may be used to identify U deposits, although this is expected to be limited to identifying occurrences within ~100 m of the surface due to the short half-life of ^{222}Rn, unless it is carried advectively to the surface. High ^{222}Rn fluxes may also reflect preferential transport to the surface through the presence of subsurface faults. Naturally occurring radioactive materials (NORM) such as residues from resource extraction activities (e.g., oil, gas, and coal industries; mineral sands processing for Th) also can be local sources of ^{220}Rn and ^{222}Rn (Ishimori et al. 2013).

In the atmosphere, the concentration of ^{222}Rn decreases with elevation in the atmosphere due to a changing balance between upward transport and decay and can be used to determine rates of atmospheric advection. The mean world-wide flux of ^{222}Rn from soils is 16 mBq m^{-2} s^{-1} (UNSCEAR 2000) though this can vary considerably and can be substantially higher in areas with underlying soils with high U concentrations. Atmospheric concentrations decrease with altitude and reflect vertical advective transport and mixing processes.

Biological Utilization and Toxicity

About 60% of the total natural radiation dose is from Rn and its decay products (Appleton 2012). The hazards of Rn were established through epidemiological studies that found increased incidences of lung cancer in uranium miners. For the general population, most of the exposure is due to increased concentrations in dwellings, and it has been estimated that ~10% of total death rate by lung cancer is attributable to Rn. The incidence rate is greater for smokers (WHO 2009).

^{222}Rn is unreactive and does not accumulate in the body. However, it decays to the sequence of very short-lived ^{218}Po (3.04 min half-life), ^{214}Pb (26.8 min), ^{214}Bi (19.9 min), and ^{214}Po (164 μs) isotopes, which attach to natural aerosols that may be inhaled and become lodged to lung epithelial cells. The alpha radiation from decay of ^{218}Po and ^{214}Po damage DNA both directly and through the generation of free radicals. Since major genetic damage can be caused by even a single alpha particle, health organizations generally consider any level of exposure potentially harmful (WHO 2009). Similarly, ^{220}Rn decays to a series of particle-reactive short-lived nuclides, including those subject to alpha decay.

Most Rn enters buildings by air advection from above the soil surface and through openings in the structure (Nazaroff 1992) and so is dependent upon atmospheric conditions. Building materials generally only contribute a small fraction of indoor Rn but may be important in areas with low soil fluxes or when concrete or blocks are used that are made using natural materials that are high in U, such as granites or alum shale (Appleton 2012). The flux from soils is almost entirely ^{222}Rn due to the long transport times relative to the half-life of ^{220}Rn, although building materials may provide a significant flux of ^{220}Rn.

Maps of the level of potential hazard due to Rn are often used to assess local risk and may be based on indoor Rn levels and dwelling construction features, geochemical characteristics and lithology of underlying rocks and soils, Rn transport

data such as soil permeability and moisture levels, and Rn soil gas concentrations (Appleton 2012).

Indoor ^{222}Rn concentrations are the result of the balance between the influxes and the rate of removal by ventilation and decay. Therefore, maintaining low Rn concentrations in high-risk locations involves limiting the flux of Rn from soils into buildings using barriers and sealing openings and enhanced ventilation below and within structures.

Summary

Radon has unique characteristics as a short-lived noble gas that is present throughout the environment. Rn can accumulate in dwellings and be a significant source of natural radiation. Rn also provides a unique geochemical tracer for very short-term environmental processes.

Cross-References

- ▶ Atmophile Elements
- ▶ Earth's Atmosphere
- ▶ Noble Gases
- ▶ Polonium
- ▶ Radioactivity
- ▶ Radium
- ▶ Thorium
- ▶ Uranium
- ▶ Uranium Decay Series

References

Appleton JD (2012) Radon in air and water. In: Selinus O (ed) Essentials of medical geology. Springer

Baskaran M (2016) Radon: a tracer for geological, geophysical and geochemical studies. Springer, Cham

Ishimori Y, Lange K, Martin P, Mayya YS, Phaneuf M (2013) Measurement and calculation of radon releases from NORM residues. IAEA technical reports series no. 474, Vienna

Marshall JL, Marshall VR (2003) Ernest Rutherford, the "true discoverer" of radon. Bull Hist Chem 28(2):76

Nazaroff WW (1992) Radon transport from soil to air. Rev Geophys 30:137–160

Porcelli D (2008) Investigating groundwater processes using U- and Th-series nuclides. Radioact Env 13:105–153

Smith CG, Swarzenski PW, Dimova NT, Zhang J (2011) Natural radium and radon tracers to quantify water exchange and movement in reservoirs. In: Baskaran M (ed) Handbook of environmental isotope geochemistry. Springer, pp 345–365

UNSCEAR (2000) Report of the United Nations Scientific Committee on the effects of atomic radiation to the general assembly. IAEA, Vienna

WHO (2009) WHO handbook on indoor radon: a public health perspective. World Health Organization, Geneva

Woith H (2015) Radon earthquake precursor: a short review. Eur Phys J Spec Top 224:611–627

Raman Microspectroscopy

András Gorzsás
Department of Chemistry, Umeå University, Umeå, Sweden

Synonyms

Hyperspectral Raman imaging; Micro-Raman spectroscopy; Raman imaging; Raman mapping; Raman microscopy

Definition

Raman spectroscopy is a spectroscopic technique based on the inelastic scattering of photons (the Raman effect), resulting in a shift of the frequency of the monochromatic light used for irradiating the sample, based on molecular vibrations and rotations (or other low frequency movement modes in a system). Microspectroscopy refers to spectroscopy performed in a spatially resolved manner.

Basic Principles and History

The inelastic scattering of photons has been postulated on theoretical grounds at the area of quantum mechanics (Smekal 1923) and was experimentally demonstrated shortly after in liquids (Raman and Krishnan 1928) and in crystals (Landsberg and Mandelstam 1928). This inelastic scattering (the Raman effect) is the basis of Raman spectroscopic methods that study molecular vibrations and rotations. In many senses, Raman spectroscopy is complementary to infrared spectroscopy, as both are probing molecular motions and symmetries that correspond to essentially the same energy level differences, although approached by different routes (Fig. 1), as Raman spectroscopy is based on the above mentioned scattering and not on absorption as is the case for infrared spectroscopy. Since only a fraction of the photons undergo inelastic scattering (Fig. 1), the Raman effect and consequently Raman spectroscopic signals are frequently weak. Most importantly for spectroscopic applications, the inelastic scattering results in a shift of the incoming light frequency (i.e., energy is either lost or gained upon interacting with the molecules of the sample), and this shift is characteristic of the molecules of the sample but independent from (although related to) the original monochromatic light frequency. Thus, conclusions regarding the presence of certain functional groups, conformations, and symmetry of the molecules in the sample can be drawn from the Raman spectrum in much the same way as from an infrared spectrum. The complementary nature of vibrational spectroscopic

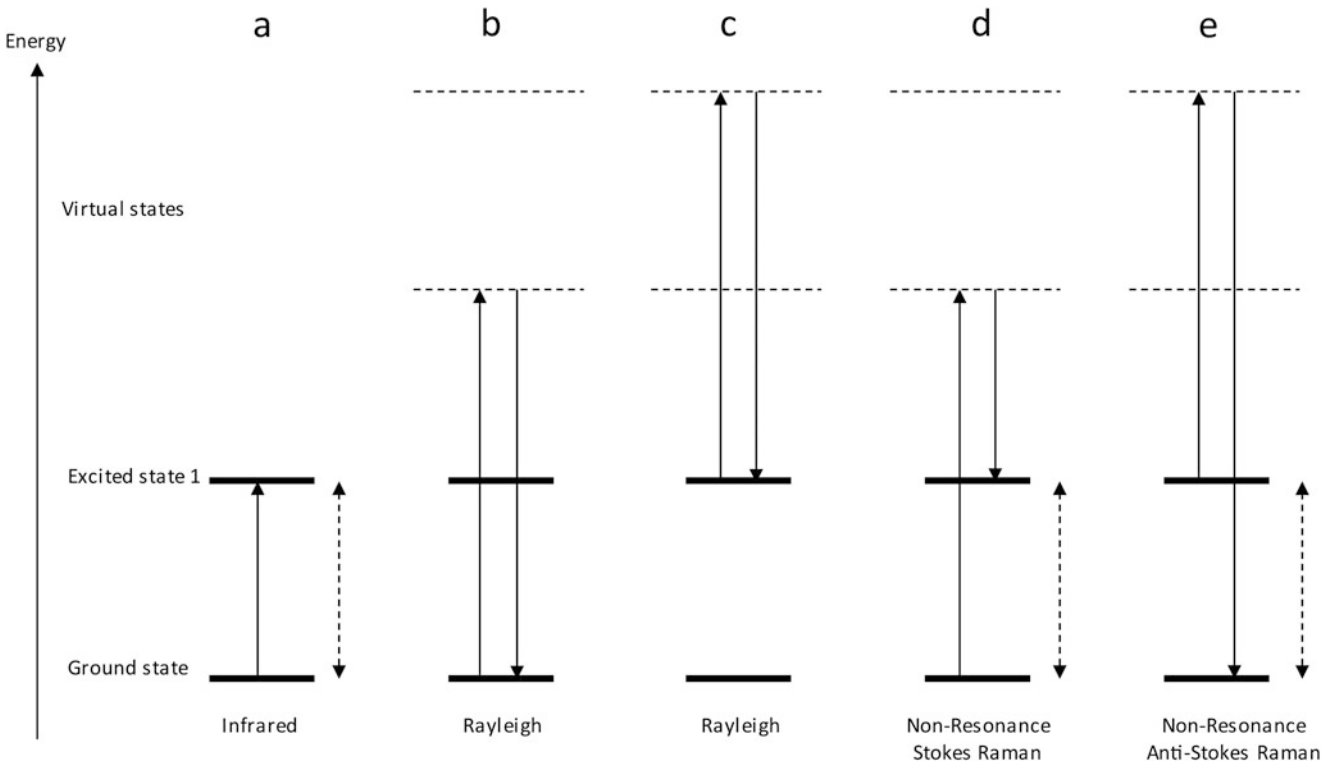

Raman Microspectroscopy, Fig. 1 Energy diagram with schematics illustrating the Raman effect. The vibrational states are marked with *bold horizontal lines* and labeled as ground or excited states (the rotational states in each vibrational state are excluded for simplicity). Virtual states are shown in *dashed horizontal lines*. The transitions are marked with *single-headed arrows*, and the energy difference is marked with *dashed double-headed arrows*. (**a**) Absorption of mid-infrared light results in a transition from the ground vibrational state to the first excited vibrational state; (**b** and **c**) Rayleigh scattering does not result in energy exchange, whether the molecules were in the ground state or the excited state originally; (**d**) during Stokes Raman scattering, the atom or molecule gains energy, the transition corresponding to that of the infrared absorption case (in **a**) but achieved differently; (**e**) a fraction of the atoms/molecules was already in an excited state (according to the Boltzmann distribution) and will lose energy during the anti-Stokes Raman scattering to return to the ground state. The energy difference is the same as in (**a**) and (**d**), but its sign is opposite (due to energy loss instead of gain). It has to be noted that only a small proportion of light is scattered, and the vast majority of the scattered photons undergo Rayleigh scattering (10^3–10^5 as much as Stokes scattering). Thus, the Stokes lines represent ca. 10^{-6}–10^{-9} of the light intensity. Since there are considerably fewer molecules in the excited state at start (Boltzmann distribution), and most of them will undergo Rayleigh scattering (according to **c**), the anti-Stokes lines have even lower intensity than the Stokes lines

techniques can be further illustrated by the fact that molecular vibrations can be either Raman active (if they involve a change in the polarization potential), infrared active (if the polarization is altered), both Raman and infrared active, or none (which can be particularly beneficial in the case of diatomic gases, such as N_2 and O_2, as it means that dry air usually does not disturb measurements).

Instrumentation

For a modern dispersive Raman spectrometers, the essential components include a light source, a sample compartment (with a possibility to focus the laser light), collection optical elements (often including filters to remove the strong Rayleigh signal, Fig. 1), a dispersing optical element (most commonly gratings) and a detection system (usually charge coupled devices, to convert photons to electric signal), and a computer to handle the system. Raman spectrometers can be equipped with a microscope attachment at the sample compartment site, allowing for spatially resolved measurements. The lateral (xy) resolution depends on the ability to focus the laser spot and is commonly in the micron range. Microscopes are often manufactured to enable the setting of a confocal pinhole, considerably improving resolution in the z-direction (and slightly in the xy direction) at the price of potentially weakened signals. Microscope accessories enable the collection of hyperspectral data, that is, generating chemical maps over 2D or 3D (especially with confocal settings) sample areas. This is usually achieved by point scanning, although array detectors have become more common recently, allowing for simultaneous scanning of a defined area (often a line) at the cost of spatial resolution limitations (based on detector size instead of laser focusing capacity).

Raman (micro)spectroscopy instruments are generally versatile and can be equipped with fiber optic probes and a set of different lasers to enable workarounds for (auto)fluorescence problems of certain materials. Raman spectrometers can also be equipped with other accessories (such as temperature and humidity control chambers, polarizers, autosamplers, immersion setups, etc.) and combined with other instruments (such as atomic force microscopes, in which case the AFM needle head serves as the Raman laser exit and entry point, allowing for generating a chemical map overlay as the topography is probed).

As a final note, Fourier-transform (FT) Raman spectrometers also exist, particularly for lasers in the near infrared range of the spectrum, where fluorescence problems are avoided. These setups often have more limited lateral resolution and employ different detectors than the corresponding dispersive setups with lower wavelength lasers.

Sample Preparation, Measurement, and Data Analysis

Preparing samples for Raman microspectroscopy is often very simple. When only the surfaces of larger objects (mm size) need to be investigated, the sample often requires no preparation specifically for the measurement and can be used as is. For smaller samples or investigating deeper layers of nontransparent heterogeneous materials, the sample may need to be prepared to provide the best signal in the shortest time. This preparation can involve sectioning or depositing (a layer of) the sample on a carrier (either standard microscopy slides or special Raman transparent carriers, made of, e.g., CaF_2 or BaF_2).

Finding the ideal measurement conditions is usually done iteratively, starting by selecting the appropriate laser (to provide the best signal with the least disturbances, such as fluorescence, heat generation, power and focusing possibilities, etc.) and the required lens (based on magnification and other properties such as medium immersion or long-working distance objectives). Exposure time, focus settings (including focus levels, focus tracking, and confocal settings), and spectral range selection follows, often interdependently. Finally, the measurement area needs to be defined, together with the step sizes, which determines the number of points (pixels or voxels) that are recorded. Together with the exposure time and the mode of spectrum acquisition, this determines the time each measurement takes. The length of measurement can be of particular importance if the sample can change over time (e.g., due to being sensitive to laser exposure or unstable or because processes with comparable time spans are monitored, etc.)

Data analysis can be extremely simple as well, in case diagnostic bands exist and can be monitored accurately. Evaluating their intensity (or checking for the presence/absence) can be performed using univariate methods (integrals or simple spectral intensity readouts) but often require preprocessing, such as the removing of cosmic rays, baseline correction, and optionally smoothing/noise filtering and intensity normalization (to compensate for out-of-focus intensity fluctuations, for instance). These preprocessing steps are often necessary before multivariate analyses as well, although some of them can be "filtered" by the multivariate methods. Multivariate analyses are more time-consuming especially for large hyperspectral datasets and frequently require some level of chemometrics knowledge from the user.

Selected Advantages and Disadvantages of Raman Microspectroscopy

General and common advantages:

1. Cost and time effectiveness. Raman microspectroscopy is generally fast and inexpensive, especially considering the high information content of the resulting spectra(l maps).
2. Minimal to no sample preparation may be required, and most phases of materials can be measured with relative ease (gases, liquids, solids).
3. A complete chemical profile of the sample is gained without the need for labelling/staining/marking or extraction (i.e., in situ, with no a priori knowledge or bias for tracking). This includes not only chemical composition but also structure (e.g., protein conformational changes, crystallinity measures, etc.)
4. Directional activity: since the laser is polarized, anisotropy, chirality, and polymer orientations can be determined together with chemical compositional and structural information.
5. High specificity, since each Raman active molecule provides a unique Raman spectral fingerprint.
6. Potentially high sensitivity (certain Raman techniques are capable of detecting single molecules of chemicals. Generally, however, concentrations down to micromolar ranges are investigated).
7. (Semi)quantitative analysis, as the intensity of the Raman signal should be proportional to the concentration of the scattering species, if other (optophysical) factors are eliminated.
8. Complementary to infrared spectroscopy: water does not disturb (except for near infrared lasers, e.g., FT-Raman), and bands are often narrower (better resolved) than in the corresponding infrared spectra.
9. High spatial resolution. Unlike in FTIR microspectroscopy, the resolution is not diffraction limited. Often, the maximum achievable resolution depends on the focus of the laser (set by the numerical aperture of the lens and the optical setup of the spectrometer as well as by

the wavelength of the laser) and the step movement accuracy of the microscope stage. Normal Raman microspectroscopy can operate in 0.1 μm spatial resolution, but coupled to AFM nanometer spatial resolution is achievable.

General and common disadvantages:

1. Since the Raman signal is inherently weak, long exposure times and high laser powers may be required (especially for samples with low concentrations or otherwise weak Raman activity). Samples may not stay intact during this time.
2. Fluorescence. Strong fluorescence can completely swamp Raman signals and is hard to circumvent, especially if inherent to the sample (e.g., autofluorescing materials) and not caused by contamination. Quenching the fluorescence by long laser exposure may work in certain cases, but frequently selecting a different laser line (often in the near infrared range) is the only solution.
3. Sample sensitivity to heat/light. Especially in the case of colored samples and high power near infrared lasers, the absorbed light may result in an extreme heat locally where the laser is focused. This, in turn, may damage the sample. Similarly, samples sensitive to light may be altered due to the high photon flux in the laser focus area.
4. Specificity may be compromised in mixtures, as overlaps may render bands nondiagnostic.

Selected Earth Science Applications of Raman Microspectroscopy

Raman (and infrared) microspectroscopy is widely used to characterize geological materials, either "as is" or sectioned/polished, in fields as broad as mineralogy, petrology, paleontology, geochemistry, and even cosmochemistry (Gillet 2002). Due to the extreme versatility and customization possibilities of the technique, even non-laboratory conditions can be studied (e.g., extreme pressures and temperatures to study mineralogy in the Earth's mantle and core, or conditions mimicking those on the surface of Mars, to study ice formation, surface reactions, etc.)

One particular area is to study minerals, as Raman microspectroscopy can provide complementary information to X-ray-based techniques regarding crystal structures and phase transitions. (It has to be noted here that materials with noncrystalline structures, such as melts or glasses, feature broad Raman bands which are harder to assign and quantify.) Reference spectra for common minerals are often compiled into searchable databases which enables quick identification even in mixtures. Spectral features have been identified and listed for the major classes of minerals, ranging from silicates to different oxides (iron, aluminum, etc.), carbonates, phosphates, and sulfates/sulfides (Gillet 2002 and references therein).

Additional Raman Spectroscopic Techniques

Resonance Raman Spectroscopy (RRS): utilizes resonance effects to increase Raman signal intensity by up to a millionfold. Frequently used for transition metal containing large biomolecules.

Coherent Anti-Stokes Raman Spectroscopy (CARS): using two very intense lasers pulsed (fixed and variable). Often used in biological imaging.

Raman Optical Activity (ROA): utilizes oppositely circularly polarized lasers. Frequently used for determining conformations and absolute configurations of chiral molecules.

Optical Tweezers Raman Spectroscopy (OTRS): used for measuring single cells or individual particles.

Tip-Enhanced Raman Spectroscopy (TERS), using AFM or STM metallic tips, allows for nanometer resolution and single-molecule sensitivity.

Surface-Enhanced Raman Spectroscopy (SERS): adsorbates on metals (often Cu, Au or Ag) of the right dimensions (or colloidal), greatly increases the intensity of the signal (by $10^{8–11}$), and is frequently used in various fields, ranging from solar cells to biology.

Summary

Raman microspectroscopy is a fast, inexpensive, nondestructive and noninvasive, label-free technique to assess the chemical composition of a broad range of materials in situ (i.e., without extractions or processing). Common setups achieve spatial resolutions in the micrometer range, and sensitivities are generally in the micromolar concentration range, although special techniques and setups allow for nanometer spatial resolutions and single-molecule detection. The technique is very versatile and can be easily tailored to specific needs.

Cross-References

- ▶ Analytical Techniques
- ▶ Carbonate Minerals and the CO2-Carbonic Acid System
- ▶ Chemical Bonds
- ▶ Clay Minerals
- ▶ Colloids
- ▶ Complexes
- ▶ Geochemical Reference Materials
- ▶ Geochemistry
- ▶ Kinetics of Geochemical Processes

▶ Native Minerals
▶ Oxide Minerals
▶ Silicate Minerals
▶ Sulfate Minerals
▶ Sulfide Minerals
▶ Surface Geochemistry

References

Gillet P (2002) Applications of vibrational spectroscopy to geology. In: Chalmers JM, Griffiths PR (eds) Handbook of vibrational spectroscopy, Volume 4, 2nd edn. John Wiley & Sons Ltd, Chichester, England

Landsberg GD, Mandelstam LI (1928) Eine neue Erscheinung bei der Lichtzerstreuung in Krystallen. Naturwissenschaften 16:557–558

Raman CV, Krishnan KS (1928) A new type of secondary radiation. Nature 121:501

Smekal AG (1923) Zur Quantentheorie der Dispersion. Naturwissenschaften. 11:873–875

Refractory Inclusions in Chondritic Meteorites

Alexander N. Krot[1] and Glenn J. MacPherson[2]
[1]Hawai'i Institute of Geophysics and Planetology, University of Hawai'i at Mānoa, Honolulu, HI, USA
[2]Smithsonian Institution, Washington, DC, USA

Definition

Refractory inclusions are submillimeter-to-centimeter-sized objects with mineralogy similar to that predicted by thermodynamic calculations to condense out of a gas of solar composition at total pressure $<10^{-3}$ bar and temperatures above ~1300 K (Fig. 1). Refractory inclusions are a minor component (<5 vol%) in all groups of chondritic meteorites (chondrites); they were also found in a comet dust returned to Earth by NASA's *Stardust* mission from the Jupiter Family Comet 81P/Wild 2. Refractory inclusions comprise two kinds of objects – Ca,Al-rich inclusions (CAIs) and amoeboid olivine aggregates (AOAs). CAIs formed by aggregation of solids that resulted from evaporation (often incomplete) and condensation in a protoplanetary disk region with high ambient temperature (at or above condensation temperature of forsterite) and approximately solar redox conditions (i.e., highly reduced). Subsequently some CAIs experienced melting, evaporation, and condensation during transient heating events, most likely in the same disk region. AOAs are aggregates of igneous and nonigneous CAIs and forsterite condensates. Most inclusions we now study clearly experienced significant and extended reprocessing during transient heating events, including solid-state recrystallization, melting, and some degree of lower-temperature back-reaction with the nebular gas. Few, if any, of the primary condensates are actually preserved among the objects we now see.

Classification of Refractory Inclusions

CAIs can be classified in terms of major minerals (listed here in order of decreasing condensation temperature, not abundance): corundum (Al_2O_3), hibonite ($CaAl_{12}O_{19}$), grossite ($CaAl_4O_7$), perovskite ($CaTiO_3$), melilite [gehlenite ($Ca_2Al_2SiO_7$) – åkermanite ($Ca_2Mg_2Si_2O_7$) solid solution], spinel ($MgAl_2O_4$), Ca-pyroxene [diopside ($CaMgSi_2O_6$) – kushiroite ($CaAl_2SiO_6$) – grossmanite ($CaTi^{4+}Al_2O_6$-$CaTi^{3+}AlSiO_6$) – davisite ($CaScAlSiO_6$) solid solution], anorthite ($CaAl_2Si_2O_8$), and forsterite (Mg_2SiO_4). Large CAIs, commonly present only in CV (Vigarano-type) chondrites, are divided into four types – Type A (dominated by melilite + spinel), Type B (made mostly of melilite + Ca-pyroxene + anorthite + spinel), Type C (composed mainly of anorthite + Ca-pyroxene + spinel), and forsterite-bearing Type B.

Both igneous and nonigneous CAIs are typically surrounded by a thin (<50 μm) sequence of nearly monomineralic layers of a similar thickness, referred to collectively as Wark-Lovering rim (Fig. 2). A complete rim sequence, observed around some CAIs, consists of an innermost spinel ± perovskite ± hibonite layer, a layer of melilite often replaced by anorthite, a layer of Ca-pyroxene, and a layer of forsterite. These rims are thought to have formed in the CAI-forming region by flash melting of outermost portion of the host CAIs, followed by evaporation, condensation, diffusion-controlled metasomatic reactions, and prolonged thermal annealing.

Bulk Chemical Compositions of Refractory Inclusions

The bulk major element chemical compositions of refractory inclusions follow approximately an equilibrium condensation path from a gas of solar composition (Fig. 3). The deviations from this path have been interpreted in terms of (1) non-equilibrium evaporation of Mg and SiO that the CAI melts have experienced during transient heating events (Grossman et al. 2000), (2) condensation of SiO into the CAI melts (Krot et al. 2007), and (3) condensation of fine-grained spinel-melilite-anorthite-rich CAIs at low total pressure, $<10^{-5}$ bar (MacPherson et al. 2004).

The bulk rare earth element (REE) compositions of CAIs are volatility controlled and divided into six groups (Fig. 4). Most CAIs have essentially unfractionated (except Eu and Yb) REE patterns (groups I, III, V, and VI), which

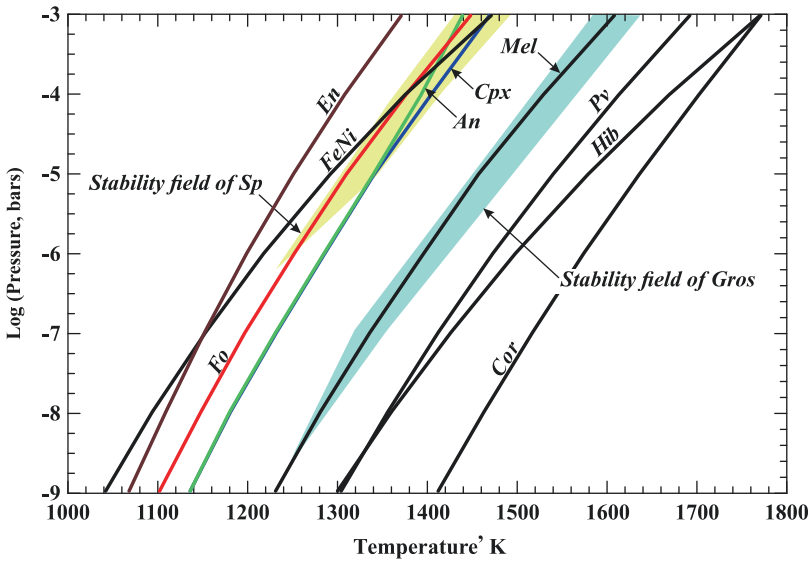

Refractory Inclusions in Chondritic Meteorites, Fig. 1 Equilibrium condensation sequence of a gas of solar composition at total pressure of 10^{-3} to 10^{-9} bar (after Petaev and Wood 2005). Mineral abbreviations: *An* anorthite, *Cor* corundum, *Cpx* Ca-pyroxene, *En* enstatite ($MgSiO_3$), *Fo* forsterite, *Gros* grossite, *Hib* hibonite, *Mel* melilite, *Pv* perovskite

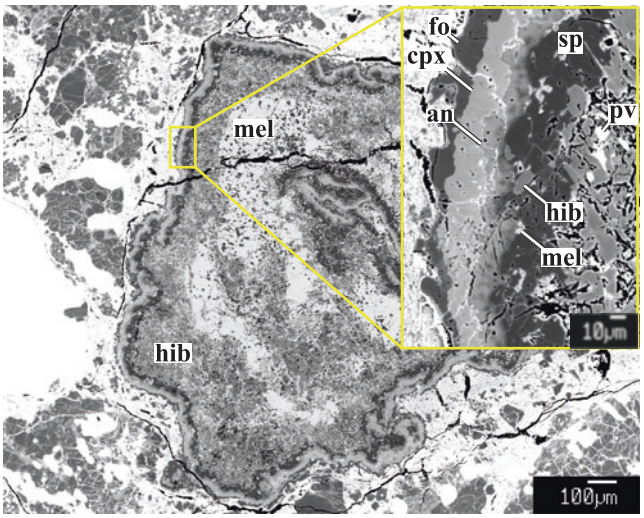

Refractory Inclusions in Chondritic Meteorites, Fig. 2 Back-scattered electron image of a CAI from a CR (Renazzo-type) carbonaceous chondrite. The CAI consists of melilite, hibonite, spinel, and perovskite. It is surrounded by a Wark-Lovering rim (see inset) composed of an innermost spinel-hibonite layer, a layer of anorthite replacing melilite, a layer of Ca-pyroxene, and a layer of forsterite. Mineral abbreviations are the same as in Fig. 1

have been interpreted in terms of complete condensation from a solar gas (Boynton 1975; Davis and Grossman 1979). Group II pattern is depleted in both the most refractory (Gd, Tb, Dy, Ho, Er, and Lu) and the most volatile REEs (Eu and Yb), and resulted from fractional condensation from a gaseous reservoir in which a component containing the most refractory REEs was removed either by condensation or by incomplete evaporation. The nature of this ultrarefractory (UR) component is still unknown, but can be potentially identified in rare CAIs having UR REE patterns, which are roughly complementary to group II (Fig. 4). The UR CAIs contain a number of μm-sized minerals highly enriched in very refractory elements (Zr, Sc, Y) such as allendeite ($Sc_4Zr_3O_{12}$), Sc-rich anosovite [$(Ti,Mg,Sc,Al)_3O_5$], davisite ($CaScAlSiO_6$), kangite [$(Sc,Ti,Al,Zr,Mg,Ca)_2O_3$], lakargite ($CaZrO_3$), panguite [$(Ti,Sc,Al,Mg)_{1.8}O_3$], tazheranite [$(Zr,Ti,Ca,Y)O_{1.75}$], thortveitite ($Sc_2Si_2O_7$), zirconolite ($CaZrTi_2O_7$), warkite ($Ca_2Sc_6Al_6O_{20}$), and eringaite [$Ca_3(Sc,Y,Ti)_2Si_3O_{12}$]. The REE patterns of these UR minerals have yet to be studied.

Formation Age of Refractory Inclusions

CAIs are the oldest solar system solids dated using ^{207}Pb-^{206}Pb absolute chronology. CAIs show significant variations in $^{235}U/^{238}U$ ratio (Brennecka et al. 2010). The U-corrected Pb-Pb age of the only four CV CAIs measured so far, 4567.3 ± 0.16 Ma (Connelly et al. 2012), is considered to represent the beginning of the solar system formation – t_0, in cosmochemical rather than astrophysical sense.

Short-Lived Radionuclides in Refractory Inclusions

Because of their antiquity, CAIs preserve evidence for short-lived (half-lives, $t_{1/2} < 10$ Myr), now extinct, radionuclides in the early solar system, including ^{10}Be (decays to ^{10}B with $t_{1/2} \sim 1.4$ Myr), ^{26}Al (decays to ^{26}Mg with $t_{1/2} \sim 0.7$ Myr), and ^{182}Hf (decays to ^{182}W with $t_{1/2} \sim 8.9$ Myr). ^{10}Be is inferred to have formed by solar energetic particle irradiation of nebular gas from which CAIs or their precursors condensed, most likely near the Sun (McKeegan et al. 2000). ^{26}Al and ^{182}Hf have an external stellar origin. ^{182}Hf was inherited from the protosolar molecular cloud and appears to be uniformly distributed in the protoplanetary disk, making it an important

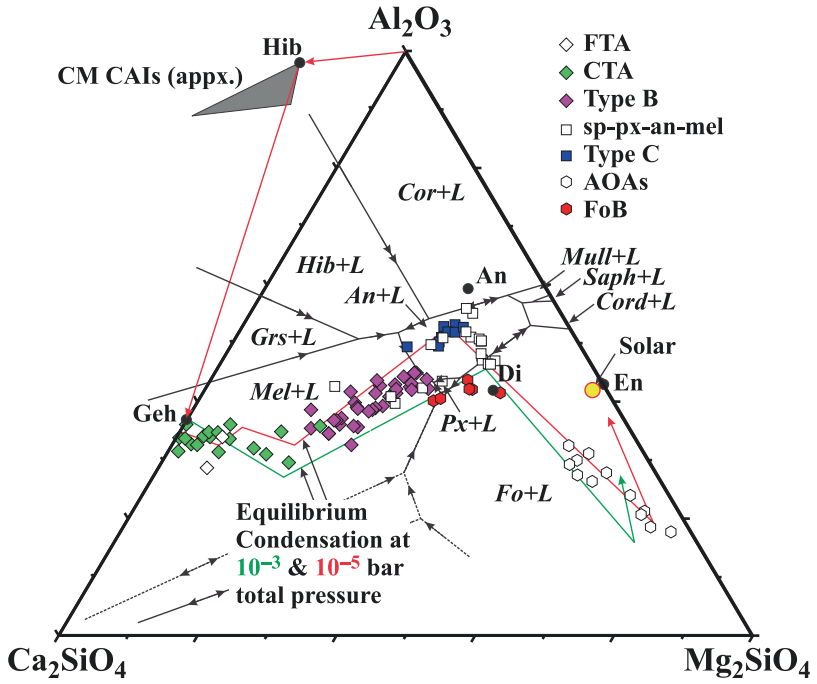

Refractory Inclusions in Chondritic Meteorites, Fig. 3 Bulk chemical compositions of AOAs and major CAI types, igneous [Compact Type A (CTA), Type B, Type C, and forsterite-bearing Type B (FoB)] and nonigneous [Fluffy Type A (FTA) and fine-grained spinel-pyroxene-anorthite-melilite (sp-px-an-mel)], in CV chondrites projected from spinel on forsterite (Mg_2SiO_4) – corundum (Al_2O_3) – larnite (Ca_2SiO_4) plane (MacPherson and Huss 2005). The *shaded* field labeled CM CAIs (appx.) indicates the general region where silicate-poor CAIs from CM (Mighei type) chondrites plot. Equilibrium condensation paths from a gas of solar composition at a total pressure of 10^{-3} (Yoneda and Grossman 1995) and 10^{-5} (MacPherson et al. 2004) bar are indicated by *green* and *red* lines, respectively. Data from Wark (1987), Grossman et al. (2000), Krot et al. (2004), and Bullock et al. (2012). Abbreviations: *Cord* cordierite, *Di* diopside, *En* enstatite, *Geh* gehlenite, *L* liquid, *Mull* mullite, *Saph* saphirine. Other abbreviations are the same as in Fig. 1

Refractory Inclusions in Chondritic Meteorites, Fig. 4 Schematic illustration of bulk rare element patterns in CAIs (from MacPherson et al. 1988)

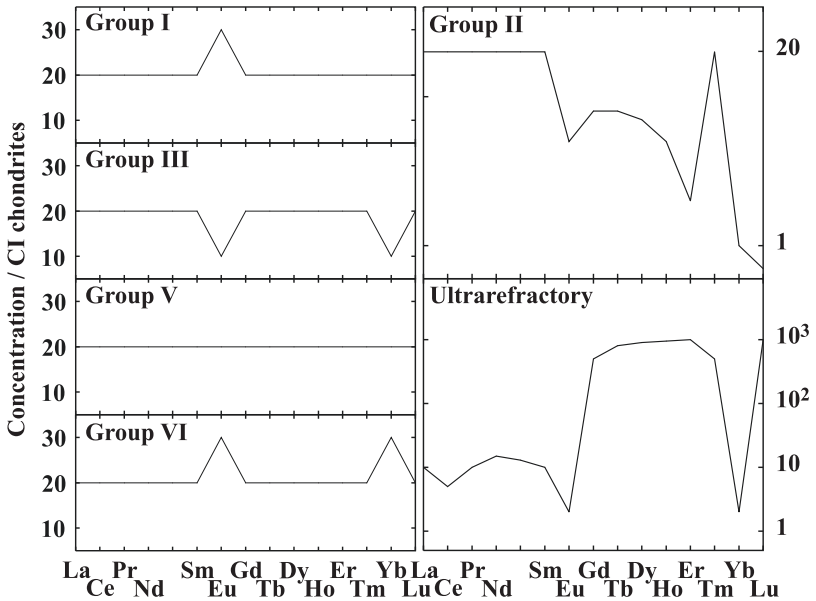

relative chronometer of disk processes (Kruijer et al. 2014). In contrast, the initial $^{26}Al/^{27}Al$ ratios [$(^{26}Al/^{27}Al)_0$] among individual CAIs from weakly metamorphosed chondrites show large variations, from $<5 \times 10^{-6}$ to $\sim 5 \times 10^{-5}$; $(^{26}Al/^{27}Al)_0$ in most CAIs, however, is $\sim 5 \times 10^{-5}$, and called the "canonical" value (MacPherson 2014). The observed variations in $(^{26}Al/^{27}Al)_0$ among CAIs have been interpreted to reflect several processes, including (i) recent addition of

^{26}Al from a neighboring massive star (supernova, Wolf-Rayet, or asymptotic giant branch stars) prior to collapse of the protosolar molecular cloud, (ii) homogenization of ^{26}Al in the disk at about the canonical level, and (iii) subsequent thermal processing of CAIs (e.g., Krot et al. 2012; Kita et al. 2013). Although there are multiple generations of CAIs (e.g., Krot et al. 2008), the heterogeneous distribution of ^{26}Al among them prevents use of ^{26}Al-^{26}Mg systematics for defining the entire duration of CAI formation. At the same time, the existence of the canonical $(^{26}Al/^{27}Al)_0$ in CAIs from different chondrite groups may suggest a homogeneous distribution of ^{26}Al in the disk by the time most CAIs formed. If this is the case, ^{26}Al has an important chronological significance for dating early solar system processes that postdate homogenization of ^{26}Al in the disk.

Nucleosynthetic Isotopic Anomalies in Refractory Inclusions

CAIs preserved nucleosynthetic isotope anomalies in many elements (W, Ba, Nd, Sm, Sr, Ca, Ti, Mg, etc.), reflecting incomplete evaporation of presolar dust and the lack of isotopic homogenization in the solar system. These anomalies are much smaller than in presolar grains formed around dying stars. The largest isotope anomalies are found in CAIs with low $(^{26}Al/^{27}Al)_0$, platy hibonite crystals (PLACs), and FUN CAIs (mass-dependent fractionation and "unknown" nuclear effects), consistent with their early formation, prior to homogenization of ^{26}Al in the disk.

Oxygen Isotopic Compositions of Refractory Inclusions

On a three-isotope oxygen diagram ($\delta^{17}O$ versus $\delta^{18}O$, where $\delta^{17,18}O = (^{17,18}O_{sample}/^{17,18}O_{SMOW} - 1) \times 1000$, and SMOW is Standard Mean Ocean Water), the terrestrial samples define a mass-dependent fractionation line with a slope of 0.52, called the terrestrial fractionation (TF) line (Fig. 5). In contrast, most extraterrestrial solids (meteorites, Moon, and Mars) deviate from the TF line (e.g., Yurimoto et al. 2008). Refractory inclusions are enriched in ^{16}O compared to other solar system solids. The majority of refractory inclusions in unmetamorphosed chondrites are isotopically uniform and have $\Delta^{17}O$ values (deviation from the TF line $= \delta^{17}O - 0.52 \times \delta^{18}O$) of about −24‰, close to the composition of the Sun inferred from measurements of the solar wind ($\Delta^{17}O = -28 \pm 2$‰) returned by the NASA's *Genesis* spacecraft (McKeegan et al. 2011). Relative to this solar value, some CAIs are ^{16}O-enriched ($\Delta^{17}O$ up to −37‰) or ^{16}O-depleted ($\Delta^{17}O$ up to −5‰). On a three-isotope oxygen diagram, most CAIs plot along carbonaceous chondrite anhydrous mineral (CCAM) line with a slope of about 1 (Fig. 5), interpreted to be a mixing line between the coexisting ^{16}O-rich and ^{16}O-poor reservoirs inherited from the protosolar molecular cloud and/or generated in the disk. Some igneous CAIs, including FUN CAIs, plot significantly to the right from the CCAM line, along mass-dependent fractionation line that deviates from the TF line by about −24‰. Mass-dependent fractionation effects are also observed in these CAIs for silicon and magnesium (Grossman et al. 2000). These effects were reproduced experimentally by melt evaporation under nearly vacuum conditions (Mendybaev et al. 2013).

CAIs and their Wark-Lovering rims in CV chondrites are often isotopically heterogeneous, with spinel, hibonite, forsterite, and pyroxenes being ^{16}O-rich relative to melilite and anorthite (Fig. 5). These observations have been interpreted as evidence for rapid fluctuations of oxygen-isotope composition of nebular gas in the CAI-forming region (Simon et al. 2011). The nature of oxygen-isotope heterogeneity in CV CAIs remains poorly

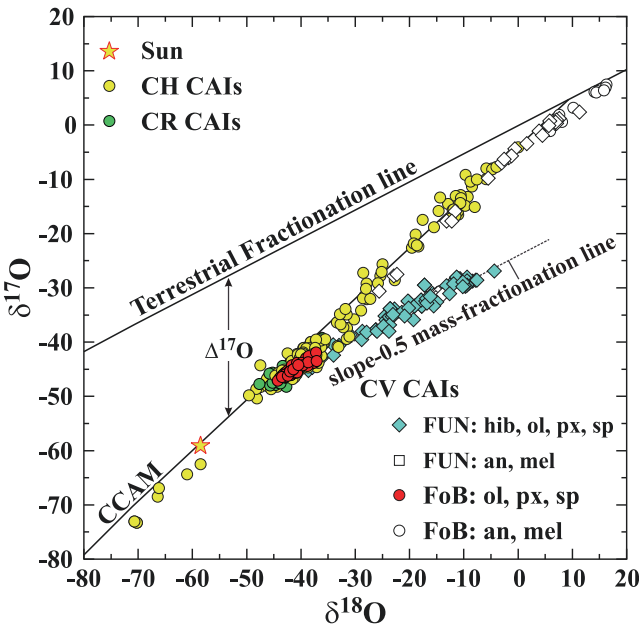

Refractory Inclusions in Chondritic Meteorites, Fig. 5 Three-isotope oxygen diagram of the inferred composition of the Sun and individual minerals in CAIs from CR, CH, and CV chondrites measured by secondary ion mass-spectrometry. Carbonaceous chondrite anhydrous mineral (CCAM) line with a slope of ~1 and the terrestrial fractionation (TF) line with a slope of 0.52 are shown for reference. Most CAIs plot along the CCAM line. Some igneous CAIs plot along slope-0.52 line that deviates from the TF line by about −24‰. Mineral abbreviations are the same as in Fig. 1. Data from McKeegan et al. (2011), Bullock et al. (2012), and Krot et al. (2008, 2014). *FoB* forsterite-bearing Type B CAIs

understood; the proposed mechanisms include gas-melt or gas-solid exchange, and condensation from nebula gas of variable composition (Yurimoto et al. 2008 and references therein). It has been also hypothesized that anorthite and melilite in CV CAIs experienced some oxygen-isotope exchange during fluid-rock interaction on the CV parent asteroid. This hypothesis has yet to be evaluated experimentally.

Radial Transport and Residence Time of Refractory Inclusions in the Protoplanetary Disk

The presence of multiple generations of CAIs in all chondrite groups indicates that refractory inclusions were episodically removed from the CAI-forming region and dispersed throughout the disk. A mechanism of this radial transport remains poorly understood; turbulent diffusion along the disk mid-plane and stellar wind above the disk are being discussed (Shu et al. 1996; Ciesla 2010). Subsequently, some refractory inclusions experienced various degrees of melting during chondrule formation 1–3 Myr after t_0, suggesting their long residence time in the disk prior to accretion into chondrite parent bodies (MacPherson et al. 2012). In thermally metamorphosed chondrites, refractory inclusions experienced various degrees of aqueous and metasomatic alteration which modified their primary nebular records (Brearley and Krot 2013).

Summary and Conclusions

Refractory inclusions are the oldest objects known to have formed in the solar system. They preserve clear evidence for the existence of the short-lived radionuclides in the early solar system, the isotopic signatures of presolar stellar nucleosynthesis, and the oxygen isotopic composition of the gaseous and possibly solid reservoirs in the early solar system. The petrologic and isotopic characteristics of refractory inclusions recorded several hundred thousand years of very high-temperature processes (evaporation, condensation, aggregation, and melting) in the inner solar system. They formed in the protoplanetary disk near the Sun, and were subsequently transported radially away and accreted into chondritic and cometary parent bodies over several Myr.

Cross-References

- ▶ Chondrites
- ▶ Magnesium Isotopes
- ▶ Oxygen Isotopes

References

Boynton WV (1975) Fractionation in the solar nebula: condensation of yttrium and the rare earth elements. Geochim Cosmochim Acta 39:569–584

Brearley AJ, Krot AN (2013) Metasomatism in the early solar system: the record from chondritic meteorites. In: Metasomatism and the chemical transformation of rock, Lecture notes in Earth system sciences, pp 659–789

Brennecka GA, Weyer S, Wadhwa M et al (2010) $^{238}U/^{235}U$ variations in meteorites: extant ^{247}Cm and implications for Pb-Pb dating. Science 327:449–452

Bullock EM, MacPherson GJ, Nagashima K et al (2012) Forsterite-bearing Type B refractory inclusions from CV3 chondrites: from aggregates to volatilized melt droplets. Meteorit Planet Sci 47:2128–2147

Ciesla FJ (2010) The distributions and ages of refractory objects in the solar nebula. Icarus 208:455–467

Connelly JN, Bizzarro M, Krot AN et al (2012) The absolute chronology and thermal processing of solids in the solar protoplanetary disk. Science 338:651–655

Davis AM, Grossman L (1979) Condensation and fractionation of rare earths in the solar nebula. Geochim Cosmochim Acta 43:1611–1632

Grossman L, Ebel DS, Simon SB et al (2000) Major element chemical and isotopic compositions of refractory inclusions in C3 chondrites: the separate roles of condensation and evaporation. Geochim Cosmochim Acta 64:2879–2894

Kita NT, Yin Q-Z, MacPherson GJ et al (2013) ^{26}Al-^{26}Mg isotope systematics of the first solids in the early solar system. Meteorit Planet Sci 48:1383–1400

Krot AN, Petaev MI, Yurimoto H (2004) Amoeboid olivine aggregates with low-Ca pyroxenes: a genetic link between refractory inclusions and chondrules? Geochim Cosmochim Acta 68:1923–1941

Krot AN, Yurimoto H, Hutcheon ID et al (2007) Anorthite-rich, igneous (Type C) Ca, Al-rich inclusions from the CV carbonaceous chondrite Allende: evidence for multistage formation history. Geochim Cosmochim Acta 71:4342–4364

Krot AN, Nagashima K, Bizzarro M et al (2008) Multiple generations of refractory inclusions in the metal-rich carbonaceous chondrites Acfer 182/214 and Isheyevo. Astrophys J 672:713–721

Krot AN, Makide K, Nagashima K et al (2012) Heterogeneous distribution of ^{26}Al at the birth of the solar system: evidence from refractory grains and inclusions. Meteorit Planet Sci 47:1948–1979

Krot AN, Nagashima K, Wasserburg GJ et al (2014) Calcium-aluminum-rich inclusions with fractionation and unknown nuclear effects (FUN CAIs): I. Mineralogy, petrology, and oxygen-isotope compositions. Geochim Cosmochim Acta 145:206–247

Kruijer TS, Kleine T, Fischer-Gödde M et al (2014) Nucleosynthetic W isotope anomalies and the Hf-W chronometry of Ca-Al-rich inclusions. Earth Planet Sci Lett 403:317–327

Larsen K, Trinquier A, Paton C et al (2011) Evidence for magnesium-isotope heterogeneity in the solar protoplanetary disk. Astrophys J 735:L37–L40

MacPherson GJ, Wark DA, Armstrong JT (1988) Primitive material surviving in chondrites: refractory inclusions. In: Kerridge JF, Matthews MS (eds) Meteorites and the early Solar System. University of Arizona Press, Tucson, pp 746–807

MacPherson GJ, Petaev MI, Krot AN (2004) Bulk compositions of CAIs and Al-rich chondrules: Implications of the reversal of the anorthite/forsterite condensation sequence at low nebular pressures. Lunar Planet Sci XXXV:#1838

MacPherson GJ, Huss GR (2005) Petrogenesis of Al-rich chondrules: evidence from bulk compositions and phase equilibria. Geochim Cosmochim Acta 69:3099–3127

MacPherson GJ, Kita NT, Ushikubo ES et al (2012) Well-resolved variations in the formation ages for Ca–Al-rich inclusions in the early Solar System. Earth Planet Sci Lett 331–332:43–54
MacPherson GJ (2014) Calcium-aluminum-rich inclusions in chondritic meteorites. In: Davis AM (ed) Meteorites, comets and planets Vol. 1, Treatise on geochemistry (eds) Holland HD , Turekian KK, pp. 139–179. Elsevier, Oxford
McKeegan KD, Chaussidon M, Robert F (2000) Incorporation of short-lived ^{10}Be in a calcium-aluminum-rich inclusion from the Allende meteorite. Science 289:1334–1337
McKeegan KD, Kallio APA, Heber VS et al (2011) The oxygen isotopic composition of the Sun inferred from captured solar wind. Science 332:1528–1532
Mendybaev RA, Richter FM, Georg RB et al (2013) Experimental evaporation of Mg- and Si-rich melts: implications for the origin and evolution of FUN CAIs. Geochim Cosmochim Acta 123:368–384
Petaev MI, Wood JA (2005) Meteoritic constraints on temperatures, pressures, cooling rates, chemical compositions, and modes of condensation in the solar nebula. In: Krot AN, Scott ERD, Reipurth B (eds) Chondrites and the protoplanetary disk, Astronomical society of the Pacific conference series, vol 341, pp 373–407
Shu FH, Shang H, Lee T (1996) Toward an astrophysical theory of chondrites. Science 271:1545–1552
Simon JI, Hutcheon ID, Simon SB et al (2011) Oxygen isotope variations at the margin of a CAI records circulation within the solar nebula. Science 331:1175–1178
Wark DA (1987) Plagioclase-rich inclusions in carbonaceous chondrite meteorites – Liquid condensates? Geochim Cosmochim Acta 51:221–242
Yurimoto H., Krot A.N., Choi B.-G., et al. (2008) Oxygen isotopes of chondritic components. In: MacPherson GJ (ed) Oxygen in the Solar System, Rev Mineral Geochem 68:141–187
Yoneda S, Grossman L (1995) Condensation of CaO-MgO-Al_2O_3-SiO_2 liquids from cosmic gases. Geochim Cosmochim Acta 59:3413–3444

Rhenium

James M. Brenan
Department of Earth Sciences, Dalhousie University, Halifax, NS, Canada

Element Data
Atomic Symbol: **Re**
Atomic Number: **75**
Atomic Weight: 186.207
Isotopes and Abundances: ^{185}Re 37.40%, ^{187}Re 62.60%
0.1 MPa Melting Point: 3185 °C
0.1 MPa Boiling Point: 5551 °C
Common Valences: −1, +2, +4, +6, +7
Ionic Radii: 6-fold: 63 pm (+4), 58 pm (+5), 55 pm (+6), 53 pm (+7)
Pauling Electronegativity: 1.9
(*continued*)

First Ionization Energy: 755.82 kJ/mol
Chondritic (CI) Abundance: 39.54 ng/g
Silicate Earth Abundance: 0.35 ng/g
Crustal Abundance: 0.188 ng/g
Seawater Abundance: 40 pmol/kg
Core Abundance: 230 ng/g

Definition

Atomic number 75 is a dense, highly refractory, transition metal with a bright silvery-white luster. Discovered in 1925, it is widely employed in the production of Ni-based superalloys and as a catalyst for gasoline production. ^{187}Re decay to ^{187}Os is used for radiometric age determinations and isotopic tracing.

History and Uses

The discovery of rhenium (atomic number 75) is attributed to W. Noddack, I. Tacke, and O. Berg, who in 1925 detected the element spectroscopically in platinum ores and in the minerals columbite, gadolinite, and molybdenite. Rhenium is the last discovered of the elements with a stable isotope. The name is derived from Rhenus, latin for Rhine.

Most Re (>80%) is consumed in the production of Ni-based superalloys, which are employed in the manufacture of aircraft engines and gas turbine fan blades. A second important application is as a component in Pt-Re alloys, utilized to catalyze key reactions to enhance the octane rating during gasoline production. Other important uses are for crucibles and electronic components. ^{186}Re and ^{188}Re are short-lived ($t_{1/2}$ = 89.3 and 17 h, respectively) isotopes produced for the treatment of bone and liver cancer.

Elemental and Physical Properties

Rhenium has an atomic weight of 186.207[1], ground state electronic configuration of $[Xe]4f^{14}5d^{5}6s^{2}$, with melting and boiling points at 0.1 MPa of 3185 °C and 5551 °C, respectively (Arblaster 1996). Rhenium is amongst the most dense of the elements (21,090 kg/m^3), similar to gold (19,300 kg/m^3) and about twice that of lead (11,340 kg/m^3). Rhenium is considered to be a highly refractory element, with a 50% condensation temperature of 1544 °C (Lodders 2003). Rhenium has one stable isotope, 185 (37.40[5]%), as well as the radioactive ^{187}Re (62.60[5]%), which undergoes beta decay to ^{187}Os, with a half-life of 4.16×10^{10} years. In addition to the neutral metal, the common oxidation states are −1, +2, +4, +6, and +7. The radius of the neutral atom is

188 pm (Clementi et al. 1967), and Re crystallizes in the hexagonal close-packed structure (space group P63/mmc) with a metallic radius of 137.5 nm (Wyckoff 1963). The size of the cation varies as follows (from Shannon 1976): 63 pm (+4, VI-fold), 58 pm (+5, VI-fold), 55 pm (+6, VI-fold), 38 pm (+7, IV-fold), and 53 pm (+7, VI-fold).

Geochemical Behavior and Reservoir Abundance

Rhenium is both highly siderophile (see entry for ▶ "Siderophile Elements") and strongly chalcophile (see entry for ▶ "Chalcophile Elements") and is grouped with other 5th and 6th row transition metals having similar chemical properties: Ru, Rh, Pd, Os, Ir, and Pt; the so-called platinum group elements (PGE; see entry for ▶ "Platinum Group Elements"). In rare cases, such as volcanic sublimates, Re occurs as ReS_2, rheniite, but more commonly dissolves as a component in molybdenite (MoS_2), owing to the geochemical similarity of Re and Mo. Re can also substitute into base metal sulfides (pyrrhotite, chalcopyrite, pentlandite), and experiments have shown that Re can readily dissolve into rock-forming minerals, such as olivine, pyroxene, and garnet, but this is highly dependent on the oxygen fugacity (summary in Brenan et al. 2016). The abundance of Re in the carbonaceous chondrite Orgueil is 39.5 ng/g (Horan et al. 2003), taken as being similar to the bulk earth concentration, which has now been highly fractionated into the core (230 ng/g; McDonough 2003), upper mantle (0.35[0.06] ng/g; Becker et al. 2006), and crust (continental: 0.188 ng/g; Rudnick and Gao 2003; oceanic: 0.736 ng/g; Peucker-Ehrenbrink et al. 2012). The relative proportions of both Re and the PGEs, as well as (age-corrected) radiogenic ^{187}Os (see below), are close to chondritic in the estimates for the primitive upper mantle (Becker et al. 2006). Abundances of these elements are higher than expected for equilibrium between metal and silicate (Mann et al. 2012) and relative abundances are unfractionated. Many believe this is the result of late accretion of chondritic materials following core formation. The rhenium content of seawater (40 pmol/kg) is >10x higher than the heavy rare-earth elements (Bruland and Lohan 2003), although the crustal abundance of Re is similar. Calculations indicate that the dominant Re species in seawater is $[ReO_4]^{2-}$ at 25 °C, pH 8.2, 0.1 MPa (Byrne et al. 1988).

Re-Os Isotopic System

Whereas most other long-lived isotopic systems used in geochronology involve lithophile elements as parent and daughter, the siderophile/chalcophile nature of the ^{187}Re-^{187}Os system is unique. Re and Os partition differently into various sulfide minerals, which allows for the dating of massive sulfide and porphyry copper ore deposits, as well as sulfide mineral inclusions in diamonds. Rhenium is incompatible and osmium is compatible during mantle melting, resulting in large differences in the Os-isotopic compositions of crust and mantle reservoirs. This allows a distinction to be made between crustal and mantle inputs to magmatic sulfide ores. Rhenium is also fractionated from osmium during the solidification of planetary cores, so this isotopic system has been used to date the formation of iron meteorite parent bodies (e.g., Walker et al. 2008). Under reducing conditions, rhenium is concentrated in organic-rich sediments, and hydrocarbons, which has been useful for dating sediment deposition, as well as tracking the source and migration of oil (Selby and Creaser 2005). Carlson (2005) and Stein et al. (2001) provide comprehensive reviews of the use of the Pt-Re-Os isotopic system in a wide range of applications.

Economic Geology

Economic concentrations of Re require >1,000-fold enrichment relative to crustal background values. Essentially all of the global Re supply is a by-product of copper mining. Re is volatile in oxidized form, so is removed from the Cu ore concentrate during smelting and captured in the flue gas. The largest supplies of Re are from magmatic porphyry ores (80%), hosted in molybdenite, with other sources found in sediment hosted stratabound deposits. Global production in 2014 was ~50,000 kg, with approximately half from Chilean copper deposits, at an average market price of ~$3,000/kg.

Summary

Rhenium is a bright, silvery-white transition metal characterized by high density and high melting temperature. The principal uses of rhenium are in the manufacturing of Ni-based superalloys and as catalysts for gasoline production. Rhenium is highly siderophile, as well as chalcophile, and is therefore concentrated in Earth's core, with complementary depletions in the silicate mantle, crust, and surface reservoirs. Rhenium has one radioactive isotope, ^{187}Re, that decays to ^{187}Os ($t_{1/2} = 4.16 \times 10^{10}$ years). Unique aspects of this isotopic system are that both parent and daughter are siderophile/chalcophile, and rhenium is concentrated in organic-rich sediments. These attributes have led to a number of novel geochemical applications, such as dating and tracing the source of magmatic sulfide ores, establishing the timing of core formation on iron meteorite parent bodies, dating sediment deposition and tracing oil migration. Extreme enrichment of rhenium relative to crustal background values is needed to produce minable ores, with significant concentrations in the mineral molybdenite, formed in porphyry copper deposits.

Cross-References

- Chalcophile Elements
- Chondrites
- Formation and Evolution of the Earth
- Natural Gas
- Ore Deposits
- Osmium
- Platinum
- Platinum Group Elements
- Rhodium
- Ruthenium
- Siderophile Elements
- Sulfide Minerals
- Transition Elements

References

Arblaster JW (1996) The thermodynamic properties of rhenium on ITS-90. Calphad 20:343–352

Becker H, Horan MF, Walker RJ, Gao S, Lorand J-P, Rudnick RL (2006) Highly siderophile element composition of the Earth's primitive upper mantle: constraints from new data on peridotite massifs and xenoliths. Geochim Cosmochim Acta 70:4528–4550

Brenan JM, Bennett N, Zajacz Z (2016) Experimental results on fractionation of the highly siderophile elements (HSE) at variable pressures and temperatures during planetary and magmatic differentiation. Rev Mineral Geochem 81:1–88

Bruland KW, Lohan MC (2003) Controls of trace metals in seawater. In: Elderfield H (ed) The oceans and marine geochemistry. Holland HD, Turekian KK (eds in Chief) Treatise on geochemistry, vol 6. Elsevier, Amsterdam

Byrne RH, Kump LR, Cantrell KJ (1988) The influence of temperature and pH on trace metal speciation in seawater. Mar Chem 25:163–181

Carlson RW (2005) Application of the Pt–Re–Os isotopic systems to mantle geochemistry and geochronology. Lithos 82:249–272

Clementi E, Raimondi DL, Reinhardt WP (1967) Atomic screening constants from SCF functions. II. Atoms with 37–86 electrons. J Chem Phys 47:1300–1307

Horan MF, Walker RJ, Morgan JW, Grossman JN, Rubin AE (2003) Highly siderophile elements in chondrites. Chem Geol 196:5–20

Lodders K (2003) Solar system abundances and condensation temperatures of the elements. Astrophys J 591:1220–1247

Mann U, Frost D, Rubie D (2012) Partitioning of Ru, Rh, Pd, Re, Ir and Pt between liquid metal and silicate at high pressures and high temperatures: implications for the origin of highly siderophile element concentrations in the Earth's mantle. Geochim Cosmochim Acta 84:593–613

McDonough WF (2003) Compositional model for the Earth's core. In: Carlson RW (ed) The mantle and core. Holland HD, Turekian KK (eds in Chief) Treatise on geochemistry, vol 2. Elsevier, Amsterdam

Peucker-Ehrenbrink B, Hanghoj K, Atwood T, Keleman PB (2012) Rhenium–osmium isotope systematics and platinum group element concentrations in oceanic crust. Geology 40:199–202

Rudnick RL, Gao S (2003) Composition of the continental crust. In: Rudnick RL (ed) The crust. Holland HD, Turekian KK (eds in Chief) Treatise on geochemistry, vol 3. Elsevier, Amsterdam

Selby D, Creaser RA (2005) Direct radiometric dating of hydrocarbon deposits using rhenium–osmium isotopes. Science 308:1293–1295

Shannon RD (1976) Revised effective ionic radii and systematic studies of interatomic distances in halides and chalcogenides. Acta Crystallogr A32:751–767

Stein HJ, Markey RJ, Morgan JW (2001) The remarkable Re–Os chronometer in molybdenite: how and why it works. Terra Nova 13:479–486

Walker RJ, McDonough WF, Honesto J, Chabot NL, McCoy TJ, Ash RD, Bellucci JJ (2008) Modeling fractional crystallization of group IVB iron meteorites. Geochim Cosmochim Acta 72:2198–2216

Wyckoff RWG (1963) Crystal structures, vol 1. Wiley, New York, p 467

Rhodium

Thomas C. Meisel
General and Analytical Chemistry, Montanuniversität Leoben, Leoben, Austria

Element Data

Atomic Symbol: **Rh**
Atomic Number: **45**
Atomic Weight: 102.90550(2) g/mol
Isotopes and Abundances: ^{103}Rh, 100%
1 Atm Melting Point: 1964 °C
1 Atm Boiling Point: 3697 °C
Common Valences: +3
Ionic Radii: 80.5 pm
Pauling Electronegativity: 2.28
First Ionization Energy: 719.7
Chondritic (CI) Abundance: 133 µg/kg (Fischer-Gödde et al. 2010)
Silicate Earth Abundance: 1.2±0.2 ng/g (Fischer-Gödde et al. 2011)
Crustal Abundance: 0.018 µg/kg (Park et al. 2012)
Seawater Abundance: 0.4–1 pmol/kg
Core Abundance: ~0.74 mg/kg (McDonough 2014)

Properties

Rhodium ($_{45}$Rh) is one of the platinum group elements (PGE) and as such is a member of the transition metals. Together with Cobalt, Iridium, and Meitnerium it is also part of the Cobalt group.

As the energy difference between the outer *s* and *d* shell is relatively small, one electron is transferred to the *d* orbitals resulting in an electron configuration of [Kr] $4d^8$ 5 s^1. The small energy difference between the valence shells allows a high number of possible oxidation states (−1, 0, +1, +2, +3, +4, +5, +6) with +3 as the principal oxidation states besides

the neutral metal. As a monoisotopic element, the atomic weight is very well determined, with a value of 102.905 50(2) g/mol. The melting point is 1964 °C, with a density of 12.4 g/cm^3 (Predel 2006), both of which are lower than those for Ru, but higher than those for Pd. The metal has cubic symmetry (fcc). The atomic radius of 1.345 Å is also in between that of Ru and Pd, but similar to Ir. Rhodium shares many properties with neighbors of the same row, Ru and Pd, and also some with the same column, Ir (e.g., similar refractory acid digestion behavior). Unlike any other PGE, Rh can be dissolved in boiling HBr/Br_2. The metal can also be dissolved by melting with potassium or sodium hydrogensulfate, while Pt, Ir, and Ru remain unaffected (Renner et al. 2001). Rhodium is the only monoisotopic PGE, making it inaccessible for isotope dilution mass spectrometry. Though accessible via neutron activation, the most common procedure for Rh analysis is NiS fire assay in combination with ICP-MS, although this method has limitations due to the impurity of reagents (Meisel and Horan 2016). Hence, little published Rh data of low-concentration samples is available for geochemical samples, in particular for basalts and sediments.

History and Use

Wollaston discovered Rh in 1803, along with Pd, through chemical experiments on large quantities of crude alluvial platinum ore with aqua regia and alkali salts. Rose-red colored precipitates that formed during the isolation process lent the name Rhodium from Greek *rhodon* (ῥόδον) or *rhodeos* (ῥόδεος) meaning "rose" or "rose-red," respectively.

The hardness, mechanical and chemical stability, and reflectivity make Rh coatings superior to all other PGE metals. With the ideal properties of a homogeneous catalyst, more than 80% of the Rh metal production is used for three-way catalytic converters in gasoline engines with currently no appropriate substitute except for Pt and Pd (Loferski 2015). The production of many important chemicals relies on the use of Pt-Rh catalysts. For example, the catalytic conversion of ammonia to nitric oxide is important for the production of nitric acid, fertilizers, and explosives.

Natural Occurrence

The Bushveld Complex (South Africa) contains more than 80% of the world's exploited resources of Rh metal. The most common Rh-bearing minerals are pentlandite, Pt–Rh–Cu sulfide, and several sulfarsenides (e.g., Hollingworthite [(Rh,Pt,Pd)AsS]), and native Rh has also been observed (O'Driscoll and González-Jiménez 2016).

The estimated mean concentration in CI chondrites is 133 μg/kg (Fischer-Gödde et al. 2010). Rhodium shows highly siderophile geochemical behavior with a metal/silicate partition coefficient of $>10^4$ (Day et al. 2016). It is highly enriched in the Earth's core and occurs, though highly depleted in the Earth's mantle, among all other PGEs and Re, in chondritic relative abundances (Day et al. 2016). This fact is remarkable, as this behavior cannot be predicted based on partitioning experiments between silicates and metals. One of the hypothesis that can explain this remarkable observation is addition of material with chondritic relative abundances to the Earth's mantle after core formation, so-called late accretion (Kimura et al. 1974; Day et al. 2016). The highly siderophile-chalcophile geochemical property of Rh makes it one of the rarest nonradioactive elements, with an estimate of 0.018 μg/kg in the Earth's crust. The current estimate for the Earth's mantle is 1.2 ± 0.2 ng/g (Fischer-Gödde et al. 2011). Previously, it had been unclear as whether rhodium belonged to the IPGE [Ir, Os, and Ru (Barnes et al. 1985)] or PPGE [Pt, Pd (Barnes et al. 1985)] group of platinum group elements. However, based on more recent Rh data, it became clear that Rh should be classified as more compatible PGE and there as a member of the Ir-PGE or IPGE group (Barnes 1999).

Biological Utilization and Toxicity

Rhodium and rhodium compounds have no biological function. Very little is known about the aqueous behavior, the mobility, and toxicity of rhodium compounds because of its rareness and low abundance in the environment. However, $Rh(OH)_3^{3-n}$ and $RhCl_3^{3-n}$ with an range of 0.4 to 1 pmol/kg and an estimated mean abundance of 0.8 pmol/kg have been described (Bruland and Lohan 2003).

Summary

The highly siderophile geochemical behavior made rhodium to be one of the rarest nonradioactive elements in the Earth's crust. Compared to the other PGE very little concentration data for geochemical is available. The chemical and mechanical stability makes Rh an ideal for metal coatings and catalytic converters. The common use as catalytic converter in automobiles has increased the interest in environmental monitoring and environmental-geochemical behavior.

Cross-References

- ▶ Formation and Evolution of the Earth
- ▶ Iridium
- ▶ Native Minerals

- ▶ Neutron Activation Analysis
- ▶ Osmium
- ▶ Palladium
- ▶ Platinum
- ▶ Platinum Group Elements
- ▶ Ruthenium
- ▶ Siderophile Elements
- ▶ Sulfide Minerals

References

Barnes SJ (1999) Elements: platinum group. In: Marshall CP, Fairbringe RW (eds) Encyclopedia of geochemistry. Kluwer, Dordrecht/Boston/London, p 218

Barnes S-J, Naldrett AJ, Gorton MP (1985) The origin of the fractionation of platinum-group elements in terrestrial magmas. Chem Geol 53:303–323

Bruland KW, Lohan MC (2003) Controls of trace metals in seawater. In: Elderfield H (ed) The oceans and marine geochemistry, vol 6. Elsevier/Pergamon, Amsterdam, pp 23–47

Day JMD, Brandon AD, Walker RJ (2016) Highly siderophile elements in Earth, Mars, the Moon, and asteroids. In: Day JMD, Harvey J (eds) Highly siderophile and strongly chalcophile elements in high temperature geochemistry and cosmochemistry, vol 81. Mineralogical Society of America, Chantilly, pp 161–238

Fischer-Gödde M, Becker H, Wombacher F (2010) Rhodium, gold and other highly siderophile element abundances in chondritic meteorites. Geochim Cosmochim Acta 74:356–379

Fischer-Gödde M, Becker H, Wombacher F (2011) Rhodium, gold and other highly siderophile elements in orogenic peridotites and peridotite xenoliths. Chem Geol 280:365–383

Kimura K, Lewis RS, Anders E (1974) Distribution of gold and rhenium between nickel–iron and silicate melts: implications for the abundance of siderophile elements on the Earth and Moon. Geochim Cosmochim Acta 38:683–701

Loferski PJ (2015) Commodity report: platinum-group metals. In: Book commodity report: platinum-group metals. Metals and minerals, vol I. Pittsburg, U.S. Government Printing Office (GPO), pp 57.50–57.11

McDonough WF (2014) 3.16 – Compositional model for the Earth's core A2. In: Turekian KK, Holland HD (eds) Treatise on geochemistry, 2nd edn. Elsevier, Oxford, pp 559–577

Meisel T, Horan MF (2016) Analytical methods for the HSE elements. In: Day JMD, Harvey J (eds) Highly siderophile and strongly chalcophile elements in high temperature geochemistry and cosmochemistry, vol 81. Mineralogical Society of America, Chantilly, pp 89–106

O'Driscoll B, González-Jiménez JM (2016) An inventory and overview of natural occurrences of the platinum-group minerals (PGM) in extraterrestrial and terrestrial rocks. In: Day JMD, Harvey J (eds) Highly siderophile and strongly chalcophile elements in high temperature geochemistry and cosmochemistry, vol 81. Mineralogical Society of America, Chantilly, pp 489–578

Park J-W, Hu Z, Gao S, Campbell IH, Gong H (2012) Platinum group element abundances in the upper continental crust revisited – new constraints from analyses of Chinese loess. Geochim Cosmochim Acta 93:63–76

Predel B (2006) Ac–Ag … Au–Zr · introduction. In: Predel B (ed) Landolt–Börnstein – group IV physical chemistry, vol 12A. Springer, Berlin/Heidelberg

Renner H, Schlamp G, Kleinwächter I et al (2001) Platinum group metals and compounds. In: Ullmann's encyclopedia of industrial chemistry, vol 28. Wiley-VCH Verlag GmbH & Co. KGaA, Weinheim, pp 317–388

Rubidium

Oliver Nebel
School of Earth, Atmosphere and Environment, Monash University, Clayton/Melbourne, VIC, Australia

Element Data
Atomic Symbol: Rb
Atomic Number: 37
Atomic Weight: 85.4678
Isotopes and Abundances:
Rb-85, 72.17%
Rb-87, 27.83%
1 Atm Melting Point: 39 °C
1 Atm Boiling Point: 688 °C
Common Valences: 1+
Ionic Radii: 1.72 Å
Pauling Electronegativity: 0.82
First Ionization Energy: 403.0 kJ/mol
Chondritic (CI) Abundance: 2.32 μg/g
Silicate Earth Abundance: 0.464 μg/g
Crustal Abundance: 49 μg/g
Seawater Abundance: 0.12 μg/g
Core Abundance: nil

Properties

Rubidium is an alkali metal of Group Ia of the periodic table with the atomic number of 37 and an average atomic mass of 85.4678, an electron configuration of [Kr] 5s1, and a valance state of +1. In elemental form, it is a very soft (0.3 Mohs scale), silvery-white metal that is extremely reactive, that is, it reacts violently with water and spontaneously ignites in air. It melts at ca. 39 °C and boils at ca. 688 °C. The element has two naturally occurring stable isotopes, Rb-85 and Rb-87, and 27 synthetic isotopes with half-lifes of ca. 86 days or less. From its two naturally occurring isotopes, Rb-87 is radioactive with a β^- decay and a half-life of ca. 49 billion years. This corresponds to a Rb decay constant of $\lambda^{87}\mathrm{Rb} = 1.393 \times 10^{-11}$ (Nebel et al. 2011a), determined by age comparison against the U-Pb system, $\lambda^{87}\mathrm{Rb} = 1.395 \times 10^{-11}$ through ingrowth experiments (Rotenberg et al. 2012), $\lambda^{87}\mathrm{Rb} = 1.396 \times 10^{-11}$ by physical counting (Kossert 2003), and a IUPAC recommended average of $\lambda^{87}\mathrm{Rb} = 1.394 \times 10^{-11}$ (Villa et al. 2015). The ratio of natural Rb isotopes can be precisely measured by plasma source mass spectrometry to ±0.05% on $^{87}\mathrm{Rb}/^{85}\mathrm{Rb}$ (Waight et al. 2002; Nebel et al. 2005). The natural

ratio appears constant in terrestrial rocks (Nebel et al. 2005) but shows small variations in chondritic meteorites (Nebel et al. 2011b).

Rubidium has a relatively low first ionization energy and the large difference between the first and second ionization potential (4.18 vs. 27.3 eV) results in its +1 atomic charge. Rubidium has an ionic radius of 1.72 Å, which is similar to that of K, Cs, and Tl.

History

The element rubidium (Rb, Latin – *rubidius*, "deepest red") was discovered by Robert Bunsen and Gustav Kirchhoff in 1861 through the extraction of rubidium salt analyses from lepidolite, a mica-group mineral. Bunsen purified Rb within 2 years of its discovery. Campbell and Wood were the first to report its natural radioactivity in 1906.

Minerals

Rubidium forms no silicate mineral of its own but can occur in some in quantities of up to a few per cent but no more than five. Following the Goldschmidt rules, it substitutes best for potassium and thus occurs predominantly in K-rich minerals such as orthoclase or mica. In felsic rocks, especially highly differentiated intrusives, such as pegmatites, it can be enriched to $\gg$1000 ppm. The residence time in oceans is ca. 800 ka. With an average Rb concentration in seawater of 0.12 ppm, it is substantially enriched compared to variable but substantially lower concentrations in surface waters, depending on ambient country rocks.

Geochemistry

Rubidium is a lithophile element and is thus hosted by the silicate portion of the Earth, with no Rb in the Earth's core. Combined with its large ionic radius, it is considered a large ion lithophile element (LILE) and mobile in aqueous solutions. The CI chondrite abundance of Rb is 2.32 ppm but highly variable due to its volatile nature, and with a half condensation temperature of 727 K, it is depleted in most early solar system materials. Hence, Rb concentrations in the bulk silicate Earth (BSE) are estimated and based on Rb/Sr and Sr abundances. In a chondritic Earth model, the $[Rb]_{BSE}$ is 0.605 ppm (Palme and O'Neill 2014). However, in a nonchondritic Earth model, and assuming $^{87}Sr/^{86}Sr_{BSE} \sim 0.71$ and a $^{87}Rb/^{86}Sr_{BSE} \sim 0.61$ (Caro and Bourdon 2010), the resultant $[Rb]_{BSE} = 0.464$. During mantle melting, it is incompatible in almost all common mantle minerals and is therefore highly enriched in the crust. The only significant host of Rb in the mantle is metasomatic phengite. Estimations for Rb concentrations in the lower, middle, and upper continental crust vary considerably and increase from 11 ppm over 65 ppm to 84 ppm, respectively, reflecting the incompatible nature of Rb. Average continental crust contains ~49 ppm Rb (Rudnick and Gao 2014).

In sedimentary systems, Rb abundances are controlled by detrital mica and Rb^+ absorption out of solutions to clay-size minerals, resulting in a threefold increase in Rb abundances in clay over silt-size fractions. Carbonates do not contain significant amounts of Rb. In metamorphic reactions, Rb is controlled by the stability phyllosilicates. It is easily redistributed into newly formed mica and due to its mobility in aqueous solutions can be easily transported, which accounts for the low Rb abundance in high-grade, dehydrated granulite facies rocks.

Utilization and Toxicity

Rubidium has only a limited commercial use in fireworks and modern laser technology and plays no critical role in biologic systems with a relatively low toxicity.

Summary

The high mobility of Rb in aqueous fluids is useful for tracing water-rock interactions and the mobility of LILE in low temperature environments. In high temperature processes, the incompatible nature of Rb during mantle melting, and igneous differentiation of primitive melts can be useful in understanding rock-forming processes. In combination with Sr, however, Rb is most useful as a geochronometer.

Cross-References

- ▶ Alkali and Alkaline Earth Metals
- ▶ Large-Ion Lithophile Elements
- ▶ Lithophile Elements
- ▶ Strontium
- ▶ Strontium Isotopes

References

Caro G, Bourdon B (2010) Non-chondritic Sm/Nd ratio in the terrestrial planets: consequences for the geochemical evolution of the mantle crust system. Geochim Cosmochim Acta 74(11):3333–3349

Kossert K (2003) Half-life measurements of Rb-87 by liquid scintillation counting. Appl Radiat Isot 59(5–6):377–382

Nebel O, Mezger K, Scherer E, Münker C (2005) High precision determinations of 87Rb/85Rb in geologic materials by MC-ICP-MS. Int J Mass Spectrom 246:10–18

Nebel O, Mezger K, van Westrenen W (2011a) Rubidium isotopes in primitive chondrites: constraints on Earth's volatile element depletion and lead isotope evolution. Earth Planet Sci Lett 305 (3–4):309–316
Nebel O, Scherer EE, Mezger K (2011b) Evaluation of the Rb-87 decay constant by age comparison against the U-Pb system. Earth Planet Sci Lett 301((1–2)):1–8
Palme H, O'Neill HSC (2014) Cosmochemical estimates of mantle composition. In: Holland H, Turekian K (eds) Treatise on geochemistry. Elsevier, Amsterdam, pp 1–39
Rotenberg E, Davis DW, Amelin Y, Ghosh S, Bergquist BA (2012) Determination of the decay-constant of Rb-87 by laboratory accumulation of Sr-87. Geochim Cosmochim Acta 85:41–57
Rudnick RL, Gao S (2014) Composition of the continental crust. In: Holland H, Turekian K (eds) Treatise on geochemistry. Elsevier, Amsterdam, pp 1–51
Villa IM, De Bievre P, Holden NE, Renne PR (2015) IUPAC–IUGS recommendation on the half life of Rb-87. Geochim Cosmochim Acta 164:382–385
Waight T, Baker J, Willigers B (2002) Rb isotope dilution analyses by MC-ICPMS using Zr to correct for mass fractionation: towards improved Rb–Sr geochronology? Chem Geol 186(1–2):99–116

Ruthenium

Thomas C. Meisel
General and Analytical Chemistry, Montanuniversität Leoben, Leoben, Austria

Element Data
Atomic Symbol: Ru
Atomic Number: 44
Atomic Weight: 101.07(2)
Isotopes and Abundances: ^{96}Ru 5.54%, ^{98}Ru 1.87%, ^{99}Ru 12.76%, ^{100}Ru 12.6%, ^{101}Ru 17.06%, ^{102}Ru 31.55%, ^{104}Ru 18.62%
1 Atm Melting Point: 2334 °C
1 Atm Boiling Point: 4150 °C
Common Valences: +4
Ionic Radii: 60 pm
Pauling Electronegativity: 2.28
First Ionization Energy: 109.7 kJ/mol
Chondritic (CI) Abundance: 688 μg/kg
Silicate Earth Abundance: 7.2 μg/kg
Crustal Abundance: 0.03 μg/kg
Seawater Abundance: < 50 fmol/kg
Core Abundance: 4 mg/kg (McDonough 2014)

Properties

The transition metal $_{44}$Ru is one of the six platinum group elements (PGE) and a member of the iron group (iron, ruthenium, osmium, and hassium).

Ruthenium has the electron structure [Kr] $4d^7$ 5 s^1. As for Rh, only one electron can be found in the *s*-shell due to the small energy difference between the *s*- and *d*-shell. The atomic radius of 1.325 Å is the lowest value within the "light" platinum group elements (PGE group) (Ru, Rh, and Pd) but has the highest melting point, 2334 °C, and density, 12.2 g/cm^3 (Predel 2006). As for osmium, the crystal structure is hexagonal close packed (hcp). Ruthenium not only shares many properties with its horizontal neighbors but also with Os, which is a member of the "heavy" PGE (Os, Ir, Pt). Unlike all the other PGE, both Ru and Os react with KOH, NaOH, and Na_2O_2 melts. Under oxidizing conditions, Ru and Os form tetraoxides, as only these two PGE can reach the oxidation state of +8. Ruthenium can also reach the following known oxidation states: −2, 0, +2, +3, +4, +5, +6, +7, +8 with +4 as the most common. Ruthenium has an atomic weight of 101.07(2) g/mol with seven stable isotopes. Isotope dilution mass spectrometry (IDMS), combined with inductively coupled mass spectrometry (ICP-MS) after acid digestion at high temperatures or after nickel sulfide fire assay, is the most common method of analysis (Meisel and Horan 2016).

History and Use

The name ruthenium is derived from Ruthenia, the Latin word for Rus', a Urals mountain region from where the samples from which ruthenium was first isolated, were derived. Ruthenium was probably discovered also in the residues after platinum extraction in aqua regia together with the other platinum group elements in the beginning of the nineteenth century but was only until 1844 when its isolation procedure, described by the Baltic German chemist Karl Ernst Claus (Карл Ка́рлович Кла́ус in Russian), was verified.

Ruthenium metal absorbs light throughout the visible spectrum making it attractive for solar energy technologies. The largest portion of the metal production goes into the electronics industry. As a versatile catalyst, Ru and ruthenium compounds have important applications in organic and pharmaceutical chemistry.

Physical, Chemical, and Geochemical Properties

Natural Occurrence

In nature, ruthenium occurs as rare native metal, as sulfides (e.g., laurite RuS_2), arsenides (e.g., ruthenarsenite [(Ru,Ni)As]), sulfarsenides (e.g., ruarsite, RuAsS), and Os–Ir–Ru alloys (O'Driscoll and González-Jiménez 2016). Ruthenium minerals are mined as by-product by the mineral processing of platinum and palladium ores (e.g., Bushveld, South Africa). A major source of Ru is anode slime created by the electro-refining process of nickel.

The estimated mean concentration of Ru in CI chondrites is 688 μg/kg (Fischer-Gödde et al. 2010). Estimates of the Earth's mantle and crust are 7.2 and 0.03 μg/kg, respectively (Becker et al. 2006; Park et al. 2012). The highly siderophile–chalcophile geochemical behavior and compatibility during mantle melting result in Ru as being one of the rarest elements in the Earth's crust. This geochemical behavior is shared with Ir and Os (thus Ru is also member of the Ir-PGE group).

Biological Utilization and Toxicity

Ruthenium and ruthenium compounds have no known biological function. Very little is known about the aqueous behavior, the mobility, and toxicity of ruthenium compounds because of its rareness and low abundance in the environment. However, $Ru(OH)_n^{4-n}$ species have been described with an abundance of less than 50 fmol/kg (Bruland and Lohan 2003). The only well-known toxic molecule is RuO_4. ^{106}Ru, as short-lived fission product formed from uranium in nuclear reactors and explosions, has been observed in the environment, possibly released as volatile RuO_4.

Summary

Ruthenium is one of the rarest PGE in the Earth's crust with a highly siderophile–chalcophile geochemical behavior similar to Ir and Os. Ruthenium shares similar resistance toward acids and solubility in alkali melts as Os and also forms volatile tetraoxide species.

Cross-References

- ▶ Iridium
- ▶ Native Minerals
- ▶ Osmium
- ▶ Palladium
- ▶ Platinum
- ▶ Platinum Group Elements
- ▶ Rhodium
- ▶ Siderophile Elements
- ▶ Sulfide Minerals

References

Becker H, Horan MF, Walker RJ, Gao S, Lorand JP, Rudnick RL (2006) Highly siderophile element composition of the Earth's primitive upper mantle: constraints from new data on peridotite massifs and xenoliths. Geochim Cosmochim Acta 70:4528–4550

Bruland KW, Lohan MC (2003) Controls of trace metals in seawater. In: Elderfield H (ed) The oceans and marine geochemistry, vol 6. Elsevier/Pergamon, Amsterdam, pp 23–47

Fischer-Gödde M, Becker H, Wombacher F (2010) Rhodium, gold and other highly siderophile element abundances in chondritic meteorites. Geochim Cosmochim Acta 74:356–379

McDonough WF (2014) 3.16 – Compositional model for the Earth's core A2. In: Turekian KK, Holland HD (eds) Treatise on geochemistry, 2nd edn. Elsevier, Oxford, pp 559–577

Meisel T, Horan MF (2016) Analytical methods for the HSE elements. In: Day JMD, Harvey J (eds) Highly siderophile and strongly chalcophile elements in high temperature geochemistry and cosmochemistry, vol 81. Mineralogical Society of America, Chantilly, pp 89–106

O'Driscoll B, González-Jiménez JM (2016) An inventory and overview of natural occurrences of the platinum-group minerals (PGM) in extraterrestrial and terrestrial rocks. In: Day JMD, Harvey J (eds) Highly siderophile and strongly chalcophile elements in high temperature geochemistry and cosmochemistry, vol 81. Mineralogical Society of America, Chantilly, pp 489–578

Park J-W, Hu Z, Gao S, Campbell IH, Gong H (2012) Platinum group element abundances in the upper continental crust revisited – new constraints from analyses of Chinese loess. Geochim Cosmochim Acta 93:63–76

Predel B (2006) Ac–Ag … Au–Zr · introduction. In: Predel B (ed) Landolt–Börnstein – group IV physical chemistry, vol 12A. Springer, Berlin/Heidelberg

S

Samarium

Michael Bizimis and Howie D. Scher
Earth and Ocean Sciences, University of South Carolina, Columbia, SC, USA

Properties

Element Data
Atomic Symbol: Sm
Atomic Number: 62
Atomic Weight: 150.363(8)
Isotopes and Abundances:
^{144}Sm 3.08(1)%
^{147}Sm 15.02(5)%
^{148}Sm 11.25(3)%
^{149}Sm 13.83(4)%
^{150}Sm 7.35(2)%
^{152}Sm 26.74(3)%
^{154}Sm 22.73(5)%
1 Atm Melting Point: 1345 K
1 Atm Boiling Point: 2067 K
Common Valences: 3+
Ionic Radii: 108 pm (eightfold coordination)
Pauling Electronegativity: 1.17
First Ionization Potential: 5.6437 eV
Chondritic (CI) Abundance: 0.148 ppm
Silicate Earth Abundance: 0.406 ppm
Crustal Abundance: 3.9 ppm
Seawater Abundance: 0.1–20 pmol/kg
Core Abundance: ~0

History and Use

Samarium was first discovered by Swiss chemist Marc Delafontaine in 1878 who named it "decipium," later proven to be a mixture of samarium and other rare earths. French chemist Paul-Emile Lecoq de Boisbaudran isolated samarium in 1879. It was purified from the mineral samarskite named for Colonel Vasili von Samarsky, a Russian mine official (Holden 2001). Commercial applications of Sm include samarium-cobalt magnets, which have a permanent magnetization second only to neodymium magnets, though Sm magnets can withstand higher temperatures before losing magnetization. Radioactive ^{153}Sm is used in a drug (^{153}Sm lexidronam) to treat painful bone metastases (Serafini et al. 1998) and to kill cancer cells in the lung, prostate, and breast. The isotope ^{149}Sm has a large neutron adsorption cross section and is used in the manufacture of control rods for use in nuclear reactors. Sm is typically concentrated along with other light rare-earth elements in late differentiated melts and typically found in commercially viable concentrations in the minerals bastnaesite and monazite associated with carbonatites or phosphate deposits (USGS 2015).

Geochemical Behavior

Samarium is a refractory, lithophile element following the Goldschmidt classification and belongs to the lanthanide rare-earth element group. It is thought to partition wholly in the silicate earth with practically no Sm in the core. Due to its relatively large ionic radius and 3+ charge, it is moderately to highly incompatible in most major rock-forming minerals and in the Earth's mantle, approaching a partition coefficient of 1 only in some garnets (Salters et al. 2002). As a consequence,

W. M. White (ed.), *Encyclopedia of Geochemistry*,
https://doi.org/10.1007/978-3-319-39312-4

Sm has lower concentration in the depleted upper mantle (0.27–0.239 ppm, Salters and Stracke 2004; Workman and Hart 2005), and higher concentration in the continental crust (3.9 ppm; Rudnick and Gao 2003) and mid-oceanic ridge basalts (3.8 ppm; Gale et al. 2013) than primitive mantle.

The most important usefulness of Sm in geochemistry is through its role in the neodymium (Nd) isotope system. ^{147}Sm decays to ^{143}Nd by α-decay and a half-life of 1.06×10^{11} years and a decay constant ($\lambda_{Sm}{}^{147}$) of 6.54×10^{-12} year^{-1}. ^{146}Sm decays to ^{142}Nd by α-decay and a short half-life estimated between 68×10^6 (Kinoshita et al. 2012) and 103×10^6 years (Marks et al. 2014). Samarium is generally more compatible than Nd in most petrogenetically significant minerals, which leads to fractionation of Sm from Nd during melting and crystallization processes. This fractionation leads, over time, to variable enrichment of ^{143}Nd over the stable ^{144}Nd in different minerals, forming the basis of ^{147}Sm/^{144}Nd geochronology and the use of Nd isotopes as key tracers of mantle processes. Due to its short half-life, ^{146}Sm is practically extinct at present. Nevertheless fractionation of the Sm/Nd system within the first 300–400 My of the Earth's history resulted in measurable fractionation of the ^{142}Nd/^{144}Nd isotope system which has been used to constrain early differentiation of the Earth and the chronology of the solar system (e.g., Marks et al. 2014; see also "▶ Neodymium Isotopes" for details).

As an intermediate rare-earth element, the comparison of samarium concentrations to that of the larger and highly incompatible light rare-earth element lanthanum (La) through the La/Sm ratio is a useful proxy for the fractionation of rare-earth element patterns, where La/Sm ratios lower than chondrite meteorites are a clear indication of a melt-depleted reservoir.

Samarium, as the other rare-earth elements, is highly insoluble in fluids at neutral pH, and its solubility increases with decreasing pH. In typical seawater composition and at pH = 8.2, Sm exists primarily as the carbonate ion species $Sm(CO_3)_2^-$ (Schijf et al. 2015). In the absence of strong organic complexing ligands, like humic acids (Sonke and Salters 2006), Sm is highly particle reactive and readily adsorbed in hydrated Fe and Mn oxide phases and particulate surfaces (Schijf et al. 2015), resulting in very low concentrations in seawater of less than 20 pmol/kg, typically around 3–5 pmol/kg (Alibo and Nozaki 1999; Tachikawa et al. 1999).

Biological Utilization and Toxicity

There is no known biological usage of Sm, likely due to its low concentration in waters that discouraged organisms for developing a use for it. Specific data for toxicity of Sm is lacking.

Cross-References

- ▶ Chondrites
- ▶ Earth's Continental Crust
- ▶ Lanthanide Rare Earths
- ▶ Lithophile Elements
- ▶ Mantle Geochemistry
- ▶ Mid-Ocean Ridge Basalts (MORB)
- ▶ Neodymium
- ▶ Neodymium Isotopes

References

Alibo DS, Nozaki Y (1999) Rare earth elements in seawater: particle association, shale-normalization, and Ce oxidation. Geochim Cosmochim Acta 63:363–372

Gale A, Dalton CA, Langmuir CH, Su Y, Schilling J-G (2013) The mean composition of ocean ridge basalts. Geochem Geophys Geosyst 14(3):489–518

Holden NE (2001) History of the origin of the chemical elements and their discoverers. BNL-NCS-63859-01/10-REV, Brookhaven National Laboratory. http://www.nndc.bnl.gov/publications/preprints/origindc.pdf

Kinoshita N, Paul M, Kashiv Y, Collon P, Deibel CM, DiGiovine B, Greene JP, Henderson DJ, Jiang CL, Marley ST, Nakanishi T, Pardo RC, Rehm KE, Robertson D, Scott R, Schmitt C, Tang XD, Vondrasek R, Yokoyama A (2012) A shorter ^{146}Sm half-life measured and implications for ^{146}Sm-^{142}Nd chronology in the solar system. Science 335(6076):1614–1617

Marks NE, Borg LE, Hutcheon ID, Jacobsen B, Clayton RN (2014) Samarium–neodymium chronology and rubidium–strontium systematics of an Allende calcium–aluminum-rich inclusion with implications for ^{146}Sm half-life. Earth Planet Sci Lett 405:15–24

Rudnick RL, Gao S (2003) The composition of the continental crust. In: Treatise on geochemistry, vol 3. Elsevier, Amsterdam, pp 1–64

Salters VJM, Stracke A (2004) Composition of the depleted mantle. Geochem Geophys Geosyst 5(Q05004). https://doi.org/10.1029/2003GC000597

Salters VJM, Longhi JE, Bizimis M (2002) Near mantle solidus trace element partitioning at pressures up to 3.4 GPa. Geochem Geophys Geosyst 3(7). https://doi.org/10.1029/2001GC000148

Schijf J, Christenson EA, Byrne RH (2015) YREE scavenging in seawater: a new look at an old model. Mar Chem 177(Part 3):460–471

Serafini AN, Houston SJ, Resche I, Quick DP, Grund FM, Ell PJ, Bertrand A, Ahmann FR, Orihuela E, Reid RH, Lerski RA, Collier BD, McKillop JH, Purnell GL, Pecking AP, Thomas FD, Harrison KA (1998) Palliation of pain associated with metastatic bone cancer using samarium-153 lexidronam: a double-blind placebo-controlled clinical trial. J Clin Oncol 16 (4):1574–1581

Sonke JE, Salters VJM (2006) Lanthanide-humic substances complexation. I. Experimental evidence for a lanthanide contraction effect. Geochim Cosmochim Acta 70(6):1495–1506

Tachikawa K, Jeandel C, Roy-Barman M (1999) A new approach to the Nd residence time in the ocean: the role of atmospheric inputs. Earth Planet Sci Lett 170(4):433–446

U.S. Geological Survey (2015) Mineral commodity summaries 2015: U.S. Geological Survey, 196 p. https://doi.org/10.3133/70140094

Workman RK, Hart SR (2005) Major and trace element composition of the depleted MORB mantle (DMM). Earth Planet Sci Lett 231:53–72

Scandium

Iain M. Samson[1] and Mathieu Chassé[2]
[1]Department of Earth and Environmental Sciences, University of Windsor, Windsor, ON, Canada
[2]Institut de minéralogie, de physique des matériaux, et de cosmochimie (IMPMC), Sorbonne universités – UPMC, Paris, France

Element Data
Atomic Symbol: **Sc**
Atomic Number: **21**
Atomic Weight: 44.95591
Isotopes and Abundances: ^{45}Sc 100%
1 Atm Melting Point: 1541 °C
1 Atm Boiling Point: 2836 °C
Common Valences: 3+
Ionic Radii: 6-fold, 74.5 pm, 8-fold, 87 pm
Pauling Electronegativity: 1.36
First Ionization Energy: 633.1 kJ/mol
Chondritic (CI) Abundance: 5.81 ppm
Silicate Earth Abundance: 16.4 ppm
Crustal Abundance: 21.9
Seawater Abundance: 2–20 pmol/L
Core Abundance: ~0

Properties

Scandium is the lightest group 3 (IIIB) element and is the lightest of the transition metals. Its atomic number (proton number) is 21, has only one long-lived isotope, and has an atomic mass of 44.95591 u. Scandium's electronic configuration is [Ar]$4s^2 3d^1$ and only occurs in the trivalent state (Sc^{3+}) in nature. Thus, unlike most other period 4 transition metals, the geochemical behavior of scandium is not affected by redox conditions and shows lithophile behavior. The effective ionic radii in six- and eightfold coordination are 74.5 and 87 pm, respectively (Shannon 1976), and its Pauling electronegativity is 1.36. Pure scandium metal has a melting point of 1541 °C at 1 atm. The International Union of Pure and Applied Chemistry considers Sc to be a rare earth element (REE) (Damhus et al. 2005); however, the ionic radius and electronic configuration of Sc are sufficiently different from yttrium and the lanthanides that it is generally excluded from discussions of the REE.

History and Use

Scandium was "discovered" by Lars Fredrik Nilson in 1879 by separation from rare earth mixtures from euxenite and gadolinite and is named for Scandinavia.

Global production of Sc is small (~10 tonnes per year) as a by-product from mining of ores of titanium, rare earths, apatite, and uranium. Bauxites are another potential source of Sc, as it gets concentrated, along with other elements, in the "red mud" residue that results from Al processing (Deady et al. 2016). The principal uses of Sc are in Sc-Al alloys and in solid oxide fuel cells. Minor amounts of Sc are also used in a variety of other applications including electronics, lasers, and lighting.

Natural Abundances

The abundance of Sc in the solar system, as estimated from chondritic meteorites, is ca. 5.81 ppm (McDonough and Sun 1995). The refractory behavior of this element in the solar nebula as well as its lithophile behavior led to the relative concentration of this element in the silicate Earth, with an estimated abundance of about 16 ppm, which is also the estimated abundance of the primitive mantle (Palme and O'Neill 2014). The abundance of Sc in the Earth's continental crust is higher, with average values of 31, 19, and 14 ppm for the lower, middle, and upper crust, respectively, and an average continental crust value of 21.9 ppm (Rudnick and Gao 2014). It occurs in higher concentrations in oceanic crust as reflected in values in MORB of between 34 and 48 ppm (Klein 2003). Thus, as with the rare earth elements, scandium is not particularly rare, and is found in similar concentrations in the crust to Pb, and is orders of magnitude more abundant than most of the precious metals in the Earth's crust.

The relatively large ionic radius to charge ratio (ionic potential) of Sc^{3+} means that it is incompatible in the structures of many of the common rock-forming minerals, such that it is generally present in low concentrations, ranging from a few ppm to a few tens of ppm. The concentration of Sc in different rock types is shown in Fig. 1. Scandium is generally incompatible in mantle rocks (Davis et al. 2013), which explains the lower Sc concentration in komatiites compared to basalts and the low Sc content of peridotites and dunites. The latter reflects low concentrations and mineral/melt partition coefficients for olivine and spinel compared to garnet, clinopyroxene, and amphibole (Davis et al. 2013; Bédard 2014; Fig. 2). The very similar ionic radii (74.5 and 72 pm in sixfold coordination) and electronegativities (1.36 and 1.31) of Sc and Mg, respectively, explain the substitution of Sc for Mg in the M1 octahedral site of clinopyroxene and M octahedral sites of amphibole. Scandium also substitutes

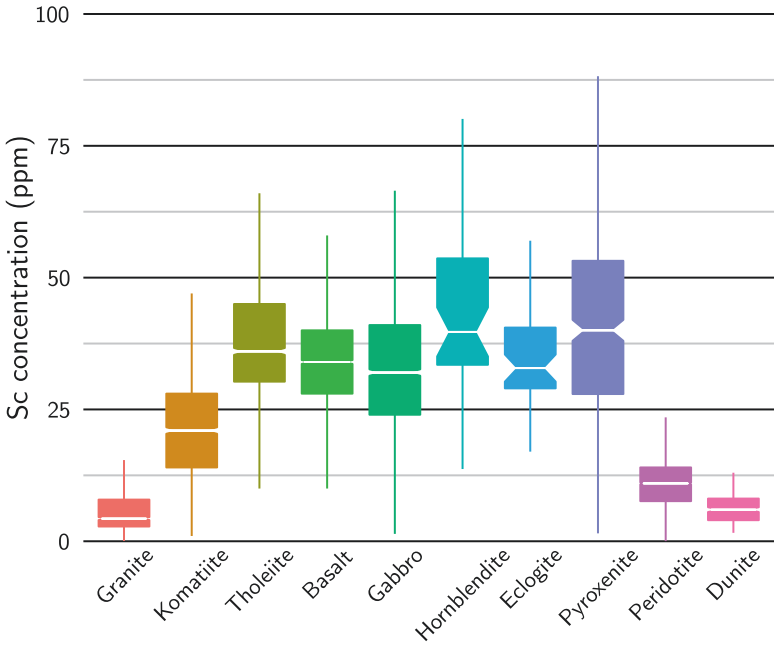

Scandium, Fig. 1 Box-and-whisker plot of Sc concentrations in some common lithologies. (Data from the GEOROC database, Sarbas and Nohl (2008); 11,846 analyses.) "Tholeiite" stands for tholeiitic basalt, whereas "basalt" includes a wide range of other basalt types. The boxes represent the first and third quartiles of the data distribution. The horizontal line represents the median, and the width of the adjacent notches provides the 95% confidence interval about the median. The "whiskers" represent the last value before 1.5 × midrange (arithmetic mean of maximum and minimum values) beyond the first or third quartile

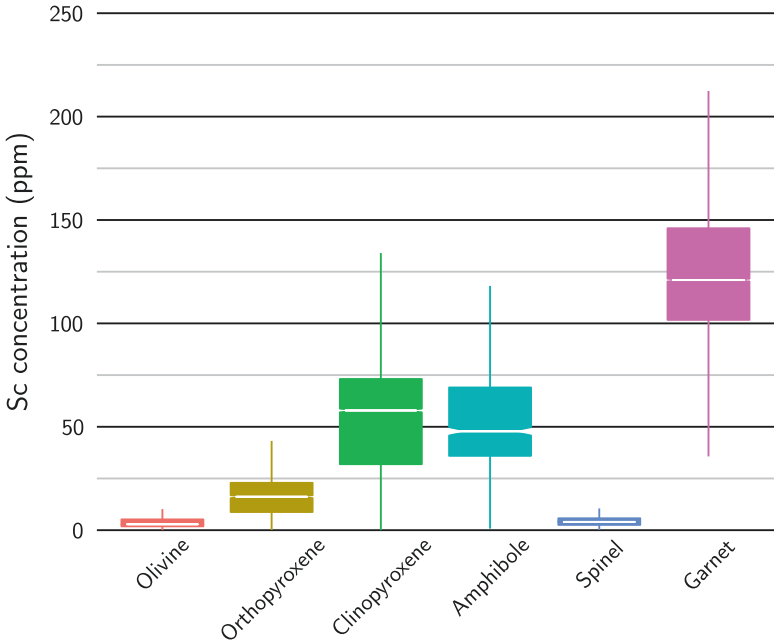

Scandium, Fig. 2 Box-and-whisker plot of Sc concentrations in various mantle-related minerals. (Data from the GEOROC database, Sarbas and Nohl (2008); 21,475 analyses.) The minerals mostly come from xenoliths of various mafic and ultramafic lithologies

for Mg due to similar ionic radii in the cubic X site of pyrope garnets (Oberti et al. 2006). Felsic rocks, such as granites, are depleted in Sc, as quartz and feldspars cannot accommodate significant amounts of Sc. Because vanadium (V) has comparable behavior to Sc, but also variable valence, V/Sc ratios are sensitive to fO_2 and have been used to provide information on the redox conditions in the mantle (Li and Lee 2004).

Scandium is residually concentrated in soils and typically reaches concentrations between about 1 and 10 ppm (e.g., Jeske and Gworek 2013). Coal can contain significant Sc. Average Sc concentrations in a wide variety of coals from Asia range from 0.85 to 16.0 ppm, with an overall average of 4.3 ppm and a maximum value of 230 ppm (Arbuzov et al. 2014). Consequently, coal fly ash can also contain significant Sc, generally several tens of ppm (e.g., Bettinelli et al 1987; Franus et al. 2015).

Although Sc generally occurs in low concentrations in common minerals and rocks, it can achieve higher concentrations in restricted environments, most notably alkaline igneous rocks, including carbonatites, in granitic pegmatites, in hydrothermal veins, and in some meteorites. It is in these environments that Sc-rich minerals occur.

Scandium Mineralogy

Minerals that contain Sc at concentrations greater than a few tens of ppm include Sc-rich varieties of minerals such as columbite, rutile, perrierite, euxenite, ixiolite, and pyrochlore (e.g., Åmli 1977; Bergstøl and Juve 1988; Wise et al. 1998), as well as minerals in which Sc is an essential element. There are relatively few minerals known that contain Sc as an essential element, and only seventeen IMA-approved minerals exist, comprising silicates, phosphates, and oxides. Silicates belong to the inosilicate (e.g., cascandite [$Ca(Sc,Fe^{2+})Si_3O_8(OH)$]), cyclosilicate (e.g., bazzite [$Be_3(Sc,Al)_2Si_6O_{18}$]), sorosilicate (e.g., thortveitite [$(Sc,Y)_2Si_2O_7$]), and orthosilicate (eringaite [$Ca_3Sc_2(SiO_4)_3$]) subclasses. Phosphates include anhydrous and hydrous species, such as pretulite [$ScPO_4$] and kolbeckite [$ScPO_4 \cdot 2H_2O$]. A number of scandium-bearing oxides have been recognized, and most of these occur in meteorites, such as allendeite [$Sc_4Zr_3O_{12}$], named for its type locality, the Allende meteorite. These minerals are rare, and, as described above, most scandium on Earth occurs as a trace component of other minerals.

Aqueous Geochemistry

Scandium concentrations in surface waters are invariably very low, generally in the parts per trillion (ppt) range. The limited data available on Sc concentrations in seawater indicate an average concentration of around 13 pmol L^{-1} (~0.6 ppt) (Horovitz 1999). This is consistent with a profile through the Pacific Ocean that shows a gradual increase from 2 pmol L^{-1} (0.09 ppt) at the surface to 20 pmol L^{-1} (2 ppt) at the ocean floor, which is considered to be a nutrient-like profile (Amakawa et al. 2007). Concentrations in river water are also very low, in the range of 1–16 ppt (Silker 1964; Tanizaki et al. 1992; Cerutti et al. 2003); however, concentrations can be higher (ppb levels) in acid mine drainage (e.g., Jerez et al. 2014).

The relatively small radius of Sc^{3+} and its trivalent nature make it a "hard" acid in the sense of Pearson (1963) and, in aqueous solutions, will preferentially bond to hard bases, including OH^- and F^-, and certain organic ligands, such as acetate. This is confirmed by available thermodynamic and experimental data which indicate that in most low-temperature environments (pH ~ 4–10), the aqueous complexes $Sc(OH)^{2+}$, $Sc(OH)_2^+$, and $Sc(OH)_3^0$ will predominate. At low pH, Sc^{3+} will predominate. With increasing temperature, the hydroxy complexes with higher ligand numbers are predicted to become increasingly important. Scandium fluoride complexes are relatively stable and could be important in fluorine-rich environments, particularly at low pH. There are few data on the aqueous solubility of the Sc minerals described above. Calculated solubilities for the phase ScOOH at 25 °C indicate low solubilities (~9 ppb) and a solubility minimum between pH ~ 6 and 10, but that under acidic conditions, solubilities can reach several hundred ppm (Wood and Samson 2006). In low-temperature phosphate-rich environments, the phase $ScPO_4$ is calculated to have even lower solubilities and would severely limit the mobility of Sc (Wood and Samson 2006), for example, in some soil environments where REE phosphates are known to occur (Aide and Aide 2012).

Biological Utilization and Toxicity

Scandium does not bioaccumulate readily in plants (Alloway 2013) and, given the concentrations found in biomaterials, is generally not considered a toxic element, except at higher than normal doses, but can have some beneficial effects on organisms (Bordean et al. 2013). Scandium chloride ($ScCl_3$) is, however, more toxic (Horovitz 2000).

Summary

Scandium, a lithophile element, is the lightest of the transition elements and has crustal abundances that generally range between 15 and 50 ppm. Scandium can occur in higher concentrations, generally in alkaline rocks, where it can form Sc minerals, but is mostly present as a trace component in a wide range of rock-forming minerals, most easily substituting for Mg. It occurs in very low concentrations in natural waters and does not easily bioaccumulate.

Cross-References

- ▶ Earth's Oceanic Crust
- ▶ Electronegativity
- ▶ Fugacity
- ▶ Geochemical Classification of Elements
- ▶ Incompatible Elements
- ▶ Ionic Radii
- ▶ Lanthanide Rare Earths
- ▶ Lithophile Elements
- ▶ Low-Temperature Geochemistry
- ▶ Magnesium
- ▶ Mantle Geochemistry
- ▶ Meteorites
- ▶ Mid-Ocean Ridge Basalts (MORB)
- ▶ Mineralogy
- ▶ Ocean Biochemical Cycling and Trace Elements
- ▶ Ore Deposits
- ▶ Oxide Minerals
- ▶ Partitioning and Partition Coefficients

▶ Silicate Minerals
▶ Soils
▶ Solubility
▶ Surface Geochemistry
▶ Trace Elements
▶ Transition Elements

References

Aide MT, Aide C (2012) Rare Earth elements: their importance in understanding soil genesis. ISRN Soil Sci 2012:783876. https://doi.org/10.5402/2012/783876
Alloway BJ (2013) Bioavailability of elements in soil. In: Selinus O (ed) Essentials of medical geology. Springer, The Netherlands, pp 351–373
Amakawa H, Nomura M, Sasaki K, Oura Y, Ebihara M (2007) Vertical distribution of scandium in the north central Pacific. Geophys Res Lett 34:L11606
Åmli R (1977) Carbonatites, a possible source of scandium as indicated by Sc mineralization in the Fen peralkaline complex, southern Norway. Econ Geol 72:855–859
Arbuzov SI, Volostnov AV, Mezhibor AM, Rybalko VI, Ilenok SS (2014) Scandium (Sc) geochemistry in coals (Siberia, Russian Far East, Mongolia, Kazakhstan, and Iran). Int J Coal Geol 125:22–35
Bédard JH (2014) Parameterizations of calcic clinopyroxene – melt trace element partition coefficients. Geochem Geophys Geosyst 15:303–336
Bergstøl S, Juve G (1988) Scandian ixiolite, pyrochlore and bazzite in granite pegmatite in terdal, Telemark, Norway. A contribution to the mineralogy and geochemistry of scandium and tin. Mineral Petrol 38:229–243
Bettinelli M, Baroni U, Pastorelli N (1987) Determination of scandium in coal fly ash and geological materials by graphite furnace atomic absorption spectrometry and inductively coupled plasma atomic emission spectrometry. Analyst 112:23–26
Bordean D-M, Cojocariu A, Horablaga M, Cojocariu L, Alda S, Nica D, Alda L, Borozan AB (2013) Scandium, element of surprises. In: 13th SGEM GeoConference on ecology, economics, education and legislation. SGEM2013 conference proceedings, Albena, vol 1, pp 865–872, 16–22 Jun 2013
Cerutti S, Salonia J, Gásquez J, Olsina R, Martinez L (2003) Determination of scandium in river water by ICP-OES with flow-injection on-line preconcentration using knotted reactor and ultrasonic nebulization. J Anal At Spectrom 18:1198–1201
Damhus T, Hartshorn RM, Hutton AT (2005) Nomenclature of inorganic chemistry: IUPAC recommendations 2005. Royal Society of Chemistry, London
Davis FA, Humayun M, Hirschmann MM, Cooper RS (2013) Experimentally determined mineral/melt partitioning of first-row transition elements (FRTE) during partial melting of peridotite at 3 GPa. Geochim Cosmochim Acta 104:232–260
Deady É, Mouchos E, Goodenough K, Williamson B, Wall F (2016) A review of the potential for rare-Earth element resources from European red muds: examples from Seydişehir, Turkey and Parnassus-Giona, Greece. Mineral Mag 80:43–61
Franus W, Wiatros-Motyka MM, Wdowin M (2015) Coal fly ash as a resource for rare Earth elements. Environ Sci Pollut Res 22:9464–9474
Horovitz CT (1999) Biochemistry of scandium and yttrium, part 1: physical and chemical fundamentals. Springer US, Boston, p 324
Horovitz CT (2000) Biochemistry of scandium and yttrium, part 2: biochemistry and applications. Springer US, Boston, p 303
Jerez J, Isaguirre AC, Bazán C, Martinez LD, Cerutti S (2014) Determination of scandium in acid mine drainage by ICP-OES with flow injection on-line preconcentration using oxidized multiwalled carbon nanotubes. Talanta 124:89–94
Jeske A, Gworek B (2013) Distribution and mobility of scandium and yttrium in selected types of soils in Poland. Chem Speciat Bioavailab 25:216–222
Klein EM (2003) Geochemistry of the igneous oceanic crust. In: Turekian KK, Holland HD (eds) Treatise on geochemistry, vol 3, 1st edn. Elsevier, Amsterdam, pp 433–463
Li Z-XA, Lee C-TA (2004) The constancy of upper mantle fO_2 through time inferred from V/Sc ratios in basalts. Earth Planet Sci Lett 228:483–493
McDonough WF, Sun S-S (1995) The composition of the Earth. Chem Geol 120:223–253
Oberti R, Quartieri S, Dalconi MC, Boscherini F, Iezzi G, Boiocchi M, Eeckhout SG (2006) Site preference and local geometry of Sc in garnets: part I. Multifarious mechanisms in the pyrope–grossular join. Am Mineral 91:1230–1239
Palme H, O'Neill HSC (2014) Cosmochemical estimates of mantle composition. In: Turekian KK, Holland HD (eds) Treatise on geochemistry, vol 3, 2nd edn, Oxford, Elsevier, pp 1–39
Pearson RG (1963) Hard and soft acids and bases. J Am Chem Soc 85:3533–3539
Rudnick RL, Gao S (2014) Composition of the continental crust. In: Turekian KK, Holland HD (eds) Treatise on geochemistry, vol 4, 2nd edn. Elsevier, Oxford, pp 1–51
Sarbas B, Nohl U (2008) The GEOROC database as part of a growing geoinformatics network. In: Brady SR, Sinha AK, Gundersen LC (eds) Geoinformatics 2008 – data to knowledge, proceedings, U.S. Geological Survey Scientific Investigations Report 2008-5172, pp 42–43
Shannon RD (1976) Revised effective ionic radii and systematic studies of interatomic distances in halides and chalcogenides. Acta Crystallogr A32:751–767
Silker WB (1964) Variations in elemental concentrations in the Columbia River. Limnol Oceanogr 9:540–545
Tanizaki Y, Shimokawa T, Nakamura M (1992) Physicochemical speciation of trace elements in river waters by size fractionation. Environ Sci Technol 26:1433–1444
Wise MA, Cerny P, Falster AU (1998) Scandium substitution in columbite-group minerals and ixiolite. Can Mineral 36:673–680
Wood SA, Samson IM (2006) The aqueous geochemistry of gallium, germanium, indium and scandium. Ore Geol Rev 28:57–102

Selenium

Monica Vasiliu and David A. Dixon
Department of Chemistry, University of Alabama, Tuscaloosa, Al, USA

Element Data
Atomic Symbol: Se
Atomic Number: 34
Atomic Weight: 78.96
Isotopes and Abundances: ^{74}Se 0.9%, ^{76}Se 9.2%, ^{77}Se 7.6%, ^{78}Se 23.7%, ^{80}Se 49.8%, ^{82}Se 8.8%

(*continued*)

1 Atm Melting Point: 490 K
1 Atm Boiling Point: 958.1 K
Common Valences: +6, +4, −2
Ionic Radii: (+VI) 42 ppm, (+IV) 69 ppm, (−II) 191 ppm
Pauling Electronegativity: 2.55
First Ionization Potential: 9.75 eV
Chondritic (CI) Abundance: 18.6 ppm
Silicate Earth Abundance: 0.075 ppm
Crustal Abundance: 0.05 ppm
Seawater Abundance: 0.9 ppb
Core Abundance: 8 ppm

Properties

Selenium (Emsley 1991, 2001; Anthoni 2006; Anders and Grevesse 1989; McDonough 2005) is a semi-metal that exists in two allotropic forms as a silvery metal and as a red amorphous powder; the former is produced from the latter by heat. The metal consists of spirals of linked selenium atoms and the red form has stacked rings each made up of eight selenium atoms. The importance of the eight ring structure is also found for sulfur. The metal form conducts electricity better in the light than in the dark, and it is used in photocells. Selenium burns in air and it is not affected by water, but it dissolves in concentrated nitric acid and alkaline solutions.

Selenium resembles sulfur and tellurium which lie above it and below it, respectively, in the Periodic Table, in terms of its chemical activity and physical properties.

History and Use

Selenium was discovered by Jöns Jacob Berzelius in 1817 in Stockholm. He was preparing sulfuric acid and found a red-brown sediment at the bottom of the chambers in which the acid was made. When heated, it had a strong smell of radishes and Berzelius thought at first that the element was tellurium, but, eventually, he realized that it was a new element, chemically similar to tellurium. He named it selenium from the Greek "selene" which means Moon to match the name tellurium from the Latin "tellus" meaning Earth. He observed that the new element was like sulfur because it vaporized on heating and can be redeposited on a cold surface as beautiful crystals known as "flowers," with bright yellow "flowers" for sulfur and red "flowers" for selenium in its nonmetallic form. Berzelius found that selenium was also present in samples of tellurium and that selenium gave tellurium the smell of radishes. Berzelius was personally affected by selenium as it can be absorbed through the skin and caused him to experience bad breath. Within a few years of its discovery, selenium was found in many minerals. Sometimes, the metallic form of selenium was refined and cast into medallions carrying pictures of its founder Berzelius.

The biggest use of selenium is as an additive to glass. There are selenium compounds that decolorize glass and others that give it a deep red color. Selenium is used to reduce the transmission of sunlight in architectural glass by giving it a bronze tint. Also it is used to make pigments for ceramics, paints, and plastics. Selenium has both photovoltaic and photoconductive properties. Thus, it is useful in photocells, solar cells, and photocopiers and in rectifiers (converting AC current to DC current). Selenium is also used as an additive to make stainless steel and to improve the abrasion resistance in vulcanized rubbers. Selenium, as sodium selenite, is used in animal feeds and food supplements. Some selenium compounds are added to antidandruff shampoos because selenium is toxic to the scalp fungus that causes dandruff.

Geochemical Behavior

Selenium is a rare element on the surface of earth and is present in the atmosphere as its methyl derivatives. Uncombined selenium is occasionally found, and there are about 40 known selenium-containing minerals, some of which can have up to 30% selenium. These minerals are rare and generally occur together with sulfides of metals such as copper, zinc, and lead. The main producing countries are Canada, the USA, Bolivia, and Russia.

Selenium occurs naturally in the environment being released through both natural processes and human activities. Selenium is present in phosphate fertilizers, and it is often added as a trace nutrient. Selenium settles from air and thus its levels in soils and waters increase. Selenium pollutes the environment around certain facilities, for example, coal-burning power stations, metal smelters which use sulfide ores, and municipal incinerators burning paper, cardboard, and tires, which contain small amounts of selenium.

Selenium in soils does not always react with oxygen and it remains fairly immobile. Selenium that is immobile and will not dissolve in water is less of a risk for organisms. Factors such as the oxygen level in the soil, soil temperature, moisture, the season, and the acidity of the soil will increase mobile forms of selenium.

Biological Utilization and Toxicity

Selenium is an essential trace element for some species, including humans. Selenium is part of the antioxidant enzyme

glutathione peroxidase, which eliminates peroxides before they form dangerous free radicals. Human bodies contain about 14 mg of selenium, and every cell in a human body contains more than a million selenium atoms. The recommended maximum daily intake is 450 micrograms. Too little selenium can cause health problems and in the same time too much can be dangerous. In excess, selenium is carcinogenic and teratogenic. Excess amounts can be readily detected as a garlic odor to the breath.

References

Anders E, Grevesse N (1989) Abundances of the elements: meteoritic and solar. Geochim Cosmochim Acta 53:197–214. http://meteorites.wustl.edu/goodstuff/chondritic_abundances.htm

Anthoni JF (2006) The chemical composition of seawater. http://www.seafriends.org.nz/oceano/seawater.htm

Emsley J (1991) The elements, 2nd edn. Clarendon, Oxford

Emsley J (2001) Nature's building blocks an A-Z guide to the elements. Oxford University Press, Oxford

McDonough WF (2005) Compositional model for the earth's core. In: Carlson RW (ed) The mantle and Core. Elsevier, Oxford, pp 547–568. http://www.knowledgedoor.com/2/elements_handbook/element_abundances_in_the_earth_s_core.html

Siderophile Elements

James M. D. Day
Scripps Institution of Oceanography, University of California San Diego, La Jolla, CA, USA

Definition

Siderophile elements preferentially partition into metal phases during cosmochemical and geochemical processes. The siderophile elements include the highly siderophile elements (HSE; Re, Os, Ir, Ru, Pt, Rh, Au, Pd), which are characterized by low-pressure metal–silicate distribution coefficients of more than 10^4; the moderately siderophile elements (MSE; including Mo, W, Fe, Co, Ni, P, Cu, Ga, Ge, As, Ag, Sb, Sn, Tl, Bi), with low-pressure metal–silicate partition coefficients that are typically more than 10, but less than 10^4; and the slightly siderophile elements (SSE; Mn, Cr, and V) (Table 1). The SSE, along with the highly chalcophile elements (HCE: S, Se, Te, Pb), and elements that otherwise exhibit atmophile, lithophile, or chalcophile affinity, can become siderophiles at specific temperatures (T), pressures (P), compositions (x), or oxygen fugacity (fO_2). An example of this phenomenon is the composition of Earth's core which, from seismological constraints, requires an alloy of FeNi metal and light elements. The nature of the light alloying element(s) remains uncertain, with Si, O, S, H, and C all considered as potential candidates, implying potential siderophile behavior of these elements at high pressures and temperatures.

Properties of the Siderophile Elements

The siderophile elements have both long-lived and short-lived radioactive isotope decay schemes and important novel stable isotope systems (e.g., Fe isotopes) embedded within them (Table 1). Of the radiogenic isotope systems, ^{182}W is the decay product of the extinct radionuclide ^{182}Hf and can be used to date core formation due to Hf partitioning into silicate portions of planets, relative to W, which partitions preferentially into metallic cores. The ^{187}Re-^{187}Os is a long-lived isotope chronometer and has found wide application, from geochronology to studies of mantle isotopic heterogeneity or the record of continental weathering from seawater $^{187}Os/^{188}Os$ composition (Shirey and Walker 1998; Harvey and Day 2016).

During condensation of elements at the formation of the solar nebula, siderophile elements sequestered in refractory metallic alloys, or into iron sulfides, depending on volatility, leading to some fractionation of the siderophile elements. Early differentiation of Earth led to siderophile elements being extracted into a metallic iron core and corresponding depletion of these elements in Earth's silicate mantle and crust. Application of low-pressure metal–silicate partition coefficients shows that the predicted abundances of some siderophile elements, especially the HSE, are higher than expected from metal–silicate partitioning in the bulk silicate Earth. The overabundance of siderophile elements in Earth's mantle has been attributed to "late accretion" of materials with generally chondritic bulk composition after core formation ceased, to account for the generally flat, chondrite-relative abundances of the HSE (Fig. 1).

Experimental partitioning studies have found that some siderophile elements have decreasing metal–silicate partitioning coefficients at high pressures. Thus, the possibility of high pressure core-mantle equilibration to account for the siderophile element – and specifically HSE – abundances in the bulk silicate Earth cannot be ruled out, but we have to account for both the abundances of these elements and the long-term ratios of Re/Os and Pt/Os that are within 5–10% of chondritic values deduced from $^{187}Os/^{188}Os$ and $^{186}Os/^{188}Os$ in terrestrial mantle rocks (e.g., Day et al. 2016). Asteroidal parent bodies, which underwent metal–silicate partitioning at low pressures, also show enrichments of siderophile elements in broadly chondritic proportions, indicating that late accretion was ubiquitous to planetary bodies. Late accretion is a natural consequence of planetary growth, whereby the end of

Siderophile Elements, Table 1 Behaviors and abundances in CI chondrites and the bulk silicate Earth (BSE) for the HSE and MSE

Element			Atomic number	Cosmochemical behavior	50% Tc (K)	Units	CI-chondrite	BSE abundance	BSE/CI	Examples of radioactive isotope systems
Phosphorus	P	MSE	15	Moderately volatile	1229	$\mu g\ g^{-1}$	1080	90	0.083	
Sulfur	S	HCE	16	High volatile chalcophile	664	$\mu g\ g^{-1}$	54,000	250	0.005	
Vanadium	V	SSE	23	Refractory	1429	$\mu g\ g^{-1}$	56	82	1.464	
Chromium	Cr	SSE	24	Transitional	1296	$\mu g\ g^{-1}$	2650	2625	0.991	
Manganese	Mn	SSE	25	Moderately volatile	1158	$\mu g\ g^{-1}$	1920	1045	0.544	
Iron	Fe	MSE	26	Transitional	1334	%	18.1	6.26	0.35	^{60}Fe-^{60}Ni ($t^{1/2}$ = 4.7 Ma)
Cobalt	Co	MSE	27	Transitional	1352	$\mu g\ g^{-1}$	500	105	0.210	
Nickel	Ni	MSE	28	Transitional	1353	$\mu g\ g^{-1}$	10,500	1960	0.187	
Copper	Cu	MSE	29	Moderately volatile	1037	$\mu g\ g^{-1}$	120	30	0.250	
Gallium	Ga	MSE	31	Moderately volatile	968	$\mu g\ g^{-1}$	9.2	4.0	0.435	
Germanium	Ge	MSE	32	Moderately volatile	883	$\mu g\ g^{-1}$	31	1.1	0.035	
Arsenic	As	MSE	33	Moderately volatile	1065	$\mu g\ g^{-1}$	1.85	0.05	0.027	
Selenium	Se	HCE/MSE	34	High volatile chalcophile	697	$\mu g\ g^{-1}$	19.7	0.075	0.004	
Molybdenum	Mo	MSE	42	Refractory	1590	$\mu g\ g^{-1}$	900	50	0.056	
Ruthenium	Ru	HSE	44	Refractory	1551	$ng\ g^{-1}$	631	7.0	0.011	
Rhodium	Rh	HSE	45	Refractory	1392	$ng\ g^{-1}$	130	1.2	0.0092	
Palladium	Pd	HSE	46	Transitional	1324	$ng\ g^{-1}$	563	7.1	0.013	^{107}Pd-^{107}Ag ($t^{1/2}$ = 6.5 Ma)
Silver	Ag	MSE	47	Moderately volatile	996	$ng\ g^{-1}$	200	8.0	0.040	
Tin	Sn	MSE	50	Highly volatile	704	$ng\ g^{-1}$	1650	130	0.079	
Antinomy	Sb	MSE	51	Moderately volatile	979	$ng\ g^{-1}$	140	5.5	0.039	
Tellurium	Te	HCE/MSE	52	High volatile chalcophile	709	$ng\ g^{-1}$	2330	12	0.005	
Tungsten	W	MSE	74	Refractory	1789	$ng\ g^{-1}$	93	13	0.140	^{182}Hf-^{182}W ($t^{1/2}$ = 8.9 Ma)
Rhenium	Re	HSE	75	Refractory	1821	$ng\ g^{-1}$	37.3	0.35	0.0094	^{187}Re-^{187}Os ($t^{1/2}$ = 42Ga)
Osmium	Os	HSE	76	Refractory	1812	$ng\ g^{-1}$	450	3.9	0.0087	
Iridium	Ir	HSE	77	Refractory	1603	$ng\ g^{-1}$	424	3.5	0.0083	
Platinum	Pt	HSE	78	Refractory	1408	$ng\ g^{-1}$	864	7.6	0.0088	^{190}Pt-^{186}Os ($t^{1/2}$ = ~460Ga)
Gold	Au	HSE	79	Moderately volatile	1060	$ng\ g^{-1}$	149	1.7	0.011	
Thallium	Tl	MSE	81	Highly volatile	532	$ng\ g^{-1}$	140	3.5	0.0250	
Lead	Pb	MSE	82	High volatile chalcophile	727	$ng\ g^{-1}$	2470	150	0.061	U-Th-Pb dating
Bismuth	Bi	MSE	83	Highly volatile	746	$ng\ g^{-1}$	110	2.5	0.023	

50% Tc = Equilibrium condensation temperatures for a solar system composition gas presented as the 50% trace element concentration
CI-chondrite carbonaceous Ivuna (type 1) chondrite, *BSE* bulk-Silicate Earth, taken as being the primitive mantle composition (after McDonough and Sun 1995; Lodders 2003).

core formation and metal–silicate partitioning enables buildup of siderophile elements in planetary mantles, in broadly chondritic abundances. For Earth, late accretion of approximately 0.8% by mass of a carbonaceous chondrite component is required to explain the abundances of the HSE in the mantle. For other planetary bodies, the amount of late

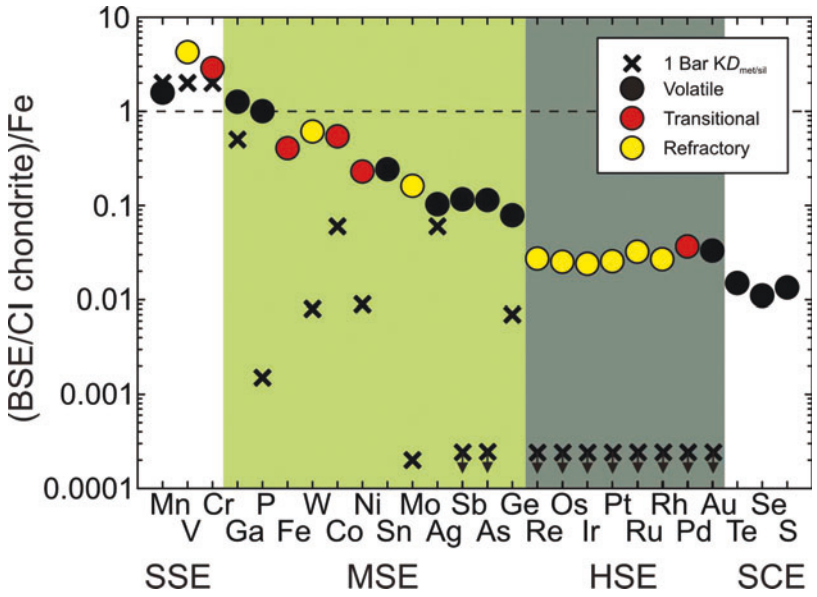

Siderophile Elements, Fig. 1 Abundances of elements in the bulk silicate Earth (*BSE*) with slightly (*SSE*), moderately (*MSE*), and highly siderophile element (*HSE*) behavior and with strongly chalcophile element (*SCE*) behavior, double-normalized to the composition of CI chondrites and to Fe content. Volatile (defined as those elements for which 50% TC < 1250 K), transitional, and refractory (50% TC > 1360) behaviors are shown. Abundances of the siderophile elements in the BSE are higher than expected from 1 atmosphere metal–silicate partition coefficients (1 Bar $KD_{met/sil}$; those with *downward arrows* = > 10^4). Higher abundances of these elements, most especially of the HSE, which are in broadly chondritic relative proportions, have been interpreted to reflect late accretion of chondritic material to Earth, after core formation was complete

accretion is less certain but is likely to be strongly tied to the timing of cessation of core formation and metal–silicate equilibration.

Cross-References

- ▶ Chalcophile Elements
- ▶ Formation and Evolution of the Earth
- ▶ Lithophile Elements

References

Day JMD, Brandon AD, Walker RJ (2015) Highly siderophile elements in Earth, Mars, the Moon, and Asteroids. Rev Mineral Geochem 81, 78 pp. https://doi.org/10.2138/rmg.2014.81.04

Harvey J, Day JMD (2016) Introduction to highly siderophile and strongly chalcophile elements in high temperature geochemistry and cosmochemistry. Rev Mineral Geochem 81(1):3–4

Lodders K (2003) Solar system abundances and condensation temperatures of the elements. Astrophys J 591:1220–1247

McDonough WF, Sun S-S (1995) The composition of the earth. Chem Geol 120:223–253

Shirey SB, Walker RJ (1998) The Re-Os isotope system in cosmochemistry and high-temperature geochemistry. Annu Rev Earth Planet Sci 26:423–500

Silicate Melts

Pascal Richet
Institut de Physique du Globe de Paris, Paris, France

Synonyms

Magmas

Definition

Produced at depth by partial melting of mantle or crustal rocks, silicate melts form as small droplets at mineral-grain boundaries. By coalescing and concentrating volatiles present at depth – primarily water and CO_2 – these droplets constitute the liquid phase that is the main component of magma. Owing to a density lower than that of the surrounding rock, the magma begins its rise to the Earth's surface, undergoing along the way complex processes known as fractional crystallization and assimilation and often carrying solid enclaves. At depths of a few tens of km, lower pressures cause volatiles to become oversaturated and to exsolve as bubbles, enhancing

the buoyancy. The process results in volcanism during which the lava emitted cools down quickly. Depending on factors such as melt viscosity and compressive or extensive geological contexts, however, all magmas do not reach the Earth's surface. Cooling then is very slow and melt crytallization eventually results in solidification of plutonic intrusions.

The Discovery of Silicate Melts

Magma owes its geochemical importance to the efficient way it transports energy and matter, at all scales, in response to pressure and temperature gradients. Ever since its formation 4.5 billion years ago, the Earth has thus primarily been shaped by magmatic processes. The discovery of this activity is rather recent, however, because from antiquity until the end of the eighteenth century it was believed that rocks were melted by subterranean combustion of matters such as sulfur, coal, or bitumen. Volcanism thus was perceived as an accidental process of very limited extent. The situation abruptly changed when de Dolomieu (1797) concluded from smart geological observations that magmas were originating instead from a region located below the then-thought primordial granite, which was itself lying on an older material from which lavas were issued. Announcing the concepts of isostasy and asthenosphere, Dolomieu concluded that this region upon which the solid crust rested all over the world was "pasty and viscous." At a given place, he noted, this source could produce large amounts of lava for very long times without leaving empty spaces collapsing under the weight of growing volcanoes, and without needing continuous supplies of combustible and of the then-known oxygen. With a source that was extending all over the Earth, magmas had at last become a major geological agent.

The Peculiarity of *Liquids*

The importance of silicate melts stems from the fact that these are *liquids*, i.e., phases characterized by a lack of long-range order and a high atomic mobility. Here the concept of unit cell thus is completely irrelevant, but not that of short-range order as oxygen coordination polyhedra similar to those of crystals can still be defined. Interatomic distances and bond angles do not take on fixed values, however, but follow instead more or less broad distributions that vary continuously with composition. Like in crystals, increasing SiO_2 contents cause an increasing polymerization of the structure. In olivines, pyroxenes, and SiO_2 polymorphs, all SiO_4 units are, for instance, connected to 0, 2, and 4 other tetrahedra by *bridging* oxygens (BO), respectively, whereas 4, 2, and 0 oxygens are left *nonbridging* (NBO). In glasses and melts, polymerization in contrast proceeds progressively through the coexistence of SiO_4 units having different numbers of bridging oxygens. This is why much attention is paid to the distribution of the so-called Q^n species, where n is the number of bridging oxygens per TO_4 polyhedra: here T designates not only Si^{4+} but also cations such as Al^{3+} and Fe^{3+} that can also be part of the silicate framework provided that they are associated with other cations (mostly alkalis and alkaline earths) to bring the overall formal charge to 4+. To describe polymerization/depolymerization, it is then useful to distinguish between network-former (T) and network-modifier (M) cations whose roles are summarized by the reaction

$$M_2O + T{-}BO{-}T = 2\ Si{-}NBO{-}M \qquad (1)$$

in the case of a monovalent M cation.

Contrary to solids where atomic positions are fixed and strongly constrained by long-range symmetry, liquids are in addition characterized by dynamic disorder, that is, by unceasing atomic rearrangements made possible by the excess thermal energy, with respect to solids, that they acquire on melting. Part of the thermal energy gained upon heating actually induces structural changes without causing temperature rises, which is the reason why melts have higher heat capacities than their crystalline counterparts. Such *configurational contributions* originating in structural changes are also found for the compressibility and thermal expansion coefficient. As a rule, they represent from 10% to more than 30% of these second-order thermodynamic properties, increasing with decreasing SiO_2 contents (cf. Mysen and Richet 2005).

From a geochemical standpoint, several important consequences follow. First, the disordered structure of melts generally allows a wide range of elements or oxides to coexist in a single phase, as illustrated by the fact that only one liquid forms upon melting of a rock made up of a number of distinct mineral phases. Second, water, CO_2, and other volatile species brought at depth by subduction zone processes can be incorporated at rather large concentrations in the newly formed magma; upon decompression their solubility is exceeded only under subsurface conditions where volatile exsolution causes sharp buoyancy increases and, thus, triggers volcanic eruptions. Third, atomic arrangements are generally more compact if ordered rather than disordered so that melts are less dense than their isochemical crystalline assemblages and, therefore, buoyant with respect to them, and the effect is enhanced not only by the dissolution of light volatiles such as water, but also by fractional crystallization since precipitation of dense ferromagnesian minerals causes the density of residual melts to decrease. Fourth, whereas crystalline phases are stable in limited pressure and temperature ranges, where changes in bond angles and distances must remain consistent with their long-range symmetry, liquids do not experience discontinuous phase transitions since

their structure keeps constantly adjusting to varying temperatures and pressures. Their lack of long-range order makes in particular possible a wide diversity of densification mechanisms, such as continuous pressure-induced changes of Si and Al from four to higher coordination by oxygen (e.g., Ghiorso 2004).

Besides, a major consequence of the progressive enrichment in SiO_2 and alkali oxides of the residual melts in all petrogenetic series is the aforementioned increasing polymerization of the structure, from the isolated SiO_4 tetrahedra and Si_2O_6 chains of olivine- and pyroxene-like units, respectively, to the three-dimensional network of SiO_4 and AlO_4 tetrahedra when the aluminosilicate compositions of rhyolites are reached. Correlatively very strong viscosity increases take place, which affect markedly rates of magma ascent and, therefore, eruption temperatures and eruptive styles. To quote a single example, rapidly rising basalts typically erupt at temperatures of about 1200 °C, which are 300 °C higher than for andesites. The viscosity difference between these melts thus increases from two orders of magnitude at 1200 °C to six at their eruption temperatures (Fig. 1): this feature accounts very simply for the difference between their effusive and explosive eruptive styles, respectively, and for the resulting morphology contrast between shield and stratovolcanoes.

Contrary to what has long been assumed, however, viscosity does not increase upon melt polymerization because of increasing entanglement of the silicate units when their average size increases. As alluded to above about mobility, the average lifetime of bonds tremendously decreases with rising temperatures so that the relative motion of silicate units involved in viscous flow must thus be pictured as a mutual interpenetration that takes place through bond exchange (Fig. 2). This is the reason why viscosity scales as the rate of bond rearrangement between oxygen and the network-forming cations Si and Al (Farnan and Stebbins 1994). All elements are involved, however, because the network-modifying cations have to move away for the activated complex to form. As a result (Richet 2009), viscosity can be expressed in terms of a constant enthalpic factor, *Be* (reflecting the average strength of the rearranging bonds) and an entropy term, *Sconf* (markedly increasing with temperature, accounting for the greater size of the units that can rearrange):

$$\log\eta = Ae + Be/TSconf, \tag{2}$$

where *Ae* is a pre-exponential factor.

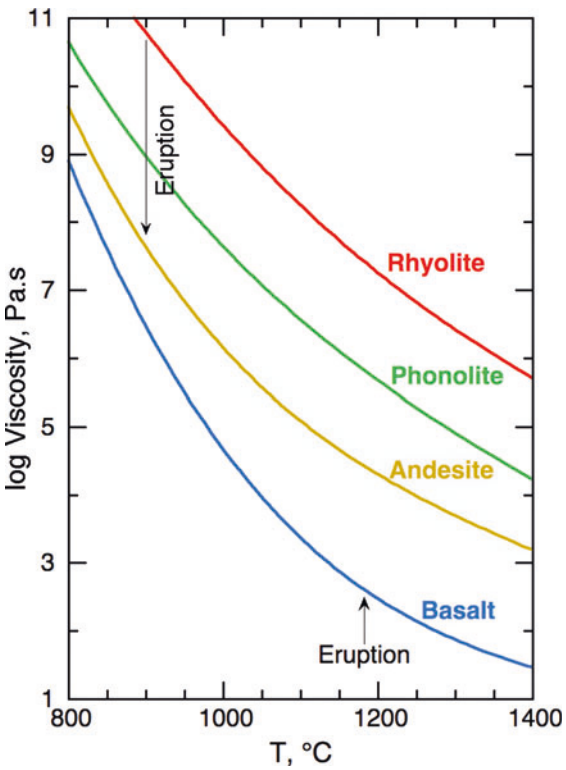

Silicate Melts, Fig. 1 Effect of melt polymerization on the viscosity, and its temperature dependence, of important lava types

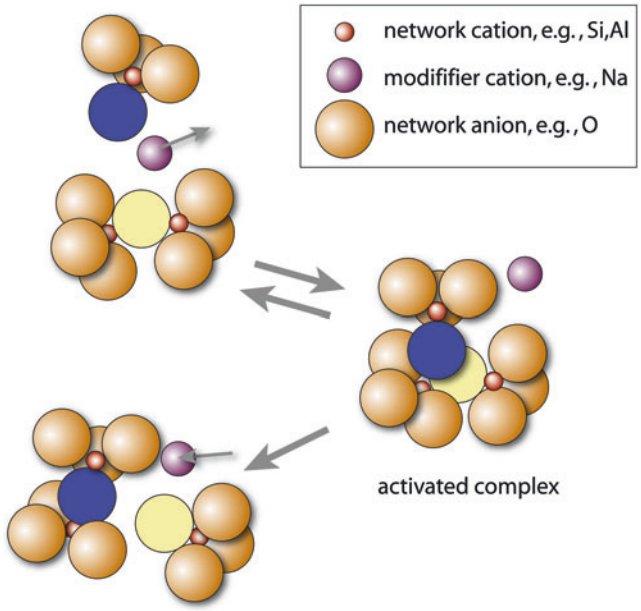

Silicate Melts, Fig. 2 Bond-exchange mechanism of viscous flow for a sodium-silicate melt (Farnan and Stebbins 1994). (*a*) Sodium moving away when a nonbridging oxygen (*dark*) of a Q^0 species gets close to the bridging oxygen (*clear*) of two Q^1 species. (*b*) Formation of an activate complex with a fivefold coordinated Si. (*c*) Decomposition of the activated complex into two new entities in which the two oxygens considered have exchanged their nonbridging and bridging characters, the original sodium atom rebonding to the new nonbridging oxygen

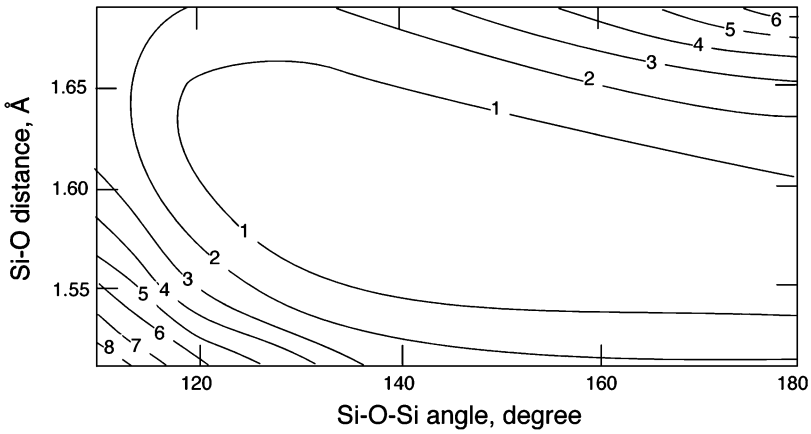

Silicate Melts, Fig. 3 Strongly contrasting energy changes induced by variations of Si–O distances and bending of Si–O–Si angles as indicated by the surface of constant energy of $H_6Si_2O_7$ clusters; 1 unit = 14 kJ/mol (Gibbs et al. 1981)

The Silica Paradox

The very strong increase of viscosity with SiO_2 content reflects the much greater strength of Si—O compared to other metal–oxygen bonds. But since fusion temperatures also increase with bond strengths, one would expect SiO_2 polymorphs to melt at much higher temperatures than minerals such as lime (CaO), periclase (MgO), or forsterite (Mg_2SiO_4). And since the most refractory crystals precipitate first upon fractional crystallization, magma differentiation should cause residual melts to become progressivly poorer in SiO_2. These two statements are, of course, blatantly contradicted by experience.

The paradox lies in the fact that bond strengths are usually considered within the framework of ionic forces, which are by definition nondirectional. Now, directionality is an inherent feature of Si—O bonding in view of its markedly covalent character. Because electron delocalization through polymerization and creation of Si—O—Si linkages is not large enough to constrain geometrically the arrangements of the SiO_4 tetrahedra, the same energy variations are, for instance, caused in $H_6Si_2O_7$ clusters by a 0.02 Å change of the Si—O bond length and by a 20° modification of the O—Si—O intertetrahedral angles (Fig. 3). Bending thus is so easy that configurational rearrangements take place without involving much energy, as most simply illustrated by the transitions of α-quartz or α-cristobalite (the high-temperature SO_2 polymorph), near 573 °C and 250 °C, respectively, to their dynamically disordered β-forms. Hence, fusion of such minerals does not require the breaking of bonds needed in ionic crystals. Magma differentiation thus is eventually a quantum-chemical effect mainly driven by the sp^3 hybridization of silicon orbitals (Richet and Ottonello 2014), which causes highly polymerized crystals to melt at temperatures much lower than would be expected from their Si—O or Al—O bond strengths. But much work, of course, remains to be done to account quantitatively for the petrogenetic series themselves in terms of such first-principles calculations.

Summary

Silicate melts owe their fundamental importance to a high atomic mobility prevailing in disordered structures. Whereas the former factor makes viscous flow possible, the latter causes buoyancy with respect to surrounding rocks and make continuous adjustments of the structure and physical properties in response to pressure, temperature, and composition changes.

Cross-References

- ▶ Fractional Crystallization and Assimilation
- ▶ Geochemical Thermodynamics
- ▶ Magmatic Process Modeling
- ▶ Mineralogy
- ▶ Partial Melting
- ▶ Silicate Minerals
- ▶ Subduction Zone Geochemistry
- ▶ Volcanism

References

de Dolomieu D (1797) Rapport fait par le citoyen Dolomieu, Ingénieur des Mines, sur ses voyages de l'an V et de l'an VI. J Mines 7:385–402

Farnan I, Stebbins JF (1994) The nature of the glass transition in a silica-rich oxide melt. Science 265:1206–1209

Ghiorso MS (2004) An equation of state for silicate melts. I. Formulation of a general model. Amer J Sci 304:637–678

Gibbs GV, Meagher EP, Newton MD, Swanson DK (1981) A comparison of experimental and theoretical bond length and angle variations for minerals and inorganic solids, and molecules. In: O'Keefe M, Navrotsky A (eds) Structure and bonding in crystals. Academic, New York, pp 195–225

Mysen BO, Richet P (2005) Silicate glasses and melts: properties and structure. Elsevier, Amsterdam

Richet P (2009) Residual and configurational entropy: quantitative checks through applications of Adam-Gibbs theory to the viscosity of silicate melts. J Non-Cryst Solids 355:628–635

Richet P, Ottonello G (2014) The earth as a multiscale quantum-mechanical system. Géosciences 346:317–325

Silicate Minerals

Ritsuro Miyawaki
Department of Geology, National Museum of Nature and Science, Tokyo, Japan

Definition

A silicate mineral is a salt of silicate anions and cations formed by geological processes. Silica minerals [SiO_2], such as quartz, cristobalite, and tridymite, and the hydrous phases [$SiO_2 \bullet nH_2O$], opal and mogánite, are often grouped with the silicate minerals. A silicate anion is an oxo acid of silicon, and commonly consists of one centered Si and four O atoms forming a SiO_4 tetrahedron, or rarely of one centered Si with six O atoms forming a SiO_6 octahedron.

Classification

Tetrahedral $(SiO_4)^{4-}$ anions are isolated in the crystal structures of nesosilicates. Forsterite [Mg_2SiO_4] of the olivine group and almandine [$Fe^{2+}{}_3Al_2(SiO_4)_3$] of the garnet super group are typical examples of nesosilicate. In the other silicates, tetrahedral $(SiO_4)^{4-}$ anions are polymerized by means of sharing the apical oxygen atom(s) to form dimers, trimers, or polymers. Solosilicates consist of the dimer $(Si_2O_7)^{6-}$ and/or trimer $(Si_3O_{10})^{8-}$, e. g., epidote [$Ca_2Fe^{3+}Al_2(Si_2O_7)(SiO_4)O(OH)$] of the epidote super group and thalénite-(Y) [$Y_3Si_3O_{10}F$]. Cyclosilicates have three- four- six- or rarely eight- or 12-membered rings of SiO_4 tetrahedra as the structural pieces. Benitoite [$BaTiSi_3O_9$] and nagashimalite [$Ba_4(V^{3+},Ti)_4(O,OH)_2[(B_2O_3)(Si_2O_{12})_2]Cl$] are examples for cyclosilicates with three- and four-membered rings, respectively. The six-membered rings are in the crystal structures of schorl [$NaFe^{2+}_3Al_6(Si_6O_{18})(BO_3)_3(OH)_4$] (Fig. 1) of the tourmaline super group and beryl [$Be_3Al_2Si_6O_{18}$]. Different type rings are sometimes combined in a crystal structure of cyclosilicate, such as hexagonal double rings, in other words, the combination of six- and four-membered rings, in osumilite [$KFe^{2+}_2Al_3(Al_2Si_{10})O_{30}$]. Inosilicates are characterized by the chain structures of silicate polymers. Single chains (pyroxenes such as augite [$(Ca,Mg,Fe)_2Si_2O_6$] (Fig. 2), and wollastonite[$CaSiO_3$]), double chains (amphiboles as actinolite [$Ca_2(Mg,Fe^{2+})_5Si_8O_{22}(OH)_2$], xonotlite [$Ca_6Si_6O_{17}(OH)_2$], and others), and triple chains (e.g., jimthompsonite[$Mg_5(Si_6O_{16})(OH)_2$]) have been known. A part of Si is sometimes replaced with Al (aluminosilicate). Micas, e.g., muscovite [$KAl_2(Si_3Al)O_{10}(OH)_2$], and most of clay minerals, e.g., serpentine group [$(Mg,Fe)_3Si_2O_5(OH)_4$)], are phyllosilicates. They are characterized by the layered structures of combined octahedral and tetrahedral sheets in a ratio of 1:1 or 2:1, and, sometimes, interlayer ions and molecules. The feature on configuration of SiO_4 tetrahedra, which share the individual three of four apical oxygen atoms with neighboring three SiO_4 tetrahedra, is hexagonal in the network. The centered Si is often replaced with Al and/or, rarely, with Fe. In the crystal structures of tectosilicate, the SiO_4 tetrahedra share all four apical O atoms to build up a three-dimensional framework. Quartz [SiO_2] is one of the typical

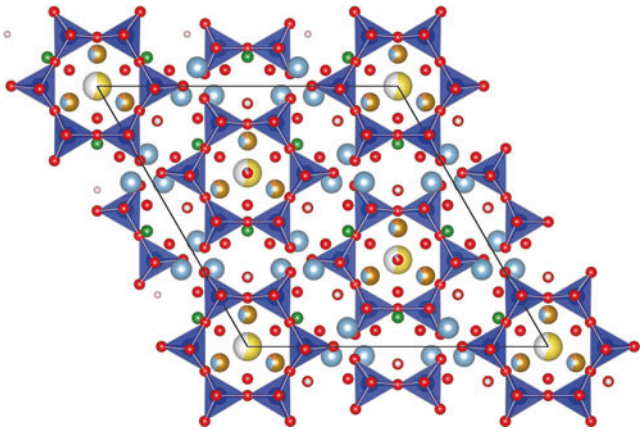

Silicate Minerals, Fig. 1 A VESTA illustration of the six-membered rings of Q^2 SiO_4 tetrahedra (*blue* in color) in schorl. The structure data are from AMCSD

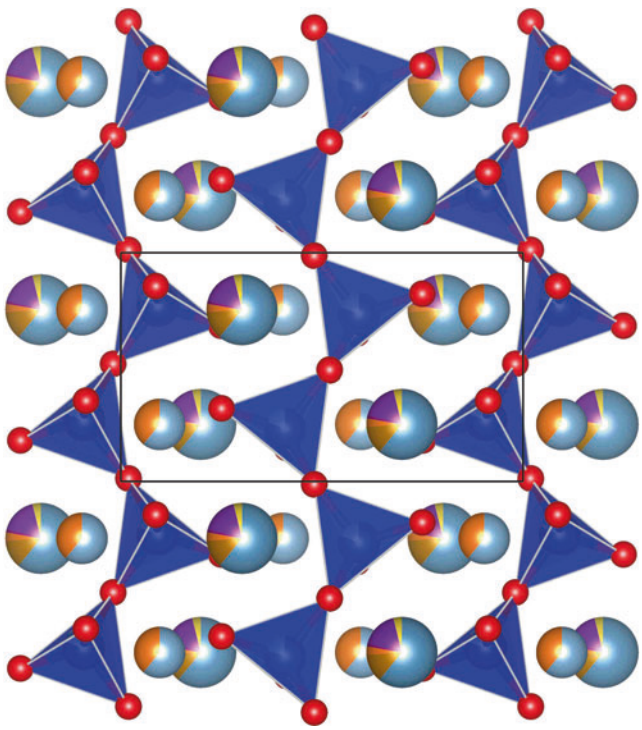

Silicate Minerals, Fig. 2 A VESTA illustration of the single chains of Q^2 SiO_4 tetrahedra (*blue* in color) in augite. The structure data are from AMCSD

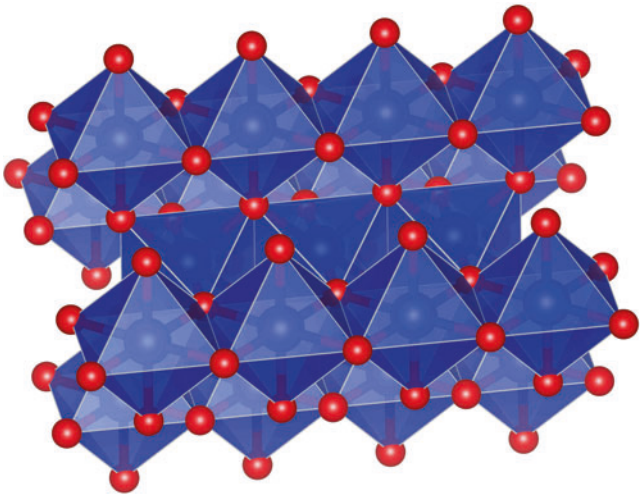

Silicate Minerals, Fig. 3 A VESTA illustration of the edge-sharing columns of SiO_6 octahedra (*blue* in color) in stishovite. The columns are connected with the others by the corner-sharing linkages. The structure data are from AMCSD

tectosilicates. Lots of aluminosilicates, e.g., microcline [$KAlSi_3O_8$] in feldspar family, nepheline[$NaAlSiO_4$] in feldspathoid family, and analcime[$NaAlSi_2O_6 \cdot H_2O$] in zeolite family, are included in this subclass.

Atomic Coordination

Octahedral SiO_6 can be observed in the crystal structures of some high-pressure phases, e.g., stishovite [SiO_2] (Fig. 3), bridgmanite [$MgSiO_3$] having the perovskite structure, and majorite [$Mg_3(MgSi)(SiO_4)_3$], a member of garnet super group consisting of SiO_6 octahedron and SiO_4 tetrahedron. These silicate minerals crystalized in the lower mantle of the Earth, or by shock during meteorite impacts. Thaumasite [$Ca_3Si(OH)_6(SO_4)(CO_3) \cdot 12H_2O$] is an unique mineral of alterations products having octahedral $Si(OH)_6$ in the crystal structure.

The coordination of O atoms around a Si in a silicate can be examined by the high resolution nuclear magnetic resonance (NMR) spectroscopy for ^{29}Si, in addition to the crystallographic data based on diffraction of X-ray and/or neutrons. The ^{29}Si-NMR spectra show a correlation between chemical shift and polymerization, Q^n notation presenting the number of bridging O atoms per a Si atom in a SiO_4 tetrahedron: Q^0 (monosilicate), Q^1 (disilicate or chain end), Q^2 (middle in a chain), Q^3 (chain branching site or middle in tetrahedral sheet), and Q^4 (sharing all O atoms in three-dimensional cross-linked framework).

Chemical and Physical Properties

Silicates are weakly soluble in pure water or acidic solutions, except for hydrofluoric acid (HF) solution, under the ambient temperature and pressure. However, groundwater and seawater contain small but measurable amounts (ppm order) of solute orthosilicate ion $(SiO_4)^{4-}$ to form extremely weak silicic acid (H_4SiO_4, in other formula, $Si(OH)_4$). High pH basic aqueous solutions (e.g., NaOH solution) and alkaline fusions (e.g., Na_2CO_3 melt) can dissolve silicate minerals. Silicates are remarkably soluble in hydrothermal waters, especially supercritical ones.

Some silicate minerals crystallize from melts, but the others from solutions such as hydrothermal solutions and hot spring water. Some are secondary minerals or weathering products after rock-forming minerals. Quartz in chert and amorphous silica in diatomite are major examples of biogenic silicates.

Most of silicate minerals have a vitreous luster. Their hardness varies over a wide range in Mohs scale; from 1 [talk: $Mg_3Si_4O_{10}(OH)_2$] to 8 [topaz: $Al_2SiO_4F_2$].

Summary

Silicate minerals constitute the majority of Earth's crust and mantle. Approximate 1500 species of silicate minerals have been described among ca 5000 mineral species approved by the Commission of New Minerals, Nomenclature, and Classification of the International Mineralogical Association (CNMNC-IMA).

References

American Mineralogist Crystal Structure Database (AMCSD). http://rruff.geo.arizona.edu/AMS/amcsd.php

Commission on New Minerals Nomenclature and Classification, International Mineralogical Association (CNMNC-IMA). http://www.ima-mineralogy.org/CNMNC_Strategy.htm

Visualization for Electronic and Structural Analysis (VESTA). http://jp-minerals.org/vesta/en/

S

Silicon

Monica Vasiliu and David A. Dixon
Department of Chemistry, University of Alabama, Tuscaloosa, AL, USA

Element Data
Atomic Symbol: Si
Atomic Number: 14
Atomic Weight: 28.0855

(*continued*)

Isotopes and Abundances: ^{28}Si 92.23%, ^{29}Si 4.67%, ^{30}Si 3.10%
1 Atm Melting Point: 1683 K
1 Atm Boiling Point: 3538 K
Common Valences: +4, −4
Ionic Radii: (+IV) 26 ppm, (−IV) 271 ppm
Pauling Electronegativity: 1.90
First Ionization Energy: 786.5 kJ/mol
Chondritic (CI) Abundance: 10.64%
Silicate Earth Abundance: 21%
Crustal Abundance: 27.7%
Seawater Abundance: 0.0001% (30 ppb at the surface, 2 ppm in the deeper layers
Core Abundance: 6%

Properties

Silicon (Emsley 1991, 2001; Anthoni 2006; Anders and Grevesse 1989; McDonough 2005), classified as a member of metalloids, is the eighth most abundant element in the universe and the second most abundant in the Earth's crust after oxygen. Silicon rarely occurs as the pure free element on Earth's crust, but it is found as oxides (silica) and as silicates. The oxides include sand, quartz, rock crystal, amethyst, agate, flint, and opal. The silicate form includes asbestos, granite, hornblende, feldspar, clay, and mica.

Silicon is a solid at room temperature and has a greater density in the liquid state than in the solid state, and, similar to water, it expands when it freezes. Silicon is a good heat conductor. In its crystalline form, pure silicon is strong, very brittle, and prone to chipping and has a gray color and metallic luster. Silicon is a semiconductor in its pure form with semiconductivity increasing by introducing small amounts of impurity. Silicon is similar to metals in its chemical behavior.

History and Use

Silicon, as silica (SiO_2) in the form of sharp flints, was among the first tools made by humans. Ancient civilizations used other forms of silica such as rock crystal and knew how to turn sand into glass. Considering silicon's abundance, it is somewhat surprising that it received very little attention from early chemists. Even though a number of chemists were close to isolating silicon, the credit for its discovery goes to the Swedish chemist Jöns Jacob Berzelius who, in 1824, obtained silicon by heating potassium fluorosilicate with potassium. The product was contaminated with potassium silicide, but he removed this by stirring it with water, with which it reacts, and thereby obtained relatively pure silicon powder which is a noncrystalline form (amorphous silicon). Berzelius called this new element silicium, but in 1831 T. Thomson named it silicon because of its nonmetallic character. Crystalline silicon, the other form of silicon, was actually discovered years later, by mistake, in 1854, by Henri Deville.

Elemental silicon is produced commercially by reducing sand with carbon in an electric furnace. High-purity silicon, for the electronics industry, is prepared by the thermal decomposition of ultrapure trichlorosilane, followed by recrystallization. These crystals can be doped with boron, gallium, germanium, phosphorus, or arsenic and are used in the manufacture of solid-state electronic devices, such as transistors, solar cells, rectifiers, and microchips. Silicon is the basis of the semiconductor industry, and silicon-based chips have been following Moore's Law for almost 50 years. Silicon dioxide (SiO_2) is the most common compound containing silicon and mostly takes the form of ordinary sand, but also exists as quartz, rock crystal, amethyst, agate, flint, jasper, and opal. Silicon is extensively used in the manufacture of glass and bricks. Silica gel, a colloidal form of silicon dioxide, easily absorbs moisture and is used as a desiccant.

Silicon forms other useful compounds: silicon carbide (SiC) is nearly as hard as diamond and is used as an abrasive; sodium silicate (Na_2SiO_3), also known as water glass, is used in the production of soaps, adhesives, and as an egg preservative; and silicon tetrachloride ($SiCl_4$) is used to create smoke screens. Silicon is also an important ingredient in silicone, a class of material that is used as lubricants, polishing agents, electrical insulators, and medical implants.

Geochemical Behavior

Silicon dioxide is found in all three types of rocks. Silicates weather leading to dissolution and erosion when exposed at the surface of the continents to water and wind. Besides bicarbonate, dissolved silica (undissociated silicic acid $Si(OH)_4$) represents a dominant species in river water at higher concentration than in seawater. The suspended silicates are only slightly affected during their transport by rivers. On a geological time scale, the input of dissolved silica by rivers to the sea must be compensated by a removal process which is only possible in the sediments. The silica cycle is closely tied to the carbon and sulfur cycle due to metamorphic processes. Of particular importance is the reaction between carbonates and silicates. Accumulation of silicates at geological time scales leads to an increase of CO_2 levels in the atmosphere, and the reverse occurs when there is preferential accumulation of carbonates in the sediments.

Biological Utilization and Toxicity

Silicon is not in particular toxic, but fine particles of silicates or silica (e.g., asbestos) can cause damage to lungs, silicosis, and different health agencies have different legal limits. People are exposed to silicon by breathing it in, swallowing it, skin contact, and eye contact. Silicon supplements are used as medicine. Silicon in various forms is used to treat weak bones (osteoporosis), heart disease and stroke (cardiovascular disease), Alzheimer's disease, hair loss, for improving hair and nail quality, improving skin healing, treating sprains and strains, and digestive system disorders. Silicone (a group of materials resembling plastic that contain silicon, oxygen, and other chemicals) is used to make breast implants, medical tubing, and a variety of other medical devices. There is some evidence that silicon might have a role in bone and collagen formation, but the clear biological role of silicon in humans is not really known.

References

Day JMD, Brandon AD, Walker RJ (2015) Highly siderophile elements in Earth, Mars, the Moon, and Asteroids. Rev Mineral Geochem 81, 78 pp. https://doi.org/10.2138/rmg.2014.81.04

Harvey J, Day JMD (2016) Introduction to highly siderophile and strongly chalcophile elements in high temperature geochemistry and cosmochemistry. Rev Mineral Geochem 81(1):3–4

Lodders K (2003) Solar system abundances and condensation temperatures of the elements. Astrophys J 591:1220–1247

McDonough WF, Sun S-S (1995) The composition of the earth. Chem Geol 120:223–253

Shirey SB, Walker RJ (1998) The Re-Os isotope system in cosmochemistry and high-temperature geochemistry. Annu Rev Earth Planet Sci 26:423–500

Silicon Isotopes

Anat Shahar
Geophysical Laboratory, Carnegie Institution for Science, Washington, DC, USA

Definition

Silicon, atomic number 14, has 24 known isotopes with mass numbers ranging from 22 to 45. Silicon has three stable isotopes: ^{28}Si with 92.23% abundance, ^{29}Si with 4.67% abundance, and ^{30}Si with 3.1% abundance.

Introduction

As the second most abundant element on Earth, silicon has been used to trace processes from as far back as 4.5 billion years ago to today. The added benefit of having three stable isotopes (^{28}Si, ^{29}Si, and ^{30}Si) that can be used to further our understanding of the silicon cycle and processes occurring on Earth and in the solar system makes silicon an increasingly powerful tool for geochemistry. Since the 1950s there have been studies aimed at analyzing silicon isotope ratios, mostly in low-temperature environments, using gas source mass spectrometry. In the early 2000s, the development and application of multiple collector inductively coupled plasma mass spectrometry was applied to Si isotopes, and the field of high-temperature silicon isotope geochemistry flourished. In this entry we focus on what has been learned from silicon isotope geochemistry to date. All isotope values are written in traditional delta notation as defined below:

$$\delta^{30/28}\mathrm{Si} = \left(\frac{\left(^{30/28}\mathrm{Si}_{\mathrm{sample}}\right)}{\left(^{30/28}\mathrm{Si}_{\mathrm{standard}}\right)} - 1 \right) * 1000 \qquad (1)$$

Low Temperature

Silicon isotopes have been used extensively to study continental weathering, oceanic primary production, and as a tool for understanding the silicon cycle today and throughout Earth's history. The silica sources to the oceans include hydrothermal fluids, seafloor (basalt) weathering, and aerosol deposition, but are dominated by riverine input, derived from weathering of the continents (e.g., Georg et al. 2009; Treguer and De La Rocha 2013). Diatoms and other silica-secreting organisms require the dissolved silicic acid (H_4SiO_4) for growth and provide the major sink for the dissolved silica in the modern ocean. These organisms and their predecessors have played a dominant role in the marine silica cycle through geologic time. Silicon isotopes have been shown to fractionate during the utilization of silicic acid by diatoms (e.g., De La Rocha et al. 1997; Hendry and Brzezinski 2014) and during continental weathering, whereby the seawater is left enriched in the heavy isotopes. The δ^{30}Si of modern seawater is ~1.1 ‰ (De La Rocha et al. 2000) which is more enriched than both the continental and hydrothermal inputs due to the light isotopes partitioning into the organisms in the ocean. The Si isotope fractionation ranges from −1.1 ‰ for diatoms to −3.5 ‰ for marine sponges (De La Rocha et al. 1997; De La Rocha 2003; Hendry and Robinson 2012). Using the δ^{30}Si of diatom silica from sediments can trace the percent removal of the nutrient dissolved silicon from surface waters in the past.

In terms of continental weathering, Georg et al. 2006 show that in order to understand the δ^{30}Si of river waters, the important parameters are the discharge of the rivers, the resulting weathering fluxes, and the concentration of dissolved silicon. Less is known about the effect of hydrothermal alteration on Si isotopes (e.g., Frings et al. 2016). On the other hand, clays, which are the products of chemically

weathered silicates, are on average lighter than igneous rocks and about 0.4 ‰ lighter than coexisting feldspars and 0.6 ‰ lighter than groundwater (Georg et al. 2009). This implies that the heavier isotopes are enriched in the fluid, which has a weaker bonding environment, antithetical to equilibrium isotope geochemistry theory.

Another fascinating use of silicon isotopes is understanding cherts (deposits of amorphous silica) which can document the evolution of the silica cycle through time and possibly be used as a paleothermometer of the ocean. Chert formation (by evaporation) also leads to an enrichment of silicon isotopes in seawater and can provide crucial insights into the sources and sinks of marine silica before the evolution of the silica-secreting organisms such as sponges and diatoms. Robert and Chaussidon (2006) reported the use of combined O and Si isotope data to argue that past seawater temperatures were close to 70 °C. It is important to note however that chert precipitation can be complicated and one needs to know the source of silica, the mechanisms of silica precipitation, and the depositional setting in order to interpret the analyses (e.g., Oelze et al. 2014). But as more models and laboratory experiments become available, the possibility exists to use these isotope ratios as a paleothermometer and as a tool for reconstructing the silicon cycle through time. Further, more laboratory measurements and geochemical markers can be used to constrain a possible paleo-proxy. A recent study (Delvigne et al. 2016) looked at combining the Si isotope record with Ge/Si ratios in order to constrain desilication in the Archean. For a more in-depth review of low-temperature Si isotope fractionation, see the review of Frings et al. 2016.

High Temperature

Early (gas source) measurements of the Si isotope compositions of high-temperature materials such as meteorites and terrestrial igneous rocks (Douthitt 1982; Molini-Velsko et al. 1986; Ding et al. 1996) found no resolvable fractionation among different reservoirs. Following the application of MC-ICPMS and HF-free sample preparation techniques (Georg et al. 2006), accurate Si isotope measurement of all types of planetary material is now reliably attainable, and small but important isotope variations have been reported.

With the intention of learning about the building blocks of the terrestrial planets, much work has gone into constraining the silicon isotope composition of chondritic meteorites. The average compositions of ordinary and carbonaceous chondrites are indistinguishable and are used as a chondritic reference frame, estimated to be $\delta^{30}Si_{chondrite} = -0.46 \pm 0.09$ ‰ (2sd) by Savage et al. (2014). On the other hand, enstatite chondrites have a distinctly light Si isotope composition which has been explained as being due to either lithophile element fractionation in the solar nebula (Fitoussi and Bourdon 2012) or inclusion of isotopically light Si in the metal phase during condensation (Savage and Moynier 2013). The bulk silicate Earth (BSE) has a $\delta^{30}Si_{BSE} = -0.29 \pm 0.07$ ‰ (2sd) which is significantly heavier than the chondritic value (Fitoussi et al. 2009; Savage et al. 2010; Armytage et al. 2011; Zambardi et al. 2013). This difference was interpreted to reflect that isotopically light Si entered the core during the Earth's differentiation. Georg et al. (2007) used first-principles calculations to test whether there would be a silicon isotope fractionation between metal and silicate and found that even at high temperature (2000 K), the silicate is enriched in the heavier Si isotopes on the order of $\Delta^{30}Si_{silicate\text{-}metal}$ ($\delta^{30}Si_{silicate} - \delta^{30}Si_{metal}$) ≈ 1.5 – 1.7 ‰.

Shahar et al. (2009, 2011) then experimentally constrained the metal-silicate Si isotope partitioning, using piston-cylinder and multi-anvil setups, the latter allowing pressures up to 7 GPa and temperatures up to 2200 °C. As with the ab initio calculations of Georg et al. (2007), the experiments consistently found the silicate enriched in the heavier isotopes and more specifically found the following temperature dependence:

$$\Delta^{30}Si_{silicate-metal} = \frac{7.45(\pm 0.41) \times 10^6}{T^2} \quad (2)$$

However, a more recent experimental study by Hin et al. (2014) investigated $\Delta^{30}Si_{silicate\text{-}metal}$ between basalt and metal and found ~40% lower degrees of isotope fractionation at a given temperature compared to the work of Georg et al. (2007), Shahar et al. (2009, 2011), and Ziegler et al. (2010) but in the same direction. It is unclear why the results differ but the composition of the experiments was quite different (Young et al. 2015).

Analyses of meteorites from Mars, Vesta, the Moon, and aubrite and angrite achondrites have all helped in our understanding of how these planetary bodies formed. For example, samples from Mars show no resolvable variation between the different meteorite groups: $\delta^{30}Si_{Shergottite} = -0.47 \pm 0.06$, $\delta^{30}Si_{Nahklite} = -0.51 \pm 0.04$, and $\delta^{30}Si_{Chassigny} = -0.47 \pm 0.06$, with an overall average of $\delta^{30}Si_{MARS} = -0.48 \pm 0.06$ (Armytage et al. 2011; Pringle et al. 2013; Zambardi et al. 2013). This value is identical to ordinary and carbonaceous chondrites suggesting that no processes have altered the silicon isotope composition of bulk Mars since its formation. On the other hand, basaltic samples from the moon show an identical value to the Earth's mantle (Armytage et al. 2012; Fitoussi and Bourdon 2012; Zambardi et al. 2013; Poitrasson and Zambardi 2015) adding further evidence that the Moon is genetically linked to the Earth.

Arguably, the most interesting meteorites analyzed to date are the angrites, an oxidized basaltic achondritic meteorite group. Two groups (Pringle et al. 2014; Dauphas et al. 2015) have measured these samples and found that the angrite

parent body mantle had a composition of $\sim -0.21 \pm 0.03$ (2sd) which is significantly heavier than all the achondrites measured and very similar to the bulk silicate Earth's value. However, unlike the Earth these meteorites are too oxidized for enough silicon to partition into their parent body's core, and thus this cannot be the explanation for the value. Therefore, new mechanisms are needed in order to explain these data. Pringle et al. (2014) suggested that the Si isotope composition of the angrites is related to volatile depletion on the parent body, whereby there is preferential loss of isotopically light Si due to impact-related kinetic isotope fractionation. However, Dauphas et al. (2015) argue that the heavy Si isotope composition of angrites is not due to planetary processes, but instead is inherited from nebula fractionation of Si isotopes (similar to the theory of Fitoussi and Bourdon 2012). These are very different hypotheses with very different ramifications; however, as is the case with high-temperature stable isotope ratios, there are many physical and chemical ways to achieve such small deviations. For a more in-depth look at high-temperature silicon isotope, see Savage et al. 2014 and Shahar et al. 2016.

Summary

In sum, while silicon isotopes have been studied for decades, there is a lot more potential in using silicon isotopes as tracers for both high- and low-temperature environments due to recent technological advances. This will be a fascinating area of research to follow.

Cross-References

- ▶ Chemical Weathering
- ▶ Chondrites
- ▶ Clay Minerals
- ▶ Earth's Core
- ▶ Germanium
- ▶ Meteorites
- ▶ Silicon
- ▶ Stable Isotope Geochemistry

References

Armytage RMG, Georg RB, Savage PS, Williams HM, Halliday AN (2011) Silicon isotopes in meteorites and planetary core formation. Geochim Cosmochim Acta 75:3662–3676

Armytage RMG, Georg RB, Williams HM, Halliday AN (2012) Silicon isotopes in lunar rocks: implications for the Moon's formation and the early history of the Earth. Geochim Cosmochim Acta 77:504–514

Dauphas N, Poitrasson F, Burkhardt C, Kobayashi H, Kurosawa K (2015) Planetary and meteoritic Mg/Si and d30Si variations inherited from solar nebula chemistry. Earth Planet Sci Lett 472:236–248

De La Rocha CL (2003) Silicon isotope fractionation by marine sponges and the reconstruction of the silicon isotope composition of ancient deep water. Geology 31:423–426

De La Rocha CL, Brzezinski MA, DeNiro MJ (1997) Fractionation of silicon isotopes by marine diatoms during biogenic silica formation. Geochim Cosmochim Acta 61:5051–5056

De La Rocha CL, Brzezinski MA, DeNiro MJ (2000) A first look at the distribution of the stable isotopes of silicon in natural waters. Geochim Cosmochim Acta 64:2467–2477

Delvigne C, Opfergelt S, Cardinal D, Hoffman A, Andre L (2016) Desilication in Archean weathering processes traced by silicon isotopes and Ge/Si ratios. Chem Geol 420:139–147

Ding T, Jiang S, Wan D, Li Y, Li J, Song H, Liu Z, Yao X (1996) Silicon isotope geochemistry. Geological Publishing House, Beijing

Douthitt C (1982) The geochemistry of the stable isotopes of silicon. Geochim Cosmochim Acta 46:1449–1458

Fitoussi C, Bourdon B (2012) Silicon isotope evidence against an Enstatite Chondrite Earth. Science 335:1477–1480

Fitoussi C, Bourdon B, Kleine T, Oberli F, Reynolds BC (2009) Si isotope systematics of meteorites and terrestrial peridotites: implications for Mg/Si fractionation in the solar nebula and for Si in the Earth's core. Earth Planet Sci Lett 287:77–85

Frings PJ, Clymans W, Fontorbe G, De La Rocha CL, Conley DJ (2016) The continental Si cycle and its impact on the ocean Si isotope budget. Chem Geol 425:12–36

Georg RB, Reynolds BC, Frank M, Halliday AN (2006) Mechanisms controlling the silicon isotopic compositions of river waters. Earth Planet Sci Lett 249:290–306

Georg RB, Halliday AN, Schauble EA, Reynolds BC (2007) Silicon in the Earth's core. Science 447:1102–1006

Georg RB, West AJ, Basu AR, Halliday AN (2009) Silicon fluxes and isotope composition of direct groundwater discharge into the Bay of Bengal and the effect on the global ocean silicon isotope budget. Earth Planet Sci Lett 283:67–74

Hendry KR, Brzezinski MA (2014) Using silicon isotopes to understand the role of the Southern Ocean in modern and ancient biogeochemistry and climate. Quat Sci Rev 89:13–26

Hendry KR, Robinson LF (2012) The relationship between silicon isotope fractionation in sponges and silicic acid concentration: modern and core-top studies of biogenic opal. Geochim Cosmochim Acta 81:1–12

Hin RC, Fitoussi C, Schmidt MW, Bourdon B (2014) Experimental determination of the Si isotope fractionation factor between liquid metal and liquid silicate. Earth Planet Sci Lett 387:55–66

Molini-Velsko C, Mayeda TK, Clayton RN (1986) Isotopic composition of silicon in meteorites. Geochim Cosmochim Acta 50:2719–2726

Oelze M, von Blanckenburg F, Hoellen D, Dietzel M, Bouchez J (2014) Si stable isotope fractionation during adsorption and the competition between kinetic and equilibrium isotope fractionation: implications for weathering systems. Chem Geol 380:161–171

Poitrasson F, Zambardi T (2015) An Earth–Moon silicon isotope model to track silicic magma origins. Geochim Cosmochim Acta 167:301–312

Pringle EA, Savage PS, Badro J, Barrat J-A, Moynier F (2013) Redox state during core formation on asteroid 4-Vesta. Earth Planet Sci Lett 373:75–82

Pringle EA, Moynier F, Savage PS, Badro J, Barrat J-A (2014) Silicon isotopes in angrites and volatile loss in planetesimals. Proc Natl Acad Sci U S A 111:17029–17032

Robert F, Chaussidon M (2006) A palaeotemperature curve for the Precambrian oceans based on silicon isotopes in cherts. Nature 443:969–972

Savage PS, Moynier F (2013) Si isotopic variations in enstatite meteorites: clues to their origin. Earth Planet Sci Lett 361:487–496

Savage PS, Georg RB, Armytage RMG, Williams HM, Halliday AN (2010) Silicon isotope homogeneity in the mantle. Earth Planet Sci Lett 295:139–146
Savage PS, Armytage RMG, Georg RB, Halliday AN (2014) High temperature silicon isotope geochemistry. Lithos 190–191:500–519
Shahar A, Ziegler K, Young ED, Ricolleau A, Schauble EA, Fei Y (2009) Experimentally determined Si isotope fractionation between silicate and metal and implications for Earth's core formation. Earth Planet Sci Lett 288:228–234
Shahar A, Hillgren VJ, Young ED, Fei Y, Macris CA, Deng L (2011) High-temperature Si isotope fractionation between iron metal and silicate. Geochim Cosmochim Acta 75:7688–7697
Shahar A, Savage P, Moynier F (2016) Stable isotope evidence for the differentiation of planetesimals. Submitted for Cambridge University Press Volume on Planetesimals
Treguer P, De La Rocha CL (2013) The World Ocean silica cycle. Annu Rev Mar Sci 5:477–501
Young ED, Manning CE, Schauble EA, Shahar A, Macris CA, Lazar C, Jordan M (2015) High-temperature equilibrium isotope fractionation of non-traditional stable isotopes: experiments, theory, and applications. Chem Geol 395:176–195
Zambardi T, Poitrasson F, Corgne A, Méheut M, Quitté G, Anand M (2013) Silicon isotope variations in the inner solar system: implications for planetary formation, differentiation and composition. Geochim Cosmochim Acta 121:67–83
Ziegler K, Young ED, Schauble EA, Wasson JT (2010) Metal–silicate silicon isotope fractionation in enstatite meteorites and constraints on Earth's core formation. Earth Planet Sci Lett 295:487–496

Silver

Helen Mango
Department of Natural Sciences, Castleton University, Castleton, VT, USA

Element Data
Atomic Symbol: **Ag**
Atomic Number: **47**
Atomic Weight: 107.8682 g/mol
Isotopes and Abundances: ^{107}Ag 51.839%, ^{109}Ag 48.161%
1 Atm Melting Point: 961.8 °C
1 Atm Boiling Point: 2162 °C
Common Valences: 2+, **1**+, 0
Ionic Radii: 129 pm (1+); 108 pm (2+)
Pauling Electronegativity: 1.93
First Ionization Energy: 731.0 kJ/mol
Chondritic (CI) Abundance: 0.201 ppm
Silicate Earth Abundance: ~0.05 ppm
Crustal Abundance: ~0.056 ppm
Seawater Abundance: <0.003 ppm
Core Abundance: ~0.15 ppm

Properties

Silver (symbol Ag) has atomic number 47 and atomic mass 107.8682 ± 2 (Haynes et al. 2014). Silver has two naturally occurring isotopes: ^{107}Ag and ^{109}Ag, with abundances of 51.839% and 48.161%, respectively (IUPAC 2015). The metallic radius of the silver atom is 144 pm (Greenwood and Earnshaw 1997). Because its outer electron configuration is $5s^1 4d^{10}$, the univalent ion (Ag^+, ionic radius = 129 pm) is more common than the divalent ion (Ag^{2+}, ionic radius 108 pm) (Shannon 1976). Pure silver has a specific gravity of 10.50 (20 °C) and a hardness of 2.5–3, with a melting point of 961.78 °C (1 atm) and a boiling point of 2162 °C (1 atm); it has a brilliant white metallic luster, a cubic crystal structure, is very ductile and malleable, has a heat capacity of 0.235 J/gK, and the highest electrical and thermal conductivities and lowest contact resistance of all the metals (Haynes et al. 2014).

History and Use

Silver has been known since ancient times. For thousands of years it has been used for jewelry, utensils, and coinage. It is currently also used in photography and the production of mirrors, solders, brazing alloys, bearings, electrical contacts, photovoltaics, dental alloys, high-capacity Ag-Zn and Ag-Cd batteries, and printed circuits (Goonan 2014; Haynes et al. 2014; USGS 2015). Photography is the largest end use, accounting for 30% of silver consumption in the United States; the increase in digital photography is reducing the use of silver in this application but has increased it in medical and industrial X-rays (Goonan 2014; Haynes et al. 2014) and as a metal ink for printing semiconductors (Yung et al. 2014). Silver is used as a catalyst in oxidation reactions, such as in the production of formaldehyde and ethylene oxide (Goonan 2014; USGS 2015). Silver iodide is used for seeding clouds (Haynes, 2014). Nanosilver has germicidal properties and is used for purifying water, sterilizing equipment, and for treating wounds (Goonan 2014).

Abundance

Table 1 gives the abundances of silver in different geologic materials.

Geochemical Behavior

Silver is found in the native state and in combination with other elements, primarily S, Sb, Se, Pb, As, Bi, Cu, and Au. It is strongly chalcophile in geologic processes, although in

Silver, Table 1 Silver abundances in geologic materials

Material	Average abundance/range
Iron meteorites	20 ppb
Chondrites	200 ppb
Lunar rocks	10 ppb
Average Earth	50 ppb
Continental crust	80 ppb
Upper crust	53 ppb
Middle crust	48 ppb
Lower crust	65 ppb
Mantle	6 ppb
Ultramafic igneous rocks	50 ppb
Mafic igneous rocks	100 ppb
Intermediate igneous rocks	70 ppb
Felsic igneous rocks	50 ppb
Metamorphic rocks	10^2–10^3 ppb
Carbonates	100–170 ppb
Sandstones	200–250 ppb
Evaporites	<100 ppb
Phosphoric/black shales	10^2–10^3 ppb
Manganese nodules	3 ppm
Abyssal clays	10 ppb
Coal/peat	<10 ppm
Petroleum	10 ppm
Soils	0.01–5 ppm
Fresh water	0.2–0.3 ppb
Ocean water	<3 ppb
Metalliferous brines	<2 ppm
Geothermal fluids	10^1–10^3 ppb
Fluid inclusions	10^1–10^3 ppm

Silver abundances in geologic materials. Data from Seward et al. (2014), Lodders (2010), Rudnick and Gao (2014), Palme and O'Neill (2014), McLean and Bledsoe (1992), Henderson (1986), Aubert and Pinta (1977), Parker (1967), McDonough (2014)

cosmochemical reactions it is moderately volatile and can exhibit both siderophile and chalcophile behavior (Woodland et al. 2005). Native silver is rarely pure; it is usually alloyed with measurable quantities of one or more of the following elements: Au, Hg, As, Sb, Bi, Te, Cu, Fe, Sn, Pb, Co, Ni, Pt, and Ir.

Silver's transport in hydrothermal solutions in ore-forming processes is greatly dependent on the presence of complexing ligands. Within the range of temperatures (<350 °C) and pH (acidic) of most hydrothermal systems, chlorosilver (I) complexes appear to be the most important transporters of silver. Figure 1 shows silver solubility in the presence of aqueous sulfur species. Silver deposition from soluble complexes can occur if pH rises or the oxidation potential of the system decreases. Although the complexes $AgCl^0$, $AgCl_2^-$, $AgCl_3^{2-}$, and $AgCl_4^{3-}$ and the silver ion Ag^+ may all exist in hydrothermal solutions, complexes of low coordination number are favored, especially $AgCl_2^-$ (Seward 1976). While fluid salinities tend to be less than 3 M in many hydrothermal systems, silver-rich magmatic brines may be responsible for high-grade ore formation (Wilkinson et al. 2013).

For the univalent silver ion in aqueous solution, at 25 °C and 1 atm, the Ag^+ ion is coordinated by four inner-sphere water ligands with an average Ag-O distance of 2.32 Å, while at 350 °C, the coordination number decreases to approximately 3, and the Ag-O bond decreases by about 0.10 Å (Seward et al. 1996). Silver is a type-B metal cation, and so has a great affinity for sulfur; Ag^+ forms strong bonds with organic ligands such as thiols and mercaptans, which allows for rapid exchange of Ag^+ onto and off the cells of organisms (Bell and Kramer, 1999).

The highest concentrations of silver in soils are found overlying Ag-bearing bedrock; the silver tends to occur in the surface A_0 horizon, suggesting that chelated complexes of humic material are important for binding silver (Levinson 1974). Soil pH appears to control the mobility of silver; Ag is more soluble in acidic conditions and fairly immobile in more alkaline conditions (pH > 4). Silver mobility is also controlled by the availability of ligands in the soil, such as SO_4^{2-}, NO_3^-, $S_2O_3^{2-}$, HCO_3^-, and organic acids (McLean and Bledsoe 1992).

Silver Minerals

Table 2 lists the most common silver-bearing minerals.

Ore Deposits

In 2014, the ten top producers of silver were Mexico, Peru, China, Australia, Chile, Bolivia, Russia, Poland, the United States, and Argentina (Silver Institute 2015). Ore deposits that are related to igneous activity account for 60% of all silver discovered, and of these, a significant amount of silver is found in clearly defined veins (Singer 1995).

Epithermal vein deposits account for approximately 17% of the silver mined in the world (Singer 1995) and have very high silver grades (500–2000 g/t Ag; Wilkinson et al. 2013). Deposits of this type are concentrated in convergent tectonic zones, associated with calc-alkaline to alkaline magmatism (Simmons et al. 2005). These deposits are mostly young (<65 million years) and shallow (<1.5 km) and are characterized by the presence of fractures, fissures, zones of leaching, and other open spaces in which ore precipitated from hydrothermal solutions (Kissin and Mango 2014). Epithermal deposits are divided into low-sulfidation (adularia-sericite) and high sulfidation (acid-sulfate) types (Heald et al. 1987). Low-sulfidation deposits are more silver-rich, with silver occurring in sulfides, sulfosalts, selenides, and tellurides, with associated electrum and base-metal sulfides such as galena, chalcopyrite, sphalerite, pyrite, stibnite, and cinnabar.

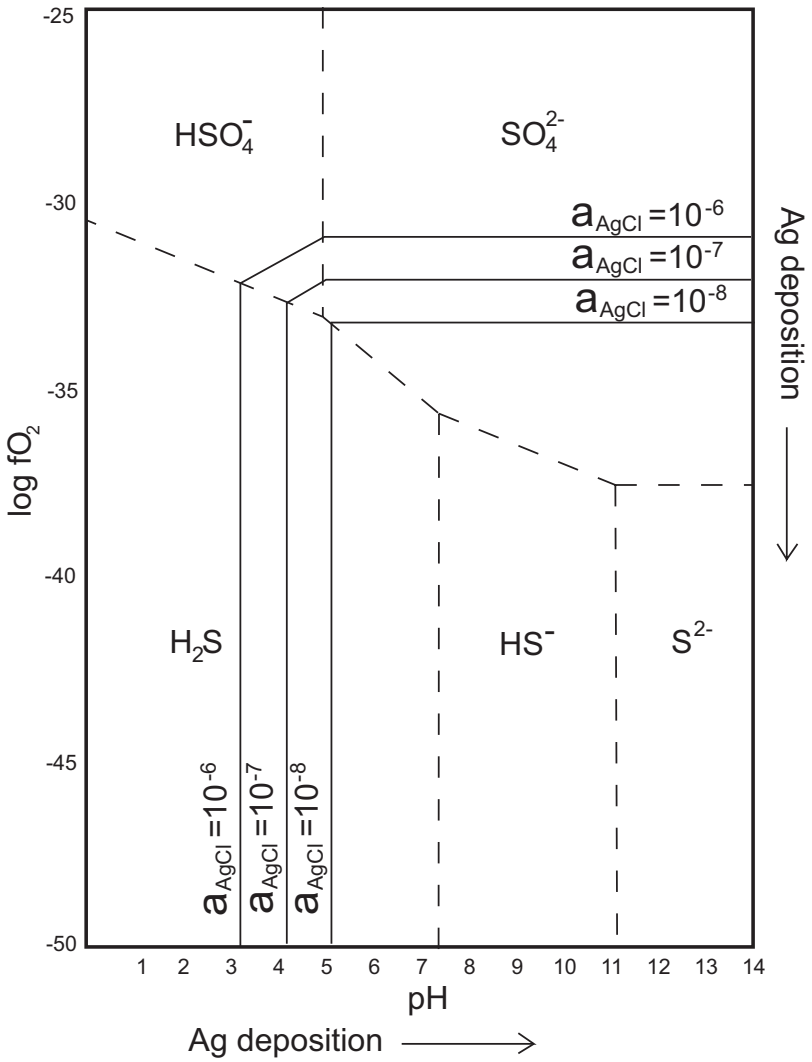

Silver, Fig. 1 pH-fO_2 diagram showing silver solubility (as activity of AgCl) superimposed on the stability fields of aqueous sulfur species (separated by *dashed lines*) at 250 °C and total sulfur activity of 10^{-1}. Silver solubility decreases as a function of increasing pH and/or decreasing oxygen fugacity (Modified from Mango et al. (2014))

Silver, Table 2 Names, mineral families, and chemical formulae of the most common Ag-bearing minerals (Carmichael, 1989)

Mineral name	Mineral family	Chemical formula
Native silver	Native element	Ag
Electrum	Native element	Ag-Au alloy
Acanthite[a]	Sulfide	Ag_2S
Argentite[a]	Sulfide	Ag_2S
Proustite	Sulfosalt	Ag_3AsS_3
Pyrargyrite	Sulfosalt	Ag_3SbS_3
Polybasite	Sulfosalt	$(Ag,Cu)_{16}Sb_2S_{11}$
Pearcite	Sulfosalt	$Ag_{16}As_2S_{11}$
Stephanite	Sulfosalt	Ag_5SbS_4
Aguilarite	Sulfosalt	Ag_4SeS
Hessite	Telluride	Ag_2Te

[a]Argentite inverts to acanthite below 179 °C

Ore minerals often grade downward from a silver- and gold-rich zone at the top to a base-metal-rich zone below. They form from near-neutral pH, reduced, gas-rich, meteoric/magmatic hydrothermal fluids (Albinson et al. 2001; John 2001; Leavitt et al. 2004; Mango et al. 2014). Examples are Guanajuato, Fresnillo, Pachuca, and Tayoltita in Mexico, and Tonopah, Round Mountain, Midas, Comstock, and Creede in the United States.

Silver-bearing epithermal veins are found in late-stage mineralization above porphyry copper deposits; the silver occurs in sulfosalts and in solid solution in sphalerite and galena (Hurtig and Williams-Jones, 2015; Sillitoe 2010).

Silver-lead-zinc veins form a major class of silver deposits (Kissin and Mango 2014). Cordilleran vein type deposits are formed from magmatic-hydrothermal solutions. Silver is found in sulfosalts such as the tetrahedrite-tennantite series and form in the temperature range of 280–320 °C. Associated minerals include pyrite, chalcopyrite, sphalerite, galena, bornite, pyrrhotite, magnetite, arsenopyrite, and chalcocite, sometimes with uranium and tungsten minerals. Cordilleran-type veins hosted in clastic metasedimentary rocks appear to lack an igneous source for the ore solutions. Silver occurs in sulfosalt minerals associated with galena, sphalerite, pyrite, pyrrhotite, magnetite, and chalcopyrite (Kissin and Mango

Silver, Fig. 2 Sample of native silver for the Kongsberg district, Norway. Sample dimensions: 3.7 × 2.5 × 1.8 cm (Photo credit: www.irocks.com)

2014). Solution temperatures average 250–300 °C. Magma, Tintic, and Coeur d'Alene in the United States and Casapalca and Cerro de Pasco, Peru, are examples of this type of ore deposit.

Five-element (Ag-Ni-Co-As-Be) veins include the Kongsberg district of Norway, from which many fine specimens of native silver have been recovered (Fig. 2). Silver is found as the native element and in sulfosalts such as pyrargyrite, proustite, and stephanite. Uranium can be a significant coproduct, and some deposits are arsenic-rich. Silver deposition occurs in the temperature range 150–250 °C, although a much wider fluctuation in temperature, as well as fluid mixing, appears to have caused mineral deposition (Kissin and Mango 2014). Deposits of this type include the Cobalt-Gowganda, Thunder Bay, and Great Bear Lake districts in Canada.

Silver veins are also found related to granite-hosted tin mineralization, such as in Cerro Rico de Potosí in Bolivia (considered to be the largest silver deposit in the world). Here, silver-rich veins are associated with hydrothermal alteration above an igneous dome (Simmons et al. 2005). In the Cornwall deposits in England, silver occurs as argentiferous galena in veins that cross-cut earlier-formed tin mineralization and appear to be associated with faulting (Jackson et al. 1989).

Silver is associated with skarn mineralization, occurring as Ag-sulfosalts in polymetallic veins within the skarn and in distal Au-Ag veins (Einaudi et al. 1981; Jackson et al. 1989; Meinert et al. 2005).

Because silver is relatively soluble when combined with common anions existing in the oxidized zone of an ore deposit, but is very insoluble in the reduced sulfide form or as a native metal, it is frequently found in supergene enrichment zones associated with hydrothermal systems (Guilbert and Park 1986; Sillitoe 2009). Silver halides found in the oxidized zone of supergene enrichment are particularly insoluble and immobile (Sillitoe 2009).

Annual silver metal production worldwide (2014) was 20,300 tons, with a reserve base of 570,000 tons (USGS 2015).

Application to Cosmochemistry

The Pd-Ag chronometer is used to set constraints on the timing of early planetesimal formation. ^{107}Pd decays to ^{107}Ag, with a half-life of 6.5 million years (Chen and Wasserberg 1996). ^{107}Pd is now extinct in meteorites, but Pd/Ag ratios can be measured; in particular, Fe-Ni metal usually has much higher Pd/Ag ratios than cogenetic sulfides, reflecting fractionation (Woodland et al. 2005). Pd/Ag fractionation processes during condensation, early accretion, and metal segregation in the solar nebula allow construction of isochrons from which accretion models of Earth formation can be constructed (Chen and Wasserberg 1996; Woodland et al. 2005).

Toxicity

Argyria is a nontoxic tissue build-up of silver that causes blue-gray skin discoloration (Goonan 2014). Most silver salts are poisonous: exposure to dust containing silver nitrate or silver oxide may cause respiratory problems, lung, throat and skin irritation, and stomach pain (ATSDR 2015). Strong bioaccumulation of Ag^{+} has been observed in benthic organisms to the point of toxicity (Bell and Kramer 1999; Eisler 1996).

Cross-References

- Chalcophile Elements
- Complexes
- Hydrothermal Solutions
- Native Minerals
- Ore Deposits
- Oxidation-Reduction Reactions and Eh-pH (Pourbaix) Diagrams
- Sulfide Minerals

References

Albinson T, Norman DI, Cole D, Chomiak B (2001) Controls on the formation of low-sulfidation epithermal deposits: constraints from fluid inclusion and stable isotope data. In: Albinson T, Nelson CE (eds) New mines and discoveries in Mexico and central America. Soc Econ Geol, Littleton. Special Publication, 8, pp 1–32

ATSDR (2015) Toxic substances portal: Silver. Agency for toxic substances and disease registry. www.atsdr.cdc.gov/phs/phs.asp?id=537&tid=97. Accessed 21 Sept 2015
Aubert H, Pinta H (1977) Trace elements in soils. Elsevier, Amsterdam
Bell RA, Kramer JR (1999) Structural chemistry and geochemistry of silver-sulfur compounds: critical review. Environ Toxicol Chem 18:9–22
Carmichael RS (1989) Practical handbook of physical properties of rocks and minerals. CRC Press, Boca Raton
Chen JH, Wasserberg GJ (1996) Live ^{107}Pd for the early solar system and implications for planetary evolution. In: Chen, Wasserburg (eds) Earth processes: reading the isotopic code, Geophysical monograph, vol 95. American Geophysical Union, Washington, DC
Einaudi MT, Meinert LD, Newberry RJ (1981) Skarn deposits. In: Skinner BJ (ed) Economic geology 75th anniversary volume. Econ Geol Pub Co, Blacksburg, pp 317–391
Eisler R (1996) Silver hazards to fish, wildlife, and invertebrates: a synoptic review. Contaminant Hazard Reviews Biological Report 32
Goonan TG (2014) The lifecycle of silver in the United States in 2009. USGS Scientific Investigations Report 2013–5178
Greenwood NN, Earnshaw A (1997) Chemistry of the elements, 2nd edn. Butterworth-Heinemann, Oxford
Guilbert JM, Park F (1986) The geology of ore deposits. WH Freeman and Sons, New York
Haynes WM, Lide DR, Bruno TJ (2014) CRC handbook of chemistry and physics, 84th edn. Taylor and Francis, Boca Raton
Henderson P (1986) Inorganic geochemistry. Pergamon Press, Oxford
Heald P, Foley NK, Hayba DO (1987) Comparative anatomy of volcanic-hosted epithermal deposits: acid-sulfate and adularia-sericite types. Econ Geol 82:1–26
Hurtig NC, Williams-Jones AE (2015) Porphyry-epithermal Au-Ag-Mo ore formation by vapor-like fluids: new insights from geochemistry modeling. Econ Geol 43:587–590
IUPAC (International Union of Pure and Applied Chemistry) (2015) Commission on isotopic abundances and atomic weights. http://www.ciaaw.org/silver.htm. Accessed 20 Sept 2015
Jackson NJ, Willis-Richards J, Manning DAC, Sarns MS (1989) Evolution of the Cornubian ore field, Southwest England. Part II. Mineral deposits and ore-forming processes. Econ Geol 84:1101–1133
John DA (2001) Miocene and early Pliocene epithermal gold-silver deposits of the northern Great Basin, western U.S.: characteristics, distribution and relation to magmatism. Econ Geol 96:1827–1853
Kissin SA, Mango H (2014) Silver vein deposits. In: Holland HD, Turekian KK (eds) Treatise on geochemistry, vol 13, 2nd edn. Elsevier-Pergamon, Oxford, pp 425–432
Leavitt ED, Spell TL, Goldstrand PM, Arehart GB (2004) Geochronology of the Midas low-sulfidation epithermal gold-silver deposit, Elko County, Nevada. Econ Geol 99:1665–1686
Levinson AA (1974) Introduction to exploration geochemistry. Applied Publishing Ltd., Calgary
Lodders K (2010) Solar system abundances of the elements. In: Goswami A, Reddy BE (eds) Principles and perspectives in Cosmochemistry. Springer, Berlin/Heidelberg, pp 379–418
Mango H, Arehart G, Oreskes N, Zantop H (2014) Origin of epithermal ag-au-cu-Pb-Zn mineralization in Guanajuato, Mexico. Mineral Deposita 49:119–143
McDonough WF (2014) 3.16 – compositional model for the Earth's core A2. In: Turekian KK, Holland HD (eds) Treatise on geochemistry, 2nd edn. Elsevier, Oxford, pp 559–577
McLean JE and Bledsoe BE (1992) Behavior of metals in soils. Technology innovation office, office of solid waste and emergency response, EPA/540/S-92/018
Meinert LD, Dipple GM, Nicolescu W (2005) World skarn deposits. In: Hedenquist JW, Thompson JFH, Goldfarb RJ, Richards JP (eds) Economic geology 100th anniversary volume. Society of Economic Geologists, Littleton, pp 299–336
Palme H, O'Neill HSC (2014) Cosmochemical estimates of mantle composition. In: Holland HD, Turekian KK (eds) Treatise on geochemistry, vol 2, 2nd edn. Elsevier-Pergamon, Oxford, pp 15–36
Parker RL (1967) Composition of the earth's crust: United States geological survey professional paper 440-D. U.S. Geological Survey, Washington, DC, 19 p
Rudnick RL, Gao S (2014) Composition of the continental crust. In: Holland HD, Turekian KK (eds) Treatise on geochemistry, vol 3, 2nd edn. Elsevier-Pergamon, Oxford, pp 1–64
Seward TM (1976) The stability of chloride complexes of silver in hydrothermal solutions up to 350°C. Geochim Cosmochim Acta 40:1329–1341
Seward TM, Henderson CMB, Charnock JM, Dobson BR (1996) An X-ray absorption (EXAFS) spectroscopic study of aquated Ag^+ in hydrothermal solutions to 350°C. Geochim Cosmochim Acta 60:2273–2282
Seward TM, Williams-Jones AE, Migdisov AA (2014) The chemistry of metal transport and deposition by ore-forming hydrothermal fluids. In: Holland HD, Turekian KK (eds) Treatise on geochemistry, vol 13, 2nd edn. Elsevier-Pergamon, Oxford, pp 1–64
Shannon RD (1976) Revised effective ionic radii and systematic studies of interatomic distances in halides and chalcogenides. Acta Cryst A32:751–767
Sillitoe R (2009) Supergene silver enrichment reassessed. Econ Geol Spec Publ 14:15–32
Sillitoe R (2010) Porphyry copper systems. Econ Geol 105:3–41
Silver Institute (2015) Silver production. In: Supply and Demand. The Silver Institute. www.silverinstitute.org/site/supply-demand/silver-production. Accessed 20 Sept 2015
Simmons SF, White NC, John DA (2005) Geological characteristics of epithermal precious and base metal deposits. In: Hedenquist JW, Thompson JFH, Goldfarb RJ, Richards JP (eds) Economic geology 100th anniversary volume. Society of Economic Geologists, Littleton, pp 485–522
Singer DA (1995) World-class base and precious metal deposits: a quantitative analysis. Econ Geol 90:88–104
USGS (2015) Silver: statistics and information. In: Minerals information. United States Geological Survey. www.minerals.usgs.gov/minerals/pubs/commody/silver. Accessed 20 Sept 2015
Wilkinson JJ, Simmons SF, Stoffell B (2013) How metalliferous brines line Mexican epithermal veins with silver. Sci Rep 3:1–6
Woodland SJ, Rehkämper M, Halliday AN, Lee D-C, Hattendorf B, Günter D (2005) Accurate measurements of silver isotopic compositions in geologic materials including low Pd/ag meteorites. Geochim Cosmochim Acta 69:2153–2163
Yung LC, Fei CC, Mandeep JS, Abdullah HB, Wee LK (2014) Synthesis of a nano-silver metal ink for use in thick conductive film fabrication applied on a semiconductor package. PLoS One 9:e97484

Sodium

Jérôme Gaillardet
Institut de Physique du Globe de Paris, Paris, France

Element Data
Atomic Symbol: Na
Atomic Number: 11

(*continued*)

Atomic Weight: 22.98977 u
Isotopes and Abundances: ^{23}Na 100%
1 Atm Melting Point: 97.7 °C
1 Atm Boiling Point: 883 °C
Common Valences: 1+
Ionic Radii: 110 pm
Pauling Electronegativity: 0.93
First Ionization Energy: 496 kJ.mol^{-1}
Chondritic (CI) Abundance: 4962 ppm
Silicate Earth Abundance: 2590 ppm
Crustal Abundance: 2.3%
Seawater Abundance: 0.47 mol/kg
Core Abundance: ~0

Properties

Sodium (Na) is an alkali metal belonging to the first column of the periodic table. Like the other alkali metals (Li, K, Rb, Cs, Fr), it is a highly reactive element that does not exist in a metallic form on Earth. It easily loses an electron and combines mostly with oxygen and halogens. Its electronic configuration is [Ne] $3s^1$ and its ionic radius is 1.1 Angstrom making Na^+ one of the largest cations.

It is mainly found in silicates, chlorides, or as the free ion Na^+ in surface fluids. It is particularly enriched in seawater as a result of its mobile behavior during fluid-rock interactions. It has an important biological role in cell homeostasis and nerve impulse circulation.

History and Use

Sodium was first isolated in 1807 by Humphrey Davy in England from the electrolysis of melted soda. The symbol has been adopted from the Latin name Natrium by the German chemist Berzelius in 1813.

Table salt has long been a very precious good for humans, often used as a food preservative agent. The word "salary" is derived from the Latin word "salarium" denoting the salt ration received monthly by the Roman soldiers.

Na is an element widely used by humans for different purposes: food (i.e., table salt), paper, glass, soap, textile, petroleum, and metal industries. NaCl is used as road salt for deicing. It is extracted essentially from seawater, rock salts (evaporites), or salt lakes. Sodium hydroxide and sodium carbonate, widely used in chemical industry, are derived from NaCl by industrial processes. The global production of NaCl is approximately 250–400 $\times$ 10^6 t/year, representing an anthropogenic Na flux of 100–160 $\times$ 10^6 t/year on the same order of magnitude than the global flux of Na to the ocean (200 $\times$ 10^6 t/year). China and the USA are the main NaCl producers.

Geochemical Behavior and Distribution

Na is about the 14th most abundant chemical element in the universe as deduced from the standard cosmic abundances. Na is 17 times less abundant in the solar photosphere that is silicon and 158 times less abundant that is carbon (Palme et al. 2014). On our planet, Na is mostly concentrated in the mantle (90–95%), the rest being in the continental and oceanic crust and in the ocean. The concentration of Na varies a lot in different Earth materials. While Na is a minor element in the mantle, it is a major element in the oceanic and continental crusts where it contributes to the stoichiometry of the major rock forming minerals.

The condensation temperature of Na is approximately 970 K at 10^{-4} bar. The concentration of Na in chondrites varies between 3300 and 6800 ppm (Li 2000). CI chondrites have mean Na concentration of 4982 ppm while the bulk silicate earth is about 2590 ppm (Palme and O'Neill 2014). This illustrates the volatile character of sodium. During the accretion of the Earth, the planet probably lost part of its initial Na. The concentration of Na in the core is not known and is usually assumed to be negligible.

Na in Magmatic Processes

According to the Goldschmidt classification, Na can be classified as a lithophile element with regard to its affinity for silicates. The estimated Na concentration in the bulk continental crust is 2.3% or 3.1% Na_2O (Rudnick and Gao 2014). Na is more concentrated in the upper part of the continental crust (2.4%). Na in crustal rocks is mainly hosted in plagioclase (e.g., albite $NaAlSi_30_8$) and alkali feldspars. It usually enters into the octahedral sites of aluminosilicates in association with Ca.

The behavior of sodium during partial melting and fractional crystallization is that of a moderately incompatible element, which means that Na will preferentially be enriched in silicate melts and rocks formed by their crystallization. Among alkali elements, Na has the highest partition coefficient between melt and solid (concentration in the solid over that in the liquid) and is thus the least incompatible of the alkalis. The bulk partition coefficient of Na between the mantle and the crust was estimated to be 0.1 by Hofmann (1988) using a simple crust-mantle differentiation model, much higher than the partition coefficient of heavier alkalis. In mid-oceanic ridge basalts (MORB), a correlation is observed between Na concentration varying between 1.3% and 2.5% (1.7–3.4% Na_2O) and axial depth (Klein and

Langmuir 1987), a feature interpreted by variations in the extent of mantle melting linked to temperature variations in the mantle.

Na in Fluid-Rock Interactions

Na is one of the most soluble elements (at least among cations) at the surface of the Earth. It mostly occurs in fluids as free Na^+ except in high temperature concentrated fluids where it can be found as complexes (e.g., with aluminum). This mobile character of Na during water-rock interaction is mainly attributed to its large ionic radius and +1 valence state (or in other words, to its low ionic potential), precluding Na from entering into precipitating minerals as dictated by Goldschmidt's rules. There are very few clay minerals containing significant amounts of Na (e.g., smectites). Na will thus be particularly enriched in fluids formed by weathering and metamorphic processes.

With chloride, sodium is the most concentrated element in seawater (0.47 mol/kg or 10.8 g/kg) suggesting that Na has accumulated over geological time in the ocean. The residence time of Na in the ocean is very long (on the order of 100 Myrs), confirming its lack of reactivity at Earth's surface conditions.

The dissolution of sea salt atmospheric aerosols produced by bubble bursting over the ocean allows Na to be one of the most abundant elements in rainwater, its concentration decreasing sharply with distance from the coast.

Sodium is also concentrated in rivers, particularly those draining igneous rocks. The mean Na concentration carried by large rivers to the ocean is 240 µmol/kg (5.5 mg/kg). About 40% of Na added each year to the ocean by rivers is derived from the chemical weathering of silicate rocks; the remaining Na originates from rain (leaching atmospheric sea salts) and evaporite dissolution (Gaillardet et al. 1999).

Accordingly, the secondary weathering products (clays and oxides) accumulating in soils or transported by rivers to the ocean are depleted in Na compared to the source rock, confirming its soluble behavior at the surface of the Earth (Viers et al. 2009). On a global scale, modern large river sediments are between 2 and 10 times depleted in Na compared to upper continental crustal rocks, with Na concentrations ranging from 2000 ppm to 15,000 ppm, on average (respectively, 0.25–2 Na_2O weight%). River sands transported as bed load are usually richer in Na due to the presence of detrital feldspars. In continental weathering studies, Na (soil profiles, modern and ancient sediments) is often used as the most mobile element to which other metal mobilities are compared.

Na in hydrothermal mid-oceanic ridge vents is slightly more concentrated (0.3–0.6 mol/kg) than seawater, indicating that Na is leached out of the oceanic lithosphere when seawater and seafloor interact at high temperature. Less is known about the off-axis low-temperature interaction between seawater and oceanic floor, but Na concentrations in fluids tend to indicate that Na is retained in the secondary minerals formed (Na zeolites, phillipsite smectite, palagonite minerals). This is corroborated by the comparison between fresh and weathered oceanic crust that shows a net gain of Na in the oceanic crust (Staudigel 2014).

In continental hydrothermal settings, Na is generally the most abundant cation in the aqueous phase, also confirming that Na is not significantly controlled by the precipitation of secondary phases.

During the evaporation of seawater in confined conditions, it is possible to precipitate Na in halite (NaCl) when Na reaches a typical concentration of 360 g/L. Halite precipitation is rare on modern Earth. It happens in modern salt marshes but happened massively in the Earth's history during particular periods (e.g., at middle and late Permian in Europe). Rare evaporitic minerals, such as natron (Na_2CO_3, $10H_20$), are also known to precipitate Na from brines in arid settings.

Joly's Sodium Age of the Earth

In a brilliant paper published in 1899, John Joly, an Irish scientist, proposed a method relying on sodium to estimate the age of the ocean and thus of the Earth. By assuming the rate of Na discharged to the ocean has remained constant throughout Earth's history, Joly used the amount of Na in the ocean and its modern delivery yield to the ocean (corrected from cyclic rain salts and evaporite dissolution) to show that the Earth should be 90–100 Myrs (Jackson 2001). We now know that Joly's estimate was not the age of the Earth but rather the residence time of Na in the ocean. He assumed that Na was not reactive in the ocean and was simply accumulating over time. This hypothesis is erroneous and several mechanisms can be invoked to recycle Na from the ocean to either crustal or mantle rocks. The enrichment of Na in the oceanic crust during its interaction with seawater, the episodic formation of saline rocks or its incorporation in authigenic phases ("reverse weathering") and carbonates, or, ultimately, the subduction of Na in the mantle are the main plausible mechanisms explaining the fate of Na in the ocean. There is, finally, a last process able to scavenge oceanic Na, which is the ion exchange with Ca onto clay surfaces occurring when Ca-rich river particles enter into the Na-rich ocean:

$$S - Ca + 2Na^+ = S - Na + Ca^{2+}$$

This mechanism is invoked to ultimately lead to the precipitation of carbonate in the ocean following the continental weathering of Na silicates.

We still lack precise knowledge of the processes scavenging Na from seawater, but it is clear that compared to K and Li, Na is less prone to be reincorporated into secondary phases.

Biological Utilization and Toxicity

Sodium has an important biological role in cell homeostasis and nerve impulse circulation.

Na is an element essential to life. Na is found in the biosphere at concentrations ranging between 10^3 and 10^4 ppm. Human blood contains 1800 ppm of Na (about 1.8 mg/L; Li 2000). It plays an important (together with potassium) role in maintaining the ionic balance in biological tissue and in not only compensating the negative charges of major biopolymers but also in maintaining osmotic pressure and electrical potentials. Very precise mechanisms of Na homeostatic behavior been developed by life, in particular for maintaining the electrical and concentration gradients necessary to produce highly energetic polymers (e.g., ATP). Active specific Na^+ (and K^+) pumps coupled to enzyme ATPase have been discovered that help to maintain the gradients across biological membranes. The circulation of messages in nerve cells of animals also implies the opening of Na^+ (and K^+) channels (Da Silva and Williams 2001).

Summary

Na is a chemical element that has been concentrated in the surface layers of the Earth, due to its affinity for the fluid phase during meting and weathering processes. The ocean is salty, because Na (together with Cl) accumulated over Earth's history which also reflects its very long residence time (80 Myrs). As a consequence of this oceanic abundance, marine and then terrestrial life took advantage of Na and used it as an essential electolyte. The high Na concentration in the interior fluids of terrestrial vertebrates is probably a legacy of the early times of oceanic life.

Cross-References

- Alkali and Alkaline Earth Metals
- Chemical Weathering
- Complexes
- Evaporites
- Geochemistry
- Geochemical Classification of Elements
- Halide Minerals
- Hydrothermal Solutions
- Hydrothermal Vents
- Lithophile elements
- Mid-Ocean Ridge Basalts (MORB)
- Ocean Biochemical Cycling and Trace Elements
- Partial Melting

References

Da Silva JF, Williams RJP (2001) The biological chemistry of the elements: the inorganic chemistry of life. Oxford University Press, New York

Gaillardet J, Dupré B, Louvat P, Allegre CJ (1999) Global silicate weathering and CO_2 consumption rates deduced from the chemistry of large rivers. Chem Geol 159(1):3–30

Hofmann AW (1988) Chemical differentiation of the earth: the relationship between mantle, continental crust, and oceanic crust. Earth Planet Sci Lett 90(3):297–314

Holland HD (2005) Sea level, sediments and the composition of seawater. Am J Sci 305:220–239

Jackson PNW (2001) John Joly (1857–1933) and his determinations of the age of the earth. Geol Soc Lond, Spec Publ 190 (1):107–119

Klein E, Langmuir C (1987) Global correlations of ocean ridge basalt chemistry with axial depth and crustal thickness. J Geophys Res 92:8089–8115

Li YH (2000) A compendium of geochemistry: from solar nebula to the human brain. Princeton University Press, Princeton

Palme H, O'Neill HSC (2014) 3.1 – cosmochemical estimates of mantle composition. In: Holland HD, Turekian KK (eds) Treatise on geochemistry, 2nd edn. Elsevier, Oxford, pp 1–39

Palme H, Lodders K, Jones A (2014) 2.2 – solar system abundances of the elements A2. In: Holland HD, Turekian KK (eds) Treatise on geochemistry, 2nd edn. Elsevier, Oxford, pp 15–36

Rudnick RL, Gao S (2014) 4.1 – composition of the continental crust. In: Holland HD, Turekian KK (eds) Treatise on geochemistry, 2nd edn. Elsevier, Oxford, pp 1–51

Staudigel H (2014) Chemical fluxes from hydrothermal alteration of the oceanic crust. In: Holland HD, Turekian KK (eds) Treatise on geochemistry, 2nd edn. Elsevier, Oxford, pp 583–606

Viers J, Dupré B, Gaillardet J (2009) Chemical composition of suspended sediments in world rivers: new insights from a new database. Sci Total Environ 407(2):853–868

S

Soils

Johannes Lehmann
Soil and Crop Science, School of Integrative Plant Science, Cornell University, Ithaca, NY, USA

Definition

Soils constitute the uppermost layer of the Earth. They exhibit pedogenic horizons as a result of physical, chemical, and biological weathering, growth of plants, transformation of minerals, accumulation of organic matter, and microbial and faunal activity.

Introduction

Soils are at the nexus of the lithosphere, atmosphere, biosphere, and hydrosphere and therefore a product of a plethora of influences that determine their genesis and properties (Jenny 1941). Soils distinguish themselves from rock by chemical, physical, and biological transformations that lead to the accumulation of organic matter and the activity of microbiota (Weil and Brady 2016). They are distinct from sediments morphologically by the presence of horizons that are formed in situ (Fig. 1), in contrast to layers present in sediments. On the one hand, temporarily or permanently submerged soils exist, for example, in mangrove ecosystems where one would normally expect ocean sediments; on the other hand, soils can develop on sediments, generating transitions between sediments and soils. In comparison, paleosols are not soils but remains of soils in the geological record (Retallack 1988).

Soil horizons are typically divided into organic or O horizons (conventionally abbreviated by letters) overlaying the mineral soil; mineral A horizons with an accumulation of organic carbon or a depletion of minerals (Fig. 1); mineral B horizons with an accumulation of minerals, clay, or organic matter from the A horizon or transformation in situ; and mineral C horizons that are weakly transformed, often only by weathering, and overlay the parent rock material (Weil and Brady 2016). Different classification systems exist (such as the "World Reference Base of Soil Resources," Food and Agriculture Organization of the United Nations and the "Keys to Soil Taxonomy," United States Department of Agriculture) that establish different criteria to distinguish soil types and horizons, either based on how the soil was formed (e.g., the German soil classification system) or what chemical and physical properties it possesses (e.g., the USDA Soil Taxonomy). Soil properties depend on the nature of the rock they develop on, deposition or erosion, climate, vegetation, and time and can vary widely.

Soil Development

Depending on climate, the development to highly weathered soils can take millions of years even in contemporary tropical environments and is best described as an evolution of soils due to inconsistency of soil-forming factors over long periods of time (Huggett 1998). During such evolution, the mineralogy changes from a domination of primary minerals that are a reflection of the underlying bedrock to the formation of phyllosilicates with a stoichiometry of silicon to aluminum of 2:1 such as illites and smectites and of iron oxides such as goethite (Weil and Brady 2016). During further soil development, silicon is predominantly lost, leading to preferential

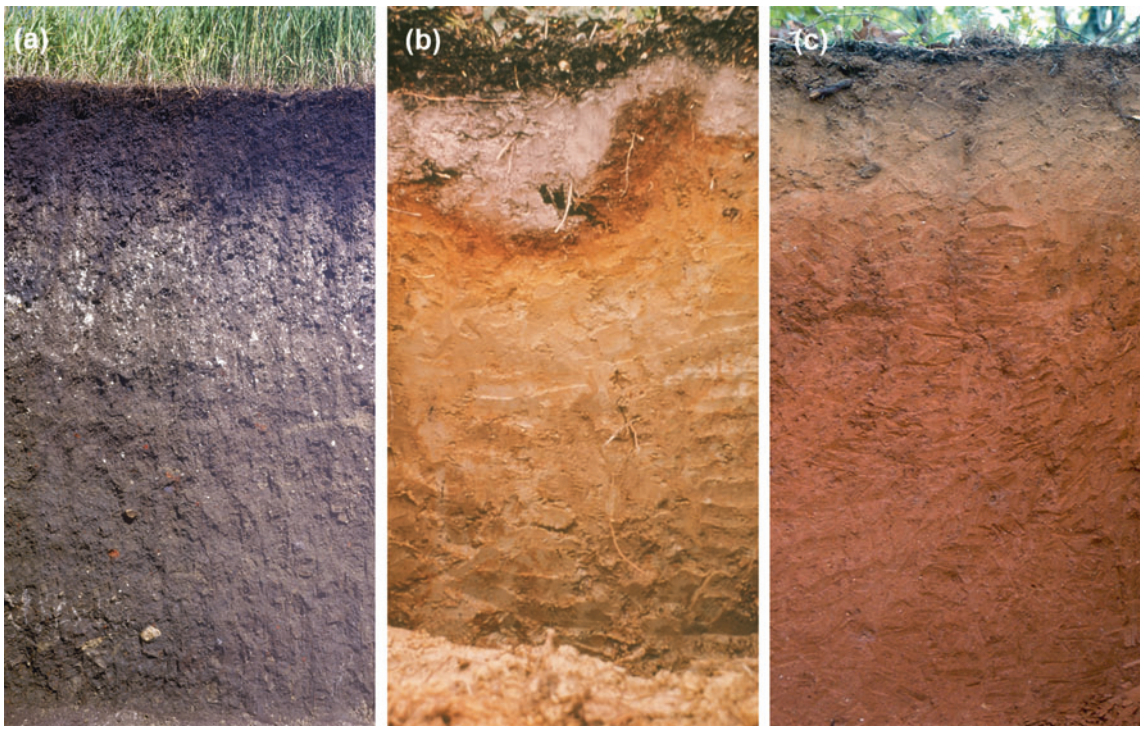

Soils, Fig. 1 Soil profiles of (**a**) a Mollisol, (**b**) a Spodosol, and (**c**) an Ultisol. Clearly visible are soil horizons with mainly organic matter accumulation in upper A horizons, a depleted E horizon in the Spodosol, and horizons with iron oxide accumulation in B horizons (Photos courtesy of USDA, Natural Resources Conservation Service)

formation of phyllosilicates with a stoichiometry of silicon to aluminum of 1:1 such as kaolinite and of aluminum oxides, until the secondary soil minerals are rich in aluminum and iron oxides. These profound changes in soil mineralogy also affect soil solution chemistry in many different ways. At early stages of soil development, weatherable cations are released, and the soil pH is determined by the parent material ranging from slightly acidic on granitic rock to slightly alkaline on limestone, and soil minerals contain little negative charge that retains cations. In contrast, successively developing 2:1 phyllosilicates such as smectites have large permanent negative charge due to isomorphic replacement of silicon by aluminum, and aluminum by iron, as well as large inner surface areas exposed during expansion of the aluminosilicate layers. The pH is still largely influenced by the parent material, while pH in turn strongly influences ion retention due to variable charge increasing negative charge with higher pH and positive charge with lower pH. Further soil development decreases the pH, increases the sensitivity of surface charge to changes in pH, and reduces the net negative charge. This proceeds until the mineral phase in oxide-rich soils develops net positive charge that does not retain any cations but can retain anions especially in subsoils that are low in organic matter.

As soil mineralogy changes over long periods of time, the release of elements such as phosphorus or calcium declines (Chadwick et al. 1999; Vitousek and Farrington 1997). Atmospheric input can then under some conditions be significant, such as in the proximity of oceans through input by sea spray (Chadwick et al. 1999) or through input of dust even by long-distance transport (Prospero et al. 2002). In addition to changes in mass balances, the interaction between solutes and mineral surfaces changes significantly with soil development and concomitant changes in mineralogy. For example, phosphorus sorption and fixation increases with an increase in iron and aluminum oxides (Vitousek and Farrington 1997), thereby decreasing ecosystem phosphorus availability.

Nitrogen is not to any appreciable extent released by weathering of primary rock. Since nitrogen is an essential nutrient for both flora and fauna and typically needed in large quantities, any soil development requires input of nitrogen from the atmosphere (Vitousek and Howarth 1991). To a great extent, this input is delivered by free-living or symbiotic microorganisms that have the capability to fix atmospheric nitrogen. During initial periods of soil development, plant productivity is primarily limited by nitrogen, whereas it may be more constrained by phosphorus availability in weathered soil. Similarly, sulfur availability is low at initial stages of soil development, but in contrast to phosphorus after these initial changes does not change greatly thereafter (Turner et al. 2016). However, atmospheric inputs from oceans (Turner et al. 2016) and anthropogenic emissions from coal (Lehmann et al. 2008c) can significantly affect isotopic composition, and in the case of coal emissions, organic sulfur forms also on the long term.

Soils and Civilizations

Soils' use and degradation are on many levels intimately connected to the development and decline of human civilizations. The word "human" itself has linguistic roots in the Latin word "humus" for soil, and many religions use imagery of mankind being born out of the Earth and becoming part of it in a cycle of life. In a more practical sense, soil fertility is the foundation for land-based food production. Early civilizations starting at 10,500 years BC began exploring crop and soil management to increase food production as an alternative to hunter-and-gatherer societies (Zeder 2008). The overexploitation of soils leading, for example, to salt accumulation in ancient Babylonia (Jacobsen and Adams 1958) also led to declines in food production and disappearance of what were once large and complex societies. Soil management did not significantly evolve further until the late eighteenth to the mid-nineteenth century when growing scientific insights provided the basis for the concept of nutrient fertilization. It took until the early twentieth century to develop the technology that enabled nitrogen fertilizer production from atmospheric dinitrogen through the Haber-Bosch process when its use started having Earth system impacts on soil productivity. Apart from food production, soils can be credited to have been the source of antibiotics such as streptomycin isolated by Selman Waksman and Albert Schatz in 1943 and of many other substances.

Soil Biota

Soils contain a tremendous amount of organisms, including both fauna and flora that build complex food webs with implications for both ecosystem diversity (Bardgett and van der Putten 2014), crop production and food quality (Lakshmanan et al. 2014), and human health (Wall et al. 2015). One gram of a given soil harbors millions of species of microorganisms, and billions of living organisms, mainly bacteria and fungi. Knowledge of soil biodiversity and resultant biogeochemistry is limited, but it is clear that biodiversity varies globally as a function of pH, climate, vegetation, and soil management (Fierer and Jackson 2006). However, clear biogeographical patterns across biomes do not seem to exist as for aboveground plant and animal composition which also implies a certain degree of de-coupling between above- and belowground biodiversity at a global scale (Bardgett and van der Putten 2014). On the scale of an individual soil, biota composition varies widely between topsoil and subsoil or over the course of a year. On an even smaller scale of

millimeters, soils are very heterogeneously populated by microorganisms as a function of soil architecture (Fig. 2a; Young and Crawford 2004), despite the large amounts of organisms per unit mass.

Soil Organic Matter

An even greater heterogeneity can be observed for soil organic matter at the relevant scale where biogeochemical processes occur (Fig. 2b and c; Lehmann et al. 2008a). Organic matter properties vary greatly between different locations in microaggregates (Milne et al. 2011), and the average organic matter composition of a soil sample does not represent the properties observed at the scale of nanometers (Lehmann et al. 2008a) as a result of different biotic and abiotic processes dependent on micro-location. Therefore, bulk soil properties of organic matter are irrelevant for evaluating soil organic matter cycling that is controlled by access of microorganisms and their enzymes to organic matter adsorbed to mineral surfaces or entrapped in aggregates and small pores (Kleber et al. 2015). On a global scale, both climate and soil mineralogy appear to be important determinants of soil carbon storage (Doetterl et al. 2015).

Soils are important for key functions of terrestrial ecosystems such as the provision of clean water and regulation of climate in addition to many other biogeochemical cycles. Soils contain three times more organic carbon than is present in the world's plants and as carbon dioxide in the atmosphere combined. The organic matter in soils is therefore a globally important ecosystem property for food security, water quality, and the climate. Soil organic matter is progressively decomposed and can be seen as a continuum ranging from large biomolecules of plant and animal origin to small decomposition products to carbon dioxide (Lehmann and Kleber 2015). The residence time of an organic molecule is less a function of its intrinsic chemical composition than a result of its solubility, adsorption to soil minerals, encapsulation in soil aggregates, the decomposer community, other energy (e.g., additions of organic matter) and electron donor/acceptors, moisture content, and temperature, among others.

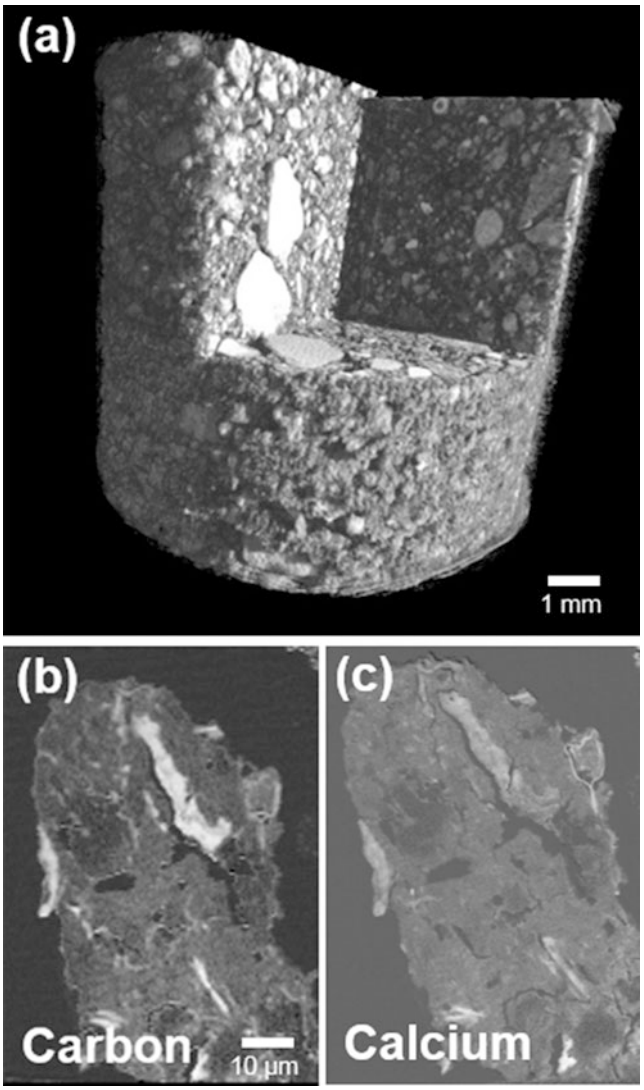

Soils, Fig. 2 High spatial heterogeneity in soil shown for (**a**) the soil physical assemblage (Young and Crawford 2004), (**b**) soil carbon (Lehmann et al. 2008a), and (**c**) soil calcium (Solomon et al. 2012) (*white areas* in (**b**) and (**c**) indicate higher amounts of the target element) (With permission from the publishers)

Fire and Soil

Vegetation fires are part of the Earth's system that are both natural and anthropogenic and have profound direct and indirect effects on soil properties and processes. Direct heat oxidizes organic matter, destroys soil biota, and changes soil mineralogy (Certini 2005). Indirectly, combustion residues such as ash increase soil pH as well as constitute an input in base cations and phosphorus. Thermally decomposed organic matter, called pyrogenic organic matter, augments persistent organic matter in soils (Lehmann et al. 2008b), increases cation retention (Liang et al. 2006), and may change cycling of biologically transformed organic matter in a process often referred to as "priming" (Woolf and Lehmann 2012).

Soil Erosion

Erosion of soil is both a natural landscape process and influenced by human activity (Amundson et al. 2015). Erosion typically removes topsoil on upper and middle slope positions and deposits it at foot slopes or exports it to streams where it may form stream or lake sediments or enter the oceans. Erosion is mainly seen as a loss of organic matter and soil fertility

(Montgomery 2007) but also as a sink of organic matter through its eventual burial (Van Oost et al. 2007) and as an input of nutrient-rich runoff (Nixon 2003). Subsoils have also only recently been recognized as containing important sources of nutrients (Lehmann 2003) and serving as an important sink of atmospheric carbon dioxide (Marin-Spiotta et al. 2014).

Soil Contamination

Anthropogenic contamination of soil is a relatively recent phenomenon in the Earth's history. Agrochemicals such as pesticides and herbicides, but also atmospheric emissions of polycyclic aromatic hydrocarbons (PAH), lead, sulfates, and nitrates, as well as direct input of dioxins, petroleum, pathogens, heavy metals, arsenic, polychlorinated biphenyls (PCB), endocrine disruptors, nanoparticles, and others may cause various human and ecosystem health issues. In some cases, however, contamination can also have natural sources, such as with arsenic originating from weathering of arsenic-rich rock, transport with ground water, and uptake into crops (Smith et al. 2000). Both the uptake into food crops and the transport to ground and surface waters are of concern and depend on retention by various adsorption mechanisms to the soil matrix as well as in the case of organic contaminants the metabolization by microorganisms. Decontamination is often difficult to achieve and may involve phytoremediation (Lasat 2002), leaching with or without added solutes, remediation using microbial additives, and mechanical barriers (Mulligan et al. 2001a, b).

Future Soil Management

Managing the diverse ecosystem services that soils provide poses a challenge in a world with greater population, greater demand on food production, and more diverse expectations such as for soils to contribute to climate change mitigation and water quality (Keesstra et al. 2016). Balancing these demands requires all stakeholders to be involved and appropriate market incentives to be developed (Tilman et al. 2002). The current renewed recognition of the importance of soil will only be successful in addressing global change challenges if the vast variability of its properties will be recognized at spatial scales from an individual molecule to the global scale and temporal scales from minutes to millions of years. Modern information technology is required to implement site- and time-specific management built on the best available science.

Summary

Soils form the upper layer of the Earth' crust and develop different properties over time depending on parent geological material, climate, vegetation, and management. On small scales where microbial or abiotic processes occur, soils are highly variable and constitute a highly dynamic system for organic matter stabilization and nutrient availability. Historically, soils provided the foundation for the development of human civilization and continue to provide key ecosystem services to sustain food production, water quality, and climate stability.

Cross-References

- ▶ Acid–Base Reactions
- ▶ Biogeochemistry
- ▶ Carbon Cycle
- ▶ Clay Minerals
- ▶ Low-Temperature Geochemistry
- ▶ Mineral Defects
- ▶ Nitrogen Cycle
- ▶ Nutrients
- ▶ Organic Geochemistry
- ▶ Phosphorus

References

Amundson R, Berhe AA, Hopmans JW, Olson C, Sztein AE, Sparks DL (2015) Soil and human security in the 21st century. Science 348:647

Bardgett RD, van der Putten WH (2014) Belowground biodiversity and ecosystem functioning. Nature 515:505–511

Certini G (2005) Effects of fire on properties of forest soils: a review. Oecologia 143:1–10

Chadwick OA, Derry LA, Vitousek PM, Huebert BJ, Hedin LO (1999) Changing sources of nutrients during four million years of ecosystem development. Nature 397:491–497

Doetterl S, Stevens A, Six J, Merckx R, Van Oost K, Pinto MC, Casanova-Katny A, Muñoz C, Boudin M, Zagal Venegas E, Boeckx P (2015) Soil carbon storage controlled by interactions between geochemistry and climate. Nat Geosci 8:780–783

Fierer N, Jackson RB (2006) The diversity and biogeography of soil bacterial communities. Proc Natl Acad Sci 103:626–631

Huggett RJ (1998) Soil chronosequences, soil development, and soil evolution: a critical review. Catena 32:155–172

Jacobsen T, Adams RM (1958) Salt and silt in ancient Mesopotamian agriculture. Science 128:1251–1258

Jenny H (1941) Factors of soil formation: a system of quantitative pedology. McGraw-Hill, New York

Keesstra SD, Quinton JN, van der Putten WH, Bardgett RD, Fresco LO (2016) The significance of soils and soil science towards realization of the United Nations sustainable development goals. Soil 2:111–128

Kleber M, Eusterhues K, Keiluweit M, Mikutta C, Mikutta R, Nico PS (2015) Mineral–organic associations: formation, properties, and relevance in soil environments. Adv Agron 130:1–140

Lakshmanan V, Selvaraj G, Bais HP (2014) Functional soil microbiome: belowground solutions to an aboveground problem. Plant Physiol 166:689–700

Lasat MM (2002) Phytoextraction of toxic metals. J Environ Qual 31:109–120

Lehmann J (2003) Subsoil root activity in tree-based cropping systems. Plant Soil 255:319–331
Lehmann J, Kleber M (2015) The contentious nature of soil organic matter. Nature 528:60–68
Lehmann J, Solomon D, Kinyangi J, Dathe L, Wirick S, Jacobsen C (2008a) Spatial complexity of soil organic matter forms at nanometre scales. Nat Geosci 1:238–242
Lehmann J, Skjemstad JO, Sohi S, Carter J, Barson M, Falloon P, Coleman K, Woodbury P, Krull E (2008b) Australian climate-carbon cycle feedback reduced by soil black carbon. Nat Geosci 1:832–835
Lehmann J, Solomon D, Zhao F-J, McGrath S (2008c) Atmospheric SO_2 emissions since the late 1800s change organic sulfur forms in humic substance extracts of soils. Environ Sci Technol 42:3550–3555
Liang B, Lehmann J, Solomon D, Kinyangi J, Grossman J, O'Neill B, Skjemstad JO, Thies J, Luizão FJ, Petersen J, Neves EG (2006) Black carbon increases cation exchange capacity in soils. Soil Sci Soc Am J 70:1719–1730
Marin-Spiotta E, Chaopricha NT, Plante AF, Diefendorf AF, Mueller CW, Grandy AS, Mason JA (2014) Long-term stabilization of deep soil carbon by fire and burial during early Holocene climate change. Nat Geosci 7:428–432
Milne AE, Lehmann J, Solomon D, Lark RM (2011) Wavelet analysis of soil variation at nanometre- to micrometre-scales; an example of organic carbon content in a micro-aggregate. Eur J Soil Sci 62:617–628
Montgomery DR (2007) Soil erosion and agricultural sustainability. Proc Natl Acad Sci 104:13268–13272
Mulligan CN, Yong RN, Gibbs BF (2001a) Remediation technologies for metal-contaminated soils and groundwater: an evaluation. Engin Geol 60:193–207
Mulligan CN, Yong RN, Gibbs BF (2001b) Surfactant-enhanced remediation of contaminated soil: a review. Engin Geol 60:371–380
Nixon SW (2003) Replacing the Nile: are anthropogenic nutrients providing the fertility once brought to the Mediterranean by a great river? Ambio 32:30–39
Prospero JM, Ginoux P, Torres O, Nicholson SE, Gill TE (2002) Environmental characterization of global sources of atmospheric soil dust identified with the Nimbus 7 Total Ozone Mapping Spectrometer (TOMS) absorbing aerosol product. Rev Geophys 40:1002
Retallack GJ (1988) Field recognition of paleosols. Geol Soc Am Sp Papers 216:1–20
Smith AH, Lingas EO, Rahman M (2000) Contamination of drinking-water by arsenic in Bangladesh: a public health emergency. Bull World Health Organ 78:1093–1103
Solomon D, Lehmann J, Harden J, Wang J, Kinyangi J, Heymann K, Karunakaran C, Lu Y, Wirick S, Jacobsen C (2012) Micro- and nano-environments of carbon sequestration: multi-element STXM-NEXAFS spectromicroscopy assessment of microbial carbon and mineral associations. Chem Geol 329:53–73
Tilman D, Cassman KG, Matson PA, Naylor R, Polasky S (2002) Agricultural sustainability and intensive production practices. Nature 418:671–677
Turner BL, Condron LM, France CAM, Lehmann J, Solomon D, Peltzer DA, Richardson SJ (2016) Sulfur dynamics during long-term ecosystem development. Biogeochemistry 128: 281–305
Van Oost K, Quine TA, Govers G, De Gryze S, Six J, Harden JW, Ritchie JC, McCarty GW, Heckrath G, Kosmas C, Giraldez JV, Marques da Silva JR, Merckx R (2007) The impact of agricultural soil erosion on the global carbon cycle. Science 318:626–629
Vitousek PM, Farrington H (1997) Nutrient limitation and soil development: experimental test of a biogeochemical theory. Biogeochemistry 37:63–75
Vitousek PM, Howarth RW (1991) Nitrogen limitation on land and in the sea: how can it occur? Biogeochemistry 13:87–115
Wall DH, Nielsen UN, Six J (2015) Soil biodiversity and human health. Nature 528:69–76
Weil RR, Brady NC (2016) The nature and properties of soils (No. Ed. 15). Pearson, Prentice-Hall Inc, New York
Woolf D, Lehmann J (2012) Modelling the long-term response to positive and negative priming of soil organic carbon by black carbon. Biogeochemistry 111:83–95
Young IM, Crawford JW (2004) Interactions and self-organization in the soil-microbe complex. Science 304:1634–1637
Zeder MA (2008) Domestication and early agriculture in the Mediterranean Basin: origins, diffusion, and impact. Proc Natl Acad Sci 105:11597–11604

Solid Solution/Exsolution

C. Noguera[1] and B. Fritz[2]
[1]Institut des Nanosciences de Paris, CNRS-Sorbonne Universités, UPMC University Paris 06, Paris, France
[2]Laboratoire d'Hydrologie et Géochimie de Strasbourg, Université de Strasbourg/EOST, CNRS, Strasbourg Cedex, France

Definition

By analogy with aqueous solution, a solid solution, sometimes called mixed crystal, is defined as an homogeneous solid-state solution of one or more solutes in a solvent. Its composition may vary in a more or less wide range of compositions, between extreme values which correspond to pure solids, known as its end-members. At variance with a mechanical mixture in which the components are mixed but not chemically bonded, mixing in a solid solution occurs at the atomic level, generally by substitution of one type of atoms by another on the same lattice. Many metal alloys, oxides, and silicates are substitutional solid solutions, but solid solutions may also be formed by insertion of foreign atoms at interstitial sites in the host crystal (interstitial solid solutions) or by loss of atoms in nonstoichiometric compounds (omissional solid solutions). The importance of solid solutions comes from the synergistic properties that they may display compared to their end-members and to their ubiquity in the natural environment.

In some cases, an homogeneous SS may become unstable with respect to its components, and phase separation, also called demixing or exsolution, may occur. More precisely, exsolution is the processes of separation of an initially homogeneous solution phase (liquid or solid) into two compositionally different immiscible phases. This process may be triggered by pressure, temperature, or composition changes but mostly by the two former for solid phases which show little volume change upon pressure.

Introduction

Solid solutions (SSs) are often encountered in chemistry, in metallurgy, as well as in the earth sciences: mineralogy, petrology, or geochemistry. In metallurgy, alloying elements are added to metals to improve their strength and their hardness or their resistance to corrosion. In the natural environment, compared to pure minerals, mixed minerals are the generality rather than the exception. Indeed, the formation of SSs is often thermodynamically preferred over the separate formation of their end-members, as can be judged by the frequent incorporation of trace elements in minerals; the ubiquity of complex oxides, silicates, or carbonates; and the scarcity of pure minerals (see Trace Elements, Clay Minerals, Oxide Minerals, Silicate Minerals, Carbonate Minerals). Two main processes lead to the formation of SSs: condensation from a melt or precipitation from a supersaturated aqueous fluid. Understanding SS formation conditions may bring insight into global element cycles, composition of natural waters, and diffusion of elements in contaminated soils and may be useful to try reconstructing past conditions.

In substitutional SSs, the process of mixing relies on the existence of local interactions between substituent (solute) and host atoms. In order that mixing takes place at the atomic level, several conditions have to be fulfilled:

- The crystal structure of the solvent should remain unchanged upon addition of the solute. End-members should thus have the same atomic structure.
- The substituting and host ions should have ionic radii differing by less than ≈15% (Hume Rothery rule) (see Ionic Radii).
- For single substitutions, the substitution has to be isoelectronic (replacing ion of the same valence as host ion). For multiple substitutions, global electric neutrality requires a coupling between charges and molar fractions. For example, substitution of Si by Al in the tetrahedral sites of phyllosilicate minerals requires a correlated charge compensation in the interlayer space or in the octahedral sites.
- The chemical affinity of host and solute atoms should be low; otherwise defined compounds are formed rather than solid solutions.

If these conditions are not fulfilled, SSs are restricted to a composition range of a few percents. Conversely, SSs which exist in a large composition range are usually made from elements which are close to each other in the periodic table.

Depending on the sign and strength of the interatomic interactions, fully disordered SSs, SSs with short-range order or defined compounds with long-range order, may form. In some instances, phase separation may take place, for example, leading to exsolution upon cooling. Simple models of mixing account for all these possibilities and allow deriving generic phase diagrams as a function of the thermodynamic conditions (temperature, pressure, composition, contact with an aqueous solution) and discussing out-of-equilibrium processes.

Mixing Properties of Substitutional Solid Solutions

The thermodynamic state (molar volume V, entropy S, enthalpy H, Gibbs free energy G) of a SS of the $A_{1-x}B_xC$ type is conveniently characterized with respect to the thermodynamic functions of its pure end-members AC and BC (McGlashan 1979) (see Geochemical Thermodynamics). When no chemical interaction takes place at the atomic level, which is the case of a *mechanical mixture*, these quantities are obtained by simple linear interpolation between those of the end-members, weighted by their respective mole fractions $X_{AC} = 1 - x$ and $X_{BC} = x$. For example, the molar volume of a mechanical mixture is equal to $V_{M\,M} = X_{AC}\,V_{AC} + X_{BC}\,V_{BC}$, which is the expression of Vegard's rule, and its Gibbs free energy is equal to $G_{M\,M} = X_{AC}\,G_{AC} + X_{BC}\,G_{BC}$.

When solution takes place, the linear relationship between the SS thermodynamic functions and those of its end-members no longer holds. Mixing quantities (ΔV_M, ΔS_M, ΔH_M, ΔG_M) are then defined by difference between V, S, H, and G and those of the mechanical mixture, e.g., $\Delta G_M = G - X_{AC}\,G_{AC} - X_{BC}\,G_{BC}$.

A first contribution to ΔG_M, of entropic origin, arises due to the disorder induced by the substitution. In the case of full randomness, it expressed as (R the gas constant):

$$\Delta S_M^{id} = -R(X_{AC}\ln X_{AC} + X_{BC}\ln X_{BC}) \qquad (1)$$

ΔS_M^{id} is a positive quantity, which lowers $\Delta G_M = \Delta H_M - T\,\Delta S_M$ (T the temperature) and thus stabilizes the SS with respect to the mechanical mixture in the whole compositional range. When ΔG_M has no other contribution than ΔS_M^{id}, the SS is said to be *ideal* (hence the superscript *id*).

However, very few SSs are ideal, as shown by numerous results of advanced calorimetric and diffraction methods (Geiger 2001; Navrotsky 2014) (see Calorimetry). This stems from so-called *excess* mixing terms, including entropy as well as enthalpy contributions. The excess mixing entropy includes the vibrational entropy and a contribution due to the decrease in the number of accessible configurations with respect to perfect randomness when short-range order exists (Benisek and Dachs 2012). The excess mixing enthalpy involves elastic and chemical terms. The elastic one, always positive, results from the lattice distortions associated to mixing which increases the internal energy of both end-members. The chemical term is associated with effective

interactions between substituent and host atoms. They are both accounted for in the following polynomial expansion of ΔH_M proposed by Guggenheim (1937) for *non-ideal* SSs:

$$\Delta H_M = X_{AC}X_{BC}A_0 + X_{AC}X_{BC}(X_{AC} - X_{BC})[A_1 + A_2(X_{AC} - X_{BC}) + \ldots] \quad (2)$$

The first term relies on the number and strength of each type of nearest-neighbor bond. Its constant A_0 depends on the energy difference between chemical bonds connecting identical or distinct species $A_0 \propto 2W_{A-B} - W_{A-A} - W_{B-B}$. Usually, the largest contribution comes from the nearest neighbors, but longer-range interactions can also be included in this term. Multi-body interactions (triplet, quadruplet, etc.) are accounted for in the higher-order terms A_1, A_2, and so on. ΔH_M varies with temperature but usually more weakly than ΔS_M^{id}.

Aside from experimental methods to determine mixing properties, the huge development of numerical simulations in the last decades has allowed calculations of alloy thermodynamic properties such as short-range order in SSs and composition-temperature phase diagrams. A methodology, known as the cluster expansion method (Kikuchi 1951; Ducastelle 1991; Vinograd and Winkler 2010), consists in parametrizing the energy of an alloy under the form:

$$E = \sum_i g_i J_i (\Pi_j p_j) \quad (3)$$

in which the index i scans all existing pairs (in which case, j takes two values), triplets (j takes three values), etc., of degeneracy g_i associated to occupation numbers $p_j = \pm 1$ in the configuration upon consideration. The coefficients J_i of the cluster expansion are determined by fitting them to the energy of a relatively small number of configurations obtained through first-principle computations (see Density Functional Theory). The convergence of the expansion is usually rapid. Only a few terms representing pairs and small triplets are necessary to obtain good accuracy on thermodynamic properties.

The cluster expansion method gives a rationale for the Guggenheim expansion. However, the latter is a mean field approximation in which the probability of finding an AB pair is replaced by the (uncorrelated) product of site probabilities X_{AC} or X_{BC}. Going beyond such an approximation, for example, by using Monte Carlo approaches, based on the cluster expansion Hamiltonian, Eq. 3, is necessary to account for fluctuations of probabilities around their mean values and for possible ordered phases (van de Walle and Asta 2002).

When only the first term in the Guggenheim expansion is important, i.e., when the strength of the interactions is independent on composition, the SS is said to be *regular*, and ΔG_M is symmetric with respect to $x = 0.5$. Depending on the sign and the value of A_0, ΔG_M displays a single minimum ($A_0/RT < 2$) or two minima ($A_0/RT > 2$), as shown in Fig. 1.

SSs which require two terms in the polynomial expansion of ΔH_M (so-called two-parameter Margules model) are called *sub-regular* SSs. The A_1 term accounts for a linear dependence of the interactions on composition. It yields an asymmetry of ΔG_M with respect to $x = 0.5$. In the infinite dilution limits, $A_0 + A_1$ and $A_0 - A_1$ represent the solubilities of B in pure AC and A in pure BC, respectively (see Solubility).

The chemical potentials μ_i of the end-members (i = AC or BC) in the SS are derived from the knowledge of the molar Gibbs free energy $G = \Sigma_i \mu_i X_i$, as:

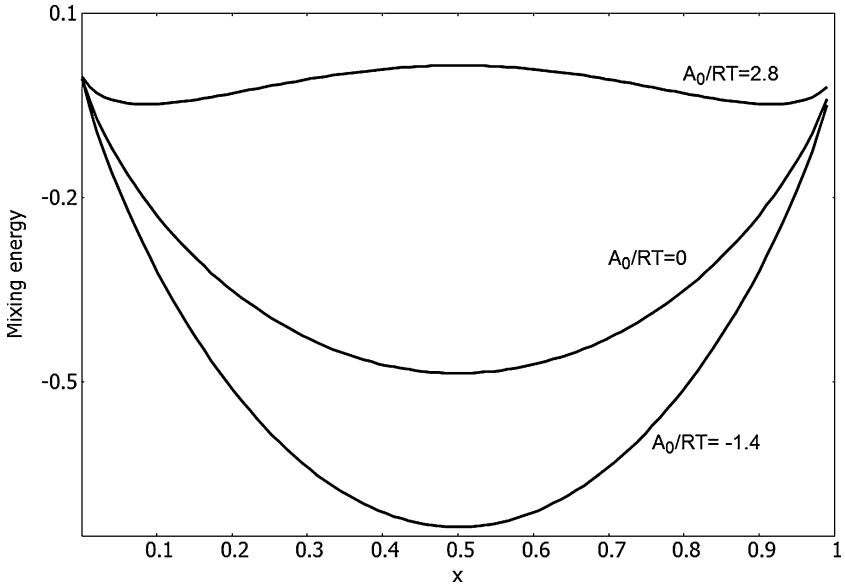

Solid Solution/Exsolution, Fig. 1 Composition dependence of the mixing Gibbs free energy of a regular SS for three values of $A_0/RT = -1.4$, 0 and +2.8

$$\mu_i = G + (1 - X_i)\left(\frac{\partial G}{\partial X_i}\right)_{P,T} \quad (4)$$

and this allows determining their activities a_i (see Activity and Activity Coefficients) through the relationship $\mu_i = G_i + RT$ Ln a_i (Neperian logarithm). For a given composition of the SS, μ_{AC} and μ_{BC} can be graphically read at the intersections of the tangent to the G curve at $x = 0$ and $x = 1$, respectively (Fig. 2, left panel). The activity coefficients $\gamma_i = a_i/X_i$ of the end-members in the SS are equal to 1 in ideal SSs, and their deviation from 1 evidences the existence of excess terms of mixing in the Gibbs free energy. Following Redlich-Kister, they read (Glynn 1991):

$$\begin{aligned} RT\ln\gamma_{AC} &= X_{BC}^2(A_0 + A_1(3X_{AC} - X_{BC}) + \ldots) \\ RT\ln\gamma_{BC} &= X_{AC}^2(A_0 - A_1(3X_{BC} - X_{AC}) + \ldots) \end{aligned} \quad (5)$$

These concepts may be generalized to the case of multiple substitutions. For example, when the two substitutions occur on different sites and are uncoupled, the solid solution, of generic chemical formula $A_{(1-x)(1-y)}B_{x(1-y)}C_{y(1-x)}D_{xy}$, has four end-members (A, B, C, D), associated to molar fractions $X_A = (1 - x)(1 - y)$, $X_B = x(1 - y)$, $X_C = y(1 - x)$, and $X_D = xy$. The molar fractions are linked not only by the usual relationship $X_A + X_B + X_C + X_D = 1$ but also by the cross product equality $X_A X_D = X_B X_C$, which results from the fact that there are only two independent composition parameters (x and y). Such solid solutions are referred to as *reciprocal* solid solutions. Contrary to the case of a single substitution, they are non-ideal with end-member activity coefficients different from 1 (Ganguly 2001), even when the mixing in each site is ideal, i.e., when ΔG_M only involves the ideal mixing entropy term:

$$\Delta S_M^{id} = -R(x\ln x + (1-x)\ln(1-x) + y\ln y + (1-y)\ln(1-y)) \quad (6)$$

Temperature-Composition Phase Diagram

Igneous rocks are formed when a magma or a lava cools and solidifies. Metamorphic rocks, for their part, result from the transformation of existing rocks when they are subject to heat and/or pressure. SSs are often encountered in these cases. The phases in presence, once thermodynamic equilibrium has been reached, can be read on a temperature-composition $T - x$ phase diagram, directly derived from the canonical ensemble expression of G discussed previously (see Phase Equilibria).

Thermodynamic Equilibrium

When the mixing Gibbs energy is negative and displays a single minimum as a function of composition, as in the case of ideal or weakly non-ideal SSs, an homogeneous mixing is energetically favorable over a mechanical mixture, and a SS exists in the whole composition range.

When ΔG_M displays two minima, as in the case of strongly non-ideal mixing, there exists a composition range $x_1 < x < x_2$, called the *miscibility gap*, in which an homogeneous SS is unstable with respect to the coexistence of two immiscible SSs α and β of compositions x_1 and x_2. Phase separation thus takes place. For such a process to be thermodynamically stable, the chemical potentials of the end-members μ_i (i = AC or BC) have to be equal in the two phases: $\mu_i^\alpha = \mu_i^\beta$. This requirement

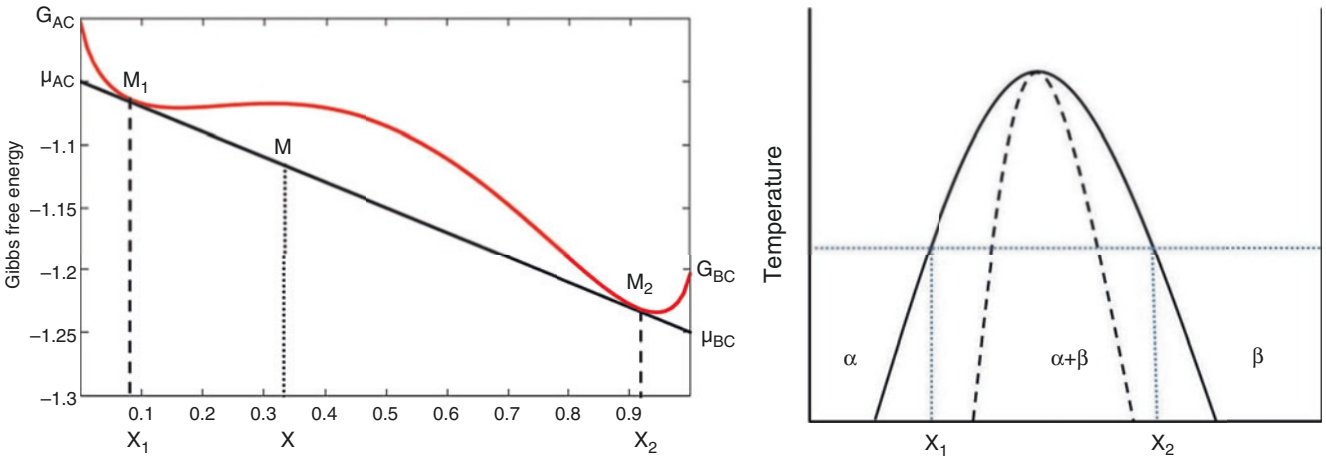

Solid Solution/Exsolution, Fig. 2 Left panel: Composition dependence of the Gibbs free energy of a strongly non-ideal regular SS at fixed temperature T ($A_0/RT = +2.8$). The plain straight line is the common tangent to ΔG_M, marking the limits of the miscibility gap $x_1 < x < x_2$. Right panel: Typical phase diagram of a strongly non-ideal SS. The region of the miscibility gap is delineated by the solvus (plain line). The spinodal line is represented by a dashed line

graphically defines the compositions x_1 and x_2 of the α and β SSs as the abscissa of the points of common tangent to the G curve (Fig. 2, left panel). The locus of these points when temperature varies is called the *solvus* (Fig. 2, right panel). For a given average composition x of the solid phase, the proportions Q_α and Q_β of the α and β phases are given by the ratios MM_2/M_1M_2 and MM_1/M_1M_2 of the tangent segments represented in Fig. 2, respectively (lever rule). When T increases at fixed pressure, the miscibility gap generally becomes narrower, because the negative contribution to G coming from the ideal entropy term increases (in absolute value) much more rapidly than the positive enthalpic contribution. Beyond a critical temperature T_M, called the *upper consolute temperature*, the region of phase coexistence vanishes, and the components of the mixture are soluble in all proportions.

The generic phase diagram displayed in Fig. 2 is highly simplistic, since only two ordered phases are considered (the end-members). The phase diagrams of metallic alloys, for example, often involve several ordered phases and several regions of miscibility gaps between them and SS phases with various compositions. Mixed carbonate minerals may also display more complex phase diagrams, the most famous example being the calcite-magnesite system with the ordered dolomite phase at 50% composition. Several numerical codes allow calculation of the phase diagrams of binary systems, e.g., the ATAT code (van de Walle 2017) and the OpenCalphad code (Fries 2013).

Exsolution Process

When a SS which is homogeneous in the temperature range $T > T_M$ enters the region of a miscibility gap, phase separation, also called demixing or exsolution, occurs. Exsolution begins at the atomic scale, but as it continues, the exsolved phase usually forms irregular patterns (lamellae, films or patches), depending on the region of the miscibility gap in which it takes place. A special curve, called *spinodal* (Fig. 2 right panel), which connects the inflection points of G inside the miscibility gap (condition $\partial^2 G/\partial x^2 = 0$), separates the latter in two regions in which the early composition fluctuations leading to exsolution are either periodic or exponentially decaying in space.

Most minerals exsolve upon appropriate conditions of temperature, pressure, and composition, e.g., feldspars, pyroxenes, amphiboles, micas, oxides, carbonates, and sulfides (e.g., Schumacher 2007). For example, the important group of feldspars, to which belong the most abundant phases of igneous rocks, can be described in the ternary solid solution system: albite $NaAlSi_3O_8$, microcline $KAlSi_3O_8$, and anorthite $CaAl_2Si_2O_8$. Albite-microcline SSs, called alkali feldspars, which are formed at high temperature, easily exsolve at low temperature, each end-member being only able to substitute a small amount of the other alkali ion. At variance, plagioclases, which are also formed at high temperature, do not exsolve. All intermediate compositions are known between their end-members albite and anorthite. These feldspar SSs play an important role as components of granitic rocks and major contributors to hydrothermal alteration or weathering processes at lower temperature.

The process of exsolution of a SS may be used in solvus geothermobarometry (see Geothermometry and Geobarometry), due to the sensitivity of the exsolved phase composition to temperature and pressure. Data on geothermometers are derived from both laboratory studies on artificial mineral assemblages, where minerals are grown at known temperatures and pressures and the chemical equilibrium measured directly, and from calibration using natural systems. They also require a theoretical thermodynamic understanding of the components and phases involved. The measurements and interpretation are not straightforward and may lead to noticeable uncertainties, because it is difficult to assess if a system has truly reached thermodynamic equilibrium. Moreover, the synthesized minerals are difficult to characterize due to their often poor crystallinity and their submicrometer sizes.

Solid Solutions Formed by Precipitation from a Supersaturated Aqueous Fluid

Another important class of SS formation processes concerns the precipitation from a supersaturated aqueous solution (AS) (see Aqueous Solutions). At variance with results obtained in the canonical ensemble (fixed P, T, and composition), the mean composition of a SS in equilibrium with a multicomponent aqueous medium is not a priori fixed but depends on the composition of the AS, which may change if external conditions do so (Glynn and Reardon 1990; Prieto 2009). In natural solutions, a large number of chemical elements are usually present which may participate to the formation of secondary minerals, either as major constituents or as trace elements in solid solutions. Clay minerals which are very commonly produced in geochemical systems (weathering sequences, hydrothermal alterations, diagenetic transformations) are striking examples of SS phases formed in the presence of an AS. They display large composition variability, by substitution in their skeleton (tetrahedral and octahedral sites) and/or cation exchange in their interlayer space (see Fluid-Rock Interactions, Hydrothermal Alteration, Weathering: Chemical). Clays as well as other SSs share the major property of being able to adapt their composition to the evolution of the fluid composition as a function of time (Tardy and Fritz 1981).

Thermodynamic Equilibrium

As a general statement, a solid of fixed composition is in equilibrium with an AS when their chemical potentials are

equal. The chemical potential of the relevant ions in the AS is equal to $\mu_{\text{ions}} = RT\ln(IAP)$, with IAP the ion activity product, and the chemical potential of the solid phase is equal to its Gibbs energy per mole, which defines its solubility product K: $\mu_{\text{solid}} = RT\ln K$ (See Solubility). Equilibrium is thus reached when $K = IAP$, or equivalently, when the saturation state of the AS with respect to the solid $I = IAP/K = 1$.

The generalization of this condition to a binary SS $A_{1-x}B_xC$ in equilibrium with an AS involves two conditions, one for each end-member i (i = AC or BC), stating that their chemical potentials are equal to the chemical potential of their corresponding ions in the AS. Using the expression $\mu_i = G_i + RT\ln X_i\gamma_i$ and introducing the solubility products K_i of the end-members and the saturation states I_i of the AS with respect to them, the conditions for thermodynamic equilibrium are:

$$\begin{aligned} I_{AC} &= (1-x_0)\gamma_{AC}(x_0) \\ I_{BC} &= x_0\gamma_{BC}(x_0) \end{aligned} \tag{7}$$

Numerical codes, like KINDIS (Madé et al. 1994) or PHREEQC (Parkhurst and Appello 2013), allow the determination of the SS characteristics in equilibrium with an aqueous solution.

Equation 7 shows that, while a BC compound would not form as a pure phase in a highly undersaturated AS ($I_{BC} \ll 1$), B ions may easily be incorporated as trace elements in the substitutional sites of an AC compound, if the AS is nearly saturated with respect to the latter ($I_{AC} \simeq 1$). This illustrates why most mineral phases produced in natural systems are not pure end-members. Conversely, quasi pure phases are strong indicators of the composition of the fluids that produced them and may be an indicator of paleo-conditions.

Stoichiometric Saturation State

Thermodynamic equilibrium conditions (Eq. 7) are equivalent to saying that the stoichiometric saturation state $I(x)$ of the AS with respect to the SS of composition x is simultaneously equal to 1 and maximum with respect to x. This can be proved by considering the stoichiometric solubility product $K(x)$ of the SS, equal to:

$$K(x) = K_{AC}^{1-x}K_{BC}^{x}\exp\left(\frac{\Delta G_M}{RT}\right) \tag{8}$$

and writing $I(x) = IAP/K(x)$, i.e.:

$$I(x) = \left[\frac{I_{AC}}{(1-x)\gamma_{AC}(x)}\right]^{1-x}\left[\frac{I_{BC}}{x\gamma_{BC}(x)}\right]^{x} \tag{9}$$

When only the condition that $I(x)$ is maximum with respect to x is fulfilled, one speaks of the *stoichiometric saturation state*. It amounts to considering the SS with respect to which the AS is the most supersaturated (Prieto 2009). Its composition x_{st} obeys the implicit equation:

$$\frac{I_{AC}}{(1-x_{st})\gamma_{AC}(x_{st})} = \frac{I_{BC}}{x_{st}\gamma_{BC}(x_{st})} \tag{10}$$

It obviously only depends on the composition of the AS through the quantity $W = I_{BC}/I_{AC} = [B]K_{AC}/[A]K_{BC}$, proportional to the ratio of activities of the exchangeable ions. Equation 10 has no analytic solution. However, it can be solved numerically quite easily for regular and sub-regular SSs (Noguera et al. 2016). It has a single root whenever ΔG_M displays a single minimum and three roots if ΔG_M has two minima. The number of solutions of Eq. 10 thus only depends on the values of the coefficients A_0 and A_1 in the Guggenheim expansion of ΔH_M.

When Eq. 10 has three roots, two correspond to a minimum of $I(x)$ and one to a maximum. Of the two minima, the one which is relevant is associated to the lowest Gibbs free energy of the system (lowest value of $-\ln I(x)$). Because the $I(x)$ curves associated to the three roots cross each other, a discontinuity in x_{st} between two values x_1 and x_2, characterized by the same Gibbs free energy, takes place for some specific value of W, as shown in Fig. 3. The discontinuity $x_2 - x_1$ marks the existence of a miscibility gap, which increases as the SS becomes more and more non-ideal. In this representation, W combines the information on the AS composition and on the solubility products of the end-members, in a more compact way than the (equivalent) classical Roozeboom plot (Mullin 1993) which displays x_{st} as a function of $[B]/([A]+[B])$ but requires one curve for each K_{BC}/K_{AC} ratio.

Out-of-Equilibrium Processes

The stoichiometric saturation state does not fully characterize thermodynamic equilibrium, but its characteristics are useful to approach nucleation and growth processes (see Crystal Growth).

Within the classical nucleation theory, assuming that the SS surface energy σ and molar volume v are weakly dependent on composition, the change in Gibbs free energy in the formation of a SS nucleus of composition x and containing n formula units reads (k_B the Boltzmann constant and X a shape factor) (Markov 1995; Noguera et al. 2016):

$$\Delta G(n,x) = -nk_BT\ln I(x) + n^{2/3}v^{2/3}X\sigma \tag{11}$$

When $I(x) > 1$, $\Delta G(n,x)$ displays a maximum as a function of n, which defines the nucleus size and the barrier $\Delta G_m(x)$ to overcome for its nucleation:

$$\Delta G_m(x) = \frac{4X^3\sigma^3v^2}{27(k_BT\ln I(x))^2} \tag{12}$$

S

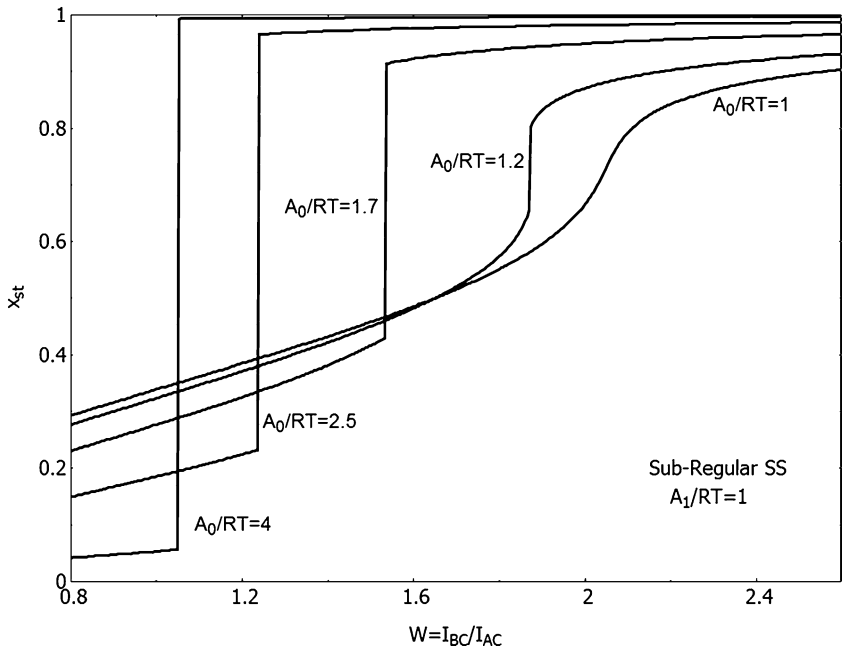

Solid Solution/Exsolution, Fig. 3 Representation of the relationship between a sub-regular SS composition x_{st} and $W = ([B]K_{AC})/([A]K_{BC})$, which characterizes the AS composition, for $A_1/RT = 1$ and various values of the Guggenheim parameters A_0/RT. When $A_0/RT \gtrsim 1.15$, the x_{st} curve displays a discontinuity

The composition x^* of the critical nuclei is then determined by the condition that the nucleation barrier is minimum with respect to x, leading to a maximum of the nucleation frequency. Since, according to Eq. 12, this amounts to finding the maximum of $\ln I(x)$, the composition of the critical nuclei is equal to x_{st}. A similar reasoning can be applied to the composition of the incremental growth layers, when growth is limited by surface reactions.

Since the composition of an AS may vary with time, either because external conditions change (temperature or seasonal cycles) or in a closed system due to the precipitation process itself, x_{st} is also due to depend on time. Time variations of the particle composition thus usually occur, which leads either to a change in the average composition (if solid-state diffusion is efficient) or to composition inhomogeneities inside the particles (composition profiles) when solid-state diffusion does not occur. Considering the typical evolution of x_{st} as a function of the AS composition W as shown in Fig. 3, the composition profiles are smooth in ideal or weakly non-ideal SSs, while they display a discontinuity for strongly non-ideal SSs. Except under very specific conditions, W does not remain fixed at the critical value of the discontinuity during the precipitation process so that demixing is much less likely than in processes at constant T, P, and x conditions. Numerical codes like KINDIS (Madé et al. 1994) or NANOKIN (Noguera et al. 2010) account for the kinetics of precipitation of SSs under various approximations.

The specificity of SS dissolution kinetics has not been considered in details so far. In dissolution processes, SSs are generally assumed to be defined compounds with a fixed composition inherited from their formation conditions. This assumption overlooks the existence of a distribution of compositions inside the particle population and the existence of composition profiles inside each particle. Moreover, when equilibrium is approached, the activity ratio of the ions released in the AS is likely closer to that in the solid phase than to the one required in the AS for thermodynamic equilibrium. The way equilibrium can be reached thus remains an open question.

Summary

Solid solutions are ubiquitous in the natural environment, due to the existence of multicomponent fluids (aqueous solutions or melts) from which they form. Their major property is their ability to continuously adapt their composition as the fluid composition evolves in time. Their phase diagrams may involve homogeneous phases in part or in the whole concentration range and regions of phase separation. Incorporation of trace elements is often thermodynamically easy, which explains the scarcity of pure minerals, particularly those formed at low temperature and pressure. While the description of their mixing properties and their equilibrium properties has greatly improved in the last decades, both experimentally and theoretically, much remains to be done to account for the kinetics of their formation and dissolution.

Cross-References

- ▶ Activity and Activity Coefficients
- ▶ Aqueous Solutions
- ▶ Calorimetry

▶ Carbonate Minerals and the CO2-Carbonic Acid System
▶ Chemical Weathering
▶ Clay Minerals
▶ Crystal Chemistry
▶ Density Functional Theory
▶ Fluid–Rock Interaction
▶ Geochemical Thermodynamics
▶ Geothermometry and Geobarometry
▶ Hydrothermal Alteration
▶ Ionic Radii
▶ Oxide Minerals
▶ Phase Equilibria
▶ Silicate Minerals
▶ Solubility
▶ Trace Elements

References

Benisek A, Dachs E (2012) A relationship to estimate the excess entropy of mixing; application in silicate solid solutions and binary alloys. J Alloys Compd 527:127–131
Ducastelle F (1991) Order and phase stability in alloys. Elsevier, New York
Fries SG (2013) http://www.opencalphad.com/
Ganguly J (2001) Thermodynamic modelling of solid solutions. In: Geiger C (ed) Solid solutions in silicate and oxide systems, EMU notes in mineralogy, vol 3. Eötvös University Press, Budapest, pp 37–70
Geiger C (2001) Thermodynamic mixing properties of binary oxide and silicate solid solutions determined by measurements: the role of strain. In: Geiger C (ed) Solid solutions in silicate and oxide systems, EMU notes in mineralogy, vol 3. Eötvös University Press, Budapest, pp 71–100
Glynn PD (1991) MBSSAS: a code for the computation of the Margules parameters and equilibrium relations in binary solid-solution aqueous solution systems. Comput Geosci 17:907–966
Glynn PD, Reardon EJ (1990) Solid-solution aqueous-solution equilibria: thermodynamic theory and representation. Am J Sci 290:164–201
Guggenheim EA (1937) Theoretical basis of Raoult's law. Trans Faraday Soc 33:151–159
Kikuchi R (1951) A theory of cooperative phenomena. Phys Rev 81:988–1003
Madé B, Clément A, Fritz B (1994) Modelling mineral solution interactions: the thermodynamic and kinetic code KINDISP. Comput Geosci 20:1347–1363
Markov IV (1995) Crystal growth for beginners: fundamentals of nucleation, crystal growth and epitaxy. World Scientific, Singapore/London/Hong Kong
McGlashan ML (1979) Chemical thermodynamics. Academic Press, London
Mullin JW (1993) Crystallization. Butterworth-Heinemann
Navrotsky A (2014) Progress and new directions in calorimetry: a 2014 perspective. J Am Ceram Soc 97:3349–3359
Noguera C, Fritz B, Clément A (2010) Simulation of the nucleation and growth of binary solid solutions in aqueous solutions. Chem Geol 269:89–99
Noguera C, Fritz B, Clément A (2016) Kinetics of precipitation of non-ideal solid-solutions in a liquid environment. Chem Geol 431:20–35
Parkhurst DL, Appello CAJ (2013) Description of input and examples for PHREEQC version 3-a computer program for speciation, batch-reaction, one-dimensional transport, and inverse geochemical calculations: U.S. Geological Survey Techniques and Methods, book 6, chap. A43, p 497
Prieto M (2009) Thermodynamics of solid solution-aqueous solution. In: Thermodynamics and kinetics of water-rock interaction, Reviews in mineralogy and geochemistry, vol 70. Mineralogical Society of America/Geochemical Society, Chantilly/St. Louis, pp 47–85
Schumacher JC (2007) Metamorphic amphiboles: composition and coexistence. In: Amphiboles: crystal chemistry, occurrence, and health issues, Reviews in mineralogy and geochemistry, vol 67. Mineralogical Society of America/Geochemical Society, Chantilly, pp 359–416
Tardy Y. et Fritz B (1981) An ideal solid solution model for calculating solubility of clay minerals. Clay Minerals 16:361–373
van de Walle A (2017) The alloy-theoretic automated toolkit (ATAT): a user guide. http://www.brown.edu/Departments/Engineering/Labs/avdw/atat/
van de Walle A, Asta M (2002) Self-driven lattice-model Monte Carlo simulations of alloy thermodynamic properties and phase diagrams. Modelling Simul Mater Sci Eng 10:521–538
Vinograd VL, Winkler B (2010) An efficient cluster expansion method for binary solid solutions: application to the halite-silvite, NaCl-KCl, system. In: Wentzcovitch R, Stixrude L (eds) Theoretical and computational methods in mineral physics: geophysical applications, Reviews in mineralogy and geochemistry, vol 71. The Mineralogical Society of America, Chantilly, pp 413–436

Solubility

Jean-François Boily
Department of Chemistry, Umeå University, Umeå, SE, Sweden

Definition

Solubility is the maximal quantity that a substance can dissolve as a solute in a host solvent, forming a saturated solution. Any additional quantity occurs as a precipitate and results in a suspension of particles. Solubility is expressed in terms of concentration units for a given temperature and pressure.

Introduction

Solubility is an essential concept needed in many areas of geochemistry to describe the ability of gases (g), liquids (l), or solids (s) to dissolve in substances. The resulting solutions are homogeneous mixtures of two or more substances, where the solvent is typically, although not necessarily, one of high mole fraction and the solute of lower mole fractions. Examples include the dissolution of sodium chloride (halite) in water, or of water in magmas. In contrast to miscibility where

substances can mix in all proportions (e.g., water and ethanol), solubility pertains to the maximal quantity that can be accomodated by the host solvent. This quantity is predominantly one determined by laboratory experiments, explained by molecular details of solute–solvent interactions, and predicted by thermodynamics.

The concept of solubility is essential for understanding and predicting numerous forms of mass transport processes in fluids of Earth's surface and subsurface. Examples include fluid flow in geothermal systems and ore deposits, diagenesis, secondary porosity generation in sedimentary basins, contaminant transport in aquifers, as well as injection of supercritical CO_2 in geological storage sites and remediation of contaminated sites. The concept is also needed in experimental simulations of geochemical reactions, such as in the study of mineral growth, nucleation and dissolution, as well as in laboratory (e.g., preparation, purification) procedures and analytical determination of natural samples. This concept is even needed in molecular simulations of geological fluids for determining the maximal number of ions that can be realistically inserted into a box of solvent molecules.

Solubility is expressed as a concentration for a given temperature and pressure. The mass fraction (w_i) of solute *i* in solvent *solv* is given by:

$$w_i = \frac{s_i}{s_i + s_{\text{sol}}} \tag{1}$$

where s_i and s_{solv} are respectively the masses of the solute and of the solvent. Other concentration units relate to w_i through:

$$[i] = 1000\,\rho_{\text{solv}}\,\frac{w_i}{M_i} \quad \text{for Molarity} \tag{2}$$

$$m_i = 1000\frac{w_i}{M_i(1-w_i)} \quad \text{for Molality} \tag{3}$$

$$x_2 = \frac{w_i}{M_i}\left(\frac{w_i}{M_i} + \frac{1-w_i}{M_{\text{solv}}}\right)^{-1} \quad \text{for mole fraction} \tag{4}$$

$$r_i = 100\frac{w_i}{1-w_i} \quad \text{for mass of solute per 100 g water} \tag{5}$$

and where ρ_{solv} is the density of the solvent and M is molecular weight.

A conventional rule of thumb for rationalizing aqueous solubility involves the concept of polarity. A polar solute is soluble in a polar solvent, like water, but insoluble in a nonpolar solvent, like benzene. Likewise, the solubility of an organic molecule in water can be largely controlled by the population and distribution of polar groups (e.g., carboxyls) on a molecule. On the molecular front, solubilization can be explained by the differences between solute/solvent interaction energies with those of solute/solute and solvent/solvent interactions. Intermolecular, ion-dipole, ion- and dipole-induced dipole as well as (London) dispersion forces govern the ability of a solvent to host solutes. Hydrogen bonding in water is notably a well-known form of interaction solubilizing hydrophilic substances. Solubility can be strongly affected by temperature due to changes in the hydrogen-bonding capability of water, explained through changes in its dipole moment (dielectric constant) and self hydrogen bonding populations and structure.

In this article, thermodynamic expressions describing solubility are presented alongside several key examples also detailing the molecular-level details of solute–solvent interactions.

Thermodynamics of Solubility

The Gibbs free energy of formation of solutes generated by the dissolution of a substance into a solvent at a given temperature (T) relates to, just as all in chemical processes, the enthalpy (H) and entropy (S) of the reaction, $\Delta G = \Delta H - T\Delta S$. The enthalpy change resulting from this reaction is accounted for by Hess' law:

$$\Delta H_{\text{soln}} = \Delta H_{\text{solute}} + \Delta H_{\text{solvent}} + \Delta H_{\text{solute-solvent}} \tag{6}$$

where ΔH_{soln} is the total heat of solution, ΔH_{solute} is the (endothermic) heat involved in separating the solute particles against intermolecular forces of the original substance (e.g., lattice energy of solids), $\Delta H_{\text{solvent}}$ is the (endothermic) heat involved in separating the solvent molecules to accomodate the solute, and $\Delta H_{\text{solute–solvent}}$ is the (exothermic) heat resulting from solute–solvent interactions. For the specific case of the dissolution of a solid in water, hydration energy (ΔH_{hydr}) is the sum of the $\Delta H_{\text{solvent}}$ and $\Delta H_{\text{solute–solvent}}$ terms and is exothermic when ion–water dipole interactions are stronger than the sum of water–water hydrogen bonds broken to accomodate the ion.

The entropic contribution to these reactions pertains to the dispersion of solutes from a solid to the solvent. In a system of *r* components, the entropy of mixing is:

$$\Delta S_{\text{mix}} = -Nk_{\text{B}}\sum_{i=1}^{r} x_i \ln x_i \tag{7}$$

where N is the number of molecules, k_B Boltzmann's constant, x_i is a mole *fraction* (also, probability of finding a component in a given site). As such, there is always a gain in entropy during as substances randomly mix in a solution. Entropy is the driving force for dissolution when no heat is exchanged, such as in the mixing of organic liquids. However, when heat is exchanged, dissolution will be favored by

reactions that are strongly exothermic to mildly endothermic. These reactions proceed until saturation is achieved, namely, at solubility, the point beyond which no additional solute can be accomodated by the solvent.

A thermodynamic description of solubility in non-ideal (real) solutions begins with the chemical potential $\left(\mu_i = (\delta G/\delta N_i)_{T,P,N_j}\right)$ of solute species i at temperature T and pressure P:

$$\mu_i = \mu_i^*(T,P) + \mathrm{RT}\gamma_i x_i = \mu_i^*(T,P) + \mathrm{RT}a_i \tag{8}$$

where μ_i^* is the chemical potential of the ideal species, γ_i is the activity coefficient, x_i the mole fraction, and the activity is given by $a_i = \gamma_i\, m_i$. When, say, a gas (g; μ_i^θ) is in equilibrium with a liquid solution (l), the chemical potential of species i will be identical in both phases:

$$\begin{aligned}\mu_i(g) = \mu_i(l) &= \mu_i^*(T,P) + \mathrm{RT}\ln\gamma_i x_i \\ &= \mu_i^\theta(T) + \mathrm{RT}\ln P_i\end{aligned} \tag{9}$$

From this equation:

$$P_i = \gamma_i x_i k_i \tag{10}$$

with

$$k_i = \exp\left(\frac{\mu_i^*(T,P) - \mu_i^\theta(T)}{\mathrm{RT}}\right) \tag{11}$$

Thus, if the mole fraction x_i is 1, we have Raoult's law (Convention I) where k_i relates to the vapor pressure of the solvent of dilute solutions or mixtures of similar types of liquids.

As many solutions cannot form high mole fractions of each substance, the main species present at high mole fractions is referred as the solvent and the minor species the solute. As stated above, *solubility* is the composition of a solution containing the *maximal* quantity of a solute that can be incorporated by a solvent. In this case, Convention II for activity coefficients (γ) stipulates distinct thermodynamic treatments for the solvent and the solutes. Thus, as in Raoult's law, the chemical potential of the solvent is expressed through:

$$\mu_{\mathrm{solv}} = \mu_{\mathrm{solv}}^*(T,P) + \mathrm{RT}\ln\left(\gamma_{\mathrm{solv}} \cdot x_{\mathrm{solv}}\right) \tag{12}$$

with $\gamma_{\mathrm{solv}} \to 1$ when the mole fraction $x_{\mathrm{solv}} \to 1$. For the solute, the chemical potential also becomes:

$$\mu_{\mathrm{solute}} = \mu_{\mathrm{solute}}^*(T,P) + \mathrm{RT}\ln\left(\gamma_{\mathrm{solute}} \cdot x_{\mathrm{solute}}\right) \tag{13}$$

except that $\gamma_{\mathrm{solute}} \to 1$ when $x_{\mathrm{solute}} \to 0$. The chemical potential of the solute (μ_{solute}^*) is that of the ideal ($\gamma_{\mathrm{solute}} = 1$) pure solute at $x_{\mathrm{solute}} = 1$ for a given T and P. Under dilute conditions solute–solute interactions are negligible, and μ_{solute} is dominated by solute–solvent interactions, and Eq. 10 is then Henry's law with the constant $k_{Hi} = k_i$. In this case, the chemical potential of the solute is one behaving as an ideal liquid under infinite dilution ($\gamma_{\mathrm{solute}} \to 1$). Stated otherwise, at equilibrium, the mass of gas dissolved in the solvent is proportional to its partial pressure in the adjacent gas phase. The temperature dependence of k_{Hi} can be expressed via the van't Hoff equation (e.g., $k_{H_i} = k_{H_i}{}^{\mathrm{ref}}\exp\left[C\left(\frac{1}{T} - \frac{1}{T^{\mathrm{ref}}}\right)\right]$, where ref denotes a reference (e.g., standard state) value and C a constant in Kelvin related to the enthalpy of the solution.

When working within solutions only and the mole fraction of the solute i is sufficiently low, the chemical potential ($\mu_{m,i}$) of species i is more conveniently expressed on a molality (m_i; moles per kg solvent) scale, such that

$$\mu_{m,i} = \mu_{m,i}^*(T,P) + \mathrm{RT}\ln\left(\gamma_{m,i} m_i\right) \tag{14}$$

and where the activity of i is $a_{m,i} = \gamma_{m,i} m_i$. In this case, the standard state is a fictious 1 molal (or molar) solution where $\gamma_{m,i} = 1$. This is a widely used convention in the realms of low temperature aqueous and hydrothermal geochemistry. Activity coefficients can be neglected for solutions containing a constant ionic strength or predicted using extended Debye-Hückel (I < 0.1 m), Güntelberg (I < 0.1 m), or Davies (I < 0.5 m) theories. The (semiempirical) Pitzer ion interaction model can alternatively be used for a wider range of ionic strengths, as, for instance, simultaneously applied for various minerals of eight component Na-K-Mg-Ca-H-Cl-SO_4-OH-HCO_3-CO_3-CO_2-H_2O system (Harvie et al. 1984).

Building upon this framework, the dissolution of, say, the binary A_xC_y solid, with the soluble anion A^{z-} and cation C^{z+}

$$A_xC_y(s) \rightleftharpoons xA^{z-}(aq) + yC^{z+}(aq) \tag{15}$$

is predicted with the equilibrium constant

$$K = \frac{a_A{}^x a_C{}^y}{a_{\mathrm{AC}}} = \gamma_A{}^x \gamma_C{}^y \cdot m_A{}^x m_C{}^y \tag{16}$$

Taking the activity of A_xC_y to 1 ($a_{\mathrm{AC}} = 1$), the *solubility product* is defined as

$$K = K_{\mathrm{sp}} = a_A{}^x a_C{}^y \tag{17}$$

where the activities of A^{z-} and C^{z+} at saturation are used to obtain K_{sp}. As such, when the ion activity product (IAP) product exceeds the solubility product (IAP > K_{sp}) precipitation occurs, but when it is below this value (IAP < K_{sp}),

dissolution occurs. Concrete examples include the solubility of silica:

$$SiO_2(s) + 2H_2O \rightleftharpoons H_4SiO_4 \quad (18)$$

with $K_{sp} = a_{H_4SiO_4}$ because $a_{SiO_2} = 1$ and $a_{H_2O} = 1$ and that of calcite with

$$CaCO_3(s) + H^+ \rightleftharpoons Ca^{2+} + HCO_3^- \quad (19)$$

with $K_{sp} = a_{Ca^{2+}} a_{HCO_3^-} a_{H^+}^{-1}$ because $a_{CaCO_3} = 1$.

As solubility is affected by the ability of the solvent to overcome the attractive forces of the solute molecules of the incipient substance, temperature increases the kinetic energy of the solvent molecules and therefore generally favors solubility. This can be generally observed in inorganic salts (Fig. 1). Still, retrograde (or reverse) solubility occurs for solids whose dissolution is exothermic, such as cerium sulfate, calcium carbonate, calcium sulfate, calcium phosphate, and magnesium silicate.

The pressure (P) dependence, in turn, is given by the differences in the partial molal volumes (ΔV) of the solids involved

$$\log\left(\frac{K_{sp,P}}{K_{sp,P_{ref}}}\right) = \frac{-\Delta V(P - P_{ref})}{2.303\ RT} \quad (20)$$

While this dependence is typically negligible for Earth surface processes, it becomes essential for predictions of deeper Earth and deep sea processes. Examples include pressure dissolution phenomena within solutions at grain boundaries under where pressure (cf. stylolites), or the enhanced solubility of calcite in oceanic bottoms (cf. carbonate compensation depth).

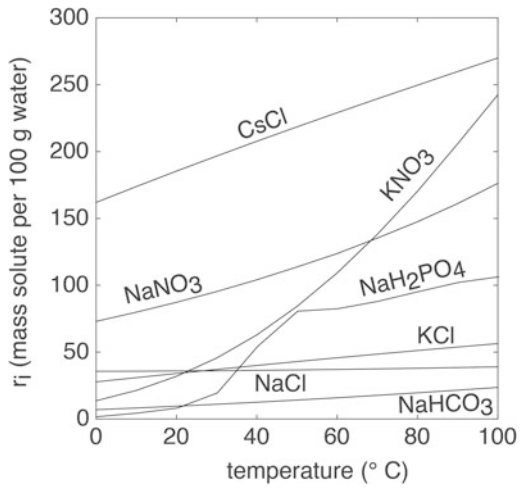

Solubility, Fig. 1 Solubility of common inorganic salts in water

Prediction of solubility can be made using thermodynamic parameters derived by experimentation and with values tabulated in comprehensive reviews on the subject (e.g., IUPAC-NIST Solubility Database). As a note of caution, databases of solubility constants can contain large variations for the same substances, such as minerals. These disprepancies can arise from numerous factors including (1) variations in crystallinity, (2) impurities or trace elements hindering congruent dissolution, (3) unaccounted complexing agents (e.g., pH buffers such as potassium hydrogen phthalate), (4) differences in equilibration criteria, (5) variations in ionic strength, and (6) heterogeneous particle size distributions. Ideally, solubility constants of solids ought to pertain to highly crystalline, pure, large monocrystalline particles of low specific surface area. Still, even for pure samples, particles of high specific surface area (cf. submicrometer-sized particles) may have shifted reaction energies. This shift can be expressed through and apparent (*app*) solubility constant with:

$$\log K_{s,app} = \log K_s + \frac{\gamma A}{3.454\ RT} \quad (21)$$

where γ is surface tension, A is the molar surface area of the solute. Tightly bound water molecules on small (e.g., nanometer-sized) particles can impact surface tension and therefore reaction energies. The impact of particle size on the thermodynamics of deydroxylation reactions of iron oxyhydroxides to iron oxides was notably demonstrated by (Navrotsky et al. 2008).

Examples of Solubility

Gases in Water

Dissolution of gases in liquids require the accommodation of the host solvent for the gaseous molecules. Those reacting with the solvent will have greater solubilities than those that are relatively inert. For example, the solubility of common gases in geochemistry is greater in the order $He < N_2 < O_2 < CH_4 < CO_2 < NH_3$. Generally, the solubilization of a nonpolar gas in a solvent first involves an endothermic component to make space for the molecule. An exothermic component then results from the formation of a hydrophobic hydration shell via van der Waals dispersion interactions (e.g., H_2O gas), forming a clathrate-like environment. Reactions are generally more endothermic in organic solvents than in water because the energy required to accomodate space for the solute is larger, and less energy is released via organic solvent–solute interactions. Thus, following Le Châtelier's principle, the solubility of gases in water is generally smaller at larger temperatures where heat is added to the system. Additionally, as dissolved salts effectively compete for hydration waters, gas solubility is

generally lowered by salinity, as, for example, shown in the case of O_2 solubility in aqueous solutions of NaCl (Fig. 2) (Benson and Krause 1984).

Gases undergoing reactions with water, such as CO_2 and NH_3 are, on the other hand, more soluble. The case of CO_2 solubility in water

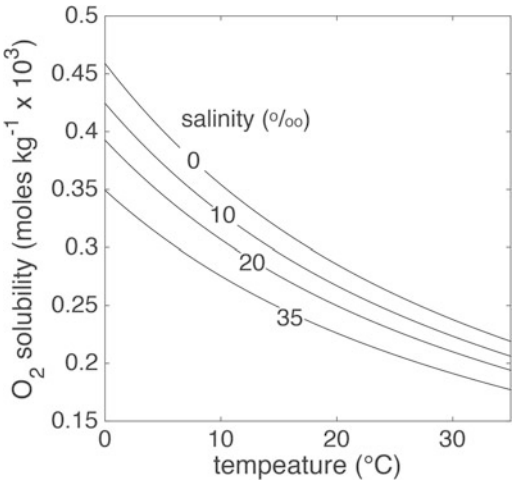

Solubility, Fig. 2 Impact of salinity (NaCl) on solubility of oxygen in water

$$CO_2(g) \rightleftharpoons CO_2(aq) \tag{22}$$

is a pivotal process to many geochemical processes and can be predicted through Henry's constant (K_H) with:

$$[CO_2(aq)] = K_H P_{CO_2} \tag{23}$$

where K_H relates to Dalton's law of partial pressure ($K_D = [CO_2(aq)]/[CO_2(g)]$ with $[CO_2(g)] = P_{CO_2}/RT$ and ($K_H = K_D/RT$). CO_2 solubility in water over a wide range of pressures and temperatures can be accurately predicted using equations of states, such as the virial-like formulation of Henry's law by (Diamond and Akinfiev 2003) (Fig. 3):

$$\ln(k_H) = (1-\xi)\ln f^0_{H_2O} + \xi \ln\left(\frac{RT}{M_W}\rho^0_{H_2O}\right) + 2\rho^0_{H_2O}\left[a + b\left(\frac{1000}{T}\right)^{0.5}\right] \tag{24}$$

where ξ is a scaling factor (-0.088) for predicting standard partial molar volume of CO_2, $f^0_{H_2O}$ is the fugacity (MPa), $\rho^0_{H_2O}$ the density ($g \cdot cm^{-3}$) of pure water, and a and b are empirial fit parameters predicting solubility over -1.5–100 °C and 0.1–100 MPa.

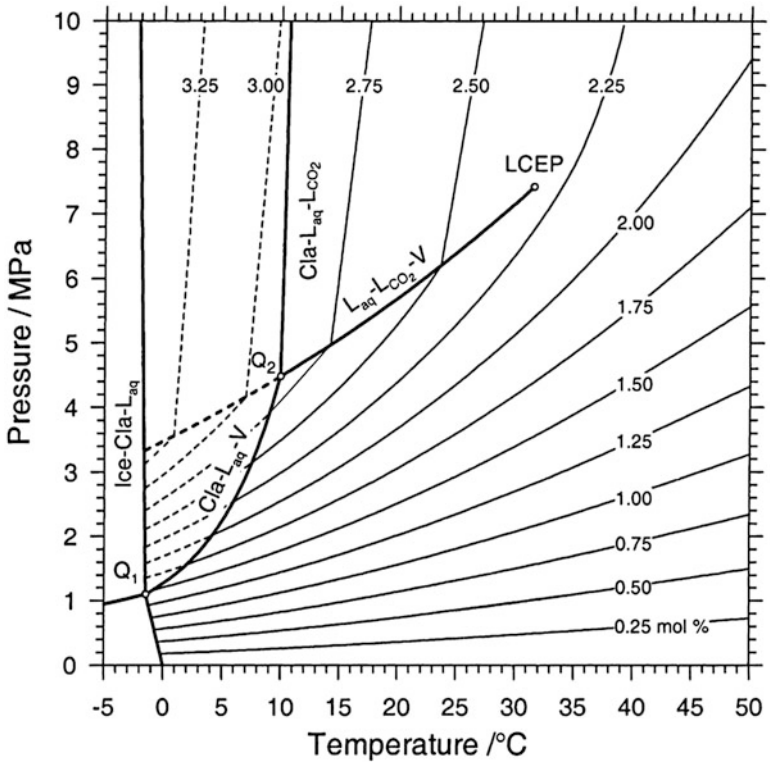

Solubility, Fig. 3 P-T diagram of solubility isopleths of CO_2. Reproduced with permission from Elsevier. Diamond LW, Akinfiev NN (2003) Solubility of CO2 in water from -1.5 to 100 degrees C and from 0.1 to 100 MPa: evaluation of literature data and thermodynamic modelling. Fluid Phase Equilib 208 (1-2):265-290. https://doi.org/10.1016/s0378-3812(03)00041-4

Soluble CO_2 (aq) can be regarded as a hydrophobe (e.g., 0.56 hydrogen bond per molecule in water (Lam et al. 2015; Kumar et al. 2007)) embedded in a cylindrical void forcing a local ordering of water. Carbonic acid (H_2CO_3), which results from the association of CO_2(aq) and H_2O, represents however about 1% of the total soluble CO_2 and has a short lifetime of ~300 ns. This lifetime was recently suggested to arise from deprotonation to bicarbonate (Adamczyk et al. 2009) and thus not to the backdissociation as often stated in textbooks. The total analytical concentration of dissolved CO_2 is expressed as $[H_2CO_3^*] = [CO_2(aq)] + [H_2CO_3]$. When accounting for the deprotonation to bicarbonate and carbonate, the total concentration ($[CO_2]_T$)of CO_2 in a solution is given by $[CO_2]_T = [H_2CO_3^*] + [HCO_3^-] + [CO_3^{2-}]$. Moreover, the pH-dependent total concentration of CO_2 in a solution exposed to an open atmosphere relates to Henry's law via:

$$[CO_2]_T = \left(K_H + \frac{K_H K_1}{[H^+]} + \frac{K_H K_1 K_2}{[H^+]^2}\right) p_{CO_2} \quad (25)$$

where K_1 and K_2 are the first and second deprotonation constants of carbonic acid, respectively. As a result, CO_2 solubility increases strongly at *pH* values exceeding the first deprotonation step from carbonic acid to bicarbonate.

Gases in Melts

The solubility of volatiles in melts can, in principle, be calculated via thermodynamic properties of a given decomposition reaction (e.g., biotite → feldspar + magnetite + water) involving a rock of a given mineralogical composition at the time of crystallization. The study of fluid inclusions also supplies estimates for the pressure during fluid entrapment. At the same time, experimental studies provided direct means at assessing the ability of melts at solubilizing gases. For instance, water solubilizes in silicate melts as OH- and molecular (H_2O_m) species. A representative H_2O dissolution reaction for melts can be written as (Zhang et al. 2007):

$$H_2O(g) \rightleftharpoons H_2O_m(\text{melt})\ K_1 \quad (26)$$

$$H_2O(\text{melt}) + O(\text{melt}) \rightleftharpoons 2OH(\text{melt})K_2 \quad (27)$$

The pressure dependence of the total solubility H_2O (H_2O_T) does not follow Henry's law as it follows the expression of the type:

$$[H_2O_T] = \frac{1}{2}[OH] + [H_2O_m] = k_1 p_{H_2O}^{1/2} + k_2 p_{H_2O} \quad (28)$$

The temperature-dependent equilibrium constant of reaction *n* is represented by

$$K_n = \frac{X_{H_2O_m}}{f^0_{H_2O}} = A_n \exp\left(-\frac{\Delta H^0_n}{RT}\right) \quad (29)$$

where X is the mole fraction of H_2O in the melt, f_{H2O} is the fugacity of water vapor, *A* is a preexponential factor, and ΔH^0 is the standard state reaction enthalpy. Improved, yet semi-empirical, expressions have been formulated to better account for composition of Fe-free silicate melts such as (Zhang et al. 2007):

$$C_w = \left(-0.231 + \frac{651.1}{T}\right)\sqrt{P} + \left(0.03424 - \frac{32.57}{T} + 0.02447 \cdot AI\right) \quad (30)$$

where C_w is the total solubility of water (weight %), *P* is pressure (MPa) and AI is a compositional parameter given by AI = Na + K − Al given in mole fractions. Predictions of mixed volatile solubility (e.g., H_2O-CO_2) can be more readily achieved via computer codes (Newman and Lowenstern 2002).

Solids in Liquids

Dissolution of an ionic solid compound, such as NaCl, produced hydrated Na^+ and Cl^- species each surrounded by a number of hydration shells. The molar enthalpy of the resulting solution corresponds to the dissolution of one mole of a molecule, such that

$$NaCl(s) = Na^+(aq) + Cl^-(aq)\ \Delta H = 3.9 kJ/mol \quad (31)$$

for pure NaCl(s), with a solubility of 35.9 g per 100 g of water at 298 K. A saturated aqueous solution of NaCl thus contains an average of ~9 H_2O per NaCl molecule. It therefore not only consists of hydrated Na^+ and Cl^- species but also of solvent-shared and contact ion pairs (e.g., $[Na(H_2O)_n Cl]^0$). Molecular simulations of NaCl aqueous solutions at elevated temperatures also suggest the possible presence of polyatomic complexes of the type $Na_xCl_y^{x-y}$, whose formation could be induced by the decrease in the dipole moment (cf. dielectric constant) of water (Driesner et al. 1998).

Dissolution of solid compounds into water and whose components undergo aqueous speciation reactions can display strongly pH- and complexation-dependent solubilities. For instance, the dissolution of gibbsite (α-$Al(OH)_3$) to Al^{3+}:

$$\alpha\text{-}Al(OH)_3 + 3H^+ \rightleftharpoons Al^{3+} + H_2O \quad (32)$$

involves the pH-dependent hydrolysis of this ion via:

$$qAl^{3+} + pH_2O + rL^{z-} \rightleftharpoons Al_q(OH)_pL_r^{3q-p-rz} + pH^+ \quad (33)$$

In the absence of a foreign ligand (L^{z-}), common species $AlOH^{2+}$ ($p,q = -1,1$), $Al(OH)_2^+$ ($p,q = -2,1$), $Al(OH)_3^+$ ($p,q = -3,1$), $Al_3(OH)_4^{5+}$ ($p,q = -4,3$), and $Al_{13}O_4(OH)_{24}^{7+}$ ($p,q = -32,13$) control gibbsite solubility. The pH-dependent concentration of aluminum is then given by the sum of the concentrations of its aqueous species ($q = 0$):

$$[Al]_{tot} = \sum_0^p \sum_0^q \sum_0^r q\left[Al_q(OH)_pL_r^{3q-p-rz}\right] \quad (34)$$

and forms the characteristic U-shaped solubility curve of many metal (oxy)(hydr)oxide minerals in water and with the solubility minimum controlled by the crystallinity of the minerals involved (Fig. 4). The slopes (s) of the solubility curves on a log (base 10) $[Al^{3+}]$ vs. pH plot are the result of the pH-dependent speciation of the aqueous species, with $s = -(3q\text{-}p)/q$ when a single species dominates the speciation (e.g., $s = -3$ for Al^+ but 0 for $Al(OH)_3^0$). Increased salt (e.g., NaCl) can favor more highly charged ions and therefore enhance solubility. Addition of metal-complexing ligands can considerably enhance solubility, such as in the case of fluoride forming various mixed aluminum-hydroxo-fluoro complexes (Fig. 4). Formation of (nano- to micro-meter thick) surface coatings can, in turn, block dissolution reactions and therefore suppress solubility. One example includes aluminum hydroxo fluoride precipitates when gibbsite is exposed to concentrated fluoride solutions. The fluoridation of apatite surfaces, forming a non-stoichiometric coating of low solubility, is another example of how passivation of mineral surfaces leads to important changes in solubility.

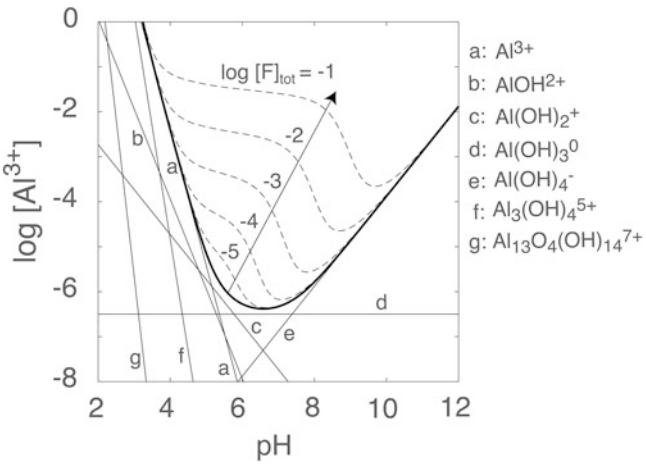

Solubility, Fig. 4 Solubility of gibbsite (α-$Al(OH)_3$) in water at 25 °C with and without NaF

Temperature and pressure effects on solubility are strongly affected by changes in aqueous speciation. This directly arises from changes in the ability of water to hydrate ions. For example, changes seen in metal (oxy)(hydr)oxides include shifts in the solubility minima to more acidic conditions with temperature and to the increase in the concentration of species of lower charge due to the decreased dielectric constant (static permittivity) of water. Born theory can be used to predict the thermodynamics of solvation of ion i:

$$\Delta G_{solv} = \omega_i\left(\frac{1}{\epsilon_r} - 1\right) \quad (35)$$

where ω is a species-dependent Born interaction parameter and ϵ_r is the relative permittivity of the solvent. Knowledge of the latter value for water (Pan et al. 2013; Sverjensky et al. 2014) enables use of Equations of State (e.g., Helgeson-Kirkham-Flowers model; (Helgeson et al. 1981) to predict thermodynamic properties of aqueous species at elevated temperatures and pressures. For example, the solubility of quartz to several kb and hundreds of °C (Sverjensky et al. 2014) can be effectively described in this fashion (Fig. 5). An alternative approach stems upon the log-log relationship of equilibriums constants with the density of water and with relative permittivity (Dolejs and Manning 2010; Marshall and Franck 1981). Accounting for variations in the solvent density (Dolejs and Manning 2010) provides advantages for rationalizing changes in solubility with temperature and pressure. This view accounts for the energetic contributions of the compression of the hydration shell (electrostriction) on the solute – which are smaller in neutrally charged and larger in highly charged aqueous species. As such, the solubility of minerals generating highly-charged species (e.g., Ca-bearing calcite, apatite, fluorite, and portlandite of Dolejs and Manning (2010)) undergo important hikes in solubility in solvents of greater density (at constant temperature). This dependence is weaker in minerals generating neutrally charged species (e.g., $Si(OH)_4^0$, $Al(OH)_3^0$ at circumneutral pH). Likewise, the retrograde solubility of minerals generating charged species tends to occur under conditions of lower solvent density (e.g., high temperature, low pressure).

Solids in Gases

Although many solid phases of interest for geochemistry are of low volatility, gaseous reactants can act as transport agent. For example, boiling of hydrothermal fluids can produce species CO_2, H_2S, HCl, SiO_2 as well as low molecular weight metals complexes (e.g., $AgCl{\cdot}(H_3O)_3(g)$; (Migdisov et al. 1999)) in high temperature steam. Transport of such species along a temperature gradient can drive crystallization reactions which can, for example, account for epithermal transport and deposition of ore deposits, such as those of gold (Hurtig

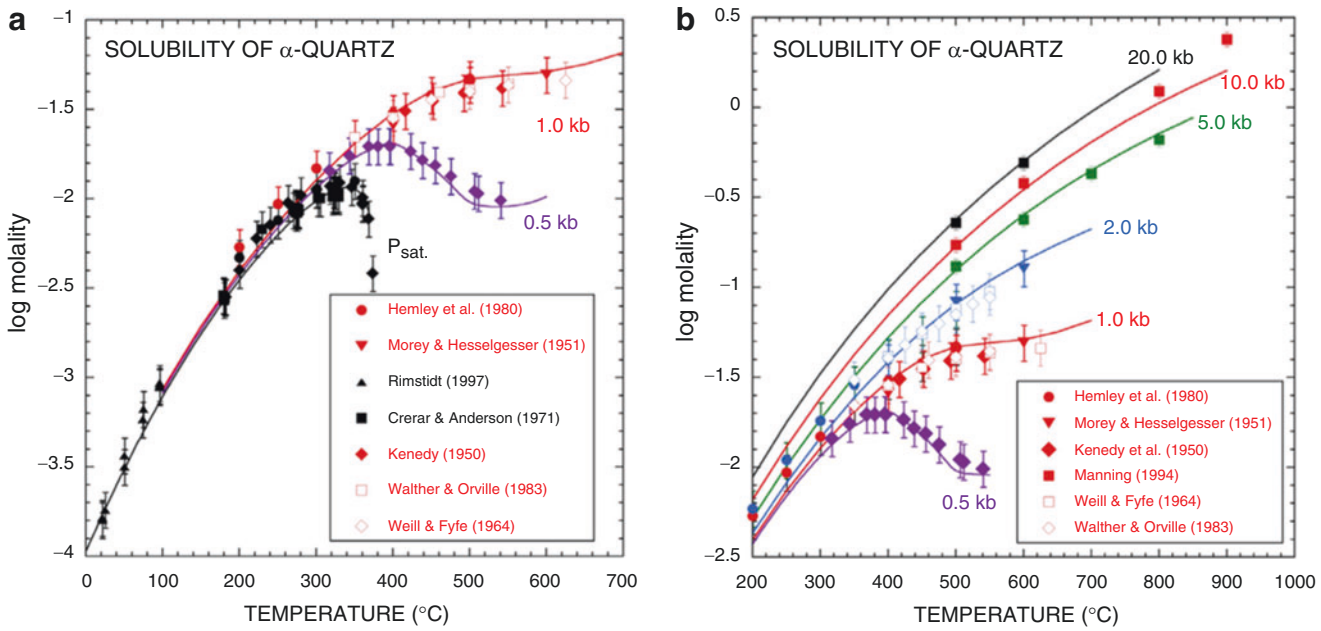

Solubility, Fig. 5 Solubility of quartz (α-SiO_2) as a function of temperature and pressure, and thermodynamic predictions. Reproduced with permission from Elsevier. Sverjensky DA, Harrison B, Azzolini D (2014) Water in the deep Earth: The dielectric constant and the solubilities of quartz and corundum to 60 kb and 1200 degrees C. Geochim Cosmochim Acta 129:125-145. https://doi.org/10.1016/j.gca.2013.12.019

and Williams-Jones 2014). Chemical vapor deposition methods are also used in the production of solid materials for technological uses.

R. Bunsen (Biot et al. 1852) first invoked vapor-driven transport to describe the formation of crystalline Fe_2O_3 by HCl-bearing volcanic gases. In the absence of a transport agent, solid/gas transfers include direct sublimation (e.g., $AlCl_6(s) \rightleftharpoons Al_2Cl_6(g)$) and decomposition sublimation (e.g., $CuCl_2(s) \rightleftharpoons CuCl(s) + ½\ Cl_2(g)$, followed by $CuCl(s) \rightleftharpoons CuCl(g)$) reactions. In contrast, a transport agent, such as HCl (g), facilitates solid/gas conversion via a reaction of the type:

$$Fe_2O_3(s) + 6HCl(g) \rightleftharpoons Fe_2Cl_6(g) + 3H_2O(g) \qquad (36)$$

The transport direction can be understood by the sign of the reaction enthalpy, in the sense that Le Châtelier's principle will stipulate that endothermic transport proceeds toward cooler while exothermic reactions to warmer reaction. As the reaction of Eq. 36 is endothermic, transport of $Fe_2Cl_6(g)$ along a thermal gradient favors deposition of hematites in colder regions, such as vents of volcanoes.

In the presence of water vapor, species can be stabilized via solubilization in small molecular clusters of water (e.g., $H_3O^+ \ldots (H_2O)_m$, with $m = 1 \leq 5$) (e.g. Lemke and Seward 2008). Gas-phase solubility metals (*or* metal fugacity) and speciation can therefore be strongly affected by steam composition and properties. For example, Hurtig and Williams-Jones (2014) show that gold solubility in steam increases with water density, such as along the water vapor saturation curve.

Summary

The concept of solubility is essential in geochemistry for describing the maximal quantity of a substance that can be dissolved in solutions. It often becomes a starting talking point for understanding whether solutions are homogeneous or prone to bear particular matter. Preditions of solubility often require a distinct thermodynamic treatment of the solute and the solvent that can be built in different modeling frameworks. Equations of states or more empirical sets of equations can be used to effectively predict solubility over a range of conditions relevant to the solvent. Examples include salinity and pH of water, partial pressures of gases, as well as pressure and temperature of water and melts. The concept of solubility thus applies to diverse aspects of Earth Sciences and enables a means for formulating predictive models on mass transport in nature.

Cross-References

- ▶ Activity and Activity Coefficients
- ▶ Aqueous Solutions
- ▶ Enthalpy
- ▶ Entropy

- Equilibrium
- Equilibrium Constant
- Fluid–Rock Interaction
- Fugacity
- Geochemical Thermodynamics
- Gibbs-Duhem Equation
- Henry's Law
- Hydrothermal Solutions
- Low-Temperature Geochemistry
- Silicate Melts
- Solid Solution/Exsolution
- Water

References

Adamczyk K, Premont-Schwarz M, Pines D, Pines E, Nibbering ETJ (2009) Real-time observation of carbonic acid formation in aqueous solution. Science 326(5960):1690–1694. https://doi.org/10.1126/science.1180060

Benson BB, Krause J Jr (1984) The concentration and isotopic fractionation of oxygen dissolved in freshwater and seawater in equilibrium with the atmosphere. Limnol Oceanogr 29:620–632

Biot BC, Henry O, Barreswil R, Pohl JJ (1852) Notizen. J Prakt Chem 56(1):53–64. https://doi.org/10.1002/prac.18520560106

Diamond LW, Akinfiev NN (2003) Solubility of CO2 in water from −1.5 to 100 degrees C and from 0.1 to 100 MPa: evaluation of literature data and thermodynamic modelling. Fluid Phase Equilib 208(1–2): 265–290. https://doi.org/10.1016/s0378-3812(03)00041-4

Dolejs D, Manning CE (2010) Thermodynamic model for mineral solubility in aqueous fluids: theory, calibration and application to model fluid-flow systems. Geofluids 10(1–2):20–40. https://doi.org/10.1111/j.1468-8123.2010.00282.x

Driesner T, Seward TM, Tironi IG (1998) Molecular dynamics simulation study of ionic hydration and ion association in dilute and 1 molal aqueous sodium chloride solutions from ambient to supercritical conditions. Geochim Cosmochim Acta 62(18):3095–3107. https://doi.org/10.1016/s0016-7037(98)00207-5

Harvie CE, Moller N, Weare JH (1984) The prediction of mineral solubilities in natural-waters – the NA-K-MG-CA-H-CL-SO4-O-HCO3-CO3-CO2-H2O system to high ionic strengths at 25-degrees-C. Geochim Cosmochim Acta 48(4):723–751. https://doi.org/10.1016/0016-7037(84)90098-x

Helgeson HC, Kirkham DH, Flowers GC (1981) Theoretical prediction of the thermodynamic behavior of aqueous-electrolytes at high-pressures and temperatures.4. Calculation of activity-coefficients, osmotic coefficients, and apparent molal and standard and relative partial molal properties to 600-degrees-C and 5 KB. Am J Sci 281(10):1249–1516

Hurtig NC, Williams-Jones AE (2014) An experimental study of the transport of gold through hydration of AuCl in aqueous vapour and vapour-like fluids. Geochim Cosmochim Acta 127:305–325. https://doi.org/10.1016/j.gca.2013.11.029

Kumar PP, Kalinichev AG, Kirkpatrick RJ (2007) Dissociation of carbonic acid: gas phase energetics and mechanism from ab initio metadynamics simulations. J Chem Phys 126(20). https://doi.org/10.1063/1.2741552

Lam RK, England AH, Smith JW, Rizzuto AM, Shih O, Prendergast D, Saykally RJ (2015) The hydration structure of dissolved carbon dioxide from X-ray absorption spectroscopy. Chem Phys Lett 633:214–217. https://doi.org/10.1016/j.cplett.2015.05.039

Lemke KH, Seward TM (2008) Solvation processes in steam: Ab initio calculation of ion-solvent structures and clustering equilibria. Geochim Cosmochim Acta 72:3293–3310. https://doi.org/10.1016/j.gca.2008.02.024

Marshall WL, Franck EU (1981) Ion product of water substance, O-degrees-C-1000-degrees-C, 1-10,000 bars – new International formulation and its background. J Phys Chem Ref Data 10(2):295–304

Migdisov AA, Williams-Jones AE, Suleimenov OM (1999) Solubility of chlorargyrite (AgCl) in water vapor at elevated temperatures and pressures. Geochim Cosmochim Acta 63(22):3817–3827. https://doi.org/10.1016/S0016-7037(99)00213-6

Navrotsky A, Mazeina L, Majzlan J (2008) Size-driven structural and thermodynamic complexity in iron oxides. Science 319(5870):1635–1638. https://doi.org/10.1126/science.1148614

Newman S, Lowenstem JB (2002) VolatileCalc: a silicate melt–H2O–CO2 solution model written in visual basic for excel. Comput Geosci 28(5):597–604. https://doi.org/10.1016/S0098-3004(01)00081-4

Pan D, Spanu L, Harrison B, Sverjensky DA, Galli G (2013) Dielectric properties of water under extreme conditions and transport of carbonates in the deep Earth. Proc Natl Acad Sci U S A 110(17):6646–6650. https://doi.org/10.1073/pnas.1221581110

Sverjensky DA, Harrison B, Azzolini D (2014) Water in the deep Earth: the dielectric constant and the solubilities of quartz and corundum to 60 kb and 1200 degrees C. Geochim Cosmochim Acta 129:125–145. https://doi.org/10.1016/j.gca.2013.12.019

Zhang Y, Xu Z, Zhu M, Wang H (2007) Silicate melt properties and volcanic eruptions. Rev Geophys 45(4). https://doi.org/10.1029/2006RG000216

Stable Isotope Geochemistry

William M. White
Department of Earth and Atmospheric Sciences, Cornell University, Ithaca, NY, USA

Definition

Stable isotope geochemistry is the study of natural variations in the isotopic composition of elements that occur as a consequence of chemical and physical processes other than radioactive decay in the Earth and Solar System.

Introduction

Although chemical processes involve only the electrons of atoms, atomic mass does play a role in the chemical and physical behavior of atoms. This leads to slightly different behavior of the various isotopes of an element, which in turn leads to variations in the ratios of isotopes within the Earth and the Solar System. Stable isotope geochemistry began with the study of a few of the lightest and most abundant elements, H, C, N, O, and S, that exhibited large variations in isotopic composition. The field began with early work of Alfred Nier of the University of Minnesota, who measured the

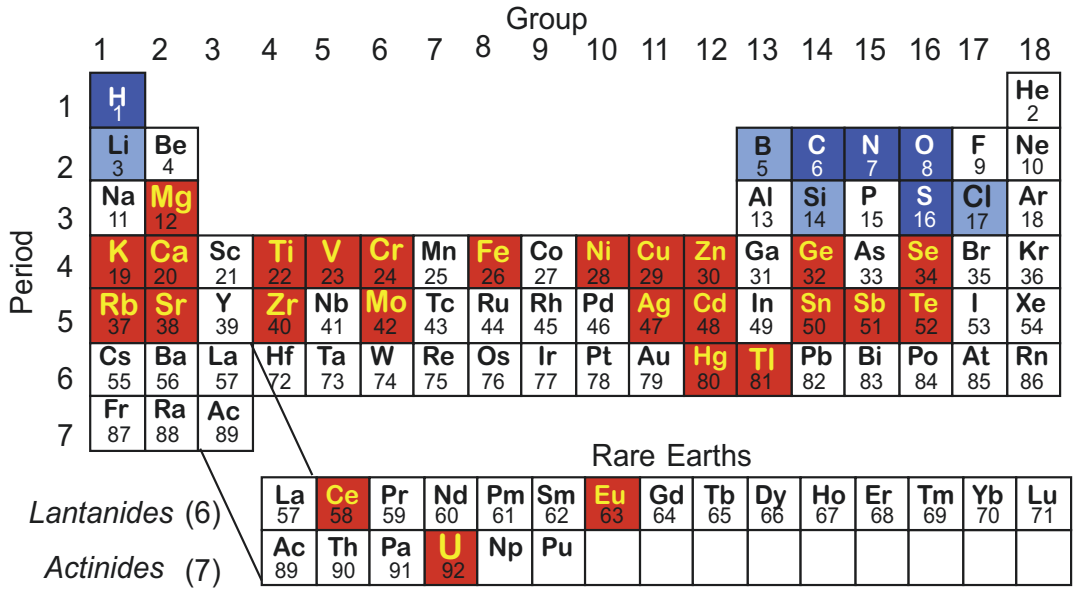

Stable Isotope Geochemistry, Fig. 1 The traditional stable isotopes are shown in *dark blue*; elements for which some work was done in the 1970s and 1980s are shown in *light blue*. Nontraditional isotopes are shown in *red*

isotopic compositions of many elements and noted variations, and of Harold Urey and his colleagues at the University of Chicago, who laid the theoretical foundations of stable isotope geochemistry (Bigeleisen and Mayer 1947; Urey 1947). Over the past decade or two, stable isotope geochemistry has expanded to include most of the multi-isotopic chemical elements, driven in part by advances in analytical techniques, most notably the development of multi-collector–inductively coupled plasma–mass spectrometers (Fig. 1). Increasing sensitivity and accuracy of other types of mass spectrometers, the development of high-resolution gas source multi-collector mass spectrometers, improvements in ion microprobes enabling in situ, micron-scale measurements of isotope ratios in solids, and advances in absorption spectroscopy and nuclear magnetic resonance spectroscopy are also contributing to this advancement. Many of these techniques are described in separate entries. This entry will review the main principles of the field: the isotope geochemistry of many specific elements is described in dedicated entries in this encyclopedia or in the entry on the element itself. In addition, the book edited by Teng et al. (2017) provides more details on many of the nontraditional stable isotopes.

Terminology

Because variations in isotope ratios are usually small, they are reported in parts per thousand or *per mil* variations, denoted ‰, from a standard. This is the delta notation, which for the $^{18}O/^{16}O$ ratio is:

$$\delta^{18}O = \left[\frac{\left(^{18}O/^{16}O\right)_{\text{sample}} - \left(^{18}O/^{16}O\right)_{\text{std}}}{\left(^{18}O/^{16}O\right)_{\text{std}}}\right] \times 1000 \quad (1)$$

The standard may be a naturally occurring substance such as air, the standard for $^{15}N/^{14}N$ ratio, or an artificially prepared laboratory standard. In some cases, more than one standard is used, in which case the standard used is denoted as a subscript, e.g., $\delta^{18}O_{\text{SMOW}}$. Many early defined natural standards, such as Standard Mean Ocean Water (SMOW), the standard for oxygen and hydrogen isotopes, have been replaced by artificial standards, most notably ones distributed by the International Atomic Energy Commission in Vienna. These are designated with a V, e.g., V-SMOW. It should also be noted that the isotopic composition of hydrogen is expressed as δD, where D designates deuterium, ^{2}H. As analytical precision has improved and the smaller variations in nontraditional stable isotopes (Fig. 1) have been explored, several analogous notations have emerged, epsilon (ε) and mu (μ), which are the relative deviations from standards in parts in 10,000 and parts per million, respectively.

When a process results in a change in the isotopic distribution of an element between phases, isotopes are said to be fractionated. The *fractionation factor*, α, is the ratio of isotope ratios in two phases, *a* and *b*, that will occur as a consequence of a process or reaction:

$$\alpha_{a-b} = \frac{\left(^{18}O/^{16}O\right)_a}{\left(^{18}O/^{16}O\right)_b} \quad (2)$$

The fractionation of isotopes between two phases is also often reported as

$$\Delta_{A-B} = \delta_A - \delta_B \tag{3}$$

Because isotope fractionations are almost always small, Δ and α can be related as:

$$\Delta \approx (\alpha - 1) \times 10^3 \tag{4}$$

or

$$\Delta \approx 10^3 \, ln \, \alpha \tag{5}$$

The upper-case delta (sometimes spoken as cap-delta) has two other uses in stable isotope geochemistry which will be described in subsequent sections.

Fractionation factors can be determined either observationally (e.g., measuring the isotope ratios of two minerals at equilibrium in a rock), experimentally (e.g., precipitating a mineral from solution), or theoretically from a knowledge of crystal/molecular bonding and quantum mechanics. When theoretical calculations are involved, isotope fractionation is also often expressed in terms of a β-factor defined as the ratio at equilibrium of the isotope ratio of the substance of interest to the isotope ratio of dissociated atoms, for example:

$$\beta_{H_2O}^{\left({}^{18}O/{}^{16}O\right)} = \frac{\left({}^{18}O/{}^{16}O\right)_{H_2O}}{\left({}^{18}O/{}^{16}O\right)_O} \tag{6}$$

The denominator is the isotope ratio in a gas of monatomic oxygen and the numerator is the isotope ratio in water in equilibrium with it. The fractionation factor can then be calculated from the ratio of β factors. For example, in the exchange of oxygen between CO_2 and water, a similar β factor for CO_2 can be written and denominators would cancel in the ratio of β factors can so that the fractionation factor may be calculated as:

$$\alpha_{CO_2-H_2O} = \frac{\beta_{CO_2}}{\beta_{H_2O}} \tag{7}$$

The advantage of this expression is that β values are closely related to the partition function of statistical mechanics.

Causes of Isotope Fractionations

Isotope fractionation can originate from both *kinetic* effects and *equilibrium* effects. Equilibrium isotope fractionations arise from the *translational, rotational, and vibrational motions* of molecules in gases and liquids and atoms in crystals because the energies associated with these motions are mass-dependent. Systems tend to adjust themselves so as to minimize energy. Thus, isotopes will be distributed so as to minimize the vibrational, rotational, and translational energy of a system. Of the three types of energies, vibrations, the only mode of motion available to atoms in a solid, make by far the most important contribution to isotopic fractionation.

All atomic motions are quantized and, as Urey (1947) and Bigeleisen and Mayer (1947) demonstrated, equilibrium fractionations can be predicted from quantum statistical mechanics. The reader can find detailed explanations elsewhere (O'Neil 1968; Sharp 2007; Hoefs 2015; White 2015; Blanchard et al. 2017). Equilibrium constants of chemical reactions, K, can be calculated from the ratio of *partition functions, Q* (which is the denominator of the Boltzmann Distribution Function), of products and reactants:

$$\mathrm{K} = \prod_i Q^{v_i} \tag{8}$$

Where v_i is the stoichiometric constant of phase i and is negative for reactants. Consequently, equilibrium fractionation factors may be predicted if the available energy states of products and reactants are known.

This approach reveals that the vibrational frequency will be lower for a bond involving a heavier isotope of an element, which in turn lowers the vibrational energy of the molecule or crystal, thus bonds involving heavier isotopes will be stronger. In a system consists of two phases with different bond energies available, the energy of the system is lowered when the heavy isotope occupies the site with the stronger bond. Thus, at equilibrium, *the heavy isotope of an element will tend partition into the phase with the stronger bond.* A second important result of the statistical mechanical approach is that isotope fractionations will be temperature dependent. The temperature dependence can be complex as mass occurs in the partition functions in several forms, but at low temperatures (up to approximately Earth's surface temperatures), equilibrium fractionation factors are generally proportional to the inverse of temperature (Fig. 2). At higher temperatures, equilibrium fractionation factors vary approximately with the inverse square of temperature. This temperature dependence is the basis of stable isotope geothermometry. It is primarily useful at low to moderate (i.e., metamorphic) temperatures. As igneous temperatures are approached, fractionations become too small to provide useful geothermometers.

Isotope fractionations may also occur due to the kinetics associated with fast, incomplete, or unidirectional processes like evaporation, diffusion, dissociation reactions, and biologically mediated reactions. Kinetic fractionations arise because molecules and ions of lighter isotopes diffuse faster (a consequence of equipartition of energy: if a lighter molecule has the same energy as a heavier one, it must be moving

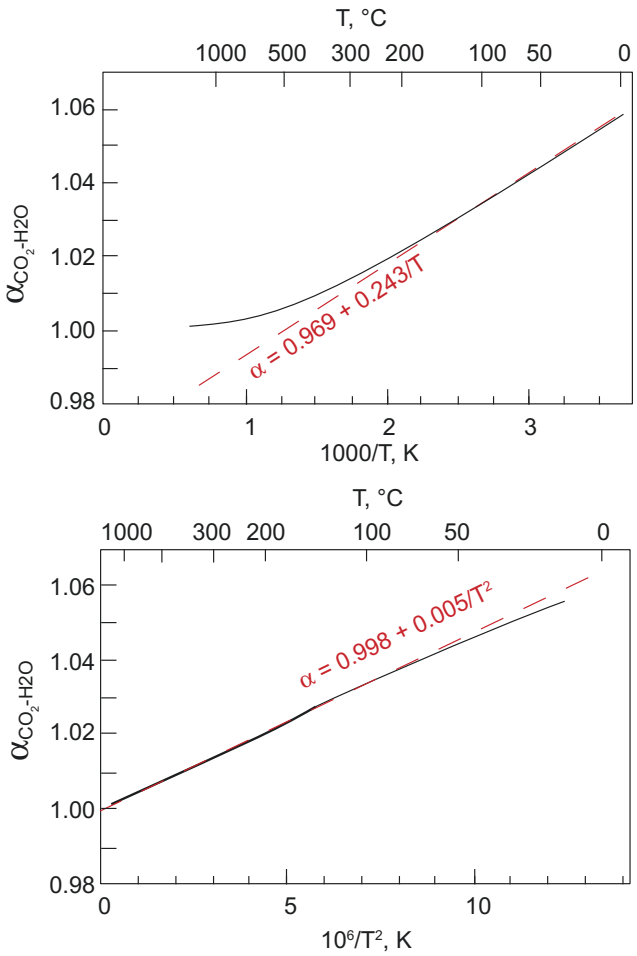

Stable Isotope Geochemistry, Fig. 2 Temperature dependence of the oxygen water-CO_2 fractionation factor. α is approximately proportional to 1/T a low temperature and $1/T^2$ at high temperature (From White (2015))

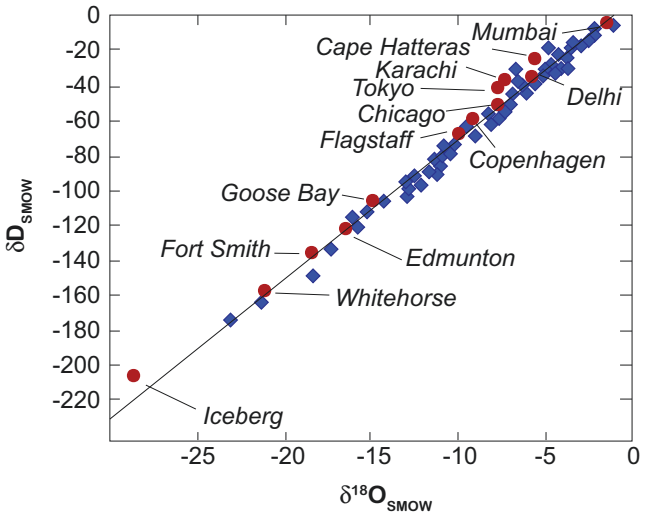

Stable Isotope Geochemistry, Fig. 3 Correlated variations in hydrogen and oxygen isotopes in precipitation define a global meteoritic water line

faster). The weaker bonds formed by lighter isotopes are more readily broken, hence light isotopes will react more rapidly. Consequently, where reactions do not achieve equilibrium, the lighter isotope will usually be preferentially concentrated in the reaction products, but where reactions attain equilibrium the equilibrium fractionations will dominate.

Kinetic fractionations often work in tandem with equilibrium ones. This is the case in the hydrologic cycle. At equilibrium, water vapor is isotopically light (low δD and δ^{18}O) relative to the liquid, but isotopically light water also evaporates more readily. Once it evaporates, the opportunity for atmospheric water vapor to equilibrate with the oceans is limited; hence, water vapor is more depleted in D and ^{18}O than predicted from equilibrium. When water vapor condenses as precipitation, an equilibrium fractionation again occurs and the rain or snow will be enriched in the heavier isotopes with limited opportunity to equilibrate with the vapor. As water vapor is carried away from its source region, precipitation will progressively deplete the remaining vapor in the heavier isotopes. Further, as the air mass moves toward the poles it cools, so that fractionations become greater. As a result of this Rayleigh condensation process, δD and δ^{18}O in polar ice can be as low as −450‰ and −50‰, respectively, and there is a strong correlation between the isotopic composition of precipitation and mean annual temperature. As this process affects both hydrogen and oxygen isotopic composition and the ocean is effectively an infinite reservoir of water, the two are strongly correlated such that $\delta D_{SMOW} \cong 8\delta^{18}O + 10$ in meteoric water something known as the *Meteoric Water Line* (Fig. 3). Deviations from this line are observed locally, for example, water that has evaporated or has mixed with evaporated water typically defines a trend of lower slope than the global meteoric water line. Hydrogen and oxygen isotopes are thus important tools in hydrology, ecology, and paleoclimate (e.g., Bowen 2010).

Mass Dependent Verses Mass Independent Fractionations

Where an element has three or more isotopes, for example, ^{16}O, ^{17}O, and ^{18}O, the variation in the ratio of any pair of isotopes will usually be strongly correlated with that of any other pair, with the extent of fractionation depending on mass difference. For example, the mass difference between ^{17}O and ^{16}O is half the difference between ^{18}O and ^{16}O and theoretically we expect the fractionation between ^{17}O and ^{16}O to be about half that between ^{18}O and ^{16}O. Specifically, fractionation factors calculated from partition functions show that the ratio of fractionation factors $\Delta^{17}O^{16}O/\Delta^{18}O/^{16}O$ should be ≈ 0.53 over the range of temperatures near the surface of the

Earth (or Mars). The empirically observed ratio for terrestrial fractionations (and also within classes of meteorites) is $\Delta^{17}O^{16}O/\Delta^{18}O/^{16}O \approx 0.52$. This relationship is known as *mass dependent fractionation* (MDF). Because of this simple and predictable relationship of fractionation between ^{18}O, ^{17}O, and ^{16}O, the $^{17}O/^{16}O$ ratio is rarely measured. In some cases, however, the variations in isotope ratios of multi-isotopic elements do not bear this simple relationship to mass difference. This is known as *mass independent fractionation* (MIF). It was first observed in oxygen isotope ratios in meteorites by Clayton et al. (1973) and interpreted as a nucleosynthetic effect; however, Thiemens and Heidenreich (1983) subsequently demonstrated mass independent fractionation of oxygen isotopes during ozone production in laboratory experiments. Recognition of these mass independent effects led to the introduction of another use of Δ in stable isotope geochemistry: it is the deviation of an isotope ratio from the expected mass dependent fractionation. For example:

$$\Delta^{17}O = \delta^{17}O - 0.52\delta^{18}O \tag{9}$$

Subsequently, mass independently fractionated O isotopes were observed in stratospheric ozone (Mauersberger et al. 1993) as well as other atmospheric gases. Mass independent fractionation of sulfur was also found in sulfides and sulfates older than the early Paleoproterozic as a consequence of the early Earth's ozone-free atmosphere (Farquhar et al. 2000) and in mercury isotopes of compounds produced by photochemical reactions (Bergquist and Blum 2007).

To date, essentially all examples of mass independent fractionations appear to involve photochemical reactions. The causes are not completely understood and likely varied. One likely cause is self-shielding, which may explain the MIF oxygen isotopes in meteorites (Clayton 2002; Yurimoto et al. 2007). This occurs when radiation with energy to photodissociate the dominant isotopic species, such as $^{12}C^{16}O$, is completely absorbed at some distance and hence not capable of initiating chemical reactions while that of a minor one such as $^{12}C^{18}O$ is not. A second factor may be the ability of excited asymmetric molecules such as $^{17}O^{16}O^{16}O$ and $^{18}O^{16}O^{16}O$ to repartition energy more readily than symmetric ones such as $^{17}O^{16}O^{16}O$ (Hiedenreich and Thiemens 1986). In heavy nuclides, differences in nuclear sizes and shapes of isotopes shift the ground electronic energy of an atom or molecule, which is known as the nuclear field effect (Bigeleisen 1996) and the extent of this effect differs for nuclei with odd and even numbers of neutrons. Finally, nuclei with odd numbers of nucleons have an intrinsic nuclear spin or nuclear magnetic moment, which gives rise to the nuclear spin effect (Buchachenko 2001). In such nuclei, nuclear magnetic moments can interact with the magnetic moments of electrons and affect the reaction rates of reactions involving excited reaction intermediates, such as those in photochemical reactions. This effect is strictly kinetic and does not affect equilibrium isotope distributions.

Further information on mass independent fractionations maybe found in the review by Thiemens (2006) as well as the entries on oxygen isotopes, sulfur isotopes, and mercury isotopes in this Encyclopedia.

Isotope Clumping

The term isotope clumping refers to the tendency of the heavy isotopes of a pair of elements, for example, ^{13}C and ^{18}O, to occur together in molecules or species with more frequency than a purely random distribution.

Molecules of the same chemical but different isotopic composition, for example, $^{12}C^{16}O_2$, $^{12}C^{16}O^{18}O$, and $^{13}C^{16}O^{18}O$, are known as *isotopologues*. Statistical mechanics predicts that the distribution of isotopes in a chemical species will not be random but rather that some of these isotopologues will be thermodynamically favored, in particular the heavier isotopes of elements (^{13}C and ^{18}O) are more likely to be "clumped" together in a single molecule than to be randomly distributed among all molecules. The reason for this is that double heavy isotope substitution generally leads to a reduction in vibrational frequency and energy greater than twice that of single substitution. Thus, clumping lowers the energy of the system as a whole compared to a merely random distribution of isotopes. The extent to which this clumping occurs is described by yet another use of the upper-case delta

$$\Delta_i = \left(\frac{R_{i-e}}{R_{i-r}} - 1\right) \times 1000 \tag{10}$$

where $R_{i\text{-}e}$ is that ratio of the observed or calculated equilibrium abundance of isotopologue i to the isotopologue containing no rare isotopes and $R_{i\text{-}r}$ is that same ratio if isotopes were distributed among isotopologues randomly. Thus, in the example of CO_2:

$$\Delta_{47} = \left(\frac{\left(\left[^{13}C^{18}O^{16}O\right]/\left[^{12}C^{16}O^{16}O\right]\right)_e}{\left(\left[^{13}C^{18}O^{16}O\right]/\left[^{12}C^{16}O^{16}O\right]\right)_r} - 1\right) \times 1000 \tag{11}$$

The subscript 47 refers to the molecular mass of $^{13}C^{18}O^{16}O$. The random distribution can be calculated directly as the probability of choosing isotopes randomly to form species. The equilibrium distribution can be calculated from partition function ratios. Ghosh et al. (2006) demonstrated that Δ_{47} could be measured in coral carbonates and that measured values variated as a function of temperature as predicted from theoretical calculations, thus demonstrating its value as a geothermometer. It has the advantage over

S

conventional isotope geothermometers that temperature can be determined from analysis of a single phase. Clumped isotope analysis has found wide application in paleoclimatology and diagenesis. One of the most interesting applications was demonstrating that dinosaurs could regulate their body temperature (Eagle et al. 2010).

Isotope clumping has also been studied in methane. Stolper et al. (2014) showed that clumping of ^{13}C and ^{2}H in methane (Δ_{18}) could be used to reliably determine its formation temperatures (and hence distinguish biogenic and thermogenic methane). In addition, kinetic effects leading to nonequilibrium distribution of isotopologues of biogenic methane (Wang et al. 2015) and methane oxidation processes (Whitehill et al. 2017), leading to new insights into them. Additional details on isotope clumping can be found in reviews of Eiler (2011, 2013), and Douglas et al. (2017).

Applications

Stable isotope geochemistry has had an enormous impact on our understanding of the Earth and the Solar System. One of its first and still greatest successes has been determining paleotemperatures, work initiated by Harold Urey and his students and associates at the University of Chicago, including Casare Emiliani (1955), who published the first $\delta^{18}O$ time series of Pleistocene carbonates in deep sea sediments and concluded the "Ice Ages" were driven by Milankovitch cycles. Records of $\delta^{18}O$ and δD in Antarctic and Greenland ice cores (Jouzel et al. 2007) have provided more detailed and accurate records of climate variability while substantiating Emiliani's original conclusions. Stable isotopes have also been invaluable in other paleoclimate and paleoenvironmental studies as well as atmospheric evolution as described in entries on those topics in this encyclopedia.

The temperature dependence of isotope fractionations has led to widespread application of isotope geothermometers, particularly in metamorphic rocks and hydrothermal systems (e.g., Valley 1986). Rocks of the crust, particularly the continental crust, have usually interacted with water and as a result have widely varying O isotope compositions. At mantle temperatures, isotope fractionations become extremely small in most cases, so that most fresh mantle rocks comprise a quite narrow range of stable isotopic compositions. As Taylor and Sheppard (1986) stated "igneous rocks whose oxygen isotopic compositions show significant variations from the primordial value (+6) must either have been affected by low temperature processes, or must contain a component that was at one time at the surface of the Earth." Cavosie et al. (2005) observed elevated $\delta^{18}O$ in zircons as old as 4325 Ma and argued that liquid water was present on the Earth by this time. Taylor and Sheppard's statement can be generalized to other stable isotopes as well, and consequently they have become useful tools in recognizing crustal assimilation by magmas (e.g., Bezard et al. 2014) and in the generation of ore deposits (e.g., Ripley et al. 2017). Stable isotopes have also proved useful in identifying recycled crustal material in the Earth's mantle (e.g., Eiler 2001; Delavault et al. 2016; Pringle et al. 2016). Meteorites and comets show considerable variation in stable isotope composition as a consequence both of fractionations and incomplete mixing of material from various nucleosynthetic sources. Stable isotopes therefore provide strong constraints on the Earth's formation and early differentiation (e.g., Fitoussi and Bourdon 2012; Halliday 2014; Huang and Jacobsen 2017).

$\delta^{13}C$ is fractionated by up to about −30‰ when inorganic carbon is fixed in organic molecules in photo- and chemosynthesis. Metabolic processes produce relatively small fractionations, so isotopically light carbon is a characteristic of all biologically produced organic matter, including petroleum, coal, and natural gas. Isotopically, light carbon in Eoarchean rocks from the Isua Belt of Greenland and the Nuvvuagittuq Belt of Canada thus provide evidence (albeit somewhat controversial) for the very early appearance of life on Earth (Rosing 1999; Dodd et al. 2017). Nitrogen is also isotopically fractionated during assimilation, but because most autotrophs can utilize only reduced (e.g., NH_3) or oxidized (NO_3^-) nitrogen and availability of this reactive nitrogen is limited and its isotopic composition varies more than inorganic carbon. The $\delta^{15}N$ of autotrophs reflects this variability as well as fractionations during assimilation. Legumes, which form a symbiotic relationship with nitrogen-fixing bacteria, contain less fractionated N than other terrestrial plants. Unlike carbon, however, other cellular processes significantly fractionate $\delta^{15}N$, particularly amino acid production, so that nitrogen tends to become isotopically heavier at each trophic level. Oxygen and hydrogen are taken up by biota as water and there is little isotopic fractionation in this process (although some fractionation occurs as a consequence of transpiration); hence, the O and H isotopic composition of biomolecules generally reflects that of the local water. Determination of the isotopic composition of carbon and other elements in specific biomolecules such as biomarkers through compound-specific isotope analysis has become important tool in biogeochemistry and organic geochemistry. Studies on H, C, O, N, and S isotopes as well as on nontraditional stable isotopes have become important tools in ecology (Peterson and Fry 1987; Fry 2006), forensics (Cerling et al. 2016), paleontology and archeology (e.g., Lee-Thorp 2008), atmospheric evolution (Pufahl and Hiatt 2012), and medicine (Albarède et al. 2017).

Summary and Outlook

Stable isotope geochemistry has had an enormous impact on geochemistry and more broadly earth and planetary sciences

generally. The impact ranges from formation of the Earth and its neighbors and mantle evolution to paleoclimate, mineral exploration, petroleum exploration, and hydrology. Following the lead of geoscientists, archeologists, forensic scientists, and biologists have also found widespread use for stable isotopes in fields ranging from paleontology and ecology to medicine.

Future impacts are likely to be greater as stable isotope geochemistry is presently experiencing a particularly rapid development. Part of this relates to exploring isotopic variations of nontraditional stable isotopes (Fig. 1): in many instances these fields are still in their infancy with yet much to be discovered. Part of it reflects exploring new directions such as mass independent fractionation and isotopic clumping. Progress is also driven by continued innovation in analytical techniques enabling smaller sample volumes, greater precision, and the analysis of specific molecules and, in the future, determine the isotopic composition of atoms at specific sites in molecules. Eiler et al. (2014) provide a more detailed review of the frontiers of stable isotope geochemistry.

Cross-References

- Analytical Techniques
- Archeological Geochemistry
- Atmospheric Evolution
- Atomic Absorption, Inductively Coupled Plasma Optical Emission Spectroscopy, and Infrared Spectroscopy
- Atomic Number, Mass Number, and Isotopes
- Biogeochemistry
- Biomarkers: Petroleum
- Boron Stable Isotopes
- Calcium Isotopes
- Chlorine Isotopes
- Chromium Isotopes
- Compound-Specific Isotope Analysis
- Copper Isotopes
- Diffusion
- Equilibrium Constant
- Formation and Evolution of the Earth
- Gas Source Mass Spectrometry (GS-MS)
- Geochemical Thermodynamics
- Hydrogen Isotopes
- Hydrologic Cycle
- Inductively Coupled Plasma Mass Spectrometry (ICP-MS)
- Iron Isotopes
- Ion Microprobe
- Kinetics of Geochemical Processes
- Lithium Isotopes
- Magnesium Isotopes
- Mantle Geochemistry
- Mercury Isotopes
- Meteorites
- Molybdenum Isotopes
- Nuclear Magnetic Resonance
- Nucleosynthesis
- Oxygen Isotopes
- Paleoclimatology
- Paleotemperatures
- Sulfur Isotopes
- Thallium Isotopes
- Zinc Isotopes

References

Albarède F, Télouk P, Balter V (2017) Medical applications of isotope metallomics. Rev Mineral Geochem 82(1):851–885

Bergquist BA, Blum JD (2007) Mass-dependent and -independent fractionation of Hg isotopes by photoreduction in aquatic systems. Science 318(5849):417–420

Bezard R et al (2014) Assimilation of sediments embedded in the oceanic arc crust: myth or reality? Earth Planet Sci Lett 395(0): 51–60

Bigeleisen J (1996) Nuclear size and shape effects in chemical reactions. Isotope chemistry of the heavy elements. J Am Chem Soc 118(15):3676–3680

Bigeleisen J, Mayer MG (1947) Calculation of equilibrium constants for isotopic exchange reactions. J Chem Phys 15(5):261

Blanchard M, Balan E, Schauble EA (2017) Equilibrium fractionation of non-traditional isotopes: a molecular modeling perspective. Rev Mineral Geochem 82(1):27–63

Bowen GJ (2010) Isoscapes: spatial pattern in isotopic biogeochemistry. Annu Rev Earth Planet Sci 38(1):161–187

Buchachenko AL (2001) Magnetic isotope effect: nuclear spin control of chemical reactions. J Phys Chem A 105(44):9995–10011

Cavosie AJ, Valley JW, Wilde SA, E.I.M.F, (2005) Magmatic δ18O in 4400–3900 Ma detrital zircons: a record of the alteration and recycling of crust in the Early Archean. Earth Planet Sci Lett 235(3):663–681

Cerling TE et al (2016) Forensic stable isotope biogeochemistry. Annu Rev Earth Planet Sci 44(1):175–206

Clayton RN (2002) Self-shielding in the solar nebula. Nature 415:860–861

Clayton RN, Grossman L, Mayeda TK (1973) A component of primitive nuclear composition in carbonaceous meteorites. Science 182(4111): 485–488

Delavault H, Chauvel C, Thomassot E, Devey CW, Dazas B (2016) Sulfur and lead isotopic evidence of relic Archean sediments in the Pitcairn mantle plume. Proc Natl Acad Sci 113(46): 12952–12956

Dodd MS et al (2017) Evidence for early life in Earth's oldest hydrothermal vent precipitates. Nature 543(7643):60–64

Douglas PMJ et al (2017) Methane clumped isotopes: progress and potential for a new isotopic tracer. Org Geochem 113:262–282

Eagle RA et al (2010) Body temperatures of modern and extinct vertebrates from 13C-18O bond abundances in bioapatite. Proc Natl Acad Sci 107(23):10377–10382

Eiler JM (2001) Oxygen isotope variations of basaltic lavas and upper mantle rocks. Rev Mineral Geochem 43(1):319–364

Eiler JM (2011) Paleoclimate reconstruction using carbonate clumped isotope thermometry. Quat Sci Rev 30(25,Äì26):3575–3588

Eiler JM (2013) The isotopic anatomies of molecules and minerals. Annu Rev Earth Planet Sci 41(1):411–441

Eiler JM et al (2014) Frontiers of stable isotope geoscience. Chem Geol 372:119–143
Emiliani C (1955) Pleistocene temperatures. J Geol 63:538–578
Farquhar J, Bao H, Thiemens M (2000) Atmospheric influence of earth's earliest sulfur cycle. Science 289(5480):756–758
Fitoussi C, Bourdon B (2012) Silicon isotope evidence against an Enstatite Chondrite Earth. Science 335(6075):1477–1480
Fry B (2006) Stable isotope ecology. Springer, New York
Ghosh P et al (2006) 13C-18O bonds in carbonate minerals: a new kind of paleothermometer. Geochim Cosmochim Acta 70(6):1439–1456
Halliday AN (2014) 2.8 – the origin and earliest history of the earth A2 – Holland, Heinrich D. In: Turekian KK (ed) Treatise on geochemistry, 2nd edn. Elsevier, Oxford, pp 149–211
Hiedenreich JE, Thiemens M (1986) A non-mass-dependent oxygen isotope effect in the production of ozone from molecular oxygen: the role of molecular symmetry in isotope chemistry. J Chem Phys 86:2129–2136
Hoefs J (2015) Stable isotope geochemistry. Springer, Berlin, p 389
Huang S, Jacobsen SB (2017) Calcium isotopic compositions of chondrites. Geochim Cosmochim Acta 201(Suppl C):364–376
Jouzel J et al (2007) Orbital and millennial antarctic climate variability over the past 800,000 years. Science 317(5839):793–796
Lee-Thorp JA (2008) On isotopes and old bones. Archaeometry 50(6):925–950
Mauersberger K, Morton J, Schueler B, Stehr J, Anderson SM (1993) Multi-isotope study of ozone: implications for the heavy ozone anomaly. Geophys Res Lett 20(11):1031–1034
O'Neil JR (1968) Hydrogen and oxygen isotope fractionation between ice and water. J Phys Chem 72(10):3683–3684
Peterson BJ, Fry B (1987) Stable isotopes in ecosystem studies. Annu Rev Ecol Syst 18(1):293–320
Pringle EA et al (2016) Silicon isotopes reveal recycled altered oceanic crust in the mantle sources of Ocean Island Basalts. Geochim Cosmochim Acta 189(Suppl C):282–295
Pufahl PK, Hiatt EE (2012) Oxygenation of the Earth's atmosphere–ocean system: a review of physical and chemical sedimentologic responses. Mar Pet Geol 32(1):1–20
Ripley EM et al (2017) Multiple S isotope studies of the Stillwater Complex and country rocks: an assessment of the role of crustal S in the origin of PGE enrichment found in the J-M Reef and related rocks. Geochim Cosmochim Acta 214(Suppl C):226–245
Rosing M (1999) 13C-depleted carbon microparticles in >3700 Ma seafloor sedimentary rocks from West Greenland. Science 283:674–676
Sharp ZD (2007) Principles of stable isotope geochemistry. Pearson Prentice Hall, Upper Saddle River, p 344
Stolper DA et al (2014) Formation temperatures of thermogenic and biogenic methane. Science 344(6191):1500–1503
Taylor HP, Sheppard SMF (1986) Igenous rocks: I. Processes of isotopic fractionation and isotope systematics. In: Valley JW, Taylor HP, O'Neil JR (eds) Stable isotopes in high temperature geological processes. Reviews in mineralogy. Mineralogical Society of America, Washington, DC, pp 227–271
Teng F-Z, Dauphas N, Watkins JM (eds) (2017) Non-traditional stable isotopes. Reviews in mineralogy and geochemistry, vol 82. Mineralogical Society of America, Washington, DC, p 885
Thiemens M (2006) History and applications of mass-independent isotope effects. Annu Rev Earth Planet Sci 34:217–262
Thiemens MH, Heidenreich JE (1983) The mass-independent fractionation of oxygen: a novel isotope effect and its possible cosmochemical implications. Science 219(4588):1073–1075
Urey HC (1947) The thermodynamics of isotopic substances. J Chem Soc 1947:562–581
Valley JW (1986) Stable isotope geochemistry of metamorphic rocks. Rev Mineral Geochem 16(1):445–489
Wang DT et al (2015) Nonequilibrium clumped isotope signals in microbial methane. Science 348(6233):428–431
White WM (2015) Isotope geochemistry. Wiley, Chichester
Whitehill AR et al (2017) Clumped isotope effects during OH and Cl oxidation of methane. Geochim Cosmochim Acta 196: 307–325
Yurimoto H, Kuramoto K, Krot AN, Scott ERD, Cuzzi JN, Thiemens M (2007) Origin and evolution of oxygen isotopic compositions of the solar system. In: Reipurth B, Jewitt D, Keil K (eds) Protostars and planets V. University of Arizona Press, Tuscon, pp 849–862

Standard States

William H. Casey[1] and Peter A. Rock[2]
[1]Department of Chemistry and Department of Earth and Planetary Sciences, University of California, Davis, CA, USA
[2]College of Math and Physical Sciences, Department of Chemistry, University of California, Davis, CA, USA

Definition

Energy states, and thermodynamic activities, are calculated relative to a chosen condition called a standard state that is required as an integration limit. For pure substances these states are usually defined at a fixed temperature and pressure. For solutions, these states are usually defined at a fixed temperature, a pressure, and a composition that has an ideal behavior for a solvent or a solute, meaning that the behavior satisfied Raoult's law or Henry's Law, respectively.

Elaboration

The concept of standard states arises from the definition of the activity function that was created by G.N. Lewis, one of the most revered American physical chemists in the early twentieth century. Lewis invented the activity function in order to preserve the simple algebraic form of the law of concentration (mass) action first enunciated by the Norwegian chemists Gulberg and Waage (Lewis and Randall 1961; Laidler 1993). If μ_i is the chemical potential of component i in a multicomponent system at temperature T and pressure, P, then the activity, a_i is defined as follows:

$$d\mu_i = -\overline{S}_i dT + \overline{V}_i dP = RTd\ \ln(a_i) \qquad (1)$$

where $\overline{S}_i$ and $\overline{V}_i$ are the partial molar entropy and partial molar volume, respectively, of component i. Note that Eq. 1 is an *incomplete* definition of the activity as there is an integration constant that is yet unspecified.

Peter A. Rock: Deceased.

We now integrate Eq. 1 at fixed temperature from a standard, or reference, state that is denoted by the superscript "o" to another (nonstandard) state:

$$\int_{\mu_i=\mu^o}^{\mu_i} d\mu_i = \int_{a_i=a^o}^{a_i} RT \ d\ln(a_i) \tag{2}$$

or

$$\mu_i - \mu_i^o = RT \ \ln\left(\frac{a_i}{a_i^o}\right) \tag{3}$$

The integration constant is required by the limit and is referred to as the "standard state."

The choice of a standard state is purely arbitrary, but the most common choice is a state for which the activity can be set equal to unity, $a_j = 1$ (exactly), which has obvious mathematical utility in that the logarithm is zero. The activity is a unitless ratio of conditions (see "▶ Fugacity"). For gases, the ratio is the fugacity relative to that of a standard state fugacity that can be derived from statistical mechanics (see Dill and Bromberg 2010, pp. 211, 242) or measured.

The standard state can be a real state that is accessible to laboratory measurement, or it can be a hypothetical state. If component i exists as a pure substance in the same type of phase (solid, liquid, or gas) as the solution (e.g., liquid water at $T <$ I00 °C, 1 atm, for an aqueous solution at $T <$ 100 °C, 1 atm), then we choose the *pure* substance at 1 atm and the temperature of the solution as the standard state for which we set $a_i = 1$ (exactly). Thus for an aqueous solution at 25 °C and 1 atm totals pressure, we choose the standard state of water as the pure liquid at 25 °C and 1 atm, for which a_i^o is equal to unity. This type of standard state is referred to as a Raoult's law (or solvent) standard state. The Raoult's law description of a solvent means that one has chosen the mole fraction concentration scale. The pure solvent has unit mole fraction; $X_i = 1$ or logarithm$(X_i) = 0$.

For nonvolatile solutes, but which are soluble in the solvent of interest (e.g., liquid water), yet which do not exist as pure liquids at the temperature of the liquid solution, we are forced to choose a hypothetical standard state. By convention we choose aqueous solutes to have a *Henryan* state of a hypothetical one molal solution with the properties of infinite dilution. The wording seems obscure but is not difficult to parse in light of the equations above. A 1 m standard state is used because the $\log(m_i = 1.0) = 0$ (whereas the solvent has a $X = 1$ standard state). Reference to the *properties of infinite dilution* means that a finite slope exists between activity and concentration that is rarely true for real one molal solutions. For this Henry's law and hypothetical solute standard state, $a_i^o = 1.0$ (exactly), where $a_i^o = m_i^o \cdot \gamma_i^o$; $m_i^o = 1.0$ and γ_i^o is the activity coefficient of component i in the standard state ($\gamma_i^o = 1.0$).

In order to establish a Henry's law standard state, experiments must be carried out on solutions of decreasing concentration ($m_i \to 0$) to establish the dilute limit where $\gamma_i \to 1.0$. Practically, the activity coefficients are estimated using a theory, with the ones based upon the Debye-Hückel theory for electrolytes being the most common. When we attain the Henryan region, $a_i = m_i$. Note that other concentration scales can also express Henryan behavior – we emphasize electrolytes and the molality scale here only as the most familiar examples. In the Henry's law region, we have for an aqueous electrolyte:

$$\mu_i = \mu_i^o + RT\ln(m_i) \tag{4}$$

Because they often work at high temperatures and pressures, the arbitrary nature of choosing solute (Henryan) or solvent (Raoultian) standard states is particularly evident to geochemists. For example, the concentration of dissolved carbonate in equilibrium with the atmosphere ($pCO_2 = 10^{-3.5}$ atm) is on the order of 10^{-5} m, which is so small that a Henryan standard state is obvious. A given volume of some metamorphic or hydrothermal fluid, however, can contain amounts of dissolved CO_2 or dissolved SiO_2 that exceed the concentration of water. For these cases it may be more convenient to employ a Raoult's law standard state (see Rock 1983) and the mole fraction concentration scales for both components in the mixture. It is hard in those cases to decide if it is silica dissolved in water or water dissolved in silica.

To elaborate further, one generally chooses a fixed-pressure standard state to describe solutions near the Earth surface, but any fixed pressure could be used as a standard state. The activities of states that differ only in pressure are related by the equations:

$$\int_1^2 d\ln(a_i) = \frac{1}{RT}\int_{P_1}^{P_2} \overline{V}_i \ dP \tag{5}$$

or

$$\ln\left(\frac{a_{i,2}}{a_{i,1}}\right) = \frac{1}{RT}\int_{P_1}^{P_2} \overline{V}_i \ dP \tag{6}$$

where in general, $\overline{V}_i$ depends on both P and T. The activity for a fixed-composition substance at pressure, P, relative to a 1 bar (10^5 Pa) standard state for that temperature, where: $a_{i,1}^0 = 1$ is:

$$\ln(a_{i,2}) = \frac{1}{RT}\int_1^{P_2} \overline{V}_i(P) \ dP \tag{7}$$

We can set $a_{i,1} = 1$ for any convenient value of P and refer all $a_{i,2}$ values to that standard state. Alternative standard states are described in Anderson and Crerar (1993).

S

Conclusions

Well-defined standard states are explicit in thermodynamic calculations and derive from the need for an integration limit. Choice of standard states, however, is purely a matter of convenience. In biological systems, for example, the standard state for H_3O^+ is not the 1.0 m solution described above, but a 10^{-7} M solution, which is closer to a physiological media like blood (see Alberty and Silbey 1992, pp. 280–282). Geochemists also move the standard states to elevated temperatures and pressures to better match the environmental conditions (see Anderson and Crerar 1993; Nordstrom and Munoz 1994) that are often far different from conditions at the Earth surface.

Cross-References

- ▶ Activity and Activity Coefficients
- ▶ Fugacity
- ▶ Geochemical Thermodynamics
- ▶ Gibbs-Duhem Equation
- ▶ Henry's Law

References

Alberty RA, Silbey RS (1992) Physical chemistry. Wiley, New York, 898 pp

Anderson GM, Crerar DA (1993) Thermodynamics in geochemistry. Oxford University Press, New York, 588 pp

Dill KA, Bromberg S (2010) Molecular driving forces: statistical thermodynamics in biology, chemistry, physics, and nanoscience, 2nd edn. Garland Science, London/New York, 756 pp

Laidler KJ (1993) The world of physical chemistry. Oxford University Press, New York, 476 pp

Lewis GL, Randall M (1961) Thermodynamics (revised by KS Pitzer and L Brewer). McGraw-Hill, New York, 724 pp

Nordstrom DK, Munoz JL (1994) Geochemical thermodynamics, 2nd edn. Blackwell Scientific Publications, Cambridge, MA, 494 pp

Rock PA (1983) Chemical thermodynamics. University Science Books, Mill Valley, 548 pp

Stoichiometry

Anna F. Oliveri

Department of Chemistry, Department of Earth and Planetary Sciences, University of California, Davis, CA, USA

Definition

The stoichiometry of a chemical reaction is the molecular ratio of individual reactants and products, typically represented as whole numbers. When the relative quantities of molecules are calculated correctly, the number of each type of atom should be equal in the reactants and products.

In a given chemical reaction, the numbers that come before each reactant and product represent the quantities, or stoichiometry, of each substance. In Eq. 1, two quantities (usually expressed in moles) of AX_3 react with three quantities of BY_2 to produce two and three quantities of AY_3 and BX_2, respectively. One mole is 6.022×10^{23} particles of a given substance. This unit is similar to a dozen and is used to organize gigantic numbers of items (molecules, atoms, etc.) into practicable proportions. The law of conservation of mass dictates that no mass (or energy) can be created or destroyed; therefore, using moles, you can see that the reaction starts and ends with 6 mol of X^-.

$$\mathbf{2AX_3 + 3BY_2 \rightarrow 2AY_3 + 3BX_2} \quad (1)$$

To determine the proper stoichiometry for a chemical equation, you must simply balance the specific types of atoms. Take the simple reaction of hydrogen peroxide decomposing into water and oxygen gas (Eq. 2). Without stoichiometry, the chemical equation indicates that each individual reaction begins with two oxygen atoms and spontaneously produces a new one, resulting in three oxygen atoms.

$$\mathbf{H_2O_2 \rightarrow H_2O + O_2} \quad (2)$$

This cannot be true, due to the law of conservation of mass. By indicating that two hydrogen peroxide molecules must react to form two water molecules and one oxygen molecules, the reaction is balanced, and mass is conserved (Eq. 3).

$$\mathbf{2H_2O_2 \rightarrow 2H_2O + O_2} \quad (3)$$

Stoichiometry is extremely useful for determining experimental concentrations, limiting reagents and molar proportions, predicting yield, and calculating percent yield. Stoichiometric ratios allow for easy mathematical conversion from one type of substance to another. If 1.0 g of H_2O_2 is allowed to decompose, how many g of H_2O will be created after complete O_2 gas evolution? Having a balanced chemical equation makes this an extremely simple question to answer; no experimental data is needed (Fig. 1).

The stoichiometric ratio, provided by the balanced chemical reaction, allows for the type of molecular conversion shown in Fig. 1. By comparing the calculated value (the predicted yield) to experimental data, the percent yield of a reaction can be determined. Conversely, if a specific quantity of product is desired, the stoichiometric ratio can be used to ascertain the needed quantities of reactants.

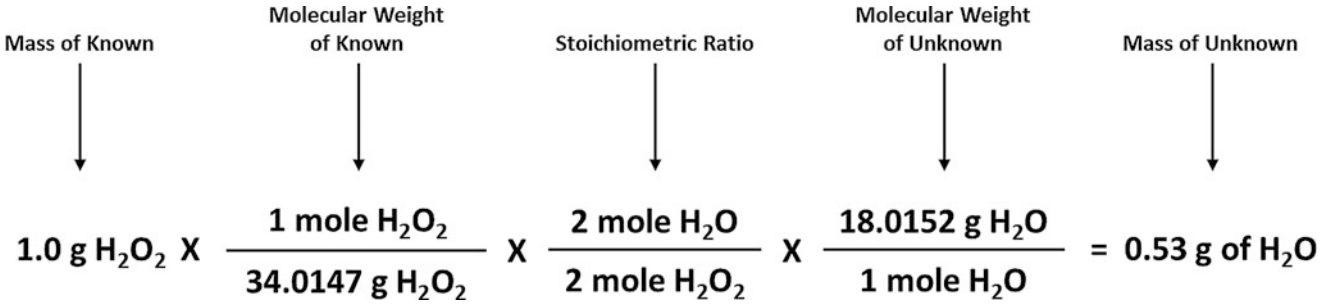

Stoichiometry, Fig. 1 Sample calculation to determine the mass of water produced when 1.0 g of hydrogen peroxide completely decomposes

Strontium

Oliver Nebel
School of Earth, Atmosphere and Environment, Monash University, Clayton/Melbourne, VIC, Australia

Element Data
Atomic Symbol: Sr
Atomic Number: 38
Atomic Weight: 87.62
Isotopes and Abundances:
^{84}Sr, 0.56%
^{86}Sr, 9.86%
^{87}Sr*, 7.00%
^{88}Sr, 85.58%
1 Atm Melting Point: 769 °C
1 Atm Boiling Point: 1348 °C
Common Valences: 2+
Ionic Radii: 126 pm
Pauling Electronegativity: 0.95
First Ionization Energy: 549.47 kJ/mol
Chondritic (CI) Abundance: 7.79 ppm
Silicate Earth Abundance: 22 ppm
Crustal Abundance: 320 ppm
Seawater Abundance: 8 ppm
Core Abundance: nil

Properties

Strontium (Sr) is an alkaline Earth element of group IIa of the periodic table. In its low temperature polymorph (transition into high temperature polymorphs at 235 °C and 540 °C), it is a soft, silvery metal (Mohs scale 1.8). It rapidly reacts to a yellowish colored oxide in air and decomposes vigorously in water. Strontium has an average atomic weight of 87.62, an electron configuration of [Kr]$5s^2$, and occurs in a 2+ valence state in natural systems.

Strontium has four naturally occurring, stable isotopes: Sr-84, Sr-86, Sr-87, and Sr-88, of which Sr-87 is subject to radiogenic ingrowth by Rb-87 beta decay. The range in $^{87}Sr/^{86}Sr$ in natural terrestrial material prevents a more precise standard atomic weight and the isotopic composition of Sr can vary substantially in rocks and minerals, depending on age and Rb content. With a half-life of ca. 49 billion years, the related ^{87}Rb-^{87}Sr isotope system is a widely applied dating tool and isotope tracer (Nebel et al. 2011). Twenty-four additional, short-lived isotopes of Sr are known, of which Sr-90 has the longest half-life with ca. 28 years.

History and Use

Strontium is named after the village Strontian, located in Sunart in the Scottish highlands. The element was first identified in 1787 from the mineral strontianite ($SrCO_3$) by Adair Crawford, which was recovered from a local lead mine and identified as a new element by Thomas Hope in 1791. It was first isolated by electrolysis by Humphrey Davy in 1808. Strontium also forms a sulfate mineral of its own (celestite, $SrSO_4$). In all other naturally occurring minerals, Sr is only present in trace amounts. In industry, Sr is frequently used in pyrotechnics for red coloring, such as fireworks and warning flares. Strontium can further be used as a compound in ferrite magnets and as chloride hexahydrate in toothpaste for sensitive teeth.

In Earth sciences, Sr is frequently used as an indicator mineral for the fractionation of plagioclase in igneous petrogenesis. In combination with Rb, it is one of the most important dating tools for igneous rocks. Radiogenic and stable isotopes of Sr are often employed as geochemical tracers in both high-temperature rocks and low-temperature chemical sediments and waters.

Geochemical Behavior

Strontium is lithophile and moderately incompatible in mantle phases. It is thus enriched in the crust compared to primitive or depleted mantle. The Earth's core contains no Sr. Accordingly, an estimation of the abundance of Sr in the bulk silicate Earth (BSE) is 22 ppm, based on a chondritic refractory element budget for Earth and a chondritic abundance of 7.79 ppm (Palme and O'Neill 2014). Strontium abundance in continental crust is estimated to average 320 ppm (Rudnick and Gao 2014). Values for Sr abundances in upper, middle, and lower continental crust vary only marginally with values of 320, 348, and 320 ppm, respectively (Rudnick and Gao 2014). These reflect the relative equal distribution of Sr in all crustal assemblages. This equates to an average D(Sr) during crust-mantle differentiation of 0.69. In magmatic systems, Sr is a trace element with abundances $\ll$1% in most rocks, except for highly alkaline or carbonatitic rocks and anorthositic rocks. Strontium readily substitutes for and partitions into the site of Ca^{2+} due to their similar charge and ionic radii (Sr^{2+} = 1.26 Å, Ca^{2+} = 1.12 Å). It preferentially partitions into anorthite and to a lesser extent into the smaller octahedral site of clinopyroxene or, if present, into clino-amphibole. Because of its incompatible nature in most igneous minerals (except plagioclase), Sr concentration increases in the melt until the onset of feldspar fractionation, often indicated by co-variations with Eu* (Eu/[Gd + Sm]). In more felsic systems, Sr is mainly hosted by plagioclase but also in Ca-bearing accessory phases, for example, apatite. In highly alkaline rocks, such as carbonatites, Sr can occur to up to lower wt% abundances. Strontium is a large ion lithophile element and considered mobile during fluid transport. In aqueous solutions, it has an effective diameter of 500 pm, similar to Ba but smaller than Ca (600 pm). Owing to its high solubility in water, Sr is relatively concentrated in the oceans (ca. 7.6 ppm) and surface waters (2 orders of magnitude lower than in oceans, depending on bed-rock geology). Subsurface brines can contain thousands of ppm Sr. There is a generally good co-variation of Sr concentration and its radiogenic isotope composition in waters, which indicates that Sr is an excellent tracer for fluid-rock interactions, mixing of aquifers and recharge areas, and fluid migration during diagenetic processes. Consequently, Sr is often re-distributed during hydrous metamorphic reactions and low-temperature fracture fills.

Strontium in seawater has a long ocean residence time between 1 and 20 Myrs (Vollstaedt et al. 2014) and reflects a mix between continental run-off and Sr exchange between oceanic crust and seawater at oceanic ridges. A high continental run-off into the oceans and relatively fast ocean mixing times result in a relatively constant global Sr concentration and isotope composition in seawater. Over geologic timescales, the Sr isotope composition of the oceans can vary in response to changes in the isotopic composition of continental run-off during fluctuations in the tectonic and erosional regimes.

Strontium has a high affinity for chemical sediments and cement. Whereas carbonates are the most abundant Sr hosts (up to 0.1 wt%) with aragonite > calcite > dolomite, phosphorites can also contain significant amounts. Strontium is further incorporated into biogenic carbonates and phosphates. Absolute concentrations and Sr/Ca in corals or other marine skeletons can serve as proxies for present and past sea surface temperature reconstructions (Devilliers et al. 1995; Corrège 2006).

Biological Utilization and Toxicity

Strontium is considered nonhazardous for organisms. The only known health risk is associated with Sr-90, which is a hazardous radioactive isotope produced by nuclear fission. Injected or consumed Sr is almost instantly cleared from blood and is readily incorporated into bone and marrow (ca. 99% of the human Sr budget). Strontium deficiency or high concentrations (up to 0.5% uptake) have no reported effect on man or farm animals (Nielsen 2004). In low quantities, Sr can be used as a medical tracer or in radiotherapy as a cancer treatment. Strontium borate is being tested as a future material for bone substitute material.

Cross-References

- ▶ Alkali and Alkaline Earth Metals
- ▶ Calcium
- ▶ Incompatible Elements
- ▶ Lithophile Elements
- ▶ Ocean Biochemical Cycling and Trace Elements
- ▶ Paleotemperatures
- ▶ Rubidium
- ▶ Strontium Isotopes

References

Corrège T (2006) Sea surface temperature and salinity reconstruction from coral geochemical tracers. Palaeogeogr Palaeoclimatol Palaeoecol 232(2–4):408–428

Devilliers S, Nelson BK, Chivas AR (1995) Biological controls on coral Sr/Ca and delta-O-18 reconstructions of sea-surface temperatures. Science 269(5228):1247–1249

Nebel O, Scherer EE, Mezger K (2011) Evaluation of the Rb-87 decay constant by age comparison against the U-Pb system. Earth Planet Sci Lett 301(1–2):1–8

Nielsen SP (2004) The biological role of strontium. Bone 35:583–588

Palme H, O'Neill HSC (2014) Cosmochemical estimates of mantle composition. In: Holland H, Turekian K (eds) Treatise on geochemistry. Elsevier, Amsterdam, pp 1–39

Rudnick RL, Gao S (2014) Composition of the continental crust. In: Holland H, Turekian K (eds) Treatise on geochemistry. Elsevier, Amsterdam, pp 1–51
Vollstaedt H et al (2014) The Phanerozoic delta Sr-88/86 record of seawater: new constraints on past changes in oceanic carbonate fluxes. Geochim Cosmochim Acta 128:249–265

Strontium Isotopes

Oliver Nebel[1] and Jessica A. Stammeier[2]
[1]School of Earth, Atmosphere and Environment, Monash University, Clayton/Melbourne, VIC, Australia
[2]Institute of Applied Geosciences, Graz University of Technology, Graz, Austria

Definition

Strontium (Sr) isotopes are widely applied tracers in geoscientific applications. One of the four stable isotopes (^{87}Sr) is subject to long-term radiogenic ingrowth by radioactive decay of rubidium (^{87}Rb). Resultant isotope variations in $^{87}Sr/^{86}Sr$, but also other stable isotope variations, can be employed to trace mixing of global reservoirs, ranging from high-temperature-pressure processes preserved in solid rock to low-temperature, environmental conditions in surface waters, oceans, chemical sediments, or biogeochemistry. A second, frequent application is the dating of rock-forming processes using the Rb-Sr decay scheme, ranging in age from the infant stages of the solar system to most recent geologic events.

Introduction to Rb-Sr Systematics

Rb-Sr systematics are based on the radioactive decay of the isotope ^{87}Rb (that today accounts for ~27% of all rubidium) to ^{87}Sr (~9% of all strontium) by beta decay with a half-life of approximately 49 billion years, corresponding to a Rb decay constant (λ^{87}Rb) of 1.394×10^{-11}/a (Nebel et al. 2011b). A prime application of the decay scheme is tracing geochemical processes using the radiogenic Sr isotope signature in rocks and minerals. As a dating technique Rb-Sr is, in principle, suitable for samples from the early stages of the solar system to a few million years before present. Modern Rb-Sr geochronology of multiple phases can achieve precisions similar to Ar-Ar dating or conventional U-Pb dating, in the order ca. ±0.2% (Nebel and Mezger 2008; Willigers et al. 2004). The thermal threshold, or closure temperature T_C, for Rb-Sr reset is between 300 °C and 400 °C, dependent on mineralogy. This renders Rb-Sr one of the most susceptible systems to thermal overprint among the long-lived lithophile element isotope systems.

Isochron relationships can further be used to test initial isotope equilibrium of phases. For this, in an isochron diagram, isotope equilibrium at t_0 is marked by the ordinate intercept of the regression line (Fig. 1) or can be calculated as initial $^{87}Sr/^{86}Sr$. The related decay equation is (with t in millions of years):

$$^{87}Sr/^{86}Sr_{present} = {}^{87}Sr/^{86}Sr_{initial} + {}^{87}Rb/^{86}Sr \times \left(e^{(\lambda \times t)} - 1\right)$$

Strontium Isotope Analyses

Strontium isotope compositions vary from subtle variations among whole rocks or mineral phases in the 5th decimal place (i.e., 0.00005) to large variations, especially in older samples. The $^{87}Sr/^{86}Sr$ can be routinely analyzed in > 50 ng Sr of purified sample material by thermal ionization mass spectrometry (TIMS). Precisions are typically ±40 ppm but can be as good as ±5 ppm with modern TIMS instruments. An alternative method is the use of multicollector inductively coupled plasma source mass spectrometry (MC-ICP-MS). This technique allows a high sample throughput and *in situ* analyses via laser ablation, but yields less precise data no better than ±100 ppm (Vroon et al. 2008) and is restricted to samples with low Rb/Sr. Collision-cell, triple-quadrupole ICP mass spectrometers, however, can be used for *in situ* Rb-Sr dating with precisions <1.5% of the sample age (Zack and Hogmalm 2016). Mass fractionation in the mass spectrometer during isotope analyses is corrected for by using a $^{86}Sr/^{88}Sr = 0.1194$ by convention, or in the case of stable isotope analyses, by correction relative to the NBS-987 isotope standards.

Radiogenic Sr Isotopes in Early Solar System Material and Bulk Silicate Earth

The initial $^{87}Sr/^{86}Sr$ composition of the solar system ($^{87}Sr/^{86}Sr_{SS}$) is best estimated by analyses of calcium-aluminum-rich inclusions (CAI) in primitive chondrites. These inclusions, composed of predominantly refractory elements, are believed to be the first solids condensed from the solar nebular. Their initial $^{87}Sr/^{86}Sr$ has recently been determined to 0.698975 ± 0.000008 (Hans et al. 2013).

Previous determination of $^{87}Sr/^{86}Sr_{SS}$ also employed initial $^{87}Sr/^{86}Sr$ of achondrites (best achondrite basaltic initial - BABI), including the pyroxene-rich angrite Angra Dos Reis (ADOR). These older analyses revealed $^{87}Sr/^{86}Sr$ isotope heterogeneity among the earliest solar system bodies. However, Hans and co-workers found variations in the stable $^{84}Sr/^{86}Sr$ in these meteorites, which they ascribe to

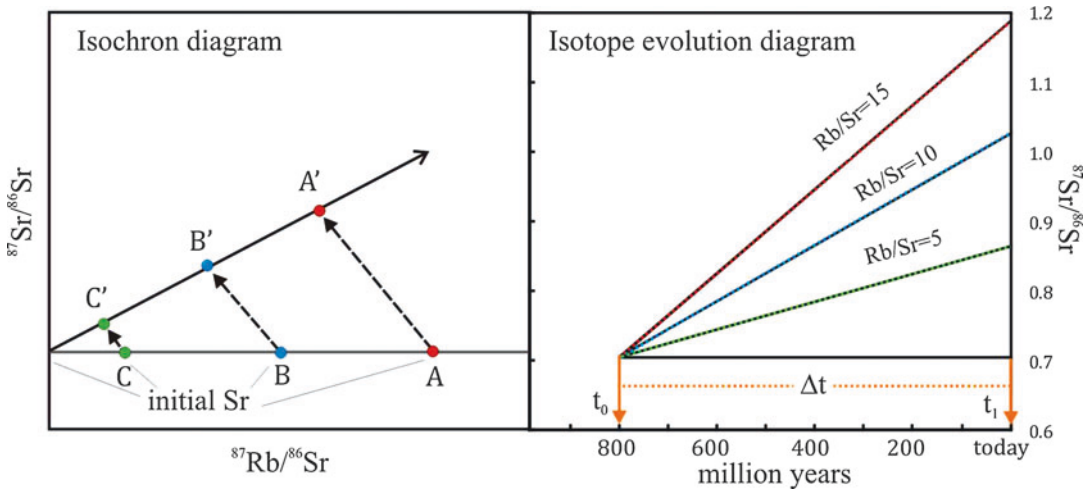

Strontium Isotopes, Fig. 1 (**a**) Rb-Sr isochron diagram showing the time-dependent evolution of three different phases, (A-C) with variable Rb/Sr that formed in isotopic equilibrium and thus have the same initial $^{87}Sr/^{86}Sr$ isotope composition. Points A'-C' reflect the present day isotope composition of phases A-C, respectively. (**b**) $^{87}Sr/^{86}Sr$ isotope evolution versus time plot (with t_0 defining the onset of radiogenic ingrowth and t_1 the time of sampling) with the respective ^{87}Sr ingrowth of three different phases as a consequence of their variable Rb/Sr

incomplete mixing of *r*-process nuclides in the solar nebula. Upon correction for these isotope variations in $^{84}Sr/^{86}Sr$ compositions (and thus also affecting $^{87}Sr/^{86}Sr$ prior to radiogenic ingrowth), the resultant $^{87}Sr/^{86}Sr_{SS}$ in angrites is identical to those in CAI. Considering the very similar formation age of angrites, within ca. two million years after CAI formation, this indicates a homogeneous initial $^{87}Sr/^{86}Sr$ of the early solar system.

A key problem in determining the $^{87}Sr/^{86}Sr$ evolution of the bulk silicate Earth (BSE) is that its average Rb/Sr is unknown, and no representative sample is available for analysis. The reason for this is two-fold: One major obstacle is that although the Sr isotope compositions of primitive chondrites can be precisely measured, the Rb/Sr of these terrestrial building blocks are highly variable due to the volatility of Rb (half-condensation temperature of ~800 K). Loss of volatile elements, including Rb, during early solar system body collisions or depletion into the early sun or the outer solar system has likely altered the chondritic Rb/Sr (Nebel et al. 2011a). Using terrestrial Sr-Nd isotope covariations in mantle-derived rocks (Fig. 2a) as a substitute yields a Sr isotope composition of $^{87}Sr/^{86}Sr_{CHUR} \sim 0.705$ in a chondritic Earth model (CHUR), or $^{87}Sr/^{86}Sr_{SCHEM} \sim 0.703 \pm 0.004$ in a subchondritic Earth model (SCHEM, (Caro and Bourdon 2010).

Radiogenic Sr Isotopes in the Crust–Mantle System

Continental crust has formed with time mainly by partial melting of the upper mantle at convergent plate margins or in plumes. During melting processes in the mantle, Rb is less compatible than Sr, which leads to a time-integrated high Rb/Sr in the crust compared to the mantle and a correspondingly high $^{87}Sr/^{86}Sr$ in crustal rocks. A sample or entire terrane separated from the mantle at one point in Earth's history will therefore diverge from the mantle's Sr isotope evolution. However, due to substantial Rb/Sr fractionation during igneous differentiation processes, the continental crust is highly heterogeneous in its $^{87}Sr/^{86}Sr$ with an average present day isotope composition of $^{87}Sr/^{86}Sr \sim 0.715$, based on loess samples (e.g., Yokoo et al., 2004).

The present day depleted mantle is also heterogeneous in its Sr isotope composition, owing to melt extraction and re-fertilization by recycled crust. Due to elevated $^{87}Sr/^{86}Sr$ and high Sr abundances in crustal rocks and their sedimentary products, crustal recycling has a strong effect on the Sr isotope composition of mantle rocks with less radiogenic $^{87}Sr/^{86}Sr$ (Armstrong 1968; DePaolo 1981). On average, global mid-ocean ridge basalts (MORB), considered representative of the upper mantle, show a depleted Sr isotope signature with the lowest reported present day value of $^{87}Sr/^{86}Sr = 0.7021$ (Fig. 2a). A key difference between the actively discussed chondritic versus subchondritic Earth models is the degree of mantle depletion. About one-third of ocean floor lavas at oceanic ridges is isotopically enriched through crustal components in a SCHEM model, opposing a nearly complete depletion in a CHUR model.

Oceanic island lavas (OIB), considered by most to be sourced by thermo-chemical anomalies from the lower mantle (plumes), also show elevated radiogenic isotope signatures associated with crustal recycling. The common model explains these signatures with a recycling process of

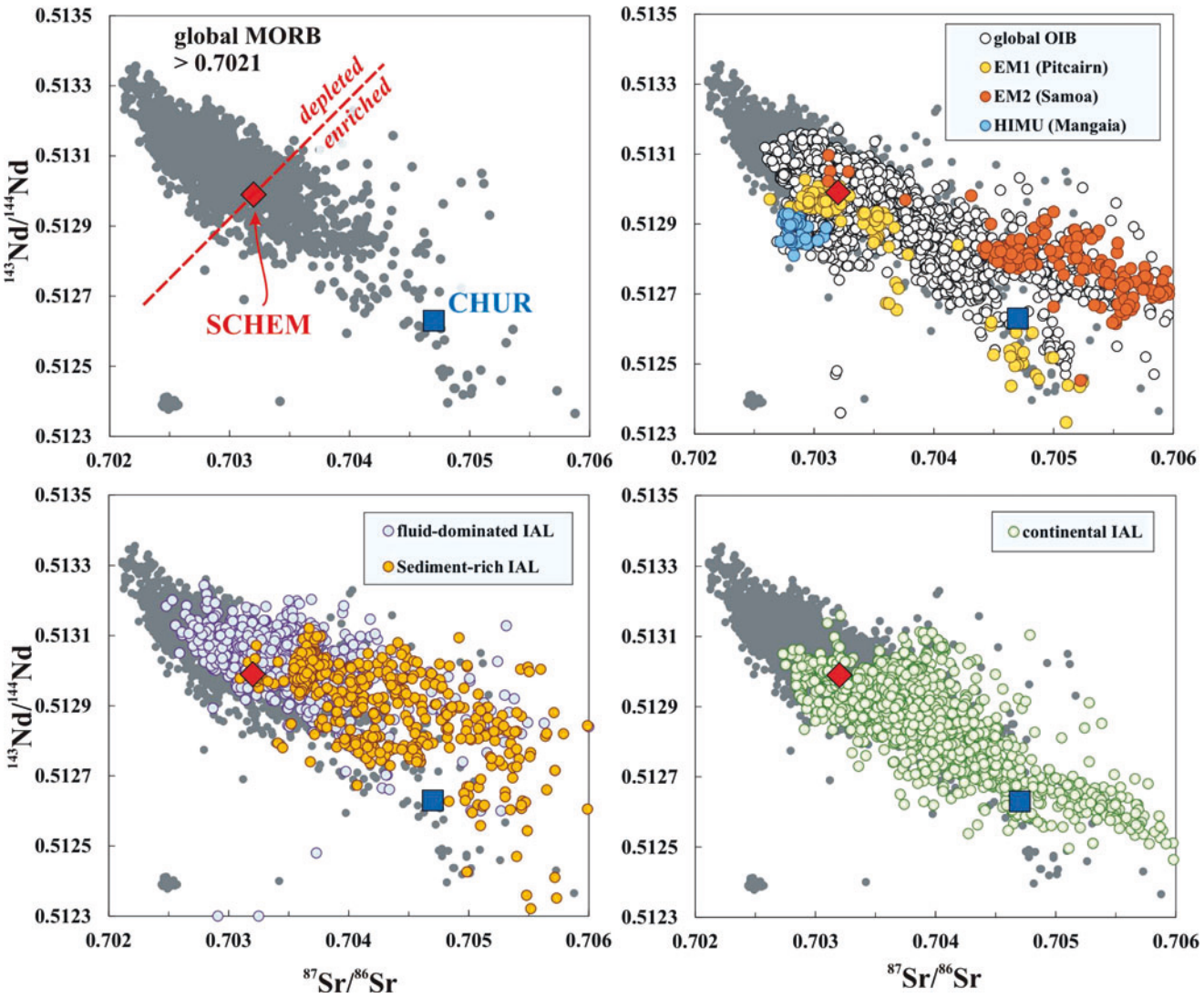

Strontium Isotopes, Fig. 2 Comparison of Sr and Nd isotope ratios in global ocean floor lavas following the rational of DePaolo and Wasserburg (1977). (**a**) Mid-ocean ridge basalts (MORB) show a clear co-variation (*gray dots*). In a subchondritic Earth model (SCHEM), 1/3 of al data are isotopically enriched, tending towards the *top-left* corner in the diagram. (**b**) Ocean Island basalts (OIB) with the three isotope end members enriched-mantle 1 and 2 (EM1, EM2) and high-μ (HIMU). (**c, d**) Subduction zone data for global island arc lavas (IAL) in comparison with MORB; MORB and OIB/IAL data taken from www.earthchem.org/petdb and http://georoc.mpch-mainz.gwdg.de, respectively. SCHEM and CHUR values as listed in Caro and Bourdon (2010)

S

subducted, crustal components into the lower mantle and their return to the surface in upwelling plumes (Hofmann and White 1982). Even though the calculated amount of crust in these rocks appears small, in the order of <5%, the radiogenic isotope character of Sr is still sufficiently indicative for the presence of crustal components in the source of these lavas. Mantle-residence times of crustal components vary substantially from <650 Myrs in some so-called enriched mantle 1 (EM1) components (Sobolev et al. 2011), based on $^{87}Sr/^{86}Sr$ in Hawaiian lavas, to >2.3 Ga in the most extreme HIMU lavas with remarkably low $^{87}Sr/^{86}Sr$. Samoan OIB show the most extreme Sr isotope values among OIB, which represent the so-called enriched mantle 2 (EM2) component. (Jackson et al. 2007).

The major sites for crust-mantle interaction is and Sr pollution of the mantle occurs at convergent margins, that is, in subduction zones. However, recycling into the mantle is incomplete, evidenced by elevated $^{87}Sr/^{86}Sr$ in most erupting island arc lavas (IAL) when compared to average MORB. The Sr isotope composition in IAL is broadly correlated to the amount of sediment that is being subducted in the subduction zone. Fig. 2c shows a plot of arcs associated with large amounts of subducted sediment (Banda and Lesser Antilles arc) with a clear offset from MORB due to partial sediment

melting. In contrast, IAL from so-called fluid-dominated arcs (Marianna, Izu-Bonin, Kermadec, and Aleutian) show intermediate signatures, often related to overprint with Sr-bearing fluids. In continental arcs (Fig. 2d, Cascades, Central American and Mexican Volcanic arc), crustal assimilation plays an important role, illustrated by lower Sr isotopes for a given Nd isotope signature when compared to intraoceanic arcs.

Stable Sr Isotopes in Geochemistry

Within the current analytical limits of ±0.02 δ^{88}Sr units (the delta notation is the deviation in $^{88}Sr/^{86}Sr$ from the NBS-987 standard times 1000), early solar system materials, including Martian rocks, are identical. In contrast, terrestrial rocks show lighter values in relation to igneous differentiation, tentatively linked to plagioclase fractionation and associated substitution of Sr^{2+} for Ca^{2+} with a preference for the heavier isotope (Charlier et al. 2012). In the low temperature environment, stable Sr isotopes show fractionation during weathering of crustal rocks and in associated soils and waters (Stevenson et al. 2016). Experimental work on biological carbonate material suggests a dependence between ambient temperature and δ^{88}Sr (Fietzke and Eisenhauer 2006). In marine carbonates sampled throughout the Phanerozoic, however, stable Sr isotope compositions show little or no dependence with temperature. Instead, the variations in δ^{88}Sr, decoupled from $^{87}Sr/^{86}Sr$, can be used to constrain the flux of Sr run-off into the oceans and associated ocean residence times (Vollstaedt et al. 2014).

Radiogenic Sr Isotopes in Surface and Ocean Water

Strontium is a large ion lithophile element (LILE) and therefore considered mobile in aqueous solutions. It has a high solubility and is readily transported in surface waters and hydrothermal fluids. In ground water, dissolution of Sr^{2+} through reaction with aquifer lithology leads to highly variable $^{87}Sr/^{86}Sr$, which can be used to trace water pathways (Jacobson and Wasserburg 2005). Because of the radiogenic nature of the continental crust, crustal weathering results in radiogenic isotope signatures in most surface waters and open oceans with an average, present day seawater $^{87}Sr/^{86}Sr \sim 0.712$ (Palmer and Edmond 1989). Continental run-off of Sr into the ocean is related to continental weathering rates, and the related ocean residence time is in the order of 1 Myr to as long as 20 Myrs in the Phanerozoic Oceans (Vollstaedt et al. 2014). Consequently, enhanced weathering due to erosion of crustal terranes with associated radiogenic $^{87}Sr/^{86}Sr$, for example, during times of peak orogenesis, results in more radiogenic Sr isotope signatures in seawater. Similarly, the contribution of juvenile $^{87}Sr/^{86}Sr$ to the ocean in times of extensive seafloor spreading, for example, during continental reorganization following the break-up of supercontinents, can alter seawater Sr isotopic composition.

Strontium is easily incorporated into Ca-bearing chemical sediments (e.g., carbonates or phosphates) or biogenic carbonate-phosphate skeletons (e.g., shells, corals). Hence, with a detailed knowledge of the $^{87}Sr/^{86}Sr$ signatures of seawater through time, the isotope signatures of Ca-bearing

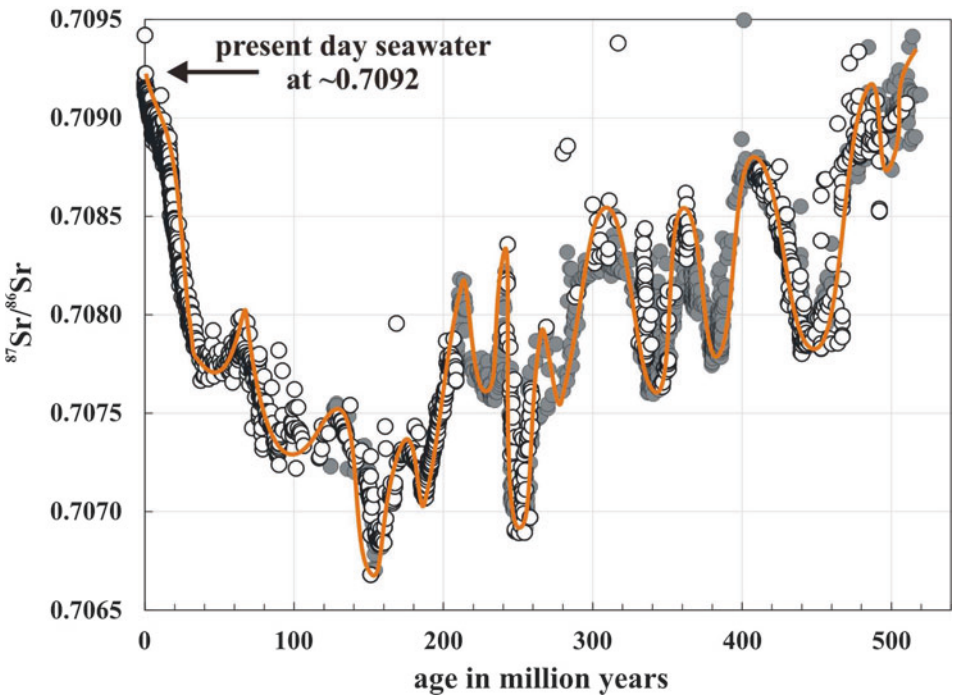

Strontium Isotopes, Fig. 3 Strontium isotope evolution of Phanerozoic seawater after Veizer et al. (1999). Filled symbols represent coherent data reported in Veizer et al. (1999); open symbols are additional literature data. The *orange line* is a moving average drawn by eye to highlight the sharp changes in $^{87}Sr/^{86}Sr$. Data compilation courtesy by Jan Veizer, accessible via http://mysite.science.uottawa.ca/jveizer/isotope_data/

marine sediments, for example carbonates, may be used to place them into a broader stratigraphic context. This process is known as Sr chronostratigraphy. Careful analyses of limestones and/or biogenic calcite with known age revealed a detailed Sr isotope evolution of seawater throughout the Phanerozoic (Burke et al. 1982; Veizer and Compston 1974). Subsequent refinements of the seawater evolution curve revealed a cyclic evolution with de- and increasing isotope signatures (Fig. 3). Notable is a constant decline in average Sr isotope composition from the Cambrian to the late Jurassic. A steady increase since then has led to a present day $^{87}Sr/^{86}Sr = 0.7092$, broadly matching Cambrian seawater isotope composition.

Sr Isotopes in Forensic Sciences

Strontium readily substitutes for Ca^{2+} in biogenic phosphates and with this also locks in the $^{87}Sr/^{86}Sr$ isotope code of the environment in which the organism grows. With this, Sr isotope compositions of bones and teeth are a valuable tracer in forensic sciences for provenances studies or to track migration routes. Application range in identifying historic human remains and their provenance using teeth, for example, the iceman discovered in Austria (Muller et al. 2003), or tracking human or bird migration through hair or feather analyses, respectively (Font et al. 2007; Font et al. 2012). Analyses in human bone, however, reflect only the last ca. 6 years of life (Price et al. 2000).

Cross-References

- ▶ Archeological Geochemistry
- ▶ Earth's Continental Crust
- ▶ Formation and Evolution of the Earth
- ▶ Inductively Coupled Plasma Mass Spectrometry (ICP-MS)
- ▶ Mantle Geochemistry
- ▶ Mid-Ocean Ridge Basalts (MORB)
- ▶ Neodymium Isotopes
- ▶ Ocean Biochemical Cycling and Trace Elements
- ▶ Oceanic Island Basalts
- ▶ Rubidium
- ▶ Stable Isotope Geochemistry
- ▶ Strontium
- ▶ Thermal Ionization Mass Spectrometry

References

Armstrong RL (1968) A model for the evolution of strontium and lead isotopes in a dynamic earth. Rev Geophys 6:175–199

Burke WH et al (1982) Variation of seawater $^{87}Sr/^{86}Sr$ through Phanerozoic time. Geology 10(10):516–519

Caro G, Bourdon B (2010) Non-chondritic Sm/Nd ratio in the terrestrial planets: consequences for the geochemical evolution of the mantle crust system. Geochim Cosmochim Acta 74(11):3333–3349

Charlier BLA et al (2012) High temperature strontium stable isotope behaviour in the early solar system and planetary bodies. Earth Planet Sci Lett 329:31–40

DePaolo DJ (1981) Trace element and isotopic effects of combined wall rock assimilation and fractional crystallization. Earth Planet Sci Lett 53:189–202

DePaolo DJ, Wasserburg GJ (1977) Sources of island arcs as indicated by Nd and Sr isotopic studies. Geophys Res Lett 4(10):465–468

Fietzke J, Eisenhauer A (2006) Determination of temperature-dependent stable strontium isotope (Sr-88/Sr-86) fractionation via bracketing standard MC-ICP-MS. Geochem Geophys Geosyst 7

Font L, Nowell GM, Pearson DG, Ottley CJ, Willis SG (2007) Sr isotope analysis of bird feathers by TIMS: a tool to trace bird migration paths and breeding sites. J Anal At Spectrom 22(5):513–522

Font L et al (2012) Strontium and lead isotope ratios in human hair: investigating a potential tool for determining recent human geographical movements. J Anal At Spectrom 27(5):719–732

Hans U, Kleine T, Bourdon B (2013) Rb-Sr chronology of volatile depletion in differentiated protoplanets: BABI, ADOR and ALL revisited. Earth Planet Sci Lett 374:204–214

Hofmann AW, White WM (1982) Mantle plumes from ancient oceanic crust. Earth Planet Sci Lett 57:421–436

Jackson MG et al (2007) The return of subducted continental crust in Samoan lavas. Nature 448(7154):684–687

Jacobson AD, Wasserburg GJ (2005) Anhydrite and the Sr isotope evolution of groundwater in a carbonate aquifer. Chem Geol 214(3–4):331–350

Muller W, Fricke H, Halliday AN, McCulloch MT, Wartho JA (2003) Origin and migration of the Alpine Iceman. Science 302 (5646):862–866

Nebel O, Mezger K (2008) Timing of thermal stabilization of the Zimbabwe Craton deduced from high-precision Rb-Sr chronology, Great Dyke. Precambrian Res 164(3–4):227–232

Nebel O, Mezger K, van Westrenen W (2011a) Rubidium isotopes in primitive chondrites: constraints on Earth's volatile element depletion and lead isotope evolution. Earth Planet Sci Lett 305(3–4):309–316

Nebel O, Scherer EE, Mezger K (2011b) Evaluation of the Rb-87 decay constant by age comparison against the U-Pb system. Earth Planet Sci Lett 301(1–2):1–8

Palmer MR, Edmond JM (1989) The strontium isotope budget of the modern ocean. Earth Planet Sci Lett 92:11–26

Price TD, Manzanilla L, Middleton WD (2000) Immigration and the ancient city of Teotihuacan in Mexico: a study using strontium isotope ratios in human bone and teeth. J Archaeol Sci 27(10):903–913

Sobolev AV, Hofmann AW, Jochum KP, Kuzmin DV, Stoll B (2011) A young source for the Hawaiian plume. Nature 476 (7361):434–437

Stevenson EI et al (2016) Insights into combined radiogenic and stable strontium isotopes as tracers for weathering processes in subglacial environments. Chem Geol 429:33–43

Veizer J, Compston W (1974) $^{87}Sr/^{86}Sr$ composition of seawater during the Phanerozoic. Geochim Cosmochim Acta 38(9): 1461–1484

Veizer J et al (1999) Sr-87/Sr-86, delta C-13 and delta O-18 evolution of Phanerozoic seawater. Chem Geol 161(1–3):59–88

Vollstaedt H et al (2014) The Phanerozoic delta Sr-88/86 record of seawater: new constraints on past changes in oceanic carbonate fluxes. Geochim Cosmochim Acta 128:249–265

Vroon PZ, van der Wagt B, Koornneef JM, Davies GR (2008) Problems in obtaining precise and accurate Sr isotope analysis from geological materials using laser ablation MC-ICPMS. Anal Bioanal Chem 390(2):465–476

Willigers BJA, Mezger K, Baker J (2004) Development of high precision Rb–Sr phlogopite and biotite geochronology; an alternative to 40Ar/39Ar tri-octahedral mica dating. Chem Geol 213(4):339–358
Zack T, Hogmalm KJ (2016) Laser ablation Rb/Sr dating by online chemical separation of Rb and Sr in an oxygen-filled reaction cell. Chem Geol 437:120–133

Subduction Zone Geochemistry

Terry Plank
Lamont-Doherty Earth Observatory, Columbia University, Palisades, NY, USA

Definition

The exchange of chemical components between the Earth's interior and exterior driven by plate subduction.

Introduction

Subduction zones are not just sites of plate convergence but regions where the interior and exterior of the Earth chemically exchange (Fig. 1). Like a factory, raw material from the Earth's exterior is fed into the subduction zone and transformed in a series of chemical reactions driven by increasing pressure (P) and temperature (T) in the sinking plate. Some of the products are buoyant and so rise, drive melting in the mantle, and return back to the Earth's crust via intrusion and volcanism. Dense waste products continue to sink into the deep mantle, perhaps to the boundary with the core. This subduction factory is ultimately responsible for generating continental crust, re-enriching the mantle, and redistributing water and carbon dioxide in the planet. The processes that occur inside the factory are hidden from view, inferred from comparison of oceanic input and volcanic output chemical fluxes, laboratory experiments that simulate high P-T reactions, thermodynamic calculations, and exhumed high-pressure rocks.

Input Materials

The input to the subduction zone is the incoming plate, which consists of three layers of fundamentally different chemical compositions: the basaltic oceanic crust created at mid-ocean ridges, its mantle residuum substrate that moves with the plate, and marine sediments that deposit on top (Fig. 1). Each of these layers interacts differently with the ocean as the plate travels from mid-ocean ridge to deep sea trench. Most information on the chemical composition of the subducting plate has come from the international scientific ocean drilling programs through direct sampling and borehole observatories.

The basaltic oceanic crust represents the melt layer segregated from the melting mantle at mid-ocean ridges, and its initial chemical composition reflects the degree of melting and history of the upper mantle source region. Hydrothermal circulation near the active spreading center then decorates the oceanic crust with secondary minerals such as smectite and Fe oxides and introduces chemical components such as H_2O, S, U, Li, B, and alkalis (Kelley et al. 2003). Carbonate veins precipitate at lower temperatures as the plate moves off the ridge axis (Alt and Teagle 1999). Near the trench, plate bending opens new fractures that hydrate the oceanic crust. The sum of these chemical interactions produces an altered basaltic crust with very different parent-daughter isotope ratios, such as high $^{238}U/^{206}Pb$ and $^{87}Rb/^{87}Sr$, which initiate distinct isotopic evolutionary paths (Kelley et al. 2005; Porter and White 2009).

The extent to which the mantle peridotite substrate reacts with the ocean is debated, but critical to the fate of water at the surface of our planet. The primary mineral in peridotite is olivine, which may undergo rapid and extensive hydration, even at ambient temperatures, to the mineral serpentine (a hydrous mineral with an abundance of H_2O, ~12–13 wt%). The peridotite section of the oceanic plate is thus a sponge to water if it can be delivered to depth. The primary evidence for serpentinization of the oceanic plate comes from a reduction in seismic velocity toward the trench, observed at the Central American, Andean, and Aleutian margins (Shillington et al. 2015). As little as 2% serpentinization of the top few km of incoming peridotite holds enough water to subduct the entire ocean every billion years (Hacker 2008). Although H_2O is the dominant chemical component attending serpentinization, other diagnostic features include elevated Cl and $\partial^{11}B$ (Vils et al. 2009; Debret et al. 2014).

Sediments deposited on the seafloor constitute the greatest chemical heterogeneity injected into the subduction zone, from pure silica chert to nearly pure calcium carbonate chalks and metal-rich red clays (Plank 2014). Marine sediments are physical mixtures of variable amounts of continental detritus, delivered by wind, rivers, and/or volcanic eruption, biogenic accumulations of primarily carbonate, opal and apatite organism hard parts, and hydrothermal particulates as the complements to seafloor alteration. All of these phases may be seeds for adsorption of chemical complexes from seawater itself, a hydrogenetic component. Globally, marine sediments are dominated by continental detritus and so have a composition very similar to that of average shales and the upper continental crust. Biogenic phases are largely diluents to most chemical species in the detritus, except for Sr, Ba, and U in carbonates, rare earth element (REE) in phosphates, and Ba associated with biogenic opal. In regions of the oceans far from wind or river inputs, sediments are dominated by

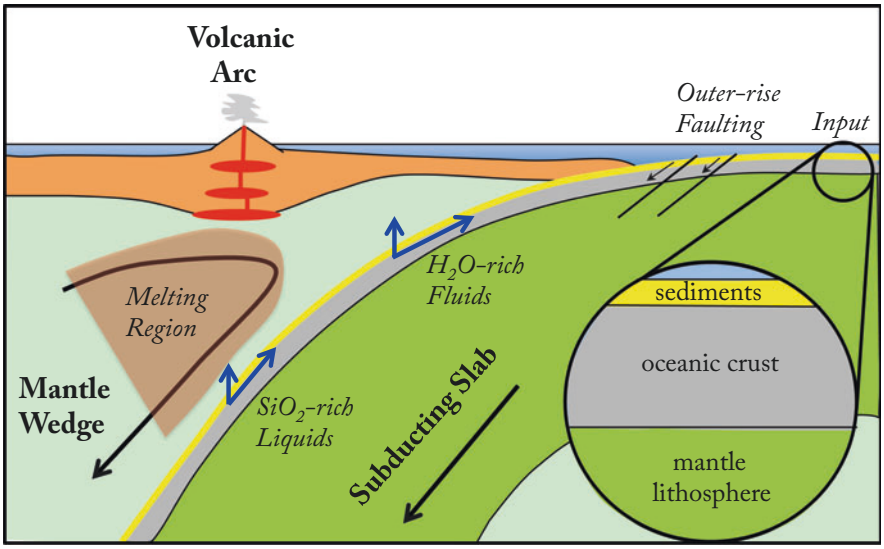

Subduction Zone Geochemistry, Fig. 1 Cartoon of subduction zone depicting some key sources and processes that affect geochemistry

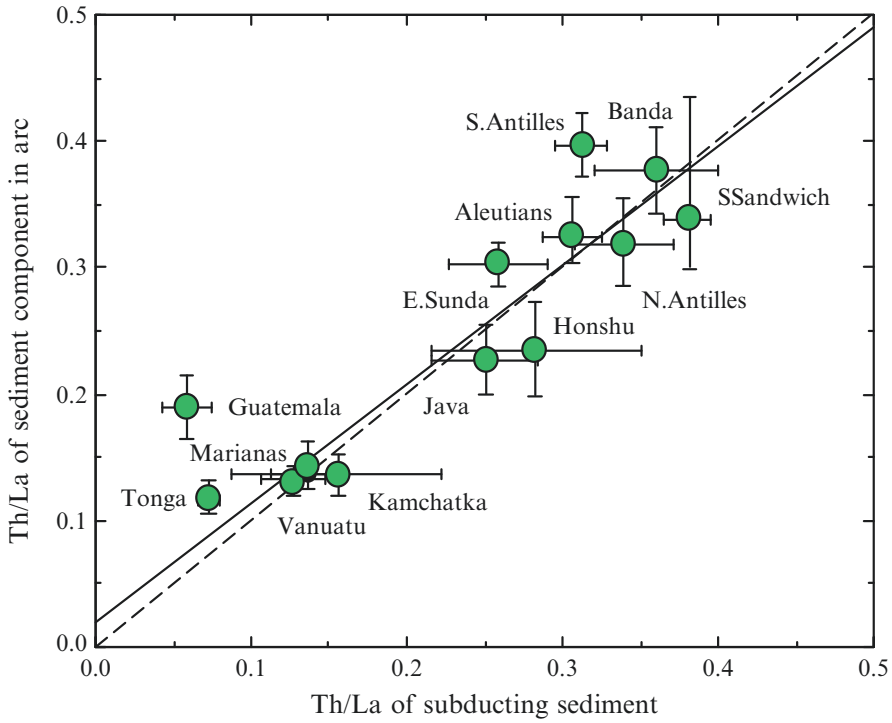

Subduction Zone Geochemistry, Fig. 2 One-to-one correlation between the Th/La of bulk sediment subducting into different trenches and Th/La measured in the corresponding arc volcanoes. This relationship demonstrates the geochemical connection between sediment input and volcanic output at subduction zones. The sediment component in each arc is calculated by linear regression of Th/La-Sm/La in basaltic samples (Plank 2005)

hydrogenetic or hydrothermal components, rich in Fe-Mn oxides, REE, Th, Pb, Co, and other metals. Unlike most planetary reservoirs, marine sediments may have distinctive Nd-Hf isotopic compositions due to the strong enrichment of REE in some phases and the lack of the heavy mineral zircon in sediments far from land (Vervoort et al. 2011). The oceanic realm also may lead to the distinctive fractionation of Ce (which is highly particle reactive when 4+) from the other dominantly trivalent REE. The sedimentary input to different subduction zones is widely variable, depending on the paleogeography and paleoceanography of each site. The unique geochemical characteristics of each sedimentary section is shared by its adjacent volcanic arc (Fig. 2), providing strong evidence for cycling through the subduction zone.

On the Way Down

As oceanic material enters the subduction zone, it begins a path of increasing T and P that drives mineral transformations,

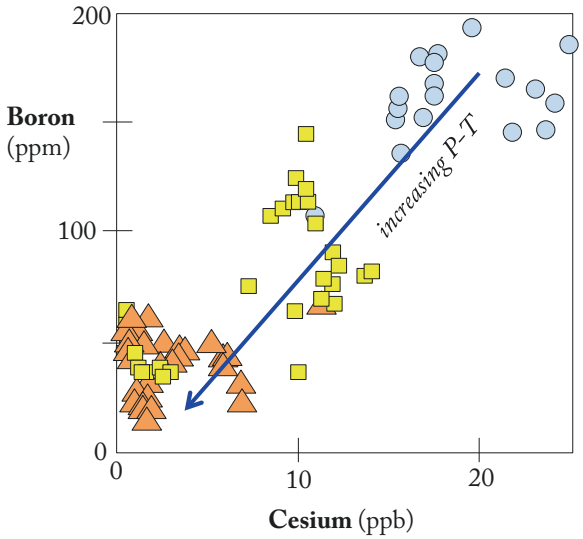

Subduction Zone Geochemistry, Fig. 3 The loss of boron and cesium during subduction, as recorded in micas from metasedimentary rocks of the Catalina Schist during increasing P (pressure) – T (temperature) grade from ~200 °C to 600 °C. *Circles* are lowest grade lawsonite-albite schists; *squares* medium grade blueschists; *triangles* higher-grade amphibolites (From Bebout (2014))

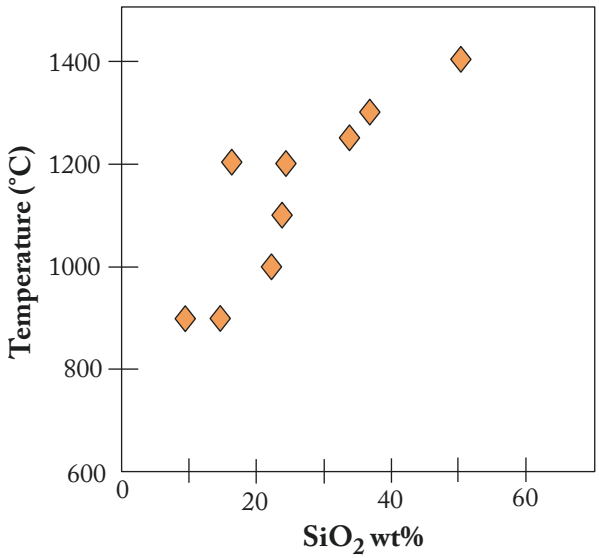

Subduction Zone Geochemistry, Fig. 4 SiO2 concentration of high P-T fluids generated in the laboratory (equilibrated with basalt at 6 GPa). Fluids evolve continuously from low-SiO2 aqueous fluids at low T to high-SiO2 melt-like supercritical fluids at high T (Figure from Kessel et al. (2005))

devolatilization reactions, fluid evolution from aqueous to solute rich, and an increase in the solubility of many trace-element-bearing minerals. Mineral reaction and fluid production in turn accompany a spectrum of fault slip behavior in the subduction zone, from slow and silent slip to the world's largest intraplate earthquakes.

The lowest P-T conditions involve compaction and dehydration of the sedimentary section as the clay mineral smectite transforms to illite and the light elements Li and B as well as alkalis Cs and Rb are liberated into a water-rich fluid (Ishikawa et al. 2008; Bebout 2014; Fig. 3). At higher P-T, the dominant minerals in the basaltic crust become lawsonite, garnet, and clinopyroxene (Klimm et al. 2008), while quartz and mica also form in sediments. A plethora of accessory mineral phases and their T-dependent solubility control the behavior of key tracers, such as REE, Th, and U in monazite and allanite, Nb and Ta in rutile, and Zr, Hf, U, and HREE in zircon (Hermann and Rubatto 2009; Skora and Blundy 2010). Serpentine minerals have a maximum stability of 600–700 °C (Schmidt and Poli 1998), but may persist to >200 km depth in the peridotite section because the slab interior heats up more slowly (Hacker 2008). Deformation within the subduction zone may create mélange (Marschall and Schumacher 2012), a mechanical mixture of sediment-basalt-peridotite that may favor the formation of distinctive minerals such as chlorite.

At higher temperatures, fluids evolved during the breakdown of lawsonite, amphibole, and mica are more solute rich, containing Si, Al, and alkalis (Manning 2004). If flushed with water-rich fluids, the top of the plate may melt at T $\geq$ 700 °C and P $\geq$ 3 GPa (Mann and Schmidt 2015). At pressures higher than 5 GPa, sediments no longer melt at a discrete solidus but instead evolve "supercritical" liquids that span a continuum of compositions (Kessel et al. 2005; Fig. 4) from dilute aqueous liquids with little dissolved silicate to melt-like silicate-rich liquids with dissolved water (Hermann et al. 2006).

The workings within the subduction zone beneath volcanic arcs are of particular interest because they prime the source of arc magmatism. The tracers of the slab include large ion lithophile elements (e.g., alkalis, Ba, Pb) that are thought to be mobile in lower T fluids and high-field strength elements (e.g., Nb, Ta, REE, Th) which are thought to be mobile only in higher T fluids/melts/supercritical liquids (Elliott 2003; Fig. 5). A range of fluid and solid compositions will exist for different subduction zone P-T paths. Young slabs (e.g., Cascadia) follow higher T/P paths than old, fast subducting slabs (e.g., Tonga; Syracuse et al. 2010). Different thermal regimes will lead to different slab fluid compositions that supply different arcs, for example, REE-poor and high Ba/La, U/Th, and B/Be at Tonga and low H_2O/Ce and high Sr/Y at Cascadia (Ruscitto et al. 2012). Sedimentary versus basaltic slab material supply different $^{143}Nd/^{144}Nd$, $^{10}Be/^{9}Be$, and $^{205}Tl/^{203}Tl$ compositions, reflecting greater mean age, cosmogenic contribution, and seawater interaction, respectively (White and Patchett 1984; Morris et al. 2002; Prytulak et al. 2013). Volcanic arcs often inherit the local subducted sedimentary fingerprints in their Th/La (Plank 2005) and $^{207}Pb/^{204}Pb$ ratios.

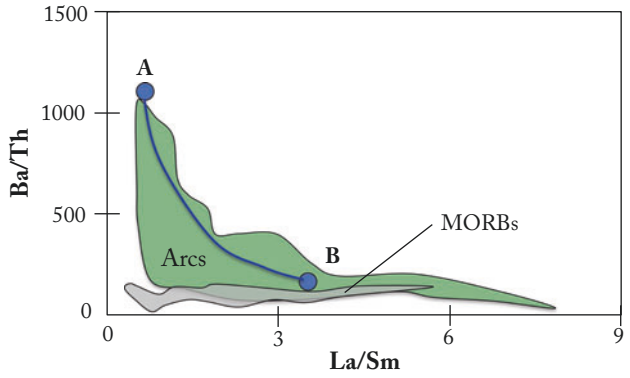

Subduction Zone Geochemistry, Fig. 5 Subduction zones produce arc basalts (*green field*) that are significantly enriched in Ba/Th compared to mid-ocean ridge basalts (*gray field*). *Line* shows expected mixing between low-temperature/altered oceanic crust fluid (1) and high-temperature/sediment melt (2) from the subduction zone (Mixing calculation and figure from Elliott (2003))

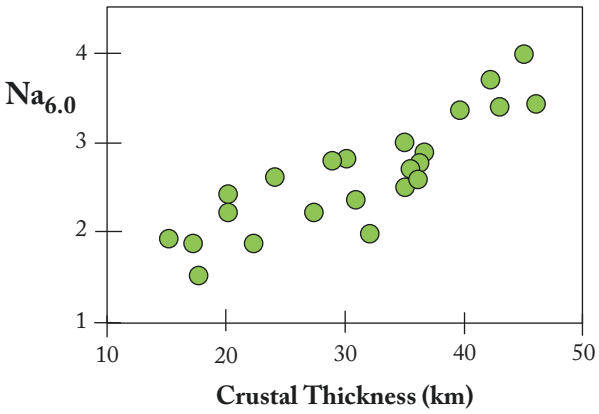

Subduction Zone Geochemistry, Fig. 6 Correlation between the thickness of the crust and the sodium concentration of basaltic magmas, averaged for different volcanic arc segments globally. This relationship is interpreted to reflect lower extents of mantle melting beneath arcs with thick crust, due to the displacement of the hot mantle wedge core to greater depths. Na6.0 is the average Na2O concentration (wt%) of volcanic rock samples with 5.5 > MgO < 6.5 wt% (Data compilation, figure, and interpretation from Turner and Langmuir (2015a))

One Man's Trash Is Another Man's. . .

The progressive removal of water, fluids, melts, supercritical liquids, and buoyant solids leaves behind a dense slab that sinks deeper into the upper mantle, the transition zone, the lower mantle, and potentially as far as the core-mantle boundary. Such processed slab material contributes to mantle heterogeneity. Carbonate and organic carbon are stubborn substances in subduction zones, some destined to become diamonds in the mantle (Walter et al. 2011; Sverjensky et al. 2014). Particularly cold P-T paths can ferry water into the lower mantle in a series of dense hydrous magnesium silicates, leading to a loss of water from the surface hydrosphere (Nishi et al. 2014). The transition zone is capable of containing oceans of water in the mineral ringwoodite, recently discovered as inclusions in high-pressure diamonds (Pearson et al. 2014). The subduction zone can deliver to the deep mantle stable isotope tracers in $^{18}O/^{16}O$, $^{7}Li/^{6}Li$, and $^{34}S/^{32}S$ that bear vestiges of their origin in the biosphere, hydrosphere, and atmosphere at Earth's surface (Eiler 2001; Farquhar et al. 2002; Elliott et al. 2006; Sleep et al. 2012). Other radiogenic isotope tracers such as $^{206}Pb/^{204}Pb$, $^{187}Hf/^{186}Hf$, and $^{87}Sr/^{86}Sr$ evolve to anomalous values due to extreme fractionation of parent from daughter isotope in subducting slabs (Chauvel et al. 2008). Such distinctive slab material is thought to surface again in rising mantle plumes, producing volcanism on ocean islands like Hawaii, Galapagos, and Samoa (Blichert-Toft et al. 1999; Jackson et al. 2007; Hofmann 2014).

Or, What Goes Down Must Come Up

Fluids evolved from the subducting plate may rise up the slab interface or into the overlying mantle (Wilson et al. 2014). The exact path of fluid flow from slab to hot core of the mantle wedge and the extent of reaction along the way are poorly known (Pirard and Hermann 2015). Weak, low-density sediment or mélange may become gravitationally unstable and rise as diapirs into the overlying mantle (Behn et al. 2011). These materials may interact with and/or drive melting in the overlying mantle wedge, the source of magmas that feed arc volcanoes.

The mantle wedged between the upper and downgoing plates may melt in two ways: (1) by the addition of slab fluid (s.l.) that lowers the mantle melting temperature or (2) by adiabatic decompression due to an upward component of plate-driven circulation, primarily in the back-arc region (Grove et al. 2002). It has also been proposed that the removal of ice loads during deglaciations may lead to enhanced decompression melting (Huybers and Langmuir 2009). Slab diapirs may also melt as they rise through the mantle wedge and heat up (Castro and Gerya 2008). This sum of processes leads to zonation in the concentration of H_2O and other slab tracers in volcanism at different distances from the trench (Pearce et al. 2005; Kelley et al. 2006; Portnyagin et al. 2007). The mantle melting signal is thought to be best recorded in elements which do not derive primarily from the downgoing plate, such as the high-field strength elements (HFSE: Nb, Ta, Hf, Zr, Ti, and Y) and Na. These elements, in turn, vary with both H_2O (Plank et al. 2013) and crustal thickness (Turner and Langmuir 2015a; Fig. 6), leading to competing models whereby slab H_2O on the one hand and wedge depth on the other control mantle melting (Turner and Langmuir 2015b). Some volcanoes erupt magmas with similar geochemical heritage (e.g., U/Th, Ba/La) for 100,000's year (Wade et al. 2005; Jicha and Singer 2006), while others

erupt an enormous diversity of primary compositions (Patino et al. 2000). The primary melts that rise out of the mantle are thought to be basalts in most cases but in some regions are high Mg/(Mg + Fe) andesites and dacites (Kelemen 1995). Such magmas appear to have been more common in the early Earth (Fig. 7).

Building Volcanoes and Continents

Magmas continue to be buoyant in the crust, particularly once they begin to exsolve volatile species (e.g., H_2O, CO_2, SO_2, halogens) to vapor. Some of the magmas born in the subduction zone will erupt out a volcano, while some will meet their "viscous death" and crystallize in the crust to become a plutonic body (Annen et al. 2006). The magma flux through the crust will affect the extent of cooling, crystallization, and final composition of the erupted or intruded magma. Magmas with short residence time in the crust will remain basaltic (with high MgO, Ni, Cr), and those with the longest residence time and/or interaction with the crust will evolve to become rhyolites (with high SiO_2 and alkalis). As magmas evolve, they may enrich in Fe (the tholeiitic trend) or deplete in Fe (calc-alkaline). Calc-alkaline trends, predominant at subduction zones and distinctive to Earth, are created from high initial water and oxygen fugacity (Sisson and Grove 1993; Zimmer et al. 2010). Trace elements that are essential constituents to accessory minerals, such as P in apatite and Zr in zircon, will show kinks along crystal fractionation paths as these minerals saturate. Magmas will variably interact, digest, and disrupt the crust they intrude, leading to decreases in $^{143}Nd/^{144}Nd$ as magmas evolve to higher SiO_2 (Sisson et al. 2014), isotopic heterogeneity within individual crystals (Davidson et al. 2001), and/or a cargo of foreign crystals (Dungan and Davidson 2004).

The continental crust and arc magmas share geochemical fingerprints, such as low La/Nb and Th/Nb (Fig. 8), which have long provided strong evidence for continent formation at

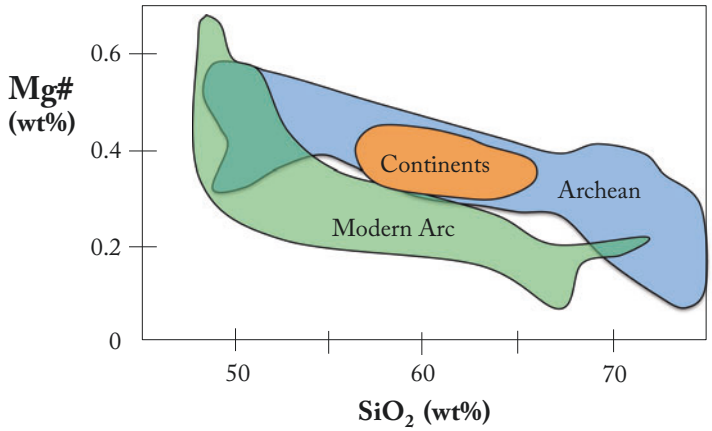

Subduction Zone Geochemistry, Fig. 7 SiO2 and Mg# (Mg/[Mg + Fe]) in Archean igneous rocks (dots), bulk continental crust (*orange field*) and typical modern Aleutian arc lavas (*green field*). Most modern subduction lavas are not compositionally similar to the continental crust (From Kelemen (1995))

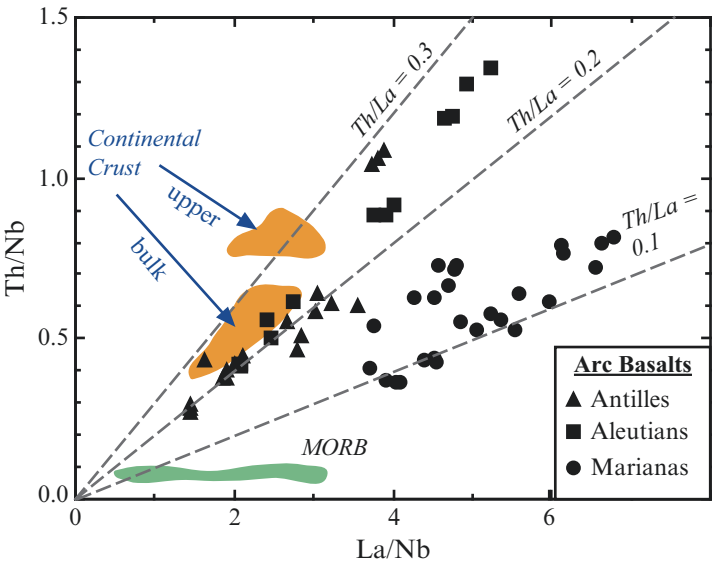

Subduction Zone Geochemistry, Fig. 8 Th/Nb vs. La/Nb in arc basalts f rom subduction zones, compared to average continental crust (orange field) and mid-ocean ridge and oceanic island basalts (green field). The high Th/Nb (depletion in Nb) is a feature shared by both the continental crust and subduction magmatism. Figure after Plank (2005)

subduction zones (Rudnick 1995; Plank 2005). Few modern arcs, however, provide a good match to the full continental fingerprint (Gazel et al. 2015), and most arc crust is significantly less silicic than bulk continental crust (Rudnick and Gao 2014). This "silica problem" has several proposed solutions (Tatsumi et al. 2008), generally falling into two categories: (a) predominance of high-silica primary magmas in the early Earth or plutonic record (Kelemen 1995; Fig. 7) and (b) subtraction of low-silica crystals by sinking of dense lower crust into the mantle (Jull and Kelemen 2001).

Timescales of Subduction Geochemistry

Radioactive isotopes and diffusion chronometry constrain the timescales of subduction geochemistry, from millions of years to minutes. Geochemical variations and U-Pb zircon geochronology track the evolution and construction of convergent margins over tens of millions of years (Lee et al. 2007). The presence of the cosmogenic and radioactive isotope ^{10}Be in arc volcanic crystals requires Be to travel from shallow sediments on the seafloor down the subduction zone and back to the surface in less than a few Ma (Morris et al. 2002). Disequilibrium in the activity of U-chain isotopes clocks transport from the slab to the surface in less than a few 100,000 years and perhaps as rapidly as a few 1000 years (Turner et al. 2003). Ar-Ar geochronology establishes the lifetime of individual volcanoes to 100–600 ka (Carr et al. 2007). Crystals erupted from volcanoes can endure several freeze-thaw cycles in magma storage regions (Cooper and Kent 2014), recorded in ^{238}U–^{230}Th crystallization ages on the order of 10,000 years. Diffusion profiles of transition metals (Ni, Fe, Mg, Cr) in primary olivine crystals are speedometers of rapid magma supply from the mantle to some volcanoes in months to years (Ruprecht and Plank 2013). The eruptive process itself may occur in minutes, fueled by the rapid loss of volatiles from melt to vapor and recorded in H_2O diffusion profiles in glass and crystals (Lloyd et al. 2014).

Mass Balances Across the Subduction Zone

Developing meaningful mass balances of different tracers across subduction zones remains an outstanding challenge. An example comes from the rare earth element Nd. The concentration and isotope ratios of Nd in sediments and basaltic crust entering subduction zones are fairly well constrained by drilling. The Nd abundance in subducting peridotite is minor, and Nd is not widely mobilized during the first 700°C of heating in the subduction zone. Its release into slab fluids/melts will be governed largely by the T-dependent solubility of the REE-rich minerals allanite and monazite. A few percent of sediment is generally sufficient to reproduce the ^{143}Nd/^{144}Nd composition of arc magmas, but the balance from subducting basaltic crust versus mantle is not currently well constrained. Other unknowns are the contributions of Nd from the preexisting arc crust, especially if it is made of young arc volcanics with similar ^{143}Nd/^{144}Nd to the intruding magma. The Nd concentrations in arc volcanics are reasonably well known for many volcanoes, but large uncertainties in the magma flux rate at arcs (volcanic and plutonic) lead to minimum uncertainties of a factor of two in the output flux of any magmaphile element. By comparing the volcanic output to the subducted input, it is clear that the Nd contributed from the slab is widely variable from arc to arc. From 0% to 60% of the Nd in volcanic arcs is derived from the slab (Porter and White 2009). Still, the net effect of subduction on the slab is relatively minor for Nd, with 100–70% of the initial slab Nd continuing into the deep mantle.

Even greater uncertainties exist for the mass balance of other chemical species, such as carbon, where current estimates are anywhere from ~0% to 80% C entering subduction zones continuing into the deep mantle (Kelemen and Manning 2015). A similar situation exists for H_2O, although the presence of the surface ocean over most of geological time places maximum constraints on the amount of water that can disappear into the mantle (Parai and Mukhopadhyay 2012). The slow subduction process adds up over geological time; an ocean of water and a mass equivalent to the entire surface pool of organic C have disappeared down subduction zones every few billion years. Variable and inefficient return may have contributed to the unusually high H/C of our planet's surface (Hirschmann and Dasgupta 2009).

Most mass balance estimates to date are like balancing a checking account that has large uncertainties on the deposits and withdrawals – this leads to an uncomfortable situation! A fundamentally different approach is gaining accuracy. Given a P-T path for a slab, it is possible to calculate where and how much departing fluid is evolved and its elemental composition using thermodynamic and partitioning data from laboratory experiments. With enough accuracy of the underlying chemical reactions, the future will see subduction mass balances predicted from calculation. Such an approach is underway with the arc basalt simulator (Kimura et al. 2009), and geochemical-thermomechanical models (Hebert et al. 2009; Baitsch-Ghirardello et al. 2014).

Summary and Conclusions

Subduction geochemistry is a rich topic, spanning from marine geology to igneous petrology, geodynamics to thermodynamics. Accordingly, diverse and multidisciplinary observations and measurements are needed to understand the full subduction cycle for any geochemical tracer. These

include the study of sediments and serpentinite from the seafloor, study of metamorphic rocks and high-pressure simulations in the laboratory, modeling of magma and mantle movement, and study of plutonic and volcanic rocks, glasses, gases, and crystals. For this reason, subduction geochemistry has generally advanced through coordinated, international programs involving hundreds of scientists, with efforts crossing the shoreline and spanning from megascale drilling to nanoscale chemical analysis. The challenges to our understanding are wide and deep, and the stakes are high – subduction has built the continents, stirred the mantle, and developed our hydrosphere and carbosphere over Earth history.

References

Alt JC, Teagle DAH (1999) The uptake of carbon during alteration of oceanic crust. Geochim Cosmochim Acta 63:1527–1535

Annen C, Blundy JD, Sparks RSJ (2006) The genesis of inter- mediate and silicic magmas in deep crustal hot zones. J Petrol 47:505–539

Baitsch-Ghirardello B, Stracke A, Connolly JAD, Nikolaeva KM, Gerya TV (2014) Lead transport in intra oceanic subduction zones: 2D geochemical–thermo-mechanical modeling of isotopic signatures. Lithos 208–209:265–280

Bebout GE (2014) Chemical and isotopic cycling in subduction zones. In: Holland HD, Turekian KK (eds) Treatise on geochemistry, vol 4, 2nd edn. Elsevier, Oxford, pp 703–747

Behn MD, Kelemen PB, Hirth G, Hacker BR, Massonne H-J (2011) Diapirs as the source of the sediment signature in arc lavas. Nat Geosci 4:641–646. https://doi.org/10.1038/ngeo1214

Blichert-Toft J, Frey FA, Albarede F (1999) Hf isotope evidence for pelagic sediments in the source of Hawaiian basalts. Science 285:879–882

Carr MJ, Saginor I, Alvarado GE, Bolge LL, Lindsay FN, Milidakis K, Turrin BD, Feigeson MD, Swisher CC (2007) Element fluxes from the volcanic front of Nicaragua and Costa Rica. Geochem Geophys Geosyst 8:Q06001

Castro A, Gerya TV (2008) Magmatic implications of mantle wedge plumes: experimental study. Lithos 103:138–148

Chauvel C, Lewin E, Carpentier M, Arndt NT, Marini JC (2008) Role of recycled oceanic basalt and sediment in generating the Hf–Nd mantle array. Nat Geosci 1:64–67

Cooper KM, Kent AJR (2014) Rapid re-mobilization of magmatic crystals kept in cold storage. Nature:480–483. https://doi.org/10.1038/nature12991

Davidson JP, Tepley FJ III, Palacz Z, Main S (2001) Magma recharge, contamination and residence times revealed by in situ laser ablation isotopic analysis of feldspar in volcanic rocks. Earth Planet Sci Lett 182:427–442

Debret B, Koga KT, Nicollet C, Andreanai M, Schwartz S (2014) F, Cl and S input via serpentinite in subduction zones: implications for the nature of the fluid released at depth. Terra Nova 26:96–101

Dungan MA, Davidson J (2004) Partial assimilative recycling of the mafic plutonic roots of arc volcanoes: an example from the Chilean Andes. Geology 32:773–776

Eiler JM (2001) Oxygen isotope variations of basaltic lavas and upper mantle rocks. Rev Mineral Geochem 43:319–364

Elliott TR (2003) Tracers of the slab. Geophys Monogr 138:23–45

Elliott T, Thomas A, Jeffcoate A, Niu Y-L (2006) Lithium isotope evidence for subduction-enriched mantle in the source of mid-ocean-ridge basalts. Nature 443:565–568

Farquhar J, Wing BA, McKeegan KD, Harris JW, Cartigny P, Thiemens MH (2002) Mass-independent sulfur of inclusions in diamond and sulfur recycling on the early earth. Science 298:2369–2372

Gazel E, Hayes JL, Hoernle K, Everson E, Holbrook WS, Kelemen P, Hauff F, van den Bogaard P, Vance E, Chu S, Calvert AJ, Carr MJ, Yogodzinski G (2015) Continental crust generated in oceanic arcs. Nat Geosci 8:321–327

Grove TL, Parman SW, Bowring SA, Price RC, Baker MB (2002) The role of an H_2O-rich fluid component in the generation of primitive basaltic andesites and andesites from the Mt. Shasta region, N California. Contrib Mineral Petrol 142:375–396

Hacker BR (2008) H2O subduction beyond arcs. Geochem Geophys Geosyst 9:Q03001. https://doi.org/10.1029/2007GC001707

Hebert LB, Asimow P, Antoshechkina P (2009) Fluid source-based modeling of melt initiation within the subduction zone mantle wedge: implications for geochemical trends in arc lavas. Chem Geol 266:306–319

Hermann J, Rubatto D (2009) Accessory phase control on the trace element signature of sediment melts in subduction zones. Chem Geol 265:512–526

Hermann J, Spandler C, Hack A, Korsakov AV (2006) Aqueous fluids and hydrous melts in high-pressure and ultra-high pressure rocks: implications for element transfer in subduction zones. Lithos 92:399–417

Hirschmann MM, Dasgupta R (2009) The H/C ratios of Earth's near-surface and deep reservoirs, and consequences for deep earth volatile cycles. Chem Geol 262:4–16. https://doi.org/10.1016/j.chemgeo.2009.1002.1008

Hofmann AW (2014) 3.3 – sampling mantle heterogeneity through oceanic basalts: isotopes and trace elements. In: Holland HD, Turekian KK (eds) Treatise on geochemistry, vol 3, 2nd edn. Elsevier, Oxford, pp 67–101

Huybers P, Langmuir C (2009) Feedback between deglaciation, volcanism, and atmospheric CO_2. Earth Planet Sci Lett 286: 479–491

Ishikawa T, Tanimizu M, Nagaishi K, Matsuoka J, Tadai O, Sakaguchi M, Hirono T, Mishima T, Tanikawa W, Lin W, Kikuta H, Soh W, Song S-R (2008) Coseismic fluid–rock interactions at high temperatures in the Chelungpu fault. Nat Geosci 1:679–683

Jackson MG, Hart SR, Koppers AAP, Staudigel H, Konter J, Blusztajn J, Kurz M, Russell JA (2007) The return of subducted continental crust in Samoan lavas. Nature 448:684–687

Jicha BR, Singer BS (2006) Volcanic history and magmatic evolution of Seguam Island, Aleutian island arc, Alaska. Geol Soc Am Bull 118:805–822

Jull M, Kelemen PB (2001) On the conditions for lower crustal convective instability. J Geophys Res 106:6423–6446

Kelemen PB (1995) Genesis of high andesites and the continental crust. Contrib Mineral Petrol 120:1–19

Kelemen PB, Manning CE (2015) Reevaluating carbon fluxes in subduction zones, what goes down, mostly goes up. Proc Natl Acad Sci 112:E3997–E4006

Kelley KA, Plank T, Ludden JN, Staudigel H (2003) The composition of altered oceanic crust at ODP sites 801 and 1149. Geochem Geophys Geosyst 4:8910

Kelley KA, Plank T, Farr L, Ludden J, Staudigel H (2005) Subduction cycling of U, Th and Pb. Earth Planet Sci Lett 234:369–383

Kelley KA, Plank T, Newman S, Stolper EM, Grove TL, Hauri E (2006) Mantle melting as a function of water content at subduction zones. Back-arc basins. J Geophys Res 111:B09208

Kessel R, Ulmer P, Pettke T, Schmidt MW, Thompson AB (2005) The water- basalt system at 4 to 6GPa: phase relations and second critical endpoint in a K-free eclogite at 700 to 1400 °C. Earth Planet Sci Lett 237:873–892

Kimura J-I, Hacker BR, van Keken PE, Kawabata H, Yoshida T, Stern RJ (2009) Arc basalt simulator version 2, a simulation for slab

dehydration and fluid-fluxed mantle melting for arc basalts: modeling scheme and application. Geochem Geophys Geosyst 10:Q09004

Klimm K, Blundy JD, Green TH (2008) Trace element partitioning and accessory phase saturation during H_2O-saturated melting of basalt with implications for subduction zone chemical fluxes. J Petrol 49:523–553

Lee CTA, Morton DM, Kistler RW, Baird AK (2007) Petrology and tectonics of Phanerozoic continent formation: from island arcs to accretion and continental arc magmatism. Earth Planet Sci Lett 263:370–387

Lloyd AS, Plank T, Ruprecht P, Hauri EH, Rose W, Gonnermann HM (2014) NanoSIMS results from olivine-hosted melt embayments: magma ascent rate during explosive basaltic eruptions. J Volcanol Geotherm Res 283:1–18. https://doi.org/10.1016/j.jvolgeores.2014.06.002

Mann U, Schmidt MW (2015) Melting of pelitic sediments at subarc depths: 1. Flux vs. fluid-absent melting and a parameterization of melt productivity. Chem Geol 404:150–167

Manning CE (2004) The chemistry of subduction-zone fluids. Earth Planet Sci Lett 223:1–16

Marschall HR, Schumacher JC (2012) Arc magmas sourced from melange diapirs in subduction zones. Nat Geosci 5. https://doi.org/10.1038/NGEO1634

Morris JD, Gosse J, Brachfeld S, Tera F (2002) Cosmogenic ^{10}Be and the solid earth: studies in geomagnetism, subduction zone processes, and active tectonics. In: Grew ES (ed) Beryllium: mineralogy, petrology and geochemistry, Reviews in mineralogy geochemistry, vol 50. The Mineralogical Society of America, Chantilly, pp 207–270

Nishi M, Irifune T, Tsuchiya J, Tange Y, Nishihara Y, Fujino K, Higo Y (2014) Stability of hydrous silicate at high pressures and water transport to the deep lower mantle. Nat Geosci 7:224–227

Parai R, Mukhopadhyay S (2012) How large is the subducted water flux? New constraints on mantle regassing rates. Earth Planet Sci Lett **317**:396–406

Patino LC, Carr MJ, Feigenson MD (2000) Local and regional variations in central American arc lavas controlled by variations in subducted sediment input. Contrib Mineral Petrol 138:265–283

Pearce JA, Stern RJ, Bloomer SH, Fryer P (2005) Geochemical mapping of the Mariana arc-basin system: implications for the nature and distribution of subduction components. Geochem Geophys Geosyst 6:Q07006. https://doi.org/10.1029/2004GC000895

Pearson DG, Brenker FE, Nestola F, McNeill J, Nasdala L, Hutchison MT, Matveev S, Mather K, Silversmit G, Schmitz S, Vekemans B, Vincze L (2014) Hydrous mantle transition zone indicated by ringwoodite included within diamond. Nature 507:221–224

Pirard C, Hermann J (2015) Focused fluid transfer through the mantle above subduction zones. Geology 43:915–918

Plank T (2005) Constraints from Th/La on sediment recycling at subduction zones and the evolution of the continents. J Petrol 46:921–944

Plank T (2014) The chemical composition of subducting sediments. In: Holland HD, Turekian KK (eds) Treatise on geochemistry, vol 4, 2nd edn. Elsevier, Oxford, pp 607–629

Plank T, Kelley KA, Zimmer MM, Hauri EH, Wallace PJ (2013) Why do mafic arc magmas contain ~4 wt% water on average? Earth Planet Sci Lett 364:168–179

Porter KA, White WM (2009) Deep mantle subduction flux. Geochem Geophys Geosyst 10:Q12016. https://doi.org/10.1029/2009GC002656

Portnyagin M, Hoernle K, Plechov P, Mironov N, Khbunaya S (2007) Constraints on mantle melting and composition and nature of slab components in volcanic arcs from volatiles (H_2O, S, Cl, F) and trace elements in melt inclusions from the Kamchatka arc. Earth Planet Sci Lett 255:53–69. https://doi.org/10.1016/j.epsl.2006.12.005

Prytulak J, Nielsen SG, Plank T, Barker M, Elliott T (2013) Assessing the utility of thallium and thallium isotopes for tracing subduction zone inputs to the Mariana arc. Chem Geol 345:139–149

Rudnick RL (1995) Making continental crust. Nature 378:571–578

Rudnick RL, Gao S (2014) Composition of the continental crust. In: Holland HD, Turekian KK (eds) Treatise on geochemistry, vol 4, 2nd edn. Elsevier, Oxford, pp 1–51

Ruprecht P, Plank T (2013) Feeding andesitic eruptions with a high-speed connection from the mantle. Nature 50:68–72. https://doi.org/10.1038/nature12342

Ruscitto D, Wallace PJ, Cooper L, Plank T (2012) Global variations in H_2O/Ce II: relationships to arc magma geochemistry and volatile fluxes. Geochem Geophys Geosyst 13:Q03025. https://doi.org/10.1029/2011GC003887

Schmidt MW, Poli S (1998) Experimentally based water budgets for dehydrating slabs and consequences for arc magma generation. Earth Planet Sci Lett 163:361–379

Shillington DJ, Becel A, Nedimovic MR, Kuehn H, Webb SC, Abers GA, Keranen KM, Li J, Delescluse M, Mattie-Salicrup GA (2015) Link between plate fabric, hydration and subduction zone seismicity in Alaska. Nat Geosci 8:961–964. https://doi.org/10.1038/ngeo2586

Sisson TW, Grove TL (1993) Experimental investigations of the role of H_2O in subduction zone magmatism and calc-alkaline differentiation. Contrib Mineral Petrol 113:143–166

Sisson TW, Salters VJM, Larson PB (2014) Petrogenesis of Mount Rainier andesite: magma flux and geologic controls on the contrasting differentiation styles at stratovolcanoes of the southern Washington Cascades. GSA Bull 126:122–144

Skora S, Blundy J (2010) High-pressure hydrous phase relations of radiolarian clay and implications for the involvement of subducted sediment in arc magmatism. J Petrol 51:2211–2243

Sleep NH, Bird DK, Pope E (2012) Paleontology of Earth's mantle. Annu Rev Earth Planet Sci 40:277–300

Sverjensky DA, Stagno V, Huang F (2014) Organic carbon species in subduction-zone fluids and implications for the deep carbon cycle. Nat Geosci 7:909–913. https://doi.org/10.1038/ngeo2291

Syracuse EM, van Keken PE, Abers GA (2010) The global range of subduction zone thermal models. Phys Earth Planet Inter 183:73–90

Tatsumi Y, Shukuno H, Tani K, Takahashi N, Kodaira S, Kogiso T (2008) Structure and growth of the Izu-Bonin-Mariana arc crust: 2. Role of crust-mantle transformation and the transparent Moho in arc crust evolution. J Geophys Res 113:B02203. https://doi.org/10.1029/2007JB005121

Turner SJ, Langmuir CH (2015a) The global chemical systematics of arc front stratovolcanoes: evaluating the role of crustal processes. Earth Planet Sci Lett 422:182–193

Turner SJ, Langmuir CH (2015b) What processes control the chemical compositions of arc front stratovolcanoes? Geochem Geophys Geosyst 16:1865–1893. https://doi.org/10.1002/2014GC005633

Turner S, Bourdon B, Gill JB (2003) Insights into magma genesis at convergent margins from U-series isotopes. Rev Mineral Geochem 52:255–315

Vervoort JD, Plank T, Prytulak J (2011) The Hf-Nd isotopic composition of marine sediments. Geochim Cosmochim Acta 75:5903–5926

Vils F, Tonarini S, Kalt A, Seitz H-M (2009) Boron, lithium and strontium isotopes as tracers of seawater–serpentinite interaction at Mid-Atlantic ridge, ODP leg 209. Earth Planet Sci Lett 286:414–425

Wade JA, Plank T, Stern RJ, Tollstrup DL, Gill JB, O'Leary JC, Eiler J, Moore RB, Woodhead JD, Trusdell F, Fischer TP, Hilton DR (2005) The May 2003 eruption of Anatahan volcano, Mariana Islands: geochemical evolution of a silicic island arc volcano. J Volcanol Geotherm Res 146:139–170

Walter MJ, Kohn SC, Arajuo D, Bulanova GP, Smith CB, Gaillou E, Wang J, Steele A, Shirey SB (2011) Deep mantle cycling of oceanic crust: evidence from diamonds and their mineral inclusions. Science 334:54–57

White WM, Patchett PJ (1984) Hf-Nd-Sr isotopes and incompatible element abundances in island arcs: implications for magma origins and crust-mantle evolution. Earth Planet Sci Lett 67:167–185
Wilson CR, Spiegelman M, van Keken PE, Hacker BR (2014) Fluid flow in subduction zones: the role of solid rheology and compaction pressure. Earth Planet Sci Lett 401:261–274
Zimmer MM, Plank T, Hauri EH, Yogodzinski GM, Stelling P, Larsen J, Singer B, Jicha B, Mandeville C, Nye CJ (2010) The role of water in generating the calc-alkaline trend: new volatile data for Aleutian magmas and a new tholeiitic index. J Petrol 51:2411–2444

Sulfate Minerals

Andrew G. Christy
School of Earth and Environmental Sciences, University of Queensland, St Lucia, QLD, Australia
Geosciences, Queensland Museum, Hendra, QLD, Australia

Definition

Sulfate minerals are mineral species in which the dominant anionic entity is the sulfate anion, $[SO_4]^{2-}$ (Chang et al. 1996; Alpers et al. 2000). About 380 valid species of sulfate minerals had been described by early 2017 (cf. www.mindat.org), which are often grouped into a broader "sulfate" anion class along with the much small number (ca. 50) of chromates, molybdates, and tungstates. Even rarer related complex anions are the sulfite ion $[S^{4+}O_3]^{2-}$ in scotlandite ($PbSO_3$), fluorsulfonate ion $[SO_3F]^-$ in reederite-(Y) ($Na_{15}Y_2(CO_3)_9(SO_3F)Cl$), and thiosulfate ($[SO_3S]^{2-}$ or $[S_2O_3]^{2-}$) in sidpietersite ($Pb_4(S_2O_3)O_2(OH)_2$).

Introduction

Sulfur is the commonest element in the Earth that occurs in both negative (S^{2-}) and positive (S^{4+}, S^{6+}) oxidation states. Hexavalent sulfur usually occurs bonded to four oxygen atoms in a tetrahedral arrangement, forming the sulfate anion $[SO_4]^{2-}$. The complex anion is held together internally by rather strong, covalent S-O bonds (bond valence = 1.5 valence units), but are bound to other cations to form a mineral structure through links that are usually lower in bond valence and more ionic in character. The formation of sulfate anion requires conditions that are oxidizing relative to those found in the deep Earth, so sulfate minerals are characteristic of near-surface environments that are oxygenated, particularly the oxidized zones of sulfide ore bodies, oxidized hydrothermal and fumarole systems and since sulfate is a common anion in the ocean and many other water bodies, in evaporites. Oxidation of sulfides to form sulfuric acid and hence sulfate minerals is frequently catalyzed by acidophile lithoautotrophic bacteria such as *Thiobacillus* and *Sulfobacillus* in cooperation with iron-oxidizing species (Nordstrom and Southam 1997; Pósfai and Dunin-Borkowski 2006). This process may be exploited for ore processing by bioleaching, and it should be noted that other species utilize the converse reaction of sulfate reduction (Southam 2012). Anhydrite ($CaSO_4$) may also crystallize as a primary mineral from oxidized, sulfur-rich magmas, although it is may not always be preserved in the geological record since it is sparingly water soluble.

Examples

Sulfate minerals may be simple, anhydrous salts of one or more cations. However, most are more complex, containing additional water, hydroxide anion, or other anionic species such as chloride or carbonate. Sulfate is also an essential but subordinate constituent in some minerals such as nosean ($Na_8[Al_6Si_6O_{24}](SO_4)\cdot H_2O$) which do not fall into the sulfate anion class (nosean is a tectosilicate of the sodalite group). Most of the anhydrous sulfate minerals are uncommon, highly water soluble, ephemeral species of fumaroles, and arid environments. However, baryte ($BaSO_4$) and celestine ($SrSO_4$) are extremely insoluble in water and are common hydrothermal gangue minerals of ore deposits, as well as occurring as evaporites. The names of these minerals are as included in the Mineral List of the International Mineralogical Association (2017); the spellings "barite" and "celestite" remain common in American usage. They have an orthorhombic crystal structure in which the large Ba and Sr cations are in 12-fold coordination by oxygen. Anglesite ($PbSO_4$), which shares the same crystal structure, is a frequent oxidation product of lead sulfide ore minerals such as galena.

Calcium sulfate occurs primarily as orthorhombic anhydrite and also as the common monoclinic dihydrate gypsum ($CaSO_4\cdot 2H_2O$), as well as the rare, metastable hemihydrate bassanite ($CaSO_4\cdot \frac{1}{2}H_2O$), which is a natural analog of synthetic "plaster of Paris." Gypsum predominates at the Earth's surface, but it is readily dehydrated to anhydrite through the increase in pressure and temperature associated with burial, with 21% volume decrease of the solid phase. Conversely, anhydrite crystallizes directly from water above 55 °C, but is readily hydrated to gypsum by the action of water at low temperature and pressure. Gypsum formed some of the largest single crystals known of any mineral (up to 12 m long), discovered in 2000 in the "Cave of Crystals" at Naica, Chihuahua, Mexico (García-Ruiz et al. 2007). Also in Mexico, the abundance of these calcium sulfate minerals in evaporitic sediments at the 65-million-year-old Chicxulub impact site is believed to have filled the atmosphere with sulfate aerosol that caused a prolonged global cooling,

exacerbating the Cretaceous-Paleogene mass extinction event (Pope et al. 1997).

While gypsum is by far the commonest hydrated sulfate mineral, this group also includes epsomite ($MgSO_4{\cdot}7H_2O$), melanterite ($FeSO_4{\cdot}7H_2O$), goslarite ($ZnSO_4{\cdot}7H_2O$), and chalcanthite ($CuSO_4{\cdot}5H_2O$), all of which are highly water soluble and are found as efflorescences resulting from sulfide oxidation, often as postmining products.

Hydroxyl-bearing sulfates tend to be less soluble in water. This group includes the green copper sulfates antlerite ($Cu_3[SO_4](OH)_4$) and brochantite ($Cu_4[SO_4](OH)_6$), which are often found in the supergene zones of copper sulfide deposits, along with carbonates such as azurite ($Cu_3[CO_3](OH)_4$) and malachite ($Cu_2[CO_3](OH)_2$) and the amorphous copper silicate chrysocolla.

Economic and Environmental Importance

The large alunite supergroup of minerals, including sixteen sulfate minerals and another nine sulfate-phosphates or sulfate-arsenates as of 2017, shares the rhombohedral structure of alunite $KAl_3[SO_4]_2(OH)_6$ and jarosite, $KFe^{3+}{}_3[SO_4]_2(OH)_6$. Alunite is formed through alteration of feldspars by acid sulfate waters, while jarosite is a widespread oxidation product of iron sulfides such as pyrite at near-surface conditions and is a common component of limonitic gossans and mine waste. It is also a characteristic mineral of formerly sulfidic soils of wetlands that have oxidized on draining to become acid-sulfate soils (Dent and Pons 1995). Jarosite is only stable under acidic conditions and liberates sulfuric acid on its decomposition to goethite at higher pH. It accumulates toxic heavy metals such as Pb and As and releases them upon decomposition (cf. Murray et al. 2014), complicating attempts to remediate such environments. Synthetic jarosite is precipitated as a low-cost and efficient means of removing iron during processing of zinc ore (cf. Dutrizac and Monhemius 1986), but its disposal presents an environmental problem because of the link to acidity. Jarosite has been detected on the surface of Mars by the NASA Mars Rover "Opportunity" using Mössbauer Spectrometry (Klingelhöfer et al. 2004); the mineral is important evidence for the former presence of liquid water on Mars.

Celestine is the principal source of strontium metal and its compounds and baryte of barium. However, the majority of baryte mined commercially is used in fine powder form as a component of drilling muds in hydrocarbon exploration. This is due to its lack of chemical reactivity, magnetism, or abrasiveness, while possessing a high density (ideally 4.48 g/cm^3). It is also used as a dense, inert white filler in paints and plastics. High absorption due to the presence of the heavy barium ion combined with its insoluble, nontoxic nature leads to it being used as a contrast agent for medical X-rays of the digestive system. Gypsum, very soft at 2 on the Mohs scale, has been used in massive form since ancient times as the easily carved sculptural medium "alabaster." It is also used for blackboard "chalk," as a fertilizer and, when partially dehydrated to bassanite, as plaster. Bassanite powder in water forms a viscous paste, which may then be shaped before gradual rehydration of the solid phase turns it back into a rigid mass of interlocking gypsum crystals (cf. Van Driessche et al. 2012).

Formation of sulfate minerals is also important in the corrosion and degradation of concrete and cement products. Sulfate-bearing waters and atmospheric sulfur dioxide attack the calcium silicates, carbonates, and hydroxides of such structural materials to produce minerals such as gypsum, ettringite, $Ca_6Al_2[SO_4]_3(OH)_{12}{\cdot}26H_2O$, and thaumasite, $Ca_3[Si(OH)_6][SO_4][CO_3]{\cdot}12H_2O$, with associated softening and volume expansion (Winter 2012).

Summary

The sulfate anion is widespread under near-surface conditions on Earth, with the result that about 7% of all known mineral species are members of the "sulfate" anion class. Most of these are rare secondary minerals produced by oxidation of sulfide-rich ore bodies, but a small number are important and sometimes rock-forming minerals. Out of these, baryte and celestine are major sources for the elements barium and strontium, respectively, while the extremely common calcium sulfate minerals have found a wide range of industrial uses since Classical times. Volume changes due to sulfate mineral formation can play a major role in degradation and erosion of engineered structures, while redox cycling between sulfide and sulfate species, usually mediated by microbes, produces minerals such as jarosite which play an important role in controlling acidity in environments such as mine waste and drained wetlands.

Cross-References

- ▶ Biogeochemistry
- ▶ Chemical Bonds
- ▶ Low-Temperature Geochemistry
- ▶ Mineralogy
- ▶ Ore Deposits
- ▶ Sulfide Minerals
- ▶ Sulfur
- ▶ Sulfur Cycle
- ▶ Sulfur Isotopes
- ▶ Supergene
- ▶ Surface Geochemistry

References

Alpers CN, Jambor JL, Nordstrom DK (2000) Sulfate minerals – crystallography, geochemistry, and environmental significance, Reviews in mineralogy and geochemistry, vol 40. Mineralogical Society of America, Washington, DC. 608 pp

Chang YY, Howie RA, Zussmann J, Deer WA (1996) Rock forming minerals, volume 5B: non-silicates; sulphates, carbonates, phosphates and halides. Longman, Harlow. 383 pp

Dent DL, Pons LJ (1995) A world perspective on acid sulphate soils. Geoderma 67:263–276

Dutrizac JE, Monhemius AJ (eds) (1986) Iron control in hydrometallurgy. Ellis Horwood Ltd/Halsted Press, Chichester/New York. 794 pp

García-Ruiz J-M, Villasuso R, Ayora C, Canals A, Otálora A (2007) Formation of natural gypsum megacrystals in Naica, Mexico. Geology 35:327–330. https://doi.org/10.1130/G23393A.1

International Mineralogical Association (2017) List of minerals. http://nrmima.nrm.se/. Sighted 6 Aug 2017

Klingelhöfer G, Morris RV, Bernhardt B, Schröder C, Rodionov DS, de Souza PA Jr, Yen A, Geller R, Evlanov EN, Zubkov B, Foh J, Bonnes U, Kankeleit E, Gütlich P, Ming DW, Renz F, Wdowiak T, Squyres SW, Arvidson RE (2004) Jarosite and hematite at meridiani planum from opportunity's mössbauer spectrometer. Science 306:1740–1745. https://doi.org/10.1126/science.1104653

Mindat. Online mineral database. www.mindat.org

Murray J, Kirschbaum A, Dold B, Mendes Guimarae E, Pannunzio Miner E (2014) Jarosite versus soluble iron-sulfate formation and their role in acid mine drainage formation at the Pan de Azúcar mine tailings (Zn-Pb-Ag), NW Argentina. Minerals 4:477–502. https://doi.org/10.3390/min4020477

Nordstrom DK, Southam G (1997) Geomicrobiology of sulfide mineral oxidation. Rev Mineral 35:361–390

Pope KO, Baines KH, Ocampo AC, Ivanov BA (1997) Energy, volatile production, and climatic effects of the Chicxulub Cretaceous/Tertiary impact. J Geophys Res 102:21645–21644

Pósfai M, Dunin-Borkowski RE (2006) Sulfides in biosystems. Rev Mineral 61:679–714

Southam G (2012) Minerals as substrates for life: the prokaryotic view. Elements 8:101–106

Van Driessche AES, Benning LG, Rodriguez-Blanco JD, Ossorio M, Bots P, García-Ruiz J-M (2012) The role of basanite as a stable precursor phase to gypsum precipitation. Science 336:69–72. https://doi.org/10.1126/science.1215648

Winter NB (2012) Understanding cement. WHD Microanalysis Consultants Ltd, Woodbridge. 206 pp

Sulfide Minerals

Andrew G. Tomkins[1] and Bree Morgan[2]

[1]School of Earth, Atmosphere and Environment, Monash University, Melbourne, VIC, Australia

[2]School of Geosciences, The University of Sydney, Camperdown, NSW, Australia

Synonyms

Sulfosalt minerals (Sulphosalt); Sulphide minerals

Definition

Reduced sulfur bonds as an anion with a significant range of metals (M) to form sulfide minerals of the general form M_aS_b, although two or more metals exist in many sulfide minerals. Sulfosalt minerals are a more complex subset of sulfide minerals of the general form $M_aX_bS_c$, where X is typically one or more of the semimetals (As, Sb, Bi). Metals typically found as major cations in sulfide minerals on Earth include Fe, Co, Ni, Cu, Zn, Mo, Ag, Cd, Hg, Tl, and Pb. Metals that can be found as, sometimes important, trace substitutions in sulfide minerals include the Platinum Group Elements (PGE: Pt, Pd, Rh, Ru, Ir, Os), Au, Ga, Ge, In, and Sn. Together, this large group of metal and semimetal cations, are referred to as chalcophile elements (meaning sulfur-loving). However, the PGE and Au behave as siderophile elements when metallic FeNi metal is present (Hayden et al. 2011). Selenium and Te are chalcogens, which substitute for, or replace S in many minerals (forming selenides and tellurides, respectively), and the semimetals As and Sb act as anions in place of S in subgroups of minerals known as arsenides and antinomides, respectively; these elements and S are important constituents of many platinum group minerals. This large range of minerals is grouped under the heading of Sulfides in the Nickel-Strunz classification system (version 10), which contains nearly 700 minerals.

Given this large number of sulfide minerals, the range of crystal structures is great (Makovicky 2006). The most abundant sulfide minerals in the accessible Earth, in estimated order of abundance, include pyrrhotite ($Fe_{1-x}S$, monoclinic with hexagonal polytypes), pyrite (FeS_2, isometric diploidal, typically cubic habit), pentlandite ($[Fe,Ni]_9S_8$, isometric hexoctahedral), chalcopyrite ($CuFeS_2$, tetragonal scalenohedral), sphalerite (ZnS, isometric hextetrahedral), and galena (PbS, cubic hexoctohedral). At the temperatures and pressures of the upper mantle, monosulfide solid solution (MSS) is the dominant sulfide phase, which exsolves upon cooling to pyrrhotite (dominant), pentlandite and chalcopyrite. Pyrite is the dominant sulfide in the upper crust but tends to break down to pyrrhotite in the mid to lower crust (e.g., Pitcairn et al. 2006; Tomkins 2010; Finch and Tomkins 2017).

Introduction

Sulfur (S) is the tenth most abundant element in the Universe, and the fifth most abundant in the Earth, so the minerals and compounds it forms play, and have played, key roles in the evolution of the Earth and its life. Sulfide minerals are the most abundant form of sulfur in the solid Earth, and contain important metal resources that are essential to modern societies, so understanding their formation and stability is fundamental to many subdisciplines of geosciences.

Sulfide Ore Deposits

Sulfide minerals are the key metal-bearing constituents of many of our most important ore deposit types. There is a wide range of ore deposit types because S is highly mobile in aqueous fluids and magmas. Various sulfide ore deposit types fall under the broad headings of magmatic, magmatic-hydrothermal, and hydrothermal ore deposits.

Our most important resources of Ni and PGE form as magmatic sulfide deposits (Cu is an important constituent of some), where mafic to ultramafic magmas become saturated in S, promoting exsolution of immiscible sulfide liquid droplets, which are able to gravitationally accumulate and sequester chalcophile elements from the silicate magma (Mungall 2014). The most important Cu and Mo deposits (Au is commonly an important constituent) form when felsic to intermediate magmas crystallize in the upper crust, releasing saline and S-bearing hydrothermal fluid, which scavenges metals from the magma and transports them to a range of structurally controlled locations where sulfide minerals form (Cooke et al. 2014). Most of the world's gold deposits formed when metamorphism in orogenic belts promoted release of fluids containing H_2O, CO_2, and H_2S from mid to lower levels of the crust, which transported Au (and Ag) into structurally controlled sites in the mid to upper crust (Tomkins 2013), where Au was deposited in close association with typically pyrite and arsenopyrite (FeAsS); a range of other sulfide minerals are also sometimes present. The most important Zn and Pb resources formed in deep sea floor settings (so-called volcanogenic massive sulfide (Hannington 2014) and sedimentary exhalative sulfide deposits (Wilkinson 2014)), involving deep circulation of warm saline fluid through igneous and/or sedimentary rocks before expulsion of metal-bearing fluids through vents on the sea floor where sulfide minerals are precipitated due to distinct temperature and fluid chemistry changes. Many of the chalcophile elements are primarily extracted as byproducts from these main sulfide ore deposit groups, including As, Bi, Co, Ga, Ge, Hg, In, Sb, Se, Te, and Tl. However, there is a wide range of other settings where sulfide-rich ore deposits form.

Sulfide Minerals in Biogeochemical Systems

Sulfide mineral precipitation in low temperature anoxic conditions is largely driven by the global biogeochemical cycling of S, Fe, and organic C and can be limited by availability of each of these components depending on system conditions. Because sulfate is abundant in modern oceans, dissimilatory sulfate reduction is the dominant process fueling microbial break down of organic matter in marine systems (Rickard and Luther 2007). Furthermore, some of the earliest life forms are thought to have gained energy by oxidizing molecular hydrogen (H_2), or methane (CH_4), while reducing sulfate (SO_4^{2-}) to sulfide, existing in an early Earth environment that lacked free oxygen (~3.9–2.4 billion years ago). In both cases, these sulfate reducing prokaryotes produce dissolved sulfide (H_2S, S^{2-} or HS^-), which then reacts with reduced divalent metal ions (M^{2+}), to be immobilized in sulfide minerals. Fe-sulfide minerals are most commonly precipitated during this process due to the high abundance of reactive iron at the Earth's surface, with reduction of Fe^{3+} to Fe^{2+} being thermodynamically favored (and thus preceding) over the reduction of sulfate (Burdige 2006).

Pyrite is the most abundant Fe-sulfide mineral produced by biologically mediated sulfate reduction (Rickard and Luther 2007). The formation of sedimentary pyrite is a complex process, generally involving the initial precipitation of metastable monosulfide precursors, including poorly crystalline mackinawite (tetragonal FeS) and greigite (cubic Fe_3S_4; Hunger and Benning 2007). The "hydrogen sulfide pathway" and the "polysulfide pathway" are widely thought to promote pyrite formation from an iron monosulfide precursor, and involve the reaction of FeS with hydrogen sulfide or polysulfide (S_n^{2-}), respectively (Schoonen 2004; Rickard and Luther 2007). The transformation of Fe-monosulfides to thermodynamically stable pyrite requires the availability of an oxidant (other than dissolved sulfide) to proceed, such as O_2, S^0 , and other S intermediates (Schoonen and Barnes 1991; Benning et al. 2000).

Sulfide Minerals and the Global Sulfur Cycle

To biogeochemists, the term sulfur cycle refers to the cycling of sulfur through organic processes in the surface environment and upper crust, as discussed above. However, there is a larger-scale, longer-term cycle whereby S is cycled through the atmosphere and hydrosphere, often via the biosphere, into the deep Earth, and eventually back into the atmosphere. This cycle can be viewed as starting with sulfur in volcanic gases, and sulfur released into rivers by weathering of sulfide minerals (mainly pyrite) in rocks exposed in mountain belts. Sulfur from these sources is introduced into the oceans, where SO_4^{2-} is the second most abundant anion. This sulfate is circulated into the oceanic crust at volcanic mid-ocean ridges and other areas of extensional faulting, where seawater promotes alteration of the rock and formation of pyrite, pyrrhotite and anhydrite ($CaSO_4$), storing S in the oceanic crust (Alt 1995). The layer of sediments sitting on top of the basaltic crust typically contains biogenic pyrite. This oceanic crust is eventually subducted into the mantle, where the pyrite and anhydrite break down during blueschist and eclogite facies metamorphism, releasing S into fluids that migrate upwards into the overlying mantle (Tomkins and Evans 2015). These fluids promote metasomatism of the mantle,

forming mainly disseminated grains of monosulfide solid solution, and making the mantle more susceptible to melting (Rielli et al. 2017). These sulfide mineral grains are partially dissolved into the magmas that develop, and these eventually make their way up to magma chambers beneath the numerous volcanoes that populate magmatic arcs. Some sulfide mineral rich ore deposits form in this environment (and are eventually eroded), and some magmas erupt through the volcanoes releasing gaseous sulfur back into the atmosphere. Because the sulfate in the oceans is thought to have become more abundant due to the evolution on the biosphere, it has been postulated that this global sulfur cycle may have driven changes in the chemistry of the deep Earth over billions of years (Evans and Tomkins 2011).

Extraterrestrial Sulfide Minerals

Sulfide minerals are common in meteorites, which represent approximately 110 asteroids, as well as Mars and the Moon. Most meteorites contain the mineral troilite (stoichiometric FeS). A small proportion of oxidized meteorites, and most of those from Mars, contain pyrrhotite ($Fe_{1-x}S$) and pentlandite ($[FeNi]_9S_8$). Pyrite (FeS_2) is found in very few meteorites but is notably abundant in an important regolith breccia from Mars (NWA 7034 and pairs). Given that S is a volatile element, rocky and rock-ice bodies that formed further from the Sun are expected to have greater abundances of sulfide minerals, and this appears to be the case for Mars compared to the Earth.

The most reduced meteorites, the enstatite chondrites and achondrites, have such little oxygen that elements such as Ca, Mg, and Mn partly combine with S to form sulfide minerals such as oldhamite (CaS), niningerite (MgS), and alabandite (MnS) and their solid solutions involving Fe. Sulfide minerals in these ultrareduced meteorites also contain elevated lathanides and actinides (Barrat et al. 2016).

Summary

Because sulfur is relatively abundant in the Earth's crust and mantle and can exist in multiple valence states in many geochemical domains, sulfide minerals have been a cornerstone of several important geochemical processes. They are the products of the anaerobic respiration utilized by some of the earliest life forms on Earth (sulfate reducing prokaryotes), which persist today in anoxic subaqueous environments. They are part of the global sulfur cycle, which transfers sulfur from the surface through subduction zones into the deep Earth and back through volcanoes. And, they are the hosts to many of our most important metal resources.

References

Alt JC (1995) Sulfur isotopic profile through the oceanic crust: sulfur mobility and seawater-crustal sulfur exchange during hydrothermal alteration. Geology 23:585–588

Barrat JA, Greenwood RC, Keil K, Rouget ML, Boesenberg JS, Zanda B, Franchi IA (2016) The origin of aubrites: evidence from lithophile trace element abundances and oxygen isotope compositions. Geochim Cosmochim Acta 192:29–48

Benning LG, Wilkin RT, Barnes HL (2000) Reaction pathways in the Fe–S system below 100°C. Chem Geol 167:25–51

Burduge DJ (2006) Geochemistry of marine sediments. Princeton University Press, Princeton, USA. p 624

Cooke DR, Hollings P, Wilkinson JJ, Tosdal RM (2014) Geochemistry of porphyry deposits. In: Scott SD (ed) Treatise in geochemistry, vol. 13: geochemistry of mineral deposits, Elsevier, Amsterdam. pp 195–218

Evans KA, Tomkins AG (2011) The relationship between subduction zone redox budget and arc magma fertility. Earth Planet Sci Lett 308:401–409

Finch EG, Tomkins AG (2017) Pyrite-pyrrhotite stability in a metamorphic aureole: implications for orogenic gold genesis. Econ Geol 112:661–674

Hannington MD (2014) Volcanogenic massive sulfide deposits. In: Scott SD (ed) Treatise in geochemistry, vol. 13: geochemistry of mineral deposits, Elsevier, Amsterdam. pp 463–488

Hayden LA, Van Orman JA, McDonough WF, Ash RD, Goodrich CA (2011) Trace element partitioning in the Fe–S–C system and its implications for planetary differentiation and the thermal history of ureilites. Geochim Cosmochim Acta 75: 6570–6583

Hunger S, Benning LG (2007) Greigite: a true intermediate on the polysulfide pathway to pyrite. Geochem Trans 8:1

Makovicky E (2006) Crystal structures of sulfides and other chalcogenides. Rev Mineral Geochem 61:7–125

Mungall JE (2014) Geochemistry of magmatic ore deposits. In: Scott SD (ed) Treatise in geochemistry, vol. 13: geochemistry of mineral deposits, Elsevier, Amsterdam. pp 195–218

Pitcairn IK, Teagle DAH, Craw D, Olivo GR, Kerrich R, Brewer TS (2006) Sources of metals and fluids in orogenic gold deposits: insights from the Otago and Alpine schists, New Zealand. Econ Geol 101:1525–1546

Rickard D, Luther GW (2007) Chemistry of iron sulfides. Chem Rev 107:514–562

Rielli A, Tomkins AG, Nebel O, Brugger J, Etschmann B, Zhong R, Yaxley G, Paterson D (2017) Evidence of sub-arc mantle oxidation by sulfur and carbon. Geochem Perspect Lett 3:124–132

Schoonen MA (2004) Mechanisms of sedimentary pyrite formation. Geol Soc Am Spec Pap 379:117–134

Schoonen MAA, Barnes HL (1991) Reactions forming pyrite and marcasite from solution: II. Via FeS precursors below 100°C. Geochim Cosmochim Acta 55:1505–1514

Tomkins AG (2010) Windows of metamorphic sulfur liberation in the crust: implications for gold deposit genesis. Geochim Cosmochim Acta 74:3246–3259

Tomkins AG (2013) On the source of orogenic gold. Geology 41:1255–1256

Tomkins AG, Evans KA (2015) Separate zones of sulfate and sulfide release from subducted mafic oceanic crust. Earth Planet Sci Lett 428:73–83

Wilkinson JJ (2014) Sediment-hosted zinc-lead mineralization: processes and perspectives. In: Scott SD (ed) Treatise in geochemistry, vol. 13: geochemistry of mineral deposits, Elsevier, Amsterdam. pp 220–249

Sulfur

James Farquhar
Department of Geology and Earth System Science Interdisciplinary Center, University of Maryland, College Park, MD, USA

Element Data
Atomic Symbol: S
Atomic Number: 16
Atomic Weight: 32.059–32.076†
Isotopes and Abundances:
^{32}S (0.9441–0.9529),
^{33}S (0.00729–0.00797),
^{34}S (0.0396–0.0477),
^{35}S (radioactive t ½ = 87 days),
^{36}S (0.000129–0.000187)
1 Atm Melting Point: >115 °C††
1 Atm Boiling Point: 444.64 °C
Common Valences: −2,0,+2,+4,+6
Ionic Radii: 0.2 (+6) to 1.78 (−2)
Pauling Electronegativity: 2.58
First Ionization Potential: 9.996 Ev
Chondritic (CI) Abundance: 5.35%
Silicate Earth Abundance: 211 ppm
Crustal Abundance: 404 ppm
Seawater Abundance: 28 mMol
Core Abundance: 1.9%
†Reflects variation of isotopic composition
††Melting Point Varies by Allotrope

Sulfur is the tenth most common element in the solar system with an abundance about half that of silicon and a little less than one tenth that of oxygen (Lodders 2003). While there are a number of nucleosynthetic pathways for production of this element, the principal nucleosynthetic pathway for production of its three lightest isotopes (^{32}S, ^{33}S, ^{34}S) is related to explosive burning of oxygen (Woosley et al. 1973) and the pathway of its rare isotope is principally via neutron rich silicon burning (Cameron 1979; McDonough 2014; Meija et al. 2016a, b; Meyer 1976; Palme et al. 2014; Rudnick and Gao 2014; Steudel 2003; Steudel and Eckert 2003; Wang and Becker 2013; Whittaker and Muntus 1970).

Properties

Sulfur in its elemental form is a yellow crystalline solid. When broken, it has a sulfurous smell. Elemental sulfur sublimates at ambient temperatures, is insoluble in water, but soluble in organic solvents such as carbon disulfide, benzene, toluene, xylenes, and chloroform, and carbon tetrachloride. The electronic structure of sulfur ([Ne] $3s^2$ $3p^4$) determines its accessible oxidation states, which range from −2 to +6, leading to a wide range of sulfur-bearing compounds in nature.

History and Use

Sulfur has had a variety of uses, including as a component in black powder, to harden (vulcanize) rubber by creating cross-linkages, in the form of mercaptan (SCH_3) as an odorant in natural gas, and as a pesticide. In nature, sulfur compounds act as cryoprotectants in cells and as natural deterrents to predation. Sulfur in various forms is also used as a fertilizer. Sulfur as sulfate is used for sulfuric acid, a component in batteries.

Geochemical Behavior

Sulfur in nature occurs in gas, liquid, and solid phase organosulfur as well as inorganic sulfur compounds. This rich chemistry, in combination with the moderately high abundance of sulfur creates a role for sulfur chemistry in the atmosphere, ocean, and solid Earth.

Sulfur is introduced to the atmosphere from a variety of natural and anthropogenic sources. Biological sources of sulfur include hydrogen sulfide, a byproduct of sulfate reduction by prokaryotes, as well as various volatile organosulfur compounds (carbonyl sulfide and methylated sulfur compounds). Atmospheric sulfur is also supplied as hydrogen sulfide and sulfur dioxide released from volcanic edifices. These include large explosive eruptions that can influence climate by injecting sulfur into the stratosphere where it is oxidized to sulfate which forms reflective aerosols, and quiescent degassing such as is observed in hydrothermal regions like Yellowstone. Anthropogenic sources of sulfur include various industrial sources such as coal burning, hydrocarbons, smelting of steel, as well as from waste treatment.

Once in the atmosphere, sulfur compounds participated in complex chemical reaction networks that produce numerous oxidized intermediates and products. Some of these products are hygroscopic and contribute to cloud formation. Other sulfur products contribute to particulate aerosols that can have consequences for air quality and also serve as loci for further chemical transformations of atmospheric compounds. The oxidation of sulfur compounds in the atmosphere also generates species that react with water to form strong acids, making them one of the key contributors to acidification of

rain, snow, and even surface waters when they occur in regions with low buffering capacity.

In the oceans, sulfur is present in both organic matter and as dissolved sulfate. Dissolved sulfate is the second most abundant anion in seawater and its catabolic reduction by microbial metabolisms in marine environments is the second most important pathway for organic carbon mineralization on geological timescales. Sulfate reduction contributes on the order of 30% of the total to organic carbon mineralization and through burial of pyrite provides a long-term geological sink for electrons that contributes significantly to the net oxidation state of Earth's surface environments.

In the solid Earth, sulfur partitions chalcophile elements and is responsible for concentration of metals in the silicate Earth. Earth's mantle is significantly depleted in sulfur relative to that seen for the solar system because of partitioning of sulfur into Earth's core (Savage et al. 2015).

Biological Utilization and Toxicity

Sulfur is an essential element for life, being a key component in the amino acids methionine and cysteine. Sulfur cross-linkages are essential for formation of proteins, and sulfur is present in keratin, a compound found in finger nails and hair. More complex organic sulfur compounds are key components for plants and microbes that are used to deter predation, for signaling and communication, and also for freezing point depression as cryoprotectants. Compounds familiar to humans through experiential, even if not explicitly recognized, include glucosinolates such as sinigrin which is a component of mustard and wasabi (horse radish), allicin which is a component of garlic that adds to its characteristic flavors and has antibiotic and anticancer properties. Antibiotic and anticancer properties have also been identified for a variety of other organosulfur compounds such as glucoraphanin and glutathione which are components of cruciferous vegetables such as broccoli and cabbage. Biological sulfur compounds often smell, sometimes pleasant, as in the low level methyl sulfides that bring the characteristic smell of the ocean, and sometimes unpleasant as in the smell of a skunk, or of rotten eggs, vegetables, or meat.

Summary

The diverse oxidation states of sulfur contribute to a rich chemistry in Geobiology and Geochemistry. In biology, sulfur cross-links proteins, is part of essential amino acids, and provides key properties for biologically relevant chemicals. In Earth's atmosphere, redox transformations contribute to aerosol formation and acidification of rain. In the oceans, the reactivity of microbially produced sulfide with iron and oxygen has made it one of the key elements for controlling whether the oceans, in part or in whole, have been oxic, ferruginous, or sulfidic. In Earth's crust and mantle, sulfide chemistry of chalcophile elements plays an important part in their concentration and distribution. In the solid Earth and its precursors, sulfur is thought to have been strongly partitioned into the metallic liquids during planetary differentiation and thus is considered a strong candidate light element for the core.

Cross-References

- ▶ Gold
- ▶ Iron
- ▶ Sulfur Isotopes

References

Cameron AGW (1979) The neutron-rich silicon-burning and equilibrium processes of nucleosynthesis. Astrophys J 230:L53–L57

Lodders K (2003) Solar system abundances and condensation temperatures of the elements. Astrophys J 591(2):1220

McDonough WF (2014) Compositional model for the Earth's core. In: Treatise on geochemistry, vol 2. Elsevier, Amsterdam, pp 547–568

Meija J, Coplen TB, Berglund M, Brand WA, De Bièvre P, Gröning M, Holden NE, Irrgeher J, Loss RD, Walczyk T, Prohaska T (2016a) Atomic weights of the elements 2013 (IUPAC Technical Report). Pure Appl Chem 88(3):265–291

Meija J, Coplen TB, Berglund M, Brand WA, De Bièvre P, Gröning M, Holden NE, Irrgeher J, Loss RD, Walczyk T, Prohaska T (2016b) Isotopic compositions of the elements 2013 (IUPAC technical Report). Pure Appl Chem 88(3):293–306

Meyer B (1976) Elemental sulfur. Chem Rev 76(3):367–388

Palme H, Lodders K, Jones A (2014) Solar system abundances of the elements. In: Treatise on geochemistry, vol 1. Elsevier, Amsterdam, pp 15–36

Rudnick RL, Gao S (2014) Composition of the continental crust. In: Treatise on geochemistry, vol 4. Elsevier, Amsterdam, pp 1–64

Savage PS, Moynier F, Chen H, Shofner G, Siebert J, Badro J, Puchtel IS (2015) Copper isotope evidence for large-scale sulphide fractionation during Earth's differentiation. Geochem Perspect Lett 1(1):53–64

Steudel R (2003) Liquid Sulfur Liquid Sulfur. In: Elemental sulfur and sulfur-rich compounds I. Springer, Berlin/Heidelberg, pp 93–106

Steudel R, Eckert B (2003) Solid sulfur allotropes sulfur allotropes. In: Elemental sulfur and sulfur-rich compounds I. Springer, Berlin/Heidelberg, pp 1–80

Wang Z, Becker H (2013) Ratios of S, Se and Te in the silicate Earth require a volatile-rich late veneer. Nature 499(7458):328

Whittaker EJW, Muntus R (1970) Ionic radii for use in geochemistry. Geochim Cosmochim Acta 34(9):945–956

Woosley SE, Arnett WD, Clayton DD (1973) The explosive burning of oxygen and silicon. Astrophys J Suppl Ser 26:231

Sulfur Cycle

Martin A. Schoonen
Brookhaven National Laboratory, Upton, NY, USA
Department of Geosciences, Stony Brook University, Stony Brook, NY, USA

Definition

The global sulfur cycle refers to the transfer of sulfur between the upper lithosphere, hydrosphere, pedosphere, biosphere, and atmosphere as a result of geological, biological, and anthropogenic processes. Sulfur passing through the cycle is subject to redox reactions with oxygen, carbon, and iron as major reactants, which lead to a tight coupling of the global cycles for these elements.

The Major Sulfur Reservoirs on Earth

Most sulfur on Earth involved in the global sulfur cycle is retained in the upper lithosphere and marine sediments (Table 1). A large unknown amount of sulfur residing in the Earth's core and mantle is effectively sequestered and excluded from the global sulfur cycle. The oceans contain most of the sulfur residing in the hydrosphere, dwarfing the amount of sulfur in lakes and rivers (Table 1). The amount of sulfur contained in soils and biomass is roughly four orders of magnitude smaller than the amount of sulfur in the oceans, while the atmosphere represents the smallest reservoir of sulfur on Earth (Table 1). Table 1 not only summarizes estimates of the amount of sulfur contained in the major reservoirs; it also indicates the most abundant forms of sulfur in each reservoir.

Sulfur Cycle, Table 1 Major sulfur reservoirs on Earth[a]

Reservoir	Major forms of sulfur	Mass (Tg S)[b]
Atmosphere	Gas: H_2S, SO_2, DMS, OCS Aerosols: H_2SO_4, $(NH_4)_2SO_4$	4.8
Pedosphere and biosphere	Sulfates, organic S, pyrite	3×10^5
Rivers and lakes	SO_4^{2-}	300
Oceans	SO_4^{2-}	1.3×10^9
Marine sediments	Pyrite, gypsum, anhydrite	3×10^8
Lithosphere	Gypsum, anhydrite, metal sulfides, sulfur	2×10^{10}

[a]Based on Brimblecombe (2014) and Jones et al. (2016)
[b]Tg is 10^{12} g

The Modern Natural Global Sulfur Cycle

The modern natural global sulfur cycle is dominated by processes involving transfer of sulfur in and out of the oceans (Sievert et al. 2007). A significant amount of sulfur is lofted into the air in the form of small sulfate-containing salt crystals; see Fig. 1. Most of the particles settle rapidly back into the ocean, but some are transported over land and are removed from the air mass through precipitation or by settlings as dry deposition. Removal of sulfate through microbial reduction in marine sediments to sulfide, followed by the formation of pyrite, is a major process that removes sulfate from the ocean (Schoonen 2004). Some sulfate is also removed from the oceans in the form of evaporate minerals and as a trace constituent of sedimentary carbonates (Staudt and Schoonen 1995). Microbial conversion of sulfate into volatile organo-sulfur compounds in marine environments also contributes to a transfer of sulfur from the ocean reservoir through the biosphere into the atmosphere (Sievert et al. 2007).

Inputs to the ocean reservoir in the natural sulfur cycle are dominated by weathering of sulfate-containing evaporative deposits and weathering of pyrite-containing sediments. Removal of volcanogenic sulfur emissions via precipitation or dry deposition into the oceans constitutes a small input, although the magnitude of this flux varies with volcanic activity (Jones et al. 2016).

The magnitudes of all the fluxes in the modern natural global sulfur cycle are difficult to reconstruct because contributions from human activity are difficult to separate from natural contributions. New approaches relying on the study of multiple S isotope systematics are promising (Tostevin et al. 2014), but it remains difficult to close the natural sulfur budget.

Sulfur Cycle Through the Earth's History

As the Earth evolved, so did the sulfur cycle (Rickard 2012; Brimblecombe 2014). Microbial processes play a significant role in the modern natural sulfur cycle (Fig. 1). Hence, on a prebiotic Earth, the sulfur cycle would have been dominated by emissions of volcanic sulfur gases – predominantly SO_2, with minor H_2S – into the atmosphere and removal of sulfur from the atmosphere through photochemical reactions. There was likely very little subaerial crust, all but eliminating gypsum deposition and dissolution as major processes at this early time. Dissolved reduced iron (Fe(II)), leached from crustal rock interacting with ocean waters, would have limited the amount of hydrogen sulfide in solution through iron sulfide precipitation. A higher heat flow on the early Earth would have promoted widespread hydrothermal circulation of ocean water through the crust. The net

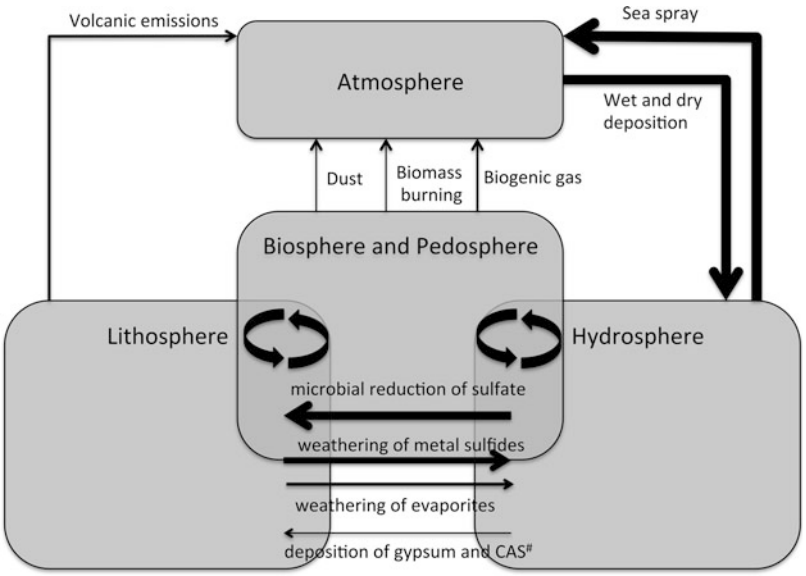

Sulfur Cycle, Fig. 1 Simplified modern natural sulfur cycle. The weight of the *arrow* indicates the relative importance of a given flux. There is considerable cycling of sulfur that involves uptake and release of sulfur within the overlaps of hydrosphere, lithosphere, and biosphere as indicated by the *curved arrows*. Anthropogenic activities have a significant effect on the natural sulfur cycle; see Fig. 2, which makes it difficult to determine the absolute magnitude of the modern natural fluxes. #*CAS* carbonate associated sulfur

effect would have been sequestration of sulfate as metal sulfide as ocean water interacted with the crust at elevated temperatures.

The emergence of life triggered significant changes in the sulfur cycle (Rickard 2012). The most profound change to the sulfur cycle occurred at the time of the transition from an anoxic atmosphere to an oxic atmosphere around 2.3 Ga as a result of the emergence of photosynthetic bacteria producing oxygen as a waste product. Detailed studies exploiting multi-S-isotope systematics point to a sulfur cycle that is largely dominated by inorganic processes up to this point in the Earth's history (Johnston 2011). Once the atmosphere contained molecular oxygen, volcanogenic sulfur emitted into the atmosphere was readily oxidized to sulfate. Besides the accumulation of oxygen in the atmosphere, the growth of continents enabled chemical weathering of sulfide-containing rocks through oxidation, resulting in the enhanced transport of sulfate to the ocean. This sets the stage for sulfate-reducing bacteria – possibly long present in the ocean but limited by the availability of sulfate – to flourish and produce sedimentary pyrite in abundance. The emergence of continents also provided settings for the formation of evaporite deposits that removed sulfate from the oceans in the form of gypsum and barite.

With microbial life established and continents forming and reforming, the sulfur cycle saw additional perturbation as a result of changes in the rate of primary production, evaporite deposition, and weathering (Brimblecombe 2014). Geological, geochemical, and isotopic studies have allowed for detailed reconstructions of these excursions. However, one of the single largest excursions in the sulfur cycle has been induced by human activity over the last two centuries.

Anthropogenic Influence on the Sulfur Cycle

Anthropogenic activities transfer a significant amount of additional sulfur into the atmosphere and hydrosphere. Most pronounced is the burning of S-containing fossil fuel, such as coal. Sulfur in coal is predominantly present as small pyrite crystals (FeS_2), which converts to gaseous SO_2 upon burning and contributes to acidification of rain. Modern scrubbing technologies remove much of the SO_2 from flue gas, but the technology is not widely implemented in China and India, which have emerged as major contributors to the atmospheric SO_2 burden (Klimont et al. 2013). In addition, mining of coal or metal sulfides creates sulfur-containing dust as well as sulfide-containing mine waste that often reacts with water and air to form acid mine drainage. Oxidation of mine waste contributes significantly to the riverine flux of sulfate out to the sea. Roasting of metal sulfide ores, a necessary step to provide society with metals such as zinc and copper, releases a significant amount of SO_2. International shipping, which relies on burning of S-rich bunker fuel, amounts to about 10% of the global anthropogenic SO_2 emissions (Klimont et al. 2013).

The magnitude of the anthropogenic perturbation of the sulfur cycle is illustrated in Fig. 2. For example, it is estimated that more than half of the sulfur transported to the oceans by rivers and 75% of the sulfur emissions to the atmosphere are anthropogenic in origin (Berner and Berner 1996).

On a global scale, the emissions of SO_2 have dropped recently (Klimont et al. 2013). Changes in economic activity

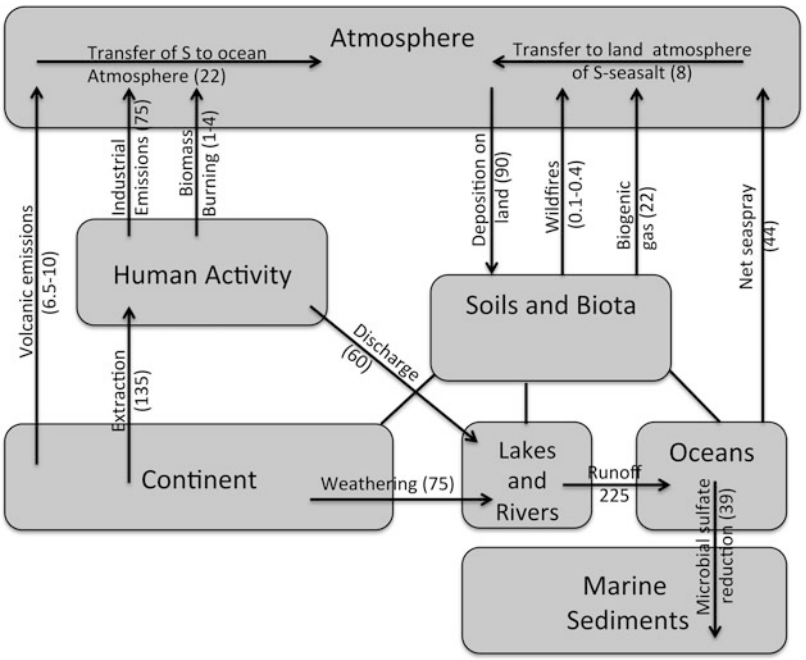

Sulfur Cycle, Fig. 2 Annual fluxes of sulfur (Tg/a). Fluxes based on Brimblecombe (2014) and Berner and Berner (1996) The flux associated with wildfires is estimated to be a factor of ten smaller than biomass burning associated with crop waste burning and land-clearing activities

have a profound effect on the demand for fossil fuel, metals, and transportation of goods via international shipping, and the recent (2005–2011) drop likely reflects the impact of a global recession. However, it is projected that economic growth in India, an expansion of international shipping, and growth of emerging economies in Africa will add to the atmospheric SO_2 burden. At the same time, stricter environmental regulations are expected to lead to a broader application of technologies to scrub SO_2 from flue gas in China, Europe, and North America. While this will lead to a long-term, sustained decrease in SO_2 emissions, it only addresses one of the anthropogenic processes that contributes to the imbalance of the global sulfur cycle (Klimont et al. 2013; Brimblecombe 2014).

Conclusions

The modern global sulfur cycle is out of balance as a result of anthropogenic activity. The sulfur cycle has changed as the Earth evolved. On the prebiotic Earth, volcanic emissions played a key role in the sulfur cycle. This cycle may have remained largely unchanged, until free oxygen accumulated in the atmosphere as photosynthetic microbes emerged. The presence of oxygen and the growth of continents fundamentally changed the sulfur cycle, with evaporate deposition, oxidative weathering of pyrite-containing rocks, and dissolution of evaporites becoming important processes. One of the outcomes was a built up of sulfate in the oceans that allowed microbial sulfate reduction to emerge as an important process. It is thought that the flux of sulfate removal from the ocean through microbial sulfate reduction has grown with the increased atmospheric sulfur deposited in the ocean as a result of human activity. Adoption of new mitigation technologies is likely to reduce the anthropogenic emissions of sulfur.

References

Berner EK, Berner RA (1996) Global Environment. Prentice-Hall, Upper Saddle River

Brimblecombe P (2014) 10.14 – the global sulfur cycle A2. In: Holland HD, Turekian KK (eds) Treatise on geochemistry, 2nd edn. Elsevier, Oxford, pp 559–591

Johnston DT (2011) Multiple sulfur isotopes and the evolution of Earth's surface sulfur cycle. Earth Sci Rev 106:161–183

Jones MT, Jerram DA, Svensen HH, Grove C (2016) The effects of large igneous provinces on the global carbon and Sulphur cycles. Palaeogeogr Palaeoclimatol Palaeoecol 441:4–21

Klimont Z, Smith SJ, Cofala J (2013) The last decade of global anthropogenic sulfur dioxide. Environ Res Lett 8

Rickard D (2012) The evolution of the sedimentary sulfur cycle, sulfidic sediments and sedimentary rocks. Elsevier, Amsterdam, pp 685–766

Schoonen MAA (2004) Mechanisms of sedimentary pyrite formation. In: Amend JP, Edwards KJ, Lyons TW (eds) Sulfur biogeochemistry – past and present. Boulder, Geological Society of America, pp 117–134

Sievert SM, Kiene RP, Schulz-Vogt HN (2007) The sulfur cycle. Oceanography 20:117–123

Staudt WJ, Schoonen MAA (1995) Sulfate incorporation into sedimentary carbonates. In: Vairavamurthy MA, Schoonen MAA (eds) Geochemical transformations of sedimentary sulfur. American Chemical Society, Washington DC, pp 332–345

Tostevin R, Turchyn AV, Farquhar J, Johnston DT, Eldridge DL, Bishop JKB, McIlvin M (2014) Multiple sulfur isotope constraints on the modern sulfur cycle. Earth Planet Sci Lett 396:14–21

Sulfur Isotopes

James Farquhar
Department of Geology and Earth System Science Interdisciplinary Center, University of Maryland, College Park, MD, USA

Isotope Data
Symbols: ^{32}S, ^{33}S, ^{34}S, ^{35}S, ^{36}S
Atomic Number: 16
Isotopic Masses:
^{32}S (31.97207100 (15)),
^{33}S (32.97145876 (15)),
^{34}S (33.96786690 (12)),
^{35}S (34.96903216 (11)),
^{36}S (35.96708076 (20))

Isotopes and Abundances:

^{32}S (0.9441–0.9529),
^{33}S (0.00729–0.00797),
^{34}S (0.0396–0.0477),
^{35}S (radioactive t ½ = 87 days),
^{36}S (0.000129–0.000187)

Standardization: V-CDT
Abundances of Isotopes of the V-CDT standardization†
^{32}S (0.950395),
^{33}S (0.007487),
^{34}S (0.041719),
^{36}S (0.000146)

†Calculated from Ding et al. (2001) using IAEA-S1 in combination with measurements from Antonelli et al. (2014) for ^{33}S and ^{36}S. (Audi et al. 2003)

Introduction

Sulfur has one relatively long-lived cosmogenic isotope ^{35}S and four stable isotopes ^{32}S (95.018%), ^{33}S (0.75%), ^{34}S (4.215%), and ^{36}S (0.017%) that have proven valuable for geochemistry. The cosmogenic isotope, ^{35}S, has a half-life of 87 days and is used as an atmospheric tracer, principally of stratospheric air masses and as a radiolabel for studies of sulfate reduction rates (Howarth and Jørgensen 1984). The four stable isotopes are used to study a wide variety of geochemical processes that extend from the atmosphere to the solid Earth, and from the present-day to time when Earth formed.

Notation

Several types of notation are used to describe variation of S isotope ratios (R): ^{34}R ($^{34}S/^{32}S$), ^{33}R ($^{33}S/^{32}S$), and ^{36}R ($^{36}S/^{32}S$). The most commonly used notation is the lower case delta notation for $^{34}S/^{32}S$:

$$\delta^{34}S = \left(^{34}R_a/^{34}R_{ref} - 1\right) \times 1000$$

which describes the deviation of a ratio of sample (a) relative to a reference (ref), and is expressed at the level of permille (‰) and normalization on the V-CDT scale using IAEA reference materials. V-CDT (Vienna Canyon Diablo Troilite) is an inferred composition for meteoritic sulfur (originally calibrated using a single troilite nodule of the Canyon Diablo meteorite) that is calibrated relative to International Atomic Energy Agency standards.

The second type of notation is the upper case delta notation to describe deviations of the $^{33}S/^{32}S$:

$$\Delta^{33}S = {}^{33}R_a/^{33}R_{ref} - \left(^{34}R_a/^{34}R_{ref}\right)^{0.515},$$

and $^{36}S/^{32}S$:

$$\Delta^{36}S = {}^{36}R_a/^{36}R_{ref} - \left(^{34}R_a/^{34}R_{ref}\right)^{1.90},$$

ratios from a composition on a reference mass fractionation array with the same $\delta^{34}S$. The exponents (0.515 and 1.90) are an approximation of low temperature chemically produced, mass-dependent isotopic fractionations. Thus the upper case delta values quantify mass-independent fractionations. Figure 1 presents mass-independent data (red) and mass-dependent data (blue) on plots of $\delta^{34}S$ versus $\delta^{34}S$ (lower case delta) and $\Delta^{34}S$ versus $\delta^{34}S$ (upper case delta).

Using the delta and capital delta notation ($\delta^{34}S$, $\Delta^{33}S$, and $\Delta^{36}S$), geochemists have been able to gain important insights into processes associated with temperature-dependent equilibrium isotope fractionations, kinetic isotope fractionation (all described below) that occur with ground state and excited state species, and to trace material transferred between different geochemical and mineralogic reservoirs.

Standards

Various standards have been used for measurement of sulfur isotopes. The original standard material was a single troilite nodule from the Canyon Diablo IAB iron meteorite (see entry on ▶ Iron Meteorites) that is archived at the USNM (museum of Natural History of the Smithsonian Institution). Because this material is limited and because of concerns about its

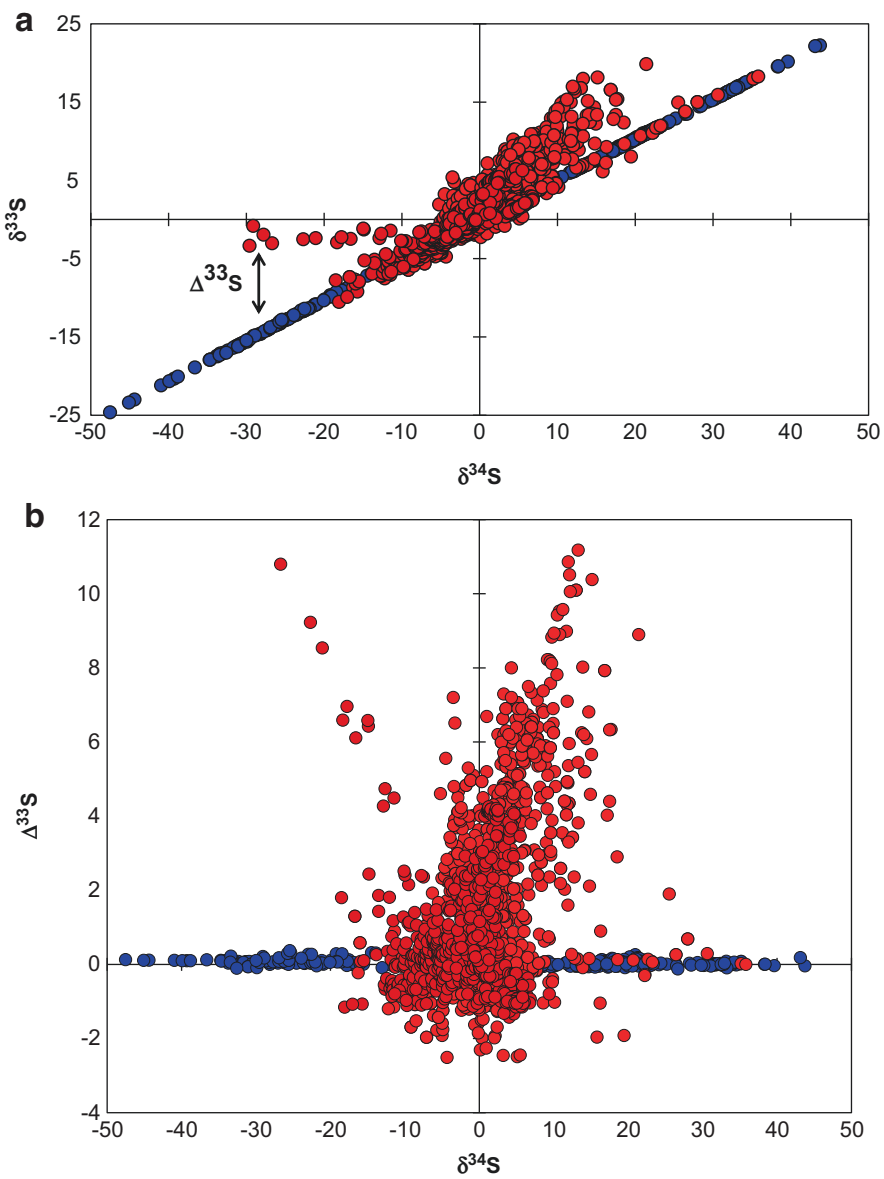

Sulfur Isotopes, Fig. 1 Plots illustrating mass-dependent data (blue) and mass-independent data (red) for lower case delta (top) and upper case delta (bottom)

homogeneity, a secondary scale was devised (the V-CDT scale) that calibrated a composition of the troilite relative to a prepared reference material IAEA S-1 (silver sulfide) that was demonstrated to be homogeneous (Robinson 1995). These standards have also been used to normalize $\Delta^{33}S$ and $\Delta^{36}S$, but further work is still needed to refine and anchor these calibrations relative to CDT and other meteoritic reference frames.

Methods of Measurement

Various strategies have been employed for measurement of sulfur isotopes, gas source isotope ratio mass spectrometry (GS-MS), ICP-MCMS (inductively coupled plasma source, multicollection mass spectrometry), TIMS (thermal ionization mass spectrometry), SIMS (Secondary Ionization Mass Spectrometry), and spectroscopic techniques.

The most commonly used approach is gas source isotope ratio mass spectrometry with either sulfur dioxide or sulfur hexafluoride as the analyte gas (Mayer and Krouse 2004; Böttcher and Schnetger 2004). The advantage of sulfur dioxide techniques is the rapidity with which the samples can be analyzed in when produced and carried by a helium carrier. The advantage of sulfur hexafluoride techniques is the lack of isobaric interferences which allow for measurements of all four stable sulfur isotopes at high precision.

ICPMS techniques have recently shown considerable promise for measurement of three of the four isotopes ^{32}S, ^{33}S, and ^{36}S for samples in solution and gas at very low abundance levels (Paris et al. 2013).

TIMS techniques also allow for $\delta^{34}S$ of small samples to be analyzed at high precision using double spike techniques. Secondary Ion Mass Spectrometry allows for in situ measurements to be undertaken on all four sulfur isotopes at a resolution of several 10s to less than 0.1 micron at lower precision.

Spectroscopic techniques have been used for remote monitoring of atmospheric and telescopic determination of isotope ratios, and methods based on spectroscopy (e.g., Christensen et al. 2007) are likely to become part of the standard tool kit for isotope geochemists as methods based on laser spectroscopy techniques are developed and refined. Since sulfur is not usually present in the form that is used for analysis, various extraction techniques are required for its extraction, purification, and chemical preparation for analysis by most of these techniques.

Mass Dependence: A distinguishing feature of isotope effects that occur for ground state species and for equilibrium isotope exchange is strong dependence of the magnitude of the produced isotope fractionation (the isotope effect) on the mass difference between isotopes being exchanged. Thus, if there is a fractionation of 50 permille for $\delta^{34}S$, which arises because of the partition coefficients for isotopic species containing ^{34}S and ^{32}S, the fractionations for species containing ^{33}S and ^{36}S will have associated shifts approximately half and twice this magnitude because the mass difference between ^{33}S and ^{32}S is approximately half that between ^{34}S and ^{32}S, and the mass difference between ^{36}S and ^{32}S is approximately twice that between ^{34}S and ^{32}S. The exact relationship is very close to that described by the reference array used to in the $\Delta^{33}S$ and $\Delta^{36}S$, and the $\Delta^{33}S$ and $\Delta^{36}S$ will both have values very close to zero. Small deviations in these values can be produced by mixing and fractionation of sulfur with different $\delta^{34}S$, and this is seen in many metabolic and biogeochemical reaction networks.

Equilibrium isotope partitioning of sulfur isotopes among mineral phases and/or aqueous phase and gas phase species is related to the way that vibrational and in the cases of gases translational and rotational energy is partitioned among various isotopic sulfur-containing substances and are determined using experimental techniques to directly measure isotope fractionations, or more recently, using theoretical (ab initio) techniques to calculate partition functions for substances (e.g., Eldridge et al. 2016). Finally, constraints can be obtained by making inferences from observations (empirical calibrations).

Ab initio calculations also allow for determinations of the isotopic partitioning characteristics of species that are not physically separable, but that need to be considered to interpret isotopic fractionations in systems at equilibrium. An example of this is given by Eldridge et al. (2016) for the bisulfite system. In this study, the isotopic partition coefficients of inseparable two bisulfite isomers were determined using ab initio techniques and then weighted using independent constraints on their isomerization coefficients to explain the partitioning of bulk bisulfite in solution as well as its unusual temperature dependence.

Chemical kinetic isotope effects (KIE) involving ground state and transition states also produce mass-dependent isotope effects. These KIE are elementary effects that are produced by unidirectional reactions and result from differences in the rates of reaction for different isotopic species. In cases where this partitioning is the primary determinant of reaction rate, the KIE for systems with more than two isotopes will yield rates that scale with mass, and thus with the mass difference (Δm) between the substituted isotopes in the reacting species. Thus the effect will reflect how the transition state (TS) is populated, and this is mass dependent.

While reaction rates and KIE are relevant for understanding the total sulfur isotopic fractionation produced by a single organism metabolizing sulfur, which has been referred to by geochemists as "vital" effects, the two constructs, KIE and vital effects, are distinct. Such vital isotope effects for sulfur can be produced by a combination of EIE and KIE that are part of the total metabolism, but KIE refer to a distinctly chemical isotope effect that is produced by differences in the rates of reaction for isotopic species. There are also differences in energy for the different sulfur isotope species involved in KIE because part of the basis for the rate control is population of the TS, which depends on quantized energy levels in the TS and the reactant state.

Mass Independence: Larger variations for $\Delta^{33}S$ and $\Delta^{36}S$ can be seen when factors in addition to the mass difference between the isotopes of sulfur contribute to the isotope of fact. The most common situation where these factors come into play is for excited state reaction kinetics, where selection factors can depend on factors other than mass, or on factors that do not scale linearly with mass.

These mass-independent isotope effects are thus most common in gas phase reactions such as those seen in photochemistry and are thus relevant for distinguishing geochemical signatures produced by atmospheric processes from those produced in condensed phase where ground state chemistry prevails.

In some kinetic isotope reactions other factors that come into play and exert an additional control on reaction rates for different isotopic sulfur species yield relationships that deviate considerably from the Δm relationships. In these cases, the effects are often referred to as mass-independent and significant nonzero $\Delta^{33}S$ and $\Delta^{36}S$ can be produced. Such additional factors can include resonance coupling between electron and nuclear spin that permit different rates of reaction (Magnetic Isotope effects – MIE) (Oduro et al. 2011), differences in the density of states that are related to the symmetry of isotopic molecules, and differences in coupling between states (Franck-Condon Factors) for isotopic molecules (Zmolek et al. 1999).

In addition to the possibility of equilibrium isotope effects, kinetic isotope effects, and various physical processes that can cause isotopic fractionation, there are also characteristic signatures relevant to interpretation of sulfur isotopes that are produced when sulfur with two different compositions is mixed or when sulfur isotopes are involved in a process that preferentially removed from a mixture (isotopic distillation).

When mixing involves pools with very different isotopic compositions, the change in isotopic composition for all four isotopes reflects the proportions of material added (or removed) and these changes scale linearly with the amount of material transferred.

In cases where the mixing is associated with a mass-dependent process (equilibrium isotope effects or KIE) the isotopic compositions of the endmembers are related by an exponential relationship, so a small deviation for mixing is seen for $\Delta^{33}S$ and $\Delta^{36}S$. This has been referred to as a mass conservation effect and has been used as a tool to study biological and biogeochemical systems (Ono et al. 2006). Mixing of isotopic pools also provides opportunities for using sulfur isotopes to trace addition of unrelated materials because of the significant magnitude of sulfur isotope compositions that is observed among different types of geological materials.

Thus, processes that mix sulfur of different isotopic compositions ($\delta^{34}S$, $\Delta^{33}S$, and $\Delta^{36}S$) can be unraveled with information about compositions or amounts of materials mixed. These different responses of $\delta^{34}S$, $\Delta^{33}S$, and $\Delta^{36}S$ to different types of processes provide a variety of different types of ways to apply sulfur isotopes in geochemistry. In the following, a few of the key applications and findings made using sulfur isotopes are described.

Geochemical Records

Atmospheric: Studies of sulfur isotopes in the atmosphere indicate that sulfur is introduced to the atmosphere by geological processes associated for the most part with volcanism, by biological activity of microbial and higher forms of life, and from anthropogenic sources such as coal and hydrocarbon combustion, steel smelting and mineral processing, as well as waste treatment.

While the amount of sulfur in the atmosphere is minor compared to that of oxygen or nitrogen, its chemistry allows it to play potentially important roles as a factor controlling rainwater pH, with aerosols that may act as cloud condensation nuclei and influence Earth's radiation balance and climate, and compounds that can be toxic and in some cases have negative health impacts. For these reasons, isotopic techniques that can be used to track its origin have been of widespread interest.

The contribution of sulfur as sulfur dioxide (SO_2) via combustion can be monitored by the isotopic composition of sulfur from combustion sources which can span a wide range of $\delta^{34}S$ values, but commonly centers on $\delta^{34}S$ values of 0–5‰. Mukai et al. (2001) demonstrated that the isotopic composition of atmospheric sulfate aerosols in China are closely correlated with the isotopic compositions of regional coal indicating a strong connection. Understanding these contributions is important because of the role played in acidification of rain resulting from the atmospheric oxidation product S(VI) [S^{6+}] reacting with atmospheric water to form sulfuric acid by reactions like

$$SO_3 + H_2O = H_2SO_4.$$

Studies of isotopic signatures of rainwater and lake water sulfate led to the suggestion that acid rain led to significant lowering of pH in lakes in the coal burning regions of North America in the late twentieth century (e.g., Caron et al. 1986). These isotope studies and others combined with other geochemical data provided critical information into a process that negatively impacted agriculture as well as higher animals including fish like trout, leading to key regulations in North America and Europe that have significantly addressed the problem.

While regulations that reduce emissions of sulfur dioxide by burning of low sulfur coal and scrubbing sulfur gases from power plant emissions in North America and Europe have had a profound effect and reversed the damages that were being seen, in other parts of the world (e.g., parts of Asia) acid rain and snow are still seen downwind of industrial activity that generate sulfur-bearing gases like sulfur dioxide. Isotopic studies continue to be used to trace the origin of this sulfur (Mukai et al. 2001).

Formation of atmospheric sulfate via natural processes from oxidation of volatile biogenic sulfur species such as dimethylsulfide (DMS – CH_3-S-CH_3) carries a more ^{34}S enriched composition with $\delta^{34}S$ values of ~18–20‰ (Patris et al. 2000; Oduro et al. 2012; Amrani et al. 2013). DMS and other methylated sulfur compounds are present at trace levels in oceanic air and contribute to the "smell" we perceive when near the ocean. The biological origin of DMS makes it potentially a forcing agent for climate that also responds to prevailing climate conditions. It has been suggested that DMS production and chemistry also play a role in climate regulation as cloud condensation nuclei, and participate in a feedback loop known as the CLAW hypothesis (Charlson et al. 1987) where biogenic oceanic DMS emission fluxes respond to, and indirectly control, insolation that is in turn controlled by cloud cover and cloud condensation nuclei (CCN) that are produced as a result of chemistry involving DMS and its oxidation products.

Other types of climate impacts of sulfur have been documented using sulfur isotopes both $\delta^{34}S$ and $\Delta^{33}S$

(Savarino et al. 2003; Baroni et al. 2007) for injections of sulfur dioxide (SO_2) by large volcanic eruptions into the stratosphere where it is oxidized to form a high-altitude layer of sulfate aerosols. These high-altitude aerosols impact Earth's radiation balance and lead to cooling such as in the year following the Pinatubo eruption or for the year without summer in 1816 which is attributed to eruption of the Indonesian volcano Tambora. The unique chemistry of photochemical oxidation to form sulfate in the stratosphere produces an anomalous signature for sulfur isotopes that evolves over the course of the deposition cycle to the ice, leaving behind a clear signal that can be used to identify evidence of these events in ice core records.

A challenge of atmospheric applications of sulfur isotopes is partitioning the contributions from various sources. Other information used for source partitioning can include additional constraints from other isotopic systems ($\Delta^{33}S$, $\Delta^{36}S$, and ^{35}S for sulfur and $\delta^{18}O$ and $\Delta^{17}O$ for oxygen in sulfate) as well as the amount (concentration) of aerosols. Constraints from $\Delta^{33}S$, $\Delta^{36}S$, ^{35}S, and $\Delta^{17}O$ are used to track atmospheric chemistry as well as contributions from stratospheric air. $\Delta^{33}S$ and $\Delta^{36}S$ provide insight into photochemical oxidation and $\Delta^{17}O$ provides constraints on the oxidation pathways. So far, isotopic compositions (principally $\delta^{34}S$ and $\delta^{18}O$) of atmospheric aerosols, of sulfate in rainwater, and of sulfate in ice cores and snow have been used to evaluate the relative importance of various biogenic, anthropogenic, and geological sources of atmospheric sulfur. The present, understanding of atmospheric chemistry and dynamics is informing understanding of isotopic measurements of $\Delta^{33}S$, $\Delta^{36}S$, $\Delta^{35}S$, and $\Delta^{17}O$. The challenge for future sulfur isotope studies will be to reverse this flow of information by developing ways to use this isotopic information to inform chemical and dynamical aspects of the atmosphere.

The deep time geological and meteorite records also preserve information about atmospheric sulfur. Signatures are seen for both $\Delta^{33}S$ and $\Delta^{36}S$ in the Archean and earliest Proterozoic (Farquhar et al. 2000). These signatures are attributed to photochemical reactions involving atmospheric sulfur compounds in a low oxygen, low ozone atmosphere that was largely transparent to the ultraviolet wavelengths needed to drive mass-independent reactions and conducive for the transfer of this signature to the rock record (Ono 2017).

A record of mass-independent sulfur is widespread in sedimentary successions from prior to about 2.4 billion years ago and the disappearance of a mass-independent signature from the sedimentary record is taken as indicative of the onset of an oxygenated atmosphere. Figure 2 illustrates this striking transition from a geological regime characterized by mass-independent sulfur preserved in the rock record prior to ~2.4 Ga, to a regime characterized by mass-dependent sulfur since ~2.4 Ga.

Oceanic: Studies of the isotopic composition of sulfur in sedimentary and water column environments have been used to reconstruct biological and abiological processes involved in the reduction and oxidation of sulfur compounds in the present-day as well as in ancient oceans.

The isotope fractionation imparted by bacteria and archaea that reduce sulfate to sulfide is enriched in light isotopes and imparts a complementary positive $\delta^{34}S$ (light isotope depletion) to oceanic sulfate. This sulfate, due to its long residence time, has a relatively homogeneous composition at $\delta^{34}S \approx 21‰$. Because the residence time of this sulfate is longer than the residence time of seawater, leading to a homogenous $\delta^{34}S$ value and an enhancement of sulfate

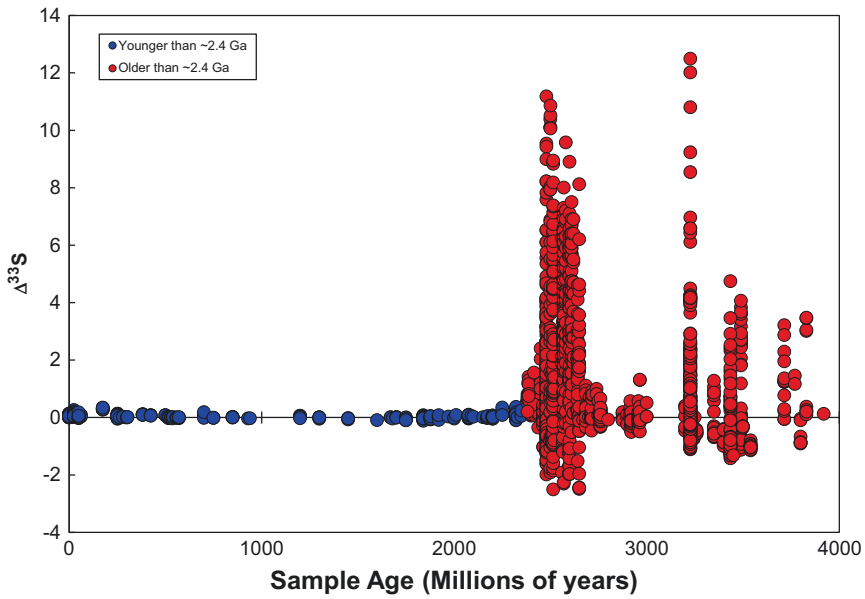

Sulfur Isotopes, Fig. 2 Plot of $\Delta^{33}S$ versus sample age, illustrating the change from a period prior to 2.4 Ga. (red symbols) when mass-independent sulfur was preserved in the geologic record to a period since 2.4 Ga (blue symbols), when mass independent signatures are not seen

concentrations over that of its sources, this has provided a tool to study the sulfur cycle in Earth's ancient oceans.

The principal source of sulfate to the oceans is and has been from the continents and includes a combination of remobilized evaporite sulfate and sulfate produced by oxidation of sulfide minerals. A secondary source is from mid-ocean ridge and back arc hydrothermal activity. These sources, in combination with sulfide sinks, maintain oceanic sulfate concentrations near 28 millimolar and with compositions that are stable over long periods of time.

The isotopic composition of oceanic sulfate has been shown using highly precise marine barite records to have possessed $\delta^{34}S$ values of ~20–21‰ through much of the Cenozoic (Paytan et al. 1998). Work by Claypool et al. (1980) had previously demonstrated swings of oceanic $\delta^{34}S$ to more positive and negative values in earlier parts of the Phanerozoic reflecting different proportions of sulfide burial and possibly variations in the magnitude of the isotope fractionation associated with buried pyrite.

The primary sulfide sink is sedimentary sulfide (iron sulfides like pyrite and organic sulfur compounds). Reduction of sulfate to sulfide that leads to the sedimentary sulfide sink is carried out by prokaryotic sulfate reducing bacteria that use S (VI) from sulfate as an electron acceptor and organic carbon as an electron donor. A significant amount of this sulfide is reoxidized, returning sulfate to the oceans and allowing these organisms to oxidize a significant amount of organic matter while producing a sink of mineralized sulfide that maintains a high sulfate concentration.

The proportion of sulfide reoxidized is intricately linked to the isotopic fractionation that is expressed between buried pyrite and oceanic sulfate. Wu et al. (2010) have shown that the $\Delta^{33}S$ of Phanerozoic sulfate also varies with time, but at a much lower level than that seen for mass-independent signatures of the early Proterozoic and Archean. These low level variations have been used in combination with a model to constrain the $\delta^{34}S$ evolution of buried pyrite and the role of sulfide oxidation (but see Leavitt et al. 2013, for an interpretation that also invokes a concomitant biological response). The work by Wu et al. (2010) suggests that larger fractionations (variation of $\delta^{34}S$ of about 40‰) prevailed for the past 250 million years and smaller fractionations ($\Delta^{34}S$ of about 30‰) for the earlier Phanerozoic.

Sulfide can also play a role in local environments. In some atypical cases where sulfide accumulates in the water column, such as in the Black Sea or in basins like the Cariaco Basin, its isotopic composition usually varies with depth and has very negative $\delta^{34}S$, sometimes as negative as −40‰. In sediments, the situation is different; as sulfate in porewater is consumed, the isotopic composition of porewater sulfate evolves to more positive $\delta^{34}S$. The ^{34}S enrichment typically increases deeper in the sediment. Likewise the isotopic composition of sulfide changes with depth from a more negative $\delta^{34}S$ higher closer to the sediment-water interface and a less negative $\delta^{34}S$ deeper in the sediment.

Factors that influence the isotopic profiles of porewater sulfate and sedimentary sulfide include the rate of porewater-seawater exchange, the role of secondary reactions (oxidation (sulfide to sulfur intermediate or sulfate) or disproportionation, a fermentative metabolism where sulfur intermediates are decomposed into sulfide and sulfate), and mass transfer of sulfate and sulfide in the system.

Sulfur isotope studies have also been conducted on water-column organic sulfur compounds like dimethylsulfide which exhibits a positive $\delta^{34}S$ in the range of 18–21‰ (Amrani et al. 2013) which is similar to oceanic sulfate and points to a connection between oceanic sulfate and the metabolic pathways responsible for production of DMS precursors.

DMS is relevant as a biogenic sulfur-bearing gas that is emitted to the atmosphere and knowledge of its isotopic composition and variability of the isotopic composition is used as one of the knowns in reconstruction of atmospheric sources (source partitioning).

Solid Earth: Sulfur is present in Earth's crust, mantle, and core. In Earth's crust, the affinity of sulfur and metals for each other makes sulfide deposits such as Volcanogenic Massive Sulfide (VMS) deposits sources of elements such as copper, zinc, lead, gold, and silver.

Sulfides are also found in high abundance in some sedimentary rocks like black shales and some coals. The characteristic positive $\delta^{34}S$ of oceanic sulfate and negative $\delta^{34}S$ of sedimentary sulfide compared to the near zero $\delta^{34}S$ of juvenile terrestrial sulfur has made it possible to track sources of sulfur in the solid Earth.

Likewise, the occurrence of mass-independent sulfur Isotopic signatures in Earth's earliest sediments provides a way to trace their contributions to solid-Earth reservoirs. Labidi et al. (2013) demonstrate evidence for such recycling, and for a more subtle sulfur isotope fractionation effect associated with core formation (^{34}S depletion in mantle sulfur) using relationships between Sr isotopes and $\delta^{34}S$ of mid-ocean ridge sulfur.

Similarly, Cabral et al. (2013) and Delavault et al. (2016) report anomalies for $\Delta^{33}S$ in oceanic island basalts that implicate recycling of ancient crustal sulfur to reservoirs in the deep mantle that are sourced by ocean island basalts. They suggest that the observation of isotopic signatures for $\Delta^{33}S$ in some ocean island basalts and diamonds has been interpreted to indicate recycling of ancient surface-derived sulfur with mass-independent characteristics (Cabral et al. 2013).

Another place where anomalous $\Delta^{33}S$ has been observed is in Martian meteorites. These meteorites preserve evidence of weathering on Mars, and the signatures have been interpreted to indicate that the sulfur present in these meteorites possesses a component indicative of atmospheric (photochemical)

oxidation. Like for terrestrial samples, this signature has also been traced to sulfide phases and indicates uptake of a sulfur-bearing component on emplacement or assimilated by the parent melts on their way to the place where they were emplaced (Franz et al. 2014).

Equilibrium isotope fractionations for sulfur isotopes are large because of significant differences in the bonding environments for sulfate minerals compared to sulfide minerals. It is possible to extract information about temperature from isotopic fractionations between sulfur-bearing minerals because partitioning of isotopes is temperature dependent and in some cases this is done. Complexity in the application of isotopic thermometers arises when minerals do not attain isotopic equilibrium or when the isotopic composition of one or more mineral used to obtain a temperature is disturbed.

It is also not uncommon for sulfide minerals and sulfate to exhibit disequilibrium because of different temperatures of formation and slow exchange of sulfur between sulfate and sulfide; it is, however, possible to extract information about disequilibrium and to gain insight into the histories different mineral phases.

The significant range of observed variation for $\delta^{34}S$ and $\Delta^{33}S$ observed in the rock record has thus made it a valuable tracer of sulfur sources, leading to a wide variety of applications of sulfur isotopes in the study of crustal rocks, and particularly in hydrothermal and ore-bearing systems.

Summary

Sulfur has four stable isotopes and is standardized relative to the V-CDT scale and measured by a number of different geochemical techniques, but predominantly by Isotope Ratio Mass Spectrometry. Sulfur isotope variations include both mass-dependent and mass-independent isotopic signatures. Mass-dependent isotopic signatures are produced by equilibrium processes and a host of processes that occur in gas, liquid, and gas phase. Mass-independent isotopic signatures are principally produced by gas phase chemistry involving excited state species and are used to trace atmospheric processes. One of the significant atmospheric signals that sulfur isotopes have been used to trace is related to the evolution of Earth's atmosphere and marks the appearance of oxygen in Earth's atmosphere. In this case, mass-independent signatures were produced and transferred to the rock record when the atmosphere had low (sub ppm) levels of oxygen and then was not transferred when oxygen levels rose above this threshold. The rich isotopic chemistry of sulfur also makes its isotopic characterization useful for study of other systems such as (i) to trace biological activity of sulfate reducers in Earth's oceans and in other environments where these organisms live, (ii) in solid earth systems where sulfur isotopes are fractionated between sulfur-bearing phases, and (iii) in cases where isotopic signatures are used as tracers of subducted surface materials.

Cross-References

- Acid Deposition
- Atmospheric Evolution
- Earth's Atmosphere
- Earth's Core
- Formation and Evolution of the Earth
- Gas Source Mass Spectrometry (GS-MS)
- Hydrothermal Alteration
- Inductively Coupled Plasma Mass Spectrometry (ICP-MS)
- Ion Microprobe
- Iron Meteorites
- Kinetics of Geochemical Processes
- Meteorites
- Ocean Salinity, Major Elements, and Thermohaline Circulation
- Oceanic Island Basalts
- Oxygen Isotopes
- Ozone and Stratospheric Chemistry
- Precambrian Geochemistry
- Stable Isotope Geochemistry
- Sulfide Minerals
- Sulfur
- Thermal Ionization Mass Spectrometry

References

Amrani A, Said-Ahmad W, Shaked Y, Kiene RP (2013) Sulfur isotope homogeneity of oceanic DMSP and DMS. Proc Natl Acad Sci 110(46):18413–18418

Antonelli MA, Kim ST, Peters M, Labidi J, Cartigny P, Walker RJ, Lyons JR, Hoek J, Farquhar J (2014) Early inner solar system origin for anomalous sulfur isotopes in differentiated protoplanets. Proc Natl Acad Sci 111(50):17749–17754

Audi G, Wapstra AH, Thibault C (2003) The AME 2003 atomic mass evaluation:(II). Tables, graphs and references. Nucl Phys A 729(1):337–676

Baroni M, Thiemens MH, Delmas RJ, Savarino J (2007) Mass-independent sulfur isotopic compositions in stratospheric volcanic eruptions. Science 315(5808):84–87

Böttcher ME, Schnetger B (2004) Direct measurement of the content and isotopic composition of sulfur in black shales by means of combustion-isotope-ratio-monitoring mass spectrometry, Ch 27. In: De Groot PA (ed) Handbook of stable isotope analytical techniques, vol 1. Elsevier, Amsterdam, pp 597–603

Cabral RA, Jackson MG, Rose-Koga EF, Koga KT, Whitehouse MJ, Antonelli MA, Farquhar J, Day JM, Hauri EH (2013) Anomalous sulphur isotopes in plume lavas reveal deep mantle storage of Archaean crust. Nature 496(7446):490

Caron F, Tessier A, Kramer JR, Schwarcz HP, Rees CE (1986) Sulfur and oxygen isotopes of sulfate in precipitation and lakewater, Quebec, Canada. Appl Geochem 1(5):601–606

Charlson RJ, Lovelock JE, Andreaei MO, Warren SG (1987) Oceanic phytoplankton, atmospheric sulphur, cloud. Nature 326(6114):655–661
Christensen LE, Brunner B, Truong KN, Mielke RE, Webster CR, Coleman M (2007) Measurement of sulfur isotope compositions by tunable laser spectroscopy of SO_2. Anal Chem 79(24):9261–9268
Claypool GE, Holser WT, Kaplan IR, Sakai H, Zak I (1980) The age curves of sulfur and oxygen isotopes in marine sulfate and their mutual interpretation. Chem Geol 28:199–260
Delavault H, Chauvel C, Thomassot E, Devey CW, Dazas B (2016) Sulfur and lead isotopic evidence of relic Archean sediments in the Pitcairn mantle plume. Proc Natl Acad Sci 113(46): 12952–12956
Ding T, Valkiers S, Kipphardt H, De Bievre P, Taylor PDP, Gonfiantini R, Krouse R (2001) Calibrated sulfur isotope abundance ratios of three IAEA sulfur isotope reference materials and V-CDT with a reassessment of the atomic weight of sulfur. Geochim Cosmochim Acta 65(15):2433–2437
Eldridge DL, Guo W, Farquhar J (2016) Theoretical estimates of equilibrium sulfur isotope effects in aqueous sulfur systems: highlighting the role of isomers in the sulfite and sulfoxylate systems. Geochim Cosmochim Acta 195:171–200
Farquhar J, Bao H, Thiemens M (2000) Atmospheric influence of Earth's earliest sulfur cycle. Science 289(5480):756–758
Franz HB, Kim ST, Farquhar J, Day JM, Economos RC, McKeegan KD, Schmitt AK, Irving AJ, Hoek J, Dottin III J (2014) Isotopic links between atmospheric chemistry and the deep sulphur cycle on Mars. Nature 508(7496):364–368
Howarth RW, Jørgensen BB (1984) Formation of 35S-labelled elemental sulfur and pyrite in coastal marine sediments (Limfjorden and Kysing Fjord, Denmark) during short-term 35SO42− reduction measurements. Geochim Cosmochim Acta 48(9):1807–1818
Labidi J, Cartigny P, Moreira M (2013) Non-chondritic sulphur isotope composition of the terrestrial mantle. Nature 501(7466):208
Mayer B, Krouse HR (2004) Procedures for sulfur isotope abundance studies, Ch. 26. In: De Groot PA (ed) Handbook of stable isotope analytical techniques, vol 1. Elsevier, Amsterdam, pp 538–596
Mukai H, Tanaka A, Fujii T, Zeng Y, Hong Y, Tang J, Guo S, Xue H, Sun Z, Zhou J, Xue D (2001) Regional characteristics of sulfur and lead isotope ratios in the atmosphere at several Chinese urban sites. Environ Sci Technol 35(6):1064–1071
Oduro H, Harms B, Sintim HO, Kaufman AJ, Cody G, Farquhar J (2011) Evidence of magnetic isotope effects during thermochemical sulfate reduction. Proc Natl Acad Sci 108(43):17635–17638
Oduro H, Van Alstyne KL, Farquhar J (2012) Sulfur isotope variability of oceanic DMSP generation and its contributions to marine biogenic sulfur emissions. Proc Natl Acad Sci 109(23):9012–9016
Ono S, Wing B, Johnston D, Farquhar J, Rumble D (2006) Mass-dependent fractionation of quadruple stable sulfur isotope system as a new tracer of sulfur biogeochemical cycles. Geochimica et Cosmochimica Acta 70(9):2238–2252
Ono S (2017) Photochemistry of sulfur dioxide and the origin of mass-independent isotope fractionation in Earth's atmosphere. Annu Rev Earth Planet Sci 45(1):301
Paris G, Sessions AL, Subhas AV, Adkins JF (2013) MC-ICP-MS measurement of δ 34 S andΔ 33 S in small amounts of dissolved sulfate. Chem Geol 345:50–61
Patris N, Delmas RJ, Jouzel J (2000) Isotopic signatures of sulfur in shallow Antarctic ice cores. J Geophys Res Atmos 105(D6):7071–7078
Paytan A, Kastner M, Campbell D, Thiemens MH (1998) Sulfur isotopic composition of Cenozoic seawater sulfate. Science 282(5393):1459–1462
Robinson BW (1995) Sulphur isotope standards. Int Atomic Energy Agency TECDOC 825:39–45
Savarino J, Romero A, Cole-Dai J, Bekki S, Thiemens MH (2003) UV induced mass-independent sulfur isotope fractionation in stratospheric volcanic sulfate. Geophys Res Lett 30(21):11
Wu N, Farquhar J, Strauss H, Kim ST, Canfield DE (2010) Evaluating the S-isotope fractionation associated with Phanerozoic pyrite burial. Geochim Cosmochim Acta 74(7):2053–2071
Zmolek P, Xu X, Jackson T, Thiemens MH, Trogler WC (1999) Large mass independent sulfur isotope fractionations during the photopolymerization of 12CS2 and 13CS2. Chem A Eur J 103(15):2477–2480

Supergene

Martin Reich
Department of Geology and Andean Geothermal Center of Excellence (CEGA), FCFM, Universidad de Chile, Santiago, Chile

Definition

The term *supergene* is used to describe processes and products that are the result of near-surface alteration and modification of originally deeply formed rocks. It is in the *critical zone* – the Earth's contact zone where air, water, biota, organic matter, and minerals interact – where combinations of geological, chemical, physical, and biological processes operate together on preexisting minerals so as to adjust to the new environmental conditions (average $T_{atm} \sim 15$ °C, $P_{atm} \sim 1$ bar, and $pO_2 \sim 0.2$ bar) (Reich and Vasconcelos 2015).

Supergene Processes and Enrichment

Supergene processes are controlled by three basic factors. The first and most important factor is the parent rock (e.g., limestone vs. andesite) and its mineral constituents (e.g., silicates vs. sulfides). The second factor is landscape, which is shaped by hydrological and pedological processes coupled with the geodynamic evolution of the crustal section under consideration. The third factor is climate, reflecting ambient temperature, availability of liquid water (i.e., rainfall intensity and seasonality), evapotranspiration rates, and biological and microbiological activity (Vasconcelos et al. 2015).

Supergene deposits form when recurrent chemical weathering promotes the dissolution, remobilization, and reprecipitation of elements at or near the Earth's surface, creating a chemically stratified weathering profile, which may extend down from a few meters to ~1000 m below the surface. Although the term *supergene* can be used to describe any process or alteration product formed by descending or ascending water at low temperature and pressure (Reich et al. 2009), its most common use relates to supergene oxidation

and enrichment of deeply buried primary (or hypogene) ore bodies that are exposed at or near the Earth's surface.

The phenomenon known as supergene enrichment refers to the secondary, in situ, accumulation of metals as a result of three essential processes: (1) the electrochemical oxidation of primary sulfides, oxides, or native metals (e.g., native copper Cu(0) to Cu(II)), (2) the transport of the released metals as soluble metal species (e.g., $CuSO_4^0$, $AuCl_4^-$), and (3) the reprecipitation of the metals by reduction (e.g., Cu(II) to native copper Cu(0)), by supersaturation (e.g., Mg^{2+} in magnesite deposits), or by cation exchange (e.g., Ni^{2+} exchange for Mg^{2+} in smectite- or serpentine-group minerals) (Reich and Vasconcelos 2015). The resultant highly enriched supergene zone or "blanket" that forms above ore deposits is usually accessible during the early stages of surface mining and contributes significantly to the overall viability of the mine.

The process of supergene enrichment of metals is commonly exemplified by copper (Sillitoe 2005). In most copper ore bodies, the stepwise hydrolysis and oxidation of primary pyrite- and chalcopyrite-bearing assemblages leads to a decrease in the pH of descending groundwaters and the liberation of soluble Cu^{2+} ions and oxidized sulfur as SO_4^{2-} anions. These dissolved species encounter progressively greater reducing conditions deep into the profile. This process is accompanied by "capping," the precipitation of iron oxyhydroxides in the leached zone from which copper is removed. The thickness of the leached cap is highly variable but can reach several hundred meters in porphyry copper deposits, particularly when the water table was deep enough during the supergene oxidation and enrichment phase (Taylor 2011).

Summary

Supergene enrichment may result in a two- to tenfold increase in metal grades for commodities such as Cu, Al, Fe, Ni, Mn, U, Au, and Zn. Supergene deposits, apart from these major metal components, can contain economic or near-economic concentrations of *critical metals* including the rare earth elements (REE), platinum group elements (PGE), Co, Be, V, Ga, In, Ge, Li, and I, making these deposits attractive targets for exploration and exploitation.

Cross-References

- ▶ Copper
- ▶ Chemical Weathering
- ▶ Fluid–Rock Interaction
- ▶ Lanthanide Rare Earths
- ▶ Lithium
- ▶ Ore Deposits
- ▶ Oxidation-Reduction Reactions and Eh-pH (Pourbaix) Diagrams
- ▶ Platinum Group Elements
- ▶ Sulfide Minerals
- ▶ Sulfur
- ▶ Transition Elements

References

Reich M, Vasconcelos P (2015) Geological and economic significance of supergene metal deposits. Elements 11:305–310

Reich M, Palacios C, Vargas G, Luo S, Cameron EM, Leybourne MI, Parada MA, Zuniga A, You CF (2009) Supergene enrichment of copper deposits since the onset of modern hyperaridity in the Atacama Desert, Chile. Mineral Deposita 44:497–504

Sillitoe RH (2005) Supergene oxidized and enriched porphyry copper and related deposits. Econ Geol 100th Anniversary Volume:723–768

Taylor R (2011) Gossans and leached cappings: field assessment. Springer, Berlin, p 146

Vasconcelos P, Reich M, Shuster D (2015) Paleoclimatic signatures of supergene metal deposits. Elements 11:317–322

Surface Geochemistry

Christian Ludwig[1,2] and William H. Casey[3]
[1]Paul Scherrer Institute (PSI), Villigen, Switzerland
[2]École Polytechnique Fédérale de Lausanne (EPFL), Lausanne, Switzerland
[3]Department of Chemistry and Department of Earth and Planetary Sciences, University of California, Davis, CA, USA

Synonyms

Interfacial geochemistry

Definition

The chemistry that occurs at the interface between two phases of matter.

Introduction

> Das Volumen des Festkörpers schuf Gott,
> ihre Oberfläche wurde vom Teufel gemacht. (W. Pauli)

The subject of surface chemistry extends across virtually all fields of the Earth sciences, although most research concerns the surface of a mineral in aqueous solutions because of the recognized importance of soil minerals to environmental

chemistry. One could equally argue that interface chemistry is just as essential to atmospheric chemistry or even oceanography, however, or the myriad other fields within Earth science that don't prominently state an interest in surface chemistry.

The term "surface" is poorly defined. It can refer to the region that is within a single-bond distance from material interface, or can extend over hundreds of nanometers, although one can encounter more restrictive definitions. The chemistry in this region is unique and exerts fundamental control over many geochemical transformations, including phase transformations, rates of diagenesis, and the metal enrichments in ore formation. This chemistry is most commonly approached by coupling simple experiments with sophisticated methods of surface analysis, such as X-ray photoelectron spectroscopy, surface-probe microscopy, and synchrotron methods. X-ray free electron laser (XFEL) methods now allow spectroscopic investigations of ultrafast surface reactions. In addition, some methods that are inherently for bulk analysis, such as XAFS or NMR spectroscopy, can be adapted to study surface processes by clever choice of the experimental conditions, such as the use of unique isotopes.

The Gibbs-Thompson Equation

The incremental energy change to create area from bulk solid is described as a partial derivative of Gibbs energy with respect to surface area:

$$\left[\frac{\partial G}{\partial A}\right]_{T,P,N_i} = \gamma \quad (1)$$

at fixed temperature *(T),* pressure *(P)* and composition *(N)* with a coefficient of proportionality *(γ)* known as the interfacial surface energy (or surface tension). Values of this energy for liquids in contact with their vapors range from 0.01–0.06 J/m^2 for condensed gases to 2 J/m^2 for liquid metals (Adamson 1982). The coefficients depend, of course, on which two phases are in contact at the interface. The change in interfacial energies with composition relate to the surface *excess* concentrations of each component and the chemical potentials of those components via the Gibbs isotherm equation.

For geologists, the surface energy presents a formidable activation barrier to phase changes. New area is created as bubbles or crystals nucleate from a melt and as etches form on a dissolving crystal. Furthermore, the energy derived by reducing the exposed surface area is large relative to changes in bulk energy if the particles are small. Therefore, large mineral particles grow at the expense of small ones and small soap bubbles coalesce in a bath of suds in a process referred to as "Ostwald ripening." Description of the surface chemistry at this scale requires no knowledge of molecular configuration or reaction mechanisms. The opposing contributions of bulk energy and surface energy make the formation of new phases an activated process, with a barrier energy that prevents reaction and must be surmounted. These subjects are treated using classical theories called "BCF" theory after the major authors in the mid-twentieth century (Burton et al. 1949, 1951).

Adsorption/Desorption at Hydrolyzed Surfaces

Description of mineral surfaces in water using Eq. 1 is unwieldy. The interfacial tensions are difficult to measure and sensitive to small changes in solution composition. They also provide no molecular insights.

Molecular interactions control much of the conspicuous surface chemistry of minerals and solid oxides. For example, oxide solids, like many ions, exhibit an amphoteric chemistry and the Brønsted acid-base chemistry of a particular mineral surface is characteristic of its composition and structure. Just as silicic acid ($H_4SiO_4^o$(aq)) is not expected to have an acid-base chemistry that is similar to aluminum ion ($[Al(H_2O)]_6^{3+}$(aq)), so too is the acid base chemistry of solid silica (SiO_2(s)) different than that of corundum (α-Al_2O_3(s)). Silica has a near-neutral surface at near-neutral pH and acidic conditions. At these conditions corundum has a positive charge on its surface from the uptake of protons. Corundum surfaces are neutral at pH $\sim$ 9, meaning that at this pH there is an equal concentration of positively and negatively charged surface sites.

Surface-complexation models emphasize reaction at ionizable functional groups (Boehm 1966). In aqueous solutions these are most commonly hydroxyls, which are abbreviated as: >Me-OH, where Me stands for the surface cation ("Metal") of the mineral surface (Schindler and Stumm 1987). For example, Brønsted reactions can be portrayed:

$$>Si-OH(s) + H_2O(l) = >Si-O^-(s) + H_3O^+(aq) \quad (2)$$

or:

$$>Al-OH(s) + H_2O(l) = >Al-OH_2^+(s) + OH^-(aq) \quad (3)$$

in a similar fashion as solutes. Although it is possible to assign the equilibrium constants to actual coordinated oxygens at the surface, as is done for acids and bases in homogeneous solution, more common for surface chemistry is the assignment of equilibrium constants to a generic site at the surface, as above. These surface-complexation models link surface

chemistry to the broader fields of coordination chemistry for metals in solution (Schindler 1991).

Besides these Brønsted reactions, surface charge can arise from substitutions of unequally charged ions in the lattice of the solid, such as Al(III) substitution into a Si(IV) site or vice versa. Surface charge attracts counterions, forming an electrostatic double layer of charged adsorbates, co-ions and counterions. The distribution of ions in this double layer, which is analogous to the counterion swarm of Debye-Hückel theory, is usually calculated by solving the Poisson-Boltzmann equations that relate electrostatic potential to the net distributions of attracted counterions and repelled co-ions. The same approach for ions in solution yields Debye-Hückel theory and solute activity coefficients. If instead of an ion sphere, a charged plate is used in the equations, one arrives at Guoy-Chapman theory of the interface and the electric double layer, which is important to colloid stabilities. Diminution of the electric field with distance from the charged surface relates to the ionic strength because aqueous ions shield one another and diminish the electrostatic force.

The contribution of electrostatic energy is commonly treated separately in surface-complexation models. This separation leads to an equilibrium expression that varies with the concentration of charge on the surface, or more correctly, with the interfacial potential, which is not equivalent. It is easy to see the origin of these electrostatic contributions – it takes less energy to protonate a negatively charged surface than a positively charged one. Thus, the electrochemical potential (μ_i) of an ion, i, has a Coulombic term and is given as:

$$\mu_i = \mu_i^o + z_i F\psi + \mathrm{RTln}(a_i) \tag{4}$$

where μ_i^o is the standard-state chemical potential of the ion, z_i is the charge of the ion, ψ is then the electrostatic potential, R is the gas constant, T is temperature in Kelvins, a_i is the thermodynamic activity (see e.g., Schindler 1991; Sverjensky and Sahai 1994) and F is the Faraday constant. Although here we emphasize oxide surfaces with charges that arise from ionization of functional groups, uncharged phases could also rise to an electrical potential if they were in contact with one another and had different dielectric constants. Electrical work would be performed in moving the ion from one phase to the other.

For ions at the mineral-water interface, the net result is that one typically observes an exponential term in models of surface equilibria that varies with a Coulombic surface potential:

$$K = K_{\mathrm{int}} e^{z_i F\psi_o/\mathrm{RT}} \tag{5}$$

where K_{int} is the *intrinsic* equilibrium constant in the reference state of no surface charge. The subscript "*int*", and the word "intrinsic", expresses the idea that K_{int} represents a chemical stability constant that is free of influence by surface charges (see Schindler 1991). Details of how these electrostatic energies are treated depends upon the model chosen to describe the surface potential and charge (e.g., the "Constant Capacitance Model," the "Triple-Layer Model" etc.; see Sposito 2004). The key result, however, is that conditional equilibrium constants for complexation reactions at an interface commonly vary by factors of 10–100 with surface charge concentration (see Sposito 1984).

Practical benefits are most important. The different models to describe surface complexation are now implemented into computer software (e.g., Westall 1980, 1987) so that adsorption onto surfaces, and competition between metals and ligands, is solved simultaneously with aqueous speciation. Coupling of aqueous speciation to surface speciation has advanced understanding of environmental toxicity. One such application is the "Biotic Ligand Model" (e.g., Di Toro et al. 2001) that couples toxicity to surface complexation on biological materials. Assessing ecological toxicity depends upon the health of indicator organisms, such as trout minnows or water fleas in various chemical settings. The surface-complexation models allow the effect of a toxicant on these indicator organisms to be related to the concentration actually adsorbed at key biological membranes (e.g., gills for fish), and allows for full competition between metals and ligands. Previously the toxicity would be inferred from the total analytical concentration of toxicant in the stream or lake, which was incomplete because of competition with other constituents for the key biologic functional groups.

Colloid stability also reflects surface chemistry in results in geographic features that are so large as to be identifiable from satellites. When the electrostatic forces are coupled to Van der Waal's forces, one gets the DLVO theories (from: ***D***erjagian, ***L***andau, ***V***erbey and ***O***verbeek) of colloid stabilities and interactions (see Bunker and Casey 2016). The essence of colloid stability is that surface charges repel one another, but Van der Waal's forces attract and these two opposing forces vary in importance depending on solution composition. The net result is a colloid stability that depends sensitively on ionic strength. Thus in the dilute waters of the Mississippi River, clays are stable as separated colloids because the electrostatic forces prevent collisions and bonding. However, when those waters mix with seawater in the New Orleans estuary, the ionic strength increases and the distance of electrostatic repulsion diminishes so much that the clay particles collide. The colloids bond to one another by Van der Waal's forces, flocculate and settle out of the water column to form the Mississippi River Delta, identifiable from space.

The links between homogeneous and interfacial chemistry cannot be overestimated. The same variables that affect classes of reactions for solutes in water also affect those reactions at mineral surfaces, and often quantitatively so. The broad classes are ligand exchange, electron exchange and chelation.

A similarity between ligand exchanges affecting metal ions in water and those metals at dissolving mineral surfaces are shown in Fig. 1.

In Fig. 1 the dissolution of a mineral with an unpolymerized fabric (e.g., MgO, periclase) is shown to resemble the exchange of waters from the solvation sphere of $[Mg(OH_2)_6]^{2+}$(aq) in water. This similarity in reactivity trends (Fig. 1) should not be surprising since one can view surface reactions like dissolution as a series of ligand exchange reactions. Instead of ligands like bound waters being replaced, it is the bridging oxygens that link the metal to the mineral (Casey and Ludwig 1995). Dissolution of an unpolymerized oxide like periclase (MgO(s)), for example, involves stepwise replacement of bridging oxygens with non-bridging oxygens until a solute like $[Mg(OH_2)_6]^{2+}$(aq) is released. Thus the same variables that affect ligand-exchange rates for ions is also commonly manifested at mineral surfaces (see Casey 1991).

The similarity arises in part because many metals have similar coordination geometries in the mineral structure and in the solute released by dissolution. The Mg(II) metal, for example, is hexacoordinated to oxygens in both the periclase structure, at the periclase-water interface, and in the $[Mg(OH_2)_6]^{2+}$(aq) ion. What differs considerably is the coordination number of the exposed oxygens. These numbers range from six-coordination to single coordination at a typical surface kink site, whereas the Mg(II) metal remains six-coordinated throughout the process. Exceptions can be found where the coordination number of the metal differs between the mineral structure and aqueous species (e.g., B (III), Al(III)), but these are relatively uncommon. None of these changes in coordination are captured by the abbreviated equations, above.

These surface reactions are important to the health of the planet as marine and lacustrine particles scavenge trace metals and organic matter. Many toxicants are removed from natural waters as the particles aggregate and settle. Similarly the reactions at interfaces are key to atmospheric chemistry as the interfaces can catalyze otherwise slow processes and can themselves generate reactive species, such as free radicals. Finally, just as injection of an electron into a multimeric aqueous complex can labilize rates of ligand exchange by weakening the bond strengths, so too can injection of an electron into an oxide surface labilize the reactions at the interface. The details differ enormously, but the general reaction trends are preserved.

Organic Molecules and Aqueous Surface Films

Non-polar molecules, such as lipids, hydrocarbons and carbohydrates, have a larger affinity for other non-polar molecules than for solvation with waters. They tend to become segregated out of an aqueous phase onto mineral surfaces, or to the air-water interface. For example, a monolayer exists at the air/water surface of marine and fresh waters that is 2–500 nm thick and considerably enriched in non-polar molecules. Likewise, chlorinated hydrocarbons and non-polar pesticides accumulate at the microlayer because of their "hydrophobic" tendencies. The extent to which these molecules are enriched at mineral surfaces varies with aqueous solubility and the molecular weight of the organic molecule.

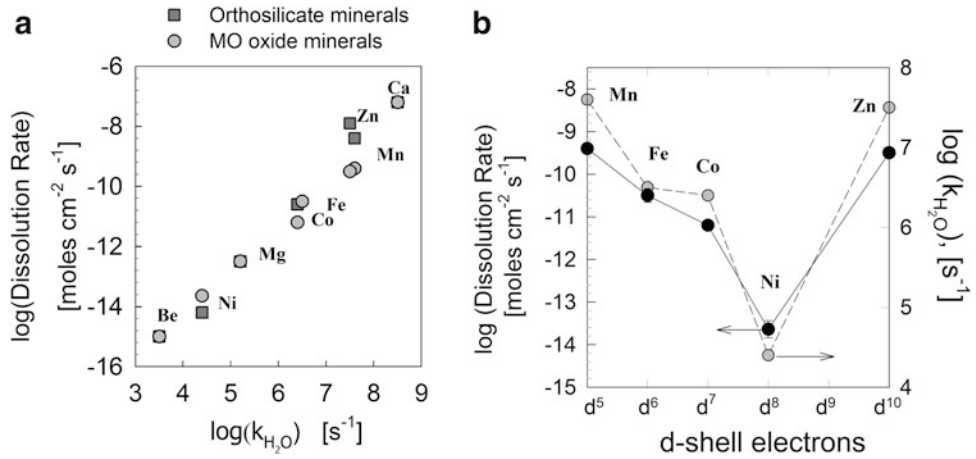

Surface Geochemistry, Fig. 1 Here the dissolution rates of sets of metal-oxide minerals having the stoichiometry: "MO" and the orthosilicate minerals having the stoichiometry "M_2SiO_4" are plotted against the logarithm of the rates of water exchange around the corresponding ion in solution (k_{H_2O} on the abscissa). In both (**a**) and (**b**) figures, "Mg," for example, indicates the dissolution rates of MgO(s) and Mg_2SiO_4 as well as the rates of ligand exchange around $[Mg(OH_2)_6]^{2+}$(aq), expressed as the logarithm of the k_{H_2O} value. In the *right-most* figure, (**b**) the rates are plotted against the number of d electrons in the metal, showing that the same crystal-field effects that control ligand exchange in solution also control reaction at the mineral interface (Adapted from Casey and Westrich 1992)

Addition of each -CH_i- group to a hydrocarbon chain increases the partitioning of the non-polar organic to mineral surfaces. Stated simply – just as our bodies can accumulate hydrophobic substances in our fatty lipid-rich organs, so too can lipid-rich parts of soil or natural waters accumulate hydrophobic molecules and these are usually at interfaces.

Life itself exists through these hydrophobic forces because they maintain integrity in the lipid bilayers of cell membranes. Likewise, the hydrophobicity of hydrocarbons in water leads to petroleum accumulation in discrete bodies. The attraction of these hydrocarbon molecules to mineral surfaces via Eq. 1 controls the wetting of pores in a reservoir and the migration of liquid hydrocarbons in strata.

Metal-ion adsorption is sometimes significantly changed in the presence of dissolved organic ligands. There are many causes but two are particularly important: competition between dissolved and surface ligands for the metal, and the formation of ternary surface complexes, as both the metal ions and the dissolved ligands coadsorb to surfaces of minerals, and these are usually oxides in the shallow Earth. This proximity can lead to a catalytic property.

Surface Catalysis

The catalytic properties of minerals were known well before Fritz Haber sampled different iron-oxide ores to develop a path for nitrogen fixation. These experiments led to the Nobel Prize (1918) and one of the most important single set of experiments in the twentieth century (with the development of cheap fertilizer, which now allows half of the people on the planet to feed themselves). The importance of this surface catalysis cannot be overstated – it staved off mass starvation in the twentieth century.

The catalytic properties of minerals fall into several categories. Some reactions relate to the electronic properties of a metal or metal oxide mineral. The semiconducting properties of minerals such as MnO_2 and TiO_2 make them particularly useful for photodegrading organic molecules (see Hocking et al. 2011). In acid-mine drainage, oxidation of pyrite to sulfuric acid involves autocatalysis by adsorbed Fe^{3+} (aq). Likewise, reactions that are catalyzed by configuration to protons commonly proceed more rapidly as adsorbates than in homogeneous systems. Protons are particularly reactive at mineral surfaces – the Brønsted acidity of water at the surface of nearly dry kaolinite has acidity comparable to concentrated sulfuric acid. The micropores of zeolites combine this high surface acidity with a confining space that keeps reactants in close proximity. Minerals such as hydrotalcite (also called layered-double hydroxides) can combine surface ionization reactions with changes in layer charge that lead to industrially useful catalysts (e.g., Gerken et al. 2011).

Enzymes function by adsorbing and stabilizing the critical molecules in a biochemical reaction and therefore are key to understanding the evolution of life on this planet. These enzymes must have initially developed abiotically, perhaps by reconfiguration of amino acids on mineral surfaces in a particularly reactive geologic setting, such as a hot spring. Thus, the core of the photosynthetic enzyme, Photosystem-II, resembles a fragment of one of the manganese-oxide minerals (e.g., Sauer and Yachandra 2002). The structural links are not accidental.

The Future

Scientists are comparing the structures of adsorbates calculated via quantum-chemical models with those determined via the spectroscopies that allow for *in situ* measurements (scanning probe microscopy, SPM; extended X-ray absorption fine structure analysis, EXAFS). The goal of this work is a set of rules analogous to Pauling's rules for solids, that predicts the structural chemistry and reactivities of adsorbates. Those interested in a more extensive discussion are referred to references in Bunker and Casey (2016) and particularly to Israelachvili (1992), Yariv and Cross (1970) and Stumm (1992).

Cross-References

- ▶ Analytical Techniques
- ▶ Atomic Absorption, Inductively Coupled Plasma Optical Emission Spectroscopy, and Infrared Spectroscopy
- ▶ Colloids
- ▶ Crystal Chemistry
- ▶ Gouy-Chapman Theory
- ▶ Kinetics of Geochemical Processes
- ▶ Mineralogy
- ▶ Nuclear Magnetic Resonance
- ▶ Oklo Natural Nuclear Reactors
- ▶ Poisson-Boltzmann Equation
- ▶ Synchrotron X-Ray Fluorescence Analysis

References

Adamson AW (1982) Physical chemistry of surfaces. Wiley, New York. 662 pp

Boehm H-P (1966) Functional groups on surfaces of solids. Angew Chem 5(6):533–622

Bunker BC, Casey WH (2016) The aqueous chemistry of oxides. Oxford University Press, New York. 620 pp

Burton WK, Cabrera N, Frank FC (1949) Dislocations in crystal growth. Nature (London, United Kingdom) 163:398–399

Burton WK, Carbrera N, Frank FC (1951) The growth of crystals and the equilibrium structure of their surfaces. Phil Trans R Soc Lond A243:299–358

Casey WH (1991) On the relative dissolution rates of some oxide minerals. J Colloid Interface Sci 146:586–589
Casey WH, Ludwig C (1995) Silicate mineral dissolution as a ligand-exchange-reaction. In: White AF, Brantley SL (eds) Chemical weathering rates of silicate minerals. Reviews in mineralogy, vol 31, Ser. ed. Ribbe HP. Mineralogical Society of America, BookCrafters, Michigan, pp 87–117
Casey WH, Westrich HR (1992) Control of dissolution rates of orthosilicate minerals by divalent metal-oxygen bonds. Nature 355:157–159
Di Toro MD, Allen HE, Bergman HL, Meyer JS, Paquin RP, Santore RC (2001) The biotic ligand model of the acute toxicity of metals: 1. Technical basis. Environ Toxicol Chem 20:2383–2396
Gerken JB, McAlpin JG, Chen J, Rigsby M, Casey WH, Britt RD, Stahl S (2011) Electrochemical water oxidation with cobalt-based electrocatalysts from pH 0–14: the thermodynamic basis for catalyst structure, stability, and activity. J Am Chem Soc 133(36):14431–14442
Hocking RK, Brimblecombe R, Chang SLY, Singh A, Cheah MH, Glover C, Casey WH, Spiccia L (2011) Water-oxidation catalysis by mineral birnessite in a geochemical-like cycle. Nat Chem 3:461–466
Israelachvili J (1992) Intermolecular and Surface Forces, 2nd edn. Academic, Santa Barbara. 674 pp
Sauer K, Yachandra VK (2002) A possible evolutionary origin for the Mn_4 cluster of the photosynthetic water oxidation complex from natural MnO2 precipitates in the early ocean. Proc Natl Acad Sci 99(13):8631–8636
Schindler PW (1991) A solution chemist's view of surface chemistry. Pure Appl Chem 63:1697–1704
Schindler PW, Stumm W (1987) The surface chemistry of oxides, hydroxides, and oxide minerals. In: Stumm W (ed) Aquatic surface chemistry. Wiley, New York, pp 83–110
Sposito G (1984) The surface chemistry of soils. Oxford University Press, New York. 234 pp
Sposito G (2004) The surface chemistry of natural particles. Oxford University Press, New York. 243 pp
Stumm W (1992) Chemistry of the solid-water interface. Wiley, New York. 425 pp
Sverjensky DA, Sahai N (1994) Theoretical prediction of single-site surface-protonation equilibrium constants for oxides and silicates in water. Geochim Cosmochim Acta 60:3773–3797
Westall J (1980) Chemical equilibrium including adsorption on charged surfaces. Am Chem Soc Adv Chem Ser 189:33–44
Westall JC (1987) Adsorption mechanisms in aquatic surface chemistry. In: Stumm W (ed) Aquatic surface chemistry. Wiley, New York, pp 4–32
Yariv S, Cross H (1970) Geochemistry of colloid systems for earth sciences. Springer, New York. 450 pp

Synchrotron X-Ray Fluorescence Analysis

Juan S. Lezama Pacheco[1] and Scott E. Fendorf[2]
[1]School of Earth, Energy, and Environmental Sciences, Stanford University, Menlo Park, CA, USA
[2]Department of Geology, Stanford University, Menlo Park, CA, USA

Definition

Synchrotron X-ray fluorescence refers to the emission of fluorescent X-ray resulting from a sample being bombarded with monochromatic X-rays generated from a synchrotron particle accelerator.

Introduction

X-ray fluorescence spectrometry is a technique based on the analysis of secondary emission of photons with an X-ray frequency (known as X-ray fluorescence) from a given sample. As a result of a primary interaction with an X-ray excitation source, inner shell electrons are ejected from the atom leaving a "hole" (or vacant orbital) in the inner orbitals. The electrons ionized in this manner are therefore referred to as photoelectrons, and the vacant orbital left by this interaction is referred as core hole. Electrons from higher orbitals decay, filling the core hole so that the atom is brought back to its lowest energy state. In order to balance the energy given by the electron decay, a photon is produced having a frequency in the X-ray range. The frequency (or energy) of this photon is *unique* to each element, changing as a function of the core hole *energy level, the atomic number*, *and electronic configuration*. Each photon given by this electronic decay is therefore unique for each type of atom in the periodic table, making the fluorescent X-ray a unique signature for each element (Elam et al. 2002). The secondary photon emission produced through a photoionization process by X-rays is referred to as **X-ray fluorescence (XRF)**. After a sample is illuminated by a primary X-ray source, the analysis of XRF lines directly fingerprints the atomic species in a sample. Moreover, as the intensity of the fluorescence emission is related to the relative amounts of each element in a given sample, direct quantification of the sample composition is possible.

Early Stages

Since its discovery by Moseley in the early 1912, the potential of XRF was recognized for its nondestructive and reliable attributes in identifying elemental composition of samples ranging from metal alloys to rocks to biological materials. Although many advances have been made, the typical layout of an X-ray spectrometer has remained relatively unchanged. Three components are needed to perform an XRF measurement: (1) X-ray source, (2) sample stage, and (3) X-ray detector. X-ray tubes are the most commonly used source in "bench-top" and other commercial systems. These sources have a spectrum dependent on the anode and the voltage. Therefore, the excitation energies are intrinsically limited, shortening the range of elements that can be studied with conventional XRF. In addition, the non-monochromatic nature of X-ray sources makes the differentiation between elements and emission lines hard to deconvolute – as the samples are excited with a continuous X-ray spectra, the

overlap between the different fluorescence lines is increased. Finally, with a few exceptions and some recent developments, XRF spectrometry has been regarded as a bulk technique. This is mainly due to the limited X-ray optics and the divergent nature of X-ray beams by typical X-ray sources, limiting the study of microscopic samples and missing the possible element correlations that could occur in the micrometer scale.

Synchrotron-XRF

Synchrotron radiation is emitted by charged particles undergoing acceleration; the particles are maintained at a velocity near the speed of light but undergo a change in direction (and thus an acceleration) while navigating a (near) circular pathway. As charged particles are accelerated through these trajectories, a "fan" of white (a collection of frequencies from UV to gamma rays) light is emitted. The white light is captured in specially aligned pipes that bring the radiation to a spectrometer. After passing though different sets of optics and mirrors, a monochromatic beam of light is obtained. The light beam can be "tuned" to different energies by passing it through a monochromator; most monochromators are a set of crystals that allow light of a specific energy or wavelength to pass based on the incidence angle of incidence, which can then be adjusted to give different energies. Additionally, secondary focusing optics allow for the control of the beam size from tens of millimeters to micron size beams. The intensity of such energy beams is approximately 10^8 times the intensity of the emitted spectra by an X-ray tube, reducing the measurement time from hours to a few seconds. All of these capabilities make synchrotron radiation the perfect X-ray source for XRF spectrometry. From here on, we will refer to XRF spectrometry using synchrotron radiation as *S*-XRF.

Instrumentation and Analysis

Just as its bench-top counterpart, S-XRF requires a detector and a sample positioning system. With the development of semiconductor technology in the 1970s, materials like Ge and Si have been used as energy-dispersive (i.e., detection of several X-ray energy intensities at once) detectors for S-XRF. As a sample is excited with an X-ray beam at a given energy, each of component elements emits its corresponding fluorescence lines. These fluorescence lines are nothing more than a discrete set of X-ray energies. Each time one of these X-rays hits the detector material (Ge or Si), it creates distinct set of electron–hole pairs. The intensity and frequency of these pulses are binned and translated into a more meaningful energy scale and intensity scale; plotting the intensity of emitted lines against their energy (Fig. 1) represents the elemental composition of the sample. Integrating the relative intensities and locating its position in an absolute energy scale allows a quantitative estimation of the relative abundances of the elements composing a sample. The absolute intensity scale can be calibrated using reference foil

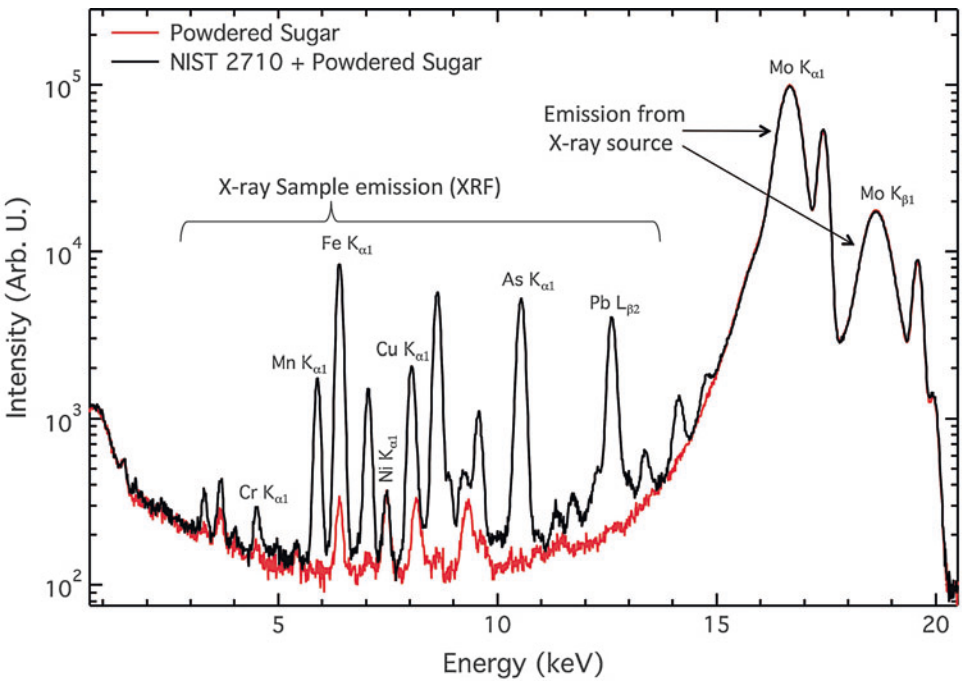

Synchrotron X-Ray Fluorescence Analysis, Fig. 1 Typical X-ray fluorescence spectra from powdered sugar and a 1:1 dilution with NIST 2710 soil standard (Montana Soil). Each emission line energy represents an element present in the sample, and the amplitude is related to the concentration of that element in the sample. Note the emission lines from the elements in the soil standard sitting *on top* of the powdered sugar matrix used in the dilution (background emission)

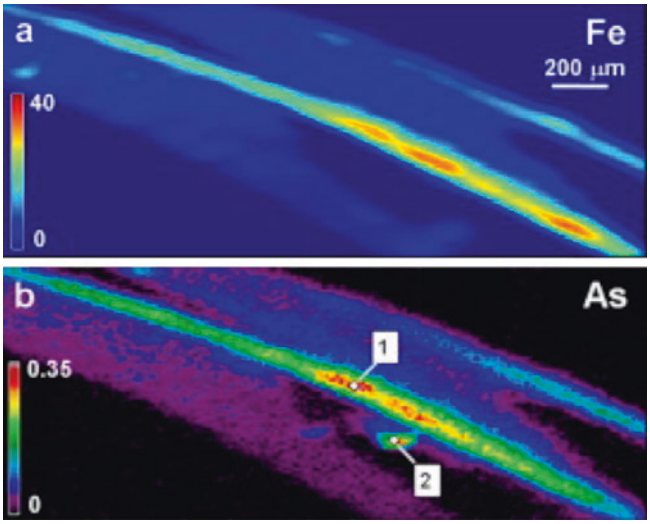

Synchrotron X-Ray Fluorescence Analysis, Fig. 2 X-ray fluorescence images of total Fe (**a**), As (**b**) on a cross section along the longitudinal axis of a rice root. Numbers with *white circles* (**b**) indicate where As *hot spots* on which further spectroscopic measurements were performed. All color scales are in pictograms of the element of interest (Adapted from Seyfferth et al. (2011))

standards, which contain definite amounts of a set of elements. The final component of S-XRF is the positioning system. Briefly, these systems usually consist of a motorized x-y-z stage with micrometer resolution movements, including frequently 2–3 rotation angle movements. Coupled to current state of the art X-ray focusing optics, it transforms S-XRF from a bulk to a technique with microscopic resolution. 2-D and 3-D maps can be generated by synchronizing the sample stage movements and the acquisition electronics and detectors. This provides a full rendering not only of the elemental composition and concentrations but the actual spatial distribution of the different elements composing a sample (Fig. 2).

The elemental mapping capability has opened S-XRF spectrometry to a more broad audience, from environmental sciences to archeology. Moreover, because the optics for synchrotron X-ray sources allows incident X-ray energies to be selected, element sensitivity is dramatically improved potential overlaps in fluorescent lines to be mitigated. By simply selecting energies below and above the X-ray ionization potential (or absorption edge) of a given element, a difference map can be generated, isolating the signal of an element and revealing potential correlations that otherwise would be hard to deconvolute.

As with many other analytical techniques, S-XRF is subject to matrix effects (i.e., changes in signal based on the composition of the material). Some of these effects are countered by either working with pictographic thin sections or by mathematically correcting for matrix effects. Matrix effects range from self-absorption (or auto-absorption) of the fluorescence by the matrix (leading to nonlinear X-ray emission), X-ray penetration depth effects (irregular sampling if excitation energies are changed), and other effects. If the overall composition of the sample is known to a certain degree, a correction can be applied. Thin sectioning helps reduce those artifacts in a less artificial manner. Lighter matrix materials (organic materials like plants and root and low Z elements) provide ideal matrices, as the background absorption is minimal.

Conclusion and Perspectives

Despite its noted uses, S-XRF is still advancing. Current developments in X-ray optics are capable of generating more intense X-ray beams in the submicron scales, allowing greater spatial resolution. Also, more intense X-rays imply greater sensitivities. Coupled with faster detection systems, not only the sensitivity but also the measurement time is decreased (from minutes to a few milliseconds).

S-XRF can be applied to dozens of systems, from plant roots to archeological materials, making an extremely versatile and powerful technique for identification and the spatial distribution of elements in a sample.

Cross-References

▶ Analytical Techniques
▶ X-ray Fluorescence Analysis

References

Elam WT, Ravel BD, Sieber JR (2002) A new atomic database for X-ray spectroscopic calculations. Radiat Phys Chem 63(2):121

Seyfferth AL, Webb SM, Andrews JC, Fendorf S (2011) Defining the distribution of arsenic species and plant nutrients in rice (*Oryza sativa* L.) from the root to the grain. Geochim Cosmochim Acta 75:6655–6671

T

Tantalum

Carsten Münker
Institut für Geologie und Mineralogie, Universität zu Köln, Köln, Germany

Element Data
Atomic Symbol: **Ta**
Atomic Number: **73**
Atomic Weight: 180.94788 ± 2
Isotopes and Abundances (CIAAW): ^{180}Ta 99.988%, ^{181}Ta, 0.01198%
1 Atm Melting Point: 3017 °C
1 Atm Boiling Point: 5458 °C.
Common Valences: 5+
Ionic Radii: 6-fold: 64 pm
Pauling Electronegativity: 1.5
First Ionization Potential: 761 kJ/mol
Chondritic (CI) Abundance: 15 ppb
Silicate Earth Abundance: 43 ppb
Crustal Abundance: 0.7 ppm
Seawater Abundance: 0.01 to 0.3 pmol/g
Core Abundance: ~0

Properties

Tantalum is a transition metal of low toxicity with the atomic number of 73. Its melting point is 3017 °C, and its boiling point is 5458 °C. Tantalum has two stable isotopes, ^{180}Ta and ^{181}Ta, with an atomic mass of 180.94788 ± 2 (CIAAW 2015). The small isotope ^{180}Ta only has an abundance of ca. 0.012% (Berglund and Wieser 2011), making it the rarest stable isotope in the solar system. A more precise measurement of natural ^{180}Ta/^{181}Ta (Weyer et al. 2002) yielded isotope abundances of 0.0001198 ± 6 for ^{180}Ta and of 0.9998802 ± 6 for ^{181}Ta. By better taking into account tailing effects during mass spectrometry, Pfeifer et al. (2017) revised the natural ^{180}Ta/^{181}Ta to 0.00011705 ± 41, yielding a revised atomic weight of 180.9478787 ± 38. Notably, ^{180}Ta is only stable in nature in its excited isomeric state, whereas in its ground state, it would decay rapidly with a half-life of ca. 8 h. In nature, Ta occurs in +5 valence state, although +4 valence is known from synthetic systems. Its atomic radius is 146 pm, and its ionic radius in +5 valence state and sixfold coordination is 64 pm, virtually identical to its geochemical twin Nb (Shannon 1976). Due to its high ratio of charge to ionic radius, Ta is classified in geochemistry as *high field strength element*.

History and Use

Tantalum was first discovered in 1802 by the Swedish chemist A. Ekeberg (Ekeberg 1803), following the discovery of the chemically similar *Niobium* 1 year earlier (named *Columbium* at the time, Hatchett 1802). The element was named after Tantalus, a Greek mythological figure, reflecting the extreme chemical inertness of Ta. It was not until 1845 that the German chemist Heinrich Rose (Rose 1845) could clearly demonstrate *Tantalum* and *Niobium* are two different elements.

Economically important Ta deposits are always bound to Nb deposits and are typically hosted by pegmatitic granites or carbonatites. The most important economical grade Ta mineral is tantalite (Ta-rich variety of columbite), and this type of mineralization is often referred to as COLTAN. Countries with the world's largest Ta deposits have traditionally included Australia and Brazil, but in Africa, Eastern Congo, Ruanda, and Burundi became increasingly important in the last years, now covering more than 50% of Ta world production (USGS 2015), despite being conflict areas. Technically, Ta is mainly used as materials for capacitors in automotive electronics, personal computers, and mobile phones. Other

W. M. White (ed.), *Encyclopedia of Geochemistry*,
https://doi.org/10.1007/978-3-319-39312-4

industrial uses include alloys for nuclear reactors, chemical equipment, and jet engines.

Geochemical Behavior

Tantalum is a highly refractory element with a 50% condensation temperature of 1573K (Lodders 2003) and has behaved lithophile during the Earth's differentiation. Ratios of Ta and similarly refractory elements like rare earth elements, Zr or Nb, are nearly constant in most groups of chondrites, and only CV chondrites rich in refractory components are depleted in Nb relative to Ta (Münker et al. 2003). The solar system abundance of Ta as estimated from CI chondrites is 15 ppb; the estimated abundance in the bulk silicate Earth is 43 ppb (Palme and O'Neill 2014). As Ta is not known to be significantly depleted in the silicate Earth relative to other refractory lithophile trace elements, it is assumed that the Earth's core contains no Ta, in line with experimental evidence (Wade and Wood 2001; Mann et al. 2009).

During silicate melting on Earth, Ta behaves highly incompatible in mantle minerals and is therefore depleted in the mantle and enriched in the crust. In the continental crust, the Ta content is estimated to 0.7 ppm with a content of 0.9 ppm and a Nb/Ta between 12 and 13 in the upper crust (Barth et al. 2000; Rudnick and Gao 2014). Relative to similarly incompatible elements like La or U-Th, however, Ta and its geochemical twin Nb are markedly depleted in the continental crust, mirroring their selective depletion in subduction zone magmas that contributed to the bulk of the continental crust. The selective depletion of Ta (and Nb) in subduction-related lavas and the continental crust is caused by their lower solubility in subduction zone fluids and by their retention in Ti-rich phases like rutile in subducting oceanic crust and possibly in subducting sediments (e.g., Zack et al. 2002; Hermann and Rubatto 2009). Together with its geochemical twin Nb, Ta is therefore a viable tracer for elemental mass balances in subduction zone systems, and employing Nb/Ta ratios in igneous and metamorphic rocks has now become an important tool to better understand silicate melting processes. Although the ionic radii reported for Ta and Nb are similar (Shannon 1976), experimental studies simulating mantle melting have shown that Ta behaves slightly less incompatible than its geochemical twin Nb (e.g., Blundy et al. 1998, Mc Dade et al. 2003). This observation argues for a slightly smaller ionic radius of Ta compared to Nb.

Due to its high valence state, Ta tends to hydrolize easily and is not very soluble in seawater, with an estimated concentration range between 0.01 and 0.3 pmol/kg, where 0.1 pmol/kg marks a typical value (Firdaus et al. 2011; Bruland et al. 2014). Compared to silicate rocks, Ta is less abundant in seawater than its geochemical twin Nb, as indicated by elevated Nb/Ta in seawater that are as high as 85 (Firdaus et al. 2011). Once more data will become available for aqueous systems, combined Nb and Ta studies may therefore have great potential to better understand weathering processes and ocean circulation.

Biological Utilization and Toxicity

Tantalum has no known biological role. Due to its inertness, it is used on bio-implants, but Ta dust can be a skin, eye, and lung irritant at high concentrations (US Centers for Disease Control and Protection 2015).

Summary

Tantalum is a highly refractory incompatible element and one of the high field strength elements. Unlike its geochemical twin, Nb, it is strictly lithophile. It has low solubility and is generally considered immobile. Compared to elements of similar incompatibility, it is depleted in the Earth's crust and in subduction zone magmas.

Cross-References

- ▶ High Field Strength Elements
- ▶ Incompatible Elements
- ▶ Niobium
- ▶ Ore Deposits
- ▶ Periodic Table
- ▶ Subduction Zone Geochemistry
- ▶ Transition Elements

References

Barth MG, McDonough WF, Rudnick RL (2000) Tracking the budget of Nb and Ta in the continental crust. Chem Geol 165:197–213

Berglund M, Wieser ME (2011) Isotopic compositions of the elements 2009 (IUPAC technical report). Pure Appl Chem 83(2):397–410

Blundy JD, Robinson JAC, Wood BJ (1998) Heavy REE are compatible in clinopyroxene on the spinel lherzolite solidus. Earth Planet Sci Lett 160:493–504

Bruland KW, Middag R, Lohan MC (2014) Controls of trace metals in seawater. In: Mottl MJ, Elderfield H (eds) The oceans and marine geochemistry, Treatise on geochemistry, vol 8. Elsevier, Amsterdam, pp 19–51

Center for Disease Control and Protection (2015) NIOSH pocket guide to chemical hazards. http://www.cdc.gov/niosh/npg/npgd0585.html

CIAAW (2015) Commission on isotopic abundances and atomic weights. http://ciaaw.org/atomic-weights.htm

Ekeberg AG (1803) Ueber ein neues Metall, Tantalum, welches zugleich mit der Yttererde in einigen schwedischen Fossilien entdeckt worden ist; nebst einigen Anmerkungen über die Eigenschaften der Yttererde, in Vergleichung mit der Beryllerde. Crells Annalen der Chemie 1:1–21

Firdaus ML, Minami T, Norisuye K, Sohrin Y (2011) Strong elemental fractionation of Zr-Hf and Nb-Ta across the Pacific Ocean. Nat Geosci 4:227–230
Hatchett C (1802) An analysis of a mineral substance from North America, containing a metal hitherto unknown. Philos Trans R Soc Lond 92:49–66
Hermann J, Rubatto D (2009) Accessory phase control on the trace element signature of sediment melts in subduction zones. Chem Geol 265:512–526
Lodders K (2003) Solar system abundances and condensation temperatures of the elements. Astrophys J 591:1220–1247
Mann U, Frost DJ, Rubie DC (2009) Evidence for high-pressure core-mantle differentiation from the metal–silicate partitioning of lithophile and weakly-siderophile elements. Geochim Cosmochim Acta 73:7360–7386
McDade P, Blundy JD, Wood BJ (2003) Trace element partitioning on the Tinaquillo Lherzolite solidus at 1.5 GPa. Phys Earth Planet Inter 139:129–147
Münker C, Pfänder JA, Weyer S, Büchl A, Kleine T, Mezger K (2003) Evolution of planetary cores and the Earth – Moon system from Nb/Ta systematics. Science 301:84–87
Palme H, O'Neill HSC (2014) Cosmochemical estimates of mantle composition. In: Carlson RW (ed) The mantle and core, Treatise on geochemistry, vol 3. Elsevier, Amsterdam, pp 1–39
Pfeifer M, Lloyd NS, Peters STM, Wombacher F, Elfers BM, Schulz T, Münker C (2017) Tantalum isotope ratio measurements and isotope abundances determined by MC-ICP-MS using amplifiers equipped with 10^{10}, 10^{12} and 10^{13} Ohm resistors. J Anal At Spectrom 32:130–143
Rose H (1845) On two new metals, pelopium and niobium, discovered in the Bavarian tantalites. Philosophical Magazine Series 3 26(171):179–181
Rudnick RL, Gao S (2014) Composition of the continental crust. In: Rudnick RL (ed) The crust, Treatise on geochemistry, vol 4. Elsevier, Amsterdam, pp 1–51
Shannon RD (1976) Revised effective ionic radii and systematic studies of interatomic distances in halides and chalcogenides. Acta Crystallogr A32:751–767
Wade J, Wood BJ (2001) The Earth's 'missing' Nb may be in the core. Nature 409:75–78
Weyer S, Münker C, Rehkämper M, Mezger K (2002) Determination of ultra-low Nb, Ta, Zr and Hf concentrations and the chondritic Zr/Hf and Nb/Ta ratios by isotope dilution analyses with multiple collector ICP-MS. Chem Geol 187:295–313
Zack T, Kronz A, Foley SF, Rivers T (2002) Trace element abundances in rutiles from eclogites and associated garnet mica schists. Chem Geol 184:97–122

Technetium

Yoshio Takahashi
Graduate School of Science, The University of Tokyo, Tokyo, Japan

Element Data
Atomic Symbol: **Tc**
Atomic Number: 43
(*continued*)

Atomic Weight: ~97.91
Isotopes and Abundances: no stable isotopes; ^{97}Tc ($T_{1/2} = 2.6 \times 10^6$ years), ^{98}Tc ($T_{1/2} = 4.2 \times 10^6$ years), ^{99}Tc ($T_{1/2} = 2.1 \times 10^5$ years)
1 Atm Melting Point: 2,157 °C
1 Atm Boiling Point: 4,265 °C
Common Valences: 7+, 4+
Atomic Radius: 138 pm (covalent)
Pauling Electronegativity: 1.9
First Ionization Energy: 702 kJ
Chondritic (CI) Abundance: ~0
Silicate Earth Abundance: ~0
Crustal Abundance: ~0
Seawater Abundance: ~0
Core Abundance: ~0

Properties

Technetium (Tc), with atomic number of 43, is an element between molybdenum (Mo) and ruthenium (Ru). Tc is the lightest element which has no stable isotopes. The isotopes known for this element are all radioactive. The isotopes with a half-life ($T_{1/2}$) of more than 1 h are ^{93}Tc ($T_{1/2} = 2.8$ h; decay mode, EC + β^+), ^{94}Tc ($T_{1/2} = 4.9$ h; EC + β^+), ^{95}Tc ($T_{1/2} = 20.0$ h; EC + β^+), ^{95m}Tc ($T_{1/2} = 61.0$ days; EC + β^+ or IT), ^{96}Tc ($T_{1/2} = 4.3$ days; EC + β^+), ^{97}Tc ($T_{1/2} = 2.6 \times 10^6$ years; EC), ^{97m}Tc ($T_{1/2} = 90.1$ days; EC, IT), ^{98}Tc ($T_{1/2} = 4.2 \times 10^6$ years; β^-), ^{99}Tc ($T_{1/2} = 2.1 \times 10^5$ years; β^-), and ^{99m}Tc ($T_{1/2} = 6.0$ h; β^-, IT). Even the longest $T_{1/2}$ of 4.2×10^6 years for ^{98}Tc is not long enough to be present from the time of the nucleosynthesis of elements that constitute the solar system. Thus, Tc found in the Earth is only produced naturally by the decay of other radionuclides or as fission products and artificially by nuclear reactions, such as in nuclear reactors and nuclear weapons. In particular, ^{99}Tc comprises 6% of the total fission products of ^{235}U and ^{239}Pu, and its long $T_{1/2}$ makes it accumulate gradually in the environment through the use of nuclear energy. As a result, knowledge on the environmental chemistry of Tc has accumulated.

Technetium is located at the center of the transition metals in the periodic table. The electron configuration of Tc is [Kr] $4d^5 5s^2$, which ensures a variety of applications in chemistry. The oxidation states known for this element are −1, 0, +1, +2, +3, +4, +5, +6, and +7 but are mainly found as Tc(VII) and Tc(IV) species. The chemical structure of Tc was investigated using a long-lived isotope, ^{99}Tc ($T_{1/2} = 2.13 \times 10^5$ years), which is readily produced by milking of ^{99}Mo produced by fission of enriched U or neutron activation of ^{98}Mo. A stable oxide of Tc is TcO_2, and a Tc species soluble in aqueous

solution is TcO_4^- under oxic conditions. Technetium becomes Tc(IV) and insoluble as $Tc(OH)_4$ or TcO_2 under reducing conditions and is only soluble as TcO^{2+} or $TcOOH^+$ under acidic conditions (Icenhower et al. 2010).

History and Use

It was thought that the discovery of this element could not be difficult, because the position of Tc was already predicted as "ekamanganese (Em)" immediately below manganese in the periodic table by Dmitri Mendeleev. Before the discovery of Tc, all stable elements were already found (the final stable element was rhenium (Re), which is below Tc in the periodic table), and two positions among the elements lighter than lead (Pb, which is the heaviest element with stable isotopes) were unoccupied, which corresponded to Tc and promethium (Pm). In 1937, Perrier and Segrè successfully isolated Tc from a molybdenum foil that had been used as a target of a deuteron beam in a cyclotron in the Lawrence Berkeley National Laboratory in California (Perrier and Segrè 1937). The element was named after the Greek word "technetos," meaning "artificial."

Geochemical Behavior

Observation of Tc in natural systems was first reported by Merrill (1952), who observed spectra from relatively young stars outside the solar system. Afterward, Tc in terrestrial environment was found as fission products of uranium (U) in pitchblende, a uranium-bearing ore (Kenna and Kuroda 1961). Natural ^{99}Tc was also detected in uranium ores from the Cigar Lake uranium deposit in Canada (Curtis et al. 1999). Migration of ^{99}Tc in Cigar Lake was observed in a limited area possibly because of the absence of pertechnetate (TcO_4^-), the mobile form of Tc, under reducing condition of the system.

Isotope ratio anomalies of Ru induced by the decay of Tc have been investigated in several systems. Excess ^{100}Ru compared with the normal isotopic ratio of Ru produced by neutron capture of ^{99}Tc was used to trace the migration of Tc in Oklo and Bangombé natural fission reactors in Gabon (Hidaka et al. 1999). An anomaly in ^{99}Ru was detected in individual presolar silicon carbide (SiC) stardust grains, which was explained by the in situ decay of ^{99}Tc in the grains. The anomalous Ru isotopes caused by the extinct Tc were used to identify the origin of presolar SiC grains (Savina et al. 2004). This study also indicated that detection of ^{99}Ru due to the decay of ^{99}Tc in early solar system materials cannot be estimated based on the amount of ^{99}Tc produced in such stars.

As mentioned previously, determination and speciation of Tc in the environment has been investigated in particular for safety assessment of radioactivity in the environment and nuclear waste management (Shi et al. 2012). Emission from nuclear reprocessing plants is primarily important (>1,874 $\times$ 10^{12} Bq), followed by global weapon fallout (140 $\times$ 10^{12} Bq) and nuclear accidents (Chernobyl and Fukushima; about 1 $\times$ 10^{12} Bq). The concentration of ^{99}Tc in the normal environment is 1–10 μBq/L (= 1.6 $\times$ 10^{-15} to 1.6 $\times$ 10^{-14} ^{99}Tc g/L) and 4–88 mBq/kg (= 6.4 $\times$ 10^{-15} to 1.41 $\times$ 10^{-13} ^{99}Tc g/g) in seawater (Japan Sea) and soil in Japan, respectively. The low concentration at this level must be measured with the appropriate pre-concentration and separation methods. Detection is mostly conducted by β counting or ICP-MS. The β counting method, a radiometric method using a low-level GM counter, is commonly used, but needs a long measurement time. The ICP-MS method is sensitive and fast, but is subject to mass interference from ^{99}Ru, which needs to be removed before analysis.

The environmental behavior of Tc has been investigated in various systems, such as the soil–plant systems on land and the marine environment (Icenhower et al. 2010). Chemical processes, including redox reactions, sorption reactions, colloid formation, and interaction with humid substances, have been investigated. Generally, Tc is enriched in solid phases, such as soil and sediment, under reducing conditions because of the formation of insoluble Tc(IV) species. By contrast, Tc is highly soluble as TcO_4^- under oxic conditions, such as in normal seawater.

Biological Utilization and Toxicity

Technetium has no known biological role. It is toxic due to its radioactivity. Technetium has a high complex-forming ability ability, which allows the synthesis of various labeled compounds of ^{99m}Tc. The short lifetime of ^{99m}Tc is appropriate for using the Tc compound for medical diagnosis and medical research. ^{99m}Tc is exclusively supplied by ^{99}Mo–^{99m}Tc generators. Although the medical application of ^{99m}Tc prevails widely the amount of ^{99}Tc released from medical use is less than 0.02 $\times$ 10^{12} Bq, which is negligible compared with those from other sources, such as reprocessing and nuclear testing (Shi et al. 2012).

Summary

Technetium (Tc) is an element without any stable isotopes but has been used as various labeled compounds in medical diagnosis. Environmental study of Tc is important, which has been developed based on the advanced high-sensitive analytical methods.

Cross-References

- Oklo Natural Nuclear Reactors
- Presolar Grains
- Radioactivity
- Ruthenium
- Uranium

References

Curtis D, Fabryka-Martin J, Dixon P, Cramer J (1999) Nature's uncommon elements: plutonium and technetium. Geochim Cosmochim Acta 63:275–285

Hidaka H, Holliger P, Gauthier-Lafaye F (1999) Tc/Ru fractionation in the Oklo and Bangombé natural fission reactors. Gabon Chem Geol 155:323–333

Icenhower JP, Qafoku NP, Zachara JM, Martin WJ (2010) The biogeochemistry of technetium: a review of the behavior of an artificial element in the natural environment. Am J Sci 310:721–752

Kenna BT, Kuroda PK (1961) Isolation of naturally occurring technetium. J Inorg Nucl Chem 7:142–144

Merrill PW (1952) Spectroscopic observations of stars of class S. Astrophys J 116:21–26

Perrier C, Segrè E (1937) Radioactive isotopes of element 43. Nature 140:193–194

Savina MR, Davis AM, Tripa CE (2004) Extinct technetium in silicon carbide stardust grains: implications for stellar nucleosynthesis. Science 303:649–652

Shi K, Hou X, Roos P, Wu W (2012) Determination of technetium-99 in environmental samples: a review. Anal Chim Acta 709:1–20

Tellurium

Yoshio Takahashi
Graduate School of Science, The University of Tokyo, Tokyo, Japan

Element Data
Atomic Symbol: **Te**
Atomic Number: **52**
Atomic Weight: 127.60
Isotopes and Abundances: ^{120}Te 0.09%, ^{122}Te 2.55%, ^{123}Te 0.89%, ^{124}Te 4.74%, ^{125}Te 7.07%, ^{126}Te 18.84%, ^{128}Te 31.74%, ^{130}Te 34.08%
1 Atm Melting Point: 450 °C
1 Atm Boiling Point: 990 °C
Common Valences: 2−, 4+, 6+, 0
Ionic Radii: sixfold Te^{2-} 221 pm, Te^{4+} 97 pm, Te^{6+} 56 pm; covalent: 137 pm
Pauling Electronegativity: 2.1
(*continued*)

First Ionization Energy: 869.3 kJ
Chondritic (CI) Abundance: 2.28 ppm[a]
Silicate Earth Abundance: 9 ppb[a]
Crustal Abundance: 5 ppb[b]
Seawater Abundance: ~2 ng/L
Core Abundance: 0.85 ppm[c]
[a]Palme and O'Neill (2014)
[b]Wedepohl (1995)
[c]McDonough (2014)

Properties

Tellurium (Te) is one of the chalcophile elements that belong to group 16 in the periodic table and has an electronic configuration of $[Kr]4d^{10}5s^25p^4$. There are eight stable isotopes from ^{120}Te to ^{130}Te. It is expected that ^{126}Te is enriched relative to other isotopes because of the decay of the short-lived nuclide tin 126 (half-life: 2.345×10^5 year) in certain phases with high Sn/Te ratio in primordial materials in the solar system, such as chondrite meteorites (Yokoyama and Walker 2016). However, clear evidence of this anomaly has not been obtained yet. Tellurium stable isotope fractionation has been found mainly as a consequence of abiotic and biotic redox reactions of Te in nature (Smithers and Krouse 1968; Baesman et al. 2007).

Te exhibits variable oxidation states of −2, 0, +2, +4, and +6, similar to selenium (Se). Although the chemical characteristics of Te are generally regarded as similar to those of sulfur (S) and selenium (Se), they are substantially different in various aspects. The ionic radii (^{CN}r; CN is the coordination number) of Te at various oxidation states are larger than those of S and Se (e.g., $^6r(S^{4+}) = 0.37$ Å; $^6r(Se^{4+}) = 0.50$ Å; $^6r(Te^{4+}) = 0.97$ Å). Consequently, isomorphic replacement of S in various compounds is more frequently observed for Se than for Te. Te has a large number of independent minerals, as shown below. Te compounds generally show more covalent or metallic bonding compared with S and Se compounds.

History and Use

Tellurium was discovered in gold telluride by Franz-Joseph Müller von Reichenstein in 1782 and named after the Latin word *tellus*, which means the Earth by Martin Heinrich Klaproth in 1798.

From an economical point of view, Au–Ag–Te minerals are unimportant because of their rarity. Instead, more ubiquitous deposits of pyrite, pyrrhotite, and chalcopyrite with smaller concentrations of Te (and Se) than in Au–Ag–Te ores are the main source of Te. The recovery of these elements

from pyrite, pyrrhotite, or chalcopyrite is relatively easy, since Te effectively accumulates in dust or anodic slugs in electrolytic copper refinery plants. Te production is approximately 220 tons per year in the USA, Russia, Sweden, Japan, Peru, and Canada (Brown et al. 2015). Te is primarily utilized in metallurgy and chemical industries as additives to (i) copper alloys and stainless steel to make processing and milling easy and to (ii) lead (Pb) to increase strength. Te has been also utilized in electrotechnical and electronics industries and photonic glasses. In particular, its use in solar cells in photovoltaics has been greatly expanding, which poses concern about the supply of Te, one of rare metals due to its low crustal abundance (Zweibel 2010; Green 2013).

Geochemical Abundances and Behavior

The abundance of Te in the solar system (4.81 atoms per 10^6 Si) is the highest among all elements with atomic number >40. However, Te is only about the 80th most abundant element in the crust, since Te is one of highly volatile elements that was not incorporated into solid planetary materials during condensation. The abundances of calcogen elements in silicate rocks and various types of chondrites have been studied to unveil the "late veneer" hypothesis that chondritic materials with volatiles were accreted to the Earth after core formation (Wang and Becker 2013).

The abundance of Te in silicate rocks is in the range of 0.4–12 ppb. Similarly, background Te concentrations in soils and sediments are at the low ppb level. Its concentration in seawater is usually less than 2 ng/L (about 16 pM), whereas the concentration is approximately one order of magnitude higher in freshwater (Belzie and Chen 2015).

Native Te exists in crystalline and amorphous forms. The specific gravity of the two at 18 °C are 6.24 and 6.0–6.2, respectively. Their melting and boiling points are 450 °C and 990 °C, respectively.

The most notable feature of Te in terms of mineralogy is the formation of Au–Ag–Te species, such as calaverite ($AuTe_2$), krennerite ($AuAgTe_2$), sylvanite ($AuAgTe_4$), and hessite (Ag_2Te) in epithermal, orogenic, and intrusion-related hydrothermal ore deposits. During the formation of these minerals, Te can be transported as gaseous species, such as H_2Te and Te_2, under reducing conditions (Grundler et al. 2013). The transport by the gaseous Te species is also important during its emission from volcanoes.

Under Earth's surface conditions, Te forms tellurite (TeO_3^{2-}) or tellurate (TeO_4^{2-}) depending on the redox condition. These ions can be fixed to the solid phase through the adsorption on Fe (hydr)oxides, such as ferrihydrite and goethite (Harada and Takahashi 2008). The adsorbed species form an inner-sphere complex on the surface of metal oxides. Meanwhile, selenate forms an outer-sphere complex. The difference in the adsorbed species results in the insoluble nature of Te compared with Se in soils or sediments under ambient conditions. Tellurite or tellurate can be fixed to the solid phase through the formation of native Te under reducing conditions. Te is highly enriched in ferromanganese nodules or crusts at the seafloor. The degree of enrichment in ferromanganese oxides relative to shale is the largest for Te compared with any other elements (Hein et al. 2003) possibly due to the isomorphous substitution of Te(VI) to Fe^{3+} or Mn^{4+} ions in ferromanganese oxides (Kashiwabara et al. 2014).

Biological Utilization and Toxicity

The environmental behavior of Te is of great importance because of its high toxicity. Specifically, tellurite is more toxic than tellurate. No biological role is known for Te. In humans, Te is exhaled in the breath of victims of Te toxicity as dimethyl telluride, $(CH_3)_2Te$, a gas with a garlic-like odor.

The size distribution of Te in aerosols shows that Te is mainly found in submicron particles, which suggests that Te is emitted as a gaseous species through its preferential emission from combustion processes and then converted into fine particles by condensation as the fumes cool or by chemical reactions in air (Chiou and Manuel 1986). Similarly, the vapor transport of radioactive Te is also important in commercial nuclear power plants related to its occurrence as a short-lived fission product. Te radioisotopes (e.g., ^{132}Te) decay to radioiodine (^{132}I), which is a hazardous radioisotope because of the accumulation of iodine into the thyroid. Te can be released with other volatile elements, such as Cs and I, nuclear reactor accidents such as at Chernobyl (1986) and Fukushima Daiichi (2011) nuclear power plants (Jantunen et al. 1991; Yoshida and Takahashi 2012).

Cross-References

- ▶ Chalcophile Elements
- ▶ Copper
- ▶ Cosmic Elemental Abundances
- ▶ Elements: Metalloids
- ▶ Formation and Evolution of the Earth
- ▶ Native Minerals
- ▶ Ore Deposits
- ▶ Oxidation-Reduction Reactions and Eh-pH (Pourbaix) Diagrams

▶ Selenium
▶ Stable Isotope Geochemistry
▶ Sulfide Minerals
▶ Sulfur

References

Baesman SM, Bullen TD, Dewald J, Zhang D, Curran S, Islam FS, Beveridge TJ, Oremland RS (2007) Formation of tellurium nanocrystals during anaerobic growth of bacteria that use Te oxyanions as respiratory electron acceptors. Appl Environ Microbiol 73:2135–2143

Belzie N, Chen YW (2015) Tellurium in the environment: A critical review focused on natural waters, soils, sediments and airborne particles. Appl Geochem 63:83–92

Brown TJ, Wrighton CE, Raycraft ER, Shaw RA, Deady EA, Rippingale J, Bide T, Idoine N (2015) World mineral production 2009–2013. British Geological Survey, Keyworth/Nottingham, p 88

Chiou KY, Manuel OK (1986) Tellurium and selenium in aerosols. Environ Sci Technol 20:987–991

Green MA (2013) Rare materials for photovoltaics: recent tellurium price fluctuations and availability from copper refining. Sol Energy Mater Sol Cells 119:256–260

Grundler PV, Brugger J, Etschmann BE, Helm L, Liu W, Spry PG, Tian Y, Testemale D, Pring A (2013) Speciation of aqueous tellurium(IV) in hydrothermal solutions and vapors, and the role of oxidized tellurium species in Te transport and gold deposition. Geochim Cosmochim Acta 120:298–325

Harada T, Takahashi Y (2008) Origin of the difference in the distribution behavior of tellurium and selenium in a soil-water system. Geochim Cosmochim Acta 72:1281–1294

Hein JR, Koschinsky A, Halliday AN (2003) Global occurrence of tellurium-rich ferromanganese crusts and a model for the enrichment of tellurium. Geochim Cosmochim Acta 67:1117–1127

Jantunen M, Reponen A, Kauranen P, Vartiainen M (1991) Chernobyl fallout in southern and central finland. Health Phys. 60:427–434

Kashiwabara T, Oishi Y, Sakaguchi A, Sugiyama T, Usui A, Takahashi Y (2014) Chemical processes for the extreme enrichment of tellurium into marine ferromanganese oxides. Geochim Cosmochim Acta 131:150–163

McDonough WF (2014) Compositional model for the Earth's core. In: Turekian KK, Holland HD (eds) Treatise on geochemistry, 2nd edn. Elsevier, Oxford, pp 559–577

Palme H, O'Neill HSC (2014) 3.1 – cosmochemical estimates of mantle composition. I. In: Turekian KK, Holland HD (eds) Treatise on geochemistry, 2nd edn. Elsevier, Oxford, pp 1–39

Smithers M, Krouse HR (1968) Tellurium isotope fractionation study. Can J Chem 46:583–591

Wang Z, Becker H (2013) Ratios of S, Se and Te in the silicate Earth require a volatile-rich late veneer. Nature 499:328–332

Wedepohl KH (1995) The composition of the continental crust. Geochim Cosmochim Acta 59:1217–1232

Yokoyama T, Walker RJ (2016) Nucleosynthetic isotope variations of siderophile and chalcophile elements in the solar system. Rev Mineral Geochem 81:107–160

Yoshida N, Takahashi Y (2012) Land-surface contamination by radionuclides from the Fukushima Daiichi Nuclear Power Plant accident. Elements 8:201–206

Zweibel K (2010) The impact of tellurium supply on cadmium telluride photovoltaics. Science 328:699–701

Terbium

Scott M. McLennan
Department of Geosciences, Stony Brook University, Stony Brook, NY, USA

Element Data
Atomic Symbol: Tb
Atomic Number: 65
Atomic Weight: 158.92535(2)
Isotopes and Abundances: ^{159}Tb, 100%
1 Atm Melting Point: 1356 °C
1 Atm Boiling Point: 3230 °C
Common Valences: +3
Ionic Radii: 92.3 pm (CN6), 104.0 pm (CN8), and 123.6 pm (CN12)
Pauling Electronegativity: ~1.2
First Ionization Energy: 565.77 kJ mol^{-1}
Chondritic (CI) Abundance: 0.0375 ppm
Silicate Earth Abundance: 0.084 ppm
Crustal Abundance: 0.60 ppm
Seawater Abundance: 0.175 ppt
Core Abundance: ~0

Properties

Terbium (Tb), named after the Swedish village of Ytterby, is a soft, ductile, malleable, dense (8.230 g cm^{-3}), bright silvery-gray metal. Its electronic configuration is [Xe]4f^{9}6s^{2}. It is relatively stable at room temperature and readily dissolves in mineral acids. It is a group 3 or IIIB inner transition element, with +3 being its only valence state in geological environments, and is one of the lanthanide rare earth elements (REE). In geochemical terminology, it is grouped with heavy rare earth elements (HREE; Gd-Lu). Terbium has one stable isotope.

More than 270 minerals contain lanthanides as essential structural constituents, but those with Tb as a significant component are restricted to Y and HREE varieties, such as xenotime [$Y(PO_4)$], gadolinite-Y [$Y_2FeBe_2(Si_2O_{10})$], bastnäsite [$REE(CO_3)F$], allanite [$(REE,Ca,Y)_2(Al,Fe^{2+},Fe^{3+})_3(SiO_4)_3(OH)$], and britholite [$(REE,Ca)_5(SiO_4,PO_4)_3(OH,F)$].

Details of properties, mineralogy, history, and uses of Tb were compiled from Goonan (2011), Chakhmouradian and Wall (2012), Zaimes et al. (2015), Gschneidner (2016), Hammond (2016), and Meija et al. (2016a, b).

History and Use

Terbium was discovered in 1843 by Carl Gustaf Mosander; early naming is somewhat confused as the names erbium and terbium were switched in 1864. The most important use of terbium is in green phosphors used in visual displays, tubes, and fluorescent lights. Secondary uses include as additives in neodymium magnets, lasers, and phosphors and in alloys used in a variety of electronic and magnetic devices.

Geochemical Behavior

The fundamental importance of Tb in geochemistry is that it is one of the small trivalent rare earth elements, among the most useful trace elements in all areas of geochemistry and cosmochemistry due to their coherent and systematic behavior as a group, largely a consequence of the "lanthanide contraction."

Terbium is typically a trace element in most rocks and minerals. It is classified geochemically and cosmochemically as a highly refractory lithophile element, with a 50% $T_{condensation}$ of 1659 K at 10^{-4} bars (Lodders 2003). In most igneous systems, Tb is incompatible with bulk partition coefficients, $D < 1$. In aqueous systems, Tb normally has very low fluid/rock partition coefficients ($\ll 1$). As a result, Tb contents of clastic sediments typically reflect their average provenance.

In seawater, Tb has very low concentrations (sub-ppt) and residence times (~570 year) with speciation dominated by Tb^{3+}, $TbCO_3^+$, and $Tb(CO_3)_2^-$. In other aqueous systems (e.g., magmatic, hydrothermal), Tb can reach ppm levels due to elevated temperatures, pH effects, and complexing with various ligands (e.g., F^-, Cl^-, OH^-).

Concentration and residence time data are from compilations in Taylor and McLennan (2009) and Nozaki (2001).

Biological Utilization and Toxicity

There are no documented biological uses for Tb. REE (including Tb^{3+}) likely substitute for Ca^{2+} in biological materials and processes. REE concentrations (including Tb) in human tissues and fluids are very low (~ppb to <ppb levels, respectively) due to very low concentrations in natural waters and low uptake rates throughout the food chain (Bulman 2003). At low levels of ingestion, there are no established toxic effects that pose a threat to human health.

Cross-References

- ▶ Incompatible Elements
- ▶ Lanthanide Rare Earths
- ▶ Lithophile Elements
- ▶ Trace Elements
- ▶ Transition Elements

References

Bulman RA (2003) Metabolism and toxicity of the lanthanides. In: Sigel A, Sigel H (eds) Metal ions in biological systems, vol. 40, the lanthanides and their interrelations and biosystems. Marcel Dekker, Basel, pp 683–703

Chakhmouradian AR, Wall F (eds) (2012) Rare earth elements. Elements 8:333–376

Goonan TG (2011) Rare earth elements – end use and recyclability. U S Geol Surv Sci Invest Rpt 2011–5094, 15pp

Gschneidner KA Jr (2016) Physical properties of the rare earth metals. In: Haynes WM (ed) CRC handbook of chemistry and physics, 96th edn. CRC Press, Boca Raton, pp 4-115–4-120

Hammond CR (2016) The elements. In: Haynes WM (ed) CRC handbook of chemistry and physics, 96th edn. CRC Press, Boca Raton, pp 4-1–4-42

Lodders K (2003) Solar system abundances and condensation temperatures of the elements. Astrophys J 591:1220–1247

Meija J, Coplen TB, Berglund M, Brand WA, De Bièvre P, Gröning M, Holden NE, Irrgeher J, Loss RD, Walczyk T, Prohaska T (2016a) Atomic weights of the elements 2013. Pure Appl Chem 88:265–291. (IUPAC Technical Report)

Meija J, Coplen TB, Berglund M, Brand WA, De Bièvre P, Gröning M, Holden NE, Irrgeher J, Loss RD, Walczyk T, Prohaska T (2016b) Isotopic compositions of the elements 2013. Pure Appl Chem 88:293–306. (IUPAC Technical Report)

Nozaki Y (2001) Rare earth elements and their isotopes in the ocean. In: Steele JH (ed) Encyclopedia of ocean sciences. Academic, London, pp 2354–2366

Taylor SR, McLennan SM (2009) Planetary crusts: their composition, origin and evolution. Cambridge University Press, Cambridge. 378pp

Zaimes GG, Hubler BJ, Wang S, Khanna V (2015) Environmental life cycle perspective on rare earth oxide production. ACS Sustain Chem Eng 3:237–244

Thallium

Josh Wimpenny
Nuclear and Chemical Sciences Division, Lawrence Livermore National Laboratory, Livermore, CA, USA

Element Data
Atomic Symbol: Tl
Atomic Number: 81
Atomic Weight: 204.3833 (2)
Isotopes and Abundances: ^{203}Tl (29.524%) and ^{205}Tl (70.476%)
1 Atm Melting Point: 577 K

(*continued*)

1 Atm Boiling Point: 1746 K
Common Valences: +1 and +3
Ionic Radii: 164 pm (+1), 102.5 pm (+3)
Pauling Electronegativity: 1.62
First Ionization Energy: 589.4 kJ mol^{-1}
Chondritic (CI) Abundance: 0.143 ppm
Silicate Earth Abundance: 0.004 ppm
Crustal Abundance: 0.5 ppm
Seawater Abundance: 10–20 ng/l
Core Abundance: 0.03 ppm

Introduction

Thallium (Tl) is a soft blue-grey metal that is present in trace quantities in the Earth's crust and is highly toxic either as a metal or as one of many compounds. It was first discovered in 1861 by William Crookes, and Tl metal was first isolated in 1862 by both Crookes and Claude-August Lamy (Peter and Viraraghavan 2005). Thallium has an atomic number of 81, atomic weight of 204.37, and is in group 13 of the periodic table. It has two oxidation states, with a 3+ state similar to other elements in group 13 (e.g., boron and aluminum) and a 1+ state. The relatively common Tl + ion is similar in charge and radius to group I elements K, Na, and Rb. It is dense (11.85 g/cm^3 at room temperature) and considered highly volatile, with a melting point of 577 K and a boiling point of 1746 K. There are two stable isotopes of Tl; ^{203}Tl (29.524%) and ^{205}Tl (70.476%). There are also several short lived radioisotopes of Tl including ^{204}Tl ($t_{0.5}$ 3.78 years), ^{202}Tl ($t_{0.5}$ 12.2 days), and ^{201}Tl ($t_{0.5}$ 73 h).

Thallium in the Earth's Crust

Thallium is widely distributed throughout the Earth's continental crust with an average concentration of ~0.5 ppm (Wedepohl 1995). In detail, there is approximately 3 times more Tl in the upper continental crust than in the lower crust, and orders of magnitude more Tl in the continental crust than is present in either the oceanic crust or mantle (Wedepohl 1995; Peter and Viraraghavan 2005; Nielsen and Rehkamper 2012). The reason for this enrichment of Tl in crustal rocks is that the isotopes of Tl have a relatively large ionic radius (Tl^+ 1.49A, Tl^{3+} 1A) that is too large to incorporate into the crystal lattice of mantle minerals olivine and pyroxene (Heinrichs et al. 1980; Shaw 1952). Thus, Tl behaves as an incompatible element during partial melting of the mantle, i.e., instead of remaining in mantle minerals Tl is preferentially incorporated into the melt. Because the Earth's crust is ultimately derived from this melt fraction, the crust becomes relatively enriched in Tl and the mantle becomes relatively depleted. The prevalence of the reduced form of Tl (+1 valence state) and similarity of its ionic radius and charge with group I elements means that, in the silicate Earth, the behavior of Tl closely corresponds to the alkali metals K^+, Rb^+, and Cs^+ (Rehkamper and Nielsen 2004). In terms of the most common rock forming minerals, Tl is usually concentrated in K^+ rich minerals such as K-feldspar and biotite, where Tl concentrations are commonly between 1 and 10 ppm (Shaw 1952; Heinrichs et al. 1980). In contrast, mantle minerals such as pyroxenes and olivine have Tl concentrations ~20–50 ppb.

As well as being a lithophile element, Tl is also chalcophile (readily combines with sulfur) so Tl readily partitions into sulfide melts (Rehkamper and Nielsen 2004). Significant quantities of Tl (Wt% levels) have been found in a small number of very rare sulfide minerals including lorandite ($Tl_2S.As_2S_3$) and huthinsonite ($PbS.(Ag,Tl)_2S.As_2S_3$). For economic purposes, the Tl-rich sulfide minerals are usually too scarce and the concentration of Tl in major rock-forming minerals too low for large-scale extraction. An example of a mining operation in which Tl is the primary target is the Xiangquan mine in China. Here the Tl is mostly present in pyrite but some lorandite and huthinsonite is also present (Zhou et al. 2005). Typically, the main source for commercial extraction of thallium is other heavy metal sulphide ores such as galena, sphalerite, and chalcopyrite. In these ores Tl can be present in the ppm level up to Wt% levels in chalcopyrite (Peter and Viraraghavan 2005). In addition, significant quantities of Tl (up to 1000 mg/kg) have been found in organic-rich shales and coal measures (Kazantzis 2000), and in deep sea sediments and manganese nodules (Peter and Viraraghavan 2005).

Thallium Behavior During Weathering

The concentration of Tl in river and seawater is typically between 10 and 20 ng/l (Flegal and Patterson 1985), though higher concentrations are observed in waters close to auriferous ore bodies and in polluted streams (Peter and Viraraghavan 2005). Thallium concentrations in soil typically range between 0.1 and 1 ppm, although values as low as 0.01 ppm and as high as 55 ppm have been observed (Kazantzis 2000; Jakubowska et al. 2007; Tremel et al. 1997). Such high concentrations in soil can be naturally derived; for example Tremel and coauthors (1997) observed 55 ppm Tl in soil derived from calcareous parent rocks that contain abundant sulphide minerals. Adsorption of Tl from solution onto oxide and phyllosilicate minerals plays an important role in controlling the Tl distribution in surface waters, soils, and crustal sediments. In particular, ferric oxides are important; adsorption of Tl+ does not take place at pH $<$ 3, but readily occurs at pH ~6.5 (Karlsson 2006). The readiness with which Tl can be adsorbed onto oxides, clay

minerals, and organic matter means that Tl will persist in soils rich in these minerals. In general the oxidation state of Tl plays a crucial role in controlling Tl uptake (Karlsson 2006). For example, in seawater Tl+ preferentially adsorbs to negatively charged Mn oxides, while Tl^{3+} adsorbs to neutrally charged FeOOH.

Anthropogenic Thallium and Toxicity

Although global production of Tl is low (around 15 t per year), it is estimated that annually between 2000 and 5000 t of Tl are released into the environment (Kazantzis 2000). The majority of this Tl is released by emissions from coal burning power plants and smelting of lead, copper, and zinc ores (Kazantzis 2000). Other significant sources of Tl include cement production and refining of nonferrous metals. Because Tl is very volatile, it is vaporized and then recondensed onto fine ash and dust particles which pass through conventional filtering systems in power plants.

In river and stream waters, the highest Tl concentrations measured are in industrial wastewaters; concentrations between 1 and 88 ppm have been observed in wastewaters from metal mines (Peter and Viraraghavan 2005). Similarly, the highest concentrations of Tl in soils are also reported in close proximity to mining areas. Close to the Silesian-Cracowian lead-zinc ore deposit, Tl concentrations of 150 ppm have been measured (Jakubowska et al. 2007). Other areas in which the concentration of Tl in soil ranges from 5 to 120 ppm include pyrite processing plants and near sulphide ores of heavy metals such as Hg, Au, and As. These high concentrations of Tl are usually confined to the topsoil, around 0–0.2 m from the surface (Jakubowska et al. 2007).

High concentrations of Tl in soil can be taken up into plants, depending on the plant type, solubility of the Tl compound, and acidity of the soil (Tl being more mobile in higher acidity waters). Concentrations of 25–50 mg/kg (dry weight) have been measured in some green cabbage, rape seed, and kale (LaCoste et al. 2001). These concentrations can exceed the concentration of Tl present in the soil and approach levels that are major potential risks for human consumption. Thallium poisoning involves inhibition of certain potassium dependent biological processes due to similarities between the ionic radius and charge of K+ and Tl+ ions. This affects the action of certain enzymes, coenzymes, and proteins and can result in gastrointestinal disturbances and central nervous system disorders (Galvan-Arzate and Santamaria 1998).

Summary

Thallium is typically present in trace quantities (sub-ppm) in the Earth's crust and mantle. Because it is a chalcophile element, relatively high concentrations up to the Wt% level can be found in sulphide minerals and ore bodies. Though the concentration of Tl in natural waters and soils is low, local to ore bodies and near to industrial ore processing plants the concentration of Tl in streams and soils can be orders of magnitude above background levels and have implications for human health if contaminated material is ingested or inhaled. Because of its extreme toxicity, it is important to understand its mobility and distribution during both natural weathering processes and anthropogenic processing.

Cross-References

- ▶ Chalcophile Elements
- ▶ Lithophile Elements
- ▶ Thallium Isotopes

Acknowledgments Prepared by LLNL under Contract DE-AC52-07NA27344.

References

Flegal AR, Patterson CC (1985) Thallium concentrations in seawater. Mar Chem 15(4):327–331

Galván-Arzate S, Santamaría A (1998) Thallium toxicity. Toxicol Lett 99(1):1–13

Heinrichs H, Schulz-Dobrick B, Wedepohl KH (1980) Terrestrial geochemistry of Cd, Bi, Tl, Pb, Zn and Rb. Geochim Cosmochim Acta 44(10):1519–1533

Jakubowska M, Pasieczna A, Zembrzuski W, Świt Z, Lukaszewski Z (2007) Thallium in fractions of soil formed on floodplain terraces. Chemosphere 66(4):611–618

Karlsson U, Karlsson S, Düker A (2006) The effect of light and iron (II)/iron (III) on the distribution of Tl (I)/Tl (III) in fresh water systems. J Environ Monit 8(6):634–640

Kazantzis G (2000) Thallium in the environment and health effects. Environ Geochem Health 22(4):275–280

LaCoste C, Robinson B, Brooks R (2001) Uptake of thallium by vegetables: Its significance for human health, phytoremediation, and phytomining. J Plant Nutr 24(8):1205–1215

Nielsen SG, Rehkämper M (2012) Thallium isotopes and their application to problems in earth and environmental science. In: Handbook of environmental isotope geochemistry. Springer, Berlin/Heidelberg, pp 247–269

Peter AJ, Viraraghavan T (2005) Thallium: a review of public health and environmental concerns. Environ Int 31(4):493–501

Rehkämper M, Nielsen SG (2004) The mass balance of dissolved thallium in the oceans. Mar Chem 85(3):125–139

Shaw DM (1952) The geochemistry of thallium. Geochim Cosmochim Acta 2(2):118–154

Tremel A, Masson P, Sterckeman T, Baize D, Mench M (1997) Thallium in French agrosystems – I. Thallium contents in arable soils. Environ Pollut 95(3):293–302

Wedepohl KH (1995) The composition of the continental crust. Geochim Cosmochim Acta 59(7):1217–1232

Zhou TF, Fan Y, Yuan F, Wu MA, Hou MJ, Voicu G et al (2005) A preliminary geological and geochemical study of the Xiangquan thallium deposit, eastern China: the world's first thallium-only mine. Mineral Petrol 85(3–4):243–251

Thallium Isotopes

Sune G. Nielsen
Department of Geology and Geophysics, Woods Hole Oceanographic Institution, Woods Hole, MA, USA

Definition

The element thallium (Tl) has two isotopes; ^{203}Tl and ^{205}Tl. Thallium isotope measurements have been conducted since the 1960s due to the hypothesized presence of the radioactive isotope ^{205}Pb (which decays to ^{205}Tl with a half-life of ~15 million years) when the solar system formed. However, it was only with the development of high precision measurements of Tl isotope ratios by multiple collector inductively coupled mass spectrometry (MC-ICP-MS) in the late 1990s that variation in ^{205}Tl/^{203}Tl was detected. In addition to significant Tl isotope variation in meteorites from the decay of ^{205}Pb, studies of terrestrial samples have revealed that Tl isotopes, despite their heavy masses, can fractionate substantially, especially in the marine environment. The most fractionated reservoirs identified are ferromanganese sediments and low temperature altered oceanic crust. These display a total isotope variation of about 35 ε^{205}Tl-units, which is more than 70 times the current analytical reproducibility. The isotopic variation can be explained by invoking a combination of conventional mass dependent equilibrium isotope effects and the nuclear field shift isotope fractionation, but the specific mechanisms are still largely unaccounted for.

Thallium isotopes have been applied to investigate paleoceanographic processes in the Cenozoic, the magnitude of hydrothermal fluid circulation through ocean crust, subduction zone and mantle recycling processes, and anthropogenic contamination of soil.

Historical Context

Thallium has two isotopes with atomic masses 203 and 205 (Table 1). This equates to a relative mass difference of <1%. Considering that conventional stable isotope fractionation theory states that the magnitude of isotope fractionation should scale with the relative mass difference of the isotopes (Urey 1947) one would not expect large stable isotope effects for Tl. The main reason behind the first Tl isotope studies was the search for radiogenic isotope variations due to decay of the now-extinct radioactive isotope ^{205}Pb (Anders and Stevens 1960; Ostic et al. 1969). Lead-205 decays to ^{205}Tl with a half-life of 15.1 Myrs (Pengra et al. 1978), whereas ^{203}Tl is stable and has no radioactive precursor. Therefore, it was believed that variable ^{205}Tl/^{203}Tl ratios would reveal the former presence of ^{205}Pb when the solar system formed. A number of studies between 1960 and 1994 all failed to register any resolvable Tl isotope variation for some selected terrestrial and a large number of extraterrestrial materials (Anders and Stevens 1960; Ostic et al. 1969; Huey and Kohman 1972; Chen and Wasserburg 1987, 1994). The failure to detect any Tl isotope variation was due to the relatively large errors (>0.2%) associated with the thermal ionization mass spectrometry (TIMS) measurements used at that time. The breakthrough came in 1999 when the first high precision Tl isotope measurements by MC-ICP-MS were published (Rehkämper and Halliday 1999). This technique provided a reduction in the uncertainty of more than an order of magnitude with errors reported at about 0.01–0.02% (Rehkämper and Halliday 1999). As with the previous Tl isotope investigations, Rehkämper and Halliday (1999) were ultimately motivated by the search for ^{205}Pb. However, analyses of a number of terrestrial samples that were meant to define the Tl isotope composition of Earth, which could then be compared to extraterrestrial findings, revealed large Tl isotope variation in excess of 15 times the analytical reproducibility. In principle, it is not possible to distinguish between ^{205}Tl/^{203}Tl variation caused by decay of ^{205}Pb and stable isotope fractionation because Tl has only two isotopes. However, the observed variation was clearly unrelated to radioactive ^{205}Pb and thus was inferred to be the result of stable isotope fractionation. Subsequent studies have confirmed that stable Tl isotope variation is common on Earth as well as in meteorites.

Thallium Isotopes, Table 1 Physical properties of thallium (Nriagu, 1998)

Melting point	577 K	
Molar weight	204.38 g	
Density	11.85 g/cm^3	
Valence states	Tl^+	Tl^{3+}
Redox potentials (V)		
$Tl_{(s)} \rightarrow Tl^+ + e^-$	+0.336	
$Tl^+ \rightarrow Tl^{3+} + 2e^-$	−1.28	
Ionic radius (Tl^+)	1.50 Å	
Ionic radius (Tl^{3+})	0.89 Å	
Isotopes	^{203}Tl	^{205}Tl

Thallium Isotope Measurements

The reason that MC-ICP-MS produces Tl isotope data far superior to TIMS is that instrumental isotope fractionation can be monitored during MC-ICP-MS measurements. Samples of Tl are introduced into the mass spectrometer as a solution (or a desolvated aerosol) into which the NIST SRM 981 Pb standard is admixed. By measuring all isotopes of Tl and Pb simultaneously and assuming that the isotope

fractionation incurred for the two elements is proportional, isotope ratios can be determined very accurately and precisely (Rehkämper and Halliday 1999; Nielsen et al. 2004) with the most recent studies reporting uncertainties of ~0.003–0.005% (Nielsen et al. 2015). Thallium isotope compositions are determined relative to the NIST SRM 997 Tl isotope standard and isotope compositions are reported as:

$$\varepsilon^{205}\mathrm{Tl} = 10^4 \times \left(\left({}^{205}\mathrm{Tl}/{}^{203}\mathrm{Tl}_{\mathrm{sample}} - {}^{205}\mathrm{Tl}/{}^{203}\mathrm{Tl}_{\mathrm{NIST\ 997}}\right) \times / \left({}^{205}\mathrm{Tl}/{}^{203}\mathrm{Tl}_{\mathrm{NIST\ 997}}\right)\right)$$

The terminology used for Tl isotope ratios is slightly different to standard stable isotope ratio conventions, which generally use the δ-notation (variations in parts per 1000). The reason for this is that the Tl isotope system was originally developed as a cosmochemical radiogenic isotope system, which by convention mostly is reported using the ε-notation (variations in parts per 10,000). Hence, the original notation was retained in order to make comparisons between cosmochemical and terrestrial data easier. In addition, the analytical uncertainty on and overall variability of stable Tl isotope ratios make the ε-notation very convenient as most data are thereby shown in whole digits with only a single figure behind the decimal point.

In order to measure Tl isotope ratios precisely and accurately it is necessary to completely separate Tl from the sample matrix (Rehkämper and Halliday 1999; Nielsen et al. 2004). The chemical separation technique relies on the fact that the trivalent Tl ion produces anionic complexes with the halogens (the technique uses either Cl^- or Br^-) in acidic solutions that partition very strongly to anion exchange resins. Conversely univalent Tl does not form strong anionic complexes and thus does not partition at all to anion exchange resins. Therefore, samples are prepared in oxidizing media by adding small amounts of water saturated in Br_2 to the samples already digested and dissolved in hydrochloric acid. This process ensures that all Tl is in the trivalent state, which will adsorb onto the anion exchange resin prepared in a quartz or teflon column. The sample matrix can then be eluted in various acidic media as long as Br_2 is present. Lastly, Tl is stripped from the resin by elution with a reducing solution that converts Tl to the univalent state. The reducing solution used is 0.1 M hydrochloric acid in which 5% by weight of SO_2 gas has been dissolved.

Applications of Thallium Isotopes

Evidence for ^{205}Pb in Meteorites

Two studies have found evidence for the presence of ^{205}Pb in the early solar system. The first study investigated Tl isotope systematics in several iron meteorites and found overall variation of ~50 ε^{205}Tl-units (Nielsen et al. 2006a). This variation was concluded to originate from both stable isotope fractionation and decay of ^{205}Pb. Measurements of multiple metal fragments of the IAB iron meteorite Toluca was found to form an isochron with $^{205}Pb/^{204}Pb \sim 7.4 \times 10^{-5}$ at the time of metal crystallization. The solar system initial $^{205}Pb/^{204}Pb$ depends on the age of Toluca metal crystallization, which is highly uncertain. The second study of Tl isotopes in meteorites investigated primarily carbonaceous chondrites and found an overall Tl isotope variation of only ~5 ε^{205}Tl-units (Baker et al. 2010). However, the majority of the carbonaceous chondrite data formed an isochron with $^{205}Pb/^{204}Pb \sim 1 \times 10^{-3}$ at the time of carbonaceous chondrite formation. Given that carbonaceous chondrites likely formed only a few million years after the start of the solar system (Kleine et al. 2005) it was concluded that the carbonaceous chondrite $^{205}Pb/^{204}Pb$ was essentially the initial of the solar system (Baker et al. 2010).

Studies of Tl Isotopes in Fe-Mn Crusts

Three studies have determined Tl isotope depth profiles for several hydrogenetic Fe-Mn crusts, which identified large systematic changes in Tl isotope compositions (Rehkämper et al. 2004; Nielsen et al. 2009, 2011). Modern surfaces of Fe-Mn crusts are characterized by $\varepsilon^{205}\mathrm{Tl} \sim 13$ (Rehkämper et al. 2002) whereas seawater is uniform with $\varepsilon^{205}\mathrm{Tl} \sim -6$ (Rehkämper et al. 2002; Nielsen et al. 2006c). Application of a constant Tl isotope fractionation factor between seawater and old Fe-Mn crust layers implied that the Tl isotope composition of seawater has experienced a single large shift in Tl isotope composition, which occured between ~55 and ~45 Ma (Fig. 1). It was proposed that the large shift in the ε^{205}Tl value of seawater in the early Cenozoic reflects a decrease in the amount of authigenic Mn oxides that were deposited with pelagic sediments in the early Eocene (Nielsen et al. 2009). Therefore, archives of the marine Tl isotope record are potentially a robust monitor of the oxidation state of seawater because the precipitation of Mn oxides requires oxygen at the sediment-water interface.

Calculation of Hyrothermal Fluid Fluxes Using Tl Isotopes in the Ocean Crust

Hydrothermal fluids are expelled from the seafloor (i) at high temperature on mid ocean ridge axes, as fueled by the magmatic energy from the crystallization and cooling of fresh ocean crust to ~300–400 °C and (ii) at lower temperatures on the ridge flanks, as the ocean crust cools slowly over millions of years. These hydrothermal fluxes play pivotal roles in controlling seawater chemistry, but the magnitude of the high temperature water flux at mid-ocean ridge axes remains widely disputed, whilst the volume of low temperature vent fluids expelled at ridge flanks is virtually unconstrained.

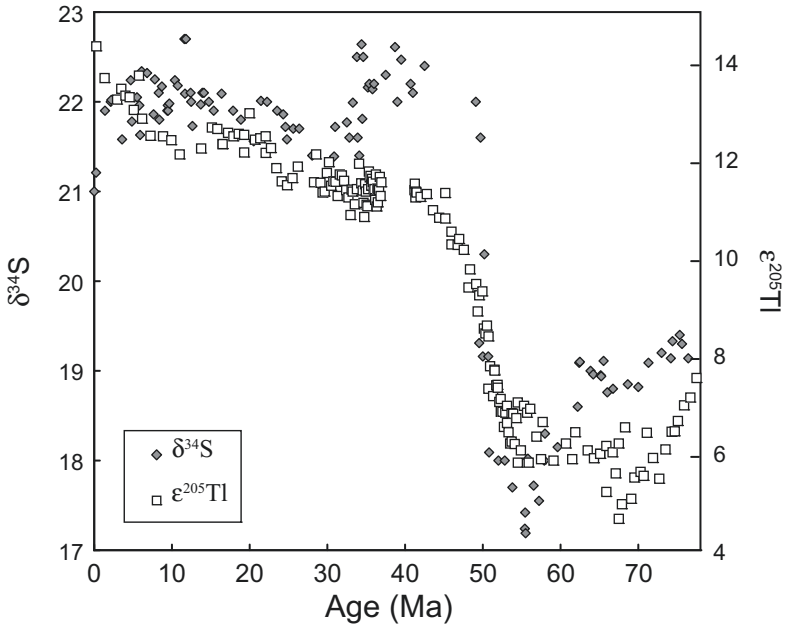

Thallium Isotopes, Fig. 1 Thallium isotope data for a Fe-Mn crust from the Pacific Ocean plotted for the last 75Myrs. The chronology of the Tl isotope curve was determined based on Os isotope data (Burton 2006) (Figure modified from Nielsen et al. (2009))

Thallium displays distinct behavior during high and low temperature hydrothermal alteration of the oceanic crust. High-T fluids effectively leach Tl from the cooling rocks with no isotope fractionation between fluid and rock, whereas low-T fluids deposit Tl into the upper part of the oceanic crust with deposition of light Tl isotopes into alteration minerals (Nielsen et al. 2006c; Coggon et al. 2014).

The high-T hydrothermal fluid flux was calculated using a mass balance between Tl in fluids and Tl available in the oceanic crust (Nielsen et al. 2006c), which yielded a range of fluid fluxes from 0.2 to 2.9 $\times$ 10^{13} kg/year. Low-T hydrothermal fluid fluxes were calculated using a similar mass balance equation between Tl supplied by seawater and the average Tl enrichment of oceanic crust altered by low-T hydrothermal fluids. It was found that 0.2–5.4 $\times$ 10^{17} kg/year of seawater is cycled through the upper 600 m of oceanic crust with an average temperature increase over ambient seawater of only 0.1–3.6 °C.

Thallium Isotopes as a Tracer for Ocean Crust Recycling in the Mantle

Thallium isotopes can be used to trace material recycled deep into the mantle because specific processes such as ocean crust alteration and marine Mn oxide precipitation causes substantial Tl isotope fractionation. Since Tl isotopes are not substantially fractionated during magmatic processes (Nielsen et al. 2016), subduction of these materials into the deep mantle should produce Tl isotope heterogeneity in regions of the mantle dominated by recycled oceanic crust and sediments.

To date, basalt samples from the Azores, Iceland and Hawaii have been investigated (Nielsen et al. 2006b, 2007). As it is unclear whether the Azores basalts were affected by post-eruptional alteration (Nielsen et al. 2007), these data will not be discussed here. Samples from Hawaii exhibit the most convincing Tl isotope evidence for presence of sediments in the mantle source (Nielsen et al. 2006b). About 10 ppm by weight of pure Fe-Mn sediment would be sufficient to explain the heavy isotope compositions recorded in these rocks.

Additional Tl isotope data for a suite of Icelandic basalts, on the other hand, did not show any significant Tl isotope variation and it could not be ascertained based on Tl isotopes if any sediment or altered oceanic crust is present in the mantle beneath Iceland (Nielsen et al. 2007).

Causes of Thallium Isotope Fractionation

In general, Tl isotope variations on Earth are fairly limited, with only a few select environments displaying significant deviations from the bulk Earth value of $\varepsilon^{205}Tl = -2$ (Nielsen et al. 2005, Nielsen et al. 2006b, Nielsen et al. 2006c, 2007). However, the overall magnitude of Tl isotope variation in natural environments on Earth now exceeds 35 ε^{205}Tl-units (Rehkämper et al. 2002, 2004; Nielsen et al. 2006c). This variability is comparable to the extent of fractionation observed for $^{56}Fe/^{54}Fe$ (Anbar 2004), which has a relative mass difference almost four times that of Tl. The larger-than-expected Tl isotope variation was shown to likely originate partially from equilibrium reactions in which so-called nuclear field shift isotope fractionation takes place (Bigeleisen 1996). Nuclear field shift isotope fractionation is not mass dependent but scales positively with the electron density close to the atom nucleus, which is generally largest

for the heavy elements due to relativistic contraction of s-orbitals for high-mass elements (Knyazev and Myasoedov 2001; Schauble 2007). The calculations that were carried out for Tl predict that an equilibrium system featuring Tl^{+} and Tl^{3+} will produce both regular mass dependent and nuclear field shift isotope effects, with isotope fractionation factors that act in the same direction (Schauble 2007).

Three experimental studies have investigated the Tl redox and isotopic effects during sorption of Tl to Mn oxide (Peacock and Moon 2012; Nielsen et al. 2013), which is the primary host of Tl in Fe-Mn rich sediments (Koschinsky and Hein 2003; Peacock and Moon 2012). These studies revealed that the MnO_2 phase hexagonal birnessite has the capacity to oxidize Tl^{+} to Tl^{3+}, following adsorption as a univalent ion (Bidoglio et al. 1993; Peacock and Moon 2012). In addition, it was found that this oxidation reaction was associated with significant Tl isotope fractionation in which the heavy Tl isotope was concentrated on the birnessite (Nielsen et al. 2013). The direction and magnitude of the isotope fractionation was consistent with that observed for natural Fe-Mn crusts (Rehkämper et al. 2002). Furthermore it was shown that natural Fe-Mn crusts are dominated by trivalent Tl (Peacock and Moon 2012) despite seawater almost exclusively contains univalent Tl (Nielsen et al. 2009). The experimental results are, therefore, consistent with the theoretical predictions in which ^{205}Tl is preferentially associated with trivalent Tl (Schauble 2007).

The Tl isotope fractionation found in low-T altered ocean crust is more poorly understood, which is in part because the host mineral for Tl in the altered oceanic crust is yet to be directly identified. Different studies have suggested that either sulfides or alkali-rich minerals contain most of the Tl added through low-T alteration (McGoldrick et al. 1979; Jochum and Verma 1996; Nielsen et al. 2006c; Coggon et al. 2014).

Summary

High precision measurements of Tl isotope ratios have only been possible since 1999, but this isotope system has already found a number of novel applications. To date, studies have revealed that Tl isotopes fractionate substantially in the marine realm with ferromanganese sediments and low temperature hydrothermal alteration displaying a total isotope variation of about 35 $\varepsilon^{205}Tl$-units. The isotopic variation can most likely be accounted for by invoking a combination of conventional mass dependent equilibrium isotope fractionation and nuclear field shift isotope effects (Bigeleisen 1996; Schauble 2007). It has been suggested that preferential oxidative sorption of ^{205}Tl onto the Mn oxide hexagonal birnesite is one of the primary mechanisms causing Tl isotope variation in the ocean and sediments (Peacock and Moon 2012; Nielsen et al. 2013).

Thallium isotopes have thus far mainly been applied to investigate past and present marine environments where Tl isotopes may be utilized as a monitor of the Mn supply rate or Mn oxide deposition rate over million year time scales (Rehkämper et al. 2004; Baker et al. 2009; Nielsen et al. 2009). Thallium isotopes can also be used to calculate the magnitude of hydrothermal fluid circulation through ocean crust. Such calculations can be performed both for high and low temperature fluids (Nielsen et al. 2006c).

Lastly, it has been shown that marine ferromanganese sediments can be detected in mantle-derived basalts (Nielsen et al. 2006b), which confirms that marine sediments subducted at convergent plate margins can be recycled to the surface via mantle plumes (e.g., Hofmann and White 1982).

References

Anbar AD (2004) Iron stable isotopes: beyond biosignatures. Earth Planet Sci Lett 217:223–236

Anders E, Stevens CM (1960) Search for extinct lead 205 in meteorites. J Geophys Res 65:3043–3047

Baker RGA, Rehkämper M, Hinkley TK, Nielsen SG, Toutain JP (2009) Investigation of thallium fluxes from subaerial volcanism-implications for the present and past mass balance of thallium in the oceans. Geochim Cosmochim Acta 73:6340–6359

Baker RGA, Schonbachler M, Rehkämper M, Williams HM, Halliday AN (2010) The thallium isotope composition of carbonaceous chondrites – new evidence for live Pb-205 in the early solar system. Earth Planet Sci Lett 291:39–47

Bidoglio G, Gibson PN, Ogorman M, Roberts KJ (1993) X-ray-absorption spectroscopy investigation of surface redox transformations of thallium and chromium on colloidal mineral oxides. Geochim Cosmochim Acta 57:2389–2394

Bigeleisen J (1996) Nuclear size and shape effects in chemical reactions. Isotope chemistry of the heavy elements. J Am Chem Soc 118:3676–3680

Burton KW (2006) Global weathering variations inferred from marine radiogenic isotope records. J Geochem Explor 88:262–265

Chen JH, Wasserburg GJ (1987) A search for evidence of extinct lead 205 in iron meteorites. LPSC XVIII:165–166

Chen JH, Wasserburg GJ (1994) The abundance of thallium and premordial lead in selected meteorites – the search for ^{205}Pb. *LPSC* XXV:245

Coggon RM, Rehkämper M, Atteck C, Teagle DAH, Alt JC, Cooper MJ (2014) Mineralogical and microbial controls on thallium uptake during hydrothermal alteration of the upper ocean crust. Geochim Cosmochim Acta 144:25–42

Hofmann AW, White WM (1982) Mantle plumes from ancient oceanic crust. Earth Planet Sci Lett 57:421–436

Huey JM, Kohman TP (1972) Search for extinct natural radioactivity of Pb-205 via thallium-isotope anomalies in chondrites and lunar soil. Earth Planet Sci Lett 16:401–412

Jochum KP, Verma SP (1996) Extreme enrichment of Sb, Tl and other trace elements in altered MORB. Chem Geol 130:289–299

Kleine T, Mezger K, Palme H, Scherer E, Münker C (2005) Early core formation in asteroids and late accretion of chondrite parent bodies: evidence from ^{182}Hf-^{182}W in CAIs, metal-rich chondrites and iron meteorites. Geochim Cosmochim Acta 69:5805–5818

Knyazev DA, Myasoedov NF (2001) Specific effects of heavy nuclei in chemical equilibrium. Sep Sci Technol 36:1677–1696

Koschinsky A, Hein JR (2003) Acquisition of elements from seawater by ferromanganese crusts: solid phase association and seawater speciation. Mar Geol 198:331–351
McGoldrick PJ, Keays RR, Scott BB (1979) Thallium – sensitive indicator of rock-seawater interaction and of sulfur saturation of silicate melts. Geochim Cosmochim Acta 43:1303–1311
Nielsen SG, Rehkämper M, Baker J, Halliday AN (2004) The precise and accurate determination of thallium isotope compositions and concentrations for water samples by MC-ICPMS. Chem Geol 204:109–124
Nielsen SG, Rehkämper M, Porcelli D, Andersson PS, Halliday AN, Swarzenski PW, Latkoczy C, Günther D (2005) The thallium isotope composition of the upper continental crust and rivers – an investigation of the continental sources of dissolved marine thallium. Geochim Cosmochim Acta 69:2007–2019
Nielsen SG, Rehkämper M, Halliday AN (2006a) Large thallium isotopic variations in iron meteorites and evidence for lead-205 in the early solar system. Geochim Cosmochim Acta 70:2643–2657
Nielsen SG, Rehkämper M, Norman MD, Halliday AN, Harrison D (2006b) Thallium isotopic evidence for ferromanganese sediments in the mantle source of Hawaiian basalts. Nature 439:314–317
Nielsen SG, Rehkämper M, Teagle DAH, Alt JC, Butterfield D, Halliday AN (2006c) Hydrothermal fluid fluxes calculated from the isotopic mass balance of thallium in the ocean crust. Earth Planet Sci Lett 251:120–133
Nielsen SG, Rehkämper M, Brandon AD, Norman MD, Turner S, O'Reilly SY (2007) Thallium isotopes in Iceland and Azores lavas – implications for the role of altered crust and mantle geochemistry. Earth Planet Sci Lett 264:332–345
Nielsen SG, Mar-Gerrison S, Gannoun A, LaRowe D, Klemm V, Halliday AN, Burton KW, Hein JR (2009) Thallium isotope evidence for a permanent increase in marine organic carbon export in the early Eocene. Earth Planet Sci Lett 278:297–307
Nielsen SG, Gannoun A, Marnham C, Burton KW, Halliday AN, Hein JR (2011) New age for ferromanganese crust 109D-C and implications for isotopic records of lead, neodymium, hafnium, and thallium in the Pliocene Indian Ocean. Paleoceanography 26:PA2213. https://doi.org/10.1029/2010PA002003
Nielsen SG, Wasylenki LE, Rehkämper M, Peacock CL, Xue Z, Moon EM (2013) Towards an understanding of thallium isotope fractionation during adsorption to manganese oxides. Geochim Cosmochim Acta 117:252–265
Nielsen SG, Klein F, Kading T, Blusztajn J, Wickham K (2015) Thallium as a tracer of fluid-rock interaction in the shallow Mariana forearc. Earth Planet Sci Lett 430:416–426
Nielsen SG, Yogodzinski GM, Prytulak J, Plank T, Kay SM, Kay RW, Blusztajn J, Owens JD, Auro M, Kading T (2016) Tracking along-arc sediment inputs to the Aleutian arc using thallium isotopes. Geochim Cosmochim Acta 181:217–237
Nriagu J (1998) Thallium in the environment, advances in environental sciences and technology. Wiley, New York
Ostic RG, Elbadry HM, Kohman TP (1969) Isotopic composition of meteoritic thallium. Earth Planet Sci Lett 7:72–76
Peacock CL, Moon EM (2012) Oxidative scavenging of thallium by birnessite: controls on thallium sorption and stable isotope fractionation in marine ferromanganese precipitates. Geochim Cosmochim Acta 84:297–313
Pengra JG, Genz H, Fink RW (1978) Orbital electron capture ratios in the decay of ^{205}Pb. Nucl Phys A302:1–11
Rehkämper M, Halliday AN (1999) The precise measurement of Tl isotopic compositions by MC- ICPMS: application to the analysis of geological materials and meteorites. Geochim Cosmochim Acta 63:935–944
Rehkämper M, Frank M, Hein JR, Porcelli D, Halliday A, Ingri J, Liebetrau V (2002) Thallium isotope variations in seawater and hydrogenetic, diagenetic, and hydrothermal ferromanganese deposits. Earth Planet Sci Lett 197:65–81
Rehkämper M, Frank M, Hein JR, Halliday A (2004) Cenozoic marine geochemistry of thallium deduced from isotopic studies of ferromanganese crusts and pelagic sediments. Earth Planet Sci Lett 219:77–91
Schauble EA (2007) Role of nuclear volume in driving equilibrium stable isotope fractionation of mercury, thallium, and other very heavy elements. Geochim Cosmochim Acta 71:2170–2189
Urey HC (1947) The thermodynamic properties of isotopic substances. J Chem Soc 69:562–581

Thermal Ionization Mass Spectrometry

John C. Lassiter
Department of Geological Sciences, Jackson School of Geosciences, University of Texas at Austin, Austin, TX, USA

Definition

Thermal ionization mass spectrometers are used for high-precision measurement of isotope ratios. Ions are produced by heating the element of interest under vacuum, focused and accelerated by applying an electrostatic potential, and then sorted by momentum (mass) using an electromagnet.

Introduction

Thermal ionization mass spectrometry (TIMS) is one of the primary methods available for high-precision isotope analysis and is used for many applications in the geological sciences and nuclear industry. A thermal ionization mass spectrometer consists of four main components: an ion source, a series of electrically charged plates used to focus and accelerate ions generated from the source, an electromagnet surrounding a "flight tube" through which the accelerated ions travel, and a detector system for measuring the intensity of ion beams after they have passed through the magnetic field.

Ion Source and Mass Analyzer

The ion source consists of one or more metal filaments. The element to be analyzed is loaded onto a filament that is heated under high vacuum by passing an electric current through the filament. The element must first be chemically purified, most commonly by ion exchange chromatography, in order to avoid potential interferences (e.g., a mass spectrometer cannot distinguish ^{87}Rb and ^{87}Sr ions because they have nearly identical mass). Typically, high-purity metals with high work functions such as tungsten, tantalum, or platinum are used for

the filament material. Heating of the filament causes the element loaded onto the filament to desorb or volatilize, and a portion of the desorbed atoms are ionized, as described by the Saha-Langmuir equation (Dresser 1968). Elements with low first ionization potentials are most susceptible to thermal ionization, producing +1 ions (e.g., Rb, Sr). However, some elements with high ionization potentials (e.g., Hf) are not easily ionized in this manner, and other elements (e.g., Os) are best measured as negative rather positive ions (as OsO_3^-).

Ions are then focused into a collimated beam and accelerated by applying controlled voltages to a series of horizontally and vertically aligned plates that contain slits through which the ions pass. The total electric potential gradient typically used is 8–10,000 V for acceleration of positive ions. Because ions desorbed from the filament possess much lower thermal energies and a narrow energy spread, ions accelerated in this manner exit the source lens array in a tightly focused beam, all having nearly identical kinetic energies. However, because the kinetic energy of an ion is described by the equation:

$$KE = \frac{1}{2}mv^2 \tag{1}$$

but the momentum of a particle is defined as:

$$M = mv \tag{2}$$

where m is the mass and v is the velocity, this acceleration results in two ions with the same charge but different mass exiting the source lens having different velocities and therefore different momenta. An ion's kinetic energy after being accelerated by the imposed electric potential is given as:

$$KE = Vq \tag{3}$$

where V is the applied accelerating voltage and q is the ion charge. After exiting the electrostatic lens, the ions pass though a magnetic field whose strength is controlled by varying the current applied to an electromagnet. The electromagnet is oriented such that the magnetic field lines are perpendicular to the path of the charged ions. Interaction with the magnetic field causes the ion paths to curve, with the radius of curvature controlled by the momentum of the charged particles, because the force exerted by the magnetic field is balanced by the centripetal force. Thus:

$$F_{\text{mag}} = qvB \tag{4}$$

where q is ion charge, v is the particle velocity, and B is the magnetic force vector. This is exactly balanced by:

$$F_{\text{cent}} = \frac{mv^2}{r} \tag{5}$$

where m is particle mass, v is again velocity, and r is the radius of curvature of the particle path. Combining the above equations, we find:

$$r = \frac{\sqrt{2mV/q}}{B} \tag{6}$$

Thus, all ions with the same charge/mass ratio follow the same curved path. Different isotopes of the same element have the same charge but different mass and therefore follow distinct, diverging paths. Ions with greater mass and therefore greater momentum follow circular paths with larger radii than lower-mass particles, and upon exiting the magnetic field, these different ions will travel along diverging paths to the detector assembly. The curvature of the ion paths can be adjusted by increasing or decreasing the strength of the applied magnetic field.

Detectors

Finally, one or more detectors are positioned at the back of the instrument to collect the different ion beams. Several detectors may be used, each positioned to collect the ions associated with each of the momentum-sorted ion beams. Alternatively, a single collector is used, with the magnetic field varied over time to sequentially position each ion beam of interest into the detector. To first order, the isotopic composition of the sample being analyzed is equal to the relative intensities of the ion beams associated with the different isotopic masses.

Several different types of detectors are commonly used to measure the intensity of the ion beams generated in a TIMS analysis. The most common type of detector is a Faraday detector. Ions enter a "cup" commonly composed of machined graphite or graphite-coated ceramic. The ions impart a small charge to the cup, which is then dissipated by applying a current equal to the number of ions impacting the cup per unit time. Thus, a 10^{-11} A current would correspond to an ion beam of equal intensity. For a beam of ions with a +1 charge, this corresponds to ~62 million ions entering the detector cup per second. Measurement of such small currents is achieved by use of high-resistance amplifiers, which convert the current into a voltage difference. Commercially available resistors used in modern mass spectrometers have resistances ranging from 10^{10} to 10^{12} Ω, and 10^{13} Ω resistors are in development (Koornneef et al. 2014). Higher resistance produces greater magnification of the signal to be measured and generally improves signal/noise ratio. However, amplifiers with very high resistance have a number of potential drawbacks, including a limited signal range where they have linear response and slower response time. Therefore, the most suitable type of amplifier to be used varies with application.

For ion beams greater than a few million ions per second, Faraday collectors provide excellent linearity and stability

and are the detector of choice for high-precision (<0.01%) isotopic measurements. However, measurement of small signals using high-resistance amplifiers is compromised by amplifier Johnson-Nyquist noise, the spurious voltage recorded by an amplifier in the absence of any real applied current due to the random thermal motion of electrons within the amplifier itself (Nyquist 1928). This noise is unavoidable and the signal/noise ratio places a limit on measurement precision at low beam intensities. Other methods of measuring small ion beams include electron multipliers and Daley detectors. These detectors work by converting ion collisions with the detector into either an electron cascade or light pulses that are then measured. Electron multipliers and Daley detectors are very effective at low-noise measurement of very small ion beams. However, they are in general less linear and less stable than Faraday collectors and have a more limited dynamic range. In addition, all measurements include uncertainty associated with counting statistics, so that the maximum possible precision of an isotopic measurement is to first order roughly equal to $1/N^{0.5}$, where N is the number of ions measured of the least-abundant isotope.

Mass Fractionation

Instrumental mass fractionation during measurement is also significant and varies systematically over time, and so must be corrected for in order to generate precise measurements. Mass fractionation occurs because lighter isotopes preferentially desorb from the filament relative to heavier isotopes. At the same time, because the sample loaded onto a filament represents a finite reservoir, the isotopic composition of this reservoir, and therefore of the desorbed species, typically becomes progressively heavier as an analysis proceeds. This Raleigh-Taylor fractionation can be corrected for by normalizing the measured isotopic ratio of two non-radiogenic isotopes to a fixed "natural" value and then applying this same correction to the ratios of other isotopes. For example, in Sr-isotope measurements, the isotopic ratio of interest is usually $^{87}Sr/^{86}Sr$, because the isotope ^{87}Sr is generated by the radioactive decay of ^{87}Rb. To correct for mass fractionation, the $^{86}Sr/^{88}Sr$ ratio is also measured and corrected to a fixed, accepted value using one of several mass fractionation laws (e.g., Wasserburg et al. 1981), and the derived correction factor is then applied to the measured $^{87}Sr/^{86}Sr$ as well to derive a value that is corrected for mass fractionation. Some elements do not have a pair of non-radiogenic stable isotopes that can be used for internal normalization (e.g., Pb-isotopes), and for some applications, it is the natural variation in stable isotope ratios that is the signal of interest (e.g., Ca-isotopes). In these cases, mass fractionation correction can in principle be achieved either through standard-sample bracketing or by adding an isotopically enriched spike to the sample. However, these methods are labor-intensive and can limit final analytical precision. For many such applications and for elements with higher first ionization potentials (e.g., Hf), isotopic measurement via MC-ICP-MS may be preferable.

Summary

Thermal ionization mass spectrometry is a highly precise method of measuring the isotopic compositions of target elements, with wide applications in geochemistry, cosmochemistry, and the nuclear industry. Although many elements previously analyzed by TIMS can also be analyzed via multi-collector inductively coupled plasma mass spectrometry quickly and precisely, TIMS is preferable for some applications, particularly where sample size is limited, due to better overall ion yield often capable by TIMS relative to other analytical methods.

Cross-References

- ▶ Geochronology and Radiogenic Isotopes
- ▶ Inductively Coupled Plasma Mass Spectrometry (ICP-MS)
- ▶ Ion Exchange Chromatography

References

Dresser MJ (1968) The Saha-Langmuir equation and its application. J Appl Phys 39:338–339

Koornneef JM, Bouman C, Schweiters JB, Davies GR (2014) Measurement of small ion beams by thermal ionization mass spectrometry using new 10^{13} Ohm resistors. Anal Chim Acta 819:49–55

Nyquist H (1928) Thermal agitation of electric charge in conductors. Phys Rev 32:110–113

Wasserburg GJ, Jacobsen SB, DePaolo DJ, McCulloch MT, Wen T (1981) Precise determination of Sm/Nd ratios, Sm and Nd isotopic abundances in standard solutions. Geochim Cosmochim Acta 45(2311):2324

Thermogravimetry

Jiri Kucerik
Institute of Chemistry and Technology of Environmental Protection, Faculty of Chemistry, Brno University of Technology, Brno, Czech Republic

Synonyms

Thermogravimetric analysis (TGA)

Definition

A technique in which the mass of a substance (and/or its reaction product(s)) is measured as a function of temperature, while the substance is subjected to a controlled temperature program (IUPAC 1997).

Background

Thermogravimetry (TG) is one of the mostly used methods of thermal analysis. Its principle is relatively simple. A crucible with a sample is placed onto the balance and subjected to a programmed temperature regime, during which sample mass is continuously monitored. The mass can stay either constant or it can change. Indeed, many thermally initiated processes accompanied by a change in sample mass can occur. A decrease can be caused due to sublimation and evaporation of volatile constituents, desorption of gasses, loss of crystalline water, oxidative degradation (if the experiment is conducted in air or oxygen), thermal decomposition (if the experiment is conducted in inert atmosphere), and reaction in which a gaseous product is evolved (e.g., decarboxylation). An increase in sample mass can be caused by an adsorption of gases, oxidation of metals, and pre-oxidation of some organic materials or heterogeneous materials in which a reactant is part of used atmosphere.

The result of TG measurement is a TG curve, which is a dependence of sample mass on either temperature or time. Figure 1 summarizes the most frequent TG curves obtained under either isothermal (time scale) or non-isothermal (temperature scale) conditions: A, sample is stable over used temperature interval; B, desorption or drying; C, single-step process (decomposition, evaporation); D, multistep processes (i.e., decomposition); E, the same as D, but sample was heated too fast; F, reaction with atmosphere (e.g., pre-oxidation) followed by decomposition; and G, reaction with atmosphere, but with a stable product.

To separate the overlapping processes (e.g., curve E), it is beneficial to express the TG records as derivative (DTG) or second derivative (DDTG) records. The thermobalances (as are TG instruments called) are often equipped so that they can also record simultaneously other signals such as differential scanning calorimetry (DSC) or differential thermal analysis (DTA). The combination of TG with these techniques allows observing also the thermal effects that are not connected with mass loss, and for this reason, it is beneficial for understanding the transitions (e.g., melting) that sample undergoes before or during changing its mass. The magnetic susceptibility of samples can be measured by thermomagnetometry, which is a hybrid TG technique based on the change of the attraction between a sample and superimposed magnetic field. TG can also be hyphenated with other

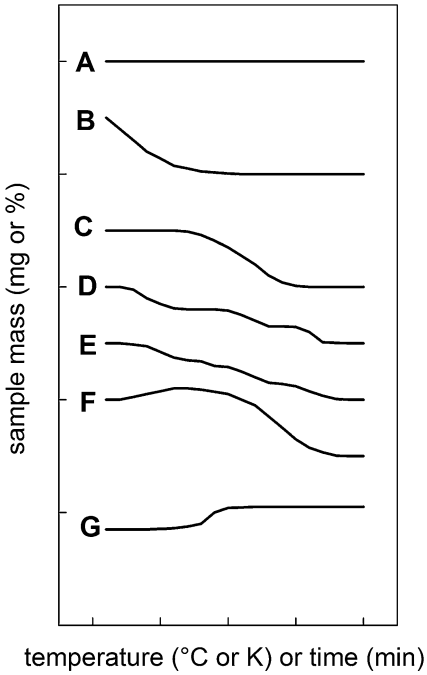

Thermogravimetry, Fig. 1 Most typical pattern of thermogravimetry curves

instruments such as Fourier transform Infrared spectroscopy (FTIR), mass spectrometry (MS), gas chromatography mass spectrometry (GSMS), or ultrahigh-resolution Fourier transform ion cyclotron resonance mass spectrometer (UHR FTICR MS) in order to analyze the composition of gases evolved during sample heating (evolved gas analysis (EGA)). This coupling is beneficial for compositional and stability analyses of complex materials.

Methodology

The TG experiments serve mostly for quantitative analysis. To a lesser extent, TG is also used for qualitative analyses or for the determination of kinetic parameters of studied processes. The purpose of the experiment is decisive for the designing of experimental conditions, and also the resulting TG curves reflect chosen experimental conditions. The most important parameters in TG analysis are heating program, type of dynamic atmosphere and pressure.

Typically, the temperature program involves linear heating and cooling ramps or periods of isothermal segments. The heating and cooling ramp rates are mostly used within the range of 1–50 °C min^{-1}, though the commercially available devices allow large spam (linear heating from 0.1 °C min^{-1} to at least 500 °C min^{-1} and ballistic heating > 2000 °C min^{-1}). Nevertheless, one should always be aware that very slow ramps require longer time for analysis, and very fast ramps cause a deviation between programmed and real temperature

of sample. The latter is caused by thermal resistance that is low for metals and high for organic and some mineral samples. In addition, fast ramps decrease the resolution of TG curve (curve E in Fig. 1), thus several processes can overlap in one "broad" process. This is undesirable for quantitative analysis that is based on an exact definition of onset and endset temperatures of investigated process. For this reason, the controlled rate thermal analysis (CRTA) known also as high-resolution TG was developed. In the CRTA method, the ramp rate is continuously adjusted (using a mathematic function) according to the instantaneous sample mass change.

A second important parameter influencing the TG curve is the type of purge gas that controls the sample environment. The flow of nitrogen, helium, or argon is used as an inert atmosphere and either air or oxygen as an oxidative atmosphere. In special cases, experimental conditions may require specific atmosphere of carbon dioxide, ammonia, or air enriched by water vapors. Conducting of experiments in air or oxygen leads to thermo-oxidative degradation, while choosing inert gases prevents samples against oxidation, and (organic) samples can be transformed by pyrolysis. If the gas produced during sample's heating is the same as purging gas, the flow rate influences the equilibrium of the investigated process, especially if the process is reversible.

Third, the TG curve is also influenced by the pressure around the sample. Usually, the pressure in a thermobalance is constant, and its influence is neglected. However, gases are frequently evolved during TG experiments, and pressure can significantly influence their dynamics. Specialized instruments allow to modulate pressure from vacuum to overpressure, because pressure-controlled TG is beneficial to study sorption/desorption processes or gasification. In addition, also the shape of sample holder (a crucible) influences the solid-gas interfaces. Therefore, it is desirable to choose such a type of holder that allows the reactive gas to diffuse into the solid material and at the same time enables the evolved gas to escape. This can also be improved by reducing the packing of material in crucible and increasing the solid-gas interface. Frequently, the interface is increased by sample grinding. However, this should be done with care because due to friction, grinding can significantly increase the temperature and change the investigated material. Last but not the least, change in density of used gases with temperature causes buoyancy affecting the balance signal. The correction of buoyancy is either a part of calibration or it is recommended to conduct a correction run under the same conditions with empty crucibles and subtract it from the measurement.

The derivative TG curve, indicating mass changes in temperature intervals, serves directly for quantitative analysis of sample's components or conversion of studied processes. The determination of kinetics of those processes can be conducted either under non-isothermal or isothermal conditions. Under non-isothermal conditions are measured mass losses in dependency on time employing several heating rates. Under isothermal conditions the masses are measured in dependency on time at several temperatures. The kinetic analysis is usually carried out to obtain activation energy, pre-exponential factor and reaction model. This kinetic triplet allows the prediction of stability of investigated material. As a rule, the degradation processes are complex; therefore, the so-called model-free methods have been introduced to facilitate the process analysis and modeling (Vyazovkin et al. 2011).

TG could be also used for qualitative analysis, but it requires strictly reproducible conditions of analysis. Obtained temperature and shape of the TG curve serve as a fingerprint. The most typical qualitative analyses are decomposition, evaporation, and sublimation or identification of metals according to the change in their magnetic properties.

Instrumentation

The instrument used in TG is a thermobalance. Currently, three main balance/furnace designs are used. First system is a vertical overhead thermobalance system with top loading. An extended version of this system is a parallel guide differential top pan balance mechanism, which enables simultaneous measurement of temperature and mass changes between an inert reference and sample. Second arrangement is also vertical, but with a sample holder hanging on a thin hangdown wire into the furnace below the balance. A reference pan may be placed on another balance in a separate chamber. Third system is a horizontal arrangement of balance, in which balance arms with thermocouples on pan carriers hold the sample and reference.

Most of the TG measurements start at room temperature, although some instruments allow to measure mass changes also at subambient temperatures (from ~ −196 °C). The highest temperature of measurement is furnace and sample limited. Most of organic materials are degraded below 1000 °C; for inorganic materials the temperatures up to ~2500 °C can be used. The accuracy of sample mass determination in TG measurements depends on the type of analysis. Modern instruments have the sensitivity <0.1 μg, but for most analyses, it is recommended to use several to tens milligrams of sample. However, in specific cases, e.g., in trace analyses, when the mass loss is expected to be extremely small, sample mass can be even in grams (if the instrument enables it). Prior to running TG experiments, the instrument requires calibration of both temperature and balance under the same conditions as the experiment. To calibrate balance, inorganic salts with known stoichiometry of decomposition are used (e.g., calcium oxalate monohydrate, calcium carbonate etc.). When simultaneous DTA and DSC are available, they can be used for calibration of furnace temperature. If not, the most frequent way is to determine Curie temperature by measuring

the metallic standards (e.g., alumel, nickel, Perkalloy, iron) in magnetic field. The detailed information on thermogravimetry and other methods of thermal analysis can be found, e.g., in Brown (1988).

Applications in Geochemistry

TG is widely used for the analysis of geological materials, but only several examples will be mentioned here. TG provides large opportunities to analyze fossil fuels such as coals or oil shales. However, the interpretation of the obtained records is not straightforward due to the complexity of processes taking part during heating of organic materials. The analysis of coals and other fossil fuels under inert conditions results in mass loss steps that correspond to contents of moisture and volatile compounds. TG is also used to monitor coking and cracking process. Under oxidative conditions, the mass losses correspond to contents of moisture and combustible part, while the residual mass represents the ash content. The change in atmosphere from inert to oxidative in the course of analysis allows the determination of fixed carbon (Ottaway 1982; Kok 2008). Using hydrogen atmosphere, the iron pyrite in residual ash can be reduced into metallic iron and consequently quantitatively detected using thermomagnetometry (Gallagher 1997).

TG is also frequently used in soil science (Plante et al. 2009). Heating of soil to 200 °C causes mainly the loss of soil moisture. Soil organic matter decomposes in two or three steps. First, there is a decomposition (up to the 400 °C) of stable part consisting of fresh residues, followed by decay of a humified part together with organo-clay complexes (up to 550 °C). The mass loss above 550 °C is due to the decomposition of soil carbonates. The loss on ignition (LOI) between 105 °C and 550 °C corresponds to the total organic matter content mainly in organic soils. In mineral soils, LOI is enhanced by intercrystalline water, decay of hydroxy groups in sesquioxides, destruction of charcoal, and the decay of some carbonates. Similarly as for other organic substrates, the interpretation of TG records of soils is complex due to a large number of simultaneous chemical and physicochemical processes. An alternative approach is the extraction of mass losses from 10 °C intervals. For a wide range of mineral soils, these intervals can be used for the determination of total soil organic carbon and nitrogen and clay contents (Siewert 2004) or modeling of soil microbiological activity represented by CO_2 production (Kucerik and Siewert 2014).

Frequently, TG is used to study the composition of minerals, which are thermally active. Their activity is determined by the conditions of rock formation. For example, igneous rocks formed under high temperatures and are thermally inert and do not provide any mass change up to 1000–1500 °C. On the contrary, igneous mineral associations formed at lower temperatures and pressures, or those that were transformed under low temperatures, are less stable. As a result, for most of the rocks, only part of their minerals can be analyzed using TG. An important part of these minerals represent water. Mass loss in particular temperature intervals allows the classification of mineral water according to the binding mechanisms. The mineral water can be divided into weakly bound water fraction adsorbed on external surfaces, in open and closed internal spaces and strongly bond water mostly in cation hydrate sheets, crystal water, and structural water. TG is useful for the interpretation of stoichiometric ratios in many minerals including oxides, hydroxides, carbonates, chalcogenides, silicates, sulfates, etc. A large collection of the TG records of various minerals and some examples of atypical applications of TG in geoscience were summarized by Földvári (2011). Additional applications in geoscience can be found in ASTM collection edited by Earnest (1988).

Summary

TG is a simple but very robust and mature technique that requires expenditure of very little sample. The analysis is quick, low cost, and provides precise and reproducible data. The thermobalances and the consumables are relatively inexpensive, and the maintenance is easy. For this reason, the technique is affordable by most laboratories and useful for both routine analyses and research purposes.

Cross-References

- ▶ Analytical Techniques
- ▶ Calorimetry
- ▶ Coal
- ▶ Petroleum

References

Brown ME (1988) Introduction to thermal analysis. Techniques and applications. Chapmann and Hall, London

Earnest CE (ed) (1988) Compositional analysis by thermogravimetry. American Society for Testing Materials STP, Philadelphia, p 997

Földvári M (2011) Handbook of thermogravimetric system of minerals and its use in geological practice. Geological Institute of Hungary, Budapest

Gallagher PK (1997) Thermomagnetometry. J Therm Anal 49:33–44

IUPAC (1997) Compendium of chemical terminology, 2nd ed. (the "Gold Book"). Compiled by McNaught AD, Wilkinson A. Blackwell, Oxford

Kok MV (2008) Recent developments in the application of thermal analysis techniques in fossil fuels. J Therm Anal Calorim 91:763–773

Kucerik J, Siewert C (2014) Practical application of thermogravimetry in soil science. Part 2: modeling and prediction of soil respiration using thermal mass losses. J Them Anal Calorim 116:563–570

Ottaway M (1982) Use of thermogravimetry for proximate analysis of coals and cokes. Fuel 61:713–716
Plante AF, Fernández JM, Leifeld J (2009) Application of thermal analysis techniques in soil science. Geoderma 153:1–10
Siewert C (2004) Rapid screening of soil properties using thermogravimetry. Soil Sci Soc Am J 68:1656–1661
Vyazovkin S, Burnham AK, Criado JM, Perez-Maqueda LA, Popescu C, Sbirrazzuoli N (2011) ICTAC Kinetics Committee recommendations for performing kinetic computations on thermal analysis data. Thermochim Acta 520:1–19

Thorium

Vincent J. M. Salters
National High Magnetic Field Laboratory and Department of Earth, Ocean and Atmospheric Sciences, Florida State University, Tallahassee, FL, USA

Element Data
Atomic Symbol: **Th**
Atomic Number: **90**
Atomic Weight: 232.038
Isotopes and Abundances: ^{232}Th, ~100%, ^{230}Th, ^{234}Th, ^{228}Th, ^{227}Th
1 Atm Melting Point: 1750 °C
1 Atm Boiling Point: 4790 °C
Common Valences: 4+
Ionic Radii: 6-fold, 108 pm; 4-fold, 112 pm
Pauling Electronegativity: 1.3
First Ionization Energy: 724 kJ/mol
Chondritic (CI) Abundance: 29.4 ppb
Silicate Earth Abundance: 79.5 ppb
Crustal Abundance: 5.6 ppm
Seawater Abundance: 0.12 ppt
Core Abundance: ~0

Properties

Thorium, Th, with an atomic number of 90, has an atomic weight of 232.038. Its melting point is 2023 K and its boiling point is in excess of 5000 K. The density of the pure metal form is 11.72 g/cm^3. Thorium is a white silvery metal that is stable at surface conditions but over months' time will oxidize and at the surface will turn gray and subsequently black. The metal is very ductile and can be rolled. Its properties are governed by its purity with the most common contaminant its oxide, which makes the material more brittle. Thorium's crystal structure changes from a cubic to a body-centered cubic structure at 1673 K.

History and Use

Berzelius first identified thorium in 1828 in the mineral thorite discovered by Esmark on the island of Lauvöya, northern Norway. The name thorium is derived from the Scandinavian god of war, Thor. Powdered Th is pyrophoric and burns brilliantly white in air. Mantles of portable gas lights take advantage of this property and are the main use of Th. Its further uses are for manufacturing of alloys (with Mg), high-quality lenses, and coating of filaments (W) for electronic tubes. ^{232}Th has further use as a nuclear fuel for the production of fissionable ^{233}U by neutron capture and followed by two electron emissions.

Isotopes and Applications

Th has five naturally occurring isotopes of which ^{232}Th has the longest half-life (14.01 Gyr; see Table 1) and is the only primordial isotope of Th that has survived on Earth. Th with U and K is the Earth's main heat-producing element. The other isotopes are part of the uranium decay series. The longest lived of these is ^{230}Th and the ^{230}Th/^{232}Th in the Earth is $\sim 5 \times 10^{-6}$; the natural abundances of the remaining isotopes are negligible. Th isotopes are used to investigate processes in which it is significantly fractionated from its parent. In aquatic systems Th isotopes are an important tool in sediment dating and determining particle fluxes in the oceans (Henderson and Anderson 2003). The ingrowth of ^{230}Th in marine corals has allowed for precise dating and calibration of the ^{14}C timescale (Bard et al. 1990). The high U/Th ratio of seawater is reflected by the coral which contains very low levels of common Th.

Thorium, Table 1 Half-lives of Th isotopes and their use in geosciences

Isotope	Half-life	Decay	Parent	Application
^{234}Th	24.1 days	β	^{238}U	Elemental scavenging, particle/carbon fluxes in the oceans, particle mixing
^{232}Th	14.01 Gyr	β	na	Trace element, Pb isotope
^{230}Th	75,584 (±110) year[1]	β	^{234}U	Elemental scavenging, sediment dating, coral growth dating, magma chamber dynamics, melt transport
^{228}Th	1.912 (±0.002) year	β	^{228}Ac	Particle/carbon flux in the oceans
^{227}Th	18.72 days	β	^{227}Ac	Particle/carbon flux in the oceans

[1]Cheng et al. (2013)

Th isotopes are also utilized for dating of volcanic rocks and mineral residence times in magmatic systems. More details are in the U series entry.

Chemistry

Thorium is an actinide element with an electronic structure (Rn)$6d^2 7s^2$. The outer electronic structure and bond characteristics resemble those of Zr and Hf which contribute to similarities in their chemical properties. Thorium is electropositive, has only one oxidation state, and in solution is tetravalent. However, the ionic radius of Th results in a quite different behavior as a trace metal in solids than Zr or Hf. The Th metal can be dissolved easily in concentrated hydrochloric acid or in aqua regia. Th(IV) easily complexed with anions in solution, and fluoride, oxalate, iodate, and phosphate salts with Th have very low solubility products making Th insoluble even under acidic solutions. This property of Th was used early on for quantitative separation and gravimetric determination from a large range of samples.

Ores and Distribution in Rocks

Thorium is a trace element in all rocks with concentrations ranging from sub-ppb to ppm levels. The tetravalent thorium ion has a high charge over radius which strongly limits its substitution for major ions and makes it a member of the high-field strength elements. Therefore, Th does not partition into most rock-forming minerals and concentrates in the melt during most melting and crystallization events. Typical partition coefficients for mineral phases during melting and crystallization are less than 10^{-3} (GERM database, https://earthref.org/GERM/).

Because of its incompatible behavior, high concentrations of Th are found in rocks that represent a small melt fraction either due to the low degree of melting or the high degree of fractional crystallization, granitic rocks and pegmatites, and differentiated alkaline magmas and epigenetic veins associated with alkaline magmas. Carbonatites can have as high as 200 ppm Th (Bizimis et al. 2003). Monazite (REE, Th)PO_4 is the most commonly occurring Th-bearing mineral and contains about 10 wt% of Th. These high concentrations of Th combined with low Pb concentrations allow the determination of monazite ages by electron or ion microprobe. Monazite is a heavy mineral (density of 4.7–5.6 g/cm^3) and can concentrate in placer deposits that can be easily mined. Such placer deposits occur among others in coastal India and Brazil and the Carolinas and north Florida coast in the USA (Van Gosen et al. 2009).

High-Temperature Geochemistry

The insolubility of Th in fluid caries through to high temperatures and metamorphic fluids also have low Th content compared to elements with similar partitioning coefficients in anhydrous mantle melt systems. The ratio of fluid-mobile elements, like Ba or La, and fluid-immobile elements, like Th or Nb, can be used in subduction environments to constrain slab contributions from fluids and melts. Ba, Th, and U behave very similar as highly incompatible elements during melting, but Ba/Th and U/Th are fractionated during fluid extraction. Fluid contributions in variably depleted mantle source composition can be assessed through La/Th versus La/Sm ratios whereby La/Sm indicates source enrichment and La/Th is an indicator for fluid addition (Plank 2005). Island arc volcanics have significant ^{230}Th deficiencies (U excesses). These disequilibria are the result of fluid addition to source of the volcanics. *More details are in the uranium decay series entry.*

Although the behavior of U and Th is similar during most magmatic processes, these elements do fractionate with Th, in general, being more incompatible. Magmatic processes lead to disequilibrium between ^{238}U and ^{230}Th. The half-life of ^{230}Th allows investigation of timescales up to 500 ka. During melting, especially mantle melting under dry conditions, Th is slightly more incompatible than U and consequently the melt will carry ^{230}Th excesses. Under mantle conditions garnet is better able to fractionate Th from U. Significant ^{230}Th excesses observed in zero-age mid-ocean ridge basalts require that melting starts in the garnet stability field. This requires that melting starts at a depth where garnet is stable and strongly constrains melting rate and melt transfer rates. In most models melting is fractional or dynamic, and the parameters that are varied are mantle and melt ascent velocity and residual porosity (McKenzie 1985). *More details are in the uranium decay series entry.*

Low-Temperature Geochemistry

At the Earth's surface, tetravalent Th has very low solubility and is particle reactive. Therefore Th concentrations in natural waters are very low. During weathering Th, which resides mostly in resistant accessory minerals, stays either in the regolith or is transported in the particulate fraction or colloidal fraction (Chabaux et al. 2003). If transported in the aqueous phase, Th complexes very strongly with humic acid (Stern et al. 2014). The retention of Th in soils can be used to date soil-forming processes by measuring ^{230}Th-^{238}U disequilibria, but studies have shown that these processes are more complex that simple U-leaching or precipitation while Th is immobile (Chabaux et al. 2003).

Biological Utilization and Toxicity

Thorium is not used by living organisms as micronutrient and there is no selective uptake in organisms. Th toxicity stems from its radioactivity only. For example, there is no drinking water maximum contaminant level for Th.

Summary

Th is incorporated in few minerals and behaves like an incompatible element during melting and crystallization. In aquatic systems Th is particle reactive and dissolved concentrations are extremely low. Its radioactivity makes it useful for age dating a variety of processes.

Cross-References

- Atomic Number, Mass Number, and Isotopes
- Earth's Continental Crust
- Epigenesis
- Geochronology and Radiogenic Isotopes
- Heat-Producing Elements (HPEs)
- High Field Strength Elements
- Incompatible Elements
- Lead Isotopes
- Lithophile Elements
- Partitioning and Partition Coefficients
- Radioactivity
- Solubility
- Subduction Zone Geochemistry
- Trace Elements
- Uranium
- Uranium Decay Series

References

Bard E, Hamelin B, Fairbanks RG, Zindler A (1990) Calibration of the ^{14}C timescale over the past 300,000 years using mass spectrometric U-Th ages from Barbados corals. Nature 345:405–409

Bizimis M, Salters VJM, Dawson JB (2003) The brevity of carbonatite sources in the mantle: evidence from Hf isotopes. Contrib Mineral Petrol 145:281–300

Chabaux F, Riotte J, Dequincey O (2003) U-Th-Ra fractionation during weathering and river transport. In: Bourdon B, Henderson GE, Lundstrom CC, Turner SP (eds) Uranium-series geochemistry. Mineralogical Society of America, Washington, DC, pp 533–576

Cheng H, Edwards RL, Shen C-C, Polyak VJ, Asmerom Y, Woodhead J, Hellstrom J, Wang Y, Kong X, Spötl C, Wang X, Alexander EC (2013) Improvements in ^{230}Th dating, ^{230}Th and ^{234}U half-life values, and U–Th isotopic measurements by multi-collector inductively coupled plasma mass spectrometry. Earth Planet Sci Lett 371–372:82–91

Henderson GE, Anderson RF (2003) The U-series toolbox for paleoceanography. In: Bourdon B, Henderson GM, Lundstrom CC, Turner SP (eds) Uranium-series geochemistry, vol 52. Mineralogical Society of America, Washington, DC, pp 493–531

McKenzie D (1985) ^{230}Th-^{238}U disequilibrium and the melting processes beneath ridge axes. Earth Planet Sci Lett 72:149–157

Plank T (2005) Constraints from thorium/lanthanum on sediment recycling at subduction zones and the evolution of the continents. J Petrol 46(5):921–944

Stern JC, Foustoukos DI, Sonke JE, Salters VJM (2014) Humic acid complexation of Th, Hf and Zr in ligand competition experiments: metal loading and pH effects. Chem Geol 363:241–249

Van Gosen BS, Gillerman VS, Armbrustmacher TJ (2009) Thorium deposits of the United States- energy resources for the future? vol 1336. US Geological Survey, Washington, DC, p 29

Thulium

Scott M. McLennan
Department of Geosciences, Stony Brook University, Stony Brook, NY, USA

Element Data
Atomic Symbol: Tm
Atomic Number: 69
Atomic Weight: 168.93422(2)
Isotopes and Abundances: ^{169}Tm, 100%
1 Atm Melting Point: 1545 °C
1 Atm Boiling Point: 1950 °C
Common Valences: +3
Ionic Radii: 88.0 pm (CN6), 99.4 pm (CN8), and 120.7 pm (CN12)
Pauling Electronegativity: 1.25
First Ionization Energy: 596.695 kJ mol^{-1}
Chondritic (CI) Abundance: 0.0256 ppm
Silicate Earth Abundance: 0.057 ppm
Crustal Abundance: 0.32 ppm
Seawater Abundance: 0.169 ppt
Core Abundance: ~0

Properties

Thulium (Tm), named after *Thule*, the original name for Scandinavia, is a soft, malleable, dense (9.321 g cm^{-3}), bright silvery-gray metal. Its electronic configuration is $[Xe]4f^{13}6s^2$. It is stable at room temperature and readily dissolves in mineral acids. It is a group 3 or IIIB inner transition element, with +3 being its only valence state in geological environments, and is one of the lanthanide rare earth elements (REE).

In geochemical terminology, it is grouped with heavy rare earth elements (HREE; Gd-Lu). Thulium has one stable isotope.

More than 270 minerals contain lanthanides as essential structural constituents, but those with Tm as a significant component are restricted to Y and HREE varieties, such as xenotime [$Y(PO_4)$], gadolinite-Y [$Y_2FeBe_2(Si_2O_{10})$], bastnäsite [$REE(CO_3)F$], allanite [$(REE,Ca,Y)_2(Al,Fe^{2+},Fe^{3+})_3(SiO_4)_3(OH)$], and britholite [$(REE,Ca)_5(SiO_4,PO_4)_3(OH,F)$].

Details of properties, mineralogy, history, and uses of Tm were compiled from Goonan (2011), Chakhmouradian and Wall (2012), Zaimes et al. (2015), Gschneidner (2016), Hammond (2016), and Meija et al. (2016a, b).

History and Use

Thulium was discovered in 1879 by Per Theodor Cleve, who separated the oxide and named it *thulia*. Reasonably pure thulium metal was first isolated in 1911. Due to its very low crustal abundances, thulium is very expensive and accordingly has relatively few applications. Minor uses include as a component in radiation sources of portable, X-ray equipment, YAG lasers, and high-temperature superconductors.

Geochemical Behavior

The fundamental importance of Tm in geochemistry is that it is one of the small trivalent rare earth elements, among the most useful trace elements in all areas of geochemistry and cosmochemistry due to their coherent and systematic behavior as a group, largely a consequence of the "lanthanide contraction."

Thulium is typically a trace element in most rocks and minerals. It is classified geochemically and cosmochemically as a highly refractory lithophile element, with a 50% $T_{condensation}$ of 1,659 K at 10^{-4} bars (Lodders 2003). In most igneous systems, Tm is incompatible with bulk partition coefficients, $D < 1$. In aqueous systems, Tm normally has very low fluid/rock partition coefficients ($\ll 1$). As a result, Tm contents of clastic sediments typically reflect their average provenance.

In seawater, Tm has very low concentrations (sub-ppt) and residence times (~2430 year) with speciation dominated by Tm^{3+}, $TmCO_3^+$, and $Tm(CO_3)_2^-$. In other aqueous systems (e.g., magmatic, hydrothermal), Tm can reach ppm levels due to elevated temperatures, pH effects, and complexing with various ligands (e.g., F^-, Cl^-, OH^-).

Concentration and residence time data are from compilations in Taylor and McLennan (2009) and Nozaki (2001).

Biological Utilization and Toxicity

There are no documented biological uses for Tm. REE (including Tm^{3+}) likely substitute for Ca^{2+} in biological materials and processes. REE concentrations (including Tm) in human tissues and fluids are very low (~ppb to <ppb levels, respectively) due to very low concentrations in natural waters and low uptake rates throughout the food chain (Bulman 2003). At low levels of ingestion, there are no established toxic effects that pose a threat to human health.

Cross-References

- Incompatible Elements
- Lanthanide Rare Earths
- Lithophile Elements
- Trace Elements
- Transition Elements

References

Bulman RA (2003) Metabolism and toxicity of the lanthanides. In: Sigel A, Sigel H (eds) Metal ions in biological systems, vol. 40, the lanthanides and their interrelations and biosystems. Marcel Dekker, Basel, pp 683–703

Chakhmouradian AR, Wall F (eds) (2012) Rare earth elements. Elements 8:333–376

Goonan TG (2011) Rare earth elements – end use and recyclability. U. S. Geol. Surv. Sci. Invest. Rpt. 2011–5094, 15pp

Gschneidner KA Jr (2016) Physical properties of the rare earth metals. In: Haynes WM (ed) CRC handbook of chemistry and physics, 96th edn. CRC Press, Boca Raton, pp 4-115–4-120

Hammond CR (2016) The elements. In: Haynes WM (ed) CRC handbook of chemistry and physics, 96th edn. CRC Press, Boca Raton, pp 4-1–4-42

Lodders K (2003) Solar system abundances and condensation temperatures of the elements. Astrophys J 591:1220–1247

Meija J, Coplen TB, Berglund M, Brand WA, De Bièvre P, Gröning M, Holden NE, Irrgeher J, Loss RD, Walczyk T, Prohaska T (2016a) Atomic weights of the elements 2013. Pure Appl Chem 88:265–291. (IUPAC Technical Report)

Meija J, Coplen TB, Berglund M, Brand WA, De Bièvre P, Gröning M, Holden NE, Irrgeher J, Loss RD, Walczyk T, Prohaska T (2016b) Isotopic compositions of the elements 2013. Pure Appl Chem 88:293–306. (IUPAC Technical Report)

Nozaki Y (2001) Rare earth elements and their isotopes in the ocean. In: Steele JH et al (eds) Encyclopedia of ocean sciences. Academic, London, pp 2354–2366

Taylor SR, McLennan SM (2009) Planetary crusts: their composition, origin and evolution. Cambridge University Press, Cambridge. 378pp

Zaimes GG, Hubler BJ, Wang S, Khanna V (2015) Environmental life cycle perspective on rare earth oxide production. ACS Sustain Chem Eng 3:237–244

Tin

William M. White
Department of Earth and Atmospheric Sciences, Cornell University, Ithaca, NY, USA

Element Data
Atomic Symbol: **Sn**
Atomic Number: **50**
Atomic Weight: 118.81 g/mol
Isotopes and Abundances: ^{112}Sn 0.97%, ^{114} Sn 0.66%, ^{115}Sn 0.34%, ^{116}Sn 14.54%, ^{117}Sn 7.68%, ^{118}Sn 24.22%, ^{119}Sn 8.54%, ^{120}Sn 32.58%, ^{122}Sn 4.63%, ^{124}Sn 5.79% ($t_{1/2} > 10^{17}$years)
1 Atm Melting Point: 232 °C
1 Atm Boiling Point: 2875 °C
Common Valences: 4+, 2+
Ionic Radii: 4+: 69 pm, 2+: 118 pm
Pauling Electronegativity: 1.96
First Ionization Potential: 708.4 kJ/mol
Chondritic (CI) Abundance: 1.63 ppm
Silicate Earth Abundance: 0.14 ppm
Crustal Abundance: 1.7 ppm
Seawater Abundance: 0.1–0.2 ppb
Core Abundance: ~0.5 ppm

Properties

Because it has a "magic number" of protons (50), the tin nucleus is particularly stable and Sn has greatest number of stable isotopes (10) of any element. The common valence states of Sn in nature are +4 and +2. Pure Sn exists in two forms: β-tin or white tin, stable at and above room temperature, is a silvery white, malleable, low-melting point metal forming a body-centered tetragonal lattice, while α-tin, or gray tin, stable below 13 °C, forms a diamond cubic structure. Bonding is covalent in the latter, and hence it is brittle and lacks typical metallic properties. This transformation severely degrades tin objects and is known as "tin pest."

History and Use

Tin is one of the most anciently known metals whose discovery is lost to history. Its chemical symbol derives from the Latin name for the metal, *stannum*. Alloying of Cu with 10–15% Sn produces bronze, a much stronger metal than Cu. The development of bronze metallurgy and consequent replacement of stone tools and weapons with bronze ones marks the end of the Neolithic Period in many parts of the world. Since Sn and Cu rarely occur together in the same deposits, bronze metallurgy also spurred the development of extensive new trade networks. Although some older bronze objects are known, widespread bronze metallurgy began around 3200–3000 BCE in the Middle East, Europe, and India and around 2000 BCE in East Asia. Some bronze was also produced by South and Central American cultures after about 200 BCE, but was used for ornamental rather than utilitarian purposes.

Pliny the Younger mentioned the use of Sn in solder in 79 BCE and solder remains one of the primary uses of Sn. Tin-plated steel cans for food storage and beverage storage has been an important use since the early nineteenth century. Tin continues to be used as an alloying metal, most notably in bronze and pewter (>90% tin and lesser amounts of Cu and Sb). Nb_3Sn is used for superconducting magnets, and zirconium-tin alloy is used for cladding nuclear fuel cells. Because of its low-melting point, liquid tin is used to "float" glass as it solidifies. Stannous fluoride (SnF_2) is a common additive to toothpastes used to promote fluoridation of tooth enamel (Greenwood and Earnshaw 1984).

Cassiterite, SnO_2, is the most common Sn mineral and primary ore of Sn and occurs primarily in pegmatites and hydrothermal veins and stockworks associated with granitic intrusions. Tin ores include both these rocks and weathering products and placers derived from them. Tin-bearing complex sulfides containing other metals, such as stannite (Cu_2FeSnS_4), occur in some of these deposits. Britain, Cornwall in particular, was a primary supplier of Sn to Europe from preclassical to recent times. As of 2015, the principal producers were China, followed by Indonesia, Burma, Peru, Bolivia, and Brazil.

Geochemical Behavior

Tin is moderately volatile with a 50% nebular condensation temperature of 704 K (Lodders 2003). It is also moderately siderophile, and consequently much of the Earth's inventory is thought to reside in its core (McDonough 2014). Within the silicate Earth, Sn behaves as a moderately incompatible lithophile element, but understanding of its behavior is limited. Sn/Sm ratios are roughly constant at ~0.32 in the mantle and mantle-derived rocks, with concentrations ranging from ~1 ppm in MORB to as high as 20 ppm in some OIB (Jochum et al. 1993; Yi et al. 1995). The Sn/Sm ratio of the bulk continental crust appears to be slightly higher (0.44; Rudnick and Gao 2014). Sn is compatible in ilmenite (Klemme et al. 2006) as well as biotite in highly evolved granites and pegmatites (Tischendorf et al. 2001).

The valence state of tin depends on oxygen fugacity and the crossover between Sn^{2+} and Sn^{4+} dominance in magmas appears to occur at oxygen fugacities near the fayalite-magnetite-quartz (FMQ) buffer (Durasova et al. 1986). The standard electrode potential for reduction of Sn^{4+} to Sn^{2+} is 0.384 ± 0.02 V (Gajda et al. 2009), implying that the 4+ form (stannic) is predominant in systems in contact with the atmosphere. The solubility of cassiterite depends on the f_{O_2}: it is more soluble at low f_{O2} where the +2 (stannous) form dominates. It also depends on temperature and melt or fluid composition, including factors such as the ratio of aluminum to alkalis, H_2O, F, and Cl content (e.g., Bhalla et al. 2005).

Tin appears to be a highly immobile element during weathering and is consequently strongly enriched in highly weathered and flushed lateritic soils and bauxites (Kronberg et al. 1982; Romer and Kroner 2014) and very impoverished in seawater (Sun and Li 2015). Marine sediments have Sn contents approximately the same to those of upper continental crust, 2–4 ppm (Li and Schoonmaker 2014).

Tin is likely present in seawater as stannic hydroxide complexes (Bruland et al. 2014), but Sn^{2+} forms strong carbonate, chloride, fluoride, and sulfate complexes (Cigala et al. 2012). These may be important in hydrothermal solutions and development of Sn ores (Müller and Seward 2001).

Tin mineralization is associated with highly evolved granites concentrated in discontinuous "tin belts," which are often associated with continental margins but not necessarily with subduction-related magmatism (Romer and Kroner 2016), and Sn is apparently not enriched in subducting lithosphere-derived fluids (Noll et al. 1996). Extreme fractional crystallization under conditions of low f_{O_2} (enhancing the solubility of Sn in the melt) is an important precondition for tin mineralization (Lehmann 1982), but high concentrations in the magma source appear to be critical as well. Essentially all Sn-rich granites are the products of crustal anatexis or have assimilated large quantities of crustal material. Romer and Kroner (2016) argue that melting or assimilation of sediments derived from intensely weathered crustal precursors is an essential precondition for development of Sn mineralization (Romer and Kroner 2016).

Tin Isotopes

Relatively few studies have been carried out on isotopic variations of Sn in nature, most of these with the objective of distinguishing tin sources in ancient bronze and other artifacts. As yet, there is no consensus on which isotope ratios are measured or on standards. Moynier et al. (2009) demonstrated mass independent fractionation in the laboratory of Sn isotopes bearing the odd-even signature of the nuclear field shift effect, but mass independent fractionations have not yet been identified in nature. Haustein et al. (2010) analyzed Sn isotope ratios in cassiterites from Sn deposits in Germany and England and found a range in isotopic composition of 0.55‰/u, with deposits isotopically homogeneous. Yamazaki et al. (2013) found a range of isotopic composition of 0.19‰/u in Asian Sn deposits. While these variations are archeologically useful, Yamazki et al. concluded that "the cause of Sn isotopic variation is yet to be established." Because Sn consists of nuclides formed in s-, r-, and p-process nucleosynthesis, isotopic variations in meteorites are expected, but studies with sufficient precision to identify them have not yet been carried out (Yokoyama and Walker 2016).

Biological Utilization and Toxicity

Tin has no known biological use. In its inorganic form, it is nontoxic, as its widespread use in food containers and toothpaste attests. Some organic tin compounds, however, are toxic. Tributyl-tin was used for a time in paints for the hulls of ships as an antifouling agent, but it proved to be an environmental toxin and is no longer used (Emsley 2001).

Summary

Tin metallurgy played a key role in the development of civilization, and Sn remains widely used today. Much of the Earth's tin is sequestered in the core, and it behaves as a moderately incompatible and highly immobile element with the highest concentrations occurring in highly evolved granites and associated hydrothermal veins. Its geochemical behavior nonetheless remains poorly understood.

Cross-References

- ▶ Atomic Number, Mass Number, and Isotopes
- ▶ Copper
- ▶ Fractional Crystallization and Assimilation
- ▶ Incompatible Elements
- ▶ Lithophile Elements
- ▶ Nucleosynthesis
- ▶ Ore Deposits
- ▶ Samarium
- ▶ Siderophile Elements
- ▶ Stable Isotope Geochemistry

References

Bhalla P, Holtz F, Linnen RL, Behrens H (2005) Solubility of cassiterite in evolved granitic melts: effect of T, f_{O2}, and additional volatiles. Lithos 80(1–4):387–400

Bruland KW, Middag R, Lohan MC (2014) 8.2 – controls of trace metals in seawater A2 – Holland, Heinrich D. In: Turekian KK (ed) Treatise on geochemistry, 2nd edn. Elsevier, Oxford, pp 19–51

Cigala RM, Crea F, De Stefano C, Lando G, Milea D, Sammartano S (2012) The inorganic speciation of tin(II) in aqueous solution. Geochim Cosmochim Acta 87:1–20
Durasova NA, Ryabchikov ID, Barsukov VL (1986) The redox potential and the behavior of tin in magmatic systems. Int Geol Rev 28(3):305–311
Emsley J (2001) Nature's building blocks: A-Z guide to the elements. Oxford University Press, Oxford, p 538
Gajda T, Sipos P, Gamsjäger H (2009) The standard electrode potential of the Sn^{4+}/Sn^{2+} couple revisited. Monatsh Chem Chem Mon 140(11):1293–1303
Greenwood NN, Earnshaw A (1984) Chemistry of the elements. Pergamon Press, Oxford. 1542 pp
Haustein M, Gillis C, Pernicka E (2010) Tin isotopy – a new method for solving old questions. Archaeometry 52(5):816–832
Jochum KP, Hofmann AW, Seufert HM (1993) Tin in mantle-derived rocks: constraints on Earth evolution. Geochim Cosmochim Acta 57:3585–3595
Klemme S, Günther D, Hametner K, Prowatke S, Zack T (2006) The partitioning of trace elements between ilmenite, ulvospinel, armalcolite and silicate melts with implications for the early differentiation of the moon. Chem Geol 234(3–4):251–263
Kronberg BI, Fyfe WS, McKinnon BJ, Couston JF, Filho BS, Nash RA (1982) Model for bauxite formation: Paragominas (Brazil). Chem Geol 35(3–4):311–320
Lehmann B (1982) Metallogeny of tin; magmatic differentiation versus geochemical heritage. Econ Geol 77(1):50–59
Li YH, Schoonmaker JE (2014) 9.1 – chemical composition and mineralogy of marine sediments A2 – Holland, Heinrich D. In: Turekian KK (ed) Treatise on geochemistry, 2nd edn. Elsevier, Oxford, pp 1–32
Lodders K (2003) Solar system abundances and condensation temperatures of the elements. Astrophys J 591:1220–1247
McDonough WF (2014) 3.16 – compositional model for the Earth's core A2 – Karl K Turekian, Heinrich D. Holland, Treatise on geochemistry, 2nd edn. Elsevier, Oxford, pp 559–577
Moynier F, Fujii T, Telouk P (2009) Mass-independent isotopic fractionation of tin in chemical exchange reaction using a crown ether. Anal Chim Acta 632(2):234–239
Müller B, Seward TM (2001) Spectrophotometric determination of the stability of tin(II) chloride complexes in aqueous solution up to 300°C. Geochim Cosmochim Acta 65(22):4187–4199
Noll PD, Newsom HE, Leeman WP, Ryan J (1996) The role of hydrothermal fluids in the production of subduction zone magmas: evidence from siderophile and chalcophile trace elements and boron. Geochim Cosmochim Acta 60(4):587–611
Romer RL, Kroner U (2014) Sediment and weathering control on the distribution of Paleozoic magmatic tin–tungsten mineralization. Mineral Deposita 50(3):327–338
Romer RL, Kroner U (2016) Phanerozoic tin and tungsten mineralization – tectonic controls on the distribution of enriched protoliths and heat sources for crustal melting. Gondwana Res 31:60–95
Rudnick RL, Gao S (2014) 4.1 – composition of the continental crust. In: Holland HD, Turekian KK (eds) Treatise on geochemistry, 2nd edn. Elsevier, Oxford, pp 1–51
Sun S, Li J (2015) Determination of Zr, Nb, Mo, Sn, Hf, Ta, and W in seawater by *N*-benzoyl-*N*-phenylhydroxylamine extraction chromatographic resin and inductively coupled plasma-mass spectrometry. Microchem J 119:102–107
Tischendorf G, Förster H-J, Gottesmann B (2001) Minor- and trace-element composition of trioctahedral micas: a review. Mineral Mag 65(2):249–276
Yamazaki E, Nakai S, Yokoyama T, Ishihara S, Tang H (2013) Tin isotope analysis of cassiterites from Southeastern and Eastern Asia. Geochem J 47(1):21–35
Yi W, Halliday AN, Lee D-C, Christensen JN (1995) Indium and tin in basalts, sulfides, and the mantle. Geochim Cosmochim Acta 59(24):5081–5090
Yokoyama T, Walker RJ (2016) Nucleosynthetic isotope variations of siderophile and chalcophile elements in the solar system. Rev Mineral Geochem 81(1):107–160

Titanium

Jay B. Thomas
Department of Earth Sciences, 204 Heroy Geology Laboratory, Syracuse University, Syracuse, NY, USA

Element Data
Atomic Symbol: **Ti**
Atomic Number: **22**
Atomic Weight: 47.867 g/mol
Isotopes and Abundances: ^{46}Ti 8.25%, ^{47}Ti 7.44%, ^{48}Ti 73.72%, ^{49}Ti 5.41%, and ^{50}Ti 5.18%
1 Atm Melting Point: 1668 °C
1 Atm Boiling Point: 3287 °C
Common Valences: 3+, 4+
Ionic Radii: Ti^{3+}: 4-fold 67 pm, Ti^{3+}: 6-fold 42 pm, 5-fold 51 pm, 6-fold 60.5 pm, 8-fold 74 pm
Pauling Electronegativity: 1.54
First Ionization Energy: 658.8 kJ/mol
Chondritic (CI) Abundance: 477 ppm
Silicate Earth Abundance: 1265 ppm
Crustal Abundance: 0.52%
Seawater Abundance: 6–250 pmol/kg
Core Abundance: ~0

Properties

Titanium is the second element in the first transition series and is a silver, lightweight metal in pure form. It has a density of 4.506 g/cm^3 at standard conditions. In nature, Ti behaves as a refractory lithophile element.

History and Use

Titanium oxide was first discovered in 1791 by mineralogist and chemist Reverend William Gregor while studying minerals in Cornwall, England (Russell 1955). In his modest laboratory in the town of Creed, Gregor analyzed the mineral ilmenite (now known to be $FeTiO_3$) collected from a stream at

Tregonwell Mill in the nearby village of Manaccan. Gregor determined that the ilmenite contained iron and the oxide of a new metallic substance he proposed be named menaccanite (originally called menachanite, menacanite, or menakanite). Later in 1791 Franz Joseph Muller also produced an unidentified substance from ilmenite. In 1795 chemist M. H. Klaproth concluded that the mineral rutile (TiO_2) contained a new element he proposed be called titankalk or titanium in reference to the strong giants of Greek mythology.

Rutile-, ilmenite-, and apatite-rich rocks called nelsonites associated with anorthosites in Nelson County, Virginia, were the primary source of Ti worldwide through the 1940s (Watson 1915; Herz et al. 1970). Anorthosite-related rocks continue to be valuable sources of Ti (Woodruff et al. 2013). The most economically important Ti resources are heavy mineral sands in which rutile, ilmenite, and leucoxene are concentrated along with other heavy minerals in alluvial, marine, and eolian placer deposits (e.g., Philander and Rozendaal 2015). Approximately 95% of Ti ore is refined to produce white-colored TiO_2 pigment, and the remainder is used to produce Ti metal (Bedinger 2015).

Titanium metal was first purified from TiO_2 by chemist M. A. Hunter at Rensselaer Polytechnic Institute (Troy, NY) in 1910 by reacting $TiCl_4$ with sodium metal in a high temperature "bomb"-type pressure vessel using a method now known as the Hunter process (Hunter 1910). In 1937 V. W. Kroll developed a similar process (Kroll 1937) in which rutile and ilmenite mineral concentrates were reacted to form metal chlorides (e.g., $TiCl_4$, $FeCl_2$) followed by reduction with magnesium metal to form $MgCl_2$ and Ti metal. The Kroll process is currently the most widely used method to produce Ti metal. Titanium metal is widely used for aerospace and nautical applications because it has a high strength to weight ratio and resists corrosion. Prosthetic implants are commonly fabricated from Ti metal because it is biocompatible and strong.

Geochemistry

Titanium does not commonly occur as a native element (Chen et al. 2000); it is usually bonded to oxygen. The electronic properties and ionic radii of Ti (element data table) strongly influence the solubility of Ti in fluids, melts, and minerals. Titanium may occur as Ti^{3+} or Ti^{4+} in minerals and melts. The blue color of some Ti-bearing minerals has been attributed to incorporation of Ti^{3+} (Johnson and Weyl 1949; Ihinger and Stolper 1986). Trivalent Ti occurs in lunar and meteoritic minerals, but it is exceptionally rare in terrestrial systems. It was believed that very low oxygen partial pressures (i.e., oxygen fugacity; fO_2) are required to stabilize Ti^{3+} (Anderson et al. 1970; Papike 2005; Borisov 2012). It is conceivable that fO_2 values in extraterrestrial systems are sufficiently low to produce melts with Ti^{3+}/Ti^{4+} higher than in melts observed on Earth; however, measurements of natural lunar basaltic composition melts and experimental analogs formed at fO_2 characteristic of the Moon (i.e., fO_2 lower than the iron-wustite oxygen buffer) show that most Ti occurs as Ti^{4+} (Krawczynski et al. 2010; Borisov 2012). This observation is supported by recent experiments which showed that Ti^{3+}/Ti^{4+} in minerals may vary widely at a fixed fO_2 because crystal chemistry can stabilize oxidation states independent of fO_2 (Doyle et al. 2014).

The accessory minerals (<1% of the rock) rutile, ilmenite, and titanite ($CaTiSiO_5$) host the majority of Ti in most crustal rocks. There are also numerous less abundant minerals that contain Ti as an essential structural constituent (i.e., their chemical formula and crystal structure are defined in part by the presence of Ti; http://rruff.info/chem=Ti/display=default/). Beyond these, many common terrestrial minerals can contain Ti in major element concentrations, including spinels, garnets, pyroxenes, amphiboles, and micas (Deer et al. 2013). Meteorites and lunar specimens commonly have the minerals hibonite, armalcolite, and grossmanite that contain major element concentrations of Ti (Sheng et al. 1991; Ma and Rossman 2009; Doyle et al. 2014). Titanium is a cathodoluminescence activator in some silicate minerals (e.g., Leeman et al. 2012, and references therein).

A wide range of Ti concentrations are observed in terrestrial and extraterrestrial rocks (Fig. 1). In terrestrial rocks the highest Ti concentrations are in mafic rocks (e.g., basalts), intermediate composition rocks (e.g., andesite, tonalite) have intermediate Ti concentrations, and the lowest Ti concentrations are observed in evolved felsic rocks (e.g., high-SiO_2 rhyolites). Sedimentary rocks contain Ti concentrations similar to intermediate composition igneous rocks (Fig. 1a).

Most extraterrestrial specimens contain Ti concentrations similar to rocks on Earth (Fig. 1b). One exception is the lunar high-Ti ultramafic glasses collected during the Apollo Moon landings (Delano 1986). The glasses are among the most unusual composition igneous materials observed in the solar system. The high-Ti ultramafic glasses have colors that range from green to yellow to orange to red and corresponding TiO_2 concentrations that range from 0.26 to 16.4 wt% TiO_2. Chondrites have lower Ti concentrations than most rocks from the Earth, Moon, and Mars (Fig. 1b).

Large Ti isotopic variations observed in solar system materials (e.g., presolar grains, hibonite grains, calcium-aluminum inclusions, chondrules, etc.) are used in cosmochemistry to study origins of the solar system (e.g., see references in Zhang 2012; Steele and Boehnke 2015). Processes such as equilibrium partitioning between phases, diffusion, and evaporation/

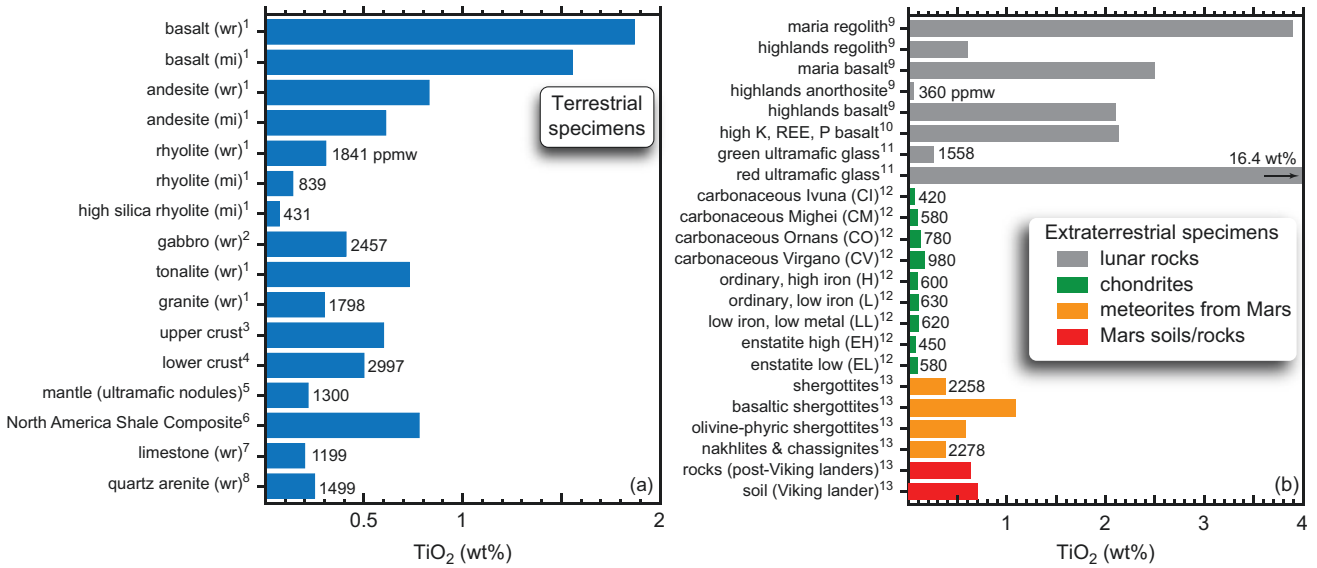

Titanium, Fig. 1 Average Ti concentrations measured in (**a**) terrestrial and (**b**) extraterrestrial specimens. Notations in parentheses for terrestrial specimens are *wr* whole rock, *mi* melt inclusion. For specimens with <0.5 wt% TiO_2, the concentrations are listed in parts per million by weight (ppm). *1*, http://georoc.mpch-mainz.gwdg.de/georoc/; *2*, Natland and Dick (2002); *3*, Taylor et al. (1981); *4*, Weaver and Tarney (1984); *5*, Sun (1982); *6*, Gromet et al. (1984); *7*, Condie et al. (1991); *8*, Boryta and Condie (1990); *9*, Taylor (1975); *10*, Hubbard et al. (1972); Rhodes and Hubbard (1973); Warren et al. (1978); Warren and Wasson (1979); *11*, Delano (1986); *12*, Wasson and Kallemeyn (1988); *13*, Bridges and Warren (2006) (Source: Jay Thomas)

condensation produced mass-dependent isotopic fractionations during early solar system assembly. Nucleosynthetic processes, radioactive decay, and cosmic-ray-induced transmutations produced mass-independent fractionations of Ti isotopes. Early solar system solids formed in different parts of the proto-solar nebula at different times; thus, Ti isotopes can be used to study physical and chemical processes that accompanied early solar system formation. Distribution of ^{46}Ti and ^{50}Ti in early solar system solids has been used to evaluate the efficiency of mixing processes in stellar-derived gas and dust in the proto-solar system. Additionally, similarity of $^{50}Ti/^{47}Ti$ ratios of earth and lunar materials supports derivation of the Moon from the Earth by impactor processes (Zhang et al. 2012).

Titanium Solubility in Fluids, Melts, and Minerals

Pressure, temperature, and system composition strongly affect the solubility of Ti in aqueous fluids, melts, and minerals. Because rutile commonly coexists with a free fluid phase in the Earth, the solubility of TiO_2 in fluids is important to equilibrium and kinetic processes that control Ti uptake and transport in earth materials. Experimental studies of rutile solubility in aqueous fluids at crustal and upper mantle conditions show that rutile is sparingly soluble in pure H_2O (Fig. 2; Antignano and Manning 2008). Rutile solubility in pure H_2O increases with pressure and temperature. Addition of Na-Al components (e.g., albite) to the fluid substantially increases solubility of TiO_2 in the fluid (Fig. 2; Antignano and Manning 2008; Hayden and Manning 2011). At 10 kbar and 700 °C, approximately 6 ppm Ti dissolves into pure water, whereas ~40 ppm Ti dissolves into an aqueous solution containing 6.3 wt% Na-Al silicate.

The solubility of TiO_2 in silicate melts is strongly affected by pressure, temperature, and composition. TiO_2 solubility in melts can be used to calculate titania activity in rutile-free magmatic systems for application of thermobarometers that involve TiO_2 equilibria (Hayden and Watson 2007; Ghiorso and Gualda 2012). Additionally, the P–T–X dependencies of rutile solubility in melts can be used to determine the extent to which rutile in magmatic source regions controls high field strength element variations (e.g., Ti, Nb, Ta) in many igneous rocks. Rutile saturation in melts was investigated by crystallizing rutile from TiO_2-saturated melts ranging in composition from rhyolite to basalt in experiments conducted from 1 bar to 35 kbar and 1000 to 1300 °C (Ryerson and Watson 1987; Gaetani et al. 2008). Rutile solubility in silicate melts increases considerably with increasing temperature and decreasing pressure (Fig. 3). The Ryerson and Watson (1987) rutile saturation model predicts that 1138 ppm Ti will dissolve into rhyolitic composition melt at 1 kbar and 700 °C, and 8855 ppm Ti will dissolve into the melt at 1100 °C and 30 kbar. Recent studies showed that TiO_2 solubility increases markedly with increasing water content in the melt (Gaetani et al. 2008).

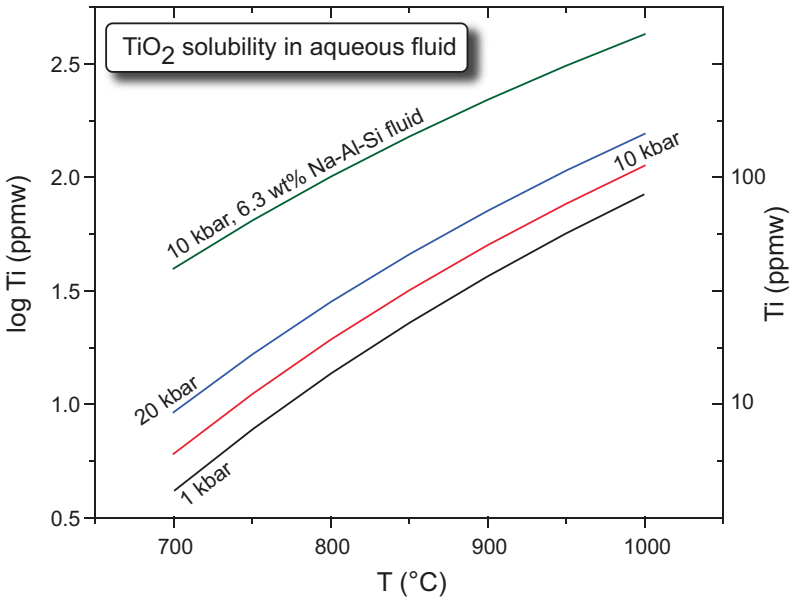

Titanium, Fig. 2 Rutile solubility in aqueous fluids (Antignano and Manning 2008). The lower three curves show the solubility of Ti in pure H_2O. The *upper red curve* shows the solubility of Ti in a fluid with 6.3 wt% silicate solution produced from dissolved albite ($NaAlSi_3O_8$) (Source: Jay Thomas)

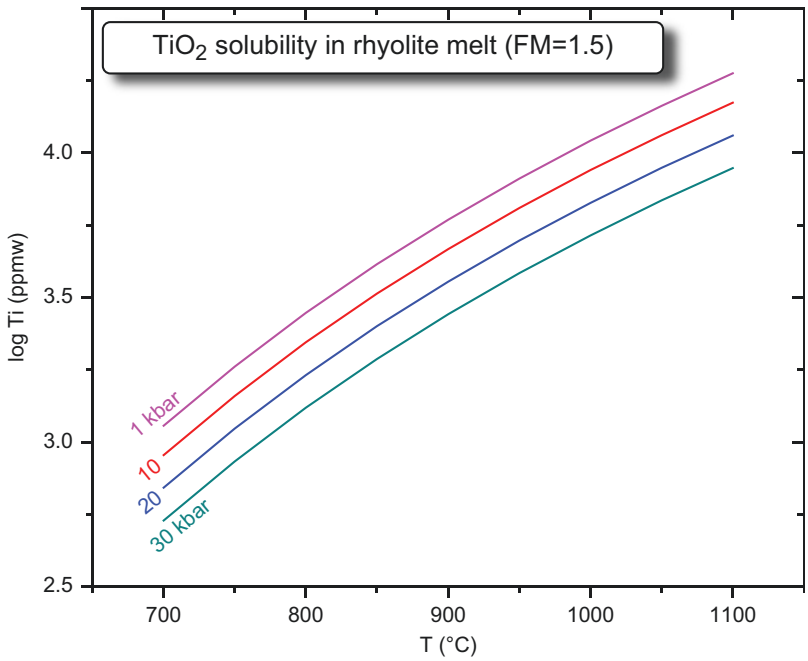

Titanium, Fig. 3 TiO_2 solubility in rhyolite composition melt (Ryerson and Watson 1987). FM is a compositional parameter (Source: Jay Thomas)

Using Ti in Zircon and Quartz to Determine Crystallization Pressure and Temperature

The minor to major element Ti content and the presence of near-pure rutile in many natural systems makes Ti an ideal candidate for thermodynamically based experimental calibrations to estimate crystallization temperature and/or pressure. Experimental studies in the ZrO_2-SiO_2-TiO_2 system showed that Ti solubility in zircon systematically increases with increasing temperature (Fig. 4; Watson et al. 2006; Ferry and Watson 2007). Zircon was co-crystallized along with rutile and quartz from SiO_2-, TiO_2-, and $ZrSiO_4$-saturated fluids and melts. The temperature dependence of Ti solubility in zircon was presented as a geothermometer "calibration" that can be used to estimate the temperature of zircon crystallization. For example, the Ti-in-zircon solubility model predicts that a zircon with 10 ppm Ti that grew in the presence of rutile and quartz crystallized at 746 °C (Fig. 4). Magma compositions that commonly crystallize zircon are not typically rutile saturated, which means that titania activity must be estimated for applications to most igneous systems (Hayden and Watson 2007; Ghiorso and Gualda 2012).

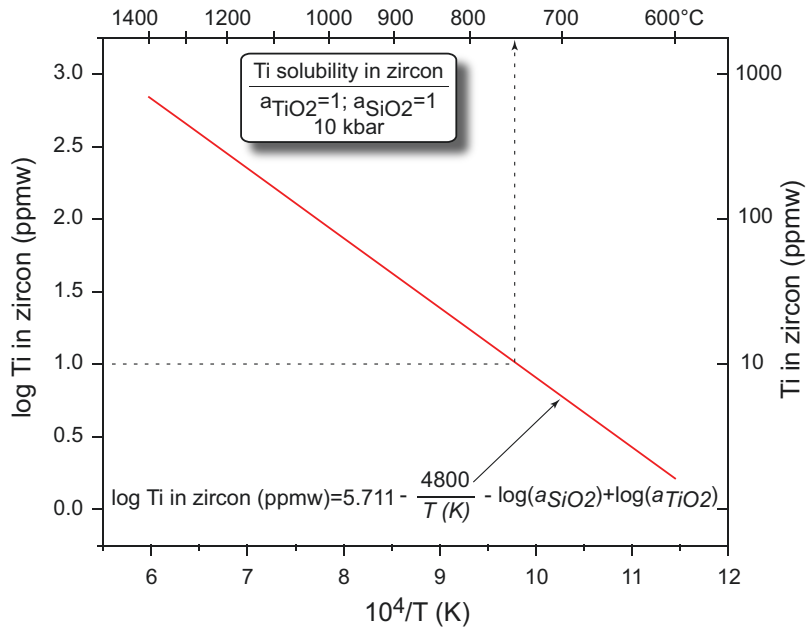

Titanium, Fig. 4 Calibration of the Ti-in-zircon thermometer (Watson et al. 2006; Ferry and Watson 2007). Activities of titania and silica in the system, $a_{TiO_2}^{\text{liquid}-\text{rutile}}$ and $a_{SiO_2}^{\text{liquid}-\text{quartz}}$, are referenced to rutile and quartz saturation, respectively (Source: Jay Thomas)

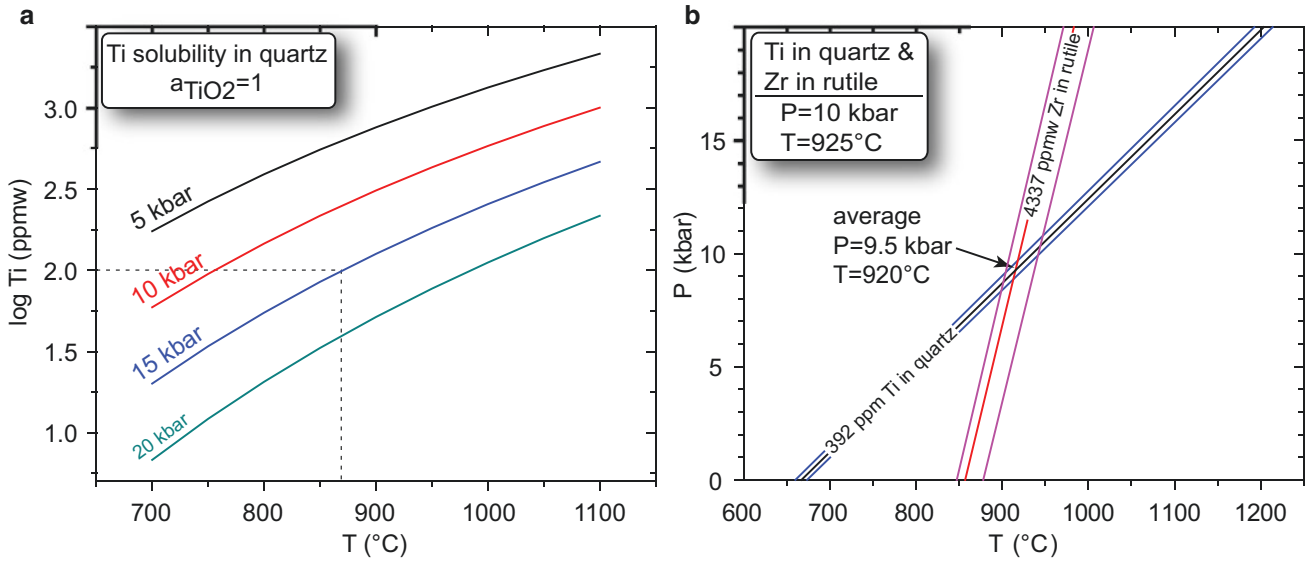

Titanium, Fig. 5 (**a**) Ti-in-quartz solubility model; isobars calculated from $\log \text{Ti in quartz (ppmw)} = -26530 + 50 \cdot T(\text{K}) - 760 \cdot P(\text{kbar}) + RT \log a_{TiO_2}^{\text{liquid}-\text{rutile}}/RT(\text{K})$, where R is the gas constant 8.3145 J/K, T is temperature in Kelvin, and $a_{TiO_2}^{\text{liquid}-\text{rutile}}$ is titania activity in the system referenced to rutile saturation (Thomas et al. 2010). (**b**) Application of the Ti-in-quartz solubility model to an experiment of Thomas et al. (2015). The average Ti-in-quartz isopleth calculated from the calibration of Thomas et al. (2010) and the average Zr-in-rutile isopleth calculated from the calibration of Tomkins et al. (2007) cross at 9.5 kbar and 920 °C, which is in excellent agreement with the P–T conditions of the crystallization experiment at 10 kbar and 925 °C (Source: Jay Thomas)

The pressure and temperature dependencies of Ti-in-quartz solubility have been quantified from experimental studies in the SiO_2-$TiO_2 \pm ZrO_2$ system (Thomas et al. 2015, and references therein). Titanium solubility in quartz systematically increases with increasing temperature and decreasing pressure (Fig. 5a). For example, the Ti-in-quartz solubility model predicts that quartz with 100 ppm Ti that grew at 15 kbar in the presence of rutile crystallized at 869 °C (Fig. 5a). The P–T dependencies of Ti-in-quartz solubility can be used as a thermobarometer when used in combination with another thermobarometer in a coexisting mineral, an independent P or T estimate of quartz crystallization, or well-constrained phase equilibria (Fig. 5b; Thomas et al. 2010; Thomas and Watson 2012; Thomas et al. 2015).

Biological Utilization and Toxicity

Titanium is not biologically utilized and is not toxic.

Summary

Terrestrial and extraterrestrial rocks have a wide range of Ti concentrations. The majority Ti in rocks is contained in accessory minerals rutile, ilmenite, and titanite. Heavy mineral sands are the most economically important Ti sources. Large variations of Ti isotopes are used in cosmochemistry to study processes that produced mass-dependent and mass-independent fractionations. In terrestrial systems there is a well-defined geochemical framework to use Ti-in-quartz and Ti-in-zircon solubilities and lattice diffusion parameters (Cherniak and Watson 2007; Cherniak et al. 2007) to develop petrogenetic models that include the pressure and temperature of crystallization (e.g., Wark et al. 2007; Thomas and Watson 2012; Breiter et al. 2014), temperature of deformation (Nachlas et al. 2014, and references therein), the time scales of thermobarometric events (Spear et al. 2012), and the provenance of quartz crystals (Ackerson et al. 2015).

Cross-References

- ▶ Chondrites
- ▶ Geothermometry and Geobarometry
- ▶ Lithophile Elements
- ▶ Nucleosynthesis
- ▶ Presolar Grains
- ▶ Refractory Inclusions in Chondritic Meteorites

References

Ackerson MR, Tailby ND, Watson EB (2015) Trace elements in quartz shed light on sediment provenance. Geochem Geophys Geosyst. https://doi.org/10.1002/2015GC005896

Anderson AT, Crewe AV, Goldsmith JR et al (1970) Petrologic history of moon suggested by petrography, mineralogy, and crystallography. Science 167:587–590. https://doi.org/10.1126/science.167.3918.587

Antignano A, Manning CE (2008) Rutile solubility in H_2O, H_2O–SiO_2, and H_2O–$NaAlSi_3O_8$ fluids at 0.7–2.0 GPa and 700–1000 °C: implications for mobility of nominally insoluble elements. Chem Geol 255:283–293. https://doi.org/10.1016/j.chemgeo.2008.07.001

Bedinger GM (2015) Titanium [Advance Release]. In: 2013 Minerals yearbook. USGS, Washington, DC, pp 78.1–78.14

Borisov AA (2012) The Ti^{4+}/Ti^{3+} ratio of magmatic melts: application to the problem of the reduction of lunar basalts. Petrology 20:391–398. https://doi.org/10.1134/S0869591112040030

Boryta M, Condie KC (1990) Geochemistry and origin of the Archaean Beit Bridge complex, Limpopo Belt, South Africa. J Geol Soc 147:229–239. https://doi.org/10.1144/gsjgs.147.2.0229

Breiter K, Ackerman L, Ďurišová J et al (2014) Trace element composition of quartz from different types of pegmatites: a case study from the Moldanubian Zone of the Bohemian Massif (Czech Republic). Mineral Mag 78:703–722. https://doi.org/10.1180/minmag.2014.078.3.17

Bridges JC, Warren PH (2006) The SNC meteorites: basaltic igneous processes on Mars. J Geol Soc 163:229–251. https://doi.org/10.1144/0016-764904-501

Chen J, Li J, Wu J (2000) Native titanium inclusions in the coesite eclogites from Dabieshan, China. Earth Planet Sci Lett 177:237–240. https://doi.org/10.1016/S0012-821X(00)00057-1

Cherniak DJ, Watson EB (2007) Ti diffusion in zircon. Chem Geol 242:470–483. https://doi.org/10.1016/j.chemgeo.2007.05.005

Cherniak DJ, Watson EB, Wark DA (2007) Ti diffusion in quartz. Chem Geol 236:65–74. https://doi.org/10.1016/j.chemgeo.2006.09.001

Condie KC, Wilks M, Rosen DM, Zlobin VL (1991) Geochemistry of metasediments from the Precambrian Hapschan Series, eastern Anabar Shield, Siberia. Precambrian Res 50:37–47. https://doi.org/10.1016/0301-9268(91)90046-D

Deer WA, Howie RA, Zussman J (2013) An introduction to the rock-forming minerals, 3rd edn. The Minerological Society, London

Delano JW (1986) Pristine lunar glasses: criteria, data, and implications. J Geophys Res 91:201–213. https://doi.org/10.1029/JB091iB04p0D201

Doyle PM, Schofield PF, Berry AJ et al (2014) Substitution of Ti^{3+} and Ti^{4+} in hibonite ($CaAl_{12}O_{19}$). Am Mineral 99:1369–1382. https://doi.org/10.2138/am.2014.4532

Ferry JM, Watson EB (2007) New thermodynamic models and revised calibrations for the Ti-in-zircon and Zr-in-rutile thermometers. Contrib Mineral Petrol 154:429–437. https://doi.org/10.1007/s00410-007-0201-0

Gaetani GA, Asimow PD, Stolper EM (2008) A model for rutile saturation in silicate melts with applications to eclogite partial melting in subduction zones and mantle plumes. Earth Planet Sci Lett 272:720–729. https://doi.org/10.1016/j.epsl.2008.06.002

Ghiorso MS, Gualda GAR (2012) A method for estimating the activity of titania in magmatic liquids from the compositions of coexisting rhombohedral and cubic iron–titanium oxides. Contrib Mineral Petrol 165:73–81. https://doi.org/10.1007/s00410-012-0792-y

Gromet LP, Haskin LA, Korotev RL, Dymek RF (1984) The "North American shale composite": its compilation, major and trace element characteristics. Geochim Cosmochim Acta 48:2469–2482. https://doi.org/10.1016/0016-7037(84)90298-9

Hayden LA, Manning CE (2011) Rutile solubility in supercritical $NaAlSi_3O_8$–H_2O fluids. Chem Geol 284:74–81. https://doi.org/10.1016/j.chemgeo.2011.02.008

Hayden LA, Watson EB (2007) Rutile saturation in hydrous siliceous melts and its bearing on Ti-thermometry of quartz and zircon. Earth Planet Sci Lett 258:561–568. https://doi.org/10.1016/j.epsl.2007.04.020

Herz N, Valentine LE, Iberall ER (1970) Rutile and Ilmenite placer deposits, Roseland district, Nelson and Amherst counties, Virginia. USGS Bulletin 1312–F, Washington, DC

Hubbard NJ, Gast PW, Rhodes JM, Wiesmann H, Church SE (1972) Nonmare basalts: part II. Proc Lunar Planet Sci 3:1161–1179

Hunter MA (1910) Metallic titanium. J Am Chem Soc 32:330–336. https://doi.org/10.1021/ja01921a006

Ihinger PD, Stolper E (1986) The color of meteoritic hibonite: an indicator of oxygen fugacity. Earth Planet Sci Lett 78:67–79. https://doi.org/10.1016/0012-821X(86)90173-1

Johnson G, Weyl WA (1949) Influence of minor additions on color and electrical properties of rutile. J Am Ceram Soc 32:398–401. https://doi.org/10.1111/j.1151-2916.1949.tb18920.x

Krawczynski MJ, Sutton SR, Grove TL (2010) Titanium valence in lunar ultramafic glasses and olivine-diogenites. Lunar Planet Sci Conf 41:1825

Kroll W (1937) Verformbares Titan und Zirkon. Z Anorg Allg Chem 234:42–50. https://doi.org/10.1002/zaac.19372340105
Leeman WP, MacRae CM, Wilson NC et al (2012) A study of cathodoluminescence and trace element compositional zoning in natural quartz from volcanic rocks: mapping titanium content in quartz. Microsc Microanal 18:1322–1341. https://doi.org/10.1017/S1431927612013426
Ma C, Rossman GR (2009) Grossmanite, $CaTi^{3+}AlSiO_6$, a new pyroxene from the Allende meteorite. Am Mineral 94:1491–1494. https://doi.org/10.2138/am.2009.3310
Nachlas WO, Whitney DL, Teyssier C et al (2014) Titanium concentration in quartz as a record of multiple deformation mechanisms in an extensional shear zone. Geochem Geophys Geosyst 15:1374–1397. https://doi.org/10.1002/2013GC005200
Natland JH, Dick HBJ (2002) Stratigraphy and composition of gabbros drilled in Ocean Drilling Program Hole 735B, Southwest Indian Ridge: a synthesis of geochemical data. In: Natland JH, Dick HBJ, Miller DJ, Von Herzen RP (eds) Proceedings of the Ocean Drilling Program, 176 scientific results. Ocean Drilling Program. https://doi.org/10.2973/odp.proc.sr.176.002.2002
Papike JJ (2005) Comparative planetary mineralogy: valence state partitioning of Cr, Fe, Ti, and V among crystallographic sites in olivine, pyroxene, and spinel from planetary basalts. Am Mineral 90:277–290. https://doi.org/10.2138/am.2005.1779
Philander C, Rozendaal A (2015) Geology of the Cenozoic Namakwa sands heavy mineral deposit, west coast of South Africa: a world-class resource of titanium and zircon. Econ Geol 110:1577–1623. https://doi.org/10.2113/econgeo.110.6.1577
Rhodes JM, Hubbard NJ (1973) Chemistry, classification and petrogenesis of Apollo 15 mare basalts. Lunar Planet Sci Conf 4:1127–1148
Russell A (1955) The Rev. William Gregor (1761–1817), discoverer of titanium. Mineral Mag 30:617–624
Ryerson FJ, Watson EB (1987) Rutile saturation in magmas: implications for TiNbTa depletion in island-arc basalts. Earth Planet Sci Lett 86:225–239. https://doi.org/10.1016/0012-821X(87)90223-8
Sheng YJ, Hutcheon ID, Wasserburg GJ (1991) Origin of plagioclase-olivine inclusions in carbonaceous chondrites. Geochim Cosmochim Acta 55:581–599. https://doi.org/10.1016/0016-7037(91)90014-V
Spear FS, Ashley KT, Webb LE, Thomas JB (2012) Ti diffusion in quartz inclusions: implications for metamorphic time scales. Contrib Mineral Petrol 164:977–986. https://doi.org/10.1007/s00410-012-0783-z
Steele RCJ, Boehnke P (2015) Titanium isotope source relations and the extent of mixing in the proto-solar nebula examined by independent component analysis. Astrophys J 802:80. https://doi.org/10.1088/0004-637X/802/2/80
Sun S-S (1982) Chemical composition and origin of the earth's primitive mantle. Geochim Cosmochim Acta 46:179–192. https://doi.org/10.1016/0016-7037(82)90245-9
Taylor SR (1975) Lunar science: a post-Apollo view. Pergamon Press, New York, p 390
Taylor SR, McLennan SM, Armstrong RL, Tarney J (1981) The composition and evolution of the continental crust: rare earth element evidence from sedimentary rocks [and discussion]. Philos Trans R Soc A Math Phys Eng Sci 301:381–399. https://doi.org/10.1098/rsta.1981.0119
Thomas JB, Watson EB (2012) Application of the Ti-in-quartz thermobarometer to rutile-free systems. Reply to: a comment on: "TitaniQ under pressure: the effect of pressure and temperature on the solubility of Ti in quartz" by Thomas et al. Contrib Mineral Petrol 164:369–374. https://doi.org/10.1007/s00410-012-0761-5
Thomas JB, Watson EB, Spear FS et al (2010) TitaniQ under pressure: the effect of pressure and temperature on the solubility of Ti in quartz. Contrib Mineral Petrol 160:743–759. https://doi.org/10.1007/s00410-010-0505-3
Thomas JB, Watson EB, Spear FS, Wark DA (2015) TitaniQ recrystallized: experimental confirmation of the original Ti-in-quartz calibrations. Contrib Mineral Petrol 169:1–16. https://doi.org/10.1007/s00410-015-1120-0
Tomkins HS, Powell R, Ellis DJ (2007) The pressure dependence of the zirconium-in-rutile thermometer. J Metamorph Geol 25:703–713. https://doi.org/10.1111/j.1525-1314.2007.00724.x
Wark DA, Hildreth W, Spear FS et al (2007) Pre-eruption recharge of the Bishop magma system. Geology 35:235–238. https://doi.org/10.1130/G23316A.1
Warren PH, Wasson JT (1979) The origin of KREEP. Rev Geophys 17:73–88. https://doi.org/10.1029/RG017i001p00073
Warren PH, Afiattalab F, Wasson JT (1978) Investigation of unusual KREEPy samples – Pristine rock 15386, cone crater soil fragments 14143, and 12023, a typical Apollo 12 soil. Lunar Planet Sci Conf 9:653–660
Wasson JT, Kallemeyn GW (1988) Compositions of chondrites. Philos Trans R Soc A Math Phys Eng Sci 325:535–544. https://doi.org/10.1098/rsta.1988.0066
Watson TL (1915) The rutile deposits of the eastern United States. USGS Bull 580:385–412
Watson EB, Wark DA, Thomas JB (2006) Crystallization thermometers for zircon and rutile. Contrib Mineral Petrol 151:413–433. https://doi.org/10.1007/s00410-006-0068-5
Weaver BL, Tarney J (1984) Empirical approach to estimating the composition of the continental crust. Nature 310:575–577. https://doi.org/10.1038/310575a0
Woodruff LG, Nicholson SW, Fey DL (2013) A deposit model for magmatic iron-titanium-oxide deposits related to Proterozoic massif anorthosite plutonic suites. USGS Scientific Investigations Report 2010–5070–K
Zhang J (2012) Titanium isotope cosmochemistry. PhD thesis, University of Chicago
Zhang J, Dauphas N, Davis AM et al (2012) The proto-Earth as a significant source of lunar material. Nat Geosci 5:251–255. https://doi.org/10.1038/ngeo1429

Trace Elements

William M. White
Department of Earth and Atmospheric Sciences, Cornell University, Ithaca, NY, USA

Definition

A trace element is one present at very low abundance in a particular system such that it obeys Henry's Law in that system.

Which Elements Are Trace Elements?

The answer depends on the system of interest; a trace element in one system may be a major element in another. Oxygen, magnesium, silicon, iron, aluminum, calcium, nickel, and calcium make up ~99% of the Earth, so all other elements could be considered trace elements. Nevertheless, for example, potassium constitutes ~1.5% of the Earth's continental

crust, where it is considered a "major element." Manganese and phosphorus are also conventionally reported along with the major oxides in rocks, even though their concentrations rarely exceed a few tenths of a percent.

One possible definition of a trace element or trace component is that it does not significantly affect the chemical or physical properties of the system as a whole. Yet trace elements can determine the color of a mineral, CO_2 profoundly affects the atmosphere's transparency to infrared radiation, and consequently Earth's climate, even in concentrations of 100's of ppmv and hydrogen dramatically affects mantle viscosity even at concentrations below 100 ppm. So this definition is not satisfactory either.

This leads to what may be the best definition of a trace element: *an element whose activity obeys Henry's Law in the system of interest*. This implies sufficiently dilute concentrations that interactions between atoms of that element are sufficiently rare that its behavior is independent of its concentration.

Geochemical and Biochemical Importance of Trace Elements

Although trace elements constitute only a small fraction of a system of interest, they provide geochemical information out of proportion to their abundance. There are several reasons for this. First, variations in the concentrations of many trace elements are much larger than those of major components, often by many orders of magnitude. Second, in any system the number of trace elements far exceeds the number of major elements. Third, the range in behavior of trace elements is large, and collectively they are sensitive to processes to which major elements are insensitive. One example is the depth of partial melting. When the mantle melts, the major element composition of those melts depends only weakly on pressure. The heavy rare earths, however, are highly sensitive to the depth of melting because they partition into garnet, which is only present at high pressure (e.g., Kay and Gast 1973). Another example is cadmium in the fossil shells of microorganisms, which has provided information about the biological productivity and circulation patterns of ancient oceans (e.g., Boyle 1988). Finally, many elements that are present only in trace quantities in the environment are biologically essential. For example, zinc, present in soils at the parts per million (ppm) level and in seawater at the parts per billion (ppb) level, is a component of many essential proteins and enzymes.

Concentration Units

Trace element concentrations are often reported in weight units as parts per million (ppm), parts per billion (ppb), or parts per trillion (ppt), which correspond to milli-, micro-, and nanograms per kilogram. Commonly used molarity units are milli-, micro-, or nano-moles per liter abbreviated as mM, μM, and pM. For atmospheric gases, volume units are more commonly used, for example, parts per million by volume (ppmv).

Cross-References

- ▶ Cadmium
- ▶ Earth's Atmosphere
- ▶ Earth's Continental Crust
- ▶ Geochemical Classification of Elements
- ▶ Henry's Law
- ▶ Lanthanide Rare Earths
- ▶ Partial Melting
- ▶ Potassium
- ▶ Zinc

References

Boyle EA (1988) Cadmium: chemical tracer of deepwater paleoceanography. Paleoceanography 3:471–489

Kay RW, Gast PW (1973) The rare earth content and origin of alkali-rich basalts. J Geol 81(6):653–682

Transition Elements

Dante Canil
School of Earth and Ocean Sciences, University of Victoria, Victoria, BC, Canada

Definition

The transition elements are defined as having an electronic configuration of partially filled d- or f-orbitals. As a group they have a range of valence states and are responsible for the variety of colors and magnetic properties in many natural minerals and glasses. The multivalent nature of transition elements makes their distribution in fluids, gases, and minerals in natural geologic systems especially sensitive to temperature and redox state.

Abundance and Distribution

Only transition metals with unfilled d-shells are considered in this chapter. There are 29 such metals, subdivided by their

position in the rows of the periodic table as first row (Sc – Zn), second row (Y to Cd), and third row (Hf – Hg) transition elements. The first row transition elements are the most abundant in the Sun, chondrites, and the bulk Earth compared to the other two groups. Iron is the most abundant transition element in the bulk Earth, maximized in concentration by nucleosynthetic processes that formed all elements (Table 1).

The transition metals can be classified as siderophile (affinity for metal), lithophile (combine readily with oxygen), or chalcophile (pairing with sulfide). The classification of transition metals as chalco-, sidero-, or lithophile, however, varies substantially with oxidation state. For example, Fe is siderophile at conditions of the core, lithophile in most of the mantle and crust, and yet is a common constituent of many sulfide minerals and melts. Some transition metals (Cd, Hg) are even atmophile given their volatility at certain conditions.

Behavior

The valence states of transition metal ions control their substitution into crystal structures and their solubility in solutions. Chemical fractionation during formation of the early Earth segregated metallic Fe to the core. Partial melting to form magmas has sequestered some of the transition elements (Cr, Ni, Fe, Co) that are more compatible in silicates or oxides of the mantle, or the crust (Sc, Ti). Exsolution of sulfides from magmas or hydrothermal fluids has focused anomalously high concentrations of other transition elements into ore deposits of the crust (Cu, Zn, Ni).

Valence State and Crystal Chemistry

The valence states for transition metal ions can vary from 1^+ to 8^+, though 2^+ and 3^+ are the most common valence states in

Transition Elements, Table 1 Properties of transition metal ions in terrestrial rocks

Element	Classification[a]	Valence states[b]	Coordination state[c]	Mineral in crust or mantle[d]
Sc	Lith	3^+	6	Px, Amp
Ti	Lith	2^+,3^+,**4^+**	4,6	Px, Amp, Ilm, Ttn, Rut
V	Lith	2^+,**3^+**,4^+,5^+	4,6	Sp, Gt, Sp
Cr	Lith	2^+,**3^+**,4^+,5^+,6^+	4,6	Sp, Px, Gt
Mn	Lith	**2^+**,3^+,4^+	6,8	Ol, Px, Sp
Fe	Lith, Chal, Sid	**2^+**,**3^+**,4^+	6,8	Ol, Px, Sp, Amp
Co	Lith	**2^+**,3^+,4^+	6,8	Ol, Px, Sp
Ni	Lith, Chal, Sid	2^+,3^+,4^+	6,8	Ol, Px, Sp
Cu	Chal	**1^+**,**2^+**,3^+	6,8	Ccp, Py, Po
Zn	Lith, Chal	2^+	6,8	Px, Sp, Sph
Y	Lith	3^+	6,8	Gt
Zr	Lith	4^+	4,6	Zrn
Nb	Lith	3^+,4^+,**5^+**	6	Ttn
Mo	Lith	3^+,**4^+**,5^+	6	Mo
Tc	Artificial	4^+,5^+,7^+	6	
Ru	Sid	**3^+**,4^+,5^+,7^+,8^+	4,6	PGM
Rh	Sid	**3^+**,4^+,5^+	6	PGM
Pd	Sid	1^+,**2^+**,3^+,4^+	4,6	PGM
Ag	Chal	1^+,2^+	4,6	Sul
Cd	Chal	2^+	4,8	Sul
Hf	Lith	4^+	4,6,8	Zrn
Ta	Lith	3^+,4^+,**5^+**	6,8	Rut
W	Lith	**4^+**,5^+,6^+	6	Sch
Re	Sid	**4^+**,5^+,6^+,7^+	4,6	Sul
Os	Sid	**4^+**,5^+,6^+,7^+,8^+	4,6	PGM
Ir	Sid	**3^+**,4^+,5^+	6	PGM
Pt	Sid	**2^+**,4^+,**5^+**	4,6	PGM
Au	Sid, Chal	3^+,5^+	4,6	PGM
Hg	Chal	1^+,2^+	4,6,8	Cinn, Sul

[a] *Lith* lithophile, *Chal* chalcophile, *Sid* siderophile
[b] Common valence state at terrestrial conditions in **boldface**
[c] Lists only most common coordination state in common crustal or mantle minerals
[d] Mineral group with significant transition metal ion substitution: *Px* pyroxenes, *Amp* amphiboles, *Ol* olivine, *Sp* spinel, *Gt* garnet, *Ilm* ilmenite, *Rut* rutile, *Zrn* zircon, *Ttn* titanite, *Mo* molybdenite, *Sul* sulfide minerals, *PGM* platinum group metal alloys, *Cinn* cinnabar, *Sch* scheelite, *Sph* sphalerite

minerals at terrestrial conditions. In common rock-forming minerals of the crust and mantle, the first row transition elements substitute mostly on octahedrally coordinated sites, less so on cubic sites (Shannon 1976). Substitution on tetrahedral sites is rare. With the exception of Fe, no common rock-forming minerals are dominated by the concentration of any given transition element. Some accessory minerals are dominated by transition elements: Ti in perovskite ($CaTiO_3$), rutile (TiO_2), and ilmenite ($FeTiO_3$); Fe and Cr in spinel group minerals; Mn in oxides; and Cu-Zn-Ni in sulfides.

Crystal-Melt Partitioning

A number of attributes of the transition metals in earth materials can inform about conditions in the Earth both now and in the past. The ratio of Fe^{3+}/Fe^{2+} in magmas is sensitive to temperature, composition, and oxygen fugacity. The change in Fe^{3+}/Fe^{2+} ratio in melts with these variables reveals the redox states for the formation of terrestrial magmas, and its changes during differentiation or melting. The range in Fe^{3+}/Fe^{2+} in magmas spans several orders of oxygen fugacity, possibly related to that of their mantle source region (Carmichael 1991).

The partitioning of Fe, Mn, Zn, Sc, and V between mantle minerals and melts varies considerably (Fig. 1) and is useful to deduce the redox state or major element and mineralogical heterogeneity of the mantle source region of basaltic magmas (Canil 1999; Le Roux et al. 2011). The element pairs Fe-Zn and Sc-V generally have the same compatibility in mantle minerals olivine and pyroxene relative to melts, except that the partition of Fe or V is redox sensitive (Mallmann and O'Neill 2009). The V/Sc or Zn/Fe in basalts from mid-ocean ridges and volcanic arcs are nearly the same, requiring their redox state during melting to be nearly equal, contrary to that inferred by their different Fe^{3+}/Fe^{2+} (Lee et al. 2005; Lee et al. 2010). This leaves a dichotomy for the high Fe^{3+}/Fe^{2+} and oxygen fugacity of many arc magmas.

The Fe/Mn and Fe/Zn is very uniform in terrestrial oceanic basalts, except for those from ocean islands (Qin and Humayun 2008). When compared to olivine or orthopyroxene, both garnet and clinopyroxene partition less Zn and more Mn relative to Fe (Le Roux et al. 2010). Thus, lithologies rich in garnet and clinopyroxene (eclogite, pyroxenite) must be significantly more abundant and mixed in with peridotite in the mantle sources of ocean island basalts relative to those of arcs and mid-ocean ridges (Davis et al. 2013).

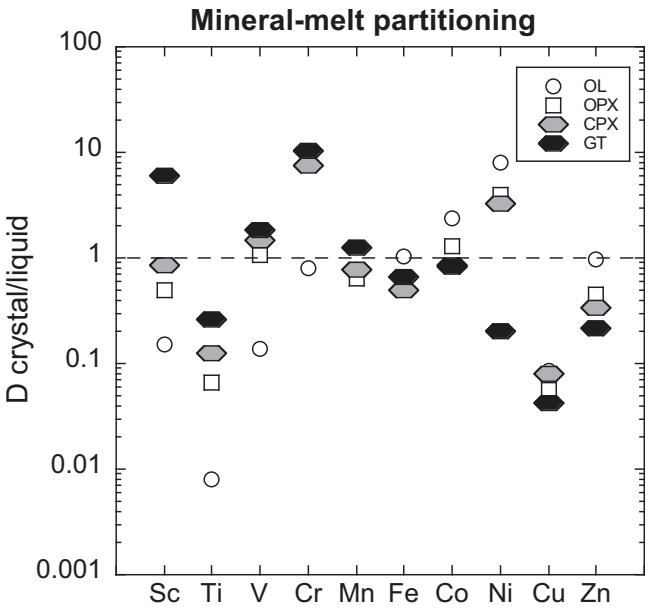

Transition Elements, Fig. 1 Plot of partition coefficients D crystal/liquid = [element concentration in crystal]/[element concentration in melt] for first row transition elements measured between mantle melts and olivine (OL), orthopyroxene (OPX), clinopyroxene (CPX), and garnet (GT) (Data from: Canil (1999), Le Roux et al. (2011), Davis et al. (2013), and Liu et al. (2014))

High–Low Spin Transition in Fe

The d-orbitals of transition metals ions can split in energy level, proportional to the charge on the ion and its coordination state. The splitting is described by crystal field theory and can affect the absorption of light (to produce color). In addition, for first row transition metals in octahedral coordination, the splitting of electrons can affect their spin state to be either high or low (Burns 1993). The spin state of a coordination complex affects its ionic radius, thus the density or molar volume of a mineral, or its magnetic properties.

The high spin state of Fe is the normal configuration, where a single electron occupies each d-orbital, whereas in the low spin state, the orbitals are paired as much as possible. High-low spin transitions in Fe predicted to occur at high pressures in Earth's lower mantle (Badro et al. 2003) have been borne out by direct experiments (Catalli et al. 2011). The two most abundant transition metal ions, Fe^{2+} or Fe^{3+}, can undergo high – low spin transitions in the lower mantle minerals ferropericlase ($Fe_{1-x}O$) and bridgmanite ($(Mg,Fe)(Fe,Al)O_3$ – perovskite). The high-low spin state transitions may be sharp or smooth throughout the temperature-pressure range of the lower mantle, depending on its composition and oxidation state (Catalli et al. 2011). Such transitions can produce anomalies in the seismic wave speed, magnetic properties, or heat transfer in the deep mantle (Lin et al. 2007).

Hydrothermal Fluids

The solubility and speciation of transition metals in fluids are affected by pH, pressure, temperature, and composition (Crerar et al. 1985). In certain pressure-temperature regimes in the upper crust and seafloor, boiling of hydrothermal fluid may occur, leading to exsolution of vapor from liquid. Transition metals such as Fe, Mn, Zn, Cu, and Au can be fractionated from one another due to complexation with specific ligands in fluids and vapors. The complexation tends to follow Pearson's (1963) rules – hard acids pair with hard bases and vice versa. For example, Cu^{+} is soft and binds with S^{-} complexes (H_2S) and HS^{-}, whereas Zn^{2+} is hard and pairs with hard bases (Cl^{-} or HCl) as ZnCl species (Pokrovski et al. 2005; Nagaseki and Hayashi 2008). In this way, transition metals such Cu and Au will concentrate in ores produced by vapor transport such as porphyry and epithermal settings, whereas as Zn, Mn, or Fe prefer the liquid/brine phase (Heinrich et al. 1999).

References

Badro J, Fiquet G, Guyot F, Rueff JP, Struzhkin VV, Vankó G, Monaco G (2003) Iron partitioning in Earth's mantle: toward a deep lower mantle discontinuity. Science 300:789–791

Burns RG (ed) (1993) Mineralogical application of crystal field theory. Cambridge University Press, New York

Canil D (1999) Vanadium partitioning between orthopyroxene, spinel and silicate melt and the redox states of mantle source regions for primary magmas. Geochim Cosmochim Acta 63:557–572

Carmichael ISE (1991) The redox states of basic and silicic magmas: a reflection of their source regions? Contrib Mineral Petrol 106:129–141

Catalli K, Shim S-H, Dera P, Prakapenka VB, Zhao J, Sturhahn W, Chow P, Xiao Y, Cynn H, Evans WJ (2011) Effects of the Fe3+ spin transition on the properties of aluminous perovskite – new insights for lower-mantle seismic heterogeneities. Earth Planet Sci Lett 310:293–302

Crerar D, Wood S, Brantley S (1985) Chemical controls on solubility of ore-forming minerals in hydrothermal solutions. Can Mineral 23:333–352

Davis FA, Humayun M, Hirschmann MM, Cooper RS (2013) Experimentally determined mineral/melt partitioning of first-row transition elements (FRTE) during partial melting of peridotite at 3 GPa. Geochim Cosmochim Acta 104:232–260

Heinrich CA, Günther D, Audétat A, Ulrich T, Frischknecht R (1999) Metal fractionation between magmatic brine and vapor, determined by microanalysis of fluid inclusions. Geology 27:755–758

Le Roux V, Lee CTA, Turner SJ (2010) Zn/Fe systematics in mafic and ultramafic systems: implications for detecting major element heterogeneities in the Earth's mantle. Geochim Cosmochim Acta 74:2779–2796

Le Roux V, Dasgupta R, Lee CTA (2011) Mineralogical heterogeneities in the Earth's mantle: constraints from Mn, Co, Ni and Zn partitioning during partial melting. Earth Planet Sci Lett 307:395–408

Lee CTA, Leeman WP, Canil D, Li ZXA (2005) Similar V/Sc systematics in MORB and arc basalts: implications for the oxygen fugacities of their mantle source regions. J Petrol 46:2313–2336

Lee CTA, Luffi P, Le Roux V, Dasgupta R, Albarede F, Leeman WP (2010) The redox state of arc mantle using Zn/Fe systematics. Nature 468:681–685

Lin J-F, Vankó G, Jacobsen SD, Iota V, Struzhkin VV, Prakapenka VB, Kuznetsov A, Yoo C-S (2007) Spin transition zone in Earth's lower mantle. Science 317:1740–1743

Liu X, Xiong X, Audetat A, Li Y, Song M, Li L, Sun W, Ding X (2014) Partitioning of copper between olivine, orthopyroxene, clinopyroxene, spinel, garnet and silicate melts at upper mantle conditions. Geochim Cosmochim Acta 125:1–22

Mallmann G, O'Neill HSC (2009) The crystal/melt partitioning of V during mantle melting as a function of oxygen fugacity compared with some other elements (Al, P, Ca, Sc, Ti, Cr, Fe, Ga, Y, Zr and Nb). J Petrol 50:1765–1794

Nagaseki H, Hayashi K (2008) Experimental study of the behavior of copper and zinc in a boiling hydrothermal system. Geology 36:27–30

Pearson RG (1963) Hard and soft acid and bases. Am Chem Soc J 85:3533–3539

Pokrovski GS, Roux J, Harrichoury JC (2005) Fluid density control on vapor–liquid partitioning of metals in hydrothermal systems. Geology 33:657–660

Qin LP, Humayun M (2008) The Fe/Mn ratio in MORB and OIB determined by ICP-MS. Geochim Cosmochim Acta 72:1660–1677

Shannon RD (1976) Revised effective ionic radii and systematic studies of interatomic distances in halides and chalcogenides. Acta Crystallogr A A32:751–767

Tungsten

George R. Helz
Departments of Geology and Chemistry, University of Maryland, College Park, MD, USA

Element Data

Atomic Symbol: W
Atomic Number: 74
Atomic Weight: 183.84
Isotopes and Abundances: ^{180}W (0.12%, $t_{½}$ 1.8x10^{18} y), ^{182}W (26.50%), ^{183}W (14.31%), ^{184}W (30.64%), ^{186}W (28.43%) (additionally 27 artificial isotopes)
1 Atm Melting Point: 3695 K
1 Atm Boiling Point: 6203 K
Common Valences: W^0, W^{3+}, W^{4+}, W^{5+}, W^{6+} (other valences not important in nature)
Ionic Radii: (Coord. No.): W^{6+}(6-fold) 76 pm, W^{6+}(4-fold) 56 pm, W^{4+}(6-fold) 80 pm
Pauling Electronegativity: 2.36
First Ionization Potential: 7.864 eV
Chondritic (CI) Abundance: 0.093 ppm
Silicate Earth Abundance: 0.013 ± 0.010 ppm
Crustal Abundance: 1.4–2.0 ppm
Seawater Abundance: 0.0092 ppb
Core Abundance: 0.50 ± 0.12 ppm

Properties

Notable properties of tungsten include its melting point (highest of any metal) and its density (exceeding all stable elements except gold and platinum group elements). Combined in tungsten carbide, it forms an abrasive with extraordinary hardness, like that of corundum. Tungsten is also the heaviest element that is essential to some prokaryotes, though not to eukaryotes (including humans). Tungsten shares Group 6 of the Periodic Table with Cr and Mo. Oxidation states below +6 are much less common for W than for Cr and Mo owing to relativistic destabilization of 5d electrons in W (Holm et al. 2011).

Tungsten's principal minerals are scheelite, $CaWO_4$, and wolframite, (Fe, Mn)WO_4. In these, W is respectively fourfold and sixfold coordinated by oxygen. Tungsten sulfides, such as tungstenite (WS_2), catamarcaite (Cu_6GeWS_8), and kiddcreekite (Cu_6SnWS_8), are rare. A few complex silicate minerals are known.

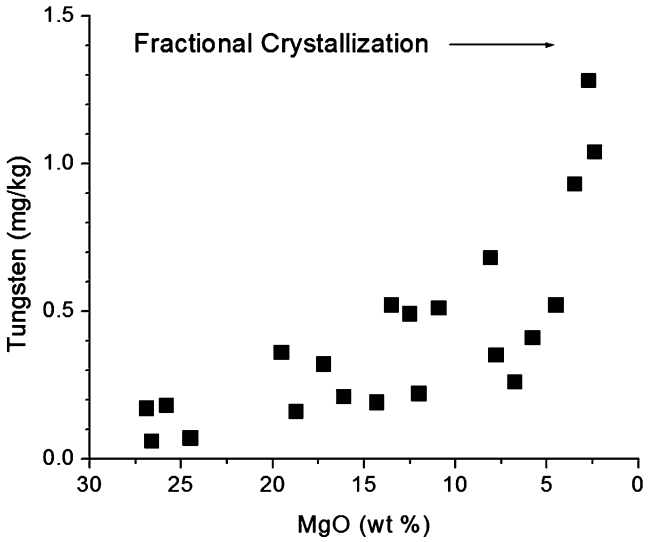

Tungsten, Fig. 1 Tungsten's incompatability during fractional crystallization illustrated in Kilauea Iki lava lake (data of Greaney et al. 2017)

History and Use

Discovery of tungsten is often attributed to Scheele, who obtained tungstic acid in 1781. Its first isolation as an element was accomplished by the brothers Elhuyar in 1783.

In 2016, China was the world's largest producer (82% of world production, 71,000 metric tons) and Vietnam the second largest (7%, 6,000 metric tons).

Tungsten's principal use is in tungsten carbide abrasives. It also finds use in wear-resistant and high-temperature alloys and in munitions, where its density is advantageous for armor-penetrating projectiles. Owing to its high melting point, it has long been favored for filaments in light bulbs and other electrical devices.

Geochemical Behavior

Tungsten is a moderate siderophile, and in consequence, more than nine-tenths of Earth's W budget resides in the core. On the other hand, in the silicate earth, W is an incompatible element, similar to U, so fractional melting and crystallization processes concentrate it in the crust, leaving a depleted mantle containing 0.008 ± 0.007 μg/g (Arevalo and McDonough 2008) (Fig. 1).

Tungsten does not display the borderline chalcophile tendencies of its Group 6 neighbor, Mo. In skarn and porphyry ore deposits, W is most often found as $CaWO_4$ or (Fe, Mn)WO_4 whereas in the same rocks Mo is found as its sulfide, MoS_2 (Hsu 1977; Wood and Samson 2000). In sulfidic pore waters from estuarine and continental shelf sediments, W is mobilized whereas Mo is precipitated (Mohajerin et al. 2016). Likewise, W is mobilized and Mo precipitated during circulation of sulfidic hydrothermal waters through the seafloor near spreading centers (Kishida et al. 2004). Experiments show that aqueous WO_4^{2-} can be thiolated to WS_4^{2-}, but only at much higher sulfide concentrations than needed to thiolate MoO_4^{2-} (Mohajerin et al. 2014).

Traditionally, five stable W isotopes have been recognized. The lightest, ^{180}W, is now known to be a low-activity α emitter ($t_{½}$ 1.8 × 10^{18} y; Cozzini 2004). Cosmochemists and geochemists have devoted most attention to ^{182}W, the daughter of radioactive ^{182}Hf ($t_{½}$ 8.9 × 10^6 y). Planetary core formation separates lithophile Hf from siderophile W, so the abundance of ^{182}W relative to other W isotopes in silicate and metal reservoirs yields information about timing of core formation and late accretion (Kleine et al. 2002).

Chemical fractionation among W stable isotopes is anticipated, but this subject largely remains to be developed. Tungstate adsorbed to Fe and Mn oxyhydroxides is isotopically lighter than aqueous tungstate, hinting at similarity in W and Mo stable isotope behavior. The fractionation mechanism involves tungsten's transfer from tetrahedral coordination in water to distorted octahedral coordination on oxyhydroxide surfaces (Kashiwabara et al. 2017).

Acidification causes dilute aqueous WO_4^{2-} to become diprotonated near pH 4. This process initiates hydration, producing octahedrally coordinated $W(OH)_6^0$. At dissolved W concentrations exceeding10^{-5} M and at pH below 5, WO_4^{2-} forms polyoxyanion oligomers (e.g., $W_6O_{20}(OH)^{5-}$; Baes and Mesmer 1976). In most natural waters, W concentrations are far too low to stabilize such species.

Even where W concentrations exceed 10^{-5} M in nature, such as in mine drainage or in rivers and lakes subject to evaporative concentration (Petrunic and Al 2005; Johannesson et al. 2000), pH is usually too high for oligomerization. Nonetheless, polyoxyanions are proposed to form in some soils, possibly stabilized by low water activity (i.e., relative humidity) in soil pore spaces, and could explain anomalous W mobility (Sun and Bostick 2015). Once formed, polyoxotungstates react sluggishly.

Present as WO_4^{2-} at about 0.05 nmol/kg, tungsten is a conservative component of seawater with a mean residence time of about 14,000 y (Firdaus et al. 2008). In river waters, its concentration is much higher and quite variable, averaging about 0.54 nmol/kg (Gaillardet et al. 2005). High dissolved (i.e., filter passing) W concentrations in rivers are due partly to colloidal transport (Pokrovsky and Schott 2002).

Shales and sandstones are similar to continental crust in their W content, but carbonate sediments are mildly depleted. In organic-rich black shales, the median W concentration is 2.9 μg/g, which is only narrowly enriched relative to crust (Ketris and Yudovich 2009). In contrast, Mo is highly enriched.

On the other hand, W is considerably enriched in marine ferromanganese nodules and crusts (50–100 μg/g; Hein et al. 2013). The principal host phases appear to be Mn oxyhydroxides rather than Fe oxyhydroxides (Kashiwabara et al. 2013).

Biological Utilization and Toxicity

Until about 30 years ago, tungsten's role in biology was viewed as solely injurious owing to interference in Mo-dependent processes (Andreesen and Makdessi 2008). Since then, beneficial utilization in a number of W-dependent enzymes has been recognized, especially in hyperthermophilic prokaryotes. Redox potentials in W enzymes are lower than in comparable Mo enzymes (Bevers et al. 2009; Holm et al. 2011). In some cases, structures of active sites in W and Mo enzymes are almost identical, yet these enzymes catalyze quite different reactions. In other cases, as in Mo nitrogenase (a N_2 reduction catalyst), the W form is inactive.

Genetic evidence shows that hyperthermophiles were among the earliest organisms. It has been proposed that W enzymes evolved before Mo enzymes, at a time when hydrothermal vents were the main source of W and Mo to the ocean (Williams and Frausto da Silva 2002).

Recognition of a cluster of leukemia cases near tungsten mines in Nevada gave rise to a hypothesis that W is an environmental carcinogen (Koutsospyros et al. 2006). So far, this hypothesis lacks firm support (Lemus and Venezia 2015). The US Occupational Safety and Health Administration has set 8-h threshold limits for air of 1 and 5 mg/m^3 for water-soluble and water-insoluble tungsten, respectively. Currently, W is not regulated in drinking water by the World Health Organization or by the US Environmental Protection Agency, but Russia has set a standard of 50 μg/L.

Summary

Tungsten and molybdenum have been described as twins due to their similar ionic radii and electronegativity. Their crustal abundances are nearly the same despite tungsten's much lower cosmic abundance. In natural waters, both are found as tetrahedral oxyanions and are conservative components of seawater. Both sorb readily to ferromanganese oxide minerals with the lighter isotopes preferentially depleted in solution. They form structurally similar minerals in the earth and enzymes in living organisms. On the other hand, key differences include tungsten's greater siderophilicity and lower chalcophilicity as well as tungsten's lower redox potential. Neither is currently regarded as problematic in the environment, although this could change as more information becomes available.

Cross-References

- ▶ Black Shales and Sapropels
- ▶ Chromium
- ▶ Colloids
- ▶ Elements: Metalloids
- ▶ Molybdenum
- ▶ Polyoxometalates and Other Metal-Oxo Clusters in Nature
- ▶ Siderophile Elements
- ▶ Tungsten Isotopes

References

Andreesen JR, Makdessi K (2008) Tungsten, the surprisingly positively acting heavy metal element for prokaryotes. Ann N Y Acad Sci 1125:215–229

Arevalo R, McDonough WF (2008) Tungsten geochemistry and implications for understanding the Earth's interior. Earth Planet Sci Lett 272:656–665

Baes CF, Mesmer RE (1976) The hydrolysis of cations. Wiley, New York, 489 pp

Bevers LE, Hagedoorn P-L, Hagen WR (2009) The bioinorganic chemistry of tungsten. Coord Chem Rev 253:269–290

Cozzini C and 23 others (2004) Detection of the natural α decay of tungsten. Phys Rev C 70:064606

Firdaus ML, Norisuye K, Nakagawa Y, Nakatsuka S, Sohrin Y (2008) Dissolved and labile particulate Zr, Hf, Nb, Ta, Mo and W in the Western North Pacific Ocean. J Oceanogr 64:247–257

Gaillardet J, Viers J, Dupre B (2005) Trace elements in river waters. In: Holland HD, Turekian KK (eds) Treatise on geochemistry, vol 3. Elsevier, Amsterdam, pp 225–272
Greaney AT, Rudnick RL, Helz, RT, Gaschnig RM, Piccoli PM Ash RD (2017) The behavior of chalcophile elements during magmatic differentiation as observed in Kilauea Iki lava lake, Hawaii. Geochim Cosmochim Acta 210:71–96
Hein JR, Mizell K, Koschinsky A, Conrad TA (2013) Deep-ocean mineral deposits as a source of critical metals for high- and green-technology applications: comparison with land-based resources. Ore Geol Rev 51:1–14
Holm RH, Solomon EI, Majumdar A, Tenderholt A (2011) Comparative molecular chemistry of molybdenum and tungsten and its relation to hydroxylase and oxotransferase enzymes. Coord Chem Rev 255:993–1015
Hsu LC (1977) Effects of oxygen and sulfur fugacities on the scheelite-tungstenite and powellite-molybdenite stability relations. Econ Geol 72:664–670
Johannesson KH, Lyons WB, Graham EY, Welch KA (2000) Oxyanion concentrations in eastern sierra Nevada Rivers 3. Boron, molybdenum, vanadium, and tungsten. Aquat Geochem 6:19–46
Kashiwabara T, Takahashi Y, Marcus MA, Uruga T, Tanida H, Terada Y, Usui A (2013) Tungsten species in natural ferromanganese oxides related to its different behavior from molybdenum in oxic ocean. Geochim Cosmochim Acta 106:364–378
Kashiwabara T, Kubo S, Tanaka M, Senda R, Iizuka T, Tanimizu M, Takahashi Y (2017) Stable isotope fractionation of tungsten during adsorption on Fe and Mn (oxyhydro)oxides. Geochim Cosmochim Acta 204:52–67
Ketris MP, Yudovich YE (2009) Estimations of clarkes for carbonaceous biolithes: world averages for trace element contents in black shales and coals. Int J Coal Geol 78:135–148
Kishida K, Sohrin Y, Okamura K, Ishibashi J (2004) Tungsten enriched in submarine hydrothermal fluids. Earth Planet Sci Lett 222:819–827
Kleine T, Munker C, Mezger K, Palme H (2002) Rapid accretion and early core formation on asteroids and the terrestrial planets from Hf-W chronometry. Nature 418:952–955
Koutsospyros A, Braida W, Christodoulatos C. Dematas D, Strigul N (2006) A review of tungsten: From environmental obscurity to scrutiny. J Hazardous Mat 136:1–19
Lemus R, Venezia CF (2015) An update to the toxicological profile for water-soluble and sparingly soluble tungsten substances. Crit Rev Toxicol 45:388–411
Mohajerin TJ, Helz GR, White CD, Johannesson K (2014) Tungsten speciation in sulfidic waters: determinaation of thiotungstate formation constants and modeling their distribution in natural waters. Geochim Cosmochim Acta 144:157–172
Mohajerin TJ, Helz GR, Johannesson KH (2016) Tungsten-molybdenum fractionation in estuarine environments. Geochim Cosmochim Acta 177:105–119
Petrunic B, Al TA (2005) Mineral/water interactions in tailings from a tungsten mine, mount pleasant, new Bruswick. Geochim Cosmochim Acta 69:2469–2483
Pokrovsky OS, Schott J (2002) Iron colloids/organic matter associated transport of major and trace elements in small boreal rivers and their estuaries (NW Russia). Chem Geol 190:141–179
Sun J, Bostick BC (2015) Effects of tungstate polymerization on tungsten (VI) adsorption on ferrihydrite. Chem Geol 417:21–31
Williams RJP, Frausto da Silva JJR (2002) The involvement of molybdenum in life. Biochem Biophys Res Commun 292:293–299
Wood SA, Samson IM (2000) The hydrothermal geochemistry of tungsten in granitoid envionments: 1. Relative solubilities of ferberite and scheelite as a function of T, P, pH and m_{NsCl}. Econ Geol 95:143–182

Tungsten Isotopes

Thorsten Kleine
Institut für Planetologie, University of Münster, Münster, Germany

Introduction

Tungsten consists of the five stable isotopes ^{180}W (0.12%), ^{182}W (26.50%), ^{183}W (14.31%), ^{184}W (30.64%), and ^{186}W (28.43%), which are produced by three different nucleosynthetic processes: the *p*- (proton capture), *s*- (slow neutron capture), and *r*- (rapid neutron capture) processes. Of the stable W isotopes, ^{180}W is produced in the *p*-process, whereas the four major W isotopes are produced by both the *s*- and *r*-processes. In addition, ^{182}W is produced by β^--decay of now-extinct ^{182}Hf with a half-life of 8.9 ± 0.1 Ma (Vockenhuber et al. 2004), leading to variable ^{182}W abundances in terrestrial and extraterrestrial samples. The short-lived ^{182}Hf-^{182} W system has been widely used as a chronometer for meteorites and the large-scale chemical differentiation of asteroids and terrestrial planets.

Origin of W Isotope Variations

Tungsten isotope variations have several distinct origins, including radiogenic, cosmogenic, and nucleosynthetic processes, as well as mass-dependent fractionation. *Radiogenic* ^{182}W variations result from the decay of ^{182}Hf and form the basis of the Hf-W system (e.g., Kleine et al. 2009). *Cosmogenic* W isotope variations predominantly affect ^{182}W in lunar samples and iron meteorites, and arise from secondary neutron capture reactions induced by the interaction with galactic cosmic rays (GCR) (Leya et al. 2003). *Nucleosynthetic* W isotope variations result from the heterogeneous distribution of presolar material. They have been observed in several components of primitive chondrites (e.g., Budde et al. 2016b; Burkhardt et al. 2012; Kruijer et al. 2014a) and in some bulk meteorites (Kruijer et al. 2017a; Qin et al. 2008). Nucleosynthetic W isotope anomalies serve as tracers of genetic relationships and have been used to demonstrate a genetic link between chondrules and matrix (Budde et al. 2016b), and between some iron meteorites and carbonaceous chondrites (Kruijer et al. 2017a). Both nucleosynthetic and cosmogenic W isotope variation must be quantified for chronological applications of the Hf-W system.

Mass-dependent W isotope fractionations during high-temperature processes seem to be limited, but small variations may occur during magmatic differentiation (Krabbe et al.

2017). More significant W isotope fractionations have been observed for low-temperature processes, such as the precipitation of W onto surfaces of Fe and Mn oxides (Abraham et al. 2015; Kashiwabara et al. 2017).

The ^{182}Hf-^{182}W System

Because Hf is lithophile (silicate-loving) and W is siderophile (iron-loving), metal-silicate fractionation results in a large fractionation of the Hf/W ratio, making the Hf-W system uniquely useful as a chronometer of planetary core formation (e.g., Harper et al. 1991). Additional Hf/W fractionation likely occurred in the mantle of planetary bodies, because W is more incompatible than Hf (Righter and Shearer 2003). Processes such as magma ocean crystallization or partial melting can therefore also be dated using the Hf-W system. Finally, the Hf-W system is a versatile chronometer for meteorites and meteorite components, because there is sufficient spread in Hf/W ratios among the constituent minerals of these rocks.

A Hf-W model age of core formation is usually determined by assuming that core formation occurred in a single instant from a reservoir that previously evolved with chondritic Hf/W. As both Hf and W are refractory elements, the assumption of chondritic Hf/W for bulk planets is reasonable. The assumption of single-stage core formation is more problematic and is only appropriate for meteorite parent bodies. By contrast, for larger bodies such as the Earth and Mars, core formation occurred by several distinct events during planetary growth. One common model is to assume that accretion and concomitant core formation occurred at an exponentially decreasing rate. This model provides a mean age of accretion as the time necessary to reach 63% of a planet's mass (Harper and Jacobsen 1996). However, the Earth's core likely formed episodically by a few giant impacts, meaning that the exponential growth model may not be appropriate (Nimmo and Agnor 2006). Moreover, the extent to which the metal cores of giant impactors equilibrated with Earth's mantle has a strong influence on the calculated model ages for core formation (Halliday 2004).

^{182}W Compositions of Meteorites and Terrestrial Planets

Tungsten isotope ratios are either normalized to ^{184}W or ^{183}W and are corrected for instrumental and natural mass-dependent isotope fractionation using either ^{186}W/^{184}W or ^{186}W/^{183}W. It is common practice to report results for both normalizations, which allows a reliable quantification of nucleosynthetic contributions to observed ^{182}W variations. This also allows quantification of small analytical artefacts on ^{183}W induced during sample preparation, where the nuclear field shift effect leads to small apparent ^{183}W deficits (Cook and Schönbächler 2016).

Tungsten isotopic data are typically expressed as the parts-per-10,000 deviation from terrestrial standard values (Alfa Aesar or NIST W 3163) as follows:

$$\varepsilon^{182}\mathrm{W} = \left(\frac{^{182}\mathrm{W}/^{184}\mathrm{W}_{\mathrm{sample}}}{^{182}\mathrm{W}/^{184}\mathrm{W}_{\mathrm{standard}}} - 1 \right) \times 10^4.$$

More recently, W isotopic data have also been reported as μ^{182}W values (=100 ε^{182}W). The ^{182}W compositions of meteorites and samples from the Earth, Moon, and Mars are summarized in Table 1 and plotted on Fig. 1.

Rapid Accretion of Protoplanets

Compared to chondrites, iron meteorites show ^{182}W deficits, whereas angrites and eucrites have ^{182}W excesses (Table 1, Fig. 1). These ^{182}W variations indicate that core formation in meteorite parent bodies occurred well within the first ~3 Ma of the Solar System. Such early differentiation is consistent with ^{26}Al-decay as the major heat source driving melting of small planetary bodies, and indicates that differentiated protoplanets accreted within ~1 Ma of Solar System history (Kruijer et al. 2017a; Kruijer et al. 2014b). A key constraint from the ^{182}W data is that the accretion of iron meteorite parent bodies predated those of the more primitive chondrite parent bodies.

Iron meteorites that are genetically linked to carbonaceous meteorites have younger core formation ages (~2.2–2.8 Ma) than noncarbonaceous iron meteorites (~0.3–1.8 Ma) (Kruijer et al. 2017a). This difference has been interpreted to indicate a later accretion at greater heliocentric distance of the carbonaceous irons (Budde et al. 2016a; Kruijer et al. 2017a), and has been used to argue that Jupiter's solid core formed within ~1 Ma of Solar System formation, leading to the spatial separation of the carbonaceous and noncarbonaceous meteorite reservoirs (Kruijer et al. 2017a).

Timescales for Mantle Differentiation

Variations in ε^{182}W values among eucrites and angrites (Fig. 1) provide evidence for magmatic activity on their parent bodies for at least until ~20 Ma and ~10 Ma after Solar System formation, respectively (Kleine et al. 2012; Touboul et al. 2015b). ^{182}W variations among Martian meteorites have been interpreted to indicate magma ocean crystallization within the first 20–25 Ma, followed by crust

Tungsten Isotopes, Table 1 Hf-W isotopic systematics of meteorites and terrestrial planets

Planetary body	$^{180}Hf/^{184}W$	$\varepsilon^{182}W$	Model age	Accretion timescale
Chondrites[a]	1.35 ± 0.11	−1.9 ± 0.1		
Iron meteorites	~0	−3.45 to −3.18	~0.3 to ~2.8 Ma[c]	~0.2 to ~1 Ma[e]
Eucrites				
Individual samples	~6 to ~40	~14 to ~35	n.a.	
Bulk silicate portion[b]	19 ± 4	20 ± 2	<1 Ma[d]	<1 Ma[e]
Angrites				
Individual samples	~5 to ~8	~2 to ~5	n.a.	
Bulk silicate portion[b]	~3 to ~8	−0.3 to ~6	<2 Ma[d]	<1.5 Ma[e]
Mars				
Individual samples	n.a.	~0 to ~3	n.a.	
Bulk Martian mantle	4.0 ± 0.5	0.37 ± 0.04	4 ± 3 Ma[c]	<10 Ma
Earth	24 ± 5	≡0	34 ± 3 Ma[c]	>34 Ma
Moon	28 ± 6	0.25 ± 0.04	n.a.	>60 Ma[f]

[a]Average composition of carbonaceous chondrites; time-integrated $^{180}Hf/^{184}W$ using the initial $\varepsilon^{182}W = -3.49$ and $^{182}Hf/^{180}Hf = (1.018 \pm 0.043) \times 10^{-4}$ determined on CAI (Kruijer et al. 2014a)
[b]Composition inferred from Hf-W isotopic evolution of eucrites (Touboul et al. 2015b) and angrites (Kleine et al. 2012)
[c]Two-stage model ages
[d]Age inferred from Hf-W isotopic evolution of mantle (Kleine et al. 2012; Touboul et al. 2015b)
[e]Obtained from thermal modeling of asteroids internally heated by ^{26}Al-decay
[f]Assumes distinct Hf/W ratios of Moon and Earth's mantle

formation until at least ~40 Ma after Solar System formation (Foley et al. 2005; Kruijer et al. 2017b).

There are no radiogenic ^{182}W variations among different lunar rock types (Fig. 1), indicating that differentiation of the Moon occurred later than ~70 Ma after Solar System formation (Touboul et al. 2007; Kruijer and Kleine 2017). By contrast, small ^{182}W variations exist among terrestrial samples (Fig. 1) (see summary in Kleine and Walker 2017). Whereas the ^{182}W excesses in some Archaean samples may reflect derivation from sources that lack some portion of the late veneer (e.g., Willbold et al. 2011), the small ^{182}W deficits observed for some ocean island basalts (Mundl et al. 2017) cannot be explained in this manner. These ^{182}W deficits were interpreted as vestiges of an early differentiation of Earth's mantle within the first 60 Ma of the Solar System. Such early differentiation processes could have also produced the ^{182}W excesses observed in Archaean samples (Touboul et al. 2012). Thus, as for Mars but unlike for the Moon, ^{182}W heterogeneities from Earth's earliest formative period have been preserved until the present-day.

Accretion Timescales for the Earth, Moon, and Mars

The mantles of the Earth and Mars have higher $\varepsilon^{182}W$ compared to chondrites, indicating that core formation at least partly occurred during the lifetime of ^{182}Hf. Although the Earth's and Mars' mantles have similar $\varepsilon^{182}W$, their Hf/W ratios are very different (Table 1), leading to distinct Hf-W ages. For Mars, the two-stage model for core formation is 4 ± 3 Ma after Solar System formation, with a mean age of accretion of ~2 Ma (Dauphas and Pourmand 2011). For the Earth, the two-stage model age is 34 ± 3 Ma, while the mean age is ~11 Ma (Kleine et al. 2002; Schoenberg et al. 2002; Yin et al. 2002). As noted above, the assumption of single stage core formation is not appropriate for large bodies, meaning that accretion probably took longer than given by the two-stage model ages. As such, Mars was probably fully formed by ~10 Ma after Solar System formation (Kruijer et al. 2017b). For the Earth the end of accretion is poorly defined, mainly because the extent of equilibration of metal and silicate during giant impacts is not known. Incomplete equilibration leads to younger calculated Hf-W ages. For instance, assuming only ~40–50% equilibration would change the Hf-W age to ~100–150 Ma, which would be consistent with the Pb-Pb age of the Earth (Rudge et al. 2010).

The Moon exhibits a small ^{182}W excess of ~25 ppm over the present-day bulk silicate Earth (Kruijer et al. 2015; Touboul et al. 2015a). This ^{182}W difference likely results from late accretion following the Moon-forming impact, which lowered the ^{182}W composition of Earth's mantle by about 10–30 ppm, but left the lunar ^{182}W composition essentially unchanged. Prior to late accretion the $\varepsilon^{182}W$ of the Moon and Earth's mantle were, therefore, indistinguishable. The lack of a resolvable radiogenic ^{182}W difference between the Moon and Earth's mantle implies formation of the Moon after extinction of ^{182}Hf, more than ~60 Ma after Solar System formation (Touboul et al. 2007). This conclusion is valid

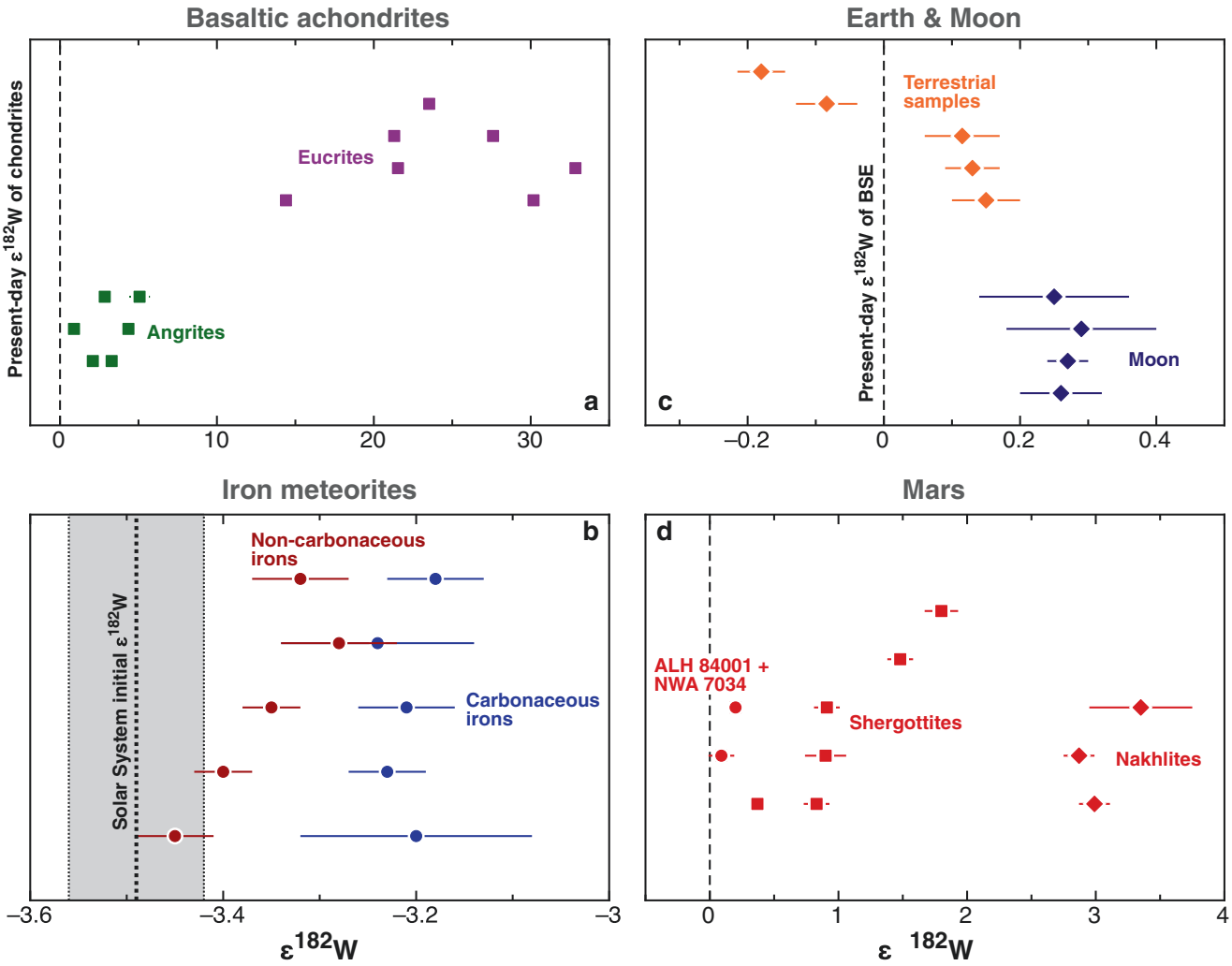

Tungsten Isotopes, Fig. 1 $\varepsilon^{182}W$ variations among extraterrestrial and terrestrial samples. Note the different scales for each panel. *Dashed line* in **a**, **c**, and **d** represents W isotopic composition of the present-day bulk silicate Earth (BSE). Note the much larger $\varepsilon^{182}W$ variations in basaltic achondrites (**a**) and Mars (**d**) compared to the Earth and Moon (**c**). (**c**) For terrestrial samples, only data for selected localities are shown, but these cover the entire range of ^{182}W variations reported to date

only if the Hf/W ratios of the lunar and terrestrial mantles are sufficiently different.

Summary

Tungsten isotope studies are widely applied to determine the timescales of planetary accretion and differentiation and have demonstrated that differentiated protoplanets accreted within ~1 Ma, Mars accreted within the first ~10 Ma, and Earth's accretion was completed no earlier than ~30 Ma after Solar System formation. The Hf-W system also serves as an important chronometer for meteorites and meteorite components, and as a tracer of late accretion. In addition, nucleosynthetic W isotope anomalies have important applications for establishing genetic links among early Solar System materials.

References

Abraham K, Barling J, Siebert C et al (2015) Determination of mass-dependent variations in tungsten stable isotope compositions of geological reference materials by double-spike and MC-ICPMS. J Anal At Spectrom 30:2334–2342

Budde G, Burkhardt C, Brennecka GA et al (2016a) Molybdenum isotopic evidence for the origin of chondrules and a distinct genetic heritage of carbonaceous and non-carbonaceous meteorites. Earth Planet Sci Lett 454:293–303

Budde G, Kleine T, Kruijer TS, Burkhardt C, Metzler K (2016b) Tungsten isotopic constraints on the age and origin of chondrules. Proc Natl Acad Sci 113:2886–2891

Burkhardt C, Kleine T, Dauphas N, Wieler R (2012) Nucleosynthetic tungstenisotope anomalies in acid leachates of the Murchison chondrite: implications for Hf-W chronometry. Astrophy J Lett 753:L6

Cook DL, Schonbachler M (2016) High-precision measurement of W isotopes in Fe-Ni alloy and the effects from the nuclear field shift. J Anal At Spectrom 31:1400–1405

Dauphas N, Pourmand A (2011) Hf-W-Th evidence for rapid growth of Mars and its status as a planetary embryo. Nature 473:489–U227

Foley CN, Wadhwa M, Borg LE et al (2005) The early differentiation history of Mars from ^{182}W-^{142}Nd isotope systematics in the SNC meteorites. Geochim Cosmochim Acta 69:4557–4571

Halliday AN (2004) Mixing, volatile loss and compositional change during impact-driven accretion of the Earth. Nature 427:505–509

Harper CL, Jacobsen SB (1996) Evidence for ^{182}Hf in the early solar system and constraints on the timescale of terrestrial accretion and core formation. Geochim Cosmochim Acta 60:1131–1153

Harper CL, Völkening J, Heumann KG, Shih CY, Wiesmann H (1991) ^{182}Hf-^{182}W: New cosmochronometric constraints on terrestrial accretion, core formation, the astrophysical site of the r-process, and the origin of the solar system. Lunar Planet Sci XXII:515–516

Kashiwabara T, Kubo S, Tanaka M et al (2017) Stable isotope fractionation of tungsten during adsorption on Fe and Mn (oxyhydr)oxides. Geochim Cosmochim Acta 204:52–67

Kleine T, Walker RJ (2017) Tungsten isotopes in planets. Ann Rev Earth Planet Sci 45: 389–417

Kleine T, Münker C, Mezger K, Palme H (2002) Rapid accretion and early core formation on asteroids and the terrestrial planets from Hf-W chronometry. Nature 418:952–955

Kleine T, Touboul M, Bourdon B et al (2009) Hf-W chronology of the accretion and early evolution of asteroids and terrestrial planets. Geochim Cosmochim Acta 73:5150–5188

Kleine T, Hans U, Irving AJ, Bourdon B (2012) Chronology of the angrite parent body and implications for core formation in protoplanets. Geochim Cosmochim Acta 84:186–203

Krabbe N, Kruijer TS, Kleine T (2017) Tungsten stable isotope compositions of terrestrial samples and meteorites determined by double spike MC-ICPMS. Chem Geol 450:135–144

Kruijer TS, Kleine T, Fischer-Godde M, Burkhardt C, Wieler R (2014a) Nucleosynthetic W isotope anomalies and the Hf-W chronometry of Ca-Al-rich inclusions. Earth Planet Sci Lett 403:317–327

Kruijer TS, Touboul M, Fischer-Godde M et al (2014b) Protracted core formation and rapid accretion of protoplanets. Science 344:1150–1154

Kruijer TS, Kleine T, Fischer-Gödde M, Sprung P (2015) Lunar tungsten isotopic evidence for the late veneer. Nature 520:534–537

Kruijer TS and Kleine T (2017) Tungsten isotopes and the origin of the Moon. Earth Planet Sci Lett 475: 15–24

Kruijer TS, Burkhardt C, Budde G, Kleine T (2017a) Age of Jupiter inferred from the distinct genetics and formation times of meteorites. Proc Natl Acad Sci 114:6712

Kruijer TS, Kleine T, Borg LE et al (2017b) The early differentiation of Mars inferred from Hf-W chronometry. Earth Planet Sci Lett 474: 345–354

Leya I, Wieler R, Halliday AN (2003) The influence of cosmic-ray production on extinct nuclide systems. Geochim Cosmochim Acta 67:529–541

Mundl A, Touboul M, Jackson MG et al (2017) Tungsten-182 heterogeneity in modern ocean island basalts. Science 356:66

Nimmo F, Agnor CB (2006) Isotopic outcomes of N-body accretion simulations: Constraints on equilibration processes during large impacts from Hf/W observations. Earth Planet Sci Lett 243:26–43

Qin LP, Dauphas N, Wadhwa M et al (2008) Tungsten nuclear anomalies in planetesimal cores. Astrophys J 674:1234–1241

Righter K, Shearer CK (2003) Magmatic fractionation of Hf and W: Constraints on the timing of core formation and differentiation in the Moon and Mars. Geochim Cosmochim Acta 67:2497–2507

Rudge JF, Kleine T, Bourdon B (2010) Broad bounds on Earth's accretion and core formation constrained by geochemical models. Nat Geosci 3:439–443

Schoenberg R, Kamber BS, Collerson KD, Eugster O (2002) New W-isotope evidence for rapid terrestrial accretion and very early core formation. Geochim Cosmochim Acta 66:3151–3160

Touboul M, Kleine T, Bourdon B, Palme H, Wieler R (2007) Late formation and prolonged differentiation of the Moon inferred from W isotopes in lunar metals. Nature 450:1206–1209

Touboul M, Puchtel IS, Walker RJ (2012) W-182 Evidence for Long-Term Preservation of Early Mantle Differentiation Products. Science 335:1065–1069

Touboul M, Puchtel IS, Walker RJ (2015a) Tungsten isotopic evidence for disproportional late accretion to the Earth and Moon. Nature 520:530–533

Touboul M, Sprung P, Aciego SM, Bourdon B, Kleine T (2015b) Hf–W chronology of the eucrite parent body. Geochim Cosmochim Acta 156:106–121

Vockenhuber C, Oberli F, Bichler M et al (2004) New half-life measurement of ^{182}Hf: Improved chronometer for the early solar system. Phys Rev Lett 93:172501

Willbold M, Elliott T, Moorbath S (2011) The tungsten isotopic composition of the Earth's mantle before the terminal bombardment. Nature 477:195–199

Yin QZ, Jacobsen SB, Yamashita K et al (2002) A short timescale for terrestrial planet formation from Hf-W chronometry of meteorites. Nature 418:949–952

U

Unified Atomic Mass Unit, Avogadro Constant, and Mole

Norman E. Holden
National Nuclear Data Center, Brookhaven National Laboratory, Upton, New York, USA

Definition

The unified atomic mass unit, u, is defined as 1/12th of the rest mass of a neutral atom of ^{12}C in its nuclear and electronic ground state. Avogadro's constant, N_A, is the number of atoms in a mole of substance, where mole, denoted *mol*, is defined as the amount of substance that contains as many elementary entities as there are atoms in 0.012 kg of carbon-12.

Unified Atomic Mass Unit

The nineteenth-century chemists had two different standards for atomic weight values: hydrogen = 1, as chosen and quoted by John Dalton (1805), and oxygen = 16, as suggested by Brauner (1889) and the German Atomic Weights' Committee (Ostwald 1903) because oxygen was a primary measurement standard. At the start of the twentieth century, chemists (Landolt et al. 1900) voted for oxygen =16. The physicist, Francis Aston, who was using a mass spectrometer to determine mass ratios of isotopes (nuclides), used the stable isotope $^{16}O = 16$ as a standard. With the discovery (Giaugue and Johnson 1929a; Giaugue and Johnson 1929b) of the oxygen isotopes, ^{17}O and ^{18}O in 1929, there was a slight difference in the two standards. The physical scale was 0.27% smaller than the chemical scale. Initially, this factor was used to convert measurements between the two different scales. However, with Dole's discovery (Dole 1935) of different atomic weight values for oxygen in air and in water, this became a variable difference between the chemical and physical standards for atomic weights that persisted for three decades. When IUPAP and IUPAC agreed to change the atomic mass scale from oxygen to carbon in 1960/1961, the physicist's definition of the atomic mass unit, *amu*, as equal to 1/16th of the mass of an atom of ^{16}O would become a unified atomic mass unit, u, defined as 1/12th of the rest mass of a neutral atom of ^{12}C in its nuclear and electronic ground state (Holden 1984). When the unification of scales was proposed, the name aston (symbol An) was proposed for the unit (Cohen, Private communication, 8 July 1981). More recently, the biochemical suggestion of the Dalton was proposed, which a number of international bodies have adopted. When the atomic weight value of a chemical element is used with the International System of Units (SI) unit of grams, the result is the gram-atomic weight or a mass of a mole of that element, i.e., the mass of Avogadro constant of atoms of that element.

Avogadro Constant and Mole

Avogadro's constant, N_A, the number of entities in the amount of substance of one mole, is a scaling factor between the microscopic (atomic scale) and the macroscopic properties of matter. It has a unit of a reciprocal mol. It is named after the Italian scientist, Amedeo Avogadro, who proposed that the volume of a gas (at a given pressure and temperature) is proportional to the number of atoms or molecules regardless of the nature of the gas (Avogadro 1811). The latest recommended value of N_A is $6.022140857\ (74) \times 10^{23}\ mol^{-1}$ in the SI, where the number in parentheses (74) is the uncertainty in the two trailing digits, "57", in the value. It is based on the 2014 adjustment of the CODATA (International Council for Science's Committee on Data for Science and Technology) recommended values of the fundamental constants of physics and chemistry. N_A expresses the ^{12}C mass in kilograms according to the expression:

$M(^{12}C) = N_A \bullet m(^{12}C)$, where $M(^{12}C) = 0.012$ kg/mol is the molar mass and $m(^{12}C)$ is the atomic mass of ^{12}C.

W. M. White (ed.), *Encyclopedia of Geochemistry*,
https://doi.org/10.1007/978-3-319-39312-4

The mole is defined as the amount of substance of a system, which contains as many elementary entities as there are atoms in 0.012 kg of carbon-12. Its symbol is "mol." When the mole is used, the elementary entities must be specified, and they may be atoms, molecules, ions, electrons, other particles, or specified groups of such particles.

It has been suggested that "amount of substance" should be replaced by the term "chemical amount." However, "chemical amount" is not a well-understood term. No conclusion has been reached in this regard.

There is a proposed new definition of the mole, which sets the magnitude of the mole by fixing the numerical value of the Avogadro constant. However, the definition of the Avogadro constant is the number of atoms in a "mole."

The effect of the new definition of the mole would reverse the situation of the Avogadro constant and the atomic mass of ^{12}C. At present, the atomic mass of ^{12}C is equal to 12 with no uncertainty, while the value and the uncertainty of the Avogadro constant is determined by measurement. With the new definition, the value of the Avogadro constant would be fixed with no uncertainty, while the value and uncertainty of the atomic mass of ^{12}C would become variable and be set by measurement. At the present time, measurements of the Avogadro constant continue and the exact value and uncertainty of the Avogadro constant has not been finalized.

Summary

The unified atomic mass unit (or Dalton) is equal to 1/12th of the rest mass of a neutral atom of ^{12}C in its nuclear and electronic ground state.

The Avogadro constant is the scaling factor between the microscopic and the macroscopic properties of matter, whose value is the number of ^{12}C atoms in their nuclear and electronic ground states in 0.012 kg of ^{12}C (designated as 1 mol).

The mole is the amount of substance (or chemical amount) of a system which contains as many elementary entities as there are atoms in 12 g of ^{12}C.

Cross-References

- ▶ Atomic Number, Mass Number, and Isotopes
- ▶ Periodic Table
- ▶ Stoichiometry

References

Avogadro A (1811) Essai d'une maniere de determiner les masses relatives des molecules elementaires des corps, et les proportions selon lesquelles elles entrent dans ces combinaisons. J Phys 73:58–76

Brauner B (1889) Die basis atomgewichte. Ber Dtsch Chem Ges 22:1186–1892

Dalton J (1805) On the absorption of gases by water and other liquids. Mem Proc Manch Lit Philos Soc 1:271–287

Dole M (1935) The relative atomic weight of oxygen in water and in air. J Am Chem Soc 57:2731

Giaugue WF, Johnson HL (1929a) An atom of oxygen, mass 18. Nature 123:318

Giaugue WF, Johnson HL (1929b) An isotope of oxygen of mass 17 in the earth's atmosphere. Nature 123:831

Holden NE (1984) The International Commission on Atomic Weights – an early historical review. Chem Int 6(1):5–12

Landolt H, Ostwald W, Seubert K (1900) Zweiter Bericht der Commission fur die Festsetzung der Atomgewichte. Ber Dtsch Chem Ges 33:1847–1883

Ostwald W (1903) Bemerkungen zu dem Berichte der internationalen Atomgewichtskommission. Z Anorg Chem 34:257–259

Uranium

Vincent J. M. Salters
National High Magnetic Field Laboratory and Department of Earth, Ocean and Atmospheric Sciences, Florida State University, Tallahassee, FL, USA

Element Data
Atomic Symbol: **U**
Atomic Number: **92**
Atomic Weight: 238.029
Isotopes and Abundances: ^{238}U, 99.2745%, ^{235}U 0.7255%, ^{234}U, ^{223}U
1 Atm Melting Point: 1,132 °C
1 Atm Boiling Point: 4,131 °C
Common Valences: 4+, 6+
Ionic Radii Tetravalent U: sixfold, 108 pm; fourfold, 112 pm
Pauling Electronegativity: 1.38
First Ionization Energy: 597.6 kJ/mol
Chondritic (CI) Abundance: 8.1 ppb
Silicate Earth Abundance: 20.3 ppb
Crustal Abundance: 1.3 ppm
Seawater Abundance: 3.2 ppb
Core Abundance: ~0

Properties

The element is named after the planet Uranus. Its symbol is U, its atomic number is 92, and its atomic weight is 238.0289. Its melting point is 1,408 K and its boiling point is 4,404 K and is considered a refractory lithophile element, with a 50%

nebular condensation temperature of 1,010 K (Lodders 2003). The specific gravity of U is 18.95 g/cm^3, which makes it the fourth in line with respect to density after Pt, Au, and W. Uranium is a white silvery metal which is pyrophoric when finely divided. It is malleable, ductile, and slightly paramagnetic. Its metal has three forms α (ορτηορομβιχ), β (tetragonal), and γ (cubic) with transition temperatures of 961 K and 1,049 K.

History and Use

Uranium was first recognized as an unknown element by Klaproth in 1789, and the metal was first isolated by Peligot in 1841. Uranium is used for inertial guidance devices, gyrocompasses, and ballast for missile reentry vehicles. Depleted uranium (depleted in ^{235}U) is used for shielding for tanks as well as armor-piercing bullets. Its metal is also used for X-ray target to produce high-energy X-rays. Enriched uranium has higher than natural abundance of ^{235}U and is used as fuel for nuclear reactors.

Chemistry

Uranium is an actinide and can be di-, tri-, tetra-, penta-, and hexavalent. Its ground-state electronic configuration is [Rn] $5f^3 6d^1 7s^2$. In nature, the two common valence states are tetravalent under reducing and hexavalent under oxidizing conditions as in the oceans. In its tetravalent state, it behaves much like Th and is particle reactive and insoluble in water. Under oxidizing conditions, it is soluble in water resulting in relatively high concentrations in surface and ocean waters. In solution, the dominant form of U is the uranyl ion, UO_2^{2+}, but U is also complexed by F^-, OH^-, SO_4^{2-}, NO_3^-, and carboxylates. In most minerals, it is tetravalent with an ionic radius 8.9 nm in sixfold coordination and 10 nm in eightfold coordination.

Concentrations of U in bulk samples are generally low, in the ppm to ppb range, and are mostly measured by inductively coupled plasma mass spectrometry (ICP-MS) or by isotope dilution. Its first ionization potential is relatively high, 6.3 eV, making it more difficult to analyze by flame photometry. Before the era of ICP-MS, U concentrations were analyzed by neutron activation or by XRF. ^{234}U abundance (activity) is also measured by alpha counting or by thermal ionization mass spectrometry (Chen et al. 1992).

Isotopes and Applications

Natural occurring uranium isotopes are ^{238}U (99.2745%), ^{235}U (0.720%), and ^{234}U (0.0055%). The present-day ^{238}U/^{235}U isotope abundance ratio is 137.88; at secular equilibrium, the ^{238}U/^{234}U isotope abundance ratio is 18236. All three natural occurring isotopes are unstable and have half-lives of 245,250 ± 490 years (^{234}U), 0.70381 ± 0.00096 G years (^{235}U), and 4.468 ± 0.0048 G years (^{238}U). The stable daughter isotope in the ^{238}U-series is ^{206}Pb; during this decay scheme, eight alpha particles are released. The ^{235}U decay series ends at ^{207}Pb and seven alpha particles are released. At the start of the solar system, the ^{238}U/^{235}U was 3.3. Any significant variations in ^{206}Pb/^{207}Pb have to be produced early in Earth's history as for the last 2Ga ^{207}Pb/^{204}Pb has changed little due to the now low abundance of ^{235}U.

Except for at the Oklo nuclear reactor (Bros et al. 1993), the present-day ^{235}U/^{238}U was long thought to be constant. Natural fractionation of uranium isotopes was first exploited by Stirling et al. (2007) and Weyer et al. (2008). Isotopic compositions are reported as δ^{238}U, which is the relative deviation, reported in per mil, of the ^{238}U/^{235}U of the sample compared to that of a standard. For most analyses, samples are spiked with ^{233}U–^{236}U for mass bias correction. The natural variation in δ^{238}U is approximately 3 ‰. These natural variations occur through low-temperature processes, and the largest differences are between oxidizing and reducing environments. Black shales are approximately 0.4 ‰ heavier than seawater. These fractionations are thought to be related to volume-dependent equilibrium fractionation where U in seawater is reduced and the ^{238}U is preferentially concentrated in the reduced U(IV) and concentrates in the sediment. During microbial reduction, the heavy isotope is also concentrated in the reduced fraction (Bopp et al. 2010). The magnitude and direction of the fractionation is consistent with theoretical prediction of the fractionations being related to differences in nuclear volume (Schauble 2007). Kinetic isotope fractionations would predict enrichments in the light isotope in the reduced phase, which is opposite to the observations. Except for near the basalt-seawater interface, altered oceanic crust also shows heavy isotope enrichment which is attributed to the penetration of seawater to deeper levels, reduction of U(VI), and addition of U to the crust (Andersen et al. 2015).

Absorption of U to Fe-Mn hydroxides also results in an isotope fractionation whereby the absorbed fraction is lighter (Weyer et al. 2008). The absorption, as observed with Mn nodules, is not associated with a change in valence state (Brennecka et al. 2011), and kinetic fractionation is expected and consistent with the sense of the observed mass fractionation.

Ores and Distribution in Rocks

Uranium is a trace element in all rocks and is mostly present in tetravalent state. Due to its large ionic radius and high charge,

uranium is not easily incorporated in crystal structures of common rock-forming minerals. Therefore, during melting, uranium enters the melt very early, and mineral melt partition coefficient is typically less than 10^{-3}. U is a large ion lithophile element as well as a high field strength element. It enters the melt easily and during crystallization is concentrated in the residual melt and is incorporated in late-stage crystallizing trace phases like zircon, apatite, xenotime, or sphene. The tendency for U to substitute in zircon makes it the premier geochronometer because, as well as being U-rich, it typically contains little or no Ph initially, it is a common accessory mineral in many rocks, and it extremely chemically and mechanically stabile. Although there are significant uncertainties, approximately 16% of the Earth's U is sequestered in the continental crust, which comprises only 0.2% of Earth's mass.

Uranium concentrations in igneous rocks are low in most mafic and ultramafic rocks, but have higher concentrations in alkaline and silica-undersaturated magmas, but can be as high as 50 ppm in carbonatites and up to 100 ppm in syenites. Marine phosphorites are the highest in U concentration (100 ppm) of sedimentary rocks. High silica granites can have 10–20 ppm of U. In most other natural materials, the concentration of uranium is low. For example, mid-ocean ridge basalts have U concentrations generally below 1 ppm.

Concentrations of U in ultramafic rocks are very low, often less than 10 ppb. It is, however, unclear where the U resides. The sum of the uranium content of the individual mineral phases is often less than the bulk rock content, indicating U is probably residing along grain boundaries or in fluid inclusions.

Uranium ores can be formed under a wide variety of conditions with uraninite (UO_2) or pitchblende as the main mineral. Ores can be formed by concentration in late-stage melts or in sedimentary rocks by being transported by fluids and precipitated at a reaction front due to more reducing conditions resulting in UO_2 precipitation.

Uranium together with Th and K are presently the three elements responsible for almost all the radiogenic heat production in the Earth, therefore knowing its concentration in the mantle because the heat production in the mantle contributes to convection, plate motion, and magmatism. A novel and expensive way to measure U concentration in the Earth is with the placement of giant liquid scintillators-based detectors deep in the crust to measure geoneutrinos (McDonough and Šrámek 2014), but this will ultimately provide a better estimate of the U content of Earth.

High-Temperature Geochemistry

In subduction zones, U is mobilized by dehydration of the slab and enriches the overlying mantle wedge with U. This conclusion is supported by the low Th/U ratios and $^{230}Th/^{238}U$ showing U excesses in island arc magmas (Turner et al. 2003). Mass balance calculations and the variations in U/Th ratios indicate that the addition of slab components is a two-step process: first bulk addition of sediment or sediment melt with unfractionated U/Th followed by a fluid addition from the altered oceanic crust more enriched in U than Th resulting in U excesses in the magmas (Turner et al. 2003).

During melting, U concentrates in the melt phase together with other highly incompatible elements. The Nb/U is constant in mid-ocean ridge basalts over a wide range of concentrations indication that their behavior is very similar during melting of a peridotite and subsequent crystallization at lower pressures. Its behavior under these conditions is also very similar to Th. One of the major shallow mantle minerals able to fractionate U from Th is garnet in which $D_{Th} < D_U$.

The cycling of Th and U in the Earth through time is constrained by the Pb isotope variations of the different Earth reservoirs. An example is that Th/U of the upper mantle is lower that what is expected based its Pb-isotopic composition measured in mid-ocean ridge basalts (Elliott et al. 1999). It has been argued that a change in behavior of U is the cause of this in that the early Earth had an anoxic atmosphere and U behaved very much like Th. With the increase in oxygen of the atmosphere, U behavior on the Earth's surface changed, and presently U is preferentially lost over Th from the slab, while in the early Earth when the ocean was anoxic, U in the altered subducted slab was tetravalent. Thus, on the early Earth, there was no low Th/U flux in to the upper mantle, like there is nowadays. The recent discovery of U isotope fractionation, including on the ocean floor (Stirling et al. 2007; Weyer et al. 2008), provides a tracer for U that has been in an oxygenated environment and allows for testing the U/Th cycle (Andersen et al. 2015). Present-day MORB are heavy in $\delta^{238}U$ (-0.268 ± 0.005 ‰) versus ocean island basalts (-0.308 ± 0.005 ‰) and island arcs (~-0.4 ‰), while altered oceanic crust $\delta^{238}U$ is -0.17 ‰ with Th/U = 0.44. This is explained as preferential loss of light, mostly sediment-derived U, to the island arc while at greater depth heavier U from the altered oceanic crust which also has low Th/U. Although there is much evidence for sediment and oceanic crust recycling in OIB sources, it is argued these sources are established before the oceans were oxygenated and therefore do not have fractionated $^{235}U/^{238}U$ (Andersen et al. 2015).

Low-Temperature Geochemistry

Under oxygenated conditions, U is hexavalent and is relatively soluble in concentrations in freshwater and in the oceans is relatively high. Seawater has over 3 ppb of

U which is high compared to elements with similar behavior in magmatic systems. Groundwaters have high ^{234}U as β-decay of ^{238}U results in recoil of the daughter product ^{234}Th in the groundwater which subsequently decays with a 24.1 day half-life through ^{234}Pa to ^{234}U. This results in an excess of ^{234}U. The exact amount of excess is dependent on the nature of the aquifer, the degree of interaction between the dissolved fraction and the aquifer matrix, as well as the colloidal fraction (Porcelli and Swarzenski 2003). ^{234}U excesses in the oceans are about 15% (Chen et al. 1986). Rivers can have larger excesses, and the excess ^{234}U in groundwaters can be extreme with ($^{234}U/^{238}U$) up to 11 (Porcelli and Swarzenski 2003). In groundwater, the ^{234}U excesses have been useful in tracing flow through subsurface conduits. In marine sediment, the $^{234}U/^{238}U$ is often measured as a check on the age disequilibria involving shorter-lived U-series radionuclides. ^{234}U has the longest half-life of the daughter isotopes in the U-series decay scheme, and thus if the disequilibrium dates the time at which it is separated from seawater, then the ^{234}U should still be present.

Biological Utilization and Toxicity

In the subsurface, a large variety of bacteria, dissimilatory metal-reducing and sulfur-reducing bacteria, have the ability to reduce hexavalent uranium. These uranium reducers seem to have in common that they thrive in anaerobic conditions where the redox potential is low enough for the reduction of U (VI) to take place (Wall and Krumholz 2006). The bacterial reduction to U(IV) renders U immobile, and stimulating bacteria in the subsurface to immobilize U have been experimented with (Anderson et al. 2003) and have shown to be effective in bioremediation by containing U contamination in the subsurface.

Uranium is toxic at intake levels of 20–40 mg and can result in kidney damage and failure. Radiological toxicity is due to the U decay that produces alpha particles. Due to the limited penetration depth of alpha particles ingestion or inhalation of uranium are the main hazards.

Summary

The geochemical behavior of uranium is strongly dependent on its valence state: hexavalent U goes in solution, while tetravalent is near insoluble. Presently U is in the hexavalent state at the oxygen-rich Earth's surface. But, before the Earth's surface was oxygenated, its behavior was markedly different. U is the parent in the U-series that ultimately lead to stable lead isotopes. This provides the opportunity for dating processes over a large range of time scales. Because of its large ionic radius, U is not easily accommodated in most crystal lattices and is incompatible, concentrates in trace phases like zircon, and enters a melt early and crystallizes out late in a sequence.

Cross-References

- ▶ Atmospheric Evolution
- ▶ Atomic Number, Mass Number, and Isotopes
- ▶ Earth's Continental Crust
- ▶ Geochronology and Radiogenic Isotopes
- ▶ Geoneutrinos
- ▶ Heat-Producing Elements (HPEs)
- ▶ Incompatible Elements
- ▶ Large-Ion Lithophile Elements
- ▶ Lead Isotopes
- ▶ Oklo Natural Nuclear Reactors
- ▶ Solubility
- ▶ Stable Isotope Geochemistry
- ▶ Thorium
- ▶ Trace Elements
- ▶ Uranium Decay Series

References

Andersen MB, Elliott T, Freymuth H, Sims KWW, Niu Y, Kelley KA (2015) The terrestrial uranium cycle. Nature 517:356–359

Anderson RT, Vrionis HA, Ortiz-Bernad I, Resch CT, Long PE, Dayvault R, Karp K, Marutzky S, Metzler DR, Peacock A, White DC, Lowe M, Lovley DR (2003) Stimulating the in situ activity of geobacter species to remove uranium from the groundwater of a uranium-contaminated aquifer. Appl Environ Microbiol 69:5884–5891

Bopp CJ IV, Lundstrom CC, Johnson TM, Sanford RA, Long PE, Williams KH (2010) Uranium 238U/235U isotope ratios as indicators of reduction: results from an in-situ biostimulation experiment at Rifle, Colorado, USA. Environ Sci Technol 44:5927–5933

Brennecka GA, Wasylenki LE, Bargar JR, Wetyer S, Anbar AD (2011) Uranium isotope fractionation during adsorption to Mn-Oxyhydroxides. Environ Sci Technol 45:1370–1375

Bros R, Turpin L, Gauthier-Lafaye F, Hiolliger P, Stille P (1993) Occurrence of naturally enriched ^{235}U: implications for plutonium behaviour in natural environments. Geochim Cosmochim Acta 57(6):1351–1356

Chen JH, Edwards RL, Wasserburg GJ (1986) ^{238}U, ^{234}U and ^{232}Th in seawater. Earth Planet Sci Lett 80:241–251

Chen JH, Edwards RL, Wasserburg GJ (1992) Mass spectrometry and applications to uranium series disequilibria. In: Ivanovich M, Harmon RS (eds) Uranium-series disequilibrium: applications to earth, marine and environmental sciences. Clarendon, Oxford, pp 174–206

Elliott T, Zindler A, Bourdon B (1999) Exploring the kappa conundrum: the role of recycling in the lead isotope evolution of the mantle. Earth Planet Sci Lett 169:129–145

Lodders K (2003) Solar system abundances and condensation temperatures of the elements. Astrophys J 591:1220–1247

McDonough WF, Šrámek O (2014) Neutrino geoscience, news in brief. Environ Earth Sci 71:3787–3791

Porcelli D, Swarzenski PW (2003) The behavior of U and Th-series nucklides in groundwater. In: Bourdon B, Henderson GM, Lundstrom CC, Turner SP (eds) Uranium -series geochemistry, vol 52. Mineralogical Society of America, Washington, DC, pp 317–361
Schauble EA (2007) Role of nuclear volume driving equilibrium stable isotope fractionation of mercury, thallium and other very heavy elements. Geochim Cosmochim Acta 71:2170–2189
Stirling CH, Andersen MB, Potter E-K, Halliday AN (2007) Low-temperature isotopic fractionation of uranium. Earth Planet Sci Lett 264:208–225
Turner S, Bourdon B, Gill J (2003) Insight into magma genesis at convergent margins from U-series isotopes. In: Bourdon B, Henderson GE, Lundstrom CC, Turner SP (eds) Uranium-series geochemistry. Mineralogical Society of America, Washington, DC, pp 255–315
Wall JD, Krumholz LR (2006) Uranium reduction. Annu Rev Microbiol 60:149–166
Weyer S, Anbar AD, Gerdes A, Gordon GW, Algeo TJ, Boyle EA (2008) Natural fractionation of 238U/235U. Geochim Cosmochim Acta 72:345–359

Uranium Decay Series

Bernard Bourdon
Laboratoire de Géologie de Lyon, Université de Lyon, Lyon, France
ENS-Lyon, Université Lyon 1, CNRS, UMR 5276 LGLTPE, Lyon, France

Definition

Uranium decay series are the products of radioactive decay of uranium isotopes (^{235}U and ^{238}U). U decay series are an essential tool of modern geochronology for ages ranging between a few years to one million years. This is due both to the excellent temporal resolution afforded by U-series dating and the ability to measure low-level geological samples. In parallel, U-series are also powerful tracers of both low- and high-temperature processes in the Earth, providing key constraints on the rates and timescales of numerous geological processes.

Basic Principles in U-Series Geochemistry

^{238}U decays to stable ^{206}Pb via a series of α and β decays. If the decay chain is undisturbed, it reaches a steady state called secular equilibrium, and the abundance of short-lived intermediate nuclides is then controlled by their half-lives. However, this secular equilibrium can be perturbed by physical or chemical processes (e.g., crystallization, water-rock interaction, or nuclear properties) that lead to a fractionation between isotopes of the U decay series. This fractionation is the basis for U-series geochemistry. The basic equations that describe the evolution of the U-series decay chain can be written for the first nuclide (^{238}U, ^{235}U, or ^{232}Th) as follows:

$$\frac{dN_1}{dt} = -\lambda_1 N_1 \tag{1}$$

where N_1 is the number of atoms of the parent isotope (i.e., ^{238}U or ^{235}U) and λ_1 the decay constant. For the nuclides that are produced by successive decay of the parent isotope, the following equation should be used:

$$\frac{dN_{i+1}}{dt} = -\lambda_{i+1} N_{i+1} + \lambda_i N_i \tag{2}$$

Given some initial conditions, this system of ordinary differential equations can be solved analytically. The solution for the first nuclide can be integrated as:

$$N_1 = N_1^0 e^{-\lambda_1 t} \tag{3}$$

and for the second nuclide:

$$N_2 = \frac{\lambda_1}{\lambda_2 - \lambda_1} N_1^0 \left(e^{-\lambda_1 t} - e^{-\lambda_2 t}\right) + N_2^0 e^{-\lambda_2 t} \tag{4}$$

where N_1^0 and N_2^0 are the number of atoms of nuclides 1 and 2 at t = 0. In the case of a long-lived nuclide such as ^{238}U or ^{235}U, the term $e^{-\lambda_1 t}$ is almost equal to 1. In this case, it can be shown that if the system is undisturbed, N_2 reaches a steady-state value:

$$N_2 = \frac{\lambda_1}{\lambda_2 - \lambda_1} N_1 \tag{5}$$

Since λ_1 is small compared to λ_2, the equation can be further simplified to $\lambda_1 N_1 = \lambda_2 N_2$. This corresponds to an equality of the activity of nuclides N_i where the activity is defined as $\lambda_i N_i$. This equation can be generalized to the whole decay chain:

$$\lambda_1 N_1 \approx \lambda_2 N_2 \approx \ldots \approx \lambda_n N_n \tag{6}$$

where the subscript 1 indicates the parent nuclide (^{238}U or ^{235}U), λ_i is the decay constant for nuclide i, and N_i is the number of nuclides of i. The return to secular equilibrium is a function of time and this property can be used for age determination. Following a fractionation event between two given nuclides, the dating method is operative if there is a resolvable difference between the value measured for the daughter nuclide and the value at secular equilibrium; this corresponds to a time of the order of six half lives. Radiometric dating with

U-series is possible when the processes causing fractionation are a discrete event. When the process itself is protracted relative to the half-life of the daughter product, then it is only possible to derive a timescale for this process or alternatively its rate. In what follows, the various methods and applications of U-series nuclides are described while highlighting the most recent advances.

^{238}U-^{234}U Dating

The main principle behind the ^{238}U-^{234}U dating method is that in low-temperature environments, ^{234}U can fractionate from ^{238}U due to nuclear effects. The first part of the ^{238}U decay chain can be written as follows:

$$^{238}U \xrightarrow{\alpha} {}^{234}Th \xrightarrow{\beta^-} {}^{234}Pa \xrightarrow{\beta^-} {}^{234}U \tag{7}$$

The half-lives of the intermediate nuclides ^{234}Th and ^{234}Pa are very short (24.1 days and 6.69 h, respectively) compared with geological processes. The ^{234}Th is ejected by recoil from the site where ^{238}U was residing, and this implies that the daughter nuclide can be more labile. If the ^{238}U resided near the boundary of a grain, the ^{234}Th can be directly ejected out of the grain. Alternatively, it can be more easily leached out of the grain during weathering reactions compared with ^{238}U because it no longer sits in an energetically stable lattice site. Collectively, these effects can lead to a fractionation between ^{238}U and ^{234}U. The experiments of Kigoshi (1971) have shown that a solution in contact with a zircon can be enriched in ^{234}U relative to its secular equilibrium abundance, due to its preferential release in the solution. Leaching experiments of granite also showed that dissolution leads to ^{234}U-^{238}U fractionation (Andersen et al. 2009). If a mineral forms in equilibrium with seawater or any water whose ^{234}U/^{238}U is known and subsequently behaves as a closed system, the following equation is used to calculate its isotopic composition as a function of time:

$$\left(\frac{^{234}U}{^{238}U}\right)_t - 1 = \left(\left(\frac{^{234}U}{^{238}U}\right)_{\text{initial}} - 1\right)_{\text{initial}} e^{-\lambda t} \tag{8}$$

This equation can be inverted to obtain the time since the mineral last equilibrated with water provided the initial ratio is known (Andersen et al. 2008).

Dating Based on ^{230}Th-^{238}U and ^{231}Pa-^{235}U Disequilibrium

These dating methods are based on the existence of chemical fractionation between ^{230}Th and ^{234}U or ^{231}Pa and ^{235}U. This fractionation arises because U and Th (and Pa) behave differently in geochemical processes. For the sake of illustration, we describe the dating of carbonates. When carbonates form by precipitation from seawater, the carbonate incorporates U (^{238}U, ^{234}U, and ^{235}U) but little ^{230}Th and ^{231}Pa which have a very low abundance in seawater but also a low partition coefficient in carbonates. As a result the initial ^{230}Th/^{234}U and ^{231}Pa/^{235}U activity ratios in carbonates are close to zero. If one assumes that the system is closed and solves (Eqs. 1 and 2), one obtains:

$$\left(\frac{^{230}Th}{^{238}U}\right) = 1 - e^{-\lambda_0 t} + \left(\left(\frac{^{234}U}{^{238}U}\right) - 1\right)\left(\frac{\lambda_0}{\lambda_0 - \lambda_4}\right)\left(1 - e^{-(\lambda_4 - \lambda_0)t}\right) \tag{9}$$

$$\left(\frac{^{231}Pa}{^{235}U}\right) = 1 - e^{-\lambda_5 t} \tag{10}$$

By measuring the activity ratios of ^{230}Th/^{238}U and ^{234}U/^{238}U, the only unknown in Eq. 9 is time t, while for Eq. 10, the measurement of ^{231}Pa/^{235}U is sufficient to derive an age. These methods have been used extensively to determine the age of corals for ages as old as 1 Ma or for dating speleothems (Hu et al. 2008). The great powers of these methods have been first the ability to determine ages precisely and second to use jointly the ^{230}Th-^{234}U-^{238}U and ^{231}Pa-^{235}U dating methods using concordia approach similar to the U-Pb technique. With this approach it is possible to ascertain that the ages have not been disturbed by a later event leading to open-system behavior. In some cases, open-system behavior has been identified and this can be due to recoil effects. Using the following equations, Thompson et al. (2003) were able to correct the ages while quantitatively estimating the effect of recoil:

$$\begin{aligned}
\frac{d^{238}U}{dt} &= -\lambda_8 {}^{238}U \\
\frac{d^{234}U}{dt} &= -\lambda_4 {}^{238}U + f_4\lambda_8 {}^{238}U \\
\frac{d^{230}Th}{dt} &= -\lambda_0 {}^{230}Th + f_0\lambda_4 {}^{234}U
\end{aligned} \tag{11}$$

where f_i represents the fraction of nuclides that are not lost from the system by recoil. An evaluation of such models is given in Scholz and Mangini (2007).

Dating Magmatic Event and Magma Storage

Upon eruption, a magma crystallizes relatively rapidly, and the difference in compatibility between U-series nuclides (in this case, U, Th, Pa, Ra) can be used for dating. By analyzing mineral phases in a volcanic rock, it is possible to use an isochron approach to obtain an age. There are two main methods: (1) dating mineral crystallization with ^{230}Th-^{238}U disequilibrium (2) dating recent events with ^{226}Ra-^{230}Th disequilibrium.

For the first method, one assumes that all mineral phases remain closed system after eruption. In this case, the following equation can be used to describe the time evolution of each mineral phase/matrix (Allègre 1968):

$$\left(\frac{^{230}Th}{^{232}Th}\right) = \left(\frac{^{230}Th}{^{232}Th}\right)_0 e^{-\lambda t} + \left(\frac{^{238}U}{^{232}Th}\right)\left(1 - e^{-\lambda t}\right) \quad (12)$$

This equation is similar to Eq. 4, except that it has been normalized by the activity of ^{232}Th, which is assumed constant over the timescale of interest. An additional assumption is that all the minerals formed in isotope equilibrium (i.e., with identical ^{230}Th/^{232}Th ratios) with the melt. In numerous cases, a comparison with eruption ages was possible and it was found that the U-Th age was older than the eruption age. These observations have enabled to develop a new range of applications where U-series are used for dating magma storage and for dating phenocryst growth (e.g., Cooper and Kent 2014).

The second method based on ^{226}Ra-^{230}Th disequilibrium makes the assumption that Ra and Ba are chemical analogues, and since there is no stable isotope of ^{226}Ra, the activity of Ra is normalized to Ba to yield an equation similar to Eq. 4. There has been criticism regarding this approach, and it was subsequently extended to a new method to take into account the difference in partitioning between Ra and Ba (Cooper et al. 2001).

Tracing Mantle Melting and Melt Migration

During partial melting of the mantle, chemical equilibrium between melt and mineral phases leads to a chemical fractionation between U-Th-Ra and U-Pa, which results in a disequilibrium of the decay chains. This disequilibrium can be used as a probe of melting processes in various geodynamic settings. First, U-series disequilibria can be used to infer the rate of melting and the porosity of the mantle during melting. Second, the ^{226}Ra-^{230}Th disequilibrium has been argued to be a tracer of the rate of melt migration.

The existence of ^{230}Th-^{238}U disequilibrium in mantle-derived magmas is surprising because Th-U fractionation should be small as mineral-melt partition coefficients of these elements are low ($D \sim 10^{-3}$). For a fractionation to take place, the mantle porosity should be of the same order of magnitude as D. In turn, this observation puts strong constraints on the porosity of the mantle (ϕ) during melting. Similarly, the observations of ^{226}Ra-^{230}Th disequilibria in mantle melts indicate that melt transport was sufficiently rapid to allow the extraction of magmas on timescales that are short relative to the half-life of ^{226}Ra (1600 years).

One important aspect of the U-series disequilibria measured in mid-ocean ridge basalts (MORB) is that they are responding to the pressure dependence of U-Th partitioning. U-Th fractionation is mostly sensitive to the first few percent of melting as both elements are highly incompatible (Blundy and Wood 2003). The mineral/melt partition coefficient of U is often greater than that of Th and Pa in most minerals (see exception below). During partial melting of the mantle beneath ridges and hotspots, if melting starts in the garnet lherzolite stability field, ^{230}Th, ^{231}Pa, and ^{226}Ra are enriched in the melt relative to U, which creates a fractionation that can be used for tracing magmatic processes (Beattie 1993). In the spinel lherzolite stability field, the budget of U is mostly in clinopyroxenes, and experiments by Landwehr et al. (2001) showed that in this case, the ratio of D^U/D^{Th} is less than 1 and decreases with decreasing pressure. Thus, melting at shallower pressure should yield ^{238}U excess in the melt. ^{238}U-^{230}Th systematics in MORB show that basalts produced from a greater depth of melting have ^{230}Th excesses larger than those produced at shallower depth (Bourdon et al. 1996; Elkins et al. 2014), thereby constraining the depth of melting for MORBs.

Another key parameter that controls the degree of U-Th-Pa fractionation is the rate of melting (McKenzie 1985). In the context of adiabatic melting beneath mid-ocean ridges and intraplate volcanism, the melting rate increases with the rate of mantle upwelling. It has been shown analytically that the U-Th or U-Pa fractionation is a direct function of the rate of mantle upwelling (Bourdon and Sims 2003). Thus, an increasing melting rate leads to a smaller ^{231}Pa/^{235}U and ^{230}Th/^{238}U in the melt. Sims et al. (1999) showed that the ^{231}Pa/^{235}U and ^{230}Th/^{238}U decreased toward the center of the hotspot which they attributed to increasing mantle upwelling rates. Hotspots with larger buoyancy fluxes and faster melting rates were shown to have smaller ^{231}Pa and ^{230}Th excesses (Bourdon et al. 2006). These observations were used to map mantle upwelling rates beneath hotspots and to infer mantle temperatures.

It is worth mentioning here that the presence of pyroxenites can affect U-series systematics during melting. Notably, the garnet mode in pyroxenite is much greater than in peridotites which means the U-Th and U-Pa fractionation is enhanced and their melting rates is much greater. Thus it is important to quantify the abundance of these lithologies to interpret U-series in mantle-derived rocks (e.g., Elkins et al. 2014).

U-Series as Tracer of Water-Rock Interaction

In the surface environment, U and Ra are more soluble than Th and Pa, which means that water-rock reactions lead to fractionation of U relative to Th and Pa. In the case of

^{234}U-^{238}U, water-rock interaction leads to preferential removal of ^{234}U in the water phase. The observed fractionation can then be used to trace the timescale of water interaction in waters, aquifers, soils, or sediments. There have been a number of applications to infer the rates of chemical weathering in soils or at the scale of a basin (e.g., Dosseto et al. 2008), the rates of dissolution in sediments (Maher et al. 2004), the ages of comminution of fine grained sediments (Lee et al. 2010), and the transport timescales of sediments (Dosseto et al. 2008).

In order to infer the timescale of chemical weathering, one needs to make assumptions about the kinetics of these reactions. Experimental work has shown that first-order reaction could be used to describe the release rate of U-series nuclides in soils (e.g., Andersen et al. 2009) in the case of silicate or carbonate rocks. One can describe this process by the following equation:

$$\frac{d^{238}U}{dt} = -k_8{}^{238}U_s \tag{14}$$

$$\frac{d^{234}U_s}{dt} = \lambda_8{}^{238}U_s - (k_4 + \lambda_4)^{234}U_s \tag{15}$$

By solving a series of coupled equations describing ^{238}U-^{230}Th-^{234}U measured in solids and dissolved form, it is possible to derive both the rate and timescale of weathering. This approach has been described in more detail in Vigier et al. (2001) and Dosseto et al. (2008). It was argued by Keech et al. (2013) that a two-stage model with first-order kinetics was a better representation of observations, and this results in differences in the calculated timescales. If one assumes as in DePaolo et al. (2006) that the dominant source of ^{238}U-^{234}U fractionation is due to recoil effect, the following equation can be written:

$$\frac{d^{234}U_s}{dt} = \lambda_8{}^{238}Us - \lambda_8 f_\alpha{}^{238}Us - \lambda_4{}^{234}U_s \tag{16}$$

where f_α represents the fraction of recoil nuclide that are ejected from the solid. By solving this equation, one can derive the age of "mineral comminution." Several studies have attempted to use this approach, and although a correct timescale can be obtained (Lee et al. 2010; Handley et al. 2013), there could be complications, owing to the fact that ^{234}U-^{238}U can be fractionated during leaching (Andersen et al. 2009) and not simply due to recoil.

Applications in the Field of Oceanography

The U-series nuclides (mainly ^{230}Th and ^{231}Pa) have become particularly powerful tools to study particle scavenging, ocean circulation, and paleoproductivity. The solubilities of Pa and Th in seawater are extremely low, and it is expected that the abundances of ^{230}Th and ^{231}Pa should be directly linked to their in situ production by decay of ^{238}U and ^{235}U. This ratio can be modified by adsorption of Th and Pa onto biogenic particles, and it has been found experimentally (e.g., Roberts et al. 2009) that the adsorption of Pa is smaller than that of Th. As a consequence, the residence time of Pa in the oceans is greater than that of Th, and this difference in adsorption properties yields variations in Pa/Th ratios in water masses relative to the production ratio. Variations in the biological productivity of the oceans are correlated with the flux of biogenic particles, and it has been found that the Pa/Th ratio increases with biogenic particle flux (Kumar et al. 1995). Therefore, this ratio measured on sediments can be used as a proxy for paleoproductivity. Most often, this proxy is not used in isolation and it is often coupled with models of paleocirculation (Siddall et al. 2005).

Another application of U-series in the oceans is the possibility to determine groundwater fluxes from continental margins to the oceans. During decay of ^{230}Th contained in solid particles, a fraction of ^{226}Ra can be ejected into the sediment pores which leads to an enhancement of this nuclide inside sediments. If freshwater circulates through the sediment, this ^{226}Ra can be fluxed out toward the oceans. This results in a local increases in ^{226}Ra concentration that can be directly scaled to the flux of groundwater, and by measuring gradients in ^{226}Ra along a shoreline, it is possible to quantify the submarine groundwater discharge (Moore 1996).

Summary

The radioactive decay chain of U and its daughters evolve to a state of secular equilibrium at a predictable rate. The extent of disequilibrium between members of the decay series can not only provide a geochronology tool for dating events such as crystallization of a magma but also provide insights into such diverse processes as mantle upwelling and melting, biological productivity, and groundwater flux to the oceans.

Cross-References

- Chemical Weathering
- Geochronology and Radiogenic Isotopes
- Magmatic Process Modeling
- Ocean Biochemical Cycling and Trace Elements
- Paleoproductivity
- Partial Melting
- Partitioning and Partition Coefficients
- Protactinium
- Radium

▶ Thorium
▶ Uranium
▶ Volcanism

References

Allègre CJ (1968) ^{230}Th dating of volcanic rocks: a comment. Earth Planet Sci Lett 5:209–210

Andersen MB, Stirling CH, Potter E-K, Halliday AN, Blak SG, McCulloch MT, Ayling BF, O'Leary M (2008) High precision U-series measurements of more than 500,000 year old fossil corals. Earth Planet Sci Lett 265:229–245

Andersen MB, Erel Y, Bourdon B (2009) Experimental evidence for ^{234}U–^{238}U fractionation during granite weathering with implications for ^{234}U/^{238}U in natural waters. Geochim Cosmochim Acta 73:4124–4141

Beattie PD (1993) Uranium–thorium disequilibria and partitioning on melting of garnet peridotite. Nature 363:63–65

Blundy J, Wood B (2003) Mineral-melt partitioning of uranium, thorium and their daughters. In: Bourdon B, Henderson GM, Lundstrom CC, Turner SP (eds) Uranium-series geochemistry, vol 52. Mineralogical Society of America, Washington, DC, pp 59–123. Rev Min Geoch

Bourdon B, Sims KW (2003) U-series and hotspot magmatism in U-series geochemistry and applications. In: Bourdon B, Henderson GM, Lundstrom CC, Turner SP (eds) Uranium-series geochemistry, vol 52. Geochemical Society and the Mineralogical Society of America, Washington, DC, pp 215–254

Bourdon B, Zindler A, Elliott T, Langmuir CH (1996) Constraints on mantle melting at mid-ocean ridges from global ^{238}U-^{230}Th disequilibrium data. Nature 384:231–235

Bourdon B, Ribe NM, Stracke A, Saal AE, Turner SP (2006) Dynamics of mantle plumes: insights from U-series geochemistry. Nature 444:713–717

Cooper KM, Kent AJR (2014) Rapid remobilization of magmatic crystals kept in cold storage. Nature 506:480–483

Cooper KM, Reid MR, Murrell MT, Clague DA (2001) Crystal and magma residence at Kilauea Volcano, Hawaii: 230Th-226Ra dating of the 1955 east rift eruption. Earth Planet Sci Lett 184:703–718

DePaolo DJ, Maher K, Christensen JN, McManus J (2006) Sediment transport time measured with U-series isotopes: results from ODP North Atlantic drift site 984. Earth Planet Sci Lett 248:394–410

Dosseto A, Bourdon B, Turner SP (2008) Uranium-series isotopes in river materials: insights into the timescales of erosion and sediment transport. Earth Planet Sci Lett 265:1–17

Elkins LJ, Sims KWW, Prytulak J, Blichert-Toft J, Elliott T, Blusztajn J, Fretzdorff S, Reagan M, Haase K, Humphris S, Schilling JG (2014) Melt generation beneath Arctic Ridges: implications from U decay series disequilibria in the Mohns, Knipovich, and Gakkel Ridges. Geochim Cosmochim Acta 127:140–170

Handley HK, Turner S, Afonso JC, Dosseto A, Cohen T (2013) Sediment residence times constrained by uranium-series isotopes: a critical appraisal of the comminution approach. Geochim Cosmochim Acta 103:245–262

Hu C, Henderson GM, Huang J, Xie S, Sun Y, Johnson KR (2008) Quantification of Holocene Asian monsoon rainfall from spatially separated cave records. Earth Planet Sci Lett 266:221–232

Keech AR, West AJ, Pett-Ridge JC, Henderson GM (2013) Evaluating U-series tools for weathering rate and duration on a soil sequence of known ages. Earth Planet Sci Lett 374:24–35

Kigoshi K (1971) Alpha recoil thorium-234: dissolution into water and uranium-234/uranium-238 disequilibrium in nature. Science 173:47–49

Kumar N, Anderson RF, Mortlock RA, Froelich PN, Kubik P, Dittrich-Hannen B, Suter M (1995) Increased biological productivity and export production in the glacial Southern Ocean. Nature 378:675–680

Landwehr D, Blundy J, Chamorro-Perez EM, Hill E, Wood B (2001) U-series disequilibria generated by partial melting of spinel lherzolite. Earth Planet Sci Lett 188:329–348

Lee VE, DePaolo DJ, Christensen JN (2010) Uranium-series comminution ages of continental sediments: case study of a Pleistocene alluvial fan. Earth Planet Sci Lett 296:244–254

Maher K, DePaolo DJ, Lin JCF (2004) Rates of silicate dissolution in deep-sea sediment: in situ measurement using ^{234}U/^{238}U of pore fluids. Geochim Cosmochim Acta 68:4629–4648

McKenzie D (1985) ^{230}Th-^{238}U disequilibrium and the melting processes beneath ridge axes. Earth Planet Sci Lett 72:149–157

Moore WS (1996) Large groundwater inputs to coastal waters revealed by ^{226}Ra enrichments. Nature 380:612–614

Roberts KA, Xu C, Hung C-C, Conte MH, Santschi PH (2009) Scavenging and fractionation of thorium vs. protactinium in the ocean, as determined from particle–water partitioning experiments with sediment trap material from the Gulf of Mexico and Sargasso Sea. Earth Planet Sci Lett 286:131–138

Scholz D, Mangini A (2007) How precise are U-series coral ages? Geochim Cosmochim Acta 71:1935–1948

Siddall M, Henderson GM, Edwards NR, Frank M, Müller SA, Stocker TF, Joos F (2005) ^{231}Pa/^{230}Th fractionation by ocean transport, biogenic particle flux and particle type. Earth Planet Sci Lett 237:135–155

Sims KWW, DePaolo DJ, Murrell MT, Baldridge WS, Goldstein S, Clague D, Jull M (1999) Porosity of the melting zone and variations in the solid mantle upwelling rate beneath Hawaii: inferences from ^{238}U-^{230}Th-^{226}Ra and ^{235U}-^{231}Pa disequilibria. Geochim Cosmochim Acta 63:4119–4138

Thompson WG, Spiegelman MW, Goldstein SL, Speed RC (2003) An open-system model for U-series age determinations of fossil corals. Earth Planet Sci Lett 210:365–381

Vigier N, Bourdon B, Turner SP, Allègre CJ (2001) Erosion timescales derived from U-decay series measurements in rivers. Earth Planet Sci Lett 193:485–499

V

Van der Waals Force

Taku Tsuchiya
Geodynamics Research Center, Ehime University, Matsuyama, Ehime, Japan

Synonyms

London dispersion force

Definition

The van der Waals force is the term used to describe weak but general forces acting between neutral atoms or molecules. Forces due to covalent bonds or electrostatic interactions between ions or ionic groups with one another or with neutral molecules are not included.

Description

This force was first introduced by van der Waals in 1873 as an attractive force among neutral atoms to account for the equation of state of non-ideal actual gases. Although he did not provide its detailed mechanisms, three different types of interactions with different physical origins have later been proposed as van der Waals force: (1) the dipole-dipole interaction, (2) the dipole-induced dipole interaction, and (3) the instantaneous dipole-induced dipole interaction (London dispersion interaction) (van Oss et al. 1988).

Among these three, the first two are found with molecules that have permanent dipoles. Only the London interaction is universal, being present in non-polarized atom-atom interactions or molecule-molecule interactions as well, and is predominantly important between the macroscopic bodies in condensed systems. Thus, the London force is responsible for bonding in solid-state rare gases and organic molecules. It is also responsible for bonding between non-charged carbon layers in graphite and in electrically neutral silicate and oxide layers in clay minerals and micas. The London force is a force caused by the dipole moments between an instantaneous dipole on one atom or molecule and the induced dipole on the neighboring ones by the instantaneous dipole. The system experiences this as an attractive van der Waals force. London used a quantum-mechanical theory based on second-order perturbation theory with charge fluctuations in one part of an atomic system that are electrodynamically correlated with charge fluctuations in another (London 1937).

There are empirical and semiempirical accounts for the van der Waals or London dispersion forces that rely on the asymptotical form $-1/R^6$ for atoms or molecules, where R is the distance between the nuclear centers of mass (Kittel 1991). This asymptotical form has been widely used in molecular simulations using pairwise interatomic model potentials. However, the London dispersion interactions constitute a quantum-mechanical phenomenon, so that their correct values at important distances like the van der Waals bond lengths are substantially different from those predicted by the asymptotic forms. Since the van der Waals force at one point depends on the charge events at another region and is a truly nonlocal correlation effect, high-level (time-consuming) quantum-mechanical (wave function) approaches were required for its quantitative evaluations (e.g., Tsuzuki et al. 2002). Due to recent developments of a practical functional form for the nonlocal correlations between electrons, density-functional theory (DFT), which has long since proven successful for dense matter and is more efficient compared to wavefunction approaches, has been extended to sparse matter (atoms or molecules with large separations across marginal charge density regions) (Dion et al. 2004; Thonhauser et al. 2007) and applied to various relevant systems, including layered systems like graphite, dimers of benzene, polymer, and the structure of DNA with intercalators. Studies of

W. M. White (ed.), *Encyclopedia of Geochemistry*,
https://doi.org/10.1007/978-3-319-39312-4

minerals with this modern technique remain limited so far and future applications are expected.

Summary

The van der Waals force is the term used to describe weak but general forces acting between neutral atoms or molecules. The London dispersion interaction in particular constitutes a quantum-mechanical phenomenon. Practical techniques to evaluate this interaction quantitatively have been developed recently, but applications to minerals are still limited so far.

Cross-References

► Density Functional Theory

References

Dion M, Rydberg H, Schröder E, Langreth DC, Lundqvist BI (2004) Van der Waals density functional for general geometries. Phys Rev Lett 92:246401. https://doi.org/10.1103/PhysRevLett.92.246401

Kittel C (1991) Introduction to solid state physics, 6th edn. Wiley, New York, 646 pp

London F (1937) The general theory of molecular forces. Trans Faraday Soc 33:8–26. https://doi.org/10.1039/tf937330008b

Thonhauser T, Cooper VR, Li S, Puzder A, Hyldgaard P, Langreth DC (2007) Van der Waals density functional: self-consistent potential and the nature of the van der Waals bond. Phys Rev B 76:125112. https://doi.org/10.1103/PhysRevB.76.125112

Tsuzuki S, Honda K, Mikami M, Tanabe K (2002) Origin of attraction and directionality of the π/π interaction: model chemistry calculations of benzene dimer interaction. J Am Chem Soc 124:104–112. https://doi.org/10.1021/ja0105212

van Oss CJ, Chaudhury MK, Good RJ (1988) Interfacial Lifshitz–van der Waals and polar interactions in macroscopic system. Chem Rev 88:927–941. https://doi.org/10.1021/cr00088a006

Vanadium

Olivier Pourret[1] and Aline Dia[2]
[1]UniLaSalle, Beauvais cedex, France
[2]Géosciences Rennes, Rennes, France

Element Data
Atomic Symbol: **V**
Atomic Number: **23**
Atomic Weight: 50.9415 g/mol
(*continued*)

Isotopes and Abundances: ^{50}V 0.25%, ^{51}V 99.75%
1 Atm Melting Point: 1910 °C
1 Atm Boiling Point: 3407 °C
Common Valences: 5+, 4+, 3+, 2+
Ionic Radii: 64 pm (in 3+, 6-fold coordination)
Pauling Electronegativity: 1.63
First Ionization Energy: 6.74 eV
Chondritic (CI) Abundance: 54.6 ppm[a]
Silicate Earth Abundance: 86 ppm[a]
Crustal Abundance: 138 ppm[b]
Seawater Abundance: ~30–37 nmol/kg[c]
Core Abundance: ~150 ppm[d]
[a]Palme et al. (2014)
[b]Rudnick and Gao (2014)
[c]Bruland et al. (2014)
[d]McDonough (2014)

Properties

Vanadium (chemical symbol, V) is a d-block transition metal, silver in color, appearing in the first long period of the periodic table between titanium and chromium. Vanadium has two stable isotopes: ^{50}V and ^{51}V, with atomic abundance of 0.25% and 99.75%, respectively. Vanadium has several oxidation forms (between 2+ and 5+). In the lithosphere, V occurs as reducing V(III) form, whereas in oxidizing conditions V prevails under V(IV) form. Vanadium(II) is particularly unstable in the environment. Vanadium(III) is more stable than V(II), but it is also gradually oxidized by the air or dissolved oxygen. Vanadium(V) is expected to be the prevailing form in waters exposed to atmospheric oxygen, whereas V(IV) may be present in reducing environments. Depending upon geometry and environment, V ionic radii vary between 36 pm and 79 pm. Vanadium has a high melting point of 1910 °C and is a mildly incompatible, refractory, lithophile (siderophile in the iron core and chondrites) element. Vanadium has an electronegativity of 1.63 on the Pauling scale and displays a first ionization potential of 6.74 eV. More details can be found in Richards (2006) and Haynes (2015).

History and Use

Vanadium was first discovered by del Rio in 1801 and was incorrectly considered as impure chromium. Vanadium was rediscovered and named by Sefström in 1830 after the Scandinavian goddess Vanadis. In 1867, Roscoe isolated V in nearly pure form by reducing V chloride with hydrogen. Vanadium of high purity (99.3–99.8%) was not produced until 1927. The V redox chemistry and its specific application

to renewable energy technologies (e.g., vanadium redox battery; a type of rechargeable flow battery using V in different oxidation states to store chemical potential energy) have already add to the demand for this element and will definitely continue to increase in the near future. Vanadium demand for construction materials is the greatest consumer of mined V - (Moskalyk and Alfantazi 2003). Indeed, vanadium is the most widely used alloying element for strengthening steels employed in buildings and bridges. Vanadium volume that is cycled through terrestrial and aquatic reservoirs can thus be expected to further growth. It results in uncontrolled V releases in the environment, and environmental issues appear in developing and developed countries (Imtiaz et al. 2015).

Geochemical Behavior

Widely and sparsely distributed, V is not found as the free metal in nature. It originates from primary sources such as ores (i.e., iron oxides deposits), metallurgical slags (i.e., processing of U and Ti ores), and petroleum residues. Other sources include vanadiferous sandstones, bauxite, coals, or oil shales.

Vanadium is widely distributed in igneous and sedimentary rocks and minerals. Among more than fifty minerals, carnotite [$K_2(UO_2)_2(VO_4)_2.3H_2O$], roscoelite [$KV^{3+}{}_2(Si_3Al)O_{10}(OH)_2$], vanadinite [$Pb_5(VO_4)_3Cl$], mottramite [$PbCu(VO_4)(OH)$], and patrónite ($VS_4$) are the most important V-carriers. It is also present in some crude oils as organic complexes. Its average content in the Earth's crust is approximately 138 ppm and is similar to that of Zn and Ni. It is, however, more dispersed in the crust than either of those elements, and concentrated mineral deposits are consequently rare. The average V contents of CI chondrites range from 54.6 ppm to 56.5 ppm. The silicate Earth has a V content of 86 ppm, the bulk Earth of 105 ppm, whereas its content in the metallic core is slightly higher (150 ppm). Vanadium contents in the bulk continental crust vary significantly from 96 ppm to 230 ppm. These aspects have been further reviewed by McDonough (2014), Palme et al. (2014), and Rudnick and Gao (2014).

Historically, geochemists' interest in vanadium has derived from the occurrence of variable redox states in Earth surface environments, +3, +4, +5, and as a consequence its application as a redox indicator (Huang et al. 2015). Indeed, V chemical speciation and solubility are strong functions of pH and Eh conditions. Incorporation of reduced V species (III, IV) in clays and other secondary minerals provides a useful redox indicator for past anoxic conditions. Moreover, V behaves as an incompatible element because V(III) is preferentially incorporated into crystals: V-bearing minerals which crystallized in equilibrium with a low fO_2 magma have a higher V content than crystals from the same magma with high fO_2 (Mallmann and O'Neill 2009). It results in an increasing interest in V partitioning during high temperature – high pressure magma differentiation processes. Studies on V partitioning among Earth's crustal reservoirs have provided critical insights into the interaction and evolution of these reservoirs. Vanadium depletion in the silicate Earth is explained by it preferential partitioning into the metallic core during "deep magma ocean" process (at high pressure and low fO_2; Wood et al. 2006). The core could contain half of the total V budget of the bulk Earth (McDonough 2014). Perspectives to exploit V stable isotope chemistry are considered: Wu et al. (2015) proposed first-principles calculations that predict V isotopes fractionation among V species with different valences in aqueous systems and during sorption of V(V) to goethite.

Vanadium is also a naturally occurring element in air, soil, plants, and water. The concentration of dissolved V in natural freshwater and seawater is generally several mg/L or lower (Bruland et al. 2014; Gaillardet et al. 2014). Vanadium concentrations in marine and nonmarine sediments are generally below 100 ppm, reflecting a net accumulation from the aqueous phase. Vanadium in trace amounts represents an essential element for normal cell growth, but it may cause adverse effects when its concentration is much greater than a few tenths of μg/L (Chatterjee 2009). Most data on the release of V into the environment have been related to industrial activities, especially from oil refineries and power plants using V-rich fuel oil, and coal crude oil is enriched in V with respect to many other trace elements, with concentrations occasionally exceeding 1 mg/L. Thus, the fraction of dissolved V in surface waters might be an environmental indicator of oil combustion or pollution (Hope 2008). Such pollution sources may be responsible for appreciable amounts of V into the environment, well above the natural background levels associated with rock weathering and sediment leaching. Fluvial dissolved V concentrations might also be indicative of the types of rocks being weathered or of the nature of the involved weathering processes. Weathering rate and source rock type, rather than solution chemistry or anthropogenic influences, appeared to be the important controlling factors on fluvial dissolved V concentrations (Hope 2008).

The oxidation rate of V(IV) to V(V) and the equilibrium between these two species in aqueous solution will regulate V prevalence in water (Pourret et al. 2012). It further depends on several factors, such as pH, V concentration, redox potential, ionic strength of the aqueous system, and biological activity. In water, V(IV) is commonly present as a vanadyl cation [VO^{2+}, $VO(OH)^{+}$], whereas V(V) exists as a vanadate oxyanion ($H_2VO_4{}^{-}$, $HVO_4{}^{2-}$). VO^{2+} is strongly adsorbed onto solid phases, including organic and oxyhydroxide phases. Adsorption of anionic V ($H_2VO_4{}^{-}$, $HVO_4{}^{2-}$) is much lower than the cations; however, VO^{2+} solubility may be greatly increased through complexation with organic matter. Whereas V(IV) is not thermodynamically stable at

pH > 7, complexation by various organic and inorganic species may considerably increase its stability. Eventually, V(V) oxidation state ion is more toxic than V(IV) ion one.

Biological Utilization and Toxicity

Whereas low concentrations of V are required for plants to positively influence chlorophyll synthesis, K consumption, or N assimilation, higher V concentrations are toxic as they cause chlorosis and limit growth. At trace amounts V is essential for normal cell growth, whereas possibly toxic at higher concentrations, especially when occurring as pentoxide (Rehder 2008). Chronic exposure may result in inflammation of bronchi and trachea, eyes and skin irritation, pulmonary edema, and systemic poisoning (Mukherjee et al. 2004).

Summary

Vanadium's occurrence receives more attention as the global demand for V increases. However, its prevalence in environment becomes a new critical issue. Vanadium has been suggested to be a potentially dangerous pollutant, and the United States Environmental Protection Agency classifies V in the priority list of environmental risk elements. Fixing the environmental issue of V is constrained by the limited understanding of V biogeochemistry relative to other d-block transition metals. A better understanding of V biogeochemical behavior may support to assess the risk to the environment and to human health and to assist in developing new remediation tools.

Cross-References

- ▶ Complexes
- ▶ Lithophile Elements
- ▶ Oxidation-Reduction Reactions and Eh-pH (Pourbaix) Diagrams
- ▶ Transition Elements

References

Bruland KW, Middag R, Lohan MC (2014) 8.2 – Controls of trace metals in seawater. In: Holland HD, Turekian KK (eds) Treatise on geochemistry, 2nd edn. Elsevier, Oxford, pp 19–51

Chatterjee M (2009) Vanadium. In: Schwab M (ed) Encyclopedia of cancer. Springer, Berlin/Heidelberg, pp 3140–3142

Gaillardet J, Viers J, Dupré B (2014) 7.7 – Trace elements in river waters. In: Holland HD, Turekian KK (eds) Treatise on geochemistry, 2nd edn. Elsevier, Oxford, pp 195–235

Haynes WM (2015) CRC handbook of chemistry and physics, 96th edn. CRC Press, Boca Raton

Hope BK (2008) A dynamic model for the global cycling of anthropogenic vanadium. Glob Biogeochem Cycles 22:GB4021

Huang J-H, Huang F, Evans L, Glasauer S (2015) Vanadium: global (bio) geochemistry. Chem Geol 417:68–89

Imtiaz M, Rizwan MS, Xiong S, Li H, Ashraf M, Shahzad SM, Shahzad M, Rizwan M, Tu S (2015) Vanadium, recent advancements and research prospects: a review. Environ Int 80:79–88

Mallmann G, O'Neill HSC (2009) The crystal/melt partitioning of V during mantle melting as a function of oxygen fugacity compared with some other elements (Al, P, Ca, Sc, Ti, Cr, Fe, Ga, Y, Zr and Nb). J Petrol 50:1765–1794

McDonough WF (2014) 3.16 – Compositional model for the Earth's core. In: Holland HD, Turekian KK (eds) Treatise on geochemistry, 2nd edn. Elsevier, Oxford, pp 559–577

Moskalyk RR, Alfantazi AM (2003) Processing of vanadium: a review. Miner Eng 16:793–805

Mukherjee B, Patra B, Mahapatra S, Banerjee P, Tiwari A, Chatterjee M (2004) Vanadium – an element of atypical biological significance. Toxicol Lett 150:135–143

Palme H, Lodders K, Jones A (2014) 2.2 – Solar system abundances of the elements. In: Holland HD, Turekian KK (eds) Treatise on geochemistry, 2nd edn. Elsevier, Oxford, pp 15–36

Pourret O, Dia A, Gruau G, Davranche M, Bouhnik-Le CM (2012) Assessment of vanadium distribution in shallow groundwaters. Chem Geol 294:89–102

Rehder D (2008) Bioinorganic vanadium chemistry. Wiley, Chichester, p 213

Richards RL (2006) Vanadium: inorganic & coordination chemistry. In: Encyclopedia of inorganic chemistry. Wiley, Chichester

Rudnick RL, Gao S (2014) 4.1 – Composition of the continental crust. In: Turekian HD, Holland KK (eds) Treatise on geochemistry, 2nd edn. Elsevier, Oxford, pp 1–51

Wood BJ, Walter MJ, Wade J (2006) Accretion of the Earth and segregation of its core. Nature 441:825–833

Wu F, Qin T, Li X, Liu Y, Huang J-H, Wu Z, Huang F (2015) First-principles investigation of vanadium isotope fractionation in solution and during adsorption. Earth Planet Sci Lett 426:216–224

Volcanic Gases

Alessandro Aiuppa[1,2] and Fabrice Gaillard[3]

[1]Dipartimento DiSTeM, Università di Palermo, Palermo, Italy

[2]Sezione di Palermo, Istituto Nazionale di Geofisica e Vulcanologia, Palermo, Italy

[3]Institut des Sciences de la Terre, Université d'Orléans-BRGM, Orléans, France

Definition

The term "volcanic gas" identifies the fluid gas phase released by active volcanoes, both during eruption and quiescence. Compositionally, volcanic gases are molecular combinations of four major elements (H, C, O, and S) but also include a variety of minor (Cl, F, N, He, Ne, and Ar) to trace components. Being generally water-dominated, volcanic gases show a spread of compositions, reflecting a

combination of source processes (magma and its geodynamic context) and interactions with local hydrothermal or hydrologic systems. Volcanic gases can be schematically distinguished among (i) "magmatic gases", being sourced by a relatively shallow magmatic source, are hot (>500 °C), and rich in SO_2 and halogens (HCl and HF), whereas (ii) "hydrothermal gases", being mostly contributed by magmatic gas-heated boiling aquifer(s), are cool, and richer in steam, CH_4, and H_2S (and virtually HCl- and HF-free). Finally, soil gases, dominated by CO_2, make the diffuse, low-temperature emissions occurring through the flanks and faults on active volcanoes.

In the Earth's interior, the volatiles species of the H-C-O-S system and the magma are intimately related since magma concentrates volatile species and volatiles trigger melting of rocks. The production of volcanic gases results from the decrease in the solubility of H-C-O-S species in melts as pressure decreases: as the magma rises from the mantle through the crust, volatile components are increasingly transferred from the melt into a vapor phase becoming volcanic gases at the surface.

Our understanding of the compositions and fluxes of volcanic gases arises from two approaches: (i) direct measurements involving in situ or remote sampling and (ii) calculations based on lava abundances in H, C, O, and S and equilibrium partition coefficients between melt and fluid. Geochemists using approaches (i) and (ii) broadly agree on the composition of volcanic gases and how it changes with temperature (magmatic vs. hydrothermal), with geodynamics (arcs, hotspots, ridges, and rifts), and with eruptive dynamics (submarine, subaerial, explosive, and effusive). The issue of gas fluxes is, however, more debated since (i) volcanoes emit gas during quiescent and eruptive periods, within their crater and on their flanks making a global and integrated assessment tentative and (ii) most of magma produced in the Earth does not erupt but remains at depth as intrusive solidifying body, whose contribution to degassing is difficult to quantify; finally, the dominant part of volcanism on Earth, which is produced at mid-ocean ridges, is submarine and ridge volcanic gases are inaccessible for sampling, implying that only indirect reconstructions allow us to estimate fluxes of volcanic gases at ridges.

Scientific Interests

Volcanic gases are studied for several reasons corresponding to several processes ranging from planetary to regional scales and occurring at various timescales. Integrated over geological times, the flux of volcanic gases is contributing to the regulation of surficial processes, including long-term climate, chemistry of surface waters, and biogeochemical processes including photosynthesis (Holland 2002; Halevy et al. 2010; Gaillard et al. 2011). Noteworthy, this regulating role has been perturbed through the ages of the Earth during the emplacement of several large magmatic provinces, producing over millions of years a tremendous amount of H, C, O, and S species with dramatic impacts on the environment recorded as mass extinctions (Iacono-Marziano et al. 2012; Self et al. 2014). At the timescale of single eruptive events, catastrophic eruptions are also able to emit large amounts of reactive gas species perturbing the chemistry of the atmosphere and stratosphere with immediate climatic effects (Robock 2000). At very short timescale, volcano monitoring constitutes a very active field on volcanic gas research. It involves using the chemical compositions of volcanic gases and their changes with time to probe the status of the magma stored at depth and to track potential changes of this status. If acquired at a sufficient temporal resolution, this chemical message can be deciphered in terms of eruptive dynamics with critical implications for mitigation of volcanic risk (Saccorotti et al. 2014). As a notable example, volcanic gas CO_2/SO_2 ratios and plume CO_2 flux emissions have recently been monitored in great details and have both shown clear precursory increases prior to eruption, reflecting pre-eruptive, deep degassing of bubble-rich magmas ascending in the crust (Aiuppa et al. 2007). Finally, volcanic gases provide key information on volatile abundances and behaviors in magmas, on the source mantle (Wallace et al. 2015), on the cycling and fate of volatiles during geodynamic processes (e.g., during subduction), and on magma-crust processes (Iacono-Marziano et al. 2012; Fischer and Chiodini 2015).

Chemical and Isotopic Composition

The composition of volcanic gases depends on (and yields insights onto) the processes that occur throughout the entire magma evolution path, from generation in the mantle, through ascent-storage in the crust, and eventually eruption.

High-temperature (>500 °C) volcanic gases have compositions that most strictly reflect conditions (volatile content and degassing history) of the source magmas. Compositionally, these so-called "magmatic" gases are typically water-dominated, with carbon dioxide (CO_2) and sulfur dioxide (SO_2) coming next in order of abundance. H_2O, CO_2, and SO_2, taken together, normally make >99 mol% of the magmatic gas phase, but the levels of H_2O enrichment vary from volcano to volcano and with geodynamic/tectonic setting. The "arc" magmatic gases that are degassed at convergent margin volcanoes, for example, are systematically more hydrous ($H_2O \gg 90$ mol%) than those seen at divergent/within plate volcanoes (where H_2O can be as low as 50 mol%) (Symonds et al. 1994; Giggenbach 1996; Oppenheimer et al. 2014). This compositional diversity is

commonly ascribed to the involvement of a recycled seawater component in arc volcanism, as isotopic (δD and $\delta^{18}O$) determinations on arc magmatic gases suggest (Taran et al. 1989; Giggenbach 1992). The contribution of recycled "sedimentary" fluids, issuing from the subducted slab, to the arc magmatic gas budget is also proved by the more HCl-rich (but HF-poor) nature of arc gases (relative to "multi-component nonarc" gases) and by their carbon (CO_2), sulfur (SO_2), and nitrogen (N_2) isotopic compositions that are intermediate between mantle and crustal sediment signatures (Fischer et al. 2002; Marty 2012; Kagoshima et al. 2015). Magmatic gases also contain appreciable amounts of H_2, CO, and N_2 (typically at 0.01 to <1 mol% level) and minor to trace amounts of noble gases (He, Ar) and heavy metals. Noble gas (He, in particular) isotopes, that are unaffected by degassing or gas-water reactions, have been particularly useful in constraining the relative contributions of the mantle, the crust, and slab fluids to arc magmatic gases (Hilton et al. 2002; Sano and Fischer 2013).

For volcanic systems in quiescent time (i.e., the majority of the Holocene volcanoes), the magma is stored at depth and the expelled magmatic gases cool and interact with crustal/meteoric fluids, so that the composition of the fluids finally reaching the surface is irremediably altered. The resulting "hydrothermal" gas discharges are compositionally distinct from "magmatic" gases, being more hydrous (H_2O often >98% mol%) and depleted in water-soluble compounds (e.g., HCl and HF) (Symonds et al. 2001). Hydrothermal gases are also typically SO_2-free, this species being converted into H_2S by gas-water-rock redox reactions taking place in the hydrothermal envelope. Gas/solutions/minerals reactions also affect carbon and hydrogen compounds, favoring the low-temperature species CH_4 and H_2O (Chiodini and Marini 1998). Hydrothermal gases keep memory of the isotopic composition of the source magma (particularly for noble gases and, partially, for carbon) but also record a larger contribution of crustal fluids and/or the impact of isotopic fractionations during low-temperature gas-water-rock interactions (Fischer and Chiodini 2015).

Techniques for Volcanic Gas Measurements and Volcano Monitoring

The multicomponent nature of volcanic gases, and their diversity of emission modes, requires that a combination of gas sampling/sensing techniques is used by geochemists.

Since the beginning of the nineteenth century, direct sampling techniques have been used to collect gas from fumaroles/vents (Fig. 1). A variety of sampling apparatus have been utilized, but the so-called "Giggenbach bottle" technique (pioneered by Werner Giggenbach in the 1970s) is the most common. This method employs evacuated glass flasks to collect acid components (CO_2, SO_2, H_2S, HCl, and HF) in a sodium hydroxide solution and noncondensable gases (N_2, O_2, H_2, CO, and noble gases) in the headspace of the bottle (Giggenbach and Gougel 1989; Symonds et al. 1994). Field collection is followed by analysis in a laboratory by standard wet chemical methods and gas chromatography.

Since the late 1960s, degassing associated to erupting volcanoes has been assessed by remote sensing observations (e.g., measurement from distal locations; Carn 2015). This has allowed the characterisation of large, open-vent gas emissions through volcanic plumes (Fig. 1b), and the quantification of volcanic gas fluxes (e.g., mass of gas released per unit time) by deriving integrated gas column amount along the cross section of a plume. All such remote sensing methods work basing upon the principles of spectroscopy, e.g., they rely upon the interaction of chemical bonds in volcanic gas species and a (natural or artificial) light source. Scattered ultraviolet (UV) sunlight, measured from ground or aircraft, has been used as the source for measuring SO_2 fluxes from volcanoes using COrrelation SPECtrometers (COSPEC). More recently, the advent of more compact and less power consuming scanning differential optical adsorption spectrometers (DOAS) has revolutionized our ability to make fully automated, continuous gas observations leading to unprecedented long SO_2 flux records of high spatial-time resolution (Galle et al. 2003; Carn 2015).

The recent introduction of Fourier-transform IR (FTIR) spectroscopy in volcanology has paved the way to real-time sensing of all major volcanic gas species (Allard et al. 2005;

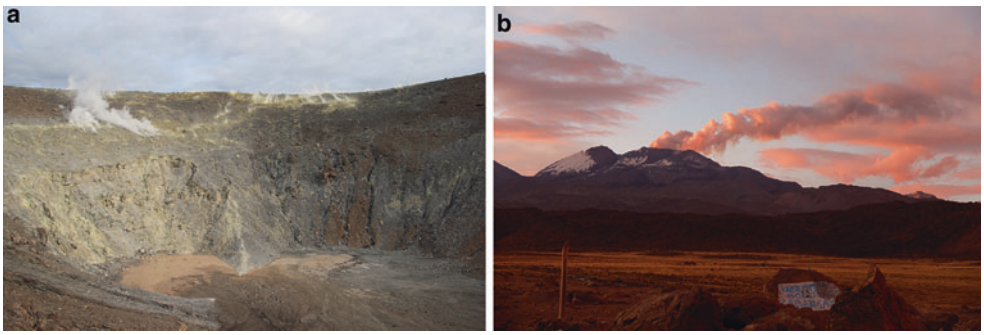

Volcanic Gases, Fig. 1 The two main modes of volcanic gas release: (**a**) fumarolic vent emissions at a quiescent closed-vent volcanoes (Vulcano Island, Italy); (**b**) an example of open-vent crater plume degassing (Sabancaya volcano, Perù) (Photos: A. Aiuppa)

Burton et al. 2007), but its use is restricted to a relatively limited number of volcano observatories, due to the expense of the instrument and high level of expertise required to interpret the data. More compact, cheaper, rugged, and user-friendly sensor units, commonly termed Multi-GAS sensors (Shinohara 2005; Aiuppa et al. 2007), are increasingly used to monitor the actual mixing ratios of volatile species (H_2O, CO_2, SO_2, H_2S, HCl, H_2) in volcanic plumes with a temporal resolution of a few seconds. At many volcanoes worldwide, these crater rim installations are complemented by use of commercial soil degassing units (based upon the "accumulation chamber" principle; Chiodini et al. 1998), targeting the "diffuse" CO_2 flux emissions issuing from soils and steaming grounds along faulted volcanic flanks and/or solfataras.

In order to address volcanic gases at a planetary scale, future direction will require measuring gas from space. It was in the 1980s that a new era in volcanology opened when the Total Ozone Mapping Spectrometer (TOMS) contributed the first satellite-based measurements of SO_2 emitted by explosive volcanic eruptions (Krueger 1983). Space-borne UV spectrometers (e.g., the Ozone Monitoring Instrument, OMI, on NASA's Aura satellite) detects SO_2 emissions from large volcanic eruptions and effectively contribute to monitoring passively degassing volcanoes, particularly those located in remote or unexplored regions (Carn 2015). The major challenge of satellites remains to extend observations to detection/quantification of other relevant volcanic species that are less abundant (H_2S, CO) or more difficult to investigate (CO_2).

Summary

Volcanic degassing, transferring H-C-O-S species from the innermost planet to the atmosphere, is a key step in the geodynamic cycle of volatiles and governs a variety of processes determining the habitability of a planetary environment. Present-day fluxes remain difficult to precisely assess, and establishing the preindustrial baseline for fluxes of C and S remains critical for understanding the dynamic nature of our planet. Several recent technical progresses allow precise field analyses; but the variety of physical expression of volcanic gases (e.g., plumes during eruption, crater fumaroles during quiescent time and diffusive emission on the flanks of volcanoes) complicates the interpretation of this chemical message sent from magma at depth. Satellite-based observations will certainly provide a planetary view of volcanic degassing that is difficult to capture with regional field data collection. Finally, fundamental research on the fate and behavior of volatiles at depth is needed to establish a theoretical framework that can be tested by empirical field observations.

Cross-References

- ▶ Carbon Isotopes
- ▶ Gas Chromatography–Mass Spectrometry (GC–MS)
- ▶ Helium Isotopes
- ▶ Hydrothermal Vents
- ▶ Magmatic Process Modeling
- ▶ Natural Gas
- ▶ Silicate Melts
- ▶ Subduction Zone Geochemistry
- ▶ Volcanism

References

Aiuppa A, Moretti R, Federico C, Giudice G, Gurrieri S, Liuzzo M, Papale P, Shinohara H, Valenza M (2007) Forecasting Etna eruptions by real-time observation of volcanic gas composition. Geology 35:1115–1118

Allard P, Burton MR, Murè F (2005) Spectroscopic evidence for a lava fountain driven by previously accumulated magmatic gas. Nature 433:407–410. https://doi.org/10.1038/nature03246

Burton M, Allard P, Murè F, La Spina A (2007) Depth of slug-driven strombolian explosive activity. Science 317:227–230

Carn S (2015) Gas, plume, and thermal monitoring. In: The encyclopedia of volcanoes, 2nd edn. Elsevier, pp 1125–1148. https://doi.org/10.1016/B978-0-12-385938-9.00065-1

Chiodini G, Marini L (1998) Hydrothermal gas equilibria: the H_2O-H_2-CO_2-CO-CH_4 system. Geochim Cosmochim Acta 62:2673–2687

Chiodini G, Cioni R, Guidi M, Raco B, Marini L (1998) Soil CO_2 flux measurements in volcanic and geothermal areas. Appl Geochem 13:543–552

Fischer TP, Chiodini G (2015) Volcanic, magmatic and hydrothermal gases. In: The encyclopedia of volcanoes, 2nd edn. Academic Press/Elsevier, Waltham, pp 779–796. https://doi.org/10.1016/B978-0-12-385938-9.00045-6

Fischer TP, Hilton DR, Zimmer MM, Shaw AM, Sharp ZD, Walker JA (2002) Subduction and recycling of nitrogen along the Central American margin. Science 297:1154–1157

Gaillard F, Scaillet B, Arndt NT (2011) Atmospheric oxygenation caused by a change in volcanic degassing pressure. Nature 478:229–232

Galle B, Oppenheimer C, Geyer A, McGonigle A, Edmonds M, Horrocks LA (2003) A miniaturised ultraviolet spectrometer for remote sensing of SO_2 fluxes: a new tool for volcano surveillance. J Volcanol Geotherm Res 119:241–254

Giggenbach WF (1992) Isotopic shift in waters from geothermal and volcanic systems along convergent plate boundaries and their origin. Earth Planet Sci Lett 113:495–510

Giggenbach WF (1996) Chemical composition of volcanic gases. In: Scarpa R, Tilling R (eds) Monitoring and mitigation of volcano hazards. Springer, Berlin/Heidelberg/New York, pp 221–256

Giggenbach WF, Gougel RL (1989) Method for the collection and analysis of geothermal and volcanic water and gas samples. Department of Scientific and Industrial Research, New Zealand, report CD2401, pp 81

Halevy I, Johnston DT, Schrag DP (2010) Explaining the structure of the Archean mass-independent sulfur isotope record. Science 329:204–207

Hilton DR, Fischer TP, Marty B (2002) Noble gases in subduction zones and volatile recycling. In: Porcelli D, Ballentine C, Wieler R (eds) Noble gases in geochemistry and cosmochemistry, Reviews in mineralogy geochemistry, vol 47. Mineralogical Society of America, Chantilly, pp 319–362

Holland HD (2002) Volcanic gases, black smokers, and the great oxidation event. Geochim Cosmochim Acta 66:3811–3826
Iacono-Marziano G, Marecal V, Pirre M, Gaillard F, Arteta J, Scaillet B, Arndt NT (2012) Gas emissions due to magma–sediment interactions during flood magmatism at the Siberian Traps: gas dispersion and environmental consequences. Earth Planet Sci Lett 357–358:308–318. https://doi.org/10.1016/j.epsl.2012.09.051
Kagoshima T, Sano Y, Takahata N, Maruoka T, Fischer TP, Hattori K (2015) Sulphur geodynamic cycle. Sci Rep 5:8330. https://doi.org/10.1038/srep08330
Krueger AJ (1983) Sighting of El Chichón sulfur dioxide clouds with the nimbus 7 total ozone mapping spectrometer. Science 220:1377–1378
Marty B (2012) The origins and concentrations of water, carbon, nitrogen and noble gases on Earth. Earth Planet Sci Lett 313–314:56–66
Oppenheimer C, Fischer TB, Scaillet B (2014) Volcanic degassing: process and impact. Treatise Geochem 4:111–179. https://doi.org/10.1016/B978-0-08-095975-7.00304-1
Robock A (2000) Volcanic eruption and climate. Rev Geophys 38 (2):191–219. https://doi.org/10.1029/1998RG000054
Saccorotti G, Iguchi M, Aiuppa A (2014) In situ volcano monitoring: present and future. In: Volcanic hazards, risks and disasters. Elsevier, Amsterdam, pp 169–202. https://doi.org/10.1016/B978-0-12-396453-3.00007-1
Sano Y, Fischer TP (2013) The analysis and interpretation of noble gases in modern hydrothermal systems. In: Burnard P (ed) The noble gases as geochemical tracers, Advances in isotope geochemistry. Springer, Berlin/Heidelberg, pp 249–317
Self S, Schmidt A, Mather TA (2014) Emplacement characteristics, time scales, and volcanic gas release rates of continental flood basalt eruptions on Earth. In: Keller G, Kerr AC (eds) Volcanism, impacts, and mass extinctions: causes and effects, Geological Society of America special paper, vol 505. The Geological Society of America, Boulder, pp 319–337. https://doi.org/10.1130/2014.2505(16)
Shinohara H (2005) A new technique to estimate volcanic gas composition: plume measurements with a portable multi-sensor system. J Volcanol Geotherm Res 143(4):319–333
Symonds RB, Rose WI, Bluth GJS, Gerlach TM (1994) Volcanic-gas studies: methods, results and applications. Rev Mineral 30:1–66
Symonds RB, Gerlach TM, Reed MH (2001) Magmatic gas scrubbing: implications for volcano monitoring. J Volcanol Geotherm Res 108:303–341
Taran YA, Pokrovsky BG, Doubik YM (1989) Isotopic composition and origin of water in andesitic magmas. Dokl Earth Sci 304:1191–1194
Wallace PJ, Plank T, Edmonds M, Hauri EH (2015) Volatiles in magmas. In: The encyclopedia of volcanoes, 2nd edn. Academic Press/Elsevier, Waltham, pp 163–182. https://doi.org/10.1016/B978-0-12-385938-9.00007-9

Volcanism

Nick Rogers
School of Environment, Earth and Ecosystem Sciences, The Open University, Milton Keynes, UK

Definition

Volcanism is the surface expression on any planetary body of the production, migration, and eruption of molten rock or magma from that body's interior.

Introduction

Magma comprises three phases – solid, vapor, and liquid – in the form of crystals and bubbles suspended in a liquid, usually molten silicate rock. The production of magma implies that any volcanically active planetary body has a source of internal energy. On Earth that source of internal energy is a combination of radiogenic heat from the long-lived radioisotopes ^{235}U, ^{238}U, ^{232}Th, and ^{40}K and residual primordial heat from the Earth's formation and core segregation. On other bodies, such as Io, one of the larger Jovian moons, the heat is derived from tidal distortions caused by its proximity to Jupiter. Other moons in the solar system show evidence of volcanism caused by the melting of thick layers of ice.

All four of the inner planets of the solar system and the Earth's moon show evidence of volcanic processes in the past, but only Earth has unequivocal evidence of current volcanic activity. It is known from a combination of remote sensing, direct observation, and meteorite samples that volcanic activity on these five planetary bodies is almost exclusively silicate based and is caused by the partial melting of their mantle and crustal layers.

Volcanism and Plate Tectonics

Modern day volcanism on Earth is intimately linked to plate tectonics and mantle convection. Volcanic rocks are found at both convergent and divergent plate margins, but the compositions of the volcanic rocks from these two tectonic environments show distinctive characteristics that reflect the processes of their generation and subsequent evolution. In addition volcanism is found away from plate margins, in so-called intraplate environments, and volcanic rocks from these locations form a third distinctive compositional group.

The dominant form of volcanic activity today is related to the eruption of basaltic magma, formed by partial melting of the mantle. Melting can be triggered by two dominant processes: decompression and the introduction of hydrous fluids. Once produced, melt migrates toward the surface as a result of matrix compaction and upward flow because the melt is less dense than the solid residue.

Decompression melting is the dominant process at divergent plate margins, where the separation of two lithospheric plates induces the underlying mantle to rise toward the surface. In so doing the mantle rises adiabatically and melts as soon as the pressure falls sufficiently, at a depth of around 75 km, and continues to the base of the newly formed oceanic crust at about 10 km (Fig. 1). The resulting magma is known as mid-ocean ridge basalt or MORB (Gale et al. 2014). The total volume of oceanic crust added by magmatic process at

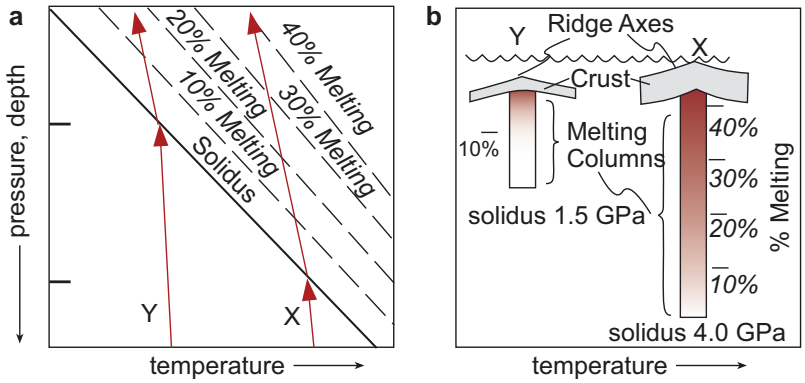

Volcanism, Fig. 1 (**a**) Pressure (depth) – temperature relationship for adiabatically upwelling mantle undergoing melting. The example Y represents the situation beneath ocean ridges where mantle of ambient temperature rises and intersects the P-T conditions on the mantle solidus at about 75 km depth. The case for hotter mantle, as in a mantle plume, is illustrated by curve X. This intersects the solidus at a higher pressure and temperature and can produce much greater volumes of melt. However, if the melting regime is overlain by oceanic lithosphere, then the top of the melting column occurs at a greater depth than shown, and the resulting melt fractions are smaller. (**b**) Illustrates the relationship between axial depth, crustal thickness, melting, and mantle temperature. Hotter mantle X produces more melt, and so a thicker crust and the ridge is maintained at a higher elevation by its buoyancy (Modified after Klein and Langmuir (1987) and White (2013))

constructive margins is between 10 and 20 km^3 per year, making ocean ridge volcanism the most widespread and extensive on Earth, yet much of this occurs unseen beneath the oceans.

Beneath ocean islands, which form on older, thicker lithosphere, the mantle temperature must be greater than that beneath mid-ocean ridges for melting to occur (Fig. 1). Such ocean island basalts (OIB) are poorer in silica than MORB but richer in incompatible elements, reflecting greater pressures and temperatures of melt generation and smaller melt fractions (Niu et al. 2011). These observations, together with the time progressive nature of volcanism along chains of ocean islands, have led to the concept of mantle plumes underlying many ocean islands.

Melting associated with convergent plate margins is related to the release of volatile components, especially water, from the subducted oceanic lithosphere, or slab, which percolate upward through the overlying mantle wedge. Water has the effect of dramatically reducing the solidus temperature of peridotite by as much as 300 °C so the introduction of water by itself is capable of inducing melting in ambient mantle (Katz et al. 2003) (Fig. 2). This can be further enhanced by decompression if tectonic activity causes the mantle to rise, for example, in a back-arc environment (Kelley et al. 2010).

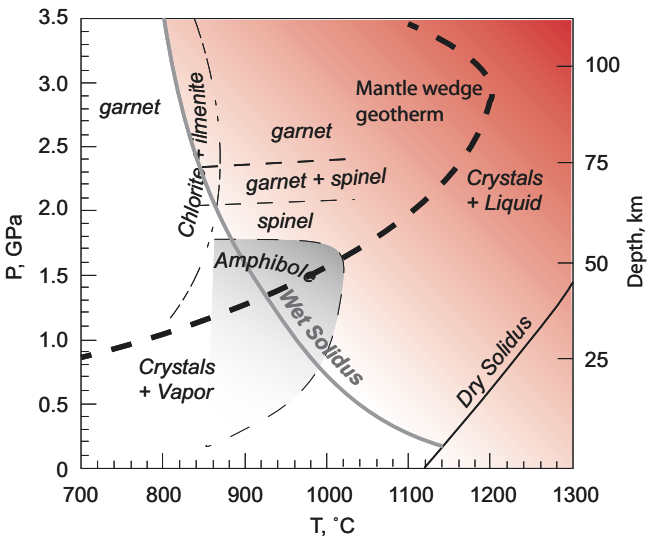

Volcanism, Fig. 2 Phase diagram for the system peridotite – water (H_2O). The dry solidus represents the melting temperature of peridotite in the absence of water, whereas the wet solidus represents the conditions under which peridotite will melt in the presence of free water – which can be many hundreds of degrees cooler than dry mantle. Other curved lines represent the stabilities of critical phases, while the *bold-dashed line* labeled mantle wedge geotherm is an example of the temperature variation with depth in the mantle above a subducting slab. The drop to lower temperatures at high pressure illustrates the cooling effect of the slab. Note how, the wedge geotherm passes through the region of melt plus crystals for peridotite + H_2O (After Grove et al. (2006) and White (2013). Wedge geotherm taken from van Keken et al. (2002))

Magma Evolution and Volcanic Eruptions

As magma emerges from the melting regime and rises toward the surface, it changes in composition as a result of cooling and crystallization. This is envisaged to happen largely in magma chambers that form when magma encounters discontinuities in the surrounding geology (e.g., the crust-mantle boundary). During cooling mafic minerals crystallize and drive the liquid toward compositions with lower MgO, CaO, and FeO and higher SiO_2, Al_2O_3, and alkali elements. These changes reduce the density of the magma which can

then rise further toward the surface, possibly halting in higher level magma chambers en route to the surface where the magma is eventually erupted as a volcanic rock (see Cashman and Sparks 2013).

Magma composition has a profound influence on both the eruptive style of volcanic rocks and the morphology of volcanic structures. Basaltic magmas form at high temperatures and with low volatile and modest SiO_2 contents, resulting in a low viscosity. They therefore tend to erupt effusively, forming sheetlike lava flows from shield volcanoes with shallow slopes. Small-volume effusive eruptions, such as those on Iceland and Hawaii, can be observed from close proximity, although they are not without their own hazards. However, larger effusive eruptions, such as the Laki fissure eruption on Iceland in 1783–1784 lasted 8 months, had a final erupted volume of 14 km^3, and caused considerable environmental and societal effects both locally on Iceland and more distantly, especially in Northern Europe as a consequence of the large masses of sulfur dioxide (120 Mt) and other gases released (Thordarson and Self 2003).

Evolved magmas rich in silica and alumina, such as andesites and rhyolites, erupt at lower temperatures and tend to have higher viscosities because of the formation of molecular networks and polymerization of Si-O and Al-O bonds. Hence, andesitic lavas produce steeper-sided cones, so-called stratovolcanoes, such as Mt Fuji in Japan. The process of differentiation has the additional effect of increasing the volatile content of a magma so that on eruption volatiles are released explosively and fragment the magma. Thus, andesites, rhyolites, and other volatile-rich magmas often erupt explosively (Fig. 3), and the resultant deposit is unconsolidated and generally described as tephra. Tephra fragments are subdivided into ash, lapilli, and bombs according to their sizes, and if the deposit becomes lithified, as a result of heating and compaction, then it is termed a pyroclastic rock.

History is scattered with records of these violent, explosive eruptions of volatile-charged magmas. That of Vesuvius in 79 CE was observed by Pliny the Younger who is credited with producing the first written description of a major volcanic event and gave his name to that type of eruption – Plinian. Plinian eruptions inject volcanic ash and gases high into the atmosphere as the large magma chamber rapidly empties. They also produce density currents or surges that are turbulent mixtures of pumice and hot gases known as ignimbrites that move down the flanks of a volcano at remarkably high speeds. Plinian eruptions frequently remove large parts of the volcanic structure, leaving hollowed out circular depressions in the center of the residual volcano known as caldera.

Plinian eruptions are spectacular and often hit the news headlines, for example, Mt St Helens in the USA (1980) and Mt Pinatubo in the Philippines (1991) were both extensively covered by the media. Even though Mt Pinatubo was the second largest eruption of the twentieth century, the death toll was less than 1000, and while any death caused by a natural hazard is to be regretted, volcanoes rank far behind hurricanes, earthquakes, floods, and famine as a source of human casualties and misery. Pinatubo is dwarfed by the 1815 eruption of Tambora in Indonesia, which at 50 km^3 volume was the largest in recent history. It had a global reach, triggering the "year without a summer" in 1816 (Oppenheimer 2003).

Further back in time, prehistoric eruptions from so-called super-volcanoes (Miller and Wark 2008) are of much greater volume: Taupo in New Zealand erupted 530 km^3 of rhyolite 25.4 +/− 0.2 ka BP (Wilson 2008), and eruptions exceeding 1000 km^3 were associated with the Yellowstone Caldera at 2.1 Ma, 1.3 Ma, and 650 ka (Christiansen 2001). The eruption of Toba in Indonesia (69 ka BP) erupted an estimated 2800 km^3 of volcanic material, and its effects on global climate are considered by some to have influenced human

Volcanism, Fig. 3 The early stage of an eruption of Sarychev Peak, Matua Island, Kuril Islands, as photographed from the International Space Station on June 12, 2009. This is an example of a Plinian or sub-Plinian eruption showing the early stage of the development of the eruption column, already 3–5 km in height and capped by a developing mushroom head. The pale gray cloud at the base of the column represents a pyroclastic flow, moving rapidly down the flanks of the volcano (NASA) http://eoimages.gsfc.nasa.gov/images/imagerecords/38000/38985/ISS020-E-09048_lrg.jpg

evolution (Petraglia et al. 2012). The effects of such a super-eruption today would be global and probably catastrophic, potentially plunging the world into a "nuclear winter" and disrupting trade and communication for years (Self 2006).

The deeper geological record includes evidence of yet more voluminous eruptions of both basaltic and rhyolitic composition (Bryan and Ferrari 2013). The former are often termed flood basalts or large igneous provinces (LIP) and may have volumes in excess of 10^6 km^3 erupted over periods of less than 10^6 years. Examples include the Deccan traps of India and the Karoo flood basalts of Southern Africa, and within these provinces individual eruptions can have volumes of hundreds of km^3. LIP events closely coincide with major breaks in the stratigraphic and fossil record and have been implicated as the causes of significant global environmental change.

Volcanism for Geochemistry

Volcanism provides one of the most effective windows on the composition of the Earth's interior, particularly the use of basaltic volcanism to map variations in the composition of the upper mantle. From the earliest analyses of trace elements and radiogenic isotopes in oceanic basalts, it was apparent that there are significant differences in the composition of MORB and OIB. The depletion of the most incompatible elements in MORB relative to enrichments of the same elements in OIB is reflected in radiogenic isotope ratios which implies that the depletion of the MORB source is long-lived. These observations rapidly evolved into models in which the uppermost mantle has been depleted by the extraction of the continental crust over geological time.

Subsequently, subtle variations have been observed in both MORB and OIB that have allowed discrete areas of particular mantle compositions to be mapped out (e.g., the DUPAL anomaly in the Southern Indian Ocean). The variation in OIB compositions has been interpreted as resulting from the mixing of various putative end-member compositions in the mantle (EM1, EM2, HiMu, etc.) that are now thought to be the imprint of recycled sediment and oceanic crust (White 2015). Variations in titanium and compatible trace elements in OIB lead to similar conclusions (Prytulak and Elliott 2007; Sobolev et al. 2007). The identification of possibly primordial material in mantle plumes, characterized by enrichments of ^{3}He over radiogenic ^{4}He, testifies to the presence of a reservoir in the deep Earth, frequently referred to as PREMA, C, or FOZO, that has retained a fraction of the volatile material from the earliest Earth and may have a more primitive composition. Most recently, systematic zonation of key isotope ratios within single ocean island chains (e.g., Hawaii and Samoa) have been related to chemical heterogeneities inherited from the source regions of mantle plumes, arguably located on the boundaries of large seismic anomalies in the lower mantle. If so, this opens up the exciting possibility of using volcanic rocks to map lateral variations in the age and composition of the lower mantle.

The composition of magmas generated above subduction zones is distinct from both MORB and OIB in that they show an enrichment in large ion lithophile elements over high field strength elements, reflecting the incorporation of subducted sediments in arc magma sources and the effects of hydrous fluids on element mobility. Isotope and trace element studies have allowed the quantification of these effects and related magma composition to the compositions of the sediments being subducted. Confirmation of recycling of materials once at the surface was achieved by the detection of the cosmogenic nuclide ^{10}Be in arc volcanic rocks.

Volcanic rocks provide geochemists with samples of quenched melts in the form of melt inclusions in phenocrysts and other glasses such as submarine basaltic pillow rinds. These are particularly valuable in that they represent liquid compositions and preserve the original dissolved volatile inventory of the magma prior to eruption. They reveal high H_2O concentrations in arc-related magmas, as expected from trace element and other compositional variations, and much lower volatile abundances in MORB and OIB (e.g., Kent 2008; Plank et al. 2013).

Geochemistry for Volcanology and Petrology

The principles of physical chemistry and thermodynamics have provided the foundations of petrology for over a century, while the evolution of analytical geochemistry now permits the analysis of element abundances and isotope ratios in rocks and minerals to an unprecedented level of precision, accuracy, and spatial scale. Geochemical analysis is now a routine aspect of many investigations of volcanic and magmatic processes and provides the basis for volcanic rock classification independent of earlier mineralogical criteria. Starting with simple models of crystal fractionation and partial melting (e.g., Bowen 1928; Shaw 1970), our current understanding of the evolutionary processes operating within and beneath volcanoes has developed to a sophisticated level involving thermodynamic models of silicate melts and the partitioning of elements between different phases (e.g., melts http://melts.ofm-research.org/, also Bohrson et al. 2014). The combination of these approaches – analysis and modeling – to cogenetic suites of volcanic rocks has led to a quantification of the effects of fractional crystallization, partial melting, crustal contamination, magma mixing and hybridization, and the roles played by fluids, especially water, in all processes from magma source to eruption.

Geochemistry provides insights into the timescales of magmatic processes, especially into the evolution of super-

volcanoes such as Taupo. The application of U-Th-Ra disequilibria is critical in determining the rates of assembly of large magma chambers prior to major eruptions (e.g., Cooper 2015), and there is an active debate as to whether such chambers are long-lived features or whether they develop over a relatively short period of time (Annen et al. 2015), thus giving less advance warning of an impending eruption. Element diffusion between zones in crystals can also be used to determine the time between the development of the zonation and quenching on eruption. Different elements diffuse at different rates and so this method can be used to probe a range of time scales (minutes to millennia) and processes that produce crystal zonation, providing the diffusion coefficients of the relevant elements and minerals are known and the magmatic temperature can be determined with some precision. The two methods often complement each other in understanding magma chamber development, while diffusion chronometry is allowing the timing of pre-eruptive magmatic events to be compared with the timing of geophysical signals of pre-eruptive unrest (see papers in Putirka 2008).

Conclusions

The interplay of geochemistry, petrology, and volcanology has been one of the most remarkable areas of scientific expansion in the Earth sciences over the past 50 years and has led to a vastly increased knowledge of the composition and evolution of the upper mantle and continental crust, of the nature of magmas and their evolution, of the link between igneous processes and the timing and styles of volcanic eruption, and of the cycling of materials through the solid Earth. As analytical methods improve, our scientific understanding of volcanic rocks and volcanic processes will be further refined, and new ideas will develop, but the complexity of volcanic systems will always present a challenge to both chemical analysis and scientific interpretation.

Cross-References

- Earth's Oceanic Crust
- Fractional Crystallization and Assimilation
- Geochronology and Radiogenic Isotopes
- Magmatic Process Modeling
- Mantle Geochemistry
- Mid-Ocean Ridge Basalts (MORB)
- Oceanic Island Basalts
- Partial Melting
- Phase Equilibria
- Silicate Melts
- Silicate Minerals
- Subduction Zone Geochemistry
- Trace Elements

References

Annen C, Blundy JD, Leuthold J, Sparks RSJ (2015) Construction and evolution of igneous bodies: towards an integrated perspective of crustal magmatism. Lithos 230:206–221. https://doi.org/10.1016/j.lithos.2015.05.008

Bohrson WA, Spera FJ, Ghiorso MS, Brown GA, Creamer JB, Mayfield A (2014) Thermodynamic model for energy-constrained open-system evolution of crustal magma bodies undergoing simultaneous recharge, assimilation and crystallization: the magma chamber simulator. J Petrol 55:1685–1717. https://doi.org/10.1093/petrology/egu036

Bowen NL (1928) The evolution of the igneous rocks. Oxford University Press, Oxford

Bryan SE, Ferrari L (2013) Large igneous provinces and silicic large igneous provinces: progress in understanding over the last 25 years. Geol Soc Am Bull 125:1053–1078. https://doi.org/10.1130/B30820.1

Cashman KV, Sparks RSJ (2013) How volcanoes work: a 25 year perspective. Geol Soc Am Bull 125:664–690. https://doi.org/10.1130/B30720.1

Christiansen RL (2001) The quaternary and pliocene yellowstone plateau volcanic field of Wyoming, Idaho, and Montana. U S Geol Surv Prof Pap 729-G:1–156

Cooper KM (2015) Timescales of crustal magma reservoir processes: insights from U-series crystal ages. Geol Soc Lond Spec Publ 422:141–174. https://doi.org/10.1144/SP422.7

Gale A, Langmuir CH, Dalton CA (2014) The global systematics of ocean ridge basalts and their origin. J Petrol 55:1051–1082. https://doi.org/10.1093/petrology/egu017

Grove TL, Chatterjee N, Parman SW, Medard E (2006) The influence of water on mantle wedge melting. Earth Planet Sci Lett 249:74–89. https://doi.org/10.1016/j.epsl.2006.06.043

Katz RF, Spiegelman M, Langmuir CH (2003) A new parameterization of hydrous mantle melting. Geochem Geophys Geosyst 4:1073. https://doi.org/10.1029/2010GC003282

Kelley KA, Plank T, Newman S, Stolper EM, Grove TL, Parman S, Hauri EH (2010) Mantle melting as a function of water content beneath the Mariana arc. J Petrol 51:1711–1738. https://doi.org/10.1093/petrology/egq036

Kent AJR (2008) Melt inclusions in basaltic and related volcanic rocks. In: Putirka KD (ed) Minerals, inclusions and volcanic processes, Reviews in mineralogy and geochemistry, vol 69, 668pp

Klein EM, Langmuir CH (1987) Ocean ridge basalt chemistry, axial depth, crustal thickness and temperature variations in the mantle. J Geophys Res 92:8089–8115

Miller CF, Wark DA (2008) Supervolcanoes and their supereruptions. Elements 4:11–15. https://doi.org/10.2113/GSELEMENTS.4.1.11

Niu Y, Wilson M, Humphreys ER, O'Hara MJ (2011) The origin of intraplate Ocean Island basalts (OIB): the Lid effect and its geodynamic implications. J Petrol 52:1443–1468. https://doi.org/10.1093/petrology/egr030

Oppenheimer C (2003) Climatic, environmental and human consequences of the largest known historic eruption: Tambora volcano (Indonesia) 1815. Prog Phys Geogr 27:230–259. https://doi.org/10.1191/0309133303pp379ra

Petraglia MD, Korisettar R, Pal JN (eds) (2012) The Toba volcanic super-eruption of 74,000 years ago: climate change, environments, and evolving humans. Quat Int 258:1–200

Plank T, Kelley KA, Zimmer MM, Hauri EH, Wallace PJ (2013) Why do mafic arc magmas contain ~ 4 wt. % water on average? Earth Planet Sci Lett 364:168–179. https://doi.org/10.1016/j.epsl.2012.11.044

Prytulak J, Elliott T (2007) TiO_2 enrichment in ocean island basalts, 2007. Earth Planet Sci Lett 263:388–403. https://doi.org/10.1016/j.epsl.2007.09.015

Putirka KD (ed) (2008) Minerals, inclusions and volcanic processes. Rev Mineral Geochem 69, 668pp

Self S (2006) The effects and consequences of very large explosive volcanic eruptions. Philos Trans R Soc 364:2073–2097. https://doi.org/10.1098/rsta.2006.1814

Shaw DM (1970) Trace element fractionation during anataxis. Geochim Cosmochim Acta 34:237–243

Sobolev AV et al (2007) The amount of recycled crust in sources of mantle-derived melts. Science 316:412–417. https://doi.org/10.1126/science.1138113

Thordarson T, Self S (2003) Atmospheric and environmental effects of the 1783–1784 Laki eruption: a review and reassessment. J Geophys Res 108:4011. https://doi.org/10.1029/2001JD002042

van Keken TE, Keifer B, Peacock SM (2002) High resolution models of subduction zones: implications for mineral dehydration reactions and the transport of water into the deep mantle. Geochem Geophys Geosyst 3. https://doi.org/10.1029/2001GC000256

White WM (2013) Geochemistry. Wiley, Chichester, 670pp

White WM (2015) Isotopes, DUPAL, LLSVPs, and Anekantavada. Chem Geol 419:10–28. https://doi.org/10.1016/j.chemgeo.2015.09.026

Wilson CJN (2008) Supereruptions and supervolcanoes: processes and products. Elements 4:29–34. https://doi.org/10.2113/GSELEMENTS.4.1.29

W

Water

Carl O. Moses
Provost and Vice President for Academic Affairs, Grand View University, Des Moines, Iowa, USA

Definition

Water (H_2O), present in the geologic environment as solid, liquid, vapor, and supercritical fluid, is one of the most important components of Earth's fluid envelope. Without water and its special properties, Earth would be a vastly different planet in many ways. Water plays critical roles in atmospheric processes, including the absorption of radiant energy and the redistribution of energy through weather mechanisms, thus fundamentally influencing climate. In the lithosphere, water serves as an essential solvent and transport medium for many of the elements, a modifier of rock physical properties, and a lubricant for tectonic processes. The biosphere also depends on water for its very existence, for its solvent properties, and, in photosynthesis, as an electron-donating nutrient.

Properties of Water

Many of water's physical and chemical properties (Table 1) are anomalous, whether by comparison with other compounds generally; by comparison with the dihydride compounds of S, Se, and Te, with which O shares a column in the periodic table; or by comparison with isoelectronic hydrides like CH_4, NH_3, and HF. Perhaps the most notable property of water is the temperature dependence of its density. Unlike most materials, the solid phase of water is less dense than the liquid phase, and as a consequence, ice floats on liquid water. Water is even more unusual in that as T increases above the melting point, density continues to increase in the liquid phase up to 3.98 °C, above which it decreases. The temperature dependence of density ensures that bodies of water freeze from the top down rather than from the bottom up and causes inverse stratification of lakes during cold weather (water $T < 3.98$ °C overlying water with $T \geq 4$ °C), which has significant implications for life in aquatic habitats. Because density is a macroscopic manifestation of molecular structure, a structural model for water must account for the unusual temperature dependence of water's density.

Many of water's other properties also have geochemical significance. If water's melting and boiling points followed the trend of other Group VIB dihydrides (Fig. 1), only water vapor would exist in the surficial Earth system; the anomalously high melting and boiling points of water allow the existence of liquid water and ice. In addition, liquid water is stable over a remarkably wide range of temperature (the difference between T_{boil} and T_{melt}). The short bond length, tetrahedral bond angle, and great strength of the O–H bonds also indicate a very stable compound. The bonding characteristics of H_2O distinguish it from the dihydrides of S, Se, and Te, all of which have longer bonds, orthogonal bond angles, and weaker M–H bonds.

Water's enthalpy of vaporization is very high, which has great significance for the climate system. A mole of H_2O liquid extracts 44 kJ of energy from its surroundings as it evaporates, which is responsible for the cooling effect associated with evaporation. Furthermore, in the vapor, that energy is in a very mobile form that can be transported at great distances by the movement of air masses before it is released in the reverse process, condensation. This transfer of "latent heat" is an important mechanism by which energy is transported from low latitudes to high latitudes by the climate system, and it is a significant component of tropical storms and convective storms. During condensation, substantial energy releases take place that can result in significant warming of upper elevations of the troposphere that can, in turn, offset some of the adiabatic cooling that takes place during uplift of an air mass. When latent heat is combined with water's high heat capacity (proportionality constant for

W. M. White (ed.), *Encyclopedia of Geochemistry*,
https://doi.org/10.1007/978-3-319-39312-4

Water, Table 1 Selected properties of water (at $T = 298.15$ K, P = 0.1 MPa (1 bar) unless otherwise noted)

Property	Data	Comments
Density, ρ	$\rho_{solid} < \rho_{liquid}$ $T_{\rho max} = 3.98$ °C $\rho_{max} = 1.0$ g/cm^3	ρ_{max} is much less than that predicted by geometric argument; unusual for solid to float on liquid; unusual for ρ to increase with temperature
Melting point, T_{melt}	0.0 °C	Both T_{melt} and T_{boil} are anomalously high and the temperature span between T_{melt} and T_{boil}
Boiling point, T_{boil}	100.0 °C	Is anomalously large (Fig. 1)
O–H bond length	95.7 pm	Small; cf. H_2S (133.6), H_2Se (146), and H_2Te (169)
H-O-H bond angle	104.5° (gas phase)	Tetrahedral angle; cf. ~90° angle for H_2S, H_2Se, and H_2Te
Enthalpy of formation, $\Delta H°_f$	−285.85 kJ/mol	Highly exothermic; much stronger bonding than endothermic formation of H_2S, H_2Se, and H_2Te
Enthalpy of vaporization, $\Delta H°_{vap}$	44.02 kJ/mol	Very high ($\Delta S°_{vap} = 118.8$ J/K/mol is also high)
Heat capacity, $C° p$	75.19 J/K/mol	Unusually high
Dissociation constant, K $W = (a_{H}+)(a_{OH}-)$	10^{-14}	Very small; cf. H_2S ($\sim 10^{-7}$), H_2Se ($\sim 10^{-4}$), and H_2Te ($\sim 10^{-3}$)
Surface tension, γ	71.97×10^{-3} J/m^2	Large
Dielectric constant, $\in$	78.4 (unitless)	Very large

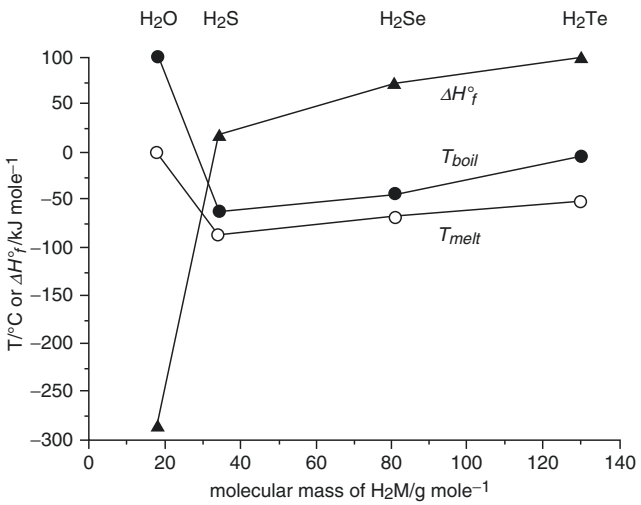

Water, Fig. 1 Comparison of melting point (T_{melt}), boiling point (T_{boil}), and $\Delta H° f$ for H_2O and other Group VIB dihydrides

the relationship between heat transfer and temperature change; see ▶ Geochemical Thermodynamics), one can appreciate the moderating effect that water has on weather patterns.

Water is a weaker acid than H_2S, H_2Se, and H_2Te, which, in part, reflects the greater M–H bond strength of water as well as the stabilizing role of H-bond formation. Water may also behave as a weak base, forming H_3O^+. This amphoteric nature of water (see ▶ Acid–Base Reactions) enhances water's influence on the solubility of rocks and gases, because water is able to react with both acids and bases.

The high surface tension of water plays a vital role in climate through the regulation of water droplet size in clouds and precipitation. Surface tension also controls the relative wetting of mineral surfaces by water and nonpolar fluids (e.g., oil) and thus influences the relative mobility of water and other fluids in porous rocks.

The dielectric constant of water reflects the ability of water molecules to separate electrical charges. For example, ions in aqueous solution with opposite charge tend to attract one another, and if they combine, the result may be the formation of a precipitate; the aggregate effect of such processes would be diminished solubility. Water is very effective in separating such charges (shielding ions from interactions with one another), thus enhancing solubility. Water is over ten times as effective in this regard as mica or Teflon, substances that one readily recognizes as excellent dielectric media.

Structure of Water

The central O of a water molecule has the electronic configuration [He]$2s^2 2p^4$, and H has the ls^1 configuration. One might expect that the formation of H_2O involves the sharing of bonding electrons between the O 2p and H ls orbitals, and this does, indeed, appear to be the dominant bonding mechanism in H_2S, H_2Se, and H_2Te. In water, however, the combination of the small size of the O and the orthogonal configuration of the 2p orbitals would bring the two H atoms too closely together; the resulting repulsion destabilizes the system. Instead, the 2 s and 2p orbitals of O combine with the H ls orbitals to form four tetrahedrally oriented sp^3 hybrid molecular orbitals, two of which are occupied by lone-pair electrons and two of which are occupied by bonding electrons. The two lone pairs repel each other somewhat more strongly than the two H atoms repel each other, so the H atoms are separated by an angle (104.5°) slightly smaller than the ideal tetrahedral angle of 109.5° (Fig. 2), while the lone pairs are separated by a slightly larger angle (113°).

The tetrahedral orientation of the H_2O molecule lends itself to a highly symmetric interaction in which H_2O molecules are hydrogen bonded to one another (Fig. 3). An electrostatic bond forms between an $H^{\delta+}$ on one H_2O and a lone

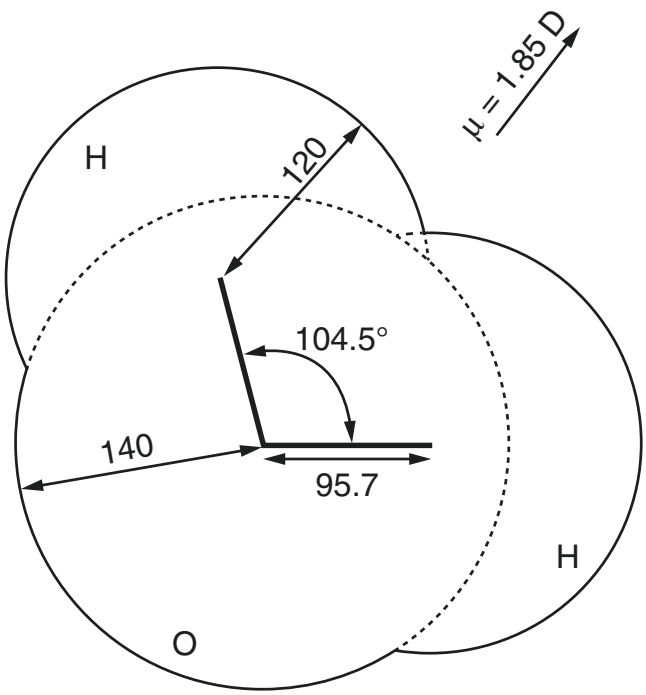

Water, Fig. 2 Schematic illustration of a water molecule; length dimensions are pm. The molecule's center of mass is displaced from the center of the O atom by about 4.5 pm along the axis that bisects the H-O-H angle. Water molecules generally behave like spheres with a radius of 141 pm. The field-free dipole moment of the molecule, μ, is oriented as shown; 1 D (debye) = 3.33×10^{-30} C m

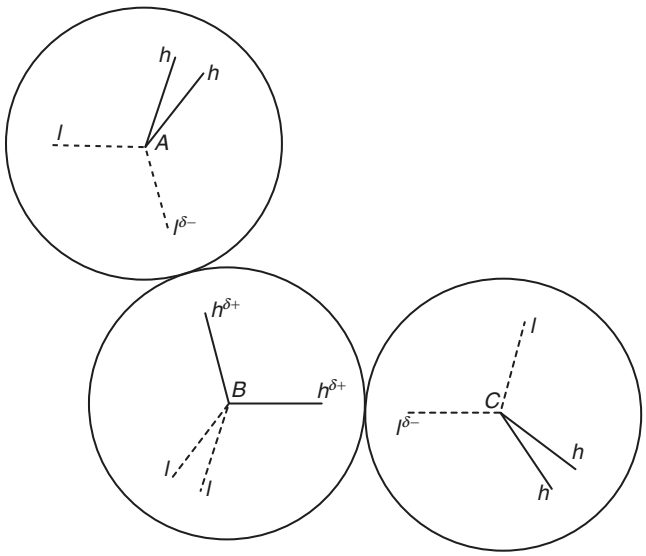

Water, Fig. 3 Relative orientation of three H-bonded water molecules; h = H atom and l = lone pair of electrons; δ indicates a fractional increment of charge (not all charges are shown). ∠H-O-H = ~105° in each molecule but ∠O-O-O (ABC) = ~109.5°, giving an extended structure of H-bonded molecules the ideal tetrahedral geometry. For clarity in illustration, the vectors of lone-pair orbitals are dashed and the water molecules are drawn as spheres

pair ($lp^{\delta-}$) on another H_2O (the δ represents a fractional charge of the indicated sign). The energy of H bonds depends somewhat on the local environment of the molecules but is on the order of 20 kJ/mol. Although small clusters of H-bonded H_2S, H_2Se, and H_2Te molecules may form, they do not grow large owing to steric hindrance resulting from the large size of the molecules and the orthogonal H-M-H and lp-M-H angles. In contrast, the evidence suggests that extensive three-dimensional networks of H-bonded water molecules dominate the structure of water.

At atmospheric pressure and $0° > T > \sim -130$ °C, ice forms a hexagonal framework structure, I_h, similar to tridymite (at lower T, an isometric polymorph like cristobalite exists, and other polymorphs are found at pressures > ~200 MPa). In the I_h structure, each H_2O is H bonded to four others in tetrahedral coordination, two via its lone pairs to H on other H_2O molecules and two via its H atoms to lone pairs on other H_2O molecules. The O-O-O angles have the ideal tetrahedral value of 109.5°, but the H-O-H angles are still ~105°, suggesting that H bonding does not fully relax the repulsive relationships among the lone pairs and H atoms on a given H_2O molecule. The I_h structure is not a close-packed structure. In fact, the observed density of ~1 g/cm^3 suggests that the four-fold coordination leaves ~62% of the volume of ice unfilled. The large open cavities, or interstices, in the ice structure are responsible for its low density.

As ice melts, large H-bonded clusters or polymers of water molecules remain intact in the liquid phase, retaining the open three-dimensional framework I h structure. H_2O monomers that are also released during melting slip inside the large interstices of the clusters. This interstice-filling process allows more H_2O molecules to fill a given volume of liquid water than the same volume of ice, hence the higher density of liquid water. Thermal agitation competes with interstice filling for control of the density of liquid H_2O. The temperature dependence of H_2O density suggests that interstice filling dominates at $0° < T \leq 3.98$ °C, and thermal processes dominate at $T > 3.98$ °C. Radial distribution function measurements indicate that, at T = 3.98 °C, ~82% of the H_2O molecules are in ice-like clusters and that, at 100 °C, ~73% are still in clusters. Clearly, H bonding yields a stable and robust configuration for H_2O molecules, but clusters have only fleeting existences, with a half-life of $\sim 10^{-10}$s (which is still ~1000 × longer than the vibrational period of an H bond and ~10 × longer than the time required for a H_2O molecule to diffuse through a distance equal to its own diameter). The interstitial model of water structure described here has been termed the "flickering cluster-monomer theory" to convey an image of the highly dynamic nature of the structure. Note that other structural models have been advanced for liquid water, but regardless of details, there is little doubt that tetrahedrally coordinated H bonds play a substantial role.

The stability of the unusual H-bonded structure of liquid water accounts for many of water's unusual properties. The high melting and boiling points, the wide range of stability for the liquid phase, the high enthalpy of vaporization, the high heat capacity, and the high surface tension are all manifestations of a very stable material. The tetrahedral coordination caused by the sp^3 hybrid molecular orbitals is responsible for the H-bonded framework structure; it is also responsible for the great stability of the O–H bonds in a given H_2O molecule, which is manifested in the strongly exothermic enthalpy of formation and the very weak acidity of H_2O in comparison with H_2S, H_2Se, and H_2Te.

Water's dielectric property is attributed to its dipole moment (Fig. 2) and the polarizability of water molecules. The dipole moment arises from the asymmetric distribution of charge, with the δ^+ of the H atoms on one "side" of the molecule and the δ^- of the lone pairs on the other side. Strictly speaking, a water molecule is a quadrupole, but the dipole treatment is sufficient for most purposes. Dipole moment is given by $2aq$, where $2a$ is the distance between the + and – charges and q is the amount of charge. If q is fixed, as in H_2O, the dipole moment may still change if $2a$ varies. In the absence of an electrical field, the dipole moments of a large population of H_2O molecules are randomly oriented, and the population generates no electrical field of its own. If an electrical field is imposed (e.g., by a solute ion or a charged mineral surface), the H_2O molecules will reorient themselves (subject to the usual constraints imposed by thermal agitation) so that their dipole moments are pointing against the external electrical field (by convention, electrical field strength vectors point from – to + charge, so the dipoles orient with their vectors pointing toward – charges). As a result, the population of oriented H_2O molecules generates a field that partly offsets the external field. The strength of the offsetting field is proportional to the dipole moment, the number of dipoles, and the degree of alignment the dipoles achieve with the external field. In a polarizable molecule, such as water, the response to the external field includes an increase in $2a$ (i.e., the molecule stretches), which increases the dipole moment and, thus, the strength of the offsetting field. Dielectric strength decreases with increasing T, reflecting the disruptive influence of thermal motion on the mutual orientation of the molecules generating the offsetting field.

The production of an offsetting electrical field by the oriented dipoles is the key characteristic of a dielectric medium and determines the extent to which the dielectric can separate opposite charges. In water, the significance of the offsetting electrical field lies in its ability to reduce electrostatic interactions among ionic solutes. A strong offsetting field "shields" an ion from others. As noted above, water is exceptionally effective in this regard.

Phase Behavior of Water

Entropy always increases on melting ($\Delta S_{melt} > 0$), so the unusual density behavior of water ($\Delta V_{melt} < 0$) leads (by the Clapeyron equation; see ▶ Entropy) to a negative slope, $\Delta P/\Delta T < 0$, for the solid–liquid boundary on a P–T phase diagram of water (Fig. 4). This boundary marks the set of (T, P) conditions for which solid and liquid coexist at equilibrium. In fact, the slope of that boundary is so steep that it is almost imperceptibly different from − infinity and leads to a temperature decrease of only 0.01 K between the triple point ($T_t = 273.16$ K, $P_t = 611$ Pa) and T_{melt} at 10^5 Pa (273.15 K and 1 bar, $\Delta P/\Delta T < -9.9$ MPa/K).

In the absence of liquid water in the local environment at $T < T_t$, the presence of ice surfaces can lead to very dry conditions owing to the sublimation process (exchange of water between solid and vapor phases). The $\Delta P/\Delta T$ slope of the solid–vapor boundary, which marks the set of (T, P) conditions for which the solid and vapor coexist at equilibrium, is always positive (Fig. 4c, d), and the vapor pressure over ice decreases from 611 Pa at T_t to 260 Pa at −10 °C (263.15 K, $\Delta P/\Delta T \approx 35$ Pa/K). The magnitude of $\Delta P/\Delta T$ for the solid–vapor boundary diminishes with decreasing T. The liquid–vapor boundary is metastable at $T < T_{melt}$ at any pressure, but supercooled water can only slightly increase P_{H2O} from its equilibrium value with ice (~10% at 263.15 K, Fig. 4e).

The $\Delta P/\Delta T$ slope of the liquid–vapor boundary, which marks the set of (T, P) conditions for which liquid and vapor coexist at equilibrium, is also always positive (Fig. 4), and its magnitude increases with increasing T from ~1000 Pa/K in the 0–100 °C range to almost 0.2 MPa/K in the 300–370 °C range. The unusual stability of the liquid phase accounts for the considerable "length" of the liquid–vapor boundary (Fig. 4), which is limited by the critical temperature, T_c (647.14 K), and the critical pressure, P_c (22.06 MPa; critical data from Lide and Kehiaian 1995). Beyond (T_c, P_c), the liquid–vapor boundary ceases to exist. If one considers an isotherm (line of constant temperature, i.e., a vertical line on the P–T diagram) at $T < T_c$ and one at $T > T_c$, one might conclude that the critical point marks the temperature limit of stability for the liquid phase. On the other hand, if one considers an isobar (line of constant pressure, i.e., a horizontal line on the P–T diagram) at $P < P_c$ and one at $P > P_c$, one might conclude that the critical point marks the pressure limit of stability for the vapor phase. The fluid that exists beyond the critical point and is neither liquid nor vapor is termed a supercritical fluid. The critical molar volume of water, $\overline{V}_c$, is 56 cm^3/mol. It may be interesting to note that, even at the relatively extreme conditions of the critical point, water's density is 0.9970 g/cm^3, i.e., still very close to 1.

A phase diagram in P–V coordinates (Fig. 5) is useful in understanding the concept of a supercritical fluid. The lines in

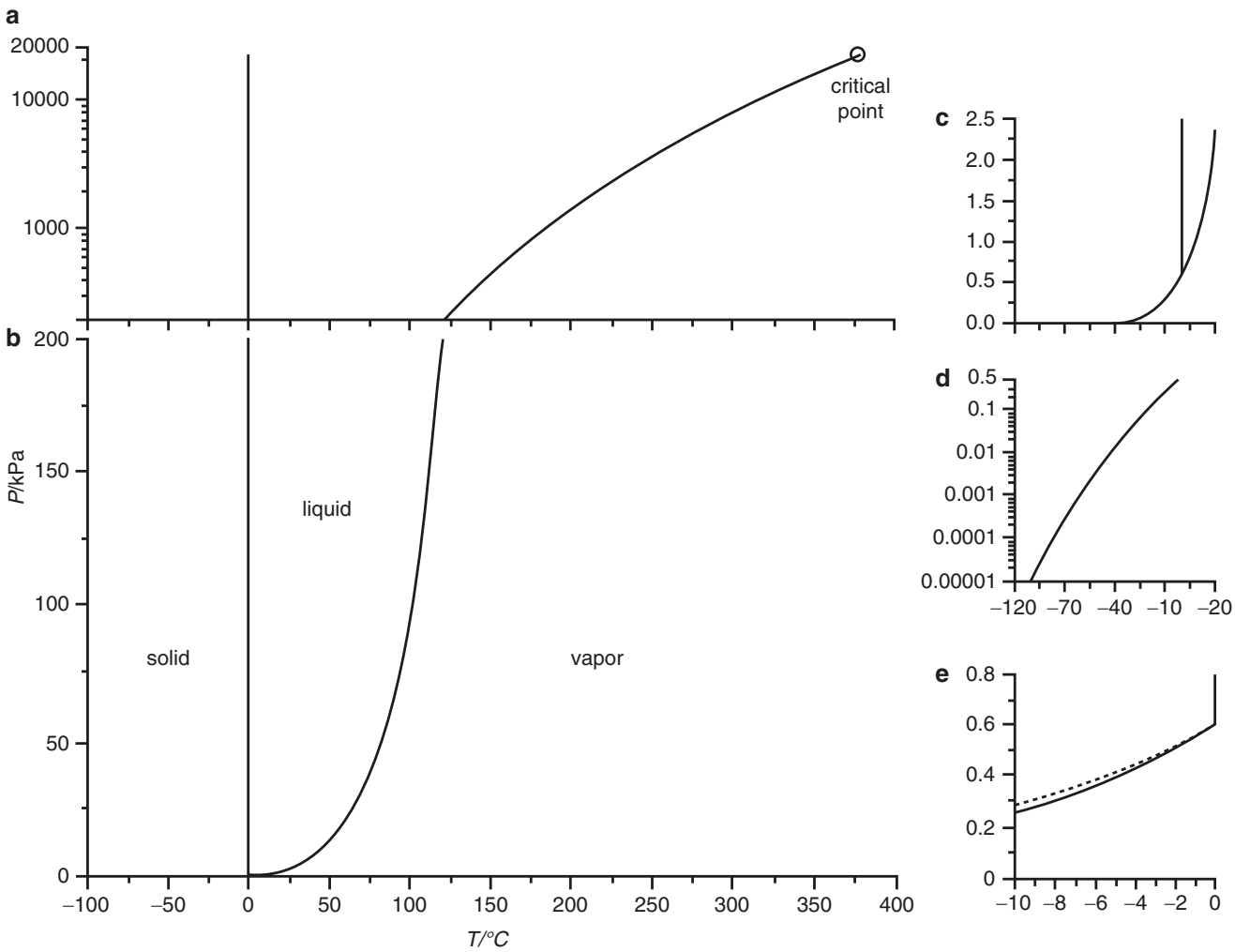

Water, Fig. 4 *P–T* phase diagram for water. (**a**, **b**) Relationship of solid, liquid, and vapor phases; note different pressure axis scales. (**c**, **d**) Region near the triple point; note change in pressure axis scales to display the solid–vapor boundary more clearly in (**d**). (**e**) Solid–vapor boundary (*solid line*) and metastable liquid–vapor boundary (*dashed line*) at $T < 0$ °C. 1 bar = 100 kPa

Fig. 5 labeled with temperatures are isotherms and represent the pressure changes that result from isothermal volume changes. Overall, each isotherm has a negative dP/dV slope, reflecting the fact that pressure increases as volume decreases and vice versa. Note that all of the isotherms steepen in slope (i.e., the magnitude of the slope increases) as volume decreases. In detail, however, some of the isotherms (those for $T < T_c$) also have an isobaric segment; this segment is longest at low temperatures and grows shorter, approaching zero length, as $T \rightarrow T_c$. In the high V, low P region of P–V space, vapor is the only stable phase for $T < T_c$, and pressure is free to vary with volume. When the pressure reaches the vapor pressure for a given temperature, liquid begins to condense. Now two phases, liquid and vapor, coexist, and the system loses a degree of freedom. Consequently, pressure remains fixed as long as both phases exist and temperature remains constant, but volume can continue to decrease (with no pressure change). When volume decreases to the point that only liquid exists and no vapor is left, the isotherm enters the low V, high P region of P–V space, liquid is the only stable phase for $T < T_c$, the system regains a degree of freedom, and pressure is free to vary with volume. Owing to the relative incompressibility of the liquid phase, the dP/dV slope is much steeper than for the vapor phase. In P–V–T coordinates (Fig. 6), the projection of the isobaric sections onto the P–T plane gives the familiar liquid–vapor boundary of Fig. 4 on which P is fixed by T (or vice versa) and liquid and vapor coexist.

With increasing temperature, the isobaric section of the isotherms (the volume range for which liquid and vapor coexist) becomes shorter until, at T_c, the isobaric section is infinitesimal. For $T > T_c$, there is no volume range for which liquid and vapor can coexist, so there is no phase transition. Note that, even in the supercritical fluid, dP/dV is shallower at

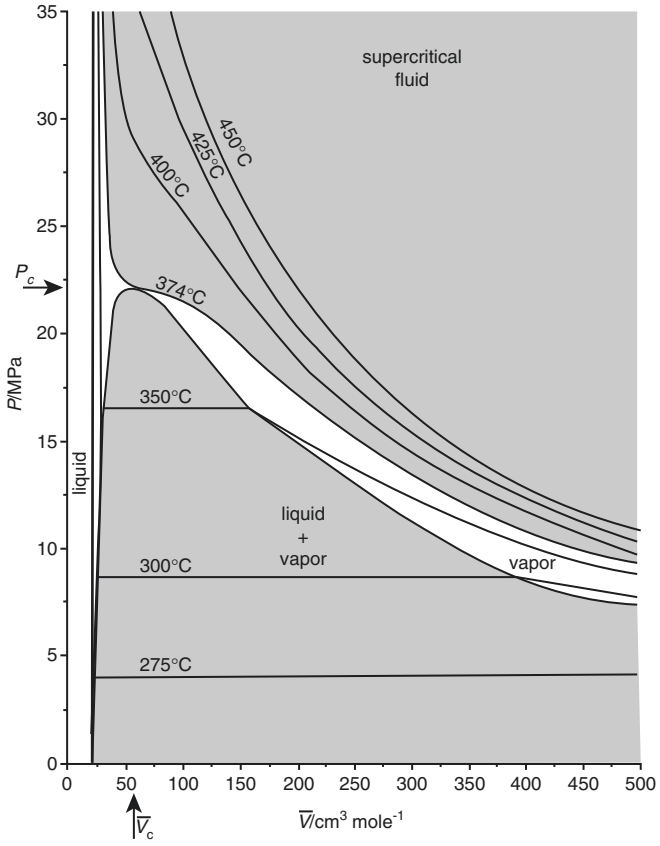

Water, Fig. 5 *P–V* phase diagram for water in the region of the critical point. The labeled lines are isotherms. Isotherms for $T > T_c$ (374 °C) pass through the liquid + vapor stability field (*the lower gray area*), in which $P \neq f(\overline{V})$. The liquid + vapor stability field does not exist for $T > T_c$. The upper gray area indicates the *P–V–T* domain for supercritical water

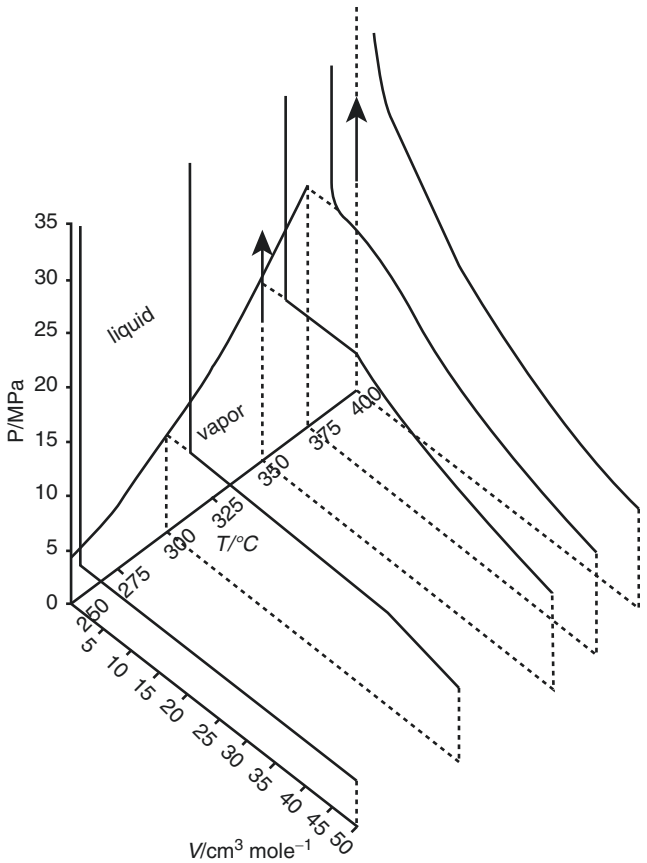

Water, Fig. 6 Constructing the liquid–vapor boundary in *P–T* coordinates (cf. Fig. 5) by projecting the isobaric segments representing liquid + vapor stability from planes of equal temperature in *P–V–T* coordinates onto the *P–T* plane. The heavy arrows represent isothermal compression paths in *P–T* coordinates at $T < T_c$ and $T > T_c$

high V and low P than it is at low V and high P. This behavior is consistent with the behavior of any fluid, including the vapor and liquid phases existing below (T_c, P_c). The key distinction of the supercritical fluid, then, is the absence of the first-order phase transition between vapor and liquid.

Supercritical water exists in many crustal settings and is geologically important for solute transport and mineral solubility relations in such problems as ore deposits, metamorphic fluids, and magmatic crystallization. Aside from temperature and pressure considerations, one of the most important properties of supercritical water is its greatly reduced dielectric strength, which enhances the formation of solute complexes. Depending on fluid composition, those complexes may increase or decrease the solubility of the solutes. Free radical reaction mechanisms are greatly hindered in the liquid phase of water but occur much more readily in supercritical water. Accordingly, supercritical water may also prove to be a useful medium for decomposing certain nonpolar organic contaminants.

The Hydrologic Cycle

In the environment, water is highly abundant and mobile. The exchanges of water among different parts of the environment are summarized in the hydrologic cycle (Table 2). The data from Berner and Berner (1987) were compiled mostly in the 1960s and 1970s, while the Trenberth et al. (2007) data were compiled between the late 1980s and early 2000s. The more recent data may be somewhat more accurate, but global estimates of the smaller reservoirs are imprecise. Berner and Berner (1987) include the biosphere as a reservoir containing 0.6×10^6 km^3 water. About 99% of Earth's modern inventory of water is in the oceans or in ice. During periods of extensive glaciation, some of the oceanic inventory is shifted to ice. Most of the remaining global inventory is in groundwater. The water content of the crust diminishes with depth, but evidence from metamorphic rocks indicates that liquid water exists at depths of at least 20 km in the crust.

Most marine precipitation is derived from marine evaporation, and most continental evaporation is returned to the

Water, Table 2 Reservoirs and fluxes in the hydrologic cycle, comparing data from Trenberth et al. (2007) and Berner and Berner (1987). Reservoirs, 10^6 km^3; fluxes, 10^6 km^3 y^{-1}

Reservoirs	Trenberth et al. (2007)		Berner and Berner (1987)	
Oceans	1335.0400 (96.95%)		1370.0000 (97.25%)	
Ice (ice sheets, sea ice, glaciers)	26.3500 (1.91%)		29.0000 (2.06%)	
Groundwater	15.5300 (1.11%)		9.5000 (0.67%)	
Surface water (lakes, rivers)	0.1780 (0.01%)		0.1267 (0.01%)	
Soil water	0.1220 (0.01%)		0.0650 (<0.01%)	
Permafrost	0.0220 (<0.01%)		n/a	
Atmosphere (liquid equivalent)	0.0127 (<0.01%)		0.0130 (<0.01%)	
Total	1377.0247		1408.7047	
Fluxes	Evaporation	Precipitation	Evaporation	Precipitation
Over oceans	0.413	0.373	0.4231	0.3857
Over land	0.073	0.113	0.0729	0.1103
Continental drainage	0.040		0.0374	

continents as precipitation. On the other hand, marine evaporation exceeds marine precipitation, while continental precipitation exceeds continental evaporation. The system is balanced by transport of water vapor from the oceans to the continents and the drainage of liquid water from the continents to the oceans. Aside from its effect on the global water budget, the net transport of water vapor to the continents is a significant part of the climatic moderating influence associated with marine air masses (as noted above, vapor transport = latent heat transport).

Water in the Lithosphere

The most familiar action of water in relation to rocks is to dissolve (chemically weather) mineral components. Minerals are soluble to varying degrees, so one would not expect the elements to be partitioned into the hydrosphere in the same relative abundances observed in the lithosphere. Excluding oxygen, the seven most abundant elements of the lithosphere, in decreasing order of abundance, are Si, Al, Fe, Ca, Na, K, and Mg. In the hydrosphere, the sequence of abundance is Cl, Na, S (as SO^{2-}_4), Mg, Ca, K, and C (as HCO^{-}_3). The differences result from differences in solubility controls, which are a combination of thermodynamic (equilibrium) and kinetic effects, ion exchange processes, and biological utilization. For example, the low abundance of aluminum in the hydrosphere chiefly reflects its low equilibrium solubility; chemical weathering processes generally transfer little Al from the solid phase to the aqueous phase. An example of the effect of ion exchange processes is the enhanced mobility of Na in the hydrosphere compared to K, which is about equal in crustal abundance to Na but has roughly 10% of the abundance of Na in the hydrosphere. An example of the effect of biota is carbon, which is not abundant in igneous rocks or, indeed, in the total solid Earth inventory. Sedimentary rocks, however, contain large quantities of carbon, which chiefly reflect interactions among the biosphere, atmosphere, and lithosphere, mediated by the hydrosphere.

Water also contributes to the physical alteration of the lithosphere. Because water expands when it freezes, rocks exposed at Earth's surface that are intruded by liquid water may experience repeated cycles of freezing and thawing with consequent decrepitation. Moving water is able to transport particles of decrepitated rock in suspension, and in many rivers, the transport of suspended solids greatly exceeds that of dissolved solids. Continental denudation makes an important contribution to marine sediments and nutrient availability in near-shore marine ecosystems. In addition, rapid continental denudation, occurring in regions of high rainfall and significant topographic relief, has recently received attention as a mechanism for tectonically "unloading" areas of continental crust and allowing substantial rates of uplift (Ruddiman and Kutzbach 1989; Kutzbach et al. 1993).

Aside from the familiar interactions between water and the rocks of the lithosphere, other significant geologic processes are influenced by water. Two examples come from structural geology and petroleum geology. The transport of large (km thick) thrust blocks over great distances along faults with low dip angles cannot be explained when realistic coefficients of friction for rock surfaces are combined with the strength of rocks; horizontal forces necessary to overcome the friction are far in excess of the forces necessary to fracture the blocks. Hubbert and Rubey (1959) recognized that fluid pressure in the fault plane would reduce the shear stress required to move block by reducing the normal component of stress on the fault. The relative incompressibility of water permits the development of sufficient hydrostatic pressures to lubricate major overthrust faults, thus allowing dramatic tectonic displacements. In petroleum geology, Hubbert (1954) recognized the important role that hydrodynamic processes play in trapping oil (or any immiscible fluid with a lower density than water's) under dipping surfaces of low permeability. Even when the flow of formation water is more or less parallel

to the low permeability surface, the buoyancy of the low-density fluid gives it a significant upward component of motion, leading to the development of a trapped stationary lens overlying the flowing water.

Water in the Atmosphere

Although the atmosphere has one of the lowest inventories of water in the hydrosphere, the dynamics of water in the atmosphere are vital to weather (and climate) and to many geochemical processes. The discussion above has already alluded to the role of evaporation and condensation in the transport of energy as latent heat through the environment by atmospheric processes. The water content of the atmosphere is highly variable in both time and space, but generally, most atmospheric water is in the troposphere, water content diminishes with altitude, air masses at tropical and temperate latitudes have a higher atmospheric water content than at sub-tropical or polar latitudes, and marine air masses have a higher water content than continental air masses.

Most of the water in the atmosphere is present as vapor; clouds consist of liquid water droplets or ice crystals. In the gas phase, atmospheric water content is expressed as the mixing ratio, $w = m_v/m_d$, where m_v is the mass of water vapor (g) and m_d is the mass of dry air (kg). The relationship between w and the partial pressure of water P_{H2O} depends on the total atmospheric pressure, P_{tot} (Eq. 1; $\varepsilon = M_w/M_d = 0.622$, where M_w and M_d are the molecular masses of water and dry air, respectively).

$$P_{H_2O} = \left(\frac{w}{w+\varepsilon}\right) P_{tot} \qquad \text{(W2)} \qquad (1)$$

The saturation vapor pressure, $P^0{}_{H_2O}$, corresponds to the vapor pressure given by the Clapeyron equation for the liquid–vapor equilibrium. To a first approximation ($\Delta H^0_{evap} \neq f(T)$ at normal environmental temperatures), $\log P^{0,\,liquid}{}_{H_2O} = 9.4 - (2354/T)$, where T is in K and $P^{0,\,liquid}{}_{H_2O}$ is in mb (1 mb = 100 Pa). The solid–vapor (sublimation) boundary gives a saturation vapor pressure with respect to ice, for which $\log P^{0,\,ice}{}_{H_2O} = 10.55 - (2667/T)$.

There is a saturation mixing ratio that corresponds to the saturation vapor pressure, $w_s = m_{v,s}/m_d$, where $m_{v,s}$ is the mass of water vapor in saturated air of the given temperature. As with the relationship in Eq. 1, the relationship between w_s and $P^0{}_{H_2O}$ depends on P_{tot} (Eq. 2; an approximation depending on the fact that $P_{tot} > P^0{}_{H_2O}$).

$$w_s = \frac{\varepsilon P^0_{H_2O}}{P_{tot}} \text{(W2)} \qquad (2)$$

Because $P^0{}_{H_2O} = f(T)$ and, therefore, $w_s = f(P, T)$, the saturation mixing ratio is a function of state in the atmosphere. Relative humidity is the ratio of the observed vapor content and the saturation vapor content, expressed as a percentage: $h = w/w_s \times 100\%$. The dew point is the temperature to which the air must be cooled (at constant pressure) to reach $h = 100\%$ (i.e., the temperature at which $w = w_s$; cooling air at constant pressure causes w_s to decrease while w is conservative). Usually, w_s is defined with respect to liquid water, but it can also be defined with respect to ice.

Clouds form when droplets of liquid water (or crystals of ice) can nucleate and grow. Condensation nuclei in the form of, for example, dust, sea salt, or biogenic aerosols are sufficiently abundant in the atmosphere for condensation to proceed by heterogeneous mechanisms at $h \approx 100\%$; homogeneous nucleation, which would require $h > 100\%$, apparently never occurs in the environment. With reference to the P–T diagram (Fig. 4), P–T conditions for water in the atmosphere are either in the vapor-phase stability field or, uncommonly, on the liquid–vapor or solid–vapor boundary; conditions in the atmosphere never enter the liquid or solid stability fields. Cloud particles have dimensions generally <20 μm and are easily kept aloft by slight updrafts. In order for precipitation to take place, the particles must grow large enough (≥1 mm, depending on vertical wind velocity) to fall. Furthermore, the particles must reach the ground surface before evaporating. Small particles (sufficiently large to fall) can reach the ground under conditions of high humidity, but if the humidity is low, very large particles may be required.

In addition to the phase transitions associated with weather and climate, water's interactions with solar and terrestrial radiation are important. Water vapor is, in fact, a "greenhouse" gas, so called because it absorbs radiant energy passing through the atmosphere. Water vapor's heat capacity is greater than that of most gases (about twice that of dry air), so water vapor is very effective at retaining the energy it absorbs. Liquid and solid water have even higher heat capacities, enhancing the ability of atmospheric water to retain energy. The more rapid cooling of the environment under low humidity conditions than under high humidity conditions is a familiar manifestation of energy absorption and retention by water vapor. The nonuniform spatial and temporal distribution of water vapor in the atmosphere is thus an important determinant of regional climate patterns.

Cross-References

- ▶ Acid–Base Reactions
- ▶ Aqueous Solutions
- ▶ Biogeochemistry
- ▶ Chemical Bonds
- ▶ Chemical Weathering

▶ Earth's Atmosphere
▶ Earth's Oceanic Crust
▶ Fluid–Rock Interaction
▶ Hydrogen
▶ Hydrologic Cycle
▶ Oxygen
▶ Van der Waals Force
▶ Water

References

Berner EK, Berner RA (1987) The global water cycle. Prentice-Hall, Englewood Cliffs, 397 pp

Hubbert MK (1954) Entrapment of petroleum under hydrodynamic conditions. Bull Am Assoc Pet Geol 37:1954–2026

Hubbert MK, Rubey WW (1959) Role of fluid pressures in mechanics of overthrust faulting: I. Mechanics of fluid-filled porous solids and its application to overthrust faulting. Bull Geol Soc Am 70:115–166

Kutzbach JE, Prell WL, Ruddiman WM (1993) Sensitivity of Eurasian climate to surface uplift of the Tibetan Plateau. J Geol 101:177–190

Lide DR, Kehiaian HV (1995) CRC handbook of thermophysical and thermochemical data. CRC Press, Boca Raton, 518 pp

Ruddiman WM, Kutzbach JE (1989) Forcing of late Cenozoic northern hemisphere climate by plateau uplift in southern Asia and the American west. J Geophys Res 94:18409–18427

Trenberth KE, Smith L, Qian T, Dai A, Fasullo J (2007) Estimates of the global water budget and its annual cycle using observational and model data. J Hydrometeorol 8:758–769

X

Xenon

Sujoy Mukhopadhyay
Department of Earth and Planetary Sciences, University of California Davis, Davis, CA, USA

Element Data
Atomic Symbol: Xe
Atomic Number: 54
Atomic Weight: 131.293 AMU
Isotopes and Abundances: ^{124}Xe, ^{126}Xe, ^{128}Xe, ^{129}Xe, ^{130}Xe, ^{131}Xe, ^{132}Xe, ^{134}Xe, and ^{136}Xe with the relative abundances of these isotopes in air being 0.095%, 0.089%, 1.910%, 26.4%, 4.017%, 21.23%, 26.91%, 10.44%, and 8.86%, respectively
Atm Melting Point: 161.4 K
1 Atm Boiling Point: 165.1 K
Common Valences: 0
Atomic Radii: 2.16 Å (van der Waals radius)
Pauling Electronegativity: 2.6
First Ionization Energy: 1170.35 kJ/mol
Chondritic (CI) Abundance: 0.17 ppb
Silicate Earth Abundance: 30–500 ppq
Atmospheric Abundance: 87 ppb
Seawater Abundance: 65 ppt
Core Abundance: Not known

Properties

Physical Properties

At standard temperature and pressure of 273.15 K and 1 atmosphere, Xe is a gas. In the Earth's interior, at pressures >8 gigapascal (GPa), Xe that is not hosted within a mineral would be present as a pure solid phase (Jephcoat 1998). Since the Xe abundance in the mantle is very low, whether pure solid Xe phases exist in the Earth's interior is not clear.

Among the stable noble gases (i.e., He, Ne, Ar, Kr, Xe), Xe can be the most easily polarized, which makes it the most soluble of the noble gases in water. Furthermore, Xe exhibits the strongest temperature dependence of solubility in water, a property that can be exploited to obtain paleotemperature from water bodies. The solubility of Xe can be expressed by Henry's Law

$$C = H \times P_i$$

where C is the dissolved concentration, P_i is the partial pressure, and H is the Henry's constant, a function of pressure, temperature, and salinity. In water, Xe solubility decreases as temperature and salinity increase (Ozima and Podosek 2002).

Xe usually has the lowest solubility of the noble gases in silicate melts and usually the highest solubility in silicate minerals (Ozima and Podosek 2002). However, in bridgmanite, the primary lower mantle mineral, Xe solubility is observed to be lower than Ar and Kr (Shcheck and Keppler 2012). In melts, Xe solubility decreases with decreasing silica content and increasing concentrations of network modifiers; i.e., solubility decreases as the melt becomes depolymerized (Lux 1987; Shibata et al. 1996, 1998). The dissolution of Xe in silicate melts appears to be controlled by its coupling to the bridging oxygen atom in the silicate melt.

Crystal-melt partitioning data for Xe, which is effectively the ratio of the solubility of Xe in the crystal to the solubility in melt, exists between basaltic liquid and the major upper mantle minerals, olivine and clinopyroxene. Earlier partitioning studies sometimes indicated partition coefficients close to 1, although these experiments might have been affected by melt contamination of crystals or adsorbed gases (Broadhurst et al. 1992; Hiyagon and Ozima 1986). Recent advances with microanalytical techniques, such as UV laser ablation, appear to largely avoid these issues with crystal-melt partition coefficients for Xe converging to values of 2×10^{-4} to 1×10^{-3} (Brooker et al. 2003; Heber et al. 2007).

W. M. White (ed.), *Encyclopedia of Geochemistry*,
https://doi.org/10.1007/978-3-319-39312-4

Diffusion data for Xe in geologic materials is limited to basaltic liquids (Lux 1987) and glasses of silica, albitic, and jadeitic compositions (Roselieb et al. 1992, 1995). In silica, albite, and jadeite glasses, the activation energy of diffusion and diffusivities increase as Si is substituted by Na and Al, possibly as a result of structural relaxation of the melt (Roselieb et al. 1995). In basaltic melt, the diffusion coefficient at 1350 °C is 3×10^{-5} cm^2/s, which is several orders of magnitude higher than expected from extrapolated values of diffusivities in silicate glasses, suggesting diffusivities cannot be extrapolated through the glass transition temperature for silicates (Lux 1987). The only available data for minerals are some step-heating experiments in Ba-rich silicates, from which the activation energy of diffusion can be estimated but not diffusivities (Hetherington and Villa 2007).

Chemical Properties

Xenon interactions with solids are often described by adsorption. Adsorption can either be in the form of physisorption or chemisorption. Physisorption usually involves interactions associated with the weak van der Waals, while chemisorption involves electron sharing or even electron transfer. Since Xe has the largest atomic radii and lowest ionization energy of the noble gases, compared to the other noble gases, it has the strongest interactions with concentrations of Xe in a wide variety of materials are often described as resulting from adsorption, such as in charcoal, clay minerals, sedimentary rocks, igneous rocks, and meteorites.

In 1962, Neil Bartlett at the University of British Columbia demonstrated that Xe was reactive enough to form chemical bonds. He produced the first noble gas compound, xenon hexafluoroplatinate, by reacting Xe gas with platinum hexafluoride. Subsequently a large number of Xe compounds have been synthesized, including halides (XeF_2, XeF_4, XeF_6, $XeCl_2$), oxides (XeO_3, XeO_4), and oxohalides ($XeOF_2$,). Additionally, bonds between Xe and C in organic compounds have been observed. Xenon also forms clathrates with a number of hosts, such as water, nitrogen, and methane ice, and formation of Xe clathrates might be a particularly relevant process in the outer solar system (Lunine and Stevenson 1985; Swindle et al. 2009; Thomas et al. 2007; Mousis et al. 2013).

Biological Properties

Xe has been developed for use in humans as an inhalation anesthetic. Its anesthetic and neuroprotective function are achieved by binding to the glycine site glutamatergic N-methyl-D-aspartate (NMDA) receptor competitively and blocking it (Franks et al. 1998). A significant advantage of Xe as an anesthetic and neuroprotector appears to be its lack of toxicity and, because of its low blood-gas coefficient, fast recovery times for patients (Goto et al. 1997). The high costs associated with Xe production, however, have so far limited its widespread usage as an anesthetic.

More recently, Xe has been tested as a treatment for post-traumatic stress disorder (PTSD) (Meloni et al. 2014). Xe inhibits NMDA receptors, which are important in memory functions and affect the synaptic plasticity in two key brain areas, the amygdala and hippocampus. In animal trials using mice, Xe was found to substantially and persistently inhibit memory reconsolidation, opening a potential new path for treating people with PTSD and other memory disorders (Meloni et al. 2014).

History and Xenon Applications in Earth Science Research

The element xenon, whose name comes from a Greek word meaning *the stranger*, was discovered by chemists Sir William Ramsay and Morris Travers in 1898. Sir Ramsay was awarded the Nobel Prize in 1904 for the discovery of xenon.

The strong temperature dependence of Xe solubility in water has been utilized in numerous groundwater studies to reconstruct continental paleotemperatures. The relative abundance of Xe with respect to the other stable noble gases in groundwaters from tropical and temperature northern latitudes suggests a 5–10 °C increase in temperatures between the last glacial maximum and the Holocene. A complication in the paleotemperature reconstructions is the presence of excess air, which leads to noble gas concentrations in excess of their predicted equilibrium solubility in water. Numerous models have been developed to account for the excess noble gases in groundwater, although it is not clear which of the models best describe the physical process responsible for the phenomenon (e.g., Aeschbach-Hertiz and Solomon 2013). However, the models do suggest that while the absolute temperatures may be sensitive to the model chosen to account for excess air, the relative changes in paleotemperature reconstructions are more robust.

Over the past decade, the relative abundance of Xe with respect to the other noble gases has been used with some success to reconstruct continental temperatures from fluid inclusions trapped in speleothems (Kluge et al. 2008; Vogel et al. 2013). These studies are often plagued by noble gas budgets in speleothems being dominated by trapped air and/or gases trapped in the calcite lattice. However, techniques have been developed to reduce the non-fluid inclusion gases, such as pre-crushing samples in a He atmosphere or combined vacuum crushing and sieving (Scheidegger et al. 2010, 2011; Vogel et al. 2013). These techniques may allow for temperature reconstructions from speleothems with an uncertainty in the range of 1–2 °C (Vogel et al. 2013).

Xe measurements in seawater, combined with measurements of the noble gases, have been used to constrain air-sea gas exchange, a process that is critical to tracing the cycle of gases that play an important role in ocean biogeochemistry (such as CO_2, N_2O, dimethyl sulfide) (Stanley et al. 2009; Hamme and Severinghaus 2007). Recently, Xe measurements, in concert with measurements of other noble gases, were used to trace the addition of glacial meltwater from Antarctica to the southern ocean (Loose and Jenkins 2014).

Xe has been a particularly useful element with which to understand the early degassing and long-term degassing associated with plate tectonics. While a significant fraction of the mantle Xe inventory was degassed into the atmosphere within a hundred million years of Earth's history (Allegre et al. 1987; Kunz et al. 1998; Moreira 2013; Mukhopadhyay 2012), recent work also indicates that subduction is regassing the mantle Xe content (e.g., Holland and Ballentine 2006; Kendrick et al. 2011; Parai and Mukhopadhyay 2015).

A particularly vexing problem associated with terrestrial Xe research is the issue of missing Xe on Earth. Briefly, while Xe, along with the heavier noble gases, is believed to have a chondritic affinity, Xe is depleted in the Earth more than Ar and Kr when compared to chondritic abundances. The depletion was recognized since the 1960s (e.g., Canalas et al. 1968) and is particularly difficult to understand, as any loss processes on Earth should preferentially deplete lighter noble gases compared to Xe. This is known as the missing Xe paradox. Two significant advances in addressing the missing Xe paradox have been made recently. The first is the discovery that the initial atmospheric composition that was mass fractionated to produce the modern atmosphere of the Earth can be successfully explained by a mix of cometary xenon measured in the short-period comet 67P/Churyumov-Gerasimenko (Marty et al. 2017) and chondritic/solar Xe (Marty 2012; Marty et al. 2017). The second discovery was made by Pujol et al. in 2011 who realized from measurements of trapped gases in 3.5–3.0 Ga barites and cherts that, in preference to the other noble gases, Xe was being lost from the atmosphere during the Hadean and Archean. While the exact mechanism driving Xe loss is unclear, the process might be related to the fact that Xe is the easiest of the noble gases to ionize with solar UV and, importantly, is the only noble gas that is more easily ionized than hydrogen. Therefore, Xe can be ionized by UV photons, whereas Kr and lighter noble gases would be more difficult to ionize, as hydrogen would absorb the photons that could ionize the lighter noble gases (Zahnle et al. 2007, 2015). Subsequently, the Xe^+ ions may get dragged away by escaping hydrogen ions along open magnetic field lines (Zahnle 2015). The missing Xe problem, which still requires a quantitative understanding, is a key component to explaining the origin and subsequent evolution of Earth's atmosphere.

Summary

Xenon is a member of the group VIIIA gases, usually referred to as noble or rare gases. While Xe is usually considered to be an inert gas, it does chemically interact with other elements. Although it primarily interacts with matter via physi- and chemisorption, it also participates in chemical bonds, and a number of Xe compounds have been synthesized with Xe oxidation states of +2 to +8. Xe is particularly effectively as an anesthetic given its low blood toxicity and is potentially a new way of treating PTSD. Xe has been used in a number of applications in earth science research including paleotemperature estimates from studies of groundwater and speleothem, air-sea gas exchange, mantle degassing, loss of terrestrial volatiles, and the origin and evolution of the atmosphere. Two significant recent advances in the study of Xe in earth sciences have been the realization that comets must have contributed Xe to Earth's early atmosphere and the missing Xe paradox was not a result of Earth's accretion, but rather due to protracted Xe loss from the atmosphere during the Hadean and Archean.

Cross-References

- ▶ Atmospheric Evolution
- ▶ Chondrites
- ▶ Noble Gases
- ▶ Paleotemperatures
- ▶ Xenon Isotopes

References

Aeschbach-Hertig W, Solomon DK (2013) Noble gas thermometry in groundwater hydrology. In: Burnard P (ed) The Noble gases as geochemical tracers. Springer, Springer-Verlag Berlin Heidelberg, pp 81–122

Allègre CJ, Staudacher T, Sarda P (1987) Rare-gas systematics -formation of the atmosphere, evolution and structure of the Earth's mantle. Earth Planet Sci Lett 81:127–150

Broadhurst CL, Drake MJ, Hagee BE, Bernatowicz TJ (1992) Solubility and partitioning of ne, Ar, Kr and Xe in minerals and synthetic basaltic melts. Geochim Cosmochim Acta 56:709–723

Brooker RA, Du Z, Blundy J, Kelley SP, Allan NL, Wood B, Chamorro EM, Wartho J-A, Purton JA (2003) The 'zero charge' partitioning behaviour of noble gases during mantle melting. Nature 423:738–741

Canalas R, Alexander EC Jr, Manuel OK (1968) Terrestrial abundance of noble gases. J Geophys Res 73:3331–3334

Franks NP, Dickinson R, de Sousa SLM, Hall AC, Lieb WR (1998) How does xenon produce anaesthesia? Nature 396:324–324

Goto T, Saito H, Shinkai M, Nakata Y, Ichinose F, Morita S (1997) Xenon provides faster emergence from anesthesia than does nitrous oxide–sevoflurane or nitrous oxide–isoflurane. Anesthesiology 86:1273–1278

Hamme RC, Severinghaus JP (2007) Trace gas disequilibria during deep-water formation. Deep-Sea Research Part I-Oceanographic Research Papers. 54. https://doi.org/10.1016/j.dsr.2007.03.008

Heber VS, Brooker RA, Kelley SP, Wood BJ (2007) Crystal–melt partitioning of noble gases (helium, neon, argon, krypton, and xenon) for olivine and clinopyroxene. Geochim Cosmochim Acta 71:1041–1061
Hetherington CJ, Villa IM (2007) Barium silicates of the Berisal complex, Switzerland: a study in geochronology and rare-gas release systematics. Geochim Cosmochim Acta 71:3336–3347
Hiyagon H, Ozima M (1986) Partitioning of noble gases between olivine and basalt melt. Geochim Cosmochim Acta 50: 2045–2057
Holland G, Ballentine CJ (2006) Seawater subduction controls the heavy noble gas composition of the mantle. Nature 441:186–191
Jephcoat AP (1998) Rare-gas solids in the Earth's deep interior. Nature 393:355–358
Kendrick MA, Scambelluri M, Honda M, Phillips D (2011) High abundances of noble gas and chlorine delivered to the mantle by serpentinite subduction. Nat Geosci 4:807–812
Kluge T, Marx T, Scholz D, Niggemann S, Mangini A, Aeschbach-Hertig W (2008) A new tool for palaeoclimate reconstruction: noble gas temperatures from fluid inclusions in speleothems. Earth Planet Sci Lett 269:407–414
Kunz J, Staudacher T, Allegre CJ (1998) Plutonium-fission xenon found in Earth's mantle. Science 280:877–880
Loose B, Jenkins WJ (2014) The five stable noble gases are sensitive unambiguous tracers of glacial melt water. Geophys Res Lett 41. https://doi.org/10.1002/2013GL058804
Lunine JI, Stevenson DJ (1985) Thermodynamics of clathrate hydrate at low and high pressures with application to the outer solar system. Astrophys J Suppl Ser 58:493–531
Lux G (1987) The behaviour of noble gases in silicate liquids: solution, diffusion, bubbles and surface effects, with applications to natural samples. Geochim Cosmochim Acta 51:1549–1560
Marty B (2012) The origins and concentrations of water, carbon, nitrogen and noble gases on earth. Earth Planet Sci Lett 313:56–66
Marty B et al (2017) Xenon isotopes in 67P/Churyumov-Gerasimenko show that comets contributed to Earth's atmosphere. Science 356:1069–1072
Meloni EG, Gillis TE, Manoukian J, Kaufman MJ (2014) Xenon impairs reconsolidation of fear memories in a rat model of post-traumatic stress disorder (PTSD). PLoS ONE 9:e106189. https://doi.org/10.1371/journal.pone.0106189
Moreira M (2013) Noble gas constraints on the origin and evolution of the Earth's volatiles. Geochemical perspectives 2:229–403
Mousis O, Lunine JI, Mandt KE, Schindhelm E, Weaver HA, Stern SA, Waite JH, Gladstone R, Moudens A (2013) On the possible noble gas deficiency of Pluto's atmosphere. Icarus 225:856–861
Mukhopadhyay S (2012) Early differentiation and volatile accretion recorded in deep-mantle neon and xenon. Nature 486:101–104
Ozima M, Podosek FA (2002) Noble gas geochemistry, 2nd edn. Cambridge University Press, Cambridge
Parai R, Mukhopadhyay S (2015) The evolution of MORB and plume mantle volatile budgets: constraints from fission Xe isotopes in southwest Indian ridge basalts. Geochem Geophys Geosyst 16:719–735
Pujol M, Marty B, Burgess R (2011) Chondritic-like xenon trapped in Archean rocks: a possible signature of the ancient atmosphere. Earth Planet Sci Lett 308:298–306
Roselieb K, Rammensee W, Butter H, Rosenhauer M (1992) Solubility and diffusion of noble gases in vitreous albite. Chem Geol 96:241–266
Roselieb K, Rammensee W, Butter H, Rosenhauer M (1995) Diffusion of noble gases in melts of the system SiO_2-$NaAlSi_2O_8$. Chem Geol 120:1–13
Scheidegger Y, Baur H, Brennwald MS, Fleitmann D, Wieler R, Kipfer R (2010) Accurate analysis of noble gas concentrations in small water samples and its application to fluid inclusions in stalagmites. Chem Geol 272:31–39
Scheidegger Y, Brennwald MS, Fleitmann D, Jeannin P-Y, Wieler R, Kipfer R (2011) Determination of Holocene cave temperatures from Kr and Xe concentrations in stalagmite fluid inclusions. Chem Geol 288:61–66
Shcheka SS, Keppler H (2012) The origin of the terrestrial noble-gas signature. Nature 490:531–534
Shibata T, Takahashi E, Matsuda J (1996) Noble gas solubility in binary CaO-SiO2 system. Geophys Res Lett 23:3139–3142
Shibata T, Takahashi E, Matsuda J (1998) Solubility of neon, argon, krypton and xenon in binary and ternary silicate systems: a new view of noble gas solubility. Geochim Cosmochim Acta 62: 1241–1253
Stanley RHR, Jenkins WJ, Lott DE, Doney SC (2009) Noble gas constraints on air-sea gas exchange and bubble fluxes. J Geophys Res-Oceans 114(C11020). https://doi.org/10.1029/2009JC005396
Swindle TD, Thomas C, Mousis O, Lunine JI, Picaud S (2009) Incorporation of argon, krypton and xenon into clathrates on Mars. Icarus 203:66–70
Thomas C, Mousis O, Ballenegger V, Picaud S (2007) Clathrate hydrates as a sink of noble gases in Titan's atmosphere. Astron Astrophys 474: L17–L20
Vogel N, Brennwald MS, Fleitann D, Wieler R, Maden C, Susli A, Kipfer R (2013) A combined vacuum crushing and sieving (CVCS) system designed to determine noble gas paleotemperatures from stalagmite samples. Geochem Geophys Geosyst 14. https://doi.org/10.1002/ggge.20164
Zahnle KJ (2015) Xenon fractionation and Archean hydrogen escape. 46th Lunar and Planetary Science Conference, Abstract#1549
Zahnle KJ, Arndt N, Cockell C, Halliday AN, Nesbit E, Selsis F, Sleep NH (2007) Emergence of a habitable planet. Space Sci Rev 129:35–78

Xenon Isotopes

Sujoy Mukhopadhyay
Department of Earth and Planetary Sciences, University of California Davis, Davis, CA, USA

Definition

Xenon is an inert gas and belongs to group VIIIA of the periodic table. Xenon has nine stable isotopes, second only to tin. The nine xenon isotopes are ^{124}Xe, ^{126}Xe, ^{128}Xe, ^{129}Xe, ^{130}Xe, ^{131}Xe, ^{132}Xe, ^{134}Xe, and ^{136}Xe. Of these isotopes, ^{124,126,128,130}Xe are nonradiogenic, ^{129}Xe is radiogenic and ^{131,132,134,136}Xe are fissiogenic. The relative abundances of these isotopes in the atmosphere are 0.095%, 0.089%, 1.910%, 26.4%, 4.017%, 21.23%, 26.91%, 10.44%, and 8.86%, respectively. The isotopic abundances in other reservoirs, such as crust, mantle, or groundwater, differ from the atmospheric abundances due to fractionation of I-Xe, U-Xe, and Pu-Xe and subsequent radioactive decay. This contribution will focus on the Xe isotopes in the solid Earth and atmosphere.

Introduction

Measurements of xenon isotopes in mantle-derived basalts provide information on processes as varied as volatile accretion, mantle degassing history, styles of mantle convection, and volatile exchange between the deep Earth and the atmosphere. The nonradiogenic isotopes ^{124}Xe, ^{126}Xe, ^{128}Xe, and ^{130}Xe are primordial with terrestrial inventories established by the balance between volatile delivery during accretion and atmospheric loss processes. The radiogenic Xe isotopes can be divided into two categories: ^{129}Xe produced by β-decay of ^{129}I and ^{131,132,134,136}Xe produced by fission from extinct ^{244}Pu and extant ^{238}U. Radiogenic ^{129}Xe was produced only during the first ~90 Myr of solar system history by β-decay of the extinct nuclide, ^{129}I ($t_{1/2}$ = 15.7 Ma). ^{129}I was the first extinct radionuclide detected in our solar system through the measurements of ^{129}Xe in meteorites (Reynolds 1963). Fissiogenic ^{131}Xe, ^{132}Xe, ^{134}Xe, and ^{136}Xe were produced from extinct short-lived ^{244}Pu ($t_{1/2}$ = 80.0 Myr) for the first ~500 million years of solar system history and continues to be produced from extant ^{238}U ($t_{1/2}$ = 4.468 Gyr). Pu and U fission, however, produce the fissiogenic Xe isotopes in distinct, characteristic proportions. Xe isotopic measurements in mantle-derived samples can, therefore, be used to deconvolve the fraction of Xe derived from Pu-fission versus U-fission. Thus, the radiogenic Xe isotopic compositions can be used to investigate the evolution of mantle volatile budgets on a variety of timescales. Here, I first provide some background on how Xe isotopes have been used to obtain information on accretion and mantle degassing timescales, and then focus on four major discoveries associated with Xe isotopes during the past decade: (1) regassing of mantle xenon, (2) preservation of heterogeneities created during Earth's accretion, (3) heterogeneous volatile accretion, and (4) loss of Xe from the atmosphere during the Hadean and Archean.

Background and Prior Work

Decay of ^{129}I on the Earth would produce ^{129}Xe, and I-Xe fractionation would induce differences in the ratio of radiogenic ^{129}Xe to nonradiogenic ^{130}Xe (^{129}Xe/^{130}Xe). Variations in ^{129}Xe/^{130}Xe ratios between different reservoirs can only be generated within the first 90 million years of solar system history. The first excess of ^{129}Xe in the solid Earth, relative to Earth's atmosphere, was detected by Butler et al. (1963) in Harding County CO_2 well gas and attributed to ^{129}I decay in the early Earth. Staudacher and Allegre (1982) measured excesses in ^{129}Xe in mid-ocean ridge basalts (MORBs) and modeled the measured ^{129}Xe excess in the Earth's mantle to suggest that Earth formed 50–75 Myrs after the formation of meteorites. In ocean island basalts (OIBs), derived from partial melting of mantle plumes, ^{129}Xe excesses were first detected in Hawaiian xenoliths (Hennecke and Manuel 1975; Kaneoka and Takaoka 1978) and later in Samoa (Poreda and Farley 1992), Iceland (Harrison et al. 1999; Trieloff et al. 2000), Shona, and Discovery seamounts (Sarda et al. 2000). These measured excesses were attributed to both early degassing as well as mixing between upper mantle Xe and atmospheric Xe (e.g., Poreda and Farley 1992; Trieloff et al. 2000).

The ^{244}Pu- and ^{238}U-produced fission isotopes of Xe (^{131,132,134,136}Xe) provide information about mantle degassing rates, particularly during the early history of the Earth (e.g., Allegre et al. 1987; Coltice et al. 2009; Kunz et al. 1998; Ozima et al. 1985; Staudacher and Allegre 1982; Yokochi and Marty 2005). ^{244}Pu and ^{238}U produce the four fission isotopes in different proportions and fission Xe yields from Pu are significantly larger than from U. A reservoir that remains completely closed to volatile loss over Earth's history has a $^{136}Xe_{Pu244}$*/$^{136}Xe_{U238}$* of ~27, where "*" refers to fissiogenic Xe (Azbel and Tolstikhin 1990; Tolstikhin et al. 2006; Tolstikhin and O'Nions 1996). ^{244}Pu became extinct at ~4 Ga. Thus, reservoirs that underwent extensive degassing over the past 4 Gyrs have lost a significant fraction of the Pu-produced fission Xe and consequently have a large proportion of ^{238}U-derived fission Xe. Importantly, $^{136}Xe_{Pu244}$*/$^{136}Xe_{U238}$* in degassed reservoirs is $\ll$27. Hence, if the Pu and U yields of the different Xe isotopes are known precisely, measurements of Xe isotopes in mantle-derived rocks can yield the fraction of Xe derived from ^{244}Pu versus ^{238}U, which in turn constrains the timing and degree of outgassing of the mantle reservoir.

The terrestrial fission Xe excesses relative to air were first detected by Boulos and Manuel (1972) in the Harding County well gases. They noted the measured compositions were consistent with a ~1:3 mixture of Pu-fission Xe and U-fission Xe. However, due to the large uncertainties, the Xe isotopic measurements by Boulos and Manuel (1972) were also consistent with pure Pu- fission or pure U-fission. Subsequent measurements with increased precision (Phinney et al. 1978; Caffee et al. 1999) put a limit of 20% for Pu-derived fission Xe in the well gases. Kunz et al. (1998) presented more precise isotopic measurements to constrain 32 ± 10% of the fission Xe to be ^{244}Pu-derived assuming that the terrestrial mantle had the same initial composition as atmospheric Xe. Assuming an initial solar composition of the mantle, Pepin and Porcelli (2006) assigned 60% of the fission Xe to ^{244}Pu. The ratio of Pu to U-derived Xe in all of these estimates suggests extensive degassing of the Earth's mantle.

Combining the I-Xe and Pu-Xe system is a particularly powerful approach to understanding volatile accretion timescales, the timing of mantle degassing and the formation of the atmosphere. The I-Pu-Xe system is interrogated from the measured ^{129}Xe/^{136}Xe ratio and using the fraction of ^{136}Xe derived from ^{244}Pu (calculated from measurements of

^{131,132,134,136}Xe) to compute the ^{129}Xe*/^{136}Xe$_{Pu244}$* ratio. Wetherill (1975) used the I-Pu-Xe and data from the Harding County well gases (Butler et al. 1963; Boulos and Manuel 1972) to estimate that the formation interval of the Earth was 127 Myr after the formation of the ordinary chondrite Bjurböle. Based on MORBs measurements, Staudacher and Allegre (1982) used the I-Pu-Xe system to compute a formation interval of 40–60 Myrs for the Earth and a mean age of 70–80 Myrs for the Earth's atmosphere. These estimates were largely confirmed through more precise measurements by Kunz et al. (1998).

Pepin and Phinney (1976) combined the I-Pu-Xe system to formulate a closure age (T) of a reservoir given by:

$$T = \frac{1}{\lambda_{244} - \lambda_{238}} \times \ln\left[\frac{\left(^{129}\mathrm{Xe} * / ^{136}\mathrm{Xe}_{Pu244*}\right)\left(^{238}\mathrm{U}/^{127}\mathrm{I}\right)_o \left(^{244}\mathrm{Pu}/^{238}\mathrm{U}\right)_o {}^{136}\mathrm{Y}_{244}}{\left(^{129}\mathrm{I}/^{127}\mathrm{I}\right)_o}\right] \ldots \quad (1)$$

where λ is the decay constant, $^{136}Y_{244}$ is the fission yield of ^{136}Xe from Pu fission, ^{129}Xe* is the radiogenic ^{129}Xe produced from ^{129}I decay, ^{136}Xe$_{Pu244}$* is the fissiogenic ^{136}Xe produced from ^{244}Pu fission and the subscript "o" refers to the initial value. The formulation yields the age when a reservoir (e.g., solid Earth, Earth atmosphere) transitions from quantitatively Xe loss to closed system retention of Xe. Using this formulation, Pepin and Phinney (1976) calculated an atmospheric closure age of ~80 Myrs after the start of the solar system, while Pepin and Porcelli (2006) calculated closure ages of ~100 Myr for both the atmosphere and the MORB source.

The ratio of ^{129}Xe*/^{136}Xe$_{Pu244}$* also provides insights into the relation between mantle Xe and atmospheric Xe. For example, the ^{129}Xe*/^{136}Xe$_{Pu244}$* ratio in the MORB source suggests that atmospheric Xe must be from a late accretionary source and not degassed from the mantle (Caffee et al. 1999; Marty 1989; Ozima et al. 1985; Yokochi and Marty 2005). The argument follows from the fact that as the half-life of ^{129}I is significantly shorter than the half-life of ^{244}Pu, at the time of atmosphere formation, a larger proportion of ^{244}Pu would not have undergone radioactive decay compared to ^{129}I. Consequently, if the atmosphere were derived from degassing of the MORB mantle, the ^{129}Xe*/^{136}Xe$_{Pu244}$* ratio in the MORB mantle source must have evolved to a lower value than the atmosphere. However, the MORB mantle has a higher ratio than the atmosphere. Consequently, Xe in the MORB source is not consistent with the composition of a reservoir that is residual to outgassing of Xe into the atmospheric. This argument was recently challenged (Boehnke et al. 2015) on the ground that ^{129}Xe*/^{136}Xe$_{Pu244}$* in MORBs may have been overestimated due to improper accounting of uncertainties in Pu fission yields when computing the value of ^{136}Xe$_{Pu244}$*.

Regassing of Mantle Xenon

Early models on the noble gas evolution of the mantle required subduction zones to be a barrier towards the transport of atmospheric noble gases into the mantle (e.g., Staudacher and Allegre 1988). Thus, while volatile elements like H, C, N, and S were supposed to be recycled back into the mantle, noble gases were supposed to have a unidirectional transport out of the mantle. As a result, differences in MORB and OIB Xe isotopic compositions were modeled to indicate differences in the degree of mantle outgassing. That is, variations in Xe isotopes in the mantle could result only from I-Xe fractionation or Pu-U-Xe fractionations associated with partial melting or magmatic degassing. In these models, the plume source was thought to be sampling a more primitive less degassed mantle source compared to the MORB source. In mantle steady state models (Porcelli and Wasserburg 1995), recycling of atmospheric Xe could occur into the MORB source, but depended on an assumed composition of the OIB source.

The subduction zone barrier was challenged in 2006 by Holland and Ballentine based on the full suite of noble gas measurements (He, Ne, Ar, Kr, and Xe) in CO_2 gases from the Bravo Dome gas field in New Mexico, USA. Holland and Ballentine (2006) demonstrated that the relative abundances of Ar, Kr, and Xe in the CO_2 gas was similar to that of the gas-rich "popping-rock" sample from the North Atlantic mid-ocean ridge (Moreira et al. 1998), and the relative abundance patterns in both samples were similar to that of seawater. This observation suggested the subduction of noble gases dissolved in seawater into the convective mantle. The non-radiogenic Xe in the mantle was modeled as a mixture of 80% recycled atmospheric Xe and 20% primordial Xe. The recycling of Xe back into the mantle is an important paradigm shift since it introduces a fundamentally different way to interpret variations in observed Xe isotopic ratios. For example, differences in ^{129}Xe/^{130}Xe ratios in mantle-derived samples do not need to arise from preservation of mantle domains with difference melt and gas extraction histories. Instead, ^{129}Xe/^{130}Xe variations could arise from differences in the amount of recycled atmospheric Xe in the mantle. Holland and Ballentine (2006) suggested that the Xe isotopic composition of OIBs were closer to atmospheric values compared to MORBs because of preferential recycling of atmospheric Xe dissolved in seawater into the OIB source.

Subsequent work by Sumino et al. (2010) and Kendrick et al. (2011) in exhumed metamorphic terranes at subduction zones confirm deep recycling of Xe. At the Higashi-akaishi peridotite body in the Sanbagawa metamorphic belt in Japan, Sumino et al. (2010) found fluid inclusion trapped in olivine crystals at a depth of 100 km. Xenon and the other noble gases in these fluid inclusions have a striking resemblance to those in marine pore fluids. Sumino et al. (2010) suggested that the marine fluids were liberated from either sediments, or the

oceanic crust, or from lithospheric mantle hydrated at the outer rise of the subduction zone. These fluids were subsequently trapped in the mantle wedge peridotite and exhumed as the Higashi-akaishi peridotite body. While the observation directly links recycling of atmospheric-derived Xe down to depths of 100 km, it is likely that the atmospheric component is being subducted deeper as not all of the subducted water is liberated and returned to the surface at subduction zones (Van Keken et al. 2011; Parai and Mukhopadhyay 2012).

Kendrick et al. (2011) further investigated the subduction of atmospheric noble gases, including Xe, through measurements of halogens and noble gases in antigorite schists from Ligurian Alps, Italy, and in olivine–enstatite rocks from Betic Cordillera, Spain. These rock assemblages sample increasingly higher pressure-temperature environments in subduction zones, reflecting the progressive breakdown of serpentine (antigorite schists) to produce olivine and enstatite residues. Kendrick et al. (2011) observed fluid inclusions in olivine–enstatite veins in the antigorite schists and interpreted them to reflect fluids generated from serpentine breakdown. These fluid inclusions had $^{130}Xe/^{36}Ar$ ratios similar to sea water, or seawater–marine sediment mixtures, although the ^{130}Xe concentrations in the fluid inclusions were higher than in seawater. Fluid inclusions trapped in the olivine–enstatite rocks were interpreted as higher pressure fluids generated by the final breakdown of serpentine, and these inclusions had $^{130}Xe/^{36}Ar$ ratios that were similar to values observed in the OIBs. Overall, the range of $^{130}Xe/^{36}Ar$ ratios seen in the fluid inclusions is broadly similar to that seen in different mantle reservoirs, with the inclusions having concentrations that are one to three orders of magnitude higher than the mantle concentrations (Kendrick et al. 2011).

While Holland and Ballentine (2006) and Sumino et al. (2010) suggested that the transport of Xe back into the mantle is associated with unbound pore fluids, Kendrick et al. (2011, 2013) argued that seawater-derived noble gases are directly incorporated into hydrous phases, like serpentine, during hydration of the lithospheric mantle. Breakdown of serpentine in subduction zones releases fluids carrying the seawater-derived noble gases, which are subsequently trapped in the breakdown products of olivine–enstatite. These fluid inclusions could be released into the shallow mantle during deformation and recrystallization of the olivine-enstatite rocks associated with downward transport of the plate. Alternatively, the fluids could be incorporated into olivine polymorphs (wadsleyite) and transported into the deep mantle (Kendrick et al. 2011).

The recycling of substantial atmospheric Xe into the mantle was also confirmed using a completely different approach from measurements of MORBs and OIBs that represent a different repository of mantle-derived material than exhumed high pressure-temperature metamorphic rocks (Mukhopadhyay 2012; Parai et al. 2012; Parai and Mukhopadhyay 2015; Tucker et al. 2012; Pető et al. 2013). From combined $^{20}Ne/^{22}Ne$-$^{40}Ar/^{36}Ar$-$^{129}Xe/^{132}Xe$ isotope mixing systematics, these authors corrected for shallow-level air contamination to determine the mantle Xe isotopic compositions. The mantle Xe isotopic compositions were then modeled as a mixture of primordial Xe, recycled atmospheric Xe, radiogenic (^{129}Xe) and fissiogenic Xe ($^{131,132,134,136}Xe$) using a least squares fitting routine. For both MORBs and OIBs, between 80% and 90% of the Xe budget was determined to be atmospheric Xe returned to the mantle via subduction. Thus, numerous lines of evidence suggest that the Xe budget of the mantle is dominated by recycled atmospheric Xe. Consequently, Xe transport into the mantle has been regassing the mantle. Furthermore, the recycling of Xe appears to be tied to recycling of water itself (Holland and Ballentine 2006; Sumino et al. 2010; Kendrick et al. 2011, 2013).

Preservation of Heterogeneities Created During Terrestrial Accretion

While differences in measured Xe isotopic composition between MORBs and OIBs have long been recognized (Hennecke and Manuel 1975; Kaneoka and Takaoka 1978; Poreda and Farley 1992; Harrison et al. 1999; Trieloff et al. 2000), the interpretation of the isotopic differences remained unclear until recently. In general, $^{129}Xe/^{130}Xe$ ratios in OIB ratios are lower than MORBs, with the highest values reaching values of 6.8–7.0 compared to MORB values of 7.8–7.9 (Holland and Ballentine 2006; Poreda and Farley 1992; Mukhopadhyay 2012; Moreira et al. 1998; Sarda et al. 2000; Tucker et al. 2012; Parai et al. 2012; Pető et al. 2013; Staudacher and Allegre 1982; Kunz et al. 1998; Trieloff et al. 2002). Since the atmospheric $^{129}Xe/^{130}Xe$ ratio (6.49) is lower than the OIB values, the differences between OIB and MORB lavas could result from a higher degree of syn- to posteruptive atmospheric contamination of OIB lavas, mixing between subducted atmospheric Xe and MORB Xe (Holland and Ballentine 2006; Poreda and Farley 1992; Trieloff and Kunz 2005), or different I/Xe ratios for the OIB and MORB sources (Allegre et al. 1987; Poreda and Farley 1992).

High precision Xe isotopic data from an Icelandic basalt, which samples the OIB source, demonstrated that the differences in $^{129}Xe/^{130}Xe$ ratios between MORBs and OIBs must result from different I/Xe ratios for the two sources (Mukhopadhyay 2012; Fig. 1). The Iceland and MORB sources, along with the atmospheric composition, are plotted in $^{129}Xe/^{130}Xe$-$^{3}He/^{130}Xe$ space (Fig. 1). Two-component mixing in this space is linear. Since the MORB and Iceland source compositions are not colinear with the atmospheric composition, adding subducted air, or a shallow-level air contaminant to a MORB source cannot produce the lower

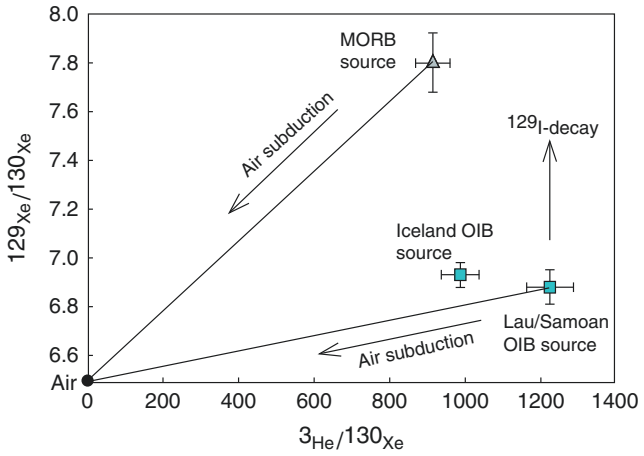

Xenon Isotopes, Fig. 1 Correlation of ^{129}Xe, produced from the decay of extinct ^{129}I, with ^{3}He for the MORB and OIB source composition. The MORB source data are from Moreira et al. (1998) while the Iceland and Lau/Samoa source data are from Mukhopadhyay (2012) and Pető et al. (2013), respectively. Two-component mixing in this space is linear and the observations demonstrate that adding recycled atmospheric Xe to the MORB source cannot generate the OIB composition

^{129}Xe/^{130}Xe ratios in OIBs. Consequently, the OIB sample from Iceland must have evolved with a different I/Xe ratio than the MORB source, and the two mantle sources must have differentiated by 4.45 Ga. Subsequent mixing between the MORB and OIB reservoirs must also have been limited, otherwise the differences in Xe isotopic composition would have been destroyed (Mukhopadhyay 2012). These first order conclusions were confirmed by Pető et al. (2013) from the northern Lau Basin, which samples the Samoan OIB source, (Fig. 1) and by Caracausi et al. (2016) from magmatic gas samples derived from the deep mantle in the Eifel volcanic area of Germany.

The observation that differences in isotopic composition produced by extinct radionuclides persist within the mantle to the present day has several important implications for understanding Earth accretion, mantle evolution, and volatile fluxes between Earth reservoirs. The lifetime of ^{129}I is concurrent with Earth's accretional timescale (e.g., Jacobsen et al. 2014). Therefore, the differences between OIB and MORB ^{129}Xe/^{130}Xe were setup during Earth's accretion. The preservation of heterogeneities created during Earth's accretion then requires that the Earth's mantle was not chemically homogenized by giant impacts and magma oceans. Likewise, the preservation of ancient heterogeneities indicate that differences between the OIB and MORB sources cannot be generated solely through processes associated with plate subduction, mantle convection or crust-mantle differentiation occurring during the past 4.4 Gyrs of Earth's history.

Differences in noble gas compositions between MORBs and OIBs have often been interpreted in the context of steady-state mantle models that require primordial noble gases in the volatile depleted MORB source to be derived from a primitive volatile-rich OIB source (e.g., Porcelli and Wasserburg 1995; Tolstikhin and Hoffmann 2005). Admixtures of the OIB-derived primordial noble gases, radiogenic noble gases produced in the MORB source, and subducted atmospheric noble gases lead to the noble gas isotopic compositions observed in MORBs. However, the steady-state model is fundamentally at odds with the observed Xe isotopic variations between MORBs and OIBs. This is because the OIB source cannot supply Xe to the MORB source unless augmented with ^{129}I-derived ^{129}Xe (Fig. 1). However, ^{129}I went extinct at 4.45 Ga. As a result, Xe and other noble gases in MORBs must primarily be indigenous to the MORB source. Consequently, the present day budget of primordial noble gases in the MORB source was set by the initial budget after the Moon-forming giant impact, 4.5 Ga of outgassing via mantle convection, and regassing of the mantle associated with recycling. Regassing is, however, not important for all the noble gases, but relevant for Ar, Kr, and Xe (e.g., Holland and Ballentine 2006; Kendrick et al. 2011, 2013).

Heterogeneous Volatile Accretion

The isotopes of Xe provide powerful constraints on Earth's accretion, particularly on the history of volatile delivery. The constraints are provided by the parent radionuclides, ^{129}I and ^{244}P. While I is a volatile element, Pu is a refractory lithophile element. Hence, the ratio of I/Pu in different reservoirs can be used to trace volatile accretion rate. The I/Pu ratio of the Earth can be interrogated through the ^{129}X*/136Xe$_{Pu244}$* ratio (e.g., Mukhopadhyay 2012). Traditionally, the ^{129}Xe*/^{136}Xe$_{Pu244}$* ratio has been used to constrain the closure time for volatile loss of a mantle reservoir (Eq. 1; Pepin 1991; Pepin and Porcelli 2006; Avice and Marty 2014). Since ^{129}I has a shorter half-life than ^{244}Pu, for reservoirs with the same initial I/Pu ratio, higher ^{129}Xe*/^{136}Xe$_{Pu244}$* ratios are indicative of earlier closure to volatile loss.

With the advent of better mass spectrometric techniques, more precise measurements of Xe isotopic ratios were made in mantle-derived material. These measurements allowed the deconvolution of Xe into radiogenic (^{129}Xe), plutogenic, uranogenic, recycled atmospheric Xe and primordial Xe, which indicated lower ^{129}Xe*/^{136}Xe$_{Pu244}$* ratios for the OIB source and higher values for the MORB source (Mukhopadhyay 2012; Tucker et al. 2012; Pető et al. 2013; Parai and Mukhopadhyay 2015; Caracausi et al. 2016). Depending on whether the primordial Xe component in the mantle was solar or chondritic, the ^{129}Xe*/^{136}Xe$_{Pu244}$* of the OIB source mantle was determined to vary between 2.1 ± 1.6 and $2.9^{+0.4}_{-0.1}$, with the corresponding range for MORBs being $7.8^{+3.1}_{-1.8}$ and $9.4^{+5.5}_{-2.7}$ (Mukhopadhyay 2012; Pető et al. 2013; Parai and Mukhopadhyay 2015). The discovery that the

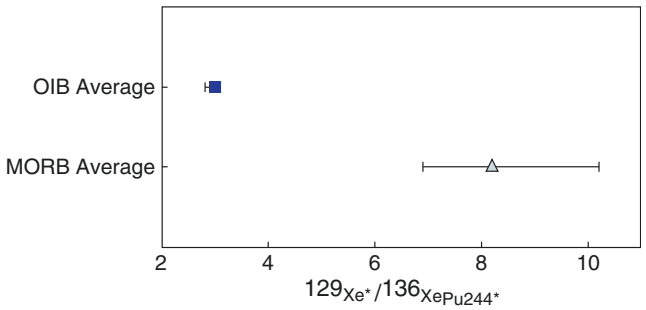

Xenon Isotopes, Fig. 2 Ratios of I- to Pu-derived Xe in OIB and MORB sources assuming a chondritic starting composition for Xe isotopes in the mantle (Caracausi et al. 2016). The OIB average was compiled from data presented in Mukhopadhyay (2012), Pető et al. (2013), and Caracausi et al. (2016). The MORB average is from Parai and Mukhopadhyay (2015) based on data presented by Tucker et al. (2012) and Parai and Mukhopadhyay (2015)

primordial Xe component in the mantle was chondritic (Caracausi et al. 2016), enabled the $^{129}Xe^*/^{136}Xe_{Pu244}^*$ ratio to be further restricted to $3^{+0.1}_{-0.2}$ for OIBs and $8.2^{+2.0}_{-1.3}$ for MORBs (Fig. 2; Schlichting and Mukhopadhyay 2017).

If the whole mantle had a homogenous I/Pu ratio, then based on Eq. (1), the higher $^{129}Xe^*/^{136}Xe_{Pu244}^*$ ratio in the MORB source would imply that the shallower MORB mantle source became closed to significant volatile loss earlier than the deeper OIB mantle source; i.e., the shallow stopped losing volatiles while volatile loss in the deeper mantle kept ongoing. Such a scenario is physically unrealistic as mantle outgassing and volatile loss occurs at the Earth's surface. A simpler and more plausible interpretation of the lower $^{129}Xe^*/^{136}Xe_{Pu244}^*$ ratio in OIBs is that it reflects a lower initial I/Pu ratio for the deeper OIB source compared to the shallower MORB source. Since I is a highly volatile element, the $^{129}Xe^*/^{136}Xe_{Pu244}^*$ provides direct confirmation of heterogeneous volatile accretion with the initial phase of Earth's accretion being volatile poor compared to the later stages of accretion. Importantly, because the signature of varying volatile accretion rate associated with Earth's formation is still preserved in the present day mantle, magma oceans and giant impacts that characterized Earth's growth from an embryo to its current size (Agnor et al. 1999; Jacobsen et al. 2014; Melosh 1990; Tonks and Melosh 1993; Tucker and Mukhopadhyay 2014) did not ever homogenize the planet; chemical signatures acquired during the embryo stage are still present in the deepest part of the Earth's mantle.

Loss of Xe from the Atmosphere During the Hadean and Archean

Atmospheric Xe is mass fractionated and enriched in the heavier isotopes by ~4%/amu compared to both solar and chondritic Xe. The mass fractionation of Xe is usually taken as a telltale sign of atmospheric Xe loss from the Earth, or in the precursor bodies that accreted to form the Earth (Pepin 1991, 2000; Pepin and Porcelli 2002; Zahnle et al. 1990a, b). The magnitude of the Xe mass fractionation is, however, quite puzzling as the isotopic composition of Kr is mass fractionated from solar by only ~0.4%/amu. A second puzzling observation with atmospheric Xe is that simple mass dependent fractionation of solar or chondritic xenon cannot produce the observed isotopic abundances in the atmosphere; the mass fractionation produces an overabundance of the heaviest isotopes ($^{134,136}Xe$) without even adding any Pu- or U-derived fission Xe that would have been produced on the Earth.

Both of these puzzling aspects of terrestrial atmospheric Xe have been written about extensively (e.g., Pepin 1991, 1992, 2000; Pepin and Porcelli 2002, 2006) and only a brief summary is given below. To solve the initial atmospheric composition, nebular Xe was supposed to have the composition of U-Xe (Pepin 1991), a mathematically constructed composition that when mass fractionated, and added to Pu-derived fission Xe, yields the atmospheric composition. While the existence of U-Xe has been long speculated, only recently has the progenitor of U-Xe been potentially identified in the comet ^{67}P/Churyumov–Gerasimenko (Marty et al. 2017). Analysis of the Xe isotopes in the coma of the comet by the Rosetta Orbiter Spectrometer show significant deficits in heavy Xe isotopes, similar to that in U-Xe. These measurements suggest that the Earth's atmosphere could be made of mixture of 22 ± 5% cometary Xe with chondritic/solar Xe (Marty et al. 2017).

The Xe isotopic fractionation observed in the present day atmosphere was modeled to result from loss of a primary solar nebular atmosphere associated with hydrodynamic escape during Earth's accretion (e.g., Pepin 1991). Hydrodynamic escape of the atmosphere would mass fractionate the light gases more than the heavier gases, leading to a higher degree of mass fractionation for Kr isotopes compared to Xe isotopes. The lower extent of mass fractionation for Kr isotopes is achieved by outgassing of mantle Kr enriched in the lighter isotopes. However, recent work indicates that mantle Kr is enriched in *heavier* isotopes compared to the atmosphere (Holland et al. 2009). Therefore, hydrodynamic escape of a primary nebular atmosphere followed by mantle outgassing cannot explain the differences in the extent of mass fractionation for Xe and Kr isotopes in the modern atmosphere.

Xenon isotopic measurements in Archean rocks also challenge the notion that Xe mass fractionation was produced by hydrodynamic escape during Earth's accretion. Srinivasan (1976) detected nonradiogenic Xe in a 3.5 Ga Archean barite that was mass fractionated compared to modern day atmosphere. Based on additional measurements in 3.5 Ga barite and 3.0 Ga cherts from the Pilbara craton in Australia, Pujol et al. (2009, 2011) documented an increase in the extent of Xe isotopic fractionation from primordial values towards modern air (Fig. 3). They suggested that this signature of evolving Xe

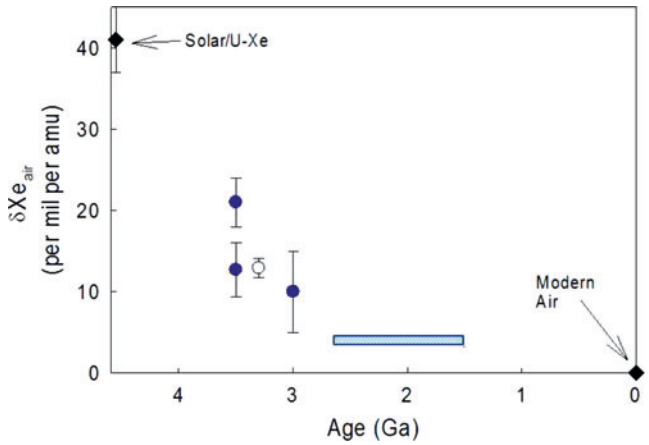

Xenon Isotopes, Fig. 3 Change in atmospheric Xe mass fractionation through time. The solid circles are data from Pujol et al. (2009, 2011) and Srinivasan (1976) from barite and chert samples from the Pilbara craton in Australia. The open circle is from quartz samples from the Barbeton Greenstone belt in South Africa (Avice et al. 2017). The hatched rectangle is based on data from deep fluids in Precambrian rocks from Timmins, Ontario, Canada (Holland et al. 2013)

isotopic fractionation from 3.5 to 3.0 Ga in the rock record was a signature of the evolving atmospheric Xe composition driven by Xe escaping from the atmosphere during the Hadean and Archean. The observation that ancient atmosphere was less fractionated then modern air has now been reproduced in other localities, including macrocrystalline quartz samples from the Barbeton Greenstone belt in South Africa (Avice et al. 2017) and deep fracture fluids in Precambrian basement rocks in Timmins, Ontario, Canada (Holland et al. 2013). These data appear to suggest a monotonic increase in mass fractionation through the Archean into the Proterozoic (Fig. 3; Pujol et al. 2009, 2011; Avice et al. 2017). Thus, significant Xe loss from the atmosphere appears to have been protracted over at least the Hadean and Archean.

A physical process that drives protracted Xe loss has not yet been conclusively identified. A key observation in the Archean rock record is that the Kr isotopes are not mass fractionated compared to modern air (Pujol et al. 2011; Avice et al. 2017). Hence, the process must only drive Xe loss and not loss of the lighter elements. Since the ionization potential of H_2 is higher than Xe but lower than Kr, Zahnle (2015) suggest that solar UV could readily ionize Xe while ionizing Kr would be considerably harder. Moreover, the ionized Kr would be readily lost through reaction with H_2 (Zahnle 2015). The ionized Xe could then get dragged away by H^+ ions along open magnetic field lines. Such a process would require a substantial flux of escaping H_2, which could be derived from oxidation of H_2O. The escaping H_2 would ultimately lead to oxidation of the Earth's surface and the rise of O_2 in the atmosphere (Zahnle 2015). The atmospheric Xe record is thus important, as it might provide the observational basis for substantial hydrogen escape in the Archean.

Summary

Measurements of Xe isotopes were utilized in the first detection of an extinct radionuclide in the solar system, ^{129}I. Xe isotopes have been used to constrain the atmospheric closure age, the formation interval of the Earth, and timescales for mantle degassing. In the past decade, several important advances in Earth Science have been made through studies involving Xe isotopes. These include convincing evidence for the transport of atmospheric noble gases associated with hydrous phases back into the mantle, key new insights into the preservation of deep mantle heterogeneities dating back to Earth's accretion, evidence of heterogeneous volatile accretion with early accretion being volatile poor, mass fractionating Xe loss from the atmosphere during the Hadean and Archean, and the discovery of the progenitor of U-Xe in comets. Looking ahead, key areas for improvement in Xe isotopes studies include measurement precision, techniques to reduce shallow level air-contamination in terrestrial samples, and a better determination of the isotopic composition of Xe generated from Pu versus U fission.

Cross-References

- Atmospheric Evolution
- Chondrites
- Formation and Evolution of the Earth
- Noble gases
- Xenon

References

Agnor CB, Canup R, Levison HF (1999) On the character and consequences of large impacts in the late stage of terrestrial planet formation. Icarus 142:219–237

Allegre CJ, Staudacher T, Sarda P (1987) Rare gas systematics – formation of the atmosphere, evolution and structure of the Earth's mantle. *Earth Planet Sci Lett* 81:127–150

Avice G, Marty B (2014) The iodine–plutonium xenon age of the Moon–Earth system revisited. Phil Trans R Soc A 372:20130260. https://doi.org/10.1098/rsta.2013.0260

Avice G, Marty B, Burgess R (2017) The origin and degassing history of the Earth's atmosphere revealed by Archean xenon. Nat Commun 8:15455. https://doi.org/10.1038/ncomms15455

Azbel IY, Tolstikhin IN (1990) Geodynamics, magmatism, and degassing of the Earth. Geochim Cosmochim Acta 54:139–154

Boehnke P, Caffee MW, Harrison TM (2015) Xenon isotopes in MORB source, not distinctive of early global degassing. Geophys Res Lett 42:4367–4374

Boulos MS, Manuel OK (1972) Extinct radioactive nuclides and production of xenon isotopes in natural gas. Nature 235:150–152

Butler WA, Jeffery PM, Reynolds JH, Wasserburg GJ (1963) Isotopic variations in terrestrial xenon. J Geophys Res 68:3283–3291

Caffee MW, Hudson GB, Velsko C, Huss GR, Alexander EC Jr, Chivas AR (1999) Primordial noble gases from Earth's mantle: identification of a primitive volatile component. Science 285:2115–2118

Caracausi A, Avice G, Burnard PG, Furi E, Marty B (2016) Chondritic xenon in the Earth's mantle. Nature 533:82–85
Coltice N, Marty B, Yokochi R (2009) Xenon isotope constraints on the thermal evolution of the early Earth. Chem Geol 266:4–9
Harrison D, Burnard P, Turner G (1999) Noble gas behaviour and composition in the mantle: constraints from the Iceland Plume. Earth Planet Sci Lett 171(2):199–207
Hennecke EW, Manuel OK (1975) Noble gases in an Hawaiian xenolith. Nature 257:778–780
Holland G, Ballentine CJ (2006) Seawater subduction controls the heavy noble gas composition of the mantle. Nature 441:186–191
Holland G, Cassidy M, Ballentine CJ (2009) Meteorite Kr in Earth's mantle suggests a late accretionary source for the atmosphere. Science 326:1522–1525
Holland G, Sherwood Lollar B, Li L, Lacrampe-Couloume G, Slater GF, Ballentine CJ (2013) Deep fracture fluids isolated in the crust since the Precambrian era. Nature 497:357–360
Jacobsen SA, Morbidelli A, Raymond SN, O'Brien DP, Walsh KJ (2014) Highly siderophile elements in Earth's mantle as a clock for the Moon-forming impact. Nature 508:84–87
Kaneoka I, Takaoka N (1978) Excess ^{129}Xe and high ^{3}He/^{4}He ratios in olivine phenocrysts of Kapuho lava and xenolithic dunites from Hawaii. Earth Planet Sci Lett 39:382–386
Kendrick MA, Scambelluri M, Honda M, Phillips D (2011) High abundances of noble gas and chlorine delivered to the mantle by serpentinite subduction. Nat Geosci 4:807–812
Kendrick MA, Honda M, Pettke T, Scambelluri M, Phillips D, Giuliani A (2013) Subduction zone fluxes of halogens and noble gases in seafloor and forearc serpentinites. Earth Planet Sci Lett 365:86–96
Kunz J, Staudacher T, Allegre CJ (1998) Plutonium-fission xenon found in Earth's mantle. Science 280:877–880
Marty B (1989) Neon and xenon isotopes in MORB: implications for the earth–atmosphere evolution. Earth Planet Sci Lett 94:45–56
Marty B et al (2017) Xenon isotopes in ^{67}P/Churyumov–Gerasimenko show that comets contributed to Earth's atmosphere. Science 356:1069–1072
Melosh HJ (1990) Giant impacts and the thermal state of the early Earth. In: Newsom H, Jones J (eds) Origin of the Earth. Oxford University Press, Oxford, pp 69–83
Moreira M, Kunz J, Allègre C (1998) Rare gas systematics in popping rock: isotopic and elemental compositions in the upper mantle. Science 279:1178–1181
Mukhopadhyay S (2012) Early differentiation and volatile accretion recorded in deep-mantle neon and xenon. Nature 486:101–104
Ozima M, Podosek F, Igarashi G (1985) Terrestrial xenon isotope constraints on the early history of the Earth. Nature 315:471–474
Parai R, Mukhopadhyay S (2012) How large is the subducted water flux? New constraints on mantle regassing rates. Earth Planet Sci Lett 317–318:396–406
Parai R, Mukhopadhyay S (2015) The evolution of MORB and plume mantle volatile budgets: constraints from fission Xe isotopes in Southwest Indian Ridge basalts. Geochem Geophys Geosyst 16:719–735
Parai R, Mukhopadhyay S, Standish JJ (2012) Heterogeneous upper mantle Ne, Ar and Xe isotopic compositions and a possible Dupal noble gas signature recorded in basalts from the Southwest Indian Ridge. Earth Planet Sci Lett 359–360:227–239
Pepin RO (1991) On the origin and early evolution of terrestrial planet atmospheres and meteoritic volatiles. Icarus 92:2–79
Pepin RO (1992) Origin of noble gases in the terrestrial planets. Annu Rev Earth Planet Sci 20:389–430
Pepin RO (2000) On the isotopic composition of primordial xenon in terrestrial planet atmospheres. Space Sci Rev 92:371–395
Pepin RO, Phinney D (1976) The formation interval of the Earth. Abstr Lunar Planet Sci Conf 7:682–684
Pepin RO, Porcelli D (2002) Origin of noble gases in the terrestrial planets. Rev Mineral Geochem 47:191–246
Pepin RO, Porcelli D (2006) Xenon isotope systematics, giant impacts, and mantle degassing on the early Earth. Earth Planet Sci Lett 250(3–4):470–485
Pető MK, Mukhopadhyay S, Kelley KA (2013) Heterogeneities from the first 100 million years recorded in deep mantle noble gases from the northern Lau back-arc basin. Earth Planet Sci Lett 369–370:13–23
Phinney D, Tennyson J, Frick U (1978) Xenon in CO_2 well gas revisited. J Geophys Res 83:2313–2319
Porcelli D, Wasserburg G (1995) Mass transfer of helium, neon, argon, and xenon through a steady-state upper mantle. Geochim Cosmochim Acta 59:4921–4937
Poreda RJ, Farley KA (1992) Rare gases in Samoan xenoliths. Earth Planet Sci Lett 113:129–144
Pujol M, Marty B, Burnard P, Philippot P (2009) Xenon in Archean barite: weak decay of ^{130}Ba mass-dependent isotopic fractionation and implication for barite formation. Geochim Cosmochim Acta 73:6834–6846
Pujol M, Marty B, Burgess R (2011) Chondritic-like xenon trapped in Archean rocks: a possible signature of the ancient atmosphere. Earth Planet Sci Lett 308:298–230
Reynolds JH (1963) Xenology. J Geophys Res 68:2939–2956
Sarda P, Moreira M, Staudacher T, Schilling J-G, Alleger CJ (2000) Rare gas systematics on the southernmost Mid-Atlantic Ridge: constraints on the lower mantle and the Dupal source. J Geophys Res 105:5973–5996
Schlichting HE, Mukhopadhyay S (2017) Atmospheric impact losses. Space Sci Rev (in review)
Srinivasan B (1976) Barites – anomalous xenon from spallation and neutron-induced reactions. Earth Planet Sci Lett 31:129–141
Staudacher T, Allegre CJ (1982) Terrestrial xenology. Earth Planet Sci Lett 60:389–406
Staudacher T, Allegre CJ (1988) Recycling of oceanic-crust and sediments – the noble-gas subduction barrier. Earth Planet Sci Lett 89:173–183
Sumino H, Burgess R, Mizukami T, Wallis SR, Holland G, Ballentine CJ (2010) Seawater-derived noble gases and halogens preserved in exhumed mantle wedge peridotite. Earth Planet Sci Lett 294:163–172
Tolstikhin I, Hofmann AW (2005) Early crust on top of the Earth's core. Phys. Earth Planet Interiors 148:109–130
Tolstikhin IN, O'Nions R (1996) Some comments on isotopic structure of terrestrial xenon. Chem Geol 129:185–199
Tolstikhin IN, Kramers JD, Hofmann AW (2006) A chemical Earth model with whole mantle convection: the importance of a core-mantle boundary layer (D″) and its early formation. Chem Geol 226:79–99
Tonks WB, Melosh HJ (1993) Magma ocean formation due to giant impacts. J Geophys Res 98:5319–5333
Trieloff M, Kunz J (2005) Isotope systematics of noble gases in the Earth's mantle: possible sources of primordial isotopes and implications for mantle structure. Phys Earth Planet Interiors 148:13–38
Trieloff M, Kunz J, Clague DA, Harrison D, Allegre CJ (2000) The nature of pristine noble gases in mantle plumes. Science 288:1036–1038
Trieloff M, Kunz J, Allègre CJ (2002) Noble gas systematics of the Reunion mantle plume source and the origin of primordial noble gases in Earth's mantle. Earth Planet Sci Lett 200:297–313
Tucker JM, Mukhopadhyay S, Schilling J-G (2012) The heavy noble gas composition of the depleted MORB mantle (DMM) and its implications for the preservation of heterogeneities in the mantle. Earth Planet Sci Lett 355–356:244–254
Tucker JT, Mukhopadhyay S (2014) Evidence for multiple magma ocean outgassing and atmospheric loss episodes from mantle noble gases. Earth Planet Sci Lett 393:254–265

Van Keken PE, Hacker BR, Syracuse EM, Abers GA (2011) Subduction factory: 4. Depth-dependent flux of H2O from subducting slabs worldwide. J Geophys Res Solid Earth 116:B01401. https://doi.org/10.1029/2010jb007922
Wetherill GW (1975) Radiometric chronology of Early solar system. Annu Rev Nucl Part Sci 25:283–328
Yokochi R, Marty B (2005) Geochemical constraints on mantle dynamics in the Hadean. Earth Planet Sci Lett 238:17–30
Zahnle KJ (2015) Xenon fractionation and Archean hydrogen escape. 46th Lunar and planetary science conference, The Woodlands, p 1549, 16–20 March 2015
Zahnle KJ, Kasting JF, Pollack JB (1990a) Mass fractionation of noble gases in diffusion limited hydrodynamic hydrogen escape. Icarus 84:502–527
Zahnle KJ, Pollack JB, Kasting JF (1990b) Xenon fractionation in porous planetesimals. Geochim Cosmochim Acta 54:2577–2586

X-Ray Diffraction

Tori Z. Forbes
Department of Chemistry, University of Iowa, Iowa City, IA, USA

Definition

X-ray diffraction is the result of coherent scattering of an X-ray beam through a solid-state crystalline phase. Single-crystal X-ray diffraction can provide information about the arrangement of atoms and overall chemical composition of mineral phases by determining the angle and intensity of the diffracted beam. Powder samples can also be analyzed using this method to identify unknown phases or mixtures, provide unit cell parameters, and determine particle sizes.

Introduction to X-rays

X-rays were first discovered by Wilhelm Conrad Roentgen in 1985 during experiments with a cathode ray tube (Bertin 1975; Reventos et al. 2012). This device consists of a specialized vacuum tube in which images can be created when electrons are accelerated or deflected onto a phosphorescent screen. During his experiments, he observed that a fluorescent screen located on a table six feet away from his experiments glowed when he activated the tube. Since these rays were previously undescribed, he named them X-rays.

We now know that X-rays are a subset of the electromagnetic spectrum that has wavelengths from 0.1 to 100 Å (10^{-10} m) (Bertin 1975). X-rays are produced in a cathode ray tube by shooting a high velocity stream of electrons at a target. The electrons in the stream collide with electrons in the target and if the oncoming electrons have the right velocity, the target electrons are knocked into a higher energy orbital. When the electrons fall back down into the lower energy orbital, X-rays are produced. Bohr's model of the atom can be used to describe this phenomenon (Fig. 1). In this diagram, an electron is knocked out of the K shell and then an electron from the L-shell then drops down to the lower energy state, releasing a photon in the process. This photon, or X-ray, has a very specific wavelength that is related to the energy difference between the two shells and referred to characteristic X-rays. If the electron does not strike a target electron, but instead interacts with the positively charged nucleus, the velocity can change and result in the formation of an X-ray, which is referred to as Bremsstrahlung radiation. Characteristic X-rays have defined energies, but Bremsstrahlung radiation has a wide range of energies based upon the wide range of kinetic energy for this reaction.

X-rays are described based upon their photon energy with soft X-rays having energies below 5 keV and hard X-rays having photon energies above 5 keV. Hard X-rays are used for diffraction techniques because of their ability to penetrate solid materials and interact with the electron clouds of the atoms present in the crystalline lattice. The wavelength (<2.5 Å) of hard X-rays is also similar to the size of atoms, providing the ability to determine their arrangement within the solid-state material.

Principles of X-ray Diffraction

When X-rays photons propagate through a substance, they can be scattered or absorbed, but it is the analysis of the coherently scattered X-rays that is utilized in diffraction techniques. For coherent scattering to take place, the X-ray beam will interact with the electrons surrounding the nucleus, creating an oscillation with the same frequency as the electric field component of the electromagnetic wave. The radiation created from this process is emitted in all directions and has the same wavelength as the incoming wave. In a crystalline solid, such as a mineral phase, millions of atoms are arranged in ordered arrays and the monochromatic X-ray beam can interact with a multitude of electrons associated with these atoms. The coherently scattered waves can interact either destructively (canceling out the amplitude of the wave) or constructively (increasing the magnitude of the wave). Constructive interaction of the X-ray beam produces wave fronts that are in phase, and this cooperative scattering effect is known as diffraction.

When an X-ray beam penetrates a crystal, the diffraction can occur as a "reflection," where the incident beam reflects back out of the crystal from these parallel planes. However, for the diffraction effect to be of measurable intensity, reflections from the individual planes must be in phase with each other to lead to constructive enhancements. The necessary

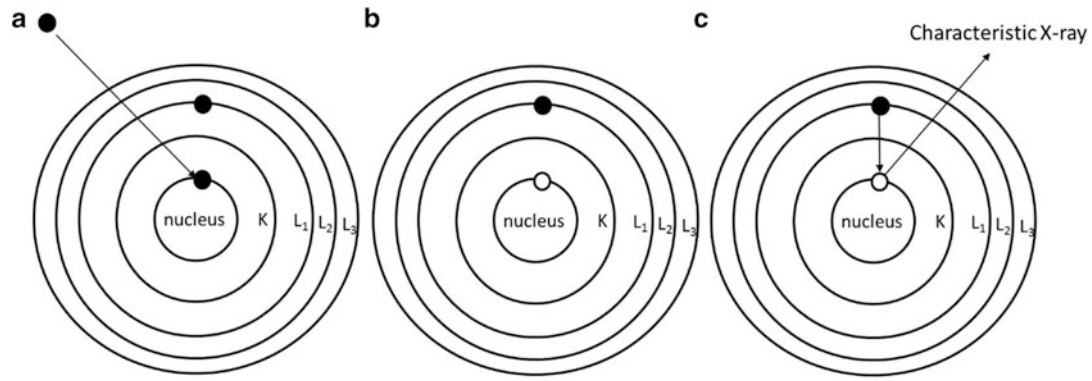

X-Ray Diffraction, Fig. 1 Characteristic X-rays are produced when (**a**) an incoming electron removes an electron from a core shell and (**b**) creates a hole. (**c**) An electron from a higher energy orbital moves to the hole and releases a photon with a specific energy or wavelength, resulting in characteristic X-ray

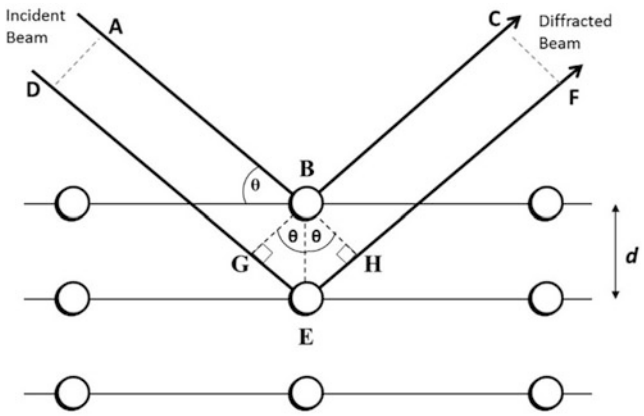

X-Ray Diffraction, Fig. 2 Diffraction of the incident X-ray beam by atomic planes in a crystalline solid can result in enhanced signals if all the waves are in phase. This can be accomplished if there is an integral wave value, as determined by Bragg's law

conditions for in-phase diffraction or "reflection" by the parallel atomic planes can be expressed using Bragg's equation. William Lawrence Bragg was a British physicist who was considered one of the first X-ray crystallographer (Reventos et al. 2012). He and his father (William Henry Bragg) determined that an integer value of the wavelength is related to the distance between the parallel atomic planes and the angle of the diffracted beam. Within the crystalline lattice, a set of parallel atomic planes can be described that are separated by a distance (d) (Fig. 2). X-rays hitting the first plane are reflected at the incident angle, θ, and must be reinforced by in-phase reflection (integral values) of the other atomic planes (e.g., second, third, fourth) for diffraction to be measurable. Therefore, the wave path along first atomic plane (ABC) is shorter than the second plane (DEF), and this value must be a whole number of the wavelength (nλ) for diffraction conditions to be satisfied. In Fig. 2, lines BG and BH are drawn perpendicular to AB and BC so that AB = DG and BC = HF. To satisfy the in-phase condition, GE + EH = nλ. The line drawn between B and E is perpendicular to the atomic planes and is equal to the interplanar spacing (d). This creates two right triangles where d sin θ = GE and d sin θ = EH. Thus, Bragg's equation states:

$$\mathbf{2d\ sin\theta = n\lambda}$$

When a single crystal ($\sim 1 \times 10^{-4}$ m) is placed into the incoming X-ray beam, then the resulting diffraction from a specific plane of diffraction results in a single reflection and rotation of the crystal is required to observe coherent scattering from all possible Bragg angles. Integration of the diffraction data allows complete characterization of the sample including the crystal system, space group, atom locations, bond lengths and angles, and chemical content of the solid (Massa 2004). It is often difficult to obtain or collect highly ordered single crystals with the correct dimensions for analysis with single-crystal X-ray diffraction. Polycrystalline material can also be analyzed using power X-ray diffraction and the large number of randomly ordered crystallites gives rise to lines of diffraction (Bish and Post 1989). The positions of these lines are related to the atomic position and thus the resulting powder X-ray diffractogram can be used as a "fingerprint" to identify mineral phases.

Instrumentation

An X-ray diffractometer is used to collect information regarding the placement and the intensity of the diffracted beam and consists of three major components: (1) X-ray source, (2) sample stage, and (3) detector. The X-ray tube consists of a tungsten filament cathode to provide the source of electrons and a target metal to produce the characteristic X-ray. Most laboratory-based systems contain molybdenum (Mo), copper (Cu), or cobalt (Co) targets that result in $K\alpha_1$ wavelengths of

0.70932, 1.5418, and 1.7902 Å, respectively (Pecharsky and Zavalij 2005). The sample stage consists of a goniometer that allows the sample to be moved through a wide range of diffraction conditions. Specialized sample cells have been designed to handle high pressure and variable temperatures to explore structural changes in mineral phases under geologically relevant conditions (Toulemonde et al. 2014). The detector converts the individual X-ray photons into voltage pulses that can be transformed into information regarding the intensity and position of the diffracted beam. Traditionally, photographic film was used to collect information on the diffracted beam, but current methods use solid-state semiconductors within one- and two-dimensional position sensitive detectors (Pecharsky and Zavalij 2005).

Uses in Geochemistry

Single-crystal X-ray diffraction has been utilized extensively in mineralogy and geochemistry to determine the structural feature of geologic media. Halite (NaCl) was the first atomic resolution structure to be determined by X-ray diffraction in 1913, and other minerals analyzed the following year include fluorite, calcite, and pyrite (Reventos et al. 2012). Since the early years, thousands of minerals have been structurally characterized, leading to an advanced understanding of the chemical and physical properties of these materials. An example of the latest structural characterization include mineral species collected from meteorites (Xie et al. 2015), high temperature and pressure phases (Golubkova et al. 2015; Merlini et al. 2015), and unusual quasicrystals (Bindi et al. 2015). While thousands of mineral phases are known, it is possible that there is still 25% of unknown mineral phases with undescribed structural features (Hazen et al. 2015).

Given the polycrystalline nature of a significant portion of geologic media, powder X-ray diffraction is a very important technique and is used for identification, evidence of chemical changes in the material, and size determination of nanoparticle samples. Structural determination of solid-state materials can also be performed using Rietveld analysis on the collected diffractogram (Bish and Post 1989). Powder X-ray diffraction has been used to investigate biomineralization processes (Pokroy et al. 2004; Villalobos et al. 2006; Cam et al. 2015) and identify clay minerals on the surface of Mars (Bristow et al. 2015), meteorite mineralogy (King et al. 2015), and composition of Mn-nodules from the Pacific Ocean (Wegorzewski et al. 2015). Advancements in powder X-ray diffraction and related techniques are currently pushing the limits on detection of crystalline ordering to investigate poorly crystalline and amorphous systems (Mikutta et al. 2014; Dideriksen et al. 2015).

Summary

X-ray diffraction techniques are used to determine the structural features of a solid material. Single-crystal methods provide the atomic arrangement and elemental composition of highly ordered mineral phases. Powder X-ray diffraction is used to identify unknown samples and mixtures (soils or sediments), determine structural parameters, and ascertain particle sizes.

Cross-References

- ▶ Analytical Techniques
- ▶ Crystal Chemistry
- ▶ X-Ray Fluorescence Analysis

References

Bertin E (1975) Principles and practice of X-ray spectrometric analysis. Plenum Press, New York

Bindi L, Yao N, Lin C, Hollister LS, Andronicos CL, Distler VV, Eddy MP, Kostin A, Kryachko V, MacPherson GJ, Steinhardt W, Yudovskaya M, Steinhardt PJ (2015) Decagonite, $Al_{71}Ni_{24}Fe_5$, a quasicrystal with decagonal symmetry from the Khatyrka CV3 carbonaceous chondrite. Am Mineral 100:2340–2343

Bish DL, Post JE (1989) Modern powder diffraction. The Mineralogical Society of America, Washington, DC

Bristow TF, Bish DL, Vaniman DT, Morris RV, Blake DF, Brotzinger JP, Rampe EB, Crisp JA, Achilles CN, Ming DW, Ehlmann BL, King PL, Bridges JC, Eignebrode JL, Sumner DY, Chipera SJ, Moorokian JM, Treimaan AH, Morrison SM, Downs RT, Farmer JD, Des Marais D, Sarrazin P, Floyd MM, Mischna MA, McAdams AC (2015) The origin and implications of clay minerals from Yellowknife Bay, Gale crater, Mars. Am Mineral 100:824–836

Cam N, Georgelin T, Jaber M, Lambe JF, Benzerara K (2015) In vitro synthesis of amorphous Mg-, Ca-, Sr-, and Ba-carbonates: what do we learn about intracellular calcification by cyanobacteria? Geochim Cosmochim Acta 161:36–49

Dideriksen K, Frandsen C, Bovet N, Wallace AF, Sel O, Arbour T, Navrotsky A, DeYoreo JJ, Banfield J (2015) Formation and transformation of a short range ordered iron carbonate precursor. Geochim Cosmochim Acta 164:94–109

Golubkova A, Merlini M, Schmidt MW (2015) Crystal structure, high-pressure, and high-temperature behavior of carbonates in the $K_2Mg(CO_3)_2$-$Na_2Mg(CO_3)_2$ join. Am Mineral 100:2458–2467

Hazen RM, Hystad G, Downs RT, Golden J, Pires AJ, Grew ES (2015) Earth's 'missing' minerals. Am Mineral 100:2344–2347

King AJ, Schofield PF, Howard KT, Russell SS (2015) Modal mineralogy of Cl and Cl-like chondrites by X-ray diffraction. Geochim Cosmochim Acta 165:148–160

Massa W (2004) Crystal structure determination. Spinger, Berlin

Merlini M, Hanfland M, Salamat A, Petitgard S, Muller H (2015) The crystal structures of $Mg_2Fe_2C_4O_{13}$, with tetrahedrally coordinated carbon, and $Fe_{13}O_{19}$, synthesized at deep mantle conditions. Am Mineral 100:2001–2004

Mikutta C, Schroder C, Michel FM (2014) Total X-ray scattering, EXAFS, and Mossbauer spectroscopy analysis of amorphous ferric arsenate and amorphous ferric phosphate. Geochim Cosmochim Acta 140:708–719

Pecharsky VK, Zavalij PY (eds) (2005) Fundamentals of powder diffraction and structural characterization of materials. Springer, New York

Pokroy B, Quintana JP, Caspi EAN, Berner A, Zolotoyabko E (2004) Anisotropic lattice distorions in biogenic aragonite. Nature 3:900–902

Reventos MM, Rius J, Amigo JM (2012) Mineralogy and geology: the role of crystallography since the discovery of X-ray diffraction in 1912. Rev Soc Geol Esp 25:133–143

Toulemonde P, Goujon C, Laversenne L, Bordet P, Bruyere R, Legendre M, Leynaud O, Prat A, Mezouar M (2014) High pressure and high temperature in situ X-ray diffraction studies in the Paris Edinburgh cell using a laboratory X-ray source. High Pressure Res 34:1–6

Villalobos M, Lanson B, Manceau A, Toner B, Sposito G (2006) Structural model for the biogenic Mn oxide produced by *Pseudomonas putida*. Am Mineral 91:489–502

Wegorzewski AV, Kuhn T, Dohrmann R, Wirth R, Grangeon S (2015) Mineralogical characterization of individual growth structures of the Mn-nodules with different Ni + Cu content from the central Pacific ocean. Am Mineral 100:2497–2508

Xie X, Yang H, Gu X, Downs RT (2015) Chemical composition and crystal structure of merrillite from the Suizhou meteorite. Am Mineral 100:2753–2756

X-Ray Fluorescence Analysis

Izumi Nakai
Department of Applied Chemistry, Tokyo University of Science, Tokyo, Japan

Definition

X-ray fluorescence (XRF) analysis is one of the best analytical techniques to perform nondestructive elemental analysis of solid or liquid samples for major and minor components. A sample is excited by bombarding with X-rays causing ejection of inner electrons with subsequent emission of the characteristic (fluorescence) X-rays of the sample. The energy of the fluorescence X-rays is a characteristic of an element, and their intensities are proportional to the number of excited atoms and thus can be used for qualitative and quantitative analysis of the sample.

Introduction

Since discovery of X-rays by Rontgen in 1895, interaction of X-rays with an atom became a target of eager study in physics research, and X-ray spectroscopy was developed (Bertin 1978). At early stage of X-ray spectroscopy development, Moseley (1913) showed that the chemical composition of a substance can be determined with the aid of X-ray spectroscopy. However, introduction of modern X-ray spectrometer for XRF analysis must wait until 1948, when Friedman and Birks built the prototype of the first modern commercial X-ray secondary-emission spectrometer with a sealed-off X-ray tube (Bertin 1978). Nowadays, XRF analysis is a well-established analytical method that is one of the fundamental techniques of element analysis and is widely used in various fields such as geochemistry, geology, archaeology, material sciences and industry (Muller 1972).

Principle of X-ray Fluorescence Analysis

The principle of X-ray fluorescence emission is well explained by Bohr's model as shown in Fig. 1: a positively charged nucleus is surrounded by electrons that travel in circular orbits (defined by their energy levels E_i) around the center and are bound to the nucleus by the Coulomb forces. These electron shells (orbits) are denoted by K, L, M, N, etc., shells in the order of increasing shell diameter (Fig. 1). The energy of an electron depends on the size of the orbit and is lower for smaller orbits. Therefore, K shell is the smallest, and E_K is the lowest.

When an X-ray photon with energy E is impinged on a K shell electron, which is bound to a nucleus with a binding energy E_b^K, the electron may be knocked out of the shell as a photoelectron if $E > E_b^K$. Then, this atom becomes an excited state with an electron vacancy in the K shell. The vacancy is filled by an electron from a neighboring outer shell (e.g., L shell), and the excess energy ($\Delta E = E_K \sim E_L$) is emitted in the form of X-rays, which is called the X-ray fluorescence K line (if from L shell, it is called the Kα line). E_b is the minimum energy necessary for the excitation of the electron in the shell. This threshold energy is called the absorption edge energy. ΔE is characteristic of an emitting element; therefore, we can accurately identify the element, qualitative analysis, by measuring ΔE, which is the energy of the emitted X-ray fluorescence line. On the other hands, since the intensity of the emitted X-ray (I) is basically proportional to the amount of the element, quantitative analysis can be performed by measuring I. These are basic principles of X-ray fluorescence analysis (Muller 1972).

The XRF spectrometer measures the energy (ΔE) and intensity (I) of the X-ray fluorescence signal emitted from a sample by irradiation of X-rays, and, thus, an XRF spectrum is obtained. The XRF spectrometer is composed of an X-ray source, sample chamber, X-ray detector, and electronic devices for signal processing, amplification, counting, and computing. There are two types of instruments to measure the XRF energy: wavelength dispersive (WD) and energy dispersive (ED) analyses (Grieken and Markowicz 2001). In ED analysis, a solid-state detector is used to measure the XRF spectrum, and the X-ray energy and intensity can be simultaneously measured with the detector. In WD analysis, the XRF signals emitted from a sample are directed into analyzing

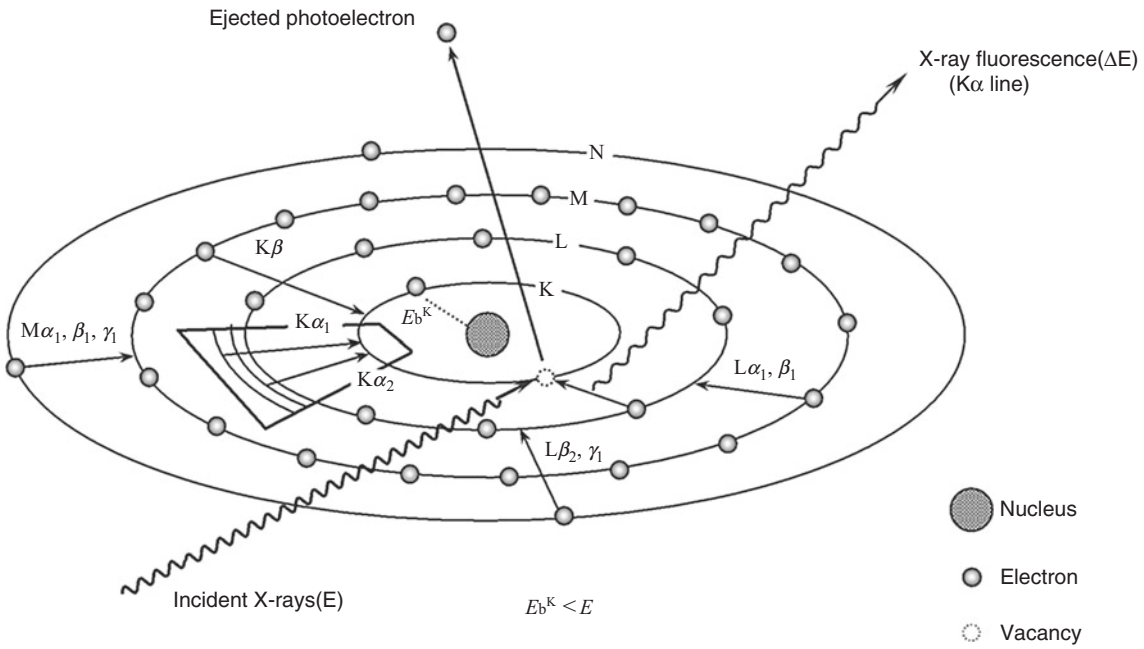

X-Ray Fluorescence Analysis, Fig. 1 Principle of X-ray fluorescence analysis. A Bohr atom showing the first four inner shells and the origin of the X-ray spectra; intraatom electron transitions are responsible for the principal X-ray spectral lines of analytical interest

crystals, diffraction grating monochromators with known d spacing. By varying the angle (θ) of incidence and the take-off on the analyzing crystal, the X-ray wavelength (λ) is selected by X-ray diffraction based on the Bragg equation of $n\lambda = 2d\sin\theta$. ED analysis has the advantage of simple components of the instruments, i.e., an X-ray source and a detector are two basic essential components, which allow miniaturization of the instrument. The weak point of ED analysis is that the energy resolution is not good, ca. 120 eV as that of WD (~30 eV). This causes the peak overlap of the neighboring elements in the spectrum. However, WD analysis requires a moving mechanism of the monochromator, which requires a large instrumental volume with a long beam pass and a strong intensity of X-ray irradiation, which may cause damage to the sample.

The XRF technique is suitable for nondestructive multielemental analysis of solid, liquid, and gas samples. Conventional instruments allow analysis of Na and heavier elements in air and in vacuum analysis of lighter elements down to Be, which can be detected with high-performance instruments. The sensitivity of quantitative XRF analysis of heavy elements is in the order of sub-ppm and somewhat worse than that of ICP-AES. The great advantage of the method is nondestructive nature, suitable for analysis of precious samples. Another advantage is that the sample preparation is easy, without the necessity of dissolving a solid sample into acid or alkali which requires chemical laboratory. XRF analysis is a type of surface analysis with an information depth of 1 μm to a few millimeters depending on the X-ray energy and the mean atomic number of samples. For quantitative analysis, a sample should be sufficiently thick (infinite thickness) and homogeneous. For quantitative analysis, a calibration curve is prepared using a standard sample of known compositions with similar matrix components to the sample. The FP (Fundamental Parameter) method is a theoretical method widely used in quantitative XRF analysis, and the X-ray intensity is theoretically calculated based on the physical parameters such as absorption factor, X-ray intensity. The least-square analysis is used to refine the concentration parameters, such that the difference between the observed and calculated intensities becomes minimum.

Recent Innovation in XRF Analysis

Hand-Held XRF Analyzer

In recent years, two big innovations emerged in XRF analysis. One is the development of a hand-held XRF analyzer (Fig. 2). The weight of the instrument is around 1 kg and can be held by one hand. With this handy instrument equipped with a battery, anyone can feel free to analyze a sample without specialized knowledge at anytime and anywhere. Examples of applications include analysis of soils with GPS data, analysis of huge rocks, ore mineral, environmental samples, etc., and can be used on location for immediate results.

Synchrotron Radiation Application

Another innovation is the fact that synchrotron radiation (SR)-XRF analysis becomes more or less a routine technique. A large number of SR facilities have been constructed

globally, and the SR-XRF technique becomes not specialized to limited number of users. SR X-rays are brilliant light source and are energy-tunable: the users can select the energy required for their experiments. The use of monochromatic X-rays in XRF analysis with a suitable X-ray excitation energy drastically increases the sensitivity of the analysis by selective excitation of a specific element of interest. SR X-rays are ideal as an excitation source in XRF analysis, and their characteristic applications were illustrated in the following example.

SR is a parallel beam, and a microbeam with 1 μmϕ focused by a total reflection mirror is practically available. The champion data of the smallest beam size are on the order of ten nanometers (Mimura et al. 2010). This micro (nano)-beam is suitable for two-dimensional analysis of geological and biological samples. Figure 3 shows an example of μ-XRF imaging of a plant, *Arabidopsis halleri*, a hyper accumulator of Cd (Fukuda et al. 2008). It is interesting to reveal where this plant accumulates a toxic Cd ion. Figure 3 (a) shows the photograph of the measured sample showing the imaging area, and the distribution of (b) Cd, (c) Zn, (d) Ca, and (e) Mn are expressed using red (the highest intensity) to blue (the lowest intensity) colors corresponding to the XRF intensities of each element. It is found that Cd was highly accumulated in a part of trichome, epidermal hairs existing on the surface of the leaves. Figure 3b, c shows a significant correlation between the XRF intensity distributions of Cd and Zn. The results showed that Cd and Zn behave in a similar way. Thus, in vivo analysis of plant and animal samples with the cellular resolution in air is possible by SR-μ-XRF analysis. A similar spatial resolution can be obtained using scanning electron microscopy–energy dispersive spectoscopy (SEM-EDS) analysis; however, analysis of living samples in air is not possible with SEM-EDS analysis. SEM-EDS analysis involves electron beam excitation, which tends to cause damage to the sample. SEM-EDS analysis is suitable for analyzing light elements, such as C, N, O, and F, but the sensitivity of heavy element analysis is relatively low at 0.1% level. In contrast, SR-μ-XRF analysis shows a ppm–ppb sensitivity for heavy elements, though the sensitivity of the analysis of light elements is low. Instead of SR application, X-ray microbeam produced by capillary optics became popular in XRF analysis in a laboratory, and an XRF microscope with a spatial resolution of 10 μm is commercially available.

The use of high-energy 116 keV X-rays in XRF analysis allows excitation of K-shell electrons of uranium ($E_b^K = 115.6$ keV), the heaviest element in nature, and the U K line spectra can be measured (Nakai 2004). The K line region of the XRF spectra of heavy elements do not overlap with any light element lines. Thus, high-sensitive analysis of geochemically important heavy elements, such as lanthanide, is possible by using high-energy XRF analysis with 116 keV X-rays.

X-Ray Fluorescence Analysis, Fig. 2 Handheld X-ray fluorescence analyzer

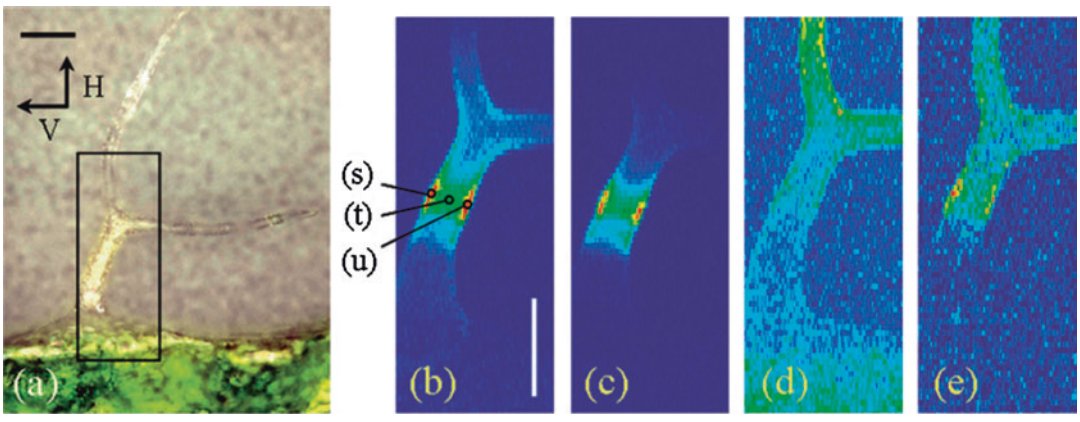

X-Ray Fluorescence Analysis, Fig. 3 μ-XRF imaging of trichome; the X-ray energy is 37 keV, the beam size is 3.8 μm (H) × 1.3 μm (V). (**a**) Photographs of the measured samples showing the imaging area. The elemental distribution maps of (**b**) Cd, (**c**) Zn, (**d**) Ca, and (**e**) Mn are shown as a color scale from *red* (the highest XRF intensity) to *blue* (the lowest XRF intensity). (Fukuda et al. 2008; Fig. 2)

Chemical State Analysis

Another characteristic application of SR-XRF analysis is chemical state analysis using fluorescence-X-ray adsorption fine structure (XAFS) spectra. A fluorescence-XAFS spectrum can be obtained by measuring the X-ray fluorescence intensity of an element from a sample as a function of the excitation energy from ca. 50 eV below the X-ray absorption edge energy (E_b) of the element to 1 keV above E_b. The fine structure of the XAFS spectrum below and above E_b is called the X-ray absorption near edge structure (XANES) spectrum, and the oscillation structure from 50 eV to 1 keV above the edge is called the extended X-ray absorption fine structure (EXAFS). The energy of E_b increases when the oxidation state of the absorber atom increases, which is called the chemical shift. With this principle, chemical state analysis of the absorber element in the microregion is possible with SR X-rays. This method is applicable to any form of the sample, solid, liquid, gas. Moreover, the analysis of EXAFS oscillation provides information about the local structure around the absorber atom (bond distance, coordination number, etc.) even from an amorphous sample without knowing any structural information. Therefore, fluorescence XAFS is very useful technique for geochemists. At early stage of SR application, XAFS was independent of XRF analysis. However, more than 30 years have passed since XAFS became a popular analytical tool, and fluorescence-XAFS measurement combined with micro-XRF analysis became a routine technique of the XRF beamline at an SR facility. Especially, a micro-X-ray absorption near edge structure (XANES) spectrum measurement with a microbeam is a powerful technique to determine the chemical form of an element in geochemical samples.

Figure 4 shows an example of the Cd-K edge XANES spectra of trichome of *A. halleri* (see Fig. 3) and the reference compounds (Fukuda et al. 2008). The Cd Kedge XANES spectra of points (s), (t), and (u) in Fig. 3b in trichome are shown in Fig. 4 as (a), (b), and (c), respectively. The comparison of the XANES spectra of the reference materials shown in Fig. 4 suggests that there is a characteristic difference in the shapes between the spectrum of Cd with S ligands: (f) CdS, (d) phytochelatin (PC)-Cd, and (e) metallothionein (Mt)-Cd, and that of Cd with O ligands: (g) CdO, (h) $Cd(NO_3)_2$aq, (i) cadmium acetate (AcCd) or N ligand, (j) hexakis(imidazole) cadmium(II) nitrate $(Im)_6Cd(NO_3)$. The covalent nature is high in the Cd–S bond, while the ionic nature is high in the Cd–O (N) bonds yielding a very flat feature for the XANES spectra of the former type. The spectra from Fig. 4a–c are similar in shape to those of compounds containing Cd with O or N ligands. Consequently, it was found that a majority of Cd in *A. halleri* was divalent and bound to O or N ligands, not to S ligands.

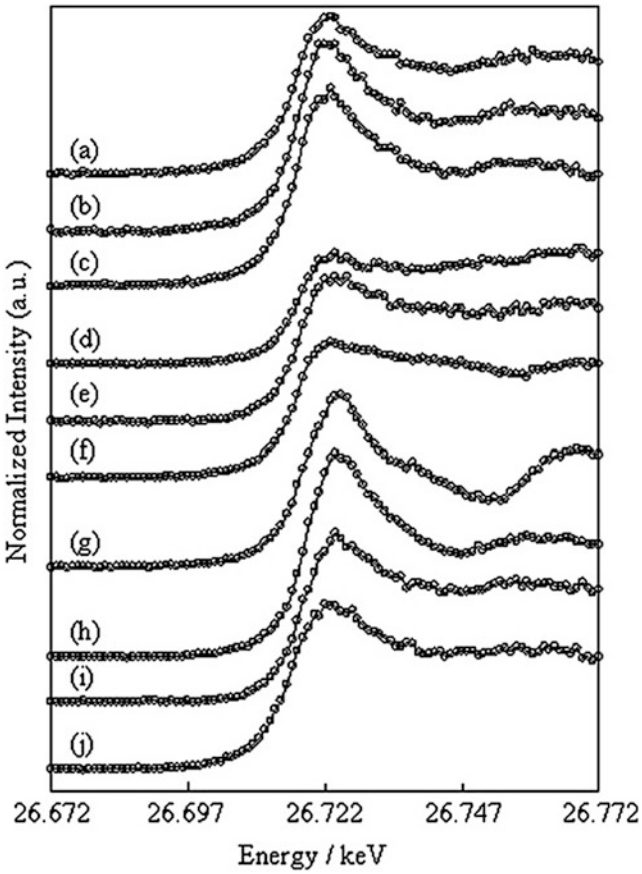

X-Ray Fluorescence Analysis, Fig. 4 Cd K-edge μ-XANES spectra of trichome of *A. halleri* and reference compounds (*a*) point s, (*b*) point t, and (*c*) point u of the trichome sample in Fig. 2b, (*d*) PC-Cd, (*e*) Mt-Cd, (*f*) CdS, (*g*) CdO, (*h*) $Cd(NO_3)_2$aq, (*i*) AcCd, (*j*) $(Im)_6Cd(NO_3)_2$. (Fukuda et al. 2008; Fig. 4)

Conclusion

XRF analysis is not an insensitive analytical method any longer. A combination of a secondary target and three-dimensional polarizing optical geometry of a spectrometer greatly reduced the background of the XRF spectrum, and analysis of heavy elements at ppb level becomes possible in a laboratory. Handheld XRF analyzers provide fast, easy, and nondestructive elemental analysis by anyone at any place, which will open a new field of XRF applications. The utilization of SR X-rays expands application fields of XRF analysis into chemical state analysis. Two-dimensional analysis with a spatial resolution of 1 μm is practically possible. With these innovations, it could be said that XRF analysis has now entered a new stage of application.

Cross-References

- ▶ Synchrotron X-ray Fluorescence Analysis
- ▶ X-ray Diffraction

References

Bertin EP (1978) Introduction to X-ray spectrometric analysis. Plenum Press, New York, pp 1–3

Fukuda N, Hokura A, Kitajima N, Terada Y, Saito H, Abe T, Nakai I (2008) Micro X-ray fluorescence imaging and micro X-ray absorption spectroscopy of cadmium hyper-accumulating plant, *Arabidopsis halleri* ssp. *gemmifera*, using high-energy synchrotron radiation. J Anal At Spectrom 23:1068–1075

Grieken Rene EV and Markowicz AA (1993) Handbook of X-ray spectrometry: methods and techniques, Marcel Dekker, Inc. New York, pp 75–180

Mimura H et al (2010) Breaking the 10 nm barrier in hard-X-ray focusing. Nat Phys 6:122–125

Moseley HGJ (1913) XCIII. The high-frequency spectra of the elements. Philos Mag 26:1024–1034

Muller R (1972) Spectrochemical analysis by X-ray fluorescence. Springer, New York, pp 11–129, pp 215–324

Nakai I (2004) High energy X-ray fluorescence. In: Tsuji K, Injuk J, Griken RV (eds) X-ray spectrometry: recent technological advance. Wiley, pp 355–372

Y

Ytterbium

J. H. L. Voncken
Faculty of Civil Engineering and Geosciences, Department of Geosciences and Engineering, Section Resource Engineering, Delft University of Technology, Delft, The Netherlands

Element Data
Atomic Symbol: **Yb**
Atomic Number: **70**
Atomic Weight: 173.054(5)
Isotopes and Abundances: ^{168}Yb 0.13%, ^{170}Yb 3.04%, ^{171}Yb 14.28%, ^{172}Yb 21.83%, ^{173}Yb 16.13%, ^{174}Yb 31.83%, ^{176}Yb 12.76%
1 Atm Melting Point: 824 °C
1 Atm Boiling Point: 1196 °C
Common Valences: 3+, 2+
Ionic Radii: (3+) 4-fold 86.8 pm, 6-fold 92.5 pm, 8-fold 98.5 pm, (2+) 6-fold 108 pm, 8-fold 114 pm
Pauling Electronegativity: 1.1
First Ionization Energy: 603.435 kJ/mol
Chondritic (CI) Abundance: 161 ppb
Silicate Earth Abundance: 441 ppb
Crustal Abundance: 1.9 ppm
Seawater Abundance: ~0.17–1.2 ng/kg
Core Abundance: ~0

Properties

Ytterbium is a silvery-white metal, with a slight yellowish tinge (see Fig. 1). Ytterbium is a lithophile element (McDonough and Sun 1995). It is soft, malleable, and quite ductile. It is slowly oxidized by air. However, this oxide layer forms a protective layer on the surface, preventing complete oxidation (Emsley 2011; Hammond 2016).

The element reacts slowly with water, and dissolves readily in dilute acids. The +3 oxidation state is predominant. In solution ytterbium exists as Yb^{3+}, associated with nine molecules of H_2O. Both Yb solutions and salts are colorless (Emsley 2011).

History and Use

Ytterbium was first discovered in 1878 by Swiss chemist Jean Charles Galissard de Marignac, 1817–1894, (Marignac 1878). He separated an Earth which he called ytterbia from erbium nitrate. About the same time, Carl Auer (1858–1929) discovered the same oxide and named it aldebaranium (Emsley 2011). Ytterbium metal was made first in 1937, but it was not pure enough for the properties to be reliably measured (Hammond 2016). In 1953, a pure sample was finally obtained (Emsley 2011).

The artificial isotope ^{169}Yb is used as a source of gamma rays for non-destructive testing and radiomedicine (Hammond 2016). Ytterbium is also used in atomic clocks (NIST 2013), and in catalysis (Emsley 2011; Mori and Kobayashi 2012). Applications are also found in alloys (Hammond 2016). The total amount of applications of Yb is, however, limited (Hammond 2016).

Geochemical Behavior

Ytterbium is a moderately incompatible trace element, and behaves as a lithophile element. As are the other lanthanides, it is highly insoluble in natural aqueous solutions and considered immobile. Because it, along with Eu and Ce, has lower nebular condensation temperatures than the other lanthanides, both chondrites and their refractory inclusions

W. M. White (ed.), *Encyclopedia of Geochemistry*,
https://doi.org/10.1007/978-3-319-39312-4

Ytterbium, Fig. 1 Ytterbium, pieces (Source: Wikipedia.nl (Ytterbium). (https://nl.wikipedia.org/wiki/Ytterbium) Photograph by W. Oelen. No changes made. Link to the license: http://creativecommons.org/licenses/by-sa/3.0/. Used with permission)

sometimes exhibit Yb anomalies (Boynton 1975). Ytterbium is found mostly in the mineral monazite (Ce, La, Th) PO_4, but also in euxenite (Y,Ca,Ce,U,Th)(Nb,Ta,Ti)$_2O_6$ and xenotime (YPO_4). It also partitions strongly into garnet. It can be extracted by ion exchange and solvent extraction (Emsley 2011).

Biological Utilization and Toxicity

Ytterbium has no known biological function and has a low acute toxicity rating (Hammond 2016).

Cross-References

- ▶ Lanthanide Rare Earths
- ▶ Lithophile Elements
- ▶ Transition Elements

References

Boynton WV (1975) Fractionation in the solar nebula: condensation of yttrium and the rare earth elements. Geochim Cosmochim Acta 39(5):569–584

Emsley J (2011) Nature's building blocks. An A-Z guide of the elements. Oxford University Press, Oxford, pp 614–616

Hammond CR (2016) CRC Handbook of chemistry and physics, 96th edition, 2015–2016, Electronic edn. CRC Press, Boca Raton

Marignac JCG (1878) Sur l'ytterbine, nouvelle terre contenue dans la gadolinite. C R Hebd Seances Acad Sci LXXXVII: 578–581

McDonough WF, Sun SS (1995) The composition of the earth. Chem Geol 120:223–253

Mori Y, Kobayashi S (2012) Organic synthesis. In: Atwood DA (ed) The rare earth elements: fundamentals and applications. Wiley, Hoboken, pp 452–453

NIST (2013) Ytterbium atomic clocks set record for stability. http://www.nist.gov/pml/div688/clock-082213.cfm. Accessed Mar 2016

Yttrium

J. H. L. Voncken
Faculty of Civil Engineering and Geosciences, Department of Geosciences and Engineering, Section Resource Engineering, Delft University of Technology, Delft, The Netherlands

Element Data
Atomic Symbol: **Y**
Atomic Number: **39**
Atomic Weight: 88.90585(2)
Isotopes and Abundances: ^{89}Y, 100%
1 Atm Melting Point: 1522 °C
1 Atm Boiling Point: 3345 °C
Common Valences: 3+
Ionic Radii: 6-fold: 90 pm, 7-fold: 96 pm, 8-fold: 101.9, 9-fold 107.5
Pauling Electronegativity: 1.22
First Ionization Energy: 599.878 kJ
Chondritic (CI) Abundance: 1.57 ppm
Silicate Earth Abundance: 4.30 ppm
Crustal Abundance: 19 ppm
Seawater Abundance: ~9 ppt
Core Abundance: ~0

Properties

Yttrium is a transition metal with a silvery-white color. It has strong chemical similarities with the lanthanides, especially with the heavier ones (Gd–Lu). Therefore it is usually classified as a (heavy) rare earth metal. It is also always found combined with rare earth metals. The most prominent ore mineral is xenotime (YPO_4). Yttrium's only stable isotope, ^{89}Y, is also its only naturally occurring isotope. The metal is readily oxidized by air, which however forms a resistant oxide film on the surface of the metal, preventing full oxidation. It is attacked by water, where it causes decomposition with the release of hydrogen gas (Emsley 2011), (Fig. 1).

History and Use

Yttria, which is an earth containing yttrium, was discovered by Finish chemist Johan Gadolin (1760–1852) in 1794 (Gadolin 1794, 1796). The material from which yttria was prepared was found in a quarry near the Swedish town of Ytterby (Hammond 2016).

Yttrium, Fig. 1 Yttrium, sublimed-dendritic, high purity 99.99%, as well as an argon arc remelted 1 cm^3 yttrium cube for comparison. Purity 99.9% (Source: Wikipedia.en (Yttrium). (https://en.wikipedia.org/wiki/Yttrium) Photograph by H. Pniok. No changes made. Link to the license: https://commons.wikimedia.org/wiki/Commons:Reusing_content_outside_Wikimedia. Used with Permission)

Friedrich Wöhler (1800–1883) obtained the impure element in 1828 (Wikipedia 2016a). Highly pure yttrium was first prepared in 1953 by Frank Spedding (1902–1984) at Ames Laboratory, Iowa (Wikipedia 2016b).

Yttrium oxide is one of the most important compounds of yttrium and accounts for the largest use. Yttrium is widely used to produce YVO_4 and Y_2O_3, which, doped with europium are widely used as a red phosphor in color televisions. Also yttrium oxide sulphide $Y_2O_2S{:}Eu_{3+}$ doped with europium is used as such (Emsley 2011; Hammond 2016).

Yttrium is also used for the production of $Y_3Fe_5O_{12}$ (yttrium iron garnet, or YIG), which is an effective microwave filter. Yttrium iron garnet is also exceptionally efficient as both a transmitter and transducer of acoustic energy.

Yttrium iron, aluminium, and gadolinium garnets (e.g., $Y_3Al_5O_{12}$) have interesting magnetic properties. Yttrium aluminium garnet, with a hardness of 8.5, is also finding use as simulated diamond. YAG (Yttrium Aluminium Garnet) doped with a variety of elements, such as Nd, Ho, Er, Yb, Ce, etc. are used as lasers (Emsley 2011; Hammond 2016).

In metallurgy, small amounts of yttrium (0.1–0.2%) are used to reduce grain size in chromium, molybdenum, zirconium, and titanium. Such amounts are also used to dope aluminium and magnesium alloys, where yttrium increases strength. There are several other alloy applications, among them an aluminium-nickel-yttrium alloy, which is used in aircraft manufacture (Hammond 2016).

In catalysis, yttrium is used as a catalyst for ethylene polymerization (Emsley 2011). Ceramic superconductors of the type $YBa_2Cu_3O_7$ ("123 superconductors," Wu et al. 1987) also rely on yttrium.

Geochemical Behavior

Like all other REE, yttrium behaves as a moderately incompatible lithophile ("rock-loving") element in igneous systems. Yttrium concentrates in magmatic liquids and late crystallizing mineral phases and is thought to have an incompatibility similar to that of rare earths Dy and Ho. Like the lanthanides, Y is highly insoluble in natural aqueous solutions and considered immobile. Yttrium favorably concentrates in xenotime, YPO_4 (Emsley 2011).

Biological Utilization and Toxicity

Yttrium has no known biological function. Some soluble yttrium salts may be mildly toxic and yttrium may be carcinogenic in some animals and may cause lung disease in humans (Emsley 2011; Occupational Safety and Health Guideline for Yttrium and Compounds (2016)).

Cross-References

- ▶ Lithophile Elements
- ▶ Lanthanide Rare Earths
- ▶ Transition Elements

References

Emsley J (2011) Nature's building blocks. An A-Z guide of the elements. Oxford University Press, Oxford, pp 617–620

Gadolin J (1794) Undersökning av en svart tong stenart ifran Ytterby stenbrott i Roslagen. Kungliga Svenska Vetenskapsakademien, Handlingar, pp 137–155

Gadolin J (1796) Von einer schwarzen, schweren Steinart aus Ytterby Steinbruch in Roslagen in Schweden, Crell's Annalen, (also: "Chemische Annalen für die Freunde der Naturlehre, Arzneygelährtheit, Haushaltungskunst und Manufacturen," or just "Chemische Annalen"), pp 313–329. See for an online version: http://reader.digitale-sammlungen.de/de/fs1/object/display/bsb10072281_00321.html?contextType=ocr

Hammond CR (2016) CRC Handbook of chemistry and physics, 96th edition, 2015–2016, Electronic edn. CRC Press

Occupational Safety and Health Guideline for Yttrium & Compounds (2016) http://web.archive.org/web/20130302060936/http:/www.osha.gov/SLTC/healthguidelines/yttriumandcompounds/recognition.html. Accessed 16 Mar 2016

Wikipedia (2016a) https://en.wikipedia.org/wiki/Friedrich_W%C3%B6hler. Accessed 16 Mar 2016

Wikipedia (2016b) https://en.wikipedia.org/wiki/Frank_Spedding#Later_life. Accessed 16 Mar 2016

Wu MK, Ashburn JR, Torng CJ, Hor PH, Meng RL, Gao L, Huang ZJ, Wang YQ, Chu CW (1987) Superconductivity at 93 K in a new mixed-phase Y-Ba-Cu-O compound system at ambient pressure. Phys Rev Lett 58(9):908–910

Z

Zinc

Joël Brugger
School of Earth, Atmosphere and the Environment, Monash University, Clayton, Australia

Element Data
Atomic Symbol: **Zn**
Atomic Number: **30**
Atomic Weight: 65.38(2) g/mol
Isotopes and Abundances: Five stable isotopes: ^{64}Zn, 49.17(75)%; ^{66}Zn, 27.73(98)%; ^{67}Zn, 4.04(16)%; ^{68}Zn, 18.45(63)%; ^{70}Zn, 0.61(10)%
1 Atm Melting Point: 419.6 °C
1 Atm Boiling Point: 907 °C
Common Valences: +2
Ionic Radii: 60 pm (4-fold) and 0.74 pm (6-fold)
Pauling Electronegativity: 1.65
First Ionization Energy: 906.4 kJ mol^{-1}
Chondritic (CI) Abundance: 312 ppm
Silicate Earth Abundance: 55 ppm
Crustal Abundance: 70 ppm
Seawater Abundance: 35 ppb
Core Abundance: <5 ppm (?)

Properties

Zinc is a bluish-white, rather soft metal. Zinc has atomic number 30 and is the first of the group IIB elements in the periodic table. It has atomic mass 65.38(2) g/mol, density 7.14 g/cm^3; its melting point of 419.6 °C is the lowest melting point of any transition metal aside from the other group IIB elements, Hg and Cd.

History and Use

Isolated examples of the use of impure zinc in ancient times have been discovered. Zinc–copper alloys ("brass") were in use as early as the fourteenth–to the tenth century BC, with isolated discoveries of other alloys dating to the twenty-fifth century BC. The naming of zinc is attributed to Swiss alchemist Paracelsus (1493–1541) after the German "Zinke," "pointy object, fork tooth, comb tooth," in allusion to its pointy habit in melting ovens. German chemist Andreas Marggraf is usually credited with the discovery of Zn as an element in 1746.

With an annual production of about 13 million tons (2013 and 2014), zinc is the fourth most commonly used metal, following iron, aluminum, and copper. The most important use of zinc is as an anticorrosion coating (>50%), followed by alloys and batteries. In the USA, other industrial uses account for about 8% of total use, including zinc oxide as a white pigment in paints and a catalyst in the manufacture of rubber; zinc chloride as a fire retardant or wood preservative; or various compounds used in organic synthesis. Zinc oxide absorbs UV light, and nanoparticulate ZnO is a common active ingredient in sunscreen.

Cosmochemistry

Zinc is the 22nd most abundant element in the solar system (1260 Zn atom per 10^6 Si atoms; 312 ppm; Anders and Grevesse 1989). The average concentration of zinc in Earth's crust is about 70 ppm (approximately as abundant as rubidium (78 ppm) and copper (68 ppm), and 53.5 ppm in the Mantle (Palme and O'Neill 2005). A Silicate-Earth value of 55 ppm is well established (McDonough and Sun 1995). Seawater contains 35 ppb Zn. Zn can behave both as a lithophile (e.g., Zn is dominantly concentrated in oxides and silicates within chondritic meteorites; Nishimura and Sandell 1964) or as

W. M. White (ed.), *Encyclopedia of Geochemistry*,
https://doi.org/10.1007/978-3-319-39312-4

a chalcophile element. Zinc concentrations are generally very low (<5 ppm) in fractionally crystallized iron meteorites, suggesting lithophile behavior during planetary differentiation. Consequently, models of Earth's chemical composition assert that Zn is present in only negligible quantities in the Earth's core (McDonough and Sun 1995). The discrepancy between solar system abundance and bulk Earth could be related to Zn volatility during large impacts or partitioning into S-rich metallic melts.

Mineralogy

Metallic zinc (Hexagonal, $P6_3/mmc$) is a very rare mineral occurring mostly in the cementation zone of polymetallic ore deposits and in volcanic sublimates (Boyle 1961; Karpov and Mokhov 2010). The divalent oxidation state is the only significant oxidation state of Zn in Nature. Zinc(II) has ionic radii of 0.60 Å (tetrahedral coordination) and 0.74 Å (octahedral coordination).

Zinc is an essential constituent of more than 200 minerals and occurs at minor to trace levels in many more. The most common Zn minerals include sphalerite and its polymorph wurtzite (ZnS), smithsonite ($ZnCO_3$), and hemimorphite ($Zn_4Si_2O_7(OH)_2 \cdot 2H_2O$). Since the ionic radius of Zn(II) is similar to that of Mg(II) and Ca(II), Zn can substitute in the crystal lattice of many common rock-forming minerals (e.g., staurolite – zincostaurolite endmember; chlorite – baileychlore endmember; calcite/dolomite – smithsonite/minrecordite endmembers).

Aqueous and Hydrothermal Geochemistry

In aqueous solutions, Zn(II) complexes with a variety of inorganic and organic ligands, including chloride, bromide, hydroxide, bisulfide, carbonate, acetate, cyanide, or amine. Zinc chloride, sulfate, and nitrate salts are readily soluble in water, whereas Zn oxides, carbonates, phosphates, and silicates are poorly soluble in water at ambient temperature. Zinc sulfide (sphalerite) is highly insoluble in reduced sulfur-bearing solutions at room temperature. The corrosion resistance of metallic Zn and its alloys is due to the formation of insoluble, thermodynamically stable Zn oxide or Zn carbonates on their surface. Zinc(II) chloride complexes are responsible for Zn transport in most crustal fluids, although thermodynamic calculations suggest that Zn bisulfide complexes (e.g., $Zn(HS)_2(aq)$) may become important at high temperatures (>500 °C) (Zhong et al. 2015).

At room temperature, the Zn(II) aquo complex displays an octahedral geometry, being coordinated to six water molecules. This octahedral $Zn(H_2O)_6^{2+}$ complex is destabilized by the addition of chloride ions in favor of tetrahedral

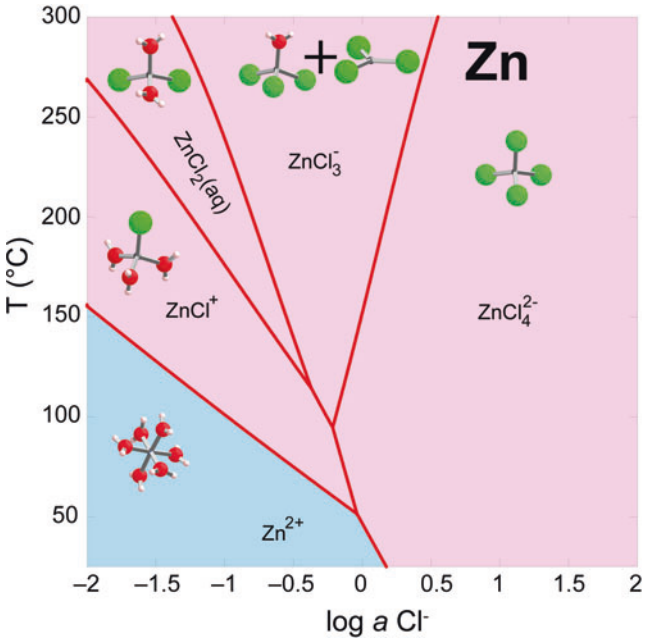

Zinc, Fig. 1 Speciation of zinc in natural fluids as a function of temperature and activity of chloride (Data from Mei et al. (2015))

complexes such as $ZnCl(H_2O)_3^+$. Similarly, the $Zn(H_2O)_6^{2+}$ complex is unstable at high temperature relative to tetrahedral $Zn(H_2O)_4^{2+}$. Tetrahedral $ZnCl_4^{2-}$ is stable in saline solutions up to high temperature; however, with increasing temperature, $ZnCl_3^-$ and $ZnCl_2(aq)$ become increasingly stable. This is especially true for $ZnCl_3^-$, which also shows a change in geometry, from predominantly tetrahedral $[ZnCl_3(H_2O)]^-$ at lower temperature to predominantly trigonal planar $[ZnCl_3]^-$ at 600 °C (Fig. 1).

Biological Utilization

Zinc is an essential trace element for humans, other animals, plants, and microorganisms alike. Zinc is an efficient Lewis acid and can therefore act as a catalyst for hydroxylation and other enzymatic reactions. In addition, the flexible coordination chemistry of Zn allows proteins using it to rapidly shift conformations to perform biological reactions. A human body contains 2–4 g Zn, and Zn is "*typically the second most abundant transition metal in organisms*" after iron (Broadley et al. 2007). For example, the protein hormone insulin contains Zn, and the metal is essential for growth, development, and reproduction in humans. Zinc deficiency results in stunted growth and in male sexual immaturity. Because of the ubiquitous and varied role of zinc in biochemical processes, its 18 synthetic radioactive isotopes are commonly used as tracers in biological studies (e.g., ^{65}Zn, $t_{1/2} = 245$ days; ^{69}Zn, $t_{1/2} = 55$ min).

Some plants are able to hyperaccumulate Zn, e.g., up to 4.0 g kg^{-1} in *Thlaspi caerulescens*.

Environmental Geochemistry and Toxicity

Since Zn plays an important role as an essential trace metal in all organisms from bacteria to humans, the metal has low toxicity compared to other elements such as cadmium, mercury, and lead. Consequently, Zn shortage in soils around the world is an important problem, although levels of Zn in excess of 500 ppm (e.g., via contamination around zinc smelters or where zinc-containing sludge is used as fertilizer) interfere with the ability of plants to absorb other essential metals such as Fe and Mn. About 2000 years ago, Zn emissions from mining and smelting totalled 10,000 tons a year. Zinc emissions peaked at 3.4 million tons per year in the 1980s and declined to 2.7 million tons in the 1990s. Anthropogenic and natural emissions occur at a ratio of 20–1 (Broadley et al. 2007).

The forms of Zn in soils may include:

- Constituents of the lattice of primary and secondary minerals, either as an essential element or in substitution for Ca, Mg (mainly)
- Adsorbed on the surface of clay minerals, Fe, Mn, Al oxy-hydroxides, and organic matter
- Immobilized in living organisms and biological residues

The Zn concentrations in weathering solutions are controlled by adsorption rather than by solubility of secondary Zn carbonates, hydroxides, and phosphates. The Zn contents in soils range mostly from 10 to 300 ppm. Several soil profile studies show that the extractable Zn contents generally decrease with depth, while total Zn is uniformly distributed throughout the profile. The content of extractable Zn usually correlates positively with that of total Zn, content of organic matter, clay content, and cation exchange capacity. An inverse correlation between the amount of extractable Zn and free $CaCO_3$, soil pH, and base saturation was also observed.

In surface waters, Zn occurs mainly bound to suspended matter (clays, Al, Fe, Mn, Si hydrous oxides). Acid mine water can locally accumulate Zn up to a high concentrations. Zinc occurs in the atmosphere mainly as fine particles (<2 μm). Atmospheric Zn results from the production and processing of Zn, nonferrous smelters, fossil fuel combustion, and car emissions.

Ore Deposits and Mineral Processing

Although Zn can become enriched via extreme magmatic differentiation in some pegmatites and agpaitic rocks, all economic Zn ore deposits share a hydrothermal origin. By far the most common economic Zn ore minerals are the cubic Zn sulfide sphalerite (ZnS) and its hexagonal polymorph, wurtzite. The most common impurities in sphalerite and wurtzite (sometimes recovered as a by-product of zinc mining) are Fe, Cd, Pb, In, Cu, and Ag; high concentrations of Ge (to 3000 ppm) and Sn occur in some localities.

The three major producing countries in 2014 were China (38%), Australia (11%), and Peru (10%). More than half of the World's Zn is produced from sedimentary exhalative (SEDEX) Zn-Pb-(±Ag,Cu,Au) massive sulfide deposits (e.g., Red Dog Mine, Alaska, USA; Mount Isa Mine, Queensland, Australia) and their putative metamorphosed equivalents (e.g., Rampura-Agucha mine, India; Broken Hill, New South Wales, Australia). Another important class of Zn deposits are carbonate-hosted "Mississippi Valley Type" Pb-Zn deposits. Their name reflects their historic occurrences along the Mississippi River in the USA, but large provinces exist in Ireland, Canada, and Australia. Some vein-type and skarn deposits (e.g., El Toqui zinc-gold mine in Chile) are also mined for Zn.

In "nonsulfide Zn deposits," sulfide-free minerals such as smithsonite ($ZnCO_3$), hemimorphite ($Zn_4Si_2O_7(OH)_2 \cdot 2H_2O$), willemite ($Zn_2SiO_4$), or the smectite sauconite ($Na_{0.3}Zn_3[(Si,Al)_4O_{10}](OH)_2 \cdot 4H_2O$) are the Zn carriers. This genetically varied class of deposits accounts for less than 10% of total Zn production, but these deposits are attractive as they have high Zn grades and less environmental impact than sulfide ore (e.g., no sulfur emissions or waste, little or no acid drainage). These deposits can form from the weathering of sulfide Zn deposits (e.g., Skorpion Mine, Karas Region, Namibia), direct hydrothermal precipitation of willemite (e.g., Beltana, South Australia; Vazante, Brazil), or high-grade metamorphism of preexisting Zn mineralization (e.g., Franklin, New Jersey, USA).

Zinc metal is produced using extractive metallurgy, typically involving: (i) grinding the ore; (ii) froth flotation to separate sphalerite/wurtzite from gangue by taking advantage of differences in the hydrophobicity of the various minerals; this results in a concentrate that contains ~50% Zn; (iii) roasting to convert the Zn sulfide to Zn oxide; the produced sulfur dioxide is used to produce sulphuric acid, which is used in the leaching process; (iv) reduction of ZnO to metallic Zn via either pyrometallurgy or electrowinning. Pyrometallurgy processing reduces ZnO with carbon or carbon monoxide at 950 °C into the metal. The metal is distilled as Zn vapor, during which metallic impurities that are not volatile are eliminated. In electrowinning, Zn is leached from the ore concentrate by sulphuric acid, and aqueous Zn is reduced by electrolysis.

Summary

Zinc (atomic number 30) is the 22nd most abundant element in the solar system (312 ppm; 70 ppm in the Earth's crust). Zinc can behave both as a lithophile or as a chalcophile element and occurs in the divalent oxidation state in Nature. Zinc is the fourth most commonly used metal, following iron, aluminum, and copper. All economic Zn ore deposits share a hydrothermal origin, with sphalerite (ZnS) as the most common Zn mineral. Zinc(II) chloride complexes are responsible for Zn transport in most crustal fluids, with Zn bisulfide complexes possibly becoming important at high temperatures. "Non-sulfide Zn deposits" (containing Zn carbonates or silicates minerals) account for less than 10% of Zn production. Zinc plays an important role as an essential trace metal in all organisms from bacteria to humans. Consequently, the metal has low toxicity compared to other elements such as Cd, Hg, and Pb, and Zn shortage in soils around the world is an important problem.

Cross-References

- ▶ Chalcophile Elements
- ▶ Hydrothermal Solutions
- ▶ Lithophile Elements
- ▶ Ore Deposits
- ▶ Sulfide Minerals
- ▶ Transition Elements
- ▶ Zinc Isotopes

References

Anders E, Grevesse N (1989) Abundances of the elements: meteoritic and solar. Geochim Cosmochim Acta 53:197–214

Boyle RW (1961) Native zinc at Keno Hill. Can Mineral 6: 692–694

Broadley MR, White PJ, Hammond JP, Zelko I, Lux A (2007) Zinc in plants. New Phytol 173:677–702

Karpov GA, Mokhov AV (2010) Microparticles of native metals, sulfides, and oxides in andesitic ashes of Karymskii Volcano. J Volcanol Seismol 4:164–179

McDonough WF, Sun S-S (1995) The composition of the Earth. Chem Geol 120:223–253

Mei Y, Sherman DM, Liu W, Etschmann B, Testemale D, Brugger J (2015) Zinc complexation in chloride-rich hydrothermal fluids (25–600 °C): a thermodynamic model derived from ab initio molecular dynamics. Geochim Cosmochim Acta 150:265–284

Nishimura M, Sandell EB (1964) Zinc in meteorites. Geochim Cosmochim Acta 28:1055–1079

Palme H, O'Neill H (2005) Cosmochemical estimates of mantle composition. In: Carlson RW (ed) The mantle and core. Elsevier, Oxford, pp 1–38

Zhong R, Brugger J, Chen Y, Li W (2015) Contrasting regimes of Cu, Zn and Pb transport in ore-forming hydrothermal fluids. Chem Geol 395:154–164

Zinc Isotopes

Frédéric Moynier
Institut de Physique du Globe de Paris, Université Paris Diderot, Sorbonne Paris Cité, Paris, France
Institut Universitaire de France, Paris, France

Introduction and Definitions

Zinc is comprised of five natural stable isotopes, ^{64}Zn (48.6%), ^{66}Zn (27.9%), ^{67}Zn (4.1%), ^{68}Zn (18.8%), and ^{70}Zn (0.6%). Due to its relatively high first ionization potential (9.4 eV), the measurement of Zn isotope ratios is very difficult by thermal ionization mass spectrometry (TIMS). This explains the very limited Zn isotope data produced before the advent of multi-collection inductively coupled plasma mass spectrometry (MC-ICP-MS). Since the first commercialized MC-ICP-MS in the late 1990s and the first high precision Zn isotope ratio measurements (Maréchal et al. 1999), more than 1000 papers have been published (source ISI Web of Science) on various geochemistry topics associated with Zn isotopes (e.g., oceanography, cosmochemistry, environmental sciences, medical sciences). Generally, the isotopic data are acquired by MC-ICP-MS by either standard bracketing (e.g., Maréchal et al. 1999; Weiss et al. 2005; Viers et al. 2007; Balistrieri et al. 2008) and only rarely by the double spike method (e.g., Bermin et al. 2006; Arnold et al. 2010). Most of the isotopic variations measured in natural samples are mass dependent (Moynier et al. 2009a) and are represented as the per mil deviation of the ^{66}Zn/^{64}Zn ratio from the JMC-Lyon standard as (Fig. 1)

$$\delta^{66}Zn = \left[\frac{\left(^{66}Zn/^{64}Zn\right)_{sample}}{\left(^{66}Zn/^{64}Zn\right)_{JMC-Lyon}} - 1\right] \times 1000$$

Zinc in Igneous Rocks and Extraterrestrial Samples

Zinc is a moderately volatile element with a 50% condensation temperature of 660 K (Lodders 2003), and the main sources of isotopic variation at high temperature are related to volatile events. Since Fe^{2+} and Zn^{2+} share similar ionic radii, the Fe/Zn ratio is not fractionated during partial melting of peridotites, and primitive basalts preserve the Fe/Zn ratio of the parental magma and therefore Zn (Le Roux et al. 2011). The Zn isotopic compositions of terrestrial igneous rocks are clustered within $0.2 < \delta^{66}Zn < 0.4$ with an estimated value for the bulk Earth of 0.28 ± 0.05 (Chen et al. 2013); the only exceptions are tektites (Moynier et al. 2009b). Tektites are terrestrial natural

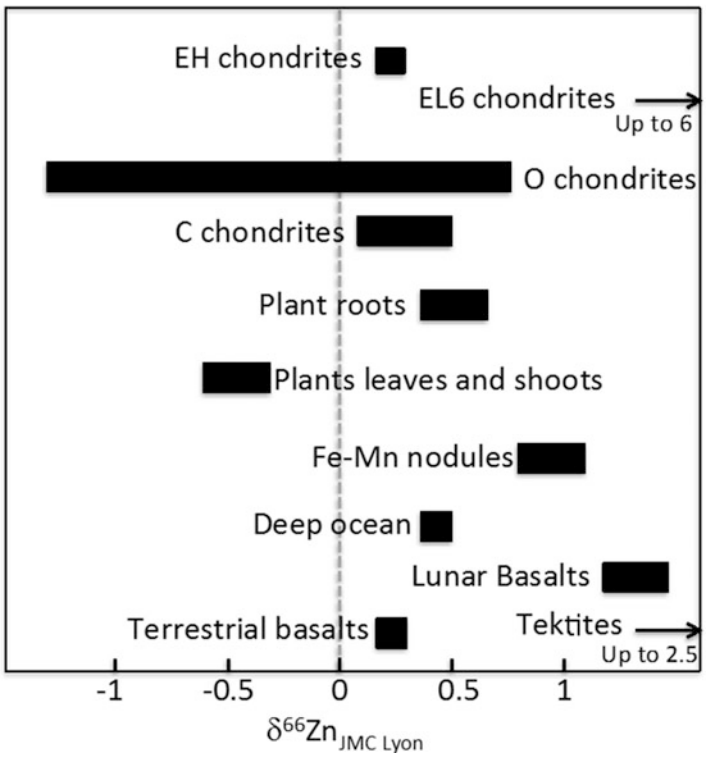

Zinc Isotopes, Fig. 1 $\delta^{66}Zn$ normalized to JMC-Lyon of different planetary reservoirs. *EH* enstatite chondrites H, *EL6* enstatite chondrites L of high metamorphic grade, *O Chondrites* ordinary chondrites, *C Chondrites* carbonaceous chondrites. Lunar basalts are enriched in the heavier isotopes of Zn compared to terrestrial basalts. Planetary samples with high volatile depletions (tektites and EL6) are highly enriched in the heavier isotopes of Zn

glasses produced during a hypervelocity impact of an extraterrestrial projectile onto the Earth's surface. They are extremely depleted in volatile elements, and they are among the driest terrestrial samples (<0.02% of water). Tektites are extremely enriched in the heavier isotopes of Zn, with $\delta^{66}Zn$ up to 2.5 per mil. This enrichment was attributed to kinetic isotopic fractionation during evaporation. Therefore, since Zn is not fractionated to a large extent during igneous processes and fractionated during evaporation, it is an ideal tracer to investigate the origin of Zn abundance variations in planetary bodies.

Zinc isotopes have been used to understand the origin of the volatile element abundance variations between chondrites (Luck et al. 2005; Albarede 2009). The negative correlation between $\delta^{66}Zn$ and 1/Zn is robust evidence against evaporation as the origin of the variability of Zn abundance between chondrite groups; rather, this suggests that the variation in the volatile element content of chondrite parent bodies was caused by nebular processes (Luck et al. 2005). This argument was later developed by Albarede (2009) to suggest that the volatile element abundances in chondrites were inherited from nebular conditions during accretion, and the Earth must have accreted "dry" and acquired its volatile elements later via impact. Following this work, Zn isotopes have been used to study the origin of the volatile element depletion of the Moon compared to the Earth (Moynier et al. 2006; Herzog et al. 2009; Paniello et al. 2012; Kato et al. 2015). The Moon is isotopically heavier than the Earth with $\delta^{66}Zn$ ~1.3. This suggests that the Moon has lost its volatile elements by evaporation either during the giant impact or during the magma ocean phase early in the Moon's history (Day and Moynier 2014). Zinc isotopes have also been used to understand the relative depletion of volatile elements in the enstatite meteorites and the depletion of volatile elements in the EL enstatite chondrites compared to the EH ones (~ factor 5). The EL6 chondrites are highly enriched in the heavier isotopes of Zn ($\delta^{66}Zn$ up to 6 per mil), suggesting that the EL parent body has lost its volatile elements during evaporation (Moynier et al. 2011). Ureilite meteorites are residues of partial melting. The Zn isotopic composition of samples with different shock degrees and volatile element abundances is positively correlated with 1/Zn, whereby samples with the lowest Zn content showed the heaviest Zn isotopic compositions. This suggests that the variations in the abundance of Zn isotopes between ureilite samples were controlled by evaporation processes (Moynier et al. 2010). In addition, the more depleted samples also exhibit a higher shock state, suggesting impacts have been responsible for the heating event.

Zn Isotopes in Surface Environments

In terrestrial environments, some of the largest isotope fractionations occur during the exchange of Zn isotopes between chemical species (e.g., carbonates, sulfides, phosphates, citrates), and changes in speciation control the isotopic

composition of aqueous solutions (e.g., Fujii et al. 2011). The same is true for the Zn isotopic fractionation in biological materials, where Zn isotopes are fractionated between the different enzymes in which Zn is bound (Moynier et al. 2013; Fujii et al. 2014). Because of the control of chemical speciation on isotopic fractionation, Zn isotopes represent a tracer for the physical and chemical conditions (e.g., pH, temperature) under which Zn isotopes were fractionated (Pons et al. 2011), the mechanisms of Zn transport in soils and plants (Weiss et al. 2005; Viers et al. 2007; Bigalke et al. 2010), biological productivity (Pichat et al. 2003; Andersen et al. 2011), and the possible changes of the metabolism associated with pathologies (Albarede 2015). In addition, Zn is a vital micronutrient that is involved in many biological processes. Zinc isotopes are fractionated during the uptake of Zn by microorganisms; the organic cellular material is enriched in the lighter isotopes (John et al. 2007), while adsorption enriches the cell's surfaces in the heavier isotopes (Gelabert et al. 2006; John et al. 2007; Balistrieri et al. 2008; Jouvin et al. 2009; Andersen et al. 2011). The Zn isotopic composition of seawater is globally heavier than the input to the ocean by ~0.2 per mil which requires an isotopically light sink of Zn incorporated into sediments (Little et al. 2014; Zhao et al. 2014) similarly to what is observed for Li and B (Paris et al. 2010; Misra and Froelich 2012).

Zinc isotopes are fractionated during the transport of Zn in plants from the roots to the aerial parts (e.g., Weiss et al. 2005; Viers et al. 2007; Moynier et al. 2009c; Aucourt et al. 2011). This fractionation has been explained by the difference of speciation of Zn between the root system (isotopically heavy Zn phosphates) and the aerial parts, rich in isotopically light malates (Fujii and Albarede 2012). Zinc isotopic fractionation between organs of sheep and mice has been observed (Balter et al. 2010; Balter et al. 2013; Moynier et al. 2013). In mice, red blood cells (RBC) and bones are enriched by 1 per mil compared to the brain and the liver (Moynier et al. 2013). These isotopic fractionations are well explained by the equilibrium distribution of isotopes between different bonding environments of Zn in different organs. In the RBC, Zn is bounded to isotopically light histidine-rich proteins, while in the brain and the liver, Zn is principally bounded to isotopically heavy cysteine-rich proteins (Moynier et al. 2013). Differences in gender and genetic background do not appear to affect the isotopic distribution of Zn, which show the potential use of Zn isotopes as a tracer for dietary Zn, and for detecting disturbances in Zn metabolism due to pathological conditions.

Zinc isotopes in 3.8 Ga serpentinites from Isua are depleted in heavy isotopes compared to the bulk silicate Earth (BSE), while serpentinites from modern mid-ocean ridge ophiolites are isotopically similar to the BSE (Pons et al. 2011). Theoretical calculation shows that the incorporation of isotopically light Zn in serpentinites requires that the serpentinization reactions occurred at high pH, with a fluid rich in carbonate at medium temperature (100–300 °C). These are the conditions that are found in modern mud volcano environments such as the Mariana forearc, where the serpentinites are also isotopically light. Therefore, Zn isotopes can be used as a pH proxy for ancient environments (Pons et al. 2011).

Summary

Evaporation/condensation processes mainly fractionate Zn isotopes in high-temperature systems and by changes in speciation at lower temperature. Zinc isotopes are little fractionated by igneous differentiation, and isotopic variations of Zn in meteorites and lunar samples have been used to constrain the origin of the variation of the volatile element abundances between solar system planetary bodies. The fractionation of Zn isotopes between different chemical species suggests that Zn isotopes could be used as pH proxy for high-pH range. The difference in the isotopic composition between the Zn uptakes in living organisms, the Zn adsorbed at the surface of the cells, and between the different species present in the ocean water makes Zn isotopes good proxy to study biochemical cycling of Zn in the ocean and changes of biological productivity with time. Finally, due to its importance in biological reactions, and the different bounding environment in the different organs, Zn isotopes have a strong potential in medical geochemistry in order to trace changes in metabolism due to medical pathologies.

Cross-References

- Biogeochemistry
- Boron Stable Isotopes
- Chondrites
- Giant Impact Hypothesis
- Inductively Coupled Plasma Mass Spectrometry (ICP-MS)
- Lithium Isotopes
- Stable Isotope Geochemistry
- Thermal Ionization Mass Spectrometry
- Zinc

References

Albarede F (2009) Volatile accretion history of the terrestrial planets and dynamic implications. Nature 461:1227–1233

Albarede F (2015) Metal stable isotopes in the human body: a tribute of geochemistry to medicine. Elements 11:265–269

Andersen MB, Vance D, Archer C, Anderson RF, Ellwood MJ, Allen CS (2011) The Zn abundance and isotopic composition of diatom frustules, a proxy for Zn availability in ocean surface seawater. Earth Planet Sci Lett 301:137–145

Arnold T, Schonbachler M, Rehkamper M, Dong SF, Zhao FJ, Kirk GJD, Coles BJ, Weiss DJ (2010) Measurement of zinc stable isotope ratios in biogeochemical matrices by double-spike MC-ICPMS and determination of the isotope ratio pool available for plants from soil. Anal Bioanal Chem 398: 3115–3125

Aucourt AM, Pichat S, Macnair MR, Oger P (2011) Fractionation of stable zinc isotopes in the zinc hyperaccumulator *Arabidopsis halleri* and nonaccumulator *Arabidopsis petraea*. Environ Sci Technol 45:9212–9217

Balistrieri LS, Borrok DM, Wanty RB, Ridley WI (2008) Fractionation of Cu and Zn isotopes during adsorption onto amorphous Fe(III) oxyhydroxide: experimental mixing of acid rock drainage and ambient river water. Geochim Cosmochim Acta 72:311–328

Balter V, Zazzo A, Moloney AP, Moynier F, Schmidt O, Monahan FJ, Albarede F (2010) Bodily variability of zinc natural isotope abundances in sheep. Rapid Commun Mass Spectrom 24: 605–612

Balter V, Lamboux A, Zazzo A, Telouk P, Leverrier Y, Marvel J, Moloney AP, Monahan FJ, Schmidt O, Albarede F (2013) Contrasting Cu, Fe, and Zn isotopic patterns in organs and body fluids of mice and sheep, with emphasis on cellular fractionation. Metallomics 5:1470–1482

Bermin J, Vance D, Archer C, Statham PJ (2006) The determination of the isotopic composition of Cu and Zn in seawater. Chem Geol 226:280–297

Bigalke M, Weyer S, Kobza J, Wilcke W (2010) Stable Cu and Zn isotope ratios as tracers of sources and transport of Cu and Zn in contaminated soil. Geochim Cosmochim Acta 74:6801–6813

Chen H, Savage P, Teng FZ, Helz RT, Moynier F (2013) zinc isotope fractionation during magmatic differentiation and the isotopic composition of the bulk Earth. Earth Planet Sci Lett 369–370:34–42

Day JM, Moynier F (2014) Evaporative fractionation of volatile stable isotopes and their bearing on the origin of the Moon. Philos Transact A Math Phys Eng Sci 372:20130259

Fujii T, Albarede F (2012) Ab initio calculation of the Zn isotope effect in phosphates, citrates, and malates and applications to plants and soil. PLoS One 7:e30726

Fujii T, Moynier F, Pons ML, Albarede F (2011) The origin of Zn isotope fractionation in sulfides. Geochim Cosmochim Acta 75:7632–7643

Fujii T, Moynier F, Blichert-Toft J, Albarede F (2014) Density functional theory estimation of isotope fractionation of Fe, Ni, Cu, and Zn among species relevant to geochemical and biological environments. Geochim Cosmochim Acta 140:553–576

Gelabert A, Pokrovsky OS, Viers J, Schott J, Boudou A, Feurtet-Mazel A (2006) Interaction between zinc and freshwater and marine diatom species: surface complexation and Zn isotope fractionation. Geochim Cosmochim Acta 70:839–857

Herzog GF, Moynier F, Albarede F, Berezhnoy AA (2009) Isotopic and elemental abundances of copper and zinc in lunar samples, Zagami, Pele's hairs, and a terrestrial basalt. Geochim Cosmochim Acta 73:5884–5904

John SG, Geis R, Saito M, Boyle EA (2007) Zn isotope fractionation during high-affinity zinc transport by the marine diatom Thalassiosira oceanica. Limnol Oceanogr 52:2710–2714

Jouvin D, Louvat P, Juillot F, Marechal CN, Benedetti MF (2009) Zinc isotopic fractionation: why organic matters. Environ Sci Technol 43:5747–5754

Kato C, Moynier F, Valdes MC, Dhaliwal JK, Day JM (2015) Extensive volatile loss during formation and differentiation of the Moon. Nat Commun 6:7617

Le Roux V, Lee CT, Turner SJ (2011) Zn/Fe systematics in mafic and ultramafic systems: implications for detecting major element heterogeneities in the Earth's mantle. Geochim Cosmochim Acta 74:2779–2796

Little SH, Vance D, Walker-Brown C, Landing WM (2014) The oceanic mass balance of copper and zinc isotopes, investigated by analysis of their inputs, and outputs to ferromanganese oxide sediments. Geochim Cosmochim Acta 125:673–693

Lodders K (2003) Solar system abundances and condensation temperatures of the elements. Astrophys J 591:1220–1247

Luck JM, Othman DB, Albarede F (2005) Zn and Cu isotopic variations in chondrites and iron meteorites: early solar nebula reservoirs and parent-body processes. Geochim Cosmochim Acta 69: 5351–5363

Maréchal C, Télouk P, Albarède F (1999) Precise analysis of copper and zinc isotopic compositions by plasma-source mass spectrometry. Chem Geol 156:251–273

Misra S, Froelich PN (2012) Lithium isotope history of Cenozoic seawater: changes in silicate weathering and reverse weathering. Science 335:818–823

Moynier F, Albarede F, Herzog G (2006) Isotopic composition of zinc, copper, and iron in lunar samples. Geochim Cosmochim Acta 70:6103–6117

Moynier F, Beck P, Jourdan F, Yin Q-Z, Reimold U, Koeberl C (2009a) Isotopic fractionation of zinc in tektites. Earth Planet Sci Lett 277:482–489

Moynier F, Dauphas N, Podosek FA (2009b) A search for 70Zn anomalies in meteorites. Astrophys J 700:L92–L95

Moynier F, Pichat S, Pons ML, Fike D, Balter V, Albarede F (2009c) Isotopic fractionation and transport mechanisms of Zn in plants. Chem Geol 267:125–130

Moynier F, Beck P, Yin QZ, Ferroir T, Barrat JA, Paniello R, Telouk P, Gillet P (2010) Volatilization induced by impacts recorded in Zn isotope composition of ureilites. Chem Geol 276:374–379

Moynier F, Paniello RC, Gounelle M, Albarede F, Beck P, Podosek F, Zanda B (2011) Nature of volatile depletion and genetic relationships in enstatite chondrites and aubrites inferred from Zn isotopes. Geochim Cosmochim Acta 75:297–307

Moynier F, Fujii T, Shaw A, Le Borgne M (2013) Heterogeneous distribution of natural zinc isotopes in mice. Metallomics 5:693–699

Paniello RC, Day JM, Moynier F (2012) Zinc isotopic evidence for the origin of the Moon. Nature 490:376–379

Paris G, Gaillardet J, Louvat P (2010) Geological evolution of seawater boron isotopic composition recorded in evaporites. Geology 38:1035–1038

Pichat S, Douchet C, Albarede F (2003) Zinc isotope variations in deep-sea carbonates from the eastern equatorial Pacific over the last 175 ka. Earth Planet Sci Lett 210:167–178

Pons ML, Quitte G, Fujii T, Rosing MT, Reynard B, Moynier F, Douchet C, Albarede F (2011) Early Archean serpentine mud volcanoes at Isua, Greenland, as a niche for early life. Proc Natl Acad Sci U S A 108:17639–17643

Viers J, Oliva P, Nonelle A, Gelabert A, Sonke J, Freydier R, Gainville R, Dupre B (2007) Evidence of Zn isotopic frationation in a soil-plant system of a pristine tropical watershed (Nsimi, Cameroon). Chem Geol 239:124–137

Weiss DJ, Mason TFD, Zhao FJ, Kirk GJD, Coles BJ, Horstwood MSA (2005) Isotopic discrimination of zinc in higher plants. New Phytol 165:703–710

Zhao Y, Vance D, Abouchami W, de Baar HJW (2014) Biogeochemical cycling of zinc and its isotopes in the Southern Ocean. Geochim Cosmochim Acta 125:653–672

Zirconium

Carsten Münker
Institut für Geologie und Mineralogie, Universität zu Köln, Köln, Germany

Element Data
Atomic Symbol: **Zr**
Atomic Number: **40**
Atomic Weight: 91.224
Isotopes and Abundances: ^{90}Zr, 51.45% ^{91}Zr, 11.22%, ^{92}Zr, 17.15%, ^{94}Zr, 17.38%, ^{96}Zr, 2.80%
1 Atm Melting Point: 1855 °C
1 Atm Boiling Point: 4371 °C
Common Valences: 4+
Ionic Radii: sixfold: 72 pm
Pauling Electronegativity: 1.33
First Ionization Potential: 640 kJ/mol
Chondritic (CI) Abundance: 3.63 ppm
Silicate Earth Abundance: 10.3 ppm
Crustal Abundance: 132 ppm
Seawater Abundance: 9–300 pmol/kg
Core Abundance: n/a

Properties

Zirconium is a transition metal of low toxicity with the atomic number of 41. Zirconium has five stable isotopes (90, 91, 92, 94, 96) with an atomic mass of 91.224(2) (CIAAW 2015). The isotope ^{92}Zr is the decay product of the now extinct ^{92}Nb with a half-life of 34.7 Ma (e.g., Münker et al. 2000; Schönbächler et al. 2002; Iizuka et al. 2016). In some chondrites and CAIs, the neutron-rich isotope ^{96}Zr is slightly enriched relative to other Zr isotopes, reflecting variable contributions from AGB stars and supernova material to early solar system matter (e.g., Akram et al. 2015).

In nature, Zr occurs in +4 valence state, although a lower valence state of +2 is known from synthetic systems. Its atomic radius is 155 pm, and its ionic radius in +6 valence state and sixfold coordination is 72 pm (Shannon 1976). Due to its high ratio of charge to ionic radius, Zr is classified in geochemistry as *high field strength element*.

History and Use

Zirconium was first discovered in 1789 by the German chemist M.H. Klaproth, who named it after the mineral *zircon*. In 1824, it was for the first time synthesized by the Swedish chemist J.J. Berzelius, although the atomic mass estimated at the time was too high due to the presence of small amounts of Hf that exhibits an extreme geochemical similarity to Zr.

Economically important Zr deposits are hosted by placer deposits, granitic rocks, or coastal sand deposits that in most cases exhibit a paired enrichment of both Zr and its geochemical twin Hf in heavy minerals. Such important economical grade heavy minerals include zircon and baddeleyite. Countries with the world's largest Zr deposits include Australia, the USA, South Africa, and Brazil, with Australia and South Africa presently supplying most of the industrially used Nb (USGS 2014). Technically, Zr is mainly used as high-temperature ceramic material, as opacifier, for laboratory crucibles and for heat-resisting equipment including space vehicle parts, turbines, and jet engines. There is also some minor use in nuclear industry.

Geochemical Behavior

Zirconium is one of the most refractory elements with a 50% condensation temperature of 1764°K (Lodders 2003), and it has traditionally been regarded as behaving lithophile during Earth's differentiation. Ratios of Zr and similarly refractory elements like Hf, Nb, or Ta are nearly constant in most groups of chondrites (Münker et al. 2003). The solar system abundance of Zr as estimated from CI chondrites is 3.63 ppm; the estimated abundance in the bulk silicate Earth is 10.3 ppm (Palme & O'Neill 2014). Because of its strongly lithophile behavior, the concentration of Zr in the core is negligibly low. Due to its virtually identical geochemical and cosmochemical properties, Zr behaves very similar to Hf, leading to a virtually constant Zr/Hf ratio in chondrites and the silicate Earth (34.3 ± 0.3; Münker et al. 2003).

During silicate melting on Earth, Zr behaves as a mildly incompatible element in mantle minerals and is therefore depleted in the mantle and enriched in the crust. In the continental crust, the Zr content is estimated to 132 ppm with a content of 193 ppm and a near chondritic Zr/Hf in the upper crust (Barth et al. 2000; Rudnick and Gao 2014). Relative to similarly incompatible elements like Nd or Sm, however, Zr (and Hf) is slightly depleted in the continental crust, mirroring its selective depletion in many subduction zone magmas that contributed to the bulk of the continental crust. The selective depletion of Zr in subduction-related lavas and the continental crust is caused by its lower solubility in subduction zone fluids and by its retention in HFSE-rich phases like zircon or rutile in subducting crust (e.g., Zack et al. 2002; Hermann and Rubatto 2009). Together with its geochemical twin Hf, Zr is therefore a viable tracer for elemental mass balances in subduction zone systems, belonging

to some of the most insoluble elements in subduction zone fluids (e.g., Pearce and Peate 1995).

Employing Zr/Hf and Zr/Sm ratios in igneous rocks has now become an important tool to better understand melting processes and the role of residual phases such as zircon, rutile, or amphibole during silicate melting. Although behaving broadly similar, Zr is slightly more incompatible during mantle melting than Hf (e.g., McDade et al. 2003), leading to higher Zr/Hf ratios in basalts if compared to depleted mantle rocks (e.g., David et al. 2000; Münker et al. 2003). Moreover, Zr/Hf ratios can serve as viable tracers for carbonatite metasomatism and for recycled eclogitic components in the mantle (e.g., Pfänder et al. 2007, 2012; Klemme et al. 2002). Ratios of Zr/Sm are important tracers for the presence of amphibole during continental crust formation (e.g., Foley et al. 2002).

Due to its high valence state, Zr tends to hydrolize easily and is not very soluble in seawater, with an estimated concentration between 9 and 300 pmol/kg (Firdaus et al. 2011; Bruland et al. 2014). Notably, Zr/Hf are elevated in seawater if compared to silicate rocks (Godfrey et al. 1996; Firdaus et al. 2011), indicating that Zr can be highly fractionated from its geochemical twin Hf in aqueous systems due to their different complexing behavior. This observation was also made for chemical sediments, as well as for high-temperature fluids and their deposits, where strong Zr/Hf fractionation was also observed (e.g., Bau 1996; Schmidt et al. 2014). Collectively, Zr/Hf ratios are therefore valuable tracers for aqueous processes in silicate rocks.

Biological Utilization and Toxicity

Zirconium has no known biological role, and most Zr compounds have been shown to have low toxicity, largely due to their low solubility.

Summary

Zirconium is a highly refractory lithophile element and one of the high field strength elements and forms the highly stable and common accessory mineral zircon. It has low solubility and is generally considered immobile. Compared to elements of similar incompatibility, it is depleted in the Earth's crust and in subduction zone magmas.

Cross-References

- ▶ Hafnium
- ▶ High field strength elements
- ▶ Incompatible elements
- ▶ Ore Deposits
- ▶ Periodic Table
- ▶ Subduction Zone Geochemistry
- ▶ Transition Elements

References

Akram W, Schönbächler M, Bisterzo S, Gallino M (2015) Zirconium isotope evidence for the heterogeneous distribution of s-process materials in the solar system. Geochim Cosmochim Acta 165:484–500

Barth MG, McDonough WF, Rudnick RL (2000) Tracking the budget of Nb and Ta in the continental crust. Chem Geol 165:197–213

Bau M (1996) Controls on the fractionation of isovalent trace elements in magmatic and aqueous systems: evidence from Y/Ho, Zr/Hf, and lanthanide tetrad effect. Contrib Mineral Petrol 123:323–333

Bruland KW, Middag R, Lohan MC (2014) Controls of trace metals in seawater. In: Mottl MJ, Elderfield H (eds) The oceans and marine geochemistry, Treatise on geochemistry, vol 8. Elsevier, Amsterdam, pp 19–51

CIAAW (2015) Commission on isotopic abundances and atomic weights. http://ciaaw.org/atomic-weights.htm

David K, Schiano P, Allègre CJ (2000) Assessment of the Zr/Hf fractionation in oceanic basalts and continental materials during petrogenetic processes. Earth Planet Sci Lett 178:285–301

Firdaus ML, Minami T, Norisuye K, Sohrin Y (2011) Strong elemental fractionation of Zr-Hf and Nb-Ta across the Pacific Ocean. Nat Geosci 4:227–230

Foley S, Tiepolo M, Vannucci R (2002) Growth of early continental crust controlled by melting of amphibolite in subduction zones. Nature 417:837–840

Godfrey LV, White WM, Salters VJM (1996) Dissolved zirconium and hafnium distributions across a shelf break in the northeastern Atlantic Ocean. Geochim Cosmochim Acta 60(21):3995–4006

Hermann J, Rubatto D (2009) Accessory phase control on the trace element signature of sediment melts in subduction zones. Chem Geol 265:512–526

Iizuka T, Lai YJ, Akram W, Amelin Y, Schönbächler M (2016) The initial abundance and distribution of 92Nb in the Solar System. Earth Planet Sci Lett 439:172–181

Klemme S, Blundy JD, Wood BJ (2002) Experimental constraints on major and trace element partitioning during partial melting of eclogite. Geochim Cosmochim Acta 66(17):3109–3123

Lodders K (2003) Solar system abundances and condensation temperatures of the elements. Astrophys J 591:1220–1247

McDade P, Blundy JD, Wood BJ (2003) Trace element partitioning on the Tinaquillo Lherzolite solidus at 1.5 GPa. Phys Earth Planet Inter 139:129–147

Münker C, Weyer S, Mezger K, Rehkämper M, Wombacher F, Bischoff A (2000) ^{92}Nb-^{92}Zr and the early differentiation history of planetary bodies. Science 289:1538–1542

Münker C, Pfänder JA, Weyer S, Büchl A, Kleine T, Mezger K (2003) Evolution of planetary cores and the Earth – moon system from Nb/Ta systematics. Science 301:84–87

Palme H, O'Neill HSC (2014) Cosmochemical estimates of mantle composition. In: Carlson RW (ed) The mantle and core, Treatise on geochemistry, vol 3. Elsevier, Amsterdam, pp 1–39

Pearce JW, Peate DW (1995) Tectonic implications of the composition of volcanic arc magmas. Annu Rev Earth Planet Sci 23:251–285

Pfänder JA, Münker C, Stracke A, Mezger K (2007) Nb/Ta and Zr/Hf in ocean island basalts - implications for crust-mantle differentiation and the fate of Niobium. Earth Planet Sci Lett 254(1-2):158–172

Pfänder JA, Jung S, Münker C, Stracke A, Mezger K (2012) A possible high Nb/Ta reservoir in the continental lithospheric mantle and consequences

on the global Nb budget – evidence from continental basalts from Central Germany. Geochim Cosmochim Acta 77:232–251
Rudnick RL, Gao S (2014) Composition of the continental crust. In: The crust, Treatise on geochemistry, vol 4. Elsevier, Amsterdam, pp 1–51
Schmidt K, Bau M, Hein JR, Koschinsky A (2014) Fractionation of the geochemical twins Zr–Hf and Nb–Ta during scavenging from seawater by hydrogenetic ferromanganese crusts. Geochim Cosmochim Acta 140:468–487
Schönbächler M, Rehkämper M, Halliday AN, Lee DC, Bourot-Denise M, Zanda B, Hattendorf B, Günther D (2002) Niobium-zirconium chronometry and early solar sytem development. Science 295:1705–1708
Shannon RD (1976) Revised effective ionic radii and systematic studies of interatomic distances in halides and chalcogenides. Acta Crystallogr A32:751–767
USGS (2014) http://minerals.usgs.gov/minerals/pubs/commodity/zirconium/mcs-2014-zirco.pdf
Zack T, Kronz A, Foley SF, Rivers T (2002) Trace element abundances in rutiles from eclogites and associated garnet mica schists. Chem Geol 184:97–122

Author Index

A
Adetunji, Jacob, 738
Aiuppa, Alessandro, 1476
Akaogi, Masaki, 186, 262
Albarède, Francis, 498
Alpers, Charles N., 895
Arevalo, Ricardo Jr., 23, 1253
Arndt, Sandra, 1094
Asimow, Paul D., 1180

B
Bach, Wolfgang, 711
Ballentine, Chris J., 1003
Barling, Jane, 950
Barnes, Sarah-Jane, 229
Baronnet, Alain J., 936
Barrat, Jean-Alix, 7
Barry, Peter H., 1003
Bebout, Gray E., 172
Bechtel, Achim, 123
Bekki, Slimane, 1135
Bentley, R. Alexander, 42
Bergquist, Bridget A., 900
Bickmore, Barry R., 21, 39, 234, 442
Bierman, Paul R., 95
Birdwell, Justin E., 1055
Bizimis, Michael, 965, 967, 1321
Black, Jay R., 297, 345
Blichert-Toft, Janne, 629, 631
Bodnar, Robert J., 488
Boily, Jean-François, 294, 706, 1359
Bonifacie, Magali, 244
Bourdon, Bernard, 1468
Bourg, Ian C., 263
Brandes, J. A., 1019
Brenan, James M., 1172, 1233, 1312
Brophy, James G., 693
Brugger, Joël, 1521
Budahn, James R., 978
Bureau, Hélène, 167, 728
Busigny, Vincent, 756, 991

C
Canil, Dante, 1452
Canuel, Elizabeth A., 191
Cartigny, Pierre, 985, 991
Casey, William H., 19, 325, 521, 554, 620, 1115, 1374, 1410
Chappaz, Anthony, 947
Chassé, Mathieu, 980, 1323
Chauvel, Catherine, 226, 719, 799, 800
Chivas, Allan R., 541
Christy, Andrew G., 1392
Ciobanu, Cristiana L., 153
Clauer, Norbert, 85
Cole, Devon B., 256
Cole, Lydia E. S., 1197
Colla, Christopher A., 521
Colleary, Caitlin, 1099
Cook, Nigel J., 153
Crossey, Laura J., 353, 492
Cuney, Michel, 1063
Curry, Joan E., 1240
Czaja, Andrew D., 1099

D
Day, James M. D., 1328
de Baar, Hein J. W., 1023, 1042
Degryse, Patrick, 42
Derry, Louis A., 615
Dia, Aline, 1474
Dixon, David A., 1, 58, 59, 171, 255, 347, 445, 622, 721, 1241, 1291, 1326, 1335
Dunlea, Ann G., 878

E
Ebel, Denton S., 1175
Eble, Cortland F., 275
Emeis, Kay-Christian, 155
Etiope, Giuseppe, 961

F
Farkaš, Juraj, 181
Farquhar, James, 1397, 1402
Faucon, Michel-Pierre, 291
Fendorf, Scott E., 1415
Föllmi, Karl B., 1231
Forbes, Tori Z., 828, 835, 1508
Foster, Gavin L., 162
Fritz, B., 1352

G
Gaillard, Fabrice, 1476
Gaillardet, Jérôme, 1344
Gamsjäger, Heinz, 455
Geiger, Charles A., 471
Genda, Hidenori, 617
Gerke, Tammie L., 864
Ghiorso, Mark, 841
Giering, Sarah L. C., 111
Glass, Jennifer B., 947
Glassley, William E., 492
Goldblatt, Colin, 62
Gorzsás, András, 1303
Goswami, Jitendra Nath, 1014
Greb, Stephen F., 275
Green, Eleanor C. R., 906
Greenwood, Richard, 7
Griffen, Dana T., 331
Griffin, William L., 980

H
Haack, Henning, 762
Hardison, Amber K., 191
Harmon, Russell S., 83
Harpp, Karen, 1201
Hartnett, Hilairy Ellen, 107, 375, 987
Hawkins, Adam J., 592
He, Meng, 136
Hein, James R., 477
Helz, George R., 1455
Herrle, Jens O., 194
Hertzberg, Jennifer E., 1166
Hirata, Takafumi, 801
Hochella, Michael F. Jr., 943
Holden, Norman E., 1463
Holland, Greg, 784
Honda, Masahiko, 541
Hoppe, Peter, 1273
Houston, Jacqueline R., 37
Hower, James C., 275
Humayun, Munir, 526, 745
Humphreys, Matthew P., 111

J
Jackson, Matthew Gerard, 1048
Jenner, Frances E., 827
Johnson, Clark M., 751
Jones, Adrian, 187
Jones, Rhian, 251

K
Kamilli, Robert J., 1175
Kawamoto, Tatsuhiko, 471
Kearns, Stuart, 439
Kelly, Thomas J., 1197
Kendrick, Mark A., 53, 241, 645
Keppler, Hans, 340
Kleber, Markus, 148
Kleine, Barbara I., 704, 715
Kleine, Thorsten, 1458
Koga, Kenneth T., 495
Komiya, Tsuyoshi, 1258

W. M. White (ed.), *Encyclopedia of Geochemistry*,
https://doi.org/10.1007/978-3-319-39312-4

Königsberger, Erich, 456
Krot, Alexander N., 1307
Kucerik, Jiri, 1435
Kujawinski, Elizabeth B., 666
Kumar, Rajnish, 535
Kurosawa, Masanori, 1185

L
Lackner, Klaus S., 34
Lang, Maik, 932
Langmuir, Charles H., 924
LaRowe, Douglas Edward, 1094
Lassiter, John C., 1433
Lawrence, Gregory B., 12
Lawson, Ian T., 1197
Lécuyer, Christophe, 156, 162, 177
Lee, Cin-Ty, 545
Lehmann, Johannes, 1347
Lerman, Abraham, 206
Lezama Pacheco, Juan S., 1415
Liang, Yan, 363
Liang, Yu-Hsuan Crystal, 950
Lichtner, Peter C., 892
Linga, Praveen, 535
Little, Brenda J., 864
Liu, Xingcheng, 303
Louda, J. William, 1247
Ludwig, Christian, 1410
Luth, Robert W., 1220
Lyons, Timothy W., 947

M
Mackenzie, Fred T., 206
MacPherson, Glenn J., 1307
Magill, Clayton R., 194
Mango, Helen, 1340
Marschall, Horst R., 162
Mascaro, Giuseppe, 701
Matsubara, Satoshi, 957
McDonough, William F., 418, 589
McKirdy, David, 1052
McLennan, Scott M., 381, 460, 525, 683, 792, 839, 1257, 1286, 1425, 1441
Medeiros, Patricia M., 530
Meisel, Thomas C., 553, 743, 1314, 1318
Middag, Rob, 1023, 1042
Miyawaki, Ritsuro, 1334
Mizell, Kira, 477
Moldowan, J. Michael, 116, 136
Montañez, Isabel P., 353, 492
Mookherjee, Mainak, 27
Moreira, Manuel, 973, 975
Morgan, Bree, 1394
Moses, Carl O., 15, 446, 447, 518, 1487
Moynier, Frédéric, 1524
Mukhopadhyay, Sujoy, 1497, 1500
Münker, Carsten, 983, 1419, 1528
Murray, Richard, W., 878
Muscente, A. D., 1099

N
Naafs, B. D. A, 1160
Nadoll, Patrick, 1120
Nagashima, Kazuhide, 736
Nakai, Izumi, 1511
Nebel, Oliver, 1316, 1377, 1379
Nielsen, Sune G., 1429
Noguera, C., 1352
Nyman, May, 1242

O
Ohlin, C. André, 19
Oliva, Priscia, 237
Oliveri, Anna F., 1376
O'Neill, Hugh StC, 652, 827

P
Palme, Herbert, 310
Palta, Monica M., 987
Pancost, R. D., 1160
Pearson, Ann, 818
Perfit, Michael, 430
Peters, Kenneth E., 116, 136, 1276
Peterson, Larry C., 1147
Petsch, Steven, 771
Philp, R. Paul, 1075
Pilgrim, Corey D., 233, 1009
Pinti, Daniele L., 60, 383
Planavsky, Noah J., 756
Plank, Terry, 1384
Porcelli, Don, 1295, 1301
Portenga, Eric W., 95
Pourret, Olivier, 291, 1474
Prytulak, Julie, 1287
Puchtel, Igor S., 1236
Putirka, Keith, 597
Püttmann, Wilhelm, 123

Q
Qin, Liping, 256

R
Reardon, Patrick, 148
Reeves, Eoghan P., 711
Reich, Martin, 1409
Reinhard, Christopher T., 256
Richardson, Justin B., 326
Richet, Pascal, 1330
Riedman, Leigh Anne, 1099
Rigali, Mark J., 1059
Roberts, Jennifer A., 378
Rock, Peter A., 325, 554, 620, 1374
Rodriguez, Leonardo Briceño, 1276
Rodriguez, Norelis D., 1057
Rogers, Nick, 1480
Rollinson, Hugh, 738
Rose-Koga, Estelle F., 495
Ross, Andrew, 1052
Rudnick, Roberta L., 392, 800
Russell, Sara, 248
Rutzke, Michael A., 76
Ryan, Jeffrey G., 93, 822, 824

S
Sakaguchi, Isao, 483
Salters, Vincent J. M., 664, 1439, 1464
Samson, Iain M., 1323
Sano, Yuji, 657, 659
Sarda, Philippe, 56
Sauer, Peter E., 696
Savage, Paul, 305
Savarino, Joël, 1135
Scher, Howie D., 965, 967, 1321
Schimmelmann, Arndt, 693, 696
Schmidt, Matthew W., 1166
Schmitz, Mark D., 586
Schönbächler, Maria, 723, 731
Schoonen, Martin A., 1399
Schwartz, Kurt, 932
Scruggs, Melissa, 513
Scudder, Rachel P., 878
Seewald, Jeffrey S., 789
Shahar, Anat, 1337
Sikes, Elisabeth, 1103
Sparks, Don, 775
Spera, Frank, 513
Sposito, Garrison, 623
Stammeier, Jessica A., 1379
Stefánsson, Andri, 704, 715
Stracke, Andreas, 867
Strąpoć, Dariusz, 100
Summons, Roger, 1266
Sun, Chenguang, 1062, 1186

T
Takahashi, Yoshio, 1421, 1423
Talukder, Asrarur, 1052
Teng, Fang-Zhen, 853, 856
Tester, Jefferson W., 592
Thomas, Jay B., 1445
Thompson, John F. H., 549
Thomson, Stuart N., 484
Tomkins, Andrew G., 1394
Tsuchiya, Taku, 1473
Tsunakawa, H., 860

U
Ungerer, Philippe, 1207

V
van Heuven, Steven M. A. C., 1023, 1042
Vasiliu, Monica, 58, 59, 171, 255, 445, 622, 721, 1241, 1326, 1335
Vervoort, Jeff, 571
Viers, Jérôme, 237
Volkman, John K., 685, 1081
Voncken, J. H. L., 1517, 1518

W
Wagner, Thomas, 194
Walker, Richard J., 1109, 1111
Wander, Matthew C. F., 21, 39, 234, 442
Wang, Xiangli, 256
Warren, John, 464, 636
Wefer, Gerold, 1163
Weis, Dominique, 811, 813
Weisberg, Michael K., 917
White, William M., 29, 91, 561, 663, 670, 1298, 1367, 1443, 1451
Wieler, Rainer, 317
Wilkinson, Jamie J., 453
Willbold, Matthias, 462
Wimpenny, Josh, 265, 1426
Woodfield, Brian F., 649
Woodhead, Jon, 767
Woosley, Ryan J., 204

X
Xiong, Xiaolin, 303

Y
Yamaguchi, Akira, 7
Yamamoto, Y., 860
Yang, Jie, 950
Young, Edward D., 1124
Yurimoto, Hisayoshi, 1129

Z
Zhang, Yi Ge, 300

Subject Index

A
Abietane, 125
Ab initio
  approach, 563
  calculations, 244, 676, 1404
  (from first principles) electronic structure calculations, 1
  electronic structure methods, 348
Abiogenic methane, 105
Abiogenic self-assembly, 1268
Abiological model, 73
Abiotic hydrocarbon-rich gas, 962
Abiotic methane, 700
Abiotic nitrogen reduction, 1000
Absolute entropy, 650
Absorption, 1299
  edge energy, 1511
  efficiency, 1136
  spectroscopy, 1368
Abundance sensitivity, 725
Abyssal peridotites, 1113
Acapulcoites, 7, 921
Acasta gneisses, 413
Accelerator mass spectrometers, 31, 324
Accelerator mass spectrometry (AMS), 95, 96, 1083
Accessory mineral, 1446
Accretion, 1236
  of Earth, 216
  timescales, 1460–1461
Acetate, 101
Acetoclastic methanogenesis, 100
Acetogenic lipids, 818
Achondrites, 7, 568, 678
Acid–base reactions, 40–41
Acid deposition, 14–15
  base cations, 14
  history of, 13–14
  landscape sensitivity, 12–13
Acidic rock, 18
Acidification of rain, 1400
Acidithiobacillus ferrooxidans, 749
Acid mine drainage, 285, 328, 564, 1400, 1414
Acid mine waste, 749
Acid-neutralizing capacity, 14
Acid rain, 285, 562, 1405
  See also Acid deposition
Acid-sulfate soils, 1393
Acritarchs, 144
Actinide elements, 653, 672, 1465
Actinium, 1287
Activation energy, 367–368, 371, 562, 790, 1214, 1437
Activation enthalpy, 20, 367, 369
Activation entropies, 20
Activation parameters, 19
Activation volume, 20, 367, 371, 562
Active transport, 112
Activity(ies), 21, 522, 523, 1374
  coefficient(s), 21, 209, 345, 366, 621, 1116, 1125, 1361
  measurement, oxygen, 1125
  radon, 1301
Activity–composition, 1220
  relation, 909, 910
Acyclic isoprenoids, 1269
Adiabatic compressibility, 212
Adiabatic melting, 406, 1181, 1480
Adsorption, 266, 272, 1432
  desorption, 1411–1413
  partitioning reactions, 41
Aeolian dust, 529
Aerobic bacteria, 142
Aerosol(s), 296, 723, 1143, 1392, 1405, 1406
  particles, 1141
AFC-assimilation fractional crystallization, 433
Ag, 1174
Age-diagnostic biomarkers, 143–145, 1083
Age of Earth, 813
Age on the Moon, 503
Age-standard approach, 486
Agglomeration, 294
Aggregation, 112
Agricola, Georgius, 670, 944, 946, 1072
Albedo, 1144, 1154
Alchemical symbol, 895
Alchemy, 670, 679
Alcohols, 276
Aldebaranium, 1517
Aldrich, T., 674
Algaenans, 689, 691, 1082
Algoma, 751
Aliphatic hydrocarbon, 685, 686, 690
Alkali and alkaline earth metals, 91, 177, 828, 1299, 1316, 1377
  chemistry and geochemical behavior, 23–24
  geological applications, 25
  migration, 441
Alkalinity, 69
Alkanes, 140, 1209, 1212, 1214, 1217
n-Alkanes, 123
Al Keggin ion, 1245
Alkenes, 685, 687
Alkenone(s), 301, 1083, 1150, 1151
  ^{13}C method, 301
  $U^{k'}_{37}$, 1168
n-Alkyl diols, 1084
Allanite, 381, 461, 525, 578, 684, 796, 839, 1257, 1425, 1442
Allègre, C., 674
Allende CV3 meteorite, 163
Allende meteorite, 679
Alloying material, 37
Allred-Rochow electronegativity, 443
Almadén, 895
Al-octahedra, 265
Al ore, 564
Alpha counting, 1288
Alpha decay, 484, 796, 1296
  radiation damage, 486
Alpha recoil, 1299, 1302
Alpha spectrometry, 1297
Alteration, 884
Altered oceanic crust, 1181, 1465, 1466
Altitude, 1136
Alumen, 27
Aluminium, 44
Aluminium-26, 501
Aluminosilicate(s), 265, 878, 882–886, 888, 889
  polymorphs, 27
Aluminum, 13, 15, 527, 1245
  avoidance principle, 28
Alunite, 1393
Amalgamation, 895
Amalgams, 895
American Chemical Society, 671
Amines, 1210, 1212
Amino acids, 48, 1082
Ammonia, 65, 695, 987
Ammonium, 986
Amoeboid olivine aggregates (AOAs), 568, 1307
Amphibole(s), 179, 945, 1193
Amphibolite-facies, 393
Anaerobic green-sulfur bacteria, 143
Anaerobic methane oxidation, 105
Anaerobic oxidation of methane (AOM), 301
Analytical derivative methods, 3
Analytical method, 371

W. M. White (ed.), *Encyclopedia of Geochemistry*,
https://doi.org/10.1007/978-3-319-39312-4

Analytical resolution, 440
Analytical techniques, 496, 561, 567, 568, 978
  compositional and isotopic analysis, 29–32
  crystalline, molecular, oxidation state, and chemical bonding characterization, 32–33
  definition, 29
Andes, 402
Andesite(s), 402, 433, 1482
Andesitic glasses, 244
Angiosperm(s), 125, 127, 132, 145
Anglesite, 1392
Angrites, 9, 528, 920
Angular momentum, 498, 1009, 1292
Anhydrite, 177, 1044, 1299, 1392, 1395
Anion, 297
  exchange resins, 733, 1430
  exclusion, 264
Ankerite, 284, 378, 753
Annamox, 988, 989
Anorthite, 1378
Anorthosites, 528, 618, 619
Anoxia, 1160, 1161
Anoxic conditions, 102, 130, 142, 149, 195, 278, 1040, 1099, 1119, 1133, 1086
  atmosphere, 1400
Antarctica, 1139
Antarctic Bottom Water (ABW), 199, 1046
Antarctic circumpolar current, 1046
Antarctic intermediate water, 1046
Antarcticite, 177
Anthopocene, 43
Anthracite, 189
Anthracitic coals, 279
Anthropogenic
  contaminants, 1114
  emissions, 896
  pCO_2, 199
  processes, 1399
  release, 660
Anthropogenic CO_2, 115, 205
  carbon budget balancing, 35–36
  emissions, environmental concern, 35
  sources, 34–35
Antibiotics, 1349
Anti-dandruff shampoos, 1327
Antiferromagnetism, 861
Antiferromagnets, 651
Antimony, 44
  trioxides, 37
Anti-neutrinos, 589, 591
Antinomides, 1394
Antioxidant enzyme glutathione peroxidase, 1328
Anti-particles, 1014
Antlerite, 1393
Antoine Laurent de Lavoisier, 1124
Apatite, 244, 246, 484, 578, 1231, 1378, 1466
APCI, *see* Atmospheric pressure chemical ionization (APCI)
Apparent rate laws, 777
APPI, *see* Atmospheric pressure photo-ionization (APPI)
Aquatic environments, 1238
Aqueous alteration, 251
Aqueous/complex speciation, 298
Aqueous electrolyte solutions, 345
Aqueous solution (AS), 492, 1356–1358
  complexation, 41
  definition, 39
  in geochemistry, 39
  structure, 39
  thermodynamic description, 39
Aqueous species, 298, 707
Aquo-complexes, 547
Aragonite, 204, 206, 207, 211, 214–215, 217, 218, 379, 465, 886, 1169
Araucariaceae, 125
Archaea, 100, 129, 133, 142, 686, 1085
  archaeal lipid classes, 819
  GDGTs of, 820
Archaeological fields, 198
Archaeological geochemistry, 42
Archean, 406
  continental crusts, 1260
  crust, 410
  rocks, 970, 1267
Archean-Proterozoic (A-P) boundary, 408
Archeological geochemistry, 567
Archeology, 562, 1372
Arc lavas, 1114
Arc magmas, 246
Arctic polar vortex, 1140
Areal porosity, 892
Argillic alteration, 705
Argon, 53, 61, 1004
Argon (Ar) isotopes
  ^{36}Ar concentrations, 54
  ^{39}Ar-^{40}Ar dating method, 56
  ^{40}Ar, 53
  $^{40}Ar/^{29}Ar$ dating, 674
  $^{40}Ar/^{36}Ar$, 55, 385
  $^{40}Ar/^{39}Ar$ approach, 580, 581
  $^{40}Ar/^{39}Ar$ geochronology, 544
  ^{40}Ar-^{39}Ar technique, 54
  atmospheric, 56
  K-Ar dating method, 57
  tracing geological processes, 57–58
Armstrong, D., 674
Aromatic hydrocarbons, 685, 688, 690
Aromatics, 1209, 1210, 1214
Arrhenius, S., 677, 678
Arrhenius diagram, 367, 368
Arrhenius rate equation, 20, 367–368, 371, 486, 790, 1214, 1277, 1283
Arsenic (As), 445, 527, 1351
  geochemical behavior, 59
  history and use, 59
  properties, 58
  toxicity, 59
Arsenides, 1394
Arterial calcification, 180
Arthritis, 160
Ash alteration, 881
As(III) oxidation, 778
Aspedamite, 1245
Asphalt, 136
Asphaltene, 103, 282, 1210, 1211
Asphaltite, 1053
Assimilation, 432, 433, 513, 841, 844, 846–850, 1444
Assimilation and Fractional Crystallization (AFC), 513
Assimilatory nitrate reduction, 987
Astatine, 59, 645
Asteroidal achondrites, 7
Asteroids, 251, 917, 1273
Asthenosphere, 1181
Astronomical forcing, 1152–1153
Ataxites, 767
Atlantic Meridional Overturning Circulation, 1289
Atmophile, 1453
Atmosphere, 295, 296, 509, 562, 1133, 1136, 1302, 1399
Atmosphere–ice sheet–ocean system, 1131
Atmospheric aerosols, 1087
Atmospheric Ar, 580
Atmospheric carbon dioxide (CO_2), 108, 110, 199, 301, 1160, 1161
  concentrations, 327
Atmospheric chemistry, 563
Atmospheric dynamics, 317
Atmospheric evolution, 62, 1372
Atmospheric gases, 663
Atmospheric helium, 660
Atmospheric Hg, 902
Atmospheric nitrogen, 987
Atmospheric O_2, 752, 754
Atmospheric pressure chemical ionization (APCI), 667
Atmospheric pressure photo-ionization (APPI), 667
Atom(s)
  definitions, 83
  nuclear structure and stability, 83–84
Atomic absorption spectroscopy (AAS), 30, 77–78, 378
Atomic diffusion, 474
Atomic emission spectroscopy, 30
Atomic mass, 1201
Atomic number, 83, 589, 1201
Atomic radius, 739
Atomic spectroscopy, 77
Atomic weight, 84
Atomistic simulations, 371
ATR-FTIR, 778
Au–Ag–Te minerals, 1423
Aubrites, 9, 920
Aufbau principle, 1292
Austin Model, 1, 2
Authigenesis
  in buried sediments, 86
  in continental aerial environments, 85
  crystal scale, 88
  definition, 85
  in hydrothermal environments, 88
  in marine environments, 86
  in volcanic ash beds, 86
Authigenic minerals, 881
Authigenic processes, 881
Automated geochemical log interpretation, 1282
Automated sample purification, 184
Available geochemical energy, 714
Average continental crust, 882
Avogadro, 442
  constant and mole, 1463–1464
  law, 21
Axonopathy, 293

B

Ba/Ca ratios, 92
Back-arc basins, 926, 929
Back-arc basin basalts (BABB), 926
Back-arc spreading centres, 711
Back scattered electron (BSE) images, 579
Bacquerel, H., 673
Bacteria, 142, 686, 1084–1085
  carotenoids, 820
  membrane bilayers of, 819
  membrane structures, 818
  tetraether lipids, 820
Bacterial mediation, 359
Bacterial siderophores, 529
Bacteriohopanepolyols (BHPs), 686–689, 819, 820, 1082
Bakken formation, 1055
Banded iron formation (BIF), 408, 509, 564, 749, 751, 753, 1066, 1069
Band gaps, 350

Barite, 91, 1299, 1392
Barium, 91, 1299
Barth, T.F.W., 677
Baryte, 1392
Basalt(s), 402, 825, 1237, 1454
Basaltic meteorites, 528
Base cations, 14
Basinal brines, 360, 1066
Basin and petroleum system modeling (BPSM), 1277, 1279, 1283, 1284
Basin modelling, 1090
Basis set of atomic orbitials, 3
Bassanite, 1392, 1393
Bastnäsite, 226, 796
Bauxite, 527, 564, 1069
Becquerel, H., 1242, 1295
Benitoite, 92
Benthic iron shuttle, 755
Benzene, 685
^{10}Be production, 96
Bering Land Bridge, 1157
Berner, R., 675, 677
Beryllium, 93–95, 1242
Berzelius, J.J., 679, 1528
Beta decay, 796, 1017, 1295, 1316
β-factor, 1369
Beta particles, 978
Beta spectrometry, 1297
Betulaceae, 125, 132
Bicadinanes, 127
Big Bang, 310, 316, 659, 1014, 1015
Bigeleisen, J., 675
Bioaccumulation, 1297
  factors, 898
Bio-calcification, 1044
Biochemicals, 694, 695, 699
Biodegradation, 689, 690, 1058, 1090, 1209, 1217, 1218
Biogenic apatite, 878, 886, 887
Biogenic coalbed methane, 104
Biogenic methane, 276
Biogenic phosphates, 1383
Biogenic quartz, 886
Biogenic sediment, 878, 880, 886–887
Biogenic silica, 113
Biogeochemical cycles, 375, 678, 1350
Biogeochemical cycling, 567, 832
Biogeochemical iron cycling, 757–758
Biogeochemical processes, 327, 894
Biogeochemistry, 551, 563–565, 673, 678, 1349, 1372, 1379
  atmospheric, terrestrial and marine, 109–110
  conceptual and numerical models, 110
  coupled biogeochemical cycles, 108–109
  definition, 107
  and science of global change, 110
  spatial and temporal scales in, 108
  stoichiometry, 108
  thermodynamic considerations, 108
Bio-intermediate, 113
Bioirrigation, 1097
Bio-limiting, 113
Biological carbon pump, 113–115
Biological fixation, 833
Biological markers, 1247
  See also Biomarkers
Biological nitrogen fixation, 328
Biological processes, 1138
Biological productivity, 880, 1526
Biological pump, 111–115
Biology, 753
Biomacromolecules
  as catalysts, 150
  as information carriers, 149–150
  as source of energy, carbon and nutrients, 149
Biomarkers, 46, 116, 195, 533, 677, 699, 818, 821, 1057, 1083, 1104, 1150–1151, 1160, 1164, 1168, 1207, 1211, 1212, 1252, 1268, 1372
  age-diagnostic, 143
  analytical methods, 136–140
  definition, 136
  hydrocarbons, 1053
  maturity ratios, 116
  precursors, biosynthesis of, 140–142
  source and environmental indicators, 142–143
  stereochemistry, 145–147
Biomass productivity, 327
Biomedicine, 308
Biominerals, 113, 947
Biomolecules, 376, 565, 1099
Biophile elements, 729, 1232
Biopolymers, 277, 772, 1100
Bioremediation, 1467
Biosignature, 1128
Biosphere, 49, 412, 562, 673, 855, 1232, 1399
Biosynthesis, 699
Biotic pigments, 1247
Biotic redox reactions, 1423
Biotite, 184
Bioturbation, 1097
Bird migration, 1383
Birnessite, 150
Bischof, G., 670, 676
Bismuth
  biological utilization and toxicity, 154
  economic geology and mining, 154
  history and use, 153
  mineralogy, 154
  properties, 153
Bittern salts, 464
Bitumen, 136, 147, 1055, 1056, 1060, 1268
Bituminous coal, 189, 279
Black Sea, 193, 1085, 1407
Black shales, 231, 1110, 1112, 1407
  depositional environments, 155
  origin of, 156
Black smoker, 711
Bloch equations, 1011, 1012
  for rotating frame of reference, 1012
Blocking temperature, 863
Blu-ray discs, 527
B3LYP, 348
Bog, 123, 127, 129, 1198
Boiling, 1455
Boltwood, B., 673
Boltzmann distribution, 452
  function, 1369
Bond angles, 32
Bond-exchange mechanism, 1332
Bond–valence approach, 333
Bond–valence sums, 333
Bone collagen, 47
Bone matrix, 180
Borax, 157, 159
Boric acid, 157
Boric anhydride, 157
Born-Oppenheimer approximation, 1
Born theory, 1365
Boron (B), 44, 162, 445, 1015, 1149, 1150
  electronic configuration, 156
  fertilizer, 160
  isotopes, 445, 675, 1161
  isotopic composition, 44
Botryococcanes, 689
Botryococcus braunii, 687, 688
Bottom water temperature, 1166
Bouazzerite, 1246
Boundaries, 744
Boundary conditions, 1291
Bowen, N.L., 676
Bowen's reaction series, 1176
Boyle, R., 677
B88P86, 348
Brachinites, 9
Bragg's equation, 1509
Bragg's law, 440, 1509
Branched alkanes, 686, 687, 689
Branched glycerol dialkyl glycerol tetraethers (brGDGTs), 127, 132, 819, 820
Brass, 44
Bravais lattices, 335
Bremsstrahlung radiation, 1508
Brewer-Dobson circulation, 1142
brGDGT, *see* Branched glycerol dialkyl glycerol tetraethers (brGDGTs)
Brice equation, 1188
Bridgmanite, 676, 747
Brines, 244, 245
Brin process, 91
Britholite, 796
British Antarctic Survey, 1139
BrO, 169, 1140
Brochantite, 1393
Broecker, W., 678
Bromine, 167–169, 637, 647, 648, 1138
  isotopes, 167, 246
Brønsted-Lowry concept, 16–17
Bronze, 44
Bronze Age, 943
  of Denmark, 48
Brown, H., 679
Brucite, 267
Brunhes-Matuyama magnetic field reversal, 323
Buffering capacity, 205
Bulk continental crust, 402
Bulk (three-dimensional) defects, 934
Bulk Earth, 413, 1431
Bulk leaching (BLEG), 551
Bulk modulus, 398, 474
Bulk partition coefficients, 406
Bulk silicate Earth (BSE), 183, 307, 634, 653, 870, 970, 984, 1113, 1236, 1317, 1329, 1338, 1380, 1420, 1528
Bullion, 622
Burial, 1094
  dating, 322
  diagenesis, 360
  diagenetic realm, 355
Bushveld Complex, 1237, 1319
  style PGE, 1065
Butane, 961

C
δ^{13}C, 184, 198, 1104
^{14}C, 187
C3 pathway, 1087
C3 plants, 197
Ca^{2+}, 1044
Ca–Al-rich inclusion (CAI), 618, 1307, 1528
Cadalane, 125, 127
Cadinanes, 125
Cadmium (Cd), 1025, 1034, 1164
  geochemical behavior, 172
  history and use, 171
  properties, 171
  toxicity, 172
Caesium, 173
  abundance, 173

Caesium (*cont.*)
behavior, 175
general behavior in fluid, 173–174
properties, 172
subduction zone cycling, 174
Calcareous deposits, 878, 886
Calcification, 114
Calcifying organisms, 179
Calcite, 177, 189, 204, 206, 207, 211, 213–215, 218, 283, 378, 379, 846–847, 849, 850, 1024, 1044, 1102
Calcium, 13, 14, 181, 462, 637, 1349
depletion, 14
electron configuration, 177
flux to river, 179
properties, 177
Calcium-aluminum inclusions (CAI), 27, 178, 252, 568, 679, 920, 1446
Calcium bromide, 178
Calcium carbonate, 113, 191, 204
formation, 69
Calcium-oxalates, 180
Calculated vitrinite reflectance, 131, 132
Caldera, 1184
California, 895
Californium-252, 979
Calorimeter, 186
Calorimetry, 558
adiabatic and thermal relaxation, 186
reaction, 186
Cancer, 256
Canonical value, 1309
Capillaries, 543
Capping, 1410
Caprocks, 1216
Carbides, 189, 957
Carbohydrates, 136, 1100, 1104
Carbon, 60, 181, 187
inorganic, 191
organic, 191
and oxygen burning, 1016
Carbonaceous chondrites (CC), 92, 157, 162, 249, 251, 311, 386, 500, 653, 918, 1173, 1234, 1313
Carbonate(s), 13, 179, 182, 184, 188, 191, 408, 509, 945, 1299
'counter' pump, 114
ion concentration, 1167
mineralogy, 357
minerals, 543, 564
minerals and CO_2-carbonic acid system, 1043
Carbonate compensation depth (CCD), 200, 880, 886
Carbonate fluorapatite (CFA), 887
Carbonatites, 189, 984, 1232, 1378, 1419
Carbon burial, 1127
Carbon cycle, 34, 36, 100, 109, 127, 130, 133, 179, 188, 562, 672, 675, 713, 1094, 1198, 1217, 1267–1268
inorganic carbon, 191
organic carbon, 191
organic matter preservation and geologic processes, 193
Carbon cycling, 129–131
Carbon dioxide (CO_2), 68, 164, 188, 191, 194, 536, 962, 1128, 1153, 1199
binding, 475
calcium carbonate formation, 69–70
carbonate-silicate thermostat, 70–71
control by ocean chemistry, 69
disposal, 494
proxy constraints, 71–72
reduction methanogenesis, 101
solubility, 849
Carbonic anhydrase, 1033
Carbonization, 189
Carbon isotope excursions (CIE), 199
Carbon isotopes, 47, 187, 195, 536, 1148, 1149, 1156
distribution, 197
emergence of life, 198
fractionation, 137
measurements, 196–197
ratios, 561
in shallow seawater, 198–199
Carbon sequestration, 36
Carbonyl sulphide, 1142
Carboplatin, 1237
Cariaco Basin, 1407
Carlin style Au, 1065
Carnallite, 464
Carotenoids, 819, 820, 1082, 1269
CASPT2, 4
Catagenesis, 116, 147, 192, 279, 353, 773, 962, 1212
Catalytic converters, 1238
rhodium, 1315
Catalytic cycles, 1138, 1139
Catalytic macromolecules, 150
Catastrophic collisions, 765
Catastrophic degassing event, 385
Catchment-wide erosion rates, 323
Catechols, 278
Catenation, 187
Cathode ray tube, 1508
Cathodoluminescence, 356, 836, 1446
imaging, 578
Cation, 297
exchange, 264
exchange capacity, 267, 269, 273
Cavendish, H., 53
Cave of Crystals, 1392
Cavity ring down spectroscopy (CRDS), 697, 1131
CB chondrites, 250
C cycle, 1081
α-Cedrene, 124
Celestine, 1392
Celestite, 1377, 1392
Cell membranes, 160
Cellulose, 275
Cell volumes, 213
Cement, 34–35
products, 1393
Cementation, 356
Cenozoic Climate History, 1154–1158
Centered lattice, 335
Central Pacific, 218
Ceramic(s), 43
manufacturing, 43
Cerium
biological utilization and toxicity, 227
geochemical behavior, 226–227
geochronology and isotope geochemistry, 227
history and use, 226
properties, 226
Certified reference materials (CRMs), 553
CFCs, *see* Chlorofluorocarbons (CFCs), 1138, 1140
Chain lengths, 1104
Chalcanthite, 1393
Chalcogenic, 527
Chalcophile, 236, 303, 547, 729, 827, 1110, 1111, 1235, 1394, 1395, 1453
Chalcophile elements, 153, 305, 812, 896, 1174, 1205, 1236, 1313
definition, 229
distribution in terrestrial rocks, 229–231
Chalcopyrite, 154, 490, 1394
Chaotic phase, 500
Chapman model, 1138
Characteristic X-rays, 1185
Charge distributions, 347
Charge radii, 901
Chassignites, 11
CH chondrites, 250
Chelates, 297
Chelation
definition, 233
role, 233
Chemical abrasion, 579
Chemical affinity, 266
Chemical bond(s), 545
definition, 234
Chemical bonding, 567
behavior, 475
Chemical compaction, 359
Chemical diffusion, 364–365, 369, 371
Chemical disequilibrium, 360
Chemical equilibrium, 195
Chemical evolution, 1176
Chemical fossil, 1083
Chemical fractionation, 1469
Chemical kinetics, 19, 474, 775, 776
Chemically isolated magma, 843
Chemical oceanography, 563, 677
Chemical periodicity, 1203–1205
Chemical potential(s), 519, 522, 560, 621, 907, 909, 914, 1361, 1374
gradient, 364, 365
Chemical precipitates, 751, 755
Chemical profile, 1305
Chemical reaction(s), 357, 776, 893, 906
Chemical relaxation technique, 778
Chemical sediments, 408
Chemical segregation, 1180
Chemical separation, 1430
Chemical speciation, 1031
Chemical thermodynamics, 561, 562, 649–651
Chemical weathering, 271, 328, 393, 529, 562, 563, 830, 832, 1471
definition, 237
geologic process, 238
laboratory research, 239
natural and experimental weathering rates, 239–240
reactions of, 238
surface protonation, 237
watershed approach, 239
WITCH model, 239
Chemisorption, 1498, 1499
Chemistry, 251
Chemocline, 467
Chemostratigraphy, 195, 199–201, 588, 903
Chemosynthetic communities, 1053
Chemosynthetic microorganisms, 714
Chernobyl reactor incident, 1298
Chert(s), 408, 881, 886
Chicxulub impactor, 1114
Chicxulub impact site, 1392
China, 895
Chirality, 145
Chitin, 1102
Chlor-alkali processing, 896
Chloride, 244

Chlorine, 242, 637, 647, 1138, 1139
  dimer, 1140
  monoxide, 1139
  radicals, 1138
Chlorine isotopes, 245–246
  fractionations, 244–245
  history, 244
  measurements, 244
Chlorinity, 243
Chlorite, 269, 273
Chlorofluorocarbons (CFCs), 1138, 1140,
Chlorophyll(s), 128, 129, 136, 677, 1024, 1081, 1211, 1212, 1247
Cholesterol, 48, 142
Chondrites, 187, 251, 306, 463, 499, 568, 679, 795, 827, 828, 865, 888, 917, 984, 1112, 1130, 1231, 1236, 1379, 1420, 1430, 1446, 1525, 1528
  ages of, 250
  alteration of, 248
  classification, 248–250
  definition, 248
  oxygen isotope composition, 249
  oxygen isotopes, 250
Chondritic uniform reservoir (CHUR), 583, 634, 969, 970
Chondritic veneer, 386
Chondrules, 499, 568, 679, 920
Chromatogram, 531
Chrome yellow, 255
Chromic oxide, 255
Chromite, 1237, 1275
Chromium, 619, 864
  discovery, 255
  geochemical behavior, 255
  properties, 255
  toxicity, 256
Chromium-54, 500
Chromium isotopes
  applications, 256
  cosmochemistry, 257
  environmental applications, 258–259
  high-temperature terrestrial settings, 257–258
  measurement, 257
  paleoredox proxy, 259–260
Chronic beryllium disease, 94
Chronometer, 629
Chrysotherapy, 623
Chrysotila spp., 1084
Chuquicamata supergiant deposit, 1068
CI chondrites, 250, 310, 311, 316, 496, 647, 896, 1329
CI-CM class meteorites, 386
Cinnabar, 895
Cis-platin, 1237
CK meteorites, 249
Cl, 1043
δ^{37}Cl, 243
Clapeyron's equation, 262–263, 452
Clarite, 280
Clarke, F.W., 562, 670–671, 679
Clastic sediments, 461, 526, 684, 839, 1426, 1442
Clathrate, 535, 536
  hydrates, 189
Claudianus, C., 488
Clausius, R., 557
Clausius inequality, 449–450
Clay(s), 159, 245, 902
  minerals, 43, 265, 266, 270, 282, 700, 1214, 1217
  swelling, 1240
Clay membranes, 263
  Debye length, 264
  electrical double layer, 264
  geochemical importance, 263
  mathematical formulation, 264
  phenomenology, 263
  unresolved issues, 264
Clayton, R., 675
Cleats, 278
Climate, 47, 328, 1104, 1143, 1409
  change, 35, 49, 894, 1141
  change mitigation, 1351
Climate proxies
  biomarkers, 1150
  elements, 1150
  fossil assemblages, 1148
  isotope systems, 1151
  stable isotopes, 1148
Clinopyroxene, 179, 927
Closed system, 842–843
Closure temperature, 372, 1379
Clouds, 1138, 1139
Clumped isotopes, 1161, 1168
  analysis, 676
  geochemistry, 543
Cluster(s), 1242
  expansion method, 1354
CM chondrites, 250, 896
CNO cycle, 1016
CO_2, *see* Carbon dioxide (CO_2)
CO_2-carbonic acid-carbonate system
  and ocean water, 217–219
  and seawater, 206–211
Coagulation, 294, 1142
Coagulum, 294
Coal, 189, 191, 193, 200, 528, 535, 677, 771, 772, 774, 961, 962, 1081, 1212, 1250, 1407, 1438
  ashes, 528
  balls, 283
  carbon cycling in peat bogs, 129
  classification, 277–280
  combustion, 901
  definition, 275
  environment of peat and coal deposition, 128
  grade, 279
  macerals, 280
  microlithotypes, 280
  mineral content, 282–286
  molecular structure, 282
  origins, 275–276
  and paleoclimate, 127
  paleovegetation, 123
  rank, 277–279
  tars, 287
  thermal maturity, 131
  utilization, 287
Coalification, 277
Coastal bitumen, 1052, 1053
Coastal ocean, 1105
Cobalt (Co), 44, 1023, 1033
  group, 744
Coccolithophores, 180
Coccolithophorids, 1024, 1168
CO chondrites, 250
Co-condense, 1142
Coenzyme cobalamin, 293
Coercivity, 863
Coesite, 1221, 1226, 1228
Cohenite, 189
Coion exclusion and counterion condensation, 625–626
Coke, 287
Colemanite, 159
Collagen, 180
Collisional erosion, 647, 765
Collision/reaction cells, 727
Colloidal gold, 623
Colloidal stability, 1240
Colloidal transport, 1457
Colloid(s), 1030
  filtration, 894
Colloid-facilitated transport, 894
Columbia Hills (Mars), 748
Columbite, 1419
Columbium, 984, 1419
Column method, 733–734
Comet 67P/Churyumov–Gerasimenko, 61
Comets, 386, 500, 1273, 1372
Comminution, 295
Compaction, 1216, 1217
Compatible, 528, 546, 1237
  element, 1110
  trace element, 408
Complete basis set (CBS) limit, 3
Complexes, 153, 546
Complex formation, 297
Complexing behaviour, 1529
Complex reaction progress, 847
Complex speciation, 345
Component, 1220
Composition of minerals, 1438
Compound-specific isotope analysis (CSIA), 31, 48, 129, 140, 300, 534, 675, 1082
Compound-specific isotope compositions, 46
Compound specific radiocarbon (^{14}C) analysis (CSRA), 1083
Compressibility, 845, 849
Computational thermodynamics, 842
Concentration analyses, 727
Concentration gradient, 363, 366
Concentrations, lithium, 823
Conceptual DFT, 350
Concordia, 814, 1469
Concrete products, 1393
Condensation, 295, 499, 500
  sequence, 679, 1176
Condensed phases, 458
Conductor-like Screening Model (COSMO), 5
Configuration interaction (CI), 2
Confined pyrolysis, 790
Confined tracks, 486
Confocal laser scanning microscopy (CLSM), 1101
Conservative, 246
  profile, 113
  seawater, 1043
Consolidation, 263
Constant concentration, 483
Constant pressure heat capacity, 651
Constant source method, 371
Constant volume calorimetry, 446
Constant volume heat capacity, 651
Constitutive relations, 894
Contaminant, 1102
  migration, 894
  transport, 833
Contamination, 1269
Continental basalt, 410
Continental crust, 392, 463, 566, 589, 591, 655, 719, 720, 795, 966, 984, 1113, 1322, 1380, 1388, 1420, 1466, 1528
Continental growth, 1260

Continental recycling, 1260
Continental rifts, 1181
Continental weathering, 85, 185, 857
Continuity equations, 1137
Continuous flow (CF), 543
Continuum, 892
Convecting mantle, 655
Convergent margins, 406
  settings, 714
Coordination complexes, 297
Coordination environment, 297
Coordination number, 739, 742, 743
Copper (Cu), 44, 537, 1033, 1313, 1424
  biological utilization and toxicity, 304
  history and use, 303
  hydrothermal processes, 303
  magmatic processes, 303
  natural waters, 304
  ore deposits, 304
  properties, 303
Corals, 35, 1024, 1169
  calcium level, 180
Core, *see* Earth's Core
Core–mantle boundary (CMB), 418, 419, 867
  dense material at, 869
  thermal boundary layers, 867
Core-mantle exchange, 1237
Core-valence, 5
Coriolis acceleration, 1046
Coriolis force, 427
Correlation consistent basis sets, 3
Corrinoid, 897
Corrosion, 1393
Corundum, 1275
Cosmic abundances, 671, 679
  of the elements, 679
Cosmic dust, 888
Cosmic element abundances, 310
  historical background, 310–311
  Sun and meteorites, 311
Cosmic ray(s), 646, 662
  flux, 317
  muons, 317
Cosmic ray exposure
  age, 320
  dating of meteorites, 785
Cosmic ray spallation, 1015–1016
  reactions, 94
Cosmic shoreline, 73
Cosmochemistry, 383, 563, 568, 678–679, 760
Cosmochronology, 746
Cosmogenic exposure dating, 243
Cosmogenic helium, 662
Cosmogenic isotopes, 566, 1402
Cosmogenic nucleosynthesis, 696
Cosmogenic nuclides, 31, 96, 317, 322–323, 571, 1297
Cosmogenic radionuclides, beryllium, 94
Cosmogenic reactions, 975
Coulombic forces, 297
Coulombic interactions, 345
Counterion condensation and coion exclusion, 625–626
Counter ions, 733
Counting statistic error, 979
Coupled-cluster (CC) theory, 2, 4
Coupled cluster with all single and double excitations plus a correction for the connected triples (CCSD(T)), 4
Coupled numerical models, 328
Coupled substitution, 1190, 1192, 1193
Covalent bonds, 545
Cracking, 118
Craig, H., 675
Crassulacean Acid Metabolism (CAM), 197
CR chondrites, 250
Crenarchaeota, 1085
Cretaceous, 180
Cretaceous–Paleogene boundary, 744
Cr isotope ratios, 865
Cristobalite, 1333
Critical endpoints, 473
Critical metals, 477
Critical point, 326
Critical zone, 308, 326, 563, 676–678
  observatories, 329
  science, 329
Crocetane, 686
Crocite, 255
Cr(III) oxidation, 779
Crude oil, 136
Crust, 854, 855, 944–945
Crustal, 529
  assimilation, 408, 1382
  differentiation, 437
  growth, 184, 410–412
  helium, 661–662
  preservation, 411
  recycling, 408
  rock, 660
Crust composition paradox, 406
Crust-mantle differentiation, 1237
Cryolite, 637
Crystal chemistry, 331
Crystal classes, 336
Crystal defects, 932
Crystal field, 1454
  splitting, 341
  theory, 340–343
Crystal field stabilization energy (CFSE), 341–343
Crystal fractionation, 406, 1067
Crystal growth, 488, 841, 851
Crystal lattice, 739
Crystallization, 830, 831, 1448
  process, 763
Crystallochemical predictions, 334
Crystal-melt mush, 433, 436
Crystal radii, 739
Crystal systems, 364
Crystal X-ray diffraction, 1509
CSIA, *see* Compound-specific isotope analysis (CSIA)
Cu, *see* copper
Cummingtonite, 413
Cumulate plutonic rock, 434–435
Cumulates, 408
Cumulative formation constant, 298
Cu-Ni sulfides, 1237
Cuparene, 124
Cupressaceae, 124, 125, 132
Curie, M., 673
Curie, Marie, 1242, 1299
Curie (Ci), 1295, 1299
  paramagnetism, 860
  temperature, 861, 863
Curie, Pierre, 1299
CV chondrite, 896
CV meteorites, 249
Cyanide, 895
Cyanobacteria, 686, 1084
Cyclosilicates, 945, 1334
Cyclostratigraphy and astrochronology, 588

D

Dacites, 432, 433
Daley detectors, 1435
Dalton's law, 1363
Dansgaard, W., 675
Dansgaard-Oeschger (D-O) events, 1157
  in Greenland ice cores, 995
Darcy's law, 264, 893
Darcy velocity, 893
Darken's equation, 366
Data analysis, 1305
Datolite, 158
Davy, Humphry, 91, 442
Davy Medal, 1201
D-block transition metal, 291
D3 correction, 350
Dead Sea, 158
Dead zones, 1232
de Boisbaudran, Paul-Émile Lecoq, 527
DeBroglie's matter waves, 1291
Debye and Einstein functions, 651
Debye-Hückel approximation, 626
Debye-Hückel equation, 22, 345
Debye-Hückel theory, 1375, 1412
Debye length, 264, 1240
Decay, 1141
  β^-decay, 589
  constants, 572, 673, 1296–1297
  series, 1287
Deccan traps, 1114
de Chancourtois, 1201
Decompression, 448
  melting, 1180, 1480
Deep Carbon Observatory, 188
Deep mantle differentiation, 1265
Deep ocean, 482
Deep phreatic zone, 358
Deep-sea, 477, 481
  hydrothermal vents, 563
Deep Sea Drilling Project (DSDP), 86, 1147
Deep water formation, 112
Deepwater Horizon, 690
Defects
  bulk (three-dimensional), 934
  classification of, 932–934
  definition, 932
  line (one-dimensional), 933
  planar (two-dimensional), 934
  point (zero-dimensional), 932–934
Deformation, 474, 906, 907, 914
Degassing, 841
Degeneracy, 1228, 1230
Dehydration, 1182
  melting, 406
Delamination, 406
Delta notation, 1402
Delta values, 182
Demethylation, 897
Dendrochronology, 1148
Denitrification, 833, 988, 989
Density, 1044
  boron, 157
  calcium, 177
  foundering, 406
Density-functional theory (DFT), 347, 1473
Dental bioapatite, 198
Denudation rates, 322
DePaolo, D., 674
Depleted mantle (DM), 583, 872, 1380
Depleted MORB mantle (DMM), 872
Deposition, 880, 884, 1142
  rates, 1097
Depositional environment, 136, 688, 691, 1056, 1057, 1104
Depositional remanent magnetization (DRM), 863
Depth profiling, 737, 738
Deserpentization, 169

Desert landscapes, 322
Desolvating nebulizer systems, 724
Detection limits, 552
  for neutron activation analysis, 979
Detrital grains, 360
Detrital inheritance, 271
Detrital zircons, 410, 578
Deuterium, 694, 696, 1169
  excess, 1170
Developed countries, 1140
D/H ratio, 387
Diagenesis, 116, 146, 270–272, 277, 453, 563, 753, 773, 795, 818, 820, 831, 886, 887, 889, 962, 1086–1087, 1161, 1217, 1411
  carbonate, 357–360
  definition, 353
  diagenetic cycle, 353–356
  evolution, 361
  processes, 184, 706, 880
  reactions, 884
  sedimentation, 477–480
  siliciclastic, 360–361
Dialysis, 529
Diamagnetism, 860
Diamond, 187, 445
  anvil cell, 676
Diamondoid(s), 690
  hydrocarbons, 1269
Diatoms, 1024
Dielectric constant, 708, 1365, 1488
Diel vertical migration, 112
Differential scanning calorimetry, 186, 1436
Differential thermal analysis, 1436
Differentiation, 545, 1482
Diffraction, 474
Diffusion, 245, 246, 264, 363, 508, 562, 567, 743, 907, 909, 914, 1369, 1450, 1484
  in anisotropic media, 364
  chemical diffusion, 364
  closure temperature, 372
  coefficients, 363, 364, 366–371, 483, 823, 892
  couple method, 371
  driving forces, 364
  effective binary diffusion, 365
  equation, 363–365, 371
  Fick's laws of, 363–364
  grain boundary diffusion, 366–367
  length, 367, 372
  matrix, 364, 366
  self and chemical diffusion relationship, 365–366
  self diffusion, 364
  thermal diffusion, 366
Diffusive flux, 363–365
Diffusive mass transfer, 892
Diffusive transport, 105
Diffusivity, 363, 366, 368, 369, 371, 527
Dikes, 434
Dimethylsulfide, 1405
Di-nitrogen, 64–65
Dinoflagellates, 144
Dinosteranes, 144, 1083
Dinosterols, 144, 1083
Dioctahedral, 267
Diogenites, 920
Diorite, 402
Diploptene, 686, 687
Dipole moments, 2, 1490
Dipterocarpaeae, 127
Discontinuous phase transition, 339
Discordia, 577
Discrete activation energy (DAE), 1283
Discrete ash layers, 883
Disequilibrium melting, 743
Dislocations, 933
Dispersed ash, 883
Dispersion, 892
Displacive transformations, 338
Disproportionation, 747
Dissimilatory microbial iron reduction (DIR), 757
Dissimilatory nitrate reduction, 988
Dissimilatory sulfate reduction, 1395
Dissolution, 356, 492, 829, 1167, 1364
  precipitation reactions, 41
Dissolved inorganic carbon (DIC), 198, 209–210, 218, 1023, 1043
Dissolved organic carbon (DOC), 200, 677, 1199
Dissolved organic matter (DOM), 375, 565, 668, 895, 1094, 1104
  bulk quantification, 376
  carbon cycle, 377
  characterization, 376–377
  sample collection, 376
Dissolved oxygen, 1025
Diterpenoids, 125–126, 1083
Dittmar, W., 677, 1043
DLVO theory, 295, 1412
D-MORB, 929
DM-PREMA array, 873
DNA, 1101
  sequencing, 1083
Dobson unit, 1136
Dodecaniobate, 1245
Dole effect, 1127
Dolomite, 206, 208, 211, 213, 215, 221, 283, 359, 886, 1044, 1045
  crystal structure and geochemistry, 378
  definition, 378
  geological significance and occurrence, 379
  history and use, 379
  kinetics of precipitation, 379
Dolomitization, 359–360, 881, 886, 1045
  crystal structure and geochemistry, 378
  definition, 378
  geological significance and occurrence, 379
  history and use, 379
  kinetics of precipitation, 379
D-orbitals, 1454
Double-double effect, 794
Double focusing ICP-MS, 726
Double-spike method, 257, 769
Drilling fluids, 91
Drilling muds, 1393
Dual inlet (DI) mass spectrometer, 543
Dumas combustion, 992
DUPAL anomaly, 873, 931, 1483
Durite, 280
Duroclarite, 280
Dust, 884
Dysprosium (Dy), 562
  biological utilization and toxicity, 382
  geochemical behavior, 382
  history and use, 381
  properties, 381

E

Eagle Ford Shale, 1055
Early diagenesis, 453
Early Eocene Climatic Optimum, 1156
Earth, 462, 528
  age determination of, 575
  atmosphere, 383
  climate, 200
  continental crust, 91, 671
  crust, 472, 811
  early crust, 412–413, 571
  formation, 566, 1372
  history, 818
  mantle, 163, 812, 945
  materials, 475
  structure, 474
  surface processes, 327
  sustainability, 945–946
Earthquake, 474, 1302
Earth's core, 568, 618, 619, 647, 828
  core composition and light element, 424
  core-mantle separation, age of, 426
  definition, 418
  formation conditions and composition, 420
  geodynamo and radioactive elements, 307, 425, 1110, 1174, 1234, 1236
  inner-outer core, 420
  physical properties of, 419
  planet and core, compositional models of, 420
  properties, 418
East Pacific Rise (EPR), 433, 434
Ebelman, J.J., 670, 678
Ebelmen-Urey reaction, 215
Eclogite, 406
Ecological effects of MeHg, 898
Ecology, 1372
ED analysis, *see* Energy dispersive (ED) analysis
Edge dislocations, 933
Effective binary diffusion coefficients, 365, 369
Effective diffusion coefficient (D_{eff}), 367
Effective ionic radii, 739–742
EH-pH diagrams, 676
Eigenfunctions, 1291
Eigenvalues, 1291
Ekamanganese, 1422
Electrical conductivity, 1043
Electrical double layer (EDL), 264, 265, 295, 1240
Electrochemistry, 647
Electrolysis, 527, 694
Electron, 1014, 1017, 1201
  capture, 589, 1296
  configuration, calcium, 177
  correlation, 2
  density, 348
Electronegativity, 234, 350, 442, 545
Electroneutrality, 264
Electron-exchange reactions, 1116
Electronic configuration, boron, 156
Electronic energy levels (UV and visible spectra), 2
Electronic spin state, 739, 743
Electronic structure calculations, 347
Electron microprobe, 378, 926
Electron microprobe analysis (EMPA), 356
Electron multipliers, 1435
Electron paramagnetic resonance (EPR), 1083
Electron probe microanalysis (EPMA), 30
  definition, 439
  electron source, 440
  quantitative analysis, 440–441
  sample preparation, 441
  X-ray mapping, 441
  X-ray spectrometers, 440
Electrophile, 17
Electroplating, 292
Electrospray ionization (ESI), 667
Electrostatic bond strength, 332
Electrostatic model, 1188–1189

Electrostatic repulsion, 1241
Electrostatic spherical analyser (ESA), 726
Element(s), 670, 671, 673, 674, 676, 677, 679, 957, 1394, 1396, 1517
  analysis, 723
  major, 915
  minor, 915
  purification, 732
  trace, 915
Elemental abundance, 854, 1205
Elemental bromine, 168
Elemental formula, 667
Elemental mapping, 1417
Elementary reaction, 19, 776
El Niño-Southern Oscillation (ENSO) system, 1150
Elution peaks, 735
Emerged continental surfaces, 509
Emiliani, Cesare, 675, 1148, 1152
Emiliania huxleyi, 1084
Emission lines, 1415
Emmons' zoning model, 1177
E-MORB, 432, 434, 929
Empirical parameterizations, 842
Enantiomers, 146
Enantiomorphic pairs, 1228, 1229
Energetics, 347
Energy, 519, 1096
  barrier, 20
  constrained, 849
  deposits/resources, 1064
Energy dispersive (ED) analysis, 1511
Energy dispersive spectrometer (EDS), 440, 1185
Energy dispersive spectroscopy, 1101
Enriched isotope, 767
Enriched mantle, 463
Enstatite, 251
Enstatite chondrites (EC), 250, 311, 385, 919, 1525
Enthalpy, 20, 446, 556–557, 562, 650, 1220, 1361
  of vaporization, 326, 1487
Entropy, 448, 514, 518, 554, 557–558, 560, 562, 621, 650, 1220, 1222, 1230, 1360, 1374
  Clapeyron equation, 452
  Clausius inequality, 449–450
  measurement, 451–452
  molecular basis, 452–453
  second law, 450
  thermodynamic concept, 448–449
Environment, 127–129, 1090
Environmental aspects of PGE, 1238
Environmental carcinogen, 1457
Environmental geochemistry, 549, 829, 1411
Environmental impacts, 1072
Environmental minerals, 943
Enzymatic synthesis, 145
Enzymes, 1414
Eocene climatic optimum, 466
Eogenesis, 353, 453
Eolian material, 884
Epidiagenesis, 453
Epigenesis, 453, 454
Epigenetic deposits, 453
Epigenetic mineralization, 1066
Epimerization, 146
Episodic growth, 507
Epithermal, 705
Epithermal gold deposits, 1068
EPR, *see* East Pacific Rise (EPR)
Epsomite, 464, 1393
Epstein, S., 675
Equation of state, 489, 1363
Equilibrium, 19, 20, 325, 455, 554, 556, 557, 559, 562, 650, 1220, 1221, 1224
  condition, 456, 457
  distribution coefficient, 733
  fractionations, 245
  isotope fractionations, 1369
  isotope partitioning, 1404
  mineralogy, 393
  state, 519
  thermodynamics, 620
Equilibrium constant(s), 20, 196, 209, 211, 212, 216, 220, 444, 1116, 1117, 1119, 1187, 1189, 1411
  of chemical reactions, 1369
  examples, 460
  solutions, 458–459
  temperature effect, 459–460
Equilibrium crystallization (EC), 514
Erbium (Er)
  biological utilization and toxicity, 461
  geochemical behavior, 461
  history and use, 461
  properties, 461
Erosion, 96, 392
  and denundation rates, 328
  rate, 97, 317
Essential nutrient, 529, 1019
Estuaries, 529, 1105
Ethane, 961
Ettringite, 1393
Eu anomaly, 408
Eucrites, 920
Eukaryote, 142, 1025
Eukaryotic phytoplankton, 1269
Euphotic zone, 1025
European Copper Shale, 1070
Europium, 618
  geochemical behavior, 462–463
  history and use, 462
  properties, 462
Euryarchaeota, 1085
Eustigmatophytes, 1084
Eutectic, 1224, 1225
  behavior, 843, 845, 847
Eutrophication, 833, 1232
Evaporate, 1142
Evaporation, 1140
Evaporite(s), 44, 168, 242, 466, 564, 1044, 1216, 1392
  basinwide, 469
  definition, 464
  deposition, 1400
  deposits, 163, 554
  lacustrine, 469
  minerals, 831
  platform, 467
Evaporite salts
  marine brine, 464–465
  nonmarine brine, 465–466
Evapotranspiration, 702
Excess mixing enthalpy, 1353
Exchangeable cations, 269
Exchangeable hydrogen, 697
Exchange-correlation functionals, 348
Exchange interaction, 861
Excited state reaction kinetics, 1404
Exploration geochemistry, *see* Geochemical exploration
Explosive nucleosynthesis, 1017
Export efficiency, 111, 115
Export flux, 111–112, 114
Exposure age, 96, 317
Exposure dating, 322
Exsolution, 339, 845, 849
  process, 1352, 1356
Extended X-ray absorption fine structure (EXAFS), 897, 1414, 1514
External detector method, 485
External-PIXE, 1185
Extinct radioactivity, 385, 503, 507, 1014
Extinct Tc, 1422
Extracellular hydrolytic enzymes, 1095
Extraterrestrial debris, 889
Extra-terrestrial hydrocarbons, 690–691
Extraterrestrial sulfide minerals, 1396
Extrinsic regime, 369

F

Facies concept, 676
Faint Young Sun Paradox (FYSP), 64, 1154
Faraday cup, 542, 543, 726, 1436
Faraday detector, 1434
Farrington, O., 679
Fatty acids, 46, 140, 1084
Fault scarps, 96
Fe colloids, 529
Fe-FeO-FeS, 527
Fe fertilization experiments, 1030
Feldspar, 184, 252, 462, 796, 945, 1378
Feller-Peterson-Dixon (FPD) method, 4
Felsic, 393
Fe-Mn crusts, 1430, 1432
Fen, 1198
Fe-Ni metal, 527
Fe peak elements, 527
Fermentation, 276
Fermentative bacteria, 101
Fernenes, 125
Ferns, 125, 132
Ferric/ferrous ratio, 843
Ferric hydroxide, 749
Ferrihydrite, 943, 1245
Ferrimagnetism, 861
Ferroan dolomite, 753
Ferrobasalts, 431
Ferromagnetism, 746, 861
Ferromagnets, 651
Ferromanganese (Fe-Mn) crusts, 477, 1424
  economic potential, 481
  formation and composition, 477
  geologic setting and distribution, 480
Ferromanganese (Fe-Mn) nodules, 477, 1424, 1457
  economic potential, 481
  formation and composition, 477
  geologic setting and distribution, 481
Ferruginol, 125
Fertilizer, 988, 1231
FeS (troilite), 316
FeTi basalts, 433
Fick's law, 363, 364, 483, 892
Field strength, definition, 664
Fingerprinting approach, 1000
Fire retardants, 37
First Ionization Potential, 527
First law of thermodynamics, 446, 554, 556
First-order phase transition, 263
First-row transition elements, 408
Fischer assay method, 1055
Fischer-Tropsch synthesis, 140
Fish consumption advisories, 898
Fissiogenic isotopes, 1061
Fission decay, 1296
Fission products, 979, 1061
Fission track
  annealing, 486

dating, 484–486, 1296
definition, 484
in minerals, 935
thermal history modeling, 486–487
Fixed volume constraint, 849
Flame AES, 78
Flame ionization detector (FID), 1278, 1279
Flocculation, 294, 296
Florencite, 796
Flue gas, 1401
Fluid, 471
aqueous, 915
composition, 489–490
hydrothermal, 907
inclusion assemblage, 489
inclusions, 488, 493, 1179
pressures, 705
samples, 544
Fluid-mobile elements, 547
Fluid-rock interaction, 356, 437, 492, 595–596, 1133
Fluorescence, 836, 837, 1306
Fluorescence-XAFS spectra, 1411, 1514
Fluorination, 1131
Fluorine, 495, 637, 646, 647
Fluorite, 495, 637, 647
Fluorsulfonate, 1392
Fluvial sediment, 97
Flux density, 483
Flux melting, 1180
Focused ion beam, 527
Food chain, 47, 1025
Foodwebs, 49
Foraminifera, 180, 199, 886, 1148, 1150, 1156, 1166
zooplankton, 1024
Forchhammer's Rule, 563
Forensic sciences, 1383
Formation waters, 244
Forschammer, G., 677
Forward modeling, 841
Fossil(s)
definition, 1099
sources and post burial processes, 1099
Fossil assemblages, 1148
Fossil fuel(s), 535, 988, 1438
combustion, 13
Foundational laws of thermodynamics, 649
Fourier, J.-B.J., 678
Fourier transform (FT), 666, 1010
Fourier transform infrared spectrometers, 1082
Fourier transform infrared (FTIR) spectroscopy, 82, 1101, 1436
Fourier-transform ion cyclotron resonance mass spectrometer (FT-ICR MS), 666–668, 1248
Fourier-transform Raman spectrometers, 1305
Fractional crystallization, 431–433, 513, 676, 841, 842, 844, 1444
and assimilation, 1330
Fractionation, 272, 699
factor, 196, 1368
Fractured porous media, 894
Framboids, 749
Francevillian series, 1060
Franck Condon Factors, 1404
Francolite, 1232
Free energy, 342, 519, 651
Free radical mechanisms, 1214
Frenkel defects, 837, 932
Frequencies, 1011
Freshwater biota, 903
Freshwater phreatic zone, 358
FT-ICR MS, *see* Fourier-transform ion cyclotron resonance mass spectrometer (FT-ICR MS)
Fugacity, 21, 1375
Fukushima Daiichi, 1424
Fukushima reactor incident, 1298
Fullerenes, 188
Fumaroles, 244, 246, 496
Fumarolic sublimates, 637
Functional groups, 732–733, 734
Fundamental Parameter (FP) method, 1512
Fusain, 281
Fusion, 694
digestions, 1112

G

Gabbros, 402, 433–436
Gadolinite, 525, 684, 839, 1425, 1442
Gadolinium (Gd)
biological utilization and toxicity, 526
geochemical behavior, 525–526
history and use, 525
properties, 525
Gaia hypothesis, 73
Galactic chemical evolution, 1131, 1274
Galactic cosmic radiation, 317
Galena, 154, 811, 815, 1394
Galinstan, 527
Gallite, 526
Gallium, 526
arsenide, 527
nitride, 527
trichloride, 527
Galvanometric optics, 804
Gammacerane, 690
Gamma (γ) radiation, 1296
Gamma ray(s), 32, 978
logging, 30
spectrometers, 30
spectroscopy, 30
Gamma spectrometry, 1297
Gamow, G., 1015
Ga-porphyrins, 528
Garnet, 528, 1192
effect, 635
geochronology, 581
Garrels, R.M., 676
Gas(es), 189, 1081, 1138, 1359
bubbles, 296
cap, 1216
Gas chromatography (GC), 48, 197, 300–301, 530, 772
Gas chromatography–mass spectrometry (GC–MS), 31, 116, 136, 685, 690, 818, 1082, 1210, 1211
Gas chromatography–mass spectrometry-mass spectrometry (GC-MS-MS), 136
Gaseous systems, 458
Gas hydrates, 648
definition, 535
bearing sediments, 197
exploitation, 539–540
locating, 537
methane production, 537–538
resources, 538
structure and characteristics, 536
Gas mass spectrometers, 660
Gas-oil ratio (GOR), 1211, 1216
Gas source, 31
Gas source isotope ratio mass spectrometry (GS-IRMS), 244, 1403
Gas source mass spectrometry (GS–MS)
noble gas mass spectrometry, 543–544
stable isotope mass spectrometry, 543
Gauss' equation, 894
Gaussian-type orbitals (GTO's), 3
GC–MS, *see* Gas chromatography–mass spectrometry (GC-MS)
GDGT, *see* Glycerol dialkyl glycerol tetraether (GDGT)
Ge, *see* Germanium
Geiger-Müller counter, 1297
Gelification, 278
Gems, 1065, 1275
Generalized gradient approximations (GGA), 348
General metabolism, 160
Genes, 1085
Genesis mission, 500
Genesis return mission, 1004
Genetic fingerprints, 1236
Genomic techniques, 551
Geobacter metallireducens, 749
Geobarometers, 561, 597, 850
Geobiology, 327
Geochemical affinity and periodicity, 1205–1206
Geochemical background levels, 552
Geochemical classification of elements, 1195
Geochemical cycle, calcium, 179
Geochemical databases, 410
Geochemical exploration
analytical techniques, 551–552
definition, 549
detection limits, 551
dispersion, 550
hand-held analytical tools, 552
isotopic analyses, 552
multi-element data, 552
multivariate statistical techniques, 552
primary dispersion, 550
quality control and quality analysis (QA/QC), 552
sampling medium and methods, 550, 551
sampling medium, geochemical background levels, 552
spatial statistical techniques, 552
surface and near-surface processes, 550–551
SWIR, 552
XRF, 552
Geochemical modeling, 345
Geochemical properties, 632–633
Geochemical reference material, 30
Geochemical weathering, 894
Geochemistry, 471, 670, 828, 829, 1115
biogeochemistry, 678
chemical oceanography, 677
Clarke, F.W., 670
cosmochemistry, 678
geochronology, 673–674
Goldschmidt, V.M., 671
igneous and metamorphic rocks, 676
organic geochemistry, 677
radiogenic isotope geochemistry, 674–675
stable isotope geochemistry, 675
Vernadsky, V., 672
Geochron, 815
Geochronology, 43, 566, 571, 673, 728, 767, 812, 1295
applications, 573
radioactive decay, equation of, 572–573
Geochronometers, 796
Geodynamics, 915
Geodynamo, 590
Geo-engineering, 115, 1141, 1144
Geofluids, 242
Geological fluids, 303
Geologic history, 410

Geologic time scale, 329, 561, 566
  chemostratigraphy, 588
  construction, 586–587
  cyclostratigraphy and astrochronology, 588
  definition, 586
Geomagnetic field, 317
Geomorphology, 322
Geoneutrinos, 29, 1466
Geophysics, 471
Geopolymers, 277, 1096
Geoporphyrins, 1247
Geosphere, 191
Geotherm, 412
Geothermal, 493
  energy, 894
  waters, 180
Geothermal systems
  definition, 592
  direct thermal use of heating, 592
  fluid-rock interactions, 595–596
  fluid sources, 593
  geographic occurrences, 592
  heat sources, 592–593
  primary fluids, 593–594
  secondary geothermal fluid, 594–595
Geothermobarometry, *see* Thermobarometry
Geothermometers, 489, 561, 676, 850, 1127, 1131, 1369, 1371
GEOTRACES, 563, 971
Gephyrocapsa spp., 1084
Germanium, 527
  geochemical behavior, 615–616
  history and use, 615
  properties, 615
Geysers, 159
Ghareb oil shale, 1056
Giant impact, 568, 1525
Giant Lunar Impact, 501, 502
Giant planets, 387
Gibbs, J.W., 558, 1220
Gibbs-Duhem equation (GDE), 457, 560, 620, 909
Gibbs energy, 450, 456, 514, 519, 555, 557, 559, 560, 602, 843, 910, 911, 1097, 1220, 1222, 1353, 1355, 1357, 1360
Gibbs-Helmholtz equation, 460, 521
Gibbsite, 267
Gibbs phase rule, 554, 621, 671, 911, 912, 1221
Gibbs standard free energy, 212
Glacial diamictites, 392
Glacial moraines, 322
Glacial periods, 1164
Glacial sediment, 97
Glass, 43, 473
Glassy/amorphous material, 947
Glauconite authigenesis, 86
Global buoyancy flux, 655
Global carbon cycle, 197, 275, 773, 774, 1104
  See also Carbon cycle
Global circulation models (GCM), 110
Global climate, 1131
  change, 98
Global cooling, 1392
Global heat flux, 655
Global Stratotype Section and Point (GSSP), 586
Global sulfur cycle, 1395–1396
Global warming, 539, 833, 1143, 1165
  and climate change, 562
Glycerol dialkyl glycerol tetraethers (GDGTs), 127, 819, 820, 1082, 1168
Goethite, 748, 752, 945, 1348
Gold, 895, 1233, 1234, 1312
  leaf, 622
  mining, 902
Goldschmidt, V.M., 310, 311, 562, 671–672, 679
Goldschmidt classification, 236, 671, 827
Goldschmidt geochemical classification of elements, 60
Goldschmidt's classification of the elements, 800
Goldschmidt's rules, 671, 1187
GOR, *see* Gas-oil ratio (GOR)
Goslarite, 1393
Gouy-Chapman model, 264
Gouy-Chapman scaling, 624–625
Gouy-Chapman theory, 623
  objective of, 623
  validation, 626–627
Gradient operator, 892
Grain boundary diffusion, 366
Granites, 406, 489, 505
Granitic rocks, 1133
Granular iron formations (GIFs), 751
Granulite-facies rocks, 393
Granulites, 393
Graphene, 188, 1267
Graphical phase diagram, 842
Graphite, 187, 279, 1273
Gravitational energy, 500
Gravitational fractionation, 995
Gray tin, 445
Graywackes, 408
Great Oxidation Event (GOE), 509, 561, 676, 678, 752, 754, 1127, 1265, 1267
Greece, 644
Greenalite, 753
Greenhouse, 1152, 1155, 1156
  eustasy, 467
  gas(es), 104, 704, 1141, 1144, 1153, 1154, 1494
  gas emissions, 1199
  gas forcing, 64
Greenland-Iceland-Norwegian Seas, 1046
Green river formation, 1056
Greenstone belt(s), 408
Greenstone belt basalts, 408
Grenville orogeny, 582
Gross primary production, 192
Ground instruments, 703
Groundwater, 159, 567, 699, 1299, 1302, 1467
Groundwater dating, 785
Guano deposits, 1232
Gunmetal, 44
Guoy-Chapman theory, 1412
Gymnosperms, 125, 127, 132
Gypsum, 177, 465, 1044, 1392, 1399

H

Haber-Bosch process, 986, 988, 1349
Hadean, 411
Hadean rocks, 1259
Hafnium, 670, 1528
Hafnium carbide (HfC), 630
Half-condensation temperature, 1380
Half-life, 183, 527, 572, 1312, 1316
  lead, 813
Half-time (t1/2), 777
Halide(s), 945
  complexes, 637
Halide minerals
  definition, 636–637
  halide complexes, 637
  oxyhydroxy-halides, 637–644
  simple halides, 637
Halite, 637, 647, 1044
Halogen(s), 553, 637, 828
  elements, 729
  geodynamics, 246
Halokinetic geometries, 469
Halons, 167, 1140
Hammersley formation, 749
Hand-held analytical tools, 552
Hand-held XRF analyzer, 1512, 1513
Hardness and softness, 350
Harmonic oscillator, 1292
Hartree-Fock calculation, 348
Hartree-Fock theory, 2
HBI alkanes, *see* Highly branched isoprenoid (HBI) alkenes
H burning, 1125
^{3}He, 384
Health effects, 160
Healthy bones, 160
Heart implant devices, 1237
Heat, 555, 650
  capacity, 186, 212, 326, 556, 562, 649, 650, 652, 1220, 1230
  conduction, 841
  content, 844–845, 848
  flow, 398
  flux, 844
  of formation, 4, 671
  production, 393, 1296
  of reaction, 186
Heat producing elements (HPE), 393, 425
Heavy metal(s), 1393
Heavy metal pollution, 154
Heavy rare earth elements (HREE), 381, 393, 461, 525, 839, 1174, 1234, 1313, 1425, 1442, 1518
Heavy water, 694
He burning, 1125
HED meteorites, 10
Heinrich events, 1157
Heisenberg uncertainly principle, 1291
Helgeson, H., 677
Heliosphere, 317
Heliothermal brine system, 467
Heliothermality, 467
Helium, 61, 1003
  burning, 1016
  element data, 657
  geochemical behavior, 658
  history and use, 658
  properties, 657–658
Helmholtz energy, 555
Hematite, 752, 755, 861
Hemes, 1247
Hemoilmenite, 862
Henry, William, 663
Henry's constant, 1363
Henry's Law, 21, 522, 663, 1188, 1189, 1361, 1374, 1375, 1451
  constants for gases, 663
  definition, 663
  equilibrium of oxygen, 663
  gas solubility, 663
  trace component, 664
Hermann-Mauguin symbols, 336
Hermite polynomials, 1292
Heteroatoms, 143
Heterogeneous chemistry, 1139
Heterogeneous equilibria, 599
Heterogeneous primary nucleation (HeN), 938
Heterogeneous reactions, 893
Heterogeneous volatile accretion, 1504
Heterotrophic, 191
Hexagonal birnessite, 1432
Hexaniobate, 1245
Hexa-valent, 1465
Hf isotope compositions, 578

Hf isotope model age, 411
Hf model ages, 583, 584
Hf-W chronometer, 618
Hf-W system, 1459, 1460
^{182}Hf-^{182}W system, 1459
^{82}Hf-^{182}W systematics, 389
3H-3He method, 662
Hibonite, 1275
High-energy ion beam, 1185
High-energy mobile muds, 1098
High field strength, 630
High field strength elements (HFSE), 546, 1528
  definition, 664
  geochemical behavior, 664
High latitudes, 1140
Highly-branched isoprenoids (HBIs), 144
Highly branched isoprenoid (HBI) alkenes, 686, 687, 1084
Highly siderophile elements (HSE), 350, 386, 1111
Highly volatile elements, 316
High nutrient low chlorophyll (HNLC), 1029
High performance liquid chromatography (HPLC), 197, 685, 732, 1082
High-precision isotope data, 732
High-pressure NMR, 1013
High-pressure research, 471
High quartz, 1221, 1222, 1226
High-resolution gas source multi-collector mass spectrometers, 1368
High-resolution mass spectrometry, 32
High resolution transmission electron microscopy (HRTEM), 1267
High-spin state, 742, 746
Highstand/Regressive Systems Tract (HST) strata, 1079
High-temperature geochemistry, 563, 566, 858
Hiseponymous equation, 603–604
Histosol, 1197
HMS Challenger, 888
H_2O, 473
H_2O-CO_2, 473
Holmium (Ho)
  biological utilization and toxicity, 684
  geochemical behavior, 684
  history and use, 684
  properties, 683
Holomixis, 467
Hominins, 43
Homogeneous primary nucleation (HoN), 938
Homogeneous reactions, 893
Hopanes, 118, 146, 819, 820
Hopanoids, 142, 1084
Hop-17(21)-ene, 129, 131
Hot springs, 384
Howard, E., 678
Howardites, 920
HPLC, *see* High performance liquid chromatography (HPLC)
HPLC-Orbitrap high resolution MS, 1248
Huancavelica, 895
Human activities, 1136
Human beings, boron poisoing, 160
Human body, calcium level in, 180
Human impacts, 98
Human perturbations, 327
Humic acids, 529
Humic and fulvic acids, 668
Humic coals, 279, 1055
Humic substances, 130, 150, 276, 1107
Humification, 276
Humin, 678
Huminite, 281
  group macerals, 281
Hund's rules, 1293
Hutton, James, 944
Hybrid GGA (HGGA), 348
Hydrargyrum, 895
Hydraulic fracturing, 1075
  fluids, 164
Hydrocarbon(s), 136, 140, 187, 189, 275, 533, 535, 648, 695, 714, 818, 820, 1052, 1053, 1055, 1119, 1208, 1210, 1212, 1214, 1216, 1217
  aliphatic, 685
  analysis and identification, 685–686
  ancient sediments, 688
  in archaea, 686
  in bacteria, 686
  in coal, 688–689
  in cyanobacteria, 686–687
  extra-terrestrial, 691
  gas, 116
  in geosphere, 687–688
  in microalgae, 687
  in petroleum, 689–690
  pollutant sources of, 690
  in vascular plants, 687
Hydrocarbonoclastic bacteria, 688
Hydrochloric acid, 242
Hydrochlorofluorocarbons, 1140
Hydrofluoric acid, 496
Hydrogen, 60, 387, 490, 498, 696, 748, 962
  atom, 146
  biological utilization and toxicity, 695
  bonding, 348, 695
  bonds (H-bonds), 236
  burning, 1016
  economy, 694
  history and use, 694
  isotopes, 47, 123, 127
  occurrence, 694–695
  properties, 693–694
  radicals, 1138
  sulfide, 748
  sulfide pathway, 1395
Hydrogenetic, 887
  sedimentation, 477
Hydrogen index (HI), 772, 1076, 1080, 1281
Hydrogenous, 887
Hydrological thermostat, 240
Hydrologic cycle, 317, 1370, 1492–1493
  component measurement, 702
  definition, 701
  energy balance and climate change\:, 703
  processes, 702
  reservoirs and fluxes, 702
  spatial and temporal variability, 703
Hydrolysis, 298, 1364
  constant, 16
Hydrolytic anion, $[Sb(OH)_6]^-$, 38
Hydrophobic, 187
  substances, 1414
Hydropyrolysis, 1082
Hydrosphere, 60, 694, 855, 1399
Hydrothermal, 179, 463, 493, 887
  activity, 677
  alteration, 270, 704, 1133, 1432
  circulation, 1045
  deposits, 154
  fluids, 163, 495, 648, 823, 825, 1066, 1430–1432
  metamorphism, 434
  mineral deposit, 1177
  ore deposits, 648, 705, 1068
  petroleum formation, 714
  precipitate, 637
  processes, 436–437, 566
  systems, 490, 789, 791, 1300, 1372
Hydrothermally-altered oceanic crust, 159
Hydrothermal solutions, 453, 709
  definition, 706
  mineral deposits, 707
  physicochemical properties of, 707–709
Hydrothermal vents, 408, 1028
  carbon cycling, 714
  water-rock interactions, 713
Hydrous pyrolysis, 790, 1060
Hydroxides, 528, 945
Hydroxyapatite, 177
Hydroxyl radical, 1136
Hyperfiltration, 263
Hyperthermophiles, 1457
Hypogene, 715
  mineral deposit formation, 716
  mineral deposit occurence, 716

I
^{129}I, 1501, 1502, 1504
Ice ages, 561
Ice cores, 1169
Icehouse, 467, 1152, 1156
Iceland, 408, 1482
ICP-MS analysis, 824
Ideal behavior, 21
Ideal-gas equation, 555
Ideal gas law, 21
Idrija, 895
Igneous differentiation, 1380
Igneous rock, 676, 1133
Ignimbrites, 1482
IIE silicate clasts, 9
Illite(s), 86, 282, 1348
Ilmenite, 1445
Imaging, 737, 738
Impact(s), 251, 253
Impact melts, 412
Impedance spectroscopy, 474
Incision rates, 96
Incompatibility, radium, 1299
Incompatible, 528, 546, 966, 1237, 1317, 1321
  behavior, 159, 244
  trace elements, 430, 432, 434, 436, 513, 930
Incompatible elements, 91, 226, 242, 408, 674, 1378, 1420
  definition, 719
  use in geochemistry, 719–720
Indium
  biological utilization and toxicity, 722
  geochemical behavior, 722
  history and use, 722
  properties, 722
Inductively coupled plasma, 31, 378, 723
Inductively coupled plasma atomic emission spectroscopy (ICP-AES), 30
Inductively coupled plasma mass spectrometers, 769
Inductively coupled plasma mass spectrometry (ICP-MS), 31, 723, 926, 1112, 1237
  polyatomic interferences, 727
  quadrupole ICP-MS, 724–725
  sampler/skimmer interface, 724
Inductively coupled plasma optical emission spectroscopy (ICP-OES), 30, 79–80

Inductively coupled plasma source mass spectrometry, 1379
Inductively coupled plasma source, multi collection mass spectrometry (ICP-MCMS), 1403
Industrial emissions, 1140
Industrial neon, 973
Industrial revolution, 34, 35, 746
Industry, 1140
Inert gases, 53, 784
Inertinites, 129, 276, 281, 772
Inertite, 280
Infiltration deposits, 1069
Infrared absorption, 30
Infrared and Raman vibrational spectra, 350
Infrared (IR) radiation, 81, 1136, 1144
Infrared spectroscopy, 772
Initial $^{87}Sr/^{86}Sr$, 1379
Initial Hf isotopic heterogeneity, 582
Initial isotope composition, 574
Initial Pb isotopic compositions, 575
Initial Pb ratio, 575
Initial rate, 777, 779, 782
Initial reaction rates, 779
Inner core (IC), 418, 420, 426
Inner-outer core boundary (ICB), 426
Inner-sphere, 266
  complex, 298
Inorganic, 833
  carbon, 191
  colloids, 328
Inosilicates, 945, 1334
In situ ^{10}Be ($^{10}Be_i$), 96–97
In-situ experiments, 472
Insoluble trace elements, 392
Interatomic distances, 32
Interdiffusion, 363, 366, 368
  coefficient, 366
Interfacial surface energy, 1411
Interferences, 727
Intergovernmental Panel on Climate Change (IPCC), 35
Interlayer, 266, 268, 269
  cations, 272
Internal differentiation, 500
Internal (mineral) isochrons, 575
Internally consistent thermochemical models, 842
International mineralogical association (IMA), 943
Interplanetary dust particles (IDPs), 1005, 1273
Interstellar medium, 1274
Intraaggregate diffusion, 776
Intracratonic, 467
Intraoceanic volcanic arcs, 712
Intraplate settings, 406
Intrinsic diffusivity, 366
Intrinsic properties, 651
Intrinsic regime, 369
Invariant point, 1220, 1225–1229
Invariant temperature, 843
Iodine, 637, 646, 647
Ion activity product (IAP), 211, 214, 1361
Ion association, 346
Ion counting detector, 725
Ion exchange capacity, 736
Ion exchange chromatography, 31, 731, 1433
  batch and column methods, 733–735
  efficiency, 735
  principles, 732
  process, 733
  retention volume, 735
  structure, 732–733
  various strategies, 735–736
Ion exchange reaction, 733
Ion exchange resin, 732–733
Ion filtration, 245
Ionic bonding, 637
Ionic potential, 546
Ionic radii, 671, 1187, 1188, 1190, 1192, 1193
Ionic radius, 546, 740, 968
  coordination number, 739
  crystal radii, 739
  determination of, 739
  effective ionic radii, 739
  electronic spin state, 739
  lithium, 823
  methods of measurement, 739
  in mineralogy and petrology, 742–743
  patterns in, 742
  radium, 1299
Ionic strength, 345, 1241
Ionisation, 725
Ionization efficiency, 667
Ionization potentials (photoelectron and X-ray spectra), 2, 630
Ion microprobe, 31, 1368
  advantages of, 737
  geo-/cosmo-chemistry and advancements, 737–738
  operation principle, 737
Ion pair, 298
I/Pu ratio, 1504, 1505
I-Pu-Xe system, 1501
IR absorption spectroscopy, 301
Iridium, 744
Iron (Fe), 44, 864, 865, 1023, 1027, 1125, 1126, 1165, 1349, 1399
  addition, 115
  age ceramics, 44
  availability, 749
  fertilization hypothesis, 749
  group of nuclides, 1017
  isotope fractionation, 32
  peak, 746
  sulfides, 862
Iron oxide, 477, 1275
Iron Age, 746, 943
Iron formations (IFs)
  definition, 751
  geologic occurrences, 751–753
  role of biology, 753–755
  seawater chemistry, 753
Iron meteorites, 307, 527, 568, 679, 863, 921, 1110, 1112, 1174, 1459
  definition, 762
  origin, 762–767
Iron-reducing bacteria, 897
Iron-reducing organisms, 749
Irreversible process, 842, 851
IR spectrometers, 82
Isheyevo carbonaceous chondrite, 994
Island arc, 159, 1381
  volcanoes, 567, 1300
Isobaric interferences, 49, 544, 727
Isobars, 84
Isochore, 489
Isochron, 968, 969
  method, 573–575, 1112
Isochrysis spp., 1084
Isomers, 146
Isomorphic exchange, 268
Isomorphic substitutions, 266
Isopimaranes, 125
Isopolyanions, 1243
Isoprenoid, 140, 686, 687, 689, 818, 820
  biochemistry, 1085
  lipids, 818
Isothermal compressibility, 211, 212, 326, 1220
Isotones, 84
Isotope, 753, 755, 1043, 1059, 1061
  anomalies, 185
  clumping, 1371–1372
  dilution, 31, 768
  and element ratios, 1163
  equilibrium, 1379
  excursions, 184
  fractionation, 182, 195, 858, 1130, 1131, 1402, 1404, 1406, 1408, 1429, 1431, 1432, 1465, 1466
  fractionation factors, 5, 1293
  geochemistry, 563, 566, 673–676
  geothermometers, 1372
  mass-balance, 183
  ratio analysis, 43, 723
  systems, 493
Isotope dilution-thermal ionization mass spectrometry (ID-TIMS), 578
Isotope ratio gas chromatography–mass spectrometry (IRGC-MS), 136
Isotope ratio mass spectrometer, 31, 46
Isotope ratio mass spectrometry (IRMS), 196, 197, 1130, 1403, 1408
Isotopic abundance anomalies, 1273
Isotopic analyses, 552
Isotopic anomalies, 322, 1015, 1019
Isotopic compositions, 361, 737, 738
Isotopic fractionation, 900, 1087
  factor, 105, 379
Isotopologues, 676, 1371
Isua, Greenland, 970
Isua supracrustal belt, 413
Italy, 895
Itsaq gneiss complex, 413
^{129}I-^{129}Xe system, 385, 388

J
Jack Hills, 412
Jacob's Ladder of functionals, 348
Jahn–Teller effect, 342
Jarosite, 748, 1393
Johannes van der Waals's analysis, 22
Joly's Sodium Age of the Earth, 1346
Jupiter-family comets, 388
Juvenile crust, 409

K
^{40}K, 53
Kakangari type chondrites (K), 250
Kamacite, 861–863
Kaolin, 266, 268
Kaolinite, 273, 282, 1349
  authigenesis, 86
K-Ar ages, 54
K-Ar dating, 674
K-Ar isotope system, 571, 579–580
Karstification, 358
Kaurane, 125
Keggin-ion, 1244
Kelp, 647
Kelvin, 673
  temperature scale, 555
Kernite, 158
Kerogen, 102, 129, 132, 142, 143, 147, 150, 155, 193, 198, 565, 677, 689, 691, 700, 789, 790, 962, 1055, 1075, 1082, 1100, 1107, 1211, 1214, 1249, 1267
  analysis techniques, 772–773
  composition, 772
  conglomerate of organic structures, 1076

definition, 771, 1076
formation, 771–772
global carbon cycle, 773
imbalances and atmospheric changes, 774
molecular structure, 1076
occurence, 771
petroleum generation, 773
role in global carbon cycle, 773–774
sedimentary rocks, 1076
thermal defragmentation of, 105
thermal degradation, 1079
thermal maturation, 773
thermolysis of, 103
types, 772, 1076
type I kerogen, 1212, 1214
type II kerogen, 1212, 1214
type III kerogen, 1212, 1214
Kerosene, 1056
Kinetic(s), 145, 562, 677, 775, 1214, 1369, 1437
of chemical reactions, 1012
fractionations, 245
inhibition, 379
parameters, 486
phenomena, 842, 851
processes, 244
rate law, 893
Kinetic isotope effects (KIE), 1404, 1405
of respiration, 1127
Kohn-Sham orbitals, 348
Komatiites, 406, 408, 505, 507, 1066, 1110, 1237
Korzhinskiĭ, Dmitriĭ Sergeevich, 843
K-rich minerals, 1317
Kr-Q, 786
Krypton, 61, 1004
cosmic ray exposure dating of meteorites, 785
extremely atmophile, 785
geochemical behaviour, 784–785
geochemical studies, 785
groundwater dating, 785
highly volatile element, 785
history and use, 784
isotope geochemistry, 785
mantle geochemistry, 785, 786
solar system studies, 786
Kukersite, 1056
Kupferschiefer, 564, 1070
Kuroko massive sulphide deposits, 1066
K/U value, 590

L

Laboratory investigation, scientific field, 471
Lactoferrin, 529
Lacunary POMs, 1246
Ladderanes, 819, 820
Laguerre polynomials, 1292
Lake, calcium level, 179
Laki, 1482
Lamosite, 1056
Landforms, 96
Land-ocean continuum, 1094
Landscape, 1409
dynamics, 97
erosion, 97
Land use, 97
Lanthanide(s), 795
contraction, 671, 684, 744, 793, 794, 1205, 1258
Lanthanide rare earth elements (REE), 461, 525, 683, 827, 1257, 1286, 1425, 1441
Lanthanite, 796
Lanthanum, 1322
geochemical behavior, 799
geochronology, 799
history and use, 799
properties, 799
toxicity, 799
Large igneous province volcanism (LIPS), 903, 1483
Large-ion lithophile element (LILE), 24, 173, 432, 436, 794, 1299, 1317, 1382, 1466
definition, 800
geochemistry, 800
origin of term, 800
Large low shear wave velocity provinces (LLSVPs), 1051
Larmor, 1011
frequency, 1009, 1010
Laser, 1305
ablation, 305
Laser ablation-inductively coupled plasma mass spectrometry (LA-ICP-MS), 31, 49, 411, 486, 489, 553, 578, 579
definition, 802
imaging, 807
in-situ dating, 806
in-situ isotope ratio measurements, 805
multi-element determinations, 803
quantification protocol, 804–805
Laser ablation multi-collector, 46
Laser ablation split stream (LASS) technique, 579
Last glacial maximum (LGM), 1045, 1157
Late accretion, 1113, 1236
Late diagenesis, 453
Late heavy bombardment, 388, 500, 1236
event, 1260
Latent heat, 845, 1180, 1487
Laterites, 271
Lateritic nickel, 1065
Late veneer, 389, 503, 1113
hypothesis, 1424
theory, 386
Lattice diffusion, 366
Lattice specific heat, 651
Lattice strain model, 743, 1188
Lattice vibrations, 651
Laurite, 1110, 1319
Laurium (Lavrion), 644
Lava flows, 430
Lavoisier, A., 563, 677, 1231
Law of Detailed Balance, 1013
Lawrencite, 637
Laws of thermodynamics, 554
Layered intrusions, 1237
Layered mantle model, 1005
Lead, 44, 813, 1173, 1234, 1312
chromate, 255
isotopes, 45, 49
isotopic analysis, 46
Leaf wax compounds, 1151
Leaf waxes, 1104
Least squares analysis, 778
Le Châtelier's principle, 1362
Legendre polynomials, 1292
Lepidolite, 822
Lever rule, 1182
Lewis acid, 299
concept, 17–18
Lewis base, 299
Lherzolite, 1470
Li, 1015
Libby, W.F., 674
Life, 1102
Life on Earth, 737
Lifetime, 1137, 1138
Ligand, 297, 1455
field theory, 340, 342
Light elements, 527
Light rare earth element, 408
Lignin phenols, 1083
Lignins, 275, 1104
Lignite, 123, 125, 127, 129, 133, 189, 278
Lime, 177
Limestone, 189, 1045
Limonite, 748
Linear alkyl benzenes (LABs), 690
Line (one-dimensional) defects, 933
Linus Pauling, 442
Lipids, 123, 127, 131, 136, 1057, 1079, 1082, 1100, 1104
bacteriohopanepolyols, 820
carotenoid distributions, 820
paleotemperatures, 820
proxies, 1088
structural classes, 818–820
Liptinites, 281, 282, 772
Liptite, 280
Liquid, 1359
chromatography, 300
immiscibility, 514
line of descent, 514, 927, 928
scintillation detector, 589
Liquid chromatography-mass spectrometry (LC/MS), 818
Lithification, 831
Lithium, 562
in aqueous solutions, 824
biological utilization, 823
concentrations three, 823
geochemical behavior five, 822
history and use, 822
ion batteries, 292
isotopes, 824
properties six, 822
subduction cycling of isotopes, 825–826
Lithoautotrophic bacteria, 1392
Lithogeochemistry, 551
Lithology, 398
Lithophile, 157, 236, 461, 546, 630, 653, 684, 763, 794, 839, 984, 1317, 1378, 1426, 1442, 1443, 1453, 1519, 1528
calcium, 178
Lithophile element, 27, 91, 168, 729, 823, 966, 1124, 1231, 1299, 1313, 1517
large ion, 91
samarium, 1321
Lithophile trace elements, 1420
Lithosphere, 1181, 1399
Local scale process, 184
Local spin density approximation (LSDA), 348
Lodranites, 7, 921
Loess, 392
London dispersion (Van der Waals) forces, 236
London force, 1473
Long chain diol index (LDI), 1089
Longitudinal relaxation time T1, 1012
Long-range atomic order, 946
Long Valley, 1184
Lonsdaleite, 188
Lord Rayleigh, 53
Lost City Hydrothermal Field, 713
Low-energy facies, 1098
Lower continental crust, 393
Lower crust, 392
Lower oceanic crust, 925
Low-grade metamorphic rocks, 705

Low quartz, 1221, 1222, 1226
Low-spin state, 742, 746
Lowstand Systems Tract (LST) strata, 1079
Low-temperature alterations, 705
Low-temperature geochemical, 832, 833
Low-temperature geochemistry, 563–564, 829–834, 858
Lu-Hf, 674
$^{176}Lu/^{176}Hf$ decay system, 839
Lu-Hf geochronology, 581
Lu-Hf model ages, 411
Luminescence, 835, 836–837
  dating, 838
  spectroscopy, 837–838
  zoning, 837
Luminosity, 1154
Lunar-forming giant impact, 618, 619
Lunar Giant Impact, 502
Lunar impact melt rocks, 1236
Lunar meteorites, 10, 922
Lunar regolith, 321
Lunar samples, 618, 619
Lupane, 125
Lutetium (Lu)
  biological utilization and toxicity, 839
  geochemical behavior, 839
  history and use, 839
  properties, 839
Lysocline, 204, 1167

M
Maceral groups, 772
Maceral(s), 276, 280–282, 1075
  types, 1056
Mackenzie, F., 677
Macromolecule, 148
Macrophytes, 127
Mad Hatter's syndrome, 898
Mafic composition, 398
Mafic silicate minerals, 860
Maghemite, 748
Magic number, 84, 91, 672, 1443
Magma, 296, 471, 705, 716, 1180, 1388, 1469–1470, 1480
  chambers, 433, 434, 1481
  degassing, 244, 713–714
  differentiation, 760, 1333
  mixing, 433, 514
  ocean, 501, 504, 528, 618, 619, 1236
  ponding, 1184
Magma, process modeling, 841
  assimilation processes, 846–850
  manifesto, 850–851
  techniques, 842
  thermodynamic models, 843–846
Magmatic, 706
  differentiation, 307
  evolution, 841, 842
  irons, 528
  processes, 430, 433, 434, 1300, 1331
  process modeling, 562
  sulfide deposits, 232, 1395
Magmatic-hydrothermal processes, 304
Magmatic-hydrothermal systems, 489
Magmatogenic ore deposits, 1066
Magnesite, 207, 211, 212, 217, 378
Magnesium, 854–855
Magnet, 726
Magnetic field, 412
  strength, 667
Magnetic isotope effects (MIE), 901, 1404
Magnetic sector mass analyzer, 541
Magnetism, 860
Magnetite, 752, 754, 861–863
Magnetosomes, 749
Magnetotactic bacteria, 749
Major element, 857
MALDI, *see* Matrix-assisted laser desorption ionization (MALDI)
Manganese (Mn), 1032
  biological utilization, 866
  geochemical behavior, 865–866
  history and use, 865
  nodules, 795
  oxides, 477
  properties, 864–865
Mangrove, 127, 132, 1197
Manhattan Project, 673, 675
Mantle, 55, 183, 430–433, 472, 566, 794, 825, 854, 925, 927, 929, 931, 1236, 1480
  chemical heterogeneity, 246
  convection, 590, 1480
  differentiation timescales, 1459–1460
  dynamics, 263
  melt fraction, 410
  melting, 433, 434
  nitrogen, 65
  overturn, 407
  peridotite, 406
  plumes, 406, 566, 674, 816, 1432, 1481, 1483
  source, 1431
  upwelling, 1289
  wedge, 406, 1182
  xenoliths, 1236
  xenon regassing, 1502
Mantle-crust, 633
Mantle geochemistry
  atmosphere, origin of, 786
  chemical geodynamics, 870–872
  convection, 867–869
  definition, 867
  facts about, 867
  geodynamics, 869–870
  heterogeneity, 872–873
  heterogeneity scale of, 873–874
  plate tectonics, 867–869
  probing, 870
  source of Earth's volatiles, 785
  synthesis, 874
  volcanism, 867–869
Many-body perturbation theory (MBPT), 2
Marcasite, 284, 749
Marine archives, 184
Marine biota, 903
Marine carbonates, 1382
Marine primary productivity, 193
Marine sedimentary mineral deposits, 477
Marine sedimentary processes, 94
Marine sediments, 92, 192, 193, 199, 537
Marine snow, 111
Marine systems, 376
Marinites, 1056
Mars, 273, 386, 496, 506, 509, 528, 865, 1393
Mars Exploration Rover, 748
Marshes, 1197
Martian meteorites, 11, 922, 1407
Martin curve, 112
Mass accuracy, 666, 667
Mass-action expression, 519
Mass analyser, 726
Mass assimilated to mass crystallize ratio, 848
Mass balance, 1045, 1431
  approach, 760
Mass bias, 727, 768, 769
Mass conservation, 893
Mass dependent, 1432
  fractionation, 92, 1130, 1371
  W isotope, 1458
Mass dispersion, 726
Mass extinctions, 744
Mass fractionation, 727
Mass fragmentography, 139
Mass independent fractionation (MIF), 509, 567, 675, 900, 1130, 1371, 1402, 1404, 1447
Mass independent fractionation of sulphur isotopes (MIF-S), 66
Mass-independent nucleosynthetic isotopic anomalies, 1236
Massive dolomites, 360
Massively parallel computing, 894
Mass peak spectrum, 724
Mass resolution, 725, 737
Mass spectrometer, 184, 723, 737, 738
Mass spectrometry, 146, 162, 530, 697, 772, 1297, 1316, 1436
Mass spectrum, 533
Mass-to-charge ratio (m/z), 724
Mass transfer, 493, 892
Matrix, 920
  in chondritic meteorites, 253
  effect, 727, 737
Matrix-assisted laser desorption ionization (MALDI), 667
Maturity, 131
Maunder minimum, 323
Maxwell, J. C., 559
Maxwell-Boltzmann equation, 77
Mayan region, 49
MBT/CBT, 1161
MBT-CBT proxy, 1088
McConnell formalism, 1012
Mechanical mixture, 1353
Medical diagnosis, 1422
Medicine, 1372
Mediterranean overflow water, 1046
Mediterranean Sea, 1044
Medium atomic order, 946
Melanin, 1102
Melanosomes, 1102
Melanterite, 1393
Melt, 471, 1364
  inclusions, 244
  migration, 1470
  productivity, 1289
  sills, 434
MELTS model, 599
Melting, 430, 432, 1317
Mendeleev, D., 527, 1242
Menezesite, 1245
Mercaptan (SCH_3), 1397
Mercury, 287, 527, 900–903
  isotopes, 1371
  mines, 895
Meridiani Planum, 748
Meridional overturning circulation (MOC), 1158
Mesocrystals, 946
Mesogenesis, 355
Mesosiderites, 10, 920
Messinian salinity crisis, 1044
Metabolic capabilities, 1096
Metaboric acid, 157
Metagenesis, 116, 147, 192, 773, 1212
Meta GGA (mGGA), 348
Metal, 43, 252, 776

authigenesis, 86
deposits, 705
Metallic bonds form, 234
Metallic Ga, 527
Metallic iron, 316
Metallicity, 310
Metalliferous sediment, 878, 887–888
Metalloids, 156, 328, 445
Metallophytes, 293
Metalloporphyrins, 677, 1081
Metallurgy, 670, 679
Metal mining, 895
Metal-oxo wall, 1244
Metal-silicate partition coefficients, 1193–1194
Metal-silicate systems, 1189
Metamorphic, 706
cycle, 472
dehydration, 857
facies, 907, 908
and igneous petrology, 563
reactions and processes, 562
recrystallization, 398
rocks, 490, 676, 825, 1133
Metamorphism, 251, 402, 495, 566, 1133, 1267
Metamorphogenic-hydrothermal ore deposits, 1071
Metapelitic rocks, 398
Metasomatic process, 453, 472
Metasomatism, 307, 1395
Metastable equilibria, 455
Metazoa, 1265
Meteoric, 706
^{10}Be, 97–98
diagenesis, 357
origin, 705
radionuclides, 320
water line, 1370
waters, 180
Meteorites, 7, 189, 273, 306–307, 317, 561, 568, 671, 673, 675, 678, 679, 786, 815, 827, 828, 917, 1014, 1015, 1018, 1090, 1125, 1132, 1175, 1273, 1371
chondrites, 248
pairing, 321
terrestrial ages, 321
Meteoritic water, 1133
Methane, 129, 130, 133, 535, 685, 686, 690, 691, 695, 748, 961, 1053, 1138, 1154, 1156, 1372
gas-hydrates, 789
hydrates, 104, 200, 1156
oxidation, 68
Methanogen, 101–102, 129, 131, 686, 689
Methanogenesis, 197, 276, 700
Methanogenic consortia, 103
Methanol-utilizing methanogenesis, 101
Methanotrophic archaea, 129
Methanotrophs, 129, 131, 1087
Methicillin-resistant Staphylococcus aureus, 749
Methylation, 897, 903
Methyl chloride, 1138
2-Methylhopanoids, 1084
Methylphenanthrene index (MPI-1), 131, 132
Methylphenanthrene ratio (MPR), 131
Mexico, 895
Meyer, M., 675
Mg/Ca, 886
paleothermometry, 1166
thermometry, 1150
Mg-silicates, 316
Mica, 266, 269, 796, 1317
Micritization, 357
Microalgae, 687, 1083
Microbes, 829, 895
Microbial (biogenic) gas, 962
Microbial community structure, 1096–1097
Microbial decomposition, 149
Microbial Fe(III) reduction, 754
Microbial loop, 376
Microbially produced methane, 197
Microbial methane, 116, 963
Microbial methanogenesis, 100, 102, 104
Microbial nitrate respiration, 949
Microbial respiration, 529
Microfossils, 754
Micrometeorites, 888, 917
Micro-milling, 48
Micronutrient, 160, 1526
Microorganisms, 1095, 1349, 1351
Microphysical processes, 1142
Micro-PIXE, 1185
MicroRaman spectroscopy, 1267
Microscope, 1304
Microstructure, 906, 914, 915
Middle continental crust, 393
Mid-Miocene Climatic Optimum, 1156
Mid-ocean ridge, 185, 430, 431, 434, 711, 720, 887, 1181, 1289, 1407
Mid-ocean ridge basalts (MORB), 229, 430, 432–433, 496, 517, 566, 567, 661, 674, 812, 842, 843, 870, 966, 969, 976, 1133, 1322, 1466, 1480, 1502, 1503
average MORB compositions, 926–927
elements and mineralogy, 927
glass, 647
lower oceanic crust, 925
radiogenic isotopes, 931
solidus, 925
trace elements, 929
volcanism, 1048
Mid-ocean spreading centers, 430
Midplane, 498
Mid-Pleistocene Transition, 1149, 1157
MIE, *see* Magnetic isotope effects (MIE)
MIF sulfur isotope, 678
Milankovich cycles, 675
Milankovitch, Milutin, 675, 1152
Milankovitch cycles, 1372
Milankovitch theory, 1131
Mineral(s), 251, 471, 706, 830, 1306
acids, 14
birth and growth, 936–937
crystalline Earth and dynamics, 936
deposits, 549, 550, 566, 712, 715–716
diagenesis, 1217
evolution, 1176
fission tracks in, 935
growth and sector zonings, 941
growth events and mineral habit changes, 940
growth mechanisms, 939–940
matrix, 1097
monazite, 1518
nanoparticles, 944
paragenesis, 672, 1175
physics, 474
precipitation, 830
primary nucleation and secondary nucleation, 937–939
radiation damage in, from self-irradiation, 934
resorption, 936, 940–941
ripening, 942
species (*see* Sulfate minerals)
surfaces, 150
synthesis, 475
zonation/zoned minerals, 912
See also Mineralogy
Mineralizing processes, 551
Mineral-melt partition coefficients, 743
amphibole, 1193
garnet, 1192
olivine, 1190
plagioclase, 1193
pyroxene, 1191
Mineral-melt systems, 1187–1189
Mineralogy, 927–929, 1175
definition, 943, 947
history, 943–944
numbers and classification, 944
present and future challenges, 945
Mine waste, 1393
Minimata disease, 898
Minimum detection limits, 441
Minnesotaite, 753
Minto Block, 413
Miscibility gap, 1355–1357
Missing Xe
problem, 386, 387, 389
Mississippi Valley type deposits, 1070
Mississippi Valley type ores, 564, 1070
Mitigate, 1144
Mixed layer illite-smectite, 271
Mixed layer pump, 112
Mixing, 105
time, 869
^{53}Mn, 865
Mn nodules, 865
Mn oxide, 1430, 1432
Mobile, 246, 1317
phase, 732–735
Model age, 582–583, 970
calculations, 1112
Moderately siderophile, 527
Moderately volatile element, 251, 316, 527, 654
Modern analog technique, 1166
Modified neglect of differential overlap (MNDO), 2
Moho, 392, 406
Mohorovic discontinuity, 392
Molar abundance, 21–22
Molarity units, 1452
Molar volume, 211, 216, 1220
Mole, definition, 1464
Molecular archaeology, 1082, 1088
Molecular fossils, 533
Molecular orbital theory, 1
Molecular simulation, 494
Molecular stratigraphy, 1085
Molecular structures (rotational spectra), 2
Mollusk, 1024
Molybdenite, 1313
Molybdenum (Mo), 1025, 1034, 1164, 1243
biological utilization and toxicity, 948–949
geochemistry, 948
history and use, 948
isotopic composition of, 949
properties, 948
Molysite, 637
Monazite, 226, 796, 1257
Monazite U-Pb geochronology, 578
Monosulfide solid solution, 1237, 1394, 1396

Monte Carlo simulations, 626
Montmorillonite, 150
Montreal Protocol, 1140
Moon, 243, 307, 462, 496, 528, 568, 617, 619, 1525
Moraines, 96
MOR-type helium, 661
Mössbauer spectroscopy, 32
Mosses, 127, 131
Mountainous river systems, 1098
Mount Pinatubo, 1143
MRCI, 4
MSSVpy, 1082
Mt. Narryer, 412
Mt Pinatubo, 1482
Mt St Helens, 1482
Mudstones, 398
Mulliken-Jaffe electronegativity, 443
Multi-anvil presses, 676
Multi-collection inductively-coupled-plasma mass-spectrometry, 1524
Multicollector, 544
Multi collector inductively coupled mass spectrometry, 723, 814, 968
Multi-collector inductively coupled plasma mass spectrometer, 757, 1368, 1429
Multi-collector inductively coupled plasma mass spectrometry (MC-ICPMS), 305, 543, 900, 1288
Multicomponent diffusion, *see* Chemical diffusion
Multicomponent solutions, 621
Multi-domain structure (MD), 863
Multi-element analyses, 979
Multiple Collector Inductively Coupled Plasma Mass Spectrometry (MC-ICP-MS), 731, 732, 735
Multiple interacting continua, 894
Multireference, 4
Multi-S-isotope systematics, 1400
Multivariant equilibria, 601
Multivariate statistical techniques, 552
Mu-meson, 1014
Murchison meteorite, 698
Muscovite, 412

N
Na^+, 1043
Nahcolite, 465
Nakhlites, 11, 922
Nanocrystals, 947
Nanodiamonds, 187, 1273
Nanomineralogy, 945
Nanoparticles, 897
Naphthenes, 1209
Native elements, 957
Native metal, 744
Natron glass, 44
Natural gas, 34, 36, 136, 192, 660, 677, 685, 689, 690, 700, 773, 774, 789, 1208, 1214, 1216, 1217
Natural Hafnium, 629
Natural nuclear reactors, Oklo
  chemical, physical and geological properties, 1060
  definition, 1059
  discovery, 1059
  formation conditions, 1059–1060
  natural fission reactors, 1061
  natural reactor operation, condition, 1060
Natural radiation dose, 1302
Natural remanent magnetization (NRM), 863
Nb^{5+}, 1243
^{142}Nd isotope, 413, 966
Nd isotopes, 408, 1151
Nd model ages, 409
ε_{Nd} notation, 969–970
^{20}Ne, 385
Near surface environment, 327
Nebular condensation, 547
Nebular mixing processes, 1236
Nebular theory, 568
Nebulizer, 724
Néel temperature, 861
Negative Ce anomaly, 227
Negative thermal ionization mass spectrometry (NTIMS), 1112, 1237
Neodymium, 562, 965, 1322
  geochemical behavior, 966
  history and use, 965
  properties, 965
  toxicity, 967
Neodymium isotopes, 44
  Earth and CHUR reservoir, evolution of, 969
  ε_{Nd} notation, 969–970
  ratio determinations, 968
  seawater, 971
  ^{146}Sm-^{142}Nd system, 970–971
  ^{147}Sm-^{143}Nd decay system, 968–969
  terrestrial reservoirs and model ages, 970
Neoformation, 270
Neolithic farmers, 43
Neomorphism, 353
Neon, 61, 973–974, 1004
Neon isotopes
  atmospheric loss, 977
  in chondrites, 976
  in Earth's mantle, 976–977
  in solids, 975–976
Neoproterozoic, 184
Nernst relation, 1116
Nesosilicates, 1334
Net primary production (NPP), 193
Neurotoxin, 898
Neutrino, 527, 1296
  detector, 527
  spallation, 496
Neutron(s), 96, 978, 1014, 1016, 1018, 1059–1060, 1242
  absorption cross-section, 525
  activation, 1315
  capture cross-section, 31, 979
  detectors, 31
  moderation, 1059–1060
  number, 83
  spallation sources, 475
Neutron activation analysis (NAA), 31, 978
New Albany Shale, 1056
Newcomb's first steam engine, 34
Nickel, 1033, 1210
  biological utilization and toxicity, 982–983
  geochemistry, 981
  history and use, 980
  ores and production, 981
  properties, 980
Nier, Alfred, 673, 1367
Niobium, 983, 1419, 1528
NIST SRM, 553, 610
Nitrate (NO_3^-), 990, 1023, 1026, 1043
Nitrides, 957
Nitrification, 833, 988, 989
Nitrite, 989
Nitrogen, 60, 143, 188, 832, 1349
  atomic mass of, 986
  crustal, 986
  fixation, 678, 987
  Haber-Bosch process, 986
  oxides, 1138
  source of, 986
Nitrogenase, 987
Nitrogen cycle, 109, 1267
  anthropogenic alterations, 990–991
  coupling of fluxes and flux balance, 990
  definition, 987
  fluxes in, 987–990
Nitrogen isotopes, 49, 544, 1149
  analytical techniques, 992–993
  archaeological investigations, 1000
  cosmochemistry, 993–994
  geodynamics, 998–1000
  paleo-diets, 1000
  to sedimentary record, 998
  stable, 992
Nitrous oxide, 65, 1138
N-methyl-D-aspartate (NMDA) receptor, 1498
N-MORB, 432
Noachian, 748
Noble gas, 53, 1301
Noble gases, 60, 317, 383, 543–544, 546, 653, 674, 784, 1188
  composition in Earth's atmosphere, 1005–1006
  cosmochemistrty, 1004
  definition, 1003
  geochronology, 1007
  ice, oceans and crustal fluids, 1006–1007
  mantle geochemistry, 1005
  in meteorites, 1004
Noble gas mass spectrometer, 543–544
Noble metals, 31
Nominally anhydrous minerals, 473
Non-equilibrium thermodynamics, 264
Non-ideal chemical behavior, 22–23
Nonlinear least square analysis, 777
Non-magmatic irons, 528
Non-mass-dependent isotopic fractionation, 543
Non-redox-dependent process, 758
North Atlantic Deep Water (NADW), 199, 1046, 1150, 1151
Northern hemisphere, 1140
Nosean, 1392
Nova explosion, 1274
Nuclear binding, 1295
Nuclear energy, 1421
Nuclear field effect, 1371
Nuclear field shift, 1431
Nuclear fission reactions, 1059
Nuclear fusion, 1016
Nuclear magnetic resonance (NMR), 694, 772, 1009, 1014, 1082, 1411
  chemical shifts2, 350
  experiment, 1010
  spectrometer, 1011
  spectroscopy, 32, 1368
Nuclear reactions, 661
Nuclear reactor, 1242
Nuclear spin, 1009
  effect, 1371
Nuclear statistical equilibrium, 527
Nuclear structure, 671, 672
Nuclear transmutation, 84
Nuclear volume, 901, 1465
Nuclear volume effect (NVE), 901
Nuclear waste, 1300
  containment, 1061

disposal, 894
Nuclear weapons, 255, 527
Nucleation, 513, 909, 1142
of minerals, 937–939
Nucleic acids, 1100
Nucleogenic reactions, 975
Nucleophile, 17
Nucleosynthesis, 310, 496, 679, 786, 822, 1274, 1286, 1296, 1444
carbon and oxygen burning, 1016
cosmic ray spallation, 1015
explosive, 1017
first nuclides, formation of, 1014–1015
helium burning, 1016
hydrogen burning, 1016
isotopic anomalies, 1015
origin and abundances of elements, 1014
p-process, 1017–1018
primordial, 1015
r-process, 1017
silicon burning and "e" (equilibrium) process, 1016
s-process, 1017
stardust, 1015
Nucleosynthetic, 1453
theory, 671
W isotope, 1458
Nuclide, 83
Nutrient(s), 108, 109, 199, 328, 789, 1019
cycling, 328
elements, 1023
input, 1165
limitation, 990, 1020
Nutrient-like distribution, 92
Nutrient-type profile, 113
Nuvvuagittuq greenstone belt, 413

O

Ocean, 86, 168, 296, 308, 384, 562, 695, 1094, 1302
circulation, 567, 971, 1300
pH, 1150
residence time, 1378
ridges, 924, 929, 931
salinity, 1089
water, 182, 698, 1133
Ocean acidification (OA), 205, 218–219
Ocean biochemical cycling, 1023
and trace elements, 1043, 1045
Oceanic anoxic events (OAE), 156, 200, 225, 262, 1099, 1164
Oceanic core complexes, 713
Oceanic crust, 179, 392, 430, 648, 712
bulk composition, 436–437
gabbroic layer, 434–436
major elements composition, 430–432
trace elements composition, 432–434
Oceanic island basalt glass, 647
Oceanic island lavas, 1380
Oceanic layer 2A, 714
Oceanic mantle, 815
Oceanic plateaus, 408
Oceanic pore-fluid signature, 1005
Ocean island(s), 1289
Ocean island basalts (OIBs), 246, 432, 517, 566, 674, 720, 812, 870, 874, 969, 976, 1113, 1407, 1466, 1481, 1501, 1503
definitions, 1048
geochemistry and crustal recycling, 1049–1050
hotspots, and mantle plumes, 1049
primordial signature, 1050
Oddo-Harkins effect, 795
Odd oxygen, 1137
Off-axis spectroscopy, 1131
Oil, 136, 189, 282, 772, 774, 789–790, 1081
families, 1057
field brines, 243
sand deposits, 1111
saturation index, 1281
shales, 1055, 1087, 1438
spill, 690, 1090
window, 116, 118, 359, 773, 1212
Oil-oil and oil-source rock correlations, definition, 1057
Oil-oil correlations, 1057–1058
Oil-oil/rock correlation, 119
Oil seeps, 1207
local ecosystems, impact on, 1053
methods of detection and sampling, 1053
seep locations, 1052–1053
Oil-source rock, 1057
correlation, 119
Oklo, 1422
nuclear reactor, 1465
See also Natural nuclear reactors, Oklo
Oleananes, 125, 145
Oligarchic growth, 500
Olivine, 251, 435, 796, 927, 928, 1190–1191, 1237, 1275
Olympic Dam style IOCG, 1065
Onuma diagrams, 743, 1187, 1188, 1192
definition, 1062
history, 1062–1063
partition coefficients of trace elements, 1062
Oort cloud, 387
Opal-A, 886
Opal-CT, 886
Open system(s), 843, 844
behavior, 513, 1112
magma chambers, 433
Operator, 1292
Ophiolite(s), 411
complexes, 430
Ophirite, 1246
Optical properties, 1105
Orange glass (lunar), 502
Orbitrap mass spectrometer, 666, 667
Ordinary, 251
Ordinary chondrites (OC), 92, 248, 311, 918
Ore, 43
Ore-bearing systems, 1408
Ore deposit, 550, 1175, 1372
formation, 495
Ore formation, 1411
Ore-forming fluids, 490
Ore-forming metals, 789
Ore forming minerals, 715
Ore-forming processes, 490
Organic acidity, 13
Organic carbon (OC), 191–193, 753, 754
Organic chemicals, 776
Organic colloids, 529
Organic complexation, 1032
Organic components, 1057
Organic compounds, 789
Organic contaminants, 834
Organic diagenesis, 1212
Organic facies
classifications, 1078–1079
definition, 1075
depositional environments, 1075, 1078
hydraulic fracturing, 1075
hydrocarbon source potential, 1076
kerogen, 1076–1077
oil and gas production, 1076
organic matter variations, 1077–1078
palynofacies and macerals, 1075–1076
sequence stratigraphy, 1079–1080
Woodford shale, 1080
Organic geochemistry, 137, 563, 565–566, 668, 677–678, 1211, 1252, 1372
Organic ligands, 529
Organic materials, 46–49
Organic matter (OM), 100, 102, 108, 110, 533, 1055, 1060, 1081, 1104, 1267, 1348–1351
composition of, 1095, 1096
deposition flux of, 1095
export efficiencies, 1095
Organic-rich shales, 1301
Organic substances, 1163
Organic sulfur compounds, 1086
Organism assemblages, 1164
Organobromines, 169
Organometallic compounds, 1210
Organophile, 547
Orogenic Au deposits, 716
Orogenic gold, 1065
Orthosilicates, 945
Osmium, 1313
geochemical behavior, 1110
history and use, 1110
properties, 1109
Os model ages, 411
Osmosis, 263
Osmotic pressure (Pa), 264
Osteoblasts, 180
Osteocalcin, 180
Osteoclasts, 180
Outcrop surface, 97
Outer core (OC), 418, 420
Outer-sphere, 266
complex, 298
Overall reactions, 19, 20
Overthickened crust, 1184
Oxaliplatin, 1237
Oxidation, 1138
Oxidation-reduction (redox) reactions, 41, 564, 1115
Oxidation state, 32, 490, 843
boron, 157
Oxidative sorption, 1432
Oxidative weathering, 192
Oxide minerals, 713
applications and economic significance, 1122–1123
definition, 1120
mineralogy, 1121
occurrence, 1122
physical and chemical properties, 1121–1122
Oxides, 343, 945, 1273
Oxygen, 60, 387, 828, 1137, 1399
in the atmosphere, 1127–1128
cosmochemical significance, 1125–1127
in Earth's core, 1125
evolution, 66
fugacity, 369, 516, 1122, 1125, 1444, 1454
isotopes, 1127
oxidation, 66
properties, 1124
sources of, 67

Oxygen (*cont.*)
stable isotopes of oxygen, 1124
stellar origins, 1125
Oxygen–exposure time, 1107
Oxygenic photosynthesis, 509, 752, 754
Oxygen index (OI), 772, 1076, 1281
Oxygen isotopes, 49, 252, 411, 567, 1148, 1149, 1151, 1155, 1371
definition, 1129
distribution in Galaxy and Solar system, 1131–1133
on Earth, 1133–1134
mass dependent fractionation relations and geothermometers, 1131
ratio and δ units, 1130
Oxygen isotopic composition, 619, 1167
Oxygen radicals, 1137
Oxyhydroxy-halides, 637–644
Ozone, 67–68, 1128, 1135
hole, 562, 1135, 1139

P
Pacific water, 660
Palaeocene–Eocene thermal maximum (PETM), 200, 1089
Palaeoclimate, 49
studies, 785
Palaeoclimatology, 534
Palaeolithic hunter-gatherers, 43
Palaeontology, 198
Paleoceanographic conditions, 477
Paleoceanography, 1288
Paleocene Atlantic Ocean sediments, 86
Paleocene-Eocene Thermal Maximum (PETM), 200, 1089, 1155, 1156
Paleocirculation, 1471
Paleoclimate, 127, 1127, 1130
Paleoclimatology, 675
Cenozoic Climate History, 1154
climate proxies, 1147
climate system and timescales of change, 1151–1154
definition, 1147
Paleoenvironmental assessment, 1088
Paleoenvironmental conditions, 128
Paleoenvironmental reconstruction, 1086
Paleoenvironments
complicating factors, 1161
definition, 1160
developments, 1161
Paleontology, 1372
Paleoproductivity, 1163, 1471
Paleo-redox conditions, 129
(Paleo)secular variation, 864
Paleoseismic studies, 96
Paleosols, 1348
Paleotemperature, 1088, 1148, 1166, 1214, 1372
Paleothermometer, 567, 1127
Paleovegetation, 123–128, 133
Paleozoic, 184
Palisades, 86
Pallasites, 10, 921
Palsa mires, 1197
Palynofacies, 1075, 1079
Paragenetic sequence, 356
Paramagnetism, 860–864
Parent rock, 1409
Parnallee meteorite, 249
Partial annealing zone (PAZ), 486
Partial melting, 406, 433, 719, 925, 1180, 1237, 1470, 1480
of mantle, 1330
Partial molar entropy, 560
Partial molar volume, 560, 1362, 1374
Partial/selective leach extraction, 551
Particle flux, 115
Particle in box, 1291
Particle-induced x-ray emission (PIXE), 30, 1185
Particle size distribution, 1142
Particulate organic carbon (POC), 902, 1199
Particulate organic matter (POM), 375, 1094, 1105, 1243
Partition coefficients, 303, 794, 796, 1062, 1063, 1183, 1258, 1470
Partition functions, 1369
Partitioning, 546
of elements, 719
Partitioning and partition coefficients
history and use, 1187
metal-silicate partition coefficients, 1193
mineral-melt partition coefficients, 1190–1193
sulfide-silicate partition coefficients, 1194
thermodynamic basis, 1187–1190
Parts per billion (ppb), 1452
Parts per million (ppm), 1452
Parts per trillion (ppt), 1452
Passive margins, 179
$^{231}Pa/^{230}Th$ ratios, 1151
Patterson, C., 673, 674, 679
Patterson Claire, 1037
Pauli Exclusion Principle, 1, 1292
Pauling electronegativity, 443
Pauling's Rules, 331
Pauli paramagnetism, 860
^{205}Pb, 1429, 1430
Pb contamination, 812
PBE, 348
Pb isotopes, *see* lead isotopes
Pb-Pb ages, 575
Pb-Pb isochron diagram, 576
Pb-Pb whole-rock isochron approach, 575
67P/Churyumov–Gerasimenko, 383, 387, 388
PDB, 1130
Peak-jumping/multi-collection, 544
Peat, 125, 127–131, 189, 193, 275, 1197
Peatification, 276
Peatlands, 1197–1198
Pedosphere, 1399
Pegmatites, 154, 566, 1066, 1067
Pegmatitic granites, 984, 1419
Pelagic clay, 887
Pelagic sediment, 888
Penesaline waters, 464
Pentlandite, 1394, 1396
Peptides, 1102
Peridotite, 1110
Periodic boundary conditions, 350
Periodic table, 226, 1242, 1292
elegance of, 1201
guide to, 1201–1203
Permafrost, 537, 894
Permeability, 493, 705, 893, 1216
Permian-Triassic boundary, 744
Permissible rotational symmetry operations, 336
Pertechnetate (TcO_4^-), 1422
Peru, 895
Pe scale, 1116
PETDB, 924, 926
Peterandresenite, 1245
Petrogenetic grid, 911, 912
Petrographic microscope, 679
Petrography, 43, 772
Petroleum, 34, 116, 136, 140, 146, 189, 192, 193, 549, 668, 677, 789, 961, 1052, 1053, 1055, 1057, 1081, 1247, 1300
composition, 1208–1211
definition, 136
distribution, 1208
exploration, 142, 1089
generation potential, 1214
global carbon cycle, 1217
history, 1207–1208
migration, 1089, 1214–1217
mineral diagenesis, 1217
and natural gas, 91
origin, 1211–1214
potential, 1080
Petrologic features, 918
Petrophysical properties, 361
pH, 14, 17, 829, 1088
boron, 159
calcium, 179
Phanaerozoic Eon, 1044
Phanerozoic organic matter, 1266
Phase, 1220
diagrams, 842, 845, 849, 850, 1181, 1220, 1222, 1228, 1231
equilibrium, 471, 489, 906, 909, 913, 915
transformations, 339, 1117
transition, 263, 472
103P/Hartley 2, 388
Phase equilibria
calculation of, 1229–1230
component, 1220
four/more components, 1224–1225
Gibbs phase rule, 1221
heterogeneous phase equilibria, 1221–1224
homogeneous phase equilibria, 1221
phase, 1220
state variable, 1220
system, 1220
three-component systems, 1224
univariant curves, 1225
variance/degrees of freedom, 1221
pH-Eh, 865
Phenolic acids, 150
Phenols, 279
Phillipsite, 86
Phi-rho-z method, 441
Phlogiston, 1124
Phosphate (HPO_4^{2-}), 184, 509, 945, 1023, 1026, 1043
Phosphatic, 1101
Phosphides, 957
Phospholipids, 142
Phosphorescence, 836
Phosphorites, 1268
Phosphorous, 109
Phosphorus, 1231–1232, 1349, 1350
Photic zone euxinia (PZE), 686, 1086
Photochemical equilibrium, 1137
Photochemical processes, 1132
Photochemical reduction, 901
Photochemistry, 901, 1137
Photoferrotrophy, 754
Photoionization, 1415
Photoluminescence, 835, 836
Photolysis, 1137
Photolyzed, 1142
Photons, 1137
Photooxidation, 1106
Photoreduction, 1032
Photosynthesis, 191, 192, 198, 818, 820, 1094, 1125
Phototrophic oxidation, 754
Photovoltaics, 527, 1424
Phreatic zone, 358
Phyllocladane, 125

Phyllosilicates, 267, 269, 272, 700, 945, 1317, 1334
Physical protection, 1097
Physisorption, 1498
Phytane, 128, 129, 141, 819
Phytoliths, 282
Phytoplankton, 180, 1023
Picrites, 406, 1237
Picritic lavas, 437
Pictograms, 1417
Pilbara Craton, 1269
Pimaranes, 125
Pinaceae, 125, 127
Pinatubo eruption, 1406
Pitzer-based model, 22
Pitzer's equations, 346
Placer(s), 564, 1069
  deposits, 1528
Plagioclase, 179, 435–436, 501, 795, 927, 1193, 1377, 1378
Plagiogranites, 435, 436
Planar (two-dimensional) defects, 934
Planck's constant, 1291
Planetary accretion, 547
Planetary achondrites, 7
Planetary cores, 527
Planetary helium, 660
Planetary melting, 316
Planetesimals, 254, 618
Planet formation, 1237
Plane waves, 350
Planktonic and benthic foraminifera, 1164
Plantary albedo, 63
Plant roots, 160
Plant wax, 1083
Plaster, 1393
Plate tectonics, 402, 504, 566, 590, 1212, 1480
Platina, 1173, 1233
Platinum, 1312
Platinum group elements (PGE), 386, 389, 393, 553, 744, 1067, 1110, 1173, 1174, 1234–1236, 1313, 1314, 1318, 1394, 1395
  deposits, 1237
  mineralization, 1237
Platinum group family, 503
Platinum group minerals, 1234
Plinian, 1482
Pliny the Elder, 488, 944
Plumes, 1380
Plume-type helium, 661
Plutonic rocks, 430, 434–435
Plutonium, 672
Podiform chromite deposits, 1066
Podocarpaceae, 125
Point (zero-dimensional) defects, 932–934
Poisoning, 160
Poisson–Boltzmann equation, 623, 1240, 1412
Polarizabilities, 2
Polar regions, 1139
Polar stratospheric clouds, 1139
Pollen, 1148, 1156
Pollutants, 1136
Pollution, 159, 562
  control and cleanup, 475
Polonium, 673, 1241, 1242
Polyaromatic hydrocarbons, 1269
Polyatomic interferences, 727
Polycadinenes, 125, 127
Polycyclic aromatic hydrocarbons (PAHs), 187, 685, 688, 690, 1087
Polyethersulfone filters, 376
Polymer, 148
Polymetallic nodules, 865
Polymorphism, 338, 1229
Polymorphs of SiO_2, 1221
Polyoxometalates, 1243
Polyoxyanions, 1457
Polyphasic nanominerals, 947
Polysulfide pathway, 1395
Pore fluid chemistry, 357, 358
Porewater, 881
Porosity, 357, 893
Porous medium, 892
Porphyrins, 136, 142, 301, 1211, 1247, 1269
Porphyry copper, 1065
  deposits, 705
Porphyry deposits, 716, 1068
Post-spinel transition, 263
Post-traumatic stress disorder (PTSD), 1498, 1499
Potassium, 183, 637, 652
  biological utilization and toxicity, 1255
  bromide, 169
  chemistry/geochemical behaviour, 1254
  dichromate, 255
  geological importance, 1254–1255
  history and use, 1253–1254
  properties, 1253
Pottery, 43–44
Pourbaix diagram, 1117–1118
PP1, 1015
PP2, 1015
p-Process, 1018
Praseodymium (Pr)
  biological utilization and toxicity, 1258
  geochemical behavior, 1258
  history and use, 1258
  properties, 1257
Prebiotic Earth, 1399
Precambrian, 751, 754, 755
Precambrian Geochemistry, 1023
Precambrian organic matter
  bitumen, 1268–1269
  carcon cycle reconstruction, 1267
  definition, 1266
  kerogen, 1267
  prevalence and preservation, 1266–1267
Precipitation, 492, 698, 702, 829, 1356–1358
Pre-exponential factor, 367
Pre-nucleation clusters, 1244
Preservation, 880, 886
Presolar grains, 499, 679, 1131, 1273, 1446
Presolar silicon carbide, 1422
Pressure(s), 706, 709
  solution, 359
PREvalent MAntle (PREMA), 872
Priestly, Joseph, 678, 1124
Primary biogenic methane, 102
Primary dispersion, 550
Primary geothermal fluids, 594–595
Primary mantle-derived magmas, 406
Primary mineral, 704, 717
Primary production, 192
Primary productivity, 179
Priming, 1097
Primitive atmosphere, 61
Primitive lattices, 335
Primitive mantle, 157, 178, 242, 1322
Primordial ^{3}He, 674
Primordial crust, 507
Primordial (planetary) helium, 660
Pristane, 128, 129, 141, 819
  phytane ratio, 128, 129, 133
Production index, 1279
Production rates of cosmogenic nuclides, 318
Programmed pyrolysis, 116, 121
Programmed temperature pyrolysis, *see* Pyrolysis
Prokaryotes, 142, 647, 1025
Promethium (Pm)
  biological utilization and toxicity, 1286
  geochemical behavior, 1286
  history and use, 1286
  properties, 1286
Propane, 961
Proper model calibration, 598
Prosthetic teeth, 1237
Protactinium properties, 1287
Proteins, 136, 947, 1100, 1102, 1104
Proterozoic-style geology, 1259
Protium, 694, 696
Protodolomite, 213
Protokerogen, 1086
Proto-lunar disk, 618, 619
Proton(s), 693, 694, 709, 1014, 1016, 1018
Proton-induced X-ray emission, 1185
Protoplanet, 618
Protoplanetary disk, 251, 618
Protoplanetary gas, 1125
Protoplanetary nebula, 187
Proto-solar cloud, 1014, 1015
Proto solar nebula, 385
Proxies, 1021, 1147–1151, 1163, 1166
Pseudohalogen, 622
Pseudopotentials, 3, 350
Pseudosection, 911, 913
  thermobarometry, 913, 914
Pteropods, 1024
P-T phase diagram, 1491
^{239}Pu, 1060
^{244}Pu, 1501, 1502
Public health, 1237
Pu-fission, 1501
P-V phase diagram, 1492
PW91, 348
Pyrite, 284, 749, 1394, 1395, 1399
Pyrobitumen, 116, 1212, 1217
Pyroclastic lavas, 502
Pyroclastic rock, 1482
Pyrogenic organic matter, 1350
Pyrohydrolysis, 244
Pyrolysis, 531, 689, 790, 897, 1055, 1082
  data interpretation, geochemical logs, 1281–1283
  geologic time, 1282–1283
  kinetic measurements, 1278–1279
  petroleum generation kinetics for rock samples, 1277–1278
  quality, quantity and thermal maturity of rock samples, 1277
  Rock-Eval pyrolysis, 1278, 1283
  and vitrinite reflectance, 1280
Pyrolytic methane, 102, 104
Pyroxene, 251, 796, 945, 1192, 1275
Pyroxenites, 1470
Pyrrhotite, 1394, 1395

Q
Q phase, 659
  and pre-solar noble gases, 1004
Quadrupolar nuclei, 1009, 1012
Quadrupole ICP-MS, 724–725
Qualitative analysis, 1437
Quantification protocol, 804
Quantitative analysis, 440–441, 1436
Quantitative metastable reaction monitoring (MRM-GCMS), 140
Quantitative XRF analysis, 1512
Quantum Design Physical Property Measurement System (PPMS), 652
Quantum-mechanical phenomenon, 1473
Quantum mechanics, 1291
Quartz, 96, 282, 412, 490, 753, 755, 945, 1333, 1449
Quartz-fayalite-magnetite O_2-buffer reaction, 520

Quartz torch, 723
Quasicrystal, 943
Quasicrystalline structure, 957
Quick-scanning X-ray absorption spectroscopy (Q-XAS), 778
Quorum sensing, 150

R
Racah parameter, 342
Radial distribution function, 1489
α-Radiation, 1241
Radiation damage, in minerals from self-irradiation, 934
Radiative/atmospheric forcing, 1153–1154
Radical, 1138
  pair, 901
Radioactive, 1316
  decay, 92, 183, 484, 672
  decay law, 1295
  disequilibrium, 1300
  element, astatine, 60
  isotopes, 505, 527, 1313
  semi-metal, 1241
  waste, 646, 1061
  waste disposal, 475
Radioactivity, 673, 1241, 1295, 1299, 1301
  exposure and hazards, 1297
Radiochronometric dating, argon isotopes, 56–57
Radiogenic heat, 590, 655
  production, 1466
Radiogenic helium, 662
Radiogenic isotope, 45, 181, 183, 432, 796, 926, 930–931, 1501
  decay systems, 1237
  geochemistry, 561, 566–568
  ratios, 674
  system, 272, 632, 1111
Radiogenic power, 653
Radiogenic systems, 814
Radioisotope imaging, 529
Radiolaria, 886, 1024
Radiomedicine, 1517
Radiometric dating, 253, 915, 934, 1468
Radionuclides, 30, 95, 317, 978
Radium, 673, 1299–1301
Radon, 1300, 1301
Raman effect, 1303
Raman microspectroscopy, 32
Raman spectroscopy, 32, 378, 489, 1101
Rank parameters, 132
Raoult's Law, 21, 522, 663, 1361, 1374, 1375
Rapid accretion, protoplanets, 1459
Rapid neutron capture, 92, 568
  See also r-process
Rare earth(s), 31
Rare earth elements (REE), 226, 381, 434, 462, 546, 553, 671, 753, 929, 930, 1063, 1205
  definition, 792
  Eu and Ce redox geochemistry, 795
  geochemistry, 793–795
  mineralogy, 796
  normalization, 795–796
  sources and uses, 796–797
Rare gases, 53, 54, 784
  See also Noble gases
Rate, 881
  constant, 781, 1214
  constants/coefficients, 777
  laws, 776–777
  of mantle upwelling, 1470
  of melting, 1470
  parameters, 782
Rayleigh condensation, 1370
Rayleigh distillation, 698, 1169
Rayleigh fractionation, 1149
Rayleigh signal, 1304
Rb decay constant, 1379
Rb-Sr dating, 272
Rb-Sr decay system, 674
Rb-Sr isochron diagram, 574
Rb/Sr isotope system, 574
Rb-Sr systems, 572
Reaction kinetics, 513
Reaction rate, 492, 893
Reaction zones, 437
Reactive porous flow, 433
Reactive transport equations, 894
Reactive transport models, 328
Reactivity, 1086, 1096, 1104
Recharge, assimilation and fractional crystallization (RAFC), 514
Recharge, magma, 841, 844, 846
Recondensation, 150
Reconstructive transformations, 338, 339
Recrystallization, 353
Recycling, 508, 884
  of mafic, 406
  of oceanic crust, 1237
Redbeds, 66
Red blood cells, 1526
Redfield, A., 678
Redfield ratio, 678, 1020, 1025
Redfield stoichiometry, 1034
Red giant(s), 679, 1125
  stars, 1274
Redox, 753, 755, 829, 1452
  kinetics, 778
  reaction, 32, 308
Redox-sensitive, 462, 529
Reference materials, 543, 553
  See also Geochemical Reference Materials
Reference spectra, 1306
Refractory, 499, 548
  component, 316
  element, 251, 965, 984, 1234, 1312, 1420, 1528
  lithophile elements, 653
  samarium, 1321
Refractory inclusions
  bulk chemical compositions, 1307
  classification, 1307
  definition, 1307
  formation age, 1308
  oxygen isotopic compositions, 1310
  radial transport and residence time, 1311
  short-lived radionuclides, 1308–1310
Regolith, 406
Regular coordination polyhedra, 332
Relamination, 402
Related lavas, 984
Relative supersaturation, 937
Relativistic effective core potentials, 3
Relativistic effects, 3
Remanent magnetization, 863
Remineralization, 112–113, 1025, 1149, 1150
Remnant magnetism, 412
Remote sensors, 703
Re-Os isotopic system, 674, 1234, 1328
Representative elemental volume, 892
Republic of Gabon, 1059, 1061
Reservoir rocks, 1075
Reservoir species, 1139
Residence time, 158, 163, 179, 184, 463, 677, 1045, 1299
  of helium, 660
Residues, 408
Resolution, 1304
Resolving power, 666, 667, 669
Resource potential, 482
Resources estimation, 536
Respiration, 988, 1025, 1094, 1125
Retene/cadalene ratio, 127
Retene, 688, 689
Retention, fission products, 1061
Retention volume, 735
Reverse weathering hypothesis, 1045
Reversibility, 449
Rhabdophane, 796
Rhenium, 670
Rheological studies, 474
Rheology, 915
Rhodium properties, 1314
Rhombohedral, 156
Rhyolites, 406, 1482
Rifts, 406
Rigid rotor, 1292
Ringwood, A.E., 676
Ringwoodite, 384
Riverine flux, 183
Riverine particles, 758
River water, 158, 529, 699
River water pollution, 179
Rock, 471, 1438
Rock-Eval, 1090
  analysis, 1055
  pyroanalyzers, 1281
  pyrolysis, 772, 1214, 1268
  pyrolysis system, 1076, 1077
Rocky planets, 413
Roedder's rules, 489, 490
Roman coins, 43
Roman pigments, 43
ROSETTA mission, 390
Rössing deposit, 1067
Rotating frame approximation, 1009, 1010
Rotating frame of reference, 1012
Rotational spectroscopy, 1293
Rotational symmetry, 335
r-process, 92, 527, 1017
R (Rumurutti-like) chondrites, 919
Ru, *see* Ruthenium
Rubidium, 175, 1316–1317, 1377, 1379
Rule of parsimony, 334
Rules of substitution, 742
Rumuruti type chondrites, 250
Runaway growth, 500
Rundle, 1056
Russell, R.D., 674
Ruthenium, 1422
  isotopes, 1236
  natural occurrence, 1319
  properties, 1318
Rutherford, E., 673
Rutile, 406, 1446

S
Sabkha, 466
Sal-ammoniac, 637
Saline formation waters, 243, 648, 1300
Saline lacustrine facies, 1058
Salinity, 209, 245, 677, 1024, 1038, 1043, 1167, 1363
Salinometer, 209
Saltern evaporites, 467
Salts, 245
Samarium
  geochemical behavior, 1321–1322
  history and use, 1321
Sample preparation, 441
Sampler/skimmer interface, 724
San Francisco Bay, 902

Sapropelic coals, 279
Sapropels, 155, 156, 1089
Satellites, 1136, 1139
Saturation state, 204, 270
Saturation vapor pressure, 1142
Scalar relativistic effects, 5
Scaling of production rates, 319
Scandium
  aqueous geochemistry, 1325
  biological utilization and toxicity, 1325
  history and use, 1323
  mineralogy, 1325
  natural abundances, 1323–1324
  properties, 1323
Scanning electron microscopy (SEM), 356, 440
Scanning electron microscopy–energy dispersive spectoscopy (SEM-EDS) analysis, 1513
Scanning probe microscopy (SPM), 1414
Scanning transmission X-ray microscopy (STXM), 1268
Scatter, 1143
Scattering efficiency, 1142
Scavenged profile, 113
Scavenging, 529, 1032
Scheele, Karl Wilhelm, 1124
Scheelite, 1456
Schönbein, C.F., 670
Schotky defects, 932
Schottky anomaly, 651
Schreinemakers, F.A., 1225
Schreinemakers' analysis, 1220
  binary systems, 1228
  one-component systems, 1228
  ternary system, 1228–1229
  univariant curves, 1226–1228
Schrödinger equation, 347, 1291
Schwertmannite, 943
Scourian granulites, 402
Screw dislocations, 933
Seafloor hydrothermal fluids, 529
Sea level, 411
  fluctuations, 184
Sea surface temperature (SST), 1148, 1160, 1161, 1378
Seawater, 158, 165, 206–211, 218, 219, 227, 463, 529, 563, 623, 646, 677, 706, 707, 712, 817, 971, 1042, 1378
  acidity, and calcium level, 180
  array, 634
  carbon isotopes in, 198
  chemistry, 753
  composition, 966, 1322
  evaporates, 464
  exposure time, 887
  masses, tracing of, 199
  radium in, 1299
Secondary biogenic methane, 102
Secondary dispersion, 550
Secondary geothermal fluid, 594–595
Secondary ionization mass spectrometers, 31
Secondary ion mass spectrometry (SIMS), 411, 527, 553, 578, 579, 993, 1101, 1131, 1268, 1273
  MegaSIMS, 738
  NanoSIMS, 738
Secondary ion microprobe, 356
Secondary minerals, 705, 716
Second law of thermodynamics, 554, 557
Sectioning, sample preparation, 1305
Secular equilibrium, 1288, 1468
Secular radioactive equilibrium, 1299
Sediment(s), 97, 531, 1081, 1104, 1164
  budgets, 97
  core, 1167
  diagenesis, 789
  transport, 97
  trap, 1166
  yield, 97
Sedimentary, 831
  basins, 353, 789
  chemistry, 563
  exhalative sulfide, 1395
  formation waters, 242
  iron isotope, 758–759
  organic matter, 116, 790
  pyrite, 1395
  rocks, 191, 193, 206, 207, 296, 392, 771, 773, 774, 818, 1076, 1133
  rock studies, 997
  sorting, 884
  systems, 357
Sedimentation, 1142
Seepage, 961
Seismic discontinuities, 472
Seismic layers, 430, 434
Seismic wave velocities, 430
Selective extraction, 897
Selective preservation, 772, 774, 1096
Selenides, 1241, 1327–1328, 1394
Selenium, 1327
Self-consistent reaction field (SCRF), 5
Self diffusion, 364, 366, 367, 369, 371
Self-shielding, 500, 979, 1126
Semi-empirical (SEMO), 2
Sensible heat, 845, 848
Sensible volume, 848
Separation factor, 735
Sequestration of organic matter, 1105
Serpentinites, 189, 1526
Serpentinization, 169
Serpentinized mantle, 1181
Sesquiterpanes, 690
Sesquiterpenoids, 123–125
Shackleton, Nicholas, 1148, 1152
Shale(s), 392, 771, 1268
  gas, 964, 1075
  oil, 1075, 1208, 1217
Shale-hosted oil, 1055
Shallow heat sources, 592
Shared polyhedral elements, 333–334
Shear modulus, 398
Sheeted dike complexes, 434
Shergottites, 11, 922
Shergotty-Nakhla-Chassigny (SNC) meteorites, 618, 619, 679, 760
Shewanella putrefaciens, 749
Shield volcanoes, 1482
Shock, 251
Short atomic order, 946
Short-lived isotopes in early solar system, 1297
Short-lived radioisotopes, 253
Short-lived radionuclides, 568, 571
Short-wave infrared (SWIR) tools, 552
Shungite, 1267
Siberian red lead, 255
Siderite, 283, 752, 754
Siderophile, 236, 547, 763, 827, 828, 984, 1315, 1443, 1453
  tendencies, 654
Siderophile elements, 291, 305, 1173, 1174, 1193, 1194, 1234, 1236, 1313, 1394
  definition, 1328
  properties, 1328–1330
Silica, 755
Silicate, 917, 1026, 1273, 1317
  clasts, IAB and IIICD irons, 7
  melts, 303
Silicate minerals, 496, 944
  atomic coordination, 1335
  chemical and physical properties, 1335
  classification, 1334
  definition, 1334
Silica tetrahedron $[SiO_4]^{4-}$, 945
Siliceous deposits, 878, 886–887
Siliciclastic systems, 360
Silicides, 957
Silicoflagellates, 886
Silicon, 445, 1024
  biological utilization and toxicity, 1337
  burning, 1016–1017
  geochemical behavior, 1336
  history and use, 1336
  nitride, 1273
  properties, 1336
  solubility, 28
Silicon carbide, 1273
Silicon drift detector (SDD), 440
Silicon isotopes
  definition, 1337
  high temperature, 1338–1339
  low temperature, 1337–1338
Silicothermic Pidgeon process, 854
Silver, 895, 1233
  application to cosmochemistry, 1343
  bromide, 167
  geochemical behavior, 1340
  and gold deposits, 705
  history and use of, 1340
  minerals, 1341
  properties, 1340
  toxicity, 1343
Simple halides, 637
Simultaneous reactions, 455
Single collector sector field mass spectrometers (ICP-SFMS), 723
Single-domain structure, 863
Sinking particles, 111, 112
Si-tetrahedra, 265
Skarn(s), 493
  deposits, 154, 705
Skeletons, calcium level, 180
Slab fluids, 406
Slab melting, 406, 1182, 1265
Slab pull, 906
Slater determinant, 5
Sleipner Field, 35, 36
Slovenia, 895
Slow neutron capture, 568
  See also s-process
^{146}Sm, 1322
^{147}Sm, 1322
Small ionic charge, 637
SMD approach, 5
Smectite, 266, 269, 273, 884, 1348
  clay, 264
Sm-Nd ages, 674
Sm-Nd geochronology, 581–582
Sm-Nd isotope system, 575
Sm-Nd systems, 572
Snowball Earth, 1265
Sodalites, 244
Sodium, 637
  biological utilization and toxicity, 1347
  dichromate, 255
  fluid-rock interactions, 1346
  geochemical behavior and distribution, 1345
  history and use, 1345
  Joly's sodium age of the earth, 1346

Sodium (*cont.*)
magmatic processes, 1345
properties, 1345
Soft-tissue pump, 114
Soil, 13, 14, 48, 142, 528, 531, 562, 565, 832, 903, 987, 1081, 1094, 1104, 1302
biodioversity, 1349
biota, 1349–1350
carbon storage, 1350
chemistry, 563
and civilizations, 1349
contamination, 1351
development, 1348–1349
erosion, 903, 1350–1351
and fire, 1350
formation, 327, 328
horizons, 1348
humus, 192
management, 1351
minerals, 1410
nitrogen, 987
organic matter, 1350
production, 97
radium in, 1299
science, 328, 1438
and water sustainability, 328
Solar abundance, 310, 311
Solar activity, 323
Solar evaporation, 464
Solar flux, 1144
Solar helium, 660
Solar Kr component, 786
Solar nebula, 498, 679, 1174
Solar nebular, 243
Solar photosphere, 647
Solar system, 251, 272, 413, 498, 571, 629, 974, 1273, 1430
abundance, 157
element abundances, 310, 313–315
Solar variability, 1143
Solar wind, 500
Solfatara fumaroles, 714
Solid, 1359
samples, 544
state nuclear magnetic resonance spectrometry, 151
Solid solutions (SSs), 154, 339–340, 910, 1353
exsolution process, 1352, 1356
ideal SSs, 1353–1358
non-ideal SSs, 1354–1358
out-of-equilibrium processes, 1357–1358
reciprocal, 1355
regular SS, 1354
stoichiometric solubility product, 1357
sub-regular SSs, 1354
temperature-composition phase diagram, 1354–1356
thermodynamic equilibrium, 1356–1357
Solidus, 925, 1180
depression, 1183
Solosilicates, 1334
Solubility, 303, 473, 528, 547, 755, 1183, 1361, 1447
curve, 1365
definition, 1359
polarity, 1360
product, 159, 1361
Soluble elements, 393
Soluble organic matter (SOM), 1079
Solute, 733–735, 1360
reflection coefficient, 263
Solutions, 1359
hydrothermal (*see* Hydrothermal solutions)
Solvation, 5
Solvent, 1359, 1360
SOPITA, 873
Sorbtion, 308
Sorby, H. C., 488
Soret coefficient, 366
Soret effect, 366
Soret separation, 514
Sorption, of organic matter, 1097
Sorption reactions, 776
Source(s), 1138
Source/sink, 893
Source identification, 902
Source rocks, 688, 690, 1057, 1075, 1076, 1078, 1211, 1212, 1214, 1216, 1217
Southern ocean, 1046
South Pole, 1139
Space groups, 338
Spain, 895
Spallation, 157, 696
reaction, 662
Spark-source mass spectrometry, 31
Spatial resolution, 1305
Spatial statistical techniques, 552
Speciation, 1365
Specific heat, 466
See also Heat capacity
Specific ion interaction theory (SIT), 22
Specific surface area, 893
Spectra, 347
Spectral reflectance, 917
Spectrophotometer, 1136
Spectroscopically, 527
Spectroscopic techniques, 1404
Speleothems, 1469
Sphagnum, 123, 129, 131
Sphalerite, 489, 527, 1394
Spherical harmonics, 1292
Spike, 768
Spin, 1292
Spinel, 528, 1275
Spin-orbit, 1293
interaction, 5
Spin transitions, 1454
Spodumene, 822
Spontaneous magnetization, 861
Spray chamber, 724
s-process, 527, 561, 1017
Sputtering, 737, 738
Squalene, 141
$^{87}Sr/^{86}Sr$, 408
Sr/Ca ratios, 1169
Sr chronostratigraphy, 1383
SR-XRF analysis, *see* Synchrotron radiation (SR)-XRF analysis
Stability, 1437
relation, 262
Stable Ca isotope, 181
Stable carbon and nitrogen isotopes, 1164
Stable carbon isotope(s), 127, 133
Stable carbon isotope ratios, 119
Stable isotope, 527, 543, 856, 963, 1148–1150, 1312, 1402, 1408, 1429
analysis, 47
geochemistry, 567, 675–676, 1367
of oxygen, 1124
ratios, 561, 567, 874, 1087
systems, 271
Stable isotopic composition of methane, 104–105
Stable isotopic systems, 162
Stagnant lid, 504
lid tectonics, 410
Standard chemical potential, 457, 458
Standard equilibrium constant, 456, 457, 460
Standard Light Antarctic Precipitation (SLAP), 697
Standard materials, 737
Standard Mean Ocean Water (SMOW), 1130
Standard state, 208, 522, 523, 1374, 1412
enthalpy change, 520
Gibbs energies, 1116
Staphylococcus, 749
Stardust, 1015
State functions, 556
State variable, 1220–1221
Static mode, 543
Stationary phases, 732, 733
Statistical mechanics, 1369
Statistical thermodynamics, 452
Steady state, 507, 1044
ozone concentration, 1138
Steam, 707, 1365
Steel(s), 746
making, 34
Stellar atmospheres, 311
Stellar nucleosynthesis, 1125
See also Nucleosynthesis
Stellar processes, 659
Step heating technique, 580
Stepwise formation constant, 298
Stepwise pyrolysis, 1082
Sterane(s), 117, 146, 1090, 1269
biomarkers, 143
Stereochemistry, 145
atoms, 331
coordination polyhedra, 331, 332
polyhedral arrangements, 332–333
shared polyhedral elements, 333
Stereoisomerization, 146
Stereoisomers, 116
Steroids, 119, 143, 1104
Sterols, 117, 1084
Stibnite, 37, 44
Stilpnomelane, 753
Stirring, 508
Stoichiometric coefficients, 893, 1226
Stoichiometric constants, 1025
Stoichiometric saturation state, 1357
Stoichiometry, 108, 1438
definition, 1376
ratio, 1376
Stone age, 943–944, 946
Stony irons, 1112
Stratiform deposits, 1066
Stratiform reefs, 1237
Stratiform sediment-hosted Cu deposits, 1070
Stratopause, 1136
Stratosphere, 63, 1128
Stratospheric ozone, 728, 729, 1371
Strato-volcanoes, 1482
Strontianite, 1377
Strontium, 211
biological utilization and toxicity, 1378
geochemical behavior, 1378
history and use, 1377
isotope, 44, 48, 509
properties, 1377
Subaqueous ash, 883
Sub-atomic particles, 1014
Subbituminous coals, 278
Sub-continental lithospheric mantle (SCLM), 655, 1111
Subducted sediment, 159, 1381
Subducting lithosphere, 474
Subduction, 906, 1431

Subduction-related lavas, 1420, 1528
Subduction–related magmas, 92
Subduction-related metamorphic rocks, 825
Subduction-type helium, 661
Subduction zone, 98, 159, 304, 402, 566, 648, 815, 1181, 1381, 1466
  description, 1384
  geochemistry, 1389
  input, 1384–1385
  mass balances, 1389
  processes, 1331
Sublimation, 1366
Submarine groundwater discharge, 1299
Submarine volcanism, 436
Sub-shells, 1201
Substitution, 1453
Suess effect, 199
Sulfate, 713, 1299
  anion $[SO_4]^{2-}$, 1392
  minerals, 1393
Sulfate-reducing bacteria, 897
Sulfide, 37, 303, 343, 713, 896, 945, 1236
  deposits, 1407
  melts, 1174, 1235
  saturation, 1237
Sulfide minerals, 154, 564
  in biogeochemical systems, 1395
  extraterrestrial, 1396
  global sulfur cycle, 1395
  ore deposits, 1395
Sulfide-silicate partition coefficients, 1194–1195
Sulfide-silicate systems, 1190
Sulfidic ocean, 1265
Sulfidic waters, 948
Sulfite, 1392
Sulfonamides, 894
Sulfosalt, 896, 1394
Sulfur, 108, 284, 1100, 1210, 1217, 1392
  bacteria, 1086
  biological utilization and toxicity, 1398
  dioxide, 1405
  geochemical behavior, 1397
  isotopes, 1397
  properties, 1397
  uses, 1397
Sulfuric acid, 285, 1142, 1405
Sulfur isotopes, 567, 676, 1371
  atmospheric, 1405–1406
  mass dependence, 1404
  mass-independence, 1404–1405
  notation, 1402
  oceanic, 1406–1407
  solid Earth, 1407–1408
  standards, 1402
Sulfur reducing bacteria, 1467
Sulphates, 945
Sulphide, 252
Sulphur, 729, 764
  cycle, 1141
  dioxide, 1142
  isotope analysis, 48
  oxidation, 1141
Sun, 310–317, 993
Sun's photosphere, 496
Supercontinent formation, 411
Super-cooled aerosols, 1141
Supercritical water, 1492
Superexchange interaction, 861
Supergene, 715
  enrichment, 1410
  ore deposits, 1069
  process, 1066
  weathering, 227
Super High Resolution Ion Microprobe (SHRIMP), 579
Superior Province, 413
Supernova, 498, 679, 746, 1015, 1018, 1231, 1274, 1296
Superplume, 407
Super-volcanoes, 1482
Supramolecular assemblies, 149
Surface catalysis, 1414
Surface protonation, 237
Surface tension, 1362, 1488
Susceptibility, 860
Sustainable milling, 1072–1074
Swelling clay, 1241
SWIR, *see* Short-wave infrared (SWIR) tools
Sylvanite, 623
Sylvite, 464, 637
Synchrotron, 946, 1415
  radiation, 474
  spectromicroscopy, 151
Synchrotron radiation (SR)-XRF analysis, 30, 1512, 1513
Syndiagenesis, 453
Syneruptive timescales, 851
Syngenesis, 453
Syngenetic deposits, 453, 1065
Synsedimentary ore deposits, 1069
Syntrophic bacteria, 101
System, 1220

T
Tambora, 1406, 1482
Tandem mass spectrometry, 533
Tannin, 149
Tantalum (Ta), 984, 1243, 1419, 1528
Taphonomic analysis, 1100
Taphonomic medium, 1268
Taraxerol, 127
Tar balls, 1053
Tar mats, 1216
Tasmanite, 1056
Taxodiaceae, 125
Technetium, 1014, 1017, 1421
Tectonic, 191, 193
  forcing, 1152
  windows, 434, 435
Tectosilicates, 945, 1334
Tektites, 307, 1524
Tellurate, 1424
Tellurides, 1394
Tellurite, 1424
Tellurium (Te), 445, 562, 1241, 1327
  native, 1424
  radioisotopes, 1424
  source of, 1423
  stable isotope fractionation, 1423
Telogenesis, 277
Telogenetic zone, 355
Temperate environments, 1097
Temperature, 1097
  gradient, 366
Tephra, 883, 1482
Tera-Wasserburg concordia diagram, 577
Terbium (Tb)
  biological utilization and toxicity, 1426
  geochemical behavior, 1426
  history and use, 1426
  properties, 1425
Terminal electron acceptors (TEAs), 1095
Term symbols for atom, 1293
Ternary system, 365
Terraces, 96
Terrestrial aquatic systems, 376, 377
Terrestrial atmosphere, 504
Terrestrial environment(s), 326, 1160
Terrestrial fractionation, 1310
Terrestrial late heavy bombardment, 61
Terrestrial mantle and crustal rocks, 759–760
Terrigenous sediments, 408, 878
Terrigenous sources, 889
Tetraborate decahydrate, 160
Tetrad effect, 794
TetraEther indeX of 86 carbons (TEX_{86}), 1088, 1150, 1161, 1168
Tetrapyrroles, 140, 1247
Tetravalent, 1465, 1467
Thallium (Tl), 1429
  adsorption, 1427
  anthropogenic and toxicity, 1428
  behavior during weathering, 1427
  concentrations, 1427
  in Earth's crust, 1427
  isotopes, 1427, 1429, 1431
  K^+ rich minerals, 1427
  oxidation states, 1427
  sulphide minerals, 1427
Thaumasite, 1393
^{232}Th decay series, 1297
^{232}Th-^{208}Pb decay scheme, 578
Theoretical mineralogy, 475
Therapies, 1237
Thermal analysis, 1436
Thermal contraction, 845
Thermal degradation, 1079
Thermal diffusion, 366, 369
Thermal diffusion coefficient, 366
Thermal expansivity, 1220
Thermal fluids, 704, 715
Thermal fractionation, 995
Thermal ionization mass spectrometers, 757, 769
Thermal ionization mass spectrometry (TIMS), 31, 49, 244, 632, 723, 731, 732, 757, 769, 814, 968, 1288, 1379, 1403, 1404, 1524
  components, 1433
  Faraday detector, 1434
  ion source and mass analyzer, 1433–1434
  mass fractionation, 1435
Thermally isolated magma, 843
Thermal maturation, 200, 789, 791
  of organic matter, 359
  petroleum generation, 773
  process, 773
  stages, 773
Thermal maturity, 116, 136, 146, 772, 773, 1090
Thermal neutron(s), 485
  capture, 321
Thermal sulfate reduction (TSR), 1217
Thermobarometer, 1447
Thermobarometry, 412, 562, 567, 676, 913–914
  activity, 602
  Bishop Tuff controversy, 598–599
  calorimetric data and activity models, 605–609
  Gibbs free energy, 602
  heat of reaction, 603
  historical background, 597
  MELTS model, 599
  multivariant equilibria, 599
  origins of, 597
  solid and liquid solution, 604
  solution models, 602
  sources of, 597–598
  univariant equilibria, 600
Thermochemical methanogenesis, 105

Thermochemical sulfate reduction, 359, 791
Thermocline, 467
Thermodynamic(s), 186, 341, 345, 472, 554, 562, 1097, 1115, 1116, 1220, 1360
  activity, 522, 621, 1412
  constants, 379
  controls, 328
  equation of state of seawater, 1044
  equilibrium, 244, 506, 677, 791, 1128
  factor, 366
  level, 707
  models, 948
  properties, 326, 1331
  solubility product, 214
Thermodynamic-kinetic-dynamical modeling tool, 851
Thermogenic gas, 962
Thermogenic methane, 279
Thermogravimetry, 1436
Thermohaline circulation, 971, 1025, 1044, 1046
Thermoluminescence, 835, 837
Thermoremanent magnetization (TRM), 863
Thin film
  solution, 483
  source, 483
Thin layer chromatography (TLC), 685
Thin layer chromatography with flame ionization detection (TLC-FID), 685
Thin source method, 371
Thiol/sulfhydryl (SH^-) groups, 897
Thiosulfate, 1392
Third-law calorimetry, 650
Third-law entropies, 558
Third law of thermodynamics, 451, 554, 558
Tholeiitic magmatic suite, 431
Thorium (Th), 590, 652, 673, 1299, 1301
  biological utilization and toxicity, 1441
  chemistry, 1440
  high-temperature geochemistry, 1440
  history and use, 1439
  isotopes and applications, 1439–1440
  low-temperature geochemistry, 1440
  ores and distribution in rocks, 1440
  properties, 1439
Three-body reaction, 1137
Thucholites, 1267
Thulium (Tm)
  biological utilization and toxicity, 1442
  geochemical behavior, 1442
  history and use, 1442
  properties, 1441
Tight oil formations, 1055
Ti-in-zircon temperatures, 412
Time dependent density functional theory (TD-DFT), 350
Time independent, Schrödinger wave equation, 1
Time-of-flight mass spectrometer, 31
Timescales, 775–776, 1483
TIMS, *see* Thermal ionization mass spectrometry (TIMS)
Tin, 44, 811
  geochemical behavior, 1444
  history and use, 1443
  isotope ratios, 46
  isotopes, 1444
  properties, 1443
Tipping points, 1158
Tissot, L., 677
Titan, 187
Titania activity, 1447
Titanite, 578
Titanite crystal structure, 332
Titanium, 44, 619, 1445
Titanium-50, 500
Titanium carbide, 1273
Titanium oxide, 1275
Titanohematite, 862
Titanomaghemite, 862
Titanomagnetite, 862
$^{205}Tl/^{203}Tl$, 1429
$\varepsilon^{205}Tl$, 1430
TLC-FID, *see* Thin layer chromatography with flame ionization detection (TLC-FID)
T-MORB, 929
Tocopherols, 128
Tonalite-trondjhemite-granodiorites, 406
Tooth enamel, 48
Torbanite, 1056
Torque equation, 1011
Total alkalinity, 114, 210–211, 218
Total atomization energy, 4
Total orbital angular momentum quantum number, 1292
Total organic carbon (TOC), 1075, 1080, 1277, 1282
Total spin angular momentum quantum number, 1292
Tourmaline, 158, 163
Trace analyses, 723, 1437
Trace constituents, 1138
Trace elements, 29, 286, 304, 392, 462, 490, 566, 719, 929–930, 979, 1025, 1164
  concentrations, 361
  concentration units, 1452
  definition of, 1452
  distribution, 850
  geochemical and biochemical importance, 1452
Trace metals, 713
Tracer diffusion, *see* Self diffusion
Transfer efficiency, 112
Transfer functions, 1148, 1151, 1166
Transferrin, 529
Transgressive Tract Systems (TST) strata, 1079
Transition elements, 792
Transition metal(s), 546, 983, 1236, 1312, 1313, 1419
Transition state (TS), 1404
Transition-state theory, 19
Translational symmetry elements, 336
Transmission electron microscopes, 946
Transmission electron microscopy, 378, 527
Transport, 880, 884–885, 1137
  efficiency, 115
  processes, 776, 1097–1098
  timescales of sediments, 1471
Transport-controlled processes, 777
Transverse relaxation time, T2, 1012
Travertine(s), 180
  deposits, 1300
Treibs, Alfred, 140, 677, 1247
Triboluminescence, 836, 837
Trichodesmium phytoplankton, 1029
Tricyclic terpanes, 690
Trioctahedral, 267
"Triple-alpha" reaction, 1016
Triple spike, 769
Triterpanes, 1269
Triterpenoid lipids, 1083
Triterpenoids, 125–127, 132
Tritium, 694, 696
Trivalent Tl, 1430, 1432
Troilite, 527, 1396
Trona, 465
Trophic level, 48
Tropical regions, 1140
Tropopause, 63, 1136
Troposphere, 1136
T-Tauri stage, 385
T-Tauri stars, 499
TTG, 505, 507
Tungsten, 1243, 1456
  isotopes, 1458–1461
Two-component chemical system, 1182
Two site exchange, 1013
Type I carbonaceous chondrites, 527
Type II supernovae, 1017, 1018, 1125
Type-I supernova, 1017, 1018

U
^{238}U, 1501
$\delta^{238}U$, 1465
U decay series, 43, 813
^{235}U decay series, 1297
^{238}U decay series, 1297, 1299
U-fission, 1501
UK'37 index, 1150
Ulexite, 158
Ultrafiltration, 529
Ultramafic, 430, 434
Ultramafic volcanic surfaces, 408
Ultrasonic wave speeds, 393
Ultraviolet radiation, 1136, 1140
Ultra volatile elements, 316
Unconventional energy sources, 535
Unconventional natural gas, *see* Gas hydrates
Unified atomic mass unit, definition, 1463
Unit cell, 334
21st United Nations Conference of the Parties, 35
1992 United Nations Framework Convention on Climate Change, 35
Univalent Tl, 1430
Univariant equilibria, 600
Univariant reactions, 1224, 1226, 1228
Unresolved complex mixture (UCM), 685
U-Pb dating, 410, 673, 674
U-Pb dating method, 806
U-Pb isotope systems, 737
U/Pb ratios, 575
U-Pb systems, 571
Uphill diffusion, 365
Upper consolute temperature, 1356
Upper continental crust, 392
Upper mantle, 507, 1313, 1466
Upwelling intensity, 1165
Uraninite, UO_2, 1059–1061, 1067, 1466
Uranium (U), 575, 590, 652, 673, 1059–1060, 1288, 1299, 1301, 1422
  biological utilization and toxicity, 1467
  chemistry, 1465
  dating magmatic event and magma storage, 1469–1470
  definition, 1468
  high temperature geochemistry, 1466
  history and use, 1465
  isotopes and applications, 1465
  low temperature geochemistry, 1466–1467
  mantle melting and melt migration, 1470
  mineralization, 1301
  ores and distribution in rocks, 1465–1466
  properties, 1464–1465
  ^{230}Th-^{238}U and ^{231}Pa-^{235}U disequilibrium, 1469
  ^{238}U-^{234}U dating, 1469
  water-rock interaction, 1470–1471
Uranophane, 1068
Ureilites, 9, 921, 1525
Urey, Harold, 673, 675, 678, 679, 1127, 1148, 1368

Ursane, 125
U-series decay chain, 571, 1300
U.S. Geological Survey, 671
U-Th-Ra disequilibria, 1484
$^{238}U/^{235}U$ ratio, 575
UV-photo oxidation, 754
UV–vis spectra, 350
U-Xe, 1505

V
Vacuum, 724
Vadose zone, 358
Valence bonds, 234
Valence-bond theory, 443
Valence electrons, 4
Vanadium (V), 1025, 1033, 1164, 1210, 1243
  biological utilization and toxicity, 1476
  geochemical behavior, 1475
  history and use, 1474
  properties, 1474
van der Waals attraction, 1241
van der Waals force(s), 295, 500, 1473
van der Waals interactions, 348
van Krevelen diagram/plots, 667, 772, 773
Van't Hoff, J., 554
Van't Hoff's equation, 20, 460
Van't Hoff's relation, 264
Variance/degrees of freedom, 912, 1221
Variational approach, 4
Vascular plants, 160, 687
Vegard's rule, 1353
Vegetation, 182, 308, 326, 329
Venus, 73–74, 505
Vermiculite, 269
Vernadsky, V., 672–673
Vesta, 496, 528, 568
Vibrational energy levels (infrared and Raman spectra), 2
Vibrational spectroscopy, 1293
Vienna Peedee Belemnite (VPDB), 196
Vienna Standard Mean Ocean Water (VSMOW), 697
Vinogradov, A., 678
Viscous flow, 543
Vital effects, 165
Vitrinertite, 280
Vitrinertoliptite, 280
Vitrinite(s), 278, 281, 772, 773, 1056
  phytoclasts, 116
  reflectance, 116, 131, 133, 1090
Vitrinization, 278
Vitrite, 280
Volatile(s), 244, 246, 499, 548, 1482
  compounds, 1317
  elements, 60, 1380
Volatility, 896
Volcanic activity, 1399
Volcanic arc, 1184
Volcanic ash, 878, 882–884
Volcanic degassing, 188
Volcanic eruptions, 1141, 1143
Volcanic forcing, 1143
Volcanic gas(es), 496
  chemical and isotopic composition, 1477
  composition, 1477
  definition, 1476
  measurement technique, 1478
Volcanic Hg, 903
Volcanic massive sulfide deposits, 705
Volcanic rocks, 826
Volcanic surveillance, 246
Volcanism, 566, 889, 903, 924, 926, 931, 1180, 1331
Volcanogenic massive sulphide (VMS) deposits, 716, 1395, 1407
Volume diffusion, 366
Volume expansion, 211
Volumetric flow rate, 893
Volumetric porosity, 892
Volumetric properties, 707
VV10, 350

W
Wark-Lovering rim, 1307
Washington, H., 671
Wasserburg, J., 674
Water, 20, 72, 410, 694, 695, 1138, 1208, 1214, 1216, 1217, 1438
  in atmosphere, 1494
  hydrologic cycle, 1492–1493
  in lithosphere, 1493–1494
  molecule, 1042
  phase behavior, 1490–1492
  properties of, 1487–1488
  and soil resources, 327
  structure, 1488–1490
Water-rock interactions, 677
Water-rock reactions, 713
Water-saturated solidus, 1181
Watershed approach, 239
Water-soluble, 244
Water table, 123, 129, 130, 358
Water vapour, 1366
Water world, 509
Wavelength dispersive (WD) analysis, 1511
Wavelength dispersive spectrometers (WDS), 440
^{182}W compositions, meteorites and terrestial planets, 1459
Weathered bedrock, 327
Weathering process, 14, 98, 163, 183, 191, 192, 270, 308, 327, 392, 496, 677, 695, 825, 884, 984, 1069, 1127, 1299, 1348, 1349, 1351, 1382, 1420
Weiss's theory, 861
Wetherill concordia diagram, 576, 578
White tin, 445
Whitlockite, 1232
Widmanstätten structure, 764–765
Wildfires, 903
Winonaites, 7
WITCH model, 239
Witherite, 92
Witwatersrand style Au, 1065
Wolframite, 1456
Woodford shale, 1077, 1080
Work, 555
Wormhole, 894
Wüstite (FeO), 1125, 1126

X
XANES, *see* X-ray absorption near edge structure (XANES) spectrum
Xenoliths, 433, 506
Xenon, 61, 1004
  biological properties, 1498
  chemical properties, 1498
  and history, 1498–1499
  physical properties, 1497–1498
Xenon isotopes, 1500
  in atmosphere, 1500
  heterogeneities preservation, terrestrial accretion, 1503
  heterogeneous volatile accretion, 1504
  loss from atmosphere during Hadean and Archean, 1505
  Pu-fission, 1501
  regassing of mantle xenon, 1502
Xenotime, 381, 461, 525, 578, 684, 796, 839, 1425, 1442, 1518
X-ray(s), 1508, 1509
  characteristic, 1508
  crystallography, 140
  signals, 440
  spectra, 1415
  spectrograph, 671
  spectrometers, 440
  spectroscopy, 630, 1511
  spectrum, 441
X-ray absorption near edge structure (XANES) spectrum, 747, 1514
X-ray diffraction (XRD), 32, 356, 378, 739, 1508–1510
X-ray diffractometer, 671, 1509
X-ray fluorescence (XRF) analysis, 1415
  advantages, 1512
  definition, 1511
  ED analysis, 1511
  fluorescence-XAFS spectra, 1514
  hand-held XRF analyzer, 1512, 1513
  prinicple, 1511, 1512
  quantitative analysis, 1512
  SEM-EDS analysis, 1513
  SR beam properties, 1513
  SR-XRF analysis, 1512–1513
  WD analysis, 1511–1512
  XANES, 1514
  X-ray spectroscopy, 1511
X-ray fluorescence (XRF) spectrometers, 46
X-ray fluorescence (XRF) spectroscopy, 30, 32, 552
X-ray mapping, 441
X-ray near-edge absorption spectroscopy (XANES), 32, 1101

Y
Yarkovsky effect, 766
Yellowstone, 1184
Younger Dryas, 1157
Young stellar objects, 254
Yttrium iron garnet, 1519
Yttrium oxide, 1519

Z
ZAF correction, 1185
Zeeman effect, 1009, 1010
Zero point energy, 195
Zeta age calibration, 486
Zinc (Zn), 527, 1023, 1033, 1452
  aqueous and hydrothermal geochemistry, 1522
  biological utilization, 1522
  environmental geochemistry and toxicity, 1523
  history and use of, 1521
  isotopes, 1524
  mineralogy, 1522
  properties, 1521
Zircon, 410, 484, 505, 508, 573, 737, 812, 814, 815, 1448, 1466, 1467, 1528
Zirconium (Zr), 984, 1528
Zircon-rich clastic sediments, 631
Zircon U-Pb geochronology, 576–578
Zooplankton, 112, 113, 1023
Zooxanthellae, 1025
Zunyite, 1246